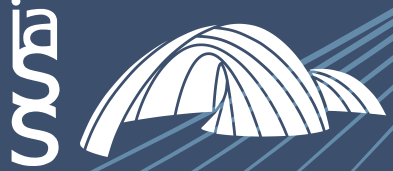
Yi Min Xie, Jane Burry, Ting-Uei Lee, Jiaming Ma - *Editors*

Integration of Design and Fabrication

Proceedings of the International Association for Shell and Spatial Structures Annual Symposium 2023



IASS 2023
July 10–14 Melbourne
Integration of Design and Fabrication

Preface

The International Association for Shell and Spatial Structures (IASS) symposia are a unique forum for engineers, architects and researchers to exchange exciting ideas and latest developments in the field of shell and spatial structures. The IASS symposia have been successfully held for over 60 years in various countries such as Brazil, China, Germany, Japan, the Netherlands, Poland, South Korea, Spain, the UK and the USA.

After three years of travel restrictions due to the worldwide COVID-19 pandemic, it is wonderful that the IASS community is able to meet face-to-face again, this time in Melbourne, Australia. The theme of the IASS 2023 symposium is *Integration of Design and Fabrication*, which is becoming an increasingly important topic with the rapid developments of digital technologies in both design and manufacturing.

The present proceedings contain a collection of 246 papers on various aspects of design, analysis, construction and maintenance of shell and spatial structures.

The editors would like to take this opportunity to thank all authors for submitting their contributions, the Scientific Committee for reviewing the abstracts and full papers, the sponsors and supporters for their generous support, and the Organising Committee and many other people for their tireless effort in making the symposium a success.

Yi Min Xie, Jane Burry, Ting-Uei Lee, Jiaming Ma

Committees

Local organising committee

Yi Min 'Mike' Xie (Co-Chair, RMIT University)
Jane Burry (Co-Chair, Swinburne University)
Ding Wen 'Nic' Bao (RMIT University)
Sascha Bohnenberger-Fehr (Swinburne University)
Canhui Chen (Swinburne University)
Sofia Colabella (The University of Melbourne)
Joe Gattas (The University of Queensland)
Ting-Uei 'Jeff' Lee (RMIT University)
Peter Lim (Lightweight Structures Association of Australasia)
Guoxing Lu (Swinburne University)
Dan Luo (The University of Queensland)
Jiaming Ma (RMIT University)
Nico Pietroni (University of Technology Sydney)
Alberto Pugnale (The University of Melbourne)
Tim Schork (Queensland University of Technology)
Mary Tomlinson (RMIT University)

International advisory committee

Görün Arun (Turkey)
Alireza Behnejad (UK)
Ken'ichi Kawaguchi (Japan)
Olga Popovic Larsen (Denmark)
Carlos Lázaro (Spain)
Juan Gerardo Oliva Salinas (Mexico)
Sergio Pellegrino (USA)
Jenny Sabin (USA)
Su-Duo Xue (China)

Scientific committee

Karim Abedi (Iran)
John F. Abel (USA)
Sigrid Adriaenssens (USA)
Masoud Akbarzadeh (USA)
Nayar Gutierrez Astudillo (Mexico)
Ding Wen 'Nic' Bao (Australia)
Minghao Bi (Australia)
Annette Boegle (Germany)
Dan Bomba (UK)
Andrew Borgart (Netherlands)
Maurizio Brocato (France)
Peter Von Buelow (USA)
Jane Burry (Australia)
Michael Burt (Israel)
Jianguo Cai (China)
Wujun Chen (China)
Yao Chen (China)
Zhihua Chen (China)
John Chilton (UK)
Kok Keong Choong (Malaysia)
Paolo Cignoni (Italy)
Jeroen Coenders (Netherlands)
Pierluigi D'Acunto (Germany)
Fevzi Dansik (Turkey)
Raj Das (Australia)
Lars De Laet (Belgium)
Niels De Temmerman (Belgium)
Alberto Domingo (Spain)
Cyril Douthe (France)
Andreas Falk (Sweden)
Feng Fan (China)
Ruoqiang Feng (China)
Günther H. Filz (Austria)
Corentin Fivet (Switzerland)
Stefano Gabriele (Italy)
Charis Gantes (Greece)
Wei Gao (Australia)
Christoph Gengnagel (Germany)
Matthew Gilbert (UK)
Arndt Goldack (Germany)
Mohamed Gomaa (Australia)
Jinghai Gong (China)
Manfred Grohmann (Germany)
Lei Gu (China)
Hong Guan (Australia)
Nayar Gutierrez Astudillo (Mexico)
Ngoc San Ha (Australia)
Muhammad Hadi (Australia)
Hong Hao (Australia)
Reinhard Harte (Germany)
Minjuan He (China)
Mahmoud Heristchian (Iran)

Xiaodong Huang (Australia)
Koichiro Ishikawa (Japan)
Tian-Jian Ji (UK)
Yoshihiro Kanno (Japan)
Shiro Kato (Japan)
Anahita Khodadadi (USA)
Seung-Deog Kim (Canada)
Jae-Yeol Kim (Korea)
Toni Kotnik (Finland)
Dmitri Kozlov (Russia)
Sudarshan Krishnan (USA)
Haresh Lalvani (USA)
Seung-Jae Lee (Korea)
Wanda J. Lewis (UK)
Qing Quan (Stephen) Liang (Australia)
Richard Jat Yuen Liew (Singapore)
Susanna Lin (Australia)
Hongjia Lu (Australia)
Yaozhi Luo (China)
Ramesh B. Malla (USA)
Hazrina Binti Mansor (Malaysia)
Priyan Mendis (Australia)
Marisela Mendoza (UK)
René Motro (France)
Shoji Nakazawa (Japan)
Tuan Ngo (Australia)
John A. Ochsendorf (USA)
Makoto Ohsaki (Japan)
Manolis Papadrakakis (Greece)
Gerry Parke (UK)
Ruy Marcelo Pauletti (Brazil)
Arno Pronk (Netherlands)
Ekkehard Ramm (Germany)
Janusz Rębielak (Poland)
Mohammad Reza Chenaghlou (Iran)
Anooshe Rezaee Javan (Australia)
Edmond Saliklis (USA)
Omidali Samavati (UK)
Jaime Sanchez-Alvarez (Germany)
Narendra K. Srivastava (Canada)
Romuald Tarczewski (Poland)
Tibor Tarnai (Hungary)
Jonathan Tran (Australia)
Brian Uy (Australia)
Petr Vegh (Canada)
Andrew Viquerat (UK)
Chris Williams (UK)
Jinzhi Wu (China)
Minger Wu (China)
Yue Wu (China)
Yi Min 'Mike' Xie (Australia)
Tetsuo Yamashita (Japan)
Yeong-Bin Yang (China)
Zhong You (UK)
Jingyao Zhang (Japan)
Lihai Zhang (Australia)
Qilin Zhang (China)
Sarah Zhang (Australia)
Lin Zhao (China)
Xiao-Lin Zhao (China)
Shiwei Zhou (Australia)
Zhongyi Zhu (China)
Yan Zhuge (Australia)
Alphose Zingoni (South Africa)

Graphic design and paper formatting committee

Minghao Bi (RMIT University)
Mohamed Gomaa (RMIT University)
Ngoc San Ha (RMIT University)
Yunzhen He (RMIT University)
Zhi Li (RMIT University)
Hongjia Lu (RMIT University)
Mary Tomlinson (RMIT University)
Tao Xu (RMIT University)

Contents

Active bending 17
Calculation method for restoring force of member and deformation occurred by in curved surface combined with flat plates and bolts
Daichi MORI, Keisuke NOMURA, Shigehiro MOROOKA 18
Expanding the design freedom of spatial patterns by combined elastic bending and twisting: a parametric study
Fereshteh KHOJASTEHMEHR, Günther H. FILZ 28
Interlocking connections for bending-active timber structures with variable stiffness
Maren ZYWIETZ, Annette BÖGLE, Ehsan TAGHIYAR 40
Investigation of cross-sections for hybrid gridshells based on bending-active formwork
Yasaman YAVARIBAJESTANI, Michael HERRMANN, Khalid M. MOSALAM, Simon SCHLEICHER 51
Study on shape control method for active bending arch structures using kerf bending technique
Yuki OZAWA, Akihito YOKOTA, Satoshi OHKI 61
Additive manufacturing/ 3D printing 70
4D printed textile formwork for robotic concrete spraying
Guillaume JAMI, Selen Ercan JENNY, Chenguyan WEI, Hamilton FORSYTHE, Nicolas FEIHL, Skylar TIBBITS, Ena LLORET-FRITSCHI 71
Additive manufacturing of fully recyclable walls solely made from renewables – a possible quantum leap in sustainable building construction
Benjamin KROMOSER, Bernhard REINHOLZ, Roman MYNA, Sara REICHENBACH, Falk LIEBNER, Rupert WIMMER 83
Additively manufactured steel joints for structural frames: concept proposal and numerical simulations
Seyed Pouya AFSHAR IMANI, Mani KHEZRI, Kim J.R. RASMUSSEN 90
An assembly-oriented novel low-carbon masonry building method with unfired 3D printed earthen blocks
Yelda GIN, Darshil U. SHAH, Michael H. RAMAGE 102
Continuous fibre additive manufacturing of topological spatial lattices for fabrication-aware design processes
Eduardo CHAMORRO, Mark BURRY, Mathilde MARENGO 114
Continuous multi-filament 3D printing for tension-compression structure components
Teng TENG, Yefan ZHI, Kun-Hao YU, Shu YANG, Masoud AKBARZADEH 126
Design optimization workflow for 3D concrete printing of spanning structures
Gonçalo DUARTE, Jose Pinto DUARTE, Nathan C. BROWN, Ali MEMARI, Shadi NAZARIAN 139
Digital Ceramics: High hyperbolic curvature fabrication technologies in paste-based additive manufacturing
Philip F. YUAN, Lei GONG 151
Liquid printed reusable dredged-based material for concrete formwork
BoSheng LIU, Tzu-Hsien LO, Cheng-Hsuan YEH 163
Local optimization of self-supporting shell structures in 3D printing: a skeleton method
Yefan ZHI, Hua CHAI, Teng TENG, Masoud AKBARZADEH 171
Model test of sunflower triple-strut cable dome structure with metal additive manufacturing nodes
Yang ZHAO, Ruolan FAN, Zhen WANG, Ruhao WANG, Shilin DONG 182
Rapid fabrication system for large-scale free-form double curved shell
Zhuoyang XIN, Guanqi ZHU, Dan LUO 189
Architectural geometry 199

A multi-objective progressive optimization method for free-form canopy based on fabrication morphology
Sijia GU, Li HAN, Philip F. YUAN 200
Designing the West Gate Tunnel portals: Timber gridshells
Andre F. PEREIRA, Benjamin COOP, Dmitry ZELENKIN, Richard WHITFIELD, Kevin BERRY 210
Form dictated by material-specific properties of a mycelium composite
Dana SAEZ, Alexandra BERTSCH, Denis GRIZMANN, Martin TRAUTZ, Anett WERNER 224
Rethinking geometry of grapevine structure proposed by Konrad Wachsmann
Tsubasa INOUE, Toshiaki KIMURA, Yosuke KOMIYAMA, Satoru KIMURA 235
Shape generation of hexagonal lattice shell consisting of edge offset mesh
Ryo WATADA, Makoto OHSAKI 244
Structural features of Dong'an lake stadium roof
Yuan FENG, Quan ZHOU, Xin An XIANG, Wen Ming CHEN, Li YAO 251
Bamboo for sustainable construction and quality of life improvement 264
Experimental evaluation of load-induced cracking in moso bamboo tubes
Dan V. BOMPA, S. Alireza BEHNEJAD, Holmer SAVASTANO Jr, Arash AZADEH, Moe POURGHAZ 265
Preliminary study on relationship between culm morphology and mechanical characteristics of Japanese bamboo
Takuo NAGAI 277
Study on compression strength of Japanese full-culm bamboo columns using short-length specimens
Keisuke OKI, Takuo NAGAI 288
Bio-inspired structures and architecture 297
Comparison of four current low-density concrete technologies emphasis on the criteria's of performance, fabrication, and mixtures
Ferdinand OSWALD, Richard HENRY, Djordje NIKOLIC 298
Vibration analysis of the real shaped bi-valve shell model created by CT images
Minori OGOSHI, Masaki TERANISHI 310
Bridge structures 318
Innovative design of a pedestrian bridge using multi-material topology optimisation
Yaping LAI, Yu LI, Peixin CHEN, Yanchen LIU, Lijun ZHAO, Jin LI, Yi Min XIE 319
Integrated bridge structure design process through finite element analysis (FEA) and pixel-based visibility culling method
Ana Gabriela LOAYZA, Taeyong KIM 331
Computational form-finding 341
A BESO aid to efficient form finding
Izak LEE, Andre BROWN 342
A novel approach to generating diverse and competitive structural designs through load perturbation in topology optimisation
Yulin XIONG, Hongjia LU, Yi Min XIE 348
A numerical comparison between geometric stiffness- and elastic stiffness-based structural shape optimization for gridshells
Gaoyuan WU, Rafael PASTRANA, Sigrid ADRIGENSSENS, Maria E. Moreyra GARLOCK 360
Cognitive multi-pattern gridshell design: a method inspired by weaverbirds' nest building strategies
Mohammad Hassan SALEH TABARI, Günther H. FILZ 373
Computational conceptual design – typological exploration of spatial truss systems through optimization
Jonas WARMUTH, Pierluigi D'ACUNTO, Corentin FIVET 385
Form finding for post tensioned, 3D printed fluid containers
Patrick SCHÄFERLING, Matthias BECKH 395
Form finding of tensile membrane structures by solving the generalized laplace equation using physics informed neural network
Sounak KABASI, Allan L. MARBANIANG, Siddhartha GHOSH 407
Form-finding of membrane structures using transfinite interpolated initial shapes
Allan L. MARBANIANG, Sounak KABASI, Siddhartha GHOSH, Subhrajit DUTTA 414

Generation of a compression-tension combined funicular polyhedral beam structure
Hua CHAI, Yao LU, Ma´rton HABLICSEK, Masoud AKBARZADEH 423
Graphic statics and topology optimization: An integrated approach to designing architecture structures
Xinjie ZHOU, Yu LI, Philip F. YUAN 432
Conceptual design 444
Conceptual design and parametric modelling of pretensioned stiffened membranes
Iuliia LEBEDEVA, Martin F. EICHENAUER, Peer HALLER 445
Structural design of flat and spiral buildings with inclined pillars
Ken NODA, Yoshiharu KANEBAKO 459
Concrete structures 469
A group-theoretic approach for constructing spherical-interlocking assemblies
Reymond AKPANYA, Tom GOERTZEN, Alice C. NIEMEYER 470
Influence of biochar in alkali-activated slag composites upon engineering properties and impact resistance
Harshani EGODAGAMAGE, Hiran YAPA, Satheeskumar NAVARATNAM, H.A.D. Samith BUDDIKA, Kate NGUYEN 482
Construction techniques 494
Anti-fragile shell aggregations on the moon
Xavier DE KESTELIER, Levent OZRUH, Jonathan IRAWAN 495
Cast glass arches, vaults and domes: case studies and design methodology
Telesilla BRISTOGIANNI, Faidra OIKONOMOPOULOU 507
Enhancing construction of complex compression-based structures through holographic-assisted assembly
Ertunç HÜNKAR, David LEE 519
Fabrication methods for topology-optimized massive glass structures
Faidra OIKONOMOPOULOU, Menandros IOANNIDIS, Anna Maria KONIARI, Telesilla BRISTOGIANNI 531
Inflatable flexible factory formwork construction: most recent construction techniques and details
Alex Morgan BELL, Tyler ROBINS 543
Research on digital design and optimisation method for large-scale reciprocal frame structure: The case of Chengdu agricultural expo exhibition hall
Philip F. YUAN, Tianyi GAO, Yingzi HU, Liming ZHANG 555
Study on the dismantling method of cable-strut tension structures
Jiaqi YANG, Yue WU, Guangyao XIN 567
Deployable and inflatable structures 578
A foldable modular structure unit inspired by kirigami
Zafira Nur Ezzati MUSTAFA, Kok Keong CHOONG, Jae-Yeol KIM 579
Comparison of biologically inspired functionally graded deployable geosystems with experimental measurements
Ann C. SYCHTERZ, Kaylee A. TUCKER 587
Manual deployment and shape determining method of guide frame for tunnel inspection by force control
Fumihiro INOUE, Momoe TERATA, Shu LI, Suzuno FUKUNAGA, Satoru NAKAMURA 599
Modular design of multistable pneumatic structures from a flat pattern of air pouches
Yiwei ZHANG, Tomoya TENDO, Tomohiro TACHI 608
Section design and performance optimization of C-cross section thin-walled deployable boom
Fengyuan LIU, Minger WU, Ping XIANG 620
Surface accuracy analysis and test on 0.5 m aperture wrap-rib deployable antenna
Han ZHANG, Minger WU, Ping XIANG 632
Design competition (WG21) 644
A reconfigurable construction system based on hypar timber components
Markus HUDERT, László MANGLIÁR 645
Clustering and optimisation of nodes, beams and panels for cost effective fabrication of free-form surfaces
Minghao BI, Yuanpeng LIU, Yi Min XIE 652
Constructing topologically optimized spatial structure using innovative mortise-and-tenon joints
Xin YAN, Ding Wen BAO, Congcong REN, Yi Min XIE 664

Controlling frills of bending-active negative curvature surface
Fuki ONO, Miwako KASE, Kotaro SEMPUKU, Mizuki SHIGEMATSU, Hiroki TAMAI, Seri NISHIMOTO, Tomohiro TACHI 676
Coupled thick-panel origami tubes along creases for stiff deployable structures
Sunao TOMITA, Kento SHIMANUKI, Kazuhiko UMEMOTO, Atsushi KAWAMOTO, Tsuyoshi NOMURA,Tomohiro TACHI 688
Triply periodic discrete surface of constant negative curvature constructed from one type of piece
Kanata WARISAYA, Seri NISHIMOTO, Toshiyuki MORISHIMA, Tomohiro TACHI 697
Digital modelling and fabrication 706
A novel modular technique for manufacturing free-form rammed earth walls
Ahmed ABDELAAL, Mohamed GOMAA, Yi Min XIE 707
Complex digital modelling for low-cost construction of East African vernacular architecture
Joanna Maria LESNA, Xavier de KESTELIER 719
Design and construction complex shell structure using U-shaped glass and steel frame with collaborative robotics and human expertise
Lei YU, Guanqi ZHU 730
Digital design, optimisation and automated construction of a curved wooden truss – housing for the BOKU Robot Laboratory
Benjamin KROMOSER, Maximilian ORTNER, Matthias BRAUN 742
Digitization and construction of steel-frame double curvature façade with a spatial element: with the example of Chongqing Center for Planning and Exhibition
Philip F. YUAN, Menghao YUAN 754
Generative design of isostatic ribbed slabs using anisotropic Reaction-Diffusion
Alessandro ZOMPARELLI, Roberto NABONI 766
Guided irregular cement geometry stacking using real-time optimization and motion tracking
Alex ORSHOLITS, Ren IMAI, Hirotaka UJIOKA, Shimpei KOJIMA, Mika ARAKI, Yusuke OBUCHI, Jun SATO 778
KNOTSHELL pavilion – Development of a low-tech approach for transferring complex digital data to building elements
Kristina Viktoria KRÖLL, Alec Bikramjit SINGH, Felipe RIOLA-PARADA 790
Morphogenesis method for thin metal plate with non-uniform stiffness distribution by applying auxetic mechanism
Hirotaka UJIOKA, Mika ARAKI, Kai MORINAGA, Masaaki IWAMOTO, Yuri IWATA, Akitoshi IWAMOTO, Miki KATSUKI, Hanano TANAKA 802
Nonlinear analysis of multi-scale coupling based on coordinated distributing method
Junjie YAO, Yanfeng ZHENG, Yaozhi LUO 814
Optical parametric component referencing for the facilitated prefabrication of timber wall elements
Felix SCHMIDT-KLEESPIES, Laurenz ANDRITZ, Cristoph DIJOUX, Alexander STAHR 824
Process simulation for enhancing self-supporting printability in 3D curvature-oriented clay form printing with an additional-axis base
Xuanyu LU, Yasushi IKEDA, Arastoo KHAJEHEE, Koki ITO 834
Sequential augmented assembly of interlocking timber elements for circular wood construction
Nima ZAHIRI 847
Structural design and construction of a large building with a 3D 'circle truss' and ETFE membrane roof
Idogawa TATSUYA, Miyasaka TAISUKE, Ueda MASAHIRO, Komiya MASAYA, Kurata TAKASHI 859
Towards upscaling membrane tensegrity shells: A design-to-fabrication workflow
Ying Yi TAN, Kenneth J. TRACY, Christine YOGIAMAN 871
Xtect: a digital intelligence platform for off-site prefabricated construction
Jackie Leong Shong YONG, Wanyu HE, Lei GU, Peiwen LI, Ying WANG 881
Dynamic response of metal spatial structures 892
Collapse mechanism under strong earthquake and seismic design of single-layer aluminum alloy latticed shells
Jinzhi WU, Yu LIU, Guojun SUN, Jianhua ZHENG, Miao FENG, Yigang ZHANG, Jie HU, Yafang GU, Xianquan CHANG 893
Influence of axial force on the dynamic response of the aluminum foam-filled 6082-T6 aluminum tube under lateral impact
Ximei ZHAI, Lingzhao MENG, Guangming CUI 905

Mechanical properties of the curvature-consistent frictional pendulum isolation system and vibration control of spherical reticulated shell
Niyi LIANG, Xudong ZHI 916
Seismic force reduction factor evaluation for double-layered domes supported by single-story substructures
Yuki TERAZAWA, Haruna SHIJO, Deepshikha NAIR, Toru TAKEUCHI 927
Seismic response modification factors of space structures in the horizontal and vertical directions
Mehdi POURSHA, Karim ABEDI, Hamed JAFARZADEH, Pouya HEIDARIAN, Ali ABDOLLAHI 937
Study on finite element numerical simulation of seismic response of suspended-dome structure
Guojun SUN, Shuo XIAO, Xiongyan LI, Cong ZHANG, Jinzhi WU, Suduo XUE 949
Dynamic response of other structures 961
Modal identifications of a scaling stratospheric airship in still air
Longlong CHEN, Wujun CHEN 962
Form-finding and structural optimisation of interlocking discrete assemblages 970
Chain mail assembly: a new model of programmable modular structure
Nabila AFIF, Gergana RUSENOVA, Charlie RANSCOMBE, Jane BURRY 971
Double-curved plate components in configurable systems
Ahmed SOLIMAN, Ellen LEEMANS, Lars DE LAET, Niels DE TEMMERMAN 983
Graphical methods 995
3D auxetic materials designed with algebraic polyhedral graphic statics
Yao LU, Márton HABLICSEK, Abdolhamid AKBARZADEH, Masoud AKBARZADEH .. 996
The extended affine method for form finding of a spoke wheel system in light of graphic statics: part 2
Hiroki TAMAI 1002
Towards homological methods in graphic statics
Zoe COOPERBAND, Robert GHRIST 1011
Gridshell and lattice structures 1023
Design and construction of the ReciPlyDome, a lightweight modular reciprocal dome
Ellen LEEMANS, Ahmed SOLIMAN, Stijn BRANCART, Niels De TEMMERMAN, Lars DE LAET 1024
Development of the design of the new Sydney Football Stadium
Alex EDWARDS, Tristram CARFRAE, Andrew JOHNSON 1035
FreeGrid: a benchmark on design and optimisation of free-edge gridshells
Luca BRUNO, Paolo CIGNONI, Stefano GABRIELE, Ernesto GRANDE, Maura IMBIMBO, Francesco LACCONE, Francesco MARMO, Elena MELE, Lorenzo RAFFAELE, Valentina TOMEI, Fiammetta VENUTI 1047
Simultaneous stress-aligned and flat-panel-aligned grids on mixed tension-compression membrane shells
Masaaki MIKI, Toby MITCHELL 1058
Sydney's Central Station upgrade – design modularity and heritage enhancement in the renewal of the Grand and Northern Concourse
Michael CHERNYAVSKY, Amy CLARK 1069
Historical concrete shells 1082
Digital tools and technologies in the preservation of historic concrete shells
Marisela MENDOZA, Mariana ESPONDA, Albero MUCIÑO-VÉLEZ, Alejandro LEALMENEGUS, Juan I. DEL CUETO RUIZ-FUNES, Nohema C. RUIZ-GÓMEZ 1083
Naiju community center by Shoei Yoh: pioneering computational architecture applying origami geometry and bamboo formwork
Masaaki IWAMOTO, Tomo INOUE, Shoichi NAKAMOTO, Nicole GARDNER, M. Hank HAEUSLER 1095
Translucent concrete shells in Ecuador
Mauricio LUZURIAGA 1105
Historical structures 1115
Pier Luigi Nervi's arch in E'42
Satoru KIMURA, Toshiaki KIMURA, Yosuke KOMIYAMA 1116
The hybrid static by Heinz Hossdorf – interaction between physical models, material and the first computers
Baris WENZEL, Eberhard MÖLLER, Benjamin SCHMID, Christiane WEBER 1122
Lattice structures 1133

Structural design of a public library with lamella shell roof
Yoshiharu KANEBAKO, Yasuhiro MOCHIZUKI 1134
Structural optimization of lattice shells with geometric nonlinearity using machine learning
Yuma YABUUCHI, Shinnosuke FUJITA 1140
Life-cycle design and assessment of structures 1151
Algorithmic investigation of structural system utility for urban development reusing existing foundations
Kiley FEICKERT, Caitlin T. MUELLER 1152
Aurecon buildings carbon sketcher: A cross-disciplinary webtool for carbon neutral building design
Max G. MARSCHALL, Jack WALKER, Daniel FITZMAURICE, Hamed SEIFI, Cindy LAM, Nathan PALEIRET, Darcy CREIGHTON, Qisi ZHENG, James ALLISON, Tristan MORGAN, Pablo SEPULVEDA, Matthew AUSTIN 1164
Autarkic office boat
Arno D.C. PRONK 1176
Designing structures from reused steel: A cost-effective carbon mitigation strategy
Juliana BERGLUND-BROWN, John OCHSENDORF 1188
Interactive design with optimum matchmaking of reused structural elements – a software implementation
Jonas WARMUTH, Jan BRÜTTING, Corentin FIVET 1200
Long-term strength prediction model for structural glass
Siyi YI, Suwen CHEN, Roberto BALLARINI 1207
Neural ODE-based data-driven approach for prediction of the creep behaviour of steel cables
Weijia ZHANG, Xingfei YUAN, Lei YUAN, Yi-Qing NI, Su-Mei WANG 1218
Optimal sensor placement of large-span spatial structures based on sensitivity analysis
Yiqun WANG, Yaozhi LUO 1226
Predicting the embodied greenhouse gas emissions of building structures through machine learning
Sandie Kate FENTON, Klaas DE RYCKE, Lars DE LAET 1233
Probability-based life cycle carbon emission assessment for space grid structures
Jianzhou YOU, Xian XU 1244
Metal gridshell structures, connections and stability 1254
Design and construction of two tree-columns supported gridshells in Canberra
Catherine POIRRIEZ, Yacine BOUZIDA 1255
Grid shell for Hamad Airport expansion in Doha
David CABALLERO, Mikel MONASTERIO, Oscar BATUECAS, Josu GOÑI, Gabriel RUIZ, Jose Miguel RICO 1263
Plastic buckling test of axially compressed aluminium latticed cylinders formed by 3D-printer
Tetsuo YAMASHITA, Kohki UCHIDA 1273
State-of-the-art review of initial imperfection field simulation methods for single-layer gridshells
Shaojun ZHU, Qiang ZENG, Xu YANG, Chenyu WU 1284
Methods and construction technologies for sustainable shell structures 1296
Bio-based composite spatial shell structures
Mostafa AKBARI Farzaneh OGHAZIAN, Ji Yoon BAE, Felecia DAVIS, Laia MOGAS-SOLDEVILA, Masoud AKBARZADEH 1297
New carbon paradigm: applications of carbon composite materials in the building industry
Shengdan YANG 1310
Textile steel - experimental investigations of textile fabrication processes for steel shell and lattice structures
Vincent WITT, Pascal KNOPF, Erik ZANETTI, Baris WENZEL, Moritz DÖRSTELMANN 1320
Morphology and configuration processing 1331
Multi-modal transportation hub: 'Fill-material-free' technology for a marine-air-land terminal
Michael BURT, Yehiel ROSENFELD 1332
Next generation parametric design 1340
Design workflows for a complex urban steel artwork
Sascha BOHNENBERGER-FEHR, Matthew TAM, Csaba BÖHM, Gergely PILLMANN, Ven IYER, Chris FOX, Tommaso PAGANI 1341

Form finding and structural analysis of free-form shells with specified horizontal projected stress distribution
Taku NAKAJIMA, Makoto OHSAKI 1351
Isogeometric deep learning framework to predict the structural performance of free-form surfaces
Kazuki HAYASHI, Makoto OHSAKI 1361
Using augmented reality for interactive value engineering of structural steel connections
Yuyu WANG, Vitor S. BOTTAZZI, Joseph M. GATTAS 1370
Using data-rich objects in geometric parametric modelling
Lennert LOOS 1382
Novel methods in modelling, optimisation and construction for reducing carbon footprint of continuous roof shells 1392
Isogeometric refinement for shells' shape optimization
Gloria Rita ARGENTO, Enzo MARINO, Valerio VARANO, Stefano GABRIELE 1393
Leaned brick shells with Mexican quoins and steel edges
Juan Gerardo OLIVA, Marcos Javier ONTIVEROS 1404
Numerical methods for geometry, form-finding and optimisation of lightweight structures 1410
A novel generatively designed and additively fabricated ankle-foot orthosis
Ryan BLAKIS, Peter DABNICHKI, Mladenko KAJTAZ 1411
An efficient shape optimisation algorithm for gridshells based on node shifting
Chao DING, Zhen WANG, Yang ZHAO, Huiping TANG, Yi Min XIE 1422
Designing the West Gate Tunnel portals: façade geometry and structure
Benjamin COOP, Andre PEREIRA, Hieu TRAN, Dwayne VAN HALEWIJN, Manning THOMSON, Atreyu DE LACY 1431
Multi-objective optimization of the large telescope structure under temperature loading
Hiroaki KAWAMURA, Ayame USUI, Chihiro IMAMURA, Akio TANIGUCHI, Kohei SHINTANI, Takayuki YAMADA, Yoichi TAMURA, Toshiaki KIMURA 1443
Nonparametric shape optimization of piecewise developable surfaces for maximum stiffness using discrete differential geometry
Makoto OHSAKI, Kentaro HAYAKAWA, Jingyao ZHANG 1451
Sizing optimization of free-form lattice shells using deep deterministic policy gradient and graph convolutional networks
Chi-tathon KUPWIWAT, Kazuki HAYASHI, Makoto OHSAKI 1458
Study on quasi-static compression performance of honeycomb structures with negative Poisson's ratio
Yiyi ZHOU, Jiabin SONG, Amardeep SINGH, Dan JIANG 1469
Tailoring Poisson's ratio of bending-active mechanical metamaterials with periodic and nonperiodic pentagonal grids
Yusuke SAKAI 1478
Towards a novel form-finding approach using matrix analysis: exploiting nodal displacements of pin-jointed frameworks
Yao LU, Hua CHAI, Masoud AKBARZADEH 1489
Optimisation methods and applications 1499
A study on the binary harmony search algorithms for an optimal design of the truss system
Hyeonju HA, Sudeok SHON, Seungjae LEE 1500
Applications of shape-optimised cold-formed steel cross-sections in roof purlin and wall stud construction
Ziqi ZHAO, Zichen WEI, Hong GUAN, Bin WANG, Huiyue QIAO 1506
Design space exploration of shell structures using quality diversity algorithms
Konstantinos SFIKAS, Antonios LIAPIS, Joel HILMERSSON, Jeg DUDLEY, Edoardo TIBUZZI, Georgios N. YANNAKAKIS 1517
Development of 3D mathematical models for tendon layout optimization by strain energy minimization
Hanna DOMNICK, Juan Pablo OSMAN-LETELIER 1529
Enhancing interactivity in structural optimisation through reinforcement learning: an application on shell structures
Gabriele MIRRA, Alberto PUGNALE 1541
Functionally graded CharCrete slabs for embodied carbon optimisation in architecture
Nikol KIROVA, Jane BURRY, Areti MARKOPOULOU, Mehrnoush LATIFI 1553

Global topology optimization of lattice shell considering constructability dependent on connection relationships of members
Naoto OKUZONO and Shinnosuke FUJITA 1565
Interactive gradient-decent optimization method for timber column-slab structures
Keerthana UDAYKUMAR, Luis OROZCO, Anna KRTSCHIL, Achim MENGES, Jan KNIPPERS 1574
Optimization of corrugation direction on corrugated shells
Kenji YAMAMOTO, Kentarou DOI 1585
Performance-based fire protection design and practical application of large-space aluminum alloy structure
Yuanwen OUYANG, Yufeng JIAO, Zhiqiang LI, Xiaowei LIU 1594
Shape optimization of hyperellipsoid long-span structures using modified height adjustment method
Yuqing QU, Zhuang GUO, Zhenhui LI, Xiao LAI, Zheng HE 1606
Slimline floor an invention by Pronk and Lichtenberg
Arno D.C. PRONK, Elke MERGNY 1616
Stress reduction effect by changing the upper and lower surfaces near the boundary of a spherical shell
Shigehiro MOROOKA, Shouhei OHYAMA 1625
Study on the influence of structural optimization techniques on architectural design, with a focus on topology optimization methods
Bunji IZUMI, Anders RØNNQUIST, Bendik MANUM 1636
The stability of laminated glass plate during anticlastic cold bending
Xiaohan HAO, Suwen CHEN 1645
Topology optimisation of free-form shells for architectural applications
Jiaming MA, Hongjia LU, Ting-Uei LEE, Zhonggao CHEN, Yi Min XIE 1657
Origami 1667
Analysis of bending behaviour in simple flexible honeycomb cores with tetradecagonal cells
Chisaki KITAJIMA, Kazuya SAITO, Taiju YONEDA, Hiroshi OKUBO, Kaoru SUEHIRO 1668
Bridging the gap – A study on foldable tubular bridges
Rupert MALECZEK, Kiumars SHARIFMOGHADDAM, Georg NAWRATIL, Clemens PREISINGER 1676
Design and evaluation of compliant hinges for deployable thick origami structures
Munkyun LEE, Tomohiro TACHI 1687
Experimental study on a type of foldable structure with asymmetrical crease line pattern
Khai Seng CHEW, Kok Keong CHOONG 1698
Multi-layered curved folding
Marcus BERNHARD, Rupert MALECZEK 1705
Multi-stability of hexagonal origami hypar structures based on group theory and symmetry breaking
Chenhao LU, Ruizhi XU, Yao CHEN, Ke LIU, Jian FENG, Pooya SAREH 1716
Panel-pin model for kinematic and equilibrium analysis of rigid origami
Kentaro HAYAKAWA, Makoto OHSAKI 1728
Study on seismic behavior of origami-based buckling-controlled concentric braces with beam-column-brace connections
Yangqing LIU, Tian DENG, Dongping MEI, Qin YU 1741
Study on the performance of the space structure using CLT folded plate structure
Kaito IKAWA, Shinta YOSHITOMI 1751
Tessellated origami surface and soft robotics
Youness YOUSEFI, Vera PARLAC 1759
Other 1772
A modified finite area element model for simulating the evolution of roof snow loads
Huamei MO, Zhiheng LUO, Ziwei TAI, Yuanyuan LI, Feng FAN 1773
Aeolus: a Grasshopper plugin for the interactive design and optimisation of acoustic shells
Gabriele MIRRA, Michael MACK, Alberto PUGNALE 1785
Analytical simulation of roof snow load on flat roofs considering a probabilistic model of wind speed
Yuanyuan LI, Huamei MO, Feng FAN 1798
Application of long span discontinuous curved lattice shell in Qingdao Airport design
Yuan FENG, Xun XIA, Xiao-bing WU, Li-wei WANG, Zhi-qing CHEN, Yan ZHANG 1805

Bridging design and fabrication: BIM application in two prefabrication projects
Hing C. LAU, Jingxiang ZHU 1811
Built environment prototyping for design-value
Darcy ZELENKO, Duncan MAXWELL 1822
CFD investigation of snow drifting on long-span dome roofs
Qingwen ZHANG, Guolong ZHANG, Feng FAN 1833
CLT requires a new approach to design: a case study in CLT folded-plate structure
Yoko MASUDA, Yuko MIYAMOTO 1844
Contribution of structural intuition at early conceptual stage in efficient workflow: A precedent study of Oscar Niemeyer
Irem SEREFOGLU, Luiza Souza WANDERLEY, Remo PEDRESCHI, Miguel Paredes MALDONADO 1855
Control objectives for adaptive slabs with integrated fluidic actuators, a comparison of effects
Markus NITZLADER, Matthias J. BOSCH, Hansgeorg BINZ, Matthias KREIMEYER, Lucio BLANDINI 1867
Effect of stochastic imperfections on the buckling of open-top storage tanks under wind loads
Liang LIU, Ying SUN, Ning SU, Zhenggang CAO 1879
Experimental study on estimation of water content and compaction of soil by SDS test
Tomoyuki SAKAMOTO, Keisuke NOMURA 1888
Numerical simulations of snow loads on long-span curved roofs
Guolong ZHANG, Qingwen ZHANG, Feng FAN 1897
Home reconstruction after the 2016 Kumamoto earthquake with a community focus
Yuuki KUROIWA 1908
Intelligent detection of ceiling damage in large public buildings based on semantic segmentation
Lichen WANG, Shihao YAN, Ken'ichi KAWAGUCHI 1917
ReconWood Slab. Computational design and structural optimization of reconfigurable timber slabs
Anja KUNIC, Roberto NABONI 1929
Research of snow distribution on the long-span roof with local obstructions
Rui LI, Qingwen ZHANG, Yu ZHANG, Feng FAN 1939
Rethink*Rotor, the reuse of rotor blades in the construction sector
Marcin ORAWIEC, Thorsten HELBIG, Ina-Marie ORAWIEC 1946
Structural design of a gymnasium with warren trusses in a grid arrangement supported by thin columns and damping braces
Eisuke MITSUDA 1956
Structural node of foundation for buildings located in seismic areas
Janusz RĘBIELAK 1964
Sydney Football Stadium redevelopment – An efficient design, manufacturing and on-site assembly approach to a complex form-found roof shell structure
Michael CHERNYAVSKY, Hudson KESTEL 1974
Teaching design uncertainty: working with unknown qualities/quantities of new and re-claimed materials 1986
A modular approach to repurposing timber structural elements
Matthew TAM, Sascha BOHNENBERGER-FEHR, Chris FOX, Tommaso PAGANI 1987
New master's education: innovative teaching of sustainable design approaches for handling uncertainty
Olga Popovic LARSEN, Sander Løkkegaard BENNER, Sebastian Bernhard SEIPELT ... 2000
Teaching of shell and spatial structures 2010
Acoustic and structural design embedded in design studio pedagogy
Sofia COLABELLA, Michael MACK 2011
Educational tools for arch and frame structures
Ayaka KONDO, Shigehiro MOROOKA 2023
Mid-to-long term reflections on a project based learning initiative in civil engineering education
Ramsha SALEEM, S. Alireza BEHNEJAD, Anesa HOSEIN 2030
Seismic retrofitting by double layer grids for HP suspension gymnasium
Kazuya MIYAGAWA, Yoshiya TANIGUCHI 2042
Tensegrity systems and cable structures 2052
Design and research on roof structure of the stadium of Sanya International Sports Industry Park
Chenyu LIANG, Zhongyi ZHU, Guangbo BAI, Yi CHEN, Xuyang DENG, Wei WANG, Xiaogang LIU 2053

Evaluation and improvement of bearing capacity of annular crossed cable net structure after local cable failure
Suduo XUE, Xuanzhi LI, Xiongyan LI, Zaigen MU 2061
Exploration on the shape and force of large-span steel structure of Chengdu open-air music park
Yuan FENG, Lian LIAO, Guangpo ZHAO, Xinyu CHE, Xiaolong DENG, Kaiguo DENG 2071
Kinematic performance of a vibration-driven six-bar tensegrity structure
Ruhe MEI, Xian XU, Ruizhi LIU 2077
Locomotive performance evaluation of the spherical tensegrity robots
Meijia WANG, Xian XU, Yaozhi LUO 2088
Static performance of an open Levy cable dome with partial CFRP cables
Weijing ZHANG, Yizhou HU 2096
Structural behaviours of arch SCS with "pin-pin" support
Akira TANAKA 2104
Suspended tensegrity: the anthropomorphic machine
Paul LOH, David. LEGGETT, Sascha BOHNENBERGER, Matthew TAM 2113
Tension and membrane structures 2124
Active control of hybrid string structure
Wucheng XU, Xuanhe ZHANG, Yanbin SHEN, Xian XU and Yaozhi LUO 2125
Application of partial factors to actions in case of membrane structures
Wolfram JÄGER, Tammam BAKEER, Andreas NIEMEIER 2136
Construction of developable freeform membrane tensegrity structures
Yuta SHIMODA, Sei HAYASHI, Hiroki AWAJI, Taichi NAKAMURA, Haruto KAMIJO, Tomoyuki GONDO, Tomohiro TACHI, Jun SATO 2147
Defining design limits for ETFE foils determined in bubble inflation tests
Felix SURHOLT, Jörg UHLEMANN, Natalie STRANGHÖNER 2158
Effect of temperature on strength of PVC coated fabrics
Chengjun GAO, Zilong ZHOU, Sen WANG, Wujun CHEN, Bing ZHAO, Jianhui HU 2170
Experimental methods and performance of membrane structures: A systematic literature review
Haonan HUANG, Yaozhi LUO 2176
FDMremote: Interactive inverse design of tensile structures with differentiable FDM
Adam BURKE, Keith LEE, Janet ECHELMAN, David FELDMAN, Caitlin MUELLER .. 2187
Fundamental study on form-finding of tensegrity-membrane structures using a dynamic relaxation method
Yohei NAGANO, Takuo NAGAI 2199
Large span membrane architecture: how to accomplish carbon neutral with innovative photovoltaic and adaptive control strategy
Yongsheng YAN, Wujun CHEN, Jianhui HU 2209
Numerical and experimental modelling of pneumatic structures
Ruy Marcelo O. PAULETTI, Karina B. ROCHA 2221
Numerical simulation of snowdrift on a membrane structure
Jialin ZOU, Xiaoying SUN, Yue WU 2233
PTFE membrane privacy screen structure for National Palace Malaysia
Migico SING, Kok Keong CHOONG, Azri Hariz CHE MALID, Chong Kiat NG 2240
Study on the wind response properties of roof structures composed of radially arranged cables considering roof deformation
Akira OSHIUMI, Naoya MIYASATO, Akira OKADA, Shuzo HIROISHI, Daisuke SHINOHARA 2246
Temperature field analysis of air-supported membrane structure for coal storage sheds
Xiuliang LU, Cong ZHANG, Xiongyan LI, Fei YAN, Suduo XUE 2255
The constitutive model of STFE membrane material
Ye YUAN, Qilin ZHANG, Xiaoqun LUO, Ruijie GU 2267
The mechanical properties of membrane material STFE
Ruijie GU, Qilin ZHANG, Xiaoqun LUO, Ye YUAN 2277
The roof structure design of the professional football stadium of Chengdu phoenix mountain sports center
Yuan FENG, Tian QIU, Liwei WANG, Yan ZHANG, Xin An XIANG 2289
Tension structures in the Asia-Pacific 2299
Steel structural design of a 60,000-seats Stadium
Yuan FENG, Yan ZHANG, Liwei WANG, Xinan XIANG, Tian QIU 2300
Timber and bio-based structures 2312

Compression resistance of digitally fabricated hollow timber columns
Stephan RAPLEY, Dan V. BOMPA, Suryakanta BISWAL 2313
Cross laminated plywood construction of a free-form roof
Paul LOH, David. LEGGETT 2324
Derivation of wind loads for shell structures using CFD analyses
Christian HEIDENREICH, André KILIAN, Josephin BÜTTNER, Sophie SCHERER 2334
Digital twins of wooden shingle envelopes
Farzaneh ESKANDARI, Yves WEINAND 2344
Experimental investigation on the bending response of reuse-ready timber slabs – The Pixel Slab System
Xavier ESTRELLA, Johnny SYRIANI, Corentin FIVET 2354
Integrative approach to a timber gridshell formed on-site
Evy Laura SLABBINCK, Hermann BLUMER, Stefan RICK, David RIGGENBACH, Martin ANTEMANN, Fabian SCHEURER 2364
Inventory-constrained design of a variable small diameter round timber structure
Kim R. BABER, Aaron BARTON, Jane R. BURRY, Canhui CHEN, Joseph M GATTAS, Christoph KOCH, Hengyi REN 2377
Material efficiency in local timber construction: unlocking the potential of English timber
Dario MARINO, Harry F. MILLS, Antiopi KORONAKI, Darshil U. SHAH, Michael H. RAMAGE 2389
Multi-material components for a sustainable built environment: integration of design by topology optimisation and fabrication by 3D printing
Hèrm HOFMEYER, Motahareh YOUSHI, Arjen H. DEETMAN 2400
Post-tensioned strapping connections for rapid assembly of low-cost timber structures
Joseph M. GATTAS, Shaobo XU, Zhengtao LU, Zhuo-Yang XIN 2412
Research on clay mixtures for sustainable building materials
Andreea-Terezia MIRCEA, Gabriela CĂLĂTAN 2424
Reversible timber only connections – an investigation into the potential of threaded dowels and swelling for reconfigurable truss components
Xan BROWNE, Olga Popovic LARSEN 2432
Structural design of Mukogawa women's university canoe club house
Naoyuki TAKAYAMA 2445
Systematically ranking of mycelium composites used for facade construction via a fuzzy comprehensive evaluation
Yaning WEI, Seyed Ali HADIGHEH, Zicheng HUANG, Anastasia GLOBA, Phillip GOUGH, Anusha WITHANA 2454
Testing on the shear performance of embedded steel tube glulam joints in arched timber structures
Chengyang HE, Minjuan HE, Zheng LI, Yongliang SUN 2464
Topology optimisation 2474
A boundary-finite element coupling framework for topology optimisation in unbounded media
Aldemar SIQUEIRA, Pérsio L.A. BARROS, Renato PICELLI, Josué LABAKI 2475
A reaction diffusion-based B-spline level set method using body-fitted mesh for structural topology optimisation
Cong WANG, Zicheng ZHUANG, Xuyu ZHANG, Yi Min XIE, Shiwei ZHOU 2485
Efficient steel-concrete slab designed using multi-material topology optimisation
Yu LI, Hao WU, Xingjie XIE, Philip F. YUAN, Yi Min XIE 2494
Non-penalization topology optimization for maximizing natural frequency using SEMDOT
Yun-Fei FU, Bernard ROLFE 2505
Optimisation of a satellite antenna bracket using the BESO method
Joshua RODRIGUES, Simon BARTER, Raj DAS 2512
Topology optimisation considering buckling in architectural design
Tao XU, Xiaoshan LIN, Yi Min XIE 2521
Topology optimisation considering subjective preferences: current progress and challenges
Zhi LI, Ting-Uei LEE, Yi Min XIE 2529
Topology optimisation of support-free structures for multi-axis additive manufacture
Qichen GUO, Hongjia LU, Jun YE 2540
Topology optimization of dynamic stiffness response of constrained damping laminate structures
Teng Xiao YAN, Chen Xiang YANG, Jiang Xu DONG 2551

Topology optimization of spatial grid structures considering member stability based on linear allowable stress iteration
Ruoqiang FENG, Hui WANG, Qi CAI 2563
Topology optimization of truss structure with nodal stability and local buckling of member constraints
Qi CAI, Yiyi ZHOU 2571
Truss topology optimisation considering constructability constraints
Ajmal Babu MAHASRANKINTAKAM, Allan L. MARBANIANG, Sounak KABASI, Siddhartha GHOSH, Subhrajit DUTTA 2580
Traditional masonry structures and innovation 2588
Tile patterning on free-form surfaces that reduces tile cutting
Chaoyu DU, Tom VAN MELE, Philippe BLOCK 2589
Transformable structures 2599
Design and development of a hybrid deployable spherical shield based on foldable plate structures and scissor systems
Kevin MORENO GATA, Alex SEITER, Juan MUSTO, Martin TRAUTZ 2600
Snap-through buckling detection and analysis method for multi-stable structures
Ruta STANKEVICIUTE, Jun SATO 2610

Active bending

► **Active bending**
Additive manufacturing/ 3D printing
Architectural geometry
Bamboo for sustainable construction and quality of life improvement
Bio-inspired structures and architecture
Bridge structures
Computational form-finding
Conceptual design
Concrete structures
Construction techniques
Deployable and inflatable structures
Design competition (WG21)
Digital modelling and fabrication
Dynamic response of metal spatial structures
Dynamic response of other structures
Form-finding and structural optimisation of interlocking discrete assemblages
Graphical methods
Gridshell and lattice structures
Historical concrete shells
Historical structures
Lattice structures
Life-cycle design and assessment of structures
Metal gridshell structures, connections and stability
Methods and construction technologies for sustainable shell structures
Morphology and configuration processing
Next generation parametric design
Novel methods in modelling, optimisation and construction for reducing carbon footprint of continuous roof shells
Numerical methods for geometry, form-finding and optimisation of lightweight structures
Optimisation methods and applications
Origami
Other
Teaching design uncertainty: working with unknown qualities/quantities of new and re-claimed materials
Teaching of shell and spatial structures
Tensegrity systems and cable structures
Tension and membrane structures
Tension structures in the Asia-Pacific
Timber and bio-based structures
Topology optimisation
Traditional masonry structures and innovation
Transformable structures

IASS 2023
July 10–14 Melbourne
Integration of Design and Fabrication

Proceedings of the IASS Annual Symposium 2023
Integration of Design and Fabrication
10–14 July 2023, Melbourne, Australia
Y.M. Xie, J. Burry, T.U. Lee and J. Ma (eds.)

Calculation method for restoring force of member and deformation occurred by in curved surface combined with flat plates and bolts

Daichi MORI*, Keisuke NOMURA[a], Shigehiro MOROOKA[a]

* Graduate Student, Graduate School of Engineering, Tokai University
4-1-1 Kitakaname,Hiratsuka,Kanagawa 259-1292, Japan
2cckm021@mail.u-tokai.ac.jp

[a] Dept. of Architecture and Building Engineering, School of Architecture and Urban Planning, Dr. Eng

Abstract

Morooka et al. proposed a method of creating a curved surface structure by stacking multiple bent flat plates and bolting them together. The shape of the plates is determined by dividing the targeted original surface, but there are differences between the model created by this method and the original surface. The purpose of this study is to investigate the cause of the difference in the shapes and to examine a division method to minimize the difference. In this method, the plates are elastically bent, and a restoring force is generated to recover the shape before bent. The restoring force acts on the next overlapping plate from the holding bolts, causing the plates to be deformed differently from the target shape. The restoring forces on all the plates, and their interaction with each other, are assumed to cause the shape difference. The validity of this assumption was confirmed by comparing the shape differences measured from the model with the displacements obtained by numerical analysis considering the restoring force. The restoring force was the reaction force obtained by forcibly deforming a single plate member to a target bending shape. The displacements were obtained by numerical analysis with the analytical model in which all plates were applied with the restoring force. On the other hand, the flat plate shape of the model depends on the division shape of the original surface, and the restoring force also changes when the division shape is changed. A general equation for the restoring force that considers the effect of the flat plate shape was developed by geometrical parametric study. By using the equation, the restoring force can be obtained even if the division shape is changed, and the displacement considering the restoring force can also be obtained. Division shapes with reduced displacement were explored.

Keywords: curved surface structure, restoring force, shape difference, numerical analysis, large deformation analysis

1. Introduction

Morooka[1] proposed a method of creating curved structures by stacking bent flat members and securing them with bolts. Figure 1 shows the steps for creating a curved surface structure. First, create the target curved surface, and then divide it into triangular facets to make it suitable for tessellation. Project the triangular elements onto a plane, and then connect neighboring elements to create quadrilateral elements. At this point, duplicate elements are allowed. Create thin flat material quadrilateral elements, overlap the common triangular parts, and secure them with bolts. Repeat this process, and gradually bend each element to create a curved structure that closely matches the target curved surface. This is a method for creating a curved structure. In this structure, the shape error that arises between the target curved surface and the model varies depending on factors such as the shape of the target curved surface, the dividing rules, and the materials used. This makes it difficult to predict the shape of the model. While it is

Copyright © 2023 by Daichi MORI, Keisuke NOMURA and Shigehiro MOROOKA. Published in the Proceedings of the IASS Annual Symposium 2023 with permission.

impossible for the shape of the model to perfectly match that of the target curved surface, it is necessary to have a method for predicting the degree of error.

Murata [2] thought that if he divided a bent flat member so that the restoring force, which is the force that returns it to its original shape, would be small, the differences in shape would also be small. However, there is a possibility that the mechanical model used to determine the restoring force does not follow the behavior of bending the flat plate during model creation. On the other hand, Watanabe [3] created a model by unifying the division rules with multiple curved surfaces and examined the correlation between the evaluation values created by the width of the member and the bending angle and the differences in shape. However, unlike Murata, Watanabe's evaluation values do not have a physical meaning, and when the division rules differ, they are not correlated.

From the above, the authors have studied a method to estimate shape error before creating a model by numerical analysis. In the model using this method, members are forcibly deformed in bending from a flat state, and the shape after deformation is maintained by restraining them with overlapping members and bolts. At this time, the bent flat plate generates a restoring force that tries to return it to its original flat shape. This restoring force acts on each plate through the bolt, deforming each plate and resulting in a shape error. In order to verify the validity of this idea, in this paper, an analytical model of the polyhedron after division is analyzed by applying a restoring force, and the shapes after deformation are compared with those of the model. The restoring force in this case is considered to be the force required to forcibly deform each flat plate member into the shape of the polyhedron. Section 2 of this paper describes how the model was constructed, and Section 3 describes the formulation of the formula for calculating the restoring force. Section 4 compares the deformed shapes by numerical analysis with those of the model and discusses the validity of the ideas presented in this paper.

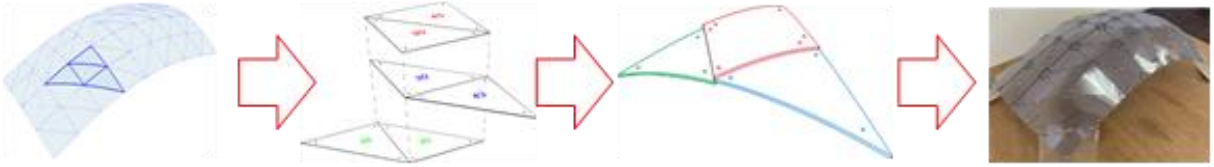


Figure 1. Assembly produce

2. Curved surface structure creation method using flat plates and bolts

2.1. Creation of 3D models and drawings

This section describes how to create a model using this method. Create a design plan for a model based on a 3D model. First, create a curved surface of the desired shape as shown in Figure 2. Next, divide the target surface into a polyhedron with triangular faces, as shown in Figure 3. Finally, project the triangular elements of the polyhedron onto a plane and create quadrilateral elements by connecting all combinations of adjacent triangles. As shown in Figure 4, the layers are divided considering the order of layering. After the bolt positions are determined, the design diagram of the model can be created. Note that the bolt positions are the intersections of the lines offset from each boundary side of the triangular elements by an arbitrary distance.

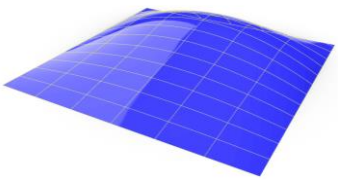


Figure 2. Curved surface

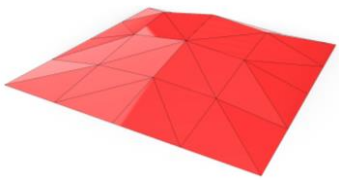


Figure 3. Divide a curved surface

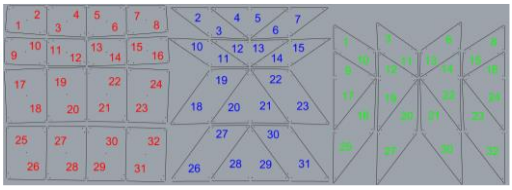


Figure 4. design drawing of the model

with triangular elements

2.2. Assembling the model

Cut out the flat plate member as shown in the design drawing in Fig. 4. Also, as shown in Figure 5, the cutting process and drilling of holes for bolts will be performed by CNC. Overlap the common triangular components of the flat components and fasten them with bolts as shown in Figure 6. Furthermore, to prevent interference between the stacked flat components when they bend, place two washers between the flat components.

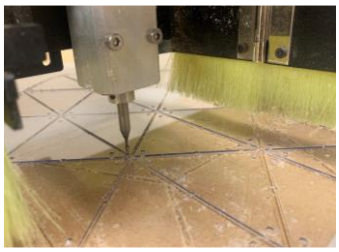


Figure 5. Cutting and drilling

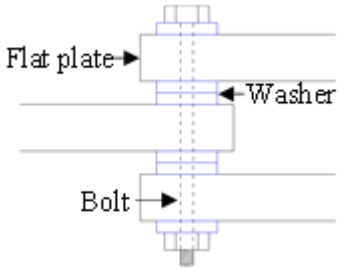


Figure 6. How to fasten flat plate members



Figure 7. Bent flat plate member

3. Formula for calculating restoring force

3.1. Concept of restoring force

The restoring force of a bent flat plate member is considered to be the force required to bend the plate, in order to return it to its original flat shape. Moreover, since each flat plate member is fixed by bolts, the restoring force was considered at the bolt position. Therefore, the restoring force was calculated as the force required to deform the plate member to a certain angle at the bolt positions. In the next section, we will describe the formulation of the calculation formula.

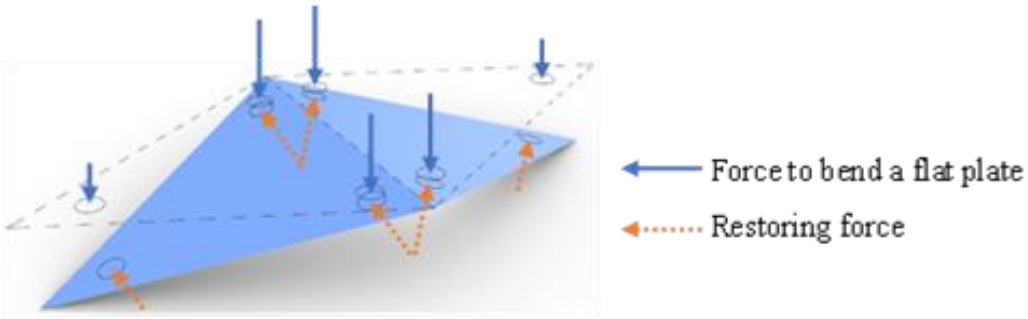


Figure 8. Concept of restoring force

3.2. Formula for calculating restoring force

The figure 9 shows a mechanical model for calculating the equation of the restoring force. We assumed one of the triangular element parts of the flat plate member as a cantilever beam and applied a concentrated force at each bolt position. The triangular elements are isosceles triangles. We define the distance from the joint of the triangular elements to the nearest bolt as l_1, the distance to the furthest bolt as l_2, and the distance between them as l_3. Calculate the force required to bend the flat component to a displacement of δ_1 and δ_2 at the bolt positions, which is represented as P_1 and P_2, respectively. Assuming that P_1 and P_2 are obtained from the shape of the polyhedron, δ_1 and δ_2 were determined using the normal angles θ between the triangular elements of the polyhedron and the distances l_1 and l_2 to the bolt positions as equation (1). (See Figure 10.)

$$\delta_1 = \frac{l_1}{\cos\theta}$$
$$\delta_2 = \frac{l_2}{\cos\theta} \tag{1}$$

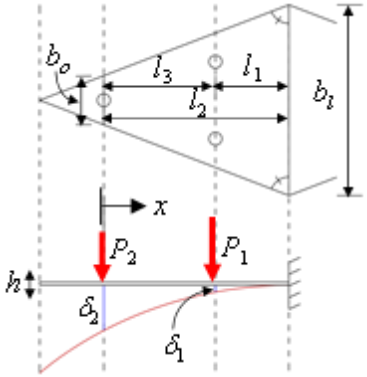


Figure 9. Mechanical model

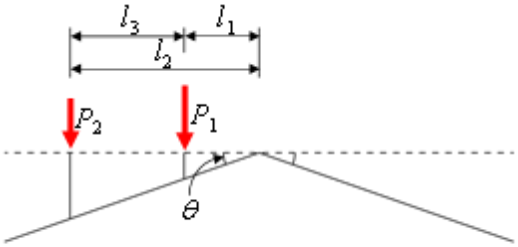


Figure 10. Size of δ_1 and δ_2

The calculation formulas for P_1 and P_2 were derived by solving the differential equation represented as equation (2) based on the theory of beams and arranging the solutions for P_1 and P_2.

$$\frac{\partial^2 \delta(x)}{\partial x^2} = -\frac{M(x)}{EI(x)} \tag{2}$$

Here, $\delta(x)$ is the deflection equation, $M(x)$ is the bending moment equation, E is the Young's modulus, and $I(x)$ is the cross-sectional quadratic moment equation at the deformed section. As shown in Figure 9, assuming the width of the fixed end side to be b_l, the width at the far bolt position to be b_o, and the thickness of the plate to be h, $I(x)$ can be expressed as equation (3).

$$I(x) = \frac{(\alpha x + \beta)h^3}{12}$$
$$\alpha = \frac{b_l - b_o}{l_2} \tag{3}$$
$$\beta = b_o$$

Additionally, the bending moment equation $M(x)$ can be expressed as equation (4).

$$M(x) = \begin{cases} -P_2 x & \text{if } 0 \le x \le l_3, \\ -(P_1 + P_2)x + P_1 l_3 & \text{if } l_3 \le x \le l_2 \end{cases} \tag{4}$$

Furthermore, equation (5) can be considered as the boundary conditions for deflection and deformation angle.

$$\begin{aligned}
&\theta(l_2) = 0 \\
&\delta(l_2) = 0 \\
&\theta(l_3)_{:0\le x\le l_3} = \theta(l_3)_{:l_3\le x\le l_2} \\
&\delta(l_3)_{:0\le x\le l_3} = \delta(l_3)_{:l_3\le x\le l_2}
\end{aligned} \tag{5}$$

From the above, by solving the differential equation in equation (2), the deflection equation can be expressed as equation (6).

$$\delta(x) = \begin{cases} \dfrac{12P_2}{Eh^3}\left\{\dfrac{\alpha x\{\alpha(2\alpha C_1 + x) + 2\beta\} - 2\beta(\alpha x + \beta)\log(\alpha x + \beta)}{2\alpha^3} + C_2\right\} & \text{if } 0 \le x \le l_3, \\ \dfrac{12(P_1 + P_2)}{Eh^3}\left\{\dfrac{\alpha x\{\alpha(2\alpha C_3 + x - 2\zeta) + 2\beta\} - 2(\alpha x + \beta)(\beta - \alpha\zeta)\log(\alpha x + \beta)}{2\alpha^3} + C_4\right\} & \text{if } l_3 \le x \le l_2 \end{cases} \tag{6}$$

Here

$$C_1 = \frac{P_1 + P_2}{P_2}\left\{\frac{(\alpha\zeta - \beta)\log(\alpha l_3 + \beta) + \alpha l_3}{\alpha^2} + C_3\right\} - \left\{\frac{\alpha l_3 - \beta\log(\alpha l_3 + \beta)}{\alpha^2}\right\}$$

$$C_2 = \frac{P_1 + P_2}{P_2}\left[\frac{\alpha l_3\{\alpha(2\alpha C_3 + l_3 - 2\zeta) + 2\beta\} - 2(\alpha l_3 + \beta)(\beta - \alpha\zeta)\log(\alpha l_3 + \beta)}{2\alpha^3} + C_4\right]$$
$$- \frac{\alpha l_3\{\alpha(2\alpha C_3 + l_3) + 2\beta\} - 2\beta(\alpha l_3 + \beta)\log(\alpha l_3 + \beta)}{2\alpha^3}$$

$$C_3 = -\frac{(\alpha\zeta - \beta)\log(\alpha l_2 + \beta) + \alpha l_2}{\alpha^2}$$

$$C_4 = -\frac{\alpha l_2\{\alpha(2\alpha C_3 + l_2 - 2\zeta) + 2\beta\} - 2(\alpha l_2 + \beta)(\beta - \alpha\zeta)\log(\alpha l_2 + \beta)}{2\alpha^3}$$

$$\zeta = -\frac{P_1 l_3}{P_1 + P_2}$$

Assuming the displacement of the bolt position as δ_1 or δ_2,

$$\begin{aligned}
&\delta(0) = \delta_2 \\
&\delta(l_2) = \delta_1
\end{aligned} \tag{7}$$

From this, solving for P_1 and P_2, the formula for calculating the restoring force can be expressed as equation (8).

$$\begin{aligned}
P_1 &= \frac{F_3G_2 - F_2G_3}{F_1G_2 - F_2G_1} \\
P_2 &= \frac{F_3G_1 - F_1G_3}{F_2G_1 - F_1G_2}
\end{aligned} \tag{8}$$

Here

$$F_1 = \left\{\frac{l_3}{\alpha} - l_3D_3 - \frac{D_1D_2}{\alpha^2} - D_5\right\}l_3 + \left\{l_2D_4 + \frac{l_3^2}{2\alpha} + \frac{\beta l_3}{\alpha^2} - \frac{\beta D_1D_2}{\alpha^3} + D_6\right\}$$

$$F_2 = \left\{ l_3 D_4 + \frac{l_3^2}{2\alpha} + \frac{\beta l_3}{\alpha^2} - \frac{\beta D_1 D_2}{\alpha^3} + D_6 \right\}$$

$$F_3 = \frac{E h^3 \delta_1}{12}$$

$$G_1 = -\frac{\beta D_1 D_2}{\alpha^3} + \frac{\beta l_3 (1 + D_2)}{\alpha^2} - \frac{l_3^2}{2\alpha} + D_6 - \left(\frac{D_1 D_2}{\alpha^2} - \frac{l_3 (1 + D_2)}{\alpha} + D_5 \right) l_3$$

$$G_2 = -\frac{\beta D_1 D_2}{\alpha^3} + \frac{\beta l_3 (1 + D_2)}{\alpha^2} - \frac{l_3^2}{2\alpha} + D_6 + \frac{\beta}{\alpha^3} (\alpha l_3 + \alpha l_3 D_2 - D_1 D_2) - \frac{l_3^2}{2\alpha} - \frac{\beta^2}{\alpha^3} \log(\beta)$$

$$G_3 = \frac{E h^3 \delta_2}{12}$$

$$D_1 = \alpha l_3 + \beta$$

$$D_2 = \log(\alpha l_3 + \beta)$$

$$D_3 = \frac{-\log(\alpha l_2 + \beta)}{\alpha}$$

$$D_4 = \frac{\beta \log(\alpha l_2 + \beta) - \alpha l_2}{\alpha^2}$$

$$D_5 = l_2 \left(\frac{1}{\alpha} - D_3 \right) - \frac{(\alpha l_2 + \beta) \log(\alpha l_2 + \beta)}{\alpha^2}$$

$$D_6 = \frac{\beta (\alpha l_2 + \beta) \log(\alpha l_2 + \beta)}{\alpha^3} - l_2 \left(D_4 + \frac{l_2}{2\alpha} + \frac{\beta}{\alpha^2} \right)$$

3.3. Validity of the formula for calculating restoring force

As this calculation formula is extremely complex, we compared its results to those of numerical analysis to confirm the validity of the formula. First, P_1 and P_2 were obtained using the formula. Assuming that l_1 is 5 mm, l_2 is 88 mm, b_l is 100 mm, b_o is 20 mm, h is 1 mm, θ is 10 degrees, and Young's modulus is 3000 N/mm^2, δ_1 is 0.87 mm and δ_2 is 15.42 mm. Solving for P_1 and P_2 using equation (8), we obtained P_1 as 534 N and P_2 as -0.664 N. Next, an analytical model was created using the numerical analysis software midas[4]. The model was created using 100 equally divided beam elements, and the width of the member was varied in steps from the fulcrum to the tip. The model was analyzed with P_1 = 534 N and P_2 = -0.664 N obtained from the calculation formula, and the deformations δ_1 and δ_2 were obtained. The δ_1 was 0.87 mm and the δ_2 was 15.10 mm. Since the values of the calculation formula and the numerical analysis are in general agreement, it can be said that the calculation formula is reasonable.

4. Numerical results of a three-dimensional model subjected to restoring forces and shape differences of the model

4.1. Geometry of the model

Figure 11 shows the shape of the model used as a comparison target. In this model, the polyhedral shape after division was created by combining triangular elements instead of dividing the curved surface. The shapes of elements 1-6 are equilateral triangles with a side length of 90mm, while elements 7-14 are isosceles triangles with a vertex length of 0.7 times the side length of an equilateral triangle measured from the boundary edge. The normal angle between the elements was set to be 10 degrees. A model and a numerical model were created with this geometry.

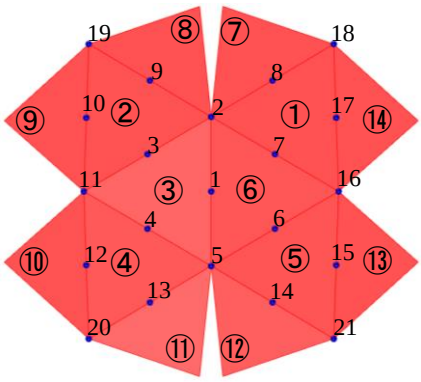


Figure 11. Subject model

4.2. Shape differences in models

The model was made as described in Section 2, Section 2. The flat plates were made of 1 mm thick PVC plates, and M3 bolts were used. The position of the bolts was set at the intersection of a line offset 5mm from the boundary edge. The outermost bolt was fixed to a base member created to match its orientation and height. Figure 12 shows a photo of the created model. The black or gray parts in the figure are the base member. The shape of the base member was determined by a 3D model, and a 3D printer was used to create the base members. The base member was constructed within 5 mm inside the bolt position. The base members were bolted to an MDF board, and its position was also determined by the 3D model. The holes in the MDF board were drilled by CNC.

After creating the model, the coordinates of the position indicated by the circular mark in Figure 11 were measured using photogrammetry. The number on the upper right corner of the blue dotin in figure 11 is the number of the measurement point. We attached measurement marks to the measuring points of the model, and took photographs from various angles. Then, we used the image processing software Metashape[5] to obtain the coordinates of the measurement marks. The difference between these coordinates and the coordinates of the corresponding points on the 3D model was calculated. In order to calculate the difference between the measurement results and the 3D model, the measured points were translated and rotated so that the first measurement point coincided and the direction from that point to the second measurement point was aligned.

Figure 13 shows the shape difference of the model. The arrows represent the x and y components of the shape difference, and the color of the markers represent the z component. The figure also shows the reference length of the arrows and the color scale. The figure shows that the shape difference in the x,y direction increases as it spreads outward from the center, and the points at the four corners are deformed toward the center, while the other points are deformed outward. In addition, the shape difference in the z direction is increasing upward. The model has a more swollen shape than the 3D model.

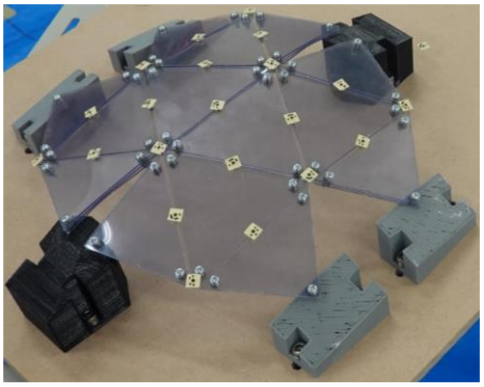


Figure 12. Created model

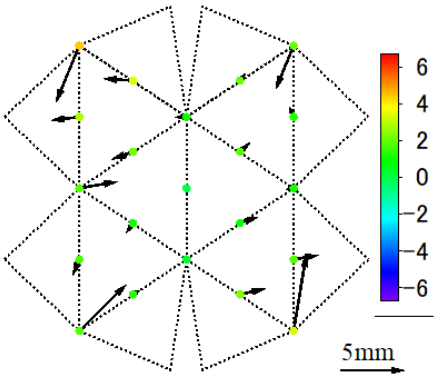


Figure 13. Shape differences in model [unit: mm]

4.3. Numerical analysis of the 3D model with applied restoring forces

Describe the numerical analysis. A numerical analysis model was created in a polyhedral shape, and the restoring force was applied to it, and calculated the displacement. Figure 14 shows the numerical analysis model. The material was assumed to have a Young's modulus E = 3000 N/mm^2 and a Poisson's ratio of ν = 0.38. The element used was a quadrilateral plate element with a thickness of 1 mm and was meshed in a square shape with a spacing of 0.5 mm (triangular shape near vertices and boundary edges). The nodes on the green line in the figure were used as pin supports. This position is on the boundary of the base member. The restoring force was obtained using the method described in Section 3. The restoring force was assumed to be the force that causes the flat plate member to return to its original shape, so when the flat plate members overlap, the restoring forces obtained for each flat plate member were combined. For example, elements numbered 1 to 6 have three overlapping flat plate members. For these elements, we assumed three boundary edges as fixed ends, calculated the restoring forces for each condition, and added up the restoring forces at each bolt position to obtain the total restoring force at that position. Numerical analysis was performed using Karamba3D[6] in Grasshopper, an extension of Rhinoceros. The analysis method used was large deformation analysis, and the number of increments was set to 100. Only the restoring force was used as the load, and no dead weight was applied.

Figure 15 shows the displacement diagram obtained from the analysis. The pink color indicates greater deformation. The maximum displacement value was 7.38 mm. The displacements at each measurement point were summarized in the same format as the shape differences of the model shown in Figure 13, and are shown in Figure 16. From the figure, the deformation in the x- and y-directions increases from the center to the outside, mostly deforming to the center; the deformation in the z-direction deforms to the upper side at the position of the apex of the triangular element and to the lower side at the position of the center of the boundary edge.

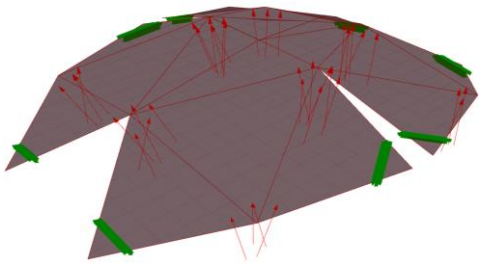


Figure 14. Numerical analysis model

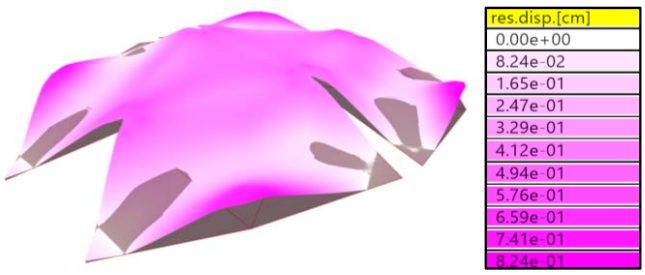


Figure 15. Deformation diagram

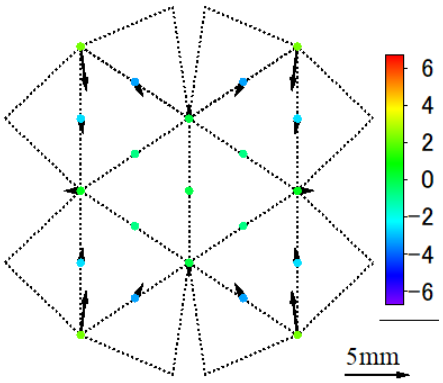


Figure 16. Results of numerical analysis [unit: mm]

4.4. Comparison of the model and numerical analysis, and discussion

The shape differences of the models were compared with the results of the numerical analysis. Figure 17 shows the shape difference of the model minus the numerical analysis.

The maximum error in the x-y directions was found to be around 2.8 mm at point 11, where the shape difference of the model was greatly deformed inward, and it is assumed that the accuracy of the measured mark position at point 11 was low. For points other than point 11, 86% of the points had errors less than 2 mm, and 38% of the points had errors less than 1 mm.

Regarding the z-direction, all points except for 18 and 20 have positive values, and the values for 18 and 20 are almost zero. This indicates that the model has a more swollen shape than the numerical analysis. The errors for the triangle vertices (points 2, 5, 11, 16, and 18-21) are small, ranging from -0.4 to 2.2 mm, while the errors for the center points of the boundary edges (points other than the vertices) range from 1.7 to 6.7 mm, indicating that the errors are large. In particular, the errors for the points farther from the reference point (points 8-10, 12-15, and 17) are even larger, ranging from 3.9 to 6.7 mm. Therefore, while the numerical analysis yields values equivalent to the model's shape differences for the triangle vertices, the errors for the center points of the boundary edges are large. Furthermore, for all points relative to the inflated model, the numerical analysis results in the center points of the boundary edges being concave.

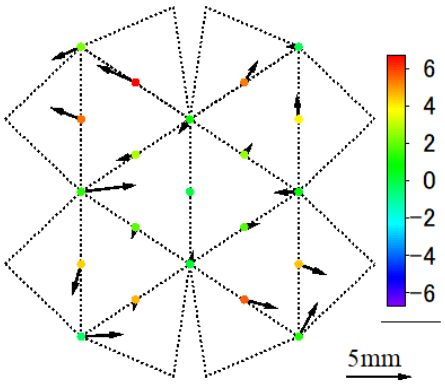


Figure 17. Comparison of geometrical differences between models and numerical analysis [unit: mm]

this suggests that this is the cause by only giving forces to the bolt positions. As a solution, it is necessary to reconsider how to calculate the restoring forces and where to apply them. In addition, during numerical analysis, as shown in Figure 18, the restoring forces are applied in the normal direction of the pre-deformation surface. However, to maintain that angle even after deformation, it is necessary to

consider a method to modify the restoring forces to face the normal direction of the deformed surface with each iterative calculation.

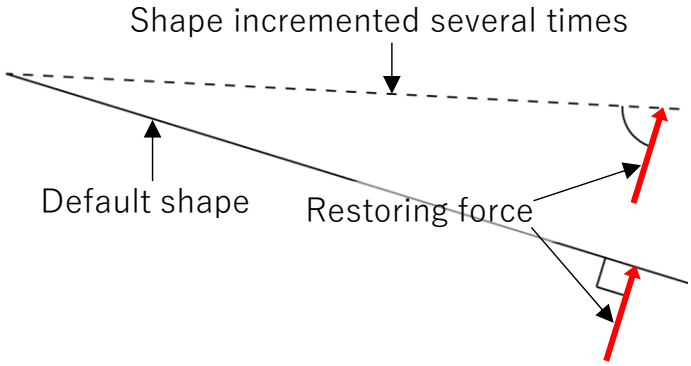


Figure 18. The direction of the restoring force after deformation

5. Conclusion

In this study, we verified a method to estimate the shape difference between a model and a 3D model in a curved structure made of a plate and bolts. We compared the deformation obtained by giving restoring force to the 3D model with that of the model, assuming that the deformation obtained by giving restoring force to the 3D model is similar to the shape of the model, and validated its validity. The restoring force was considered as the force that the plate member forming the model tries to return to its original position. Also, this force was considered as the force required to bend the plate member to the target position. The formula for calculating this restoring force was formulated by treating the plate member as a beam element and solving the mechanical model where force was applied to the bolt position.

From the comparison of the shape difference between the model and the numerical analysis, it is suggested that the errors at the vertices of the triangles are small, and the shape difference can be estimated by numerical analysis. On the other hand, the errors are large at the center of the boundary edge of the triangles, indicating the need to reexamine the concept and application of the restoring force, the method of applying it, and the numerical analysis approach.

References

[1] Morooka S. and Nomura K., Difference between drawings and assembled models in curved surface combined with flat plates and bolts, *Proceedings of the IASS-SLTE 2014 Symposium*, Brasilia, Brazil, Sep. 2014

[2] Murata S., Nomura K. and Morooka S., The influence given by the different element division method on shape of the curved surface structure consisting of flat plates and bolts, *Summaries of Technical Papers of Annual Meeting, Architectural Institute of Japan* (CD-ROM), Sep. 2018, pp.781-782

[3] Watanabe S. and Nomura K., Relationship between Deformation and Shape Difference of Flat Plate Members in Shell Structure made of Flat Plates and Bolts, *Summaries of Technical Papers of Annual Meeting, Architectural Institute of Japan* (CD-ROM). Sep. 2021, pp.623-624

[4] Midas iGen, 2023.3, https://www.midasuser.com/jp

[5] Metashape, 2023.3, https://oakcorp.net/agisoft/

[6] Karamba3D, 2023.3, https://karamba3d.com/

IASS 2023
July 10–14 Melbourne
Integration of Design and Fabrication

Proceedings of the IASS Annual Symposium 2023
Integration of Design and Fabrication
10–14 July 2023, Melbourne, Australia
Y.M. Xie, J. Burry, T.U. Lee and J. Ma (eds.)

Expanding the design freedom of spatial patterns by combined elastic bending and twisting: a parametric study

Fereshteh KHOJASTEHMEHR[a,*], Günther H. FILZ[a]

[a,*] Universität Innsbruck, Faculty of Architecture, LSU Lightweight Structures Unit
Technikerstrasse 21c, 6020 Innsbruck, Austria
Fereshteh.Khojastehmehr@uibk.ac.at

Abstract

Elastic bending, nowadays referred to as bending active, of initially straight elements has become increasingly popular in the construction of spatial structures, such as elastic gridshells. According to our previous review [1], despite the introduction of modern gridshells over 80 years ago, their geometric patterns tend to be similar and a clear relationship between the pattern and the Gaussian curvature of the surface could not be observed. To gain more design freedom in creating bespoke architectural and structural patterns, in addition to elastic bending the potential of torsion as a design driver may be explored [2]. However, the naturally emerging shape of the strips and their geometrical limitations imposed by the material need to be understood [3]. This paper presents a parametric study on combined bending and twisting of one single or several interacting, linear wooden strips. Presently, our main focus is on the two aspects of the minimum achievable bending radius and pattern curvature and the maximum twistability of the strips in the elastic range of the material. Our investigations and experiments are conducted in both digital and physical environments starting from the strips and patterns rather than from a form-found predefined shape, to which the patterns are applied. Our studies (i) show the geometrical possibilities of wooden strips in terms of elastic bending and twisting, in dependence from their cross-section and support conditions, (ii) identify the limitations of wooden strips in terms of geometrical rules, and (iii) compare the digital modelling to physical prototypes. Feature-driven, the created patterns are applied to different shapes. These features can be structurally informed, taking into account, for example, the Gaussian curvature of the target surface, fabrication-driven, or architecturally driven, such as the density of patterns, visibility, depth of the surface, or other aesthetic aspects. Future investigations will include different cutting patterns of the strips, further increasing the technical and architectural design space.

Keywords: spatial structures, elastic gridshell, torsion, geometrical pattern, Gaussian curvature, architecture

1. Introduction: a review on elastic bending and torsion

Spatial structures are a type of structures that can be made out of curved or linear elements. While using linear elements is more common in spatial space structures, curved elements are used in grid spatial structures, gridshells. The material used for curved elements is mostly wood and its fabrication process in architectural structures is possible with different methods of pre-forming using CNC milling machines, non-industrial techniques [4, 5, 6] or natural self-shaped methods [7], and post-forming using the potential of elastic bending. Spatial structures that use the advantage of elastic bending can be used for different purposes. They can be a lattice structure such as Rise project [8], Mangrove [9], Vartwisted & Varschoba [10], Loop [11], elastic habitat [12], triaxially woven structures [13], bio-inspired lamellar structure [14], and zip-bent prototype [15] or elastic gridshells that can have different subcategories of regular such as Essen pavilion [16], Multihalle Mannheim [17], Toledo gridshell [18, 19], Portalen pavilion [20] and irregular patterns including examples of SG2012 gridshell [21], Mantashell [22], UWE research pavilion [23], geodesic winding gridshell [24], inside/out gridshell [25], and computational

Copyright © 2023 by Fereshteh KHOJASTEHMEHR and Günther H. FILZ. Published in the Proceedings of the IASS Annual Symposium 2023 with permission.

bamboo [26]. While elastic gridshells are efficient structures in terms of material use, structural behavior, and facilitation in transportation, their geometric patterns tend to be similar and a clear relationship between the pattern and the Gaussian curvature of the surface could not be observed [1]. Complex forms can be realized by the use of twists for changing the direction of the strip and the use of strong or weak axis of the lath in the elastic elements in simple grids. This is useful when combining two different patterns, for example combining a pattern with elements perpendicular to the surface using their strong axis with patterns that are aligned on the surface and use their weak axis. In addition to responding to the curvature shift, the twist may change the overall shape of the structure and increase the design freedom in elastic spatial structures. Using twists in geometries is not new and dates back to past times [27]. Twist refers to the action of turning or warping one object around another one [28]. Torque is also defined as a force that results in rotation or torsion [29, 30]. Elastic torque has been used in different research but still, its power on spatial structures is not fully explored. Elmas et al. [31] showed the power of twisting in designing efficient cantilevered beam structures. Twist as a design derivative has been introduced for combining elastic strips with fabric [32]. Naboni et al. [15] developed a method for the fabrication of elastic elements with a zip-bending possibility that enable the potential of twisting in curved wooden elements.

By combining bending with twisting in elements with elastic behavior, this paper introduces innovative structures that can improve the quality of elastic spatial structures in terms of geometrical, architectural, structural, and environmental aspects. In particular, this paper (i) shows the geometrical possibilities of wooden strips in terms of elastic bending and twisting, depending on their cross-section and support conditions, (ii) identifies the limitations of wooden strips in terms of geometrical rules, and (iii) compares the digital modeling to physical prototypes from birch plywood strips. Simultaneously we provide an evaluation of the applied digital simulations. Our method is based on experiments in the digital and physical environment. The physical prototypes are used to evaluate the simulations and improve them in terms of realistic results. The two design methods that are used in most elastic gridshells are top-down (shape-first) and bottom-up (pattern-first) [33]. In our research, we start with a pattern-first approach and explore the possible forms for elastic strips in terms of geometrical rules and restrictions including the minimum and maximum possible curvature. In the next steps, we will combine these understanding and geometric rules with shape-first where an overall shape is considered as a first input but the structural form at the end can follow the material behavior and self-organizing principles.

2. A geometric approach to elastic-forming

We explore the geometrical features of patterns that are formed based on a combination of elastic bending and twisting. By twist, we mean the action of twisting of material around a longitudinal axis resulting in a torqued shape. The observation consists of one-strip explorations, two-strip connections and joint planes, and the exploration of a network of strips. Figure 1 shows the feasible range for one strip in combined elastic bending and twisting with hinged supports in a defined platform.

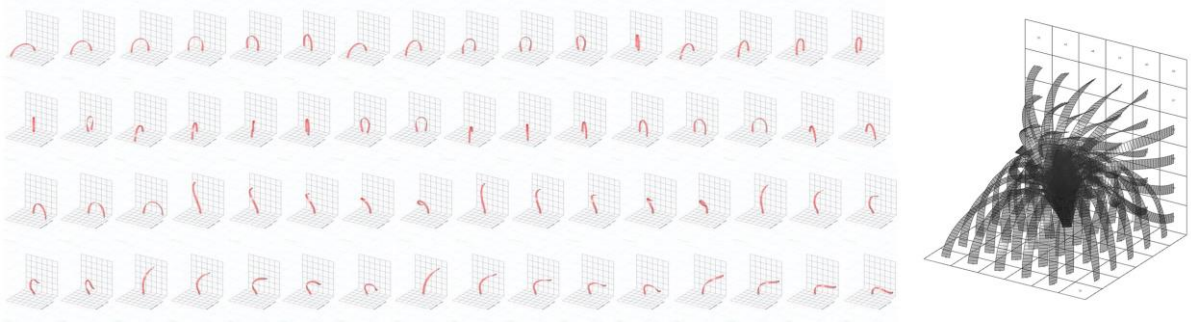


Figure 1. Parametric study and feasible range for one strip in combined elastic bending and twisting with hinged supports.

The focus of our work is on the two aspects of the minimum achievable bending radius and pattern curvature and the maximum twistability of the strips in the elastic range of the material. The bending radius depends on the length of the elements and the support conditions. It seems clear that in longer strips, with the same width and thickness of material, the bendability of the material increases. For example, in comparing two strips with the size of 10 mm x 100 mm and 10 mm x 200 mm, and a thickness of 0.6 mm, the strip with the length of 200 mm shows more flexibility. But in the same length and proportions of the strip and same support conditions and changing the span, different minimum and maximum bending radius are achieved (Figure 2). As the smallest and largest bending circles show, for both hinged and fixed supports the minimum bending radius is usually in the middle of the curve, and the maximum bending radius is at the ends of the strip.

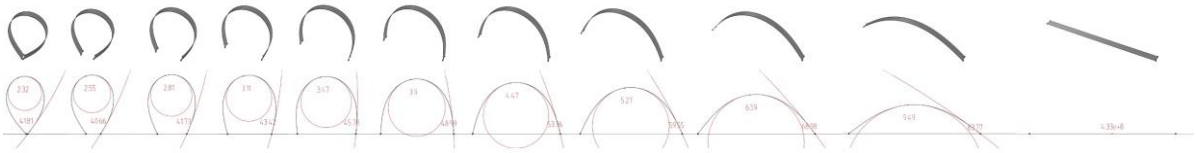
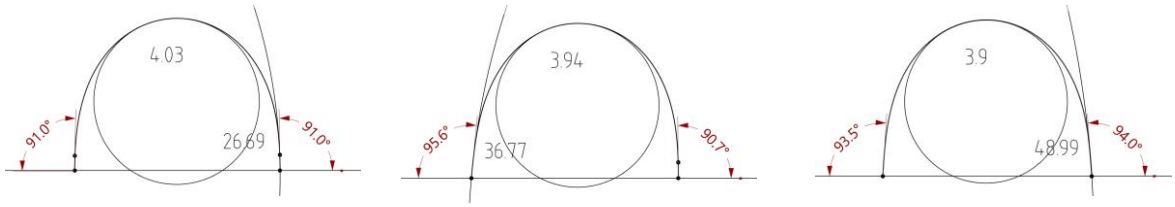


Figure 2. The smallest and largest bending radius for one strip with proportions of 1/20.

By changing the supports from fixed to hinged, a smaller minimum bending radius, and larger maximum bending radius can be achieved. Figure 3 shows one strip with the same proportions and three different support types. Also, the outer angle at the fixed support is almost 90 degrees and increases by changing to hinged supports which means more flexibility in the curvature is possible for hinged supports.



fixed-fixed hinged-fixed hinged-hinged

Figure 3. Examples of support types in one strip and their corresponding curvature radius and angles at supports, left: fixed-fixed, center: hinged-fixed, and right: hinged-hinged.

The elastica curve of strips for four different proportions of 1/20, 1/10, 1/6.66, and 1/5 show the same bending radius, that means by keeping the same length and thickness of the material and changing the width of the strips, the bendability of the material in straight line stays almost the same (Figure 4).

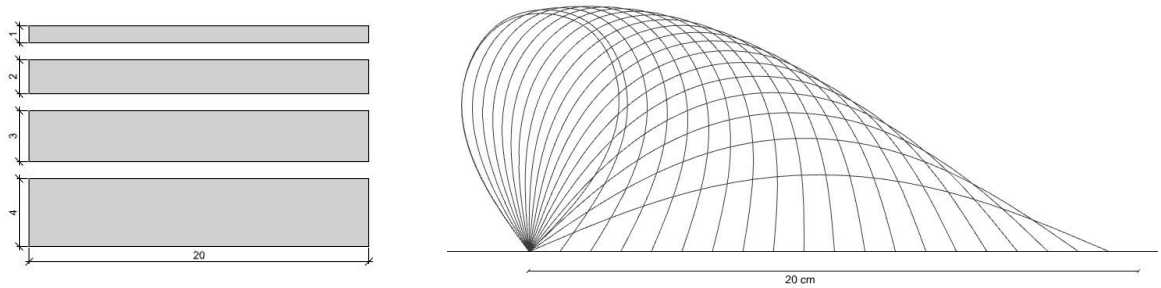


Figure 4. Four strip proportions and the corresponding curvature for 20 spans.

The effect of proportions however is understandable when introducing twist by rotating one or both endpoints of a strip, or by shifting one or both endpoints of a strip from the initially straight axis, or by combining both aforementioned options. Figure 5 shows four strips with different proportions, the same

span of 40 mm, hinged supports, and a rotation angle of 90 degrees. By keeping the same span and twist angle but changing the proportions from 1/20 to 1/5, the minimum bending radius reduces which means higher curvature is allowed. As shown below, the minimum bending radii for the strips with the sizes of 10 mm x 200 mm, 20 mm x 200 mm, 30 mm x 200 mm, and 40 mm x 200 mm are 24.9 mm, 23.7 mm, 22.1 mm, and 17.6 mm respectively. One possible reason is that by increasing the width of the material, the number of osculating circles, fitting the points of the surface, will be increased and smaller circles can result.

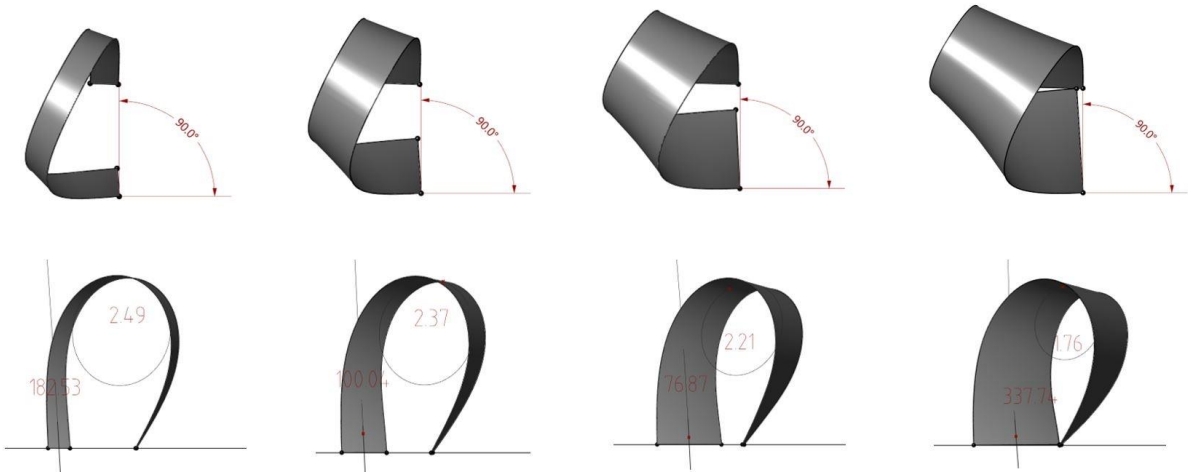


Figure 5. The minimum and maximum bending radius for four strips with the span of 40 mm, and the twist angle of 90 degrees (up: top view, down: side view).

To better compare the relevance of twist, strip proportions, and the bending radius, we explore and compare the minimum bending radii of four 90-degree twisted strips with four proportions of 1/20, 1/10, 1/6.66, and 1/5 and in three different spans of 40 mm, 100 mm, and 180 mm (Figure 6). As the charts show, the minimum bending radius for each of these spans is almost the same between all these proportions when there is no twist. By increasing the twist degree, the effect of change in proportions and the minimum bending radius is more understandable. In both spans 40 mm and 100 mm, the behavior of the material is similar, the higher bending curvature is achievable in wider strips, proportion of 1 to 5, and in larger twist angles, 90 degrees. In span 180 mm, however, it is somehow different where the smallest bending radius is achievable by the twist angle of 67.5 degrees. Also, almost in each of the angles and in all spans, the minimum bending radius has the smallest amount for strips with proportions of 1/5 and the largest amount for strips with proportions of 1/20.

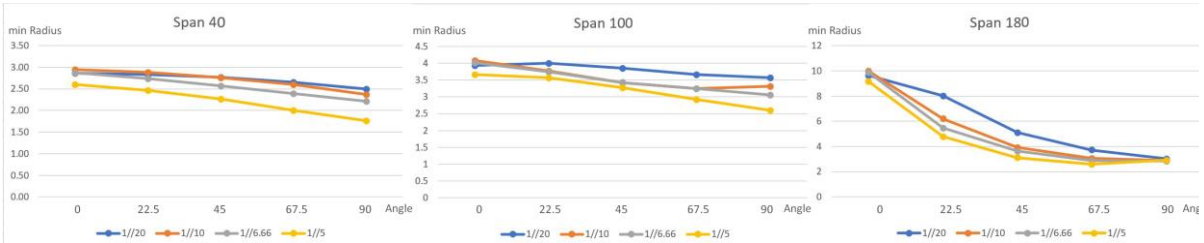
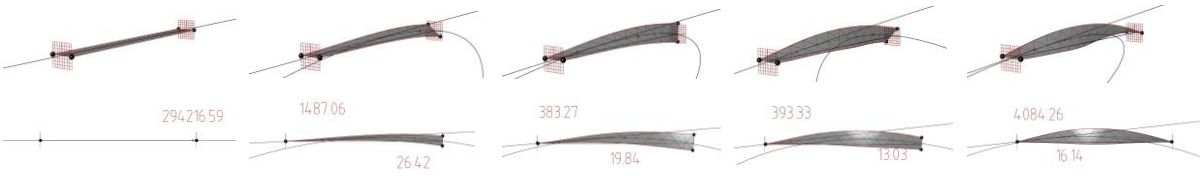


Figure 6. The minimum curvature radius for one strip with four proportions of 1/20, 1/10, 1/6.66, and 1/5, three spans of 40 mm, 100 mm, 180 mm, and the twist angle of 90 degrees.

Twisting one strip can be helpful for curvature shifts and changing the direction of the weak axis of the material. It also helps to have different curvature radius in places where higher curvature is needed. The effect of the twist of one strip on the minimum and maximum bending radius is shown in Figure 7. The

strip has the proportions of 1 to 10 and 5 twisting degrees of 0°, 45°, 90°, 135°, and 180° at its right end and around the strip axis. As it is shown, the minimum bending radii for these degrees are 2942165.9 mm, 264.2 mm, 198.4 mm, 130.3 mm, and 161.4 mm which means the minimum bending radius for one strip by considering the twist in its axis (parallel to the length of the strip) is 135 degrees between these explored twist angles.

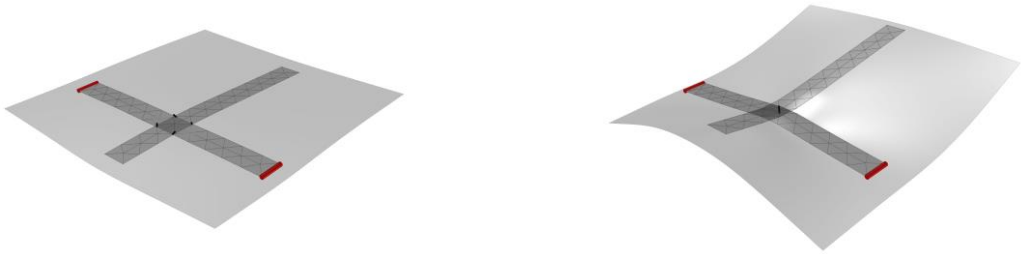


0 45 90 135 180

Figure 7. The effect of different twist angles on the minimum and maximum bending radius of one strip with proportion of 1/10 (top: perspective view, down: side view).

2.1. Connections of elements

Joining twisted elements to create a connected network raises challenging geometrical questions with practical relevance. We consider two joint types, a fixed one, where translations and rotations are blocked, and a pinned one where only translations are blocked. Figure 8 shows two strips with the same proportions of 1/20, two support edges, and two different joints pinned or fixed connecting them. The other two edges are considered free to let the structure self-form the curvature. The change in the connection type will also change the curvature of the resulting structure and therefore change the output surface that is generated based on the curvature of these strips. A visual explanation of how this surface is generated is shown in Figure 9. As shown below, pinned joints due to allowing for rotations, enable higher surface curvature and might be more suitable options for parts of the structure that need a higher curvature. To clarify the curvature intensity as a result of each connection we introduce the deformation value (dv) of the surfaces that represents the difference between the minimum and maximum z value of all the points on the two strips in millimeters. As the values show, using pinned joints in these two strips results in a surface deformation that is almost 10 times larger than with fixed joints.



dv = 2.11 mm dv = 20.78 mm

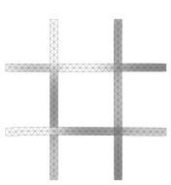
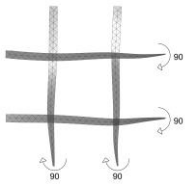
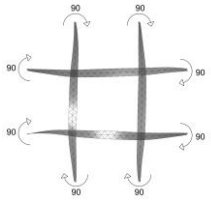
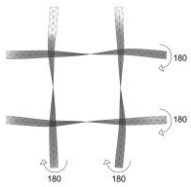
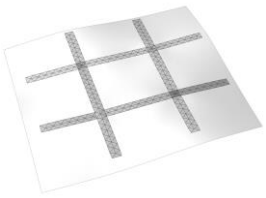
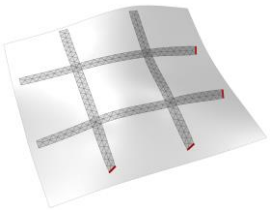
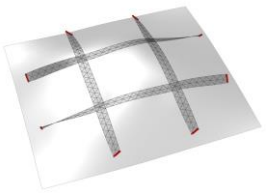
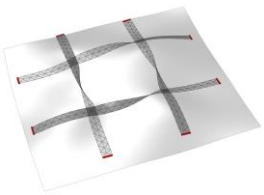
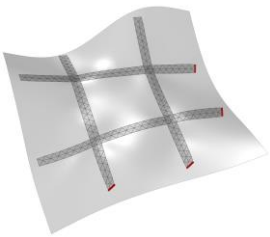
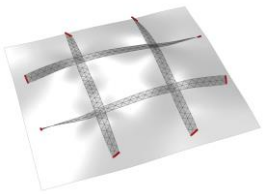
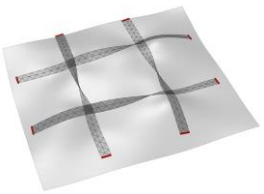
Figure 8. Two types of connection between two strips and the corresponding surface curvature result; left: fixed, right: pinned (if there is a red line at the end it means that the end points are supports).

2.2. Pattern of strips and surface curvature

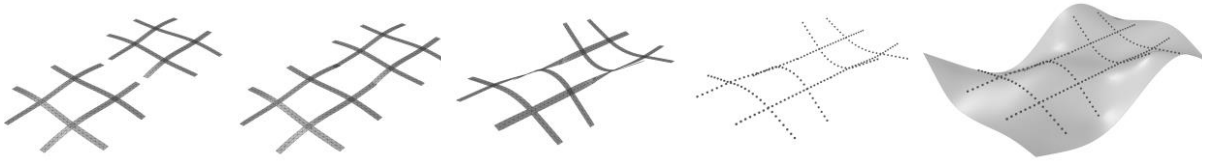
In a pattern-first approach and by considering a simple rectangular grid, we twisted four strips with a proportion of 1/20 and explored how twist imposes a curvature on the structure. Table 1 shows four types of twists on these four strips with different joint types of fixed and pinned and the corresponding surface curvature that is post-generated for visualization reasons. In types 2 and 3 all of the strips are 90 degrees twisted in one or both ends. The twist angle of type 4 is increased for all strips to 180 degrees at one end each. Similar to Figure 8, to clarify the curvature intensity in each pattern we use the deformation value of the surfaces of the strips in a pattern. The twisted end edges are considered supports to apply the curvature on the form. As shown in types 3 and 4, when all of the strips` ends are considered

supports, the final surface curvature is almost the same in the two different joint types and the change has a range of 0.98 mm. This means that the effect of change in the joint types is more understandable when there is a mix between the free end edges and the support ones, such as types 1 and 2.

Table 1. Four patterns with four types of twist and the corresponding surface curvature for two joint types.

	Type 1	Type 2	Type 3	Type 4
joint type				
fixed				
	dv = 3.82 mm	dv = 31.63 mm	dv = 12.82 mm	dv = 10.95 mm
pinned				
	dv = 37.37 mm	dv = 51.62 mm	dv = 11.84 mm	dv = 11.32 mm

As mentioned, the surfaces shown in Table 1 are added to the digitally generated strips to visualize the curvature of the structural elements using a patch surface. In Rhino3D, a patch surface is defined as a surface that fits to a defined set of meshes, curves, points, or point clouds [34]. Figure 9 shows the process of combining two 4-strips patches into one pattern by twisting the connection between them. To simplify the modeling in both digital and physical environment, we use the same size of the strips and consider changing the distance of the two patches and connecting them with an overlap value of 10 mm. We achieve similar results, especially in digital environment, if we consider two continuous strips instead of having separate pieces. To visualize the shape, we add a patch surface to show the effect of twist on the final surface curvature. This is to make it clear that we start with strips and not with a surface.



a b c d e

Figure 9. From left to right; (a) the two 4-strips patches, (b) connecting the two patches with an overlap of 10 mm, (c) twisting the joints in between, (d) extracting the points of the strip meshes, and (e) the resulting patch surface from the mesh points.

As it is shown in Figure 9, twisting the connection between the two patches by 90 degrees provides the possibility to convert a convex shape into a concave shape. Figure 10 shows this shift in the curvature in a graphical way. The circles of curvature show the direction of the surface curvature in two parts of the pattern.

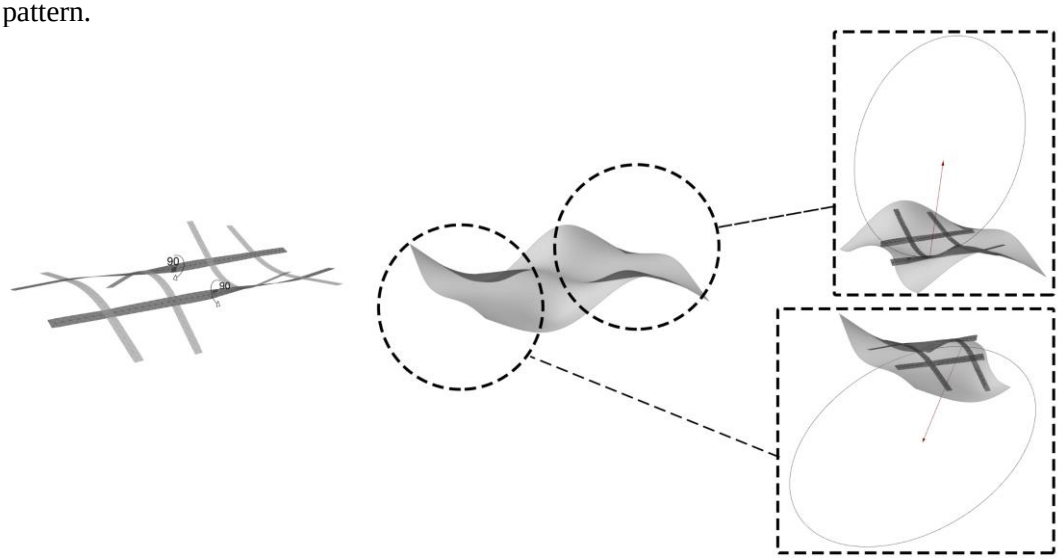
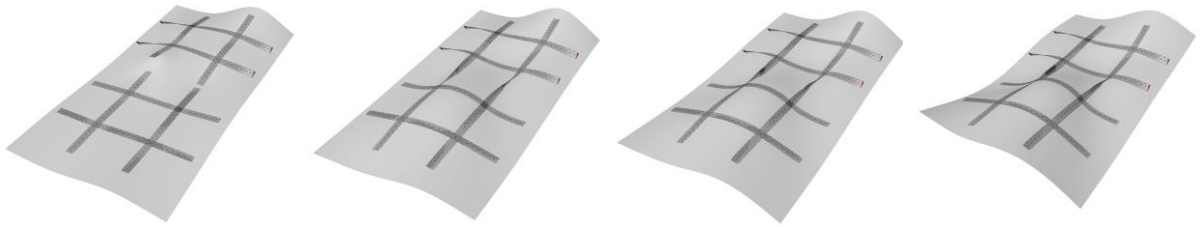


Figure 10. Two separate patches with different curvature directions are connected together and 90 degrees twisting the connection made the conversion between them possible.

Similar to the pattern shown in Figure 9, the amount of overlap, respectively the distance between separate patches defines the effect of the twist on the whole structure. Figure 11 shows one pattern consisting of two separate 4-strips patches in 4 states before connecting and connecting with three different overlap values of 10 mm, 20 mm, and 30 mm. In all of these patterns, only 4 edges are kept in their place to show the effect of twist on the whole structure.

The patch surface is also added to show the change in the curvature of the final form. The dv values show that by increasing the overlap (shortening the distance) in the connection, the twist results in higher curvature for the whole form which means that the effect of twist is not locally on the connection part and can influence the whole curvature of the form. It should be noticed that the overlap of the strips causes extra stiffness to the whole structure and results in less flexibility for bending and twisting. We therefore limit the overlap to a range of 30 mm in our small-scale models.

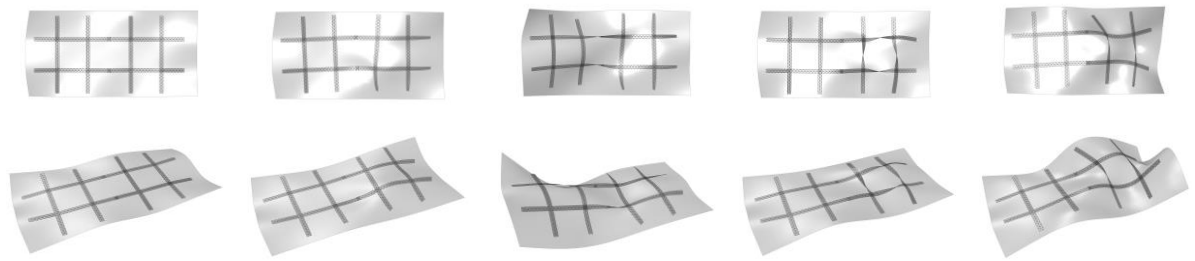


dv = 22.72 mm | dv = 24.24 mm | dv = 26.58 mm | dv = 39.92 mm

a | b | c | d

Figure 11. A pattern made of two 4-strips patches, (a) without connection between the section, and connection with overlap of (b) 10 mm, (c) 20 mm, and (d) 30 mm. The red lines at the end of the edges represents the supports.

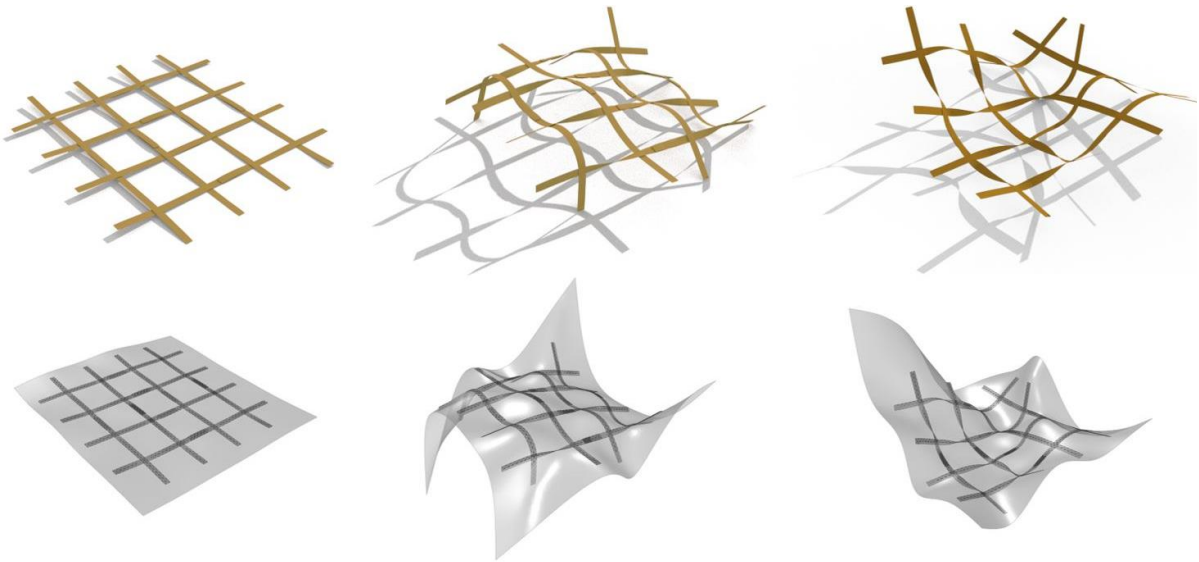
The same process was applied to eight strips with the same size and proportions as in the experiment in Table 1. By adding to the number of strips and extending the pattern, the change in the surface curvature is clearer. Figure 12 shows how the output surface has different curvatures by twisting these strips in five different versions with the same overlap value of 10 mm.



dv = 9.06 mm | dv = 22.09 mm | dv = 73.82 mm | dv = 20.22 mm | dv = 71.56 mm

Figure 12. Five different twist types for eight strips and the corresponding surface curvature in two views of top (up) and perspective (down).

Continuing the process with more strips, the change in the curvature is more clearly shown in Figure 13 where 16 strips are connected together with the same square pattern and type of joints (fixed), but with three different levels of twist. Now the effect of twist on the curvature and the shadow is very different from the flat grid. Different degrees of twists in elements result in different surface curvatures, also shown with the deformation values, and can be used for different functions and design demands. To reach a self-organized form and let the structural forms shape themselves only based on the material behavior, twist, and joints, the endpoints are not considered supports.



dv = 12.33 mm | dv = 88.18 mm | dv = 142.41 mm

Figure 13. A square pattern with 16 strips (left) and two versions of twisting the strips (center and right).

3. Findings on geometrical explorations of elastic elements

3.1. Geometrical considerations and rules

We refer to geometric rules that make restrictions for elastic elements in the process of post-forming. One important rule is the minimum bending radius for the curved strip, which depends on the material dimensions and elasticity. The maximum radius is not a problem because the material starts from the

flat state and returns to flatness due to its elasticity. We used birch plywood strips with the size of 10 mm x 200 mm and the thickness of 0.6 mm for our scaled models. Here, the minimum bending radius is 12.0 mm. In the digital environment, less than this value is possible but when adding the material properties and trying to fabricate it that would not be possible. The maximum twistability is also another important factor, which of course depends on the strip length. For our scaled models and a predefined length of 200 mm this value is limited to 180 degrees, especially in a network of strips where the twist in one strip affects the other ones as well. Twist degrees in the range of 270° result in breakage of the strip as the tension in the material dramatically increases. Figure 14 shows the twist test in three states of 180°, 270°, and the breakage as a result of tension in the material for one strip with the aforementioned size and thickness.

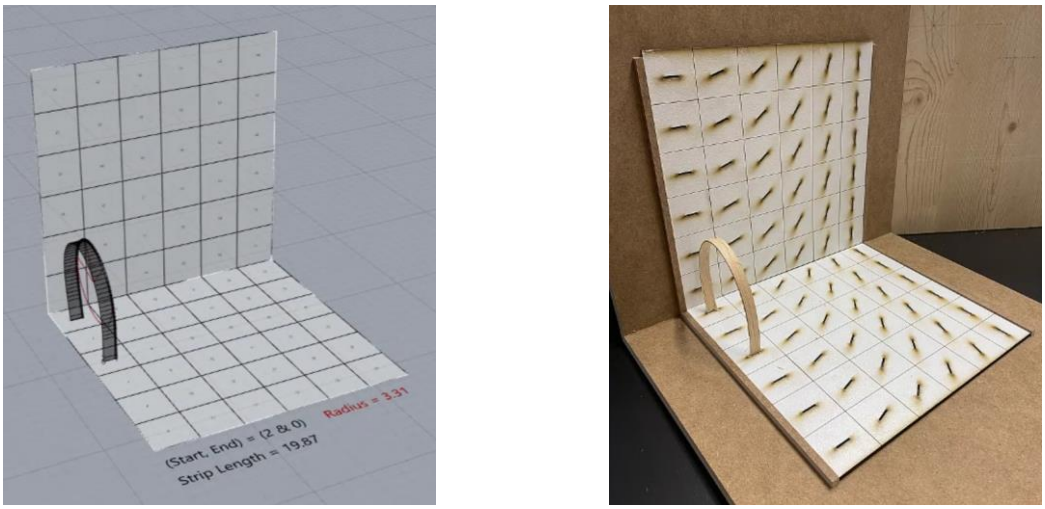


a b c

Figure 14. The maximum twistability of material: (a) 180 degrees twist, (b) 270 degrees twist, and (c) the break result of the high tension in the material.

3.2. Digital simulation vs physical simulation

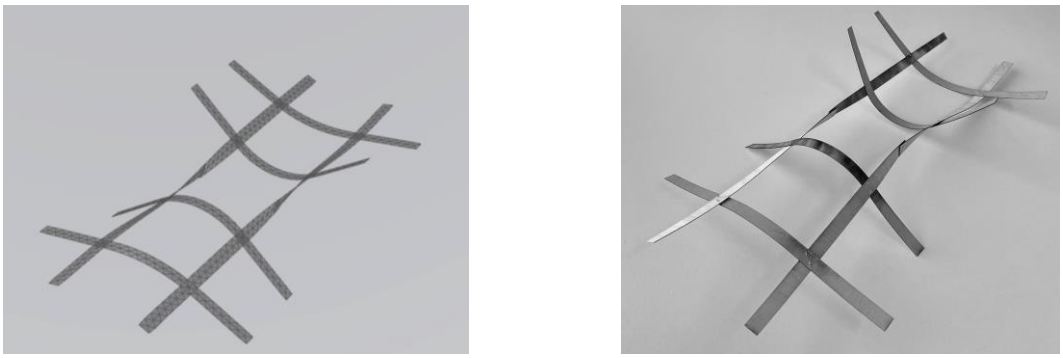
The simulation is physics-based modeling using Kangaroo Physics. The specific rules are set to simulate the elastic behavior of the material in bending and twisting. The material stretch in the modeling is limited to 0.6 mm. To test and evaluate our simulation, we consider birch plywood strips with the size of 10 mm x 200 mm and the thickness of 0.6 mm consisting of three layers for our scaled models. An experimental platform of two perpendicular planes with a grid of 6*6 consisting of cells with a dimension of 20 mm x 20 mm on each plane is considered as a first step and the curvature of one strip with different start and end points is investigated. The results from the digital simulation are also compared to the physical models of the same built platform. Figure 15 shows the same state of one strip in two different environments of digital and physical. The minimum bending radii are compared between the two models and the results shows that they are closely aligned. The model building verified the digital model being in a range of 0.6 mm accuracy. This is considered acceptable for small-scale results and not of practical relevance. For larger scales, the relative deviations may be even smaller, even though imperfections of material etc. may play a bigger role.



bending radius = 33.1 mm bending radius = 33.0 mm

Figure 15. Comparison between digital simulation (left) and physical prototype with plywood (right).

The behavior of the system is also checked in a network of strips with the same size of 10 mm x 200 mm and the thickness of 0.6 mm with or without twists. Figure 16 shows the simulation and the physical prototype of a square pattern consisting of twisted elements. As shown, the curvature in the final form is similar in both of the models. To verify our results, we calculated the deformation value of the physical model in parallel to the digital one and the results show the deviation of a maximum of 1.4 mm, which is assumed acceptable for the small-scale prototypes. It should be noted that there might be small errors in the physical prototypes because of the connection methods, using staples instead of four connecting points as in the digital simulation.



dv = 60.6 mm dv = 62.0 mm

Figure 16. Comparison between the digital simulation (left) and the physical prototype from birch plywood strips (right) of a square pattern with twist.

4. Discussion, conclusion, and future work

This paper shows the possibilities of twist for elastic spatial structures that include changing the curvature of the form from convex to concave shape and increasing the design freedom in elastic gridshells. The process follows a pattern-first approach and explores the possible forms and surface curvatures by twisting the strips, considering different joints and support conditions. The proposed approach improves and increases the variety in the design of elastic spatial structures by following the material behavior in a self-organized process. We show the first results of using twist in small-scale prototypes and they are acceptable due to having minor deviations. For larger scales still, the accuracy and similarity of the physical and digital environment could be improved. The effect of twist on the structural performance and the maintenance of the material should be evaluated in large-scale prototypes and by adding the vertical and lateral forces. In the next steps, we will work on shape-first approaches and combine the knowledge from the pattern-first with it. This will lead to the design of elastic structures based on an approach that starts from a defined surface but is not limited to it. Modifications in the curvature of the final form is possible based on considering the material behavior. The application of these structures can be from small-scale products such as furniture to large-scale projects including buildings with different functions.

Having control over the design of spatial structures results in generating improved forms. The resulting structures can have different pattern types and different profiles based on the designer's wishes such as the need for interior lighting or controlling the views to the outside. We can imagine lamellas with profiles perpendicular to the surface curvature guiding views or controlling natural light. Conversely, the grids and profiles could be denser and less transparent if they follow geodesic curves as strips. Also, from a structural perspective, the intentional use of strong and weak axes of the strip material can be used to adjust structural performance as needed. Such complex requirements and shapes allow architectural and structural designers to generate spaces that respond to environmental, structural and architectural wishes and necessities. Although the use of twist can pose some challenges to the manufacturing process and specific geometric rules regarding material elasticity must be considered, we expect significant impact on the design space and thus design outcomes for elastic gridshells.

References

[1] F. Khojastehmehr, M. H. Saleh Tabari, and G. H. Filz, "A review on the curvature and geometrical patterns of elastic gridshells: exploring structural and architectural potentials," Proceedings of the IASS 2022 Symposium affiliated with APCS 2022 conference, pp. 2573–2586, 2022.

[2] G. H. Filz, S. Elmas, and A. A. Markou, "The structural geometry of a beam element from 4 torqued strips," in Structures and Architecture, P. J. Cruz and M. F. Hvejsel, Eds., London: CRC Press, pp. 150–158, 2022.

[3] C. Gengnagel, A. Holger, and E. Lafuente, "Active Bending in Hybrid Structures," Form–Rule| Rule–Form, pp. 12–27, 2013.

[4] H. Kang, "A study on the technique and process of bending wood". KFS J 21(6):459–468, 2010.

[5] J. Benson, "Woodworker's guide to bending wood: techniques, projects, and expert advice for fine woodworking". Fox Chapel Publishing, 2016.

[6] M. Schulte, S. Mankouche, J. Bard, and T.Y. Ng, "Digital steam bending: re-casting historical craft through digital techniques". In: Considering research: reflecting upon current themes in architecture research, 2011.

[7] S. Bechert, L. Aldinger, D. Wood, J. Knippers, and A. Menges, "Urbach Tower: Integrative structural design of a lightweight structure made of self-shaped curved cross-laminated timber". In Structures, Vol. 33, pp. 3667-368, Elsevier, 2021.

[8] M. Tamke, D. Stasiuk, and M. Ramsgard Thomsen, "The Rise – Material Behaviour in Generative Design," in *Proceedings of the 33rd Annual Conference of the Association for Computer Aided Design in Architecture (ACADIA)*, Cambridge (Ontario), Canada, pp. 379–388, 2013.

[9] T. Bessai, "ending-active bundled structures: Preliminary research and taxonomy towards an ultra-light weight architecture of differentiated components," 2013.

[10] Vartwisted & varschoba. [online]. Available: http://archiv.koge.at/?page_id=2408 (accessed: Apr. 10 2023)

[11] PS1 Loop. [online]. Available: https://www.howeleryoon.com/work/745/ps1-loop (accessed: Apr. 14 2023)

[12] Elastic habitat. [online]. Available: http://architettura.it/architetture/20070319/index.htm (accessed: Apr. 14 2023).

[13] P. Ayres, A. G. Martin, and M. Zwierzycki, "Beyond the basket case: A principled approach to the modelling of kagome weave patterns for the fabrication of interlaced lattice structures using straight strips," in Advances in Architectural Geometry, pp. 72–93, 2018.

[14] Y. Yavaribajestani and S. Schleicher, "Bio-Inspired Lamellar Structures", in *Proceedings of the 39th Annual Conference of the Association for Computer Aided Design in Architecture (ACADIA)*, Austin, Texas, pp. 122-129, 2019.

[15] R. Naboni, A. Kunic, D. Marino, and H. Hajikarimian, "Robotic zip-bending of wood structures with programmable curvature", Architecture, Structures and Construction, 2(1), 63-82, 2022.

[16] J. Chilton and G. Tang, *Timber Gridshells*, New York, Routledge, 2016.

[17] E. Happold and W. I. Liddell, "Timber lattice roof for the Mannheim Bundesgartenschau," in *Structural Engineer*, pp. 99–135, 1975.

[18] B. D'Amico, A. Kermani, H. Zhang, A. Pugnale, S. Colabella, and S. Pone, "Timber gridshells: Numerical simulation, design and construction of a full scale structure," *Structures*, vol. 3, pp. 227–235, 2015, doi: 10.1016/j.istruc.2015.05.002.

[19] B. D'Amico, A. Kermani, and H. Zhang, "Form finding and structural analysis of actively bent timber grid shells," *Engineering Structures*, vol. 81, pp. 195–207, 2014, doi: 10.1016/j.engstruct.2014.09.043.

[20] *Portalen Pavilion / Map13 Barcelona + Summum Engineering + Edyta Augustynowicz.* [Online]. Available: https://www.archdaily.com/949152/portalen-pavilion-map13-barcelona-plus-summum-engineering-plus-edyta-augustynowicz (accessed: Jun. 6 2022).

[21] SG2012 Gridshell. [Online]. Available: https://www.matsys.design/sg2012-gridshell (accessed: Jun. 8 2022).

[22] Mantashell. [Online]. Available: https://www.matsys.design/mantashell (accessed: Jun. 8 2022).

[23] J. Harding, S. Hills, C. Brandt-Olsen, and S. Melville, "The UWE research pavilion 2016," in *Proceedings of International Association for Shell and Spatial Structures Annual Symposia*, 2017.

[24] G. H. Filz, "Geodesic Winding of Minimal Surfaces: the architecture, structure and geometry of an irregular grid-shell pavilion assembled from thin plywood strips," in *Annual Symposium of the International Association for Shell and Spatial Structures (IASS), 2021*.

[25] E. Schling, M. Kilian, H. Wang, J. Schikore, and J. Pottmann, "Design and construction of curved support structures with repetitive parameters". In Advances in Architectural Geometry, 2018.

[26] S. Suzuki, E. L. M. Slabbinck, and J. Knippers, "Computational Bamboo: Digital and Vernacular Design Principles for the Construction of a Temporary Bending-Active Structure," in *Impact: Design With All Senses*, C. Gengnagel, O. Baverel, J. Burry, M. Ramsgaard Thomsen, and S. Weinzierl, Eds., Cham: Springer International Publishing, pp. 224–236, 2020.

[27] J.H.E. Cartwright, D.L. Gonzalez, "Möbius Strips Before Möbius: Topological Hints in Ancient Representations", The Mathematical Intelligencer, Vol 38(2), pp. 69-76, 2016.

[28] https://dictionary.cambridge.org/dictionary/english/twist (accessed 12.2022)

[29] https://www.merriam-webster.com/dictionary/torque (accessed 12.2022)

[30] https://dictionary.cambridge.org/dictionary/english/torque (accessed 12.2022)

[31] S. Elmas, G. H. Filz, A. A. Markou, and J. Romanoff, "Zero Gravity: a novel cantilever beam utilizing elastic torsion for structures and architecture". In Proceedings of IASS Annual Symposia, International Association for Shell and Spatial Structures (IASS), Vol 27, 2020.

[32] E. L. Slabbinck, A. Körner, and J. Knippers, "Torsion as a design driver in plate-bending-active tensile structures" in Proceedings of IASS Annual Symposia, International Association for Shell and Spatial Structures (IASS), Vol 14, pp. 1-10. 2017.

[33] M. H. Saleh Tabari, F. Khojastehmehr, G. H. Filz, "Parametric thinking for decision-making in elastic gridshell design" in Proceedings of International Association for Shell and Spatial Structures (IASS) Annual Symposia, pp. 3352–3365, 2022.

[34] http://docs.mcneel.com/rhino/5/help/en-us/commands/patch.htm (accessed Mar. 29 2023).

IASS 2023
July 10–14 Melbourne
Integration of Design and Fabrication

Proceedings of the IASS Annual Symposium 2023
Integration of Design and Fabrication
10–14 July 2023, Melbourne, Australia
Y.M. Xie, J. Burry, T.U. Lee and J. Ma (eds.)

Interlocking connections for bending-active timber structures with variable stiffness

Maren ZYWIETZ[a,*], Annette BÖGLE[b], Ehsan TAGHIYAR[b]

[a,*] HafenCity University Hamburg
Henning-Voscherau-Platz 1, 20457 Hamburg, Germany
maren.zywietz@hcu-hamburg.de

[b] HafenCity University Hamburg

Abstract

Material and energy shortages make efficient material use, reuse and recycling urgent issues in 21st century construction. Wood as a renewable raw material is back in focus, with potential use in lightweight and structurally efficient gridshells. Many timber gridshells use the principle of bending-active structural behaviour, with their shape largely determined by material and cross-sectional properties. However, commonly used timber with non-biodegradable glue and inseparable steel connections cannot be returned to the material cycle. Consequently, this challenges sustainable building practices. This paper presents a reconfigurable modular system for elastically bent solid timber laths using interlocking connections and segmented cross-sections, while providing novel design possibilities through variable stiffness. The results of the research show that circular design in bending-active timber structures can contribute to quality craftsmanship and a new language in architecture and engineering.

Keywords: timber, bending-active structures, variable stiffness, sustainable construction, circular design, interlocking connections

1. Introduction

1.1. Background

Gridshells are a type of structural system that allow for large spans with minimal material usage due to their structural efficiency. One well-known example is Frei Otto's lightweight timber gridshell in Mannheim, which is an early example of a bending-active structure created by the deflection of previously planar elements [1]. The shape of bending-active structures is significantly influenced by the bending stiffness of the structural elements. Since the bending stiffness is the product of Young's modulus and area moment of inertia, material properties as well as the cross-sectional area thus essentially determine the geometry. Timber has gained importance in this context as part of the shift towards a sustainable circular economy in the construction industry and is frequently used for gridshells [2].

To meet the requirements of the circular economy, load-bearing structures must use materials that can be recycled into biological or technical material cycles and have detachable connections that can be separated by material type at the end of their service life. This ensures that the materials and components can be reused or recycled.

Glulam, which is commonly used in construction, only partially meets these requirements due to its non-biodegradable glue. One possibility for glulam is to reuse it in new configurations after a structure has reached the end of its life. The recovery of previously used elements is already being researched in the engineering field and addresses, for example, their optimised use in different structural typologies such

Copyright © 2023 by Maren ZYWIETZ, Annette BÖGLE and Ehsan TAGHIYAR. Published in the Proceedings of the IASS Annual Symposium 2023 with permission.

as trusses and lattice shells, both in the design phase and of reclaimed components (see [3],[4]). Solid wood materials should also be put to further use first. However, their application eliminates the compelling need for reuse, as they can also be returned to the biological cycle without leaving any residues.

Commonly used steel connections on gridshells cannot be separated from the wood after use in many cases, which can be considered problematic in terms of their recyclability. Modern timber engineering uses metallic screws, dowels, steel sheet fittings and nail connections. These can be easily calculated, and their use is also covered by the relevant standards. This guarantees economical use, whereas solid wood connections are rarely used in respect of the necessary craftsmanship of carpenters and the associated costs. However, because of the transformation to a circular economy, solid wood joints are experiencing a renaissance in scientific research, also because of their long tradition all over the world. For example, first classifications of traditional interlocking timber connections have been carried out with respect to their moment capacity for modern building construction [5]. In addition, interlocked connections are also used in built research pavilions, for example in bending-active shell structures [6] and Interlocking Particle Structures [7]. Noticeably, this research explores interlocking connections of shell- and plate-like timber structures. Novel interlocking connections of beam-like timber elements, especially beyond the connections at the beam ends, represent a special case which is yet to be investigated.

1.2. Aim and research questions

Due to their dependence on material and cross-section properties, bending-active structures represent a special type of structural behaviour. Regarding the use of this principle in gridshells, further development possibilities can be identified against the background of the scarcity of resources in the construction industry. Building on the parameters of materiality and connections, this publication therefore explores the potential of circular design for bending-active timber structures.

The aim of the work is to develop a reconfigurable modular system for bending-active members, which uses solid wood connectors and at the same time leads to novel design possibilities through variable stiffnesses due to segmented cross-sections.

The following research questions will be addressed:

(1) What are the possibilities of variable stiffnesses on bending-active systems?
(2) What are the boundary conditions for such a system under the premise of circular design? What properties must materials and cross-sections meet in order to be implemented?
(3) What can a modular system look like in practice and what challenges arise in manufacturing?

2. Methods

Different methods are used to answer the highlighted research questions. These are based on a combination of experimental and computational investigations.

System stiffnesses in closed systems can be modified either by couplings of members or by variable bending stiffnesses of the individual cross sections. To get a sense of the possibilities of variable stiffness distribution over beam length, small preliminary studies were first made using paper strips. These are intended to show the flexibility in design and construction that is possible with variable stiffnesses on bending-active systems.

Since the bending stiffness of a structural element depends to a large extent on the material properties as well as the cross-sectional dimensions, as described above, these two properties were analysed in turn in order to subsequently develop a toolkit.

In general, timber as a building material can be divided into solid wood and wood-based materials according to construction principles. Since the presented project is to consist of fully recyclable

materials that do not require glue layers, the selection is limited to solid wood. For bending-active structures in particular, sawn timber and veneer are suitable due to the necessary low cross-sectional heights. In order to identify which wood is capable of elastic bending at the same time, an analysis of different wood species was carried out in the next step. As a regenerative and renewable material, solid wood has certain mechanical and rheological properties that have different effects on the structural behaviour.

The next step is the analysis of solid wood joints to allow the coupling of members at their joints as well as over their cross-sectional length in a single type. Old techniques of traditional carpentry will be used to determine suitable methods for the construction of the demonstrator.

Based on the knowledge gained from the analyses, a modular system will be developed that allows the connection of battens both longitudinally and transversely. The result of this experimental approach is a kit of timber laths and wood-to-wood joints, which will be realised as full-scale prototypes made of a suitable wood species available in Germany.

Finally, an analytical study demonstrates the applicability of the developed principle using the example of a bending-active structural element.

3. Research findings

3.1. Preliminary study

In this study, the influence of a variable stiffness distribution on the shape of a simple curved paper strip was investigated. Higher levels of stiffness have been achieved by adding more layers of paper. The figure shows a paper strip with a constant cross-section, a paper strip with higher stiffness at the third points and a paper strip with higher stiffness in the middle. As expected, there is a clear influence on the bending radii and thus on the shape of the sheet. It can be concluded that variable stiffnesses over the cross-section length can change the design and the structure can be adapted depending on the stiffness distribution.

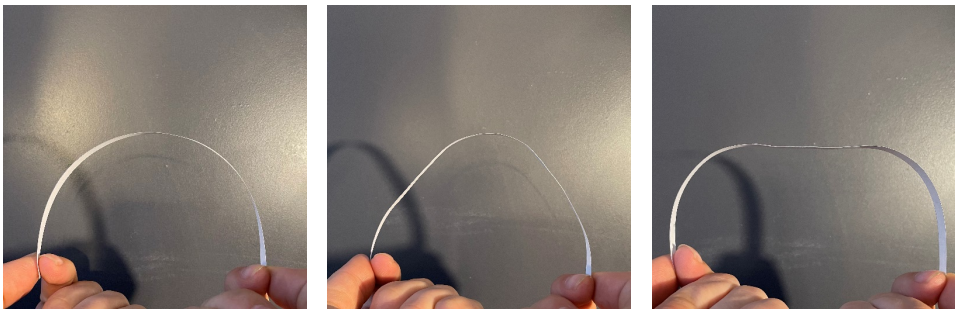


Figure 1. Preliminary study.

3.2 Results of the analyses

The results of the analyses of solid wood species and traditional carpentry joints are presented below.

3.2.1. Solid wood species

In this analysis, mechanical and rheological properties of different untreated woods were compared. Special attention was paid to the availability of the woods in Europe, so that globally available woods were not considered in detail.

The mechanical properties include the flexural modulus of elasticity E_m and the flexural strength f_m. These values were taken from DIN 68364 and not from DIN EN 338, the standard usually used for construction timber. The reason for this is that simple comparative values were sought to obtain an overview of the mechanical properties of woods. A classification into strength classes and grading

classes is not yet available at this early stage of the analysis. The minimum bending radius for a cross-section height of 11 mm and the ratio of modulus of elasticity and bending strength were determined from the available characteristic values following [8]. These values are tabulated below for eleven woods native to Europe.

The rheological properties include creep, stress relaxation and creep rupture strength and are not shown in the table.

Table 1. Mechanical properties of hardwood native to Europe [9].

Wood species	E_m [N/mm²]	f_m [N/mm²]	Ratio f_m/ E_m [MPa/GPa]	Bending radius r_{min} [cm]
Black walnut	11,850	133	11.2	49.00
Robinia	13,600	150	11.0	49.87
Limewood	8,800	88	10.0	55.00
Alder	9,500	91	9.6	57.42
Black cherry	10,250	98	9.6	57.53
Maple	10,500	95	9.0	60.79
European hornbeam	14,500	130	9.0	61.35
Chestnut	9,000	80	8.9	61.88
Birch	14,000	120	8.6	64.17
Beech	14,000	120	8.6	64.17
Ash	13,000	105	8.1	68.10

The mechanical properties of hardwoods are more suitable for bending-active structural behaviour than softwoods. Due to the availability of lime wood, it was selected for use in the demonstrator.

3.2.1. Traditional carpentry joints

In this project, a brief analysis of traditional carpentry joints in timber construction was carried out.

In general, timber connections can be classified into different schemes (see [10], [11]). One possibility is to divide them by application, by joint type (butt, tenon, leaf, etc.) or joint form. In this work, a distinction is made regarding the form of the connection: Thus, two components can be connected either longitudinally, across corners or crosswise. For each of these shapes, there are different types of connection, which differ in their ability to transmit forces. Another reason for choosing a particular wood-to-wood connection can also be the manufacturing effort. In a bending-active system, both normal forces and bending moments must be transmitted through the joints. With regard to this special situation, the dovetail joint is considered particularly advantageous for further research work: The form-fitting connection enables the transmission of these forces and can be realised as a butt joint as well as a cross and end joint. This means that a basic type of connection can be implemented for all requirements.

3.3. Design and manufacturing of a modular system

Based on the previous findings, the details for the identified connections were designed. Transportability and manageability also played a role in the design. For this reason, the maximum member length for the demonstrator was limited to one metre.

3.3.1. Stiffness matrix

The special feature of this design is the adaptability of stiffnesses over the beam length. The aim was to allow a sliding coupling of different cross-section parts in order to keep the total cross-section height and width variable. The authors call this form of coupling a stiffness matrix. Figure 2 illustrates a possible principle of division into different elements, which are held together by clamps. The cross-section resembles a matrix in its appearance, with the number of elements varying along the length of the beam. This results in variable stiffnesses for the overall structure.

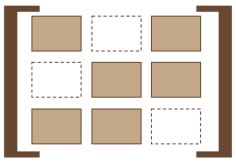


Figure 2. Principle of stiffness matrix.

Due to the variable coupling possibilities, the final cross-sectional dimensions result from the design or the desired system geometry. In the present demonstrator, a maximum of two cross-sections were coupled together in a two-dimensional manner. However, a multi-layer cross-section structure is also possible. A single cross-section layer has a height of eleven millimetres. In the following, the middle, non-milled part of the wood is referred to as the core beam. Coupled together, a higher cross-section can thus be achieved, which results in a higher moment of resistance against bending moments.

Two different variants were considered for the demonstrator. One option is the interlocking of the beams in the transverse direction, which are held in position by wooden dowels. In this variant, there is no stepless adjustment possibility; the coupling of cross sections depends on the interlocking distances.

The favoured variant is the use of dovetail joints in the longitudinal direction, so that the core beams can be joined together over the entire length. In this case, the connection is not made via dowels, but is given via the form fit.

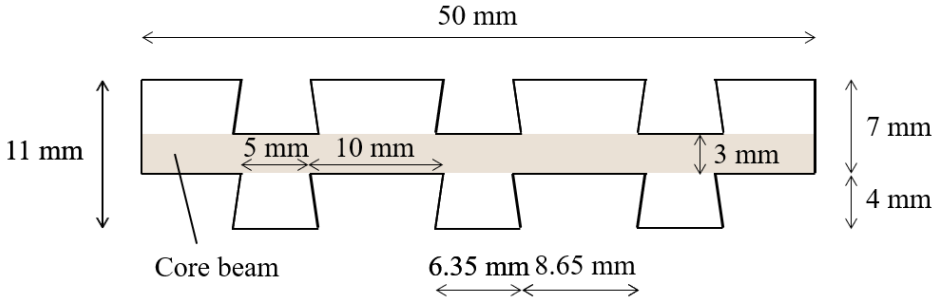


Figure 3. Final dimensions of the cross-section.

In principle, there are two possible ways of producing this connection. One is to mill the laths from a larger cross-section of wood. CNC control makes it possible to produce the joints very precisely. The other manufacturing possibility is the adhesive bonding of individual laths, whereby attention must be paid to the circularity of the joint.

In this project, the second manufacturing option was used because the necessary size of the CNC milling machine was not available. Due to the set requirement of fully recyclable and biodegradable construction, a study of suitable adhesives was therefore carried out. Animal glues, which are obtained by boiling out animal waste, are an interesting option. These differ in their adhesive strength and elasticity depending on the starting material. For this project, fish glue was chosen, which has the elasticity necessary for bending-active structures. To withstand shear, additional wooden needles were arranged across the grain direction of the wood, which can transfer the forces that occur in case the glue fails.



Figure 4. Two coupled cross-section layers.

3.3.2. Butt joints

Butt joints are intended to achieve the strongest bending-resistant coupling of two elements at their end faces. For butt-jointed beams, there are different possibilities depending on the number of cross-sectional layers.



Figure 5. Joining continuous beams.

A butt joint with more than one cross-sectional layer can be realised by continuous beams. Here, it is important to ensure a sufficient overlap length so that the beams do not slip during bending due to the resulting shear forces.

When connecting beams with a single cross-section, the type of connection depends on the thickness of the core beam.

If the core beam is thicker (>5 mm), the beams can be drilled in the transverse direction. A possible connection here results from cutting the ends of the beams so that the resulting tabs can be drilled in the transverse direction and then connected with a wooden dowel.

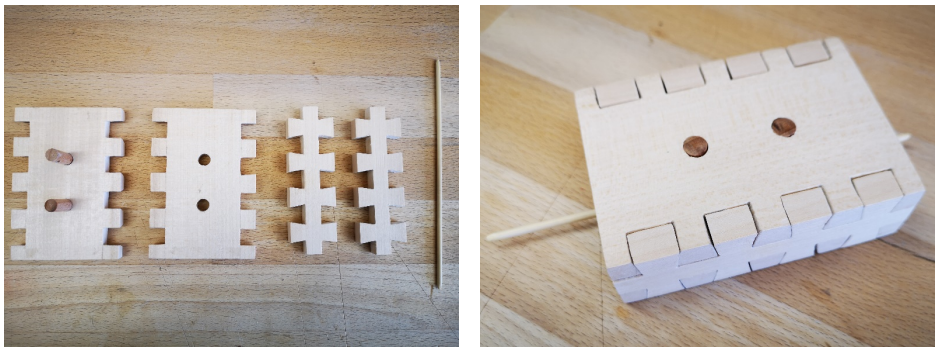


Figure 6. Sleeve enclosing the end faces of core beams <5 mm.

If the core beam is thin (<5 mm), drilling in the transverse direction is not possible. Therefore, at the end face a sleeve is provided with which the end faces are enclosed. This is the case in the built example. Under the influence of bending, the lateral pieces of wood interlock with the upper and lower part of the sleeve. The occurring forces are transferred by pressure and friction between the teeth. The position of the butted beams within the sleeve is secured by two wooden dowels. In the special case of coupling a beam with two cross-sectional layers and a beam with one cross-sectional layer, an additional piece of wood can be used.



Figure 7. Sleeve-joined beams subjected to bending.

3.3.3. Cross connections

This connection must join two intersecting beams in a bending-resistant manner. A gear wheel was used as a reference object so that the angles of the beams can vary. This can realise the desired angles through the toothing and is the basis for the designed shaped piece. The angle is fixed with a wooden dowel. One or more cross-sectional layers can be inserted into the upper part of the shaped piece. This connection only works for bending in the y-direction and attention must be paid to the grain direction of the wood.



Figure 8. Cross connections.

3.3.3. End connections

The developed end connection has two functions. On the one hand, it forms a termination of the end face of the cross-section layers and thus satisfies a design requirement, but at the same time also prevents slipping of beams, should they consist of several cross-section layers. On the other hand, another beam can cross if necessary. The principle is therefore similar to the already described cross connection and is realised with the help of a gear wheel.

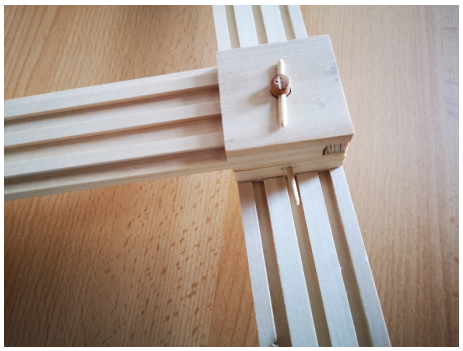


Figure 9. End connection.

3.4. Application of the principle in analytical study

In this section it is examined to what extent the developed principle can be applied to a bending-active structural element. For this purpose, Grasshopper, and the programme Kiwi3D were used. The reference object is the catenary, which represents the optimum shape for a load under its dead weight. The aim of the study was to come as close as possible to this line with the help of short bending-active segments.

First, the given catenary was generated as a curve with a constant cross-section, a length of 9 metres and a span of 4 metres using Grasshopper. Subsequently, a second line with a length of 9 metres was created, the cross-section of which can vary over this length. To realise this, the "Python Script Component" was used. In this way, the previously developed cross-section was modelled in the programme with its dimensions as well as the mechanical properties of the material. The segmented curve is initially arranged flat on the plane and can be brought into its final shape with the help of a movable support at one end of the beam. The Kiwi3D programme then calculates any stresses that occur, resulting in the elastically deformed output geometry.

Due to the different stiffness, the weight of the structure changes from section to section. Since the catenary represents the shape adopted by a freely hanging chain of constant cross-section, the elastica curve using variable stiffnesses will not work in pure compression. Nevertheless, both curves will be approximated to demonstrate the bending capabilities of the variable stiffness structure.

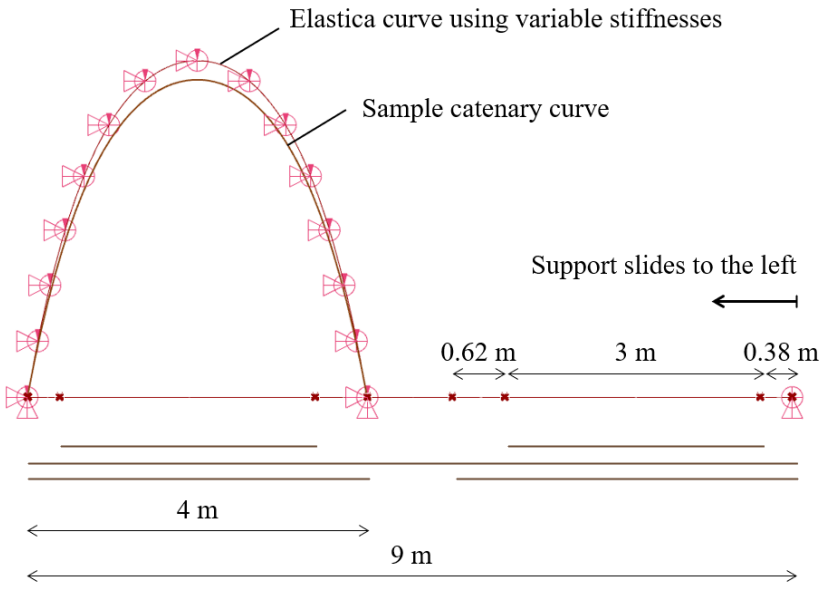


Figure 10. Optimised configuration of modules

To verify the deviations between the sample curve and the bent beam, control points were created at certain distances on both curves, the distances of which were added together. The aim of the optimisation was thus to minimise this sum, whereby lengths, distances, and the number of layers of the segments were adjusted manually.

The manually optimised configuration with its dimensions can be taken from Figure 10. As expected, the stress analysis shows stress concentrations between the segments. These points will be discussed in the following section.

4. Discussion

The study presents interesting results regarding the impact of circular design methods on interlocking systems of bending-active beam elements.

By focusing on design and craftsmanship, the results extend the current state of research on interlocking connections, especially regarding the possibility of interlocking beams along their length in a novel way. The literature studies and analyses of suitable materials and connections show that traditional timber construction provides a wide range of possibilities.

The high level of craftsmanship involved in wood-to-wood connections may increase the perceived value of wood as a material. Despite standardisation, wood looks different and can be processed differently depending on its origin and type of wood. This was also observed during the construction of the demonstrator. Increasing the appreciation of the material could be highly desirable in terms of a circular economy, as it could help to ensure that manufactured components are more likely to be reused and remanufactured at the end of their life than components designed to be discarded. Furthermore, the processed wood shows the labour, carpentry and engineering skills that have been invested in it.

Interlocking connections also make an important contribution to circular construction through their reversibility, but in unmixed timber construction they can also be returned to the biological material cycle as a whole. But it is not only the circularity, but also the possibility of varying forms in connection with bending-active structures that opens new possibilities of use and longer service lives.

Regarding the possibilities of variable design through changeable cross-sections, the present study can only be seen as a first contribution. A comprehensive investigation of the influence of variable stiffnesses on the shape and design of load-bearing structures will follow.

Within the scope of the analyses, European wood species were presented and compared with each other with regard to their mechanical properties and suitability for bending-active structural behaviour. If availability and sustainability reasons are disregarded and non-European tree species are considered, different conclusions could be drawn. Furthermore, different timbers can be chosen for members and joints, which would result in a different load-bearing behaviour.

In the designed cross-section, the different layers are coupled on top of each other to resist bending in the y-direction. Another possibility is to extend the cross-section in the y-direction. Likewise, the proposed stiffness matrix method could be applied. This would have a significant influence on the resistance to impacting bending moments. This is an important aspect that can be explored by further research, particularly due to the bending-active behaviour of the structure and the resulting twisting of the cross-sections.

Due to the fish glue used, the developed system can currently only be used under indoor conditions, as this dissolves on contact with warm water. Conventional component adhesives, however, do not bond components together in a separable way, so that appropriately manufactured components can only circulate in the technical material cycle. The authors therefore welcome research into fully biodegradable glues and can envisage their use in research projects. In addition, the construction method used of glue and wooden nails reaches its mechanical limits due to the shear stresses that occur. As an alternative, the partial cross-sections can also be milled from a solid cross-section. However, the material

consumption for milling the joint is very high. For the cross-section developed in this project, for example, the loss is approximately 25%. For this reason, it must be discussed whether the waste of a biodegradable material can be justified compared to the use of a component adhesive.

In order to allow the beams to slide, tolerances have to be strictly adhered to. By using a CNC milling machine to produce the cross-sections, the accuracy of fit can also be further improved. In addition, creep loads, and the effects of humidity have not been considered and are the subject of further research.

When generating inverted catenaries using variable cross-sections, the individual beams have so far only been optimised manually. Here, a computer-aided optimisation can be developed that calculates the best configuration under given boundary conditions. On the other hand, the stress peaks that occur may require an adjustment of the built cross-sections. The best solution probably lies between the optimum arrangement of individual cross-sections and a construction-based solution. Furthermore, a study of the principle in large-scale systems may also be considered.

5. Conclusion

This study investigated the potential of circular design for bending-active timber structures. Building on the parameters of materials and connections, both experimental and computational studies were used to answer the research questions.

To explore the design scope through variable stiffnesses, small preliminary studies were first carried out, which showed the influence of variable bending stiffnesses on cross-sections, especially over the cross-section length. Under the premise of circular design, suitable materials and connection options for a built system were then analysed. The results from various European wood species showed that hardwoods have good properties for this purpose, so that lime wood was ultimately chosen for the demonstrator. Dovetail joints were chosen for the built example due to the form-fitting nature of the joints. Based on the previous analyses, a modular system was conceptualised and subsequently implemented in the built example. Furthermore, the principle of the stiffness matrix was presented, with which the beam stiffnesses could be successfully varied over the beam length on the prototype. Finally, the developed principle was transferred into a computer model and tested for its design applicability.

The results of the project show that circular design affects the materials, cross-sections and connections of bending-active structures in different ways and is in general possible. The study focused on the design and fabrication of a demonstrator. Possibilities for improvement were identified in the manufacturing methods. In addition, further studies on form finding with variable cross-sections were proposed to further verify the developed principle.

The developed reconfigurable modular system enables a wide range of new design possibilities. Particularly in view of the need for a circular economy in the building industry and the associated reusability and recyclability of materials, the required quality of craftsmanship has a positive effect on the respectful use of materials. The interlocking connections, their reversibility, and the possibility to vary the structural system can lead to a longer acceptance and therefore a longer service life of load-bearing structures. Thus, interlocking connections in bending-active timber structures are an interesting way of contributing to a new design language in architecture and engineering.

References

[1] J. Lienhard and J. Knippers, "Biegeaktive Tragwerke," *Bautechnik*, vol. 92, no. 6, pp. 94–402, Jun. 2015, doi: 10.1002/bate.201500007.

[2] D. Naicu, R. Harris, and C. Williams, "Timber gridshells: Design methods and their application to a temporary pavilion," in *WCTE 2014 - World Conference on Timber Engineering, Proceedings*, Aug. 2014.

[3] J. Brütting, G. Senatore, and C. Fivet, "Design and fabrication of a reusable kit of parts for diverse structures," *Automation in Construction*, vol. 125, p. 103614, May 2021, doi: 10.1016/j.autcon.2021.103614.

[4] Y. Huang, L. Alkhayat, C. D. Wolf, and C. Mueller, "Algorithmic circular design with reused structural elements: method and tool," in *International fib Symposium - Conceptual Design of Structures 2021*, Sep. 2021. doi: 10.35789/fib.proc.0055.2021.cdsymp.p056.

[5] J. Moradei et al., "Structural Characterization of Traditional Moment-Resisting Timber Joinery," in *Proceedings of the IASS Symposium 2018*, 2018.

[6] H. Dahy, "'Materials as a Design Tool' Design Philosophy Applied in Three Innovative Research Pavilions Out of Sustainable Building Materials with Controlled End-Of-Life Scenarios," *Buildings*, vol. 9, no. 3, p. 64, Mar. 2019, doi: 10.3390/buildings9030064.

[7] C. A. Aranha, M. Hudert, and G. Fink, "Interlocking birch plywood structures," *International Journal of Space Structures*, Jun. 2021, doi: 10.1177/09560599211022219.

[8] J. Lienhard, H. Alpermann, C. Gengnagel, and J. Knippers, "Active Bending, a Review on Structures where Bending is used as a Self-Formation Process," *International Journal of Space Structures*, vol. 28, no. 3 & 4, pp. 187–196, 2013.

[9] DIN 68364:2003-05, Kennwerte von Holzarten - Rohdichte, Elastizitätsmodul und Festigkeiten

[10] K. Zwerger, *Das Holz und seine Verbindungen. Traditionelle Bautechniken in Europa, Japan und China*. Birkhäuser Basel, 2015

[11] W. Graubner, *Holzverbindungen: Gegenüberstellungen japanischer und europäischer Lösungen.* Stuttgart: Deutsche Verlags-Anstalt, 2004.

Proceedings of the IASS Annual Symposium 2023
Integration of Design and Fabrication
10–14 July 2023, Melbourne, Australia
Y.M. Xie, J. Burry, T.U. Lee and J. Ma (eds.)

Investigation of cross-sections for hybrid gridshells based on bending-active formwork

Yasaman YAVARIBAJESTANI*, Michael HERRMANN[a], Khalid M. MOSALAM[b], Simon SCHLEICHER[c]

* University of California, Berkeley, Department of Architecture
College of Environmental Design (CED)
232 Wurster Hall, #1800, Berkeley, CA 94720-1800

[a] structure GmbH Stuttgart and Technische Hochschule (TH) Lübeck
[b] University of California, Berkeley, Department of Civil and Environmental Engineering and Pacific Earthquake Engineering Research Center
[c] University of California, Berkeley, Department of Architecture

Abstract

In previous studies, the authors have presented the concept of building hybrid gridshells as an effective method for spanning large distances with very little material. In this approach, the structure consists of carbon fiber-reinforced polymer (CFRP) strips, which serve as lost formwork in the construction of a concrete gridshell. Preliminary digital simulations and physical tests have shown promising performance gains, but have also raised important questions about the structural behavior of the hybrid cross-sections that require further investigation. Motivated by this challenge, this study aims to investigate the material properties of composite CFRP-concrete cross-sections through physical experiments. A total of eighteen test specimens were produced and divided into six groups, which differed in terms of their internal and external reinforcement and bonding properties between the two materials (full or partial bonding). All specimens were tested in a four-point bending arrangement to evaluate the performance of the proposed CFRP-concrete cross-section. The loading and deflection were recorded and discussed in detail. The results of these tests show that the flexural capacity of gridshell beams, which have a full bond between CFRP and concrete, is more than 300% higher than that of the concrete-only control beams. This confirms that the type of connection between the layers has a significant influence on the load-bearing and bending capacities. Moreover, these test results show that the bending strength and stiffness of the developed hybrid cross-section offer significant improvements over the concrete-only control beams. In conclusion, this study proves that externally bonded CFRP strips not only serve as an effective stay-in-place formwork for the fabrication of concrete gridshells, but also exhibit a beneficial composite effect in the interaction between the two materials of a hybrid cross-section.

Keywords: bending-active formwork, hybrid cross-section, material properties, experimental method, concrete, carbon fiber reinforced polymer, composite structures, hybrid gridshells

1. Introduction

Concrete shell structures are an efficient means of spanning large distances with little material. However, their construction requires a significant amount of labor, which makes the process time-consuming and costly. To address this challenge, researchers have introduced new methods of constructing concrete shells and gridshells using bending-active structures with minimal and easy-to-build formwork. The idea behind bending-active structures is to use large elastic deformations of

Copyright © 2023 by Yasaman YAVARIBAJESTANI, Michael HERRMANN, Khalid M. MOSALAM and Simon SCHLEICHER. Published in the Proceedings of the IASS Annual Symposium 2023 with permission.

originally straight or planar building elements to create structures with complex curved geometries [1]. Moreover, these bending-active structures bring formal design freedom and can be applied to both synclastic (centers of curvature located on the same side of the surface) and anticlastic (centers of curvature located on opposing sides of the surface) geometries [2] [3]. Using this technique, the authors have further demonstrated that it is possible to build elastic gridshells from millimeter-thin carbon fiber reinforced polymer (CFRP) strips, in which the strips can serve both as stay-in-place formwork as well as potential tensile reinforcement in the production of lightweight hybrid gridshells [4]. This concept is beneficial because it addresses one of the biggest challenges in dealing with concrete, namely its low tensile capacity compared to its high compressive strength. While conventional concrete structures counteract this material weakness by adding steel reinforcing bars, which results in thicker cross-sections, the authors investigated the use of CFRP as a material for the stay-in-place formwork and external reinforcement to further reduce the cross-section of the hybrid gridshell. CFRP is a very suitable material in this context and is often chosen for retrofitting or repairing concrete structures, as it is durable, has very high tensile strength, and is available in various forms such as sheets, strips, or rovings [5].

The proposed hybrid concrete and CFRP gridshell takes advantage of the inherent strengths of the two materials while achieving the goal of large spans with low material usage. However, for this hybrid system to be used effectively, a complete understanding of the material's behavior and its limitations is required, both by the engineers who design this innovative system and by the construction workers who handle the material. In addition to the mechanical strength, the modulus of elasticity is one of the most important characteristics in structural design, controlling the stiffness and accordingly deformation and serviceability. A number of studies have investigated the bending behavior of various concrete mix designs and cross-sectional designs, the effect of various amounts of internal reinforcement, the type and amount of external reinforcement (e.g., glass fiber reinforced polymer (GFRP), and CFRP), the percentage of pre-loading, the shear and flexural debonding mechanisms of the fiber reinforced polymer (FRP) layers, and different configurations of the external reinforcement [6]–[12]. However, there are not many studies that focus on the flexural strength in hybrid concrete-CFRP structures, especially in the context of using this material combination for hybrid gridshells based on bending-active formwork. Previous to this work, authors performed a parametric sensitivity analysis for such hybrid concrete and CFRP gridshell structures using digital simulations [13]. As a further step, this study aims to perform a preliminary experimental investigation of the material properties of this hybrid cross-section and to provide some initial design guidelines for its implementation. For this purpose, a series of four-point bending tests were carried out, which will be discussed in more detail in the following sections.

2. Methodology

The tests were conducted at the Civil and Environmental Engineering (CEE) Department at the University of California, Berkeley. The purpose of the tests was to investigate the behavior of hybrid beams made of CFRP strips and concrete. In addition, an analytical study of the proposed hybrid cross-section was performed to compare its results with the experimental results and confirm the reliability of the obtained experimental data.

2.1. Experimental study

A total of eighteen specimens were fabricated and divided into six groups (3 specimens each), including: (i) concrete (C), (ii) concrete with internal GFRP mesh (C Mesh), (iii) concrete-CFRP bonded together by nail connectors (C-CFRP Nail), (iv) concrete (with internal GFRP mesh) and external CFRP, interconnected by nail connectors (C-CFRP Nail Mesh), (v) concrete-CFRP interconnected by epoxy resin (C-CFRP Epoxy), and (vi) concrete (with internal GFRP mesh) and external CFRP interconnected by epoxy (C-CFRP Epoxy Mesh). Finally, three concrete cylinders were fabricated on which compression tests were performed.

2.1.1. Test specimens and material

All beams were 30.4 cm long, 5.08 cm wide, and 1.4 cm deep (referring to the concrete layer). The concrete cylinders were 20.32 cm high and 10.16 cm in diameter. Figure 1 shows the dimensions and connection details of the tested beams in this study. All beam and cylinder specimens were cast from the same batch of Sikacrete®-752 3D concrete with a water-cement ratio of 17% and cured in the fog chamber for 28 days. In addition, nine of the beams were reinforced with an embedded GFRP grid at the midplane of their cross-sectional height. Six of the eighteen test specimens connect the CFRP strip to the concrete through nails. This was achieved by attaching the nails to the CFRP strips with epoxy and later pouring the concrete onto them. The 10 nails are distributed in two parallel rows along the length of the beams, spaced 6 cm apart and 3.2 cm from the short edge. The CFRP strip used for 12 of the specimens has a thickness of 0.2 cm.

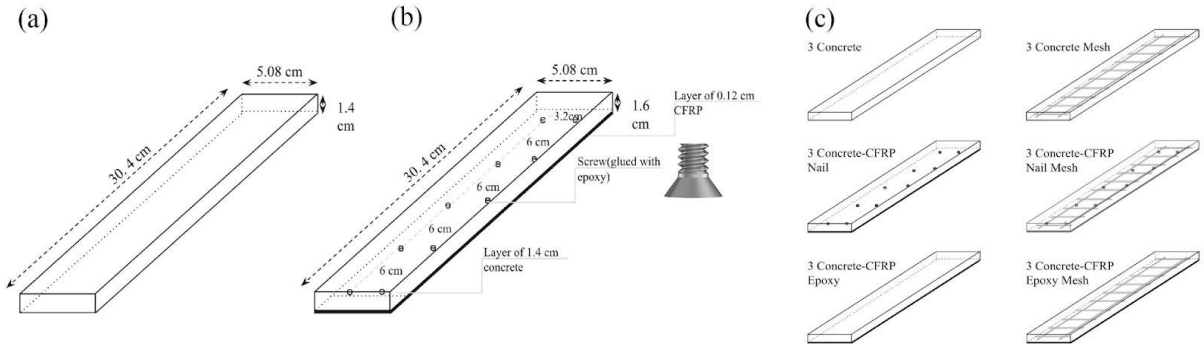


Figure 1. (a) Dimensions of specimens without CFRP (b) Specimens with CFRP and nail connector arrangement for C-CFRP Nail beams (c) Configuration details of the individual beam categories.

2.2. Compression test

28 days after casting, three concrete cylinders were tested for compression using the ASTM C39 procedure and the Forney Compression Machine (700K capacity), as shown in Figure 2.

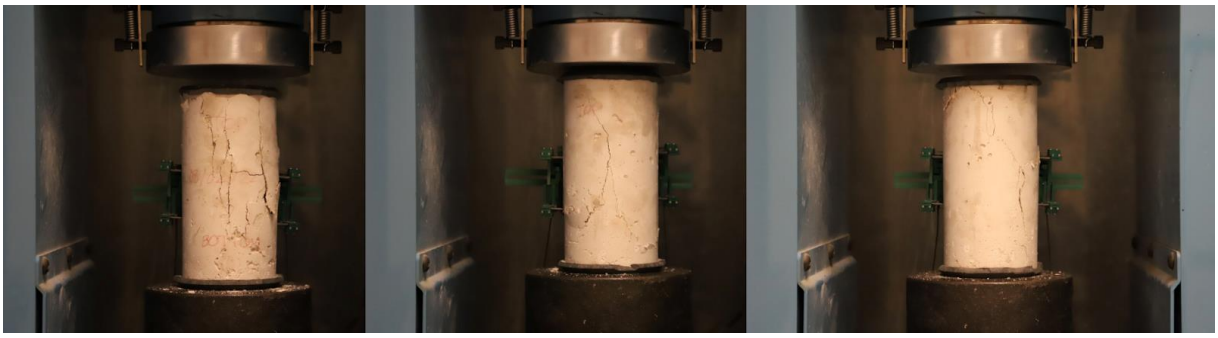


Figure 2. Three concrete cylinder specimens after performing the compression test.

We determined the compressive strength of the concrete using Equation 1 [14] and the failure loads obtained from the compression tests.

$$f_c = \frac{F}{A_c} \tag{1}$$

in which:

F: failure load (N)

A_c: area of the specimen on which the load was applied (mm^2)

The mean strength values, f_c of concrete cylinder, obtained was 31.55 MPa (N/mm^2).

2.2.1. Young's Modulus calculation from the compression test

The static pressure modulus of elasticity is the ratio between a compressive stress difference and the corresponding so-called elastic deformation per unit length [15]. The modulus of elasticity is calculated using the stresses (σ_o and σ_i) and strains (ε_o and ε_i) at points $0.33f_c$ and 0.5 N/mm², respectively, and the associated measuring length l_o of the extensometer (used for calculating the strain values from the displacement measurements), from Equation 2: The mean value for the concrete's longitudinal modulus of elasticity, E, was 33,718 N/mm².

$$E = \frac{\Delta\sigma}{\Delta\varepsilon} = \frac{\sigma_o - \sigma_i}{\varepsilon_o - \varepsilon_i} \tag{2}$$

with:

E: Modulus of elasticity [N/mm²]

σ_o: Test stress at $0.33f_c$ [N/mm²]

σ_i: Test stress of 0.5 N/mm²

ε_o: Strain measured at σ_o

ε_i: Strain measured at the stress of 0.5 N/mm²

2.3. Four-point bending test

The beams were externally instrumented and tested under four-point bending. Two vertical loads were applied symmetrically with respect to the mid-span of the beams with a constant bending moment region of 7.62 cm. All the beams were simply supported and had an effective span of 22.86 cm. Figure 3 shows the experimental setup in detail, along with the dimensions. The applied load and vertical displacements were monitored throughout the tests. Displacement was measured at mid-span using linear variable differential transformers (LVDTs). The applied two concentrated loads to the beam were monitored using load cells. All data obtained from the load cells and the LVDTs were recorded using a data acquisition system.

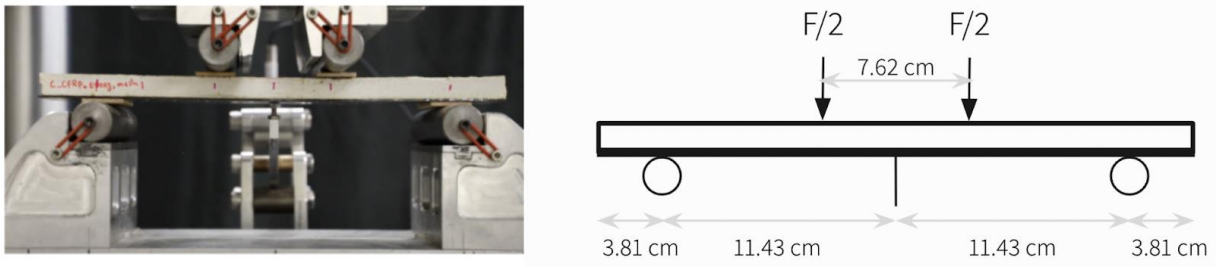


Figure 3. Left: Experimental setup. Right: Dimensions, loading, and support conditions

2.4. Analytical study

The transformed properties of the hybrid cross-section are calculated via the modular ratio n, which is described as shown below and used to obtain the transformed concrete section from the composite section (Equations 3-9). This value determines the reduced cross-section values of the lower (CFRP) layer. The original C-CFRP and transformed calculated concrete cross-sections are shown in Figure 4.

$$n = \frac{E_{CFRP}}{E_c} \tag{3}$$

$$A_{CFRP,tr} = A_{CFRP}.n \tag{4}$$

$$I_{CFRP,tr} = I_{CFRP}.n \tag{5}$$

$$A_i = A_{CFRP,tr} + A_C \tag{6}$$

$$Z_i = \frac{A_{CFRP,tr}.Z_{CFRP,tr}+A_C.Z_C}{A_i} \quad (7)$$

$$I_i = I_{CFRP,tr} + A_{CFRP,tr}.\Delta Z_{CFRP,tr}{}^2 + I_C + A_C.\Delta Z_C{}^2 \quad (8)$$

$$W_i = \frac{I_i}{Z_i} \quad (9)$$

With:

ΔZ_*: Distance of partial center of gravity from the total center of gravity

$*_{CFRP}$, $*_C$: CFRP layer, Concrete Layer

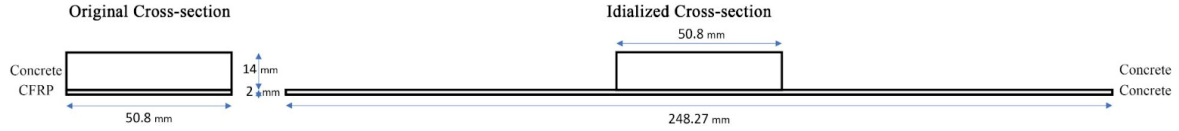


Figure 4. Left: Original concrete-CFRP cross-section. Right: Transformed concrete cross-section.

The cracking moment is calculated using the mean concrete tensile strength f_{ctm}. This is according to Equations 10 and 11, calculated from the concrete's compressive strength. The calculated transformed concrete cross-section and the cracking moment, force, and its associated displacement are presented in Tables 1 and 2.

$$f_{ctm} = 0.3.(f_{ck})^{\frac{2}{3}} [N/mm^2] \quad (20)$$

$$M_{cr} = W_i.f_{ct,eff} \quad (31)$$

with $f_{ct,eff}$: Flexural stress in concrete

Table 1. Transformed cross-section properties.

n	Zi (mm)	I_i (mm⁴)	f_{ck} (N/mm²)	f_{ctm} (N/mm²)	W_i (mm³)	M_{cr} (N.mm)
4.9	5.7	30495	32	3	2964	8879

Table 2. Analytical calculation of P_{cr} and Δ_{cr} associated with the transformed cross-section.

I(mm⁴)	E(N/mm²)	L(mm)	a(mm)	M_{cr}(N.mm)	P_{max}(N)	Δ_{max}(mm)
30,495	33,718	229	76	8,879	117	0.024

3. Discussion

Figure 5 shows the load-displacement diagrams for each of the specimens in the four-point bending test. The plots represent the sum of the loads from the two load cells versus the measured deflection of the beam at mid-span. Figure 6 shows the load-deflection diagram of the C-CFRP Epoxy and C-CFRP Epoxy Mesh specimens compared to the calculated stiffnesses up to the cracking moment M_{cr}, where the cracking moment is calculated using Equation 11. Figure 7 shows the test setup for the four-point bending test and the appearance of the specimens after testing.

In Figure 5a, which shows the concrete-only specimens, i.e. control specimens, an almost linear behavior is observed until the ultimate load is reached, after which the load suddenly drops to zero since the specimens are brittle and have no reinforcement. The calculated modulus of elasticity of these concrete beams from the four-point bending test (32,875 N/mm²) is compatible with the calculated modulus of

elasticity from the compression test of the concrete cylinder (33,718 N/mm²). The maximum load capacity of specimens C_1 and C_2 is lower than that of specimen C_3 because they had some preliminary damage at the edges of their cross-sections.

For the concrete mesh specimens (Figure 5b), after the crack initiation at about 200-267 N, some strength gain is observed due to the internal GFRP mesh reinforcement, which also increases the ultimate load capacity by up to 30%.

Figure 5c shows that the C-CFRP Nail beams experience an initial steep strength drop related to the delamination of the CFRP layer and a second drop due to the brittle failure of the concrete layer.

Figure 5d shows the C-CFRP Nail Mesh beams initially experiencing delamination of the CFRP layer, followed by cracking within the concrete layer and some strength gain due to the internal GFRP mesh reinforcement.

Figures 5e and 5f show that the initial stiffness of the C-CFRP Epoxy specimens with and without internal reinforcement decreases sharply as a result of the delamination of the CFRP layer and subsequent failure of the concrete layer. However, the ultimate strength of these two groups are much higher than the other 4 groups (about 300% higher, load capacity of 1,200 N compared to only 300 N).

In the C-CFRP Epoxy Mesh category, one specimen was completely broken when removed from the casting formwork, while another specimen showed minor cracking. The calculated flexural stiffness (EI) values for C-CFRP Epoxy Mesh specimens 1 and 2 were determined to be about 1,350,000 (KN.mm²) and 202,000 (KN.mm²), respectively. However, due to the large difference between the results of these two specimens and to ensure the validity and generality of the results, it is planned to repeat a four-point bending test on this particular category of specimens. This set of specimens display a significant improvement in their ultimate load capacity compared to the concrete control beams.

The analytical calculations for the C-CFRP Epoxy specimens with and without reinforcement mesh suggest that the first crack should occur at approximately 516 N, as shown in Figure 6. However, the onset of cracking took place at about 800 N, possibly due to the epoxy preventing crack development up to a higher load.

Finally, the flexural strength (EI) of each specimen is calculated using Equation 12, and the average flexural stiffness of the three specimens in each category is shown in Table 3.

$$EI = \frac{Fa(3L^2-4a^2)}{24\Delta max} \tag{42}$$

Where:

EI = flexural stiffness (N.mm^2)

P = total point load (N)

a = distance from support to the point load (mm)

L = length of the span under consideration (mm)

Δ_{max} = mid-span deflection (m)

Table 3. Average flexural strength (EI) of each category of beams.

Specimen Category	**C**	**C Mesh**	**C-CFRP Nail**	**C-CFRP Nail Mesh**	**C-CFRP Epoxy**
Average EI (N.mm^2) (uncracked)	570,051,659	582,398,188	611,749,422	648,362,988	632,864,071

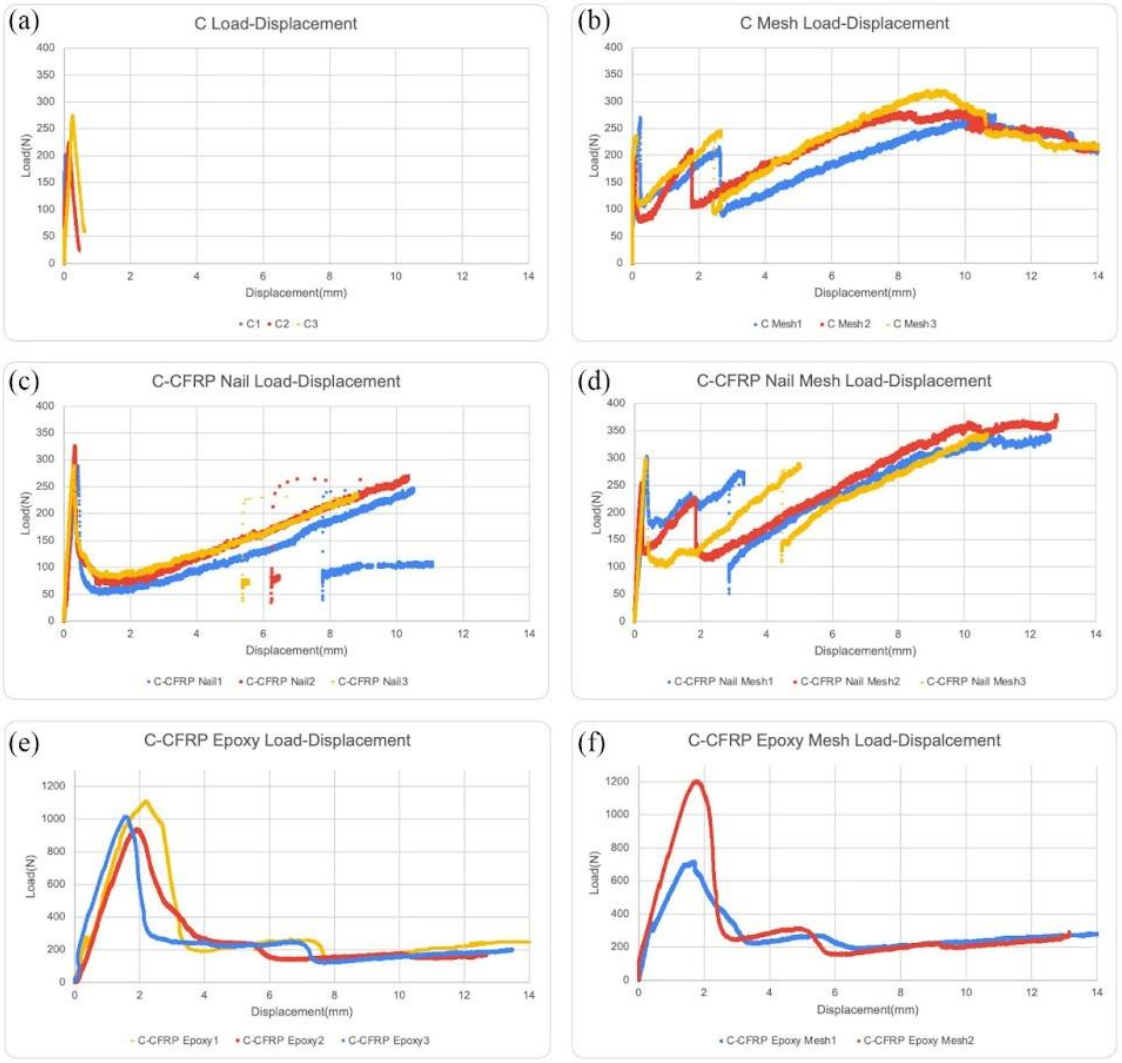


Figure 5. Load-deflection relationships of each category of the specimens under the four-point bending test: (a) Concrete (b) Concrete Mesh (c) Concrete-CFRP Nail (d) Concrete-CFRP Nail Mesh (e) Concrete-CFRP Epoxy (f) Concrete-CFRP Epoxy Mesh

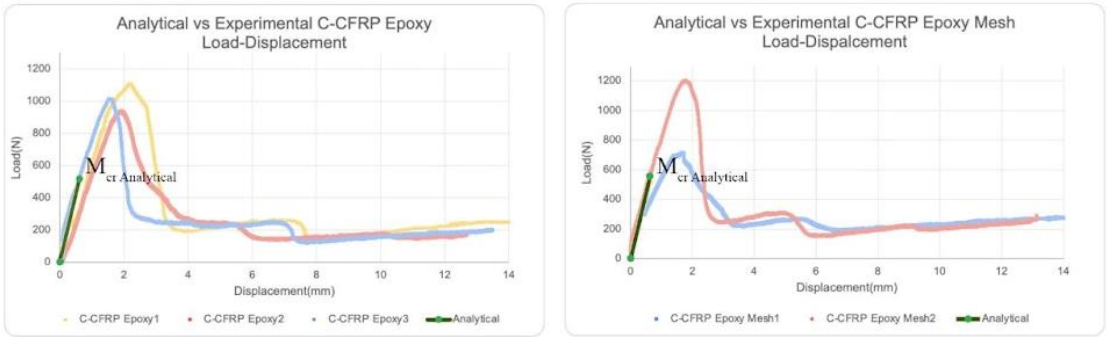


Figure 6. Analytical M_{cr} for hybrid C-CFRP cross-section vs. experimental load deflection of C-CFRP Epoxy with and without mesh.



Figure 7. Beams after performing the four-point bending test (each row, from left to right): (a) C 1-3 (b) C Mesh 1-3 (c) C-CFRP Nail 1-3(d) C-CFRP Mesh Nail 1-3 (e) C-CFRP Epoxy 1-3 (f) C-CFRP Epoxy 1-3.

4. Summary and conclusion

This study investigates the flexural behavior of eighteen beam specimens, six of which were reinforced with CFRP strips via an epoxy adhesive or nail shear connectors. The test variables studied in the experimental program were the internal GFRP mesh reinforcement, the external CFRP layer, and the type of connection between the external CFRP and the concrete. All specimens were tested under four-point bending, and three concrete control specimens were used for the comparative strength. In addition, to the experimental tests, simplified transformed section analyses were conducted.

Based on the experimental and analytical studies, the following observations and conclusions were made:

- All hybrid beams failed due to delamination of the CFRP strips, confirming the importance of proper shear connections between the two layers.
- For the hybrid specimens with nails, it is observed that the composite behavior does not fully develop, which may be due to the weak connection between the nails and the CFRP layer and the small force transfer area between the nails and the CFRP layer.
- For the hybrid specimens with epoxy resin, the composite properties have a significant influence on the performance of the cross-sections. These specimens have a higher ultimate flexural capacity (up to 320% more compared to the control beams), and a significant decrease in flexural stiffness is observed after delamination of the CFRP layer.
- For the specimens without CFRP layer, the internal mesh reinforcement contributes to the increase of the ultimate flexural capacity of the specimens (to about 30% of the original crack load of the specimen). However, for hybrid cross-sections, the ultimate load-bearing capacity depends more on the composite action of the hybrid cross-section rather than by the presence of the internal mesh.
- In the case of hybrid cross sections, the addition of the mesh also helps to restore the stiffness lost due to cracking in the concrete. It can also be seen that the delamination of the CFRP layer greatly reduces the stiffness of the cross-section.
- The first crack in most specimens occurs at a force of about 220-300N (about 25% of the ultimate load of the specimens with epoxy). For the C-CFRP Epoxy specimens, the experimental cracking moment is higher than the calculated cracking moment, which could be attributed to the crack-preventing effect of the epoxy.

Acknowledgements

The authors would like to thank the Department of Civil and Environmental Engineering (CEE) and the Department of Architecture at UC Berkeley's College of Environmental Design (CED) for accommodating this study. Special thanks are also due to the Al Falah Fellowship, Hellman Fellowship, and Bakar Fellowship for their generous financial and intellectual support of the authors. We also wish to acknowledge the support provided for this research by Dr. Cruz Carlos, CEE concrete lab manager, for his guidance and discussion on conducting physical testing and analysis, and all the laboratory technical staff members. Finally, we would like to extend our thanks to this project's undergraduate student assistants, Seoyoung Oh, and Zaina Mosalam for their excellent work and assistance during this study.

References

[1] J. Knippers, J. Cremers, M. Gabler, and J. Lienhard, *Construction Manual for Polymers+ Membranes: Materials, Semi-finished Products, Form finding, Design*. Walter de Gruyter, 2012.

[2] R. La Magna, S. Schleicher, and J. Knippers, "*Bending-active Plates*," *Adv. Archit. Geom.*, vol. 2016, pp. 170–87, 2016.

[3] Y. Yavaribajestani and S. Schleicher, "Bio-Inspired Lamellar Structures," 2019.
[4] S. Schleicher and M. Herrmann, "Constructing hybrid gridshells using bending-active formwork," *Int. J. Space Struct.*, vol. 35, no. 3, pp. 80–89, Sep. 2020, doi: 10.1177/0956059920924189.
[5] T. Uomoto, H. Mutsuyoshi, F. Katsuki, and S. Misra, "Use of fiber reinforced polymer composites as reinforcing material for concrete," *J. Mater. Civ. Eng.*, vol. 14, no. 3, pp. 191–209, 2002.
[6] W. Nawaz, M. Elchalakani, A. Karrech, S. Yehia, B. Yang, and O. Youssf, "Flexural behavior of all lightweight reinforced concrete beams externally strengthened with CFRP sheets," *Constr. Build. Mater.*, vol. 327, p. 126966, 2022.
[7] S. T. Smith and J. Teng, "FRP-strengthened RC beams. II: Assessment of debonding strength models," *Eng. Struct.*, vol. 24, no. 4, pp. 397–417, 2002.
[8] M. M. Ali, D. J. Oehlers, and S.-M. Park, "Comparison between FRP and steel plating of reinforced concrete beams," *Compos. Part A Appl. Sci. Manuf.*, vol. 32, no. 9, pp. 1319–1328, 2001.
[9] H. Nordin and B. Täljsten, "Testing of hybrid FRP composite beams in bending," *Compos. Part B Eng.*, vol. 35, no. 1, pp. 27–33, 2004.
[10] I. A. Shehata, L. A. Carneiro, and L. C. Shehata, "Strength of short concrete columns confined with CFRP sheets," *Mater. Struct.*, vol. 35, pp. 50–58, 2002.
[11] H. Rahimi and A. Hutchinson, "Concrete beams strengthened with externally bonded FRP plates," *J. Compos. Constr.*, vol. 5, no. 1, pp. 44–56, 2001.
[12] Z. Wu, W. Li, and N. Sakuma, "Innovative externally bonded FRP/concrete hybrid flexural members," *Compos. Struct.*, vol. 72, no. 3, pp. 289–300, 2006.
[13] Y. Yavaribajestani, M. Herrmann, and S. Schleicher, "Parameter sensitivity analysis of hybrid gridshells with bending-active formwork," in *Innovation, Sustainability and Legacy-Proceedings of the IASS Annual Symposium 2022*, Beijing, China, September 19-23, 2022.
[14] D. Duthinh and N. J. Carino, *Shear design of high-strength concrete beams: a review of the state-of-the art*. US Department of Commerce, Technology Administration, National Institute of standards and technology, 1996.
[15] DIN 1048-5: 1991-06, "Prüfverfahren für Beton–Teil 5: Festbeton, gesondert hergestellte Probekörper," 1991.

IASS 2023
July 10–14 Melbourne
Integration of Design and Fabrication

Proceedings of the IASS Annual Symposium 2023
Integration of Design and Fabrication
10–14 July 2023, Melbourne, Australia
Y.M. Xie, J. Burry, T.U. Lee and J. Ma (eds.)

Study on shape control method for active bending arch structures using kerf bending technique

Yuki OZAWA[*], Akihito YOKOTA[a], Satoshi OHKI[b]

[*] School of Architecture, Shibaura Institute of Technology
y-ozawa@shibaura-it.ac.jp

[a] VUILD, inc.
[b] Graduate student, Shibaura Institute of Technology

Abstract

Kerf bending (KB) is a technique to reduce bending stiffness and enabling curvature by providing openings or cutouts in inflexible flat materials. This study focuses on the application of the KB technique for unidirectional bending and proposes a shape control method for active bending arch structures to attain target shapes. The efficiency of this approach is validated through experimental and analytical examinations. There are a multitude of slit patterns utilized in KB, in this study a simple pattern of parallel lines in the orthogonal direction to the span was employed. By manipulating the distribution of two design parameters, "slit spacing" and "slit ratio", the bending stiffness of rigid plane material is altered and the deformed shapes can be controlled. Four distinct geometric shapes were set as target shape: semi-circle, sine wave, parabola, and catenary. Since bending deformation is solely generated through the movement of pin-supported points, the bending moment distribution $M(x)$ on attainment of the target shape can be easily calculated from the support reaction force P and the point height y, and the required stiffness distribution can be obtained through $M(x)$ and the curvature distribution κ of the target shape. By combining information about the required curvature distribution and the slit arrangement - stiffness reduction relationship, the optimal slit arrangement can be determined.

Keywords: active bending, arch, kerf bending, shape control, slit pattern, laser cutter, stiffness reduction

1. Introduction

In recent years, as digital processing technology has become more common, there have been cases where materials have been given properties that were not originally available. One example is "kerf bending (KB)," a technique that reduces bending rigidity by inserting slits or openings in a rigid plane material to make it easier to bend. This technique does not require any special equipment other than a cutting machine, and is expected to be applicable to a wide range of fields from product design to architecture, as it can be easily and quickly bent into various materials.

T. Oshima et al. proposed an analytical model for elastic materials with 2D repetitive slit patterns[1]. They modeled the relationship between the local geometry and resultant global elasticic modulus. O. Z. Güzelci et al. studied cut patterns that can be manually and freely formed on 3D surfaces[2]. S. Zarrinmehr et al. presented a relief cutting method to turn rigid planar surfaces into flexible ones using meander pat- terns that consist of interlocked Archimedean spirals[3]. A. Kalama et al. study kerf bending, where material is removed at strategic locations on the surface of a plate to locally weaken it and make it easier to bend aiming to understand the interrelationship between cutting patterns and properties such as bending curvature and material resistance to load[4]. D. Mitov et al. studied a method for designing cutting patterns based on geometry and material processing for the production of double curved architectural panels for materials widused for interior wall finishes, such as wood and

Copyright © 2023 by Yuki OZAWA, Akihito YOKOTA and Satoshi OHKI. Published in the Proceedings of the IASS Annual Symposium 2023 with permission.

plasterboard[5]. M. Capone et al. proposed a method to make ruled double curved surfaces by making used of kerf bending[6]. R. Chen et al. studied kerf cut patterns for designing complex free-form shapes[7]. Two types of cut patterns, square and hexagonal, were assumed and the relationship between different cutting densities and kerf patterns for elongation, bending and torsional deformation was considered. B. R. Lorenzoni focused on the geometric accuracy of MDF kerf bending and examined the design, cutting, bending, 3D scanning and analysis of target geometries to form accurate cylindrical shapes[8].

Although a certain number of papers have studied the relationship between kerf cut pattern and bending stiffness, machining accuracy to obtain an accurate shape, etc., there have been no studies that have proposed a method to actively control the shape formed by varying the cut pattern. This study focuses on KB technology for unidirectional bending of wood board materials such as MDF boards. By applying it, it is aimed to propose a method to control the shape of the arch structure formed by the active bending to achieve an arbitrary target shape, and to verify its effectiveness.

2. Calculation of stiffness distribution

To control the shape of active bending arch structures, it is necessary to determine the stiffness distribution along the length of the material that can achieve the target shape. The stiffness distribution can be expressed as a distribution of reduction ratio when the stiffness of a member without slits is set to 1. This reduction ratio distribution is called $C(x)$ here, and the calculation of $C(x)$ is shown in the following section.

2.1. Basic theory

Consider a beam-like member supported by a left-end pin and a right-end pin roller like shown in Figure 1. If the member is transformed into an arch shape only by applying a leftward pushing force P at the right end, the moment distribution $M(x)$ can be simply expressed as follows using the deformation $f(x)$ in the y direction.

$$M(x) = P \cdot f(x) \tag{1}$$

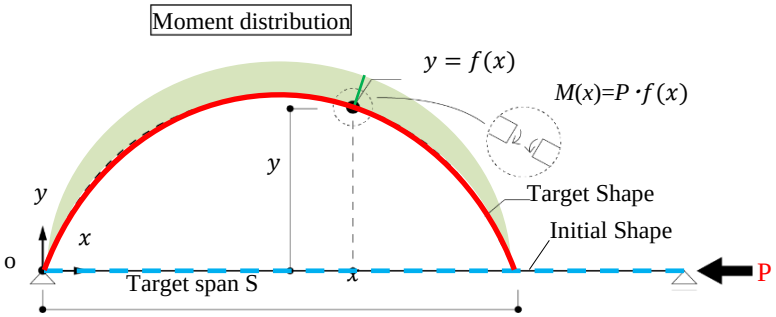


Figure 1. Moment distribution of active bending arch structure

If $f(x)$ matches the target shape and the effect of self load can be ignored, the stiffness distribution $K(x)$ required to achieve the shape can be expressed as follows using $M(x)$ and the curvature distribution $\kappa(x)$ of the target shape.

$$K(x) = \frac{M(x)}{\kappa(x)} \tag{2}$$

The curvature of a beam that produces a large deformation is expressed by the following equation

$$\kappa(x) = \frac{f''(x)}{(1+f'(x)^2)^{1.5}} \tag{3}$$

The stiffness distribution $K(x)$ of the plate material with slits is defined as follows using the distribution of reduction ratio in stiffness due to slitting: $C(x)$, Young's modulus of the material: E, and sectional secondary moment: I.

$$K(x) = C(x) \cdot EI\,, \quad (0 < C \leq 1) \tag{4}$$

From equations (1)-(4), the distribution of the reduction rate of stiffness $C(x)$ required to achieve the target shape can be expressed as follows

$$C(x) = \frac{f(x) \cdot (1 + f'(x)^2)^{1.5} \cdot P}{f''(x) \cdot EI} \tag{5}$$

2.2. Target shape formation method and design

In this section, the stiffness distribution is obtained for each target shape. The model assumed is a 400mm length, 100mm width, 2.5mm thick MDF board. The magnitude of forced displacement will be unified as δ = 145.35mm, which is a semicircular arch when the target shape is a circular arc. Hence, the span (L-δ) after forced displacement for both models is 254.65 mm, and the radius r for the semicircular arch is 127.325 mm (Figure 2).

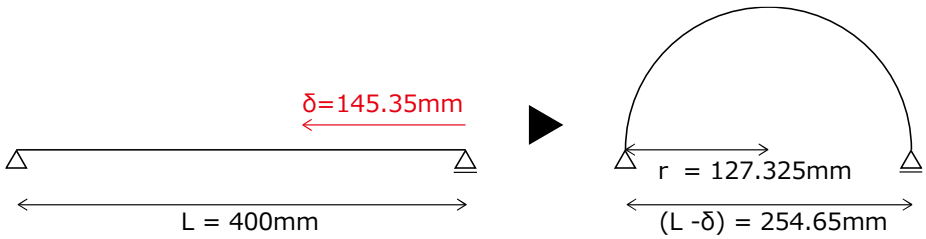


Figure 2. Overview of arch shape generation method

Figure 3 shows the required stiffness ratio distribution for the four target shapes (semicircle, catenary, sine, and parabola) obtained by using the procedure shown in 2.1. The horizontal axis is expressed the distance from right edge in the arch length direction, and the vertical axis is expressed the required stiffness ratio by standardizing the maximum value as 1.

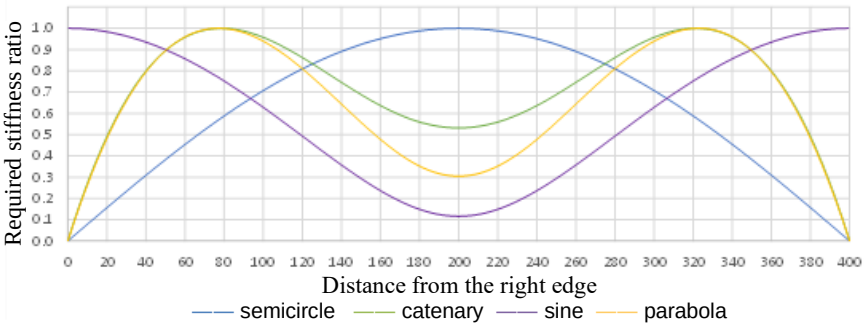
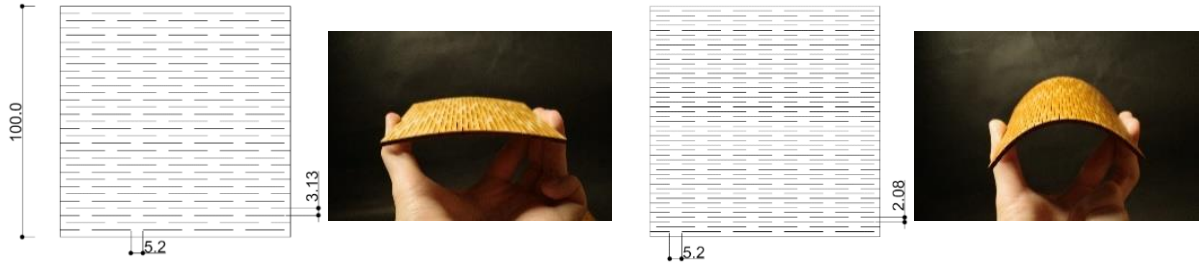


Figure 3. Distribution of required stiffness ratio

3. Design for slit arrangement

3.1. Slit setting

There are various patterns of slit shapes used in KB technique, however in this study the simple pattern with a series of horizontal parallel lines as shown in Figure 4 is used. This pattern is most commonly used in KB with a single curvature and is considered to have an excellent balance of strength and flexibility [2]. It has also been shown that the narrower the slit spacing and the larger the proportion of slits in the width direction, the easier it tends to bend. In this study, two variables, "slit spacing" and "slit ratio," are set as the design parameters for design. Here, "slit ratio" Indicates the percentage of openings by slits in the width direction. The distribution of these variables is manipulated to vary the stiffness of the face material and control the deformation shape. The slits are arranged so that the center positions of adjacent slits are mutually different from each other.



(a) When the slit spacing is wide (b) When the slit spacing is narrow

Figure 4. Slit arrangement and bending flexibility

3.2. Evaluation of bending stiffness by FEM analysis

To verify the relationship between cut pattern and bending stiffness, FEM analysis using a plate element model is performed. An overview of the model is shown in Figure 5. Midas/iGen is used as the analysis program. The models are MDF plates of 200 mm length, 100 mm width and 2.5 mm thick with various slit arrangement. The material properties are set to Young's modulus E = 4000 N/mm^2 and Poisson's ratio: 0.2. Linear analysis were performed under the condition that a centralized loads were applied to a simple beam(Figure 5). The load condition is set so that the total load is about 200 N in the center of the plate beam, and the self weight is not considered.

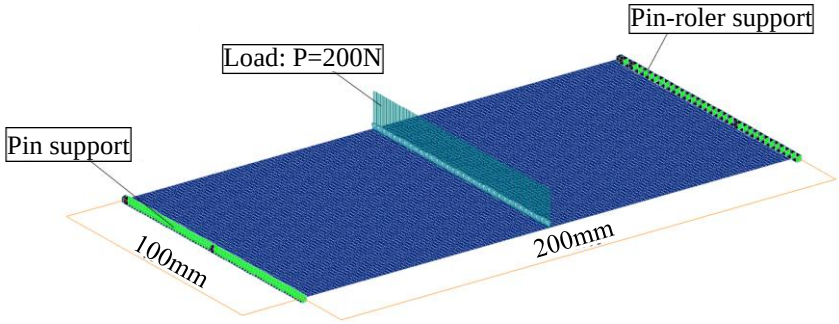


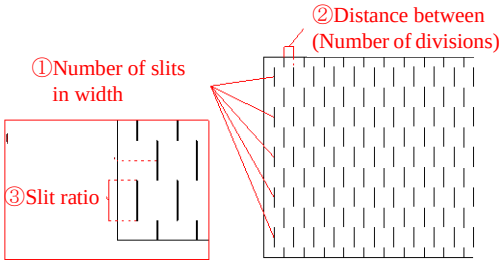
Figure 5. Analysis model

3.3. Analysis parameters

The analytical parameters are shown in Table 1. As shown in the figure in the table, when the number of slits is 5 and the slit ratio is 50%, the length of one slit is 10 mm.

Table 1. Analysis Parameters

Example of notation) S-N5-4mm-50% ① ② ③		
①Number of Slit N	②Slit spacing w[mm]	③Slit ratio c(%)
5 10	1 (200) 2 (100) 3.03 (66) 4 (50) 5 (40) 5.88 (34) 7.14 (28) 8 (25) 9.09 (22) 10 (20)	10 20 30 40 50 60 70 80 90



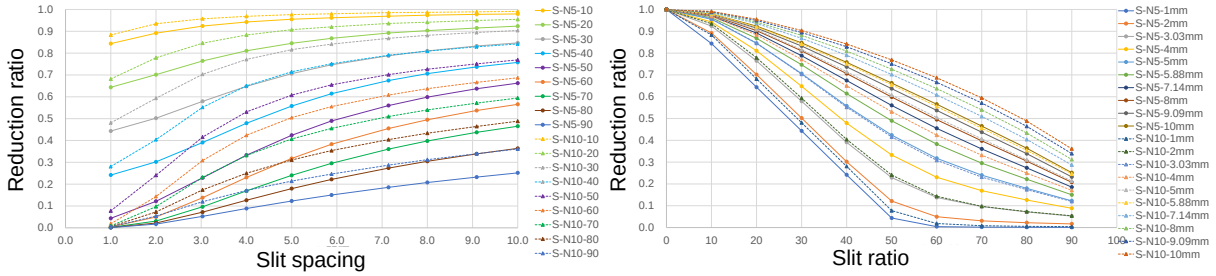
3.4. Analysis overview and bending stiffness evaluation method

Using the deflection δ obtained from the analysis results, the rate of reduction is back-calculated from the deflection theoretical equation for a simple beam loaded with a centralized load.

$$C = \frac{PL^3}{48EI\delta}$$

where P is the center concentration load (here P=200N), L is the length (L=200mm) and I is the sectional secondary moment(I=100×2.5^3/12=130.208mm^4).

The analytical results are shown in Figure 6. The relationship between slit spacing and slit ratio and stiffness was confirmed.



(a) Slit spacing - Stiffness ratio (b) Slit ratio - Stiffness ratio

Figure 6. Each parameter - Stiffness reduction ratio relationship

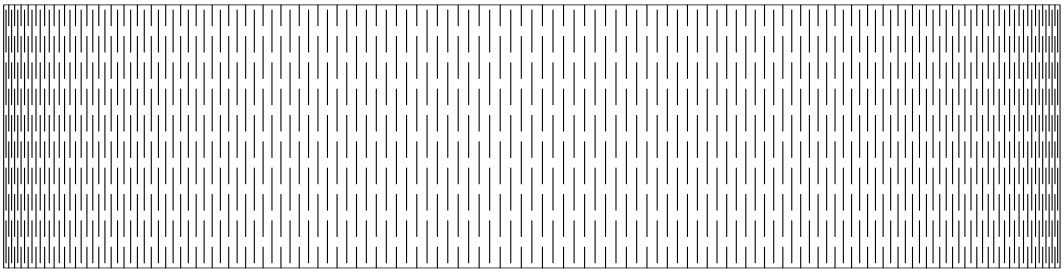
3.5. Slit pattern design

By combining the required stiffness distribution shown in Figure 3 and the relationship between slit pattern - stiffness ratio shown in Figure 6, the slit arrangement that can achieve the target shape by active bending can be determined. As indicated in 3.4, there are two design methods for slit arrangement.

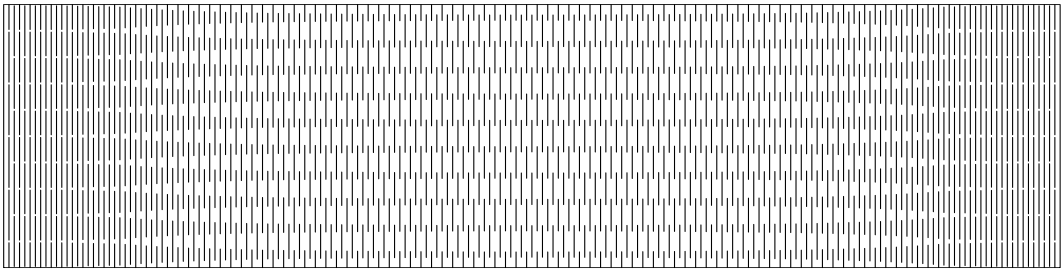
(1) Slit spacing method

(2) Slit ratio method

Figure 10 shows the slit patterns determined by each method for semicircle shape.



(a) Slit arrangement by slit spacing method

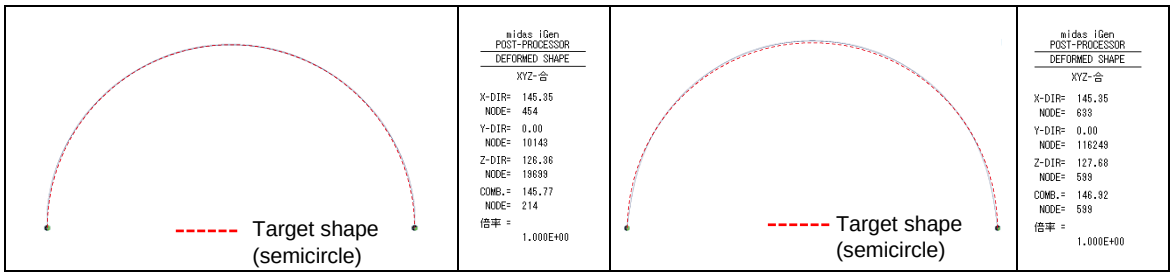


(b) Slit arrangement by slit ratio method

Figure 7: Slit pattern for semicircle shape

3.6. Confirmation by geometric nonlinear analysis

The designed slit pattern models are modelled by Midas/iGen, and a geometric nonlinear analysis considering large deformation is performed to confirm if the target shape can be formed. The arch shapes are formed by applying leftward forced displacement at the right edge of the models. In order to generate rise deformation stably, an initial irregularity of 1/800 with respect to the length was added to the center of each model. Figure 8 shows the analysis results of a semicircle as an example. From the analysis results, it can be confirmed that the shape is almost equal to the target shape.



(a) Designed by slit spacing method (b) Designed by slit ratio method

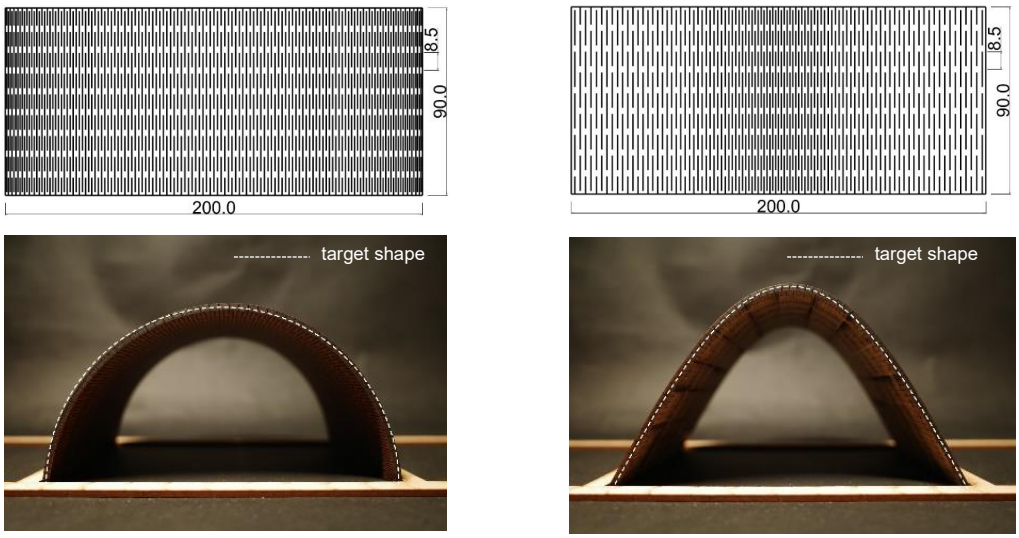
Figure 8: Analysis results for semicircle shape models

4. Experiments with scaled models

To confirm the effectiveness of the proposed method, scaled models was actually produced and the arch shape were formed by active bending. This chapter presents a summary of the results. A Trotec Laser laser processing machine Speedy 4002 was used to prepare the specimens. Slit widths ranged from 0.2 to 0.4 mm, with an average of 0.3 mm.

4.1. Simple experiment

A simple experiment using a small-scale model of 90 mm x 200 mm x 2.5 mm is shown in Figure 9. The cut pattern was designed using the method of changing the slit spacing. It was confirmed that the target shape was achieved for both targeted shape of the semicircle and the sine curve.



(a) Semi-circle (b) Sine curve

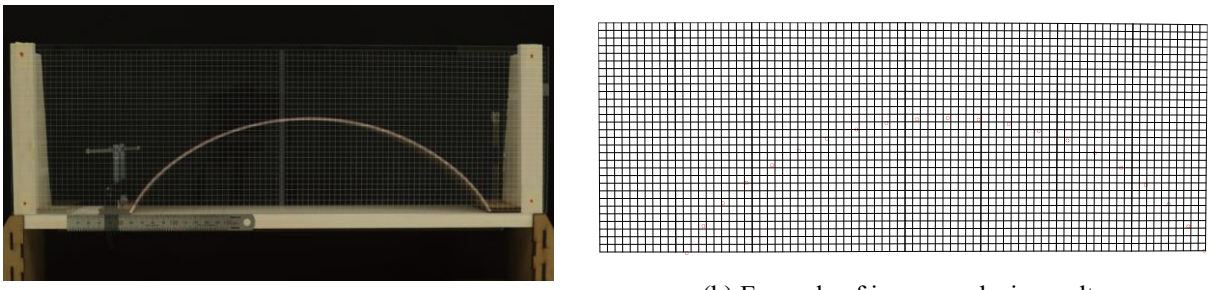
Figure 9. Shape control by varying slit spacing

4.2. Detailed experiment

More detailed experiments were carried out and are reported here.

The test specimen preparation conditions are the same as in 2.2. The specimen were made by 2.5mm thick MDF board with 400mm length and 100mm width and were machined with slits in the pattern shown in Figure 7. A Trotec Speedy 400 laser cutter was used for the slitting process.

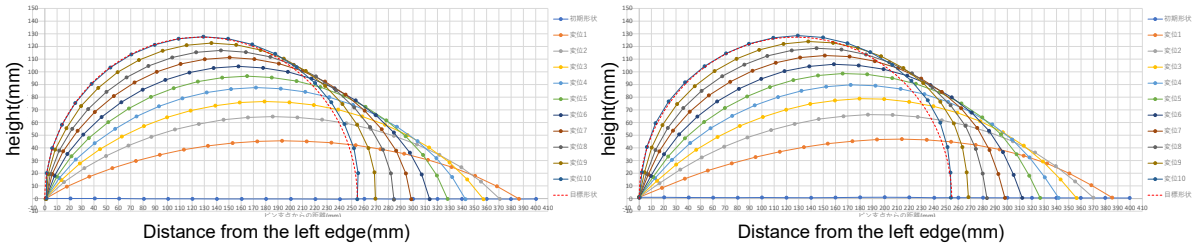
A forced displacement of up to 145.35 mm on the left side was applied in 10 steps to the right supporting point, forming a final semi-circular arch. The overview of experiments is shown in Figure 10. Measurement points are marked on the test specimen beforehand at intervals of 20 mm along the length direction. An acrylic plate with grids marked at 5 mm intervals is placed in front of the test specimen and the co-ordinates of the measuring points at each step are measured by image analysis using still images.



(a) Test specimen and test equipment (b) Example of image analysis results

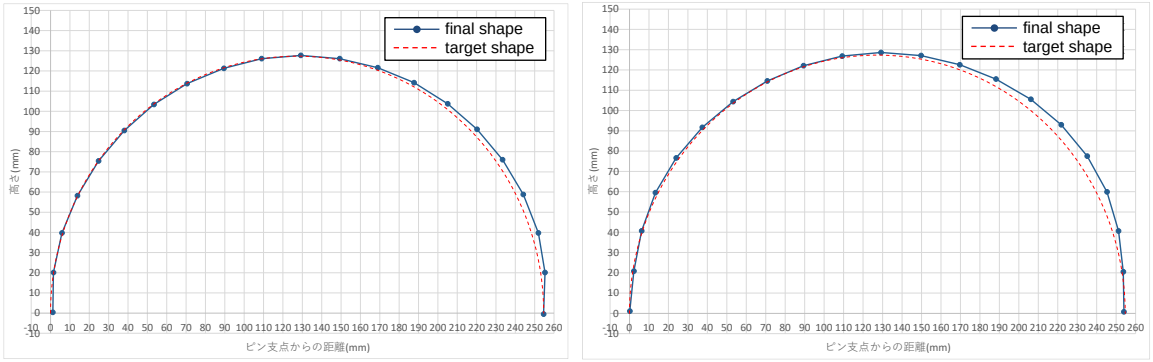
Figure 10. Overview of detailed experiments

Figure 11 shows a progress of deformation at each step and final shape of the specimen forming a semicircle. The final shape formed by each specimen is shown in Figure 12. The test results showed a maximum error of about 2% with respect to the span. Despite some errors, the shape was generally equal to the target shape. The error is thought to be due to the effects of gravity and the initial bias in the stiffness of the material, and partly due to the effects of material non-linearity.



(a) Designed by slit spacing method (b) Designed by slit ratio method

Figure 11: Test results of semicircle target models



(a) Designed by slit spacing method (b) Designed by slit ratio method

Figure 12: Comparison of final and target shape

5. Conclusion

This study proposed a shape control method for active bending arch structures by combining with kerf bending technique. In this study a simple slit pattern of parallel lines in the orthogonal direction to the span was employed. It is possible to vary the stiffness of inflexible plane board by adjusting the length and spacing of the slits to achieve the target arch shape.

In this study, four distinct geometric shapes were set as target shape: semi-circle, sine wave, parabola, and catenary. The required stiffness distribution can be obtained through $M(x)$ and the curvature distribution κ of the target shape. By combining information about the required curvature distribution and the slit arrangement-stiffness reduction relationship, the optimal slit arrangement can be determined. Simple experiments and geometric nonlinear analysis have demonstrated the effectiveness of the method.

If the span is large in relation to the stiffness, the effect of gravity may be greater. Correction methods that take into account the effect of gravity are still under investigation.

References

[1] Taisuke Ohsima, Tomohiro Tachi, Hiroya Tanaka, Yasushi Yamaguchi, "Analysis and design of elastic materials formed using 2D repetitive slit pattern", *Proceedings of IASS Annual Symposia*, IASS 2015 Amsterdam Symposium, 2015

[2] Orkan Zeynel Güzelci, Zeynep Bacınoğlu, Sema Alaçam, "*Enhancing Flexibility of 2D Planar Materials By Applying Cut Patterns For Hands On Study Models*", SIGraDi 2016, XX Congress of the Iberoamerican Society of Digital Graphics 9-11, November, 2016 - Buenos Aires, Argentina, 2016

[3] Saied Zarrinmehr, Mahmood Ettehad, Negar Kalantar, Alireza Borhani, Shinjiro Sueda, Ergun Akleman, "Interlocked archimedean spirals for conversion of planar rigid panels into locally flexible panels with stiffness control", *Computers & Graphics*, 66 (2017) 93–102, 2017

[4] A.-M. Kalama, D. Tzoni and I. Symeonidou, "Kerf bending: A genealogy of cutting patterns for single and double curvature", *Proceedings of the 7th International Conference on Geometry and Graphics*, 2020

[5] Dejan Mitov, Bojan Tepavčević, Vesna Stojaković, Ivana Bajšanski: "Kerf Bending Strategy for Thick Planar Sheet Materials", *Nexus Network Journal*, Aug. 2018.

[6] Mara Capone, Emanuela Lanzara, Kerf bending: ruled double curved surfaces manufacturing, SIGRADI 2018

[7] Renzhe Chen, Coby Turman, Mingliang Jiang, Negar Kalantar, Michael Moreno, Anastasia Muliana, Mechanics of kerf patterns for creating freeform structures, Springer-Verlag GmbH Austria, *part of Springer Nature 2020*, 2020

[8] Barbara Ruschel Lorenzoni, Fabio Pinto da Silva, "Geometric analysis of the MDF kerf-bending structure accuracy", *International Journal of Space Structures*, Volume 37 Issue 2, June 2022

Additive manufacturing/ 3D printing

Active bending
► **Additive manufacturing/ 3D printing**
Architectural geometry
Bamboo for sustainable construction and quality of life improvement
Bio-inspired structures and architecture
Bridge structures
Computational form-finding
Conceptual design
Concrete structures
Construction techniques
Deployable and inflatable structures
Design competition (WG21)
Digital modelling and fabrication
Dynamic response of metal spatial structures
Dynamic response of other structures
Form-finding and structural optimisation of interlocking discrete assemblages
Graphical methods
Gridshell and lattice structures
Historical concrete shells
Historical structures
Lattice structures
Life-cycle design and assessment of structures
Metal gridshell structures, connections and stability
Methods and construction technologies for sustainable shell structures
Morphology and configuration processing
Next generation parametric design
Novel methods in modelling, optimisation and construction for reducing carbon footprint of continuous roof shells
Numerical methods for geometry, form-finding and optimisation of lightweight structures
Optimisation methods and applications
Origami
Other
Teaching design uncertainty: working with unknown qualities/quantities of new and re-claimed materials
Teaching of shell and spatial structures
Tensegrity systems and cable structures
Tension and membrane structures
Tension structures in the Asia-Pacific
Timber and bio-based structures
Topology optimisation
Traditional masonry structures and innovation
Transformable structures

IASS 2023
July 10–14 Melbourne
Integration of Design and Fabrication

Proceedings of the IASS Annual Symposium 2023
Integration of Design and Fabrication
10–14 July 2023, Melbourne, Australia
Y.M. Xie, J. Burry, T.U. Lee and J. Ma (eds.)

4D formwork for robotic concrete spraying

Guillaume JAMI[a,*], Selen Ercan JENNY[a,*], Chenguyan WEI[a], Hamilton FORSYTHE[b], Nicolas FEIHL[a], Skylar TIBBITS[b], Ena LLORET-FRITSCHI[a,c]

[a,*] Gramazio Kohler Research, ETH Zurich, Switzerland
jami@arch.ethz.ch, ercan@arch.ethz.ch

[b] Self Assembly Lab, MIT, USA
[c] Fabrication and Material Aware Architecture, Academy of Architecture, USI, Switzerland

Abstract

Globally, concrete is the second most used material after water. On average, three tons of concrete is consumed per person per year, while each ton of concrete added to the atmosphere contributes one ton of greenhouse gases. Because of this negative environmental impact, research institutions, architects, and construction professionals seek to reduce concrete usage in the built environment. Material-optimized structures offer one approach; however, such structures often require custom-made formworks that are disposed of after a single use and are thus expensive and waste-generating. Recently, several unconventional solutions for formwork have emerged that produce material-optimized structures without generating significant waste, including the examples of lost-, stay-in-place, and dynamic-formworks. This paper examines 4D-printing technology, which is tested in terms of scalability to produce a building component through fiber-reinforced concrete (FRC) spraying. With an empirical study, we evaluate two different 4D-printing techniques: 1) textile 4D-printing and 2) thermoplastic 4D-printing, both enabling the production of self-shaping, lightweight textile formworks. Furthermore, we present the first prototypical results and discuss the challenges and next steps for 4D-printed formworks that promise a more sustainable use of concrete.

Keywords: 4D-printing, concrete spraying, formwork, digital fabrication, architecture

1. Introduction

Concrete is the second most used construction material after water [1], and it is one of the most significant sources of CO_2 emissions worldwide [2]. Even though efforts are made to find new ways to mix concrete using less CO_2, current incentives are not sufficient to reduce emissions. Additionally, using less bulk material overall is necessary, which is possible by casting materially optimized structures. However, custom formworks are required to cast such forms, which are used only once, and they generate a significant amount of waste [3] as well as increase construction costs by up to 70% compared to the standard [4]. Therefore, making technological improvements to formwork systems is critical to move towards a more sustainable way of building [5].

Innovation in formworks is driven by several goals: decreasing production time, reducing costs, advancing geometric complexity, increasing material efficiency, or reducing environmental impacts. Since the early 2000s, researchers have explored concrete 3D printing [6] and 3D printed thin formworks [7]. This paper explores the architectural potentials and fabrication principles for creating self-shaping lightweight, 4D-printed formworks. Such formworks could enable new design possibilities, as they are lightweight, self-shaping, applicable at a large scale, and compatible with various concrete

Copyright © 2023 by Guillaume JAMI, Selen Ercan JENNY, chenguyan WEI and Hamilton FORSYTHE. Published in the Proceedings of the IASS Annual Symposium 2023 with permission.

mixtures.

4D-printed objects are actuated or activated by environmental changes, such as heat, humidity, or tension. [8]. Although such 4D-printing has the potential to function as a flexible system at an architectural scale, the current state-of-the-art in 4D-printing only allows to produce small-scale elements (smaller than 100 mm in size). The study presented in this paper, however, scales the existing 4D-printing technologies to realize architectural and structural applications. To achieve this, a workflow is developed that is applicable to different 4D-printing techniques as shown in Figure 1. This workflow comprises the following steps: (A) Firstly, the object is 3D-printed using a specific print path. Secondly, (B) the object is activated and geometrically transformed. Thirdly, (C) the transformed object, which consists of plastic and textile, is sprayed with a custom mortar mix with a thickness of less than 1 mm on average and the transformation is stabilized. Finally, (D) the result, the bespoke 4d formwork, is sprayed with concrete.

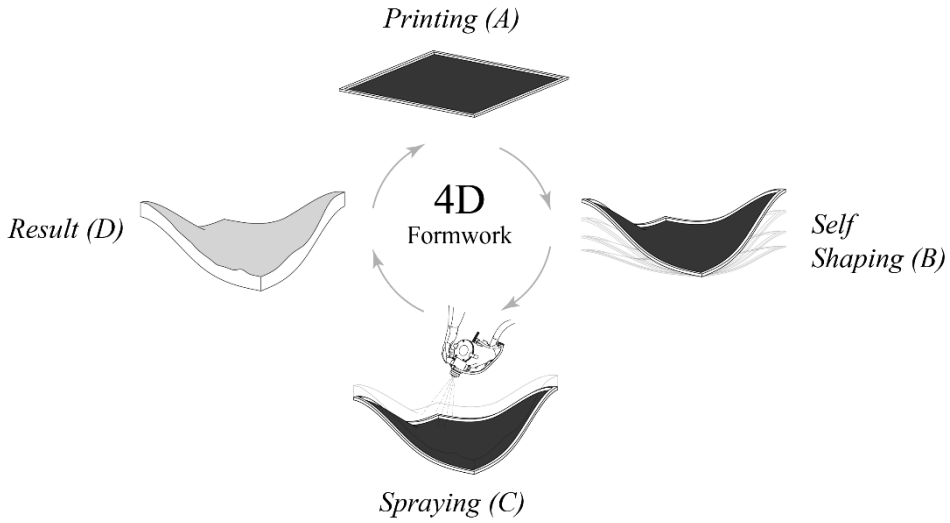


Figure 1. 4D formwork fabrication steps.

2. Relevant Work

2.1. Textile formworks

The concept of using thin textile formworks for concrete has been explored for centuries. It was first used in the Roman period, for which one example is the concrete vault under the Villa Medici in Rome [9]. The textile formworks were revisited later in history by Gustav Lilienthal in the early Industrial Revolution era and then by others throughout the 20th century [9]. More recently, Mark West, founder of the Center for Architectural Structures and Technology (CAST) at the University of Manitoba, re-introduced the concept of thin textile formwork [10]. Their work initially experimented with a method using fabric as formwork to create expressive columns (Figure 2, (A)) and as well as material-optimized beams. Despite offering considerable design freedom, these explorations have yet to make it into architectural structures, mainly due to their unpredictability, which makes it difficult to use them in interfacing with other systems, such as tension cables, foundations, and reinforcement. Another project, Knit Candela, by Mariana Popescu [11], aims to use knitted textiles as lost formworks to precisely fabricate double-curved structurally optimized shell structures. This research uses computational

methods to generate knitted patterns and fabricate textiles suspended on wooden scaffolding systems (Figure 2, (B)), which is more precise and predictable than the CAST method. It demonstrated a fabric-knitted formwork used to fabricate a double-curved shell structure, which was produced and exhibited in architectural scale. The knitted formwork is tensioned and sustained by a secondary timber structure and scaffolding, allowing the textile to stay in place while a layer of concrete is applied. The resulting shell expresses the freedom and flexibility allowed by such fabric formwork. However, despite being a very promising process, the heavy scaffolding structure used to create this pavilion does not fulfill the goal of allowing geometrical freedom using a light and self-standing formwork without extra structural material.

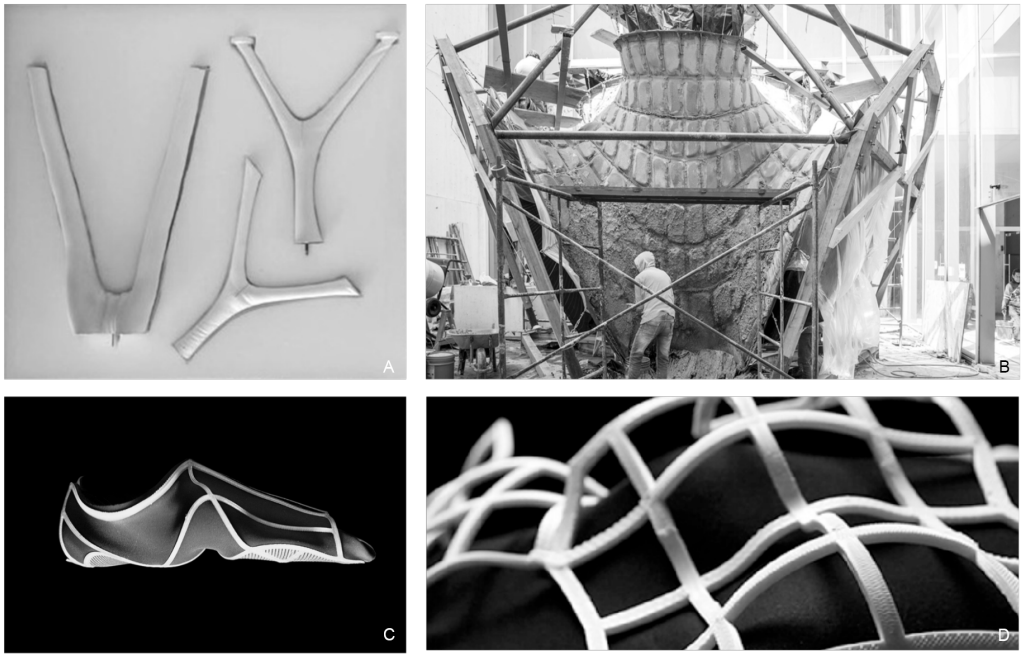


Figure 2: (A) Fabric formwork Y-column by CAST at the University of Manitoba. (B) Knit Candela pavilion by Zaha Hadid Architects and Block Research Group, 2018. (C) 4D-printed shoes by MIT Self-Assembly Lab, 2015. (D) Thermoplastic 4D-printed frame, Carnegie Mellon University, 2018.

2.2. 4D-printing

To the author's knowledge, the general definition and theory of 4D-printing was first introduced in 2013 by the Self-Assembly Lab at MIT [12]. This definition describes 4D-printing as an additive manufacturing strategy in which an additional factor, an environmental "stimulus" such as light, humidity, heat, or speed, is used to activate a controlled transformation of the material [13]. Among various existing 4D-printing techniques, two are directly related to the study presented in this paper: Thermoplastic 4D-printing and textile 4D-printing. This study compares the potential and limitations of these two 4D-printing techniques for developing *4D formwork,* a term that is coined in this paper.

2.2.1. Thermoplastic 4D-printing

The thermoplastic 4D-printing technique enables the transformation of FDM 3D-printed objects into 4D objects, relying on the residual stress in an FDM 3D-printed object. These objects can be actuated and transformed into 4D objects by heating them above the glass transition phase, using specific print paths. Research has shown that the bending angle and deformation shape of the element are affected by

changing the overall length of the actuator and the proportions of the two sections, as well as the printing layer height and velocity. Research from CMU [14] demonstrates the design potential of this method and its high level of controllability (Figure 2, (D)). However, the prototypes have so far been small - limited to 100-150 mm - and use only PLA. The possibility of scaling up this technique to further architectural applications thus remains an untapped area.

2.2.2. Textile 4D-printing

Textile 4D-printing technique emerged when 3D-printing technology became easily accessible and allowed printing to be carried out on various supports or beds, including textiles [15]. As this method produces roughly predictable transformations, it can be used to design self-shaping objects, such as shoes or fashion garments. One example is the Active Shoe (Figure 2, (C)) project developed at MIT [16]. Other research, such as the work of Lotte Scheder Bieschin on membrane-actuated stiffness gradient composites (MASGC) [17], or similar research conducted at URJC Madrid in collaboration with Disney Research on the computational design and automated fabrication of Kirchhoff-Plateau surfaces [18] demonstrate that the results of a self-shaped membrane can be predicted and classified or simulated with a dedicated optimization algorithm. Such research presents that the design rules guiding the self-shaping deformation are known to depend on the tension applied to the textile, the print path geometry, the printing material properties, and the time allowed for the deformation. However, neither has demonstrated architectural scale applications.

This paper uses existing knowledge of both thermoplastic 4D-printing and textile 4D-printing, substantially upscaling both 4D-printing technologies and combining them with an existing concrete spraying technology, Glass Fiber Reinforced Concrete spraying (GFRC).

3. Material and Methods

To assess the feasibility of the 4D formwork for concrete structures, custom digital design tools were developed, and a series of experiments were conducted to test and validate the proposed formwork. The experimental setup, which allows for an iterative design process, uses the developed set of digital design and fabrication tools, which are explained in the following section. The iterative design and fabrication process follows four steps: design generation, printing, activation of the reaction, and 3D scanning.

3.1. Fabrication setup

The printing setup uses the same base technology for both 4D-printing techniques. As shown in Figure 3, the textile 4D-printing relies on (A) a *UR10* robotic arm with (B) a custom-made filament extruder end-effector, with a 1200 mm square print bed. The thermoplastic 4D-printing uses (C) a *BigRep One* printer with a 1000 mm print bed. On the *UR10* robotic arm, (D) an *Intel RealSense Depth Camera D435i* is mounted to scan and compare the physical result to the digital model in Rhino. For logistic reasons, all prototypes are scanned with the *UR1*0 setup.

All prototypes are printed using PLA NX2 filament [19]. To activate the prints, two different activation platforms are used as shown in Figure 3. The textile 4D-printing results are activated on (E) a platform by cutting the textile around the print without moving it from the print bed. For thermoplastic 4D-printing, the printed elements are placed in (F) a water tank. To activate the deformation, the water temperature is raised to 65°C using an array of water heating resistance.

Once deformed, prototypes are moved to the spraying setup and minimally fixed to a horizontal surface. Prototypes are first sprayed vertically with a 1 mm-thin layer of mortar using (G) a *PFT Swing L FC Airless pump*. This thin-layer locks in the final shape of the transformed print when it hardens and

supplies enough rigidity to support the next layer. After curing for 24 hours, the prototypes are sprayed with GFRC using the setup from *Aerocrete*, a project that introduces a novel spraying technology for the production of slender, bespoke concrete elements [20]. Within the scope of this paper, this setup includes (H) an *MK3 Powertex Facing Coat Spray Gun* that chops glass fibers into 20 mm lengths and then pushes the material with the fibers through (I) a nozzle using pressured air.

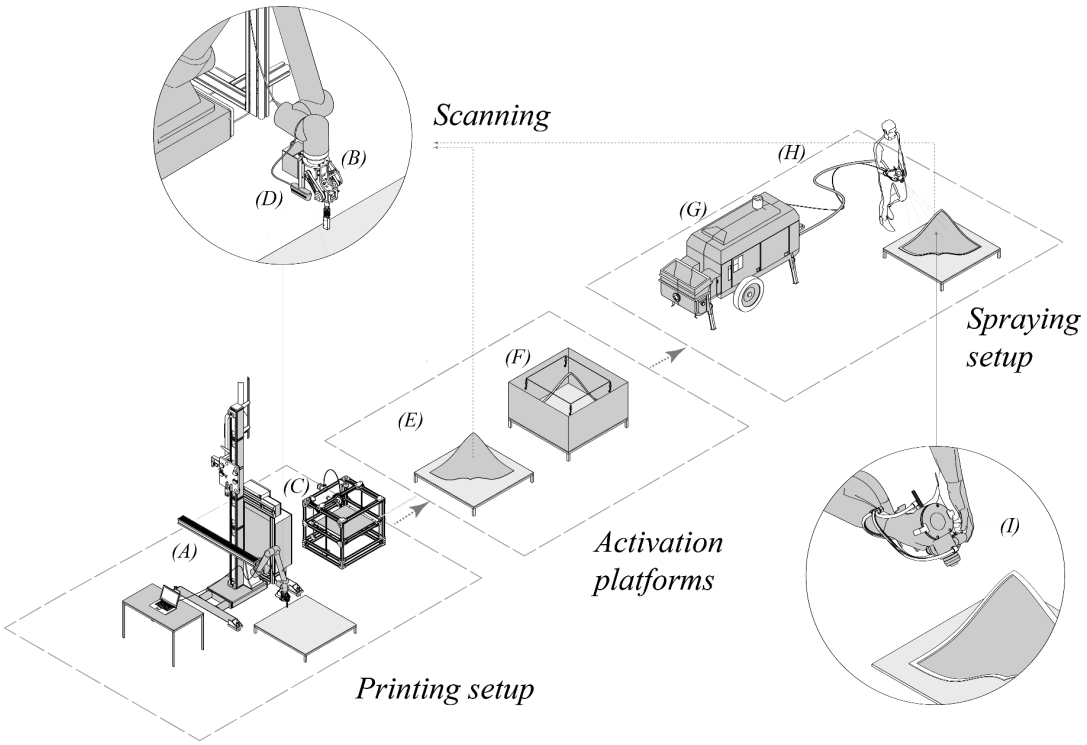


Figure 3. Fabrication setup. (A) *UR10* robotic arm, (B) Custom-made filament extruder end-effector, (C) *BigRep One* printer, (D) *Intel RealSense Depth Camera D435i,* (E) Textile 4D-printing activation platform, (F) Thermoplastic 4D-printing activation platform - water tank (G) *PFT Swing L FC Airless pump,* (H) *MK3 Powertex Facing Coat Spray Gun,* (I) Close up of the nozzle.

3.2. Digital design tools

Digital design tools rely on existing software to generate a print path based on a target geometry. The print path is designed and visualized in Rhino [21] Grasshopper [22]. Both 4D-printing techniques rely on custom Python components developed within the open-source, python-based framework COMPAS, specifically, the COMPAS Slicer library [23]. The input geometries and parameters are converted to *.json* files or *.gcode* and sent to the fabrication setup for printing. The design tool also includes software components that convert the parameters into boundary representation (Brep) to visualize the print volume in Rhino, which serves as a visual interface.

3.2.1. Thermoplastic 4D-printing tool

For thermoplastic 4D-printing, the user can draw the targeted geometry directly in Rhino. As shown in

Figure 4, during the curvature analysis process, the tool first takes the curvature value (k) of uniformly distributed points on the input curve. Then by evaluating the product of *k* between two adjacent points, the input curve is divided into concave and convex segments. The k product of two adjacent points at the concave and convex transition area is *(kn × kn + 1 < 0)*. At the other locations, the k product is *(kn × kn + 1 > 0)*. When the k product equals 0, then *(kn × kn + 1 = 0)*, which indicates that the input is a line. For *(kn < 0),* the curve is convex; for *(k > 0)*, the curve is concave; for *(kn × kn + 1 = 0),* the curve is straight. Based on the results of these calculations, a custom print path is generated. Finally, based on the segmentation of the curve, the tool helps to arrange the actuator and constraint sections and their corresponding print path. This computational process aims to ensure that the shape of the physical specimen after the transformation is consistent with its original digital input.

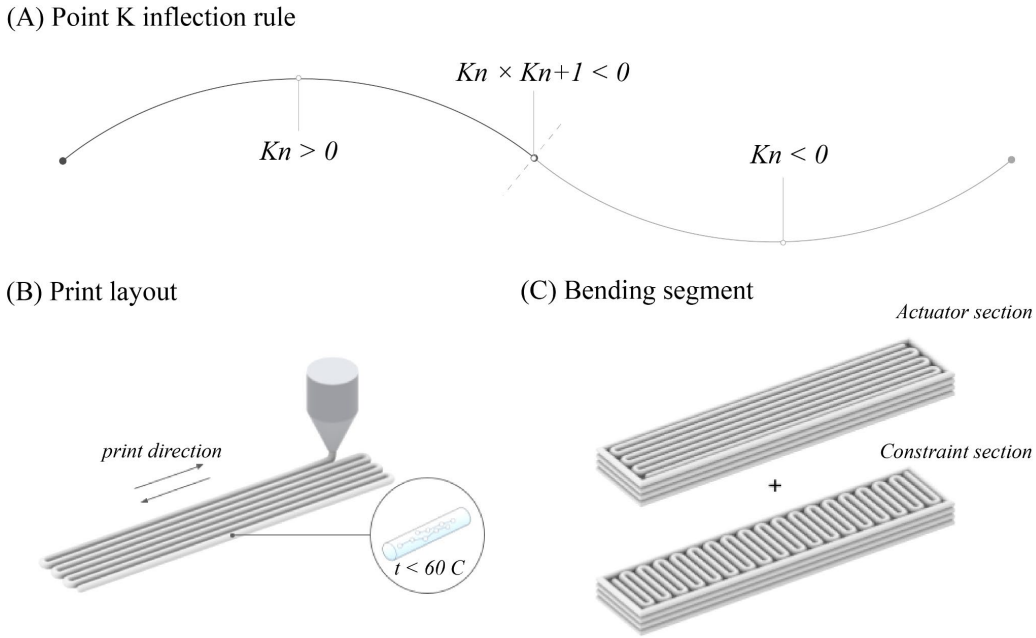


Figure 4. Thermoplastic 4D-printing actuator design rules. (A) Geometric rules defining the curve inflection. (B) Print direction. (C) Combination of the actuator and the constraint sections.

3.2.2 Textile 4D-printing tool

As introduced in Section 3.1, the textile 4D-printing consists of an FDM 3D-printing process on a pre-tensioned fabric covering the printing bed. The textile tension and the printed pattern allow for a three-dimensional deformation of the element once the tension is released (Figure 5). The digital design tools developed for textile 4D-printing are used to determine the print path, the layer height, the layer width, the number of layers, and the print speed. The layer height and width are the parameters that inform the beam cross-section based on empirical observation of each printed result. Print paths are generated using COMPAS Slicer library, and the resulting 3D print is visualized and validated in Rhino Grasshopper before sending it to the fabrication setup. This visualization includes the print path simulation, waiting time at each print point, and extrusion rate, all of which ensure successful print results.

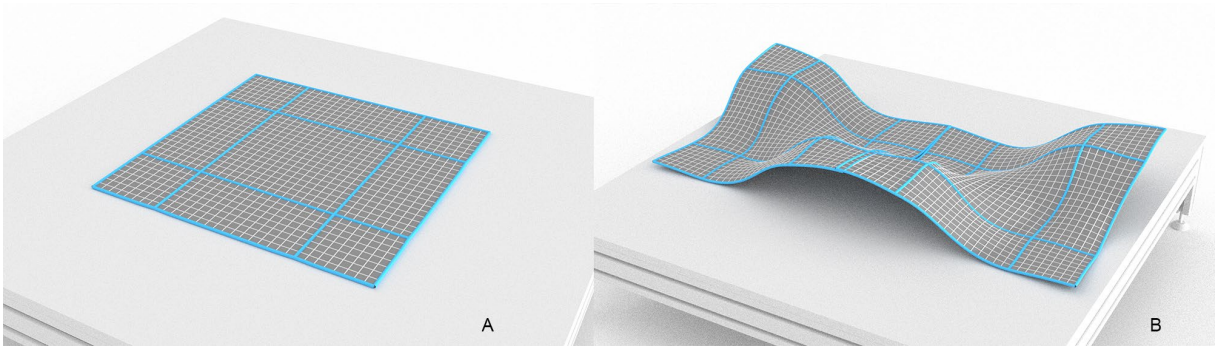


Figure 5. Textile 4D-printing: (A) Print before the tension is released, and (B) after the tension is released.

4. Experiments, results and discussion

This section explains the testing procedure to evaluate the feasibility of a large-scale 4D-printed concrete formwork. The first part focuses on the development of thermoplastic 4D-printing as a substructure for the formworks. The second part focuses on the steps involved in textile 4D-printing, ranging from the initial understanding of this technique to the prototypes. The third part details the testing and emergence of hybrid methods embedding the textile 4D-printing and the thermoplastic 4D-printed frame in one solution, which were then used in the production of the Open Column.

4.1. Thermoplastic 4D-printing experiments

Thermoplastic 4D-printing relied on the shrinking behavior of the shape memory polymer in a preheated water tank (Figure 6). During the printing process, polymer chains in the material were aligned along the extrusion direction and locked in a stretched position. When the material was reheated to above its glass transition temperature, the tension started to release, and the part tended to decrease in length along the direction of the printing path. Meaning, once reheated, the actuator section tended to shrink, and the constraint section (as introduced in Section 3.2.1) maintained its length, which caused the element to bend. The amount of shrinkage could be influenced by many factors, such as printing parameters, triggering temperatures, and material properties. Therefore, experiments compared and evaluated the feasibility of various material properties and fabrication parameters, and bending methods, as well as aimed to conduct material mechanism tests.

Most significantly, experiments confirmed previous findings; the bending angle could be controlled through the arrangement of the actuator and constraint layer. However, the thermoplastic 4D-printing result - the thermoplastic-activated mesh - was not viable as formwork for two reasons. First, the sprayed concrete did not fill the cells equally, resulting in an irregular surface. Secondly, the reaction of cement with the PLA frame created breakage because of the chemical reaction between the plastic mesh and the cementitious material. Those results guided us to protect the mesh from the concrete with a textile.

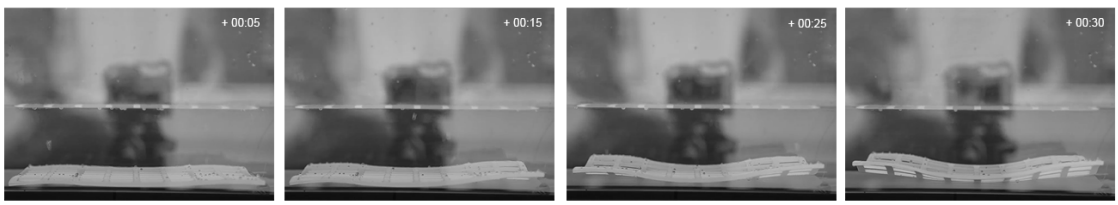


Figure 6. Thermoplastic 4D-printed prototype transformation in 65°C water tank.

4.2. Textile 4D-printing experiments

The initial experiments aimed to find an equilibrium between the tension of the pre-stretched textile and the compression resistance of the print path. The hierarchy between the inner print path and the outer print border governed the global shape of the printed textile. Meaning, the infill, referred to as a sub-pattern, controlled the local transformation and aimed to reinforce the global shape (Figure 7). These experiments helped to establish procedures for adjusting the thickness of the printed lines on the textile and controlling the connection between corners and parallel printed lines of a single pattern. Also, they enabled the calibration of the line thickness, the print speed, and the selection of a suitable textile for the process.



Figure 7. Transformation variations of textile 4D-printed prototypes with different sub-patterns.

To operate a robust print setup, wait times were derived from the point-to-point angle of the toolpath, while the print speed remained constant for the rest of the print path. The more advanced testing phase consisted of applying the parameters to a large variety of printable patterns (Figure 8) to explore the possibilities offered by such a 4D-printing strategy as well as to narrow the research scope down to a pattern that can support the GFRC spraying process.

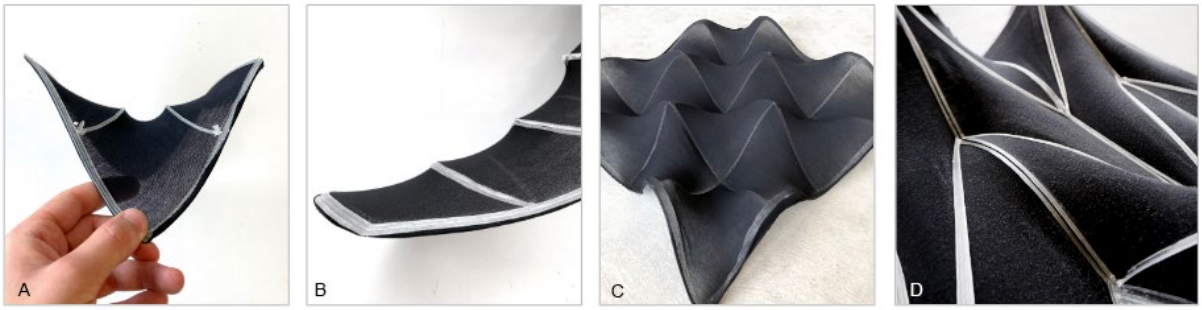


Figure 8. (A) Square with linear pattern, (B) Rectangle with linear pattern, (C) Square grid, (D) Diamond pattern.

For testing the spraying, the first series of experiments aimed to evaluate the capabilities of textile 4D-printing for medium-scale, modular building panels (Figure 9). Each design geometry was 750 mm by 750 mm, and the results created the final 1500 mm x 750 mm x 350mm (W x L x H) prototype panels. To stabilize the formwork, a custom mortar mix with a thickness of less than 1 mm on average was sprayed prior to the GFRC layer. The prototypes were then each sprayed with a GFRC layer and a finishing concrete layer and had an average thickness ranging between 5mm and 8mm.

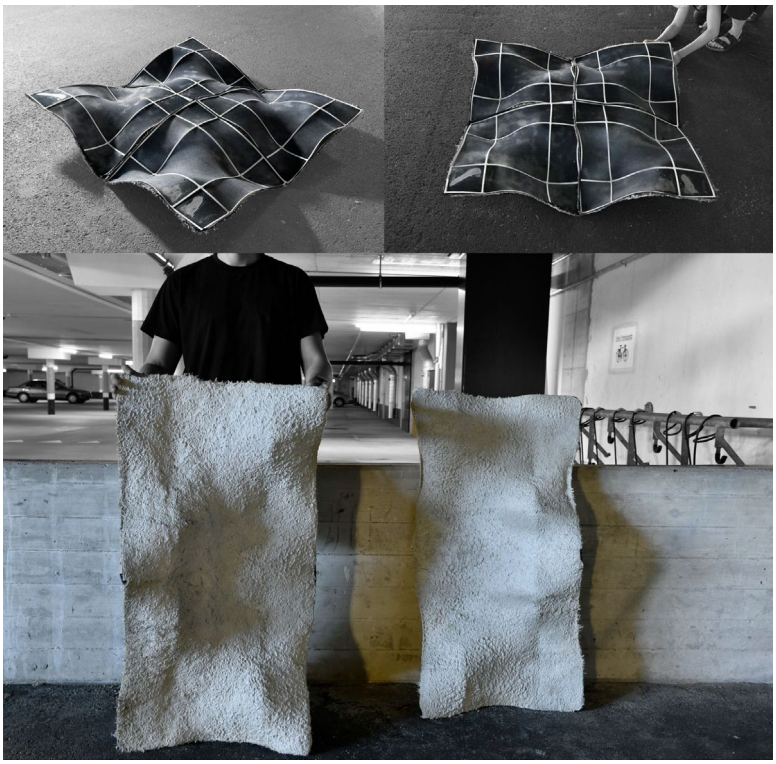


Figure 9. Textile 4D-printed modular panels and GFRC spraying.

4.3. Open Column

The Open Column (Figure 10) incorporates the two techniques presented in Sections 4.1 and 4.2. The goal was to take advantage of those complementary approaches and create a large-scale, doubly curved self-standing demonstrator, which was designed as a 2400 mm high vertical element. The Open Column structure was not optimized however, this particular form was chosen to express the design potentials of this 4D formwork fabrication technique while complying with the limitations described in Sections 4.1 and 4.2. In addition, it aimed to show two different surfaces of the 4D formwork, where the outside surface displayed the sprayed texture, and the inside surface showcased the textile as well as the thermoplastic frames. This demonstrator was composed of six custom-shaped thermoplastic 4D-printed frames. Each thermoplastic frame measured 750 by 840 mm with 25 mm beam edges. The frames were individually triggered at 65°C in a 200 L water tank. First assembled horizontally, the frames were glued together to receive the 2500 mm by 1500 mm textile reinforced with 3D printed ribs. The textile ribs were spaced 100 mm apart to ensure continuous tension and reinforce the textile between the frames. The frames and the textile were welded and sealed together using a hot blade to avoid using additional chemicals. To ensure the stability of the shape, 8 mm steel bar reinforcements were tied to the structure in both directions. This larger-scale demonstrator shows how concrete mass and time impacted and increased the deviation between the targeted shape and the actual result. Nevertheless, this was the first architectural scale 4D-printed formwork of its kind.



Figure 10. 2700 mm high open-column produced with 4D formwork, resulting from the combination of the two 4D-printing techniques and GFRC spraying.

5. Conclusions and outlook

The large-scale prototyping in this research demonstrates the potential of 4D-printing scalability and the use of it as 4D formwork for concrete structures. This research provides the first steps towards a formwork that can be lighter, thinner, and less labor-intensive to produce. The possibility to computationally pre-program a given 3D geometry and transfer it in a flat shape opens up the possibility of efficiently transporting large-scale formworks. This technology works thanks to physical reactions and material compatibility, using widely available materials – PLA, warm water, concrete, and textiles. In addition, the technology will be accessible and easily replicable for research and industry, thanks to the use of the open-source COMPAS framework.

Looking forward, further studies will have various options to optimize this process, for example, water tanks could be heated using natural and sustainable energies like sunlight. Also, building at a larger scale is very likely to lead to simpler and more standardized processes, so further research could investigate the behavior of much larger textile 4D-printed and thermoplastic 4D-printed prototypes.

Finally, improving the precision of these formworks will remain essential to their further development. Current prototypes presented in this research show a gap of 2 to 8mm between the physical and the 3D model in the central parts of the membranes, but we observe a 40 to 80 mm deviation at the edge. These inaccuracies in the final results demonstrate the need to investigate this technique further to reach a more stable and precise process. However, the demonstrators still confirm the potential of 4D-printing as a novel formwork production, taking the first steps for technological improvements to move toward a more sustainable way of building. They provide a perspective on how advanced digital techniques and non-standard formwork production could help to meet the sustainability goals of the near future.

Acknowledgments

This research was partially supported by the Swiss Innovation Agency and the Innosuisse program (Project no. 41139.1 IP-ENG). The authors acknowledge the guidance of Prof. Fabio Gramazio and Prof. Matthias Kohler and the support of MAS ETH in the Architecture and Digital Fabrication program. The authors would like to thank Nizar Taha, Theo Buergins, and Joris Burger for providing support, with the spraying process and the 3D-printing setup, respectively. Buergins Creations is acknowledged for its logistic and technical support and sponsorship.

References

[1] J. Watts, "Concrete: The most destructive material on earth," The Guardian, pp. 1–9, 2019.

[2] Dorking, The Global Cement Report – 12th Edition. Tradeship Publication, 2017. (Accessed October 7, 2022).

[3] J. Burger, E. Lloret-Fritschi, F. Scotto, et al., "Eggshell: Ultra-thin three-dimensional printed formwork for concrete structures," 3D Printing and Additive Manufacturing, vol. 7, no. 2, pp. 48–59, Apr. 1, 2020, ISSN: 2329-7662, 2329-7670. doi: 10.1089/3dp.2019.0197. [Online]. Available: https://www.liebertpub.com/doi/10.1089/3dp.2019.0197 (accessed on September 7, 2022).

[4] Schipper HR, Grunewald S. Efficient material use through smart, flexible formwork method. In: ECO-Crete Int. Symp. Environ. Friendly Concr. Iceland: Reykjavik, 2014; pp. 1–8.

[5] E. Lloret, From smart, dynamic casting to a growing family of Digital Casting Systems. Pergamon, 2020.

[6] J. Xiao, G. Ji, Y. Zhang, et al., "Large-scale 3d printing concrete technology: Current status and future opportunities," Cement and Concrete Composites, vol. 122, p. 104-115, Sep. 2021, ISSN: 0958-9465. doi: 10.1016/j.cemconcomp.2021.104115. [Online]. Available: https://linkinghub.elsevier.com/retrieve/pii/S0958946521001839 (accessed on June 7, 2022).

[7] J.Burger, et al. "Design and fabrication of a non-standard, structural concrete column using eggshell: ultra-thin, 3D printed formwork." Second RILEM International Conference on Concrete and Digital Fabrication: Digital Concrete 2020. Springer International Publishing, 2020.

[8] F. Zhang, L. Wang, Z. Zheng, Y. Liu, and J. Leng, "Magnetic programming of 4d printed shape memory composite structures," Composites Part A: Applied Science and Manufacturing, vol. 125, p. 105-571, Oct. 2019, ISSN: 1359-835X. doi: 10.1016/j.compositesa.2019.105571. [Online]. Available: https://linkinghub.elsevier.com/retrieve/pii/S1359835X19303203 (accessed on June 7, 2022).

[9] V. Diederik, M. West, and P. Block. "History and overview of fabric formwork: using fabrics for concrete casting." Structural Concrete 12.3 (2011): 164-177.

[10] M. West. The fabric formwork book: Methods for building new architectural and structural forms in concrete. Routledge, 2016.

[11] M. A. Popescu, "KnitCrete: Stay-in-place knitted formworks for complex concrete structures," Ph.D. dissertation, ETH Zurich, Zurich, Switzerland, 2019. doi: 10.3929/ETHZ-B-000408640. . http://hdl.handle.net/20.500.11850/408640 (accessed on June 7, 2022).

[12] T. Skylar, Self-Assembly Lab: Experiments in Programming Matter. Boca Raton, FL, USA: Taylor & Francis, 2016.

[13] A. Menges and S. Reichert, "Material capacity: Embedded responsiveness," Architectural Design, vol. 82, no. 2, pp. 52–59, Mar./Apr. 2012.

[14] G. Wang, H. Yang, Z. Yan, et al., "4dmesh: 4d printing morphing non-developable mesh surfaces," in Proceedings of the 31st Annual ACM Symposium on User Interface Software and Technology, Berlin, Germany, Oct. 11, 2018, pp. 623–635. doi: 10.1145/3242587.3242625. https://dl.acm.org/doi/10.1145/3242587.3242625 (accessed on 07/05/2021).

[15] D. B. Sitotaw, D. Ahrendt, Y. Kyosev, et al., "Additive manufacturing and textiles—State-of-the-art," Applied Sciences, vol. 10, no. 15, p. 5033, Aug. 2020.

[16] Self-Assembly Lab, "Active Shoes,". https://selfassemblylab.mit.edu/active-shoes. (Accessed: Mar. 10, 2023).

[17] L. Aldinger, G. Margariti, A. Körner, et al., "Tailoring self-formation fabrication and simulation of membrane-actuated stiffness gradient composites," in Proceedings of IASS Annual Symposia, 2018, pp. 1–8.

[18] J.Pérez, M.Otaduy, and B.Thomaszewski. "Computational Design and Automated Fabrication of Kirchhoff-Plateau Surfaces." ACM Transactions on Graphics (TOG) 36, no. 4 (2017): 1-12.

[19] Extrudr, "Extrudr - high-quality filament,". http://www.extrudr.com. (Accessed: Dec 27, 2022).

[20] N. Taha, A. N. Walzer, J. Ruangjun, et al., “Robotic AeroCrete – a novel robotic spraying and surface treatment technology for the production of slender reinforced concrete elements,” in collab. with J. P. Sousa, J. P. Xavier, and G. Castro Henriques, 10 p. 2019, Artwork Size: 10 p. Medium: application/pdf Publisher: ETH Zurich. doi: 10.3929/ETHZ-B-000387276. http://hdl.handle.net/20.500.11850/387276 (accessed on Mai 7, 2021).

[21] Robert McNeel & Associates, Rhinoceros 3D, 2020. https://www.rhino3d.com/. (Accessed: December 18, 2022).

[22] Robert McNeel & Associates, Grasshopper 3D, 2020.. (Accessed: December18, 2022).

[23] I. Mitropoulou and J. Burger, "COMPAS SLICER: Slicing functionality for COMPAS," Zenodo, Jun. 28, 2020. doi: 10.5281/zenodo.5910846. . https://compas.dev/compas_slicer/. (Accessed: Mar. 10, 2023).

IASS 2023
July 10–14 Melbourne
Integration of Design and Fabrication

Proceedings of the IASS Annual Symposium 2023
Integration of Design and Fabrication
10–14 July 2023, Melbourne, Australia
Y.M. Xie, J. Burry, T.U. Lee and J. Ma (eds.)

Additive manufacturing of fully recyclable walls solely made from renewables – a possible quantum leap in sustainable building construction

Benjamin KROMOSER[a,*], Bernhard REINHOLZ[a], Roman MYNA[a], Sara REICHENBACH[a], Falk LIEBNER[b], Rupert WIMMER[c]

[a,*] Institute of Green Civil Engineering, Department for Civil Engineering and Natural Hazards
benjamin.kromoser@boku.ac.at

[b] Institute of Chemistry of Renewable Resources, Department of Chemistry
[c] Institute of Wood Technology and Renewable Materials, Department of Material Sciences and Process Engineering
University of Natural Resources and Life Sciences, Vienna

Abstract

Bioresources like wood, its lignocellulosic constituents or other abundant biopolymers are of returning, enormous interest for our society. This includes their use as construction materials which is due, among others, to their great potential for lowering the carbon footprint of this industry sector. This advantage can be amplified by implementation of smart solutions allowing for multiple reuse of biopolymer based construction elements. Based on a recent study revealing the unique bonding/debonding capabilities of hot-pressed mixtures of equal quantities of corn starch and sodium lignosulfonate ("*BIOMIX*", [1]), this paper presents a novel technological approach targeting the additive manufacture of recyclable bio-based wall elements [1]. It is based on dry blending of wood particles with *BIOMIX* in a weigth ratio of 1:1 (referred to as "*BIOMIX-w*"), subsequent adjustment of a certain surface moisture, extrusion through a printing nozzle and final application of heat and pressure to facilitate bonding within and between the printed layers. Different from conventional adhesives, the bonds between the individual constituents can be re-opened by joint exposure to steam and gentle shear force, allowing for lossless reprocessing and recycling of all constituents.

Keywords: additive manufacturing, 3D printing of renewables, biobased construction materials, structural optimisation, sustainable building construction

1. Introduction

Global warming driven by the ever-increasing emission of greenhouse gases and the impending shortage of fossil resources have recently amplified global efforts towards a more biobased, circular economy. This development has also reached the building industry where sustainability is increasingly considered a key pillar that carries ecological, economical and societal responsibility [2]. This development is of particular importance as the construction industry is among those business segments that consume the most energy and raw materials, and simultaneously release large quantities of air pollutants [3]. Timber constructions are more favourable in this regard, but still far from being a showpiece considering sustainability. In Austria, almost 40% of all processed trees end up as by-products like saw dust, bark or wood chips [4], with the majority being thermally utilized releasing approximately 1.8 kg of carbon dioxide per kilogram of combusted material into the atmosphere. These numbers illustrate, that the wood construction sector only insufficiently takes advantage of the great ecologic potential of wood as one of the most valuable gifts of nature. This obstacle of low efficiency can be overcome by structural

Copyright © 2023 by Benjamin KROMOSER, Bernhard REINHOLZ, Roman MYNA, Sara REICHENBACH, Falk LIEBNER and Rupert WIMMER. Published in the Proceedings of the IASS Annual Symposium 2023 with permission.

optimization of buildings, co-utilization of by-products in material applications, and efforts to promote the transition towards implementation of circularity in wood product utilization [5].

Besides inefficient material usage, it is to note that the construction sector is increasingly lacking skilled craftsmen and craftswomen, especially in industrialized countries. This is of particular significance as the construction rates continue to mismatch the pace of rising demand for living space nourished by population growth and rising prosperity.

These diverging developments in the construction sector can be counteracted by implementation of fully automated design and construction processes. This paper proposes a newly developed approach for additive manufacturing of fully recyclable walls solely made from renewable resources, covering the entire lifecycle of a sustainable building construction, i.e. manufacture, multiple re-utilization and final composting.

Based on the unique properties of hydrophilic polysaccharides and the amphiphilicity of lignin, both providing excellent compatibility with wood, a novel "*BIOMIX*" blend has been recently developed that demonstrates intriguing adhesive properties for a broad variety of materials, including wood and concrete [6]. This fundamental work – targeting optimization of the blend and hot-press conditions as well as indicative tests of hydrolytic bond line cleavage – was the starting point for the advanced concept of up-scaled additive manufacturing presented here, which additionally includes wood particles as ternary filler (like stones in concrete) for *BIOMIX* (referred to as "*BIOMIX-w*") as well as hydrolytic disintegration under application of gentle shear force [1]. Thus, the novel 3D-printing approach comprises all of the above key aspects of sustainability in the construction sector.

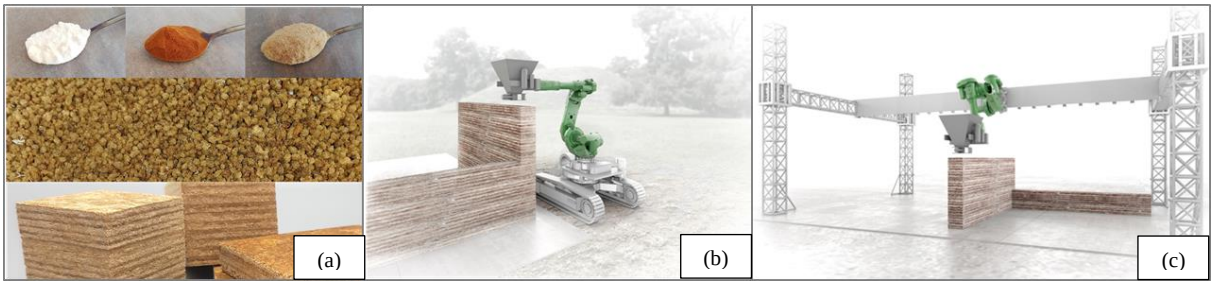


Figure 1: *BIOWALL* printing strategies

Using the example of spruce sawdust mixed with the components of *BIOMIX* in a 2:1:1 weight ratio, it had been demonstrated that an apparently dry blend of "*BIOMIX-w*", adjusted to a certain moisture content, can be processed semi-automatically either as fully-integrated alternative or via a granulate-based approach (Figure 1(a)). For full automation an industrial robot for either prefabrication or onsite 3D-printing could be a viable solution. As the printing head is an independent module, the carrier system can be alternatively connected e.g. to a portal system, as presented in Figure 1 (b)+(c). The produced *BIOWALL* specimens were furthermore confirmed to feature excellent recyclability by shear-aided moistening which provides a maximum of flexibility with regard to reshaping by printing. Since disintegration of *BIOWALL* succeeds at mild conditions, this process step is virtually lossless and preserves the chemical integrity of the individual components to full extent, the material can be reused in multiple cycles.

2. Preliminary data of semi-automated wall printing and environmental impact

Processing of *BIOMIX-w* can be accomplished following two different routes (Figure 2). The first approach, referred to as the fully-integrated concept, comprises of dry mixing three components, i.e. starch, lignosulfonate and wood particles, inside the printing head and offers the possibility of tribo-electric charging for the generation of additional porosity aiding sorption of moisture during subsequent processing (Figure 2a). The second approach includes the production of a granular *BIOMIX-w* blend for improved moisture uptake by capillarity as an intermediate step before printing (Figure 2b; [1]).

First tests exploring the potential of the above-mentioned approaches were conducted using solely *BIOMIX-w* at the standard wood-to-starch-to-lignin ratio of 2:1:1 (reference). Further tests included blends of *BIOMIX-w* with additives like sodium chloride powder or ash from beech bark, as well as processing of granular *BIOMIX-w* pre-manufactured by mixing the wood, starch and lignin in a ratio 2:1:1 under rotation using either spruce or oak sawdust as wood component.

Processing of these mixtures into small-scale *BIOWALL* specimens was accomplished employing the four-stage semi-automatic scheme outlined recently [1]. In brief, the respective *BIOMIX-w* blends – generated by dry mixing of the components (Figure 2(a)) or using pre-manufactured granules (Figure 2(b)) – were extruded through the discharge nozzle. Then, water in liquid phase was sprayed onto both sides of the thin layers to ensure partial solubilization of the adhesive components starch and lignin. Subsequently, the extruded layers were individually transferred manually into a heated hydraulic press to facilitate bonding within and between the layers. Once the desired height of the specimen was reached (typically more than 10 layers), they were equilibrated at standard climatic conditions (20°C, 65% rel. humidity) for one week and subsequently cut to obtain the size desired for the flexural (160 mm x 40 mm x 40 mm) and compressive testing (40 mm x 40 mm x 40 mm).

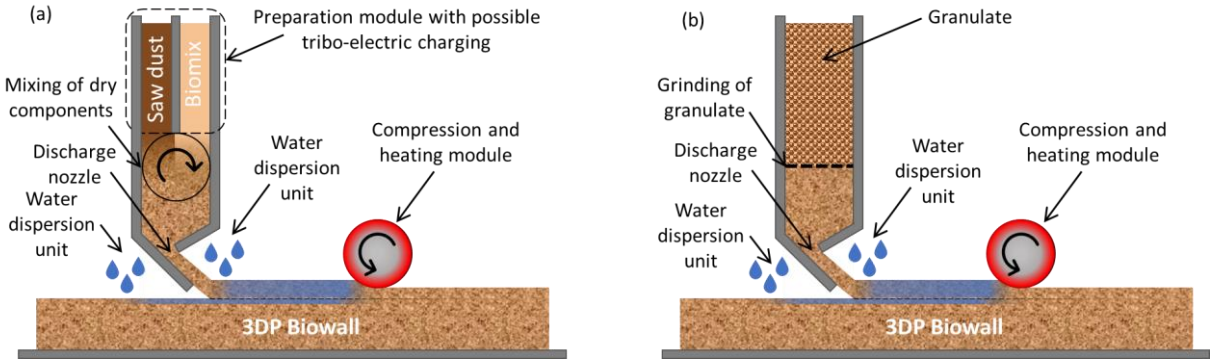


Figure 2: Schematic of the research printing approaches: (a) fully-integrated ; (b) granulate-based [1].

The results, shown in Figure 3, clearly confirm that both compressive and flexural strength of the layer-by-layer *BIOWALL* #1-3 assemblies prepared by the fully-integrated approach with *BIOMIX-w* strongly depend on their apparent density and, hence, by the used process conditions. Using *BIOWALL* #3 as reference the data furthermore reveal, that the addition of either powdered NaCl or ash from beech bark at mass ratio of approx. 30% relative to *BIOMIX-w* has only a marginal impact on the mechanical properties, despite their significant contributions to the bulk density of the specimens prepared. Processing of these blend types at harsher hot-press conditions is subject of ongoing work.

The usefulness of pre-manufacturing granular *BIOMIX-w* is not evident at first glance from the data of Figure 3, since the density-normalized mechanical performance of the respective assemblies does not exceed that of variant *BIOWALL* #3, no matter whether spruce (44,79wt% water) or oak (16,81wt% water) sawdust was used. However, due to the better options for controlling homogenous moistening and considering the shorter pressing times required (120 vs. 180 seconds), the granulate based approach will be further pursued.

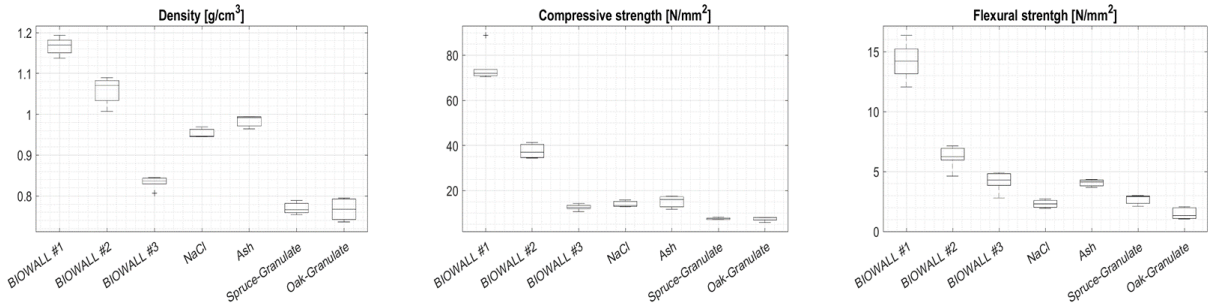


Figure 3: Mechanical properties of first test series

Besides mechanical testing, a preliminary life cycle assessment (LCA) was conducted evaluating the environmental impact of the additive Biowall production steps A1-A3, which comprises raw material supply, transport, and processing. Besides energy consumption (renewable and non-renewable resources), the potentials for global warming, ozon depletion (reference trichloofluoromethane; CFC-11), acidification and eutrophication were roughly estimated (Figure 4). Distinction is made between primary and secondary resources, where primary describes a material that is specifically produced for an application while secondary resources refer to by-products or even waste materials. The LCA results confirm that starch has the highest environmental impact, followed by lignosulfonate. Therefore, this project also envisages testing of secondary resources for potential replacement of one or even both primary resources.

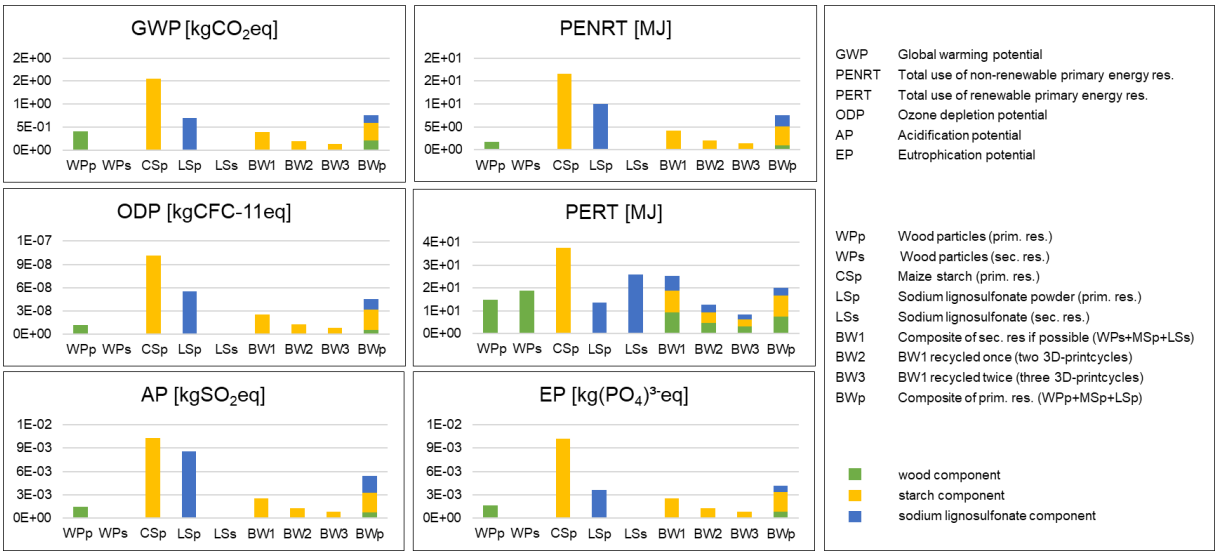


Figure 4: LCA of the *BIOWALL* material [1]

3. Fully automated production process

The independent development of printing head and carrier system as a key element of this project ensures a maximum of flexibility with regard to production techniques or even the site where the *BIOWALL* is printed. Depending on factors, such as climatic or weather conditions, manpower or accessibility of the construction area, the modular concept allows for either offsite prefabrication on an industrial robot system maintaining constant conditions, transport of respective blends to the construction site using a mobile portal system or its onsite prefabrication and feeding into the printing head using a mobile carrier system, as shown in Figure 1 (b)+(c).

Currently three main technologies are available for 3D-printing: 1) Extrusion of highly viscous pastes like melted thermoplastics which solidify upon cooling or cement paste that requires subsequent drying,

2) application of liquid layers hardening by physical or chemical crosslinking like photo-polymerisation and 3) melt-bonding of fine-grained powder similar as accomplished by direct selective laser sintering of metals [7]. Different from all aforementioned approaches, this paper introduces a novel technology targeting additive manufacturing of wood providing the strong asset of multiple recyclability and re-printing at zero synthetic adhesive requirement.

The sequence of final steps currently taking place in the printing head are 1) dry extrusion of *BIOMIX-w*, 2) double-sided moistening of the layer formed and 3) simultaneous application of pressure and heat (*cf.* Figure 2). While automated discarding and moistening has been satisfyingly implemented, further optimization in terms of heating temperature and rate as well as pressure regime is required for the final hot-press stage. This is necessary to shorten the current impracticably long heating times of 2-3 minutes, required to remove the excess of moisture for each of the most recently printed *BIOMIX-w* layers, to a reasonably short time period in the seconds range.

In particular the replacement of the current spray-moistening by steam is promising due to its higher wetting surface, faster penetration of small pores, and formation of thinner and more homogeneous moisture layers, thus supposedly promoting homogeneous solubilization, gelatinization and plasticization of *BIOMIX-w* components. Success provided, significantly less water and, hence, energy for its removal would be needed. Alternatively, it is to be tested to what extent the addition of water can be entirely omitted when *BIOMIX* is blended with fresh sawdust, which typically contains 12-50% wt.% water, instead of only up to 11wt.% in the case of dry sawdust used within the initial experiments (*cf.* Figure 3). This measure, implemented by a upstream process stage producing a granular *BIOMIX-w* blend, would clearly reduce technical complexity, energy and water consumption, at simultaneously improved process reliability with a more even moisture distribution.

In order to provide proof of concept for both alternative approaches, test specimens were produced analogous to those of the preliminary tests. Suitable compression rates and hot-press conditions (15-30 sec, temperatures higher than 150°C) were determined to ensure uniform apparent bulk density (ca. 1.0 g cm^{-3}) as a prerequisite for comparing their mechanical performance. Intriguingly, a significant reduction of pressing time could be achieved compared to the initial experiments. While it was still 30 seconds during steam moistening, the pressing was reduced to 15 seconds when fresh sawdust was used to prepare granular *BIOMIX-w* in the additionally implemented upstream process stage. Mechanical performance of the obtained samples (Figure 5(a)) was assessed after equilibrating them at 65%RH and 20°C for one week.

The behavior of the specimens under compression can be seen in Figure 5(c). The dry and moistened specimens are compared to the *BIOWALL* #2 specimens from the previous tests as they are all in a region of similiar density. For this density the moistened granulate-based approach shows the highest compressive strength (Figure 5(c) middle) together with a higher compression rate than that of the dry granulate-based approach (Figure 5(b)). Thus looking at the modulus of elasticity the values for the specimens produced without water addition are the highest. Although needing six or even twelve times the pressing time, the *BIOWALL* #2 specimens cannot exceed the characteristics of the specimens made from granulate.

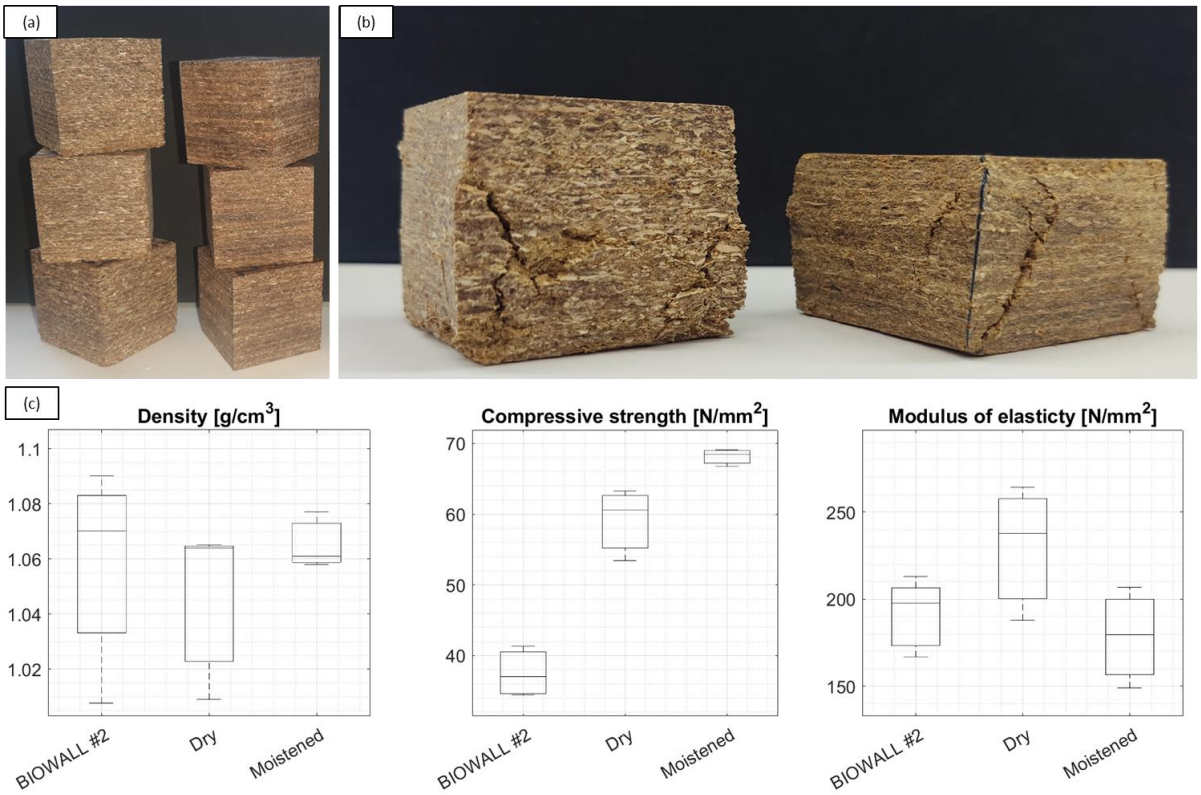


Figure 5: Compression tests of granulate-based small-scale specimens: (a) dry specimens (left) and moistened specimens (right); (b) test specimens after compression test; (c) mechanical properties

The first fully automated tests using a robot system relied on a combination of both steam moistening of the granular material prior and post discharging to promote intra- and inter-layer bonding. Removal of excess water was accomplished by connecting the discharging nozzle with a module consisting of a heated rotating cylinder to apply pressure and a heated plate to extend the time of heat input as the contact area between solely the cylinder and material bed would be too small. This first prototype of the modified printing head was mounted on an IRB 7600-325/3.1 industrial robot system at the robot laboratory of the Institute of Green Civil Engineering (ABB Group; Figure 6(a)), operated at a printing speed of 1 m min^{-1}.

However, despite maintaining a heating temperature over 200°C, three heating passages per layer were required for sufficient drying, as areas with high water content still present after the first and second repetition (dark regions in Figure 6(b)). The first three layers – each being 1,5 mm thick – of a *BIOWALL* assembly printed with the industrial robot system are shown in Figure 6(c)+(d). After removing the assembly from the printing bed and subsequent cooling, thermomechanical warping was observed (Figure 6 (d)) as known from FDM 3D-printing technologies.

While these tests can be regarded as proof of concept, further technology and material development is required since the mechanical performance of the samples did not yet reach that of the preliminary batch tests due to insufficient ensemble of material characteristics and production management.



Figure 6: Pictures of the first fully automated 3D printing tests. Printing head connected to the robot system (a), heating of the first layer (b), three-layer *BIOMIX-w* assembly prior to (c) and after detaching from the printing bed (d)

4. Conclusion

The results of this work confirm that fully automated 3D-printing of wood particles, embedded into a fully biobased adhesive system, is feasible. Improvement of moisture, heat and pressure management as well as material will be subject of ongoing work to unfold the full potential of the novel bio-blends for additive manufacturing of BIOWALL systems. Based on the results of this optimisation work, the life cycle assessment of this study will be further refined.

Acknowledgements

This research is funded by FFG, the Austrian Research Promoting Agency under the THINK.WOOD initiative (project 41132360). Furthermore, the authors would like to acknowledge their company partners Rubner Holzindustrie Gesmb, CRS Control & Robot Service GmbH and AustroCel Hallein GmbH.

Beside that the authors would like to thank Lorenz Matzinger and Eleonore Weininger for their valuable contributions centred around the recyclability of BIOMIX-w in the course of the 2022 Student Talent Action granted by FFG (Project 44703140), as well as Raphaela Hellmayer for supervising that work.

References

[1] B. Kromoser, S. Reichenbach, R. Hellmayr, R. Myna, und R. Wimmer, “Circular economy in wood construction – Additive manufacturing of fully recyclable walls made from renewables: Proof of concept and preliminary data”, Constr. Build. Mater., Bd. 344, S. 128219, Aug. 2022, doi: 10.1016/j.conbuildmat.2022.128219.

[2] M. Pfeiffer, A. Bethe, und C. P. Pfeiffer, Nachhaltiges Bauen: wirtschaftliches, umweltverträgliches und nutzungsgerechtes Bauen. München: Hanser, 2022.

[3] F. Krausmann, C. Lauk, W. Haas, und D. Wiedenhofer, “From resource extraction to outflows of wastes and emissions: The socioeconomic metabolism of the global economy, 1900–2015”, Glob. Environ. Change, Bd. 52, S. 131–140, Sep. 2018, doi: 10.1016/j.gloenvcha.2018.07.003.

[4] “Branchenbericht 2019/2020: Ein Rohstoff voller Leben. Holz.”, Fachverband der Holzindustrie Österreichs, 2020. [Online]. Verfügbar unter: https://www.wko.at/branchen/industrie/holzindustrie/branchenbericht-2019-2020.pdf

[5] C. Mair und T. Stern, “Cascading Utilization of Wood: a Matter of Circular Economy?”, Curr. For. Rep., Bd. 3, Nr. 4, S. 281–295, Dez. 2017, doi: 10.1007/s40725-017-0067-y.

[6] R. Hellmayr u. a., “Heat bonding of wood with starch-lignin mixtures creates new recycling opportunities”, Mater. Today Sustain., S. 100194, Juli 2022, doi: 10.1016/j.mtsust.2022.100194.

[7] S. Das und J. J. Beaman, “Direct Selective Laser Sintering of Metals”, US 6,676,892 B2, 13. Januar 2004

IASS 2023
July 10–14 Melbourne
Integration of Design and Fabrication

Proceedings of the IASS Annual Symposium 2023
Integration of Design and Fabrication
10–14 July 2023, Melbourne, Australia
Y.M. Xie, J. Burry, T.U. Lee and J. Ma (eds.)

Additively manufactured steel joints for structural frames: concept proposal and numerical simulations

Seyed Pouya AFSHAR IMANI[a,*], Mani KHEZRI[a], Kim J.R. RASMUSSEN[a]

[a,*] School of Civil Engineering, The University of Sydney, Sydney, 2006, New South Wales, Australia
safs3478@uni.sydney.edu.au

Abstract

Connections are essential components of steel structural systems as their properties greatly influence the global response and control the collapse behaviour. The conventional approach for the design and analysis of structural frames offers a narrow range of pre-defined connection types and limited scope for optimising their rigidity and strength, and the fabrication of connections is labour-intensive. The novel and advantageous features of Wire Arc Additive Manufacturing (WAAM) can be exploited to address these challenges and produce connections with superior characteristics. This study aims to investigate the potential application of additively manufactured connections for steel frames by introducing an alternative conceptual design achieved by topology optimisation showing a superior structural performance to that of conventionally designed connections. An extended bi-directional evolutionary structural optimization (BESO) technique based on discrete variables is adopted to deliver optimised connections considering material non-linearities. Numerical simulations are carried out on simple beam-column connections to quantify the structural benefits achievable by topology optimisation compared to a conventional design solution. Moreover, the structural performance of a two-storey steel frame assembled using the optimised connection solutions is compared to that of a frame constructed using conventional welded connections.

Keywords: topology optimisation (TO), bi-directional evolutionary structural optimisation (BESO), additive manufacturing (AM), steel frame, conceptual design, structural connection

1. Introduction

Topology optimisation is recognised as a means of achieving advanced and economically rewarding structural designs [1]. Among the most recent and well-known topology optimisation strategies for continuum structures, the Homogenization Method [2], Solid Isotropic Material with Penalisation (SIMP) Method [3], Level-set Method [4] and Evolutionary Structural Optimisation (ESO) Method [5] are widely referenced in the literature. The ESO method is grounded on the idea of gradually removing material from inefficient parts of a structure to evolve towards an optimum solution. The Bi-directional Evolutionary Structural Optimisation (BESO) which was further developed from the ESO method [6], also enables material to be added simultaneously at efficient locations of the structure. In pursuing a more realistic design, the implementation of material non-linearity in optimisation algorithms has also been investigated [7]. In the context of connection components produced through additive manufacturing (AM), the highly non-linear stress-strain behaviour under large deformations is important as is fabrication-related constraints imposed on the geometry of the optimised topology. Inclusion of minimum feature and cavity sizes that are bound by the resolution of printing and post-treatment machining tools [8] accounting for self-supporting geometric features [9] and anisotropy in mechanical response [10] are examples of such fabrication-related constraints imposed on topology optimisations.

Applications of AM in the construction of metallic structures have been reported by several groups, including Arup's design of an optimised space node using powder-based methods [11], and MX3D's

Copyright © 2023 by Seyed Pouya AFSHAR IMANI, Mani KHEZRI and Kim J.R. RASMUSSEN. Published in the Proceedings of the IASS Annual Symposium 2023 with permission.

fully functional steel pedestrian bridge, for which the design capacity was also determined through numerical and experimental investigations [12]. While the early uses of metal additive manufacturing in construction have primarily featured modest-scale components such as façade nodes and small connections, the fabrication of large-scale components are currently being developed using the more recent WAAM technique. Therefore, it is expected that a framework suitable for the optimisation and design of large-scale additively manufactured structural components will be in demand in the near future, as pursued in this paper.

The paper is organised as follows: Section 2 describes the optimisation exercise, performed by integration of a Python-based extended BESO script with the well-established Finite Element (FE) package ABAQUS [13] as the analysis engine. Section 3 presents numerical simulations on a simple connection between a beam and a column, designed through structural optimisation and using conventional structural connections, and subjected to various load cases. Section 3 also compares the structural responses of two-storey frames featuring optimised and conventional structural connections. Section 4 draws conclusions from the study.

2. Structural optimisation methodology

2.1. Bi-directional Structural Optimisation (BESO) for continuum structures

2.1.1. Sensitivity numbers

Structural optimisation problems aim to place the material at the most effective location for a design domain subjected to predefined objectives, constrains, loads and boundary conditions and are generally formulated with the objective to maximise stiffness. In order to maximise the stiffness of the structure while ensuring that the structure can bear loads up to the maximum design load (F^*), the complementary work (W^c) depicted in Figure 1 shall be minimised. The basic problem can be described mathematically as:

$$\textbf{Minimise}: f_1'(x) = W^c = \left[\frac{1}{2}\lim_{n\to\infty} \Delta F^T (U_i + U_{i-1})\right] \tag{1}$$

$$\textbf{Subject to}: K(U)U = F$$

$$R = F - F^{int}(U) = 0$$

$$V^* - \sum_{i=1}^{nelem} x_e v_e = 0$$

where U and F represent the nodal displacement and force vectors, respectively, the stiffness matrix $K(U)$ is a function of U in a non-linear problem sourced from material or geometrical non-linearities, i denotes the increment number in the total of n load increments and V^* is a prescribed target volume fraction for the optimisation task. Since BESO is a discrete optimisation procedure, design variables x are assigned to individual finite elements (e). In a "soft-kill" scheme, these binary variables can be taken either of the following values:

$$x = x_{min} \ \ (\text{void}) \text{ or } 1.0 \ \ (\text{solid}) \tag{2}$$

While the solution for the equilibrium of linear elastic problems can be determined explicitly, when the response of the structure is non-linear, an iterative scheme needs to be adopted [7] which typically reduces the residual error **R** between the external and internal force vectors to 0 to achieve an equilibrium solution.

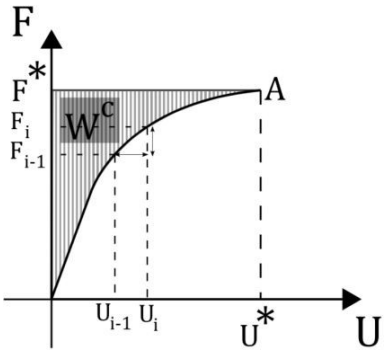


Figure 1. Load-displacement curve for a non-linear continuum structure.

2.1.2. Sensitivity numbers

Considering a non-linear load-displacement behaviour (Fig. 1), the variation of the elemental strain energy with design variable x_e can be derived as [7]:

$$\alpha_e = x_e^{p-1} \lim_{n\to\infty} \sum_{i=1}^{n} \left(E_{e,i} - E_{e,i-1}\right) = x_e^{p-1} E_{e,n} \tag{3}$$

in which $E_{e,n}$ specifies the final elemental strain energy comprised of elastic and plastic components. The smoothed sensitivity number ($\hat{\alpha}_e$) is then calculated to eliminate the mesh-dependence of the solution [14]:

$$\hat{\alpha}_e = \frac{\sum_v (w(r_{v,e})\alpha_e)}{\sum_v w(r_{v,e})} = \sum_v \frac{w(r_{v,e})}{\sum_v w(r_{v,e})} \alpha_e \tag{4}$$

where the weight factor is determined based on the number of *v* elements in the vicinity of element *e* as:

$$w(r_{v,e}) = \max(0, r_{min} - r_{v,e}) \tag{5}$$

where $r_{v,e}$ specifies the Euclidean distance between the centres of elements *v* and *e* and r_{min} specifies the prescribed filter radius, typically taken as ~ 2–3 times the element length (l_e). In order to relax the convergence of the solution, the elemental sensitivities are averaged between the *j*th and *j*-1th iteration yielding the modified elemental sensitivity number as:

$$\hat{\alpha}_e = \frac{\hat{\alpha}_{e,j} + \hat{\alpha}_{e,j-1}}{2} \tag{6}$$

Prior to removal/addition of any elements, the target evolutionary volume for the next iteration needs to be determined:

$$V_{j+1} = V_j(1 \pm ER) \quad (j = 1, 2, 3, \dots) \tag{7}$$

where ER denotes the evolutionary rate, typically taken as 1% or 2%. Depending on whether the objective volume (V^*) has been reached, the target volume may increase or decrease. Once the objective volume has been achieved, it will be kept constant. The elements are then sorted according to their sensitivity numbers ($\hat{\alpha}_e$) and compared to a threshold sensitivity α_{th} aiming to deliver the target volume, retaining elements possessing the highest sensitives and deleting elements with the lowest sensitivities at each iteration [15]. The convergence criterion for the complementary energy is checked at each iteration:

$$\text{error}_j = \frac{\left(\sum_{k=1}^{N} W_{j-k+1}^c\right) - \left(\sum_{k=1}^{N} W_{j-k-N+1}^c\right)}{\sum_{k=1}^{N} W_{j-k+1}^c} \leq \text{tol} \tag{8}$$

where *N* describes the integral number and is usually taken between 2–5 [7].

2.2. Multiple load cases

The optimisation of structural connections needs to consider that the building is subject to multiple load cases (gravity, wind, earthquake, etc.) and combinations thereof over the course of its design life. In order to account for the contribution of each load case in determining the overall performance of the structure, the elemental sensitivity numbers ($\hat{\alpha}_e$) introduced in Eq. (4), are instead calculated using the sum of elemental strain energy values of all different load cases [15] as:

$$\alpha_e = \sum_{m=1}^{M} \alpha_{e,m} \tag{9}$$

Where m denotes the number of load case in the total of M cases considered for the simulation and $\alpha_{i,m}$ represents the ith elemental sensitivity number corresponding to mth load case. Furthermore, the objective function is modified to include:

$$W_j^c = \sum_{m=1}^{M} W_{j,m}^c \tag{10}$$

where $W^c_{j,m}$ indicates the complementary work done at each iteration by each load case m contributing to the overall work done by the structure at each iteration W^c_j.

2.3. Material non-linear model

The connection was assumed to be manufactured from AISI 316L stainless steel, for which, in the elastic range, the isotropic response is defined by a Young's modulus of 190 GPa [16] and Poisson's ratio of 0.3. In the ABAQUS finite element package, they are defined using the *ELASTIC, TYPE = ISOTROPIC for three-dimensional simulations. Moreover, in order to account for plastic deformations beyond the yield point, a two-stage Ramberg-Osgood material model was used to describe the full-range stress-strain relationship [16]:

$$\varepsilon = \frac{\sigma}{E_0} + 0.002\left(\frac{\sigma}{\sigma_{0.2}}\right)^n \qquad for\ \sigma \le \sigma_{0.2} \tag{11}$$

$$\varepsilon = \frac{\sigma-\sigma_{0.2}}{E_{0.2}} + \varepsilon_u\left(\frac{\sigma-\sigma_{0.2}}{\sigma_u-\sigma_{0.2}}\right)^m + \varepsilon_{0.2} \qquad for\ \sigma > \sigma_{0.2} \tag{12}$$

where $\sigma_{0.2}$, E_0 describe the 0.2% proof stress and initial Young's modulus, n and m denote the strain-hardening and degree of hardness components, respectively. The implementation in ABAQUS was completed using the *PLASTIC command and specifying a multi-linear curve (Fig. 2) of true stress against true plastic strain, as obtained from the engineering stress-strain curve (Eqs. (11,12)) also shown in Figure 2.

Table 1. Input parameters for AISI 316L stainless steel [16].

$\sigma_{0.2}$ (MPa)	σ_u (MPa)	ε_u (%)	n	m
316	616	51	5.88	2.2

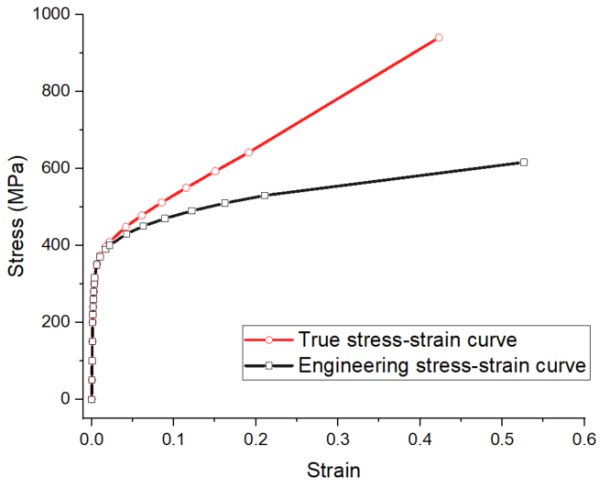


Figure 2. Plot of engineering stress-strain using two-stage Ramberg-Osgood relationship.

3. Numerical simulations

3.1. Structural frames and connections

Frame structures are the most widely used systems in the construction of residential and commercial buildings. Connections of such systems are employed to withstand and transfer the combined forces imposed by all connecting structural elements (i.e. beams, columns, lateral bracings, etc.) towards the supporting base. Consequently, it is crucial that they maintain strength and stability while all the connecting elements are in service. In other words, connections must be able to transfer the full capacity of their connecting members. In the context of engineering design, frames must function under a combination of gravitational loads such as permanent (dead) and imposed (live) actions as well as lateral forces such as wind- and earthquake-induced actions. A three-storey commercial frame with a total height of 15 m has been considered for the current study as is shown in Figure 3. The beams and columns in the system have total lengths of 8 meters and 4 meters, respectively, and I-shaped cross-sections with overall depths of 360 mm and 300 mm respectively as is shown in Figure 3.

The assessment of the structural behaviour of the frame system was conducted using the Ultimate Limit State (ULS) provisions of the Australian loading standard AS1170 considering gravity and earthquake loads. An importance level of 2 (ordinary) and a design life of 50 years were assumed in the design. The permanent (dead, G) and imposed (live, Q) actions were determined in accordance with AS1170.1, while the lateral earthquake loads (E) were determined using the provisions of Section 5.4.2 of AS1170.4 for a structure with an overall height less than 15 meters ($F_i = K_s[k_p Z S_p/\mu]W_i$). The combinations of actions considered for the strength assessment were obtained from Section 4.2.2 of AS1170.0, as shown in Table 2, resulting in a total of 9 load cases. A geometric and material non-linear analysis of the frame was undertaken using the material model defined in Table 1.

Table 2. Load combinations for strength.

Item	Name	Combination
1	Gravity	$1.2G + 1.5Q$
2	Earthquake-x	$1.0G + \psi_e Q \pm 1.0E_x \pm 0.3E_y$
3	Earthquake-y	$1.0G + \psi_e Q \pm 0.3E_x \pm 1.0E_y$

NOTES:

1. The reduction factor ψ_e was selected as 0.3 for residential building.

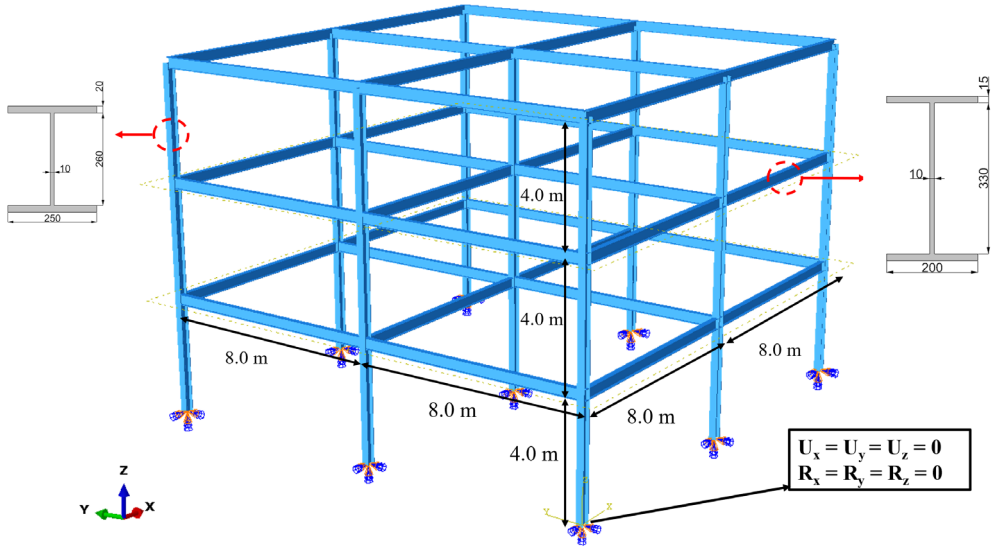


Figure 3. Isometric view of the structural frame and boundary conditions. Sectional dimensions are expressed in millimeters.

3.2. Engineering design

Conventionally, steel members are connected through bolting or welding. The latter is assumed in this study. The conventional welded connection between the beam and column shown in Figure 4 can be designed for strength by providing sufficient capacity to transfer all predicted structural actions from the frame analysis, as summarised in Table 3. The thickness of the fillet weld group can then be determined in accordance with Clause 9.6.3.10 in AS4100.2020 as:

$$v_w^* \leq \phi v_w = \phi \times (0.6 f_{uw} t_t k_r) \tag{13}$$

$$t_t = \frac{v_w^*}{\phi \times (0.6 f_{uw} k_r)} \tag{14}$$

Considering an E55 grade electrode, with a minimum ultimate nominal strength of 620 MPa, the required nominal throat thickness of 6.4 mm will be required.

Table 3. Stress components applied on the weld group considering a unit thickness for the weld group (t_t = 1 mm).

Stress component	**Gravity** (MPa)	**Earthquake-x** (MPa)	**Earthquake-y** (MPa)
$f_a = \frac{N^*}{A}$	20.7	25.7	20.7
$f_{vx} = \frac{V_x^*}{A}$	171.6	172.6	133.4
$f_{bx} = \frac{M_x^* \times (D/2)}{I_{xx}}$	1831.3	1850.4	1429.3
$f_{vy} = \frac{V_y^*}{A}$	0	0	0
$f_{by} = \frac{M_y^* \times (b_1/2)}{I_{yy}}$	0	0	0
$f_r = \sqrt{(f_a + f_{bx} + f_{by})^2 + (f_{xy})^2 + (f_{vy})^2}$	1860.0	1884.0	1454.0

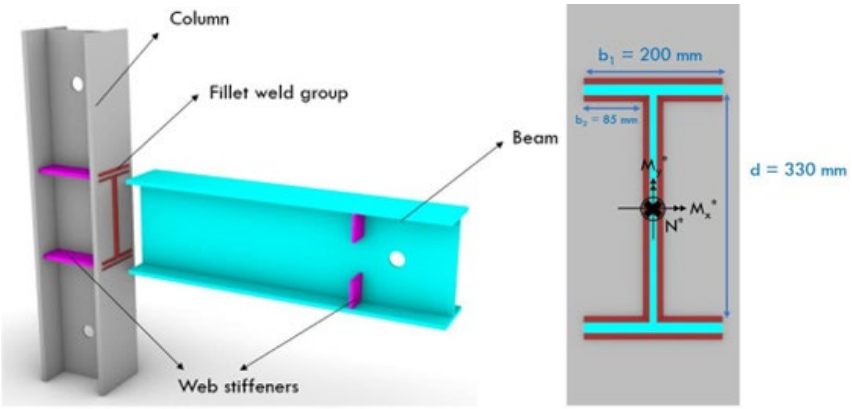


Figure 4. Engineering design: (a) isometric CAD view of the connection components, (b) active structural actions on the group of weld.

3.3. Optimisation of additively manufactured connection

The beam-column joint introduced in Section 3.2 is designed for additive manufacturing using the topology optimisation scheme presented in Section 2. In order to initiate the optimisation, a design domain needs to be defined. A rectangular design domain of 720 × 480 × 250 mm was chosen as shown in Figure 5. In order to generate the design stress flow through the connection, the structural actions obtained from the frame analysis described in Section 3.1 were applied to the top of the column and tip of the beam as tractions while the lower end of the column was fixed (Fig. 5b). The finite element mesh was created using a total of 33612 C3DR8 three-dimensional solid elements in ABAQUS.

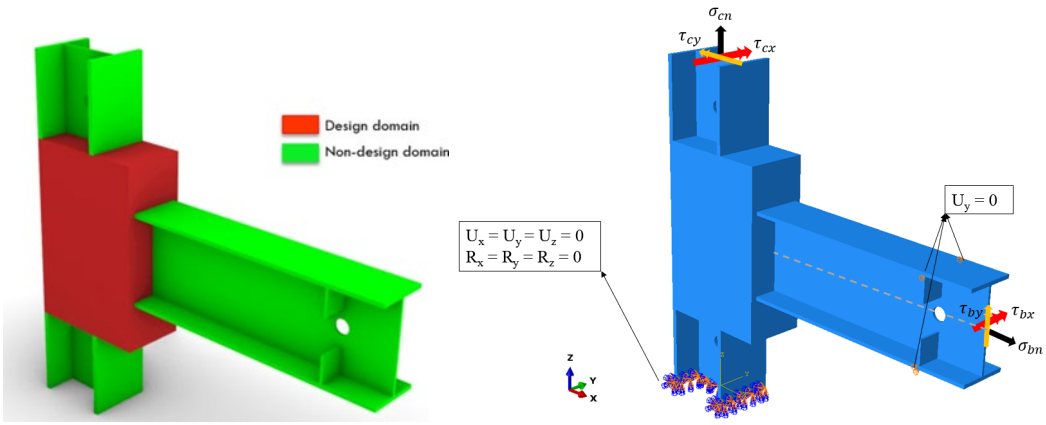


Figure 5. Initial design domain: (a) isometric CAD view, (b) applied boundary conditions in ABAQUS.

The topology of the final design of the optimised joint, presented in Figure 6, is distinctively different from that of the conventional welded joint (Fig. 4). In the optimisation, the target volume fraction was set to match the total mass of the conventional welded connection within a small margin. The mass of the final design was determined as 100.7 kg, which was within 5% of the total weight of the convectional welded connection shown in Figure 4. A total of 77 iterations were completed during the optimisation task after which only 7096 design variables (x_e) in the design domain were forced to be solid. Figure 7 shows the evolution of the topology and the distribution of von Mises stress. The latter demonstrates where the material is least stressed and helps to understand the gradual change of topology. The reinforced areas near the flanges of the beam are apparent, while the less effective central region of the web has gradually been eliminated. Furthermore, the primary compressive stress flow resulting from

the combined axial and bending actions on the column has been redirected through the connection zone to converge towards the flow of compressive stress in the lower flange of the beam.

The final stage of the conceptual design process for an optimised topology involves the smoothening of the finite element model into a manufacturable part and subsequent evaluation of the strength and behaviour of the optimised design. The final smoothed geometry was achieved by applying non-uniform rational B-splines (NURBS) to the boundary nodes of the tessellated FEM mesh. This task could be cumbersome, given the stepwise tessellated faces and existing non-manifold edges. For this purpose, the additive manufacturing CAD software Fusion 360 [17] was implemented to first re-construct the solid geometry from the ABAQUS-generated STL file, then smooth and export the geometry to ABAQUS for FE re-evaluation.

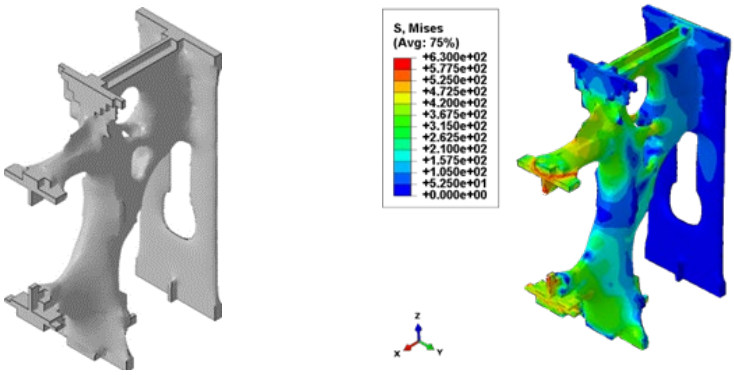


Figure 6. Manufacturable joint: (a) smoothed CAD design for the optimised joint, (b) von Mises stress distribution (MPa).

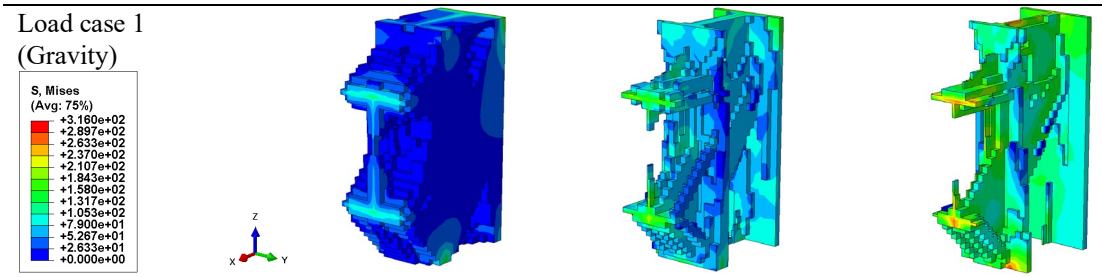
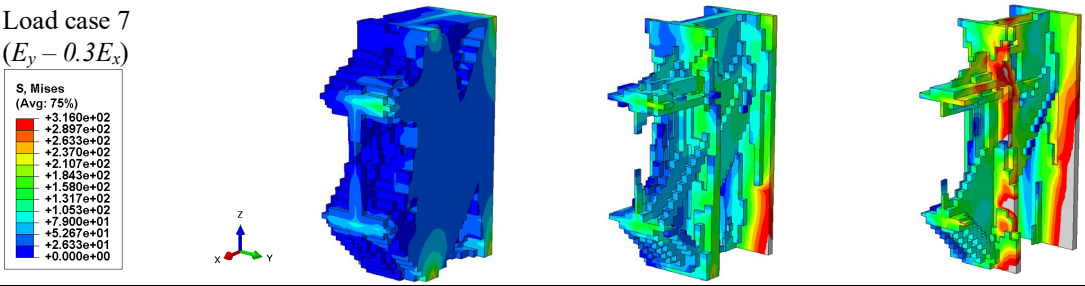
Iteration	**10**	**50**	**70**
Load case 1 (Gravity)			
Load case 7 ($E_y - 0.3E_x$)			
Mean compliance ($N.mm$)	10.34×10^6	12.65×10^6	15.59×10^6
Volume fraction (V/V_0)	0.82	0.36	0.24

Figure 7. Topological evolution with von Mises stress distribution field for the material non-linear stiffness design for various load cases (peak stress of 316 MPa is plotted as red).

The smoothed final geometry was assessed for structural strength and integrity. For this purpose, the moment-rotation curve of the optimised connection was compared to that of the conventional welded

connection presented in Section 3.2. The material properties used for the weld group in the simulation of the conventional welded connection are shown in Table 4. The moment-rotation curves are shown in Figure 8.

Table 4. Input parameters for E5518-C1 H5R electrode [18].

$\sigma_{0.2}$ (MPa)	σ_u (MPa)	ε_u (%)
550	620	26

As can be seen from Figure 8, both the ultimate strength and deformation of the optimised joint are superior to its conventional counterpart. Due to their critical role, connections are generally designed to be the last structural components to fail in structural frameworks. Hence, the ability to sustain large inelastic deformations (ductility) is a desired characteristic of connections. The relative ductility index, defined as the ratio between the ultimate and yield rotation capacities ($\mu = \theta_u/\theta_y$), was used to quantify the difference in the performance of the optimised and conventional connection designs [19]. Table 5 summarises the ultimate moments and ductility indices achieved by the two designs.

Table 5. Applied tractions at the beam and column faces.

Design	**Ultimate moment capacity** M_u (kN.m)	**Yield rotation** θ_y (mRad)	**Yield rotation** θ_u (mRad)	Relative ductility
Optimised connection	423.3	9.7	60.9	6.3
Conventional connection	390.1	6.8	31.1	4.6

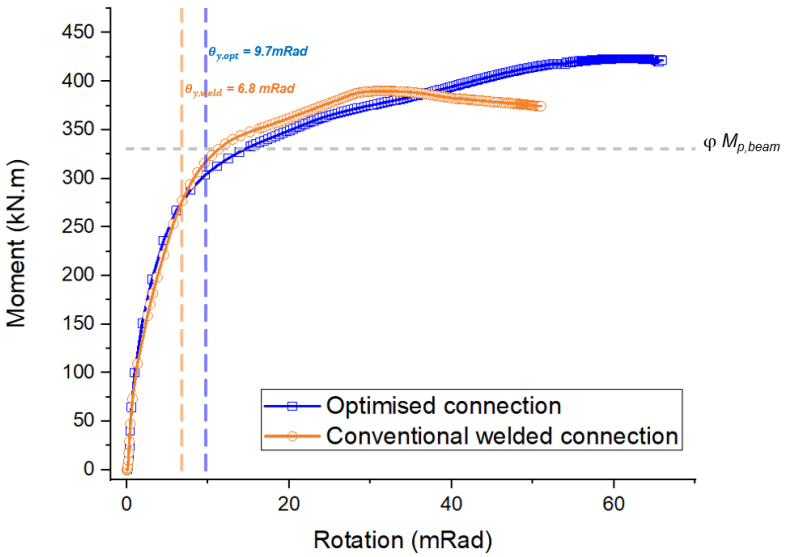


Figure 8. Moment-rotation curves for the two designs.

3.4. Optimisation of structural frame with additively manufactured connections

A further assessment on the performance of the optimised joint is made by considering the response of a complete frame. For this purpose, a two-storey steel frame constructed from beams and columns of the same dimensions shown in Figure 3 is chosen for this study (Fig. 10). Initially an optimisation of a "top floor" joint connecting a single beam and column was completed using the same objective function used for the optimisation in Section 3.3. The evolution of the optimised topology is shown in Figure 9,

obtained using 82 iterations to match the weight of the conventional connection counterpart. The performance of the frame has been evaluated for the gravity and earthquake ULS load cases, considering the moments carried by the connections and the members. Figure 11 shows the bending moment distributions for the frames with optimised and conventional connections about the major axis of structural elements. The peak bending moments in the floor beam of the first floor at mid-span and near the connections have been reported in Table 6. It can be seen that by using optimised joints, the mid-span moments are reduced by 12% –13%, whilst the end moments increase by 55% and 89% for the gravity and earthquake load cases, respectively, indicating the optimised joints provided a higher degree of end fixity to the beam at the connections than the conventional connections, while not generating moments larger than the mid-span moments. Moreover, it can be observed that due to the higher stiffness provided by the optimised connections, the bending moments in the columns near the connections increase by 41% and 37% for the gravity and earthquake load cases, respectively.

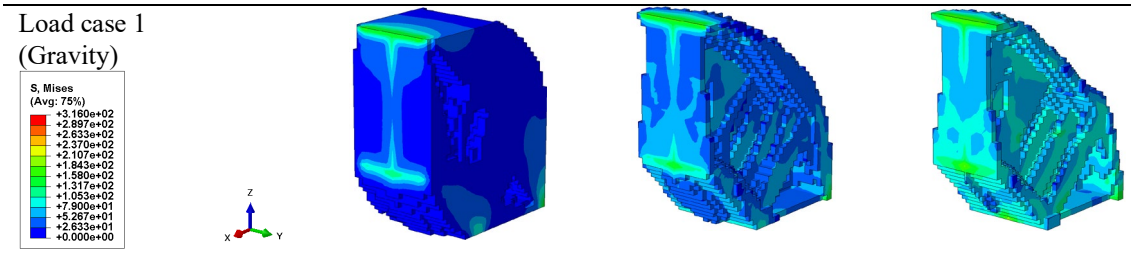
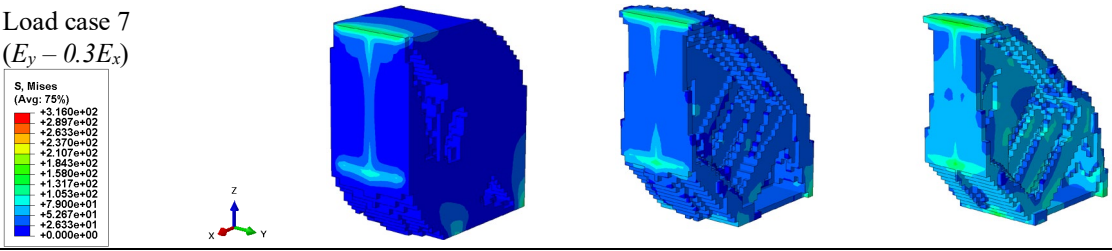
Iteration	**10**	**50**	**70**
Load case 1 (Gravity)			
Load case 7 ($E_y - 0.3E_x$)			
Mean compliance ($N.mm$)	4.45×10^6	4.90×10^6	5.44×10^6
Volume fraction (V/V_0)	0.82	0.36	0.24

Figure 9. Topological evolution with von Mises stress distribution field for the material non-linear stiffness design for the top joint under various load cases (peak stress of 316 MPa is plotted as red).

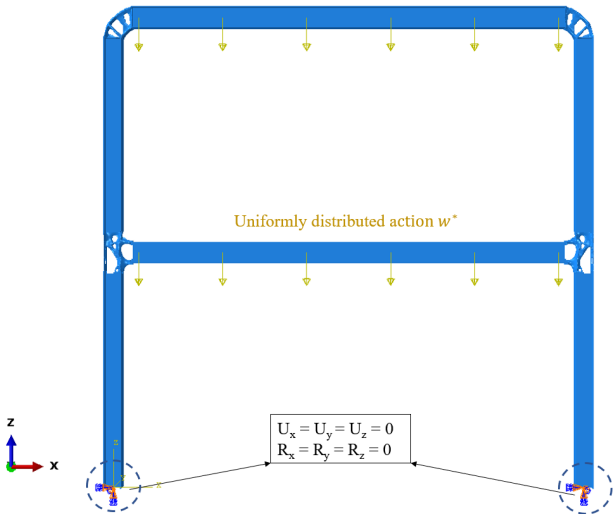


Figure 10. Front view of the studied frame using optimised joints (ULS gravity actions are shown).

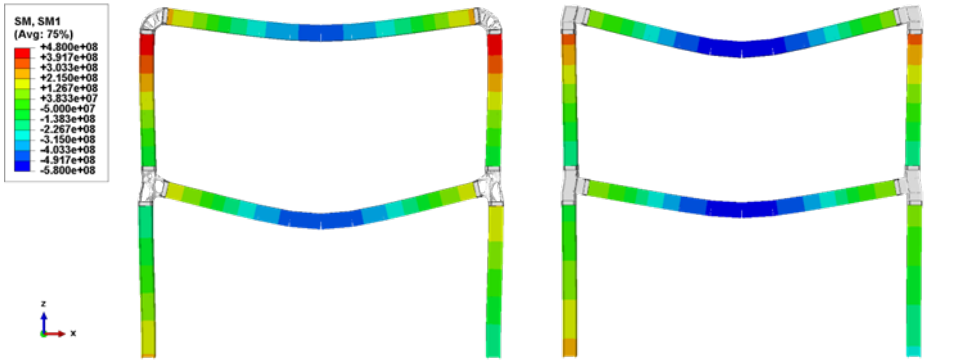
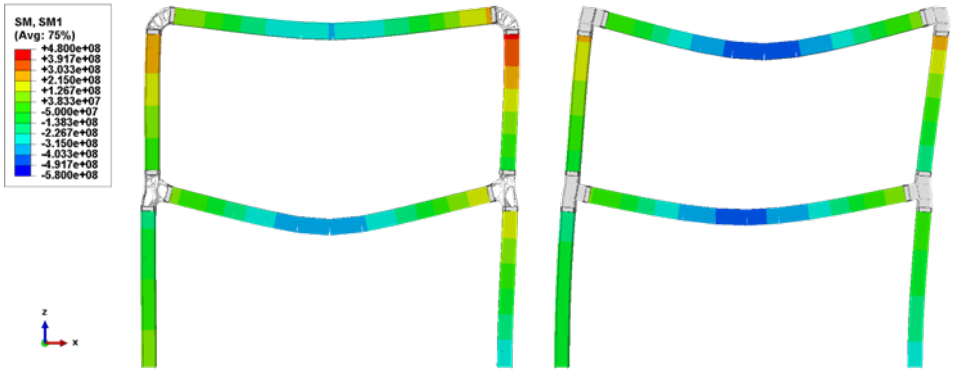
Ultimate Limit State	**Optimised frame**	**Conventional frame**
Gravity		
Earthquake		

Figure 11. Bending moment distribution about the major axis of structural elements with deformed shape corresponding to each design under the ultimate loads (ULS case).

Table 6. Summary of the structural actions in the first floor of the frame (Maximum moment at the support (M_{max}).

Frame type	Gravity case		Earthquake case	
	Mid-span	connection	Mid-span	connection
	kN.m	kN.m	kN.m	kN.m
Optimised connection	471.3	194.7	375.3	194.7
Conventional connection	540.3	125.7	425.7	102.9
Ratio (opt./conv.)	0.87	1.55	0.88	1.89

NOTE: The moments at the connections are taken at a section 280 mm away from the face of the column.

4. Conclusion

The paper describes a framework for investigating the potential application of optimised joints fabricated by advanced manufacturing with a particular focus on the steel framing systems used in commercial and residential buildings. The first part of the paper developed a methodology for the optimisation of a frame structural connection considering multiple load cases. The numerical simulations of the optimised connections showed promising advantages in terms of strength, ductility and stiffness compared to their conventional connection counterparts. In the future, more elaborate connection layouts with multiple connecting members accounting for potential WAAM-related constraints can be developed to enhance the performance of such optimised connections and further demonstrate their advantages over conventional connection designs.

Acknowledgements

This work was supported by the Australian Research Council (ARC) Discovery Project DP210103103. The authors also acknowledge the use of the University of Sydney's high-performance computing cluster, Artemis.

References

[1] G. Rozvany, "Historical review of layout optimization," in *Structural optimization, proceedings of the IUTAM symposium on structural optimization, Melbourne*, 1988.

[2] M. P. Bendsøe and N. Kikuchi, "Generating optimal topologies in structural design using a homogenization method," *Computer methods in applied mechanics and engineering,* vol. 71, no. 2, pp. 197-224, 1988.

[3] M. P. Bendsøe and O. Sigmund, "Material interpolation schemes in topology optimization," *Archive of applied mechanics,* vol. 69, pp. 635-654, 1999.

[4] J. A. Sethian and A. Wiegmann, "Structural boundary design via level set and immersed interface methods," *Journal of computational physics,* vol. 163, no. 2, pp. 489-528, 2000.

[5] Y. M. Xie and G. P. Steven, "A simple evolutionary procedure for structural optimization," *Computers & structures,* vol. 49, no. 5, pp. 885-896, 1993.

[6] O. M. Querin, G. P. Steven, and Y. M. Xie, "Evolutionary structural optimisation (ESO) using a bidirectional algorithm," *Engineering computations,* vol. 15, no. 8, pp. 1031-1048, 1998.

[7] X. Huang and Y. Xie, "Topology optimization of nonlinear structures under displacement loading," *Engineering structures,* vol. 30, no. 7, pp. 2057-2068, 2008.

[8] Y. He, Z.-L. Zhao, K. Cai, J. Kirby, Y. Xiong, and Y. M. Xie, "A thinning algorithm based approach to controlling structural complexity in topology optimization," *Finite Elements in Analysis and Design,* vol. 207, p. 103779, 2022.

[9] M. Bi, P. Tran, and Y. M. Xie, "Topology optimization of 3D continuum structures under geometric self-supporting constraint," *Additive Manufacturing,* vol. 36, p. 101422, 2020.

[10] X. Wang *et al.*, "Space Node Topology Optimization Design Considering Anisotropy of Additive Manufacturing," *Applied Sciences,* vol. 12, no. 18, p. 9396, 2022.

[11] S. Galjaard, S. Hofman, and S. Ren, "New opportunities to optimize structural designs in metal by using additive manufacturing," in *Advances in Architectural Geometry 2014*: Springer, 2014, pp. 79-93.

[12] P. Kyvelou, C. Buchanan, and L. Gardner, "Numerical simulation and evaluation of the world's first metal additively manufactured bridge," in *Structures*, 2022, vol. 42: Elsevier, pp. 405-416.

[13] *ABAQUS (2016) CAE 2016*. (2016).

[14] X. Huang and Y. Xie, "Convergent and mesh-independent solutions for the bi-directional evolutionary structural optimization method," *Finite elements in analysis and design,* vol. 43, no. 14, pp. 1039-1049, 2007.

[15] Z. H. Zuo and Y. M. Xie, "A simple and compact Python code for complex 3D topology optimization," *Advances in Engineering Software,* vol. 85, pp. 1-11, 2015.

[16] K. J. Rasmussen, "Full-range stress–strain curves for stainless steel alloys," *Journal of constructional steel research,* vol. 59, no. 1, pp. 47-61, 2003.

[17] *Autodesk Fusion 360*. [Online]. Available: https://www.autodesk.co.uk/products/fusion-360

[18] C. P. Ltd. *Welding Consumables Pocket Guide*, 2008. [Online]. Available: https://www.welding.org.au/wp-content/uploads/2015/07/CIGWELD-Filler-Metals-PocketGuide-2008.pdf.

[19] A. Tamboli, *Handbook of structural steel connection design and details*. McGraw-Hill Education, 2010.

Proceedings of the IASS Annual Symposium 2023
Integration of Design and Fabrication
10–14 July 2023, Melbourne, Australia
Y.M. Xie, J. Burry, T.U. Lee and J. Ma (eds.)

An assembly-oriented novel low-carbon masonry building method with unfired 3D printed earthen blocks

Yelda GIN[a,*], Darshil U. SHAH[a], Michael H. RAMAGE[a]

[a,*] University of Cambridge, Department of Architecture
Centre for Natural Material Innovation, Cambridge, UK
yg362@cam.ac.uk

Abstract

Conventional earthen building methods such as cob and adobe are relevant for developing countries but labour-intensive, expensive and slow for developed countries. Automation in construction has been increasingly favourable in developed countries, especially buildings constructed with 3D printed cementitious materials. 3D printed earthen materials demonstrate a better environmental performance compared to 3D printed cementitious materials due to the energy intensive manufacturing of cement. Moreover, conventional earthen methods, such as cob, create earthen buildings with solid sections while 3D printing allows a hollow section and various infill designs using less material. Despite the benefits, the research on the mechanical strength of 3D-printed earthen structures is still limited. The lack of data on the mechanical performance of 3D printed earthen structures, is one of the obstacles preventing the mainstream construction industry from approaching this novel building method. Our research investigates an assembly-oriented novel low-carbon masonry building method with unfired 3D-printed earthen blocks and explores its adaptability to the mainstream construction industry with a critical comparison based on mechanical properties.

Keywords: 3D printing, construction techniques, digital modelling and fabrication, earthen architecture, low carbon construction, automation

1. Introduction

Manufacturing of industrial construction materials contributes up to one-third of all carbon dioxide emitted by the construction industry[1]. Conventional materials like steel and concrete are high embodied energy materials because of the energy required to provide high temperatures necessary for their production [2]. In contrast, unfired earth requires no industrial processing and is generally available at the excavation site or locally. Moreover, earthen buildings can balance humidity and regulate indoor temperatures, eliminating the need for mechanical heating and cooling systems, further reducing the carbon footprint of the building [3].

Nearly a third of the world's population lives in earthen dwellings [4]. Nonetheless, earth is still not considered a conventional building material. Earth is generally perceived as a primitive material only used for dwellings in rural areas or developing countries. Yet, there are numerous contemporary earthen buildings for various architectural purposes built for various economic classes and urban environments in developed and developing countries. Moreover, earth is an excellent material for constructing with the principles of the circular economy [5]. For example, Brussels Cooperation in Belgium creates earthen building elements from 36 million tonnes of earth excavated from the Belgian construction sites, which would otherwise be waste [6]. This approach is promising to create innovative and sustainable future urban habitats within a circular economy.

Copyright © 2023 by Yelda GIN , Darshil U. SHAH and Michael H. RAMAGE. Published in the Proceedings of the IASS Annual Symposium 2023 with permission.

2. 21st century mud

2.1. Why 3D printing with earth?

During a lecture at the Pratt Institute in 1973, Louis Kahn had his famous conversation with a brick, asking the brick what it wants to be, later added that the same conversation could happen with concrete or marble, emphasising the importance of understanding the nature of each material or "honoring the material" [7]. Today architects and designers take this discourse even further with computational design and digital fabrication. Gramazio and Kohler [8] observe that the advanced design and fabrication techniques blur the boundaries between data and material along with programming and construction, creating a "digital materiality" which "enriches material by information". Additive manufacturing methods such as 3D printing are revolutionising architecture and design by enabling the manufacture of data-driven complex forms created by computational design, which would be hard and expensive for conventional craft and making to realise. By placing the material exactly where its needed, structural stability could be gained with less material. Developed countries are increasingly investing in automation in construction and labour intensive nature of the conventional earthen building methods prevents its uptake by the mainstream construction industry. Population growth combined with the high cost of housing makes access to affordable housing one of the most critical concerns of the 21st century. On-site robotic 3D printing with concrete is a novel construction strategy suggested as a fast and affordable solution for housing. For example, a house in Nantes(France) is the first habitable 3D printed concrete building constructed in 54 printing hours and claimed to be 20% cheaper than conventional concrete construction [9]. This construction system eliminates material waste caused by the use of formwork. However, 3D printed concrete is more carbon intensive than conventional concrete due to plasticiser added to the mix to be able to 3D print. 3D printed earthen buildings are a low-carbon alternative to 3D printed concrete [10], while adapting to the construction industry in developed countries and automating the building process. Without adding chemical stabilisers, the earth from the site or locality could be re-printed until the desired result is achieved. First housing prototypes built with on-site robotic 3D printing with earth, such as Casa Covida [11] by Rael&San Fratello in the USA, Tecla [12] by World`s Advance Saving Project (WASP) and Mario Cucinella Architects in Italy, and Tova [13] by Institute for Advance Architecture of Catalonia (IAAC) in Spain present a natural and low-carbon alternative to 3D printed concrete houses. Since the uptake of steel and concrete after World War II, earth has been neglected as a rural and weak material. The juxtaposition of this humble material with cutting-edge technology also removes this bias and creates a contemporary "21st Century Mud".



Figure 1-2-3. Traditional earthen building methods such as cob and adobe are labour intensive and slow.



Figure 4. Tecla [12], Photo credit: Iago Corrazza.



Figure 5.Tova [13], Photo credit:Gregori Civeru.







Figure 6-7-8. On-site 3D printing of Tecla[12] photo credit:WASP, Casa Covida[11], photo credit: Emergent Objects and Tova[13], photo credit: Gregori Civeru.

2.2 On site vs off-site (prefabricated) 3D printing with earth

On-site additive manufacturing with earth has several environmental and financial benefits. Earth has an advantage for regions where wood and concrete are expensive and require long-distance transport. This process does not need scaffolding and is largely waste-free. However, the construction site must be protected as earthen walls are prone to erosion by rain and strong winds. Strong directional sunlight also creates irregularities in geometry and cracking, if one side of the wall dries much faster than the other side so shading is essential. On the other hand, off-site construction is not weather dependent, making all year fabrication possible in a climate-controlled environment.

Although on-site additive manufacturing offers continuity of the construction, there is only a certain height that can be printed in session, then it is necessary to wait for the walls to dry and gain strength before continuing with the printing. Off-site prefabrication of earthen blocks allows continuous fabrication where blocks can be stacked for drying. The control over the production with expert staff also avoids mistakes caused by craftsmanship on site, ensuring a result without discrepancies, making it more favourable to the mainstream construction industry. Also, prefabrication enables better precision and tolerances for earthen blocks that shrink in volume and weight while drying. The prefabricated rammed earth walls of Ricola Herb Centre by Martin Rauch is a recent example of how a prefabrication approach was welcomed for a contemporary building while using the local earth from the construction area. Experimental research projects such as Terraperforma [14] and Digital Adobe [15] investigates a similar approach with robotic fabrication. Despite several advantages, off-site production also presents challenges, such as transporting and assembling heavy earthen blocks. Building construction hubs close to the site to fabricate earthen blocks combined with fast robotic assembly on site could solve these challenges.




Figure 9-10 : IAAC Terraperforma [27] Image credit: Gabriel Frederick.

3. Prefabricated 3D printed earthen blocks

3.1 Fabrication process

As demonstrated in detail in our research paper for IASS 2022 [15], we have designed and 3D printed eight earthen blocks with KUKA KR 60 high-accuracy robot and a custom-designed extruder at the Welsh School of Architecture, using local clay-rich soil from Cardiff. The goal was to print robust earthen blocks with minimum material using block geometry and infill strategies.

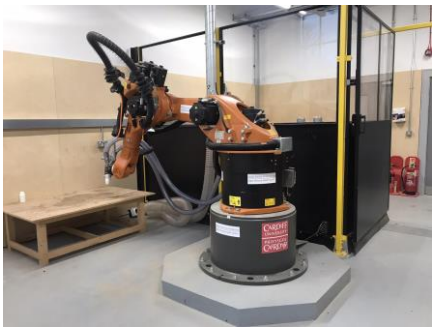




Figure 11,12,13. KUKA KR60 six axis high accuracy industrial robot, the dual extruder [16] and the custom fabricated steel end effector connecting 3D printed nozzle to the pressure hoses.

Blocks were designed with Rhinoceros® Grasshopper® with a parametric design approach, introducing parameters based on wall thickness, number of wall layers, layer height, number of undulations, and width, length control which allowed us to produce and test multiple iterations without the need to design each block from scratch.

During the prototyping process, several blocks were tested while an optimum robot speed at 0.09 m/s, 0.1 m/s extruder speed and soil mix viscosity was defined. The outcomes of the prototyping process confirmed successful data for block parameters such as layer height, number of layers and undulations to finalise the block and infill geometries. Simultaneously, the final earth mix recipe was confirmed as 61% soil, 0.3%straw, 22% sand and %17 water. This recipe was fluid enough to ensure a continuous material flow from the extruder through the pipe and to the nozzle while solid enough to print the blocks without buckling.

Once the prototyping process was finalised, we printed eight blocks that transformed in size, form and infills to create the tapering and slightly rotating wall once assembled. Printing each block took less than 5 minutes, at a rate that demonstrating the potential for fast production.

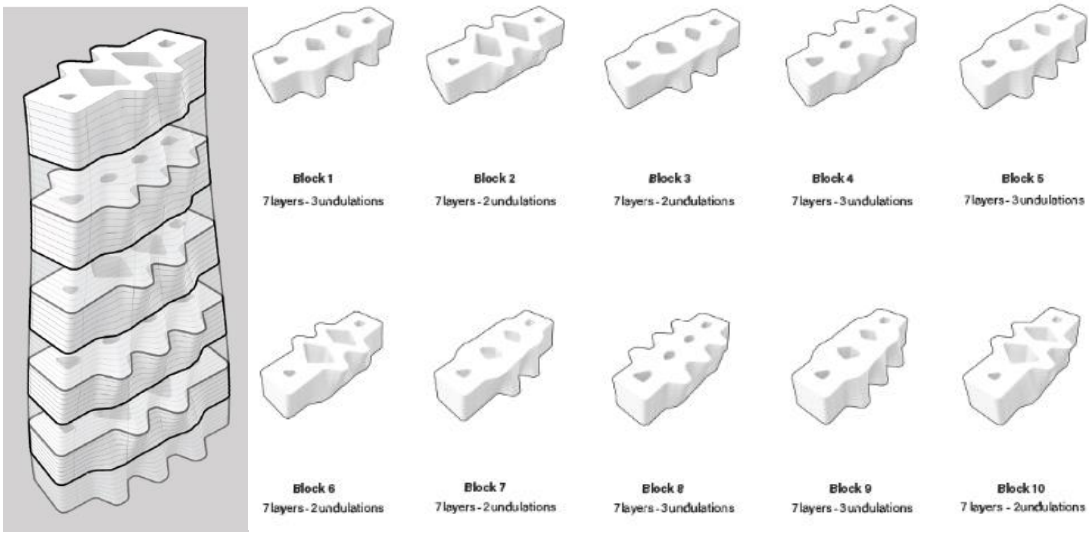


Figure 14: Final design optimisation and blocks to be printed with undulations and infills blending into the wall form. Images courtesy of MSc CMA students, Cardiff University, 2022: Afnan Aldulaijan, Ashley Vias, Dorsa Boroujerdifard, Darshan Chavan, Deval Ambavi, Louai Jaber, Mohammad Omar Eqbal, Sapta Sunusae and Selda Pourali Behzad.

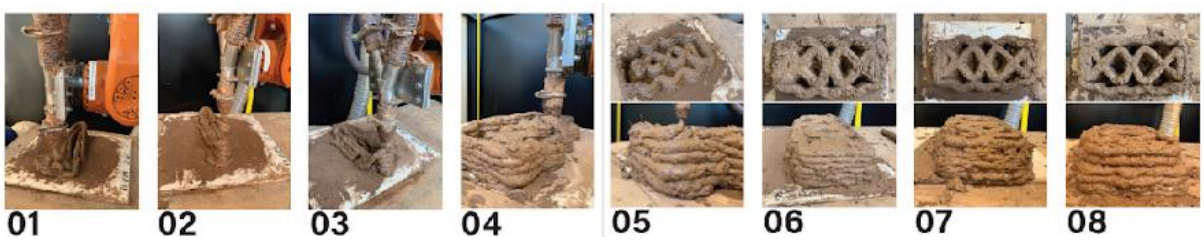


Figure 15. Trials with various robot speeds and layer heights while keeping the extrusion speed at 0.1 m/s and printing with the 25 mm nozzle.

3.2 Drying and assembly of blocks

Printed blocks were left to dry in a heated room for a month. Avoiding the temperature and humidity fluctuations allowed the blocks to dry without significant deformations in form. During the drying period, blocks lost 15% in weight as the water evaporated. Once fully dry, blocks were stacked on each other after being sanded and wetted with the same soil mix used as mortar. The same mortar recipe with adding more water and eliminating the straw can be robotically sprayed on the 3D printed samples to smooth the surface of the blocks, if needed. The assembly process has shown discrepancies between the block design, 3D printed blocks and dried specimens due to the unpredictable nature of the printing and drying process, which presents a challenge for the adaptation to the mainstream construction industry, where predictability and precision are essential. Nonetheless, prefabrication in a controlled environment presents the opportunity to improve the precision of the process by multiple calibrations exempt from weather conditions and accurate prediction of the final geometry after the drying period. This optimisation process to fabricate the blocks is essential to develop various assembly methods and block connections.



Figure 16, 17. Assembled wall and the assembly process.

4. Mechanical properties of 3D printed blocks

4.1 Introduction

As mentioned in the previous sections, 3D printing with earth can enable building robust structures using less material as material scarcity becomes increasingly critical. Cob is a technique of mixing clayey earth and fibres such as straw and then applying them by hand with pushing them to create a monolithic wall. The plastic nature of cob also makes it ideal to use it for 3D printing, with increasing the amount of water to make the mix printable, as previously mentioned. It can be argued that conventional cob is an additive manufacturing method where the mix is gradually added by hand to create walls, while 3D printing cob, automates and accelerates this process. Moreover, conventional earthen methods, such as cob, create earthen buildings with solid sections while 3D printing allows a hollow section and various infill designs using less material. 3D printing also enables the designer to use the gaps in the infill for insulation or ventilation. Despite the benefits of this new approach, the research on the mechanical strength of 3D-printed blocks is still limited. To our knowledge, only three research papers are published on the subject [18] [19] [20]. The lack of data on the mechanical performance of 3D printed earthen structures prevents engineers and contractors from approaching this novel building method. More data and research on the mechanical properties of 3D printed earthen blocks is essential to accelerate the mainstream industry's uptake of this novel building method.

Compressive strength is the main mechanical property when defining the integrity of earthen structures as it shows the loadbearing capacity [21]. Gomaa et al. [18], looked into sixteen research papers, including conventional cob's compressive strength, and found that values fall between 0.4-1.35 MPa. Previous research on the compressive strength of 3D printed earthen specimens is documented as between 1.2 and 1.8 MPa for a cob-like mix using alginate seaweed polymer instead of straw [19], 0.87 MPa for 3D printed cob cylinders [18], and 2.32 Mpa for a 3D printed load-bearing element by WASP [20]. Our compression tests aimed to find out where our specimens fall in this range and compare the compressive strength of each specimen to see if the geometry and the thickness of the block infill affect the compression strength.

4.2 Test specimens



Figure 18,19,20. Test Specimens, Block A, Block B, Block C. Photo Credit: Lina Ahmad.

Three 3D printed blocks, fabricated with the process and material mix explained in section 3 were selected as test specimens. The infill geometry, number of undulations and thickness of the blocks are slightly different for each specimen. The width of specimens are 15 cm at the narrowest and 20 cm at the widest. The heights of the specimens are 7-8 cm and the length of the specimens is 35-36 cm.

4.3 Test preparation, equipment and method

Before the testing, quick-setting dental plaster was applied to the top of the blocks to have a flat surface to ensure uniform load distribution and avoid stress concentrations that could lower the compressive strength values. In addition, prior to dental plaster application, the holes on the blocks were filled temporarily to avoid plaster penetrating inside the block.



Figure 21,22,23. Dental plaster application to flatten the block surface prior to testing.

1MN Servo-hydraulic fatigue testing machine was used for testing to accommodate the size of specimens. First, compression platens were installed and the height of the platens were adjusted according to the block heights. Subsequently, each specimen was subjected to a uniform axial load. Initially, the load was applied at a conservative 0.001418 mm/s to Specimen A and the test took about

50 min. Then, the speed was increased approximately five times to 0.008255 mm/s for specimens B and C, and the test took about 25-30 min for each specimen.

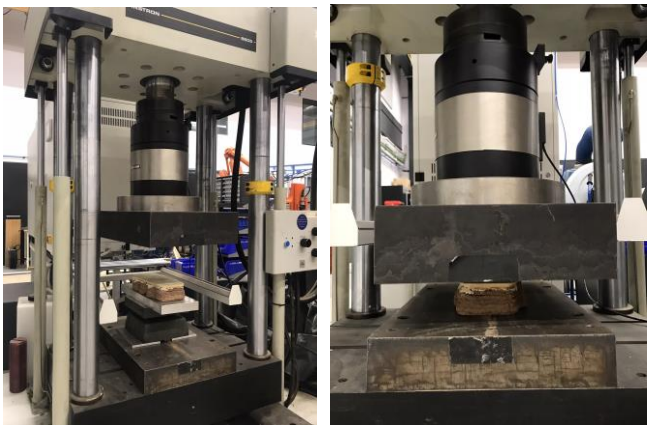


Figure 20. 1MN Servo-hydraulic fatigue testing machine used for the compression tests.



Figure 21. Typical failure at the corners and along the perimeter was observed for all specimens.

4.4 Test Results

The testing machine has generated data for force (kN) vs displacement (mm). The stress was calculated based on $\sigma = P/A$ formula, where P is the applied force and A is the cross-section area of the block. The axial strain was calculated based on the $\varepsilon axial = \Delta/L$ formula, where Δ is the displacement and L is the length of the blocks.



Figure 22. Specimens before and after testing (broken pieces are disposed of).

The irregular infill geometry makes it harder to get an accurate cross-section area with manual dimensioning. Therefore, we extracted each block's accurate cross-section areas from the scanned models of the blocks using Rhinoceros®.

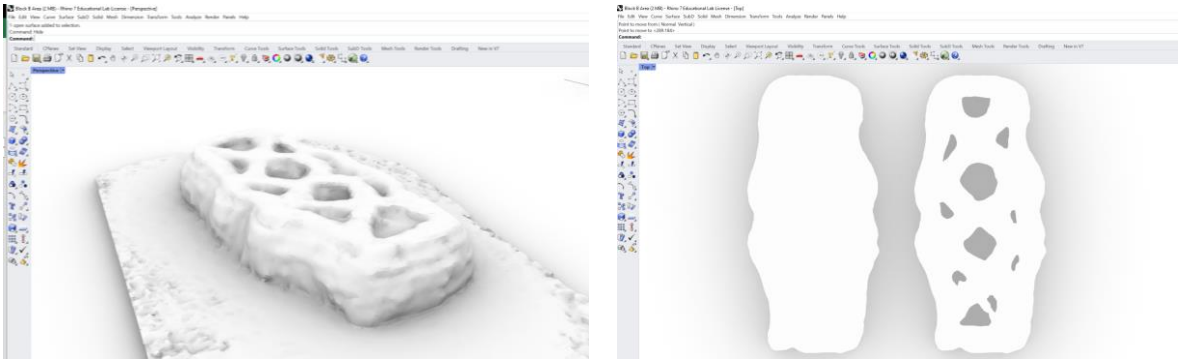


Figure 23. 3D scanned specimen B in Rhinoceros® and cross-section area with and without the gaps in the block.

Table 1. Area and solidity comparison of test specimens

Cross Section Areas (mm^2)	**Specimen A**	**Specimen B**	**Specimen C**
Infill gaps included	54000	48500	56500
Infill gaps excluded	41261	42744	50087
Block Solidity	76.4%	88.1%	88.6%

Based on blocks cross-section areas (gaps excluded) shown above, the compressive strength of Specimen A is 1.7 MPa, Specimen B is 4.4 MPa and Specimen C is 3.1 MPa. When the compressive strength is calculated based on cross-section areas with gaps included, then the compressive strength of Specimen A is 1.3 MPa, Specimen B is 3.8 MPa and Specimen C is 2.8 MPa. All blocks performed well considering the average conventional cob compression strength and previously recorded compression strength of the 3D-printed cob. The stress-strain diagram for each block is shown below.

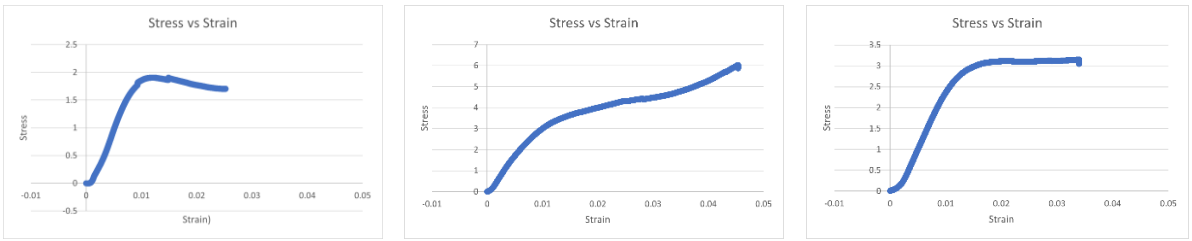


Figure 24. Stress-Strain Diagrams for Specimen A, B and C.

A similar behavior was observed for specimen A and C on these diagrams, where a linear rise ended with the peak and reached a plateu after a small reduction in slope. On the other hand, Block B has shown an irregular behaviour where the linear rise has started again after reaching a plateau. This irregularity might be caused by the dental plaster holding the pieces together and delaying the brittle response. Hence, the first peak before reaching the plateau has been considered for specimen B while calculating maximum compressive strength and the second peak is ignored.

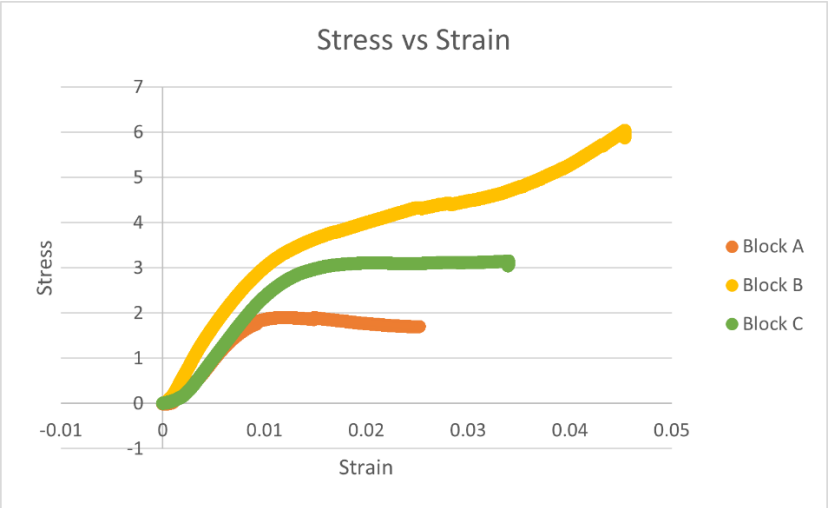


Figure 24. Stress-Strain Diagram, comparison between Block (Specimen) A,B and C.

As mentioned in the previous section, during the prototyping process, the block form was updated with more significant undulations to gain better structural stability and avoid buckling, while 3D printing and interlocking waves were added to the infill geometry to work as buttresses. However, the compression test has shown that while the buttress strategy increases the structural strength of the block, the undulations of blocks on the perimeter have no effect. Additionally, although specimens A and C have similar geometry, specimen C performed much better under axial load due to thicker infill layers. Specimen C also had a stronger buttress connection than Specimen A, which supported its strength too. While dental plaster helped attain a uniform load distribution, it might have held the blocks together longer than usual, preventing an expected brittle behaviour after blocks reached their maximum strength and demonstrating an unusually long plateau in stress-strain diagrams.

5. Conclusion

3D printing enables short supply chains and localised fabrication while providing an opportunity to use less material and ensuring structural stability with geometric optimisation. Prefabrication of the 3D printed earthen blocks has the potential to mitigate the uncertainties about the earthen block fabrication and provide precision in a controlled environment while enabling rapid fabrication for a greater demand. Precision and rapid fabrication can accelerate the adoption of earthen construction by the mainstream construction industry in the developed world. However, the lack of data about the properties of 3D-printed earthen construction creates doubt for construction professionals. Our research explored the mechanical properties and compression strength, in particular, of 3D-printed earthen blocks. As mentioned above, our research has demonstrated that geometry, infill strategies and the infill's thickness affect the compression strength of the 3D printed blocks. Moreover, our specimens performed well compared to the average conventional cob compression strength and previously recorded compression strength of the 3D-printed earthen elements. However, further tests are required to investigate the role of infill geometry on compression strength. In addition, different fibres could be used to explore it`s effect on the strain response of the blocks. This design and fabrication method is promising to allow bespoke block and infill geometries to be created and fabricated using local earth. The increase in the availability and affordability of 3D printing equipment, combined with the increase in the data about the performance of 3D printed earthen structures, will spread it`s use as a novel low-carbon building method in the mainstream construction industry.

Acknowledgements

We would like to acknowledge the diligent work and contributions of Prof Wassim Jabi, Kamal Haddad, and the Welsh School of Architecture, MSc Computational Methods in Architecture students in 2022, Afnan Aldulaijan, Ashley Vias, Dorsa Boroujerdifard, Darshan Chavan, Deval Ambavi, Louai Jaber, Mohammad Omar Eqbal, Sapta Sunusae and Selda Pourali Behzad. We also extend our gratitude to Lina Ahmad who helped us with the scanning, photographing and shipment of the 3D printed earthen blocks. We would like to thank Pieter Dresneck and Phil McLaren for their help during testing. YG acknowledges the EPSRC and the Cambridge Trust for the financial support for her PhD research and the Department of Architecture, the University of Cambridge, for the Faculty Fieldwork Funding awarded for this research project.

References

[1] UN, "United Nations World Urbanization Prospects", 2018. Available: https://www.un.org/development/desa/publications/2018-revision-of-world-urbanization-prospects.html.

[2] Habert, G., Castillo, E., Vincens, E. and Morel, J.C., "Power: A new paradigm for energy use in sustainable construction". *Ecological Indicators*, vol 23, pp. 109-115, 2012.

[3] Minke, G., *Building with Earth. Design and Technology of a Sustainable Architecture. (6th ed.)* Basel; Boston: Birkhauser-Publishers for Architecture, 2009.

[4] UNESCO "World Heritage Paper", in: *Proceedings of the UNESCO International Colloquium on the Conservation of World Heritage Earthen Architecture*, Paris, France. 17-18 December 2012, L. Eloundou, T. Joffroy, Eds.

[5] Fabbri, A. and Morel, J. C., "Earthen materials and constructions", *Nonconventional and Vernacular Construction Materials*, pp. 375–401, 2020.

[6] Cooman, K. D., "Down to earth: earth building in Europe and Africa by BC Architects & Materials & Studies", *Architectural Review*, 1468, pp. 66-69, 2020.

[7] Poerschke, U., "On concrete materiality in Architecture", *Architectural Research Quarterly*, 17(2), pp.149–156, 2013.

[8] Gramazio, F. and Kohler, M., *Digital Materiality in Architecture*, Baden: Lars Müller Publishers, 2008.

[9] Cowan, M., "The world`s first family to live in a 3D-printed home", *BBC*, 6 July, 2018. Available at: https://www.bbc.com/news/technology-44709534, 2018.

[10] Alhumayani, H., Gomaa, M., Soebarto, V. and Jabi, W., "Environmental assessment of large-scale 3D printing in construction: A comparative study between cob and concrete", *Journal of Cleaner Production*, 270, 2020.

[11] Rael, R., San Fratello, V., Curth A., Arja L., "Casa Covida-Mud Frontiers III", in *ACADIA 2020 Distrubuted Proximities*, Online, October 24-30, 2020, Yablonina M., Marcus A., Doyle S., Del Campo M., Ago V., Slocum B., Eds.

[12] Parkes, J., "Tecla House 3D-printed from locally sourced clay", *Dezeen*, 23 April, 2021. Available at: https://www.dezeen.com/2021/04/23/mario-cucinella-architects-wasp-3d-printed-housing/

[13] Estudiantes del programa 3D Printing Architecture 2021-2022, "Prototype Tova", *ArchDaily, 30 August, 2022.* Available at: https://www.archdaily.com/988078/prototype-tova-posgrado-3d-printing-architecture-iaac

[14] IAAC, "Terra Performa", 2017. Available at: http://www.iaacblog.com/programs/terra-performa/

[15] IAAC, "Digital Adobe", 2018. Available at: https://iaac.net/project/digital-adobe/

[16] Gin, Y., Haddad K., Jabi W., Shah D., Ramage, M. “Robotic 3D printing with earth: A case study for optimisation of 3D printing building blocks”, in: *Proceedings of IASS Annual Symposia. Vol. 2022. International Association for Shell and Spatial Structures (IASS)*, 2022.

[17] Gomaa, M. et al., "3D printing system for earth-based construction: Case study of cob", *Automation in Construction*, 124 (January), 2021.

[18] M. Gomaa, J. Vaculik, V. Soebarto, M. Griffith, and W. Jabi, “Feasibility of 3DP cob walls under compression loads in low-rise construction,” *Constuction and Building Materials*, vol. 301, no. July, p. 124079, 2021.

[19] A. Perrot, D. Rangeard, and E. Courteille, “3D printing of earth-based materials: Processing aspects,” *Constuction and Building Materials*, vol. 172, pp. 670–676, 2018.

[20] E. Ferretti, M. Moretti, A. Chiusoli, L. Naldoni, F. De Fabritiis, and M. Visonà, “Mechanical Properties of a 3D-Printed Wall Segment Made with an Earthen Mixture,” *Materials (Basel).*, vol. 15, no. 2, 2022.

[21] Q. M. Pullen and T. V. Scholz, “Index and engineering properties of Oregon Cob,” *J. Green Build.*, vol. 6, no. 2, pp. 88–106, 2011.

IASS 2023
July 10–14 Melbourne
Integration of Design and Fabrication

Proceedings of the IASS Annual Symposium 2023
Integration of Design and Fabrication
10–14 July 2023, Melbourne, Australia
Y.M. Xie, J. Burry, T.U. Lee and J. Ma (eds.)

Continuous fibre additive manufacturing of topological spatial lattices for fabrication-aware design processes

Eduardo CHAMORRO[a,*], Mark BURRY[b], Mathilde MARENGO[a]

[a,*] Institute for Advanced Architecture of Catalonia, Barcelona, Spain
eduardo.chamorro@iaac.net

[b] Swinburne University of Technology School of Design in the Faculty of Health Arts and Design

Abstract

The architecture, engineering and construction additive manufacturing field has witnessed rapid development in recent years facilitated by the development of digital fabrication processes and geometrical design workflows. However, there has been limited research on non-planar 3D toolpath optimization tailored for continuous fibre additive manufacturing processes, other than layer-by-layer deposition. This paper addresses a novel design for manufacturing framework for building structural 3D spatial lattices with continuous fibre additive manufacturing processes through an optimisation form-finding method based on stress-lines generation. This fabrication-aware method overcomes the traditional challenges of non-regular topology sequencing, improving material efficiency, weight and structural performance compared to standard 3D lattices. The proposed method produces load-bearing designs for functionally graded lattice cellular topologies that respond to stress distribution and structural requirements. From a structural design perspective, specific non-standard load-based lattice geometries, have the potential to significantly reduce material usage, a major drawback of composite materials in AEC. This research presents a framework to manufacture a globally continuous 3D spatial lattices toolpath for 2.5D structural designs, which takes advantage of the benefits of continuous fibre placement as structural reinforcement for composite elements.

Keywords: additive manufacturing/3D printing, computational form-finding, construction techniques, lattice structures, robotic fabrication, material optimization, continuous fabrication, optimization methods and applications

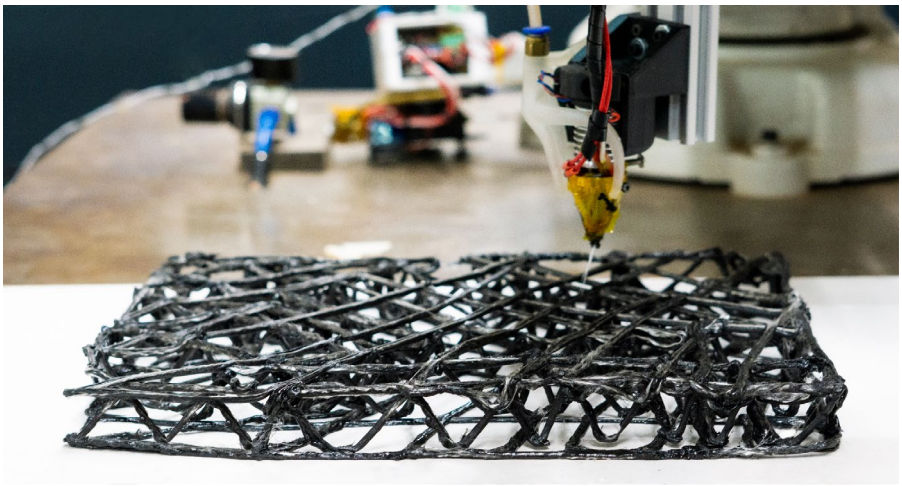


Figure A.1 Continuous fibre additive manufacture spatial lattice prototype

Copyright © 2023 by Eduardo CHAMORRO, Mark BURRY and Mathilde MARENGO. Published in the Proceedings of the IASS Annual Symposium 2023 with permission.

1. Introduction

Nowadays the major constraint for the integration of high-performance materials and additive manufacturing (AM) techniques in construction, is the cost of the material supplied [1]. 3D printing should be used for what it does best [2], which includes optimizing workflows. Conventional methods of additive manufacturing are affected both by gravity and the printing method. As well, layer-by-layer AM is either constrained by material usage or limited geometrically by the inherent overhang capabilities of the material in deposition. For composite AM to be able to reach 'volume' construction on the construction market, it must form part of an integrated, digital continuum in which the performative impact performance-wise on deployment cost and structural improvement/proficiency-outweighs aesthetics alone.

Architects with their role as designers typically prioritize aesthetics while structural engineers focus on the practicalities of building techniques. The integration of advanced computational tools and fabrication techniques has enabled architects to push the boundaries of traditional design, integrating in the design practice, "the architecture of the parametric and data" as part of the design process. This evolution of design has allowed architects to create structures that are not only visually stunning but also highly functional and sustainable.

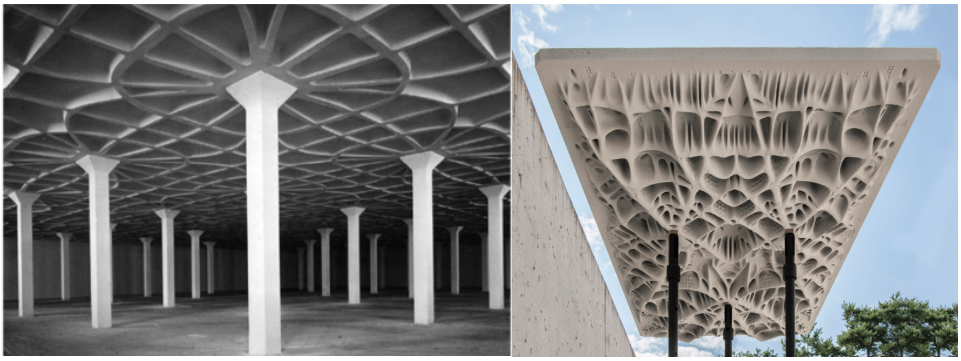


Figure 1.1 (Left) Gatti Wool Factory. Image credit: Ma, Jiaming et al. 2022, Figure 1.2. (Right) -Topology optimization of a slab with three supports. Image credit: DBT ETH

One of the earliest recorded examples of this approach can be found in the work of Vitruvius, a famous Roman architect and engineer who proposed that a building should embody three fundamental principles: firmitas, utilitas, and vetustas [3]. Firmitas, or strength, refers to the structural integrity of the building, while utilitas, or utility, is concerned with its functional purpose and how it can best serve its intended users. Finally, vetustas, or beauty, speaks to the aesthetic and visual appeal of the building. This cross-disciplinary application of fields such as engineering in the modern architectural practice developed the concept of "strength through geometry", terminology coined by Philippe Block for the definition of structures with optimized material usage through its geometrical shape and material manufacturing optimization.[4] or the work developed at the Digital Building Technologies at ETH (Fig 1.2), where they work on computational methods, such as the optimization of size, shape, and topology of material distribution to ensure the efficient distribution of concrete for a given part resulting in high complexity geometries that can achieve significant material reduction at the cost of problematic and intricate fabrication processes, that is overcome by additive manufacturing technologies [5]. As well, there has been growing interest in using advanced materials from fields such as aerospace and biology in architectural practice. For instance, lightweight, high-strength materials such as composite materials make it possible to design buildings with complex shapes and structures that were previously impossible usually, at the cost of high manufacturing complexity [6] (Fig 1.3 and 1.4).

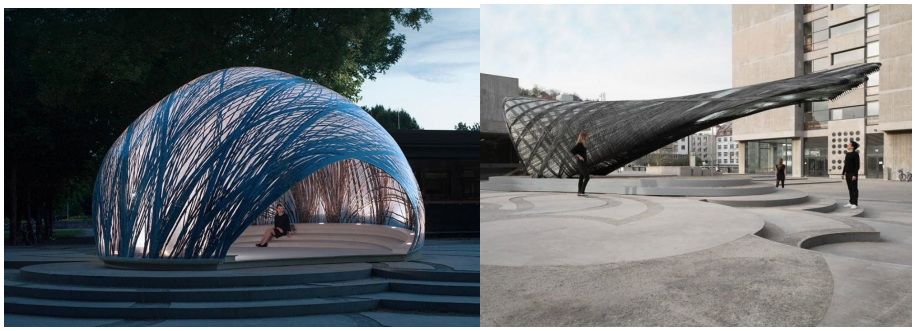


Figure 1.3. (Left) ICD/ITKE Research Pavilion 2012: FRP monocoque shell pavilion; (b) full-scale winding test Image Credit: University of Stuttgart, Figure 1.4. (Right) -ICD/ITKE research pavilion 2016/2017.Image Credit: University of Stuttgart.

1.1. Research aim

The presented research outlines the exploration of a niche of architectural possibilities on the combination of continuous fibre with AM such as continuous fibre-reinforced plastic (CFRP) technology for the fabrication of structurally optimized spatial lattices, that structurally benefits from the material-load capabilities through advanced composite AM fabrication techniques. The experimental case study for this research on a computational workflow is the Messerschmidt- Bölkow-Blohm (MMB) beam problem for a distributed load. This case study has been partially AM robotically fabricated as a proof-of-concept prototype of the accounted methodology. (Fig.1.5)



Figure 1.5. Photocollage above is the combination of the partially 3D printed spatial lattice prototype explained in this paper and the full digital model of the calculated scenario.

2. Additive manufacturing and spatial lattices

2.1. 3D printed spatial lattices

Several academic institutions accounted as Digital Structures Group and MediaLab at MIT, ICD ITKE, Gramazio Kohler research group (Fig 2.4) and Laboratory of Composite Materials and Adaptive Structures at ETH, among others, have researched the geometrical capabilities of lattices structures with additive manufacturing or sequential assembly and its high load-bearing capabilities to material per weight. [18] Prior examples of space lattice make use of a repetitive unit's arrangement in a regular topology syntax, conforming rows or grids that are added to each other. The uniform topologies sometimes with variable cell sizing ensure reduced path planning complexity and sequencing even when applied on twisted forms or ruled surfaces. The usage of material efficiently is done by the variations of

the distance between the inner and outer cells, a span of the individual cross-section of the node's members or grid geometry/topology [7]. These regular and variable topologies offer limited structural optimization and geometric freedom (Fig 2.2).

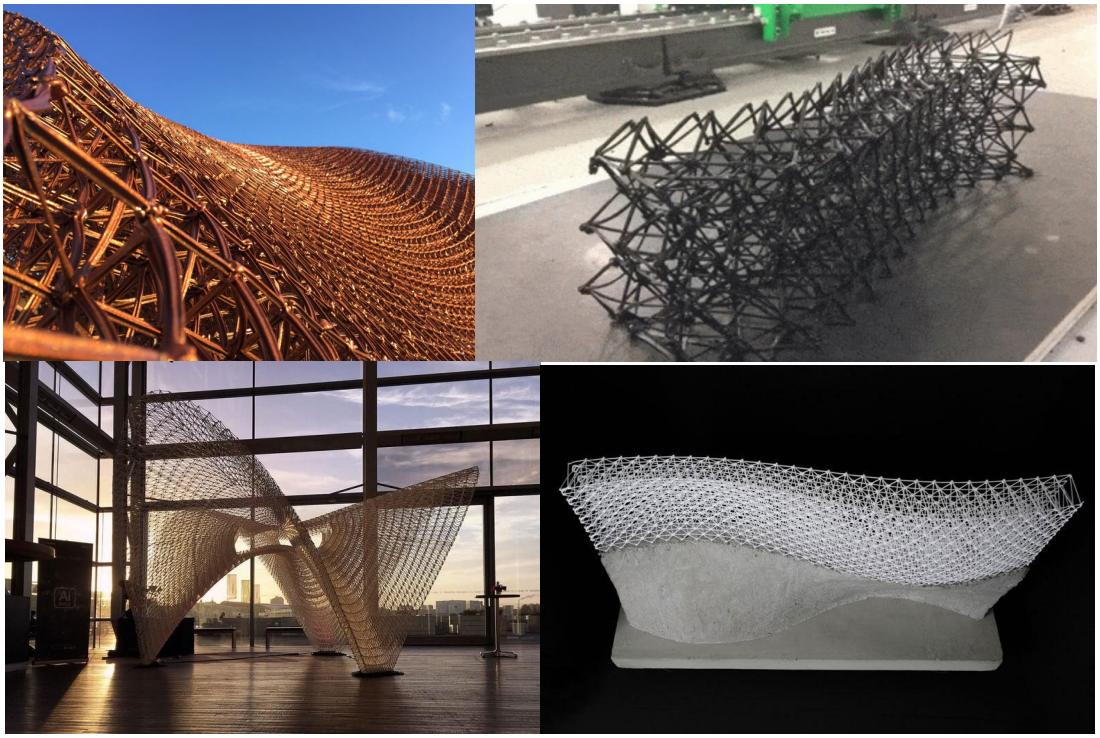


Figure 2.1. (Top-Left) - SHoP Pavilion Miami Image Credit: Branch technology. Figure 2.2. (Top-Right) - Cellular fabrication C-FAB. Image Credit: Branch Technology. Figure 2.3. (Bottom-Left) - Daedalus Pavilion. Image Credit: AI Build. Figure 2.4. (Bottom-Right) - Mesh Mould. Image Credit: ETH Zurich NCCR.

In conclusion, the load paths for a structurally loaded regular spatial lattice in a conventional space frame exhibit directional discontinuities due to the members not necessarily aligning with the overall force flow in the structure. As a result, there is less than optimal utilization of materials. However, recent advances in geometrical path-planning techniques have led to the development of irregular lattices that are even more optimized for strength-to-weight ratios. In this regard, new manufacturing technologies and methods could enhance the application of these lightweight structures with lightweight materials in construction.

2.1. Continuous fibre additive manufacturing

One of the major updates, when we analyze the current technologies under development for highly resistant and lightweight materials available for additive manufacturing, is the introduction and enlargement of continuous fibre manufacturing processes (CFAM). The current research on this topic exists in the engineering and material scientist fields [8], [9] and has been focused on the underlying mechanics [10] chemistry [11], [12], and performance of the physical output [13], [14], as well as material behaviour properties [15],[16] (Fig.2.5).

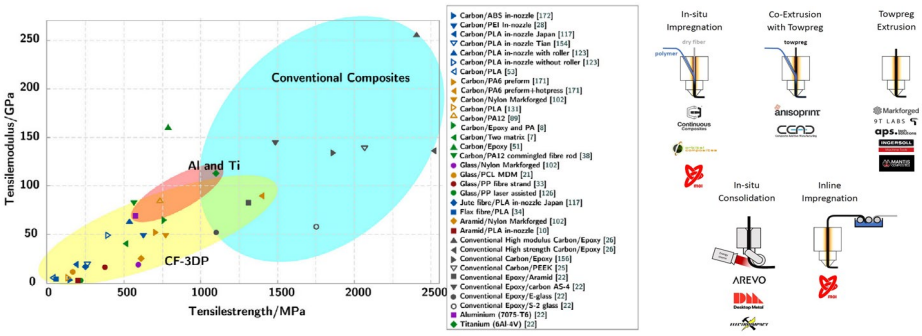


Figure 2.5. (Left) - Tensile strength / Tensile modulus material comparison chart of multiple academic publications on CF-3DP. Image Credit: [18] P. Zhuo et al, 2021. Figure 2.6. (Right) - Concepts for direct fibre integration. Image Credit: Alexander Matschinski, Virtual Symposium on AFP and AM, TU Munich, Chair of Carbon Composites (LCC), Sep. 2020

The development of CFAM techniques is driven by the industry's demand for highly engineered parts (Fig 2.6). Various companies develop these processes, starting with Anisoprint, which uses Composite fibre Co-extrusion (CFC), Markforged and Desktop Metal, which use Continuous Fiber Reinforcement (CFR) technology to create technical parts on desktop and industrial 3D printers and newer companies, such as 9T Labs, Arevo, Mantis Composites, AREVO and CEAD's that can achieve true 3D paths and z-direction reinforcement, allowing those companies to fabricate fully freeform shapes at large scale. With the development of additive manufacturing deposition techniques and material implementation processes for continuous fibre 3D printing, the possibility of more structurally efficient lightweight architectures bears high potential as newer techniques enhance design freedom and flexibility in geometry design [17]. The introduction of continuous fibre in 3d printing is the next step of additive manufacturing. In that way, there is potential to create new fabrication routes for composite-made architectures such as lattice structures.[19]

2.2.1. Hardware

During this research, an end-effector extruder for continuous fibre-reinforced plastic was used (Fig 2.7). This one integrates several continuous PLA plastic filaments combining them with glass fibre yarns in a pull-extrusion integrative method (CFRP), it was ad-hoc designed based on other academic research's [16][20][21][25]. The mechanical platform was an existing 6-axis robotic arm ABB IRB140, connected to a positive air pressure system and electronically controlled with an Arduino-based programmable controller PLC. Both pneumatic and PLC systems are digitally controlled by the robotic arm controller box to proceed with the on/off operation, pressure and speed control, on-the-fly based on the different toolpaths operations.

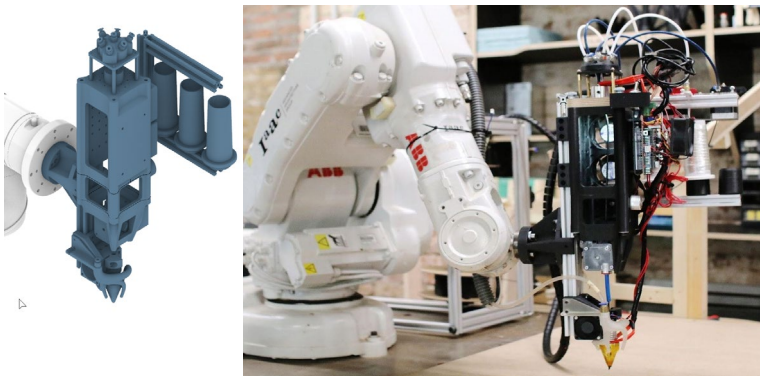


Figure 2.7. Pulltruder-extruder end effector, dry continuous impregnation for continuous fibre manufacturing developed ad-hoc for this research. 3D Cad model (left). Prototype extruder(right)

3. Design for manufacturing & computational methodology

3.1. Stress lines form-finding

There has been limited research on computational design techniques that account for high anisotropy behaviour such as continuous fibre 3d printing, and spatial lattices topologies [19],[23]. In which the material works anisotropically at compression and tension. On the other hand, it has been found correlation between complex lattice patterns found in biological forms and the structural properties of principal stress trajectories [22]**.** Principal stress lines are a representation of the directions of purely axial stress in space (Fig 3.1.). By aligning bar-type elements with the carried load, the material can be directly oriented to meet stress constraints, which can be especially advantageous in situations where little material is required. There is existing research on the generation of fabrication-ready geometries based on stress lines for additive manufacturing (SLAM) [23].

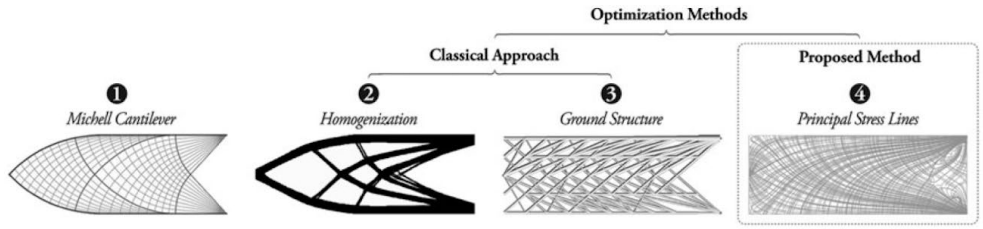


FIG. 5. Convergence of optimization results obtained from **(2–3)** classical optimization methods and both the **(1)** Michell structures and the **(4)** principal stress lines of the corresponding design domain.

Figure 3.1. Additive manufacturing along Principal Stress Lines. Image credit: Tam, K.-M.M. and Mueller, C.T. (2017)

The generative method proposed creates printable paths that follow the stress forces along the materials on a surface it is explained through the presentation of several recursivity algorithms that iteratively start a vector-finding process among the constituent finite element nodal stresses on an initial F.E.M calculation for a specific case study. The algorithmic approach for continuous stress line form-finding not only matches the mechanical characteristics of the fibre composites, which need to have a continuity among the fibre direction to be able to maximize the stiffness and stress capabilities of the materials but also the problems inherent in continuous fibre AM composites. In CFAM is mandatory to have a toolpath with the least number of discontinuities, as the deposition process needs to prioritize the continuity of fibre among its structure to reduce the need for external intervention to section the fibres or an end-effector with cutting capabilities and increase the structural behaviour.

3.2. Stress lines to continuous lattice formation

For the lattice formation, we can distinguish two-level hierarchical structured components obtained across the geometrical lattice. At the first level of resolution, the load paths follow the placement of the main overall force-flow calculated in the SLAM method, at the second level of resolution, the bi-dimensional polygonised matrices are interconnected by the parallel projection of their crossing vertices, followed by reconstruction of the planar defined geometries in a 3-dimensional formation. The projection level of the vertices is constrained by the end-effector capabilities and its conical nozzle point design, stated at a 50mm distance between the first level stage resolution.

Specifically, the final design is not initially modelled in 3D; rather, becomes a 3-dimensional model by the composition of bidimensional matrices that are interconnected with the 3D versions of the same. (Fig.3.2) Cell sizing is informed and driven by the manufacturing criterion of maximum and minimum spacing in their generation of stress lines.

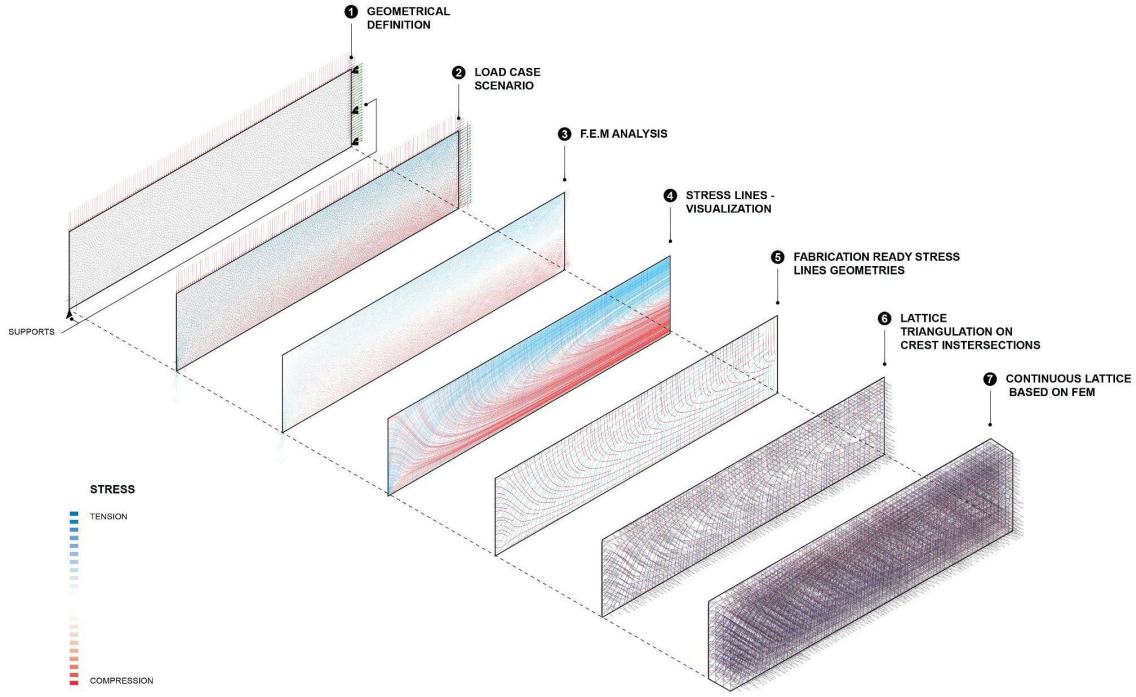


Figure 3.2. Description of the generative method: (1) geometrical definition and boundary constraints, (2) load-case structural scenario, (3) finite element vector result from the load-case scenario, (4) stress-lines interpolation from structural programs, (5) stress-line fabrication aware tracing, (6) stress-line crossing interpolation for crest generation, (7) stacking of bidimensional layers on the 3-dimensional design domain.

Manufacturing-wise, hierarchies follow primarily the two-dimensional substrate resulting from the SLAM followed thoroughly by the vertical interconnecting members. Giving as result a planar-triangulation-planar (P-T-P) lattice formation, that is evenly repeated until the initial volume is filled. The inner and outer layers of it have an identical topology, with a connecting topology between each pair of corresponding nodes, acting as a bracing element for stability. By utilizing carefully-oriented multi bar-type elements, the material continuity can be directly kept by sequencing the polylines on a cartesian space based on the averaged distance to the design space origin, splitting the sequence in stress polylines sequence, continued by the compression ones, allows for continuity of the different elements by force classification, closing the cell lattice between the elements as the material keeps continuity during the print reduce fibre cutting operations, as seen in figure 3.4.

For each individual resulting cell the triangulation topology is constructed by establishing the valleys of it the mid-point of the individual member of each major stress line and the crest at the intersection of these, creating edges on the inner and outer layer, of two possible diagonals for each intersecting set of lines (Fig 3.6). However, the limitation of this strategy is the presence of gaps between the non-reaching boundary lines resulting in non-uniform spacing, resulting in crossing elements that have no structural focus (Fig 3.3).

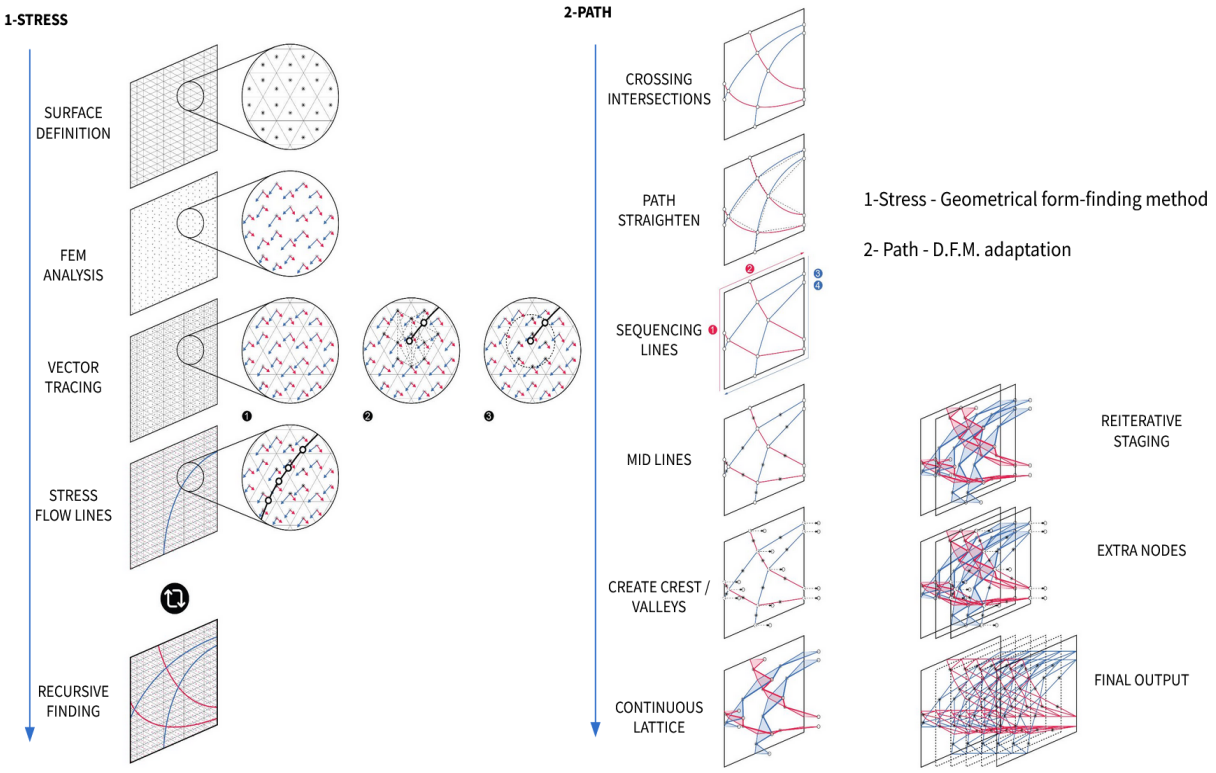


Figure 3.3. Description of the generative method: (1) geometrical definition of stress lines (2) path for manufacturing adaptation and lattice formation.

To effectively incorporate CFAM and topological spatial lattices into fabrication-aware design processes. Continuously arranging the fibres along the lattice-like linear elements of the structure allows for the optimization of material usage and reduces weight while maintaining its structural integrity. This process is more critical when the manufacturing process of continuous fibre deposition relies on the continuity of the fibre for maximum strength and minimizing cutting fibre operations.[21] (Fig 3.7). A continuous print path planning strategy greatly improves the deposition sequence and simultaneously reduced the collision checking operations. The external collision objects have been reduced to a variety of points conforming to the spatial lattice geometry. Instead of using collision checking among mesh to mesh, the points conforming to the spatial lattice are tested to be in the interior of the end-effector basic geometries which greatly improves the calculation time and keeps good detection of possible collisions. This process in the case of lattice additive manufacturing techniques serves as a close match as the material deposited in the workspace is of reduced size and dimension compared to its linear topology.

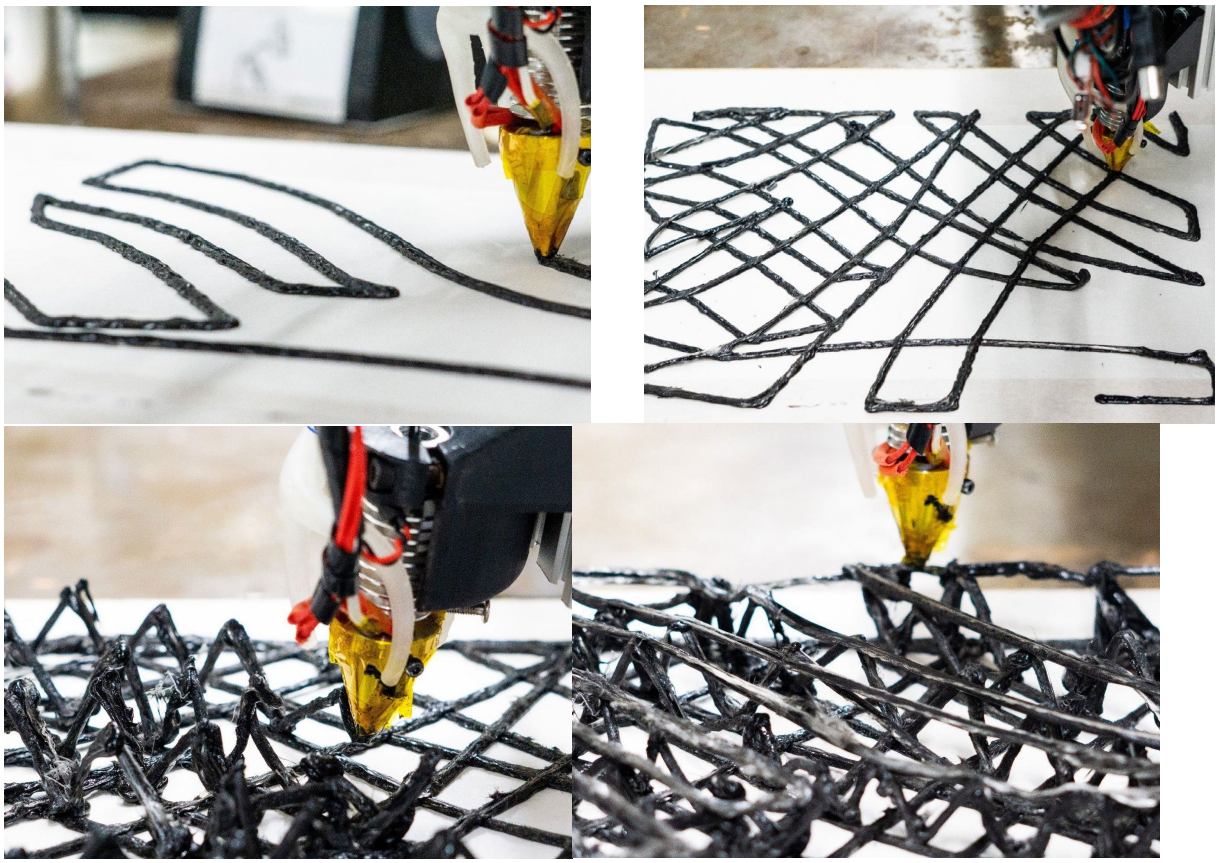


Figure 3.4. (Top-Left) - Continuity path between among the lines with the same force-flow. Figure 3.5. (Top-Right) - Secondary set of compression element continuity. Figure 3.6. (Bottom-Left) - Stress triangulation. Figure 3.7. (Bottom-Right) - Secondary in air stress print layer.

The methodology used for the fabrication sequencing was developed through a series of preliminary material tests, searching for the adequate parameters regarding, material setting time, cantilever maximum spans, geometrical deviation, extruding, horizontal and vertical deposition speed as well as necessary cooling or set time of the material to reach its solid-state mechanical properties.

3.3. Structural re-analysis

In this design for manufacturing workflow which is structurally driven the total supported load relative to the self-weight of the generated case study digital model was reanalysed for its verification as the mechanical performance is a critical aspect for its validation. The spatial lattice line simplified line model was analyzed in KARAMBA 3D, which is a finite element analysis (FEA) plugin for Rhinoceros 3D and Grasshopper 3D modelling environment. The main materials characteristics used in the FEA scenario, are a Young's Modulus of 5000 kN/cm^2, (50MPA), an In-plane shear modulus of 2000 kN/cm^2, a specific weight of 17.45 kN/m^3, for the in-plane ones and the rest of the anisotropy characteristics of the material were fed, based on the aforementioned researchers stated in chapter 2.1. The cross-section resulting from the AM method used, a 4mm diameter linear element in this case was used. A linear elasticity simulation was run using the initial load and support scenario but in this final validation the whole design element was calculated, not the half Messerschmidt- Bölkow-Blohm (MMB), being the design domain a volume of 0.3 x 0.1 x 3 m and a distributed load of 4kn/m^2.

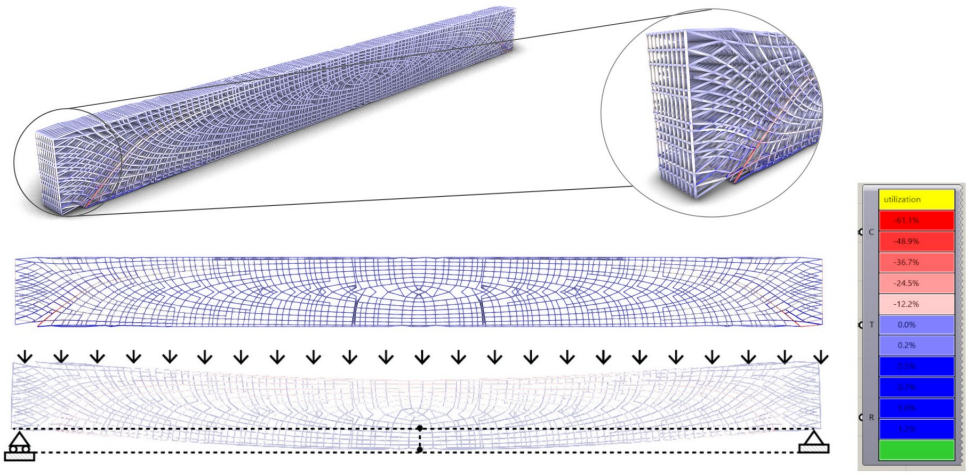


Figure 3.8. Line model analyzed of the structure under a distributed load with PLA+continuous fibreglass material characterization and cylindrical members of 4mm diameter resulting from a CFRP 3D printed extrusion.

The analysis of the resulting structure shows where the principal stresses are driven (red-blue) and the maximum and minimum material utilization on the different lattice elements, being on a visual inspection equally distributed. The diagram in Figure 3.8. is an enhanced image (50x for visualization purposes) of the actual model displacement deformation for this 3m span beam, which is 0.245cm. The total weight for the calculated model is estimated to be 29.88kg.

4. Conclusions and outlook

We have presented a design for manufacturing workflow for continuous fibre lattice additive fabrication and investigated the correlation between continuous path planning and structurally driven stress lines F.E.M. to direct model translation. The characterization of the structural load-bearing capabilities relies on the simple consideration of final structural re-analysis for its validation. Some possible directions for future works are suggested, and the possibility for further optimisation seems achievable. Reiterative stress-line formation and lattice triangulation are mainly driven at the moment by purely manufacturing constraints and the final model can be further lightened by the final output analysis and element reduction as well the possibility of further optimization is therefore inherited in the path-creating process, as the finite element matrix used for calculation occupies the whole initial design domain for the stress line finding algorithm. Reduction of the finite elements used for that process limits the total amount of stress lines created and consequently, material deposited.

Although the proposed method is in its early stages of development, the significance of this research is to confirm that lightweight additively manufactured lattices can be material and topology optimized when coupling structurally driven topology form-finding techniques enhanced with high-performance composite 3d printing techniques. By leveraging the benefits of form-found design and additive manufacturing and considering the multifunctional performance requirements of large-scale structures, this project aims to exploit new opportunities for lightweight architectural design.

Acknowledgements

The authors gratefully acknowledge the support of the Swinburne University of Technology and the Institute for Advanced Architecture of Catalonia, PhD offshore program DR-DES.

References

[1] R. Soar and D. Andreen, "The role of additive manufacturing and physiomimetic computational design for Digital Construction," *Architectural Design*, vol. 82, no. 2, pp. 126–135, 2012.

[2] G. Gardiner, "Continuous Fiber Manufacturing (CFM) with Moi Composites," *CompositesWorld*. [Online].Available:https://www.compositesworld.com/articles/continuous-fiber-manufacturing-cfm-with-moi-composites. [Accessed: 30-Dec-2023].

[3] V. Pollio, I. D. Rowland, T. N. Howe, and M. Dewar, *Vitruvius: Ten books on architecture*. Cambridge: Cambridge University Press, 1999.

[4] "Strength through geometry and Material Effectiveness," Building Better - Less - Different: Circular Construction and Circular Economy, pp. 72–78, 2022.

[5] Jipa, Andrei & Bernhard, Mathias & Meibodi, Mania & Dillenburger, Benjamin "3D-Printed Stay-in-Place Formwork for Topologically Optimized Concrete Slabs," *TxA Emerging Design + Technology*. 2016.

[6] J. Solly, N. Früh, S. Saffarian, L. Aldinger, G. Margariti, and J. Knippers, "Structural design of a lattice composite cantilever," *Structures*, vol. 18, pp. 28–40, 2019.

[7] D. Piker and R. Maddock, "Continuous robotic spatial 3D printing of topologically irregular space frames," *Impact: Design With All Senses*, pp. 502–516, 2019.

[8] Omuro, R, Ueda, M, Matsuzaki, R, Todoroki, A & Hirano, Y 2017, 'Three-dimensional printing of continuous carbon fiber reinforced thermoplastics by in-nozzle impregnation with compaction roller', Paper presented at 21st International Conference on Composite Materials, ICCM 2017, Xi'an, China, 20/08/17 - 25/08/17.

[9] J. P. Nunes, J. F. Silva, and P. J. Novo, "Processing Thermoplastic Matrix TOWPREGS by pultrusion," *Advances in Polymer Technology*, vol. 32, no. S1, 2012.

[10] M. Heidari-Rarani, M. Rafiee-Afarani, and A. M. Zahedi, "Mechanical characterization of FDM 3D printing of continuous carbon fiber reinforced PLA composites," *Composites Part B: Engineering*, vol. 175, p. 107147, 2019.

[11] A. Thakur and X. Dong, "Printing with 3D continuous carbon fiber multifunctional composites via UV-assisted coextrusion deposition," *Manufacturing Letters*, vol. 24, pp. 1–5, 2020.

[12] G. Zocchi, "New developments in 3D printing of Composites : Photocurable resins for UV-assisted processes," *Home page*, 28-Sep-2016. [Online]. Available: https://www.politesi.polimi.it/handle/10589/124844. [Accessed: 30-Mar-2023].

[13] A. N. Dickson, H. M. Abourayana, and D. P. Dowling, "3D printing of fibre-reinforced thermoplastic composites using fused filament fabrication—a review," *Polymers*, vol. 12, no. 10, p. 2188, 2020.

[14] A. Adumitroaie, F. Antonov, A. Khaziev, A. Azarov, M. Golubev, and V. V. Vasiliev, "Novel continuous fiber Bi-Matrix Composite 3-D printing technology," *Materials*, vol. 12, no. 18, p. 3011, 2019.

[15] P. Zhuo, S. Li, I. A. Ashcroft, and A. I. Jones, "Material extrusion additive manufacturing of continuous fibre reinforced polymer matrix composites: A review and outlook," *Composites Part B: Engineering*, vol. 224, p. 109143, 2021.

[16] R. Matsuzaki, M. Ueda, M. Namiki, T.-K. Jeong, H. Asahara, K. Horiguchi, T. Nakamura, A. Todoroki, and Y. Hirano, "Three-dimensional printing of continuous-fiber composites by in-nozzle impregnation," *Scientific Reports*, vol. 6, no. 1, 2016.

[17] Eichenhofer, M., Maldonado, J. I., Klunker, F., Ermanni, P., Materials, C., Extrusion, F. C., Structures, F. F., & Composites, T. "Analysis of Processing Conditions for a Novel 3D Composite Production Technique". *20th International Conference on Composite Materials*, *July* 19–24, 2015.

[18] T. Shelton, "Cellular fabrication," *Technology|Architecture + Design*, vol. 1, no. 2, pp. 251–253, 2017.

[19] M. Eichenhofer, J. C. H. Wong, and P. Ermanni, "Continuous lattice fabrication of ultra-lightweight composite structures," *Additive Manufacturing*, vol. 18, pp. 48–57, 2017.

[20] S. Kuschmitz, A. Schirp, J. Busse, H. Watschke, C. Schirp, and T. Vietor, "Development and processing of continuous flax and carbon fiber-reinforced thermoplastic composites by a modified material extrusion process," *Materials*, vol. 14, no. 9, p. 2332, 2021.

[21] N. Li, Y. Li, and S. Liu, "Rapid prototyping of continuous carbon fiber reinforced polylactic acid composites by 3D printing," *Journal of Materials Processing Technology*, vol. 238, pp. 218–225, 2016.

[22] D. A. W. Thompson, *On growth and form*. Cambridge: Cambridge University Press, 1968.

[23] K.-M. M. Tam, K. T. Mueller, J. R. Coleman, and N. W. Fine, "Stress Line Additive Manufacturing (SLAM) for 2.5-D shells," *Journal of the International Association for Shell and Spatial Structures*, vol. 57, no. 4, pp. 249–259, 2016.

[24] Y. M. Xie, "Generalized topology optimization for architectural design," *Architectural Intelligence*, vol. 1, no. 1, 2022.

[25] J. H. Li, X. D. Huang, Y. Durandet, and D. Ruan, "A review of the mechanical properties of additively manufactured fiber reinforced composites," *IOP Conference Series: Materials Science and Engineering*, vol. 1067, no. 1, p. 012105, 2021.

Proceedings of the IASS Annual Symposium 2023
Integration of Design and Fabrication
10 – 14 July 2023, Melbourne, Australia
Y.M. Xie, J. Burry, T.U. Lee and J. Ma (eds.)

Continuous multi-filament 3D printing for tension-compression structure components

Teng TENG[a,*], Yefan ZHI[a], Kun-Hao YU[b], Shu YANG[b], Masoud AKBARZADEH[a,c]

[a,*] Polyhedral Structures Laboratory, Weitzman School of Design, University of Pennsylvania, Philadelphia, USA
Pennovation Center, 3401 Grays Ferry Ave. Philadelphia, PA, 19146
tteng@upenn.edu

[b] Department of Materials Science and Engineering, University of Pennsylvania, Philadelphia, USA
[c] General Robotic, Automation, Sensing and Perception (GRASP) Lab, School of Engineering and Applied Science, University of Pennsylvania, Philadelphia, USA

Abstract:
In this research, we propose a Multi-Filament Fused Deposit Modelling (MFFMD) printer and a respective generator that can be used to produce structural parts with locally tailored functional properties. 3D-printed structural components can highly benefit from multi-material printing with tuneable functional properties. Currently, multi-material printing is mainly achieved using multiple separate nozzles, leading to discontinuous flow in switching materials. This limitation results in material interface delamination, minimal control in the continuous transition of material properties, and longer production time.To address this, we first design and build an MFFMD printer with a single customized nozzle allowing seamless switching between multiple filaments. We then develop a method that generates a continuous toolpath of a given geometry and differentiates materials based on various stress conditions at particular regions. To illustrate, we fabricate a Pratt truss as an example of a tension-compression structure as a case study. In one go, the MFFMD printer deposits resistant filament, respectively, at tension- or compression-concentrated regions based on local stress conditions. Comparative load tests are conducted to validate the performance enhancement of multi-filament prints against single-filament prints. Our proposed method is a prototypical study conducted at a small scale. While it mainly uses thermal plastic filaments, it can be expanded to other construction materials and scales in the future. The contribution of this paper is multiple. In addition to the prints' structural performance enhancement through the development of the MFFMD printer and slicing tool, the results also provide a tangible visualization of the mechanical and geometrical properties of printed components, facilitating design communications across disciplines.

Keywords: additive manufacturing, multi-material printing, functionally graded material, structural performance, mechanics visualization

1. Introduction

This paper describes a novel method that uses cutting-edge multi-material additive manufacturing technology to continuously print tension-compression structures. The method allows the structure's material properties can be tailored locally based on its' stress patterns through numerical control of material deposition and composition regulation. The method results in the structure's mechanical performance enhancement.

Copyright © 2023 by Teng TENG, Yefan ZHI, Kun-Hao YU, Shu YANG and Masoud AKBARZADEH. Published in the Proceedings of the IASS Annual Symposium 2023 with permission.

3D printing offers considerable advantages in the design and fabrication of tension-compression structures, enabling greater design freedom, rapid prototyping, material and cost efficiency, and on-demand manufacturing. This technology facilitates the creation of complex geometries, custom components, and the integration of multiple functions while promoting sustainability through reduced material waste and optimized designs. Despite its benefits, when using 3D printing technology to produce structural components for construction purposes, limitations are explicit concerning material properties, printing resolution, and scalability must be considered to ensure its suitability for specific projects.

In the construction of tension-compression structures, taking truss as an example, the utilization of single and homogeneous materials presents numerous challenges, often resulting in suboptimal performance and structural inefficiencies. One such challenge arises from the limited material properties inherent in a single homogeneous material, which may lack the necessary combination of strength, stiffness, ductility, and fatigue resistance required for both tension and compression members [1]. This can lead to inefficient use of the material and compromise the overall structural integrity. Moreover, structures made from a single material are more susceptible to common modes of failure, such as corrosion or fatigue [2]. As a consequence, the entire structure is at an increased risk of degradation, whereas a combination of materials could help diversify the failure modes and enhance the structure's resilience. Additionally, using a single material may result in a heavier structure than necessary, impeding its efficiency and practicality. For example, a truss structure composed entirely of steel could be excessively heavy, whereas a combination of steel and aluminum could provide an optimal balance of strength and weight [3]. Therefore, employing a combination of materials can mitigate these challenges and lead to more effective tension-compression truss structures.

In recent years, various innovative methods have been developed to improve the fabrication and assembly of truss structures. Liu et al. (2018) [4] proposed a continuous carbon fiber reinforced thermoplastic lattice truss, which offers enhanced mechanical properties and manufacturing flexibility. This approach leverages the benefits of carbon fiber reinforcement to create lightweight and high-performance trusses. Another significant development in the field is the large-scale 3D printing of metal structure components, as demonstrated by Assunção et al. (2018) [5]. This technique enables the fabrication of complex geometries and rapid production, making it a promising solution for the construction of truss structures. Furthermore, Foster+Partners [6] explored the potential of 3D printing steel trusses, showing the feasibility of employing advanced manufacturing methods to create robust structural elements. Lastly, Kovacs et al. (2017) [7] introduced a method for 3D printing truss joints, facilitating rapid truss assembly and reducing the overall construction time. These advancements collectively showcase the potential of modern fabrication techniques in revolutionizing the design and manufacturing of truss structures.

Current research on 3D-printed truss structures primarily focuses on utilizing a single homogeneous material for the fabrication of components, neglecting the impact of local load conditions and material properties on overall structural performance. Although some studies [8] have considered local stress lines in the design of 3D printing toolpaths, the primary material employed remains homogeneous. Single homogeneous materials are inefficient in addressing the complex internal load distribution within tension-compression truss structures, especially in slender truss members prone to buckling under compressive forces, compromising structural integrity[9]. We propose the use of multi-material 3D printing to construct truss structures with different materials tailored to specific load requirements, thereby enhancing overall performance and stability. However, current studies on the subject of multi-material additive manufacturing focus less on construction purposes [10], [11], [12].

To tackle the aforementioned challenges, a viable methodology must be developed, enabling the additive manufacturing of tension-compression structures in an integrated manner. This strategy should involve the application of locally tailored material properties, contingent upon the stress distribution and loading conditions of the designed structure.

As a pilot study, this paper is situated from the fabrication perspective and discusses the multi-material printing technique and methodology. We select classic 2d truss structures as a trial to validate the performance enhancement through the proposed method.

In this paper, our primary objectives are twofold: First, we aim to integrate the design-make process of multi-material 3D printed tension-compression structures, leveraging the advantages of additive manufacturing technology to create a seamless workflow from design to fabrication. Second, we strive to enhance the mechanical properties of the resulting structures, enabling more robust and efficient performance compared to traditional single-material approaches. By achieving these objectives, we hope to demonstrate the potential of multi-material 3D printing in revolutionizing the construction of tension-compression structures and addressing the limitations of existing methodologies.

2. Methodology

In truss structures, members predominantly experience axial loads, manifesting as either tensile or compressive forces acting along their longitudinal axes. To ensure stability and load-bearing capacity, the materials employed in these members must exhibit adequate resistance to deformation, specifically elongation or shortening, under the influence of the applied forces. Utilizing fiber-reinforced materials with fibers aligned in the longitudinal direction can enhance the tensile strength and stiffness of the members, making them well-suited for withstanding tensile loads. Conversely, non-fiber-reinforced materials demonstrate fine compressive strength when oriented along their short axial direction, rendering them more appropriate for resisting compressive forces in truss members.

The fabrication of a truss structure as holistic through multi-material additive manufacturing necessitates several critical steps. Firstly, tensile and compressive members within the structure must be identified. Subsequently, the local segment orientation is determined based on the stress distribution. Utilizing the stress condition, a toolpath is designed, and appropriate materials are assigned for each member. The material data is then integrated into the toolpath and converted into G-code, which guides the 3D printer during the manufacturing process. The 3D printer employed, whether a commercial or customized system, must possess the capability to process and deposit multiple materials simultaneously, ensuring accurate and efficient fabrication of the truss structure.

We here use the classic Pratt truss as a case study to demonstrate our approach.

2.1. Identify stress situation for truss member

The Pratt truss is situated in a three-point bending scenario (Figure 1a). The load condition primarily involves vertical loads distributed across the structure through tension in diagonal members, compression in vertical members, and in addition, compression and tension, respectively, in the top and bottom chords. While the two outermost vertical members do not receive force in the three-point bending load case, they are treated as tension members in a typical Pratt truss setup where the bottom points receive a live load. Figure 1b shows a simulation run by Karamba3D.

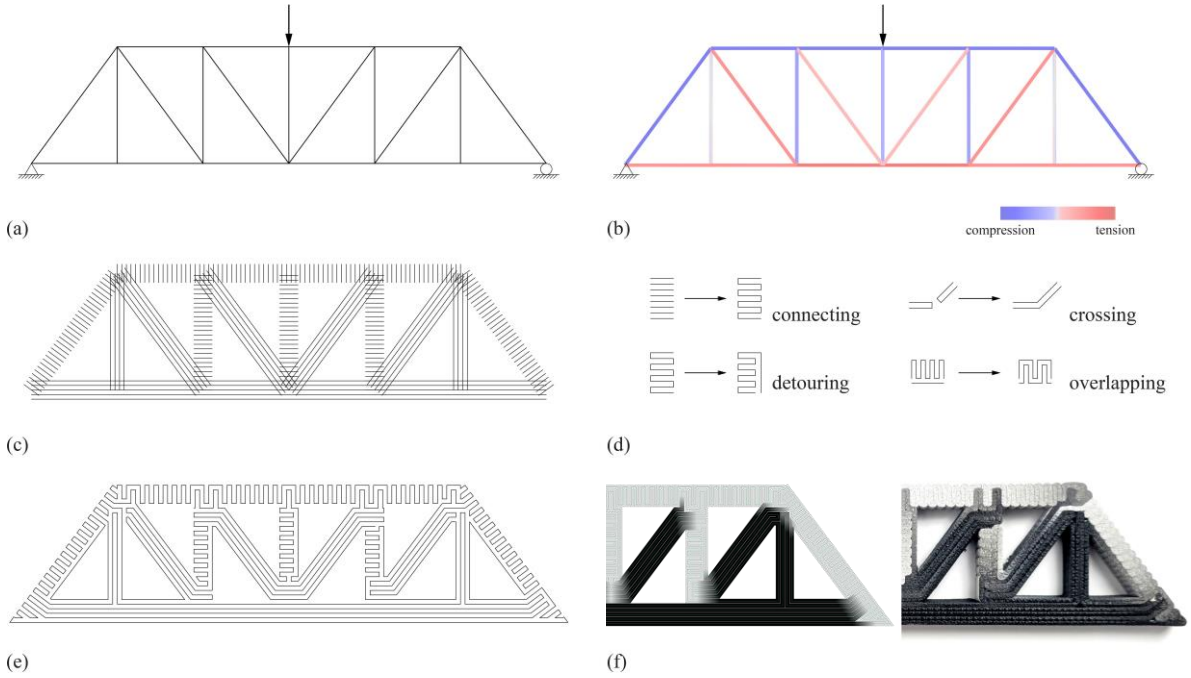


Figure 1. Multi-material printed truss toolpath generation process: (a) Input curves; (b) axial force conditions solved by Karamba3D; (c) raw curves according to the axial forces; (d) post-processing methods to form a continuous toolpath; (e) the final toolpath; (f) left: multi-material visualization of the print, right: multi-material printing

2.2. Translating stress pattern into continuous toolpath design

The mechanical property of a parallel print is similar to that of wood lumbers: the longitudinal direction takes more tensile forces while the tangential direction takes more compression. To utilize such knowledge, the local orientation of the toolpaths is determined by the stress situation (tension or compression). When the rod takes tensile forces its toolpaths are parallel to the rod direction; when it takes compressive forces its toolpaths are vertical. Figure 1c shows this step of generating raw toolpaths as discontinuous lines.

A continuous toolpath for 3D printing significantly saves production time and avoids underfilling and overfilling to enhance the bound [13]. In our case, post-processing (Figure 1d) is introduced to make the toolpath continuous. The curves are connected, primarily in a zig-zag fashion to form several loops. The loops are then merged by crossing and detouring. Finally, at the joints, we modify the toolpaths to create overlapping for better bounding.

The continuous planar toolpath is shown in Figure 1e. Multi-material information is then embedded to print the tensile part using carbon fiber filament and the compressive part using regular PLA filament. Figure 1f shows the visualization of the material-coded toolpath with the printed object.

2.3. Hardware modification

Improving the mechanical performance of structural components through multi-material additive manufacturing involves not only designing toolpaths based on local stress conditions but also utilizing special-

ized equipment for multi-material printing. In this regard, we made minor modifications to a conventional Fused Deposition Modeling (FDM) 3D printer to meet our demands.

Firstly, in terms of hardware, considering the challenges associated with material transition and bonding, we abandoned the use of a multi-nozzle, multi-filament mechanical system for multi-material printing. Although multi-nozzle systems are the most common approach for multi-material 3D printing and can fully facilitate multi-material printing, material transitions mainly rely on nozzle switching. This results in explicit interfaces between materials, which under load conditions, especially tensile forces, can lead to relatively weak bonding adhesion between materials and potentially compromise the overall structural strength.

To address this issue, we developed a detachable single-nozzle multi-filament extruder (Figure 2) to composite the proposed Multi-Filament Fused Deposit Modelling (MFFMD) printer. This extruder comprises a brass 3-in-1-out nozzle connected to three E3D V6 heatsink/heat throat kits. Each kit is connected to a corresponding stepper motor via an individual teflon hose. The brass nozzle is specially designed with three input chambers and one output chamber. The three input chambers merge at the nozzle's center and then connect to the output chamber. We set the output chamber's diameter at 1 millimeter, and the length at 5 millimeters, and the nozzle was fabricated using selective laser sintering. The three stepper motors are responsible for feeding the three filaments, which are then sent through the hoses into the three E3D V6 heatsink/heat throat kits for melting before being extruded through the output.

Meanwhile, the 3-in-1-out nozzle necessitates the addition of two extra stepper motors to the machine's stock configuration. Consequently, it is essential to replace the original printer motherboard, which conventionally supports only four axes (X, Y, Z, and E0). The new motherboard must support the aforementioned four axis as well as two additional feeding stepper motors (E1 and E2). In this study, we employed the BTT Octopus series multi-axis motherboard. This motherboard not only accommodates the standard three linear axes but also provides support for an additional five axes on the extruder, with the potential to integrate three more axes in future developments. At the firmware level, we adopted Marlin 2.1.2 and overwrote certain contents to enable the mixing extruder functionality. This allows for simultaneous adjustments of multiple feeding motor rotational speeds during the printing process.

2.4. Multi-material deposition

The firmware modification facilitates multi-material deposition using a single-nozzle, multi-filament configuration. However, conventional slicing software lacks comprehensive support for multi-material printing with this setup. To address this limitation, we developed a Rhino/Grasshopper-based G-code generator that enables users to input the designed toolpath of the target structure, along with material indications, and generate G-code compatible with the modified single-nozzle, multi-filament printer.

In general, the key steps for generating G-code for single-nozzle multi-material 3D printing involve using M163 and M164 commands to set up and store the configurations for each filament used and then printing the desired toolpaths with the corresponding filaments. Initially, each filament is activated for extrusion, while the others are deactivated, and the setup is stored. This process is repeated for all filaments involved in the printing process. Next, the pre-defined filament setups are called up using the T command sequentially. The corresponding toolpaths are printed by moving the extruder to the specified coordinates while extruding the appropriate amount of the selected filament at a predetermined speed. These steps enable a single-nozzle 3D printer to successfully perform multi-material printing by

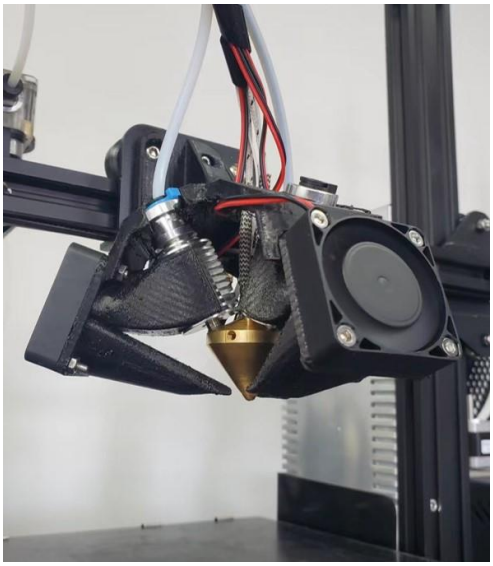


Figure 2. 3-in-1-out nozzle designed for Multi-material (filament) printing

switching between different filaments during the printing process. Listing 1 is a short G-code for printing two lines with two different filaments, Table 1 explains the G-code commands and their meanings when printing multi-material.

Listing 1: G-code for printing three lines with three filaments.

```
M163 S0 P1
M163 S1 P0
M163 S2 P0
M164 S0

M163 S0 P0
M163 S1 P1
M163 S2 P0
M164 S1

M163 S0 P0
M163 S1 P0
M163 S2 P1
M164 S2

...

T0
G1 X0 Y0 Z1 E0
G1 X10 Y0 Z1 E10
T1
G1 X20 Y0 Z1 E20
T2
G1 X30 Y0 Z1 E30
```

Due to the extrusion of different filaments is proceed through the same nozzle, in addition to the identical

Table 1. Description of G-code commands, lowercase letters are values to fill in.

Command	Description
`M163 Ss Pp`	Set the weight for extruder motor *s* to *p*
`M164 Ss`	Store the current mix as tool index *s*
`Tx`	Select the previously stored tool index *x*
`G1 Xx Yy Zz Ee`	Move to (x, y, z) and extrude to *e*

or similar matrices of filament, the extruded materials exhibit a highly cohesive bonding. This bonding is essential for achieving reliable, robust, multi-material 3D printing with a single nozzle system. The following pseudocode describes the composition procedure of the G-code used for single-nozzle multi-material printing.

To ensure the overall strength of the printed structural components, we opted to connect all the force-informed toolpaths into a single continuous polyline instead of multiple line segments. This approach ensures the continuity of the printer's extruder movement to result in a continuous extruded filament through a single nozzle. However, this toolpath is mathematically a curve that is composed of multiple segments sharing endpoints. Each segment is assigned a corresponding resistant filament based on the local stress conditions of the structure using the T command in G-code.

In addition, to switch between different filaments, the new material will push out residual material once the new material's corresponding stepper motor begins feeding. Hence, the advancement of material switching is necessary, meaning that the endpoint of each segment needs to move forward for a certain length on the continuous toolpath. For our setup, we use the volume of the output chamber of the nozzle to determine the advancement length.

By using the above method to generate force-informed and multi-material-embedded toolpaths, we successfully 3D printed a three-material Pratt truss (Figure 3) to demonstrate our printability, in where the color distribution is based on Finite element analysis result of a three-point bending simulation. The blue color indicates the stress-concentrated area, and the green color indicates where it withstands less stress.

3. Results

3.1. Experimental setup and testprocedure

To validate the improvement in the mechanical performance of the components fabricated using our proposed method, We prepared two truss samples (Figure 4) to conduct a three-point bending test. Each sample was printed with a layer height of 0.8 mm and an extrusion bandwidth of 2mm. The dimensions of all samples were 250mm in length, 65mm in height, and 16 mm in thickness. The printing time for each sample was approximately one hours. For the experimental specimen, we utilized HATCHBOX white PLA as the compressive material, which was deposited at the compressive members. In contrast, OVERTURE Carbon Fiber reinforced PLA filament was used as the tension-resistant material deposited at the tensile members. For the single material control group specimen, HATCHBOX white PLA was employed as the primary material. All test specimens were printed at a temperature of 200°C and a speed of 30mm/sec. Calculated from toolpath length, the multi-material experimental specimen contains 52.5% of the toolpath that withstands tensional stress while another 47.5% of the toolpath is bearing compression stress. The multi-material experimental specimen is weighted as 166g, while the single-material control group specimen is weighted as 179g.

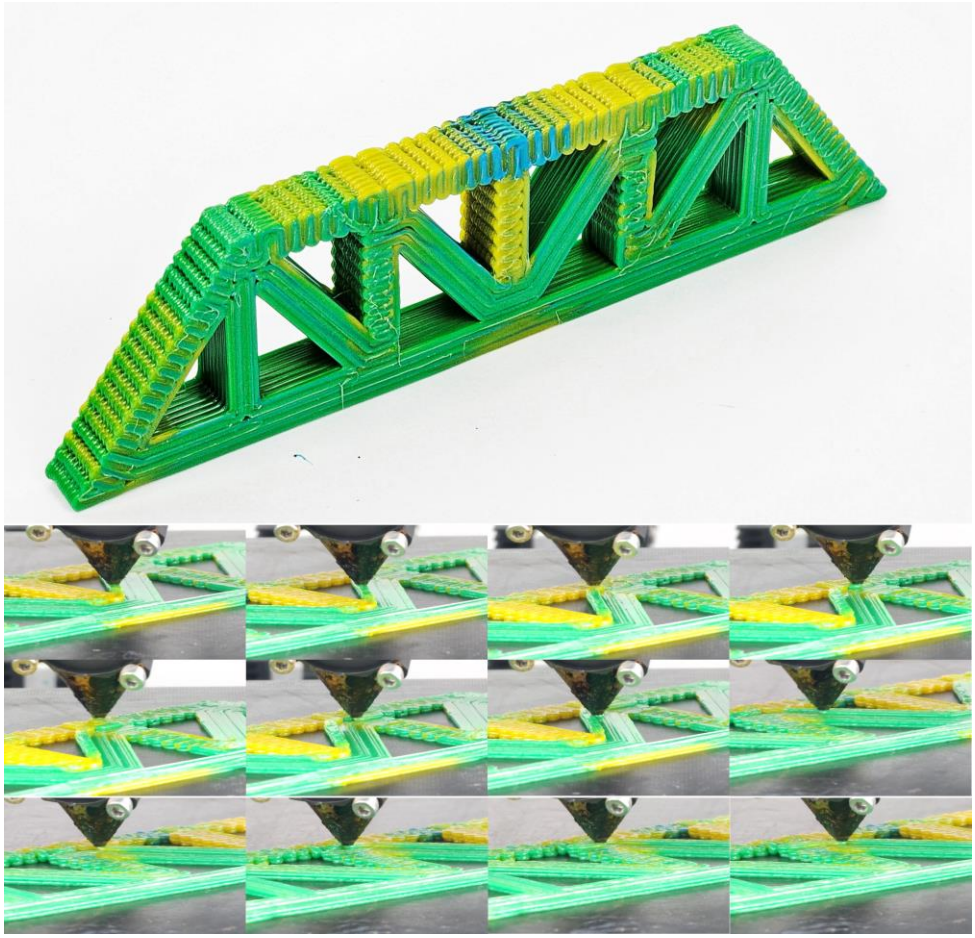


Figure 3. Upper: Printed Pratt truss with three different filaments: yellow PLA Filament, green PLA Filament and blue PLA Filament. Lower: the three-filament continuous printing process.

We utilized an Instron 4206 testing machine to perform the three-point bending tests. Each sample was positioned on the two lower supports of the fixture, and the loading nose was aligned to the center of the top chord of the truss specimen. The span length for the test was set at 220mm.

We first ensured that the loading nose was correctly aligned and centered. We then set the loading rate at 10 mm/min and initiated the test by applying force to the center of the truss using the upper loading nose. Throughout the test, the testing machine continuously recorded the applied force and the resulting displacement of the truss. We continued to apply force until the truss either fractured or yielded and repeated the test for both specimens.

3.2. Results and observations

The three-point bending test as shown in Figure 6 determines the maximum load both specimens can withstand. As shown in Figure 5, the single-material control specimen yielded under a load of 0.83 kN. In contrast, the multi-material experimental specimen reaches the yield point at 1.16 kN, and one of the compressive members begins to buckle, causing overall plastic deformation in the truss. As expected, the multi-material experimental specimen exhibits a higher stiffness than the single-material specimen.

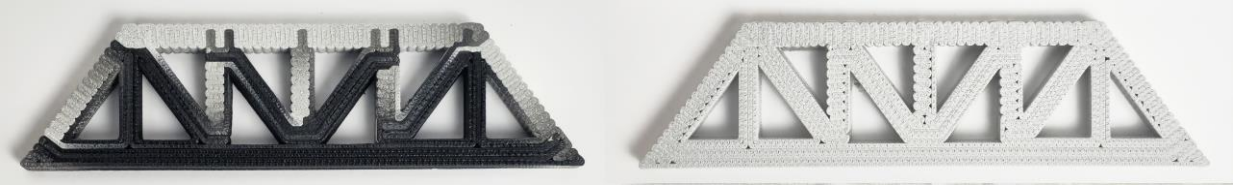


Figure 4. Two samples for three-point bending test. Left: multi-material experimental specimen printed with HATCHBOX white PLA and OVERTURE Carbon Fiber reinforced PLA. Right: single material control group specimen printed with HATCHBOX white PLA only.

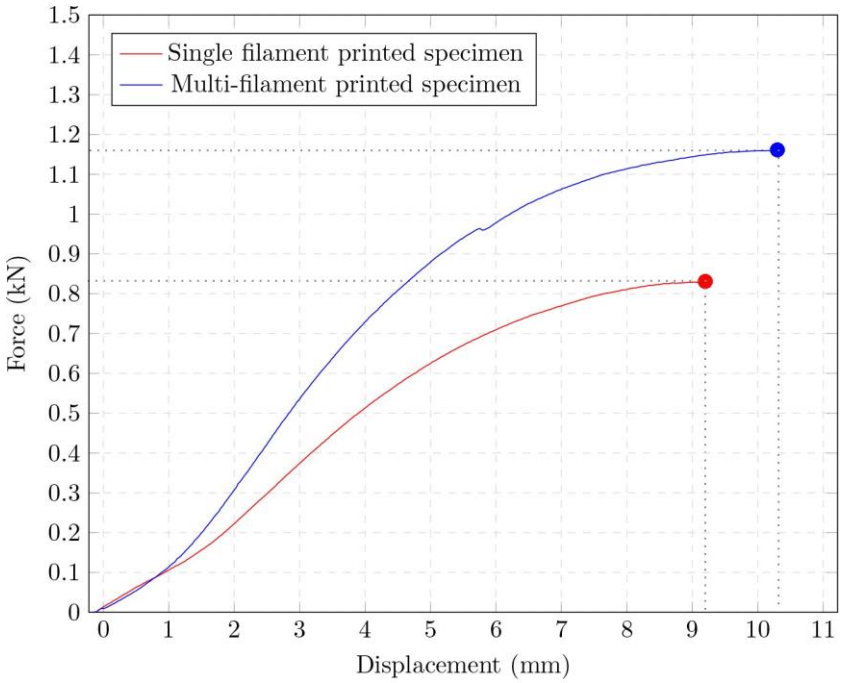


Figure 5. Result of three-point bending test

Figure 5 also presents the load-displacement curves obtained from the three-point bending tests for the different specimens. The load-displacement curves demonstrate that the multi-material specimen possesses substantially higher toughness compared to its single-material counterpart. The toughness is measured by the area under the stress-strain curve up to the fracture point. In our three-point bending test, we employ the trapezoidal rule for numerical integration to calculate this area:

$$\text{Area} \approx \frac{1}{2}\sum_{i=1}^{n-1}(\varepsilon_{i+1} - \varepsilon_i)(\sigma_{i+1} + \sigma_i) \tag{1}$$

where ε_i and σ_i represent the displacement and force values, respectively, for the i-th data point, and n is the total number of data points.

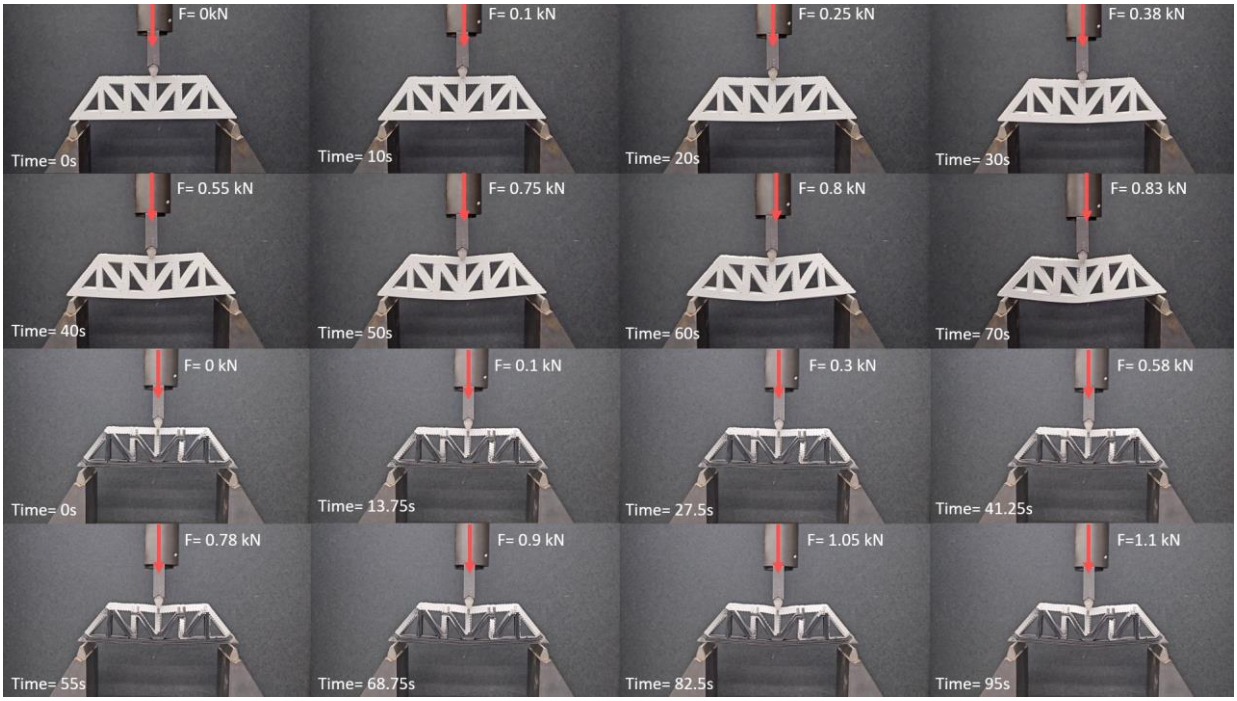


Figure 6. Three-point bending test of two PLA truss specimens. Upper two rows: single material (Regular white PLA) printed controlled sample. Lower two rows: Multi-material (Regular white PLA and carbon fiber enforced black PLA) printed experimental sample.

The numerical analysis revealed that the multi-material sample exhibits approximately 67% higher toughness compared to the single-material counterpart.

Due to the high elastic deformation capacity of PLA filament, we did not observe the behavior of two specimens under fracture conditions after the structure yielded under applied external loads. Therefore, we conducted another test using PETG to examine the fracture behavior of multi-material printed structures when the load was applied. In Figure 7, A subsequent three-point bending test was performed, applying continuous load until fracture to investigate the specimen responses beyond material yield points. The control specimen was fabricated using standard white PETG, while the experimental specimen was composed of carbon-fiber-reinforced black PETG and standard white PETG. The examination of the fractured specimens post-testing revealed no initiation of cracks at the material transition regions, suggesting that the single nozzle configuration effectively mitigates delamination under tensile loading. A comparison between the post-test multi-material and single-material samples demonstrated that one tensile member in the single-material sample experienced failure and disintegration. In contrast, the corresponding tensile element in the multi-material sample remained undamaged. The primary cause of fracture in the multi-material sample can be attributed to the buckling of the adjacent compressive members.

4. Conclusion

This paper presented a groundbreaking method that harnesses the potential of state-of-the-art multi-material additive manufacturing technology to print tension-compression structures in a continuous manner. This innovative technique paves the way for unique opportunities in the development of structures

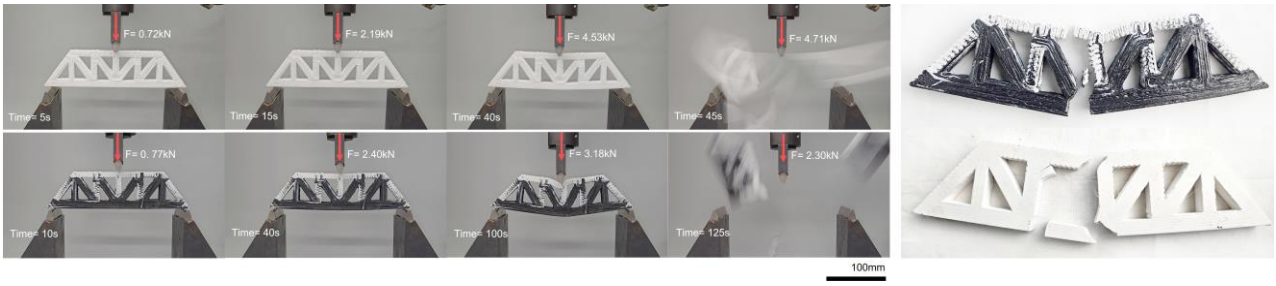


Figure 7. Left: three-point bending test for examing structure's fracture behavior. Upper left row: single material (Regular white PETG) printed controlled sample. Lower left row: Multi-material (Regular white PETG and carbon fiber enforced black PETG)printed experimental sample. Right: A comparison between the post-test multi-material and single-material samples. Upper right image:multi-material specimen, Lower right image:single-material specimen

that possess enhanced mechanical properties. The proposed method enables local customization of the structure's material properties based on stress patterns by accurately controlling material deposition and composition regulation. As a result, this approach not only improves the mechanical performance of the structure but also optimizes material usage and reduces overall material waste. Distinguished from traditional manufacturing techniques and in collaboration with stress-informed toolpath design, the proposed method capitalizes on the versatility of heterogeneous materials to fabricate high-performance tension-compression structures with unprecedented capabilities. The current methodology is constrained by the build volume of the 3D printers, limiting the dimensions of fabricable structures. Additionally, the technique presently accommodates only 2D extrusion, potentially restricting the development of intricate and complex geometries. Furthermore, the existing setup is incompatible with the utilization of construction materials, such as concrete, for additive manufacturing purposes.

Future work should focus on adapting the multi-material extruder for compatibility with robotic systems, thereby enhancing fabrication freedom and scalability. Extending the method to accommodate 3D extrusion is crucial for enabling the creation of more complex structures and designs. Moreover, exploring the integration of construction materials, such as concrete, into the printing process is essential to broaden the range of potential applications in the construction industry.

The wider implications of the proposed multi-material printing system have far-reaching effects that extend well beyond the realm of additive manufacturing. By facilitating local tailoring of components, this pioneering method enables the development of high-performance structures with potential applications in diverse industries, such as aerospace, automotive, and civil engineering.

The system allows for the fabrication of objects with multiple material properties in a singular process, streamlining production workflows, reducing the need for subsequent assembly, and considerably mitigating inefficiencies in manufacturing and construction sectors. Furthermore, the establishment of this groundbreaking technology will offer invaluable insights for researchers across diverse disciplines to construct the single-nozzle multi-cartridge (SNMC) printer for multi-material applications at varying scales.

As a result, the comprehensive ramifications of this innovative system will not only promote the progres-

sion of interdisciplinary research but also contribute to a new era of efficient, sustainable, and advanced manufacturing solutions. By embracing the possibilities offered by multi-material additive manufacturing, we move closer to a future where design and functionality are seamlessly integrated, creating structures and components that redefine our understanding of efficiency and performance.

Acknowledgements
This research was also funded by the National Science Foundation CAREER Award (NSF CAREER-1944691 CMMI) and the National Science Foundation Future Eco Manufacturing Research Grant (NSF, FMRG-2037097 CMMI) to Dr. Masoud Akbarzadeh.

References

[1] J. Zhao, X. Lu, J. Liu, C. Bao, G. Kang, M. Zaiser, and X. Zhang, "The tension-compression behavior of gradient structured materials: A deformation-mechanism-based strain gradient plasticity model," *Mechanics of Materials*, vol. 159, p. 103912, 2021.

[2] S. Mall, D. Katwyk, R. Bolick, A. D. Kelkar, and D. Davis, "Tension–compression fatigue behavior of a h-vartm manufactured unnotched and notched carbon/epoxy composite," *Composite structures*, vol. 90, no. 2, pp. 201–207, 2009.

[3] K. J. Doherty, A. Yiournas, J. A. Wagner, and Y. Murty, "Structural performance of aluminum and stainless steel pyramidal truss core sandwich panels," tech. rep., ARMY RESEARCH LAB ABERDEEN PROVING GROUND MD, 2009.

[4] S. Liu, Y. Li, and N. Li, "A novel free-hanging 3d printing method for continuous carbon fiber reinforced thermoplastic lattice truss core structures," *Materials & Design*, vol. 137, pp. 235–244, 2018.

[5] E. Assunção, L. Quintino, F. Martina, S. Williams, I. Pires, and A. Lopez, "Lasimm-am production of large scale engineering structures," 2018.

[6] "Foster + Partners breaks new ground with LASIMM 3d printing technology — Foster + Partners — fosterandpartners.com." https://www.fosterandpartners.com/news/ foster-plus-partners-breaks-new-ground-with-lasimm-3d-printing-technology. [Accessed 07-Apr-2023].

[7] R. Kovacs, A. Seufert, L. Wall, H.-T. Chen, F. Meinel, W. Müller, S. You, M. Brehm, J. Striebel, Y. Kommana, *et al.*, "Trussfab: Fabricating sturdy large-scale structures on desktop 3d printers," in *Proceedings of the 2017 CHI conference on human factors in computing systems*, pp. 2606–2616, 2017.

[8] K.-M. M. Tam and C. T. Mueller, "Additive manufacturing along principal stress lines," *3D Printing and Additive Manufacturing*, vol. 4, no. 2, pp. 63–81, 2017.

[9] D. Bondok, H. Salim, and G. Urgessa, "Quasi-static responses and associated failure mechanisms of cold-formed steel roof trusses," *Engineering Structures*, vol. 231, p. 111741, 2021.

[10] W. Liu, Y. S. Zhang, M. A. Heinrich, F. De Ferrari, H. L. Jang, S. M. Bakht, M. M. Alvarez, J. Yang, Y.-C. Li, G. Trujillo-de Santiago, *et al.*, "Rapid continuous multimaterial extrusion bioprinting," *Advanced materials*, vol. 29, no. 3, p. 1604630, 2017.

[11] D. Han and H. Lee, "Recent advances in multi-material additive manufacturing: methods and applications," *Current Opinion in Chemical Engineering*, vol. 28, pp. 158–166, 2020.

[12] M. Vaezi, S. Chianrabutra, B. Mellor, and S. Yang, "Multiple material additive manufacturing–part 1: a review: this review paper covers a decade of research on multiple material additive manufacturing technologies which can produce complex geometry parts with different materials," *Virtual and Physical Prototyping*, vol. 8, no. 1, pp. 19–50, 2013.

[13] M. Bi, L. Xia, P. Tran, Z. Li, Q. Wan, L. Wang, W. Shen, G. Ma, and Y. Xie, "Continuous contour-zigzag hybrid toolpath for large format additive manufacturing," *Additive Manufacturing*, vol. 55, p. 102822, 04 2022.

IASS 2023
July 10–14 Melbourne
Integration of Design and Fabrication

Proceedings of the IASS Annual Symposium 2023
Integration of Design and Fabrication
10–14 July 2023, Melbourne, Australia
Y.M. Xie, J. Burry, T.U. Lee and J. Ma (eds.)

Design optimization workflow for 3D concrete printing of spanning structures

Gonçalo DUARTE[a,*], Jose Pinto DUARTE[b], Nathan C. BROWN[a], Ali MEMARI[a], Shadi NAZARIAN[b]

[a,*] Department of Architectural Engineering, The Pennsylvania State University
gfd5123@psu.edu

[b] Stuckeman School of Architecture and Landscape Architecture, The Pennsylvania State University
jxp400@psu.edu

Abstract

The process of 3D concrete printing (3DCP) and early age material behaviour introduce design constraints related to overall form and toolpath design. These requirements are particularly acute in the case of spanning structures. To avoid printing failure and identify forms that are amenable for 3D printing, a workflow is proposed to optimize forms based on buildability constraints and user preferences. The workflow encompasses four steps: generation of an initial structure based on predefined parametric models and user input, generation of an appropriate toolpath, structural simulation in early and hardened states, and structural optimization of the form and toolpath considering buildability, serviceability, and printability constraints. The workflow was validated by designing and printing a 1.2-meter tall cross-vault. The optimization process focused on studying the scale effect, by comparing how the cross-vault design changes with the area to be enclosed; fabrication process, by evaluating how different construction processes influence the design; and structural performance vs printing quality. Results indicate higher slenderness for larger scale solutions, which is explained by the increased printing time per layer and thus material strength. Additionally, optimization results indicate that increasing printing time per layer through specific fabrication strategies led to material savings up to 50%, and is key to fabricate solutions that are slender, functional, and display better printing quality.

Keywords: 3D Concrete Printing (3DCP); digital fabrication; conceptual design; buildability; structural performance; optimisation; shells, Hangai Prize applicant

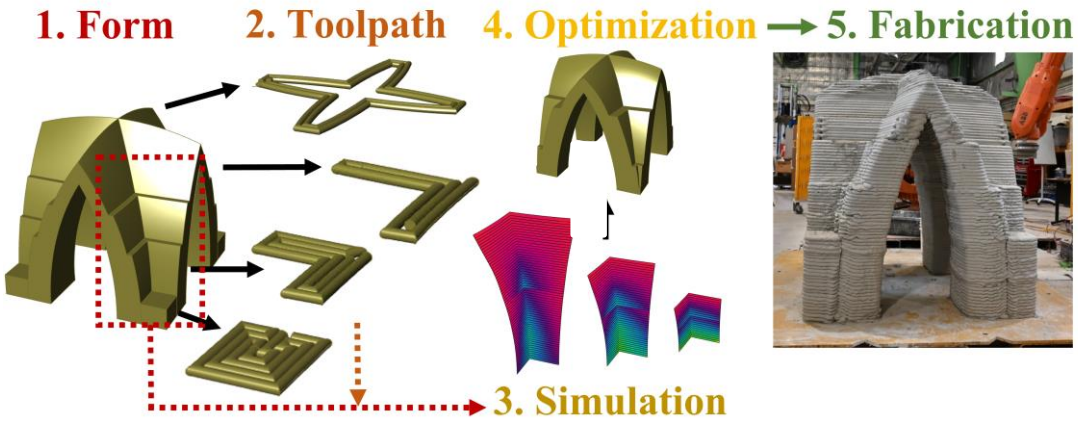


Figure 1. Proposed design optimization workflow description and application to the design of a 3DCP cross-vault.

Copyright © 2023 by Gonçalo DUARTE, Jose Pinto DUARTE, Nathan C. BROWN, Ali MEMARI and Shadi NAZARIAN. Published in the Proceedings of the IASS Annual Symposium 2023 with permission.

1. Introduction

The world population has experienced exponential growth in the past 100 years because of technological developments that led to the industrial revolution, and advances in medicine and sanitation that allowed disease control. As a result, one of the greatest challenges of our time is to provide affordable housing for millions of people still living in degrading conditions. To solve the shortage of affordable housing, it is necessary to develop innovative construction techniques to overcome the current limitations of the construction industry, while decreasing its ecological footprint. Additive construction is seen as a promising solution because of fast construction rates and use of sustainable printing mixtures, as seen in home construction by Apis Cor, ICON, and Wasp, to name a few cases. Additionally, this technology promotes the use of locally available materials for the mix-design, which has also been an argument for its potential use for lunar and Martian construction. A challenge in the widespread use of additive construction is the fabrication of spanning structures, in particular roof structures. In fact, most recent industry solutions involve printing straight or curved walls and installing the roof with a different technological system, which leads to additional costs and does not exploit the full potential of the technology. Alternatives such as prefabricating discretised parts [1] or large-scale 3D printed formwork for slabs [2] allow the exploration of the architectural freedom that is possible to achieve with this technology, but they require on-site assembly and formwork. Recent work has also explored scaffold-free fabrication [3,4], but this has largely been limited to small-scale spanning structures. Thus, the fabrication of enclosures for additive construction is still an ongoing challenge.

In addition to roof fabrication, design for additive construction presents several challenges. In fact, the current methods to design structures require a multitude of software for different design stages, such as 3D modelling of the basic design, toolpath generation, structural analysis, and in case of using an industrial ABB robotic arm, Rapid code generation. This process is fragmented and time consuming and does not facilitate design optimization. Therefore, there is a need to develop a design optimization framework directed for additive construction.

To overcome the challenges mentioned above, this paper proposes a workflow to optimize printed forms based on printability, buildability, and hardened constraints. The workflow is supported by a design platform developed in Grasshopper that encompasses four main components: (1) shape generator, which generates an initial structure based on predefined parametric models and user input; (2) toolpath and filament generator, which depends on the choice of fabrication process; (3) structural performance simulator, which performs layer by layer structural analysis of the part during printing and in its hardened state; (4) performance-based constrained optimizer. The proposed design optimization workflow facilitates design for additive construction by providing a single platform combining form generation, toolpath generation, structural analysis, and optimization. This work also demonstrates that 3D printing technology is adequate to fabricate small-scale and construction scale roof structures. Additionally, this work studies the influence of scale, layer printing time, and filament design in the structural optimization of roof structures for additive construction.

2. Performance-based design and optimization for additive construction

Design for additive construction involves two inter-related concepts, namely form and toolpath. Many historic structures feature forms and processes that rely on compression as the main structural principle and are, therefore, suitable for printing in concrete without formwork. Previous work [6] identified structures consisting of load-bearing walls and shells, such as pointed vaults and domes, as examples of roof structures suitable for additive construction. The rules for designing these structures can be codified into a shape grammar that can be converted into a parametric model for ease of implementation [7]. Alternatives to parametric modelling include form finding methods such as the force density method [4] and dynamic relaxation [8], which have been adopted in the design and fabrication of funicular shells. Toolpath design follows the overall shape generation and has been a part of research projects that

incorporate shape grammar-based algorithms [7], patch grammars [3], transfinite mapping [9], and a combination of principal stress lines and parametrized control curves [4].

The extension of the overall shape and toolpath generation into a workflow is dependent on analysing early age buildability. A challenge in the study of 3D printed concrete in early age is integrating structural performance indicators into an optimization workflow, which requires simplified models that reduce processing time and are easily automated. Several methods for structural performance for additive construction include limit state equilibrium analysis, discrete element methods, and finite element analysis. Limit state equilibrium has been adopted to evaluate collapse based on the critical angle, as seen in Carneau *et al.* [5], but was limited by not considering the dynamic state of the material caused by the thixotropic behaviour over time. Discrete element modelling has been adopted in 3DCP [1], but this example involved discretised masonry structures. Limit analysis also contains assumptions such as no tensile capacity, infinite compressive strength, and infinite friction coefficient. These assumptions do not represent the early age buildability, in which the material displays a viscoelastic behaviour and a well-defined friction coefficient. Finally, finite element analysis (FEA) has been used to estimate the early-age modes of collapse [11, 12] and has found a good level of agreement between simulations and printing experiments. The work by [3] incorporated a workflow that combined a form finding algorithm with structural stability analysis using FEA, but without considering buildability constraints based on the time-depending material properties. The work by [4] incorporated a design optimization workflow for funicular vaults that optimized a compound function based on the toolpath length and the displacement field of the shell. However, the impact of buildability constraints and respective modes of collapse were not discussed. Both workflow applications described were limited to the context of small-scale shells and did not discuss implications for construction-scale fabrication.

The workflow presented in this paper extends knowledge by allowing the structural optimization of a given structure based on design constraints that depend on buildability, serviceability, and printability. Buildability constraints consider the toolpath solution obtained from a concentric-based toolpath generator, the layer-by-layer performance, variable material properties over time, and the analysis of the modes of collapse: plastic collapse, elastic buckling, and flexural collapse, which were evaluated using a structural simulator developed and validated in a previous publication [12]. Serviceability constraints provide a proxy for excessive deflection and drift for service wind loads. Printability constraints are incorporated as a proxy for printing quality in terms of expected filament geometry. This conference paper shows the application of the workflow to the case study of a cross-vault structure.

3. Methodology

The proposed design optimization workflow and the supporting platform are represented in Figure 2. The platform is comprised of five main components, each corresponding to a step in the workflow: (1) form generator, which generates a 3D model of a shell based on the geometric and printing variables defined by the user; (2) filament analyser, which considers the printing variables and outputs as a proxy for printability a set of constraints based on filament geometry and quality; (3) toolpath generator, which generates a toolpath solution based on the fabrication strategy and printing variables defined by the user; (4) structural simulator, which slices the generated shell model into layers, calculates their ages, assigns the respective material properties based on the toolpath design, and outputs a set of constraints that represent a proxy for buildability and serviceability; and (5) performance-based optimizer, which takes such constraints and the geometric and printing variables, and uses toolpath length, which is proportional to structural mass, as the objective function. The use of the workflow in the of design a cross-vault structure, followed by validation through experimental printing tests, is described below as a way of illustration.

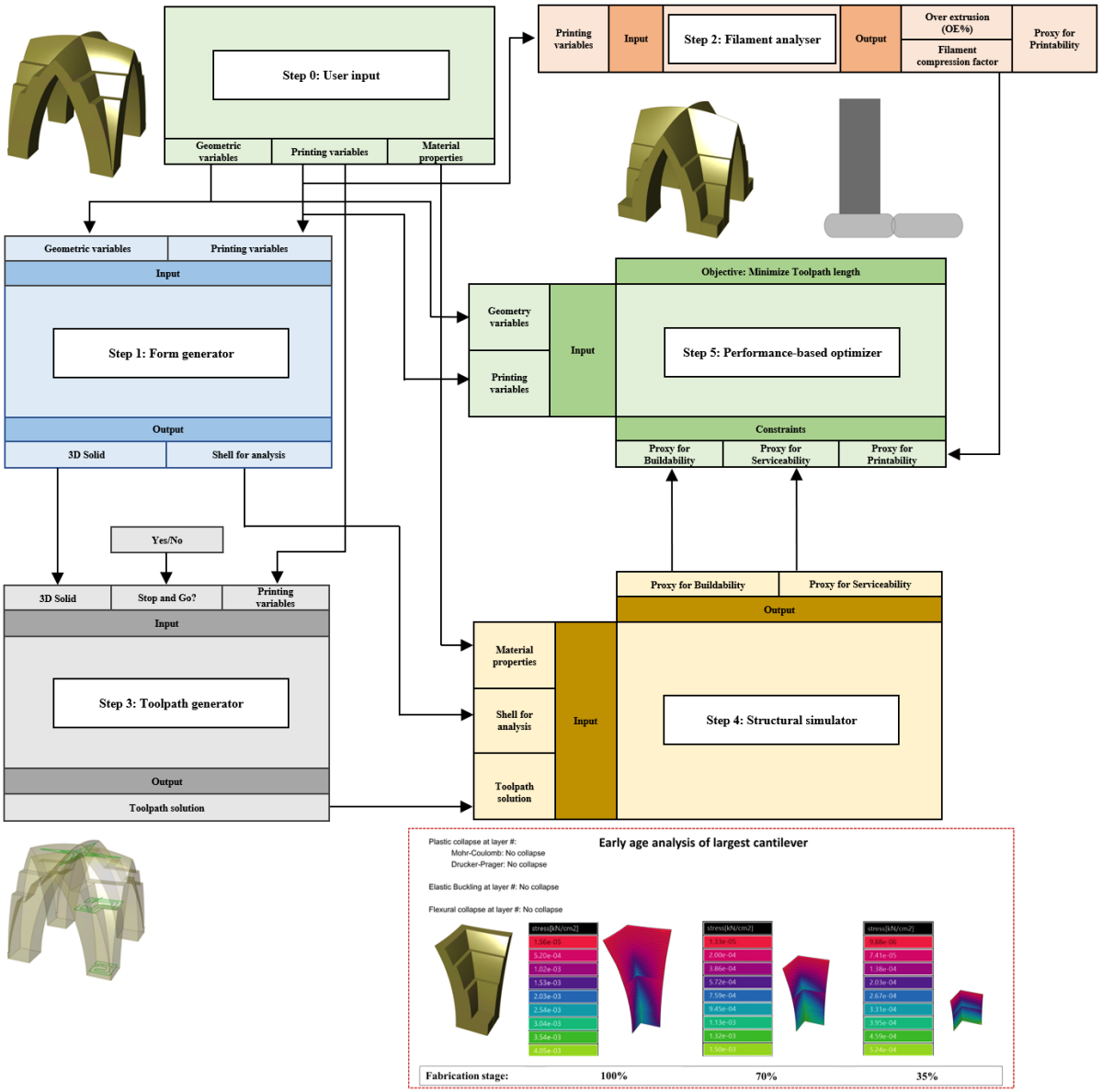


Figure 2. Proposed design optimization workflow.

3.1. Step 1: Form generator

The first step in the workflow is to use a parametric design system to generate an overall form, based on a shape grammar for roof structures. This grammar includes shape rules to generate a variety of roof structures, from vaults (cross-vault, cloister vault, barrel vault) to domes. The representation of a cross-vault solution is presented in Figure 3. The grammar was translated and encoded into a parametric design system that generates the desired 3D designs based on user input, such as the area to be enclosed and the type of vault or dome (Figure 4). The output is a 3D model of the desired structure, which will be input into the toolpath generator, and a shell representation of the same structure, which will be used for structural analysis.

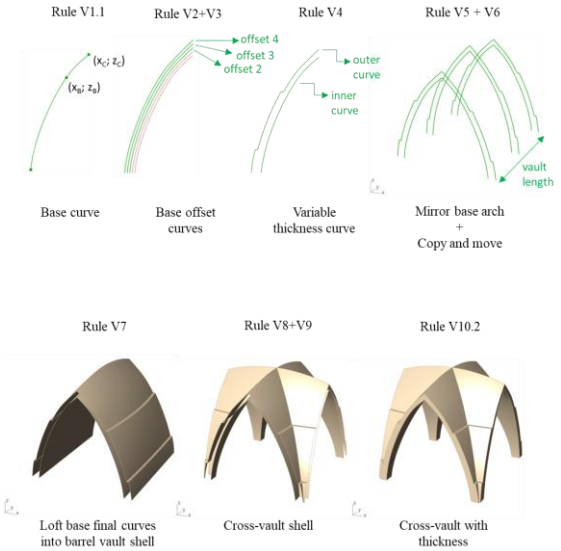


Figure 3. Shape grammar representation for a cross-vault solution.

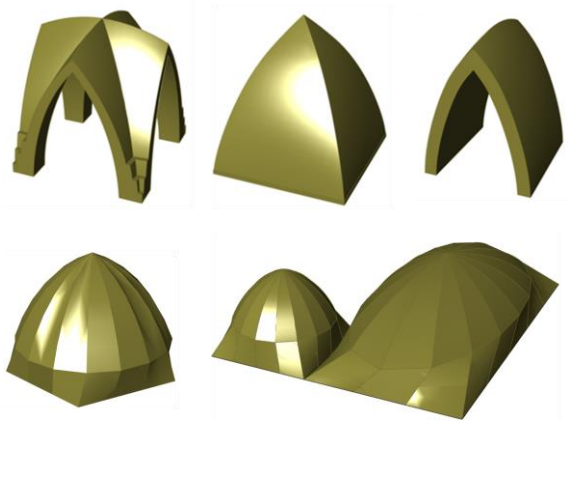


Figure 4. Design generation based on user-defined variables.

3.2. Step 2: Filament analyser

The task of toolpath design requires knowledge of the variables that affect the extruded filament which depend on the geometry of the nozzle as well as the printing settings. The following variables are considered in filament design:

- Φ – nozzle diameter (m)
- h (h_{layer} or $h_{filament}$) – filament height (m)
- Q – extrusion flow rate (m^3/s)
- v_R – robot speed (m/s)
- w – filament width (m)
- $w_{eq,nozzle}$ – filament width for a rectangular section equivalent to the nozzle cross-section (constant extrusion flow rate and robot speed);
- $w_{expected}$ – filament width assuming an equivalent rectangular section (variable extrusion rate and robot speed);
- $w_{toolpath}$ – selected filament width for toolpath design.
- a – radius of the round edge of the filament, which assumes that the edges of the filament have an ellipsoidal shape once $w_{expected}$ exceeds $w_{eq,nozzle}$.
  - If $w_{expected} = w_{eq,nozzle}$: $a = 0$
  - If $w_{expected} \neq w_{eq,nozzle}$ & $w_{expected} > w_{eq,nozzle}$: a = Eq. (4)

The variables presented above are included in mathematical expressions to design filaments for 3D concrete printing (3DCP). Filament design depends on the printing process and should be oriented towards assuring adequate structural performance and printing quality. Figure 5 shows the cross sections of the extruded filament and the nozzle. An equivalent rectangular section for the filament is obtained if the expected filament width $w_{expected}$ is equal to $w_{eq,nozzle}$, with the latter corresponding to a filament cross-section equal to the cross-section of the nozzle (Eq. 1).

$$w_{eq,nozzle} = \frac{\pi \Phi^2}{4h} \text{ (33.78 mm when } \Phi = 25.4 \text{ mm)} \quad (1)$$

Depending on both the extrusion flow and robot speed, the expected filament width $w_{expected}$, might exceed $w_{eq,nozzle}$. The value of $w_{expected}$ can be determined using Eq. 2. This value considers that the

expected cross-section of the filament is rectangular. However, the edges of the section will not be flat because of material behavior. It will be assumed that the edges of the section will be ellipsoidal. As a result, the actual cross-section is a composition of rectangular and ellipsoidal shapes (Fig. 5), where the horizontal axis *a* of the ellipse can be determined by Eq. 3.

$$w_{expected} = \frac{Q}{v_R * h} \quad (2) \qquad a = \left({}^{2 * w_{expected}}/_{\pi}\right) - \left({}^{\Phi^2}/_{2h}\right) \quad (3)$$

In the scenario of adjacent filaments, the prescribed distance between their center lines consists of the toolpath width, $w_{toolpath}$ which can be defined to ensure some overlapping and maximize printing quality. Printing quality stems from two main criteria: dimensional accuracy – the fabricated element has the same dimensions as the 3D model; and filament quality – adjacent filaments are properly bonded, there are no voids (A_{infill}), over extrusion is minimal. The latter criterion is illustrated in Fig. 6. Filament design for printing quality depends on the relation between the area with voids A_{voids}, and over lapping area A_{int}, between adjacent filaments, which will be represented by the over extrusion factor, $OE\%_f$. If *OE%* is greater than 0 there is overextrusion, if it less than 0% there is underextrusion. To optimize printing quality, OE% should be as close as possible to 0% (Eq. 4).

$$OE\%_f = \frac{OE\%_{limit}}{|OE\%|} > 1 \quad \text{Where,} \quad OE\%_{limit} = 5\% \quad (4)$$

$$OE\% = \frac{A_{int} - A_{voids}}{A_{voids}} * 100$$

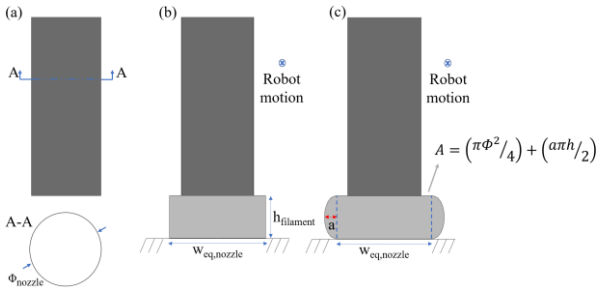


Fig. 5: (a) Nozzle and respective cross-section; (b) equivalent rectangular printed filament; expected printed filament.

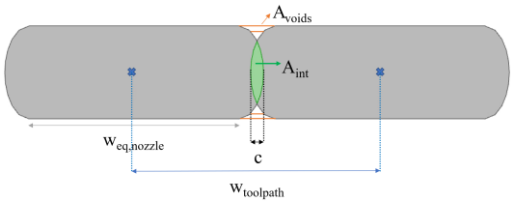


Fig. 6: (a) Overlapping between adjacent filaments spaced by the toolpath width ($w_{toolpath}$), resulting in a overlapping area (A_{int}) and an area with voids (A_{voids}), which will be partially infilled by A_{int}.

Other indicators for printing quality include the nozzle compression factor NC_f, which should be as low as possible but enough to guarantee proper bonding between successive layers (Eq. 5), and the filament yielding factor, S_f, which should be low enough to avoid filament yielding due to excessive tensile stresses generated at the end of the nozzle (Eq. 7).

$$NC_f = \frac{NC}{NC_{limit}} > 1 \quad \text{Where,} \quad NC_{limit} = 0.75 \quad NC = {}^{h_{layer}}/_{\Phi} \quad (5)$$

$$S_f = \frac{S}{S_{limit}} > 1 \quad \text{Where,} \quad S_{limit} = 1.75 \quad S = {}^{w_{expected}}/_{\Phi} \quad (6)$$

3.3. Step 3: Toolpath generator

The next step is to generate the toolpath design for the printing of the 3D roof structure generated in Step 1. The toolpath generator (Figure 7) takes the vault design as input, slices it into layers, identifies the type of surface at each layer (namely closed solid; open hollow; closed hollow; multiple sections), and generates a concentric toolpath based on the specified toolpath width and height. Another available

option concerns the fabrication process, which for layers with multiple surfaces, includes printing a full component (e.g., a complete "leg" of a cross-vault) at a time (fabrication process 1 or FP1), or printing a layer of each member in sequence, thereby introducing travel moves (fabrication process 2 or FP2). The choice of the fabrication process will have a direct impact on structural performance during printing since it impacts the printing time per layer, and therefore material properties.

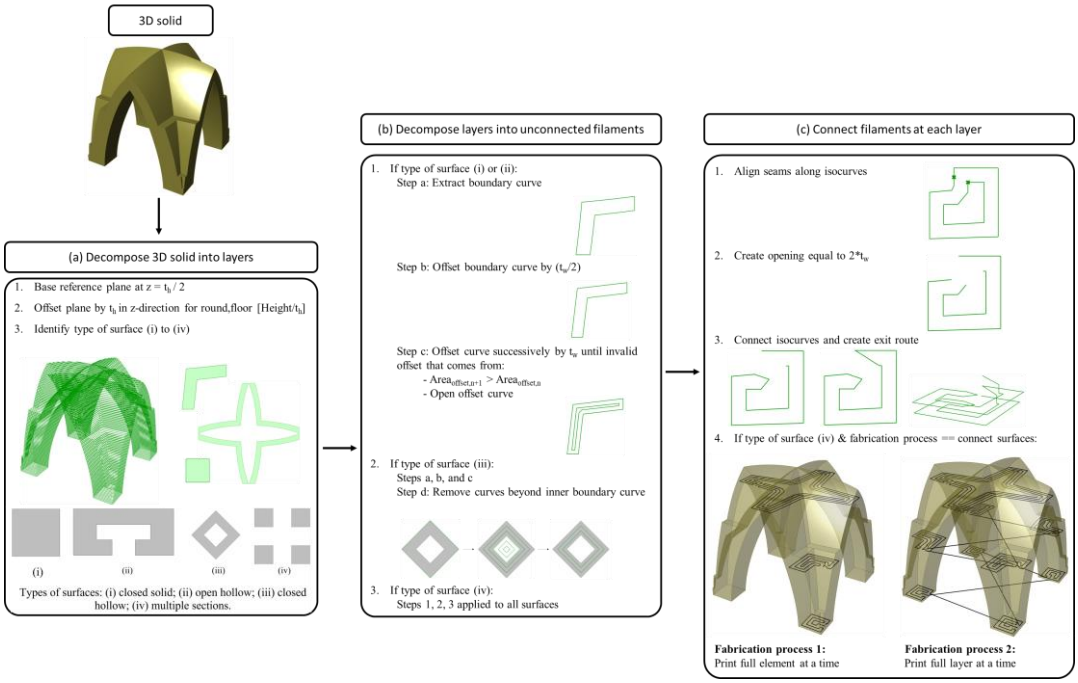


Figure 7. Toolpath generation algorithm

3.4. Step 4: Structural simulator

Step 3 is determining the structural behavior of the structure by performing a finite element analysis using *Karamba3D*, a *Grasshopper* plug-in. The simulation of structural performance includes two separate analyses (Figure 8), namely an early age buildability analysis, and a hardened state serviceability analysis. The simulator performs structural numerical modelling of candidate solutions by taking the shell model and dividing it into layers whose height is equal to the toolpath layer height. It also assigns material properties to each layer as a function of the cumulative printing time at each layer, which is directly calculated from the length of the toolpath solution generated in Step 2. A mesh is then generated for each layer using triangular shell elements.

The early age buildability analysis takes the largest cantilever and analyses the buildability of the element at three different stages, namely, when it is 35%, 70%, and 100% completed, and compares the numerical modelling results with early age criteria for plastic collapse, elastic buckling, and flexural collapse, following the procedure described in [12] with the material properties determined in [13]. Deadload was the only load considered in early age buildability analysis, which represents the weight of the printed layers. The plastic collapse criterion PC_c used is the Mohr-Coulomb criterion, which depends on cohesion C and the angle of friction φ, and compares it with the maximum principal stress at each layer σ_I (Eq. 7). The elastic buckling criterion EB_c is established based on the buckling load factor B_F, which depends on the critical stress σ_{crit}, and is calculated from a linear elastic analysis considering second order effects (Eq. 8). Finally, the flexural collapse criterion FC_c [12] considers the modulus of rupture over time and an adjustment factor α, which accounts for second order effects from layer deformation and compares it with the maximum tensile stress at the top fiber at each layer $\sigma_{t,max}$

(Eq. 9). The three-criterion described constitute a proxy for buildability. The superscript *k,n* in Equation 9 expresses the stress value at layer *k* after printing *n* layers. Therefore, $\sigma_I^{k,n}$ represents the principal stress σ_I at layer *k* after printing *n* layers.

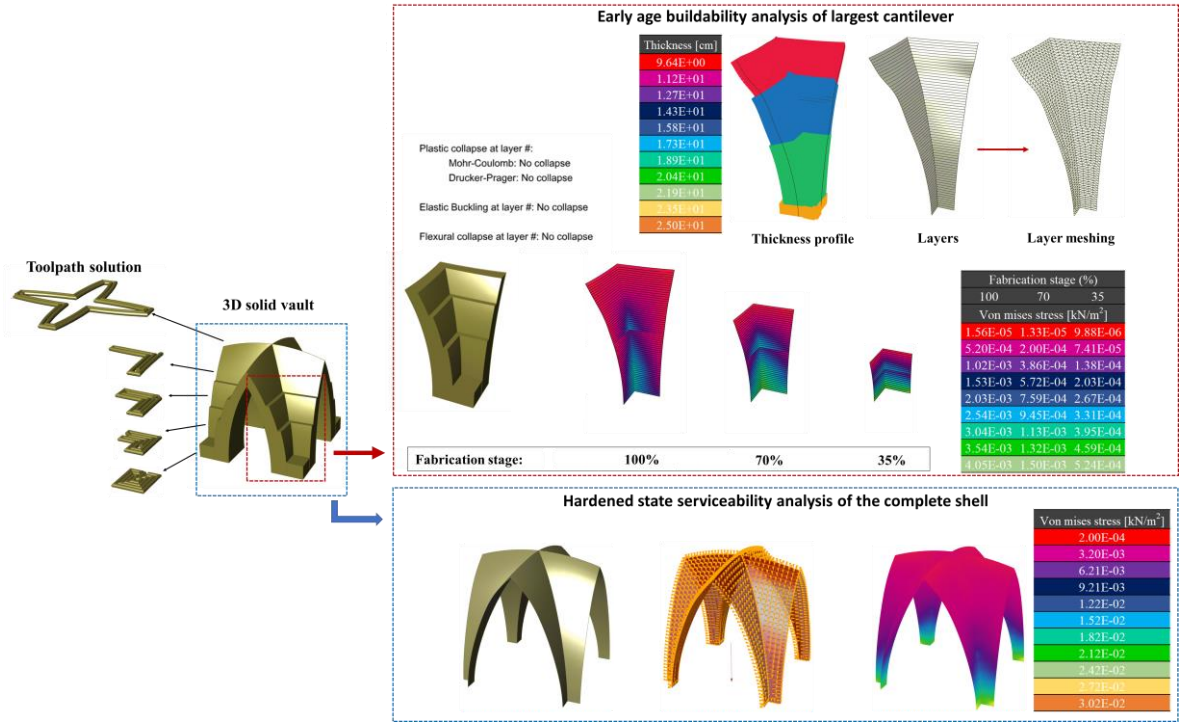


Figure 8. Early age buildability and hardened state serviceability analysis.

Plastic collapse criterion:
$$PC_c = \sigma_I^{k,n} - \left(2C(t)^{k,n} \sqrt{\frac{1+\sin\varphi}{1-\sin\varphi}} + \sigma_{III}^{k,n} \sqrt{\frac{1+\sin\varphi}{1-\sin\varphi}} \right) \leq 0 \quad (7)$$

Elastic buckling criterion:
$$EB_c = B_F = \sigma_{crit}^{n\ layers} / \sigma_{c,max}^{k,n} > 1 \quad (8)$$

Flexural collapse criterion:
$$FC_c = \sigma_{t,max}^{k,n} - \alpha \times 0.50 \times R(t)^{k,n} < 0; \quad \alpha = 0.65 \quad (9)$$

The goal of the hardened state serviceability analysis is to provide a proxy for serviceability that detects excessive displacements, such as excessive deflection δ_v, (Eq. 10) and excessive drift δ_h (Eq. 11), for a wind load scenario applied to the complete shell representation of the vault. The vault length and height are expressed by L and H, respectively.

Deflection criterion:
$$\delta_v - {}^{L}/_{240} < 0 \quad (10)$$

Drift criterion:
$$\delta_h - {}^{H}/_{500} < 0 \quad (11)$$

3.5. Step 5: Performance-based optimizer

The role of the optimizer is to find the best design, which consists of the solution that minimizes the objective function and respects a set of given constraints. For this study, the objective function is the toolpath length T_L because it is directly related with both the overall printing time and structural mass,

thus being an adequate objective for structural optimization. In addition, three types of constraints were defined, namely, constraints that serve as a proxy for: (i) printability – level of over extrusion (Eq. 4), nozzle compression factor (Eq. 5), and filament yielding factor (Eq. 6); (ii) buildability – plastic collapse (Eq. 7), elastic buckling (Eq. 8), and flexural collapse (Eq. 9); and (iii) serviceability – deflection (Eq. 10) and Drift (Eq. 11). Previous optimization results have identified the need to include the influence of buildability in the objective function due to its large influence on the overall solution. Therefore, the plastic collapse indicator (Eq. 8) was added under a penalty term p into the objective function (Eq. 12). This study proposes penalty-based, constrained gradient-free optimization as a valid method to optimize structures for 3D concrete printing. The proposed optimization strategy employs the gradient free algorithm Linear Cobyla and uses the component Radical from the plugin DSE for Grasshopper.

Objective function:		$T_L + p * PC_c$	(12)
Subjected to constraints:	Printability	Eq (4); Eq (5); Eq (6)	
	Buildability	Eq (7); Eq (8); Eq (9)	
	Serviceability	Eq (10); Eq (11)	

3.5.1. Cross-vault optimization

The case study used to illustrate the use of the proposed framework consists in designing a cross-vault structure to enclose two different areas with a cross-vault, namely a 4 ft x 4 ft (small scale) and a 10 ft x 10 ft (full scale). The optimization process focuses on studying three main aspects: (i) scale effect, by comparing how the cross-vault design changes with the area to be enclosed; (ii) fabrication process, by determining how different construction processes (see Section 3.3) influence the design; and (iii) influence of the boundary conditions. The goals of the small-scale optimization are to study the influence of increasing the printing time of each layer by changing the fabrication process and introducing a waiting time between successive layers. The large-scale optimization focuses on comparing how the fabrication process and boundary conditions impact design solutions.

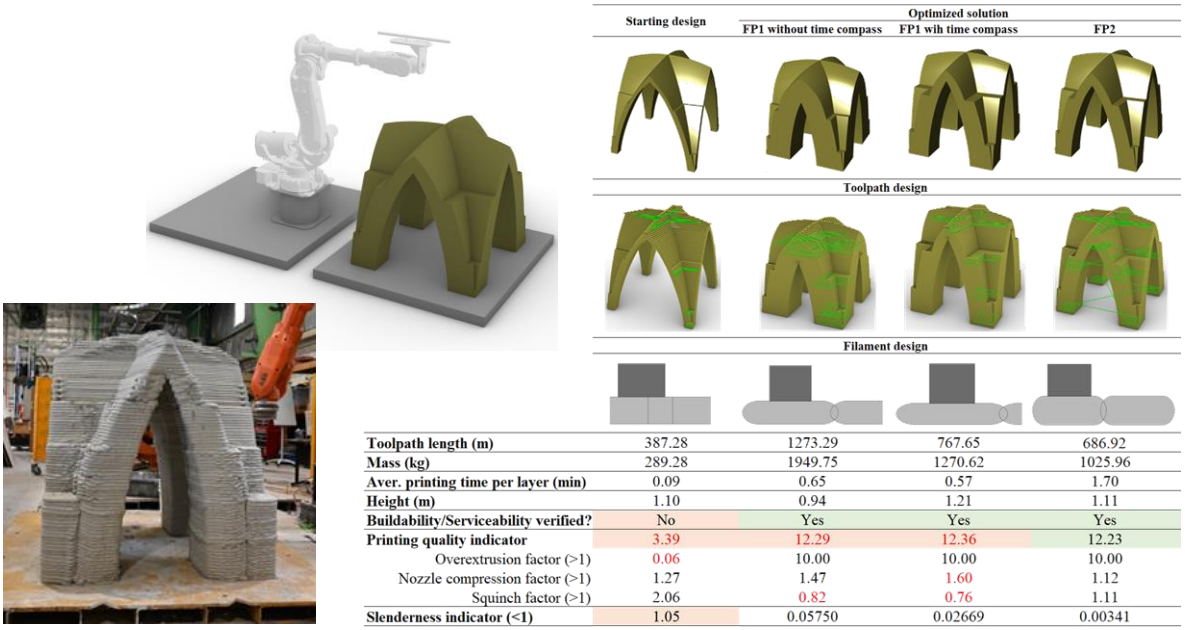
4. Preliminary results and discussion

Preliminary results for both the small-scale and large-scale cross-vault optimization are described below, followed by a discussion of the relevance of optimization in the context of 3DCP. For the optimization, the initial designs were chosen as slender vaults that did not verify the design constraints.

4.1. Small-scale cross-vault optimization

The results of the small-scale cross-vault optimization are depicted in Figure 9, where the optimized solutions verify both buildability and serviceability constraints. However, some of the printability constraints were not met under fabrication process 1 (FP1). Results also illustrate a clear relation between the printing time per layer and toolpath length. The optimization results with FP1 without a waiting time presented the largest mass and toolpath length, which is explained by the need for a larger cross-section to increase the printing time and, therefore, strength to accommodate stresses from deadload and guarantee buildability. In addition, the relevance of printing time in early age buildability was shown by a decrease in toolpath length of 34.83% when incorporating a waiting time Δt that guarantees a printing time per layer of 34 seconds, which has been shown to be de time required for a layer to stop deforming under the weight of subsequent layers for the material used in this study [7]. Finally, when optimizing the cross-vault considering fabrication process 2 (FP2), the average printing time per layer increased from 0.57 min to 1.70 min, which resulted in a solution with a toolpath length 10.5% shorter and 19.26% less material. Therefore, small-scale optimization results indicate how early age buildability depends on the printing time per layer, which is largely influenced by the printing strategy. A small-scale cross-vault was successfully printed using FP1 (Figure 9), which shows that

buildability was respected. However, it did not display high printing quality, which confirms the printability constraints not met when using FP1.

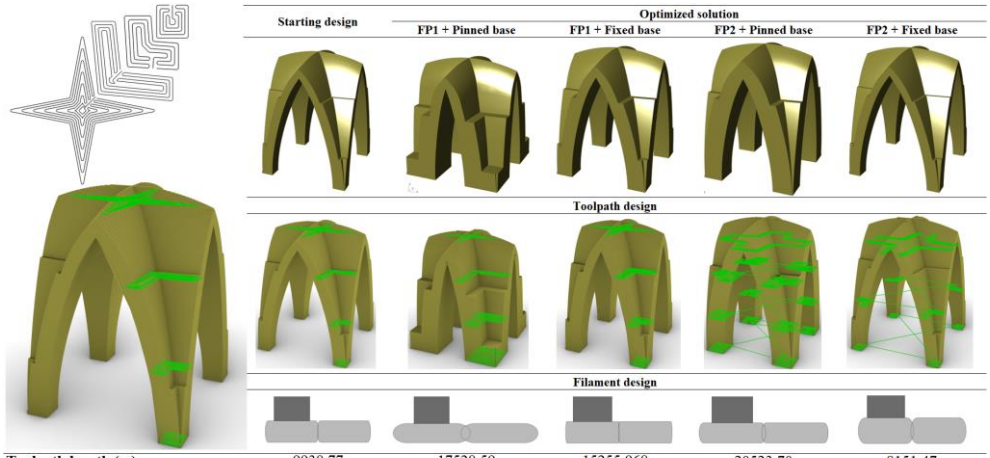


Toolpath length (m)	387.28	1273.29	767.65	686.92
Mass (kg)	289.28	1949.75	1270.62	1025.96
Aver. printing time per layer (min)	0.09	0.65	0.57	1.70
Height (m)	1.10	0.94	1.21	1.11
Buildability/Serviceability verified?	No	Yes	Yes	Yes
Printing quality indicator	3.39	12.29	12.36	12.23
Overextrusion factor (>1)	0.06	10.00	10.00	10.00
Nozzle compression factor (>1)	1.27	1.47	1.60	1.12
Squinch factor (>1)	2.06	0.82	0.76	1.11
Slenderness indicator (<1)	1.05	0.05750	0.02669	0.00341

Figure 9. Small-scale optimization results and printing validation.

4.2. Large-scale cross-vault optimization

Large scale cross-vault optimization results are presented in Figure 10 and show that to respect design constraints, solutions using a pinned base required double the mass when compared with the initial design, while fixed base solutions show an increment in mass of 42.27% with FP1, and a decrease of 6.09% with FP2. These results are explained by the fact that a fixed base generates lower stresses and in FP2 the same layer of all the legs of the structure is printed before moving on to the next layer, which increases the printing time per layer and, therefore, the layer strength. A similar trend was observed in the toolpath length, where slender solutions resulted in shorter toolpath length. Buildability explains the impact of both boundary conditions and fabrication process on these results. Boundary conditions affect the stresses on the structure, while fabrication process directly influences the cumulative printing time and, therefore, the age of the printed layers (Figure 11) and, therefore, their strength. The impact of the fabrication process is not limited to buildability. In fact, solutions with FP2 present additional benefits: (i) improved printing quality, due to higher average printing time per layer, which increases the strength of the filaments, causing them to deform less under the weight of subsequent layers and therefore have a cross-sectional area smaller, thus displaying better printing quality; (ii) higher slenderness, since solutions are less robust and therefore present a smaller elastic buckling factor because the critical stress is smaller. The slenderness indicator stems as the inverse of the elastic buckling factor; (iii) increased functionality, as the usable area is larger than in solutions with FP1 for same boundary conditions. The described results indicate that increasing printing time per layer either through specific fabrication strategies or by manipulating printing setting such as the robot speed is key to fabricate solutions that are slender, functional, and display better quality. However, it should be noted that excessive time between layers can lead to worsened bonding between layers, which impacts structural performance.



Toolpath length (m)	9938.77	17528.59	15255.968	20523.70	8151.47
Mass (kg)	12044.27	26343.48	17135.40	25180.34	11310.30
Aver. printing time per layer (min)	0.15	2.82	1.93	10.37	6.26
Height (m)	3.80	3.39	3.73	3.79	3.77
Buildability/Serviceability verified?	No	Yes	Yes	Yes	Yes
Printing quality indicator	17.78	3.13	5.05	3.70	8.13
Overextrusion factor (>1)	15.31	0.91	3.47	1.24	5.81
Nozzle compression factor (>1)	1.27	1.36	0.79	1.36	1.06
Squinch factor (>1)	1.20	0.86	0.79	1.10	1.26
Functionality indicator (>1)	1.29	0.76	1.20	1.14	1.29
Slenderness indicator	0.06317	0.00238	0.00685	0.01154	0.01646

Figure 10. Large scale optimization results.

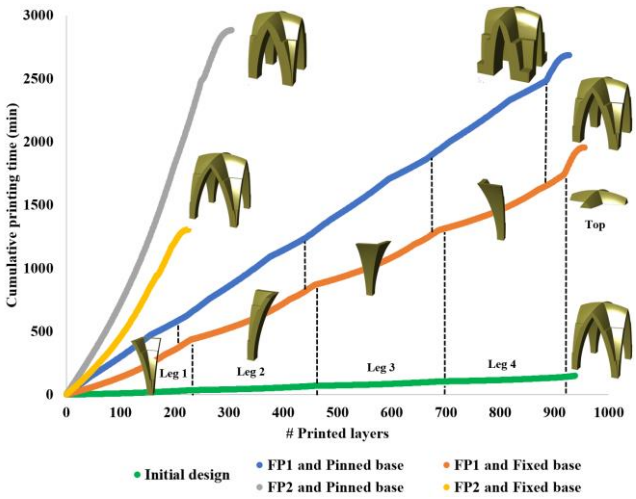


Figure 11. Cumulative printing time per layer based on the fabrication process (FP) and boundary conditions.

5. Conclusions

This paper proposes a design optimization workflow for spanning structures for 3DCP. It is demonstrated by optimizing a cross-vault structure under several conditions and validated by printing of a small-scale cross vault (Figure 9). The optimization considered two alternative fabrication strategies and boundary conditions to determine their impact on the optimized design. The level of fixation to the base was found to influence early age buildability as much as the fabrication strategy, since the former affects the stresses, while the latter directly impacts material strength by changing the printing time per layer and thus the layer age. Differences of minutes in the age of printed layers were shown to largely influence the early age buildability of 3DCP structures at small- and large-scales. Similarly, optimization results indicate a relation between printing quality and printing time per layer. This work proposes a design optimization workflow that enhances design for additive construction by providing a platform that includes shape generation, toolpath generation, structural analysis, and optimization. It adopts

constrained optimization to design both small-scale and construction scale roof structures for 3DCP. Future work will demonstrate the workflow on forms beyond the initial cross-vault example.

Acknowledgements

This research was funded by The Pennsylvania State University, X-Hab 3D, The Portuguese Foundation for Science and Technology (FCT), Golf Concrete Technology (GCT), Hilti Foundation, and Xtreme Habitats Institute. The authors express their gratitude to Dr. Sven Bilén, Dr. Aleksandra Radlińska, Mr. Nathan Watson, Mr. Hanbin Cheng, Mr. Zhengyu Wu, and Ms. Nusrat Tabassum for their valuable insights and contributions to this research.

Declaration of interests

Two of the co-authors, Jose P. Duarte, and Shadi Nazarian, have equity in a company, X-Hab 3D, whose activity is concrete printing.

References

[1] S. Bhooshan, V. Bhooshan, A. Dell'Endice, J. Chu, P. Singer, J. Megens, T. Van Mele, P. Block, The Striatus bridge, *Journal of Architecture, Structures and Construction*, vol. 2, pp. 521–543, 2022.

[2] J. Burger, T. Huber, E. Lloret-Fritschi, J. Mata-Falcon, F. Gramazio, M. Kohler, Design and fabrication of optimised ribbed concrete floor slabs using large scale 3D printed formwork, *Journal of Automation in Construction*, vol. 144, 2022.

[3] M. Motamedi, R. Mesnil, R. Oval, O. Baverel, Scaffold-free 3D printing of shells: Introduction to patching grammar, *Journal of Automation in Construction*, vol. 139, 2022.

[4] A. Curth, T. Brodesser, L. Sassa, C. Mueller, Multi-objective optimization of 3D printed shell toolpaths, *Proceedings of the IASS Annual Symposium 2020/21*.

[5] P. Carneau, R. Mesnil, N. Roussel, O. Baverel, "Additive manufacturing of cantilever - From masonry to concrete 3D printing", *Journal of Automation in Construction*, vol. 116, 2020.

[6] G. Duarte, N. Brown, A. Memari, J.Duarte, "Learning from historical structures under compression for concrete 3D printing construction", *Journal of Building Engineering*, vol. 43, 2021.

[7] N. Ashrafi, S. Nazarian, N. Meisel, J. P. Duarte, "A grammar-based algorithm for toolpath generation: Compensating for material deformation in the additive manufacturing of concrete", *Journal of Additive Manufacturing*, vol. 55, 2022.

[8] M. Motamedi, R. Mesnil, R. Oval, M. Charrier, O. Baverel, Scaffold-free Robotic 3D Printing of a Double-layer Clay Shell, *Proceedings of the IASS Annual Symposium 2020/21*.

[9] Q. Wan, L. Wang, G. Ma, "Continuous and adaptable printing path based on transfinite mapping for 3D concrete printing", *Journal of Automation in Construction*, vol. 142, 2022.

[10] M. Rippmann, A. Liew, T. Van Mele, P. Block, Design, fabrication and testing of discrete 3D sand-printed floor prototypes, Materials Today Communications, vol. 15, pp. 254–259, 2018.

[11] R.J.M. Wolfs, F.P. Bos, T.A.M. Salet, "Early age mechanical behaviour of 3D printed concrete: Numerical modelling and experimental testing", *Cement and Concrete Research*, vol. 106, pp.103–116, 2018.

[12] G. Duarte, J. P. Duarte, N. Brown, A. Memari, J. P. Gevaudan, "Design for early age structural performance of 3D printed concrete structures: a parametric numerical modelling approach", under review in the *Journal of Automation in Construction*, 2022.

[13] G. Duarte, J. P. Duarte, A. Memari, N. Brown, J. P. Gevaudan, "Towards a model for structural performance in concrete printing based on buildability and toolpath design", *Journal of Building Engineering*, vol. 69, 2023.

IASS 2023
July 10–14 Melbourne
Integration of Design and Fabrication

Proceedings of the IASS Annual Symposium 2023
Integration of Design and Fabrication
10–14 July 2023, Melbourne, Australia
Y.M. Xie, J. Burry, T.U. Lee and J. Ma (eds.)

Digital Ceramics: High hyperbolic curvature fabrication technologies in paste-based additive manufacturing

Philip F. YUAN*, Lei GONG[a]

[a,*] Tongji University
College of Architecture and Urban Planning, Tongji University, 1239 Siping Rd., Shanghai, China
philipyuan007@tongji.edu.cn

Abstract

We present a robotic clay printing technique that uses non-quick-setting paste-based materials and a six-axis robotic arm to quickly fabricate and manufacture complex-shaped surfaces with high hyperbolicity. To analyze the effect of the construction methods on double curvature, the surface prototype is obtained from rotating the cosine-type curve as the generatrix around the y-axis by one turn. This study analyzes the shaping principles and limitations of the primary Contour Craft (CC) and then investigates the complex hyperbolic fabrication technique via multiple sets of improved toolpath planning schemes and associated technological parameters, using paste-based clay as raw material. Employing a customized pneumatic tool to extrude clay, the superior schemes were discovered and extracted over the course of several studies. As the cases are printed and evaluated, craft characteristics parameters that meet the standards for creating high-curvature objects can be deduced, resulting in better-performing Hybrid Craft (HC). It fully preserves and replicates the excellent morphology fitting capabilities of Contour Craft (CC), matching surfaces with target features, while the toolpath arrangement, which is adapted from Lattice Craft (LC), addresses UV bi-directional structural support for hyperbolic surfaces, maintaining the design representation and resolving collision and reachability issues. We create and fabricate hyperbolic digital surfaces over a variety of digital models to illustrate our versatility.

Keywords: high hyperbolic curvature, toolpath planning, hybrid crafts, paste-based material, additive manufacturing

1. Introduction

Sustainable construction has improved using additive manufacturing of earth-based materials. However, the compression and sluggish solidification of these materials under gravity makes it difficult to make construction components of specific shapes, especially curvatures. Some designers have employed drying devices on the robot flange, safe redundant boundaries, and the optimum processing speeds to overcome material property-induced deformation. Other designers have added chemical quick-setting components to earth-based materials to solidify and strengthen quickly to reduce nonlinear depositional distortion between layers. However, these antiquated processes are expensive and hard to copy, and innovation never reaches the method level. It lacks universality for extensive promotion.

In this paper, we explore the mechanism of shaping hyperbolic surfaces of paste-based materials through toolpath planning for clay printing, and the adopted construction method was initially used to develop an early concrete contour craft [1]. It was previously impossible to physically construct complex-shaped clay components, but with the advent and development of robotics and digital fabrication, designers can now control the manufacturing parameters of the clay extrusion process.

Copyright © 2023 by Philip F. YUAN and Lei GONG. Published in the Proceedings of the IASS Annual Symposium 2023 with permission.

However, attempts to investigate the complex deformation behavior of clay during extrusion in the context of constructing large curvature components are rarely documented, current research is still restricted to planes or curved surfaces with a small range of curvature, and the goal of producing precise and highly adaptable building components remains elusive. This research, based on previous work on the geometry of the Contour Craft and Lattice Craft toolpath, proposes a Hybrid Craft approach that represents a highly challenging morphology produced in clay and thus presents an appropriate microscopic characteristic. Both the material's vertical deformation caused by gravity and the precise distribution of the UV dimension of the high-curvature surface components must be satisfied.

This work is part of the non-quick-setting material performance research that uses toolpath planning and process parameter management to improve clay 3D printing formation. Hybrid Craft, combining Contour Craft and Lattice Craft, enhances high hyperbolic component printing accuracy while lowering costs, according to the authors. This strategy can enable the use of readily available, environmentally friendly, and even living biomaterials in modern manufacturing technology to achieve more flexible design goals.

2. Related work

2.1. Clay material

Clay, which is a classic green sustainable building material, just like other natural, paste-like materials, offers a potential reduction in the embodied CO2 that the production of buildings using conventional materials emits. In addition, it also has excellent insulation and fire resistance performance. Due to its excellent material properties, clay has a long history of use. Hundreds of years ago, early humans began using the coil technology of clay to create simple vessels[2]. This ancient behavior conforms to the principles of modern extrusion 3D printing in terms of method logic. Clay materials' inability to quickly solidify and form structural strength after extrusion is the most noticeable trait during extrusion printing[3]. Thus, employing clay for printing typically leads to unanticipated results, so a robotic processing technique that matches clay's material behavior is needed. Layer-by-layer clay extrusion in material extrusion additive manufacturing leaves visible traces on 3D-printed surfaces. Clay layers created when wet can sag[4]. This microscopic deformation caused by material characteristics and gravity might abruptly explode, producing local collapse or destabilization. We address material weaknesses and maximize clay's benefits through other means.

Recent improvements in additive manufacturing of paste-based materials show promise for sustainable building construction, despite significant downsides. WASP and the IAAC use robots to extrude and deposit clay along a linear print path. The Big Delta (WASP) and Pylos (IAAC) projects show how clay may be used to build large structures rapidly and cheaply[3].

2.2. Toolpath planning

As toolpath planning plays an essential part in our work, we frame it in a more concrete context of path arrangement problems where a large body of work of high curvature surface-shaping is available in digital fabrication[5]. Contour craft (CC) is a recent layered fabrication technology that has great potential in the automated construction of whole structures, which was initially used to develop the early contour crafting methods for concrete[1]. It can produce a smooth and accurate finish on the outer and top surfaces of each layer, as well as greatly cut costs and construction times, by eliminating the need for formwork used in conventional concrete construction[6].

Lattice Craft is an extreme example of clay 3D printing that makes use of a unique technique created by Alothman[3]. The lattice geometry best exemplifies severe fabrication uncertainty because of its generally delicate form, which is vulnerable to significant deformations during printing and drying .

2.3. Curvature matters

The advent of digital fabrication has enabled the production and manufacturing of many complex customized components that were previously unimaginable. Technological advancements have not only increased productivity, but they have also brought a new paradigm revolution in aesthetics. The primary motivations for contemporary interest in form customization of architectural elements include a qualitative, design-driven desire for new forms. Additive manufacturing technology can relatively quickly produce unique components with complex geometric features, especially hyperbolic surface features, without fixed mold costs[2].

In addition to building complex curvature surfaces to meet certain form requirements, shells are also a typical efficient material structural system that generates their load-bearing capacity through curvature changes. In the past, complex surfaces were mostly made of reinforced concrete supplemented with formwork, with little research on hyperbolic elements made with non-quick-setting material additions. Simply assigning curvature features to structural surfaces does not automatically generate any structural capabilities; On the contrary, the curvature distribution of the surface needs to be carefully designed to establish sound structural principles[7]. Today, the main challenge faced by complex surfaces is, on one hand, the cost of constructing formworks, which is usually occupied by traditional labor-intensive manual masonry costs. On the other hand, its application appearance is limited to regular surface shapes. With the help of extrusion-based methods for complex hyperbolic surfaces, this study aims to solve the dilemma of formwork cost and shape limitation.

3. Method

Under the paradigm of digital manufacturing, the materialization process of high curvature complex shape models that were previously impossible has become practical and implementable. This is mainly attributed to two aspects. This is largely the result of two factors. On the one hand, researchers have modified the material properties to adapt the construction raw materials to the construction requirements of complex shapes. On the other hand, by optimizing and improving the construction process (specifically, path planning and parameter control), new process paths are being explored to investigate the application scenarios of related technologies.

This study will begin with the latter and investigate the application frontiers of non-rapid setting materials within the field of digital construction.

3.1. Curvature extraction

Curvature is a quantity that depicts the degree of curvature of a geometric body, such as how much a surface deviates from a plane or how much a curve deviates from a straight line. Prior to the introduction of digital construction technology, many studies disassembled special-shaped components into basic, developable surface components to facilitate the construction process. However, the manufacturing and processing of complex curvature components are less involved.

3.1.1. Digital prototype

In order to obtain a mathematically analyzable hyperbolic digital prototype, this experiment employs a cosine curve as a generatrix to rotate around the y-axis of the Cartesian coordinate system one cycle to obtain an infinitely extended surface. Then, as shown in Figure 1, a surface centered at the origin and defined within a period is chosen.

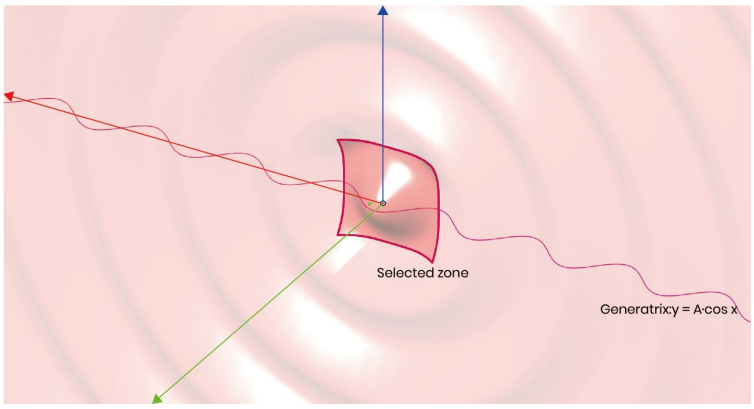


Figure 1. Selected surface and its generatrix

The cosine curve is chosen as the generatrix because, in addition to its mathematical analytical advantages, it has a high degree of operability in comparison to other curves. The curvature of the generatrix can be altered by modulating its amplitude and frequency, thereby altering the curvature distribution of the rotating surface. The following is the standard format for a cosine curve.

$$y = \mathrm{A} \cdot \cos(\omega x \pm t) \#(1)$$

This study attempts to describe as intuitively as possible the distribution of curve curvature. The initial frequency of the curve is therefore set to 1 and the initial phase to 0. The only factor that influences any shift in the curve's curvature is its amplitude. Consequently, the mathematical expression of the generatrix and its distribution of curvature is:

$$\Gamma: \begin{cases} y = \mathrm{A} \cdot \cos x \\ z = 0 \end{cases} \#(2)$$

$$\mathrm{K} = \frac{|A\ \cos x|}{\left(1 + A \sin^2 x\right)^{\frac{3}{2}}} \#(3)$$

The spatial geometric properties of the surface obtained through rotation operations are completely determined by the rotation angle of the generatrix and rotation axis, or by the consideration of control variables. All rotation axes in this study are y-axis, and the rotation angle is 360 °. The mathematical expression of the obtained rotation surface is as follows.

$$r(u, v) = (v \cos u, \cos v, v \sin u)$$

$$u, v \in (-\infty, \infty) \#(4)$$

3.1.2. Normal curvature

Compared to two-dimensional curves, a surface has countless tangents at a point, and normal curvature is the quantity used to describe and characterize the degree of curvature of a surface in a certain direction. From the definition of normal curvature in differential geometry, the ratio of the second fundamental form to the first fundamental form of a surface is a function of the point (u, v) of the surface and the tangent direction du/dv at that point, which is called the normal curvature K_n of the surface along the tangent direction du/dv at that point, namely:

$$k_n = \frac{II}{I} = \frac{L\,du^2 + 2M\,du\,dv + Ndv^2}{Edu^2 + 2F\,du\,dv + Gdv^2} \#(5)$$

where：

$$E = r_u \cdot r_u,\ F = r_u \cdot r_v,\ G = r_v \cdot r_v$$

$$L = r_{uu} \cdot n = -r_u \cdot n_u$$
$$M = r_{uv} \cdot n = -r_u \cdot n_v = -r_v \cdot n_u$$
$$N = r_{vv} \cdot n = -r_v \cdot n_u$$

K_n is only related to the tangent direction (du/ds, dv/ds) of the curve. In fact, we can consider this as a property of the surface, or more precisely, the property of the surface at a certain point and direction. Therefore, normal curvature is more like maintaining the curvature of a curve on a surface.

3.1.3. Principal curvature

In differential geometry, the two principal curvature at a given point on a surface measure how curved a surface at a given point is in different directions at that point. In a nutshell, a surface has the maximum and least normal curvature if it has normal curvature in every direction. The principal curvature is the difference between these two values, and the principal curvature direction is the direction of the tangent to the corresponding curve at this location.

At any point P on surface X, the characteristic direction {e1, e2} of Weingarten mapping becomes the main direction of the surface at point P. The normal curvature {k1, k2} of the surface along the main direction is the characteristic value of the corresponding Weingarten mapping, which is called the principal curvature of the surface at that point, namely:

$$W(dr) = \lambda\, \boldsymbol{dr}$$
$$-(n_u du + n_v dv) = \lambda(\boldsymbol{r_u du + r_v dv})$$
$$\begin{cases} -(n_u du + n_v dv) \cdot r_u = \lambda(\boldsymbol{r_u du + r_v dv}) \cdot r_u \\ -(n_u du + n_v dv) \cdot r_v = \lambda(\boldsymbol{r_u du + r_v dv}) \cdot r_v \end{cases}$$
$$\begin{vmatrix} L - \lambda E & M - \lambda F \\ M - \lambda F & N - \lambda G \end{vmatrix} = 0$$
$$k_1 k_2 = \frac{LN - M^2}{EG - F^2}$$
$$k_1 + k_2 = \frac{LG - 2MF + NE}{EG - F^2} \#(6)$$

As seen in Figure 2, the umbilical point serves as the origin of the surface that was chosen for this study. As a result, the two principal axes of curvature are equal, and any direction might be the main direction. However, this research chooses X direction and Z direction as the selected main directions since the logic of robot design is frequently three-dimensional orthogonal. The surface's major curvature in these two directions is the curvature of the curve projected on the plane spanned by the curve in the principal direction and N, respectively. The surface's normal vector at this point is N.

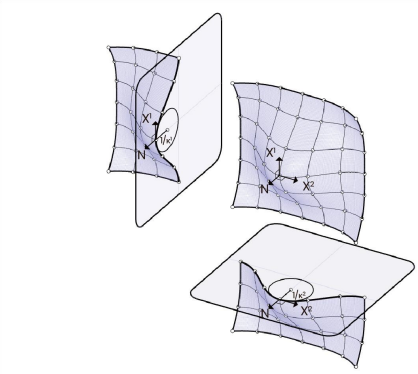


Figure 2. Principal direction and principal curvature

This experiment permits investigating the accurate depiction of the two primary curvature distributions mentioned above in various schemes, which introduces the idea of Gaussian curvature and makes it easier to investigate the impact of the construction method on the surface's curvature.

3.1.4. Principal curvature

In differential geometry, the Gaussian curvature of any point on a surface is the product of the principal curvature k_1 and k_2 of that point. It is an intrinsic measure of curvature, that is, its value only depends on how the distance on the surface is measured, not how the surface is embedded in space.

First, we can simplify the two principal curvature of the hyperboloid into developable surface in the principle direction, and start with a single surface with zero Gaussian curvature, as shown in Figure 3. These two single surfaces are similar in morphology to those obtained by extruding a generatrix along a fixed direction.

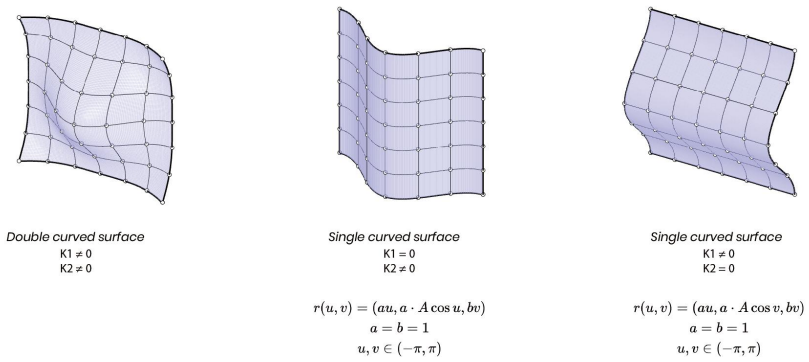


Figure 3. Selected hyperboloid and single surfaces

3.2. Toolpath generation

3.2.1. Primary Contour Craft

The primary contour craft is a method for representing a model's exterior contour that uses continuous material extrusion. This study set four different curvature classifications by varying the amplitude of the generatrix (A=1, A=0.75, A=0.5, A=0.25) in order to investigate how responsive pertinent processes are to various curvatures. Extrusion-based additive construction follows a bottom-up construction philosophy. As a result, if the component's curvature changes significantly when the Z-axis is the primary direction, there will be some overhang. The largest challenge in producing large curvature shapes with non-rapid setting materials is the inability to quickly create structural strength.

As shown in Figure 4, the initial contour process in the early hyperboloid printing experiment has a good effect on the construction of the rotating hyperboloid with A=0.25, but it has a poor effect on the construction of the rotating hyperboloid with A=1, and there is significant deformation in the middle and lower portions of the component.

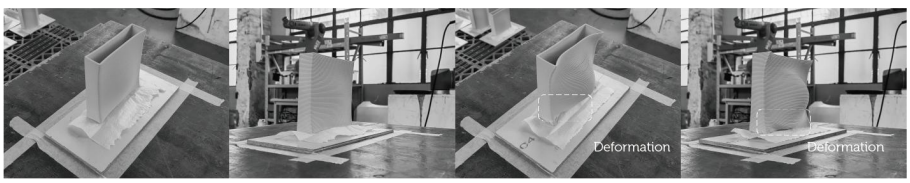


Figure 4. Hyperboloid printing experiments

In the experiment of single curved surface printing, the initial contour craft has a good effect on the construction of single curved surfaces with K_1 of 0 and K_2 of not 0. For single curved surfaces with K_1 being 0 and K_2 not being 0, small curvature surfaces with A=0.25 also exhibit local deformation and cracking, while large curvature surfaces with A=1 exhibit overall instability and the printing process cannot continue, as shown in Figure 5.

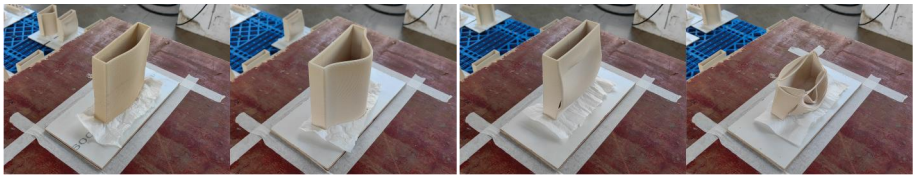


Figure 5. Single curved surface printing experiments

Due to clay's slow rate of solidification, the material's viscosity after extrusion plays a major role in preserving the component's overall stability. The material that is deposited compresses the bottom level of still-fresh clay as the number of printing layers rises. The lower component will be compressed by the rising center of gravity on the upper portion of the component, and the center of gravity will change as a result of the gradually protruding shape, leading to local deformation of the component in the absence of further support. Models with minor curvature changes in the K_1 direction are ideal for non-rapid setting material printing, which is based on the contour technology's forming theory.

3.2.2. Improved Contour Craft

Strip support. According to the two images on the left side of Figure 6, adding a strip support increases the construction stability of a single curved surface's curvature with A=0.5 in the K_1 direction. However, when working with higher curvature components, like A=0.75, strip supports continue to make the components unstable. Although strip support can expand the area of contact between the curved surface and the supporting structure and can keep the component stable by using the material's unidirectional viscosity, it has very little capacity to accommodate significant curvature.

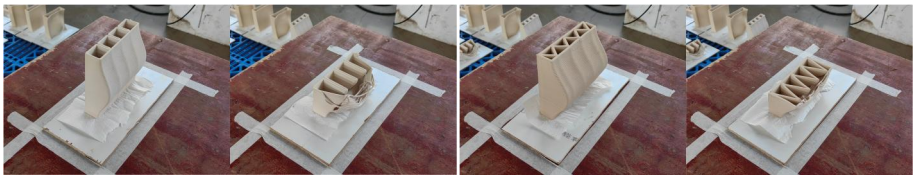


Figure 6. Left: single curved surface with strip supports; Right: single curved surface with folded supports

Folded support. The author also tried a path arrangement based on folded plate support to overcome the aforementioned problem. The folded plate support structure (Figure 7) simultaneously creates a triangular robust load-bearing structure and vertical support through the folded section. According to the printed experimental results (as shown in the right figures of Figure 6), the folded plate support was effective in constructing a single curved surface with an A value of 0.75; however, it failed to do so when the A value was 1.

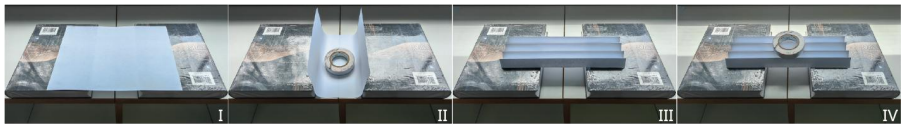


Figure 7. Paper folding plate bearing tests

This is because, regardless of the supporting structure, it can only effectively support the component's bigger overhanging portions along the longitudinal axis. The difficulty to be solved in the following

stage is how to create a support structure that is bidirectional since the two approaches discussed earlier did not create it.

Cross grid support. Due to the difficulty in achieving a strict X-direction support structure for Contour Craft, the author attempts to solve the above problem by diagonally crossing grid paths. In the XZ plane, the support structure of diagonal components can be vectorized into orthogonal supports. From the printing results of a single curved surface with A=1, it can be seen that the diagonal grid support solves the problem of component instability and deformation in the cantilever section. However, the path of this structure itself is cumbersome, resulting in an increase in the weight of the printing material. In the later stage of printing, due to a change in the center of gravity, the component capsizes towards the overhanging direction. However, in the construction experiment of hyperboloid with A=1, the shift of component gravity center was not severe, so the printing task was successfully completed (Figure 8).



Figure 8. Double curved surface with cross grid support

3.2.3. Lattice Craft

Practical engineering relies on component weight. Solving component self-weight is the next research aim to make components viable with bidirectional structural support. Contour Craft is a continuous path arrangement that accurately describes component contours and preserves digital models well. Supporting structures are needed to create a given shape, which increases component self-weight and gravity-induced local deformation and instability. We will focus on the discrete path and use other methods to alleviate the shortcomings in future study. Therefore, we will focus on a special construction method - Lattice Craft, which uses a special process called "spatial print trajectories," developed by the authors[3]. The original continuous path planning method discretized the inter layer printing unit into a certain number of lattice units. The unit path in the printing process is a single path inside the discretization lattice units, and the robot must complete the path inside one lattice unit before moving to the next printing target. Figure 9 shows Lattice Craft creating a spatial grid-like supporting structure inside the component. Compared to Contour Craft, this path planning can significantly lower structure self-weight and shape it.

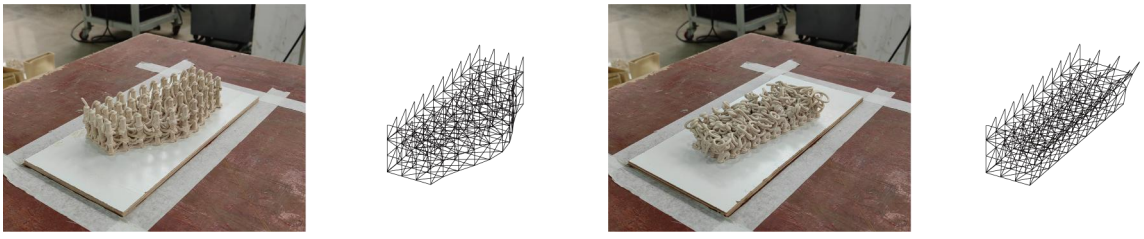


Figure 9. Lattice Craft and its path

For non-quick-setting materials, this approach has various drawbacks: 1. Vertical components in a lattice cell must be vertical to build support strength quickly (Figure 9), hence only single-curved components with K1=0 can be produced; 2. curve, and the lattice cell size cannot be too small, it is

difficult to approximate the original curve after wireless subdivision, which leads to poor surface smoothness and does not achieve high curvature construction in the strict sense (Figure 10); 3. Lattice Craft can only form a spatial structure, not a 3D spatial surface, limiting its application scenario. This method usually yields a constructive spatial structure rather than an expressive one.

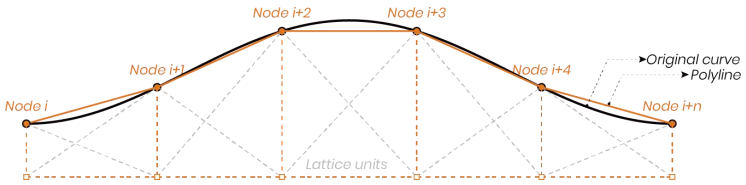


Figure 10. Fitting the original curve with polyline

3.2.4. Hybrid Craft

List all the benefits of Lattice Craft and Contour Craft in detail. The former is better at fitting surfaces, but the supporting structure can make the structure heavier overall. The latter has the advantage of being lighter overall, but is less effective at fitting surfaces. Based on this, this study suggests a Hybrid Craft with benefits that support each other. In particular, the surface of the part is printed layer by layer with Contour Craft to make a smooth surface, while the supporting part of the part is made with individual lattice units with Lattice Craft to make a strong but lightweight structure.

From the real-world printing test (Figure 11), it is clear that Hybrid Craft can make hyperboloid parts well. This method can keep the benefits of the two Crafts we've already talked about while building high hyperbolic surface components that don't distort locally.

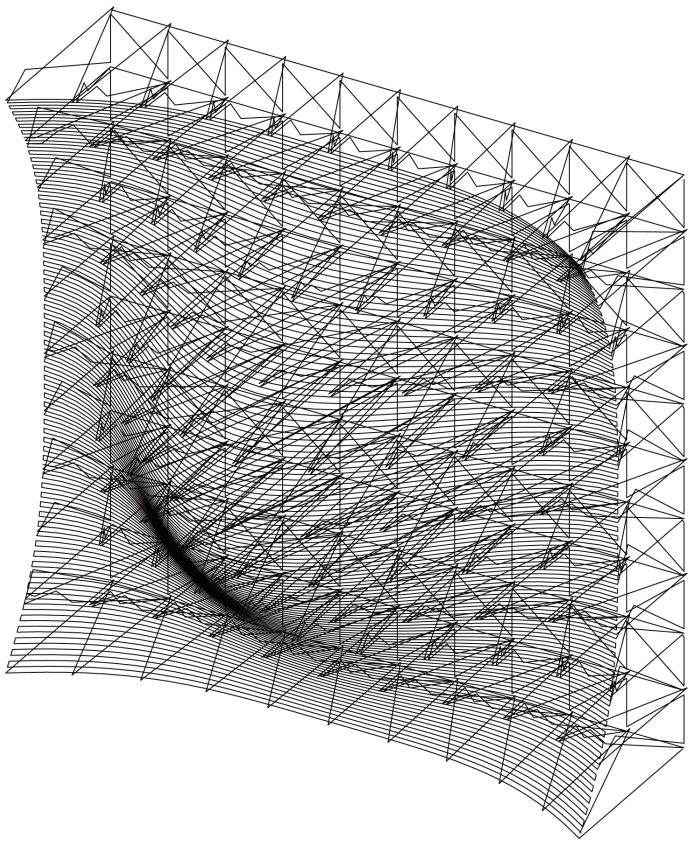


Figure 11. Toolpath for Hybrid Craft

3.3. Parameter debugging

3.3.1. Clay moisture

The amount of water in slurry materials that don't set quickly is a very important sign that has a lot to do with how thick clay materials are. On the one hand, the amount of water in slurry-based materials should stay within a certain range. On the other hand, the amount of water in slurry-based materials should be fairly consistent. Printing is interrupted when stored clay cannot be pushed out during building (Figure 12 left). The author found that unequal clay raw material mixing causes uneven humidity after repeated studies. Low-water mud is hard to extrude and forms a cavity at the pumping end of the tool head, making feeding impossible.

3.3.2. Clay compaction

Printing success depends on humidity and clay slurry compactness. Clay printing is accurate, therefore an air cavity in the slurry will generate cavitation explosion during building and destroy the printing components (Figure 12, right). Clay slurry can be compacted by stirring or vacuum degassing.



Figure 12. Left: Uneven moisture leads to extrusion interruption; Right: Air bubble explosion

3.3.3. Toolpath optimization

Non-rapid setting slurry ingredients make vertical rod printing difficult in Lattice Craft and Hybrid Craft. In order to complete the construction of vertical components, the robot's running speed must be slowed to accumulate mud, which will make the vertical components thicker. The paths of the first and last sections of the vertical components must also be adjusted. In the study (Figure 13), the author tried numerous closure routes and found Obstuse to Act, which prevents the rod from tipping due to tool head collisions and material stickiness.

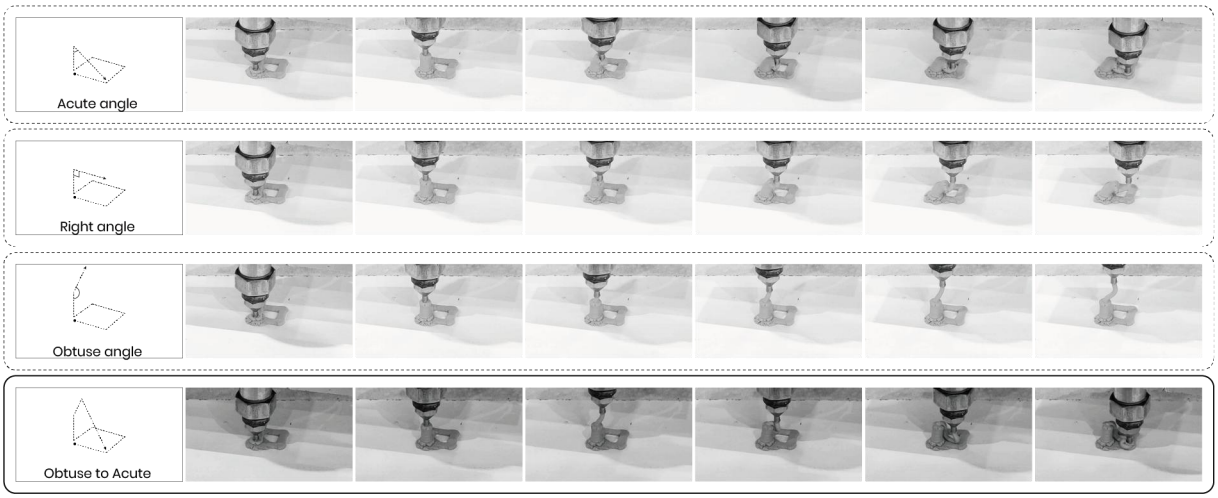


Figure 13. Path optimization

4. Results

4.1. Fabrication setup

The entire experiment was completed through a pneumatic slurry extrusion system that is mounted to an kuka kr30 industrial robot. Standard wet clay is loaded into a pressure Standard wet clay is loaded into a pressure tank attached to the extruder assembly under fixed supply of air pressure at 2.7 bar. The clay is pushed to the extruder assembly, where a motorized augur with controlled RPM regulates and sets the flow of clay. The clay body is prepared using cone 10 stoneware clay and water at 1 kg of clay to 70 g of water.4.2. Fabricated Models. The toolpath for the lattice geometry is generated by FURobot in the Grasshopper3D environment.

4.2. Demonstration

Hybrid Craft takes advantage of both processes. Contour Craft builds complicated surfaces with high precision, while Lattice Craft creates a spatial grid-like support framework for a highly versatile printing process. The challenge with path planning for this process is combining discrete and continuous methods into a single Hybrid method.Continuous path planning emphasizes contour lines between layers and uses "layers" as the unit. After each layer, the print head moves to the next layer's beginning spatial coordinate and prints in the opposite order.

The discrete path planning method is usually based on the "grid" unit, and its design goal is usually an independent path within the grid cells. After each cell path, it restarts the next cell path at its end position and repeats several times until all cell paths within the layer are completed, then moves to the next layer for printing in the opposite direction (Figure 14).



Figure 14. Hyperbolic components of hybrid craft

5. Conclusion

5.1. Forming principle discussion

Through different path planning, Contour Craft can achieve the printing of many complex surfaces. Introducing reinforcement structures such as strip ribs, folded plate ribs, and cross ribs can improve the flexibility of this process in shaping high hyperbolic surfaces.

Lattice Craft discretizes path planning. It divides the surface model into grid voxels. Printing uses a single discretization grid block preset unit path. Tool head must finish a grid block before going to the next printing target. The robot guided extrusion pumping system prints supporting components by maintaining low motion and high extrusion rates in the vertical direction, then prints connecting components by maintaining high motion and low extrusion rates in the horizontal direction. To anchor local nodes using material extrusion, the corner area is paused.

Hybrid Craft uses discrete and continuous construction. Layered technology shapes surfaces and spatial technology completes their supporting structure. The robot builds the model using complicated

speed control and pause point settings under suitable material parameters. The spatial grid-like support system reduces weight and may load forces in two orthogonal directions.

5.2. Future work

The evaluation of deformation in this experiment, which is simply a component of the robot clay technology project, now only considers the extreme deformation that can be seen with the naked eye and the collapse brought on by general instability. Future research will concentrate on 3D structured light scanning camera deformation prediction and route correction in high-precision construction.

Acknowledgements

This research was supported by the Shanghai Municipal Science and Technology Major Project (2021SHZDZX0100) , the Fundamental Research Funds for the Central Universities, the National Natural Science Foundation of China under the Joint Grant Fund (U1913603), the Collaborative Education Project of the Ministry of Education (202102560007) and the Science and Technology Innovation Action Plan for Social Development (21DZ1204500) of Shanghai Science and Technology Commission in 2021.

References

[1] B. Khoshnevis, "Automated construction by contour crafting—related robotics and information technologies," Automation in Construction, vol. 13, no. 1, pp. 5–19, Jan. 2004, doi: 10.1016/j.autcon.2003.08.012.

[2] Z. Seibold, K. Hinz, J. L. García del Castillo, N. Martínez Alonso, S. Mhatre, and M. Bechthold, "Ceramic Morphologies. Precision and control in paste-based additive manufacturing," presented at the ACADIA 2018: Re/Calibration: On Imprecision and Infidelity, Mexico City, Mexico, Mexico City, Mexico, 2018, pp. 350–357. doi: 10.52842/conf.acadia.2018.350.

[3] S. AlOthman, H. C. Im, F. Jung, and M. Bechthold, "Spatial Print Trajectory: Controlling Material Behavior with Print Speed, Feed Rate, and Complex Print Path," in Robotic Fabrication in Architecture, Art and Design 2018, J. Willmann, P. Block, M. Hutter, K. Byrne, and T. Schork, Eds., Cham: Springer International Publishing, 2019, pp. 167–180. doi: 10.1007/978-3-319-92294-2_13.

[4] B. Gürsoy, "From Control to Uncertainty in 3D Printing with Clay," presented at the eCAADe 2018: Computing for a better tomorrow, Łódź, Poland, Łódź, Poland, 2018, pp. 21–30. doi: 10.52842/conf.ecaade.2018.2.021.

[5] Z. Ma et al., "RobotSculptor: Artist-Directed Robotic Sculpting of Clay," in Symposium on Computational Fabrication, Virtual Event USA: ACM, Nov. 2020, pp. 1–12. doi: 10.1145/3424630.3425415.

[6] N. Leach, A. Carlson, B. Khoshnevis, and M. Thangavelu, "Robotic Construction by Contour Crafting: The Case of Lunar Construction," International Journal of Architectural Computing, vol. 10, no. 3, pp. 423–438, Sep. 2012, doi: 10.1260/1478-0771.10.3.423.

[7] M. Bechthold, "Digital Design and Fabrication of Surface Structures," Fabrication: Examining the Digital Practice of Architecture [Proceedings of the 23rd Annual Conference of the Association for Computer Aidd Design in Architecture and the 2004 Conference of the AIA Technology in Architectural Practice Knowledge Community / ISBN 0-9696665-2-7] Cambridge (Ontario) 8-14 November, 2004, 88-99, Jan. 2004.

IASS 2023
July 10–14 Melbourne
Integration of Design and Fabrication

Proceedings of the IASS Annual Symposium 2023
Integration of Design and Fabrication
10–14 July 2023, Melbourne, Australia
Y.M. Xie, J. Burry, T.U. Lee and J. Ma (eds.)

Liquid printed reusable dredged-based material for concrete formwork

BoSheng LIU*, Tzu-Hsien LO[a], Cheng-Hsuan YEH[a]

[a,*] Feng Chia University
bsliu@fcu.edu.tw

Abstract

A dredged-based material infused in the additive manufacturing (AM) method using the Rapid Liquid Printing (RLP) technique was applied to fabricate recyclable concrete formwork. The investigation of the printed dredged-based material and AM printing technique demonstrates its potential for custom concrete formwork in mass production. Contrary to the existing concrete formwork casting method, this research RLP additive manufacturing process and its material improve the formwork's adaptability, mobility, and reusability compared to the conventional formwork method. This paper will present the critical findings of Silt Dredged Material (Silt DM) mixed with non-petroleum-based soy-based hydrogenated vegetable glycerides material, and unhydrolyzed beeswax-based esters material printed in water that can instantly harden. The silt DM based material mixture's unconfined compression value is related to RLP extrudability, and workability that coordinate with the printing process. This RLP dredged-based material and technique are predictable, repeatable, and the instant hardened characteristic, making it possible to deliver a higher degree of fabricability suitable for greater design freedom. The material properties allow for a fast-printing process that has great potential to scale up to a sizeable architectural production.

Keywords: rapid liquid printing, dredged-based material, reusable material, 3D printed formwork, reusable concrete formwork

1. Background & introduction

Reinforced concrete (RC) structures are one of the most conventional structural typologies in Taiwan and its neighbouring southeast nations. According to the Ministry of Economic Affairs of Taiwan, more than 90% of existing structures are made of RC, with the remaining percentage split between steel structures and steel-reinforced concrete (SRC) hybrid systems. The conventional RC casting method uses wooden formworks as the primary material to create the casting body for building structures. Each wooden formwork can last for 5 to 9 uses before becoming part of the landfill. Although wood panels are still one of the primary materials for RC structures, plastic and aluminium formworks are gaining popularity within the construction industry due to their longevity, which can last up to 300 uses before recycling. However, the final lifespan of the used formwork is challenging to recycle due to impurity material and other chemical components mixed with the used formwork, resulting in the material mostly ending up in a landfill.

Meanwhile, Taiwan's appetite for premixed concrete and its RC structures has only been increasing yearly, with an average increase of 5.7% from 10.17 million tonnes in 2017 to 13.65 million tonnes in 2022 [1]. This increase translates to a rise in yearly carbon emissions (CO_2) and the total volatile organic compounds (TVOCs) in material processing and construction. This issue is not unique to Taiwan but is happening globally. As a collective body increasing CO_2 and TVOC emissions, it influences the global climate and exacerbates temperature fluctuations. To prevent extreme climate changes, governing bodies have declared Net-Zero Emission by 2050, using the Sustainable Development Goals (SDGs) to

Copyright © 2023 by BoSheng LIU, Tzu-Hsien LO and Cheng-Hsuan YEH. Published in the Proceedings of the IASS Annual Symposium 2023 with permission.

help individual nations determine national contributions (NDCs). In the context of architecture and building construction, researchers and designers have turned to additive manufacturing (AM, also known as 3D printing) as one of the potential solutions because the AM technology is cost-effective in all-scale production while offering an opportunity to use less material for the final product and could satisfy overall requirements.

In the architecture and building construction industries, AM technology is often associated with fusion deposition modelling [2] FDM, also known as layer-by-layer printing) that can extrude a wide range of materials such as metals, polymers, ceramics, composited materials (e.g., premixed concrete), and more. 3D printing concrete [3] (3DCP, i.e., printing premixed or custom-mixed concrete) is the most commonly seen application in the whole building industry, including the most eye-catching companies like ICON Build, Concrenetics, XtreeE, Peri Group, Vicat Group, and more. 3DCP uses the FDM technique, allowing the mixed concrete to pump up to the nozzle and deposit the freshly mixed concrete on top of the designated location via the digitally generated control path, allowing the freshly mixed concrete to fuse with the lower concrete. The process is completed once the concrete is cured and solidified. The 3DCP's FDM process has limitations [4]: (1) The accuracy of the outcome heavily depends on the machine holding the 3DCP extruder. (2) It is not likely to print overhangs (i.e., cantilevers) because the fusing material may not cure fast enough. (3) Adding vertical structural reinforcement is one of the significant challenges using the current 3DCP method. (4) Anisotropic characteristics in the structural performance can be found in the printed concrete structure [5]. (5) The finished printed structure's surface needs post-processing on the exterior due to the layer stacking process, resulting in uneven strands' finish. (6) Printing material performance and consistency during the action or the idol printing process. (7) The challenge of evaluating printed structures lies in the industry's agreed-upon standards.

A variation to the 3DCP method was published by Hank et al., 2020 [6] and Li et al., 2021 [7] integrated Rapid Liquid Printing (RLP) [8] [9] method to create an Injection 3D Concrete Printing (I3DCP) process. The I3DCP method involves extruding the concrete material (M1) into a chemical or natural-based rheological environment (M2, i.e., gel-like material) that supports the deposited M1 material. This I3DCP method can bypass the conventional FDM horizontal strands, providing a solution to the material's anisotropic characteristic. Additionally, the deposited material can be extruded to create overhang forms, providing previously unseen advantages. However, this method has a few drawbacks: (1) The M1 material injects into the M2 environmental volume, which increases the overall volume and subsequently pressures the already deposited material, influencing the final geometric precision. (2) There is uncertainty about the M1 material overlaying or overlapping on the already deposited M1. (3) Concrete creep and shrinkage are difficult to predict and estimate. (4) The reusability and recyclability of the M2 material require further study. (5) When the M1 material is deposited inside the M2 environment, M2 is often not fully visible from the external environment, resulting in the printed outcome having to wait until it is fully cured and solidified to evaluate whether to reprint.

This paper aims to provide an alternative perspective to 3DCP and I3DCP, not by re-engineering the construction process using novel technology but by using custom mixed dredged material (DM) with the RLP fabrication method to improve the existing concrete construction process. Based on the earlier paragraphs about concrete formwork, novel 3DCP, and I3DCP challenges, this paper proposes using dredged material mixed with non-petroleum-based material deposited inside the room temperature water using the RLP method to create customizable 100% reusable concrete formwork. One significant advantage of using dredged material is its abundance as a natural resource that often contains high amounts of clay, silt, sand, and organics. The dredging process is often considered a national interest or national security issue. In Ohio's Lake Erie alone, the US Army Corps of Engineers (USACE) must remove 1.15 million cubic meters (1.5 million cubic yards) of annual sediments from harbors and recreational ports. Some dredged materials are suitable for the built environment, as demonstrated by Liu and Coffman (2016)[10], while once the DM is processed, it can be further used in infrastructure

[11]. However, by law or code, many dredged materials are often categorized as unusable due to the dredging location or by the dredging action and its content's uncertainty (the result in this case).

Previous investigations on fresh dredged material (FDM) printing[12] [13] focused on various methods to create DM vault structures, including conventional tile vaults made from DM compressed stabilized tiles (DM-CST) and 3D printed DM vaults using different locations' dredged material (e.g., Ohio's Lake Erie harbors and one of the coastal ports in southern Louisiana). The 3D printing dredged material investigation focused on the mixture ingredients and their FDM characteristics: extrudability, buildability, workability[3], and durability [14]. While the selected works contribute to the foundation of engineered mixture with dredged material and their applications, deploying outside the research and lab environment has a severe challenge due to the laws or codes in the USA and Taiwan that prohibit DM as the structural building material. As a result, the following research proposes using DM as a substitute for concrete formwork material.

2. Dredged material

2.1. Dredged material source

A diverse landscape of mountains, rivers, and coastlines can characterize Taiwan's national geography. The island is known for its steep slopes that often descend from the mountains to the rivers and the sea. For example, Yu-Shan Mountain, which is 3,952 meters high, is less than 150 kilometres from the nearest west coastline. Taiwan's steep mountain slopes and river valleys create a unique and breathtaking landscape. However, these steep slopes can also lead to hillside erosion and the transport of suspended sediments over long distances. As a result, Taiwan's rivers, streams, and reservoirs contain significant amounts of dredged material.

In this case, the collected DM is from the Jhong-Gang River, which has a typical steep river stream geography in Taiwan (Figure 1). The river is 54 kilometres long, and its upstream is at an elevation of 2616 meters with an average flow velocity of 15 m3/s. The Jhong-Gang River has one Ta-Pu reservoir, which requires dredging to maintain its water storage volume. The dredged material is often processed via soil treatment facilities or sedimentary basins. The washed gravel and sand have significant economic value and are usually sold to concrete mixture or construction companies, while the silt and clay become by-products of the process.

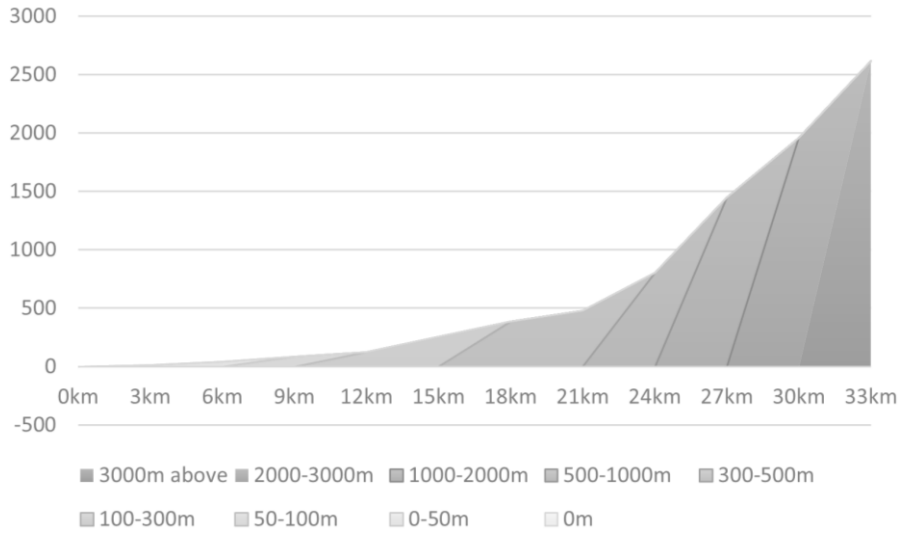


Figure 1. Jhong-Gang River's Elevation Changes from the upstream to the river mouth. The elevation date is pair with the aerial view. Information sourced from Jhong-Gang River ecosystem report and planning [15].

The collected downstream Ta-Pu reservoir's DM has been treated through sedimentary basins (Figure 2), a common practice in Taiwan. The sedimentary basins allow the dredged sediments to be naturally washed down and deposited in various basins. Each basin contains different particle classifications like gravel, sand, silt, and clay. This research first sieves unwanted dredged material through No. 100 mesh to remove unwanted elements and other organic matter. The DM sample selection process follows the ASTM D2487-17 collection process and uses the wet sieve analysis method to wash through No. 400 mesh. The sample resulted in fine silt particles smaller than 0.037 mm. The fine silt sample was later tested via hydrometer, resulting in a consistency of 4% clay and 96% silt, which is classified as silt textural soil classification.



Figure 2. Sedimentary basins next to Jhong-Gang River and the facility is specifically to treat dredged material from the Ta-Pu reservoir.

2.2. DM workability and compression test

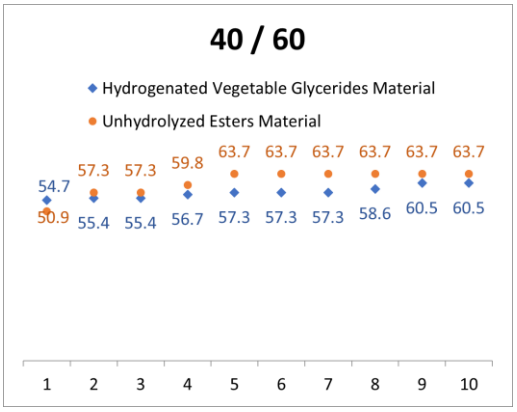
Building on the prior DM research [12] [13] [14], the freshly mixed DM material behaves differently in different soil classifications. For example, clayey DM has a more glutinous behaviour than silt-based DM. Additionally, silt-based DM has minimal sticky characteristics, which makes it suitable as the main ingredient for AM extruding processes. Instead of using water as a binding agent or a catalyst to activate the binding agent, the research investigates various non-petroleum-based materials as the binding agent with the silt DM (M1). These materials are injected into room temperature water (M2) to 3D print (RLP) concrete formwork techniques. The two critical binding agents are soy-based hydrogenated vegetable glycerides material and unhydrolyzed beeswax-based esters material. These materials are chosen because they can instantly change from liquid to solid when they come into contact with room temperature water. They are reusable and can be naturally digested and broken down by aerobic bacteria once their lifespan is completed.

An initial material compression test was carried out to investigate the mixture percentage among the binding agent, silt DM, and its mixture solid phase strength. The material workability investigation studied two binding agents: soy-based hydrogenated vegetable glycerides material and unhydrolyzed beeswax-based esters material. The hydrogenated vegetable glycerides material was heat-controlled at 60°C, and the unhydrolyzed esters material was controlled at 70°C. Each binding agent was tested with

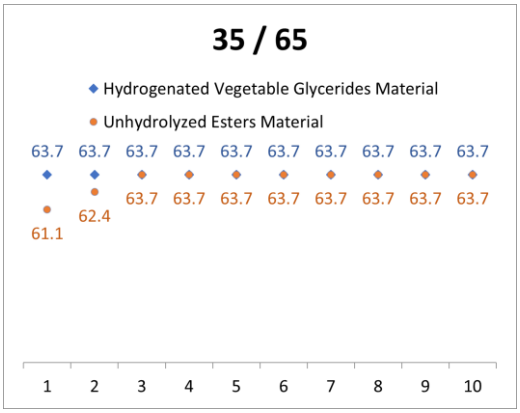
six different mixtures ranging from 80% binding agent and 20% silt DM to 20% binding agent and 80% silt DM. The extrudable and workability mixtures are 40% binding agent and 60% silt DM (i.e., 40/60), 35% binding agent and 65% silt DM (i.e., 35/65), and 30% binding agent and 70% silt DM (i.e., 30/70). Due to the glutinous level, a DM percentage of 30/70 or higher is unworkable and not extrudable.

The two binding mixtures noticeably different when it is in liquid and solid forms. The hydrogenated vegetable glycerides material's liquid is denser like syrup consistency while cured harder and the unhydrolyzed esters material is less dense like water while cured softer. Each mixture test sample was randomly selected 10 out of 30 and tested through a compression penetrometer ranging from 0 to 5 MN/m2 (MPa). As a result, the hydrogenated vegetable glycerides-based mixture has a wide range of mixture proportion possibility and the unhydrolyzed esters material has limited mixture combinations (Figure 3 (b and c)). The hydrogenated vegetable glycerides-based mixtures' 40/60 were tested with an average of 57.3 kPA (Figure 3 (a)), and both the 35/65 and the 30/70 withstood 63.7 kPa (Figure 3 (b ~ c)) without failing. Finally, the unhydrolyzed esters-based mixtures' 40/60 were tested with an average of 60.7 kPA (Figure 3 (a)), However the both the 35/65 and the 30/70 barely passed at 63.7 kPa (Figure 3 (b ~ c)) and deformations can be observed at the test samples.

(a)



(b)



(c)

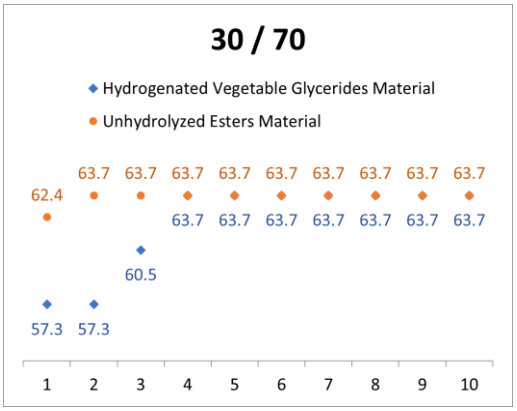


Figure 3. M1 material mixture proportion and compression strength. (a) 40% binding agent and 60% silt DM. (b) 35% binding agent and 65% silt DM. (c) 30% binding agent and 70% silt DM.

2.3. Injection printing process

In the initial injection printing process (RLP), each M1 mixture was extruded via the compressing chamber, and the pressure buildup was inconsistent, resulting in uneven extrusion (Figure (a)) inside the water environment (M2). Although the extruder equipment is not complete, one important finding was

discovered: when the M2 volume was completely full, as shown in Figure (b), the volumetric pressure of M2 was enough to affect the first printing layer of M1 inside the water tank. As a result, printed objects would detach from the tank's base. However, buildability would be fine when the M2 volume increases along with the M1's layer height (Figure 5), and it is highly possible to print overhangs and cantilevers using this method. When the M1 touches M2 only briefly, the M1 material is workable before it completely hardens. It requires further study to determine the extruding temperature and the hardening time gap to inform the printing speed.

(a) (b)

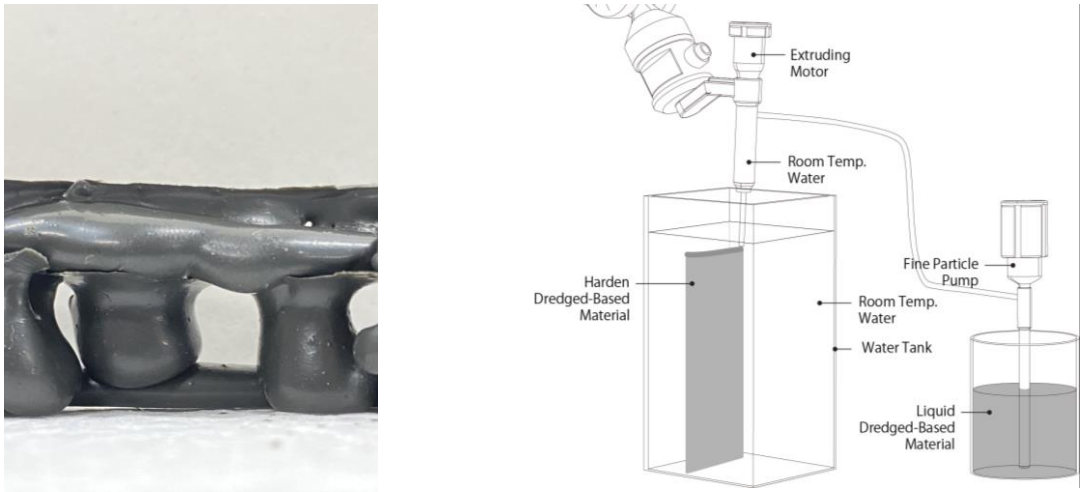


Figure 4. (a) Initial injection printing result. (b) Injection printing setup diagram.

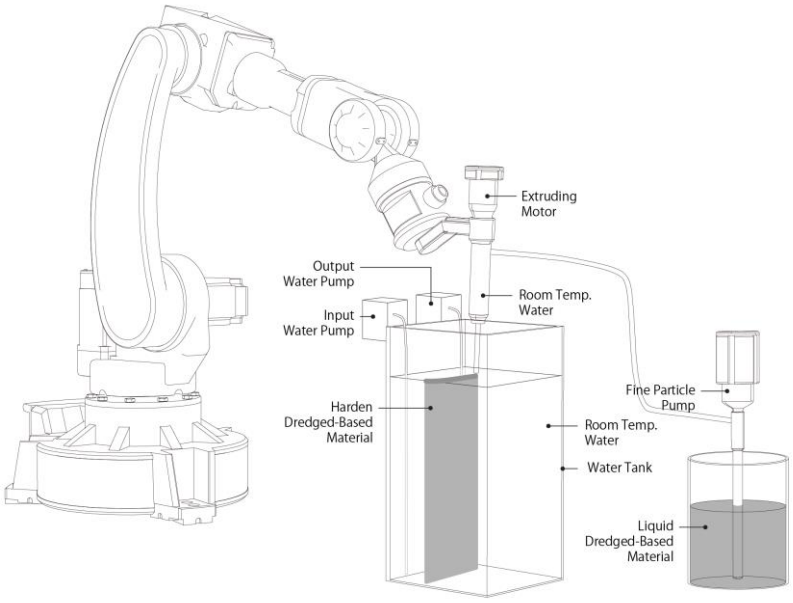


Figure 5. The injection set up including two water pumps to digitally control water height.

4. Conclusion: submission of contributions

The present paper discusses an initial investigation into the DM injection printing (RLP) technology, wherein M1 material is injected into M2 fluid with different rheological properties. The study evaluated

two variations of M1 material, namely silt DM mixed with soy-based hydrogenated vegetable glycerides material and silt DM mixed with unhydrolyzed beeswax-based esters material, using compression tests to determine their strength. Although the two binding mixture performances are different but it still yet enough data to draw a conclusion on which binding agent is better. More of the testing data needs to come from shear stress strength, material buildability, and more.

In the case of printing process, two printing methods were employed: M2 volume fully filled with M1 injection, and M2 volume rising along with M1 injection. It was concluded that the latter method performed better than the former. The results of this material mixture investigation combined with the silt DM injection printing technique satisfied the initial study requirements and suggest that this method is suitable for further research.

Although the research is a proof-of-concept and it has highlighted specific potentials, several challenges, and unknown factors also require further investigation. Firstly, while the solidified material strengths of M1 were studied, its liquid strengths were not, necessitating a shear strength study to understand better the moment M1 extrudes from the nozzle and to determine the design constraints of the printing object. Secondly, the M1 printing consistency and nozzle design must have the ability to maintain or increase their temperature during the printing process. Thirdly, the overlap condition of M1 material deposits is unknown. Lastly, it is still being determined how the printed M1 material will perform during the conventional concrete curing process and whether it will impact concrete strength.

It is important to emphasize that the DM injection printing technique relies on a solid connection between the fabrication process and material parameters. These elements cannot be viewed in isolation. Therefore, to make progress in research, it is essential to have a coordinated effort between material design, structural design, and fabrication process.

Acknowledgements

The authors would like to thank *Taichung Cultural Education Foundation for Architecture* for providing the funding and offer the opportunity to kick-start “Liquid printed reusable dredged-based material for concrete formwork”. I also want to thank student worker Meng-Ze Du for helping material investigation. And special thanks to Professor Cheng-Chia Huang and Li Qin mechanical contractor in Taiwan for assisting me to acquire Ta-Pu reservoir’s dredged material.

References

[1] D.-Y. Chen , "Analysis of Taiwan's cement and its products manufacturing industry in 2023," Taiwan Industry Economics Services, Taipei, 2022.

[2] S. H. Masood, "10.04 - Advances in Fused Deposition Modeling," *Comprehensive Materials Processing,* vol. 10, pp. 69-91, 2014.

[3] C. Gosselin, R. Duballet, P. Roux, N. Gaudillière-Jami, J. Dirrenberger and P. Morel , "Large-scale 3D printing of ultra-high performance concrete – a new processing route for architects and builders," *Materials and Design 100,* vol. 100, pp. 102-109, 2016.

[4] B. Panda, Y. W. D. Tay, S. C. Paul and M. Tan, "Current challenges and future potential of 3D concrete printing," *Materialwissenschaft und Werkstofftechnik,* vol. 49, no. 5, pp. 666-673, 2018.

[5] Y. W. D. Tay, B. Panda, S. C. Paul, N. A. N. Mohamed, M. J. Tan and K. F. Leong, "3D printing trends in building and construction industry: a review," *Virtual and Physical Prototyping,* vol. 12, no. 3, pp. 261-276, 2017.

[6] N. Hack, I. Dressler, L. Brohmann, S. Gantner, D. Lowke and H. Kloft, "Injection 3D Concrete Printing (I3DCP): Basic Principles and Case Studies," *Materials,* vol. 13, no. 1093, 2020.

[7] C. Li, X. Zhou and X. Liu, "Integrating The Bio-digital Aesthetic Value and Architecture Potential of RLP-Concrete 3D Printing Technology," *IOP Conf. Series: Earth and Environmental Science,* vol. 768, 2021.

[8] K. Hajash, B. Sparrman, C. Guberan, J. Laucks and . S. Tibbits, "Large-Scale Rapid Liquid Printing," *3D PRINTING AND ADDITIVE MANUFACTURING,* vol. 4, no. 3, 2017.

[9] C. d. Pasquier, T. Chen, S. Tibbits and K. Shea, "Design and Computational Modeling of a 3D Printed Pneumatic ToolkitforSoftRobotics," *Soft Robotics,* vol. 5, 2017.

[10] R. Liu and R. Coffman, "Lightweight Aggregate Made from Dredged Material in Green Roof Construction for Stormwater Management," *Materials,* vol. 9(8), no. 611, 2016.

[11] S. Bhairappanvar, R. Liu and R. Coffman, "Beneficial Uses of Dredged Material in Green Infrastructure and Living Architecture to Improve Resilience of Lake Erie," *Infrastructures,* vol. 3, no. 4, 2018.

[12] J. Hillegas, R. Liu, B. Liu, A. Sanchez and Q. Huang, "Engineering Properties Influencing Clayey Materials for Additive Manufacturing," in *Conference: International Association for Shell and Spatial Structures*, Boston, USA, 2018.

[13] B. Liu and R. Liu, "3D Printed Vault Using Dredged Material," in *Conference: International Conference on Emerging Technologies In Architectural Design*, Toronto, Canada, 2019.

[14] B. Liu and R. Liu, "Performance-Based Computational Design and Fabrication for A Resilient Solution: Dredged Material for Masonry Vault Construction," *The Plan Journal,* vol. 6, no. 2, 2021.

[15] D.-R. Zhu, "Wetland Ecological Corridor Survey and Conservation Workshop Plan," Miaoli County Government, Miaoli County, 2013.

Proceedings of the IASS Annual Symposium 2023
Integration of Design and Fabrication
10–14 July 2023, Melbourne, Australia
Y.M. Xie, J. Burry, T.U. Lee and J. Ma (eds.)

Local optimization of self-supporting shell structures in 3D printing: a skeleton method

Yefan ZHI[a,*], Hua CHAI[a], Teng TENG[a], Masoud, AKBARZADEH[a,b]

[a,*] Polyhedral Structures Laboratory, Weitzman School of Design, University of Pennsylvania, Philadelphia, USA Pennovation Center, 3401 Grays Ferry Ave. Philadelphia, PA, 19146
yefanzhi@upenn.edu

[b] General Robotic, Automation, Sensing and Perception (GRASP) Lab, School of Engineering and Applied Science, University of Pennsylvania, Philadelphia, USA

Abstract:

This paper presents an optimization method to create self-supporting shell structures for 3D printing (3DP) purposes. Compared to other methods of construction, 3DP can facilitate the fabrication of freeform, complex shell structures. However, for objects printed at the architectural construction scale, the 3DP supports are typically hard to remove, causing considerable material and energy waste and requiring additional postprocessing work. Making the geometry self-supporting is a challenging alternative to neutralize these downsides of 3DP. We propose a post-slicing optimization method to make porous shell structures self-supporting for 3DP by reducing the overhang when necessary. The method is applicable to shell structures that, when printed, only consist of walls without infills or caps. After slicing, we represent the planar wall toolpaths using medial axes and maximal disks. The method then examines the proximity between the medial axes of adjacent layers to build a skeleton model and makes adjustments when the overhang exceeds a limit. Finally, the planar toolpaths are updated through linkage to the medial axes. An example of a Triply Periodic Minimal Surface (TPMS) geometry is illustrated. In this paper, we offer a computational framework for the local optimization process. Instead of imposing limitations at the beginning of the design process, it adjusts a finished design to form self-supporting geometry. It investigates the geometry through an organized series of toolpaths and preserves the shell structure's local thickness and curvature continuity. While recent self-supporting optimization research mainly inspects geometries of fixed vertical sections, our method fully develops 3DP's potential in manufacturing free-form shell structures and can be of vast application on various scales.

Keywords: 3D printing, shell structure, structural optimization, Hangai Prize applicant

1. Introduction

1.1. Self-supporting structures for architectural additive manufacturing

Additive manufacturing, primarily 3D Printing (3DP), has revolutionized the way objects of different scales are designed and manufactured. It gives architects the ability to flexibly create complex functional and exotic geometries that are difficult to achieve with traditional manufacturing methods [1]. How- ever, architectural additive manufacturing, with concrete 3DP as a most prevalent practice, also faces limitations in mass production. While conventional layer-based 3DP utilizes support structures that are printed together with the geometry and removed afterward, at the architectural construction scale they are typically hard to remove and create considerable material and energy waste and require additional post-processing work [2].

Copyright © 2023 by Yefan ZHI, Hua CHAI, Teng TENG, Masoud and AKBARZADEH. Published in the Proceedings of the IASS Annual Symposium 2023 with permission.

Overhanging, hole, and edge features in the print geometry usually require support structures [3]. This paper is situated in the trend of designing self-supported structures and neutralizing the downsides of support structures. Making the geometry self-supporting is a challenging task. Extensive research has been conducted to globally optimize the topology using methods involving moving morphable compo- nents [2, 4, 5]. However, instead of being the *post-processing* to a pre-designed geometry, the *global* topology optimization process incorporating self-supporting constraints is more like the *design process* itself. The principles of topology optimization restrict the freedom of architects in experimenting with novel structural prototypes. Their outcomes are usually limited to multifurcating structures with fixed sections such as the Messerschmitt–Bölkow–Blohm (MBB) beam.

In this paper, we propose an alternative to creating a self-supporting structure by locally optimizing a present geometry that is in general printable but can be vulnerable at certain locations. The main characteristics of a vulnerable region in the print are identified as bridges, overhangs, and angles [6] when the geometry is viewed *as geometry*, or in other words, the mesh or boundary representation as the slicing input. Our method will scrutinize the geometry *as toolpaths* after the conventional slicing is finished. The unprintable characteristics, all referred to as *overhangs* in this paper, will then be manifested as the planar offset between layers of toolpaths. Utilizing a post-slicing skeleton model we will be able to calculate and reduce the overhangs when necessary and thus make the geometry self-supporting.

1.2. 3D printed shell structures

The process of 3DP is essentially linear extrusions. Compared to the traditional casting method, it is advantageous in creating shell structures with holes and multifurcations which then become innovative architectural components such as the wall, column, beam, and dome elements with tailored functions [7–11]. This sustainable approach with minimized material usage to design and fabricate lightweight structures with high structural performance has thus gained more attention.

This paper will look at lightweight porous shell structure components that, when printed in concrete, only consist of walls without infills or caps. Typically, they are prefabricated in the factory and then transported to the site for assembly, as opposed to the other two fashions of 3D printing formworks or an entire building [12]. When combined with structural form-finding, they make efficient discrete systems [13]. Triply Periodic Minimal Surface (TPMS), as one of the lightweight structural prototypes, has been extensively tested and researched. Due to their minimal surface area, TPMS structures possess a high surface area-to-volume ratio. The periodic and continuous nature of TPMS structures also allows the efficient distribution of external loads throughout the material. When a force is applied to one point on the structure, the load is distributed across multiple points, reducing the overall stress experienced by any single point. This distribution results in better overall mechanical stability and resistance to deformation [14]. This paper uses Diamond TPMS as a case study and demonstrates the respective potential of our optimization proposal.

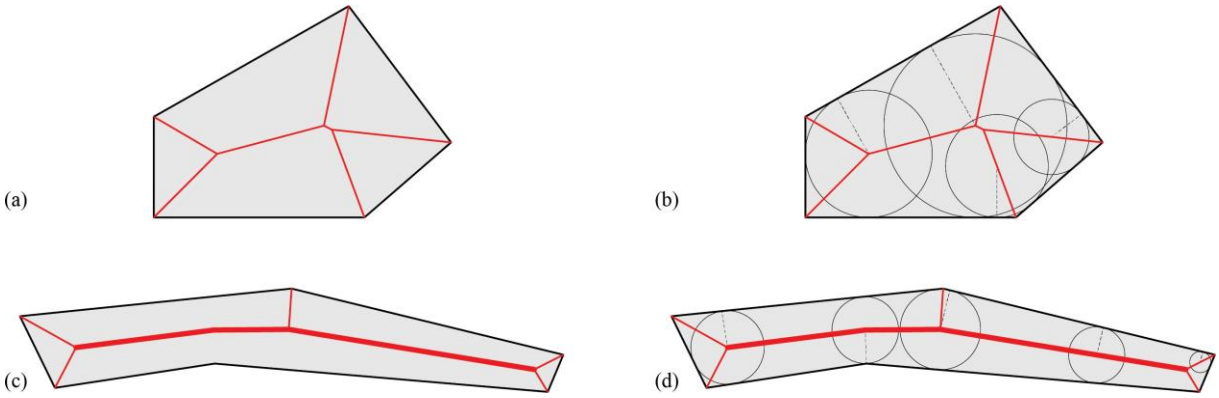


Figure 1. Medial axis (red) and some maximal disks of (a) (b) a regular polygon; and (c) (d) a slender polygon.

1.3. Medial axis and skeleton model

Introduced by Blum [15] in 1967, the *medial axis* is an efficient way to describe a 2D shape. It is essentially the set of points in a shape that have at least two closest points on the shape's boundary (Figure 1a, c). For each point on the medial axis, a unique *maximal disk* can be drawn if we use the distance between that point and the closest points on the boundary as its radius (Figure 1b, d). The points in all the maximal disks are within the original shape and all the points in the original shape are covered by some maximal disks. We call the combination of the medial axis and each point's local radius (of its maximal disk) a *disk representation* of the shape. We can mutually transform between the boundary representation and the disk representation of the original shape. This method is also applicable to planar domains with holes [16] where instead of being a *tree*, the medial axis will incorporate *cycles*.

This paper proposes printing the two sides of shell structures in two parallel curves so that the toolpaths a) are closed contours with seams for better finishing quality and b) can be continuous while accommodating multifurcations in the plane. To do so, the input geometry is a shell with thickness and volume. Given a printing direction (*z*-axis of the printer), it is sliced into one or multiple closed contours in each plane. If the structure is in general printable, the contours enclose slender domains representing the solid part of the shell (gray parts in 4). Figure 1c, d show that for a slender domain, a main axis (thickened) representing the direction and position of the geometry is observed. It offers an efficient representation where the radii of most maximal disks are similar. Thus we transfer the slender domains created into medial axes for optimization. And the disk radii are recorded as vectors to preserve the shell structure's local thickness and curvature continuity in our method.

The precise calculation of medial axes in polygonal or curved shapes is a complex and slow task [17]. We use an approximate method to compute medial axes and then examine the proximity between the medial axes of adjacent layers. Adjustments are made when the overhang exceeds a limit. Finally, the planar toolpaths are updated through vector linkages to the medial axes. This *skeleton* method will be explained in detail in the Methodology section. Note that while the concept skeleton is used by computer scientists as an extension of the medial axis of a 2D geometry, this paper uses it to refer to an entire 3D print geometry organized in a hierarchical data structure.

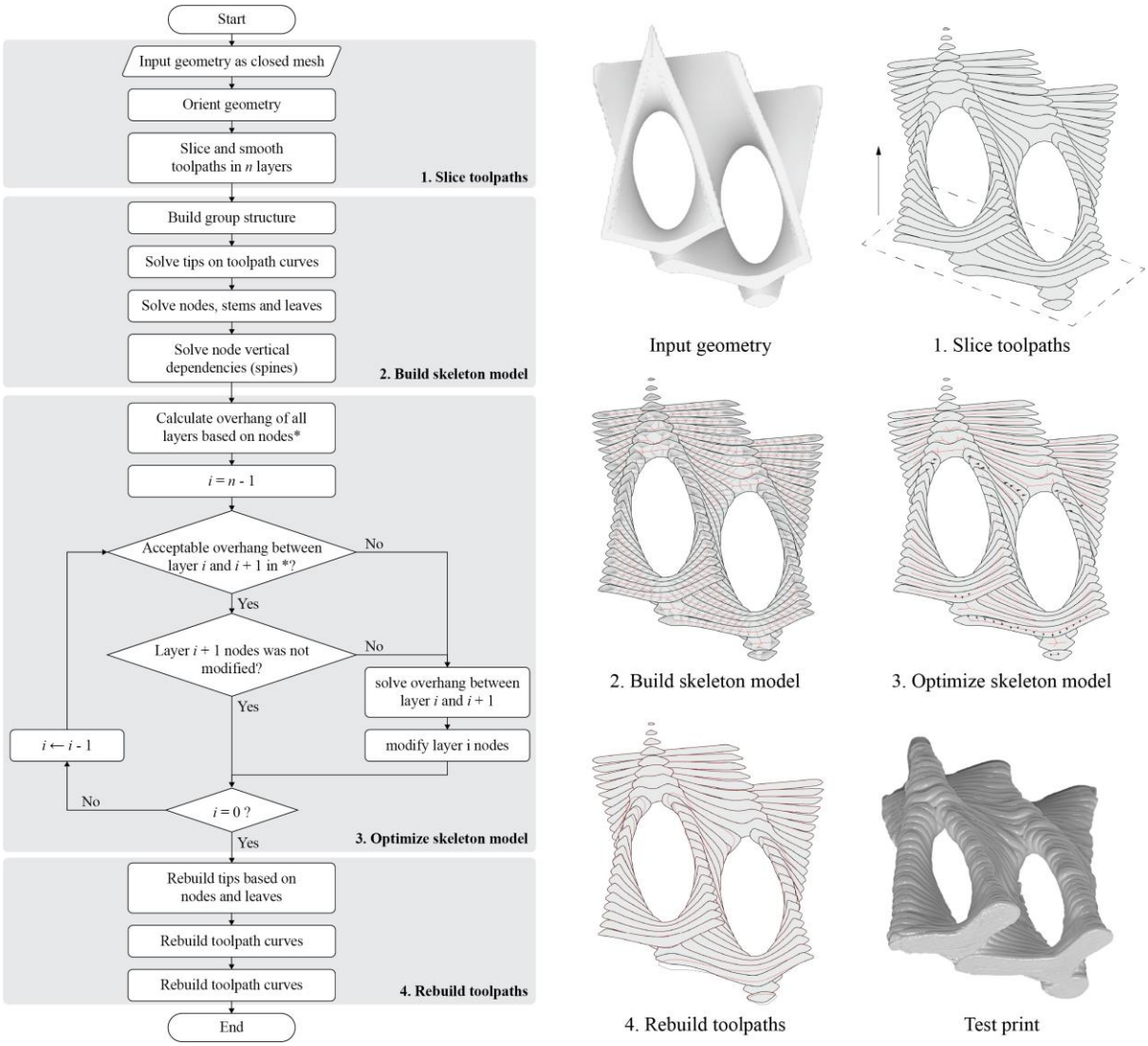


Figure 2. The computational flowchart for reducing the print overhang utilizing the skeleton model method, show- ing the geometry at different stages.

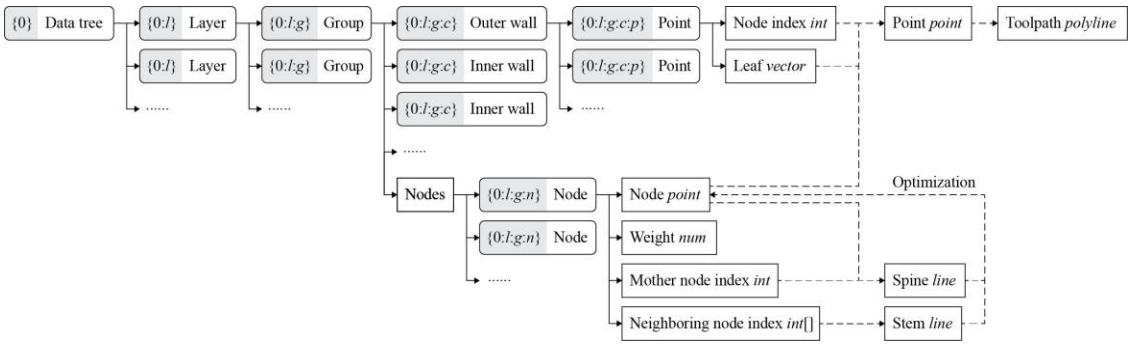


Figure 3. Main data structure of the geometry optimization.

2. Methodology

Figure 2 offers an overview of the optimization framework. It comprises four major steps: slice tool- paths; build the skeleton model; optimize the skeleton model; and finally, rebuild the toolpaths. Figure 3 illustrates the computational data structure where points are stored in relative positions to nodes of the medial axes. A case study of a Triply Periodic Minimal Surface (TPMS) geometry (Figure 2b) generated using the volumetric modeling plugin *Axolotl* [18] for *Grasshopper* is illustrated.

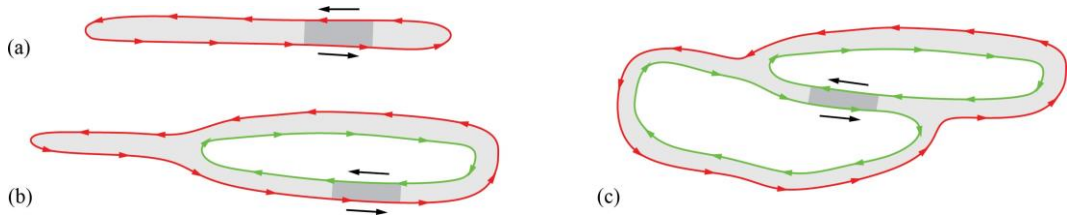


Figure 4. Outer walls (red, counterclockwise) and inner walls (green, clockwise) of groups with (a) no holes; (b) one hole; and (c) multiple holes.

2.1. Slice toolpaths

Our method applies to both parallel and non-parallel slicing of solid geometries. A concrete 3DP geome- try as a structural component usually uses its flat top and bottom faces as contact surfaces for assemblage. The two faces are part of the input of the slicing or can be found using a convex hull analysis. They de- termine the slicing planes in between that intersect the geometry to create closed contour curves.

2.2. Build skeleton model

In each plane or *layer*, the contours are then sorted based on their cross-inclusion relations to form several *groups*. As illustrated by Figure 4, each group indicates a solid domain (shown as gray). A group is formed by one *outer wall* and can have several *inner walls* each indicating a hole. In the data tree, they form a list of curves where the outer wall is the first curve (Figure 3). The printing directions of the walls are also unified to have the parallel layers printed in reversed directions and thus have increased bounding.

Our approach to calculating the medial axis is developed based on the Voronoi diagram approximation method by Brandt and Algazi [19]. (Another application of the method in 3DP is the extrusion rate control to create variable print width [20].) We start by refitting the *toolpath curve* using a compact polyline whose adjacent vertices have a prescribed maximal distance. The vertices are then extracted as a list of *points* (Figure 5a). Based on the discrete points a Voronoi diagram can be solved and purged to show the inner structure of the domain (Figure 5b). The half cells form a redundant, approximate planar skeleton structure. We then merge the adjacent vertices of the Voronoi diagram within a tolerance into *nodes* to make the representation more efficient (Figure 5c). The end nodes (having only one neighbor) too close to the boundary are also purged recursively to extract only the “bones” of the slender geometry. Referring to the original Voronoi diagram, the linkages between nodes are calculated as *stems*. With the node-stem structure formed, each toolpath point is projected to the closest node and regarded as offsetted from it by a *leaf* vector (Figure 5d). Note that here we use nouns describing plants because our geometric structure is similar to plants

such as shameplants and ferns in plane.

To examine the overhang between layers, we solve the vertical dependencies between nodes of adjacent layers. When the supporting condition of a node is examined, the node is referred to as the *daughter node*. For each daughter node, the closest node in the previous layer is found as its *mother node*. The last component of the skeleton mode, the *spines* are then created by connecting the daughter nodes and their mother nodes (Figure 5e).

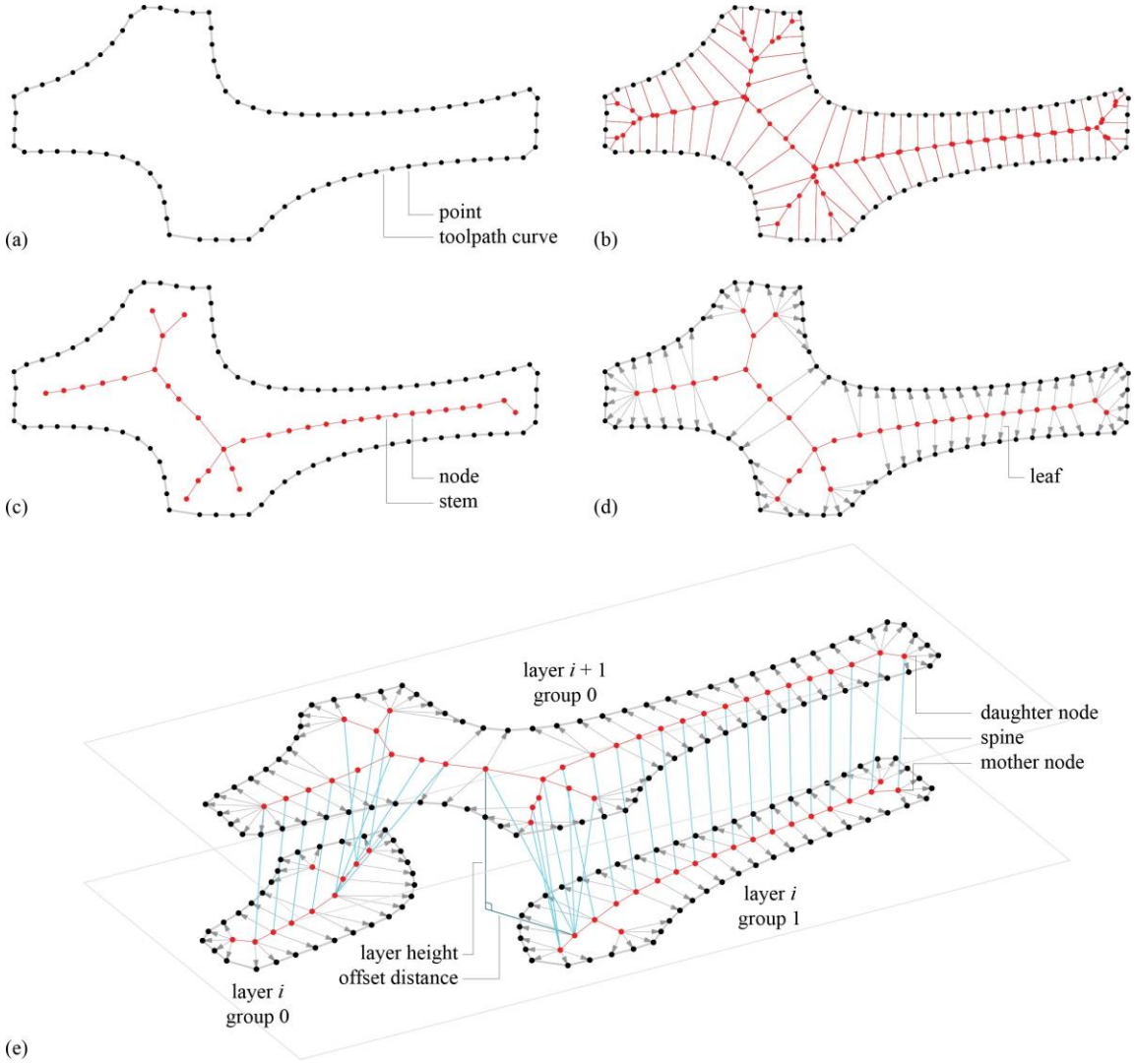


Figure 5. Skeleton model building process: (a) convert the input *toolpath curve* into a compact polyline and extract *points*; (b) solve the Voronoi diagram and the vertices inside the domain; (c) merge the vertices to create *nodes*, purge those too close to the boundary, and create *stem* connections between nodes; (d) find the closest node to each point to create *leaf* vectors; and (e) find each *daughter node* in layer $i + 1$ the closest *mother node* in layer i and connect them to form *spines*.

2.3. Optimize skeleton model

The goal of our local optimization method is to reduce overhang between layers. Ideally, the local overhang distance is defined as the offset distance between the new toolpath and the previous one that supports it (Figure 6). It can be calculated by projecting a point on the new toolpath to the

previous slicing plane and finding its distance to the closest toolpath curve. We use pairs of mother and daughter

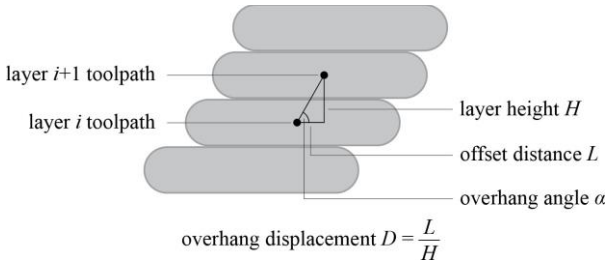


Figure 6. Ideal definition of overhang displacement.

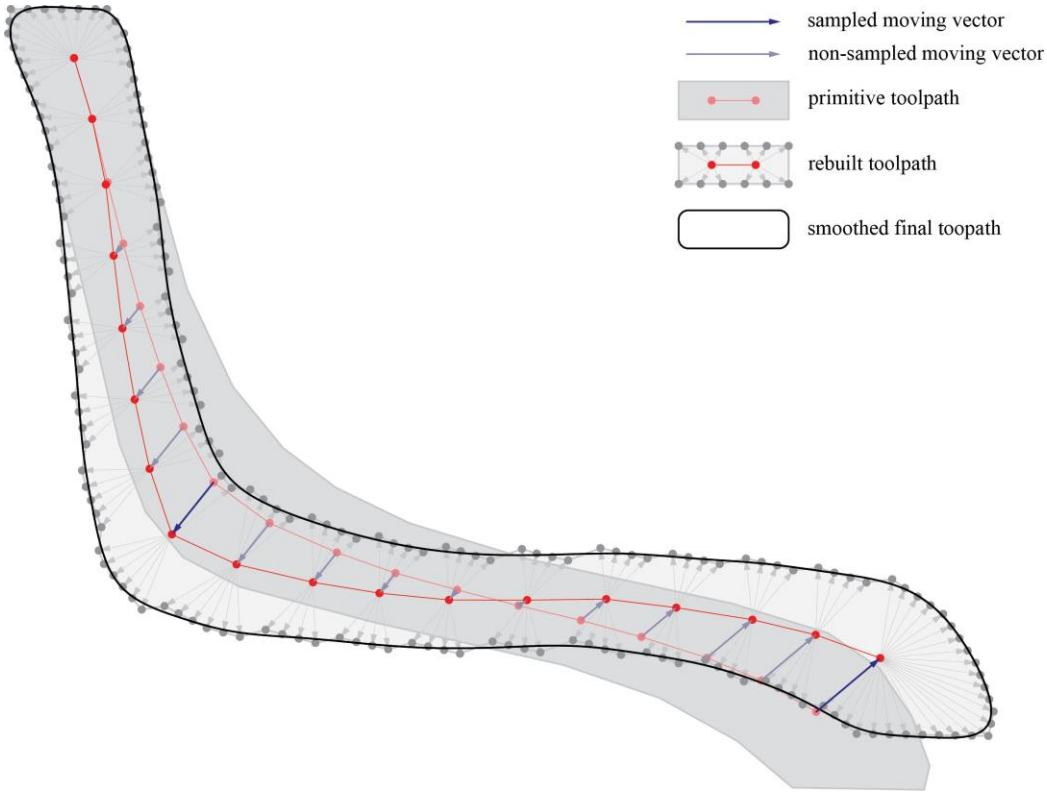


Figure 7. Example of optimizing a group where two nodes are sampled.

nodes, instead of the points to calculate the offset distance and the overhang displacement. The offset distance of all the points that rely on the same daughter node is thus treated as the projected length of the node's spine in the mother layer plane (Figure 5e). Note that the radii of the two nodes also affect the actual offset distance. However, when the radius is significantly larger than half of the shell thickness, it means the surface orientation is largely tilted, and in this extreme case allowing more tolerance in offset by neglecting the change in radii can help maintain the overall shape of the geometry.

Our method requires a predetermined overhang displacement optimization goal (0.9 in the case study). As shown by Figure 2a, after a round of pre-check, the local optimization process examines

each layer in a certain order. Usually, the contact surface of the top and bottom faces should be preserved in their original shapes and the merging regions close to the top are more dangerous than the diverging regions close to the bottom. Therefore, our method follows a top-down order in inspecting layers.

Examining each pair of adjacent payers, we adjust the mother layer (layer i) to better support the daughter layer (layer $i + 1$). Each mother node receives *moving vectors* required by the daughter nodes to reduce their overhang displacement when necessary. One mother node can have multiple daughter nodes. The vector with the largest magnitude is used to move the mother node, which means that at times our method cannot eliminate all excessive overhangs.

A node is *sampled* if it received a moving vector as the mother node. However, its neighbors should also be adjusted to preserve curvature continuity. The moving vectors of the *non-sampled* nodes are calculated based on their distance to the sampled nodes. The distance is the length of the path between the two nodes on the graph formed by nodes and stems. It acts as a variable to linearly reduce the sampled moving vector in solving non-sampled moving vectors. In the example of Figure 7, only two mother nodes are sampled, meaning their overhangs exceed the prescribed limit. When we tune the nodes in a continuous way using both sampled and non-sampled moving vectors, the curvature continuity of the node-stem graph is preserved as in the original geometry.

2.4. Rebuild toolpaths

The rebuilding of toolpaths is straightforward. By adding back the leaf vectors to the new nodes, the points of the new curves are recomputed as shown in Figure 7. The rebuilt toolpath is then smoothed recursively to form the final toolpath. The entire optimization process thus mimics the kinematics of a snake skeleton and the thickness and curvature continuity is preserved in the new shell walls.

3. Results

Our case study features a 35 × 70 × 70mm Diamond TPMS with a 2mm thickness as the input geometry. We use an in-house developed PET-G printer with a 1.65mm diameter nozzle to simulate the concrete 3DP in a 1/10 scale. The print width is 2mm and the layer height is 1mm. 0.9 is set as the optimization threshold. The computation process of slicing and optimizing takes around 60 seconds. The primitive and optimized toolpaths differ mainly in merging regions (Figure 8a). The branches holding the bridge are dragged towards each other to reduce the overhang (Figure 8b, d). Figure 8c shows the cumulative distribution of the overhang. The overhang at each node is weighted by the length of the toolpath projected to it. As a result, the percentage of toolpaths sufficing the requirement of 0.9 raised from 91% to 99%.

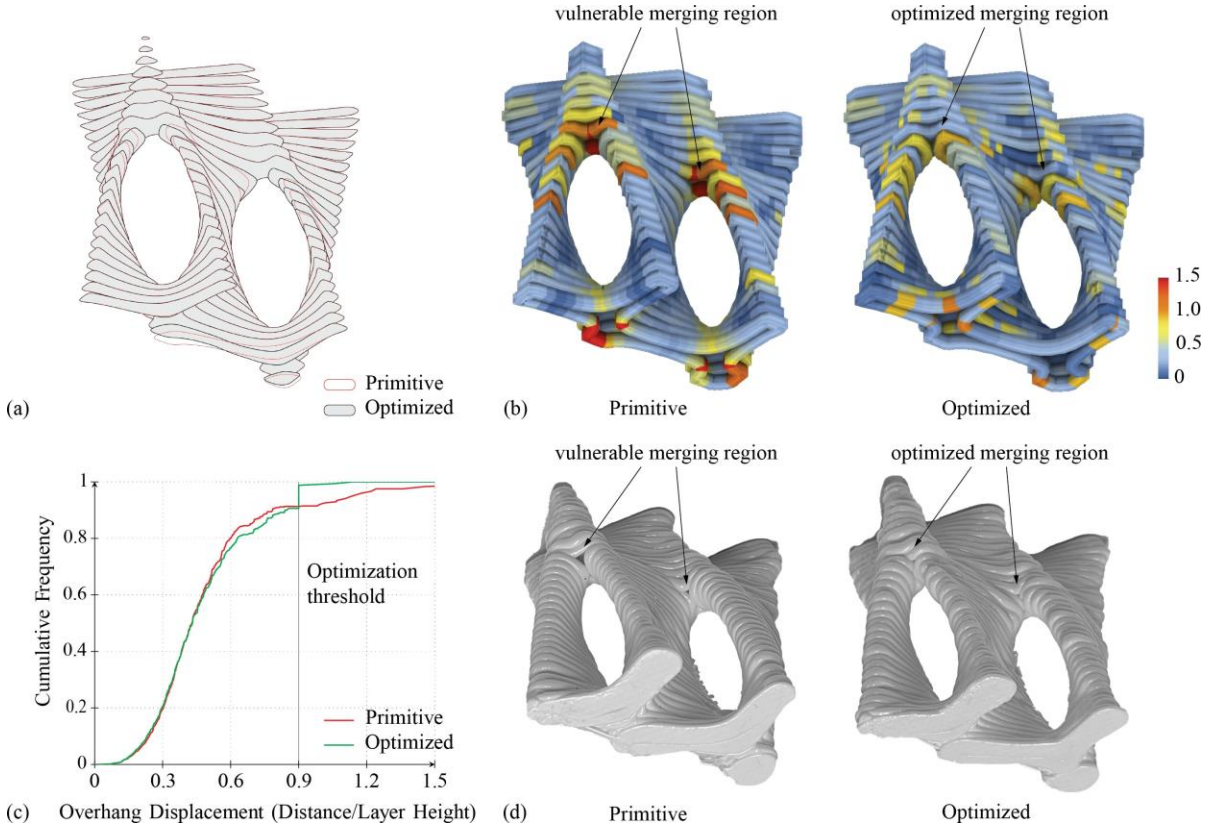


Figure 8. Optimization results of a Diamond TPMS geometry, 0.9 is set as the maximal overhang displacement: (a) toolpaths; (b) volumetric visualization showing overhang displacement; (c) cumulative distribution of printing overhang displacement; and (d) test prints.

4. Conclusion

In this paper, we offer a computational framework for the local optimization process. Instead of imposing limitations at the beginning of the design process, it adjusts a finished design to form self-supporting geometry. It investigates geometry through an organized series of toolpaths. It is a pivot exploration to assist in manufacturing free-form shell structures and can be of vast application on various scales. Meanwhile, it has the following limitations that require future work:

The method is highly resolution-dependent. The resolution and tolerance parameters, especially the overhang threshold, determine the quality of the optimized print. When the method is applied to different scales and diverse geometries, a systematic study of those parameters is required.

While our method features a top-down sequence, the order in which the layers should be organized and optimized is still open to discussion. One possible solution is to relate the overhang message with the Reeb graph structure of the geometry and decide on an optimization sequence accordingly. (An application of the Reeb graph in 3DP is provided by [21].) In addition, a constraint over the geometry's boundary parts is also a feature required by using such prints as structural components.

Finally, our local optimization can change the force flow and thus the structural performance of prints. A comprehensive, comparative study is required to investigate its limits and downsides. Cracking and vibration in the printing process of branching shell structures, discussed by [22], is also another factor affecting the printability and final quality that need to be evaluated in addition to being self-supported.

Acknowledgements

The authors gratefully acknowledge the support provided by the Advanced Research Projects Agency – Energy (ARPA-E) Grant of U.S. Department of Energy (DE-AR0001631), the National Science Foun- dation CAREER Award (NSF CAREER-1944691 CMMI), and the National Science Foundation Future Eco Manufacturing Research Grant (NSF, FMRG-CMMI 2037097) awarded to Dr. Masoud Akbarzadeh.

References

[1] B. Khoshnevis, "Automated construction by contour crafting—related robotics and information technologies," *Automation in Construction*, 2004.

[2] K. V. Bhat, G. Capasso, S. Coniglio, J. Morlier, and C. Gogu, "On some applications of generalized geometric projection to optimal 3d printing," *Computers & Graphics*, vol. 102, pp. 199–212, 2022.

[3] J. Jiang, X. Xu, and J. Stringer, "Support structures for additive manufacturing: A review," *Journal of Manufacturing and Materials Processing*, vol. 2, no. 4, 2018.

[4] A. T. Gaynor and J. K. Guest, "Topology optimization considering overhang constraints: Eliminat- ing sacrificial support material in additive manufacturing through design," *Structural and Multidis- ciplinary Optimization*, vol. 54, pp. 1157–1172, Nov. 2016.

[5] X. Guo, J. Zhou, W. Zhang, Z. Du, C. Liu, and Y. Liu, "Self-supporting structure design in additive manufacturing through explicit topology optimization," *Computer Methods in Applied Mechanics and Engineering*, vol. 323, pp. 27–63, 2017.

[6] M. Fernandez-vicente, M. Canyada, and A. Conejero, "Identifying limitations for design for man- ufacturing with desktop fff 3d printers," *International Journal of Rapid Manufacturing*, vol. 5, 12 2015.

[7] R. van Woensel, T. van Oirschot, M. Burgmans, M. Mohammadi, and K. Hermans, "Printing ar- chitecture: An overview of existing and promising additive manufacturing methods and their appli- cation in the building industry," *The International Journal of the Constructed Environment*, vol. 9,

pp. 57–81, 06 2018.

[8] C. Gosselin, R. Duballet, P. Roux, N. Gaudillie`re-Jami, J. Dirrenberger, and P. Morel, "Large-scale 3d printing of ultra-high performance concrete – a new processing route for architects and builders," *Materials & Design*, vol. 100, 03 2016.

[9] A. Anton, E. Skevaki, P. Bischof, L. Reiter, and B. Dillenburger, "Column-Slab Interfaces for 3D Concrete Printing," in *Proceedings of the 42nd Annual Conference of the Association for Computer Aided Design in Architecture (ACADIA)*, 2022.

[10] G. Vantyghem, W. De Corte, E. Shakour, and O. Amir, "3d printing of a post-tensioned concrete girder designed by topology optimization," *Automation in Construction*, vol. 112, p. 103084, 2020.

[11] L. Prasittisopin, T. Sakdanaraseth, and V. Horayangkura, "Design and construction method of a 3d concrete printing self-supporting curvilinear pavilion," *Journal of Architectural Engineering*, vol. 27, no. 3, p. 05021006, 2021.

[12] J. Xiao, G. Ji, Y. Zhang, G. Ma, V. Mechtcherine, J. Pan, L. Wang, T. Ding, Z. Duan, and S. Du, "Large-scale 3d printing concrete technology: Current status and future opportunities," *Cement and Concrete Composites*, vol. 122, p. 104115, 2021.

[13] H. Chai, M. Bolhassani, and M. Akbarzadeh, "Structural form-finding of multi-span undulating funicular beam structure," in *Proceedings of IASS 2022 symposium affiliated with APCS 2022 con- ference*, (Beijing, China), September 19-22 2022.

[14] Y. Wu, J. Fang, C. Wu, C. Li, G. Sun, and Q. Li, "Additively manufactured materials and structures: A state-of-the-art review on their mechanical characteristics and energy absorption," *International Journal of Mechanical Sciences*, 2023.

[15] H. Blum, "A Transformation for Extracting New Descriptors of Shape," in *Models for the Perception of Speech and Visual Form* (W. Wathen-Dunn, ed.), pp. 362–380, Cambridge: MIT Press, 1967.

[16] H. I. Choi, S. W. Choi, H. P. Moon, and N.-S. Wee, "New algorithm for medial axis transform of plane domain," *CVGIP Graph. Model. Image Process.*, vol. 59, pp. 463–483, 1997.

[17] O. Aichholzer, W. Aigner, F. Aurenhammer, T. Hackl, B. Jüttler, and M. Rabl, "Medial axis com- putation for planar free–form shapes," *Computer-Aided Design*, vol. 41, no. 5, pp. 339–349, 2009. Voronoi Diagrams and their Applications.

[18] M. Bernhard, M. Hansmeyer, and B. Dillenburger, "Volumetric modelling for 3d printed architec- ture," in *Advances in Architectural Geometry 2018*, (Göteborg, Sweden), pp. 392–415, 09 2018.

[19] J. W. Brandt and V. Algazi, "Continuous skeleton computation by voronoi diagram," *CVGIP: Image Understanding*, vol. 55, no. 3, pp. 329–338, 1992.

[20] P. F. Yuan, Q. Zhan, H. Wu, H. S. Beh, and L. Zhang, "Real-time toolpath planning and extrusion control (rtpec) method for variable-width 3d concrete printing," *Journal of Building Engineering*, vol. 46, p. 103716, 2022.

[21] I. Mitropoulou, M. Bernhard, and B. Dillenburger, "Nonplanar 3d printing of bifurcating forms,"

3D Printing and Additive Manufacturing, 10 2021.

[22] H. ming Zhao, Y. He, J. zhong Fu, and J. jiang Qiu, "Inclined layer printing for fused deposition modeling without assisted supporting structure," *Robotics and Computer-Integrated Manufactur- ing*, vol. 51, pp. 1–13, 2018.

IASS 2023
July 10–14 Melbourne
Integration of Design and Fabrication

Proceedings of the IASS Annual Symposium 2023
Integration of Design and Fabrication
10–14 July 2023, Melbourne, Australia
Y.M. Xie, J. Burry, T.U. Lee and J. Ma (eds.)

Model test of sunflower triple-strut cable dome structure with metal additive manufacturing nodes

Yang ZHAO[a,b], Ruolan FAN[a], Zhen WANG[*], Ruhao WANG[a], Shilin DONG[a]

[*] Advanced Materials Additive Manufacturing Innovation Research Center, Hangzhou City University, Hangzhou, 310015, China
wangzhen@zucc.edu.cn

[a] Space Structures Research Center, Zhejiang University, Hangzhou 310058, China
[b] School of Civil Engineering, Shaoxing University, Shaoxing 312000, China

Abstract

The combination of topology optimization and metal additive manufacturing technology is a new effective approach to realize integration of design and fabrication for nodal joints in spatial structures. The variable density method method was employed to optimize the topology of two typical nodes in cable dome, namely, the inner-ring cable-strut node and the outer-ring upper chord node. Stainless steel additive manufacturing of the two topology nodes was completed by selective laser melting (SLM) technology. In order to study the behavior of metal additive manufacturing nodes under actual 3D loading conditions, two structural models using conventional nodes and two of them replaced by metal additive manufacturing nodes were experimentally studied for a sunflower triple-strut cable dome model with a diameter of 10 m. Construction forming and static loading tests under full-span were carried out on the cable dome model. The results showed that the topology nodes fabricated by SLM technology instead of conventional nodes have little influence on overall behavior of the cable dome, which verified the validity and feasibility of adopting metal additive manufacturing nodes in practical engineering.

Keywords: cable dome structure, nodal joint, topology optimization, metal additive manufacturing, model test

1. Introduction

Topology optimization is an optimization process based on structural conceptual design, that is, the given initial space is taken as the design variable, and the optimal topology shape or material distribution satisfying certain constraints is sought. A reasonable initial form of the structure can be obtained through topology optimization [1-2]. By introducing the process of continuum topology optimization into the design of spatial structure nodes, node forms with reasonable mechanical properties, less material consumption, novel and beautiful shapes and satisfying diversified demands can be obtained [3-4].

However, the nodes obtained by topology optimization usually have irregular and complex geometric shapes, which can hardly be realized by traditional manufacturing technology. In recent years, additive manufacturing technology, an emerging technology with global attention, provides a new and effective way for the manufacture of topology optimization nodes due to its characteristics of fast and free forming [5-6]. Metal additive manufacturing is a manufacturing method based on 3D model data, which mainly uses powder or wire material as raw material, and uses laser, electron beam, electric arc and other high power heat source to melt and solidify materials quickly and then forms products layer by layer [7-8].

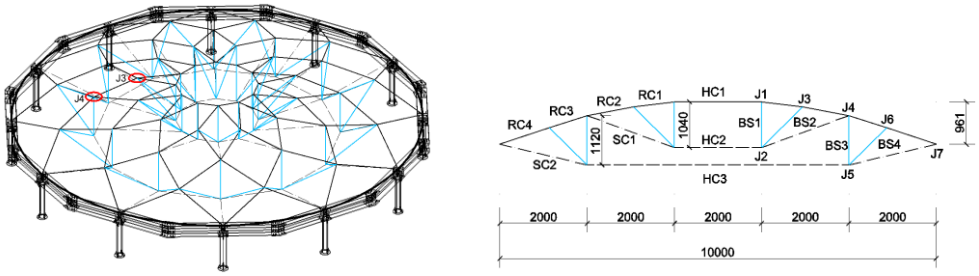
In this paper, the topology optimization of two typical nodes for sunflower triple-strut (type I) cable dome structure, inner-ring cable-strut node and the outer-ring upper chord node, is carried out. Stainless steel additive manufacturing of the two topology nodes was completed by the SLM technology. For a cable dome model with a diameter of 10 m, the construction forming and static loading tests were carried

Copyright © 2023 by Yang ZHAO, Ruolan FAN, Zhen WANG, Ruhao WANG and Shilin DONG. Published in the Proceedings of the IASS Annual Symposium 2023 with permission.

out respectiely on two structural models using conventional nodes and two of them replaced by metal additive manufacturing topology nodes. Then, the mechanical behavior of metal additive manufacturing nodes under actual 3D loading conditions were studied.

2. Cable dome structure model and typical nodes

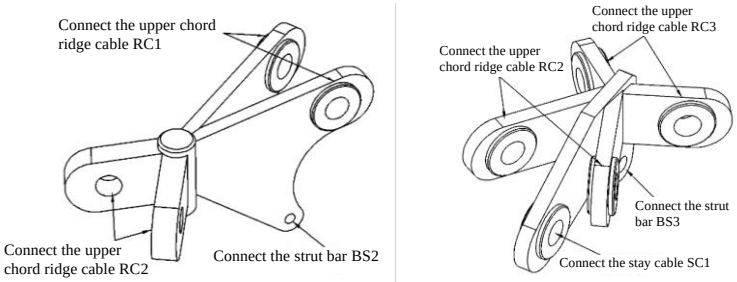
Sunflower triple-strut cable dome structure is one of a series of new cable dome structure system proposed by Dong in recent years [9]. In this section, the structure design and experimental study of a sunflower triple-struc (Type I) cable dome structure with a diameter of 10 m were carried out. Along the circumferential direction, the model consists of 12 trusses of ridge cable (RC), stay cable (SC), hoop cable (HC), strut bar (BS) and rigid ring beam, with a rise-span ratio of 0.1. The members of the model include 48 ridge cables, 24 stay cables, 72 strut bars and 3 hoop cables, and the total number of nods is 84, among which 12 are connected with rigid ring beam. Fig. 1 shows the three-dimensional diagram and section diagram of the model. High vanadium cable is used in cable dome structure model with elastic modulus of 1.6×10^5 N/mm^2 and tensile strength of 1670 MPa. The strut bars, nodal joints and rigid ring beams are made of Q355B low-alloy high-strength structural steel with elastic modulus of 2.06×10^5 N/mm^2 and yield strength of 355 MPa.



(a) (b)

Figure 1. Cable dome structure model (a) three-dimensional daagram, (b) section diagram.

The nodal joints of the cable dome structure model are usually completed by welding or casting process. The connection between the member and the node is hinged, and the design of the node ensures that all the internal forces of the cable and strut members line converge at a point, and the node will not produce bending moments in the plane. The two ends of the tensile cable or pressure strut are fixed on the pin-plate of the nodal joint through the hinge pin, so that there is no in-plane bending moment at the node, but it has a certain out-of-plane bending stiffness.



(a) (b)

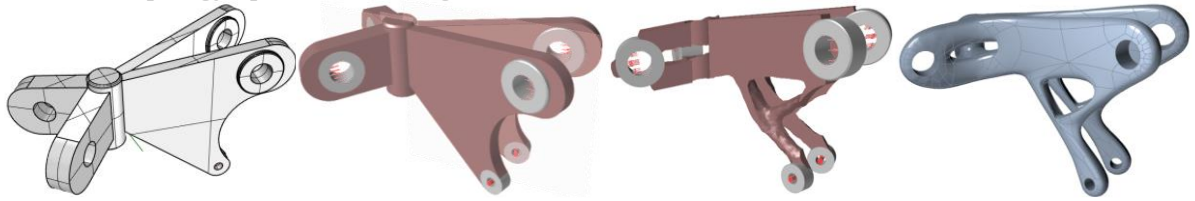
Figure 2. Conventional nodal joints (a) inner-ring cable-strut node J3, (b) outer-ring upper chord J4.

According to different forms, positions and sizes of nodes, the nodes of this model can be divided into 7 types: inner-ring upper chord cable clamp node J1, inner-ring lower chord hoop cable clamp node J2, inner-ring cable-strut node J3, outer-ring upper chord node J4, outer-ring lower chord hoop cable clamp node J5, outer-ring cable-strut node J6 and outer-ring ring-beam node J7. Fig.2 shows the two representative nodes J3 and J4 (hereinafter referred to as conventional nodal joints) designed by conventional methods. In this paper, ANSYS is used to calculate the cable dome structure model to obtain the cable-strut balance design prestress based on strong nodes and weak members under the most

unfavorable loading condition, and take this as the most unfavorable loading condition to optimize the design of two conventional nodal joints.

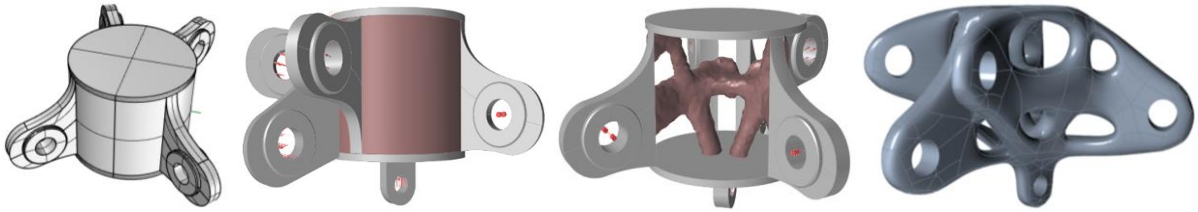
3. Topology optimization and metal additive manufacturing of typical nodes

Common topology optimization methods of continuum structure include homogenization method, variable density method [10], level set method, bidirectional evolutionary structural optimization method (BESO) [11], etc. Among them, variable density method describing structure topology with constant unit density is the most mature method with high computational efficiency and good computational stability, and has been widely used in ANSYS, ABAQUS, Solidthinking, Hyperworks and other commercial software. BESO method has also been applied to Ameba commercial plug-in developed based on Rhino Grasshopper platform [12]. In this section, variable density method method is used for topology optimization design.



(a) (b) (c) (d)

Figure 3. Topology optimization design with minimization of mass for node J3 based on variable density method (a) original Rhino model, (b) original Inspire model, (c) Inspire optimization result, (d) Evolve redesign node.



(a) (b) (c) (d)

Figure 4. Topology optimization design with minimization of mass for node J4 based on variable density method (a) original Rhino model, (b) original Inspire model, (c) Inspire optimization result, (d) Evolve redesign node.

Firstly, Solidthinking Inspire software is applied to carry out optimization design with minimization of mass as optimization objectives. After completion of optimization, optimization results are imported into Solidthinking Evolve software for redesign. The corresponding optimization result and redesign nodal joints of node J3 and node J4 are shown in Fig.3 and Fig.4 respectively. For the node J3, the mass of the optimization node is 2.45 kg, which is 37.5% less than that of the original node. For the node J4, the mass of the optimization node is 4.21 kg, which is 46.5% less than that of the original node.



(a) (b)

Figure 5. 316L stainless steel nodal joints made by SLM technology (a) inner-ring cable-strut node J3, (b) outer-ring upper chord node J4.

First, the STL file is imported into the Magics software for the pre-processing of model position adjustment and support, and the BP software is used for slicing and related parameters adjustment. The software BLT-MCS is used for printing setup and equipment control, and SLM technology is used for layering and overlay molding. Then the heat treatment of the molding part and the bottom plate is carried

out together to prevent the deformation of the 3D printing node. Then the post-treatments including wire-electrode cutting and support removal are carried out togother, followed by grinding, polishing and sand blasting surface treatment. Finally, vernier caliper is used for precision measurement, and the error between the printing product and the original model is controlled within ±0.2 mm. Two 316L stainless steel nodal joints made by SLM technology are shown in Fig.5.

4. Model test of structure with metal additive manufacturing nodes

4.1. Tensile forming of the model

It is pointed out in literature [9] that there is only one overall prestressed mode in sunflower triple-strut (type I) cable dome structure. By tensioning the outer-ring stay cable so that its internal force reaches the design prestress, then the internal force in the whole structure member is that the design prestress. The graded batch tension scheme is adopted, which is divided into three levels of tension, that is, the first level of tension is 0.5 times the stay cable force, the second level of tension is 0.75 times the stay cable force, and the third level of tension is 1.0 times the stay cable force. In the process of each level of tension, twelve outer-ring stay cables are divided into three batches of tension, and four symmetrical outer-ring stay cables are tensioned in each batch. The photo of the structure model after tensile forming is shown in Fig.6. The assembly effect of conventional original design node and metal additive manufacturing node by SLM technology for nodes J3 and J4 are shown in Fig.7.



Figure 6. Cable dome structure model after tensile forming



(a) (b) (c) (d)

Figure 7. Assembly effect of conventional original design node and metal additive manufacturing node (a) conventional node J3, (b) additive manufacturing node J3, (c) conventional node J4, (d) additive manufacturing node J4.

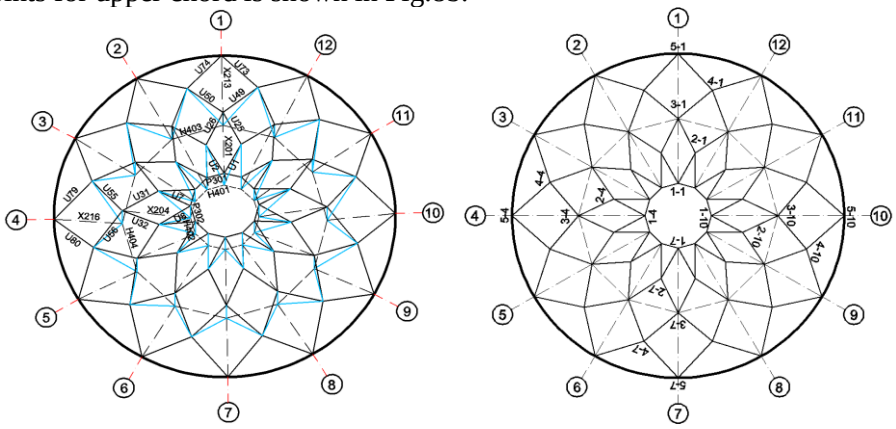
Before and after the replacement of the node J3 and node J4, the two structural models are tensioning respectively, and the internal forces of member and the elevations of node are measured in the initial state, and then compared with the ANSYS finite element results. The results show that the internal forces of member and the elevations of node are basically consistent with the ANSYS results, except for the inner-ring diagonal struts and the inner-ring upper chord ridge cables with less designed prestress, which indicate that replacing the node J3 and node J4 with the additive manufacturing nodes has little influence on the initial state of the cable dome structure model.

4.2. Static loading test scheme of the model

Two cable dome structure models using conventional nodes (model 1) and two of them replaced by stainless steel additive manufacturing topology nodes (model 2) are tested respectively. The loading modes is set to full-span loading. Apply a total uniform loading of 0.4 kN/m^2, divided into three levels

of proportional loading. The loading is carried out by the way of lower chord nodes mounting, and the loading object is 20 kg steel weight block of standard mass.

The sunflower triple-strut (Type I) cable dome structure is an axially symmetric structure. Theoretically, the data of the whole structure can be obtained by measuring only one struss of the internal force and node displacement. However, considering the error of the test model and other factors, the actual distribution of internal forces and node displacements may be uneven. Considering the symmetry and the limitation of the number of measuring points, the arrangement scheme of measuring point in the test is as follows: 1) Cable force measuring points of the cables: One cable force sensor is arranged in each of the two trusses of the cables at the position of axis ① and axis ④, which are perpendicular to each other, and two cable force sensors are arranged in each of the three hoop cables. The arrangement of cable force measuring points for cable is shown in Fig.8a. 2) Internal force measuring points of the struts: Strain gauges are arranged in the middle of the two trusses of the struts at the positions of axis ① and axis ④, which are perpendicular to each other. In order to eliminate the error of eccentric force for the struts, a three-way resistance strain gauge is arranged on the positive and negative sides of all the strut measuring points respectively. 3) Node stress measuring points: eight measuring points are arranged at the inner-ring cable-strut node J3 by SLM technology, and nine measuring points are arranged at the outer-ring upper chord node J4 by SLM technology. 4) Node displacement measurement points: Reflective plates are affixed to the upper surface of all nodes, and coordinate acquisition is carried out by total station instrument, so as to obtain node displacement. The arrangement of node displacement measuring points for upper chord is shown in Fig.8b.



(a) (b)

Figure 8. Arrangement diagram of part measuring points (a) cable force measuring points of the cable, (b) node displacement measuring points of upper chord.

4.3. Comparison of test results and FE results

Fig.9 shows the measured internal forces of part cables in the two models under full-span loading and the comparison with the FE results. It can be seen that the variation trend of the measured cable forces is consistent with the FE results, and most of the errors are within 10%. With the increase of loading, the internal forces of outer-ring ridge cables, inner-ring ridge cables and inner-ring upper chord hoop cables first decrease and then increase. With the increase of loading, the internal force of the outer-ring stay cables and inner-ring lower chord hoop cables first increases and then decreases. The internal forces of the cables before and after the replacement of the metal additive manufacturing nodes are both linear change. The node displacements are small, that is, the corresponding overall stiffness is large, indicating that the replacement of the metal additive manufacturing nodes does not influence the overall stiffness of the structure model.

Fig.10 shows the variation curves of internal forces for the outer-ring stay cables X213 and 216 under full-span loading. It can be seen that the measured internal forces of the structure show a linear change trend and are in good agreement with the FE results. The structure is always in the elastic working stage during the whole test process and basically returns to the initial state after unloading. Fig.11 shows the

comparison of the node displacements for one struss of ridge cable in the cable dome structure under the uniform full-span loadings of 0.4 kN/m^2. It can be seen that all nodes of the ridge cable have downward displacement, which is no more than 8 mm. The closer the node is to the support, the smaller the node displacement is, and the curve variation is basically consistent with the FE results.

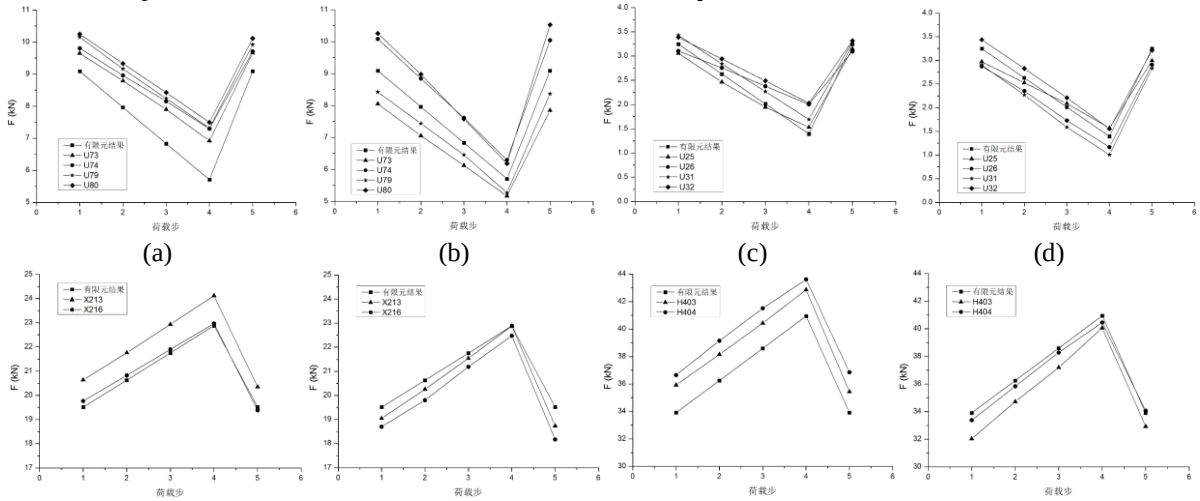


Figure 9. Internal forces of part cables for the two models under full-span loading (a) outer-ring ridge cables for model 1, (b) outer-ring ridge cables for model 2, (c) inner-ring ridge cables for model 1, (d) inner-ring ridge cables for model 2, (e) outer-ring stay cables for model 1, (f) outer-ring stay cables for model 2, (g) inner-ring lower chord hoop cables for model 1, (h) inner-ring lower chord hoop cables for model 2.

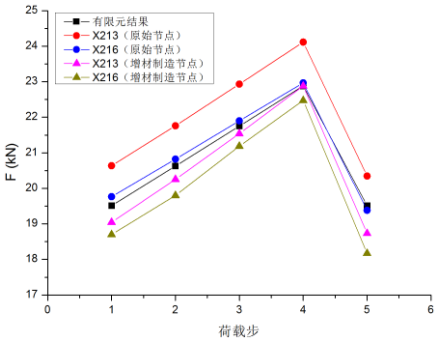


Figure 10. Variation of internal forces for outer-ring stay cables with loading step

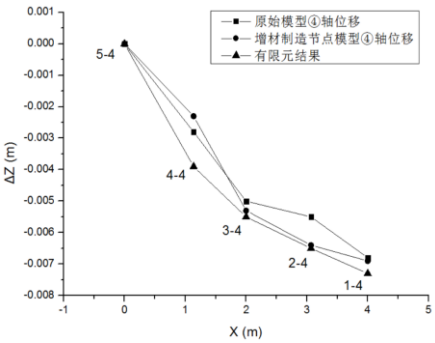


Figure 11. Comparison of node displacements for one struss of ridge cable

It can be seen from the above results that the topology nodes fabricated of metal additive manufacturing instead of conventional design nodes has little influence on the overall behavior of the cable dome structure, which preliminarily verifies the validity and feasibility of adopting metal additive manufacturing nodes in practical engineering. In addition, due to the low loading level of this test, the bearing capacity and failure mechanism of metal additive manufacturing nodes need to be further studied.

5. Conclusion

By using Solidthinking Inspire software based on variable density method, the topological optimization is carried out on two typical nodes of sunflower triple-strut (type I) cable dome structure, namely, inner-ring cable-strut node and outer-ring upper chord node. The SLM technology has been used to fabricate two stainless steel additive manufacturing nodes based on minimization of mass topology optimization. Full-span static loading test is carried out on the two cable dome models, which use all conventional nodes and two nodes are replaced by stainless steel additive topological optimization nodes. With the increase of test loading, the measured internal forces and node elevations showe a linear trend and are

in good agreement with the FE results. The change of node displacements is small, indicating that the structure is always in the elastic working stage in the whole test process, and the overall stiffness is high. Replacing the additive manufacturing node does not influence the overall stiffness of the structure.
Replacing the conventional design nodes with the topology optimization nodes fabricated of metal additive manufacturing has little influence on the overall behavior of the cable dome, which preliminarily verifies the validity and feasibility of adopting metal additive manufacturing nodes in practical engineering. In addition, due to the low loading level of this test, the bearing capacity and failure mechanism of metal additive manufacturing nodes need to be further studied.

References

[1] O. Sigmund and K. Maute, "Topology optimization approaches: a comparative review," *Structural and Multidisciplinary Optimization*, vol. 48, no. 6, pp. 1031–1055, 2013.

[2] Y. Su, J. Y. Zhang, M. Ohsaki and Y. Wu, "Topology optimization and shape design method for large-span tensegrity structures with reciprocal struts," *International Journal of Solids and Structures*, vol. 206, pp. 9-22, 2020.

[3] Y. Zhao, M. C. Chen and Z. Wang, "Additive manufacturing oriented topology optimization of nodes in cable-struc structures," *Journal of Building Structures*, vol. 40, no. 3, pp. 58-68, 2019. (in Chinese)

[4] A. Mortazavi, "A new fuzzy strategy for size and topology optimization of truss structures," *Apploed Soft Computing*, vol. 93, pp. 106412, 2020.

[5] D. Espalin, D. W. Muse, E. MacDonald and R. B. Wicker, "3D printing multifunctionality: structures with electronics," *The International Journal of Advanced Manufacturing Technology*, vol. 72, no. 5-8, pp. 963-978, 2014.

[6] W. Gao, Y. Zhang, Ramanujan D, et al, "The status, challenges, and future of additive manufacturing in engineering," *Computer-Aided Design*, vol. 69, pp. 65-89, 2015.

[7] W. Xu, "Direct additive manufacturing techniques for metal parts: SLM, EBM, laser metal deposition," *Encyclopedia of Materials: Metals and Alloys*, vol. 3, pp. 290-318, 2022.

[8] L. Gardner, P. Kyvelou, G. Herbert and C. Buchanan, "Testing and initial verification of the world's first metal 3D printed bridge," *Journal of Constructional Steel Research*, vol. 172, pp. 106233, 2020.

[9] S. L. Dongoing, H. C. Liu and X. L. Zhu, "Initial prestress determination, parametric analisis and tentative design of a novel Levy-type cable dome structure with tri-strut layout," *Journal of Building Structures*, vol. 42, no. 1, pp. 1-17, 2021. (in Chinese)

[10] M. P. Bendsøe and O. Sigmund, "Material interpolation schemes in topology optimization," *Archive of Applied Mechanics*, vol. 69, no. 9, pp. 635-654, 1999.

[11] Y. M. Xie, G. P. Steven, "A simple evolutionary procedure for structural optimization," *Computers & Structures*, vol. 49, no. 5, pp. 885-896, 1993.

[12] Y. L. Xiong, Z. L. Zhao, H. Lu, W. Shen and Y. M. Xie, "Parallel BESO framework for solving high-resolution topology optimisation problems," *Advances in Engineering Software*, vol. 176, pp. 103389, 2023.

IASS 2023
July 10–14 Melbourne
Integration of Design and Fabrication

Proceedings of the IASS Annual Symposium 2023
Integration of Design and Fabrication
10–14 July 2023, Melbourne, Australia
Y.M. Xie, J. Burry, T.U. Lee and J. Ma (eds.)

Rapid fabrication system for large-scale free-form double curved shell

Zhuoyang XIN*, Guanqi ZHU[a], Dan LUO[a]

* School of Architecture, University of Queensland, Brisbane, Australia
z.xin@uq.net.au

[a] School of Architecture, University of Queensland, Brisbane, Australia

Abstract

Additive manufacturing in the construction industry has reformed traditional construction approaches, allowing for the realization of customizable structure design in low cost and low waste manner. This paper explores a new additive construction system, namely additive lamination manufacturing (ALM), to construct large-scale structural components. The ALM utilizes Fibre Reinforced Polymer (FRP) fabric materials and the lamination approach to extrude the formwork structure, along with the robotic technique to achieve the desired fabrication accuracy. The adaption of conventional manual lamination technique into robotic construction enables the technique to build very structural components in mouldless and support-free process. This paper further compares the fabricated components performance with different composite materials, and the optimal materials are then used to fabricate a double curved shell structure.

Keywords: design customization, structural optimization, FRP composite material, freeform formwork construction, Hangai Prize applicant

1. Introduction

1.1. Additive manufacturing in construction industry

The additive manufacturing in construction industry has revolved the construction approaches with high material utilization, low labour cost and easy project management. Well-established additive manufacturing methods, for example contour crafting[1] and concrete printing[2], commonly utilized cementitious materials to construct structures via layer-by-layer material deposition. Those techniques are suitable for the fabrication of structure components in any 2.5-dimensional geometry or 3D geometry with low sloping angle in upright direction. The full-fledged family home[3] (Fig. 1a) and eco-house TECLA[4] (Fig. 1b) are the two examples demonstrating how additive manufacturing can be effectively employed in the construction of residential house.

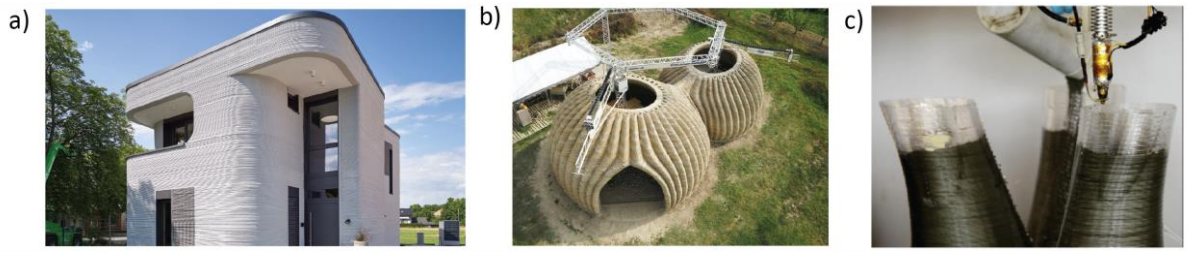


Figure 1. (a) The full-fledged family home[3]. (b) Eco-house TECLA[4]. (c) Egg-shell formwork[5].

In addition to constructing structural components, additive manufacturing can also be utilized to

Copyright © 2023 by Zhuoyang XIN, Guanqi ZHU and Dan LUO. Published in the Proceedings of the IASS Annual Symposium 2023 with permission.

fabricate formwork, for example the egg-shell formwork[5] (Fig. 1c). Although this application requires an additional step to cast the material, the resulting component gain more homogeneous material property and eliminates the issue of weak inter-layer bonding capacity in material due to the one-time casting process. This highlights the potential of additive manufacturing in formwork fabrication, as it can improve the overall quality and durability of the final product.

Nevertheless, achieving mass customization while maintaining efficiency, enhanced performance, and sustainability has posed a persistent challenge in the field of architecture design and construction. This challenge is particularly pronounced when dealing with freeform geometries, as existing additive manufacturing techniques are often limited by geometry constraints. As illustrated in Fig. 2a, the current layer-by-layer deposition printing method suffers from the drawback of being unable to achieve large inclined angles without external support for both component and formwork fabrications. This limitation becomes more evident in the case of geometries with significant cantilever angles, where additional material and time may be wasted in printing support elements to ensure proper fabrication.

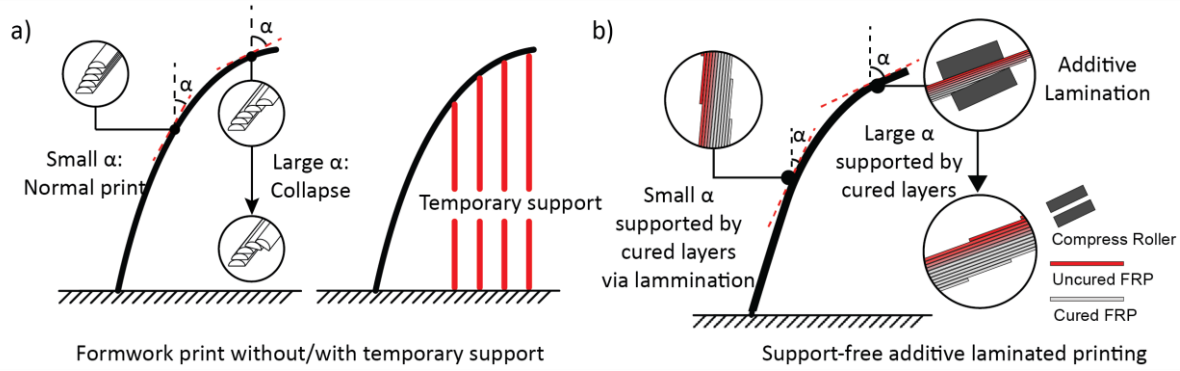


Figure 2. (a) Layer-by-layer deposition 3D printing limitation. (b) FRP lamination 3D printing benefit.

1.2. Reinforcing material in AM

In order to achieve higher performance and more flexible geometries, there is a need for material reinforcement strategies to be integrated into current 3D printing methods. One approach that has shown promise in enhancing the performance of 3D printed products is the incorporation of fiber materials, with MarkForged printer[6] being a typical example. Research has demonstrated improvements in product behaviour through the use of fiber reinforcement, albeit limited to reinforcement within layer[7-9].

Nevertheless, fiber reinforcement also exhibits potential in addressing the weak bonding capacity between layers in 3D printing techniques. This is due to the flexible geometry and superior tensile strength of fiber material[10, 11], which can facilitate effective reinforcement across layers and improve the bonding capacity.

1.3. Motivation

The concept of this paper is inspired from the conventional FRP Fibre Reinforced Polymer (FRP) lamination[12], where layers of fiber material are sequentially laminated and combined with chemical binders to gain achieve desired strength. The lamination approach allows for slight offsets between layers, enabling the product to incrementally grow in length. It is therefore reasonable to adapt 3D printing technologies to FRP lamination, with the aim of achieving a superior interlayer bonding capacity compared to the conventional layer-by-layer deposition method and fabricate the large inclined angle geometry without external support as shown in Fig. 2b.

This paper explores a new design and construction system, namely additive lamination manufacturing (ALM). The ALM utilizes FRP fabric materials and the lamination approach to extrude the formwork

structure, along with the robotic technique to achieve the desired fabrication accuracy, as shown in Fig. 3a.

2. Preliminary design and progress

2.1. Preliminary ALM system development

The system has been preliminarily developed as a proof of concept, namely the 1st generation ALM system (1G ALM SYS). The 1G ALM SYS primarily involves a designated end-effector assembled on the robot arm, as shown in Fig. 3b. The end-effector was composed by a metal framework E and multiple rollers A-D. While the robotic arm ran, the end-effector can passively drive the FRP material to implement the FRP formwork winding process, as shown in Fig. 3c. Two materials utilized in the system are plain-weave glass fiber fabric and lamination epoxy resin, as shown in Fig. 3d.

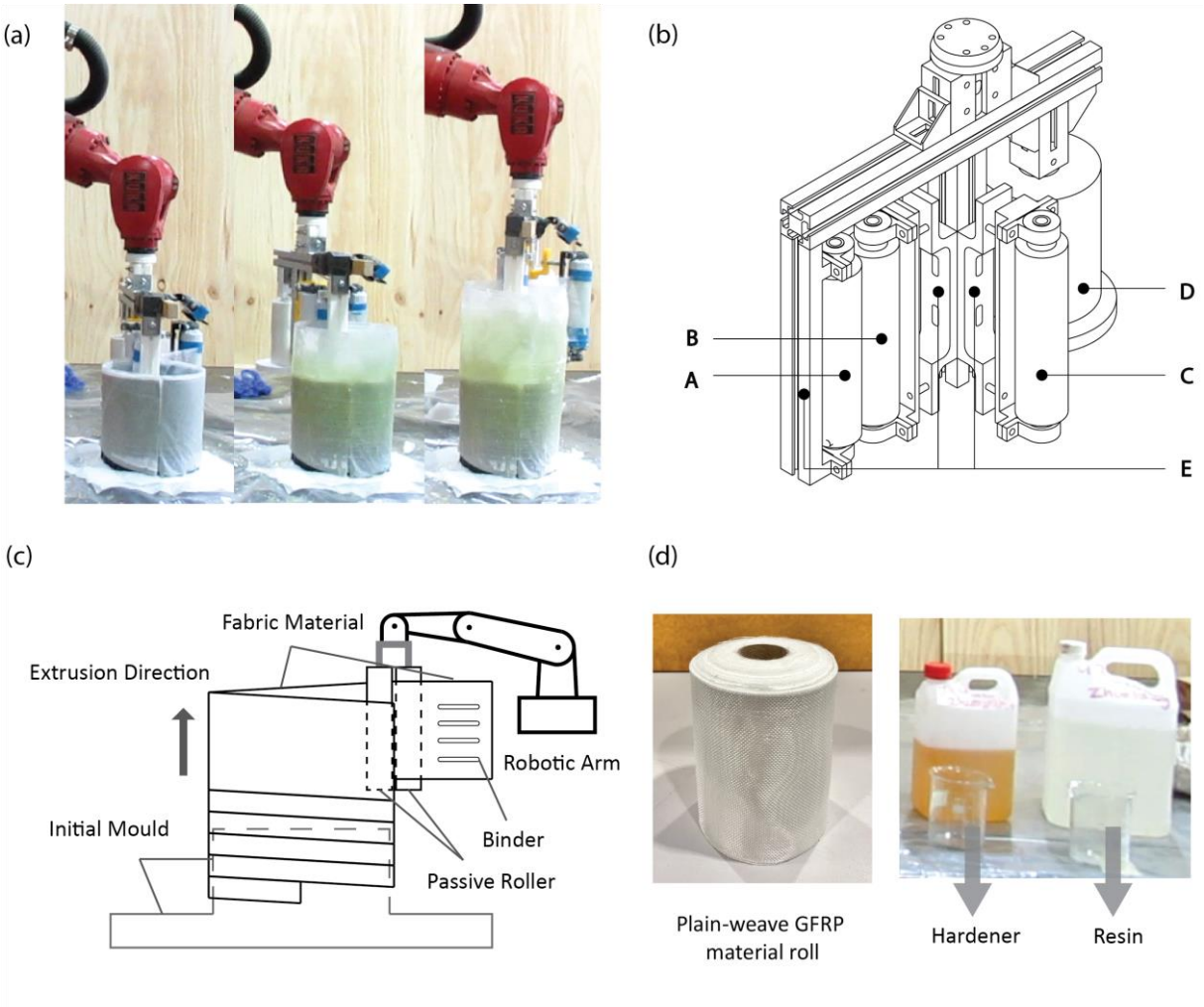


Figure 3. (a) ALM system overview. (b) End-effector sketch. (c) Winding mechanism sketch. (d) Composite material.

The 1G ALM SYS workflow consists of three recurring procedures. The first is the robotic fabric winding to attach the FRP material on the mould. The following is the resin application to manually apply the resin on FRP material and form a composite material. The final is the material curing to solidify the FRP material to provide new moulds for the subsequent robotic fabric winding. All the three procedures will be repeated until the formwork is finished.

Two upright formwork prototypes have been fabricated, one utilizing a standard circular cross section while the other employing a non-standard cross section as shown in Fig. 4a. The findings demonstrate the feasibility of 1G ALM SYS in 2.5 dimensional free-form formwork fabrication.

2.2. Limitation

Some drawbacks have been identified, the first of which is the time consuming. This is due to the utilization of lamination epoxy resin which possesses a short pot-life and long curing time under ambient temperature. To prevent the resin from exceeding its pot-life, the resin mixing process must be carried out in small quantity at a time. As a result, the fabrication requires numerous resin mixing work to continuously apply the resin. Additionally, the FRP composite's intermediate state is significant for formwork winding process as it requires sufficient stiffness to serve as a temporary mould for the subsequent material winding. Consequently, a significant amount of curing time is required during the winding process to attain the desirable material stiffness. Both of these procedures significantly reduce the fabrication efficiency and cause frequent system interruptions.

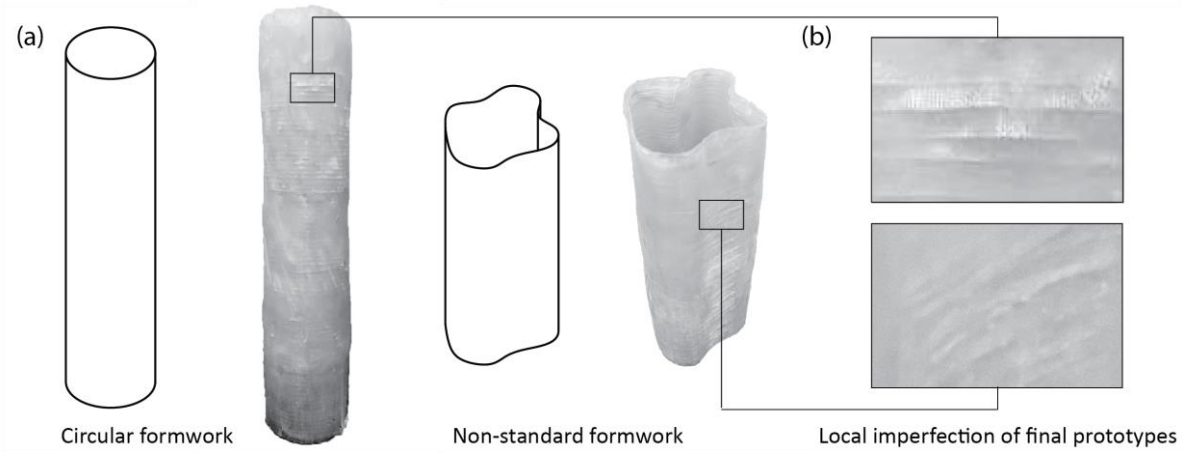


Figure 4. (a) Two upright formwork prototypes. (b) Local imperfection examples.

The second drawback to consider is the geometry imperfection. The 1G ALM SYS employs a plain weave E-glass fiber fabric which possesses remarkable pliability. Despite being mixed with uncured resin, the fabric remains susceptible to deformation. Any external interruption such as the dragging of fiber fabric roll, the sticking from winding roller with the accumulation of excess resin, the manual resin application and the application of heat from heating gun to accelerate the curing process, can result in the local imperfection of fabric material or even affect the cross section geometry. as shown in Fig. 4b.

The use of plain weave E-glass fiber fabric and lamination epoxy resin in 1G ALM SYS was observed to be a challenging fit for this rapid fabrication system. Therefore, extensive research is required to identify suitable material, as the development of appropriate materials is crucial for the successful development of any new 3D printing system[13].

3. Material innovation

The limitations in the 1G ALM SYS were apparently manifested from the preliminary prototyping, highlighting the need for improvement to address its drawbacks, especially regarding to the material. Consequently, efforts have been made to explore alternative materials that could be suitable for use in the ALM system.

3.1. Resin option

The substitution of the lamination epoxy resin is essential for minimizing the time waste and improving fabrication quality. Ultraviolet rays cured resin or UV resin is selected because it can stay in workable

state for a long time and can be cured rapidly once exposed to UV light. There are commonly two types of UV resin in the market, thermoplastic UV acrylic resin and thermoset UV epoxy resin[14]. With the consideration of the exposure to changing environment of fabricated formwork, UV epoxy resin is a preferable material in formwork fabrication to increase the stability of final product.

3.2. Glass fiber options

The plain weaved glass fiber fabric utilized in 1G ALM SYS is highly malleable. While mixing with uncured epoxy resin, it is still prone to deformation even with small, unexpected interruption during robotic winding process. Despite the intended use of UV resin will alleviate such instances by rapidly curing the fiber and making it resistant to interruption, a new material namely self-stick grid glass fiber fabric is still sourced as an alternative option. The self-stick glass fiber fabric has already been pre-impregnated with glue, providing a degree of stiffness while also being malleable.

3.3. Performance of composite material

In order to compare the performance of different composite material, four different combinations were prepared using two kinds of UV resin and two types of glass fiber. A simple flexural stiffness test adapted from ASTM D1388[15] is implemented. As shown in Fig. 5a, the testing set up comprises a sliding platform, a block weight and an angle platform inclined at an angle of 41.5°. The tested samples with a width of 25mm and length of 200mm as shown in Fig. 5b, were placed on the sliding platform and manual slid in 10mm/s, until the sample ends touch the inclined platform and the overhang distance c was measured. If the samples did not touch the inclined platform, they were positioned with 50mm on the sliding platform, left hanging out in the space, and photographed for comparison.

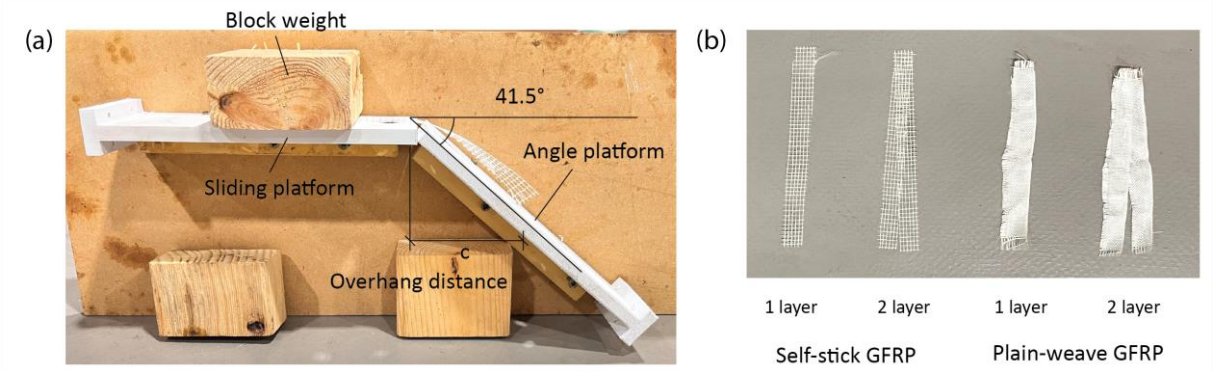


Figure 5. (a) Flexural stiffness test set-up. (b) Tested samples.

As summarized in Table 1, the outcome visually indicates that the stiffness of both types of fabric strips is lower when mixed with UV acrylic resin compared to UV epoxy resin. Additionally, the self-stick GFRP is stiffer than the plain-weave GFRP in the uncured state, but their performance is similar when mixed with the resin, indicating that the composite material stiffness is mainly contributed by the resin rather than the fiber. Furthermore, the minimum curing time of UV acrylic resin is 1 minute, while UV epoxy resin cures in just 10 seconds, making it about six times faster to cure the composite material. In conclusion, UV epoxy resin provides higher flexural stiffness and faster curing time, making it the preferred choice for the later prototyping process.

4. Prototyping comparison

In this section, the fabrication of two prototypes using UV epoxy resin, combined with plain-weaved GFRP and self-stick GFRP, respectively, is described. The performance of the prototypes during fabrication is then compared.

4.1. End-effector development

The end effector in 1G ALM SYS was observed producing large dragging force on the fiber material. As a results, modifications were made to the current 2nd generation ALM system (2G ALM SYS). The first modification involved installing two bearings for the fiber roller holder to reduce the friction during material delivery, as shown in Fig. 6a. Additionally, an extra space was provided to attach one UV torch to cure the material.

Table 1. Flexural stiffness testing results

Overhanging Distance c (N/A for not touch)				
Resin Type		Uncured	UV Acrylic	UV Epoxy
Min Curing Time		0	1 min	10 s
Plain-weave GFRP	Single Layer	53mm	85mm	N/A
				
	Double Layer		N/A	N/A
				
Self-stick GFRP	Single Layer	N/A	110mm	N/A
				
	Double Layer		N/A	N/A
				

4.2. Prototyping progress

The geometry was designed as a curved tube as shown in Fig. 6b to evaluate the performance of ALM fabrication in constructing non-linear extruded formworks. The tube has a length of 400mm and a diameter of 200mm, with a maximum curvature of 0.005mm^{-1}. Both types of fiber material utilized have a width of 75mm, which is the only common dimension available for the two materials. The overlapping number was set at 15.

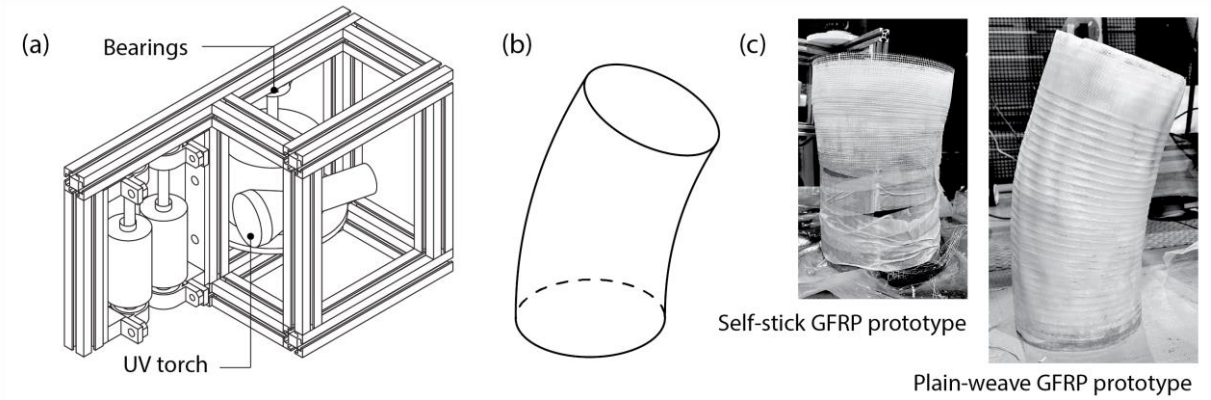


Figure 6. (a) Modified end-effector in 2G ALM SYS. (b) Designed curved tube geometry. (c) Two prototypes with 2G ALM SYS.

The fabrication process is similar to that of the 1G ALM SYS including the robotic winding and resin application. However, curing process is no longer necessary as the UV torch simultaneously cures the UV epoxy resin during lamination. The precedent material can rapidly gain certain stiffness to provide the new mould for the subsequent layer lamination. The final two prototypes are shown in Fig. 6c. The outcome demonstrates that 2G ALM SYS enables rapid fabrication, with a 2-hour production time for a 400mm long component, which is about 3.2 times increase in speed compared to the 1G ALM SYS. The new system also enhances the operability of the process and enables better control of formwork quality.

4.3. Discussion

Some benefits and drawbacks are observed during the two prototyping process. The plain-weave fabric prototype exhibits a high malleability property, rendering it suitable for shaping into any geometry, particularly in the bending section. The material can absorb the resin sufficiently to gain required composite material property and achieve full stiffness. The fabric layers are homogeneous as shown in Fig. 6c while less dragging force to interrupt the formwork geometry. Nevertheless, local imperfections still exist as shown in Fig. 7a. The winding roller with springs is challenging to press the material ideally and once the winding process surpass the initial mould, the fabric wrinkle and formwork delamination will occur.

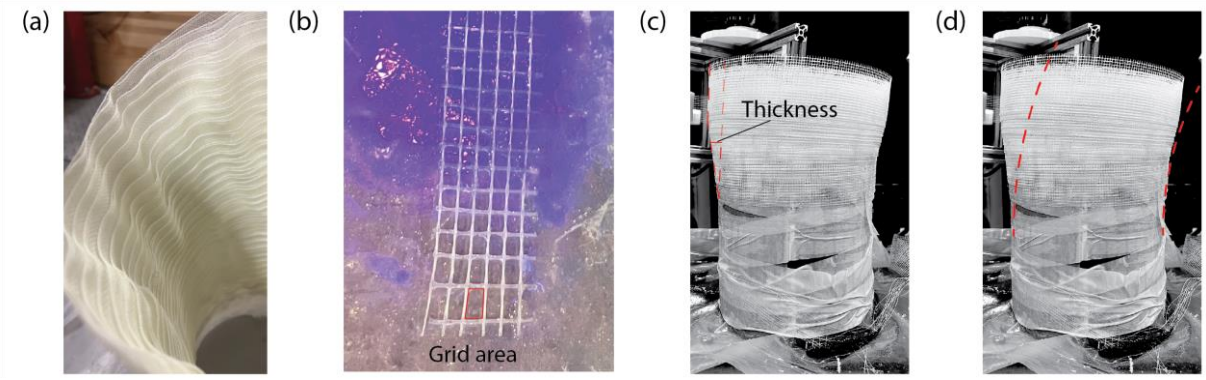


Figure 7. (a) Local imperfection examples in plain-weave fabric prototype. (b) Grid area in self-stick fabric. (c) Accumulating thickness illustration. (d) The profile deviation illustration.

In terms of the self-stick fabric prototype, which has been pre-impregnated, no local fabric wrinkle was observed on the exterior surface, resulting in a smooth and continuous cross section profile for the final prototype, as shown in Fig. 6c. However, the resin absorption capability is lower than that of the plain-weaved fabric as the material has been impregnated and the UV epoxy resin can only fill the grid area instead of penetrating the fiber material, as shown in Fig. 7b. This can lead to a higher likelihood of UV resin filling failure, inducing the composite material to form inadequately and the final prototype to lack sufficient strength. Additionally, the self-stick material has a relatively large thickness. As the formwork continues to extrude, the thickness will accumulate as shown in Fig. 7c, and the prototype will expand outward like a funnel as shown in Fig. 6c, affecting the weaving quality significantly. Furthermore, due to the pre-impregnation of the material, the self-stick fiber has less deformation capability than the plain-weave fiber, and the prototype deviated from the designed profile particularly in the bending location as shown in Fig. 7d.

4.4. Comparison

Thus far, ALM system has been utilized to fabricate several prototypes utilizing different material combinations. In this section, three prototypes with different materials are compared and their advantages and disadvantages will be highlighted in order to select a preferred composite material for the subsequent construction of a double curved shell prototype.

This paper presents three prototypes fabricated with different materials. The first prototype (P_L) utilizes plain-weave fabric and lamination epoxy resin and is produced using the 1G ALM SYS. The second prototype (P_UV) also uses plain-weaved fabric, but the curing process is eliminated by utilizing UV epoxy resin and is fabricated using the 2G ALM SYS. The third prototype (S_UV) is made with self-stick fabric and UV epoxy resin and is also produced using the 2G ALM SYS. Three prototypes are compared in Table 2 in terms of their material winding quality, geometry flexibility, fabrication operability, labour cost and fabrication speed.

P_L prototype exhibits medium winding quality due to the manual interruption and the need for additional resin curing time, leading to local imperfection on the prototype. In contrast, P_UV prototype performs high winding quality due to the fast-curing resin and less manual interruption. S_UV, on the other hand, displays poor winding quality in curved profile due to reduced material deformability. Thus, plain-weave fibers provide high flexibility, while self-stick fibers offer low flexibility. The operability of prototypes that utilize UV epoxy resin is superior to those employing lamination epoxy resin, although not classified as high due to the associated labour costs. The speed of prototypes using UV resin is significantly higher than that of prototypes utilizing lamination epoxy resin. Based on the comparison outcome, the composite material comprising plain-weave glass fiber and UV epoxy resin is the optimal material for use in future prototyping process.

Table 2. Performance comparisons of three fabricated prototypes

PTOTOYPES	**P_L**	**P_UV**	**S_UV**
QUALITY	Medium	High	Low
FLEXIBILITY	High	High	Low
OPERABILITY	Low	Medium	Medium
LABOUR	High	Medium	Medium
SPEED	Low	Medium	Medium

5. Free-form double curved shell prototype design

Existing prototypes fabricated by ALM are in linear or curved profile with various cross sections and can only serve as column or beam components. Building upon the successful fabrication experience with 2G ALM SYS for free-form linear element geometry, the potential of the ALM system in shell structure fabrication is being explored through the design of a free-form double-curved shell geometry, as shown in Fig. 8a.

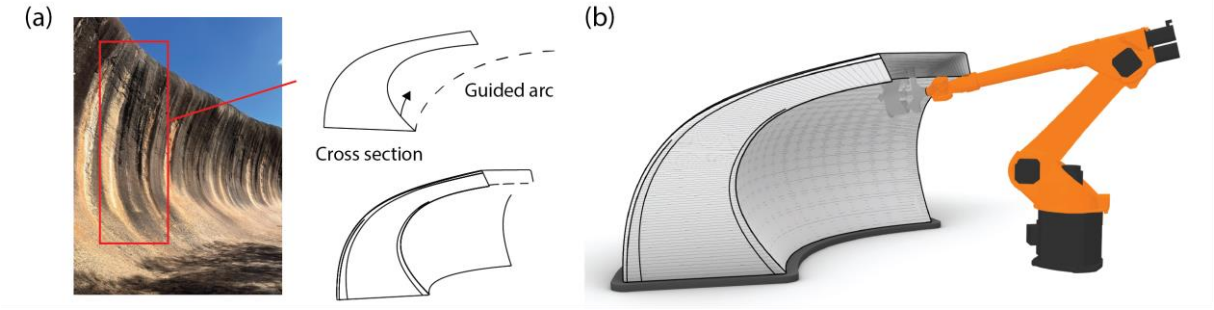


Figure 8. (a) The design progress of double-curved shell geometry. (b) Full-scale shell structure construction rendering.

The shell prototype is inspired from the wave rock in Perth. The generation of the shell begins with a cross section that has a wider foundation and a thinner top, which bends in one direction. Then, the

geometry is swept along an arc to generate a double curved 3D shape. Finally, the four edge corners are filleted to facilitate the fabrication using the ALM system. Although the prototype has not yet been fabricated due to time constraints, a medium-scale version of the shell will be fabricated before the IASS day, and the fabrication of the full-scale version, shown in Fig. 8b, will depend on the availability of time and workspace.

6. Conclusion

This paper has investigated the potential of the additive manufacturing system ALM in the construction of large-scale free-form structures. Several composite materials were evaluated and compared based on their performance with ALM system. As a result, a preferred composite material was selected based on its superior fabrication efficiency, product quality and cost-effectiveness. This material or similar alternatives will be utilized in future system development to further explore the capabilities of the ALM system in the construction industry.

Acknowledgements

The authors gratefully acknowledge UQ Structure Lab to provide working space for all the robotic work.

References

[1] B. Khoshnevis and R. J. M. T. Dutton, "Innovative rapid prototyping process makes large sized, smooth surfaced complex shapes in a wide variety of materials," vol. 13, no. 2, pp. 53-56, 1998.

[2] S. Lim *et al.*, "Fabricating construction components using layered manufacturing technology," in *Global Innovation in Construction Conference*, 2009: Loughborough University Leicestershire, UK, pp. 512-520.

[3] M. Köpp. "Inside Germany's first-ever printed 3D-house." https://www.themodems.com/lifestyle/inside-germanys-first-ever-printed-3d-house (accessed.

[4] WASP. "TECLA." https://www.3dwasp.com/en/3d-printed-house-tecla/ (accessed.

[5] A. Szabo, "Design and Fabrication of Thin Folded Members with Digital Concrete Processes," ETH Zurich, 2020.

[6] Markforged. "High Strength 3D Printing With Continuous Fibres." https://markforged.com/ (accessed.

[7] M. Mohammadizadeh, A. Imeri, I. Fidan, and M. Elkelany, "3D printed fiber reinforced polymer composites-Structural analysis," *Composites Part B: Engineering*, vol. 175, p. 107112, 2019.

[8] F. Ning, W. Cong, J. Qiu, J. Wei, and S. Wang, "Additive manufacturing of carbon fiber reinforced thermoplastic composites using fused deposition modeling," *Composites Part B: Engineering*, vol. 80, pp. 369-378, 2015.

[9] L. J. Love *et al.*, "The importance of carbon fiber to polymer additive manufacturing," *Journal of Materials Research*, vol. 29, no. 17, pp. 1893-1898, 2014.

[10] D. Lau, "Hybrid fiber-reinforced polymer (FRP) composites for structural applications," in *Developments in fiber-reinforced polymer (FRP) composites for civil engineering*: Elsevier, 2013, pp. 205-225.

[11] M. Motavalli, C. Czaderski, A. Schumacher, and D. Gsell, "Fibre reinforced polymer composite materials for building and construction," in *Textiles, polymers and composites for buildings*: Elsevier, 2010, pp. 69-128.

[12] H. Rahmani, S. H. M. Najafi, and A. Ashori, "Mechanical performance of epoxy/carbon fiber laminated composites," *Journal of Reinforced Plastics and Composites,* vol. 33, no. 8, pp. 733-740, 2014.

[13] T. T. Le, S. A. Austin, S. Lim, R. A. Buswell, A. G. Gibb, and T. Thorpe, "Mix design and fresh properties for high-performance printing concrete," *Materials and structures,* vol. 45, pp. 1221-1232, 2012.

[14] ThreeBond."UV-curing resin." https://www.threebond.co.jp/en/technical/seminar/ucuringvresin/ (accessed.

[15] *ASTM D1388-18 Standard Test Method for Stiffness of Fabrics*, 2018.

Architectural geometry

Active bending
Additive manufacturing/ 3D printing
► **Architectural geometry**
Bamboo for sustainable construction and quality of life improvement
Bio-inspired structures and architecture
Bridge structures
Computational form-finding
Conceptual design
Concrete structures
Construction techniques
Deployable and inflatable structures
Design competition (WG21)
Digital modelling and fabrication
Dynamic response of metal spatial structures
Dynamic response of other structures
Form-finding and structural optimisation of interlocking discrete assemblages
Graphical methods
Gridshell and lattice structures
Historical concrete shells
Historical structures
Lattice structures
Life-cycle design and assessment of structures
Metal gridshell structures, connections and stability
Methods and construction technologies for sustainable shell structures
Morphology and configuration processing
Next generation parametric design
Novel methods in modelling, optimisation and construction for reducing carbon footprint of continuous roof shells
Numerical methods for geometry, form-finding and optimisation of lightweight structures
Optimisation methods and applications
Origami
Other
Teaching design uncertainty: working with unknown qualities/quantities of new and re-claimed materials
Teaching of shell and spatial structures
Tensegrity systems and cable structures
Tension and membrane structures
Tension structures in the Asia-Pacific
Timber and bio-based structures
Topology optimisation
Traditional masonry structures and innovation
Transformable structures

IASS 2023
July 10–14 Melbourne
Integration of Design and Fabrication

Proceedings of the IASS Annual Symposium 2023
Integration of Design and Fabrication
10–14 July 2023, Melbourne, Australia
Y.M. Xie, J. Burry, T.U. Lee and J. Ma (eds.)

A multi-objective progressive optimization method for free-form canopy based on fabrication morphology

Sijia GU[a], Li HAN[b], Philip F. YUAN[a,*]

[a,*] College of Architecture and Urban Planning, Tongji University
No. 1239 Siping Road, Yangpu District, Shanghai, China
philipyuan007@tongji.edu.cn

[b] Shanghai Fab-Union Technology Co., Ltd.

Abstract

As a new trend of architectural system, free-form structure expands the possibilities of architectural form and spatial experience. However, in the real construction process, the lack of connection between the parameters of fabrication morphology and the misalignment of the workflow lead to unsatisfactory results in appearance. The paper proposes a multi-objective progressive optimization method based on fabrication morphology during the process from parametric design to fabrication. The method explores the geometric relationships among free-form surface, component geometry, function, and fabrication feasibility, which could be implemented in 3D modelling. To verify the effectiveness of the method, a project of a lightweight glass canopy structure was executed. The project practiced the fabrication-based optimization method for free-form canopy structures, making a complement for the method with specific digital tools and details in the process. At the same time, the successful implementation of the project demonstrates the effectiveness of the multi-objective progressive optimization method in bridging the gap between design and construction, which allows a good reproduction of the original design while controlling the difficulty of the fabrication and the cost. The working method of revealing the parameters of design and fabrication morphology in the research will help to empower better design and construction of free-form architectural system.

Keywords: free-form structure, optimization, fabrication morphology, lightweight canopy structure



Figure 1. Picture of the project about lightweight glass canopy.

Copyright © 2023 by Sijia GU, Li HAN and Philip F. YUAN. Published in the Proceedings of the IASS Annual Symposium 2023 with permission.

1. Introduction

The free-form structure has become one of the most striking trends in contemporary architecture due to its unique form [1]. The free-form surface was first proposed by the mathematician French mathematician Be´zier and then used for the design of automobile bodies [2]. Nowadays, we can see more and more buildings using free-form structures with complex geometric forms. Some precedents are the Cathedral of Saint Mary in San Francisco and the Philips Pavilion in Brussels [3]. Numerous projects based on free-form structures refresh the perception of architectural geometry, creating an unprecedented spatial experience.

For canopy structures, the application of free-form structures has attracted a wide range of interest from architects and engineers. On the one hand, it brings new forms for architectural design. On the other hand, it poses considerable challenges for fabrication. In other words, there exists an ongoing issue of how to bridge the gap between design and fabrication, so that a desired appearance could be obtained with elements related to fabrication under control [4].

The organization of the architecture itself as a complex system plays an important role in bridging design and fabrication. Due to its large volume and diverse functions, architecture works as a complex system integrated with various elements. The process from design to fabrication is usually a process of rationalizing the virtual model into physical building components. For physical components of the canopy structure, it consists of numerous components in different materials and shapes, such as columns, keels, sub-keels, panels, and auxiliary components that help them work together. These components belong to different subsystems under the whole architectural system, such as the structural system and maintenance system. Thus, when it comes to fabrication, it is a question of how to combine the various subsystems in a self-organized way under a whole building system.

The organization of component systems can be inspired by the research on structural morphology. As one of the most active research areas in architecture, structural morphology aims to bridge the gap between civil engineering and architecture [5]. structural morphology makes architecture a whole in the sense of structure by studying the relationship between the four parameters of form, force, material, and structure in a building system. In this system, the two parameters "form" and "structure" need to be coupled with each other to satisfy the balance of materials and forces [6]. For the architectural design and modelling process, how to express the relationship between the parameters geometrically becomes a key issue.

Studies on architectural geometry have contributed to clarifying the parametric relationship between form and structure [7]. Considerable research has been done by pioneers in order to study the relationship between form and structure. For example, Frei Otto used soap bubbles as a physical model [8] to explore their relationship. A similar approach is Antoni Gaudi's form-finding experiments with hanging chains [9]. With the popularity of computer modelling techniques, some structural form methods based on numerical simulations have been proposed, such as shell structure optimization methods, height adjustment methods, and NURBS-GM methods [10].

Besides, the integration of building functions is an important dimension [11]. For numerous components, they perform different functions, such as supporting, rain protection, drainage, smoke exhaust, and so on. Various types of different parameters are also involved in the whole design process. The way of coupling these parameters has a significant impact on the final completed form of the canopy. In addition, fabrication is another important factor, in which feasibility, difficulty, and cost are taken into consideration [12].

2. Proposal

Based on the research, the paper proposed a multi-objective progressive method for canopy structure based on fabrication morphology, making an explosion to the relationship between parameters involved in the parametric design and fabrication process.

In order to clarify the containing aspect of the method, four main influencing factors are summarized in the process from parametric design to fabrication according to the previous research. They are smooth surface, component geometry, fabrication, and function. And these four factors are respectively oriented to the following issues:

1. For free-form structures, creating smooth surfaces in the design process makes a good beginning for being able to perform rational construction [10]. The aesthetics of the form and construction problems would be brought about by the broken patchwork of free-form surfaces.

2. The way to combine the morphological distribution logic of the keel, secondary keel, panel, or other components to the smooth surface.

3. The problem of how to control the difficulty and cost of the fabrication process by optimizing the geometry of the building components.

4. The method for intervening with functions such as drainage and smoke exhaust based on existing components.

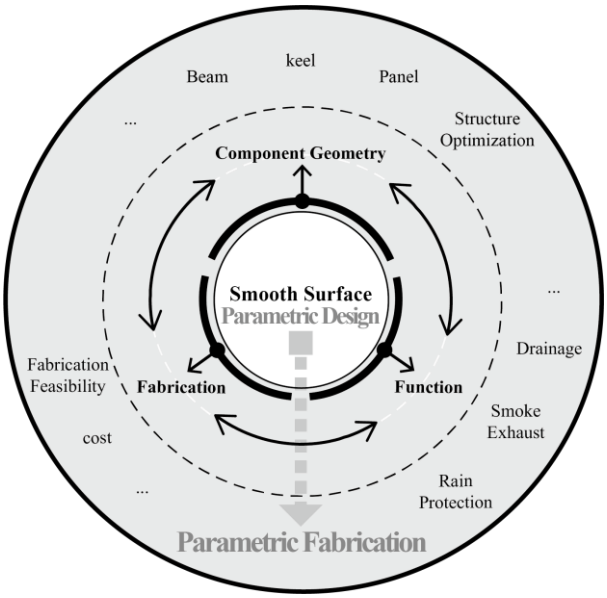


Figure 2. Four main influencing factors in the process from parametric design to construction

For the above problems, the following methods are given in the multi-objective progressive optimization method for free-form canopy based on fabrication morphology:

1. Smooth surfaces are the beginning of the process from parametric design to fabrication. The Non-Uniform Rational B-Splines (NURBS) is an effective method for generating smooth free surfaces. There are two methods of creating NURBS surfaces, one is to create fitted surfaces and the other is to create curves to build surfaces [13]. To judge the smoothness of the surface, curvature visualization is one of the methods [14]. Highlight detection also works.

2. For the component geometry, it's crucial to ensure that the geometry logic aligns with the surface morphology. For example, the positioning line of the keel can be derived from the structure line of the surface. In order for all components to agree on a consistent morphological logic, a positional relationship needs to be established between them. For example, secondary keels have to be positioned according to the main keels.

3. For fabrication, factors such as cost feasibility should be considered, which can be controlled through geometric optimization of the components. One effective method is geometric dimensionality reduction. For example, a double-curved keel can be transformed into a single-curved keel, while a single-curved

secondary keel can be transformed into a straight line, and a curved panel can be transformed into a flat surface. Another way is the standardization of component specifications.

4. When planning functional interventions, such as drainage and smoke extraction, it's important to consider the geometric form of existing components to ensure consistency in their geometric order. The determination of these interventions should be done in conjunction with the existing components' geometric form.

3. Empirical evidence

To validate the above proposal, a real project involving a lightweight free-form canopy structure was implemented using a multi-objective progressive method based on fabrication morphology.

3.1. Basic information

The project is located in Shanghai, China. The sponsors aimed to optimize the geometry of the building to improve its form and appearance while controlling costs. Before optimization, three problems were identified in the initial canopy design:

1. The curved surfaces of the canopy structure were not smooth, resulting in an uneven distribution of keel axis curvature and aesthetic concerns regarding the appearance.

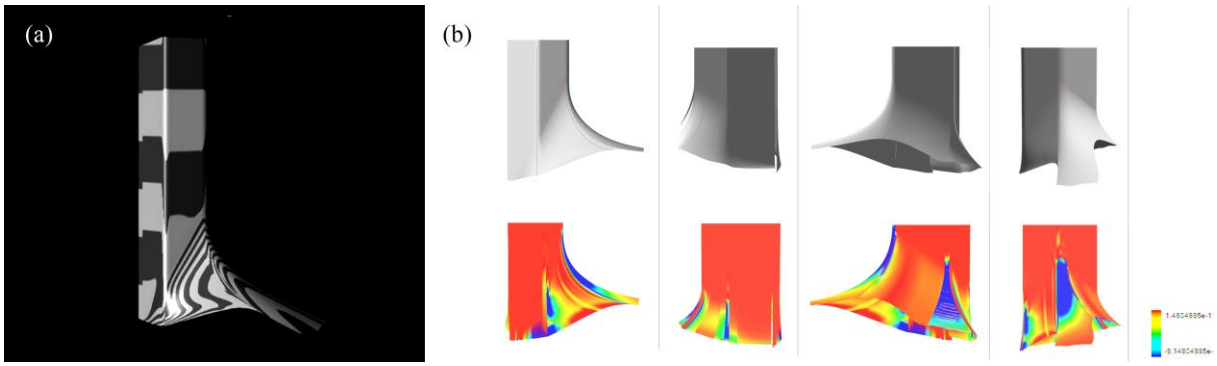


Figure 3. (a) The high light detection results of the original design surface. (b) The visualization of original design curvature on the surface.

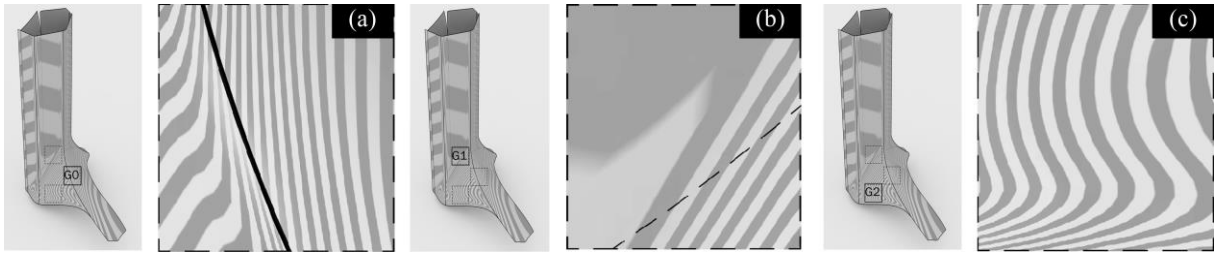


Figure 4. (a) The smoothness of G0 between the two facets. The zebra pattern cannot be connected. (b) The smoothness of G1 inside the facet. The zebra patterns are connected but not smooth. (c) The smoothness of G2 inside the facet. The zebra patterns are relatively smooth.

2. The geometric logic of the components in the canopy was not compatible with the curved surface. The discrepancy between the main keel line and the curved structure line resulted in uneven keel curvature, which had an impact on fabrication. Additionally, the differing orthogonal logic geometry languages of triangular panels and keels reduced the quality of the overall appearance.

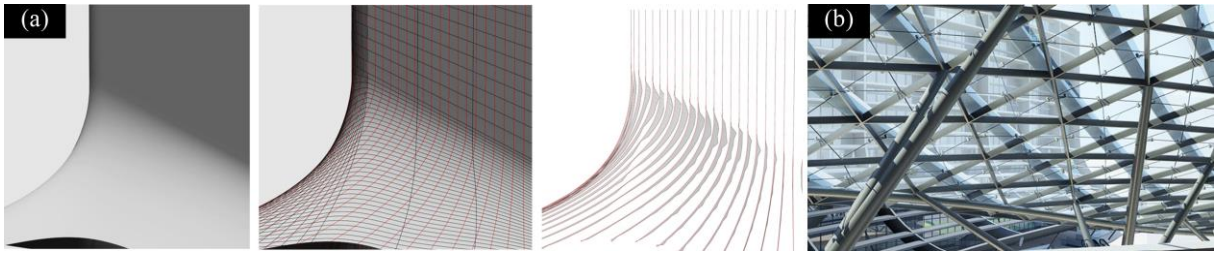


Figure 5. (a) The logic of the structural line and the main keel line in the original design is not consistent, resulting in uneven keel curvature changes. (b) The triangular panels failed to fit into the form logic of the keel.

3. The drainage elements of the canopy were not consistent with the geometric logic of the main structure. The huge drainage ditch had an adverse effect on the appearance of the canopy.

3.2. Smooth surface

In order to enhance the appearance of the original canopy, a multi-objective progressive optimization method based on fabrication morphology was employed. The optimization process began with improving the curved surface design. As a highly versatile method for generating smooth surfaces [12], the sectioning generating method was used, which employs curves in sections to create surfaces.



Figure 6. The process of generating smooth surfaces.

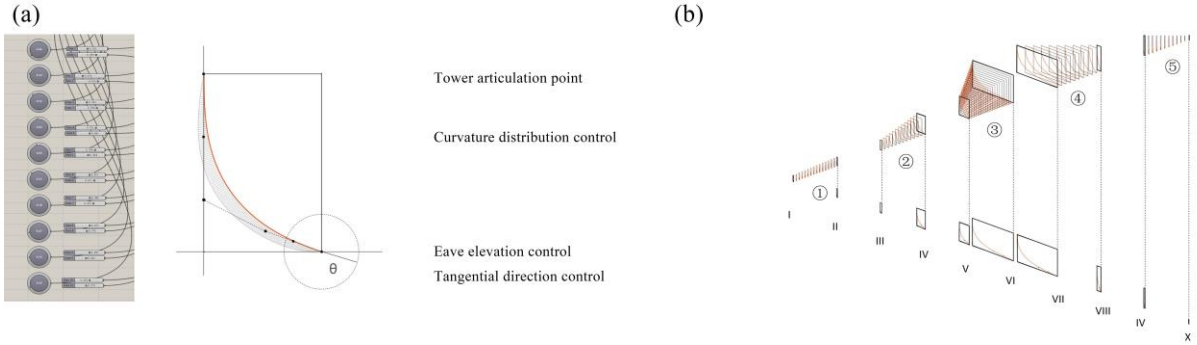


Figure 7. (a) Geometric control mechanism. (b) Generative mechanism of the beam curves.

First, a series of cross-sections were determined based on the overall shape of the building. Next, the curves in the cross-sections are adjusted to control the smoothness of the curve. The project used control at least 3 control points to achieve G2 smoothness at the tower articulation point, and at least 6 control points within the surface to ensure G3 smoothness in the interior of the surface. Then, the section control

curves were then mapped to obtain 5 surfaces. A series of section control curves were generated in excess between the 10 basic section control curves. By connecting the curve control points, section curves were obtained for the articulation between the 5 surfaces to achieve blending between the surfaces. Finally, loft all the section curves to generate the final smooth surface.

3.3. Component geometry

The geometric design of the components aims to achieve two goals. On the one hand, the overall form of all the components needs to be appropriate to the surface form. On the other hand, the geometric logic language between the components is supposed to be consistent.

Keels play a dominant role in the structural form of the entire canopy. In the project, the keels were positioned according to the position of the main structural columns and the form of the reference surface, which transformed the free-form surface into single curved keel curves.

In the process of transforming the keel positioning curve into the geometry of the components, it is necessary to determine the cross-sectional shape and direction of the components. Rectangular shapes were used because of their efficiency. Additionally, the direction of the surface normal vector was used to determine the keel thickness direction, ensuring uniform changes in the cross-section of the member, which had a positive impact on the production and assembly of the components. The position of the horizontal keels was determined based on the vertical keels.

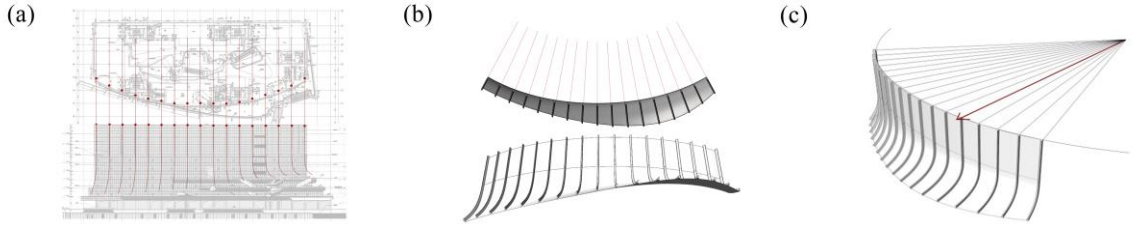


Figure 8. (a) Positioning the vertical keels through the columns. (b) Realizing all vertical keels as a single curve. (c) Determining the section direction of the vertical keels.

The panels should be designed to conform to the shape of the reference surface. In the fabrication process, panels often cannot exist as a single surface. The continuous surface needs to be divided into multiple discrete panels. In this project, the panels were divided twice. The first division was based on the horizontal keel direction. For a better appearance and fabrication ease, the primary division of the panels was positioned optimally according to the spacing of the horizontal keels. Thereafter, the secondary division of the panels was based on the vertical keels.

3.4. Fabrication

During the design-to-fabrication process, geometric optimization for the shape of components based on fabrication feasibility and cost control is important. Standardization of components and reduction of geometric complexity are two effective approaches.

For the single-curve keel in the project, the curvature of the single-curved keels varied across different sections, making it difficult to customize each keel section to the original curvature during fabrication. The curvature of the keels needed to be standardized and optimized. Therefore, a circular arc fitting optimization method was used to optimize the shape of the vertical keels. The algorithm logic can be divided into the following six steps:

1. Given an expected error value.

2. If the chord height < $\triangle x$, optimize directly to a straight line.

3. If the chord height > $\triangle x$: (a) The curve is shifted to both sides by a distance of $\triangle x$. (b) A circular arc tangent to the two new curves is made over the curve endpoints. (c) Then the arc over the curve

endpoints and the radius value between the radii of the above two circles meet the optimization requirements, so a suitable interval of [R-min, R-max] is obtained.

4. Express all the suitable intervals as a vertical line segment.

5. If there exists a horizontal line R can pass through n straight line segments, then the arcs corresponding to these line segments can all be optimized as arcs of radius R.

6. Repeat the above algorithm until all circular arcs are covered.

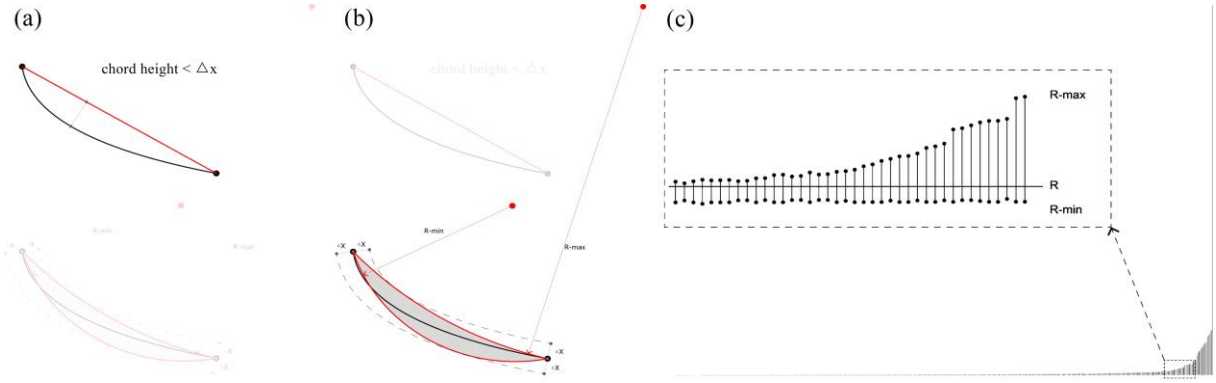


Figure 9. (a) The solution when the chord height < △x. (b) The solution when the chord height > △x. (c) The circular arc fitting optimization method for keels.

Finally, the vertical main keels were divided into 18 types of radius arcs, taking into account the elevation effect. Using an error calculation method, the average error was obtained as 9.5, the maximum error was 43.8, and the median error was 12.0. The overall form was generally consistent with the original design.

In addition, as a consideration for cost control, the geometry dimension of the secondary keels and panels was reduced in the project. The single-curved form of the secondary keels was optimized to a straight line. Similarly, the 3D curved panels were transformed to 2D flat panels.

3.5. Function

After determining the shape and logic of the basic components, the design of component nodes needed to be considered with respect to functional issues, such as ventilation, drainage, and smoke exhaust. In this project, the node design primarily focused on drainage and smoke exhaust concerns.

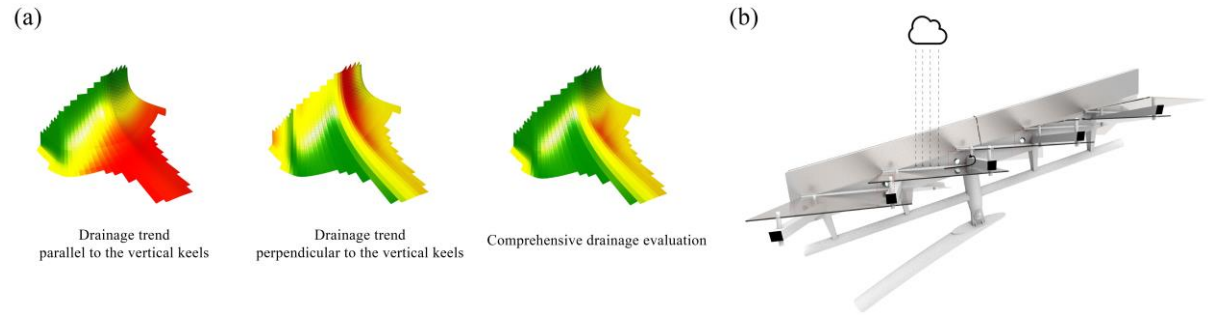


Figure 10. (a) Drainage evaluation. (b) The adaptability of the node to drainage.

For drainage, based on the optimized components, the connection nodes between components were adjusted based on drainage requirements. The drainage measures were carried out in two directions, which were parallel to the vertical keel and perpendicular to the vertical keel. In the direction parallel to the vertical keel, the panels were interlocked. All panels were rotated along the plane parallel to the vertical keel. At the same time, the end of the first panel and the front of the second panel were

overlapped. By placing the horizontal keels in between, on the one hand, the presence of the horizontal keels was hidden, making the surface of the canopy look simpler. On the other hand, the horizontal keels blocked rainwater from leaking into the space under the canopy along the panels. In the direction perpendicular to the vertical keel, the vertical keels opened holes near the panel so that the rainwater could be evacuated along the vertical keel direction. The final rainwater infusion effect is shown in the figure below.

For the adaptability to the function of smoke evacuation, when the two adjacent panels meet, the transverse keel did not completely seal the space between the adjacent panels in the node. Web bars were set between the two panels. This made a gap between adjacent panels, which was conducive to smoke evacuation.

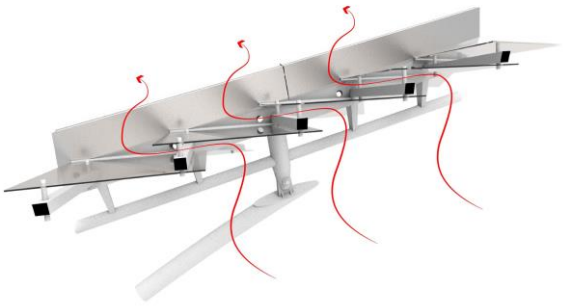


Figure 11. The adaptability of the node to smoke evacuation.

4. Feasibility analysis

The multi-objective progressive optimization method for free-form canopy based on fabrication morphology exhibits exceptional performance in the comparison of the fabrication morphology before and after optimization.

Before optimization, the vertical keel axis curvature variation was significantly uneven, which resulted in an unsmooth surface. This uneven variation was evident in both curvature visualization and highlight inspection, leading to an unfavorable appearance of the finished project.

After optimization, the optimized surface performed better in the highlight inspection. And the vertical keels became uniform in curvature variation based on a smooth surface. Furthermore, components like horizontal keels and panels also showed a better appearance.

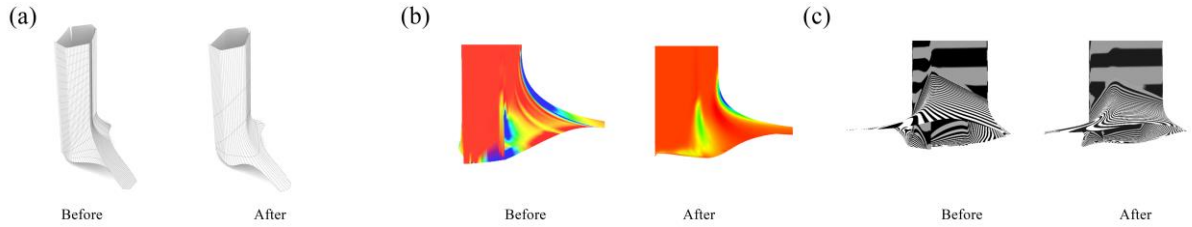


Figure 12. (a) Comparison of curvature quality. (b) Comparison of curvature of curved surfaces. (c) Comparison of highlight detection results.

In addition, for the component geometry, the logic used to generate the keels did not align with the surface morphology before optimization. And the glass panel position distribution of the triangles did not match the position of the keels. After the re-optimization of the logical relationship between the curved surface, keels, and glass panels, the canopy finally exhibited a significant improvement in its appearance.

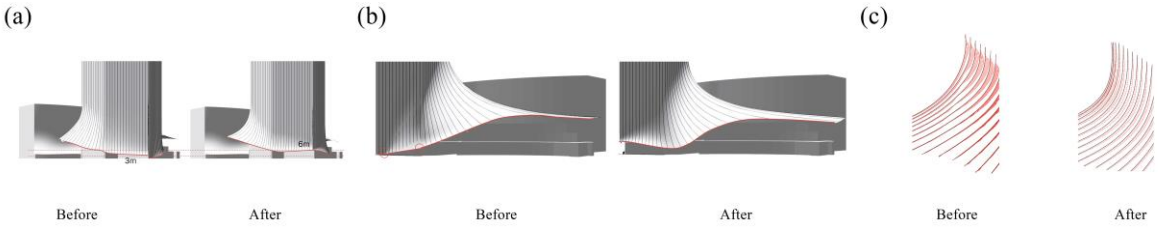


Figure 13. (a) Comparison of elevation appearance. (b) Comparison of elevation appearance. (c) Comparison of curvature of curved surfaces.

In terms of functional organization, interventions of the components required for drainage and smoke exhaust were aligned with the geometric logic of keels and panels.

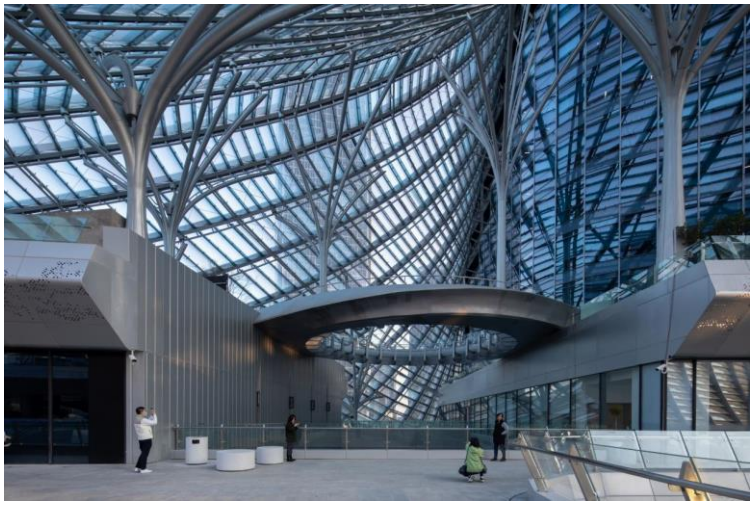


Figure 14. Picture of the interior appearance after optimization.

5. Conclusion

The paper presents a multi-objective progressive optimization method for free-form canopy based on fabrication morphology. The method aims to address four key factors encountered in the process from parametric design to fabrication in building projects. These factors include the smoothness of the design surface, the consistency of the geometric component logic, the fabrication-based component optimization, and functional nodes intervention. The smoothness of the free-form surface can be achieved by using the NURBS surface modelling method. The consistency of the geometric component logic is ensured by extracting geometric component positioning curves from the structural curves of the surface. At the same time, different types of components should be positioned to achieve a consistent geometric order. The geometry optimization based on fabrication can be achieved by component standardization and geometry dimension reduction. Nodes involving other functions need to intervene while maintaining the consistency of the logic ordering different components.

In order to verify the effectiveness of the method, a real project of a lightweight free-form canopy was executed in Shanghai, China. The project complemented the method with a concrete operational approach. The success of the project demonstrates the effectiveness of the multi-objective progressive optimization method in bridging the gap between design and fabrication. It can achieve a good reproduction of the original design while controlling the difficulty and the cost during fabrication.

Overall, the multi-objective progressive optimization method for free-form canopy based on fabrication morphology proposed in the paper aims to establish a parametric link between design and fabrication in the way of architectural geometry, hoping to inspire the design and fabrication of free-form canopy structures.

Acknowledgements

The implementation of the canopy structure project in the paper benefited from the collaborative efforts of all the participants. In the project, Professor Mike Xie from RMIT, Wei Shen, Qiang Zhou, Jin Wang, and Yanning Jiang from Ameba Engineering Structure Optimisation Research Institute made contributions to the structural design. Professor Philip F. YUAN from Tongji University, Li Han from Shanghai Fab-Union Technology Co., Ltd., Tianrui Zhu, Shaoying Lei, and Yuhao Fu from Archi-Union Architects contributed to the architectural geometry optimization.

In addition, this paper is supported by the National Natural Science Foundation of China under the Joint Grant Fund (U1913603), the Shanghai Municipal Science and Technology Major Project (2021SHZDZX0100) and the Fundamental Research Funds for the Central Universities, and the Collaborative Education Project of the Ministry of Education (202102560007).

References

[1] H. Pottmann, "Geometry of architectural freeform structures," in Proceedings of the 2008 ACM symposium on Solid and physical modeling, Stony Brook New York: ACM, Jun. 2008, pp. 9–9. doi: 10.1145/1364901.1364903.

[2] K. Linkwitz, "About formfinding of double-curved structures," Engineering Structures, vol. 21, no. 8, pp. 709–718, Aug. 1999, doi: 10.1016/S0141-0296(98)00025-X.

[3] E. Gawell, "Non-euclidean geometry in the modeling of contemporary architectural forms," Journal Biuletyn of Polish Society for Geometry and Engineering Graphics, vol. 24, 2013.

[4] T. Lu, S. Wang, K. Wu, L. Wang, C. Liu, and W. Yang, "Intelligent Construction Technology of Hyperbolic Curtain Wall," JWA, vol. 6, no. 4, pp. 76–82, Jul. 2022, doi: 10.26689/jwa.v6i4.4028.

[5] E. Stach, "Structural morphology and self-organization," presented at the DESIGN AND NATURE 2010, Pisa, Italy, Pisa, Italy, Jun. 2010, pp. 29–40. doi: 10.2495/DN100041.

[6] R. Motro, "AN APPROACH TO STRUCTURAL MORPHOLOGY," in An Anthology of Structural Morphology, WORLD SCIENTIFIC, 2009, pp. 15–32. doi: 10.1142/9789812837219_0002.

[7] H. Pottmann, M. Eigensatz, A. Vaxman, and J. Wallner, "Architectural geometry," Computers & Graphics, vol. 47, pp. 145–164, Apr. 2015, doi: 10.1016/j.cag.2014.11.002.

[8] B. Burkhardt, "Soap-film and soap-bubble models," in PHYSICAL MODELS, B. Addis, Ed., 1st ed.Wiley, 2020, pp. 569–585. doi: 10.1002/9783433609613.ch19.

[9] P.-H. Liu, "AN EXPLORATORY STUDY OF THE GEOMETRICAL ELEMENTS IN GAUDI'S ARCHITECTURE," International journal of arts and sciences, Dec. 2015.

[10] Y. Xia, Q. Li, and Y. Wu, "Computational morphogenesis of free-form shells based on the NURBS technique and the Hybrid Optimization Method," May 2015.

[11] M. Bagneris, R. Motro, B. Maurin, and N. Pauli, "Structural Morphology Issues in Conceptual Design of Double Curved Systems," International Journal of Space Structures, vol. 23, no. 2, pp. 79–87, Jun. 2008, doi: 10.1260/026635108785260560.

[12] Y. Zou, H. Huang, X. Xia, and X. Wang, "Design Optimization of Curved Curtain Wall Based on SPEA II-GA-BPNN Algorithm," Advances in Civil Engineering, vol. 2022, pp. 1–19, May 2022, doi: 10.1155/2022/2548647.

[13] H. Park, K. Kim, and S.-C. Lee, "A method for approximate NURBS curve compatibility based on multiple curve refitting," Computer-Aided Design, vol. 32, no. 4, pp. 237–252, Apr. 2000, doi: 10.1016/S0010-4485(99)00088-3.

[14] Z. Wan and E. Schling, "Structural principles of an asymptotic lamella curtain wall," Thin-Walled Structures, vol. 180, p. 109772, Nov. 2022, doi: 10.1016/j.tws.2022.109772.

IASS 2023
July 10–14 Melbourne
Integration of Design and Fabrication

Proceedings of the IASS Annual Symposium 2023
Integration of Design and Fabrication
10–14 July 2023, Melbourne, Australia
Y.M. Xie, J. Burry, T.U. Lee and J. Ma (eds.)

Designing the West Gate Tunnel portals: Timber gridshells

Andre F. PEREIRA[a,*], Benjamin COOP[a], Dmitry ZELENKIN[a], Richard WHITFIELD[a], Kevin BERRY[a]

[a,*] Taylor Thomson Whitting (TTW)
andre.pereira@ttw.com.au

Abstract

This study presents the architectural geometry and structural engineering work developed by TTW for the West Gate Tunnel Project (WGTP), a 4-kilometre toll road under construction in Melbourne. The portal structures, situated above the tunnel dive structures, feature architectural timber transition elements at the tunnel entrances and exits. Two patterns were examined for the geometric discretisation of the timber structures: diagonal (diamond-shaped) and triangular grid. The diagonal grid scheme employed genetic algorithms to approximate the portal envelope to simple surfaces, subject to constraints such as surface tangent continuity, base support positions, and road vehicle clearance. The diamond-shaped topology was generated using geodesic curves on the simplified envelope and COBYLA optimisation. Furthermore, the number of node connection types was minimised through mesh relaxation and custom form-finding techniques. The triangular grid scheme featured primary parallel hoops and secondary diagonal infill members. The opening angle between primary and secondary timber members was determined through constrained optimisation. A limited number of bracket connections were established for the primary timber members. Both schemes employed in-house structural timber design libraries compliant with AS 1720.1:2010, integrating them into the structural optimisation processes. The combination of optimisation techniques, custom timber design libraries, and automated analysis workflows facilitated cost reduction and improved fabrication while preserving the architectural design integrity.

Keywords: architectural geometry, gridshell structures, optimisation methods and applications, timber, structural design, topology optimisation

1. Introduction

The West Gate Tunnel Project is a transformative project that will deliver an essential alternative to the West Gate Bridge, facilitating faster and safer commutes while diverting thousands of trucks from residential streets. The project encompasses three key components: the tunnel structure, an elevated roadway section, and an upgraded section of the West Gate Freeway.

Three primary portal structures are situated at the entrances and exits of the tunnel. Designed by architects Wood Marsh, the portals feature architectural timber transition elements, known as the Eel Nets, leading into the tunnel, and a concrete ventilation structure with a feature clad steel diagrid [1]. The Eel Net timber structures, inspired by the Aboriginal nets and traps used to catch eels by the indigenous inhabitants of the land, serve as a cohesive architectural element, providing a seamless transition between the open and tunnel environments.

The timber structures take the form of structural gridshells constructed out of glue laminated timber. The largest of the structures, the Northern Portal, is located adjacent to Yarraville Gardens on Whitehall Street, with the timber component measuring 116 metres long, 39 metres wide, and 40 metres high (Figure 1). Most of the figures, results and numbers in this paper refer only to the Northern portal.

Copyright © 2023 by Andre F. PEREIRA, Benjamin COOP, Dmitry ZELENKIN, Richard WHITFIELD and Kevin BERRY. Published in the Proceedings of the IASS Annual Symposium 2023 with permission.

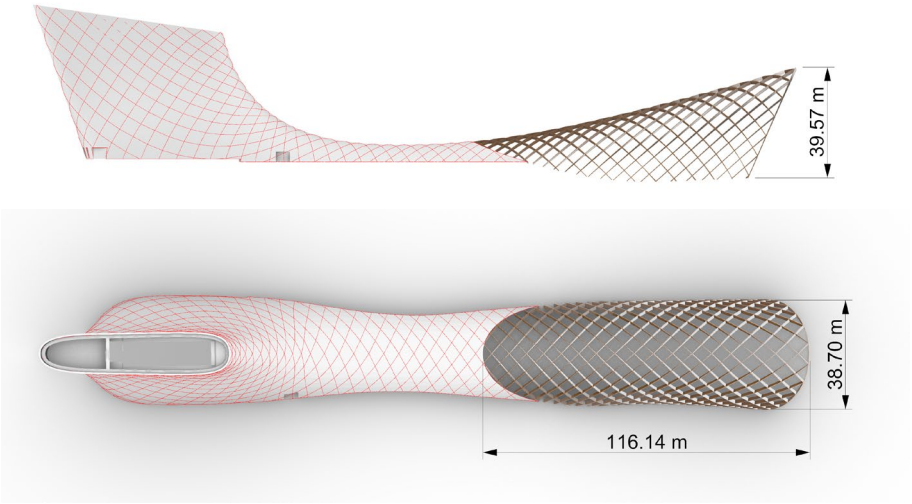


Figure 1. Northern timber portal dimensions and original diagonal gridshell topology.

Taylor Thomson Whitting (TTW) were engaged by the managing contractor for the tunnel project, CPBJH Consortium, to advance the architectural concept design for the timber structures. The concept design aimed to determine the structural feasibility of the architectural scheme, assess the structure's impact on the supporting tunnel structure, and identify potential areas for optimisation to benefit the project as a whole. TTW's work contributed to the successful awarding of a subcontract package.

A constraint led design approach was adopted, considering structural design standards, durability, vehicular impact, transportation, fabrication, erection and maintenance. The scope of this paper, however, is limited to the generation of the geometry (and associated topology) of the timber portals and the structural optimisation work carried out to design the timber members. We utilised computational design and optimisation methods to establish an automated end-to-end process, enabling the effective analysis and validation of numerous design iterations. This approach facilitated the identification of optimal solutions and, ultimately, the delivery of a high-performing and visually striking timber structure.

This paper is organised into three main sections. Sections 2 and 3 describe the geometry work developed for the two different structural gridshell topologies considered – diagonal and triangular. Section 4 addresses the work conducted for the structural design and optimisation of the timber members and connections.

2. Geometry: diagonal gridshell

The initial gridshell design (as proposed by the Architect) featured a two-way diagonal structural grid, as illustrated in Figure 1. The initial design had two primary issues. Firstly, every timber member exhibited curvature in two directions. Secondly, all members and all nodes were unique.

As the timber members' axis traced around the proposed shape, this required members curved about both axes and twisted along their length with the degree of curvature/twist varying non-uniformly along the members. Twisted members reduced or eliminated uniqueness in member types and node connections; however, it considerably limited timber fabrication partners while substantially expanding costs. In addition, very few fabricators can offer twisted timber glulam members. While there are methods to alter the shape to eliminate the twist, the resulting geometrical modifications to the envelope would be substantial and significantly affect the appearance of the timber structures. As such, this approach was not considered feasible. We addressed this with a step change in timber member rotation at the node positions and converting all members to arcs (and therefore planar).

This section outlines the work undertaken by the project team during the first half of 2018. By adjusting the overall shape and topology of structural members, we aimed to enhance structural performance, cost efficiency, and buildability by increasing the repetition of member and node families while preserving the architectural vision.

2.1. Methods

The geometry optimisation process consisted of three primary steps: (1) envelope surface rationalisation, (2) initial topology generation, and (3) topology optimisation. The goal of the first step was to create surface envelopes that rationalised the envelope, laying the foundation for an optimised topology. The second and third steps focused on organising structural members in patterns that enhanced the repeatability of nodes and member radii.

2.1.1. Relevant connection node parameters

The connection node was designed to have a circular steel hollow core and end plates welded to it. The timber members' glued rods were bolted to the end plates (Figure 2). The parameters considered for clustering different families were the three angles shown in Figure 2:

1. Alpha (α): angle between consecutive members on the plane perpendicular to the node;
2. Beta (β): angle between node direction and tangent of the member at the node;
3. Gamma (γ): twist angle between node direction and member plane.

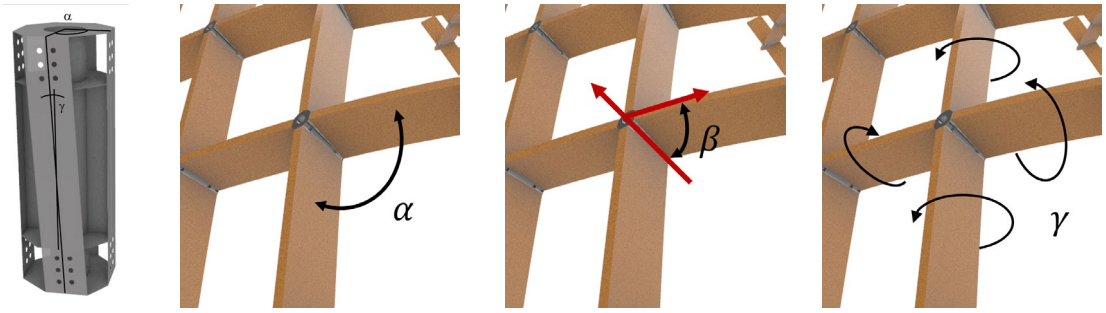


Figure 2. Parameters used for node cluster description: Node normal shown as red arrow, angles α, β and γ were used to describe node cluster family.

The beta angles (β) were considered to be zero for all nodes, as all arcs should meet the node at a 90º angle. Therefore, only alpha and gamma were considered for the clustering exercise.

2.1.2. Envelope rationalisation

We adapted the freeform architectural envelope to simple surface patches, derived from cylindrical and conical patches. Our initial step involved identifying the best-fit cylindrical surface for the envelope's top section, illustrated in yellow in Figure 3. This surface served as a reference for fitting the other surface panels.

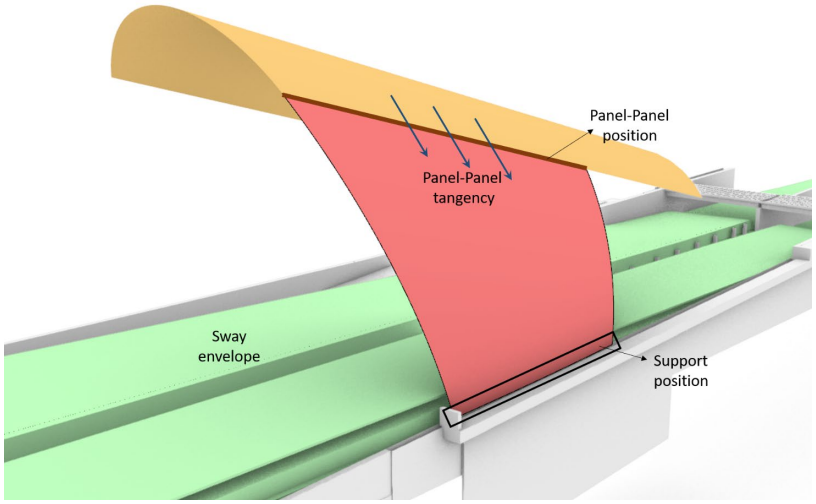


Figure 3. Form finding envelope through rational shapes. Constraints in surface fitting considered for the optimisation process: panel-panel continuity, support location and sway envelope.

We employed a genetic algorithm method (Galapagos [2] plug-in for Grasshopper/Rhino) to determine the multiple parameters that defined optimal conical surfaces (example shown in red in Figure 3) for the remaining envelope sections. Local search methods would have been valid approaches given the nature of the optimisation problem. The following architectural constraints needed to be met:

1. Panel-support interface: the surface edge at the base must coincide with the concrete capping beam of the tunnel dive structure retaining walls.
2. Panel-panel interface: adjacent surface panels must share edge positions and tangent vectors to ensure surface continuity and smooth transitions between surface patches;
3. Vehicle kinematic envelope: the fitted surface must provide adequate clearance for the outline of the space occupied by passing vehicles in motion, considering effects such as tilt, sway, etc.

2.1.3. Initial topology generation

The starting layout of the two-way diagonal topology was established by intersecting two sets of geodesic curves, each spanning a different direction and approximately mirrored about the central axis of the surface. Geodesics, defined as the shortest paths on curved surfaces, form helices when generated on cylinders. By arranging helices in a two-way grid, we can ensure consistent member profiles and node connection alpha and gamma angles throughout the entire topology. However, these properties are not present on conical patches.

To identify parallel geodesic curve sets across non-cylindrical patches, the following process was employed:

1) The top cylindrical section was divided into panels using equally spaced geodesic curves;
2) For each conical surface, initial geodesic curves in both directions were determined to maximise tangency with top cylinder members;
3) A final set of curves, aiming to be as parallel as possible to the initial geodesics from step 2, was calculated.

The generation of curves in steps 2 and 3 was achieved using the Constrained Optimisation by Linear Approximation (COBYLA) method. We used COBYLA to find the parameter t of the support level line that resulted in tangent or parallel geodesics. This process is illustrated in Figure 4.

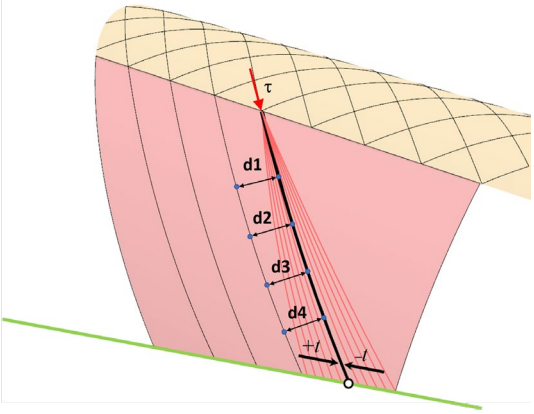


Figure 4. Finding geodesics curves that maximise tangency between curves of different surface panels and parallelism between curves on the same surface patch.

The geodesics found exhibit torsion along their length approximating to the direction of the surface normal sampled at various points along the curve. Because the structure in this area was not intended to be clad, it was not necessary to align the curve to be normal to the surface. Between points of intersection, the twisting geodesics were discretised as circular arcs, each having two parameters: total length and radius. The radius is the most relevant parameter in terms of buildability. To reduce variation in member radii, we clustered member radii into groups of similar values. Subsequently, the radii within these clusters were replaced with their corresponding mean values.

2.1.4. Structural node rationalisation

The use of rational surface patches and our topology generation approach resulted in connection nodes with small variability. However, the resulting configuration still presented a dispersion of alpha angles that required additional steps to maximise the repetition of node families. Gamma angles did not require further improvement since these were set by the relative rotation of consecutive arcs.

Alpha angles were improved through dynamic relaxation to the structural grid using the Kangaroo live physics plugin for Rhino/Grasshopper [3]. We combined base overall shape Kangaroo 'goals' to impose geometric boundary conditions (front arch node position anchors, node proximity to envelope, and top gridshell ridge nodes along generating curve) and a custom 'goal' to guide alpha angles to desired values.

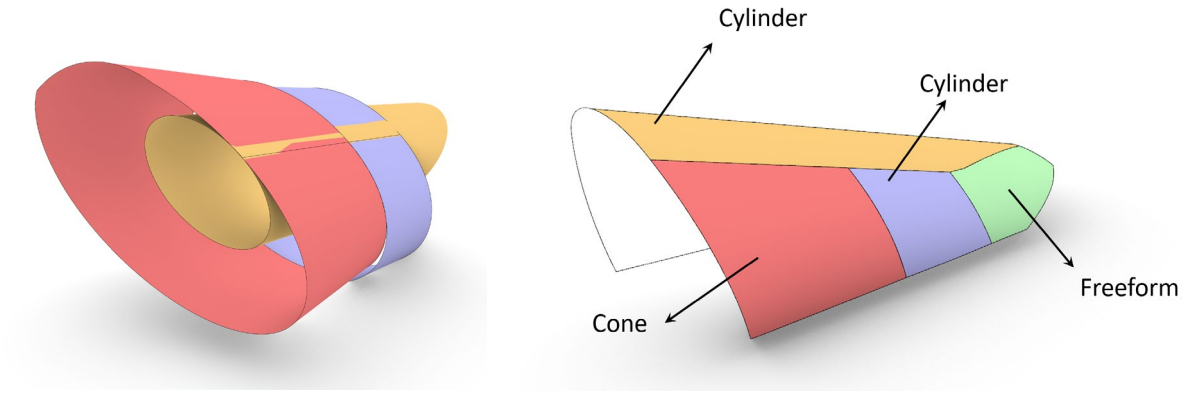
Upon convergence, we took the 'relaxed' structural gridshell and used Accord's [4] mean shift clustering algorithm, with a bandwidth of 0.115, to identify connection node families. Mean shift data points were defined as a sorted and normalised list of angles, in degrees. We clustered both connection node parameters (alpha and gamma) separately and obtained two distinct sets of alpha and gamma connection families. The resulting tolerances were 0.7 degrees for the alpha angle and 0.4 degrees for the gamma angle distributions.

Final node types were defined by the combination of individual alpha and gamma families.

2.2. Results

2.2.1. Envelope rationalisation

The surface envelope was rationalized into seven distinct patches, of which three were cylindrical and two were conical. Freeform surface patches were used in the back region, adjacent to the vent shaft cladding. Figure 5 displays the resulting surfaces and patches obtained from this initial step.



(a) (b)

Figure 5. Example of surface reconstruction for the North portal, composed of two cylinders, one cone, and a freeform region. Expanded surfaces shown in (a) and final trimmed arrangement shown in (b).

2.2.2. Gridshell topology and structural node rationalisation

The rationalised surface envelopes in conjunction with clustering optimisation allowed to reduce the time required for preparing different formworks. As a result, labour costs were also reduced.

Figure 6 and Figure 7 show the distribution of alpha angles for our initial grid topology (generated from the methods described in Section 2.1.3) and for the relaxed gridshell (Section 2.1.4). In the regions that exclude of the front arch, top ridge, and base supports (all of which required a unique connection types), the alpha angles were concentrated around either 79.1 or 101.6 degrees, initially within a range of about 10 degrees. The dynamic relaxation of the gridshell successfully reduced the range of most alpha angles down to 0.9 degrees. Figure 8 shows the final alpha and gamma angles.

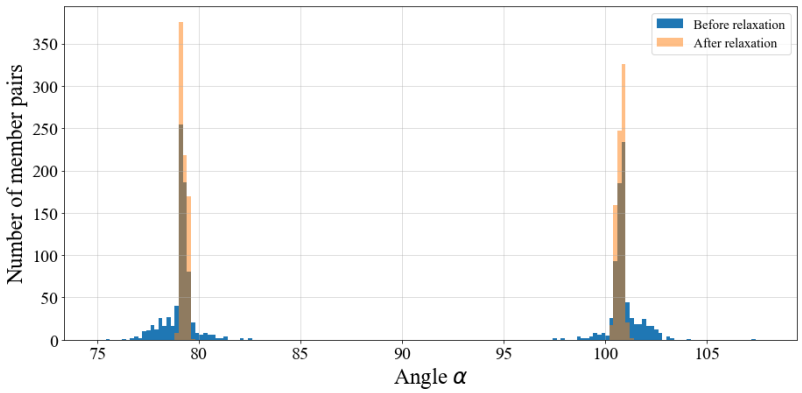


Figure 6. Histogram showing alpha angles before and after mesh relaxation (excl. front arch and top ridge nodes).

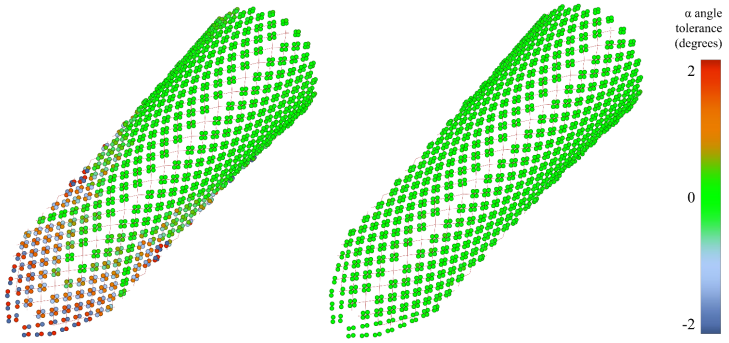
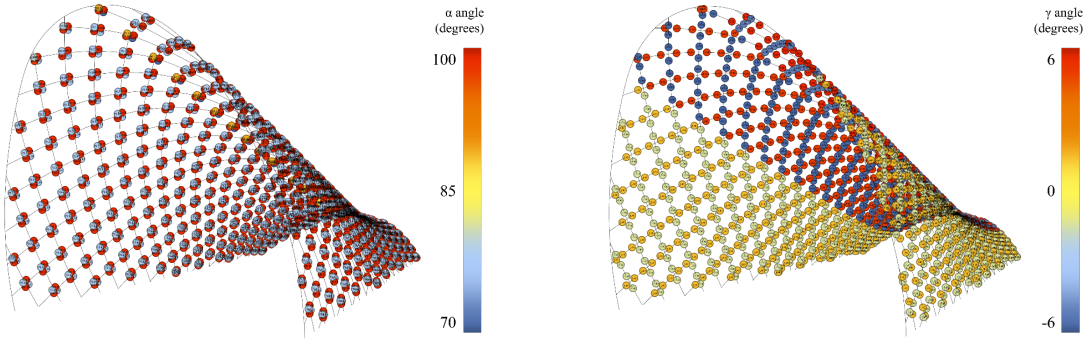


Figure 7. Alpha angle deviation from target angles before (left) and after (right) mesh.



(a) (b)

Figure 8. (a) Alpha angles obtained after relaxation. (b) Gamma angles.

Connection node angles were clustered in the alpha and gamma space into 25 and 12 families, respectively, within the tolerances defined in Section 2.1.4. The cluster families obtained for each case are shown in Figure 9 below. When combining alpha and gamma clustering, 32 total families of nodes are required in the obtained topology, 21 of which lie on the freeform surface shown in Figure 5. When compared to the original concept, developed prior to TTW's engagement, the geodesics approach required roughly 10x fewer families of nodes and as such 10x fewer sets of tooling to fabricate. Figure 10 below shows the 311 cluster families for the initial concept against the geodesics approach.

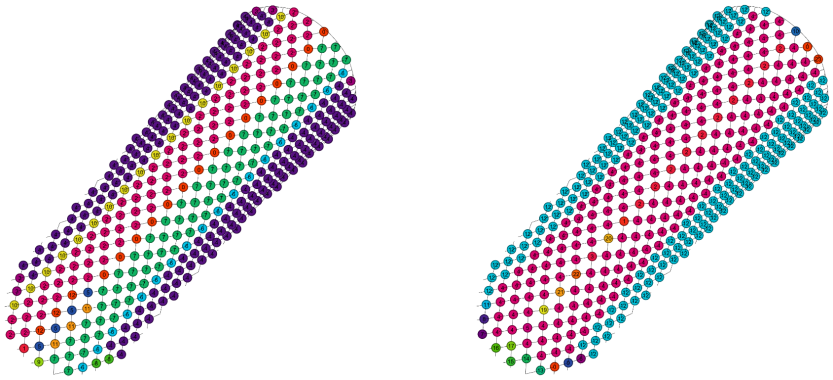
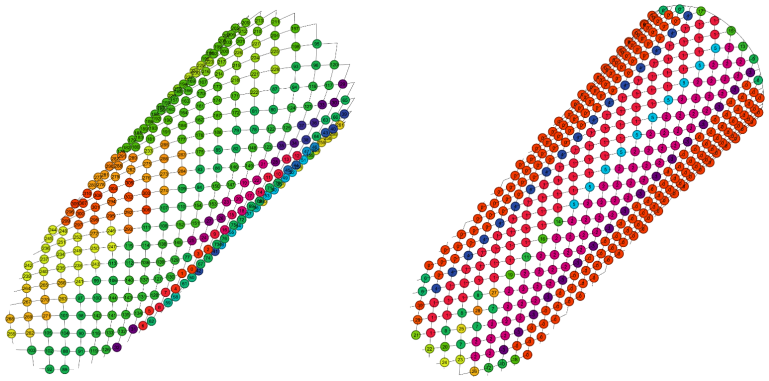


Figure 9. Clustering families when alpha (left) and gamma (right) are computed in isolation. 25 different alpha families were obtained within a tolerance of 0.7 degrees. For gamma, 12 families were required within a tolerance of 0.4 degrees.



Cluster family	Repetitions
0	175
1	69
2	67
3	17
4	17
5	10
6	5
7	3
8	3
…	…

Figure 10. Node families required for the initial concept (left) and in the topology described in this section (right). The initial concept was not rationalised and required 311 unique nodes, while the current approach was resolved with 32 families.

3. Geometry: triangular gridshell with parallel hoops

To facilitate erection, an alternative scheme featuring two 'hierarchies' of architecture was proposed: primary parallel 'hoops' and secondary diagonalised infill members, as shown in Figure 11. The scope of TTW's geometric work for this scheme involved discretising the surface envelope in such a way that both the timber members and the cladding panels exhibited consistent patterns and smoothly transitioned between different areas. This work was conducted during the latter part of 2019.

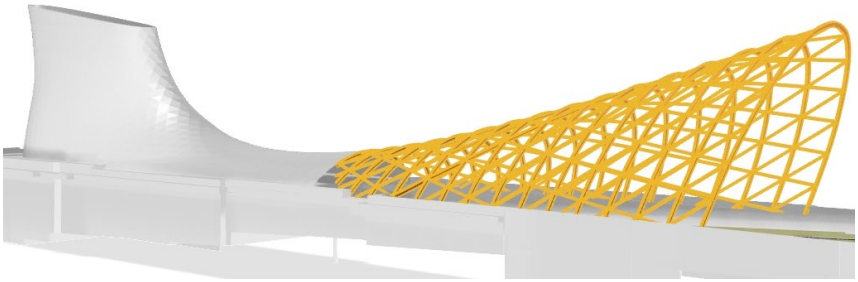


Figure 11. North Portal - Parallel hoop scheme

3.1. Methods

3.1.1. Parallel Hoop Formation

With the original geometry being based on the non-rational surface, the curvature along the length of the beam varied in accordance with the original shape and was asymmetric. After discussions with timber manufacturers, it became clear that planar curved glulam beams could be constructed with varying curvature along their length at no additional cost. For this reason, consistent curvature was not part of the rationalisation of the hoops. Instead, the hoops were converted into Bezier curves and made symmetric. From a visual perspective, the human eye can discern curvature down to the 3rd derivative of a curve (with the first, second, and third derivatives being slope, curvature, and rate of change of curvature, respectively). As such, at the connection between members, not only should the curvature of the members match but also the rate of change of curvature, so that this is not perceived as a discontinuity of the hoop. Therefore, knowing that these members would be subdivided for shipping purposes, the Bezier curves created were of the third degree, with knot vectors based on the chord length of the sampling points. The curves and curvature graphs for the original and proposed hoops can be found in Figure 12.

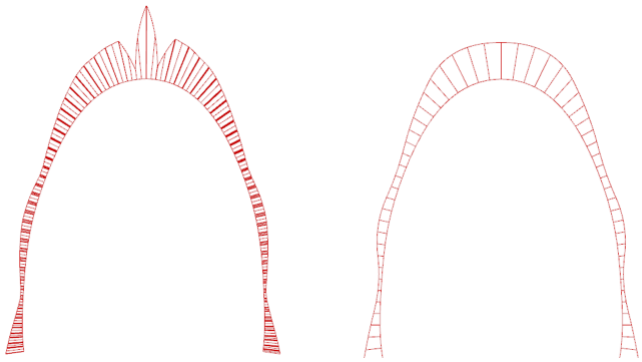


Figure 12. Comparison of non-rational hoop curvature with smoothed symmetric curvature.

3.1.2. Discretising the envelope

The parallel hoops from the timber structure set the rhythm for the panel arrangement in the cladding section. We opted for generating both timber topology and cladding panels simultaneously to achieve a smooth transition between the 'Eel Net' structures and Vent Shaft panels. Figure 13 illustrates the process. A sequence of planes, starting parallel to the planes of hoops of the timber structure, were gradually varied along the Vent Shaft cladding region. The curves resulting from the intersections between the surface envelope and planes were utilised to create the cladding's edges of the Vent Shaft. These curves were then divided into equal length portions to generate the vertices of the panels. Coop et al. 2023 [1] describes the work by TTW for the concept design of the vent aluminium façade and supporting structural steel.

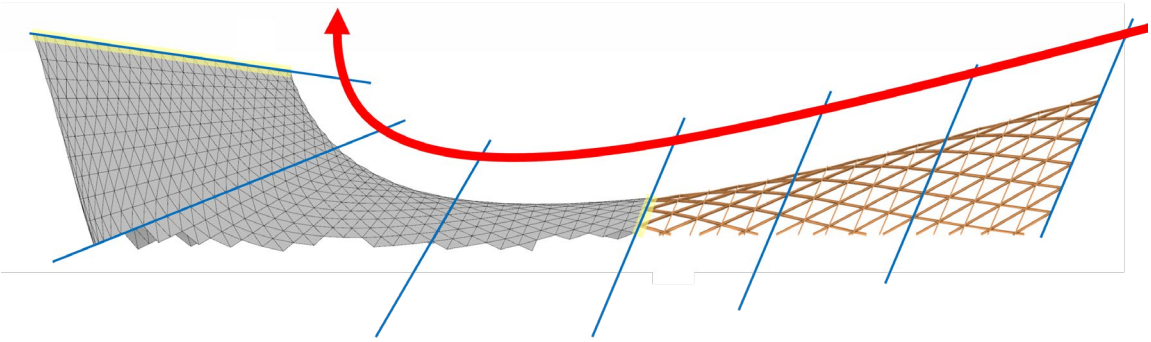
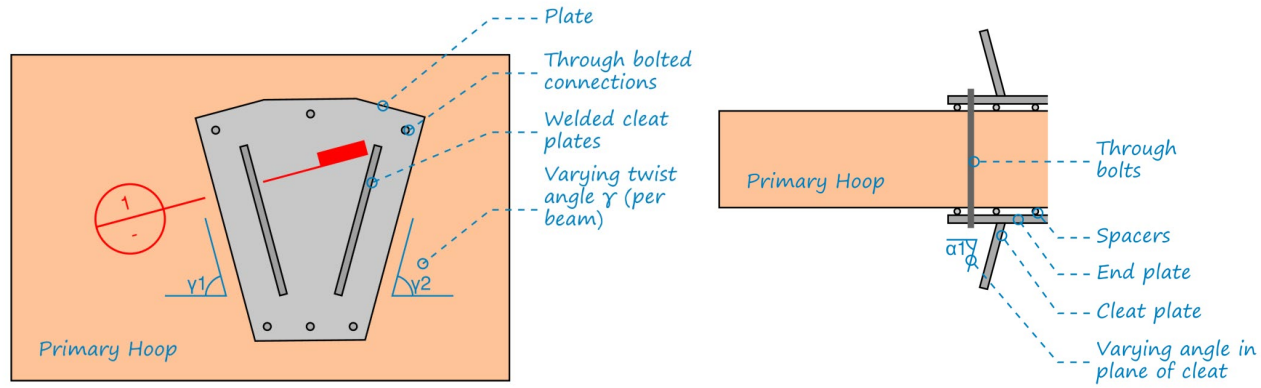


Figure 13. Full envelope discretisation approach. The parallel hoop planes were used to define some of the cladding panel edges.

Akin to the scheme described in Section 2, as the member axis trace around the proposed shape, an inherent twist occurs. The same rationalisation of the timber members into arcs was used for the gridshell method, with the same alpha (α), beta (β), and gamma (γ) angles existing at the primary and diagonal connection interface. The connection concept is illustrated in Figure 14.

This detail removes the complexity of fabrication associated with the gamma angle in the connection node presented in Section 2, and therefore, alpha was the only parameter we rationalised. The alpha angle would be materialised in the connection as the bracket angle between primary and secondary members, and its rationalisation would reduce the number of jigs required for connection fabrication.



Elevation on Connection *Section1 - 1*

Figure 14. Connection Details Showing α and γ.

Rationalising alpha angles for this scheme was significantly simpler when compared to previous approaches. Alpha and gamma angles are intrinsically associated. By rotating the secondary timber member (modifying gamma), the alpha angle would change according the Rodrigues' rotation formula [5]. We used COBYLA to find the smallest rotation of the timber members such that the respective connection alpha angles would snap to a prescribed list of values, as illustrated in Figure 15.

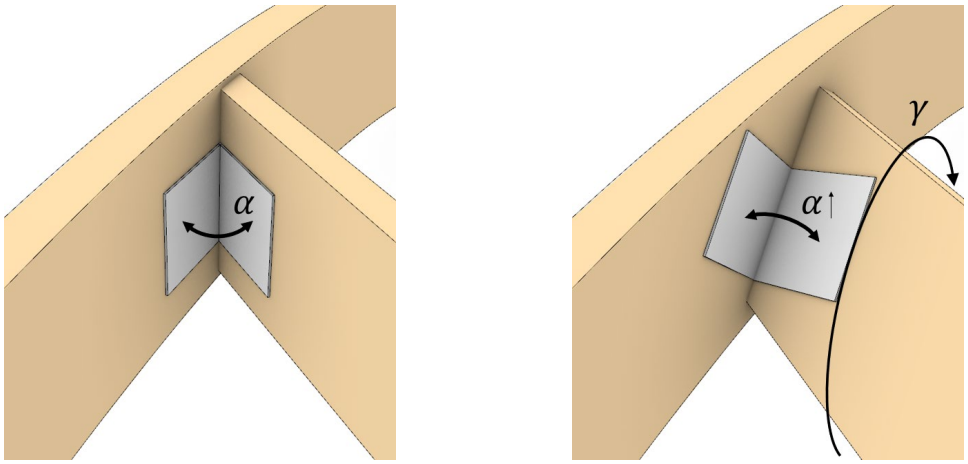
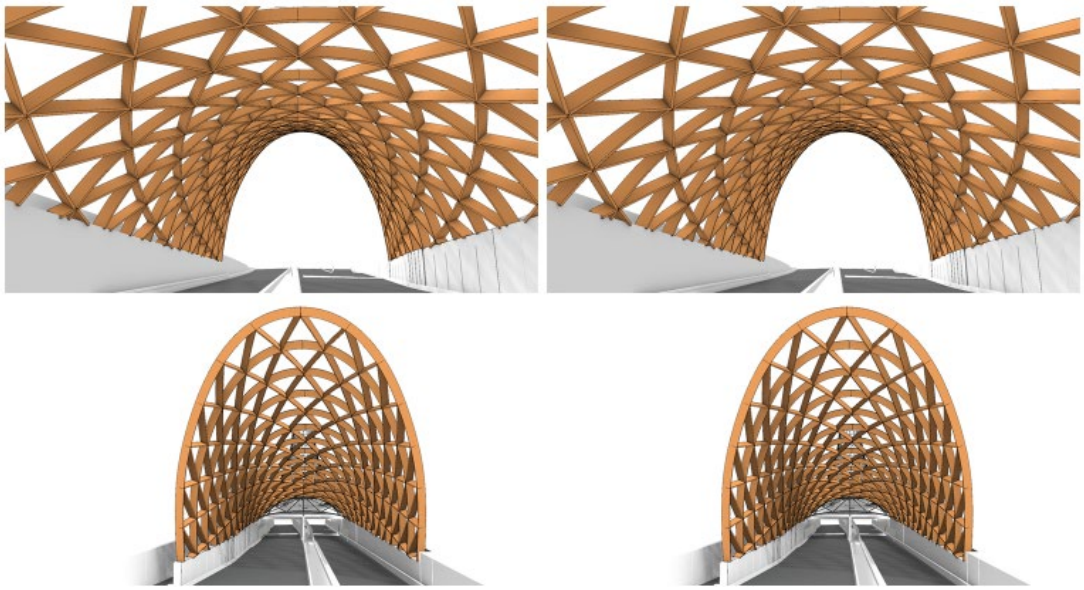


Figure 15. Through very slight timber member rotations, we were able to prescribe defined alpha angles for the node connections. Figure shows an exaggerated case.

3.2. Results

Our approach to discretising the envelope allowed us to address certain constraints and challenges, such as reducing the range of panel sizes, improving repeatability of panel angles and providing a visually striking design that followed the parametrisation of the envelope surface. Figure 16 shows the resulting timber topology.

A study was undertaken to assess the effects of using straight glulam secondary members on the visual appearance of the overall structure, as demonstrated in Figure 16. The visual impact was subtle; however, the merits of utilising straight members were substantial from a cost perspective. This was due to both a saving in manufacturing of the glulam and a reduction in transportation costs, owing to the ability to stack straight members more efficiently in a shipping container.



(a) (b)

Figure 16. Comparison of Straight Diagonals vs Curved Diagonals with Rectangular Glulam Members (Northern Portal).

4. Timber structural design

4.1. Challenges

During the structural design process, we faced several significant challenges. Firstly, calculating wind loads on the Eel Nets proved challenging due to variations in size, rotation, elevation, shading, and other factors among members. Secondly, the diagonal, diamond-shaped scheme structures exhibited high deformations from self-weight. Lastly, the timber structures demonstrated a high sensitivity to connection stiffness.

Our initial attempt to calculate wind loads involved a brute force approach. We created a script that calculated all the factors for every wind direction on each member, in accordance with the code requirements. However, the resultant wind loads were found to be higher than anticipated. After consulting with Windtech Consultants, it was decided to calculate the wind loads on the shell and then distribute the loads onto individual members based on their tributary areas. By assuming that penetrations could be disregarded to ensure conservative design, we significantly simplified the loading process.

For the diagonal grid, the self-weight of the timber was found to be the primary cause of deformation, particularly in the North portal of the diamond-shaped scheme. To account for this, we developed a construction sequence and performed a nonlinear staging analysis to capture locked-in stresses and deformations that occur during the construction phase.

In our beam model, we accounted for the flexibility of the steel node connections. We modelled the nodes using plate elements in Strand7 and extracted the corresponding moment-rotation curves, which were then incorporated into the beam FEM model. Initially, we intended to use a stiff core, with vertical plates welded to end-plates on each connecting member. However, this approach proved to have too much rotational flexibility. After several design iterations, we stiffened up the node by adding top and bottom flanges (Figure 2).

4.2 Workflow

For both schemes, in-house libraries were used for timber member checks in accordance with AS 1720.1:2010. Our timber design components were integrated into the structural optimisation processes.

The design process for the timber methods was fully automated by a Grasshopper script utilising Strand7 for finite element analysis and in-house timber design modules. Strand7 interoperability was achieved by TTW's in-house Grasshopper plugin called Kookaburra. The script took the geometry prescribed in the schemes above and grouped members based on user inputs. Each group had a range of allowable sections assigned to them. An iterative process assigned each group to a given section and proceeded to analyse the structure, complete member checks for all members, and, based on the worst-case utilisation of each group, determine if an increase or decrease in member size was suitable.

An increase in section size occurred if any member in a group exceeded a utilisation of 90%, whilst a decrease would trigger if all members were under a utilisation of 70%. The iterative nature of this process also required modifying the boundary constraints of the FEA model. A change in section depth, for example, resulted in a change in connection stiffness. As such, the script designed would change these properties dynamically in the Strand7 model as each section was changed during the iterations.

A degree of engineering judgement was required during this optimisation process. A certain percentage of members were allowed to exceed their utilisation limit in some design cases, and unique solutions such as steel reinforcement details were considered for such members. This was the case for the diagonal grid scheme on the Northern portal, where the sharp front arch angle resulted in high triangulation forces at the base to prevent overturning, as shown in Figure 17. Whilst not governing in the design manual, engineering checks were also completed for serviceability criteria such as maximum deflection after the optimisation process was completed to ensure that these did not become the governing case.

4.3. Results

4.3.1. Diagonal gridshell

Under self-weight, the majority of the timber members experienced compressive forces. The primary exception to this is within the first four lengths of timber, either side of the dive, that connect the front arch to the supporting wall without arching over the dive. These members carry significant tensile forces to restrain the front arch. Figure 17 (left) shows highlighted the structural timber members of largest utilisation ratio and a deflection plot of the timber gridshell.

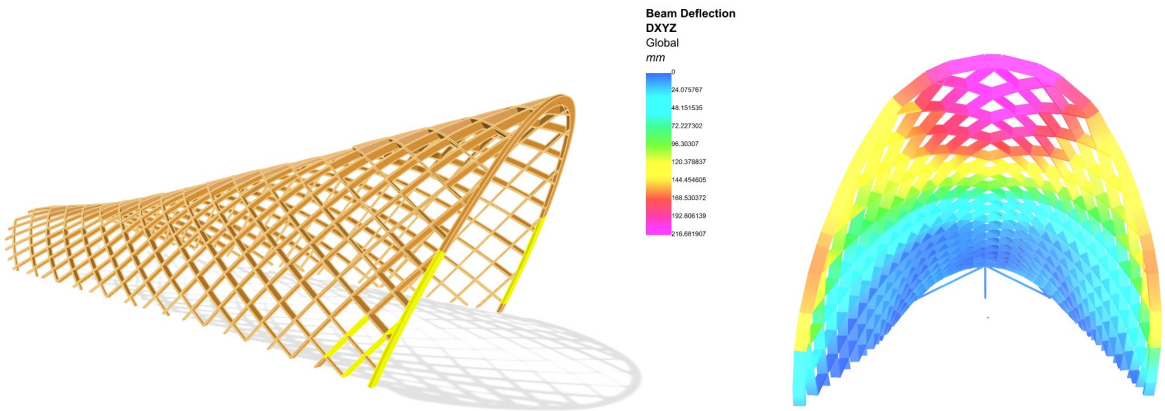


Figure 17. North Portal (1) Allowed over utilised members in yellow, caused due to the front arch wanting to rotate forward (2) Beam deflection contour plot

4.3.2. Triangular gridshell

While the described process allowed TTW to evaluate every member in the structure individually, the results of allowing each diagonal member to be optimised on its own resulted in a wide range of timber sizes being used across the structure (Figure 18).

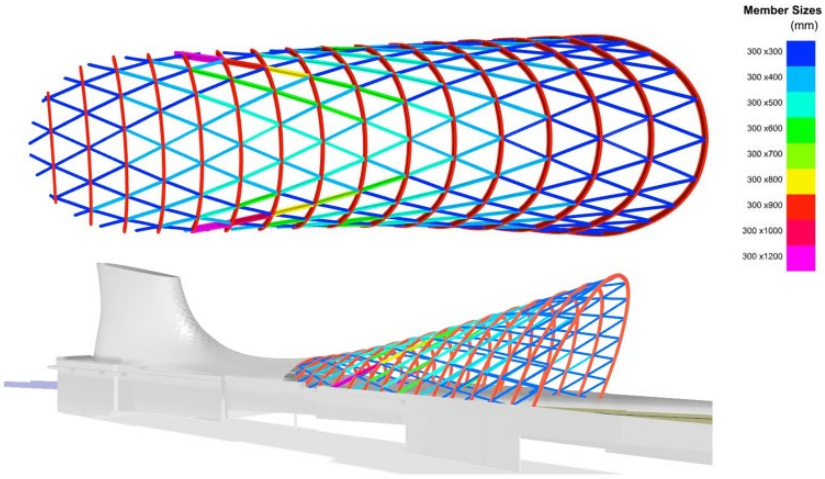


Figure 18. North Portal optimisation result for single size primary and variable diagonal sections

This did not align with the architect's vision for the structure, which eventually called for a single member size for the diagonals and another for the hoops, as per Figure 19. This limited the use case for optimisation and, as such, the main benefit of the automated design process became the ability to rapidly adapt to changing input geometries as we tested variants of each scheme.

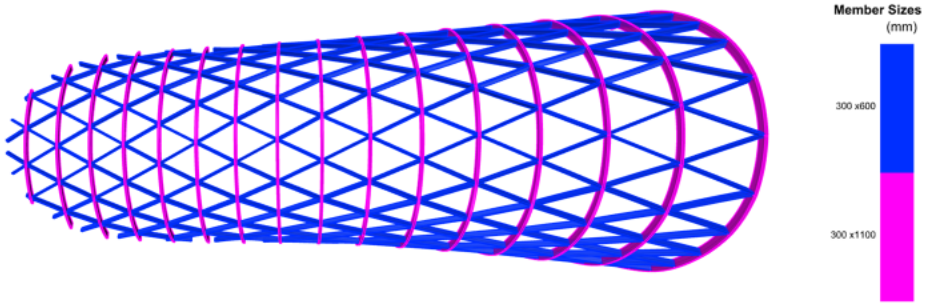


Figure 19. North Portal Final Geometry

5. Conclusions

This paper showcases the advantages of harnessing computational methods in the design of large-scale, geometrically intricate timber structures. By integrating parametric design, structural optimization techniques, and timber design libraries, we successfully established an automated, end-to-end process that enabled efficient analysis and validation of numerous design iterations. Our approach not only

facilitated the discovery of optimal solutions but also contributed to cost reduction and enhanced fabrication processes while preserving the integrity of the original architectural vision.

Acknowledgements

The authors would like to express our sincere gratitude to the whole West Gate Tunnel team for their invaluable collaboration and support throughout this project. Special thanks go to Dean Anderson, Hii King and John Haralabakos from CPBJHJV for their expertise, insights, and commitment to the project's success. We also extend our appreciation to Armin Voelske, Moshe Chong, and Roger Wood from Wood Marsh for their innovative vision, guidance, and unwavering dedication to the design process. Their collective contributions were instrumental in realising the goals and objectives of this complex timber structure.

Author Dmitry Zelenkin is currently affiliated with BG&E Consulting Engineers. Richard Whitfield is currently affiliated with Integraph Pty Ltd and Ark Pl Pty Ltd.

References

[1] Coop B., Pereira A., Tran H., Van Halewijn D., Whitfield R., Thomson M., and De Lacy A. "Designing the West Gate Tunnel portals: Façade geometry and structure." In Proceedings of IASS annual symposia, vol. 2023, International Association for Shell and Spatial Structures (IASS), 2023.

[2] Rutten, D., 2013. Galapagos: On the logic and limitations of generic solvers. *Architectural Design*, 83(2), pp.132-135.

[3] Piker, D., 2013. Kangaroo: form finding with computational physics. *Architectural Design*, 83(2), pp.136-137.

[4] Souza, C. et al. 2017. The Accord.NET Framework (v3.8.0) [Computer software].

[5] Rodrigues, O. *Journal de Mathematiques* 5, 380 (1840)

Proceedings of the IASS Annual Symposium 2023
Integration of Design and Fabrication
10–14 July 2023, Melbourne, Australia
Y.M. Xie, J. Burry, T.U. Lee and J. Ma (eds.)

Form dictated by material-specific properties of a mycelium composite

Dana SAEZ[a,*], Alexandra BERTSCH[a], Denis GRIZMANN[a], Martin TRAUTZ[a], Anett WERNER[b]

[a,*] RWTH Aachen University, Faculty of Architecture, Chair of Structures and Structural Design (Trako),
Schinkelstraße 1, 52062 Aachen, Germany
saez@trako.arch.rwth-aachen.de

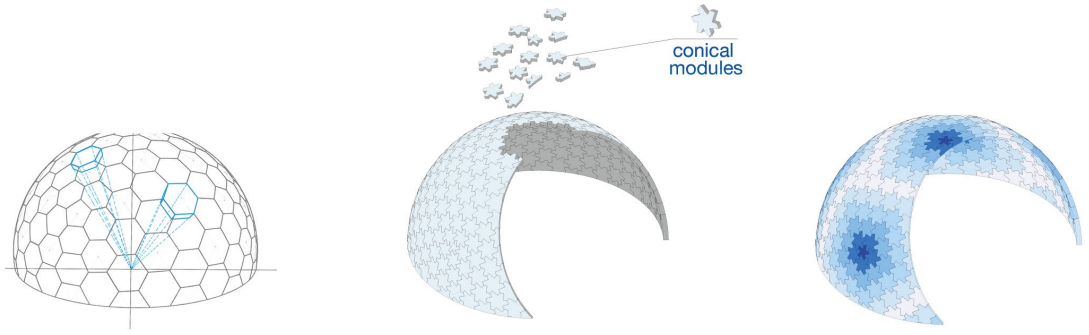
[b] Group Enzyme Technology, Chair Bioprocess Engineering, Faculty of Mechanical Science and Engineering,
Institute of Natural Materials Technology, Technical University of Dresden, 01069 Dresden, Germany

Abstract

Mycelium-based composites are a suitable alternative to replace oil-based materials since they can rapidly build up complex structures with extreme precision to 'take shape' into larger structures. This paper discusses the relationship between a given geometry and its corresponding constructive system specially tailored to mycelium-based materials. Within this context, we present the Myco Pavilion, as case study for a deep understanding of the material properties of mycelium-based materials and critically analyze how they influence the transformation of a given geometry. The goal was to integrate a bottom-up design process where we developed a construction system based on material-specific construction details. The use of standardized materials such as wood or metal could represent a challenge for double curved structural typologies, transforming the curved into polygonal forms for constructive reasons. On the contrary, fungal mycelium can occupy almost any negative given formwork. The hemisphere typology offers optimized possibilities for the use of fungal mycelium as a balanced structure. This typology can only absorb pressure and must therefore be relieved of tension, condition that correspond to the mechanical properties of mycelium-based composites. For material manufacturing reasons, the hemisphere was divided into modules connected by a material-specific joinery system [Fig. 1]. This system allowed us to explore a variety of joinery-patterns to increase the modules' connection surface, leading to better binding and a stronger cohesion between the parts.

Keywords: fungal mycelium, bio-composites, biomaterials, building biomaterials, mechanical performance, binding capacity, parametric form-finding

Copyright © 2023 by Dana SAEZ, Alexandra BERTSCH, Denis GRIZMANN, Martin TRAUTZ and Anett WERNER. Published in the Proceedings of the IASS Annual Symposium 2023 with permission.



(a) (b) (c)

Figure 1. Joinery system: (a) implementation of hexagonal modules with conical shapes as a constructive solution for hemispheres, (b) conical modules actualized with a material-based joinery system, and (c) mycelium-based modular joinery system based on the Goldberg Polyhedron.

1. Introduction

The construction industry is responsible for approximately 30% of global CO2 emissions and resource consumption as well as 30% of European energy consumption [1]. Therefore, there is an urgent need to develop strategies and concepts to confront climate emergencies. These should include not only thoughtful design and sustainable construction, but also low tech, cradle-to-cradle (C2C), or energy plus concepts. In this context, mycelium-based composites are a suitable alternative to oil-based materials. They can rapidly build up complex structures with extreme precision to take shape of larger structures. This paper discusses the relationship between a given geometry and an emerging design system specially.



Figure 2. The Myco Pavilion in the festival context.

Within this research, we present the case study 'Myco Pavilion' [Fig. 2] as the basis for a deep understanding of the material properties of mycelium-based materials to critically analyze how such

properties can dictate morphological transformation of a given geometry. The goal is to integrate a bottom-up design process where a complete construction system is developed on the basis of material-specific construction details. The use of standardized materials such as wood or metal for double-curved structural typologies could represent a challenge, transforming curved forms into polygonal ones for constructive reasons. On the contrary, fungal mycelium composites can occupy almost any negative given formwork. We use a mycelium and chip wood composite developed by Trako and Dr.-Ing A. Werner for MycoMatrix, research project funded by the German Federal Ministry of Education and Research (BMBF). It consists of a precise combination of the basidiomycete *Ganoderma lucidum* and beechwood chips manufactured under specific environmental conditions. The resulting matrix is a conglomerate with different properties that allow technical applications.

The selected mycelium-based building material is applied to design a sustainable pavilion near RWTH University's main building in Aachen's city center. The project proposes a unique roofing structure for the main stage in the context of a music, theater, and culture festival. Therefore, to fulfill programmatic requirements, we selected a hemisphere-like typology to be fabricated with the mycelium-composite elements. As a statically balanced structure, the hemisphere-like typology offers optimized use of fungal mycelium. Since the selected mycelium-based composite can difficultly resist bending and torsion moments, the selected typology can absorb pressure and must therefore be relieved of tension.

Although the selected mycelium-based material can be negatively formed, it represents a challenge due to manufacturing constraints. That is why the hemisphere has to be discretized into modules. The discretization allows a deep understanding of the binding capacity of fungal mycelium by developing a material-specific joinery system to connect the modules. The system allows us to explore a variety of patterns to increase the connection surface [Fig. 3], leading to better binding and a stronger cohesion between the parts.

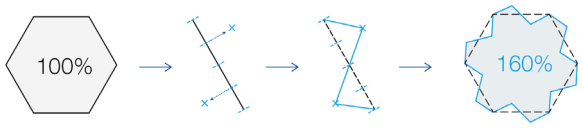


Figure 3. Parametric form-finding principle for increasing the joint area.

The in-depth study of the structural system is essential for addressing material-specific constraints. Consequently, a joinery system based on puzzle balls and the Goldberg polyhedron is analyzed and subsequently applied, considering the aforementioned constraints. Following the joining principles of puzzle balls, the modules are designed to be conically smaller towards the center and curved on the inner and outer surfaces. A detailed study of the geometry is also based on the Goldberg polyhedron. Since the Goldberg polyhedron is a polygonal shape that describes only faces, a connection of the puzzle joinery system was essential to enlarge its edges and, consequently, the binding surface to achieve material-specific requirements. Hence, the planar surfaces become curved modules that can be manufactured with the mycelium-based material. The complex intersection between topology, structural, and material constraints result in applying parametric modeling tools to optimize the Myco Pavilion's design and joinery system.

Prototyping some of the modules within this research requires not only a deep understanding not only of the material properties but also of the modules own construction system and geometry. Manufacturing the modules needs a complex formwork design process; for that reason, we decided to apply additive manufacturing (AM). AM allows us to design unique yet reusable formworks that enable growing the mycelium material under particular environmental conditions [2]. The prototyping helps test the designed joints and proves the feasibility of the design criteria on a scale of 1:2, resulting in the determining strategy within the Myco Pavilion design process.

2. Materials and methods

2.1. Structural typology and joinery system

In the beginning, a given structural typology is chosen to analyze and understand basic static properties of the future construct. In this case, the preferred structural typology is a hemisphere. Spheres are geometrically unique constructions known for having all points with the same distance from the center and same curvature both in two and three dimensions. Spheres are bodies of revolution. In such rotational bodies, there is a distinction between the meridians in the vertical direction and the latitudinal circles in the horizontal plane of the curvature. In the case of deformations or disturbances of the balanced system, increased tensile forces may occur.

As a statically balanced structure, the hemisphere typology offers great potential for using the mushroom mycelium. The fungal mycelium material can occupy all kinds of given forms. The mycelium-based modules are supported by their cross-section and designed as a non-planar system. In this typology, the overall modular system can only absorb pressure and must thus be relieved of tension. The structure is thinned at the top through an adapted cross-section to reduce the load on the components below.

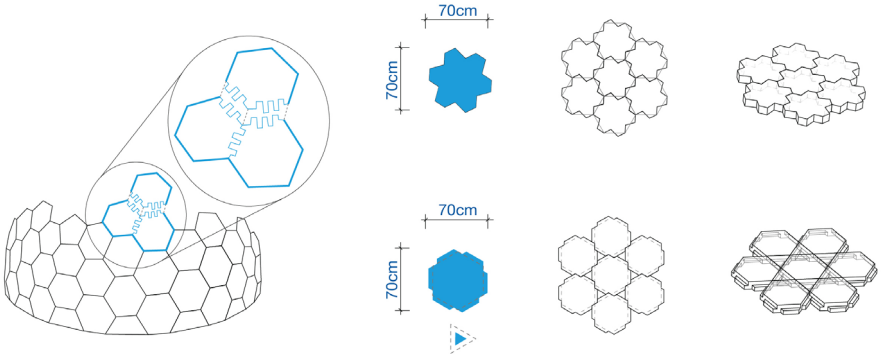


Figure 4. Hemisphere based on the Goldberg Polyhedron. (Left) First approach to geometry discretization and joinery system; (Right) two interlocking or clipping strategies for the modules.

For manufacturing reasons, the hemispherical typology has to be discretized into modules on the basis of the Goldberg polyhedron, which belongs to the icosahedra family and always shows 12 pentagons. The areas in between are filled with hexagons in circles and rows. The number of hexagons and their variants in shape and size depend on the size of the sphere.

As a polygonal shape, the Goldberg polyhedron presents a construction challenge requiring a joinery strategy [Fig. 4 left]. In our case, the material selection and its material-specific binding capacity play a key role. The joinery principle was based on the idea of the puzzle ball where modules are clipped [Fig. 4 right]. and are conically smaller towards the center and curved on the inside. The conical characteristic of the modules presented another geometrical constraint to be considered since the surface of the modules is curved, and the edges are straight.

The Goldberg polyhedron and the puzzle ball system serve as the basis for developing a novel joinery system where the mycelium grows among the interstitial space between the modules acting as a glue. Also, increasing the joint area between the modules with a jagged interface improves the material's binding capacity. Parallelly, an interlocking pattern of the joint was developed to increase the whole system's stability. In this context, the precise coordination of the angles and sizes of the various components is essential to achieve the exact fit of the interlocking connections.

2.2. Material-based joinery system

The selection of the mycelium-based composite consisting of *Ganoderma lucidum* and beechwood chips is based on the ongoing research project MycoMatrix conducted by Trako and Dr.-Ing. A. Werner. One of the research goals is to optimize the fabrication process of the bio-based material. Therefore, six manufacturing steps were determined: 1) Lignocellulosic material selection; 2) Homogenization; 3) Sterilization; 4) Inoculation; 5) Growth; and 6) Denaturation [2], [3]. Further development of the growth step serves as one of the construction strategies adopted for the pavilion's design. By unfolding step 5 in a two-step growth, the binding capacity of the matrix material plays a key role. After inoculation (step 4), the obtained mixture is placed in formworks to shape the modules of the composite material. They are incubated under specific environmental conditions for a week to obtain a cross-linked mycelium growth around the wood substrate. After this first incubation stage, the modules have to be extracted from the formworks and placed together through their binding interface. This second incubation stage takes place under the same environmental conditions for a period of two to three more weeks.

Due to geometry constraints, the mycelium composite modules require the development of a joinery system, which in this case, is based on the binding capacity of the material and its corresponding two-step growth. In similar geometries, the static complexity of the components is usually undertaken either by the edges of their surfaces [Fig. 1]. If the inner and outer surfaces of the modules are planar, the curvature of the whole construction must be completely absorbed in the connection between the parts. This condition leads to complex teeth-like edges shaping. Although it allows three-dimensional interlocking that could be favorable for static reasons, it is unfavorable for constructive reasons since it doesn't allow repetition of the modules. Assuming that the inner and outer surfaces of the modules are curved, the edges between them should be conical and straight—from a simple to a more precise edge shaping, reducing formwork manufacturing complexity. Therefore, we continue with the latter variant which involves an intermediate degree of individuality of the parts: thirteen different modules, excluding the opening edge and bottom's special modules. However, it requires complex negative formwork modeling and manufacturing.

2.3. Parametric modeling

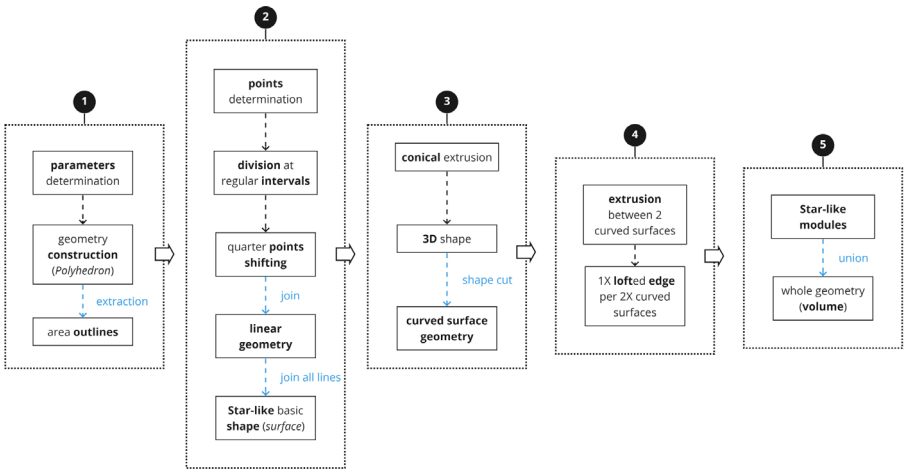


Figure 5. Parametric modeling workflow: general overview from step 1 to 5.

A parametric digital model is developed with the help of the visual programming tool Grasshopper for Rhinoceros [4] and RhinoPolyhedra [5]. The workflow can be divided into five main steps described in

Fig. 5. The parametric modeling enables us to work with a series of possible solutions which could be quickly transformed by improving or adapting the modules to the primary geometry constraints.

Footnotes should not be used. In the rare case where notes are necessary, please use Endnotes.

Step 1. RhinoPolyhedra creates polyhedra in different kinds and sizes, including the Goldberg polyhedron. The diameter and position can be varied on-demand based on the designed geometry. Subsequently, the outer lines of the polygon surfaces and the surfaces themselves are extracted due to design optimization requirements.

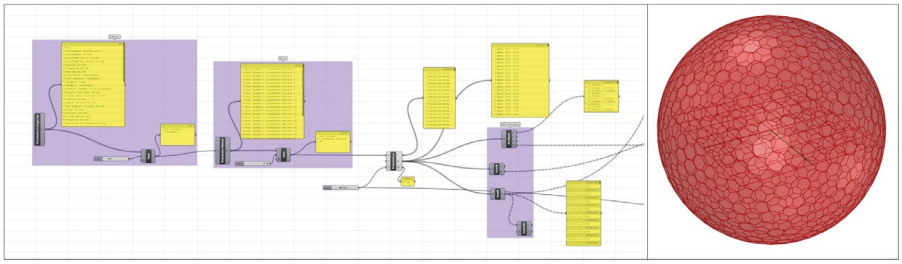


Figure 6. Step 1: Modeling of the geometry with RhinoPolyhedra.

Step 2. The outer edges of the polygons are divided into single lines. Start and endpoints are defined on these lines, and three points are in between at regular intervals. A specific parameter shifts the quarter points in the plane of the line in the opposite directions: one in one order and the other in the other direction - each orthogonally. This principle is shown in Fig. 2. The new points are reconnected to form a line and be joinined to the adjacent lines of the original polygon to create a star-like shape.

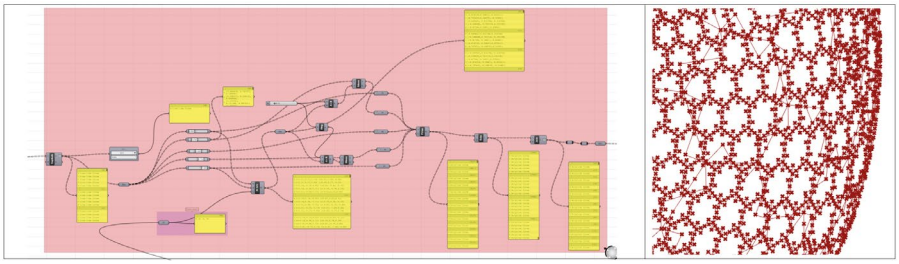


Figure 7. Step 2: from polygon to star-like shapes.

Step 3. The star-like shapes are extruded to the center, giving them their final conical shape. The extrusions are cut with two spheres to obtain the curved surfaces of the modules. The inner sphere is slightly shifted upwards, resulting in a smaller cross-section in the upper part in relation to the lateral pieces that transfer the compressive stress to the ground.

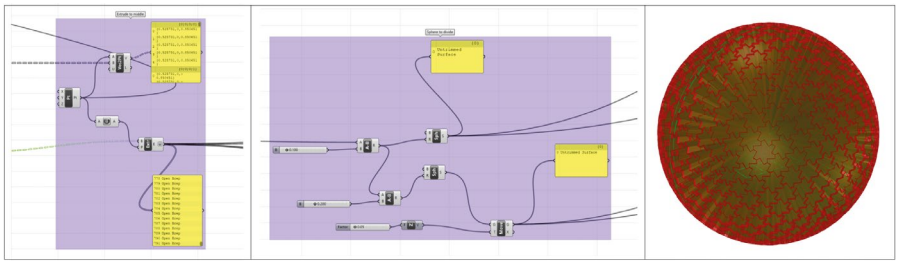


Figure 8. Step 3: curved surfaces.

Step 4. The previous steps result in two curved surfaced polyhedra. Consequently, the edges are lofted, and the modules' surfaces and corresponding lofts can be sorted in the parameter list.

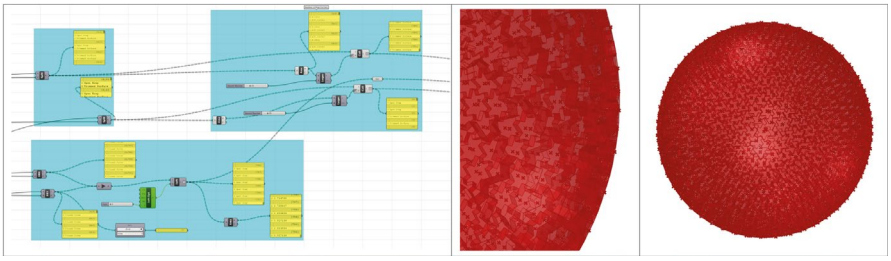


Figure 9. Step 4: conical edges of the modules.

Step 5. Finally, the resulting surfaces and lofted edges are joined to form the final multiple possible geometry variants of the Myco Pavilion. The division into a hemisphere and cutting of the opening are done in Rhino afterwards.

2.4. Function-specific design decisions

Due to function-specific requirements, the hemisphere requires a corresponding opening. The opening design represented a challenge for structural loads as well as constructive reasons. Thus, a series of studies on properly opening the hemisphere is conducted. As shown in Fig. 10, a straight cut is possible in different variants. The version highlighted in blue illustrated in Fig.10 fulfills the programmatic requirements of the Myco Pavilion. It has a shape whose mass can distribute the compression loads in a balanced way, and, at the same time, the load transfer disruption provoked by the opening is minimized.

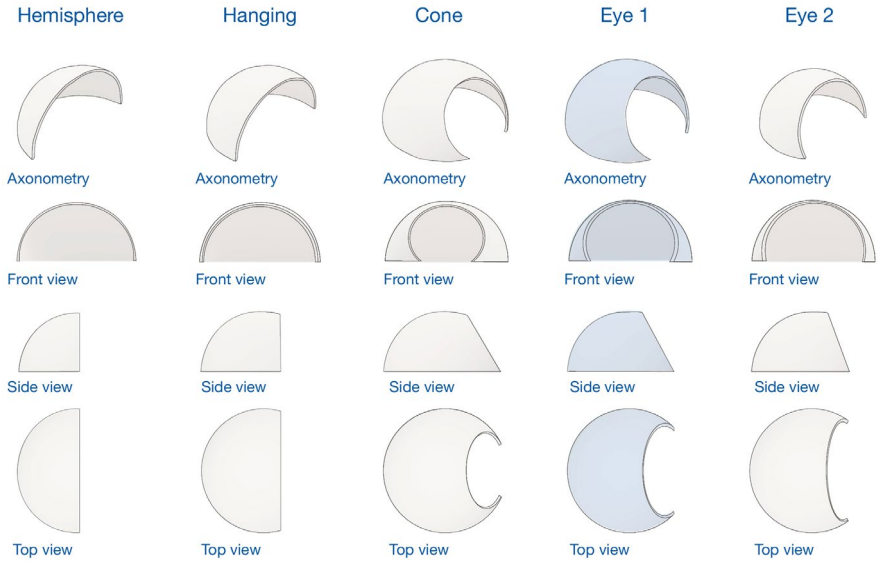


Figure 10. Opening studies. The selected opening is highlighted in blue.

Since the opening interrupt the static equilibrium, and the mycelium-based composite cannot withstand the additional stresses that may occur, the design of an extra support element is necessary. The first consideration is the reinforcement through a mycelium-based cantilever, as it can usually be found in shell structures. However, this first approach is discarded since we saw it questionable whether this principle can be applied with this material based on its deadweight effect. In conclusion, an arch-supported variant is developed—the L-profiled wood arch allows to hold the structure at the top and absorb the additional forces. At the bottom part of the pavilion, a U-profiled wood element serves to contain the stresses arising from the hemisphere.

3. Results

3.1. Final design

Since the Myco Pavilion [Fig. 11] requires extra support at both the opening and the base to allow proper load transfer and stability, the details between the different materials, wood, and mycelium-based composite are specially considered. Consequently, a friction-fit connection is selected for the proper joint of both materials.

A U-profile is selected for the surrounding base to secure the pavilion against slipping, breaking out, or deformation of the hemisphere. The Myco Pavilion is considered to be lightweight with a density of approx. 41.9 kg/m3, with a total weight of approximately 1,215.1 kg. Therefore, protection against wind forces has to be provided. Possibilities for this are anchoring the mycelium-based modules to the U-profile. For example, wooden boards or textile sheets can be used to anchor the structure. Since the design involves curved shapes, the solution with ingrown wooden panels is unsuitable. At the same time, the integration of ingrown textiles may not be friction-fit enough. Thus, the final design considers the ingrown of wooden rods inside the modules during the incubation process to strengthen the connection by anchoring.

The curved parts are to be manufactured with laminated veneer panels of easily bendable woods such as beech, oak, ash, or elm. The curvature is more workable with these materials than with solid wood panels. Due to prior investigations [3], mycelium-based modules should not come into contact with the glue found in laminated veneer since it increases the risk of contamination.

While curved components are designed with veneers, horizontally lying panels, such as the staircase or the floor, are designed with multi-layer wood panels. The floor structure must also compensate for the topographical position so that the system can stand level and no altered force flows occur due to inclination. Therefore, the floor understructure consists of reusable level-able metal feet that absorb possible unevenness of the ground. They have a special head on which the multi-layer boards can be placed. Truncated cone-shaped components secure the panels, and the central cylinder allows subsequent fine adjustments.

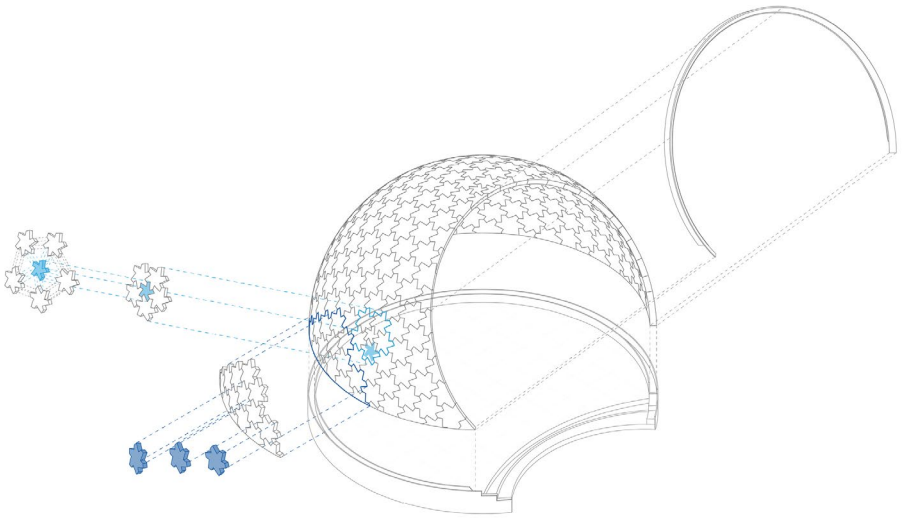


Figure 11. Myco Pavilion's exploded view: puzzle-like composition of mycelium-based modules and floor structure of wooden elements.

The modules on the bottom of the Myco Pavilion (U-profile joint) and those in direct contact with the opening (L-profile joint) are considered special modules. The special modules can also re-use the already developed negative formworks (thirteen different). Extra 3D printed special parts should be produced to fill in the gaps under the required specifications of the cut segments of the opening and the bottom part of the pavilion. Consequently, no new formworks have to be manufactured, only the individual fill-ins. Although it could represent a disadvantage in manufacturing terms, it is essential to highlight that due to the temporary condition of the pavilion, after the festival, all modules can be disassembled and composted.

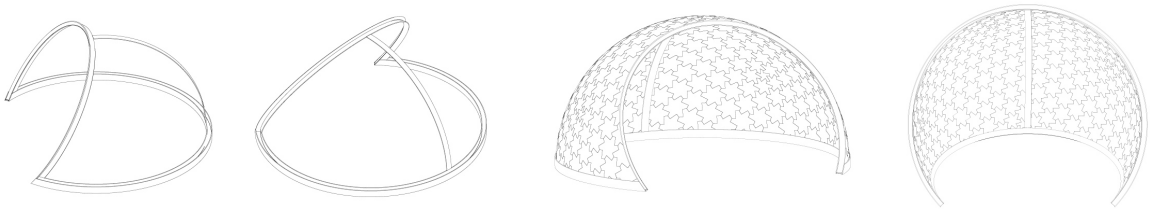


Figure 12. Opening arch and optional extra arch in perpendicular direction.

As described in chapter 2.4, the opening is supported by an L-profile made of bent multi-laminar wood. These are also additionally connected to the mycelium-based modules by ingrown wooden rods. If needed further support, another arch can be used perpendicular to the opening support. The addition of another arch could help hold the pavilion up in the center axis and simultaneously support the tilted design to hold the opening [Fig. 12].

3.2. Mycelium-based modules prototyping

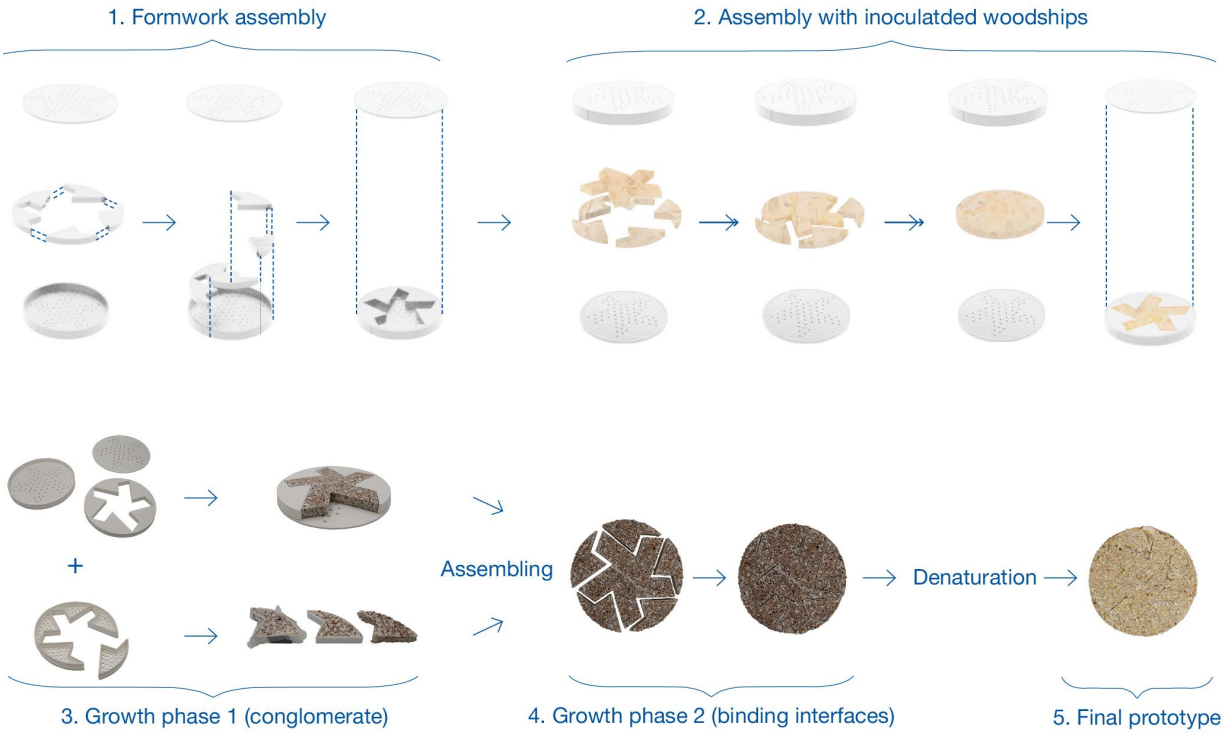


Figure 13. Design and manufacturing of the modules' prototypes and their corresponding AM-formworks.

Due to the mycelium-based composite's experimental characteristics, module prototyping plays a crucial role in the design process. It allowed an implicit perception of the material qualities that drives a certain level of understanding which could hardly be achieved without it [6].

The formwork that shapes the prototype [Fig. 13] presents a kind of complexity that makes additive manufacturing (AM) an accurate solution. The selected part of the Myco Pavilion that was prototyped is part of the designed joinery system and proves that it could be successfully implemented. In addition, the prototype provides further insights into the building material and the planned constructions.

The formwork was perforated for sufficient ventilation, and these ventilation holes were covered with Parafilm [7] during the two-step growth process to inhibit contamination. Once the formwork was properly designed and manufactured with the help of AM, the fungal mycelium and wood chips mixture was inserted and compacted with the top part of it.

After the first growth phase (described in chapter 2.2), the mold was rotated upside-down, and the mycelium-based modules were removed from this first formwork. The formwork was divided so that individual parts could be easily taken out. All modular parts were then put together on a second formwork without division which enabled the second-step growth and consequently the expected binding effect.

3.3. Assembly

Due to the conical shape of the modules, the assembly for second-step growth represents a considerable challenge. This paper proposes an assembly strategy for the pavilion's erection. After the first-growth phase of the individual modules, they should be assembled from the outside with the help of an inflatable structure, starting from the bottom up [Fig. 14]. This concept is based on the formwork studies for lightweight concrete shells using pneumatic structures by W. Sobek [8]. Also, environmental conditions for the mycelium-based composite cultivation, such as the required temperature for mycelia denaturation, could be integrated into this system, e.g., by adding warm air to the interior of the inflatable.

After assembly, second-step growth, and proper denaturation of the mycelium-based modules, the inflatable formwork could be deflated and removed.

Finally, this concept could also grant possible fitting tolerances for mycelium building blocks by using a slightly bigger inflatable.

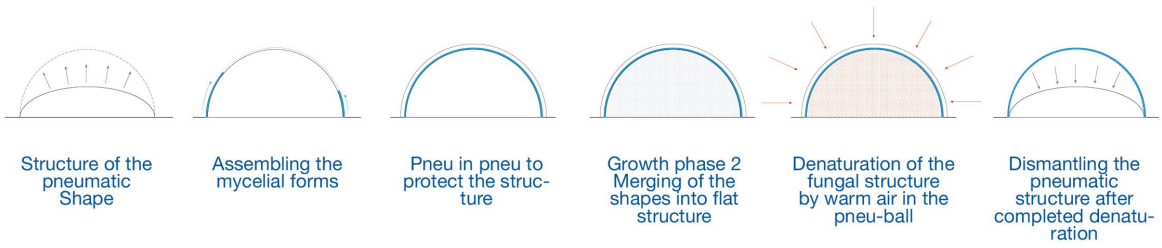


Figure 14. Assembly of the mycelium-based modules into the Myco Pavilion.

4. Discussion

The Myco Pavilion presents itself as a design with great potential for applying the described mycelium-based composite. The temporary nature of the program also supports the selection of the material due to its compostability and the upcycling possibility of old wood in the form of substrate integrating the whole design concept into the circular economy. Also, considering programmatic requirements as the outdoor setup, it is essential to highlight that the selected fungi, *Ganoderma lucidum*, present

hydrophobic characteristics. The fungal matrix tends to form a strong layer of hyphae on the superficies of the construction elements, which could grant waterproofing to the construction. Anyhow, after a series of experiments on the material's workability conducted by the MycoMatrix research team, the addition of an extra coating layer is recommended. This coating should be oil-based to avoid the fungi's hydrophobic nature.

The successful prototyping evidence the feasible application of the proposed material-specific joinery system with two-step growth manufacturing. Mono-materiality reduces the system's material entropy, which discards the use of additional mortar or glue to join the pavilion's constructive modules. The proposed interlocking system could also be further improved on the Y axis, but in that case, the overall section of the modules should be increased. The joinery system also enables the development of complex design details, which were adequately developed with the help of visual programming tools. Understanding the physical and mechanical characteristics of the mycelium-based material opens the game for novel ways of applying this material to structural typologies that require elaborated technical development. To achieve full validation of the design strategies presented in this paper, the complete realization and construction of the project should be necessary on a full scale.

Acknowledgements

The authors would like to extend special thanks to Trako's assistant team members: Raman Suliman, Steliyana Yancheva, Lea Scholz, Helena Krapp, and Hlib Novosolov.

References

[1] United Nations Environment Program. Global Status Report for Buildings and Construction: Towards a Zero Emission, Efficient and Resilient Buildings and Construction Sector; United Nations Environment Program: Nairobi, Kenya , 2020.

[2] Saez, D.; Grizmann, D.; Werner, A.; Trautz, M. Analyzing a fungal mycelium and chipped wood composite for use in construction. In Proceedings of the IASS Annual Symposium 2020/21, Guilford, UK, 23–27 August 2021.

[3] Saez, D.; Grizmann, D.; Trautz, M.; Werner, A. Developing sandwich panels with a mid-layer of fungal mycelium composite for a timber panel construction system. In Proceedings of the World Conference on Timber Engineering, Santiago, Chile, 9–12 August 2021.

[4] McNeel, R. & others, 2010. Rhinoceros 3D, Version 6.0. Robert McNeel & Associates, Seattle, WA.

[5] Fugier, D., 2014. RhinoPolyedra for Rhinoceros 3D, Version 7.0.7506.

[6] Jones, M.; Mautner, A.; Luenco, S.; Bismarck, A.; John, S. Engineered mycelium composite construction materials from fungal biorefineries: A critical review. Mater. Des. 2020, 187, 108397. https://doi.org/10.1016/j.matdes.2019.108397.Author, F.: Article title. Journal 2(5), 99–110 (2016).

[7] Amcor | Parafilm M All-Purpose Laboratory Film | Flexible Packaging [WWW Document], n.d. https://www.amcor.com/product-listing/parafilm-m-all-purpose-lab-film-fpf003 (accessed 2022.06.10).

[8] Sobek, W. Auf pneumatisch gestützten Schalungen hergestellte Betonschalen. PhD dissertation, Universität Stuttgart, Stuttgart, Germany. 1987.

IASS 2023
July 10–14 Melbourne
Integration of Design and Fabrication

Proceedings of the IASS Annual Symposium 2023
Integration of Design and Fabrication
10–14 July 2023, Melbourne, Australia
Y.M. Xie, J. Burry, T.U. Lee and J. Ma (eds.)

Rethinking geometry of grapevine structure proposed by Konrad Wachsman

Tsubasa INOUE[b], Toshiaki KIMURA[a,*], Yosuke KOMIYAMA[c], Satoru KIMURA[d]

[a,*] Graduate School of Design and Architecture, Nagoya City University
tkimura@sda.nagoya-cu.ac.jp

[b] Graduate School of Design and Architecture, Nagoya City University
[c] Department of Architecture and Architectural Engineering, Kyoto University
[d] Department of Architecture and Urban Design, Ritsumeikan University

Abstract

Konrad Wachsmann proposed the Grapevine Structure (GS) in 1953 (Figure 1). GS has a shape with regularity, which is obtained by connecting a unit in a pattern. A unit can be determined subject to a geometrical algorithm. The algorithm for GS is described in his book [1]. Note that GS has yet to be realized in practical design. However, a 3D model has been reproduced, and a full-scale physical model was exhibited at Biennale Venice 2018 [2]. GS is a unique pre-fabrication technique with the freedom to select cross-sections of members, while its detail and structural properties have yet to be discussed well. The authors think it is significant to focus on GS and explore the possibility of new architectural geometry realizing more construction efficiencies. This study focuses on the GS to apply as an actual structure. Based on the previous literature, GS is reproduced using 3D CAD. Through observing the obtained geometry and comparison with the original model and previous example, we proposed an improved generating algorithm. Then, the reproduced geometry is discretized using finite elements, and linear static FE analysis is conducted to discuss the mechanical properties. The potential applications of the Grapevine structure for architectural geometry will be discussed through numerical examples.

Keywords: conceptual design, morphology, architectural geometry, reverse engineering, FE analysis

1. Introduction

Many studies have explored the design intention or design philosophy of famous structural engineers by investigating the mechanical behavior of existing buildings designed by them. Paris *et al.* studied the herringbone patterned masonry domes without shore or formwork in the 16th century [4]. They showed the effectiveness of the pattern using Discrete Element Modelling and limit state analysis. Tomas and Montrull focused on F.Candela's concrete shell [5]. The optimization result of the shape of the L´Oceanogràfic at Valencia indicated that slight changes in the shape are enough to achieve the improvements. Barazzeta *et al.* investigated the work designed by Pier Luigi Nervi [6]. They investigated the structural behavior of the airplane hangers, which have already destroyed, using numerical analysis. Andrzejewski and Shaffer investigated the Location Orientation Manipulator, which is proposed by Wacksman and his students in the 1960s [7].

Konrad Wachsmann designed various buildings considering the modularization of joint designs and components. The U.S. air force aircraft hangar (1951) can be mentioned as a representative work. He proposed the Grapevine Structure (GS) in 1953, as shown in Fig. 1. Connecting a unit in a pattern, the shape of the GS can be obtained. Furthermore, a unit can be determined according to a geometrical algorithm. In recent years, a 3D model has been reproduced by Burkhalter *et al.*, and a full-scale

Copyright © 2023 by Toshiaki KIMURA. Published in the Proceedings of the IASS Annual Symposium 2023 with permission.

monument was exhibited at Biennale Venice 2018 [2, 3]. GS is a unique pre-fabrication technique with the freedom to select cross-sections of members. However, its detail and structural properties have not been discussed well. The authors think it is significant to focus on GS and explore the possibility of new architectural geometry realizing more construction efficiencies.

In this study, we focus on the GS proposed by Wachsmann to generate its structure and observe its mechanical characteristics as an architectural structure. GS is reproduced using 3D CAD by referring to the previous literature. Through observing the obtained geometry and comparison with the original model and previous example, we proposed an improved generating algorithm. Then, the reproduced geometry is discretized using finite elements, and linear static FE analysis is conducted to discuss the mechanical properties. The potential applications of the GS for architectural geometry will be discussed through numerical examples.

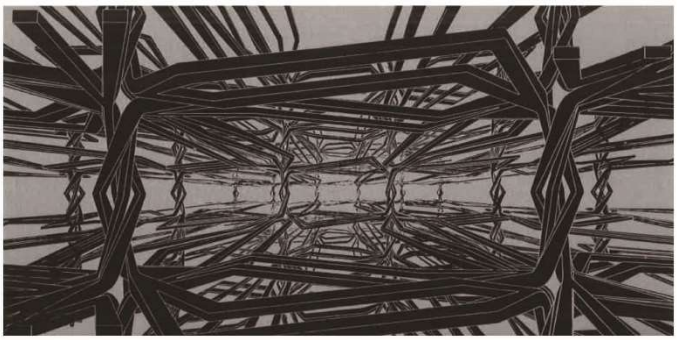


Figure 1. Conceptual image of Grapevine structure proposed by Konrad Wachsmann [1].

2. Grapevine structure

We reproduce Wachsmann's GS (GS-W), which is shown in reference [1], using 3D CAD (Rhinoceros) and Grasshopper, which is a graphical programming editor. The algorithm for generating GS-W can be summarized as follows,

Step 1 Create a cube *A* with a side length of *x* m.
Step 2 Project a square *B* with a side length of *y* m onto the center of gravity of each face of *A*. Its six sides are parallel to each face of *A*.
Step 3 Extrude two rectangles *C* with *B* as faces.
Step 4 Create a cube *D* by intersecting *C*.
Step 5 Create a new cube *E* tangent to the side of *D*.
Step 6 Rotate *E* by *p* degrees and create a new cube *F*.
Step 7 Divide the top and sides of *F* into *s* pieces. On each face, select one of the divided faces.
Step 8 Using the two surfaces and arcs created in Step 7, create the joint element of the basic module.
Step 9 Project *E* onto *A*. Then, create a strip shape on the side of *A* with the same height as *E*.
Step 10 Divide the shape created in Step 9 into t rectangular faces. Then, select two faces.
Step 11 Create the horizontal component of the basic module using the element faces created in Step 8 and the two faces selected in Step 10.
Step 12 Project the top surface of *F* onto the top surface of *A*.
Step 13 Divide the surface created in Step 12 into *u* rectangular faces. Then, select one face.
Step 14 Create the vertical component of the basic module using the faces of the joint element and the faces created in Step 13. Join the components to create basic module *X*.
Step 15 Rotate and duplicate *X* by *q* degrees around the center of gravity of *A*.
Step 16 With the center of gravity of *A* as the center, the group of units obtained in Step 15 is

duplicated vertically and symmetrically. Finally, the basic unit by GS-W is obtained.

Figure 2 represents the whole generation sequence. Figures 3 and 4 represent the basic module and basic unit by GS-W (hereafter named pattern A and pattern B from left to right), respectively.

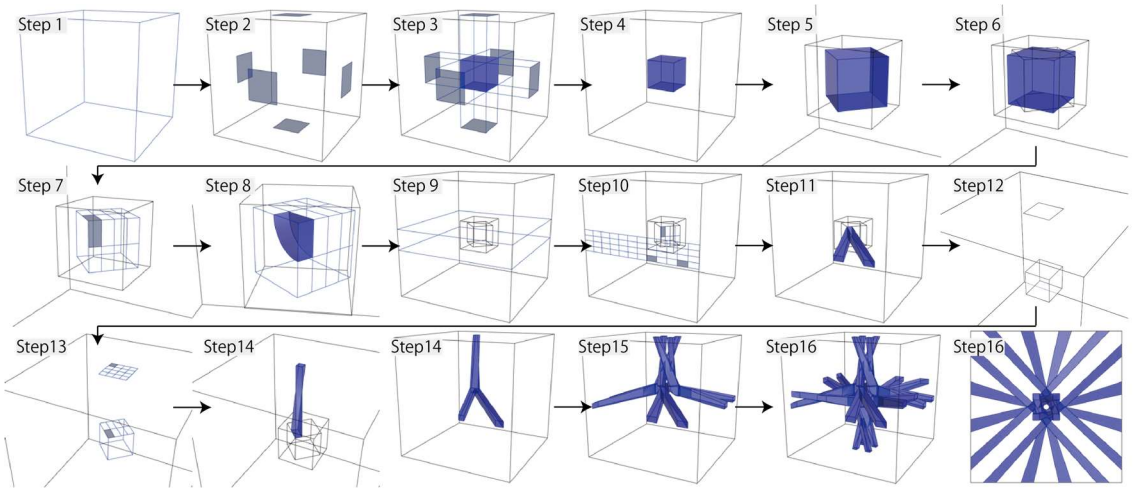


Figure 2. Generating sequence of GS geometry.

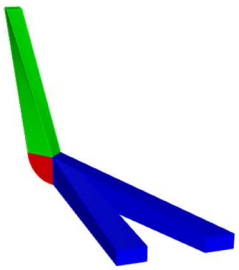


Figure 3. Basic module by GS-W (green: vertical component, blue: horizontal component, and red: joint element).

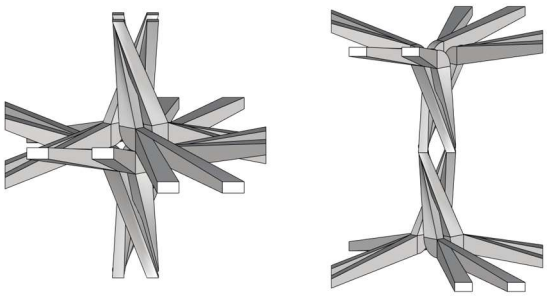
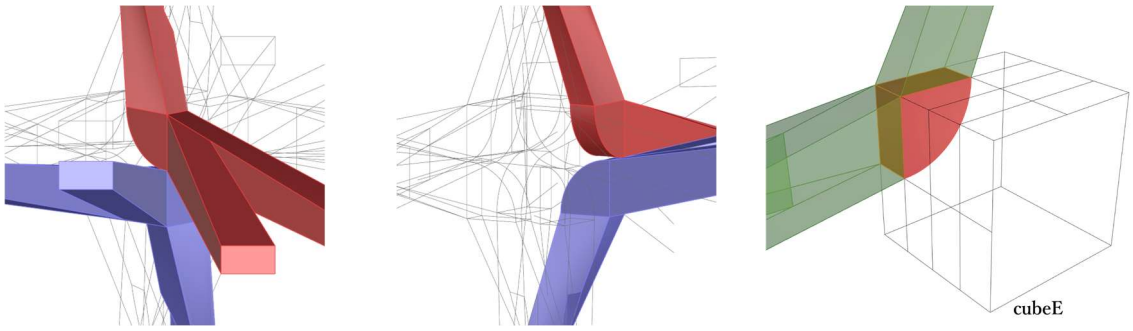


Figure 4. Basic unit by GS-W (left: pattern A, and right: pattern B).

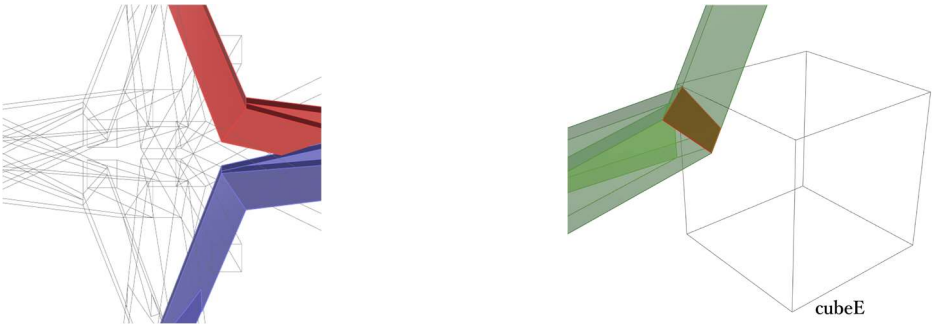
Figure 5(a) represents the joint of Pattern A with the enlarged view. The procedure for generating the joint element of Step 8 is extracted from the whole sequence and shown in Figure 5(b). It can be found that, in the case of pattern A by the GS-W procedure, the upper and lower units are contacted with a tiny area due to a fan-like shape generated in Step 8. From the view of the practical design, a sufficient joint area needs to connect units. Figure 6 shows the shape, which is generated according to the algorithm of

the previous case [2] (hereafter, GS-B). In the case of GS-B, it is hard to find a suitable connection between the upper and lower units because there is a gap between both units.



(a) (b)

Figure 5. Enlarged view of basic unit according to GS-W: (a) Joint of Pattern A, and (b) Procedure for generating joint component (Step8).



(a) (b)

Figure 6. Enlarged view of basic unit to GS-B: (a) Joint of Pattern A, and (b) Procedure for generating joint component.

In this study, we improve an algorithm of Step 8 (named GS-RW). The revised procedure (Step 8') can be expressed as follows,

> Step 8' Divide F into two parts at the top and bottom, and create a new face B' inside. Further, divide B' into $v \times w$ pieces, then select one face. Form a joint component from the divided face and the two faces created in Step 7.

Figure 7 represents the procedure of Step 8' and an obtained shape of a joint component in GS-RW. Note that v and w are assigned as v=w=4 in this study.

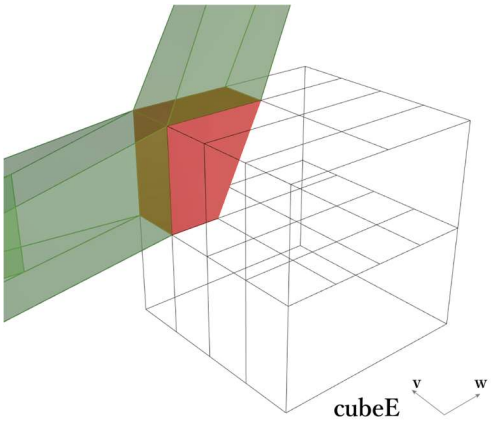


Figure 7. Procedure of Step 8' and shape of obtained joint component by GS-RW.

Figure 8 shows the shapes obtained by GS-RW and the enlarged view of the basic unit of pattern A. The shape with the red and blue colors represents the upper and lower units, respectively. Figure 8 shows that the significant connection between the upper and lower units is obtained compared with the shapes of GS-W and GS-B. Considering the stress state, the joint area can also be optimized if v and w are controlled during the generation process.

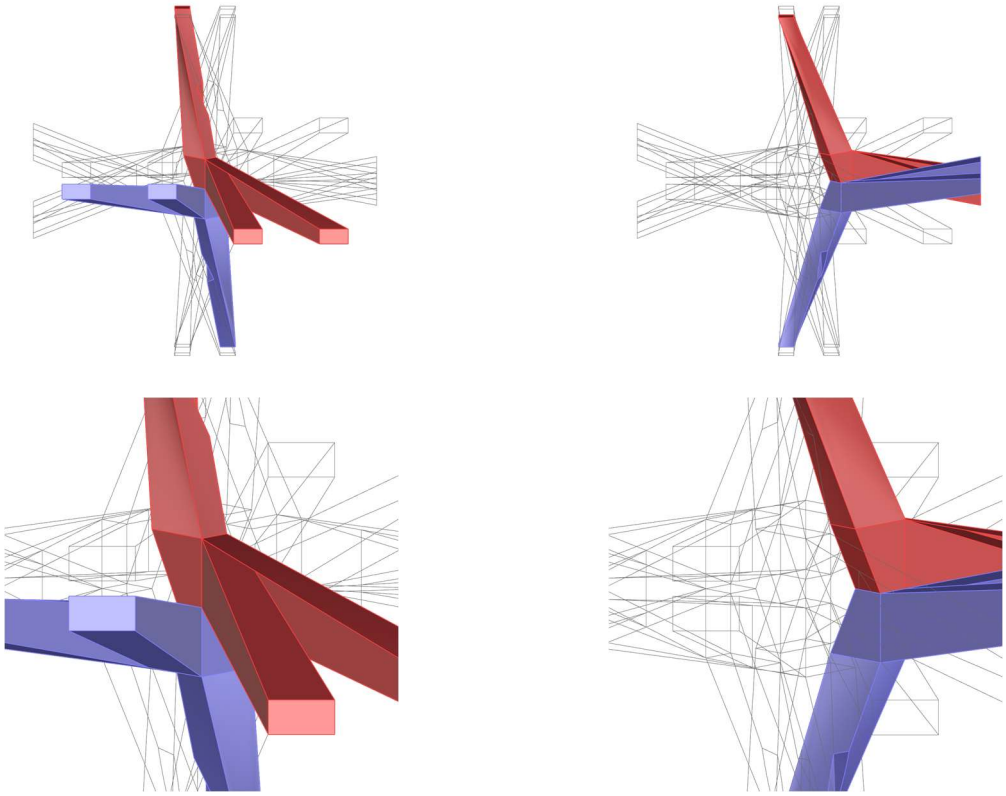
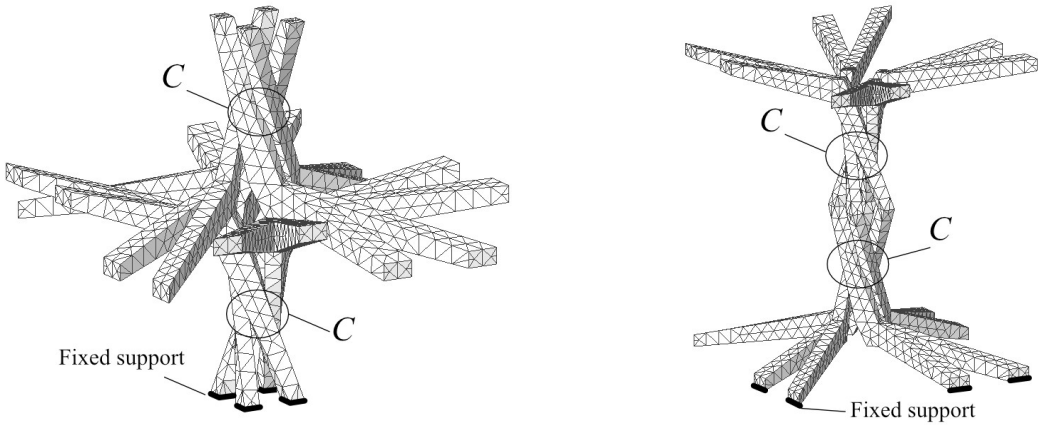


Figure 8. Enlarged view of basic unit by GS-RW.

3. Investigation of mechanical properties

We conducted linear static FE analysis for GS geometry. MIDAS iGen, which is a general FE analysis software is used for solving linear-elastic static analysis. A shape obtained in section 2 is discretized into five-node pyramid elements. The bottom surfaces of GS geometry, as shown in Fig. 9, are fixed supports. The material is concrete with Young's modulus of 21 GPa. Note that basic units are adhesively connected with each other at the domain of *C*, as shown in Fig. 9. For investigating the mechanical properties of GS geometry, four load conditions are assigned in the numerical example. A unit load of 1 kN is assigned on the tip of the horizontal component. The sum of the absolute values of the loads is set to be the same (16 kN) in all cases. Fig. 10 represents the loading pattern.

Table 1 shows the result of FE analysis. The maximum displacement in each direction is listed. Notably, we express d_{xy} and d_{xyz} as $d_{xy} = \sqrt{d_x^{\,2} + d_y^{\,2}}$ and $d_{xyz} = \sqrt{d_x^{\,2} + d_y^{\,2} + d_z^{\,2}}$, respectively. Stress distribution in the case of pattern A subjected to load of CLV can be seen in Fig. 11. Fig. 12 represents the distribution of displacement against CLT. As seen in Table 2, it can be observed that GS geometry has good stiffness against the vertical load. As seen in Fig. 11, it can be found that the vertical and horizontal components behave as the conventional beams and columns, respectively. Contrarywise, a large displacement can be confirmed when the structure is subjected to lateral and torsional loads, as seen in Table 1 and Fig. 12, due to the geometry, which is formed by a rotating array of basic units. From a view of practical design, GS geometry as a building structure is needed proper reinforcement for specific loading conditions. On the other hand, this structural behavior suggests a possibility of a unique microscopically arranged material.



(a) (b)

Figure 9. FE model: (a) pattern A, and (b) pattern B.

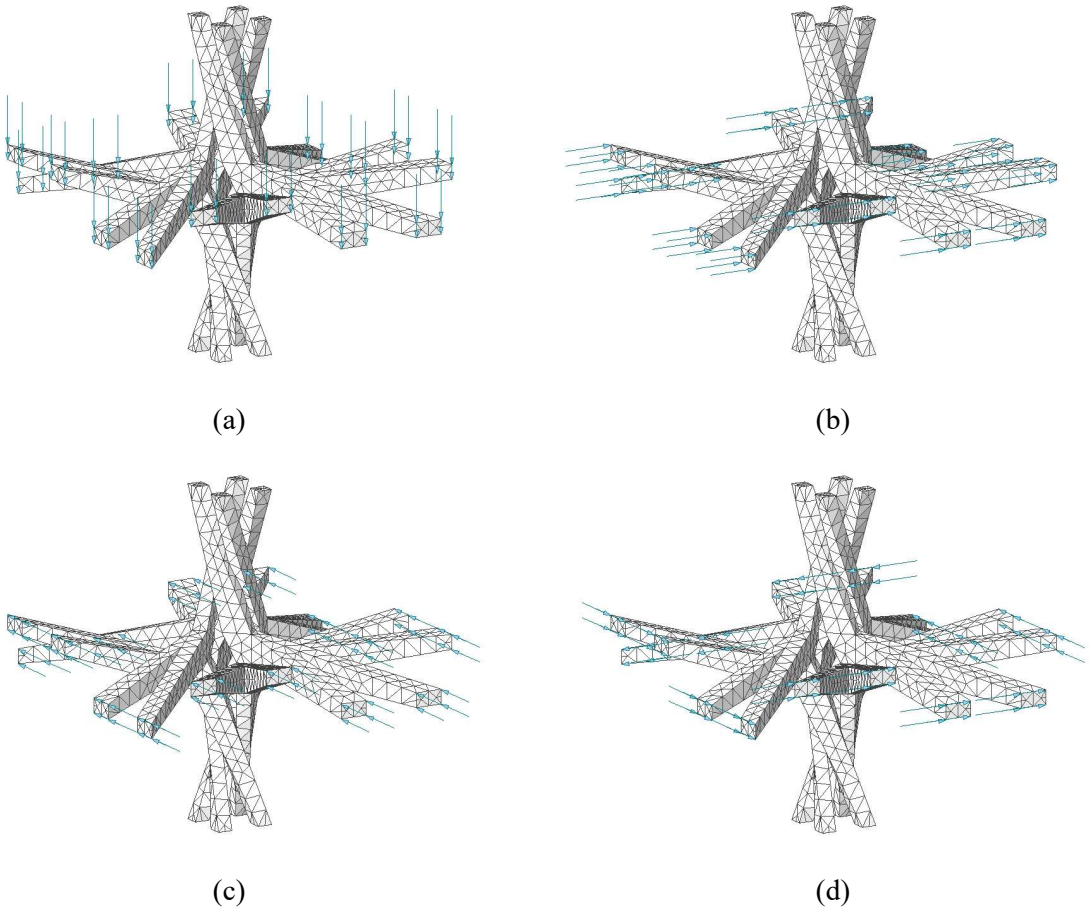


Figure 10. Distribution of nodal loads in case of pattern A: (a) CLV, (b) CLHx, (c) CLHy, and (d) CLT.

Table 1. Maximum displacement in each loading case (unit: mm).

		$\lvert d_x \rvert_{\max}$	$\lvert d_y \rvert_{\max}$	$\lvert d_z \rvert_{\max}$	$d_{xy\max}$	$d_{xyz\max}$
Pattern A	CLV	0.15	0.15	**0.41**	0.15	0.43
	CLHx	1.43	0.64	0.94	1.54	1.79
	CLHy	0.63	1.42	0.93	1.52	1.77
	CLT	2.93	2.93	0.37	**3.86**	3.86
Pattern B	CLV	0.50	0.50	**1.76**	0.62	1.85
	CLHx	10.21	1.40	5.88	10.30	11.54
	CLHy	1.43	10.22	5.89	10.32	11.56
	CLT	7.23	7.24	0.60	**9.49**	9.51

Notion: $d_{xy\max} = \max(\sqrt{d_x^{\,2} + d_y^{\,2}})$, $d_{xyz\max} = \max(\sqrt{d_x^{\,2} + d_y^{\,2} + d_z^{\,2}})$

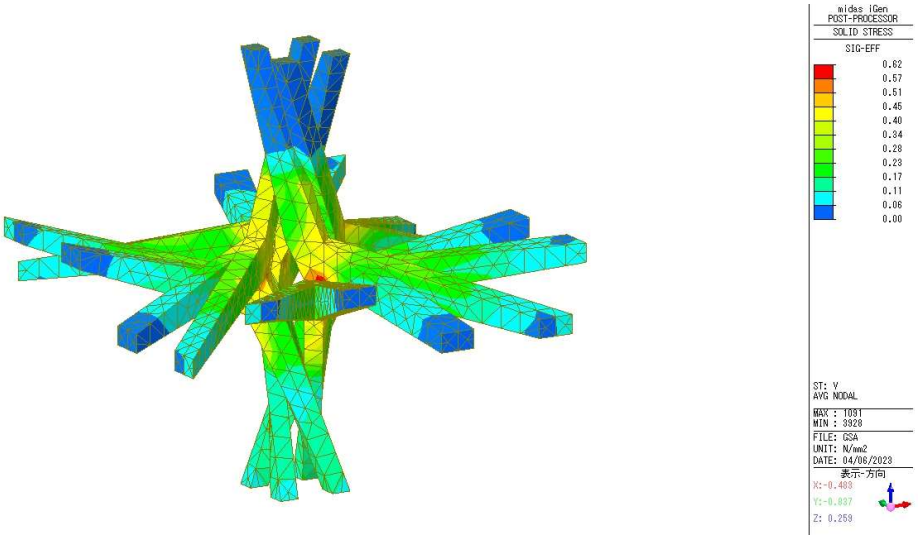
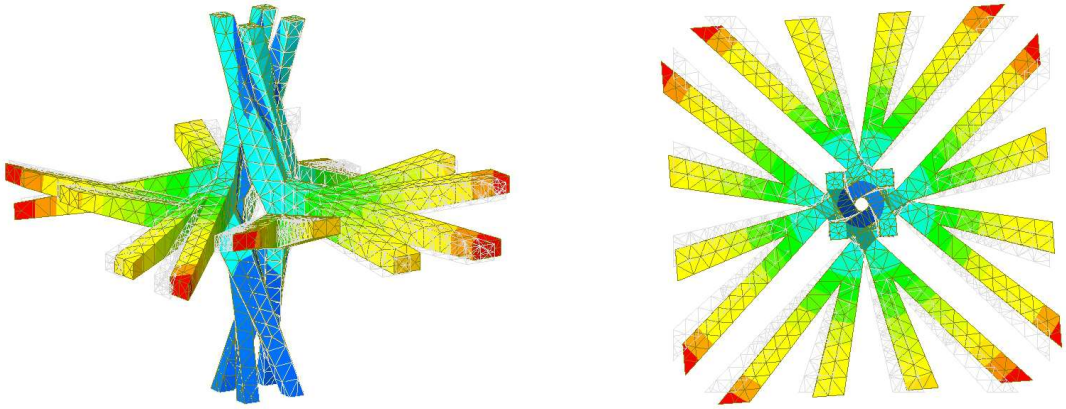


Figure 11. Distribution of von-Mises stress in case of pattern A with nodal loads of CLV.



(a) (b)

Figure 12. Distribution of von-Mises stress in case of pattern A with nodal loads of CLT.

4. Conclusion

In this study, we reproduce the GS proposed by Wachsmann observe its mechanical characteristics as an actual structure. Referring to the previous literature, GS is reproduced by using 3D CAD software. Through observing the obtained geometry and comparison with the original model and previous example, we propose an improved generating algorithm. Additionally, linear static FE analysis is conducted to investigate the mechanical properties. The potential applications of the GS for architectural geometry are discussed through numerical examples. The main conclusion can be summarized as follows,

(1) We reproduced the GS geometry based on Wachsman's algorithm written in previous literature. Through reproduction using 3D CAD, we identify an issue regarding the arrangement of the joints. Furthermore, a properly jointed geometry can be obtained by the updated algorithm.

(2) FE analysis is performed using the updated GS geometry under various loads. It can be confirmed that the GS geometry has good rigidity subjected to vertical load. On the other hand, it can be found to deform significantly subjected to lateral and torsional loads.

Designing GS geometry as a building structure, it should be properly reinforced for specific loading conditions. On the other hand, it suggests that this structure have very different stiffnesses in different directions. The authors think there is a possibility of a unique microscopically arranged material and further investigation of the physical behavior is needed.

References

[1] K.Wachsmann, *The Turning Point of Building: Structure and Design*, Reinhold Publishing Corp., 1961.
[2] M. Burkhalter, C. Sumi, F. Gramazio, M. Kohler, and H. Mayer, *Konrad Wachsmann and the Grapevine Structure*, Park Book, 2018.
[3] M. Burkhalter, C. Sumi, *"Konrad Wachsmann's Grapevine Structure: Timber Variations on a Pre-Existing Concept,"* Architectural Theory Review, Vol. 25: Issue 1-2, pp. 267-278, 2021.
[4] V. Paris, A. Pizzigoni, and S. Adriaenssens, "Statics of self-balancing masonry domes constructed with a cross-herringbone spiraling pattern," *Engineering Structures*, Vo. 215, 110440, 2020.
[5] A. Tomas and P. Marti, Optimality of Candela's concrete shells: a study of his posthumous design, *Journal of International Association for Shell and Spatial Structures*, Vol. 51(1), pp. 67–77, March 2010.
[6] G. M. Barazzeta, E. Mossa, C. Poggi, and M. Simoncelli, "The airplane hangars of Pier Luigi Nervi: digital and scaled models, " *Journal of the International Association for Shell and Spatial Structures*, Vol. 61, No. 3, pp. 187-200, September 2020.
[7] E. Andrzejewski, M. Shaffer, "Assembling the Assembler: Reanimating the "Lost" Motion Machine of Wachsmann, Bollinger, and Mendoza, " *Technology|Architecture + Design*, Vol. 6, Issue 1, pp. 90-99, 2022.

Proceedings of the IASS Annual Symposium 2023
Integration of Design and Fabrication
10–14 July 2023, Melbourne, Australia
Y.M. Xie, J. Burry, T.U. Lee and J. Ma (eds.)

Shape generation of hexagonal lattice shell consisting of edge offset mesh

Ryo WATADA*, Makoto OHSAKI[a]

* Department of Architectural and Environmental Design, Osaka Sangyo University, Japan
3-1-1 Nakagaito, Daito, Osaka, 574-8530, JAPAN
watada@edd.osaka-sandai.ac.jp

[a] Department of Architecture and Architectural Engineering, Kyoto University, Japan

Abstract

In the process of designing latticed shells, it is important that the lattice members have the same cross-section (height) and no torsion to avoid eccentricity at the joints and reduce the manufacturing cost, which is known as the property of edge offset mesh (EO mesh). In this study, we propose a two-level optimization approach to generating hexagonal meshes which satisfy the properties of EO mesh for all edges. Using the proposed method, a lattice shell can be designed so that all beams are torsion-free and all beam sizes are equal. In our method, each face of the EO mesh is sequentially added in a manner that the new face is always parallel with the Koebe mesh determined by Möbius transformation from a planar circular net. It is possible in our method to control the shape of each face more directly and individually than the existing methods by varying the edge length parameters of each face. The proposed method generates an EO mesh whose shape is close to a predefined target surface. An example shows that the proposed method can be applied to design of hexagonal lattice shell structures in which all beams and joints have no torsion, all beams have the same height, and therefore, requires less cost and time for construction.

Keywords: edge offset mesh, mesh offset, hexagonal lattice shell, Möbius transformation, torsion-free node, optimization

1. Introduction

Latticed shells are composed of straight lattice beams and are widely applied to the design of architectural roofs. A latticed shell can be regarded as a pair of a polygonal mesh M and its offset mesh M' as shown in Fig. 1 to incorporate the heights of beams. Mesh M consists of nodes $\boldsymbol{x}_i \in \mathbb{R}^3$ and edges e_{ij}, and the offset mesh M' consists of the same number of offset nodes $\boldsymbol{x}_i{}'$ and edges $e_{ij}{}'$. A line passing through $\boldsymbol{x}_i$ and $\boldsymbol{x}_i'$ is called *node axis* A_i. A quadrilateral bounded by two edges e_{ij} and $e_{ij}{}'$, and two node axes A_i and A_j is called *central plane* [1] and describes the symmetry plane of a lattice beam.

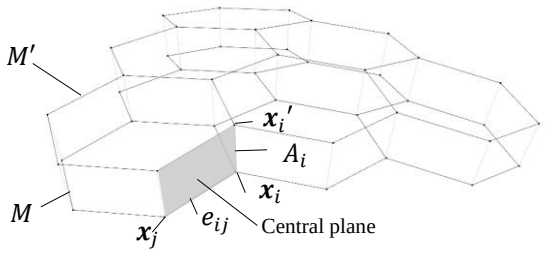


Figure 1. Mesh M and its offset mesh M' determine quadrilateral central planes describing the symmetry planes of the beams

Copyright © 2023 by Ryo WATADA and Makoto OHSAKI. Published in the Proceedings of the IASS Annual Symposium 2023 with permission.

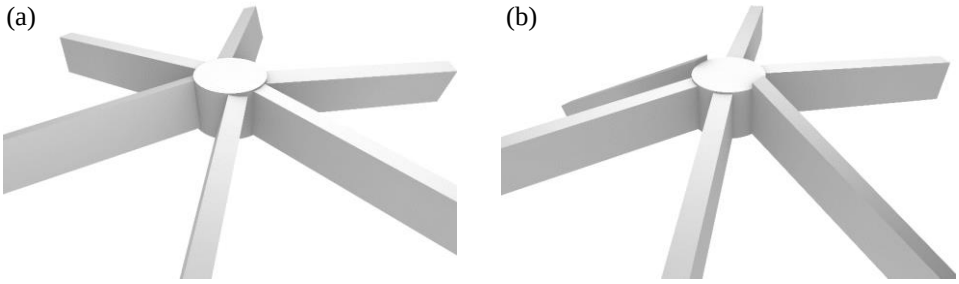


Figure 2. (a) A node with geometric torsion, (b) Kinks due to variation of vertical angles

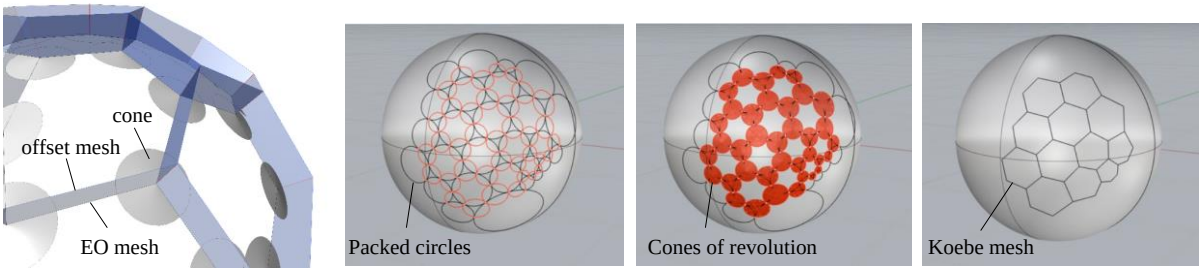
Lattice shell structures constructed by a mesh and its offset mesh generally have several geometric difficulties for construction as shown in Fig. 2. Geometric torsion as shown in Fig. 2(a) occurs when there is no common node axis which is contained in the all central planes of incoming beams. Figure 2(b) shows kinks due to variation of vertical angles between node axis and central axes of beams. Constructing a mesh with planar faces without torsion and kink is highly important for reducing cost and time for construction.

An *edge offset mesh (EO mesh)* is a offset mesh in which the distance of corresponding parallel edges e_{ij} and $e_{ij}{}'$ equals d for every edge [1]. It is known that a latticed shell composed of EO mesh has planar faces with no geometric torsion and kink. A condition for EO meshes is that all edges attached to a node are on a same cone of revolution whose axis is consistent with the node axis, as shown in Fig. 3(a).

Assume two meshes M_1 and M_0 which have the same numbers of nodes and edges with the same connectivity. The mesh M_1 is regarded as *parallel* with the mesh M_0 if the corresponding edges of M_1 and M_0 are all parallel. It is known that a mesh M is EO mesh if and only if M is parallel with a *Koebe mesh* as shown in Fig. 3(d). Koebe meshes are generated from circles packed on a sphere as shown in Fig. 3(b) in black. The edges of the Koebe mesh are determined as common tangent lines of adjacent circles, and nodes of the Koebe mesh are defined as intersections of the tangent lines, as shown in Figs. 3(c) and 3(d). In Fig. 3(c), red cones of revolution are tangent to adjacent edges and have axes passing the center of the sphere.

For obtaining EO meshes from Koebe meshes, Pottmann et al. [1] proposed optimization-based approach. In their method, the variables of the optimization problem are nodal coordinates of the EO mesh and the corresponding Koebe mesh, where the distance to a reference surface and a function representing the fairness of the mesh are considered as the objective functions. Conditions that the obtained meshes only have the planar faces and are parallel with a Koebe mesh are incorporated in penalty functions which are added to the objective functions. The obtained meshes have the property that the distances of all of the edges are approximately constant (*approximate offset*).

Koebe mesh is obtained from the patterns of adjacent circles as shown in Figs. 3(b)-(d). For considering the transformation keeping the angle between adjacent circles unchanged, Möbius geometry [2] has



(a) (b) (c) (d)

Figure 3. EO mesh and related cones of revolution: (a) EO mesh, (b)-(d) Generating a Koebe mesh from circles packed on a sphere

been used in previous researches, e.g., by Liu et al. [3]. Pottmann et al. [1] regarded the offset transformation for generating an EO mesh as one of the Laguerre transformations.

In this study, we propose a method using *two-level optimization approach* to obtain a hexagonal latticed shell satisfying the properties of EO mesh, and its shape is close to the predetermined surface. Two-level optimization consists of *mesh-level* and *face-level*. In our method, variables in a mesh-level optimization are parameters related to Möbius transformation which control the shape of Koebe mesh. For each solution of the mesh-level optimization, the face-level optimization procedures are sequentially executed for each face when it is newly added to an EO mesh, where the variables of the face-level optimization are the edge lengths of each new face so that the new face keeps parallelity to the tentatively decided Koebe mesh. The obtained mesh is an EO mesh where all edge offsets are strictly constant and the planarity of each face and beam is maintained. The effectiveness of this method is demonstrated by a numerical example.

2. Methodology

2.1. Generating Koebe mesh by Möbius transformation

Consider $z \in \mathbb{C}$ as a complex variable. A Möbius transformation on the complex plane is expressed as

$$f(z) = \frac{az + b}{cz + d}, \qquad (a, b, c, d \in \mathbb{C}, ad - bc \neq 0) \tag{1}$$

Figure 4(a) shows a base 2D circle pattern P_0 and its Möbius transformed pattern on the complex plane, which we simply called XY plane in this study. Equation (1) can alternatively be written as follows:

$$f(z) = \rho e^{i\theta}\left(\frac{1}{z + \alpha} + \beta\right) \tag{2}$$

where α and β are complex numbers, ρ is a positive real number, θ is a real number satisfying $-\pi \leq \theta < \pi$ and i is the imaginary unit. Assuming $\alpha = \alpha_{\mathrm{R}} + i\alpha_{\mathrm{I}}$ and $\beta = \beta_{\mathrm{R}} + i\beta_{\mathrm{I}}$, the Möbius

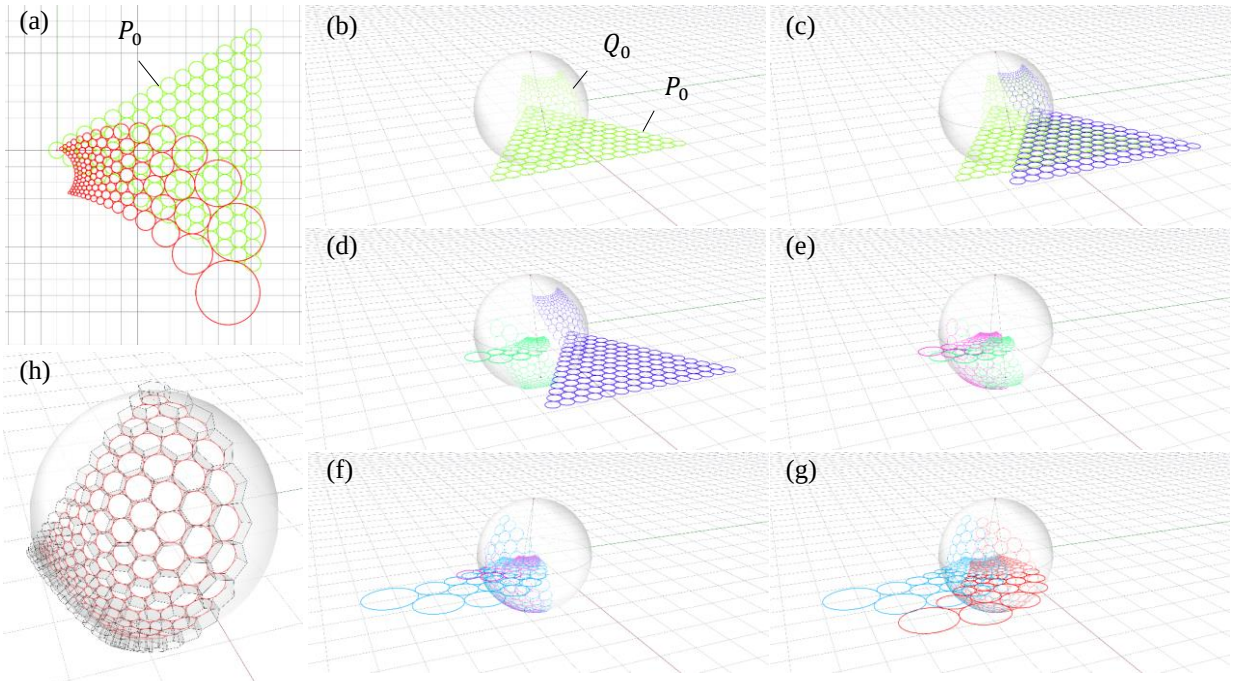


Figure 4. Möbius transformation on the complex plane; (a) Base 2D circle pattern P_0 and its transformed pattern, (b) Inverse stereographic projection from XY-plane to the north pole of a unit sphere, (c)-(g) Decomposition of Möbius transformation, (h) Obtained circle pattern Q on the unit sphere and corresponding Koebe mesh M

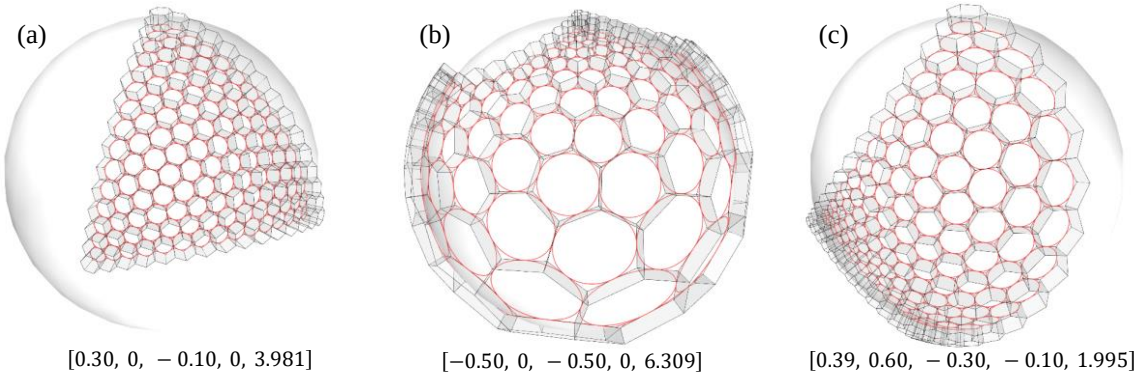


Figure 5. Generation of Koebe meshes by various Möbius transformation parameters from P_0 with the corresponding Möbius transformation parameters $[\alpha_R, \alpha_I, \beta_R, \beta_I, \rho]$

transformation can be determined by six real parameters $\alpha_R, \alpha_I, \beta_R, \beta_I, \rho$ and θ, which we call *Möbius transformation parameters* in this study. The circle pattern P_0 can be expressed as a circle pattern Q_0 on a unit sphere by inverse stereographic projection as shown in Fig. 4(b). Then, the transformation expressed by Eq. (2) acting on P_0 on the XY-plane and Q_0 on the unit sphere can be described as a combination of following steps; translation $z \to z + \alpha$ as shown in Fig. 4(c), inversion and reflection with respect to the real axis $z \to 1/z$ as shown in Fig. 4(d), translation $z \to z + \beta$ as shown in Fig. 4(e), dilation $z \to \rho z$ as shown in Fig. 4(f), and counterclockwise rotation $z \to e^{i\theta} z$ as shown in Fig. 4(g). After the Möbius transformation, rigid body rotation of the obtained circle pattern on the unit sphere to a specified position derives a circle pattern Q on the unit sphere, which generates a corresponding Koebe mesh M as shown in Fig. 4(h) with the corresponding five parameters $\alpha_R, \alpha_I, \beta_R, \beta_I$ and ρ, where the sixth parameter θ is omitted because it only causes rigid body rotation. Figure 5 shows various Koebe meshes and the corresponding Möbius transformation parameters.

2.2. Sequential face generation of EO mesh

EO meshes can be generated as a parallel mesh of a Koebe mesh as shown in Fig. 6. In this study, we propose a sequential face generation method of EO mesh keeping the parallelity to the Koebe mesh as shown in Fig. 7. The number of parameters for the face generation method depends on the number of

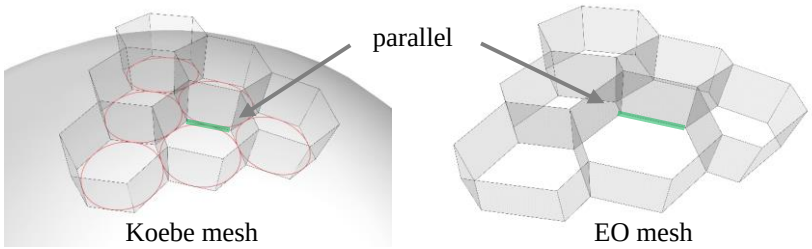


Figure 6. EO mesh as a parallel mesh of a Koebe mesh.

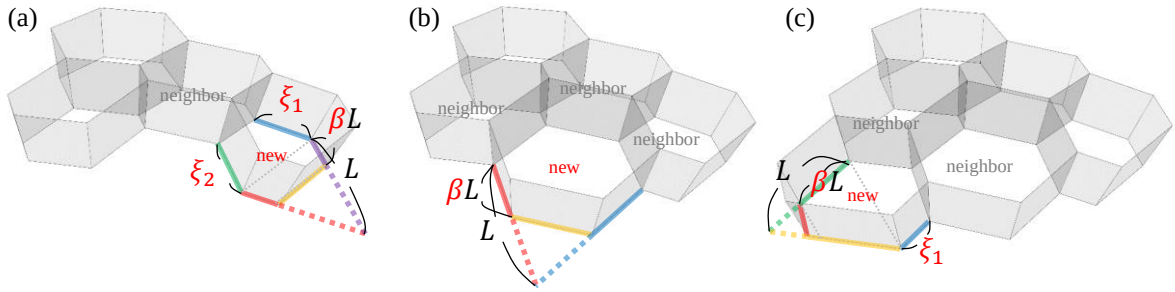


Figure 7. Sequential face generation of EO mesh; (a) One neighboring face, (b) Three neighboring faces, (c) Two neighboring faces

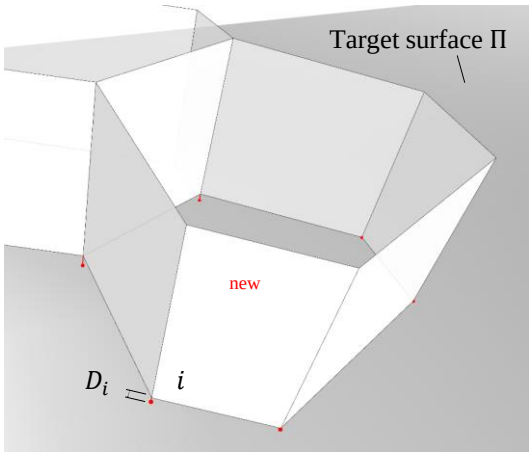


Figure 8. Distance D_i between node i and predetermined target surface Π

already set neighboring faces:

1. If the number of already set neighboring faces is one, the new face can be defined by two edge length parameters ξ_1 and ξ_2 and one edge length ratio parameter β as shown in Fig. 7(a).
2. If the number of already set neighboring faces is three, the new face can be defined by one parameter β as shown in Fig. 7(b).
3. If the number of already set neighboring faces is two, the new face can be defined by two parameters ξ_1 and β as shown in Fig. 7(c).

Parameters ξ_1, ξ_2 and β are defined so that the new face is close to a predefined target surface Π as shown in Fig. 8. Let D_i denote the distance between Π and node i in the new face f. For each face, parameters ξ_1, ξ_2 and β are defined by the following *face-level optimization problem FP*.

$$\begin{aligned} &\text{minimize} && \widehat{D}_f = \max_{i \in I_f} D_i \\ &\text{subject to} && \xi_i^{\mathrm{L}} \le \xi_i \le \xi_i^{\mathrm{U}} \qquad (FP) \\ & && \beta^{\mathrm{L}} \le \beta \le \beta^{\mathrm{U}} \end{aligned}$$

This optimization problem has at most three variables; i.e., each problem is very small.

Repeating the calcuration of $\widehat{D}_f$ and the generation of a new face, all faces are generated and the sum of $\widehat{D}_f$ denoted by $\widehat{D}_{\mathrm{SUM}} = \sum_f \widehat{D}_f$ is obtained. Under the condition that the base 2D circle pattern P_0 is unchanged, the sum $\widehat{D}_{\mathrm{SUM}}$ is uniquely determined with respect to the Möbius transformation parameters $\alpha_{\mathrm{R}}, \alpha_{\mathrm{I}}, \beta_{\mathrm{R}}, \beta_{\mathrm{I}}$ and ρ which control the shape of the referenced Koebe mesh.

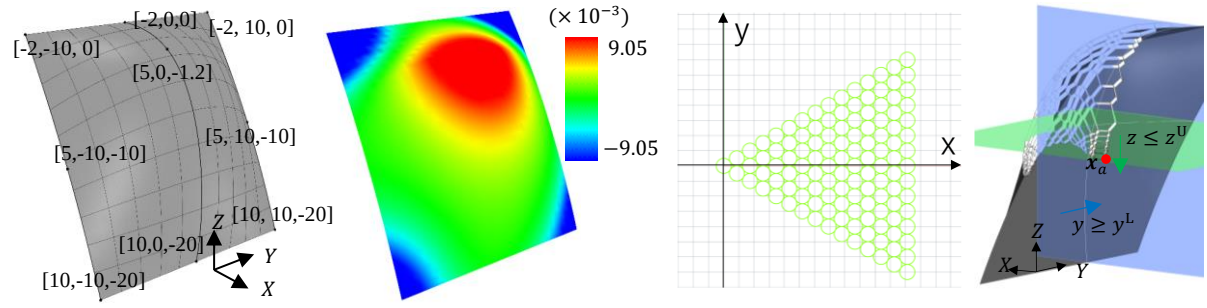
The EO mesh which mostly follows the target surface Π is determined by minimizing the following objective function OBJ with respect to $\alpha_{\mathrm{R}}, \alpha_{\mathrm{I}}, \beta_{\mathrm{R}}, \beta_{\mathrm{I}}$ and ρ, which we call *mesh-level optimization*:

$$OBJ = \widehat{D}_{\mathrm{SUM}} + F_{\mathrm{penalty}} \tag{3}$$

where $F_{\mathrm{penalty}}(\ge 0)$ is a penalty function for considering some additional geometric constraints which is equal to 0 when the constraints are satisfied.

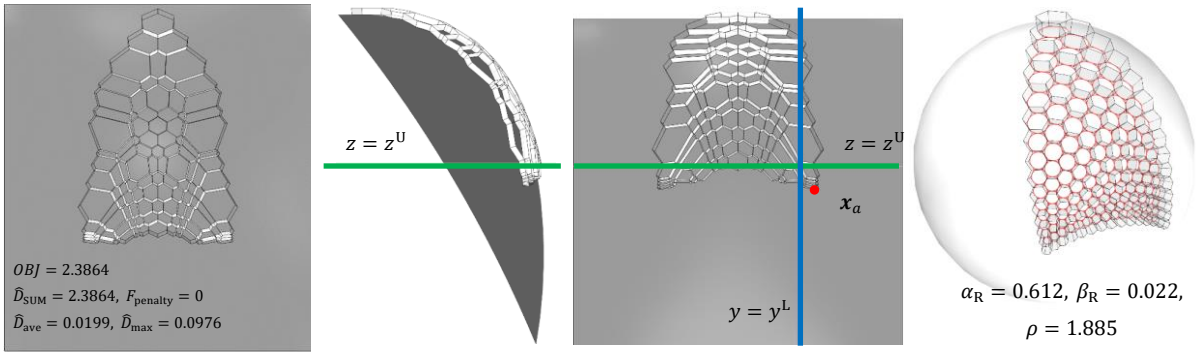
3. Numerical example

As a numerical example, we find an EO mesh which approximates a target surface Π as shown in Fig. 9(a). The surface Π is an interpolated NURBS surface including nine control points as illustrated in Fig. 9(a), and is symmetric with respect to the central XZ-plane. The Gaussian curvature of Π is distributed



(a) (b) (c) (d)

Figure 9. A numerical example; (a) Target surface Π, (b) Gaussian curvature distribution of Π, (c) Base 2D circle pattern P_0, (d) Geometric constraints of node $\boldsymbol{x}_a$



(a) (b) (c) (d)

Figure 10. Obtained EO mesh; (a) Bird's-eye view, (b) XZ view, (c)YZ view, (d) Associated Koebe mesh and corresponding Möbius transformation parameters

as shown in Fig. 9(b). The base circle pattern P_0 is as shown in Fig. 9(c), in which radii of all circles are 0.1. For consideration of the symmetry, only three Möbius transformation parameters α_{R}, β_{R} and ρ are considered and only half of the faces have independent variables ξ_i and β. The boundaries β^{L} and β^{U} of FP are 0.1 and 0.6, respectively, and ξ_i^{L} and ξ_i^{U} are $0.2L_{\mathrm{B}}$ and $1.3L_{\mathrm{B}}$, respectively, where L_{B} is the average of edge lengths in the neighboring faces. As additional geometric constraints, F_{penalty} is set to have a large positive value if a corner node $\boldsymbol{x}_a$ is not included in the region $y \geq y^{\mathrm{L}}$ or $z \leq z^{\mathrm{U}}$ as shown in Fig. 9(d), where y^{L} and z^{U} are assigned as 3.6 and –9.0, respectively. The distance D_i is calculated using RhinoCommon API. The face-level optimization FP is solved sequentially by SciPy SLSQP, and the mesh-level optimization minimizing OBJ in Eq. (3) is solved by modeFRONTIER 2022R3 Simulated Annealing Solver.

Figures 10(a)-(c) show the obtained EO mesh. It is seen from the figure that the shape of the obtained mesh well approximates the target surface and the node $\boldsymbol{x}_a$ satisfies the geometrical constraints. The average of $\hat{D}_f$ denoted by $\hat{D}_{\mathrm{ave}}$ and the max of $\hat{D}_f$ denoted by $\hat{D}_{\mathrm{max}}$ are 0.0199 and 0.0976, respectively, as shown in Fig. 10(a). Associated Koebe mesh and the corresponding Möbius transformation parameters are illustrated in Fig. 10(d).

4. Conclusion

In this study, a two-level optimization approach has been proposed to obtain a hexagonal latticed shell with EO mesh whose shape is close to a predefined target surface. The numerical example shows that the proposed method generates the EO mesh whose shape is similar to the predefined freeform target surface, strictly satisfying requirements of constant edge offset distance and face planarity.

Acknowledgements

This work was supported by JST CREST JPMJCR1911.

References

[1] H. Pottmann, Y. Liu, J. Wallner, A. Bobenko and W. Wang, "Geometry of multi-layer freeform structures for architecture," *ACM SIGGRAPH 2007 papers*, pp. 65–es, 2007.

[2] A. Bobenko and Y. B. Suris, Discrete Differential Geometry: Integrable Structure, American Mathematical Society, 2008.

[3] Y. Liu, H. Pottmann, J. Wallner, Y. L. Yang and W. Wang, "Geometric modeling with conical meshes and developable surfaces," *ACM SIGGRAPH 2006 papers*, pp. 681–689, 2006.

IASS 2023
July 10–14 Melbourne
Integration of Design and Fabrication

Proceedings of the IASS Annual Symposium 2023
Integration of Design and Fabrication
10–14 July 2023, Melbourne, Australia
Y.M. Xie, J. Burry, T.U. Lee and J. Ma (eds.)

Structural features of Dong'an lake stadium roof

Yuan FENG[*], Quan ZHOU[a], Xin An XIANG[a], Wen Ming CHEN[a], Li YAO[a]

[a,*] China Southwest Architectural Design and Research Institute Corp. Ltd
866 Tianfu Avenue North Section, Chengdu, China
xnyfy@vip.163.com

Abstract

The Dong'an Lake Sports Park Stadium will serve as the main venue for the opening ceremony of the 31st World University Games. Its roof is a perfect circle with a projected diameter of 295m and a cantilever length of 45m. In order to show the history and culture of Chengdu, the Sun Bird pattern was presented on the roof. Through fine structural design, the architectural vision was realized on the light roof with extra-long, large-span and large- overhang. Different from the conventional design, a 25m wide viewing platform of 300m long around the perimeter of the roof was set on the large-span steel roof, enabling visitors to overlook Dong'an Lake Park from different angles and enjoy the beautiful scenery of the landscapes. A single-layer arc cross grid was preferred as the platform support. Four cylinders providing vertical traffic for the 29m platform were arranged on the south side of the building. Considering the complex spatial relationship between the steel roof, large platform and vertical traffic cylinders, a refined design was carried out. In this paper, the technical innovations of the structural design to meet the requirements of architectural functions and cultural creativity were explained in terms of the selection of structural system, optimization of structural arrangement, resolution of complex space and realization of rapid construction.

Keywords: stadium roof, sun bird pattern, high altitude viewing platform, large-span, complex spatial relationship

1. Project overview

The 31st World University Games will be held in Chengdu, and Dong'an Lake Stadium will be the main venue for the opening ceremony, which will not only meet the requirements of the event and its later operation, but also carry the mission to showcase Chengdu as a city with a long history and culture to the world. The architectural scheme uses a "flying saucer" shape to express the image of Chengdu University Games with a sense of technology and sports, symbolizing hope, brightness, and unity. The roof and the infield present the Sun Bird pattern, expressing the combination of the cultural heritage of Sichuan and the spirit of the World University Games across time and space. An extra-long high altitude viewing platform is set up on the roof to provide a beautiful view of Longquan Mountain and Dong'an Lake (Figure 1-3).

Copyright © 2023 by Yuan FENG, Quan ZHOU, Xin An XIANG, Wen Ming CHEN and Li YAO. Published in the Proceedings of the IASS Annual Symposium 2023 with permission.



Figure 1. Aerial view of the northwest corner of the stadium



Figure 2. A distant view of the southeast side of the stadium

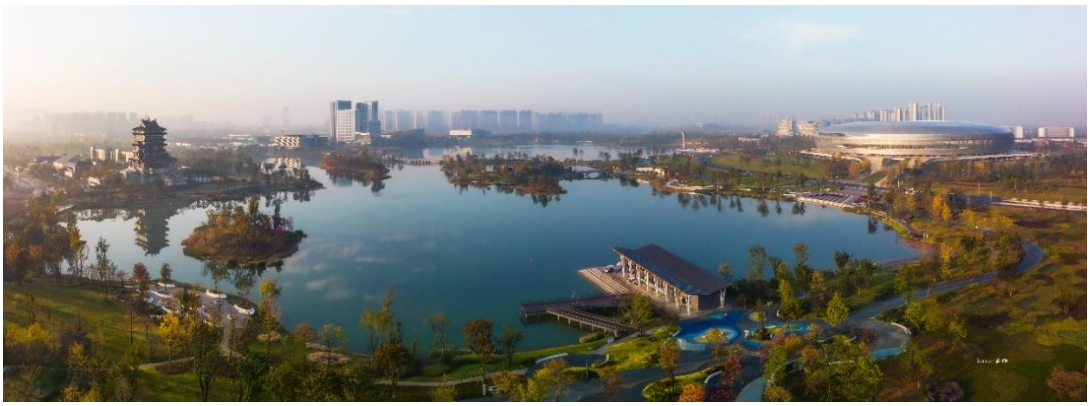
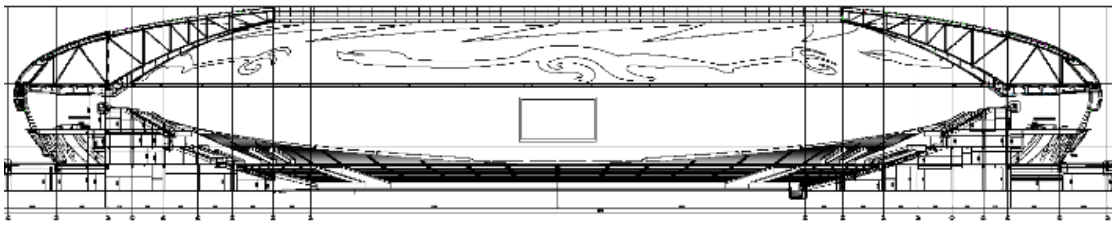


Figure 3. The stadium with a view of the mountains and the lake

The construction area of Dong'an Lake Stadium is about 120000 m^2, which is a Grade A stadium with 40000 seats. There are 5 floors above the ground, with a building height of 49.8m, and the highest point of the concrete grandstand is 22.4m [1]. The diameter of the roof is 295m, and the overhanging length of the canopy is 45m (Figure 4-5). The roof structure consists of 88 cantilever trusses, of which 44 main trusses are supported by concrete columns and 44 secondary trusses are supported by inner three-dimensional transfer trusses. The facade consists of 88 groups of crossed circular tubes forming a single-layer grid, supported by finished hinge bearings on the 7.000m platform.

(a)



(b)

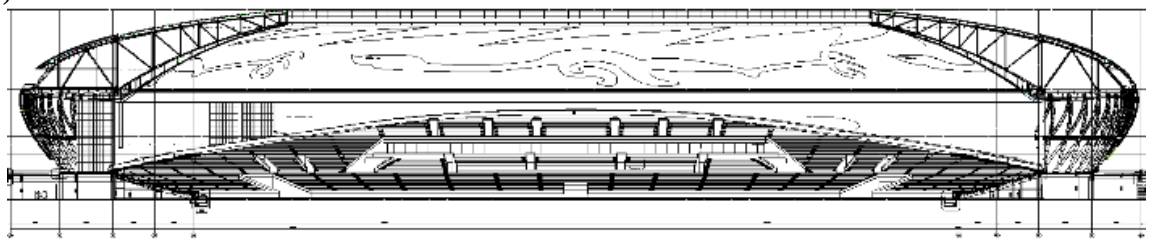


Figure 4. Stadium section drawing: (a) east and west sectional view of the stadium, (b) south and north sectional view of the stadium

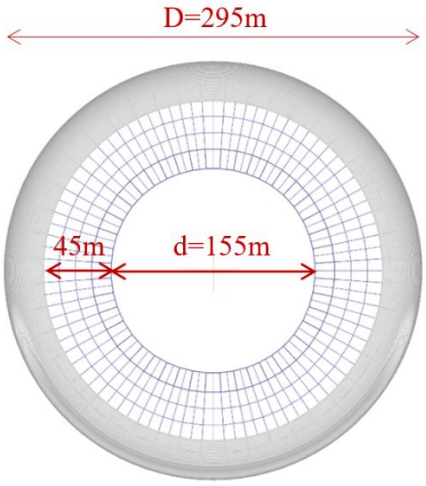


Figure 5. Schematic diagram of roof structure size

2. Structural features of the stadium

2.1. Perfect realization of the sun bird pattern

The Sun Bird pattern is presented on both the upper and lower surfaces of the stadium roof, and the long and splendid history and culture can be felt both outside and inside the stadium. The Sun Bird pattern needs to be printed on the roof covering material, and the design compared various roof materials and finally adopted glass roof. The colored glass can better represent the pattern, and the material has good

durability and self-cleaning property. The total area of roof glass is approximately 27000 square meters, which is assembled by 12540 pieces of colored glazed glass. The Sun Bird pattern on the lower surface is completed by polyester fiber grid membrane, which is hung on the lower chord of the steel roof as the ceiling of the field (Figure 6-7).



Figure 6. The sun bird pattern is presented on the glass roof

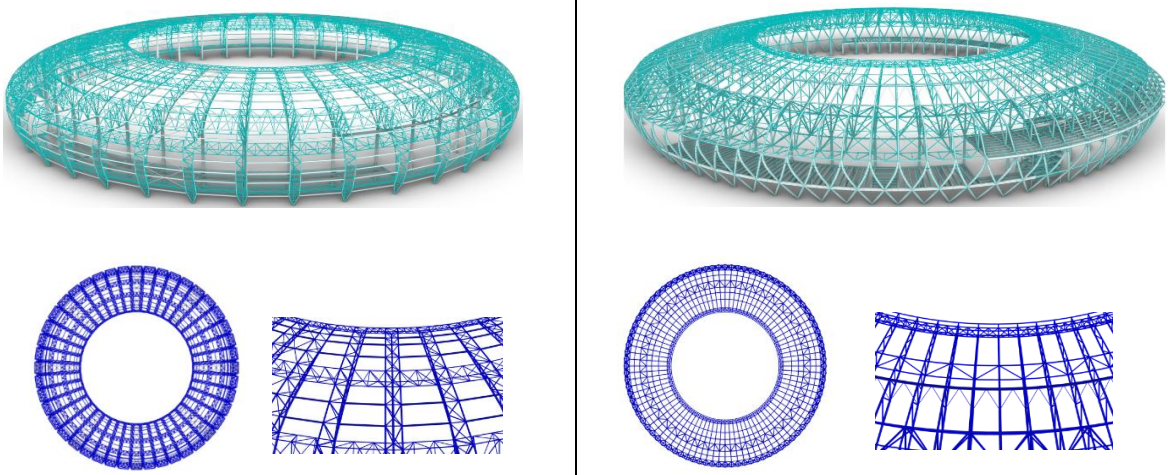


Figure 7. The sun bird pattern is presented on the lower chord membrane

Two structural forms, plane truss and triangular space truss, were compared in the overhang part of the structure. The triangular space truss structure has good overall stability, but due to the large number of members, it will be printed on the inner ceiling membrane in daylight, affecting the Sun Bird pattern. The plane truss projection surface has fewer members, so the plane cantilever truss was ultimately selected (Figure 8).

For the plane truss with a 45-meter overhang, in order to solve the problem of out-of-plane stability of the plane truss, in addition to the edge sealing truss, two annular trusses are installed in the overhang area. One of the annular trusses is located at the boundary between the sun and the bird, and the other truss evacuates the bottom chord to provide out-of-plane support with web members (Figure 9-10). At the same time, efforts are made to achieve the alignment relationship between the glass unit and the rod

to reduce the impact of excess roof lines. By adjusting the curvature of the top chord of the truss and the size of the glass parting plate, and at the same time adjusting the arrangement of the webs of the truss, the structural reasonableness was finally judged by the angle formed by the webs (Figure 11). The shape of the overhanging joist was also determined by combining the curvature of the lower chord membrane.



The triangular space truss　　The plane truss

Figure 8. Comparison of roof structure schemes

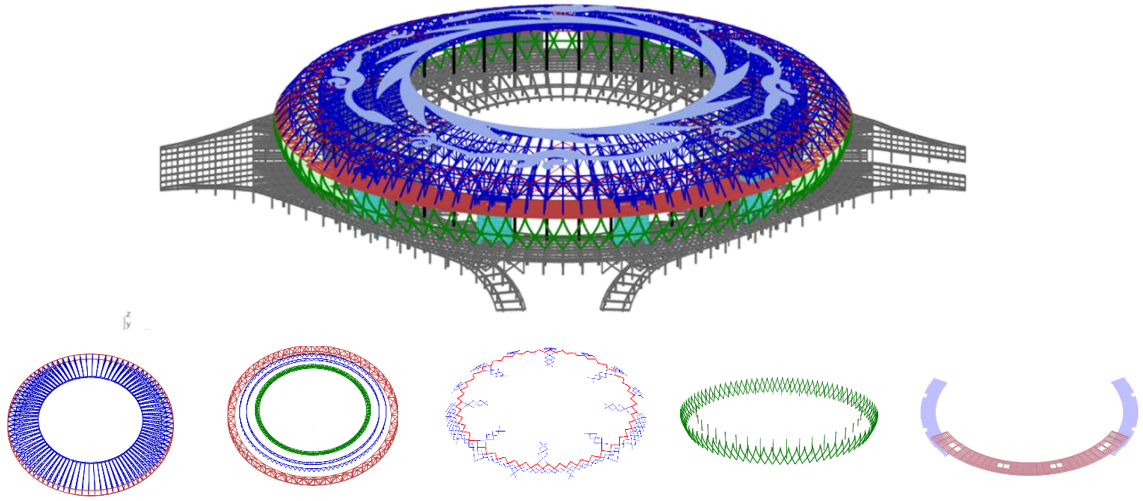


Figure 9. Structural composition of the stadium

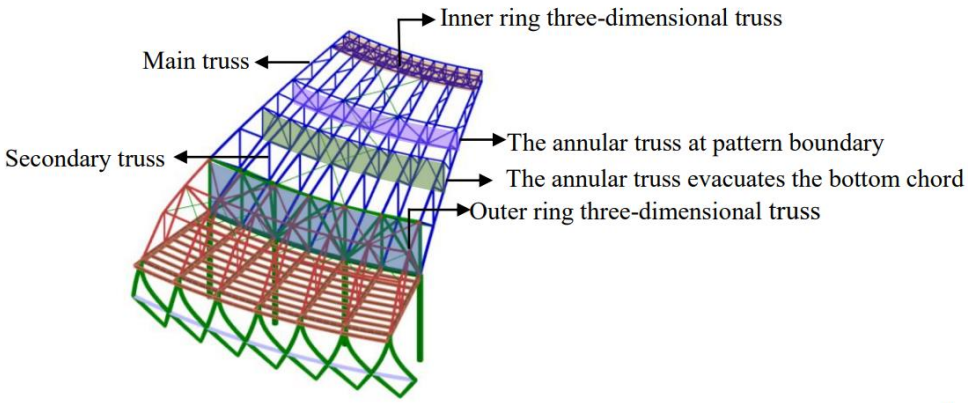


Figure10. Schematic diagram of each partition of the structure



Figure 11. Comparison of roof structure model and completed effect

2.2. Complex spatial relationship between the steel roof, viewing platform and the vertical traffic cylinders

Different from the conventional design, a 25m wide high altitude viewing platform of 300m long around the perimeter of the roof was set on the large-span steel roof, while two viewing platforms of approximately 165m long and 20m wide were set on the elevation of 16.6m, enabling visitors to overlook Dong'an Lake Park from different angles and enjoy the beautiful scenery of the landscapes. In order to reach the 29m viewing platform directly from the ground and meet the evacuation demand of the observation platform, four vertical traffic cylinders need to be designed for setting stairs and elevators. Due to the large size of the traffic cylinders, it is impossible to avoid the planar truss, which results in the lower chord of the truss passing through the vertical traffic cylinders, and the steel roof cannot be detached from the traffic cylinders. In order to shorten the force transmission path of the secondary truss, the lower chord of the secondary truss is connected to the vertical traffic cylinders, which better solves the deformation coordination and connection among the tube, floor, and truss (Figure 12-13). The effect of roof construction is shown in Figure 14-15.

The four vertical traffic cylinders on the south side connect the 7m platform and the 29m observation platform, while the 16.6m observation platforms on the east and west sides connect the curved single-layer cross grid of the facade with the grandstand structure. At the same time, the 16.6m observation platform is connected to the south core cylinder, and the curved single-layer cross grid of the facade is supported on the 7m large platform. Based on the complex spatial relationship between the steel roof, large platform and the vertical traffic cylinders, shrinkage and creep of the concrete were taken into account during the construction stage analysis. The single model and assembly model were considered for envelope, and the design parameters were considered in different regions to achieve a refined design.

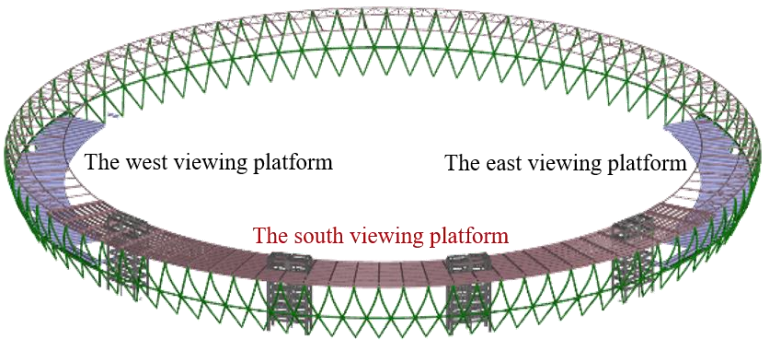


Figure 12. Diagram of the viewing platforms

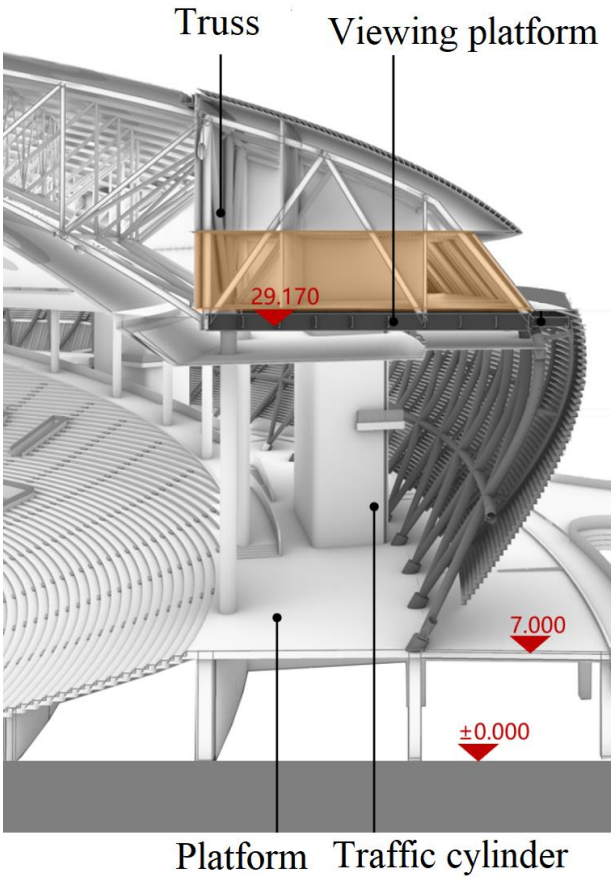


Figure 13. Section drawing of high altitude viewing platform



Figure 14. Actual view of the high altitude platform



Figure 15. The photo of the completed roof structure

2.3. Rapid construction

The construction period of the project is extremely tight, with only 23 months from construction to operation, while the average construction period of similar projects in China is 3-4 years, which poses a great challenge to both design and construction. To meet the needs of rapid construction, the stadium roof was shaped in a circle and then the circle was divided into 88 standard units to achieve

standardization and modularization of the structural system and curtain wall system. The advantages of efficient prefabrication and assembly of steel structures were exploited to improve construction efficiency and save time significantly. Figure 16 shows the roof structure under construction.



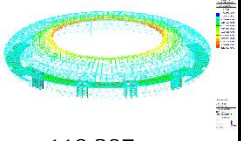
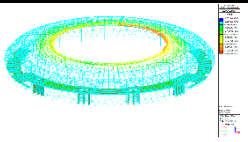
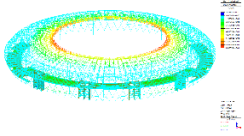
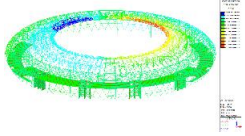
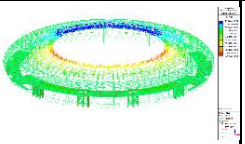
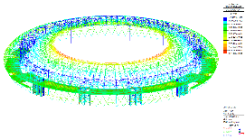
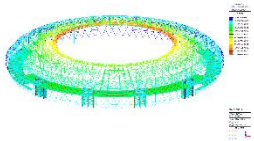
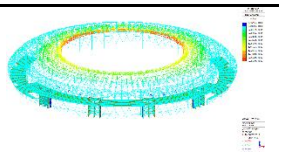
Figure 16. The roof structure under construction

3. Analysis of the roof structure

3.1. Static performance analysis of the roof structure

Considering that there are many types of rods in this project, in order to finely distinguish the importance level of rods, the rods are divided into three levels: general members, important members and key members. The static calculation of the roof structure shows that the stress ratios of the members meet the performance target requirements. The deflection-span ratio under the envelope load condition is 1/199, which meets the code [2] requirements, as shown in Table 1.

Table 1. Vertical displacement of the structure

Load case	1.0 D +1.0 L	1.0 D+1.0 L（East）	1.0 D+1.0 L（South）	1.0 D +1.0W（East）
Displacement	 -118.387mm	 -105.589mm	 -88.633mm	 -171.557mm
Load case	1.0 D +1.0 W（South）	1.0 D+1.0 T- rise	1.0 D+1.0 T-down	Envelope condition（1.0 D+1.0 W +0.7 L +0.6 T-down）
Displacement	 -130.926mm	 -54.436mm	 -137.461mm	 -226.399mm

3.2. Seismic performance analysis of the roof structure

In order to truly reflect the influence of the lower concrete structure on the upper steel structure during the earthquake, a synergistic analysis of the general assembly model was carried out. The first 4 modes of the structure are shown in Table 2, and the low-order vibration mainly focuses on the horizontal vibration of the roof, not the torsional vibration. The stress ratio of each group of rods in the response spectrum analysis meets the design requirements. Under the time history analysis of the rare earthquake (Table 3), the maximum stress ratio of key members was 0.853. The stress ratios of the remaining members were all less than 1.0, which satisfied the performance target requirements.

Table 2. The first 4 modes of the structure

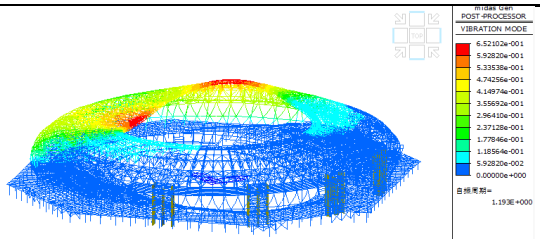
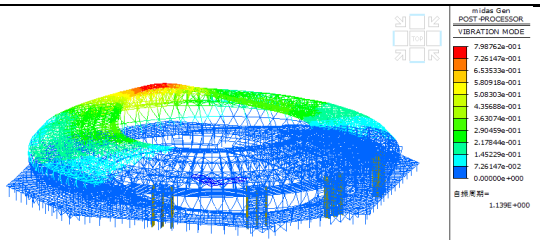
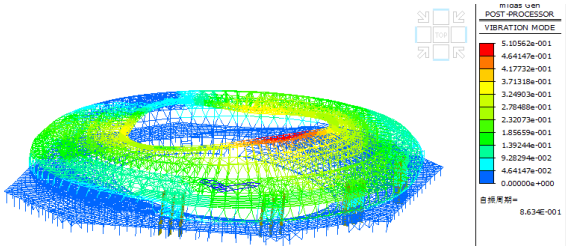
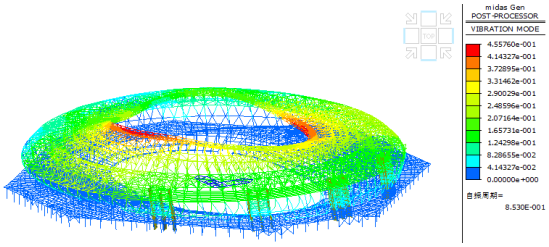
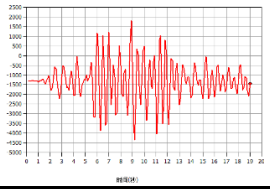
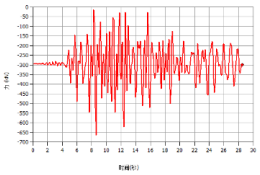
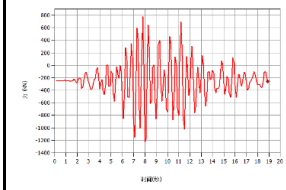
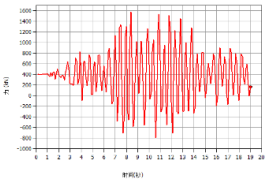
	
T1=1.193 X-direction vibration on the northeast side of the roof	T2=1.139 Y-direction vibration on the northeast side of the roof
	
T3=0.863 Y-direction vibration on the south side of the roof	T4=0.853 X-direction vibration on the east-west of the roof

Table 3. The time history analysis results of the rare earthquakes

Chord near the support	Remaining cantilever truss chords	Convert truss	Facade single-layer cross grid
			
Stress ratio 0.818	Stress ratio 0.820	Stress ratio 0.853	Stress ratio 0.701

3.3. Stability analysis of the roof structure

The stability analysis of the roof structure was carried out by using the general finite element software ANSYS, considering the double nonlinearity, and using the arc length method to track the equilibrium path of the structure to obtain the load-displacement whole process curve [3]. The stability analysis program was prepared considering the structural characteristics. The maximum initial geometric defect was taken as L/300, and the bilinear follow-through strengthening model was adopted to consider the material nonlinearity. The stability of the structure was analyzed under three load conditions of 1.0 dead load + 1.0 live load, 1.0 dead load + 1.0 east half-span live load and 1.0 dead load + 1.0 south half-span live load. Through the whole process analysis, the ultimate bearing capacity coefficients under the above conditions are 3.79, 4.52 and 4.80 respectively, which are greater than 2 and meet the code requirements. The load-displacement curves of 1.0 dead load + 1.0 live load is shown in Figure 17.

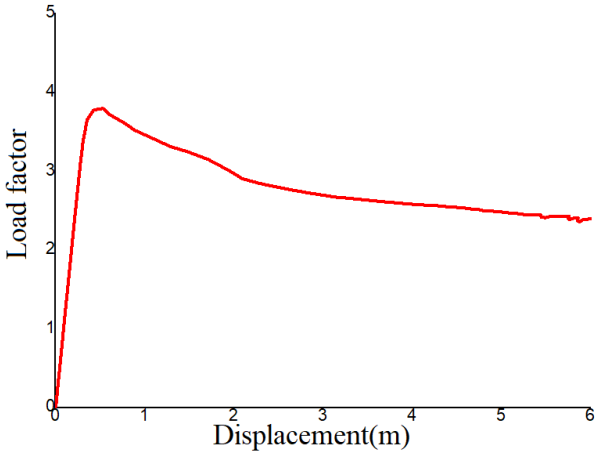


Figure 17. The load-displacement curves of 1.0 dead load + 1.0 live load

3.4. Analysis of structural consecutive collapse resistance

The transient dynamic analysis of the structure was carried out by MIDAS Gen. The damage of the roof was analyzed by removing the roof support columns and truss members separately. The stresses and displacements after removing the main truss chords of the roof are shown in Figure 18. The vertical displacement of the node after the vibration stops is 13.7mm, and the maximum stress of the adjacent upper chord is 89MPa, which is less than the yield strength of steel. When one supporting column is removed, the stress of the two horizontal transfer truss webs near the removed supporting column is 196MPa, and the stress of the remaining roof members is less than 160MPa. The bearing capacity ratio of the adjacent frame columns is 0.35, all of them are in elastic state, and the structure has strong resistance to continuous collapse.

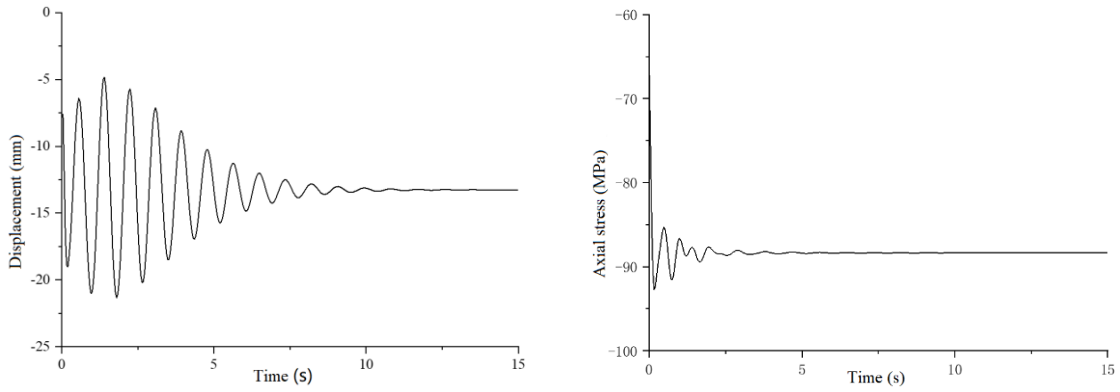


Figure 18. Stress and displacement of the structure after removing the roof main truss chord

3.5. Finite element analysis of the joints

ABAQUS was used to perform finite element analysis of the typical joints. The distribution location of each key joint is shown in Figure 19. Joint 1 has more members and the angle between the members is small, so it is difficult to weld, and finally cast steel joints were used. The calculation results of typical joints are shown in Figure 20. Excluding the local stress concentration, the stress in other parts of joint 9 is less than 290Mpa, and the yield bearing capacity is about 2.1 times the design load.

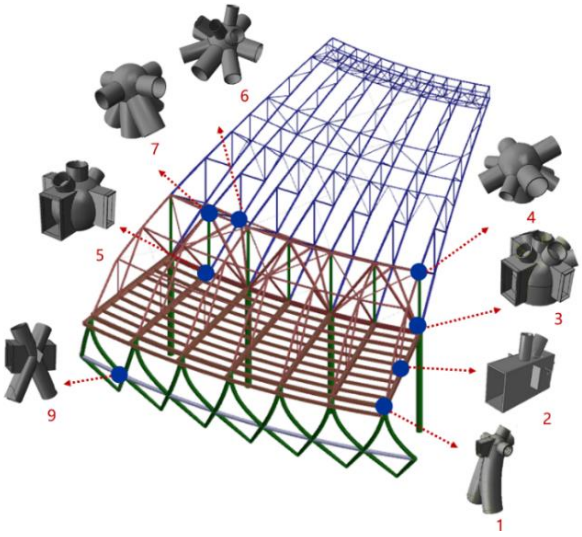


Figure 19. Diagram of key joints arrangement

(a) (b)

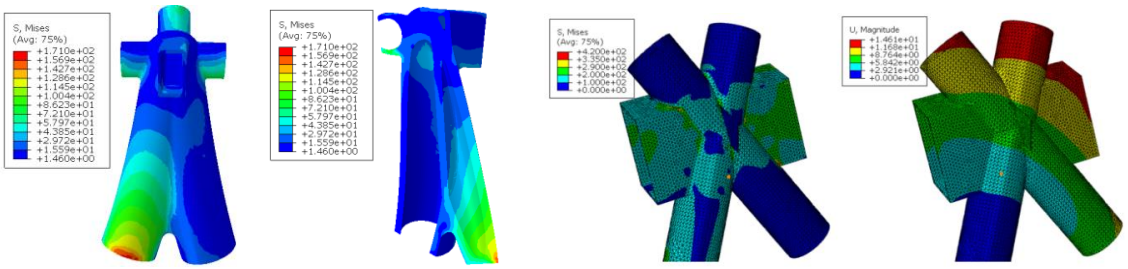


Figure 20. Typical joints calculation results: (a) analysis results of joint 1, (b) analysis results of joint 9

4. Conclusion

The perfect presentation of the Sun Bird pattern on the roof of Dong'an Lake Stadium expresses the combination of the cultural heritage of Sichuan and the spirit of the World University Games across time and space. The combination of ultra-long viewing platforms and steel structure roof creates a new architectural model for the stadium structure. The use of standardized design and prefabricated assembly has broken the time record for rapid construction of stadiums.

The clarity of structural logic display, the coordination of components and architectural space, and the refinement of joint details are key elements of structural design. While achieving the beauty of architecture, the structure itself can also be a part of the beauty of architecture. Projects with reasonable structural system, integration of architectural shape and structural force, and concise and beautiful joints can often leave a deep impression and achieve a perfect integration of structure and architecture.

Acknowledgements

Dong'an Lake Sports Park has been fully opened in June 2022, thanks to every designer and constructor who put their heart and soul into the construction of the stadium.

References

[1] Y. Feng, W. M. Chen and Q. Zhou, et al. “Structural design of Chengdu Dong'an Lake Sports Park Stadium,” *Building Structure*, vol. 50, pp.22-29, 2020.

[2] Technical Specification for space frame structures: JGJ 7—2010. Beijing: China Architecture & Building Press, 2010.

[3] Nakasone Y, Yoshimoto S, Stolarski T A, *Engineering analysis with ANSYS software*. Oxford, UK: Butterworth-Heinemann, 2006.

Bamboo for sustainable construction and quality of life improvement

---

Active bending
Additive manufacturing/ 3D printing
Architectural geometry
► **Bamboo for sustainable construction and quality of life improvement**
Bio-inspired structures and architecture
Bridge structures
Computational form-finding
Conceptual design
Concrete structures
Construction techniques
Deployable and inflatable structures
Design competition (WG21)
Digital modelling and fabrication
Dynamic response of metal spatial structures
Dynamic response of other structures
Form-finding and structural optimisation of interlocking discrete assemblages
Graphical methods
Gridshell and lattice structures
Historical concrete shells
Historical structures
Lattice structures
Life-cycle design and assessment of structures
Metal gridshell structures, connections and stability
Methods and construction technologies for sustainable shell structures
Morphology and configuration processing
Next generation parametric design
Novel methods in modelling, optimisation and construction for reducing carbon footprint of continuous roof shells
Numerical methods for geometry, form-finding and optimisation of lightweight structures
Optimisation methods and applications
Origami
Other
Teaching design uncertainty: working with unknown qualities/quantities of new and re-claimed materials
Teaching of shell and spatial structures
Tensegrity systems and cable structures
Tension and membrane structures
Tension structures in the Asia-Pacific
Timber and bio-based structures
Topology optimisation
Traditional masonry structures and innovation
Transformable structures

IASS 2023
July 10–14 Melbourne
Integration of Design and Fabrication

Proceedings of the IASS Annual Symposium 2023
Integration of Design and Fabrication
10–14 July 2023, Melbourne, Australia
Y.M. Xie, J. Burry, T.U. Lee and J. Ma (eds.)

Experimental evaluation of load-induced cracking in moso bamboo tubes

Dan V. BOMPA*, S. Alireza BEHNEJAD[a], Holmer SAVASTANO Jr[b], Arash AZADEH[b], Moe POURGHAZ[c]

* School of Sustainability, Civil and Environmental Engineering, University of Surrey
Guildford, GU2 7XH, UK
*d.bompa@surrey.ac.uk

[a] School of Sustainability, Civil and Environmental Engineering, University of Surrey, Guildford, GU2 7XH, UK
[b] Department of Biosystems Engineering, Faculty of Animal Science and Food Engineering, University of São Paulo, Brazil
[c] Department of Civil, Construction, and Environmental Engineering, North Carolina State University, Raleigh, NC, United States

Abstract

Bamboo is increasingly considered a suitable alternative to established construction materials due to its superior sustainability and relatively low environmental impact. This material has been adopted in construction both in natural and engineered forms in temporary works and structural elements, respectively. Like other biomaterials, bamboo is sensitive to moisture producing permanent deformations that can affect its mechanical properties. To evaluate the influence of moisture on the compression, shear and splitting response of moso bamboo, a detailed experimental investigation is carried out. Culm tubes with aspect ratio (H/D) of 1.0 and 3.0 were tested under the above loading conditions to failure either in oven-dry, ambient-dry or fully saturated conditions. Apart from conventional measurements, the use of digital image correlation techniques enables a detailed assessment of the stress localisation characteristics, including crack initiation and propagation within the bamboo wall tube. Comparative assessments in terms of compression, shear and splitting resistance as a function of moisture and aspect ratio are performed and discussed. The results show that an increase in moisture from oven-dry to ambient-dry to wet conditions shows a proportional decrease in strength by up to 43%, but a slight increase in ductility, as a function of the loading type. Short samples achieved between 5.1-163.6% higher maximum average stress compared to the long samples, indicating increasing the sample aspect ratio decreases the tube strength.

Keywords: moso bamboo, compression, shear, splitting, moisture, crack kinematics, biobased materials

1. Introduction

Natural bamboo has been attracting wider usage in construction as it is a fast-growing renewable raw material and with good mechanical properties when compared with other conventional materials [1,2]. The bamboo plant is better at capturing and storing carbon from the atmosphere compared with timber if it is sustainably grown [3]. Once reaching maturity it creates 15 times more wood per hectare than tree forests [4]. In comparison to conventional construction materials, both full-culm natural and engineered bamboo have a lower environmental impact [5]. Thus, the potential of natural bamboo as a material for sustainable construction and circular economic development is unprecedented. The material was at the centre of the COP27 agenda in response to the wider decarbonisation goals [6].

Copyright © 2023 by Dan V. BOMPA, S. Alireza BEHNEJAD, Holmer SAVASTANO Jr, Arash AZADEH and Moe POURGHAZ. Published in the Proceedings of the IASS Annual Symposium 2023 with permission.

Bamboo forests serve as a carbon sink and offer significant environmental benefits due to their rapid growth and regrowth after harvesting [7]. Locally sourced bamboo can provide a more environmentally friendly alternative to conventional mineral-based materials, primarily due to transportation distances and other factors. For single-story housing over the lifecycle of the building, locally sourced full culm bamboo is the most efficient material [8]. Bamboo, which originally comes from Southeast Asia [7], is now widespread in Asia, Africa, and Latin America, with roughly 1300 species covering about 0.8% of the world forested area. Moso bamboo, which is the most abundant species in China, is thus significant for testing and potentially developing strength/capacity grading for structural purposes. Despite the extensive historical use of bamboo in construction, rigorous testing and documentation of its mechanical properties are limited [9,10].

Bamboo can be regarded as a naturally occurring composite material that has a complex microstructure and unique properties, in which its properties vary along the thickness of the culm [11]. Such materials are referred to as functionally graded. The strength of natural bamboo comes from densely populated fibres at the culm exterior. Although bamboo has a high strength to weight ratio, it is weak perpendicular to fibres, making it prone to splitting, which regularly governs its structural design. Culms experience failure due to maximum tangential tensile stress, specifically in splitting, rather than in compression, bending, or shear [12,13]. Due to these properties the material has a great potential for structural applications, particularly in axial load carrying applications such as columns and trusses [14], provided that the tangential stresses are maintained below the splitting strength, otherwise splitting occurs.

The parallel-to-grain compression and shear properties of bamboo culms are typically evaluated through axial compression tests on tubular elements having the same diameter and length. For the compression tests the load is uniformly applied to the culm element, whilst for shear test a bowtie-shaped device is used to create four shear planes. The perpendicular-to-grain compression strength is obtained through edge bearing tests, in which a culm element is subjected to compression [15]. The tensile strength of bamboo in a direction perpendicular to the culm can be determined using the split pin test, in which a bamboo tube is pulled apart by a pin passed through a circular hole [15]. The presence and size of this hole influence both the tensile and compressive strength of the bamboo culm [16]. It was previously shown that the resistance of bamboo materials highly depends on the test method [17].

Like other biomaterials, bamboo is sensitive to moisture producing permanent deformations that can affect its mechanical properties. These degrade as the moisture content increases up to the fibre saturation point (around 30%), with less significant degradation beyond this point [18]. The same study showed that immersion in water for a day can achieve the fibre saturation point, causing a 25% reduction in compressive strength compared to air-dry conditions. With regard to the response to various humidity levels, it was shown that bamboo achieves the highest strength values at 60-80% humidity with a subsequent decline in strength beyond that range [18]. All studies indicated that humidity typically increases the ductility of the samples, otherwise having a relatively brittle response.

Existing studies evaluated the mechanical properties of bamboo culms through samples with a height-to-diameter ratio of 1.0. It is well known that stub tubes under compression are prone to failure due to end effects [19]. Conversely, slender tubular members are prone to local buckling. Similarly, in splitting, the crack kinematics and rate of propagation depend on the available length. Shorter tube elements under the split pin test would fail quicker than longer tubes. Due to the inherent stress distribution and end effects in compression, stub elements are likely to give unconservative estimates, whilst in splitting these would provide overly-conservative estimates. A more realistic sample ratio would consider the inter-nodal length, as the diaphragm act as internal restraint to local tube buckling.

To evaluate the influence of moisture on the mechanical properties of moso bamboo, an experimental investigation is carried out. Culm tubes with aspect ratio (H/D) of 1.0 and 3.0 were tested to failure either in oven-dry, ambient-dry or fully saturated conditions, to evaluate the stress localisation characteristics, including crack initiation and propagation within the bamboo wall tube. Comparative assessments with regard to strengths and aspect ratio are performed and discussed. This study is part of

a wider research project aiming at assessing the performance of natural and engineered bamboo under mechanical and environmental loading, developing constitutive relationships and evaluating the life-cycle sustainability of these materials.

2. Experimental methodology

2.1. Specimen details and conditioning

In this paper P. Pubescens (moso) culms with a diameter of around 70 mm and a tube thickness of 7 mm were used. Samples with two aspect ratios of height-to-length of approximately 1.0 and 3.0 were extracted randomly from 5 × 4.0 m culms by cutting with a circular saw. These aspect ratios correspond with specimens of around 70 and 210 mm length. The samples were taken from inter-nodal regions which were in good visual condition and did not show any shrinkage cracks. The inter-nodal regions were marked at each cut end with the sample number, described below, for future correlation of cross-sectional fibre distribution with mechanical strengths.

A total of 90 samples were prepared, equally divided into compression, shear and splitting tests. For the splitting tests, a central hole was drilled using a 13 mm drill bit to allow for a 12 mm pin to pass through. For each test type, three conditioning types were considered. This includes ambient-dry, oven-dry and wet conditions. Prior to conditioning the sample geometry was carefully measured with a digital calliper at a minimum of three locations. These include three measurements of top and bottom diameter, top and bottom tube thickness and tube height. The weight of the samples was measured using a digital scale with an accuracy of 0.1 g.

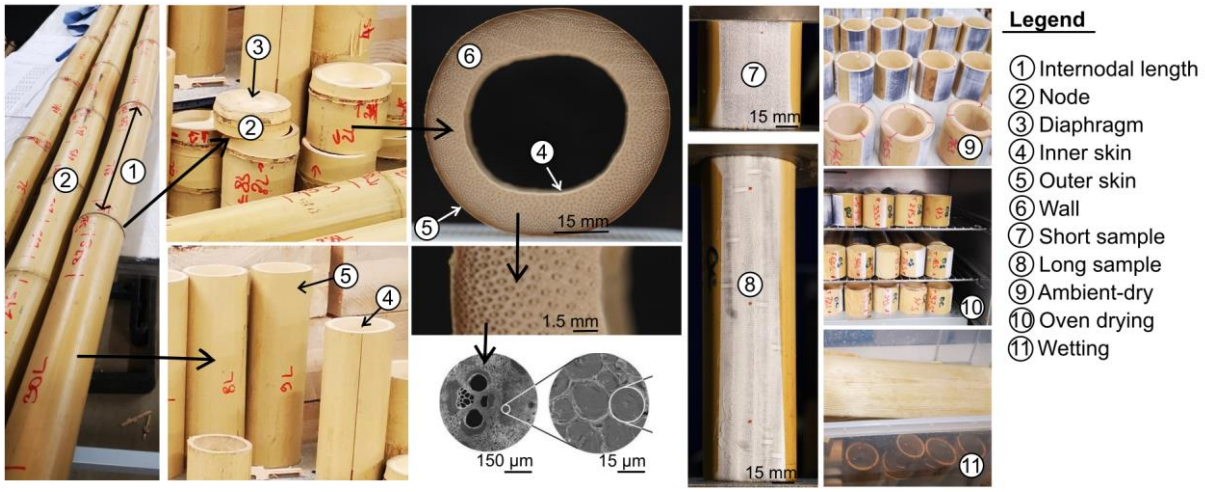


Figure 1. Details of the bamboo culms, terminology, specimen geometry and conditioning (the diagram with the bamboo microstructure is adapted from Ref. [20]).

Ambient dry samples were kept in standard laboratory conditions at 20±2°C and relative humidity of 40±5%. Oven-dry samples were dried for a period of 48h at 30°C. A low temperature for drying was considered to minimise the influence of forced drying to moisture kinematics. A preliminary study on drying showed that temperatures above 30°C are not suitable for drying this type of bamboo, particularly for the case of relatively thin tubes which split during the process. Wet samples were submersed in tap water for 48 hours in a plastic container, which is sufficient to achieve the fibre saturation point as indicated in the literature.

After oven-drying or water immersion, the sample weight was measured again with the same device, to evaluate the mass loss or gain, respectively. The average mass loss due to oven drying for all samples was 4.2±0.7%, whilst the average mass gain due to water submersion was 36.6±8.8%. Sample ID follows the B*xxACT*, in which xx is the sample number, A=S,L refers to the aspect ratio (S for short

H/D=1.0, and L for long H/D=3.0), C=A,O,W is for the conditioning (A is for ambient-dry, O is for oven-dry, and W is for wet), and T=C,B,S is for the testing type (C for compression, B for bowtie shear, S for pin splitting). For example, Sample B20LAB refers to a long bamboo tube with H/D=3.0, tested in ambient-dry conditions under bowtie shear.

2.2. Testing arrangements and instrumentation

The compression and shear samples were tested in an Instron Satec 600 kN machine provided with a data acquisition system (Figure 2). The machine bottom grip was replaced by a steel support with a flat plate, and a supplementary support plate to position the specimens. At the top grip, the machine had a hinge to ensure smooth load transfer without any influence for potential very small inclinations of the top surface of the samples. The compression samples were supported by a thick steel plate and the load was applied through the hinge. For the shear tests, top and bottom bowtie devices were used to create four shear planes for the sample subjected to compression. These tests are widely used to evaluate the shear resistance of bamboo culms. For the splitting tests an Instron 250 kN machine was used. This had a 12 mm pin device passing through the 13 mm hole drilled through the bamboo tube. At the top of the tube a rubber strip and a tee were positioned to apply a compressive load which produces splitting in the tube. All tests were carried out in displacement control at a rate of 0.5 mm/min.

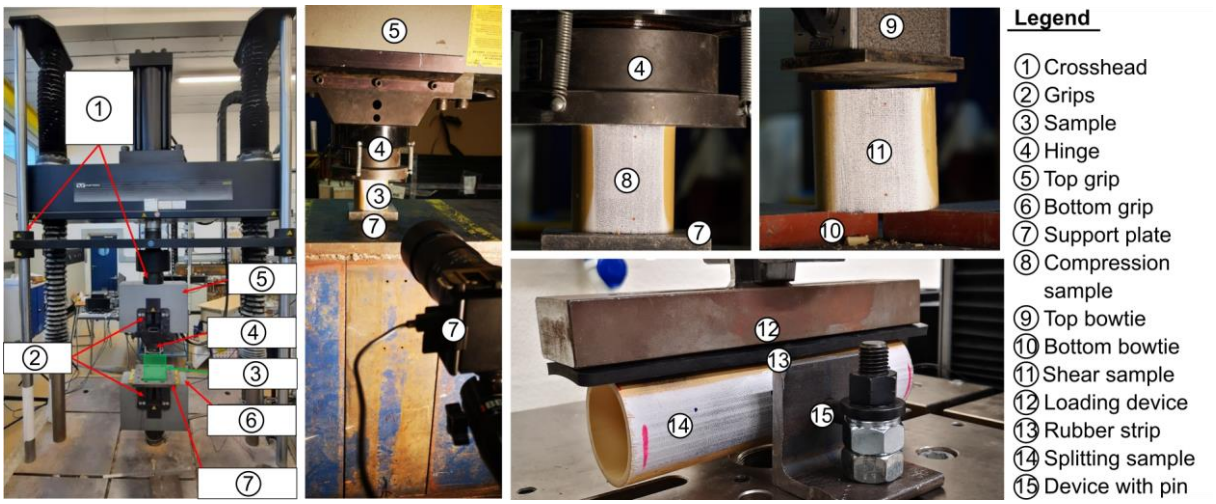


Figure 2. Testing arrangements and instrumentation

To evaluate strain development and crack kinematics, an in-house digital image correlation (DIC) was used. This DIC adopted a non-contact system that uses one high-sensitivity APS-C type (23.5 × 15.6 mm), Exmor CMOS sensor camera with USB 3.0 interface to provide accurate and practical measurements for material and specimen tests. The camera had a resolution of 24.2 Megapixel. To prepare the specimens, they were painted white and speckled with 1.00 mm black dots using black ink and stamping system. Prior to testing, a calibration procedure was done by adjusting the aperture, lighting, and focus while taking photos of a calibration plate. A frequency of 0.1 Hz was used to record the images. After testing, the DIC data was processed to obtain deformation vector fields, and surface strains which are used to identify stress concentrations. For processing the images, Ncorr, an open-access MATLAB-based 2D digital image correlation program was used [21].

3. Test results

3.1. Compression tests

As mentioned in Section 2, bamboo tube samples with a diameter of around 70 mm and wall thickness of 7.0 mm were tested under axial compression. Samples with two aspect ratios were tested in ambient-dry, oven-dry and wet conditions. Figure 3 shows the axial load – deformation response and the main

failure modes observed during the tests. The stress is the machine force divided by the measured cross-sectional area of the sample, whilst the deformation is the sample shortening divided by its length. Grey curves show test data, and black curves are the average response. The average geometrical properties per specimen group are shown in Table 1. The compressive strength of ambient dry long samples (LAC) was 74.0 MPa. Oven-drying increased the strength by 7.97% (LOC), whilst wetting reduced the strength by 43.9% (LWC). Short ambient dry samples (SAC) achieved on average a maximum stress of 66.5 MPa, which is 10.1% lower than the corresponding long elements (LAC). For the short specimens, oven-drying increased the strength by 33.8% (SOC) and wetting reduced it by 25.4% (SWC) compared to the SAC counterparts.

The stiffness properties followed a similar trend with the strength, as a function of the conditioning. With regard to the inelastic response, beyond the linear-elastic proportionality limit, ambient-dry samples (LAC and SAC) had a constant plateau with some ductility. The LOC and SOC samples, showed slight hardening, whilst LWC and SWC showed post-peak softening. This behaviour was associated with a brittle response for oven-dry elements and ductile crushing for the wet samples. The former failed by complete separation and explosive spalling of tube splits, whilst the latter more gradually. The failure modes, shown in Figure 3, were either through outward or inward buckling, both for long and short tubes. It is shown that moisture reduces compression strength, stiffness and ductility, whilst drying increases these properties at the expense of a more brittle response. The short stub specimens exhibited a strength that was 5.1% greater than that of the long samples for all conditions.

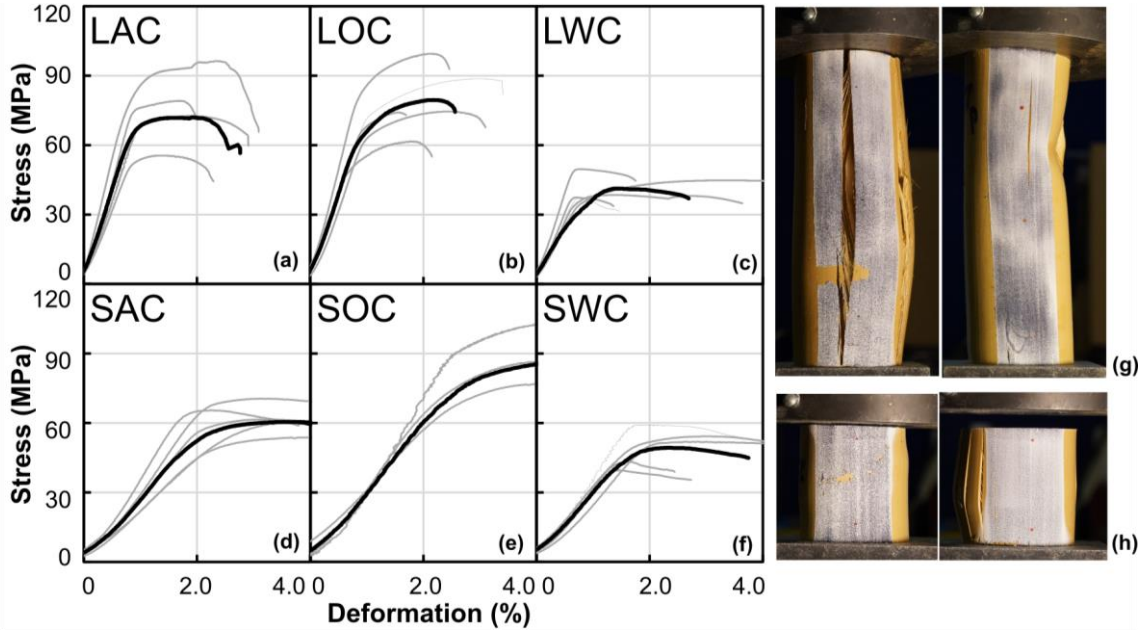


Figure 3. Compression test results for sample group: a) LAC, b) LOC, c) LWC, d) SAC, e) SOC, f) SWC; specimen failure: g) outward buckling (left) and inward buckling (right), h) inward buckling (left) and outward buckling (right) (note: grey curves represent the response of each specimen, and the black curve is the average).

3.2. Shear tests

Figure 4 shows the stress deformation response of the samples tested in bowtie shear by applying a compressive load from the machine. The stress is the machine force divided by the measured cross-sectional area of the four shear planes, whilst the deformation is the sample shortening divided by its length. Grey curves show the test data for each sample, whilst the black curve is the average of all tests from a group. The sample diameters and tube thicknesses were around 70 mm and 7 mm, respectively, as for the compression tests (Table 1). In addition to the deformational response, Figure 4 also shows selected specimens after testing. The shear strength of ambient dry long samples (LAB) was 5.7 MPa.

Oven-drying increased the strength by 36.8% (LOB), whilst wetting reduced the strength by 28.1% (LWB). Short ambient dry samples (SAB) achieved on average a maximum stress of 13.5 MPa, which is 136.8% higher than the corresponding long elements (LAB). For the short specimens, oven-drying increased the strength by 3.7% (SOB) and wetting reduced it by 34.8% (SWC) versus SAB counterparts.

The stiffness properties followed a similar trend with the strength, i.e. lower stiffness corresponds to lower strength and vice-versa. With regard to the kinematics, the sample response can be represented largely by a linear elastic curve for the oven-dry samples (LOB and SOB), and with some gradual softening around 85% of the peak stress for the remaining ambient-dry (LAB and SAB) and wet (LWB and SWB) samples. As for the compression tests, this behaviour was associated with a brittle response for oven-dry elements and ductile shear splitting for the wet samples. The former failed by complete separation and explosive spalling of tube splits, whilst the latter failed more gradually. The failure modes, shown in Figure 2, were generally through one or two shear planes. It is shown that moisture reduces sample stiffness and shear strength, whilst drying increases these properties. On average, the short samples exhibited a strength that was 105.1% higher than the long samples across all conditioning situations.

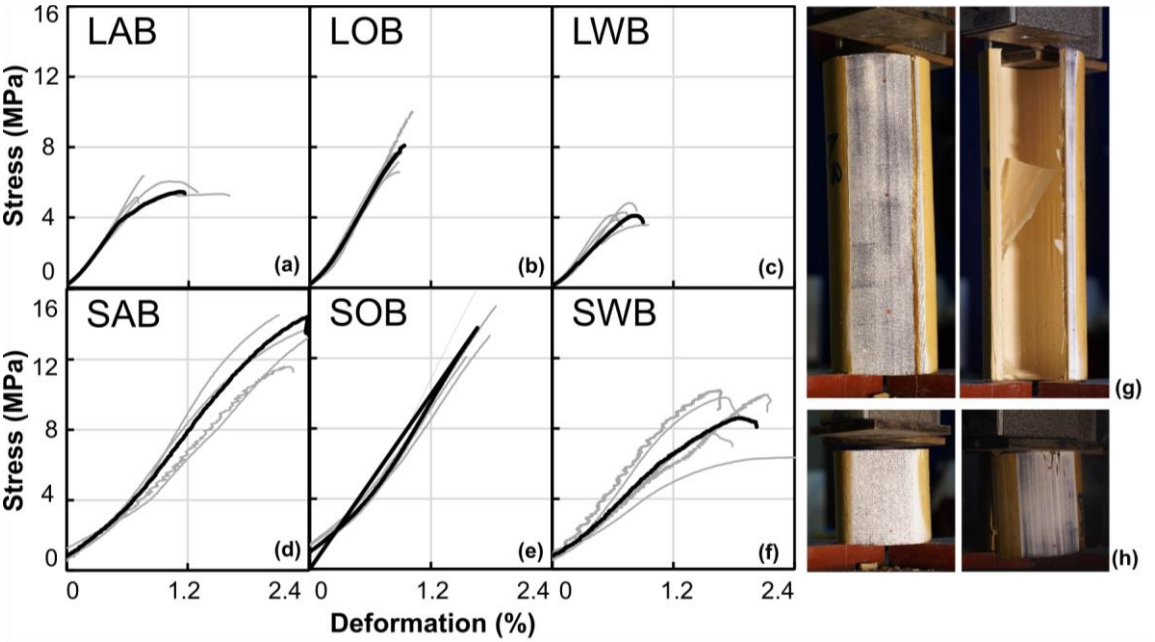


Figure 4. Shear test results for sample group: a) LAB, b) LOB, c) LWB, d) SAB, e) SOB, f) SWB; specimen failure: g) splitting through one plane (left) and full spalling of part of the tube (right), h) typical shear crack (left), rotation by the shear plane (right) outward buckling (note: grey curves represent the response of each specimen, and the black curve is the average).

3.3. Splitting tests

The stress-displacement curves and failure patterns of the bamboo tubes tested under pin splitting are shown in Figure 5. The stresses were evaluated by dividing the machine load to the cross-section of the splitting plane, whilst the displacement corresponds to the value recorded by the machine. As in the other figures, grey curves show the test data for each sample, whilst the black curve is the average of all tests from a group. The sample diameters and tube thicknesses were around 70 mm and 7 mm, respectively, as for the compression and shear tests (Table 1). The splitting strength of ambient dry long samples (LAS) was 1.3 MPa. Oven-drying reduced the strength by 30.8% (LOS), whilst moisture reduced the strength by 15.4% (LWS). Short ambient dry samples (SAS) achieved on average a maximum stress of 3.4 MPa, which is 161.6% higher than the corresponding long elements (LAS). For

the short specimens, oven-drying decreased the strength by 11.8% (SOB) and wetting reduced it 35.3% (SWS) in relation to the SAS counterparts.

With regard to the stiffness, it is shown that these are similar for all long or short specimens, regardless of the conditioning. As indicated by the curves, ambient-dry (LAS and SAS) and oven-dry (LOS and SOS) had a linear elastic response with a sudden drop after the peak. This indicates instantaneous splitting, which is similar to the brittleness levels identified in the other test types. Wet samples, on the other hand, showed some softening before the peak and a softer post-peak response. This indicates some form of tension stiffening due to moisture. It is worth noting that the splitting tests had higher variation than the compressive and shear, and in most cases the differences in maximum stress for different conditioning is within the standard deviation (Table 2). Considering the average strengths and associated standard deviation it is shown that ambient- and oven-dry samples have similar stiffness and strength for the same sample length. Moisture reduces sample splitting strength. The short samples exhibited a strength that was 163.6% higher than the long samples across all conditioning situations.

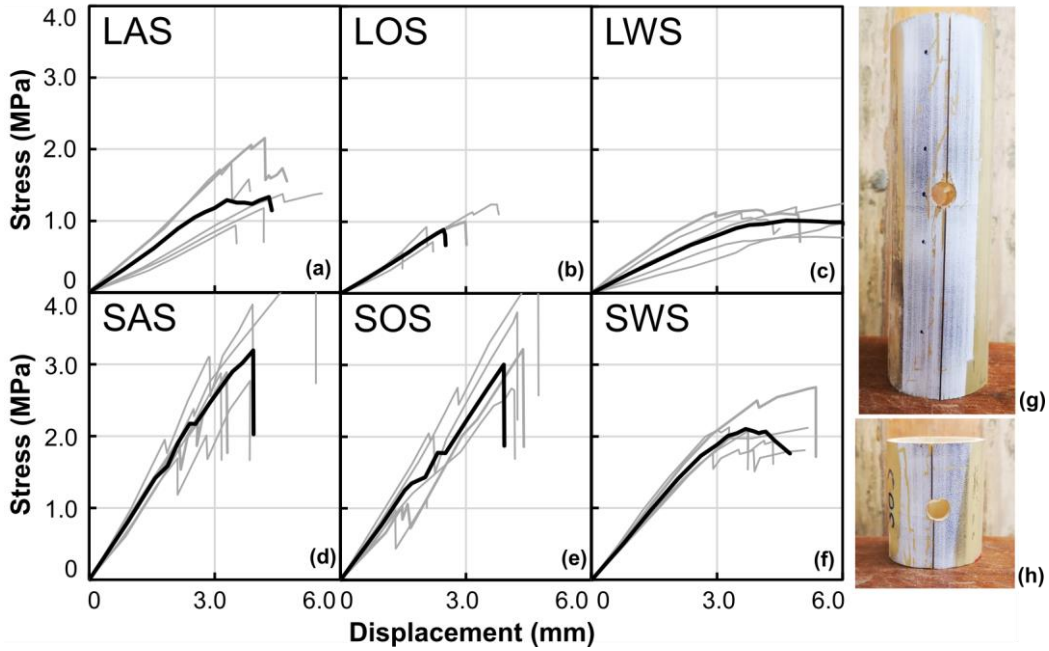


Figure 5. Splitting test results for sample group: a) LAS, b) LOS, c) LWS, d) SAS, e) SOS, f) SWS; splitting failure for g) long specimens, h) short specimens (note: grey curves represent the response of each specimen, and the black curve is the average).

3.4. Kinematics and average strengths

Figure 6 shows strain distributions at the surface of short and long tube specimens. Blue colour are associated with negative stress values indicating compression, whilst red colour is for tension. Figure 6a,b shows the shear behaviour of short elements and Figure 6c,d of the long shear samples. The surface strain maps obtained from the processing of the digital image correlation data show a concentration of compression at the top bowtie edge prior to shear splitting occurring. These maps correlate well with the failure patterns shown in Figure 4. Near the compression stress localisation, the sample had a tension governed response, due to a slight rotation of the hinge around the shear crack initiation point. As shown in Figure 6d, the maximum strain is around 2%, which is above the average deformation at failure for the long samples. The strain maps suggest that for tube specimens under bowtie shear, the failure crack initiates at the top of the sample, at compression strains above the average sample stress.

As shown in Figure 6e,d,g,f failure of the tube samples under compression is either governed by high compressions strains at the middle of the specimen (short sample in Figure 6e), or by a concentration of

compression within the length of the sample. These kinematics correspond with the failure patterns recorded after testing the specimens shown in Figure 3g,h. The short sample in Figure 6a failed in outward buckling, whilst the tube from Figure 6h in inward buckling. The other two compression samples from Figure 6f,h tested in wet conditions had both inward buckling failures evidenced by the compression strain localisation. The maximum strains in all compression samples were between 2-6%, which is about twice the ultimate average strain shown in Figure 3. The strain maps of the compression samples confirm the failure modes observed after testing and indicate ranges at which instability occurs.

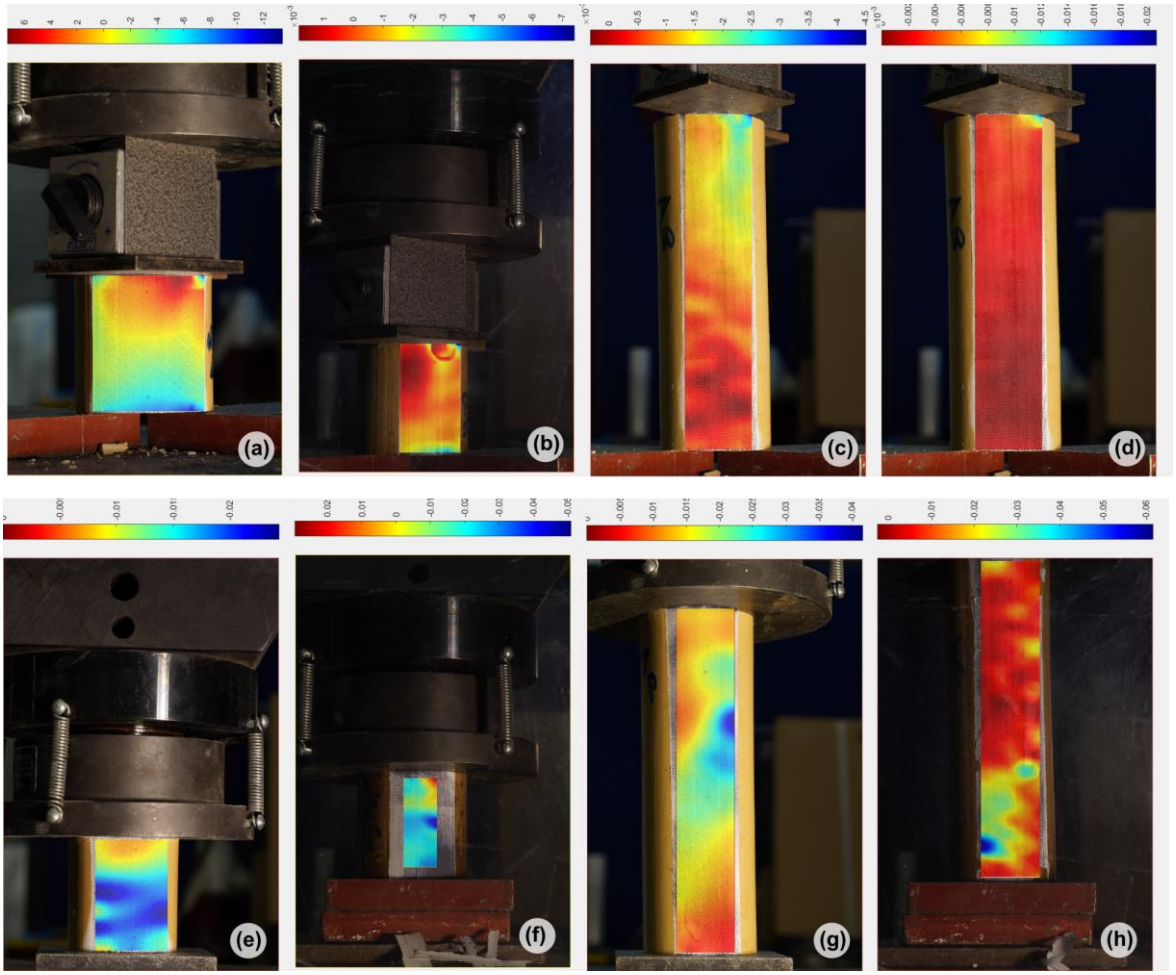


Figure 6. Stress distribution at the face of samples for selected cases: localisation at the bowtie edge in a) a short ambient dry sample, b) a short wet sample, c) a long ambient-dry sample, d) an oven-dried sample; localisation under compression: e) centre of a short tube due to outward buckling in ambient dry conditions; inward buckling initiation f) at mid-height of a wet element, g) centre-top of an ambient dry sample, h) bottom of a wet sample.

Figure 7 shows the comparative average strength for all the tests carried out in this paper. As noted above for the compression samples, the increase in moisture from oven-dry to ambient-dry to wet conditions shows a proportional decrease in strength, but a slight increase in ductility. Overall short stub compression elements had an average strength for all conditioning situations that was 5.1% higher than that of the long samples. A similar trend is observed for the bowtie shear samples, which show a decrease in strength with decrease in moisture, as well as a slightly more pseudo-ductile response, evidenced by a slight post-peak softening. On average, the short bowtie shear samples exhibited a strength that was 105.1% higher than the long samples across all conditioning situations. Finally, the splitting response was governed by higher variance within the same dataset, showing that ambient- and oven- dry samples had similar strengths, and as above, moisture had a detrimental influence on the splitting strength. The

short pin splitting samples exhibited a strength that was 163.6% higher than the long samples for all conditioning situations.

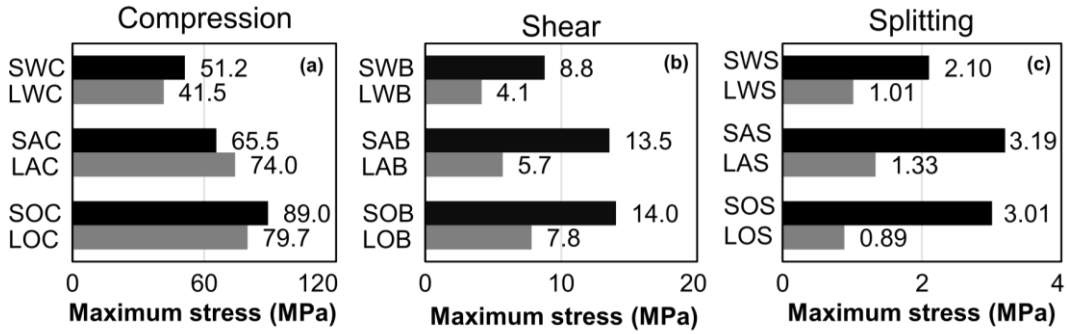


Figure 7 Maximum stress for: a) compression tests, b) shear tests, c) splitting tests.

The bar charts in Figure 7 and above discussion points indicate that short samples with aspect ratio of 1.0 fail at larger average stress levels compared to the long samples with an aspect ratio of 3.0. These tests suggest that tube slenderness influences the overall response, as shown in other twin-walled sections [22]. As shown in the literature, to reliably assess axially loaded tubular members, further experimental assessment on specimens with higher aspect ratios ($H/D \geq 3.0$) would be necessary. Stub tubes with an aspect ratio of $H/D \approx 3.0$ typically provide an accurate representation of the member behaviour, avoid consideration of end effects, they would not experience global buckling and accurately reflect stress and strain distributions. Samples with aspect ratios below $H/D < 3.0$ may be prone to local failures to end effects. These points correlate well with the experimental observations, crack kinematics and average maximum stresses recorded by specimens. When it comes to splitting, longer specimens are expected to have lower average stress compared to shorter specimens since the crack needs to propagate through a relatively longer distance.

Table 1. Sample details and maximum average stress.

Sample group (-)	Test type (-)	Diameter (mm)	Tube thickness (mm)	Height (mm)	Maximum stress (MPa)
LAC	Compression	69.5±2.9	6.2±0.6	207.6±1.0	74.0±15.2
SAC		67.8±4.8	7.2±1.8	68.2±1.6	66.5±6.0
LOC		67.4±4.0	5.7±0.6	208.2±1.0	79.7±14.6
SOC		69.9±1.5	7.7±3.2	68.4±1.7	89.0±13.4
LWC		69.1±3.5	6.9±1.5	208.1±0.8	41.5±5.5
SWC		69.6±3.2	6.2±0.9	67.7±1.0	49.6±8.0
LAB	Shear	69.7±3.0	6.6±1.1	207.8±0.7	5.7±0.5
SAB		67.1±3.3	6.7±1.7	67.8±0.9	13.5±1.3
LOB		68.0±2.1	5.9±0.7	208.2±1.8	7.8±1.3
SOB		68.2±2.3	7.1±1.3	67.8±1.1	14.0±1.7
LWB		70.2±2.3	6.7±1.1	208.7±1.5	4.1±0.5
SWB		69.8±1.9	6.1±0.4	68.1±1.1	8.8±1.7
LAS	Splitting	71.6±0.3	6.1±0.1	207.6±0.7	1.3±0.3
SAS		68.1±2.5	8.3±1.5	71.1±1.8	3.4±0.8
LOS		72.1±0.8	7.0±0.7	210.3±0.3	0.9±0.3
SOS		63.3±1.4	9.4±0.7	72.7±1.1	3.0±1.2

LWS		64.7±5.5	6.0±0.8	209.8±0.4	1.1±0.2
SWS		66.9±6.3	6.2±1.1	71.3±0.9	2.2±0.3

In full culms, these effects may be influenced by the presence of the diaphragm and inter-nodal length, which may be used for evaluating reliably the strength characteristics of bamboo culms. Using elements with a H/D ratio of 1.0 for evaluating mechanical properties may result in overestimating the material properties, potentially leading to unreliable estimates for designing such members. To further investigate these points, the tests described in this paper can serve as a validation dataset for nonlinear numerical procedures adopted in finite element models. These can be used to obtain a detailed insight into the maximum normal and shear stress and evaluate the limit condition of bamboo tubes. The detailed test measurements, coupled with numerical models and results from literature, will allow for the definition of expressions for evaluating the key mechanical properties used in the design of structural bamboo culms.

4. Conclusions

This paper presented an experimental investigation into the influence of moisture on the compression, shear, and splitting behaviour of moso bamboo. The study involved testing culm tubes with aspect ratios (H/D) of 1.0 and 3.0 under different conditioning, including oven-dry, ambient-dry, and fully saturated conditions, until failure. In addition to conventional measurements, digital image correlation techniques were employed to assess the stress localisation characteristics, including crack initiation and propagation within the bamboo wall tube. Comparative evaluations were performed and discussed, examining the compression, shear, and splitting resistance as a function of moisture and aspect ratio. The main results are presented below.

For the compressive strength, oven-drying increased the strength on average by 22.9%, whilst wetting reduced the strength on average by 34.6% for both short and long samples with respect to ambient-dry samples. Similar trends were obtained for bowtie shear with the oven-dry samples having on average 20.3% higher strength than the corresponding ambient dry samples, and the fully saturated samples by 31.5% compared to the same reference case. The splitting tests showed a higher variation within the same sample group and both oven-dry and wet specimens had lower average strength by 21.3% and 25.3% compared to the elements tested in ambient conditions.

The results indicated that short samples with an aspect ratio of 1.0 fail at larger average stress levels compared to the long samples with an aspect ratio of 3.0. These tests suggest that tube slenderness influences the overall response, as shown in other twin-walled sections. Short stub compression elements had an average strength for all conditioning situations that was 5.1% higher than that of the long samples. Short bowtie shear samples exhibited a strength that was 105.1% higher than the long samples, whilst the short pin splitting elements were stronger by 163.6% than their slender correspondents.

The tests showed a brittle response for oven-dry elements characterized by complete separation and explosive spalling of tube splits, and gradual ductile crushing for the wet samples, with the ambient-dry samples in the middle. The compression failure modes were either through outward or inward buckling, both for long and short tubes. The shear kinematics were similar to those of the compression mode. The shear failures were generally through one or two shear planes. Splitting test curves exhibited a linear elastic response followed by a sudden drop after the peak, indicating instantaneous splitting and brittleness levels similar to other tests. Wet samples showed softening before the peak and a softer post-peak response, indicating moisture-induced tension softening.

Acknowledgements

This research has been supported by funding provided by the University Global Partnership Network (UGPN) through the project "Bamboo for Sustainable Construction and Quality of Life Improvement" and the School of Sustainability, Civil and Environmental Engineering at the University of Surrey. The support is gratefully acknowledged.

References

[1] C. Tan, H. Li, M. Ashraf, I. Corbi, O. Corbi, and R. Lorenzo, "Evaluation of axial capacity of engineered bamboo columns". *Journal of Building Engineering*, 34:102039, 2021,

[2] C. Gritsch, K. Abranson, G. Camayo, M. Rashid, R. Murphy, X. Londoño, and J.C. Camargo, "Anatomical culm analysis of Guadua angustifolia in relation to age, site, and physico-mechanical properties". In *Proceedings International Symposium Guadua* (pp:188-193), 2004.

[3] UNCC (United Nations Climate Change), "Innovation Hub at COP27 to Promote Transformative Climate Solutions". Online. 31 Oct 2022. Available at: https://unfccc.int/news/innovation-hub-at-cop27-to-promote-transformative-climate-solutions (accessed 22-Dec-22)

[4] E. Zea Escamilla, G. Habert, J.F. Correal Daza, H.F. Archilla, J.S. Echeverry Fernández, and D. Trujillo, "Industrial or traditional bamboo construction? Comparative life cycle assessment (LCA) of bamboo-based buildings". *Sustainability*, 10(9):3096, 2018

[5] P. Van Der Lugt, A.A.J.F. Van den Dobbelsteen, and R. Abrahams, "Bamboo as a building material alternative for Western Europe? A study of the environmental performance, costs and bottlenecks of the use of bamboo (products) in Western Europe". *Journal of Bamboo and Rattan*, 2(3), pp.205-223, 2003.

[6] P. Verma, "From nuclear power to bamboo: The climate solutions at COP27", 11-Nov-2022. Online at: https://www.washingtonpost.com/technology/2022/11/11/cop27-climate-change-solutions/ (accessed 22-Dec-22)

[7] X. Song, G. Zhou, H. Jiang, S. Yu, J. Fu, W. Li, W. Wang, Z. Ma, and C. Peng, "Carbon sequestration by Chinese bamboo forests and their ecological benefits: assessment of potential, problems, and future challenges". *Environmental Reviews*, 19(NA), pp.418-428, 2011.

[8] J.G. Vogtländer, N.M. van der Velden, and P. van der Lugt, "Carbon sequestration in LCA, a proposal for a new approach based on the global carbon cycle; cases on wood and on bamboo". *The International Journal of Life Cycle Assessment*, 19, pp.13-23, 2014.

[9] D. Trujillo, S. Jangra, and J.M. Gibson, "Flexural properties as a basis for bamboo strength grading." *Proceedings of the Institution of Civil Engineers-Structures and Buildings*, 170(4), pp.284-294, 2017.

[10] A. Azadeh, K. Ghavami, H.S. Junior, R.D Toledo Filho, and N.P. Barbosa, "Static flexural behavior of bamboo as a functionally graded material and the effect of heat on dynamic flexural modulus." *Journal of Building Engineering*, 34, p.101949, 2021.

[11] S. Askarinejad, P. Kotowski, F. Shalchy, and N. Rahbar, "Effects of humidity on shear behavior of bamboo." *Theoretical and Applied Mechanics Letters*, 5(6), pp.236-243, 2015.

[12] O.A. Arce-Villalobos, "Fundamentals of the design of bamboo structures." (Doctoral dissertation, Technische Universiteit Eindhoven), 1993.

[13] A. Azadeh, A. Quiroga-Flores, K. Ghavami, N.P. Barbosa, R. Toledo Filho, and H. Savastano, "An Investigation of Bamboo Shear Test Methods and the Influence of Heat on Bamboo Shear Strength." *Available at SSRN 4370392.*

[14] D. Mitch, K.A. Harries, and B. Sharma. "Characterization of splitting behavior of bamboo culms." *Journal of Materials in Civil Engineering*, 22(11), pp.1195-1199, 2010.

[15] B. Sharma, K.A. Harries, and K. Ghavami. Methods of determining transverse mechanical properties of full-culm bamboo. Construction and Building Materials, 38, pp.627-637, 2013.

[16] J. Deng, F. Chen, G. Wang, and W. Zhang. «Variation of parallel-to-grain compression and shearing properties in moso bamboo culm (Phyllostachys pubescens).” *BioResources*, 11(1), pp.1784-1795, 2016

[17] A. Huang, Q. Su, Y. Zong, X. Chen, and H. Liu, “Study on Different Shear Performance of Moso Bamboo in Four Test Methods.” *Polymers*, 14(13), p.2649, 2022.

[18] Q. Xu, K. Harries, X. Li, Q. Liu, and J. Gottron, “Mechanical properties of structural bamboo following immersion in water.” *Engineering Structures*, 81, pp.230-239, 2014

[19] A. Mujdeci, D.V. Bompa, and A.Y. Elghazouli, “Confinement effects for rubberised concrete in tubular steel cross-sections under combined loading.” *Archives of Civil and Mechanical Engineering*, 21, pp.1-20, 2021.

[20] S. Mannan, J. Paul Knox, and S. Basu, “Correlations between axial stiffness and microstructure of a species of bamboo.” *Royal Society Open Science*, 4(1), p.160412, 2017.

[21] J. Blaber, B. Adair, and A. Antoniou. “Ncorr: open-source 2D digital image correlation matlab software.” *Experimental Mechanics*, 55(6), pp.1105-1122, 2015.

[22] A. Mujdeci, Y.T. Guo, D.V Bompa, and A.Y. Elghazouli, “Axial and bending behaviour of steel tubes infilled with rubberised concrete.” *Thin-Walled Structures*, 181, p.110125, 2022.

IASS 2023
July 10–14 Melbourne
Integration of Design and Fabrication

Proceedings of the IASS Annual Symposium 2023
Integration of Design and Fabrication
10–14 July 2023, Melbourne, Australia
Y.M. Xie, J. Burry, T.U. Lee and J. Ma (eds.)

Preliminary study on relationship between culm morphology and mechanical characteristics of Japanese bamboo

Takuo NAGAI[a,*]

[a,*] Department of Architecture and Design, The University of Shiga Prefecture
2500 Hassakacho, Hikone-city, Shiga, Japan
nagai.t@ses.usp.ac.jp

Abstract

In recent years, there has been increasing interest in using bamboo as a building material. However, there are still many challenges to promoting the structural use of bamboo, including understanding its mechanical properties, quantitatively evaluating its durability, and developing construction methods. The mechanical properties of bamboo vary significantly depending on the part and shape of the culm, and its anisotropic nature means that its physical properties exhibit significant anisotropy along the fiber parallel and perpendicular directions. Systematic development of these properties requires further experimentation, as research is still ongoing. Therefore, in this study, we conducted a preliminary investigation into the morphology and mechanical properties of Japanese bamboo: *Phyllostachys edulis* and *Phyllostachys bambusoides*. The geometric properties of the culm morphology were clearly expressed by standardizing culm length and other dimensions based on culm diameter at the base. Of the various mechanical properties examined, the strength and elastic modulus in the fiber parallel direction varied greatly depending on culm morphology and position. In contrast, sensitivity to culm morphology and position was low for strength in the fiber perpendicular direction, and little influence was observed.

Keywords: bamboo, Phyllostachys edulis, Phyllostachys bambusoides, structural morphology, plant-structure-optimization

1. Introduction

In recent years, there has been a significant increase in research on using bamboo as a building material [1]. This trend is driven by the need for a decarbonized society, the adoption of United Nations SDGs goals, and a growing interest in materials with low environmental impact. Additionally, with the global population predicted to peak between 2050 and 2090, mainly in developing countries, bamboo is seen as a promising material to meet the explosive demand for housing construction in these regions. Furthermore, the mechanical characteristics of bamboo culms (lightweight, cylindrical shape, high rigidity, and strength) make them highly suitable as a framework for spatial structures, with numerous pioneering examples already in existence [2, 3]. In the future, bamboo is expected to become increasingly important as a material for constructing spatial structures as well as housing structures.

While bamboo is well-known for its excellent mechanical properties in the fiber direction, which is the strong axis, its properties perpendicular to the fiber are much weaker and smaller than those in the strong axis [4, 5]. Weakness in the direction perpendicular to the fiber can cause bending failure of bamboo culms and failure of types of joint with fasteners. Therefore, evaluating the mechanical properties perpendicular to the fiber is crucial for the structural use of bamboo [6].

In this study, we investigate the structural morphology of Japanese bamboo: *Phyllostachys edulis* ("Moso" in Japanese) and *Phyllostachys bambusoides* ("Madake" in Japanese) for the development of bamboo structures in the future. We measure the geometries: positions of nodes, culm diameter, and

Copyright © 2023 by Takuo NAGAI. Published in the Proceedings of the IASS Annual Symposium 2023 with permission.

culm-wall thickness to specify the culm structure. We observe the physical and mechanical properties of bamboo culms by investigating the distribution of specific gravity, compressive strength parallel to the fiber, bending strength perpendicular to the fiber, and shear strength over the entire height of the culms. Based on these measurements, we discuss the relationship between the geometries and the mechanical properties of full-culm bamboo. Furthermore, we explore how bamboo reinforces the "weak point" due to the geometric effects, such as nodes, tapered shape of the culm, etc., as a strategy for plant-structure optimization.

2. Bamboo materials for the study

The bamboo species selected for this study were *P. edulis* and *P. bambusoides*, both of which were collected from a bamboo forest (35°15'N, 136°09'E) located in Omihachiman-city, Shiga Prefecture, Japan. The forest contains adjacent both bamboo species groves. The samples used in this study were at least three years old, and their age was determined by visual inspection. Culm diameter at breast height was divided into three categories: 60-80 mm, 80-100 mm, and over 100 mm, and samples were collected to ensure that each category had roughly the same number of samples.

The harvesting procedure involves cutting the culm at the base just above the visible surface of the adventitious roots, and then cutting the upper end of the culm at a position above the first branch, where the culm diameter is 30 mm or less when viewed from the base side. The samples were stored for six months to one year in a well-ventilated, semi-outdoor area that was protected from direct rain exposure. Afterward, various processing and measurement operations were carried out.

An example of the results of a mass change of the samples is shown in Fig. 1. The horizontal axis represents the number of days after harvesting (T), and the vertical axis represents the ratio of the mass of each sample (M_T) to the mass immediately after harvesting (M_0), i.e., M_T/M_0. M_0 was measured within half a day after harvesting. The mass change of all samples did not stabilize, and it was found that natural drying under the storage conditions described above did not reach the equilibrium moisture content within about one year. The moisture content of each sample was measured immediately after the mechanical testing.

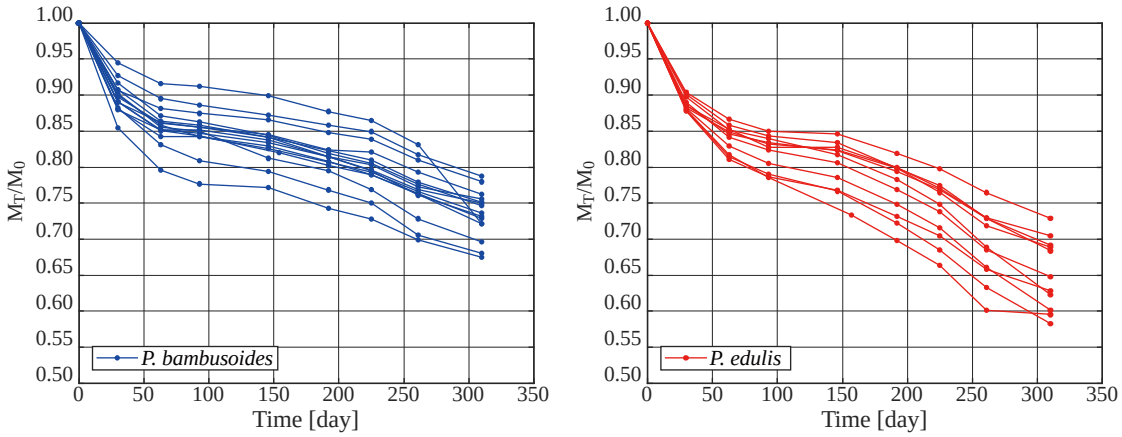


Figure 1. Example of transition of mass ratio M_T/M_0 of bamboo culms for this study.

3. Culm geometries

3.1. Measurement method

Fig. 2 shows the measurement method for culm morphology. The node directly above the underground rhizome, which is visible on the surface, is defined as "Node-1" (N-1). The nodes and internodes are

labeled sequentially from N-1 to the top of the culm as N-2, N-3, ..., N-j, ... and In-1, In-2, In-3, ..., In-j, ..., respectively. The center of In-1 is defined as "Cin-1" (Center of internode-1), and the centers of the other internodes are defined similarly as Cin-2, Cin-3, ..., Cin-j, ...

The coordinate X along the culm is defined with N-1 as the origin, positive in the upward direction toward the top of the culm, and the node of the first branch from the bottom is defined as "Node of branch-1" (Nb-1). The measured dimensions are the coordinate X_N and culm diameter D_N at each node, the culm diameter D_{In} and culm wall thickness t at the center of each internode. The coordinate X_{In} at the center of each internode is defined as the average of the coordinates of the adjacent nodes. These measurements are performed at every node and center of internode within the measurement range. Culm diameter is measured by tape measure, and calculated by dividing the circumference by π. Culm wall thickness is measured using calipers at two of the four points that divide the circumference into four equal parts (N, S, E, and W), and calculated as the average of the values at the two points.

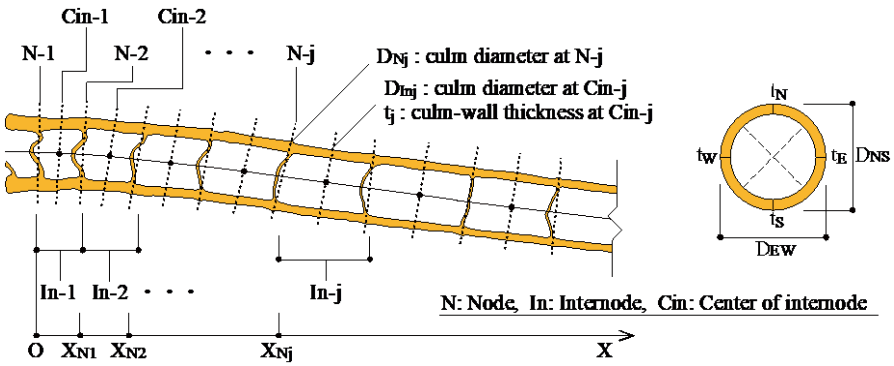


Figure 2. Measurement method of bamboo culm geometries.

3.2. Results of measured culm geometries

The relationship between N, In, and each measured value is shown in the left column of Fig. 3, while the relationship between X and each measured value is shown in the right column. Since the length of bamboo culms varies, the general tendencies of culm morphology are more easily understood by examining N and In rather than X. First, it is clear that there are significant differences in the external shape of culms between *P. edulis* and *P. bambusoides*. For example, the culm diameters, D_{In} of *P. edulis* are very large near the base and decrease rapidly upward, whereas those of *P. bambusoides* are relatively constant for a certain distance from the base and then gradually decrease. The internode length, L_{In}, is smallest near the base and largest in the middle for both species, with a decreasing tendency toward the top, but the L_{In} near the base of *P. edulis* is significantly smaller than that of *P. bambusoides*. These tendencies are similar to the results of previous studies [6], [7], [8].

On the other hand, culm wall thickness t shows a similar tendency for both species, decreasing rapidly near the base, becoming less steep thereafter, and becoming linear. Additionally, the wall thickness t of *P. edulis* is larger than that of *P. bambusoides* for most of the samples.

Fig. 4 shows the results of normalization of each measured value, which demonstrates the geometrical characteristics of the bamboo culm more clearly. The horizontal axis on the right-hand side represents the normalized coordinate X/D_{In1}, where D_{In1} is the culm diameter at the center of internode 1 (Cin-1). As Inoue *et al*. [9] mentioned that the culm diameter at the base are dominant factors in determining the bamboo culm morphology as well as species, this normalized coordinate is considered an important index for generalizing the characteristics of the bamboo culm morphology.

The vertical axis in (a) and (b) of Fig. 4 represents the aspect ratio of the internode length to the culm diameter (L_{In}/D_{In}), which increases monotonically from the base to the top. When comparing bamboo species, they are almost equal at the top, but *P. edulis* is smaller overall and below 1 at the base.

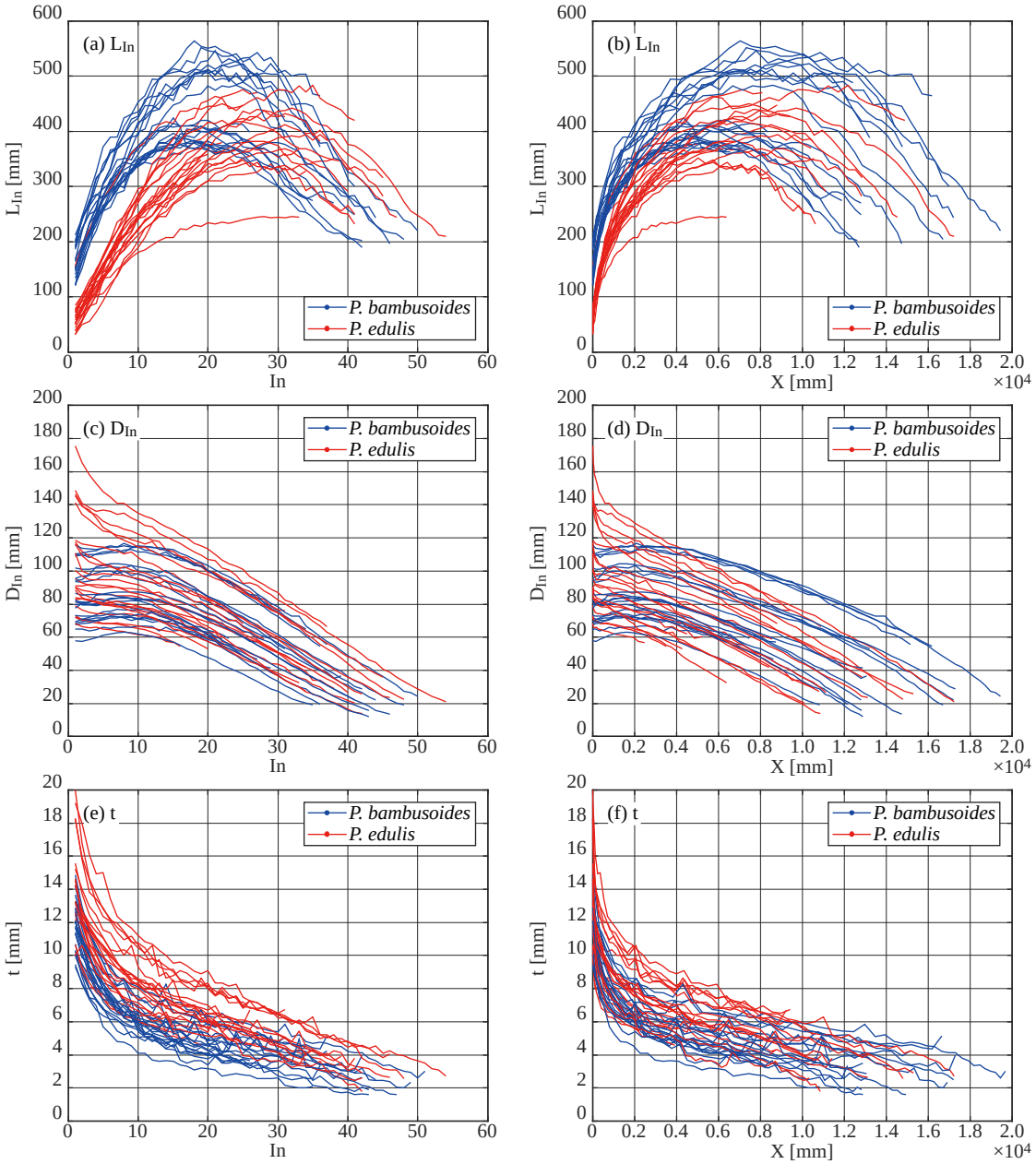


Figure 3. Left row: measured dimensions vs node index N and internode index In, right row: measured dimensions vs culm coordinate X.

The vertical axis in (c) and (d) represents the internode diameter ratio to the culm diameter at Cin-1, D_{In1} (D_{In}/D_{In1}). These figures clearly demonstrate the distinct differences in culm morphology between bamboo species. The vertical axis in (e) and (f) represents the wall thickness-to-diameter ratio (t/D_{In}) of the culm, which is obtained by dividing the wall thickness at the center of internode by the culm diameter at that location. The t/D_{In} of *P. edulis* is larger than that of *P. bambusoides*, with an average of about 0.1

and 0.08, respectively. In both species, t/D_{In} is maximum at the base, minimum in the middle, and increases again at the top.

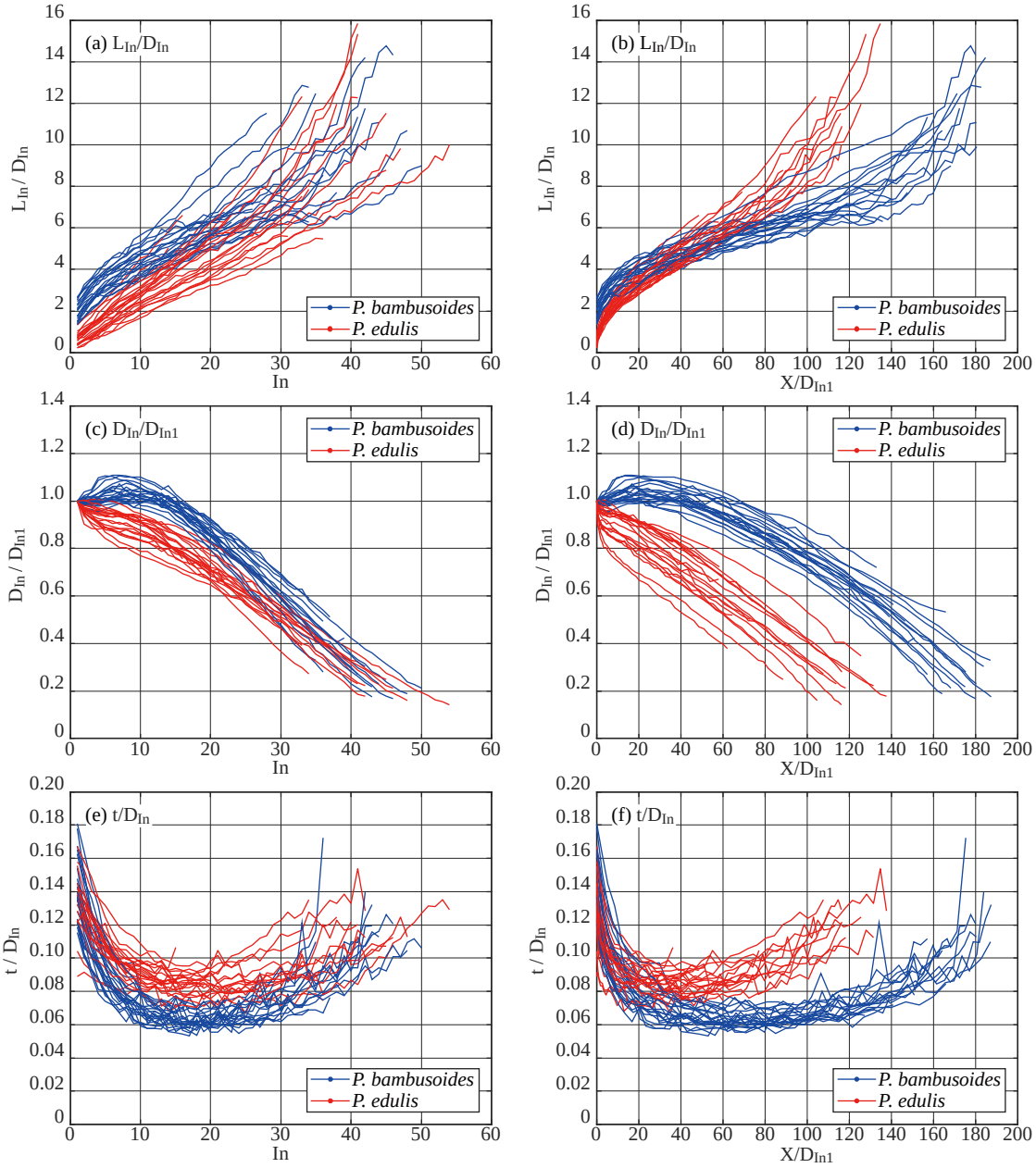


Figure 4. Left row: generalized dimensions vs node index N and internode index In, right row: generalized measured dimensions vs generalized culm coordinate.

Fig. 5(a) represents the relationship between D_{In} and t. There is a very strong proportional relationship between D_{In} and t in both bamboo species. However, near the base, t is relatively much thicker than D_{In}, and the correlation between those is locally disrupted. The vertical axis of Fig. 5(b) is the width-thickness ratio of the culm wall, t/D_{In}. In both species, t/D_{In} is not constant, and it is found that t/D_{In} increases as D_{In} decreases, except for the local increase in culm wall thickness near the base.

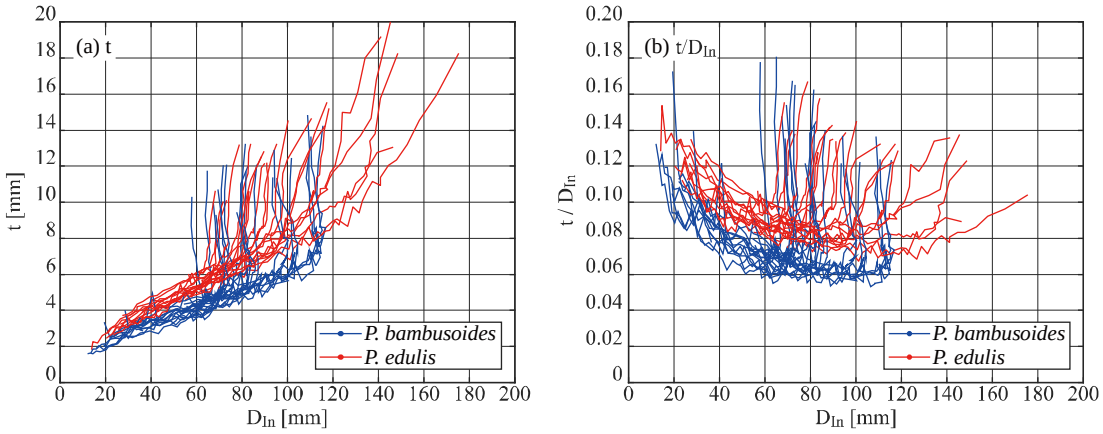


Figure 5. Relationship between culm diameter and culm wall thickness at center of internodes.

4. Mechanical properties

4.1. Testing method of mechanical properties

Fig. 6 shows the method of specimen collection and preparation for mechanical testing. In order to grasp the distribution of mechanical properties over the entire length of the culm, the culm was divided into segments of equal length, and specimens were collected from each segment for mechanical testing. The segment length, L_S, was defined as the length obtained by dividing the lower portion of the culm from the first branch node (Nb-1) into three equal parts and labeled Segment-1 to 3 from the basal end. The upper portion of the culm above Nb-1 was also divided into segments of length L_S, labeled Segment-4, 5, etc. from the basal end side. Specimens were collected from near the center of each segment, and the mechanical properties obtained from the mechanical testing were taken as representative values for that segment.

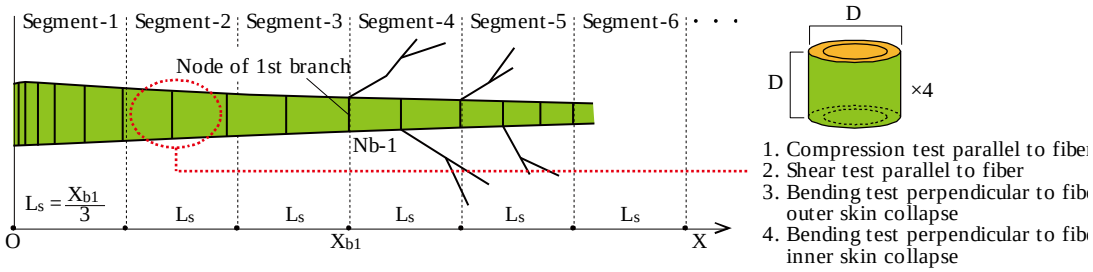


Figure 6. Sampling method of test specimen from bamboo culms.

Three types of mechanical properties are measured: F_c, which is the fiber parallel direction compressive strength, F_s, which is the shear strength, and ${}_TF_{bo}$, which is the outer bending strength in the fiber orthogonal direction. The specimens for F_c testing are of two types: with and without nodes. The reasons for selecting these properties are as follows. Firstly, since the test specimens for all the tests are small and have the same dimensions (test specimen length $\geqq$ culm diameter D), many test specimens can be obtained from a single culm. Secondly, F_c is highly correlated with tensile strength and bending strength [1], [4], and it is considered possible to estimate the changes in fiber parallel direction properties on the culm without conducting tensile and bending tests. The reason for investigating F_s and ${}_TF_{bo}$ is that the failure of the culm wall occurs mostly in response to orthogonal stresses, and the shear strength and fiber orthogonal direction bending strength are important properties for identifying the culm collapse mode. We can obtain that the bending failure of full-culm bamboo culms is caused by the Brazier effect

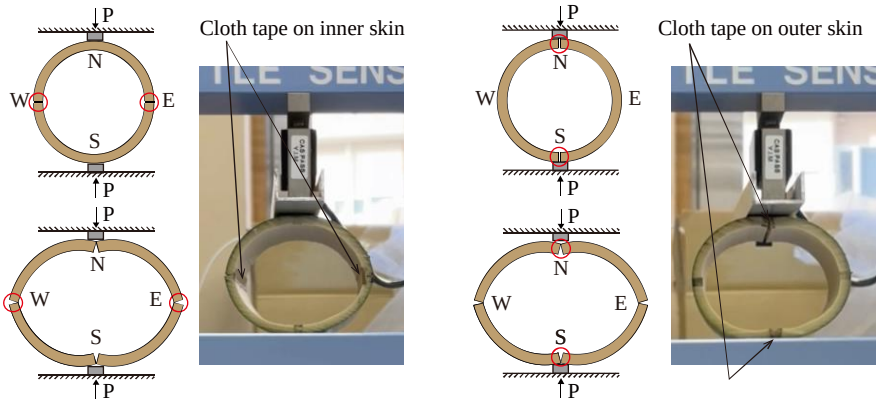
(flattening of the cross-section) that occurs during culm bending [10], with the bending failure in the fiber orthogonal direction of the culm wall outer surface being the cause. Therefore, ${}_{T}F_{bo}$ is considered an especially important property value for using round culms as bending members.

The test methods and specimen sizes used were based on ISO 22157 [11], but ${}_{T}F_{bo}$ was measured using a hinge-attached lateral compression test method shown in Fig. 7. We used the test method in which the bending failure occurred at either point E or W. The equations for calculating ${}_{T}F_{bo}$ and the bending Young's modulus (${}_{T}E_{bo}$) are provided as follows.

$$ {}_{T}F_{bo} = \frac{3P_{\max}R}{th^2} \tag{1}$$

$$ {}_{T}E_{bo} = \frac{\pi R^3}{4} \cdot \frac{P_{60} - P_{20}}{\delta_{60} - \delta_{20}} \tag{2}$$

Here, R is the radius from the centroid of the section to the core of the wall thickness, h is the depth length of the test specimen, P_{max} is the maximum load, P_{20}, P_{60}, δ_{20}, and δ_{60} are the load and displacement at 20% and 60% of the maximum load, respectively.



(a) EW-hinge bending test, Outer skin collapes at NS

(b) NS-hinge bending test, Outer skin collapes at EW

Figure 7. Modified test method of bending test perpendicular to fiber.

Note that in this method, the stress on the left and right sides of the hinge is not exactly the same, so it is assumed that the load is evenly distributed between the left and right sides when calculating each value. On the other hand, Molari *et al.* [12] proposed a method to statically determinate the test specimens by processing the cylindrical bamboo into C-shape, but it was difficult to keep the test specimens stabilized posture during loading, so this method was not adopted in this study. In addition, after various mechanical tests, the moisture content (MC) and oven-dry density (ρ_{dry}) of the test specimens are measured. These measurements are also carried out according to the ISO 22157 method.

4.2. Results of mechanical test

Fig. 8 shows the relationship between MC and various strengths, and Fig. 9 shows the relationship between ρ_{dry} and various strengths. Table 1 summarizes the mean values and coefficients of variation (CV) for each property. The specimens used in this study were allowed to dry naturally for a certain period after harvesting, so the MC of most of the specimens was between 10% and 20%. While there were not many samples with an MC above 25%, a clear trend was observed where the strength of F_c decreased as the MC increased. Regarding ρ_{dry} and various strengths, a particularly strong correlation

was observed for F_c. The correlation for F_s and ${}_TF_{bo}$ was smaller compared to F_c, but a relatively large positive correlation was observed between ρ_{dry} and F_s for *P. edulis*.

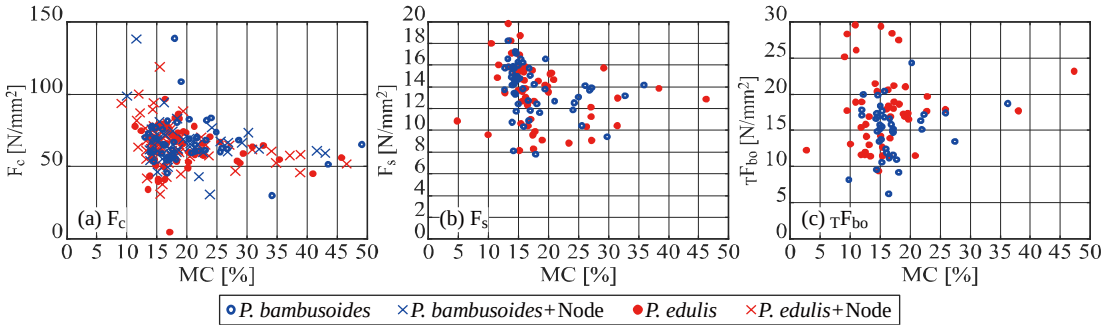


Figure 8. Relationship between moisture content ratio and various strengths.

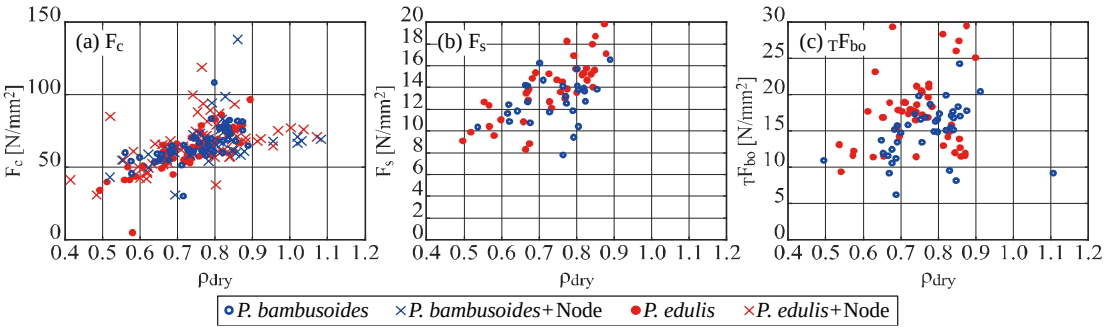


Figure 9. Relationship between oven-dry specific gravity and various strengths.

Table 1. Mean value and CV of various strengths and physical properties.

	F_c	F_c*	F_s	F_{bo}	ρ_{dry}	MC	F_c	F_c*	F_s	${}_TF_{bo}$	ρ_{dry}	MC
	N/mm^2	N/mm^2	N/mm^2	N/mm^2	-	%	N/mm^2	N/mm^2	N/mm^2	N/mm^2	-	%
Mean value	67.5	66.5	13.6	15.0	0.74	20.4	62.3	66.6	13.1	18.6	0.69	19.3
CV [%]	23.7	23.9	29.6	31.5	27.6	46.1	23.6	23.2	31.8	37.3	29.7	46.6

NOTE: F_c* = compression strength of specimen with node.

5. Discussing the relationship between culm geometries and mechanical properties

Fig. 10 shows the relationship between segment of culm and normalized coordinate X/D_{In1} and ρ_{dry}. In both species, ρ_{dry} tends to increase from the base to the top. In the left figure, Avg means the mean value of each segment. Fig. 11 shows the relationship between In, X/D_{In1}, and various strengths. Fig. 12 shows the relationship between D_{In} and various strengths. It was evident that F_c increased towards the top of the culm from the base, and a strong correlation with D_{In} is observed. As shown in the previous chapter, F_c has a stronger correlation with ρ_{dry} than other strengths and clearly varies depending on the position on the culm. The comparison of F_c between at nodes and at internodes shows no significant difference in both bamboo species. For F_s and ${}_TF_{bo}$, the correlation with In and X/D_{In1} is considerably smaller than that with F_c, and particularly for F_s, there is almost no correlation. While the scatter is larger than F_c, ${}_TF_{bo}$ also shows a slight correlation with F_s and a clear tendency to increase from the base to the top, similar to F_c.

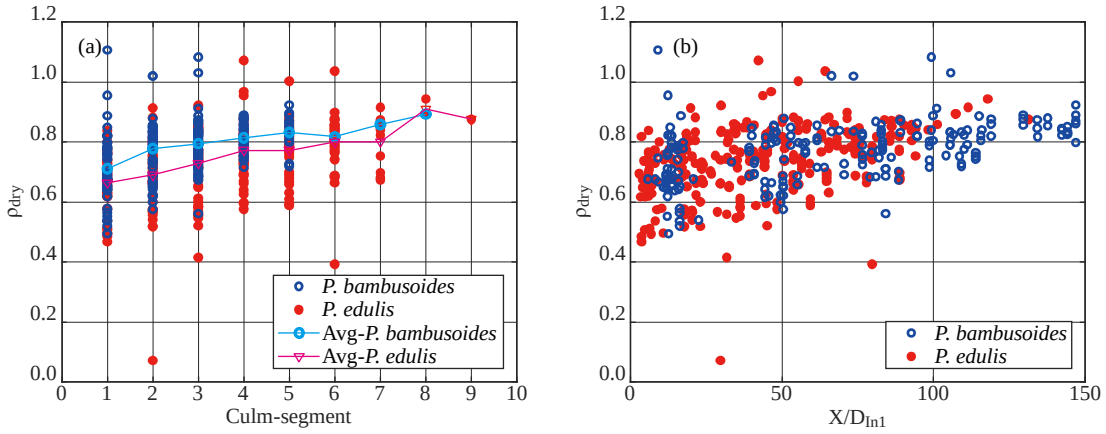


Figure 10. Relationship between relative location on the bamboo culm and oven-dry specific gravity.

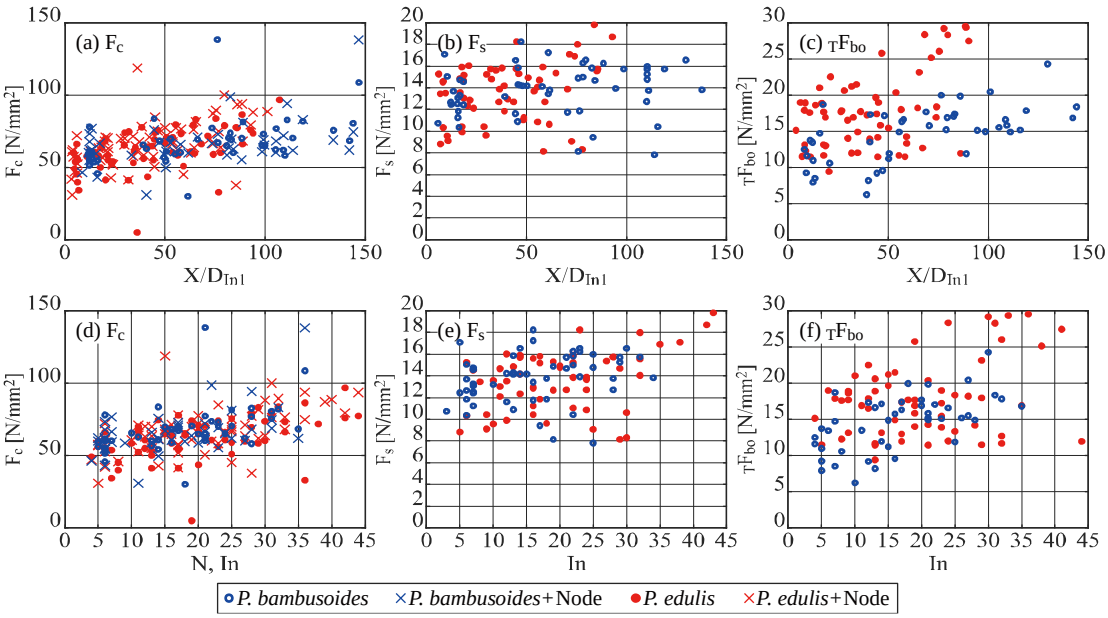


Figure 11. Relationship between relative location on the bamboo culm and various strengths.

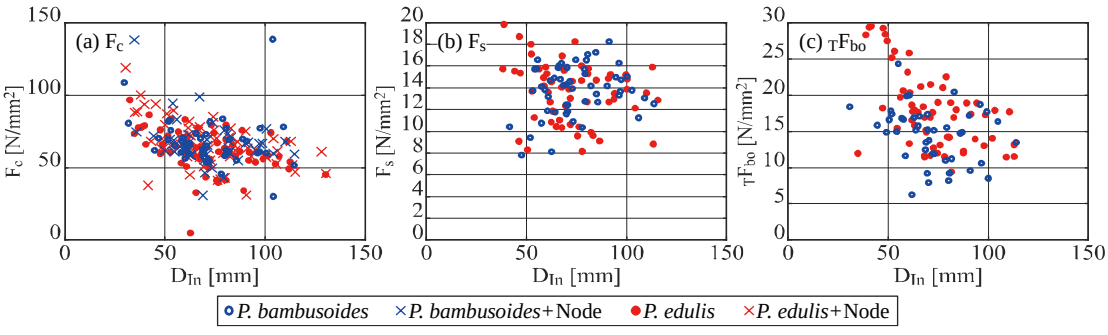


Figure 12. Relationship between culm-diameter and various strengths.

The tendency of increasing strength and stiffness from the base to the tip end of a bamboo culm is a characteristic observed in many bamboo species e.g., *Guadua*. This is mainly due to the increasing

density of vascular bundles towards the tip end (e.g., [1], [4]). Therefore, properties that depend on vascular bundle density (e.g., tensile/compressive strength and Young's modulus in the fiber parallel direction) generally exhibit higher performance at the tip end compared to the base end.

Finally, we show our preliminary results of the bending Young's modulus E_b of bamboo culms. The test specimens were bamboo culms harvested within 1-2 months after harvesting (MC ranged from 12-96%). The test method was a three-point bending test with a span of 1.6-2 m, and E_b was calculated from the load-deflection curve until a deflection of about 1/200 of the span was reached. Fig. 13(a) shows the relationship between the cross-sectional area A_{av} and E_b of the bamboo culms, and Fig. 13(b) shows the relationship between the culm diameter D_{av} and E_b. A_{av} and D_{av} are the average values of the both ends cross-sectional areas of the test specimen. In both species, a clear correlation was observed between the cross-sectional size and E_b. In addition, in both species, E_b ranged from 15-20 GPa at D = 50 mm and from 7-12 GPa at D = 100 mm, indicating a significant difference in E_b depending on the cross-sectional size.

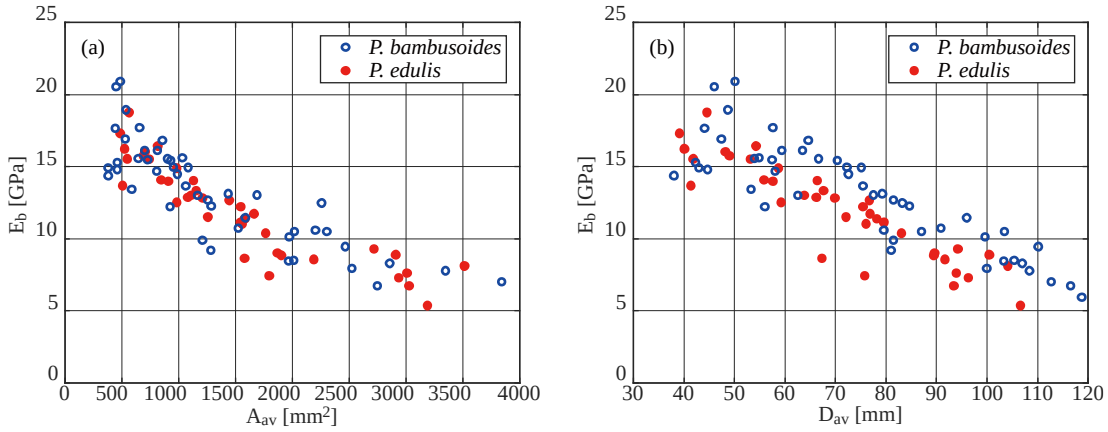


Figure 13. Relationship between cross-sectional area of bamboo culms and bending Young's modulus.

6. Concluding remarks

In this study, we conducted a fundamental investigation on the relationship between the culm morphology and mechanical properties of Japanese bamboo (*P. edulis* and *P. bambusoides*). Both bamboo species showed distinct differences in culm morphology, with a linear decrease in culm diameter from the middle to the top, but with a sudden increase in culm diameter near the base for *P. edulis* and relatively stable diameter for *P. bambusoides* up to around 5 meters from the base. On the other hand, culm wall thickness was generally greater in *P. edulis*, but the change along the culm axis was similar for both species.

Among the investigated mechanical properties, the axial compressive strength showed the strongest correlation with culm geometry. The bending Young's modulus was suggested to vary greatly depending on the cross-sectional size. From these results, it is suggested that the axial strength and stiffness, which strongly depend on the properties of the vascular bundles, are greatly influenced by culm geometry and density, while the strength in the transverse direction (shear strength, transverse bending strength, etc.) may be less affected by the position on the culm or cross-sectional dimensions.

In the future, we aim to expand the sample size and perform statistical formulation of the relationship between mechanical properties and culm geometry, with the goal of further promoting the use of bamboo structures.

Acknowledgements

We gratefully acknowledge the support received for this study from The Maeda Engineering Foundation through research grants for the fiscal years 2021 and 2022, as well as the Grant-in-Aid for Scientific Research (21K14292, 21H00373 in the New Academic Area Research category), specifically for the "Plant-Structure-Optimization". Our sincere appreciation goes to these organizations for their invaluable assistance.

References

[1] K. A. Harries and B. Sharma, Eds., *Nonconventional and Vernacular Construction Materials: Characterisation, Properties and Applications*. Woodhead Publishing, 2019.

[2] J. G. Oliva, M. Trujillo, S. Ezeta, R. Abud, M. I. Verhulst, "Bamboo gridshells for rural housing in Mexico," in *Proceedings of IASS 2022 Symposium affiliated with APCS 2022 Conference, Innovation·Sustainability·Legacy*, Beijing, China, Sep. 19-22, 2022, pp. 3328-3336.

[3] N. Vo Trong, *Towards a Reliable Bamboo Architecture: The construction, structure, and space of bamboo architecture through the use of bundled joints, repeating frame units, and bending elements*, Doctoral thesis, Waseda University, 2022.

[4] J. Janssen, *Mechanical Properties of Bamboo*. Kluwer Academic Publishers, Dordrecht, The Netherlands, 1981.

[5] S. Amada, T. Muneoka, Y. Nagase, Y. Ichikawa, A. Kirigai, and Y. Zhifei, "The mechanical structures of bamboos in viewpoint of functionally gradient and composite materials," *J. Compos. Mater.*, vol. 30, no. 7, pp. 800-819, 1996.

[6] Y. A. Akinbade, *Mechanical and Morphological Characterization of Full-Culm Bamboo*, Doctoral thesis, Swanson School of Engineering, Univ. of Pittsburgh, 2020.

[7] H. Shima, M. Sato, and A. Inoue, "Self-adaptive formation of uneven node spacings in wild bamboo," *Phys. Rev. E*, vol. 93, no. 2, pp. 022406-1-022406-9, 2016.

[8] A. Inoue, M. Sato, and H. Shima, "A new taper index based on form-factor: application to three bamboo species (*Phyllostachys* spp.)," *Eur. J. For. Res.*, vol. 140, pp. 1533-1542, Sep. 2021.

[9] A. Inoue, S. Tochihara, M. Sato, and H. Shima, "Universal node distribution in three bamboo species (Phyllostachys spp.)," *Trees*, vol. 31, no. 4, pp. 1271-1278, Apr. 2017.

[10] T. Nagai, K. Oki, Y. Nagano, and Y. Kihara, "Fundamental investigation on bending failure mechanism and bending strength of full-culm bamboo - comparative verification of bending stress generated in bamboo culm wall with Brazier effect theory, numerical analysis and experimental results," *J. Struct. Eng.*, vol. 69B, Apr. 2023. (in Japanese)

[11] ISO 22157, Bamboo structures – Determination of physical and mechanical properties of bamboo culms –, 2019.

[12] L. Molari and J. J. García, "On the radial variation of the transverse mechanical properties of bamboo," *J. Build. Eng.*, vol. 33, no. 1, p. 101557, Jan. 2021.

IASS 2023
July 10–14 Melbourne
Integration of Design and Fabrication

Proceedings of the IASS Annual Symposium 2023
Integration of Design and Fabrication
10–14 July 2023, Melbourne, Australia
Y.M. Xie, J. Burry, T.U. Lee and J. Ma (eds.)

Study on compression strength of Japanese full-culm bamboo columns using short-length specimens

Keisuke OKI*, Takuo NAGAI[a]

* Graduate school of Environmental Science, The University of Shiga Prefecture
2500, Hassaka-cho, Hikone-city, Shiga, Japan
oe52koki@ec.usp.ac.jp

[a] Department of Architecture and Design, The University of Shiga Prefecture

Abstract

This study aims to establish a method for estimating the compression strength of full-culm bamboo columns. To achieve this, the comparison between results of buckling tests using small specimens of Japanese representative bamboo species and numerical analyses is discussed. The results showed that the buckling load of the full-culm bamboo column can be estimated with high accuracy by FEM linear buckling analysis, taking into account the variation of the bamboo culm cross-sectional area and bending Young's modulus. However, since various physical properties such as moisture content and dry density can affect bending Young's modulus, it is necessary to clarify their relationship with each property. This research contributes to a better understanding of how to evaluate compression strength in full-culm bamboo columns and could inform future studies on sustainable building materials.

Keywords: full-culm bamboo, compression strength, linear buckling analysis, *Phyllostachys bambusoides*, *Phyllostachys edulis*, Hangar Prize applicant

1. Introduction

The construction industry, including architecture and civil engineering, accounts for approximately 40% of the world's greenhouse gas emissions, consumption of fossil fuels, and industrial waste emissions. In addition, there is an expected exponential demand for housing construction, particularly in developing countries with rapid population growth in the future, which underscores the need for the construction industry to transform into a sustainable industrial structure. Against this background, bamboo is attracting great expectations as a sustainable building material with low environmental impact since its fast growth, regenerative properties, and abundant resources.

Various challenges still need to be addressed in order to utilize bamboo in building structures, including the systematic organization of physical and mechanical properties of bamboo materials and construction methods, and the establishment of protective treatment methods for durability improvement. Evaluating the compression strength of bamboo is an essential challenge to overcome when using full-culm bamboo poles as columns or trusses. While pioneering research on bamboo scaffoldings by Yu *et al*. [1], [2] and numerous studies and proposals have been conducted, such as the establishment of design formulas in ISO 22156 [3] and design codes [4], [5], many of these assume that the bamboo culms are uniform and homogeneous beam-column elements with a constant cross-section. This can lead to extremely conservative compression strength estimates. On the other hand, in recent years, attempts have been made to evaluate the effects of the taper characteristics of bamboo culms with respect to buckling strength and the influence of initial irregularities in bamboo culms, in order to calculate more practical design strengths [6], [7].

Copyright © 2023 by Keisuke OKI and Takuo NAGAI. Published in the Proceedings of the IASS Annual Symposium 2023 with permission.

In this study, we investigate the calculation method of compression strength for bamboo culms by comparing the results of buckling tests using small specimens of Japanese representative bamboo species and numerical analyses.

2. Research methods

2.1. Bamboo materials for the study

The bamboo species investigated in this study were Moso (*Phyllostachys edulis*), Madake (*Phyllostachys bambusoides*), both of which were collected from bamboo forests in Omihachiman-city, Shiga Prefecture, in Japan (35.15'N, 136.09'E). The bamboo forest consists of adjacent Moso and Madake stands. The bamboo samples used in this study were aged three years or older, and their age was visually determined.

After harvesting, the bamboo culms were stored in a semi-outdoor area with good ventilation that was not directly exposed to rain. All processing and testing were conducted within three months from harvesting. No special protective treatment was applied due to the short storage period.

2.2 Research process

Since bamboo culms are variable cross-section members with changing dimensions along the culm axis, they cannot be modeled as simple, homogeneous members with a constant cross-section. Therefore, to estimate the buckling strength of bamboo culms, a finite element model that takes into account the cross-sectional variation was used, and linear buckling analysis was performed. To obtain the required values of the cross-sectional dimensions and bending Young's modulus of each part of the bamboo culm, the following experimental and measurement procedures were performed.

First, a bending test was conducted on the bamboo culm to determine its bending stiffness from the load-deflection relationship. The bending test was a small-deflection test in which the stress and strain in the specimen remained within the elastic range to avoid inducing plastic deformation. Subsequently, to prevent changes in moisture content, the buckling test was conducted promptly. In this study, experiments were conducted on small specimens with a column length of 1600 mm due to equipment limitations. After the buckling test, the bamboo culm was cut at the center of each node, and the cross-sectional dimensions were measured, and the moisture content was determined. To ensure a uniform distribution of aspect ratios ranging from 40 to 150 for the buckling test specimens, the cross-sectional sizes were selected accordingly. A total of 38 Moso specimens and 48 Madake specimens were tested.

3. Measurement and modelling of culm shape of full-culm bamboo poles

Fig. 1(a) shows the method for measuring the shape of the bamboo culm specimens. The measurement items were the length of each internode (L_{IN}), the culm diameter (D) at the center of each internode, and the culm wall thickness (t) at the four points (N, E, S, and W) where the cross sections intersect. After the buckling test, the bamboo culm was cut at the corresponding position and measurements were taken. D was calculated by measuring the circumference of the culm at the center of each internode with a tape measure and dividing by π. Although the actual cross section of the bamboo culm is not a perfect circle, this study assumes a perfect circle with diameter D for the analysis. The culm wall thickness t was defined as the average value of the wall thickness at the four points where the cross sections intersect at right angles.

Fig. 1(b) shows the FEM modeling method used to calculate the bending Young's modulus. The nodes of the model were located at the corresponding coordinates of nodes of the bamboo culm, and the internode between them was connected with planar (2D) beam elements with a uniform cylindrical cross section. The characteristic values of the beam element cross-section were determined using the cross-sectional dimensions measured at the center of each internode. Therefore, the FEM model approximated

the cross-sectional variation of the bamboo culm in the axial direction as a stepped model. Nodes were also placed at the load point at the center of the span and at the support points at both ends. The boundary conditions at the support points were set as one end pinned and the other end roller supported.

Fig. 1(c) shows the FEM modeling method used for buckling analysis. Based on the bending analysis model, nodes were added at the midpoints (centers of the internodes) between the nodes to obtain a smoother buckling mode shape. The boundary conditions at both ends were set as one end pinned and the other end roller supported.

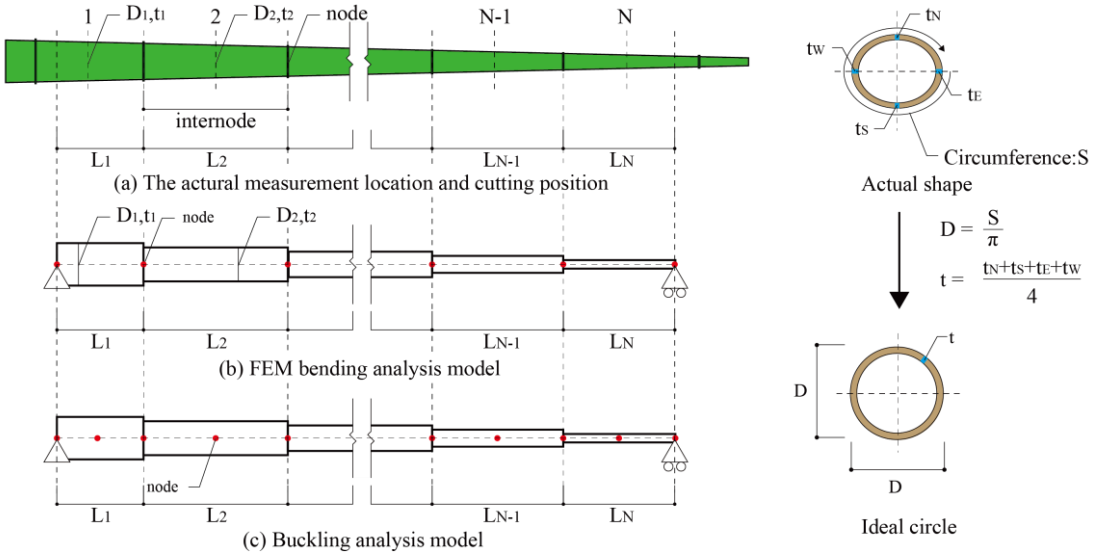


Figure 1. Measurement method and FEM modeling of dimensions for round bamboo columns.

4. Micro-deformation bending test of full-culm bamboo poles

4.1. Test methods and calculation methods of bending Young's modulus

Fig. 2 shows the bending test method. The bending test was a three-point bending test in which the specimen was loaded at the center of the span, and the load point was located near the center of each internode to avoid the nodes. The span of the specimen was determined to satisfy the conditions that the bending stress at the load point was less than 30 N/mm^2 when the deflection at the load point was about 1/200 of the span and the shear span ratio was 10 or greater, following the method specified in ISO 22157 [7]. The upper limit of the bending stress was estimated to be about one-third of the bending strength (approximately 100 N/mm^2) of Moso and Madake. As a result, the span between the supports varied depending on the specimen, ranging from 1700 to 2000 mm.

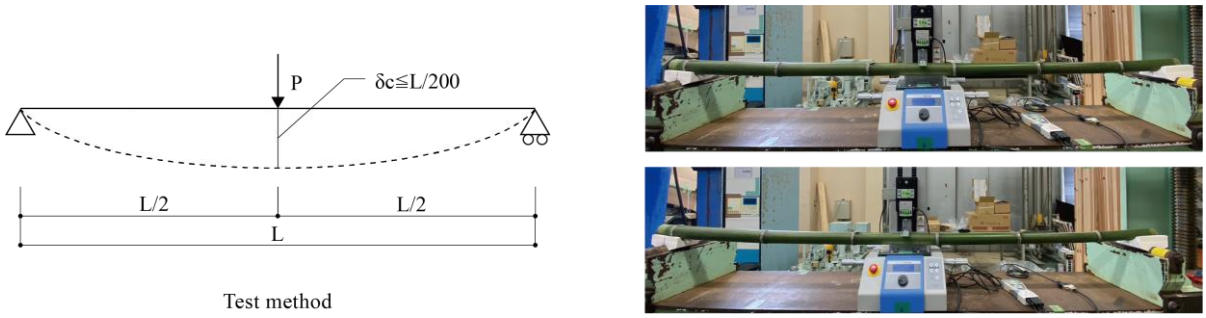


Figure 2. Method of Micro-deformation test.

Fig. 3 shows the method used to calculate the bending Young's modulus (E_b). First, the gradient k was obtained by connecting two points on the load-deflection curve obtained from the bending test. Next, linear elastic analysis using the bending analysis model shown in Fig. 1(b) was performed, and E_b was determined such that the ratio k' of the load P to the deflection δ_c in Eq. (1) was equal to k.

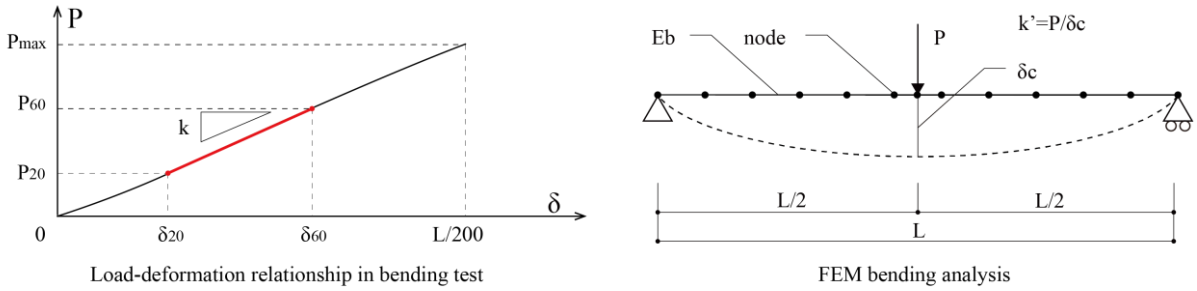


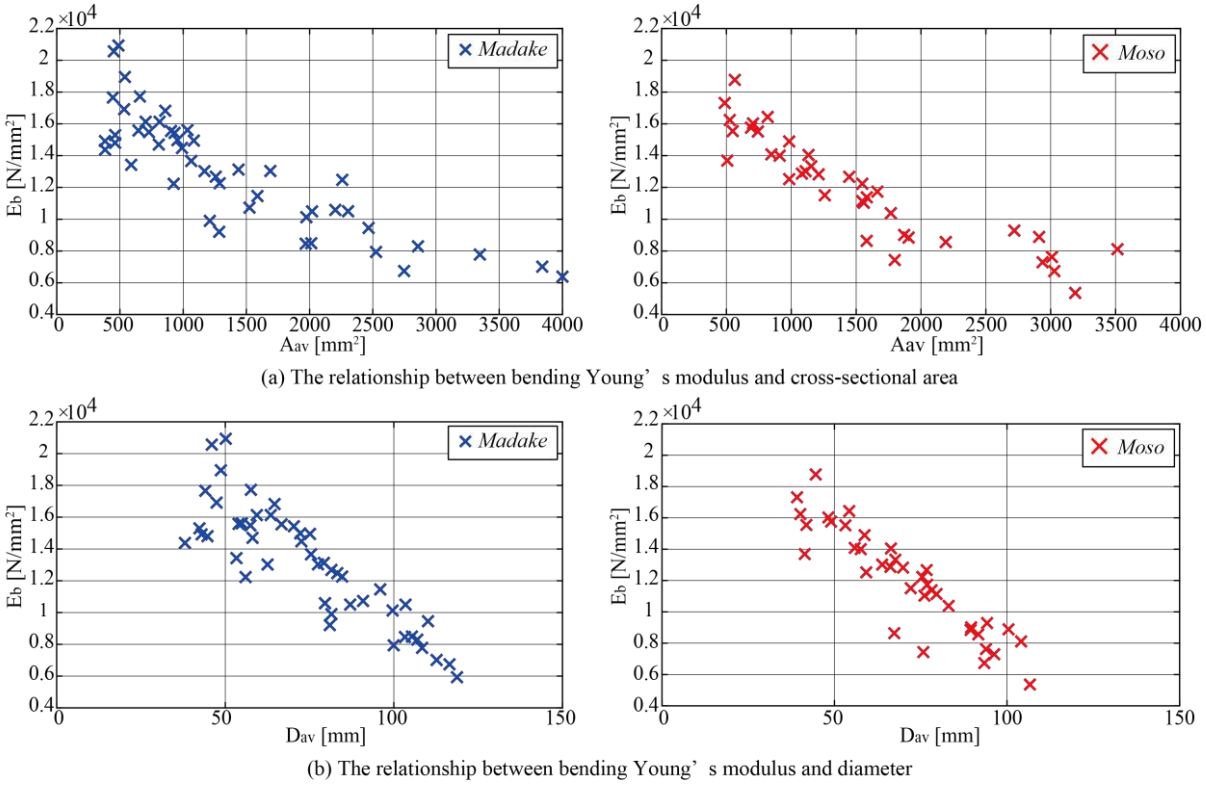
Figure 3. Method for calculating bending Young's modulus.

$$k = \frac{P_{60} - P_{20}}{\delta_{60} - \delta_{20}} = k'(E_b) \quad (1)$$

Here, P_{20}, δ_{20}, P_{60}, and δ_{60} represent the load and displacement at 20% and 60% of the maximum load, respectively.

4.2. Experimental results

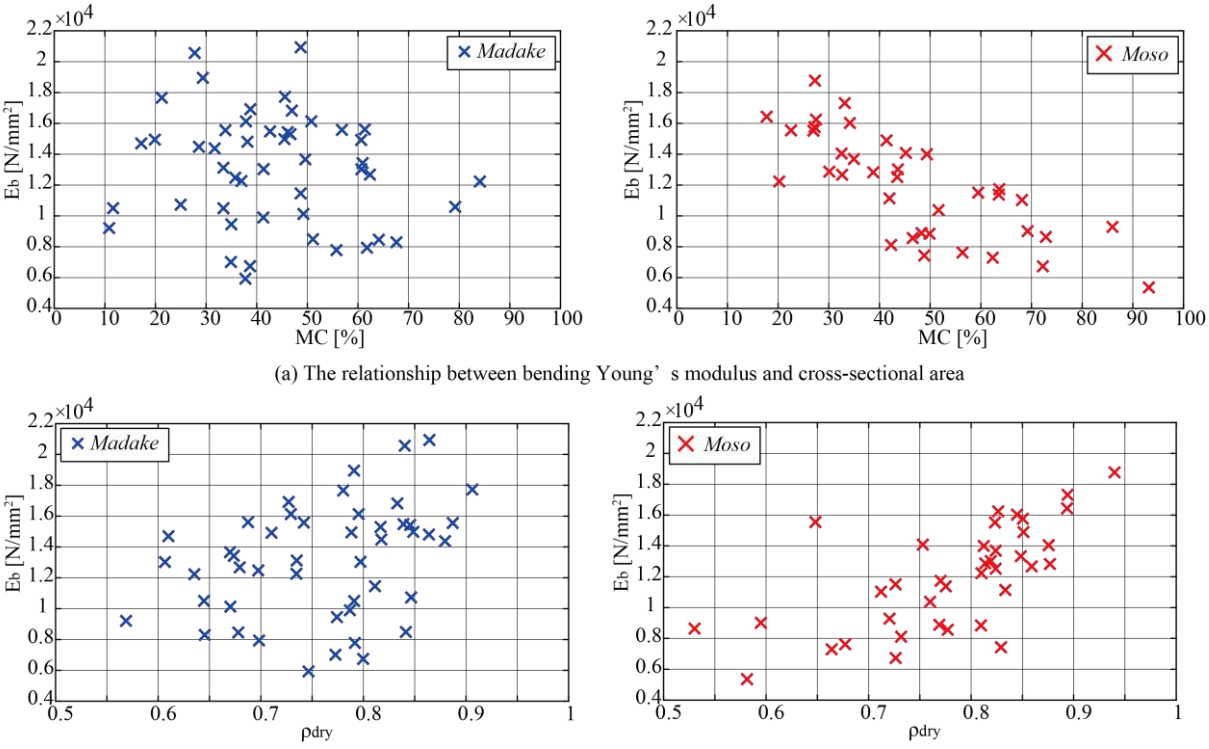
Fig. 4 shows the relationship between the average cross-sectional area (A_{av}) and the bending Young's modulus (E_b) of the test specimens. A_{av} is defined as the average of the cross-sectional area at both ends of the test specimen. For both Moso and Madake, a clear correlation between the cross-sectional size and E_b was observed. The E_b values for D = 50 mm were 15,000-20,000 N/mm^2, and those for D = 100 mm were 7,000-12,000 N/mm^2 for both species, indicating a significant dependence of E_b on the cross-sectional size. It is well known that many bamboo species have a negative correlation between the cross-sectional size and the axial properties, such as tensile, compressive, and bending strength in the longitudinal direction. This is because the volume density of vascular bundles in the cross-section increases relatively towards the top of the bamboo culm [8], [9].



(a) The relationship between bending Young' s modulus and cross-sectional area

(b) The relationship between bending Young' s modulus and diameter

Figure 4. Relationship between cross-sectional size and bending Young's modulus.



(a) The relationship between bending Young' s modulus and cross-sectional area

(b) The relationship between bending Young' s modulus and diameter

Figure 5. Relationship between the oven-dry specific gravity, moisture content and the bending Young's modulus.

In Fig. 5, the relationship between moisture content (MC), oven-dry density (ρ_{dry}), and E_b is shown for both Moso and Madake. A negative correlation between MC and E_b, and a positive correlation between ρ_{dry} and E_b were observed for Moso. This suggests that it is difficult to determine the bending Young's modulus from the cross-sectional area alone, as MC can also affect material properties. However, for Madake, a clear correlation was not observed, and the large variation in the scatter plot raises questions about the relationship between material properties. Further investigations are necessary to clarify the correlations between different material properties for Madake.

5. Buckling test of full-culm bamboo poles

5.1. Test methods

Fig. 6 shows the method for conducting the buckling test on the bamboo columns. The test specimens were prepared by cutting them to a length of 1600 mm after conducting the bending tests. Aluminum alloy ball joints were attached to the top and bottom load points to serve as pin supports.

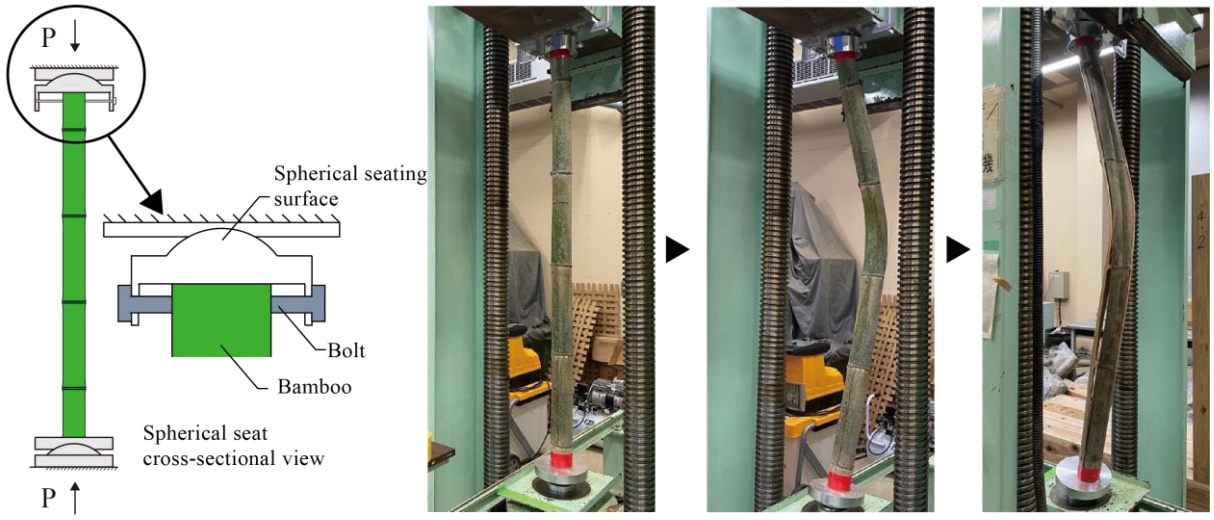


Figure 6. Method of buckling test for full-culm bamboo columns.

5.2. Comparison between test results and linear buckling analysis

Fig. 7 shows an example of the results of the buckling test. In both Moso and Madake, the relationship between the load and deformation up to the maximum load is linear and the axial rigidity hardly changes regardless of the load magnitude. In addition, it was confirmed that the greater the equivalent slenderness ratio λ_{eq}, which will be described later, the faster the load decreases after the maximum load, and the smaller the maximum load, the gentler the subsequent load decrease becomes. In this study, the experimentally obtained maximum load P_{max} was defined as the buckling load.

The analytical value P_{cr} of the buckling load was defined as the first-mode buckling load obtained by linear buckling analysis using the model in Fig. 1(c). The bending Young's modulus E_b obtained in the previous chapter was used for each test specimen. Fig. 8 shows a comparison of the experimental and analytical values. The two values are distributed evenly above and below the 1:1 slope. Table 1 shows the mean and coefficient of variation of the ratio P_{cr}/P_{max} between the analytical and experimental values. The mean values for both Moso and Madake are very close to 1.0, and the coefficients of variation are both less than 10%. Therefore, it can be concluded that the buckling load of the full-culm bamboo

column can be accurately determined by linear buckling analysis if the sectional changes of the bamboo culm and the bending Young's modulus in the small deformation range are properly evaluated.

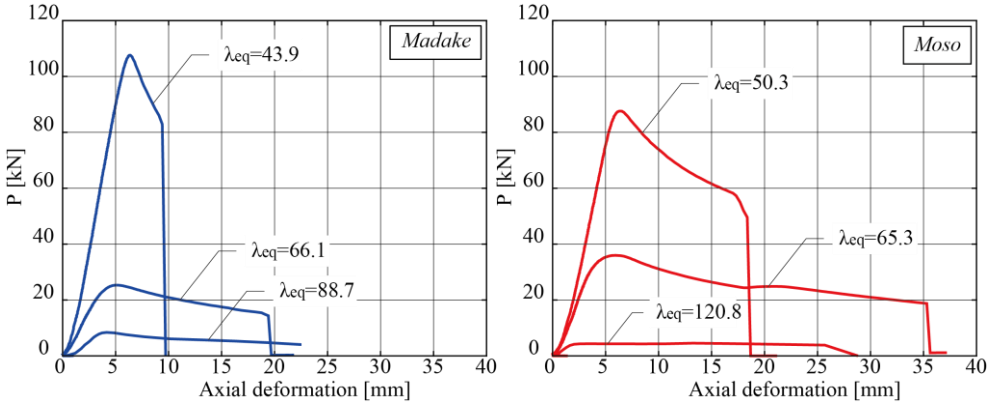


Figure 7. The example of load-axial displacement relationship in the buckling test

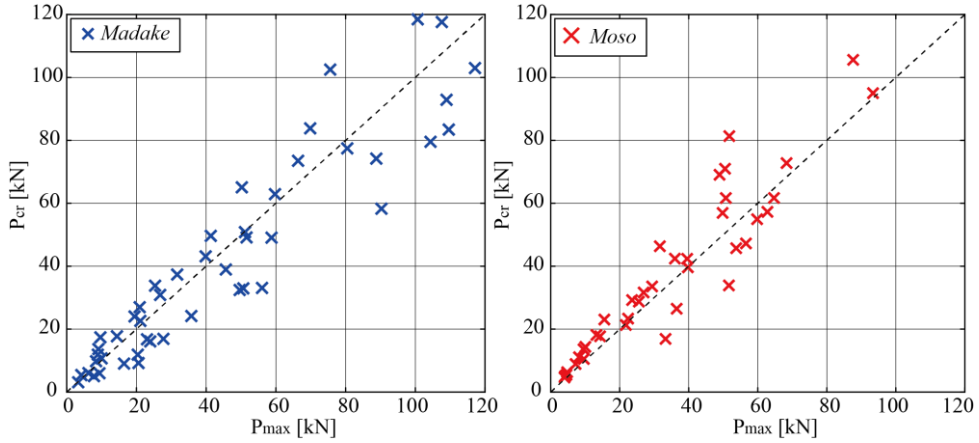


Figure 8. Comparison of buckling loads between experiments and linear buckling analysis.

Table 1. The mean value and coefficient of variation (CV) of the ratio of the analytical buckling load to the experimental buckling load.

Bamboo speceis	Mean value of P_{cr}/P_{max}	CV [%] of P_{cr}/P_{max}
Madake	0.99	9.1
Moso	1.04	3.1

5.3. Equivalent uniform cross-section model for bamboo column

The buckling load of a column member subjected to axial force is generally expressed as a function of the slenderness ratio. However, the radius of the cross-section of a bamboo culm is not uniform, and the slenderness ratio cannot be defined. Therefore, an equivalent uniform section model with the same buckling load as the one obtained by FEM is derived, and the equivalent slenderness ratio λ_{eq} is determined as following equation.

$$I_{eq} = \frac{P_{cr}L^2}{\pi^2 E_b} \tag{2}$$

Here, L represents the length of the specimen (1600 mm). Additionally, λ_{eq} is calculated using the following equation.

$$\lambda_{eq} = \frac{L}{\sqrt{I_{eq}/A_{av}}} \tag{3}$$

Here, A_{av} denotes the average cross-sectional area of the specimen at both ends. The compression strength of both the experimental and analytical values is determined using A_{av}, and is calculated using the following formula.

$$\sigma_{cr} = \frac{P_{cr}}{A_{av}}, \quad \sigma_{\max} = \frac{P_{\max}}{A_{av}} \tag{4}$$

In addition, the Euler buckling curve using λ_{eq} is expressed as follows.

$$\sigma_{cr} = \frac{\pi^2 E_b}{\lambda_{eq}^2} \tag{5}$$

Fig. 9 shows the relationship between λ_{eq} and the experimental maximum stress σ_{max}. The two curves in the figure represent the Euler buckling curves using the maximum and minimum bending Young's moduli for each bamboo species obtained from the bending tests. Most of the experimental results fall between the two Euler buckling curves, and there is a general trend of decreasing buckling strength with increasing slenderness ratio, although the scatter is large. Therefore, it is important to evaluate the bending Young's modulus of the member appropriately for calculating the buckling strength, as mentioned earlier.

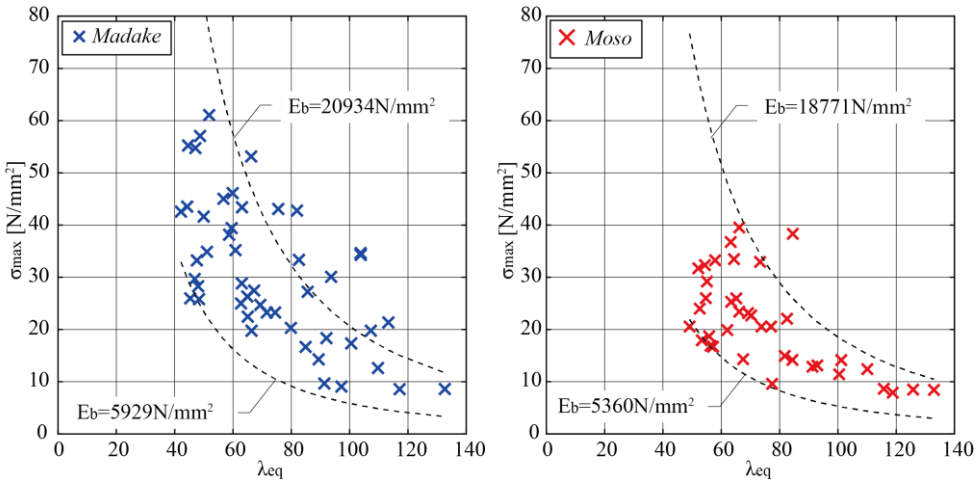


Figure 9. Relationship between slenderness ratio and compression stress of experimental results.

6. Conclusion

In this study, we investigated the method for determining compression strength of bamboo. The following findings were obtained.

The purpose of this study was to establish a method for estimating the compression strength of full-culm bamboo columns, and a comparison was made between buckling tests with small-scale specimens and numerical analysis. The buckling load of the full-culm bamboo column can be estimated with very high accuracy by FEM linear buckling analysis, taking into account the variation of the bamboo culm cross-sectional area and bending Young's modulus. However, since the bending Young's modulus is thought

to be affected not only by the cross-sectional size but also by various physical properties such as moisture content and dry density, it is necessary to clarify the relationship with each property. Additionally, the full-culm bamboo columns used in this study were small in size, so the variation in the bending Young's modulus within a single specimen was considered to be small, which may have facilitated the estimation of the buckling load by assuming homogeneity in the buckling analysis. Therefore, future studies will examine test specimens with column heights (2-3m) that are typically found in general buildings.

Acknowledgements

We gratefully acknowledge the support received for this study from The Maeda Engineering Foundation through research grants for the fiscal years 2021 and 2022, the Grant-in-Aid for Scientific Research (21K14292), as well as the Grant-in-Aid for Scientific Research (21H00373) in the New Academic Area Research category, specifically for the "Plant-Structure-Optimization". Additionally, many of the experiments in this research were conducted as a graduation thesis research project by Ayumi SAGUCHI (The univ. of Shiga pref.). We express our sincere appreciation for their invaluable assistance.

References

[1] W. K. Yu, K. F. Chung, and S. L. Chan, "Column buckling of structural bamboo," *Eng. Struct.*, vol. 25, no. 6, pp. 755-768, May 2003.

[2] W. K. Yu, K. F. Chung, and S. L. Chan, "Axial buckling of bamboo columns in bamboo scaffolds," *Eng. Struct.*, vol. 27, no. 1, pp. 61-73, Jan. 2005.

[3] ISO 22156, "Bamboo structures – Bamboo culms – Structural design," Jun. 2021.

[4] NSR-10, G12, "Normativa Colombiana de Construcción Sismo Resistente en Guadua," 2009.

[5] K. A. Harries, J. Bumstead, M. Richard, and D. Trujillo, "Geometric and material effects on bamboo buckling behavior," *ICE Proc. Struct. Build.*, vol. 170, no. 4, pp. 236-249, 2017.

[6] E. T. Bahtiar, D. Malkowska, D. Trujillo, and N. Nugroho, "Experimental study on buckling resistance of Guadua angustifolia bamboo column," *Eng. Struct.*, vol. 228, no. 111548, Feb. 2021.

[7] ISO 22157, "Bamboo structures – Determination of physical and mechanical properties of bamboo culms –," 2019.

[8] K. A. Harries and B. Sharma, Eds., *Nonconventional and Vernacular Construction Materials: Characterisation, Properties and Applications*, Woodhead Publishing, Nov. 2019.

[9] S. Amada, T. Munekata, Y. Nagase, Y. Ichikawa, A. Kirigai, and Y. Zhifei, "The mechanical structures of bamboos in viewpoint of functionally gradient and composite materials," *J. Compos. Mater.*, vol. 30, no. 7, pp. 800-819, 1996.

Bio-inspired structures and architecture

Active bending
Additive manufacturing/ 3D printing
Architectural geometry
Bamboo for sustainable construction and quality of life improvement
► **Bio-inspired structures and architecture**
Bridge structures
Computational form-finding
Conceptual design
Concrete structures
Construction techniques
Deployable and inflatable structures
Design competition (WG21)
Digital modelling and fabrication
Dynamic response of metal spatial structures
Dynamic response of other structures
Form-finding and structural optimisation of interlocking discrete assemblages
Graphical methods
Gridshell and lattice structures
Historical concrete shells
Historical structures
Lattice structures
Life-cycle design and assessment of structures
Metal gridshell structures, connections and stability
Methods and construction technologies for sustainable shell structures
Morphology and configuration processing
Next generation parametric design
Novel methods in modelling, optimisation and construction for reducing carbon footprint of continuous roof shells
Numerical methods for geometry, form-finding and optimisation of lightweight structures
Optimisation methods and applications
Origami
Other
Teaching design uncertainty: working with unknown qualities/quantities of new and re-claimed materials
Teaching of shell and spatial structures
Tensegrity systems and cable structures
Tension and membrane structures
Tension structures in the Asia-Pacific
Timber and bio-based structures
Topology optimisation
Traditional masonry structures and innovation
Transformable structures

IASS 2023
July 10–14 Melbourne
Integration of Design and Fabrication

Proceedings of the IASS Annual Symposium 2023
Integration of Design and Fabrication
10–14 July 2023, Melbourne, Australia
Y.M. Xie, J. Burry, T.U. Lee and J. Ma (eds.)

Comparison of three current low-density concrete technologies emphasis on the criteria's of performance, fabrication, and mixtures

Ferdinand OSWALD[b,*], Richard HENRY[a], Djordje NIKOLIC[b]

[*] School of Architecture and Planning, Creative Arts and Industries (CAI),
The University of Auckland.
ferdinand.owald@auckland.ac.nz

[a] Civil and Environmental Engineering, Faculty of Engineering, University of Auckland.
[b] School of Architecture and Planning, The University of Auckland.

Abstract

By utilizing low-density aggregates in concrete, it is possible to achieve reductions in weight, density, and the carbon footprint of concrete. The study found that improved thermal performances are also possible with all three of the technologies: Infra-Lightweight concrete, Ultra-lightweight concrete, and functionally graded concrete. This paper serves as an analysis of the contemporary homogeneous and inhomogeneous low-density concrete technologies that succeed in exhibiting the aforementioned characteristics. The highlighted advantages of these technologies showcase innovative advancements in the field of concrete technology and the potential for concrete to be used in a wider range of site and environmental conditions worldwide.

Keywords: low-density concrete, infra-lightweight concrete, ultra-lightweight concrete, functionally graded concrete

1. Introduction

This article provides an overview of various low-density concrete systems, specifically focusing on their compressive load-bearing and thermal performance. The article also considers the mixture compositions and fabrication processes of these concrete types. The research aims to contribute to the broader objective of reducing weight and material usage in the concrete construction industry. Areas of interest include structural optimization, the incorporation of aggregates, and specific material compositions and fabrication methods.

Weight and material reduction can be achieved through structural optimization of building components. Notable examples of this approach include the works of Pier Luigi Nervi (1891-1979) [1] and Angelo Mangiarotti (1921-2012) [2], who employed optimized structural designs that minimized material usage while shaping the aesthetics of their designs. The DFAB House project by ETH Zurich is another recent example, where 3D printing was used to create customized formwork for structural components, achieving formal structural optimization. These examples demonstrate how a design-oriented approach can lead to reduced material consumption and weight.

Another avenue for weight and material reduction is the addition of aggregates and specific material compositions, resulting in low-density concrete composites. Extensive research has been conducted on the properties of these composites, and this article focuses on the most advanced technologies in this area.

Copyright © 2023 by Ferdinand OSWALD, Richard HENRY and Djordje NIKOLIC. Published in the Proceedings of the IASS Annual Symposium 2023 with permission.

While structural elements made of standard concrete can be optimized to reduce dead loads, they typically require additional material layers when used in external building envelopes. In contrast, low-density concrete systems with lower thermal conductivity pursue a monolithic, monomaterial wall approach, achieving weight and material savings. This approach allows for the combination of structural performance and thermal insulation within a single material, thereby enhancing resource efficiency and recycling rates. The ultimate goal of advancements in this field is to provide materials that meet or exceed structural and thermal requirements while consuming less material, thus reducing the carbon footprint of the concrete industry.

The current state of research in this field is characterized by studies that focus on specific low-density concrete technologies and their performance. This analysis serves as a platform for further research in the field of low-density concrete, offering an overview and comparative study of the technologies under consideration.

2. Literature review

2.1. Lightweight concrete

Although lightweight concrete has been in use in various forms around the world for centuries, Peck describes a renaissance of this technology in the mid-20th century, "Lightweight concrete technology was developed in the 1960s with the goal of reducing concrete structural components' own weight without changing their load-bearing capabilities" [3].

Patrick Gartman's house in Chur, Switzerland, 2003, is an example of monolithic concrete design. The house is built of lightweight concrete containing expanded glass with thermal conductivity of 0.36W/mK. The concrete Gartman developed for this project has since been called 'insulating concrete', although this was not a technical term at the time [3].

2.2. Three concrete case studies

This study addresses low-density concrete as a potential alternative to conventional concrete in terms of establishing industry best practices for (external) wall-based concrete constructions. Given the common attributes of the concrete systems covered in this study, a concise overview is presented that depicts the performance of each example against a set of criteria. These attributes are a monolithic morphology and insulating properties that combine to provide a concrete typology for single-layer construction which has the potential to meet current energy efficiency requirements in parts of the world. The technologies addressed in the study are as follows:

(1) Infra-lightweight Concrete (ILC). This system is comprised of concrete layers with varying properties that in combination work to decrease component density, increase thermal performance, and facilitate load-bearing capacities [4].

(2) Ultra-lightweight Concrete (ULC). This technology is another variant of lightweight concrete with its main point of difference being the use of fly ash and binders that allow for a more densely packed matrix of expanded glass aggregates. Depending on its matrix and mixture, ULC is intended to have load-bearing capacities as well as increased thermal performance in comparison to conventional concrete (Yu et al. 2015) [5].

(3) Functionally graded concrete (FGC). This technology also contains artificially produced aggregates that work to decrease density within a component while providing thermal insulation. Another effect of gradation throughout a component made from FGC is an increase in the efficiency of the use of the material by reducing its overall mass [6].

2.3. Cross-sectional structure descriptors

In the first step, three material properties are defined: monolithic, homogeneous, and inhomogeneous. In the second step, the three material properties – monolithic, homogeneous, and inhomogeneous – are assigned to the three technologies for low-density concrete infra-lightweight concrete (ILC), ultra-lightweight concrete (ULC), and functionally gradient concrete (FGC).

Homogeneous / homogeneity

'A homogeneous material consists of the same or a similar kind or nature and is of uniform structure or composition throughout,' as in the Merriam-Webster dictionary, accessed 28 April 2022.

Inhomogeneous / inhomogeneity

'An inhomogeneous material is the condition or an instance of not being homogeneous and is where a material has a part that is not homogeneous with the larger uniform mass in which it occurs,' as in the Merriam-Webster dictionary, accessed 28 April 2022.

Monolithic

'A monolithic material is cast as a single piece, moulded or composed of material without joints or seams, and consists of or forms a single unit.' as in the Merriam-Webster dictionary, accessed 28 April 2022.

2.4. The aim of this study

Considering the previous discussion, this study has the following objectives:

- identify contemporary advanced low-density monolithic concrete technologies;
- define homogeneous and inhomogeneous concrete;
- identify the solutions provided by advanced low-density monolithic concrete technologies;
- identify thermal performances of advanced low-density monolithic concrete technologies;
- identify future benefits of advanced low-density monolithic concrete technologies; and
- identify opportunities for further development within this field of research.

3. Materials and methods

3.1 Analysis criteria

3.1.1 Technology description

An introductory description is given for each technology. Aspects of this introduction include names and information about the researchers, the institution with which the technology is associated, and the country of origin of each technology.

3.1.2 Technology type and solutions offered

The technology type describes the current status of each technology (project, prototype, or product). The solutions offered by each technology are also described.

3.1.3 Mixture

The mixture of each concrete technology is given and displayed graphically.

3.1.4 Morphology

The structure refers to any concrete technology as if a cross-section were cut through a sample. This is linked to the mix and is used to describe the overall porosity of each type of concrete and whether it is a homogeneous or stratified system.

3.1.5 Fabrication method
An image and a short description of the fabrication process are given for each concrete technology.

3.1.6 Future research
Possible aspects of research are suggested to describe what information is currently lacking in the research and to allow for future adaptation of the present work.

3.1.7 Thermal Performance
The thermal performance of each technology is given based on its thermal resistance using a 50-mm example (R-value) and its thermal transmittance (U-value). The R-value is defined by the New Zealand Standards Council as the 'sum of the surface resistances on each side of the building element' according to the current energy efficiency standard [7]. The U-value is defined as 'a measure of the thermal transmittance of a building element (e.g., a wall or window) or a given thickness of material (e.g., insulation), with lower values indicating better insulating properties,' as in the Merriam-Webster dictionary, accessed 29 April 2022.

3.2 Procedure
The method used in this research is a comparative review. A literature review was conducted, summarised in Section 2, to identify criteria and data relevant to the research objective and to discuss and compare the case studies provided. The research process proceeded in four phases: Planning Phase (purpose and protocol), Selection Phase (case study search and screening), Extraction Phase (quality assessment and data extraction) and Execution Phase (analysis of results and review) [8]. In the planning phase, the aim of the research and the protocol were defined. The protocol included a review procedure of relevant databases using specific keywords to build the framework of lightweight concrete and to identify a set of criteria to perform the investigation on case studies.

The literature search was conducted using four research databases (ScienceDirect, Google Scholar, Scopus, and Web of Science), technical information sheets from industry and proprietary systems manufacturers, and several resources already available to the authors (i.e., books and websites). The selected keywords produced a large variety of scientific journal articles. Secondary keywords added were 'porous concrete' and the names of specific technologies such as 'functionally graded concrete', 'ultra-lightweight concrete', and 'infra-lightweight concrete'. Additional resources on specific topics were added during the writing of this study. Peer-reviewed academic articles were researched through online databases such as Francis & Taylor and Elsevier.

4. Results

Table 1. Overview of technology type, structure, fabrication, institute, and country of origin for all three of the concrete technologies.

Technology	**Technology Type**	**Structure**	**Fabrication**	**Institution**	**Country of origin**
Infra-Lightweight	Prototype	Inhomogeneous	Computer Operated	Berlin Institute of Technology – department of design and construction – solid construction.	Germany
Ultra-Lightweight	Project	Homogenous	Conventional methods	Eindhoven University of Technology	Netherlands
Functionally graded v1	Prototype	Inhomogeneous	Computer Operated	Institute for Lightweight Structures and Conceptual Design, University of Stuttgart	Germany
Functionally graded v2	Prototype	Inhomogeneous	Computer Operated	Institute for Lightweight Structures and Conceptual Design, University of Stuttgart	Germany

4.1 Ultra-lightweight concrete (ULC)

4.1.1 Technology description

Similar to lightweight concrete, ULC is a homogeneous material that has both insulating and load-bearing properties [5]. ULC contains expanded glass and fly ash [5]. Research on this technology at Eindhoven University in the Netherlands was completed in 2015 by Yu, Spiesz and Brouwers [5].

4.1.2 Technology type and solutions offered

ULC is a prototypical material with potential use in monolithic structures, such as wall or façade elements [5]. Similar to FGC, the goal is to obtain a single-layer material that has both insulating and load-bearing properties, thus reducing the need for additional insulation [5]. ULC has a thermal conductivity of 0.12 (W/mK) and a density ranging from 600-750 kg/m³. The single-layer matrix of this technology is also well suited for recycling, as there are no glued-on layers as in a conventional concrete building. ULC can also be used as a highly insulating concrete used as a core layer within other concrete composites, as is the case with ILC, and has a 28-day compressive strength of around 10-12 Mpa [5].

4.1.3 Mixture

Figure 1 shows the mixture of ULC [5]. Both the expanded glass and fly ash are products of reuse and therefore contribute positively to the environmental sustainability of ULC by reducing the amount of cement required. However, fly ash is a by-product of the coal industry – something many countries are turning away from Wesche [9].

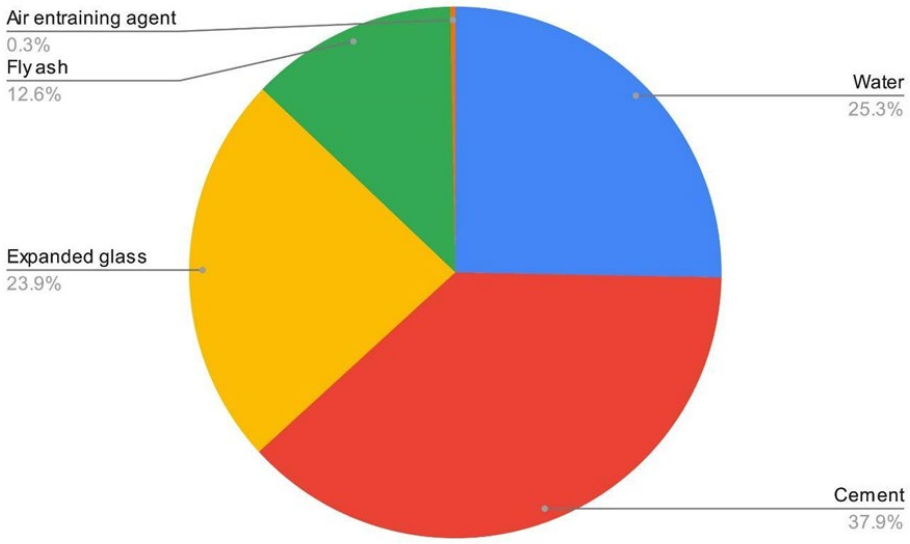


Figure 1. Chart showing the mixture composition of ultra-lightweight concrete

4.1.4 Morphology

The structure of ULC is homogenous through its cross section with visible porous aggregates [5]. Figure 2 shows an isometric drawing of an example wall component of ultra-lightweight concrete.

4.1.5 Thermal performance

R-value at 50 mm thickness: 0.4 m²K/W [5].

U-value at 50 mm thickness: 2.4 W/(m²K) [5].

4.1.6 Fabrication method

The mix for ultra-lightweight concrete is produced using a planetary concrete mixer and is therefore similar to standard concrete production processes, making it suitable for both prefabrication and in-situ use [5]. This process is illustrated in Figure 3.

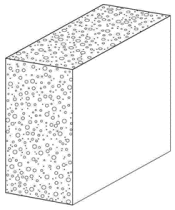


Figure 2. Isometric drawing of an example wall component of ultra-lightweight concrete.

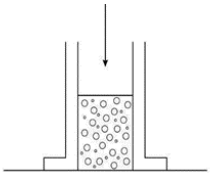


Figure 3. Diagram showing the fabrication process of ultra-lightweight concrete.

4.1.7 Future research

In the future, research could be undertaken in the area of structural design to understand how reinforcement works with this technology. Structural connections and joints could also be designed and tested to determine their performance in the context of a building. Due to the lightness of the material compared to standard concretes, they would also benefit from seismic testing.

4.2 Infra-lightweight concrete (ILC)

4.2.1 Technology description

Unlike conventional concrete or lightweight concrete, ILC is an inhomogeneous material with two distinct properties that alternate in cross-section. The outer layers are stronger and designed to meet load-bearing requirements, while the core is made of a lighter concrete mix that provides thermal insulation. Research in this area is being carried out by the Technical University of Berlin. The team members are Claudia Losch, Arno Richter, and Mike Schlaich [4].

4.2.2 Technology type and solutions offered

Due to its layered morphology, an ILC wall can provide both load-bearing and insulating properties in a single material', which could eliminate the need for additional insulation [4].The core of the structure consists of a lower density concrete with a high proportion of expanded glass and expanded clay, while the outer, stronger layers provide the required load-bearing properties [3]. In addition, photocatalytic layers enable a reduction in air pollutants [4]. Another application of ILC is the 'building simply' project led by Florian Nagler, where the material is used in much thicker external walls of 500 mm depth. This strategy has the potential to increase the thermal performance of exterior walls and allows for in-situ construction instead of prefabrication. The thicker application of this material also means that steel reinforcement is not required in the Central European context due to low seismic activity [10].

4.2.3 Mixture

Figure 4 shows an example mixture of ILC in percentages [4]. These values aggregate both the core and outer shell concrete mixes, which account for 33% and 67% of the total cross-sectional area, respectively. For the mix shown, it is assumed that 25% of the total composition is water to better understand the quantities compared to the other 3 concrete mixes.

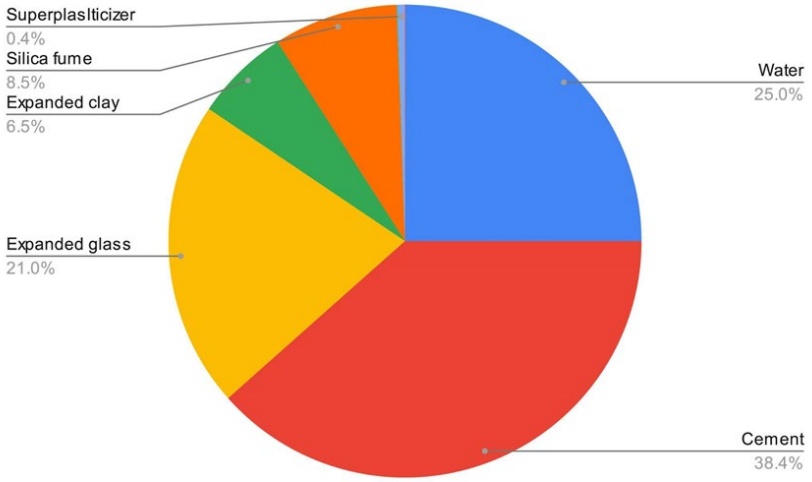


Figure 4. Chart showing the mixture composition of infra-lightweight concrete.

4.2.4 Morphology

ILC has a core that is tailored to provide a lighter product and insulative properties, with a density of 456 kg/m3 and thermal conductivity of 0.088 (W/mK). The outer layers have a higher density of 804 kg/m³, compressive strength of 15.8 MPa for load-bearing properties, and thermal conductivity of 0.169 (W/mK) [4]. The layers are formed like a sandwich panel, but where each layer is joined to another during the casting and curing process to make a monolithic building component [4]. Figure 5 shows an isometric drawing of an example wall component of infra-lightweight concrete.

4.2.5 Thermal performance

R-value of 0.345 m²K/W considering 2x10 mm shell layers and a 30 mm core [4].

U-value of 2.9 W/(m²K) considering 2x10 mm shell layers and a 30 mm core [4].

4.2.6 Fabrication method

ILC is made in stages, with the outer shell poured into a horizontal mould, followed by the core mix and another layer of shell mix [4]. In this way, the outer surfaces act as lost formwork for the inner mix. A certain amount of time must elapse between the individual phases so that the different concretes do not mix [4]. This process is illustrated in Figure 6.

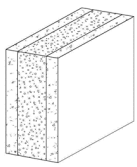


Figure 5. Isometric drawing of an example wall component of infra-lightweight concrete.

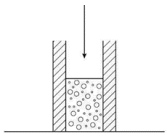


Figure 6. Diagram showing the fabrication process of infra-lightweight concrete.

4.2.7 Future research

The team from the Technical University of Berlin points out that their proposed calculations on the loading properties of ILC and possible design approaches need to be verified by further research [4]. The possible use of glass fibre rods for crack strengthening is also being investigated by the team and

could be compared to steel in terms of performance, both thermally and structurally [3]. Seismic testing is another area the team could investigate and could make the technology internationally applicable.

4.3 Functionally graded concrete (FGC)

4.3.1 Technology description

Gradient concrete is also an inhomogeneous and monolithic material like ILC; however, there is a relevant difference in the mixture of the concrete and the graded nature of the material's matrix. Instead of using a lightweight aggregate to decrease density, the team at the University of Stuttgart, Institute of Lightweight Structures and Conceptual Design (ILEK) has opted for air cavities, created using concrete hollow spheres [6]. FGC is a prototype that is still being researched. The main research headed by Werner Sobek, Walter Haase and Lucio Blandini [11]. The evolution of the team is dynamic. Currently, the research is now in the third generation of PHD (1. Michael Hermann, 2. Daniel Schmeer, 3. David Nigl).

4.3.2 Technology type and solutions offered

By avoiding the use of lightweight aggregates, the team at Stuttgart is working on decreasing the overall concrete used in building. Currently, this can be reduced by up to 62% when combined with carbon fibre reinforcing [11]. Additionally, the overall weight of a structural component can be reduced by 42%, which makes the use of concrete construction on sites with softer ground more viable [11]. Currently, the use of hollow spheres can reduce the mass of FGC by 50% without compromising the load-bearing capacity [12]. In addition to these factors, FGC also has insulating properties that can provide sufficient thermal comfort according to EnEV 2014 specifications, depending on the climate [13]. So far, FGC is a prototype material, but ILEK is currently working on an experimental university laboratory using FGC elements, as explained in an interview with W. Haase (personal communication, 25 February 2021).

4.3.3 Mixture

Figure 7 shows an example mixture of FGC in percentages [14]. The example used for the purpose of this study follows the composition of 'MIITS' concrete mixture, which is one among many test mixtures to date [14].

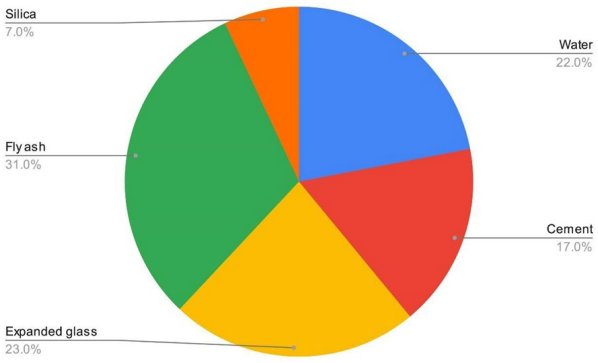


Figure 7. Chart showing the mixture composition of gradient concrete.

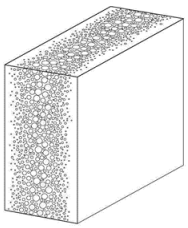


Figure 8. Isometric drawing of an example wall component of gradient concrete.

4.3.4 Morphology
There are currently two variations of FGC. Micrograded concrete features a "continuous variation of porosity" achieved by the use of lightweight admixtures, such as expanded glass and foam-forming aggregates, or through targeted placement of material regarding the requirement [15]. Pore sizes vary from 1 to10 mm diameters in micrograded FGC [15]. Mesograding on the other hand is characterized by larger cavities varying from 10 to 250mm in diameter, which are achieved with "mineral hollow bodies" [15]. The structure of FGC is inhomogeneous in cross-section and has a graded, varying porosity due to the air cavities inside the component. Conceptually, FGC is a multi-layered structure in which the outer layer with integrated reinforcement defines the shape, provides impermeability and facilitates load-bearing capacity, while the inner layer serves as thermal insulation and has the potential to reduce the overall mass [12]. Figure 8 shows an isometric drawing of an example wall component of gradient concrete.

4.3.5 Thermal performance for mixture MIISG (LM)
R-value at 50 mm thickness: 0.55 m²K/W [15].

U-value at 50 mm thickness: 1.8 W/(m²K) [15].

4.3.6 Fabrication method
The initial production of FGC was done with a manually poured, layered system that formed a sandwich slab with denser concrete on the outside and micrograded concrete on the inside, as shown in Figure 9 [15]. This is similar to the integral formwork fabrication that is used to produce ILC. ILEK then developed a two-part gradient spray technology that sprays the concrete in thin layers, while simultaneously compacting and achieving the desired degree of porosity within the component [6]. This process is illustrated in Figure 10 and is another example of micrograding [15]. However, Figure 11 shows the latest method of production, which uses automatically placed concrete hollow balls, an example of mesograding (Schmeer and Sobek 2019). The concrete spheres are robotically placed in the desired locations in combination with poured concrete, with wet-on-wet application ensuring that each layer bonds [15]. The diameter of the hollow spheres ranges from 1-10 mm at the micro-level and 10-250 mm at the macro-level [12].

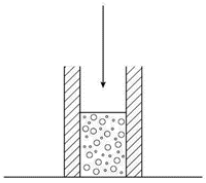


Figure 9. Sandwich diagram.

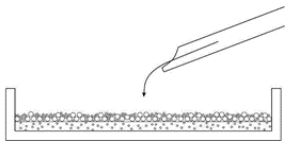


Figure 10. Spray diagram.

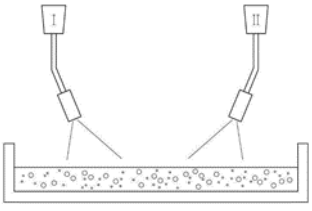


Figure 11. Hollow sphere diagram.

4.3.7 Future research
The market acceptance of FGC continues. However, one area that could be further explored is the performance of FGC in seismic testing. FGC is favourable to the industry as it reduces both weight and material usage. Further development of the mix in terms of its resistance to seismic activity would help make FGC applicable to a wide range of site conditions and environments. In the future, the mix could also be adapted to be more sustainable by replacing the use of fly ash with a substitute material.

5. Discussion

5.1 Solutions provided

The results presented in the study agree with the results of previous studies and are indicative of increasing interest in the field of low-density concretes. The solutions offered by the concrete technologies/systems discussed aim to reduce weight and increase thermal performance to obtain a monolithic building element that does not require additional insulation. The benefits of these factors for the construction industry would be very positive. The use of less material allows for more environmentally sustainable buildings, while the potential of monolithic construction indicates an improvement in recyclability. These are significant improvements over traditional concrete systems. The thermal performance of all three technologies has great potential in monolithic concrete construction, especially FGC, ULC, and ILC. The differences between them are evident. Gradient concrete (MIISG(LM)) reaches the lowest U-value of 1.8 W/(m²K) at a thickness of 55 mm [12].

5.2 Future benefits

In theory, all the technologies in this study can be seen as an improvement over conventional concrete, their main benefits being the reduction in weight, reduction of materials used, insulative potential, and the fact that they are all monolithic, single-leaf systems that are easier to recycle than layered systems. However, this depends on the type of application being considered. In many cases, the stronger and more durable traditional concrete will still be preferred. However, considering wall panels for low-rise buildings, lightweight alternatives may be preferred.

5.3 Gradient concrete

Gradient concrete has the greatest potential but is also the least mature of the technologies covered in this study. With gradient concrete, a 50 % weight reduction is possible, allowing concrete to be used in a wider range of locations, while its insulating properties allow for more comfortable buildings, i.e., performance beyond the bare minimum requirements [12]. Gradient concrete results in a 50-60% lighter concrete that requires fewer resources to produce and reduces emissions by 45-60% [11]. It is a purely mineral, multifunctional element made of a single material with insulating properties that is recyclable. In building construction, the weight of concrete floor slabs accounts for up to 70% of the total structural mass. The design of gradient concrete leads to a significant reduction in the weight of floor slabs and load-bearing walls, thus reducing the overall load-bearing structure [11]. This means, for example, that substantial buildings can be constructed on sites that are currently restricted due to the weight of concrete structures. Gradient concrete has reduced emissions by using less material and energy and the change in porosity over the component cross-section enables efficient control of thermal insulation properties [11]. The University of Stuttgart based Institute of Lightweight Structures and Conceptual Design (ILEK), is currently working on a project to construct an experimental university laboratory using functionally graded concrete elements. The first buildings with graded concrete slabs are currently in the preliminary design phase.

5.4 Limitations of this study

One of the preferred topics for further research directions among the prototype technologies discussed in this article is the area of structural connections, especially when thinking about how these

technologies might behave in an earthquake compared to conventional concrete. This highlights one limitation of this study as the research could have included seismic resistance as a criterion in the search for case study technologies. Another limitation is that the research did not include any contemporary concrete technologies that make use of alternative organic materials in their composition. This is another stream of research that is being developed within the topic of contemporary concrete technologies.

6. Conclusions

The solutions provided by the technologies discussed in this article highlight the need for the construction industry to enhance conventional standards. The use of lower density materials reduces the overall amount of material required, while the monolithic nature of these concrete technologies offers improved potential for effective recycling. Although the technologies examined in this study share a monolithic morphology, their cross-sectional structures vary: ULC is homogeneous, while ILC and FGC are inhomogeneous. It is worth noting that despite these differences, all three technologies possess load-bearing capacity.

The thermal performance offered by these technologies is also of great significance, as it enables professionals to advocate for healthier buildings in a broader range of climates. While the study indicates that all three technologies provide insulation, gradient concrete exhibits the greatest potential in this regard, depending on the specific mix and porosity achieved in a given component. These advantages combine to present a new approach to future concrete construction. The reduction in mass and weight, insulation properties, load-bearing capacity, and recyclability all point to the potential for a more environmentally sustainable monolithic approach to building with concrete, as well as the possibility of using concrete in a wider variety of climates and soil types.

However, further development is needed to address the seismic performance of ULC, ILC, and FGC to enhance their applicability at a geographical level. Since these technologies have cross-sectional structures that significantly differ from conventional concrete, conducting seismic testing would be a beneficial next step for their development, particularly in terms of designing joints and connections used with prefabricated structural elements. Additionally, when considering the precast approach to construction using these technologies, it is important to address thermal bridging between panel edges and connections between various components. Although these aspects are not covered in this paper, they should be taken into account for future research. Furthermore, comparing low-density concretes to conventional concrete in terms of environmental sustainability and conducting more research on mixes and component composition would be valuable, especially as there is an increasing interest in utilizing naturally obtained substitutes for concrete ingredients and reinforcement.

Overall, the findings of this study highlight the potential benefits of these concrete technologies and suggest avenues for further investigation and development in the field.

Acknowledgements

This research was funded by the University of Auckland, Faculty of Creative Industries and Arts: Faculty Research Development Fund (FRDF 9506/3722714) and supported by the School of Architecture and Planning: Performance Based Research Fund (PBRF A2105). The article text has been reviewed by the ELSEVIER Language Editing Plus Service and the professional proof reader Elizabeth Ardley.

References

[1] P.L. Nervi, *Aesthetics and Technology in Building: The Twenty-first-century Edition*. Urbana, IL: University of Illinois Press, 2018.

[2] T. Herzog, *Bausysteme von Angelo Mangiarotti*, München: Technische Universität München, 1998.

[3] M. Peck, "Modern Concrete Construction Manual: Structural Design, Material Properties, Sustainability", Munich: DETAIL, pp. 36–39, 2014.

[4] C. Losch, A. Richter, and M. Schlaich, "Structural behaviour of multifunctional inhomogeneous infra-lightweight concrete elements." *Journal of the FIB 2021*, vol. 6, pp. 2628-2642, 2020. doi:10.1002/suco.201900378

[5] Q. Yu, P. Spiesz, and J. Brouwers. "Ultra-lightweight Concrete: Conceptual Design and Performance Evaluation." *Cement & concrete composites, vol.* 61: pp. 19–28, 2015. doi:10.1016/j.cemconcomp.2015.04.012

[6] M. Herrmann, W. Sobek, and W. Haase, *Gradient Concrete: Investigations into the Weight Optimisation of Uniaxial Components Subjected to Bending and Shear Forces*, University of Stuttgart: Institute for Lightweight Design and Construction, 2015.

[7] Standards New Zealand, NZS 4218:2009, 2009. Accessed 6 April 2022. https://www.standards.govt.nz/shop/nzs-42182009/

[8] M. Alavi and D. Leidner. "Review: Knowledge management and knowledge management systems: Conceptual foundations and research issues." *MI Q 25*, vol. 1, pp. 107-136, 2001. doi:10.2307/3250961

[9] K. Wesche, "Fly Ash in Concrete Properties and Performance: Report of Technical Committee 67-FAB", *Use of Fly Ash in Building*, New York: Taylor & Francis, 1991.

[10] F. Nagler, "Simply Building by Florina Nagler", *Bauwelt magazine*, Bauverlag BV GmbH, Berlin, Germany, 2021.

[11] M. Herrmann and W. Sobek. *Development of Weight-Optimised, Functionally Graded Precast Slabs*, University of Stuttgart: Institute for Lightweight Design and Construction, Stuttgart, Germany, 2019.

[12] D. Schmeer, D. Schonemann, O.Arkhipkina, W. Haase, H. Garrecht, O. Sawodny and W. Sobek, *Entwicklung einer ökologischen und ökonomischen Bauweise durch den Einsatz vorgefertigter multifunktionaler Wandbauteile aus gradiertem Beton*, Fraunhofer IRB Publishing House, Germany, 2020.

[13] P. Heinz, M. Herrmann and W. Sobek, "Herstellungsverfahren und Anwendungsbereiche für funktional gradierte Bauteile im Bauwesen (Abschlussbericht Forschungsinitiative Zukunft Bau)" Universität Stuttgart: ILEK, Stuttgart, Germany, 2011.

url:https://www.irbnet.de/daten/baufo/20128035526/F_2811_Abschlussbericht.pdf
https://www.irbnet.de/daten/baufo/20128035526/F_2811_Abschlussbericht.pdf

[14] W. Sobek, „Leichtbau im Bauwesen: Ein Praxis-Leitfaden zur Entwicklung und Anwendung ressourcen- und emissionsreduzierter Bauprodukte", Baden-Wuerttemberg: ILEK, Germany, 2018.

[15] D. Schmeer and W. Sobek, „Beton Kalender 2019: VI Gradientenbeton", Ernst & Sohn GmbH & Co. KG, Germany, 2019.

Proceedings of the IASS Annual Symposium 2023
Integration of Design and Fabrication
10–14 July 2023, Melbourne, Australia
Y.M. Xie, J. Burry, T.U. Lee and J. Ma (eds.)

Vibration analysis of the real shaped bi-valve shell model created by CT images

Minori OGOSHI*, Masaki TERANISHI[a]

* Graduate School of Science and Technology, Niigata University.
Niigata University, 8050, Ikarashi 2-no-cho, Nishi-ku, Niigata 950-2181, Japan
f21n004h@mail.cc.niigata-u.ac.jp

[a] Institute of Science and Technology, Niigata University.

Abstract

Natural thin-shell structures have been in focus owing to their interesting forms and features. A seashell form is considered in terms of its potential for application to architecture structural systems. Besides, biomimetics has flourished in the architectural filed recently so that the features of seashells' form deserve more attention. Herein, we study the mechanical and geometric features of bivalve shells. In addition to these studies, a dynamic analysis should be conducted to apply seashell features to structural systems, and we modified to shell element from solid element of the model with a low computational load for the dynamic analysis on finite element (FE) analysis reflected bivalve shell form. This study presents a natural vibration analysis of the bivalve-shell form using modified FE models to reveal its vibration features. The analysis was performed multiplied equally by the size of real buildings. By comparing this with the results of the FE model reflected a hemisphere form same as building size, the response properties of the FE models reflected bivalve shell form to vibration are revealed. Up to the 100th order mode, the shell model had a broader range frequency than the dome model by natural vibration analysis. Consideration of the cumulative mass participation showed that the shell model has fewer natural period to consider when structural designed than the dome model in the case of vertical vibration.

Keywords: biomimetics, seashell, vibration analysis, image-based finite element analysis

1. Introduction

Biomimetics has become a key instrument in a wide range of engineering technologies. It is utilized in the form of train head, folding systems of space structure in the fields of mechanics, material science, and robot engineering [1-4]. Thus, biomimetics is crucial in engineering technology, and structural engineering in architecture recently as well. For example, foundational research has flourished to learn from various living things, such as research focusing on the growth patterns of trees and leaves and the ability of plants to grow themselves [5-7]. While a few examples of partial applications exist, these are not widely used in structural systems [8-12]. This is because the mechanical properties of natural organisms have not been revealed in detail, as evidenced by the fact that fundamentals are still the primary focus on the previous studies. However, other fields of architecture have been used in decorative design, such as the botanical form as a pattern [13, 14] and the ventilation system from the termite nest system [8], and a strong affinity exists between architecture and biomimetics. Therefore, we have focused on seashells, particularly bi-valve shell, which have a form similar to architectural spatial structures.

Previously, natural thin-shell structures have been the focus of study owing to their interesting forms and features such as seashells, eggshells, and soap films [15]. Among these structures, the forms of the

Copyright © 2023 by Minori OGOSHI and Masaki TERANISHI. Published in the Proceedings of the IASS Annual Symposium 2023 with permission.

seashell evolve and can be optimized to adapt to their habitat. The seashell form has been considered for potential applications in architectural structure systems [15, 16]. Research on seashells is ongoing in various fields. Biology and paleontology factor the ecology and relationships of each species, geology, and natural history discuss their role in the long history of Earth, and morphology discusses the geometric features of their shells [17-19]. These factors are evidently interrelated. This knowledge should be beneficial in new fields such as biomimetic application studies. Many studies have been conducted on the relationship between the ecology of shells and their forms, and various experiments have been conducted on their strength [20-22]. In one of them, the mathematical model of the seashell was used to elucidate mechanical properties [20]. This is a good example of how findings from an independent issue in one field can be used for another issue in another field within seashell topic. In particular, the mathematical model of seashell is considered useful in the field of building structure because various formulas have been proposed depending on the type of expression desired [17, 18, 23, 24], and shape expressions based on these formulas can also be used in CAD and other applications. Previous studies have primarily focused on molluscs' habitat. However, the advantages it offers as a spatial structure in human life are unknown.

To clarify basic knowledge, we studied the mechanical and geometric features of the bivalve shell form [25, 26]. In [26], a static analysis was performed for a bivalve shell form through image-based finite element (FE) analysis. Results were matched with geometric features, and their relationships were verified. However, many dynamic forces act on buildings, and this is a crucial factor to be considered. When architectures are subjected to dynamic loads, such as earthquakes and typhoons, spatial structures comprising a structural system that bivalve shell features can refer to are generally used as shelters. Therefore, the response should be elucidated to these loads.

This study presents a natural vibration analysis of the bivalve shell form to reveal its vibration features using an FE model, which reflects the form of the bivalve shell. The model used in this study has a small computational load while maintaining detailed geometric features for dynamic analysis [27]. By comparing this with the results of the FE model, which reflects the form of a simple dome, the response properties of the bivalve shell form to vibration are demonstrated.

2. Methods

In this study, the specimens used in previous studies [26, 27] were employed. This section describes the specimen and method used to develop the FE models. The FE models reflecting the form of the specimen and a simple spherical dome were developed. Finally, this section describes the conditions for vibration analysis.

2.1. Specimen

The specimen used in this study was a shell fragment from seven-month-old *Fulvia mutica* cultivated in Ishikawa Prefecture, Japan. As shown in Figure 1 [26], the specimen was cleaned; its size was approximately 50 mm (X direction) × 50 mm (Y direction) × 30 mm (Z direction). This species was selected because it is a species of *Veneroida* with large internal space in bivalve shells, and it is edible,

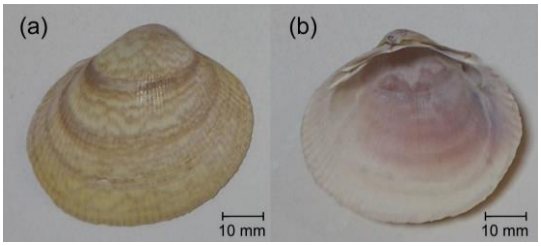


Figure 1. (a) Front and (b) back surface of specimen [26].

easily accessible, and familiar to humans. The specimens were scanned using X-ray computed tomography (CT) apparatus (Skyscann2211, Bruker Corp.). The scanning details are described in [26]. CT images were the same as those in previous studies [26, 27].

2.2. Developing the analysis models

2.2.1. Seashell model

A seashell model was developed using the CT images obtained in Section 2.1. The detailed method is described in previous studies [26, 27]. First, CT images' resolution value was decreased for the computational costs of image processing and FE analysis. The CT images were reduced to 180 μm / voxel and fragments were removed. Furthermore, the CT images were through several filters to prevent false solutions. These were processed by Image-J (Wayne Rasband and contributors National Institutes of Health, ver.1.53e), which is the software for image processing, and MATLAB (MathWorks, ver. R2020a), which is the programming language for science technology. An STL model was developed based on CT images processed through Invesalius (Center for information Technology Renato Archer, ver. 3.1) with a threshold value set at 55. Invesalius is the software for reconfiguration the CT images. The STL model in this state can be used to obtain an FE model composed of solid elements with an FE mesh creation software. However, we expect the computational cost of dynamic analysis using the solid FE model to be significantly higher. Therefore, an FE model modified to reduce computational load was proposed to convert the element type from solid to shell [27]. In this study, a modified model that reduced computational load was applied for dynamic analysis. Three types of FE models, reflecting each surface form, were obtained with this method. In this study, the FE model reflecting the front surface, which showed properties closest to the actual shape (the model configuration with the solid element) in [27], was selected. The properties of the STL and FE models used in this study are listed in Table 1. In this study, the FE model described in this section is called as the shell model.

2.2.2. Dome model

A model reflecting a simple hemispherical dome was created with three-dimensional modeling software. The rise and span were suited to the span of the shell model. After outputting the STL file format, this model was divided into a more detailed mesh using Hypermesh, which is a meshing software with the same number of elements as the shell model. The size of each element was also adjusted with the software. The FE model described in this section is called as the dome model in this study.

2.3. Conditions for the analysis

In this study, natural vibration analysis was performed on both the shell and dome models. As shown in Figure 2, the boundary conditions were considered to be pinned at the periphery and the coordinate space was set. The material properties of the models were considered to be those of ordinary concrete, where the Young modulus was 2.17×10^4 MPa, the Poisson's ratio was 0.2, and specific gravity was 24.0 kN / m^3. The analysis was performed using Abaqus (SIMULIA, ver.2019), a general-purpose FE analysis software, and S3 elements were used in Abaqus for both models. Additionally, shell element enabled the thickness distribution of these FE models to be easily changed. The thickness distribution and mean thickness of the specimens were obtained through the method in [26] into the shell and dome

Table 1. Details of each model.

Model	Nodes	Elements	Min element size [mm]	Max element size [mm]
STL model	158 718	317 430	0.000674	1.054
Shell model	94 683	188 351	0.00209	0.338
Dome model	176 091	351 254	0.00442	0.175

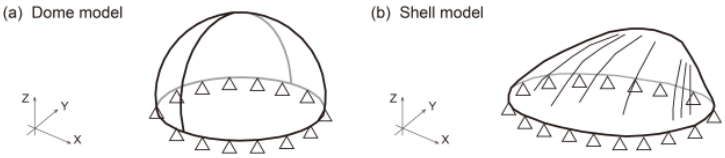


Figure 2. Conditions for the vibration analysis on (a) Dome model and (b) Shell model.

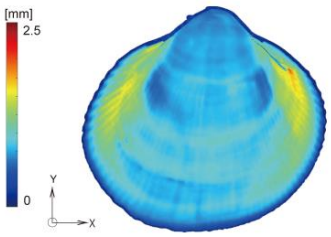


Figure 3. Distribution of thickness [26].

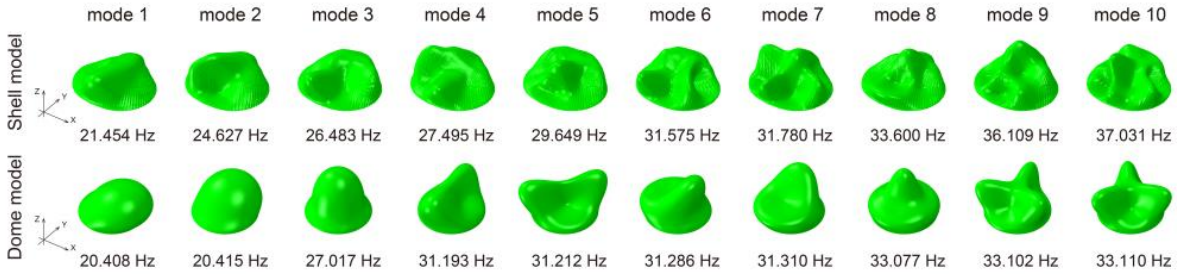


Figure 4. Deformations of the natural frequency first to tenth modes. Deformation diagrams are magnified by 5000.

models. The thickness distribution is shown in Figure 3 [26]. The mean thickness was 0.838 mm. All model sizes and thicknesses were multiplied by 500 times as the actual architectural building size before analysis. This was because the real bivalve shell size was extremely small to consider accurate deformation properties owing to the prediction of excessive entire movement when the next planned history analysis was performed using this result. This was considered on a human scale.

3. Results

Figure 4 shows the deformation diagrams and the natural frequency values of the lower-order modes on both models. The deformations of the lower-order modes were not complex in both models under the 5th mode. After the 5th mode, the deformations of the shell model showed a complex form. Deformations of the dome model maintained a simple symmetry after the 5th mode same as under the 5th mode. The dome model deformed to response for vibration wave as a whole, while the shell model's deformation concentrated on abdomen area on every mode shown in Figure 4. Therefore, when the shell model is attacked by vibration wave, large deformations would occur in the abdomen area. On the other hand, the shell model's deformation on the umbo area was small on the lower-order modes. This feature is same as the case of the elastic analysis under the dead weight [26], and [21] reported that deterioration (e.g., scraping) at the apex area of the shell reduces the mechanical capacity of the entire shell. In the case of time history response analysis as a next step, focusing on the umbo area is likely to get the beneficial knowledge about seashell form.

Figure 5 (a) shows the transitions of the frequency values up to 100th modes of both models. As shown in Figure 4, the first frequency values of both models were similar. At the lower-order modes under the 5th mode, the dome model covered wider range of the frequency. After the 5th mode, the slope of the frequency values became smaller on the dome model. However, the slope of the frequency values was constant on the shell model. The shell model and the dome model also had approximately same the first natural period so that there was no difference in point of the susceptibility to resonance for long-period earthquakes, which is an important point on the seismic analysis. In addition, when the shell model is attacked by vibration wave, there is a high probability of the shell model getting resonance with respect to short-period wave than the dome model. Subsequently, the transitions of cumulative mass

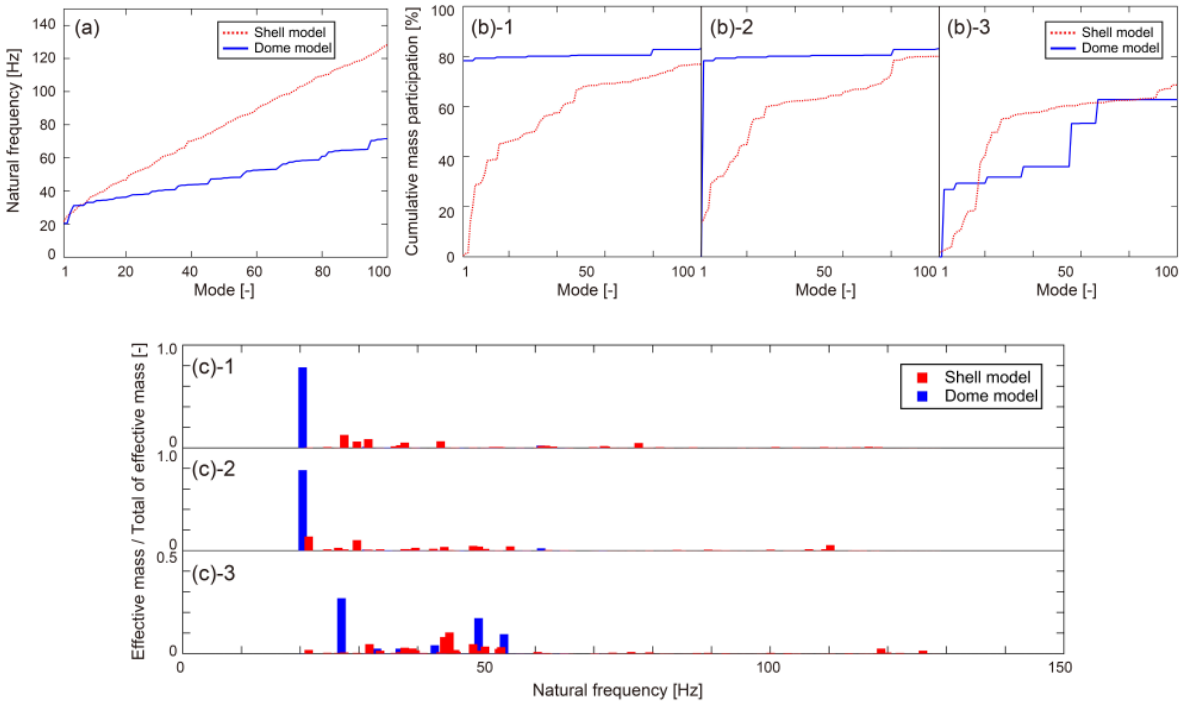


Figure 5. (a) Natural frequency transition of both models. (b) Cumulative mass participation in each direction, (-1) is X direction, (-2) is Y direction, and (-3) is Z direction. (c) Ratio of the effective mass distribution in each direction, (-1) is X direction, (-2) is Y direction, and (-3) is Z direction.

participation were examined to ascertain the contribution of each mode, and the cumulative mass participation up to the 100th mode was used to determine how much of the total was covered for each direction on both models. Figure 5 (b) shows the cumulative mass participation up to the 100th modes. The final cumulative mass up to the 100th mode for all directions almost matched on both models.

Figure 5 (b)-1 and (b)-2 show the transition curves of the horizontal direction. The cumulative mass participation of the dome model almost occupied on the lower-order modes, on the other hand, the cumulative mass participation of the shell model distributed wider range. Even beyond the mode indicated by Figure 4, the transition curves of cumulative mass participation were increasing at a constant slope in the case of the shell model. Figure 5 (b)-3 shows the transition curve of the vertical direction. In the case of the dome model, the cumulative mass participation of lower-order modes were smaller than the horizontal direction. In addition, there were also the large cumulative mass participation on the vertical direction after the 50th mode. In the cases of horizontal direction, the cumulative mass participation of the shell model did not exceed the dome model's one up to the 100th mode, but in the case of vertical direction, the cumulative mass of the shell model exceeded the dome model's one and became almost unaltered around the 20th mode. When consideration the structure attacked by vibration wave, the number of vibration eigenvalues to be considered on vertical wave in the case of the shell model is less than the dome model, whereas the number of vibration eigenvalues to be considered on horizontal wave in the case of the dome model is less than the shell model.

Moreover, in the case of the dome model, the transition curves of cumulative mass participation for X direction (Figure 5 (b)-1) and Y direction (Figure 5 (b)-2) were almost matched because of the horizontal geometry was symmetrical. However, the transition curves of cumulative mass participation were similar in the case of every direction on the shell model as well even though the model's geometry was not symmetrical for every direction. Therefore, the effective mass ratio of each frequency value was considered to confirm distribution of these. Figure 5 (c) shows the effective mass ratio for frequency

values of each mode. In the case of the dome model, the ratio in the vicinity of 20 Hz, which indicated by the first mode, occupied almost the total on the horizontal direction. In the case of vertical direction on the dome model, the mode which had the ratio same as lower-order mode appeared after 50 Hz. On the other hand, the shell model's effective mass ratio distributed between 20 Hz and 80 Hz randomly for every direction. The transition curves of cumulative mass participation for each direction were similar, but the effective values and the distribution of frequency in the case of the shell model seems to be different for each direction. Additionally, the mode which had the ratio same as lower-order mode appeared after 100 Hz in the case of the shell model. The shell model needs considerations for every direction, X, Y, and Z, by each mode on dynamic analysis because the effective mass ratio of the shell model distributed randomly and wider compared the dome model. The wide distribution of the mode which has large mass participation ratio on the shell model is different feature from the dome model. Whether this is a better feature for the structure or not must require the results of the next step, time history response analysis, and this study alone is not sufficient to judge. When these results are matched with acceleration response spectrum of typical earthquake, they have outstanding natural period between 0.2 s and 0.8s. The shell model has natural period distributed wider range under 0.05s. In the case of construction which has mechanical behavior nearly same as the shell model on vibration wave, it's hard to say because substructure and base ground condition also affect it, designing the natural period short by construction its light is an effective countermeasure against resonance.

4. Conclusion

In this study, the FE model reflected bi-valve shell form using shell element was used to perform the natural vibration analysis, and the results were compared with those of the dome model to verify the features of the bi-valve shell form with responded to vibration wave. This study can be summarized as follows:

1. In the range up to the 100th order, the shell model had a broader range frequency than the dome model by natural vibration analysis.

2. Consideration of the cumulative mass participation showed that the dome model has fewer natural period to consider when structural designed than the shell model in the case of horizontal vibration, however in the case of the vertical vibration, the shell model has fewer natural period to consider.

3. The shell model needs considerations for every direction by each mode on vibration condition like earthquake, because the effective mass ratio of the shell model distributed randomly and wider compared the dome model. Whether this is a better feature for the structure or not must require the results of the next step, time history response analysis, and this study alone is not sufficient to judge.

4. When referring to acceleration response spectrum of typical earthquake, the shell model's natural period was shorter than the outstanding natural period by the spectrum of the typical earthquake. In the case of construction which has mechanical behaviour nearly same as the shell model on vibration wave, designing the natural period short by construction it light is an effective countermeasure against resonance.

5. The dome model deformed as a whole, while the shell model's deformation concentrated abdomen area and the deformation of umbo area was small for every mode on the natural vibration analysis. On the other consideration for example, time history response analysis and more, focusing on the umbo area is likely to get the beneficial knowledge about seashell form.

Future works should focus on studying the following points:

1. We should discuss the participation factor and the sensitivity of response to each property that could not be discussed in this paper by the vibration analysis.

2. About the distribution difference of the natural period on both models found from this study, we will examine from time history response analysis whether which feature is better with respect to vibration wave.

3. We are going to continue our research with the aim of proposing a new method of morphogenesis using the features of the bi-valve shell's form obtained in this study and other the features already published on [26] about static loading.

Acknowledgements

This work was supported by Japan Society for the Promotion of Science (JSPS) Grant-in-Aid for JSPS Research Fellow Grant Number JP21J22129.

References

[1] Kim. S. J, Lee. J. H, "Parametric shape modification and application in a morphological biomimetic design," *Advanced Engineering Informatics*, 29(1), pp.76–86, 2015.

[2] Meloni. M, et. al., "Engineering origami: a comprehensive review of recent applications, design methods, and tools," *Advanced Science*, 8(13), 2000636, 2021.

[3] Chen. P. Y, et al., "Biological materials: functional adaptations and bioinspired designs," *Progress in Materials Science*, 57(8), pp.1492–1704, 2012.

[4] Lepora. N. F, et al., " The state of the art in biomimetics," *Bioinspiration & biomimetics*, 8(1), 013001, 2013.

[5] J. Hunt, et al., "A Design Tool for Spatial Tree Structures," *Journal of the International Association for Shell and Spatial Structures (IASS)*, vol.50, pp.3–10, 2009.

[6] Runions. A, et al., "Modeling and visualization of leaf venation pattern," *ACM SIGGRAPH 2005 Papers*, pp.702–711, 2005.

[7] R. Hosomi, et.al., "Derivation and Numerical Analysis of Huge Design Methodology in a Sustainable Structure System Studied from the Strategies of Mechanical optimization in Plants. (No.1 Research Summary)," *Summaries of Technical Papers of Annual Meeting, Architectural Institute of Japan (Structure I)*, pp.971–972, 2019. (in Japanese)

[8] Badarnah. L, "Form follows environment: Biomimetic approaches to building envelope design for environmental adaptation," *Buildings*, 7(2), 40, 2017.

[9] Rian. I. M., & Sassone, M., "Tree-inspired dendriforms and fractal-like branching structures in architecture: A brief historical overview," *Frontiers of Architectural Research*, 3(3), pp.298–323, 2014.

[10] Nicolas PREVOST, et al., "Building crossings in wicker: flexible construction of a postformed footbridge in active bending stiffened during service phase", *Proceedings of the IASS Annual Symposium*, pp.1514–1525, 2022.

[11] Jian ZHOU, et al., "Structure design of the steel roof of Hangzhou Xiaoshan International Airport Terminal 4", *Proceedings of the IASS Annual Symposium*, pp.1483–1494, 2022.

[12] Naleway. S. E, et al., "Structural design elements in biological materials: application to bioinspiration," *Advanced materials*, 27(37), pp.5455–5476, 2015.

[13] N. Frangos, et al., "A Bio-Informed Topology Optimization Algorithm Based in Leaf Venation Structures", *Proceedings of the IASS Annual Symposium*, pp.129–136, 2019.

[14] F. Otto, et.al., *Naturliche Konstruktionen Formen und Konstruktionen in Natur und Tecknik und Prozesse ihrer Entstehung*, Deutsche Verlags-Anstalt GmbH, 1986. (in Japanese)

[15] S. Hildebrandt, Anthony Tromba, *Mathematics and Optimal Form*, Scientific American Books, 1994. (in Japanese)

[16] E. Stach, "Form-optimizing in biological structures—the morphology of seashells. An Anthology of Structural Morphology," *World Scientific*, pp. 173–187, 2009.

[17] D. M. Raup, "The Geometry of Coiling in Gastropods," *Proc.N.A.S.*, vol.47, pp.602–609, 1961.

[18] Takao Ubukata, "Morphology of Hinge and Shell form in Bivalvia: Geometric Constraints Derived from Space Conflict between Umbones," *Paleontological Society*, JSTOR Terms and Conditions, vol.26, No.4, pp.606–624, 2000.

[19] Hans Meinhardt, *The Algorithmic Beauty of Sea Shells*, Springer, 2009.

[20] Johnson. E. H, "Experimental tests of bivalve shell shape reveal potential tradeoffs between mechanical and behavioral defenses," *Scientific Reports*, 10(1), pp.1–12, 2020.

[21] Taylor. D, "Impact damage and repair in shells of the limpet Patella vulgata," *Journal of Experimental Biology*, 219(24), pp.3927–3935, 2016.

[22] Jiang. H, et al., "Designed for the enhancement of structure mechanostability and strength: Suture-serrate margins of bivalve shells," *Journal of the Mechanical Behavior of Biomedical Materials*, 103, 103586, 2020.

[23] Cortie. M. B, "Models for mollusc shell shape," *South African Journal of Science*, 85, pp.454-460, 1989.

[24] Picado. J, "Seashells: the plainness and beauty of their mathematical description," *MAA Mathematical Sciences Digital Library*, pp.1-18, 2009.

[25] M. Ogoshi, et al., "Stress evaluation of real shape of bi-valve shell by image-based finite element analysis", *Proceedings of the IASS Annual Symposium*, pp.1622–1629, 2019.

[26] M. Ogoshi, et al., "A geometric and mechanical analysis of real shaped bi-valve shell by using X-ray computed tomography images", *Journal of Structural and Construction Engineering*, Vol.87, No.795, pp.445–453, 2022. (in Japanese)

[27] M. Ogoshi, et al., "Finite element analysis of the bi-valve shell based on solid and shell elements", *Proceedings of the IASS Annual Symposium*, pp.3229–3238, 2022.

Bridge structures

Active bending
Additive manufacturing/ 3D printing
Architectural geometry
Bamboo for sustainable construction and quality of life improvement
Bio-inspired structures and architecture
► **Bridge structures**
Computational form-finding
Conceptual design
Concrete structures
Construction techniques
Deployable and inflatable structures
Design competition (WG21)
Digital modelling and fabrication
Dynamic response of metal spatial structures
Dynamic response of other structures
Form-finding and structural optimisation of interlocking discrete assemblages
Graphical methods
Gridshell and lattice structures
Historical concrete shells
Historical structures
Lattice structures
Life-cycle design and assessment of structures
Metal gridshell structures, connections and stability
Methods and construction technologies for sustainable shell structures
Morphology and configuration processing
Next generation parametric design
Novel methods in modelling, optimisation and construction for reducing carbon footprint of continuous roof shells
Numerical methods for geometry, form-finding and optimisation of lightweight structures
Optimisation methods and applications
Origami
Other
Teaching design uncertainty: working with unknown qualities/quantities of new and re-claimed materials
Teaching of shell and spatial structures
Tensegrity systems and cable structures
Tension and membrane structures
Tension structures in the Asia-Pacific
Timber and bio-based structures
Topology optimisation
Traditional masonry structures and innovation
Transformable structures

IASS 2023
July 10–14 Melbourne
Integration of Design and Fabrication

Proceedings of the IASS Annual Symposium 2023
Integration of Design and Fabrication
10–14 July 2023, Melbourne, Australia
Y.M. Xie, J. Burry, T.U. Lee and J. Ma (eds.)

Innovative design of a pedestrian bridge using multi-material topology optimisation

Yaping LAI[a,b,*], Yu LI[c,d], Peixin CHEN[b], Yanchen LIU[b], Lijun ZHAO[b], Jin LI[b], Yi Min XIE[d,*]

[a,*] School of Civil Engineering, Chongqing University, Chongqing, 400045, China
[d,*] Centre for Innovative Structures and Materials, School of Engineering, RMIT University, Melbourne, 3001, Australia
laiyaping@tylin.com.cn; mike.xie@rmit.edu.au

[b] T.Y. Lin International Engineering Consulting (China) Co. Ltd, Chongqing, 401121, China
[c] College of Architecture and Urban Planning, Tongji University, Shanghai, 200092, China

Abstract

To facilitate commuters crossing the railways near the high-speed rail station in Shenzhen, China, a five-span pedestrian bridge with a main span of 152 m is being planned. We propose an innovative pedestrian bridge design based on multi-material topology optimisation, which realises the process from conceptualisation to detailed design considerations. This bridge is expected to satisfy unique architectural and engineering challenges, providing an iconic, cost-effective and low-maintenance solution, and complying with various construction requirements. The superstructure was designed for a variable-depth spinal-shaped girder in the centre of the deck with an elegant curving facade, from which one pathway cantilevers on either side. On the one end of the bridge, due to the considerable difference in elevation between the bridge deck and the ground, we provided a two-level Fibonacci-type spiral-shaped bicycle ramp. It is supported by a series of organic tree-branch-shaped piers obtained from topology optimisation. The elegant profile of this bridge creates an enjoyable and dynamic crossing experience with scenic views in all directions. In this paper, the main aspects of the construction requirements and challenges, conceptual development process, form-finding with the bi-directional evolutionary structural optimisation (BESO) strategy, structural design, and construction method of the bridge are presented.

Keywords: bridge design, form finding, finite element analysis, topology optimisation, spinal-shaped girder, tree-inspired branching pier

1. Introduction

Bridges are man-made structures that overcome barriers and facilitate human traveling. Thanks to developments in design theories, modern bridges with larger spans and superior structural performance are emerging. However, the homogenisation of traditional design methodology and ideology usually causes bridge structures almost the same pattern. To date, topology optimisation has become an effective strategy for architects and engineers to probe elegant and high-performance structures. Without relying on the initial configuration of form and structure, this state-of-the-art technology can inspire designers to achieve innovative bridge structures that will be efficient, lightweight, and versatile [1]. Overview of several topology optimisation methods, evolutionary structural optimisation (ESO) [2, 3] and its enhanced version bi-directional evolutionary structural optimisation (BESO) [4] are two of the most commonly used in architectural and structural design. Recently, the multi-material bi-directional evolutionary structural optimisation (MBESO) method [5, 6], which was proposed by Li and Xie, has been capable of solving multiple material topology optimisations. Hence, lighter and more effective

Copyright © 2023 by Yaping LAI, Yu LI, Peixin CHEN, Yanchen LIU, Lijun ZHAO, Jin LI and Yi Min XIE. Published in the Proceedings of the IASS Annual Symposium 2023 with permission.

structural forms can be achieved by using the MBESO method in the conceptual design of bridges [7, 8].

Nevertheless, the bridges obtained by topology optimisation typically feature irregular and complex nonlinear geometric appearances, which are difficult or expensive to realise by conventional construction techniques. Currently, various bridges with unique forms and excellent structural performance have been obtained through topology optimisation methods, but rarely of these been reported to be successfully built. Due to the huge scale that bridges typically exhibit, their design is quite different from the design and manufacture of mechanical or industrial products. Successful implementation according to the design intentions requires a combination of the current technology level and construction logic. Given this, it is essential that topology optimisation techniques are introduced into bridge design with full consideration of constructability in addition to fulfilling safety, economics, and durability.

In this paper, we proposed a novel and unique pedestrian bridge according to the construction requirements and challenges of a real project and then optimised its structure using the MBESO method. Inspired by the obtained forms from topology optimisation, we conceived this bridge based on the multiple objectives and constraints such as construction boundary conditions, functional requirements, aesthetic appeal, and structural mechanical performance. The major aspects related to design considerations and structural analysis are presented.

2. Overview of the project

2.1. Project profile

A pedestrian bridge with a main span of 152 m is planned to be built in Shenzhen, China, to improve accessibility for commuters to cross the rails adjacent to the high-speed train station. The bridge should be designed and built not only to meet the commuting function but also to achieve novelty, aesthetics, and uniqueness.

2.2. Construction requirements and challenges

Shenzhen is an attractive emerging city in southern China. The business centre of the high-speed rail station, where this pedestrian bridge is located, is one of the most animated urban areas. The construction requirements and challenges of this project are as follows:

(1) The boundary around the project is complex and restrictive factors are multifarious. Water source protection zone, ecological control lines, fundamental agricultural land, etc. must be considered comprehensively.

(2) The bridge crosses a road and several high-speed railways are in operation. Due to the stringent requirements of rail operations for a newly built bridge overhead, the construction must be completed at the fastest speed within the time window specified by the railway administration department.

(3) The owner has high requirements for the landscape and implementation of the bridge. The project needs to be a masterpiece for the community. The bridge should enhance the aesthetic taste of the city and become a landmark to shape the influence of the city.

3. Conceptualization of the novel pedestrian bridge

3.1. Concept development

For the consideration of minimising the maintenance of the cross-bridge on the operating rails and the electrical protection of the overhead contact line system, the railway administration department disallows the structure of steel or steel-concrete composite structure bridge across. As the project is located in the central business district, surrounded by numerous high-rise buildings, the bridge should

blend in with the environment and adopt a low-profile form according to the urban design. Therefore, cable-supported bridges with lofty pylons are unsuitable, while concrete girder and arch bridges are economical and reasonable solutions with minor maintenance work. Shenzhen is a seaside city with a thick cover of soft soil foundation. If a deck arch bridge (as shown in Figure 1a) is adopted, the arch seats cannot be located directly on the rock foundation. The enormous long-term horizontal thrust from the arch is prone to cause soil creep, thus endangering the bridge itself and the railways. A prestressed concrete (PC) girder bridge (as shown in Figure 1b) with variable cross-section may be appropriate, however, as the main span is 152 m, the girder depth at the main pier requires 11 m following the conventional design. However, similar to deck arch bridges, variable cross-section PC girder bridges will cause excessive elevation lift of the bridge deck. This would significantly increase the climb length of such a ramp for bridges that need to pass bicycles. Thus, conventional structural solutions have disadvantages.

How to reduce the girder depth, but still meet the bearing capacity requirements of such a long-span bridge? Given this situation, we propose to set part of the load-bearing structure above the bridge deck based on the variable-section girder bridge, forming a distinctive combination consisting of a spine structure and variable-section girder (as shown in Figure 1c). This lowers the deck elevation by two meters compared to a conventional PC girder, significantly reducing the ramp length. However, if we do not improve on this unique structure, it will seem too bulky. Therefore, we optimised this structure by using the MBESO method to achieve a strikingly elegant bridge with high efficiency.

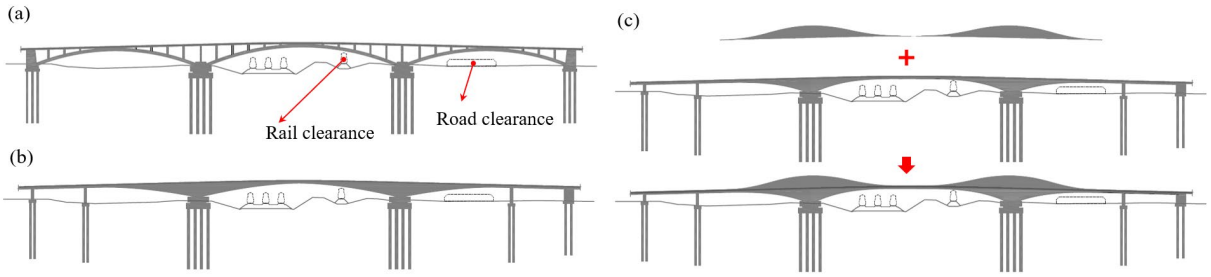


Figure 1. Concept development process: (a) deck arch bridge with flat arch, (b) variable-section PC girder bridge, (c) variable-depth spinal-shaped PC girder bridge.

3.2. Structural optimisation

3.2.1. Topology optimisation settings

Given that the length and height of the bridge structure are significantly greater than the width of the cross-section and that the load is primarily concentrated in the vertical plane, the structural model can be simplified to a plane stress problem, and this project uses a 2D topology optimisation algorithm. Compared with 3D topology optimisation, the 2D topology optimisation method can present more details with more FEA elements, making it more suitable in this case.

This project involves a series of topology optimisation calculations, with material parameters mostly remaining the same across these cases. The parameters for the two materials used for tension and compression are: steel with E_t = 200 MPa and concrete with E_c = 50 MPa. The allowable stresses for the two materials are: $[\sigma_s]$ = 200 MPa and $[\sigma_c]$ = 50 MPa. The magnitude of the line load on the flat bridge deck and the curved pedestrian walkway is set to q_1: q_2 = 2: 1. In different cases, the total number of elements in the design domain varies, but the size of individual elements remains the same, with four-node rectangular elements measuring 0.1 m × 0.1 m in length. If the design domain is a complete rectangle, the total number of finite elements is 292,340, sufficient to show small structural details. Other topology optimisation parameters are set as follows: the evolution rate *er* is set to 2%, and the filter radius is r = 0.5 m.

3.2.2. Evolution of the Initial Design Domain

Adjusting the initial design domain is a simple way that can directly influence the topology optimisation result. For a new structural form, like the one studied in this paper, an ideal optimised structure can be obtained by continuously adjusting the design domain, until a suitable design domain is determined.

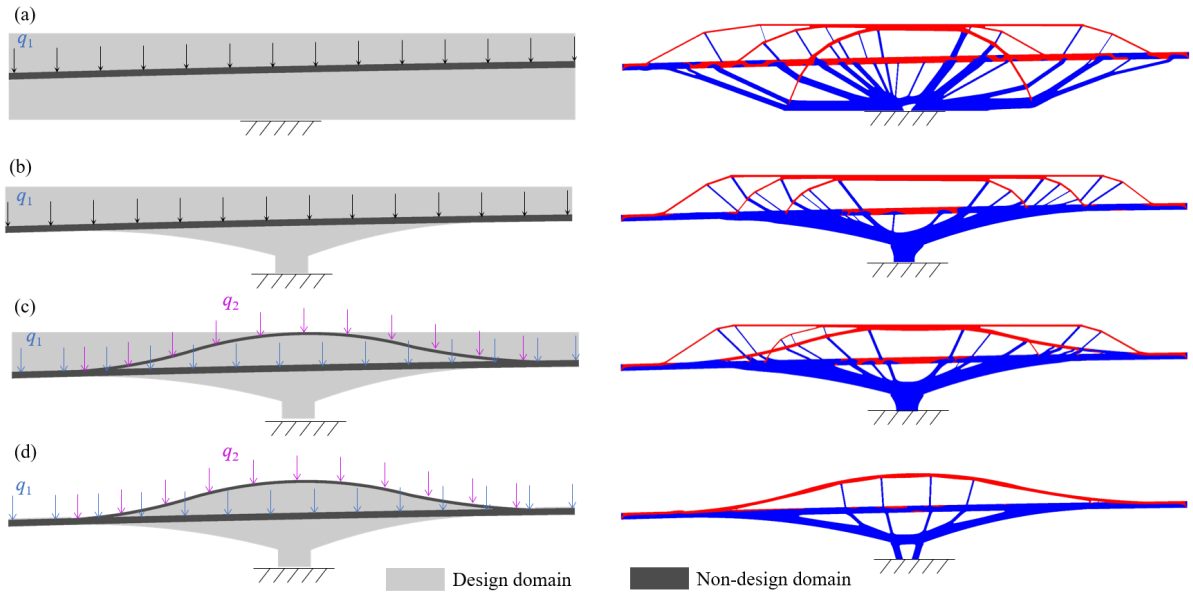


Figure 2. Various design domains, support and loading conditions, and corresponding topology optimisation results: (a) complete rectangular design domain, (b) design domain with the space below the bridge deck removed, (c) design domain with added non-design space for pedestrian walkways, (d) design domain with the space above the pedestrian walkway removed.

Figure 2 shows a series of topology optimisation results achieved by modifying the design domain boundaries. In Figure 2a, the optimised structure is obtained using the rectangular design domain, with the bridge deck as a non-design domain and fixed boundaries at the bridge piers. The blue compressed materials are radially distributed around the pier, providing support to the bridge deck, while the red tensioned materials are mainly concentrated above the bridge deck to resist bending. The force transmission path and the synergistic mode between the two materials are reasonable, but some components do not meet the functional requirements of the bridge, such as the inclined branches that almost touch the ground, obstructing traffic under the bridge deck. Therefore, the design domain boundaries in these local areas need to be adjusted. In Figure 2b, the redundant space under the bridge deck is removed, and the optimised structure presents a simple form, with blue compressed materials forming tree-shaped columns, and tensioned members above the bridge deck forming a bow-shaped inverted beam string structure system. To meet the functional requirements of pedestrians, the design domain after setting the non-design domain above the bridge deck is shown in Figure 2c, and accordingly, the optimised result also includes the pedestrian area. Furthermore, by restricting the space above the bridge deck, the tensioned members above the pedestrian walkway can be removed, and these cable-like tensioned members are merged into a single tension cable, as depicted in Figure 2d.

3.2.3. Driving topology optimisation by setting non-design domain

In Figure 2, setting non-design domains ensures that the topology optimisation results meet the functional requirements of the structure, such as retaining the bridge deck and pedestrian walkway in the results. In addition, by setting non-design domains appropriately, the evolution direction of topology optimisation direction can be driven to an ideal design reference prototype. In Figure 3a, the design domain is further adjusted based on the optimised result in Figure 2d by adding the lower chord arch of the bridge as a non-design domain, increasing the target volume fraction to 0.8, and adjusting the filter

radius to r = 1.0 m. The optimised result shows a stable tree-like structure with four inclined columns radiating from the piers and elegant curved lines of tensioned material. In Figure 3b, to obtain diverse designs, the area where the vertical columns are located is added as a non-design domain. Due to the existence of this non-design domain, the material within a certain range around the central column converges towards the vertical columns in the topology optimisation process, resulting in an optimised structure with three columns. Both of these structural forms have certain design reference values, and it is evident that setting non-design domains in very small areas can lead to completely different topology optimisation structures.

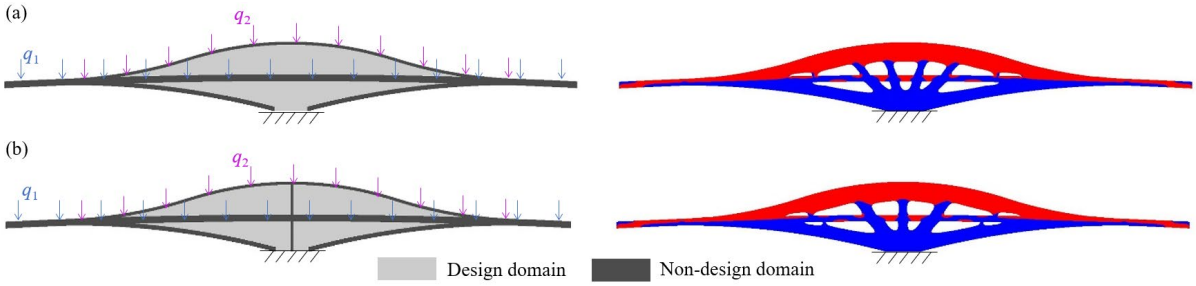


Figure 3. Driving topology optimisation direction by setting non-design domain: (a) optimisation result without setting the middle vertical column as non-design domain, (b) optimisation result with the middle column set as a non-design domain.

3.2.4. Setting different filter radius

In addition to employing non-design domains, adjusting the filter radius in topology optimisation provides an effective means to influence the direction of optimisation and achieve diverse structural designs. Expanding on the settings demonstrated in Figure 3a, increasing the filter radius to r = 3.0 m yields an entirely different topologically optimised structure, as showcased in Figure 4. The structure obtained with a smaller filter radius features slender and more members, including 4 inclined columns. On the other hand, the structure produced with a larger filter radius has fewer, sturdier members, incorporating only 2 inclined columns. When designing structures for practical engineering applications, the selection of an appropriate topology optimisation outcome should be comprehensively considered based on other factors such as construction complexity and aesthetic value.

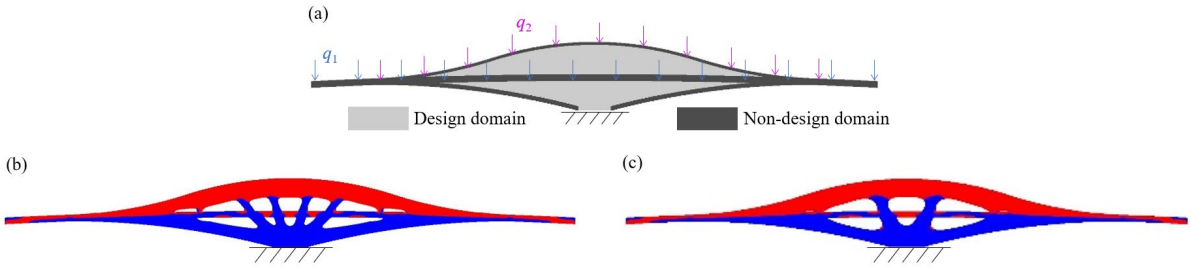


Figure 4. Obtaining diverse topology optimisation results by adjusting the filter radius: (a) design domain, support, and load conditions, (b) topology optimisation result obtained with a filter radius of 1.0 m, (c) topology optimisation result obtained with a filter radius of 3.0 m.

4. Structural design

4.1. Overall design

Based on the boundary conditions and various constraints of the bridge site, this bridge was designed as a five-span with a span arrangement of (41+85+152+85+41) m and a width of 17 m. The design for the superstructure is a variable-depth spinal-shaped PC girder with an elegant curving facade in the centre of the deck, from which one pathway cantilevers on either side. The stairway above the spinal-shaped

girders (SSGs) gradually rises to the top at the main pier, which offers scenic views of the surroundings. The segregated twin pathways allow the faster commuter bicyclists to be safely separated from the slower pedestrians. Figure 5 shows the rendering of the proposed bridge.

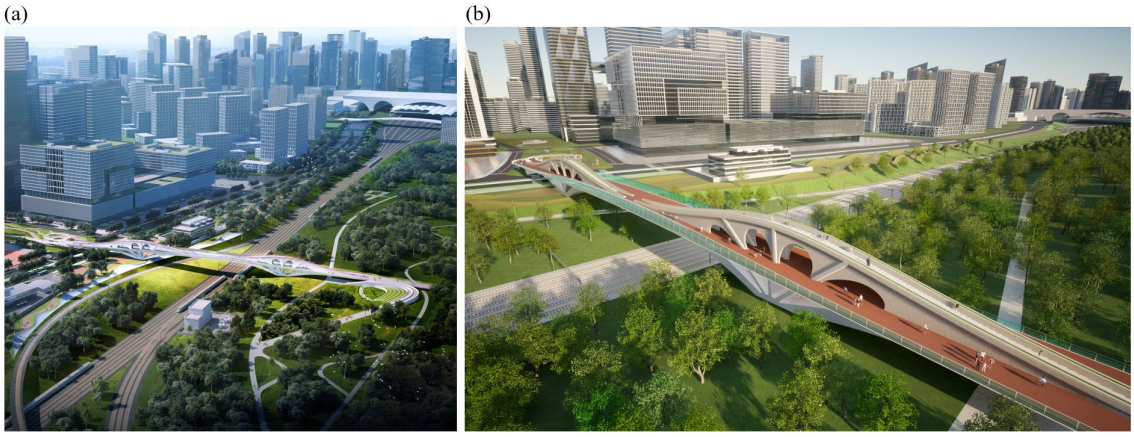


Figure 5. Rendering of the proposed bridge: (a) aerial view, (b) close-range perspective view.

4.2. Construction method

To minimise the safety risk and disruption to the railways during the bridge construction, we propose to use of the horizontal swivelling construction method for the superstructures. For ensuring weight balance during rotation, the superstructure is arranged symmetrically along the main pier. First, each section of the superstructure was cast by the temporary support along the direction of the railways, until the maximum cantilever state was formed before horizontal swivelling. Afterward, the hinges are sealed immediately after the superstructure is in place to avoid large displacements caused by small rotations of the ball hinges. Finally, the spinal-shaped superstructures are closed with the side span cast-in-place sections and the mid-span rigid hinge is installed. Figure 6 shows the construction method of the bridge.



Figure 6. Schematic diagram of the construction method: (a) cast-in-place of the superstructures, (b) horizontal swivelling process, (c) horizontal swivelling in place.

4.3. Structural design

4.3.1. Spinal-shaped superstructure

Based on the form-finding by the MBESO method, we manually simplified and adjusted the shape of the bridge slightly, and then detailed the design of this structure with full consideration of constructability. The superstructure (as shown in Figure 7) was designed as a thin-walled concrete structure with a regular curved surface. Both the main girder and the lower chords are of the single-box three-cell structure with aligned webs, which naturally transition through a converging section. The abreast SSGs are set above the deck and aligned with the middle webs of the main girders. A top slab is set between the two SSGs to strengthen the integrity of the structure, while the pedestrian steps can be set on it. By making arch-shaped holes in the webs of the SSGs (which are inefficient areas), the bridge not only reduces its self-weight but also seems lighter. Besides, people can reach the other side of the

deck through these holes, and the interior of the SSGs creates a space for pedestrians to get shelter from the sun and rain. The top of the SSGs are inverted horseshoes, in which most of the longitudinal prestressed tendons of this bridge are arranged, and only a few parts are configured in the top and bottom slabs of the main girder. In the lateral direction, due to the considerable cantilever length of the girder flange, the lateral prestressed tendons are configured in the top slabs.

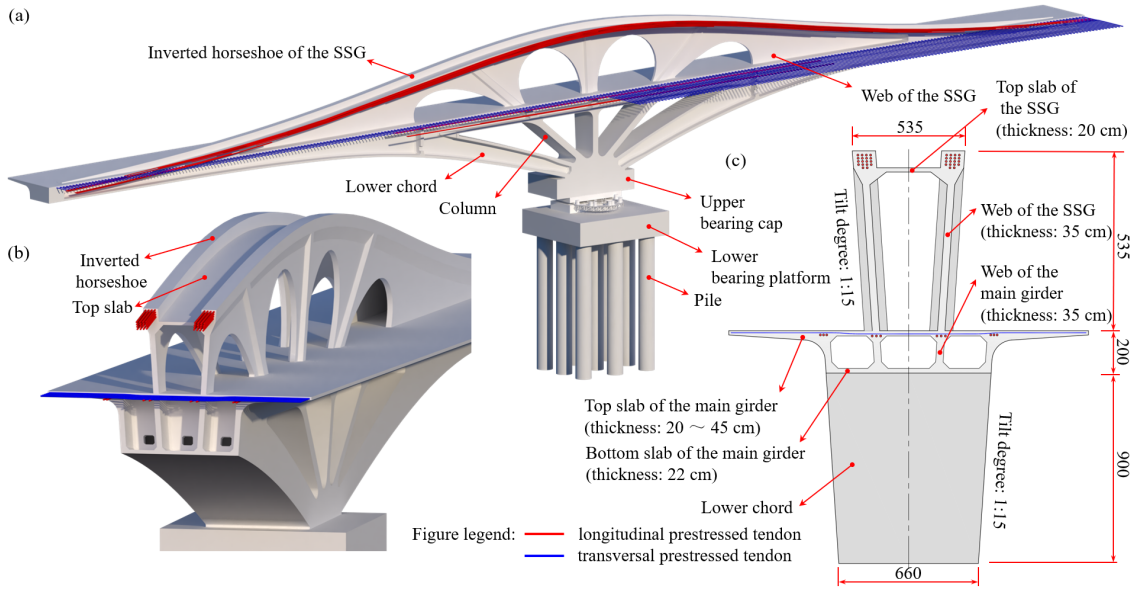


Figure 7. Schematic diagram of superstructure: (a) schematic along the axial direction, (b) schematic along the lateral direction, (c) typical cross-section of the superstructure (unit: cm).

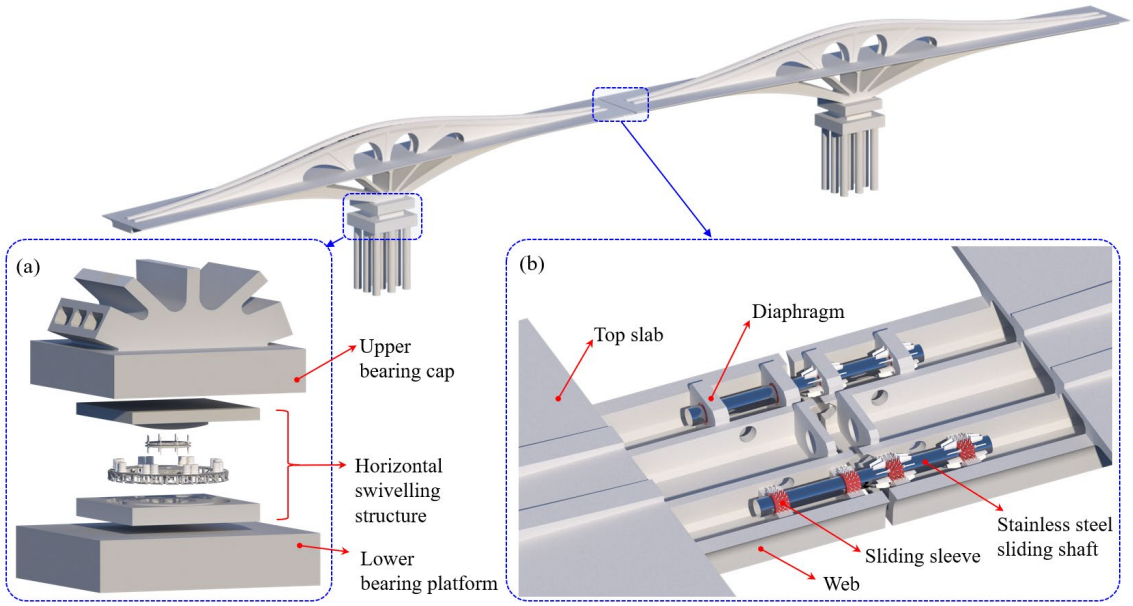


Figure 8. Schematic diagram of horizontal swivelling structure and rigid hinge expansion device: (a) horizontal swivelling structure decomposition diagram, (b) rigid hinge expansion device.

4.3.2. Horizontal swivelling structure

The horizontal swivelling structure consists of rotation, traction, and balancing system (as shown in Figure 8a). The core component is the ball hinge, which is installed below the upper bearing caps and

offers horizontal rotation around a positioning steel shaft in the centre of the main pier under the action of continuous tension jacks, thus driving the overall horizontal swivelling of the superstructure.

4.3.3. Rigid hinge expansion device

Since the bearing caps of the main piers are equipped with horizontal swivelling structures, without space to install movable bearings. To reduce the adverse effect such as temperature influence on the bridge while ensuring the continuity of the deck, we propose to disconnect the main girders at mid-span and install a rigid hinge expansion device (as shown in Figure 8b). This solution releases the longitudinal degrees of freedom of the main girders and limits the remaining degrees of freedom.

4.3.4. Bicycle ramp

On the one end of this bridge, due to the considerable difference in elevation between the bridge deck and the ground as well as the site area constraints, we provide a two-level variant Fibonacci spiral-shaped bicycle ramp with a 3.5% slope (as shown in Figure 9a). The superstructure of the bicycle ramp adopts a continuous steel girder with a depth of 30 cm for a lighter appearance. To reduce the spans of the superstructure and achieve a more uniform force, we adopted the tree-inspired branching (TIB) piers obtained from the Ameba [9]. The curved continuous steel girder is supported by a series of organic TIB piers, which conforms to the principle of minimum transfer path and reflects the convergence process of force flow from top to bottom and from dispersion to concentration. Thanks to the efficient load transfer, the bicycle ramp structure is elegant and rational, creating an enjoyable and dynamic traversing experience with scenic views in any direction (as shown in Figure 9b).

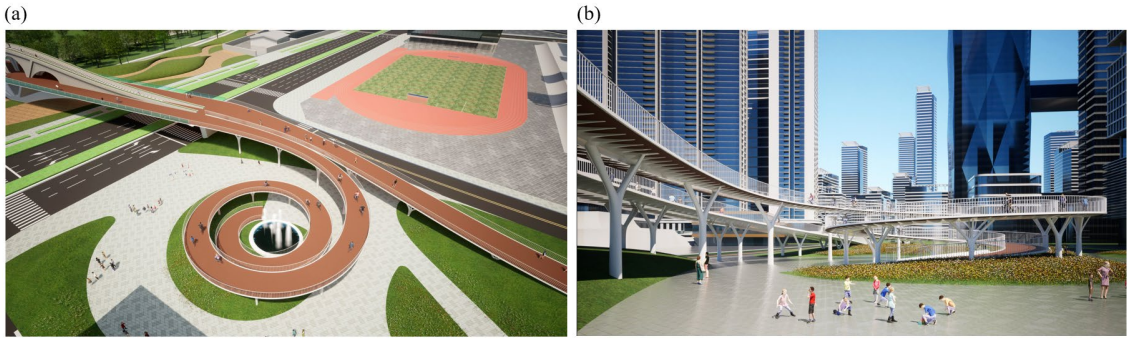


Figure 9. Rendering of the bicycle ramp: (a) aerial view, (b) close-range perspective view on the ground.

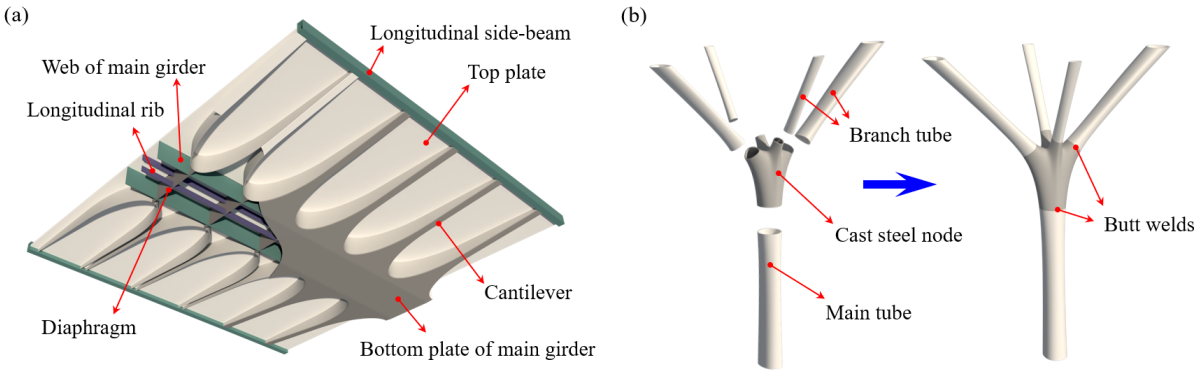


Figure 10. Structural schematic of the continuous steel girder and the TIB pier: (a) details of steel girder segment, (b) TIB pier decomposition diagram.

For achieving the organic shape, the TIB piers require a natural and harmonious transition at the intersection of the main and branch tubes. We absorbed the unique merits of cast steel members. The tree-shaped cast steel nodes are used to replace the nodes where the main and branch tubes intersect,

through integral casting. It is connected by butt welds instead of coherent welds, and the welds are dispersed, avoiding the stress concentration of welds brought by the use of steel tube coherent welding. The structural schematic of the continuous steel girder and the TIB pier is shown in Figure 10.

5. Structural analysis

5.1. Finite element model

To analyze the structural performance of the proposed pedestrian bridge, a detailed finite element model (FEM) was established using Midas/FEA NX. All structures were simulated with solid elements, except for prestressed tendons, which were simulated with tendon elements. The model was discretized into 3,408,842 solid and 22,062 tendon elements, with a mesh size of 0.1 m and 0.5 m, respectively. The constraints of the structure were: fixed constraints at the bottom of the bearing cap and simple constraints at the side supports. Since rigid hinges are provided in the mid-span, symmetric restraint and release of axial restraint were used.

5.2. Design parameters

The relevant parameters of the design loads are as follows:
(1) According to the design specification [10], Table 1 summarizes the parametric values of concrete and prestressed strands. A second-stage dead load of 16.8 kN/m was applied to the superstructure including deck pavement and railings.

Table 1. Parametric values of concrete and prestressed strands.

Material	Material grade	ρ (kg/m^3)	E_c (GPa)	$f_{cu,k}$ (MPa)	f_{cd} (MPa)	f_{td} (MPa)	f_{pk} (MPa)	f_{pd} (MPa)
Concrete	C50	2,600	34.5	50.0	22.40	1.83	/	/
Prestressed strand	1,860	7,850	195	/	/	/	1,860	1,260

Note: ρ = density; E_c = elastic modulus; $f_{cu,k}$ = standard value of cubic compressive strength; f_{cd} = design value of axial compressive strength; f_{td} = design value of axial tensile strength; f_{pk} = standard value of tensile strength; f_{pd} = design value of tensile strength.

(2) Prestressing loads: The prestressed strand's tension control stress value is 0.72 times its standard tensile strength, namely 1,339.2 MPa. The effective prestressing force in the tendons has taken full account of various prestress losses, such as: ① concrete shrinkage and creep, ② tendon relaxation, ③ anchorage deformation, ④ friction between tendons and pipes, etc., all calculated according to the specifications.

(3) Temperature effect: An Overall temperature variation range of ± 25 °C. The gradient temperature for the superstructure was set at 14 °C for the positive difference and 7 °C for the negative difference.

(4) Live load: The pedestrian load was considered at 3.5 kN/m^2, including a full crowd on the whole bridge deck and a full crowd on one side of the deck.

5.3. Static response

The effects of pedestrian load, concrete shrinkage and creep, second-phase dead load, temperature effect, and their combined effects were taken into consideration in the structural analysis. Figure 11 shows the stress distribution at the ultimate limit state in each structural component, which clarifies the load transfer path of the superstructure.

As can be seen from Figure 11, the maximum principal tensile stress is 1.8 MPa and the maximum principal compressive stress is 18.7 MPa. Only a few spots where stresses are concentrated at the corners of the structure, but these regions are minor and the stresses dissipate fast. Except for the localized stress

concentrations, the principal compressive and tensile stresses in the superstructure are all below the design value of material strength with sufficient safety reserves.

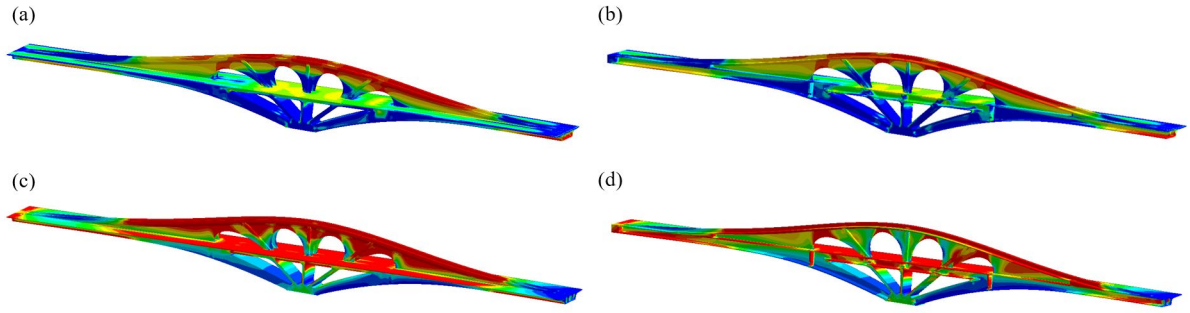


Figure 11. Stress distribution of the superstructure (unit: stress in MPa): (a) maximum principal tensile stress distribution of external surface, (b) maximum principal tensile stress distribution of inner surface (along the axial direction), (c) maximum principal compressive stress distribution of external surface, (d) maximum principal compressive stress distribution of inner surface (along the axial direction),

Since the maximum mid-span vertical deflection under the live load is 125.6 mm (the sum of the absolute values of positive and negative deflection), the deflection-to-span ratio is 1/1,209 (less than 1/600), which is sufficient to meet the requirements.

5.4. Dynamic response

Based on FEM, the analysis of structural dynamic response characteristics was performed. The structural self-weight and the second-phase dead load were converted into mass in the FEM. The natural vibration frequency of the bridge for the first-to-four and first-to-eight orders is shown in Figure 12 and Table 2, respectively.

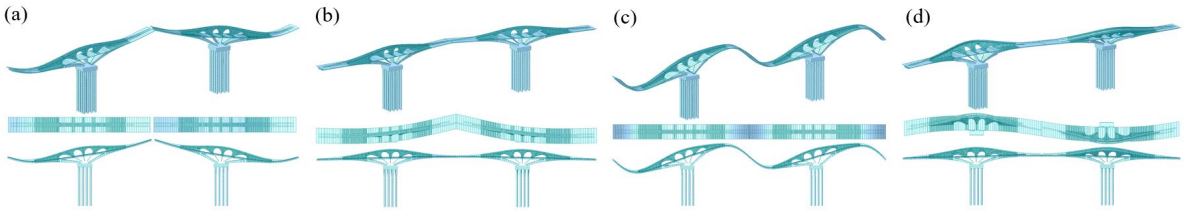


Figure 12. Vibration modes of the proposed bridge: (a) first order, (b) second order, (c) third order, (d) fourth order.

Table 2. First-to-eighth order vibration modes of the bridge.

Mode order	Frequency (Hz)	Vibration characteristics
1	0.714	symmetrical vertical bending
2	0.977	symmetrical horizontal bending
3	1.162	asymmetric vertical bending
4	1.683	asymmetric horizontal bending
5	1.757	symmetrical horizontal bending
6	1.782	symmetrical vertical bending
7	2.877	asymmetric vertical bending
8	2.930	asymmetric horizontal bending

With the ever-increasing span of pedestrian bridges and their fundamental frequency decreases, pedestrian-induced vibration and walking comfort issues become increasingly prominent. Therefore, vibration comfort level can be evaluated for different crowd density conditions by combining the

sensitive frequency range evaluation guidelines [11] and relevant codes [12–14]. The sensitive frequency range is 1.25 to 4.60 Hz for vertical vibrations and 0.50 to 1.20 Hz for transverse vibrations. When the self-oscillation frequency of a pedestrian bridge is outside the above sensitive frequency range, it can be considered as naturally meeting the requirements of pedestrian-induced vibration. Otherwise, it is necessary to check whether the acceleration response of the pedestrian bridge under the crowd walking load satisfies the walking comfort condition. Therefore, the second, sixth, and seventh order modes need to be verified for the pedestrian-induced vibration acceleration response, and the results are shown in Table 3.

Table 3. Pedestrian-induced vibration acceleration response.

Mode order	Vibration direction	Frequency (Hz)	Peak acceleration (m/s^2)	Specification limit value (CL1 level)(m/s^2)	Evaluation conclusion
2	lateral	0.977	0.066	0.1	fulfilling the requirements
6	vertical	1.782	0.499	0.5	
7	vertical	2.877	0.185	0.5	

6. Structural efficiency comparison with a continuous girder bridge

A structural efficiency comparison between the SSGs bridge and a conventional variable-section PC continuous girder bridge was conducted to assess the value of the novel SSGs bridge, as shown in Table 3. In this comparison, the span configuration, deck width, load, and other design criteria were the same.

Table 4. Comparison of the structural efficiency between the proposed bridge and conventional variable-section PC girder bridge.

Structure system		SSGs bridge	Conventional girder bridge
Quantity of materials	C60 concrete (m^3)	5,900.6	6,902.0
	Prestressed strand (t)	261.8	336.9
	Rebar (t)	885.1	1,035.3
Structural self-weight per square meter (kg/m^2)		2,796.6	3,276.8

It can be seen from Table 4 that the SSGs bridge requires less material than the conventional variable-section PC girder bridge. The innovative pedestrian bridge obtained from the MBESO method eliminates inefficient parts of the structure and enables such a long-span bridge technically and economically efficient.

7. Conclusion

In this study, an innovative long-span pedestrian bridge over several high-speed rails was designed using the multi-material bi-directional evolutionary structural optimisation (MBESO) method. In the topology optimisation process, several strategies, including setting various design domains, fixing and prohibiting part of the design space, and specifying different filter radii were adopted to achieve an optimised conceptual design. After manually simplifying and slightly adjusting the form-finding result from the MBESO method, we conducted detailed design of the structure with full consideration of constructability. In addition to the unique and elegant appearance, this bridge also shows excellent structural performance in terms of static and dynamic responses. Furthermore, a comparison between the proposed bridge and a conventional variable-section prestressed concrete continuous girder bridge under the same conditions reveals that the new design has higher structural efficiency.

As topology optimisation techniques are increasingly developed, it will be feasible for engineers to use them as intelligent tools to help design innovative bridges with high structural performance. Currently, although this technology is not yet able to consider all of the complex factors in engineering design (e.g. the construction logic and constructability of large-scale projects), the design does not need to follow a fixed routine. The designers can gain valuable insights from the outcomes of topology optimisation. On

this basis, further rethinking the structural solution by combining human cognition and wisdom, with simplifying complexity, an elegant structure may be found near its rationality.

Acknowledgements

This project was supported by the Australian Research Council (FL190100014, DP200102190) and the Technological Innovation and Construction Science and Technology Project of Chongqing City (cstc2022-1-5-3).

References

[1] Y. M. Xie, K. Yang, Y. He, Z. L. Zhao and K. Cai, "How to obtain diverse and efficient structural designs through topology optimization," in *Form and Force: Proceedings of the IASS Annual Symposium 2019*, Barcelona, Spain, October 7–10, 2019, C. Lázaro, K. U. Bletzinger and E. Oñate, Eds.

[2] Y. M. Xie and G. P. Steven, *Evolutionary Structural Optimization*, Springer, 1997.

[3] X. Huang and Y. M. Xie, Evolutionary topology optimisation of continuum structures: methods and applications. Chichester: Wiley, 2010.

[4] L. Xia, Q. Xia, X. Huang, and Y. M. Xie, "Bi-directional evolutionary structural optimization on advanced structures and materials: a comprehensive review," *Archives of Computational Methods in Engineering*, vol. 25, pp. 437–478, 2018.

[5] Y. Li and Y. M. Xie, "Evolutionary topology optimization for structures made of multiple materials with different properties in tension and compression," *Composite Structures*, vol. 259, article 113497, 2021.

[6] Y. Li, P. F. Yuan, and Y. M. Xie, "Topology optimization of structures composed of more than two materials with different tensile and compressive properties," *Composite Structures*, vol. 306, article 116609, 2023.

[7] Y. Li, Y. Lai, G. Lu, F. Yan, P. Wei, and Y. M. Xie, "Innovative design of long-span steel–concrete composite bridge using multi-material topology optimisation," *Engineering Structures*, vol. 269, article 114838, 2022.

[8] Y. Lai, Y. Li, M. Huang, L. Zhao, J. Chen, and Y. M. Xie, "Conceptual design of long span steel-UHPC composite network arch bridge," *Engineering Structures*, vol. 277, article 115434, 2023.

[9] Q. Zhou, W. Shen, J. Wang, Y. Y. Zhou, and Y. M. Xie, "Ameba: A new topology optimisation tool for architectural design," in *Creativity in Structural Design: Proceedings of the IASS Symposium 2018,* July 16–20, 2018, MIT, Boston, USA Caitlin Mueller, Sigrid Adriaenssens, Eds.

[10] Ministry of Transport of the People's Republic of China. Specifications for design of highway reinforced concrete and prestressed concrete bridges and culverts (JTG 3362-2018), *China Communications Press*, 2018.

[11] Ricciardelli F, Demartino C, "Design of footbridges against pedestrian-induced vibrations," *Journal of Bridge Engineering*, 21(8), C4015003, 2016.

[12] European Committee for Standardization.Euro Code, Basis of Structural Design-Annex A2:EN1990. Brussels, 2002.

[13] International Standardization Organization. Bases for design of structures serviceability of buildings and pedestrian walkways against vibration: ISO10137. Geneva, Switzerland, 2005.

[14] British Standards Institution.British standard specification for loads; steel, concrete and composite bridge, Part 2: BSI 5400. London, 2006.

IASS 2023
July 10–14 Melbourne
Integration of Design and Fabrication

Proceedings of the IASS Annual Symposium 2023
Integration of Design and Fabrication
10–14 July 2023, Melbourne, Australia
Y.M. Xie, J. Burry, T.U. Lee and J. Ma (eds.)

Integrated bridge structure design process through finite element analysis (FEA) and pixel-based visibility culling method

Ana Gabriela LOAYZA[*], Taeyong KIM[a]

[a,*] Harvard Graduate School of Design
aga.loayza@gmail.com

Abstract

Through industrial evolution, bridges could accommodate various requirements, from transportation to harmony with surroundings. However, ensuring minimum visual impact over their surrounding environment has not been ordinary criteria in the traditional design solutions due to the structural implications. Through an integrative view between minimal design and engineering, this study proposes a novel bridge design method using a building system of multiple slender columns in the design of pedestrian bridges. The method seeks to maximize the structural performance and material efficiency, while minimizing the visual impact of the bridge, relaying in a two-fold structural and visual analysis which assists iterations on the section and culling of columns, following allocation options that create different group densities, transit paths, and boundary conditions along the perimeter of the bridge. The analysis uses a parametric design method that computes the results of Finite Element Analysis (FEA), shape optimization, and visibility analysis based on the provided bridge structure design. Rhino 3D and grasshopper programs are used as a platform where predefined definitions, customized C# components, and the Millipede plugin assemble the procedure, to drive decision-making on bridge design. Outcomes are delivered through numeric values and graphical analysis. Through this pipeline, it is possible to estimate deflection, smallest section for each column, and visibility levels from inside and outside of the bridge from masked rendering images. This method helps unveil the hidden implications of early design decisions during the prototyping phase, while exploring the possibilities of a minimal building system.

Keywords: finite element analysis, visibility analysis, bridge, conceptual design, morphology, optimization, steel structure

1. Introduction

The profession and the executions of bridge structural engineering are as old as the human race [1]. And the development of civilization and industrial evolution increased the need for stronger and wider crossing. Especially, the inventions of the new transports such as automobiles and trains and their surging populations increased the demands of the bridges that can accommodate high traffic flow. The introduction of the steel materials and the availability of them in the market replaced the wooden trusses, leading to the longer spans supporting the heavy loads [4]. In accordance with the structural analysis, there have been efforts to improve the design features of the bridges introducing the harmonious or integrating approach to the landscape: the use of specific colour scheme, the choice of the structure, and adding ornamented features. Current design of the bridges became more diverse with the support of the computational design methods [8]. The form-finding methods and the optimization tools allowed the final design of the bridge as close as the conceptual design [5]. However, there are limited number of studies concentrated on the numerical analysis of the visual impact of the bridge design on the surroundings, fulfilling the structural requirements of the bridge.

Copyright © 2023 by Ana Gabriela LOAYZA and Taeyong KIM. Published in the Proceedings of the IASS Annual Symposium 2023 with permission.

Through the integrated study of the history, contemporary computational design process of the bridge, this study introduces a novel perspective on how to balance the visual and aesthetic notions with structural behaviour, using slender steel columns as a building element within defined computational and parametric pipeline with multiple stages: parametric design, finite element analysis, shape optimization, and visibility analysis.

2. Design background

The idea of columns as vertical elements is associated with both the structural safety and the spatial implications of their allocation in space, which is possible to see across architectural and infrastructural examples. On one hand, columns are a traditional element in the framework of structural configurations, subject different dimensioning, and modulation in space according to material and spatial needs. Le Corbusier's Villa Savoye's principles involved the use of columns (pilotis) to obtain a free plan, reducing the presence of such vertical elements to only an honest structural need. [10]

On the other hand, the perception of an enclosure and limits of an architectural space requires elements that build a physical or virtual boundary in between conditions. The sense of boundary depends as much as on the elements used to construct a boundary, as on its arrangement. For the enclosure to be perceived, there is no need for an impenetrable limit or physical surface [11]. As an example of classical architecture, the Parthenon creates a spatial condition with a specific number of columns along a rectangular perimeter, achieving a bounded outdoor and a sense of limit and enclosure.

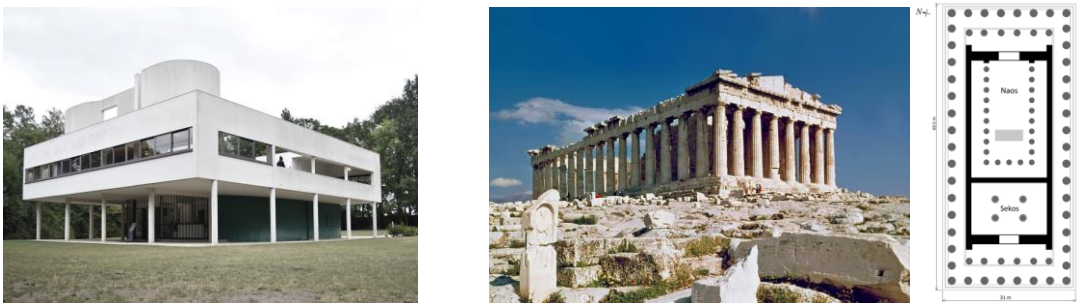


Figure 1. (Left) Le Corbusier's Villa Savoye, Poissy. [Source: Image by author*]. (Right) The Parthenon, Ancient Greece. Photo by *Steve Swayne* CC BY 2.0. (Right) Floor Plan of The Parthenon. [Source: Io Herodotus. CC BY-SA 4.0]

The use of iron during the Industrial revolution and steel in later decades allowed the transition from wood. These bridges attempted longer spans while using thin elements in their configuration [12]. At the same time, the overall configuration provides a sense of enclosure around the circulation path without the need of surfaces.



Figure 2. Bollman truss in Savage, Maryland, US. Built in 1869, moved to Savage in 1887. [Source: Public domain]

Contemporary examples such as Carmody Groarke's Regents Pavilion or Junya Ishigami's Japanese Pavilion display the qualities of vertical elements in ad hoc placement. The density and allocation of vertical elements determine different barrier grades and meanings of lightness and transparency.



Figure 3. (Left) Carmody Groarke. Regents Place Pavilion. Photograph by Luke Hayes. Source: lmoa.info (Right) Interior view of Kanagawa Institute of Technology Workshop. [Source: © junya.ishigami+associates]

From this window, this paper argues for a simultaneous interpretation of vertical thin elements as structural components and barrier elements to shape a bridge, aiming for minimal design operations and economy.

3. Design application

The paper presents a method of analysis for a building system based in multiple thin vertical columns as main elements of assembly for pedestrian bridges. Such system was customized for the design of pedestrian bridges suitable for contexts where a non-invasive formal quality and minimal visual footprint is required. For instance, natural contexts, historic urban spaces, or indoor bridge interventions.

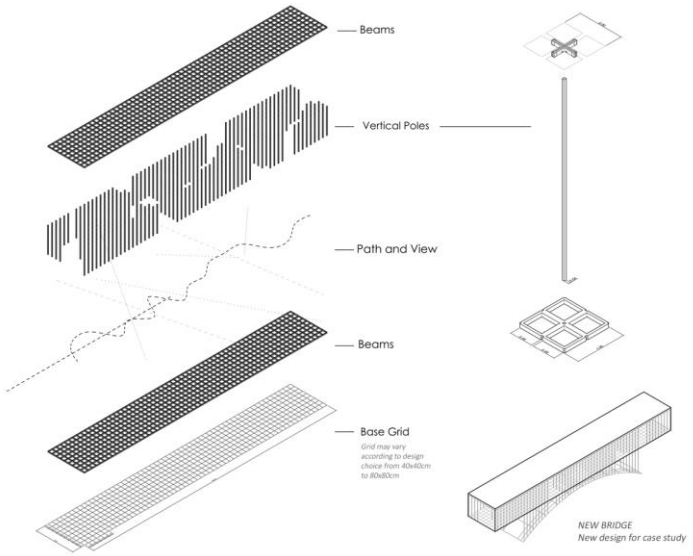


Figure 4. Diagram of columns and components of the bridge, showing the underlaying modulation (grid), columns, beams, and overall shape. [Source: Author of this paper, 2023]

The prefabricated thin steel columns meet steel beams within a rectangular boundary, modulated by a dense orthogonal base grid. Together, columns and beams shape a transitable enclosed path across two

points, where the concentration and allocation of columns along the boundaries of the bridge define the circulation paths and provide different grades of physical and visual permeability.

The study is meant to assist in early design stages for the application of this building system, to introduce structural considerations with anticipation.

4. Method

The study relies in a two-part analysis where structural performance calculations and visual impact tests act in mutual feedback, providing numerical values for both types of analysis as the designer engages in the bridge design process.

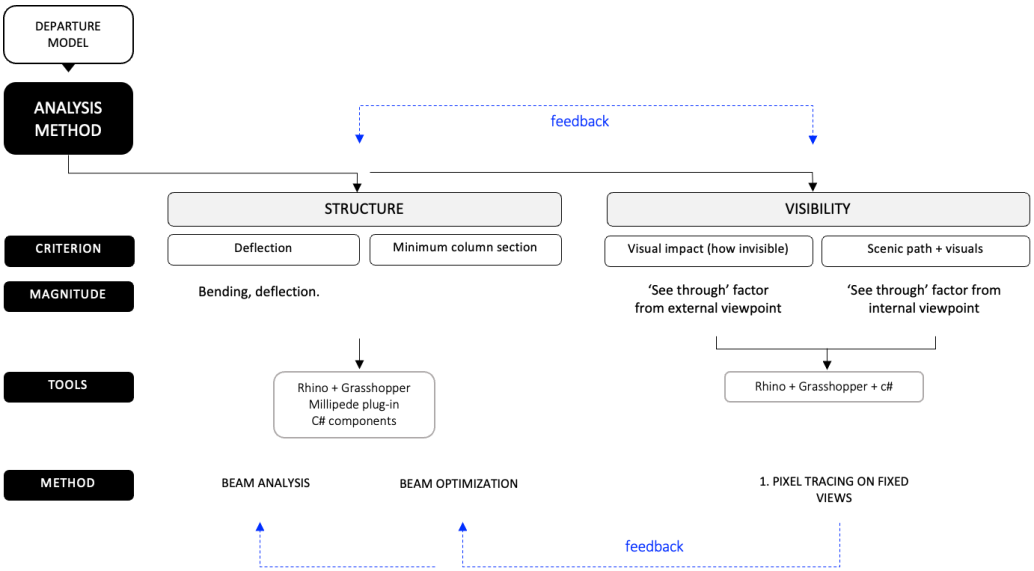


Figure 5. Overall logic of analysis. [Source: Author of this paper, 2023]

The structural assessment addresses the performance of the general assemblage regarding the material and section. From the first pipeline, The Finite Element Analysis and shape optimization of the structures are proceeded with the values of the parameters decided by the designers to understand the deflection and vulnerable areas of the bridges [3], [6], [9]. From the other pipeline, the visibility is computed by the pixel-based visibility culling methods. The images for the visibility analysis can show the inside out view along the paths of the bride, and the 360 degrees of the outside in view. The pixel dimensions of each image are 1588 by 787 pixels. And each image depicts bridge, relevant scape, and irrelevant scape with three distinct colour coded geometries: white, red, and black.

After going through the entire pipeline, the designers can iterate this process until the final decision of the bridge design. This method can provide a solution to minimize the amount of material in each column, and its number. Meanwhile, it also computes the visibility of the bridge that affects the surrounding environment. To present the process, this paper uses an arch pedestrian bridge assembled with the thin steel columns building system as a case study.

Rhino, grasshopper, and millipede plugin are used as tools to create a digital model and run the analysis.

4.1. Parametric design

As the starting point, the parametric design process allows the designer to change the shape and the number of the pedestrian's paths that affects the distribution of the vertical columns. The designer can

decide the design features of the bridge's overall form and set the parameters for both structure analysis and visibility at later stages.

The material of the bridge was set to steel. The beams and columns are made of squared shaped structures. The length of the bridge is 48 m. And the width of it is 7.2 m. The thickness of the slabs is the same as the thickness of the column structures. The columns are generated on the squared shaped grid layout. The designer can decide the density of the columns by changing the column density parameter. The layout of the column is also affected by path curves, and path width parameters, culling the columns within the specific distance to the path. The design of the paths can be modified or added by changing the shape or the number of curves. In this paper, the general load on the bridge was set above 5600 N/m^2, considering the distributed load of pedestrians and livestock on the footbridge [7]. Depending on the requirements, the designers can customize their own sets of parameters [Table 1] [Figure 6].

Table 1. Design Parameters [Source: Author of this paper, 2023].

Name	Value Type	Description
Bridge Length	Positive Number	This parameter changes the length of the bridge.
Bridge Width	Positive Number	This parameter changes the width of the bridge.
General Load	Positive Number	The general load can be set by this parameter. The user can also decide the direction of the load.
Column Density	Natural Number	This parameter decides the density of the columns supporting the roof of the bridge.
Column Height	Positive Number	The height of the columns that support the roof can be set by this parameter
Path Curve	Curve	It is possible to import multiple curves to design the path of the bridge. The columns of the bridge within specific distance are removed, making paths for the bridge users
Path Width	Positive Number	The designer can set the width of the bridge using this parameter.
Slab Thickness	Positive Number	This parameter is the slab thickness of the roof and the road.
Beam Thickness	Positive Number	This parameter defines the thickness of the square beam the supports the roof and the road of the bridge.
Beam Width	Positive Number	This parameter defines the width of the square beam the supports the roof and the road of the bridge.
Column Thickness	Positive Number	This parameter defines the width of the square columns that support the roof of the bridge.
Column Width	Positive Number	This parameter defines the width of the square columns that support the roof of the bridge.
Material	Material	This study uses steel for the structure
Support	Boolean	This parameter can decide the location of the support and type of the support. In this research, we set all the supports to fixed supports.

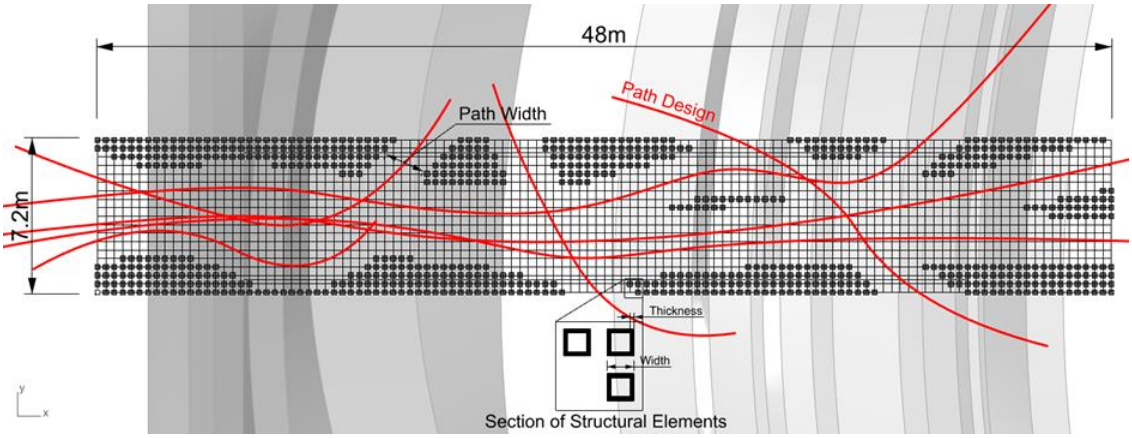


Figure 6. Parametric bridge design diagram [Source: Author of this paper, 2023].

4.2. Finite element analysis

The finite element method is widely used in various problems in civil engineering. And there are number of studies testing the buckling and deformation of the structure with given steel structure. As the millipede plug-in also supports the function of testing deformation behavior of the structure based on the FEM, it is possible to incorporate the pre-defined parameters that decide the shape of the bridge with the deformation analysis. In this study, two different cases of structure were tested by adding webs between the floor slab and arch structure. Comparison of the two cases shows that adding extra webs between the slab and arch significantly reduces both the local and global deformation behaviors of the bridge. But different solutions can be suggested by the designer. And adding more columns can also be an effective solution for this problem.

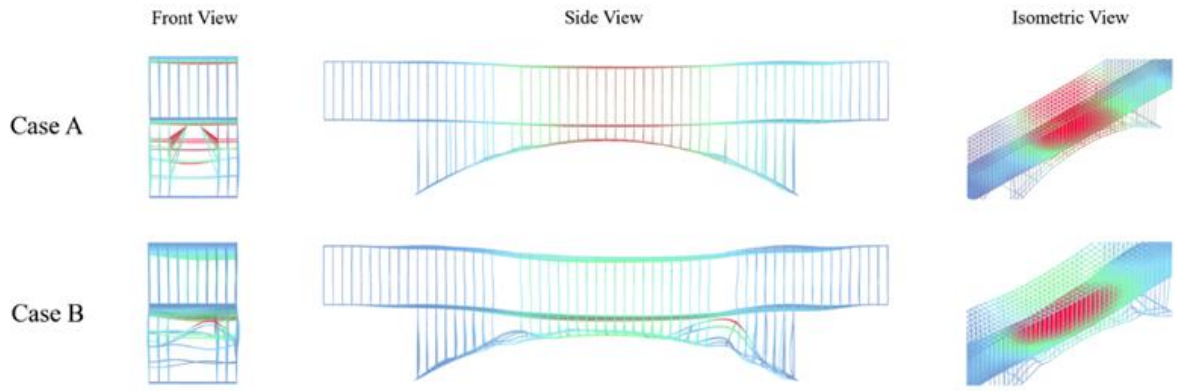


Figure 7. Deflection computed by finite element method. Case A shows the result of adding extra webs between the arch and floor slab. And Case B shows the deformation behavior without the webs. Deflection is exaggerated 500 times more than the computed value. [Source: Author of this paper, 2023].

4.3. Shape optimization

There are three distinct categories of structural optimization: sizing, shape, and topology optimization [6]. In this paper, Shape optimizing method is applied to the structure of the bridge, computing the optimized shape of the structure based on the given shapes and the loads [Figure 8]. The results of the tests show that columns, arch, and floor structure may require extra materials to increase structural

performance. And the optimized shapes of the columns are different depending on the locations of them. So, it is possible to increase the material efficiency by adjusting the thickness and width of specific columns and using relatively less material on the roof.

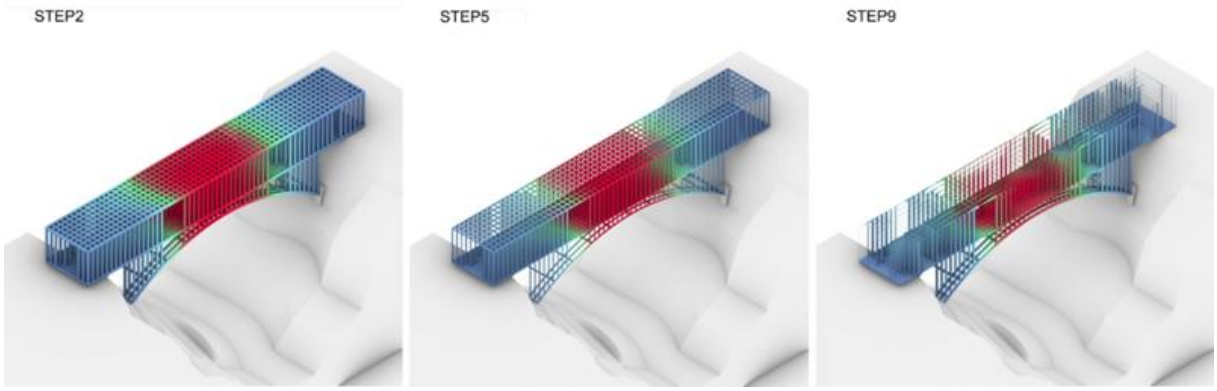


Figure 8. Topology Optimization by different steps [Source: Author of this paper, 2023].

4.4. Visibility analysis

Visibility culling method is often used to decrease the computing time of the rendered scenes [2]. In this stage, pixel-based visibility culling method is used to compute the visibility of the scene around the bridge [Figure 9]. Two collections of the images, interior and exterior image collections, are used to calculate the average number of pixels of relevant scape scenes. The interior image collection is generated from the frame of the camera, moving along the pedestrian path of the bridge. And the exterior images are captured with the camera frame that turns 360 degrees around the bridge. During the iteration of the pipeline, the averages of the visibilities from different sets of design parameters are compared to find out the best set. When *Px* is the total number of pixels of an image and *Pa* is the relevant scape pixels the visibility *V* is calculated as follows:

$$V = Pa/Px \cdot 100 \quad (1)$$

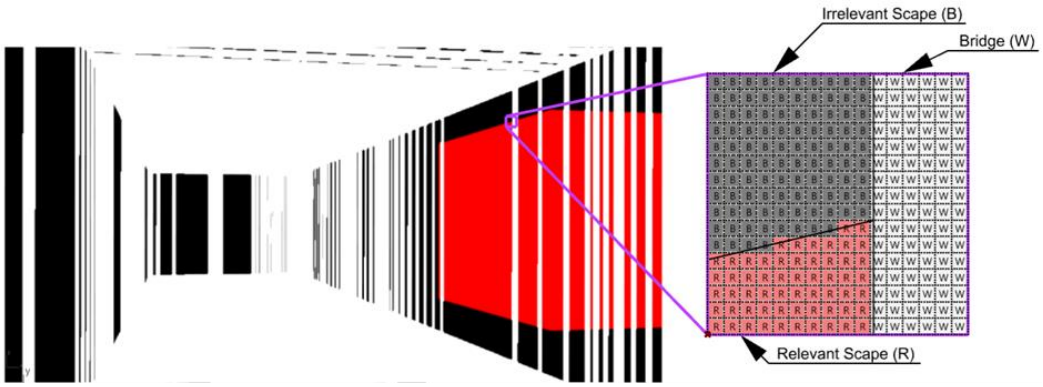


Figure 9. Pixel-based visibility culling [Source: Author of this paper, 2023].

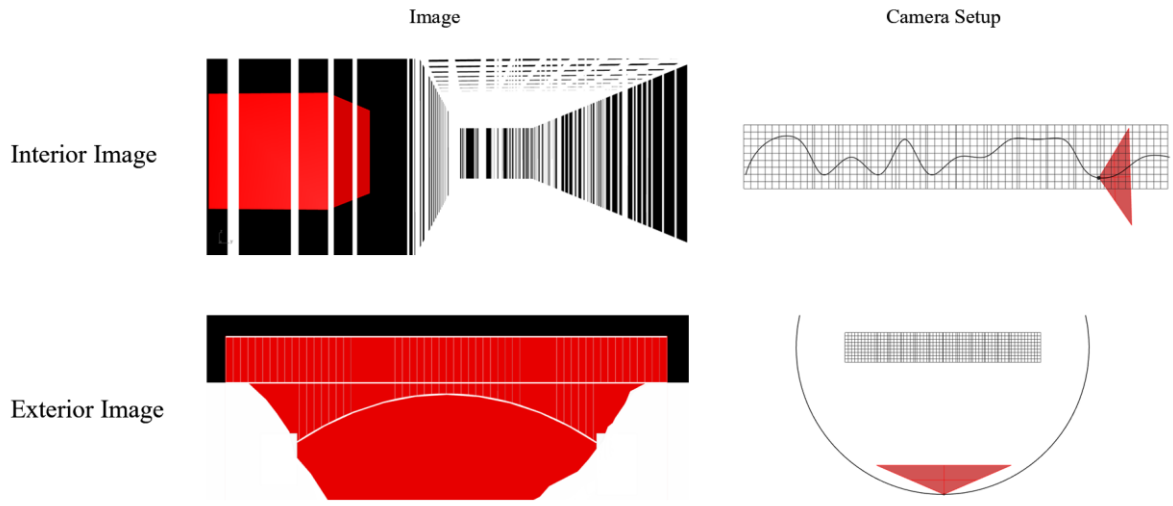


Figure 10. Camera setup example of interior and exterior views. Thick black curves are camera paths. Red triangles are camera scenes. [Source: Author of this paper, 2023].

5. Results and discussion

The result of this research shows that the iteration of the pipeline gives the designer good amount of information for the design decision. As shown in the beam analysis of the case study specific bridge, the deflection responds to the general assemblage of the bridge and grouping of vertical studs. Once the overall configuration of the bridge has been defined, it is possible to optimize columns sections. Making specific structures thinner will not necessarily derive in surging values of deflection, making the column section a flexible parameter to explore through optimization tasks.

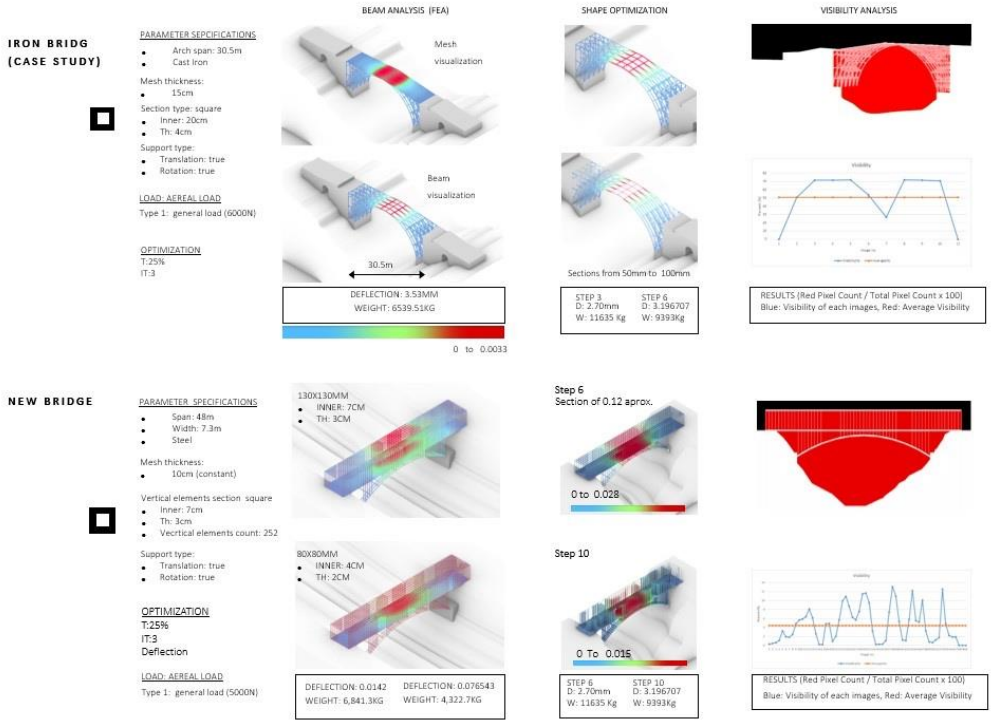


Figure 11. Analysis results of the sample bridges. [Source: Author of this paper, 2023].

The three primary limitations relate to the structure of the parametric design, the colour coding for the visibility test, statistical analysis tool. The parameters of this bridge design came from the historic study of the bridge the contemporary architectural case study, introducing the methods of improving the quality of visibility. For this reason, applying the new theme or concept of design requires enough knowledge about the computational design, and even computer language. The limitation from visibility test come from the colour coding and camera movements. This paper introduced the use of three distinct colours to differentiate the objects in each view. To make the hierarchical colour codes with various levels, the designer should set different rendering colours for each geometry The current camera movements are also set to the pedestrian path and the rotation views. The visibility analysis can also be done from fixed exterior point of views which would help to measure how light or non-invasive the bridges generate visual impact over the context.

Lastly, as the results from each stage are unique, there should be an effort to unitize the results and make statistical analysis tools to guarantee an objective interpretation of the data.

6. Conclusion

The study seeks for the minimal use of material and structural elements to design a bridge with constant information flow from numerical values obtained from finite element analysis, shape optimization, and visibility test. The future work envisions the compatibility to the unique design themes. The user-friendly setup of parameters may expand the freedom of the design decision. The application of the statistical analysis tools for structure and visibility can help the designers to compare the data from each stage and improve the accuracy of the design decisions.



Figure 12. Bridge in different locations [Source: Author of this paper, 2023].

Even though the further structural engineering is required to satisfy the building and design code of the site, the results could assist the better design decision for aesthetic purposes, safety, efficiency of the resources. Depending on the projects, the significance of the result from each stage can vary. In some cases, the visibility of specific scenery can outweigh the shape optimization result. So before and while iterating the pipeline, it is important to set the hierarchy of each result.

Acknowledgements

We would like to thank our Harvard GSD instructor Sawako Kaijima for her guidance during Fall 2020. Additional thanks to our colleague Axel Algarate for his contribution to this work.

References

[1] Henry Grattan Tyrrell, History of Bridge Engineering. Legare Street Press, 2022.

[2] S. Nirenstein, E. Blake, and J. Gain, "Exact From-Region Visibility Culling," 2002.

[3] Ehab Ellobody, Finite element analysis and design of steel and steel-concrete composite bridges. Amsterdam ; Boston: Elsevier, 2015.

[4] A. Gonzalez, M. Schorr, B. Valdez, and A. Mungaray, "Bridges: Structures and Materials, Ancient and Modern," Management of Critical Infrastructure [Working Title], Jan. 2020, doi: https://doi.org/10.5772/intechopen.90718.

[5] J. Smits, "The Art of Bridge Design: Identifying a design approach for well-integrated, integrally-designed and socially-valued bridges," A+BE | Architecture and the Built Environment, no. 3, pp. 1–212, Mar. 2019, doi: https://doi.org/10.7480/abe.2019.3.3734.

[6] M. P. Bendsøe and O. Sigmund, Topology optimization : theory, methods and applications. Berlin: Springer, 2003.

[7] ILO/ASIST, "Footbridges. Manual for Construction at Community and District Level," www.ilo.org, Jun. 01, 2004. https://www.ilo.org/emppolicy/pubs/WCMS_ASIST_8083/lang--en/index.htm (accessed Mar. 26, 2023).

[8] D. Wallin and M. Wasberg, "Parametric design of building structures in cooperation with architects : Usage and evaluation of structural plug-ins in 3D visualisation software," 2016. https://www.semanticscholar.org/paper/Parametric-design-of-building-structures-in-with-%3A-Wallin-Wasberg/0865c220ac3b40b8406ec8776c135ba0bff219fd (accessed Mar. 26, 2023).

[9] G. Allaire, C. Dapogny, and F. Jouve, "Shape and topology optimization," Geometric Partial Differential Equations - Part II, pp. 1–132, 2021, doi: https://doi.org/10.1016/bs.hna.2020.10.004.

[10] A. - Plug, "Villa Savoye, Poissy. By Le Corbusier. September 2009.," Flickr, Sep. 12, 2009. https://www.flickr.com/photos/11401580@N03/3944656527 (accessed Mar. 26, 2023).

[11] D Michelle Addington and D. L. Schodek, Smart materials and new technologies : for the architecture and design professions. Oxford: Architectural Press, 2006.

[12] D. B. Steinman, "BRIDGES," Scientific American, vol. 191, no. 5, pp. 60–73, 1954 [Online]. Available: https://www.jstor.org

Computational form-finding

Active bending
Additive manufacturing/ 3D printing
Architectural geometry
Bamboo for sustainable construction and quality of life improvement
Bio-inspired structures and architecture
Bridge structures
► **Computational form-finding**
Conceptual design
Concrete structures
Construction techniques
Deployable and inflatable structures
Design competition (WG21)
Digital modelling and fabrication
Dynamic response of metal spatial structures
Dynamic response of other structures
Form-finding and structural optimisation of interlocking discrete assemblages
Graphical methods
Gridshell and lattice structures
Historical concrete shells
Historical structures
Lattice structures
Life-cycle design and assessment of structures
Metal gridshell structures, connections and stability
Methods and construction technologies for sustainable shell structures
Morphology and configuration processing
Next generation parametric design
Novel methods in modelling, optimisation and construction for reducing carbon footprint of continuous roof shells
Numerical methods for geometry, form-finding and optimisation of lightweight structures
Optimisation methods and applications
Origami
Other
Teaching design uncertainty: working with unknown qualities/quantities of new and re-claimed materials
Teaching of shell and spatial structures
Tensegrity systems and cable structures
Tension and membrane structures
Tension structures in the Asia-Pacific
Timber and bio-based structures
Topology optimisation
Traditional masonry structures and innovation
Transformable structures

IASS 2023
July 10–14 Melbourne
Integration of Design and Fabrication

Proceedings of the IASS Annual Symposium 2023
Integration of Design and Fabrication
10–14 July 2023, Melbourne, Australia
Y.M. Xie, J. Burry, T.U. Lee and J. Ma (eds.)

A BESO aid to efficient form-finding

Izak LEE[a], Andre BROWN[b,*]

[a] NOC Ltd
izakjack@outlook.com

[b,*] School of Architecture, Victoria University of Wellington, New Zealand
andre.brown@vuw.ac.nz

Abstract

The desire for material economy and efficient structural performance has been prevalent for many years [1–3]. The research in this paper adds a new perspective and strategic means of achieving efficient performance of architectural structural systems [4,5] through the lens of topological optimization. Through the applications of computational bi-directional evolutionary structural optimization (BESO), the research presented illustrates how architectural design can be supported by a digital environment that automatically proposes reconfigurations by reprioritizing material to areas of maximum efficiency; the idea of form follows force. This is achieved through translation of BESO to a workable technology that can take traditional frame layouts or sketch proposals for a structural scheme, and present the designer with an array of efficiency-conditioned alternatives. The fluid non-orthogonal BESO outcomes consequently display greater structural efficacy when responding to the parameter-based loading conditions and initial geometry. We are not aware of a similar customised application of BESO technology as an architectural design and development tool.

Keywords: topological optimisation, BESO, form, force, material efficiency, design tool

1. Introduction: scope and intentions

The technological developments aimed at material economy and efficient structural performance is a natural aspect of progress towards a more sustainable approach to delivering new buildings or retrofitting and modification of existing buildings. Key figures have made significant contributions to this evolution [1–3], an evolution where contemporary computational means have been shown to have the potential to provide further tools to support the associated design processes [4–6].

In this paper explore the idea of a somewhat loose strategic approach in relation to design support relating to topological optimisation of structure in architecture. The system that we have developed aims to provide a development environment where the form of a structure is primarily, and directly, responsive to the physical forces exerted on the structure. The BESO-enabled environment is intended both to give a means of reconfiguring the structure to behave more efficiently in terms of load carrying, and to propose new efficient configurations that may not have been considered.

Copyright © 2023 by Izak LEE and Andre BROWN. Published in the Proceedings of the IASS Annual Symposium 2023 with permission.

2. Process

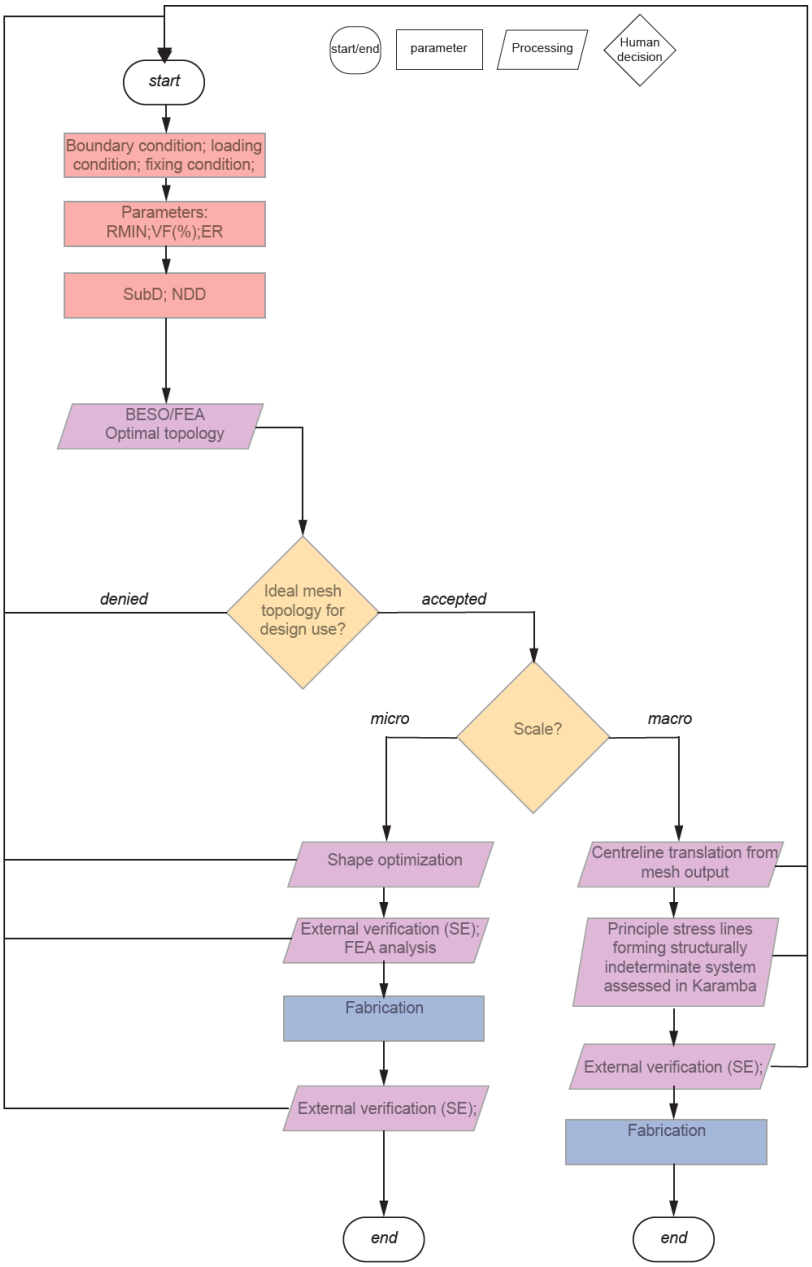


Figure 1. Computational Process Schematic

The process adopted is summarised Figure 1. The BESO facility is enabled through the Ameba plug-in for the scripting addition Grasshopper, an algorithmic node based interface, to the free-form modelling software Rhino. Selmi and Yesim [9] undertook an interesting and comprehensive comparative study of different Grasshopper Plugins for Topology Optimization in Architectural Design. In this they also refer to Millipede, an additional stress line analysis solver, that is also used in the later aspects of our study.

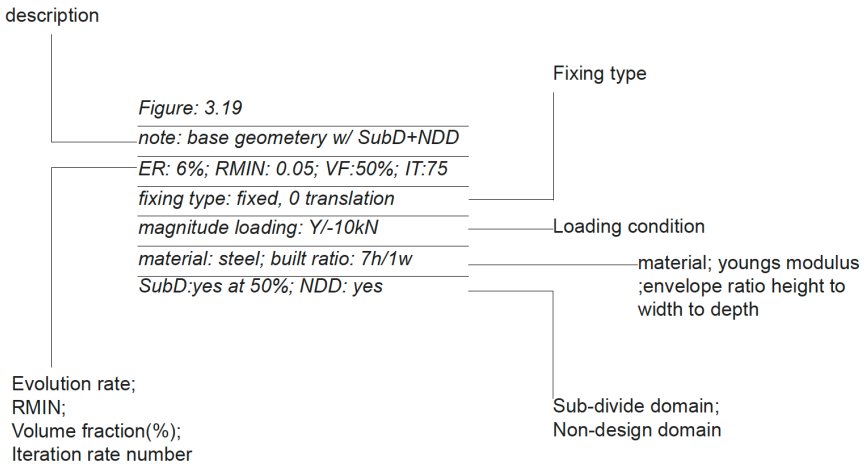


Figure 2. Key to notation used on output structural configurations proposed by the system

The basic procedure that we adopted incorporating the BESO approach is described by the computation schematic in Figure 1. Loadings are simplified for the purposes of illustration. Structural diagrams are produced by the system are annotated as shown in Figure 2. The scope of work was at three scales: S as micro elements, M as residential and pavilion scales, and L as larger multistorey structural systems. There is a branch in the process shown in in Figure 1 that indicates the stage where the process splits into different scales and the different

3. Illustrative cases

3.1. Initial trials

The first tests of the system were undertaken with simple cases of a flat plane with intermediate floors subject to (i) vertical loading and then (ii) a vertical face subject to horizontal loading (Figure 3)

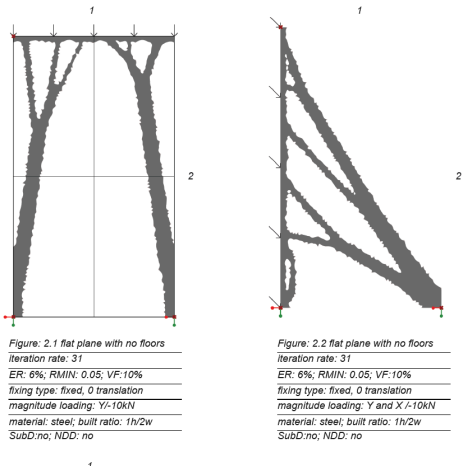


Figure 3. First test cases

3.2. Initial frame analyses

With the basic system established, we then looked at a multi-storey structure and the proposed optimal layouts both for the floor and it supports, and for the end frame on the wall. We could vary the percentage

of the area/volume that the wall structure or any other part of the structure would occupy. In figure 4 below the percentage material is relatively high and so the end wall is consequently relatively solid.

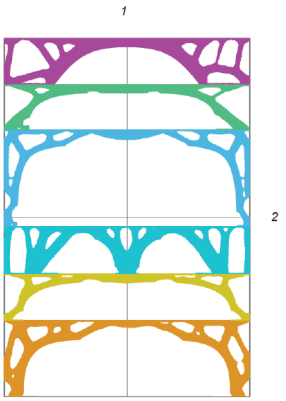


Figure: 2.7 flat plane w/ floor NDD
iteration rate: varying
ER: 6%; RMIN: 0.05; VF:10%
fixing type: fixed, 0 translation
magnitude loading: Z /-10kN
material: steel; built ratio: 1h/2w
SubD:no; NDD: yes, floors

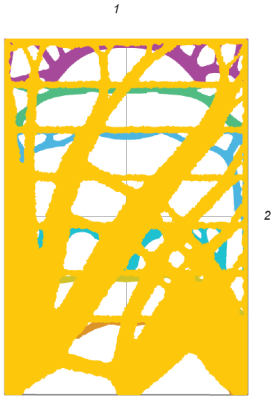


Figure: 2.8 addition of items
iteration rate: varying
ER: 6%; RMIN: 0.05; VF:10%
fixing type: fixed, 0 translation
magnitude loading: Z /-10kN
material: steel; built ratio: 1h/2w
SubD:no; NDD: yes, floors

Figure 4. First frame test cases

The Mitchell truss [10] is a classic in terms of optimal response to load carrying. Figure 5 shows a reasonably conventional tower structure that was modelled. Firstly loads replied in a reasonably conventional manner giving a combination of gravity and dead loads in the vertical election and wind loads in the horizontal direction. The optimised response that the system proposes is shown in the second image in Figure 5.

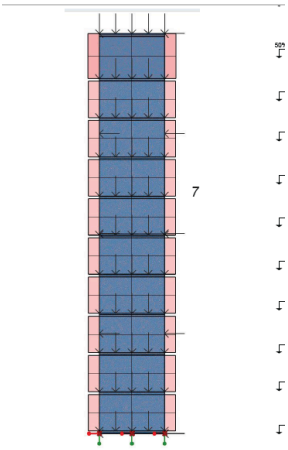


Figure: 2.17
note: base geometery w/ SubD+NDD
ER: 6%; RMIN: 0.05; VF:10%; IT:0
fixing type: fixed, 0 translation
magnitude loading: Y/-10kN
material: steel; built ratio: 7h/1w
SubD:yes; NDD: yes

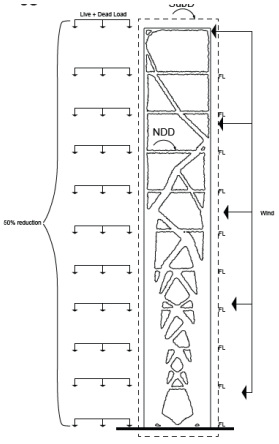


Figure: 2.20
note: base geometery w/ SubD+NDD
ER: 6%; RMIN: 0.05; VF:10%; IT:102
fixing type: fixed, 0 translation
magnitude loading: Y/-10kN
material: steel; built ratio: 7h/1w
SubD:yes; NDD: yes; Dimension: 2D

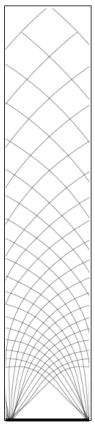


Figure: 2.23
note: Mitchell truss diagrid
ER: 6%; RMIN: 0.05; VF:50%; IT:
fixing type: fixed, 0 translation
magnitude loading: Y/-10kN
material: steel; built ratio: 7h/1w
SubD:yes at 50%; NDD: yes

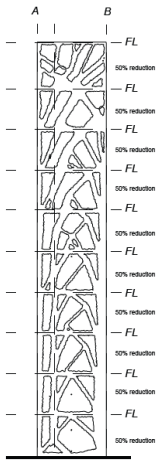


Figure: 2.25
note: base geometery w/ SubD+NDD
ER: 6%; RMIN: 0.05; VF:50%; IT:67
fixing type: fixed, 0 translation
magnitude loading: Y/-10kN
material: steel; built ratio: 7h/1w
SubD:yes at 50%; NDD: yes

Figure 5. (i) Conventional tower (i) initial proposal (ii) Mitchell truss overlay (iii) resulting proposed form

The third drawing in Figure 5 is an overlay of the Mitchell truss on to the frame as a starting point and the fourth drawing is the resulting proposed form after the BESO- enabled analysis.

3.2. Extension to 3D frames

The technique was subsequently expanded into the third dimension. The results for test frame are shown in figure 6.

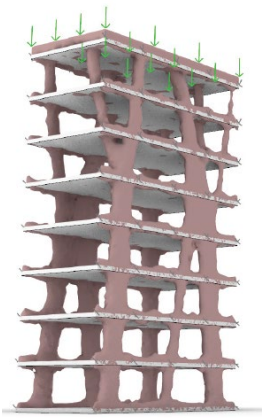


Figure 6. Extension into 3D

The work has further been developed and extended to apply to smaller building elements such as staircases. Additionally, we have looked at modernist buildings that are ruthlessly rectilinear and 'minimal'. It is interesting to apply the analytical tool to such buildings to see how a more biological and structurally efficient system changes the nature and form of such buildings.

4. Conclusion

The work described in this paper saying that developing a tool to support the architectural designer during the process in which there is a desire to produce structural form that optimise this material use.

In the case of the designer using the technology as a prompt to suggest forms that resist loading in a more efficient way, the architectural designer becomes a *curator of tool* that can be refined and reconfigured. That tool shows how the reprioritization of material to areas of efficient load sharing and transmission can drive the symbiosis of engineering performance and architectural outcome. Forms proposed by the system can be easily exported to more traditional engineering analysis software like Karamba 3D. The centre lines are extracted, either internally within Grasshopper or extracted as a line drawing on each façade as a 2d plane. In addition to addressing ideas of structural efficiency, the technology developed also responds to contemporary capabilities presented by digital fabrication such as concrete printing. Such technologies, as we know, mean that non-rectilinear form is more easily facilitated.

Applied within a contemporary computer mediated design environment BESO is shown to be a potentially useful tool in the practitioner's kitset. The computer and its computational script operated as a co-designer, side by side the human as aid. Consequently the BESO tool can be viewed as a *computational sketching tool.* Resultant meshes are often not precise due to practical resolution issues, however the mesh following the direct line of force offers sufficient indication of optimal response to a structural problem, how one can go about rationalizing a structural scheme, and offers conceptual typologies that expand the scope of architect's possibilities of a given project.

References

[1] A.G.M. Michell, LVIII. The limits of economy of material in frame-structures. *Lond. Edinb. Dublin Philos. Mag. J. Sci.* 1904;8:589–597. doi: 10.1080/14786440409463229.

[2] F. Otto, B. Rasch, *Finding Form : towards an architecture of the minimal*, Axel Menges, 1995

[3] A. Brown,, *Peter Rice: The Engineers Contribution to Architecture*, RIBA Publications, 2000.

[4] M. Killian, D. Pellis, J. Wallner and H. Pottman, "Material-minimizing forms and structures", *ACM Transactions on Graphics*, Vol. 36, No. 6, Article 173, Nov 2017.

[5] Y. M. Xie, K. Yang, Y. He, Z. L. Zhao and K. Cai, "How to obtain diverse and efficient structural designs through topology optimization," in *Form and Force: Proceedings of the IASS Annual Symposium 2019*, Barcelona, Spain, October 7–10, 2019, C. Lázaro, K. U. Bletzinger and E. Oñate, Eds.

[6] Q. Li, "Form Follows Force: A theoretical framework for Structural Morphology, and Form-Finding research on shell structures", *PhD thesis*, TU Delft, Architecture and the Built Environment, 2018,

[7] M.P. Bendsøe, O. Sigmund, "Material interpolation schemes in topology optimization" *Archive of applied mechanics*, 69 (9-10) pp. 635-654, 1999.

[8] A. Baumgartner, L. Harzheim, C. Mattheck, SKO (soft kill option): the biological way to find an optimum structure topology, *International Journal of Fatigue*, Volume 14, Issue 6, Pages 387-393, 1992.

[9] M. Selmi and Z. Yesim, "A Comparative Study of Different Grasshopper Plugins for Topology Optimization in Architectural Design", *GU Jounal of Science, Part B,* Art, Humanities, Design and Planning, 10(3): 323-334, 2022.

[10] A.G.M. Michell, LVIII. The limits of economy of material in frame-structures. *Lond. Edinb. Dublin Philos. Mag. J. Sci.* 1904;8:589–597. doi: 10.1080/14786440409463229.

IASS 2023
July 10–14 Melbourne
Integration of Design and Fabrication

Proceedings of the IASS Annual Symposium 2023
Integration of Design and Fabrication
10–14 July 2023, Melbourne, Australia
Y.M. Xie, J. Burry, T.U. Lee and J. Ma (eds.)

A novel approach to generating diverse and competitive structural designs through load perturbation in topology optimisation

Yulin XIONG[a,*], Hongjia LU[a], Yi Min XIE[a,*]

[a,*] Centre for Innovative Structures and Materials, School of Engineering,
RMIT University, Melbourne, 3001, Australia
yulin.xiong@student.rmit.edu.au; mike.xie@rmit.edu.au

Abstract

Topology optimisation has gained popularity as a powerful tool for creating elegant and innovative forms for architectural and structural designs. However, balancing structural performance, aesthetics and functional criteria can be challenging. To address this problem, we have developed a novel approach based on the bidirectional evolutionary structural optimisation (BESO) method to generate diverse designs. In this approach, the optimisation process is perturbed by applying randomly varied angles to the applied loads, and the interim results are presented to the designer for selection based on their aesthetic and functional preferences. By incorporating human guidance, this approach enables a trade-off between exploring diverse solutions and integrating the designer's preferences into the optimisation process, making it suitable for architectural and structural designs. Furthermore, serialised diverse designs can be easily generated by using combinations of perturbations at different iteration steps. Potential applications of this approach in architectural and structural designs are presented, demonstrating the ability of the proposed method to produce optimised solutions that effectively integrate the designer's functional requirements and aesthetic preferences.

Keywords: topology optimisation, BESO, diverse designs, form finding, Hangai Prize applicant

1. Introduction

Topology optimisation is a widely recognised computational design tool in engineering and architecture that enables designers to create optimised structures tailored to specific conditions, such as design domain, load and support conditions. Numerous topology optimisation techniques have been developed [1–5]. Among them, the bidirectional evolutionary structural optimisation (BESO) method [6–9] has received considerable attention in architectural and structural designs. Aesthetically pleasing and high-performance designs have been created using BESO-type methods [10–12].

While traditional topology optimisation techniques focus on generating a single optimised solution, the ability to generate diverse and competitive designs has become increasingly crucial for designers. By comparing and selecting the best solution based on their aesthetic intuition or other functional requirements, designers can make better-informed decisions and develop more effective solutions. This growing need for diverse and competitive designs in topology optimisation has led to increased research and development efforts.

Several studies have contributed to this topic by proposing various strategies for generating diverse designs in topology optimisation. Wang et al. [13] achieved diverse designs by introducing graphic diversity constraints in 2D optimisation problems. Yang et al. [14] propose five simple strategies to obtain diverse and competitive designs, which can be easily integrated into commonly used topology optimisation techniques. He et al. [15] presented three stochastic approaches: penalising elemental sensitivities, changing initial designs and integrating the genetic algorithm into the BESO method. These methods obtain diverse solutions by adding noise to the optimisation process.

Copyright © 2023 by Yulin XIONG, Hongjia LU and Yi Min XIE. Published in the Proceedings of the IASS Annual Symposium 2023 with permission.

Other researchers have explored diverse designs by controlling structural features. For instance, Zhao et al. [16] proposed an approach to control the number and size of the interior holes of structures, and He et al. [17] developed an approach to control the number of structure members. Although the perturbation noise approach enables designers to explore various design possibilities in these two methods, it may not necessarily capture their preferences in the optimisation process. In contrast, the feature control approach allows for more-accurate design customisation but limits the exploration of the design space to predefined features.

In this work, we presented a novel approach to generating diverse and competitive structural designs. An extensive collection of diverse designs can be achieved by applying angular perturbations to loads at different iteration steps. Furthermore, designers' selections can be incorporated into the optimisation process so that designers can efficiently identify the desired solutions according to their specific requirements. Overall, this approach provides a powerful tool for exploring the design space and achieving innovative and optimised designs.

This paper comprises the following sections. The load perturbation approach is described in Section 2. We use an example of apple growth to demonstrate our algorithm's ability to generate multiple solutions in Section 3. Section 4 shows the applications of the human-guided process and the serialised diverse designs. Finally, conclusions are drawn in Section 5.

2. Methodology

2.1. Review of the traditional BESO method with self-weight loads

This study aims to develop a diverse design approach based on the BESO method. First, we introduce the topology optimisation formulation. The optimisation objective is to minimise the average structural compliance of all the multiple load cases. The mathematical representation of the optimisation problem is:

$$\begin{aligned} \text{Minimise} \quad & C = \frac{1}{2}\sum \boldsymbol{f}^{(l)}\boldsymbol{u}^{(l)} \\ \text{Subject to} \quad & \boldsymbol{K}\boldsymbol{u}^{(l)} = \boldsymbol{f}^{(l)} \\ & v_f = \sum_{j=1}^{n} V_j x_j \Big/ \sum_{j=1}^{n} V_j \le V^* \\ & 0 < x_{\min} \leqslant x_i \leqslant 1, \end{aligned} \tag{1}$$

where C is the structural compliance, $\boldsymbol{K}$ is the global stiffness matrix, $\boldsymbol{f}^{(l)}$ is the global force vector, $\boldsymbol{u}^{(l)}$ is the displacement vector for the *l*-th load case and x_i refers to the *i*-th design variable, which can take a value of either 1 for the solid elements or a prescribed $x_{\min}$ for the void elements. Note that $x_{\min}$ is greater than zero to prevent possible singularity issues in the finite element analysis. In this study, $x_{\min}$ is set to 0.001. v_f represents the structural volume fraction constraint, while n, V_j and V^* are the total number of elements, the volume of the element j and the target volume fraction, respectively.

In addition, when considering design-dependent self-weight loads, the relationship between the material property and the design variable is established according to the following material interpolation scheme [18]:

$$E_i = E_0 \frac{x_i}{1 + q(1 - x_i)}, \tag{2}$$

where E_i is the Young's modulus of the material for the element i, E_0 is the Young's modulus of the solid material (i.e., $x_{solid} = 1$) and q is the penalty factor, which is larger than zero for topology

optimisation problems considering design-dependent self-weight loads [19]. The gradient of compliance for the design variable can be derived using the adjoint method [20]:

$$\alpha_i = \frac{1}{q+1}\frac{\partial C}{\partial x_i} = \begin{cases} -\dfrac{v_i \rho_0 g}{q+1}\boldsymbol{G}\boldsymbol{u}_i^{(l)} + \dfrac{1}{2}\boldsymbol{u}_i^{(l)}\boldsymbol{K}_0\boldsymbol{u}_i^{(l)}, & \text{if } x_i = 1 \\ -\dfrac{v_i \rho_0 g}{q+1}\boldsymbol{G}\boldsymbol{u}_i^{(l)} + \dfrac{1}{2[1+q(1-x_i)]^2}\boldsymbol{u}_i^{(l)}\boldsymbol{K}_0\boldsymbol{u}_i^{(l)}, & \text{otherwise} \end{cases}, \tag{3}$$

where α_i, $\boldsymbol{K}_0$ and $\boldsymbol{u}_i^{(l)}$ denote the sensitivity of element i, the solid elemental stiffness matrix and the displacement of element i for the l-th load case, respectively. The symbols g and $\boldsymbol{G}$ represent the gravitational acceleration and the gravity load vector, respectively.

Note that the sensitivity values need to be processed further with an elemental filter [21] and then averaged with historical values [12]. Further details about these steps can be found in [22].

2.2. The load perturbation method

A perturbation angle is added to the force $\boldsymbol{f}^{(l)}$ to achieve diverse designs:

$$\begin{aligned} \boldsymbol{f} &= \boldsymbol{f}_i^{(t)} + \boldsymbol{f}_j^{(t)} \\ \boldsymbol{f}_i^{(t)} &= f_i \cos\left(\theta \pm \epsilon^{(t)}\right) \\ \boldsymbol{f}_j^{(t)} &= f_j \sin\left(\theta \pm \epsilon^{(t)}\right), \end{aligned} \tag{4}$$

where $\boldsymbol{f}_i^{(t)}$ and $\boldsymbol{f}_j^{(t)}$ are the components of $\boldsymbol{f}^{(t)}$ in different directions for the t-th iteration, θ is the original load angle and $\epsilon^{(t)}$ is the perturbation angle for the t-th iteration.

As depicted in Figure 1, $\epsilon^{(t)}$ is randomly selected within a specified range [-ε, ε] at each iteration. Since the BESO method employs an iterative process that progressively applies minor structural modifications until the algorithm converges, we introduce perturbations by starting with a large ε value in the initial iterations and then gradually decreasing ε to zero. This approach enables the algorithm to explore various design alternatives and concentrate on minimising compliance for the given loads at the convergence point. In addition, an extensive collection of diverse structures can be generated by modifying the ε values used in the different stages of the optimisation process.

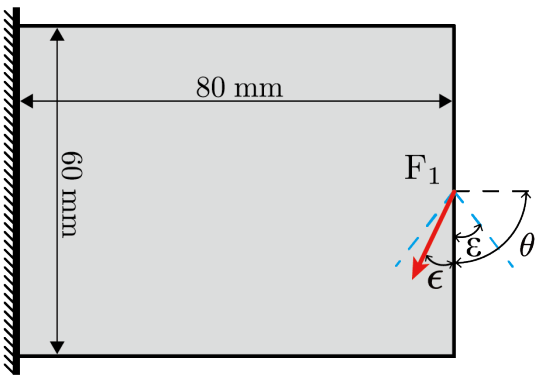


Figure 1. Illustration of a force with a perturbation angle.

3. Example 1: diverse apple shapes

This section presents an intriguing example demonstrating the load perturbation approach's ability to generate diverse solutions. The growth of an apple is a complex process influenced by various physiological and environmental factors, such as load, light and temperature. Xie and Steven [23] used

the evolutionary structural optimisation method to optimise the shape of an 'apple' under its own weight. Based on this, we use the load perturbation method to investigate the assortment of apple shapes that can be achieved by introducing random horizontal perturbation forces during growth.

The initial model is shown in Figure 2. By taking advantage of the symmetry condition, half of the domain is considered. Approximately 280,000 triangle plane stress elements are used to mesh the half domain. A non-designable stalk measuring 12 mm long and 2 mm wide is incorporated to create a 'hanging' apple. The top of the stalk is fixed, and the primary load applied on the domain is gravity, donated as G.

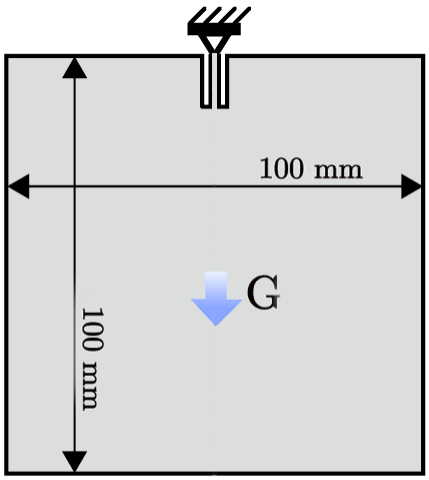


Figure 2. Design domain and boundary conditions of an apple under gravity loading.

We employ a small ball hanging from the stalk as the initial design to simulate an apple's growth, as illustrated in Figure 3(a). In the iterative process, we use the elements in direct contact with the apple structure in the current iteration as material candidates so that the material (i.e., apple pulp) is added layer by layer. Following the approach in [23], the BESO technique is applied to select the added material with a volume fraction v_f of 20%, a filter radius of 2 mm and an evolutionary ratio of 2%. Note that by adding elements from the apple structure boundaries based on the stress level, we obtain shapes with uniform stress on the surface. Figures 3(b) and 3(c) display the interim results, while the final solution is shown in Figure 3(d), which closely resembles the result reported in [23].

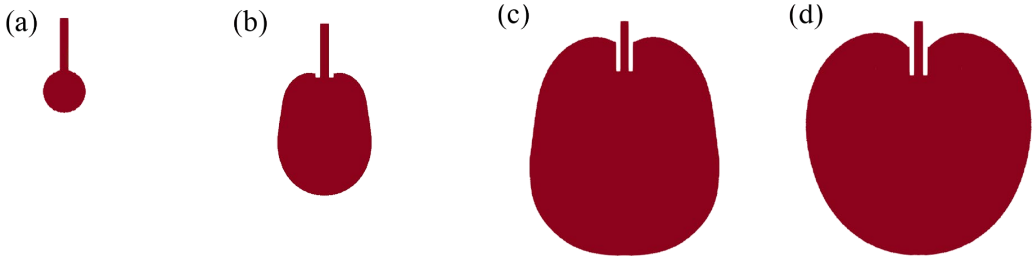


Figure 3. Optimisation process of an apple: (a) initial design, (b) interim solution of the third iteration, (c) interim solution of the tenth iteration and (d) final solution.

Using the same BESO parameters, the load perturbation approach is applied to generate diverse apple shapes. The range of the load perturbation angles is set to $[-60°, 60°]$. Variations of perturbation angles lead to three apples with distinct shapes. The original result is shown in Figure 4(a), which is an oval-shaped apple with a long length and a relatively narrow width, making it more susceptible to wind loads.

The second result (see Figure 4(b)) is a round apple with a similar width at the top and bottom. The third apple (see Figure 4(c)) also has a round shape but has a flattened region at the bottom that is wider than the region near the stalk; this apple is also shorter than the second round apple. The last apple (see Figure 4(d)) is short and wide, with an inwardly recessed area at the bottom. Most of the material accumulates horizontally, resulting in a curved shape.

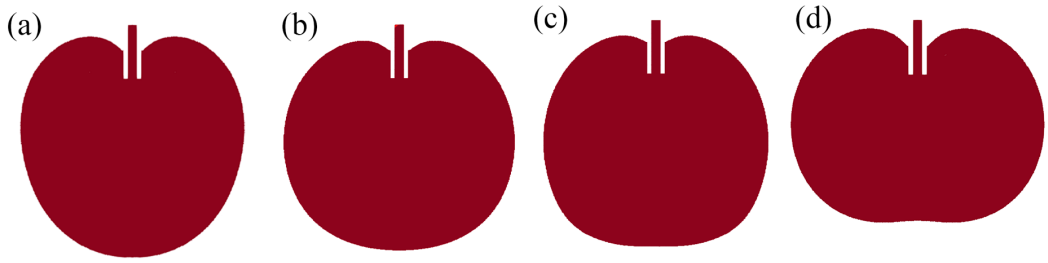


Figure 4. Apples with diverse shapes: (a) oval-shaped apple (the original result), (b) round apple, (c) round apple with a flat bottom and (d) short and wide apple.

From these results, it is clear that introducing horizontal perturbation forces significantly influences the shape of the apple. The width of the apple increases when the applied horizontal perturbation loads are relatively large. In contrast, the material tends to accumulate more in the vertical direction when gravity loading dominates. Note that in this example, all apple shapes are forced to be symmetrical. If symmetrical boundary conditions were not imposed, the positive and negative horizontal perturbation forces would result in more material remaining on the apple's left or right side.

4. Example 2: human-guided dome design

In this section, a dome with a radius of 32 m is designed using the load perturbation approach. The inner circle of the dome has a radius of 4 m, and its height is 5 m. The loading and boundary conditions are shown in Figure 5(a). A design-dependent self-weight load is applied to the dome, and pinned supports are applied on the edges. The optimisation takes advantage of the symmetry—it considers a quarter of the design domain and discretises it into approximately 1.32 million tetrahedral elements. The target volume fraction is $V^* = 60\%$, the filter radius is set to 0.5 m, and the Young's modulus and Poisson's ratio are 30 GPa and 0.3, respectively. The optimised result using the traditional BESO method is shown in Figure 5(b).

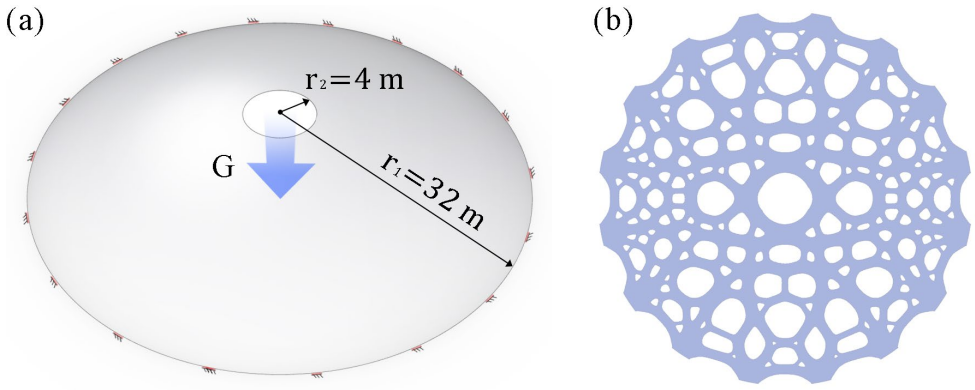


Figure 5. A dome design: (a) loading and boundary conditions of a dome, where G represents gravity, and (b) topology-optimised result obtained using the traditional BESO method.

In this example, load perturbations are added throughout the optimisation process, with the range of perturbation angles decreasing as optimisation progresses through iterations. When the volume fraction

$v_f > 90\%$, the range of the perturbation angle is $[-10°, 10°]$ (i.e., $\varepsilon = 10°$). When $v_f \in [80\%, 90\%]$, $\varepsilon = 8°$. When $v_f \in [70\%, 80\%]$, $\varepsilon = 5°$. The perturbation angle remains at zero until the optimisation converges.

Using various perturbation angles during the iterative process can generate diverse solutions, but this abundance of options can complicate decision-making. To tackle this problem, we incorporate human selection into the iterative process, taking advantage of BESO's history-dependent feature (i.e., the solution for the next iteration is modified based on the solution of the current iteration). BESO's high computational efficiency enables the simultaneous execution of multiple cases with different perturbation angle values [21]. The interim results from these parallel cases can be presented to the designer, who can then intervene in the optimisation process by selecting one preferred interim result to continue. Once an interim result is selected, multiple new cases are initiated using the chosen result as the starting point, with different perturbation values applied in the subsequent steps for each case. One or multiple selections can be made based on the designer's requirements. Since force perturbation gradually reduces during the iterative process, selections made in later stages lead to diverse designs with higher similarity. Consequently, this approach effectively balances the exploration of different design possibilities by incorporating the designer's preferences.

To illustrate the effectiveness of our human-guided process, we present an example in Figure 6. In this example, when v_f is reduced from 100% to 90%, the interim result β is selected. Without further interference in the later process, the load perturbation approach can lead to diverse solutions with vastly different geometries. Figure 7 displays six of these diverse solutions, with relative compliance values of 0.999, 1.004, 0.992, 0.999, 0.986 and 1.001 compared to the original design. These minor performance differences demonstrate that our proposed approach can effectively explore different design possibilities without substantially compromising performance.

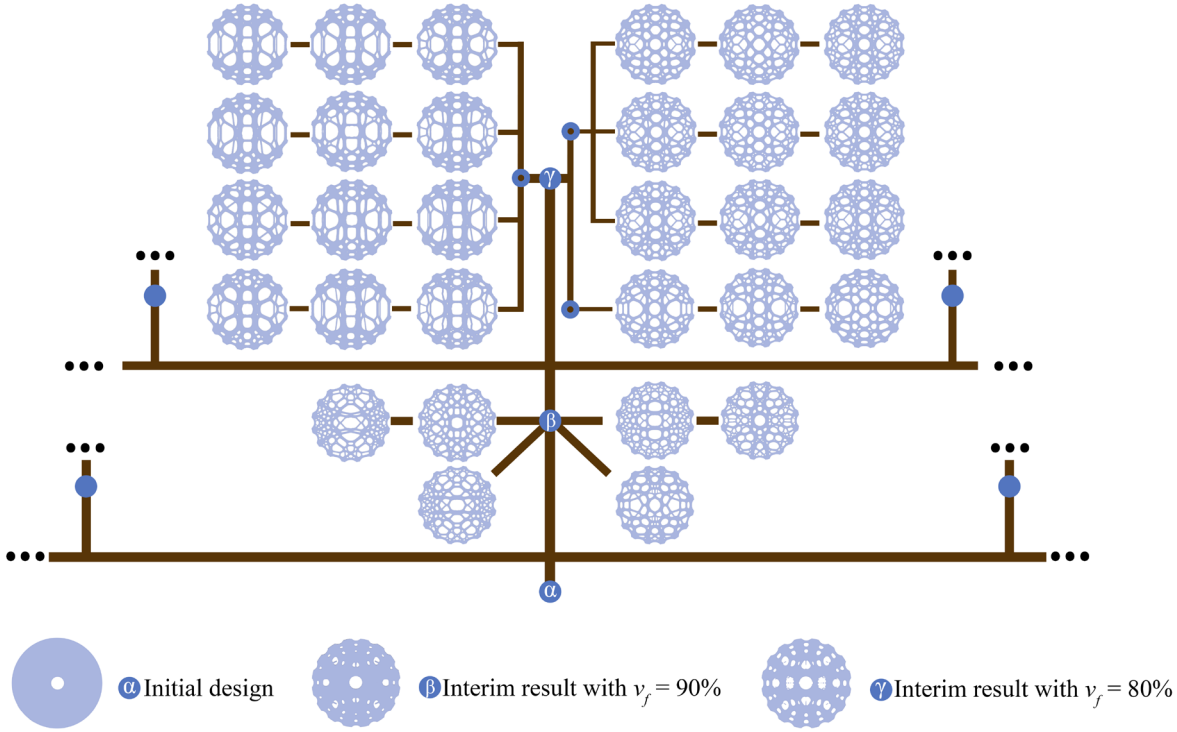


Figure 6. A tree of the diverse domes, where blue nodes represent interim optimisation results. The tree can grow horizontally to explore different design possibilities or vertically to introduce the designer's specific preferences.

Based on the selection of β, further selections can be made to better incorporate the designer's preferences into the optimisation process. In this example, we select the interim result γ at $v_f = 80\%$ (as shown in Figure 6). When solutions from only one selection in Figure 7 are compared with those from two selections, we observe that solutions become more similar as the number of selections increases. For clarity, we present 24 diverse solutions divided into three categories based on their structural topology in Figures 8, 10 and 12.

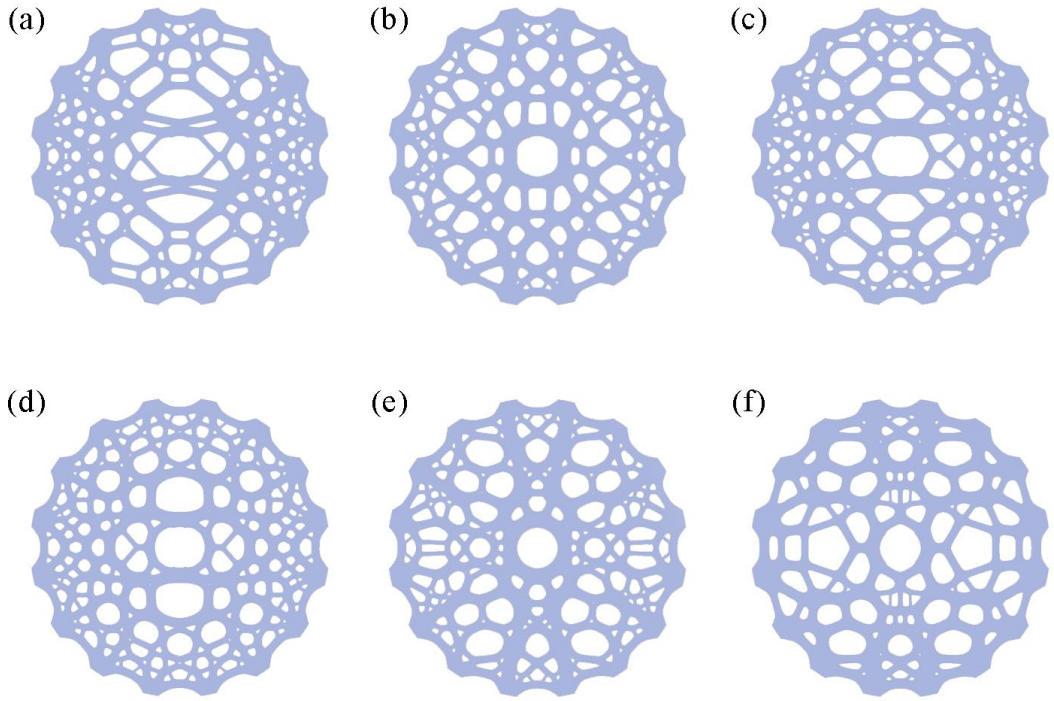


Figure 7. Diverse dome designs selected by humans from interim result β (see Figure 6).

The three designs in Category 1 primarily differ in the yellow regions of the designs. For the domes in Figure 8, the structures in the yellow regions of Figure 8(a) contain three vertical members, while Figures 8(b) and 8(c) feature X-shaped components. Compared to Figure 8(c), Figure 8(b) includes four small holes near the X-shaped component. The relative compliance values for these designs are 0.994, 0.987 and 1.014, respectively. A 3D rendering of the dome in Figure 8(c) is shown in Figure 9.

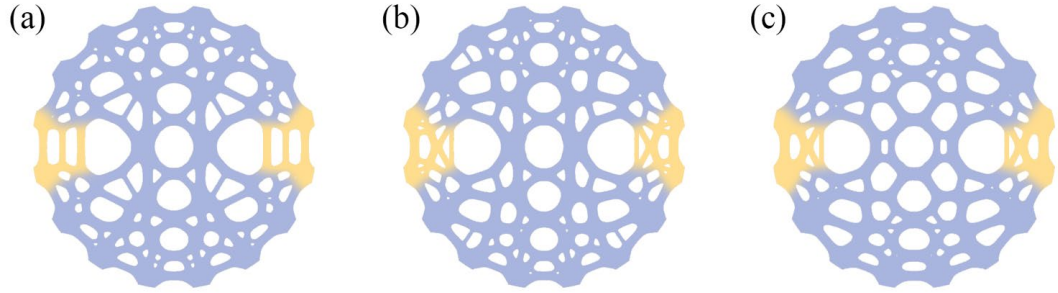


Figure 8. Category 1 of diverse dome designs with human selections from interim results β and γ (see Figure 6). The primary differences between the domes are predominantly noticeable in the yellow regions.

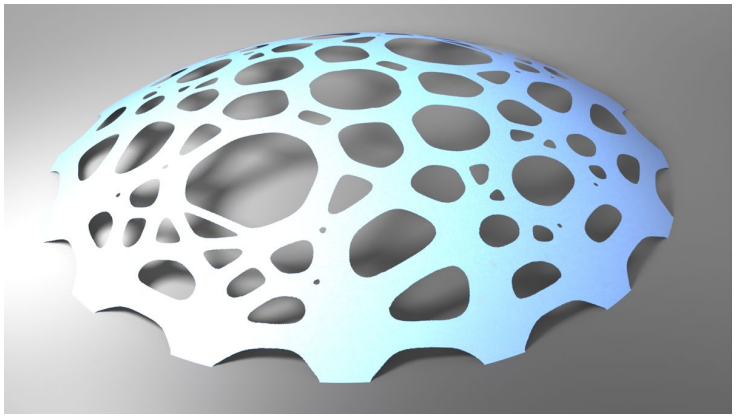


Figure 9. Rendered dome of the design in Figure 8(c).

Category 2 is similar to Category 1 but has two additional X-shaped components on either side of the central hole. As shown in Figure 10, the middle portions of the yellow regions in these designs are distinct. The intermediate structures can be classified into X-shaped and asterisk-shaped structures. All designs exhibit a similar pattern in the upper and lower parts of the yellow region, but the number and size of the holes in this region differ. The difference in structural compliance between these designs and the original design ranges from −3.347% to 1.846%. A 3D rendering of the dome in Figure 10(f) is shown in Figure 11.

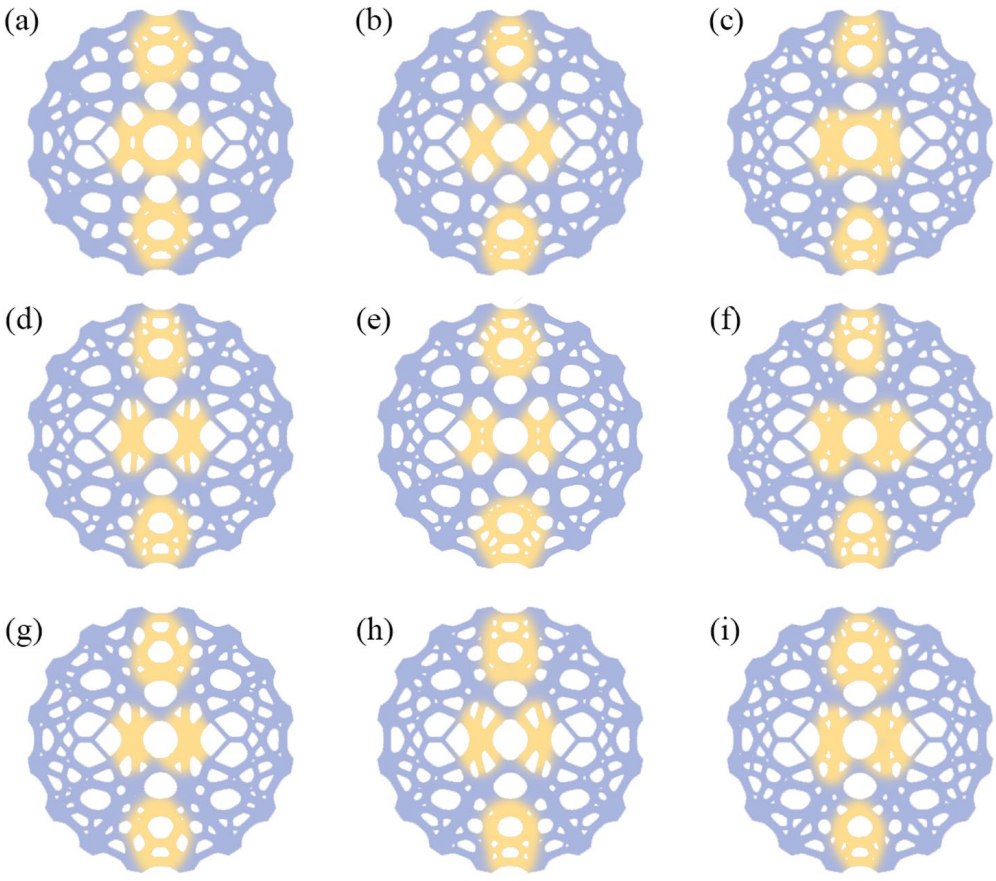


Figure 10. Category 2 of diverse dome designs with human selections from interim results β and γ (see Figure 6). The primary differences between the domes are predominantly noticeable in the yellow regions.

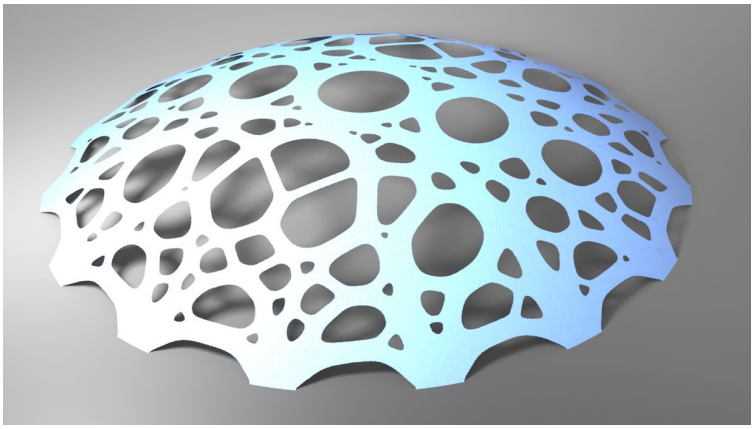


Figure 11. Rendered dome of the design in Figure 10(f).

Category 3 is notably distinct from Categories 1 and 2, with the most prominent feature being the two thick chords that span the entire structure. As shown in Figure 12, all designs have a triangular part in the yellow region, but the number, position and thickness of the members connecting this triangular part differ. The difference in structural compliance between the designs in Figure 12 and the original design ranges from −3.011% to 2.074%. A 3D rendering of the dome in Figure 12(g) is shown in Figure 13.

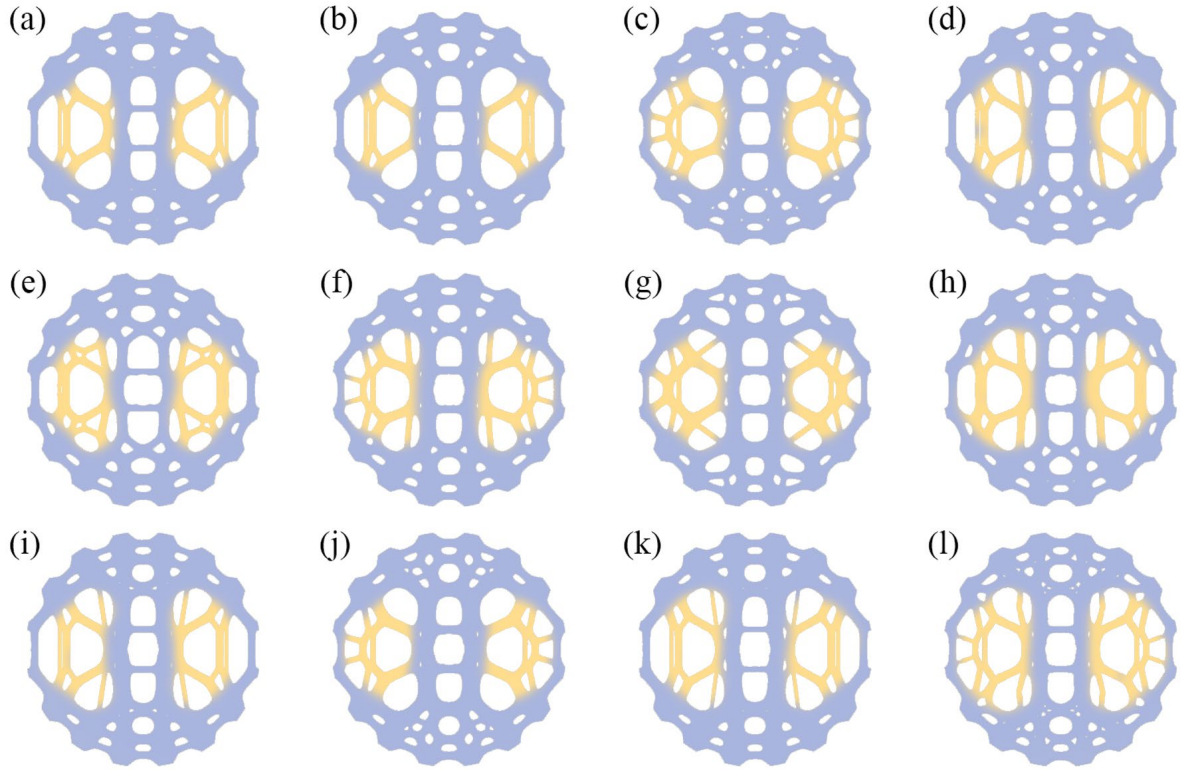


Figure 12. Category 3 of diverse dome designs with human selections from interim results β and γ (see Figure 6). The primary differences between the domes are predominantly noticeable in the yellow regions.

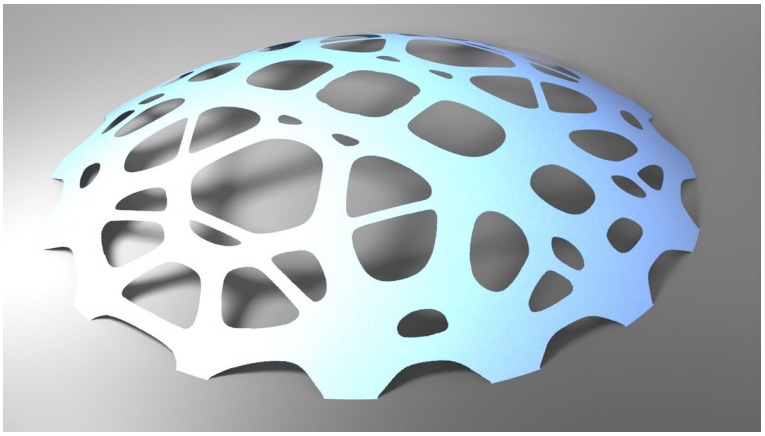


Figure 13. Rendered dome of the design in Figure 12(g).

The tree in Figure 6 can be further expanded according to the designer's requirements. For example, additional designer selections can be introduced after selecting structure γ to incorporate more designer's preferences (i.e., expanding the tree vertically). Alternatively, the designer can change the previous selection on structure β or γ to start a new branch to explore more design possibilities (i.e., expanding the tree horizontally).

In addition, it is worth noting that the proposed approach can generate serialised diverse designs with controlled similarities by introducing different numbers of selections. When designers need to generate a series of similar designs, they can explore the tree generated by this approach to compare and select multiple designs that align with their aesthetic intuition or other functional requirements. A conceptual series of diverse designs for domes is shown in Figure 14.

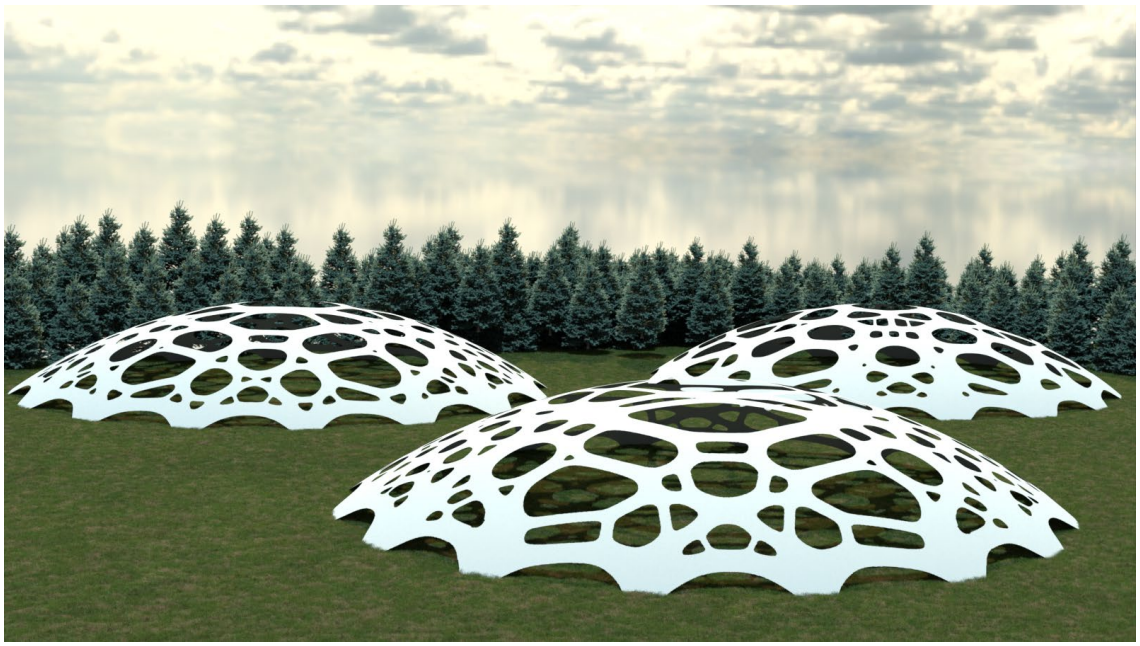


Figure 14. Serialised diverse designs for domes.

5. Conclusions

This paper proposes a novel approach to generate diverse and competitive structural designs by incorporating angular perturbations to loads during the topology optimisation process. In addition, a human-guided design process allows for the identification of desired solutions that align with the

designer's aesthetic preferences or other functional requirements. The similarity between diverse solutions increases as more human selections are introduced, effectively balancing the exploration of design possibilities with the consideration of designers' preferences.

Furthermore, the proposed approach is straightforward and can be integrated into various topology optimisation problems. We demonstrate the effectiveness of our approach through examples of apple growth and dome design. This work provides a fresh perspective on helping designers create elegant and efficient designs using topology optimisation.

Acknowledgements

This research was supported by the Australian Research Council (FL190100014).

References

[1] M. P. Bendsøe, "Optimal shape design as a material distribution problem," *Structural Optimization*, vol. 1, pp. 193–202, 1989.

[2] Y. M. Xie and G. P. Steven, "A simple evolutionary procedure for structural optimization," *Computers & Structures*, vol. 49, pp. 885–896, 1993.

[3] M. Y. Wang, X. Wang and D. Guo, "A level set method for structural topology optimization," *Computer Methods in Applied Mechanics and Engineering*, vol. 192, pp. 227–246, 2003.

[4] X. Guo, W. Zhang and W. Zhong, "Doing topology optimization explicitly and geometrically—a new moving morphable components based framework," *Journal of Applied Mechanics*, vol. 81, Article 081009, 2014.

[5] X. Huang, "On smooth or 0/1 designs of the fixed-mesh element-based topology optimization," *Advances in Engineering Software*, vol. 151, Article 102942, 2021.

[6] X. Y. Yang, Y. M. Xie, G. P. Steven and O. M. Querin, "Bidirectional evolutionary method for stiffness optimization," *AIAA Journal*, vol. 37, pp. 1483–1488, 1999.

[7] O. M. Querin, V. Young, G. P. Steven and Y. M. Xie, "Computational efficiency and validation of bi-directional evolutionary structural optimisation," *Computer Methods in Applied Mechanics and Engineering*, vol. 189, pp. 559–573, 2000.

[8] X. Huang, Y. M. Xie and M. C. Burry, "A new algorithm for bi-directional evolutionary structural optimization," *JSME International Journal Series C Mechanical Systems, Machine Elements and Manufacturing*, vol. 49, pp. 1091–1099, 2006.

[9] X. Huang and Y. M. Xie, "Convergent and mesh-independent solutions for the bi-directional evolutionary structural optimization method," *Finite Elements in Analysis and Design*, vol. 43, pp. 1039–1049, 2007.

[10] Y. M. Xie, "Generalized topology optimization for architectural design," *Architectural Intelligence*, vol. 1, Article 2, 2022.

[11] C. Cui, H. Ohmori and M. Sasaki, "Computational morphogenesis of 3D structures by extended ESO method," *Journal of the International Association for Shell and Spatial Structures*, vol. 44, pp. 51–61, 2003.

[12] Y. Lai, Y. Li, M. Huang, L. Zhao, J. Chen and Y. M. Xie, "Conceptual design of long span steel-UHPC composite network arch bridge," *Engineering Structures*, vol. 277, Article 115434, 2023.

[13] B. Wang, Y. Zhou, Y. Zhou, S. Xu and B. Niu, "Diverse competitive design for topology optimization," *Structural and Multidisciplinary Optimization*, vol. 57, pp. 891–902, 2018.

[14] K. Yang, Z.-L. Zhao, Y. He, S. Zhou, Q. Zhou, W. Huang and Y. M. Xie, "Simple and effective strategies for achieving diverse and competitive structural designs," *Extreme Mechanics Letters*, vol. 30, Article 100481, 2019.

[15] Y. He, K. Cai, Z.-L. Zhao and Y. M. Xie, "Stochastic approaches to generating diverse and competitive structural designs in topology optimization," *Finite Elements in Analysis and Design*, vol. 173, Article 103399, 2020.

[16] Z.-L. Zhao, S. Zhou, K. Cai and Y. M. Xie, "A direct approach to controlling the topology in structural optimization," *Computers & Structures*, vol. 227, Article 106141, 2020.

[17] Y. He, Z.-L. Zhao, K. Cai, J. Kirby, Y. Xiong and Y. M. Xie, "A thinning algorithm based approach to controlling structural complexity in topology optimization," *Finite Elements in Analysis and Design*, vol. 207, Article 103779, 2022.

[18] M. P. Bendsøe and O. Sigmund, "Material interpolation schemes in topology optimization," *Archive of Applied Mechanics*, vol. 69, pp. 635–654, 1999.

[19] X. Huang and Y. M. Xie, "Evolutionary topology optimization of continuum structures including design-dependent self-weight loads," *Finite Elements in Analysis and Design*, vol. 47, pp. 942–948, 2011.

[20] X. Huang and Y.-M. Xie, "A further review of ESO type methods for topology optimization," *Structural and Multidisciplinary Optimization*, vol. 41, pp. 671–683, 2010.

[21] Y. Xiong, Z.-L. Zhao, H. Lu, W. Shen and Y. M. Xie, "Parallel BESO framework for solving high-resolution topology optimisation problems," *Advances in Engineering Software*, vol. 176, Article 103389, 2023.

[22] X. Huang and Y. M. Xie, *Evolutionary Topology Optimization of Continuum Structures: Methods and Applications*, John Wiley & Sons, 2010.

[23] Y. M. Xie and G. P. Steven, *Evolutionary Structural Optimization*, Springer, 1997.

IASS 2023
July 10–14 Melbourne
Integration of Design and Fabrication

Proceedings of the IASS Annual Symposium 2023
Integration of Design and Fabrication
10–14 July 2023, Melbourne, Australia
Y.M. Xie, J. Burry, T.U. Lee and J. Ma (eds.)

A numerical comparison between geometric stiffness- and elastic stiffness-based structural shape optimization for gridshells

Gaoyuan WU[a,*,†], Rafael PASTRANA[b,†], Sigrid ADRIAENSSENS[a], Maria E. Moreyra GARLOCK[a]

[a,*] Department of Civil and Environmental Engineering, Princeton University, United States of America
gaoyuanw@princeton.edu

[b] School of Architecture, Princeton University, United States of America
arpastrana@princeton.edu
[†] These authors have contributed equally to this work

Abstract

Gridshells can span long distances efficiently if they have an adequate form. Numerical form-finding methods coupled with optimization algorithms generate such efficient shapes for gridshells based on different stiffness assumptions. These stiffness assumptions may condition the optimality of the generated shape. This paper presents a comparative study between the constrained force density method (FDM) and the finite element analysis (FEA)-based shape optimization (FSO) in the generation of shapes of gridshells that make the optimal use of material as quantified by their strain energy. Three different gridshells with fixed horizontal projection are optimized for minimal strain energy with each form-finding method: a barrel vault, a dome and a gridshell with complex plan view. The optimized gridshell are evaluated after optimization in terms of their strain energy, their maximum height and the incurred optimization runtime. High-performance numerical computing is utilized to execute experiments efficiently and automatic differentiation is leveraged to conveniently obtain the value of the derivatives needed to solve the shape optimization problems herein. The findings of this work provide insights on the strengths and weaknesses of these two form-finding methods, and open new research directions for the practical design of lightweight structures that can mitigate the carbon footprint of the built environment.

Keywords: form finding, shape optimization, force density method, finite element analysis, high-performance computing, automatic differentiation, hangai prize applicant

1. Introduction

One of the goals of structural shape optimization is to arrive at a shape for a structure that bears load using the minimal amount of material as measured by its strain energy [1]–[3] and we limit the scope to the shape optimization of gridshells for this goal herein. Numerical form-finding methods like the force density method (FDM) [4] coupled with gradient-based optimization and the finite element analysis (FEA)-based shape optimization (FSO) [2] generate such efficient shapes for gridshells based on different stiffness assumptions.

The FDM takes as input the geometric stiffness of a gridshell modeled as a network whose elements only resist axial forces. The geometric stiffness of structure is calculated based on the *force densities*: the expected ratio between the internal force and the length of the elements of the network. The FDM calculates the 3D coordinates of the nodes of the network based such that the network is in a state of static equilibrium with a design load. To minimize the material usage of a gridshell with FDM, one then solves an optimization problem that calibrates the force densities in the network such that the total load path of the gridshell is minimal [5]–[7]. The minimization of the load path is equivalent to the minimization of the strain energy in the geometric-stiffness domain for a fully stressed design of a pin,

Copyright © 2023 Annual by Gaoyuan WU, Rafael PASTRANA, Sigrid ADRIGENSSENS and Maria E. Moreyra GARLOCK. Published in the Proceedings of the IASS Symposium 2023 with permission.

jointed bar network [7]. The structural response of the FDM-optimized shape needs to be assessed with a FEA in a second and separate stage after assigning material properties and cross-sections to obtain the strain energy of the structure.

In contrast, FSO directly receives the material and cross-section properties of the members of a gridshell as inputs to characterize its elastic stiffness matrix. Moreover, FSO assumes that the elements of the structure can take axial forces, shear forces and bending moments, thus capturing a more nuanced structural response of the structure. The shape that makes an optimal use of material is generated with FSO after minimizing the total strain energy of the gridshell via optimization with the nodal coordinates as the design variables. Despite the structural elements have a bending stiffness at the outset, the minimization of strain energy also diminishes the bending behavior of a structure [1]–[3], making FSO consistent with the assumptions in FDM. Thanks to the FEA coupling, FSO achieves coherence between the shape generation and structural analysis but at the cost of iteratively performing a potentially expensive FEA throughout the optimization process.

While extensive work on successfully applying these two approaches to the shape optimization of gridshells exists separately, a unified comparison between FDM and FSO is missing. In this paper, a numerical study is conducted that compares FDM and FSO in the task of generating optimal shapes for gridshells that minimize material consumption. This study quantifies the effect of the different stiffness assumptions each of these two form-finding methods make on the optimality of the form-found shapes they generate as measured by their total strain energy, geometrical attributes, and the resulting computational cost for optimization. To evaluate their strain energy, the gridshell elements are dimensioned according to two different sizing strategies.

After introducing the theoretical underpinning of both methods (Section 2. Form finding methods), FDM and FSO are applied to three different gridshells with fixed horizontal projection: a barrel vault, a dome and a gridshell with free-form plan (Section 3 Numerical study). Both form-finding methods, as well as the experiments carried out in the study, are implemented in JAX [8], a Python library for high-performance numerical computing and automatic differentiation (AD) [9]. A discussion of the findings of the study and future research directions are provided in Section 4. Discussions.

2. Form finding methods

2.1. The force density method (FDM)

The FDM models a structure as a pin-jointed bar network. For a network with m edges and n nodes, a connectivity matrix $\boldsymbol{D} \in R^{m \times n}$ establishes the relationship between the edges and the nodes of the structure. The entry $\boldsymbol{D}_{ij} = +1$ if node j is the start node of edge i, and $D_{ij} = -1$ if the j-th node is the end node of i. Otherwise, $D_{ij} = 0$. The matrix D is decomposed into two submatrices: $\boldsymbol{D} = [\boldsymbol{D}_{IN}\ \boldsymbol{D}_F]$ where $\boldsymbol{D}_{IN}$ includes all the columns of the matrix corresponding to the free nodes and $\boldsymbol{D}_F$ consists of the columns representing the fixed nodes. The force density q_i is defined as $q_i = F_i/L_i$, where F_i is the expected force and L_i is the expected length of the i-th edge. Given a force density vector $\boldsymbol{q} \in R^m$ and the matrix $\boldsymbol{D}$, the 3D coordinates of the free nodes of a structure in static equilibrium are obtained after solving a linear system of equations:

$$\boldsymbol{x}_{IN} = (\boldsymbol{D}_{IN}^T \boldsymbol{Q} \boldsymbol{D}_{IN})^{-1} (\boldsymbol{p}_{X,IN} - \boldsymbol{D}_{IN}^T \boldsymbol{Q} \boldsymbol{D}_F \boldsymbol{x}_F) \tag{1}$$

$$\boldsymbol{y}_{IN} = (\boldsymbol{D}_{IN}^T \boldsymbol{Q} \boldsymbol{D}_{IN})^{-1} (\boldsymbol{p}_{Y,IN} - \boldsymbol{D}_{IN}^T \boldsymbol{Q} \boldsymbol{D}_F \boldsymbol{y}_F) \tag{2}$$

$$\boldsymbol{z}_{IN} = (\boldsymbol{D}_{IN}^T \boldsymbol{Q} \boldsymbol{D}_{IN})^{-1} (\boldsymbol{p}_{Z,IN} - \boldsymbol{D}_{IN}^T \boldsymbol{Q} \boldsymbol{D}_F \boldsymbol{z}_F) \tag{3}$$

where $\boldsymbol{Q} = diag(\boldsymbol{q})$ is the diagonal matrix of the force densities; $[\boldsymbol{p}_{X,IN}\ \boldsymbol{p}_{Y,IN}\ \boldsymbol{p}_{Z,IN}]$ are the loads applied to the nodes of the structure; and $[\boldsymbol{x}_F\ \boldsymbol{y}_F\ \boldsymbol{z}_F]$ are the 3D coordinates of the fixed nodes. The internal force F of k-th edge of the structure are calculated as the element-wise product between the force density vector q and its length in the static equilibrium state:

$$F_k(\boldsymbol{q}) = q_k L_k(\boldsymbol{q}), \qquad k = 1, \ldots, m$$

A structure that minimizes material volume has a low strain energy [2]. Directly minimizing strain energy with the FDM is unfeasible as this form finding method does not provide information about the displacement or the elastic stiffness of a structure to calculate its strain energy. However, for a fully stressed, pin-jointed bar structure, minimizing its total *load path* $V(\boldsymbol{q})$ is an equivalent approach to reducing its strain energy:

$$\begin{aligned} &\text{Minimize} && V(\boldsymbol{q}) = \textstyle\sum_{i=1}^{i=m} |F_i(\boldsymbol{q})| L_i(\boldsymbol{q}) \\ &\text{Subject to} && \left|X_i - X_{i,INI}\right| \le \varepsilon_X, \quad i = 1, \ldots, n \\ & && \left|Y_i - Y_{i,INI}\right| \le \varepsilon_Y, \quad i = 1, \ldots, n \end{aligned} \tag{4}$$

Constraints can be added to the optimization problem defined by Eq. (4) to preserve the horizontal projection of the structure on the plan view. In these constraints, X_i, Y_i denote the coordinates of the i-th node in static equilibrium; $X_{i,INI}$ and $Y_{i,INI}$ are the initial coordinates of the i-th free node; and ε_X and ε_Y are tolerance thresholds whose values are typically small. This constrained optimization problem can be solved efficiently with a gradient-based optimizer, like the sequential least-square programming (SLSQP) [10]. The derivatives required by the optimizer, such as $\frac{\partial V}{\partial \boldsymbol{q}}$, are automatically calculated with AD (see Section 2.3 Software implementation).

2.2. Elastic stiffness-based shape optimization

The FEA-based shape optimization (FSO) incorporates the elastic stiffness of a structure directly into the form finding process and the members used are 3D frame elements with bending stiffness. An optimal shape is found by solving an optimization problem wherein the total strain energy of a structure is minimized, as well as the bending behavior. The FSO problem reads:

$$\text{Minimize} \qquad C(\boldsymbol{z}) = \frac{1}{2} \boldsymbol{f}^T \boldsymbol{u}(\boldsymbol{z}) \tag{5}$$

where C is the strain energy (i.e. the compliance) of the structure; $\boldsymbol{z}$ denotes the design parameters, which are the Z-coordinate of all the design nodes in the domain; $\boldsymbol{f}$ is the generalized load vector; $\boldsymbol{u}(\boldsymbol{z})$ is the displacement. To solve the optimization problem listed in Eq. (5) via gradient-based optimization, the *sensitivity* of the objective function, $\frac{\partial C}{\partial \boldsymbol{z}}$, must be obtained. The adjoint sensitivity method [11] is implemented herein for the sensitivity derivation and the sensitivity with respect to the i-th design variable then reads:

$$\frac{\partial C}{\partial z_i} = \frac{\partial \boldsymbol{f}^T}{\partial z_i} \boldsymbol{u} - \frac{1}{2} \boldsymbol{u}^T \frac{\partial \boldsymbol{K}}{\partial z_i} \boldsymbol{u} \tag{6}$$

Where $\boldsymbol{K}(\boldsymbol{z})$ is the elastic stiffness matrix, as characterized by the material properties and cross-sectional properties. Assuming that the applied loads are independent from the Z coordinates of the structure, the sensitivity is simplified to:

$$\frac{\partial C}{\partial z_i} = -\frac{1}{2}\boldsymbol{u}^T \frac{\partial \boldsymbol{K}}{\partial z_i}\boldsymbol{u} \tag{7}$$

The calculation of $\frac{\partial C}{\partial z_i}$ is decomposed into two separate tasks: i) conducting a FEA to obtain $\boldsymbol{u}$ and ii) calculating $\frac{\partial \boldsymbol{K}}{\partial z_i}$. Similar to Section 2.1. The force density method (FDM), the calculation of $\frac{\partial \boldsymbol{K}}{\partial z_i}$ is obtained with AD. This required derivative is then input to a gradient based optimizer to solve the optimization problem.

With the adjoint sensitivity obtained, the FSO problem becomes an unconstrained optimization problem and can be solved by various gradient-based optimizers. To make the numerical comparison in the following section consistent, SLSQP, the same optimizer as the one used for FDM-based optimization, is selected herein to solve FSO.

2.3 Software implementation

The authors have implemented both form-finding methods in JAX, a Python library for high-performance numerical computing and automatic differentiation. These implementations have been released as open-source software packages: JAX FDM [12] and JAX-SSO [13] for FDM and FSO, respectively. Thanks to JAX, some of the important features of these packages to automate and accelerate form-finding compared to standard form-finding implementations include: function *vectorization* to parallelize function evaluations; *just-in-time* (JIT) compilation to transform Python code into a leaner, lower-level level representation that can be executed by a computer more efficiently; and *automatic differentiation* (AD) to automatically get the exact value of the derivatives of the objective function w.r.t. the form-finding design parameters required to generate the optimal shapes in this study (see Section 3 Numerical study). Interested readers are referred to the repositories of the software packages for details.

3 Numerical study

3.1 Scope and comparison framework

The study focuses on three different gridshell of growing complexity whose members have axial, shear and bending resistance. The comparison framework for the outputs of FDM and FSO is shown in Figure 1. In this study, the optimality of a structure in terms of material usage is quantified by measuring its strain energy. Low strain energies are desirable [1]–[3]. The framework starts with the initialization of the structure, which includes the initial geometry and boundary conditions. The applied loads are then specified.

For the geometric stiffness-based FDM, the minimization of the total load path of a structure given by Equation (4) is formulated and solved iteratively with SLSQP, a gradient-based optimizer. The value of the force densities of the structure are the design variables. The solution to this optimization problem converges when the relative change of $V(\boldsymbol{q})$ between two consecutive iterations is smaller than a prespecified value ε_{tol}. Material and cross-section properties are assigned to the load path optimized structure to assess its strain energy via FEA, as illustrated in Figure 1. The required material properties include the allowable axial stress σ_{MAX}, Young's modulus E, and shear modulus G, which can be arbitrarily selected. In this study, the cross-section properties are selected according to two different strategies, based on the internal forces output by FDM: i) constant cross-sections (suitable for fabrication

efficiency); ii) customized cross-sections (preferable for structural efficiency). In both strategies, rectangular sections with a depth to width ratio ($\frac{h}{b}$) of 1.5 are used. For the constant-area case, the maximum absolute value of the axial force F_{MAX} obtained with FDM as per Equation (4) and the allowable stress σ_{MAX} are used to determine the constant cross-section as $A = F_{MAX}/\sigma_{MAX}$. In contrast, we customize the cross-sectional area for each element in the second case: the sectional area of the i-th element is calculated by $A_i = MAX\{\frac{F_i}{\sigma_{MAX}}, A_{MIN}\}$ where A_{MIN} represents a prespecified minimum area value to avoid numerical instabilities, as $\frac{F_i}{\sigma_{MAX}}$ alone may give a sectional area that is close to zero.

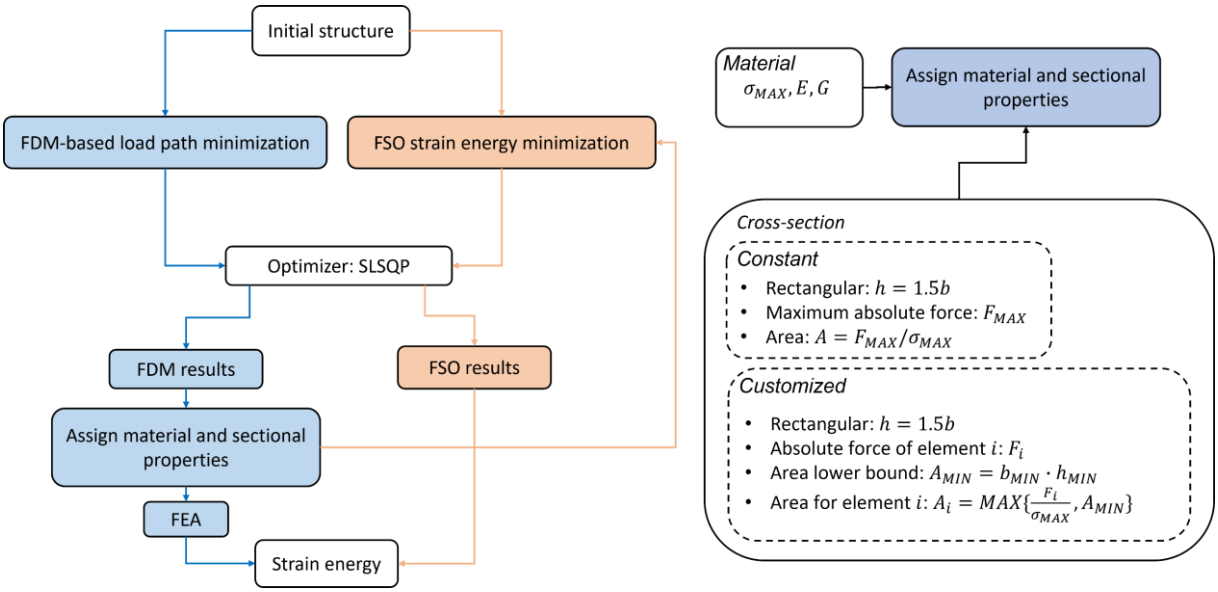


Figure 1 Comparison framework between FDM and FSO (left) and description of constant and customized strategies for the assignment of cross-section properties (right).

For elastic stiffness-based FSO, material and cross-section properties are the inputs to the optimization problem that directly minimizes strain energy. For consistency, the same properties determined after optimizing the load path of a structure with FDM are taken as inputs to the FSO-based form finding. SLSQP iteratively updates the Z coordinates to minimize the total strain energy until convergence. The same convergence criterion used in FDM is used in FSO. The strain energy measured in the last iteration as FSO is used for comparison purposes. The characteristics of the optimized geometry and the value of final strain energy resulting from both form-finding methods are discussed. In addition, the computational time to solve the optimization problems is discussed for reference purposes only. In all the experiments, the prespecified Young's modulus E is 37.9 GPa and the Poisson's ratio is 0.3. The allowable axial stress σ_{MAX} is 10 MPa. For FDM, the coordinate deviation thresholds ε_X and ε_Y are both set to 0.05 m. The stopping criterion of optimization is $\varepsilon_{tol} = 10^{-5}$.

3.1 Barrel vault

3.1.1. Problem setup

A barrel gridshell in 3D is studied (Figure 2.a). The gridshell consists of a 15 by 15 grid where the spans in the X and Y directions are 15 m each. The gridshell has 225 nodes and 420 structural members, and a starting height of 2.45 m. The 30 nodes along two longitudinal edges of the barrel vault are restrained with pin-supports. The other 195 nodes are free to move during form-finding. The load applied to every

node has a magnitude of 500 kN. In FDM, there are 420 design parameters, corresponding to force densities; in addition, there are 390 constraints, corresponding to the X and Y coordinate constraints on the 195 free nodes. In contrast, there are 195 design parameters in the FSO problem, corresponding to the Z coordinate of the free nodes, and no constraints.

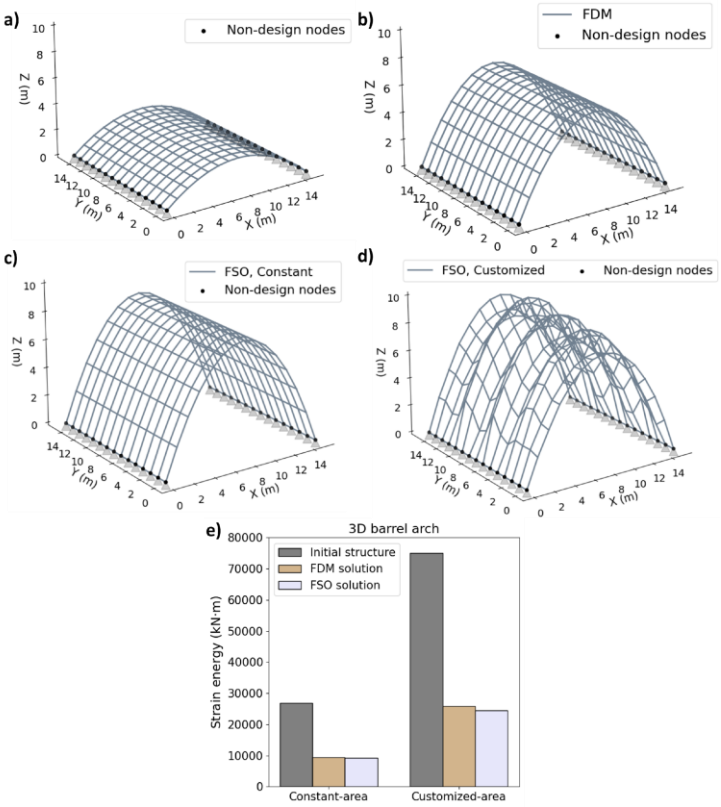


Figure 2 Barrel vault. a) Initial geometry. Optimal shapes: b) FDM; c) FSO, constant cross-section; d) FSO, custom cross-sections. e) Strain energy summary

3.1.2. Case 1: constant cross-sections

For the initial barrel, the load path is 1.38×10^7 kN·m. Solving the FDM-based optimization with the SLSQP optimizer takes 12 iterations, and the total load path decreases by 34.7% to 8.99×10^6 kN·m. The final geometry output by FDM is illustrated in Figure 2.b. It is a parabolic barrel with a height of 6.52 m. As per the constant cross-section strategy, the rectangular cross-section assigned has a width of 504 mm and a depth of 756 mm. The FEA shows that the total strain energy decreases from an initial value of 26966.72 kN·m to 9414.74 kN·m, manifesting a reduction of 65.1% from FDM-based optimization. In FSO, the optimization terminates after 11 iterations. The SLSQP optimizer successfully decreases the strain energy down to 9182.95 kN·m, which is 2.5% lower than the FDM solution. The final geometry from FSO is shown in Figure 2.c, and it has a height of 8.25m.

In this example, both methods successfully find an efficient geometry that minimizes strain energy. Although the SLSQP optimizer takes around 10 iterations in both methods to converge, the computational time is different due to the difference in the problem formulation: the geometric stiffness-based FDM takes 36.0 seconds to converge while the elastic stiffness-based FSO solution is found within 8.5 seconds. One plausible reason why FDM takes longer is that there are more design parameters and constraints when compared to FSO.

3.1.3. Case 2: customized cross-sections

For each rectangular cross-section, the minimum area is set as: $A_{MIN} = 250 \times 375 = 93750$ mm^2. Based on the FEA results, the FDM solution has a total strain energy of 25796.70 kN·m, which indicates a reduction of 65.6% compared to the initial geometry whose total strain energy is 75009.51 kN·m. When it comes to FSO, the optimization terminates after 58 iterations and outputs the minimized total strain energy of 24490.72 kN·m, which is 5.0% less than the FDM solution. However, the final geometry output by FSO is not smooth (Figure 2.d). While the form-found geometry follows the shape of arches along the X direction, the frames show zigzag patterns along the Y direction. The jagged geometry might be the result of a non-uniform gradient vector, which is triggered by the implementation of customized cross-sections. This problem can be resolved in the future by methods like sensitivity filtering or geometry parameterization [14]. For the customized-area case, FDM successfully finds a 3D barrel arch geometry that reduces the total strain energy. The optimization time needed for FDM is 36.0 seconds. On the contrary, although FSO greatly reduces the strain energy of the structural system and converges faster (12 seconds), it fails to provide a smooth geometry which could be important for aesthetic reasons.

3.2 Dome

3.2.1. Problem setup

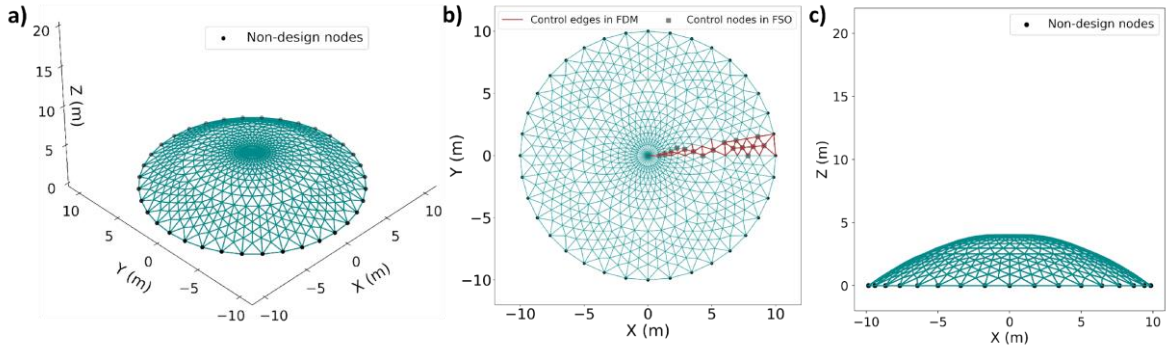


Figure 3 Initial geometry of a circular dome: a) perspective view, b) plan view and c) elevation.

The configuration of this example is adapted from an example in the work by Liew [7]. The initial geometry and its projected views can be seen in Figure 3. The initial geometry of this gridshell is triangulated, consisting of 613 nodes and 1800 structural members. The projection on plan is a circle with its center at the coordinate origin and a radius of 10 m (Figure 3.b). The height of the structure is 4.03 m. The 36 nodes on the perimeter are pin-supported and fixed. The original load applied is a 100 kPa distributed area load and it is later converted to point loads applied on the structural nodes. Despite the considerable number of nodes and edges, the radial symmetry of the initial structure and the loading condition can reduce the number of design parameters in both FDM and FSO. For FDM, the design parameters are the force densities of the 34 edges, as highlighted in Figure 3.b. For the rest of the edges, if the edge shares the same distance to the origin as one of the 34 highlighted edges, an identical force density value as the highlighted edge will be assigned. In FSO, the Z coordinates of the 17 highlighted nodes are set as the design parameters (Figure 3.b). The Z coordinates of other nodes are similarly set via radial symmetry.

3.2.2. Case 1: constant cross-sections

The initial circular dome has a total load path of 570412 kN·m and this value decreases by 40.8% to 337565 kN·m by implementing the FDM-based optimization. The load path optimization takes 37 iterations to converge, and the final geometry is illustrated in Figure 4.a and Figure 4.b. The optimized geometry has a height of 7.99 m that is 98.3% taller than the initial geometry. The constant cross-section is a rectangle with a width of 242 mm and a depth of 363 mm. The FEA shows that the total strain energy of the system is reduced from 30.50 kN·m to 17.70 kN·m, representing a decrease of 42.0% (Figure 4.g). With the same constant section assignment, the FSO takes 44 iterations to converge and outputs a total strain energy of 12.82 kN·m, which is 27.6% lower than FDM (Figure 4.g). The shape product by FSO is illustrated in Figure 4.c and Figure 4.d. The FSO solution has a height of 11.97 m, taller than the FDM solution. In addition, the central zone of the FSO solution is more curved than the FDM solution, manifested by the larger bump near $X = 0$ m and $Y = 0$ m.

The optimization takes 25.85 seconds for FDM and 65.76 seconds for FSO. The reason for the faster optimization in FDM-based optimization is the reduced number of design parameters and constraints thanks to the symmetry. While there are fewer design parameters in FSO which saves the time of calculating $\frac{\partial \boldsymbol{K}}{\partial z_i}$ in the sensitivity evaluation stage, conducting FEA for the displacement $\boldsymbol{u}$ is more computationally consuming than obtaining the static equilibrium from FDM, explaining the difference in the optimization time.

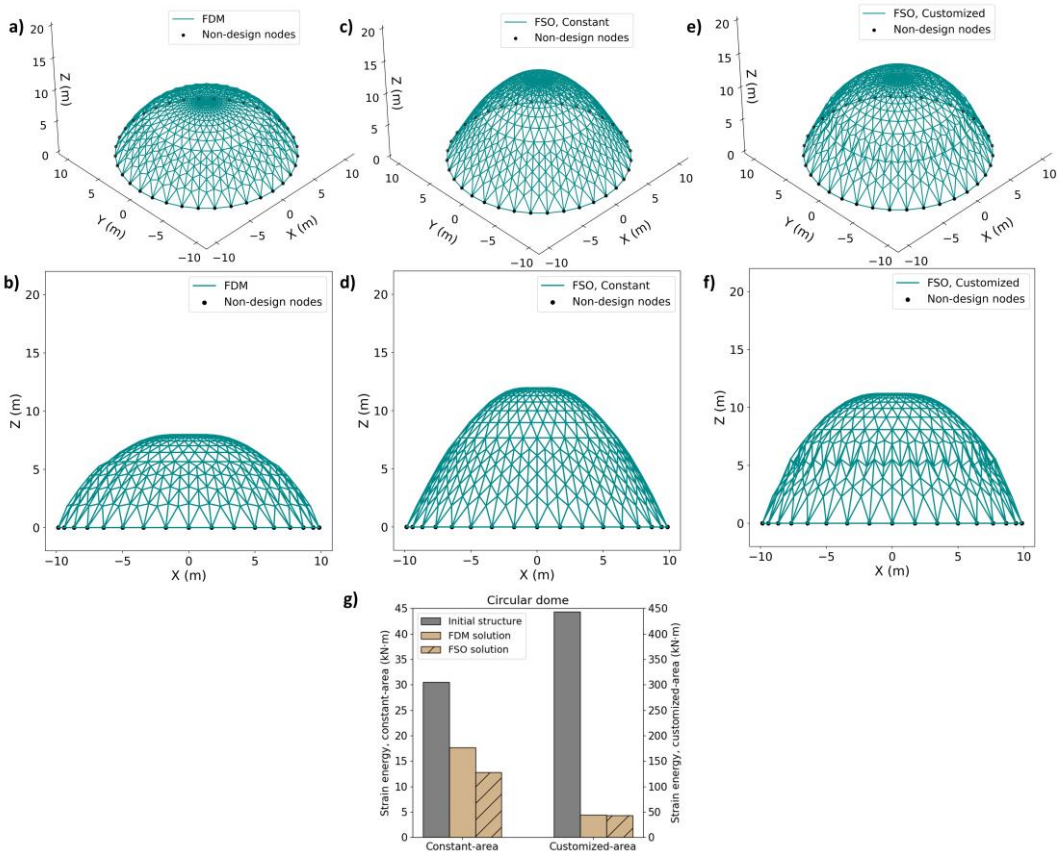


Figure 4 Dome, optimal shapes. FDM: a) perspective and b) elevation. FSO, constant cross-section: c) perspective and d) elevation. FSO, custom cross-sections: e) perspective and f) elevation. g) Strain energy summary

3.2.3. Case 2: customized cross-sections

The minimum sectional area is set as $A_{MIN} = 5 \times 7.5 = 37.5$ mm^2. With the customized sectional area assignment, the initial geometry has a total strain energy of 443.18 kN·m. With the FDM solution, this value is reduced by 90.0% to 44.51 kN·m. With FSO, the strain energy decreases to 43.45kN·m after 39 iterations and this value is 2.2% lower than the FDM solution. The form-found geometry is illustrated in Figure 4.e and Figure 4.f, and it has a maximum height of 11.21 m. Compared to the FSO solution with constant cross-sections, this geometry is less smooth at $Z = 5$m when the mesh pattern changes for the gridshell (Figure 4.f). The smoothness transition of frames can also be noticed in the FDM solution (Figure 4.b) when the gridshell pattern changes but it is less abrupt. Similar to the constant-section case, the FSO takes more time than FDM: it takes 63.84 seconds to converge compared to 25.85 seconds of FDM.

3.3 Gridshell with free-form plan

3.3.1. Problem setup

Both form-finding methods are applied to optimize the geometry of a complex gridshell roof over an exhibition center, inspired by the Mannheim Multihalle. The initial structure is shown in Figure 5.a. It spans 60 m along the X direction and 80m along the Y direction. When $Y = 0$ m and $Y = 80$ m, there are two openings that serve as gates to the main exhibition area. The width of the gates is about 10 m. The gridshell consists of 440 nodes and 1215 structural members. The 92 nodes on the boundary are fixed with pin supports. The initial structural height is 10.96 m and a downward load of 1000 kN is applied to each node. In FDM, there are 1215 design parameters and 696 constraints. In FSO, the number of design parameters is 348.

3.3.2. Case 1: constant cross-sections

In FDM, the starting geometry has a total load path of 1.41×10^7 kN·m and this value is reduced by 46.8% to 0.75×10^7 kN·m after 69 iterations in SLSQP. The optimized geometry is illustrated in Figure 5.b. Through the entrance to the main exhibition area, an arch shape can be observed. Above the main exhibition area, a doubly curved dome geometry is found. Around $X = 25$ m, the form-found geometry has a saddle-like geometry manifested by its negative Gaussian curvature, while it has positive Gaussian curvature elsewhere in the main exhibition area. The constant cross-section assigned is a rectangular section with a width of 286 mm and a depth of 429 mm. The FEA results show that the strain energy is reduced from 5711.46 kN·m to 2660.66 kN·m, representing a reduction of 53.4% (Figure 5.f).

With FSO, the strain energy is reduced to 1917.53 kN·m after 378 iterations (Figure 5.f), which is 27.9% lower than the FDM solution. The lower strain energy of the FSO solution implies that the resulting gridshell makes more efficient use of material than the FDM solution. Figure 5.c presents the final geometry obtained by FSO. An interesting observation is that, instead of having a saddle point around X=25 m like the one in the FDM solution, the main exhibition area has positive Gaussian curvature. The structural height of the FSO shape is 28.47 m, which is 45.7% taller than the FDM solution whose height is 19.54 m. Although FSO takes more iterations to converge than the FDM-based optimization, the time FSO takes is 102.63 seconds, 6.49 times faster than FDM, which needs 666.28 seconds to converge.

3.3.3. Case 2: customized cross-sections

Customized cross-sections are assigned to the structural members in this case. The minimum sectional area is $A_{MIN} = 100 \times 150 = 15000$ mm^2. For FDM, the final geometry has a total strain energy of 18627.58 kN·m, showing a decrease of 62.7% from the initial value of 49927.71 kN·m. With the customized cross-sections, the FSO converges after 365 iterations and outputs a final strain energy of

11646.79 kN·m (Figure 5.f). Comparing the optimized strain energy values of both methods, the elastic stiffness-based solution is 37.5% lower. The form-found geometry of FSO has a height of 28.18 m and it is shown in Figure 5.d. This form-found geometry is different from the FSO solution in the constant-area case, as it manifests negative Gaussian curvature near $X = 25$m, which is similar to the FDM solution. However, the form-found geometry in this case is much taller than the FDM solution and its saddle geometry is not as significant as the one seen in the FDM solution. Regarding the computational time, the FSO takes only 96 seconds as opposed to the 662.28 seconds needed by the FDM-based optimization.

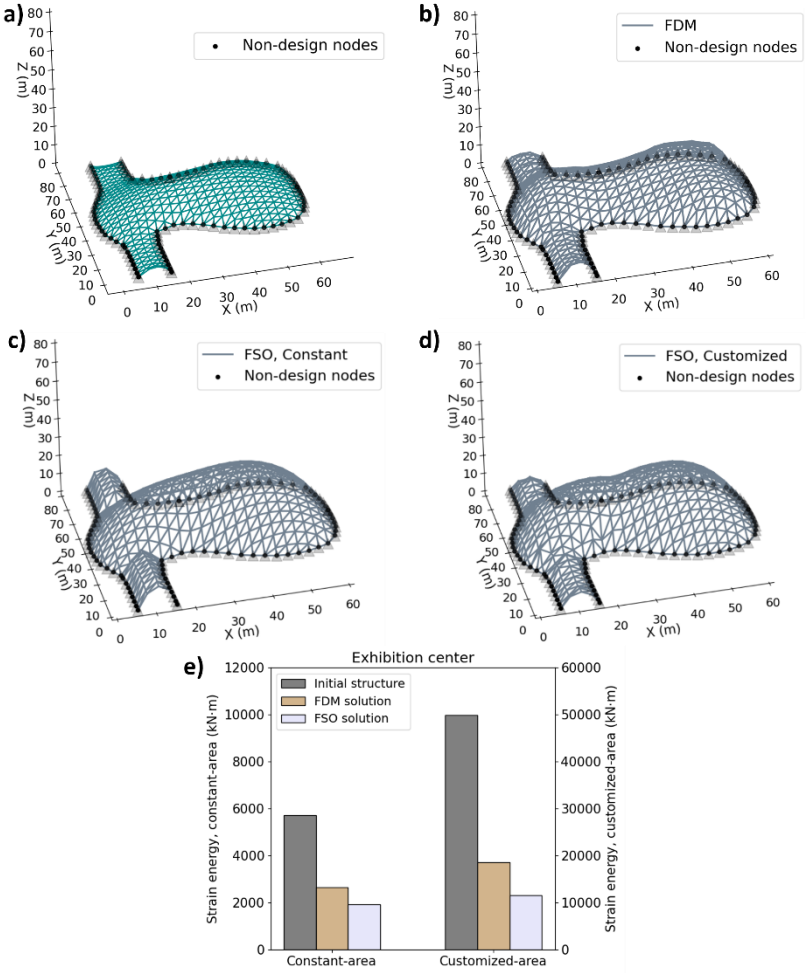


Figure 5 Free-form gridshell. a) Initial geometry. Optimal shapes. b) FDM; c) FSO, constant cross-section; d) FSO, custom cross-sections. e) Strain energy summary

4. Discussions

A summary of the outcome of the experiments in the comparative study is provided in Table 1 where we include the optimized strain energy ratio, the maximum structural height and the optimization time needed. The optimized energy ratio is calculated by the ratio between the strain energy of the optimized structure and that of the unoptimized structure, which is used to quantify the efficiency improvement of the optimized structure in terms of material usage compared to the unoptimized one. Overall, assigning constant cross-sections yields designs with higher optimized strain energy ratio than those who have

cross-sections sized in a customized way in both form-finding methods. In a critical case (dome), the use of constant cross-sections makes the optimized strain energy ratio go up by 32.34% for FSO and 47.99% for FDM, compared to their counterparts with customized cross-sections. The lowest difference in the normalized strain energy ratio between constant and custom cross-sections for a single method is observed in the FDM-optimized barrel vault (0.5%).

Based on the assumptions outlined in Section 3.1 Scope and comparison framework, FSO with custom cross-sections consistently generates gridshell shapes that have the lowest optimized strain energy ratio. The FSO-optimized geometries reduce the total strain energy of the gridshells to at least a third of their initial, unoptimized values: 32.65%, 23.32% and 9.8% for the barrel vault, the gridshell with free-form plan and the dome structure, respectively. This finding is reasonable as FSO directly optimizes the shape of a gridshell for strain energy and activates the bending and shear capacity of the structural elements, unlike FDM-based optimization which minimizes total load path, a proxy metric for strain energy, and restricts the gridshell elements to bear load only under truss action.

Table 1 Summary of experimental results

	Strain energy ratio [%]				**Height [m]**			**Time [s]**		
	FDM		FSO		FDM	FSO		FDM	FSO	
	Constant	Custom	Constant	Custom		Constant	Custom		Constant	Custom
Barrel	34.91	34.39	34.05	**32.65**	**6.52**	8.25	9.68	36	**8.5**	12
Dome	58.03	10.04	42.03	**9.8**	**7.99**	11.97	11.21	**25.85**	65.76	63.84
Free-form	46.58	37.3	33.57	**23.32**	**19.54**	28.47	28.18	666.28	102.63	**96**

Nevertheless, FDM is an effective approach to reduce the material usage of a gridshell, on par with FSO when the elements of a gridshell are sized with custom cross-sections. In half of the experiments in the study, FDM produces shapes whose strain energy ratio is at most 2% higher than those of the shapes output by FSO. The average difference in the normalized strain energy ratio in this custom cross-section regime is 5.32% between these two methods. For example, the difference in the strain energy reduction between FDM and FSO was 1.76% for the barrel vault and only 0.24% for the dome. This difference increases by one order of magnitude in the constant cross-section regime: the strain energy ratios of the FSO solutions are 13.01% and 16% lower than the FDM solution in the free-form roof case and the dome case, respectively. These findings suggest that FSO is more suitable than FDM to reduce the strain energy of complex gridshells. In addition, for the gridshells whose members cross-sections cannot be sized proportionally to their internal force and thus cannot achieve a fully stressed state potentially due to fabrication constraints, FSO is more ideal. More experiments should follow to confirm this trend.

One of the trade-offs that FSO makes to minimize strain energy is to raise the height of the gridshell. In 5 out of the 6 experiments in the study, the gridshell geometries output by FSO are at least 40% taller than those generated by FDM. For the free-form gridshell, for example, the height of the FDM-optimized gridshell is 19.54 m whereas that of the FSO optimal is at least 28 m, irrespective of the use of constant or custom cross-sections. While tall gridshells are more structurally efficient than shallow ones in this study, their increased height can conflict with architectural requirements in practical applications, which often pose limits on the total height of a structure. Because of these limitations, it would be interesting to explore the effect of height constraints on the strain energy of the optimized gridshells for both FDM and FSO in more detail.

FDM is on average 2.46 times faster to optimize the shape of the dome than FSO in the example that leveraged radial symmetry to reduce the size of the optimization problem. However, calculating optimal gridshell shapes is in general more efficient with FSO in both cross-section regimes, taking only 1/4 and

1/6 of the optimization time elapsed with FDM for the barrel vault and the free-form roof, respectively. The connectivity of the barrel, the dome and the free-form gridshells in the comparative study have 1.86, 2.93, 2.76 times more edges than nodes. Hence, one plausible explanation for this difference in performance is that FSO solves optimization problems that are at least half of the size of those addressed by FDM in terms of number of design variables, thanks to its formulation which scales up linearly with respect to the number of nodes in the gridshell (FSO sets the Z coordinate of the gridshell as design variables). Another explanation for the difference in computational performance between FSO and FDM is that the latter solves a constrained optimization problem to fix the horizontal projection of the gridshells on plan, whereas the former only deals with an unconstrained optimization problem. One way to alleviate this computational cost in the future is to replace FDM with the thrust network analysis (TNA) [15], another geometric stiffness-based form-finding method which fixes the horizontal projection of the structure without resorting to constrained optimization.

The strain energy contribution from axial forces is further evaluated for the shapes output by FSO as illustrated in Table 2. For all the FSO-optimized structures, the vast majority of the strain energy is produced by axial stresses, irrespective of the cross-section assignment strategy used. This contribution has a minimum value of 97.91% and maximum value of 99.99%, illustrating the contribution of the bending is at most 2%. This result confirms that the FSO-optimized gridshells resist external loading predominantly via axial forces, demonstrating the underlying consistency of FSO and FDM despite the difference in the types of structural elements used in the form finding process.

Table 2 Contribution of the strain energy from axial action in FSO

	Strain energy - FSO			
	Constant		Custom	
	Value [kNm]	Axial [%]	Value [kNm]	Axial [%]
Barrel	9182.95	**99.92**	24490.72	**97.91**
Dome	12.82	**99.67**	43.45	**99.99**
Free-form	1917.53	**99.87**	11646.79	**99.93**

5. Conclusions

In this work, we compare the geometric stiffness-based FDM and elastic stiffness-based FSO in terms of finding the optimal form of gridshells that minimize the material usage as quantified by the strain energy. The results show that the load path minimization based on FDM is an effective approach in reducing the material usage though it is purely geometric. For FSO, as it incorporates the elastic stiffness, it performs better than FDM in terms of strain energy reduction for the optimized structures. The FSO-optimized structures are usually taller than their FDM counterparts. In terms of the computational time, FSO is usually faster as it solves an unconstrained optimization problem while the FDM-based optimization is constrained. There exist limitations in this work, and they lead to promising future research directions. For instance, finding a strategy to combine the merits of both methods to assist the inverse design problems is of great importance. Nevertheless, this paper provides insights on the strengths and weaknesses of two widely used form-finding methods, opening new research directions that will facilitate better design of lightweight shell structures that greatly benefit the built environment.

Acknowledgements

The authors would like to thank the colleagues and friends at Princeton University for their insights and support.

References

[1] K.-U. Bletzinger and E. Ramm, "Form finding of shells by structural optimization," *Eng. Comput.*, vol. 9, no. 1, pp. 27–35, Mar. 1993, doi: 10.1007/BF01198251.

[2] K.-U. Bletzinger and E. Ramm, "Structural optimization and form finding of light weight structures," *Comput. Struct.*, vol. 79, no. 22, pp. 2053–2062, Sep. 2001, doi: 10.1016/S0045-7949(01)00052-9.

[3] K.-U. Bletzinger, R. Wüchner, F. Daoud, and N. Camprubí, "Computational methods for form finding and optimization of shells and membranes," *Comput. Methods Appl. Mech. Eng.*, vol. 194, no. 30–33, pp. 3438–3452, Aug. 2005, doi: 10.1016/j.cma.2004.12.026.

[4] H.-J. Schek, "The force density method for form finding and computation of general networks," *Comput. Methods Appl. Mech. Eng.*, vol. 3, no. 1, pp. 115–134, Jan. 1974, doi: 10.1016/0045-7825(74)90045-0.

[5] J. C. Maxwell, "On reciprocal figures and diagrams of forces," *Lond. Edinb. Dublin Philos. Mag. J. Sci.*, vol. 27, no. 182, pp. 250–261, 1864.

[6] W. F. Baker, L. L. Beghini, A. Mazurek, J. Carrion, and A. Beghini, "Maxwell's reciprocal diagrams and discrete Michell frames," *Struct. Multidiscip. Optim.*, vol. 48, pp. 267–277, 2013.

[7] A. Liew, "Constrained Force Density Method optimisation for compression-only shell structures," *Structures*, vol. 28, pp. 1845–1856, Dec. 2020, doi: 10.1016/j.istruc.2020.09.078.

[8] "JAX: composable transformations of Python+NumPy programs." Google, Mar. 16, 2023. Accessed: Mar. 16, 2023. [Online]. Available: https://github.com/google/jax

[9] A. G. Baydin, B. A. Pearlmutter, A. A. Radul, and J. M. Siskind, "Automatic differentiation in machine learning: a survey," *J. Marchine Learn. Res.*, vol. 18, pp. 1–43, 2018.

[10] D. Kraft, "A software package for sequential quadratic programming," *Forschungsbericht- Dtsch. Forsch.- Vers. Luft- Raumfahrt*, 1988.

[11] D. A. Tortorelli and P. Michaleris, "Design sensitivity analysis: Overview and review," *Inverse Probl. Eng.*, vol. 1, no. 1, pp. 71–105, Oct. 1994, doi: 10.1080/174159794088027573.

[12] R. Pastrana and S. Adriaenssens, "JAX FDM: Auto-differentiable and hardware-accelerated force density method." 2022. doi: 10.5281/zenodo.7258292.

[13] G. Wu, "A framework for structural shape optimization based on automatic differentiation, the adjoint method and accelerated linear algebra." arXiv, Nov. 23, 2022. Accessed: Dec. 04, 2022. [Online]. Available: http://arxiv.org/abs/2211.15409

[14] M. Firl, R. Wüchner, and K.-U. Bletzinger, "Regularization of shape optimization problems using FE-based parametrization," *Struct. Multidiscip. Optim.*, vol. 47, no. 4, pp. 507–521, Apr. 2013, doi: 10.1007/s00158-012-0843-z.

[15] P. Block and J. Ochsendorf, "Thrust network analysis: a new methodology for three-dimensional equilibrium," *J. Int. Assoc. Shell Spat. Struct.*, vol. 48, no. 3, pp. 167–173, 2007.

IASS 2023
July 10–14 Melbourne
Integration of Design and Fabrication

Proceedings of the IASS Annual Symposium 2023
Integration of Design and Fabrication
10–14 July 2023, Melbourne, Australia
Y.M. Xie, J. Burry, T.U. Lee and J. Ma (eds.)

Cognitive multi-pattern gridshell design: a method inspired by weaverbirds' nest building strategies

Mohammad Hassan SALEH TABARI[a,*], Günther H. FILZ[a]

[a,*] Universität Innsbruck, Faculty of Architecture, LSU Lightweight Structures Unit
Technikerstrasse 21c, 6020 Innsbruck, Austria
Mohammad.saleh-tabari@uibk.ac.at

Abstract

Elastic gridshells are a sub-category of shell structures, covering long-span with high performance and low materiality using actively bent elements. Our literature review and previous studies revealed some difficulties in integrating spatial grid patterns with multiple purposes such as architectural, environmental, structural, etc. during the form-finding process. Additionally, the possibility of changing the initial parameters such as grid pattern during the form-finding may be helpful to increase the final form variation. Indeed, an approach based on multi-objective integration and the possibility of parametrical change may encourage architects to incorporate these structures more effectively into their designs. Inspired by weaverbirds' nest building strategies and variation in pattern topology, we propose a model as "cognitive form finding" that extracts surface curvature features to identify and apply suitable pattern topologies. Consequently, we link the generated pattern topologies with an interactive physics engine to generate the overall form. In this paper, we implement our proposed method and illustrate its potential in simple geometries. Case studies show the flexibility and impact of significant changes in early-stage decision-making on the final form while staying in a feasible range of structural patterns. Our proposed method aims to increase the influence and flexibility in the early design process of the gridshell and pave the way to increased variations in patterns and final forms.

Keywords: spatial structures, elastic gridshell, geometrical pattern, gaussian curvature, architecture, structural performance, morphology, computer vision

1. Introduction to gridshell design and pattern arrangement

1.1. Gridshell design process

Shell structures are characterized by a curved, often doubly curved, surface. Gridshells, also referred to as lattice shells or reticulated shells, are structures that exhibit the shape and strength of double-curvature shells but are composed of a grid rather than a solid surface. As a result of the differences in the used material, differences in the construction and assembly processes arise. Elastic gridshells are a sub-category of shell structures, and gridshells respectively. They are long-span structures characterized not only by high performance and low material use but also by the continuity of actively bent elements. The generated patterns and the detailing of the intersections influence the visual appearance, the structural performance, and the final form of the gridshell. There are several approaches to designing gridshells [1]. Propose the following approaches a funicular approach, an analytic approach, a combined approach from the previous, and a construction-based approach that nowadays may include fabrication aspects. Funicular gridshells start from a predefined pattern and by inverting the shape of a hanging chain model under self-weight, a pure compression structure is obtained. From a designer's viewpoint [2], this method may restrict the varieties of shell geometries, as they are often resulting in dome-like structures [3]. In this approach, the predefined pattern has to be modified to adopt the surface curvature. The

Copyright © 2023 by Mohammad Hassan SALEH TABARI and Günther H. FILZ. Published in the Proceedings of the IASS Annual Symposium 2023 with permission.

analytic approach defines a grid as a pattern of nodes and lines on a pre-defined surface. Usually, form-finding is nowadays achieved using computers and the surface is defined and mathematically populated with a desired grid. Here, the needed immediate accuracy of the surface geometry and the selected grid may restrict the design freedom. A combined approach between the two approaches is possible and was used for example for the Weald and Downland gridshell. In this case, the gridshell was developed from the architectural concept using physical models. The form-finding of construction-based approaches and processes uses a flat grid and pushes the support nodes toward a desired support configuration, while also pushing the grid upwards. In a repetitive process, various parameters can be adjusted to modify the geometry, overall dimensions, or material limitations. In this approach, the pattern is related to a predefined surface type.

Designing gridshells is closely related to form-finding, which describes the process of defining the shape of a structure featuring a complex geometry. However, geometry and structural aspects are in a direct relationship, when dealing with form-finding processes of spatial lightweight structures. Usually considered a core competence of engineering, such approaches are mostly problem-solving-oriented, where results are evaluated by comparison with pre-defined requirements [4]. However, an increased variety in designs may be achieved, if early-stage parameters, including the pattern topology, can be considered and flexibly changed during the process of design. Based on our previous research on the relation between the surface curvature and the pattern in gridshell design, we can conclude that potentials/weaknesses of changing the pattern locally over the surface were not yet fully explored.

1.2 Morphology as a response to design criteria

In nature, birds more specifically weaverbirds, are fascinating craft experts who build their nests. Studies revealed that they have differentiation in their nest pattern morphology that helps them to be adapted to the environment (Figure 1). Male examples have low to no repeatability of the morphology [5] , because individual builders modify their behavior depending on their experience/environment [6]. The final surface geometry of the nest is roughly defined for the birds [7] and they construct it with various materials [8], arranging it in a specific order [9] based on cognitive selection [10]. Weaverbirds' nest-building method is hierarchical in a way that when a piece of material is failed to stick on the initial push they often shift to some other spot and try again [8]. The trial-and-error process of weaverbirds helps them to learn how to locally adjust the nest morphology while constructing it. This strategy of changing morphology as a response to reach adaptation is worth more investigation to be applied in architectural design. Gridshells as structural forms have great potential to implement the weaverbird's morphology change strategy responding to the design criteria.



Figure 1. Weaverbirds has cognition of the surface that they want to build and arrange the material to build the target surface [10].

1.3 Pattern morphology control

This research aims to provide a new method of gridshell design, inspired by weaverbirds' strategy, with the potential for local adjustment in the form-finding process. This method could result in an adaptive design. From a systematic point of view on the gridshell design process, starting from a shape so-called "shape-first" follows the top-down approach, while starting with a pattern of elements so-called "pattern-first" follows a bottom-up approach [11]. We are looking for a new method, which is a mixture of both of them in the design process. Naturally designed models are operationally neither formed entirely top-down nor bottom-up [12]. In our research, we hypothesize this mixture is a key point to achieving

adaptive form-finding. The mixed method of bottom-up and top-down results in a design process where the final form is the result of multiple sub-processes equilibrium that has converged internally and interacted with the whole afterward. Therefore, the formation of form follows the theory of systems having a micro-macro effect [13–19], which is not organized by itself like self-organizational models [19, 20]. The essential properties of such systems are the increase in order [15, 16, 19, 21], no external control, and adaptability [19]. Adaptability can find different target goals based on the design perspective such as sustainability, economics and etc. If we have a design concept that has characteristics of adaptation, as we propose here, then we can set various target goals and set up the design process. More potentials will be explained by examples in the last chapter. In order to reach the explained goal, we implemented multiple investigations that are presented in this paper. Firstly a deep computer vision [22, 23] method has been applied to our gathered dataset [11]. The possibility of pattern prediction based on surface curvature change and new pattern generation with a deep learning model has been investigated and is presented in the chapter3. The results of the experiments guided us to develop a smart computational design environment that we call pre-informed geometry modeling and is presented in chapter 4. Following chapter 2 presents some basic geometrical definitions and general terminologies before getting deeper into the investigations. Finally, the potential of our developed method and future vision is provided.

2. Surface morphology and pattern curves

As mentioned in the first chapter, gridshells are structural forms composed of continuous elements. Therefore, in computational geometry, their surface is often considered a smooth surface [24]. The changes in the surface curvature are mostly depending on the curves on it [25]. Individually evaluated curves on a surface can be analyzed by the coordination system of the curve direction vector as X direction, the surface normal vector as Z direction, and the third axis perpendicular to them as Y [25, 26]. Figure 2 represents the two principal curves on an exemplary surface, Kg, Kn, and Tg at a single point on the interaction of two curves. By evaluating a series of points on the domain of each curve on a surface, we can measure the geodesic torsion Tg, normal curvature k, and geodesic curvature T over the curve [27, 28]. Information of Tg, Kn, and Kg indicate that any deformation of the surface has a direct effect on the curves of the surface, and consequently on the pattern morphology and vice versa.

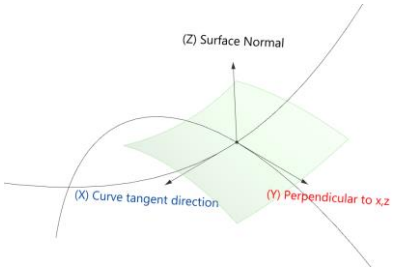


Figure 2. The local coordinate system of a certain point on a curve of a surface. Rotation of the curve around axis (Z), surface-normal direction, at an evaluated point, causes a change in geodesic curvature represented as Kg. Rotation of the curve around axis (X), Curve tangent, at an evaluated point, causes a change in geodesic torsion represented as Tg. Rotation of the curve around axis (Y), at an evaluated point, causes a normal curvature represented as Kn.

2.1 Surface types based on curvature

With the measurement of the Gaussian Curvature “K” and Mean Curvature “N” [29] of surfaces it is possible to divide surface types into three main categories monoclastic, synclastic, and anticlastic [30]. Figure 3 shows an example of these three surfaces. Synclastic surfaces have the same direction in both principal curvatures throughout the surface. For a synclastic surface, in a case where the surface curvature is constant in all points, the surface shape is that of a sphere dome (Figure 3-a). Monoclastic surfaces, also known as zero-Gaussian curvature surfaces, have zero curvature in one direction. Figure 3-b shows an example of half of a cylinder monoclastic surface. Anticlastic surfaces, in contrast, have

one positive and one negative principal curvature throughout the surface (Figure 3-c). Additionally, a surface is considered constant mean curvature (CMC) [31] when it has constant, equal principal curvature across all points. Minimal surfaces and sphere domes are examples of CMC surfaces. Figures 3-a and 3-c are members of CMC surfaces. Architectural designers do not necessarily want to have a form composed of only one surface type. In fact, sometimes design concepts are free-form surfaces that consist of multiple surface types. Figure 12 shows 4 free-form surfaces. Lacking attention to the designed surface curvature variation causes problems in realization. These problems are usually solved by changes in the concept design or additional support structures.

In the following explanation, we consider geometry modeling in centimeter metric with 4 decimal thresholds. In order to understand the surface type, we developed an algorithm that divides a surface by a distance of 1cm and evaluates the Gaussian curvature and mean curvature on each point. For a given surface the developed script calculates mean and Gaussian curvature for all evaluated points on a surface and generates two 1-dimensional vectors that we call respectively "Mean Curvature Vector", and "Gaussian Curvature Vector". If the Gaussian curvature vector of a surface is all zero it means the surface is monoclastic. If all of the Gaussian Curvature Vector values have a positive sign, the surface is synclastic. If the Gaussian Curvature Vector has a negative sign, then the surface is anticlastic. If the Mean Curvature Vector of a surface has a constant value the surface is CMC type. From this part of the paper, we consider three colors to show the surface curvature type; blue for synclastic surface, orange for monoclastic surface, and green for anticlastic surface type.

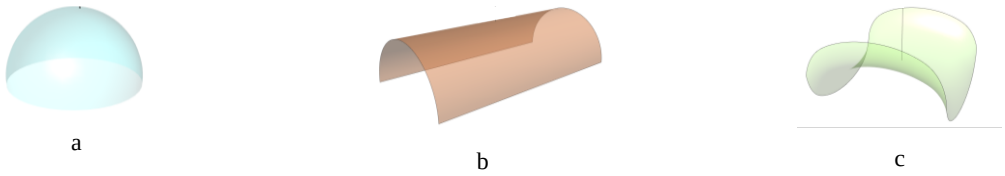


Figure 3. Three surface types based on curvature, a: sphere dome with Synclastic surface, b: Half of a cylinder surface with Monoclastic type, and c: Minimal surface with Anticlastic surface type.

2.2 Curves on a surface

In this paper, we consider three categories of curves on a surface to generate a pattern:

A. Geodesic lines: Given a regular surface M, a geodesic curve x is the shortest path between two points on a surface, with constant geodesic curvature kg=0 [27, 28]. Geodesic lines apply to any type of surface (Figure 4-a)
B. Asymptotic curves: Given a regular surface M, an asymptotic curve is formally defined as a curve x on M with constant normal curvature kn= 0 in the direction of x tangent for all domains of x. Asymptotic curves only exist on Anticlastic surface regions [27, 28] (Figure 4-b).
C. Principal curves: Given a regular surface M, a principal curve is formally defined as a curve x on M with constant geodesic torsion Tg= 0 in all domains of x [27, 28]. Principal curves exist on all surface types (Figure 4-c).

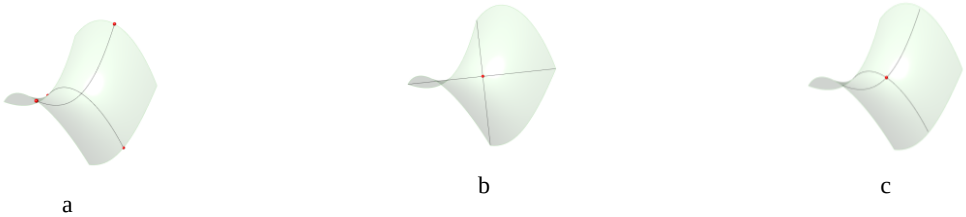
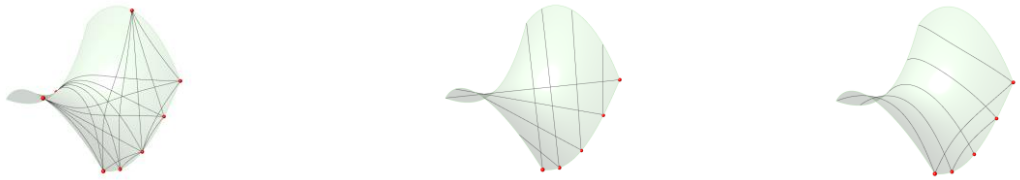


Figure 4. Three categories of curves on a surface, a: Geodesic lines from 2 pairs of points on a minimal surface, b: Asymptotic lines in 2direction of one point on the center of a minimal surface, and c: Principal lines in 2direction of one point on the center of a minimal surface.

2.3 Pattern of curves on a surface

For the sake of explanation, we assume an anticlastic surface (Non-Rational B-Spline Surfaces) M as a design concept geometry. With the evaluation of two pairs of points on the M domain, it is possible to generate geodesic lines in between them. The pair points coordination, the topology of start and end-points, and surface curvature affect the pattern morphology. Figure 5-a shows a sample pattern of geodesic curves on a surface with 5 points on one edge of each of them is connected to all individual points on the other edges. Because surface M is anticlastic, with an evaluation of a series of points it is possible to generate a pattern with asymptotic curves. Figure 5-b shows the pattern of asymptotic curves starting from 5 points on one edge of a surface. With the same series of points on M, it is also possible to create a pattern with principal curves. Figure 5-c shows the pattern of principal curves starting from 5 points on one edge of a surface. In both principal curves and asymptotic patterns surface curvature and point set coordination effects the pattern morphology.

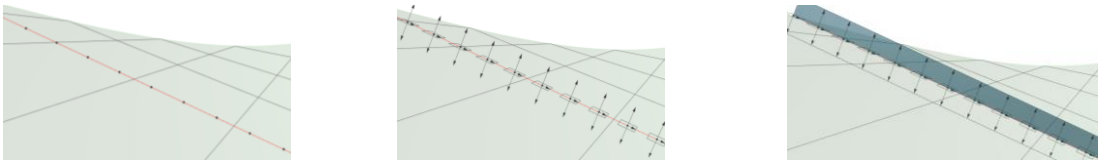


a b c

Figure 5. Patterns of curves on a surface, a: Geodesic lines with a topology of 3 start points on the first three edges and 5 end points on a 4th edge, b: Asymptotic lines with 5 points on a 4th edge, and c: Principal lines with 5 points on a 4th edge.

2.4 Adding profile to curves

It is possible to numerically add a profile to a curve on a surface based on its curvature features (Kg, Tg, and Kn) following the ruled surface [26] method. For a given curve on a surface, evaluate a number of points on the curve, and equally move them on both sides along their local surface normal vector. The result is two series of points above and beneath the surface. Connecting each point series as a spline curve gives us the two edges of the profile. Figure 6 shows the point movements and profile edges generation for a segment of an exemplary curve. The change in the length of the normal vector changes the profile width. If the initial curve is a geodesic line then the edges must be rotated over the curve's tangent direction axis by 90 degrees to lie on the surface. For an asymptotic curve there is no need for any rotation, and the associated profile aligns with the curve´s surface normal. For a principal curve type, rotation over the curve must guarantee a torsion-free profile.



a b c

Figure 6. Generating profiles on a surface, a: select a curve on a surface, b: evaluate a series of points on the curve and move them on their local surface normal vector on 2 sides, and c: generate spline curve form each series of points and generate a ruled surface between them.

3. Data analysis for cognitive pattern setting

With the scope of this paper, we re-evaluated our previous dataset [11]. This data-set consists of 980 NURBS surfaces and a pattern of curves on them. We developed a local rendering pipeline to export the NURBS surface as a matrix of numbers, in four steps. (i) Orient all surfaces on the xy plane in a way each one has the maximum footprint that touches the XY plane. (ii) Generate a bounding box that contains all oriented surfaces. (iii) Divide the rendering frame into a grid of 128 rows and columns. (iv) Move each point of the grid point in the Z direction with the length of the bounding box height.

For bounding box generation, Figure 7-a shows all oriented surfaces on the XY plane and the bounding box contains them all inside. A face of a bounding box on the XY plane that includes all surfaces inside itself is the reference rendering frame. With regards to the Z direction, if a point intersects a surface, the distance between the intersection point and the grid point is the normal displacement value. Figure 7-b shows the rendering frame grid points. The arrow in Figure 7-b shows the direction vector to move points for the intersection. The points that have an intersection with a surface along the Z direction are displayed in green color. Otherwise, if there is no intersection for a point of a grid the normal displacement value is zero. The result is an array matrix with a size of 128*128*1 that represents a surface as a numerical value. We do the same process of orientation for the surface pair pattern curves as well. We divide curves into 100 segments, map the segment points on a reference rendering frame and find their closest point on the frame. The points of the frame that are selected gain a value of 1 and others take a value of 0. The result is an array matrix with a size of 128*128*1. Figure 7-c shows the pixelization of a pattern in a render frame. Both matrixes are remapped between a value of 0.0 to 255.0 to be represented as an image for visualization. Considering the data conversion as a custom rendering pipeline we can easily serialize the numerical data in JSON, PNG, or CSV format and export. We developed an automated code using Rhino.Compute to export all data as dictionary objects to the MongoDB database.

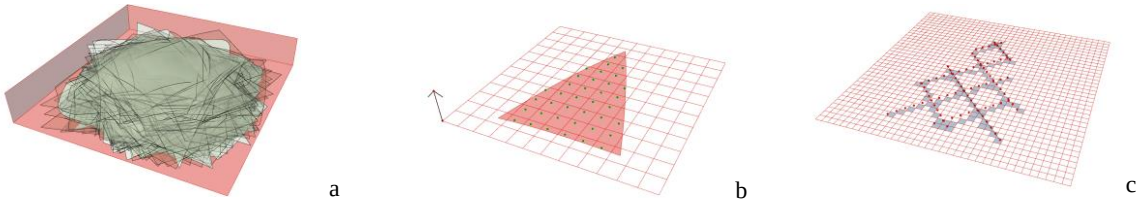


Figure 7. Data set for surfaces and patterns, a: the bounding box with all 980 oriented surface segments inside, b: the rendering frame grid points, c: the pixelization of a pattern in a render frame.

3.1. Deep exploration

Once we have geometrical data as numerical matrixes, it is possible to analyze them with computer vision methods. First, we use a mixed algorithm of a deep neural network and PCA [32, 33] to reduce the data dimensions and cluster them with K-Means clustering afterward. For the neural network, we use a pre-trained VGG-16 [23] network from tensorflow.keras backend. We check the feature maps of VGG-16's models each layer on several random pattern inputs and find that the first 12 layers are enough for the machine to understand the curves' direction and pattern. VGG-16 model converts the input pattern into a vector with the size of 40060 after 12 layers. Figure 8-b shows the feature maps captured from the network in layer 12. We then use the PCA model to find suitable potential features out of 4060. After some experiments with k-Means clustering, we find 200 features effective. As a result, we have a dataset with a size of 980 *200. The unsupervised k-Means clustering results in the three features curve orientation, free endpoints, and density. Figure 8-a shows the clustering results samples. In the second step, we trained a VAE [34] model to check if is there any potential in the provided data of the literature to have a new generation of the pattern out of it. VAEs have the potential to both generate new data and analyze the data [35]. The generated patterns of the trained model do not necessarily follow the curvature features suitable for a specific surface type.



cluster 0 oriented patterns with lower density and more free end points	cluster 1 mostly perpendicular patterns with low density and more free end points	cluster 2 oriented patterns with higher density and less free end points	cluster 3 mostly perpendicular patterns with higher density and more less end points

Figure 8-a. Clustering with a pre-trained VGG model and PCA with 500 features.

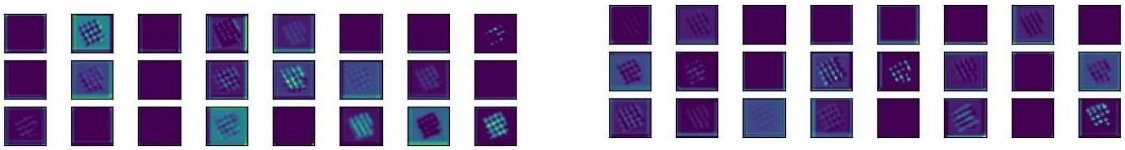


Figure 8-b. 48 feature maps of a pattern in layer 12th of the VGG-16 model.

Figure 9. shows the generated latent space in two dimensions. The point structure of the latent space of the VAE model represents a Fibonacci sequence, which could mean there is a hierarchical structure in the data, where each data point is composed of smaller sub-components. It means the patterns are a subset of each other and therefore it is hard for the machine to find significant differentiation to create new patterns from them.

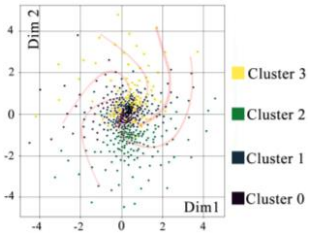


Figure 9: The latent space of the VAE model mapped on 2 dimensions.

3.2 Result of the investigation

One of the main problems is the complexity of knowing how easy it is to fabricate the predicted pattern. Because the data input does not have curvature features related to the surface, results require post-evaluation. In post-evaluation, the curves will be checked if they work to align the surface curvature or result in large unexpected deformation. The process to make the model robust is as follows:

1) Combine the already gathered dataset with a collection of the elastic gridshells pattern images
2) Combine a new set of elastic gridshell surfaces and patterns with newly generated models
3) Train a model with newly added data with an additional evaluation engine to check the machine-generated data and add a new dimension to the latent space matrix to inform the system if the pattern is suitable or not.

Because in this research, we are looking for a method to reach results that are easy to be built and have standard features as an architectural geometry, the result of the experiments recommends us to a pre-informed modeling. In pre-informed modeling, we generate new data in a specific order that helps us to involve the curve and surface geometrical features in training. The next chapter explains the primary development of this method.

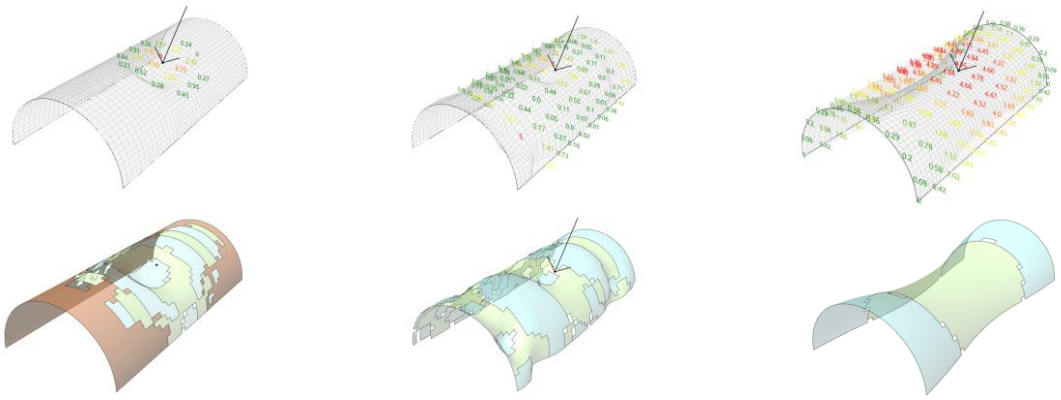
4. Smart pre-informed modeling

The pre-informed modeling environment is where not only the designer generates the surface geometry, but also can see the generated surface features, have design hints about patterns applicable on a surface, add physical behavior, and generates a form. In this chapter we first explain the method we used to make the design environment geometrically informed and afterward, we show some case studies of modeling in such a system, finally, we will discuss the potential of our developed model and what features we will add to it in the future. In our method we equipped the CAD environment with a smart assistant with the following features:

1) Identifies the surface geometry and gives the summary of the possible patterns that the surface locally can have.
2) Provides the utilities to deform the surface geometry precisely to have meaningful curvature variation.
3) Merges the patterns, adds profiles, and defines the final form.

4.1 Meaningful surface deformation

We developed a surface deformation workflow in grasshopper3d to change the surface Gaussian curvature vector. It is possible to evaluate several points on the initial surface and apply push or pull to them. The surface is sub-divided to generate grid points. It is possible to define the percentage of the grid points to be affected by the implied force and control the weighting of the force on the select points with a Bezier graph. Push means deformation is in direction of the surface normal at the evaluated point, otherwise, it is in the opposite of the normal direction. Figure 10 shows how changing push-force-vectors and weights result in various deformation. Figure 10 illustrates how the weight of the force and its distribution affects the numbers of unique curvature type segments, their size, and gradient changes in the generated free-form surface Gaussian curvature vector.



a b c

Figure 10. Deformations on a surface, a: pushing deformation on a low number of points but intense weight, b: pushing deformation on a higher number of points with cosine weighting distribution, and c: pushing deformation on a higher number of points with cosine weighting distribution.

After explained surface deformation the Gaussian curvature vector is updated. The Gaussian curvature vector matrix then is checked with the Density-Based Spatial Clustering (DBSCAN) model [36]. The DBSCAN is an unsupervised model of machine learning that based on element density checks a vector and makes sub-clusters. The Gaussian curvature vector consists of elements with negative (represents anticlastic region) and positive (reparents synclastic region) signs. Therefore, the result of the DBSCAN is a subset of regions of the surface with different curvature types. Checking the surface Gaussian curvature vector update, after deformation, gives us useful information. For example, a surface with multiple fluctuations on the curvature vector (previous figure middle) has a geodesic curve with various geodesic torsion and normal curvature. Various change in these two parameters results in the complexity to find a suitable profile direction for the strip for fabrication. Figures 11-a and b show the effect of surface deformation on a geodesic line in the middle of Figures 10-b and 10-c surfaces.

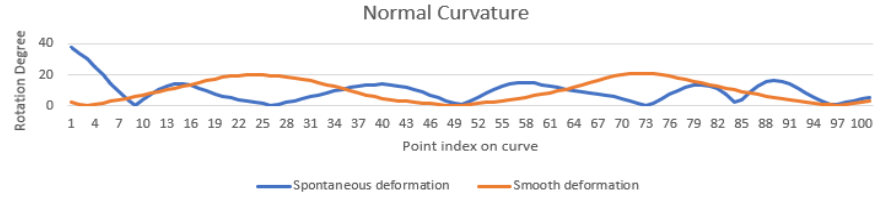


Figure 11-a. The changes of the normal curvature over a geodesic line in the middle of Figures 10-b and 10-c surfaces. The orange curve represents the curve in Figure 10-c and the blue curve is on the curve on Figure 10-b.

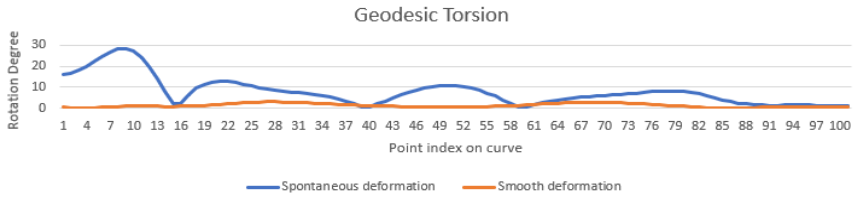


Figure 11-b. The changes of the geodesic curvature over a geodesic line in the middle of Figures 10-b and 10-c surfaces. The orange curve represents the curve in Figure 10-c and the blue curve is on the curve on Figure 10-b.

It is possible to split the deformed surface into multiple surface segments based on the DBSCAN results on the Gaussian curvature vector. Each segment has a specific curvature type with specific curve parameters. The segment numbers, outline, maximum/minimum curvature deviation, and sizes affect the pattern morphology and the final form. Integrating the deformation method with DBSCAN makes it possible to check the four aforementioned parameters in real time and visualize them. This visualization helps to be aware of the changes in surface curvatures and provides more control. Figure 12 shows an example of surface deformation on the original monoclastic and anticlastic surfaces that results in different segmentations. In this case, we can control surface regions' Gaussian Curvature Vectors to reduce the complexity in adding the profile.

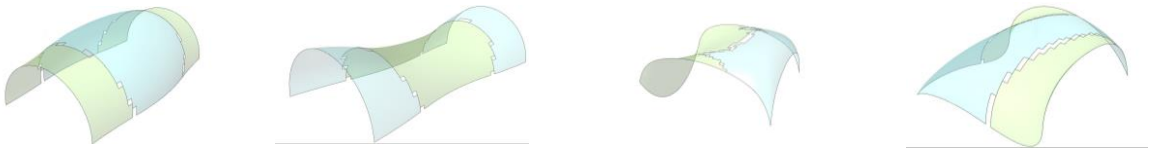


Figure 12. Surface deformations. 2 left figures are pulling and pushing deformation on a monoclastic surface. 2 right surfaces are pulling and mix of pull and push on an anticlastic surface.

Figure 12 illustrates how a simple change in direction of deformation changes the surface regions. The first two surfaces from the left in Figure 12 are generated by pulling and pushing the surface from the center. While pulling results in 1 synclastic and 2 anticlastic surfaces, pushing changes them to 1 anticlastic and 2 synclastic at the edges. Having an anticlastic region in the center means that we can have elements perpendicular to the surface and having synclastic makes it more relevant for elements tangential to the surface. Based on the geometrical theories explained in chapter 2, we can check the surface regions to understand the feasible patterns on them. Because of the parametric deformation and real-time feedback on the Gaussian Curvature Vector update, it is also possible to define preferred surface region changes as an objective for surface deformation and generate multiple variations. Figure 13 shows an example of controlling the surface deformation with a target of reaching 2 anticlastic at corners and one synclastic in the center with our developed method.

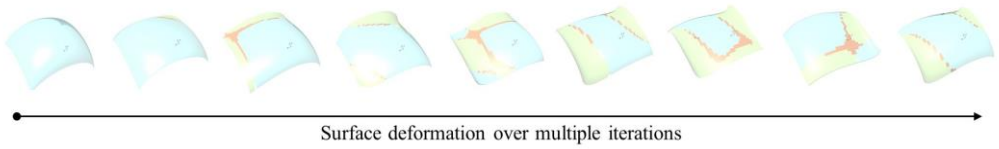


Figure 13. Unsupervised form-finding with an objective of having 2 anticlastic and one synclastic surface region.

4.3 Merging the patterns and final form-finding

Once we have finalized the surface based on each surface region's surface type, we can arrange their patterns. The final step is to merge the multiple region patterns to have continuous members on the surface. Figure 14 illustrates an example of a setting pattern on 3 regions of our deformed surface from Figure 13.

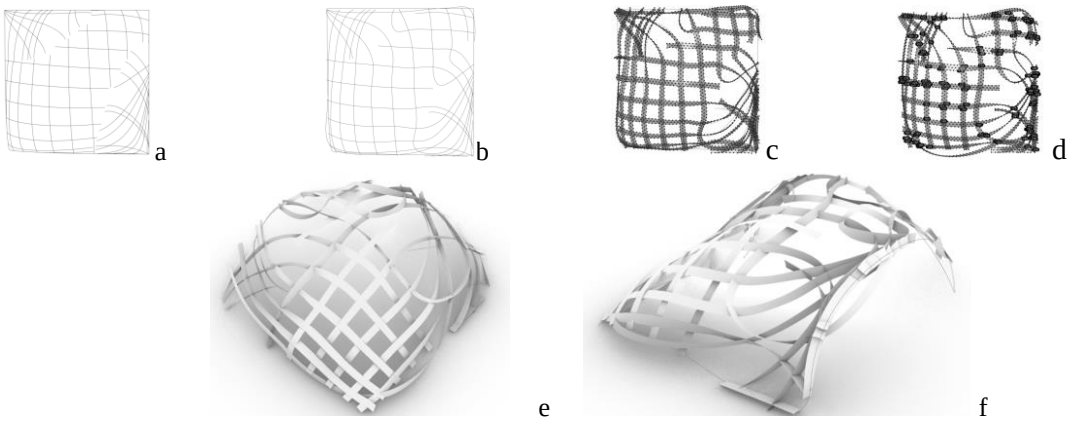


Figure 14. a. Set a pattern for each surface region. Here because two sides are anticlastic regions asymptotic curve is applied. In the center region simple grid pattern with geodesic lines is applied. b. merging different pattern curves to make continuous curve elements. c. adding a profile to curves based on their curvature properties. d. defines connection and anchor points for dynamic relaxation. e and f. finalized form-finding.

To merge patterns, we developed an algorithm that connects the different regions' pattern curve endpoints. If endpoints are in a distance of less than 3.5 cm they will be connected. Depending on starting from what region first, the order of connection will be different. Each node can select one neighbor. Therefore, the region that the connection is started from has more options in neighbor selection. Figure 15 b. shows a second possibility of merging the pattern on the surface of Figure 14. It is possible to add or remove connections afterward manually. Because after merging patterns curves' curvature will be modified, the rotation of the profile on them is not constant. Depending on which region of synclastic or anticlastic a part of the curve is its profile has a rotation of 90 degrees (geodesic line) or 0 degrees (asymptotic curve). We developed an algorithm to automatically find connections between mesh elements where pattern curves had intersected. It is possible to add and remove the connection afterward manually as well. Figure 14 d shows the connections between the profile meshes before dynamic relaxation. Kangaroo physics engine is used for dynamic relaxation.

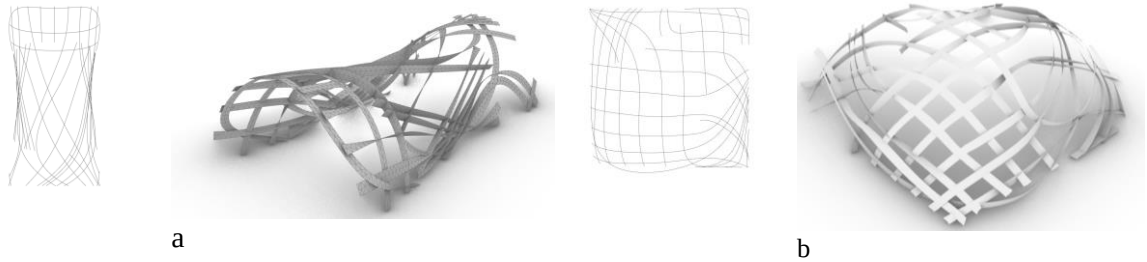


Figure 15. Multi-pattern form finding examples, a: application of method on a deformed monoclastic surface, b: change in pattern merge of the previous surface.

5. Discussion

Clearly, there are some technical issues, limitations, and errors we faced during this project so far. To control the surface deformation, we use an optimization approach that evaluates the deformation based on 2 parameters, the number of regions with different curvature types, and the area of each region. Therefore, the process is iterative and presently adds time and computational cost to the design process. With automated data generation, it is possible to generate a dataset of deformed surfaces based on set requirements. We are able to train a model based on the generated data to increase the speed and variation in this part. In order to split the surfaces, we consider surface curvature regions at the moment, while it is also possible to have segments with a mixture of curvatures to start from. We may develop an interactive space where designers either can select the region manually or have variations and/or a

mix of curvatures as well. The dynamic relaxation methods we used has some inaccuracies. The observed inaccuracy may be argued by the mesh segmentation that affects the bending behavior. The mesh segmentation also has an effect on the connection of elements as well. We will adapt our algorithm that connects the mesh elements to reduce the unexpected error of mesh crossover.

6. Potential of the cognitive method and future works

In this project, we set up the design process from a geometrical perspective. We created gridshells without repetitive geometry. When looking at the figures that are shown in Figure 14 and 15, it is obvious that we currently manage to generate and find geometrical solutions between different patches and their patterns. Usually gridshells are highly efficient spatial structures with optimized material use. Even though, they are generated by physics engines at least under gravity load, our geometries are presently neither structurally evaluated nor optimized. We are aware, that proposed geometries may not meet a grade optimization of a uniform mesh, which on the other hand comes at the cost of design freedom. As mentioned earlier, the proposed method creates a process with possibilities of adaptation and interactive workflow. The reverse of such a method is starting from the designers´ perspective and their design goals. In this case, the geometrical analysis and interaction have to be found and to be interactively proposed for the intended design concept. In our ongoing research, we are developing a model that learns from earlier experiments to provide geometrical and structural solutions that meet the design intent and purposes. In our future work, we will firstly clarify and improve the above-mentioned issues. Secondly, we will develop a model that learns from crafting similar to what weaverbirds do in their learning process. The benefit of such a model is to pave the use of gridshell for non-uniform concept designs. Indeed, architects will experience more design freedom and generate advanced geometrical forms through interactive design processes.

References

[1] D. Naicu, R. A. Harris, and C. Williams, “Timber Gridshells: Design methods and their application to a temporary pavilion,” pp. 10–14, Aug. 2014.
[2] P. Block, T. Van Mele, M. Rippmann, and N. Paulson, “Beyond Bending: Reimagining Compression Shells, Edition Detail,” 2017.
[3] M. Miki and T. Mitchell, “Interactive Exploration of Tension-Compression Mixed Shells,” 2022.
[4] S. Ylirisku and G. H. Filz, “Resolving 7 Tensions in-between Design and Engineering Education: Cases for Reflective Studio Practice,” in *Asociación Española de Ingeniería Estructural, 2018.*
[5] P. T. Walsh, M. Hansell, W. D. Borello, and S. D. Healy, “Repeatability of nest morphology in African weaver birds,” *Biology letters*, vol. 6, no. 2, pp. 149–151, 2010.
[6] P. T. Walsh, M. Hansell, W. D. Borello, and S. D. Healy, “Individuality in nest building: do southern masked weaver (Ploceus velatus) males vary in their nest-building behaviour?,” *Behavioural processes*, vol. 88, no. 1, pp. 1–6, 2011.
[7] N. E. Collias and E. C. Collias, “An Experimental Study of the Mechanisms of Nest Building in a Weaverbird,” *The Auk*, vol. 79, no. 4, pp. 568–595, 1962.
[8] L. M. Guillette and S. D. Healy, “Nest building, the forgotten behaviour,” *Current Opinion in Behavioral Sciences*, vol. 6, pp. 90–96, 2015.
[9] M. Hansell and R. Overhill, *Bird Nests and Construction Behaviour*: Cambridge University Press, 2000.
[10] I. E. Bailey, K. V. Morgan, M. Bertin, S. L. Meddle, and S. D. Healy, “Physical cognition: birds learn the structural efficacy of nest material,” *Proceedings of the Royal Society B: Biological Sciences*, vol. 281, 2014.
[11] F. Khojastehmehr, M. H. Saleh Tabari, and G. H. Filz, “A review on the curvature and geometrical patterns of elastic gridshells: exploring structural and architectural potentials,” in *IASS Beijing Symposium: Proceedings of IASS Annual Symposia*, 2022.

[12] P. Nicholas, D. Stasiuk, and T. Schork, "The social weavers: considering top-down and bottom-up design processes as a continuum," in *ACADIA, Proceedings of the 34th Association for Computer Aided Design in Architecture*, 2014.
[13] G. Nicolis, "Physics of far-from-equilibrium systems and self-organization," in *In The new physics*, 1993.
[14] J. Crutchfield, "Is anything ever new? considering emergence.," in *SANTA FE INSTITUTE STUDIES IN THE SCIENCES OF COMPLEXITY-PROCEEDINGS*, 1994.
[15] F. Heyligen, "Self-organization, emergence and the architecture of complexity," in *Proceedings of the 1st European*, 1989.
[16] F. Heyligen, "The Science of Self-Organization and Adaptivity," *The encyclopedia of life support systems*, vol. 5, pp. 253–280, 2002.
[17] J. Odell, "Objects and Agents Compared," *TheJournal of Object Technology*, pp. 41–53, 2002.
[18] H. van Dyke Parunak and S. Brueckner, "Entropy and self-organization in multi-agent systems," in *Proceedings of the fifth international conference on Autonomous agents*, 2001.
[19] T. de Wolf and T. Holvoet, "Emergence Versus Self-Organisation: Different Concepts but Promising When Combined," in *Engineering Self-Organising Systems: Methodologies and Applications*, 2005.
[20] M. Dempster, "A Self-Organising Systems Perspective on Planning for Sustainability," Ph.D. Thesis, University of Waterloo, School of Urban and Regional Planning, 1998.
[21] C. Shalizi, *Causal Architecture, Complexity and Self-Organization in Time Series and Cellular Automata, 2001*.
[22] J. Chai, H. Zeng, A. Li, and E. W. Ngai, "Deep learning in computer vision: A critical review of emerging techniques and application scenarios," *Machine Learning with Applications*, 2021.
[23] K. Simonyan and A. Zisserman, "Very Deep Convolutional Networks for Large-Scale Image Recognition," *arXiv preprint*, 2014.
[24] J. M. Sullivan, "Curvatures of Smooth and Discrete Surfaces," *Discrete differential geometry*, 2007.
[25] E. Schling and R. Barthel, "Repetitive Structures," in *Proceedings of the Design Modelling Symposium*, 2020.
[26] C. Tang, P. Bo, J. Wallner, and H. Pottmann, "Interactive Design of Developable Surfaces," *ACM Trans. Graph.*, vol. 35, no. 2, pp. 1–12, 2016.
[27] E. Schling, D. Hitrec, and R. Barthel, "Designing Grid Structures Using Asymptotic Curve Networks," in *Humanizing Digital Reality: Design Modelling Symposium*, 2017.
[28] C. Tang, M Kilian, P. Bo, J. Wallner, and H. Pottmann, "Analysis and design of curved support structures," in – *Advances in Architectural Geometry*, 2016.
[29] M. Garman and J. Bonnie, *Curvature of Surfaces in 3-Space*: Maryland Shared Open Access Repository, 2009.
[30] R. Naboni, S. Sartori, and L. Mirante, "Adaptive-Curvature Structures with Auxetic Materials," *Advanced Materials Research*, vol. 1149, pp. 53–63, 2018.
[31] J. M. Sullivan, "A Complete Family of CMC Surfaces," Dec. 2004.
[32] I. T. Jolliffe and J. Cadima, "Principal component analysis: a review and recent developments," *Philosophical transactions. Series A, Mathematical, physical, and engineering sciences*, 2016.
[33] L. Smallman and A. Artemiou, "A Literature Review of (Sparse) Exponential Family PCA," *Journal of Statistical Theory and Practice*, pp. 1–19, 2022.
[34] D. P. Kingma and M. Welling, "Auto-Encoding Variational Bayes," 2013.
[35] G. Mirra and A. Pugnale, "Comparison between human-defined and AI-generated design spaces for the optimisation of shell structures," *Structures*, vol. 34, pp. 2950–2961, 2021.
[36] M. M. R. Khan, M. A. B. Siddique, R. B. Arif, and M. R. Oishe, "ADBSCAN: Adaptive Density-Based Spatial Clustering of Applications with Noise for Identifying Clusters with Varying Densities," in *2018 4th International Conference on Electrical Engineering and Information & Communication Technology (iCEEiCT)*, 2018.

Proceedings of the IASS Annual Symposium 2023
Integration of Design and Fabrication
10–14 July 2023, Melbourne, Australia
Y.M. Xie, J. Burry, T.U. Lee and J. Ma (eds.)

Computational conceptual design – typological exploration of spatial truss systems through optimization

Jonas WARMUTH*, Pierluigi D'ACUNTO[a], Corentin FIVET[b]

* Structural Xploration Lab, Ecole Polytechnique Fédérale de Lausanne (EPFL)
Fribourg Switzerland, Passage du Cardinal 13B, CH-1700 Fribourg
jonas.warmuth@epfl.ch

[a] Professorship of Structural Design, Technical University of Munich, Munich, Germany
[b] Structural Xploration Lab, Ecole Polytechnique Fédérale de Lausanne (EPFL), Fribourg Switzerland, Passage du Cardinal 13B, CH-1700 Fribourg

Abstract

Exploring a wide range of design options is crucial for every sound conceptual design process. In the conventional structural design workflow, optimization techniques are generally employed to generate well-performing design options. However, focusing only on performative criteria may result in a lack of design exploration and diversity, narrowing down the design brief too early and neglecting essential aspects beyond pure performance. In response, this paper introduces a new method for the generation of structural forms that emphasizes both performance and the exploration of a diverse set of design briefs. The method employs layout optimization in a new way and aims to find close-to-optimal yet diverse structures. First, a parametric ground structure is generated. Second, this ground structure is used to produce a structure in equilibrium based on different user-defined goals. By varying ground structures and balancing the different goals, the method produces a series of designs that are both diverse and well-performing. The applicability of the method is demonstrated through several case studies. Results show that this method allows for the real-time generation of multiple design options, including both well-known and less well-known, but not less valid, typologies. Using this approach, designers can move beyond the limitations of established typologies and explore a new variety of structural forms.

Keywords: computational design, design exploration, interactive design, conceptual design, layout optimization, form-finding

1. Introduction

Traditionally, the process of designing structures involved reliance on hand-sketches, physical models, and well-established typologies. With advancements in computational power this process was extended to include digital format. As a result, designers have been enabled to integrate geometric and performance metrics in the design.

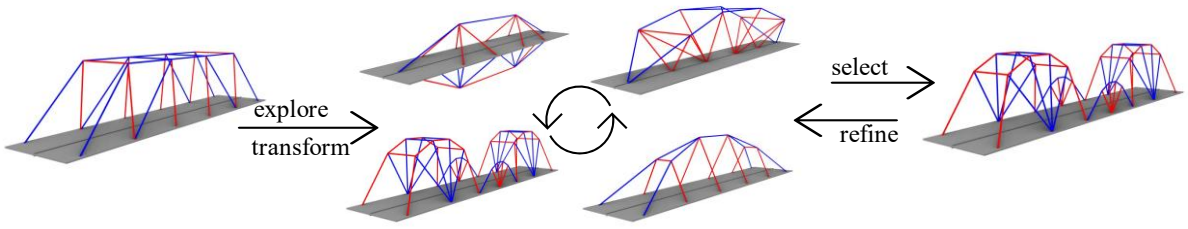


Figure 1. Designing structures by transformation operations and layout optimization

Copyright © 2023 by Jonas WARMUTH, Pierluigi D'ACUNTO and Corentin FIVET. Published in the Proceedings of the IASS Annual Symposium 2023 with permission.

Computational design has opened up a new realm of design possibilities, where feedback on an intended design is instantly available, leading to an entirely new approach of exploring and designing structures. This also brought the benefit of generating a significantly larger number of design alternatives, thereby expanding the design space and promoting exploration. With these increased possibilities, the fundamental goals of conceptual structural design could be addressed more effectively – exploring structures beyond pre-defined catalog types while ensuring adequate performance.

1.1 Related work

In this regard, computational tools have been developed to assist designers in this task. Typically, so called meta-heuristic optimization methods, such as genetic algorithms, have been employed to explore structural forms. An early example is ParaGen [1] by von Buelow. This tool operates on structures whose topology is predefined. The evolutionary exploration mechanism controls nodal coordinates and imposes the nodes' relocation until specific design criteria are satisfied. Mueller and Ochsendorf [2] contributed to the development of performance-informed design, which resulted in the creation of StructureFit. This approach employs genetic algorithms to enable designers to investigate and enhance design candidates by selecting parents for crossover and mutation. The topology of the design candidates is determined by the designer's input, with the examples presented in a 2D format. Harding and Shepherd [3] worked on meta-parametric design, resulting in Biomorpher [4], a plug-in for Grasshopper that employs interactive genetic algorithms to explore and optimize any parametric definition created by the designer. Mirtsopoulos and Fivet [5] presented a generative approach based on grammar rules and combined it with the interactive genetic algorithms in Biomorpher. A major advantage of employing meta-heuristic optimization algorithms is their capability to handle a diverse array of problems due to their independence from differentiable (in-)equations. Nonetheless, a significant challenge associated with their use is that the underlying computations may lead to computationally expensive procedures. More recently, a generative structural design workflow has been proposed that integrates the Combinatorial Equilibrium Modelling form-finding method [6] with a machine-learning-based clustering technique to facilitate the exploration of multi-dimensional spaces of structural design solutions [7]. While these methods can provide good solutions, it is essential to carefully balance design constraints to ensure practical outcomes. If constraints are excessively rigid, it may hinder design exploration. Furthermore, the process of generating results is a black box, making it challenging to establish a clear link between input and output. Regarding performance only, mathematically sound optimization techniques are often used to generate well-performing structures. He et al. [8] have proposed a computationally efficient optimization framework, in which a linear programming truss layout optimization is employed to generate close-to-optimal designs. Park et al. [9] discussed the potential use of layout optimization at the conceptual design stage. Both methods utilize optimization routines as a primary means of generating design alternatives. However, relying solely on optimization techniques can lead to prematurely narrowed designs, without sufficient exploration of other alternatives. This can result in an excessive focus on optimization itself, which may be appropriate for pure engineering tasks, but may not allow for sufficient exploration of structural forms when other factors beyond performance are important, as it is the case in the conceptual design stage.

1.2 Contributions

Optimization approaches can still be beneficial if they are integrated as sub-routines within a broader design process. Therefore, this paper aims to showcase how optimization can be leveraged without being the primary driving force, but rather a helpful tool in generating structurally sound designs while simultaneously promoting exploration. The focus lies on connecting structural performance with individual design preferences by using layout optimization in a new way. This allows to generate a diverse set of close-to-optimal structural forms that are yet visually distinct. A significant advantage of the presented method is that it operates in real-time allowing designers to directly manipulate and transform design briefs, resulting in an intuitive and seamless workflow. The method achieves a balance between exploration and rationality by imposing customized node-placing in combination with discrete

layout optimization. To summarize, this paper's contributions are: (1) the introduction of a new feedback-driven design framework for exploring structural forms in real-time, and (2) the use of discrete layout optimization in a new application focused on typological exploration.

2. Method

The method presented in this paper can be employed in two distinct ways: (1) for the creation and exploration of structural forms from the ground up, or (2) for the refinement and local transformation of an already existing design brief. This is achieved by using discrete layout optimization to create strut-and-tie models in static equilibrium, as they are known from graphic statics [10] and used by many architects and structural engineers. Section 2.1 of this paper outlines the overarching framework of the method, while Section 2.2 delves into the customized ground structure approach. In Section 2.3, the mathematical formulation for the discrete layout optimization is presented.

2.1 General framework

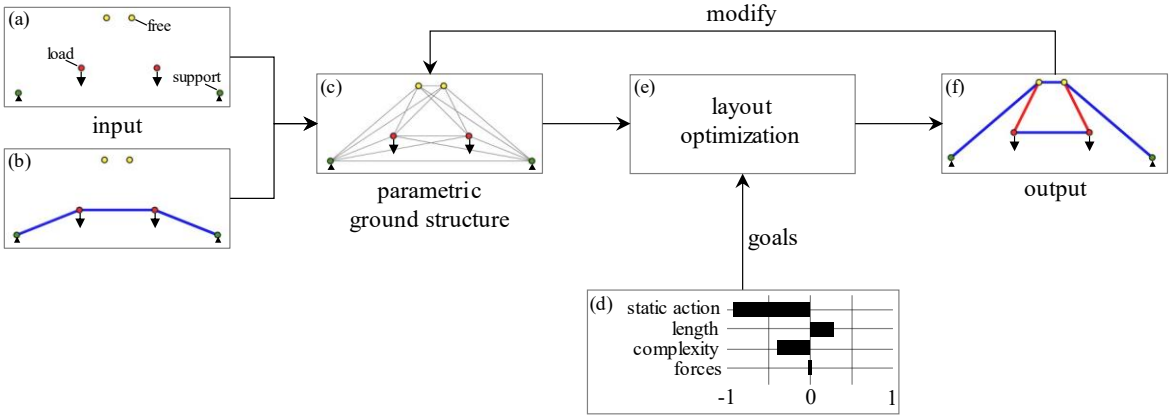


Figure 2. Workflow of the presented method

The general procedure of the method is summarized in Figure 2. The initial step in this process involves supplying input data. Figure 2(a) illustrates the three types of nodes that comprise the input data: support nodes (green), load nodes (red), and free nodes (yellow). Additionally, as illustrated in Figure 2(b), a pre-existing structure can be incorporated as needed. Once the input data is provided, a ground structure is generated by interconnecting all nodes (Figure 2c). It is important to note that the positioning of the nodes serves as one of two junctures where the designer can influence the resulting structure. The second point of influence is through the delineation of design goals, as shown in Figure 2(d). In this paper, these goals comprise four distinct categories: volume, length, complexity, and forces. However, additional, less trivial goals are available and would add even more relevance to the search process.

In order to weigh these design goals against each other, users can assign a real value between -1 and 1 for each of them, where a value of -1 represents a minimization, a value of +1 a maximization, and a value of 0 a neutral value indicating that the goal is not a priority for the optimization. When optimizing for volume, only values between -1 and 0 make sense since maximizing the volume of a structure is usually not desirable. However, for the sake of consistency, the range 0 to +1 can also be used. Regarding length, a value of -1 aims for shorter bars in the output structure, a value of +1 for longer bars. Complexity is derived from the number of bars and nodes existing in the output structure, where -1 aims for as less bars and nodes as possible and +1 for as many as possible. The 'Forces' input works slightly differently. A value of -1 requests all bars in compression, while a value of +1 requests all bars in tension. Values in between interpolate between both extremes. This means that a value of +0.8 tries to have most of the bars in tension but allows for some bars in compression. In summary, these goals influence the outcome of the layout optimization (Figure 2e) together with the custom ground structure

from Figure 2(c). Another peculiarity of the method used here is that instead of volume, the so-called static action is used:

$$\sum_{T} F_T L_T + \sum_{C} F_C L_C \tag{1}$$

Static action is calculated as the sum of the products of bar lengths by their force magnitude, separating bars in tension (T) from bars in compression (C). In early-stage design where no material has yet been decided upon, or where a constant material resistance in tension and compression is assumed throughout, static action can be understood as a substitute for volume. Thus, the terms volume and static action are used equally in this paper. Finally, the result of the process is shown in Figure 2(f). This result can be further modified by jumping back to step 2(c) i.e., by adding or removing nodes or by moving nodes to obtain a new custom ground structure. This enables designers to explore different kinds of structures for as many iterations wanted.

2.2 Extended ground structure approach

The discrete layout optimization used here is based on the ground structure approach, first proposed by Dorn et al. [11]. It consists in a fixed grid of nodes interconnected by bars. The optimal structure is found by only keeping a sub-set of all available bars and removing all obsolete bars. Over the years other strategies for discrete layout optimization were developed. Some start with a sparse structure and iteratively add nodes or bars to the structure. One well-known method, the growth method, was developed by Martinez et al. [12]. Instead of starting with a densely connected ground structure where all nodes are already available, it adds one node at a time to reduce computational cost. However, it can only deal with statically determinate 2D problems. The approach proposed here can be perceived as a combination of the two aforementioned strategies. Unlike the conventional ground structure approach that employs a predefined grid of nodes, the proposed approach allows the user to place nodes in desired locations, which are then interconnected to create a custom ground structure for the subsequent topology optimization. Therefore, the optimized ground structure is significantly influenced by the nodes selected by the designer. By this method, the designer has the ability to enforce their preferences and specify the locations where nodes and bars may or may not occur. The nodes that are placed beforehand can be altered or removed at any point during the process, and the designer can observe the effects on the final structure in real-time. This allows direct interaction with the design brief. Alternatively, the nodal positions could also be defined randomly in an automated way, which leads to the direct generation of a large set of diverse design outputs.

2.3 Layout optimization

The discrete layout optimization employed in this paper is formulated as an extension of the already mentioned ground structure approach by Dorn et al. [11] as a LP problem. Building on this, a mixed integer linear programming (MILP) formulation is proposed to allow for the definition of the goals explained in Figure 2(d).

2.3.1 Linear programming formulation

As already mentioned, the discrete layout optimization used here is based on the plastic layout optimization formulation for volume minimization. It consists of setting up a ground structure and solving the following LP problem:

$$\min_{\mathbf{a},\mathbf{q}} V = \mathbf{l}^T\mathbf{a} \tag{2a}$$

subject to

$$\mathbf{Bq} = \mathbf{f} \tag{2b}$$

$$\sigma_T \mathbf{a} - \mathbf{q}_k \geq 0 \tag{2c}$$

$$\sigma_C \mathbf{a} + \boldsymbol{q}_k \geq 0 \tag{2d}$$

$$\mathbf{a} \geq 0 \tag{2e}$$

where V is the total static action (≈ volume) of all members, **l** is a vector of all bar lengths, and **a** is a vector of all bar cross section areas. **B** is the equilibrium matrix containing the direction cosines of all bars. **q** is the vector of bar internal forces, and **f** the vector of external nodal loads. σ_T and σ_C are stress limits in tension and compression. The advantage of using this LP formulation is that it is computationally efficient which is an important feature for any interactive tool for the conceptual design stage. Design goals, as described in Figure 2(d), are not described yet in this formulation. Therefore, the current formulation needs to be extended.

2.3.2 Mixed integer linear programming formulation

One way to extend the previous formulation is to introduce additional constraints and variables. For this, binary assignment variables for nodes and bars are used, as they have already been used by Fairclough and Gilbert [13] and Brütting et al. [14]. The formulation used here is similar to the one of Fairclough and Gilbert. This extends the formulation to a MILP problem which can mean that computational complexity increases. However, it allows the addition of several goals, herein formulated as constraints:

$$M\mathbf{w} - \mathbf{a} \geq 0 \tag{2f}$$

$$Mv_j - \sum_{i \in N_j} a_i \geq 0 \tag{2g}$$

$$\mu_L \leq \sum_{i=1}^{n} w_i \leq \mu_U \tag{2h}$$

$$\vartheta_L \leq \sum_{j=1}^{m} v_j \leq \vartheta_U \tag{2i}$$

$$\mathbf{w}, \mathbf{v} \in \{0, 1\} \tag{2j}$$

Equation 2f denotes whether a potential bar in the ground structure is assigned to the final structure (w_i = 1) or not (w_i = 0), where **w** is the vector of binary assignment variables for each bar in the ground structure. *M* is a sufficiently large number which can be seen as an upper bound for cross section areas. Equation 2g denotes the existence of a node following the same principle. To provide this, the sum of the areas of all bars ($\sum a_i$) connected to the respective node is used. Here, N_j is the set of bar indices for all connected bars. **v** is another vector of binary assignment variables indicating the existence of a node j where $v_j \in \{0, 1\}$. μ_L and μ_U are lower and upper bounds for the number of bars and nodes, respectively. This allows to control the number of bars and nodes in the output structure.

3. Results

All examples in this section were run on an Intel Core i9-11900H @ 2.50GHz with 32.0 GB of RAM. To solve the MILP formulation, Gurobi 10.0.1 [15] was used. Sections 3.1 and 3.2 present a case study in 2D, where Section 3.1 demonstrates the exploration of structures generated from scratch with no additional input, while Section 3.2 demonstrates the local transformation of an existing structure to achieve structures with similar performance and appearance. Section 3.3 extends the study to 3D, highlighting the capabilities of the proposed method. Notably, all results presented in this section were obtained in real-time, taking only a few milliseconds to compute.

3.1 Structural exploration

Figure 3(a) shows the setup for this case study with three loads of value *F* and two supports. The design domain is indicated by the gray box and has a length of *L* and a height of *L/2*. Figure 3(b) shows the goals as black bars ranging from -1 to +1 (see Section 2.1). These goals can be changed to obtain different results. Support and load nodes do not move, while free nodes may move, vanish, or appear.

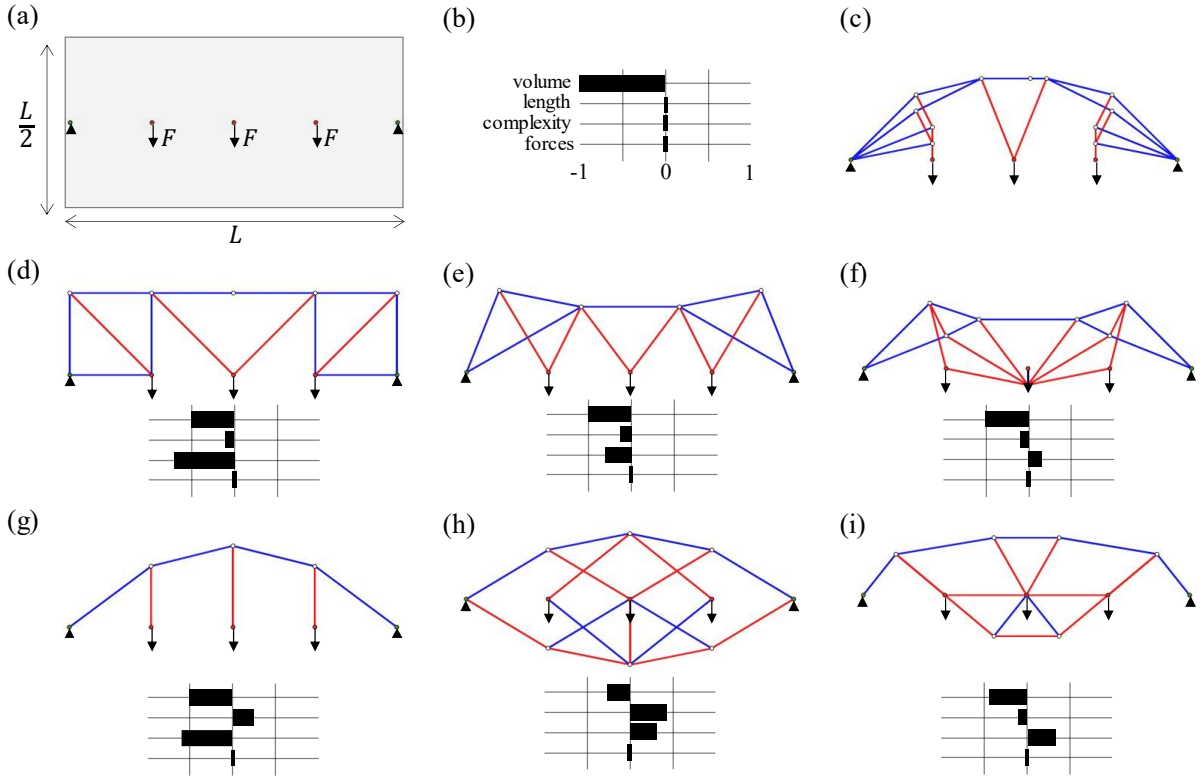


Figure 3. Case study for a structural exploration from ground up: (a) initial set up of load and support conditions; (b) input goals leading to (c) first iteration; (d-i) other results (top) resulting from other choices of input goals (bottom).

Table 1. Result metrics for the ground up exploration presented on Figure 3.

Name	Static action [FL]	Nodes [-]	Bars [-]	avg. Length [L]	Difference [-]
(c)	**21.3**	16	24	0.186	- 42%
(d)	**36.7**	10	14	0.280	± 0%
(e)	**26.1**	9	13	0.283	- 29%
(f)	**30.2**	12	20	0.211	- 18%
(g)	**21.7**	8	7	0.252	- 41%
(h)	**37.5**	11	17	0.284	+ 2%
(i)	**28.5**	11	16	0.208	- 22%

The obtained structures can be observed in Figure 3(c)-(i). Result (c) shows the 'optimal' structure if only the minimization of static action is a goal and a fully connected dense ground structure is available. It is rather a theoretical result used to benchmark results (d)-(i). Structure (d) denotes a 'classical' truss structure. Therefore, (d) is used as a reference to measure the difference of static action. The black bars underneath indicate the values chosen for the design goals. Table 1 shows the results belonging to the structures in Figure 3, containing their static action, normalized by *FL*, the number of nodes and bars,

the average length of the bars, normalized by *L*, and the difference of static action compared to the one of the reference structure (d), i.e. 36.7*FL*. All obtained structures perform similarly or significantly better than the truss in (d), while (c) performs best with 21.3*FL*. Except for (h) all structures perform 18% to 41% better. The amount of bars and nodes used is varying from 7 to 24 and 8 to 16, respectively.

3.2 Structural transformation

In this case study, the structure from Figure 3(g) is taken as a starting point and shown in Figure 4(a). Support and load conditions remain the same as in the previous example. Again, support and load nodes do not move, while free nodes may move, vanish, or appear. The intention is to transform Figure 4(a) to obtain similar arch-like looking results and explore the range of possibilities for a given type of structure. Figure 4(b)-(f) show the obtained transformed structures with the respective goals underneath. Table 2 shows the result metrics in the same way as Table 1 does.

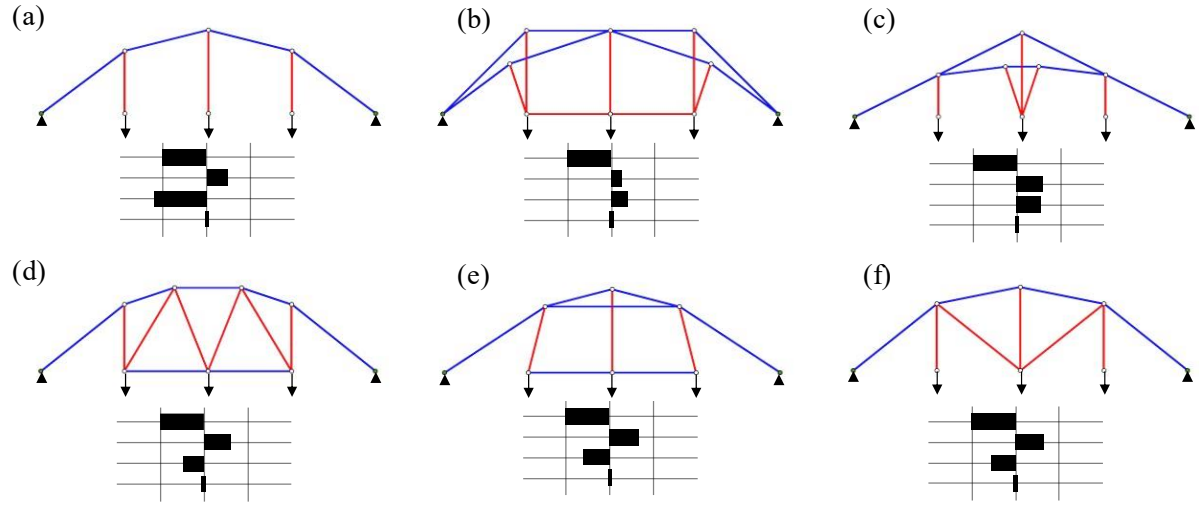


Figure 4. Case study for a structural transformation: (a) initial structure; (b-f) transformations (top) resulting from a change of input goals (bottom).

Table 2. Result metric for the structural transformation

Name	Static action [FL]	Nodes [-]	Bars [-]	avg. length [L]	Difference [-]
(a)	**21.7**	8	7	0.252	± 0
(b)	**22.2**	10	13	0.300	+ 2%
(c)	**25.9**	10	13	0.252	+ 19%
(d)	**22.2**	9	13	0.244	+ 2%
(e)	**24.1**	8	9	0.299	+ 11%
(f)	**21.9**	8	9	0.271	+ 1%

Moreover, all obtained structures perform similarly with static action deviations up to +11%, except for (c) deviating by +19% compared to the starting structure. Their amount of nodes and bars ranges from 8 to 10 and 7 to 13, respectively, while the average lengths ranges from 0.244 to 0.300.

3.3 3D bridge structure

This case study serves as an illustrative example of the extension of the introduced method to the third dimension, as demonstrated in Figure 5 where 40 different bridge structures of varying layout and

geometry are displayed. Underneath, a diverse selection of four structures for potential further investigations is shown.

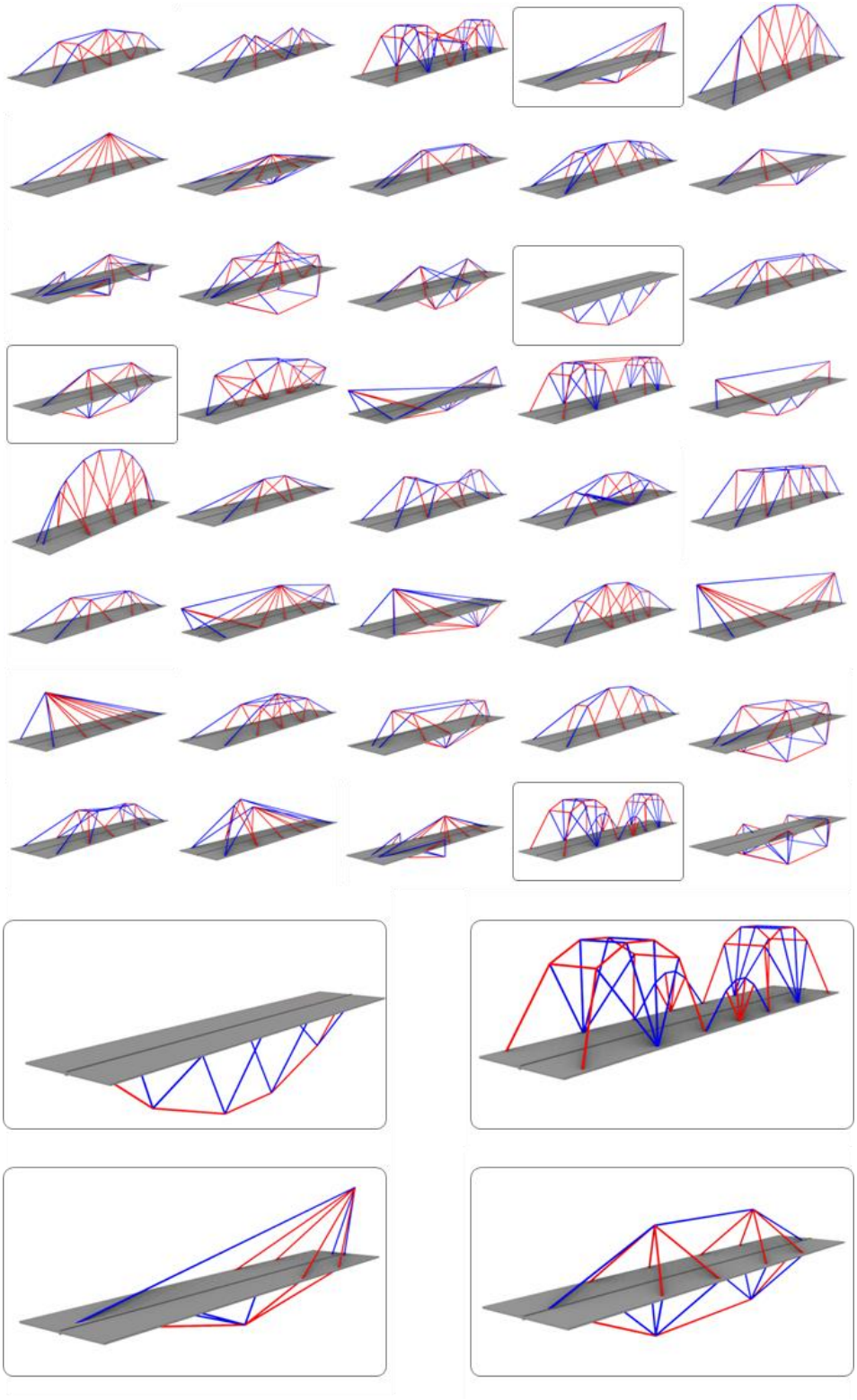


Figure 5. Sample of 40 generated structures with four selected structures to further investigate

4. Discussion

The present study reveals a diverse range of forms and types for spatial structures, as demonstrated by the case studies. These structures exhibit a variety of known types, such as arches and trusses, as well as new, uncategorized forms. Remarkably, the study finds that the diverse array of structures performs within a similar range in terms of static action. This suggests that designers may choose from a variety of forms and types for qualitative preferences without compromising performance. Moreover, the MILP problem introduced in this paper requires significantly less computational resources compared to similar MILP formulations in the literature, e.g. the one from Fairclough and Gilbert [13]. One explanation for this is that the current approach does not employ a densely connected ground structure, resulting in the utilization of fewer nodes and bars. However, there currently are several limitations and trade-offs. Form-active structures such as arches or cables are not always readily identifiable, as their nodes must be conveniently pre-positioned, which calls for combining current algorithms with complementary geometric search. Furthermore, more complex structures with a larger number of nodes and bars may pose challenges in control, and changing one node at a time only may not lead to a significant change. To address these limitations, the development of methods that bundle sets of nodes for efficient analysis and transformation is required. Also, even though this tool is meant for early-stage conceptual design, the integration of early stability checks and construction feasibility checks would make the transition to the next phases of the design process more straightforward. Finally, the development of additional goal parameters should allow users to gain control over more complex formal features and hence an even more straightforward control over the search process. These improvements will be the subject of future publications by the authors.

5. Conclusion

This paper introduced a new method for the generation and exploration of structural forms for the conceptual structural phase of the design process. The approach provides designers with the flexibility to choose between the unbridled exploration of various forms or the refinement of an already advanced design brief. The method uses layout optimization in a new way, which involves the creation of a parametric ground structure and the subsequent generation of structures in equilibrium based on different design goals. Primary advantages of this method are (1) its ability to navigate a solution space that is unrestrained from predefined typologies, (2) its ability to operate in real-time, enabling designers to modify their intended design interactively, and (3) its ability to only generate structural typologies that make sense from both points of views of static equilibrium and construction rationality or other custom goals.

Future developments of this method relate to the implementation of a geometry optimization step to allow for the generation of form-active structures and the implementation of additional design goals, hence allowing more design opportunities to tame the search of new structural typologies. The algorithms will soon be made available as a Grasshopper plugin for Rhino3D.

With this method, designers may break away from established typologies and explore a vast new set of sound structural forms. Furthermore, this method facilitates the simultaneous consideration of both performance and diversity, ensuring that the final design is not only well-performing but may also be distinctive and inventive. Therefore, this introduced method constitutes a valuable addition to the computational conceptual design process, providing designers with a persuasive tool for generating and exploring structural forms. The approach offers flexibility and adaptability to designers, empowering them to develop creative, high-quality designs that cater to the specific requirements of their projects.

References

[1] P. von Buelow, “Paragen: Performative Exploration of Generative Systems,” *J. Int. Assoc. Shell Spat. Struct.*, vol. 53, no. 4, pp. 271–284, Dec. 2012.

[2] C. T. Mueller and J. A. Ochsendorf, "Combining structural performance and designer preferences in evolutionary design space exploration," *Autom. Constr.*, vol. 52, pp. 70–82, Apr. 2015, doi: 10.1016/j.autcon.2015.02.011.
[3] J. E. Harding and P. Shepherd, "Meta-Parametric Design," *Des. Stud.*, vol. 52, pp. 73–95, Sep. 2017, doi: 10.1016/j.destud.2016.09.005.
[4] J. Harding and C. Brandt-Olsen, "Biomorpher: Interactive evolution for parametric design," *Int. J. Archit. Comput.*, vol. 16, pp. 144–163, Jun. 2018, doi: 10.1177/1478077118778579.
[5] I. Mirtsopoulos and C. Fivet, Eds., "Grammar-based generation of bar networks in static equilibrium with bounded bar lengths," *Proc. IASS Annu. Symp. 202021 7th Int. Conf. Spat. Struct.*, 2021.
[6] P. O. Ohlbrock and P. D'Acunto, "A Computer-Aided Approach to Equilibrium Design Based on Graphic Statics and Combinatorial Variations," *Comput.-Aided Des.*, vol. 121, p. 102802, Apr. 2020, doi: 10.1016/j.cad.2019.102802.
[7] K. Saldana Ochoa, P. O. Ohlbrock, P. D'Acunto, and V. Moosavi, "Beyond typologies, beyond optimization: Exploring novel structural forms at the interface of human and machine intelligence," *Int. J. Archit. Comput.*, vol. 19, no. 3, pp. 466–490, Sep. 2021, doi: 10.1177/1478077120943062.
[8] L. He *et al.*, "Optimization-driven conceptual design of truss structures in a parametric modelling environment," *Structures*, vol. 37, pp. 469–482, Mar. 2022, doi: 10.1016/j.istruc.2021.12.048.
[9] P. Park, M. Gilbert, A. Tyas, and O. Popovic-Larsen, "Potential Use of Structural Layout Optimization at the Conceptual Design Stage," *Int. J. Archit. Comput.*, vol. 10, no. 1, pp. 13–32, Mar. 2012, doi: 10.1260/1478-0771.10.1.13.
[10] P. D'Acunto, J.-P. Jasienski, P. O. Ohlbrock, C. Fivet, J. Schwartz, and D. Zastavni, "Vector-based 3D graphic statics: A framework for the design of spatial structures based on the relation between form and forces," *Int. J. Solids Struct.*, vol. 167, pp. 58–70, Aug. 2019, doi: 10.1016/j.ijsolstr.2019.02.008.
[11] W. Dorn, R. Gomory, and H. J. Greenberg, "Automatic design of optimal structures," *J. Mècanique*, vol. 3, pp. 25–52, 1964.
[12] P. Martínez, P. Martí, and O. M. Querin, "Growth method for size, topology, and geometry optimization of truss structures," *Struct. Multidiscip. Optim.*, vol. 33, no. 1, pp. 13–26, Jan. 2007, doi: 10.1007/s00158-006-0043-9.
[13] H. Fairclough and M. Gilbert, "Layout optimization of simplified trusses using mixed integer linear programming with runtime generation of constraints," *Struct. Multidiscip. Optim.*, vol. 61, no. 5, pp. 1977–1999, May 2020, doi: 10.1007/s00158-019-02449-7.
[14] J. Brütting, J. Desruelle, G. Senatore, and C. Fivet, "Design of Truss Structures Through Reuse," *Structures*, vol. 18, pp. 128–137, 2019, doi: 10.1016/j.istruc.2018.11.006.
[15] "Gurobi Optimization LLC." 2023. Accessed: Mar. 30, 2023. [Online]. Available: https://www.gurobi.com/

IASS 2023
July 10–14 Melbourne
Integration of Design and Fabrication

Proceedings of the IASS Annual Symposium 2023
Integration of Design and Fabrication
10–14 July 2023, Melbourne, Australia
Y.M. Xie, J. Burry, T.U. Lee and J. Ma (eds.)

Form finding for post tensioned, 3D printed fluid containers

Patrick SCHÄFERLING[a,*], Matthias BECKH[a,*]

[a,*] TU Dresden, Faculty of Architecture, Chair of structural design
Zellescher Weg 17, 01069 Dresden
structural-design@tu-dresden.de

Abstract

The 3D printing technology of mineral materials offers the possibility of manufacturing geometrically complex shapes. However, it is still difficult to integrate reinforcement into printed geometries. This production-related limitation results in a significant restriction in the load-bearing capacity of printed components. Therefore, the technology has been mainly used for decorative components so far. 3D-printed load-bearing structures should not be derived from conventional shapes of reinforced concrete but rather from their inherent functional and structural requirements. In this paper, we explore the strategy of combining large-scale 3D-printed, purely compression-loaded components with post-tensioned, unbonded tendons to generate statically and economically efficient systems. The separation into mineral, purely compression-loaded, and metallic, tension-loaded elements allows the advantages of the printing technology and the material's specific load-bearing behaviour to be exploited, as well as enabling better recyclability through the separation of construction materials. Using the example of large fluid containers, the form finding for systems under hydrostatic pressure and their construction with the described static system of separated compression and tension elements is investigated. These containers are considered highly relevant structures in the wake of the energy transition and climate change.

Keywords: form finding, 3d printing, post-tensioning, optimization, parametric design, concrete shells, lightweight construction, production-driven design

1. Introduction

1.1. Reason for investigation

3D concrete printing (3DCP) is developing into a competitive production method for a wide range of construction tasks, even in widespread use [1], [2]. However, current development aims more at substituting traditional construction methods and their associated shapes [3], [4]. The geometric design and structural potential of additive manufacturing technology remain largely untapped. So, the aim of this research project is twofold: first, to drastically reduce the required materials by optimizing structural shapes; and second, to avoid composite construction and thus allow for easy recyclability.

Our focus lies on construction systems for infrastructural buildings, especially liquid containers. In the infrastructure sector, more attention is paid to functional and economic aspects than to individual design aspects. Liquid containers are used in a wide variety of applications. In the course of the energy transition and the associated use of fluctuating renewable energies, an increased demand for such storage systems, both as water and heat storage, is to be expected [5], [6].

1.2. Used tools

The form-finding was developed entirely in the Rhinoceros 3D and Grasshopper [7] environment. For form finding, the Kangaroo 2 [8] solver was used, which works with the dynamic-relaxation method. We decided to use these tools because of the available APIs for Rhino and Grasshopper, as well as the comprehensive documentation of Kangaroo, which allows the implementation of self-programmed

Copyright © 2023 by Patrick SCHÄFERLING and Matthias BECKH. Published in the Proceedings of the IASS Annual Symposium 2023 with permission.

'custom goals'. Through prior experience with programming in this environment, we were able to take the first steps quickly. Overall, an even more flexible form-finding tool with more possibilities (e.g., different load cases, envelope load cases) would be desirable.

1.3. Methodological approach

We are developing a specific form-finding setup for 3DCP structures in combination with unbonded, post-tensioned concrete containers based on the underlying static principles. From two-dimensional graphic statics, equations are derived to 'goal objects' for the digital form finding. With this procedure, the complexity of the system can be successively increased to gain a deeper understanding of the relationships between form and force and their corresponding shapes. In this paper, the investigation of the two-dimensional thrust lines and its conclusions are discussed. Afterwards, the principles are translated into three-dimensional space. These results are only a glimpse, as they have not been concluded yet. However, they give insights into the problems that still must be solved in this ongoing research project.

2. Form finding in two-dimensional space

In the following chapter, the applied loads and their derivation from the structure are briefly presented. The basic relationships between form and force are evaluated based on selected load combinations. Correlations between material consumption and container volume can be derived by introducing the evaluation criterion 'efficiency ratio'.

2.1. Dead load

The first load effect on the container wall is the dead load of the purely pressure-loaded (3DCP) shell, as described in figure 1a. The calculation of the dead load is realized with a discretized representation of the thrust line, represented by a polyline element. Loads are derived from each line segment of the polyline and applied to the segment's end points. The magnitude results from the product of the segment's length l and the length-related dead weight g_0 of the used material and wall thickness. Varying wall thicknesses within the container wall are not intended at this early stage, so the calculated line load can be uniformly distributed to each segment's end points. Dead load acts vertically in the global coordinate system (-Z) and is therefore applied in the positive Z direction (acting upwards) in the form-finding process [9], [10].

2.2. Hydrostatic pressure

The hydrostatic pressure is calculated analogously to the dead load. It derives from the length l of the polyline segments and the fluid-specific, length-related pressure p_v. In addition, the corresponding water level is included in the calculation, as shown in Figure 1b. The load is determined using two partial loads for each line segment of the discretized thrust line. The first part is a constant, uniform line load over the entire segment, corresponding to the pressure at the upper segment end, $p_1 * l$. The second part, the linearly increasing load component p_2, is calculated from the height difference over the segment's length (V[0]-V[1])/2 * l. These two load components are proportionally applied to the end points of the polyline segment. The force direction is normal to the surface or line, so care must be taken to ensure a consistent line direction in the 3D model. Otherwise, the calculated pressure direction can flip in the thrust line. Since the reference point for the water level can also depend on the shape of the thrust line (container height can also be part of the form finding, e.g., with a rolled support point on the top end, see figure 9), its coordinates can be bound to a control point of the discretized thrust line, which is calculated in the algorithm [9], [10].

The discretization of the geometry leads to a significantly higher discretization-related deviation for the hydrostatic pressure than for the dead load. Theoretically, the force components at a control point of the polyline from connecting segments should be equal. However, this is not the case due to the distribution of the increasing load component over the length of the discretized line segment. With sufficiently fine discretization, this circumstance can be considered. With an idealized discretization (lim l_0 → 0) and isolated hydrostatic pressure, a constant normal force in the entire thrust line can be expected.

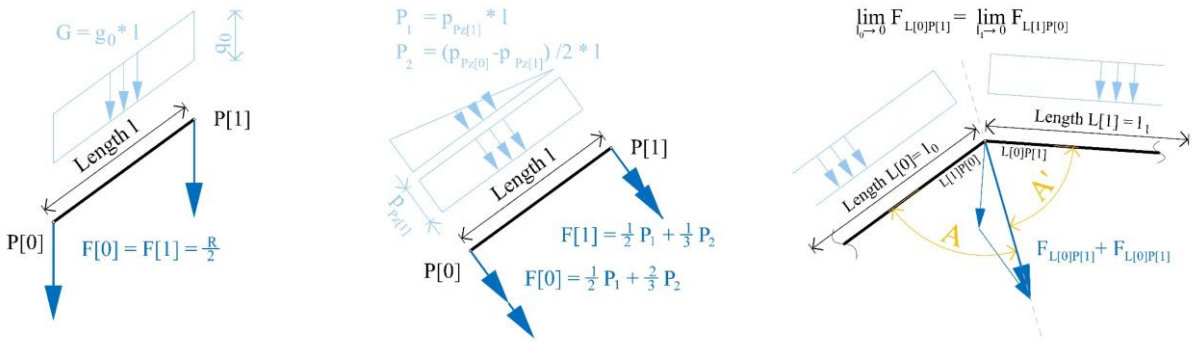


Figure 1. f.l.t.r.: (a) dead load calculation, (b) water pressure,
(c) constant normal force in thrust line under isolated hydrostatic pressure

2.3. Tension only elements

The load-bearing geometry in the form-finding process is calculated with spring elements. The spring force F is derived from the spring constant D and the length change Δl. At each line end point, half the spring force is applied coaxially to the spring axis, with the direction corresponding to the sign of the length change [9], [11].

To distinguish between purely compression-loaded and tension-loaded elements, the general spring equation was supplemented with a correction in the program. A pure tension element (e.g., post-tensioning elements) may only absorb compressive forces in the form finding process. It may therefore react to shortening (Δl < l0) with a corresponding counterforce, but not to lengthening (Δl > l0). This is realized in the program by a length-dependent correction. When Δl > l0 the calculated force will be reduced to zero. The force directions remain unchanged. Due to the reversal of the force direction in the form finding procedure, there is a risk of buckling with purely tension-loaded elements during the form finding procedure.

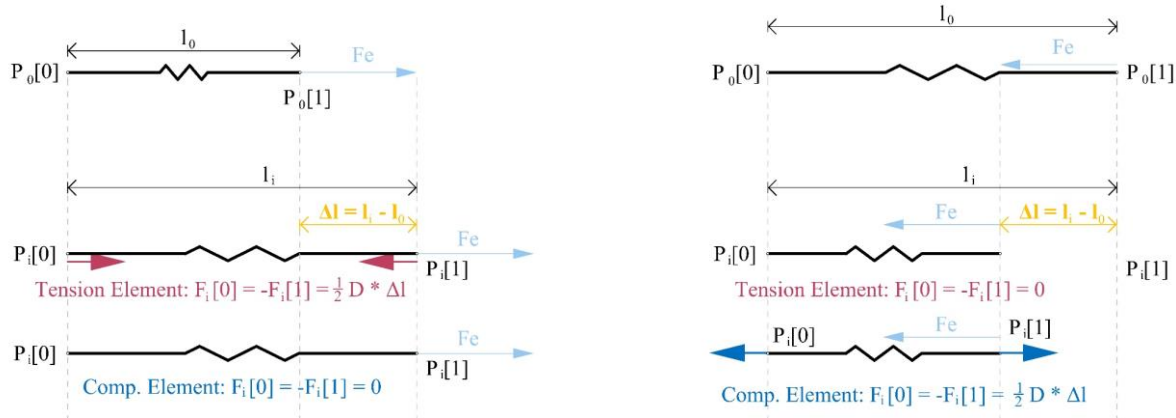


Figure 2. left: spring element under tension and corresponding reaction of tension and compression only elements; right: form-finding spring element under compression and corresponding reaction of tension and compression only elements

2.4. Compression only elements

A pure compression element (e.g., an unreinforced concrete container wall) may only absorb tensile forces in the form-finding process. A corresponding force will be applied to the line end points by lengthening ($\Delta l < l_0$). The applied forces are set to zero if the element is shortened.

2.5. Supports

Supports are calculated like a very strong spring element between its original point and the current point in the iterative solver, which always pulls it towards the origin. Support conditions (t_x, t_y, t_z) can be set by multiplying the vector's dimensions [12].

2.6. Different water levels

The forces of lower water levels can be dissipated within the thrust line of the maximum filling level in rotationally symmetrical containers. The missing dynamic pressure can be compensated with corresponding annular compression forces in the concrete shell. However, depending on the slope of the shell, these compensating annular forces can cause significantly higher internal compression forces than the load of a higher fill level, which is why these internal forces are also decisive for the dimensioning of the shell thickness. To calculate these internal forces, a new type of goal element is introduced.

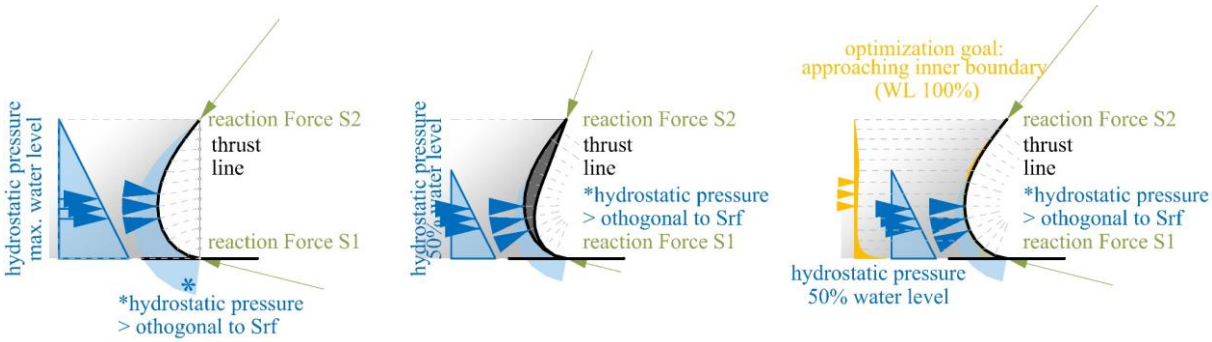


Figure 3. process of a form finding goal for lower water levels

Its mechanic is derived from the desired behavior of always approaching the thrust line geometry of a completely filled container. It is calculated in a second form-finding step after the initial one with a maximum water level. The behavior is achieved by applying additional, only horizontal-acting, concentrated loads to the control points of the thrust line. Its magnitude is derived from the horizontal distance to the thrust line of the first form-finding step. To prevent annular tension forces, the magnutude is corrected to zero depending on the acting direction of the concentrated loads (in our case, the -X direction will be corrected to 0).

2.7. Efficiency ratio

To enable an initial economic and ecological classification of different parameters and resulting shapes, we compare the resulting cross-section curves with a unitless "efficiency ratio". It is calculated from a predefined container volume in relation to the corresponding built volume of the container wall (m^3/m^3). For this purpose, the two-dimensional thrust line from the form finding is revolved around to determine the cylinder-equivalent radius b from its volume. This is supplemented with r to revolve the curve to the predefined container volume V. This results in the wall's area A, which is multiplied by the weight used for the wall's dead load in the form-finding process.

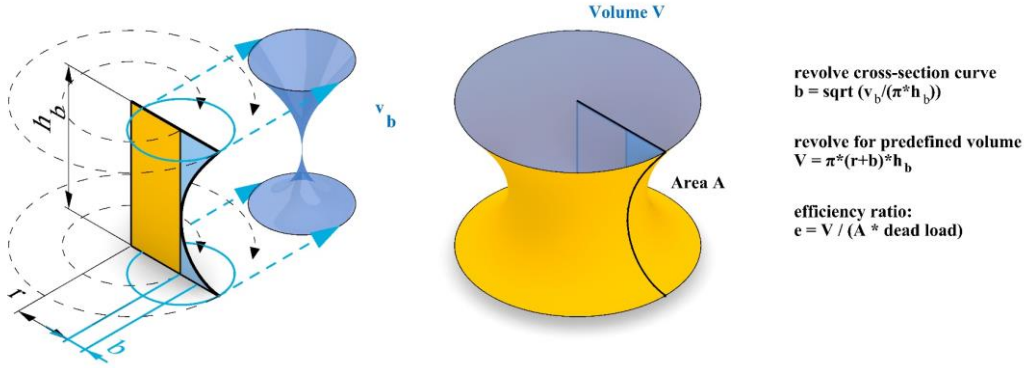


Figure 4. calculation steps of the described 'efficiency ratio'

2.8. Examples

Thrust lines for different input parameters are shown below. The ratio of dead load to hydrostatic pressure is mainly decisive for the shape of the thrust line. For this reason, only load proportions are given here (in %). A length- and height-based reference water pressure of 10 kN/m^2 and a reference dead load of 10 kN/m were assumed (100%). Loads are calculated as line loads, as described in paragraphs 2.1 and 2.2. These values were chosen for presentation in this paper to create a clearly perceptible variance and gain a better understanding of the dependencies. Real conditions for single extrusion walls would be sought near values of 100% water pressure (approx. $9.81kN/m^2$) and 20-30% dead load (approx. 3DCP wall thickness 7-8cm, $22kN/m^3$).

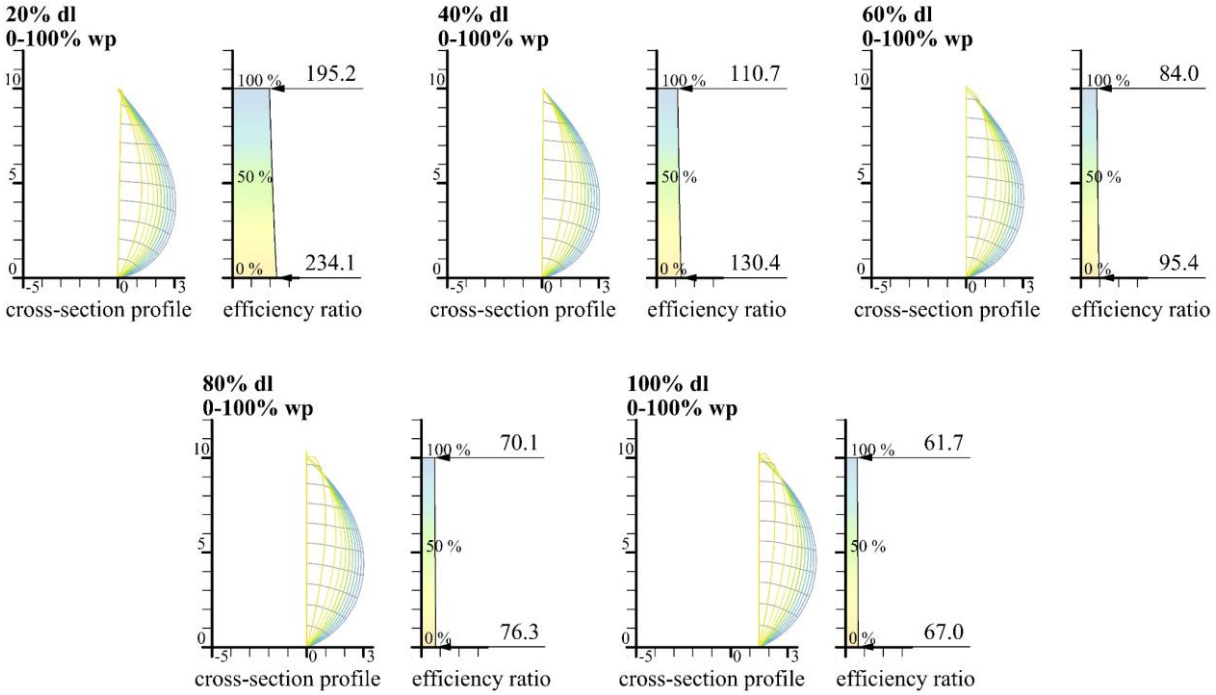


Figure 5. Thrust lines for different dead load factors (dl) with varying water pressure (wp), both ends with pinned supports.

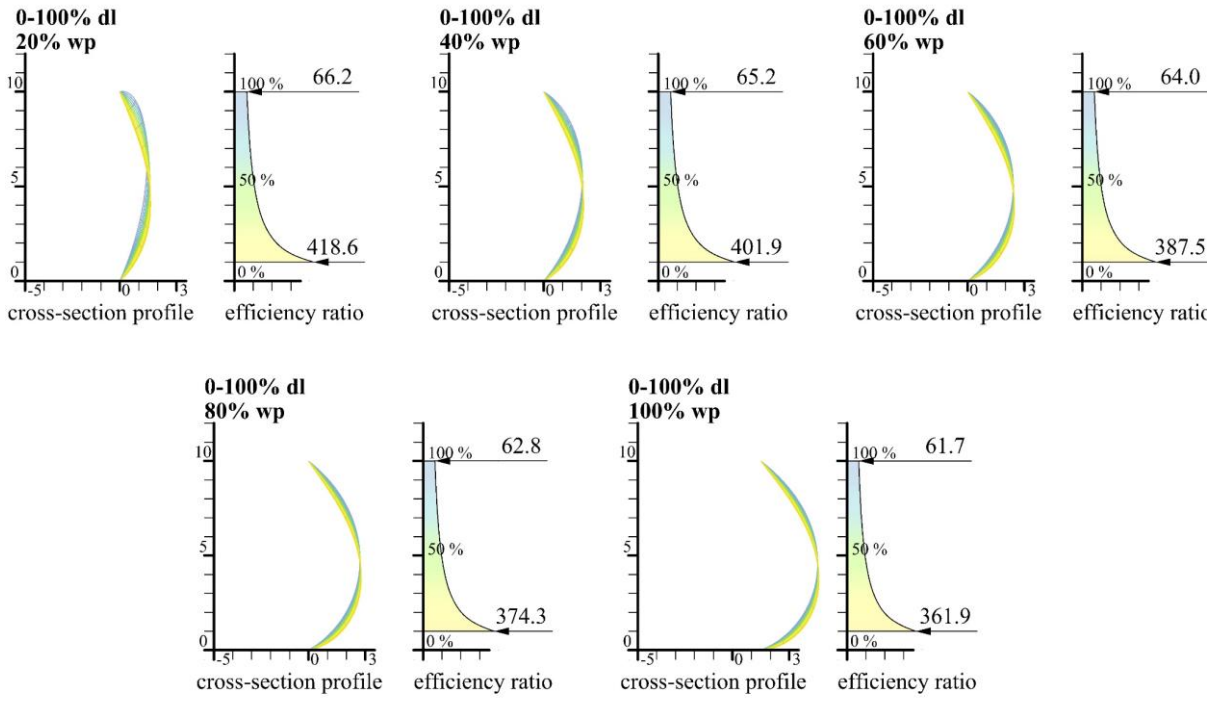


Figure 6. Thrust lines for different water pressure factors (wp) with varying dead load (dl), both ends with pinned supports.

As can be clearly seen in figures 5 and 6, the curvature shifts significantly upward due to a higher dead load. A slight reduction of the curvature can be observed. The efficiency ratio decreases significantly with increasing wall thickness, so the flatter thrust line with a higher mass in the container wall cannot compensate with a correspondingly higher container volume.

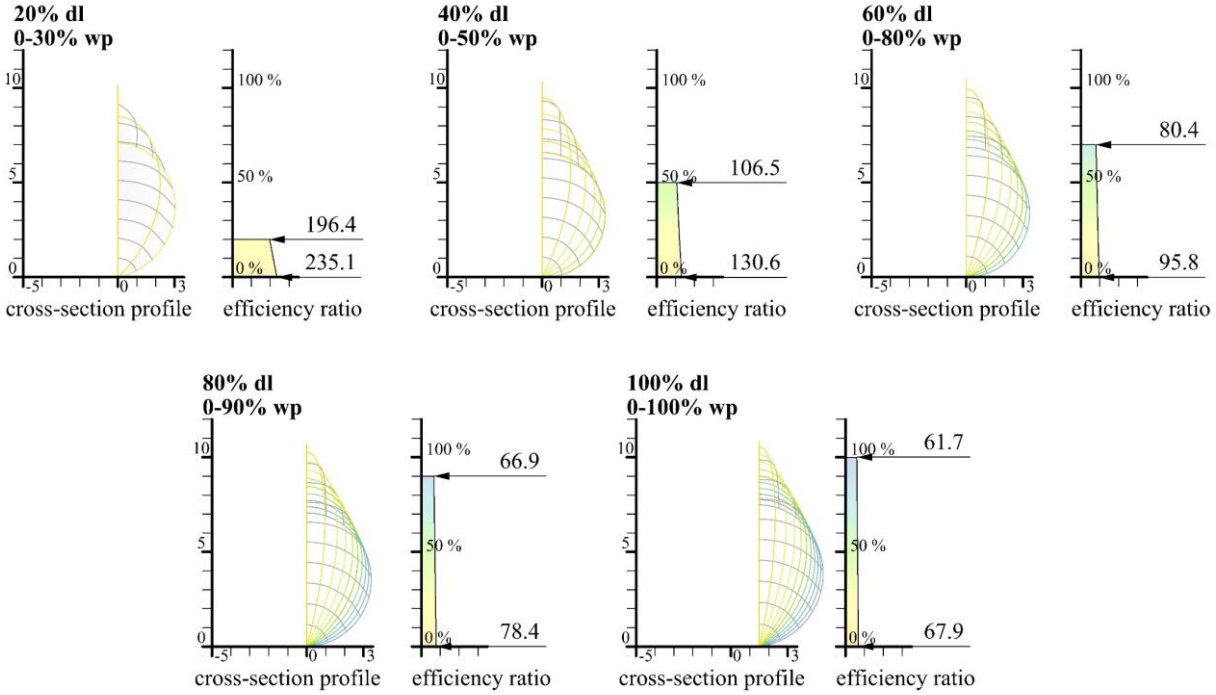


Figure 7. Different dead load factors (dl) with varying water pressure (wp), upper end with vertical roller support

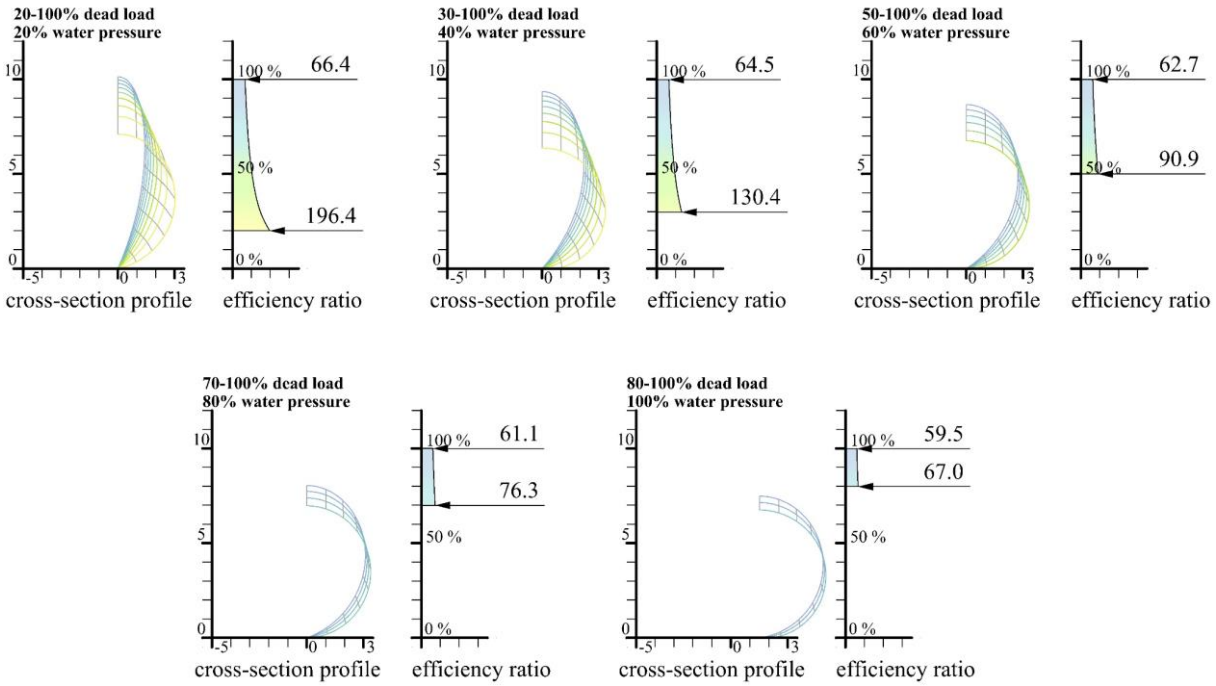


Figure 8. Varying water pressure (wp) with different dead load factors (dl), upper end with vertical roller support

Figures 7 and 8 show various support curves for load combinations with the upper support as a vertical roller support. With this support condition, all acting forces from the container are transferred to the ground through the purely compression-loaded shell without additional support structures. Annular tension forces are only short-circuited at the upper and lower edges of the container via post-tensioning tendons. The analysis shows that a certain dead load must always prevail as a prerequisite for a corresponding water pressure. For lower ratios of dead load to water pressure, no solution is found in the form-finding. This behavior is caused by the translation of the upper support point. It only absorbs vertical forces, so the support curve must always end exactly horizontally in the upper support. The higher the dead load component, the flatter the thrust line, and the higher the position of the upper support point. In this structural system, the efficiency of the container is reduced with increasing dead load (wall thickness). However, this effect becomes significantly smaller with increasing wall thickness.

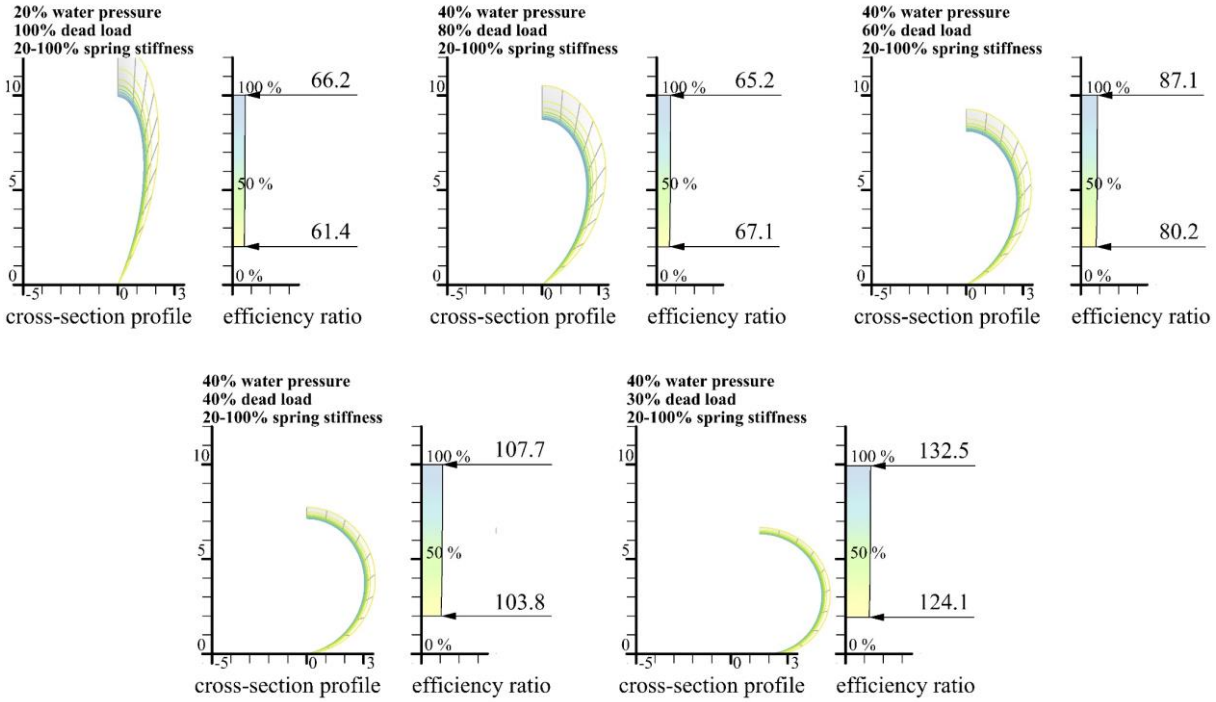


Figure 9. Varying spring stiffness with different dead load factors and water pressure, upper end with vertical roller support

Figure 9 shows the calculated spring stiffness's influence on the thrust line elements. Support conditions are derived from Figures 7 and 8. The stiffness value determines the resulting force density in the shell. The influence on the shape of the support curve and thus on the efficiency is relatively small because of the support conditions. It also decreases with higher load values. With a roller support on the top, the spring stiffness should therefore be selected accordingly high to utilize the load-bearing capacity of the shell as far as possible.

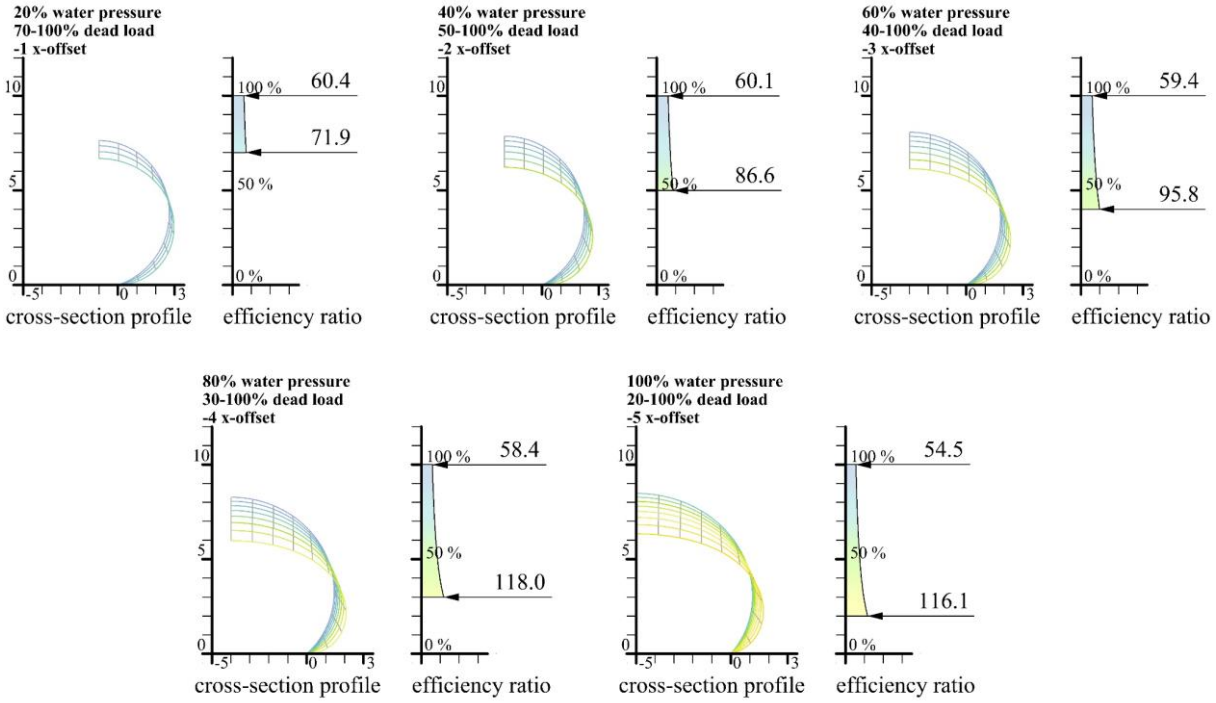


Figure 10. Varying dead load with different water pressure values, upper end with vertical roller support, different offset of upper support points

Figure 10 shows the thrust line with a pinned support at the bottom and a rolled support at the top. Based on historical examples of water tanks, the influence of a horizontal expansion over the height of the tank is examined. An increase in efficiency can be observed up to an opening angle of approx. 40°. A thicker tank wall continues to have a rather negative influence on efficiency.

2. From two-dimensional to three-dimensional space

The transfer of the principles from surface to space is associated with some difficulties. In the following, we briefly present our current state of work.

3.1. Dead load

The dead load in three-dimensional space is calculated by a corresponding discretized ‘thrust surface'. Mesh objects are most suitable; their geometric surface representation is determined by discretization via points (the so-called mesh vertices). To prevent anisotropy in rotationally symmetrical bodies and thus radial deformation in the shell during the form finding, it should be created as a uniform quad mesh, i.e., consisting of partial surfaces each described by four corner points. The problem with discretized meshes, however, is that the exact surface area is not defined by the representation of 3 or 4 surface corner points. There are an infinite number of surfaces that can be formed based on identical corner points. The area of them can always be different. Again, the finer the discretization, the smaller the deviation of the calculation algorithm gets. Our chosen approach determines the surface area with the surface area of the tetrahedron from the four corner points. The dead load is allied to each of the four corner points according to 1/8th of the tetrahedron area. The load direction remains the global Z-direction according to the two-dimensional calculation.

3.2. Hydrostatic pressure

Due to the maximum fine mesh, which is already required for the dead load calculation, the calculation of the 3D dynamic pressure was strongly simplified to save computing time. Our computational

approach is analogous to a homogeneous pressure on the mesh. The area of the mesh faces and the distribution of the force are calculated analogously to the dead load. Pressure values p(h) are calculated by the mesh area a times the area-dependent pressure force g (9.81 kN/m² for water) times the vertical distance to the maximum water level h. A differentiated consideration of the varying pressure within the mesh faces is not considered due to the required fine mesh.

3.3. Tension / Compression only elements, supports

These elements are also represented in three-dimensional space by linear, reticulated spring elements. Therefore, a dimensional adjustment of the used points and vectors is sufficient here. An adjustment of the calculation method is not necessary.

3.4. Examples of three-dimensional form finding for containers

The following shapes are results, or first attempts, at a more sophisticated design of the containers. The aim was to reduce the maximum inclination of the printed wall, as printing angles over 20° can cause layer adhesion problems during the printing process. From the 2D examination, it can be concluded that the primary lever to reduce the slope is the ratio of dead load to hydrostatic pressure. Unfortunately, studies have also shown that an increase in wall thickness is only associated with disproportionate volume gains. In the 3D models, new ways were examined to increase the vertical load component in the shell without increasing the overall wall thickness. These results are only glimpsed and not described in detail, as their investigation has not yet been completed.

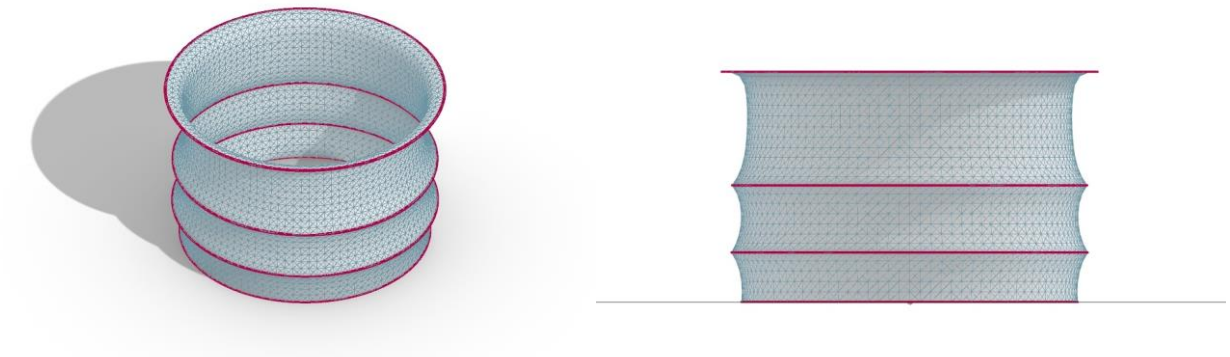


Figure 11. Container with various annular tendons, staggered according to the pressure curve
blue: pressure-loaded concrete shell, red: post-tensioning tendons.

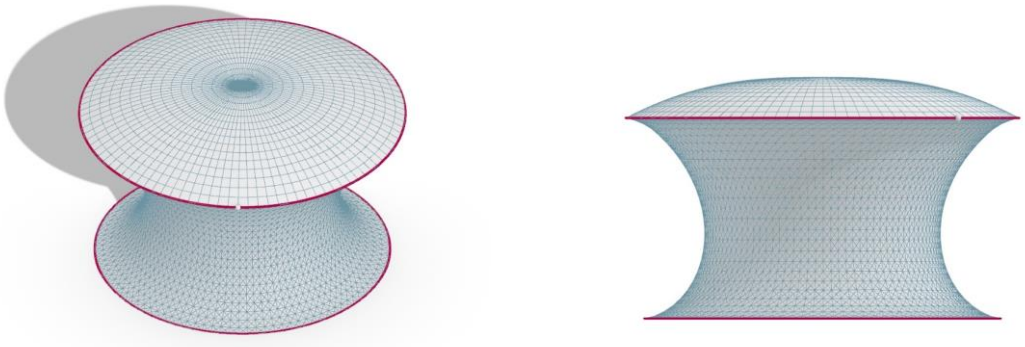


Figure 12. A roof on the container for additional vertical loads
blue: pressure-loaded concrete shell, red: post-tensioning tendons.

4. Conclusion

The implementation of the hydrostatic pressure in the form finding worked out quickly and purposefully with the available tools. The isolated results were always plausible and comprehensible. In combination with dead loads and different support conditions, however, a high level of complexity is quickly generated. By adding just a few components, the behavior of the form can only be predicted with difficulty. Even small variations in the boundary conditions can lead to completely changed results or even the failure of the form finding (no equilibrium state found). Further detailed studies of the relationships are therefore needed. Theoretically, the generated, rotationally symmetric, pressure-only shape can also derive different filling levels in the same cross-section by compensating ring forces. However, these are not directly part of the form-finding. The plausibility of the assumptions should be checked in the next step of the investigations by a complete structural analysis of the structure. The possibility of parallel simulation of different load cases in the form finding would be a helpful extension of the method to further increase the theoretical efficiency.

References

[1] G. Ma, R. Buswell, W. Wilson, L. Wang, J. Xu, Z. Scott, "Technology readiness: A global snapshot of 3D concrete printing and the frontiers for development", *Cement and Concrete Research*, vol. 156, March 2022. [Online]. Available: https://www.sciencedirect.com/science/article/pii/S0008884622000655 [Accessed May 10, 2023].

[2] V. Mechtcherine et al., "Extrusion-based additive manufacturing with cement-based materials – production steps, processes, and their underlying physics: a review", *Cement and Concrete Research*, vol. 132 , June 2020. [Online]. Available: https://www.sciencedirect.com/science/article/abs/pii/S0008884619317132. [Accessed May 10, 2023].

[3] N. Stoiber, B. Kromoser, "Topology optimization in concrete construction: a systematic review on numerical and experimental investigations." *Structural and Multidisciplinary Optimization*, vol. 64, pp.1725–1749, Oct. 2021. [Online]. Available: https://link.springer.com/article/10.1007/s00158-021-03019-6. [Accessed May 10, 2023].

[4] E. Ivaniuk, S. Müller, T. Neef, V. Mechtcherine, "Strategies for integrating reinforcement into 3D concrete printing at TU Dresden" *Open Conference Proceedings*, vol. 1, pp. 23-35, Nov. 2021. [Online]. Available: https://www.tib-op.org/ojs/index.php/ocp/issue/view/3/8. [Accessed May 10, 2023].

[5] H.-M. Henning, A. Palzer, " Was kostet die Energiewende? Wege zur Transformation des deutschen Energiesystems bis 2050", pp. 50, Nov. 2015. [Online]. Available: https://www.ise.fraunhofer.de/de/veroeffentlichungen/studien/was-kostet-die-energiewende.html. [Accessed May 10, 2023].

[6] J. Brandes, M. Haun, D. Wrede, P. Jürgens, C. Kost, H.-M. Henning, "Wege zu einem klimaneutralem Energiesystem. Die deutsche Energiewende im Kontext gesellschaftlicher Verhaltensweisen", Nov. 2021. [Online]. Available: https://www.ise.fraunhofer.de/de/veroeffentlichungen/studien/wege-zu-einem-klimaneutralen-energiesystem.html. [Accessed May 10, 2023].

[7] Rhinoceros 3D, Version 7 SR19, [Online Download], Seattle, WA: Robert McNeel & Associates, 2022.

[8] D. Piker, "Kangaroo: Form Finding with Computational Physics"; *Architectural Design*, vol. 83, no. 2, pp. 136,137, March / April 2013.

[9] U. Riedel, „*Studienbuch Technische Mechanik 1: Statik starrer Körper"*. Iserlohn: Wissenschaftliche Genossenschaft Südwestfalen, 2021, pp. 93-115.

[10] D. Piker, "DynamicWeight1D Github Library", May 2016. [Online]. Available: https://github.com/Dan-Piker/K2Goals/blob/master/DynamicWeight1d.cs. [Accessed May 10, 2023].

[11] D. Piker, "Spring element of Github Library", May 2016. [Online]. Available: https://github.com/Dan-Piker/K2Goals/blob/master/Spring.cs. [Accessed May 10, 2023].

[12] D. Piker, "AnchorXYZ element of Github Library", May 2016. [Online]. Available: https://github.com/Dan-Piker/K2Goals/blob/master/AnchorXYZ.cs. [Accessed May 10, 2023].

IASS 2023 July 10–14 Melbourne Integration of Design and Fabrication

Proceedings of the IASS Annual Symposium 2023
Integration of Design and Fabrication
10–14 July 2023, Melbourne, Australia
Y.M. Xie, J. Burry, T.U. Lee and J. Ma (eds.)

Form finding of tensile membrane structures by solving the generalized laplace equation using physics informed neural network

Sounak KABASI [a,*], Allan L. MARBANIANG[a], Siddhartha GHOSH[b]

[a,*] Indian Institute of Technology, Bombay
Powai, Mumbai, Maharashtra- 400076
sounak.kabasi001@gmail.com

[b] Structural Safety, Risk & Reliability (SSRR) Lab, Department of Civil Engineering, Indian Institute of Technology Bombay, Mumbai 400076, India

Abstract

Tensile membrane structures are becoming more popular day by day as more and more designers are opting for membrane structures due to their light weight, high material usage efficiency and their unmatched ability of spanning large areas. The designer has to undertake a methodology known as "form finding" as the form of the structure is unknown beforehand and depends on the given stress conditions and boundary conditions. In essence, the form finding aims to find a configuration of the structure that is in static equilibrium. However, mainstream form finding algorithms suffer from several issues such as selection of initial form, severe computational burden for high dimensional problems, parameter sensitivity, mesh distortion, etc. Hence, the authors propose a new method for form finding of TMS based on the theory of a general curved interface. This theory is conventionally applied to understand the contours of lipid vessels, cell membranes, etc. by solution to the general Laplace equation which is derived from the comparison of the mechanical and thermodynamical approach of describing the phenomena of curved interfaces. The proposed methodology involves the solution of a modified form of this equation by employing a newly developed method in the field of supervised learning known as Physics Informed Neural Network. The proposed meshless method is seen to be independent of dimensionality of the problem as well as the initial shape.

Keywords: tensile membrane structure, form finding, neural network, laplace equation, physics informed neural network, curved interfaces, machine learning

1. Introduction

Tensile membrane structures (TMS) have gained huge traction in recent years for permanent construction of important structural members. Constructed with the help of light-weight fabrics, they can be easily used to cover large areas. Hence, they are primarily used as roofing structures of airports, stadiums, shopping malls, parking spaces, etc. The fabric material employed for constructing TMS is incapable of resisting shear and flexure. The stability of TMS is primarily derived from the membrane action of in-plane prestresses and the anticlastic configuration. The intensity of the applied prestress should be such that the membrane does not face tearing or wrinkling failure. An important advantage of TMS is that they can be prefabricated, thus resulting in higher quality control than conventional structures like RCC, steel or masonry structures. Another advantage of such structures is the architectural freedom that flexible membranes can offer. TMS has been designed to obtain several aesthetically pleasing structures. The main design philosophy of TMS design stems from a procedure known as "form finding." The form of the TMS is not known in advance and is dependent on the

Copyright © 2023 by Sounak KABASI, Allan L. MARBANIANG and Siddhartha GHOSH. Published in the Proceedings of the IASS Annual Symposium 2023 with permission.

prescribed boundary and stress conditions. During this stage, the TMS is expected to be in stress equilibrium subjected to the prescribed boundary conditions by forming the double-curved anticlastic surface. The overall structural performance of the TMS depends on the form finding algorithm employed. It is expected that the form finding framework will produce optimal structural forms that meet the functional and durability requirements while also being affordable and aesthetically acceptable. [1, 2] provides a list of traditional form finding algorithms along with their criticisms. Some of these drawbacks include computationally costly calculation of stiffness matrix due to inclusion of material properties in stiffness-based methods, constructionally impractical results obtained from Force Density methods, and lack of clarity in choosing optimum hyper-parameters in Dynamic equilibrium based methods. Furthermore, various issues faced by mesh based traditional methods also include mesh distortion and floating meshes and computational burden for high dimensional problems. [2] explored Finite element based and DR based form finding for TMS and found that the obtained results are highly susceptible to convergence issues in case of an incorrect selection of initial shape. Furthermore, there is no unique solution of the mesh topology on the surface for a defined prestress in the mesh dependent methods, resulting in singularity concerns that must also be addressed. Additionally, a group of TMS researchers performed a round robin form finding exercise and observed that the results varied significantly across the different strategies employed and hence, underlined the importance of a method that gave consistent results.

This research proposes a new mesh-free algorithm for TMS form finding. This unique form finding strategy makes use of the theory of a general curved interface that is mostly used in the scientific domains of biophysics and colloidal sciences in conjunction with the 'Physics Informed Neural Network' (PINN) [3], which is an exceptionally convenient yet conceptually straightforward technology in the domain of data-driven solutions of partial differential equations (PDE). In this study, the theory of general curved surfaces and its relation to the form finding of TMS are explored. A more suitable equation specialized towards TMS is derived and this equation is solved using the PINN. The proposed methodology involves the solution of a modified form of this equation by employing a newly developed method in the field of supervised learning known as Physics-Informed Neural Network (PINN). It is seen that, unlike the first PINN-based method developed by the authors for TMS form-finding [2] for minimal TMS, the method proposed here can handle anisotropically prestressed TMS (non-minimal) as well. The proposed meshless method is seen to be independent of the initial shape, mesh distortion, and material properties. Different numerical form-finding case studies are presented to show the validity, accuracy and advantage of the proposed meshless form-finding method.

The rest of the manuscript is organized in the following order. Sec. 2 introduces the theory of a general curved interface and its relation to the form finding of TMS. A brief discussion on the framework of PINN is given in Sec. 3. The proposed methodology of the form finding of TMS is described in Sec. 4 followed by the form finding case studies in the subsequent chapter (Sec. 5). The manuscript ends with some concluding remarks in Sec. 6.

2. Theory of curved interfaces and its relation to form finding

There are two broad ways in which the theoretical and mathematical description of a general curved interface is approached. The first approach comes from a mechanical stand of view arising from the Kirchhoff-Love theory of plates and shells [4]. Although a benchmark in mechanical sciences, this theory is often applied to describe the surface of bio-membranes and lipid bilayers owing to its strong mathematical foundations based on two dimensional continuum mechanics, differential geometry, and tensor analysis. The second approach originates from Gibbs theory of capillarity [5] which is based on thermodynamics and is frequently cited in the domains of physical chemistry and surface sciences. [6] provided a detailed literature review of these two approaches and pondered on the relationship between the two widely different approaches used to describe the same phenomena. They came to the conclusion that the two approaches were actually equivalent and complemented each other and discovered the form of an elegant Generalized Laplace Equation. They suggested that this equation can be used to describe

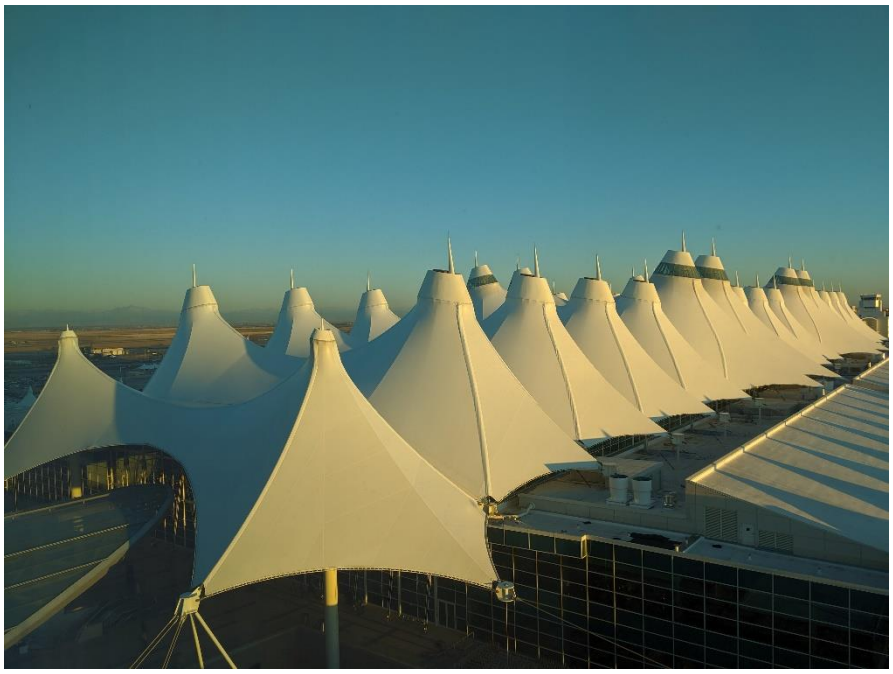


Figure 1. TMS example: Denver International airport [Wikimedia Commons]

the surface of any curved surfaces, thin films or membranes. The Generalized Laplace equation as derived in detail by [6] is given by:

$$2H\sigma + 2D\eta - 0.5\left(a^{\alpha\beta}B + q^{\alpha\beta}\Theta\right)_{\alpha\beta} = P_{II} - P_I \tag{1}$$

where,

$$\begin{aligned} \sigma &= 0.5\left(\sigma_x + \sigma_y\right) \\ \eta &= 0.5\left(\sigma_x - \sigma_y\right) \\ B &= M_1 + M_2 \\ \Theta &= M_1 - M_2 \end{aligned} \tag{2}$$

H and D are mean curvatures and deviatoric curvatures [7] at a point on the surface respectively. P_I, P_{II} are the pressures in the bulk phases. σ_x, σ_y are the eigenvalues of the surface stress tensor. M_I, M_{II} are the eigen values of the surface moment tensor. $a^{\alpha\beta}$ is the surface metric tensor and $q^{\alpha\beta}$ is the deviatoric curvature tensor. It is known that tensile membrane structures cannot resist bending stresses. Therefore, M_I , M_{II} are equal to zero. Hence, $B, \Theta = 0$. Additionally, no external loading is considered during form finding. Therefore, Eq. 1 can be reduced to the form found surface equation of TMS and can be written as:

$$H\sigma + D\eta = 0 \tag{3}$$

Due to the $\pm$ sign in the expression of $D = \pm\sqrt{H^2 - K}$ [7], where, K is the Gaussian curvature, it becomes tricky to solve Eq. 3 directly for form finding purpose. Furthermore, the square root term may also cause different numerical instabilities. Instead of solving Eq. 3 directly, $H\sigma - D\eta$ (analogous to the weight function in Finite element analysis) is multiplied on both sides of the equation and the integral given by Eq. 4 is solved (using Monte Carlo integration with N_f number of collocation points) as:

$$\begin{aligned} &\int_{\Omega}\left(H\sigma+D\eta\right)\left(H\sigma-D\eta\right)=0 \\ &\sum_{i=1}^{N_f}\left[\left(H\sigma\right)^2-\left(H^2-K\right)\eta^2\right]=0 \end{aligned} \tag{4}$$

3. Physics-informed neural network

Physics informed neural networks (PINNs) [3] are a type of neural network architecture that can learn from physics-based constraints. These constraints can be incorporated into the network's architecture as additional terms in the loss function. The general form of the loss function for a PINN is:

$$\mathrm{L}=\frac{1}{N_u}\sum_{i=1}^{N_u}\left|z(x_i)-\tilde{z}(x_i)\right|_2^2+\frac{\lambda}{N_f}\sum_{j=1}^{N_f}\left|f(x_j)\right|_2^2 \tag{5}$$

where N_u and N_f are the number of training points (for boundary/initial conditions) and physics-informed points, respectively. $\tilde{z}(x_i)$ is the predicted solution at the input x_i, and $z(x_i)$ is the true solution at the same point which is typically in the form of boundary constraints. $f(x_j)$ represents the residual of the governing equations at the input x_j, and λ is a hyper-parameter that controls the relative importance of the data (boundary/initial conditions) and physics terms in the loss function. PINNs can be used to solve a variety of physics problems, such as fluid dynamics, solid mechanics, etc. [2,3]. They are particularly useful when analytical solutions are not available or are difficult to obtain, as they can learn to approximate the solution directly from data and physics-based constraints. Overall, PINNs represent a promising approach for combining machine learning and physics-based modeling, and have the potential to revolutionize the way we approach complex physics problems.

4. Proposed approach

The approximate partial differential equation that governs the shape of the form found shape of TMS subjected to a general initial prestress condition is given by Eq. 4. This section introduces a framework for finding the solution of this equation with the help of PINN, thus finding an approximate equation of the form found shape while respecting the given boundary conditions within a low tolerance value. The basic idea of the proposed framework lies in finding the unknown solution, $z(x,y)$ of the Eq. 4 by approximating the solution of the partial differential equation using a neural network, $\tilde{z}(x,y)$. The proposed algorithm for form finding of TMS is elaborately described below:

Step 1: Boundary collocation points, $\left(x_u^i, y_u^i, z^i\right)_{i=1}^{N_u}$ and domain collocation points, $\left(x_f^i, y_f^i\right)_{i=1}^{N_f}$ are generated using Uniform distribution and Latin Hypercube sampling [8] respectively, where the x and y co-ordinates of the boundary collocation points are given by x_u^i and y_u^i respectively and z^i are the corresponding z coordinates which are to be dictated by the prescribed boundary conditions. x and y coordinates of the domain collocation points are represented by x_f^i and y_f^i respectively.

Step 2: The weights (W) and biases(B) of the neural network, $\tilde{z}(x,y)$ are initialized using Xavier Initialization [9]. The input layer of the neural network consists of two neurons and the output layer consists of just one neuron. The vectors of x and y coordinates of the collocation points are fed into the two input neurons which finally yields the vector of the unknown z coordinates of the form found shape.

Step 3: Using auto-differentiation, determine H, D [7] and find f as discussed in Sec. 3. In this case, Eq. 4 is to be approximated by f. To be specific, let's define f as f_{GLE} given by

$$f_{GLE} = \left[(H\sigma)^2 - \left(H^2 - K\right)\eta^2 \right] \tag{6}$$

Step 4: Update W and B of $\tilde{z}(x, y)$ by minimizing the loss function, E (Eq. 7) i.e. the sum of the MSE (Eq. 8) and standard deviation of the squared errors (Eq. 9).

$$E = MSE_u + MSE_f + STD_u + STD_f \tag{7}$$

$$MSE_u = \frac{1}{N_u}\sum_{i=1}^{N_u} \left| \tilde{z}\left(x_u^i, y_u^i\right) - z^i \right|^2 ; MSE_f = \frac{1}{N_f}\sum_{i=1}^{N_f} \left| f\left(x_f^i, y_f^i\right) \right|^2 \tag{8}$$

$$STD_u = \sqrt{\frac{\sum_{i=1}^{N_u} \left(|\, \tilde{z}(x_u^i, y_u^i) - z^i \,|^2 - MSE_u \right)^2}{N_u - 1}} ; STD_f = \sqrt{\frac{\sum_{i=1}^{N_f} \left(|\, f(x_f^i, y_f^i) \,|^2 - MSE_f \right)^2}{N_f - 1}} \tag{9}$$

MSE_u and STD_u are the error functions to be minimized for enforcing the boundary conditions whereas MSE_f and STD_f are minimized for enforcing the physical law defined by Eq. 4. The addition of the standard deviation in the error function improves the accuracy of the final solution [2]. In this study, the L-BFGS-B optimizer [10] is used for the training process as was suggested in [3].

Step 5: Once the convergence criteria of the optimizer is met, the PINN can be used as an approximate explicit analytical equation of the form found shape which can be subsequently used to generate the z coordinate of any given set of the x and y coordinates within the prescribed domain. Therefore, the coordinates of the form found shape of the TMS under the given boundary conditions and the initial stress conditions can be found from the ordered triplet (x, y, z).

5. Numerical study

This particular example deals with a frame supported non-minimal TMS $(\sigma_x \neq \sigma_y)$. The domain of x and y have been taken as [-2.5,2.5] m and [-5,5] m respectively. The height of the high points relative to the lower vertices is taken as 1 m. The boundary collocation points are shown in Fig. 2 (a). The final shape obtained using 2 hidden layers and 20 neurons per hidden layers [2] for $(N_u, N_f) = (30000,120)$ using the proposed PINN framework are shown in Fig. 2 (b) and Fig. 2 (c) for (σ_x, σ_y) = (4,3) kN/m and (2,4) kN/m, respectively. The prediction error at the boundaries are calculated as a percentage of the maximum TMS dimension and are found to be 0.36 % and 0.47 % respectively which signifies that the proposed PINN is able to accurately simulate the prescribed boundary conditions. The unbalanced residual forces calculated as shown in [2] are found to be 9.86×10^{-5} kN and 3.93×10^{-4} kN respectively which shows that the proposed method yields form found TMS that are in static equilibrium (acceptable tolerance 10^{-2} kN [12, 13]). The time required for convergence is 15 seconds on a 16 GB RAM standard work station (GPU is not used in this case).

6. Conclusion

This study explores the applicability of a general form of the Laplace Equation for the form finding exercise. This equation originates from the theory of general curved surfaces which is usually characterized by the mechanical approach and the thermodynamical approach. Based on this theory, an equation for form finding of TMS is proposed. This partial differential equation is solved using a

recently introduced algorithm in the domain of supervised learning known as Physics Informed Neural networks. It is seen that the proposed framework can be used for both isotropic (formulation reduces to [2] in this case i.e. $\sigma_x = \sigma_y$) and anisotropic initial prestress conditions and forms a robust tool for the form finding exercise unlike the PINN based method proposed in [2] which is only applicable for minimal TMS. Furthermore, the proposed framework has all the advantages of PINN-based framework proposed in [2] with respect to conventional mesh-based form finding frameworks like independent of the initial shape (since initial PINN parameters are initialized randomly) and material properties while also being immune to mesh distortion issues (as it is mesh-less). The proposed method does not require any discretization and the boundary can be enforced at discrete point similar to what is done in point collocation methods even for very complex frame-supported TMS. However, this manuscript presents an initial study to test the applicability of this novel mesh-less approach and needs to be tested on a larger variety of TMS case studies in the future. Furthermore, the proposed method is not applicable for cable-supported TMS as the boundary in such cases is not fixed as in frame-supported TMS. So, this PINN based form finding method needs to be explored further so as to increase the applicability to more general cases of TMS.

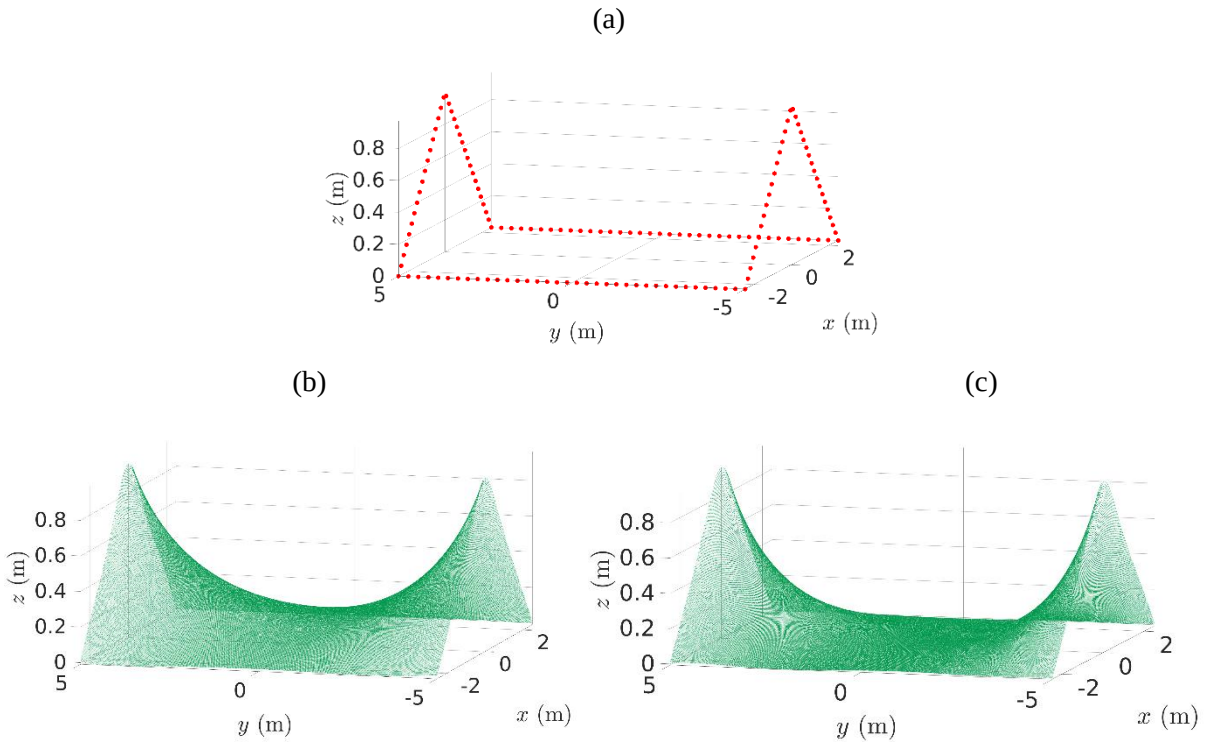


Figure 2. (a) Boundary collocation points, Form found surface for $(\sigma_x, \sigma_y) =$ (b) (4,3) kN, (c) (2,4) kN

Acknowledgements

The authors would like to express their gratitude to the Science and Engineering Research Board (SERB), India for providing the financial assistance under a research grant (CRG/2018/000498).

References

[1] D. Veenendaal and P. Block, "An overview and comparison of structural form finding methods for general networks," *International Journal of Solids and Structures*, vol. 49, pp. 3741-3753, 2012.

[2] Sounak Kabasi, A. L. Marbaniang, and S. Ghosh, "Physics-informed neural networks for the form finding of tensile membranes by solving the Euler–Lagrange equation of minimal surfaces," *Thin-Walled Structures*, vol. 182, pp. 110309, 2023.

[3] M. Raissi, P. Perdikaris, and G. E. Karniadakis, "Physics-informed neural networks: A deep learning framework for solving forward and inverse problems involving nonlinear partial differential equations," *Journal of Computational Physics*, vol. 378, pp. 686–707, 2019.

[4] Ciarlet, Philippe G, "Mathematical elasticity: volume II: theory of plates*," Studies in Mathematics and its Applications*, vol. 27, pp.1-499, 1997.

[5] G. J. Willard, *The scientific papers of j. Willard gibbs: Dynamics*. Dover Publ., 1961.

[6] P. Kralchevsky, J. Eriksson, and S. Ljunggren, "Theory of curved interfaces and membranes: mechanical and thermodynamical approaches," *Advances in colloid and interface science*, vol. 48, pp. 19–59, 1994.

[7] E. P. Lane, *Metric differential geometry of curves and surfaces*. Chicago, 1940.

[8] M. D. McKay, R. J. Beckman, and W. J. Conover, "A Comparison of three methods for selecting values of input variables in the analysis of output from a computer code," *Technometrics*, vol. 21, pp. 55-61, 1979.

[9] X. Glorot and Y. Bengio, 2010, March. Understanding the difficulty of training deep feedforward neural networks. In *Proceedings of the thirteenth international conference on artificial intelligence and statistics*, March 2010, JMLR Workshop and Conference Proceedings.

[10] D. C. Liu and J. Nocedal, "On the limited memory BFGS method for large scale optimization," *Mathematical Programming*, vol. 45, pp. 503-528, 1989.

[11] W. J. Lewis, *Tension structures -Form and behaviour*. Thomas Telford Publishing, 2003.

[12] B. H. V. Topping and P. Ivanyi, *Computer aided design of cable membrane structures*. Saxe-Coburg Publications, 2007.

A. L. Marbaniang, S. Dutta, and S. Ghosh, "Updated weight method: an optimisation-based form-finding method of tensile membrane structures," *Structural and Multidisciplinary Optimization*, vol. 65, pp. 169, 2022.

IASS 2023
July 10–14 Melbourne
Integration of Design and Fabrication

Proceedings of the IASS Annual Symposium 2023
Integration of Design and Fabrication
10–14 July 2023, Melbourne, Australia
Y.M. Xie, J. Burry, T.U. Lee and J. Ma (eds.)

Form-finding of membrane structures using transfinite interpolated initial shapes

Allan L. MARBANIANG[a,*], Sounak KABASI[a], Siddhartha GHOSH[b], Subhrajit DUTTA[c]

[a,*] Department of Civil Engineering, Indian Institute of Technology Bombay, Mumbai 400076, India
allanmarbaniang@gmail.com

[b] Structural Safety, Risk & Reliability (SSRR) Lab, Department of Civil Engineering, Indian Institute of Technology Bombay, Mumbai 400076, India
[c] Department of Civil Engineering, National Institute of Technology Silchar, Silchar 788010, India

Abstract

Tensile membrane structures (TMS) are efficient, sustainable, and aesthetically pleasing structures. These structures are made up of a membrane fabric that has negligible bending stiffness. The membrane structures resist external loading due to the stiffness provided by the internal membrane prestress and anticlastic curvature. The initial equilibrium shape of these structures is a function of the initial prestress and boundary conditions and is not known beforehand. This shape has to therefore be found by a process called form-finding. Most mesh based form-finding methods depend significantly on the definition or choice of the initial shape; e.g., the dynamic relaxation method requires an initial starting solution to initialise the form-finding process. Other geometry based approaches such as the recently developed optimisation-based updated weight method, also requires the weights to be defined with respect to an initial reference configuration that gets updated. The choice of the initial shape is therefore crucial as it affects the final solution and overall convergence. This study proposes the choice of the initial solution using a transfinite interpolation function derived from the initial boundary conditions. This approach is applied on both dynamic relaxation and updated weight methods for demonstration. Form-finding solutions using the interpolated initial shapes are compared with the results of those that use simplified starting points, in terms of efficiency and convergence metrics. The comparison is done for both frame and cable-supported TMS.

Keywords: form-finding, transfinite interpolation, optimisation, tensile membranes

1. Introduction

The appeal of tensile membrane structures (TMS) lies in their affordability, minimal weight, eco-friendliness and visually appealing design [1]. TMS comprise of flexible membranes that are supported by cables or rigid frame structural elements. These structures are efficient because of their ability to span large distances with minimal material use. The membrane structure is flexible and resists external loads through the action of the internal in-plane forces and the curvature of the surface. The fabric comprises of orthogonal fibres weaved along the ‘warp’ and ‘weft/fill’ direction. The initial shape of these structures is unknown and must be found through a process known as form-finding. TMS are flexible and take an initial shape depending on the internal prestress and boundary condition. The objective of form-finding is to find the equilibrium shape having the target design prestress distribution. Physical form-finding methods have been mostly replaced by numerical form-finding methods with varying approaches. [2] categorised different form-finding methods into the dynamic equilibrium methods [3], geometric [4] and stiffness-based methods [5]. A recent optimisation-based approach, the updated weight method was also developed for the form-finding of both frame and cable supported TMS

Copyright © 2023 by Allan L. MARBANIANG, Sounak KABASI, Siddhartha GHOSH and Subhrajit DUTTA. Published in the Proceedings of the IASS Annual Symposium 2023 with permission.

[6]. Because form-finding methods, such as the dynamic relaxation method, are highly nonlinear, an initial solution is required as a starting point. In the updated weight method, an initial reference configuration is required to define the weights. The choice of the initial shape is usually assumed at the mid-height or a as planar configuration. However, this initial solution can influence the overall convergence and final solution.

In this study, a transfinite interpolated function is used to find the initial shape for a predefined boundary condition. The interpolation function is constructed with respect to the values imposed at the boundary points. This initial shape is used for popular form-finding methods such as the dynamic relaxation method (DR) [3] and the updated weight method (UWM). Different numerical case studies using the proposed approach are preformed and compared with the standard initial shapes to show the overall advantage of the proposed formulation.

The paper is organised as follows. Sec. 2 gives an introduction to the dynamic relaxation method and the updated weight method. The theory of the adopted transfinite interpolation and its implementation in form-finding is detailed in Sec. 3. Numerical studies are then presented in Sec. 4. Final concluding remarks are given in Sec. 5.

2. Form-finding techniques

2.1. Background

In form-finding, the membrane continuum is discretised into finite elements. The use of constant strain triangle elements (CST) is a popular choice to discretise the membrane domain [7]. Another popular method is to represent each triangular membrane element by pseudo-cable elements having side length L_j for each j th side (j=1, 2, 3). The membrane thickness is included in the membrane prestress (which is expressed in kN/m). In the pseudo-cable representation of the membrane element, the natural side force vector $\mathbf{t}$ force due to the internal stresses, along each element side t_j is given as

$$\mathbf{t} = AL^{-1}\mathbf{G}^{\mathrm{T}}\boldsymbol{\Phi}^{-1}\boldsymbol{\sigma} \tag{1}$$

where A is the area of the element, $L = diag\left(L_1, L_2, L_3\right)$, $\boldsymbol{\sigma} = \begin{bmatrix} \sigma_w & \sigma_f & 0 \end{bmatrix}^T$ is the target stress along the warp and fill directions. The transformation matrix $\boldsymbol{\Phi}^{-1}$, rotates the initial prestress from the material fibre (defined globally with respect to the fabric properties) to the local basis direction (defined locally for an element). The matrix $\mathbf{G}$ transforms the stresses defined in the local basis to the natural stress vectors along the triangular element side lengths [1, 8].

Cable elements are discretised by line elements having length l with n denoting the target internal cable force.

2.1. Dynamic relaxation method

In the dynamic relaxation method (DR) [3, 8]**,** a pseudo dynamic problem having fictitious mass and damping properties is considered. The method is based on the principle that any system subjected to an out-of-balance force will only come to rest when it is in equilibrium. The out of balance forces, due to the member forces, causes this lumped mass system to oscillate about an equilibrium position. The oscillations reduce to an equilibrium state under the action of damping or by monitoring the kinetic energy. The equation of motion of an unconstrained node m at time t is [3]

$$\mathbf{R}_m^t = \mathbf{M}_m^t \ddot{\mathbf{u}}_m^t \tag{2}$$

where $\mathbf{R}_m^t$ is the residual force at node m at time t in all the components, $\mathbf{M}_m^t$ is the assumed nodal lumped mass and $\ddot{\mathbf{u}}_m^t$ is the acceleration at the node at time t. Using a central difference form for $\ddot{\mathbf{u}}_m^t$, Equation (2) then become

$$\dot{\mathbf{u}}_m^{t+\Delta t/2} = \dot{\mathbf{u}}_m^{t-\Delta t/2} + \frac{\Delta t}{M_m}\mathbf{R}_m^t \tag{3}$$

where $\dot{\mathbf{u}}_m^{t+\Delta t/2}$ and $\dot{\mathbf{u}}_m^{t-\Delta t/2}$ are the velocities at different time increments. $\mathbf{R}_m^t$ is the residual force due to internal prestress force at $\mathbf{x}_m^t$, and a single mass M_m is taken for all components at node m. The geometry is updated in the next time increment using the following equation

$$\mathbf{x}_m^{t+\Delta t} = \mathbf{x}_m^t + \Delta t\, \dot{\mathbf{u}}_m^{t+\Delta t/2} \tag{4}$$

The residual $\mathbf{R}_m^t$ at a time increment t is found from the summation of the residual forces due to the natural side forces $\mathbf{t}$ and cable forces n, due to the target prestress and cable forces at the current configuration. M_m is taken as the maximum of the mass components at the node.

$$M_m^t = \max\left(\mathbf{M}_m\right) = \max([M_{mx}\ M_{my}\ M_{mz}]) \tag{5}$$

where the mass M_{mx} of node m in component direction x is found according to [8]. Kinematic damping is used to dampen the oscillation motion towards an equilibrium state by monitoring the value of the kinetic energy of the whole system. At each peak in the kinetic energy, the process is restarted, while maintaining the current nodal positions and setting the initial velocity and kinetic energy equal to zero.

2.2. Updated weight method

In UWM, the weighted function of the geometric shape is minimised. The objective function for UWM is defined as

$$f_{UW} = \sum_{i=1}^{N_m}\sum_{j=1}^{3} W_i^{\,j}\left(L_i^j\right)^2 + \sum_{i=1}^{N_c} w_i (l_i)^2 \tag{6}$$

where L_i^j and $W_i^{\,j}$ are the side length and corresponding weight of the j th side for the i th membrane element, w_i and l_i define the cable weight and length respectively for the i th cable element. The weights are found with respect to a reference configuration $\mathbf{x}_{ref}$ as

$$W_i^{\,j} = \frac{t_i^j}{2\left(L_i^j\right)_{ref}} \quad \text{and} \quad w_i = \frac{n_i}{2(l_i)_{ref}} \tag{7}$$

where $\left(L_i^j\right)_{ref}$ and $\left(l\right)_{ref}$ are the pseudo-cable length of the membrane and cable length respectively in $\mathbf{x}_{ref}$. This reference configuration is initially taken as a flat planar configuration. The form found shape for a particular set of weights is given by the given standard optimisation formulation given as

$$\mathbf{x}^* = \min\ f_{UW} \tag{8}$$

The equilibrium solution after solving each optimisation step is used as the next reference configuration $(\mathbf{x}_{ref} = \mathbf{x}^*)$. The corresponding weights are recalculated, and the optimisation process is repeated until convergence. The detailed implementation and algorithm of UWM is given in [6].

3. Implementation of transfinite initial shape

3.1. Transfinite interpolation

TMS are usually either frame or cable supported. Frame supports comprise of linear line elements that are rigid. In cable-supported TMS, the boundary edge of the membrane is supported by cables that are fixed at boundary points. The transfinite interpolation in this study makes the use of approximate distance functions defined with respect to any boundary element [9]. In this section, the distance functions for the line segment and boundary point are given.

Line segment: The approximate distance function $p(\mathbf{x})$ at any point $\mathbf{x}$ with respect to any line segment joining any two points $\mathbf{x}_1 = (x_1, y_1)$ and $\mathbf{x}_2 = (x_2, y_2)$, having a length, $L_R = \sqrt{(\mathbf{x}_2 - \mathbf{x}_1)^{\mathrm{T}} \cdot ? \mathbf{x}_2 - \mathbf{x}_1)}$ is given as

$$p(\mathbf{x}) = p(x, y) = \sqrt{b^2 + \frac{(a-c)^2}{4}} \tag{9}$$

where the parameters a, b and c are given as follows:

$$\begin{aligned} a &= \sqrt{b^2 + c^4}; \\ b &= \frac{1}{L_R}\left[\left(\frac{L_R}{2}\right)^2 - \sqrt{(\mathbf{x} - \mathbf{x}_m)^T . (\mathbf{x} - \mathbf{x}_m)}^2\right]; \\ c &= \frac{(x - x_1)(y_2 - y_1) - (y - y_1)(x_2 - x_1)}{L_R} \end{aligned} \tag{10}$$

where the mid-point of the line segment is defined as $\mathbf{x}_m = \frac{\mathbf{x}_1 + \mathbf{x}_2}{2}$.

Boundary points: The function $p(\mathbf{x})$ at any point $\mathbf{x}$ with respect to any boundary point $\mathbf{x} = (x_p, y_p)$ is given as

$$p(\mathbf{x}) = p(x, y) = \sqrt{(x - x_p)^2 + (y - y_p)^2} \tag{11}$$

3.2. Initial shape implementation

In DR, the standard initial starting solution is usually taken at the mid-height. as the starting solution. In the case of UWM, a flat configuration is used to as the initial reference configuration. In this study,

however, we use the transfinite interpolant function to interpolate the initial shape for DR and the reference configuration for UWM. The interpolated initial shape is defined as

$$N(\mathbf{x}) = N(x, y) = \sum_{i=1}^{N_{BC}} N_i^W(\mathbf{x}) z_i(\mathbf{x}) \tag{12}$$

where $z_i(\mathbf{x})$ is the value of the imposed boundary. The interpolating weights $N_i^W(\mathbf{x})$ is given as

$$N_i^W(\mathbf{x}) = \frac{p_i^{-1}}{\left(\sum_{j=1}^{N_{BC}} p_j^{-1}\right)} \tag{13}$$

for all N_{BC} number of boundary elements. The initial solution satisfies the imposed boundary condition. In both DR and UWM, a meshed domain is defined and the z co-ordinate of all the nodes of the mesh is found using Equation (12) and used as the initial shape.

4. Numerical study

In this section, a numerical study of the use of the transfinite interpolation is done for both DR and UWM. The case studies consist of both a frame and cable supported hypar having a width and breath of 6 m, with the maximum height at 2 m. An isotropic desired prestress of 3 kN/m and cable force of 30 kN (in the cable supported example) is taken. In both the studies a comparison of the solutions by using the conventional and transfinite interpolated shape are shown. DR converges when the maximum absolute residual force is less than 10^{-3} kN with a time step of t=1 s and the mass calculated according to Sec. 2.1. In UWM the weight update converges when the maximum standard deviation of the equilibrium stress is less than 10^{-2} kN/m. The numerical problems are implemented in *MATLAB* on a Windows 11 system.

4.1. Frame-supported hypar

A frame supported hypar is taken with all the boundary edges fixed (Figure (1)). The standard initial starting solution for DR is shown in Figure (1a), while the initial reference solution for UWM is shown in Figure (1b). The transfinite initial starting point using Equation (12) is shown in Figure (1c). It can be seen from Figure (2a), that the mesh is highly distorted in the final form-found shapes using DR using the standard initial shape. Using the transfinite initial shape, however leads to a much more uniform looking mesh (Figure (2b)). This is helpful especially in a method such as DR where mesh distortion can occur and the solution convergence can get stuck. The form-found shapes for UWM, between the transfinite and standard approach are however very similar (Figure (3a) and (3b)). This is because of the fact that in UWM, a planar initial reference configuration allows for a homogeneous distribution of initial weights, resulting in a well distributed mesh in the equilibrium configuration. The stress distribution (along the 'warp' and 'fill') on the equilibrium shape for UWM after the first weight update is shown in Figure (4) for both the cases. The median is shown by the horizontal line, with the top and bottom box edges representing the 75th and 25th percentile values respectively. The whiskers represent the maximum and minimum values. It can be seen that the stress distribution after the first weight update is relatively slightly better in the transfinite interpolated case. The number of iterations for convergence for both DR and UWM is shown in Table 1. It can be seen that the number of iterations is significantly reduced for the case of DR.

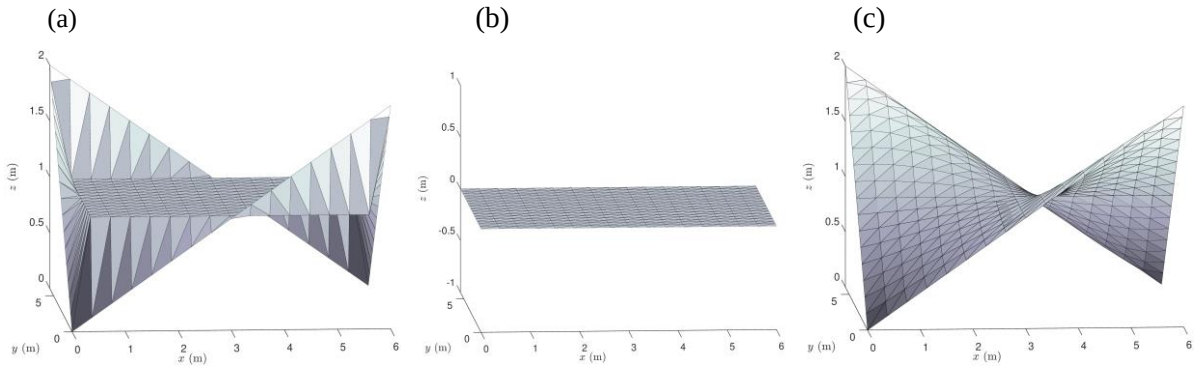


Figure 1. (a) Initial solution shape for DR; (b) Initial reference shape UWM; (c) Transfinite interpolated initial shape

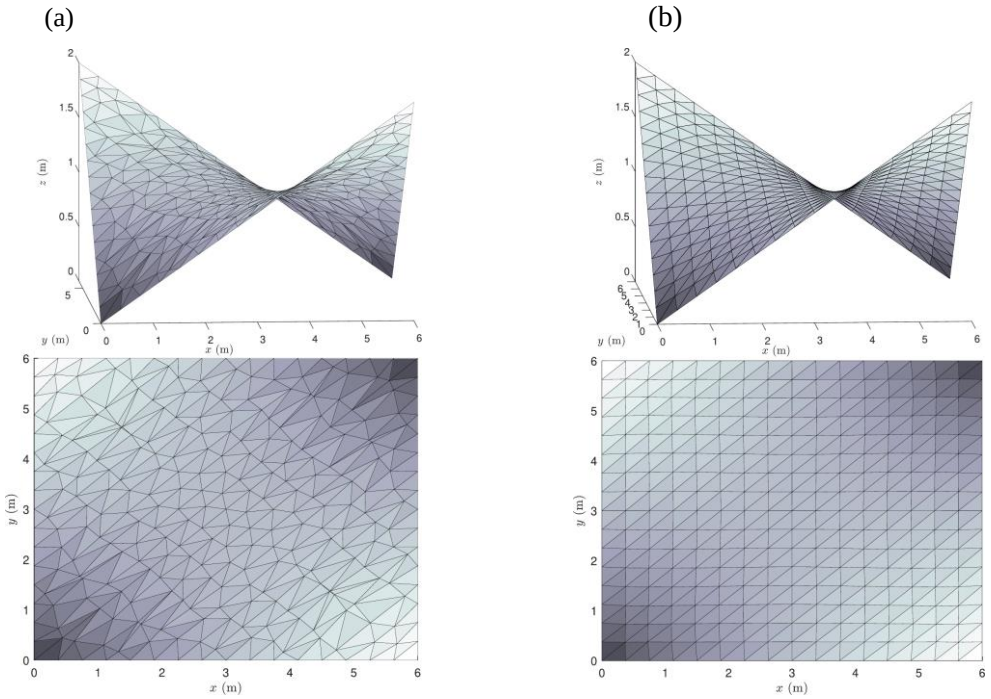


Figure 2. Form-found shape for DR for (a) Standard (b) Transfinite interpolated initial shape for frame supported hypar

Table 1. Number of iterations for convergence

	DR		UWM	
	Transfinite	Standard	Transfinite	Standard
Frame-supported	25	232	2	2
Cable-supported	394	431	4	5

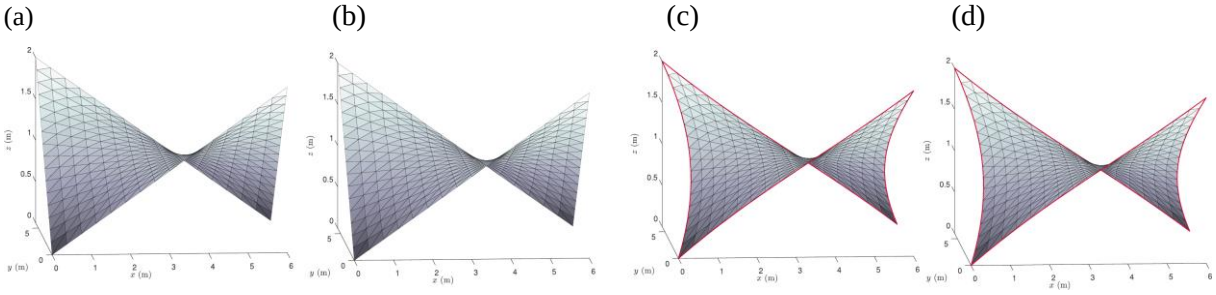


Figure 3. Form-found shape for UWM for frame supported using (a) Standard (b) Transfinite interpolated initial shape; for cable supported using (c) Standard (d) Transfinite interpolated initial shape

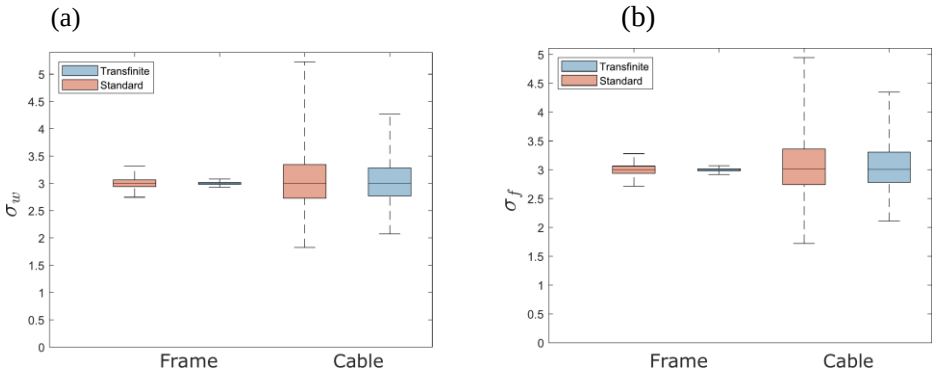


Figure 4. Stress distribution after first UWM weight update iteration for (a) σ_w (b) σ_f

4.1. Cable-supported hypar

The cable-supported hypar is shown in Figure (5) with the boundary cables fixed at four boundary points at the vertices. Figures (5a) and (5b) show the standard initial shape for DR and UWM respectively. Figure (5c) shows the transfinite interpolated shape generated by using the four boundary points in the distance function in Equation (12). In the case of DR, it is seen from Figures (6a) and (6b), that an improvement in mesh distribution is seen for the transfinite interpolated case. Similarly, to the previous section, there is no significant improvement for the form-found shapes using UWM as the final mesh in the standard solution is already well distributed (Figures (3c) and (3d)). However, it can be seen from Figure (4) that the stress distribution after the first weight update is significantly better for the transfinite interpolated case. At the first weight update iteration, the maximum standard deviation in the stress distribution in the standard case is 0.56 kN/m and 0.45 kN/m for the transfinite case. Table 1 shows that the number of iterations is reduced in the transfinite interpolated case for both DR and UWM.

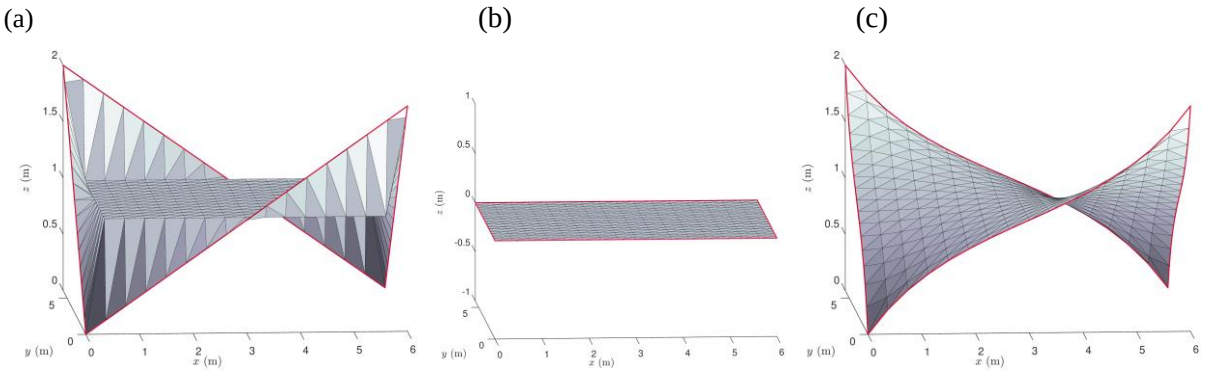


Figure 5. (a) Initial solution shape for DR; (b) Initial reference shape UWM; (c) Transfinite interpolated initial shape

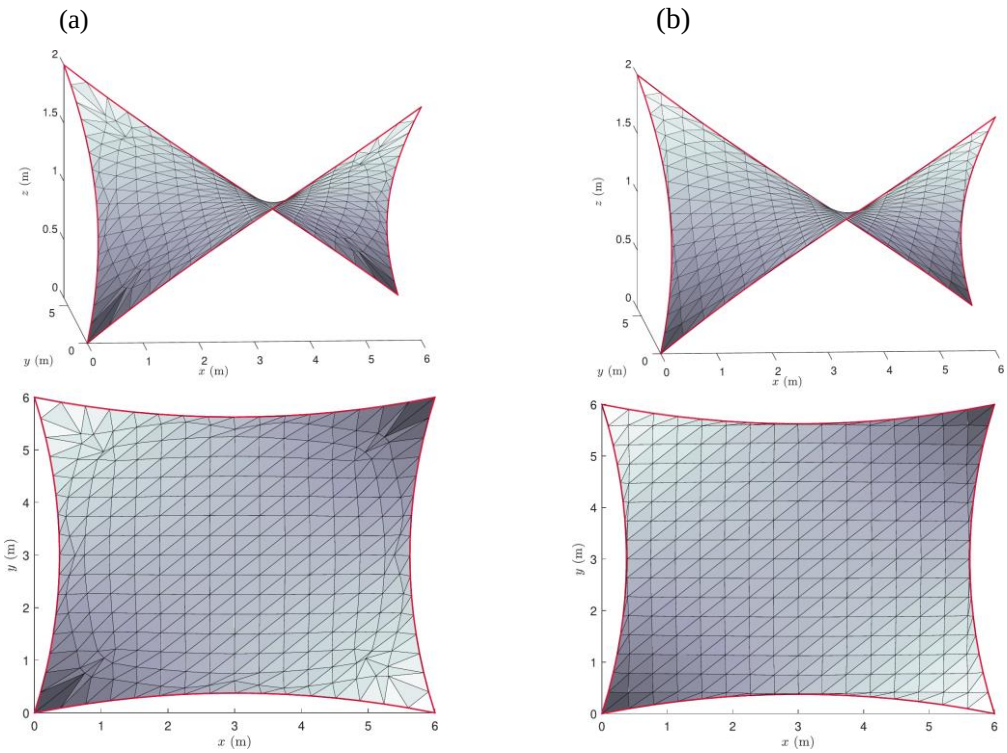


Figure 6. Form-found shape for DR for (a) Standard (b) Transfinite interpolated initial shape for cable supported hypar

5. Conclusion

The success of the form-finding process depends on the form-finding method employed and various hyper parameters. One such step is in defining the initial starting solution. In this study, the initial shape is found using the transfinite interpolation. The function can be constructed with respect to defined boundary line segments and points. The initial shape is used as the starting solution in DR and the initial reference configuration in UWM. It is seen that the proposed approach is advantageous and brings improvements in mesh uniformity, convergence and stress distribution. The method is highly effective for DR where the mesh in the final solution is highly improved along with a reduction in the total number

of iterations. Overall, the proposed method is expected to provide a more robust initial shape selection for different form-finding methods.

Acknowledgements

The authors would like to express their gratitude to the Science and Engineering Research Board (SERB), India for providing the financial assistance under a research grant (CRG/2018/000498)

References

[1] B. Bridgens and M. Birchall, "Form and function: The significance of material properties in the design of tensile fabric structures", *Engineering Structures*, vol. 44, pp. 1–12, 2012.

[2] D. Veenendaal, and P. Block. "An overview and comparison of structural form finding methods for general networks", *International Journal of Solids and Structures*, vol. 49(26), pp. 3741–3753, 2012.

[3] M.R. Barnes, "Form finding and analysis of tension structures by dynamic relaxation", *International Journal of Space Structures*, vol. 14(2), pp. 89–104, 1999.

[4] H.J. Schek, "The force density method for form finding and computation of general networks", *Computer Methods in Applied Mechanics and Engineering*, vol. 3, pp. 115–134, 1974.

[5] W.J. Lewis, "The efficiency of numerical methods for the analysis of prestressed nets and pin-jointed frame structures", *Computers and Structures*, vol. 33(3), pp. 791–800, 1989.

[6] A.L. Marbaniang, S. Dutta, and S. Ghosh, "Updated weight method: an optimisation-based form-finding method of tensile membrane structures", *Structural and Multidisciplinary Optimization*, vol. 65(6), pp. 169, 2022.

[7] B. Tabarrok, and Z. Qin, "Nonlinear analysis of tension structures", *Computers and Structures*, vol. 45(5), pp. 973–984, 1992.

[8] B. Topping, and P. Ivanyi, *Computer aided design of cable membrane structures*. Stirling, United Kingdom: Saxe-Coburg Publications, 2007.

[9] N. Sukumar and A.Srivastava, "Exact imposition of boundary conditions with distance functions in physics-informed deep neural networks", *Computer Methods in Applied Mechanics and Engineering*, vol. 389, 2021.

IASS 2023
July 10–14 Melbourne
Integration of Design and Fabrication

Proceedings of the IASS Annual Symposium 2023
Integration of Design and Fabrication
10 – 14 July 2023, Melbourne, Australia
Y.M. Xie, J. Burry, T.U. Lee and J. Ma (eds.)

Generation of a compression-tension combined funicular polyhedral beam structure

Hua CHAI[a,*], Yao LU[a], Ma´rton HABLICSEK[b], Masoud AKBARZADEH[a,c]

[a,*] Polyhedral Structures Laboratory, Weitzman School of Design, University of Pennsylvania, Philadelphia, USA
Pennovation Center, 3401 Grays Ferry Ave. Philadelphia, PA, 19146
hchai@upenn.edu

[b] Department of Mathematics, Leiden University, Leiden, Netherlands
[c] General Robotic, Automation, Sensing and Perception (GRASP) Lab, School of Engineering and Applied Science, University of Pennsylvania, Philadelphia, USA

Abstract:

This paper presents a robust form-finding method by implementing algebraic polyhedral graphic statics to generate compression-tension combined beam structure. Compared to iterative graphic statics modeling, the advanced algebraic method can define the inputs and constraints of complex geometries rapidly and precisely. The previous development of the undulating beam system relies on manipulating the Geometric Degree of Freedom (GDoF). The transforming process of GDoF is only operated in form diagram, same force diagram is utilized for finalizing the design with the combination of both form modules. Indeed, investigating these steps from the procedural implementation is not an evident process. In contrast, applying the algebraic method will provide a clearer direction for the user to modify the initial design parameter without extra manual adjustment easily. Moreover, different from the existing algebraic method that needs non-intersected planar surfaces as the potential input to construct the cells, the proposed method is to convert intersected geometries to convex polyhedrons that share the same planar surface as the input. The cells will be flipped by changing the force diagram's normal direction. The presented approach allows for a comprehensive understanding of equilibrium and constraint requirements in form and force diagrams.

Keywords: form-finding, graphic statics, beam design, algebraic 3D graphic statics

1. Introduction

The pursuit of efficient and innovative structural designs has driven the development and exploration of a wide range of form-finding methods. Graphic statics, a well-established technique, has consistently proven invaluable for designers and engineers over a hundred years [1–3], offering a clear understanding of the relationship between form and forces. The visual and intuitive nature of graphic statics has made it particularly effective for analyzing planar systems.

As an extension of the conventional graphic statics method, 3D Graphic Statics (3DGS) explored the possibilities of designing complex spatial structures. The method allows for the simultaneous analysis of multiple forces acting on the structure, making it easier to consider different loading scenarios and optimize the design accordingly [4, 5]. By understanding the force distribution and equilibrium within the structure, designers can optimize the structural members for material efficiency, minimize weight, and maximize structural performance.

The majority of 3DGS implementations depend on procedural techniques [6] or iterative algorithms that use local node operations [7, 8]. Procedural methods can be time-consuming and difficult to generalize across various inputs, while iterative algorithms based on node operations provide a unified solver,

Copyright © 2023 by Hua CHAI, Yao LU, Ma´rton HABLICSEK and Masoud AKBARZADEH. Published in the Proceedings of the IASS Annual Symposium 2023 with permission.

controlling edge lengths, vertex locations, and face areas under a single framework. However, these algorithms require an input angle tolerance for terminating iterations, leading to some deviation in the output and longer runtimes for more complex geometries. Furthermore, they cannot construct reciprocal diagrams for non-convex polyhedrons representing combined tension-compression systems, limiting the solution space exploration.

On the other hand, algebraic formulations of reciprocal diagrams offer an alternative perspective for implementing polyhedron-based 3DGS. These formulations provide more robust and faster numerical processes than existing methods, enabling greater flexibility, reduced computation time, and higher accuracy when manipulating reciprocal diagrams.

1.1. Related work

1.1.1. Computational implementations of 3DGS

Integrating computational methods and digital tools has expanded the scope and potential of polyhedral graphic statics, enabling more efficient analysis and optimization of three-dimensional structures. The properties of polyhedral forms can be combined with various fabrication techniques, such as 3D printing and origami, to create spatial frame systems with diverse design features [9–11]. Moreover, polyhedron-based 3D Graphic Statics can produce cellular solids featuring unique micro-architectures. Current studies demonstrate that subdividing force diagrams by subdivision can change these structures into highly efficient, low-density shellular funicular configurations [12]. These studies illustrate the versatility and effectiveness of polyhedral graphic statics in addressing the challenges of contemporary structural design.

1.1.2. Algebraic graphic statics

Alongside the traditional graphical approach in 2D graphic statics, researchers have explored incorporating algebraic methods, which streamline the analysis and design process for two-dimensional structures by formulating and solving equilibrium equations. Micheletti [13] introduced the concept of algebraic duality in reciprocal diagrams of self-stressed frameworks, which was then termed algebraic graphic statics by Van Mele and Block [14]. This tool calculates internal force distribution using connected lines as input and derives edge lengths by ensuring the 2D closeness of polygons. This method allows for obtaining internal and external force magnitudes. Alic and Å kesson [15] later extended this to a bi-directional approach, enabling manipulation of both force and form diagrams and updating reciprocal diagrams instantly, making it an effective interactive form-finding tool in 2D.

1.1.3. Algebraic 3D graphic statics

Building upon the principles of graphic statics, the methodology has been developed to incorporate three-dimensional systems, leading to the establishment of algebraic 3D graphic statics. Hablicsek et al. [16] developed an algebraic framework for 3D Graphic Statics, where reciprocal polyhedral diagrams are represented by a linear system of equations ensuring planar closeness of polyhedron faces. This method computes dual diagrams with high accuracy and allows for user input to control edge lengths, offering flexibility in exploring the solution space [17]. However, it lacks precise control over vertex location and edge lengths. Akbarzadeh and Hablicsek [18] proposed a quadratic formulation that can handle assigned area and edge lengths, enabling manipulation of force diagrams with desired face areas and exploration of various equilibrium states.

1.2. Problem statement and objectives

As previously discussed, 3DGS has demonstrated significant potential for diverse applications across various materialization strategies. However, current implementations have yet to take full advantage of the capabilities that 3DGS has to offer. For instance, the iterative method is limited to compressive

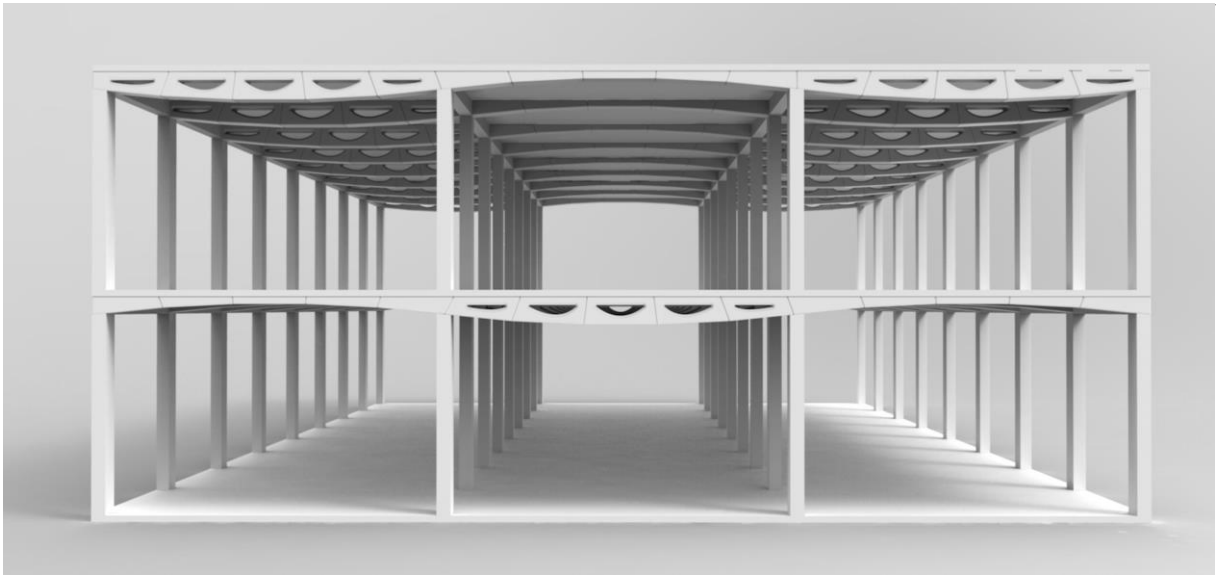


Figure 1. Undulating beam structure with potential porous materialization for all the modules.

form finding, which is usually utilized for the compression-dominant structure and is computationally demanding for intricate geometries.

While the algebraic formulation of 3DGS allows for a comprehensive exploration of the solution space, it needs to have the same precision in controlling edge lengths in reciprocal diagrams that the iterative method provides. This is a crucial aspect that needs to be addressed to maximize the potential of 3DGS for practical applications.

The other challenging part of the method is to develop an efficient and robust way for form-finding to further determine an updated force diagram and generate a corresponding form diagram that satisfies these constraints. This process should apply to a wide range of complex three-dimensional structures, facilitating the analysis and optimization of form and forces in spatial systems. To address the problem stated above, the following objectives have been identified:

- Check the property of the geometric relationships that define the force groups, including global, compression, and tension.
- Develop an algorithm that uses algebraic edge constraints to update the force diagram and generate a corresponding form diagram that adheres to these constraints.
- Demonstrate the effectiveness and versatility of the proposed method through the case study of an undulating beam structure that represents the compression and tension combined loading scenarios.

To tackle these issues, this paper aims to present an enhanced algebraic formulation of 3DGS that incorporates edge constraints. This advanced formulation offers precise control over edge lengths without compromising the inherent advantages of flexibility and accuracy. A more detailed explanation of vertex constraint can be found in the research of Lu et al. [19].

2. Methodology

In this section, we present the methodology of algebraic 3DGS, specifically focusing on the utilization of edge constraints to design structures that incorporate both compression and tension nodal groups. As the continuation study of the previous research [20], we will demonstrate the design process through the

example of the same repeatable undulating beam structure shown in Figure 1.

In 3DGS, polyhedral reciprocal diagrams play a crucial role in representing both form and force diagrams. These diagrams feature a well-defined topological and geometrical hierarchy, including vertices (v), edges (e), faces (f), and cells (c). The unique arrangement within these diagrams ensures that each edge shares a common vertex with its adjacent edges. The edges and faces in reciprocal diagrams exhibit specific directions, which are essential for maintaining the structural integrity of the diagrams. The right-hand rule is applied to achieve consistency, guiding the alignment of face normals and edge directions [16]. This rule ensures that face orientations remain consistent within each cell and maintain cell orientations throughout the diagram. As a result of this structure, neighboring faces in the reciprocal diagrams share two versions of the same edge but with opposing directions. Similarly, adjacent cells exhibit two versions of an identical face, each with contrasting normal directions. This detailed arrangement showcases the intricacies of the polyhedral reciprocal diagrams in 3DGS and their significance in both form and force representation.

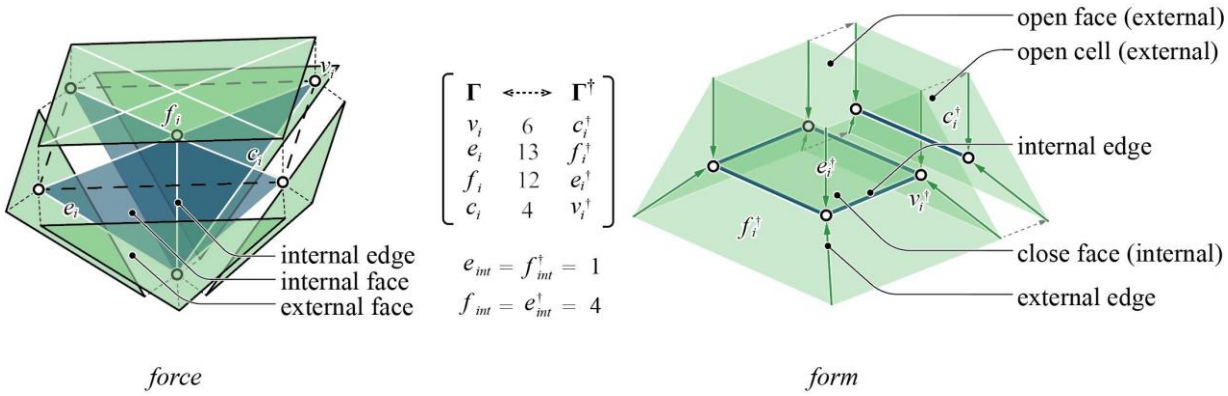


Figure 2. Left: force diagram; Right: form diagram.

A four-applied loads example is illustrated to show the topological relationship between polyhedral diagrams (Figure 2). The starting diagram or the first input is called *primal*, Γ, which can either be a form diagram or a force diagram and the reciprocal diagram is called *dual*, $\Gamma^\dagger$. The ones of the dual are identified as a dagger symbol (†). In general, both two diagrams share a reciprocal relationship, with the primal diagram's elements—vertices v, edges e, faces f, and cells c—mapping to the corresponding elements in the dual diagram—cells ($c^\dagger$), faces ($f^\dagger$), edges ($e^\dagger$), and vertices ($v^\dagger$). This reciprocity leads to an equal number of dual elements in both diagrams, such as the primal's edges (e) matching the dual's faces ($f^\dagger$) and the primal's vertices (v) matching the dual's cells ($c^\dagger$). Additionally, adjacency is preserved between the corresponding elements in both diagrams and each edge (e_i) in the primal is perpendicular to its corresponding face ($f_i^\dagger$) in the dual.

The force diagram's external faces correspond to the external edges in the form diagram that represent applied loads and reaction forces, typically depicted in green. While all elements in the force diagram are closed, the form diagram contains open elements. External edges in the form diagram have vertices at only one end, making them open-ended, and any faces or cells with open edges are also considered open. In contrast, closed faces in the form diagram are deemed internal and correspond to the force diagram's internal edges.

2.1. Analysis of form and force diagrams

The previous IASS paper presented an initial form generated using 2D graphic statics, which was then manipulated geometrically to increase design freedom for constructing updated modules. Detailed force distribution was also utilized to locate the column when merging the two units together. Figure 3 shows the extruded version of single force diagram connecting two modules that are generated from GDoF. The applied loads are evenly distributed at the top, and the supports are illustrated to identify the merging locations.

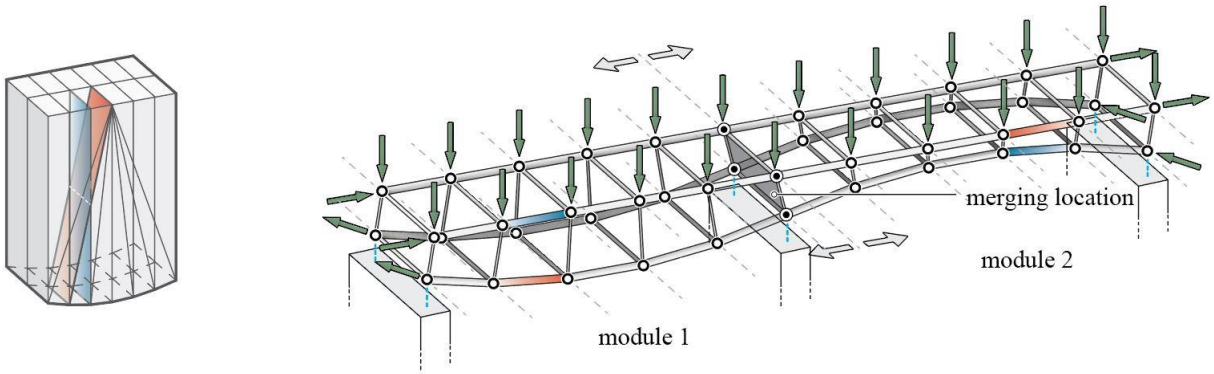


Figure 3. Left: single force diagram of two modules combined; Right: its corresponding form diagram shows the undulation of the geometry and the merging location.

Considering the current limitations of the algebraic graphic statics method, which does not allow intersected faces as input parameters, it is essential to analyze the geometric relationship of the initial force diagram. This analysis enables designers to gain a deeper understanding of structural behavior, paving the way for the development of improved methods and approaches that address these limitations. The key idea focuses on transforming intersected cells into non-intersected convex cells. Investigating this transformation process can help uncover potential strategies to overcome the existing constraints. Importantly, the geometric data is contained within the individual elements. The original relationship is preserved as long as the geometry remains unaltered by adding or subtracting faces, allowing for the free manipulation of moving locations. This approach offers a promising avenue for enhancing the applicability and effectiveness in solving complex geometric problems.

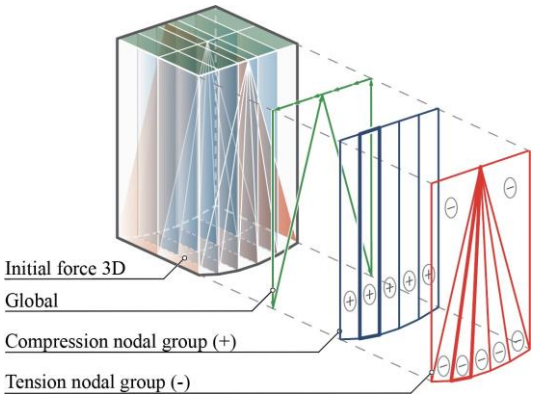


Figure 4. Analysis of different nodal groups in the tension and compression combined force diagram.

Figure 4 presents a detailed representation of the various nodal groups within the force diagram, effectively dividing it into global, compression, and tension forces. To classify these groups based on the connection to the global forces, a positive (+) value represents the compression that shared the edges with applied loads, and the negative (-) is for tension cells that have the same edges with reaction forces. The force diagram effectively demonstrates the intricate relationships in 2D, describing the connections between the edges. In the case of the 3D version, it is essentially a simple extrusion from the 2D representation, maintaining the same relationships between the elements. The global forces, denoted by the color green, remain unchanged throughout the process.

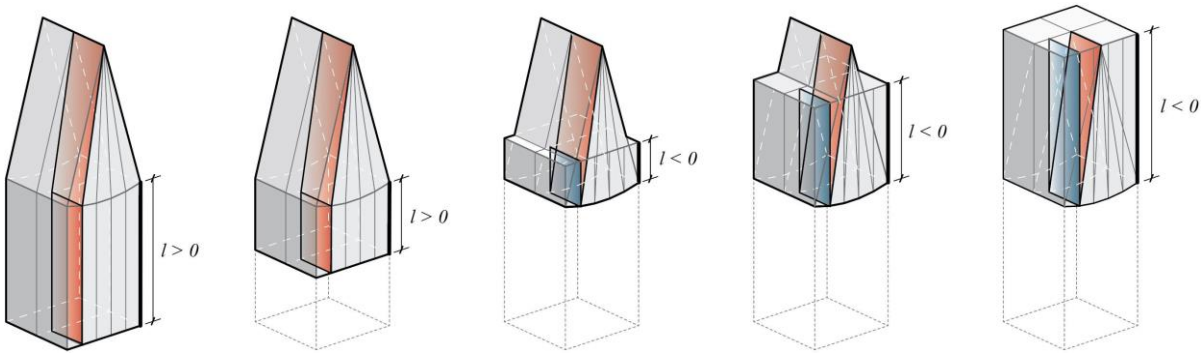


Figure 5. Edge length switched from a positive number to negative to finalize the form diagram.

2.2. Algebraic form-finding

In this section, the equilibrium equation of algebraic implementation will be explained. Firstly, each edge of the force diagram is perpendicular to its corresponding face in the form diagram, resulting in the unit direction vector of edge $e_i^{\dagger}$ in the form diagram being equal to the unit normal vector of face f_i in the force diagram. Then define $\mathbf{N}x$, $\mathbf{N}y$, and $\mathbf{N}z$ as [$f_{int} \times f_{int}$] diagonal matrices with diagonal entries representing the x-, y-, and z- coordinates of the unit normal vectors of the internal faces in the force diagram, respectively. Based on prior research in the algebraic method, the [$e_{int} \times f_{int}$] connectivity matrix $\mathbf{C}_{e_{int} \times f_{int}}$ displays the relationship between faces and edges in the form diagram. Consequently, the closeness can be expressed accordingly:

$$\begin{aligned} \mathbf{C}_{e_{int} \times f_{int}} \mathbf{N}_x \mathbf{q} &= \mathbf{0} \\ \mathbf{C}_{e_{int} \times f_{int}} \mathbf{N}_y \mathbf{q} &= \mathbf{0} \\ \mathbf{C}_{e_{int} \times f_{int}} \mathbf{N}_z \mathbf{q} &= \mathbf{0} \end{aligned} \tag{1}$$

Combing the above equations to an equilibrium matrix multiple by the potential edge length as shown here:

$$\mathbf{A}\mathbf{q} = \mathbf{0} \tag{2}$$

so $\mathbf{A}$ is a [$3e_{int} \times f_{int}$] equilibrium matrix can be represented as

$$\mathbf{A} = \begin{pmatrix} \mathbf{C}_{e_{int} \times f_{int}} \mathbf{N}_x \\ \hline \mathbf{C}_{e_{int} \times f_{int}} \mathbf{N}_y \\ \hline \mathbf{C}_{e_{int} \times f_{int}} \mathbf{N}_z \end{pmatrix} \tag{3}$$

Every solution for $\mathbf{q}$ represents a potential combination of edge lengths in the form diagram that ensures the closeness of all internal faces within the form diagram.

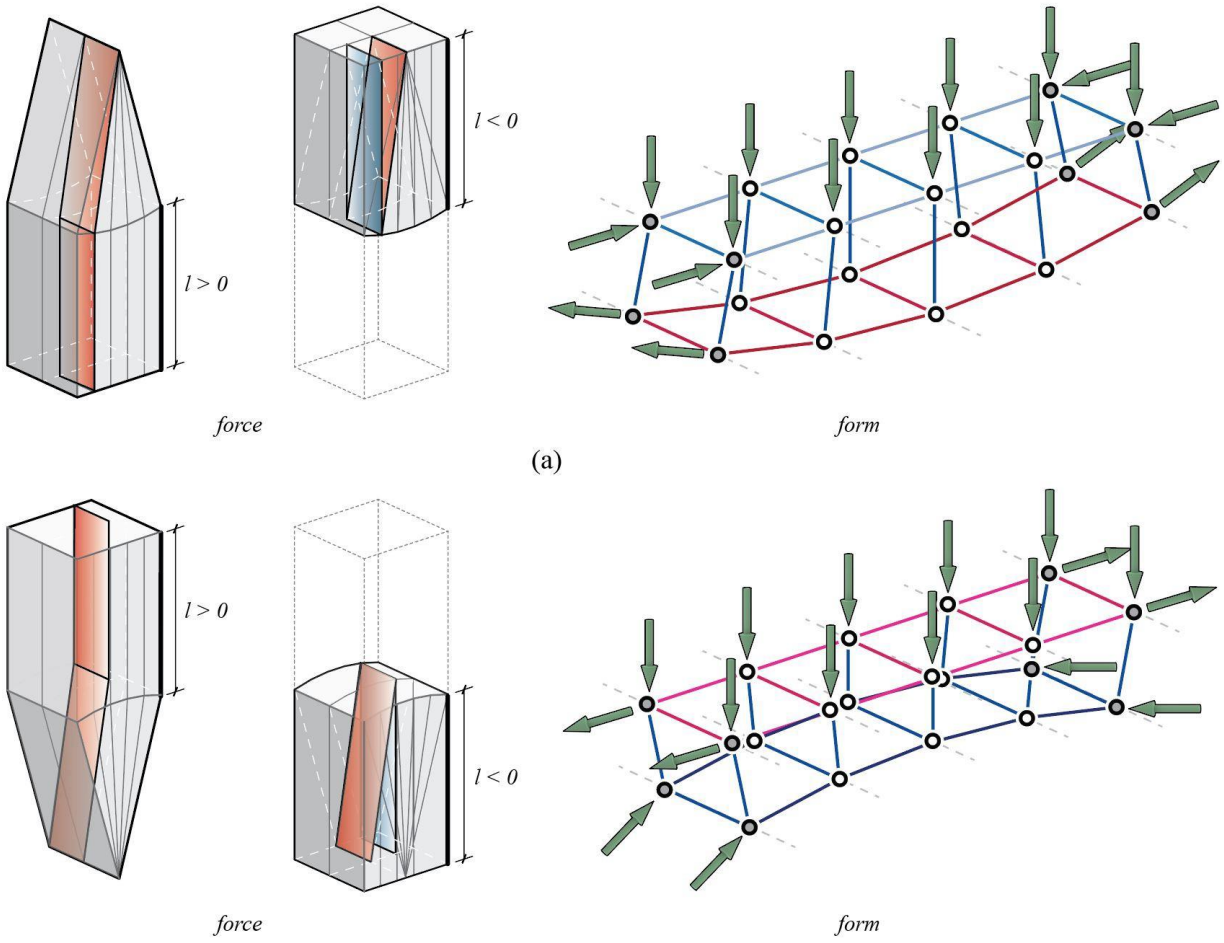


Figure 6. The transition from compression/tension only to intersected force diagram and corresponding form diagram. (a) the reciprocal polyhedral diagrams of the first module (b) mirrored force diagram as the input to generate the second module.

2.3. Additional edge constraints operation

Edge constraints set target lengths for the internal edges in the form diagram, and each constrained edge requires one additional constraint equation. For example, if the i-th internal edge $e_i^\dagger$ is constrained to a target length l, its constraint equation may be written as

$$\mathbf{b}_i^\top \mathbf{q} = l \tag{4}$$

where $\mathbf{b}_i$ is the $[f_{int} \times 1]$ column vector with all entries zero (0) except at the index of $e_i^\dagger$ where it's one (1). For a total number of b constrained edges, all b edge constraint equations may be assembled in the matrix form as

$$\mathbf{Bq} = \mathbf{l} \tag{5}$$

where the rows of the $[b \times f_{int}]$ edge constraint matrix $\mathbf{B}$ are the row vectors $\mathbf{b}_i^\top$, and $\mathbf{l}$ is a $[b \times 1]$ column vector with the entries being the target lengths.

2.4. Constrained solutions

All equilibrium equations, edge constraint equations, and vertex constraint equations are assembled as a system of non-homogeneous constrained linear equilibrium equations written as follows:

$$\mathbf{Mq} = \mathbf{t}. \tag{6}$$

Here the $[(2e_{int} + b + 3(p - 1) + 2l + n) \times f_{int}]$ matrix **M** is named the constrained equilibrium matrix, obtained by vertically stacking the equilibrium matrix **A** and the edge constraint matrix **B**

$$\mathbf{M} = \begin{pmatrix} \mathbf{A} \\ \mathbf{B} \end{pmatrix}. \tag{7}$$

The $[(2e_{int} + b + 3(p - 1) + 2l + n) \times 1]$ column vector **t** is obtained by vertically stacking the $[2e_{int} \times 1]$ zero vector, the vector **l**, and the vector **d**. Each solution of **q** represents a set of edge lengths of the form diagram that satisfy all equilibrium requirements and constraints.

The form diagram may face issues of over-constraining when constraints conflict with planarity or compete with each other, leading to overdetermined equilibrium equations with no solution. In these cases, the least-square solution offers the closest possible solution by minimizing the Euclidean norm while still attempting to satisfy all equilibrium and constraint requirements.

Figure 5 describes a process by which the final force diagram for the structure can be generated. This is achieved by assigning negative values to specific edges, allowing the structure's bottom part to merge with the top part. The decision to assign negative values is based on the changeable edge length, which affects the force distribution in the structure. It is important to note that the IDs of the fixed edges must be determined to ensure that the structure shifts within the predefined boundary conditions. This is necessary to prevent the structure from moving beyond acceptable limits.

3. Conclusion and future work

In conclusion, this research presents an analysis of the topological relationship between reciprocal polyhedral diagrams. The connectivity matrix and equilibrium matrix are used to express the closeness between the force diagram and its corresponding form diagram. Additional linear equations are introduced to account for edge constraints, resulting in a system of non-homogeneous constrained linear equilibrium equations. The least-square solution is utilized to find the closest solution in cases of over-constraining or incompatibilities among constraints (Figure 6). This approach enables a comprehensive understanding of the equilibrium and constraint requirements in form and force diagrams, paving the way for further exploration and optimization in structural design.

Acknowledgements

This research is funded by the Advanced Research Projects Agency–Energy (ARPA-E) of the U.S. Department of Energy (DE-AR0001631) and the National Science Foundation CAREER Award (NSF CAREER-1944691 CMMI) and the National Science Foundation Future Eco Manufacturing Research Grant (NSF, FMRG-2037097 CMMI) to Dr. Masoud Akbarzadeh.

References

[1] K. Culmann, *Die Graphische Statik*. Zürich: Verlag Meyer und Zeller, 1864.
[2] L. Cremona, *Graphical Statics: Two Treatises on the Graphical Calculus and Reciprocal Figures*

in Graphical Statics. Translated by Thomas Hudson Beare. Oxford: Clarendon Press, 1890.

[3] J. C. Maxwell, "On Reciprocal Figures and Diagrams of Forces," *Philosophical Magazine Series 4*, vol. 27, no. 182, pp. 250–261, 1864.

[4] M. Akbarzadeh, T. Van Mele, and P. Block, "3D Graphic Statics: Geometric Construction of Global Equilibrium," in *Proceedings of the International Association for Shell and Spatial Structures (IASS) Symposium*, 2015.

[5] A. McRobie, W. Baker, T. Mitchell, and M. Konstantatou, "Mechanisms and States of Self-stress of Planar Trusses Using Graphic Statics, part II: Applications and Extensions," *International Journal of Space Structures*, vol. 31, no. 2-4, pp. 102–111, 2016. [Online]. Available: http://dx.doi.org/10.1177/0266351116660791

[6] M. Akbarzadeh, "3d graphic statics using reciprocal polyhedral diagrams," Ph.D. dissertation, ETH Zurich, Zurich, Switzerland, 2016.

[7] PSL, "PolyFrame," https://www.food4rhino.com/app/polyframe, Aug 2018. [Online]. Available: https://www.food4rhino.com/app/polyframe

[8] A. Nejur and M. Akbarzadeh, "Polyframe, efficient computation for 3d graphic statics," *Computer-Aided Design*, vol. 134, p. 103003, May 2021.

[9] M. Akbarzadeh, A. Tabatabaie Ghomi, M. Bolhassani, M. Akbari, A. Seyedahmadian, J. Sun, H. Yao, , J. Miziumski, and K. Papalexiou, "Saltatur: Node-based assembly of funicular spatial concrete," in *Proceedings of the 40th Annual Conference of the Association for Computer-Aided Design in Architecture (ACADIA)*, 2021.

[10] Y. Lu, M. Cregan, P. Chhadeh, A. Seyedahmadian, M. Bolhassani, J. Schneider, J. Yost, and M. Akbarzadeh, "All glass, compression-dominant polyhedral bridge prototype: form-finding and fabrication," in *Proceedings of IASS Symposium and Spatial Structures Conference 2020/21, Inspiring the next generation*, Guildford, UK, August 23-27 2021.

[11] M. Akbari, Y. Lu, and M. Akbarzadeh, "From design to the fabrication of shellular funicular structures," in *Proceedings of the Association for Computer-Aided Design in Architecture (ACADIA)*, 2021.

[12] M. Akbari, A. Mirabolghasemi, M. Bolhassani, A. Akbarzadeh, and M. Akbarzadeh, "Strut-based cellular to shellular funicular materials," *Advanced Functional Materials*, p. 2109725, 2022.

[13] A. Micheletti, "On generalized reciprocal diagrams for self-stressed frameworks," *International Journal of Space Structures*, vol. 23, no. 3, p. 153–166, Sep 2008.

[14] T. Van Mele and P. Block, "Algebraic graph statics," *Computer-Aided Design*, vol. 53, pp. 104 – 116, 2014. [Online]. Available: http://www.sciencedirect.com/science/article/pii/S0010448514000682

[15] V. Alic and D. Åkesson, "Bi-directional algebraic graphic statics," *Computer-Aided Design*, vol. 93, pp. 26 – 37, 2017. [Online]. Available: http://www.sciencedirect.com/science/article/pii/S0010448517301446

[16] M. Hablicsek, M. Akbarzadeh, and Y. Guo, "Algebraic 3d graphic statics: Reciprocal constructions," *Computer-Aided Design*, vol. 108, pp. 30 – 41, 2019. [Online]. Available: http://www.sciencedirect.com/science/article/pii/S0010448518303026

[17] M. Akbarzadeh and M. Hablicsek, "Algebraic 3d graphic statics: Constrained areas," *arXiv preprint arXiv:2007.15133*, 2020.

[18] M. Akbarzadeh and M. Hablicsek, "Algebraic 3d graphic statics: Constrained areas," *Computer-Aided Design*, vol. 141, p. 103068, Dec 2021.

[19] Y. Lu, M. Hablicsek, and M. Akbarzadeh, "Algebraic 3d graphic statics with edge and vertex constraints: A comprehensive approach to extending the solution space for polyhedral form-finding," *Computer-Aided Design*, In peer-review.

[20] H. Chai, M. Bolhassani, and M. Akbarzadeh, "Structural form-finding of multi-span undulating funicular beam structure," in *Proceedings of IASS 2022 symposium affiliated with APCS 2022 conference*, Beijing, China, September 19-22 2022.

IASS 2023
July 10–14 Melbourne
Integration of Design and Fabrication

Proceedings of the IASS Annual Symposium 2023
Integration of Design and Fabrication
10–14 July 2023, Melbourne, Australia
Y.M. Xie, J. Burry, T.U. Lee and J. Ma (eds.)

Graphic statics and topology optimization: An integrated approach to designing architecture structures

Xinjie ZHOU[a], Yu LI[a], Philip F. YUAN[a,*]

[a,*] College of Architecture and Urban Planning, Tongji University
Siping Road 1239, 200092, Shanghai
philipyuan007@tongji.edu.cn

Abstract

This paper presents a method for optimizing the structure of a railway station. In contrast to traditional techniques that manipulate the structure's geometry using a single optimization method, the approach proposed in this paper employs a multi-strategy solution. Specifically, it utilizes two structural optimization design tools, namely BESO and graphic statics. By combining these two methods, the truss structure in a railway station can be effectively optimized. The algorithm implementation of the graphic statics component primarily relies on vector-based graphic statics. This approach tackles the discretization issue in topology optimization and significantly enhances the efficiency of design iterations.

Keywords: performance-based design, structural optimization, graphic statics, topology optimization

1. Introduction

The architectural design process needs to be further digitalized due to the increasing complexity of building functions and the diversification of architectural design objectives. The convergence of computer science, material science, mechanical engineering, architecture, and other disciplines, along with the advancement of digital architecture, has given rise to performance-based design thinking as a prominent approach in digital design. This approach has replaced the traditional focus on pure "formalism."

Structural performance-based design is a crucial aspect of performance-based design. In recent years, numerous structural design tools have emerged, leading to active intervention of structural design in the architectural design process [1]. Additionally, architects have expanded the application of structural design tools beyond mere structural performance-based design, aiming to facilitate the mutual integration of structure and form. Among these tools, graphic statics and topology optimization play vital roles in structural performance-based design.

1.1 Graphic statics

Graphic statics, formally established in the second half of the nineteenth century, combines both constructive and generative aspects. The foundations of graphic statics were laid by James Clerk Maxwell in his article published in 1864 [2]. It consists of a form diagram and a force diagram that are reciprocal, enabling simultaneous control of form and force flow.

Swiss engineer Robert Maillart pioneered the application of graphic statics to explore new materials for reinforced concrete. He designed several elegant and efficient bridges and roof systems using graphic statics, including the Tavanasa Bridge (1906) [3], the Chiasso shed (1924) [4], and the Salginatobel Bridge (1930) [5], among others. Graphic statics enabled Robert Maillart to efficiently explore the balance between the aesthetic and efficiency aspects of architectural form. Architect Christian Kerez

Copyright © 2023 by Xinjie XHOU, Yu LI and Philip F. YUAN. Published in the Proceedings of the IASS Annual Symposium 2023 with permission.

and structural engineer Joseph Schwartz collaborated on projects such as the Apartment Building on Forsterstrasse, the House with One Wall, and the School Building in Leutschenbach [6], utilizing graphic statics to construct their architectural free forms in a rational manner.

With the increasing digitization of architectural design, complex arithmetic processes can now be delegated to computers, leading to a resurgence of graphic statics in structural design. In contrast to numerical computational methods, graphic statics is preferred for its ability to seamlessly integrate form and structure. In recent years, researchers have dedicated significant attention and effort to the development and advancement of graphic statics.

There are currently two primary research directions in graphic statics, one based on vectors and the other on polyhedra. Several software tools have been developed for graphic statics form-finding based on these approaches. Andrei Nejur et al. introduced Polyframe [7], a 3D graphic statics tool utilizing polyhedra, but it is limited to calculating purely compressed structures. Lee developed COMPAS3gs [8], a set of 3D graphic statics tools based on polyhedra; however, it does not support automatic optimization based on constraints. The VGS tool (Vector-based 3D Graphic Statics) developed by Pierluigi D'Acunto et al. solves graphic statics using a vector approach [9], enabling iterative optimization. Nevertheless, one limitation of graphic statics is that it requires a thorough understanding of structural principles on the part of the designer.

1.2 Multi-material BESO

Topology optimization is a vital method for achieving performance-based design in structures. Compared to graphic statics, topology optimization offers advantages in material layout optimization. Presently, the prominent topology optimization techniques include the Solid Isotropic Material with Penalization (SIMP) method [10], the Level Set method [11], and the Bi-directional Evolutionary Structural Optimization (BESO) method [12]. Among these methods, the BESO method is favored by architects and engineers due to its user-friendliness and fast calculation. Mature commercial software tools, such as Ameba [13], are already available for implementing the BESO method.

However, most of the previous methods, including the classical BESO method, have been developed based on a single material and do not consider the optimization of structures with multiple materials possessing different tensile and compressive properties [14]. Recently, Li and Xie [15], [16] extended the single-material BESO method by dividing the structure into tensile and compressive regions during the topology optimization process. They assigned different materials to these regions based on the tensile or compressive state of the finite element analysis (FEA) elements, enabling the topology optimization of structures composed of two materials. Subsequent research and applications have demonstrated the excellent practical value and potential of this method in the design of large-span and composite structures [17].

1.3 Motivation

BESO is a powerful and widely recognized technique used to determine optimal geometries for designing efficient systems. However, one challenge with BESO is that the structure it generates is typically continuous, which means that it needs to be discretized into multiple parts for construction in later stages. This discretization process can sometimes make it difficult to interpret the resulting discrete structure.

Graphic statics is an exceptionally effective tool for the structural design of truss structures. It relies on reciprocal graphical relationships between the form diagram and force diagram, enabling the quick determination of force magnitudes for each component without the need for complex structural calculations. This efficient approach significantly reduces the time required for design and simulation. However, it is important to acknowledge that obtaining the initial form using graphic statics requires significant structural experience.

We propose an integrated approach to structural optimization. Unlike traditional techniques that manipulate the structure's geometry using a single optimization method, our approach utilizes a multi-strategy solution. In this paper, we present a method that combines two structural optimization design tools, namely BESO and graphic statics, to address the problem. By leveraging both of these tools, we aim to enhance the effectiveness of structural optimization.

2. Method

Given the distinct advantages of graphic statics and BESO, this paper adopts a two-stage approach, employing topology optimization and graphic statics at different design stages to leverage the strengths of both methods. The topology optimization is applied initially to generate a form, which is then transformed into a graphic statics representation by extracting the primary force flow. This enables the overall structural design, as depicted in Figure 1.

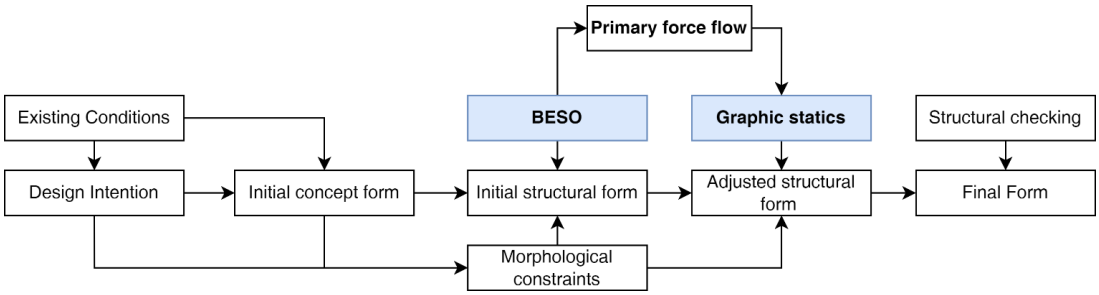


Figure 1. Structural design process of this paper

2.1. Conceptual form-finding stage

Form creation holds immense significance in architectural design. Within the field of architecture, practitioners are continually engaged in developing architectural forms and exploring various approaches to form creation. This exploration has given rise to the concept of "form-finding," which involves analyzing external conditions and responding to the design intentions of the architect. Form-finding, therefore, represents a systematic design strategy and method employed to achieve specific design goals within given constraints. It encompasses both rational reasoning and perceptual judgment. In the context of this paper, the conceptual stage refers to the architect's initial conception of form during the early proposal phase, setting the foundation for subsequent structural form-finding endeavors.

2.2. Initial structure form-finding stage

In recent times, the division between architects and structural engineers has resulted in a certain level of detachment between the form and structure of buildings. A sufficient understanding of structural principles is crucial for architects in order to develop structural concepts. Therefore, the collaboration between architects and structural engineers is often necessary to create distinctive building structures. The approach presented in this paper can, to some extent, assist architects in formulating preliminary structural concepts and expedite the initial process of generating such concepts.

The development of the initial structural concept primarily relies on the multi-material BESO algorithm. By specifying the initial design domain, loads, supports, and relevant parameters, we can readily obtain the structural form. However, adjusting the solution using the multi-material BESO algorithm is not straightforward, especially when dealing with complex building designs. Additionally, the computational speed of existing computers is inadequate for running this algorithm efficiently. Consequently, if we solely rely on this method for structural solutions, the time required for design iterations would significantly increase. As a result, we utilize the multi-material BESO algorithm for the formation of the initial concept, allowing us to generate the initial concept scheme in a single operation (see Figure 2).

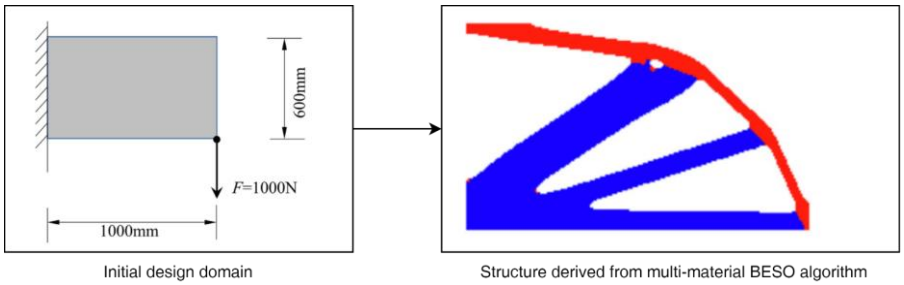


Figure 2. Initial structure form-finding stage, Modified from [15]

2.3. Conversion from BESO to graphic statics

The force flow method is a structural design approach that clarifies and analyzes the transfer mechanism of forces within a member. It conceptualizes force transfer as force flow and depicts the path of force flow through force lines. The density of force lines corresponds to the intensity of force flow, which directly correlates to stress magnitude. By utilizing the BESO (Bi-directional Evolutionary Structural Optimization) technique, we can efficiently ascertain the primary flow direction of the main force flows. This allows us to quickly identify the principal force flows required to achieve the desired design objectives in structural design.

CEM (Combined Equilibrium Modeling) [18] is a graphic statics tool that utilizes topological diagrams. It is based on the Plasticity Theory and its Lower Bound Theorem [19]. This theorem primarily aims to fulfill the structural limit states (ULS), with particular emphasis on static equilibrium conditions [20]. CEM's objective is to facilitate the active and consistent generation of discrete network models that differ in terms of topology and combinations. These networks should not necessarily be perceived as physical structures but rather as spatial representations of equilibrium forces [21]. By focusing solely on the balance between external and internal forces, CEM allows for the analysis, visualization, and integration of the relationship between geometry and structural behavior in a comprehensible manner using graphic statics.

The CEM tool is employed to convert the primary force flows into the necessary topological diagram. Subsequently, by adjusting the lengths of pertinent components or the magnitude of internal forces, we obtain the force diagram using graphic statics (refer to Figure 3).

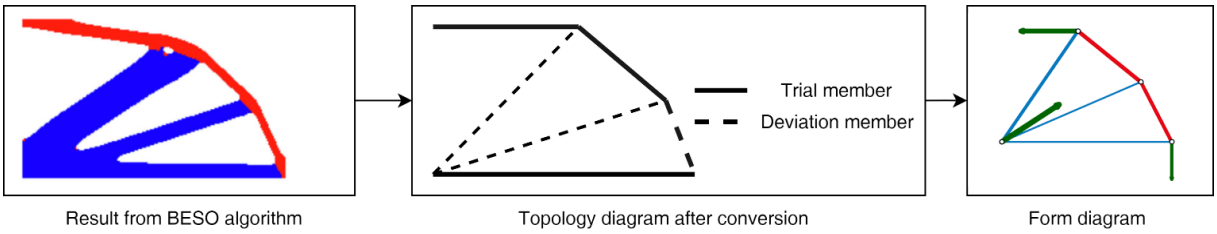


Figure 3. Conversion from BESO to graphic statics, Modified from [15]

2.4. Form adjustment stage

With the above method, we can obtain the form and force diagrams solutions for tuning. With the vector-based graphic statics tool, we can pass various constraints and optimization objectives and quickly obtain the desired optimization model. The constraint in this step generally refers to the morphological constraint we need to reach rather than the mechanical concept of constraint. In this way, we can optimize the structural form of the remaining parts of the structure while keeping some parts' shape and achieving a more efficient form within the tolerances (Figure 4).

We can use V as an indicator of the efficiency of the structure:

$$V = \sum_{i=0}^{n} L_{Fi} \times L_{F^*i} \quad (1)$$

where L_{Fi} refers to the length of the i-th component of the shape diagram solution, L_{F^*i} refers to the length of the force diagram's line segment corresponding to the form diagram's i-th component.

By employing this evaluation index, we can enhance structural efficiency through two approaches: firstly, by reducing the lengths of members in the form diagram, and secondly, by minimizing the lengths of members in the force diagram. However, as the aforementioned method revolves around optimizing a single operating condition, it is essential to validate the structure to ensure its reliability.

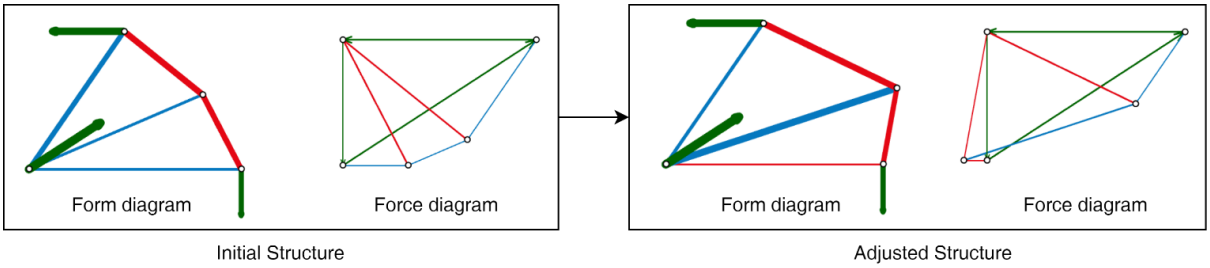


Figure 4. Form adjustment stage

3. Case Study

3.1 Background of the case

The project is situated in Chongming, Shanghai, which is an alluvial island located at the mouth of the Yangtze River in the eastern part of the Yangtze Delta. Chongming Island is the third-largest island in China and holds the distinction of being the largest estuarine alluvial island as well as the largest sand island in the country. The island features a flat, fertile landscape with abundant forests, making it renowned for its agricultural productivity and being recognized as the land of fish and rice. Given Chongming's significant agricultural foundation, the proposal aims to reconnect with the island's ecological roots by constructing a high-speed railway station amidst the fields. The underground placement of the public transportation system allows for substantial public space to be reclaimed on the surface. This approach seeks to bring nature back to the residents and visitors, creating a green urban center within Chongming.

The project's concept is called "The Tail of the Yangtze River," drawing inspiration from the meandering shape of the Yangtze River, which is the longest river in China. The design incorporates wings that unfurl along both sides of the station building, and the overall form features simple and sleek horizontal lines. At the main entrance, these lines are subtly elevated, symbolizing the entrance and creating a welcoming gesture for passengers arriving from various parts of the world (refer to Figure 5).

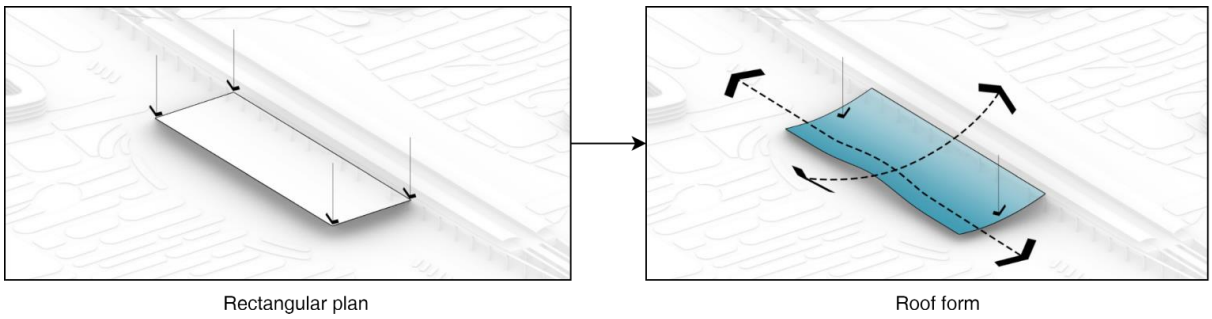


Figure 5. Concept Form Generation

The subject of this study is a railway station hall characterized by a rectangular floor plan. The structural system consists of multiple trusses that are arranged parallel to each other. Figure 6 illustrates the cross-sectional view of the structure. As the trusses exhibit a high degree of similarity, the project can be simplified to a 2D planar structure. The prominent feature of the design is a substantial overhang measuring 16 meters in length.

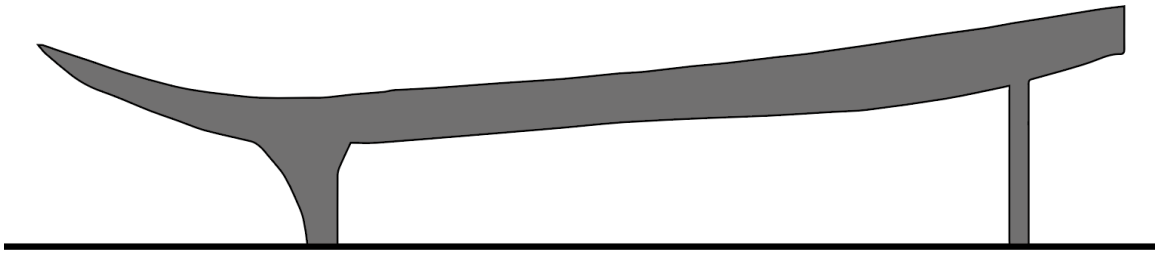


Figure 6. Initial section of the train station hall.

Initially, the design of the roof structure followed a traditional approach as depicted in Figure 7. The primary load-bearing structure of the roof consists of plane trusses and columns. The roof load is transferred to the main truss through secondary beams and further transmitted to the ground via linear and curved columns. However, this solution presented two challenges. Firstly, the roof windows were unable to be opened, limiting the amount of sunlight that could enter the interior space. Secondly, the presence of columns on the façade resulted in a segmented glass curtain wall, which compromised the heat insulation efficiency. As a result, it became necessary to introduce two additional support columns on the front elevation to ensure continuity in the curtain wall.

Additionally, due to the minimal presence of equipment ducts on the roof, there is no need to enclose the ceiling structure. Therefore, a redesign of the roof structure is required.



Figure 7. Roof structure designed using conventional methods

3.2 BESO form-finding process

The simplified design domain is shown in Figure 8, where the roof section is simplified as a curve and set as a non-design domain with a specific thickness on which the uniform load is distributed. The region under the roof is set as the design domain. On the north side of the building, due to the space limitation, only one row of columns is kept, which is also set as the non-design domain.

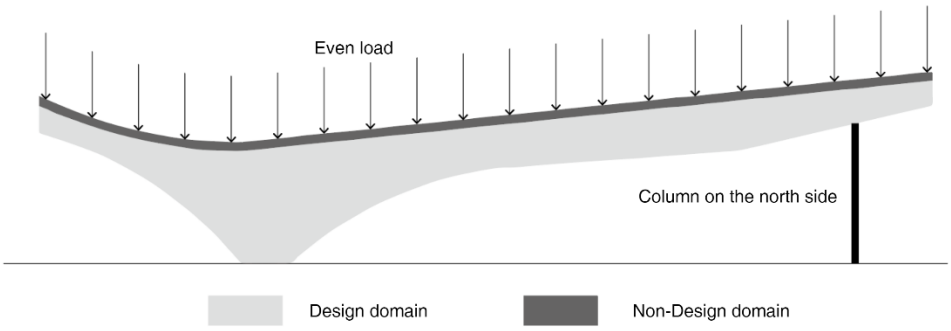


Figure 8. Design domain for topology optimization of the hall

The design domain undergoes multi-material topology optimization, even though the primary structural material intended for use is steel. It is important to note that the mechanical properties of steel may vary between tension and compression. The target volume for the topology optimization is set to 0.4, indicating that the final structure's total volume will be 40% of the volume of the original design domain illustrated in Figure 8. Figure 9 provides an overview of the crucial steps involved in the optimization process.

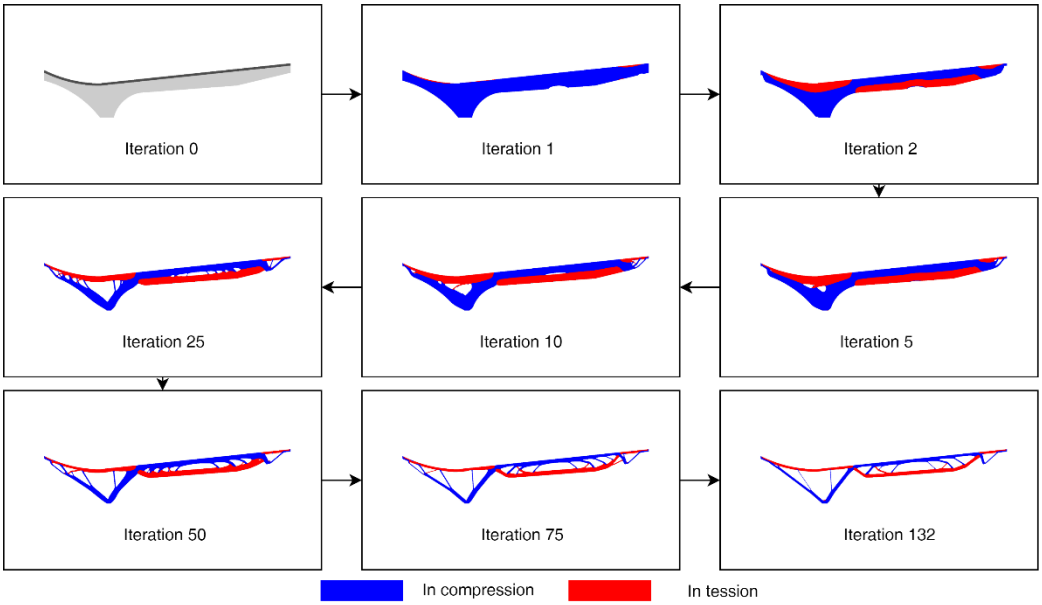


Figure 9. The process of topology optimization

After 132 iterations, the structure eventually converges to its optimized form. In the right span of the structure, the upper side experiences compression, while the lower side is subjected to tension. The topologically optimized structure necessitates additional refinement for further design. This structure comprises three primary components: the main compressed members, the secondary compressed members, and the tendons. Together, they form a stable and interconnected structural system.

By following the aforementioned method, we have obtained the initial solution for the structural design using the multi-material BESO approach. The structure exhibits an approximate triangular form on the left side. However, the inclination of the inner members is excessive, which adversely affects the utilization of the interior space. Additionally, a weak point is identified in the middle of this frame, potentially resulting in structural instability under different operational conditions. Consequently,

further adjustments and modifications are necessary to address these issues and enhance the overall design.

3.4 From BESO to graphic statics

The results obtained through the multi-material BESO algorithm reveal the presence of two primary force transfer paths within the structure. One path is predominantly subjected to compression, exhibiting a shape reminiscent of an arch. The other path is primarily subjected to tension (see Figure 10).

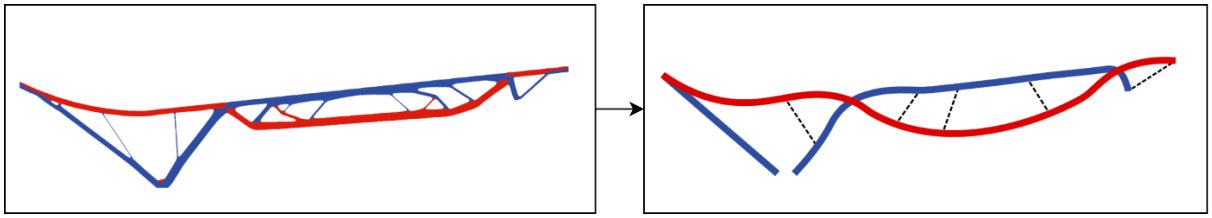


Figure 10. Extraction of force flow

To convert the two identified force transfer paths into graphic statics, we create corresponding topology diagrams. Figure 11 displays the topology diagram, which is based on a truss-like triangular structure for stability. Two trials represent the primary force flows obtained from the multi-material topology optimization, while the third trial represents the required column on the right side of the project. Several deviation members connect these three trials. In the CEM approach, the trial members can have adjustable lengths, and the deviation members can determine the magnitude of the internal forces (as shown in Figure 12). The lengths and positions of these members are crucial factors that influence the final form of the structure.

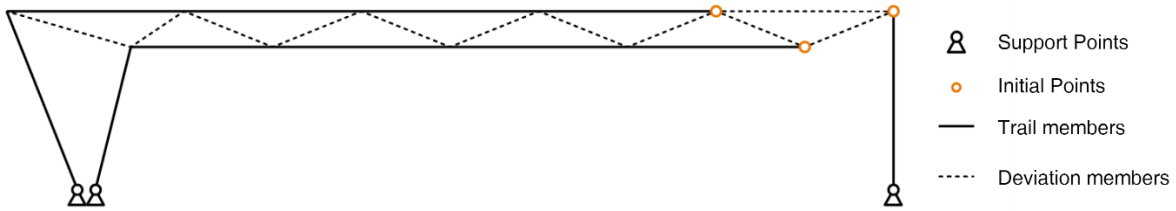


Figure 11. Constructing topological diagrams from force flow results

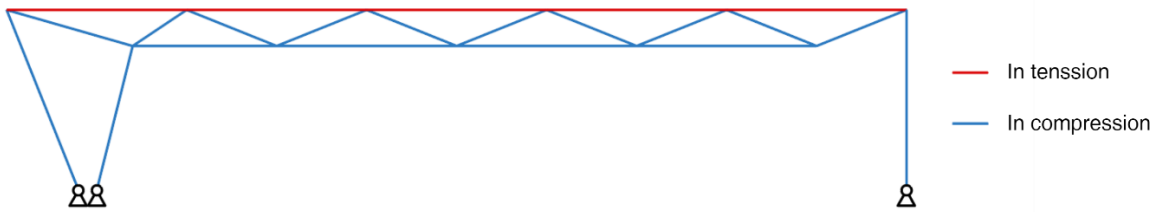


Figure 12. The set tensile-pressure relationship

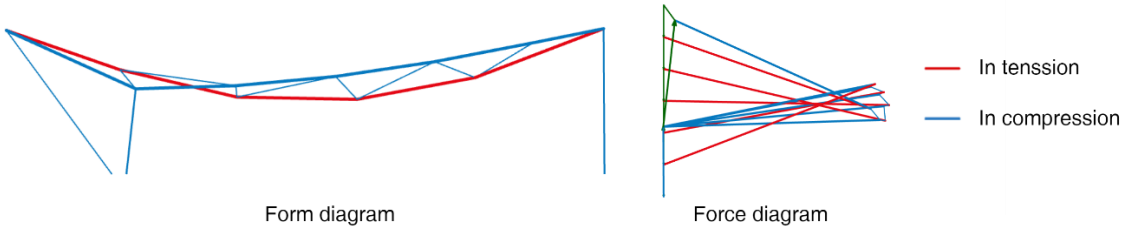


Figure 13. Generated initial graphic statics form diagram and force diagram

Following the CEM calculations, we acquire the initial form and force solutions. Figure 13 illustrates that the force flow within the structure, constructed using this method, aligns with the force flow obtained from the topology optimization. In contrast to the bars within the interior calculated through previous topology optimization, the existing structure no longer encroaches upon the interior space. However, some members in the model still possess excessive length-to-slenderness ratios, indicating room for further enhancement in terms of their efficiency.

3.3. Adjustment process based on graphic statics

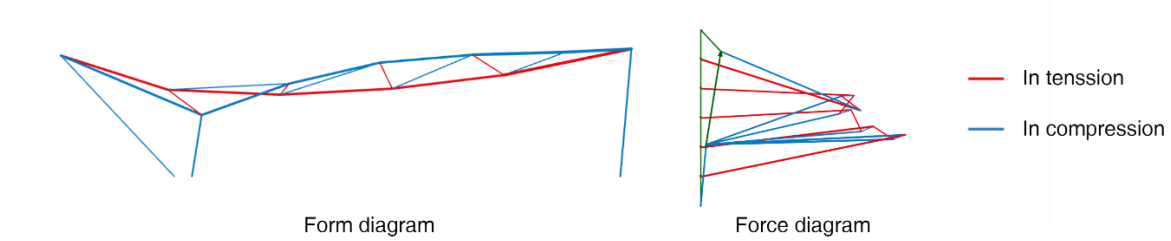


Figure 14. Adjusted structure

The existing shape and force diagrams are input into VGS (Vector-based Graphic Statics) for further adjustment and analysis. By controlling the overall form and fine-tuning the entire structure, we aim to enhance its efficiency. During the adjustment process, certain constraints are applied to specific aspects of the design. Firstly, the façade, being a crucial element of the project, is constrained to minimize the impact of efficiency optimization on its form. Consequently, it undergoes minimal changes. Secondly, the position of the supports is related to the interior area and is therefore also constrained. Lastly, the size of the interior space needs to be ensured, so the lower part of the roof is constrained as well. Taking these constraints into account, we optimize the structure by modifying the tension-compression relationship of the web members. As a result, the V decreases by 14.2%. The optimized structure exhibits a slight upward raise in the form of the roof. This alteration has a minimal impact on the building's appearance and is thus deemed acceptable (refer to Figure 14).

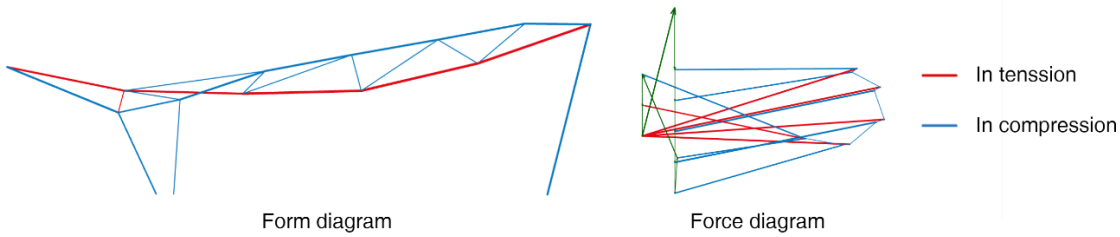


Figure 15. Adjustment of components on the façade

Nevertheless, the columns in the overhang direction were observed to be excessively long and slender, requiring further adjustments. To address this issue, we made additional modifications to the columns on the façade, taking into account the original form diagram. Simultaneously, we slightly increased the thickness of the roof to enhance structural efficiency. As a result, the final outcome successfully reduces the length of the columns on the façade while maintaining the same V value (Figure 15).

3.4. Post-design process

To enhance the overall structural strength, a modification was made to the tension beam by dividing its upper chord into two sections, ensuring out-of-plane stability (as shown in Figure 16). This configuration also allows for the inclusion of a sunroof. Additionally, certain nodes in the structure were reinforced to improve stability. In the final design, the number of web members was increased to reduce the length-to-slenderness ratio of the members, further optimizing structural efficiency (Figure 17).

Furthermore, for aesthetic purposes, the supporting columns on the façade were replaced with curved columns (Figure 18). These design adjustments collectively contribute to the final structure's strength, stability, and visual appeal.

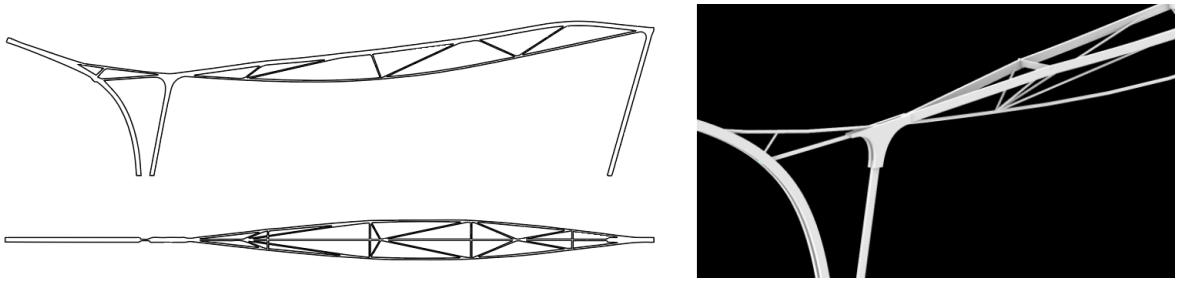


Figure 16. Post-processed structure



Figure 17. Interior effect of the railway station hall



Figure 18. The effect of the façade of the railway station hall

4 Discussion

By implementing the approach described above, the final structure successfully addresses the initial challenges while preserving the desired architectural design. The separation of the two sets of columns in the façade ensures the integrity of the curtain wall, thereby improving the building's insulation properties. Additionally, the structural design allows for the inclusion of skylights, enhancing natural lighting within the interior space. The case study serves as evidence that the method proposed in this paper is both rapid and effective in designing structural forms for buildings with multiple objectives.

Indeed, the present method does have certain limitations that should be acknowledged. Firstly, it is currently confined to two-dimensional structural design, and the transition to three-dimensional design is achieved through post-processing techniques. Further research and development are required to extend the method to three-dimensional structures. Secondly, the conversion from the multi-material BESO algorithm to graphic statics heavily relies on human observation, which may introduce subjectivity and limitations. There is a need for further exploration and investigation into automated extraction methods to enhance objectivity and efficiency in this process.

5 Conclusion

The proposed integrated design approach that combines the multi-material BESO algorithm and graphic statics offers a novel and efficient method for coupling building form and structural design. By utilizing the multi-material BESO algorithm, the initial structural solution is obtained, leading to the generation of an efficient initial structure form. The force flow patterns derived from this initial form serve as a foundation for further structure refinement using graphic statics. The effectiveness of this approach is demonstrated through its application in the design of a railway station hall. Overall, this integrated design approach showcases the potential and benefits of combining these two methods to achieve optimized and well-integrated building structures.

Acknowledgements

This project is supported by the Shanghai Municipal Science and Technology Major Project (2021SHZDZX0100), the National Key Research and Development Program “Inter-government Cooperation in International Science and Technology Innovation” (2022YFE0141400) and the National Natural Science Foundation of China (U1913603).

References

[1] L. L. Beghini, J. Carrion, A. Beghini, A. Mazurek, and W. F. Baker, “Structural optimization using graphic statics,” *Struct Multidisc Optim*, vol. 49, no. 3, pp. 351–366, Mar. 2014, doi: 10.1007/s00158-013-1002-x.

[2] J. C. Maxwell, “XLV. On reciprocal figures and diagrams of forces,” *The London, Edinburgh, and Dublin Philosophical Magazine and Journal of Science*, vol. 27, no. 182, pp. 250–261, 1864.

[3] D. P. Billington, “The revolutionary bridges of Robert Maillart,” *Scientific American*, vol. 283, no. 1, pp. 84–91, 2000.

[4] D. Zastavni, “The structural design of Maillart’s Chiasso Shed (1924): a graphic procedure,” *Structural Engineering International*, vol. 18, no. 3, pp. 247–252, 2008.

[5] C. Fivet and D. Zastavni, “Robert Maillart’s key methods from the Salginatobel Bridge design process (1928),” *Journal of the International Association for shell and spatial structures*, vol. 53, no. 1, pp. 39–47, 2012.

[6] G. Frank, C. Kerez, and H. Frei, “Christian Kerez 2000-2009,” *El Croquis*, vol. 145, 2009.

[7] Nejur Andrei and Akbarzadeh Masoud, “PolyFrame, Efficient Computation for 3D Graphic Statics,” *Computer-Aided Design*, vol. 134, no. prepublish, Art. no. prepublish, 2021.

[8] J. Lee, “Computational Design Framework for 3D Graphic Statics,” ETH Zurich, 2018.

[9] P. D'Acunto, J.-P. Jasienski, P. O. Ohlbrock, C. Fivet, J. Schwartz, and D. Zastavni, "Vector-based 3D graphic statics: A framework for the design of spatial structures based on the relation between form and forces," *International Journal of Solids and Structures*, vol. 167, pp. 58–70, 2019, doi: 10.1016/j.ijsolstr.2019.02.008.
[10] A. Rietz, "Sufficiency of a finite exponent in SIMP (power law) methods," *Structural and Multidisciplinary Optimization*, vol. 21, no. 2, pp. 159–163, 2001.
[11] N. P. Van Dijk, K. Maute, M. Langelaar, and F. Van Keulen, "Level-set methods for structural topology optimization: a review," *Structural and Multidisciplinary Optimization*, vol. 48, no. 3, pp. 437–472, 2013.
[12] X. Y. Yang, Y. M. Xie, G. P. Steven, and O. M. Querin, "Bidirectional evolutionary method for stiffness optimization," *AIAA journal*, vol. 37, no. 11, pp. 1483–1488, 1999.
[13] Q. Zhou, W. Shen, J. Wang, Y. Y. Zhou, and Y. M. Xie, "Ameba: A new topology optimization tool for architectural design," in *Proceedings of IASS Annual Symposia*, International Association for Shell and Spatial Structures (IASS), 2018, pp. 1–8.
[14] Y. M. Xie, "Generalized topology optimization for architectural design," *Architectural Intelligence*, vol. 1, no. 1, pp. 1–11, 2022.
[15] Y. Li and Y. M. Xie, "Evolutionary topology optimization for structures made of multiple materials with different properties in tension and compression," *Composite Structures*, vol. 259, p. 113497, 2021.
[16] Y. Li and Y. M. Xie, "Evolutionary Topology Optimization of Spatial Steel-Concrete Structures," *Journal of the International Association for Shell and Spatial Structures*, vol. 62, no. 2, pp. 102–112, 2021.
[17] Y. Li, Y. Lai, G. Lu, F. Yan, P. Wei, and Y. M. Xie, "Innovative design of long-span steel–concrete composite bridge using multi-material topology optimization," *Engineering Structures*, vol. 269, p. 114838, 2022.
[18] P. Ole Ohlbrock and J. Schwartz, "Combinatorial equilibrium modeling," *International Journal of Space Structures*, vol. 31, no. 2–4, pp. 177–189, Jun. 2016, doi: 10.1177/0266351116660799.
[19] A. Muttoni, J. Schwartz, and B. Thürlimann, "Bemessung von Betontragwerken mit Spannungsfeldern," Birkhäuser Verlag, Design of Concrete Structures with Stress Fields, 1997.
[20] A. A. Gvozdev, "The determination of the value of the collapse load for statically indeterminate systems undergoing plastic deformation," *International Journal of Mechanical Sciences*, vol. 1, no. 4, pp. 322–335, 1960.
[21] M. Rippmann, L. Lachauer, and P. Block, "Interactive vault design," *International Journal of Space Structures*, vol. 27, no. 4, pp. 219–230, 2012.

Conceptual design

Active bending
Additive manufacturing/ 3D printing
Architectural geometry
Bamboo for sustainable construction and quality of life improvement
Bio-inspired structures and architecture
Bridge structures
Computational form-finding
► **Conceptual design**
Concrete structures
Construction techniques
Deployable and inflatable structures
Design competition (WG21)
Digital modelling and fabrication
Dynamic response of metal spatial structures
Dynamic response of other structures
Form-finding and structural optimisation of interlocking discrete assemblages
Graphical methods
Gridshell and lattice structures
Historical concrete shells
Historical structures
Lattice structures
Life-cycle design and assessment of structures
Metal gridshell structures, connections and stability
Methods and construction technologies for sustainable shell structures
Morphology and configuration processing
Next generation parametric design
Novel methods in modelling, optimisation and construction for reducing carbon footprint of continuous roof shells
Numerical methods for geometry, form-finding and optimisation of lightweight structures
Optimisation methods and applications
Origami
Other
Teaching design uncertainty: working with unknown qualities/quantities of new and re-claimed materials
Teaching of shell and spatial structures
Tensegrity systems and cable structures
Tension and membrane structures
Tension structures in the Asia-Pacific
Timber and bio-based structures
Topology optimisation
Traditional masonry structures and innovation
Transformable structures

IASS 2023
July 10–14 Melbourne
Integration of Design and Fabrication

Proceedings of the IASS Annual Symposium 2023
Integration of Design and Fabrication
10–14 July 2023, Melbourne, Australia
Y.M. Xie, J. Burry, T.U. Lee and J. Ma (eds.)

Conceptual design and parametric modelling of pretensioned stiffened membranes

Iuliia LEBEDEVA*, Martin F. EICHENAUER[a], Peer HALLER[a]

* Chair of Structural Design, Technische Universität Dresden
Anennstrasse 1, Dresden, Germany
iuliia.lebedeva@tu-dresden.de

[a] Institute of Steel and Timber Construction, Technische Universität Dresden

Abstract

The research focused on the conceptual development of innovative architectural forms that meet both aesthetic and practical criteria by combining physical experimentation with computer simulation. The physical form-finding technique was employed in the experimental approach, utilizing models generated from pretensioned fabric as a membrane and various glued-on grid patterns as stiffeners. The relaxation of the prestressed fabric resulted in the formation of anticlastic surfaces. The influence of different patterns of rigid elements, prestress intensity, and direction were investigated. Tensegrity structures were also examined using the same method. The results of the physical experiments were utilized as a basis for parametric modelling in the Grasshopper add-on for Rhino3D. The optimization of the final shape was achieved by varying the parameters, such as the configuration of the stiffeners and membrane strength. The transfer of designs to the digital environment allowed for more accurate shaping of the elaborated structures, and subsequent optimization and development of a detailed model. The resulting prestressed stiffened membrane structures exhibit great potential for practical application as pavilions, roofs, and awnings.

Keywords: conceptual design, form finding, membrane structures, parametric modelling

1. Introduction

Nature has long been a source of inspiration for various fields of science and design, including architecture. Bionics, the study of living organisms and their structures, has been used as a design concept for developing structures that are both aesthetically pleasing and functionally efficient. Bionic architecture aims to mimic the harmonic shapes and structural principles of living organisms [1]. In this study, we focus on the exoskeleton of insects as a design concept.

Insects possess a complex system of support and movement, known as the exoskeleton. This cuticle consists of an elastic membrane supported by a network of rigid rods or plate-shaped segments, known as sclerites. The muscles, tendons, and apodemes within the insect body work together to stretch the membrane, which returns to its initial configuration when the tension is released. This interaction of rigid and flexible elements of the exoskeleton affects the position and movement of the insect body [2].

By exploring the complex interplay of rigid and flexible elements in these natural systems, architects and engineers can develop new materials and construction methods that are more sustainable, efficient, and aesthetically pleasing. Torres and Borenstein [3] further investigated the structural analysis of insect exoskeletons and proposed that their complex hierarchical structure could be used to develop new materials and structural designs for use in architecture. When applied to architecture, the structure of insect exoskeletons can be compared to pretensioned stiffened tensile membrane structures. Sclerites

Copyright © 2023 by Iuliia LEBEDEVA, Martin F. EICHENAUER and Peer HALLER. Published in the Proceedings of the IASS Annual Symposium 2023 with permission.

are equivalent to rigid edges and stiff elements such as rods or beams, while the muscle work of stretching the membrane can be calculated using structural analysis. By changing the pattern of stiffness and characteristics of pretensioning, various variations of shapes and reliefs can be obtained.

Tensegrity structures offer a potential solution for prestressed and locally stiffened membrane structures. Tensegrity systems are defined as "a system in a stable self-equilibrated state comprising a discontinuous set of compressed components inside a continuum of tensioned components" [4] (p.19). Wang, Zhang, and Wu [5] reviewed the applications of tensegrity structures in architecture, highlighting their versatility and adaptability in a variety of contexts. In this article, the case is considered when the membrane serves as the continuous tensioned component, while rigid struts and rods act as the compressed elements. Such a structure is in a state of spatial equilibrium and offers broad potential for inspiration and experimentation.

1.1. Structural behaviour

Generally, lightweight membrane surface structures are classified as form-active structures, which are characterized by loading with only tensile or compressive stresses in the axial direction [6]. The membrane is in a pure state of tension, and the geometry of the structure must follow the flow of forces [7]. The stress state in the edge details depends on the type of elements, i.e., flexible or rigid. Rigid elements are loaded in compression and may be stressed in bending [8].

The stiffness of a membrane structure is influenced by various factors, such as the surface curvature, the value of prestress, and the characteristics of the materials used [9]. In general, prestressing acts as a uniformly distributed load perpendicularly to the rigid elements and causes compressed elements to bend. The elements resist bending to maintain their original shape through their stiffness. This can also be recognized from the internal tensile forces, which depend on the value of the prestressing force and the spans [6].

External loads are transferred from the membrane to the supports and foundations through rigid elements. The ratio of external loads to their weight is significantly higher for lightweight structures than for typical building structures. Therefore, it is essential to carefully consider the design of such structures because external loads such as wind, snow, and rain have a significant effect on the deformation of the structures. Structural analysis should be performed with loads without partial safety factors to account for large deformations of membrane structures. Self-weight and prestressing loads must be taken into account for all load combinations. However, pretensioning may not affect the maximum forces in the calculations for the structural system as it can largely dissipate under the total design loading [10].

In theory, the stiffness of tensegrity structures can be achieved independently of any external loads by self-stress, which allows the system to keep itself in equilibrium, which was illustrated from linear to three-dimensional systems with struts and cables [4]. However, in practice, appropriate support systems and bracers are needed for better stability.

1.2. Execution

According to Ochsendorf and Filippi [11], a membrane structure is made of a flexible material with a thickness that is much less than its surface area. The material must be resilient and able to protect against environmental influences. Textiles, polymers, and even thin metal plates can be used as membrane material. The material must also have mechanical strength, fracture toughness, light transmittance, protection from weather and fire, and be suitable for enclosing and economical. However, there is no single material that meets all requirements, and the choice of material depends on the specific function, location, and application requirements. For mechanically pre-tensioned structures, coated textile materials such as PVC-coated polyester fabric and PTFE-coated glass fabrics are generally used [12].

Rigid elements are subject to compressive forces and bending, as described before. Steel profiles, glued wooden beams, or metal tubes are usually used for this purpose [12].

The design phase is the most time-consuming part of building membrane structures. On the other hand, assembly is the fastest part of the process. One of the main advantages of membrane structures is that with good quality, almost no maintenance is required, and often only a visual examination is sufficient [13].

2. Materials and methods

2.1. Physical form finding

To investigate forms that are suitable for implementation in architecture, such as roofs, awnings, and shells, several models were constructed. These models were composed of an elastic nylon fabric with orthogonal weave orientation to simulate a textile membrane and a rigid frame of flat wood sticks.

The fabric was attached to the cork backing using nails hammered along the edge of the backing and stretched in one or two directions. A grid of wooden sticks was then glued onto the stretched fabric while the rods remained unconnected. After the glue was allowed to dry, the fabric was removed from the fixers, leading to the deformation of the entire structure. The fabric surface bends in each "cell" due to the opportunity of the tissue to relax only within the closed contour of the framework. The rods rotate until the deformation of the fabric is complete, changing their original horizontal position so that one end forms a high point and the opposite end forms a low point, which serves as the anchor point. The rotation stops when the fabric is relaxed. This process results in the formation of rigid elements that create a frame of minimal surfaces, leading to the generation of an anticlastic hyparic surface.

The final shape is influenced by the geometry of the rigid bar mesh and some parameters, such as the direction and intensity of the pretension.

2.2. Parametric modelling

To advance the exploration of prestressed and locally stiffened membranes, their models were integrated into a digital environment. This was achieved through the utilization of the Grasshopper plugin, which is designed for use with the Rhino3D software. The integration of Kangaroo 2 into the Grasshopper plugin provides the capability to model form-active systems parametrically [14]. This allows for the simulation of various form-active structures with prestressed and locally stiffened membranes, thereby enabling the exploration of their behaviour under different conditions and the optimization of their design parameters.

3. Results

3.1. Physical form finding

3.1.1. Intensity of pretension

In this study, the effect of pretensioning intensity on the final geometry of a membrane structure was investigated through the physical examination of five specimens. A rigid frame in the shape of a square with a side length of 115 mm was glued onto a piece of the fabric. The perimeter along which the fabric was stretched was kept the same for all samples at 205x270 mm.

The intensity of tension was determined by the degree of elongation, which is calculated as the ratio between the change in the length of the fabric and the original length.

Once the fabric was removed from the nails, it relaxed inside the rigid frame, resulting in the formation of a saddle surface, which caused the opposite ends of the rods to rise. The final shape of the structure was a parabolic hyperboloid, as shown in Figure 1.

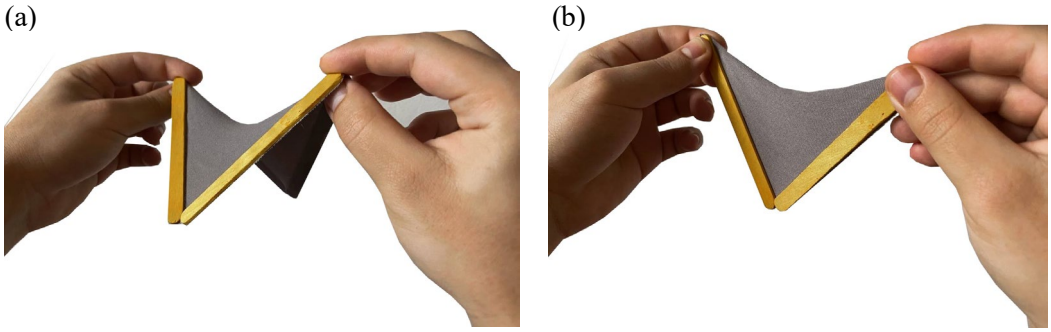


Figure 1. Parabolic hyperboloid surface: (a) unfolded state; (b) folded state.

To quantify the lift height of the rod ends, a perpendicular line was dropped from the upper ends of the rods to the level of the lower ends, using a metric ruler with a precision of +/-0.6 mm. The lift height *H*, as shown in Figure 2a, was measured and recorded for each specimen. Table 1 presents the results of this measurement, which vary depending on the level of pretension. The change in length of the fabric *Δl* was calculated as the difference between the original length of the fabric and the base on which it was stretched. The strain of the fabric, indicating the level of pretension, was calculated as the ratio of the change in length *Δl* to the original length *L*.

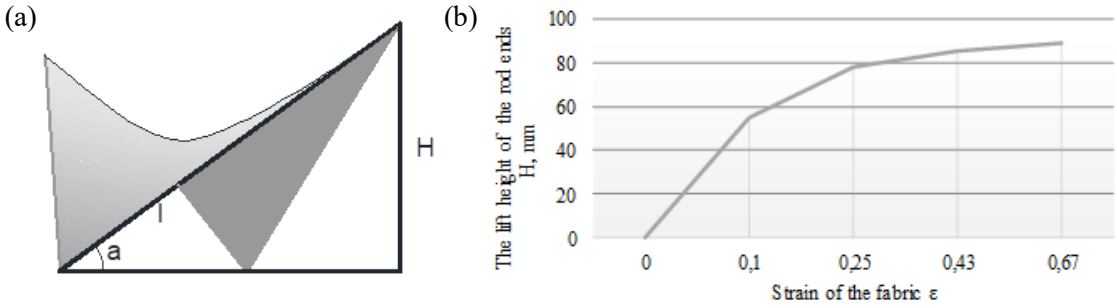


Figure 2. (a) scheme of the resulting parabolic hyperboloid with notations, (b) relationship between strain of the fabric and the height of lifting the rods ends.

The relationship between the fabric elongation during pretensioning and the amount of lifting of the rod ends in the final position was examined by plotting the results shown in Table 1 on Figure 2b. The results indicate that the intensity of pretensioning is greater when the original dimensions of the fabric are smaller because of the greater strain of the fabric. As the prestress intensity increases, the angle *a* between the base level and the rod, which determines the slope of the structure, also increases.

Table 1. Results of the experiment with different intensity of pretension.

Sample	Original length of fabric L, mm	Length of base l, mm	Change in length of fabric Δl, mm	Strain of fabric ε	The lift height of the rod ends H, mm
1	270	270	0	0,00	0
2	243	270	27	0,10	61
3	216	270	54	0,25	78
4	189	270	81	0,43	85
5	162	270	108	0,67	89

3.1.2. Direction of pretension

Two membrane structures were fabricated for physical examination in this study. One was made with uniaxial initial tensioning, while the other was fabricated with biaxial prestress. Both specimens were constructed with a square rigid frame of 65 m in side length, which resulted in a parabolic hyperboloid after relaxation. The green specimen was stretched in only one direction, while the red specimen was tensioned homogeneously, i.e., with equal tension in both directions (see Figure 3).

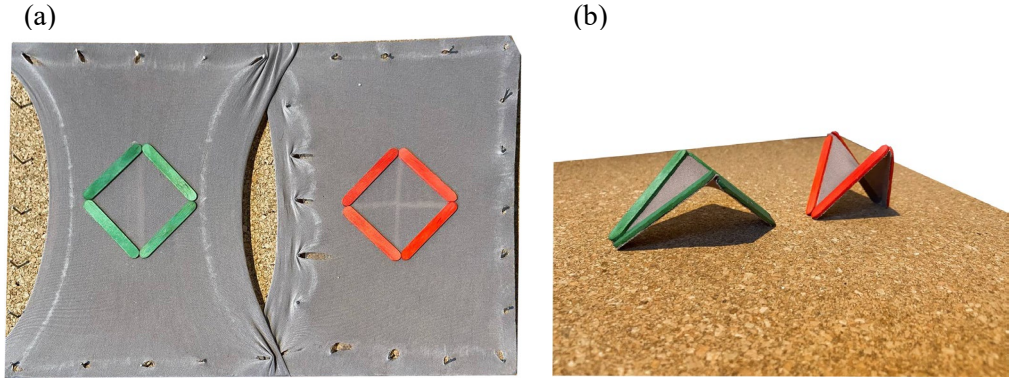


Figure 3. Specimens in the initial and final stages: (a) pretensioned fabric with a glued frame, (b) final geometry after relaxation and cutting out.

It was observed that different prestressing of the same rigid elements led to the same geometry but with different heights and curvature. The rod ends of the biaxial pretensioned membrane lifted less than those of the uniaxial pretensioned membrane. In the latter, the main curvatures were identical.

During the formation of the final geometry of the hyperbolic paraboloid, the rod ends rose at the nodes where the membrane was first relaxed. Furthermore, the highest nodes of the shape could also be inverted manually in a symmetrical manner.

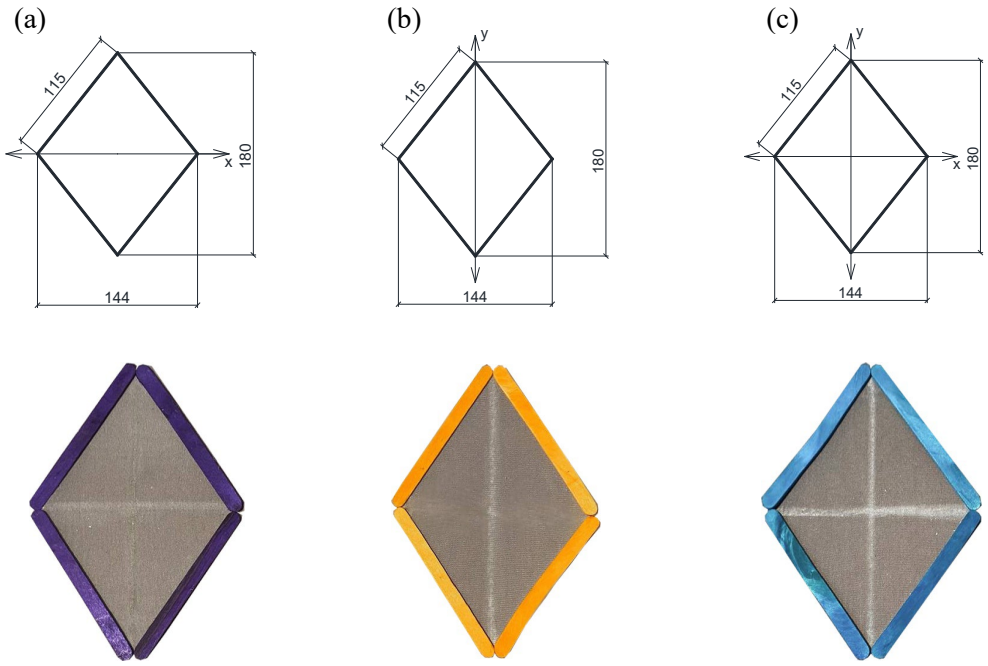


Figure 4. Specimens under tension with a glued rhombus frame and their drownings. Direction of pretension is pointed by a line: (a) with transverse pretension, (b) with longitudinal pretension and (c) with biaxial pretension.

To investigate the effect of geometry on the principal curvatures, three specimens were fabricated with a rhombus as the rigid element. The purple specimen was prestretched along the x-direction, the orange one along the y-direction, and the blue specimen biaxial prestressed (Figure 4).

The rod ends were lifted higher when prestressed in the direction of the long diagonal than when prestressed in the short diagonal, resulting in a flatter and more elongated shape. The curvature ratio remained proportional to the original dimensions with uniform preload, and the blue sample was a mixture of the others (Figure 5).

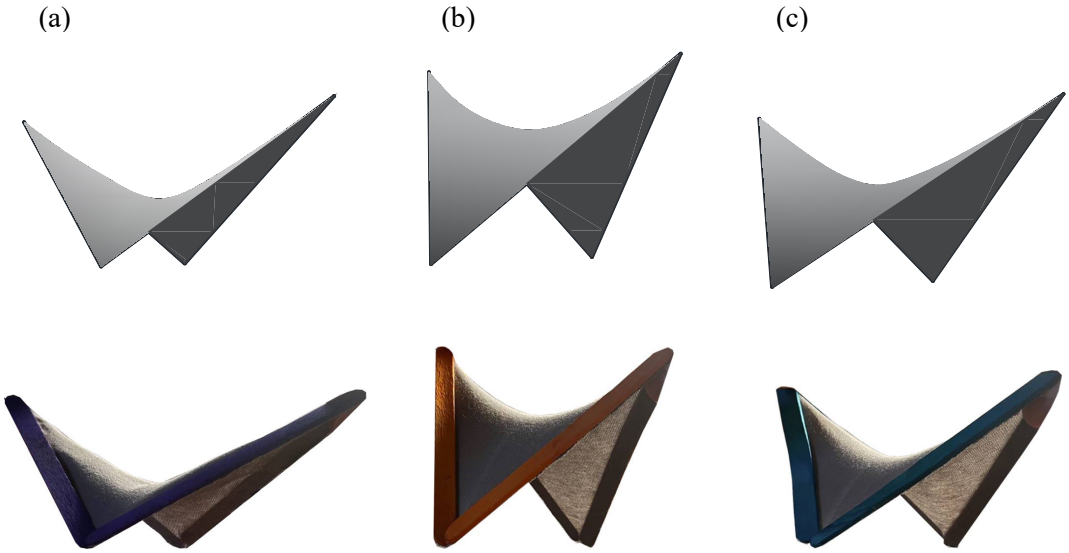


Figure 5. Final geometry of specimens with a rhombus frame and their drawings: (a) with transverse pretension, (b) with longitudinal pretension and (c) with biaxial pretension.

3.1.3. Stiffening patterns of cell structures

The geometry of the rigid members was found to be the most critical factor influencing the geometry of the entire structure. Therefore, changing the relative position of the stiffeners enabled the production of a variety of architectural forms. In this work, several experiments were conducted, and all structures were constructed with homogeneous pretensioning along the main orientation axes of the fabric weave.

Initially, a simple model (№1) was constructed, which comprised of identical parallelograms having equal side lengths (= 115 mm) and angles of 60º and 120º (Figure 6). This model can be inverted and employed on either side depending on the desired nodes of the high points.

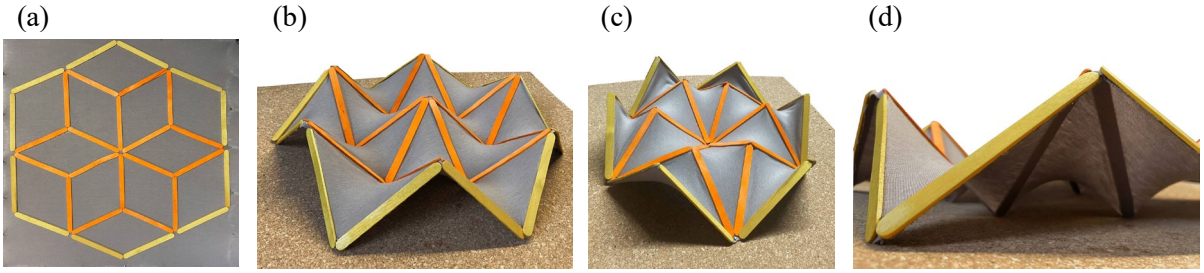


Figure 6. Specimen №1: (a) before relieving pretension, (b) after relieving pretension, (c) After turning and (d) side view.

A wide range of designs can be produced by merging rectangles and parallelograms. Pattern №2-5 were developed using 65 mm sticks, with parallelograms featuring angles of 45º and 135º (Figure 7).

Although these structures can be used for diverse purposes, they do possess a notable drawback, namely that additional internal supports might be required in the lowest nodes to bear external loads. In contrast, tensegrity structures do not face this issue.

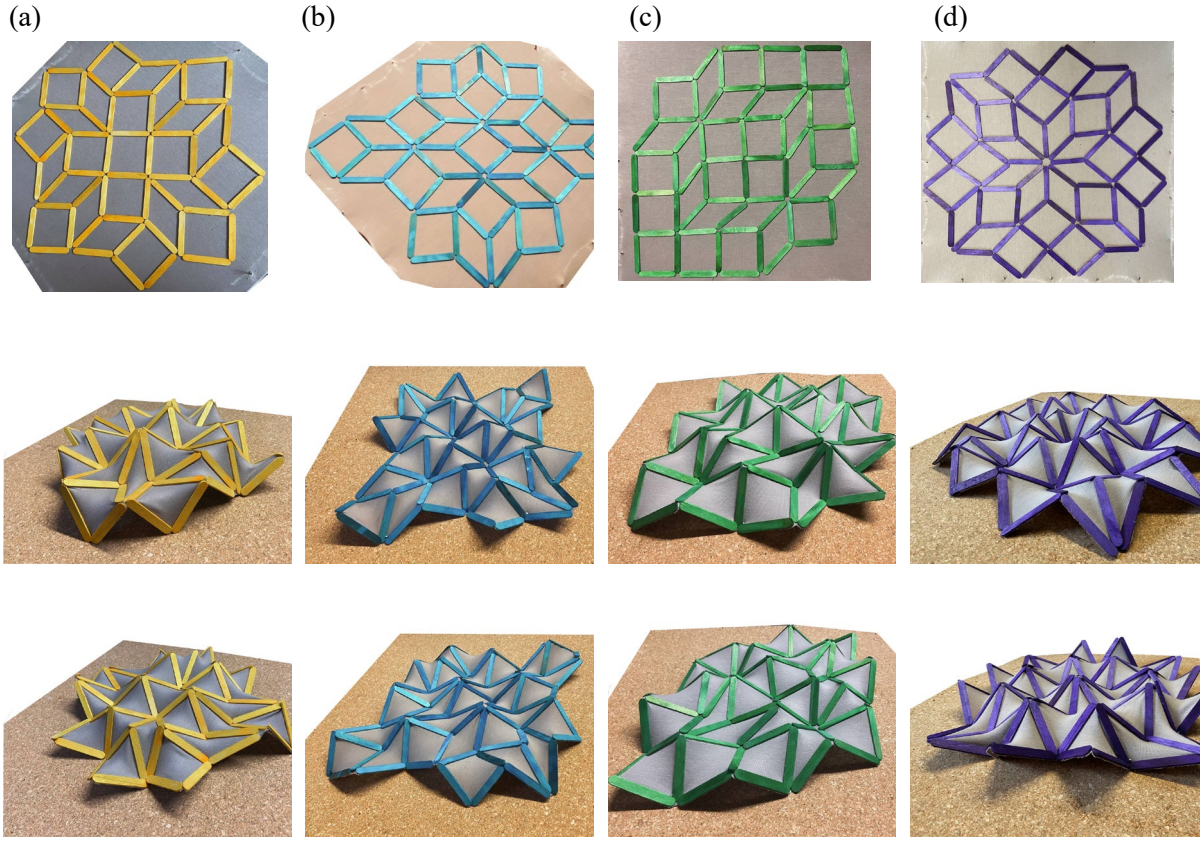


Figure 7. Specimens before and after relieving pretension and after turning out: (a) specimen №2, (b) specimen №3, (c) specimen №4 and (d) specimen №5.

3.1.4. Tensegrity structures

Tensegrity structures are a class of efficient structures that are composed of a combination of compressive and tensile elements in a state of self-stress, providing stability and equilibrium. The distinguishing characteristic of tensegrity is that the rigid struts are not directly connected to each other, but are instead supported by a network of tensioned elements. [4]. One specific type of these structures is membrane tensegrity, which replaces the tensioned cables with a continuous tensile membrane. It is based on the idea that the tensile elements should be a continuum of tensile components [15].

Physical prototypes of membrane tensegrity structures have been implemented in various ways. The common method involves connecting thin rods to the membrane at their ends, causing local stretching [16]. However, this method can be difficult to implement. An alternative approach involves using a connection fabric and rods along their entire length, as described before, which simplifies the process.

To construct a membrane tensegrity structure using this method, a symmetrical pattern of individual flat wooden sticks is glued to the prestressed fabric. The pretension is released and the ends of the outer wooden sticks are fixed as supports. The prestress is then transferred to the wooden rods as compressive forces, resulting in pure internal compression [17]. The model with sets of simple straight lines (Figure 8) is based on the the MOOM Pavilion project, a similar structure on a large scale [18].

(a) (b)



Figure 8. Pavilion with straight beams: (a) before relieving pretension and (b) after relieving pretension.

The use of rigid elements composed of a few sub-elements with different directions and locations relative to each other can result in various configurations, such as I-beams, crosses of beams, and others (Figures 9-11).

(a) (b) (c)



Figure 9. Pavilion with cross beams: (a) before relieving pretension, (b) after relieving pretension and (c) side view.

(a) (b) (c)



Figure 10. Pavilion with I-beams: (a) before relieving pretension, (b) after relieving pretension and (c) side view.

(a) (b) (c)



Figure 11. Pavilion with V-beams: (a) before relieving pretension, (b) after relieving pretension and (c) side view.

This method of form finding has the potential to generate multiple forms that can be effectively employed in architectural practice. A significant advantage of this method is its high degree of variability, which is attributable to the alteration of prestressing parameters and the pattern of rigid elements. Another advantage is the low cost of equipment required to perform experiments, which facilitates the creation of tensegrity systems, in particular.

Finally, this approach offers a simple and efficient way to construct membrane tensegrity structures in the stage of form finding using available materials and straightforward construction techniques.

3.2. Parametric modelling

3.2.1. Cell structures

The whole algorithm is shown in Figure 12a. Figure 13 demonstrates the resulting models of structures, based on the physical models.

The modelling of rigid elements and membrane behaviour is achieved using a combination of components in the Grasshopper plugin. The Length component, based on Hooke's law, is used to represent the rods and their stiffness, while the Angle component defines the geometric stiffness of the substructure (see Figure 12a, a red block). In addition, a reduction of rod's stiffness to 15% is applied to mimic the natural behaviour of rods compressed by the tension of the stretched membrane, which cause rod's shrinkage along their length, and to take into account an initial assumption of spring behaviour [18].

The behaviour of a membrane is realized by a mesh of springs with certain stiffnesses (a light blue block). The Mesh from Lines component in the Weavebirds plugin creates a mesh without binding to rods. The combination of the List Item, 4Point Surface and Mesh Brep components results in a mesh in each cell. Afterward, the Line components are applied again. The upper component in a purple block has a high value of strength and a stiffer interaction of the mesh with rods. The lower component in a blue block has a strength close to one, simulating the flexibility and mobility of the membrane surface.

Based on the experimental physical models, two lists of nodes were introduced to constrain points to the ground through the AnchorXYZ component so that our structure remains on the surface while we restrict the movement only along the z-axis. Changing between the sheets allows to create two different shapes, one from the other by rotating them (a green block). The Floor component is used to support the formation of the structure above ground level (a violet block). Components of a yellow block serve to apply forces to the structure.

The central part of the algorithm involves integrating all the components and obtaining the final result through the Solver component (outside blocks). The final output is visualized (see dark blue blocks).

3.2.2. Tensegrity structures

The algorithm for tensegrity structures is demonstrated in Figure 12b, while Figure 14 displays the parametric models of tensegrity with straight lines, crosses, I-beams, and V-beams based on physical models.

The first part of the algorithm contained in an orange block allows for the configuration of the struts in simple structures to be changed. The input consists of multiple elements, such as lines, crosses, I-beams, and others, which are sub-elements of the entire structure. Geometric parameters such as the angle of rotation of the elements, the number of columns and rows, and the distance between them can be modified, creating a network of sub-elements. A pink block corresponds to a red block in the previous example.

The second significant difference is the use of a special Delaunay mesh to simulate the membrane as a cable, with the endpoints of the struts serving as vertices (a purple block). This enables the natural structural behaviour of the membrane in tensegrity structures to be largely mimicked. The approach of using a Delaunay mesh to simulate the membrane is also supported by previous studies [19, 20].

The violet block contains the same procedure as in Figure 12a. A dark violet block corresponds to the yellow block. Other steps of the algorithm are identical to the previous one.

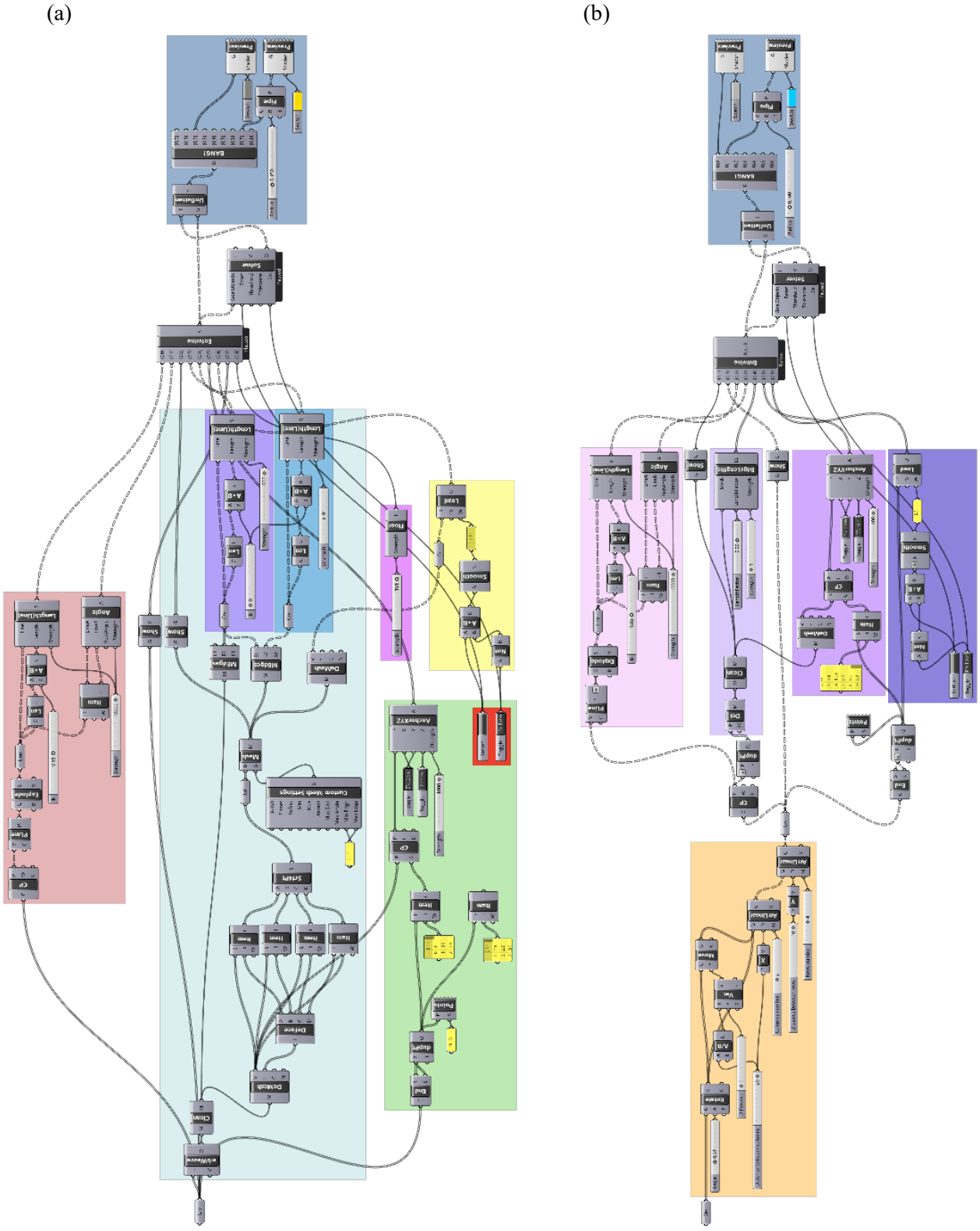


Figure 12. The algorithm in Grasshopper: (a) for cell membrane structures, (b) for tensegrity structures. (The pictures are rotated 90° to make them more readable.)

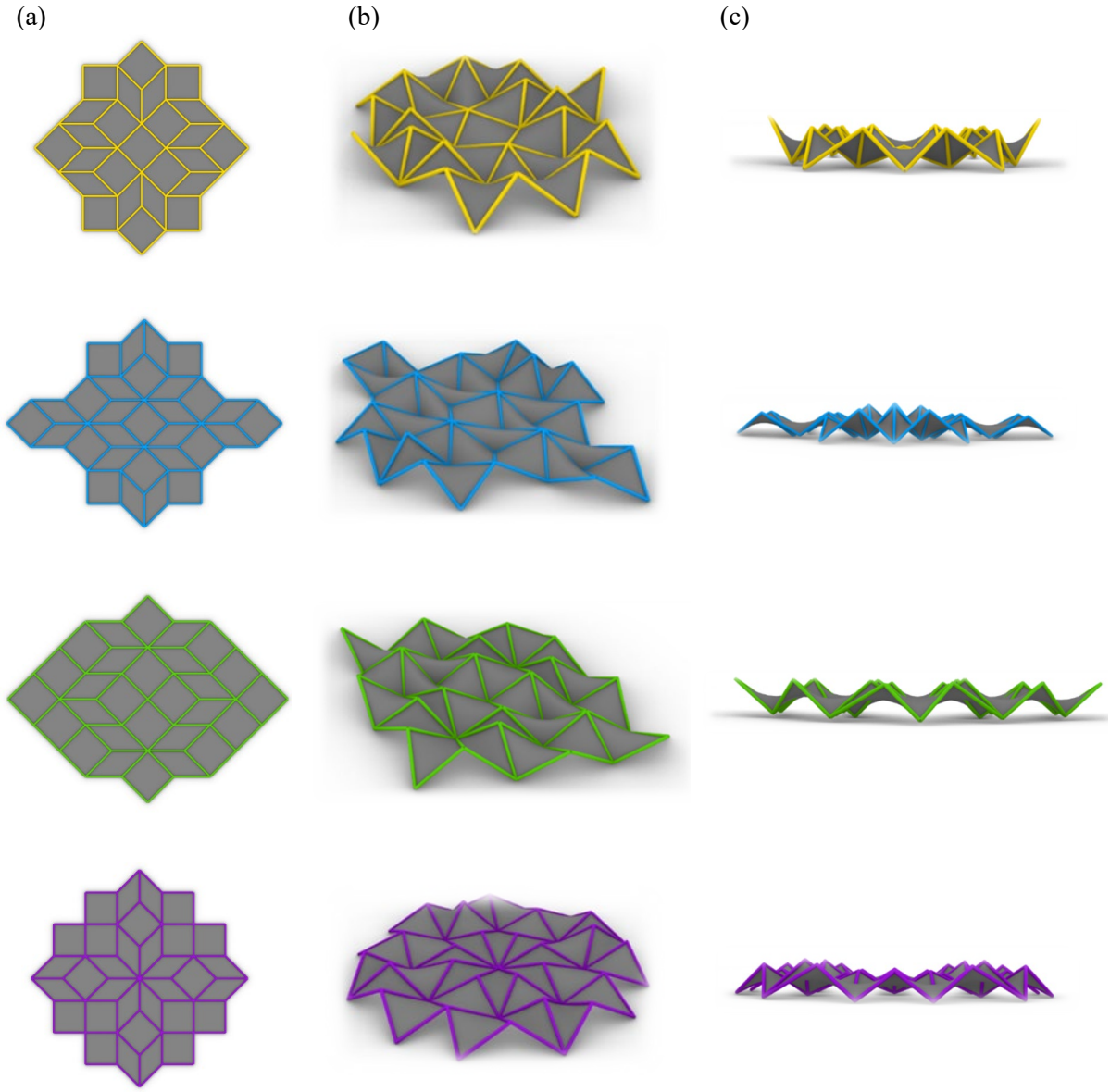


Figure 13. Parametric models of cell structures: (a) before relieving pretension, (b) after relieving pretension, (c) side view.

Many different layouts of strut configurations by Wang and Li serve as the source of inspiration for modelling these tensegrity structures [21]. In this work, such prototypes were utilized for modelling tensegrity in Grasshopper (Figure 15).

To conclude, parametric modelling is a suitable choice for digital form-finding. This method allows for the intended shape to be simulated and the properties of parts to be easily modified, helping to optimize geometry and find the ideal shape. Modelling in Grasshopper offers extensive possibilities for the required simulation of structures.

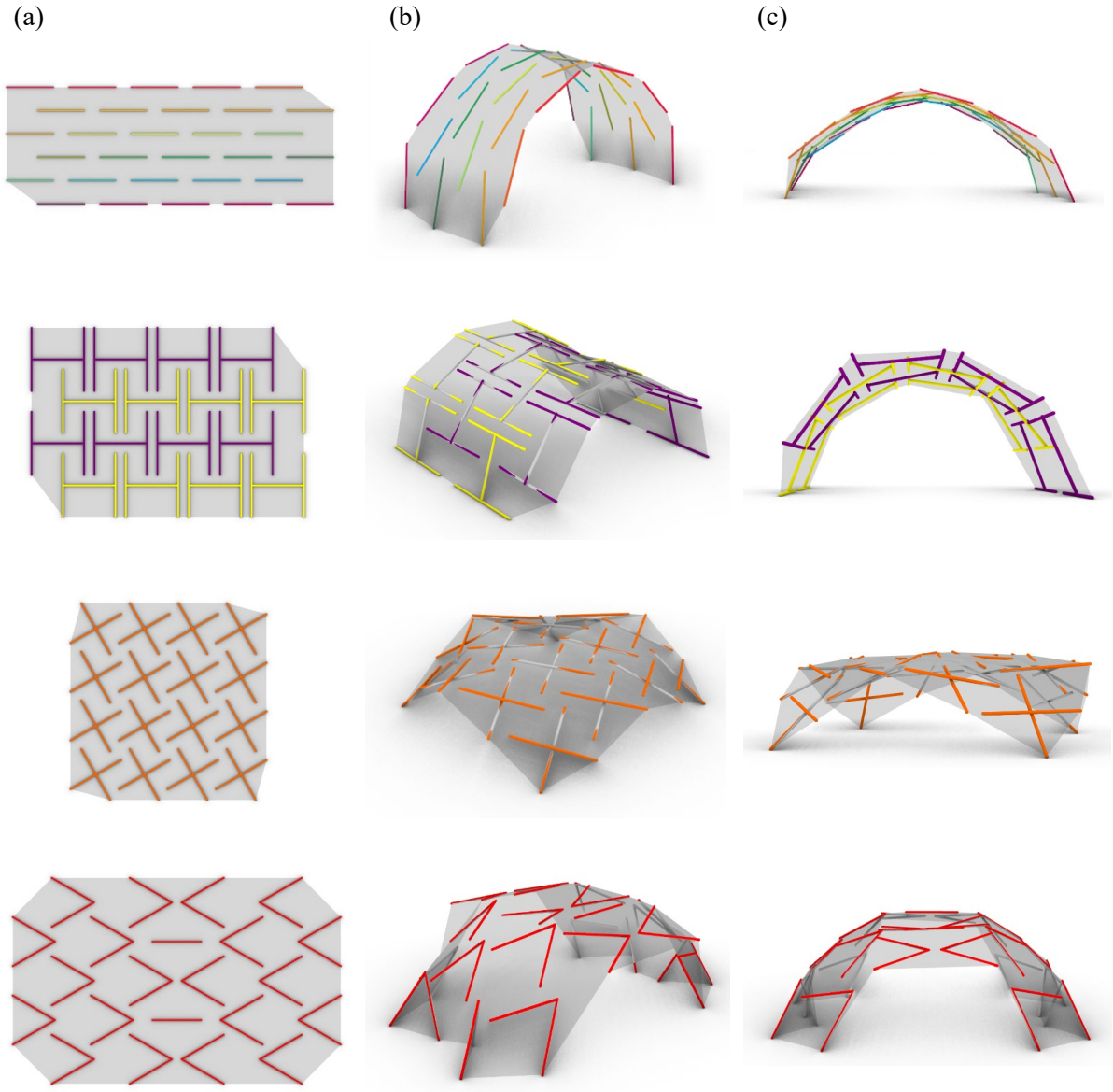


Figure 14. Parametric models of tensegrity structures: (a) before relieving pretension, (b) after relieving pretension, (c) side view.

4. Discussion

In this study, a prototype method for shape modeling was introduced based on existing types of forms and methods of finding them. The experiment involved a pretensioned fabric with a glued grid of wooden sticks, where the relaxation of the prestressed fabric contributed to the forming of specific anticlastic surfaces by energy release. The influence of the pattern of rigid elements, intensity, and direction of pretensioning on the final shape was investigated. The results showed that increasing pretension intensity results in a greater inclination of the entire structure. Hyperbolic curvature also depends significantly on the direction of prestress – uniaxial or biaxial. The overall geometry of the structure is changed by the relative position of rigid elements, resulting in a wide variety of possible shapes that can be applied in architecture. Samples of tensegrity structures were built using the same form-finding method, which simplifies the modeling process compared to the conventional method for creating tensegrity.

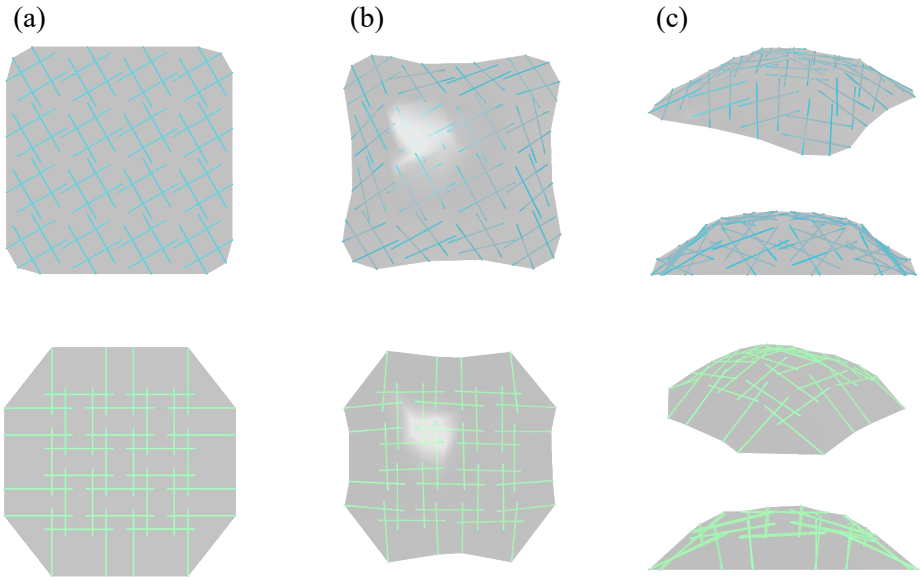


Figure 15. Parametric model of tensegrity according to layouts from [13]: (a) before relieving pretension, (b) after relieving pretension, (c) side view.

Furthermore, the experiments were digitized and simulated using Rhino6 and Grasshopper software, which offers even more options to optimize the final shape by changing the stiffening configuration, membrane strength, and deformability. This digital approach produces correct forms corresponding to physical shapes, leading to successful modeling and rationalization of the considered structures.

The final algorithms developed in this study can be extended to more detailed models, further structural analysis, and implementation in BIM. The resulting designs of the pretensioned and stiffened membrane structures have great potential for application in practice as pavilions, roofs, and awnings. These structures can demonstrate effective structural behavior and can be very spectacular from an architectural point of view. Overall, this study highlights the effectiveness of the physical and digital form-finding methods used in the design of pretensioned stiffened membrane structures. The results provide valuable insights into the factors that influence the final shape and geometry of such structures, paving the way for their practical application in various architectural contexts.

References

[1] A. Pugnale and A. Mateo, "Bionic design methods in architecture: a review," *Advanced Engineering Informatics*, vol. 31, 2017, pp. 43-59.

[2] E. U. Haque and M.N. Alam, "Biomimicry in architecture: A review on design methods and parameters," *Frontiers of Architectural Research*, vol. 6(4) , 2017, pp. 439-457.

[3] L. Torres and J. Borenstein, "Structural analysis of insect exoskeletons and implications for bionics design", *Applied Mechanics Reviews*, vol. 71(2), 020802, 2019.

[4] R. Motro, *Tensegrity: structural systems for the future,* Kogan Page Publishers, 1998.

[5] L. Wang, X. Zhang, and Z. Wu, Review on the tensegrity structures: "A brief introduction and applications in architecture", *International Journal of Advanced Structural Engineering*, 13(3), 2021.

[6] J. Knippers, J. Cremers, M. Gabler, and J. Lienhard, Construction manual for polymers + Membranes, Institut für international Architektur-Dokumentation GmbH &Co, 2011, p. 136, 145.

[7] R. Rivera, *Membrane Structures. First Steps towards Form Finding.* Membranas Estructurales, 2014, p. 23.

[8] M. Seidel, *Tensile Surface Structures. A Practical Guide to Cable and Membrane Construction.* Ernst & Sohn, p. 73, 2009.

[9] S. Pellegrino, "Membrane structures in architecture," Annual Review of Materials Science, vol. 24, pp. 49-79, 1994.

[10] M. Balz and H. Denchner, “Design Loading Conditions,” In *European Design Guide for Tensile Surface Structures*, TensiNet, pp. 192-202, 2004.

[11] J. Ochsendorf and M. Filippi, “Membrane structures: A critical analysis,” In *Shell Structures in Civil and Mechanical Engineering*, Springer, pp. 23-56, 2018.

[12] R. Blum, H. Bogner, and G. Nemoz, "Material Properties and Testing," in *European Design Guide for Tensile Surface Structures*, TensiNet, 2004, pp. 220, 224.

[13] K. Gipperich, R. Canobbio, S. Lombardi, and M. Malinowski, “Fabrication, Installation and Maintenance,” In *European Design Guide for Tensile Surface Structures*, TensiNet, pp. 253, 255-259, 2004.

[14] D. Piker, "Kangaroo: Form finding with computational physics," [Online]. Available: https://www.food4rhino.com/app/kangaroo-physics.

[15] R.E. Skelton and M.C. de Oliveira, *Tensegrity systems*, Springer, 2009.

[16] K. Tracy, S.S. Gupta, Y.N.S. Loo, J.W. So, A. Pal, T. Wortmann, R. Bamford, “Exploring Spatial Membrane Tensegrity Shell Structures,” *Proceedings of the ACADIA-2019*, Austin, USA, October 24-26, pp.111-112, 114, 2019.

[17] C. Popp and M. Bischoff, “Design and construction of tensegrity structures,” In *Handbook of Tensile Membrane Structures* (pp. 197-232), CRC Press, 2012.

[18] K. Kojima, *MOOM Tensegric membrane structure*, GA, pp. 149-151, 2011

[19] J. Zhu, J. and L. Zhang, L., “Analysis and optimization of a tensegrity antenna mast structure,” *International Journal of Antennas and Propagation*, pp. 1-10, 2014

[20] J. Zhou and Q. Li, “Analysis of cable-tensioned tensegrity structures with delaminated cables,” *International Journal of Structural Stability and Dynamics*, 16(5), pp. 1-19, 2016

[21] B.B. Wand and Y.Y. Li, “From Tensegrity Grids to Cable-Strut Grids,” *International Journal of Space Structures*, Vol. 16(4), 2001

IASS 2023
July 10–14 Melbourne
Integration of Design and Fabrication

Proceedings of the IASS Annual Symposium 2023
Integration of Design and Fabrication
10–14 July 2023, Melbourne, Australia
Y.M. Xie, J. Burry, T.U. Lee and J. Ma (eds.)

Structural design of flat and spiral buildings with inclined pillars

Ken NODA[a,*], Yoshiharu KANEBAKO[b]

[a,*] Kanebako Structural Engineers
3-12-14, Nishi-gotanda, Shinagawa-ku, Tokyo, Japan
noda@kanebako-se.co.jp

[b] Kanebako Structural Engineers; Tokyo Institute of Technology

Abstract

This paper is the structural design proposal for a bridge-like observatory with a spiral stairway. The building is located on a top of a mountain. Moreover, the site is undulating and complex ground containing many rocks. The main issues in the structural design were as follows:1. Design of forms considering both architectural aesthetics and structural rationality; 2. Implementation of systems which properly resist seismic forces on undulating ground; and 3. Reduction of underground rock excavation in foundation construction. The authors proposed a structural system with a L-shaped beams on inclined pillars. It effectively uses the pillars as seismic elements. This system was achieved by using slender pillars to provide sufficient horizontal stiffness, while minimizing the amount of rock excavation by using fewer foundations.

Keywords: structural design, L-shaped beam, inclined pillars, undulating ground

1. Introduction

With the development of technology, it has become possible to realize any form of structure. Under such circumstances, it would be important for structural engineers to consider structurally reasonable systems, not by brute force, but by structural design ingenuity. The authors have focused on the relationship between the curved structures and pillars, have been studying effective structural systems that combine them for complex forms [1]. The authors also studied a frustum shaped structures with diagonal members and ascertained its effectiveness [2].

This paper presents the structural design of the Senkoji Peak Observatory, which appears to float atop the mountain. This observatory, called “PEAK”, has a total length of 63m. While most observatories extend above the ground into the sky, this project is unique in that it is in the form of a horizontal bridge.



Figure 1. Bird’s-eye view.



Figure 2. Ground level view.

Copyright © 2023 by Ken NODA and Yoshiharu KANEBAKO. Published in the Proceedings of the IASS Annual Symposium 2023 with permission.

The building consists of three elements: an observation platform, a spiral stairway, and a vertical elevator shaft, as shown in Figures 1 and 2.

The ground is undulating and interspersed with numerous granite formations. These require high costs to excavate. Furthermore, the area below the observation platform is used as a park. In order to obtain a sufficient view from the park and to ensure the integrity of the park, the support structure was required to be free of many members so as not to become an obstacle. To solve the issues, the authors proposed a new structural system that effectively uses inclined pillars.

2. Building overview and issues

2.1. Building overview

Senkoji Peak Observatory was completed in 2022, in Onomichi-city, Hiroshima Pref., Japan. Table 1 summarizes the overview. The city faces the Seto Inland Sea, is characterized by mountains on its back and few flat areas, and is known as a city of slopes. Figure 3 shows a view from the seaside; the building is located at the top of the mountain. Figure 4 shows a view from right above.

Table 1. Building overview

Location	Onomichi-city, Hiroshima Pref.
Owner	Onomichi-city
Architect	AS
Structural Engineer	Kanebako Structural Engineers
Contractor	Taisei Corporation
Complete Date	March, 2022

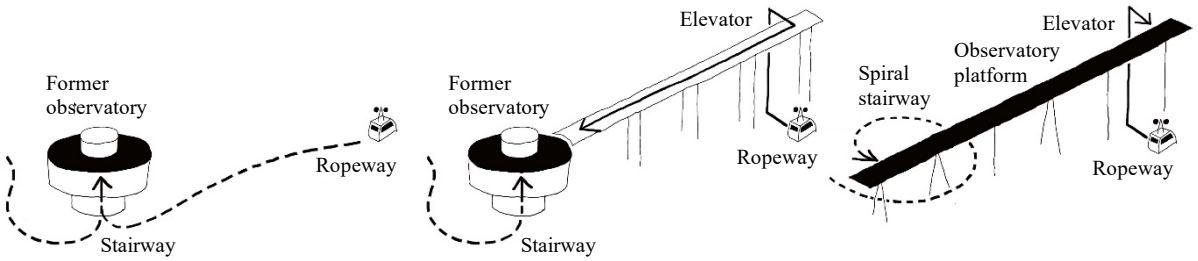


Figure 3. View from the seaside.



Figure 4. View from above.

This is a project to reconstruct an observatory and ropeway station at the top of Mt. Senkoji. Figure 5 shows the diagram transition of this project. The former observatory did not have an elevator and was not accessible, as it was on a different level from the ropeway station building, requiring a climb up the hill. In the schematic design phase, a bridge-type structure was proposed for the approach from the station to the existing observatory for accessibility. Later, the former observatory was demolished due to insufficient seismic resistance, however the view from the bridge-type approach was retained. The authors sought a simpler form, aiming for a horizontal deck floating at the top of the mountain. A spiral stairway was built where the former observatory was located.



a. Before the renovation b. Initial draft c. Final proposal

Figure 5. Diagram transition.

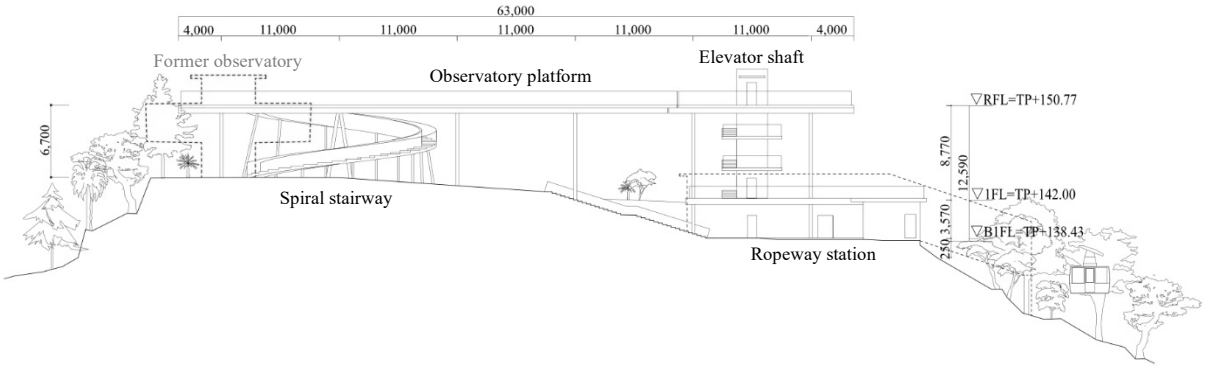


Figure 6. Longitudinal elevation (TP means elevation level).

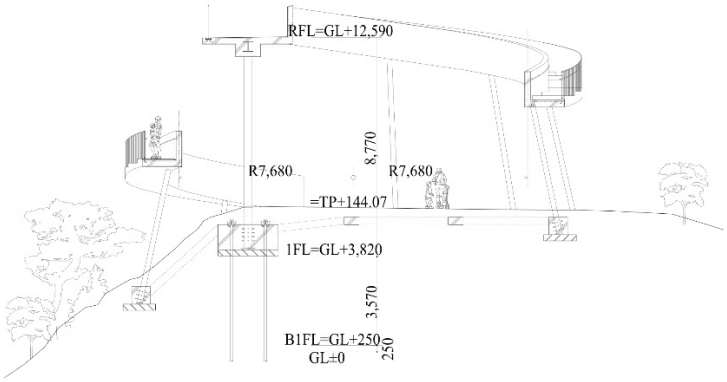


Figure 7. Section of the spiral stairway.



Figure 8. Site condition.

The site is the precincts of the Senkoji Temple, located near the top of Mt. Senkoji, and is used as a park. As shown in Figures 6 and 7, the ground level is undulating; Figure 8 shows that it interspersed with numerous granites. The former observatory stood on the western edge of the site, and the former ropeway station was to the east.

The building consists of two parts: one on the east side with a ropeway station, elevator shaft and observation platform; the other on the west side with an observation platform and a stairway. The platform level of each building is the same, however the east wing is one story deeper than the west wing, depending on the topography. The east wing is a three-story building, including the penthouse for the elevator, while the west wing is a one-story building.

In order to preserve the environment and atmosphere of the park, buildings above the ground were to be kept to a minimum such as the platform of the observatory; the elevator shaft on the east side and the stairs on the west side were installed as a connection path to the platform. The platform is flat and straight, the elevator shaft on the east side is rectangular prism, and the stairs on the west side are spirals with a large circular diameter and a constant slope.

The entire platform is 63m long, of which the east side is 18m and the west side is 45m. The width of the platform is 3.64m. For the ropeway station, the length of the longitudinal direction is approximately 22m; the length of the transverse direction is approximately 12m; the elevator shaft is approximately 3m square. The spiral stairway has the inner diameter of approximately 15m and the path width of 1.5m.

The building is made of RC, with the platform and spiral stairway supported by steel columns; the main girder of the platform is made of SRC.

2.2. Issues

The key to the structural design was to build the observatory, especially the spiral stairway, on top of this complex ground, while maintaining unobstructed atmosphere below the platform as a park. The main issues in the structural design were as follows:

1. The architectural form is a combination of geometrically simple shapes: an elongated platform, a rectangular-prism shaped shaft, and a spiral stairway. The site also functions as a park, so it was necessary to minimize the number of pillars and other obstructions. Therefore, it had to propose a system that would minimize the number of support members and effectively resist horizontal forces, while taking the form into account in the architectural concept.
2. Because the site is located on a mountaintop, the ground surface is highly undulating, which causes variation in column length. However, a rigid frame structure is not efficient because horizontal forces are concentrated on the short columns. Therefore, it should be proposed a system to enhance horizontal stiffness for the topography and height differences of the structure.
3. The site is densely covered with rocks, mainly granite, scattered throughout the ground. Because of the high cost of rock cutting, the challenge was to minimize the amount of rock cut when constructing the foundation.

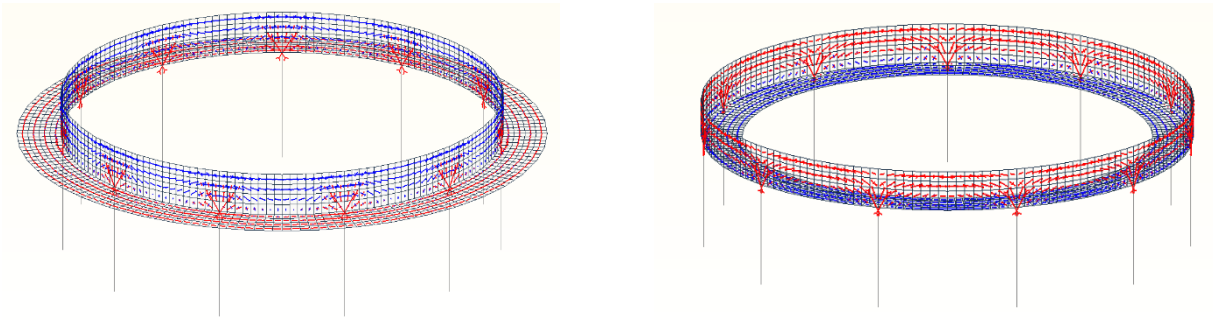
3. Analysis

3.1. Model

The building was analysed by using an FEM. Slabs and walls were modelled plane elements with in-plane and out-plane stiffness; columns, beams and footing beams were modelled beam elements. The model was considered during the design of the whole structure, and was analysed by considering dead loads, live loads, snow loads and seismic forces. This project, especially the spiral staircase, generates bi-directional axial forces and bending moments in plane elements. For the proportioning of member sections, the design method was used to design plane elements with in-plane and out-of-plane bending moments that take into account the movement of the neutral axis.

3.2. Structural behaviour

Prior to the analysis of the characteristics of the spiral stairway, this section will focus on a ring structure with an L-shaped disk composed of plane elements at the top and supported at equal intervals by pillars at the corner of the L-shape. In general, L-shaped frames are unstable when the shape is straight rather than circular because of the torsional behaviour of the L-shape around the supported point. However, if it is curved, it is stable because the torsional stress, i.e., the radial bending stress, is balanced by the circumferential bending stress. Here, although a circular shape is shown in Figure 9, etc., it does not have to be particularly closed.



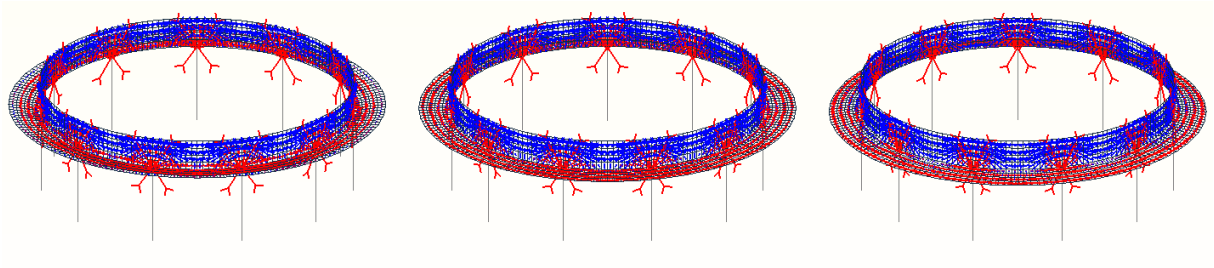
a. Supported on the inner side.

b. Supported on the outer side.

Figure 9. Axial force diagram.

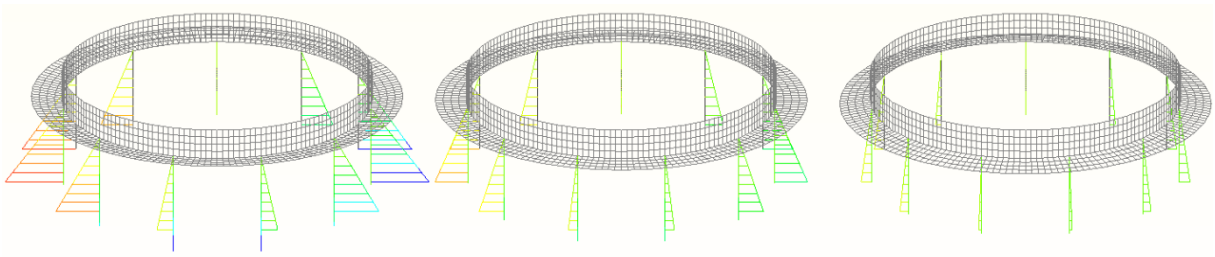
Firstly, consider the location of the supports. The L-shape assumes RC slabs and walls, and a frame supported by steel pipe pillars. The pillars are rigid at the bottom and pinned at the top. Figure 9 shows the axial force diagram under dead loading. Figure 9.a shows a structure supported on the inside with a cantilever slab on the outside, and Figure 9.b shows a structure supported on the outside. Red and blue in the figures indicate compressive and tensile forces, respectively. In this project, the L-shaped portion is assumed to be of RC. Considering the shear force transition of the slab by seismic forces, the system shown in Figure 9.a, where the slab is subjected to compressive forces under dead load, is preferable.

Secondly, the radial slope of the slab face of the L-shaped frame is discussed. Figure 10 shows the axial force diagram of plate elements and Figure 11 shows the bending moment diagram of pillars under dead load. The slope of the slab in each figure is: 'a' is higher on the outer edge, 'b' is flat, and 'c' is higher on the inner edge. Due to the difference in the slope of the slab, a tension ring is occurred at the slab edge in Figure 10.a and a compression ring in Figure 10.c. This means that near the top of pillars, compression and tension occur, respectively, opposite to the slab periphery. The top of pillars is deformed inwardly as a result of the L-shaped torsional deformation, as can be seen in Figure 11.b, where bending stresses are induced in the bottom of pillars. By varying the radial gradient on the disk, the stresses on the columns are increased or decreased in Figures 11.a and 11.c. Although it is effective to radially slope the slab so that the outside is lower for a more efficient structure, the slab is not radially sloped in this project because it is a staircase, so it is radially stepped for ease of use.



a. Higher on the outer edge. b. Flat. c. Higher on the inner edge.

Figure 10. Axial force diagram for difference in radial slope of slab.

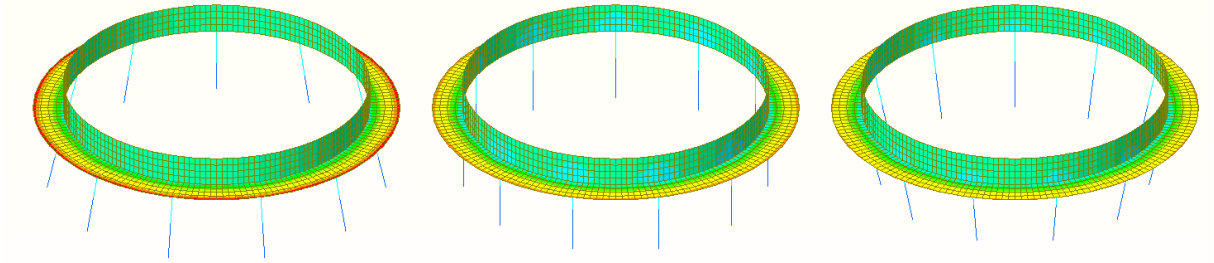


a. Higher on the outer edge. b. Flat. c. Higher on the inner edge.

Figure 11. Bending moment of pillars for difference in radial slope of slab.

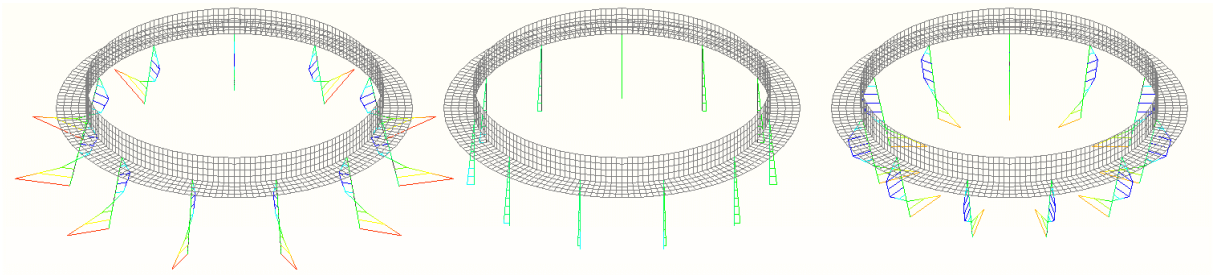
Thirdly, the inclination of the columns is discussed. Figure 12 shows contour diagrams of the vertical displacement of the slab under dead load, and Figure 13 shows bending moment of the pillars. In each figure, the columns are tilted in the following three forms: 'a' shows the bottom of pillars spread outward, 'b' shows vertical, and 'c' shows the bottom of pillars narrowed inward. Each column is tilted in a radial direction. In Figure 12, red indicates greater displacement. In other words, in Figure 12.a, the vertical displacement of the slab edge is large, and in Figure 12.c, the displacement is small. Figure 13 shows that the tilting of the column increases the bending moment due to the eccentric bending effect caused by the dead weight of the L-shaped portion. As mentioned with respect to Figure 11, even in the vertical case, as shown in 13.b, there is a bending moment that causes tension in the outward direction

of the circle due to the torsion of the L-shape. This effect is added to the eccentric bending effect for inwardly tilted pillars and subtracted for outwardly tilted pillars. Therefore, it seems structurally reasonable to support vertical loads with outwardly tilted pillars.



a. Inwardly tilted pillars. b. Vertical pillars. c. Outwardly tilted pillars.

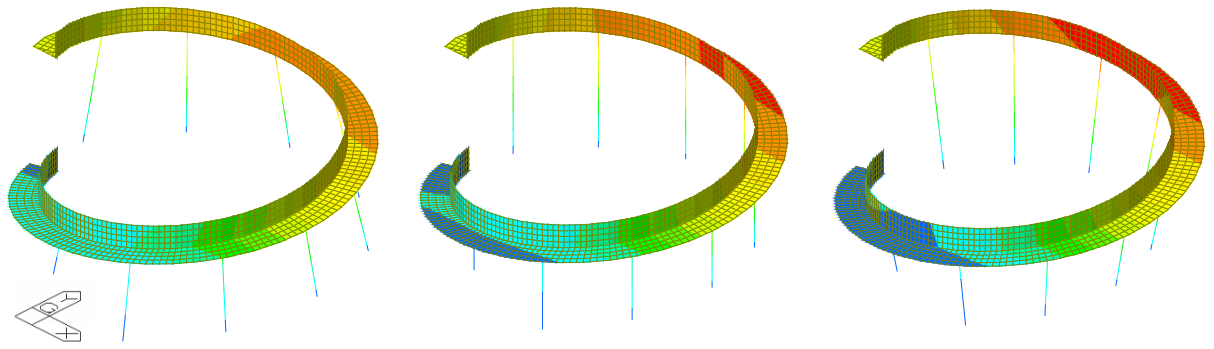
Figure 12. Vertical displacement for difference in pillar inclination.



a. Inwardly tilted pillars. b. Vertical pillars. c. Outwardly tilted pillars.

Figure 13. Bending moment of pillars for difference in pillar inclination.

Finally, considerations are made for the spiral shape. In the spiral shape, the pillar length is shorter and the horizontal stiffness is higher in the area closer to the ground, causing the pillar to behave in a twisting behaviour by seismic forces. In such a case, it would be effective to install circumferential walls or braces, however this is unsuitable for this project because of the openness required under the structure. The effect of horizontal deformation caused by tilting the pillars in the radial direction is shown in Figure 14. This contour plot represents the horizontal displacement of the slab due to seismic forces. Red indicates large displacement. The X direction in the figure is the direction of seismic force application. The models assume this project, and the pillar lengths are set according to the actual ground level. In Figures 12 and 13, tilting the columns outward was more advantageous, however in Figure 14, tilting outward is not necessarily more advantageous due to greater torsional deformation; the relative difference in horizontal displacement at low and high levels differs by about 17% between Figure 14.a and 14.c. Therefore, sufficient attention should be paid to the inclination in the actual design. In this project, the pillars were tilted inward in consideration of architectural aesthetic.



a. Inwardly tilted pillars. b. Vertical pillars. c. Outwardly tilted pillars.

Figure 14. Horizontal displacement for difference in pillar inclination.

4. Structural design

4.1. Design and realization

While most observatories extend above the ground into the sky, this project is unique in that it is in the form of a horizontal bridge. Through the design process, the search for a simpler form led to the consolidation of columns to create the expression of a horizontal platform floating above the mountain. In addition, the distinctive spiral staircase was also required to be a light structure. The spiral stairway and platform each feature L-shaped structures. Figure 15 shows the structural organization of the entire building.

Due to the unique nature of the massive rock formations scattered throughout the site, it was an important issue to consolidate the pillars to reduce the amount of excavation as much as possible. In order to reduce the cost of rock excavation, the former building locations were followed as much as possible to minimize excavation for new foundations. The spiral stairway was excavated to reduce the amount of excavation by decreasing the foundation beam size.

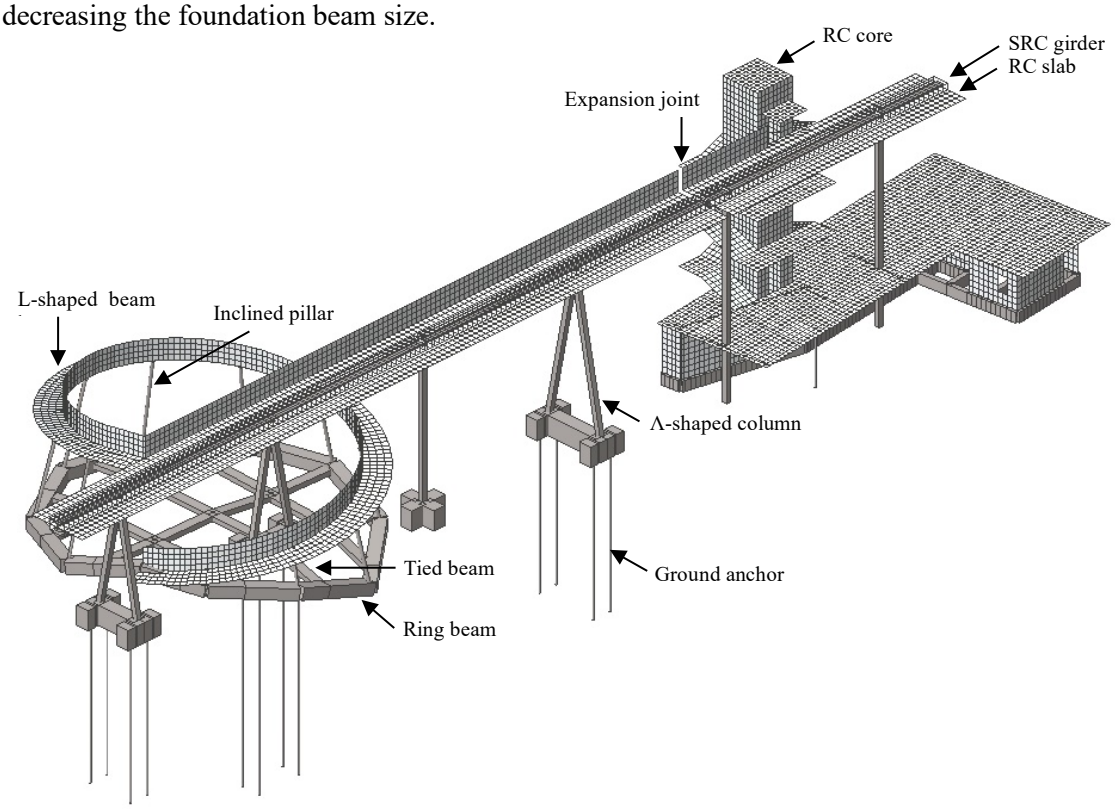


Figure 15. Structural arrangement.

4.1.1. Platform and shaft

In the schematic design phase, the structural system was envisioned to be a light structure, such as a tree-like structure, with two rows of columns with canes and beams composed of small size members that would be easy to transport, taking into account that the building is located on a mountain top.

As shown in Figures 16 and 17, the platform consists of an SRC main girder with 750 x 1,000, that is provided at the centre of the bottom of the L-shape, and a 200mm thick cantilevered slab floor. The uneven distribution of the load is resisted by the torsional stiffness of the SRC girder. Because of the long bridge geometry, there was a high degree of freedom in the location of support points. Column locations were designed to minimize the amount of framing and rock cuttings while avoiding localized depressions and exposed rock, with a span of11m. The length of the columns varies with the difference

in elevation of the ground, with a height to the platform of about 6.7m at the western end, about 9.2m near the centre, and about 12.5m at the eastern end. If the columns are designed to rigid frame system, horizontal forces will be concentrated on the short columns. Therefore, Λ-shaped columns, made of 300 mm square steel pipes, were used to resist axial forces in the direction of the applied force, regardless of the length of the member. They are arranged in a balanced manner. The columns were made thinner as an axial force resisting system, and an attempt was made to realize a floating observation platform.

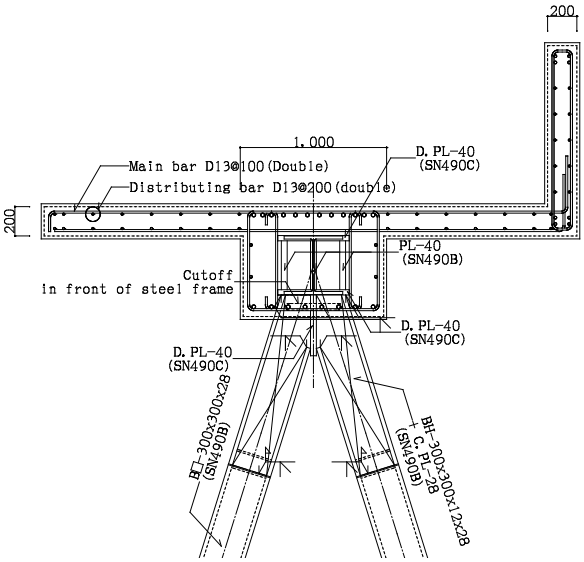


Figure 16. Detail of platform.



Figure 17. Construction of platform.

The elevator shaft, which is the starting point of the approach from the station, is constructed with RC walls. An artificial ground consisting of a 400 mm thick RC slab was provided on the middle floor to gently connect with the ground on the west side. The RC core could be used as a seismic core. The seismic wall thickness was set at 200-300 mm. Considering the overall horizontal stiffness balance, the stiffness of the RC core, which is located on the east side, is too high, causing the entire structure to cause eccentric behaviour. Further, the shaft side is also one story deeper on the elevation due to the undulating topography, so it is unbalanced in the elevation. Therefore, of the total length of 63m, 18m on the shaft side was constructed of RC and the other 45m was constructed of steel, structurally separated and functionally connected using expansion joints. As shown in Figures 18 and 19, The expansion joints are made with fluoroplastic sliding bearings attached to the steel frame of the SRC girders, and the east side is placed on the west side. In addition, since the frame is exposed as it is, the temperature fluctuation of the frame due to solar heat and other factors is significant. By dividing the building into separate buildings, seismic elements with high horizontal rigidity in the longitudinal direction can be concentrated in each building, and the effect of thermal distortion is also controlled.

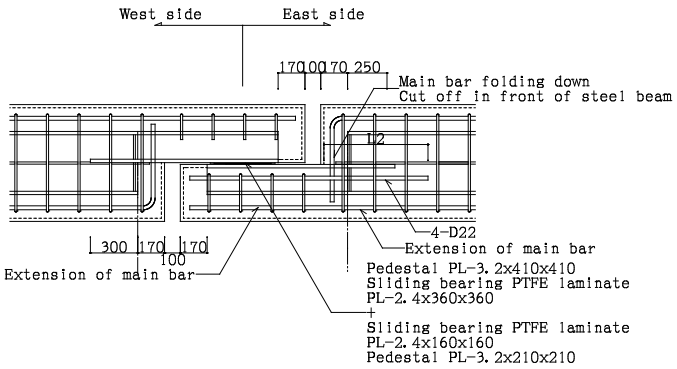


Figure 18. Detail of expansion joint.



Figure 19. Construction of expansion joint.

In the west building, the Λ-shaped steel columns are designed to resist the horizontal forces, and two are placed at both ends and one in the centre in the long direction. Torsion due to eccentricity in the longitudinal force is resisted by Λ-shaped columns in the shortitudinal direction. The columns are made of square steel tubes and are designed so that buckling will not occur on the compression side even under horizontal forces that are expected to occur in an earthquake with ground acceleration of 600 gal. Because the Λ columns of the platform have large variable axial forces due to horizontal forces in relation to the dead loads, the ground anchors were used to resist the foundation uplift.

4.1.2. Spiral stairway

A spiral stairway with a steep slope and a small diameter could be constructed without pillars due to the effect of the spiral, but in this plan, the slope is shallow, and the inner diameter is large to ensure the necessary depth dimensions for the dance floor at each level. Due to the greater influence of out-of-plane bending and torsion actions under dead load, the structure was supported by pillars with a pitch of approximately 4.6 m. Figures 20 to 22 indicate that steel capitals were provided at the top of pillars to account for stress transfer through punching. Inside the stairway has an RC beam that also serves as a handrail, enhancing bending and torsional stiffness. Horizontal stiffness is enhanced by an RC cantilevered slab that serves as a stepped floor. These form an L-shaped structure. The L-shaped beam, one side of the L-shape is about 1.5m, made of RC were 200 mm thick, and the steel inclined pillars were φ200 in diameter.

In the seismic design aspect, instead of transmitting the inertia force of the entire stairway to the platform, the supports are designed to resist the inertia force of about half of the stairway's load-bearing area. Inertia forces are transferred to the columns via stud bolts in the steel plates of the capitals. The radial arrangement of inwardly inclined pillars is expected to have the effect of suppressing torsional deformation during horizontal loading.

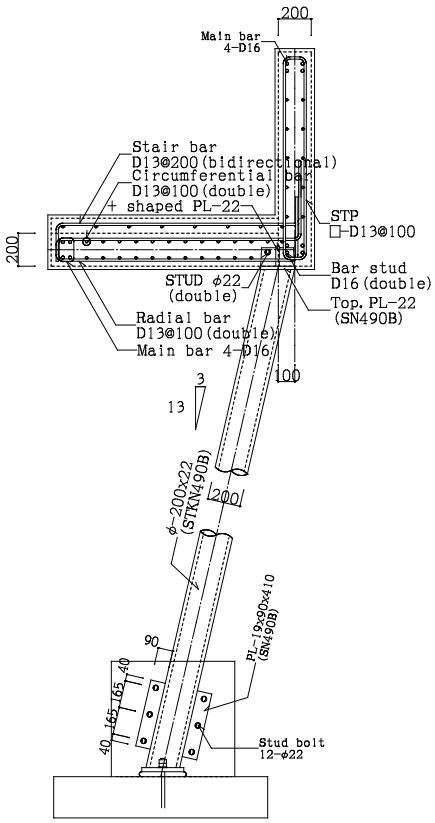


Figure 20. Structural arrangement.



Figure 21. Construction of stairway.



Figure 22. View from below.

4.3. Foundation design

The stratigraphic composition is composed of a dense concentration of hard rock, mainly granite, topped by 1 to several meters of fill. A direct foundation with rock as the support layer was designed, and soil improvement was designed to cope with the unevenness of the support layer.

In the spiral stairway, the 700mm height foundation beams were arranged in a ring shape to connect the pillar bases while adjusting to the undulations of the ground in order to resist thrust from the inwardly inclined columns. The 300mm height foundation beams are arranged in a grid pattern to serve as tie-bars. Consideration is given to reducing the amount of rock cuttings by minimizing the beam size. Moreover, as shown in Figure 23, 3D scans were made to determine the existence of rocks and landforms, and the point cloud data was shared among the parties involved to rationalize foundation planning and rock cutting areas. Using point cloud data, the foundation beams were planned so that they would not interfere with the rock to minimize the extent of rock removal as shown in Figure 24.

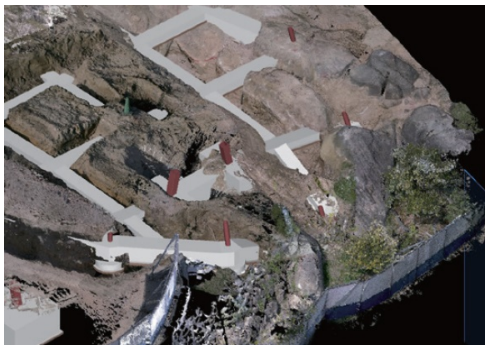


Figure 23. Point cloud data of the site by 3D scan.



Figure 24. Construction of foundation.

5. Conclusions

This paper describes the structural design of an observatory built on the mountaintop with complex ground condition.

Focusing on the spiral stairway, it was analysed the structural characteristics of a circular structure with L-shaped corners supported by columns. In order to apply the structure to the actual structure, it is supported by inwardly inclined columns, and about half of the inertia force is resisted by the columns.

In the platform, a girder is provided at the centre of the bottom of the L-shape, and a structural system with axial force resisting Λ-shaped columns is used to accommodate the different column lengths caused by the undulating ground. The platform was divided into two buildings to balance the stiffness of the entire building and to take thermal stress into consideration.

The foundation was designed to minimize the amount of rock cuttings using point cloud data obtained from a 3D scan of the ground.

Acknowledgements

We would like to thank everyone involved in the planning, design, and construction of this project. Figures 1 to 7 and 23 were provided by AS.

References

[1] K. Noda and Y. Kanebako, “Structural Design for a Building with Shell and Flat Slab Hybrids,” *Journal of the International Association for Shell and Spatial Structures,* vol.58, pp.259-266, 2017.12.

[2] K. Noda and Y. Kanebako, “Structural Design of Frustum Shaped Spatial Structures,” *Proceedings of the 12th Pacific Structural Steel Conference*, Paper No.C000165, 2019.11.

Concrete structures

Active bending
Additive manufacturing/ 3D printing
Architectural geometry
Bamboo for sustainable construction and quality of life improvement
Bio-inspired structures and architecture
Bridge structures
Computational form-finding
Conceptual design
► **Concrete structures**
Construction techniques
Deployable and inflatable structures
Design competition (WG21)
Digital modelling and fabrication
Dynamic response of metal spatial structures
Dynamic response of other structures
Form-finding and structural optimisation of interlocking discrete assemblages
Graphical methods
Gridshell and lattice structures
Historical concrete shells
Historical structures
Lattice structures
Life-cycle design and assessment of structures
Metal gridshell structures, connections and stability
Methods and construction technologies for sustainable shell structures
Morphology and configuration processing
Next generation parametric design
Novel methods in modelling, optimisation and construction for reducing carbon footprint of continuous roof shells
Numerical methods for geometry, form-finding and optimisation of lightweight structures
Optimisation methods and applications
Origami
Other
Teaching design uncertainty: working with unknown qualities/quantities of new and re-claimed materials
Teaching of shell and spatial structures
Tensegrity systems and cable structures
Tension and membrane structures
Tension structures in the Asia-Pacific
Timber and bio-based structures
Topology optimisation
Traditional masonry structures and innovation
Transformable structures

IASS 2023
July 10–14 Melbourne
Integration of Design and Fabrication

Proceedings of the IASS Annual Symposium 2023
Integration of Design and Fabrication
10–14 July 2023, Melbourne, Australia
Y.M. Xie, J. Burry, T.U. Lee and J. Ma (eds.)

A Group-Theoretic approach for constructing spherical-interlocking assemblies

Reymond AKPANYA*, Tom GOERTZEN[a], Alice C. NIEMEYER[a]

[a,*] Lehrstuhl für Algebra und Darstellungstheorie - RWTH Aachen University
akpanya@art.rwth-aachen.de

Abstract

A topological interlocking is an assembly of blocks constrained by a fixed frame such that each set of blocks is kinematically constrained. Estrin et al. [3] provide a recent overview of progress in the study of topologically interlocking assemblies. Using a group-theoretic approach, we construct interlocking assemblies of different polygonal surfaces. Given such a polygonal surface, we can compute its automorphism group and check for identified faces, i.e., faces that are identified under the symmetry of the given surface. The number of classes of identified faces corresponds to the number of different types of blocks in the resulting assembly. Next, we deform faces to obtain an interlocking structure. In this paper, we give examples of interlocking assemblies which form platonic solids or tubular interlocking structures. For our examples we use an algorithmic approach that can be easily generalized to arbitrary tessellations of spheres and tubes.

Keywords: 3d-printing, computational form finding, carbon reinforced concrete (CRC), textile reinforced concrete (TRC), topological interlocking, platonic solids, tubular structures, carbon nanotubes, interlocking shells, spherical interlockings, Hangai Prize applicant

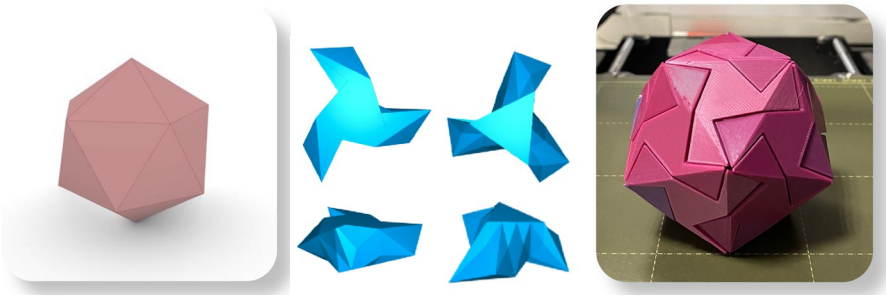


Figure 1. Construction of a spherical interlocking assembly based on the icosahedron by deforming the faces of the platonic solid, (left) an icosahedron, (middle) different perspectives on the resulting interlocking block, (right) assembly of the 3D printed blocks to form the topological interlocking assembly

1. Introduction

Since antiquity Stereotomy (lit. the art of cutting solids) has been employed to design structures which are aesthetically pleasing and structurally sound by employing gravity and the design of a stone. Perhaps best summarised in the words of Perrault (as cited in [14]), Stereotomy is based on the principle of using *the weight of the stone against itself by making it hover in space through the very weight that should make it fall down*.

While most applications employ this principle to exploit the force of gravity to a construction's advantage, the idea of underlying Abeille tiles and the modern idea of topological interlocking [2] go beyond this: they use Stereotomy to design blocks that can be assembled inside a fixed frame such that

Copyright © 2023 by Reymond AKPANYA, Tom GOERTZEN and Alice C. NIEMEYER. Published in the Proceedings of the IASS Annual Symposium 2023 with permission.

each block is not only constrained by its neighbouring blocks in one direction (towards the ground) but in all directions.

In recent years, many topological interlocking assemblies have been proposed and have been shown to have many advantageous properties (see e.g. [3] for an overview). The osteomorphic blocks proposed in [10] are very versatile and can be arranged in different ways to form 3D structures. Others have proposed blocks that can be assembled to form a tubular structure fixed by frames at either end, see [8].

We propose several new blocks that facilitate spherical and tubular interlocking assemblies. We modify a group-theoretic method introduced in [4] to design blocks that facilitate a planar interlocking assembly to the case of spherical or tubular structures. It turns out that in designing blocks for non-planar assemblies another problem arises: While each individual block may be constrained when its neighbours are fixed, it might be possible to move all blocks simultaneously, each in a different direction, thereby rendering the assembly less stable.

One example of such an assembly is that of a sphere, where each block is obtained by the group-theoretic method described above. When assembled into a sphere, all blocks can simultaneously be moved away from the centre of the sphere along the line to its centre of gravity. This problem may also arise in a tubular interlocking assembly, where it may be possible that all blocks are simultaneously moved away radially from the central line of the tube.

Depending on the applications of these structures, these problems may influence their performance. While a tunnel may experience mostly gravitational forces and forces directed towards its interior, a pillar in the shape of a hollow tube might be subjected to different forces. For example, during seismic activity it is possible that all blocks are subjected to an outwards force.

We give some examples of spherical and tubular interlocking assemblies which display this weakness and present methods for designing blocks which overcome this problem.

2. Topological interlocking

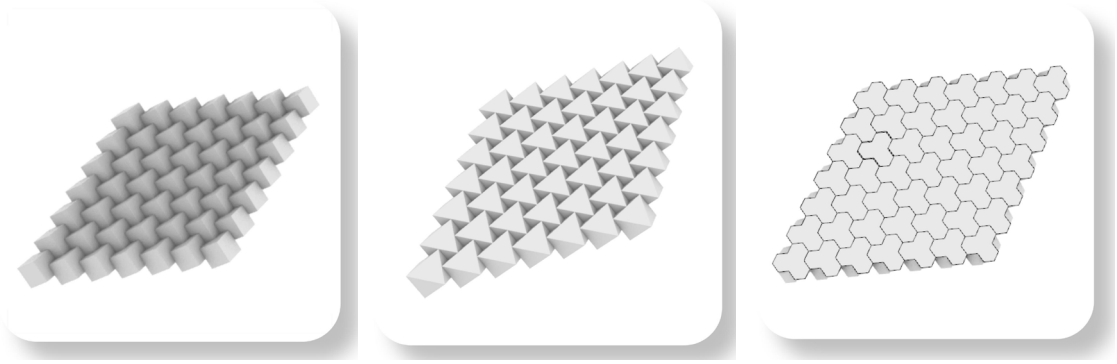


Figure 2. Left: Topological interlocking assembly of cubes [1]. Middle: An assembly of compressed octahedra (obtained by truncating cubes) Right: Filling the gaps or using the Escher-Trick (see [4])

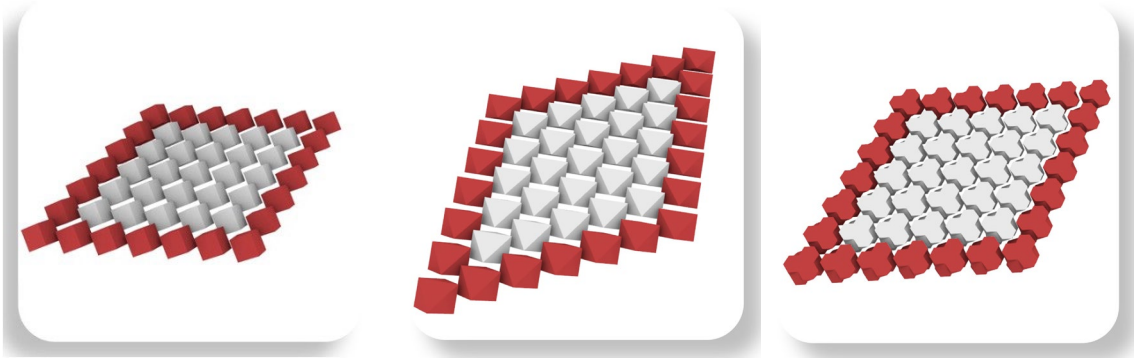


Figure 3. Exploded views of the assemblies given in Figure 2 with frame marked in red.

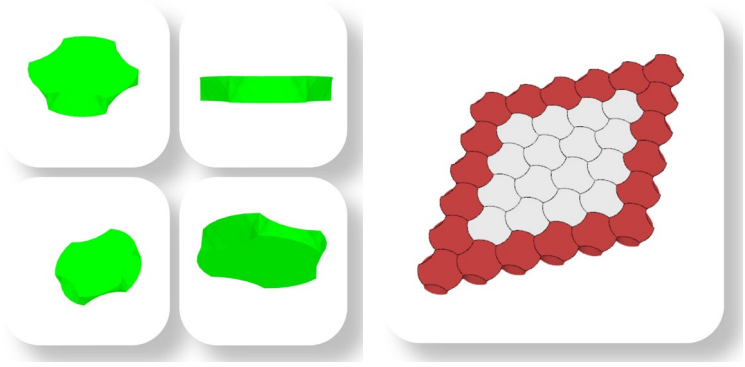


Figure 4. In [8] the authors give a smooth version of the block from the assembly in Figure 2 (right).

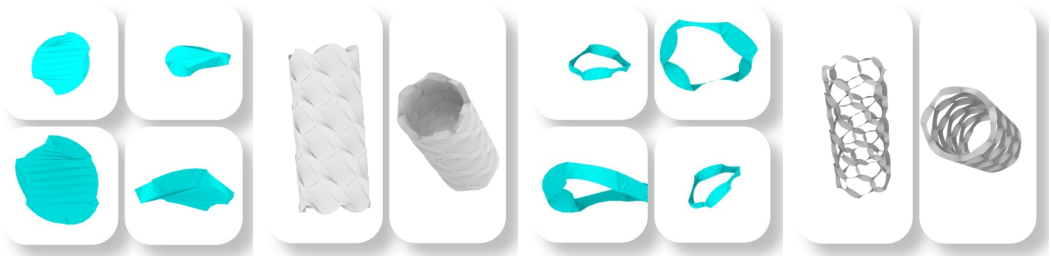


Figure 5. Deforming the block from Figure 4, we obtain a tubular interlocking assembly (see [8])

A topological interlocking (short TI) assembly consists of several blocks which are in loose contact with each other such that fixing a subset of blocks, called the "frame", restrains any motion of any arbitrary set of blocks in the assembly. The term and concept of TI assemblies were first introduced by Dyskin et al. in [2].

Before making this definition more precise we will give some examples of TI assemblies and shed light on methods that yield candidates for TI assemblies.

In [1], the authors give an assembly of cubes arranged in a hexagonal fashion, see Figure 2, such that the middle section is given by hexagons. By truncating the cubes, we obtain another interlocking assembly consisting of compressed octahedra, see Figure 2. By closing the gaps between blocks and thus enlarging the pairwise contact surfaces of any two blocks we obtain another assembly shown in Figure 2. The latter assembly can be obtained by the methods presented in [4] via the Escher-Trick. For all those assemblies we can select the outer most blocks as part of the frame (marked in red in Figure 3), to obtain a TI assembly.

A similar approach to obtaining candidates for TI assemblies starts with a hexagonal prism. Next, side faces of the prism can be paired, and a part is removed from one face and this exact part is added onto the paired face. Starting with a tessellation of hexagonal prisms, the pairing of the faces corresponds to orbits under the action of a crystallographic space group (see [4]).

In [8], the authors use this approach to obtain a smoothed version of the block (Figure 4) which can be deformed to obtain a TI assembly which has the shape of a cylinder, see Figure 5. In [8], the authors use the CAD system Rhino [9] to map this block onto a cylinder (tube). In [13], the authors further investigate generalizations of this block and constructed 3D-printed prototypes.

The assemblies in Figure 2 all use a frame consisting of the most outer blocks, see Figure 3 for an exploded view with frame marked in red. In the following sections tubular shaped assemblies with a frame consisting of the top and bottom blocks and thus two non-connected frame components are shown.

Motivated, by these examples we can state the definition of a TI assembly, taken from [4].

A pair $((X_i)_{i\in I}, J)$ consisting of an assembly $(X_i)_{i\in I}$ *of blocks* with an index set I and a subset $J \subset I$, called "frame", is called a *topological interlocking assembly* or *topological interlocking* (TI for short) if all the blocks given by $I \setminus J$ are kinematically restrained, that is we **cannot** find a finite non-empty subset $\emptyset \neq S \subset I \setminus J$ and for all $i \in S$ non-trivial continuous movements $\gamma_i: [0,1] \to SE(3)$ with $\gamma_i(0)$ is the trivial motion in the set of all three-dimensional rigid motions $SE(3)$ such that the family $\left(Y_i^t\right)_{i\in I}$ with $Y_i^t = \gamma_i(t)X_i, i \in S$ and $Y_i^t = X_i, i \notin S$, is an assembly for each $t \in [0,1]$.

In the definition above, the blocks $X_i \subset \mathbb{R}^3$ are three-dimensional subsets of the set $\mathbb{R}^3$, where in the examples shown in Figure 3 and 5, the blocks are all congruent to each other. However, the stated definition also allows assemblies of non-congruent blocks, see for instance [7]. In [6], the authors give a method for proving the interlocking property using infinitesimal motions. In [5], the authors analyse interlocking blocks from [4] as a basic unit for large shells and show that they possess favourable properties relative to their density.

In the following sections, we will give further examples of tubular interlocking assemblies and spherical assemblies and take a first step in the direction of a mathematical generalization of this concept.

3. Construction of spherical and tubular interlocking blocks

In [4] a method is introduced to construct topological interlocking blocks by deforming fundamental domains of planar crystallographic groups. The next goal is to generalise this method to construct blocks, whose topological interlocking assembly forms surfaces such as a sphere or a cylinder. Starting from a tessellation of a sphere or a cylinder, it is natural to ask whether topological interlocking blocks for these surfaces can be constructed by deforming tiles of the given tessellation.

Here, a tessellation is an arrangement of 2D-geometric shapes covering the whole surface, without gaps and intersections. For example, mapping the edges of a platonic solid onto the surface area of a sphere gives rise to a tessellation of the sphere.

For simplicity, we formulate the generalized construction for polyhedral surfaces whose vertices all lie on the unit sphere or a cylinder of radius one. The spherical and tubular case then follow by considering polyhedral surfaces with spherical and tubular faces instead of planar faces.

Let P be a convex polygonal surface with faces $f_1, \dots, f_m$ and vertices $V_1, \dots, V_n$ satisfying $\sum_{i=1}^n V_i = 0$ and $\| V_i \| = 1$ for all $1 \leq i \leq n$. Since the faces of P can be viewed as a tessellation of the polygonal surface, we aim to construct interlocking blocks by deforming these faces into tiles of a polygonal surface that arises from scaling the vertices of P with a non-negative real number.

Let therefore $\{t_1, \dots, t_m\}$ be another tessellation of the polygonal surface P with simple polygons t_i for $1 \leq i \leq n$, such that the vertices of the face f_i lie on the boundary of t_i. For a real number $a \in \mathbb{R}$ with

$a > 1$ the scaled polygonal surface aP can be tessellated by $\{at_1, \dots, at_m\}$. We now aim to construct blocks $X_1, \dots, X_m \subseteq \mathbb{R}^3$ such that $\{X_1 \cap bP, \dots, X_m \cap bP\}$ is a tessellation for any polygonal surface bP with $b \in [1, a]$. A set of blocks $X_1, .., X_m$ satisfying this condition can be realized by continuously deforming the tile f_i into the tile at_i. We then obtain a candidate for a TI block that can be assembled to reconstruct the polygonal surface.

The package [11] contains functions to compute blocks to realize a given polygonal surface whose faces consist of regular polygons as an assembly of TI blocks. The blocks used in this construction have piece-wise linear boundary and are constructed by the following deformation:

Let $(V_1, \dots, V_l)$ be the ordered vertices of a face f that forms a regular polygon and $f_1, \dots, f_l$ be the neighbour faces of f, so that f and f_i are both incident to the vertices V_i and V_{i+1}. Furthermore, let $m_i, n_i \in \mathbb{R}^3$ be vectors so that m_i is contained in the plane placed at the origin parallel to f, the vector n_i is contained in the plane placed at the origin and parallel to f_i and

$$\langle m_i, V_{i+1} - V_i \rangle = \langle n_i, V_{i+1} - V_i \rangle = 0. \tag{1}$$

We then obtain a continuous deformation of f by the following geometric shape:

$$(V_1, w_1^1, w_2^1, w_3^1, V_2, \dots, V_n, w_1^n, w_2^n, w_3^n), \tag{2}$$

whereby for $1 \leq i \leq n$ and $t \in R_{\geq 0}$ the vectors w_1^i, w_2^i, w_3^i are given by

$$\begin{aligned} w_1^i &= V_i + \frac{1}{4}(V_{i+1} - V_i) + tm_i, \\ w_2^i &= V_i + \frac{1}{2}(V_{i+1} - V_i), \\ w_3^i &= V_i + \frac{3}{4}(V_{i+1} - V_i) + tn_i. \end{aligned} \tag{3}$$

In Figure 6 the described deformation is applied to a triangle, a square and a pentagon that lie in the plane.

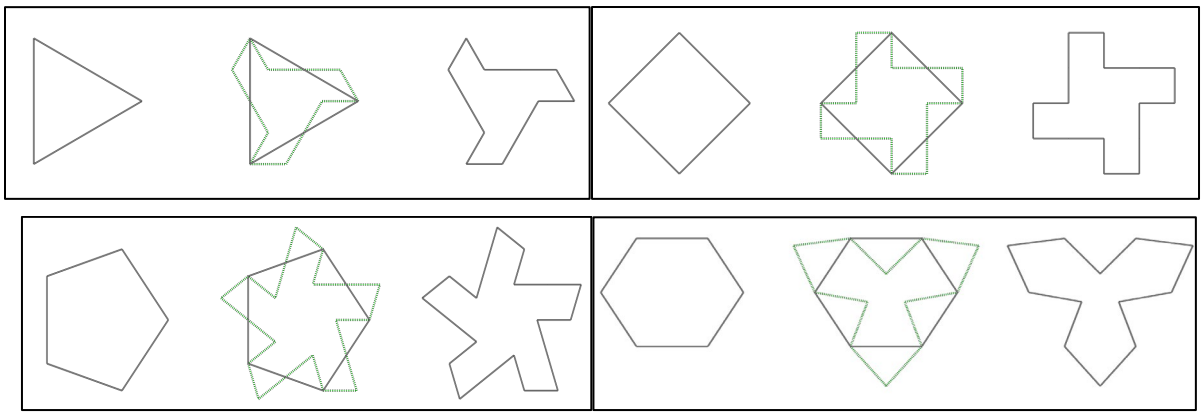


Figure 6. Deforming different regular polygons to construct a new tile of a polygonal surface

Note, by using suitable parameters to describe the above deformation we can limit the number of different blocks needed for this assembly to the number of orbits of the automorphism group of P on

its faces. Figure 7 shows the blocks that are obtained by applying the described construction to the surface of a tetrahedron, cube or dodecahedron.



Figure 7. Interlocking blocks that arise from the deformation of an equilateral triangle (left), a square (middle) and a pentagon (right)

By assembling copies of the constructed blocks, we can realize the platonic solids as an TI assembly, see Figure 8.



Figure 8. Platonic solids constructed by an assembly of interlocking blocks

Note, the tetrahedron can be realized as an TI assembly with an empty frame. The assembly of blocks that realize the octahedron or the dodecahedron forms a TI assembly by choosing the top and the base block as the frame. The constructed icosahedron and octahedron on the other hand are not that stable. In Figure 6 these two structures are held together by gluing together the different blocks.

3.1. Examples of spherical interlocking blocks

In this section we present interlocking blocks based on the platonic solids that allow us to realise spheres by assembling copies of an interlocking block.

Let therefore P be the surface of a platonic solid and S a sphere both centred at the origin so that P is fully contained in S . As mentioned above, mapping the edges of P onto the sphere leads to a tessellation of S consisting of spherical faces. By continuously deforming the faces of P onto the spherical faces of S , we obtain the interlocking blocks presented in Figure 9.

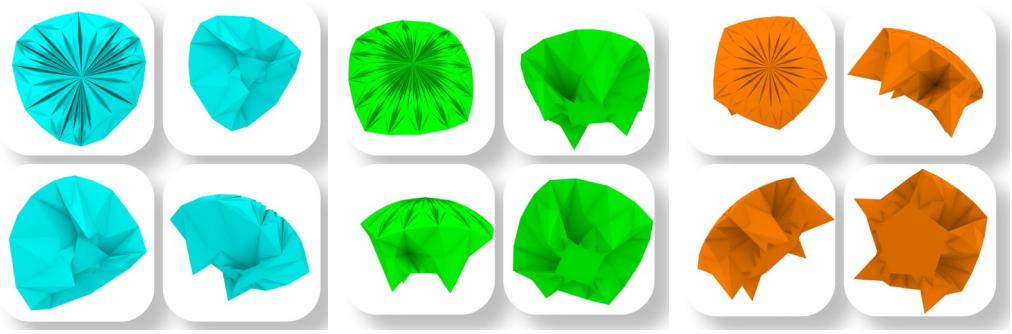


Figure 9. Various views of interlocking blocks based on the tetrahedron (left), the cube (middle) and the dodecahedron (right)

Assembling copies of the introduced blocks gives rise to topological interlocking assemblies in the shape of the platonic solids, see Figure 10.



Figure 10. Spheres realized as an assembly of constructed blocks

Note, the above assemblies based on the tetrahedron, cube and dodecahedron do not require any additional binders to stabilize the whole structure whereby the blocks in Figure 8 of the octahedron and icosahedron are glued together.

3.2. Examples of tubular interlocking blocks

In this section we discuss the construction of blocks that form tubular structures. Moreover, we illustrate the problem of creating TI blocks, introduced in Section 1, that do not allow disassembling the tube

constructed from copies of a block by simultaneously moving all copies radially from the central line of the tube.

In [4] a topological interlocking block for a planar assembly is constructed by placing a rectangle with side lengths 1 and 2 and a square with side length $\sqrt{2}$ in two parallel planes and continuously deforming the domains into each other. Algebraically the rectangle and the square form fundamental domains of a certain wallpaper group. Here, we call the process of deforming one fundamental domain into another the *Escher Trick,* as this method has been applied by M.C. Escher to create his artwork. In [7], the authors give an alternative approach for generating tubular structures using this block by introducing additional angle blocks. The above procedure can be modified by transforming three different fundamental domains for the same wallpaper group placed in three parallel planes into each other. We call this the *double Escher Trick.* A planar TI assembly yields a tubular TI assembly by mapping a section of the planar assembly onto a cylinder. Using the described double Escher Trick and mapping the resulting assembly onto a cylinder, yields the blue block in Figure 11 that can be assembled as a tube as shown in the same Figure.

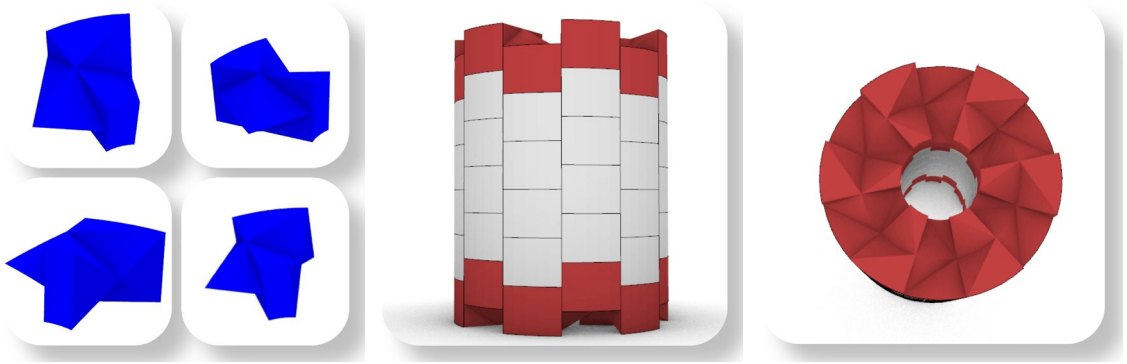


Figure 11. Various views of the interlocking block with a base and top tubular rectangle and a tubular rectangle in the middle with the corresponding assembly; frame is coloured in red

Now, assume that the frame of the assembly shown in Figure 11 is chosen to be empty. This assembly does not form a TI assembly because moving all blocks radially outwards from the central line of the tube is a set of continuous movements that does not result in non-trivial intersections of copies of the constructed block in the assembly, see Figure 12. For practical applications this might be problematic.

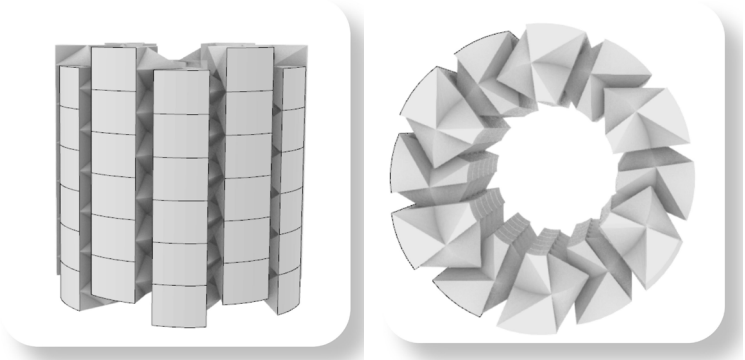


Figure 12. Various views of TI assembly forming a tower with blocks moving radially

It is well known that the load capacity of columns can be significantly increased by spiral reinforcements. This indicates that it is important to design tubular structures where the interlocking property of the assembly itself prevents the movement of collections of blocks radially outwards. For

example, without preventing radially outward movement, seismic motions may dislocate a frame that solely fixes the assembly at the top and the base, whereby the whole column could collapse.

A block whose assembly prevents the described outward movements can be created by examining the brick wall tessellation of the Euclidean plane, see Figure 13.

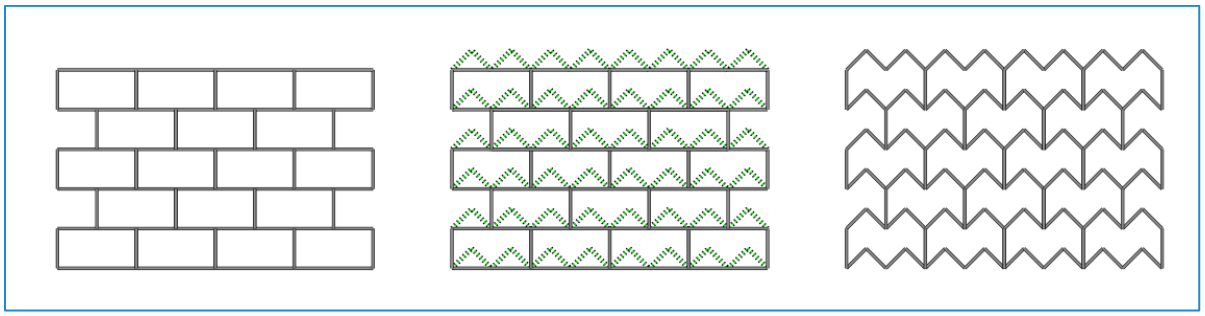


Figure 13. Deforming the brick wall tessellation of the Euclidean plane into another tessellation of the plane

Up to translation, a tile of the brick wall tessellation can be described by the following ordered list of 2D coordinates:

$$[(0,0)^t, (2,0)^t, (2,1)^t, (0,1)^t]. \tag{4}$$

Let a be a real number with $0 \leq a \leq 1$. Deforming the above tiles using the Escher Trick yields the polygon given by the following list of ordered 2D coordinates

$$\left[(0,0)^t, \left(\frac{1}{2}, a\right)^t, (1,0)^t, \left(\frac{3}{2}, a\right)^t, (2,0)^t (2,1)^t, \left(\frac{3}{2}, 1+a\right)^t (1,1)^t \left(\frac{1}{2}, 1+a\right)^t, (0,1)^t\right], \tag{5}$$

which gives rise to a new tessellation of the Euclidean plane. By placing these two tessellations in two different parallel planes and continuously deforming each tile into another, a TI block, that allows planar assemblies, is created, see Figure 14.

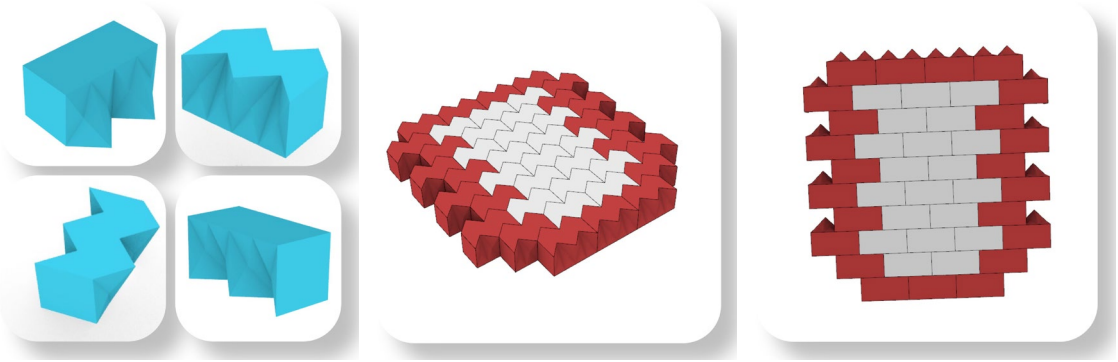


Figure 14. Various views of a TI block based on the brick wall tessellation and the corresponding planar assembly; frame is coloured in red

If we then deform the block as presented in Figure 15, it is possible to assemble angular tubes. Varying different parameters such as the diameter of the block and number of blocks that form a ring of the assembled tube, we obtain different angular tubes.

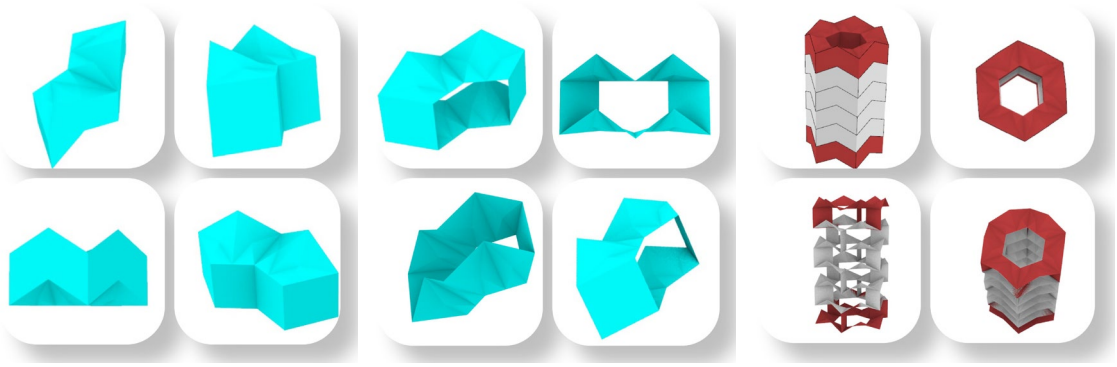


Figure 15. Various views of a TI block based on the brick wall tessellation (left), Various views of the TI block with outer and inner faces removed (middle), Various views of the corresponding topological interlocking assembly; frame is coloured in red

We can also apply the double Escher Trick and map the corresponding planar TI assembly onto a cylinder to obtain another TI block. With the tessellations shown in Figure 13 we can create the TI blocks and the tubular assembly shown in Figure 16.



Figure 16. Various views of a TI block based on the brick wall tessellation and the corresponding assembly to form a tube

As shown in Figure 17, the presented blocks prevent the simultaneous radially outwards movement of all blocks of the assembled tubes.

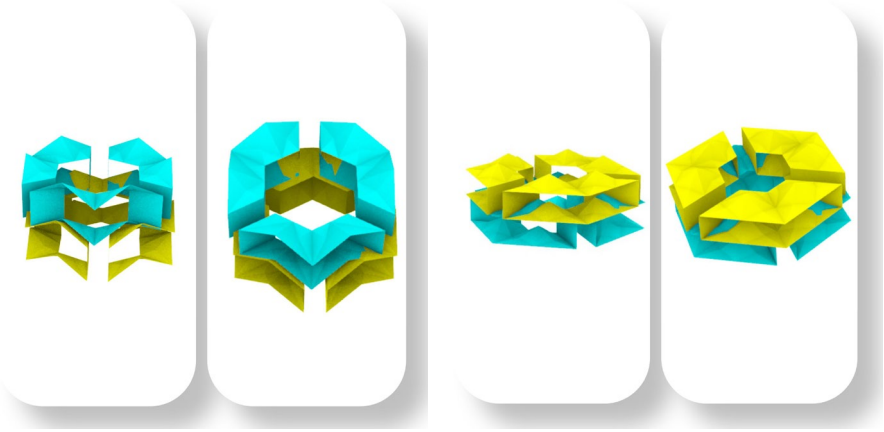


Figure 17. Various views of the TI assembly based on the brick wall tessellation with all blocks moving radially outwards

4. Conclusion

Building on a method to construct planar interlocking assemblies by modifying fundamental domains of planar crystallographic groups, a method for constructing topologically interlocking assemblies for spherical and tubular structures has been developed. An additional complication in designing good interlocking assemblies for these cases is that some assemblies might allow radially outwards simultaneous movement of all blocks. We give an example of a tubular interlocking allows for such movements and another which prevents such movements. In a forthcoming paper, proofs of the interlocking properties of the given assemblies will be given and the behaviour of tubular and spherical interlockings will be further investigated.

4. Acknowledgement

The authors gratefully acknowledge the funding by the Deutsche Forschungsgemeinschaft (DFG, German Research Foundation) in the framework of the Collaborative Research Centre CRC/TRR 280 "Design Strategies for Material-Minimized Carbon Reinforced Concrete Structures – Principles of a New Approach to Construction" (project ID 417002380).

The second author was partially supported by the FY2022 JSPS Postdoctoral Fellowship for Research in Japan (Short-term), ID PE22747.

References

[0] A. Belov-Kanel, Arcady Dyskin, Yuri Estrin, E. Pasternak, and I. Ivanov-Pogodaev. *Interlocking of convex polyhedra: towards a geometric theory of fragmented solids*. Moscow Math. J., 10, 01 2009.

[1] Arcady Dyskin, Y. Estrin, A.J. Kanel-Belov, and Elena Pasternak. *A new concept in design of materials and structures: assemblies of interlocked tetrahedron-shaped elements*. Scipta Materialia, 44:2689–2694, 2001.

[2] Yuri Estrin, Vinayak R. Krishnamurthy, and Ergun Akleman. *Design of architectured materials based on topological and geometrical interlocking*. J. Mater. Res. Technol., 15:1165–1178, 2021.

[3] Tom Goertzen, Alice Niemeyer, and Wilhelm Plesken. *Topological interlocking via symmetry*. In Proc. of the 6th fib International Congress 2022. Novus Press, Oslo, Norway, 06 2022.

[4] Iurii Vakaliuk, Tom Goertzen, Silke Scheerer, Alice Niemeyer, and Manfred Curbach. *Initial numerical development of design procedures for TRC bioinspired shells*. In IASS/APCS Annual Symposium 2022, 09 2022.

[5] Ziqi Wang, Peng Song, Florin Isvoranu, and Mark Pauly. *Design and Structural Optimization of Topological Interlocking Assemblies*. ACM Transactions on Graphics (SIGGRAPH Asia 2019), 38(6), 2019. Article No. 193.

[6] Reymond Akpanya, Tom Goertzen, Sebastian Wiesenhuetter, Alice C. Niemeyer, Jörg Noennig. Topological Interlocking, Truchet Tiles and Self-Assemblies: A Construction-Kit for Civil Engineering Design. Accepted at Bridges 2023 Conference in Halifax, Canada.

[7] Wenzheng Xu, Xiaoshan Lin, Yi Min Xie. A novel non-planar interlocking element for tubular structures. Tunnelling and Underground Space Technology Journal, Volume 103, 2020, 103503, ISSN 0886-7798, https://doi.org/10.1016/j.tust.2020.103503.

[8] Website McNeel Europe SL, Rhinoceros 3D, Version 7.0, https://www.rhino3d.com/.

[9] Dyskin A V, Estrin Y, Pasternak E, et al. Fracture resistant structures based on topological interlocking with non-planar contacts. Advanced Engineering Materials, 2003, 5(3): 116–119

[10] R. Akpanya, M. Baumeister, T. Goertzen, A. Niemeyer, and M. Weiß. "SimplicicalSurfaces, Version 0.6." 2023. https://github.com/gap-packages/SimplicialSurfaces.

[11] S. G. Subramanian, M. Eng, V. Krishnamurthy, and E. Akleman. Delaunay lofts: A biologically inspired approach for modeling space filling modular structures. Computers & Graphics, 82, 05 2019.
[12] Ermolai, V., Sover, A. and Nagîţ, G. (2022) "Design and physical validation of a non-planar interlocking element for tubular structures," *IOP Conference Series: Materials Science and Engineering*, 1235(1), p. 012003. Available at: https://doi.org/10.1088/1757-899x/1235/1/012003.
[13] Richard Etlin. Stereotomy: The Paradox of an Acrobatic Architecture. In Giuseppe Fallacara, ed., Stereotomy: Stone Architecture and New Research (Paris: Presses des Ponts, 2012), 14-35.

Proceedings of the IASS Annual Symposium 2023
Integration of Design and Fabrication
10–14 July 2023, Melbourne, Australia
Y.M. Xie, J. Burry, T.U. Lee and J. Ma (eds.)

Influence of biochar in alkali-activated slag composites upon engineering properties and impact resistance

Harshani EGODAGAMAGE*, Hiran YAPA[a], Satheeskumar NAVARATNAM[b], H.A.D. Samith BUDDIKA[a], Kate NGUYEN[b]

* School of Engineering, RMIT University/ Faculty of Engineering, University of Peradeniya
RMIT University, 264, Plenty Road, Mill Park, VIC 3082, Australia
S3892528@student.rmit.edu.au

[a] Faculty of Engineering, University of Peradeniya
[b] School of Engineering, RMIT University

Abstract

Amongst the additives in cementitious mortar, biochar is popular as a green material that enhances engineering properties. Its ability in densifying the microstructure is responsible for these improvements. Meanwhile, literature reveals that supplementary materials (e.g. silica fume), which densifies the microstructure, increase the impact resistance of concrete. However, such elaborations are unexplored for biochar. Meantime, alkali-activated slag (AAS) is known to be a sustainable replacement for Portland cement. Thus, it is of interest to assess the feasibility of supplementing biochar in AAS composites in terms of strength and impact performance. The effects of the biochar type, biochar replacement level and Na_2O content were considered in the mix design optimization using the Taguchi method. It was found that the 2% rice husk biochar (RB) increased the early strength by 16.5% while the 5% RB enhanced the 28-day strength by 27.5% compared to the control specimen. The impact resistance of the alkali-activated slag concrete (AASC) samples with 10% Na_2O and with 0%, 2%, 4% and 6% RB was measured using a drop weight test. In comparison to the biochar free sample, 6% RB improved the impact number at the first crack and the failure by 185% and by 180% respectively. Moreover, 6% RB improved the 28-day strength of AASC by 44.6% compared to the control mix. These improvements are due to the water absorption property and internal curing effect of biochar.

Keywords: alkali-activated slag composite, compressive strength, impact resistance, rice husk biochar, sewage sludge biochar, Taguchi method

1. Introduction

Alkali-activated materials (AAMs) are considered as excellent sustainable replacements for ordinary Portland cement (OPC) [1, 2]. AAMs are produced by activating an aluminosilicate precursor by an alkaline activator. Since the majority of aluminosilicate materials (e.g. fly ash and slag) are industrial waste products, the production emits low level of greenhouse gases and that result in environmentally and economically sustainable outcomes [1, 2]. Meanwhile, Alkali-activated slag (AAS) is recognized for its ability to attain considerable strength at ambient temperatures. However, some alkaline activators such as sodium silicate are carbon intensive as they are normally manufactured by the 1200–1400 ^{0}C fusion of sodium carbonate and sand [3]. Therefore, the use of alkaline activators with low carbon footprint (e.g. sodium carbonate) is highly encouraged [1, 2, 4].

Over the recent past, biochar gained considerable attention as an additive in cementitious mortar due its ability in improving the sustainability and mechanical properties. Porous biochar can absorb and sequester CO_2 without affecting the properties of mortar [5, 6]. In addition, biochar is reported to

Copyright © 2023 by Harshani EGODAGAMAGE, Hiran YAPA, Satheeskumar NAVARATNAM, H.A.D. Samith BUDDIKA and Kate NGUYEN. Published in the Proceedings of the IASS Annual Symposium 2023 with permission.

improve the mechanical properties of cementitious mortar, especially the compressive strength. Gupta and Kua [7] reported an increment in compressive strength of cementitious mortar at the ages of 1- and 28-days by 20-25% due to the addition of 0.5-1 wt.% mixed wood sawdust biochar. Chen found that 2 wt.% sewage sludge biochar could enhance the compressive strength of OPC mortar by 29.3% and 5.8% at the ages of 1-day and 28-days, respectively. Moreover, an increment in the 28-day compressive strength of cementitious concrete by 20.4% with the addition of 5 wt.% rice husk biochar (RB) is reported by [8]. However, further increment of RB content up to 10% reduced the compressive strength by about 13%. These strength enhancements are due to the high-water absorption and retention properties of porous biochar. It absorbs a portion of the added water to the mix, reducing the effective water to binder ratio (w/b), thus densifying the microstructure [9, 10]. Moreover, the absorbed water is retained in biochar, maintaining healthy internal moisture. This favours the hydration mechanism, which can result in enhanced formation of hydration products, leading to further densification of the microstructure [5, 11, 12]. Even though numerous studies evidenced by the success of biochar as an additive in cementitious mortar, limited attempts have been taken to identify the suitability of biochar as a supplement in AAM mixes [13, 14]. However, because of its potential to absorb and retain water, biochar could also have an ability to improve the performance of AAM mixes as well. Therefore, it is of interest to study the feasibility of using biochar as a supplement in AAS mixes.

In the meantime, the impact resistance of cementitious concrete has been reported to be improved by the addition of supplementary materials like silica fume, which can densify the microstructure. Gupta [15] reported an increment in the number of impacts required (drop hammer impact test) for the failure of OPC concrete from 65 to 67 and 72 respectively when the silica fume dosage was increased from 0% to 5% and 10%. Similarly, Nili [16] observed an improvement in the number of impacts for the first crack and failure of the cementitious concrete, by 6.9 and 6.5 times, respectively, with the addition of 8% silica fume by the cement weight. Moreover, Ameri [17] discovered that in OPC concrete, replacing natural sand with 60% of copper slag (CS) could improve the impact energy at the initial crack level by 42% and at the failure by 50%, compared to the non-CS mix. The densified microstructure resulting from the CS addition is responsible for these improvements. In this context, it is possible to expect that biochar would have the ability in improving the impact resistance of concrete as well. However, no studies have been carried out to verify this hypothesis. Moreover, improved impact resistance is highly beneficial for concrete structures subjecting to vehicular crashes, terrorist attacks and collisions due to earthquakes. Exploring the biochar's possibility in improving the impact resistance, would widen the application of biochar supplemented alkali-activated slag concrete (AASC) even in structures subjecting to impact forces as well. Therefore, this research study was further extended up to investigate the effect of biochar on the impact resistance of the AASC.

First part of the study focused on the identification of the feasibility of supplementing biochar in alkali-activated slag mortar (AASM). Three major affecting factors (Biochar type -BT, replacement level of biochar with slag -RL and Na_2O content by the weight of the binder -Na_2O-E) were considered in identifying an optimum AASM mix in terms of flow and compressive strength. Taguchi design of experimental method was used for the mix design optimization [18, 19]. Second part of the study was developed to understand the influence of biochar on the strength and impact resistance of the AASC. Thus, based on the identified optimum values of the selected parameters (BT and Na_2O-E), four different AASC mixes were cast with 0%, 2%, 4% and 6% biochar content. Each mix was tested for slump, 28-day compressive strength and the impact resistance. Drop hammer impact test based on the ACI 544 committee was used to evaluate the impact resistance of the AASC mixes.

2. Methodology

2.1. Materials

2.1.1. Ground granulated blast furnace slag (GGBS), alkaline activators and aggregate

GGBS was collected from the Siam City Cement (Lanka) Limited. The median particle size (D_{50}) of GGBS was measured using a laser diffraction particle size analyzer and found to be 6 µm. The chemical composition of slag assessed by the X-ray fluorescence (XRF) spectrometry is shown in Table 1. Analytical grades of Na_2CO_3 (99.9% purity) and NaOH pellets (98.5 – 100.5% purity) were dissolved in distilled water to prepare the alkaline solution. Saturated surface dry coarse aggregates were used in this study. Both coarse and fine aggregates were graded according to ASTM C33 (particle size distribution curves are shown in Figure 1). The maximum size of the coarse aggregates was 12 mm. The specific gravities of coarse and fine aggregates were 2.75 and 2.65 respectively.

Table 1. Chemical composition of GGBS (%)

Oxide	CaO	SiO_2	Al_2O_3	MgO	Fe_2O_3	K_2O	Na_2O	SO_3	MnO	P_2O_5	LOI
Percentage (%)	40.39	35.35	12.19	6.18	0.75	0.3	1.09	0.1	0.13	0.05	1.4

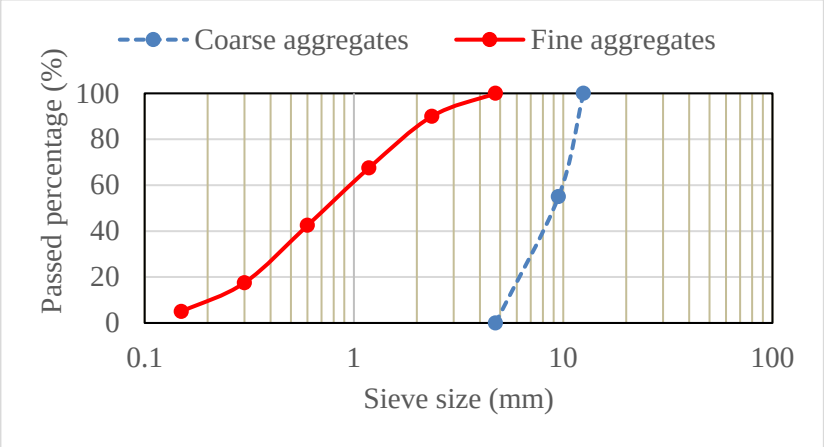


Figure 1. Particle size distribution of fine and coarse aggregates

2.1.2. Preparation of biochar

Three different biochar types, prepared from Rice husk and sewage sludge (gathered from two different treatment plants) were considered in this study. Before pyrolysis, the rice husk was cleaned with tap water, after that oven-dried at 80 ^{0}C for 48 hours. Similarly, sewage sludge samples were oven-dried at 105 ^{0}C for 24 hours until the weight became constant. Following that, sewage sludge was crushed into fine particles and passed through a 5 mm sieve in order to increase the pyrolysis efficiency. Prepared biomasses were filled into sealed crucibles separately, after which the crucibles were placed inside a Yamato FO-310 muffle furnace for pyrolysis. Pyrolysis was conducted at 500 ^{0}C as low temperatures conserve energy and the amorphous silica content [9]. However, as temperatures less than 500 ^{0}C can retain toxic substances available in sewage sludge, those temperatures were not used in this study to avoid ecological risks [9, 20]. The heating rate and the residence time were selected as 10 ^{0}C/min and 60-minutes respectively. Low heating rates and high residence times (slow pyrolysis) can smoothen the volatiles and organics release, thus enhancing the micropore fraction of biochar [5, 21]. Moreover, the yield of biochar becomes high and flammability is less in the slow process [21]. However, prolonging

the residence time beyond 60-minutes requires more energy, thus it is not economical. Finally, biochar was well-ground using a mortar and pestle, after which it was sieved through a 75 µm sieve.

2.2. Methods

2.2.1. Characterization of biochar

pH of all the biochar types was determined by mixing biochar and distilled water at a mass ratio of 1:10 [22]. After stirring the solution for 30-minutes, it was stabilized for 1 hour, after which the pH was assessed using a pH meter. pH values of the biomasses before and after pyrolysis are listed in Table 2.

Table 2. pH values of biomasses before and after pyrolysis

Biomass	pH	
	Before pyrolysis	After pyrolysis
RH	-	8.02
SSA	6.55	6.77
SSB	6.37	7.00

RH – Rice husk, SSA – Sewage sludge collected from wastewater treatment plant A, SSB - Sewage sludge collected from wastewater treatment plant B

The chemical compound compositions of biochar determined by X-ray fluorescence are tabulated in Table 3. SiO_2 was the major chemical compound found in all the three biochar types. In RB, SiO_2 content was 35.61%, which was the highest silica content among all the biochar types used in this study. The particle size distribution (PSD) of only RB and GGBS particles (Figure 2) were measured using a particle size analyzer, as RB was selected as the optimum biochar type (discussed in section 3.1). It was found that the median particle size of RB was 7.9 µm, while that was 6 µm for GGBS. This shows that RB did not impart an effective filler effect in this study as it was reported in the previous studies [5, 11].

Table 3. Oxide composition of biochar

Oxide composition (%)	SiO_2	Al_2O_3	Fe_2O_3	CaO	MgO	K_2O	Na_2O	P_2O_5	ZnO	Mn_2O_3	LOI
RB	35.61	0.03	0.02	0.33	0.14	0.57	0.05	0.1	-	0.06	62
SBA	32.99	14.67	15.84	4.06	1.15	0.66	0.82	-	-	-	30
SBB	23.94	15.58	6.05	2.06	2.17	0.99	1.01	3.76	0.07	-	45

SBA – pyrolyzed SSA, SBB – pyrolyzed SSB

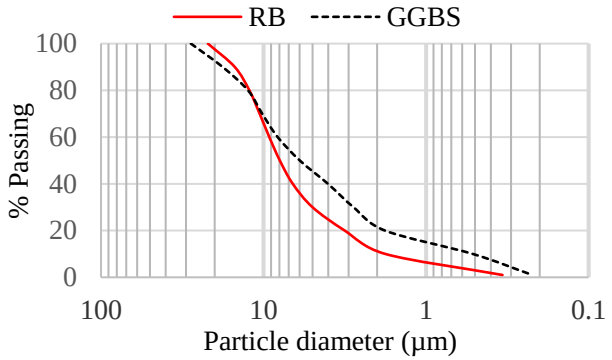


Figure 2. Particle size distribution of GGBS and RB

The water absorption capacity of biochar was measured using the 'tea bag method' [10, 11]. A quantity of 5g of dry biochar was placed inside a tea bag after which it was fully submerged in a water beaker.

Along with that an empty tea bag was also immersed in the water beaker to determine the water absorption only by biochar. The weight of the tea bags was measured at regular time intervals until there was no change in the mass. The water absorption capacity of RB, SBA and SBB was found to be 2.02 g/g dry biochar, 1.08 g/g dry biochar and 1 g/g dry biochar, respectively.

2.2.2. Mix proportion, mixing and curing

An optimum AASM mix design was selected using the "Taguchi method" based on the flow, 3- and 28-day compressive strength [18, 19]. In the mix design optimization, the considered parameters and levels of those are shown in Table 4. These parameters and their levels were selected depending on the trials and the data collected from previous studies [2, 4, 8, 9]. In both mortar and concrete preparation, the w/b and Na_2CO_3 to NaOH molar ratio were maintained as 0.5 and 10:15, respectively [4]. For mortar mixes, the sand to binder ratio was 3 [23], while for concrete mixes the coarse aggregates to total aggregates ratio was 0.57 [24]. Based on the optimum mix design identified for AASM (section 3.1), the biochar type and Na_2O content used in the AASC mixes were RB and 10%, respectively. For AASC mixes, the biochar replacement level was increased up to 6% by 2% intervals, to determine the maximum biochar replacement level in terms of improved impact resistance and the 28-day compressive strength. In [6], Praneeth reported an increment in the 28-day compressive strength of cement (80%)-fly ash (20%) composites when increasing the biochar content up to 6%. However, a reduction in the compressive strength was observed with the enhancement of the biochar dosage beyond 6%. The response of the AASC with the increased biochar content beyond 6% needs to be explored in the future. In concrete mixes, the required coarse and fine aggregates proportions were calculated using the absolute volume method. The mortar mix proportions based on the Taguchi orthogonal array are listed in

Table 5. The concrete mixture details and the slump values are given in Table 6.

2 hours prior to starting both mortar and concrete mixing the alkaline solution was prepared in order to ensure that the solution is at room temperature before adding to the mix [25]. To mix biochar well with slag, those were manually mixed before mortar mixing and subsequently mechanically mixed in the Hobart mixer at low speed for 4-minutes. Next, the alkaline solution was added and continued mixing for another 2-minutes at the same speed. Finally, sand was added to the mix and mixed at a high speed for 3-minutes [23]. Standard steel moulds (50 x 50 x 50 mm^3) [26] were used to cast mortar and then it was vibrated for a maximum of 45 seconds by placing it on a vibrating table. Until 3-days, the samples were cured inside the sealed bags, after which they were demoulded. After demoulding, the samples were continuously cured inside the sealed bags until the testing age.

In concrete mixing, coarse and fine aggregates were dry mixed for 2-minutes in a 120 L concrete mixer. Then the manually mixed slag and biochar mixer was added to the mixer and mixing was continued for another 3-minutes. Then the mixing was continued for further 4-minutes after adding the alkaline solution [27]. At the completion of the mixing, the concrete was poured into cubic and cylindrical steel moulds (100 x 100 x 100 mm^3 and 150 x 300 mm) [28] and vibrated for 1-minute using a vibrating table. Curing process was similar to that with the mortar samples.

Table 4. Factors and levels of Taguchi experimental design

Factor	Level 1	Level 2	Level 3
BT	RB	SBA	SBB
RL	1%	2%	5%
Na_2O-E	6%	8%	10%

Table 5. Mortar mixture proportions based on the Taguchi orthogonal array L_9 (3^3)

Run	BT	RL (%)	Na_2O-E (%)	Slag (g)	Biochar (g)	Na_2CO_3 (g)	NaOH (g)	Sand (g)	Water (g)
RB1-6	RB	1	6	445.5	4.5	34.6	8.7	1350	223.0
RB2-8	RB	2	8	441.0	9.0	46.2	11.6	1350	222.4
RB5-10	RB	5	10	427.5	22.5	57.7	14.5	1350	221.7
SBA1-8	SBA	1	8	445.5	4.5	46.2	11.6	1350	222.4
SBA2-10	SBA	2	10	441.0	9.0	57.7	14.5	1350	221.7
SBA5-6	SBA	5	6	427.5	22.5	34.6	8.7	1350	223.0
SBB1-10	SBB	1	10	445.5	4.5	57.7	14.5	1350	221.7
SBB2-6	SBB	2	6	441.0	9.0	34.6	8.7	1350	223.0
SBB5-8	SBB	5	8	427.5	22.5	46.2	11.6	1350	222.4

Table 6. Concrete mixture proportions

Mix No	RB (%)	Slag (Kg/m^3)	Biochar (Kg/m^3)	Activator (Kg/m^3)		Aggregates (Kg/m^3)		Water (Kg/m^3)	Slump (mm)
				Na_2CO_3	NaOH	Coarse	Fine		
RB0	0	450	0	57.7	14.5	951	692	225	104
RB2	2	441	9	57.7	14.5	951	692	225	101
RB4	4	432	18	57.7	14.5	951	692	225	94
RB6	6	423	27	57.7	14.5	951	692	225	72

2.2.3. Testing procedure

The compressive strength and the flowability of the mortar samples were determined according to ASTM C109 [26] and ASTM C1437 [29], respectively. In concrete mixes, the compressive strength and slump were measured conforming to BS EN 12390-3 [30] and ASTM C143 [31], respectively. The compressive strength testing was performed using a 3000 kN compression testing machine. The loading rate for the mortar samples was 1.5 kN/s while that for the concrete samples was 6 kN/s. The average result of three samples was considered as the compressive strength for both mortar and concrete samples.

The impact resistance of the AASC samples were tested as per the guidelines of ACI Committee 544 [32]. For each concrete mix, a 150 x 250 mm cylinder was cast and at the age of 28-days, it was cut into three 64 mm height discs for subjecting to drop weight impact test. As illustrated in Figure 3, the concrete disc is placed on the steel base plate with four positioning lugs. A weight of 4.54 kg was dropped repeatedly from a height of 457 mm on the steel ball (63.5 mm diameter) placed on top of the sample. The number of impacts till the first visible crack (L_1) and the failure (L_2) were noted. The total impact energy, depicted in Eq. (1), determines the impact resistance.

$$\text{Impact energy} = n \times m \times g \times h \quad (1)$$

Where n is the number of impacts for the first crack and failure, m is the mass of the drop weight (4.54 kg), h is the drop height (457 mm) and g is the gravitational acceleration (9.81 m/s^2).

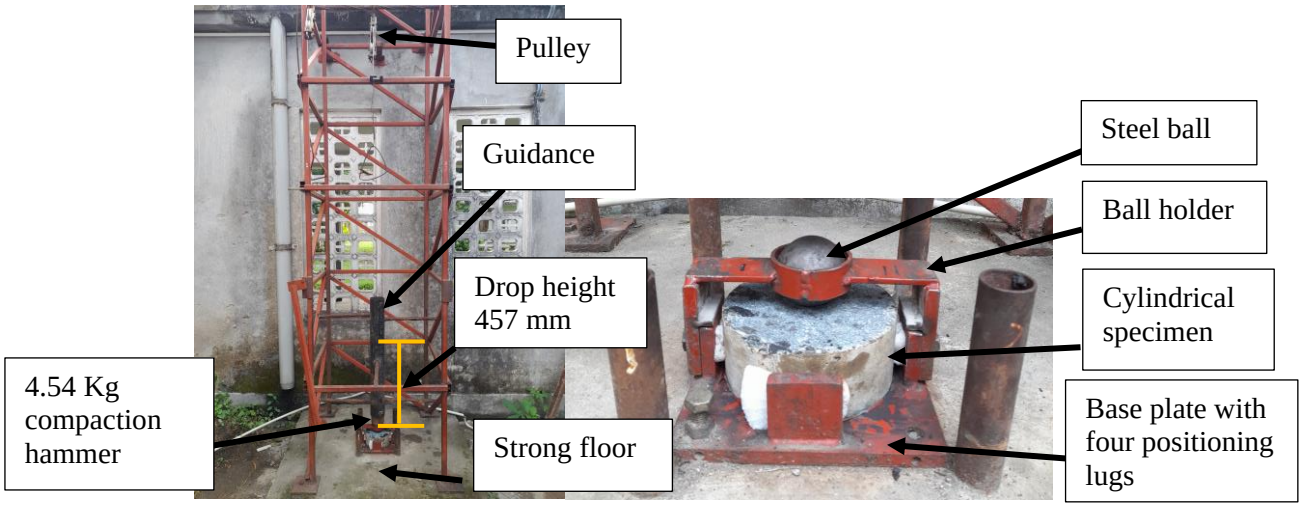


Figure 3. Drop weight test apparatus

3. Results and discussion

3.1. Determination of optimum mortar mix design

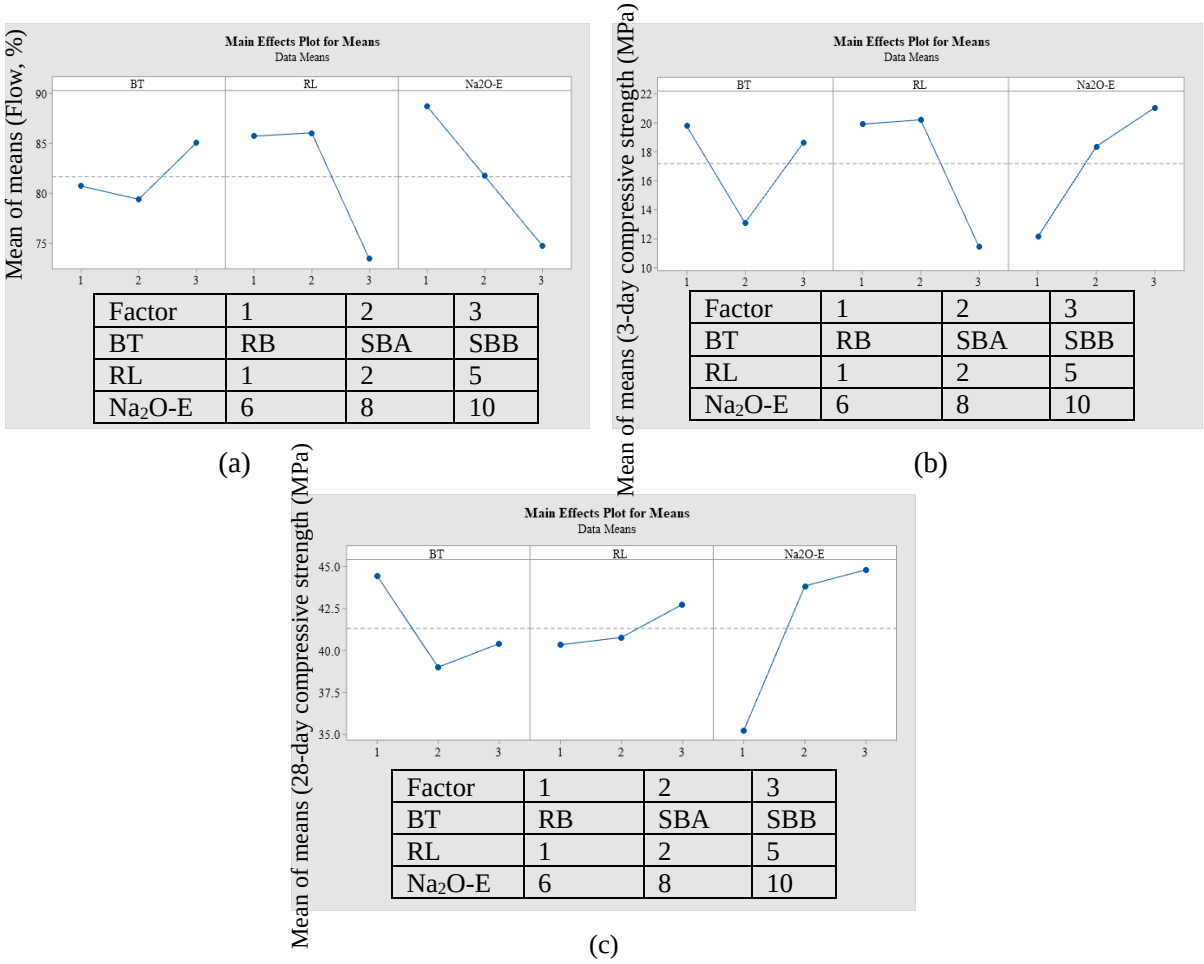
The average flowability, 3- and 28-day compressive strength of the AASM mixes cast according to the Taguchi method are shown in Table 7. Minitab software was used to analyse the results and the resulting main effect plots are given in Figure 4.

According to Figure 4(a), the highest flow is yielded by SBA2-6. Increasing biochar replacement level from 2% to 5%, caused a reduction in the flow. However, it is limited to 13 mm. Similarly, raising Na_2O content from 6% to 10% dropped the flow by 14 mm. Moreover, the response of flow to the change in biochar type is very low. Figure 4(b) illustrates that RB2-10 achieves the highest 3-day compressive strength. This is in agreement with the previous studies mentioning the ability of biochar in improving the early compressive strength when the biochar content is around 2% [5, 9]. The sensitivity of the 3-day compressive strength to the biochar replacement level is considerably higher (increasing biochar content from 2% to 5% reduced the 3-day compressive strength by about 44%). In consideration of the 28-day compressive strength, RB5-10 exhibits a better performance (Figure 4(c)). Considering the overall performance, the RB2-10 combination seems to be more promising towards the early strength improvement. However, while looking at the latter compressive strength development, RB5-10 seems to perform better than RB2-10.

Table 7. Flow and compressive strength results

Run	Flow (%)	Compressive strength (MPa)	
		3-day	28-day
R1-RB1-6	94	18.0 (0.2)	37.6 (0.8)
R2-RB2-8	83	21.7 (0.2)	43.8 (0.9)
R3-RB5-10	65	19.7 (0.3)	52.0 (0.9)
R4-SBA1-8	83	18.8 (0.3)	43.2 (1.5)
R5-SBA2-10	79	20.5 (0.1)	42.2 (0.9)
R6-SBA5-6	76	0.0*	31.7 (1.0)
R7-SBB1-10	80	22.9 (0.3)	40.3 (0.3)
R8-SBB2-6	96	18.4 (0.2)	36.4 (1.1)
R9-SBB5-8	79	14.6 (0.5)	44.6 (0.2)

* the mix did not set at 3-days; the standard deviations of the compressive strength results are denoted within the brackets.



Factor	1	2	3
BT	RB	SBA	SBB
RL	1	2	5
Na_2O-E	6	8	10

(a)

Factor	1	2	3
BT	RB	SBA	SBB
RL	1	2	5
Na_2O-E	6	8	10

(b)

Factor	1	2	3
BT	RB	SBA	SBB
RL	1	2	5
Na_2O-E	6	8	10

(c)

Figure 4. Main effect plots for: (a) flow; (b) 3-day compressive strength; and (c) 28-day compressive strength

3.2. Effect of biochar on the compressive strength of AASM

As both RB2-10 and RB5-10 combinations seemed to improve the compressive strength of the AASM, 3- and 28-day compressive strength of those mixes were compared with a biochar free AASM mix with 10% Na_2O content (RB0-10). The results are illustrated in Figure 5. In comparison to the RB0-10, 2% RB improved the 3-day compressive strength by 16.5% while 5% RB decreased it by 12.1%. In terms of 28-day compressive strength, RB2-10 combination showed a limited increment of 7.4% relative to RB0-10. However, 5% RB showed a significant improvement of the 28-day compressive strength by 27.5% compared to the biochar free mix. These results, agree with other studies where the lower replacement levels of biochar (around 2 wt.%) increased the compressive strength, especially at the early ages [5, 9]. Meanwhile, Zeidabadi et al. [8] observed an increment in the 28-day compressive strength of cementitious concrete by 20.4% with the addition of 5 wt.% biochar. Porous biochar tends to absorb a portion of the alkaline solution, declining the solution/binder ratio of the mix [14]. This results in a reduction in the capillary porosity and the alkali content of the mix. Declining the capillary porosity densifies the microstructure, improving the compressive strength [9, 10]. However, lowering the alkali content leads to a reduction in the compressive strength [33]. Therefore, a combined effect of these two determines the observed compressive strength values. This might be a reason for the reduced 3-day compressive strength of the RB5-10. Together, the internal curing action of biochar, contributes to enhancing the compressive strength. The ability of biochar to act as an internal curing agent has been reported in the previous studies [5, 12]. Choi [12] reported that the weight loss over time for mortar samples with biochar due to moisture evaporation is low compared to that of the biochar free mortar sample.

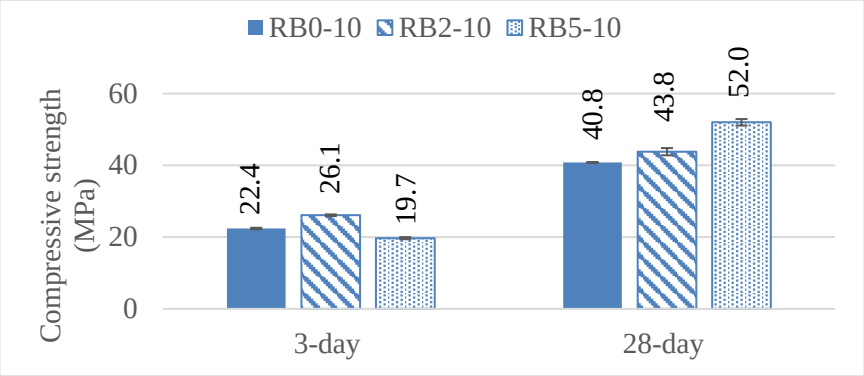


Figure 5. Compressive strength of AASM at 3- and 28-days

3.3. Effect of biochar on the compressive strength of AASC

The 28-day compressive strength results of AASC with different RB dosages are shown in Figure 6. Similar to the AASM mixes, increasing the biochar dosages enhanced the 28-day compressive strength of the AASC. The strength enhancement with the addition of 2%, 4% and 6% RB was 20.1%, 31.5% and 44.6%, respectively compared to the biochar free concrete samples. As previously discussed, biochar's ability to absorb and retain the solution is responsible for these improvements.

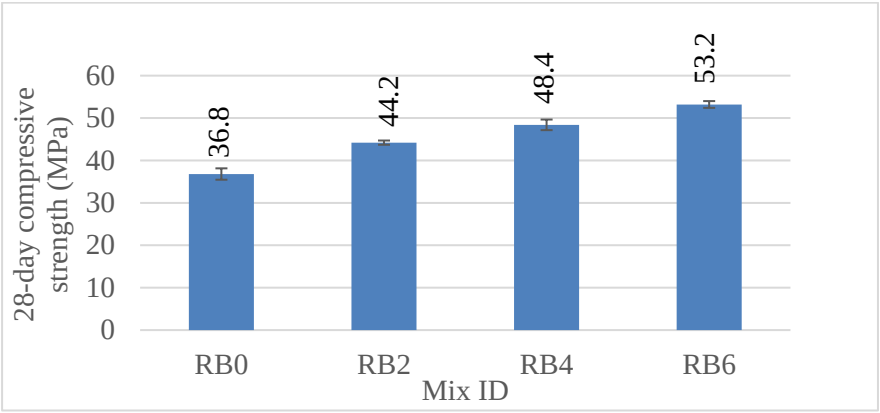


Figure 6. 28-day compressive strength of AASC with different biochar dosages

3.4. Effect of biochar on the impact resistance of AASC

The impact energies of the biochar supplemented AASC mixes at the age of 28-days are shown in

Table 8 and Figure 7. Increasing biochar dosage from 0% to 2%, 4% and 6% demonstrates an increasing trend in the impact resistance. It is visible that RB6 has gained the highest impact resistance where the impact energies at the first crack and failure are increased by 184.5% and 180.4%, respectively compared to the RB0. As anticipated, this increment in impact resistance is due to the densification effect caused by RB on the AASC. Reduction in the capillary pores of the mix and enhanced formation of the hydration products due to the addition of RB, leads to densifying the concrete mix. Egodagamage et al. [34] revealed the ability of RB to densify the microstructure of the AASM. In addition, previous studies observed the contribution of biochar to densify the microstructure of mortar [9, 10]. Similarly, enhancements in the impact resistance of concrete due to the densification effect caused by different supplements such as silica fume have been reported previously [15, 16, 17].

Table 8. Drop weight test results of AASC specimens

Mix No	Impact Numbers (L1/L2)				L1	L2	Impact energies (J)	
	S1	S2	S3	Mean	SD	SD	First crack	Failure
RB0	171/174	185/188	186/189	181/184	8.4	8.4	3684	3745.1
RB2	178/180	185/188	190/192	184/187	6	6.1	3745.1	3806.1
RB4	377/380	392/394	386/388	385/387	7.5	7	7836.1	7876.8
RB6	510/511	516/517	518/519	515/516	4.2	4.2	10482.1	10502.5

L1 and L2 are the number of impacts till the first visible crack and failure. SD- standard deviation

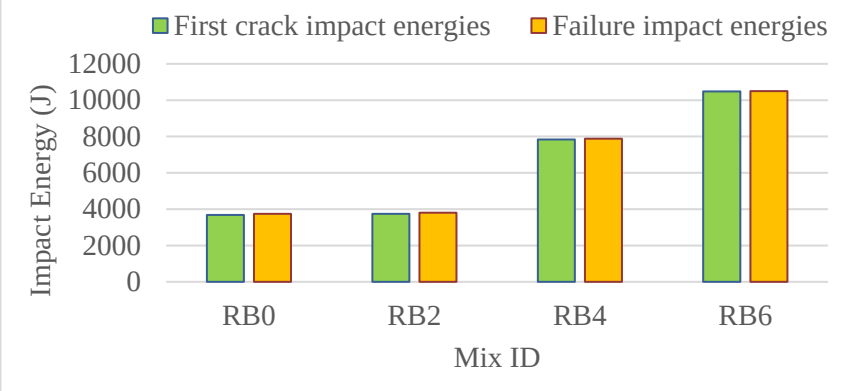


Figure 7. Impact energies of AASC mixes

4. Conclusions

Considering the early age compressive strength development of the alkali-activated slag mortar (AASM), the combination with 2% rice husk biochar (RB) and 10% Na_2O was more promising. The mix increased the early compressive strength by 16.5% in comparison with the biochar free mix (RB0-10). The 28-day compressive strength increment was limited to 7.4%. Meanwhile, 5% RB with 10% Na_2O combination (RB5-10) reduced the early age compressive strength by 12.1% relative to RB0-10. However, this mix gained a considerable 3-day compressive strength of 19.7 MPa. In addition, a significant compressive strength increment of 27.5% was shown for the RB5-10 at the age of 28-days. Therefore, depending on the application, both 2% and 5% RB are suitable to be supplemented in AASM. RB's high-water absorption and retention properties are attributed to these strength improvements.

In terms of impact resistance of alkali-activated slag concrete, 6% RB with 10% Na_2O yielded the largest impact energy, which is higher by around 180% compared to the mix without biochar. Biochar's ability to densify the microstructure resulted in this impact resistance enhancement. In addition, RB6-10 achieved a 28-day compressive strength of 53.2 MPa, which is 44.5% greater than the biochar free concrete mix.

Acknowledgements

This project is funded as part of the CRC project "upcycling solutions for hazardous claddings and co-mingled waste". The assistance provided by the Siam City Cement (Lanka) Limited and the Materials/Environmental Laboratories of the Civil Engineering Department of the University of Peradeniya is also greatly acknowledged.

References

[1] A. F. Abdalqader, F. Jin and A. Al-Tabbaa, "Development of greener alkali-activated cement: utilisation of sodium carbonate for activating slag and fly ash mixtures," *Journal of Cleaner Production,* vol. 113, pp. 66-75, 2016.

[2] B. Akturk, S. Nayak, S. M. ASCE, S. Das, A. M. ASCE and A. B. Kizilkanat, "Microstructure and Strength Development of Sodium Carbonate–Activated Blast Furnace Slags," *Journal of Materials in Civil Engineering* , vol. 31, p. 04019283, 2019.

[3] X. Gao, X. Yao, T. Yang, S. Zhou, H. Wei and Z. Zhang, "Calcium carbide residue as auxiliary activator for one-part sodium carbonate-activated slag cements: compressive strength, phase assemblage and environmental benefits," *Construction and Building Materials,* vol. 308, p. 125015, 2021.

[4] Z. Jiao, Y. Wang, W. Zheng and W. Huang, "Effect of dosage of sodium carbonate on the strength and drying shrinkage of sodium hydroxide based alkali-activated slag paste," *Construction and Building Materials,* vol. 179, pp. 11-24, 2018.

[5] S. Gupta, H. W. Kua and C. Y. Low, "Use of biochar as carbon sequestering additive in cement mortar," *Cement and Concrete Composites,* vol. 87, pp. 110-129, 2018.

[6] S. Praneeth, R. Guo, T. Wang, B. K. Dubey and A. K. Sarmah, "Accelerated carbonation of biochar reinforced cement-fly ash composites: Enhancing and sequestering CO2 in building materials," *Construction and Building Materials,* vol. 244, p. 118363, 2020.

[7] S. Gupta and H. W. Kua, "Carbonaceous micro-filler for cement: Effect of particle size and dosage of biochar on fresh and hardened properties of cement mortar," *Science of the Total Environment,* vol. 662, pp. 952-962, 2019.

[8] Z. A. Zeidabadi, S. Bakhtiari, H. Abbaslou and A. R. Ghanizadeh, "Synthesis, characterization and evaluation of biochar from agricultural waste biomass for use in building materials," *Construction and Building Materials,* vol. 181, pp. 301-308, 2018.

[9] X. Chen, J. Li, Q. Xue, X. Huang, L. Liu and C. S. Poon, "Sludge biochar as a green additive in cement-based composites: Mechanical properties and hydration kinetics," *Construction and Building Materials,* vol. 262, p. 120723, 2020.

[10] S. Gupta and H. W. Kua, "Effect of water entrainment by pre-soaked biochar particles on strength and permeability of cement mortar," *Construction and Building Materials,* vol. 159, pp. 107-125, 2018.

[11] S. Gupta, H. W. Kua and S. D. Pang, "Biochar-mortar composite: Manufacturing, evaluation of physical properties and economic viability," *Construction and Building Materials,* vol. 167, pp. 874-889, 2018.

[12] W. C. Choi, H. D. Yun and J. Y. Lee, "Mechanical Properties of Mortar Containing Bio-Char From Pyrolysis," *Journal of the Korea institute for structural maintenance and inspection,* vol. 16, pp. 67-74, 2012.

[13] R. Farges, A. Gharzouni, B. Ravier, P. Jeulin and S. Rossignol, "Insulating Foams and Dense Geopolymers from Biochar By-Products," *Journal of Ceramic Science and Technology,* vol. 09, pp. 193-200, 2018.

[14] J. Prabahar, B. Vafaei, E. Baffoe and A. Ghahremanineezhad, "The Effect of Biochar on the Properties of Alkali-Activated Slag Pastes," *Construction Materials,* vol. 2010001, pp. 1-14, 2022.

[15] T. Gupta, R. K. Sharma and S. Chaudhary, "Impact resistance of concrete containing waste rubber fiber and silica fume," *International Journal of Impact Engineering,* vol. 83, pp. 76-87, 2015.

[16] M. Nili and V. Afroughsabet, "Combined effect of silica fume and steel fibers on the impact resistance and mechanical properties of concrete," *International Journal of Impact Engineering,* vol. 37, pp. 879-886, 2010.

[17] F. Ameri, J. d. Brito, M. Madhkhan and R. A. Taheri, "Steel fibre-reinforced high-strength concrete incorporating copper slag: Mechanical, gamma-ray shielding, impact resistance, and microstructural characteristics," *Journal of Building Engineering*, vol. 29, p. 101118, 2020.

[18] R. Mohebi, K. Behfarnia and M. Shojaei, "Abrasion resistance of alkali-activated slag concrete designed by Taguchi method," *Construction and Building Materials,* vol. 98, pp. 792-798, 2015.

[19] M. N. Hadi, N. A. Farhan and M. N. Sheikh, "Design of geopolymer concrete with GGBFS at ambient curing condition using Taguchi method," *Construction and Building Materials,* vol. 140, pp. 424-431, 2017.

[20] J. Xing, L. Li, G. Li and G. Xu, "Feasibility of sludge-based biochar for soil remediation: Characteristics and safety performance of heavy metals influenced by pyrolysis temperatures," *Ecotoxicology and Environmental Safety* , vol. 180, pp. 457-465, 2019.

[21] H. Maljaee, R. Madadi, H. Paiva, L. Tarelho and V. M. Ferreira , "Incorporation of biochar in cementitious materials: A roadmap of biochar selection," *Construction and Building Materials,* vol. 283, p. 122757, 2021.

[22] A. Zielinska, P. Oleszczuk, B. Charmas, J. Skubiszewska-Zieba and S. Pasieczna-Patkowska, "Effect of sewage sludge properties on the biochar characteristic," *Journal of Analytical and Applied Pyrolysis*, vol. 112, pp. 201-213, 2015.

[23] J. Zhang, H. Tan, L. Cai, X. He, W. Yang and X. Liu, "Ultra-fine slag activated by sodium carbonate at ambient temperature," *Construction and Building Materials,* vol. 264, p. 120695, 2020.

[24] O. Nanayakkara, C. Gunasekara, M. Sandanayake, D. W. Law, K. Nguyen, J. Xia and S. Setunge, "Alkali activated slag concrete incorporating recycled aggregate concrete: Long term performance and sustainability aspect," *Construction and Building Materials,* vol. 271, p. 121512, 2021.

[25] B. Akturk and A. B. Kizilkanat, "Improvement of durability and drying shrinkage of sodium carbonate activated slag through the incorporation of calcium hydroxide and sodium hydroxide," *Construction and Building Materials,* vol. 243, p. 118260, 2020.

[26] ASTM, "Standard Test Method for Compressive Strength of Hydraulic Cement Mortars (Using 2-in. or [50-mm] Cube Specimens," *ASTM*, 2013.

[27] C. S. Thunuguntla and T. D. G. Rao, "Effect of mix design parameters on mechanical and durability properties of alkali activated slag concrete," *Construction and Building Materials,* vol. 193, pp. 173-188, 2018.

[28] T. B. S. Institution, "Testing hardened concrete: Part 1: Shape, dimensions and other requi rements for speci mens and moul ds," *BS EN 12390-1*, 2012.

[29] ASTM, "Standard Test Method for Flow of Hydraulic Cement Mortar," *ASTM*, 2013.

[30] E. 12390-3, "Testing hardened concrete - part 3: compressive strength of test specimens," *EN 12390-3*, 2001.

[31] A. C143, "Standard Test Method for Slump of Hydraulic-Cement Concrete," *ASTM C143*, 2012.

[32] A. 544.2R, "Measurement of Properties of Fiber Reinforced Concrete," *American Concrete Institute, USA*, 1999.

[33] R. J. Thomas and S. Peethamparan, "Stepwise regression modeling for compressive strength of alkali-activated concrete," *Construction and Building Materials,* vol. 141, pp. 315-324, 2017.

[34] H. Egodagamage, H. Yapa, H. S. Buddika, S. Navaratnam and K. Nguyen, "Effective use of biochar as an additive for alkali-activated slag mortar production," *Construction and Building Materials,* vol. 370, p. 130487, 2022.

Construction techniques

Active bending
Additive manufacturing/ 3D printing
Architectural geometry
Bamboo for sustainable construction and quality of life improvement
Bio-inspired structures and architecture
Bridge structures
Computational form-finding
Conceptual design
Concrete structures
► **Construction techniques**
Deployable and inflatable structures
Design competition (WG21)
Digital modelling and fabrication
Dynamic response of metal spatial structures
Dynamic response of other structures
Form-finding and structural optimisation of interlocking discrete assemblages
Graphical methods
Gridshell and lattice structures
Historical concrete shells
Historical structures
Lattice structures
Life-cycle design and assessment of structures
Metal gridshell structures, connections and stability
Methods and construction technologies for sustainable shell structures
Morphology and configuration processing
Next generation parametric design
Novel methods in modelling, optimisation and construction for reducing carbon footprint of continuous roof shells
Numerical methods for geometry, form-finding and optimisation of lightweight structures
Optimisation methods and applications
Origami
Other
Teaching design uncertainty: working with unknown qualities/quantities of new and re-claimed materials
Teaching of shell and spatial structures
Tensegrity systems and cable structures
Tension and membrane structures
Tension structures in the Asia-Pacific
Timber and bio-based structures
Topology optimisation
Traditional masonry structures and innovation
Transformable structures

Proceedings of the IASS Annual Symposium 2023
Integration of Design and Fabrication
10–14 July 2023, Melbourne, Australia
Y.M. Xie, J. Burry, T.U. Lee and J. Ma (eds.)

Anti-fragile shell aggregations on the moon

Xavier DE KESTELIER[a,*], Levent OZRUH[b], Jonathan IRAWAN[a,*]

[a,*] HASSELL
Level 1, 6-14 Underwood Street, N1 7JQ, London
xdekestelier@hassellstudio.com

[b] OZRUH

Abstract

Research on shell structures has been pursued by many in the AEC industry. Looking at contemporary precedents of shell designs - from subdivided vaults to continuously 3D printed, to discrete assembly -, we argue that they all rely on high precision and therefore have very low tolerance to construction errors. Whilst high precision is a manageable concern in controlled, accessible sites, we argue that a different approach is needed for remote sites like the Moon. As an alternative approach, we propose a construction system that is anti-fragile - a term coined by mathematical statistician Nassim Nicholas Taleb to describe a quality that gains from disorder and randomness instead of losing. As a result, the project proposes an aggregation system of hexapods as a radiation protection shell for Lunar Habitats. This approach offers a construction system that is anti-fragile to a notable degree of randomness; allowing low tolerance in how the aggregates are placed as the system is highly flexible in its interlocking mechanism. Although we use a pre-optimized, continuously smooth shell geometry to guide the hexapod aggregation process, no aggregate on its own has a crucial role in the integrity of the overall structure. This presents a novel shell design with its embodied carbon distributed evenly across its aggregates that can shrink, grow or be reconfigure the structure for future needs of human habitation on the Moon.

Keywords: anti-fragility, aggregation, randomness, dome structures, hexapod, interlocking, reconfigurability, low precision, disorder, regolith, shell structures, radiation protection



Figure 1. Aerial Visualisation of Hassell's Hexapod Aggregation Design as a Radiation Protection Shell on the Moon Credit: Hassell + Imigo

Copyright © 2023 by Xavier DE KESTELIER, Levent OZRUH and Jonathan IRAWAN. Published in the Proceedings of the IASS Annual Symposium 2023 with permission.

1. Introduction

1.1. Background

1.1.1. Case-study project

The research discussed on this paper is born out of a project Hassell is working on as part of the ESA Open Space Initiative Platform (OSIP) research grant. Titled as Lunar Habitat Framework, the project is looking at creating a framework for designing a scalable Lunar Habitat system that can grow to accommodate from 6 to 144 people.

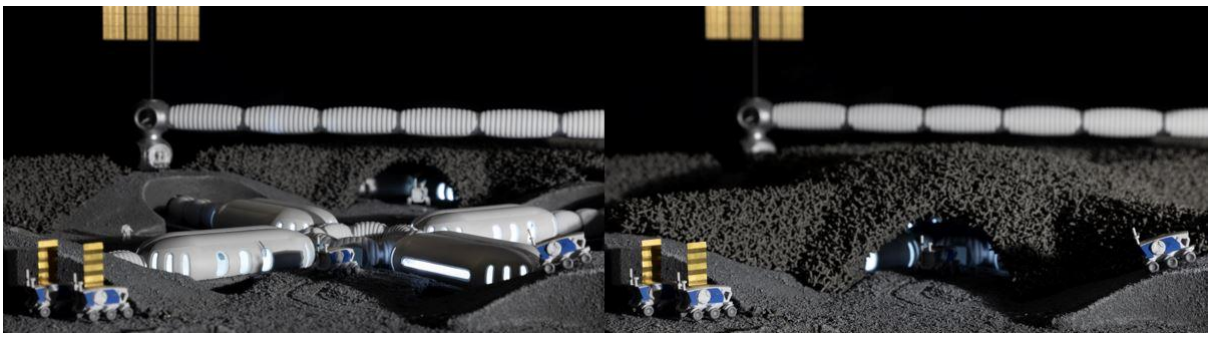


Figure 2. Physical Model of a segment from the Hassell Lunar Habitat Framework for ESA. The pair of photos highlight what sits beneath the radiation protection shell as inflatable habitats. Credit: Hassel

1.1.2. Lunar context & materiality

The location for the project is on the South Lunar Pole near the Shackleton Crater. The Moon is a highly extreme site for human habitation & construction. With no atmosphere, humans will need novel, infrastructure to access to water & oxygen whilst being subjected to high degrees of radiation. In our Lunar Habitat Framework, we propose a variety of systems to establish material cycles within pressurized, inflatable modules in which most of the human activity shall take place. Yet, these inflated habitat systems do very little when it comes to protecting from the Sun's radiation. As a solution to this problem, we propose radiation protection shell structures built with aggregates that are made of sintered Lunar Regolith; relying on in-situ material reutilisation as a means of sustainable construction growth.

2. Methodology

The design process for this research relied heavily on digital simulations. Hassell used advanced visual effects software HoudiniFX to simulate how aggregates behave in collision in a highly efficient manner in computational terms.Using HoudiniFX has allowed to have a good understanding on how hexapods - which have a geometry with concave characte -, interlock as a system of aggregates. The software is able to compute their concave form with minimal loss of information by using solvers such as Bullet and Rigid Body Dynamics. This approach makes our simulation a closer approximation to the reality than other methods like Particle-Based Simulations that treat each aggregate as a particle or a convex

form such as sphere which could have created deceptive results as the aggregates would not interlock but rather touch each other at certain points [1].

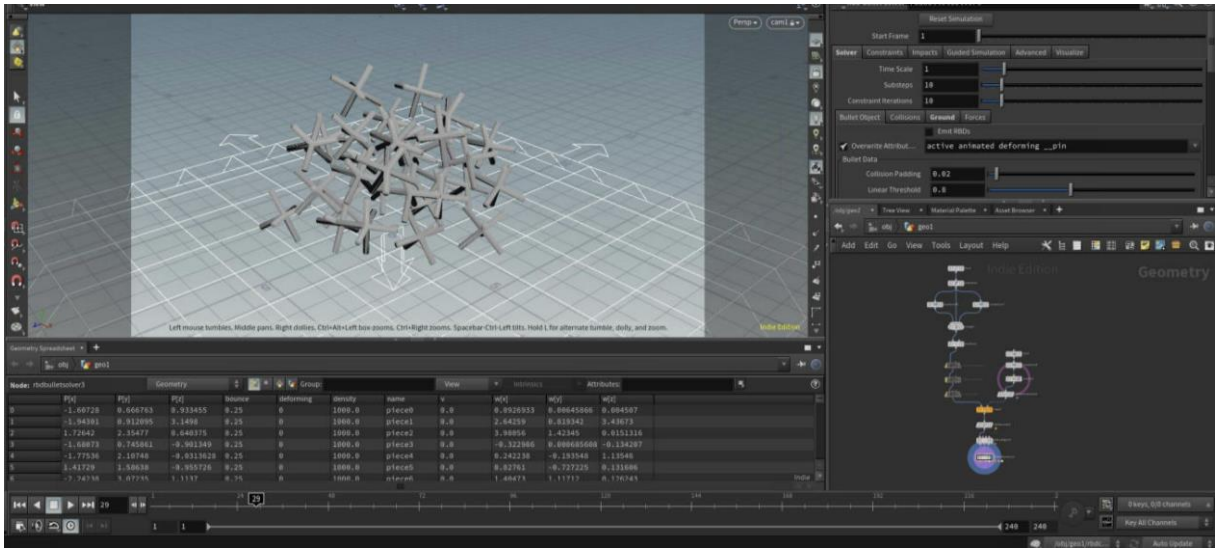


Figure 3. Houdini interface showing the procedural / algorithmic nature of where the designer is asked to create algorithmic procedures with node trees on the bottom right and their relevant parameters on the top right as a means of design. Credit: Hassell

3. Shift in design thinking

3.1 Key principles

In the last decade, there has been a significant number of precedents for continuously 3D printed, monolithic shell structures as a protection layer for habitats on the Moon & Mars [2]. The design we present here is radically different from this approach as we associate numerous concerns of scalability, sustainability and maintenance within a framework that is to grow to accommodate 144 people. Constrained to the material availability on the construction site, continuous 3D printing requires a high degree of precision with a low degree of tolerance for error for the shell to be pressure-retaining and watertight. Furthermore, a monolithic approach would lock fully the embodied carbon in its construction and does not offer any flexibility for repair / reuse due to its fixed / continuous nature. The construction would also require complex scaffolding / formwork systems. Each shell would be fixated to the form of their initial design without the ability to grow or to be reconfigured [3]. When it comes to breaking the continuity in the construction of shell structures, there is numerous novel examples on earth with both bespoke as well as the discrete approach. Although the discrete offers a great potential in reducing the amount of part typology, it nevertheless requires high precision in assembly. Therefore, our research started with the two following requirements in mind: singularity in building block and as low precision as possible for the assembly: a novel, modular aggregation that gains from disorder. This way not only the the embodied energy of a large volume is broken down, but the system is less fragile to error and adaptation to a future reconfiguration. In summary, we seek to establish a true bottom-up thinking like

the historical context of the use and development of bricks on earth-based construction systems (Figure 4) which offer a great degree of variation on the architectures it can produce (Figure 5).



Figure 5. Use of brick for vault applications. Mapungubwe Interpretation Centre by Peter Rich Architects (Left), Mortuary Chapel for the Soriano Manzanet Family by Vegas & Mileto Architects (Right). Credit: Peter Rich Architects (Left) Vegas & Mileto Architects (Right).

As a departure point, we present the following key principles for our design: discrete assembly with a single type of pieces, a high degree of flexibility in orientation of the piece during assembly, lower requirements for manufacturing precision and an aggregation-based system rather than a subdivision / grid based one. Our main inspiration comes from tetrapods which are used on Earth - particularly in Japan - as wave-dissipating blocksto prevent erosion caused by weather and to enforce coastalstructures like seawalls and breakwaters (Figure 6). Whilst tetrapods work well on being stack around simple forms, we augmented the design module to hexapods to allow for more interlocking around curved geometries that shell design will need as a compression only structure. A novel precedent that uses hexapod aggregate systems is the ICD Aggregate Pavillion 2018 [4].



Figure 6. Aerial View of tetrapods being used as coastal barriers. Credit: Institution of Civil Engineers

3.2. From order (grid / subdivision) to disorder (aggregation)

There has been a considerable number of precedents for shell designs in outer space as well as on Earth applications. We present an in-depth look in key examples under three categories: (1) Vaults with Subdivided Elements, (2) Continuous 3D Printing, (3) Discrete Blocks. (Figure 7).

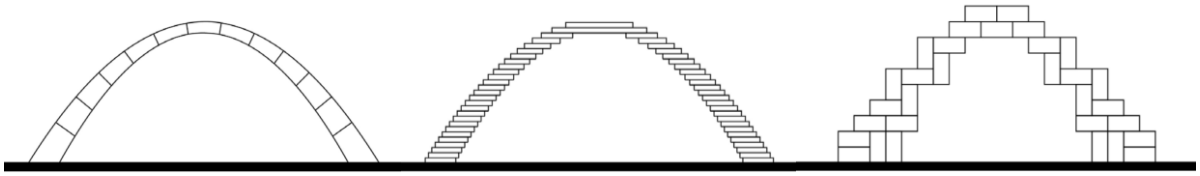


Figure 7. Three contemporary approaches to shell design: Subdivided Elements, Continuous 3D Printing, and Discrete Blocks. Credit: Hassell

3.2.1. Vault with subdivided elements

This category refers to shells as compression structures built by sub-division of an optimised global geometry into smaller parts. Key examples include Armadillo by Philippe Block [5] and Hyperbody Studio Foam Shell by TU Delft [6]. Both examples achieve great spans and open spaces and are built with high precision parts with novel assembly.

3.2.2. Continuous 3D printing

These structures are continiously 3D printed as monolithic structures, using local resources like Regolith on the Moon or Mars. In the case of Hassell's Mars Habitat [7], there are swarm of different robots building simultaneously different parts of a continious structure. In contrast, the Olympus project, a proposal by ICON, BIG & Search+ looks at continious 3D printed shells by a singular, large robot. [8]

3.2.3. Discrete blocks

Contrasting from the first two categories where global geometries dictate towards a single, optimised solution, here we see examples of bottom-up assembly discourse where parts define the whole. Notable work in this discourse to look at are Regolight by Liquifier Systems [9] and Discrete Assembly Concept by Foster + Partners [10].

Although each of the above mentioned precedents are of novel form and construction techniques, we nevertheless argue that an aggregation system acts as the best option to mitigate uncertainty and low precision tolerance within the lunar environment. The main advantage of an aggregation system is that it allows for both extra pieces as well as removal of some existing pieces. This is an approach where the piece is decided first, and the final global geometry is derived from this piece. In this case our piece is a hexapod and although it is 3D modelled as a smooth and simple Euclidean geometry for design, simulation and analysis purposes, in reality each piece can be manufactured with low precision with certain degree of roughness (Figure 8).

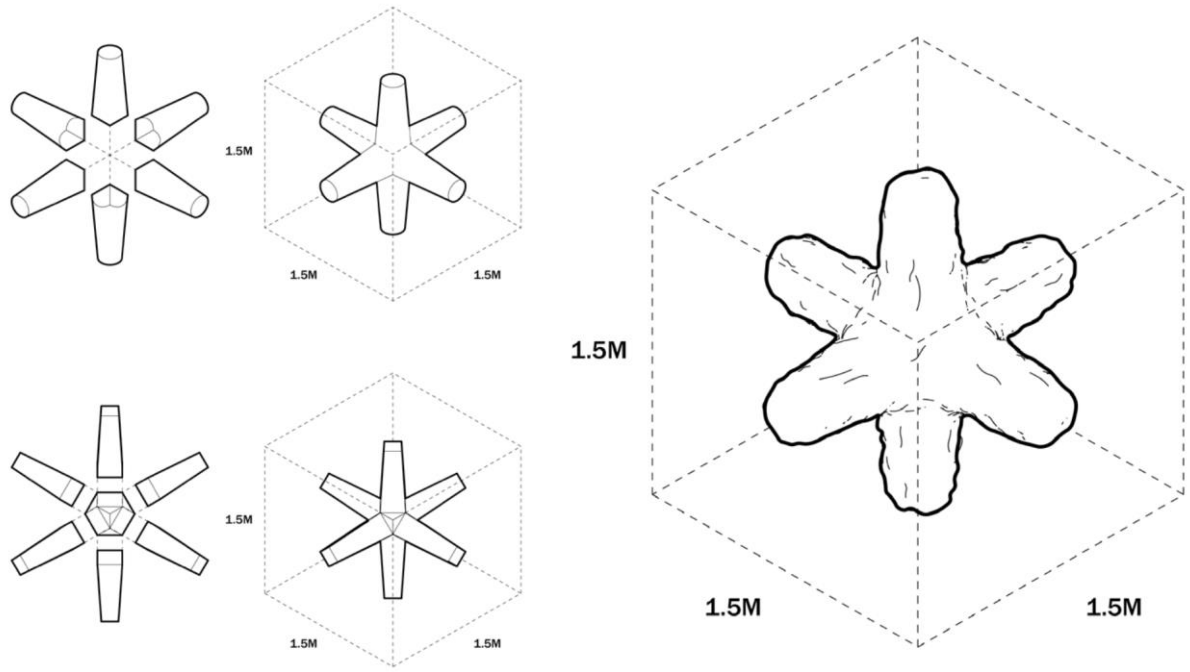


Figure 8. Different modelling of the hexapod design. Top left is used for Houdini Simulations, bottom left for structural analysis in Karamba and the version on the right is to induce how a hexapod could look like in reality as an aggregate made with sintered Regolith. Credit: Hassell

Overall, random aggregation approach differentiates itself from the above mentioned category of Sub-divided Vault Elements where it is the global geometry that is decided first and the piece(s) are subdivisions of the global geometry, allowing only a fixed number of pieces to create the structure and making each one of them necessary for the overall integrity of the structure. Our design process relies heavily on simulations as a means of calibration as for each design iteration we start with the piece first and try to populate a target surface or volume in a similar fashion to how it would be constructed. Therefore, the core of the construction method directly derives what the final design is. The design of the protection shell has evolved extensively by testing varying modes of construction, size, and form of the aggregate piece as well as the global geometry. The final state of the design relies on an inflatable formwork to build a central dome shape which then expands into an X shape by the diagonal contour slicing of four legs. Each hexapod fits inside a 1.5m x 1.5m x 1.5m bounding box

4. Design process & simulations

4.1. Conic structures

Prior to the final design and construction sequence we present later, we started our research in the hexapod aggregation by simple concentric build-ups of straight and curved - section cones. This set of exercises were useful to understand the key parameters that derive the success or failure of a design iteration: size of the hexapod, size of the target geometry (cone), and steepness (height of the target geometry divided by its radius). All the three parameters need to work together as in isolation there is no ideal value for any of them but ideal combination as a set of three. As the system has an inward / concave tendency for collapsing inwards rather than outwards, the structures would naturally become ever more stable during their construction process (Figure 9).

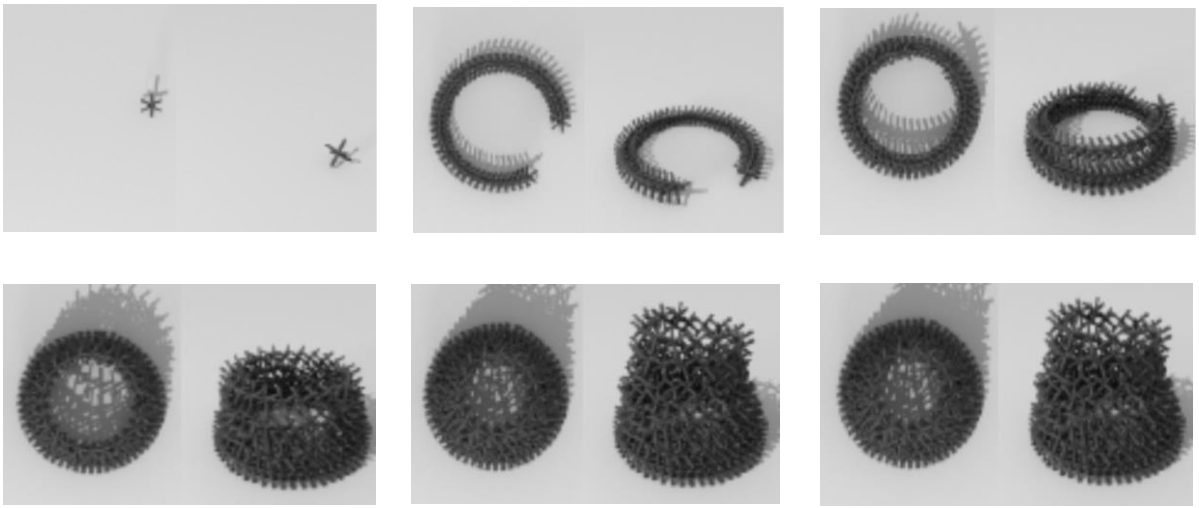


Figure 9. Key frames of the conic array drop test. Credit: Hassell

4.2. X shape / 4-legged vault

As a next step and to be able to test the effect of different values for each of the parameters mentioned above, we developed a more efficient system of simulating the collapse of non-intersecting aggregates. Instead of dropping the aggregates piece by piece, we project a large, non-intersection collection of the aggregates right above the formwork. In doing so each one of the aggregations have a different orientation vector.The algorithm loops over this logic to populate the target geometry as quickly as possible by dropping collections of aggregates instead of one by one. This reduces the overall computational time required as one does not to wait for each aggregate to drop and rest one by one. (Figure 10).

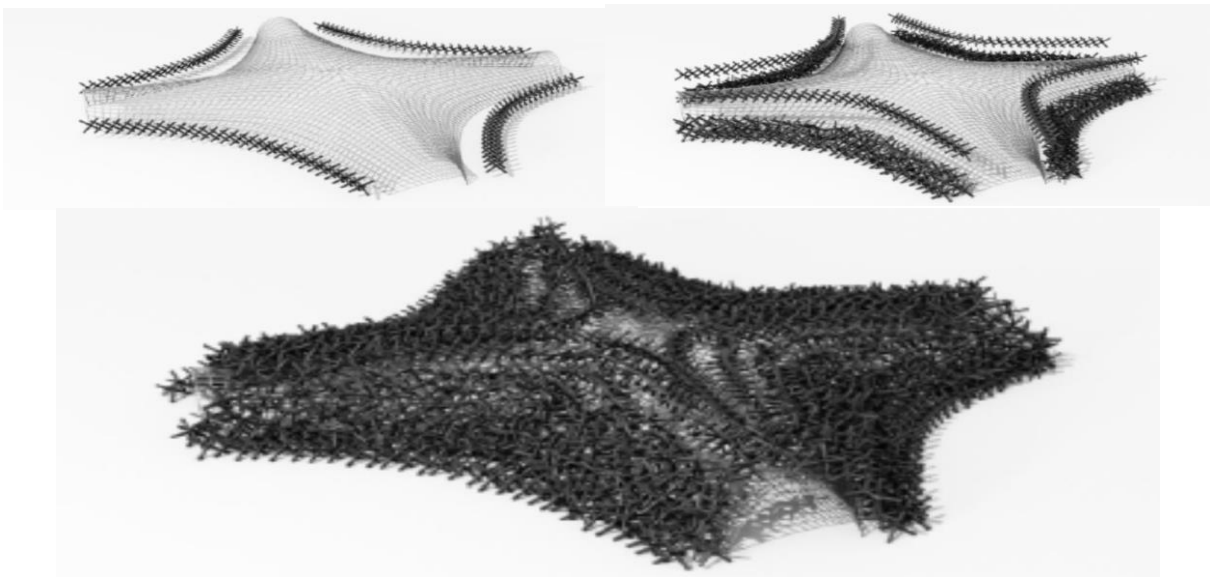


Figure 10: Aggregations collectively dropped on an X shape formwork.

As the design of the rest of the habitat framework evolved simultaneously it became clear that the next stage of evolution for the protection elements was to form an X shape on top view - as a vault with for legs. The initial set of simulations imagined a wireframe like formwork in the shape of the target geometry. This way one could rely on the formwork and simply populate the hexapods on it without any pre-engineering of a stacking sequence for the hexapod aggregation. This meant however that for each build-up of protection element, there is a need for a highly bespoke metal formwork, diminishing the true structural potential of the hexapods by making them merely insulation-like elements. Unlike the cone geometry, when an X like shape is contoured inwards the pieces stack in a convex manner, in other words they try to fall into the wrong side of the arbitrary contour they follow in construction. This results in the need for at least a temporary formwork structure holding the pieces until the construction is finished after which the formwork can be removed. Yet if we rationalize the X shape into 4 legs coming out of a vault, then the required formwork could be eliminated or reduced in size. In this approach the dome would be built prior to the legs so that the legs cannot influence the dome anymore. Here we rationalize the concave sides of the X shape to be generated by deletion of 4 sides of a uniform dome (Figure 11). What is not deleted at the perimeter of the dome is then extended outwards to create the legs. This way the dome and the legs are derived from two separate but clear structural thinking, whereby the dome is built prior to the legs and works without the legs as well if needed. To build the dome stage, we use a temporary inflatable formwork with 8 bending-active steel arches rest on it. The aggregate pieces are then populated on the inflatable formwork, with the steel arches acting as a formwork for the 8 openings. Once this is complete, 4 of the 8 openings are treated as the start of the extended legs. The contour slicing therefore follows the same profile as the opening to create the legs, built diagonally layer by layer.

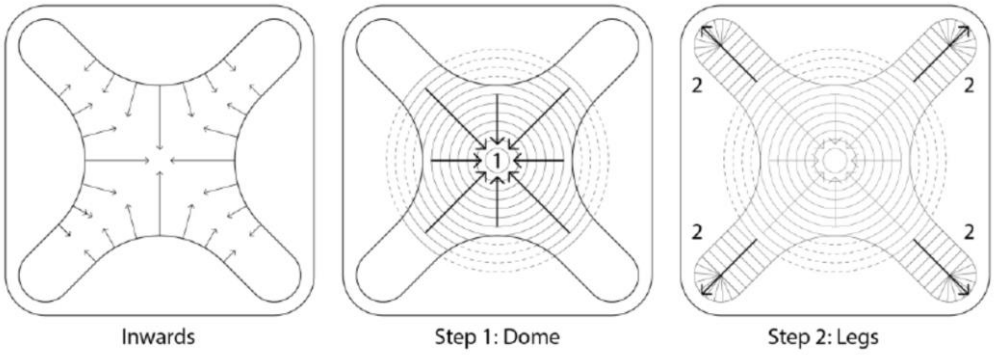


Figure 11: Dome to Legs approach explained. Credit: Hassell

5. Construction sequence

After evaluating both approaches to the general construction logic, we further developed the Dome to Legs strategy into a full construction sequence. At this point in time, the method of stacking up the aggregates is ballistic shooting with robots on site - which is the core focus of the research for Lunar

Modular Robotics project -. Figure 12 explains the key steps of the construction and do not detail out the technology for stacking-up the aggregates around the formwork and the inflatable modules:

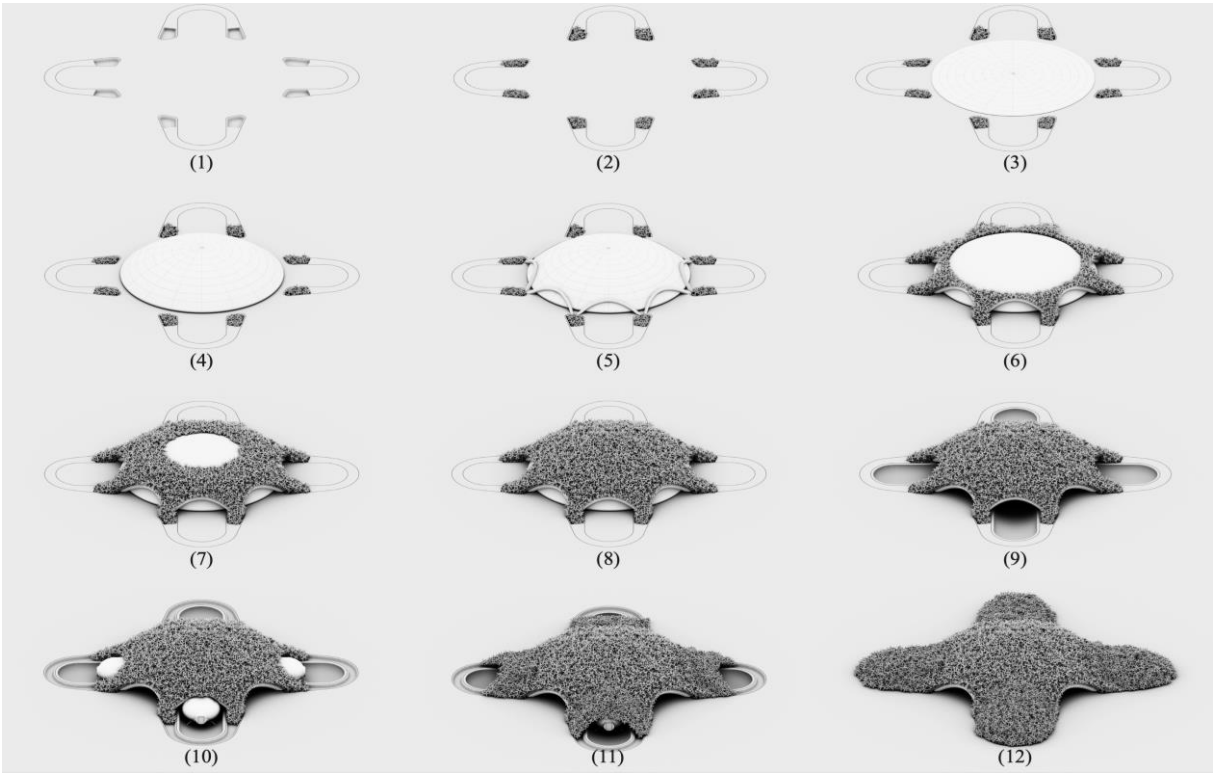


Figure 12: (1) First part of the pit dug out, (2) first layer of foundation aggregates placed, (3) inflatable formwork placed, (4) formwork inflated, (5) bending-active arcs positioned on formwork, (6-7) dome structure in construction with aggregates, (8) dome structure completed, (9) inflatable formwork removed, (10) habitats positioned under dome structure, (11) further aggregation to complete legs branching out from the dome, (12) construction completed. Credit: Hassell

6. Structural parameters

The structural understanding presented in this repor have mainly relied on digital simulations.Working closely with Format Engineers on finding an optimum design for the shell structure's guide geometry, we treated the central dome structure as compression shell and the legs acting as shear connection. In the absence of any wind forces on the Moon, where "moonquakes" are rare occasions, the digital simulations did not need to incorporate additional forces to lunar gravity. How the hexapods that do not interlock will behave; to what degree they will fall down and get damaged as a result of that will be a key question to answer with physical testing. In the final construction sequence discussed in this report, we propose that the inflatable habitats would only be placed after the dome is complete. For the legs, the habitats could be over-pressurized to act as a formwork during the construction. Integration of physical testing will be carried out on our next ESA – OSIP project titled as "Lunar Modular Robotics" on which we are working with University of Toronto. This next chapter will focus on the physical fabrication and performance analysis of the structure. As a replicant of regolith, we will be using voxel-based sand 3D printing as a fabrication method. Manufactured in different scales, the 3D-printed hexapod prototypes will then be tested for structural performance and interlocking behaviour. Below we present a collection of key details about the guide form and the structure derived from Format's report which will also play an instrumental role in setting out the physical testing in the next ESA-OSIP project.

6.1. Horizontal dimensions

The X shape shell sits on a 75m x 75m rectangle which is the reconfigurable grid cell for the Lunar Habitat Framework. Whilst the radiation protection shell stays fixed, what is underneath it as habitat modules are reconfigurable; from 1 big greenhouse to a combination of 4 medium or large habitable modules. The dome part of the X shell spans for 49 meters and has 8 openings, 4 of which is then closed with the leg part. The remaining 4 opening allows visual connection for the habitants inside with the outside world.

6.2. Form finding

The cross section of the guide shell will have an impact on defining the forces within the structure. Minimizing bending in the shell geometry will result in the thinnest required depth. The shape of the cross section will be ideal when no bending is carried under its own weight. In that sense, we isolate the dome part within the overall structure and use a inverted chain model to come-up with the compression only under moon gravity - which is around %16.5 of Earth gravity -. The results showed that arc geometry is more efficient than catenary due to the stress around openings of the dome geometry.

6.3. Height

The dome part of the guide shell is a revolved arc with openings. The height of the dome will determine the curvature of its geometry; the height of the dome will have a direct impact on material usage as well. Based on the horizontal dimensions discussed above, we found that 13m is an optimum height for the dome based on its Area / Buckling value.

6.4. Thickness

Using the same guide shell geometry, we can obtain the inflated formwork geometry by offsetting it inwards. Furthermore, to achieve an optimum thickness for the shell structure itself, we scale X/Y and Z dimensions of the guide shell independently to create a target volume for the aggregates to populate. This way, the target volume could be thicker at the bottom and thinner and the top.

6.5. Inflatable formwork

The inflatable formwork will create a closed volume, with additional surfaces along the floor being required for support. Its double curvature global form geometry will be created by using cutting patterns. This makes the fabric itself singly curved - develop from flat pieces - and the number of splits in fabric will determine: (1) how smooth inside of the shell is, (2) how consistent the thickness is at each height.

6.6. Edge support

Support conditions are vital for the edge of the shell structure, where it touches the ground. Here, lateral and vertical forces must be resisted. Notch cut into ground will be useful as a shear key and can putt horizontal forces into the ground. Furthermore, openings of the dome must be properly detailed to provide safe boundary conditions for the shell to work. In that sense, additional structure may be required to support the dome construction temporarily in these areas. Two options that can be applicable

are planar 3D trusses that are prefabricated on Earth or arches created with bags filled with Lunar Regolith (Figure 13).



Figure 13: A close approximation of arches that could be done with bags filled with Lunar Regolith. In this Earth application the bags are filled with sand.

6.7. Legs

Although the dome structure was based on revolved arcs, the legs are optimized into catenary section with no openings except the connection to the dome structure. Apart from the end cap of the legs the rest of its guide geometry is singly curved. Due to the aggregation nature of the system the transition from catenary form of the legs to the arcs of the dome is handled smoothly as low accuracy of the interlocking blends them. Figure 14 gives an overall idea on how the stacking up sequencing for each part works.

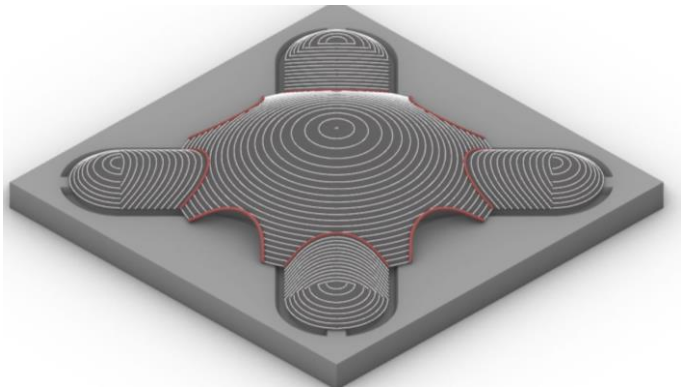


Figure 14: Guide paths for each section of the X shell. The legs are two stages; starting with a diagonal contour approach that is than finished off with horizontal stacking.

7. Conclusion

The paper offers an insight into a shift away from highly controlled design & construction methods into systems that gain from low-precision and disorder. When designing for extreme environments, we often see over-engineered control as the sole means to success of long-term survival of the building. With this paper, we propose an alternative way where disorder is not only tolerated (robustness) but more importantly is used to the overall design's advantage (anti-fragility). We position the research behind shell design as a balancing act between bottom-up module - fabrication oriented designing & top-down optimization / brief oriented designing. On the one hand, the final shell design is a direct multiplication

of a single type aggregate, making qualities like performance, aesthetics or thickness a direct product of quantity. On the other hand, how the quantities of aggregates are distributed relies on the pre-engineered, continuous shell geometry which is used to organize the randomly positioned aggregates around a more defined area than in the case of coastal barriers. Leveraging both ways of designing, we make the design as optimized and yet also as flexible as possible at the same time.

Acknowledgements

Research derived from ESA OSIP – Lunar Habitat Framework. Principal Design / Contractor: Hassell (Team: Xavier de Kestelier, Jonathan Irawan, Levent Ozruh, Joanna Maria Lesna). Structural Engineering: Format Engineers

References

[1] D. Baraff and A. Witkin, "Partitioned Dynamics,", The Robotics Institute – Carnegie Mellon University, p.1 1997. [Available: https://www.cs.cmu.edu/~baraff/papers/partition-tr.pdf [Accessed March. 29, 2023].

[2] "Projects,", spacearchitect.org [Online]. Available: https://spacearchitect.org/projects/ [Accessed: March 29, 2023].

[3] USA. The National Aeronautics and Space Administration (NASA): NASA Centennial Challange, - International Astronautical Congress Washington, DC, USA. [2019] Available: https://ntrs.nasa.gov/api/citations/20190032473/downloads/20190032473.pdf [Accessed March. 29, 2023]

[4] K. Dierichs and A. Menges, "Granular Construction: Designed Particles for Macro-Scale Architectural Studies" in *Autonomous Assembly: Designing for a New Era of Collective Construction* Vol.87 No.4, pp.88-93 July 2017

[5] P. Block, M. Rippmann, T. Van Mele and D. Escobedo, "The Armadillo Vault: Balancing Computation and Traditional Craft, " in *Fabricate 2017*, London: UCL Press, pp. 286-293.

[6] J. Feringa and A. Søndergaard, "Fabricating Architectural Volume: Stereotomic Investigations in Robotic Craft " in *Fabricate 2014*, London: UCL Press, pp. 76-84.

[7] J. Irawan, X. De Kestelier, N. Argyros, B. Lewis and S. Gregson, "A Reconfigurable Modular Swarm Robotic System for ISRU (In-Situ Resource Utilisation) Autonomous 3D Printing in Extreme Environments" in *Design Modelling Symposium Berlin*, Berlin: Springer, pp. 685-698.

[8] M. Yashar, M. Morris, R. Pailes-Friedman, W. Elshanshoury, M. Esfandabadi, D. Gomez, A. Guzeev, V. Netti and A. Rajkumar, "Project Olympus: Off-World Additive Construction for Lunar Surface Infrastructure," in *Proceedings of the 50th International Conference on Environmental Systems, July 12-15, 2021, Location* .Lisbon, Portugal:https://www.researchgate.net/profile/Melodie-Yashar/publication/353742380_Project_Olympus_OffWorld_Additive_Construction_for_Lunar_Surface_Infrastructure/links/610dc3ee1e95fe241ab69d1f/Project-Olympus-Off-World-Additive-Construction-for-Lunar-Surface-Infrastructure.pdf. [Accessed:March 29, 2023].

[9] B. Imhof, D. Urbina, P. Weiss, M. Sperl "Advancing Solar Sintering for Building a Base On The Moon," in *Proceedings of the 69th International Astronautical Congress, September 25-29, 2017, Adelaide* .: International Astronautical Federation 2017 https://liquifer.com/wp-content/uploads/2020/03/2017_Advancing_REGOLIGHT-IAC-17C2913x37414.pdf. [Accessed:March 29, 2023].

[10] M. Konstantatou, M. Dall'Igna, S. Wilkinson, I. Gallou, D. Piker "Learning lessons from Earth and Space Towards Sustainable Multi-planetary Design" *Spool* Vol.8 No.2 October 2021 https://spool.ac/index.php/spool/article/view/191/192 [Accessed:March 29, 2023].

IASS 2023
July 10–14 Melbourne
Integration of Design and Fabrication

Proceedings of the IASS Annual Symposium 2023
Integration of Design and Fabrication
10–14 July 2023, Melbourne, Australia
Y.M. Xie, J. Burry, T.U. Lee and J. Ma (eds.)

Cast glass arches, vaults and domes: case studies and design methodology

Telesilla BRISTOGIANNI*, Faidra OIKONOMOPOULOU[a]

* TU Delft, Faculty of Architecture and the Built Environment
t.bristogianni@tudelft.nl

[a] TU Delft, Faculty of Architecture and the Built Environment

Abstract

Cast glass is an excellent candidate for achieving fully transparent arch, vault and dome structures. By casting, voluminous, free-form glass components can be produced that fulfil the complex geometry requirements, offer increased compressive strength and maximize the incoming sunlight. Nonetheless, the application of cast glass in such structures is seldom seen; manufacturing challenges, uncertainties over the strength of the material, missing guidelines on the assembly methods of the components, lack of engineering norms, and the associated research and development costs to overcome those barriers, are some of the key discouraging factors. This paper explores several realised case studies of small-scale, cast glass arches, vaults and domes, where the TU Delft Glass Research group was involved in the R&D process, as well as unrealised case studies developed by the group (Fig. 1). The main challenges and developed solutions for each project are described, focusing on three main aspects: (i) the manufacturing challenges linked with achieving the desired curvature, (ii) the assembly method and mechanical validation of the system, and (iii) the construction ease of the system. Based on the comparative study of the selected projects, the paper aims to provide a design methodology for future projects employing cast glass curved structures.

Keywords: structural glass, cast glass components, cast glass shells and arches, glass casting and post-processing, adhesive bonding, interlocking components, adaptive moulds

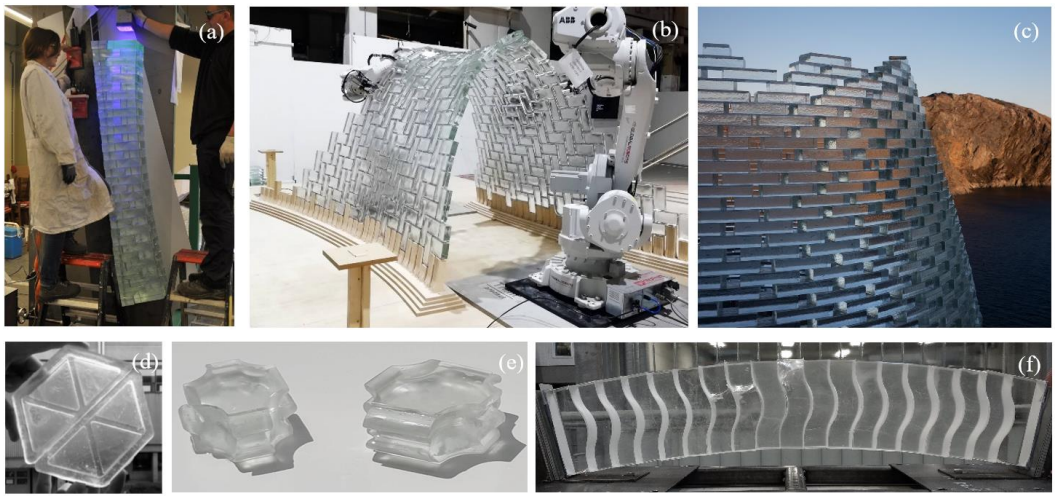


Figure 1. Cast glass case studies: (a) architrave assembly for the Crystal Houses Façade, Amsterdam (MVRDV), (b) robotically assembled LightVault, London (Princeton, SOM) (c) Qaammat pavilion in Greenland (Konstantin Arkitekter), (d) ribbed components for a geodesic dome (T. Bristogianni) (e) interlocking glass voussoirs cast with an adjustable mould (F. van der Weijst), (f) prototype for a cast glass interlocking bridge (A. Snijder).

Copyright © 2023 by Telesilla BRISTOGIANNI and Faidra OIKONOMOPOULOU. Published in the Proceedings of the IASS Annual Symposium 2023 with permission.

1. Introduction

With the Industrial Revolution enabling the use of cast and wrought iron in building structures, large-span, glazed vault and dome structures were made possible, significantly increasing the incoming daylight in public buildings of the Victorian era (Fig. 2a, b). Ever since, transparent roofs fascinated the architectural world, sustaining continuous engineering developments that refined their typology (Fig. 2c). Nonetheless, in essence, the same structural model is being reproduced over the years: a metal load-bearing structure, cladded with glass. Technological developments in the field of structural glass during the last three decades, however, showcased in smaller scale structures, the functional and aesthetical benefits of maximized transparency and light income (Fig. 2d), as these result from employing float glass as the structural element and minimizing, if not omitting, the use of steel. This can be achieved by taking advantage of the high compressive strength of glass, yet the two-dimensionality of float glass imposes buckling-related limitations and shaping challenges, which prevent the realization of larger-span all-glass curved structures. In this context, cast glass could be an excellent candidate for achieving compressive, fully transparent curved structures of larger spans, as with casting, robust components of complex geometry and considerable thickness can be achieved. Yet, the use of cast glass as a structural material is still in an experimental phase; lack of manufacturing, quality control and engineering norms coupled with a lack of design data, prevents its use in structural applications. Therefore, its suitability in such structures has been so far tested in small-scale realized projects, and with prototypes that evaluate the casting ease, mechanical performance and assembly method of the cast components. This paper explores several realised case studies of small-scale, cast glass arches, vaults and domes where the TU Delft Glass Research Group was involved, addressing the following main points:

(i) manufacturing challenges: in this case, the strategy for achieving the desired curvature of the structure is addressed in relation to the shaping limitations of cast glass, the resulting number of different component shapes and moulds, and the requirements for post-processing.

(ii) assembly methods: the choice of a permanent or temporary adhesive bonding versus a dry-assembly solution by using interlocking components and dry-interlayers is discussed. Where applicable, the output from the mechanical validation of the assembled glass system is provided.

(iii) construction ease: insights on the assembly method and sequence are provided, covering a range of solutions from scaffolding and layer-by-layer building, to rotating frames and robotic arms.

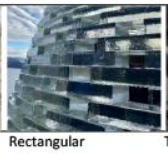
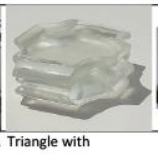


Figure 2. The evolution of (large-span) glass roofs and the increase of the glass-to-steel ratio: (a) Oxford University Museum of Natural History, 1861, (b) Palm House at Kew Gardens, 1848, (c) Queen Elizabeth II Great Court at the British Museum, 2000, and (d) Davies Alpine House at Kew Gardens, 2006.

2. Case studies

Table 1 provides an overview of cast glass arch, vault and dome structures that have been developed and -in cases- realised, with the involvement of TU Delft. Different aspects concerning the manufacturing process, assembly method and construction solution followed for each specific project are discussed below.

Table 1. Overview of cast glass case studies comprising arch, vault, or dome structures.

Case study details	Project name & location	Crystal Houses, Amsterdam	Glass Masonry Bridge, Delft	LightVault, London	Qaammat Pavilion, Greenland	Geodesic cast glass dome	Glass Vaults	The Glass dome
	Credits & sources	MVRDV, TU Delft, abt [1, 2]	TU Delft [3-6]	SOM, Princeton, TU Delft [8-11]	Konstantin Arkitekter, TU Delft [12-13]	TU Delft [14]	TU Delft [15-16]	TU Delft [17]
	Status	Realised	R&D	Realised	Realised	Case study	Case study	Case study
	Structure type	Arched architrave	Arch	Vault	Semi-circular walls, inclined, perforated	Dome	Vault	Shallow dome
	Structure size (LxWxH, m)	[1.26 (window), 1.89 (door)]x0.21x0.33	14.08x2.2x1.1	2.6x1.6x2	≈3.2x3.7x2	ø20x10	16.5x10.3x2.4	ø35.97x7.45
	Image							
Manufacturing	Component shape	Rectangular, tapered	Rectangular, tapered, 1 curved interlock	Rectangular	Rectangular	Trapezoid, pentagon, ribbed	Triangle with tongue/groove interlock, spherical node	Double sphere
	Component size (LxWxH, mm)	(58-62)x210x(44-215)	100x162x350	Main: 246x116x53 Half: 123x116x53	Main: 246x116x53, corner: 121x116x53	(440-520)x(940-1000)x96	(330-782)x(330-782)x100, ø258	220x125x92
	no. of different components	22 (window)+ 32 (door)+ 5 (corner)	1 + 2 (corner)	1+1 (half)	1 + 1 (corner)	20	1249 interlocking triangles, 1 node	1
	Production Method	Hot pouring	Hot pouring	Hot pouring	Hot pouring	Kiln-casting	Kiln-casting	Kiln-casting
	Mould type	Stainless steel	Stainless steel	Stainless steel	Stainless steel	Silica-plaster investment	Silica-plaster investment based on wax models cast with adjustable mould	Silica-plaster investment
	Post-processing	CNC grinding & polishing	None	None	None	Grinding	Grinding	Grinding
Assembly method	Bonding type	Adhesive	Interlocking, dry interlayer	Adhesive	Adhesive	Adhesive	Interlocking, dry interlayer	Interlocking, dry interlayer
	Bonding characteristics	UV-curing acrylate (DELO 4468)	Polyurethane rubber sheet	2 component multi-purpose epoxy putty (PIG™)	2-component polyurethane adhesive (3M™ DP 610), 2-component structural silicone (Dowsil Exp.)	UV-curing acrylate (DELO 4494)	Rubber dry interlayer	TPU dry interlayer
	Joint thickness (mm)	0.25	1	≤20	1 (3M), 2-3 (DOW)	1	3	2
	Validation method	Applicability tests, 4-point bending	Mid-span loading, shear test	Applicability tests, full scale mock-up	Applicability tests, full-scale mock-up	Component mock-up	Component mock-up	Component mock-up
Construction ease	Assembly method	Prefabricated with rotating mould	Dry assembly on site	Construction with 2 robotic arms	Row by row bricklaying	Row by row bricklaying	Row by row bricklaying	Row by row bricklaying
	Scaffolding on site	Not required	Required	Not required	Not required	Required	Required	Required

2.1. Crystal Houses Façade

The Crystal Houses façade in Amsterdam, designed by MVRDV, is a reinterpretation of the original 19th century brick façade in cast glass. As such, 12 architraves, 10 to be placed over the windows (1.26m span) and 2 larger ones over the doors (1.89m span) were designed, following the same structural system of the cast glass façade (Fig. 3d). This system comprises cast glass components (produced by Poesia) bonded brick by brick on site, using a stiff, transparent UV-curing acrylate of 0.25mm thickness [1]. The selected adhesive, due to its low viscosity, was applied at the horizontal brick surfaces only; vertical application would lead to non-homogeneous results due to the downward flow of the adhesive prior to curing. In addition, due to the adhesive's minimum optimum thickness, extreme dimensional precision had to be met, dictating, among others, the CNC grinding and polishing of the bricks to meet the desired tolerances [1]. Realizing the architraves was therefore an additional challenge, as (i) the cast glass bricks had to be tapered and bonded to precision to reproduce the exact curvature, (ii) the top side of the architraves had to be perfectly straight –within the 0.25mm tolerance range- to accommodate the glass brickwork above, and (iii) the adhesive could not be applied on site, as this would imply its vertical application. To solve the above challenges, 54 different steel moulds were required to achieve the desired geometry of the tapered bricks (544 pieces in total), and the vertical surfaces of the bricks were further CNC-post processed to meet the tolerances. The architraves were then prefabricated at the TU Delft Glass lab, using a rotating steel frame that allowed the horizontal application of the adhesive at every brick layer, and the creation of a straight line at the top side of the architraves (Fig. 3a,b). The prefabricated components were then craned on site, and special corner brick pieces (five per side) were adhesively bonded one by one to the side of the architraves to keep it in place (Fig. 3c). To ensure that the architraves could withstand their own weight before becoming incorporated in the wall system, a destructive 4-point bending test was conducted in a door architrave specimen. The specimen failed at 6.7MPa [2], withstanding 41.6KN which was more than double of the service load specified by the project engineers (abt).



Figure 3. Cast glass architraves for the Crystal Houses Façade: (a, b) rotating steel frame ensuring for the horizontal application of the UV-curing adhesive and for achieving a straight surface at the top of the architrave, (c) the architraves were temporarily rested on a steel frame until the surrounding wall bricks were adhered, (d) final result of the façade (image credits: MVRDV)

2.2. Glass Masonry Bridge

The Glass Masonry Bridge (Fig. 4a, non-realized project) is a pedestrian bridge designed for the TU Delft campus [3]. The arch-formed bridge consists of cast, interlocking glass components, dry assembled with a polyurethane (PU) rubber interlayer inbetween. One main component (Fig. 4b) is used -of a slightly tapered geometry to achieve the desired curvature- while two different corner components are designed to connect the bridge with the foundations. To reduce the complexity and costs of the production process, the post-processing of the glass surfaces is avoided, and dimensional deviations are expected to be absorbed by the rubbery interlayer. Several interlocking geometries were tested based on their interlocking performance [3, 4] but also on the complexity of the casting process and the compatibility of the geometry to the glass properties (e.g. sharp angles were avoided). A smooth, curved interlock was opted and validated by testing kiln-cast specimens (1:2 scale) in shear [5] (Fig. 4c) and compression [4]. These experiments indicated that poor contact between the interlocking surfaces can lead to the generation of point loads and subsequent fracture. A larger specimen (1m span), comprising components (1:2 scale) that were waterjet cut out of cast glass bricks, was tested in bending (Fig. 4d), showing satisfactory shear resistance, yet further testing involving a larger span and different load combinations is required [6]. For the assembly of the Glass Masonry Bridge, a secondary Glass Truss Bridge has been constructed below, to serve as scaffolding [7].

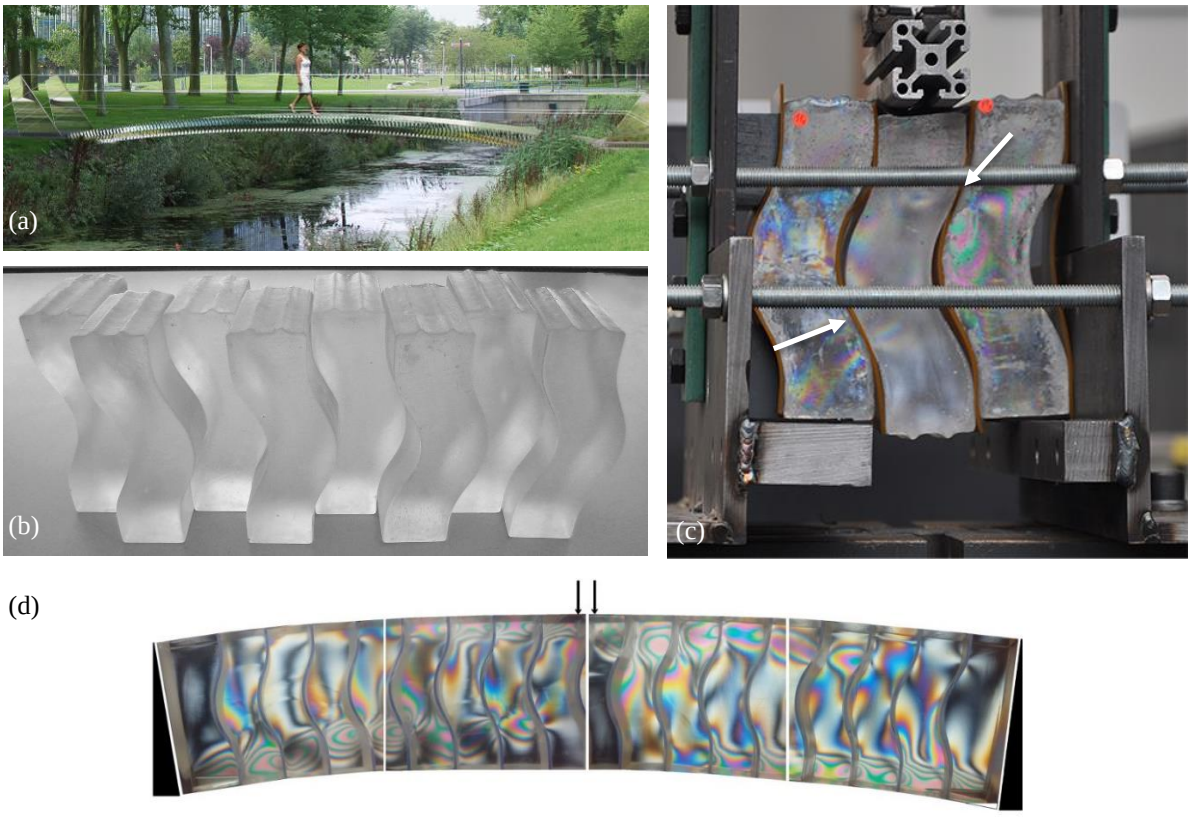


Figure 4. Cast Masonry Bridge: (a) 3D-visualization of the bridge, (b) kiln-cast glass components in 1:2 scale, showing the interlocking principle, (c) testing in shear combined with photography using cross-polarized light indicated the generation of point loads instead of the full cooperation along the interlocking surface, (d) photograph using cross-polarized light of a loaded 1m arch segment made from waterjet-cut components out of cast glass bricks.

2.3. LightVault

The LightVault, designed by SOM and Princeton University c.r.e.A.te lab and Form Finding Lab, is a double curved glass brick vault following a herringbone pattern [8]. It was designed to be built without the use of scaffolding, but with the aid of two robotic arms that would place the bricks in the precise location (Fig. 5a). The structure is realized in its majority with the use of one type of rectangular, non-tapered cast glass brick (309 pieces, produced by Poesia) that is not post-processed after casting, while a small number of half-sized bricks (29 pieces) are strategically inserted to reduce the occurring gaps in the structure. Nonetheless, due to the use of one rectangular geometry and taking into account the dimensional deviations occurring from casting, wedge-shaped gaps of significant thickness between the brick interfaces were created, the majority of which were optimized to be below 17.5mm [9]. A fast curing Epoxy Patty of 20mm gap-filling capability was selected as the intermedium [9, 10], minimizing the time the robotic arm would hold the brick in place to 12-15min (25min for the middle arch) [11]. Several prototypes were constructed to evaluate the assembly order, suggesting that the building of a broader brick wall section at the base, would enhance the temporary stability of the system (Fig. 5b, c).

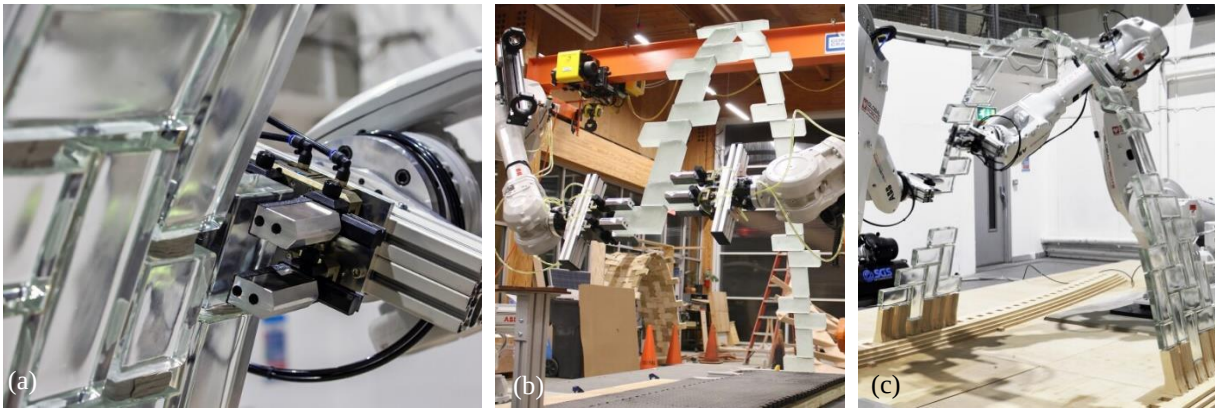


Figure 5. Robotically assembled cast glass vault: (a) robotic arm placing a half-sized glass brick (image credits: M. Grzeskowiak/SOM), (b) unstable assembly configuration (image credits: I. X. Han/ Princeton University), (c) redesigned assembly order to ensure the temporary stiffness of the system (image credits: I. X. Han & E. Bruun, Princeton University).

2.4 Qaammat Pavilion

The Qaammat Pavilion in Greenland, designed by Konstantin Arkitekter, comprises two semi-circular, perforated walls that follow a frustum shape (Fig. 6a, c). The walls were constructed with the use of a basic rectangular cast glass brick (1100 pieces) and a limited amount of half-sized bricks for the edges (bricks produced by Wonderglass). The bricks were not post-processed and were adhered with two different types of 2-component adhesives. At the bottom rows, where larger gaps between the bricks occur due to the developed geometry, a clear polyurethane of high stiffness, >3.7MPa shear strength and 1mm gap-filling capacity was selected [10, 12]. For the middle and top rows, where less stresses are developed but also higher deviations are built up from the occurring variations at the bricks' height due to casting, a more flexible, white structural silicone of 2-3mm gap filling capacity and circa 1MPa shear strength was applied, developed by DOW specifically for this project [13]. The bricks were laid row by row with the aid of CNC-cut PVC templates that would control their placement (Fig. 6b). The use of scaffolding was avoided by selecting 2-component, fast curing adhesives, which reach their set-time within 4-20min. To ensure the temporary fixing of the bricks until the set-time is reached, double-sided tape spacers were placed between the bricks, holding them in position and securing the desired thickness of the adhesive layer.

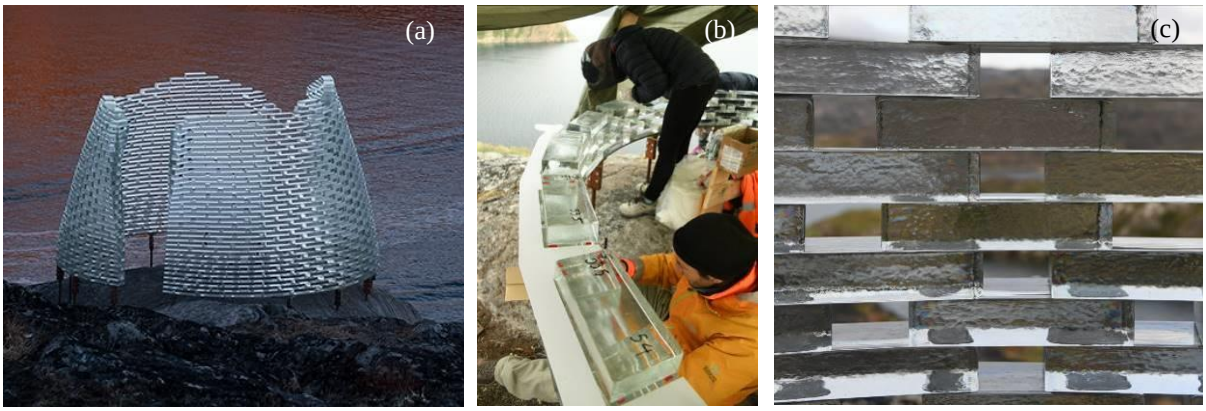


Figure 6. The Qaammat Pavilion in Greenland: (a) Aspect of the finalized project (Image credits: Julien Lanoo), (b) row by row brick laying on site, using PVC templates, (c) detail of the perforated cast glass wall.

2.5 Geodesic cast glass dome

This dome is a theoretical study on how to achieve the minimum number of different components to realize a 20m span cast glass dome [14]. The components should not overly exceed a maximum mass of 10kg, to ensure a realistic annealing time during casting, and to facilitate the assembly process. To fulfil the above criteria, Buckminster Fuller's Geodesic dome configuration was preferred versus a horizontal ring division. Using a geodesic dome frequency of 22, 20 different pieces are required; 19 hexagons and 1 pentagon. To further reduce the mass, the pieces were divided in half, and a ribbed geometry was preferred instead of a constant thickness (Fig. 7a, b). The pieces were slightly tapered and adhered together with a UV-curing acrylate that could accommodate up to 1mm tolerances. A scaffolding would be required for the construction of the dome. Prototyping of the components in 1:5 scale was conducted, to evaluate the suitability of the designed shape in relation to the casting process (Fig. 7b). Larger bevel angles are advised for the rib edges.

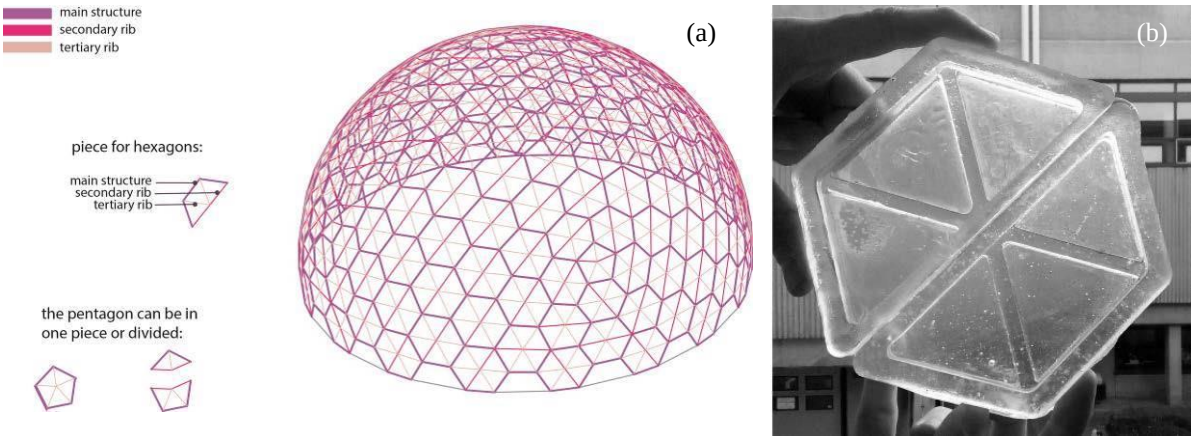


Figure 7. Concept for a cast glass geodesic dome: (a) division of the components and distinction of rib thicknesses, (b) 1:5 kiln-cast glass mock-up.

2.6 Glass Vaults

This project studies the realization of free-form transparent shell structures, by employing interlocking cast glass voussoirs [15, 16]. The voussoirs interlock thanks to their tongue or groove -shaped side surfaces, and the pieces are dry-assembled with the use of a rubber interlayer in between. Node components are also introduced at the intersection points of the voussoirs. To achieve such a complex system, voussoirs of distinct geometries are required. Adjustable moulds in triangular, quadrangular and hexagonal configuration (Fig. 8a) are therefore devised that adjust the length and angles of the components' edges, and the type and angle of the interface geometry (tongue or groove). As a proof of concept, a shell roof structure is designed for the courtyard of the Armamentarium in Delft (Fig. 8c), and an algorithm is developed to tessellate the double-curved surface into triangular components, and to assign the interface types and angles for each component. 1250 pieces are designed, varying in mass from 5.4 to 38.5kg, and with an average mass of 24.6kg. The node pieces are identical and require one mould only. The ability of the mould to adjust to the generated designs was further tested by constructing distinct models of voussoirs in wax. These wax models were thereafter used to produced investment moulds for kiln-casting the voussoirs in glass (Fig. 8b).

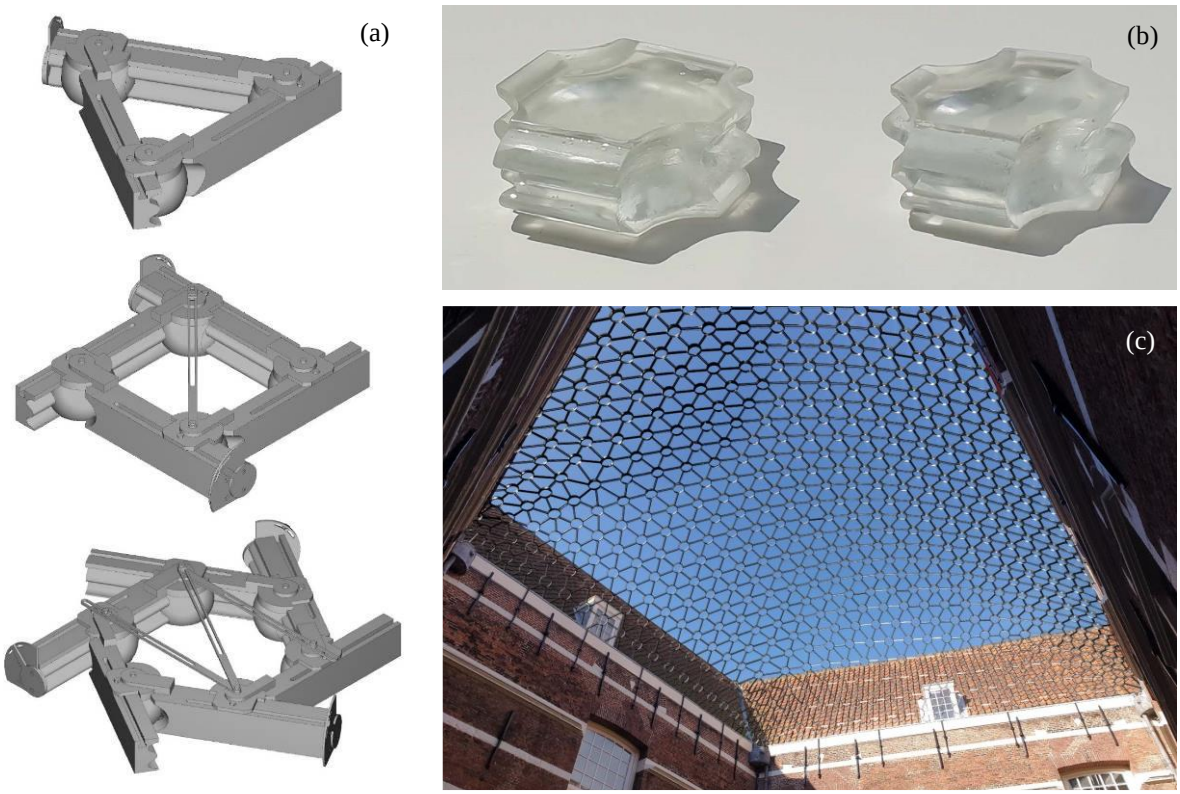


Figure 8. Concept for achieving free-form interlocking glass shell structures: (a) adjustable mould system in triangular, quadrangular and hexagonal configuration, (b) kiln-cast voussoirs using investment moulds produced with the lost-wax technique; the wax models were produced from adjustable moulds, (c) case study of a free-form shell out of interlocking cast glass components, designed to cover the courtyard of the Armamentarium in Delft.

2.7. The Glass dome

The Glass dome aviary project studies the construction of a dry-assembled cast glass dome using one omnidirectional interlocking component [17] (Fig. 9a). The component is designed by blending three spheres of different size (Fig. 9d), ensuring an interlock in both ring (horizontal, Fig. 9c) and arch (vertical, Fig. 9b) direction. The component has a 2.5kg mass, facilitating the annealing process during casting, and the assembly process. Thermoplastic polyurethane (TPU) interlayers, produced by compression molding, are placed between the glass components both in arch and ring direction. The interlayers in arch direction are identical, while those in ring direction differ in each row due to the changing curvature. A wooden substructure is suggested for assembling the dome, after which a customized compressive steel ring is fixed at the top, while a tension ring is applied at the bottom. To validate the castability and validity of the design, five components were kiln-cast in 1:2 scale (Fig. 9e). Challenges with air-entrapment were identified due to the enclosed mould design, and the introduction of mould vents is suggested to prevent the encountered problem.

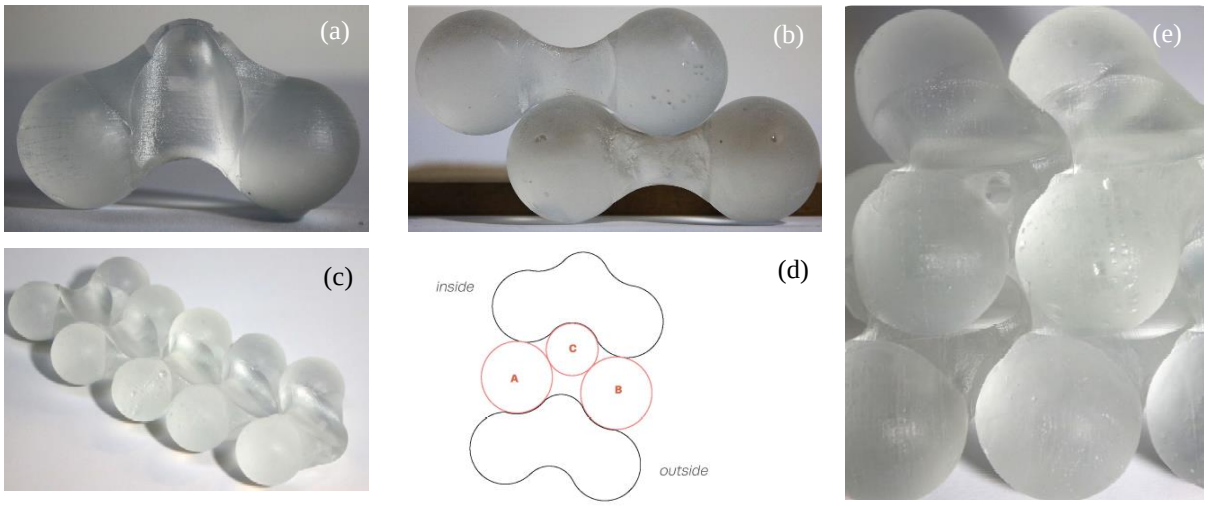


Figure 9. Omnidirectional interlocking cast glass component for a dome structure: (a) top view of the component, (b) array of the components along the arch direction, (c) array of the components along the ring direction, (d) design of the component based on 3 spheres of distinct dimensions to ensure interlock in both horizontal and vertical direction, (e) assembly of the components in both ring and arch direction.

3. Design guidelines

The presented case studies show the design choices made regarding the shape, mass and number of different components, the type of bonding (permanent, interlocking), and the method of assembly, in order to realize the desired curved cast glass structures. Based on this experience, and in combination with basic principles applied to the casting process [18], design guidelines can be developed for future applications. The main design choices are discussed below and presented in Figure 10:

Regarding the general shape of the structure, this should be principally working in compression, to benefit from the high compressive strength of glass. Double-curved, asymmetric geometries increase by definition the number of different components, and normalization of the shape is advised to prevent a plethora of distinct pieces that strain the production process and delay the assembly. Nonetheless, in case of complex geometries, two options are worth considering regarding the design of the component:

(i) using one global geometry and solving the tolerances in the interface. This interface can be an adhesive of high gap-filling capacity (e.g. an epoxy patty) or a stiff, customized dry interlayer (e.g. 3D printed plastic pieces)
(ii) using distinct components produced by adjustable moulds, to reduce the production costs.

In parallel, the bonding strategy between the components needs to be determined. Adhesively bonded structures can be very stiff –based on the adhesive type and bond thickness, but lead to permanent, non-dismountable solutions. Dry-interlocking systems, although less stiff, promote circularity, but also increase the casting complexity; high-precision of the interlocking interfaces is required to achieve homogeneous transfer of the load and thus avoid peak stresses, which increases the production costs. In both cases, the redundancy of the system should be evaluated, ensuring a safe structure even in the event of breakage of a few components. As structural norms and guidelines on the design and calculation of such cast glass structures do not exist, mechanical testing of characteristic mock-ups of the system is necessary, to validate the dimensioning of the structure and the choice of interface material.

Regardless of the solution path selected, several guidelines should be followed for the design of the cast glass components. The mass of each component desirably should not exceed a maximum of 10kg, to reduce the annealing time during the casting process, but also to facilitate the handling of the piece during assembly. To further facilitate the annealing process, abrupt changes in thickness along the piece should be avoided, while sharp edges are also not favourable in terms of casting and construction. Organic, spherical geometries are favourable in terms of annealing, but require closed or press-moulds; careful introduction of vents in those moulds should prevent air-entrapment defects at the surface of the glass components.

Some form of scaffolding is –in most cases- unavoidable, yet, the use of robotic arms is a proven solution for avoiding scaffolding in adhesively bonded double-curved systems. For achieving configurations of high-precision, the preassembling of segments of the structure (again adhesively bonded system) with the use of frames and guides should be considered. Lastly, for minimizing the scaffolding requirements, the brick-by-brick laying per row and the (almost) horizontal application of a fast curing adhesive should be opted for.

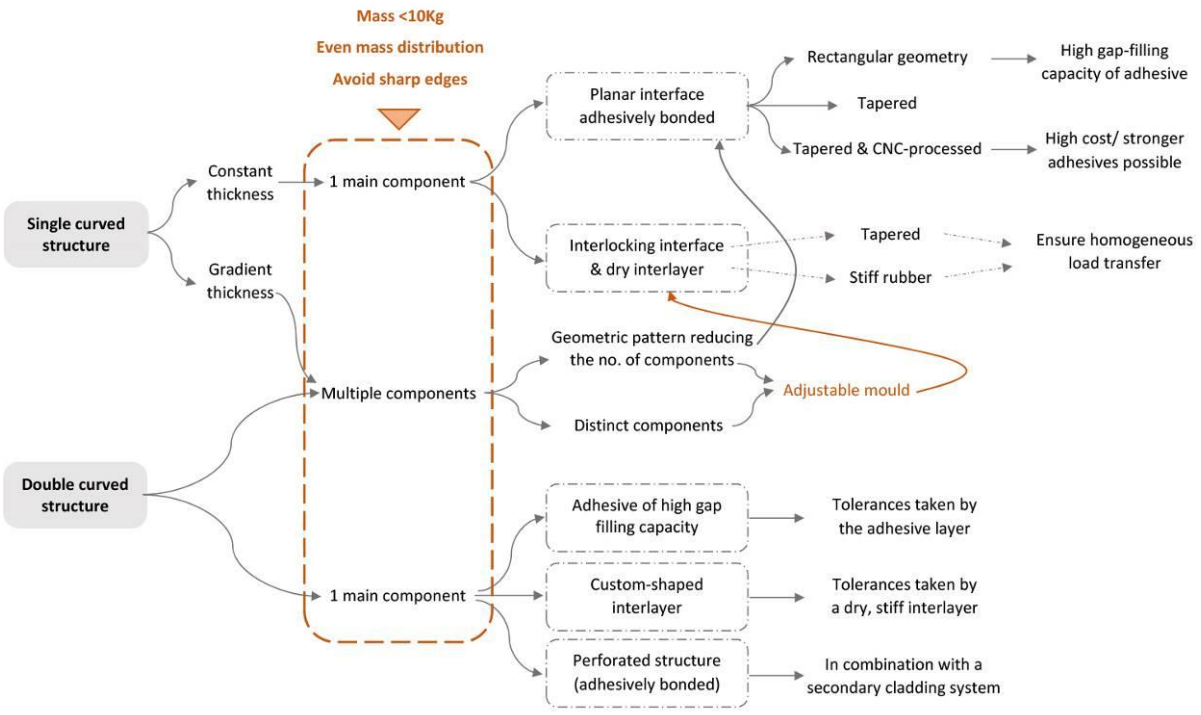


Figure 10. Design selections for achieving single and double curved cast glass structures.

4. Conclusions

Although cast glass is an excellent candidate for materializing strong and transparent arch, vault and dome structures, realized structures using cast glass components are rarely seen. Discouraging factors responsible for this include the lack of engineering data, coupled with the complexities imposed on the casting process due to the (double) curved geometries and the associated high costs. From the studying of a few realized case studies and theoretical projects, guidelines arise concerning the choices to be made on the design of the component, the connection method and the assembly process. These evolve around the decision of absorbing the tolerances at a component level –resulting to multiple different shapes- or at the interface –leading to either thick adhesive layers or custom-shaped dry interlayers. The choice of an adhesive medium versus a dry rubber interlayer has further consequences on the stiffness, demountability, and allowable tolerances of the system. The casting parameters play the most crucial role, as the reduction of the number of different moulds, the reduction of the mass, and the avoidance of post-processing, all work towards the reduction of the production costs and time, making the structure more feasible. Experimental validation of a mock-up of the chosen system is always required for ensuring a safe structure.

References

[1] F. Oikonomopoulou, T. Bristogianni, F. A. Veer, and R. Nijsse, "The construction of the Crystal Houses façade: challenges and innovations," *Glass Structures & Engineering,* vol. 3, no. 1, pp. 87-108, 2018/03/01 2018.

[2] F. Oikonomopoulou, "Unveiling the third dimension of glass. Solid cast glass components and assemblies for structural applications.," PhD, Architecture and the Built Environment, TU Delft, Delft, 2019.

[3] A. Snijder, J. Smits, T. Bristogianni, and R. Nijsse, "Design and Engineering of a Dry Assembled Glass Block Pedestrian Bridge," in *Conference on Architectural and Structural Applications of Glass (CGC5)*, Ghent, Belgium, 2016: Universiteit Gent.

[4] I. Sombroek, "Structural cast glass; A research process of design and experiment towards a feasible geometry for a cast glass element," Master of Science, Architectural Engineering and Technology, Architecture and The Built Environment, Delft University of Technology, Delft, 2016.

[5] T. Bristogianni, F. Oikonomopoulou, F. Veer, A. Snijder, and R. Nijsse, "Production and Testing of Kiln-cast Glass Components for an Interlocking, Dry-assembled Transparent Bridge," presented at the Glass Performance Days 2017 Conference Proceedings, Tampere, 2017.

[6] M. Aurik, A. Snijder, C. Noteboom, R. Nijsse, C. Louter, "Experimental analysis on the glass-interlayer system in glass masonry arches," *Glass Structures & Engineering*, vol. 3, pp. 335-353, 2018.

[7] A. H. Snijder, R. Nijsse, and P. C. Louter, "The glass truss bridge," *Heron*, vol. 63 (1/2), pp. 139-157, 2018.

[8] I. Han, E. Bruun, S. Marsh, M. Tavano, S. Adriaenssens, and S. Parascho, *From Concept to Construction: A Transferable Design and Robotic Fabrication Method for a Building-Scale Vault*. 2020.

[9] S. Parascho, I. X. Han, A. Beghini, M. Miki, S. Walker, and E. P. G. Bruun, "LightVault: A Design and Robotic Fabrication Method for Complex Masonry Structures," 2021.

[10] F. Oikonomopoulou and T. Bristogianni, "Adhesive solutions for cast glass assemblies: ground rules emerging from built case studies on adhesive selection and experimental validation," *Glass Structures & Engineering*, vol. 7, no. 2, pp. 293-317, 2022/08/01 2022.

[11] S. Parascho, I. Han, S. Walker, A. Beghini, E. Bruun, S. Adriaenssens, "Robotic vault: a cooperative robotic assembly method for brick vault construction," *Construction Robotics*, vol. 4, 12/01 2020.

[12] F. Oikonomopoulou, T. Bristogianni, M. van der Velden, and K. Ikonomidis, "The adhesively-bonded glass brick system of the Qaammat Pavilion in Greenland: From research to realization," *Architecture, Structures and Construction,* vol. 2, no. 1, pp. 39-62, 2022/05/01 2022.

[13] V. Hayez, B. Aksoy, F. Oikonomopoulou, T. Bristogianni, and K. Ikonomidis. (2021) The Qaammat Pavilion: A story of innovation, collaboration and inclusion. *Intelligent Glass Solutions*. 79-89.

[14] T. Bristogianni, F. Oikonomopoulou, F.A. Veer, R. Nijsse, "Design and production of a structural cast glass element for a transparent dome," in *Insights and Innovations in Structural Engineering, Mechanics and Computation : Proceedings of the 6th International Conference on Structural Engineering, Mechanics and Computation, SEMC,* Cape Town, 2016, pp. 1662-1667: CRC Press.

[15] F. van der Weijst, "Glass Vaults: Introducing an adjustable mould for casting glass voussoirs for transparent shell structures," MSc, Architectural Engineering + Technology, TU Delft, Architecture and the Built Environment, Delft, 2019.

[16] F. van der Weijst, F. Oikonomopoulou, and M. Bilow, "An Adjustable Mould for the Casting of Glass Voussoirs for the Construction of Fully Transparent Shell Structures," in *Challenging Glass 7 Conference on Architectural and Structural Applications of Glass,* Ghent, 2020.

[17] E. Janssens, "The Glass Dome: Design technology for a dry assembled and cast glass dome," MSc, Architectural Engineering + Technology Department, TU Delft, Architecture and the Built Environment, Delft, 2018.

[18] F. Oikonomopoulou, T. Bristogianni, L. Barou, F.A. Veer, R. Nijsse, "The potential of cast glass in structural applications. Lessons learned from large-scale castings and state-of-the art load-bearing cast glass in architecture," *Journal of Building Engineering,* vol. 20, pp. 213-234, 2018/11/01/ 2018.

IASS 2023
July 10–14 Melbourne
Integration of Design and Fabrication

Proceedings of the IASS Annual Symposium 2023
Integration of Design and Fabrication
10–14 July 2023, Melbourne, Australia
Y.M. Xie, J. Burry, T.U. Lee and J. Ma (eds.)

Enhancing construction of complex compression-based structures through holographic-assisted assembly

Ertunç HÜNKAR*, David LEE[a]

[a,*] School of Architecture, Clemson University, Clemson, SC 29634
ehunkar@clemson.edu

Abstract

This research explores the use of holographic building techniques to facilitate the construction of compression-based stacking structures with extreme cantilevers and arched spans inspired by the block stacking problem. Geometric operations including mirroring, scaling, and shifting are used to transfer the loads of each cantilever structure component to one another without the use of glue or fasteners, allowing the structure to stand without support. Three studies are introduced. In the first, the mathematical problem is parameterized using computational tools with a series of tests of an arced cantilever of X-shaped components. In the second study, we focused on arched structures as the scale of to more directly approach the stacking problem. In the third study, we explored the limits of height using limited materials available, including diminishing part lengths and nonuniform scaling of the archetype "arch" structure. Utilizing computational tools and the integration of holographic projection of geometry during the assembly process added precision and constructability. Using these tools, we were able to easily test and iterate on different design options in a virtual environment before physically constructing them. Additionally, holographic projection eliminated the need for physical measurements, support or alignment materials.

Keywords: computational modeling, structural design, holographic assembly, holographic building techniques, virtual reality, augmented reality, arched spans, extreme cantilevers, glue-less assembly, holographic projection

1. Introduction

Compression-based stacking structures, such as arches and cantilevers, have been fundamental to architecture and engineering for centuries. However, the construction of such structures presents several challenges, especially when dealing with extreme cantilevers or arched spans. Traditional building techniques often rely on glue or fasteners to keep components together, which can be impractical or impossible to use when constructing certain types of compression-based structures. So, constructing these structures without support can be a significant challenge due to the need for precise alignment and careful weight distribution.

Holographic building techniques have been gaining popularity in recent years and offer a promising alternative to traditional building methods[1]. By projecting virtual geometry during the assembly process, these techniques allow for more precise alignment and weight distribution, leading to greater stability and structural integrity. In this paper, we present a novel approach to constructing compression-based structures using holographic building techniques.

The block stacking problem, also known as the Leaning Tower of Lire[2], is a classic paradox in statics that has been studied extensively over the years. Researchers have developed a variety of solutions to this problem, making it a useful starting point for exploring the construction of complex compression-based structures. Our approach involves using computational tools to parameterize the mathematical problem of the block stacking paradox and simulate the structures in a virtual environment. This allows

Copyright © 2023 by Ertunç HÜNKAR and David LEE. Published in the Proceedings of the IASS Annual Symposium 2023 with permission.

us to easily test and iterate on different design options before physically constructing them, saving time and resources in the construction phase.

Our research aims to contribute to the field of architecture and engineering by exploring a novel approach to constructing compression-based structures using holographic building techniques and computational tools. The goal is to overcome the limitations of traditional building techniques and expand the possibilities for complex and innovative architectural designs. By using holographic projection during the assembly process, we can achieve greater precision in alignment and weight distribution, leading to greater stability and structural integrity. Additionally, by simulating the structures in a virtual environment using computational tools, we can test and iterate on different design options before physically constructing them, saving time and resources in the construction phase.

Through our research, we hope to provide insights into the benefits and limitations of holographic building techniques and computational tools in constructing complex compression-based structures. We aim to address the challenges posed by extreme cantilevers and arched spans, and explore the possibilities for new and innovative architectural designs. Ultimately, our research has the potential to revolutionize the way that compression-based structures are constructed and contribute to the advancement of the field of architecture and engineering. In the following sections, we will present our methodology and results in detail, and discuss the implications of our findings for the broader field.

2. Background

The construction of compression-based stacking structures has been an essential part of architecture and engineering for centuries, with arches and cantilevers being some of the most iconic examples of these structures. However, building these types of structures without support or glue can be challenging, and traditional building techniques often rely on these materials to keep components together. Recent advancements in technology, such as computational tools and holographic building techniques, have opened up new avenues for the construction of complex compression-based structures. In this chapter, we will provide a background on compression-based structures, the challenges involved in their construction, and the technologies that have been developed to overcome these challenges.

2.1. Traditional Building Techniques for Compression-Based Structures

Compression-based structures such as arches and cantilevers have been used in architecture and engineering for centuries. These structures rely on the principle of compression to support loads, which means that the weight of the structure is distributed along its length, rather than being concentrated at specific points[3]. However, building these structures can be challenging, particularly when dealing with extreme cantilevers or arched spans.

Traditional building techniques for compression-based structures often involve using glue or fasteners to hold the components together[4]. For example, in the construction of arches, the stones or bricks are laid in a specific pattern, with the weight of each stone or brick distributed to the adjacent ones. Mortar is then used to fill the gaps between the stones, providing additional stability and preventing the stones from moving.

In the case of cantilevers, traditional building techniques often involve using braces or supports to hold the structure in place while it is being constructed. This is necessary to ensure that the weight of the cantilever is distributed evenly and that it does not collapse under its own weight. Once the structure is complete, the braces or supports are removed, and the cantilever is able to support itself[5].

While these traditional building techniques have been used successfully for many years, they have limitations when it comes to constructing complex compression-based structures. Constructing these structures without support can be a significant challenge due to the need for precise alignment and careful weight distribution.

As a result, new building techniques have emerged in recent years that offer alternative approaches to constructing compression-based structures. One such approach is the use of holographic building techniques, which we will explore in more detail in the following sections.

2.2. Limitations of Traditional Building Techniques for Compression-Based Structures

Despite the long history of compression-based structures, traditional building techniques have several limitations that can make construction difficult, particularly for structures with extreme cantilevers or arched spans. One significant challenge is the need for precise alignment of each component. Even slight deviations from the intended position can lead to structural instability and collapse. This need for precise alignment can be particularly challenging for structures with complex geometries, which can be difficult to measure and align accurately.

Another limitation of traditional techniques is the need for additional support materials, such as scaffolding or bracing. These materials can be costly and time-consuming to install, particularly for large or complex structures. Additionally, the use of these materials can limit the design possibilities, as they can obstruct access to certain areas or limit the range of possible component configurations.

Glue or fasteners are commonly used in traditional building techniques to keep components together. However, the use of these materials can be impractical or impossible for certain types of compression-based structures[6]. Also, traditional building techniques can be limited in their ability to accommodate complex geometries. Structures with complex geometries, such as those with curved or irregular shapes, can be difficult to construct using traditional techniques, particularly when dealing with extreme cantilevers or arched spans. This limitation can limit the range of possible designs and limit the creativity of architects and engineers.

These limitations have led to the development of new and innovative building techniques, such as holographic building techniques, that offer potential solutions to these challenges. Holographic building techniques offer a promising solution to the challenges and limitations of traditional building techniques for compression-based structures. By projecting virtual geometry during the assembly process, holographic techniques allow for more precise alignment and weight distribution, leading to greater stability and structural integrity. This approach also eliminates the need for physical measurements, support, or alignment materials[7].

Overall, holographic building techniques offer a promising solution to the challenges and limitations of traditional building techniques for compression-based structures. By allowing for more precise alignment and weight distribution, holographic techniques can lead to greater stability and structural integrity, making it possible to construct more complex and innovative architectural designs. In the next section, we will present our approach to using holographic building techniques in the construction of compression-based structures with extreme cantilevers and arched spans.

2.3. Holographic Building Techniques as a Solution

Holographic building techniques have emerged as a promising solution to the challenges and limitations of traditional building techniques for compression-based structures. These techniques utilize virtual reality and augmented reality to project holographic images of the structure's geometry during the assembly process[11]. This enables builders to visualize the final structure before its construction, to identify any potential issues, and to test different design options virtually, reducing errors and saving time and resources in the construction phase.

One of the primary advantages of holographic building techniques is the ability to achieve greater precision in alignment and weight distribution, which is crucial for compression-based structures. With traditional building techniques, precise alignment and weight distribution can be difficult to achieve, leading to instability and potential collapse of the structure. Holographic building techniques eliminate

the need for manual measurements and alignment, allowing builders to achieve greater accuracy in the assembly process[8].

Furthermore, holographic building techniques can also reduce the use of materials and resources in the construction phase. With traditional building techniques, builders may need to use additional support or alignment materials, adding to the overall cost and complexity of the construction process. Holographic building techniques eliminate the need for additional materials, resulting in more cost-effective and efficient construction.

2.4. Current State of Field

Over the past few years, construction techniques that use holographic technology to project a virtual model of a structure onto the construction site have emerged, providing new opportunities for building compression-based structures. This approach eliminates the need for physical measurement, support, or alignment materials, resulting in a significant reduction in construction time and cost. An instance of such an approach is found in the Hyphae House and the Paperless Worksite[9], where researchers employed augmented reality on smartphones to construct complex structures without using CNC technology. Despite some placement issues with the blocks, the technology exhibited potential as a construction and visualization method.

Another example of this holographic building technique is the Allbrick Feature Wall[10], where researchers worked with All Brick and the University of Tasmania to create a small feature wall using an interactive mixed reality model that displayed the precise location of each brick. By eliminating the need for templates, drawings, or physical measurements, the estimated 2-week build time was significantly reduced to only 6.5 hours of bricklaying. Holographic instructions were developed by sorting bricks by height and showing one course at a time, with further improvement by showing only an outline of the top face of each brick as a virtual boundary during placement. The HoloLens's precision was well within the tolerances of general construction, as confirmed by a lidar scan of the project.

Despite these advances, there are still challenges in the compression-based structures field. Understanding and researching the structures' behavior under different loads and conditions, particularly those with cantilevers or arched spans, is critical.

3. Methodology

In this chapter, we will detail the methodology used to approach the block stacking problem. We begin by describing the parameterization of the mathematical problem using computational tools, which involves the creation of a dynamic parametric model and subsequent physical model to test its accuracy. We will then move on to discuss three specific studies undertaken within this framework, including the arced cantilever of X-shaped components, arched structures, and limits of height using limited materials. Finally, we will examine the utilization of holographic projection of geometry during the assembly process, providing insights into the advantages and limitations of this approach.

3.1. Parameterization of the mathematical problem using computational tools

The block stacking problem is a well-known paradox in statics that has been extensively studied over the years. The objective of this problem is to stack blocks along the edge of a table in a way that keeps the center of gravity of the assembly on or within the non-overhang side of the table.(Figure 1.). In order to use this problem as a design input, we have created a parametric model of the problem using linear elements.

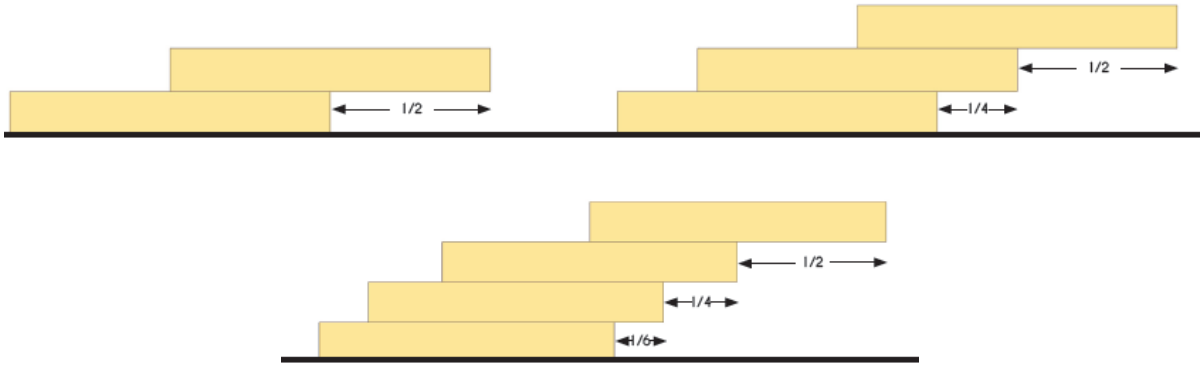


Figure 1. Block Stacking Problem Diagram

This parametric model allows us to explore the relationship between the number of elements and the cantilever distance in a dynamic and interactive way. We have color-coded the model to indicate the cantilever distance, with red indicating the maximum distance and green indicating the minimum distance. This dynamic model has provided us with valuable insights into the behavior of the system and has helped us to identify potential design improvements.

With the information gleaned from the dynamic model, we proceeded to build a physical model of the block stacking problem (Figure 2.). The physical model consists of 4.5-inch long wooden pieces stacked in a manner similar to the parametric model. However, the vertical distance between the wooden pieces in the physical model is greater than 4.5 inches to accommodate supporting pieces.

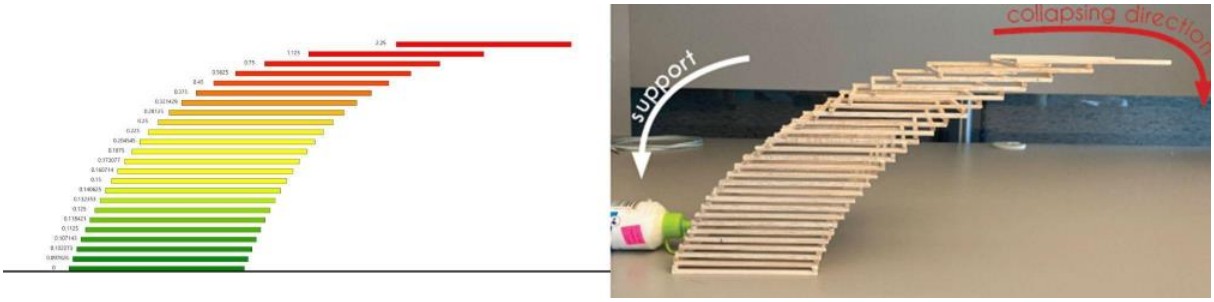


Figure 2. First Iteration Parametric Model & Physical Model

In our initial attempt to build the physical model, we found that it collapsed without any support. This led us to come up with a new iteration of the design. We decided to reduce the length of the wooden pieces as we stacked them higher, as this would provide us with a stronger chance of achieving a self-supporting structure. Thanks to the parametric nature of our model, it was relatively easy to come up with these types of variations and explore their impact on the system.

Since the parametric model is created with parameters, it was easy to come up with variations to improve the physical model. For instance, by reducing the length of the material from 4.5 inches to 2.7 inches, we were able to create a physical model that stands on its own, step by step (Figure 3.). This process allowed us to fine-tune the physical model until we achieved the desired outcome. In contrast to the physical model, the digital model required the addition of supporting lateral wood pieces in every space, due to the lack of lateral stability in the stacking direction. This was necessary to prevent the pieces from falling over immediately, as the digital model only tested the stacking direction from bottom to top. Thus, this modification added an extra level of complexity to the models, and the entire process of creating both the physical models took approximately 1.5 working days, due to the precision required

in the small shifting distances.

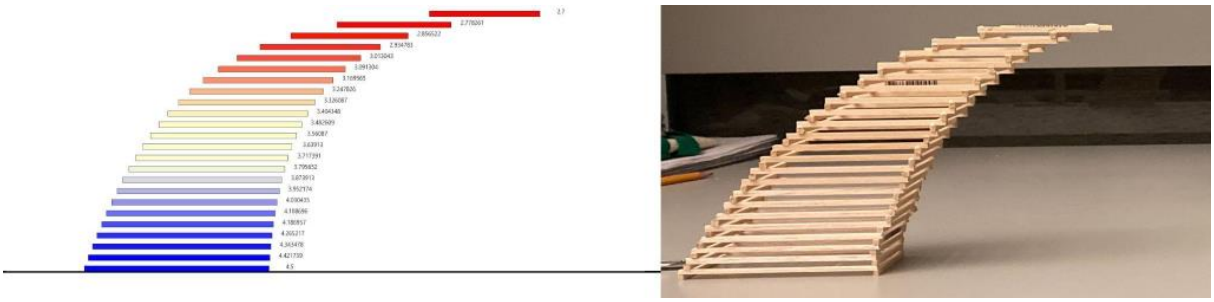


Figure 3. First Iteration Parametric Model & Physical Model

In summary, we utilized a parametric model to analyze the block stacking problem, which enabled us to visualize the problem dynamically and generate insights that helped us create a self-supporting physical model. Through this process, we were able to gain a deeper understanding of the block stacking problem and develop an effective solution.

3.2. Three studies: arced cantilever of X-shaped components, arched structures, and limits of height using limited materials

After conducting experiments with physical models, we decided to prototype different variations of the stacking strategy. Our first prototype aimed to construct an arched cantilever surface with X-shaped stacking components for a portion of the entire structure (Figure 4.). The X shape allowed us to change the stacking angle to construct the portion of the surface more precisely. However, the prototype resulted in a collapsed structure. The angled components created a shear force that shifted the center of gravity, causing the structure to collapse. From this experiment, we learned two important things. First, X-shaped components with different angles can lead to a shift in the center of gravity, resulting in structural collapse. Second, there was no support for the cantilever as it grew with less and less support underneath. These outcomes helped us improve the structural capabilities of our next prototypes.

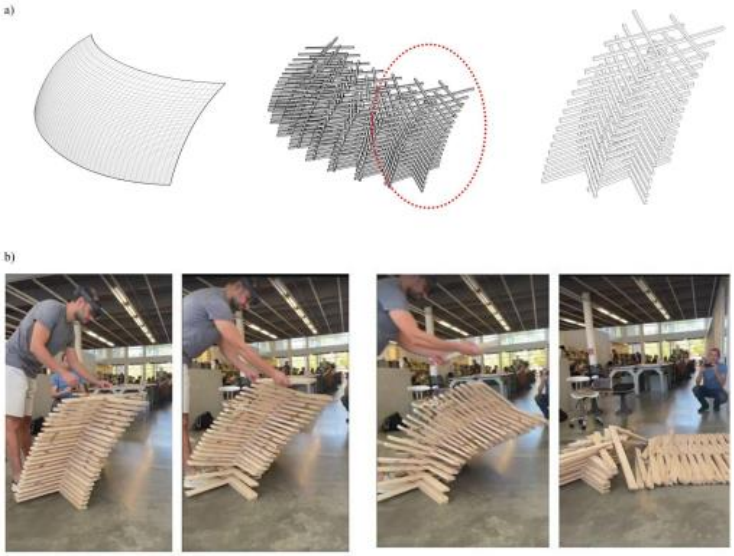


Figure 4. (a) Cantilever Surface and its portion with X shaped Components, (b) Collapsed prototype

Learning from the first prototype, our second prototype utilized 90 degree rotating stacking components from our physical models. We started by decreasing the total height of the prototype, allowing us to use

more wood pieces in opposite directions to support the initial cantilevering piece. We started with a stool-scale stacking, creating a stool by stacking pieces on top of each other. To enhance the stool's structural capacity, we had two units that were similar to each other except for one being mirrored and shrunken down in its width to create an interlocking connection with the initial unit. Following the same idea, we created a bench using a similar procedure, designed to have its initial unit interlocked with the supporting unit of the bench. This enabled us to create both pieces in a way that they support each other (stool to bench). When weight is applied to these furniture pieces, the stacking system locks itself in place, similar to a compression-based structure (Figure 5.).



Figure 5. Stool and bench formation

The success of this prototype encouraged us to proceed with a larger installation. However, we had two important constraints to consider: the number of wood pieces and the length of wood pieces. While we had a parametric model that generated new lengths, we decided to use the wood pieces that were available in our inventory. We sorted the wood pieces from long to short, from the ground up, using a parametric model that took into account the available wood pieces. By doing so, we aimed to use different lengths to create structural stability where the installation touched the ground (Figure 6.).

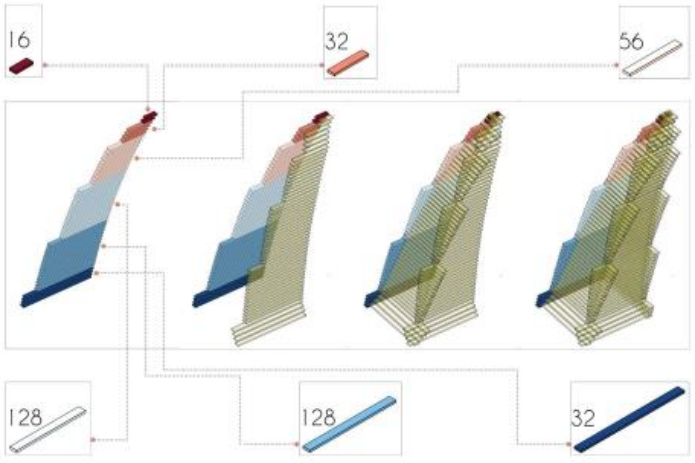


Figure 6. Material Inventory and Distribution

Unlike the second prototype, both units supported the initial unit, created as the same and then shifted to create an interlocking connection. In the end, we successfully built the installation with the available material we had (Figure 7.). The installation demonstrated the potential of the stacking strategy to create a stable structure, even with limited materials. It also highlighted the importance of considering the availability and characteristics of the materials when designing a structure, as well as the need for careful planning and execution to ensure the structural stability of the final product.

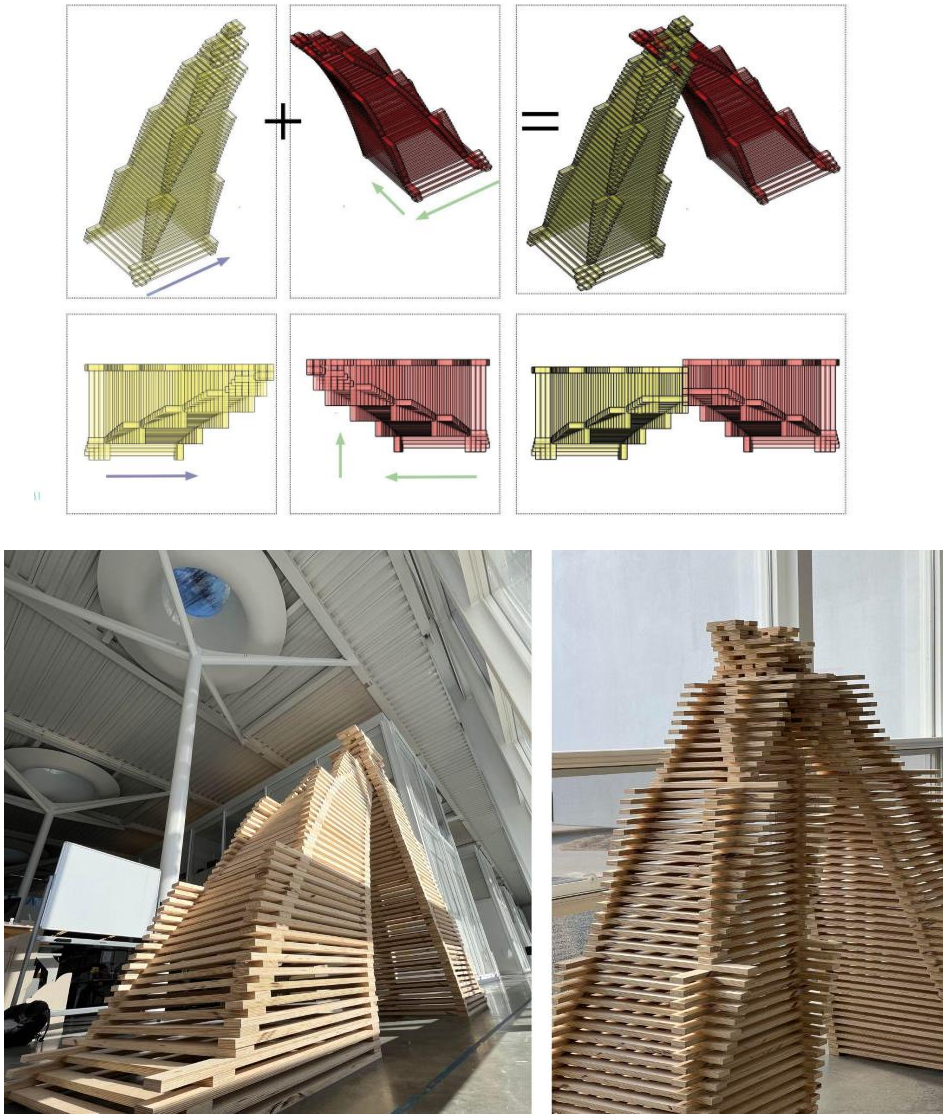


Figure 7. Installation Formation & Finished Prototype

3.3. Utilization of holographic projection of geometry during the assembly process

For all three prototypes that the researchers attempted to build, holographic projection techniques were used to project the computational model onto the site location. This allowed the researchers to perform construction without relying on physical measurements or 2D drawings, which was particularly important for wood stacking due to the small distance on each stacking layer. A straightforward construction technique was followed. First, the model was prepared as a parametric model and visualized with an Augmented Reality headset. This preparation required time to set up the most efficient adjustments. The researchers started by color-coding each wood piece based on its height, but this

created too many colors to follow. They decided to go with only two colors for the stacking, with level 0 in orange and level 1 in blue. This alternating color rule was followed to put the wood pieces. The parameters were set up in a way that this sequence could be controlled by an external phone that had 'Fologram' and/or HoloLens. All this setup was done in grasshopper.

Secondly, a QR code was generated to align the digital model to the physical construction site. The researchers taped the printed QR code on the area where they wanted to build so that they could restart the device and start again where they left off if they encountered technical issues such as running out of battery, losing the model, or HoloLens stopped working, etc. This setup was fundamental for each of the three prototypes, although there were some differences and additions in different phases.

For instance, while prototyping the arced surface geometry with X-shaped components, the researchers used a gravity simulation to detect where the structure would collapse before building the whole portion of it. Kangaroo was used in grasshopper to perform the simulation, which had promising results (Figure 8.).

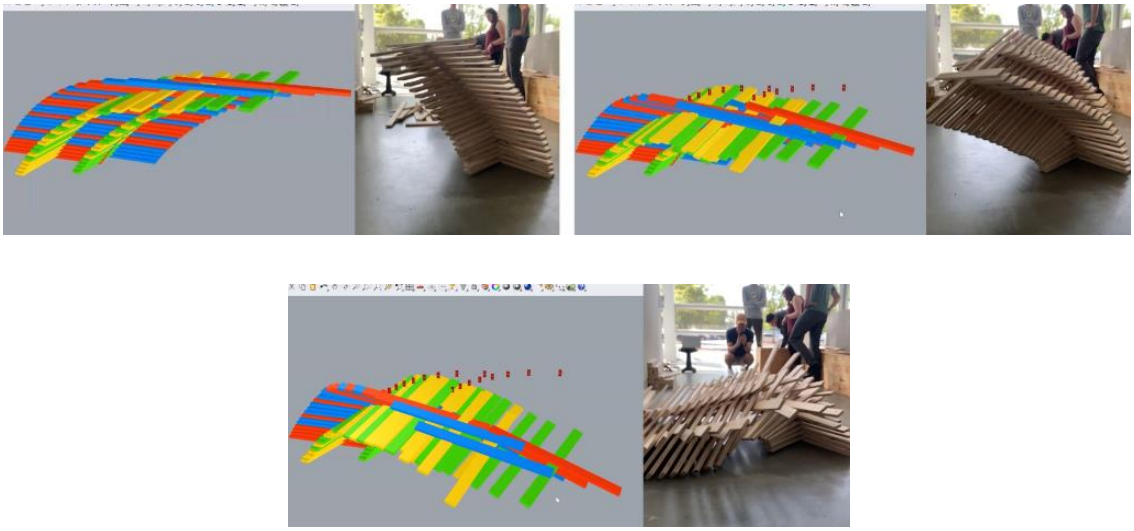


Figure 8. Gravity Simulation that shows the collapse digitally

However, the inefficiency in terms of the time it took to run (over an hour) made the researchers decide not to stick to the simulation. In this prototype, holographic projection was used in a shaded view (Figure 9.).



Figure 9. Shaded holographic projection

But the shaded view created problems in that the researchers could not track the real wood piece when they had HoloLens due to the projection type. Therefore, they switched the projection method from shading to wireframe, which worked better because they could easily align the edges of the wood pieces on the wireframe view. It also avoided any freezing due to heavier geometries that were generated by shaded views. So for the second "Arched structures and their performance" and third "Height limitations of limited materials in block stacking" prototypes, wireframe projection was used (Figure 10.)

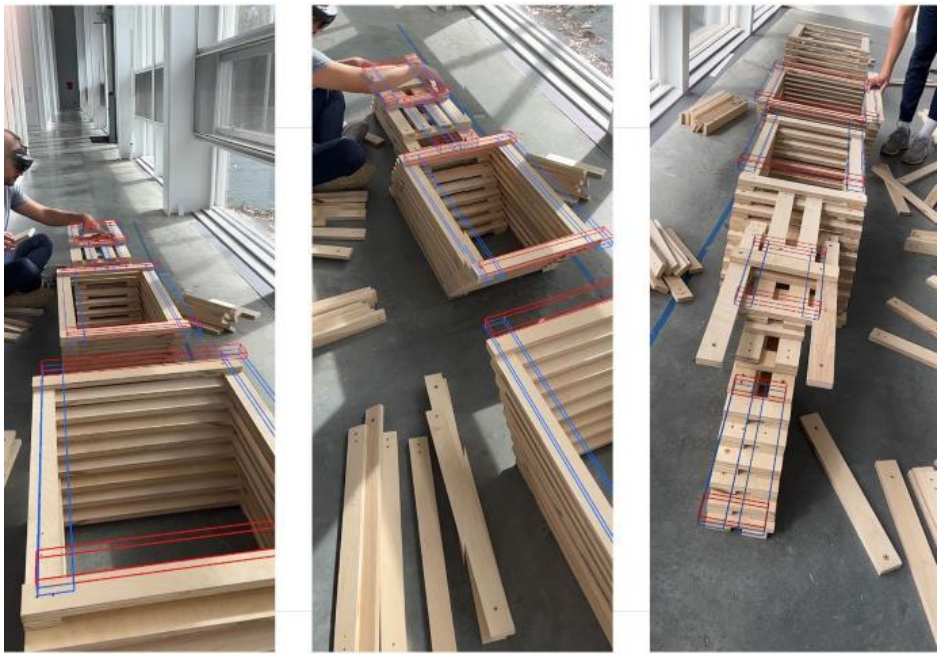


Figure 10. Shaded holographic projection

Holographic projection was used for the construction of all these experiments due to the dynamics of the project that the researchers were working on. It helped them locate the wood pieces in exact locations, even though they shifted slightly on each layer. This was crucial because this notion of movement on each stacking layer enabled the researchers to create these self-standing structures by controlling the center of gravity. Any error while placing them might cause unexpected collapses during the construction phase, but none were encountered. By using holographic projection, the structural design performed in a way that the researchers reached their goal without using glue, fasteners, or any other connection detail.

4. Results

The implementation of computational tools and holographic projection has resulted in a number of significant benefits for the design and construction process. Perhaps most notably, these techniques have enabled the creation of precise and highly constructable design options. By using these tools, we are able to create highly accurate digital models that can be easily translated into physical structures. This has allowed for an unprecedented level of precision in the design and construction process, greatly reducing the likelihood of errors or inefficiencies.

Also, the use of computational tools and holographic projection has also eliminated the need for physical measurements, support, or alignment materials. This has resulted in significant cost savings and reduced waste, as well as a more streamlined and efficient construction process. With these techniques, designers and builders can create complex structures with ease, without the need for extensive support or alignment structures.

Overall, the implementation of computational tools and holographic projection has greatly improved the efficiency, accuracy, and sustainability of the design and construction process. With these tools, designers and builders can create highly precise and constructable designs, while also reducing costs and waste. As the technology continues to develop, it is likely that we will see even more innovative and impactful uses of these techniques in the future.

5.Discussion

The field of architecture has been revolutionized by the use of computational design tools that allow architects to explore complex forms that were once impossible to create, thereby expanding the design solution space. However, traditional design annotation methods can be inefficient, especially in construction environments with limited fabrication means and skilled laborers. To address these challenges, the recent use of holographic projection technology in experimental architectural projects has shown promising results. By projecting computationally generated geometries onto the field of vision using wearable devices or smartphones, architects can create an immersive environment for implementers. Interactive holography provides architects with the ability to translate design intentions into intelligent instructions instead of static drawings, offering a significant opportunity to reduce construction complexity and potentially increase precision[11].

Nonetheless, there may be limitations to the size and complexity of structures that can be constructed using holographic projection-based techniques. While the method has shown promise in constructing small-scale prototypes, it may not be feasible for larger or more complex structures such as bridges or skyscrapers. The construction of these types of structures would require more advanced and robust holographic projection systems, as well as extensive testing and validation to ensure that they are safe and reliable. Another limitation is that the current technology may not be accessible or affordable for all builders and architects. The cost of developing and implementing holographic projection-based systems may be prohibitive for smaller firms or individual builders, limiting the potential impact of this technology on the broader construction industry.

Our work was conducted only on interiors, meaning the structures were not exposed to environmental conditions such as wind, rain, snow, and others. It is crucial to address this limitation in future research by reconsidering the connection details between wood stacks and other materials used in construction. Additionally, the usability of this methodology for real-life structures such as bridges needs to be tested and verified in real-world applications. While holographic-assisted assembly is a promising technology, it requires further development and testing to ensure its effectiveness and reliability in real-world applications.

6.Conclusion

Holographic projection technology has the potential to revolutionize the construction industry by providing a new way of visualizing and planning construction projects. The ability to create 3D holographic models of building designs allows architects, engineers, and builders to better understand the structure of a building before it is constructed, making the construction process more efficient and cost-effective.

Our project aimed to explore the potential of holographic projection technology in the construction industry through the development of a prototype holographic projection system. We used a combination of hardware and software components to create a system capable of projecting 3D holographic models onto a physical space. Our methodology involved testing and refining various components of the system, such as the projector and the software used to create the 3D models. We also conducted user testing with architects and engineers to gather feedback and improve the usability of the system.

While our project was successful in creating a functional holographic projection system, there are still limitations and challenges that need to be addressed. One limitation is that our work was conducted only

on interiors, meaning the structures weren't exposed to environmental conditions such as wind, rain, and snow. Future research could consider the connection details between wood stacks in outdoor settings to ensure the reliability of this methodology in different environmental conditions. Another limitation is the usability of this methodology for real-life structures such as a bridge. Despite the strength and reliability of the methodology, this technique of building should be tested and verified outside with real use, which could create new challenges and improvements in the existing technique. Additionally, the current cost of holographic projection technology is relatively high, which may limit its adoption in the construction industry. Further research is needed to explore cost-effective solutions and how to integrate holographic projection technology into existing construction workflows.

Looking forward, there are several possible research directions that could help to address these limitations and improve the potential of holographic projection technology in the construction industry. For example, research could focus on developing more affordable holographic projection systems, improving the accuracy and resolution of holographic models, and exploring how holographic projection technology can be integrated into existing construction workflows to enhance collaboration and efficiency.

References

[1] L. Lok, A. Samaniego, and L. Spencer, 'Timber de-standardized', in *Proceedings of the 41th Annual Conference of the Association for Computer Aided Design in Architecture, ACADIA, 2021.*

[2] P. B. Johnson, 'Leaning Tower of Lire', *American Journal of Physics*, vol. 23, no. 4, pp. 240–240, 1955.

[3] Sakarovitch, J 2003 'Stereotomy, a multifaceted technique', *Proceedings of the First International Congress on Construction History*, Madrid

[4] S. Parascho, I. X. Han, A. Beghini, M. Miki, S. Walker, E. P. G. Bruun, and S. Adriaenssens, "LightVault: A Design and Robotic Fabrication Method for Complex Masonry Structures," in *Advances in Architectural Geometry 2020*, O. Baverel, C. Douche, R. Mesnil, C. Mueller, H. Pottmann, and T. Tachi, Eds. Paris: Presses des Ponts, 2021, pp. 350-375.

[5] D. Wendland, 'Traditional Vault Construction Without Formwork: Masonry Pattern and Vault Shape in the Historical Technical Literature and in Experimental Studies', *International Journal of Architectural Heritage, vol. 1, no. 4, pp. 311–365, 2007.*

[6] P. Foraboschi, "Masonry does not limit itself to only one structural material: Interlocked masonry versus cohesive masonry," *Journal of Building Engineering*, vol. 26, p. 100831, 2019.

[7] H. Nassereddine, A. S. Hanna, D. Veeramani, and W. Lotfallah, "Augmented reality in the construction industry: Use-cases, benefits, obstacles, and future trends," *Frontiers in Built Environment, vol. 8, 2022*.

[8] D. Mitterberger, K. Dörfler, T. Sandy, F. Salveridou, M. Hutter, F. Gramazio, and M. Kohler, "Augmented bricklaying," *Construction Robotics, vol. 4, no. 3-4, pp. 151–161, 2020.*

[9] V. Sardenberg, A. L. Rolim, D. Digiandomenico, A. Figueiredo, R. R. Aguiar, and C. Duarte, "The hyphae house and the paperless worksite," *Blucher Design Proceedings, 2021.*

[10] G. Jahn, C. Newnham, N. Berg, M. Iraheta, and J. Wells, 'Holographic Construction', 12 2019

[11] S. Liu, Z. Wei, and S. Wang, "On-site Holographic building construction: A case study of aurora," *CAADRIA proceedings, 2022.*

Proceedings of the IASS Annual Symposium 2023
Integration of Design and Fabrication
10–14 July 2023, Melbourne, Australia
Y.M. Xie, J. Burry, T.U. Lee and J. Ma (eds.)

Fabrication methods for topology-optimized massive glass structures

Faidra OIKONOMOPOULOU*, Menandros IOANNIDIS[a], Anna Maria KONIARI[a], Telesilla BRISTOGIANNI[a]

[*] Delft University of Technology, Faculty of Architecture + The Built Environment
f.oikonomopoulou@tudelft.nl

[a] Delft University of Technology, Faculty of Architecture + The Built Environment

Abstract

Recent research at TU Delft has highlighted the potential of using structural Topology Optimization (TO) for designing large monolithic cast glass structures of maximized stiffness with minimal mass. The mass efficiency of these structures results in considerably shorter annealing times and, consequently in improved manufacturability in terms of time, energy and cost efficiency. Nonetheless, the geometrical complexity and customization of the resulting forms renders them challenging in terms of fabrication. Exploring the manufacturability of such intricate glass structures, in this paper we discuss the different possible fabrication methods for three-dimensional glass structures of complex and customized geometries, via a review of existing literature, experimental work and prototyping. Specifically, with the aim of addressing all possible manufacturing solutions, we look into the following fabrication methods: (i) casting in disposable moulds; (ii) waterjet cutting and lamination of float glass panes and; (iii) additive manufacturing of glass. We assess these methods based on a set of criteria linked to the structural performance, visual quality, fabrication limitations and sustainability. Accordingly, we discuss the potential, challenges and practical limitations of each fabrication method for real-world applications of TO glass structures. Subsequently, we propose the integration of alternative constraints into the TO formulation, so that customized TO tools that better reflect each fabrication method can be created.

Keywords: topology optimization, glass fabrication methods, construction techniques, customized geometry, cast glass, glass structures, shape complexity, disposable moulds

1. Introduction

Ongoing research at TU Delft [1-3] has highlighted the potential of using structural topology optimization (TO) for the design of monolithic, three-dimensional cast glass structures of complex and customized geometries for architectural and structural applications. By maximizing the stiffness while maintaining minimal mass, the design of monolithic, load-bearing glass structures of substantial dimensions can be achieved with considerably shorter annealing times; the castings of the glass mirror blanks of the giant telescopes are a characteristic such example (fig.1, left) [4]. Promising topology optimized structural glass applications include free-form glass shells and nodes [3], glass slabs, bridges [2] and columns (fig.1). So far, the research has focused on the development of a TO formulation for cast glass structural components that allows for an asymmetric stress behaviour and incorporates constraints to ensure feasible annealing times [1] and, in turn, improved manufacturability in terms of time, energy and cost efficiency. Still, there has been little exploration on the fabrication methods of the resulting complex and customized shapes. Thus, this paper reviews the different possible fabrication

Copyright © 2023 by Faidra OIKONOMOPOULOU, Menandros IOANNIDIS, Anna Maria KONIARI and Telesilla BRISTOGIANNI. Published in the Proceedings of the IASS Annual Symposium 2023 with permission.

methods for three-dimensional glass structures of customized, complex geometries generated by TO. In specific, with the aim of addressing all possible manufacturing solutions we intentionally depart from cast glass as the only possible expression of such geometrically complex forms, and we look as well into alternative fabrication methods (fig. 2). Hence, we explore: (i) casting in disposable moulds; (ii) waterjet cutting and lamination of float glass panes and; (iii) additive manufacturing of glass.

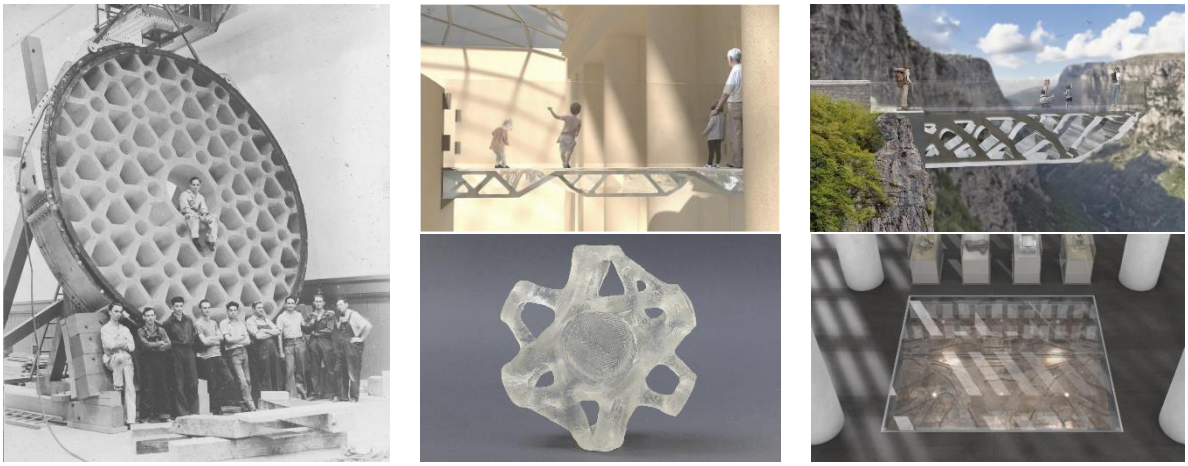


Figure 1. From left clockwise: Cast glass mirror blank of the Hale-1 telescope following a honeycomb structure (image credits: The Rakow Library, Corning Museum of Glass). Impressions of TO cast glass bridges (image credits: A.M. Koniari and M. Ioannidis) and floor (image credits: I. M. Stefanaki), and prototype of a TO cast glass node (image credits: W. Damen).

2. Methodology

To assess the aforementioned methods, we first establish a set of criteria linked to the structural performance, visual quality and fabrication limitations; towards sustainability, the waste generation and recyclability of the glass components are also addressed. Accordingly, we discuss the potential, challenges and limitations of each method based on literature review and on our main observations from experimental and prototyping work. Towards the creation of customized TO tools that better reflect each fabrication method, we propose the integration of alternative constraints into the TO formulation.



Figure 2: From left to right: Examples of free-form shapes in glass using (i) casting in disposable moulds (sculpture by Karen LaMonte), (ii) waterjet cutting and lamination of float glass panes at a prototype made in TU Delft and (iii) additive manufacturing of glass (image by C. Inamura)

3. Assessment criteria

With the aim of generating customized, complex geometries in glass, the three different fabrication methods are assessed on aspects related to the (i) structural performance, (ii) optical performance, (iii) fabrication limitations and (iv) sustainability. In specific:

(i) structural performance is evaluated in terms of the inherent strength and the integrated redundancy of the resulting glass components/structure;

(ii) optical performance concerns both the resulting transparency, as well as the finishing surface quality of the components (fig.3);

(iii) fabrication limitations are particularly linked to shape and size limitations of the chosen manufacturing methods, need for post processing and ease of fabrication;

(iv) sustainability regards the waste generation during fabrication and the recyclability of the resulting components.

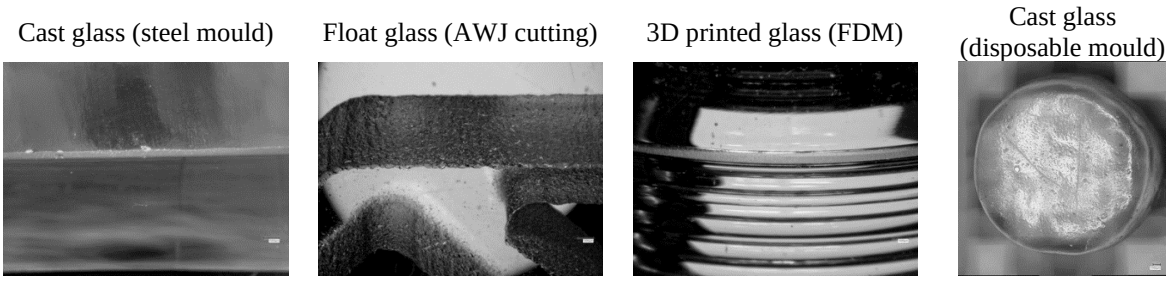


Figure 3: Microscope photos of the finishing surface quality of the different fabrication methods.

As the different assessment criteria are interconnected, they can directly impact each other. For example, the surface finish quality can influence the strength of the glass component, as well as the need for post-processing. Given the novel application of these fabrication methods for structural applications, there are limited if any comparable quantitative data in the forenamed aspects, which can lead to misleading observations. Thus, a qualitative assessment is made as more representative.

4. Fabrication methods

4.1. Casting in disposable moulds

Casting enables the creation of virtually any shape and size in glass. Nonetheless, currently in architecture, structural cast glass components are typically limited to solid blocks, similar in size to standard terracotta bricks [5]. This limited size is mainly due to the excessively lengthy annealing time required in massive glass pieces, which can span up to multiple months [4], and can subsequently result in prohibitive energy and manufacturing costs. The component's geometry and selected glass composition are the most influential factors of the annealing time. Essentially, the higher the thermal expansion coefficient of glass and/or the larger the cross-sectional thickness of the component, the exponentially longer the annealing time required. The optimization of the stiffness-to-weight ratio of cast glass components, e.g. via structural TO, and the use of glass compositions of lower thermal expansion coefficient (e.g. borosilicate glass) can greatly reduce the annealing time and subsequently, allow for larger overall dimensions.

For customized and geometrically complex components such as the one resulting using TO, disposable moulds and kiln-casting are preferred over permanent metal moulds and hot-pouring, as they are considerably cheaper and allow for a significantly higher freedom in shape[1]. Prototyping work at TU Delft has pointed towards two alternative disposable mould fabrication methods for kiln-casting: (i) silica-plaster (e.g. Crystal Cast) investment moulds using a was positive model[2] of the desired geometry that is steamed out (lost wax-technique), as shown in fig.4, and (ii) 3D-printed sand moulds (fig.6). The former, typically used in intricate-shaped glass art castings, are in principle laborious and yield

[1] Considerably more expensive multi-component steel moulds can be used for the casting of complex geometries in glass; nonetheless, such moulds cannot incorporate undercuts.
[2] For highly intricate shapes, the wax positive model can be produced using 3D-printing or sintering of wax. Research in both methods at TU Delft suggests that sintering produces more refined, smooth textures.

compromised dimensional accuracy. An alternative offering higher accuracy, yet also resulting in considerably higher manufacturing costs, is milled alumina-silica fibre ceramic moulds, such as the ones employed in the castings of the giant mirror blanks (see fig.5) [6]. For architectural applications, 3D-printed sand moulds are considered more suitable, due to their low cost, quick production, scalability and high accuracy (up to ± 0.1 mm, defined by the grain size of the sand) [6]. Previous and current experimental work at TU Delft, has shown that 3D-printed sand moulds using inorganic binders are the most promising option for kiln-cast glass components [6]. 3D-printed sand moulds can currently be produced up to 4m x 2m x 1m in dimensions by *Voxeljet printer* VX4000; nonetheless, larger, multi-piece moulds that interlock together can exceed these dimensions.



Figure 4: Left: Process of producing a silica-plaster mould process employing a wax positive. Right: Wax model (top) and resulting cast component (right). Image credits: W. Damen





Figure 5: Milled alumina-silica fibre ceramic mould (left) for the casting of the Giant Magellan Telescope mirror blanks and segment of glass produced in such a mould (right)

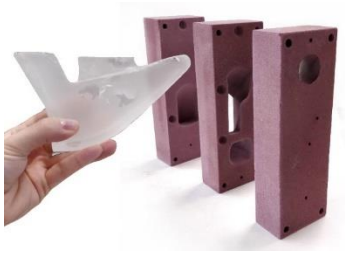


Figure 6: 3D-printed sand mould and produced glass component

4.1.1. Structural performance

Similarly to float glass panes, cast glass displays isotropic material properties. Glass's brittle failure is typically triggered by inherent flaws. Massive cast glass pieces are prone to the inverse scale effect: the larger the component, the higher the probability of critical flaws within it, thus the lowest its probabilistic strength [7]. In addition, the lack of a large-scale, automated and controlled production and of quality control standards for cast glass, contribute to an increased occurrence of defects compared to the fully-automated and strictly controlled float glass production [5, 8, 9]. The lack of sufficient strength data and of inherent redundancy in the structure, result to a decreased overall strength of cast glass compared to float and enforce the use of increased safety factors. Thermal tempering that can increase glass's tensile strength, is not advised for volumetric glass components, particularly of ones of intricate geometry, due to their bulky and uneven cross-section[3]. All the above, mandate a significant increase in material use when designing with cast glass compared to float.

[3] In thermal tempering of (float) glass, the material is first heat up and then rapidly cooled down, resulting in the outer surfaces being into compression and the inner surfaces being into tension. In volumetric glass components and/or in perplex cross-sections, tempering in a controlled manner would be extremely challenging, due to the considerably larger temperature deviations between the centre and the surfaces of the glass.

A monolithic glass structure lacks redundancy in case of failure. Possible engineering solutions that allow for redundancy, are the lamination of a float glass layer (if possible in terms of shape), or the segmentation of the structure to enable enhanced redundancy against crack propagation. In this direction, cast glass structures made of interlocking units are a promising solution with inherent redundancy [10]. Finally, initial prototype and experimental work at TU Delft suggests that glass beams with embedded metal reinforcement during casting can have increased ductility, exhibit a warning mechanism prior to ultimate fracture and secure a post-failure load-bearing capacity [11].

4.1.2. Optical performance

The monolithic nature of cast glass allows, in principle, for increased transparency. Nonetheless, the transparency of kiln-cast glass elements is affected by several factors, including the type of glass, firing temperature and annealing schedule, type of mould (fig.3) and coatings applied on it, and post processing. Transparency can be increased if a low-iron glass recipe is used that omits any colouring (e.g. of green tint). Transparency is mainly compromised in the finishing surface quality: grains of the disposable moulds tend to adhere to the glass, resulting in an opaque and rough surface, mandating post-processing, which in turn results in compromised dimensional accuracy and higher manufacturing costs. To achieve a fully transparent and smooth finishing quality of glass cast in disposable moulds, the application of mould coatings is necessary. Previous research at ETH focusing on foundry casting in 3D-printed sand moulds fabricated with inorganic binders and coated with a combination of *Zirkofluid* and graphite-water dispersion yielded promising results [12]. Current experimental work at TU Delft focuses on the further investigation of coatings that can yield a completely smooth and transparent surface quality in kiln-casting[4]. So far, series of kiln-cast prototyping experiments in several annealing schedules using two types of 3D-printed sand moulds (quartz or ceramic sand printed with inorganic binder), sponsored by *ExOne*, and a combination of coatings, sponsored by *Hüttenes-Albertus*, indicate that the combinations with the best finishing quality are (i) molds printed with quartz sand coated with *Arkopal B5* and (ii) molds printed with synthetic (ceramic) sand coated with *Crystal Cast* and *Zirkofluid*® 6672 or 1219 (see fig.7). In specific, kiln-casting experiments at 870˚C at the *TU Delft lab* facilities suggest that direct application of *Zirkofluid* coatings on the mold surface lead to partial adhesion of the sand and coating to the glass (fig.7b). When a substrate layer of *Crystal Cast* is added under the coatings it leads to a better surface quality and no sand consolidation (fig.7d-f). Given the above, 3D-printed molds of a material similar to Crystal Cast could as well be a promising solution.

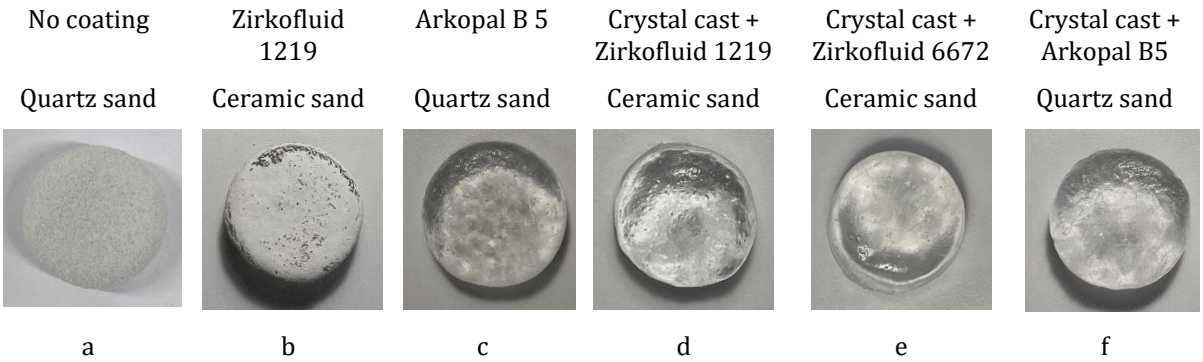


Figure 7: Glass surface of glass specimens kiln-cast at 870˚C in coated 3D printed sand moulds.

4.1.3. Fabrication limitations

The use of disposable moulds allows for great freedom in the shape and size of the cast glass components, as exhibited in existing cast glass art pieces of massive dimensions and/or of highly

[4] Compared to foundry casting, kiln-casting requires a considerably more prolonged heating cycle of the moulds.

intricate shapes [4]. The use of interlocking 3D-printed sand moulds can enable considerably large castings; the potential size of a structure utilizing such moulds has been exhibited in concrete castings, such as the *SMART SLAB* by ETH, where 3D-printed sand moulds were used for the underlying formwork [13]. In essence, the size of the glass casting is confined to the size of the kiln. Even so, custom-made kilns can be built to accommodate large castings, as proved by the castings of the *Giant Magellan Telescope* and of multi-ton glass sculptures by *Roni Horn* [4]. The component's annealing time can be considered the governing factor in limiting the glass component's overall size. Castings of massive cast glass blanks requiring up to 1 year of annealing have been recorded [4], yet such prolonged times would be prohibitive for applications in the built environment. Nonetheless, with the aid of TO, the generation of massive pieces of optimized stiffness-to-mass ratio can be achieved, which in turn can yield feasible annealing times and associated energy costs.

There are limitations in relation to shape though. Shape limitations are greatly linked to the proper annealing of the glass component and to the mould's geometry and strength. For example, abrupt changes in the component's thickness should be avoided as they would result in uneven cooling of the glass. The size and geometry of overhangs, and of very thin voids, should be as well associated with the mould's strength. Furthermore, the use of a mould hinders completely enclosed cavities.

Post-processing, in particular polishing, may be necessary to obtain the desired smooth, glossy finishing surface and to omit dimensional deviations due to the natural shrinkage of glass occurring during cooling [14]. The effect of natural shrinkage can be reduced in some cases by employing spin-casting [4]. Polishing can be challenging in cavities that are not easily accessible by the relevant equipment.

4.1.4. Sustainability

Being monolithic, cast glass can be recycled in a closed-loop. Its recyclability can be compromised, if a sacrificial layer is laminated for safety/redundancy, due to contamination by the lamination foil. The ability to cast directly the desired shape prevents the generation of glass waste. Finally, in the case of 3D-printed sand moulds, their water dissolvable composition enables the remaining sand to be reused.

4.2. Waterjet cutting and bonding of float glass panes

By abrasive waterjet (AWJ) cutting and bonding together multiple float glass layers, freeform, layered 3D glass structures can be made. In this process, three distinct fabrication steps are involved: The float glass production, the waterjet-cutting of the individual glass panes to the desired shape, and finally their bonding or lamination. In specific, AWJ cutting is a subtractive manufacturing method, used for a broad range of materials, including metals, stone and glass; it employs high-pressure waterjets with fine abrasive grains to cut the workpiece material. A computer-controlled head and nozzle with up to 5-axis allow for precise cutting under varying angles and the flow rate and abrasive size can be adjusted for optimal cutting and surface quality of the edge [15]. AWJ cutting of glass panes can lead to rough or non-perpendicular edges (kerf angle, see fig.3), necessitating the post-processing (polishing) of the edge in order to avoid undesirable stress concentrations. Once the individual sheets are AWJ-cut, they should be bonded together. Extensive literature research suggests that industrially fabricated examples using lamination are typically confined to 5-6 layers; one of the largest known multi-layer laminations is the 11-layered *Glass Wippe* by EOC Engineers. Multi-layered structures, such as the horizontally-layered glass sheet sculptures of the 6 m high *Glass Sphinx* (NL) and the 3 m high *Glass Angel* (NL), and the vertically-layered *Laminata House* (NL) opted out of lamination, but also of a conventional adhesive application, as structural glass adhesives are yet to be developed for bonding large surfaces of glass in stacked configurations [16]. Instead adhesive tapes were used for assembling the Glass Angel [17] and

the Glass Sphinx [18]; in *Laminata House*, the individual sheets were cut and pre-adhered on site in sets of 10 using a 2-component silicon compound, then installed in place using a silicone-based sealant.

4.2.1. Structural performance

The structural properties of float glass are well-documented with engineering values provided by several standards (e.g. DIN 18008, EN 16612:2019, NEN 2608:2014, ASTM E1300-00). Owing to the highly automated process and strict quality control in float glass production, float glass presents the highest engineering strength values (for soda-lime glass) among the three discussed fabrication methods. The tensile strength of float glass can be further increased via tempering. The inherent redundancy due to the bonding/lamination of multiple layers and the well-documented, predictable strength of float glass lead to the use of reduced safety factors in this case. The strength can, however, be compromised due to edge flaws introduced by AWJ-cutting; although these can be minimized by post-processing/polishing the edges. It should be noted that layered glass structures are in essence, anisotropic: they present considerably higher strength in parallel to the glass panes than in (long-term) loads perpendicular to the laminate, where, an effective thickness of the laminated or bonded glass should be considered [19].

4.2.2. Optical performance

In principle, float glass panes are of high optical quality. Yet, the transparency of a freeform, layered glass component made of float panes depends on the number and orientation of the glass layers, the overall shape and the viewing angle. In specific, a structure can be perceived as fully transparent when viewed perpendicular to the laminates, and completely opaque when seen parallel to the laminates. Polishing of the cut edges (fig.3) is essential for obtaining a smooth finish surface.

4.2.3. Fabrication limitations

A variety of machinery and materials are used in this method, resulting overall in a complex and costly process. Although individual glass panes can size up to 24m x 3.21m, further size limitations are imposed by the subsequent processing steps. Although AWJ typically has a cutting table of 4m x 2m, it can be customized to accommodate larger sizes. For example, the *yc waterjet* company has produced customized AWJ cutting tables up to 4m x 12m in size for 3-axis AWJ and 3m x 8m for 5-axis AWJ. The total thickness of the layered glass structure is subject to the type of bonding: lamination can be easily achieved for 5-6 layers of glass (each of a max. 25 mm thickness), and has been recorded for up to 11 layers. Beyond this number of layers, a customized adhesive solution should be followed, further adding to the costs and possibly affecting the overall strength.

In terms of shape freedom, a major limitation is that the desired geometry should be made by the bonding of virtually flat elements. In addition, the lamination or bonding process can render challenging the creation of undercuts and voids, as uneven pressure loads can occur during the lamination, which can lead to the eventual failure of the glass. Overall, lamination of multiple layers is challenging and can increase considerably the overall fabrication cost. If the glass sheets are bonded together with an adhesive, its uncontrollable overflow in non-accessible areas can compromise the final visual result. If an adhesive tape is used instead, the tape lines can be visible. Lastly, considerable accumulated dimensional offsets can occur, even with the high accuracy level of float glass thickness and the use of thin tape, as in the example of the *Glass Sphinx* where an accumulated height offset of 4 cm was recorded [20]. Finally, as the AWJ cutting results in a rough surface, subject as well to edge flaws, post-processing of the edge is necessary, which can be challenging in hard-to-access areas of the cut glass piece.

4.2.4. Sustainability

The subtractive nature of AWJ results in considerable glass waste. The discarded cut-out glass pieces, can be recycled by remelting; although this is an energy-intensive process. Once assembled, laminated/ bonded glass components are in principle hard to recycle, due to the difficult separation method and the inevitable contamination of the glass by the interlayers/adhesives.

4.3. Additive manufacturing (AM) of glass

Additive manufacturing (AM) of glass is still in an early stage of development, yet it displays great potential for the fabrication of freeform glass structures. Several AM methods have been explored, but most concern smaller elements [21]. The prevailing AM method for bigger glass elements is *Fused Deposition Modelling* (FDM). FDM involves a continuous filament feeding through a computer-controlled heated nozzle; it is the only method so far with available, yet limited, structural data on glass [22]. Such an AM method for printing silica glass, G3DP, was first developed by *Micron3DP* and *MIT*. G3DP is based on a dual heated chamber concept. The upper part, essentially a kiln cartridge, operates at ~1040°C and pours the molten glass through a nozzle to the desired shape. The object is built within the lower annealing chamber which keeps the glass hot enough so that the next layer of structure adheres to it while the glass can cool down controllably. A second version, G3DP2, allowed for more accurate prints and improvements in speed and printable volume. It includes a digitally integrated thermal control system to accompany the various stages of glass forming and a 4-axis motion control system for flow control, spatial accuracy and precision and faster production rates with continuous deposition of up to 30 kg of molten glass [23]. Up to now, AM of glass has been confined to small-scale objects. The largest in scale project is the *Glass II* [24], which concerns the fabrication of 3m-tall free-standing, pre-stressed hollow glass columns of intricate geometry, each consisting of 15 segments [25].

4.3.1. Structural Performance

AM glass components present anisotropic structural performance. [26] states a 40% difference between the major and minor axis. Loading perpendicular to the plane of the layer (major axis) displays the best performance. More extensive, yet still limited, testing has been performed by [22] in annealed and chemically tempered samples under 3-point bending, suggesting a tensile strength of 51 MPa in the major axis and 41 MPa in minor axis for annealed glass; whereas chemically-strengthened glass samples presented high deviation in the strength, leading to inconclusive results. Due to the small size of the tested samples, the high variation in the resulting values and the use of 3-point instead of 4-point bending tests (which would result in less favourable flexural strength values), in the work of [22] a safety factor of 10 is used. Moreover, the interface between two consecutive layers can display poorer mechanical properties than the rest of the volume. Improper adhesion of the layers can lead to delamination and failure of the sample, as shown by preliminary 3-point bending tests parallel to the layers conducted by [26]. However, the layered structure may be able to stop slow-crack growth. Still, to derive engineering strength values for 3D printed glass components extensive experimental validation remains necessary.

4.3.2. Optical Performance

Similarly to laminated glass components, due to its visible layering, 3D-printed glass using FDM displays directional transparency (see fig.2 and fig.3). In order to achieve the desired, glossy result, the finishing surfaces (top and bottom sides) should be polished using cerium oxide [26].

4.3.3. Fabrication Limitations

3D-printing of glass has a high potential in creating components with complex inner features. Yet, it can only occur within a highly controlled annealing chamber; hence, similarly to cast glass, the glass object is confined to the size of the annealing chamber. Contrary to kiln-casting, two kilns are required in this method, one for the printing cartridge and one for the annealing of the printed object. Currently, the maximum printable area is 320 mm x 320 mm x 350 mm with a flow rate of 5.2 kg/h [22] and a max. capacity of 30 kg of glass [23]. For an element of 10kg in weight, 1 hour is needed for the printing and 8 hours for annealing [25]. Further shape limitations linked to FDM, include overhang limitations which may necessitate supports, and the generation of shapes that can be produced by a continuous thread.

4.3.4. Sustainability

3D-printed glass can be considered a 100% recyclable and waste-free production method.

5. Conclusions

Table 1 provides a qualitative comparison of the different fabrication methods for complex, customized structural cast glass components, such as the ones derived using TO.

Table 1: Qualitative comparison of the different fabrication methods

Criteria		Cast	Waterjet cutting and bonding of float glass	Additive manufacturing
Structural	strength	+ medium	++ high	- low
	redundancy	- no	++ high	- no
Optical	resulting transparency	++ high	+ medium - low	- low
	finishing quality	- medium-low	++ high	+ medium
Fabrication limitations	size freedom	++ high	+ medium	- low
	shape freedom	++ high	+ medium	+ medium
	post-processing	- high	+ medium	++ medium-low
	fabrication cost	- high	+ medium	- high
Sustainability	waste generation	++ low	- high	++ low
	recyclability	++ high	- low	++ high

Waterjet cutting and bonding of float glass presents the best structural performance overall, mainly due to the well-documented and highly controlled properties of float glass, and the inherent redundancy of a multi-layered solution. Adding to the above the possibility of increasing the tensile strength of the components by tempering and the use of reduced safety factors compared to the other two methods, this fabrication method probably yields the most lightweight structure. On the downside, transparency in this case is subject to the directionality of the layers. Moreover, there are considerable limitations in both the size and the shape of the resulting piece. It is also considered the least sustainable solution, as it produces substantial glass waste and the final component cannot be easily recycled back to glass.

Cast glass is the preferred solution in terms of resulting transparency, sustainability, shape and size freedom. The governing restriction size-wise is the annealing time, which, however, can be considerably reduced by an optimized geometry and by choosing a glass composition of low thermal expansion coefficient. An inherent disadvantage is that post-processing of the finishing glass surface is essential, due to the use of disposable moulds for the fabrication of customized components; although, research at both ETH and TU Delft on mould coatings already yields promising results towards obtaining a good surface quality directly in demoulding. In terms of structural performance, cast glass components present lower strength values compared to float. This is attributed to the less controlled casting process and the lack of relevant quality standards, as well as to the inverse scale effect in large glass components. All the above result in the use of increased safety factors, which in turn yield a heavier structure compared to float glass. A monolithic glass structure lacks redundancy, but different engineering approaches, such as segmentation or lamination of a sacrificial layer, could improve the safety of the structure.

Lastly, AM of glass, although still at experimental stage, is perhaps the most sustainable solution as it results in virtually zero waste; it can potentially require the least post-processing as well. Yet, this method results in visible layering of the deposited glass, compromising the overall transparency, presents the lowest structural performance and is subject to multiple fabrication limitations; although some of them, such as limitations in size, can be linked to its infant stage of development.

6. Discussion

Based on the prioritized performance criteria, the most suitable fabrication method can already be pre-selected, as shown in fig.8. Accordingly, to create practical tools that better reflect the needs of the chosen manufacturing method, different adjustments can be incorporated to the TO formulation (fig.8).

Regarding structural performance, the isotropic or anisotropic nature, the risk of defects during the fabrication, as well as compromises in the surface quality can reduce the structural integrity of the final component. Therefore, they largely influence the applied limits for tensile and compressive strength through relevant increased or decreased safety factors, while they also affect the selection of the appropriate material failure criterion in the TO formulation [27, 28].

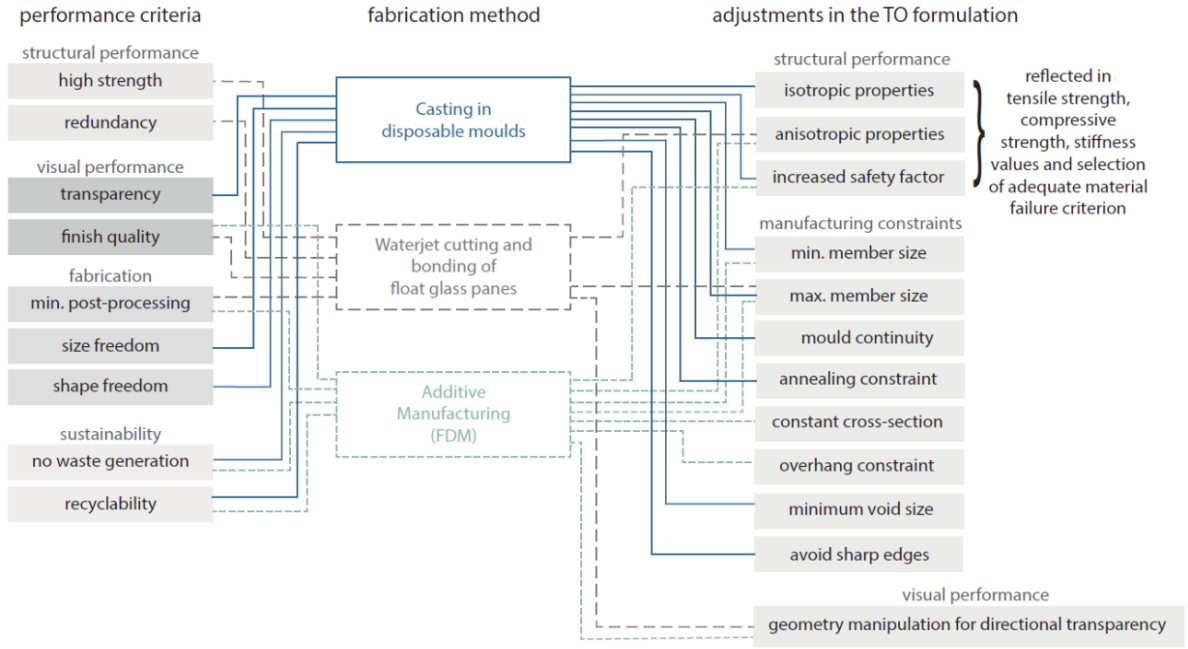


Figure 8: Flowchart showing how the prioritized performance criteria impacts the selection of the most suitable fabrication method, which in turn is reflected in the integration of different constraints in the TO formulation.

Additionally, different practical fabrication-related aspects need to be addressed according to each method. These are related primarily to the size of each member that composes the total complex geometry. Particularly, in the case of 3D printing, the cross section should have a constant dimension that can be created with the available nozzle size, while in waterjet cutting, a minimum member size should be ensured to avoid breakage during the cutting process. In the case of casting, both minimum and maximum member size constraints should be applied. In the latter case, the maximum cross section size should consider both the annealing time limit and the need for an even and smooth gradient of thickness in the geometry [1]. The need for homogeneous mass is also related to the need for elimination of sharp edges in the shape, since these cool down faster than the overall geometry leading to cracks directly in the cooling process. Moreover, a minimum void size should be applied to ensure a sufficient mold thickness to resist the hydrostatic pressure thar arises through casting. Both minimum member and minimum void size can be incorporated with multiple phase projection [29], while the maximum dimension can be applied through the maximum length scale constraint[1, 30]. Lastly, it is also important to eliminate closed cavities in order to ensure mold continuity and allow for effective demolding after casting. This can be applied through the Virtual Temperature Method [31].

In the case of 3D printing, additional aspects that should be considered in the TO formulation are the need to ensure a continuous thread, as well as restrictions in critical overhang angle, which is already studied in similar applications with AM techniques. Lastly, in all cases, the TO formulation can be adapted to comply with design criteria that can ensure directional transparency in the geometry.

Acknowledgements

The authors would like to thank ExOne and Hüttenes-Albertus for material sponsorship, Chikara Inamura for providing images of AM glass, and Evenline for providing a sample of 3D printed glass.

References

[1] A. M. Koniari, C. Andriotis, and F. Oikonomopoulou, "Minimum mass cast glass structures under performance and manufacturability constraints," in *CAAD Futures 2023*, Delft, 2023.

[2] F. Oikonomopoulou, A. M. Koniari, W. Damen, D. Koopman, M. I. Stefanaki, and T. Bristogianni, "Topologically optimized structural glass megaliths: Potential, challenges and guidelines for stretching the mass limits of structural cast glass," in *Eighth International Conference on Structural Engineering, Mechanics and Computation*, Cape Town, A. Zingoni, Ed., 2022: CRC Press.

[3] W. Damen, F. Oikonomopoulou, T. Bristogianni, and M. Turrin, "Topologically optimized cast glass: a new design approach for loadbearing monolithic glass components of reduced annealing time," *Glass Structures & Engineering*, vol. 7, pp. 267–291, 2022.

[4] F. Oikonomopoulou, T. Bristogianni, L. Barou, F. A. Veer, and R. Nijsse, "The potential of cast glass in structural applications. Lessons learned from large-scale castings and state-of-the art load-bearing cast glass in architecture," *Journal of Building Engineering*, vol. 20, pp. 213-234, 2018.

[5] F. Oikonomopoulou and T. Bristogianni, "Adhesive solutions for cast glass assemblies: ground rules emerging from built case studies on adhesive selection and experimental validation," *Glass Structures & Engineering*, 2022.

[6] F. Oikonomopoulou, I. Bhatia, F. van der Weijst, W. Damen, and T. Bristogianni, "Rethinking the Cast Glass Mould. An Exploration on Novel Techniques for generating Complex and Customized Geometries," in *Challenging Glass 7*, C. Louter, J. Belis, and F. Bos, Eds., 2020.

[7] F. Oikonomopoulou, "Unveiling the third dimension of glass. Solid cast glass components and assemblies for structural applications.," PhD PhD, Architecture and the Built Environment, TU Delft, Delft, 2019.

[8] T. Bristogianni, F. Oikonomopoulou, F. A. Veer, and R. Nijsse, "The effect of manufacturing flaws in the meso-structure of cast glass on the structural performance," in *Seventh International Conference on Structural Engineering, Mechanics and Computation (SEMC)*, Cape Town, A. Zingoni, Ed., 2019: Taylor & Francis.

[9] T. Bristogianni, "Anatomy of cast glass: The effect of casting parameters on the meso-level structure and macro-level structural performance of cast glass components," PhD, Materials-Mechanics- Management & Design, TU Delft, Delft, 2022.

[10] F. Oikonomopoulou, T. Bristogianni, L. Barou, F. A. Veer, and R. Nijsse, "Interlocking cast glass components. Exploring a demountable, dry-assembly structural glass system," *HERON*, vol. 63 (1/2), pp. 103-138, 2018.

[11] T. Bristogianni and F. Oikonomopoulou, "Reinforced glass: Structural potential of cast glass beams with embedded metal reinforcement," in *Eighth International Conference on Structural Engineering, Mechanics and Computation*, Cape Town, A. Zingoni, Ed., 2022: CRC Press.

[12] R. Giesecke and B. Dillenburger, "Three-dimensionally (3D) printed sand molds for custom glass parts," *Glass Structures & Engineering*, vol. 7, pp. 231-251, 2022.

[13] K. Graser *et al.*, "DFAB HOUSE - A Comprehensive Demonstrator of Digital Fabrication in Architecture," in *Fabricate 2020: Making Resilient Architecture*, London, J. Burry, J. Sabin, B. Sheil, and M. Skavara, Eds., 2020: UCL Press, pp. 130-140.

[14] F. Oikonomopoulou, T. Bristogianni, F. A. Veer, and R. Nijsse, "The construction of the Crystal Houses façade: challenges and innovations," *Glass Structures & Engineering*, journal article pp. 1-22, 2017.

[15] M. ShivajiRao and S. Satyanarayana, "Abrasive water jet drilling of float glass and characterization of hole profile," *Glass Structures & Engineering,* vol. 5, pp. 155-169, 2020.
[16] F. Oikonomopoulou, T. Bristogianni, M. Van der Velden, and K. Ikonomidis, "The adhesively-bonded glass brick system of the Qaammat Pavilion in Greenland. From research to realization," *Architecture, Structures and Construction,* 2022.
[17] R. Nijsse, "Glass Walls Carrying the Roof and Withstanding the Wind Load on the Facade: Conservatory of the Museum in Dordrecht and Raaks Glass Cube in Haarlem," in *Challenging Glass 3. Conference on Architectural and Structural Applications of Glass*, Delft, F. Bos, C. Louter, R. Nijsse, and F. A. Veer, Eds., 2012: IOS Press, pp. 111-120.
[18] F. Bos, T. van der Heijden, and P. Schreurs, "The Glass Sphinx: A Massive Stacked Glass Sculpture," in *Challenging Glass 3. Conference on Architectural and Structural Applications of Glass*, Delft, F. Bos, C. Louter, R. Nijsse, and F. A. Veer, Eds., 2012, vol. 1: IOS Press, pp. 47-56.
[19] L. Galuppi and G. Royer-Carfagni, "The effective thickness of laminated glass: Inconsistency of the formulation in a proposal of EN-standards," *Composites Part B: Engineering,* vol. 55, pp. 109-118, 2013.
[20] F. Bos, T. Van der Heijden, and R. Geurts, "The glass sphinx : theory to reality," in *Challenging Glass 4 and COST Action TU0905 Final Conference*, Lausanne, C. Louter, F. Bos, J. Belis, and J. Lebet, Eds., 2014: CRC Press Taylor & Francis Group, pp. 551-558.
[21] D. Zhang, X. Liu, and J. Qiu, "3D printing of glass by additive manufacturing techniques: A review," *Frontiers of Optoelectronics,* vol. 14, pp. 263-277, 2021.
[22] C. Inamura, M. Stern, D. Lizardo, P. Houk, and N. Oxman, "Additive Manufacturing of Transparent Glass Structures," *3D Printing and Additive Manufacturing,* vol. 5, pp. 269-283, 2018.
[23] MIT Media Lab. "GLASS II." MIT Media Lab. http://matter.media.mit.edu/environments/details/glass-ii#prettyPhoto (accessed 2018).
[24] C. Inamura. "GLASS II - APPLICATION." Inamura, C. https://www.chikara-inamura.com/GLASS/GLASS-IIAPPLICATION (accessed 2023).
[25] C. Inamura, "Glass Additive Manufacturing," in *Challenging Glass 6 Conference*, ed. Belgium 2020.
[26] J. Klein, "Additive manufacturing of optically transparent glass," Master of Science, School of Architecture and Planning, MIT, Boston, 2015.
[27] A. M. Mirzendehdel, B. Rankouhi, and K. Suresh, "Strength-based topology optimization for anisotropic parts," *Additive Manufacturing,* vol. 19, pp. 104-113, 2018.
[28] M. Bruggi and P. Duysinx, "Topology optimization for minimum weight with compliance and stress constraints," *Structural and Multidisciplinary Optimization,* vol. 46, pp. 369–384, 2012.
[29] J. K. Guest, "Topology optimization with multiple phase projection," *Computer Methods in Applied Mechanics and Engineering,* vol. 199, no. 1-4, pp. 123-135, 2009.
[30] J. K. Guest, "Imposing maximum length scale in topology optimization," *Structural and Multidisciplinary Optimization,* vol. 37, pp. 463-473, 2009.
[31] S. Liu, Q. Li, W. Chen, L. Tong, and G. Cheng, "An identification method for enclosed voids restriction in manufacturability design for additive manufacturing structures. ," *Frontiers of Mechanical Engineering,* vol. 10, pp. 126–137, 2015.

IASS 2023
July 10–14 Melbourne
Integration of Design and Fabrication

Proceedings of the IASS Annual Symposium 2023
Integration of Design and Fabrication
10–14 July 2023, Melbourne, Australia
Y.M. Xie, J. Burry, T.U. Lee and J. Ma (eds.)

Inflatable flexible factory formwork construction: most recent construction techniques and details

Alex Morgan BELL[a,*], Tyler ROBINS[a]

[a,*] Automatic Construction Inc
New York, NY
alex@automatic-construction.com

Abstract

Inflatable flexible factory formwork construction presented here, replaces the onsite labor of cast in place concrete construction with inexpensive-to-transport-and-manufacture flexible formwork which is erected using pumps. This flexible formwork is erected using pumps that supply a) air for shoring, and b) a cementitious material, such as concrete, for the building's structure. The buildings constructed with inflatable flexible formwork are identical in constituent parts, placement, size, architecture, safety and building code compliance to cast-in place concrete buildings. Constructed using drop stitch fabrics, the formwork contains traditional steel reinforcement to create conventional flat walls, floors and roofs. The form is held in position (shored) by pressurized air while cementitious material is injected. In this paper, updates on buildings constructed, cost and experience are detailed.

Keywords: concrete structures, construction methods, inflatable structures, fabric formwork, practice-based research



Figure 1. Buildings under construction: (a) inflatable shoring, (b) flat walls, (c) cast buildings.

1. Introduction

In the United States, the construction sector's productivity has fallen over the last 70 years [1]. The pace of urbanization continues and the UN projects that the rate of global urbanization will grow from 55% to 68% in the next 30 years with 2.5 billion more people living in cities [2].

In conventional concrete construction the building of the formwork, reinforcement and waterproofing is the most expensive construction step and should be the focus of any productivity improvement effort, "[F]ormwork is the single largest cost component of a concrete building's structural frame [3]."

To increase productivity at a global scale, society needs a building system to create conventional concrete construction with reinforcement conforming to current building codes that will be faster to

Copyright © 2023 by Alex BELL and Tyler ROBINS. Published in the Proceedings of the IASS Annual Symposium 2023 with permission.

erect, cheaper to purchase and transport, present relatively few restrictions on building design and require fewer work-hours per building. The inflatable flexible factory formwork (IFFF) construction system meets all these requirements.

2. Inflatable Flexible Factory Formwork (IFFF (I3F)): construction process

2.1. Design

Inflatable flexible factory formwork (IFFF) construction starts with the architecture and engineering designs. The average cast in place (CIP) buildings structural designs remain unchained with IFFF. The plans will be augmented to include construction drawings for the inflation of the shoring and the schedule for the building's construction. During the design phase, architects and engineers will be able to iterate on the design for manufacturability, balancing customization and cost by consulting with the IFFF factories' published capabilities. CAD tooling will include IFFF software plugins to allow for instantaneous quotes of build time and cost, permitting contemporaneous iteration by engineers and architects comparable to procedures followed in electronics manufacturing. Once a design has been finalized and approved by the relevant parties, including the local building departments, the designs will be sent to the IFFF factories for manufacture.

2.2. Factory

Depending on the size of the structure, the IFFF factories will deliver a single form, series of forms or sub components of forms for extremely large buildings. The connections between the forms will be as specified in the plans; normally spliced rebar. The IFFF factories will connect sections of rebar together with flexible joints or include openings for inserting rebar onsite and join fabric together to assemble the formwork. The IFFF factories will build into the form the inflatable shoring according to the construction plans. Once complete, tested and certified, the forms will be folded to a compact size and shipped to the job site.

2.3. Job Site

At the job site, workers will follow the factory construction assembly plan specifying the order in which forms are removed from transport and assembled. Depending on the size of the structure, smaller construction equipment such as skid steers may be all that is required to unroll and stack the forms. For larger buildings, truck cranes will help position the forms in place. The base form will require precise placement on the jobsite via laser line while subsequent uninflated forms will be stacked and connected to the first form. QR codes, hand held computers, and sensors would likely be included on larger buildings to assist with and provide oversight.



Figure 2. Images show progress erecting building.

Common concrete line pumps, air compressors, and ready mix trucks already common on the job site will be used. Using standard fittings the inflatable shoring and concrete pumps will be connected to the forms, starting with the first floor and the inflation of the series of shoring chambers. Sensors will monitor pressure in each chamber for any issues and will control air flow.

Concrete ready mix trucks will deliver self-consolidating concrete, as specified in the construction plans, to the concrete pumps which will fill the first floor forms while shoring remains in place for the full term of the plan. After the length of time specified in the construction plan, usually 1 day minimum, the next floor shoring will be inflated and concrete pumps will fill the second floor. After the concrete strength has reached the required level per floor and shoring is removed, the subsequent trades will begin finishing each floor.

2.4. Formwork details

Fabric formwork is currently used to construct inexpensive domed buildings but remained limited because of the domed shape [4]. Drop-stitch fabric technology, used in IFFF, creates the necessary flat surfaces. Drop stitch fabric is made of two sheets of woven material which are connected via robotic looms with periodic connections between the two layers.



Figure 3. Drop stitch fabric.

The process, patented by the Goodyear Company and called 'air mat' was used in inflatable airplane prototypes in the 1960s. At the time, the material's price was prohibitively expensive and it never found widespread use. In the early 2000's material science and electronic loom technology advanced to the stage that the material became sufficiently inexpensive that it could be used in inflatable water sports for rigid surf boards and gymnastic mats. Drop stitch can not be purchased for less than $10 per square meter and the prices continue to fall.

The woven exterior of the drop stitch can be covered in an additional airtight layer of plastic. In most applications this layer is pvc plastic which is bonded to the fabric to make the forms air tight. However, forms can be specified as both sides air permeable or air permeable only in one side for instance the interior or exterior of a building.

2.5. Pressure

The current assembled structures maintain a pressure up to 200 kPa. The current point of failure at higher pressures is the rupture of the drop stitch thread. For hydrostatic pressure durring concrete pours the highest pressure at the fastest rates of pour for 4.5 meter high walls is 140 kPa which is well within current technology. Material and construction advancements may increase pressure tolerances; for example, current heavy lift bags (designed to elevate thousands of tons with small inflated mats) used in shipping and rescue operations sustain pressures of over 700 kPa.

2.6. Tolerances

The formwork is created on automatic looms with stated tolerances of +/- 1 mm over a 100 meter length of material, well within the convention construction requirements. Whether manually or automatically assembled in the IFFF factories, meeting the conventional tolerance requirements is well within current tolerances for manually created drop stitch surf boards and air mats with current technologies.

2.7. Resistance to puncture & self plugging

The formwork does not need to be airtight because concrete consolidates and plugs holes in formwork. In tests, the authors have determined that holes up to 2 times the average size of the aggregate plug with minimal leakage. The self plugging character of concrete permits stabilization around rebar protrusion, industrial zippers and fabric lashing methods used to attach forms. This is consistent with traditional formwork which also contains many holes which plug.

2.8. Constructing forms

Drop stitch fabric can be formed with either plastic welding, glueing with a solvent, sewing or lashing. Welding lends itself more easily to automation and there currently exist a number of plastic welding companies that specialize in automated pvc tarpaulin welding solutions. Glueing with special pvc cement provides a less expensive, but potentially more labor intensive option.

2.9. Environmental

The formwork can be stripped off or left in place. Ideally the formwork will stay in place as it can provide a vapor barrier and increase tensile strength. When left in place the formwork can be covered as in a conventional wall with traditional facade and insulation on the outside and drywall or plaster on the inside walls.

Drop stitch fabric can be made with almost any plastic, most commonly woven polyester with a pvc coating. Both plastics are inert and extremely long lasting as long as they remain unexposed to ultraviolet light. The plastic not embedded in the concrete can be covered by a traditional facade, painted, or doped for uv resistance.

When left in place, the formwork will be governed by residential code R608.4 and must meet R302.9 flame spread and smoke development index. Both woven polyester and pvc have a flame spread index of less than 25, and a smoke developed index of less than 50 well within IBC building code.

Both pvc and polyester are widely used throughout modern homes from plumbing to furniture, clothes and more. IFFF factories will certify that their fabrics are low-VOC.

2.10. Compressive and tensile testing

A section of formwork was core drilled after 28 days and the compressive strength of the core was compared to a control test cylinder. Across three test cylinders the compressive strength remained a consistent average of 30 mPa with no statistically significant variation between test cylinder and formwork cylinder.

A beam form was created that was 10 cm by 10 cm by 1 meter and a plain concrete beam was cast as well as a drop stitch beam. The beams were supported on each end and force was applied in the middle of the beam until failure. Over three sets of tests, the drop stitch beam's failure point was on average 19% higher than the plain beam suggesting increased tensile strength. Additional tests are ongoing.

2.11. Reinforcement

Reinforcement is used in concrete construction to provide tensile strength (concrete being significantly stronger in compression than tension.) Steel reinforcement in the form of rebar is the most popular form of reinforcement although other methods are available including GFRP, post tensioning cables, and fibers.

While woven material adds to the tensile strength, IFFF will accommodate traditional rebar use and placement. There are two options for IFFF and reinforcement: rebar inserted in the factory or on the jobsite. For jobsite insertion, premade holes in the forms are prepared with rebarwheels so that construction teams, after inflating the shoring, can push rebar into the holes. The rebar inserted is kept in place in the form by the dropstitch and rebar wheels. Traditional tying of the rebar is not required. Conventional rebar placement uses plastic and metal chairs, spacers and wire ties to secure the rebar against movement during the concrete pour.



Figure 4. Rebar in form example.

In conventional construction two sections of rebar are spliced together either by overlapping and tying or by using a mechanical rebar coupler. Similarly, rebar will be overlapped or mechanically coupled. The second option is for IFFF factories to place the rebar throughout the forms and keep the rebar in place by tying between the fabric forms and using standard plastic wheel spacers.



Figure 5. Render rebar and spacers.

In order to allow the forms to fold for transport the rebar will be linked with eyelets or hinged rebar couplers at periodic intervals which allows the rebar to hinge while retaining tensile strengths (see building code section for coupler approvals).

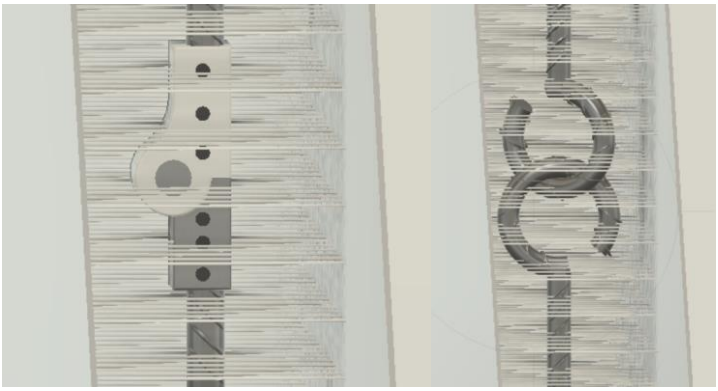


Figure 6. Hinged class b coupler and hook rebar.

IFFF will connect into foundations as in conventional construction by tying the forms into the exposed reinforcement of the foundations. For slab on grade, IFFF can be used without any foundation by specifying in the plans for a thicker slab.

Because the permanent formwork prevents corrosion, the distance the rebar is embedded below the surface of the concrete 'cover' will be less onerous in IFFF construction. However, initially, in order to speed penetration in the market, the rebar will be placed with spacers to meet current cover requirements.

In the future fiber reinforced concrete whether glass, fiber or metal could be used to decrease the amount of rebar required. Further iterations could increase the pressure of the shoring to give the ceilings a slight curvature during casting, forming a slight arch and decreasing the tensile forces.

2.12. Architecture

IFFF will maintain the current flexibility architects have in designing cast in place buildings. As in conventional construction there will be cost savings to using common sizes and shapes for IFFF factories.

The stripped walls are a similar texture to current forms with some variances. In the future surface finish and geometric design could provide aesthetic benefits to architects such as curved or patterned walls.



Figure 7. Stripped walls.

As discussed in the formwork section, the forms can be a vapor barrier or not depending on requirements. In the case of a vapor barrier the resulting building would be tighter than traditional construction with CMU block and wood framing. In further iterations of IFFF, the walls could be formed of two separate forms with an air gap between. This air gap could be then pumped full of insulative materials to create a seamless and insulated concrete wall.

Initial IFFF buildings will provide openings for windows, stairs and some mechanical connections. As IFFF gains adoption it will serve as the foundation for further advancements across the trades. Because the building will be constructed according to the digital plan; conduit, plumbing, hvac and other connections can be provided in the superstructure. The walls would come with mechanical threaded inserts already cast in the outer and inner walls so that the installation of the facade would require only bolting into the set inserts. Similarly, future iterations of IFFF could include interior walls cast separately of light weight concrete, aerated plaster, foams, or other materials to rapidly construct interior walls. These further advancements in automation would build upon IFFF and provide further productivity gains across construction.

2.13. Compression material options: concrete and more

A variety of materials can be pumped into the forms to make up the structure and provide the compressive strength of the building. For most applications the material will be concrete but any pumpable and hardening material can be used.

The use of self consolidating or self compacting (scc) concrete will allow the concrete to flow easily through the forms without required vibration. Non scc concrete can be used with vibration. A special item to consider is the aggregate size and the spacing of the drop stitch material. In general drop stitch spacing should be twice the size of the aggregate used. If larger aggregate sizes are used they can prevent flow in the forms. IFFF factories will allow drop stitch spacing to be specified in the ordering process.

IFFF has been prototyped with aircrete to form lightweight cement structures and polyurethane expanding foam, both providing lightweight and insulative structures. Other materials such as Hempcrete, soil crete, compacted earth, Alker are all lower cost and environmentally friendly options that could be created at the job site and pumped into the forms. The concrete industry's efforts to replace cement with lower C02 emitting binders would complement the IFFF building system.

2.13. Shoring

In conventional cast in place concrete construction, the shoring is used to temporarily support formwork until the concrete has strengthened sufficiently. The erection of the shoring takes place with the creation of the formwork and adds to the cost in labor and time of conventional concrete construction. To support

IFFF either conventional shoring or inflatable shoring can be used. The benefit to inflatable shoring is the IFFF factories will deliver the forms with the shoring pre-attached or in some cases separate from the forms.

Depending on the geometry of the forms the inflatable shoring can be reused or returned to the IFFF factory for recycling into further forms. When using inflatable shoring the IFFF factory will provide an air manifold which connects to each form. The plans will specify a series of compressors to be used on the jobsite. The manifolds include a pressure regulator which will maintain pressure in the shorings.

Sabotage is a problem for all construction and with flexible formwork it is potentially easier for a saboteur to destroy formwork, requiring enhanced in person security on site or remote monitoring in order to prevent unauthorized entry into the construction site.

2.14. Building department approval

IFFF was developed to meet current international building codes and rely on currently approved materials. The NYC 2014 Building Code was chosen as it is one of the most restrictive in the United States. IFFF will meet the entirety of the NYC building code; areas of particular interest are highlighted below.

NYC Building Code 2014 - Chapter 17 Structural Tests and Special Inspections- 1704.4 Concrete Construction

IFFF factories will allow for periodic inspection and reports from concrete construction special inspectors on the formwork and reinforcement. The forms will also include inspection flaps and view ports so that inspectors in the field can inspect the forms and reinforcement.

NYC Building Code 2014 - Chapter 19 - Concrete

ACI 6.3.1 - The embedded polyester fibers are not harmful to concrete. See reinforcement for discussion of added strength but for 6.3.1 assumption is no additional strength.

ACI 7 - The reinforcements used will meet the requirements of ACI section 7. Specifically minimum bend radius as defined in table 7.2.

ACI 12.14.3 Mechanical and Welded splice - The hinged rebar couplers used will exceed the 1.25fy of the bar as specified and couplers used will be ICC-ES certified and meet ASTM A1034.

ACI 13.3.8.5 - Two Way Slab - IFFF couplers will be class b tension lap splice where designated.

NYC Building Code 2014 - Chapter 33 - 3305.3 Concrete Formwork

ACI 3305.3.2 Design of Concrete Formwork - Shoring and formwork designs will come prepared by the factory with the formwork.

ACI 3305.3.3 Formwork Inspection and Observation - As detailed for Chapter 17, inspection ports and certification will be provided. IFFF is currently undergoing testing for ASTM E84 testing for Flame Spread and Smoke Development Index.

2.15. Sustainability

Concrete, a mixture of aggregate and cement, is the most widely used material on earth and its overall carbon footprint reflects this. Portland cement, the most common cement type, has a high embodied emission and is the focus of replacement efforts to develop a more environmentally sustainable product.

Recent efforts have shown that carbonation of cement in concrete can also be used for carbon sequestration. There are multiple companies and research papers that have shown that introducing carbon dioxide into the concrete allows the cement to absorb the carbon dioxide creating a stronger concrete and sequestering the carbon [5]. In most papers the focus for sequestration during curing is

focused on precast plants where the concrete could be placed in a carbon rich atmosphere. Cast in place has been largely ignored due to the impossibility of placing conventional cast in place concrete in a carbon rich atmosphere. However, with the introduction of IFFF which are sealed forms, cast in place concrete can potentially serve as an even greater carbon sequestration point with onsite pumps pumping air into the forms during the 30 day cure period to have the concrete filter and store the carbon.

Automatic Construction has been prototyping a combination of IFFF and accelerated carbonation. The paper [6] details experiments in which the process has been able to sequester all the CO2 released in the calcification of the limestone. And further, the latest results show that the rate of sequestration continues and the building material appears to continue to sequester CO2. This opens up the possibility of IFFF construction + carbonation being a net sink of CO2.

Overall, there are compelling reasons to believe IFFF will improve the sustainability of construction: a) as discussed in the section on compressive materials, IFFF construction can use any pumpable material such as recent formulations of green concrete, mass timber, or hempcrete b) IFFF buildings promise to be more efficient to heat and cool due to the vapor barrier provided by the air tight forms c) IFFF buildings will use less concrete than conventional cast in place structures due to precision manufacturing d) IFFF construction could allow for carbon sequestration on a massive scale.

2.16. Estimates of cost and time reduction

Current prototype IFFF buildings are being made at $215.00 USD per square meter. These prices for single prototypes suggest that the price will fall with scale. In order to compare costs, a 10 floor building, 315 Linwood in Brooklyn NY, was considered from detailed plans and construction accounting. The conventional cast in place superstructure cost $6M vs an estimated $1.2M for IFFF construction. As IFFF buildings are built at greater scale, a more detailed accounting of the cost difference across regions and building types will drive IFFF adoption. Initial estimates suggest that at prototype prices IFFF is already $\frac{1}{5}^{th}$ the cost of conventional construction and will certainly improve in price at scale.

It is difficult to estimate the time savings from IFFF at this stage of technological maturity. Best in class conventional cast in place construction operates on a 2 day cycle adding a floor every two days. The majority of the delay in IFFF will be waiting for the concrete to strengthen while in conventional construction the additional day is required for formwork construction. In buildings shorter than 20 stories the cycle is more commonly 10 days. It is estimated that IFFF construction could decrease times to 1 day cycles achieving a 2x speedup over the current best in class.

The biggest savings in cost and time come from the replacement of onsite labor. Activities from screeding, tying rebar, placing rebar, and the hand building of forms for each floor are all replaced by the onsite pump and single pump operator.

2.17. Beyond buildings

This paper has focused on IFFF for conventional building construction however applications also exist for other concrete structures.

IFFF can be used to create tunnels in which nested flexible tubes are laid in the ground or in water and then filled creating concrete reinforced tunnels. Potentially lowering the cost of under river tunnels.

Inground pools manufactured with conventional forms could be replaced with IFFF allowing for quicker and less expensive setup.

In exotically hard to reach locations, such as future construction on other planets, IFFF's low cost of transport in combination with local materials would be one of the only options to construction. There already exists literature on combining binders with mars or moon dust to create a cementitious product perfect for filling inflatable flexible factory forms.

3. Construction to date

Automatic Construction Inc has built single storey structures in NY, USA using the IFFF method detailed here. All construction to date has been small structures in the 10-30 square meter range. Structures have had flat roofs and pitched roofs. Structures have either used 10 cm or 20 cm walls.

4. Replication of results

IFFF and drop stitch are impressive technologies that should be used more. Below are suggestions for drop stitch/ IFFF projects.

4.1. Drop stitch material

- Drop stitch material is available on Alibaba from a variety of producers. A smaller roll of fabric can be purchased as a sample. The options are primarily 5cm, 10cm, and 20cm for thickness with either PVC or TPU coating. Some larger manufacturers such as Duletai also provide manufacturing of both materials and end products.
- Ecommerce sellers such as Amazon and AliExpress sell square dropstitch inflatable sections as gym mats. These are often excellent ways to get started experimenting, pumping and working with the material. Search "Air Mat Gymnastics" to purchase.
- Drop stitch can be cut with scissors and is easy to cut into panels for fabrication.
- For the edges of the drop stitch the best solution is to glue or weld vinyl coated tarpualine.
- There are a few options for fabricating the drop stitch into structures
    - HH-66 vinyl cement is the best glue to use.
    - Sewing drop stitch is possible with a heavy duty or leather sewing machine
    - Hot air welding requires more skill than gluing and the fumes are potentially more hazardous. However its less expensive and can be faster. Handheld plastic welders are available for low cost.
    - Radio and ultrasonic welders are a more expensive option.
    - The company Weldmaster, as well as others, provided automated solutions for fabric assembly.
- Inflatable contractors are also available who will fabricate and ship drop stitch structure. The contractors will require a design document. Example contractors are AirBox ltd or search " Drop Stitch Inflatable Manufacturer."
- In general, custom drop stitch configurations such as larger spacing for larger aggregate or other permutations are possible but require minimum orders of 1000 square meters.

4.2. Couplers

- HR valves are the standard for air inflation. The air valve will be easily clogged with concrete and should be positioned at the highest point in the forms.
- Concrete couplers should be custom made for the concrete pump connection. The two primary types are HD couplers and Camlock. To attach to the drop stitch requires a backplate which is inserted into a hole in the drop stitch. Then the flange of the coupler is bolted or riveted to the backing plate. Couplers can be manufactured out of steel, aluminum or plastic.
- The amount of concrete vibration required depends on the concrete mix design, the drop stitch spacing vs aggregate size and the distance the concrete has to flow. External vibrators can be

bolted to either the coupler or to similar couplers connected across the forms. Internal vibrators can be inserted into small holes in the forms to increase the movement of the concrete.



Figure 8. Concrete HD coupler in IFFF.

4.3. Pumps

- Air pumps for inflatables will work especially with HR valves. For inner shoring its helpful to have the ability to set the pressure. You can either use a HR valve air gauge or air pump with a pressure regulator.
- Depending on the concrete mix and desired flow rate there are a few options for concrete pumps.
    - Concrete line pumps are available for rental and come with an operator. The line pumps in the United States use HD couplers. Most concrete pumping companies will have reducers to a smaller diameter hose which is easier to handle and connect to the forms. Concrete line pumps can be extremely powerful. Start with a smaller form to gain experience. Set the volume control knob on the pump at its lowest setting and pump slowly to start.
    - Large construction diaphragm pumps for instance the Wacker Neuson PDI series connects with a camlock connection and can pump air crete and most flowable mortars. For small scale prototypes, you can also use diaphragm pumps (either hand operated or 12 volt electric) which are manufactured for bilge pumping.
    - Mortar pumps are available as either electric or gasoline/diesel powered. They usually have a maximum aggregate size but are smaller and easier to use.

4.4. Concrete mixes

- The main variables are aggregate size and concrete flow when choosing a mix. Maximum aggregate size should be less than drop stitch spacing. The concrete should be self consolidating or at least have a high flow/spread. A spread of 50 cm in a inverted cone test is best. Additions of super plasticizer are common in most ready mix locations. For aggregate size, the smallest options are usually a “block fill” variety.
- Another option for prototyping is to use air crete which can be mixed onsite and foamed. The air crete pumps much easier than traditional concrete.
- Expanding polyurethane foam is an option; however, for larger structures the expense is considerably higher than cement options.

5. Conclusion

Inflatable flexible factory formwork (IFFF) construction has the potential to improve global construction productivity without requiring compromises in architecture, new building materials, or untested building designs. Globally the construction industries lack of productivity is creating skyrocketing housing costs

and inadequate housing for the hundreds of millions of people moving to cities each year. IFFF relies on factories to produce formwork with lower onsite labor requirements in a compact and shippable form.

IFFF relies on inexpensive and readily available pumps to supply the unloading, placing and erecting of the structure. IFFF creates robotically precise buildings whose digital foundation will unlock further productivity gains across all building trades.

References

[1] A. Goolsbee and C. Syverson, *The strange and awful path of productivity in the U.S. Construction Sector*, 2023. doi:10.3386/w30845

[2] P. Bocquier, "World Urbanization Prospects," Demographic Research, vol. 12, pp. 197–236, May 2005, doi: https://doi.org/10.4054/demres.2005.12.9.

[3] R. L. Peurifoy and G. D. Oberlender, Formwork for concrete structures. New York: Mcgraw-Hill, 2011.

[4] "Welcome to Monolithic," Monolithic.org. https://www.monolithic.org/monolithic (accessed May 09, 2023).

[5] Monkman, Sean. "Calculating Sustainability Impacts of CarbonCure Ready Mix." (2019).

[6] A. Bell, "Rapid Complete Carbonation in Porous Cement Building Products," papers.ssrn.com, Jan. 28, 2022. https://papers.ssrn.com/sol3/papers.cfm?abstract_id=4148065 (accessed May 09, 2023).

IASS 2023
July 10–14 Melbourne
Integration of Design and Fabrication

Proceedings of the IASS Annual Symposium 2023
Integration of Design and Fabrication
10–14 July 2023, Melbourne, Australia
Y.M. Xie, J. Burry, T.U. Lee and J. Ma (eds.)

Research on digital design and optimisation method for large-scale reciprocal frame structure: The case of Chengdu agricultural expo exhibition hall

Philip F. YUAN[a,*], Tianyi GAO[b], Yingzi HU[c], Liming ZHANG[c]

[a,*] College of Architecture and Urban Planning, Tongji University, Shanghai, China
philipyuan007@tongji.edu.cn

[b] Shanghai Research Institute for Intelligent Autonomous Systems, Tongji University, Shanghai, China
gerryvito@outlook.com
[c] College of Architecture and Urban Planning, Tongji University, Shanghai, China

Abstract

Due to the continuous iteration of digital design and construction technologies, innovation of design paradigm liberates social productivity significantly while it also creates a new possibility of mass customization for architectural individualization and diversity. This thinking of architecture allows architects to accomplish profound design concepts and intentions, such as structural optimization, construction efficiency, and material usage. At the same time, digital design tools and algorithms also powerfully awaken the relevance of tradition and local culture, which is also an essential meaning of technological innovation for social development. The timber reciprocal frame structure is a building structure form with a long history, which has played an important role in history with its concise and practical characteristics. In the field of architecture and engineering, the current trend of combining traditional material and craft with digital technology is promoting the development of timber structure buildings, creating more elegant, environmentally friendly, and low-carbon buildings for humanity. This paper introduces the integrated design and optimisation process, with robotic construction method of large-scale timber reciprocal frame structure, taking the Chengdu Agricultural Expo Exhibition Hall as an example.

Keywords: reciprocal frame structure, shell structure, structural optimisation, digital fabrication

1. Introduction

With the popularization and application of computational design tools and architecture robotics, the intelligent construction platform not only provides a highly flexible system for architectural prefabrication but will also promote the integration of different architecture production processes [1]. In recent years, the rapid development of tools, including computers and robotics, has driven the digital transformation of construction industry [2]. Digital parametric design tool, represented by Rhino and Grasshopper, is a notably developing advanced manufacturing technology in the last 30 years. with the advantage of free manufacturing of three-dimensional structures and material saving, which has been widely used in innovative product exploitation and small-scale manufacturing. However, with the emerging architectural robotics technology, mass customization has become another popular direction for architects to explore. The development in this research field can serve both academia and industry in terms of promoting robotic algorithms, hardware, and applications in construction industry [3]. With the widespread use of architectural robotics technology, the manufacturing industry may no longer depend on traditional factories, which centralize production factors such as labour, capital, and equipment on a large scale, but rather shift to a more flexible production method based on industrial robotics that requires less investment. Combined with the digital construction method of human-

Copyright © 2023 by Philip F. YUAN, Tianyi GAO, Yingzi HU and Liming ZHANG. Published in the Proceedings of the IASS Annual Symposium 2023 with permission.

machine collaboration, digital design tools and robotic production has significant potential for practical large-scale manufacturing scenarios [4].

With challenges such as the unreliability of the naturally grown timber overcome during the last decades with novel digital technologies, prefabricated engineering timber has been one of the most digitally advanced sector within the construction industry [5]. It can reduce material waste, onsite labor, and erection time which can lead to improved safety and overall quality while reducing costs [6]. Additionally, by substituting wood, bamboo, and other plant fibers for energy-intensive materials such as concrete and steel in building construction, greenhouse gas emissions from material manufacturing can be greatly reduced [7]. The timber reciprocal frame structure is a building structure form with a long history, which has played an important role in history with its concise and practical characteristics. In recent years, with the development of digital and intelligent design in architecture, the timber reciprocal frame structure has been widely applied and developed. In the field of building structures, the combination of traditional timber material and digital technology is promoting the development of timber structure buildings, creating more beautiful, environmentally friendly, and safe buildings for humanity. This paper aims to explore the application of timber reciprocal frame structure in buildings and the future direction of its digital development. Firstly, this paper will introduce the basic shell geometry selection, pattern generation, and design concept. Secondly, the constructability is optimised based on genetic algorithm in the perspective of timber elements' dimension and joint angles. Furthermore, the robotic fabrication process has been illustrated to prove that the constructability optimisation can significantly reduce the manufacturing cost. Finally, structural performance calculation of reciprocal frame structure unit has been shown for the timber beam categorising. In summary, this paper discusses digital design and optimisation workflow for large-scale reciprocal frame structure based on mass customization scenario, taking the large-scale shell structure of Chengdu Agricultural Expo Center as an example (Figure 1).



Figure 1. A photograph of the completed project of Chengdu Agricultural Expo Center

2. Methodology

2.1. Reciprocal frame structure pattern generation

The optimized and rationalized shell surface is generated through particle-spring shape-finding algorithm, which serves as the foundation for the subsequent stage of designing a coherent structural system supporting the extension of the shell space. In the design phase, the primary aim is to create a large-span, column-free space within the shell while maintaining its structural integrity. The initial proposal used a dense ribbed timberen beam to achieve this goal. However, after exploration and modelling test, a modified frame structure was determined, and it replaced the dense ribbed timber beams with a reciprocal frame structure (Figure 2). It supports the extension of the shell space and provide a column-free interior. In the phase of designing this reciprocal frame structure, 11 Archimedean paving of orthogonal polygons are selected as the basic pattern for the reciprocal geometry library (Figure 3). This selection was made according to their compatibility with the continuous shell space and their ability to provide stable structural support. This use of reciprocal frame structure allowed for a more coherent and efficient structural system, resulting in a large-span, column-free space within the shell, which was essential for achieving the desired spatial morphology.



Figure 2. Dense-ribbed timber beams and reciprocal frame structures

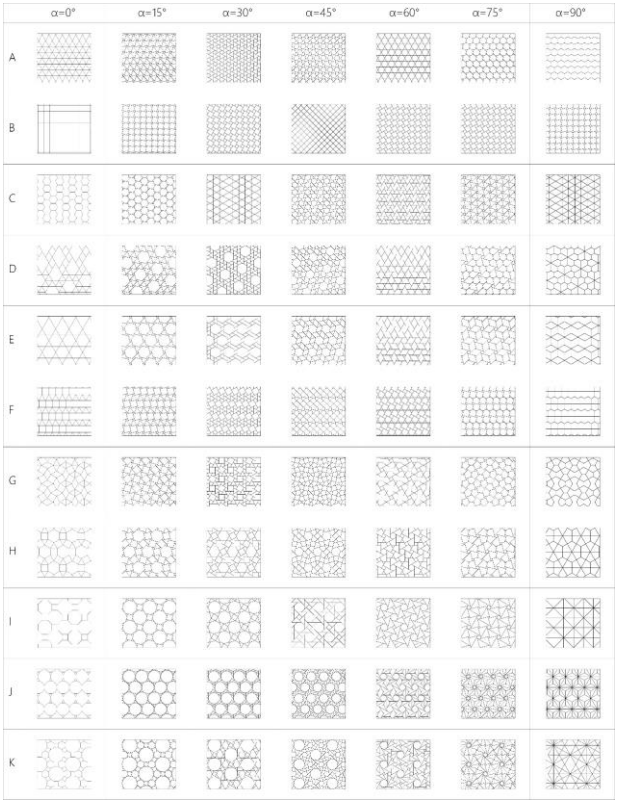


Figure 3. Reciprocal Geometry Gallery

After obtaining a prototype library of rationalized shell surfaces and planar reciprocal geometry, this project started to explore the three-dimensional transformation of reciprocal geometry using rod shape-finding mechanics and projection methods. The primary objective was to achieve an angle-preserving mapping from the plane rod to the shell surface parent, which could ensure that the reciprocal geometry remained undisturbed in both x and y directions. To achieve this, the reciprocal frame structure grid in-plane is adjusted to cover the entire shell surface. This approach resulted in a plane curve that could be fully fitted to the shell surface, which was critical for achieving optimal structural performance (Figure 4).

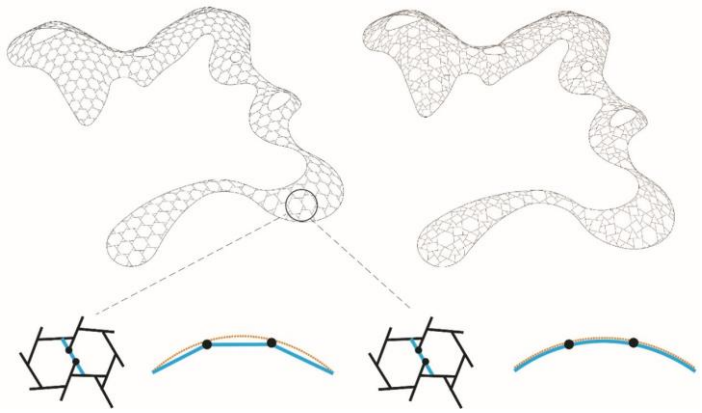


Figure 4. Left: the unit rod generated by the particle-spring method Right: the unit rod generated by the projection method

Two levels of comprehensive screening determine the construction feasibility and structural functional suitability of the hexagonal reciprocal grid. After consideration, a C-grid modified pattern is selected to reduce the impact of right angles in space while reflecting the spatial ductility of the shell structure in the design concept. Figure 5 illustrated that when the C-grid modified pattern is rotated to 16.1°, it achieves a unique reciprocal state where the intersection point is located at the third equilibrium point. This state optimizes the overall structural performance and stability of the grid C modified pattern. In addition, the smallest triangular cells in the reciprocal grid meet basic construction requirements, while the other functions including light positioning and arrangement can be completed in the later process. Figure 6 shows the final result of this refinement process. In summary, this project successfully achieved an angle-preserving mapping from the plane rod to the shell surface parent by using a hexagonal reciprocal grid with a C-grid modified pattern. This approach resulted in improved structural performance and spatial ductility, which is critical for the design of shell structure in the perspective of architecture.

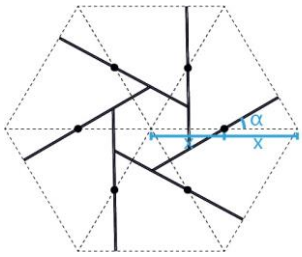


Figure 5. Mesh transformation for reciprocal geometry

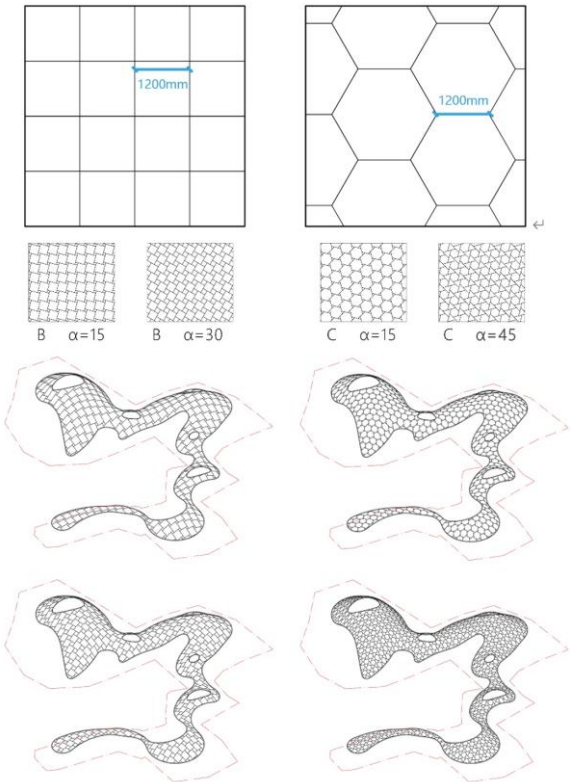


Figure 6. B, C mesh of reciprocal geometry shell surface application

2.2. Constructability optimization of the reciprocal frame structure

In the processing of mapping 3D reciprocal frame structure line model to the shell surface, several types of structural issues referring to the constructability are addressed in this project. These issues are addressed in the optimization of the overall reciprocal timber structure that intersected with the curve boundary in three dimensions (Figure 7)."

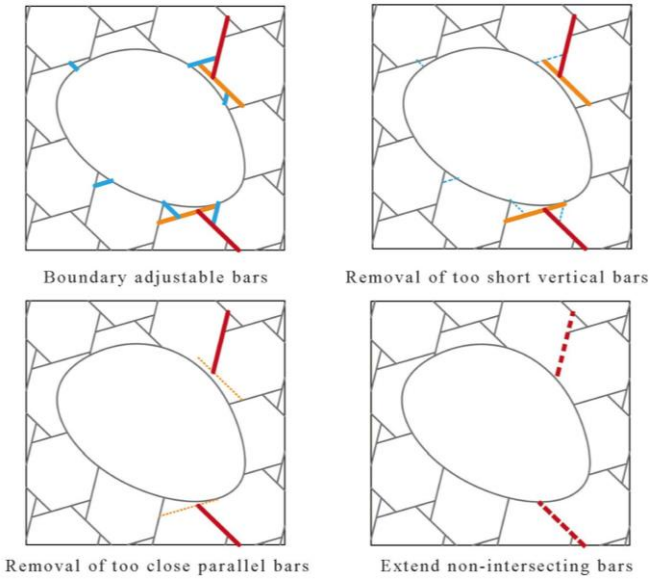


Figure 7. Boundary optimization based on constructability

In order to optimize the reciprocal frame structure, our team implemented a three-step process. Firstly, all timber rod elements with lengths less than 580mm are screened and removed. These short members are typically caused by cutting the triangular units of the reciprocal frame structure with the outer boundary. This crucial step aimed to eliminate unnecessary structural elements and improve the overall stability of the structure. Secondly, all near-parallel members with lengths less than 300mm from the edge line are screened and removed. These members can cause redundancy in mechanical properties and difficulties in positioning during on-site construction. After that, the construction processes are streamlined, and the overall efficiency of the structure is improved. Thirdly, the endpoints of all line segments intersected with other bars are checked and are extended until it intersected with another line segment (Figure 8). This intended to ensure that all structural elements were properly connected and supported, resulting in a more stable and robust structure. Overall, this boundary optimization approach ensures the final structural stability and aesthetical appearance of this reciprocal frame structure.

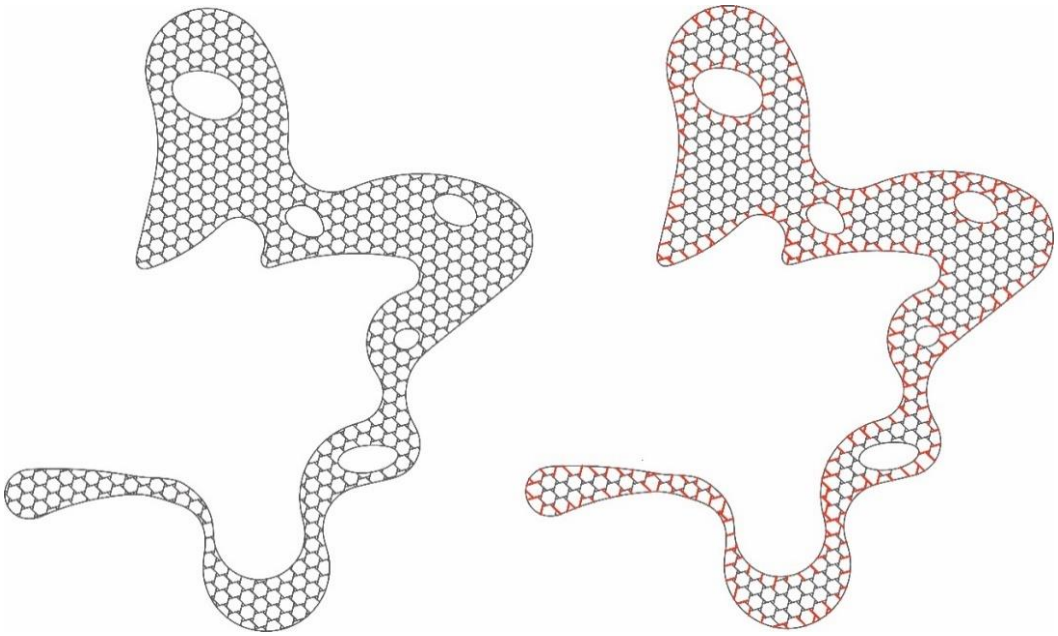


Figure 8. Left: Before boundary optimization Right: After boundary optimization

After completing the boundary-adaptive structure optimization above, it is imperative to geometrically rationalize the unit bars within each reciprocal frame structure. The positioning line of the reciprocal frame structure, derived through projection, manifests as a planar Non-Uniform Rational B-Splines (NURBS) curve with multiple control points. This curve facilitates construction-oriented optimization by controlling the error range and constructing circular arc lines through the extraction of the curve's geometric feature points. To achieve this, the endpoints and midpoints of each rod and curve are extracted independently, enabling the construction of circular arcs conforming to the original NURBS curve. Consequently, the rod positioning line could have promising geometric performance and possibility of reconstruction. In addition, it is crucial to consider the numerical difference in the radius value of the fitted arc from a prefabrication standpoint in a timber processing factory. The timberen rod exhibits various arc radius, which significantly increases the capital and time costs associated with the fabrication process. Hence, the arc radius is optimized, generalized, and integrated, building upon the initial fitting results (Figure 9). This approach ensures a more efficient fabrication process, reducing both the time and resources required for the construction of reciprocal frame structures.

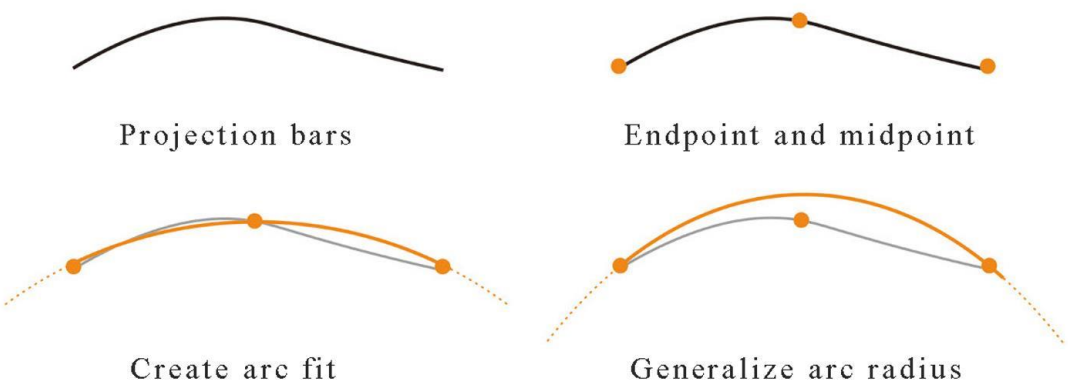


Figure 9. Preliminary fit of rods

This project conducted a comprehensive analysis of arc radius to develop a methodology for generating secondary generalized arcs. Specifically, the first step is to sort arc radius from large to small and assign sequential numbers to each arc. Then, the identified intervals of arcs with similar radius and determined median radius of each interval can serve as the unified radius for the elements. Next, this project used the generalized radius and two control endpoints to iteratively construct a secondary generalized arc. However, it is necessary to control the structural error value generated between the obtained secondary induction arc and the initially mapped rod during this process. To address this issue, the design team extracted four key data: maximum error, minimum error, average error, and median error between the rods. The error indicator was then set as the mean value of these four data. Finally, the feasible radius induction schemes were filtered out by controlling the defined error indicator threshold below 6cm. Figure 10 provides a visual representation of this process. Overall, this radius optimization methodology for fabrication and construction provides a systematic and effective approach for generating secondary generalized arcs with high precision and accuracy. Predictably, this approach has the potential to be applied in a wide range of discipline, including engineering, architecture, and manufacturing, improving the efficiency and quality of complex geometrical constructions significantly.

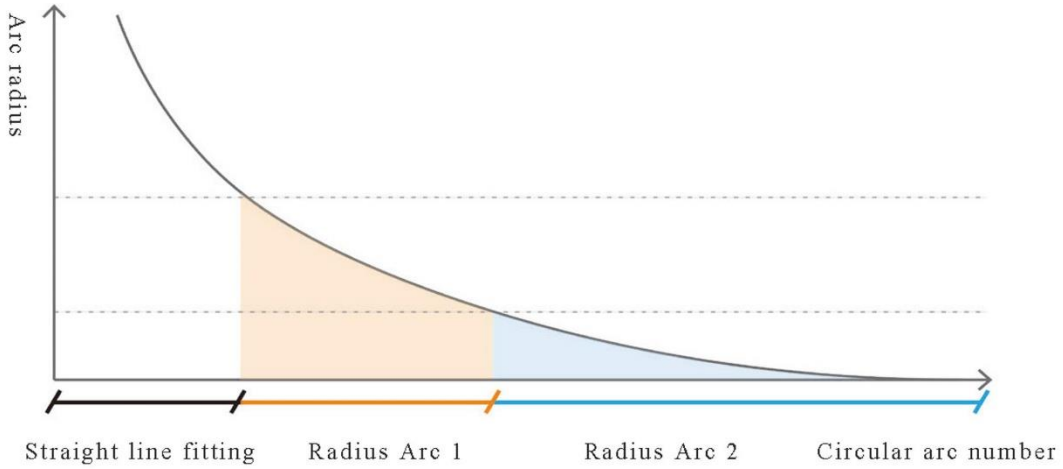


Figure 10. The radius of the induction arc

The digital optimization tool utilized in this project is genetic algorithm carrying out different attempts to divide the induction intervals and test the induction radius. By repetitively calculating and optimizing the steps of the induction radius of the circular arc, it can optimize the radius for improved efficiency. From the initial manual induction of 5 intervals and 5 types of radius optimizations, this project finally obtains only 2 intervals and 2 types of radius circular arc. For rods with oversized arc radius, which are infinitely closed to a straight-line arc, are replaced with straight rods. After that, an optimal inductive solution with an error index of less than 6cm was obtained. To streamline the fabrication process, the rods type of reciprocal frame structure finally can be concluded into three types: straight rods, 3.9m radius circular arc rods, and 9.0m radius circular arc rods. This optimization remarkably reduced the processing and construction costs of factory prefabricated rods through a geometric calculation within a reasonable error range (Figure 11). To include this step, it is rational to state that through the optimization by genetic algorithms, the constructability of the overall shell structure was crucially modified.

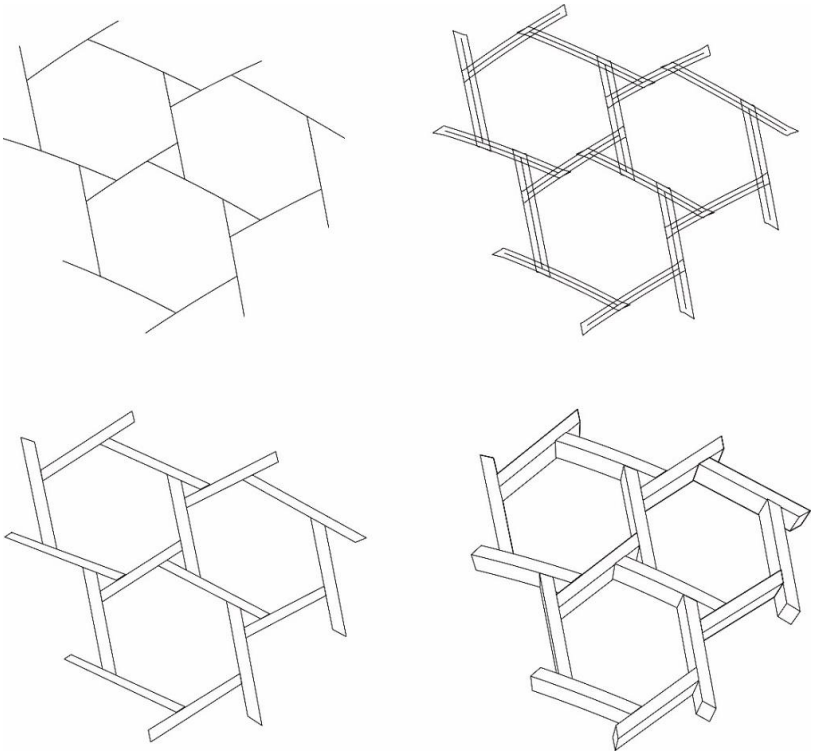


Figure 11. Structural bar conversion of reciprocal frame line mold

2.3. Robotic fabrication of timber reciprocal frame structure

The optimized structural form of the single-curved timber beam in the design process asked for high demands of accuracy and efficiency in the processing of these elements. The laminated timber form, size, hole position, and slot position required for the entire project are all different, while the machining accuracy of each node must be controlled within ±2 mm to meet the requirements of prefabricated assembly. The timber fabrication robotics based on an industrial six-axis robot arm can fully utilize its precise and efficient processing capabilities, making mass customized production of complex timber elements possible (Figure 12). The robotics is equipped with an 18000 rmp spindle motors and can complete all the milling and drilling process of the rods by converting the tool head (milling cutter). The Grasshopper plugin FURobot can convert the architectural model into a path for robotics. Through simulation, it can ensure the smooth fabrication progress and directly generate offline programs. For the same node, the robotics needs a series of processing information. Firstly, the path for rough processing of the timber needs to be formulated, milling out the required overall form from a complete timber material. Then, additional processing paths are required for details such as bolt holes and slots. In addition to architectural geometric information, no other information is required for this process. The mass customization processing method of the robot effectively guarantees the rational completion of mass-produced components, not only improving processing accuracy but also effectively reducing processing time and cost.

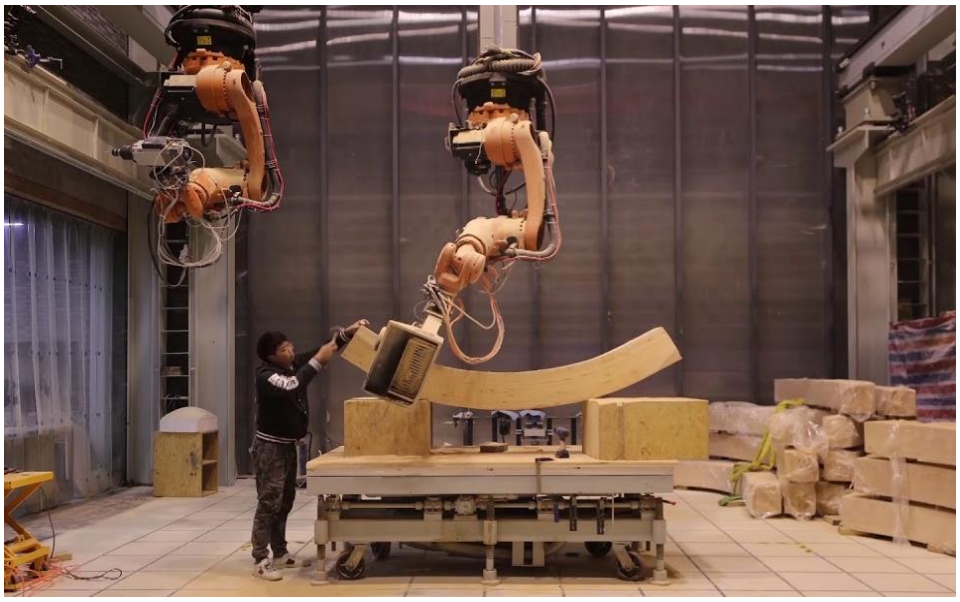


Figure 12. Robotic timber fabrication technology

3. Result: structural performance calculation of reciprocal frame structure unit

In the structural analysis result, the preliminary structural mechanics calculation of the existing structure showed that the overall bending moment and stress of the project could be maintained within a more controllable range while the variation range of the axial force was slightly larger than expected (Figure 13). The rods were grouped together. In additional, the size, material and node design were considered in different axial force areas.

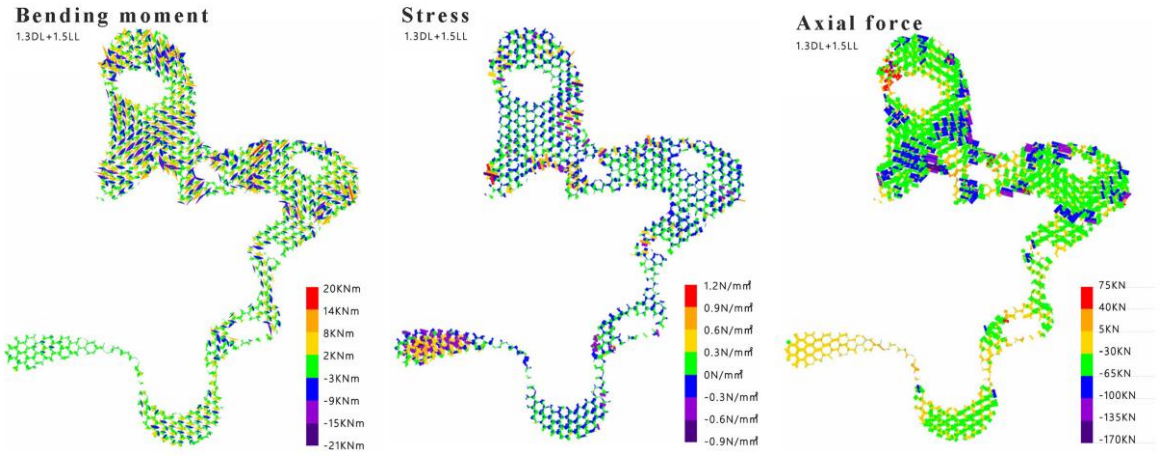


Figure 13. Structural performance calculation

The detailed fabrication strategy our team developed is categorizing timber beams into several parts. To be specific, four types of timber structure unit beams are determined based on mechanical performance calculations. The B1 and B2 beams, which are subject to less axial force, use glued laminated timber

beams with a cross-section of 450*180mm. The B3 beams, which are subject to the greatest axial force, are replaced with more stable timber veneer square steel beams due to their own tensile and compressive requirements and a smaller overall quantity. Since the outermost structural ring beams at the boundary of the rationalized curve and the five skylight openings require better structural stability and better fabrication precision, our team defined them as B4 type beams, using Φ355*16mm round steel beams as the main material (Figure 14). The team also designed different types of nodes based on steel fork plates, bolts, steel nails and other structural members for various types of unit beam members. In this way, a complete theoretical study and construction-oriented digital geometric design of the reciprocal timber structure from the geometric characteristics to the structural performance level has been developed. At the same time, the implementation and effectiveness of its basic form is evident.

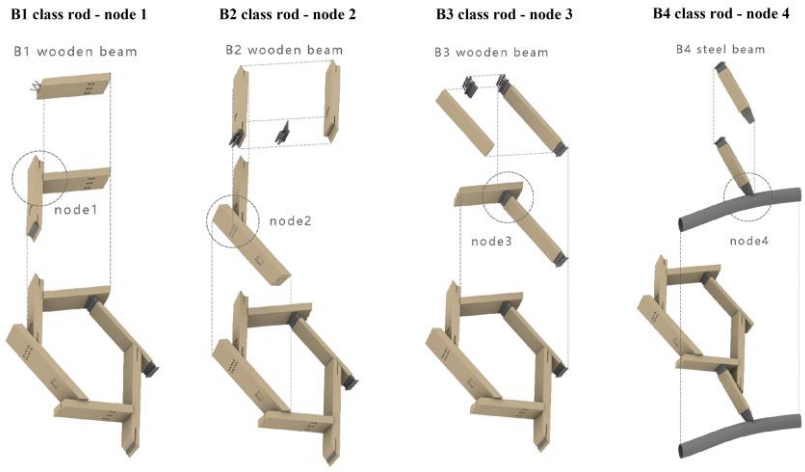


Figure 14. Form and node construction of each type of structural unit

4. Summary

This article presents a project that explores the digital design and fabrication process of a long-span shell roof with a reciprocal frame structure. Overall, this project utilizes digital design tools and genetic algorithms to efficiently prefabricate irregular timber components, from the generation of structural patterns based on an Archimedean paving of orthogonal polygons to the development of reciprocal frame structure geometries with structural performance. During the process of 3D form-finding and structural optimization, the basic planar reciprocal geometry is mapped onto complex hyperbolic shell surfaces, and further optimized using the particle-spring method to enhance the overall spatial structure and interlocking angles. Ultimately, this load-bearing structural system of hexagonal unit timber beams forms a reciprocating force system in the complex hyperbolic space, achieving optimal structural efficiency and material utilization.

In conclusion, the integrated design and optimisation process promotes a paradigm shift in architectural practice. This continuous development of digital technologies integrates performance principles with geometric principles related to shape, structure, and materials to motivate customized material processing in performance-based fabrication. Research and practice in performance-based construction using geometric principles is undoubtedly driving the advancement of digital design, construction research, and industry transformation.

Acknowledgements

This article is supported by the Shanghai Municipal Science and Technology Major Project (2021SHZDZX0100) and the Fundamental Research Funds for the Central Universities; National Natural Science Foundation of China (Grant No. U1913603)

References

[1] P. F. Yuan, H. S. Beh, X. Yang, L. Zhang, and T. Gao, “Feasibility study of large-scale mass customization 3D printing framework system with a case study on Nanjing Happy Valley East Gate,” *Frontiers of Architectural Research*, vol.11(4), pp. 670-680, 2022.

[2] D. Schodek, M. Bechthold, J. K. Griggs, K. Kao, and M. Steinberg, *Digital Design and Manufacturing: CAD/CAM Applications in Architecture and Design*. Wiley, 2004.

[3] B. Xiao, C. Chen, and X. Yin, "Recent advancements of robotics in construction," *Automation in Construction*, vol. 144, 2022, doi: 10.1016/j.autcon.2022.104591.

[4] P. F. Yuan et al., "Robotic 3D printed lunar bionic architecture based on lunar regolith selective laser sintering technology," *Architectural Intelligence*, vol. 1, no. 1, 2022, doi: 10.1007/s44223-022-00014-9.

[5] H. Chai, C. So, and P. F. Yuan, "Manufacturing double-curved glulam with robotic band saw cutting technique," *Automation in Construction*, vol. 124, 2021, doi: 10.1016/j.autcon.2021.103571.

[6] S. Bhandari, M. Riggio, S. Jahedi, E. C. Fischer, L. Muszynski, and Z. Luo, "A review of modular cross laminated timber construction: Implications for temporary housing in seismic areas," *Journal of Building Engineering*, vol. 63, 2023, doi: 10.1016/j.jobe.2022.105485.

[7] Z. Duan, Q. Huang, and Q. Zhang, "Life cycle assessment of mass timber construction: A review," *Building and Environment*, vol. 221, 2022, doi: 10.1016/j.buildenv.2022.109320.

IASS 2023
July 10–14 Melbourne
Integration of Design and Fabrication

Proceedings of the IASS Annual Symposium 2023
Integration of Design and Fabrication
10–14 July 2023, Melbourne, Australia
Y.M. Xie, J. Burry, T.U. Lee and J. Ma (eds.)

Study on the dismantling method of cable-strut tension structures

Jiaqi YANG[a], Yue WU[a,*], Guangyao XIN[a]

[a,*] School of Civil Engineering, Harbin Institute of Technology, Harbin, China
wuyue_2000@163.com

Abstract

Building deconstruction combats the negative environmental effects of traditional demolition by reducing the amount of waste materials and be embraced more than demolition. In order to promote the application of building deconstruction for prestressed structures, the dismantling methods of cable-strut tension structures were investigated in this study. Four possible dismantling methods were proposed based on the idea of releasing inside prestress by relaxing cables, and their mechanical state of the structure during dismantling, dismantling efficiency and cost of the four methods were compared using the numerical simulation method based on VFIFE. Results indicated that the method of relaxing radial cables and method of dropping inner rings has more advantages, while the method of relaxing inner ring cables and method of relaxing radial cables in batches increase the risk of dismantling works. Then, a dismantling experiment was carried out that confirmed the dismantling method of dropping inner rings is feasible and the numerical simulation method is accurate.

Keywords: building deconstruction, wheel-spoke cable-strut tension structures, dismantling method, numerical study, experimental study

1. Introduction

Traditional demolition produces numerous waste products, causing harmful impacts on the environment and society, such as land occupation, groundwater pollution and air contamination [1]. As a result, scholars have proposed the concept of building deconstruction to reduce the negative economic and environmental impacts of demolition. Building deconstruction refers to the systematic dismantling of buildings to recover the maximum amount of reusable and recyclable materials in a safe environmentally responsible, cost-effective manner [2]. Therefore, it has economic and environmental benefits over traditional demolition and tends to become the main strategy [3]. Dismantling refers to the systematic removal of as-built buildings while maintaining the integrity of the building materials and plays an important role in building deconstruction [4]. Several studies have been conducted on dismantling of high-rise buildings [5-7].

The cable-strut tension structure is a self-balanced system composed of continuous cables and discontinuous compression struts [8]. The most interesting features of the cable-strut tension structural system is light weight and high efficiency of force transmission, which have attracted attention from engineers for decades [9]. Therefore, it has been widely used in numerous large-span spatial structures recently such as the Maracana Stadium in Brazil, the Busan Stadium in South Korea [10] and the Shenzhen Bao'an Stadium in China [11]. And lots of studies focused on its erection process. Guo et al. [12] gave four erection methods and designed a tensioning experiment of a scale model that adopted cable-strut tension structural system to verify the feasibility. Yuan and Dong [13] proposed a construction simulation inverse method of prestressed structures based on the inverse process of erection.

However, the dismantling of cable-strut tension structures has received little attentions. As time goes on, a large number of cable-strut tension structures will be demolished due to the degraded performance and inadequate use as time goes on, while there are some challenges resulting from complex structural

Copyright © 2023 by Jiaqi YANG, Yue WU and Guangyao XIN. Published in the Proceedings of the IASS Annual Symposium 2023 with permission.

system need to be addressed, such as complex force transferring path, adverse effects of internal force release. Therefore, this study conducted experiment and numerical analysis on the dismantling method of the typical cable-strut tension structure, wheel-spoke structural system, giving a reference for the dismantling project of the same type of prestressed structures.

2. The dismantling methods

The cable-strut tension structures usually be erected by dragging radial cables using winches and tension devices. Studies have demonstrated that demolishing these structures by directly cutting off cables results in prestress release, producing a vibration that affects surrounding people and buildings [14]. Therefore, the dismantling of cable-strut tension structures is achieved through the relaxation of cables, and the relaxed cable is defined as the active cable. Taking the wheel-spoke prestressed structures which is the typical cable-strut tension structure for instance, four dismantling methods were proposed in reference to the erection of the wheel-spoke cable-strut tension structures.

The first dismantling method is achieved by relaxing radial cables, and the main steps are as follows: (1) arrange some relaxation devices on lower radial cables; (2) relax lower radial cables gradually to make the structure slack, and meanwhile, remove all struts and lower cables; (3) relax upper radial cables until the upper inner ring reach the ground; (4) remove the remaining components, and the dismantling is completed.

The second dismantling method is achieved by relaxing inner ring cables, and the main steps are as follows: (1) arrange some relaxation devices on upper or lower inner ring cables; (2) relax inner ring cables gradually to the desired length; (3) arrange some relaxation devices on lower radial cables and relax them, and meanwhile, remove all struts and lower cables; (4) arrange some relaxation devices on upper radial cables and relax them until the upper inner ring reach the ground; (5) remove the remaining components, and the dismantling is completed.

The third dismantling method is achieved by relaxing radial cables in batches, and the main steps are as follows: (1) arrange some relaxation devices on lower radial cables; (2) relax odd-numbered and even-numbered lower radial cables alternately, and meanwhile, remove some struts and lower cables gradually; (3) arrange some relaxation devices on upper radial cables and relax them until the upper inner ring reach the ground; (5) remove the remaining components, and the dismantling is completed.

The fourth dismantling method is achieved by relaxing radial cables and dropping inner rings, and the main steps are as follows: (1) arrange some hoisting points at the inner ring in the centre of the structure; (2) arrange some relaxation devices on lower radial cables, and relax them gradually to make the structure slack, and meanwhile, remove some struts and cables; (3) drop the inner rings by relaxing hoisting ropes until the upper radial cables become slack, and the remove all upper radial cables; (4) drop the inner rings continuously until they reach the ground; (5) remove the remaining components, and the dismantling is completed.

3. Numerical study

3.1. Numerical simulation method based on VFIFE

Due to the nonlinear finite element method has several challenges caused by the singularity of the stiffness matrix of assembly with geometrical instability. Therefore, the vector form intrinsic finite element (VFIFE) was proposed to solve strong nonlinear problems such as large deformation, fracture, and collision. Therefore, this study adopted the VFIFE method to simulate the dismantling process of the wheel-spoke cable-strut tension structures. The main principles of the simulation method are as follows.

The strut is simulated using the 3D bar element which can only bear the axial force. Assuming that a bar element moves in a path element ($t_a \sim t$), the internal force at time t can be calculated as follows:

$$F_t^{int} = F_{ta}^{int} + \Delta F_t^{int} = F_{ta}^{int} + EA\Delta\varepsilon \tag{1}$$

where F_{ta}^{int} is the internal force at time t_a, ΔF_t^{int} is the internal force increment from time t_a to t, E is the Young's Modulus, A is the cross-section area, $\Delta\varepsilon$ is the strain increment.

The cable element is simulated using a straight-line model. The solving process of internal force is the same as the 3D bar element. The difference is that the cable element cannot be compressed. Therefore, the internal force is set to zero when the cable element is slack under compression and expressed as follows:

$$F_t^{int} = \begin{cases} F_{ta}^{int} + \Delta F_t^{int} & \text{tension} \\ 0 & \text{compression} \end{cases} \tag{2}$$

The relaxation of cables is achieved by applying temperature loads, and the internal force increment of the cable element can be calculated as follows:

$$\Delta F_t^{int} = EA\left[\Delta\varepsilon - \alpha\left(T_t - T_a\right)\right] \tag{3}$$

In addition, the outer ring beam of the structure can be defined as the 3D beam element in the numerical model that can bear axial force, shear force, bending moment and torque simultaneously, and each node of the 3D beam element having six degrees of freedom. Assuming that the 3D beam element moves in a path element ($t_a \sim t$), the internal force increment vectors are written as follows:

$$\Delta\hat{\mathbf{F}}_t^{int} = \begin{bmatrix} \Delta\hat{f}_1^1 \\ \Delta\hat{f}_1^2 \\ \Delta\hat{f}_1^3 \\ \Delta\hat{f}_2^1 \\ \Delta\hat{f}_2^2 \\ \Delta\hat{f}_2^3 \end{bmatrix} = \begin{bmatrix} -\dfrac{EA}{l_a}\hat{\Delta}_e \\ \dfrac{6EI_3}{l_a^2}\left(\hat{\varphi}_1^3 - \hat{\varphi}_2^3\right) \\ \dfrac{6EI_2}{l_a^2}\left(\hat{\varphi}_1^2 - \hat{\varphi}_2^2\right) \\ \dfrac{EA}{l_a}\hat{\Delta}_e \\ -\dfrac{6EI_3}{l_a^2}\left(\hat{\varphi}_1^3 - \hat{\varphi}_2^3\right) \\ -\dfrac{6EI_2}{l_a^2}\left(\hat{\varphi}_1^2 - \hat{\varphi}_2^2\right) \end{bmatrix}, \quad \Delta\hat{\mathbf{M}}_t^{int} = \begin{bmatrix} \Delta\hat{m}_1^1 \\ \Delta\hat{m}_1^2 \\ \Delta\hat{m}_1^3 \\ \Delta\hat{m}_2^1 \\ \Delta\hat{m}_2^2 \\ \Delta\hat{m}_2^3 \end{bmatrix} = \begin{bmatrix} -\dfrac{GI_1}{l_a}\hat{\varphi}_1^1 \\ \dfrac{EI_2}{l_a}\left(4\hat{\varphi}_1^2 + 2\hat{\varphi}_2^2\right) \\ \dfrac{EI_3}{l_a}\left(4\hat{\varphi}_1^3 + 2\hat{\varphi}_2^3\right) \\ -\dfrac{GI_1}{l_a}\hat{\varphi}_1^1 \\ \dfrac{EI_2}{l_a}\left(2\hat{\varphi}_1^2 + 4\hat{\varphi}_2^2\right) \\ \dfrac{EI_3}{l_a}\left(4\hat{\varphi}_1^3 + 2\hat{\varphi}_2^3\right) \end{bmatrix} \tag{4}$$

Based on the above theory, the numerical simulation procedure of dismantling process for the prestressed structures is proposed in this study shown in Figure 1.

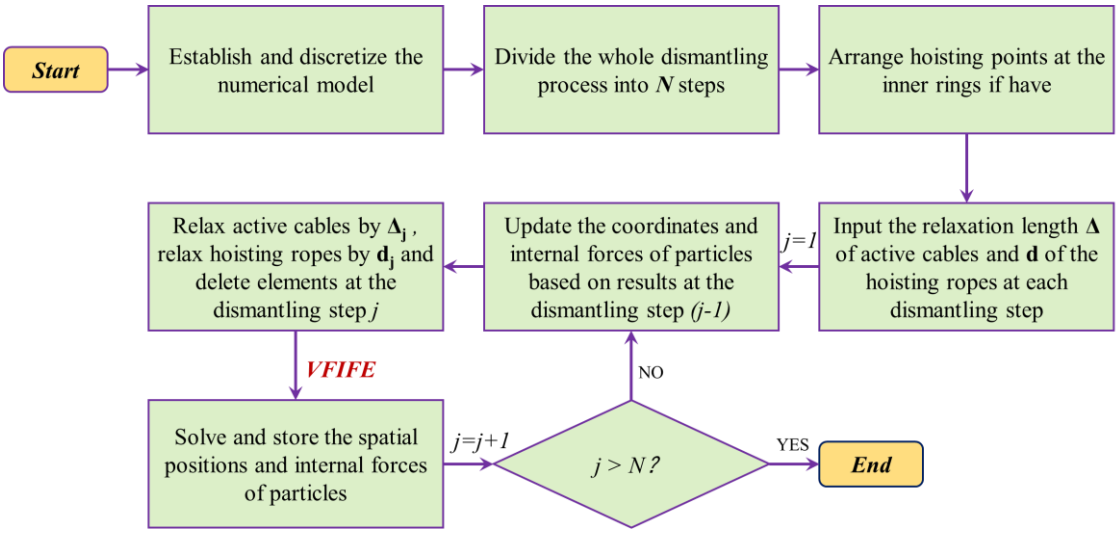


Figure 1. The numerical simulation procedure of the dismantling process

3.2. Comparative analysis of dismantling methods

This section compared the four dismantling methods in terms of mechanical state, dismantling efficiency and cost of relaxation devices. The model for comparative analysis is shown in Figure 2 that is a traditional wheel-spoke cable-strut tension structure. The main components of the model including upper radial cables, lower radial cables, inner ring cables (upper and lower ring), crossed cables between inner rings, four circle struts, outer ring beams and columns. The horizontal projection of the outer ring and inner ring in the model is the circle with the span of 160 m and 80m, respectively. The height of inner rings is 20m.

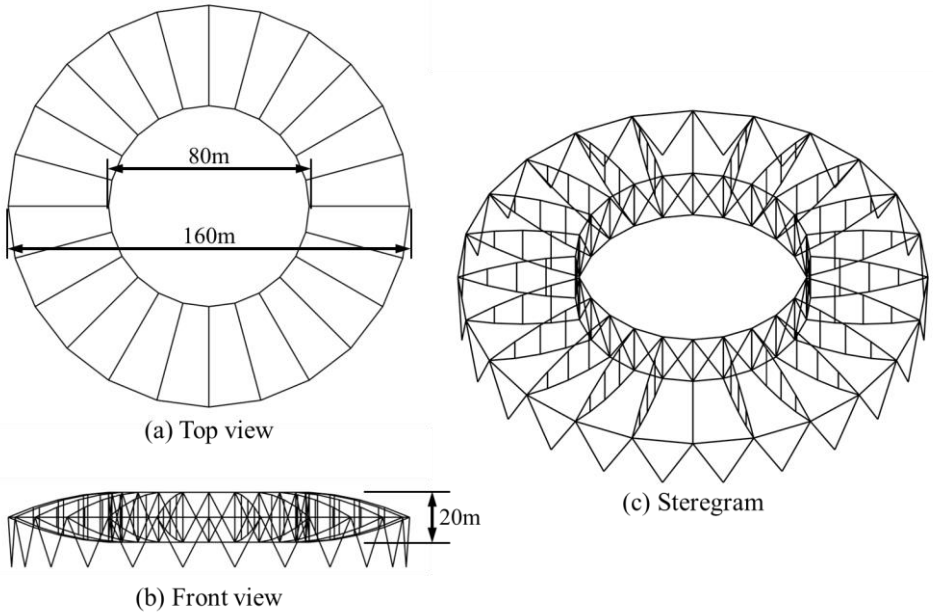


Figure 2. The model for comparative analysis

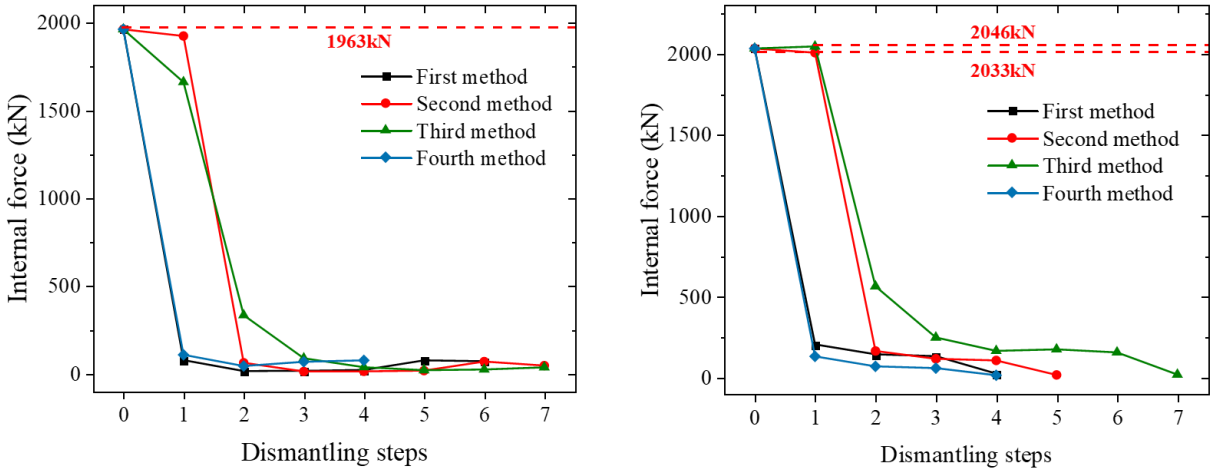
The dismantling efficiency when removing struts at outer circles can be measured by the average relaxation length of the active cables. Table 1 lists the average relaxation lengths of active cables for four dismantling methods. We can know that the relaxation length of the fourth method is the smallest,

which indicates that the fourth method has higher efficiency when relaxing active cables to remove struts.

Table 1. The average relaxation lengths of active cables for four dismantling methods

	First circle struts	Second circle struts	Third circle struts
First method	291	100	496
Second method	260	86	413
Third method	397	100	255
Fourth method	205	120	0

The internal forces of cables during dismantling of four methods are shown in Figure 3. The model is very sensitive to the relaxation of cables and was slack gradually during dismantling. This means it is effective to dismantle wheel-spoke cable-strut tension structures according to the idea of releasing prestress by relaxing cables. In addition, the load-bearing capacity of the relaxation device is determined by the internal force of the active cable during dismantling. The higher the load-bearing capacity requirement, the higher the design cost. As shown in Figure 3, the load-bearing capacity of the relaxation device for lower radial cables should be greater than 2033 kN, 2033 kN, 2046 kN and 2033 kN for the first, second, third and fourth methods, respectively. And the relaxation devices for upper radial cables should be greater than 1963kN for four methods. Therefore, the third dismantling method has least economic advantage due to the high requirement of relaxation device. This study also found that the crossed cables adjacent to the relaxed inner ring cables increased by more than ten times in the second dismantling method, which will greatly increase the risk of dismantling work.



(a) Upper radial cables (b) Lower radial cables

Figure 3. The internal forces of cables during dismantling

According to the above analysis, relaxing inner ring cables in second method and relaxing lower radial cables in batches in third method are adverse for dismantling wheel-spoke cable-strut tension structures. Therefore, the first method of relaxing radial cables and the fourth method of dropping inner rings are advised in this study. The fourth method has higher dismantling efficiency than first method.

4. Experimental study

4.1. Experimental model

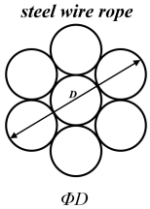
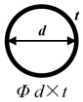
The experimental model is shown in Figure 4 that adopted the wheel-spoke cable-strut tension structural system. It comprises upper cables, lower cables, upper ring cables, lower ring cables, crossed cables between upper and lower inner rings, struts and an outer ring beam. The upper cables are crossed with each other, and the lower cables are orthogonal with the inner ring cables. The columns and braces are arranged between the outer ring beam and the steel support platform.

The horizontal projection of the experimental model is an ellipse, whose major and minor axis lengths are 12.675 m and 11.750 m, respectively. The maximum cantilever length is 3.010 m. The elevation of the upper ring cable, lower ring cable and the outer ring beam is 2.904 m, 1.932 m, and 2.340 m, respectively. The properties of components in the experimental model is listed in Table 2. As shown in Figure 5, There are 56 upper cables (UCs) and 56 lower cables (LCs) in the experimental model. The connections between cables and steel components are shown in Figure 6.

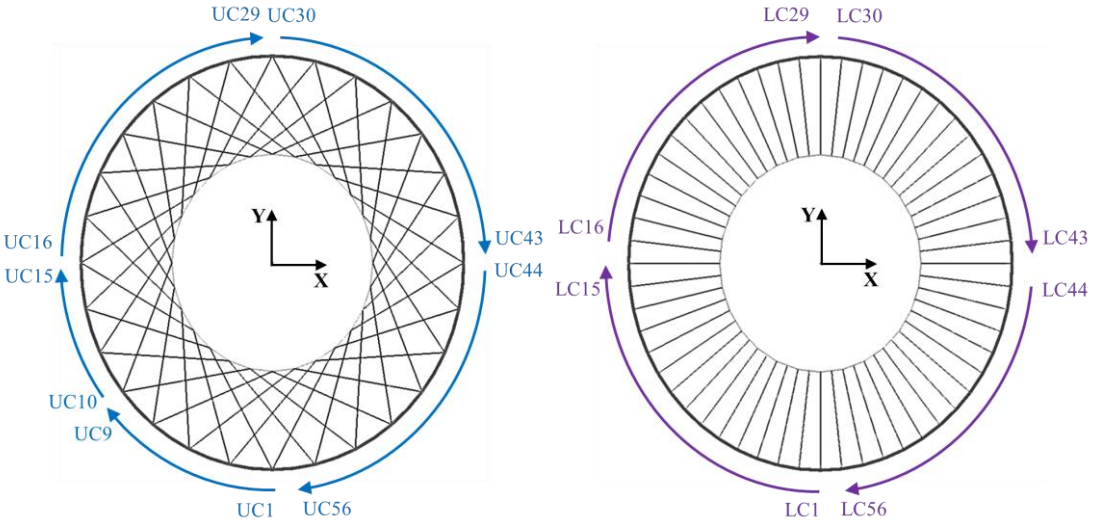


Figure 4. Experimental model

Table 2. The properties of components in experimental model

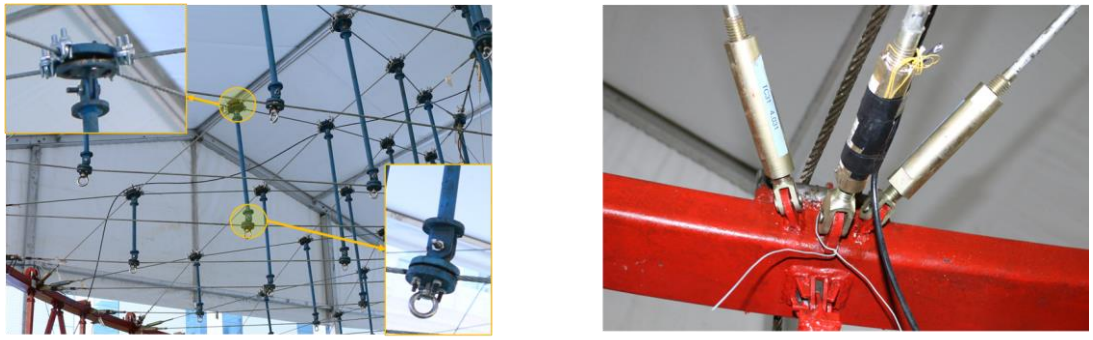
Component name	Type	Cross section (mm)	Young's modulus (N/mm^2)	Density (kg/mm^3)
Upper ring cable	steel wire rope  ΦD	Φ11	1.60×10^5	6.5×10^3
Lower ring cable		2Φ14	1.60×10^5	6.5×10^3
Upper cable		Φ6	1.60×10^5	6.5×10^3
Lower cable		Φ7	1.60×10^5	6.5×10^3
Cross cable		Φ3.6	1.60×10^5	6.5×10^3
Strut	circular steel tube  Φ d×t	Φ25×2 Φ20×2	2.10×10^5	7.85×10^3

Outer ring beam	square steel tube □$b\times h\times t_1\times t_2$	□60×120×5×5	2.10×10^5	7.85×10^3
Column and brace		□40×30×1.5×1.5	2.10×10^5	7.85×10^3



(a) Upper cables (b) Lower cables

Figure 5. The schematic diagram of the numbering of upper and lower cables



(a) Struts and cables (b) Outer ring beam and cables

Figure 6. The connections between cables and steel components

4.2. Dismantling scheme

The dismantling scheme of the experimental model was made according to the fourth method described in Section 2. The lower cable was regarded as the active cable and relaxed using the relaxation device. The dismantling process is described in detail as follows:

Stage 1: The first stage is to arrange seven hoisting points at structural center using the masts and chain hoists, as shown in Figure 7. Afterward, the hooks of the chain hoist are connected to upper ring cable nodes. The length of the iron chain with the hook can be adjusted manually.

Stage 2: In this stage, the odd-numbered lower cables (LC1, LC3, …, LC53, LC55) are considered active. They are relaxed in three steps (steps 1 - 3). The outer struts at the fifth circle are removed after step one, and the outer struts at the third circle are removed after step two. The active cables are relaxed at step three until they became slack. After undergoing all three steps, the odd-numbered lower cables are removed.

Stage 3: The even-numbered lower cables (LC2, LC4, …, LC54, LC56) are considered active in this stage. They are relaxed in four steps (steps 4 - 7). The outer struts at the sixth, fourth and second circles are removed after steps four, five and six, respectively. The active cables are relaxed at step seven until they are slack, and the even-numbered lower cables are removed at this step.

Stage 4: In this stage, the iron chains with the hook of the hoist chain are relaxed, dropping the residual model until the upper cables are slack at step eight. Subsequently, the slack upper cables are removed.

Stage 5: This stage is to relax the iron chains with the hook of the hoist chain until the lower ring cables reach the ground. Afterward, the crossed cables, inner struts and lower ring cables are removed.

Stage 6: This stage involves dropping the inner rings to the ground, removing the remaining components, and sorting them for storage.

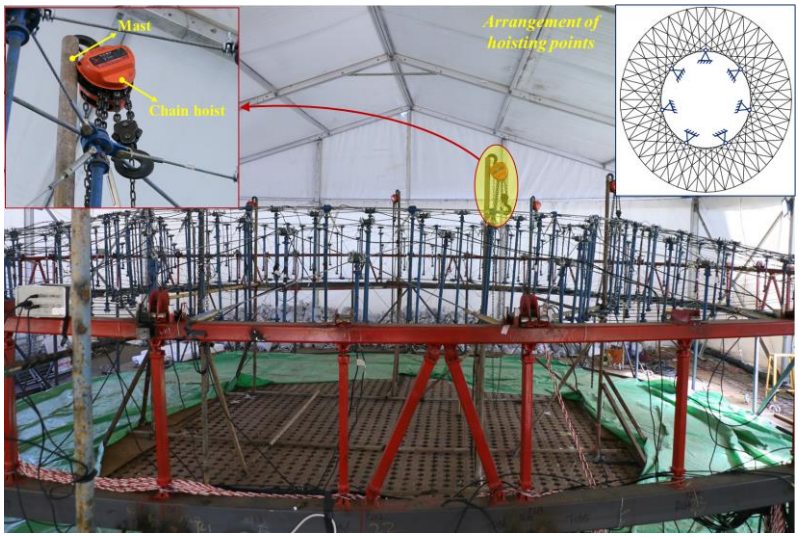


Figure 7. Arrangement of hoisting points

The designed relaxation device is shown in Figure 8. It consists of two force-transmission steel blocks, two threaded rods and two fixtures. The force-transmission steel block can be divided into two pieces connected by four bolts to facilitate installation. A single cable can be tensioned and relaxed by the mean of screwing nuts at the end of threaded rod to make two force-transmission steel blocks close to or away from each other.

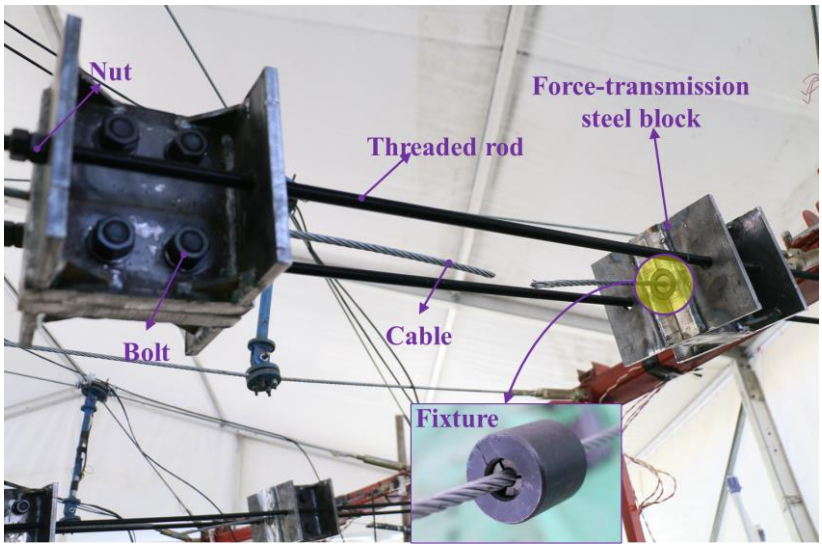
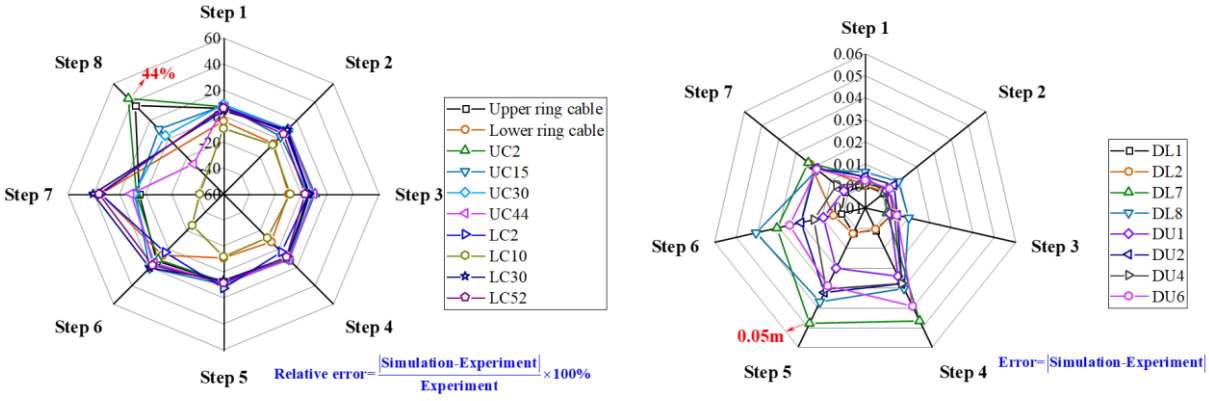


Figure 8. The relaxation device of a single cable

4.3. Results and discussion

The dismantling process of the experimental model was simulated successfully through the proposed numerical simulation method. The damping coefficient was 100, and the time step was 0.0001 s. The calculation stopped when the unbalanced force at each particle was less than 0.1 N.

The errors between experimental and numerical results during dismantling are shown in Figure 9. As we can see, the maximum relative error of the internal force is 44%, which is large and occurs in UC2 at step eight, but the absolute error is only 72 N obtained by the absolute value of the difference between the experimental and the simulated results, which is not large. And the maximum deviation of the nodal vertical displacement is 0.05 m that is 1/255 of the structural span, which occurs in DL7 at step five. The measured errors, accumulative errors and control errors are main reasons that large errors occur during dismantling. In summary, the numerical simulation method proposed in this paper can assist practitioners to formulate the dismantling process with high accuracy.



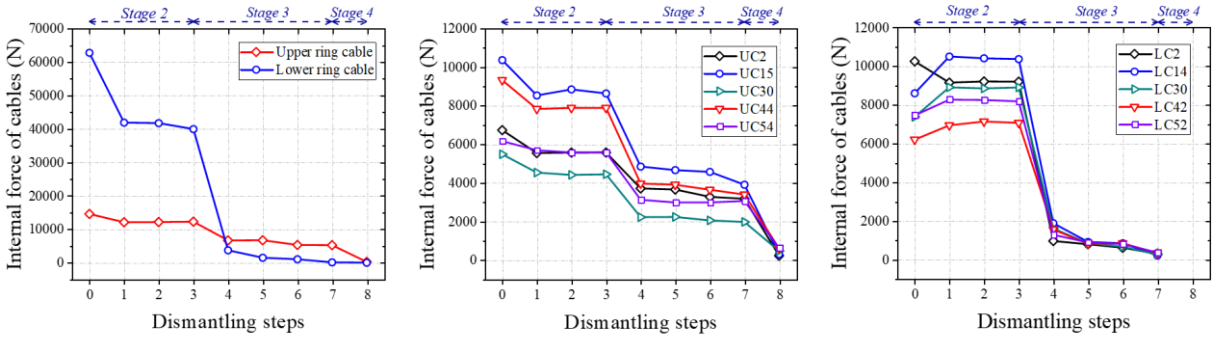
(a) The relative errors of the internal force (unit: %)

(b) The errors of the nodal vertical displacement (unit: m)

Figure 9. Errors between experimental and numerical results during dismantling

Moreover, the internal forces of cables during dismantling are shown in Figure 10. We can see that the prestress of the experimental model is almost completely released as the relaxation of the active cable and the drop of the inner ring, which reduces the adverse effects of the removal of components. This

indicates the dismantling scheme of the experiment model is feasible. Therefore, the wheel-spoke cable-strut tension structure can be dismantled successfully using the method of dropping inner rings.



(a) Inner ring cables (b) Upper cables (c) Lower cables

Figure 10. The internal forces of different cables during dismantling

5. Conclusions

The dismantling methods of cable-strut tension structures are studied, and the main conclusions are as follows:

(1) It is effective to dismantling the cable-strut tension structures based on the principle of releasing inside prestress by relaxing cables.

(2) The method of relaxing inner ring cables and relaxing lower radial cables in batches are adverse for dismantling wheel-spoke cable-strut tension structures. And the method of relaxing radial cables and the method of dropping inner rings has more advantages on efficiency, safety and economy. This can be used as the reference for practical dismantling projects.

(3) The numerical simulation method based on VFIFE is accurate in tracking the dismantling process of cables-strut tension structures, which provides an effective tool for the numerical analysis and validation of dismantling process.

Acknowledgements

This research was conducted with financial support from the National Natural Science Foundation of China (Grant NO. 52078163).

References

[1] X. Hu and Y. Zhou, Vanhullebusch S, Mestdagh R, Cui ZY, Li JB, “Smart building demolition and waste management frame with image-to-BIM,” *Journal of Building Engineering*, vol. 49, pp. 104058, 2022.

[2] G. Bradley Guy, *Building Deconstruction*, R.S. Means, 2010.

[3] A. Akbarnezhad, KCG. Ong and L. R. Chandra, “Economic and environmental assessment of deconstruction strategies using building information modeling,” *Automation in construction*, vol. 44, pp. 1-5, 2014.

[4] J. Xiao, L. Zeng, B. Xia and T. Ding, “Theoretical framework and fundamental method for deconstruction engineering,” *Journal of Building Engineering*, vol. 43, pp. 197-206, 2022.

[5] M. Kayashima, Y. Shinozaki, T. Koga and H. Ichihara, “A New Demolition System for High-Rise Buildings,” In: CTBUH 2012 9th World Congress, Shanghai, China.

[6] R. Mizutani, “Jack Down Building Demolition Method-KC & D (The Kajima Cut and TakeDown Method),” *Journal of the Society of Mechanical Engineers*, vol. 114, pp. 424-425, 2011.

[7] W.J. Van Jaarsveldt, R.S. Walls and E. Van Der Klashorst, "Experimental testing and finite element modelling of steel columns weakened to facilitate building demolition," *International Journal of Steel Structures,* vol. 18, pp. 1483-1496, 2018.

[8] I. Mungan and J F. G. Abel, *Fifty Years of Progress for Shell and Spatial Structures: In celebration of the 50th Anniversary Jubilee of the IASS (1959-2009),* IASS Jubilee Book, 2012.

[9] Z. Sābetghadam, "Improving Spoke Wheel Roofs with the Geometry of Rasmi-Bandis," *Nexus Network Journal volume,* vol. 21, pp. 479-490, 2019.

[10] B. S. Jeon and J. H. Lee, "Cable membrane roof structure with oval opening of stadium for 2002 FIFA World Cup in Busan," In: Proceedings of sixth Asian-Pacific conference on shell and spatial structures, South Korea, 2000.

[11] G. Y. Tian, Y. L. Guo, B. H. Zhang, K. Wang and S. Y. Zhao, "Experiment on sensitivity to construction tolerance and research on tolerance control criteria in spoke structural roof of Bao'an Stadium," *Journal of Building Structures,* vol. 32, pp. 11-18, 2011.

[12] Y. L. Guo, G. Y. Tian, K. Wang, B. H. Zhang and S. Y. Zhao, "Tensioning experiment on spoke structural roof of Bao'an Stadium," *Journal of Building Structures,* vol. 32, pp. 1-10, 2011.

[13] X. F. Yuan and S. L. Dong, "Inverse analysis of construction process of cable dome," *Journal of Building Structures,* vol. 22, pp. 75-79, 2001.

[14] S. S. R. Pereira, M. D. C. Magalhaes and H. Gazzinelli, "An alternative technique to the demolition of a prestressed concrete box-girder bridge: A case study," *Case Studies in Construction Materials,* vol. 6, pp. 192-197, 2017.

Deployable and inflatable structures

Active bending
Additive manufacturing/ 3D printing
Architectural geometry
Bamboo for sustainable construction and quality of life improvement
Bio-inspired structures and architecture
Bridge structures
Computational form-finding
Conceptual design
Concrete structures
Construction techniques
► **Deployable and inflatable structures**
Design competition (WG21)
Digital modelling and fabrication
Dynamic response of metal spatial structures
Dynamic response of other structures
Form-finding and structural optimisation of interlocking discrete assemblages
Graphical methods
Gridshell and lattice structures
Historical concrete shells
Historical structures
Lattice structures
Life-cycle design and assessment of structures
Metal gridshell structures, connections and stability
Methods and construction technologies for sustainable shell structures
Morphology and configuration processing
Next generation parametric design
Novel methods in modelling, optimisation and construction for reducing carbon footprint of continuous roof shells
Numerical methods for geometry, form-finding and optimisation of lightweight structures
Optimisation methods and applications
Origami
Other
Teaching design uncertainty: working with unknown qualities/quantities of new and re-claimed materials
Teaching of shell and spatial structures
Tensegrity systems and cable structures
Tension and membrane structures
Tension structures in the Asia-Pacific
Timber and bio-based structures
Topology optimisation
Traditional masonry structures and innovation
Transformable structures

Proceedings of the IASS Annual Symposium 2023
Integration of Design and Fabrication
10–14 July 2023, Melbourne, Australia
Y.M. Xie, J. Burry, T.U. Lee and J. Ma (eds.)

A foldable modular structure unit inspired by kirigami

Zafira Nur Ezzati MUSTAFA[a] , Kok Keong CHOONG[*], Jae-Yeol KIM[b]

[*] School of Civil Engineering, Universiti Sains Malaysia
14300 Nibong Tebal, Penang, Malaysia
cekkc@usm.my

[a] Toyohashi University of Technology, Aichi, Japan
[b] Hyupsung University, Gyeonggi, Republic of Korea

Abstract

Kirigami originates from origami where cutting and folding are combined. The idea of kirigami has been employed in kinematic structure where movement of stretching and folding are made possible. Foldable modular structure unit inspired by kirigami is explored in this study. It is aimed at achieving a foldable structure which has the benefits of minimum space storage requirement and ease in transportation. Kirigami inspired foldable structures have seen application in furniture design. This study focuses on application of idea of kirigami in structures such as bus stops, exhibition booths and structures of temporary nature. In order to achieve a structural concept of kirigami inspired modular foldable structure unit, this study has experimented with three different planar geometrical shapes upon which kirigami patterns are cut: hexagonal, square and triangle shapes. The cut kirigami patterns on different planar geometrical shape are chosen such that the corresponding 3D structure is formed after folding of the planar shape. After considering the ease of arranging modular units in different patterns(such as back-to-back, side-by-side) to form structures with different outlook, the one with triangular geometrical planar shape has been chosen. The study has also experimented with the construction of a full scale kirigami inspired triangular foldable modular unit made of wooden panel to test the feasibility of the proposed idea.

Keywords: kirigami, deployable structure, modular structure

1. Introduction

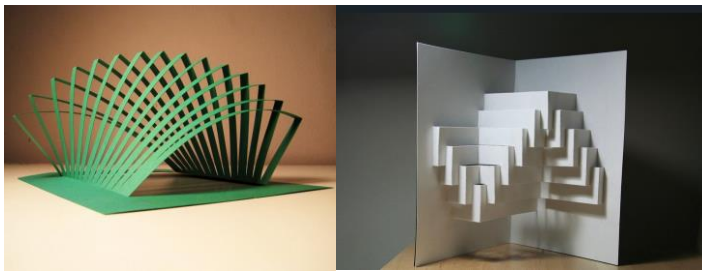
The concept of kirigami originates from origami where cutting and folding are combined. It is used in kinematic structure where stretching and folding are possible. The use of kirigami to form different architecture objects was pioneered by Chatani[1]. Taking advantage of properties of kirigami, method to design kirigami pattern[2] and computational tool for design of kirigami-inspired lightweight metamaterial[3] have been proposed. A review of recent advances in kirigami design has been compiled by Tao et al[4]. Figure 1 shows examples of objects achievable using kirigami. An example of application of idea of kirigami in furniture design is shown in Figure 2.

This study explores the possibility of applying the characteristics of kirigami to the design of foldable modular structure units. The idea is to use the units to form different structure through different arrangement pattern as shown in Figure 3 which has the benefits of minimum space storage requirement and ease in transportation. This study focuses on application to structures such as bus stops, exhibition booths, and any other types of structure for temporary usage.

The layout of the paper is as follows: i. the experimental study on basic plan geometry, kirigami pattern and folding process of foldable modular unit is first described; ii. detailed study on possible layouts of

Copyright © 2023 by Zafira Nur Ezzati MUSTAFA, Kok Keong CHOONG and Jae-Yeol KIM. Published in the Proceedings of the IASS Annual Symposium 2023 with permission.

arrangement to form different final structures are next presented; iii. the construction of a full scale foldable modular unit is described.



(a) (b)

Figure 1. Kirigami arts [https://parametrichouse.com/kinetic-architecture-2-2/].



Figure 2. Kirigami inspired furniture [https://www.toxel.com/inspiration/2012/03/03/rising-furniture/].

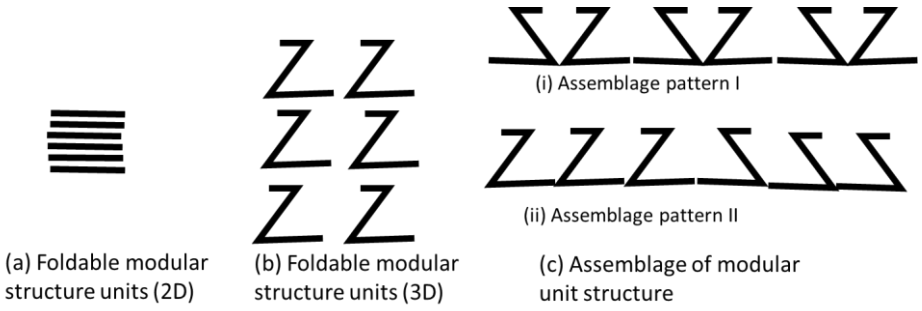


Figure 3. Assemblage of foldable modular structure units.

2. Experimental study on foldable modular structure units

The process of design of a suitable foldable modular structure unit involves: i. investigation of possible shape of plan geometry and choice of kirigami pattern, ii. checking of unfolding shape and iii. selection of the suitable design. Choices of the plan geometry and size of the modular unit are to be decided by the designer. It is important to take note that the plan geometry affects the posible arrangement pattern of modular units while kirigami pattern affects the unfolding process and the final unfolded shape of the modular unit. The type of kirigami structure adopted is the so-called 90° angle type[5] where the single

sheet of paper is folded into two via bending and cutting. Three types of plan geometry were considered: triangle, square and hexagon. The plan geometry was first drawn using AUTOCAD and then mirrored. Kirigami pattern was then added. The pattern was chosen in such a way that a final wall-roof modular structure unit could be formed in the unfolded state. Figures 4 to 6 show the process of design of modular structure unit with plan geometry of triangle, square and hexagon, respectively.

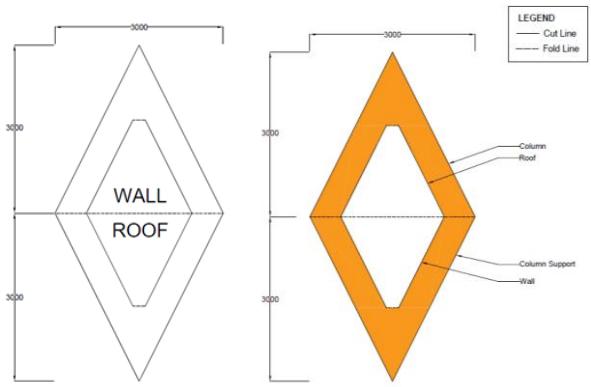


Figure 4. Process of design of triangular modular structure unit.

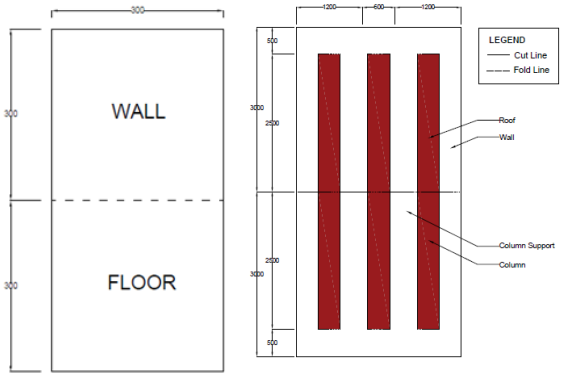


Figure 5. Process of design of square modular structure unit.

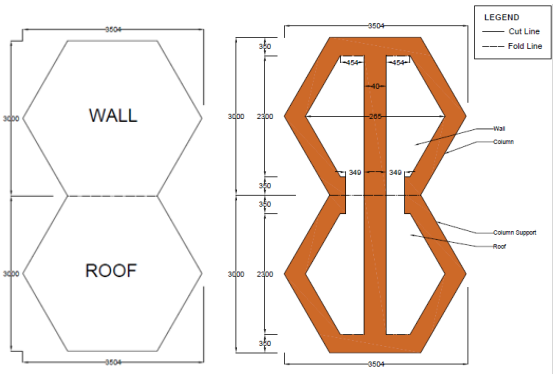


Figure 6. Process of design of hexagonal modular structure unit.

Paper models where then formed based on AUTOCAD drawing with proper cut lines. Figures 7 to 8 show the unfolded shape of the modular structure unit based on plan geometry of triangle, square and hexagon.

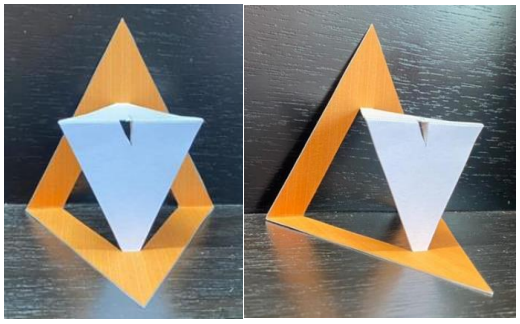


Figure 7. Unfolded shape of triangular modular structure unit.

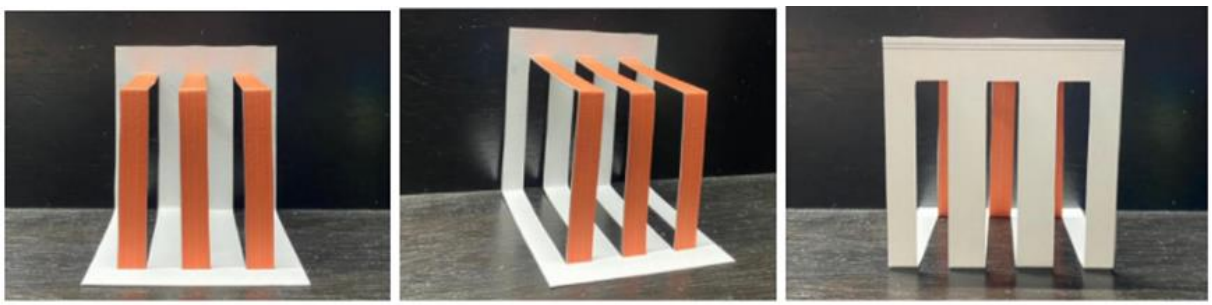


Figure 8. Unfolded shape of square modular structure unit.

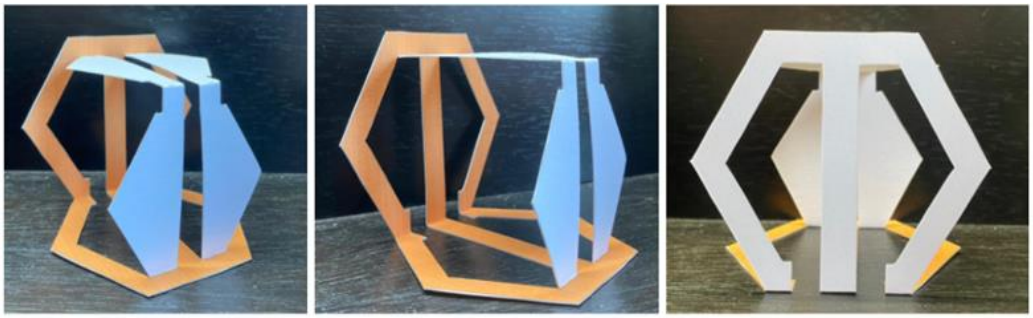


Figure 9. Unfolded shape of hexagonal modular structure unit.

Triangular foldable modular structure unit as shown in Figure 4 and 9 was chosen for further investigation into different possible structure through different arrangement or assemblage patterns of the units. Figure 10 shows the planar drawing of the foldable triangular modular structure unit used for further investigation while Figure 11 shows the paper model of the unfolded triangular modular structure unit. Outcomes of arrangement patterns with units being placed side-by-side and back-to-back were studied. Figures 12 and 13 show the structures formed by placing the unit back-to-back and side-by-side, respectively. By combining of groups of structure formed by side-by-side placement of the triangular modular units, a larger closed loop structure can be formed as shown in Figure 14. The

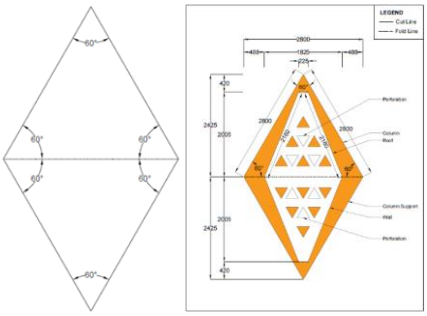


Figure 10. The triangular modular structure unit chosen for further study.

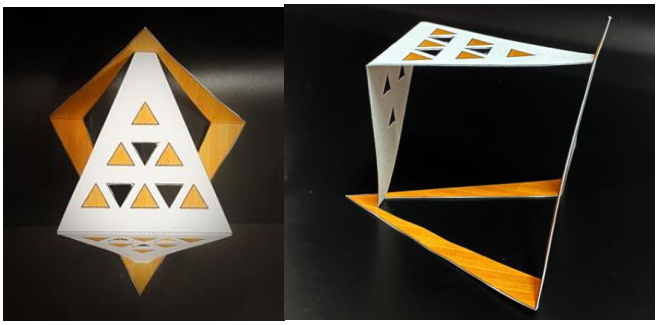


Figure 11. Paper model of the triangular modular structure unit in unfolded state.

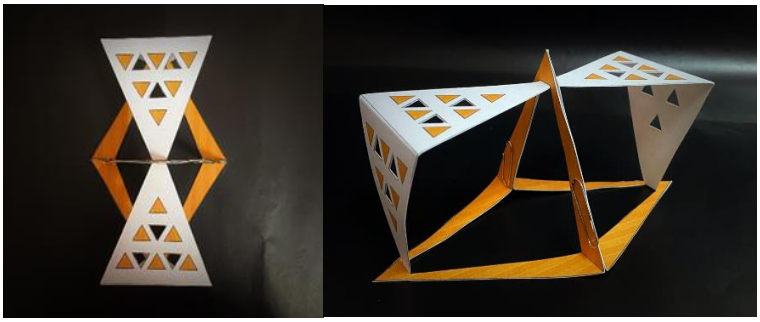


Figure 12. Twin modular unit formed by back-to-back placement of the triangular modular unit.



Figure 13. Structure formed by side-by-side placement of the triangular modular unit.

possibility of forming double layer structure using the triangular modular structure unit was also explored as shown in Figures 15 and 16.

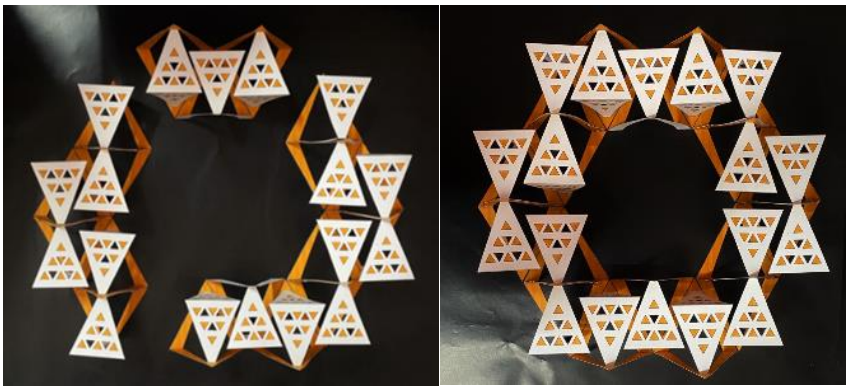


Figure 14. A close-loop structure is formed by combining groups of modular units placed side-by-side.

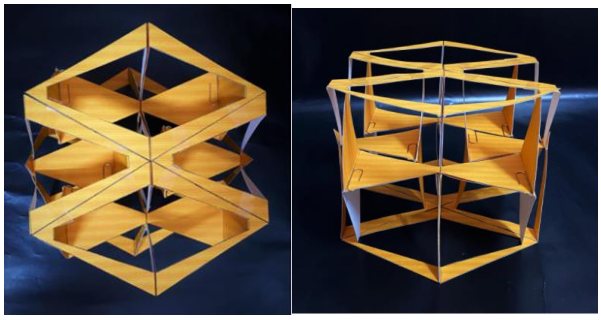


Figure 15. A basic double-layer structure formed using the triangular modular units.

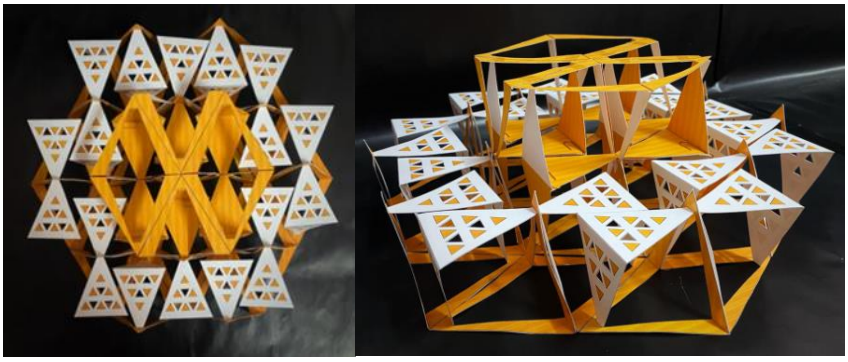


Figure 16. Combination of single-layer and double-layer units formed by the triangular modular units.

3. Physical model of the foldable triangular modular unit

A physical model measuring 2.8 m × 2.425 m (size of base triangle) and 2.425 m (height) was constructed. Plywood with thickness of 12 mm was used. Modular units which were cut based on dimension given in Figure 10 was first made (see Figure 17). Then, hinges were installed in location

of fold lines as shown in Figure 18. The unfolded shape of the physical model of the foldable triangular modular unit is shown in Figure 19.



Figure 17. Parts of the triangular modular unit.

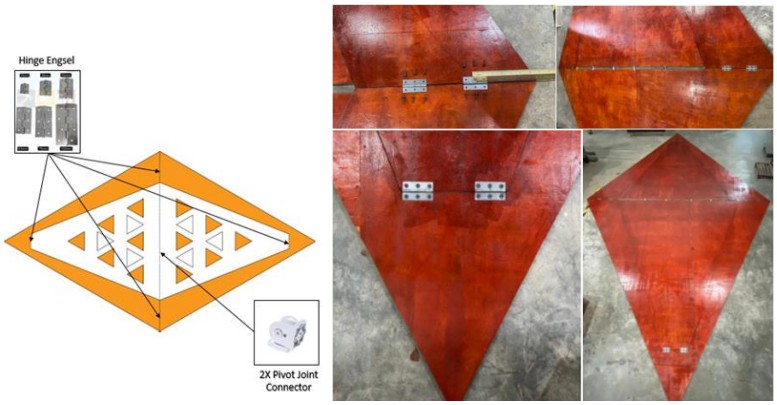


Figure 18. Locations of hinges.

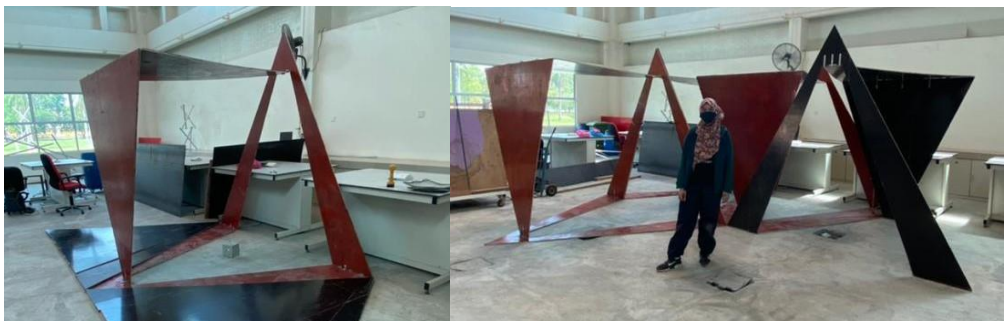


Figure 19. The completed physical model of foldable triangular modular unit.

4. Conclusion

Foldable modular structure unit inspired by kirigami which can be arranged in different pattern to form different structure was proposed. A physical model of the chosen foldable triangular modular structure unit was construction to investigate the practicality of the proposed modular unit. Future study to improve hinge design and to study the structural behaviour of the proposed unit should be carried out in order to bring the proposed idea towards reality.

Acknowledgements

This research was supported by Basic Science Research Program through the National Research Foundation of Korea(NRF) funded by the Ministry of Education (NRF-20192B4014562).

References

[1] M. Chatani, *Pop-Up Origamic Architecture*, Ondorisha Publication, 1985.

[2] J.Liu, G. Chuang, H.C.Sang and J.E.Sabin, "Programmable Kirigami: Cutting and Folding in Science, Technology and Architecture," in *Proceedings of the ASME 2019, International Design Engineering Technical Conference and Computers and Information in Engineering Conference, IDETC/CIE2019*, Anaheim, CA, USA, August 18-21, 2019.

[3] H. Zhang and J. Paik, "Kirigami Design and Modelling for Strong, Lightweight Metamaterials" *Advanced Functional Materials,* 32, 2107401, 2022.

[4] J. Tao, H.Khosravi, V.Deshpande and S. Li, "Engineering by Cuts: How Kirigami Principle Enables Unique Mechanical Properties and Functionalities*", Advanced Science,* 10, 2204733, 2023.

[5] N. Ando, N.Yamahata, S.Masumi and M.Chatani, "Shape Grammar and Form Properties of Architectural Figures*", Journal for Geometry and Graphics*, Vol.5, No.1, pp. 23-33, 2001.

IASS 2023
July 10–14 Melbourne
Integration of Design and Fabrication

Proceedings of the IASS Annual Symposium 2023
Integration of Design and Fabrication
10–14 July 2023, Melbourne, Australia
Y.M. Xie, J. Burry, T.U. Lee and J. Ma (eds.)

Comparison of biologically inspired functionally graded deployable geosystems with experimental measurements

Ann C. SYCHTERZ[*], Kaylee A. TUCKER[a]

[a,*] University of Illinois at Urbana-Champaign
205 N. Mathews Ave. Urbana, IL 61801
asychter@illinois.edu

Abstract

Deployable structures provide novel methods for resisting tensile forces for underground geosystems. A rotationally deploying geosystem has been developed and can be improved upon through the design of the material construction of the awns. A rigidity-based graded design is biologically inspired and is matched with the expected function of the geosystem. This paper presents an experimental methodology to design and test the optimization of the existing geosystem through the use of functionally graded materials (FGMs). The paper also presents awn grading patterns using FGMs and their experimental results using the developed methodology. By concentrating stiffer material at the bottom of the awn, the awn will deploy out of plane. This is expected to lead to a higher resistance capacity for the system as increases the projected surface area of the awn. A parametric design script will translate planar patterns onto the curved awns and they will be manufactured by a multi-material 3D-printer. This paper determines whether the presented experimental methodology is appropriate for testing material optimization of the awns. It also utilizes this process to design functionally graded materials that improve geosystem performance. The design and experimental methodologies successfully allow for the understanding of how FGMs can be applied to the geosystem. Improving the performance of the geosystem through functionally graded materials would allow for more sustainable construction.

Keywords: deployable, compliant, geosystem, parametric design, experimental validation, functionally graded materials

1. Introduction

1.1 Deployable structures

Deployable structures are structures that move from a compact state to an expanded state, changing shape as they change size [1]. Tuneable flexibility is possible depending on the type of joints and materials used in the structure [2]. Rigid deployable structures, like scissor structures [3] are comprised of materials with high stiffness and need joints in order to deploy. These structures may require locking connections [4]. Single-use deployable structures, used in solar sails and other space applications [5] often feature flexible materials. Despite their decreased stiffness in comparison to rigid materials, flexibility allows for more optimal material use. A hybrid between these two extremes, rigid-flexible deployable structures—examples of which include deployable masts with flexible cables [6]—contain a combination of rigid and flexible elements. This combination of materials can also be seen in applications where flexible, compliant joints connect rigid elements [2]. Deployable structures have been constructed aboveground and in space applications but have not yet been extended to underground uses.

Copyright © 2023 by Ann C. SYCHTERZ and Kaylee A. TUCKER. Published in the Proceedings of the IASS Annual Symposium 2023 with permission.

1.2 Compliant structures

Compliant structures utilize plastic or elastic deformations to change shape. These shape changes are generally concentrated in a particular element, whereas deployable structures usually change shape on a system-level scale. Requiring a balance between stiffness and flexibility, these structures are least compliant when they maximize stiffness and are most compliant when they minimize stiffness [7]. Compliant structures are also advantageous because they are lightweight, decreasing transportation requirements [8], [9]. These advantages have made compliant structures popular for a wide range of applications including endoscopic cameras [10], aviation parts [10], and—within the building sector—façade components [11]. Despite their utility, compliant structures have not yet been widely used in structural applications.

1.3 Geotechnical structures

Pile anchors are a type of underground foundation system that must resist compression from gravity and tension from friction. Driven pile anchors are advantageous due to their versatility in withstanding a wide variety of load and soil conditions [12]. However, they can have environmental effects during installation [13]. While there are some downsides to using anchor piles, they are advantageous as foundation elements due to their versatility.

Existing research has been done regarding geosystems involving static or shape-changing protrusions. Static radial fins installed on the perimeter of an anchor pile installed in sand were found to better resist uplift loads [15]. Deployable anchor piles have also been explored. For this system, once the pile is installed in sand, wings hinge outward to provide resistance to uplift loads [17]. As of now, geotechnical research has involved static or rigid body motion. The advantages of compliant systems have not yet been explored in geotechnical engineering applications.

1.4 Bio-inspired design

Deployable and compliant structures are found in nature [1], [11]. Leaves unravelling and flowers blooming are two examples of biological deployable compliant mechanisms [18]. Bio-inspired systems have also been developed within the field of civil engineering. Large-scale origami structures inspired by the folding mechanisms of leaves, petals, and insect wings have been developed using joints in place of folds [19]. These origami structures use a deployable compliant system as a precedent, but the compliant features are not preserved in the final design.

1.5 Functionally graded materials

A material is considered functionally graded when changes in the properties of the material are closely matched with the function of the part in which it is used [20]. Functionally graded materials (FGMs) can have advantages as they can match material properties to function [21]. These materials have been used in a wide variety of applications at both small and large scales. At a small scale, artificial ligaments [22] and microfluidic valves [23] have been developed using FGMs. Large scale architectural work has also leveraged these materials. Agricultural shading devices have been created from 3D-printed biopolymers, using different materials to control insect attraction, structural integrity, and solar protection [24]. Knitted textiles have also been created using different stitch patterns as materials to control shading patterns [25]. FGMs have been used at larger scales but have not yet been applied to structural or geotechnical systems.

2. Overview

2.1 Structure description

This work considers a geosystem (Figure 1) that is comprised of a cylindrical tension-loaded pile covered in a system of compliant fin-like attachments. These compliant elements, called awns, deploy

into the sand through rotation. Foundational work of this paper focuses on only a few awns rather than the whole surface of the pile. When deployed, the awns undergo bending as they change shape and size. This entraps soil and increases surface friction.

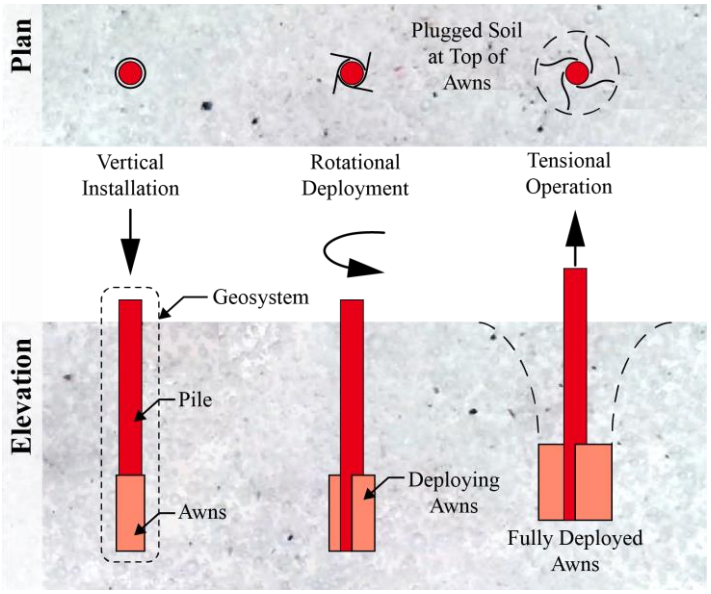


Figure 1. Schematic illustration of the geosystem showing system installation, deployment, and operation.

2.2 Physical fabrication

Additive manufacturing—using a Stratasys Objet500 Connex3 resin 3D printer [26]—was used to fabricate the test members. This machine is capable of printing multi-material parts with a layer thickness of 25 microns over a build volume of 0.5 m x 0.4 m x 0.3 m. GrabCAD Print [27], a software that allows for material selection and model setup, is used to send models to the printer.

Materials with various levels of flexibility are available on the Objet500 Connex3 printer and can be combined with each other to create additional materials with intermediate qualities (Table 1).

Table 1. Polymer materials, their composition, and their properties.

Material Name	**Material Composition**	**Tensile Strength**
VeroMagentaV	100% Acrylic-like resin; Fully rigid	65 MPa [28]
VeroCyan	100% Acrylic-like resin; Fully rigid	65 MPa [28]
Agilus30	100% Rubber-like resin; Fully flexible	3.1 MPa [29]
FLXA-MT-S95-DM-vivid	95% VeroMagentaV, 5% Agilus30; Semi-flexible	62 MPa
FLXA-CT-S95-DM	95% VeroCyan, 5% Agilus30; Semi-flexible	62 MPa

The first three materials noted in Table 1 were used as-is. These included two rigid, acrylic-like materials—VeroMagentaV and VeroCyan—and one flexible, rubber-like material—Agilus30. The following two materials in Table 1 are combinations of the previous materials. The fourth material is a combination of the rigid and flexible materials at a ratio of 95% VeroMagentaV and 5% Agilus30. This produced a semi-flexible magenta polymer called FLXA-MT-S95-DM-vivid. Combining VeroCyan and Agilus30 in the same way produced a similar polymer in cyan called FLXA-CT-S95-DM. This ratio of rigid to flexible material produces a somewhat flexible material and is the most rigid of material

combinations that the Objet500 printer can produce. The tensile strength of FLXA-MT-S95-DM-vivid and FLXA-CT-S95-DM were found by calculating a weighted average of their constituent materials.

3. Methodology

3.1 Awn stiffness variations - global

Initial tests of the geosystem used the semi-flexible polymer, FLXA-MT-S95-DM-vivid [30] as the material was flexible enough to allow the awns to deploy. However, it was important to gain an understanding in how stiffness played a role in the deployability of the system. The variations described here vary the material of the awns to determine whether awns printed in the stiffer VeroMagentaV material would adequately deploy.

An awn with a thin profile was produced in VeroMagentaV and was compared with previously tested awns printed in FLXA-MT-S95-DM-vivid. The VeroMagentaV awn was significantly more rigid than the FLXA-MT-S95-DM-vivid awn.

3.2 Awn stiffness variations - graded

The following set of variations explored awns that program increased stiffness within an awn. These functionally graded awns were inspired by plant structures and concentrated stiffer material at the bottom of the awn to allow for more deformation towards the top of the awn and more stiffness towards the bottom (Figure 2).



Figure 3. Biologically-inspired FGMs applied to a deployable compliant geosystem: (a) geosystem model, (b) leaf, as inspiration and (c) pattern applied onto awn.

Introducing stiffer material at the bottom of the awn would allow the top portion of the awn to deform outwards while keeping the bottom of the awn deploying in the XY plane. This outward deformation would increase the projected surface area of the awn and improve the performance of the awn.

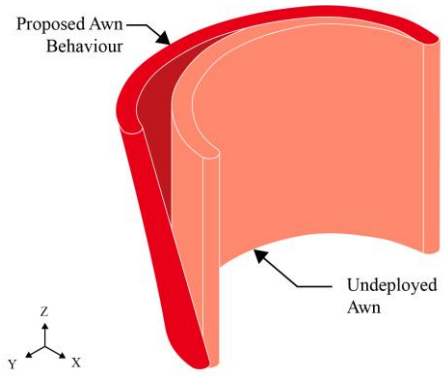


Figure 2. Representation of proposed awn deployment behaviour.

The grading patterns were inspired by the veins in leaves and were drawn flat before being projected onto the curved awns (Figure 4). A baseline awn (Figure 4a) and three patterned awns were compared. The first patterned awn (Figure 4b) had symmetrical linear leaf veins and was positioned so that the

central vein was at the centre of the awn. The second pattern (Figure 4c) featured asymmetric linear leaf veins and was positioned lower on the awn – the centre vein was located at a height of 1/4 times the height of the awn. The last pattern (Figure 4d) was placed at the bottom of the awn and was comprised of two arcs. These two arcs were analogous to the centre vein and the upward-facing vein as seen in the third pattern (pattern c).

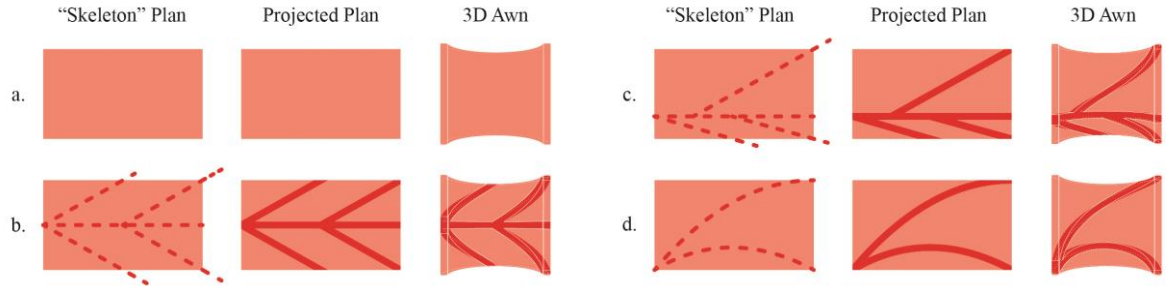


Figure 4. Tested graded patterns and the percentage of rigid material.

In order to transfer the patterns from flat, two-dimensional drawings to a highly-curved three-dimensional awn, Grasshopper—a parametric design tool within Rhinoceros 3D [31]—was utilized. The plugins Parakeet, Pufferfish, Heteroptera, Human, and Telepathy [32]–[36] were also used.

First, an awn footprint was loaded into the definition (Figure 5a). This curve provided the base for the application of the pattern. Each awn was comprised of two connected curves – an inner curve and an outer curve. Once deconstructed (Figure 5b), each curve was discretised into ten linear elements (Figure 5c). The length of these linear curves was defined as l_o for the outer curve and l_i for the inner curve. The linear curves were moved so that they were offset from the original curve (Figure 5d). This ensured that the pattern can be projected in one direction and intersect with the original, non-discretised curve. These offset discretised curves provided the base for the construction of rectangles that were constructed to have the height of the awn (h) (Figure 5e).

The outer pattern canvas was created by generating a rectangle with the length of the ten linear curves (l_o) and the height of the awn (h). The pattern canvas was divided along the horizontal axis so that smaller separator rectangles were created that were the same width as the length of the discretised curves. This process was repeated for the inner curve (Figure 5f). The outer rectangle was baked into the Rhinoceros workspace and a skeleton-like pattern was explicitly drawn in Rhinoceros (Figure 5g). Lines that intersected with the edge of the pattern canvas at an angle were extended so that they would intersect with the edge correctly when thickened. The line-based pattern was loaded into the Grasshopper file and was offset so that each line became 1 mm thick (Figure 5h). This thickened pattern was used throughout the rest of the definition.

The pattern was split into segments corresponding to the separator rectangles. The segments were sorted and reorganized so that ten data branches were created. Each data branch corresponded with and contained the segments located in a single separator rectangle (Figure 5i). The pattern was mapped from the separator rectangles on the larger pattern canvas to the separator rectangles on the smaller one (Figure 5j). These patterns were then mapped from the separator rectangles to the rectangles created from the offset discretised curve (Figure 5k, 5l). The pattern was merged so that unnecessary lines were removed (Figure 5m) and was projected to a surface created by extruding the non-discretised curve (Figure 5n). The solid objects were built from two parts. The first part was created by generating surfaces to fit within the projected curves (Figure 5o) and the second part was formed by connecting the inner and outer curves through the Sweep2 command (Figure 5p, 5q). These two collections of surfaces were joined to create the solid objects (Figure 5r). The final geometry was comprised of a solid awn extruded from the original awn footprint and a collection of solid objects that together create the pattern (Figure 5s).

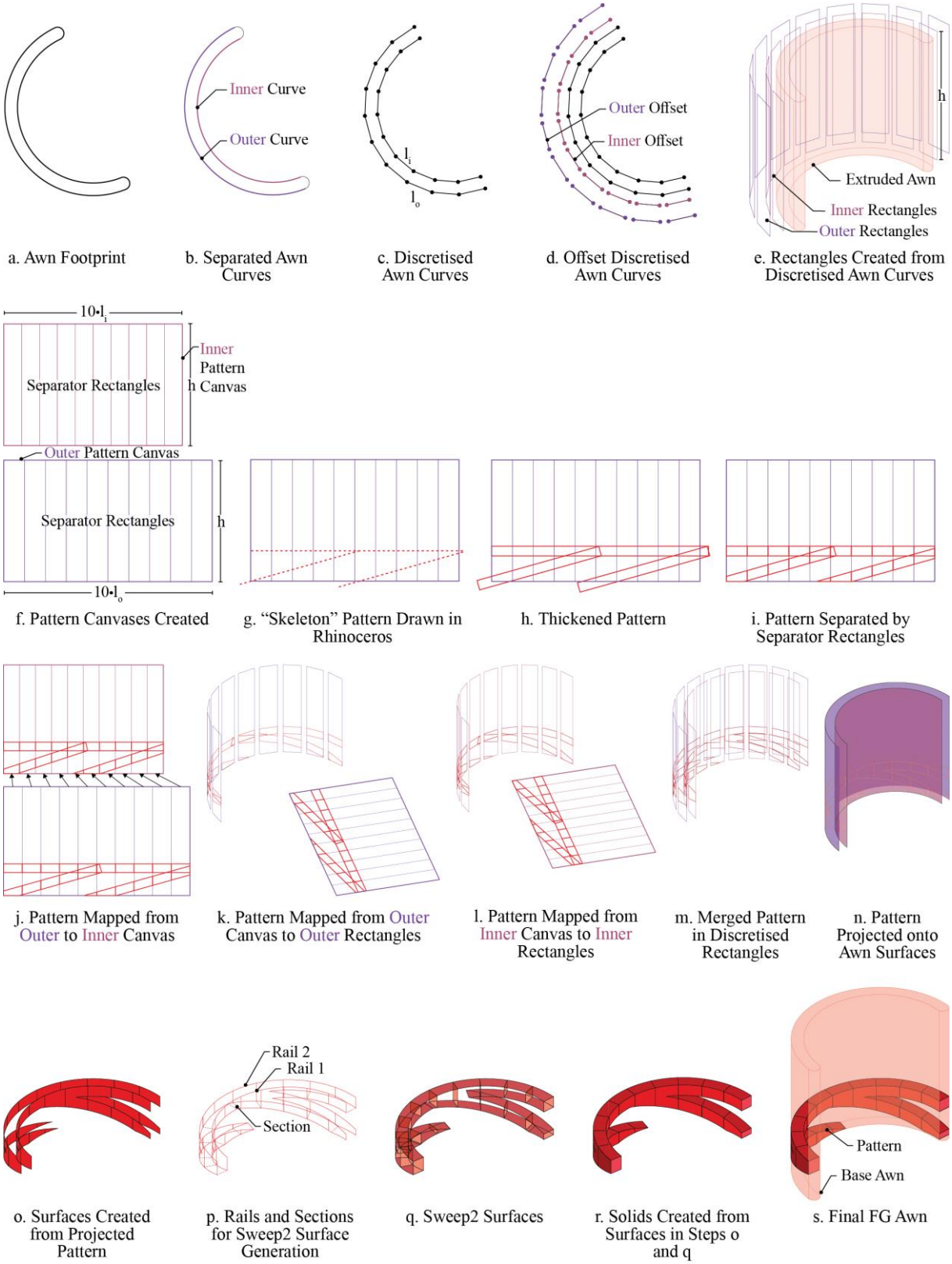


Figure 5. Step-by-step sequence showing generation of a functionally graded patterned awn using the parametric workflow.

A few adjustments were made to the model to facilitate testing. The base awn shape was extended in one direction and a 1 mm wide line was printed in FLXA-CT-S95-DM to ensure that the awn was placed in the same location for each test. Two holes, each with a radius of 1.25 mm, also were created.

Once the three-dimensional model was complete, the awns were printed (Figure 6). The functionally graded awns were loaded into GrabCAD Print to set up the print and used two materials: a semi-flexible background material (FLXA-MT-S95-DM-vivid) and a stiff pattern material (VeroMagentaV). After printing, tracking markers were placed on the awns to show where the start and end of the original awn curve were, excluding the support extension of the awn.

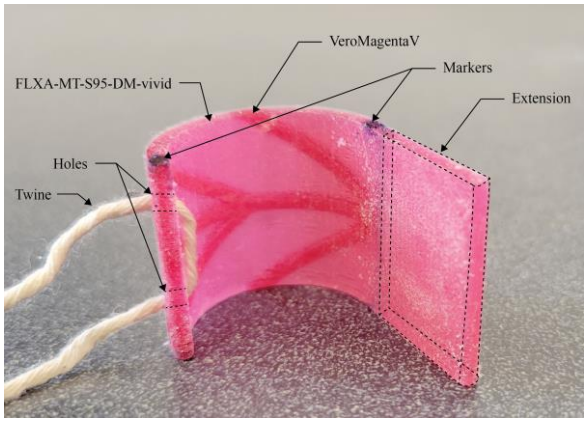


Figure 6. Printed awns for testing, showing materials and parts.

The functionally graded patterns were analysed by performing tension tests on the awns. Cotton kitchen twine was threaded through the two holes on the testing sample so that a knot could be tied on the outside of the awn with 6.4 cm of slack. A PASCO PASPORT High Resolution Force Sensor [37] was placed on the end of the twine. This force sensor has a range of ± 50 N and a resolution of 0.002 N. A piece of 1.905 cm plywood was mounted to a table and the awn was clamped to the edge of the plywood (Figure 7).

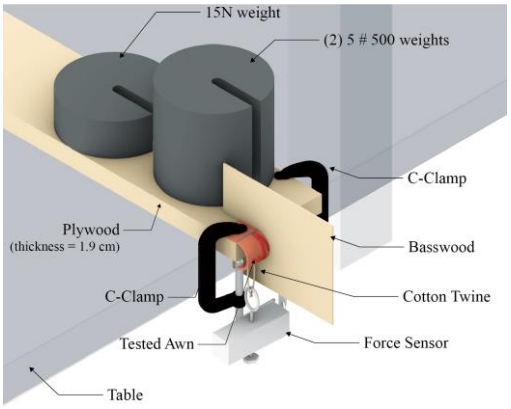


Figure 7. Tension test setup with labels.

An Inswan INS-1 document camera [38] was set up to capture an elevation view of the awn to measure displacement. The PASCO force sensor was recorded on PASCO's Capstone software [39] with a collection rate of 25 Hz. In order to synchronize the force and displacement data, the two outputs were simultaneously recorded with a screen recorder, Open Broadcaster Software (OBS) Studio [40].

The tension tests were performed by loading the awn with 10 N of force, unloading it, and then repeating twice more for a total of three tests. The load was applied instantaneously as plastic deformation and creep are not considered in the scope of this work. The experiment was repeated with the camera facing

the other direction so that both sides of the awn could be analysed (Figure 8). All tests were performed to view the bottom of the awn first and then repeated to view the top.

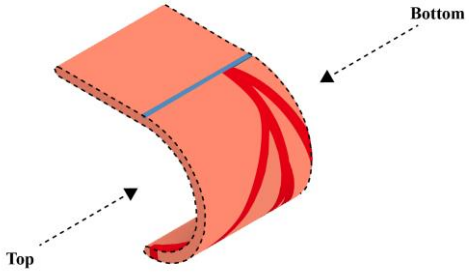


Figure 8. Representation of document camera direction and corresponding awn profiles.

Video frames were extracted from the recordings from the document camera before the test began and at each loading. As the collection rate of the force data was not able to be set to match the frame rate of the displacement data, the still image was extracted for the first frame that recorded a force above 10 N. To process the data, the curves were traced in Rhinoceros 3D. A composite curve was calculated by finding the arithmetic mean of the three loaded curves generated for each pattern. This curve was then compared to the unloaded curve and is discussed in Section 4.2.

4. Results

4.1 Awn stiffness variations - global

When the rigid awns were tested in sand, it was found that the awns did not appreciably deploy (Figure 9).

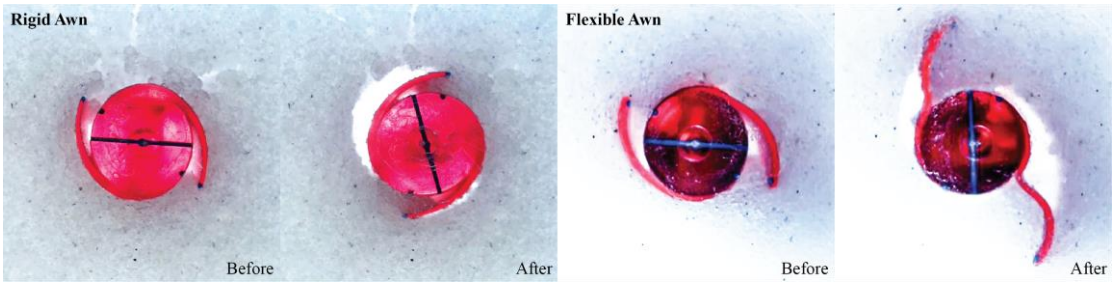


Figure 9. Geosystem with (left) rigid thin awn and (right) flexible awn before and after deployment.

Table 2. Average deployment of rigid and flexible awns.

	Rigid Awns	Flexible Awns
Average Deployment (mm)	0.57	12.41

As shown in Table 2, the rigid awns had deployments under 1 mm. This can be considered negligible, especially in comparison to the 12.41 mm average deployment than can be seen with the flexible awns. Therefore, increasing the stiffness of the awn produced an awn that was incapable of deployment. A more targeted approach is necessary to increase the stiffness of the awns without sacrificing the deployability of the system.

4.2 Awn stiffness variations – graded

The percent elongation of the awns was determined and compared (Figure 10) for both the top and bottom of the awn, as defined in Figure 8.

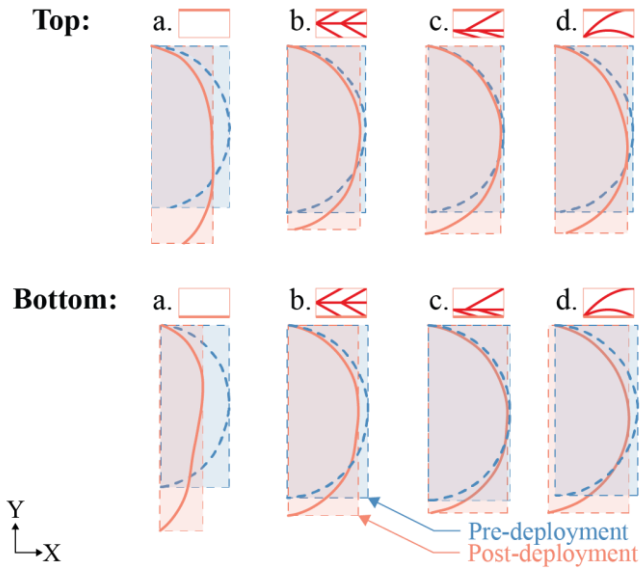


Figure 10. Awn profiles from top and bottom shown before deployment (blue) and after deployment (pink).

Table 3. Percent elongation in the Y direction for the top and bottom of the awn

	a.	b.	c.	d.
Top	22.3%	10.0%	13.0%	12.7%
Bottom	26.9%	10.4%	7.0%	10.3%

Pattern a, a control awn that did not contain a graded pattern, predictably had the most elongation (Table 3). As this awn only contained the semi-flexible FLXA-MT-S95-DM-vivid material, it was the most flexible of the awns tested. Due to the increased stiffness from the pattern in the functionally graded material, the overall stiffness of the awns was greater in patterns b-d compared with a. Pattern b, the symmetrical pattern, showed equal elongation on the top and the bottom of the awn. In contrast, the two asymmetrical patterns—c and d—underwent far more elongation on the top of the awn than the bottom.

These patterns could be helpful in the design of deployable compliant geosystems. A symmetrical pattern like pattern b may help if the geosystem requires slightly stiffer awns than can be achieved with the FLXA-MT-S95-DM-vivid material alone. This type of pattern distributes stiffness evenly throughout the awn. The two asymmetrical patterns—c and d—could be particularly useful because the bottom of the awn elongates less than the top. The bottom of the awn remains flexible enough to deploy but the top of the awn is more flexible. When applied in context on the geosystem, this type of awn can potentially bend out of plane, allowing for a larger projected surface area and more contact with the soil above. Pattern c may be more useful if less flexibility is needed at the bottom of the awn as more material is concentrated there than in pattern d.

6. Conclusions and future work

The parametric design method presented in this paper successfully allows for the design of functionally graded awns. This design method transfers flat patterns to highly curved surfaces for use in deployable compliant geosystems. The work presented here provides a parametric method for the design and an experimental methodology for the assessment and behaviour of the these patterns.

Future work will include more detailed analysis of these and additional patterns. Additionally, these patterns will be applied in context and tested as a full geosystem.

Acknowledgements

The authors gratefully acknowledge support from the National Science Foundation (Award #2207296) and University of Illinois at Urbana-Champaign and the State of Illinois.

References

[1] S. Pellegrino, *Deployable Structures*. Wien-New York: Springer Verlag, 2001.

[2] X. Zhang, R. Nie, Y. Chen, and B. He, "Deployable Structures: Structural Design and Static/Dynamic Analysis," *J Elast*, vol. 146, no. 2, pp. 199–235, Nov. 2021, doi: 10.1007/s10659-021-09860-6.

[3] Y. Akgün, C. J. Gantes, W. Sobek, K. Korkmaz, and K. Kalochairetis, "A novel adaptive spatial scissor-hinge structural mechanism for convertible roofs," *Engineering Structures*, vol. 33, no. 4, pp. 1365–1376, Apr. 2011, doi: 10.1016/j.engstruct.2011.01.014.

[4] C. J. Gantes, J. J. Connor, R. D. Logcher, and Y. Rosenfeld, "Structural analysis and design of deployable structures," *Computers & Structures*, vol. 32, no. 3, pp. 661–669, Jan. 1989, doi: 10.1016/0045-7949(89)90354-4.

[5] J. Block, M. Straubel, and M. Wiedemann, "Ultralight deployable booms for solar sails and other large gossamer structures in space," *Acta Astronautica*, vol. 68, no. 7, pp. 984–992, Apr. 2011, doi: 10.1016/j.actaastro.2010.09.005.

[6] G. Tibert and S. Pellegrino, "Deployable Tensegrity Masts," presented at the 44th AIAA/ASME/ASCE/AHS/ASC Structures, Structural Dynamics, and Materials Conference, Apr. 2003. doi: 10.2514/6.2003-1978.

[7] M. Frecker, "Synthesis through Topology Optimization," in *Handbook of Compliant Mechanisms*, John Wiley & Sons, Ltd, 2013, pp. 93–107. doi: 10.1002/9781118516485.ch7.

[8] L. L. Howell, S. P. Magleby, and B. M. Olsen, *Handbook of compliant mechanisms*. Chichester, West Sussex, United Kingdom Hoboken, New Jersey: John Wiley & Sons, Inc, 2013.

[9] S. Kota and G. K. Ananthasuresh, "Designing compliant mechanisms," *Mechanical Engineering-CIME*, vol. 117, no. 11, pp. 93–97, Nov. 1995.

[10] "Example Application," in *Handbook of Compliant Mechanisms*, John Wiley & Sons, Ltd, 2013, pp. 277–317. doi: 10.1002/9781118516485.ch13.

[11] J. Lienhard, S. Schleicher, and J. Knippers, "Bio-inspired, Flexible Structures and Materials," in *Biotechnologies and Biomimetics for Civil Engineering*, F. Pacheco Torgal, J. A. Labrincha, M. V. Diamanti, C.-P. Yu, and H. K. Lee, Eds. Cham: Springer International Publishing, 2015, pp. 275–296. doi: 10.1007/978-3-319-09287-4_12.

[12] C. Aubeny, *Geomechanics of Marine Anchors*. Boca Raton: CRC Press, 2017. doi: 10.4324/9781351237376.

[13] A. Colaço, P. Alves Costa, C. Mont'Alverne Parente, and A. Silva Cardoso, "Ground-borne noise and vibrations in buildings induced by pile driving: An integrated approach," *Applied Acoustics*, vol. 179, p. 108059, Aug. 2021, doi: 10.1016/j.apacoust.2021.108059.

[14] Y. V. S. N. Prasad and S. N. Rao, "Lateral Capacity of Helical Piles in Clays," *Journal of Geotechnical Engineering*, vol. 122, no. 11, pp. 938–941, Nov. 1996, doi: 10.1061/(ASCE)0733-9410(1996)122:11(938).

[15] J. Tom, C. O'Loughlin, D. White, A. Haghighi, and A. Maconochie, "The effect of radial fins on the uplift resistance of buried pipelines," *Géotechnique Letters*, vol. 7, Mar. 2017, doi: 10.1680/jgele.16.00142.

[16] B. Wilde, H. Treu, and T. Fulton, "Field Testing of Suction Embedded Plate Anchors," presented at the The Eleventh International Offshore and Polar Engineering Conference, Jun. 2001.

Accessed: Feb. 11, 2022. [Online]. Available: https://onepetro.org/ISOPEIOPEC/proceedings/ISOPE01/All-ISOPE01/ISOPE-I-01-208/7989

[17] M. Sakr, A. Nazir, W. Azzam, and A. Sallam, "Model study of single pile with wings under uplift loads," *Applied Ocean Research*, vol. 100, p. 102187, Jul. 2020, doi: 10.1016/j.apor.2020.102187.

[18] J. F. V. Vincent, "Deployable Structures in Biology," in *Morpho-functional Machines: The New Species*, Tokyo, 2003, pp. 23–40. doi: 10.1007/978-4-431-67869-4_2.

[19] D. Baerlecken, R. Gentry, M. Swarts, and N. Wonoto, "Structural, Deployable Folds — Design and Simulation of Biological Inspired Folded Structures," *International Journal of Architectural Computing*, vol. 12, no. 3, pp. 243–262, Sep. 2014, doi: 10.1260/1478-0771.12.3.243.

[20] N. Oxman, S. Keating, and E. Tsai, "Functionally Graded Rapid Prototyping," *Proceedings of VRAP: Advanced Research in Virtual and Rapid Prototyping in: "Innovative Developments in Virtual and Physical Prototyping "*, pp. 483–489, Sep. 2011, doi: 10.1201/b11341-78.

[21] K. Dierichs and A. Menges, "Functionally Graded Aggregate Structures: Digital Additive Manufacturing With Designed Granulates," presented at the ACADIA 2012: Synthetic Digital Ecologies, San Francisco (California), USA, 2012, pp. 295–304. doi: 10.52842/conf.acadia.2012.295.

[22] T. Khan, "State of the art review of Functionally Graded Materials," May 2019, doi: 10.1109/ICOMET.2019.8673489.

[23] S. J. Keating, M. I. Gariboldi, W. G. Patrick, S. Sharma, D. S. Kong, and N. Oxman, "3D Printed Multimaterial Microfluidic Valve," *PLOS ONE*, vol. 11, no. 8, p. e0160624, Aug. 2016, doi: 10.1371/journal.pone.0160624.

[24] J. M. Lesna and P. Nicholas, "De gradus - Programming heterogeneous performance of functionally graded bio-polymers for degradable agricultural shading structures.," presented at the CAADRIA 2020: RE:Anthropocene, Bangkok, Thailand, 2020, pp. 383–392. doi: 10.52842/conf.caadria.2020.2.383.

[25] M. R. Thomsen *et al.*, "Knit as bespoke material practice for architecture," p. 10.

[26] "Objet500 Connex3." Stratasys Ltd., Eden Prairie, MN, 2014. [Online]. Available: https://www.stratasys.com/en/3d-printers/printer-catalog/objet-350-500-connex3-printers

[27] "GrabCAD Print." Stratasys Ltd., Eden Prairie, MN, Mar. 21, 2023. [Online]. Available: https://grabcad.com/print

[28] Stratasys, "Vero Material Data Sheet," *Stratasys*, 2021. https://stratasysstorage01.file.core.windows.net/ssys-websites-files-prod/Public1/Materials/Polyjet/Vero%20Family%20(Rigid)/Vero%20Family%20-%20EN%20Data%20Sheet%20PolyJet%20Material.pdf?sv=2017-04-17&sr=f&sig=T7J4HP%2FJKo2O8Pl3U350YFJfJ%2BfI%2BmDaHpdpiYQmbf0%3D&st=2022-08-27T14%3A11%3A05Z&se=2023-08-28T14%3A11%3A05Z&sp=rwl

[29] Stratasys, "Agilus30 Material Data Sheet," *Stratasys*, 2022. https://www.stratasys.com/siteassets/materials/materials-catalog/polyjet-materials/agilus30-colors/mds_pj_agilus30_cmy_0422a.pdf?v=4991e7

[30] K. Tucker and A. C. Sychterz (forthcoming), "Analyzing Geosystems with Deployable Compliant Mechanisms for Enhanced Tension Capacity," *Proceedings of the Canadian Society of Civil Engineering Annual Conference 2022*.

[31] "Rhinoceros." Robert McNeel & Associates, Seattle, Washington, Feb. 08, 2022. [Online]. Available: https://www.rhino3d.com/

[32] Esmaeil Mottaghi and Arman Khalilbeigi, "Parakeet." PARAGEN, Dec. 28, 2022. [Online]. Available: https://www.food4rhino.com/en/app/parakeet

[33] Michael Pryor, "Pufferfish." Nov. 23, 2021. [Online]. Available: https://www.food4rhino.com/en/app/pufferfish

[34] Amin Bahrami, "Heteroptera." Heliorippple Studio, Sep. 11, 2022. [Online]. Available: https://www.food4rhino.com/en/app/heteroptera

[35] Andrew Heumann, "Human." Aug. 05, 2019. [Online]. Available: https://www.food4rhino.com/en/app/human

[36] M. Syp and A. Heumann, "Telepathy." nbbj digital, Nov. 09, 2017. [Online]. Available: https://www.food4rhino.com/en/app/telepathy

[37] "PASPORT High Resolution Force Sensor." PASCO Scientific, Roseville, CA. Accessed: Mar. 24, 2023. [Online]. Available: https://www.pasco.com/products/sensors/pasport/ps-2189

[38] "INS-1 Document Camera." INSWAN. Accessed: Mar. 22, 2023. [Online]. Available: https://www.inswan.com/en/INS-1

[39] "PASCO Capstone." PASCO Scientific, Roseville, CA, 2022. [Online]. Available: https://www.pasco.com/products/software/capstone

[40] "OBS Studio." OBS Project, Oct. 04, 2021.

IASS 2023
July 10–14 Melbourne
Integration of Design and Fabrication

Proceedings of the IASS Annual Symposium 2023
Integration of Design and Fabrication
10–14 July 2023, Melbourne, Australia
Y.M. Xie, J. Burry, T.U. Lee and J. Ma (eds.)

Manual deployment and shape determining method of guide frame for tunnel inspection by force control

Fumihiro INOUE[a,*], Momoe TERATA[b], Shu LI[b], Suzuno FUKUNAGA[b], Satoru NAKAMURA[c]

[a,*] Shonan Institute of Technology
inoue@mech.shonon-it.ac.jp

[b] Graduated School of Shonan Institute of Technology
[c] Institute of Technology, Tokyu Construction

Abstract

This study describes a new shape control method for inspection guide frames that can change according to the shape of obstacles in tunnels. The guide frame is an arch structure that linearly connects VGTs (Variable Geometry Truss) composed of extended actuators and hinges, and its shape can be determined by controlling the length of each actuator. Changing the guide frame by automatic control required confirmation of the position and size of obstacles, and the speed of shape change was slowed in consideration of safety, so it took a lot of time. Against this background, we have developed a feedback control method that allows the guide frame to be freely deformed by placing a pull with a force sensor on a part of the frame and pulling it in the desired direction. Based on the information from the force sensor, the axial force acting on the guide frame was analuzed by using the finite element method, and established a mechanism that can change its shape according to the magnitude of the attractive force. This control method is a simple method of manually deforming the guide frame, and it can be applied to a variety of shapes, and it is effective in terms of safety because the shape can be changed instantly in an emergency.

Keywords: automated inspection system, guide frame, shape adaptation, variable geometry truss, obstacle detection, force control

1. Introduction

Road structures such as bridges and tunnels, which were built in large quantities during the high growth period, have been aging, and in recent years, many structures have increased large -scale repair. Since the tunnel is difficult to modfiy after completion, regular inspections have grasped the progress of deterioration, and maintenance and renewal based on future forecasts are being maintained. In general, regular inspection of the road tunnel regulates the traffic of the car, and the point of the inspection and the auxiliary detectors are performed as close as possible to the inspection site in a high -altitude work vehicle. However, due to the wide inspection range, it takes time to see close visibility and pounding, and long -time traffic regulations are required.

In this study, as shown in Fig. 1, we will construct an inspection system for the outer wall surface that allows movement while avoiding obstacles (disposal equipment, lighting, display boards, etc.) inside the tunnel without the usual traffic control. The stage of practical application has been already reached. In this development, the authors are mainly in charge of development related to variable shape control of inspection guide frames. So far, the three-dimensional laser system that detects obstacles in tunnels have been constructed, and also



Figure 1. View of tunnel inspection system

Copyright © 2023 by Fumihiro INOUE. Published in the Proceedings of the IASS Annual Symposium 2023 with permission.

developed a model device that enables the configuration and shape change of the guide frame, established a method for simulating the shape of the guide frame that avoids obstacles[1].

On the other hand, since the guide frame is operated by an actuator via a motor, it cannot easily change its shape. In addition, considering safety, a mechanism and control to easily move the guide frame in an emergency are also required. Therefore, in order to easily manipulate the shape of the guide frame by human operation, we investigated a deployment method using a force control method. The operator applies a force in the desired direction to move the guide frame, and by transmitting the information of the force sensor to each actuator, the length and speed of its expansion and contraction can be changed. As a result, we aim to develop a force control system that can change the shape of the guide frame.

2. Overview of Tunnel Inner Wall Inspection System

The Tunnel Inspection System aims to replace human close visual inspection and hammering inspection work with robot technology, and is equipped with an inspection unit that automatically detects cracks and floats in the lining concrete. Fig. 2 shows an overview of the tunnel inspection system. Depending on the conditions of the tunnel, a gantry frame type or an aerial work vehicle type equipped with an inspection arm can be used to shorten work time and save labour, while also enabling highly accurate acquisition of the position and shape of floats. In addition, it is possible to efficiently create an inspection report using the acquired inspection data. [2,3,4] The features of this inspection system are shown below.

(1) Flexible Guide Frame: The shape of the guide frame can be freely changed according to the tunnel shape and equipment.

(2) Traveling protection Frame: A frame that runs inside the school and protects third parties from falling concrete pieces during inspections.

(3) Crack Inspection System: Acquire images and unevenness at the same time to identify differences such as cracks and dirt, enabling high-precision detection

(4) Hammering Test Unit: Automatically judge using AI (Artificial Interagency) from the noise of hitting concrete, record the location of the deteriorated part, and display it on the screen

(5) Repair Expert system: Based on the inspection, we propose the optimal repair method that meets the LCC (Life Circle Cost)

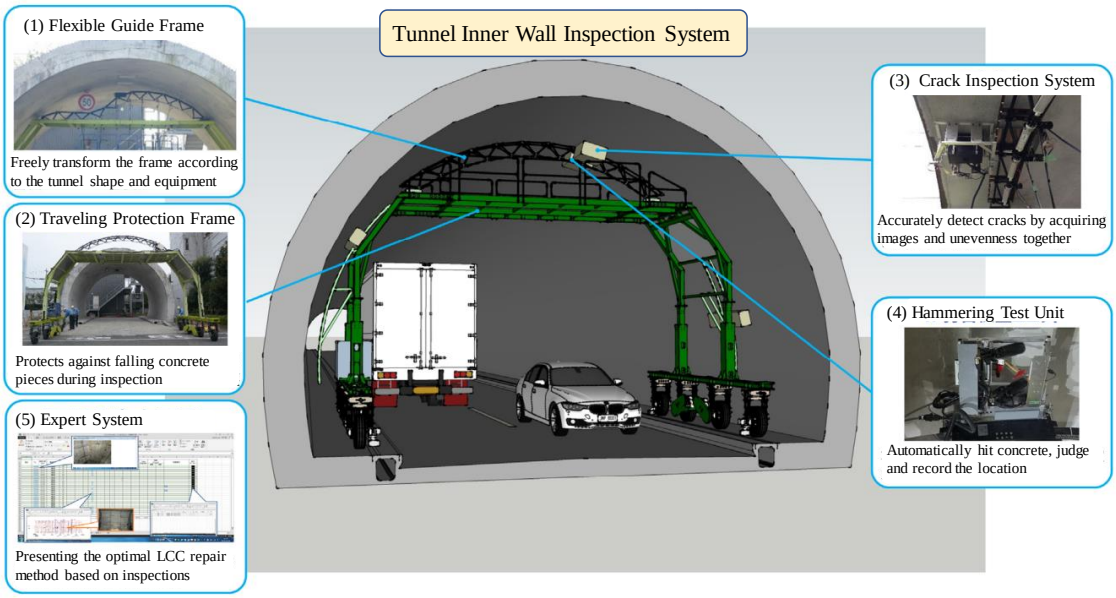


Figure 2. Overview of the tunnel inner wall inspection system and the introduced new technologies

3. Manual deployment experiment of guide frame

3.1. Image of change in shape of guide frame due to manual operation

In this chapter, in order to establish a method that can easily deform the shape of the inspection guide frame, analysis and model experiments using manual operation and force control were performed.Fig.3 shows an image of manual operation of the guide frame. Since the guide frame is composed of multiple VGTs and both ends of the frame are simply supported, part of the shape change affects the entire frame. The operator applies a force F the desired direction to move the end of the guide frame, and by transmitting information from the force sensor to each actuator, changes the extension/retraction length and speed.

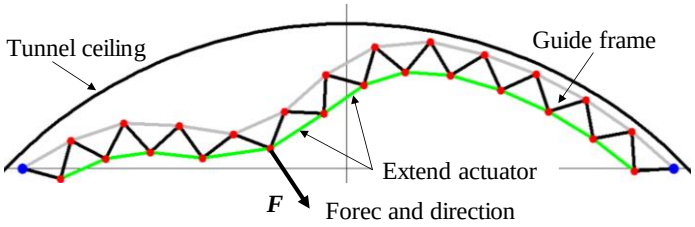


Figure 3. Image of manual operation of the guide fram

3.2. Flow of force control and force sensor

Fig.4 shows the feedback control flow for the shape of the VGT by manual operation and view of force sensor and extended actuator. By operating (pushing or pulling) the manual handle installed on the top of the guide frame, external force is applied to the force sensor. The external force is converted to voltage V, and VGF is activated when $|V|$ is within the control range of VGF ($V_{\text{Min.}}$ and $V_{\text{Max.}}$). Otherwise, stop. In addition, the VGF was extended and shrink according to the direction of the force, and the velocity was proportionally controlled according to the value of $u = k\,|V|$. By continuously running this control flow, the guide frame is gradually changed by manual operation.

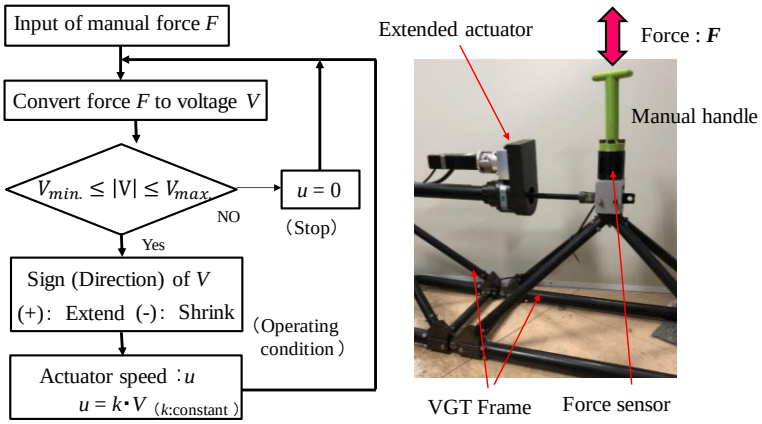


Figure 4. Feedback control flow and VGT actuator and force sensor

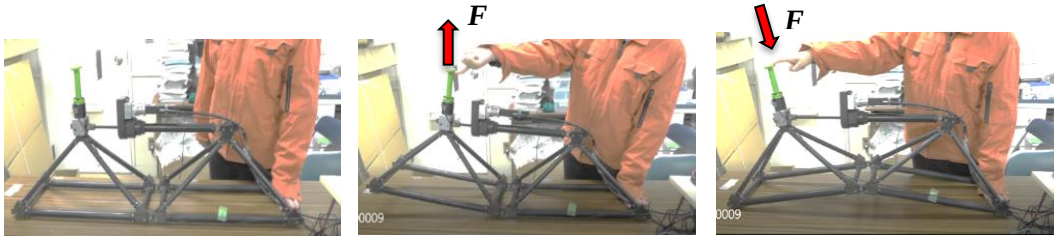
3.3. Force control experiment by manual operation

In order to apply manual force control to the actual guide frame, as a basic experiment, a simple force control experiment combining multiple VGTs was carried out.

3.3.1. Case of one VGT frame

Fig.5 shows the state of the experiment with one VGT. In the initial state where no force is applied (Fig.5-(a)), it remains stationary. As shown in Fig.5-(b), when an upward load (pulling force) is applied,

the frame length becomes shorter and the VGT transforms into a U shape. When the magnitude of the applied force was changed, the frame length velocity changed accordingly. Similarly, as shown in Fig. 5-(c), when an upward load (push force) is given, it can be seen that the shape is greatly transformed into a W shape.

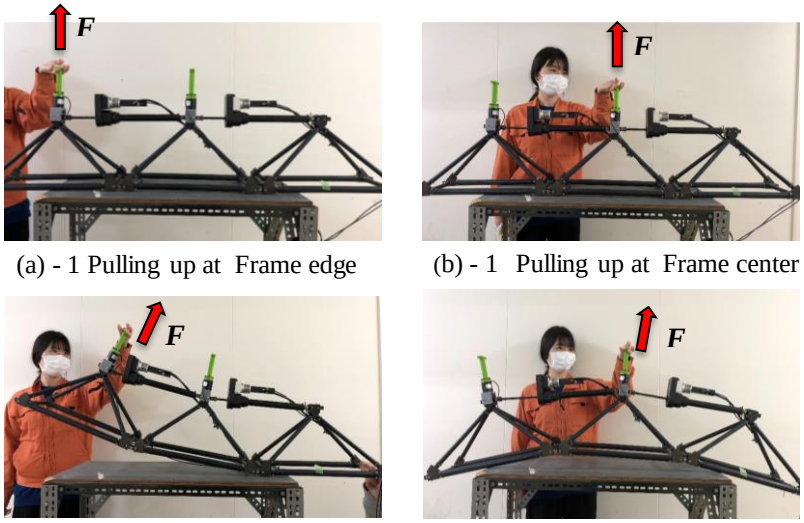


(a) Initial State ($F = 0$) (b) Pulling up ($F > 0$) (c) Pushing down ($F < 0$)

Figure 5. Shape change of one VGT actuator controlled by manual opetation

3.3.2. Case of two VGTs frame

Fig.6 shows the operation test. The shape gradually changes from the initial state (Fig.6 (a)-1: tip of frame, (b)-1: center of frame) when force is applied, and as a result, Fig.6 (a)-2 It became a convex shape change, and in Fig. 6 (b)-2, it became a concave shape change. When the magnitude of the applied force was changed, the frame length velocity changed accordingly. By controlling according to Fig. 4, the actuator that extends differs depending on where the force is applied, so the overall shape also changes. By using this method, the shape of the guide frame can be easily changed by manual operation is possible.



(a) - 1 Pulling up at Frame edge (b) - 1 Pulling up at Frame center

(a) - 2 Change to convex shape (b) - 2 Change to concave shape

Figure 6. Shape change of two VGT actuators controlled by manual opetation

4. Shape analysis of guide frame imitating force control

4.1. Purpose and method of analysis

The guide frame used in the actual site needs to operate multiple VGT mechanisms, and in order to change the shape of the guide frame composed of multiple trusses, it is necessary to measure the force acting on each truss member. [1]. Here, we applied a downward force to a part of the frame and analyzed the force acting when the shape changed by the finite element method, and investigated the force inside the actuator and the truss displacement. In order to change the shape of a guide frame composed of multiple trusses, it is necessary to measure the force (axial force) acting on each truss member. Here,

we applied a downward force to a part of the frame and analyzed the force adopted for the VGF when the shape was changed.

4.2. Shape analysis of guide frame

4.2.1. Basic Structure of guide frame

The proposed guide frame was constructed on several VGT (Variable Geometry Truss) elements [5],[6],[7]. This VGT was very simple truss structure composed of extendable members, fixed members and hinges, as showing in Fig. 7. By controlling the lengths of the extendable members, it was possible to create various truss shapes. When extendable members are extended simultaneously as indicated in Fig.8, the VGT structure was changed like a spring stretching from (a) to (b). When the extendable members are extended alternately, the structure was changed to a circular shape (c) Moreover, when they are extended optionally and their length were controlled, the structure could be changed into any intended shape (d).

The basic shape of guide frame was assumed to be an arch structure and its two edges were supported on the protection frame. Though the guide frame was changed flexibly by VGTs shape, the shape was limited by upper side of tunnel wall and traffic space area. So, to avoid projecting obstacle in the tunnel space, it was necessary to correspond to the shape of the guide frame close to the section shape of the obstacle as much as possible. Knowing the obstacle location and shape from the drawing map before inspection, the shape of obstacles as speed plate, blower and side lights were able to simulate by motion analysis. In an actual measurement, the shapes of obstacle were detected by the data of LRF continually.

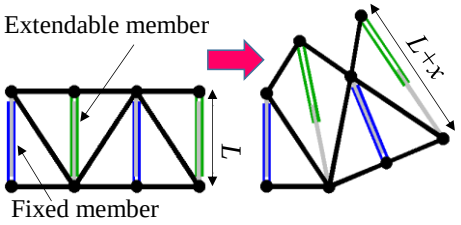


Figure 7. Basic structure of VGT

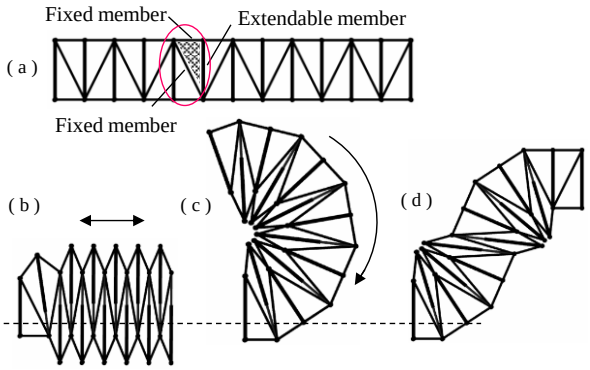


Figure 8. Example of shape change of VGT structure

4.2.2. Basic Equation and Shape of Frame

As analysing the arch structure composed of VGT, the whole of guide frame was assumed to be a cantilever structure as indicated as shown in Fig.9. The frame can replace a robot manipulator combining two fixed-length members in series. When the supported edge of frame was $q(x_0, y_0)$, the top $q(x, y)$ of the x, y co-ordinates of the frame combined with n ($n \geqq 2$) VGT sets was given by Eq. (1) and Eq.(2) using each hinge angle θ_j.(j=1, 2, 3, · ·n),

$$q(x,n) = l_0 \cdot \sum_{k=1}^{n} \cos\left\{\sum_{j=1}^{k} \theta_j\right\} \quad (1) \qquad q(y,n) = l_0 \cdot \sum_{k=1}^{n} \sin\left\{\sum_{j=1}^{k} \theta_j\right\} \quad (2)$$

Where, l_0 was the length of diagonal member of the frame. To transform the shape of arch frame, some hinge positions on the frame only had to change in proportion to target shape. However, for an intended frame shape fixed by equations (1) and (2), it was quite difficult to solve these equations analytically and to decide the angle because the frame was a very highly redundant. In this case, inverse kinematics analysis was applied [8]. Considering a temporal change of the whole of the frame, the top edge

modifying the original point by inverse analysis to all VGT angle velocity $\dot{\theta}_i$, the shape change was absorbed according to the arch.

$$J^{\#} = J^T \cdot (J \cdot J^T)^{-1} \qquad (3)$$

$$\dot{\theta}_n = J^{\#} \cdot \dot{q}_n(x_n, y_n) \qquad (4)$$

Where, J^{-1} indicates inverse Jacobean Matrix (2×n). However J^{-1} isn't necessarily decided because $\boldsymbol{J}$ is not a regular system in n>2. In this case, the suitable matrix such a pseudoinvesre matrix $\boldsymbol{J}^{\#}$ was generally inducedinstead of $\boldsymbol{J}^{-1}$**.** Iterating such modification of shape changes, the shape of original arch was able to carve partially to extent in which the obstacle could be evaded.

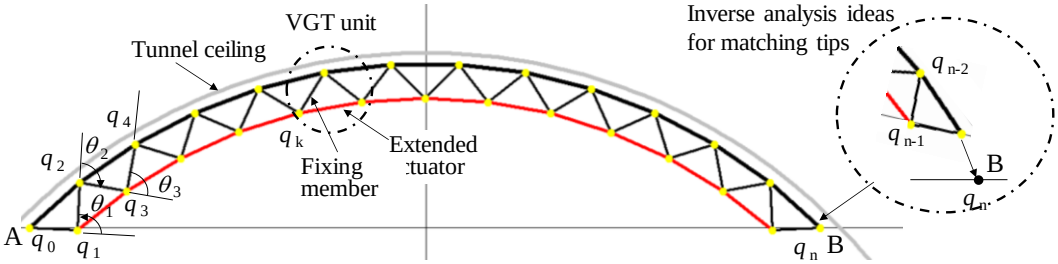


Figure 9. Analysis model of a guide frame composed of VGT

4.3. Structural analysis of guide frame by finite element method

The FEM (Finite Element Method) is an analytical method that divides a continuum such as a member into finite-sized elements and obtains the displacement and stress acting on each element to obtain various values acting on the entire member. Since the force acts on the truss member only in the axial direction, the axial force acting on the frame and actuator of each truss is analysed. Fig.10 shows the analytical drawing of the frame by finite element analysis. Displacements at both ends of each element are ($u_{k,i}$, $v_{k,i}$), ($u_{k,j}$, $v_{k,j}$), axial forces are ($F_{x,i}$, $F_{y,i}$), ($F_{x,j}$, $F_{y,j}$) , the stiffness equation of the truss is given by Equation (5). Here, the component matrix is given by equation (6). By applying this relationship to the entire guide frame and obtaining the displacement of each element, the axial force acting on the actuator is obtained.

$$\begin{bmatrix} F_{x,i} \\ F_{y,i} \\ F_{x,j} \\ F_{y,j} \end{bmatrix} = [K] \begin{bmatrix} u_{k,i} \\ v_{k,i} \\ u_{k,j} \\ v_{k,j} \end{bmatrix} \qquad (5)$$

$$[K] = \frac{AE}{L} \begin{bmatrix} cos^2 a & sina \cdot cosa & -cosa & -sina \cdot cosa \\ cosa \cdot sina & sin^2 a & -cosa \cdot sina & -sin^2 a \\ -cos^2 a & -sina \cdot cosa & cos^2 a & sinac \cdot osa \\ -cosa \cdot sina & -sin^2 a & cosa \cdot sina & sin^2 a \end{bmatrix} \qquad (6)$$

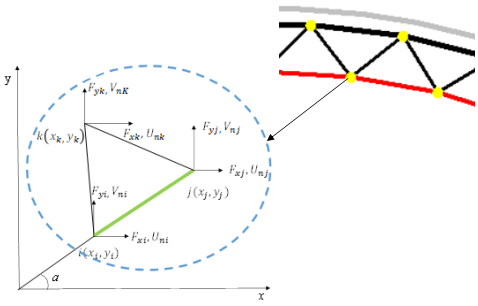


Fig.10 Application of FEM to guide frame

4.4. Shape change of guide frame assuming force control

The force and displacement of the VGT actuator when force (tensile force or compressive force) is applied to a part of the guide frame by manual operation was simulated by the finite element method according to the change of shape. As for the analysis parameters of the guide frame, the values of the

actual model machine (total dead weight: about 140 kg, initial vertical load of each VGF: 7.5 N (outside), 26 N (inside)) were used, and the manual operation The applied load was a relatively small load of F = 10N. In the analysis, the force acting on each member due to its own weight was calculated in advance, and then the analysis including the manual load was performed.

4.4.1. Obstacle avoidance on the side part

By applying a load to the manual operation, if the change in the force acting on each actuator was tensile force, the actuator was extended, and if it was compressive force, control was performed to retract the actuator. A constant proportional to the change in force was found for the extension speed of the actuator, and the speed of each actuator was determined. The step time for analysis was 0.1 second, and up to 200 steps were executed.

Fig. 11 shows the shape of the guide frame that changes according to this load. Fig. 12 shows the changes in the axial force (force excluding the force due to its own weight) acting on the actuator part (bottom chord) of each VGT due to this hand load. The guide frame changes in the manual direction according to the number of steps. A tensile load acts on the VGF near the manual load, and a compressive load acts on the VGF near the end. It can be seen that the guide frame moves downward in the manual direction according to the number of steps. On the other hand, the guide frame on the opposite side has a change that swells like a curve. A tensile load acts on the VGF near the manual load, and a compressive load acts on the VGF near the end. It can be seen that both ends are supported and the forces are balanced according to the uneven shape of the guide frame.

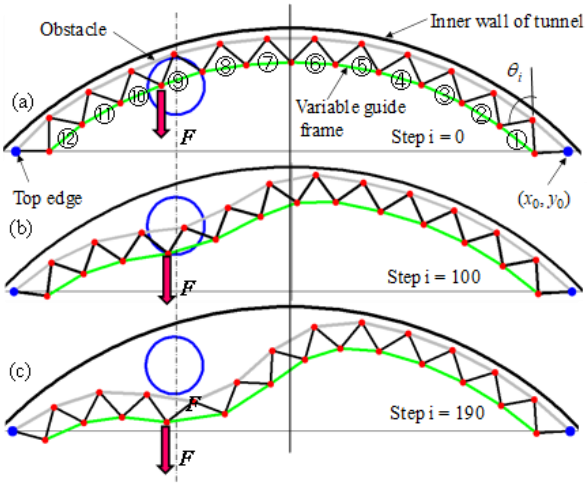


Figure 11. Shape change of guide frame simulated by manual control (Side Obstacle)

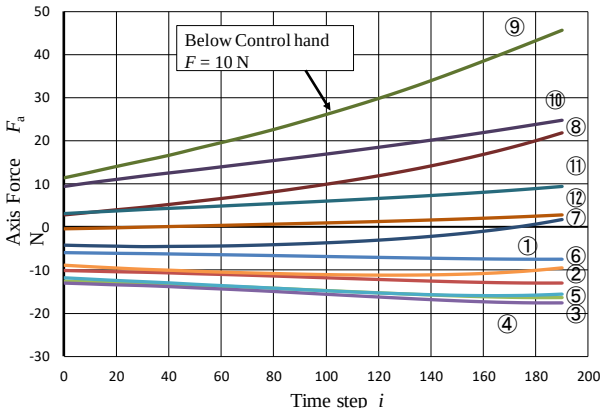


Figure 12. Axis force of actuators of guide frame simulated by manual control (Side Obstacle)

4.4.2. Obstacle avoidance in the central part

Using the same control method as in 4.4.1, the shape of the guide frame was analysed by applying a manual load to the center in order to avoid the obstacle in the center. Fig. 13 shows changes in the shape of the guide frame, and Fig. 14 shows changes in the axial force acting on each VGT actuator. The axial force of each actuator was almost equal on the left and right, and the values were almost symmetrical. Tensile force was observed in the actuator near the manual load, and compressive force was observed in the actuator near the end.

Based on the above, in the actual machine, a force sensor is attached to each actuator, and once the speed of the VGT according to the sign and load is determined, the shape is changed manually. Basically, it can be handled by force control according to the feedback flow shown in Fig. 3. In previous methods,

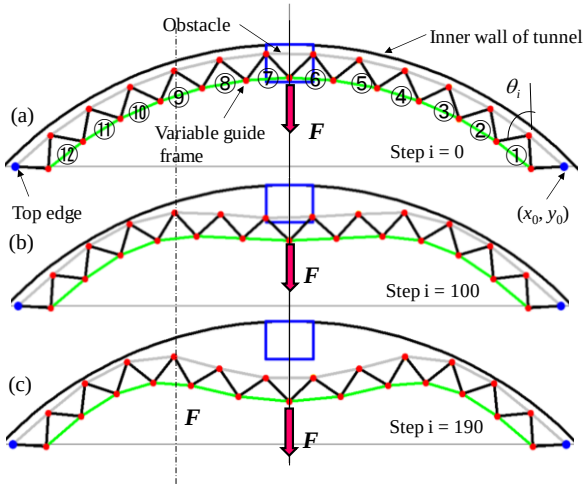


Figure 13. Shape change of guide frame simulated by manual control (Center Obstacle)

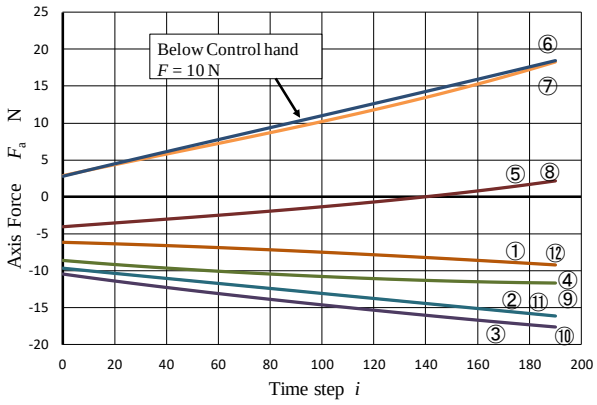


Figure 14. Axis force of actuators of guide frame simulated by manual control (Center Obstacle)

the position of the obstacle was measured by a laser, and the guide frame was automatically opened and closed based on its shape. In this case, the speed of opening and closing is very slow and not necessarily efficient. In the manual operation proposed here, the operator actually sees the shape of the obstacle, so the operation is more efficient, and fine adjustments can be made easily. It is also possible to perform the operation in case of emergency, which will greatly contribute to safety.

5. Conclusion

In this study, by using a deformable frame that can adapt to the tunnel shape, we have developed a tunnel inspection system that can inspect the inner wall surface without the usual traffic control. In order to make it easier to use the guide frame of the developed inspection system, we investigated a force control method that can easily change the shape of the guide frame by manual operation. We conducted manual experiments using multiple VGF mechanisms and confirmed that the shape can be changed according to the feedback flow. For application to the entire guide frame, it is necessary to operate multiple actuators, and the axial force of each actuator due to manual loading was analyzed. From the analysis results, it was confirmed that the sign and magnitude of the axial force changed depending on the part where the manual load was applied.

In the future, we would like to install a force sensor on the actual guide frame and determine the speed of the actuator according to the sign and value of the load generated by manual loading, aiming at practical application.

Acknowledgements

Finally, the author thanks all who supported the development of the movable arch structure and its accompanying external panel. Further, this work was supported by Council for Science, Technology and Innovation, “Cross-ministerial Strategic Innovation Promotion Program (SIP), Infrastructure Maintenance, Renovation, and Management”. (Funding agency: NEDO)

References

[1] F. Inoue, S.Kwon, S. Nakamura,” Shape Adaptation of the Inspection Guide Frame in Tunnels to Avoid Obstacles Detected by Laser Range Finder”, Journal of Robotics and Mechatronics, Vol.31, No.6, 2019, PP.752-761.

[2] S. Nakamura, A. Yamashita, F. Inoue, at el, "Inspection Test of a Tunnel with an Inspection Vehicle for Tunnel Lining concrete", Journal of Robotics and Mechatronics, Vol.31, No.6, 2019, PP.762-771.

[3] Fujii H, Yamashita A and Asama H, "Defect Detection with Estimation of Material Condition Using Ensemble Learning for Hammering Test", Proc. of the 20 16 IEEE International Conference on Robotics and Automation, pp.847-3854 , Stockholm (Sweden), 2016.

[4] Fumihiro Inoue, Soonsu Kwon et al, "Study on Shape Determination Method and Operation Experiment of Inspection Guide Frame to Avoid Obstacle in Tunnel", Proc. of the IASS Annual Symposium 2019, October 2019, Barcelona, Spain, PP.1-8, 2019.

[5] Inoue F, "Shape Control of Variable Guide Frame for Tunnel Wall Inspection", Proc. of 34th Int. Symp. on Automation and Robotics in Construction, Taipei, Taiwan, pp.675-682, 2009.5.

[6] Inoue F, "A Study on Optimum Shapes and Motion of Movable Arch Structure By Variable Geometry Truss", Proceeding of The 9th Asian Pacific Conference on Shell and Spatial Structures (APCS2009) , Nagoya, Japan, pp.121-128, 2009.5.

[7] Inoue F, Nakamura S, "Development of Variable Guide Frame to Inspect Inner Wall Tunnel", Proceedingsof the 6th International Conference on AdvanceMechatronics (ICAM2015), Tokyo, Japan, PP. 284-285,2010.

[8] Inoue F, "A Study on Adaptive Structure Applying Variable Geometry Truss (Mechanism of Movable Arch Roof with External Panel)"Journal of Robotics and Mechatronics, Vol. 21, No.2, pp.172-178, 2009.

IASS 2023
July 10–14 Melbourne
Integration of Design and Fabrication

Proceedings of the IASS Annual Symposium 2023
Integration of Design and Fabrication
10–14 July 2023, Melbourne, Australia
Y.M. Xie, J. Burry, T.U. Lee and J. Ma (eds.)

Modular design of multistable pneumatic structures from a flat pattern of air pouches

Yiwei ZHANG[a], Tomoya TENDO[a], Tomohiro TACHI[*]

[*] Graduate School of Engineering and Graduate School of Arts and Sciences, the University of Tokyo
Komaba 3-8-1, Meguro-Ku, Tokyo 153-8902, Japan
tachi@idea.c.u-tokyo.ac.jp

[a] Graduate School of Engineering and Graduate School of Arts and Sciences, the University of Tokyo, Komaba 3-8-1, Meguro-Ku, Tokyo 153-8902, Japan

Abstract

We introduce a novel family of structures that can be inflated from a plane to form a three-dimensional surface using articulated straight pouches with inextensible membranes. Specifically, we propose a modular design using a quadrangle surrounded by four slender pouches, whose inflation causes the surface to form a saddle shape. We show a fabrication method using heated nylon films with heat adhesives separated by paper mask patterns inside. We first show a geometric model to explain and predict the out-of-plane deformation and the bi-stability effect inherited in this structure. Through a geometric analysis and an elastic simulation of a pouch, we show that lowering the width-length ratio of pouches reduces the imperfection of shapes. We further propose a method for controlling the height of saddles using concentric patterns. We then extend structural modules into multiple-grid systems and identify the multi-stable behaviours of the overall structure.

Keywords: pneumatic structures, air pouch, multi-stable structures, structural morphology, modular design, Hangai Prize applicant

1. Introduction

Air-inflated pneumatic structures, i.e., structures formed by closed membrane sections, have been extensively used for realizing lightweight structures. In recent studies, researchers focus on novel aspects of air-inflated structures as the method to create three-dimensional surfaces and motions from planar states by utilizing inextensible membranes. Niiyama et al. [1] realize a transformable air actuator by inflating tubular pouches patterned on double-layered sheets. Siefert et al. [2] studied the out-of-plane bending of air tubes induced by the incompatibility caused the inflation. Panetta et al. [3] used a similar idea to program a pattern of laid-out flat air tubes that can be inflated to achieve a target three-dimensional (3D) surface. These approaches are characterized by the use of inextensible membranes that are pulled and deformed by air pressure, which is in contrast to conventional air-inflated pneumatics that focus more on the air as the structural element than the membrane. However, when inextensible air pouches are inflated, the induced bending of the tubular pouch caused wrinkles on the surface. These wrinkles may lead to structural failure if the scale of structures becomes larger. To apply the approach of air-induced out-of-plane surface transformation to a large-scale structure, the wrinkling problem has to be solved.

In this study, we propose a novel structural unit with segmented straight air pouches connected by foldable creases. The articulation will allow for a structure with a large amount of out-of-plane surface deformation with fewer effects of wrinkles. Specifically, we propose a modular design using a quadrangle surrounded by four slender pouches, whose inflation causes the surface to form a saddle shape. Unlike existing surface inflatables, the pouches remain straight after inflation and thus are free of wrin-

Copyright © 2023 by Yiwei ZHANG, Tomoya TENDO and Tomohiro TACHI. Published in the Proceedings of the IASS Annual Symposium 2023 with permission.

kling. The proposed module has two stable positions that can be programmed to form different surfaces by tessellating the modules.

We first show the manufacturing and inflation steps of the unit structures in Section 2. We show a geometric model to explain and predict the unit's out-of-plane deformation and the bi-stability effect in Section 3. We study the imperfection of the geometric models to show that lowering the w/l ratio of pouches reduces the imperfection in Section 4. We further propose a method for controlling the out- of-plane deformation for the structural unit using concentric patterns of pouches in Section 5. Finally, we extend structural modules into multiple-grid systems and identify the multi-stable behaviors of the overall structure in Section 6. We introduce a notation that labels the shape of each stable state by '+1's and '-1's. We propose a dynamic-relaxation-based simulation model to predict the stable states for a given assignment of labels.

2. Manufacturing and inflation

The proposed unit structure is manufactured by utilizing the 2D patterning based on CNC-cutting of sheet materials and heat adhesive nylon pouch. The process mainly consists of three stages (Figure 1): Cutting The process of fabrication starts with the preparation of sandwich-like paper and nylon sheets. We finish our design in Rhinoceros, export it to the Silhouette paper plotter, and cut copy paper out of the pattern. Then cut out the nylon pouch and place the pattern inside.

Heating In order to let the two layers of nylon sheets weld, we set the temperature at 180 ◦C and the pressure at 8kg for 45s. The process needed to be done twice to make sure the sheet is well merged. Inflation Finally, we cut through the pre-laid air hole and seal one side with tape. We then attach an air compressor and inflate the planar structure with a pressure around 150 − 180kpa. The interior of the structure is nearly vacuum such that it takes several times to inject and release such that the structure can be fully inflated.

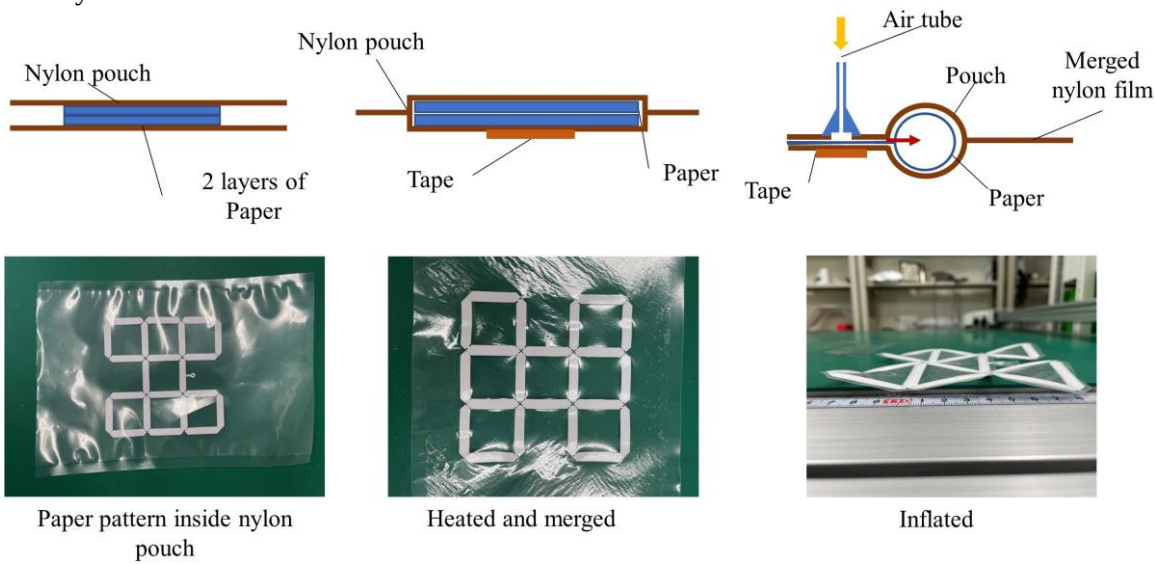


Figure 1: The fabrication process.

3. The structural unit and its geometric model

3.1. Overview of the structural unit

Our basic structural unit is a flat quadrilateral sheet consisting of 4 straight air pouches (Figure 2). The sheet is a composition of two layers of heat-adhesive nylon sheets with paper masks laid in between. When we sandwich these layers and apply heat by ironing, the paper sheets act as the insulator keeping the two layers separate while the remaining sheets get fused. This creates 4 closed straight air pouch sections (with air channels connecting them). When we pump air into the air pouches, each of them inflates into a cylindrical shape and then performs the transformation from a flat sheet to a 3D shape.

Here we call the width of each tube air pouch of the structural unit in its planar state w. Ideally, if the air pouch is entirely inflated, the two layers of paper mask and material form the boundary of a circular cross-section (Figure 2-2). Hence the projected width $w'$of the air tube after inflation is calculated as $2w/\pi$ given the condition that the material is not extensible against air pressure. This width difference provides the effect of in-plane shrinkage and causes the surface to deform into 3D. The width difference is calculated as:

$$\Delta w = w - w' = (1 - 2/\pi)w \approx 0.36w \tag{1}$$

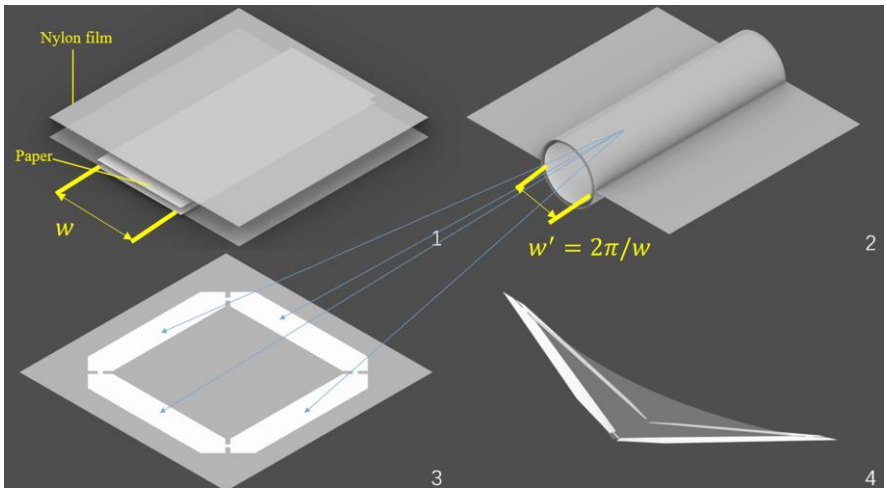


Figure 2: 1. Paper masks are laid in between nylon sheets. 2. Straight air pouches being inflated. 3. Four straight air pouches compose a single structural unit. 4. The deformation of a structural unit.

To understand the out-of-plane deformation of a single structural unit, we consider a quadrilateral MNPQ (Figure 3) and then take a quarter of the quadrilateral MNO, where MN is one side of the structural unit and O is the center. Let H be the midpoint of MN. The structural unit transforms into M 'N 'P 'Q', while keeping the origin O' = O when the projected length OH is reduced by the width difference Δw of an air pouch, i.e., OH on the plane becomes OH' = l/2 - Δw/2. Consequently, vertices M and P move in the z direction by h and N, Q move by -h. In arbitrary quadrangular cases (Figure 3) △MHO ≃ △M 'H'O, we can calculate the distance from the unit center to all edges, OH' as an example:

$$h^2 + \left(\frac{l}{2} - \frac{\Delta w}{2}\right)^2 = \left(\frac{l}{2}\right)^2 \tag{2}$$

Which accordingly tells the actual height h of the structure unit:

$$h = \frac{1}{2}\sqrt{\Delta w(2l - \Delta w)} \tag{3}$$

Equation (3) reveals that the deformation of the structural unit is decided by w/l. In a slender case of the pouch, when $w/l \ll 1$, the relatively high h/l is approximately proportional to $\left(\frac{w}{l}\right)^{\frac{1}{2}}$.

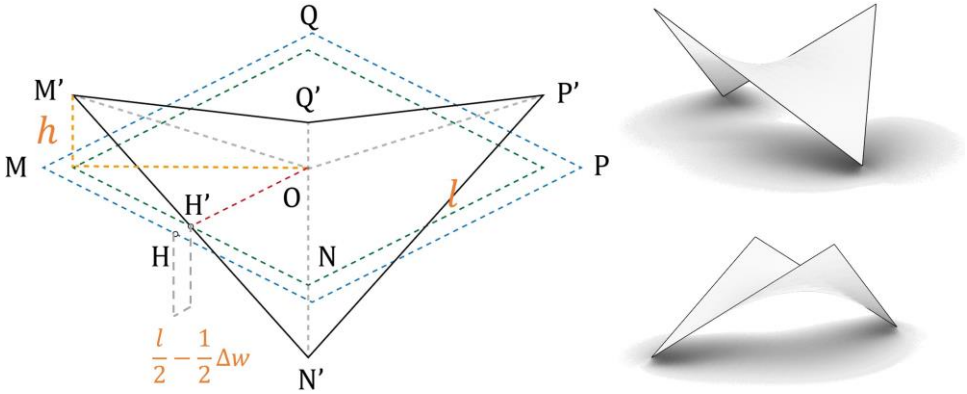


Figure 3: The geometric model and the bi-stable states for a structural unit.

3.2. The bi-stability

All elements of the paper are to be in the font Times New Roman. These guidelines give the basic layout, and the out-of-plane deformation induced by the air inflation breaks the four-fold symmetry of the entire pattern into two-fold symmetry. The structural unit needs to find a new equilibrium position such that the out-of-plane deformation happens. When it deforms, the unit needs to choose two upward vertices and two downward vertices from either the group of vertices (M, P) or (Q, N) (Figure 3 Right). Consequently, there are two possible ways for the vertex pairs to go. This bifurcation causes the structure to have two stable positions and the snapping behavior between the two stable states.

4. Detail discussions on the geometry for the structural unit

In the abovementioned geometric model, we assumed that the pouch deforms into a perfect cylinder. However, the cap part of an air tube will cause shape imperfection because it does not fit the transformation from plane to three-dimensional shape. The imperfection causes (1) length shrinkage (Figure 4 Left) and (2) non-constant shrinkage in width (Figure 4 Right) that is accompanied by wrinkles. The intrinsic mismatch between the planar state and three-dimensional shape is unavoidable, but it can be minimized. In the following sections, we show that these imperfections and wrinkling can be mitigated by making the w/l ratio small enough. Specifically, length shrinkage is an order of w/l ratio. Also, our numerical simulation revealed that non-constant width shrinkage is reduced by a smaller w/l ratio. In other words, the w/l ratio should be kept as small as possible for the least imperfection of pouch shapes. We use $w/l \leq 0.2$ in our design for the physical model for better shape prediction and structural soundness.

4.1. Length shrinkage for a pouch at the cap part

The imperfection causes the change in the height of the cap and thus in the total length. To study the imperfection, we consider that some of the materials between the cone part and the cylindrical part are "removed". Physically, the unnecessary material gets wrinkled. We consider the deployed state of the cone-shaped cap, and the cylindrical body to be a perfect match. We develop them along the suture lines between the cap and the body to obtain the flat state of a cone and cylinder. If we let the angle and the radius of the cap in the flat state be denoted by α *and* r, respectively, the height (the distance from the cap top to the suture line) of the cone r' in the inflated state is given by the equation:

$$r' = r \cdot \sqrt{1 - \left(\frac{\alpha}{\pi}\right)^2} \tag{4}$$

Therefore, the length shrinkage of the whole pouch is:

$$\Delta l = r - r' = r \cdot \left(1 - \sqrt{1 - \left(\frac{\alpha}{\pi}\right)^2}\right) = O(r) = O(w) \tag{5}$$

Here, we conclude that the size of the cap is only proportional to the width of the tube. This suggests that the strain in length direction decreases $\Delta l/l \rightarrow 0$ as the tube gets slender $w/l \rightarrow 0$.

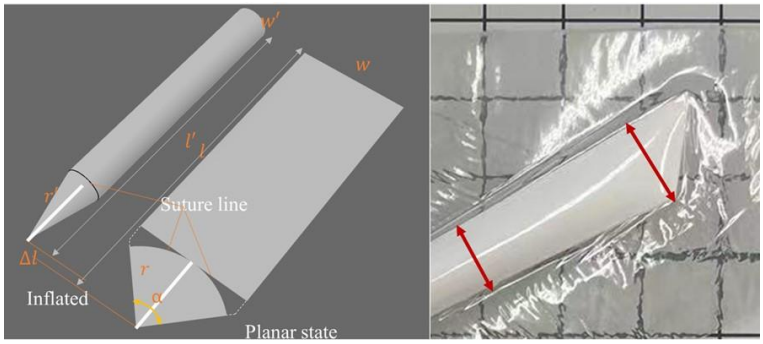


Figure 4: Left: Imperfect match for planar and 3D shape. Right: Non-constant shrinkage in the pouch width.

4.2. Width difference along a pouch and its verification

To check the effect of non-constant width shrinkage, we performed a numerical experiment with triangulated mesh based on the dynamic relaxation method using springs representing inextensibility, angular springs representing bending stiffness of sheets, and the pressures for the inflation process (Figure 5). We implemented this setting using Kangaroo 2 in Grasshopper of Rhinoceros 7.

We simulated two models of (w, l) =(10,mm,50mm),i.e.,w/l = 0.2,and (w, l) = (10mm,100mm),i.e., w/l = 0.1. To analyze the imperfection in width shrinkage, we measured the non-uniform inflated width w'(x') as the function of the position x' ∈ [0, l'] along the length direction of the pouch. Figure 7 shows the plot of w'(x') for the case w/l = 0.2 and 0.1. We set the precision tolerance to 5% of the ideal width $2w/\pi$. The region of precision i.e., the region within w'(x') ∈ [0.95 × (2w/π),1.05 × (2w/π)] is 86.4% of the length of the body for w/l = 0.2. The region of precision for w/l = 0.1 is 97%. We observed that the region of imperfection is local near the cap, and thus its size is expected to be the order of w. Therefore, they can be neglected when w/l ratio is small. We also observed a similar result from the

shape of physical air pouches (Figure 8). For practices, we choose $w/l \leq 0.2$ for a better appearance. These discussions support our geometric model in (Section 3.) if w/l ratio is small enough.

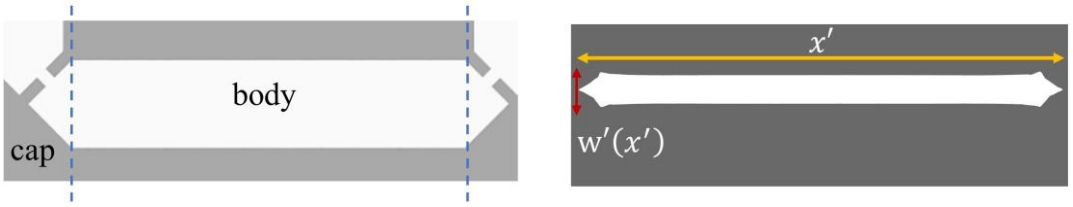


Figure 5: Top: Body part in the layout. Bottom: x' stands for half pouch width, and $w'(x')$ stands for width.

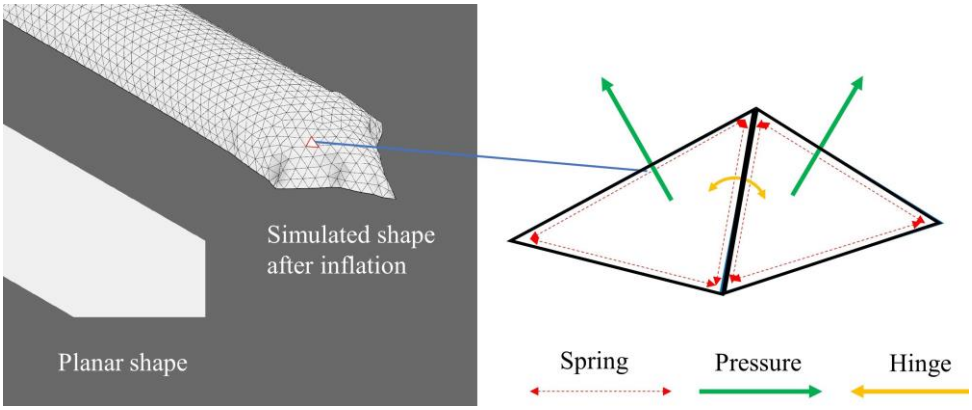


Figure 6: The simulation contains 3 kinds of constraints: The "spring" keeps the length of mesh edges imitating the in-extensible nature of the material. The "pressure" simulates the air pressure. The "hinge" of the edge within the adjacent mesh faces shows the effect of the thickness coming from the nylon sheet.

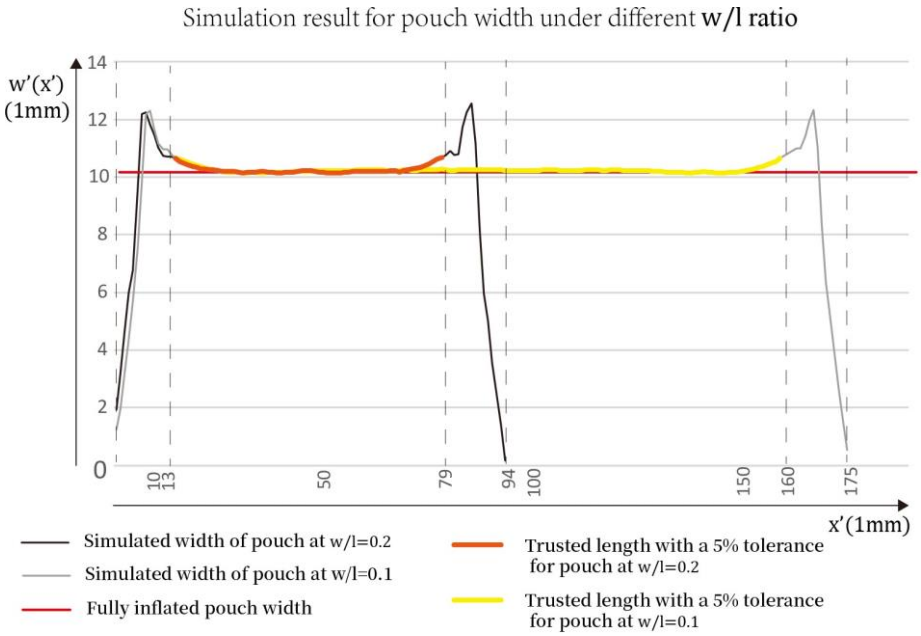


Figure 7: The simulation results for pouches at w/l ratio of 0.2 and 0.1.

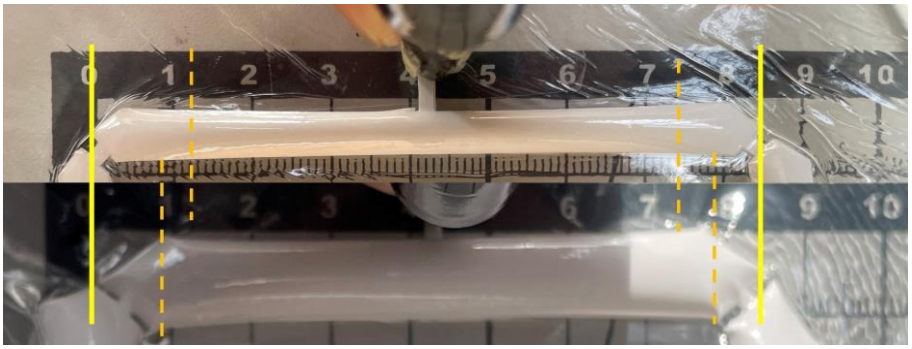


Figure 8: Comparison of the width differences of physical air pouches. Top: a pouch of $w = 8mm$ and $l = 84mm$. Bottom: a pouch of $w = 16mm$ and $l = 84mm$.

5. Actuation control using aligned pouch pattern

5.1. Actuation control

To improve the precision and reduce the effect of wrinkling, it is ideal to reduce w/l. However, the out-of-plane actuation measured as h/l also becomes small when w/l is small. Inspired by the shape study from K.Liu et al.[4], we found it is necessary to adjust Δw effectively while keeping the actual proportion w/l small. To achieve this goal, we show an approach of adding aligned air tube sets in one unit from the boundaries to the center.

To produce effective Δw while keeping the pouch proportion, we align slender pouches in parallel. Specifically, for a ring composed of four pouches, we align a smaller concentric ring composed of four pouches inside the ring. We take a pouch unit with three rings of aligned air tubes (Figure 9) as an instance. For air tubes adjacent to each other one or two small air channels are designed to let the air go through.

The straightforward prediction model for the concentric ring model is to use the summation of all aligned pouches $\sum \Delta w_i$ and replace the single width difference Δw of Equation (3). We evaluate this model in the following subsection, while we conclude that this model requires improvement.

$$h = \frac{1}{2}\sqrt{\sum \Delta w_i (2l - \sum \Delta w_i)} \tag{6}$$

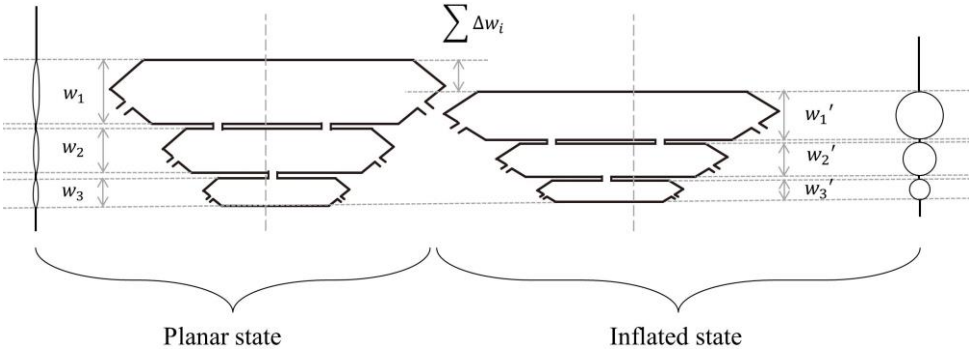


Figure 9: The deformation for the pattern with aligned air pouches before and after inflation.

5.2. Evaluation

We performed experiments to verify our geometric model. We compare three kinds of units: the original unit, the unit with 2 rings of pouches, and the unit with 3 rings of pouches (Figure 10). The length of the unit is $l = 84\,mm$, and the width of the pouches are $w_1 = 14\,mm, w_2 = 10\,mm, and\ w_3 = 7.14\,mm$ from the outer to the inner pouches. We inflate them all at the pressure of 150 kPa and measured their vertical displacement. For each specimen, we measured the height three times and took the average to obtain $H_{average}$ and calculated its half h_{actual} (Table 1). We compare h_{actual} with the corresponding value h according to our geometric model to verify whether our method of adjusting the unit actuation is plausible.

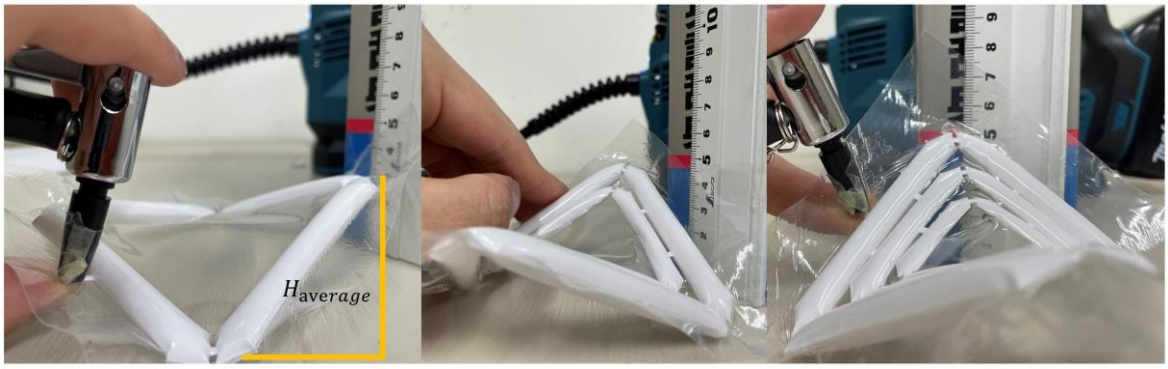


Figure 10: Measuring the vertical displacement of each unit

	$1\ Ring\ (mm)$	$2\ Rings\ (mm)$	$3\ Rings\ (mm)$
$w/l\ ratio$	$1/6$	$1/6$	$1/6$
$Haverage\ (mm)$	27.3	43.4	46
$hactual\ (mm)$	13.7	21.7	23
$h\ (mm)$	14.39	18.64	21.05
$Deviation$	-4.79%	16.42%	9.26%

Table 1: The result for comparison between the normal unit and alignment layout pattern.

The result of the comparison shows that more actuation is indeed generated by adding rings of air pouches. However, the actual height deviates from the height predicted by the geometric model; the deviation defined as $(h_{actual} - h)/h$ is added as the bottom row of Table 1. The deviation shows that the unit with a single ring transforms into a slightly lower value than the expected geometric model. This is justified by the imperfection caused by the bending stiffness and in-plane stretch of the material that makes the section of the pouches non-circular. However, we obtained non-straightforward results for the case with two and three rings, where the actual height is higher than the predicted height. This suggests that the straightforward model of simply adding the width differences in Equation (6) misses some effect that happens in the actual material. An improved model to predict the behavior of multiple

rings needs to be investigated.

6. Multi-stable grid pattern

So far, we have focused on the shape of a single structural unit. To achieve a larger surface, we propose expanding the structural unit into a grid system. By combining multiple units yields a multi-stable structure that can be programmed into many deployed states.

6.1. Different connections and grid pattern layout

Here we evaluate two types of square unit grids based on their orientation: *the aligned grid* that repeats squares along their edges, and *the diagonal grid* that repeats squares along their diagonals (Figure 11 (a)). Also, the connection between units is another detail that affects the final shape of the structure. Here with the illustration of Figure 11 (b), each connection between two adjacent units is either a single hinge or a pouch. We call them *hinge connection* and *pouch connection*, respectively. The pouch units connected by the hinge connection deform more independently because the hinge connection is softer. Also, the bending between neighboring units is concentrated at the hinge line. On the contrary, the pouch connection resists bending by a whole pouch. In an ideal model, a hinge connection is considered a revolution joint, while a pouch connection is considered a rigid connection.

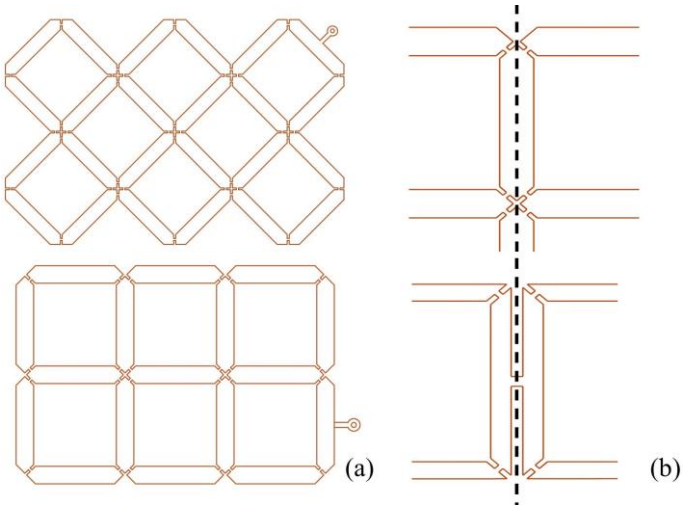


Figure 11 (a): Up: The diagonal grid. Bottom: The aligned grid. (b): Up: The pouch connection. Bottom: The hinge connection.

6.2. Notation method

To state each stable state simultaneously for a structure with multiple units, we mark each unit +1 and −1 based on its bi-stable behavior (Figure 12). Through this approach, we can determine any shape with only a matrix containing a bunch of +1 s and −1s. We name a structure consisting of all +1s or −1s the two ultimate states and the structure alternating +1s and −1s the two neutral states. With the help of +1s and −1s, we can directly tell different stable states (shapes) of one structure. Since each unit has a bi-stability, the n-unit grid system has 2^n possible nominal stable states. In reality, the structure may not

have so many possible combinations for +1s and −1s. We will verify some of them below.

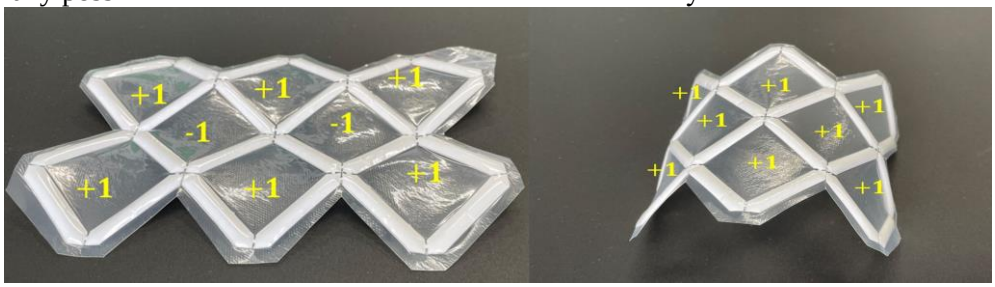


Figure 12: The +1 and −1 notations for two ultimate states. Left: A neutral state. Right: An ultimate state.

6.3. Possible and impossible states

Figure 12 is a model for a diagonal grid constructed with the pouch connection. In the neutral state (Figure 12 Left), the whole system forms a flat but wavy shape. in one of its ultimate states (Figure 12 Right), the shape is similar to a Yoshimura pattern in origami, thus the diagonal grid provides a perfect analog of a vault shape. Figure 13 shows the physical example of an aligned grid constructed with the pouch connection. It is similar to the diagonal grid in its neutral state. But when it turns to an ultimate state, the grid will scroll inwards to a cylinder whose ruling directions are parallel to the polyline created through a combination of adjacent diagonal lines among pouch units (Figure 13 Right). Note that the curvature directions of the ultimate state for both cases align with the diagonal directions of the unit. This is because the unit's principal curvature directions of the hyperbolic paraboloidal shape are aligned with the diagonal direction.

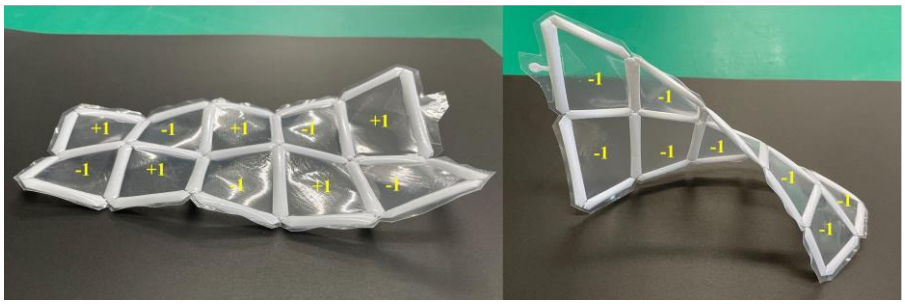


Figure 13: Left: A neutral state. Right: An ultimate state

The ultimate and neutral states exist for every combination of diagonal or aligned grids, and pouch or hinge connections. However, the existence of other states cannot be ensured for some combination of layouts and connections. Here we give an example of non-existing patterns in Figure 14. Here, we compare $2 \times n$ aligned grids with hinge and pouch connections. Some non-ultimate or non-neutral patterns applied to the pouch connection automatically turn back to a neutral state. In hinge connection, the state stayed in a correct assigned pattern for the $2 \times n$ aligned grid. This phenomenon suggests that even n-unit grid has nominally 2^n possible states, some of the states are not always workable in reality. To understand the possible and impossible states, we need to understand the compatibility between units. A model with a hinge connection can be considered as rigid origami with non-planar quadrangular panels, while the pouch connection is considered as the tessellation of rigid bodies connected rigidly. In reality, the hinges allow elastic deformation; thus, it is more allowing than the rigid model. The stability

under the elastic energy makes some modules able to exist or not. To consider the elasticity, we perform a bar-and-hinge-based simulation to check the feasibility of physical models.

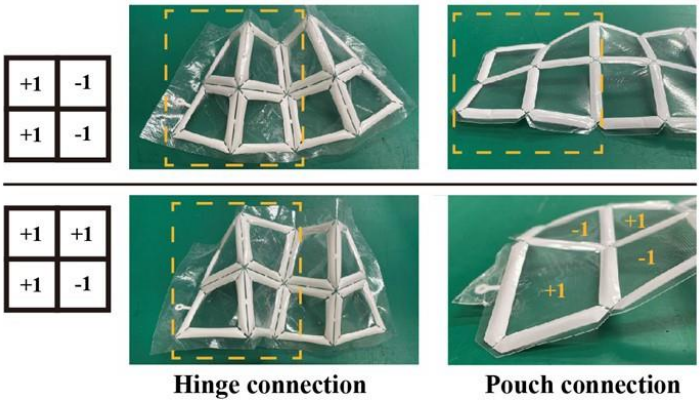


Figure 14: Hinge connections work for both notation but pouch connections fail at a combination of three +1s and one −1s.

6.4. Shape prediction

We model each unit as four triangles using M', N', P', Q', O in the geometric model (Section 3.). The target length of each edge of the triangle is set to the length of the geometric model after the inflation. We realize this length constraint as a linear spring. We also provide angular springs between four triangles. to represent the out-of-plane bending stiffness of the module (Figure 15).The connections between modules are modeled as angular springs, where the spring stiffness of the hinge connection is lower for free rotation at unit boundaries, and the pouch connection is higher to resist bending. We performed a simulation of this spring system on Kangaroo 2. To specify +1 or −1 of the model at the flat state, the target angle of the angular springs between four triangles in the module is initially set to the angle measured from M', N', P', Q', O in the corresponding +1 or −1 state. After the simulation

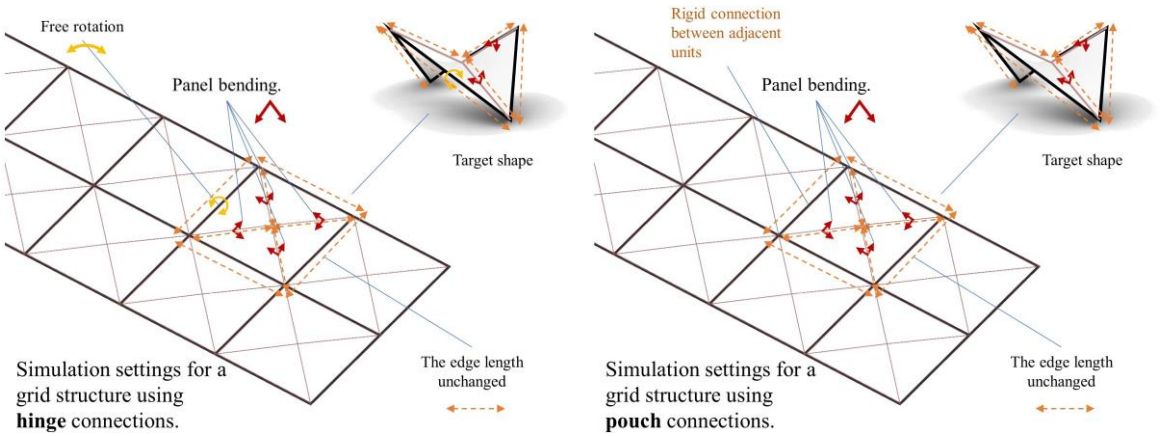


Figure 15: For grids with both connection types, we set all the unit boundaries are rigid and divide a unit into 4 triangular panels then assign each edge between the panels with opposite angles to imitate the bifurcated deformation according to the shape of a single structural unit.

finds a specific +1 or −1 pattern, we set the target angle of the angular springs to 0 to remove the bias.

6.5. Simulation result and conclusion

In the pouch connection model, we obtained the resulting shapes of the neutral and ultimate states as desired. Even after the removal of the bias, the shape stayed in the correct state. We also tested this simulation setting in some other patterns as shown in Figure 16 Left and middle, the resulting 3D shape was able to turn back to a flat piece, which was its initial state when the folding angle is reduced to 0. For the hinge connection model, we similarly obtained the resulting shapes of the neutral state and ultimate state. However, the state is not stable, and the model with hinge connection transforms as a one-DOF mechanism (Figure 16 Right).

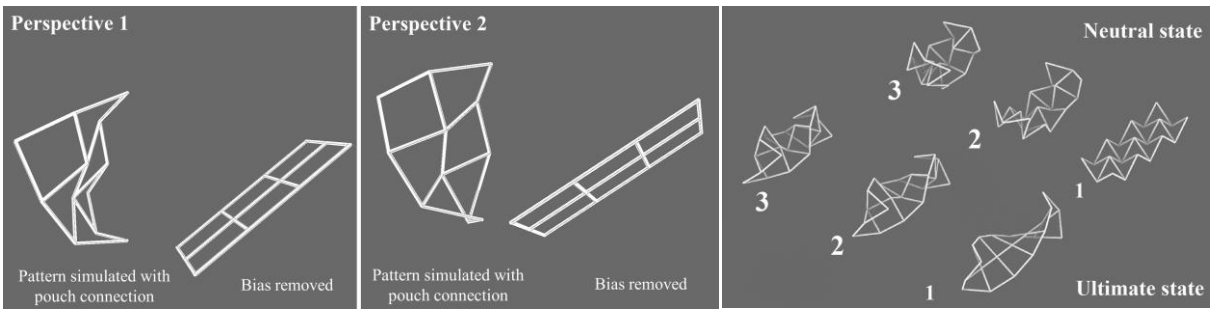


Figure 16 Left and middle: The simulated result for an arbitrary pattern made with pouch connection and the shape returned to a flat piece after the rest angle is reset to 0. Right: The shape sequence of the one DOF motion under the simulation result of hinge-connected patterns.

Acknowledgements

This work is partially supported by Takenaka Corporation.

References

[1] R. Niiyama, D. Rus, and S. Kim. Pouch motors: printable/inflatable soft actuators for robotics. In *2014 IEEE International Conference on Robotics and Automation (ICRA)*, pages 6332–6337. IEEE, 2014.

[2] E. Sie´fert, E. Reyssat, J. Bico, and B. Roman. Programming curvilinear paths of flat inflatables. *Proceedings of the National Academy of Sciences*, 116(34):16692–16696, 2019. DOI: 10.1073/pnas.1904544116. eprint: https://www.pnas.org/doi/pdf/10.1073/ pnas.1904544116. URL: https://www.pnas.org/doi/abs/10.1073/pnas. 1904544116.

[3] J. Panetta, F. Isvoranu, T. Chen, E. Sie´fert, B. Roman, and M. Pauly. Computational inverse design of surface-based inflatables. *ACM Transactions on Graphics (TOG)*, 40(4):1–14, 2021.

[4] K. Liu, T. Tachi, and G. H. Paulino. Invariant and smooth limit of discrete geometry folded from bistable origami leading to multistable metasurfaces. *Nature Communications*, 10, Sept. 2019. DOI: 10.1038/s41467-019-11935-x. (Visited on 02/21/2021).

IASS 2023
July 10–14 Melbourne
Integration of Design and Fabrication

Proceedings of the IASS Annual Symposium 2023
Integration of Design and Fabrication
10–14 July 2023, Melbourne, Australia
Y.M. Xie, J. Burry, T.U. Lee and J. Ma (eds.)

Section design and performance optimization of C-cross section thin-walled deployable boom

Fengyuan LIU*, Minger WU[a], Ping XIANG[a]

[a,*] Department of Structural Engineering, Tongji University
1239 Siping Road, Shanghai 200092, China
2011155@tongji.edu.cn

Abstract

The C-cross section thin-walled deployable boom (C boom) has a high storage ratio and can be used in various deployable structures. In the state of storage, the C boom should have no material failure, and in the working state, it should provide high bending stiffness and natural frequency to make the structure stable. This paper studies the mechanical properties of C booms in folded and deployed states. The change of maximum stress in the folding process of C booms and the boundary effect on the stress are studied in ABAQUS. The C boom with variable cross-section and the perforated C boom are proposed and studied to reduce mass and improve stiffness. The bending stiffness and natural frequency of these two types of booms are studied and compared with C booms with the same mass.

Keywords: deployable boom, C boom, optimization, variable cross-section, perforated

1. Introduction

A deployable boom can be stored in a small volume, and it can deploy by releasing stored strain energy to make the boom in working states. The C boom has a low manufacturing cost and can deploy easily, and it can be used as the support frame of deployable space structures such as antennas, solar sails, and solar panels.

The C boom should meet the requirements in both folded and deployed states. In the state of storage and during the process of storage, the C boom should have no material failure and enough steady-state moments as the power for the deploying process, while in the working state, it should provide high bending stiffness and natural frequency to make the structure stable. The yielding control criterion of C boom during the pure bending state is derived and verified by the FE model[1]. The natural frequency of C booms has been derived from experimental data, a FE model, and a beam model[2]. The length of the ploy region under the folding state of the C boom is derived, according to the classical long-wave solution of deformation of an initially cylindrical shell[3]. The classical solution of the steady-state moment of the C boom in the folding state is modified considering the boundary layer effect in the hinge region[4]. Most researches focused on the mechanical properties of common standard C booms, but there are few studies on C booms with variable cross sections or holes, which is an effective method to reduce the mass of booms.

This paper mainly studies the mechanical properties of the C boom in folded and deployed states, and the C boom with variable cross sections and the perforated C boom are proposed and studied to reduce mass and improve performance. Firstly, the change of maximum stress in the whole folding process of C booms, and the influence of the boundary effect on the maximum stress are studied in ABAQUS. Then, C booms with variable cross sections and the perforated C boom are designed to improve the deployed stiffness, and the bending stiffness and natural frequency of these two kinds of booms are analyzed by parametric studies. Finally, the bending stiffness and natural frequency of these two kinds

Copyright © 2023 by Fengyuan LIU, Minger WU and Ping XIANG. Published in the Proceedings of the IASS Annual Symposium 2023 with permission.

of booms and C booms with the same mass are compared to verify their contribution to improving the unfolding stiffness.

2. Performance of C boom at folded state

The key to the performance of C boom at folded state is to control the maximum stress in the folding process and the folded state to not exceed the yield strength so that the boom remains elastic and can fully release the elastic potential energy during the deploying process. This section studies the change of maximum stress during the folding of the C boom. In the process of folding, the boundary will also affect the stress of the C boom, which is related to the length of the ploy region.

2.1. Stress in the process of folding

The folding process is accompanied by the sudden change of bending moment, and the size and position of the maximum stress will also change during the formation and development of the localized fold. In the process of folding, the formation of the hinge is a dynamic process, but the time of this process is very short, and the performance studied in this paper is little affected by the inertia force, so the static solver is adopted to simulate the folding process. This paper creates finite element models using the stabilizing parameter set to default values within the static option from ABAQUS and studies the change of the maximum stress of the whole model $S_{\max,b}$ during the process from the natural state to the 180 ° folding of the C boom. And $S_{\max}$ is the maximum value of $S_{\max,b}$. The model adopts S4R shell elements, and to provide an appropriate balance between accuracy and computational expense, an element is divided every 2 ° along the arc of the section. The semi-structure and plane symmetry conditions are used, and the finite element results in this paper are mirror images. As shown in Figure 1, the sections at both ends of the C boom are coupled and constrained to PC1 and PC2 respectively, and a 90 ° angle is added to PC1 and PC2 respectively so that the C boom can be folded 180 °.

(a) (b) (c)

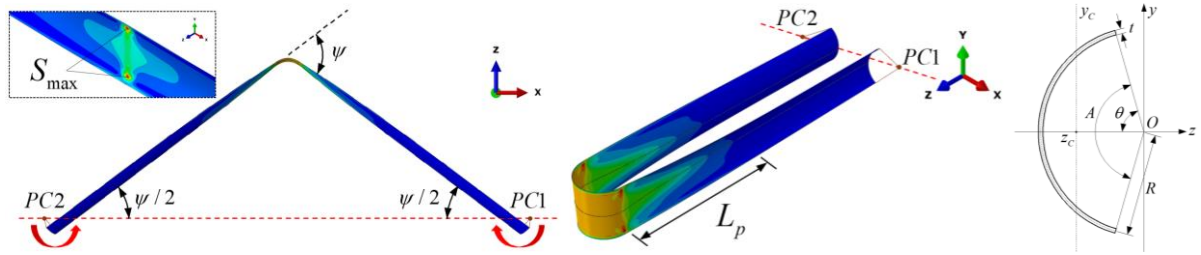


Figure 1. The finite element model: (a) the process of folding, (b) after folding, (c) cross-section geometrical dimension of the C boom

The material of C booms in this paper is 301 stainless steel, and its material properties are shown in Table 1. As shown in Figure 1, the unstressed cross-section of C booms is taken to be a circular arc of thickness t, the subtending angle A at the radius R, and $\theta=(A/2)\cdot(\pi/180)$. In this section, t =0.1mm, and the values of $R=10,15,20,25,30,35,40$mm, and $A=60,70,80,90,100,110,120$ degrees.

To make the stress not affected by the boundary, the length of the C boom L is taken as

$$L=\pi R+4L_p \tag{1}$$

$$L_p=\frac{(R\theta)^2}{\pi}\left[\frac{1-\nu^2}{120}\right]^{\frac{1}{4}}\frac{1}{\sqrt{Rt}} \tag{2}$$

to ensure that there is a section of the area without transverse deformation on both sides of the hinge after the C boom is folded 180 °. The length of the ploy region L_p in formula (2) is derived according to the classical long-wave solution of deformation of an initially cylindrical shell[3]. The simulation results show that formula (2) can well estimate the length of the ploy region, thus avoiding the influence of boundary on stress.

Table 1. Material properties of C booms

Young's modulus of elasticity for material E （Mpa）	200000
Poisson's ratio ν	0.3
Density ρ （kg/m^3）	7850

The variation of $S_{\max,b}$ and section bending moment M with the bend angle of the hinge ψ during folding is shown in Figure 5. It can be found that when M suddenly changes, $S_{\max,b}$ also changes. When the section reaches the steady-state bending moment, the $S_{\max,b}$ also remains steady, and it can be calculated[1] by the formula for the steady-state maximum stress

$$S_{\max,\text{steady}} = \frac{E}{1+\nu} \cdot \frac{t}{R} \tag{3}$$

However, according to the $S_{\max,b}$ curve, the maximum value of $S_{\max,b}$ does not occur in the steady state, but within a short range after a sudden change of M. Therefore, $S_{\max,b}$ in the folding process of C booms is studied.

As shown in Figure 2, when R and A are small, the maximum value of $S_{\max,b}$ occurs after the elastic hinge is formed, and the value is close to $S_{\max,\text{steady}}$. In this case, the maximum value of $S_{\max,b}$ in the folding process can be approximately calculated by the formula (3). When R and A are large, $S_{\max,b}$ will exhibit a "jump" phenomenon during the formation of the hinge, and there is a significant difference between the maximum value of $S_{\max,b}$ and $S_{\max,\text{steady}}$. For example, when R=40mm and A=110 °, the maximum value at which $S_{\max,b}$ "jumps" is approximate twice the value of $S_{\max,\text{steady}}$. The mises stress is shown in Figure 1 and $S_{\max,b}$ occurs in the region where the transverse curvature of the fold changes abruptly. When the $S_{\max,b}$ "jumps" phenomenon occurs, formula (3) cannot be used to estimate the maximum stress during the folding process, but specific numerical simulation is required.

(a) (b) (c) (d)

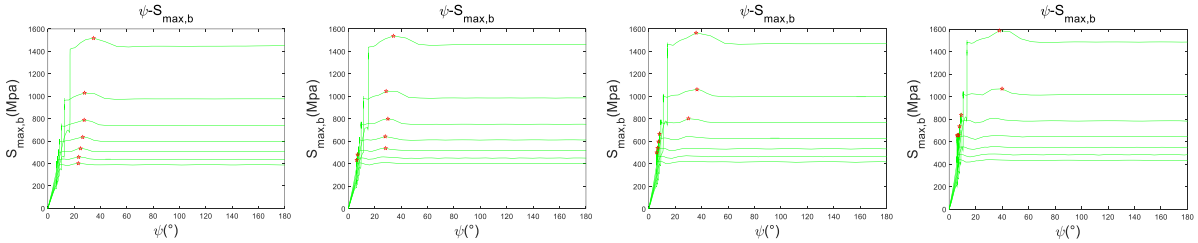


Figure 2. Maximum stress of C booms during the folding process: (a) A=60 °, (b) A=70 °, (c) A=80 °, (d) A=90 ° (curves from top to bottom represent R=10,15,20,25,30,35,40mm, respectively, and pentagrams represent the maximum values of $S_{\max,b}$)

2.2. Folding stress affected by boundary

C booms are typically used as support frames or hinges in deployable structures, with at least one end fully fixed. The hinge cannot infinitely approach the fixed end due to the ploy region. And section 2.1 studies this kind of folded state without boundary effects. However, when there is a design requirement or external force that forces the hinge to approach the fixed end, the stress of the boom will change. And this section studies this boundary effect on $S_{\max,b}$.

Based on the results of the finite element model in Section 2.1, as shown in Figure 3, after the C boom is folded 180 °, PC2 is fixed, and PC1 is pulled towards the opening direction of the hinge for a distance. Define x_{PC2} as the distance between PC2 and the endpoint of the hinge near the PC2. $S_{\max,b}$ during the pulling process is studied.

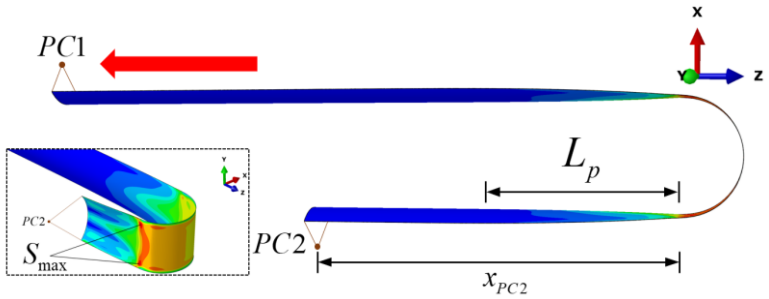


Figure 3. Pulling process of the C boom

As shown in Figure 4, when $x_{PC2}/L_p>1$, $S_{\max,b}$ remains approximately unchanged. When $x_{PC2}/L_p<1$, $S_{\max,b}$ begins to increase sharply, and boundary begins to affect the shape and size of the ploy region. At the same time, the longitudinal radius of curvature of the hinge also decreases. $S_{\max,b}$ occurs at the boundary of the hinge near the PC2, as shown in Figure 3. When $x_{PC2}/L_p=0.5$, $S_{\max,b}$ can be increased to 1.5-2 times the original value. Therefore, in engineering design, it is necessary to consider the impact of the hinge position x_{PC2} on the maximum stress during folding. Generally, x_{PC2} is compared with L_p, and the value of L_p can be calculated by Formula (2). When $x_{PC2}/L_p>1$, the boundary effects on $S_{\max,b}$ can be ignored, and the maximum value of $S_{\max,b}$ can be approximately calculated by the result of folding in Section 2.1. When $x_{PC2}/L_p<1$, a specific numerical simulation is required to determine the maximum value of $S_{\max,b}$, but this kind of design is not recommended unless necessary.

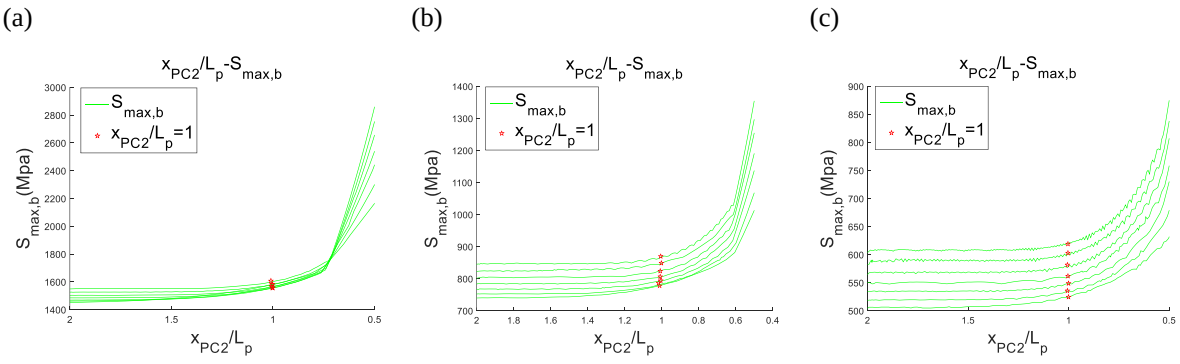


Figure 4. Maximum stress of C booms during the pulling process: (a) R=10mm, (b) R=20mm, (c) R=30mm (curves from top to bottom represent A=120, 110, 100, 90, 80, 70, 60 degrees, respectively)

3. Performance of C boom at deployed state

After the unlocking device is triggered, the C boom will release the stored elastic potential energy and expand to the final working state. The key to the performance of C booms at deployed state is sufficient stiffness. The common indicators for evaluating stiffness are bending stiffness and the natural frequency. Based on these two indicators, this section studies the impact of the size parameters of C booms on the stiffness at deployed state, and proposes two methods to improve the stiffness, namely, variable cross-section C boom and perforated C boom.

3.1. Parametric study on C boom

This section conducts a parametric study on the stiffness of C booms at deployed state. The material properties are shown in Table 1, and in this section, t =0.1mm, R = 10,15,20,...,60,65,70mm, A = 60,70,80,...160,170,180 degrees, L =500,600,700,800,900,1000mm.

3.1.1. Bending stiffness

Considering the small deformation of deployed C boom, its bending stiffness can be calculated according to the mechanics of material. As shown in Figure 1, θ is half of A, S is the area of the section, the y_C-axis is the centroid axis parallel to the y-axis, z_C is the z-coordinate of the y_C-axis, and I_{yO} and I_{yC} are the area moments of inertia relative to the y and y_C axes.

$$\theta = \frac{A}{2} \cdot \frac{\pi}{180} \tag{4}$$

$$S = 2R\theta t \tag{5}$$

$$I_{yO} = 2\int_0^{\theta} Rt\left(R\cos\alpha\right)^2 d\alpha \tag{6}$$

$$z_C = \frac{1}{S}\left(2\int_0^{\theta} Rt\left(-R\cos\alpha\right)d\alpha\right) \tag{7}$$

$$I_{yC} = I_{yO} - Sz_C^2 = \frac{R^3 t}{\theta}\left(\theta\sin\theta\cos\theta + 2\cos^2\theta + \theta^2 - 2\right) \tag{8}$$

The trend of EI_{yC} with R and A is shown in Figure 6, where EI_{yC} is positively correlated with R and A. When R >30mm and A >100 °, EI_{yC} increases significantly.

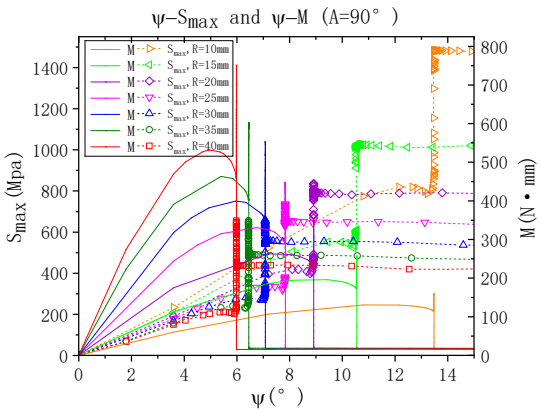


Figure 5. Bending moment and maximum stress with ψ

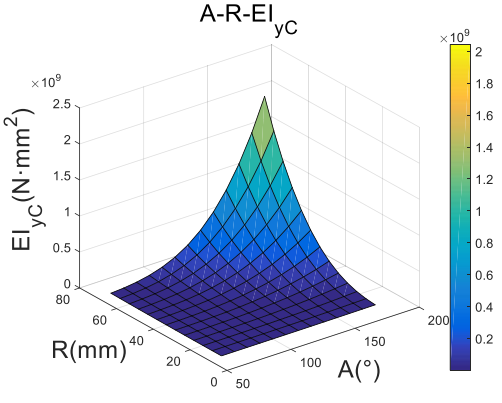


Figure 6. Bending stiffness of the C boom

3.1.2. Natural frequency

The natural frequency reflects the overall stiffness of the component. Generally, C booms are required to have a high natural frequency to ensure a stable working state. This section studies the first-order natural frequency of the cantilevered C boom f_c. Its material properties, elements, and size parameter values are the same as those of the finite element model in 2.1. The simulation results are shown in Figure 7.

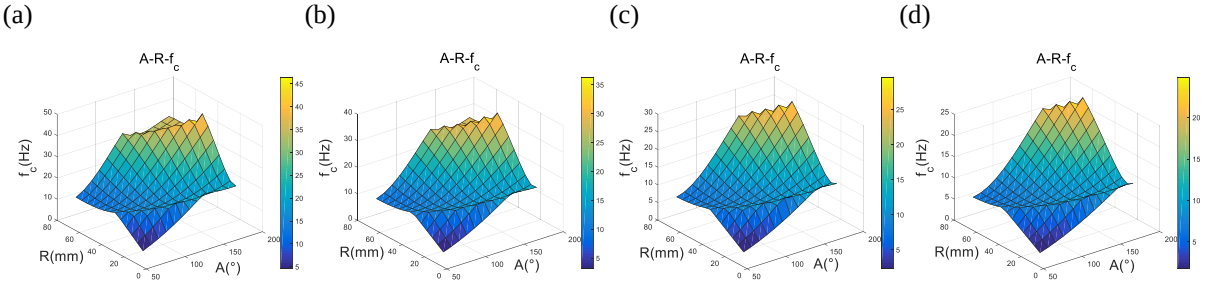


Figure 7. The first-order natural frequency of cantilever C booms: (a) L =500mm, (b) L =600mm, (c) L =700mm, (d) L =800mm

It can be seen that the trend of f_c with R and A is not monotonous, but there will be two peak lines corresponding to smaller and larger cross-sectional dimensions, respectively. When R and A are small, f_c has a significant increase with the increase of the cross-sectional dimension. When R and A cross the first peak line, f_c decreases slightly, and then rises significantly to the second peak line. When R and A cross the second peak line, f_c will have a significant decrease and remain stable within a certain range. Therefore, in engineering design, if a higher f_c is desired, the combination of R and A near the second peak line can be selected.

3.2. C boom with variable cross-section

In deployable structures, C booms are commonly used as support frames and bear uniform linear loads or concentrated loads at the ends. The section near the fixed end usually bears a greater bending moment than the distal end. From the perspective of mass reduction, the cross-section along the longitudinal direction should be variable.

This section suggests a C boom with a variable cross-section, as shown in Figure 8. In this kind of boom, R is uniform, while the subtending angle A_{vc} linearly decreases from A_2 at the fixed end to A_1 at the free end along the longitudinal direction. With the fixed end as the origin of the x-axis, A_{vc} at the coordinate x is

$$A_{vc}(x) = A_2 - \frac{A_2 - A_1}{L} x, \text{ where } A_1 \le A_2,\ x \in [0, L] \tag{9}$$

3.2.1. Bending stiffness

Because the bending stiffness of a C boom with variable cross-section varies along the longitudinal direction, it cannot be used to evaluate the stiffness of the boom. However, it is possible to compare whether the stiffness of a C boom with variable cross-section has improved compared to that of a C boom with the same mass according to specific working conditions. This section focuses on the application of ribs as support members in the wrap-rib deployable antenna. Due to accuracy requirements, when the mesh surface of the antenna is tensioned, the deformation of the ribs should be

controlled within the allowable range. The tension of the mesh facing the ribs is equivalent to a uniformly distributed load along the longitudinal direction, and the displacement of the free end of the ribs also reflects the overall deformation of the ribs. In this section, a cantilevered C boom with variable cross-section is established, and a uniformly distributed load $q = 10^{-3} N/m$ is applied on its middle line, to obtain the displacement z_{vc} of the free end of the boom along the load direction, as shown in Figure 9. The material properties are shown in Table 1. The method for determining a C boom with the same mass is to ensure that the material, t, R and L are the same as those of a C boom with variable cross-section, and determine a C boom with a subtending angle A_{emvc} to make it have the same mass as the C boom with variable cross-section, which gives

$$\rho t R A_{emvc,rad} L = \int_0^L \rho t R A_{vc,rad}(x)\, dx \tag{10}$$

where

$$A_{emvc,rad} = \frac{A_{emvc}}{180} \cdot \pi \,, \quad A_{vc,rad}(x) = \frac{A_{vc}(x)}{180} \cdot \pi \tag{11}$$

(a) (b)

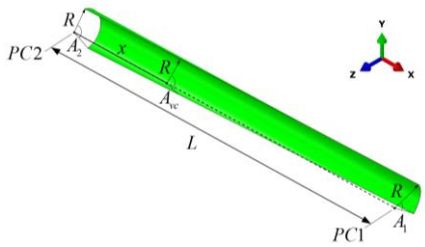


Figure 8. The C boom with the variable cross-section

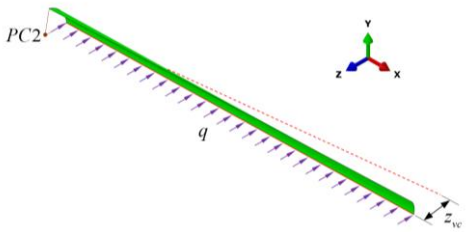


Figure 9. The uniformly distributed load

Apply the same boundary conditions and loads to the C boom with the same mass to obtain the displacement of the free end along the load direction z_c. Here, Rat_z is defined as $Rat_z = z_{vc} / z_c$. A parametric study is carried out, in which t =0.1mm, R =10,20,30,40,50,60,70mm, A_1 =60, 80, 100, 120, 140, 160, 180 degrees, $A_2 = A_1 + 20,...,180$ degrees, and L =500,600,700,800mm. The simulation results are shown in Figure 10.

(a) (b) (c) (d)

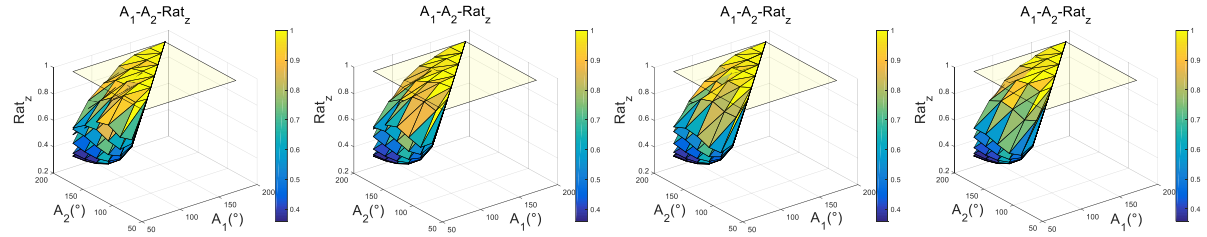


Figure 10. The ratio of displacement $Rat_z = z_{vc} / z_c$: (a) L =500mm, (b) L =600mm, (c) L =700mm, (d) L =800mm (the 7 curved surfaces in each figure correspond to R =10-70mm, and the yellow plane represents $Rat_z = 1$)

It can be seen that all curved surfaces are below the 1 plane, that is, for C booms with variable cross sections, $z_{vc} < z_c$. When A_1 is smaller and A_2 is larger, the displacement decreases more significantly,

and the minimum displacement can be reduced to 0.3-0.4 times the original value. Therefore, under the action of uniformly distributed load, the stiffness of the C boom with variable cross-section is improved compared to the C boom with the same mass, and the smaller A_1 is and the larger A_2 is, the more significant the stiffness improvement will be.

3.2.2. Natural frequency

This section studies the first-order natural frequency of a cantilevered C boom with variable cross-section f_{vc}. The material properties, elements, and parameter values are the same as those of the finite element model in 3.2.1., and the simulation results are shown in Figure 11.

It can be seen that with the decrease of A_1 and the increase of A_2, the first-order natural frequency of C booms with variable cross sections will also increase, indicating higher stiffness. To compare the natural frequency of the C boom with the same mass, the first-order natural frequency of it is calculated using the same model as in Section 3.2.1. Here, $Rat_{f,vc}$ is defined as $Rat_{f,vc} = f_{vc} / f_{c,vc}$, and the simulation results are shown in Figure 12.

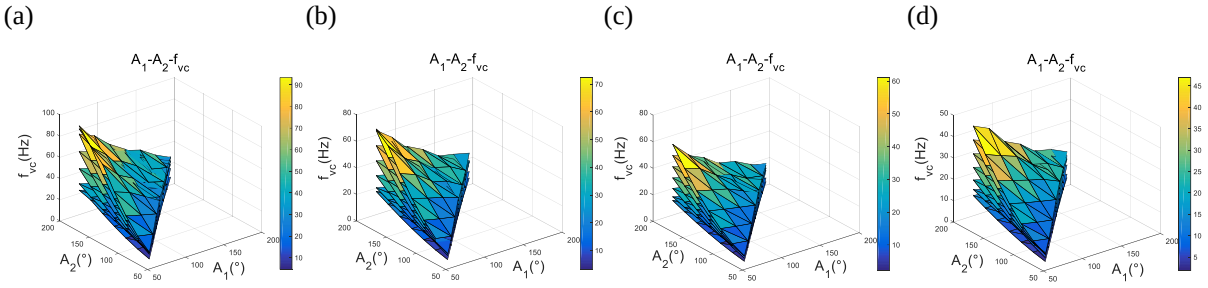


Figure 11. The first-order natural frequency of cantilevered C booms with variable cross sections: (a) L =500mm, (b) L =600mm, (c) L =700mm, (d) L =800mm (the 7 curved surfaces in each figure correspond to R =10-70mm)

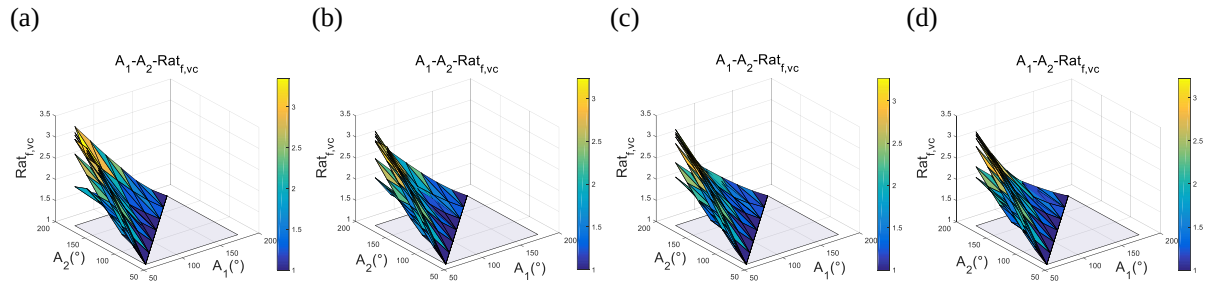


Figure 12. The ratio of first-order natural frequency $Rat_{f,vc} = f_{vc} / f_{c,vc}$: (a) L =500mm, (b) L =600mm, (c) L =700mm, (d) L =800mm (the 7 curved surfaces in each figure correspond to R =10-70mm, and the purple plane represents $Rat_{f,vc} = 1$)

It can be seen that the C boom with variable cross-section has a higher first-order natural frequency, that is, a higher stiffness, compared to the C boom with the same mass. When A_1 is smaller and A_2 is larger, the stiffness increases more obviously, which is consistent with the conclusion in Section 3.2.1.Therefore, in engineering design, C booms with variable cross sections can be used to reduce the mass of components and improve stiffness.

3.3. Perforated C boom

This section suggests a perforated C boom, which is made by drilling some holes in the C boom. The specific method is to divide the projection surface of the opening direction of the C boom into several squares, with the side length d of the square being $1/n$ times the width of the belt spring. In this paper, n is taken as 5. Correct L so that it is equal to an integer multiple of d and is closest to the design length, so that the holes are evenly distributed along the longitudinal direction of the boom. Draw a circle with the center of the square as the center and D as the diameter. Here, H is defined as $H = D/d$, where $H \in [0,1)$. Remove the projection of the circular region on the boom and the drilling is completed, as shown in Figure 13. Here, the hole ratio Rat_{hol} is defined as the ratio of the mass of the perforated C boom m_{hol} to the mass of the original C boom m_c.

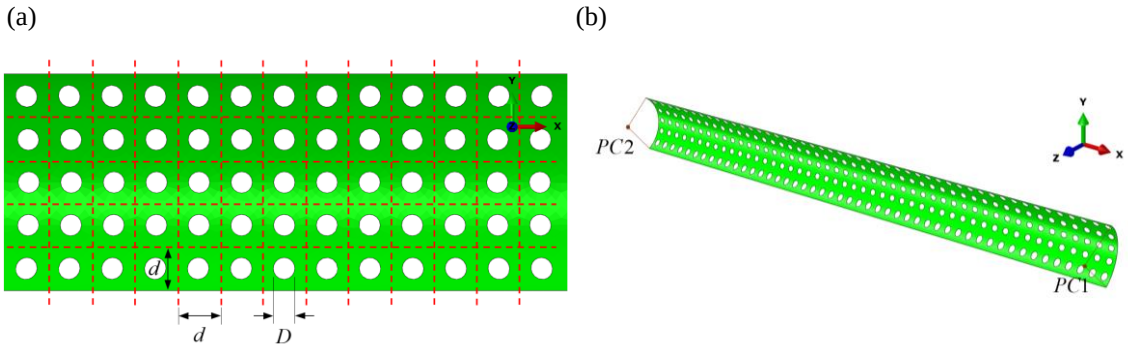


Figure 13. Perforated C boom: (a) distribution of holes on the projection plane, (b) distribution of holes in the boom

3.3.1. Bending stiffness

Due to the uniform distribution of holes along the longitudinal direction, it can be approximately assumed that the bending stiffness of the perforated C boom along the longitudinal direction is the same, and therefore it can be used to evaluate the stiffness of the boom. The bending stiffness can be obtained by numerical simulation of pure bending. As shown in Figure 13, the sections at both ends of the boom are coupled and constrained to PC1 and PC2 respectively, then a 1 ° angle around the y-axis is added to PC1 while PC2 is fixed. The bending moment of the boom section $M_{y,1\deg}$ is extracted and the bending stiffness can be derived as $EI_{hol} = 180 M_{y,1\deg} L/\pi$. The material properties are shown in Table 1. To ensure the accuracy of the simulation results, at least 8 elements are distributed along each hole edge in the finite element model.

By changing H, perforated C booms with different Rat_{hol} can be obtained, and a parametric study on EI_{hol} is carried out, in which t =0.1mm, L =500mm, R =10,20,30,40,50,60,70mm, A =60, 80, 100, 120, 140, 160 degrees, and H =0.1,0.2,0.3,0.4,0.5,0.6,0.7. The simulation results are shown in Figure 14.

As can be seen from Figure 14, the higher the hole ratio, the smaller the bending stiffness. However, drilling also reduces the mass of the boom, so the bending stiffness of the C boom with the same mass was studied. The method for determining a C boom with the same mass is to ensure that the material, t, R and L are the same as those of a perforated C boom, and determine a C boom with a subtending angle A_{emhol} to make it have the same mass as the perforated C boom, which gives

$$\rho t R A_{emhol,rad} L = m_{hol} \tag{22}$$

where $$A_{emhol,rad} = \frac{A_{emhol}}{180} \cdot \pi \tag{33}$$

The bending stiffness of the C boom with the same mass EI_{emc} can be obtained using the same method of loading and bending stiffness calculation as the perforated C boom. Here, Rat_{EI} is defined as $Rat_{EI} = EI_{hol} / EI_{emc}$, and the simulation results are shown in Figure 15.

(a) (b)

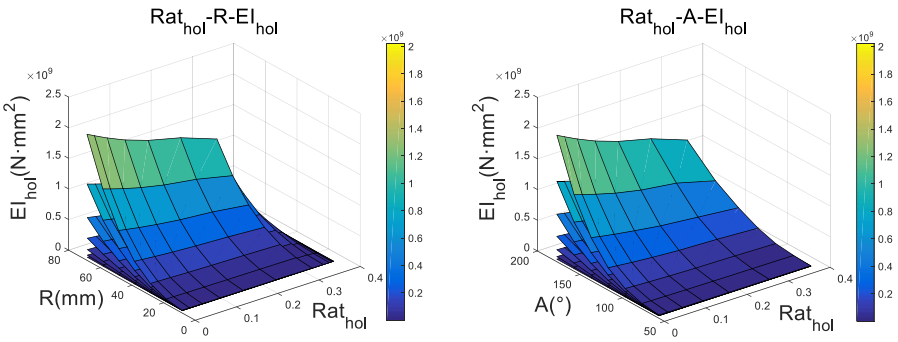


Figure 14. The bending stiffness of the perforated C boom EI_{hol} : (a) trend of EI_{hol} with Rat_{hol} and R (curved surfaces from top to bottom represent A =180, 160, 140, 120, 100, 80, 60 degrees, respectively), (b) trend of EI_{hol} with Rat_{hol} and A (curved surfaces from top to bottom represent R =70,60,50,40,30,20,10mm, respectively)

(a) (b)

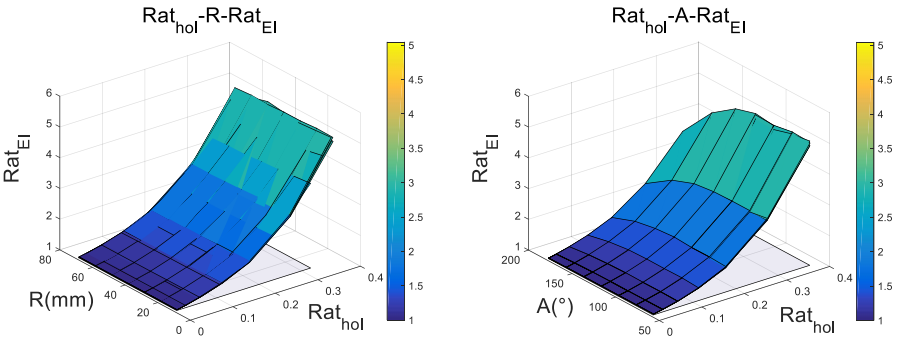


Figure 15. The ratio of bending stiffness Rat_{EI} : (a) trend of Rat_{EI} with Rat_{hol} and R, (b) trend of Rat_{EI} with Rat_{hol} and A (there are 7 surfaces in each figure representing different A and R, but they almost coincide)

It can be seen that compared to C booms with the same mass, perforated C booms have higher bending stiffness. And the higher Rat_{hol}, the more significant the improvement in bending stiffness.

3.3.2. Natural frequency

This section studies the first-order natural frequency of a cantilevered perforated C boom f_{hol}. The material properties, elements, and parameter values are the same as those of the finite element model in 3.3.1., and the simulation results are shown in Figure 16 and Figure 17.

As can be seen, the higher Rat_{hol}, the smaller f_{hol}. However, the trend of f_{hol} with A and R is not monotonic, but there is a peak line, that is, each R corresponds to an A, making f_{hol} reach an extreme point. To compare the natural frequency of the C boom with the same mass, the first-order natural frequency of it is calculated using the same model as in Section 3.3.1. Here, $Rat_{f,hol}$ is defined as $Rat_{f,hol} = f_{hol} / f_{c,hol}$, and the simulation results are shown in Figure 18 and Figure 19.

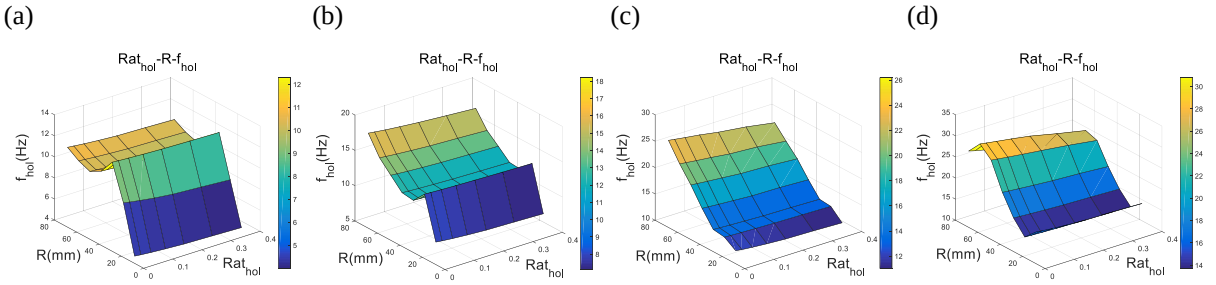


Figure 16. The trend of f_{hol} with Rat_{hol} and R: (a) A=60°, (b) A=80°, (c) A=100°, (d) A=120°

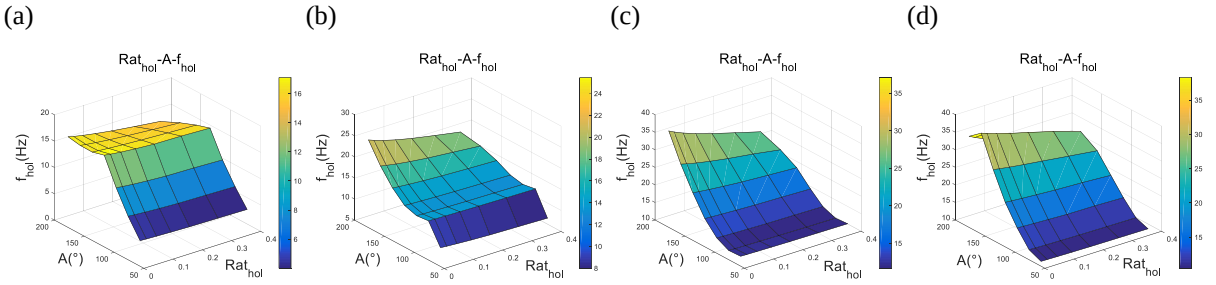


Figure 17. The trend of f_{hol} with Rat_{hol} and A: (a) R=10mm, (b) R=20mm, (c) R=30mm, (d) R=40mm

It can be seen that most perforated C boom has a higher first-order natural frequency, that is, a higher stiffness, compared to the C boom with the same mass. And the higher Rat_{hol}, the more significant the improvement in stiffness, which is consistent with the conclusion in Section 3.3.1. However, there are also some perforated C booms whose f_{hol} is lower than $f_{c,hol}$. For example, when R=70mm, A =160 °, and Rat_{hol} =0.3482, f_{hol} is only 67.11% of $f_{c,hol}$.

Therefore, in engineering design, perforated C booms can be used to reduce the mass of components and improve stiffness. However, in pursuit of higher natural frequencies, it is necessary to distinguish according to Figure 16-19 or conduct specific numerical simulations.

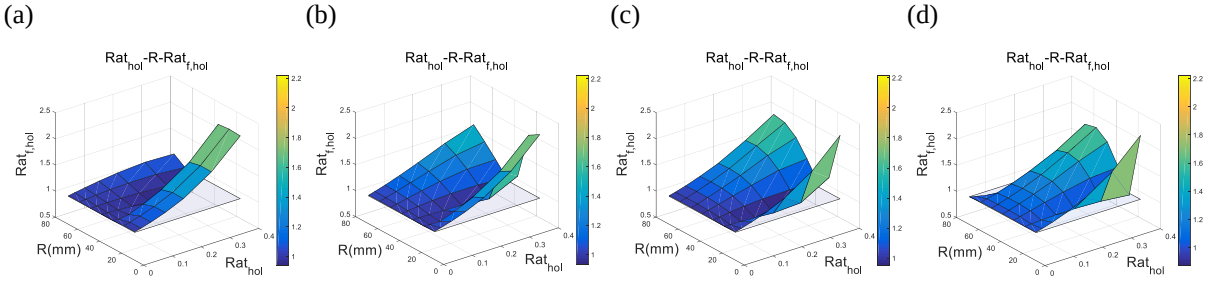


Figure 18. The trend of $Rat_{f,hol}$ with Rat_{hol} and R: (a) A=60°, (b) A=80°, (c) A=100°, (d) A=120°

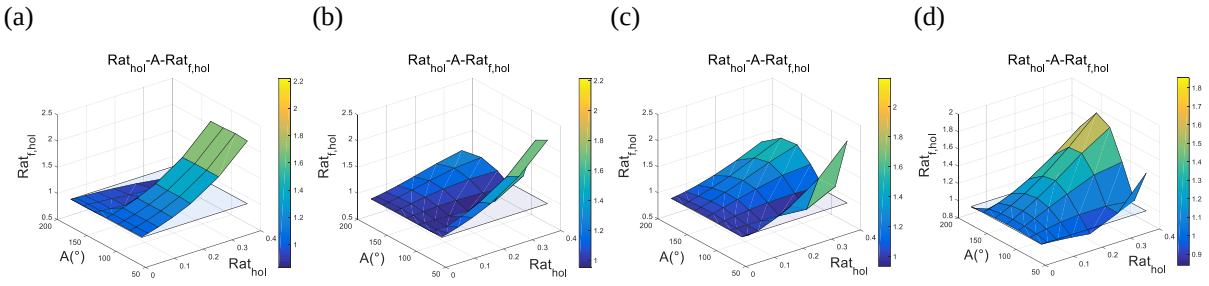


Figure 19. The trend of $Rat_{f,hol}$ with Rat_{hol} and A: (a) R=10mm, (b) R=20mm, (c) R=30mm, (d) R=40mm

4. Conclusions

This paper studies the mechanical properties of the C boom in folded and deployed states. The maximum stress during the folding process of C booms is studied. When the cross-section size is large, the maximum stress will exhibit a "jump" phenomenon. The boundary also affects the stress. When the distance between the hinge and the fixed end is less than the length of the ploy region, the maximum stress will increase sharply. The bending stiffness and first-order natural frequency of deployed C booms are studied. The C boom with variable cross section and the perforated C boom is suggested and studied to reduce the mass and improve the stiffness. The bending stiffness of these two types of booms is improved compared to C booms with the same mass, and the first-order natural frequency is also improved except for a small number of perforated C booms.

References

[1] Ji-can. XUAN, Fu-ling. GUAN and Jun. WANG, “Yielding control of tape spring for deployable structures during the pure bending buckling,” *SPATIAL STRUCTURES,* vol. 15, pp. 81-84+95, 2009.

[2] J. Shore, A. Viquerat, G. Richardson et al, “The natural frequency of drum-deployed thin-walled open tubular booms,” *Thin-Walled Structures,* vol. 170, 2022.

[3] K. A. Seffen, B. Wang, and S. D. Guest, “Folded orthotropic tape-springs,” *Journal of the Mechanics and Physics of Solids,* vol. 123, pp. 138-148, 2019.

[4] C. R. Calladine and K. A. Seffen, “Folding the Carpenter's Tape: Boundary Layer Effects,” *Journal of Applied Mechanics-Transactions of the ASME,* vol. 87, 2020.

IASS 2023
July 10–14 Melbourne
Integration of Design and Fabrication

Proceedings of the IASS Annual Symposium 2023
Integration of Design and Fabrication
10–14 July 2023, Melbourne, Australia
Y.M. Xie, J. Burry, T.U. Lee and J. Ma (eds.)

Surface accuracy analysis and test on 0.5 m aperture wrap-rib deployable antenna

Han ZHANG*, Minger WU[a], Ping XIANG[a]

[a,*] Department of Structural Engineering, Tongji University
1239 Siping Road, Shanghai 200092, China
zhanghan0731@foxmail.com

Abstract

To meet the demand for deployable antennas with high storage ratio and lightweight， a wrap-rib deployable antenna was developed in this paper. The antenna was less than 0.6 kg in weight, 0.5 meter in aperture and could be stowed in 1.5 U (10 cm× 10 cm× 15 cm). Paraboloidal mesh reflector was designed for X-band operation. The reflector was composed of ribs, metal mesh and side cables. The ribs were not only the driving elements of the reflector but also the fixing boundary of the metal mesh. C-shaped cross section was adopted for the ribs. The wrapping process of C-shaped stainless steel rib was analyzed theoretically and numerically. It was verified that ribs were in elastic state during wrapping process. Based on surface accuracy required by X-band， the number of ribs was determined as 16 and the focal length to aperture ratio of the reflector was 0.45. The reflector surface was found through shape finding analysis in which both the deformation of ribs and the distribution of tension in mesh were considered. The optimal curve of ribs was designed by minimizing the surface error through genetic algorithm. Two prototype antennas were assembled and the shapes of reflector surface were measured before and after shaking table tests. The surface RMS error was 0.8-1.0mm and had little change after multi-deployment.

Keywords: deployable antenna, wrap-rib, shape finding analysis, surface accuracy test, repeat accuracy

1. Introduction

Spaceborne deployable antenna structure can be stowed during transportation and storage, and can be deployed to a stable working state when in orbit. According to the shape of the reflector, deployable antenna can be divided into three types: solid reflector antenna; inflatable reflector antenna and mesh reflector antenna. The mesh reflector antenna has the advantages of light weight and high storage ratio, and it is easy to realize large aperture. According to the different supporting structures, the mesh reflector antenna can be divided into radial-rib antenna, wrap-rib antenna and truss antenna.

The CubeSat is a kind of microsatellites. A standard unit (1 U) of the CubeSat is a cube with an effective size of 10 cm× 10 cm× 10 cm and a mass not exceeding 1 kg. Compared with traditional satellites, the characteristics of microsatellites represented by CubeSat can be summarized as follows: microsatellites are small in size, light in weight, and easy to achieve a rocket to launch more than one satellite; the design life of microsatellites is often short, but the development cycle is also short and the cost is low; multiple microsatellites can form a distributed space system to achieve global coverage, and the single microsatellite has a high degree of integration, which can adopt modular design.

With the large increase in the demand for microsatellite, the modularization and standardization of microsatellite can realize the advantages of low cost, high performance and short development cycle. The research and development of standardized deployable antenna for microsatellites has important engineering application value.

Copyright © 2023 by Han ZHANG, Minger WU and Ping XIANG. Published in the Proceedings of the IASS Annual Symposium 2023 with permission.

The small size and light weight of microsatellites put forward many harsh requirements for the deployable antenna carried by them, such as: extreme lightweight, minimal storage volume, high surface accuracy, etc. The mesh reflector antenna has good results in surface accuracy, storage efficiency, mass and aperture. It has good comprehensive performance. Compared with radial-rib as given by SERC and JPL, the stiffness of wrap-rib is smaller, so the surface accuracy of wrap-rib antenna is slightly lower. But the wrap-rib antenna structure is simpler. The weight is lighter. And the storage efficiency is higher.

The paraboloidal reflector antenna installed on a microsatellite such as CubeSat can greatly enhance the satellite's communication capability. The Space Engineering Research Center of the University of Southern California (SERC) has developed a radial-rib deployable antenna. The antenna was 0.5 meter in aperture and could be stowed in a load area of 10 cm× 10 cm× 16 cm in Colony I CubeSat. The antenna consists of 30 ribs, each of which has two rotating hinges for deployment [1]. NASA Jet Propulsion Laboratory (JPL) developed a novel Ka-band radial-rib deployable antenna for Rain Cube CubeSat. The antenna consists of 30 ribs, and it could be stowed in 1.5 U (10 cm× 10cm × 15cm) [2-4].

The radial-ribs of the antennas as given by SERC and JPL are each 30 rigid rods with a rotating hinge in the middle. The antenna reflector of the Colony I CubeSat is deployed by using the spring to push out of the storage container. The antenna reflector of the Rain Cube CubeSat is deployed by using the screw to push out of the storage container. The two antenna reflectors have high and stable surface accuracy, but the structure is complicated. So the installation is slightly complicated. The storage efficiency is slightly low. The mass is slightly heavy. And the deployment reliability is slightly low.

In this paper, a wrap-rib deployable antenna was developed. The ribs of the antenna are 16 thin-walled rods with 0.1mm thick C-shaped cross section. The reflector is deployed by the drive of the elastic potential energy stored in the elastic wrapped ribs. The reflector structure is slightly simple. So the installation is slightly simple. The storage efficiency is slightly high. The mass is slightly light. And the deployment reliability is slightly high. Through the key position design and standardized installation technology, the reflector has a good and stable surface accuracy. Moreover, The height adjustment structure of the feed and the design of stowing the reflector through the shells make the installation, testing and stowing of the deployable antenna very convenient.

In this paper, the curve of wrap-rib was optimized. Two prototype antennas were constructed to analyzed and tested the surface accuracy of reflector.

2. Concept and design

A wrap-rib deployable antenna was developed in this paper. The antenna was less than 0.6 kg in weight, 0.5 meter in aperture and could be stowed in 1.5 U (10 cm× 10 cm× 15 cm). Paraboloidal mesh reflector was designed for X-band operation. The antenna includes locking and unlocking device, deployable reflector, deployable shell, and deployable feed, as shown in Figure 1. The deployable reflector, deployable shell and deployable feed are deployed by the drive of some elastic members. Locking and unlocking device includes rope for storage, endotherm knife and other components.

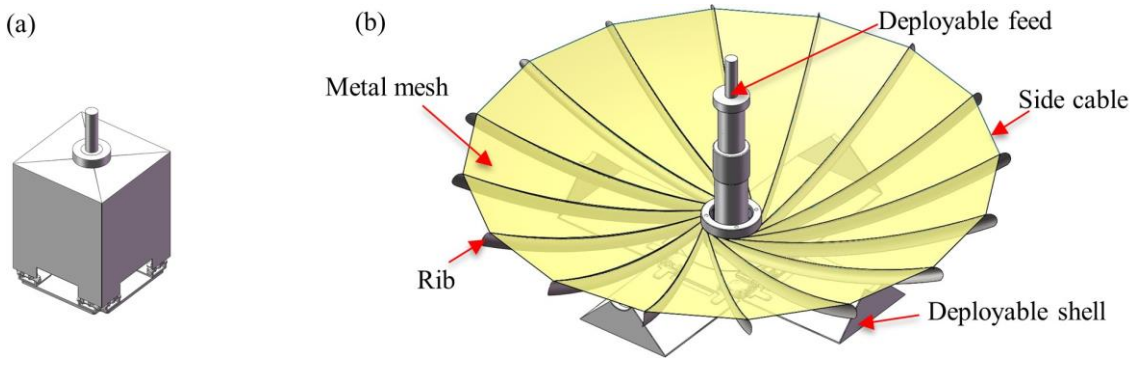


Figure 1. Configuration of wrap-rib deployable antenna: (a) stowed state, (b) deployed state.

The deployable reflector is composed of ribs, metal mesh and side cables. The root of every rib is fixed on the central hub of the antenna. The edge of the metal mesh is tensioned by the side cables. High strength and high elasticity materials such as stainless steel can be selected for the ribs, which can meet the requirements of space environment and ensure that ribs remain elastic in the wrapping process. The cross section of the ribs can adopt lenticular shape, C shape or double C shape, which have high flexural rigidity. C-shaped cross section is easy to process, so the ribs of prototype adopt C-shaped cross section in this paper. The deployable shell includes shells, pin shafts, torsional springs and locking device. The deployable feed includes telescopic sleeve, sleeve spring, feed, feeder and height adjustment structure.

The sequence of the stowing process is: reflector → shell → feed → locking device. The reflector is stowed by wrapping the ribs around the central hub, and the mesh should be located above the ribs to avoid being squeezed. Then the four shells are rotated around the pin shafts and locked. The stowed shells prevents the reflector from deploying. The deployable feed is stowed by compressing sleeve spring, and the claw at the top of the deployable feed in the stowed state prevents the four shells from deploying. Finally, the deployable feed is locked in the stowed state by a pre-tightened rope and the spiral-shaped feeder is secured in the sleeve. The section of stowed state antenna is shown in Figure 2

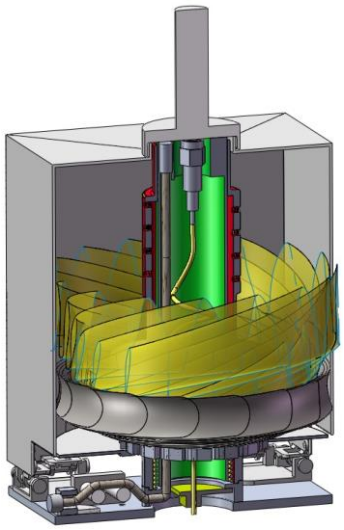


Figure 2. The section of stowed state antenna

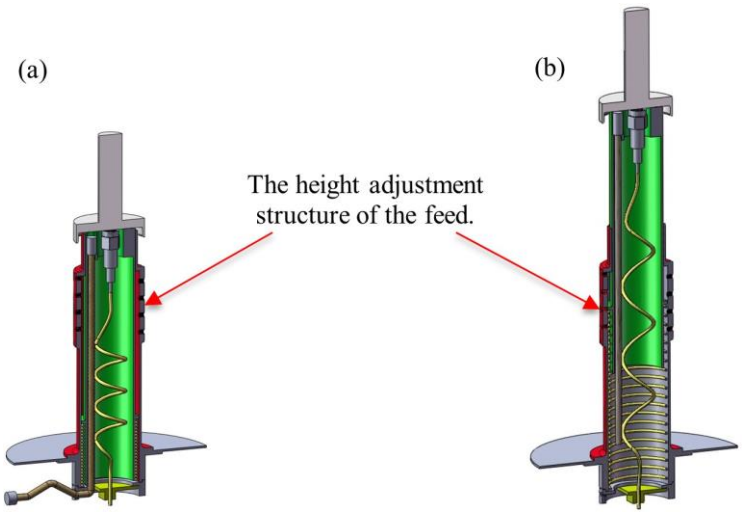


Figure 3. The section of deployable feed: (a) stowed state, (b) deployed state.

The sequence of the deploying process is: unlocking device → feed → shell → reflector. The antenna can be deployed by applying electricity to the endotherm knife. Firstly, by using the endotherm knife to cut the pre-tightened rope, the deployable feed is deployed under the push of the sleeve spring, and the feeder is elongated. Then, the claw at the top of the deployable feed do not restrain the four shells, which are deployed and locked in the deployed state by the drive of torsion springs at the pin shafts. Finally, the reflector is deployed by the drive of the elastic potential energy of the wrapped ribs, and the mesh of reflector is tensioned by ribs. The stowed state and deployed state of deployable feed is shown in Figure 3, and the outer sleeve contains the height adjustment structure of the feed.

The reflector surface is paraboloid when it is deployed. Four shells are simultaneously rotated outward 90°, then locked on the back of the reflector. The deployable feed is pushed near the focus of the reflector. The deploying process is shown in Figure 4. In the deployed state, the position of the shells and the feed are locked, and the mesh of reflector is tensioned by ribs.

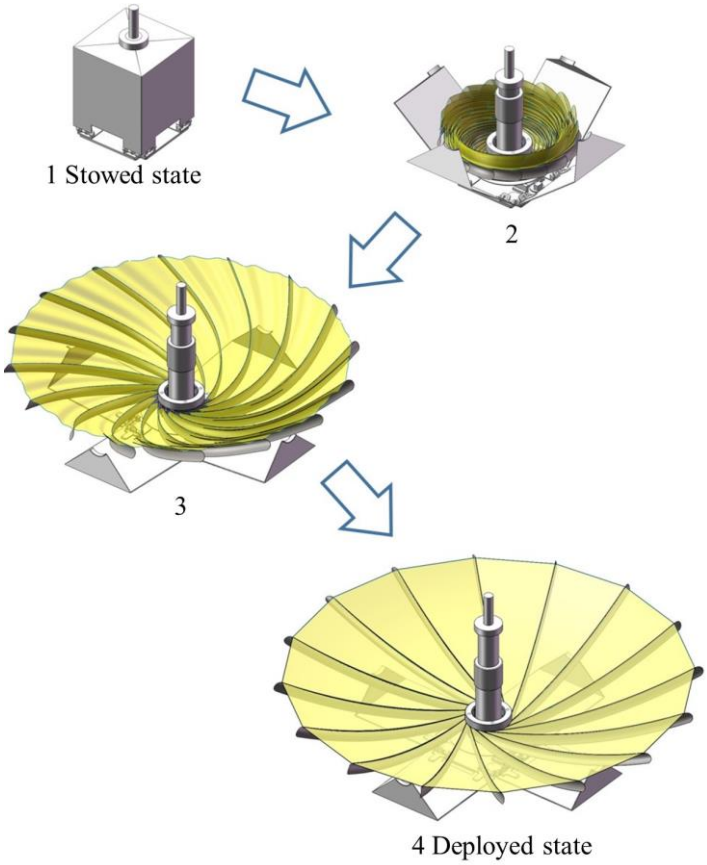


Figure 4. Deploying process

3. Rib and its wrapping analysis

3.1. Cross section of rib

Metal mesh should be tensioned and ribs support the mesh, so the cross section of rib should make the rib have enough flexural rigidity. Also, the rib should be in an elastic state under stowed state. In this paper, C-shaped cross section stainless steel rib is adopted. The cross section is flattened and wrapped for storage. In the deployed state, the cross section is restored to C-shape to provide better flexural rigidity. The geometric parameters of C-shaped cross section include radius of curvature R, thickness t and central angle θ, as shown in Figure. 5. After the cross section is flattened, it is wrapped around the

central hub of the antenna. In the stowed state, the wrapping radius r of wrapped rib is half of the outside diameter of central hub.

Based on the flexural rigidity and stress in the stowed state of rib, the following design parameters were selected in this paper: R = 15 mm, θ = 56°, t = 0.1 mm, r = 25 mm.

The ribs should be made of high strength and high elastic modulus materials to meet the requirements of space environment. In this paper, high strength stainless steel is used to make the ribs of the test prototype. The elastic modulus of the material is 206 GPa and the tensile strength is 1300 MPa.

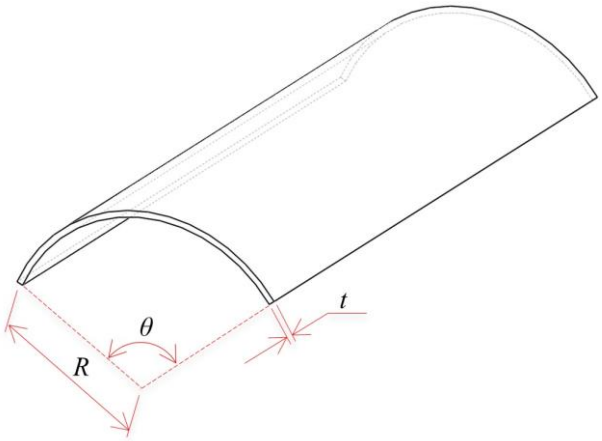


Figure 5. The cross section of wrap-rib

3.2. Approximate theoretical analysis of wrapping process

The approximate theoretical analysis of the wrapping process of rib was carried out. Ignoring the curve shape along the length of the rib, the wrapping process of the C-shaped cross section straight rib around the 2r diameter cylinder was analyzed. The theoretical analysis model is shown in Figure 6. The x direction refers to the direction along the rib length, and the y direction refers to the direction along the cross section. the convex surface of the rib is wrapped tightly to the central hub.

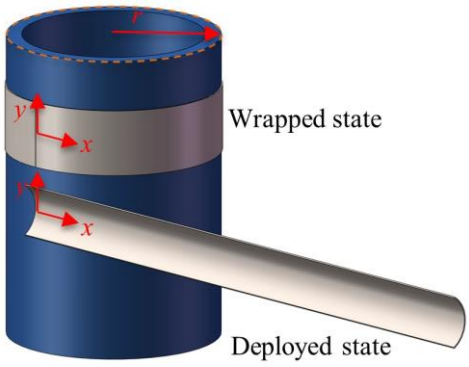


Figure 6. Analytical model of wrapping process

The wrapping process of C-shaped cross section rib includes two processes: section flattening and wrapping. According to the thin shell theory [6], equations (1) ~ (3) represent the stress-strain relationship at the position where the distance from the central surface is z.

$$\sigma_x = \frac{E}{1-\mu^2} z(\Delta k_x + \mu \Delta k_y) \tag{1}$$

$$\sigma_y = \frac{E}{1-\mu^2} z(\Delta k_y + \mu \Delta k_x) \tag{2}$$

$$\tau_{xy} = 0 \tag{3}$$

$\triangle k_x$ and $\triangle k_y$ are the curvature changes in the x and y directions, respectively. Ignoring the slight differences of curvature changes along the thickness direction, and considering the two processes of flattening and wrapping, the curvature changes can be obtained as shown in equation (4):

$$\Delta k_x = \frac{1}{r}, \Delta k_y = \frac{1}{R} \tag{4}$$

The magnitudes of two principal stresses on the convex surface of wrapped rib are shown in equations (5) and (6):

$$\sigma_1 = \frac{Et}{2(1-\mu^2)}(\frac{1}{R} + \mu \frac{1}{r}) \tag{5}$$

$$\sigma_2 = \frac{Et}{2(1-\mu^2)}(\frac{1}{r} + \mu \frac{1}{R}) \tag{6}$$

The cross section parameters (t = 0.1mm, R = 15mm) and the wrapping radius (r = 25mm) were substituted, and the elastic modulus and Poisson's ratio of stainless steel were considered, then the Mises stress was calculated as equation (7) :

$$\sigma_M = \sqrt{\sigma_1^2 + \sigma_2^2 - \sigma_1 \sigma_2} = 821.5\text{MPa} \tag{7}$$

3.3. Numerical analysis of wrapping process

The antenna reflector in this paper is a paraboloid. The curve of rib which is the boundary of the mesh is temporarily considered as a parabola. And the actual design curve of rib was slightly adjusted after subsequent optimization design in the Section 4 of the paper. Finite element software ABAQUS was used to analyze the wrapping process of parabolic single rib. The curve equation along the length of the rib is temporarily taken as $z = x^2 / 900$ (0 mm$\leqslant$ x $\leqslant$ 250 mm). In order to realize the tight wrapping of rib around the central hub, two additional 50 mm diameter cylinders were added to the numerical analysis model, both of which were set as rigid bodies. The reference points of the two cylinders were controlled for displacement loading. First, the C-shaped cross section rib was flattened, then turn one cylinder forward and reverse the other cylinder, and the rib was tightly wrapped around the cylinder. Limited sliding contact is arranged between the two sides of the rib and the surface of the cylinder, and the friction coefficient is set at 0.2. The finite element analysis model is shown in Figure 7. The Mises stress nephogram of the concave side and convex side after wrapping is shown in Figure 8.

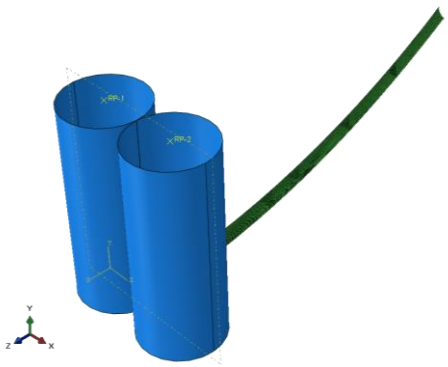


Figure 7. FEM model of wrapping process

As shown in Figure 8, the maximum Mises stress under wrapped state was 942.9 MPa on concave side and 946.9 MPa on convex side. The maximum Mises stress calculated by the finite element method was slightly larger than the approximate theoretical value, that is because the finite element model considered the curve shape along the length of rib and the contact friction.

In this paper, stainless steel ribs (material tensile strength: 1300 MPa) were fabricated. Through the wrapping test, the rib maintained a good elastic state, and no obvious plastic deformation was observed.

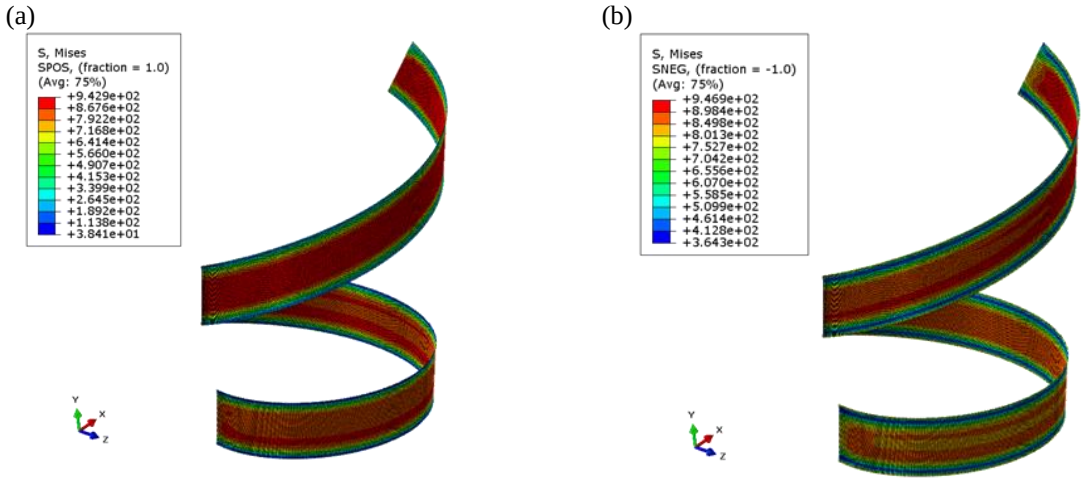


Figure 8. Mises stress of wrapped rib: (a) concave side, (b) convex side.

4. Surface accuracy analysis of reflector

4.1. Number of ribs

The number of ribs is mainly determined by the surface accuracy requirement of the reflector. The more the number of ribs, the higher the surface accuracy of reflector can be achieved, but the more complex the structure is. Without considering the machining error and installation error of the actual model, the back-pillow effect of the reflector and the rib deformation, the surface accuracy of reflector with different number of ribs and different focal length to aperture ratio of the reflector is roughly estimated, and the estimated RMS are defined as RMS-E. Three focal length to aperture ratio f/D (D = 500 mm) were set: 0.3, 0.45 and 0.5. Ribs were arranged in the tangent direction of the central hub. The mesh between ribs was assumed to be the flat plane. The calculated RMS-E values of reflector are shown in Figure 9.

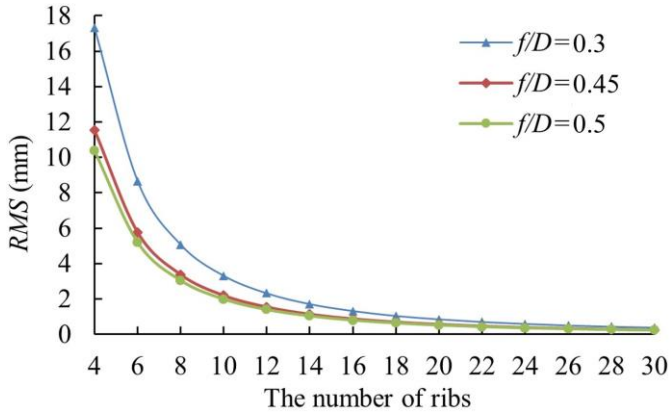


Figure 9. Relationship between number of ribs, f/D and RMS-E

The deployable antenna is considered to be used in X-band operation. Surface accuracy RMS less than 1 mm can meet the requirements of X-band antenna. In this paper, the focal length to aperture ratio of reflector is 0.45, the number of ribs is 16, and the RMS-E value is 0.88 mm.

4.2. Surface accuracy considering rib deformation and back-pillow effect

Compared with radial-rib as given by SERC and JPL, the stiffness of wrap-rib is smaller. Under the tension of the mesh and the side cable, the rib will have elastic deformation at deployed state. Also, there will be back-pillow effect on the mesh surface. To evaluate the surface accuracy of the reflector, it is important to determine the shape of the reflector through reasonable shape finding analysis. For this reason, the ribs are taken as elastic boundary of mesh, and the deformation of ribs is considered in the process of shape finding. The shape of the reflector with uniform tension is obtained by iterative calculation.

The finite element model of reflector was established by ANSYS software for shape finding analysis. In the shape finding analysis, the pre-tension of the mesh surface was set at 2 g/cm (The thickness of the mesh is 0.08 mm, so the prestress is 0.025 MPa), and the force of the side cable was set according to the vertical span ratio which is 1/10. The shape finding analysis process is as follows:

(1) Establish the finite element model of the deployed reflector, including the ribs, mesh and cables. Virtual small elastic moduli are used for the mesh and cables.

(2) Set the predetermined prestresses for the mesh and cables and then carry out FE calculations.

(3) Update the structure shape with the deformed shape.

(4) Repeat steps (2) and (3) for several iterations, until the stresses in the mesh and cables are close to the predetermined prestresses.

The Mises stress distribution of the mesh was obtained after 50 iterations, as shown in Figure 10. The maximum node displacement increment with the number of iterations is shown in Figure 11.

It can be seen from Figure 10 that the tension of the mesh after 50 iterations is close to the pre-set 0.025MPa, and the stress distribution is relatively uniform. In Figure 11, after 12 iterations, the maximum node displacement increment of each iteration is less than 0.1mm. From the uniformity of stress distribution and maximum node displacement increment, we can know that the reflector has reached the equilibrium position after 50 iterations, and the shape finding analysis has been completed.

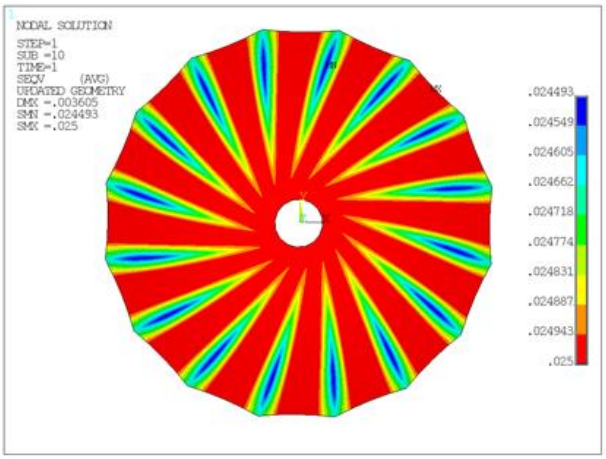


Figure 10. Mises stress distribution of mesh after 50 iterations

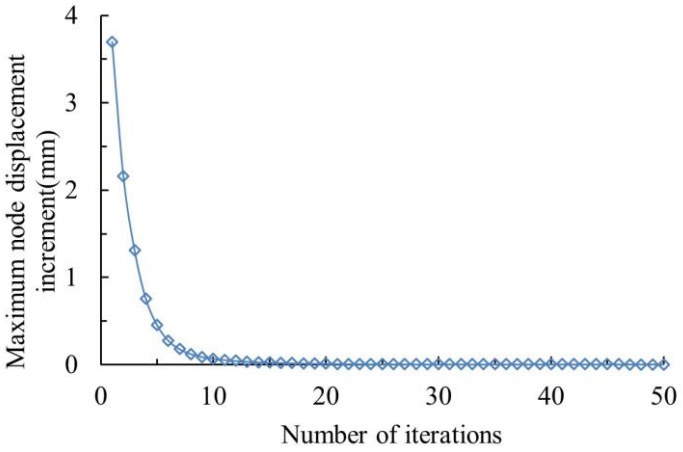


Figure 11. Maximum displacement increment in iterations

The ribs after the shape finding analysis have a rotation deformation about the central axis of reflector. The coordinates of the reflector after shape finding were extracted, and the RMS value of the reflector is 1.22 mm, which is larger than the RMS value of 0.88mm in the non-tension state before shape finding analysis.

4.3. Optimization for the curve of rib

Due to rib deformation and back-pillow effect, the surface accuracy of reflector is obviously reduced. The surface accuracy of reflector can be improved by optimizing the rib shape.

In this paper, the curve equation along the length of rib is set as a parabolic equation $z = ax^2+bx+c$ (0 mm$\leqslant x \leqslant$ 250 mm). Coefficient c could be set as 0 in describing the shape of rib. Aiming at the minimum RMS value of the reflector, coefficients a and b of the equation were optimized by genetic algorithm [7]. According to the initial values of coefficients which were a_0 = 1/900 and b_0 = 0 as given in Section 3.3, the value ranges of optimization variables were set as 1/1000 $\leqslant a \leqslant$ 1/800 and -0.01 $\leqslant b \leqslant$ 0.01. There were 100 individuals in each generation. The variation rate was set as 5%, and the termination criterion was that the propagation generation reached 40. The evolution process is shown in Figure 12. After the 29th generation, the change of the optimal RMS value between the two adjacent generations was less than 0.001 mm. Taking the optimization results of the 40th generation, the curve equation of rib is z = 0.001102 x^2 – 0.007368 x (0 mm$\leqslant x \leqslant$ 250 mm), and the RMS value of the reflector is 0.71 mm, which is less than 0.88 mm (see Section 3.3) or 1.22 mm (see Section 4.1). By optimizing the shape of rib, the surface accuracy of reflector is effectively improved.

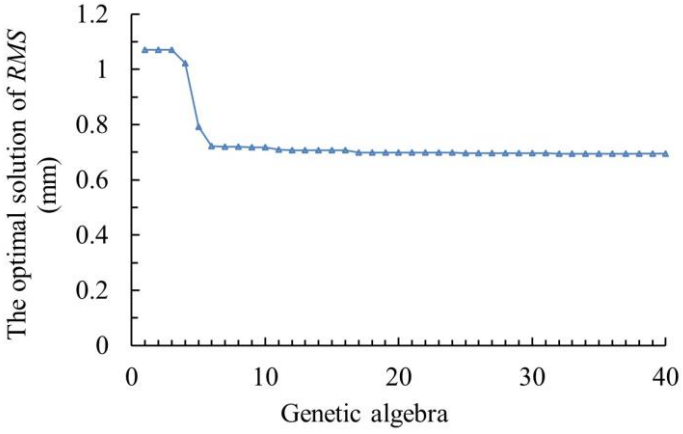


Figure 12. RMS optimization process

5. Measurement of surface accuracy

5.1. Measurement scheme

Two prototypes of 0.5m aperture wrap-rib deployable antenna were assembled.

Non-contact photogrammetry is used to measure the surface accuracy of the reflector of prototype. The measuring system includes camera, light lamp, calibration frame, marking point and supporting post-processing software system.

In this paper, the spacing of target points is 20 mm, and the error of surface accuracy caused by the spacing of target points is about 0.03 mm, which is far less than the RMS value of the reflector. The spacing of target points can meet the measuring accuracy of the reflector.

Take some pictures of the reflector with target points. After the target points are captured, the image processing software is used for post-processing to obtain the target points coordinates, as shown in Figure 13 and Figure 14.



Figure 13. Prototype of deployable antenna with target points on its reflector

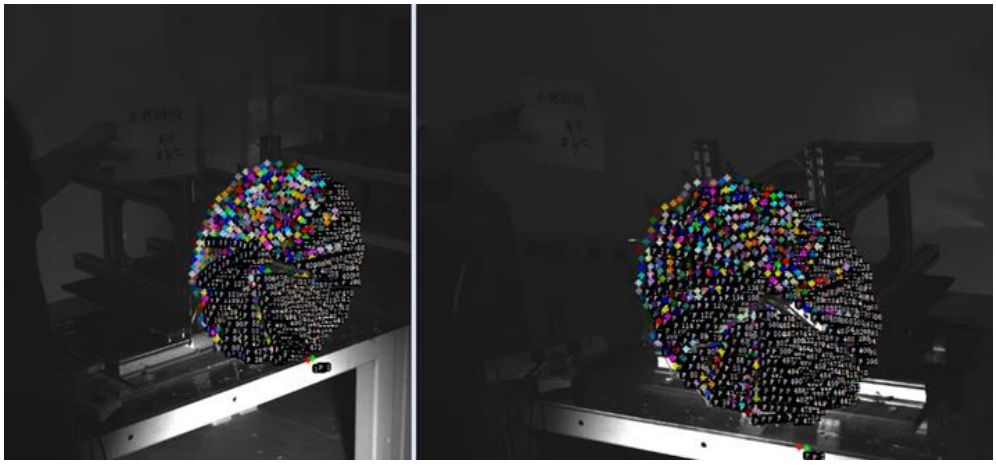


Figure 14. 3D coordinates of target points

After surface fitting of the target points, the fitted parabolic equation was obtained (see Figure 15). By comparing the coordinates of the target points with the fitting paraboloid, the RMS of the reflector was calculated.

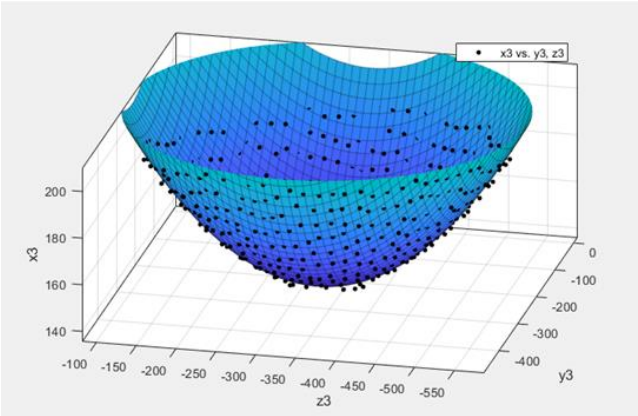


Figure 15. Paraboloid fitting

The surface accuracy of the reflector was tested under five conditions. They are:

(1) The prototype had not been stowed after assembled;

(2) The prototype had been stowed and deployed for the first time;

(3) After shaking table test, the prototype had been stowed and deployed for the second time;

(4) The prototype had been stowed and deployed for the third time;

(5) The prototype had been stowed and deployed for the fourth time.

5.2. Measurement results

1) RMS based on self-fitting paraboloid

The self-fitting paraboloid is taken as the target paraboloid in each condition. The RMS measurement and calculation results are shown in Table 1.

Table 1. RMS based on self-fitting paraboloid

Condition	(1)	(2)	(3)	(4)	(5)
RMS (mm): prototype A	0.98	0.90	0.86	0.86	0.86
RMS (mm): prototype B	0.81	0.79	0.83	0.76	0.79

2) RMS based on the fitting paraboloid of condition (1)

The fitting paraboloid of condition (1) is taken as the target paraboloid in each condition. The RMS measurement and calculation results are shown in Table 2.

Table 2. RMS based on fitted paraboloid of condition (1)

Condition	(1)	(2)	(3)	(4)	(5)
RMS (mm): prototype A	0.98	0.92	0.89	0.88	0.92
RMS (mm): prototype B	0.81	0.85	0.83	1.00	0.82

The RMS of the two prototypes was 0.8-1.0 mm, and the repetition accuracy is good. According to that the surface accuracy RMS of the reflector should be no more than 1/30 wavelength (about 1mm for X-band), the two prototypes can meet the surface accuracy requirement of X band operation.

6. Conclusions

A wrap-rib deployable antenna was developed in this paper. The antenna was 0.5 meter in aperture and could be stowed in 1.5 U. Paraboloidal mesh reflector was designed for X-band operation. The shape of ribs was optimized. Two prototype antennas were assembled to analyze and test the repetition accuracy of the reflector.

The stainless steel ribs adopt C-shaped cross section in this paper. The wrapping process of C-shaped stainless steel rib was analyzed theoretically and numerically. It was verified that ribs were in elastic state during wrapping process. Based on surface accuracy required by X-band， the number of ribs was determined as 16 and the focal length to aperture ratio of the reflector was 0.45.

A shape finding iterative algorithm was suggested which consider both the deformation of ribs and the distribution of tension in mesh. On this basis, The optimal curve of ribs was designed by minimizing the surface error through genetic algorithm. The theoretical RMS of the optimized reflector is 0.71 mm.

Two prototype antennas were assembled and shapes of reflector surface were measured before and after shaking table tests. The RMS of the reflector was calculated based on the self-fitting paraboloid and the condition (1) fitting paraboloid respectively, and the RMS was 0.8-1.0mm. After shaking table test and several times stowage and deployment, the surface accuracy of reflector has no obvious change, and has relatively stable repetition accuracy. The prototype can meet the surface accuracy requirement of X-band.

References

[1] Aherne M, Barrett T, Hoag L, et al. Aeneas-Colony I meets three-axis pointing[C]. The 25th Annual AIAA/USU Conference on Small Satellites, 2011.

[2] Chahat N, Hodges R E, Sauder J, et al. CubeSat Deployable Ka-Band Mesh Reflector Antenna Development for Earth Science Missions[J]. IEEE Transactions on Antennas & Propagation, 2016, 64(6): 2083-2093.

[3] Chahat N, Hodges R E, Sauder J, et al. Deep Space Network Telecommunication CubeSat Antenna: Using the deployable Ka-band mesh reflector antenna[J]. IEEE Antennas & Propagation Magazine, 2017, PP(99): 1-1.

[4] Sauder J F, Chahat N, Hirsch B, et al. From Prototype to Flight: Qualifying a Ka-band Parabolic Deployable Antenna (KaPDA) for CubeSats[C]// Aiaa Spacecraft Structures Conference, 2017: 1-8.

[5] Wu Minger, XIANG Ping, WU Zhuangzj, et al. High receptor-ratio wound rib type expandable antenna structure: China, CN108767418[P]. 2018-11-06. (in Chinese)

[6] Seffen K A, Pellegrino S. Deployment dynamics of tape springs[J]. Proceedings of the Royal Society A: Mathematical, Physical and Engineering Sciences, 1999, 455(1983): 1003-1048.

[7] Wu Minger, Zhang Fu, Xiang Ping. Shape Finding and Optimization of Deployable Reflectors for Small Satellites[C]// 3rd International Conference of Advanced Lightweight Structures and Reflector Antennas, Georgian, 2018: 261-265.

Design competition (WG21)

Active bending
Additive manufacturing/ 3D printing
Architectural geometry
Bamboo for sustainable construction and quality of life improvement
Bio-inspired structures and architecture
Bridge structures
Computational form-finding
Conceptual design
Concrete structures
Construction techniques
Deployable and inflatable structures
► **Design competition (WG21)**
Digital modelling and fabrication
Dynamic response of metal spatial structures
Dynamic response of other structures
Form-finding and structural optimisation of interlocking discrete assemblages
Graphical methods
Gridshell and lattice structures
Historical concrete shells
Historical structures
Lattice structures
Life-cycle design and assessment of structures
Metal gridshell structures, connections and stability
Methods and construction technologies for sustainable shell structures
Morphology and configuration processing
Next generation parametric design
Novel methods in modelling, optimisation and construction for reducing carbon footprint of continuous roof shells
Numerical methods for geometry, form-finding and optimisation of lightweight structures
Optimisation methods and applications
Origami
Other
Teaching design uncertainty: working with unknown qualities/quantities of new and re-claimed materials
Teaching of shell and spatial structures
Tensegrity systems and cable structures
Tension and membrane structures
Tension structures in the Asia-Pacific
Timber and bio-based structures
Topology optimisation
Traditional masonry structures and innovation
Transformable structures

IASS 2023
July 10–14 Melbourne
Integration of Design and Fabrication

Proceedings of the IASS Annual Symposium 2023
Integration of Design and Fabrication
10–14 July 2023, Melbourne, Australia
Y.M. Xie, J. Burry, T.U. Lee and J. Ma (eds.)

A reconfigurable construction system based on hypar timber components

Markus HUDERT[a,*], László MANGLIÁR[a]

[a,*] Aarhus University, Department of Civil and Architectural Engineering
Inge Lehmanns Gade 10, 8000 Aarhus C, Denmark
mhu@cae.au.dk

Abstract

With the aim of contributing to a higher degree of circularity in the building construction sector, and a more efficient use of resources, the here presented research explores the potential of upcycling scrap wood into hypar-shaped modular construction components, to be used as basic units in reusable and reconfigurable construction systems. The work employs empirical methods and pursues a research by design approach. In addition to introducing a new approach toward upcycling scrap wood, we also present a novel method for building hypar components from planar wooden pieces. Furthermore, the paper features a design proposal for a pavilion that is intended as a contribution to the IASS 2023 Design Competition. This pavilion is also expected to serve as a proof of concept for the above-mentioned construction and upcycling method. We conclude with an overview of future research and an indication of potential applications of the presented construction system. On a more general note, the work suggests going beyond the use of shell structures as monolithic and static artefacts. By investigating reusable and reconfigurable shell-based structures, it adds to and expands on existing research on segmented shells.

Keywords: timber and bio-based structures, modular timber structures, circular construction, hyperbolic paraboloids, reconfigurable structures, upcycling scrap wood, conceptual design, methods and construction technologies for sustainable shell structures, digital modelling and fabrication

1. Introduction

Reducing the environmental impact of the building construction sector has emerged as one of the prime challenges for practitioners and researchers in Architecture, Engineering, and Construction (AEC) over the past few years. As stated previously [1], increasing the use of timber can be one way of addressing this challenge. Preconditions for this are short routes of transport and certified sustainable forest management. For a truly sustainable use of timber, it is equally important to extend the service life of wooden components as much as possible, and to unlock alternative material sources such as scrap wood. This research explores the potential of upcycling scrap wood into modular construction components with a hypar geometry, to be used as part of reconfigurable construction systems.

A hypar is a certain type of doubly ruled surface. According to [2], a ruled surface is defined as “a surface generated by a moving straight line with the result that through every point on the surface a line can be drawn lying wholly in the surface.” A similar definition is provided in [3]: “Cylinders, cones, one-sheet hyperboloids, and hyperbolic paraboloids are surfaces that carry families of straight lines. Thus, they could also be generated by moving a straight line.”

The capacity of hypar structures for merging load-bearing and stabilizing functionalities with architectural qualities [4] becomes evident in numerous built examples. Depending on the construction method and the material used, hypar structures can consist of discrete, similar, and sometimes even identical elements. This could contribute to the reusability of their basic elements [5]. As modular

Copyright © 2023 by Markus HUDERT and László MANGLIÁR. Published in the Proceedings of the IASS Annual Symposium 2023 with permission.

entities or units, timber hypar components could become an alternative solution to conventional prefabricated building components.

In addition to being based on simple straight lines, hypars have yet another compelling geometric property. As pointed out in [6], "[…] flat quads can be created by connecting the corresponding points of intersection of the generatrices in diagonal direction." In [6], this property is highlighted in the context of using glass panels as cladding for hypar steel grid shells. The here presented research investigates the potential of employing this property for segmented timber shell components, as illustrated in *Figure 1*.

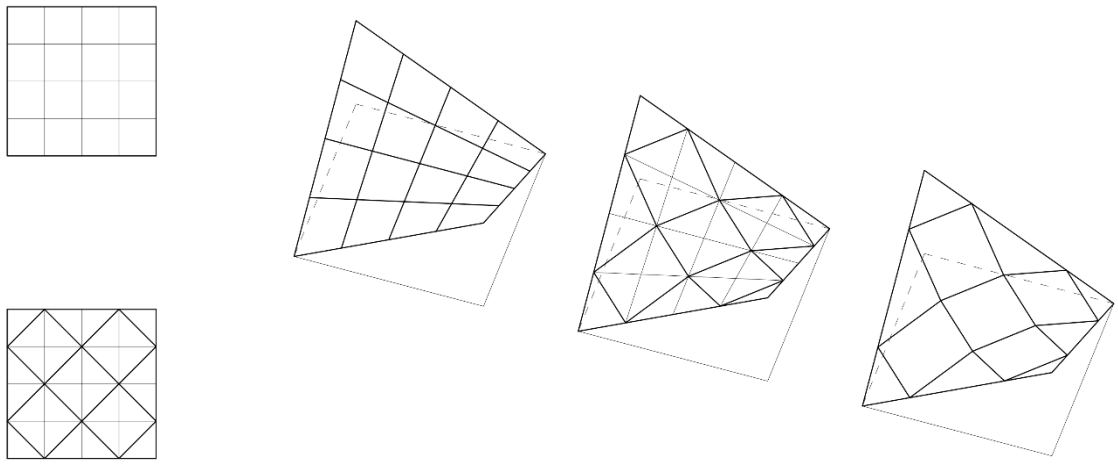


Figure 1. Left: Top view of a hypar with five equally spaced rulings (top) and a quadrilateral mesh based on top of these rulings (bottom). Right: Stepwise generation of a quadrilateral mesh based on the rulings of a hypar with a square base.

2. Design space explorations

This research explores the potential of upcycling scrap wood into modular construction components with a hypar geometry, to be used as part of reusable and reconfigurable construction systems. The design space of multi-hypar structures fundamentally depends on the geometry of the basic hypar unit. So far, two different hypar geometries have been studied as a basic unit for multi-hypar configurations.

The first one approximates a Schwarz P minimal surface when multiplied twelve times, as shown in *Figure 2*. This geometry can also be found in some of Ángel Duarte's mathematics-inspired sculptures, as well as in projects he developed together with Heinz Isler [7]. Duarte's work was identified as a relevant precedent while preparing teaching material for the MSc course "Tectonics in Engineering and Architectural Design" in the fall semester of 2020. The starting point for constructing the geometry of this hypar is a square in which a smaller and 45° rotated square is inscribed, using the midpoints of the larger square's edges as corners of the smaller one. Following this, the edge lines of the smaller square are rotated up by 45° in pairs of two, using the neighboring edges as rotation axes. Then, the now inclined edge lines are extended so that they connect and form a closed tetrahedral polyline. The four spatially articulated edges are then mirrored around their center point. The two intersecting polylines define the outlines of twelve identical, albeit differently oriented hypars.

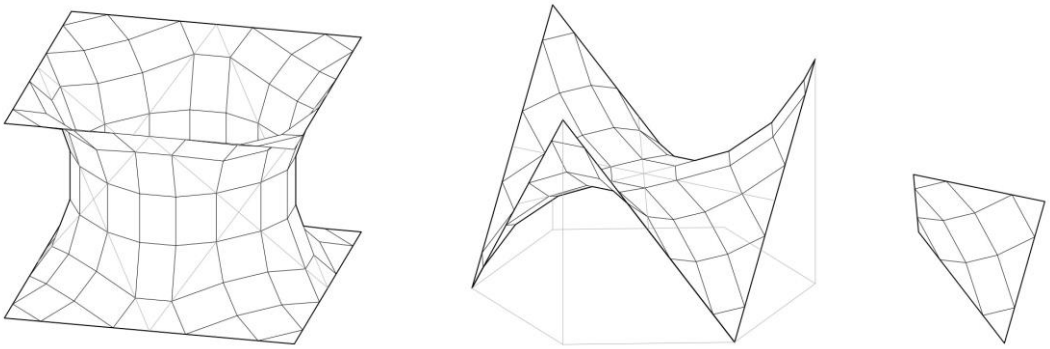


Figure 2. Two options of using patches of an approximated Schwarz P surface: in closed Schwarz P surface condition (left) with twelve patches, and as an open configuration with six patches, to be used for example as a pavilion (right), using planar quad meshing.

The second hypar geometry is based on a cube, meaning that the edges of the hypar surface are identical to the diagonals of a cube's faces. Six of such hypars can be combined into star-shaped higher-order units, as shown in *Figure 3*. The possibility of doing so was observed in the outcome of a combinatorial design workshop that was part of the MSc course "Tectonics in Engineering and Architectural Design" in the fall semester of 2021.

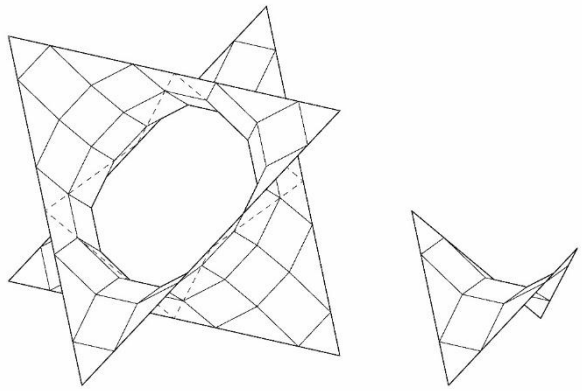


Figure 3. Six identical hypars, with a hypar surface that can be inscribed in a cube, can be combined into a star-shaped higher-order unit. This example also shows how neighboring triangular mesh faces, on the boundary of adjacent hypars, can be merged into quads.

3. Design and fabrication of a pavilion

The here presented pavilion design is the outcome of an ongoing research project that investigates the potential of upcycling scrap wood into modular construction components based on hypar geometry. The construction method used takes advantage of a geometric particularity of hypars, which enables the creation of quad meshes aligned diagonally with the rulings. Thus, it becomes possible to fabricate such double-curved shell components from planar wooden pieces.

In addition to introducing a novel construction method, and a novel approach towards upcycling scrap wood, the pavilion highlights the potential of using hypars as modular construction components. The underlying hypar geometry is based on a cube. As explained above, six of such hypar components can be combined into star-shaped higher order units, six of which are included in the proposed design. As an entity, the pavilion displays properties similar to those of periodic surfaces, see *Figure 6*.

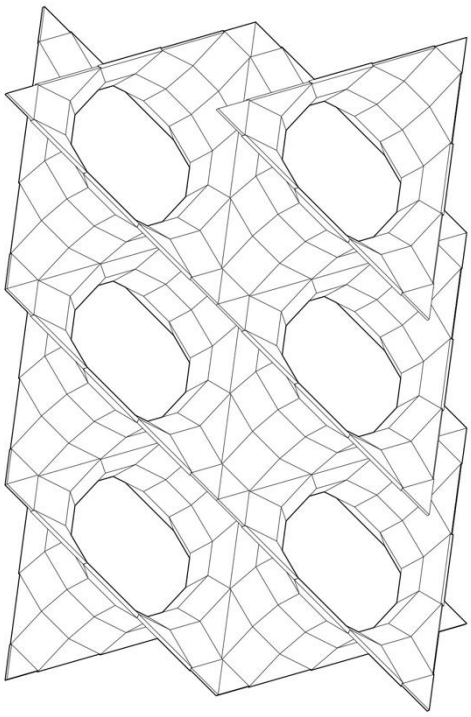


Figure 4. Axonometric view of the pavilion design, which incorporates six higher-order units. The pavilion has an approximate length of 180 cm, a width of 90 cm, and a height of 270 cm.

When moving around it, its appearance smoothly transitions between open and closed. Potential applications of this modular system could be façade elements, loadbearing walls, room dividers, skylights, or other.

For the exhibition at IASS 2023, we aim to build this pavilion, respectively demonstrator, out of scrap wood pieces, connected with wooden dowels or similar, and partially with glue. The joints between the higher order units will be designed to be reversible, allowing for the disassembly and future reuse of the components, potentially in a variety of different configurations.

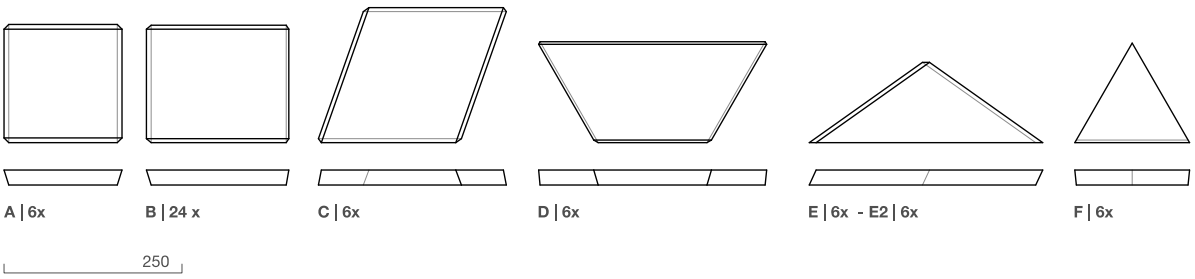


Figure 5. Top and side views of six different panel geometries.

3.1. Geometry and construction

The design space of modular hypar structures is partially determined by the way in which an immaterial hypar geometry is brought into the physical world. A closed volumetric hypar can be generated by equal distance offset, or by one-directional extrusion of the hypar surface.

There are several methods of constructing timber shell components with a hypar geometry. The most common approach is probably that of generating a grid shell, which can be achieved by extruding the rulings of the hypar, or by placing straight elements on these rulings. Another method is to combine mutually rotated layers of timber boards into assemblies similar to Cross Laminated Timber (CLT), and to connect them to an edge beam [8, 9]. Yet another option could be steam bending, which would imply size constraints and a relatively high consumption of energy.

The here proposed method enables the construction of segmented shells with wooden panels, which are geometrically described as convex polyhedrons, defined by the intersecting half-spaces of their six boundary planes.

The planar segments of a hypar are given by the diagonals of the subdivided hypar's quad meshes. The result is a planar quad mesh, which needs to be offset to obtain the geometry of the final segmented shell structure. This would be relatively easy if the hypar-based mesh would be conical. Only conical meshes have the property that their offset results in planar edge and mesh faces in equal distance, as in conical meshes, all quads adjacent to one vertex are tangent to a common cone.

However, similar to other quad-meshes based on doubly curved surfaces, the hypar-based mesh is not conical, which leads to flawed results when applying standard offset procedures. One way of solving this issue is mesh adjustment, for example via the *conicalize* function that is part of the interactive physics/constraint solver Kangaroo, which is included in the current version of Grasshopper. Another option would be to chamfer the corners of the offset quads [10].

As using these options could cause fabrication challenges and increase design complexity, we apply a method where the panels are defined as convex polyhedrons that are generated by the intersecting half-spaces placed on their boundary planes. Two of these are the inner and outer offset planes of the origin plane of the panel, and the four other are the boundary planes placed along the shared edges with the neighbouring panels. These edge boundary planes are laying along common edges, and are aligned with the average of the normal vectors of the two connected faces. It is noteworthy that in the case of synclastic surfaces, the boundary plane of the vertex neighbour faces, located on the respective vertices, should be added to the definition as well.

The resulting panels will share their long edges, provided they have the same thickness and their planar edge surface. Due to the non-conicality of the basic mesh, their offset vertices will not coincide, which is tolerable in this case. This method also enables a straightforward definition of segments made of materials with different thickness.

3.2. Joints, connections, and assembly

The pavilion is comprised of six modules, or higher-order units. Each of these higher-order units consist of six hypars with a low mesh-subdivision resolution. There are four main types of panels within one higher-order unit: triangular, rectangular, rhombic, and trapezoid shapes. The rhombic and trapezoid panels are the result of merging two or three triangular panels adjacent to the individual hypars' edges or corners, as indicated in *Figure 4*.

With a 270 cm high pavilion design, one higher-order unit has an edge length of 120 cm and consists of 60 panels. The edge length of the panels is between 16 and 30 cm, and the panel thickness is approximately 20 mm. The segments of the higher order units are milled out of scrap wood pieces, mainly from plywood or LVL, and optionally from solid wood boards. These pieces are glued and joined by internal dowel-like connections, such as cylindrical dowels, biscuit connectors, or tongue and groove joints with loose tongues. The challenge of assembling elements with various angles is addressed in the joint design, and here with the dowel orientation, which is based on a pre-defined assembly sequence. One possibility is to join the panels into strips, which are then merged into one half of a higher-order unit.

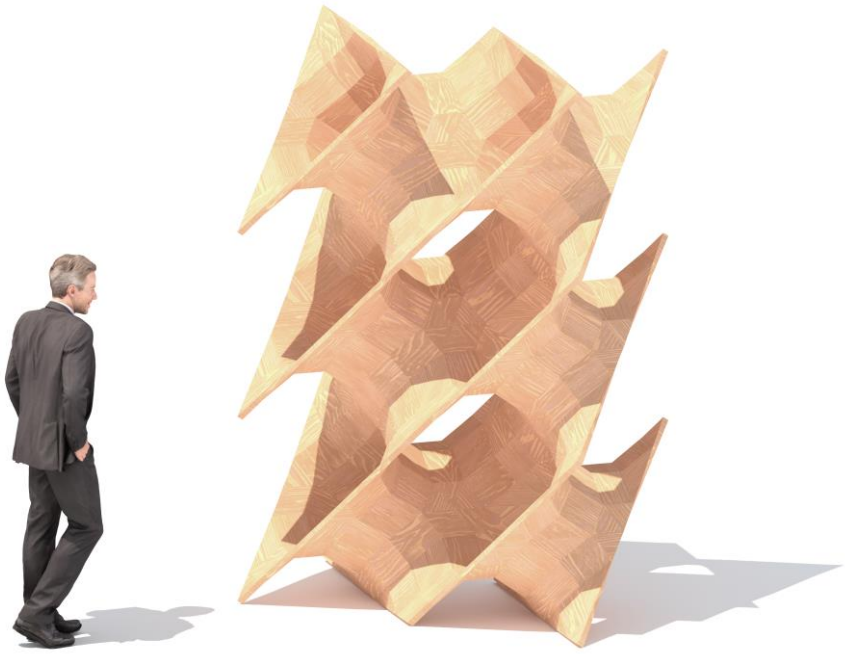


Figure 6. Rendered axonometric view of the pavilion.

Two halves are then glued together to form one whole. A simple formwork and tension belts are envisioned to apply pressure on the glued surfaces during the curing process, a method that could be applied for each edge. The joints between the higher order units will be designed to be reversible, allowing for the disassembly and future reuse of the components, potentially in a variety of different configurations. One option is that the modules are connected with dowel connections, and secured by wooden wedges or screws. An alternative method is the use of mechanisms with easier access, such as hinge- or clamp-like metal fasteners.

The final design and joinery solution also depends on the fabrication method and its constraints. The panels can be fabricated in various ways, most favorably via 5-axis CNC milling, but possibly also with a robotic arm, or with a traditional circular saw. The above-mentioned joinery solution describes the current design stage of the demonstrator. Later on, we plan to develop and compare different joinery on full-scale prototypes, mainly with cylindrical wooden dowels, biscuit connectors and finger joints.

4. Conclusion and future work

In this paper, we propose to upcycle scrap wood into hypar timber components, to be used as basic elements of modular and reconfigurable construction systems. We provide insights on the design space of multi-hypar structures and elaborate on the different factors that have an impact on it. We present the design of a pavilion that implements a novel construction method for hypar shaped segmented timber shell components, using scrap wood as material.

Currently ongoing studies investigate the potential of using hypars with irregularly spaced rulings as a means of incorporating or adapting to material stock with specific geometric properties. We are also preparing a survey that will inquire on the quality and quantity of wood scrap produced in selected areas of Europe, the results of which will allow us to refine the target definition of the optimization process.

Additional studies will be required to obtain deeper insights on the structural properties of the above-described structures, by means of numerical and experimental testing. Here it will be interesting to study the impact of the connection details as well as the overall composition and orientation of different multi-hypar configurations.

Future studies will also explore the potential of double-layer configurations. Building with two layers instead of one could facilitate the inclusion of insulation or other functions. Shifting the paneling patterns of the two layers against each other – similar to the mutually shifted tiles in Catalan vaults [11] – could support water and wind tightness. More importantly, this could also lead to advantages regarding the structural performance.

Acknowledgements

The possibility of combining six cube-based hypars into star-shaped higher-order units was observed in the outcome of an online-workshop on combinatorial design. During the workshop, the students worked with Grasshopper and the plug-in WASP. The workshop was part of the MSc course "Tectonics in Engineering and Architectural Design" in the fall semester of 2021, and carried out by the developer of the WASP plug-in, Andrea Rossi.

References

[1] L. Mangliár and M. Hudert. Re:Shuffle. Paper presented at the Fifth International Conference on Structures and Architecture, Aalborg, Denmark, July 6–8, 2022.

[2] Merriam-Webster. No date. Ruled surface. In Merriam-Webster.com dictionary. Accessed March 23, 2023. https://www.merriam-webster.com/dictionary/ruled%20surface.

[3] H. Pottmann, A. Asperl, M. Hofer and A. Kilian. Architectural Geometry: first edition. Exton: Bentley Institute Press. 2007.

[4] T. S. Sprague. "'Beauty, Versatility, Practicality': the Rise of Hyperbolic Paraboloids in post-war America (1950-1962)." *Journal of Construction History, Special Issue: Construction History in the Americas* 28, no. 1 (2013): 165-184.

[5] M. Hudert, "Connecting lines: investigating the potential of ruled surface structures for circular construction," in *Conceptual Design of Structures: Proceedings of the International fib Symposium 2021,* Attisholz Areal, Switzerland, September 16-18, 2004, C. Fivet, P. D'Acunto, M. Fernández Ruiz and P. O. Ohlbrock (Eds.), fédération internationale du béton (fib), 2004. pp. 469-476.

[6] H. Schober. "Graphic Design Principles for Grid Shells with Flat Quadrilateral Meshes." In *Transparent Shells*, edited by Hans Schober (Berlin: Ernst & Sohn, 2015), pp. 87-90. *DOI:* 10.1002/9783433605998.

[7] M. Ludwig. "Relations between Félix Candela, Heinz Isler, and Ulrich Müther." In *Candela Isler Müther: Positions on Shell Construction. Positionen zum Schalenbau. Posturas sobre la construcción de cascarones,* edited by Matthias Beckh, Juan Ignacio del Cueto Ruiz-Funes, Matthias Ludwig, Andreas Schätzke and Rainer Schützeichel, 16-23. Basel: Birkhäuser. 2020.

[8] M. Arnold and P. Aondio. "Hyperbolic Paraboloid Shells made of Engineered Wood." Paper presented at the Doktorandenkolloquium Holzbau „Forschung + Praxis", Stuttgart, Germany, March 5–6, 2020.

[9] Hyperbolisch-parabolische Schale aus Holz. Bauen + Wohnen, (17), Heft 10, 1963.

[10] I. Stotz, G. Gouaty and Y. Weinand. "Iterative geometric design for architecture." *Journal of the International Association for Shell and Spatial Structures,* vol. 50, num. 1 (2009): 11-20.

[11] G. R. Collins, "Antonio Gaudí: Structure and Form," in *Perspecta*, Vol. 8 (1963), pp. 63-90, 1963.

Proceedings of the IASS Annual Symposium 2023
Integration of Design and Fabrication
10–14 July 2023, Melbourne, Australia
Y.M. Xie, J. Burry, T.U. Lee and J. Ma (eds.)

Clustering and optimisation of nodes, beams and panels for cost-effective fabrication of free-form surfaces

Minghao BI[*], Yuanpeng LIU[a], Yi Min XIE[a,*]

[*] Centre for Innovative Structures and Materials, School of Engineering, RMIT University, Melbourne, Victoria 3001, Australia
minghao.bi@rmit.edu.au; mike.xie@rmit.edu.au

[a] Centre for Innovative Structures and Materials, School of Engineering, RMIT University, Melbourne, Victoria 3001, Australia

Abstract

Free-form surfaces have been increasingly adopted in contemporary architectural designs to create unique and elegant structures. However, fabricating these doubly curved surfaces using panel and frame systems may pose great challenges to building construction, as the three main components—nodes, beams and panels—usually exhibit vastly different shapes. While previous studies attempted to reduce the shape variability for one or two of these components, clustering and optimisation of all three remain underexplored. In this work, we present a mesh-based computational design framework that clusters and optimises nodes, beams and panels together to reduce the shape variety of elements for free-form surfaces. The proposed method uses a vertex-based similarity metric to partition panels into a user-specified number of groups and cluster beams based on the associated edge lengths. Box-constrained optimisation is then employed to obtain congruent faces and matching beam lengths while satisfying gap size, fairness and shape preservation constraints. Finally, connection holes on the spherical surfaces of nodes are clustered and optimised to allow their use at multiple locations. The practicality of the proposed method is demonstrated through the design and fabrication of a full-scale pavilion with doubly curved surfaces, which resulted in a significant reduction in the number of different nodes, beams and panels.

Keywords: clustering, optimisation, free-form surface, space frame structure, mesh, Hangai Prize applicant

1. Introduction

Free-form surfaces are becoming increasingly popular in architecture due to their exceptional aesthetic qualities and unique elegance that distinguish them from the typical uniformity in building designs. However, manufacturing these surfaces with conventional methods could present immense difficulties and high expenses due to their intricate geometries and varying surface curvatures. Such complexities have prompted researchers and practitioners to develop innovative rationalisation strategies to simplify fabrication, improve structural performance and enhance the affordability of free-form surfaces [1–5].

Several rationalisation strategies have been proposed to address the manufacturing challenges of free-form structures [6–8]. One such approach involves the planarisation of mesh faces, which aims to realise complex curved surfaces through a set of discrete planar faces, thereby reducing manufacturing costs. Apart from triangular meshes, whose faces are naturally planar, this concept has been employed in quadrilateral meshes [9] and hexagonal meshes [10]. Another approach focuses on reducing the shape variety of different elements (i.e., nodes, beams and panels) to facilitate the mass production of standardised components and consequently lower the production cost and ease construction. Given these

Copyright © 2023 by Minghao BI, Yuanpeng LIU, Yi Min XIE. Published in the Proceedings of the IASS Annual Symposium 2023 with permission.

benefits, this method has been adopted to reduce joint variability [11, 12], reuse nodes and beams for diverse structures [13], cluster beams during truss layout optimisation [14] and tile free-form surfaces using sets of panels [15–18]. This strategy can help reduce the number of moulds for casting-based and vacuum-forming manufacturing, simplify the setup and improve quality control of other fabrication techniques, including computer numerical control (CNC) machining and 3D printing. However, previous studies have primarily focused on clustering and optimising one or two of the three main elements (i.e., nodes, beams or panels). Simultaneous consideration of all three shows promise but remains largely unexplored.

In this paper, we present a novel mesh-based computational design framework that clusters and optimises nodes, beams and panels together to reduce the shape variety of elements in free-form surfaces. The framework uses the vertices, edges and faces of a given triangular mesh to represent the nodes, beams and panels of the target free-form surface. The method employs a vertex-based similarity metric to partition panels into a user-specified number of groups, and beams are clustered based on associated edge lengths. Box-constrained optimisation is used to obtain congruent faces and matching beam lengths while satisfying gap size, fairness and shape preservation constraints. Additionally, connection holes on the spherical surfaces of nodes are clustered and optimised for use in multiple joint positions. To demonstrate the effectiveness of the proposed method, we designed and fabricated a full-scale pavilion with doubly curved surfaces (3.23 m × 3 m × 1.8 m) based on an optimised free-form mesh. As shown in Figure 1, the constructed pavilion structure demonstrates a significant reduction in the number of different nodes, beams and panels.



Figure 1. A full-scale pavilion was constructed to demonstrate the practicality of the proposed method. (a) Optimised free-form mesh, (b) rendered model, where panels in the same group have the same colour and (c) constructed pavilion using 3D-printed nodes, timber beams and laser-cut acrylic panels.

The paper is structured as follows. Section 2 describes the methodology for clustering and optimising nodes, beams and panels of free-form surfaces. Section 3 presents numerical studies for three different doubly curved shapes. Section 4 details the design and construction results of a full-scale pavilion. Finally, Section 5 concludes by highlighting the key features of the proposed method.

2. Methodology

The proposed method is based on a global framework that alternates between clustering and optimisation of elements in a triangular mesh. Beams and panels are grouped into user-specified numbers of clusters using the method described in Section 2.1. Next, a box-constrained optimisation framework, as outlined in Section 2.2, is applied to steer members in the same group towards a congruent shape, with additional constraints to control gap size, fairness and closeness to the input mesh. Finally, nodes are evenly assigned to groups and optimised to allow their use in multiple joint locations, as described in Section 2.3.

2.1. Clustering of beams and panels

2.1.1. Similarity metric

The similarity metric in this work is a numerical measure that quantifies the shape difference d between two different members. In the case of straight beams, the shape difference d_b between member p and q is calculated as the difference between the two associated edge lengths:

$$d_b(p,q) = l_p - l_q \tag{1}$$

where l_p and l_q are the edge lengths for p and q, respectively.

To compute the shape difference d_p between two panels on mesh faces m and n, a three-step process is employed based on previous work [18]. Firstly, the corners of n are arranged in six permutations relative to m's reference corners 'abc', from which six possible correspondences are determined (see Figure 2). Secondly, the corresponding corners are mapped using the principle of least squares rigid motion [19], in which corners ABC are transformed to A'B'C' to minimise the sum of squared distances ($\|aA'\|^2 + \|bB'\|^2 + \|cC'\|^2$). Finally, the lowest summed value of squared distances between transformed corners and reference corners is chosen as d_p, and the edge correspondence (i.e., $\overline{AC}$ to $\overline{ac}$, $\overline{AB}$ to $\overline{ab}$, and $\overline{BC}$ to $\overline{bc}$) is recorded for subsequent optimisation. In Figure 2, the last permutation yields the lowest shape difference d_p of 3.5.

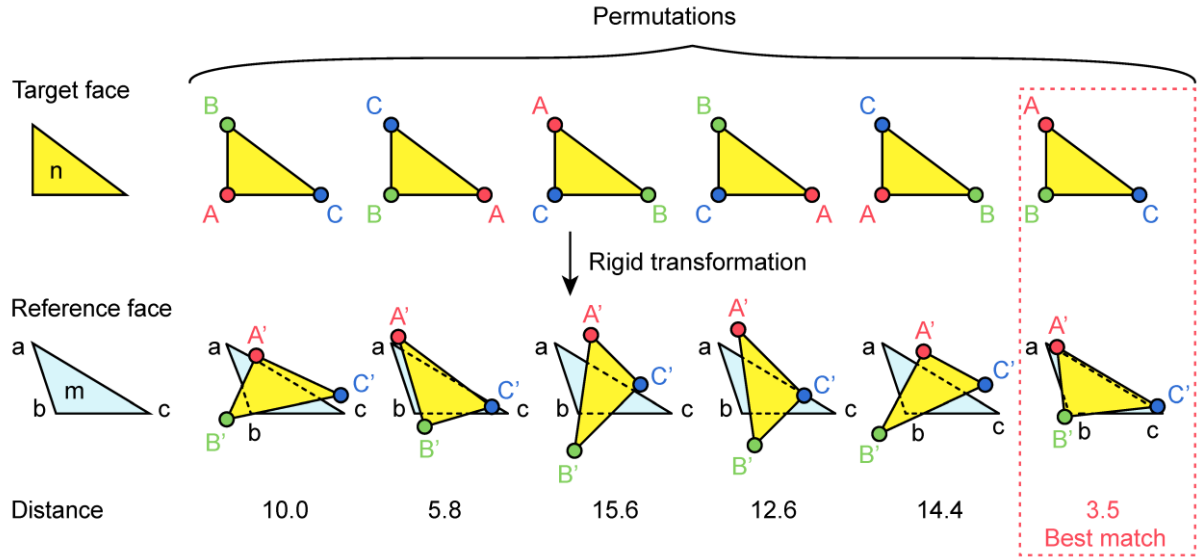


Figure 2. A three-step process is used to calculate the shape difference d_p between two panels.

2.1.2. Clustering method

The clustering approach for beams and panels uses the farthest point sampling strategy [20], gradually increasing the number of clusters until reaching the user-specified limit. First, one member is selected as the initial centroid, and all other elements are affiliated with it. Next, the shape difference of each element with respect to the centroid is computed, and the one with the largest value becomes the new centroid. In the subsequent iteration, each element is evaluated against the new centroid. Elements achieving a smaller shape difference than in the previous iteration are assigned to the new centroid, forming a new clustering configuration. By repeating this process, the final clustering configuration ensures that elements with similar geometry are grouped. In this work, the user-specified numbers of clusters for beams and panels are denoted as N_b and N_p, respectively.

2.2. Optimisation of beams and panels

2.2.1. Geometric formulation of beams and panels

The geometric formulation of beams and panels based on mesh vertices is illustrated in Figure 3. Mesh edges (pink dashed lines) represent beams between adjacent mesh vertices (pink circles). In construction practices, gaps are intentionally left between panels and beams to account for thermal expansion and construction errors. The gap size should adequately accommodate connectors and beams while avoiding the formation of major visual defects, thereby balancing practicality and aesthetics. To meet these requirements, we represent panels as a slightly smaller region (shown in blue) bounded by mesh edges (indicated by pink dashed lines) and determine their corners using a vertex-based relationship, as follows:

$$A^* = A + \overrightarrow{\boldsymbol{AA^*}} = A + \boldsymbol{v_{AB}} + \boldsymbol{v_{AC}} = A + \frac{\overrightarrow{\boldsymbol{AB}}}{|\overrightarrow{\boldsymbol{AB}}|} * \rho_{AB} + \frac{\overrightarrow{\boldsymbol{AC}}}{|\boldsymbol{AC}|} * \rho_{AC} \tag{2}$$

$$\rho_{max} > \rho > \rho_{min} > 0$$

where the panel corner A^* and mesh vertex A are related through scaled vectors $\boldsymbol{v_{AB}}$ and $\boldsymbol{v_{AC}}$ in the directions of $\overrightarrow{\boldsymbol{AB}}$ and $\overrightarrow{\boldsymbol{AC}}$, respectively, with ρ as a design parameter that governs gap size. The bounds for ρ are set by the user-specified upper limit ρ_{max} and lower limit ρ_{min}. By introducing the gap size parameter ρ, the equality constraints for beams and panels are differentiated (e.g., $|\overrightarrow{\boldsymbol{AB}}| \neq |\overrightarrow{\boldsymbol{A^*B^*}}|$), which provides more design freedom in the optimisation process. The proposed method involves two sets of design parameters: the XYZ coordinates for each mesh vertex (represented by pink circles) and two gap size parameters ρ (e.g., ρ_{AB} and ρ_{AC}) for each panel corner (represented by blue circles). For a triangular mesh consisting of A vertices and B faces, there are $3A + 6B$ design parameters to be optimised.

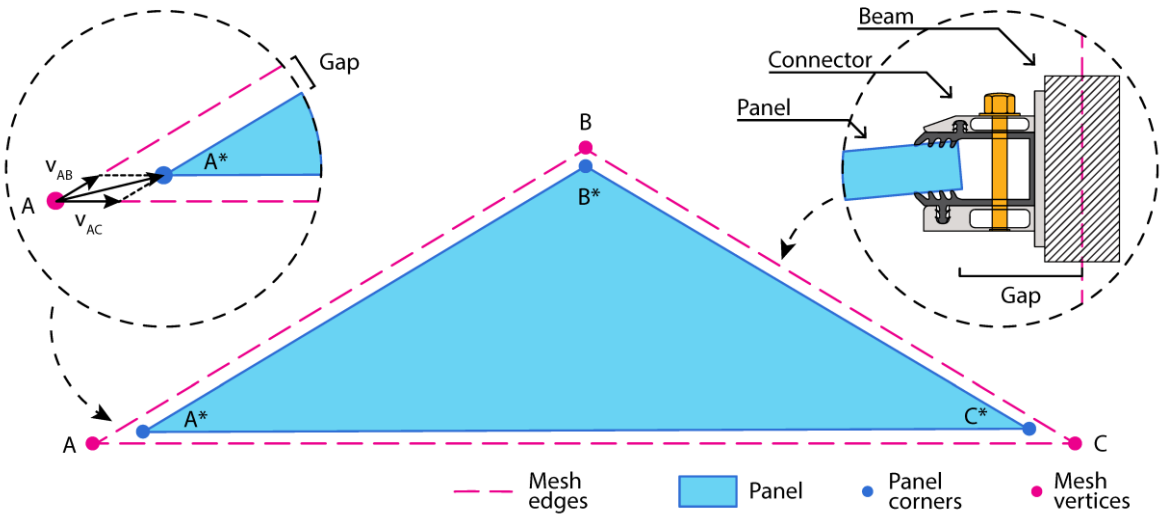


Figure 3. The proposed method represents beams using mesh edges in pink dashed lines and formulates panel corners (A^*, B^*, C^*) based on the gap size parameter ρ and the neighbouring mesh vertices (A, B, C) to ensure sufficient space for connectors.

2.2.2. Gap size constraint

The proposed method uses two approaches to control the gap size. Firstly, the gap size parameter ρ is subject to box constraints within a user-specified range, as described in Equation (2). Secondly, a gap size term F_g is introduced, as follows:

$$F_g = \sum_{i}^{n} (\rho_i - \rho_{ave})^2 \tag{3}$$

$$\rho_{ave} = \frac{\sum_i^n \rho_i}{n}$$

where the individual and average gap size parameters are denoted by ρ_i and ρ_{ave}, respectively. In total, there are n gap size parameters. Optimisation ensures that the gap sizes between panels and beams become more consistent throughout the structure.

2.2.3. Congruent panel constraint

The proposed method equalises the edge lengths of panels clustered in previous steps (Section 2.1) to obtain congruent panels for triangular meshes. To this end, a panel shape term F_p is introduced, as follows:

$$F_p = \sum_j^m \left(e_j - e_{ave}\right)^2$$
$$e_{ave} = \frac{\sum_j^m e_j}{m} \tag{4}$$

where e_j and e_{ave} denote the individual and average edge lengths within a group of m candidates, respectively.

2.2.4. Fairness constraint

Achieving smooth and aesthetically pleasing surfaces is of utmost importance in free-form architectural designs. Therefore, a fairness term F_f based on the principle of Laplacian smoothing [21] is formulated, as follows:

$$F_f = \sum_k \left(v_k - \frac{1}{\langle N(v_k) \rangle} \sum_{p \in N(v_k)} v_p \right) \tag{5}$$

where $N(v_k)$ represents the set of one-ring neighbouring vertices of v_k, and $\langle N(v_k) \rangle$ denotes the number of elements in this set. This term helps avoid sudden curvature changes between adjacent nodes and promotes smooth surfaces on the optimised mesh.

2.2.5. Original shape preservation

The proposed method constrains the displacement of mesh vertices from their initial positions to preserve the geometric features of the input mesh. This is achieved by imposing box constraints on mesh vertices using a user-specified maximum movement distance d_{max}, as follows:

$$v_x^* - d_{max} < v_x < v_x^* + d_{max}$$
$$v_y^* - d_{max} < v_y < v_y^* + d_{max} \tag{6}$$
$$v_z^* - d_{max} < v_z < v_z^* + d_{max}$$

where v^* and v are the initial and optimised vertex positions, respectively.

2.2.6. Beam length constraint

Beam lengths are equalised using the beam length term F_b to ensure congruency within each cluster, as follows:

$$F_b = \sum_h^w (l_h - l_{ave})^2 \tag{7}$$

$$l_{ave} = \frac{\sum_h^w l_h}{w}$$

where l_h and l_{ave} represent the individual and average beam length within a group of w candidates, respectively.

2.2.7. Global objective function

Combining the subgoal terms F_g, F_p, F_f and F_b gives the global objective function F for optimisation:

$$F = \omega_g F_g + \omega_p F_p + \omega_f F_f + \omega_b F_b \tag{8}$$

where ω_g, ω_p, ω_f and ω_b represent the weights assigned to the gap size, congruent panel, fairness and beam length terms. The minimisation of the objective function F is accomplished using nonlinear conjugate gradient optimisation with box constraints [22]. Applying box constraints to the gap size parameters ρ and vertex positions v helps to meet the functional requirements without excessively complicating the optimisation process.

2.2.8. Post-processing

Despite the significant reduction in shape differences achieved through optimisation, members in the same cluster may still have small discrepancies, preventing them from being manufactured using the same mould. As a solution, each beam and panel is replaced by the average shape in their corresponding cluster. After replacement, two parameters are computed and compared against user-specified thresholds: the maximum percentage change in beam length before and after the replacement, which should be lower than the threshold t_b, and the minimum and maximum gap between new corners and adjacent mesh edges, which should fall in the range of $t_{p.min}$ to $t_{p.max}$. If either criterion fails, the number of clusters (N_b for beams and N_p for panels) should be increased to provide more design freedom for optimisation. This process is repeated until the optimised mesh meets all requirements.

2.3. Node clustering and optimisation

After optimising the mesh by achieving congruent panels and matching beam lengths, the next step is to evenly distribute and merge nodes to enable their use in multiple joint locations. Building on previous work [13], the proposed method implements node clustering and optimisation in three steps (see Figure 4). The algorithm randomly selects candidates for each cluster to achieve an even distribution of nodes among clusters (see Figure 4 (a)), where high-valence nodes are prioritised for grouping with low-valence ones to minimise congestion. Once the nodes to be merged in a cluster are identified, we seek the optimum rotation of each node to distribute their connection holes evenly on the spherical surface. Each node is considered a rigid body within a cluster, and connection holes on the node share the same rotation along XYZ axes (see Figure 4 (b)). The global objective function for node optimisation F_n aims to find the optimum rotation angles of nodes in all clusters and is expressed as:

$$F_n = \sum^{C} \sum_{i \in H}^{H} \sum_{j \in H}^{H} \frac{1}{d(R(\gamma_a, \beta_a, \alpha_a)i, R(\gamma_b, \beta_b, \alpha_b)j)} \tag{9}$$

where C and H denote the set of all node clusters and all connection holes centres in the present cluster, respectively; i and j refer to two individual connection holes centres that locate on node a and b, respectively, $d(\ldots)$ calculates the Euclidean distance between two points in 3D, and R is a rotation matrix:

$$R(\gamma, \beta, \alpha) = \begin{bmatrix} \cos\beta\cos\gamma & \sin\alpha\sin\beta\cos\gamma - \cos\alpha\sin\gamma & \cos\alpha\sin\beta\cos\gamma + \sin\alpha\sin\gamma \\ \cos\beta\sin\gamma & \sin\alpha\sin\beta\sin\gamma + \cos\alpha\cos\gamma & \cos\alpha\sin\beta\sin\gamma - \sin\alpha\cos\gamma \\ -\sin\beta & \sin\alpha\cos\beta & \cos\alpha\cos\beta \end{bmatrix} \tag{10}$$

where the rotation angles α, β and γ are along the XYZ axes. During optimisation, connection hole centres in close Euclidean distance contribute significantly to the objective function and are avoided. To prevent overlap between connection holes, the minimum distance between their centres L_{min} can be computed based on hole radius r, hole depth D and node radius R (as shown in Figure 4(c)):

$$L_{min} = 2\sin\left(\tan^{-1}\frac{r}{R-D}\right) * D \tag{11}$$

If the distance between connection hole centres falls below the minimum allowable value L_{min}, the algorithm will attempt a new node clustering scheme as in step one or increase the total number of node clusters N_n.

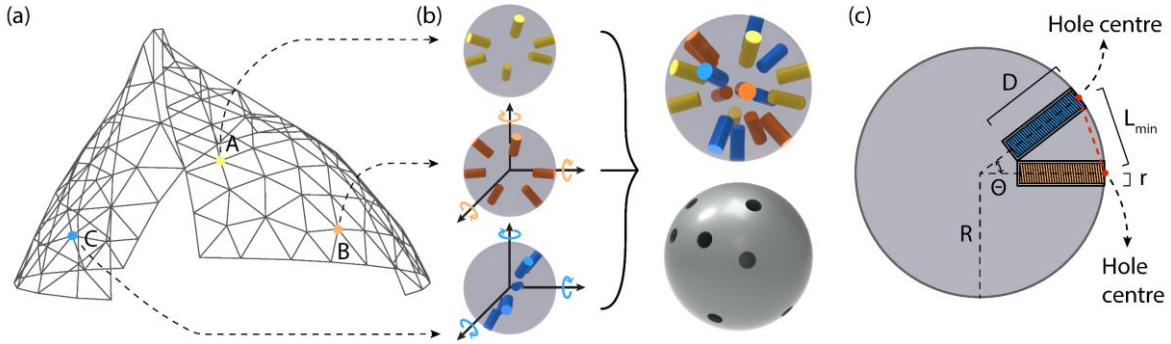


Figure 4. Node clustering and optimisation are achieved in three steps: (a) distribute nodes randomly into clusters based on vertex valence, (b) optimise node orientation to maximise the distance between connection holes' centres on the spherical surface and (c) check against the minimum allowable distance between connection holes' centres to avoid overlaps.

2.4. Workflow

The workflow of the proposed method is illustrated in Figure 5.

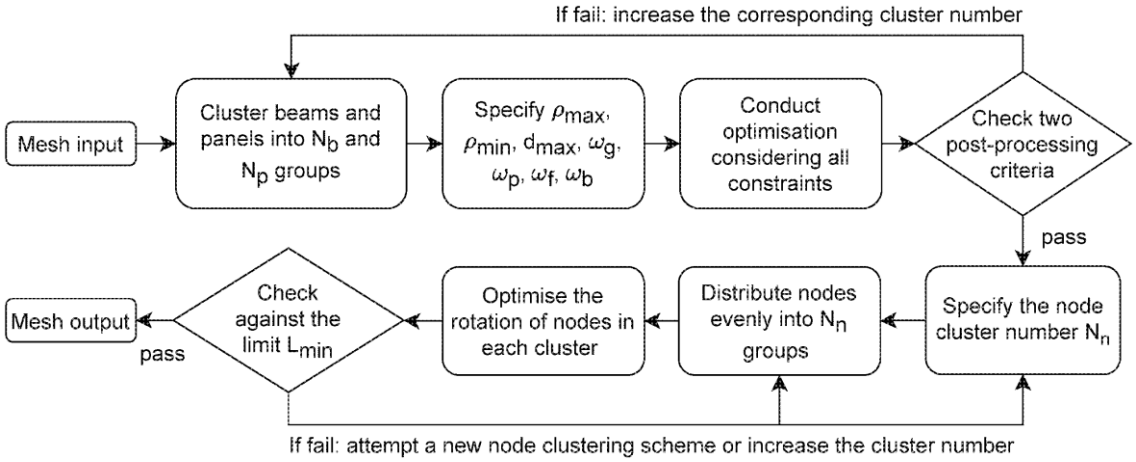


Figure 5. Workflow of the proposed method.

3. Numerical analysis

The effectiveness of the proposed method is tested on three free-form surfaces, as shown in Figure 6. The gap size parameters ρ_{min} and ρ_{max} and the maximum vertex displacement limit d_{max} are set to 2%, 4% and 2% of each mesh's average edge length. The weights assigned to the four subgoal terms ω_g, ω_p, ω_f and ω_b are 1, 1, 3 and 5, respectively. ω_f and ω_b are given larger weights to increase the surface smoothness and reduce the error in beam lengths. Following average shape replacement, the

percentage change in beam length t_b should be lower than 0.01%, while the minimum and maximum gap between new corners and adjacent mesh edges, $t_{p.min}$ and $t_{p.max}$, should be within the range of 2% to 4% of the average edge length. Elements within the same cluster are matched in colour for visualisation. Table 1 summarises the results of clustering and optimisation for the three free-form surfaces. On average, the number of different panels, beams and nodes has been reduced by 87.4%, 88.5% and 79.5%, resulting in a substantial decrease in both fabrication costs and construction difficulties.

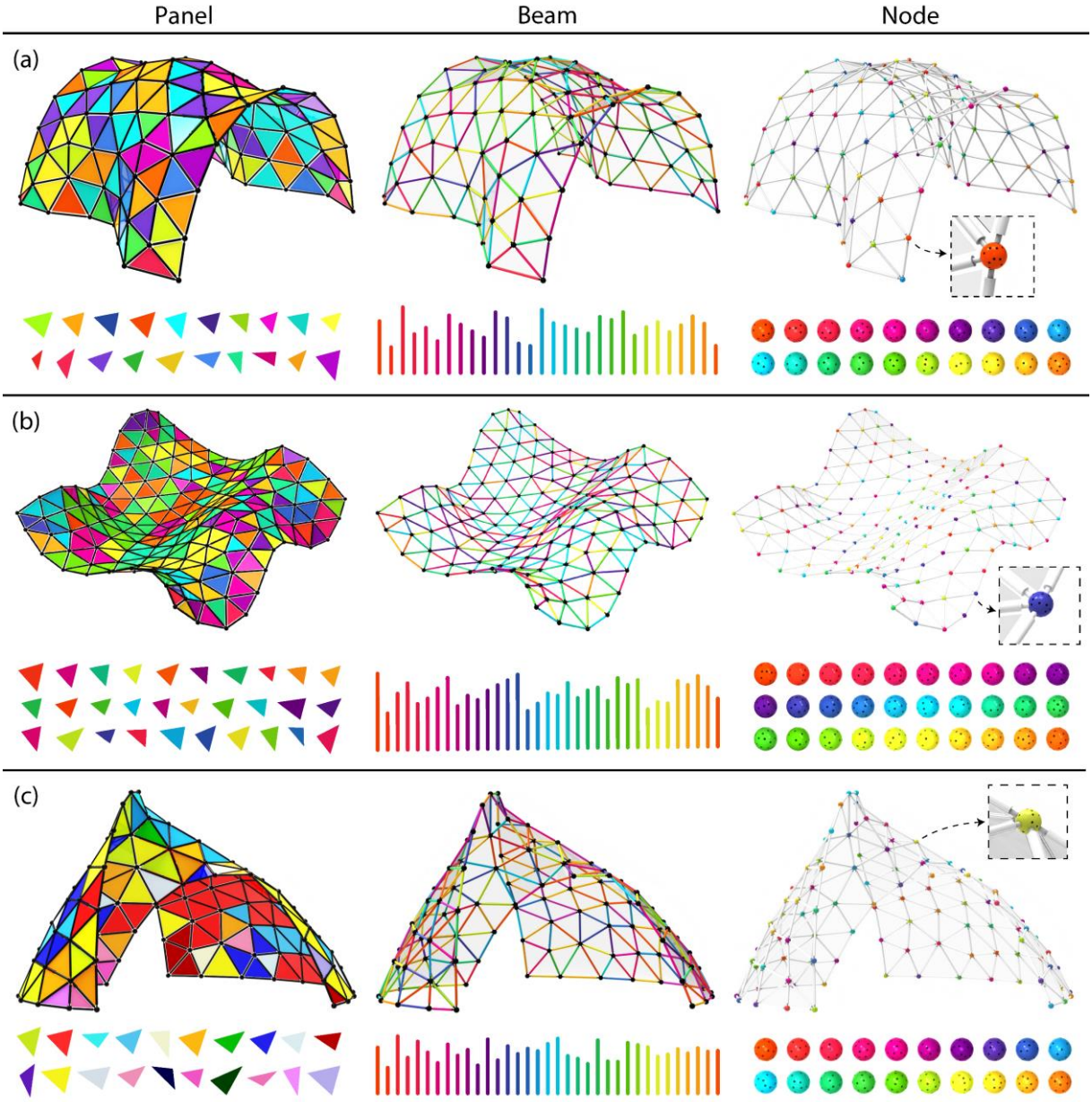


Figure 6. Clustering and optimisation results for three free-form surfaces: (a) tunnel, (b) wave and (c) pavilion. Elements within the same cluster are matched in colour for visualisation.

Table 1. Reduction in the number of panels, beams and nodes after clustering and optimisation.

Cases	**Panel**			**Beam**			**Node**		
	Original	New	Change	Original	New	Change	Original	New	Change
Tunnel	156	20	87.1%	251	30	88%	96	20	79.1%
Wave	241	30	87.6%	383	35	90.9%	143	30	79.0%
Pavilion	160	20	87.5%	261	35	86.5%	102	20	80.4%
Average	–	–	*87.4%*	–	–	*88.5%*	–	–	*79.5%*

4. Application to a full-scale pavilion

4.1. Design details

A full-scale pavilion was designed based on the optimised result of the pavilion case in Section 3 to showcase the practical application of the proposed method. The pavilion, as depicted in Figure 7 and Figure 8, has dimensions of 3.23 m × 3 m × 1.8 m and features laser-cut transparent acrylic panels, timber rods as beams and 3D-printed nodes at joints. To fill the gaps between panels and beams, aluminium-strengthened U channels have been used as connectors, which are affixed to timber rods using industrial-grade chemical adhesives. Beams are connected to nodes using M4 hanger bolts and couplers, allowing for easy assembly and disassembly. Nine segments of heavy timber plates are joined together at the base of the pavilion to provide stability for the entire structure.

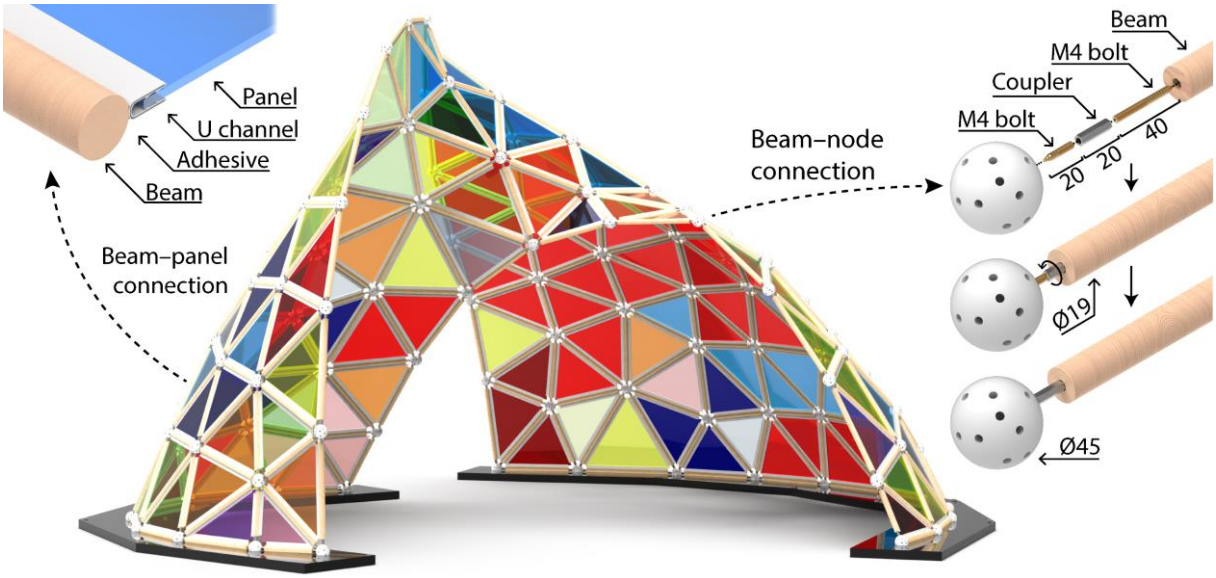


Figure 7. 3D model of a full-scale pavilion designed using the proposed method.

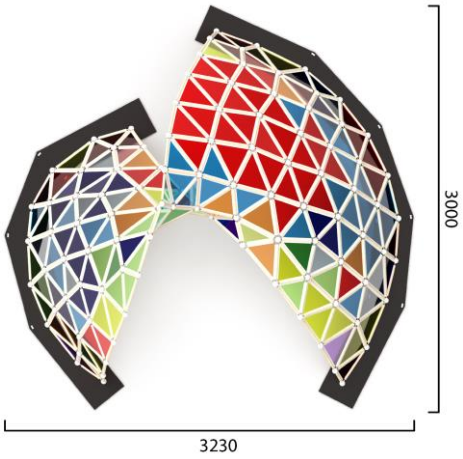


Figure 8. Top view of the pavilion design.

4.2. Construction

The preparation and construction of the full-scale pavilion were conducted in a multistep process. In the laboratory, 261 timber rods and nine bases were mechanically cut, while 102 nodes were 3D printed and 160 panels were laser cut (see Figure 9(a) for the fabricated components). The pavilion frame was then constructed in modules and transported to the construction site. The timber bases were placed on the ground and joined together to establish a stable foundation. Different modules were then combined to form the self-supporting frame of the pavilion, and the panels were assembled using U channels and chemical adhesives. A video showing the pavilion construction is provided in the supplementary file.

The completed pavilion is depicted in Figure 9(b). Although some minor discrepancies were noticed due to fabrication and construction errors, the construction results closely resemble the simulated model presented in Figure 7. Lighting was added to the frame of the structure, as shown in Figure 10, to enhance the pavilion's aesthetic appeal at night. The pavilion's successful construction confirms the feasibility of the proposed method, demonstrating that free-form surfaces can be constructed using clustered components without compromising aesthetics. The efficient use of materials can also reduce manufacturing costs and alleviate fabrication and construction difficulties.

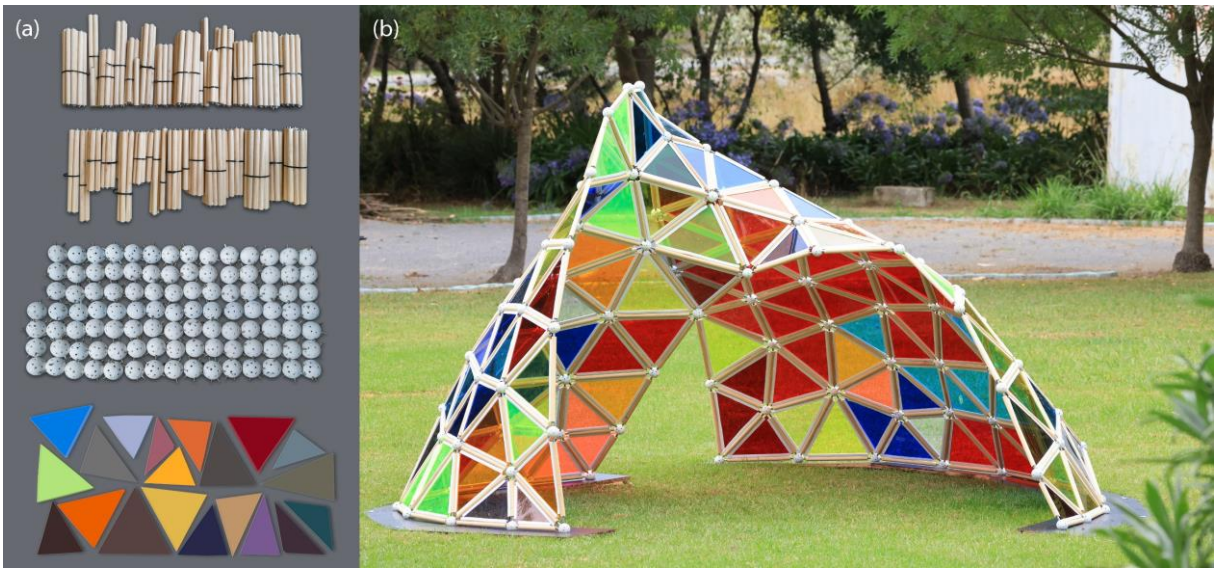


Figure 9. (a) 261 timber rods, 102 nodes and 160 panels were fabricated and grouped in 35, 20 and 20 clusters, respectively; (b) the constructed result closely resembles the simulated model.



Figure 10. Side views of the assembled pavilion during the day and at night.

5. Conclusion

This paper presents a novel design framework that clusters and optimises nodes, beams and panels together to reduce the shape variety of elements in free-form surfaces. Given a mesh as input, the proposed approach clusters beams and panels into user-specified numbers of groups based on geometric shape similarity. Then, a box-constrained optimisation method is applied to obtain congruent panels and matching beam lengths while satisfying gap size, fairness and shape preservation constraints. Finally, nodes are clustered and optimised for use at multiple joint locations. The proposed method is evaluated on three different free-form surfaces, revealing an average reduction of 87.4%, 88.5% and 79.5% in the number of different panels, beams and nodes, respectively.

The effectiveness of the proposed method is further validated by constructing a full-scale pavilion based on one of the case studies. The successful assembly of the pavilion confirms the practicability of the proposed method, as the target free-form surface can be constructed using clustered components without sacrificing aesthetic quality. The cost-effective approach developed from this study offers a potential solution to rationalising large-scale free-form architectural designs. Our future research will extend the proposed method to consider the structural performance of shell and spatial structures.

Acknowledgements

The authors would like to thank Chongjun Bi, Bing Li, Qianyun Sun, Tao Xu, Yunzhen He, Jiaming Ma and Zicheng Zhuang for helping prepare and assemble the pavilion, Huang Meng and Yongbao Liu for providing the construction site, Xiang Gao for helping fabricate the components and Xiangju Meng for assistance in preparing the video.

References

[1] I. M. de Oliveira, R. M. de Oliveira Pauletti and L. C. Meneghetti, "Connection system for gridshell structures using parametric modeling and digital fabrication," *Automation in Construction*, vol. 109, Article 102996, 2020.

[2] C. Millar, T. Mitchell, A. Mazurek, A. Chhabra, A. Beghini, J. N. Clelland, A. McRobie and W. F. Baker, "On designing plane-faced funicular gridshells," *International Journal of Space Structures*, vol. 38, pp. 40–63, 2023.

[3] N. Emami, H. Giles and P. von Buelow, "Structural, daylighting, and energy performance of perforated concrete shell structures," *Automation in Construction*, vol. 117, Article 103249, 2020.

[4] R. Mesnil and O. Baverel, "Pseudo-geodesic gridshells," *Engineering Structures*, vol. 279, Article 115558, 2023.

[5] B. D'Amico, A. Kermani, H. Zhang, A. Pugnale, S. Colabella and S. Pone, "Timber gridshells: numerical simulation, design and construction of a full scale structure," *Structures*, vol. 3, pp. 227–235, 2015.

[6] G. Austern, I. G. Capeluto and Y. J. Grobman, "Rationalization methods in computer aided fabrication: a critical review," *Automation in Construction*, vol. 90, pp. 281–293, 2018.

[7] L. Coar, J. Hare, L. De Laet, Y.-J. Cha, G. Suh, J. Piper and V. Jiang, "A study of digital and physical workflows used for the creation of fabric-formed ice shells with bending active frames," *International Journal of Space Structures*, vol. 36, pp. 13–25, 2021.

[8] S. Brancart, O. P. Larsen, L. De Laet and N. De Temmerman, "Rapidly assembled reciprocal systems with bending-active components: the reciplydome project," *Journal of the International Association for Shell and Spatial Structures*, vol. 60, pp. 65–77, 2019.

[9] Y. Liu, H. Pottmann, J. Wallner, Y.-L. Yang and W. Wang, "Geometric modeling with conical meshes and developable surfaces," *ACM Transactions on Graphics*, vol. 25, pp. 681–689, 2006.

[10] Y. Li, Y. Liu and W. Wang, "Planar hexagonal meshing for architecture," *IEEE Transactions on Visualization and Computer Graphics*, vol. 21, pp. 95–106, 2015.

[11] Y. Liu, T.-U. Lee, A. Koronaki, N. Pietroni and Y. M. Xie, "Reducing the number of different nodes in space frame structures through clustering and optimization," *Engineering Structures*, 2023.

[12] A. Koronaki, P. Shepherd and M. Evernden, "Rationalization of freeform space-frame structures: reducing variability in the joints," *International Journal of Architectural Computing*, vol. 18, pp. 84–99, 2020.

[13] J. Brütting, G. Senatore and C. Fivet, "Design and fabrication of a reusable kit of parts for diverse structures," *Automation in Construction*, vol. 125, Article 103614, 2021.

[14] H. Lu and Y. M. Xie, "Reducing the number of different members in truss layout optimization," *Structural and Multidisciplinary Optimization*, vol. 66, Article 52, 2023.

[15] Z.-Y. Liu, Z. Zhang, D. Zhang, C. Ye, L. Liu and X.-M. Fu, "Modeling and fabrication with specified discrete equivalence classes," *ACM Transactions on Graphics*, vol. 40, Article 41, 2021.

[16] C.-W. Fu, C.-F. Lai, Y. He and D. Cohen-Or, "K-set tilable surfaces," *ACM Transactions on Graphics*, vol. 29, Article 44, 2010.

[17] M. Singh and S. Schaefer, "Triangle surfaces with discrete equivalence classes," *ACM Transactions on Graphics*, vol. 29, Article 46, 2010.

[18] Y. Liu, T.-U. Lee, A. Rezaee Javan, N. Pietroni and Y. M. Xie, "Reducing the number of different faces in free-form surface tessellations," *Automation in Construction*, 2023 (under review).

[19] O. Sorkine-Hornung and M. Rabinovich, "Least-squares rigid motion using SVD," *Computing*, vol. 1, pp. 1–5, 2017.

[20] Y. Eldar, M. Lindenbaum, M. Porat and Y. Y. Zeevi, "The farthest point strategy for progressive image sampling," *IEEE Transactions on Image Processing*, vol. 6, pp. 1305–1315, 1997.

[21] C. C. L. Wang, "Towards flattenable mesh surfaces," *Computer-Aided Design*, vol. 40, pp. 109–122, 2008.

[22] W. W. Hager and H. Zhang, "A survey of nonlinear conjugate gradient methods," *Pacific Journal of Optimization*, vol. 2, pp. 35–58, 2006.

Proceedings of the IASS Annual Symposium 2023
Integration of Design and Fabrication
10–14 July 2023, Melbourne, Australia
Y.M. Xie, J. Burry, T.U. Lee and J. Ma (eds.)

Constructing topologically optimized spatial structure using innovative mortise-and-tenon joints

Xin YAN[a], Ding Wen BAO[b,c,*], Congcong REN[d], Yi Min XIE[b,*]

[b,*] Centre for Innovative Structures and Materials, School of Engineering, RMIT University, Melbourne, 3001, Australia
nic.bao@rmit.edu.au
mike.xie@rmit.edu.au

[a] Tsinghua University, Beijing, 10080, China
[c] School of Architecture and Urban Design, RMIT University, Melbourne, 3001, Australia
[d] School of Architecture and Urban Planning, Beijing University of Civil Engineering and Architecture, Beijing, 102627, China

Abstract

Topology optimisation methods have been implemented on many architectural projects, and their design layouts always are fabricated with additive manufacturing methods due to their complex organic forms. However, there are still some difficulties that limit the application potentials of additive manufacturing in real projects, including size limitations of the fabrication devices, construction cost and transportation probabilities. Therefore, different from the conventional fabricating methods, this research achieves topologically optimized models using a subtractive manufacturing method with timber mortise-and-tenon joints from the Chinese traditional wooden tectonic system. In this paper, an initial shell model with specific plane angles is generated for Bi-directional Evolutionary Structural Optimization (BESO) due to the carpentry assemble requirements. Then, different classical mortise-and-tenon joints are selected to connect timber parts in different force-transferring paths and fabrication limitations, including plugging joints, connecting joints, and steering joints. Finally, with the convenience of on-site augmented reality (AR) assisted techniques, the lightweight timber parts can be easily assembled only by several people in an extremely short time. This project presents an effective and innovative way to achieve material efficiency and lightweight through a combination of innovative advanced tools and traditional woodworking techniques. These timber joints can be also used in architectural design in the context of Chinese traditional tectonics. The prototype pavilion is proof of the concept for the great potential in applications of on-site modular buildings, installations, and artworks.

Keywords: BESO, mortise-and-tenon joint, topology optimization, timber structures

1. Introduction

Topology optimization has gained continuously growing attention in architecture design due to its potential for generating elegant and lightweight structures with high structural performance. During the last two decades, there are several classical topology optimization methods have been developed widely and deeply, e.g., Homogenization method [1, 2], the solid isotropic material with penalization (SIMP) method [3, 4], the evolutionary structural optimization (ESO) [5, 6], Bi-directional evolutionary structural optimization (BESO) [7, 8] and the level-set method (LSM) [9, 10]. And there are two main tendencies of topology optimisation in architectural research fields. On one hand, more and more contemporary architectural projects absorb topology optimisation as their concept design sources, e.g., Akutagawa River Side in Takatsuki City [11], tree-like pavilions [12], Qatar National Convention

Copyright © 2023 by Xin YAN, Ding Wen BAO, Congcong REN and Yi Min XIE. Published in the Proceedings of the IASS Annual Symposium 2023 with permission.

Centre & Shanghai Zendai Himalayan Art Centre [13, 14], concrete slab [15], Volu Dining Pavilion [16], and so on. On the other hand, topology optimisation methods can also be introduced for structural form analysis for traditional architectures, e.g., Sagrada Familia [17], Palazzeto Dellospori of Rome [18], Chinese wooden mortise and tension joints [19], Chinese rainbow bridge [20], etc. However, there is seldom research combining the above two directions to perform a new structural-effective architectural design with traditional tectonic form features and constructing probabilities.

Furthermore, although most classical topology optimisation methods are effective in finding the globally optimised solutions around the whole design domain, there are usually some objective constraints or subjective preferences which also play important roles in architectural form-finding. Faced with these non-structural requirements, many researchers have been developing lots of modified topology optimisation methods for specific aims, e.g., introducing detail constraints for concept design [21, 22], eliminating enclosed voids [23], obtaining self-supporting optimized models [24], generating diverse truss structures[25], simulating leaf morphogenesis [26], etc. And in this project, the carpentry manufacture techniques of mortise-and-tenon joints make special demands on the topologically optimised layouts, which requires modified BESO algorithms as well as customised finite element analysis models.

Therefore, an innovative structural design-fabrication working-flow based Multi-volume constraint BESO method [27] and Chinese traditional mortise and tension joint carpentry are introduced with a pavilion project named X-Form 3.0 in this paper. Compared with its two previous versions (X-Form 1.0 & 2.0) [12, 28], X-Form 3.0 consists of timber components connected with mortise and tension joints, which means that the fabrication of this project is subtractive manufacturing rather than additive manufacturing in the past projects. Therefore, this paper proposes a new structural topology optimisation workflow oriented to subtractive manufacturing. And with the Chinese traditional mortise and tension joints, this installation can be transferred easily with several light slender parts and assembled on-site with a few people, which shares the great potential in applications of on-site modular buildings, installations, and artworks.

2. Structural form-finding

2.1. Multi-volume constraint BESO method (MV-BESO)

To form a structural design with slender tree-like components, the multi-volume constraint BESO (MV-BESO) method [27] is introduced. This is because conventional topology optimization methods are aimed at achieving the solution which maximizes the structural performance under a certain global volume fraction constraint and always form continuum solid parts instead of slender rods. However, the Multi-volume BESO aims to achieve the same object with several local volume fraction constraints and share the ability of adjusting local structural designs. The basic problem of MV-BESO is different from the description of conventional topology optimization methods, and it can be written mathematically as below:

$$min\ C(\boldsymbol{X}) = \frac{1}{2}\boldsymbol{U}^T\boldsymbol{K}\boldsymbol{U} = \frac{1}{2}\sum_{i=1}^{N} x_i^p \boldsymbol{u}_i^T \boldsymbol{k}_i \boldsymbol{u}_i \tag{1}$$

$$subject\ to\ SUBV_k(\boldsymbol{X}_k) = \sum_{i=1}^{N_k} x_i v_i \le SUBV_k^* \tag{2}$$

in which C , $\boldsymbol{X}$, $\boldsymbol{U}$, $\boldsymbol{K}$, N are the objective function (compliance), design variable vector, displacement vector, global stiffness matrix and total element number in the global domain, respectively. $SUBV_k^*$, $\boldsymbol{X}_k$ and N_k are the local target volume, local design variable vector and local element number of *k*-th sub-domain. The terms v_i , x_i , k_i and $\boldsymbol{u}_i$ are the volume, design variable, stiffness matrix and nodal

displacement vector for *i*-th element. Particularly, the value of x_i is alternatively x_{min} (a prescribed small positive value, e.g., 0.001) or 1.

For stiffness optimization, the sensitivity α_i for *i*-th element, which is the criterion for design variable x_i, can be calculated as the gradient of compliance with respect to the design variable [29],

$$\frac{\partial C(\boldsymbol{X})}{\partial x_i} = -\frac{1}{2} p x_i^{p-1} \boldsymbol{u}_i^T \boldsymbol{k}_i \boldsymbol{u}_i \tag{3}$$

$$\alpha_i = -\frac{1}{p}\frac{\partial C}{\partial x_i} = \begin{cases} \frac{1}{2}\boldsymbol{u}_i^T \boldsymbol{k}_i \boldsymbol{u}_i & \text{when } x_i = 1 \\ \frac{x_{min}^{p-1}}{2}\boldsymbol{u}_i^T \boldsymbol{k}_i \boldsymbol{u}_i & \text{when } x_i = x_{min} \end{cases} \tag{4}$$

And when the penalty coefficient *p* tends to infinity, the sensitivity number α_i becomes the one in hard-kill BESO method [29],

$$\alpha_i = -\frac{1}{p}\frac{\partial C}{\partial x_i} = \begin{cases} \frac{1}{2}\boldsymbol{u}_i^T \boldsymbol{k}_i \boldsymbol{u}_i & \text{when } x_i = 1 \\ 0 & \text{when } x_i = x_{min} = 0 \end{cases} \tag{5}$$

The above sensitivity is usually modified to solve the mesh-dependent problem [30], using a filtering scheme:

$$\tilde{\alpha}_i = \frac{\sum_{j=1}^{N} w_{ij}\alpha_j}{\sum_{j=1}^{N} w_{ij}} \tag{6}$$

$$w_{ij} = \max(0, R_{min} - d_{ij}) \tag{7}$$

in which d_{ij} is the distance between the center of the *j*-th element and the *i*-th element. R_{min} and α_i are the filter radius and the original sensitivity of the *j*-th element.

To achieve a convergent solution, another historical average of $\bar{\alpha}_i$ in different iterations is introduced [30]:

$$\bar{\alpha}_i = \frac{\tilde{\alpha}_i^{(n)} + \tilde{\alpha}_i^{(n-1)}}{2} \tag{8}$$

In MV-BESO method, for *k*-th sub-domain, the element sensitivities are ranked in each iteration to determine a threshold with local target volumes of next iteration, $SUBV_k^{(n)}$, which is defined based on the current volume $SUBV_k^{(n-1)}$ and the evolutionary ratio δ.

$$SUBV_k^{(n)} = SUBV_k^{(n-1)}(1-\delta) \tag{9}$$

The threshold can be used to evaluate if the element shall be changed in a such way that if one solid element's sensitivity is lower than the threshold, its design variable will be switch from 1 to x_{min}, and the design variable of a void element will be changed from x_{min} to 1 as well if its sensitivity is higher than the threshold.

The cycle of FEA and BESO evolution continues until the following convergence criterion defined in the variation of the objective functions is satisfied [30]:

$$\frac{\left|\sum_{i=1}^{N}\left(C_{k-i+1}-C_{k-N-i+1}\right)\right|}{\sum_{i=1}^{N}C_{k-i+1}} \leq \tau \tag{10}$$

where k is the current iteration number, τ is an allowable convergence error (τ = 0.001 in this paper), which means stable compliance at least in successive 10 iterations.

2.2. Topology optimization with structural predesign

As Fig.1 shows, the pavilion in this project has a centrosymmetric free-form roof with width and length of about 3960mm and 3900mm, respectively. The curved roof is consisted of several quadrilateral or triangular plates (grey parts) and supported by three equal tree-like wooden structures (blue parts). Therefore, in the following structural form-finding process, only one-sixth part is introduced with symmetric condition settings.

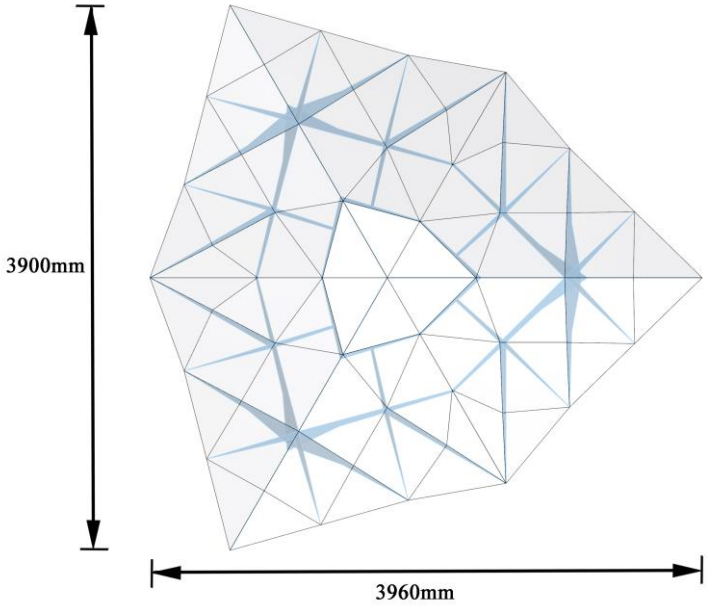


Figure 1. The top view of whole X-Form 3.0 pavilion.

The timber structure components are required to be hexagonal or octagonal columns to leave the spaces for mortise-and-tension joints carpentry works, which means that the timber components need to link each other with the fixed plane angles of 0, 45, 90, 135, or 180 degrees. Therefore, as illustrated in Fig.2, an initial shell model with the specific plane angles is generated as the basic design domain for the topologically optimised form-finding. Moreover, the above initial design domain is divided into 30 sub-domains and 6 non-design domains to get the locally optimised structure design with MV-BESO method effectively.

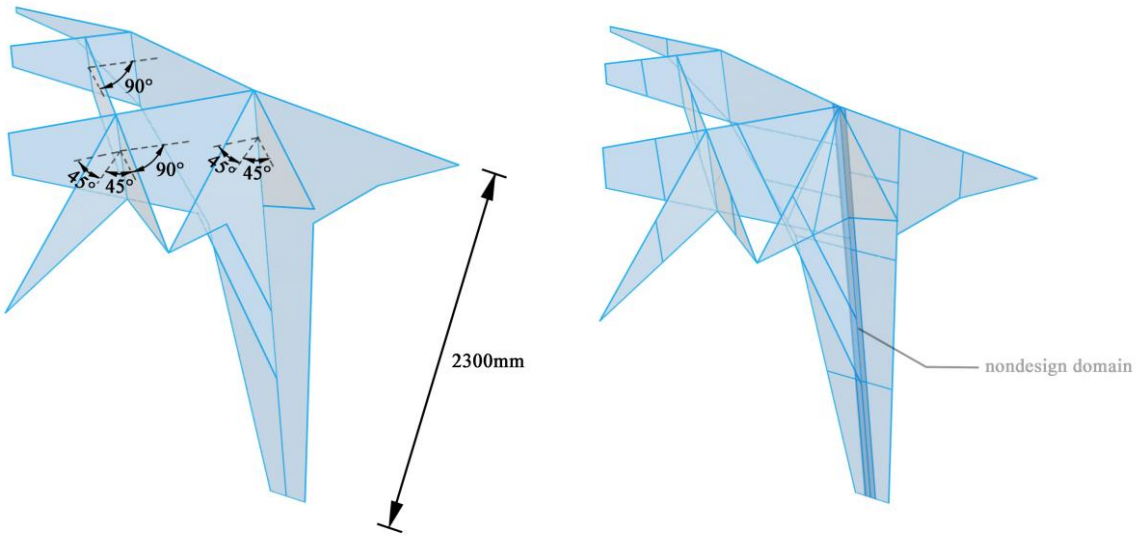


Figure 2. Initial model and sub-domain settings for MV-BESO methods.

Fig.3 illustrates some typical stages of MV-BESO stiffness optimisation process from iteration 1 to iteration 94. This FEA model is divided into 100,000 shell elements with the thickness of 10 mm. The material assumption is assumed as Young's Modulus of 700 MPa and Poisson ratio of 0.45. The MV-BESO parameters are Rmin of 20 mm and ER of 1%. All the local volume fraction constraints for sub-design domains are 45%. With the boundary conditions and loading cases (Fig.4 a), it is obvious that each sub-design domain removes its materials during the evolutionary loop. After 94 iterations, the final optimised structural layout is generated and reshaped as octagonal rods according to the requirements from carpentry work (Fig.4 b).

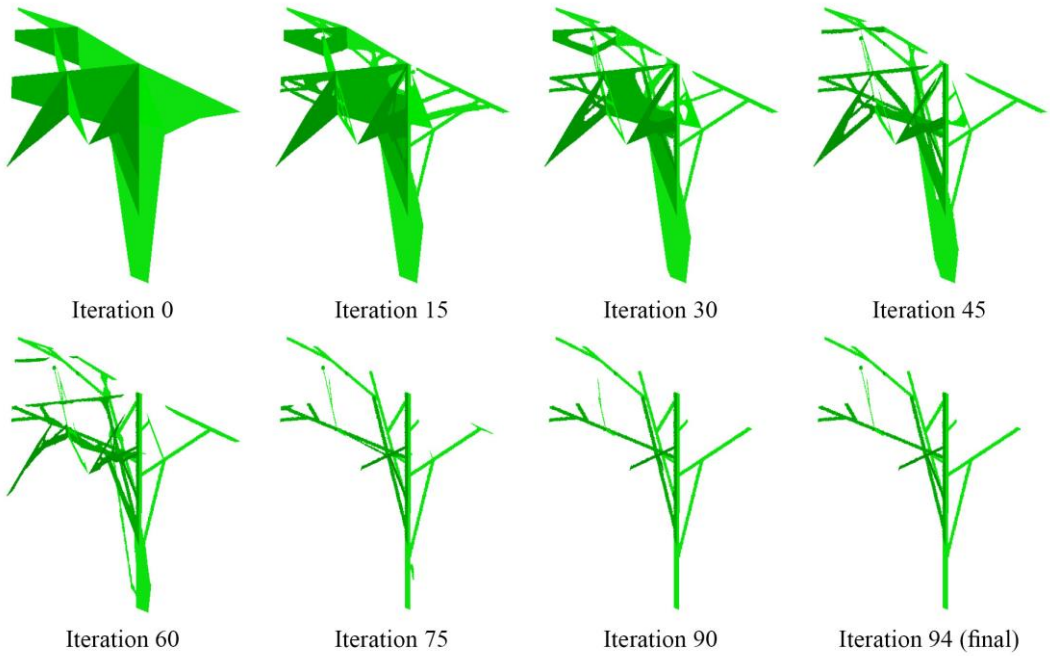
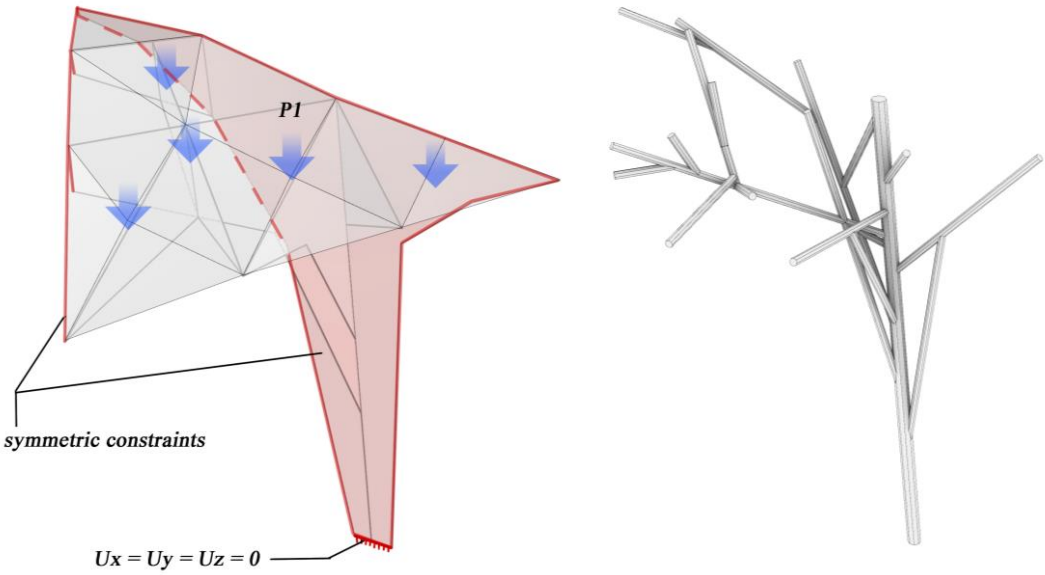


Figure 3. MV-BESO evolutionary history of X-Form 3.0.



(a) (b)

Figure 4. Boundary conditions & load case (a) and modified structural layout(b).

3. Wooden mortise-and-tenon joint and on-site assembles

One of the project's aims is to form an innovative wooden working flow which can be transferred and assembled easily, so the above optimised structure with MV-BESO needs to be divided into several slender timber rods with the maximal length of 1500mm and section diameters from 60mm to 20mm. Then, several different kinds of Chinese traditional mortise-and-tenon joints are introduced to link different structural members without any nails. The selected mortise-and-tenon joints are straight mortise-and-tenon, dovetail mortise-and-tenon, silver ingot mortise-and-tenon, mantis head mortise-and-tenon, and sleeve-shoulder mortise-and-tenon, etc.

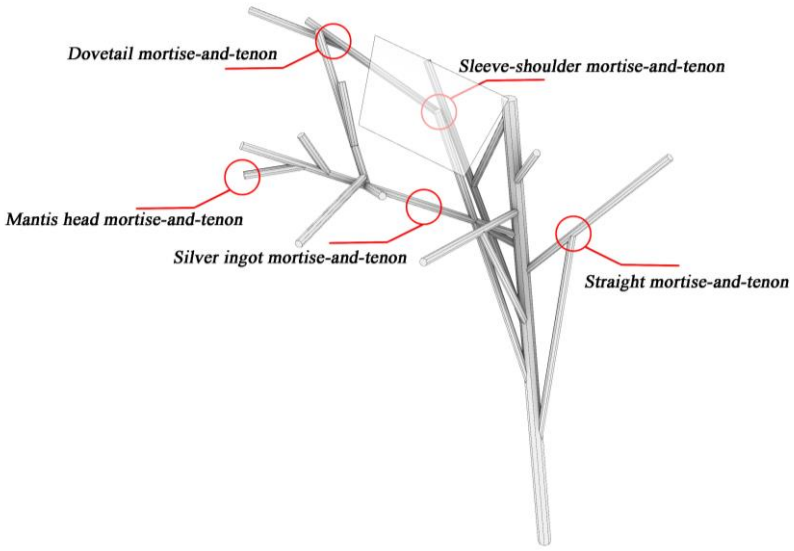
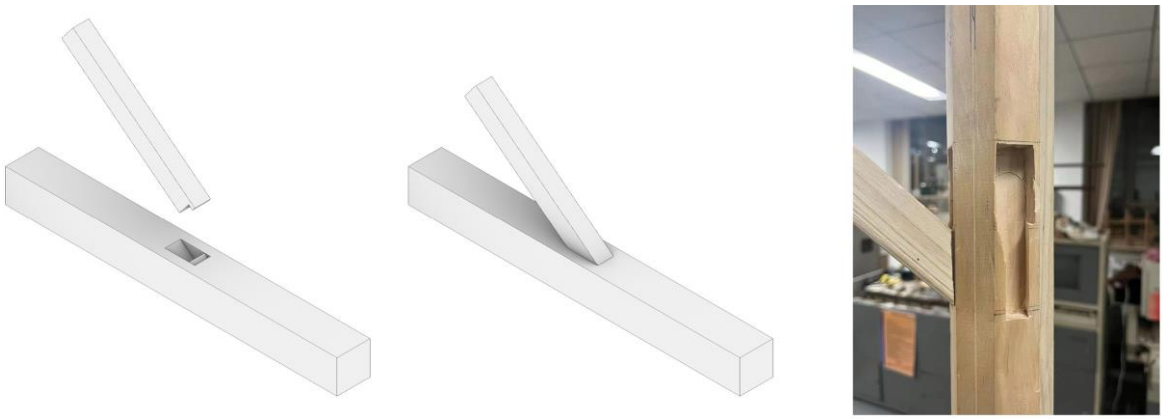


Figure 5. Diagram of different mortise-and-tenon distributions in X-Form 3.0.

3.1. Plugging joints

In this pavilion fabrication, the most commonly used plugging joint is straight mortise-and-tenon joint, which is usually applied to insert the end of one rod into the middle of another rod (**Fig. 6**). With this joint, it is really convenient to form a structural rod like a "tree branch". Therefore, it is very suitable for generating tree braches.

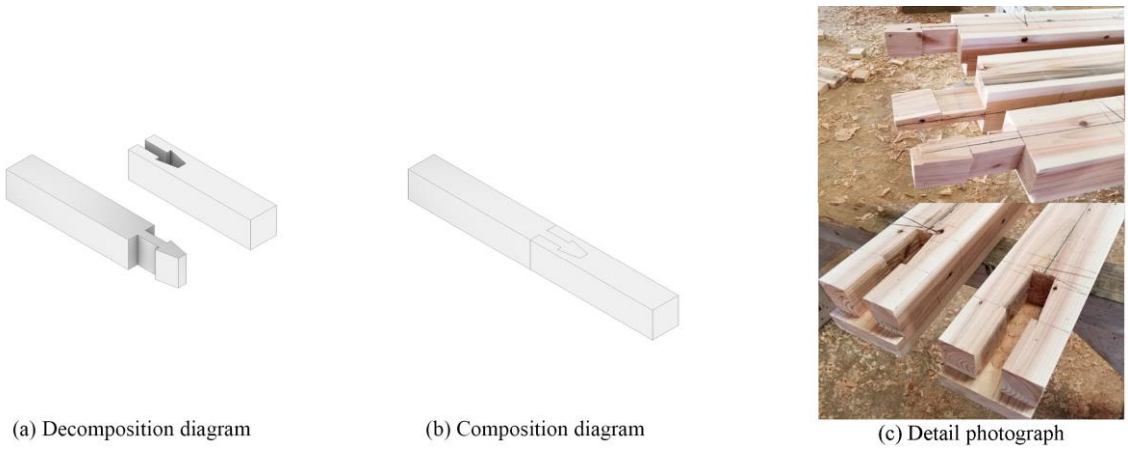


(a) Decomposition diagram (b) Composition diagram (c) Detail photograph

Figure 6. Diagrams of straight mortise-and-tenon joint.

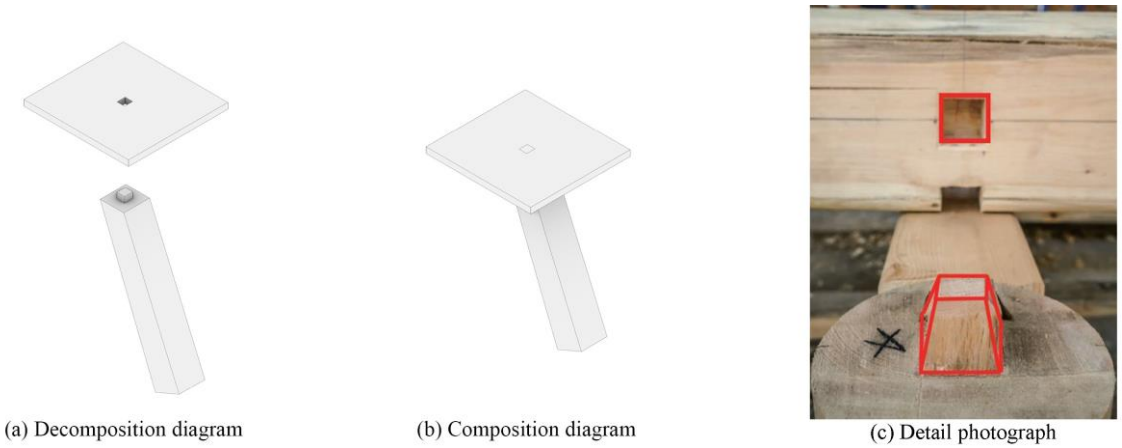
3.2. Connecting joints

The word "connecting joints" here represents the mortise-and-tenon joints which are implemented for the main purpose to link two structural parts, instead of generating new parts or new directions. And there are two kinds of connecting joints in this pavilion, which are mantis head mortise-and-tenon joint and sleeve-shoulder mortise-and-tenon joint, respectively (**Fig. 7-8**). The former one is used to combine two parallel rods into one. It is really necessary to link the three tree supports together with the mantis head mortise-and-tenon joint. And the function of sleeve-shoulder mortise-and-tenon joint is to fix roof panel to the top of tree branch.



(a) Decomposition diagram (b) Composition diagram (c) Detail photograph

Figure 7. Diagrams of mantis head mortise-and-tenon joint.

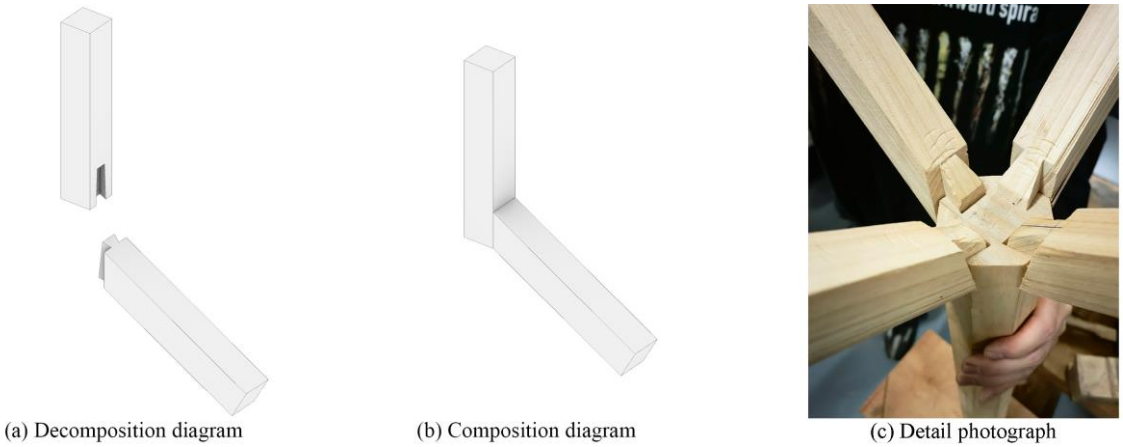


(a) Decomposition diagram (b) Composition diagram (c) Detail photograph

Figure 8. Diagrams of sleeve-shoulder mortise-and-tenon joint.

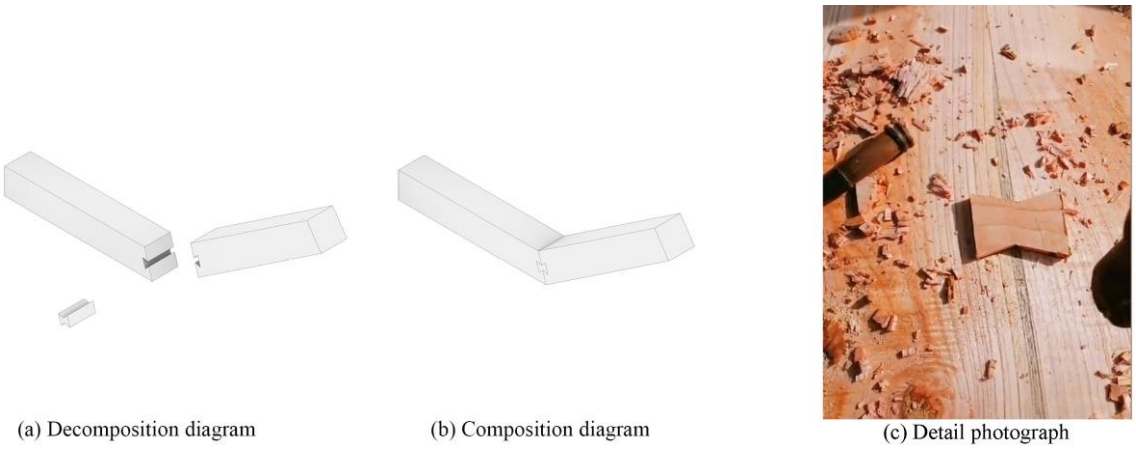
3.3. Steering joints

The last kind of mortise-and-tenon joint in this project is steering joint, and it is the main component to change rod direction. As Fig. 9-10 shows, both dovetail mortise-and-tenon joint and silver ingot mortise-and-tenon joint can undertake this task. One biggest difference between the two joints is that dovetail mortise-and-tenon joint can only link light parts, while silver ingot mortise-and-tenon joint is always used in the main structure components.



(a) Decomposition diagram (b) Composition diagram (c) Detail photograph

Figure 9. Diagrams of dovetail mortise-and-tenon joint.



(a) Decomposition diagram (b) Composition diagram (c) Detail photograph

Figure 10. Diagrams of silver ingot mortise-and-tenon joint.



Figure 11. Rendering view of X-Form 3.0.

3.4. Augmented reality on-site assembles

Taking the advantages of mortise-and-tenon joints, X-Form 3.0 is carrying-friendly and assembling-friendly. For example, the whole weight of wooden material is only 24kg, and the slender structural rods can be divided into two suitcases easily. Furthermore, the mortise-and-tenon joints also share the

advantages of on-site assembling with Fologram. Fologram is an augmented reality equipment which can transform 3D models into full-size construction guides through augmented reality glasses such as Hololens. This program is dedicated to overlaying digital guidance in the workspace to assist in the construction of complex projects that require a series of measurements, verification and targeted management, enabling step-by-step guidance for masonry work during construction. Thus, using Fologram, anyone can easily and effectively assemble the rods together (Fig. 12).

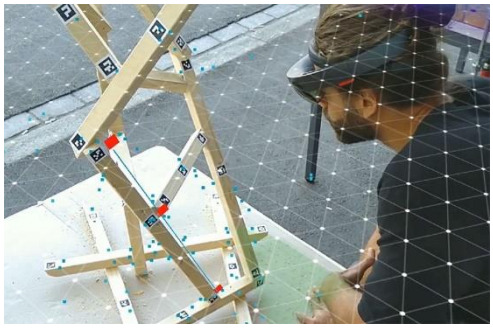


Figure 12. Fologram augmented reality construction technology.

4. Conclusion

This paper introduces the whole working flow of X-Form 3.0 including structural form-finding, joint fabrication and on-site assemble. The most notable contribution of X-Form 3.0 is that it presents a successful example to integrate topology optimisation based form-finding method with Chinese traditional wooden tectonics.

Firstly, a modified BESO method, MV-BESO method, is introduced to form the slender structural rods for timber fabrication. To achieve this, it is necessary to pay more attention to the initial model design according to carpentry requirements. Then, five different mortise-and-tenon joints are implemented to appropriately link different structural members. In this phase, the traditional carpentry also plays a great role in the fabrication because there are always some complex shapes in the mortise-and-tenon joints which can not be fabricated by robots. Finally, taking the advantage of mortise-and-tenon joints, the team can conveniently transfer all the structural components and assemble them on-site with Fologram. Furthermore, it is notable that X-Form 3.0 is only a preliminary attempt to integrate topology optimisation with traditional subtractive manufacturing, and there are still some parts which require more in-depth studies, e.g., an effective BESO method to generate timber rods, a robotic fabrication method to make complex wooden joints, and so on.

This innovative pavilion is a demonstration of the combination of new design and traditional construction techniques, explaining the design and construct process of the pavilion through exploration of emerging technologies in both digital design and subtractive manufacturing, which shares great significance for architects, engineers, and designers.

Acknowledgements

The authors gratefully acknowledge the financial support provided by the Australian Research Council (FL190100014) and National Natural Science Foundation of China (51908543).

References

[1] M. P. Bendsøe, "Optimal shape design as a material distribution problem," *Structural optimization*, vol. 1, pp. 193-202, 1989.

[2] M. P. Bendsøe and N. Kikuchi, "Generating optimal topologies in structural design using a homogenization method," *Computer methods in applied mechanics and engineering*, vol. 71, no. 2, pp. 197-224, 1988.

[3] M. P. Bendsøe and O. Sigmund, "Material interpolation schemes in topology optimization," *Archive of applied mechanics,* vol. 69, no. 9, pp. 635-654, 1999.
[4] M. P. Bendsøe and O. Sigmund, *Topology optimization: theory, methods, and applications*. Springer Science & Business Media, 2003.
[5] Y. M. Xie and G. P. Steven, "A simple evolutionary procedure for structural optimization," *Computers & structures,* vol. 49, no. 5, pp. 885-896, 1993.
[6] Y. M. Xie and G. P. Steven, "Optimal design of multiple load case structures using an evolutionary procedure," *Engineering Computations,* vol. 11, no. 4, pp. 295-302, 1994, doi: 10.1108/02644409410799290.
[7] X. Huang, Y. M. Xie, and M. C. Burry, "Advantages of bi-directional evolutionary structural optimization (BESO) over evolutionary structural optimization (ESO)," *Advances in Structural Engineering,* vol. 10, no. 6, pp. 727-737, 2007.
[8] X. Huang and Y. Xie, "A new look at ESO and BESO optimization methods," *Structural and Multidisciplinary Optimization,* vol. 35, no. 1, pp. 89-92, 2008.
[9] M. Yulin and W. Xiaoming, "A level set method for structural topology optimization and its applications," *Advances in Engineering software,* vol. 35, no. 7, pp. 415-441, 2004.
[10] G. Allaire, F. Jouve, and A.-M. Toader, "Structural optimization using sensitivity analysis and a level-set method," *Journal of computational physics,* vol. 194, no. 1, pp. 363-393, 2004.
[11] H. Ohmori, "Computational Morphogenesis: Its Current State and Possibility for the Future," *International Journal of Space Structures,* vol. 26, no. 3, pp. 269-276, 2011.
[12] D. W. Bao, X. Yan, and Y. M. Xie, "Fabricating topologically optimized tree-like pavilions using large-scale robotic 3D printing techniques," *Journal of the International Association for Shell and Spatial Structures,* vol. 63, no. 2, pp. 122-131, 2022.
[13] T. Ito, A. Isozaki, and M. Sasaki, "Morphogenesis of Flux Structure," 2007.
[14] C. Cui, H. Ohmori, and M. Sasaki, "Computational morphogenesis of 3D structures by extended ESO method," *Journal of the International Association for Shell and Spatial Structures,* vol. 44, no. 1, pp. 51-61, 2003.
[15] A. Jipa, M. Bernhard, M. Meibodi, and B. Dillenburger, "3D-printed stay-in-place formwork for topologically optimized concrete slabs," in *Proceedings of the 2016 TxA Emerging Design+ Technology Conference*, 2016: Texas Society of Architects, pp. 97-107.
[16] S. Bhoosan, "Collaborative Design: Combining Computer‐Aided Geometry Design and Building Information Modelling," *Architectural Design,* vol. 87, no. 3, pp. 82-89, 2017.
[17] J. Burry, P. Felicetti, J. Tang, M. Burry, and M. Xie, "Dynamical structural modeling: a collaborative design exploration," *International Journal of Architectural Computing,* vol. 3, no. 1, pp. 27-42, 2005.
[18] X. Yan, D. W. Bao, K. Cai, Y. F. Zhou, and Y. M. Xie, "A new form-finding method for shell structures based on BESO algorithm," in *Proceedings of IASS Annual Symposia*, 2019, vol. 2019, no. 17: International Association for Shell and Spatial Structures (IASS), pp. 1-8.
[19] C. B. Duan, S. Y. Shen, D. W. Bao, and X. Yan, "Innovative design solutions for contemporary Tou-Kung based on topological optimisation," *Architectural Intelligence,* vol. 2, no. 1, p. 10, 2023.
[20] X. Meng, Q. Zhou, W. Shen, and Y. M. Xie, "Structural and architectural evaluation of Chinese rainbow bridge and related bridge types using BESO method," in *Proceedings of IASS Annual Symposia,* 2018, vol. 2018, no. 2: International Association for Shell and Spatial Structures (IASS), pp. 1-8.
[21] X. Yan, D. Bao, Y. Zhou, Y. Xie, and T. Cui, "Detail control strategies for topology optimization in architectural design and development," *Frontiers of Architectural Research,* vol. 11, no. 2, pp. 340-356, 2022.
[22] Z. Li, T.-U. Lee, and Y. M. Xie, "Interactive Structural Topology Optimization with Subjective Scoring and Drawing Systems," *Computer-Aided Design,* p. 103532, 2023.

[23] Y. Xiong, S. Yao, Z.-L. Zhao, and Y. M. Xie, "A new approach to eliminating enclosed voids in topology optimization for additive manufacturing," *Additive Manufacturing,* vol. 32, 2020, doi: 10.1016/j.addma.2019.101006.

[24] M. Bi, P. Tran, and Y. M. Xie, "Topology optimization of 3D continuum structures under geometric self-supporting constraint," *Additive Manufacturing,* vol. 36, 2020, doi: 10.1016/j.addma.2020.101422.

[25] Q. Cai, L. He, Y. Xie, R. Feng, and J. Ma, "Simple and effective strategies to generate diverse designs for truss structures," *Structures,* vol. 32, pp. 268-278, 2021, doi: 10.1016/j.istruc.2021.03.010.

[26] J. Ma, Z.-L. Zhao, S. Lin, and Y. M. Xie, "Topology of leaf veins: Experimental observation and computational morphogenesis," *Journal of the Mechanical Behavior of Biomedical Materials,* vol. 123, p. 104788, 2021.

[27] X. Yan, Y. Xiong, D. W. Bao, Y. M. Xie, and X. Peng, "A Multi-volume constraint approach to diverse form designs from topology optimization," *Engineering Structures,* vol. 279, p. 115525, 2023.

[28] D. W. Bao, X. Yan, R. Snooks, and Y. M. Xie, "Design and construction of an innovative pavilion using topological optimization and robotic fabrication," in *Proceedings of IASS Annual Symposia*, 2019, vol. 2019, no. 5: International Association for Shell and Spatial Structures (IASS), pp. 1-8.

[29] X. Huang and Y. M. Xie, *Evolutionary topology optimization of continuum structures: methods and applications*. John Wiley & Sons, 2010.

[30] X. Huang and Y. M. Xie, "Convergent and mesh-independent solutions for the bi-directional evolutionary structural optimization method," *Finite Elements in Analysis and Design,* vol. 43, no. 14, pp. 1039-1049, 2007, doi: 10.1016/j.finel.2007.06.006.

IASS 2023
July 10–14 Melbourne
Integration of Design and Fabrication

Proceedings of the IASS Annual Symposium 2023
Integration of Design and Fabrication
10–14 July 2023, Melbourne, Australia
Y.M. Xie, J. Burry, T.U. Lee and J. Ma (eds.)

Controlling frills of bending-active negative curvature surface

Fuki ONO[b], Miwako KASE[c], Kotaro SEMPUKU[c], Mizuki SHIGEMATSU[c], Hiroki TAMAI[c], Seri NISHIMOTO[a], Tomohiro TACHI[a,*]

[a,*] The University of Tokyo
3-8-1 Komaba, Meguro-Ku, Tokyo 153-8902
tachi@idea.c.u-tokyo.ac.jp

[b] Taiyo Kogyo Corporation
[c] Nikken Sekkei Ltd.

Abstract

Frilly ruffles appearing in natural forms, such as coral and leaves, are induced by in-plane differential growth. Previously, we proposed a mechanism using bending-active scissors that reproduces these self-organized ruffles through the incompatibility of in-plane deformation produced by scissor units; however, the study left unsolved questions. This study analyzes the symmetry-breaking process of deployment and zero-stiffness wave-like motion after deployment through simulation. We propose how to control this wave-like motion by pulling the group of threads. We fabricated a meter-scale structure by assembling bar and pivot parts made of vulcanized fiber, chemically processed cellulose paper. The joint parts are utilized the material's plasticity in a wet state and stiffness in a dried state.

Keywords: bending active scissors, zero-stiffness, negative gaussian curvature, frills and ruffles, buckling

1. Introduction

Frilly ruffles in biological forms such as coral and lettuce leaves are a great inspiration for architectural and product design [1]. Such buckled surfaces induced by in-plane differential growth are ubiquitous in nature [2, 3]. Previously, we proposed a mechanism based on bending-active scissors that effectively reproduces these self-organized ruffles through the incompatibility of in-plane shear deformation produced by bending-active scissor units [4]. Although we obtained the desired ruffled form, the process of symmetry breaking, the form after the buckling, and their behavior were not fully investigated.

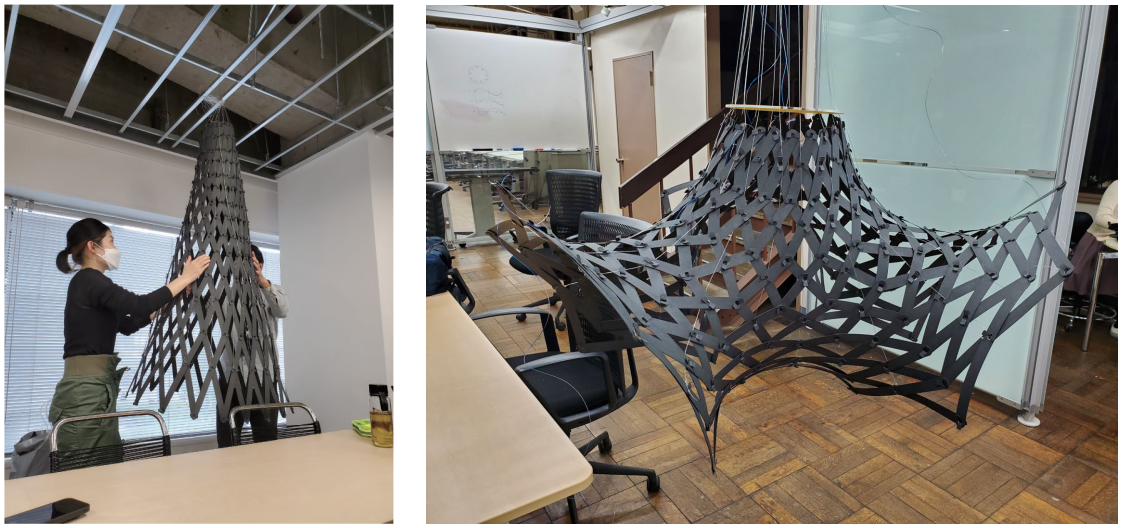
In this study, we analyze the process of symmetry breaking through simulation to understand the buckling process better. We show that the number of frills is affected by the balance between the in-plane and out-of-plane stiffness. We identify the families of locally stable configurations with different rotational symmetry, where states within the same family are connected to each other through a wave-like quasi-zero-stiffness motion.

We show how to control this wave-like motion along the perimeter by pulling the group of threads in a coordinated way. We provide a method for obtaining the control motion of threads by inversely computing from our simulated geometric model. Then, we verify the actuation using the simulation model.

We fabricated a meter-scale structure by assembling bar and pivot parts cut out from sheets of vulcanized fiber, which is chemically processed cellulose paper. The fabrication of joint parts utilizes the material's

Copyright ©2023 by F. ONO, M. KASE, K. SEMPUKU, M. SHIGEMATSU, H. TAMAI, S. NISHIMOTO and T. TACHI. Published in the Proceedings of the IASS Annual Symposium 2023 with permission.

plasticity in a wet state and elasticity in a dried state. We show the fabrication process and the joint's detailed design.



(a) (b)

Figure 1: Our structure in a meter scale.

2. Geometric model

We follow the notation and the principles of the structure from Ono and Tachi [4]. The structure is based on bending-active scissors that can deform between a linearly folded state and a surface of constant negative Gaussian curvature. We use flat members for the scissors so they can only bend in the normal direction of the surface, so it can be considered as a type of geodesic grid shells [5]. Since the straight element is kept straight in the in-plane direction (geodesic), the mechanism has one degree of freedom (DOF) in-plane transformation, allowing for easy control of the deployment. However, this motion produces the angle excess at the vertex and non-zero Gaussian curvature leading to frustration if the mechanism is kept in a plane. The frustration of in-plane scissor deformation effectively reproduces differential growth, which results in the out-of-plane buckling of the surface into a ruffled form.

In our mechanism, m polar scissors [6] units of different sizes are vertically connected to form a mirror-symmetric column, and n columns are connected rotationally symmetrically to form a surface of revolution (Figure 2). The shape of the i-th scissors ($i = 1, \dots m$) from the bottom of a column is defined by the short edge length r_i and the long edge length R_i, and its deployed configuration can be expressed by the lower bottom $x_i \in [0, 2r_i]$ of the isosceles trapezoid that each scissors unit spans. x_i becomes larger as the unit deploys (Figure 4). Also, the length of the upper base X_i is given by $X_i = \frac{R_i}{r_i} x_i$.

Consider one column of the entire mechanism. Then, adjacent units are related as $x_{i+1} = X_i$, so the deployment state of each module is sequentially determined once x_1 of one end of the column is determined. Because of the in-plane rigidity of members, the structure forms a 1 DOF mechanism in an intrinsic sense. The mirror symmetry of the one-column allows the columns to be connected to each other with rotational symmetry, and the entire mechanism also works in a one-DOF manner intrinsically. Since there exists a state where $x_i = X_i = 0$, the entire mechanism can be folded into a compact cylindrical shape, $x_i = 0$ for any r_i, R_i.

The curvature of the surface can be explained by the curvature of the polyline forming the boundary of the one-column (red curves in Figure 4). The Gaussian curvature of the entire surface is zero when the

polyline becomes a straight line (middle of Figure 4), positive when the polyline is convex (left side of Figure 4), and negative when the polyline is concave (right side of Figure 4). Thus, the opening and closing of the scissors deform the polyline and result in changing the intrinsic curvature of the entire surface.

We design such that the deployed state has a constant negative curvature. We compute the shapes of each unit using the constant negative curvature condition gives a relationship between the area A_i and the angle θ_i by the Gauss-Bonnet equation [4]. Here, we constructed a model with $n = 18$ and $m = 8$. In the simulation models (Section 3. and 4.), we set the lengths of the bars to

$$r_1, \ldots, r_8 = 44.1, 40.4, 36.1, 37.5, 44.9, 57.3, 74.6, 97.0 \text{ mm} \quad (1)$$

$$R_1, \ldots, R_8 = 44.1, 52.6, 52.1, 53.6, 62.1, 77.2, 98.6, 127.1 \text{ mm}. \quad (2)$$

In this model, x_1 deploys from 0 to $x_1^{\text{target}} = 28.8$ mm, when it reaches the constant negative curvature state with frills.

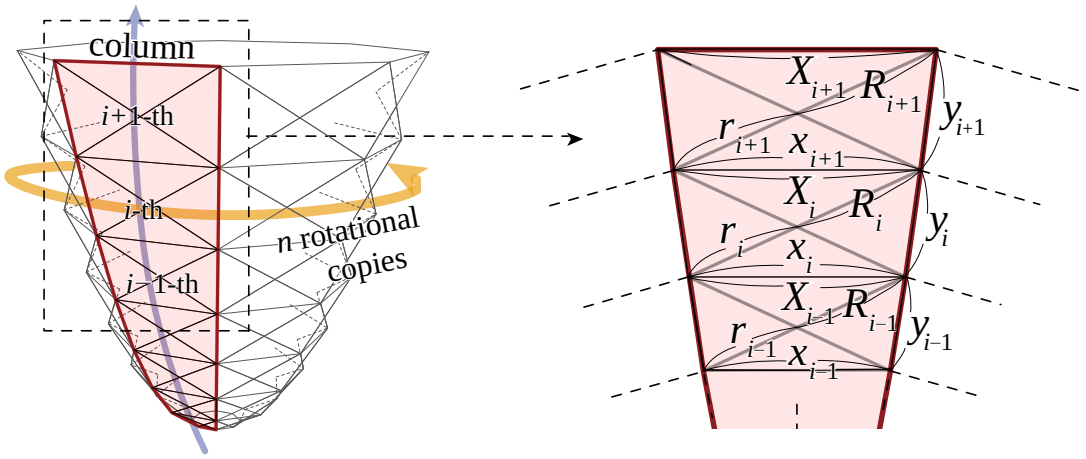


Figure 2: Notations and design parameters for the design. Left: entire structure comprising n rotational copies of one column (colored). Right: close-up view of one column.

3. Analysis of frills

We create a computational bar-and-hinge model to simulate the elastic behavior of our structure. Under this model, we first simulate and analyze the deployment process from the cylindrical state to a target frilled state. From a single simulation instance, we provide a smooth interpolation of the target surface, from which we can create a single parameter family of solutions to the obtained frilled state. We iden-

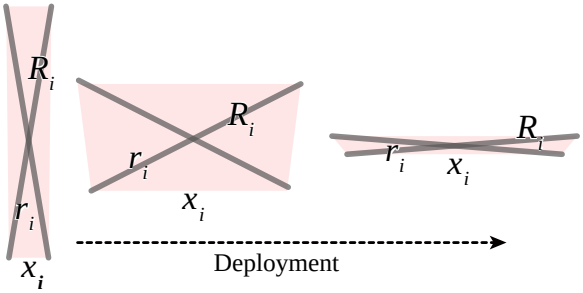


Figure 3: Change in X_i as scissors deploy.

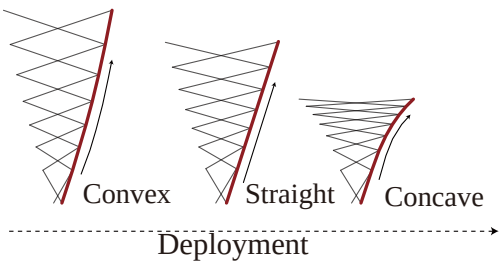


Figure 4: Change in the column's boundary polyline.

tify that these solutions have the same potential energy and that there exists a one-DOF zero-stiffness wave-like motion for a frilled state. Moreover, we show that the number of frills is determined by the proportion between the out-of-plane bending and in-plane stiffnesses.

3.1. Simulation model

Instead of directly modeling a scissor element that can bend and twist and be joined by pivots, we approximate the system as a partially homogenized shell under an equilibrium of in-plane stiffness and out-of-plane bending stiffness. Here, we modify the bar-and-hinge model [7, 8] that model the in-plane stiffness using bars (springs) and out-of-plane stiffness using hinges (angular springs). We solved the equilibrium state using *Kangaroo 2* [9] using provided goals and custom goals.

Figure 5 shows the composition of constraints in the bar-and-hinge model. To represent the in-plane stiffness, we let the unit trapezoid with a single pair of scissors consist of four bars along the diagonal scissor elements and four bars along the bases and the legs of trapezoids. We found that applying the same stiffness to all eight bars resulted in an overconstrained system that led to jaggy and unstable results. To solve this issue, we set the full stiffness to only six bars, namely the four diagonal bars and two bases, while keeping the legs' stiffness very small. Empirically, we chose 0.015 of the full stiffness bars, which makes the legs not the main element to carry the load but act as the regularization term to avoid artifacts due to discretization. For the bar elements, we used *length* in Kangaroo 2, which is a straight spring system.

To represent the out-of-plane stiffness, we use a customized *hinge* component that represents the angular springs between two triangles. The stiffness of each hinge is computed to equate with the beam with a cross-section of $w \times t$.

The following is the list of constraints, potential energy U, and the names of goals used in Kangaroo. Here, E represents Young's modulus.

1. **In-plane** The linear springs that keep each r_i, R_i, and x_i at their original length. $U_{\text{in}} = \frac{1}{2} Ewt \left(\frac{\ell - \ell_0}{\ell_0} \right)^2$, where ℓ is the length of each bar and ℓ_0 is the target length of the bar. We used [Lenght(line)]
2. **Regularization** The linear springs that regulate discretization artifacts. We keep y_i at the ideal length, but with a small value $U_{\text{reg}} = \frac{p}{2} Ewt \left(\frac{\ell - \ell_0}{\ell_0} \right)^2$, where $p = 0.015$. [Length(line)]
3. **Out-of-plane** The angle springs that keep the quadrangles planar to represent the out-of-plane stiffness. $U_{\text{out}} = \frac{1}{2} \frac{Elt^3}{8h} \rho^2$, where ρ is the fold angle between two triangles, l is the length of the hinge, and h is the sum of heights of the triangles sharing the base. [Hinge]
4. **Boundary condition** Constraints that keep the bottom vertices of the mechanism in an ideal position on the same plane. [Anchor]

Note that our model is not accurate enough to predict the exact load and energy from the given dimension. Instead, the model focuses more on how the overall behavior is dimensionally affected by parameters. Our system is governed by the balance between the in-plane and out-of-plane stiffness of the surface, where the former is proportional to the thickness t and the latter is proportional to the cube of the thickness t^3. Therefore, we vary t to calibrate and control the system's behavior. Specifically, our model computed with the thickness of $t = 3\,\text{mm}$ reproduced a similar result to our fabricated physical models with thinner material $t = 1\,\text{mm}$. Therefore, we varied t from $2\,\text{mm}$ to $4\,\text{mm}$ and performed the rest of the simulation.

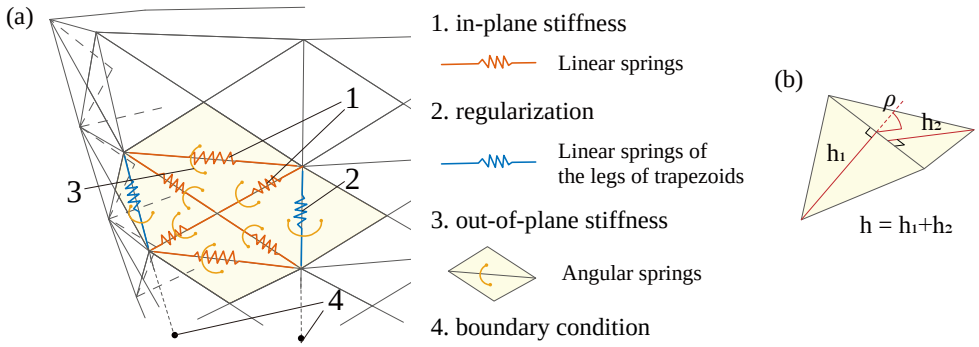


Figure 5: (a) Constraint conditions of the simulation model. (b) The fold angle ρ and heights of the triangles h.

3.2. Deployment results

We simulated the deployment process from the rotationally symmetric state to the desired ruffled form, using the model created as described in Section 3.1.. We changed x_0 from $14.4\,\mathrm{mm}$ (rotationally symmetric state) to $28.8\,\mathrm{mm}$ (fully deployed state) in 1000 steps; for each step, we performed a sufficiently large number of steps (average 35.6 steps) of iterations in Kangaroo 2 solver, to emulate a quasi-static process.

For all parameters $t = 2, 3, 4\,\mathrm{mm}$, the mechanism first deploys while keeping the rotational symmetry; but when it reaches a limit, the mechanism loses its rotational symmetry and forms a ruffled surface. Figure 6 shows the potential energy of the mechanism associated with this symmetry-breaking buckling process. We plot the graphs with the x_1 on the horizontal axis and the potential energy on the vertical axis. First, the mechanism deploys without any in-plane energy introduced. Just after x_1 passes the limit of the geometric model with rotational symmetry [4], the in-plane potential energy increases rapidly, and the structure reaches a highly frustrated state. Then, the symmetry breaks with a reduction of the in-plane potential energy and an increase of out-of-plane potential energy.

Typically, the resulting forms have an N-fold rotational symmetry, i.e., there are N repetitions of ups and downs within one cycle. We call this number N the frill number N. We found that the frill numbers differ for different thicknesses and change during deployment (Figure 6).

Specifically, for (a) $t = 2\mathrm{mm}$ case, the symmetry changed from $N = \infty$ (circular symmetry) to $N = 4$. (b) for $t = 3\mathrm{mm}$, the symmetry first changed from $N = \infty$ to $N = 4$ and took many steps of iteration after the deployment to change into $N = 3$. (c) for $t = 4\mathrm{mm}$, the symmetry moved from $N = \infty$ to $N = 4$, and then $N = 2$. Although the final stable state is affected by the thickness, the results suggest the existence of (near) metastability at different frill numbers.

3.3. Frill number analysis

We examine the metastability of and the transition between the states with 2, 3, and 4 frills, i.e., if they are the global or local minimum energy states for different thicknesses. To compare the energy states of the mechanism with different frill numbers, we run the same simulation with the initial state of frill number values of 2, 3, and 4 computed from different thickness settings. A typical transition process was in Figure 7, where the horizontal axis shows the timestep and the vertical axis shows the potential energy. First, in ~ 200 steps, the energy drops and reaches the plateau state while keeping the shape almost identical. However, later with 5 to 10 times more steps, the form falls into a different local minimum energy state but with the same frill numbers. High hinge fold angles suggest that these states

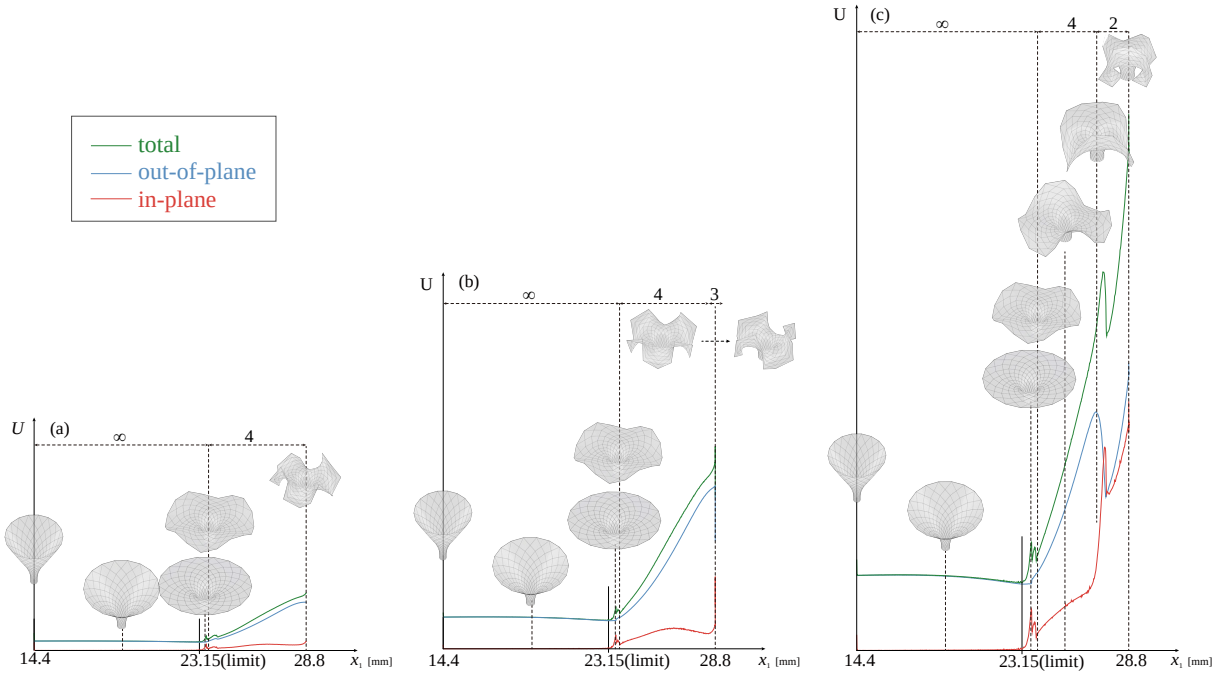


Figure 6: Plot of the potential energy U respect to the shift change x_i. Here we use $\sum U_{\text{in}} + \sum U_{\text{reg}}$ is used as the in-plane energy, and $\sum U_{\text{out}}$ is used as the out-of-plane energy.(a) $t = 2\text{mm}$, $N = \infty \to 4$, (b) $t = 3\text{mm}$, $N = \infty \to 4 \to 3$, (c) $t = 4\text{mm}$, $N = \infty \to 4 \to 2$. The vertical short bar at 23.15 mm is the theoretical limit for the geometric model with rotational symmetry.

after transition may not be a real phenomenon but an artifact of our bar-and-hinge model.

Figure 8 compares the potential energy of these plateau states for different t. This suggests that the chosen state in the forward deployment state is not necessarily the minimum energy state. However, it requires a finer elastic model to fully describe the metastability of the structure.

3.4. Interpolated surface and phase-shifting motion

Macroscopically, the original cylindrical configuration has a circular symmetry, i.e., it can be rotated at an arbitrary angle about an axis $N = \infty$. Also, the in-plane deployment that aims at the constant Gaussian curvature everywhere has the same intrinsic symmetry. However, the wave-like frilled form loses this continuous symmetry and becomes N-fold symmetric. Because of the original intrinsic symmetry, there is a one-parameter family of possibilities for where the mountain and valley of the frills are located, thus the "phase" of the frills. We model such a phase shift.

We first construct an interpolated parametric surface model from the discrete simulation result. From the grid of points on the corner of trapezoids, $\mathbf{p}(i, j)$ for $i = 0, \ldots, n-1 \mod n$ and $j = 0, \ldots, m$, we interpolate them with the periodic NURBS surface $\mathbf{f}(u, v)$ for $u \in [0, 2\pi)$ and $v \in [0, 1]$, such that $\mathbf{p}(i, j) = \mathbf{f}\left(\frac{2\pi i}{n}, \frac{j}{m}\right)$ (Figure 9 (a)).

We first align the center to the z axis and use cylindrical coordinate $\mathbf{f} = (f_\theta, f_r, f_z)$. Then, the N-fold rotational symmetry of the simulated result can be verified by the following operation:

$$\begin{pmatrix} f_\theta(u + 2\pi/N, v) \\ f_r(u + 2\pi/N, v) \\ f_z(u + 2\pi/N, v)) \end{pmatrix} = \begin{pmatrix} f_\theta(u, v) + 2\pi/N \\ f_r(u, v) \\ f_z(u, v)) \end{pmatrix}. \tag{3}$$

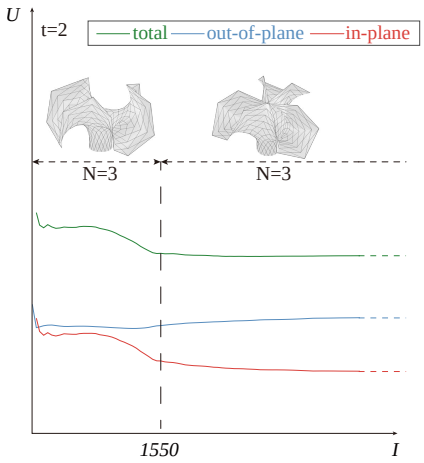


Figure 7: Plot of the potential energy U with respect to the steps of iteration for $t = 2\text{mm}$ starting from $N = 3$ initial state. The form transitions into another state with $N = 3$ symmetry.

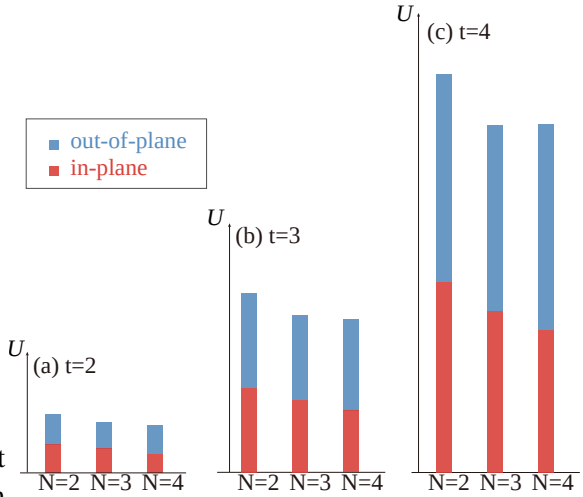


Figure 8: The potential energy of differ-ent N

Now, the phase of the frills of the interpolated surface can be shifted by angle δ by the following map $\mathbf{f} \to \mathbf{f}'$ (Figure 9 (b)):

$$\begin{pmatrix} f'_\theta(u,v) \\ f'_r(u,v) \\ f'_z(u,v)) \end{pmatrix} = \begin{pmatrix} f_\theta(u-\delta,v)+\delta \\ f_r(u-\delta,v) \\ f_z(u-\delta,v)) \end{pmatrix}. \tag{4}$$

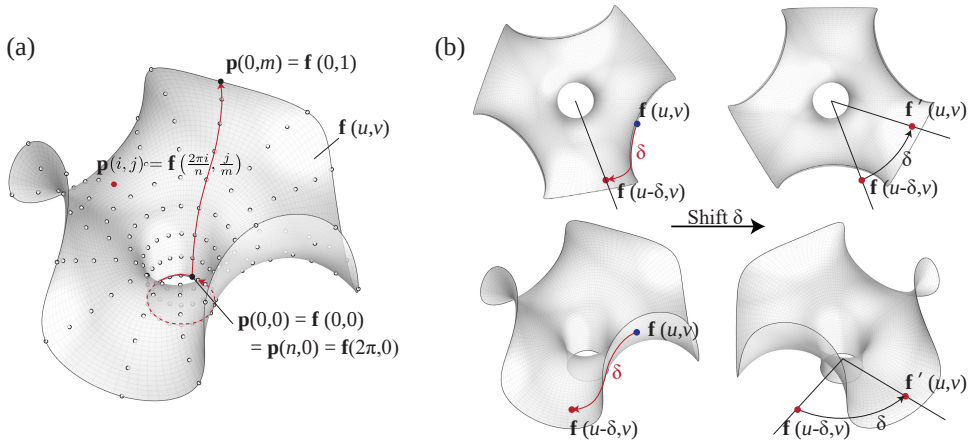


Figure 9: (a) The grid point $\mathbf{p}(i,j)$ and interpolated surface $\mathbf{f}(u,v)$. (b) Shifting the phase of the frills by angle δ by map $\mathbf{f} \to \mathbf{f}'$.

Here, we use (u,v) to keep track of the positions of the actual material, i.e., a point at $\mathbf{f}(u,v)$ moves to $\mathbf{f}'(u,v)$ by this phase shifting operation. Note that the addition of δ to the angle represents the rotation of the image of the surface, while the subtraction of δ to the parameter represents that the material itself stays not globally rotated. After this operation, we can sample the point coordinate $\mathbf{p}'(i,j) = \mathbf{f}'\left(\frac{2\pi i}{n}, \frac{j}{m}\right)$ to recover the scissors structure with a phase-shift.

We performed the bar-and-hinge simulation of Section 3.1. using the shifted scissors structure as the initial state while adding weak springs to bring the points to $\mathbf{p}'(i,j)$. Figure 10 shows the plot of the

strain energy of the structure with respect to the shift change of $\delta \in [0, 360°)$. We experimented for $N = 2, 3, 4$ cases with a fixed thickness of $t = 3\text{mm}$ with a $n = 18$ model.

We observed a nearly horizontal plot of energy with 18 bumps of in-plane energy. These bumps are attributed to the discrete structure caused by the radial division by $n = 18$ The amplitude of bumps is large for $N = 2$ and $N = 3$ and smaller for $N = 4$. The higher amplitude of the bumps in $N = 2$ and 3 may come from that n is the integer multiple of N when the hinge elements are aligned at the peaks of the ruffles, so the effect of the discretization is strongly reflected in the overall energy. It is still open if this effect is an artifact of computation or may appear in the real object; in the latter case, choosing the number of elements that are not integer multiple of N may lead to a smoother actuation.

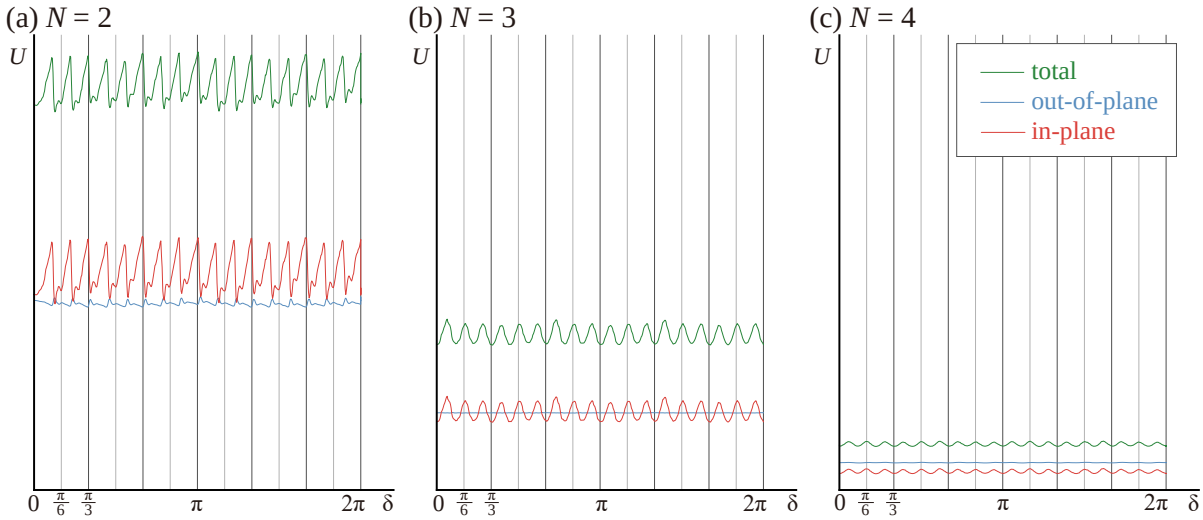


Figure 10: Plot of the strain energy with respect to the shift change of δ. (a) $N = 2$, (b) $N = 3$, (c) $N = 4$.

4. Phase change control

4.1. Concept

As simulated in Section 3.3, the wave-like frilled form after deployment is not stable in one position, allowing the frilled position to be shifted with almost zero force. This motion is a wave-like motion along the perimeter. We propose a method to control such motion by applying a tensile force to the perimeter of the structure. Specifically, the threads that pull the structure together are attached so that they connect the hinges on the perimeter with points on the central axis. We generate such motion by moving the end of the thread on the central axis side vertically to apply tensile forces.

To allow for a smooth motion, we apply the idea of a three-phase alternation. Specifically, we group the vertical movements into three groups $g = 0, 1, 2$ with different phases separated by $1/3$ of the wavelength. The threads in the same group are placed every $2\pi/N$, so there is a $3N$ threads in total (Figure 11).

4.2. Control path generation

We identify the path of the vertical movement of the endpoint on the central axis side of the thread that is required to generate a wave-like motion. We use the phase-shifted interpolated surface of a simulated

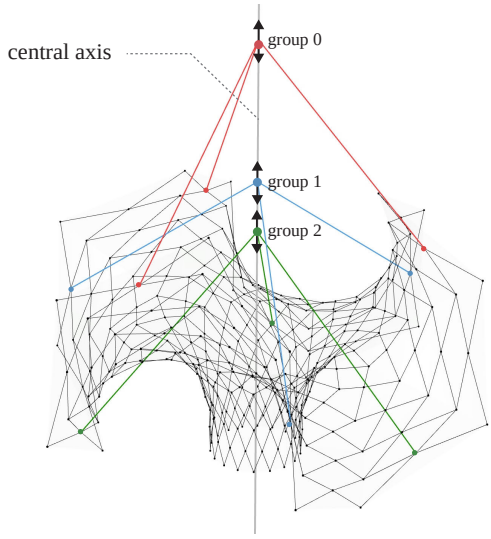


Figure 11: Vertical movements in three groups.

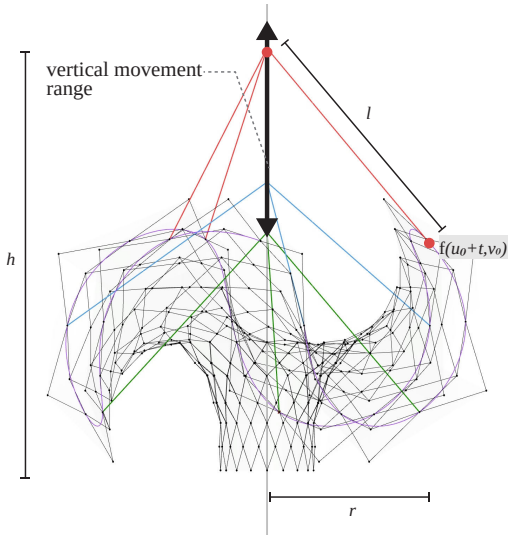


Figure 12: Notation to determine the vertical movements of the endpoints over time.

result $\mathbf{f}'(u, v)$ given in Section 3.4. The $3N$ points of control are given by

$$(u, v) = \left(\frac{2\pi}{N}n + g, 1\right), \tag{5}$$

where $n = 0, 1, \ldots, N-1$ and $g = 0, 1, 2$. Here,the height h of the endpoints on the central axis side at time t is given by the following equation (Figure 12):

$$h = \sqrt{l^2 - r_f(u_0 + t, v_0)^2} + z_f(u_0 + t, v_0), \tag{6}$$

where l is the length of the thread. Using this control, the thread is expected to be in tension at all times without sagging. The trajectory when t is varied from 0 to 2π is shown in Figure 11. By following this trajectory and moving the points on the central axis of the thread up and down, the structure can be smoothly moved in a wave motion. Note that the wavelengths of three groups with different phases are shifted by $1/3$.

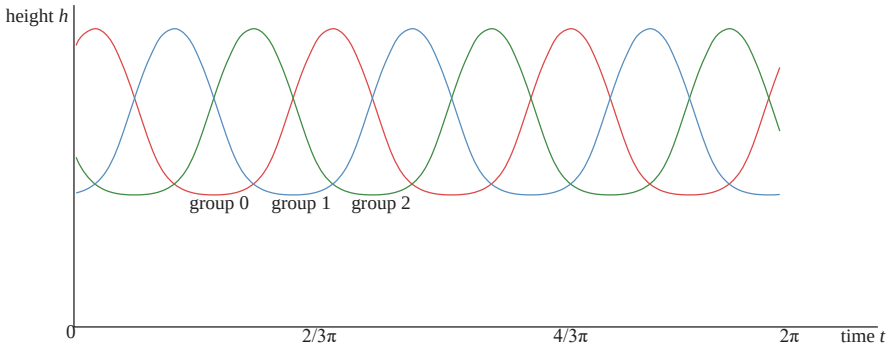


Figure 13: The height change of points on the central axis of the thread.

4.3. Evaluation by simulation

We simulate the wavy motion of the structure that is generated in the previous section. This simulation is based on Section 3.1., with the following constraints and mechanical properties added to generate such a motion. The material is assumed to be POM with Young's modulus of $E = 3 \times 10^2 \mathrm{N/mm^2}$ and the density of $1.41\,\mathrm{g/cm^3}$.

Gravitational force To approximate the deformation of the physical model, a force in the direction of gravity is applied to all pivots. For simplicity, the force applied to a single pivot is defined as the weight of the entire structure divided by the number of pivots. [load]

Tensile member A tensile member is represented as two serially connected linear springs. The middle split prevents compressive force from being applied. We used [Length(line)].

We simulated the motion for a 3-frilled model (Figure 14) and observed a continuous wave-like motion without any significant sagging of all tensile members. When actuated, the perimeter endpoints oscillate in a figure of 8.

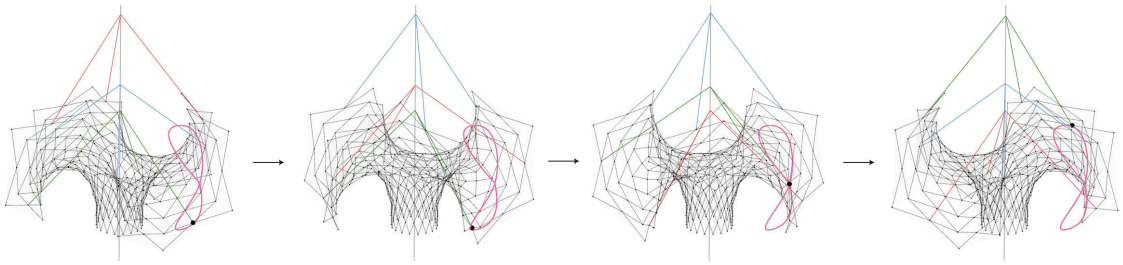


Figure 14: Sequential images of the phase change. The perimeter pivot draws like a figure of 8.

5. Fabrication / pavilion design

We designed a meter-scale pavilion that can be compactly folded and transported (Figure 1). Our structure is a 1.7 times scaled version of the simulation model shown in (1) and (2). It transforms into an elongated cylindrical shape when open, it is about $2000\,\mathrm{mm}$ in diameter, and when closed, it is about $200\,\mathrm{mm}$ in diameter. The total weight of the structure is $1.8\,\mathrm{kg}$.

We chose $1\,\mathrm{mm}$ thick sheets of vulcanized fiber (HB-77, Hokuetsu Toyo Fibre) sheets as sustainable, lightweight, and easy-to-fabricate materials. This material is made of cellulose fibers treated with chemicals to break them down to the nano-level. The fibers are tightly intertwined, making the material hard and tenacious. It is also highly biodegradable and has a smaller environmental footprint than plastics and metals. For fabrication, we utilize the property that softens and becomes plastic when moist while it hardens and becomes elastic when dry.

We made our design modular; we assembled multiple units that can be removed and added depending on the required size or partially replaced to repair the damage to the structure. All pavilion components are cut using a laser cutting machine. The maximum size of the components is determined by the size of the machine ($600\,\mathrm{mm} \times 450\,\mathrm{mm}$).

The module design is inspired by the techniques of making pivots in a pop-up book. A polar scissors unit is composed of two types of members; one is a bar-shaped member, and the other is a cross-shaped connecting member (Figure 15). The bar has three holes (top, center, and bottom) where a cross-shaped hinge slides in. The tip of the cross-shaped hinge is tapered to prevent it from falling out of the hole.

When assembling, the cross-shaped hinge is soaked in water before passing through the hole. After the joint is passed, the hinge module is dried using an iron (Figure 1) so that it becomes hard again.

The scissor units of 8 different sizes are rotationally symmetrically connected in 18 rows to form a cylindrical shape. Finally, the nylon threads are passed through the diagonals of the units, which are used to control the deployment of the pavilion (Figure 16). Note that the diagonal threading system for deployment is separate from the system that controls the wave-like motion. The control system for wave-like motion is still under development.

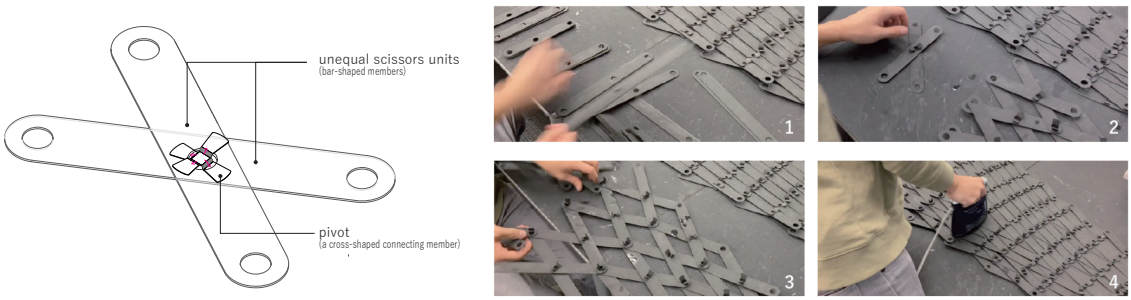


Figure 15: Joint details and assembly process.

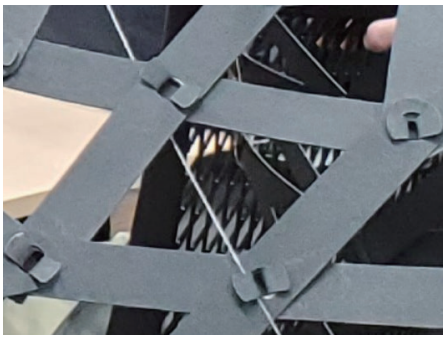


Figure 16: Diagonal threads to control the deployment.

6. Outlook

We envision that the structure we propose can be used for a variety of architectural applications, taking advantage of its characteristic movement. For example, our structure may be used as a work booth in an office space, reducing the oppression of the typical work booth closed off by walls. We hope that the bioinspired and biophilic nature of the structure improves the user's ability to concentrate, reduce stress, and increase intellectual productivity (Figure 17).

We still have future works to be done. As for theory, the metastability of the N-fold frills is still not fully analyzed. A more accurate model may be necessary to explain these interesting phenomena. As for practice, the physical control of phase-shifting motion is still a challenge we plan to accomplish.

Acknowledgments

This project is supported by NIKKEN Sekkei. We thank our colleagues who joined the brainstorming workshop for this project. We thank Shintaro Ueno, Masaharu Kii, Mei Yaya, and Hibiki Totsuka for the help in manufacturing the models.



Figure 17: Personal booth in an office space.

References

[1] I. NERVOUS SYSTEM. Nervous System blog. https://n-e-r-v-o-u-s.com/blog/ ?p=6721.

[2] P. M. Sobota and K. A. Seffen. Nonlinear growing caps. In *Proceedings of IASS Annual Symposia*, volume 2018 of number 14, pages 1–8. International Association for Shell and Spatial Structures (IASS), 2018.

[3] K. K. Yamamoto, T. L. Shearman, E. J. Struckmeyer, J. A. Gemmer, and S. C. Venkataramani. Nature's forms are frilly, flexible, and functional. *The European Physical Journal E*, 44(7):95, 2021.

[4] F. Ono and T. Tachi. Growth deformation of surface with constant negative curvature by bending-active scissors structure. In *Proceedings of the International Association for Shell and Spatial Structures 2022*, 2022.

[5] S. Pillwein, K. Leimer, M. Birsak, and P. Musialski. On elastic geodesic grids and their planar to spatial deployment. *ACM Transactions on Graphics*, 39:125, July 2020. DOI: 10.1145/3386569.3392490.

[6] F. Escrig. Expandable space structures. *International Journal of Space Structures*, 1(2):79–91, 1985.

[7] E. Grinspun, A. N. Hirani, M. Desbrun, and P. Schröder. Discrete shells. In *Proceedings of the 2003 ACM SIGGRAPH/Eurographics symposium on Computer animation*, pages 62–67. Citeseer, 2003.

[8] E. Filipov, K. Liu, T. Tachi, M. Schenk, and G. H. Paulino. Bar and hinge models for scalable analysis of origami. *International Journal of Solids and Structures*, 124:26–45, 2017.

[9] D. Piker. https://github.com/Dan-Piker/K2Goals.

IASS 2023
July 10–14 Melbourne
Integration of Design and Fabrication

Proceedings of the IASS Annual Symposium 2023
Integration of Design and Fabrication
10–14 July 2023, Melbourne, Australia
Y.M. Xie, J. Burry, T.U. Lee and J. Ma (eds.)

Coupled thick-panel origami tubes along creases for stiff deployable structures

Sunao TOMITA[a], Kento SHIMANUKI[a], Kazuhiko UMEMOTO[a], Atsushi KAWAMOTO[a], Tsuyoshi NOMURA[a],Tomohiro TACHI*

* The University of Tokyo
3-8-1 Komaba, Meguro-Ku, Tokyo, Japan
tachi@idea.c.u-tokyo.ac.jp

[a] Toyota Central R&D Labs., Inc., 41-1, Yokomichi, Nagakute, Aichi 480-1192, Japan

Abstract

The coupling of origami tubes realizes extremely stiff yet deployable structures used for temporary structures, such as emergency shelters and infrastructure. However, thickness accommodation is a crucial problem in the coupling of thick-panel origami tubes. To solve this problem, we propose the coupling of origami tubes along the creases for easy coupling of thick-panel origami tubes. As thick origami tubes can generate one-degree-of-freedom (DOF) motions based on a hinge-shift technique, coupling of origami tubes mirrored along creases also provides one-DOF motions because of the mirror symmetry along the creases. Therefore, the proposed coupling method facilitates the fabrication of coupled thick-panel origami tubes using existing hinges, such as piano hinges or fabrics. To demonstrate that the proposed coupling method contributes to the high stiffness of the coupled origami tubes, an eigenvalue analysis of linear dynamical systems defined by bar and hinge models is performed. A wide gap in eigenfrequencies is obtained between the one-DOF mode (i.e., 7th mode) and elastic modes (i.e., higher than the 7th mode), indicating that the one-DOF motion provides flexible deployment, and the elastic deformations retain high stiffness throughout the deployment process. In addition, meter-scale coupled origami tubes are fabricated based on the proposed coupling method.

Keywords: origami tubes, stiff deployable structures, bar and hinge model

1. Introduction

Deployable structures play an important role in the rapid and easy construction of contemporary structures, such as solar sails [1], emergency shelters [2], and infrastructures [3, 4, 5]. In these applications, it is necessary to design the deployable structures to have enough mechanical properties, such as load-bearing capability, after development.

Geometrical designs based on coupled origami tubes are effective in adding unique mechanical properties to deployable structures. Furthermore, coupling of Miura-ori provides lockable morphing mechanisms [6]. In previous studies, origami metamaterials with negative Poisson's ratios [7] and extremely stiff deployable structures, referred to as zipper-coupled tubes [8], were proposed based on Miura ori. Tachi-Miura polyhedra are also composed of origami tubes [9, 10, 11], which lead to auxeticity [12],

Copyright ©2023 by Sunao TOMITA, Kento SHIMANUKI, Kazuhiko UMEMOTO, Atsushi KAWAMOTO, Tsuyoshi NOMURA and Tomohiro TACHI. Published in the Proceedings of the IASS Annual Symposium 2023 with permission.

load-bearing capability [13], and high- energy absorption [14]. In these origami structures, origami tubes are coupled along origami panels. Therefore, deployability is ensured when origami tubes are fabricated using thin plates that are difficult to fabricate using thick panels.

Construction using thick panels is necessary to enhance the load-bearing capability of deployable structures [15]. In previous studies, although thickness accommodation for thick-panel origami was investigated [16, 17, 18], thickness accommodation for coupling origami tubes has not yet been fully established.

This study presents the coupling of origami tubes mirrored by creases. Using thick origami tubes that generate one-degree-of-freedom (DOF) motion based on a hinge-shift technique, the coupling of origami tubes mirrored along the creases also provides one-DOF motion because of the mirror symmetry along their creases. Therefore, the proposed coupling method facilitates the easy fabrication of coupled thick-panel origami tubes using existing hinges. Furthermore, because the rotational direction of each coupled tube is the same as that of the zipper-coupled tubes, the proposed coupling provides high stiffness. To demonstrate this observation, an eigenvalue analysis of linear dynamical systems defined by bar and hinge models [19, 20, 21, 22] was performed to evaluate the stiffness via eigen frequencies. Furthermore, the design concept for the pavilion is explained, and a prototype of a meter-scale coupled tube is fabricated using wooden panels and fabric hinges.

2. Geometry of coupled origami tubes

2.1. Miura-ori tube

This subsection describes the geometry of Miura-ori tubes. The dimensions of Miura-ori unit cell are defined as shown in Figure 1 (a). Using the length of Miura-ori a, b, the internal angle of the parallelogram α, and the half dihedral angle $\theta \in [0, \pi/2]$, the dimensions of the unit cells are defined as follows:

$$L_x = 2b\frac{\cos\theta\tan\alpha}{\sqrt{1+\cos^2\theta\tan^2\alpha}}, \tag{1}$$

$$L_y = 2a\sqrt{1-\sin^2\theta\sin^2\alpha}, \tag{2}$$

$$H = 2a\sin\theta\sin\alpha, \tag{3}$$

and

$$V = b\frac{1}{\sqrt{1+\cos^2\theta\tan^2\alpha}}. \tag{4}$$

The Miura-ori tubes were created by coupling Miura-ori to that mirrored along x-y plane, as shown in Figure 1 (b).

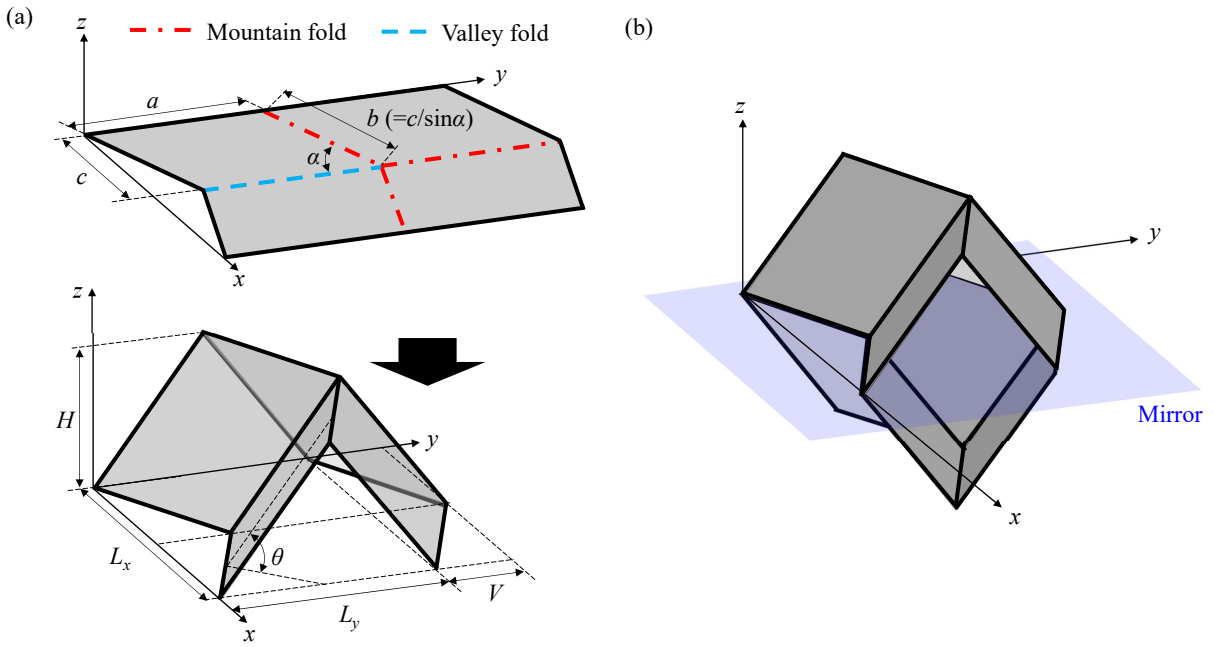


Figure 1: Geometry of Miura-ori tube (a) Unit cell of Miura-ori sheet (b) Miura-ori tube created by coupling mirrored Miura-ori sheet.

2.2. Coupled origami tubes along creases

This subsection briefly introduces the geometries of coupled Miura-ori tubes consisting of five unit cells with parameters $a = 1$, $c = 1$, and $\alpha = 55^o$. Examples of coupled tubes along faces, i.e., aligned coupled tubes and zipper-coupled tubes, introduced by Filipov et al. [8] are shown in Figure 2 (a) and (b), respectively. To avoid face contact in the coupling of origami tubes, this study proposes coupling tubes along the creases, as shown in Figure 2 (c). The coupled tubes are composed of Miura-ori tubes mirrored along the creases, providing reflection symmetry along the creases, as shown in XY-plane in Figure 2 (c).

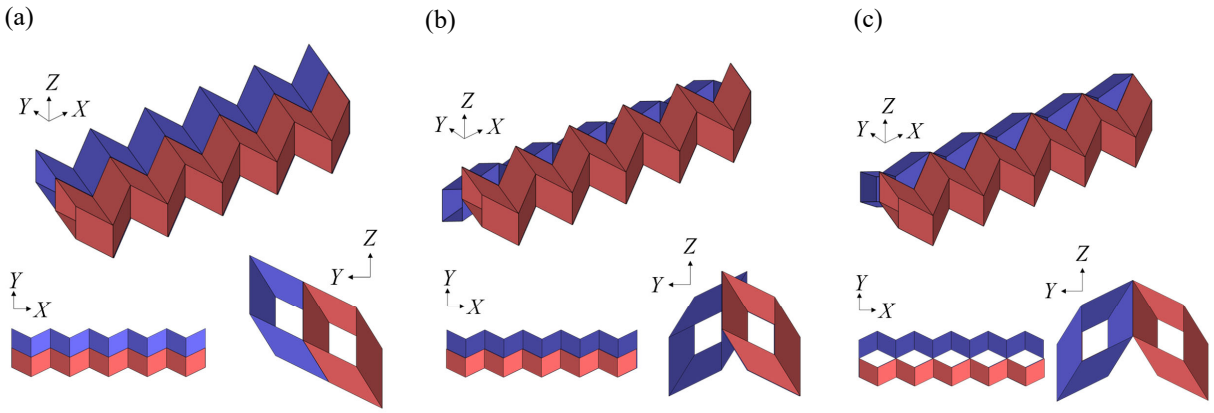


Figure 2: Geometry of coupled Miura-ori tubes. (a) Coupling aligned Miura-ori tubes. (b) Coupling zipper Miura-ori tubes. (c) Coupling mirrored Miura-ori tubes along creases.

2.3. Thickness accommodation

The thickness accommodation of mirror-coupled tubes and their motions are introduced. Tachi discussed the thickness accommodation for Miura-ori tubes using hinge-shift techniques, which provide flat foldability, rigid foldability, and one-DOF motion using thick panels [23]. Based on the thickness accommodation, the mirrored geometries along the creases in the proposed coupled tubes also retain one-DOF motion owing to the mirror symmetry along the coupled creases, as shown in Figure 3. Furthermore, the cross-sections of the coupled tubes have opposite rotations of the cross-section in the Miura-ori tubes, as shown in Figure 4. These opposite directions of rotation occur in zipper-coupled tubes and contribute to the high stiffness of coupled tubes [8]. Therefore, the proposed coupling leads to not only the realization of one-DOF motions but also the high stiffness of deployable structures.

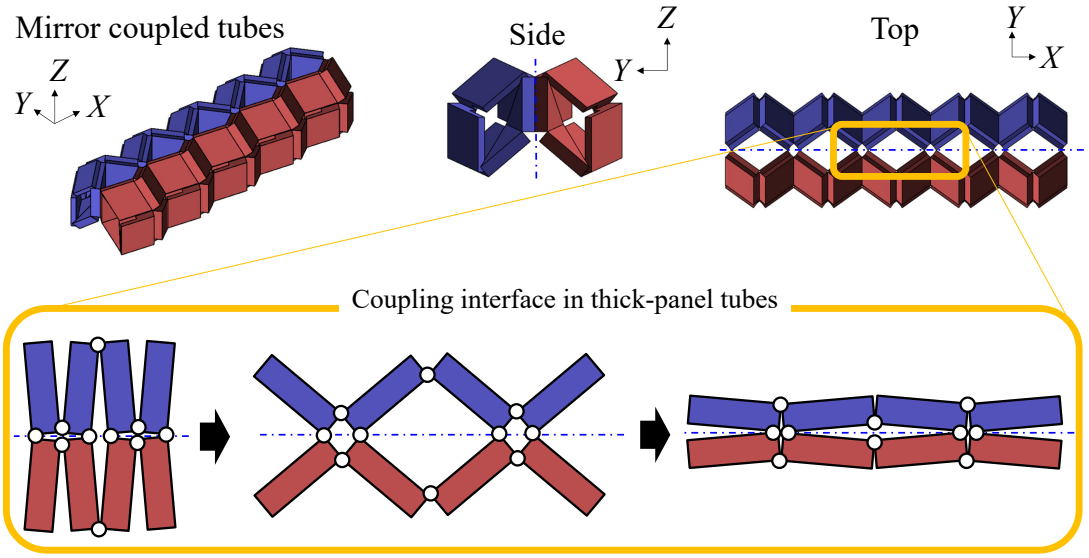


Figure 3: Motion of thick panels at the interface of coupling tubes. The mirror symmetry along the creases retains one-DOF motion after the coupling of Miura-ori tubes.

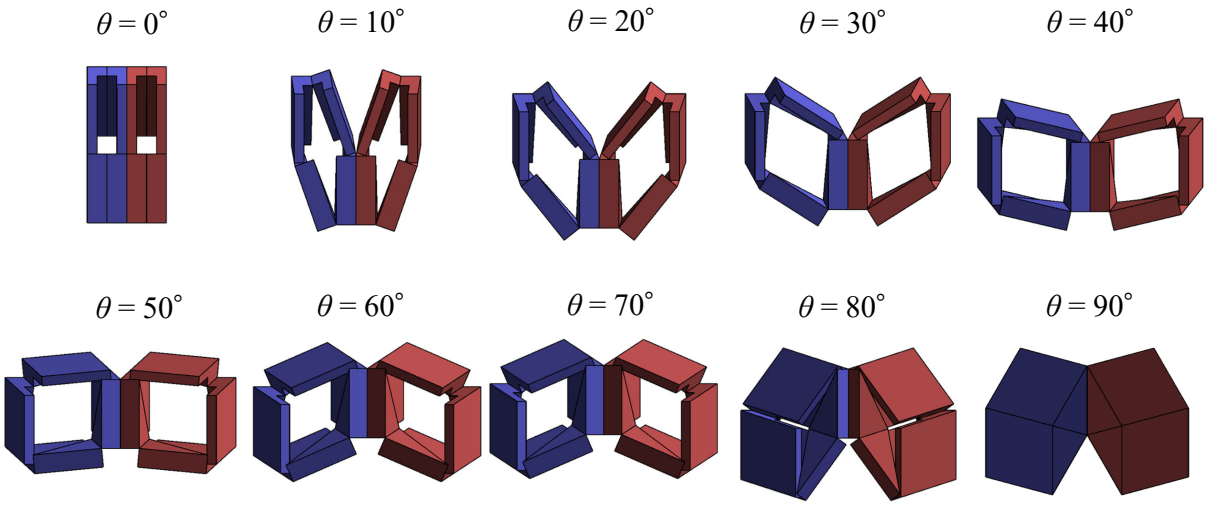


Figure 4: Motions of the cross-section of coupled tubes. The red and blue tubes rotate in opposite directions.

3. Stiffness of coupled origami tubes

3.1. Bar and hinge models for eigenvalue analysis

To evaluate the stiffness of the origami tubes, eigenvalue problem defined using the stiffness and mass matrices $\mathbf{K}$ and $\mathbf{M}$ are solved, as follows:

$$\mathbf{K}\mathbf{v}_i = \lambda_i \mathbf{M}\mathbf{v}_i, \tag{5}$$

The bar and hinge models are constructed using the N5B8 approach that expresses their panels using five nodes and eight bars. Eigenvalues λ_i and eigenmodes $\mathbf{v}_i$ are associated with the stiffness of each deformation. The mass matrix $\mathbf{M}$ is defined as a diagonal matrix composed of concentrated masses, assuming that the mass of the panels is equally distributed on each node. The stiffness matrices of the bar and hinge models are implemented based on MERLIN developed in [21, 22]. The geometry of the Miura-ori tube is presented in Subsection 2.2.. The Young's modulus, density, Poisson's ratio, and thickness of the panels are 10^6, 1, 1/3, 0.01 used in [8], respectively. The scaling factor of the stiffness of the hinges along the creases is set to 40, as used in [20].

3.2. Stiffness in basic coupled pattern

As shown in Figure 5 (a), the aligned-coupled tubes have small gaps between the one-DOF modes (i.e., 7th mode), and torsional modes appear in the 8th and 9th modes. However, zipper-coupled and the proposed coupled tubes have large gaps between the one-DOF mode and elastic modes, as shown in Figure 5 (b) and (c), because the opposite rotations of the cross-section in the Miura-ori tubes cancel each torsional deformation. The wide gaps indicate that the one-DOF motion provides flexible deployment, and the elastic deformations retain a high stiffness throughout the deployment process. Therefore, the proposed coupling method enables the easy coupling of thick-panel Miura-ori tubes without losing the unique mechanical properties of zipper-coupled tubes.

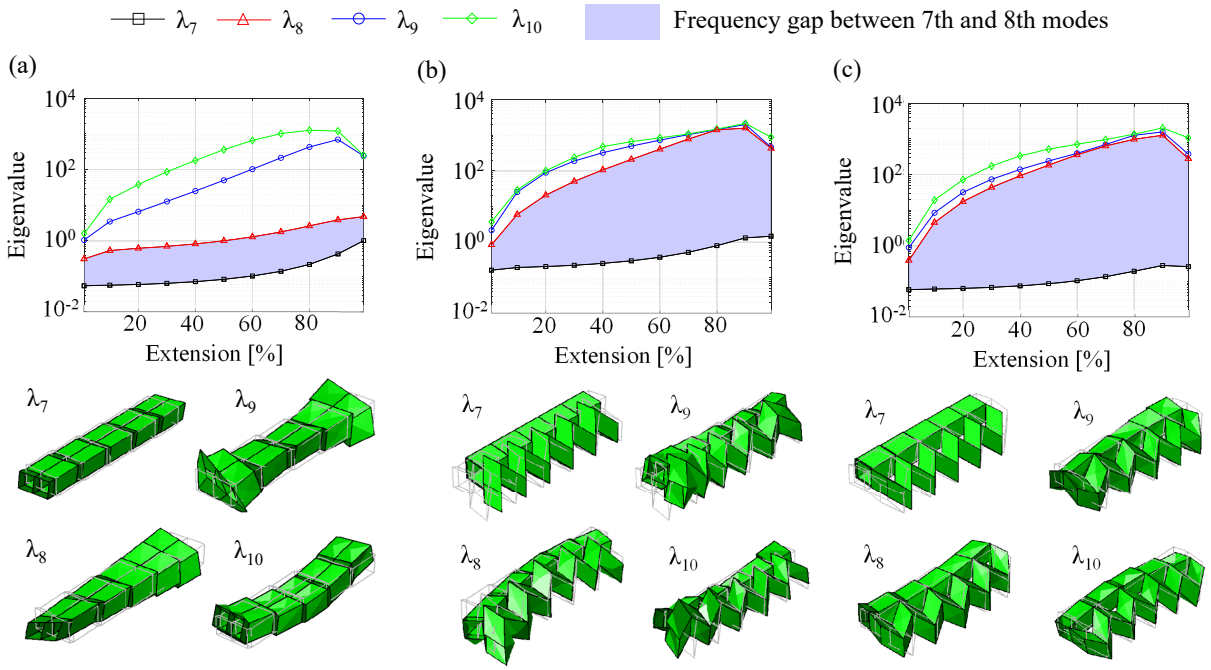


Figure 5: Eigenvalues of bar and hinge models. (a) Coupling the aligned Miura-ori tubes does not contribute to increasing the eigen frequency of torsional modes, such as 8th and 9th modes. (b) Coupling zipper Miura-ori tubes and (c) Coupling mirrored Miura-ori tubes along creases having a large frequency gap between the 7th and 8th modes.

4. Fabrication using thick panels

4.1. Concept of pavilion

As discussed in the previous section, the proposed coupling leads to high stiffness, flat-foldability, rigid-foldability, and one-DOF motions. These characteristics facilitate high transportability and the rapid construction of stiff structures. We demonstrate the deployment of 3-meter-high coupled tubes from a suitcase (Figure 6) to clearly demonstrate these key concepts to the audience in the pavilion. Although the coupled tubes are fabricated using thick panels, the one-DOF motion of the Miura-ori tubes was maintained, and the tubes were completely folded by appropriate thickness accommodation. The designed structure of the pavilion significantly affects our understanding of the compact foldability and novel mechanical properties of the proposed structures.

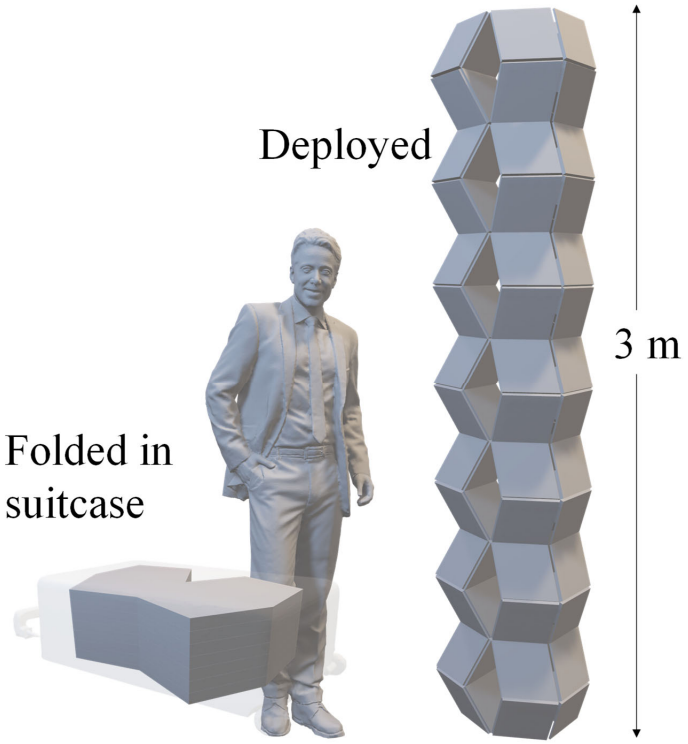


Figure 6: Design for pavilion. The deployment of 3-meter-high coupled tubes from a suitcase is demonstrated.

4.2. Prototype of fabricated coupled tubes

As a prototype of the pavilion, coupled origami tubes were fabricated on a meter scale using panels and fabric hinges. The unit of Miura-ori tube is defined by Miura ori with parameters $a = 350$ mm, $c = 350$ mm, and $\alpha = 75^o$. The tubes consisted of three Miura-ori tubes. The materials of the panels and fabric hinges were 12-mm-thick wooden panels and 0.5-mm-thick nylon sheets, respectively. The origami tubes were coupled using nylon sheets for hinges. Therefore, the coupling interfaces behave similar to hinges, and one-DOF motions are retained after coupling.

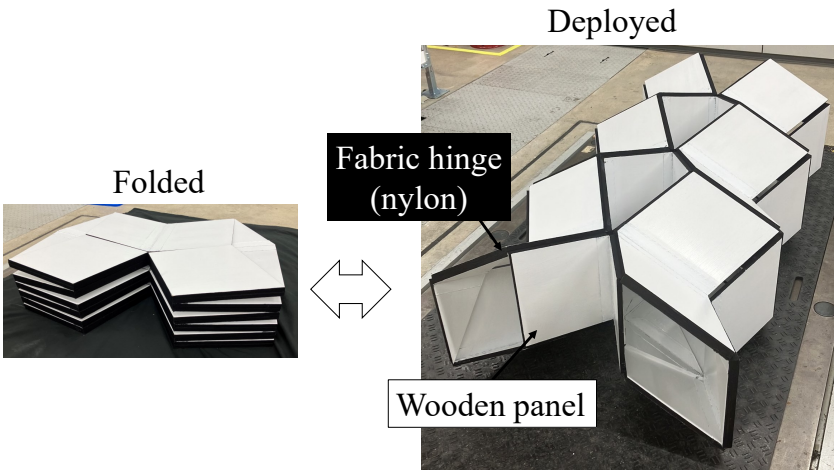


Figure 7: Coupled Miura-ori tubes fabricated by wooden panels

5. Conclusion

We present the coupling of Miura-ori tubes mirrored along their creases for easy thickness accommodation during the coupling of thick-panel Miura-ori tubes. The proposed coupling leads to high stiffness owing to the opposite rotation of the cross-sections. To demonstrate high stiffness, we indicated wide frequency gaps between the one-DOF and elastic modes via an eigenvalue analysis of the bar and hinge models. To express the compact foldability and high stiffness of the proposed structures, a pavilion design was proposed, and a proto-type of the pavilion was fabricated using thick panels and fabric hinges.

References

[1] K. Miura. Method of packaging and deployment of large membranes in space. *The Institute of Space and Astronautical Science report*, 618:1–9, 1985.

[2] D. Melancon, B. Gorissen, C. J. García-Mora, C. Hoberman, and K. Bertoldi. Multistable inflatable origami structures at the metre scale. *Nature*, 592(7855):545–550, 2021. DOI: 10.1038/s41586-021-03407-4.

[3] I. Ario, M. Nakazawa, Y. Tanaka, I. Tanikura, and S. Ono. Development of a prototype deployable bridge based on origami skill. *Automation in Construction*, 32:104–111, 2013. DOI: 10.1016/j.autcon.2013.01.012.

[4] K. Chanthamanivong, I. Ario, and Y. Chikahiro. Smart design of coupling scissors-type bridge. *Structures*, 30:206–216, 2021. DOI: 10.1016/j.istruc.2020.12.044.

[5] Y. Chikahiro, I. Ario, P. Pawlowski, C. Graczykowski, and J. Holnicki-Szulc. Optimization of reinforcement layout of scissor-type bridge using differential evolution algorithm. *Computer-Aided Civil and Infrastructure Engineering*, 34(6):523–538, 2019. DOI: 10.1111/mice.12432.

[6] J. M. Gattas and Z. You. Geometric assembly of rigid-foldable morphing sandwich structures. *Engineering Structures*, 94:149–159, 2015. ISSN: 0141-0296. DOI: 10.1016/j.engstruct.2015.03.019.

[7] M. Schenk and S. D. Guest. Geometry of miura-folded metamaterials. *Proceedings of the National Academy of Sciences*, 110(9):3276–3281, 2013. DOI: 10.1073/pnas.1217998110.

[8] E. T. Filipov, T. Tachi, and G. H. Paulino. Origami tubes assembled into stiff, yet reconfigurable structures and metamaterials. *Proceedings of the National Academy of Sciences*, 112(40):12321–12326, 2015. DOI: 10.1073/pnas.1509465112.

[9] K. Miura and T. Tachi. Synthesis of rigid-foldable cylindrical polyhedra. In *Symmetry: Art and Science*.

[10] T. Tachi and K. Miura. Rigid-foldable cylinders and cells. *Journal of the International Association for Shell and Spatial Structures*, 53(4):217–226, 2012.

[11] H. Yasuda, T. Yein, T. Tachi, K. Miura, and M. Taya. Folding behaviour of tachi–miura polyhedron bellows. *Proceedings of the Royal Society A: Mathematical, Physical and Engineering Sciences*, 469(2159):20130351, 2013. DOI: 10.1098/rspa.2013.0351.

[12] H. Yasuda and J. Yang. Reentrant origami-based metamaterials with negative poisson's ratio and bistability. *Physical Review Letters*, 114(18):185502, 2015. DOI: 10.1103/PhysRevLett.114.185502.

[13] H. Yasuda, B. Gopalarethinam, T. Kunimine, T. Tachi, and J. Yang. Origami-based cellular structures with in situ transition between collapsible and load-bearing configurations. *Advanced Engineering Materials*, 21(12):1900562, 2019. DOI: 10.1002/adem.201900562.

[14] S. Tomita, K. Shimanuki, H. Nishigaki, S. Oyama, T. Sasagawa, D. Murai, and K. Umemoto. Origami-inspired metamaterials with switchable energy absorption based on bifurcated motions of a tachi-miura polyhedron. *Materials & Design*, 225:111497, 2023. DOI: 10.1016/j.matdes.2022.111497.

[15] P. P. Pratapa and A. Bellamkonda. Thick panel origami for load-bearing deployable structures. *Mechanics Research Communications*, 124:103937, 2022. DOI: 10.1016/j.mechrescom.2022.103937.

[16] T. Tachi. Rigid-foldable thick origami. *Origami*, 5(5):253–264, 2011.

[17] Y. Chen, R. Peng, and Z. You. Origami of thick panels. *Science*, 349(6246):396–400, 2015. DOI: 10.1126/science.aab2870.

[18] R. J. Lang, K. A. Tolman, E. B. Crampton, S. P. Magleby, and L. L. Howell. A review of thickness-accommodation techniques in origami-inspired engineering. *Applied Mechanics Reviews*, 70(1), 2018.

[19] K. Liu and G. H. Paulino. Nonlinear mechanics of non-rigid origami: an efficient computational approach. *Proceedings of the Royal Society A: Mathematical, Physical and Engineering Sciences*, 473(2206):20170348, 2017. DOI: 10.1098/rspa.2017.0348.

[20] E. T. Filipov, K. Liu, T. Tachi, M. Schenk, and G. H. Paulino. Bar and hinge models for scalable analysis of origami. *International Journal of Solids and Structures*, 124:26–45, 2017. DOI: 10.1016/j.ijsolstr.2017.05.028.

[21] K. Liu and G. H. Paulino. Merlin: a matlab implementation to capture highly nonlinear behavior of non-rigid origami. *Proceedings of IASS Annual Symposia*, 2016(13):1–10, 2016.

[22] K. Liu and G. Paulino. Highly efficient nonlinear structural analysis of origami assemblages using the merlin2 software. *Origami*, 7:1167–1182, 2018.

[23] T. Tachi. One-dof cylindrical deployable structures with rigid quadrilateral panels. In *Symposium of the International Association for Shell and Spatial Structures (50th. 2009. Valencia). Evolution and Trends in Design, Analysis and Construction of Shell and Spatial Structures: Proceedings*. Editorial Universitat Politècnica de València.

IASS 2023
July 10–14 Melbourne
Integration of Design and Fabrication

Proceedings of the IASS Annual Symposium 2023
Integration of Design and Fabrication
10–14 July 2023, Melbourne, Australia
Y.M. Xie, J. Burry, T.U. Lee and J. Ma (eds.)

Triply periodic discrete surface of constant negative curvature constructed from one type of piece

Kanata WARISAYA[a], Seri NISHIMOTO[a], Toshiyuki MORISHIMA[b], Tomohiro TACHI[a,*]

[a,*] The University of Tokyo
Tokyo, 153-8902 Japan
tachi@idea.c.u-tokyo.ac.jp

[b] Kawakami Sangyo Co., Ltd.

Abstract

Shellular structures, i.e., cellular structures composed of a single smooth 2-manifold surface, have recently received attention in the context of architecture, structures, and materials. This study aims to efficiently construct shellular structures using sheet materials by dividing the surfaces into a single type of piece by using the geometry of hyplanes, discrete surfaces of constant negative curvature consisting of congruent triangles. We realize the shellular structure homeomorphic to but slenderer (or thicker) than Schwarz's D-surface with a variant of the hyplanes. Each piece with integrated joints were fabricated by cutting and perforating a sandwich panel of polypropylene. We build a pavilion that can be assembled and disassembled and compactly folded for convenient storage and transportation.

Keywords: advanced manufacturing and materials, Shellular structure, tessellation, modular construction, origami

1. Introduction

Shellular structures are cellular structures consisting of a single smooth 2-manifold surface in the form of a hollow three-dimensional truss. Typical examples of such surfaces are triply periodic minimal surfaces (TPMSs) such as Schwarz's P-surface, Schwarz's D-surface, and Schoen's gyroid surface. Their high strength, low density, and property of dividing space into two portions have attracted attention in the fields of materials [1] and architecture [2]. They also have a variety of applications such as infill for 3D printing [3] and a heat-exchanger [4].

If we attempt to construct a Shellular structure from a flat panel, it needs to be divided into some pieces because of its negative Gaussian curvature. Depending on the division method, different types of pieces may be needed. For easier manufacture and construction, a method that can divide the surface into fewer types of pieces, especially into a single type, is preferred.

We propose a method for discretizing the surface of Shellular structures with a single type of piece by applying hyplanes [5], discrete surfaces of constant negative curvature ($K = -1$ surfaces) composed of congruent triangular faces. We show an immersion of a type of hyplanes in $\mathbb{R}^3$; more specifically, we give an intrinsically isometric covering of a hyplane to a surface homeomorphic to the D-surface. Similar to our study, there have been studies that divide TPMSs into one type of triangle in a smooth [6]

Copyright ©2023 by Kanata WARISAYA*, Seri* NISHIMOTO*, Toshiyuki* MORISHIMA *and Tomohiro* TACHI.
Published in the Proceedings of the IASS Annual Symposium 2023 with permission.

or a discrete sense [7]. In these examples, the surface is divided into triangular minimum units of the surface based on its global symmetry (or even subdivided). In contrast, our discrete surface has a couple of triangles corresponding to the unit of the surface by not subdivision but by adding another triangle to the original triangular unit. This resulted in a discrete D-surface with a smoother and slenderer (or thicker) form, which has the potential for architectural applications as it can reduce the proportion of space for load bearing and increase the proportion of space that people utilize.

We create this surface as a pavilion to demonstrate its application to architecture (Figure 1). The surface is divided into a type of developable piece consisting of eight triangular faces connected in a strip using its global symmetry. We fabricate the pieces with the joints attached to the boundary edges by cutting and perforating a Plapearl [8], a lightweight sandwich panel of polypropylene. The pieces can be assembled and disassembled without damage and can be reused as no additional parts are required for the joint. The pieces can also be folded compactly for convenient storage and transport.

In Section 2., we first recall the definition of the hyplane and calculate the triangle that constitutes it. Then, we show that two variants of hyplanes can construct surfaces homeomorphic to the D-surface. In Section 3., we describe our pavilion design, including modules, joint system, material, and fabrication.

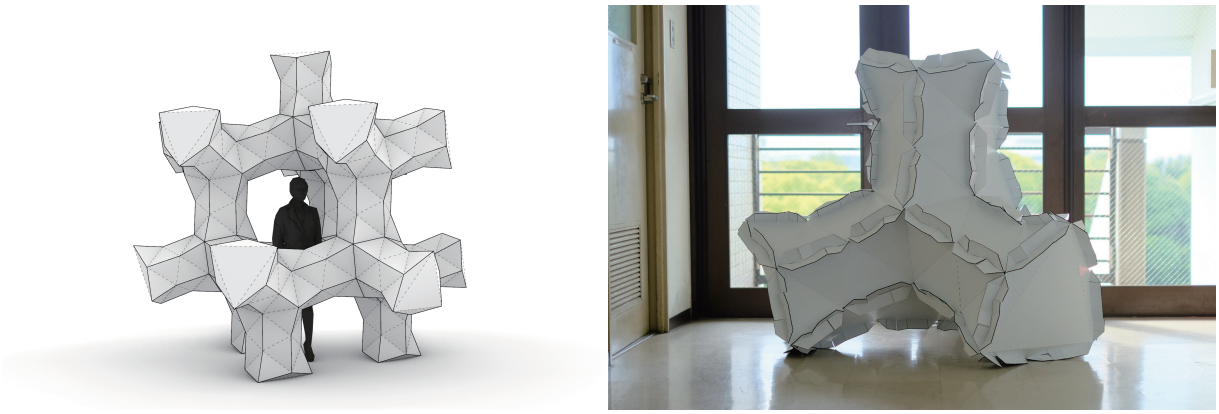


Figure 1. Left: our pavilion of a triply periodic discrete $K = -1$ surface constructed from one type of triangle, which appears to be a slender D-surface. Right: a partial mock-up of our pavilion.

2. Triply periodic discrete $K = -1$ surface

This section shows a method for dividing a surface of a Shellular structure by one type of triangle. Surfaces allowing for such division include surfaces of constant Gaussian curvature (K-surfaces), such as the sphere ($K = 1$), the Euclidean plane ($K = 0$), and the hyperbolic plane ($K = -1$), which can be tiled by one type of Schwarz triangles [9] so that adjacent triangles are mirror reflection about a plane that contains the shared edge. The immersion of the tiling of the hyperbolic plane in $\mathbb{R}^3$ creates a saddle-shaped surface, whose discrete analogue is called hyplane [5].

In Section 2.1., we recall the definition of the h yplane. In Section 2.2., we triangulate a surface homeomorphic to the D-surface so that it is an immersion of the types of hyplanes. Then we show the possibility of intrinsically isometric immersion by discussing the design freedom of the configuration of the triangles.

2.1. Hyplane

We recall the definition of the hyplane [5]. For a triad of positive integers (a, b, c), (a, b, c)-hyplane is a polyhedral surface that satisfies following conditions:

C1 $\frac{1}{a}+\frac{1}{b}+\frac{1}{c}<\frac{1}{2}$;
C2 all faces are congruent to $\triangle ABC$;
C3 any pair of adjacent faces is the mirror reflection about a plane that contains the shared edge;
C4 A, B, C create a degree-a, b, c vertex, respectively.
C5 discrete Gaussian curvature is constant on every vertex.

C1 is for the surface to have negative curvature, while C2-C4 defines the tiling structure on a surface. C3 implies that if a (b, or c, resp.) is odd, the triangle needs to be isosceles $AB = AC$ ($BC = BA$, or $CA = CB$, resp.), and thus $b = c$ ($c = a$, or $a = b$, resp.). Figure 2 shows an example of $(6, 6, 8)$-hyplane and the face triangle.

For C5, there are variations in the definition of discrete Gaussian curvature. Here, we define the discrete Gaussian curvature on a vertex as an angle defect divided by the area associated with the vertex. We divide a triangle into three kite areas by perpendicular lines from the incenter to each edge and assign each area to the vertex it contains (Figure 2 Left). This method divides the polyhedral surface into patches of regular polyhedra (Figure 2 Right).

Now we consider hyplanes composed of congruent isosceles triangles: (a, a, c)-hyplanes. Let the radius of the incircle of the triangle r and the ratio of the length of AC split by the foot of the perpendicular lines $s : (1 - s)$, where $0 < s < 1$. The triangle with $\angle A = \angle B = \theta_1, \angle C = \theta_2$ composing (a, a, c)-hyplane can be calculated by the equation about the Gaussian curvature:

$$\frac{2\pi - a\theta_1}{ars} = \frac{2\pi - c\theta_2}{cr(1-s)}, \tag{1}$$

where $2\theta_1 + \theta_2 = \pi, \cos\theta_1 = s$. This leads to

$$\frac{2\pi - a\theta_1}{a\cos\theta_1} = \frac{(2-c)\pi + 2\theta_1}{c(1-\cos\theta_1)}. \tag{2}$$

This equation for θ_1 cannot be algebraically solved as it has members of θ_1 and $\cos\theta_1$. We obtained a numerical solution of $\theta_1 \sim 0.97382$ for $(a, c) = (8, 6)$, and $\theta_1 \sim 1.12596$ for $(a, c) = (6, 8)$. The Gaussian curvature is $\sim \frac{-0.33518}{r}$ for $(a, c) = (8, 6)$, and $\sim \frac{-0.18304}{r}$ for $(a, c) = (6, 8)$.

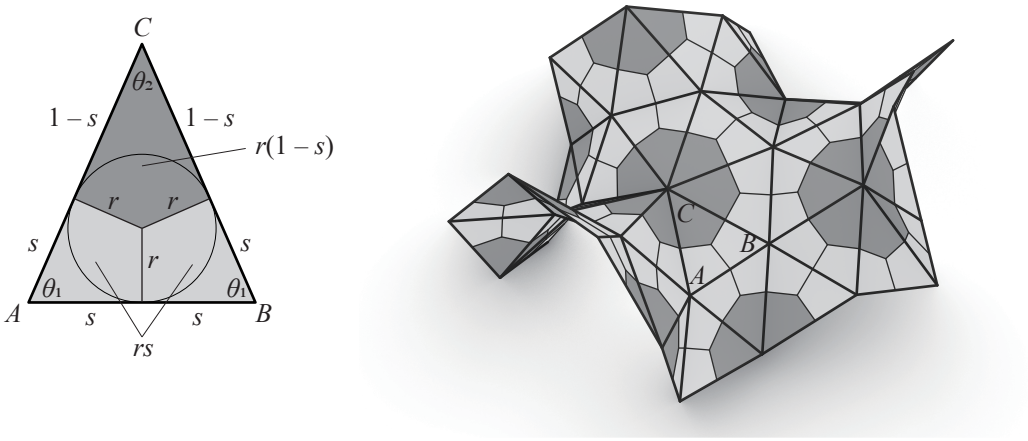


Figure 2. The geometry of (6,6,8)-hyplane. We divide the triangular face by perpendicular lines from the incenter to each edge to assign an area to a vertex. The area is used for calculating the Gaussian curvature.

2.2. Triply periodic hyplane

In this section, we show that the two types of hyplanes we obtained in Section 2.1., $(8, 8, 6)$-hyplane and $(6, 6, 8)$-hyplane, can cover a surface which is homeomorphic to the D-surface, through intrinsically isometric transformation. Figure 3 Left shows the hyplanes homeomorphic to the D-surface we obtained. We focus on the nodal module of the surface to discuss its existence (coloured in green). Figure 3 Right illustrates the conditions for the module. We divide the module into the units of $\frac{1}{24}$ by mirror planes which are determined by the global symmetry of the D-surface (shown in blue). We also provide a regular hexagonal prism on the boundary of the module which is required for the connection of the modules (shown in orange). The lines determined by the intersection of the planes and the prism are named l_1, l_2, l_3, l_4.

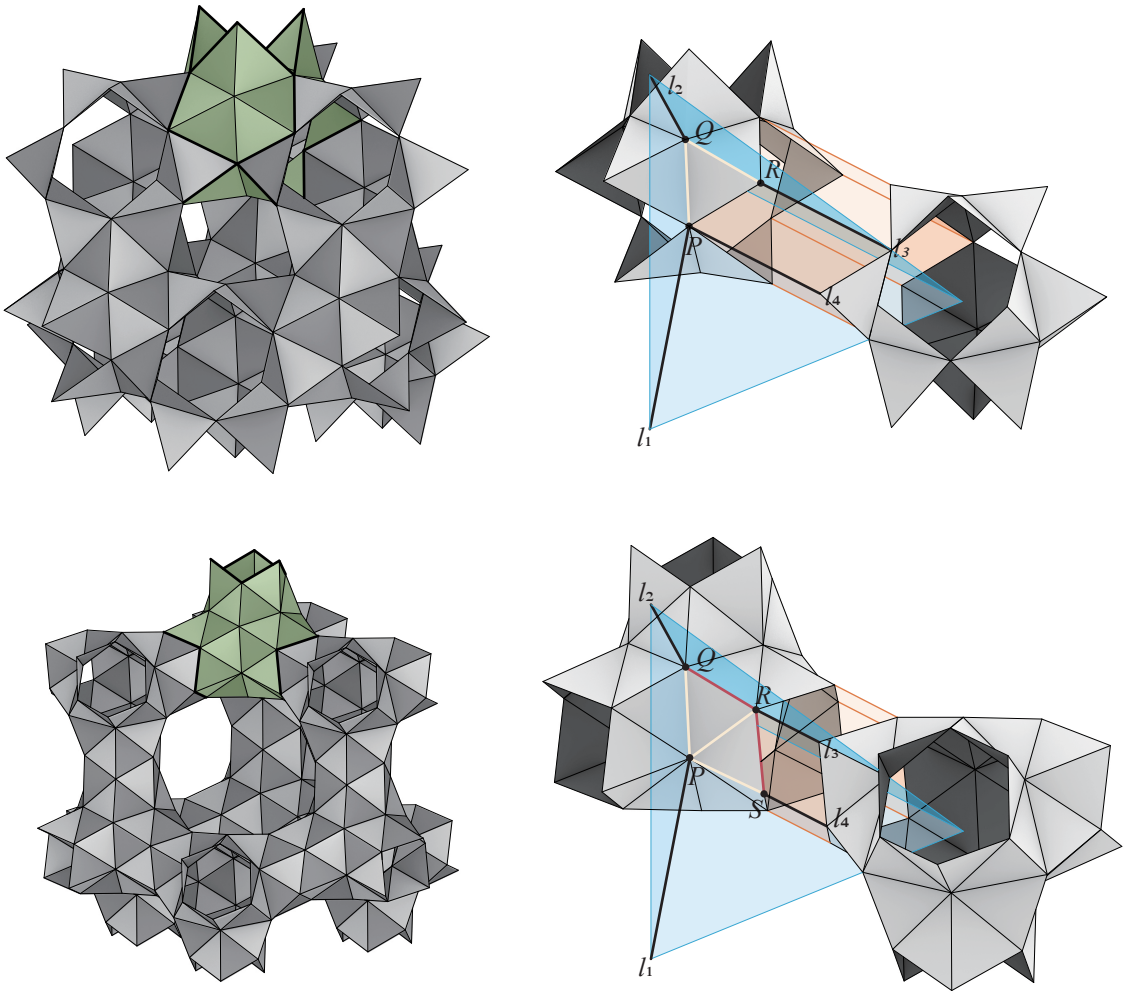


Figure 3. Left: The $(8, 8, 6)$-hyplane (Upper) and the $(6, 6, 8)$-hyplane (Lower) homeomorphic to the D-surface. We focus on the nodal module of the surface coloured in green. Right: the geometric constraints for the nodal module of the surface to have the triple periodicity.

$(8,8,6)$**-hyplane** See Figure 3 Upper. We consider the configuration of the unit $\triangle PQR$ with $PQ = QR$. P is a point that moves on both l_1 and l_4, which means it is fixed on the intersection of l_1 and l_4. Thus the variables we have are

V1 Q on l_2;
V2 R on l_3.

These variables need to satisfy the constraint:

C1 $PQ = QR$.

This system has a 1 degree of freedom with 2 variables and a 1 constraint.

$(6,6,8)$**-hyplane** See Figure 3 Lower. In this case, we consider the configuration of the unit $\triangle PQR$ with $PQ = PR$ and $\triangle PSR$ with $PS = PR$. This means the module has twice as many faces as that of the (6,8,8)-hyplane. We have the following variables:

V1 P on l_1;
V2 Q on l_2;
V3 R on l_3;
V4 S on l_4.

These variables need to satisfy the constraint:

C1 $PQ = PR$;
C2 $PS = PR$;
C3 $QR = SR$,

so that $\triangle PQR$ and $\triangle PSR$ are congruent isosceles triangles. This system also has a 1 degree of freedom with 4 variables and 3 constraints.

In the cases of both $(8,8,6)$ and $(6,6,8)$, the configuration has a 1 degree of freedom. Therefore it should include the solution of the triangle we obtained in Section 2.1., which constructs the hyplane. We obtained the numerical solution by using Kangaroo2 [10] on Rhino/Grasshopper.

Through solving in Kangaroo2, we found a surface composed of the same triangle can take different configurations while keeping its triple periodicity. Figure 4 shows the two possible configurations of the (6,6,8)-hyplane. These configurations can be switched to each other by snap-through buckling.

The D-surface, which is a minimal surface, has the property of bisecting space. In contrast, the proposed triply periodic $(6,6,8)$-hyplane has the appearance of a slenderer (or thicker) D-surface, dividing space into larger and smaller portions. The volume ratio of the two portions is calculated to be $\sim 0.757 : 0.243$, by supposing the space tessellation by rhombic dodecahedron onto the surface from its symmetry and computing the two volumes in a rhombic dodecahedron partitioned by the surface (Figure 5). This slender D-surface reminds us of triply periodic constant mean curvature (CMC) surfaces [11].

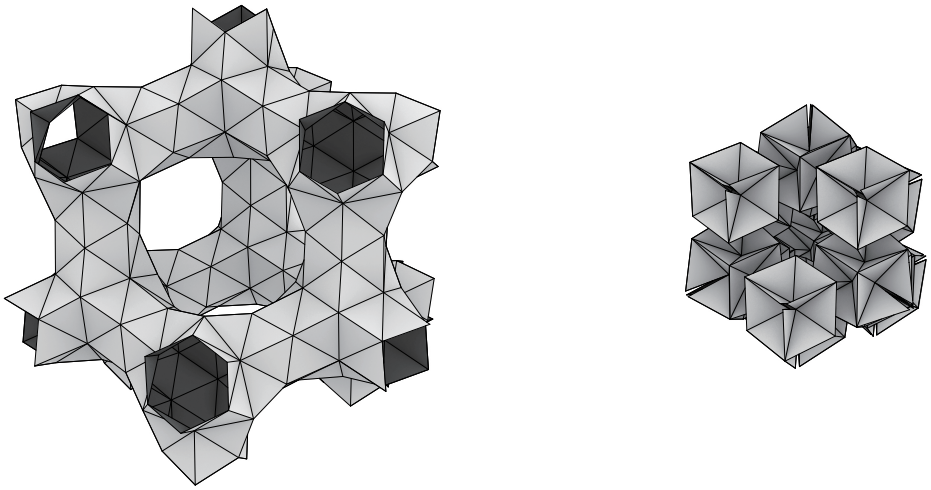


Figure 4. Two possible configurations of the $(6, 6, 8)$-hyplane with triple periodicity. They can be switched to each other through snap-through motion.

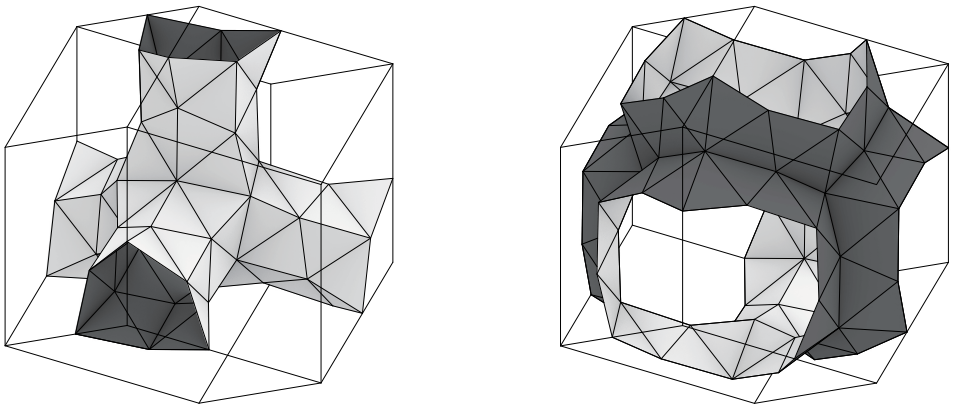


Figure 5. The part of (6,6,8)-hyplane with a triple periodicity which corresponds to the unit of space tessellation by rhombic dodecahedra.

3. Pavilion design

In Section 2., we obtained the slenderer D-surface composed of a single type of triangle by applying $(6, 6, 8)$-hyplane. This enables the construction of the surface from one type of triangular piece with improved manufacturability. Compared to $(8, 8, 6)$-hyplane, the structure will behave more like a shell due to the smoother discretization. In addition, the surface divides space into larger and smaller portions, reducing the space for load bearing and increasing the space that people utilize. We demonstrate this potential for architectural application through the practical building of the pavilion.

We construct a part of the surface with an infinite extent in space. Figure 6 shows two possible trimming of the surface we considered for design. The front side of the surface is more visible in one design and the back side is more visible in the other design. We chose the left one with fewer naked boundary edges to reduce the number of degrees of freedom of the structure. We determined the dimension of the pavilion so that a side of the space is large enough to accommodate a person on one side (Figure 1).

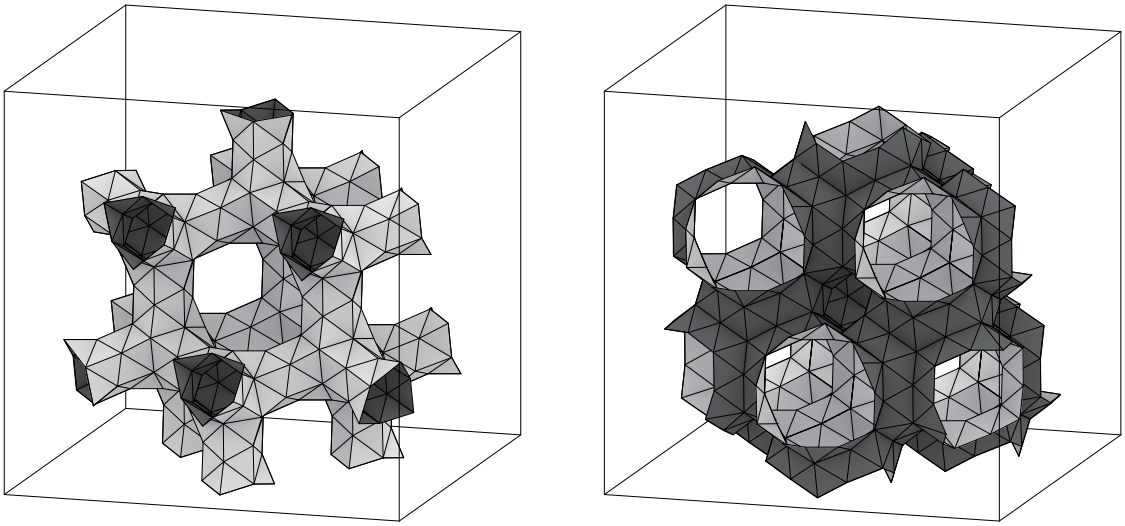


Figure 6. Two possible designs of our pavilion in the box of $3\,\mathrm{m} \times 3\,\mathrm{m} \times 3\,\mathrm{m}$.

3.1. Module

Figure 7 shows the modules of our pavilion. Although each triangular face of the surface could be a single piece, for more efficient construction, the piece should consist of several faces connected at edges as fold lines and still be developable. Therefore, using the global symmetry of the surface, we divide the surface into pieces with eight faces connected in a strip (A). Near the boundary of the surface, there are half-trimmed pieces composed of four faces (B). Caps are also provided to close the boundary of the surface to stabilize the structure (C).

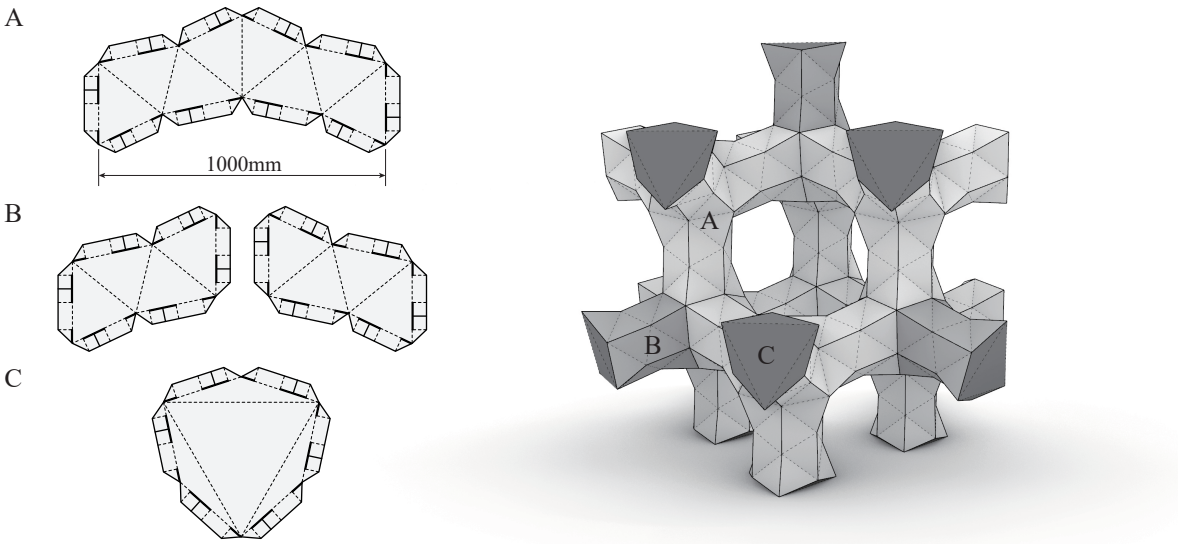


Figure 7. The pieces of our pavilion. A: a Strip of 8 faces (72 pieces), B: a mirrored pair of half-trimmed strips (12 pieces for each), and C: a cap for stabilizing the structure (16 pieces).

3.2. Joint and material

In order to join the modules together, we add regions for joints on the boundary of the pieces (Figure 7). We adopted a paper-craft technique for the joints (Figure 8). The regions for joints have cut lines, fold lines, and clearances for accommodating the thickness of the material. We fold the fold lines to make fingers (Left), then engage the fingers (Middle), and finally open the fold lines again to fix the joints (Right).

The material we use is Plapearl [8] produced by Kawakami Sangyo Co., Ltd., a three-layer polypropylene board consisting of an air bubble sheet sandwiched between two flat sheets. Plapearl is capable of cutting and embedding living hinges by perforation using CNC. Though the board has a thickness of $3\,\mathrm{mm}$, we need a minimum thickness accommodation of the joint due to the material's elasticity. The structure of the board containing air allows its lightweight of $0.5\,\mathrm{kg/m^2}$. The entire pavilion weighs about $17.6\,\mathrm{kg}$.

This construction system allows the components to be manufactured by creating cut lines and fold lines on one type of material. The pieces can be repeatedly assembled and disassembled without damage because they do not require additional parts for the joint. They can also be folded compact enough to pack in suitcases, enabling convenient storage and transport. The structure can also be grown by increasing the number of strips.

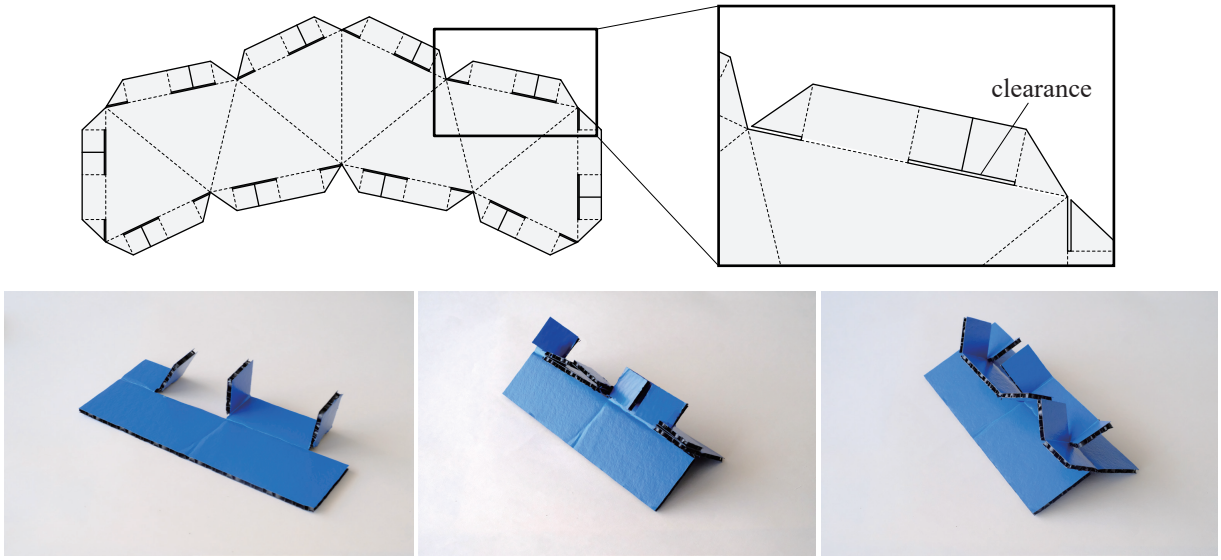


Figure 8. Paper-craft joint method with Plapearl. Upper: clearances for accommodating the thickness of the board. Lower: the process of joining. Fold the fold lines to make fingers (Left), engage the fingers (Middle), and develop the fold lines to fix (Right).

4. Conclusion

This paper showed $(8, 8, 6)$-hyplane and $(6, 6, 8)$-hyplane can construct a surface homeomorphic to Schwarz's D-surface. In the case of $(6, 6, 8)$-hyplane, the surface forms a slenderer D-surface with smoother discretization, dividing space by the ratio of $\sim 0.757 : 0.243$. We also described the design of the pavilion we construct. We divide the surface into one type of developable strip based on the global symmetry of the surface. The pieces with integrated joints are fabricated by cutting and perforating a Plapearl. The paper-craft technique is adopted for the joint, which does not require additional parts to join the pieces.

Future work includes the identification of the bending stiffness of the hinge by perforation of Plapearl, the structural analysis of the pavilion as a shell structure, and the generalization of the discretization method into other types of TPMS or Triply periodic CMC surfaces.

Acknowledgments

This work is supported by Kawakami Sangyo Co., Ltd. We thank Yoshiaki Araki for his helpful comment regarding the hyplane.

References

[1] S. C. Han, J. W. Lee, and K. Kang. A new type of low density material: shellular. *Advanced Materials*, 27(37):5506–5511, 2015.

[2] M. Akbari and M. Akbarzadeh. Continuous approximation of shellular funicular structures. *Bulletin of the International Association for Shell and Spatial Structures*, 2022.

[3] UltiMaker. Ultimaker cura. https://ultimaker.com/software/ultimaker-cura.

[4] YKK AP Inc. Window on the future. https://www.ykkap.co.jp/consumer/satellite/sp/window-future/, 2021.

[5] K. AHARA. Hyplane—polyhedral models of hyperbolic plane. *Forma*, 21(1):5–18, 2006.

[6] S. Ramsden, V. Robins, and S. Hyde. Three-dimensional euclidean nets from two-dimensional hyperbolic tilings: kaleidoscopic examples. *Acta crystallographica. Section A, Foundations of crystallography*, 65:81–108, Mar. 2009. DOI: 10.1107/S0108767308040592.

[7] U. Reitebuch, M. Skrodzki, and K. Polthier. Discrete gyroid surface. In *Proceedings of bridges 2019: Mathematics, art, music, architecture, education, culture*, pages 461–464, 2019.

[8] Kawakami Sangyo Co., Ltd. Plapearl. https://www.putiputi.co.jp/products/876.

[9] H. Schwarz. Ueber diejenigen fälle, in welchen die gaussische hypergeometrische reihe eine algebraische function ihres vierten elementes darstellt. ger. *Journal für die reine und angewandte Mathematik*, 75:292–335, 1873.

[10] D. Piker. Kangaroo 2. https://github.com/Dan-Piker/K2Goals, 2015.

[11] D. Anderson, H. Davis, J. Nitsche, and L. Scriven. Periodic surfaces of prescribed mean curvature. In *Physics of Amphiphilic Layers: Proceedings of the Workshop, Les Houches, France February 10–19, 1987*, pages 130–130. Springer, 1987.

Digital modelling and fabrication

Active bending
Additive manufacturing/ 3D printing
Architectural geometry
Bamboo for sustainable construction and quality of life improvement
Bio-inspired structures and architecture
Bridge structures
Computational form-finding
Conceptual design
Concrete structures
Construction techniques
Deployable and inflatable structures
Design competition (WG21)
► **Digital modelling and fabrication**
Dynamic response of metal spatial structures
Dynamic response of other structures
Form-finding and structural optimisation of interlocking discrete assemblages
Graphical methods
Gridshell and lattice structures
Historical concrete shells
Historical structures
Lattice structures
Life-cycle design and assessment of structures
Metal gridshell structures, connections and stability
Methods and construction technologies for sustainable shell structures
Morphology and configuration processing
Next generation parametric design
Novel methods in modelling, optimisation and construction for reducing carbon footprint of continuous roof shells
Numerical methods for geometry, form-finding and optimisation of lightweight structures
Optimisation methods and applications
Origami
Other
Teaching design uncertainty: working with unknown qualities/quantities of new and re-claimed materials
Teaching of shell and spatial structures
Tensegrity systems and cable structures
Tension and membrane structures
Tension structures in the Asia-Pacific
Timber and bio-based structures
Topology optimisation
Traditional masonry structures and innovation
Transformable structures

IASS 2023
July 10–14 Melbourne
Integration of Design and Fabrication

Proceedings of the IASS Annual Symposium 2023
Integration of Design and Fabrication
10–14 July 2023, Melbourne, Australia
Y.M. Xie, J. Burry, T.U. Lee and J. Ma (eds.)

A novel modular technique for manufacturing free-form rammed earth walls

Ahmed ABDELAAL[a], Mohamed GOMAA[a], Yi Min XIE[*]

[*] Centre for Innovative Structures and Materials, School of Engineering,
RMIT University, Melbourne, 3001, Australia
mike.xie@rmit.edu.au

[a] Centre for Innovative Structures and Materials, School of Engineering,
RMIT University

Abstract

Rammed earth (RE) is a traditional building technique that has been gaining popularity as a sustainable and low-cost alternative to conventional building methods. However, the lack of established processes for constructing free-form rammed earth structures, as well as the increasing cost of labour, hinder its uptake in contemporary design. This research proposes an innovative method of rammed earth manufacturing that combines modular design and digital fabrication techniques to leverage the potential of mass customisation and mass production. A production system for modular RE tiles with intricate curvatures is introduced, where the tiles can be aggregated to create continuous free-form RE walls. The tiles are computationally designed to allow variations through rotation and/or flipping of tiles. The aggregation of 16 identical tiles yields 128 wall design variations with continuous curved designs. Moreover, the number of potential variations rises to 512 when using four different tile designs. This encompasses both customisation of the overall system and standardisation of the module. This method merges the benefits of rammed earth construction with those of modular integrated construction (MiC), which involves off-site production of fully completed 3D modules. The new system also enables improved mobility and manageability, which elevates transportation and assembly efficiency. The proposed system offers a novel approach that can provide an alternative to conventional RE construction processes, offering higher productivity, sustainability and efficiency of the built environment.

Keywords: rammed earth, mass customization, mass production, modular design, free-form, 3D tile aggregation, digital fabrication, modular integrated construction (MiC)

1. Introduction

Rammed earth (RE) is an ancient building method that utilises natural resources such as aggregate, clay, lime and sand to construct walls [1, 2] Earth is one of the oldest construction materials that has been utilised in architecture for millennia due to its abundance, low cost and bioclimatic qualities that withstand harsh weather [3]. RE is an earth-based construction technique that has been utilised for ages in many parts of the world. It entails combining dry soil with water then compacting the mixture into successive lifts within a formwork to produce structures. Because of the near-dry state of the mixture and the creation through compression process, RE has the highest mechanical and structural strength among the many earth construction techniques [4, 5]. In terms of compression strength and erosion resistance, stabilised RE compares favourably to masonry or concrete blocks, while its raw material is less expensive. The entire cost of rammed earth building varies depending on geography and labour cost [6]. RE constructions have been witnessing an increased interest and development lately. Since 1970, Western Australia has led the world in the development of cement-stabilised rammed earth (CSRE), which is now considered an established construction method in that region. Yet, there is a considerable

Copyright © 2023 by Ahmed ABDELAAL, Mohamed GOMAA and Yi Min XIE. Published in the Proceedings of the IASS Annual Symposium 2023 with permission.

lack of utilising advanced construction techniques to manufacture free-form RE geometries. This research aims to investigate and introduce a novel method for manufacturing rammed earth walls that can substantially enhance the conventional practice of RE construction through overcoming major drawbacks in design versatility and on-site process efficiency. This research comes as a part of a large project at RMIT University's Centre for Innovative Structures and Materials (CISM) that aims to harness the qualities of digital manufacturing technologies to efficiently produce novel free-form earth construction.

2. Rammed earth construction

In rammed earth construction, walls serve as the primary structural elements. The soil used in RE mixture is subsoil excavated at a depth of more than 1 m below ground. Subsoil consists of gravel, sand, silt and clay. Particle size distribution classifies the quantity and ratios between components. A good range of particle sizes is recommended to contain a balanced mix of coarse and fine aggregates [7]. To ensure the quality of the rammed earth mixture, on-site testing and/or lab analysis is required. A good mixture should have a high sand percentage (30–50%) and no more than 8% clay. Clay is a natural binder that improves compaction and mechanical performance of soil. Other binders such as cement are also used to strengthen the construction [8]. RE offers various benefits in the built environment such as sustainability, energy efficiency, durability and aesthetic appeal, while it utilises natural and locally accessible resources with minimal embodied energy use and high recyclability [9, 10]. However, there are significant drawbacks to rammed earth in a modern context. The construction process is labour-intensive and requires highly experienced workers, which leads to higher costs compared to standard building methods [10]. Moreover, the maximum allowable structural height is relatively low [4, 11]. On the other hand, the time-consuming process of constructing, aligning, inspecting, stripping, cleaning, relocating and storing the formwork often exceeds the time spent on transporting and compacting the raw earth [12]. Despite these challenges, recent advancements have improved the quality and efficiency of rammed earth production, such as using metal formwork and pneumatic rammers [12–14].

3. Modular systems

Modular integrated construction (MiC) is a method of producing finished modules in off-site facilities and transporting them to the construction site for installation. Off-Site Construction (OSC) technologies such as prefabrication, panelisation and hybrid-construction utilise this technology [15]. MiC method was significantly leveraged and presented in two major projects in 2019. The first project is a 40-storey residential skyscraper built in Singapore using concrete MiC modules with a height of 140 m, which is considered the tallest MiC-based tower in the world. The second project is a 135 m high tower in Croydon, UK, which stands as the world's second tallest MiC-based tower [15]. MiC's popularity and rising use are attributed to its proven advantages in increasing the construction process efficiency and improving building quality. MiC encourages on-site and off-site work overlap which minimises the risk of delay. In addition, it eliminates 90% of on-site tasks [16] , while it reduces accidents by 80% [17], capital costs by 10% [18] and waste by 76% [17]. Over the past decade, the use of MiC modules has increased. This growth is demonstrated by developments such as modular buildings [22], positive impact evaluations of government initiatives to promote MiC [23], increased effectiveness of MiC module installation [24]. By utilising a 3D modular method (Figure 1), productivity can be improved by 25% to 50% [25]. However, this technology has various problems such as the high initial investment costs [19, 20], possible challenges in transportation and logistics of the modules [20].

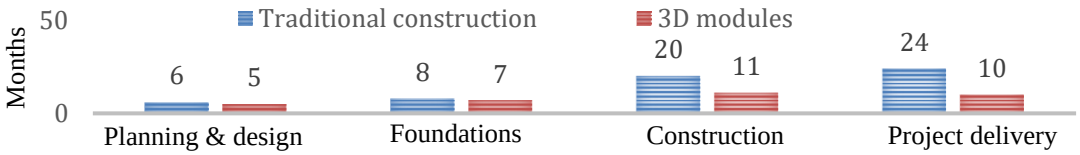


Figure 1. Example project construction duration (Months) [25].

4. Modular rammed earth

Modular rammed earth is an innovative construction technique that merges the environmentally friendly principles of rammed earth with the efficiency of modular building methods. This method involves prefabricating rammed earth wall sections in a controlled environment, which ensures consistent quality and reduces the impact of weather on the construction process. Once completed, these sections are transported to the construction site and assembled using heavy machinery, offering a faster, more efficient and more sustainable construction process compared to traditional rammed earth techniques. Hence, modular rammed earth construction offers benefits in terms of scalability, flexibility and cost-effectiveness, making it easy to rearrange or expand structures to accommodate changing needs or preferences. Moreover, the reduced construction time and labour costs associated with prefabricated components further enhance its appeal for projects with tight deadlines or budget constraints. As a result, modular rammed earth is gaining popularity in sustainable construction projects worldwide for both residential and commercial applications [2, 4, 26].

4.1 Introducing modular systems to rammed earth

Both monolithic/linear formwork and modular form work systems have similarities and distinctions where they offer various benefits to different building types. Monolithic/linear formwork refers to the use of multiple form work parts, usually in the form of boards or sheets, to construct a continuous and monolithic building components on site. On the other hand, modular formwork refers to the use of similar or identical mould units that generate sections or blocks of a large building through assembly. Integrating modular systems with RE can enhance the construction process through offering higher accuracy, better quality control, reduced waste and shorter construction timeframes compared to conventional on-site procedures. Also, modular construction could potentially overcome some of the limitations associated with rammed earth, such as the skilled labour requirements, since it requires less trained labour and can be utilised in any environment [30]. Current methods of RE prefabricated walls are often produced off-site and then transported to the installation location [26]. This is similar to the part-to-module prefabrication in modular construction, which refers to the process of producing individual components that are later assembled into larger modules for easy transportation and installation on-site [31]. However, rammed earth walls are generally larger and heavier than components of modular systems, and their construction requires special equipment and experienced workers. Modular systems, on the other hand, are more transportable and adaptable to a wider variety of architectural demands and designs [2, 32–34]. Introducing a modular system to rammed earth construction can help overcoming some of its limitations while maintaining the unique characteristics and benefits of rammed earth.

4.2 Case studies

Over the past two decades, efforts have been made to create prefabricated RE wall components off-site. This prefabrication process can offer enhanced quality control through factory production, reduce construction time and make RE construction more feasible in densely populated areas. However, the current prefabricated RE wall sections are large and require special equipment for assembly, leading to increased shipping and handling costs that can make the overall project cost more expensive. Several case studies have explored the use of prefabrication for both stabilised and unstabilised rammed earth structures [35]. For instance, since 1997, numerous prefabricated unstabilised rammed earth buildings and projects have been documented in the literature [36, 37]. One notable example is the work of Lehm Ton Erde, which has constructed buildings using prefabricated rammed earth panels. Figures 2 and 3 demonstrate the installation process of these prefabricated rammed earth panels.

In 2020, an Australian start-up firm ‘Form Earth’ unveiled a modular system prototype for automated production of RE walls. That system uses a compact unit with a material hopper, compaction device, and slip formwork. It is transportable and can function both off-site and on-site. The material hopper spans the length of the slip form and adds a complete layer of rammed earth mixture for each load. The compaction tool moves

within the formwork to undertake the ramming operation. The formwork slides higher with each completed lift and the process is repeated to construct succeeding lifts (Figure 4).



Figure 2. Alnatura Campus by Lehm Ton Erde [38].



Figure 3. Prefabricated rammed earth panels delivered and assembled on-site by Lehm Ton Erde [38].



Figure 4. Prefabricated rammed earth panels by Form Earth [39].

Another approach was presented by Hurtado and Eloualid in 2016, which is considered one of the early attempts to bring digital fabrication into RE modular manufacturing. The project utilises CNC laser cutting to create metal and plywood formwork components. The metal mould is retrieved from a single sheet and folded and tack-welded into the correct geometry before being placed within a plywood box to form the final brick mould (Figure 5). The additional soil mixture is rammed to make a rammed earth brick and the bricks are arranged to create the appropriate wall height. This concept provides a modular method for constructing a self-shading wall with enhanced thermal efficiency and intriguing appearance. However, material feeding, compaction and assembly are fully dependent on human labour [40].

In 2017, a project under the name of 'Community action walls' was presented by a team from Istanbul Bilgi University [41]. This project marks the first documented attempt to use digital manufacturing in the creation of formwork for modular rammed earth. The mould was carved from hard Styrofoam blocks using a robotic hot-wire cut process and the soil mixture was manually compacted. The manufactured rammed earth blocks were assembled into wall panels (Figure 6).



Figure 5. Modular prefabricated brick using a folded mould [40].



Figure 6. Modular rammed earth using hard styrofoam blocks as mould [41].

The presented case studies demonstrate the viability of using modular systems for RE architecture, such as prefabricated walls, or small forms such as blocks, which highlighted the potential to achieve different architectural forms and improve construction efficiency. These studies emphasise the need to investigate the design and manufacture of free-form, movable walls.

5. Novel modular system for freeform rammed earth

This research introduces an adaptable modular system for rammed earth that merges the qualities of RE with the efficiencies of MiC. The proposed system uses a collection of modular RE tiles with intricate curvatures for off-site manufacturing. This facilitates mass customization and large-scale production while ensuring consistent quality and reducing construction waste and on-site labour. The modular design allows flexibility in design, manufacturing and construction processes. This fusion between RE construction and MiC lays the groundwork for more sustainable, visually appealing and versatile building solutions.

5.1 Free-form Surfaces design process

The design of the modular rammed earth tiles is encompassed by an array of design variables (Figure 7), offering a multitude of possibilities for modifications through the simple acts of rotation and/or flipping. This flexibility empowers architects and designers to craft a diverse range of creative, visually intriguing structures tailored to their demands and unique vision. Through offering such versatility, the system can accommodate various design elements and respond to the ever-changing demands of the construction industry, making it a highly sought-after solution by architects, designers and clients alike. Furthermore, a seamless integration into various architectural contexts, from contemporary applications to traditional techniques, is facilitated by the inherent flexibility of the modular rammed earth tiles. By streamlining the design process and fostering seamless integration into different contexts, this innovative construction solution is poised to redefine the way sustainable, aesthetically appealing and customisable building projects are approached.

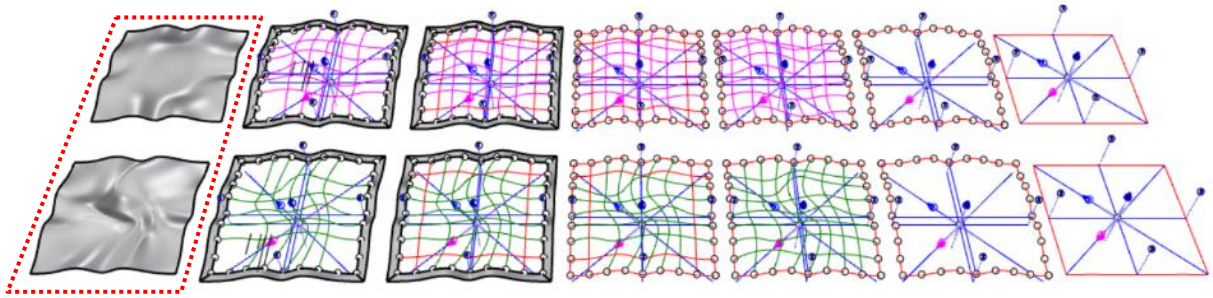


Figure 7. Design variables control of the tile itself.

The design of the tile commenced with a planar rectangle (Figure 9-a), symbolising one of the two primary faces of the tile. The aim was to create its edges as eight matching segments, which would enhance the potential for producing curvature and assist in aligning the geometric side edges. In more detail, the plan involved constructing each side edge from two segments that are mirrored around the

four-sided edges of the geometry. Subsequently, these eight mirrored edges were modified by moving their control points in the Z direction, creating a curved boundary that would become the surface edge and the main elements for the curvature. To accomplish this, it was necessary to reposition the curve's control points, which would be part of the continuous curvature (Figure 9-b). Following the division of each edge into a specified number of divisions, which was carried out for all eight edges, a set of points was constructed to designate them. Utilising these points as anchors for the control point curve along the U and V directions of the surface, the network representing the surface's curvature started to be constructed. As a result, the seamless connection of these curvatures was ensured by the precise alignment of their control points. Each of the curved edges of the tile is formed from a pair of symmetrical segments.

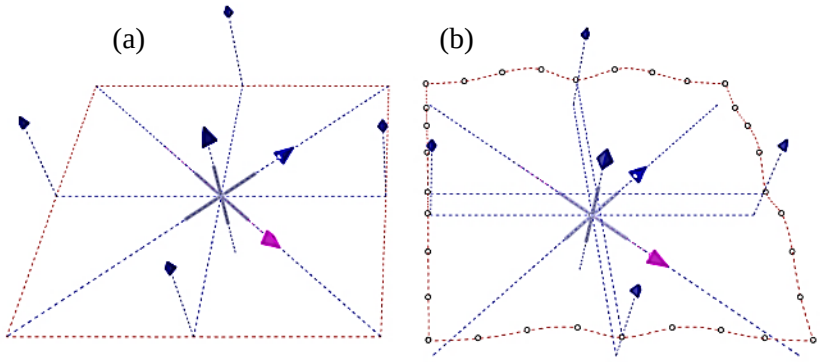


Figure 9. Deforming the boundary: (a) Tile baseline, (b) Modified boundary in Z direction.

Following that, a network of curves was established between the U and V axes of the surface, uniformly dividing the four curved planar edges. At this stage, two distinct curvature networks were generated while maintaining identical edges, resulting in continuous curvature between them. To generate the surface, the first UV curve in the network from all around the edges was to be disregarded in the subsequent step, allowing the curvature network to relax more towards the boundary. The primary objective, ultimately, was to achieve continuous curvature between the tiles (Figure 10).

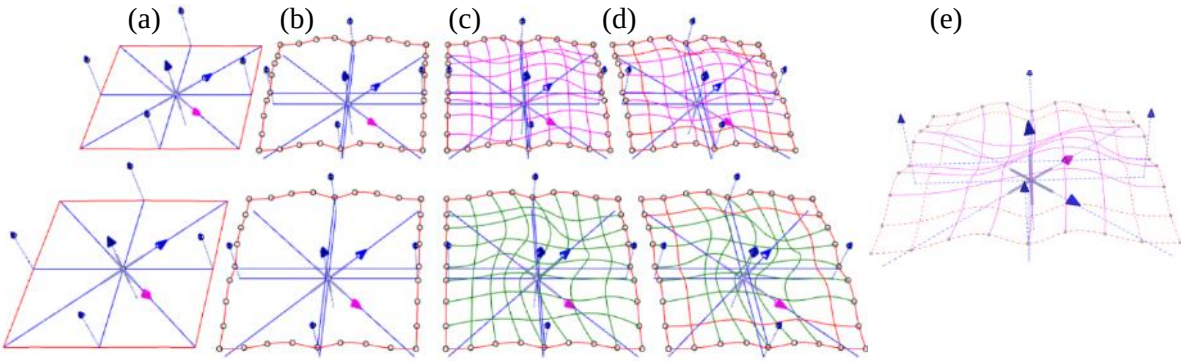


Figure 10. Surface network of curves: (a, b) Edge curvature processing (c) Curvature network creation (d) Removing curves in U and V direction for curvature relaxation (e) Final curvature network.

The aim is to produce two distinct surfaces with matching edges and continuous curvature across all transformations. Although removing the first curve in the network around the edges assists in relaxing the curvature towards the edge, it may not be sufficient. The more complex the curvature at the centre of the surface is, the greater the distance for relaxation is needed. To address this, a secure tangency guide is incorporated (Figure 11). This guide is a single curved surface perpendicular to the edges, which acts as a boundary to direct the curvature relaxation during surface creation.

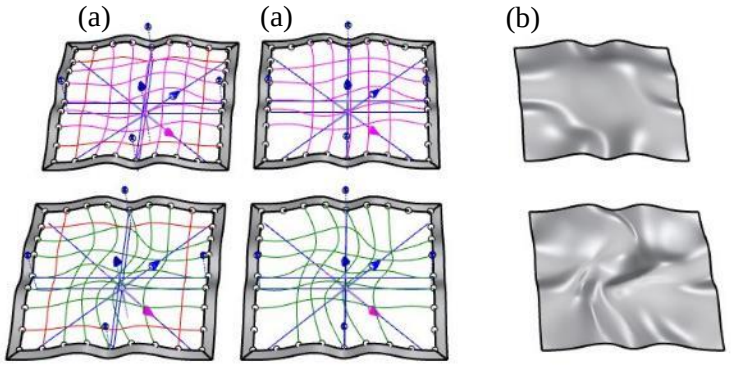


Figure 11. (a) Tangency guide (b) Final surface.

5.2 Tiles Aggregation and Assembly process

The outcome of the previous steps was a tile featuring two unique faces with four identical boundaries. When positioning the tiles adjacent to each other, the variables that affect the final wall design change from manipulating the curvature network to rotating and/or flipping the tile. Consequently, the continuity of the curvature can be transformed to change the final appearance of the wall, leading to a unique design with a continuing curvature each time the assembly order is manipulated (Figure 12). These modular tiles can be manufactured off-site with minimal equipment and required labour, then easily transported to the construction site. Also, this approach allows for modifications and repairs to be conducted more efficiently, contributing to the system's sustainability.

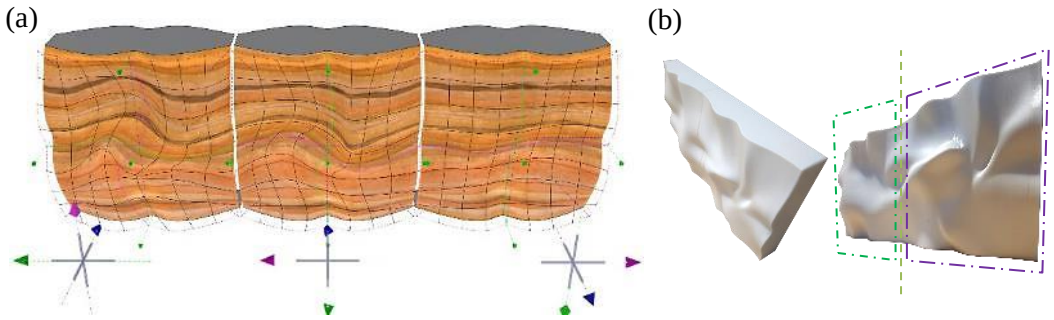


Figure 12. Tiles aggregation: (a) Same tile but flipped and rotated (b) The two distinct tile faces (the dotted lines represent the planes between the two distinct tile faces).

The tile concept can be realized in one of two ways (Figure 13). The first possibility involves creating two unique parts that are rammed as separate tiles and then attached together. The second possibility follows the same idea but includes the addition of insulation material between the tiles to enhance their thermal performance. This approach, which features two connected parts, is inspired by the sandwich structure concept [42].

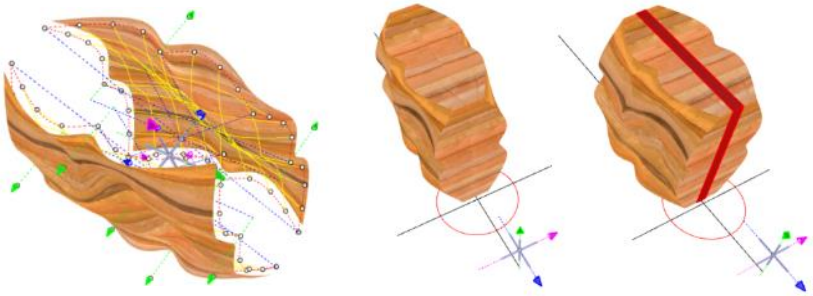


Figure 13. The envisaged design of the 3D tile.

Two design proposals were envisaged using the new 3D RE modular tiles to generate a 200 cm × 200 cm wall, with each tile measuring 50 cm × 50 cm and featuring two distinct faces. The first proposal involved using two different tiles to generate 128 wall design alternatives upon aggregation. The second proposal involves using four different tiles, resulting in 512 wall design alternatives (Figure 14).

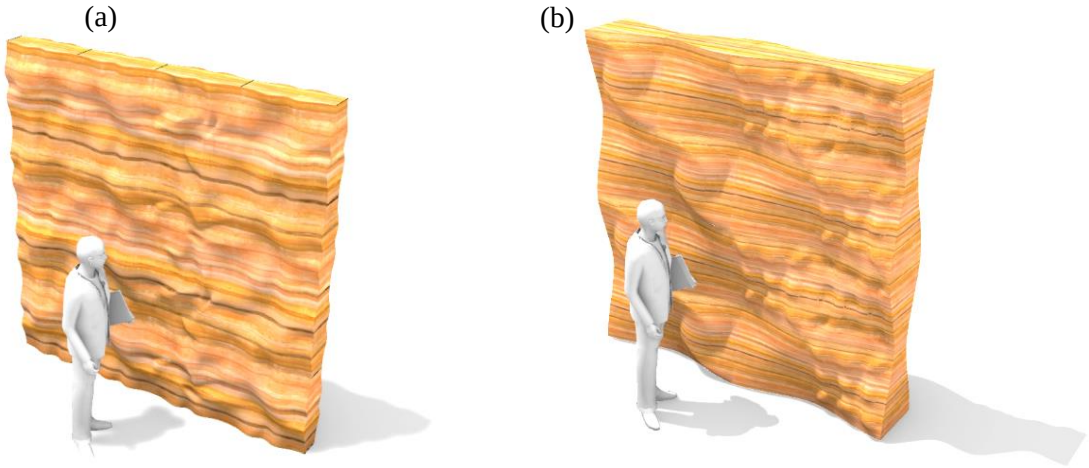


Figure 14. The envisaged two design proposals: (a) using two different tiles, (b) using four different tiles.

5.4 Fabrication Process

The formwork is composed of a curved base and a cubic frame/enclosure. The curved base is digitally manufactured through computer numerical control (CNC) milling from hardwood. The tile creation starts by adding fresh earth mixture inside the cubic mould and onto the curved base, followed by ramming the mixture manually for the first layer of soil, then with a pneumatic rammer for the remaining layers (Figure 15). This method ensures that the modular rammed earth tiles will have precise and intricate curvatures. The produced RE tile has dimensions of 50 cm × 50 cm and the depth of the produced RE tile can be easily adjusted through the cubic frame to serve various architectural requirements and construction purposes (e.g., structural, non-structural elements). The fabrication process also considers the incorporation of necessary additives, such as binders, to enhance the strength and durability of the modular RE tiles. The integration of these materials is carefully balanced to preserve the sustainability benefits of the rammed earth system while achieving the required structural performance (Figure 16).

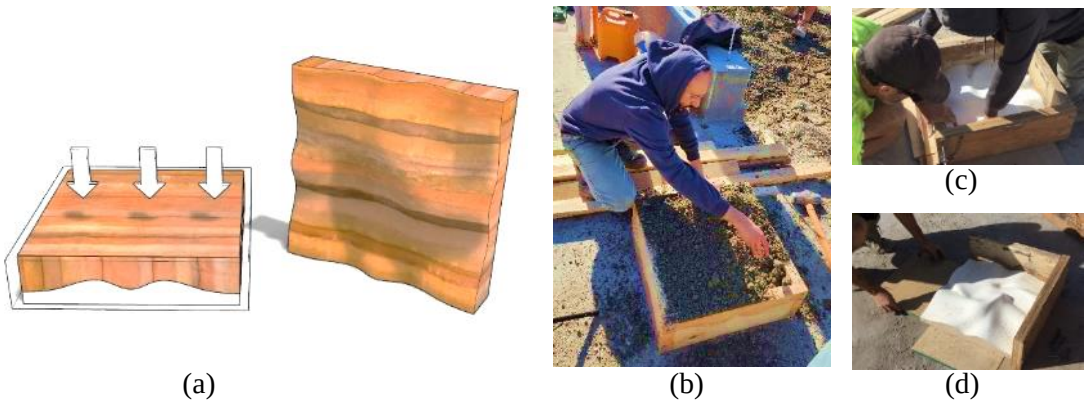


Figure 15. Fabrication process: (a, b) using the hybrid mould (curved CNC milled base and the cubic wooden boundary), (c, d) assembling the cubic wooden boundary of the hybrid mould.

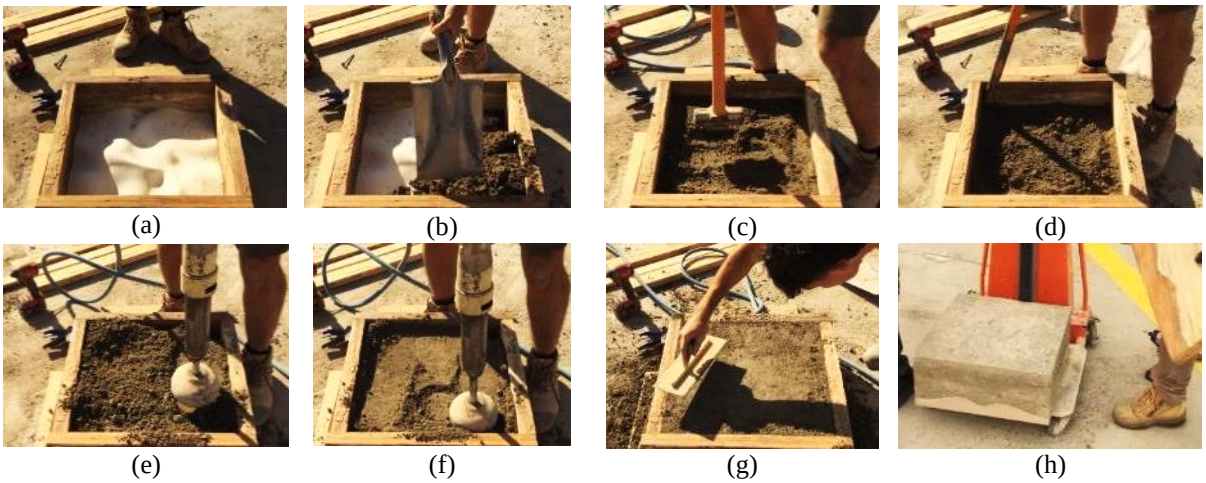


Figure 16. Tile production: (a) the hybrid mould, (b to d) manual ramming, (e to f) pneumatic ramming, (g) finishing, (h) disassembling the hybrid mould's cubic boundary.

The proposed modular rammed earth system in this research combines the sustainability of rammed earth construction with the efficiency of modular integrated construction (MiC) to create a novel approach to sustainable and efficient building practice. By using locally abundant materials, the system reduces environmental impact through off-site production and assembly. Furthermore, the mass customization and mass production aspects of the system offer a scalable solution to accommodate growing market demand. as all tiles have matching edges from all sides (Figure 17).

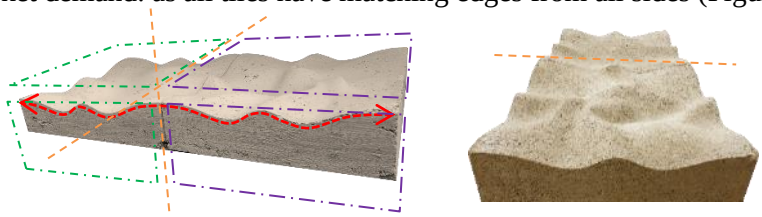


Figure 17. Rammed earth aggregated two distinct tiles (the dotted lines representing the planes between the two distinct tile faces).

6. Discussion and concluding remarks

The proposed system in this study offers a promising approach to manufacturing free-form rammed earth walls. It addresses the challenges associated with both rammed earth construction and modular integrated construction (MiC). By combining the sustainability of rammed earth with the efficiency of MiC, this innovative approach has the potential to contribute significantly to a more sustainable and efficient built environment. Further research and development are needed to refine the system and validate its effectiveness in full-scale construction. This includes replacing the cement in the soil mix with bio-binders. Future improvements are planned to enhance the workability and adjustability of the hybrid mould. These enhancements will include testing the feasibility of ramming both sides of the tile at the same time (Figure 18).

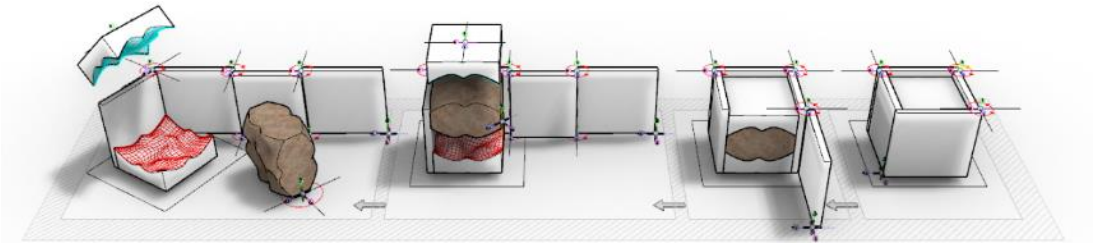


Figure 18. Further mould development to be tested.

References

[1] H. Niroumand, M. F. M. Zain and J. Maslina, "Rammed earth theory in earth architecture," *African Journal of Agricultural Research*, vol. 9, pp. 432–435, 2014.

[2] H. Niroumand, R. Akbari, K. Khanlari, A. B. Gültekin and J. A. Barcelo, "A systematic literature review of rammed earth walls," *Soil Mechanics and Foundation Engineering*, vol. 58, pp. 295–301, 2021.

[3] A. Preciado and J. C. Santos, "Rammed earth sustainability and durability in seismic areas as a building material," *IOP Conference Series: Earth and Environmental Science*, vol. 410, 12108, 2020.

[4] P. Walker, R. Keable, J. Martin and V. Maniatidis, *Rammed Earth: Design and Construction Guidelines*, IHS BRE Press, 2005.

[5] M. R. Hall, R. Lindsay and M. Krayenhoff, *Modern Earth Buildings: Materials, Engineering, Constructions and Applications*, Woodhead publishing ltd, 2012.

[6] H. Anysz, Ł. Brzozowski, W. Kretowicz and P. Narloch, "Feature importance of stabilised rammed earth components affecting the compressive strength calculated with explainable artificial intelligence tools," *Materials*, vol. 13, no. 10, 2317, 2020.

[7] M. I. Gomes, T. D. Gonçalves and P. Faria, "Unstabilized rammed earth: characterization of material collected from old constructions in south portugal and comparison to normative requirements," *International Journal of Architectural Heritage*, vol. 8, no. 2, pp. 185–212, 2014.

[8] N. C. Consoli, L. Festugato, da and R. C. Cruz, "Key parameters for strength control of rammed sand–cement mixtures: Influence of types of Portland cement," *Construction and Building Materials*, vol. 49, pp. 591–597, 2013.

[9] S. Serrano, L. Rincón, B. González, A. Navarro, M. Bosch and L. F. Cabeza, "Rammed earth walls in Mediterranean climate: material characterization and thermal behaviour," *International Journal of Low-Carbon Technologies*, vol. 12, pp. 281–288, 2016.

[10] A. Preciado and J. C. Santos, "Rammed earth sustainability and durability in seismic areas as a building material," *IOP Conference Series: Earth and Environmental Science*, vol. 410, 012108, 2020.

[11] M. Vasilios and W. Peter, "Structural capacity of rammed earth in compression," *Journal of Materials in Civil Engineering*, vol. 20, no. 3, pp. 230–238, Mar. 2008.

[12] M. Dabaieh, *Building with Rammed Earth*, Lund university, 2014.

[13] G. Giuffrida, R. Caponetto and M. Cuomo, "An overview on contemporary rammed earth buildings: technological advances in production, construction and material characterization," in *IOP conference series: Earth and Environmental Science*, IOP Publishing, 2019, 012018.

[14] D. Easton, *The rammed earth house*, White River Junction, Vermont, USA: Chelsea Publishing Company, 1996.

[15] S. Abdelmageed and T. Zayed, "A study of literature in modular integrated construction-critical review and future directions," *Journal of Cleaner Production*, vol. 277, 124044, 2020.

[16] I. laili Jabar, F. Ismail and A. A. Mustafa, "Issues in managing construction phase of IBS projects," *Procedia-Social and Behavioral Sciences*, vol. 101, pp. 81–89, 2013.

[17] M. Kamali and K. Hewage, "Life cycle performance of modular buildings: A critical review," *Renewable and sustainable energy reviews*, vol. 62, pp. 1171–1183, 2016.

[18] C. T. Haas, J. T. O'Conner, R. L. Tucker, J. A. Eickmann and W. R. Fagerlund, "Prefabrication and preassembly trends and effects on the construction workforce," *Center for Construction Industry Studies*, 2000.

[19] T. J. Chai, C. S. Tan, T. K. Chow, P. C. H. Ling and H. B. Koh, "A Review on prefab industrialised building system modular construction in malaysia: The perspective of non-structural studies," *The Advances in Civil Engineering Materials: Selected Papers of the ICACE 2018 held in Batu Ferringhi, Penang Malaysia*, 9–10 May 2018, pp. 11–21, 2019.

[20] W. Ferdous, Y. Bai, T. D. Ngo, A. Manalo and P. Mendis, "New advancements, challenges and opportunities of multi-storey modular buildings–A state-of-the-art review," *Engineering Structures*, vol. 183, pp. 883–893, 2019.

[21] A. A. Rahim and S. L. Qureshi, "A review of IBS implementation in Malaysia and Singapore," *Planning Malaysia*, vol. 16, pp.4–11, 2018.

[22] S. Srisangeerthanan, M. J. Hashemi, P. Rajeev, E. Gad and S. Fernando, "Review of performance requirements for inter-module connections in multi-story modular buildings," *Journal of Building Engineering*, vol. 28, 101087, 2020.

[23] J. Li, H. Liu, J. Zuo, R. Xia and G. Zillante, "Are construction enterprises ready for industrialized residential building policy? A case study in Shenzhen," *Sustainable Cities and Society*, vol. 41, pp. 899–906, 2018.

[24] S. Liu, A. Mansoor, B. Kugyelka, A. Bouferguene and M. Al-Hussein, "On-site assembly of modular building using discrete event simulation," in *2019 Winter Simulation Conference*, IEEE, 2019, pp. 3008–3018.

[25] Nick Bertram, Steffen Fuchs, Jan Mischke, Robert Palter, Gernot Strube and Jonathan Woetzel, "Modular construction: From projects to products," 2019. Accessed: Mar. 14, 2023. [Online]. Available: https://www.mckinsey.com/capabilities/operations/our-insights/modular-construction-from-projects-to-products

[26] G. T. Ciurileanu and I. Horvath, "Modular building using rammed earth," *Acta Technica Napocensis: Civil Engineering & Architecture*, vol. 55, no. 2, pp. 173–181, 2012.

[27] B. Khadka, "Rammed earth, as a sustainable and structurally safe green building: a housing solution in the era of global warming and climate change," *Asian Journal of Civil Engineering*, vol. 21, pp. 119–136, Feb. 2020.

[28] G. Giuffrida, R. Caponetto, F. Nocera and M. Cuomo, "Prototyping of a novel rammed earth technology," *Sustainability*, vol. 13, no. 21, 11948, 2021.

[29] M. Gomaa, S. Schade, D. W. Bao and Y. M. Xie, "Automation in rammed earth construction for industry 4.0: Precedent work, current progress and future prospect," *Journal of Cleaner Production*, vol. 398, 136569, 2023.

[30] V. Maniatidis and P. Walker, "A review of rammed earth construction," *Innovation Project "Developing Rammed Earth for UK Housing", Natural Building Technology Group, Department of Architecture & Civil Engineering, University of Bath*, vol. 12, 2003.

[31] F. E. Boafo, J.-H. Kim and J.-T. Kim, "Performance of modular prefabricated architecture: Case study-based review and future pathways," *Sustainability*, vol. 8, no. 6, 558, 2016.

[32] H. Niroumand, M. F. M. Zain and M. Jamil, "Modern rammed earth in earth architecture," *Advanced Materials Research*, vol. 457–458, pp. 399–402, 2012.

[33] Q.-B. Bui, J.-C. Morel, B. V. V. Reddy and W. Ghayad, "Durability of rammed earth walls exposed for 20 years to natural weathering," *Building and Environment*, vol. 44, no. 5, pp. 912–919, 2009.

[34] G. Giuffrida, R. Caponetto and M. Cuomo, "An overview on contemporary rammed earth buildings: technological advances in production, construction and material characterization," in *IOP conference series: Earth and Environmental Science*, IOP Publishing, 2019, 012018.

[35] B. V. V. Reddy and B. V. V. Reddy, *Compressed Earth Block and Rammed Earth Structures*, Springer Nature Singapore Pte Ltd, 2022.

[36] M. Rauch, "Earth house with European Standard: a review of the project 'rammed earth house'by the company Lehm Ton Erde Baukunst GmbH (Soil clay earth building art Ltd.) in Schlins, Austria," in *International Symposium on Earthen Structures*, 2007, pp. 22–24.

[37] M. Sauer, *Martin Rauch, refined earth: construction & design with rammed earth*, Detail-Institut für internationale Architektur-Dokumentation GmbH & Company KG, 2015.

[38] Lehm Ton Erde Baukunst GmbH, "Alnatura Campus," 2017. https://www.lehmtonerde.at/en/projects/project.php?pID=97 (accessed Mar. 14, 2023).

[39] David freeman, "Form earth," 2020. https://formearth.com/ (accessed Mar. 14, 2023).

[40] E. Hurtado and I. Eloualid, "Engineered cast earth," 2016.

[41] [POTplus] Design Research Group Fulya Özsel Akipek and Tuğrul Yazar, "https://potplus.org/common-action-walls/," *https://potplus.org/common-action-walls/*, 2017.

[42] H. Mei, H. Li, Z. Jin, D. Yang, C. Liang, L. Cheng, L. Zhang, 3D-printed SiC lattices integrated with lightweight quartz fiber/silica aerogel sandwich structure for thermal protection system," *Chemical Engineering Journal*, vol. 454, 140408, 2023.

IASS 2023
July 10–14 Melbourne
Integration of Design and Fabrication

Proceedings of the IASS Annual Symposium 2023
Integration of Design and Fabrication
10–14 July 2023, Melbourne, Australia
Y.M. Xie, J. Burry, T.U. Lee and J. Ma (eds.)

Complex digital modelling for low-cost construction of East African vernacular architecture

Joanna Maria LESNA[a], Xavier de KESTELIER[a,*]

[a,*] Hassell Studio
London, United Kingdom
xdekestelier@hassellstudio.com

Abstract

The technological advances in computer-aided design allow architects to digitally model and fabricate complex structures. However, these are typically utilised within large, well-funded teams in developed countries. Drawing on a philanthropic partnership between creative activists TO:, international architecture studio Hassell and Ugandan based architecture firm Local Works, this project demonstrates the potential for utilizing cutting-edge technology to construct buildings using the most suitable materials, thereby maximizing performance and sustainability in even the most remote locations.. This aims to provide equal opportunities to support the most vulnerable. The Bidi Bidi Music Academy and Art Centre project merges the use of sophisticated design tools with traditional construction methods to develop a complex structure in one of the largest refugee settlements worldwide. The intricate geometry of the building addresses three primary design objectives: (1) creating a culturally significant structure that instills pride in the local community and establishes a sense of identity for the area, including the inclusion of an education space with excellent acoustic properties; (2) providing environmental protection through the creation of shaded and naturally ventilated communal spaces; and (3) supporting life by incorporating a water collection system for drinking and sanitation. The paper describes process of developing and evaluating the pre-defined global geometry of the Academy (top-down) for the bespoke functions in relation to the local material properties and fabrication methods (bottom-up). The project emphasises the translation of complex elliptical global form into simple elements and guides for the construction by newly trained local workers of the refugee settlement. This publication aims to expand the use of computer-aided techniques for digital modeling in the architectural industry, particularly within impoverished urban areas. Addressing global social and environmental challenges calls for innovative approaches that uplift local communities and inspire the world. The project proves that eco-friendly building materials and construction technologies can be cost-effective while adhering to stringent building standards. Complex and optimized digital models can be translated into straightforward components that local labor can produce and assemble, thereby minimizing the carbon footprint.

Keywords: multi-scalar modelling, material performance, acoustics, BIM, mixed reality technologies, Compressed Stabilized Earth Block, CSEB, Sub-Saharan Africa, vernacular, low-cost construction

Copyright © 2023 by Joanna Maria LESNA and Xavier de KESTELIER. Published in the Proceedings of the IASS Annual Symposium 2023 with permission.



Figure 1. Visualization of the Bidi Bidi Music Academy and Art Centre (north entrance).

1. Introduction

1.1. Context

1.1.1 Bidi Bidi refugee settlement

Bidi Bidi refugee settlement is the largest refugee settlement in Africa, the second largest in the world. A small village on the South Sudan border, Bidi Bidi became officially recognized as a refugee settlement in August 2016. According to UNHCR statistics, as of August 2019 Uganda was hosting over 1.3 million refugees, making it the largest host country in Africa. Since then, Bidi Bidi has grown to cover nearly 250 km and is now home to a population of nearly 250,000 refugees - over 42,000 households, the majority of whom are South Sudanese refugees forced to flee their homes due to violent conflict. (UNHCR 2020) The Bidi Bidi Music and Arts Centre will provide a platform for gifted artists based in the Bidi Bidi settlement, and their facilities will aid in healing process for a community that has suffered in immerse trauma.

1.1.2 Local climate

Northern Uganda is located a few hundred miles north of the equator, the area is hot and dry throughout the year and particularly in the winter. The key environmental challenge of the designing in this climate is to provide an efficient protection from the sun as well as heavy rainstorms, including driving rain at almost horizontal angles.

1.1.3. Context of Music and Arts Centre

The objective of the Music and Arts Centre is to offer a space for music, art, and various cultural activities for the Bidi Bidi refugee settlement community. The facility comprises a performance area, recording studio, music classroom, changing rooms, and storage space. Recognising the central role of music in South Sudanese culture and the settlement's current lack of resources to foster such programs,

the centre will serve as a crucial hub for creative expression and individual empowerment, contributing to the healing process for a community that has endured immense trauma.

1.2. Local resources

1.2.1. Compressed Stabilized Earth Blocks

In Uganda, locally produced bricks require a substantial amount of wood as fuel for the firing process. The supply of wood near the Bidibidi settlement is limited due to deforestation for firewood. Scarcity of firewood is also a common source of conflict between refugees and host communities in Northern Uganda. Implementing alternative technology could help preserve the environment.

Compressed Stabilised Earth Block (CSEB) technology is one such alternative that has gained increasing recognition, particularly in East Africa (UN-HABITAT, 2009). CSEBs are construction blocks made from a mixture of soil and a stabilizing agent, compressed using various types of manual or motor-driven press machines. Compared to alternatives like fired bricks, CSEBs offer lower construction costs at similar quality levels and significantly reduce environmental impact. The blocks are fabricated on-site and cured over time, eliminating the need for fuel such as wood and thereby preventing environmental degradation.

1.2.2. Water

Bidi Bidi lacks a general water supply. Near the site, there is a manually operated borehole from which the community collects water for drinking and sanitation purposes. However, the water is contaminated due to limited sanitation infrastructure. Uganda frequently experiences intense tropical storms. Meteorological data for Northern Uganda indicates that there are 31 rain events per year, with each releasing over 10mm of precipitation within 15 minutes.

One of the primary design objectives was to harvest rainwater and provide water storage that would last throughout the dry season. By employing digital tools, the designers could calculate, visualize, and optimize the amount of water collected from the building's roof. This process allowed for predictions of water usage within the facility, and the excess collected water is intended to be shared with the community.

2. Methodology

Since the advent and widespread availability of parametric 3D modeling software in the early 2000s, architects have been able to design and realize complex forms. The utilization of computational methods in architectural design has become commonplace in practice, incorporating performance analysis as an integral component of the design process (Kolarevic and Malkawi, 2005).

However, the employment of these advanced tools and the development of complex geometric shapes has typically been limited to larger projects with substantial budgets. In contrast, the Music and Art Centre project, characterized by its high cultural aspirations, was undertaken pro bono by the architectural firm Hassell Studio and engineering firm Arup. In this instance, parametric design and digital analysis tools were utilized to minimize the need for an extensive design team. Design development and optioneering were efficiently carried out through iterative modifications of the parametric model. Early integration of wind and solar analysis during the design process facilitated the optimization of the overall design. Additionally, augmented reality (Hololens) and virtual reality (Twinmotion) technologies were employed for community engagement within the camp.

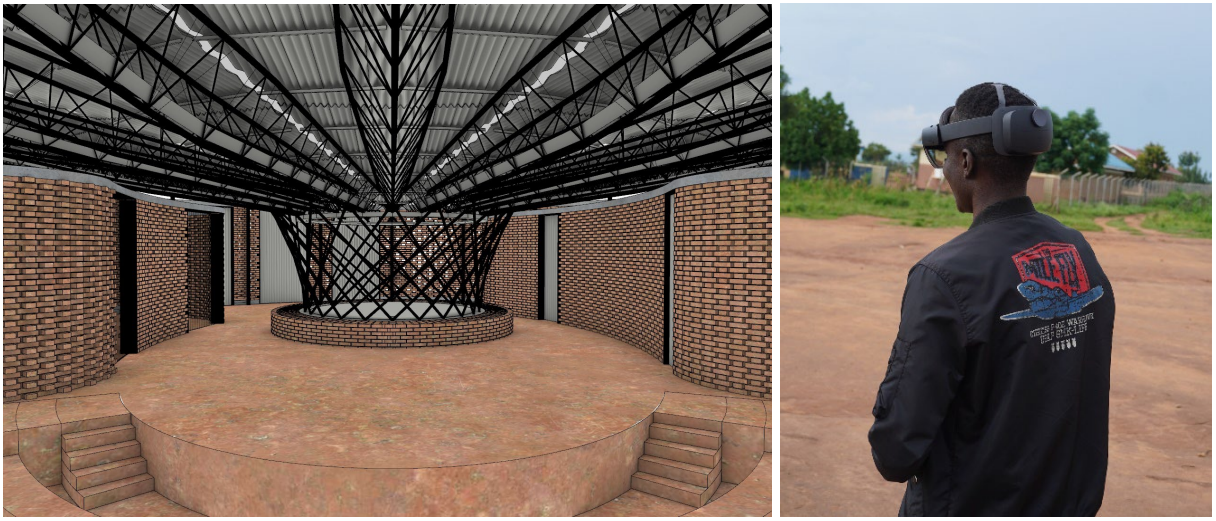


Figure 2. Visualising the project on site through Microsoft Hololens

3. Geometry

3.1. Planning and form development

The building's overall plan is elliptically shaped, a geometry derived from its relationship to the site. Situated along the existing footpath leading to a borehole, the structure serves as a creative and social hub for the local community, inviting individuals to pass straight through the building or walk along its curved façade.

An ellipse features two foci, each of which holds not only mathematical significance but also essential architectural functions in this design. The first focus, an oculus, permits daylight to enter and channels rainwater from the expansive roof to water collection tanks. The second focus serves as a stage for the amphitheatre, accommodating local artist performances and community events.

The amphitheatre constitutes the primary design function and is accessible from the south, facilitating community gatherings and spotlighting performing artists. The building's design follows the terrain's slope to utilize the natural gradient for amphitheatre seating.

Additional rooms are situated along the ellipse's short axis: a music classroom featuring a translucent polycarbonate corrugated pivoting door for natural light is located to the left of the amphitheatre, while changing rooms for performers, storage for music equipment, and a recording studio are found to the right. As visitors proceed towards the northern exit along the long axis, they pass through the multifunctional foyer-art exhibition space and oculus.

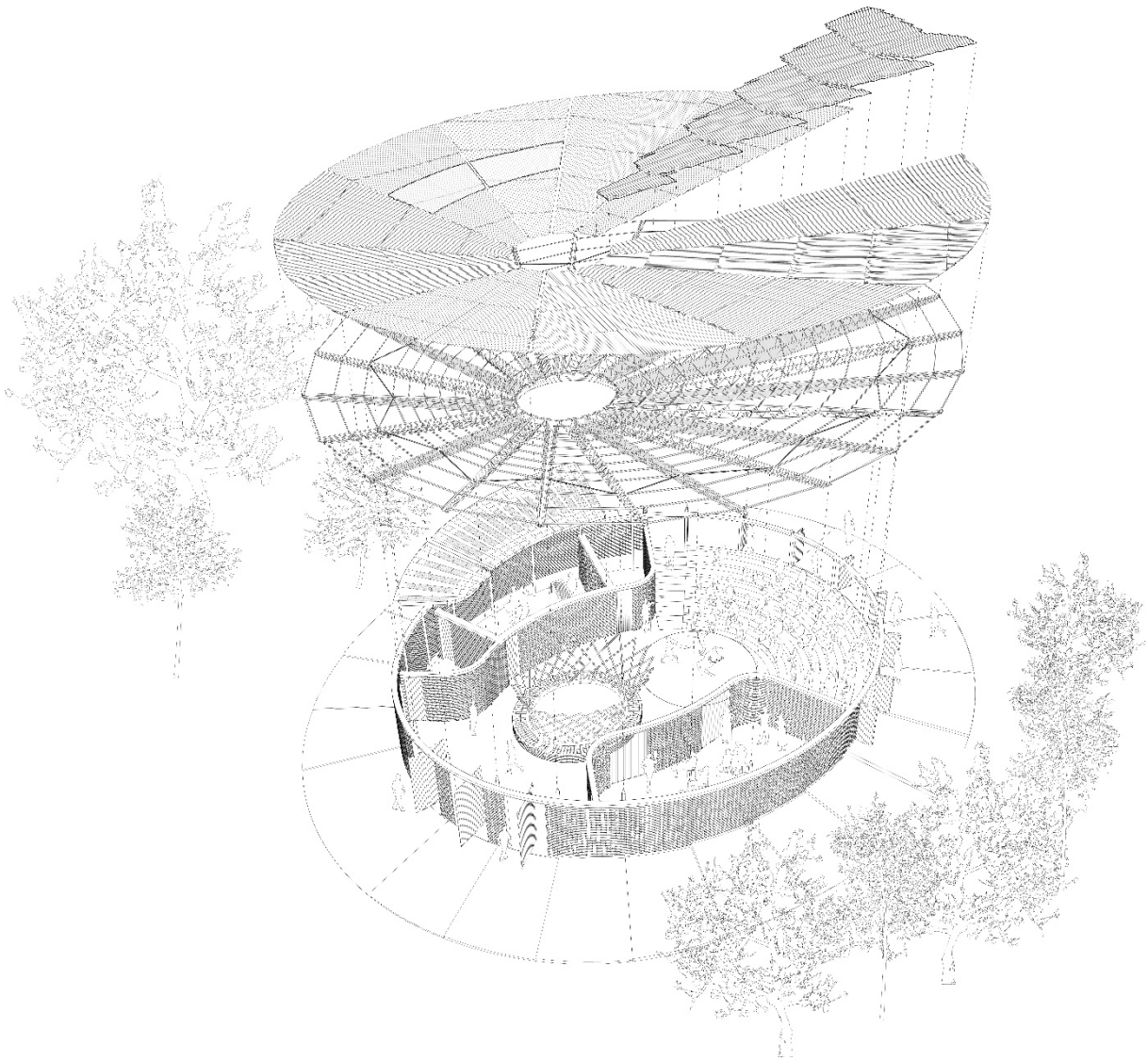
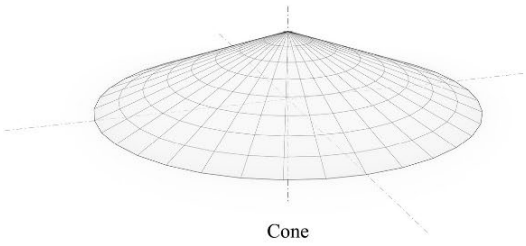
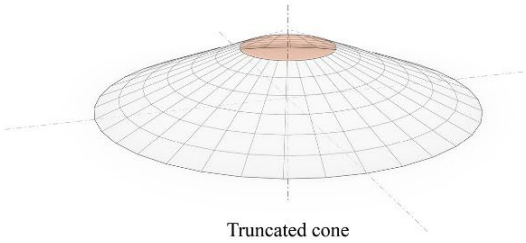


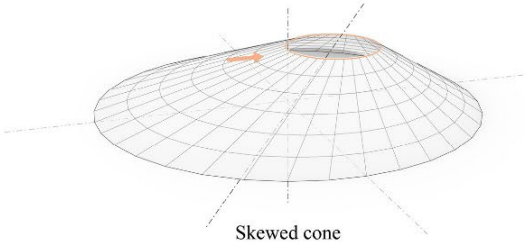
Figure 3. Exploded axometric drawing of the Bidi Bidi Music Academy and Art Centre.



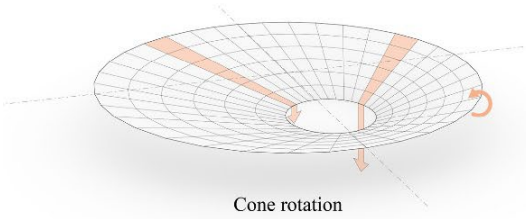
Cone



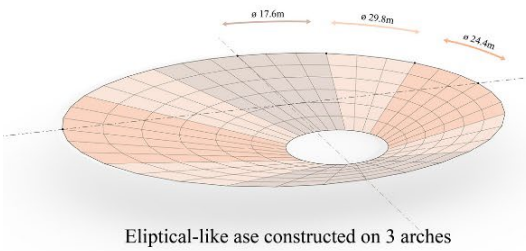
Truncated cone



Skewed cone



Cone rotation



Eliptical-like ase constructed on 3 arches

3.2. Structure and roof

The roof geometry adheres to the building's elliptical shape, extending approximately 2 meters beyond the building envelope. This overhang serves to protect the brick wall against erosion caused by heavy rainfall. Furthermore, the roof safeguards the interior from rainfall and direct sunlight.

3.2.1. Roof geometry

The roof is designed as a large funnel, collecting rainwater at the centre of the building. To facilitate proper flow on the roof surface, a minimum slope of 6% is required. The oculus, symmetrically positioned within one of the two foci of the elliptical curve, results in a roof slope varying between 6% and 11% due to differing distances from the roof's edge and the oculus.

Initially, the roof's geometry comprised a double-curved surface, which precluded a quadrilateral flat panel solution. To reduce costs and simplify manufacturing and assembly, the double-curved geometry needed conversion into a developable surface, enabling mapping onto planar quadrilateral panels. This optimization was achieved through torsal ruling of the surface, ensuring the same tangent plane at all points of the same ruling. One geometry capable of utilizing torsal ruling for isometric mapping is a cone (Pottmann et al., 2007). Given the planar curved external profile of the roof based on three arcs and the oculus's centre, the geometry can be translated into a basic cone.

The oculus's opening was fashioned by removing surfaces near the cone's vertex, resulting in a truncated cone geometry. The geometry was then transformed into a skewed cone by shifting the vertex along the ellipse's long axis, as the oculus resides in one of the ellipse's two centers. This alteration rendered the geometry reflexively symmetrical along the long axis. Subsequently, the cone was inverted, employing its lateral faces to direct rainwater towards the oculus. Analogous to the roof's edge, the oculus's curve is based on an ellipse composed of three arcs with varying radii and identical lengths. Consequently, three distinct truncated, skewed, and inverted cones were utilized to

construct the roof's form, symmetrical along the long axis.

3.2.2. Structure and construction strategy

Due to lack of wood in Bidi Bidi, the roof structure is made of light weight steel which is pre-fabricated in Kampala, the capital of Uganda. The roof decking is made out off widely available corrugated panels.

The geometry of the roof was divided based on the 3 arches into 24 parts, which 12 of them are symmetrical. Then, the parts were divided into groups of two, and the corrugated aluminium cladding was positioned parallel to the common edge of the 2 parts. This way the corrugation guides the rainwater in one direction, directing it to the oculus. (Figure 6)

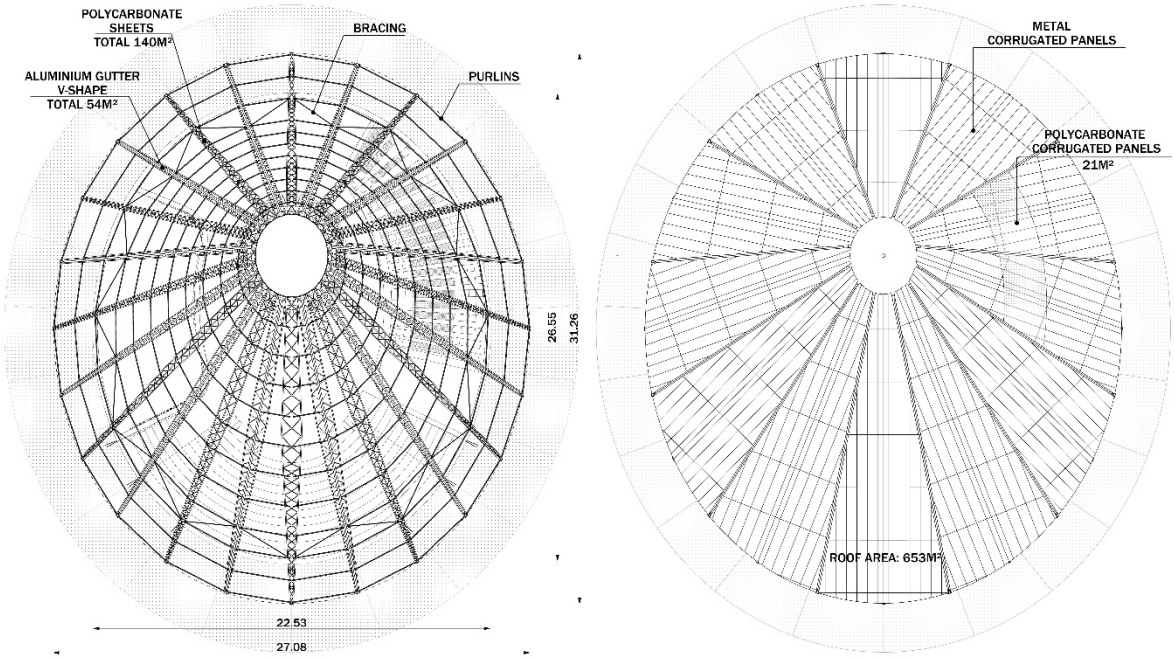


Figure 4. Drawings of the roof structure

However, due to the conical shape of the roof and corrugation pattern, one of the edges would need a drainage. Therefore, the gutters in-between every second roofing part were introduced. V-shaped gutter lying in the truss is partially made of aluminium, and partially made of polycarbonate. This allowed an additional indirect daylight to enter the interior space.

The truss structure follows the edges of the bespoke roofing parts, and it is organised radially to the oculus. It lays on columns attached to the external brick wall and central hyperbolic paraboloid column around the oculus. By using hyperbolic paraboloid one can produce the structure out of straight steel elements (Whitehead 2003).



Figure 5. Full scale mock up of structure and CEB wall at the offices of Localworks.



Figure 6. Interior render of the performance area

3.3. Brick walls: daylight, ventilation and acoustic performance

Integration of the multiple scales, geometrical and material performance as well as fabrication process constrains into early-stage design allows to create complex architectural model. However, this complexity doesn't need to be reflected in the fabrication and assembly processes. To reduce the costs, only one module of CEB with the dimensions 250x120x90mm is used for the wall construction. By changing the position and pattern of the CEB unit, we are designer is able to create a wall which varies in performance: acoustics, natural ventilation, daylight diffusion but also aesthetics. The performative variety of the predefined rooms according to the specific usage is possible to program using a multi-

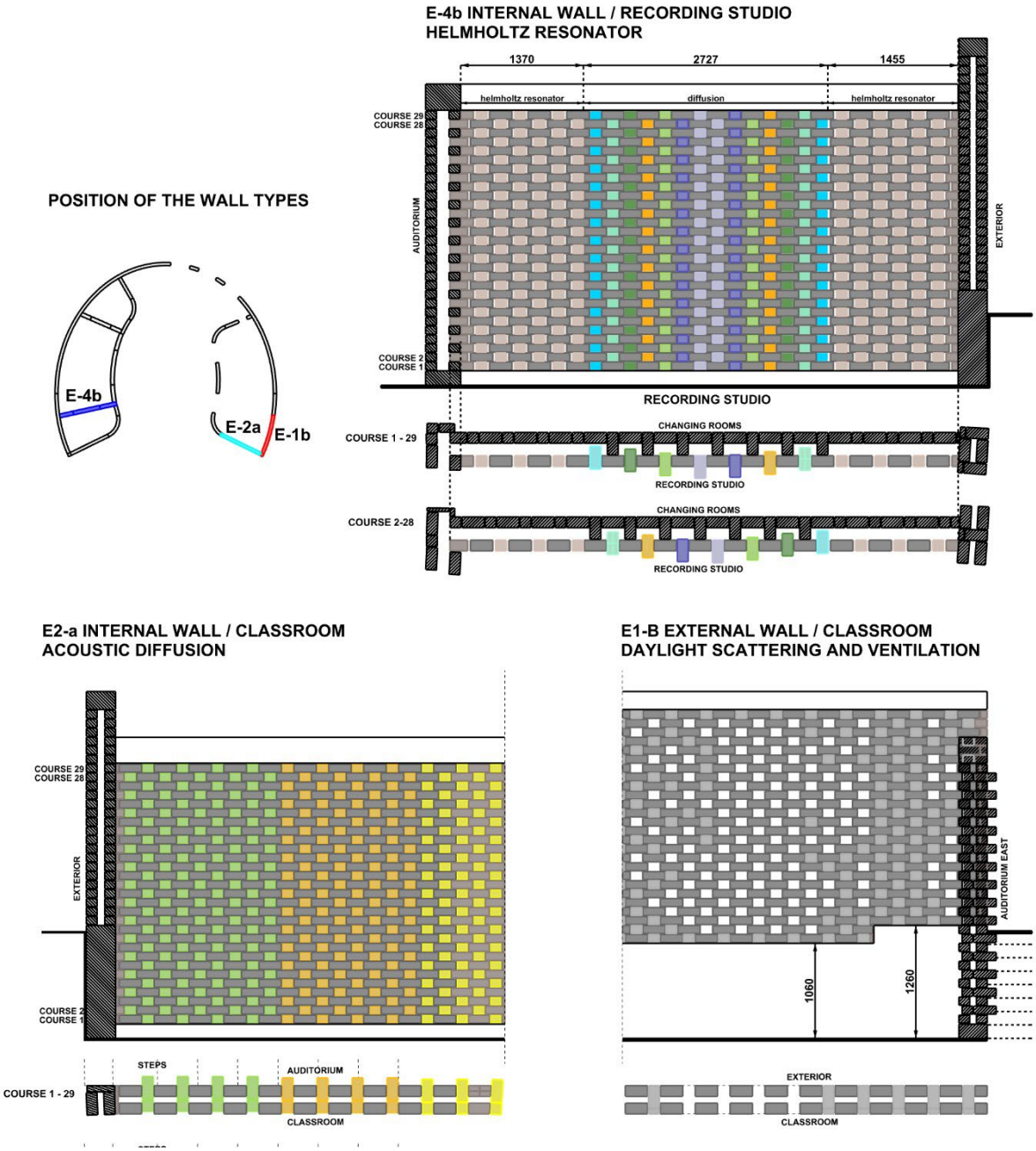


Figure 7. Drawings of the different brick patterns.

scalar approach of digital modelling and generation of bricks in various arrangement. This is followed by digital simulations and consultations with local architect and an engineer.

The spaces of recording studio, amphitheatre area and music classroom need specific acoustic performance embodied in the geometry. The complexity of the surfaces was created by altering the geometry of the wall by changing the arrangement and patterns of the CEB units. Walls of recording studio consist of two types: 1) Sound diffusers- these are made by altering protrusion distance between 70-30mm and are located in the middle of the wall length; 2) Sound absorber using Helmholtz resonator brick array, located in the corners of the room. This type consists of 3 brick layers as in the top view from inside: 1) brick layer with 3mm holes to get the sound wave into the resonator; 2) cavity gaps with fibrous absorber, 1m wide divided with unit of brick; 3) flat and closed brick layer based on Flemish bond. In a wide frequency range, the resonators have insufficient performance. Hence, the suitable size for each resonator needs to be studied and tested to widen the frequency range of sound absorption (Basirjafari 2020).

Recording studio needed to be design as a closed space, because of noises. However, walls in the music classroom and amphitheatre have additional functions.

To prevent the low but intense morning and evening sun from penetrating deep into the building – and their sides facing north and south as transparent as possible – to maximise on natural daylight and airflow. The bricks are arranged in the way that the header in the Flemish bond is removed to allow daylight to the room and naturally ventilate the space. The pattern was programmed based on the daylight analyses and users' experience and combined with acoustic patterns.

The project uses physical prototypes, mock-ups and mixed reality smart glasses as a means to explore and evaluate the methods presented. The workflow creates opportunities for feedback across the design chain and increased flexibility in effecting changes.

4. Conclusion

This publication is intended to broad the application of computer aided techniques for digital modelling in the architectural industry of the urban poor. The world's social and environmental challenges require novel approaches that elevate the local and inspire the global. The project demonstrates that environmentally friendly building materials and construction technologies can be made more affordable while still meeting rigorous building standards. Complex and optimised digital model can be translated to simple elements which the local labour is able to produce and assemble, which results in reducing the carbon footprint to minimum.

Translation of the complex elliptical and double curved geometry is a result of the fabrication possibilities in the refugee settlements and digital optimisation followed by structural analyses. Geometry of elliptical skewed cone is translated by using 3 arcs as a base instead of ellipse. Therefore, the planar tessellation of metal roof elements was possible for low-cost construction.

Furthermore, the digital tools present the opportunity for incorporating performance analysis into the architectural design process. This paper proves that this can lead to a complex performance by using simple materials and fabrication techniques.

Acknowledgements

The Bidi Bidi Music & Arts Centre was funded by the TO.org donor community. Project concepted by TO.org.

Project team: Hassell Studio (Xavier de Kestelier, Joanna Maria Lesna, Sara Huc, Nikolaos Argyros), Local Works (Felix Holland, Kevin O'Hara, Edson Agume, Wilson Sendikwanawa, Allan Ssemakula, Ayiorwoth Emily, Geoffrey Addah). Engineering was done by Arup (in the concept phase) and Local Works. Acoustic consultation and testing performed by Arup (Matthew Gray). Music programming was

created by Playing for Change Foundation and SINA Loketa in collaboration with TO.org Creative Activists.

References

[1] S. Basirjafari, "Innovative solution to enhance the Helmholtz resonator sound absorber in low-frequency noise by nature inspiration," *J Environ Health Sci Engineer 18*, pp. 873–882, 2020.

[2] B. Kolarevic, "Information master builders. Architecture in the Digital Age: Design and Manufacturing," *Washington: Taylor & Francis*, pp. 56–62, 2005.

[3] B. Peters and T. S. Olesen, "Integrating Sound Scattering Measurements in the Design of Complex Architectural Surfaces: Informing a parametric design strategy with acoustic measurements from rapid prototype scale models," *In FUTURE CITIES: 28th eCAADe Conference Proceedings*, edited by Gerhard Schmitt et al., pp. 481–491, 2010.

[4] H. Pottmann, A. Asperl, M. Hofer and A. Kilian, "Architectural geometry," First edn. Edited by D. Bentley. Exton, *Pa.: Bentley Institute Press*, 2007.

[5] UNHCR, "Uganda Settlement Profile: Bidi Bidi," *UNHCR, January 2018. Bidi Bidi Refugee Settlement Master Plan*, 2020.

[6] H. Whitehead, "Laws of Form," In: B.Kolarevic, (ed.): "Architecture in the Digital Age. Design and Manufacturing," *London: Taylor & Francis*, pp. 83-100, 2003.

IASS 2023
July 10–14 Melbourne
Integration of Design and Fabrication

Proceedings of the IASS Annual Symposium 2023
Integration of Design and Fabrication
10–14 July 2023, Melbourne, Australia
Y.M. Xie, J. Burry, T.U. Lee and J. Ma (eds.)

Design and construction of complex shell structure using U-shaped glass and steel frame with collaborative robotics and human expertise

Lei YU[a,*], Guanqi ZHU[b]

[a,*] Bond University
14 University Drive, Robina, QLD 4266, Australia
leyu@bond.edu.au

[b] University of Queensland

Abstract

This research focuses on designing and constructing a unique extension space using a 60-meter-long and 6-meter-wide curve ruled glass shell structure. The project implemented a well-coordinated data flow across various stages from design to construction, utilising digital design techniques and robotic technology. A digital model of the shell structure was created in the Rhinoceros 3D environment to facilitate the data distribution between design software and construction machines, particularly for the robot system. U-shaped glass panels were used to achieve this innovative space for both interior and exterior surfaces, with a steel structural frame embedded in the U-shaped glass modules. An on-site robot arm system was employed to assist human workers in ensuring the accuracy of the installation of the steel frame, contributing to cost savings in building materials and time efficiency. This experimental project investigates the potential of automation in construction for free-formed buildings in different stages of project delivery. This paper highlights the benefits of using advanced manufacturing and digital design techniques, specifically in complex shell structures, and discusses future developments in the industry.

Keywords: complex shell structure, digital design and fabrication, on-site robotic construction, advanced manufacturing, U-shaped glass panel, collaboration in human and robot, automation in construction

1. Introduction

In the past decade, digital design data has rapidly developed and is widely deployed in the building industry. Building Information Modelling (BIM) [1] is the dominant platform for delivering design data to construction. In addition, multiple types of computer numerical control (CNC) activities take place to address conventional tasks such as laying bricks [2], pouring concrete [3], and surveying construction [4]. Despite these advancements, there are still gaps in accuracy control and flexibility management when transferring information from digital design models to machinery, specifically for in-situ construction and assembly. For instance, if multiple teams and construction materials are not well considered in the programming phases, delays or additional costs might occur due to the automatic machines encountering unforeseen obstacles. Moreover, if the steel structure is deformed slightly by temperature changes or applying payload, but the machines still run the code with un-updated information, accidences such as collision and property damage will occur at a high percentage rate. Human experts' involvement is required to avoid these discrepancies. Consequently, managing the data flow and implementing software to hardware becomes a critical challenge for researchers and practitioners.

Copyright © 2023 by Lei YU and Guanqi ZHU. Published in the Proceedings of the IASS Annual Symposium 2023 with permission.

The building industry recognised the value of using industrial robot arms designed for versatility and adaptation to various applications. Researchers and stakeholders realised that these potential advancements, such as improved accuracy, reduced safety hazards, saved cost, and shortened delivery timeframe [5], offer significant benefits. With a large category of robot modules and configurable end effectors, a single robot arm station or multiple robot arms as a team can execute various jobs on demand. A robot arm system can overtake or reduce conventional construction machines, increasing efficiency and sustainability. Furthermore, robot arm systems can be easily reprogrammed in case of construction deviations from the digital model during a real-time site survey [6], which helps bridge the gaps between design and construction. This advanced solution prevents unexpected time costs in construction and allows architects and contractors to maintain projects' quality as it happens.

This research examined an experimental project to integrate the design and construction process by encouraging collaboration and coordination between human experts and robots. It involved schematic design, design development, project management, prefabrication, and on-site construction. These processes brought together architects, structure engineers, computer programmers, construction workers and a robot arm system in a tightly organised effort. As a result, the U-shape glass panels and steel frame were assembled to form a transparent shell structure that reflects the proposed architectural design scheme. During the shell installation, the capacity of a robot arm system was also enhanced for a broader coverage on a pair of rails to allow its end effector to reach any location as demanded. Furthermore, the industry robot arm can be configured to perform distributed roles in different construction positions. For instance, before moving onto the rails, this robot station was also hired to fabricate 1339 U-shaped glass panels, each with different lengths and edge angles.

2. Design concept, methodology and approach



Figure 1. An adaptive reuse by U-shaped glass shell and steel frame, completed in 2022 (Photo by Yuguang Liu)

2.1 Design concept

The project is an adaptive reuse of an existing building (Fig 1) in an obsolete industrial area. The client was interested in adapting robotic technology with a glass panel system. We took this opportunity to play a complete role in managing design data flow through all phases with a single design team. The existing brick house stands at the site's entrance, where they expected the new building to be intricately connected to the 50-year history of this community, with two sets of abandoned railways running through it. The project aims to turn this area into a modern cultural and art centre. We designed a transparent glass shell that expanded from the existing brick house to metaphorise the transition from the past to the future. This glass shell blends naturally into the old house on one side and is free-standing

on the other side, resulting in a smooth, spiral transition in the middle.

Additionally, the glass wall contrasts sharply with the existing brick wall, creating an inspiring landmark for attracting visitors. The new extension also contributes an open plan space of 310 sqm. The design objective is to seamlessly integrate the new with the old house with the latest design and create a particular sunny space that is visually stunning and functional for its intended purpose (Fig 2).

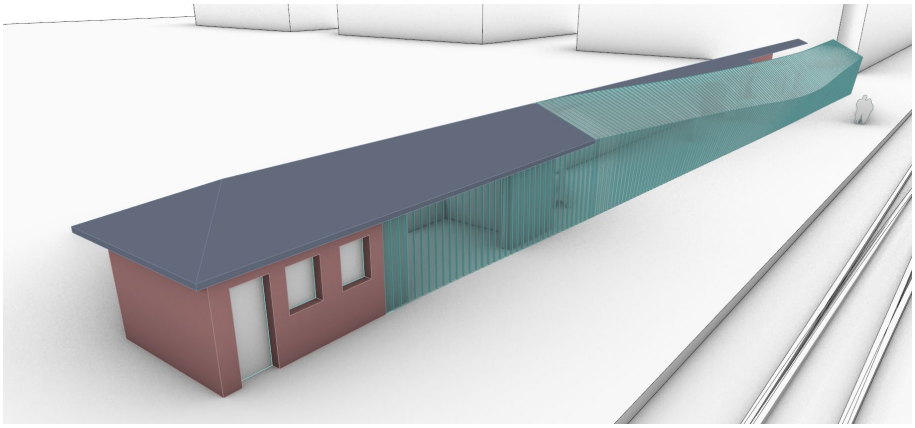


Figure 2. Concept - a transparent shell expanded out from the existing building

2.2. Building material and structure design

To construct glazing space and form the shell, U-shaped glass panels were chosen because it is a popular choice for modern building facades. Compared to the planar glass panel [7] [8] [9], U-shaped glass can provide a simple and cost-effective solution for a curved façade without the need for a mullion system [10]. The manufacturer of the U-shaped glass, ASG, provides specifications that were used in our calculations, which demonstrated that a simple support beam could have a maximum length of 6.47m. This equation assumes I (inertia) is set as 1/100, reflecting the local structural code, E is the Young's Modulus of their U-shape glass panel provided by ASG, and *w* is the wind load set as 0.5n/m. This result is particularly well-suited for our design since the top level of this shell structure is not taller than 5m, and the roof span is no longer than 6m.

$$Lmax = \sqrt[4]{\frac{384*E*I}{5*w}} \tag{1}$$

The curved façade and roof surface can be achieved by using a method called section multiplication. It involves dividing the curved surface into small sections and creating each section by slightly modifying its profile by changing the previous one's shape, foot location, and joint angle. This process is repeated from one end to the other, with gradual variations of the glass modules spacing every 275mm. Consequently, it creates a 10mm seam between the two modules because the U-shaped glass panel is 265mm wide. To meet the aesthetic requirement and provide thermal insulation during winter, the U-shaped glass panel is double-sided on interior and exterior surfaces. Two panels are placed face to face to create a single module, and their bent sides meet each other to form a hollow core with a clearance of 250*120mm.

SGI, the structure consultant, has embraced this approach and is committed to concealing the structure within the glass wall (Fig 3). To reach this goal, we have decided to insert the steel frame by fitting the customised steel studs (120*90mm) inside the hollow core of U-shaped glass panels every 12 modules. In addition, two round beams underneath each side of the north and south roof connect these sectional steel frames into a cohesive structure. The design and development of the structure system follow the design principle of ensuring that the top corner of the glass shell is free from any visual obstacle, maintaining a clear and crystal effect on the other two side corners as well.

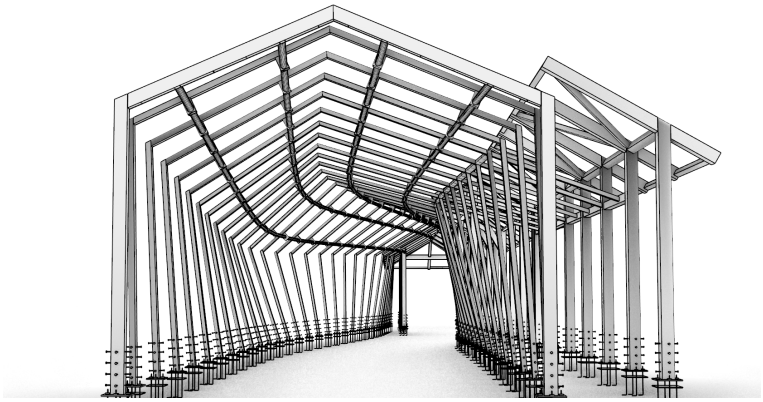


Figure 3. Steel frame structure

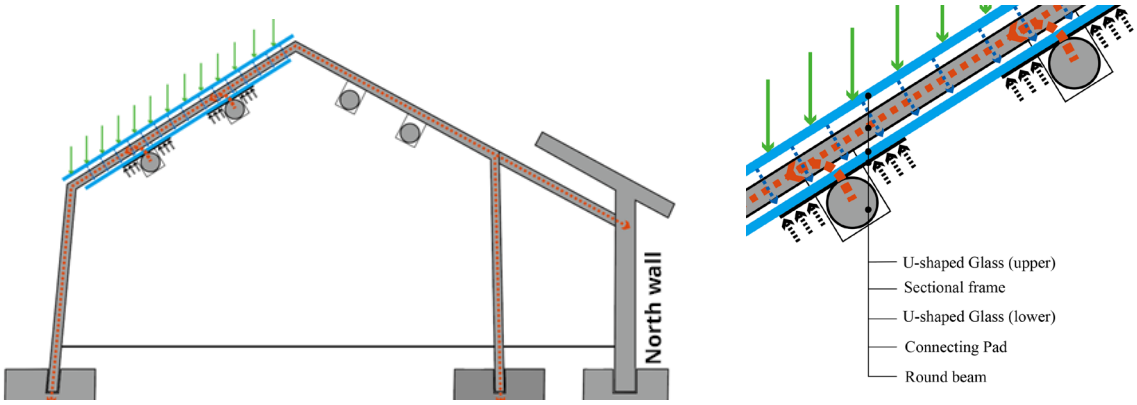


Figure 4. Section of steel design for permanent structure load and force

Four circular beams are responsible for bearing all roof loads, including the dead loads of U-shaped glass panels, metal connectors, lighting fixtures, ventilation system, and the live loads of moisture precipitation such as rain, snow, and ice together with wind loads (Fig 4). The roof steel frames in the glass core supported the loads on the four beams. Ultimately, the side steel frames transfer the upper load from the top steel frame downwards to the foundation. The glass modules in the façade and the interior partition wall are mostly self-supporting and occur in two positions: leaning inwards and outwards. The ones leaning inwards do not need any structural treatment. However, for the other position, a prestressed stainless-steel cable is anchored between the upper corner of the glass module and the lower round beam to prevent glass panels from falling outwards. The steel frame is secured by a series of connecting beams welded to the northern wall's primary columns.

2.3. Prefabrication

The primary challenge in constructing a glass shell structure is ensuring that the U-shaped glass panels and the steel frame are appropriately coordinated to prevent damage to the glass panel. Despite the structure engineer's best effort to reduce the section size of the steel studs embedded in the hollow space, there is only 20mm between the glass panel and the steel frame. This narrow space raises a challenge because the glass panels must be produced and toughened before the completion of the steel frame's construction, leaving no room for modification if the steel frame is installed below the required tolerance level. Any deviation of the steel frame from the digital model beyond +/-10mm will result in a smaller space (of less than 10mm), where a collision with glass panels could occur and damage the glass. Therefore, all U-shaped glass panels should be prefabricated precisely to follow the design data, leaving the challenge entirely in the steel frame construction.

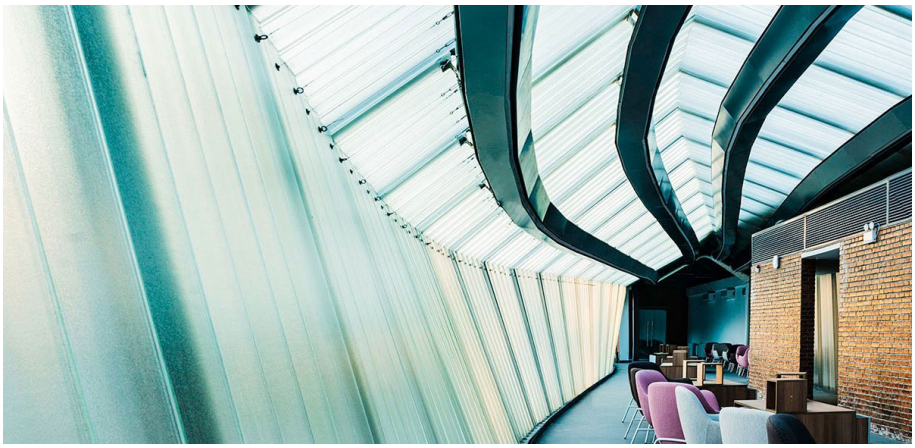


Figure 5. Interior view of the glass shell space



Figure 6. Robot system cuts U-shaped glass panels in the manufacturer site. (Photo by Ji Shi)

U-shaped glass panels can be engineered and tested to comply with various building codes and safety standards, such as ASTM E3100 for glass strength and ASTM E2353 for hurricane resistance [11]. The typical supplied U-shaped glass panel is 7mm thick, 6000mm long, 265mm in outer width and has two 65mm folded rims. We developed and test-proven a robotic glass-cutting technique from previous projects. We adopted the grinding-through technique with a diamond blade to fabricate the unique panels. Cutting U-shaped glass panels in irregular angles and shapes, especially in sharp corners at the edge of folded rims, can result in high-rate failures using the general cutting method by the stroke cutter. The grinding speed control in different cutting stages is also critical to minimise breakage because the inappropriate speed will cause cracks due to microscopic crevices and stress points. The whole prefabrication statistically has a 10% failure rate in the cutting and toughening process compared to a 3-5% loss in the general cutting technique. We also invited the skilful glass-cut expert to manually make the panels in this project. It turned out to be a 50% failure, and it took an undetermined amount of time to fix the edges to the suitable shapes with the angled grinder by hand - the same task took at most 5 minutes for each panel by the robotic cutting station. This 'on-site' prefabrication, where we moved our robot station to ASG's factory (Fig 6), also helps reduce material waste, as glass cullet can be returned to raw supply immediately.

We hired a KUKA KR120 R3900 prime to produce these unique glass panels, which fully packed a 25m cargo truck. In addition, an 8mm seam is offset for every mitre joint of the glass panels, which is used for inserting the connecting pad and leaving some space to cope with the deviation during installation.

The robotic cutting system can produce every panel with an accuracy of +/-0.5mm in length and +/-0.1 in angles, satisfying the design requirements.

2.4. Project Integration

2.4.1. Digital Workflow

Designing and constructing this project was managed and executed through a digital workflow [12]. A central model was created using Rhinoceros 3D + Grasshopper software environment that generated, optimised, extracted, and streamed data to link every project delivery phase. The dataset worked dynamically across different phases [13], progressive developments, and various tasks, such as site planning, design and development of architecture and structure, robot and CNC coding, project management, and fabrication.

At the beginning of managing the project, we found limited reference to the U-shaped glass mitre joints with fractal angles and no examples of installing the steel structure inside the core of the glass panels. As a result, we decided to make a 1:1 mockup of a typical portion of this project with technical support from ASG. After successfully proving this structural solution worked well through this mockup, we finalised the digital model, generated the final version of the data set and moved on to the fabrication phase.

This project comprised 31 sectional steel modules covered by 1339 unique U-shaped glass panels. The steel frame installation was carried out with a precision of +/- 10mm to guarantee all glass panels can be placed appropriately above the steel frame without any apparent visual flaw across the geometrical transition. This data set was subdivided into two streams: a subcontractor will fabricate the steel components manually. At the same time, our team used a robotic cutting system to automate the fabrication of U-shaped glass panels. Once both groups had delivered the structural components to the construction site, we used a mobile robotic island to assist with precisely installing the steel structure as a collaborative process. Compared to the regular steel structure, this steel frame had a data set of unaligned positions and fractal angles that were hardly measured by conventional construction techniques. Therefore, we introduced an on-site robot arm system to transform this complex data set into reachable locations with an accurate industrial standard.

The toughened U-shaped glass is fragile and easily breaks under impact around a sharp corner. In the final installation stage, after the steel frame was built, a team of skilled workers safely installed the panels (Fig 12 &13). A total station, a surveying instrument that combines the functionality of an electronic theodolite and an electronic distance meter (EDM), was used in this stage to ensure every joint of the glass panels matches the data set within a tolerance of +/-5mm. Construction silicone gel was applied to seal the seams between glass panels manually.

Due to our design team being involved in this construction, the digital workflow implemented for this project was highly flexible, allowing for seamless synchronisation of every process. The robot workflow can automatically convert the dataset to accurate installation activities in the software environment, making the construction process more efficient and controllable. Consequently, using robot arm systems as collaborative co-workers facilitates instant response to unforeseen problems when the design and programming teams operate as one team during construction. For example, if the site-survey feedback indicated that the digital model did not accurately reflect the site condition, the support team immediately fixed the data set and reprogrammed the robot system to enable a smooth workflow without delay. An assessment will also be generated instantly and visually to evaluate if these changes will affect the following tasks and give responsive adjustments to the data flow.

2.4.2. Tooling – robot implementation in different roles

The robot end effector can perform tasks with the same effect as human hands but sometimes with better results. The potential benefits of reducing human activities in construction work are also recognised.

We have been exploring robotic technology to streamline the data from the BIM model to the robot end effector to minimise human interference that can cause errors. KUKAprc, a plugin of Grasshopper, is used to generate robot code directly from the up-to-date 3D model, consisting of a data package of the working path and actuation for the end effector.

During construction, the robot arm was outfitted with various end effectors and received different sets of codes to perform specific tasks. The locations of each building component were defined in a Cartesian coordinate, along with the locations where the end-effectors completed their assigned functions. There were two tasks for developing the end effectors in this project: cutting the U-shape glass panels with various lengths and side angles; assisting workers with placing steel structural components in unique locations. Both benefit from the robot system's native flexibility and accuracy.



Figure 7. Robot end effector design and application for assisting with steel-frame construction.

The first effector was designed using a spindle router and a circular diamond blade for cutting glass panels. Each U-shaped glass panel was secured in a 3D printed fixture, and the robotic system completed two cuts as one task. This task occurred in the glass manufacturing site because the glass panel can only be shaped before the toughened process; a post-treatment of U-shaped glass is only available at ASG throughout the country. The second end effector, comprised primarily of pneumatic actuators and a servo motor, gripped and aligned two steel components at each connecting joint for designated angles(Fig 7). The lower pneumatic actuator first grabs the side column's top point firmly at the specific location; then, the servo motor drives the upper pneumatic actuator to the exact angle to await the upper steel beam. After both beams contact at the correct position and the fold angle, a professional welder will fuse them into a single piece. This task was processed one after another, with each section module secured by temporary bracings in case of any deformation before the circular connecting beams connected them into a uniform frame. This task only required three people at most (one for operating the robot system, one for welding work and one crane driver) to be involved with the robot station as a work unit, which was more cost-effective and safer than the general method using additional workers to locate the building components and necessary fixtures hold it in place during the welding process.

2.4.3 Site challenge and mobilised robot island.

Due to the complexity of construction sites, it was not feasible to level the ground to an industrial standard for robot islands, such as those seen in prefabrication factories or automobile assembly lines [14], to expand the working coverage. To solve this problem, we installed a pair of rails to enable the robotic end effector to reach every upper joint of the shell structure's 60m-long steel frame(Fig 8). The KUKA KR150 R3100 prime robotic arm was deployed again to take over the mobile island. It was a customised trolley on rails powered by a 3000W servo motor, capable of carrying the 1500Kg robot arm and stabilised by a 2000Kg sand tank as a counterweight. In case of any vibration during the operation

resulting in unstable end effector functions, the trolley was equipped with two brakes on each side, controlled by pneumatic actuators to firmly lock it on the rails as needed. The robot arm was programmed with its end effector's payload at a maximum weight of 150kg and a full speed of 0.5m/s.

There were discrete marks on the top rail surface under every other steel frame(Fig 9), indicating the positions where the robot arm was programmed to execute relative actions. Once the robot island was aligned at a mark point and its breaks were fully engaged, the corresponding codes were launched to assist with steel frame installation accordingly. This process ran one after another until the last steel frame was completed. This simple and cost-effective mechanism provided a solution for reaching a big construction site with complex terrain conditions. However, these rails must be technically levelled to allow an ideal working environment for the robot and removed after the construction. Nevertheless, in our design, this pair of rails can still serve the customised trolleys with various functions, such as coffee tables, bookshelves, billboards, etc., allocated across the shell space.

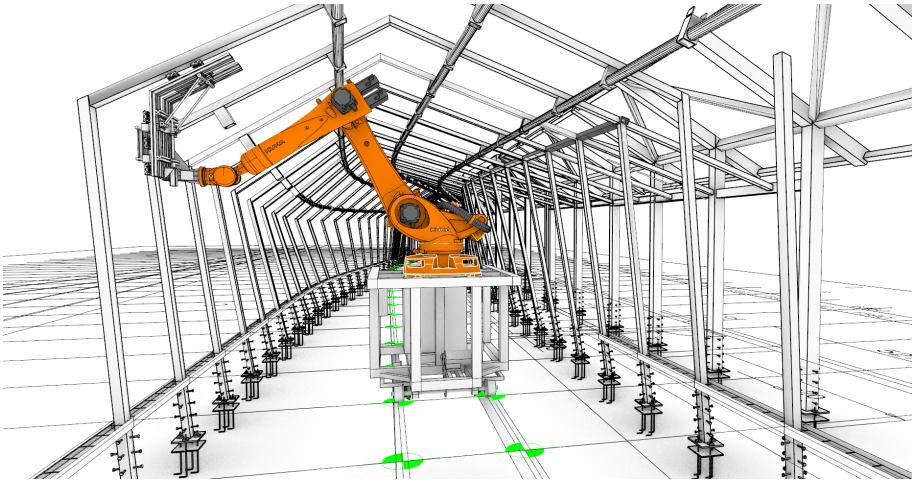


Figure 8. KUKA robot island driving on a pair of rails.

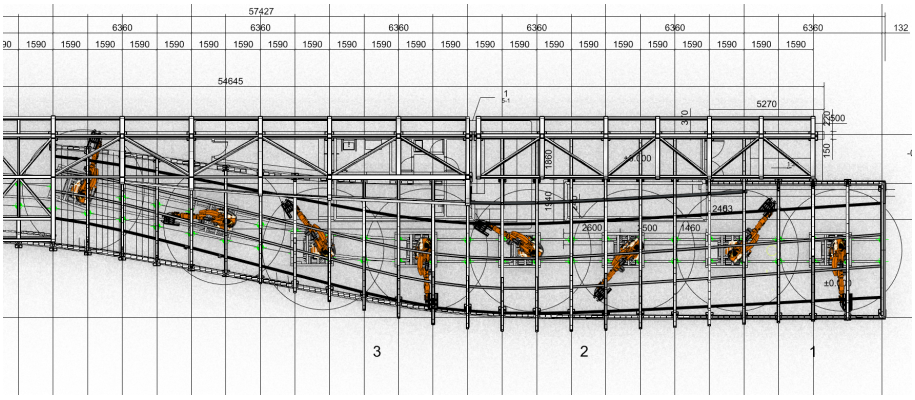


Figure 9. Marked spots for locating mobile robot island to enlarge its working coverage

2.5. Robot and Human Collaboration in Construction

Construction work is a multifaceted process that demands various skills and techniques. Each project presents unique challenges that require individualised solutions. In the context of this project, welding the steel frame was an essential aspect that must be executed to a high standard to meet the strict requirement for installing U-shaped glass panels. As such, every mitre joint of the steel frame was welded within the specified tolerance. Given numerous angles and locations, the robot arm was introduced to grip and secure the frame components in the right places before the welder started work. With a payload of 150 kg, the robot arm can carry most steel components over 4m from the ground

level. If some components exceed this payload, a crane truck can hang it into a position where the robot arm gripped the joint position firmly, ready to weld the top part. Situated in a queue of referred points robotic system runs a robotic G-code [15] to assist human workers in assembling the steel structure more efficiently and confidently(Fig 10).



Figure 10. Robot assists in structure installation.

This experiment illustrates how robots can collaborate with humans on construction sites in an extended mode other than working in factory conditions. In this productive environment, the robot arm functions as a partner that can exactly give a response to the G-code for finishing tasks. It facilitates a straightforward and highly coordinated workflow with fewer transformation procedures than the general process. This is because this work mode deals with specific problems in the environment where all immediate conflicts happen in real-time, which can be simulated, assessed, and resolved by robotic workflow.

This reciprocal teamwork promotes a new construction mode in the building industry. The project contractor manages how to coordinate human workers and robots to complete various tasks by reloading different robotic end effectors and managing correspondent silked workers and technicians. This flexible combination has merits to take over the transition in different stages of the digital workflow for high productivity and safety management, particularly for on-site construction.

However, we must also recognise that the industrial robot arm has been developed for the automatic assembly line where no people can have overlapped working space with these heavy-load machines. Therefore, a safety conduct code must also embrace robots working on the construction site with human workers in proper safety control management. Additionally, the industrial robot arm system should be modified to fit the building industry once the manufacturer and stakeholders believe the building industry will contribute a valuable share to the significant market.

Finally, it is essential to note that this research is an experimental practice by our team, who have years of experience and knowledge in robot technology. We won't encourage duplication of this research without sufficient preparation and skill in this field.

3. Conclusion

This project serves as a combination of research and practice, providing a case for the following:

- Creating a ruled surface shell structure using U-shaped glass and steel frame.
- Employing industrial robot arm technology to perform multiple roles from fabrication to installation.

- Using digital dataflow to manage design, fabrication and construction in a straightforward process and at all possible chances is a primary goal to experiment with the benefit of digital design and fabrication.
- Encouraging the collaboration between robot systems and people to deliver flexible solutions for complex design on the construction site.

Automation in construction [16] is a rapidly growing field with multi-facets to revolutionise the industry, making construction processes faster, safer, and more efficient. Digital design techniques and robotic technology are two aspects of automation that are particularly important in this regard. This project proves how these methods can turn concepts into physical outcomes. Usually, these technologies can help regular projects with more predictable efficiency. The linear process to deliver this glass shell structure demonstrates an integrated solution with structural engineers, manufacturers, and construction workers, offering insight into the potential of automation in construction for leveraging innovative and sustainable buildings.

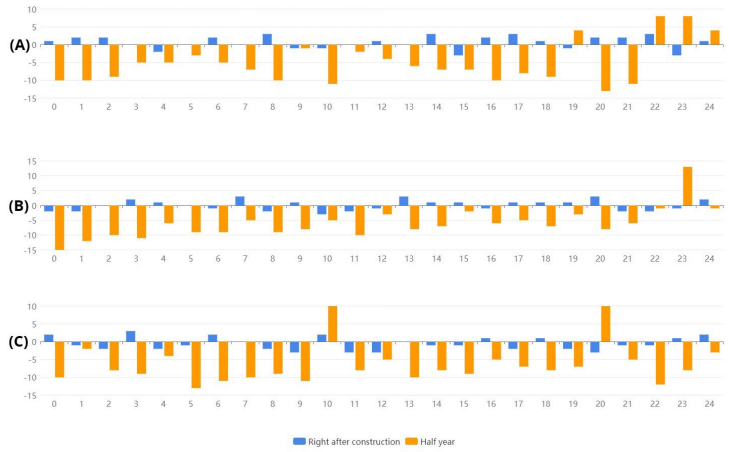


Figure 11. Steel frame survey for joints deviation in mm, vertical axis – deviation, horizontal axis – sectional frame sequent number (1 month & 6 months after).

Despite the fact that this glass shell structure has a positive outcome in reflecting the digital model, there are still some aspects that require further developments for future projects:

- The robot arm system needs to be more flexible to adapt to site conditions. In this project, we must hold the entire team to wait for any modification of robotic code on the construction site, resulting in some unexpected low-efficiency moments. We consider an advantage if tasks can be synchronised between the designer and the site manager for a forehead problem-solving mode.
- The construction materials, particularly steel, need more consideration and pre-calculation. Steel is susceptible to temperature and easily deformed over time. From two sets of surveys on the upper three corners of each sectional steel frame, significant changes occurred in 6 months during the Covid19 lockdown. Due to the distortion caused by temperature change and gravity, some of the joints sagged more than 10mm(Fig 11). A few even broke the tolerance limit, resulting in extensive efforts to revert the bias while installing glass panels.
- Instant site surveys technology, such as GPS and 3D scanning, is an advanced option for achieving better dynamic dataflow. Any conflict or deviation from the centre model can be predicted, assessed and resolved beforehand.



Figure 12. Skilled workers install U-shaped glass panels.



Figure 13. Robot rails are reused for glass installation.

Acknowledgements

We sincerely thank the structural consultant SGI team - Jing Zuo, Winter Ma and Yue Yu in the Beijing office for their significant effort. We acknowledge the support of ASG glass supplier-Yongsong Yang and Kangjian Pan for their professional assistance. We recognise the dedication of our team, Dr Lei Yu, Diaoqian Yang, Jianmin Zhu and Ji Shi, for the additional challenge posed by the Covid lockdown.

References

[1] J. Goulding, F. P. Rahimian, S. Abrishami and A. Ganah, "Virtual generative BIM workspace for maximising AEC conceptual design innovation: a paradigm of future opportunities," *Construction Innovation,* vol. 15, no. 1, pp. 24-41, 2015.

[2] Z. Dakhli, Z. Lafhaj and S. K. Shukla, "Robotic mechanical design for brick-laying automation," *Cogent Engineering,* vol. 4, no. 1, p. 1361600, 2017.

[3] L. Yu, D. Luo and W. Xu, "Dynamic Robotic Slip-Form Casting and Eco-Friendly Building Façade Design," *ROBARCH 2018: Robotic Fabrication in Architecture, Art and Design 2018,* p. 421–433, 2018.

[4] A. Gawel, H. Blum, J. Pankert, K. Krämer, L. Bartolomei, S. Ercan and F. Gramazio, "A Fully-Integrated Sensing and Control System for High-Accuracy Mobile Robotic Building Construction," *International Conference on Intelligent Robots and Systems (IROS),* 2019.

[5] B. Johannes and S. Brell-Cokcan, "Adaptive Robot Control - New Parametric Workflows Directly from Design to KUKA Robots," in *eCAADe 2015 RealTime*, 2015.

[6] S. Ercan, S. Meier, F. Gramazio and K. Matthias, "Automated Localisation of a Mobile Construction Robot with an External Measurement Device," in *International Symposium on Automation and Robotics in Construction (ISARC)*, 2019.

[7] A. Schiftner and J. Balzer , "Statics-Sensitive Layout of Planar Quadrilateral Meshes," in *Advances in Architectural Geometry*, 2010.

[8] W. CJK, "The analytic and numerical definition of the geometry of the British Museum Great Court," in *Mathematics & design*, Geelong, Core.ac.uk, 2001, pp. 434-440.

[9] S. Fabian, M. Stefan, T. Martien and T. Christoph, "Metal and Glass Grid-Shell Design: Flexible Integration of Digital Design and Fabrication Tools," in *Proceedings of IASS Annual Symposia, IASS 2018 Boston Symposium: Shell structure*, Boston, 2018.

[10] S. Adriaenssens, L. Ney, E. Bodarwe and C. Williams, "Finding the Form of an Irregular Meshed Steel and Glass Shell Based on Construction Constraints," *Journal of Architectural Engineering,* vol. 18, no. 3, 2012.

[11] R. Green, "The Challenges of Writing a Structural Standard for Glass," in *Challenging Glass Conference Proceedings*, 2016.

[12] P. Loh, D. Leggett and D. Prohasky, "Robotic fabrication of doubly curved façade system - Constructing intelligence in the digital fabrication workflow," in *24th International Conference on Computer-Aided Architectural Design Research in Asia, CAADRIA 2019*, Wellington, 2019.

[13] T. Wortmann and B. Tuncer, "Differentiating parametric design: Digital workflows in contemporary architecture and construction," *Design Studies,* vol. 52, pp. 173-197, 2017.

[14] J. Qian, B. Zi, D. Wang, Y. Ma and D. Zhang, "The Design and Development of an Omni-Directional Mobile Robot Oriented to an Intelligent Manufacturing System," *Sensors,* vol. 17, no. 9, 2017.

[15] J. Braumann and S. Brell-Cockcan, "Parametric Robot Control - integrated cad/cam for architectural design," in *integration through computation- ACADIA 2011*, 2011.

[16] Q. Chen, B. Garcia de Soto and B. T. Adey, "Construction automation: Research areas, industry concerns and suggestions for advancement," *Automation in Construction,* vol. 94, pp. 22-38, 2018.

[17] L. Sass and R. Oxman, "Materialising design: the implications," *Design Study,* vol. 27, pp. 325-355, 2006.

Proceedings of the IASS Annual Symposium 2023
Integration of Design and Fabrication
10–14 July 2023, Melbourne, Australia
Y.M. Xie, J. Burry, T.U. Lee and J. Ma (eds.)

Digital design, optimisation and automated construction of a curved wooden truss – housing for the BOKU Robot Laboratory

Benjamin KROMOSER[a,*], Maximilian ORTNER[a], Matthias BRAUN[a]

[a,*] University of Natural Resources and Life Sciences, Vienna (BOKU)
Peter Jordan Strasse 82, 1190 Vienna
benjamin.kromoser@boku.ac.at

Abstract

Timber truss systems are very efficient load-bearing structures. They allow for great freedom in design and are characterised by a high material utilisation in combination with a low environmental impact. Unfortunately, the extensive effort in design and production have made the manufacturing and application of these structures, at this day and age, a rarity. The authors' goals are to industrialise the design and optimise the production process in order to compete with plate girders, which are characterised by an easy production yet comperatively low material utilisation. The housing of the new robot laboratory of the Institute of Green Civil Engineering at BOKU Vienna is considered a special use case for their current research activities regarding resource-efficient wooden truss structures. In addition to optimising the structure to minimise the environmental impact the production process was performed by the robot building its own house. The main support structure was designed inspired by the work area of the robot resulting in a curved wooden truss. The two research areas: (1) Optimisation of the truss geometry and (2) Optimisation of the joints by using solely wood-wood connections, are addressed in this paper. The numerical optimisation strategy is based on a parametric design of the truss and the use of a genetic solver for the optimisation regarding a minimal material consumption. Furthermore, results of the tensile and compression behaviour of the chosen wood-wood connections are presented.

Keywords: industrialised production, resource-efficient timber structures, structural optimisation, genetic optimisation algorithm, timber trusses, wood-wood connections, engineered wood products

1. Introduction

Wood is a natural inhomogeneous anisotropic material with discontinuities due to defects as for example pitch pockets, branches, fibre twist etc. When used for building construction the original material undergoes multistage sorting and processing [1]–[3]. These processes, and, if applied, gluing, allow for a compensation of the defects resulting in smoother and consequently better material properties. In addition, subsequent geometry changes due to an adjustment of the equilibrium moisture can be reduced. The drawback regarding these products is that the production process is accompanied by many subtractive machining operations. The yield rate sinks to 25 - 35% within the processing of the tree trunk into the finished building component. Consequently, good mechanical properties and advantageous behaviour regarding geometric deformations are the opposite of a low yield of the raw material.

Based on these facts, it can be clearly shown that structural optimisation of building components is of highest importance for an efficient use of the material. Unfortunately, this basic principle is being partly ignored by the wood construction industry in the industrialised countries, which currently clearly focuse on saving costs rather than natural resources, since material costs are (still!) low in comparison to those for personnel. Elements produced using industrialised manufacturing processes are cheaper and therefore preferred to resource-saving yet more complicated structures. Wooden trusses, for example,

Copyright © 2023 by Benjamin KROMOSER, Maximilian ORTNER and Matthias BRAUN. Published in the Proceedings of the IASS Annual Symposium 2023 with permission.

are rarely implemented nowadays having been replaced by plate girders, especially for shorter spans, due to economic reasons even though the material yield rate is comparatively lower. [4]

The aim of the authors is to industrialise the design and production process of wood structures in order to allow for a more efficient usage of the valuable material wood while still being economically feasible. The authors split the research development in three subprocesses: (1) Optimisation of the geometry of the supporting structures, (2) Optimisation of the joints, (3) Optimisation of the production technology and the interface between the Computer Aided Design (CAD) and the Computer Aided Manufacturing (CAM). Subprocesses (1) and (2) are addressed within this paper. Work performed in area (3) can be for example found in [5]–[8].

In the robot laboratory of the newly-founded Institute of Green Civil Engineering at BOKU Vienna investigations of different numerical controlled subtractive and additive manufacturing processes can be investigated. The housing of the robot laboratory was part of the currently pursued research strategies and served as the first prototype application.

2. Parametric design and optimisation

The fundamental idea for the new robot laboratory was for the robot, which was set up first, to build its own housing. The shape of the housing was inspired by the work area of the robot, as shown in Section A-A in Figure 1. The main supporting structure was executed as a curved truss solely made from wood and wooden materials without using any steel components. To design the construction, the plug-in Grasshopper [9] for the CAD software Rhinoceros [10] was used, allowing for the creation of a parametric model with variables which were changed throughout the optimisation process in order to obtain different configurations of the truss. The following parameters were defined as variable: number of subdivisions, distance between subdivisions, alignment of the diagonal members and cross section of the members of the truss. The main goal of the optimisation was to minimise the environmental impact while still obtaining the desired load-bearing behaviour.

2.1. Evolutionary algorithm

The Grasshoppers evolutionary solver was used to determine the most efficient truss by varying the previously mentioned geometric parameters. The optimisation strategy of the solver is based on the principle of genetic evolution and consists of five steps to optimise a so-called fitness value [11]. The fitness value represents the numerical parameter which can be optimised by the solver. The goal is to either minimise or maximise the fitness value. In this project a single-objective optimisation was applied, with only one numerical value being optimised in the calculation process at a time.

Subsequently the five optimisation steps of the evolutionary solver are explained. (1) An initial population (different trusses) is randomly assembled by the algorithm from the single slider variables. (2) The fitness values of the resulting trusses are evaluated and qualitatively ranked according to their performance. (3) Trusses are chosen by the algorithm according to a determined selection procedure for further analysis. (4) The variables of the selected trusses are recombined similar to genetic reproduction, to obtain better solutions for the structure. (5) Steps (3) and (4) are repeated until one of the three abort criteria (calculation time exceeded, no improvement, best result achieved) is reached.

2.2. Evolutionary optimisation algorithm

The aim of the optimisation was to achieve the lowest possible wood consumption while maintaining the required static load-bearing capacity while simultaneously complying with the requirements regarding serviceability (deformation). The internal forces of the structure were calculated using the plug-in Karamba3D [12]. The static calculation was conducted according to Eurocode 5 (EN1995-1-1:2019-06-01) and the current Austrian application document within a separately integrated self-programmed tool box. In addition to the calculation of the deformation of the truss, buckling and cross-

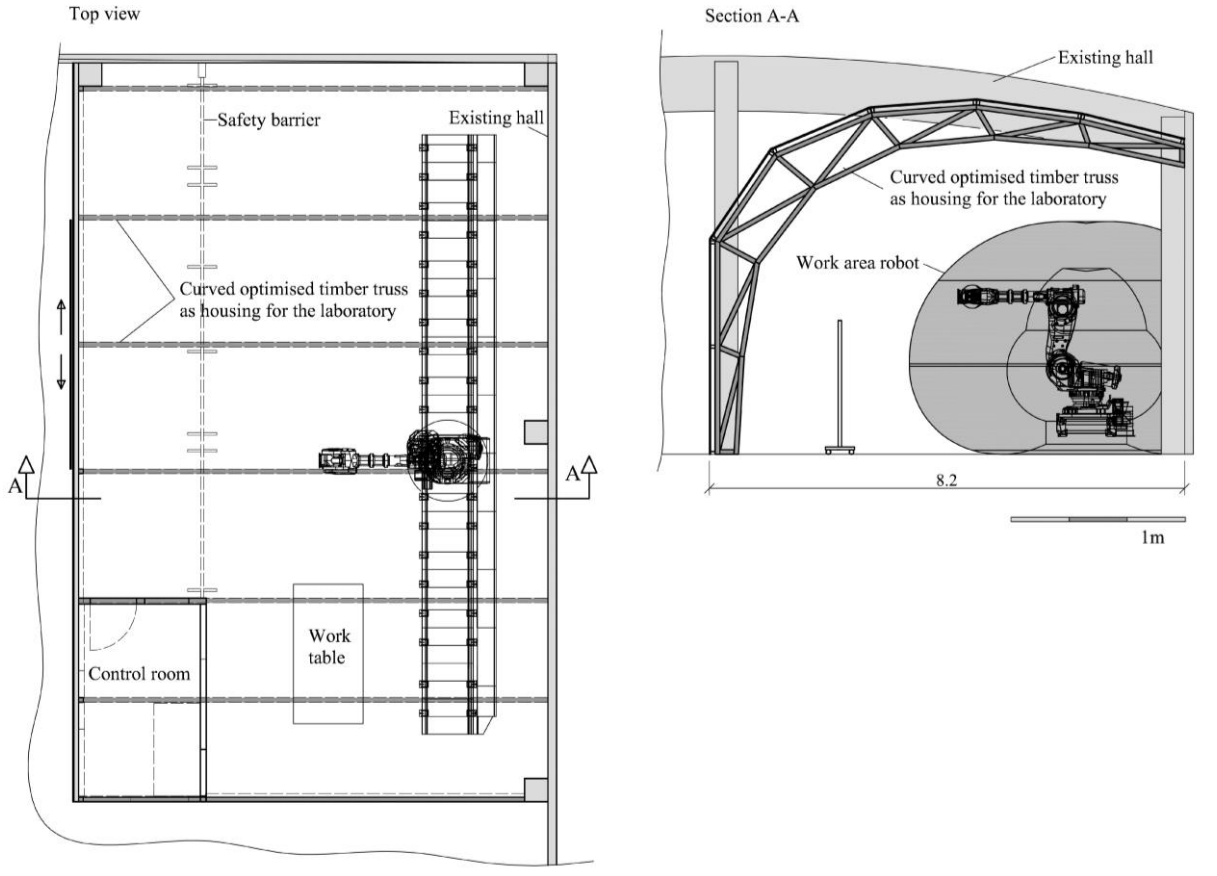


Figure 1. Top view and cross section of the robot laboratory with the curved optimised timber truss structure.

section analysis were carried out. The calculation focused on the individual truss members based on a two-dimensional model which prohibits any global buckling of the structure (the nodes were modelled in 2D and therefore fixed out-of-plane).

3. Results

3.1. Reference model

At the beginning a first version of the truss, as shown in (left), was conceptualised based on the authors' engineering know-how. The predefined floor area, the existing roof of the hall as well as the working area of the robot served as boundary conditions. All results of the optimisation are compared to this first reference truss (12 segments, alternating diagonal struts and regular spacing between the subdivisions).

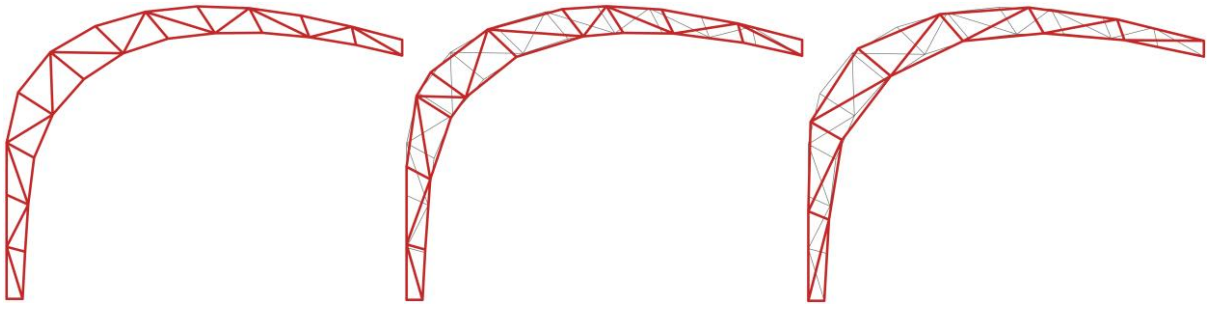


Figure 2. left: Reference model with 12 segments, alternating diagonals and regular spacing between the subdivision; middle: Uneven distribution of subdivisions; right: Final implementation of the housing.

3.2. Boundary conditions

The geometry of the truss is determined by the available area in the existing hall where the robot laboratory is located. It spans from the middle of the hall, where it is fixed directly to the floor, to a support attached to the wall at a height of 4.92 m, resulting in a truss span of 8.20 m.

The geometry of the upper and lower chord is affected by several boundary conditions. The accessibility to the robot laboratory through a 3.20 m high sliding door made it necessary for the truss to not be curved up to that height. The upper part of the truss on the other hand had to follow the shape of the glulam beam of the roof construction of the hall. Based on these limitations the authors decided to focus on the optimisation of the inner structure as well as the cross section of the truss itself. Consequently, the global geometry was not part of the optimisation and the geometries of the upper and lower chords were set as fixed curves.

The applied loads for the supporting structure consist of the dead weight plus the load of the board panelling with 1.0 kN/m, which is applied to the truss at the nodes. The truss is situated inside a machine hall, therefore weather influences like snow and wind are neglected. An additional load of 3.0 kN is applied between 2.0 m and 3.2 m from the existing machine hall wall (the wall to which the right end of the truss is attached). This load is also introduced into the truss via a node and is intended to allow the attachment of cables of possible future experimental setups.

3.3. Optimisation results

Within the optimisation single parameters can be selected individually in order to be changed by the algorithm. The results are summarised in Table 1. Depending on which fitness value is defined and which parameters are released for optimisation, different truss configurations are generated.

Table 1. Results with different fitness values (optimisation with constant cross section).

Fitness value	Reference model	Deformation	Normal force	Mass
Subdivisions [n]	12	13	8	6
Buckling [-]	0.46	0.81	0.70	0.90
Cross section [-]	0.39	0.30	0.30	0.37
Deformation [mm]	7	5	8	7
Weight [kg]	147.5	145.4	137.6	125.5
Resource reduction [%]	-	-1.4	-6.7	-14.9

The authors pursued the optimisation focusing on different fitness values. The early optimisation processes were calculated with deformation as the fitness value. For these calculations the value was set to be as low as possible. The results were very stiff trusses, with deformations smaller than 5 mm, a value of less than one sixth of the limit of 32 mm according to Eurocode 5 (EN1995-1-1:2019-06-01). The resulting material savings of 1.4 % were not considered as relevant improvements.

The next attempt was optimising the structure using the maximum absolute normal force (both compression and tension forces). The compression forces were considerably reduced by the algorithm (-22 %), while the tension forces decreased only slightly (-6 %). The goal of achieving an optimal structure through the even distribution of the occurring normal forces in all struts and chord beams of the truss resulted in a mass reduction of 6.7 %.

The previously described optimisation approaches did not lead to a minimisation of the material quantity and thus the environmental impact. The optimisation was most successful when the fitness value was set as the total mass of the construction, with it being directly proportional to the wood consumption. This resulted in a significant reduction of 14.9 % compared to the reference model.

Only chosen variables were released within the optimisation for the truss configuration of the housing. The distance between the divisions was defined evenly in order to meet aesthetic requirements. Figure 2 (middle) shows a truss with an uneven distribution of the subdivisions. In addition, the cross section of the chords and struts was set to 80 x 80 mm in regard to the envisaged node configuration.

For the final implementation of the housing, shown in Figure 1 and Figure 2 (right), a truss with 7 segments, regular spacing between the subdivisions and free diagonal member arrangement was defined, requiring 129.4 kg of timber, 18.1 kg less than the reference model.

If the entire truss structure is calculated on a pure theoretical basis, without the consideration of node configurations or national standards, the mass can be reduced even further. By allowing the algorithm to change the cross-sectional dimensions of the chords and struts a reduction of the material consumption by about 60 % is possible. For this case the truss would need more subdivisions, use smaller cross sections and have a total weight of 59.3 kg for the 8.2 m span.

4. Joining of the truss members

The load-bearing behaviour of timber trusses is particularly influenced by the material properties, the geometry and the joint performance. Based on this fact, the authors also focus on investigating the load-bearing behaviour of the joints as part of their research. The main requirement of the research was to transfer the loads without using any steel elements in order to minimise the environmental impact. Following the research presented in [13], a easily produced node element was used that can connect truss members at different angles while also allowing the transfer compressions and tensile forces. In this particular case, the authors chose plywood panels which would be notched into the truss members before being fixed with wooden pegs. For a first characterisation of the chosen configuration and due to the fact that plywood plates in combination with wooden pegs are not covered by Eurocode 5 the authors performed compression as well as tensile tests on the all-wood connections to find the optimal design as well as wood species and to investigate the occurring load-bearing mechanisms.

4.1. Design of the wood-wood connections

For the above-mentioned curved optimised truss, spruce (C24) with a cross section of 80 x 80 mm was chosen for all truss members, making this the first boundary condition for the joint design. Due to manufacturing tolerances however, the cross sections of all provided specimens turned out to be 78 x 78 mm. The node elements (plates) were made from plywood panels and were inserted into the truss members and fixed with wooden pegs. According to [14] the spacing of the pegs in the direction of force was chosen with three times the peg diameter (3d). As the cutting depth for notching the truss member for the plywood panel was limited by the manufacturing process to 115 mm, the diameter of the pegs was set to 14 mm. The combination of all geometric boundary conditions resulted in a total of four pegs per connection.

4.2. Experimental investigations on pegged joints with different wood species of the pegs

In this test series the influence of the wood species of the pegs on the mechanical behaviour of the connection was investigated. The authors manufactured the connections with the robot and tested a total of nine configurations in regard to the transmission of tensile forces (with three specimen each). The test setup is shown in Figure 3.

According to [14], the thickness of the plywood panel should be approximately equal to the diameter of the pegs diameter to ensure an adequate load-bearing behaviour and a ductile failure of the connection. For the first tests birch plywood panel was chosen with a thickness of 15 mm (BI15). The following wood species were examined for the pegs: thermo ash (TA), ash (A), oak (O), larch (L), beech (B), spruce (S), beech LVL along the layers (B_LVL_0), beech LVL perpendicular to the layers (B_LVL_90).

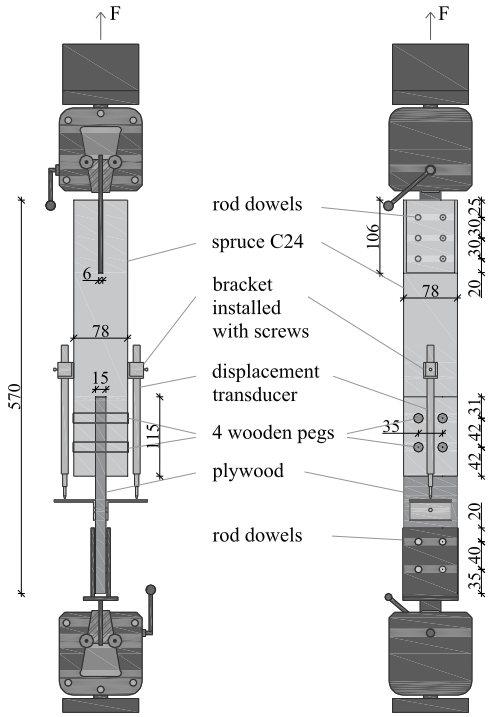


Figure 3. Test setup for the tensile connections [mm].

The tested configurations and results are summarised in Table 2 and Figure 4, respectively. The result curves represent regressive lines of summarising the three specimens of every configuration. To limit the deformation in the final structure, the stiffness in the joint should be as high as possible. The results of the experimental investigation show that the combination of beech pegs and 15 mm birch plywood (B-BI15) provided the highest stiffness. However, in this configuration, the failure for this configuration occurred in the plywood panel next to the pegs in a brittle manner after a short period of softening (see Figure 5). As brittle failure is unwanted, a further series of tests was carried out. The 15 mm birch plywood was replaced with 18 mm beech plywood to ensure that the failure would not occur in the plywood panel. With the combination of 14 mm beech pegs and 18 mm beech plywood (B-BI18), it was not only possible to achieve ductile failure, but also to increase the load-bearing capacity from 25.01 kN in the first series up to 29.56 kN (see Figure 4).

Table 2. Test configurations of the tensile tests.

Configuration	Wood species of pegs	Ø of the pegs [mm]	Wood species of plywood	Thickness of plywood [mm]
TA-BI15	Thermo ash	14	birch	15
A-BI15	ash	14	birch	15
L-BI15	larch	14	birch	15
O-BI15	oak	14	birch	15
B-BI15	beech	14	birch	15
S-BI15	spruce	14	birch	15
B_LVL_0- BI15	beech LVL	14	birch	15
B_LVL_90-BI15	beech LVL	14	birch	15
B-B 18	beech	14	beech	18

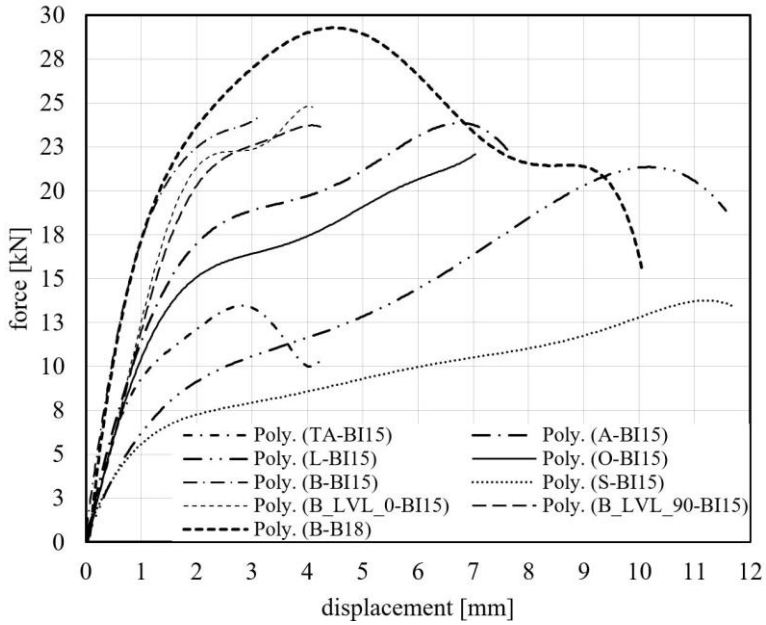


Figure 4. Comparison of the influence of the wood species of pegs on the load-bearing capacity and stiffness of the tensile joint of test series I (xx-BI15) and the ultimately chosen combination from series II (B-B18). Results are shown as regressive lines of the mean values of three specimens each. Coefficient of determination R2>0.992 (xx-BII5) and R2=0.949 (B-B18).

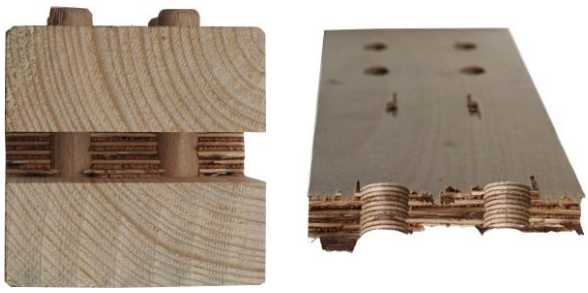


Figure 5. Test specimen from configuration B-BI15 after failure; truss member with beech dowels (left), birch plywood plate (right).

4.3. Experimental investigations on buckling of beech plywood

In some cases, the design of the curved truss resulted in acute angles between the truss members, as shown in Figure 9. Hence, a free length of the plywood panel of up to 650 mm had to be implemented. Since the joints of the truss structure do not only have to transmit tensile stresses but also compressive stresses, the risk of out-of-plane buckling of the slender plywood panel had to be ruled out. To investigate the influence of different free lengths of the plywood panels regarding buckling failure, a series of compression tests was performed. The test setup is shown in Figure 6.

As the truss nodes are stressed in different directions, three orientations of the main load-bearing direction of the plywood panel were tested. The joints consisted of 18 mm beech plywood panels inserted into the truss members and fixed with four wooden pegs (beech) with a 14 mm diameter. The joint configuration was chosen according to test Series 2 of the tensile tests, presented in Section 4.2. The aim was to transfer the compression loads not only through the peg/plywood joint but also through the contact surface between the beech plywood panel and the spruce truss member. The free length in this test series was set to 250 mm and increased in 100 mm steps up to 650 mm. Each step of free length

was tested in an angle of 0°, 45° and 90° of the plywood's main load-bearing direction to the direction of force. The investigated configurations are summarised in Table 3. In order to obtain feasible results three specimens per configuration were tested. The test results are shown in Figure 8.

Table 3. Test configurations of the compression tests.

Configuration	Free length of the plywood	Angle of the plywood's load-bearing direction [°]	Wood species of the pegs	Ø of the pegs [mm]
25-0	25	0	beech	14
25-45	25	45	beech	14
25-90	25	90	beech	14
35-0	35	0	beech	14
35-45	35	45	beech	14
35-90	35	90	beech	14
45-0	45	0	beech	14
45-45	45	45	beech	14
45-90	45	90	beech	14
55-0	55	0	beech	14
55-45	55	45	beech	14
55-90	55	90	beech	14
65-0	65	0	beech	14
65-45	65	45	beech	14
65-90	65	90	beech	14

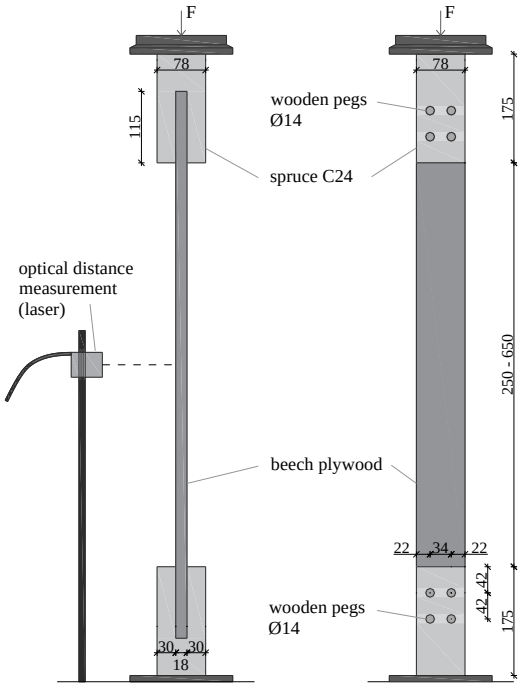


Figure 6. Illustration of the test setup for the compression tests to investigate local buckling failure [mm].

As expected, the results of the test series prove that the load-bearing capacity decreases with an increase of free length. A test specimen under load showing buckling is depicted in Figure 7. In each configuration of free length the specimens with an angle of 45° between the main load-bearing direction and the direction of force show the lowest load-bearing capacity. Each specimen with an angle of 0° between the orientation of the main layers of the plywood and the direction of force, labelled xx-0 in, provided the highest load-bearing capacity for each defined plate length.



Figure 7. Test specimen under compression.

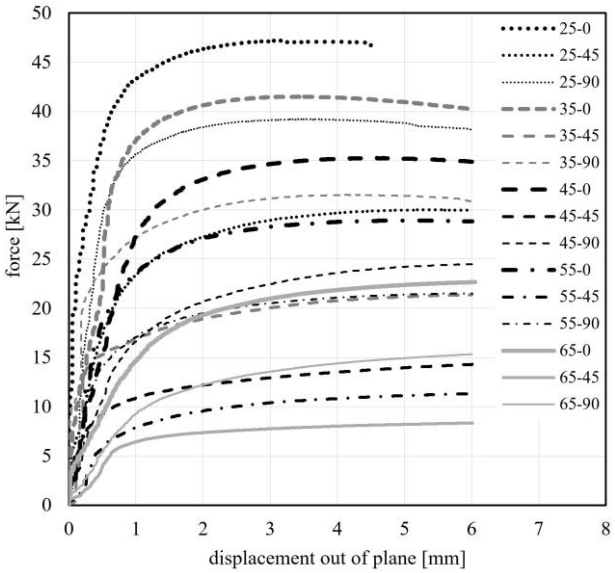


Figure 8. Comparison of the influence of the orientation of the load-bearing direction and the free length of the plywood panel on the load-bearing capacity. Mean values of three specimens each. Legend: free length in cm – angle between load-bearing direction and force direction, e.g. 25-45 means 250 mm of free length and an angle of 45° between load-bearing direction of the plywood and direction of force.

The findings show that the governing stress direction in the truss node has to coincide with the load-bearing direction of the plywood in order to fully utilise its potential. Furthermore, it was observed that the bending shape was similar to Euler case 4, leading to the assumption that the designed joints act like rigid ends.

4.4. Final design of the truss joints

For the final design of the curved truss, the members consist of spruce with a cross section of 80 x 80 mm (78 x 78 mm). One joint design was chosen for all joints to simplify the manufacturing process. Thus, four beech pegs with a 14 mm diameter and 18 mm beech plywood panels are used for the joints. A rendering of the upper part of the final design can be seen in Figure 9.



Figure 9. Rendering of the upper part of the curved timber truss.

5. Conclusions

Industrialising the complete process chain shows great potential for the wood construction sector allowing for an increase in resource efficiency and the ability to compete with other construction materials regarding economic efficiency. Within this context the present paper focuses on the optimisation of the geometry and the connections of trusses by solely using wood as the construction material for all building elements. The housing of the BOKU Vienna robot laboratory was chosen as the first pilot project.

The optimisation of the geometry by use of a parametric model and a genetic solving algorithm allowed for a reduction of the required construction material by 14.9 % in comparison to the first design based on engineering knowledge. For this case the cross section of the truss members was predefined to 80 x 80 mm. A theoretical optimisation of the cross section showed further reduction potential of 60 %.

A pure wood-wood connection was chosen using plywood as the connection panel and wooden pegs as shear connectors to minimise the environmental impact of the load-bearing structure.

A test series of tensile investigations was performed to determine the influence of the wood species of the pegs on the mechanical behaviour of the connection. The results show that using beech pegs provide the stiffest connection and the highest load-bearing capacity. Furthermore, the investigations showed that special attention needed to be paid to the interaction between peg diameter and the thickness of the plywood panel in order to ensure ductile failure of the pegs. To estimate local buckling failure in the plywood panel, compression tests were conducted giving information on the influence of the free length. The results show the importance of the main load-bearing direction of the plywood panel.

All the acquired knowledge was then applied within the pilot project where the team of the Institute of Green Civil Engineering built the structure, as seen in Figure 10, in the autumn of 2020.



Figure 10. Finished housing for the robot laboratory

Acknowledgements

The authors gratefully acknowledge the company Rubner Holzbau GmbH for the good cooperation and support. Furthermore, the authors thank the entire team of the Institute of Green Civil Engineering as the structure for the housing of the laboratory was produced in many hours of hard labour of every single one of them!

References

[1] J. Bodig and B. A. Jayne, *Mechanics of wood and wood composites*. Van Nostrand Reinhold, 1982.

[2] E. Möller, 'Tendenzen im Holzbau', *Bautechnik*, vol. 90, no. 1, pp. 42–46, Jan. 2013, doi: 10.1002/bate.201200069.

[3] R. Shmulsky and P. D. Jones, *Forest Products and Wood Science: An Introduction*. John Wiley & Sons, 2011.

[4] B. Kromoser and M. Braun, 'Towards efficiency in constructive timber engineering - design and optimization of timber trusses', in *Proceedings of the IABSE Congress 2019*, New York, USA, 06.09 2019.

[5] M. Pantscharowitsch and B. Kromoser, 'Automated Subtractive Timber Manufacturing—Joinery Machines Versus Industrial Robots', *Journal of Manufacturing Science and Engineering*, vol. 145, no. 6, Mar. 2023, doi: 10.1115/1.4056924.

[6] M. Pantscharowitsch and B. Kromoser, 'Influence of machining parameters on subtractive manufacturing of elementary geometries in glued-laminated timber using an industrial robot', *Wood Material Science & Engineering*, vol. 0, no. 0, pp. 1–19, Mar. 2022, doi: 10.1080/17480272.2022.2051734.

[7] M. Pantscharowitsch, J. Witzeneder, and B. Kromoser, 'Increasing efficiency of an industrial robot when machining timber beams – introduction of a parametric solving model to determine optimised stacks', *Wood Material Science & Engineering*, vol. 0, no. 0, pp. 1–17, Mar. 2023, doi: 10.1080/17480272.2023.2183897.

[8] M. Pantscharowitsch and B. Kromoser, 'Investigation of industrial robots vs joinery machines for milling pockets in glulam: Comparison based on surface quality and 3D Scans', *Civil Engineering Design*, vol. 4, no. 1–3, pp. 25–34, Jun. 2022, doi: 10.1002/cend.202100049.

[9] McNeel Europe, 'Kangaroo - Grasshopper', Jan. 28, 2020. https://www.grasshopper3d.com/group/kangaroo (accessed Jan. 28, 2020).

[10] McNeel Europe, 'Rhino 6 für Windows', Jan. 2020. https://www.rhino3d.com/de/ (accessed Jan. 28, 2020).
[11] V. Nissen, *Einführung in evolutionäre Algorithmen: Optimierung nach dem Vorbild der Evolution*. Springer-Verlag, 2013.
[12] Bollinger und Grohmann ZT GmbH, 'Karamba3D – parametric engineering', Jan. 2020. https://www.karamba3d.com/ (accessed Jan. 28, 2020).
[13] B. Kromoser and T. Pachner, 'Optiknot 3D – free formed frameworks out of wood with customized knots produced by FDM additive manufacturing: Experimental investigations, design approach and construction of a prototype', *Polymers*, vol. 12, no. 4, 2020, doi: https://doi.org/10.3390/polym12040965.
[14] W.-S. Chang, A. Thomson, R. Harris, P. Walker, and J. Shanks, 'Development of All-Wood Connections with Plywood Flitch Plate and Oak Pegs', *Advances in Structural Engineering*, vol. 14, no. 2, pp. 123–131, Apr. 2011, doi: 10.1260/1369-4332.14.2.123.

IASS 2023
July 10–14 Melbourne
Integration of Design and Fabrication

Proceedings of the IASS Annual Symposium 2023
Integration of Design and Fabrication
10–14 July 2023, Melbourne, Australia
Y.M. Xie, J. Burry, T.U. Lee and J. Ma (eds.)

Digitization and construction of steel-frame double curvature façade with a spatial element: with the example of Chongqing Center for Planning and Exhibition

Philip F. YUAN*, Menghao YUAN[a]

* College of Architecture and Urban Planning, Tongji University, Shanghai 200092, China
philipyuan007@tongji.edu.cn

[a] Shanghai Research Institute for Intelligent Autonomous Systems, Tongji University, Shanghai 200092, China
lyleyuan1990@gmail.com

Abstract

The study and practice of linear building façade systems have been relatively mature, through which the realm has cultivated an integrated and comprehensive design and construction framework. As the need for the complexity of architectural form in the design market increases, there is an ever-growing challenge to the existing façade design and construction system with the emergence of forms with double curvature and other types of complexity. Although digital toolsets have been around in the field to cope with such problems, their uses have long been scattered across the entire design and construction workflow, not presenting a unified trend where a highly efficient coordination system is established, and building information is generated and managed in totality so that the barriers between different construction bodies are overcome to facilitate communication, reduce risks and optimize costs. This article, with the example of the construction process of the Chongqing Center for Planning and Exhibition, aims at tackling this challenge through discussions on establishing a unified design and construction workflow centered around an exclusive digital fabrication team and a digital framework, making Building Information Modelling a crucial vessel for data management, and how the construction process is empowered by such frameworks and information.

Keywords: complex façade, building façade, construction coordination, digital fabrication, BIM

1. Introduction

As one of the most technically demanding branches of the construction industry, complex curved surface architectural façades present a significant challenge, particularly in the design and construction of double-curved façades [1]. While the industry has introduced digital tools and workflows to address these challenges and establish certain working paradigms, the intelligent integration of project stakeholders remains elusive due to insufficient knowledge of digital technology and a shortage of professional talent. Given the construction industry has always been labor-intensive, the current close-loop working mode of mainstream construction projects is becoming increasingly inadequate in the face of more advanced and innovative architectural design schemes, especially during the project development stage where it is difficult to plot and unify drawing information [2], and where effective delegation of workload and integration of outcomes is almost impossible. Therefore, establishing a digital construction workflow to fully leverage the unparalleled advantages of Building Information Modelling (BIM) in integrating complex geometric design and construction processes is the future trend of the construction industry [3].

Copyright © 2023 by Philip F. YUAN and Menghao YUAN. Published in the Proceedings of the IASS Annual Symposium 2023 with permission.

This paper demonstrates the data generation, evolution, and empowerment process of the entire façade construction workflow for the Chongqing Planning Exhibition Gallery's new building project (Figure 1), and argues that the use of an independent digital construction team to control and process data throughout the entire construction workflow has a positive impact on optimizing construction efficiency, improving overall project quality, shortening construction periods, and reducing construction costs. This paper aims to provide useful insights into the promotion and application of digital workflows and building information data in construction projects.

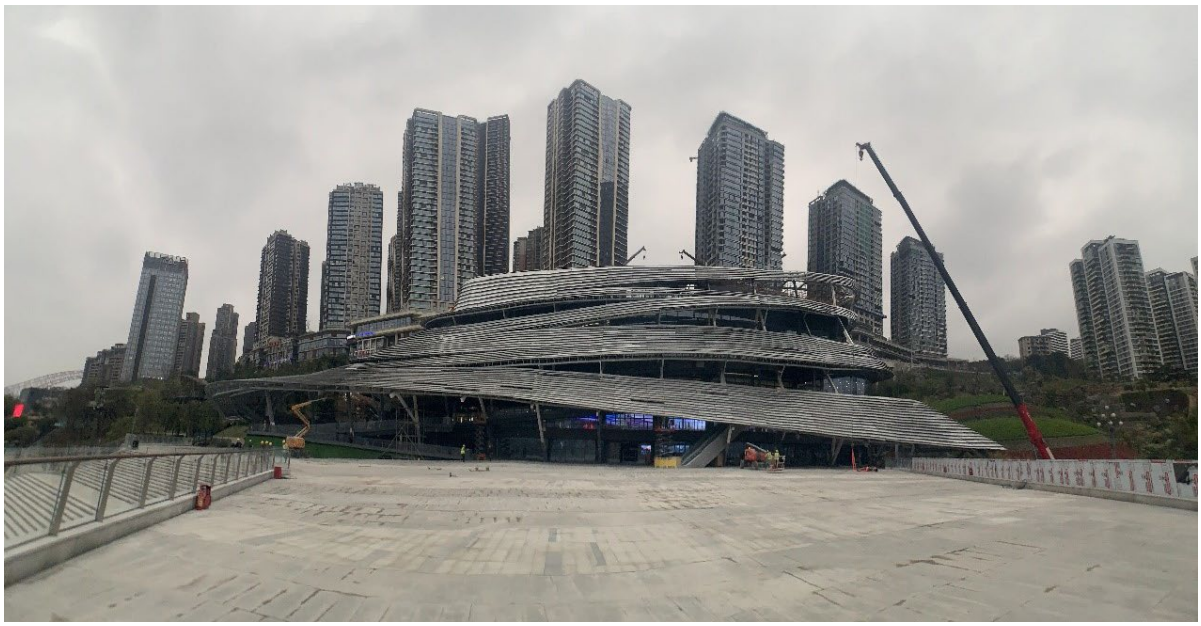


Figure 1. Chongqing Center for Planning and Exhibition (2022).

2. Generation of initial data

All the construction data of the façade can be traced back to the final version of the hyperboloid-shaped skin that was determined in the conceptual design phase. In a complex façade design, the skin and structure are interrelated. With the form of the skin determined, the structure emphasizes the surface layer of the form, which reveals and reinforces the logical core of the structure and is a genuine and logical response of the structure to the skin. Due to the semi-outdoor grey space designed between the skin and the main building, all the secondary structures of the façade can only be supported by the main steel structure, which is similar to an external skeleton. Therefore, the construction structure of the entire façade comes from the superimposition and interaction of two types of initial data, namely the skin and the structure, to varying degrees.

2.1. Initialization of façade data

The façade design primarily consists of non-linear hyperboloid shapes, with only a small portion of the back side of the building being flat, and the rest having non-zero curvature in the UV direction. After freezing the surface design, the deepened panel units are overlapped in a staggered manner and adjusted in length based on changes in curvature, resulting in a more coordinated and rational overall design for the façade pattern (Figure 2). Additionally, the open overlapping connection method with staggered joints can significantly improve the fault tolerance of the façade panel joints from a structural perspective, providing greater buffering space for design development and construction work.

During this stage, the complexity of the hyperboloid shapes is simplified by reducing the continuously changing curvature to gradually planar panel units. In the process of reducing the three-dimensional hyperboloid shapes to two-dimensional planar panel units, core initial data for the skin are generated,

such as the numbering system for the panel units, gradient sizes, relative positions, normal directions, joint distances, and planar angles.

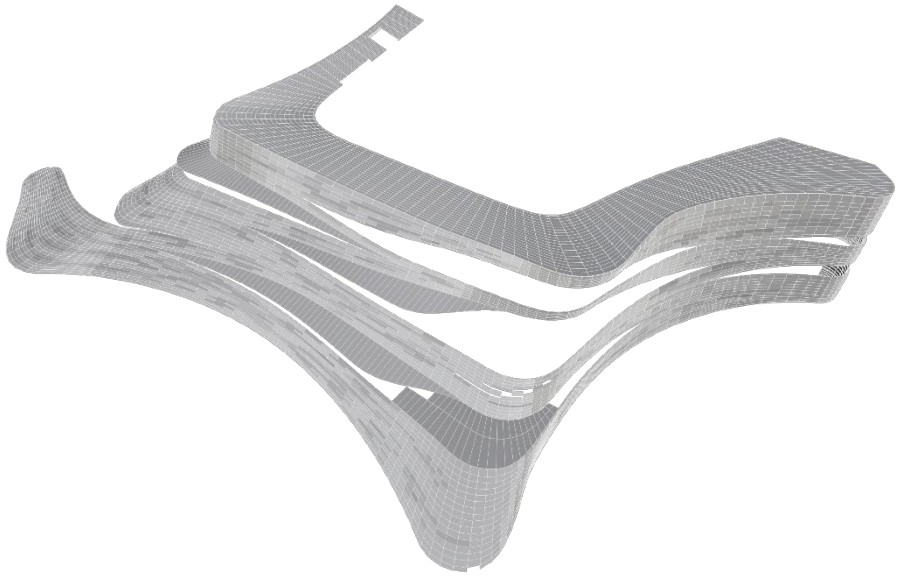


Figure 2. Façade panel units for further development.

2.2. Initialization of structural data

In the design of façades, the final form depends on the cladding scheme, while meeting the load-bearing requirements. Due to the adoption of transverse panel units with staggered joints for the hyperboloid cladding, the supporting framework is arranged using longitudinal and diagonal square-section steel beams, as well as transverse circular-section steel beams, with reference to the cladding curvature. Given the significant difference in curvature between the primary steel structure and the façade panel units, purlin systems are inserted to connect the panel units and steel structure as secondary structures. After freezing the position of the purlins, the design development of the exterior façade panel units can be independently carried out from the internal steel structure adjustment. Once the façade is completed, any design and installation errors are eliminated through the overall structure of the steel structure, purlins, and ear plates. Therefore, it is generally advisable to adopt an exterior-to-interior process from the cladding to the structure for the development of complex façade schemes.

As the corresponding framework among the façade panel units, purlins, and steel structure (Figure 3) gradually takes shape, the initial hyperboloid cladding is transformed into a façade unit system and a purlin system that can be orthogonally decomposed, with the potential adjustment space gradually fixed. This lays a good foundation for mid-term batch production and later precise and efficient construction.

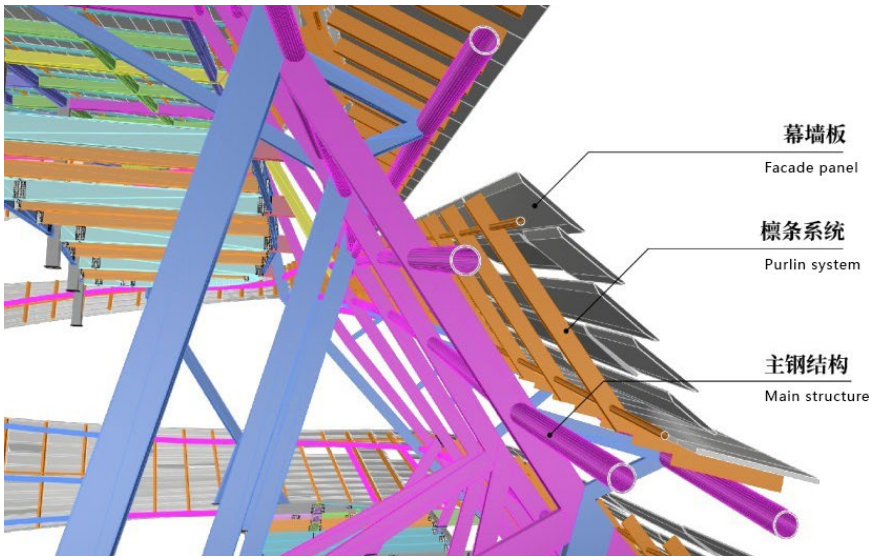


Figure 3. Façade composition: panel—purlin—main structure.

3. Development of construction data

The success of the project lies in creating a BIM model of the façade, which contains rich geometric and segmentation information that develops into a thorough construction data package at a later stage [4]. During the development process of façade design, after the scheme is finalized, the panel system and purlin system of the façade unit serve as mutually supporting constraints, leading to the derivation of more specific data for guiding precise development and large-scale production.

3.1. Batching & numbering

Taking into account factors such as structural design, manufacturing techniques, production cycles, and construction schedules, a total of 5,980 façade units were divided into 14 zones and underwent developing work in batches. Considering that the entire façade system adopts either a butt-joint or overlapping joint method with zone boundaries as the dividing line, the 14 zones were numbered using two methods: longitudinal and transverse gradients, with the zone break points as the boundary (refer to Figure 4).

The use of a numbering system as a unique identification symbol within the global scope of the project is adopted. The use of this numbering system is consistent throughout the entire project and is incorporated into the workflow loop composed of three sub-processes: façade design development, manufacturer production, and on-site installation. This system facilitates the smooth and orderly progress of the project rapidly and efficiently.

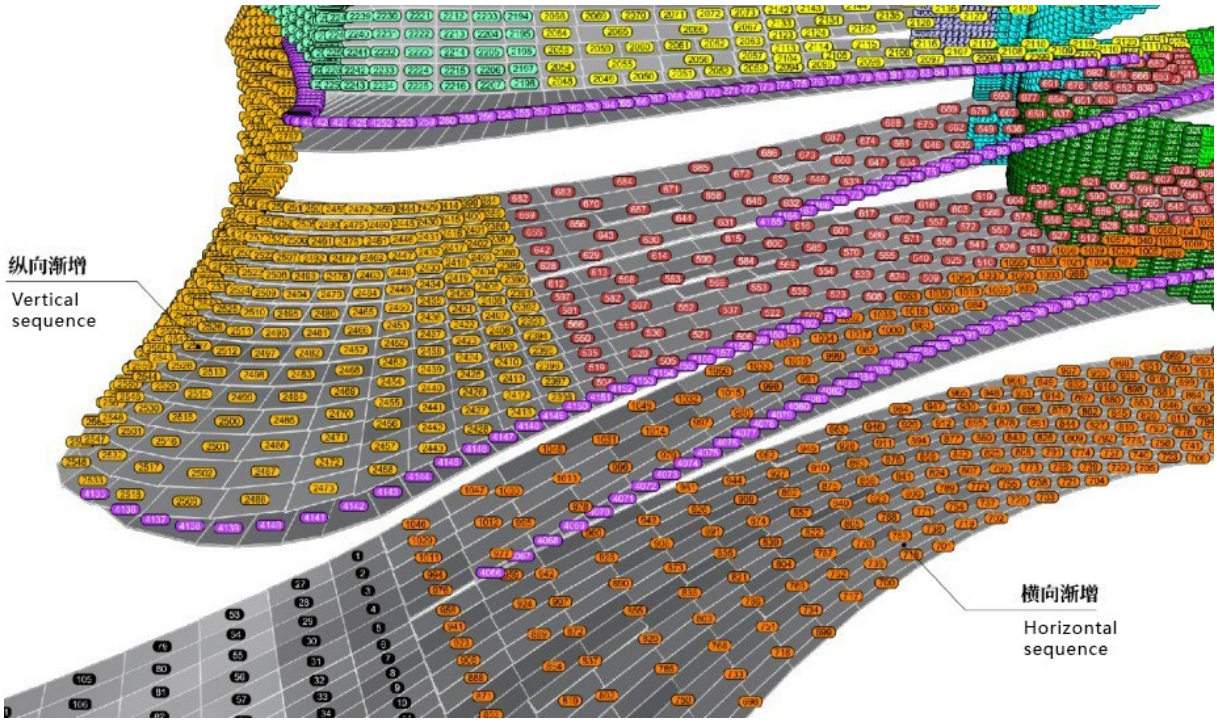


Figure 4. The two numbering systems for panel clusters.

3.2. Data generation for core components

Combining two different numbering methods from the previous step, a grouping algorithm program was applied to match the 14 partitioned façade panels with their corresponding mullions in Rhino3D and Grasshopper platforms. This process resulted in the derivation of geometric data, including vertex coordinates, normal directions, seam distances, and plane angles, which resolved issues such as displacement of points, excessively long review cycles, and high labor costs that could occur with manual development. The core content of this development phase was mainly reflected in the following three aspects.

3.2.1. Accurate grooving and hole-punching of façade panels

Once the grouping algorithm is completed, the panel units can be further perforated. Based on structural calculations and technical support from the aluminum plate manufacturer, technical drawings were obtained (Figure 5). Each panel needs to be perforated with 12 bolt holes, ranging from 120mm to 150mm in length, along the direction of the internal ribs of the panel to connect the angle steel and ear plate, and finally correspond to the purlins. Due to approximately half of the panel units being arranged in staggered rows, each purlin corresponds to both a certain number of end holes and a certain number of middle holes (Figure 6/7), with different reference lines for the two types of holes. As a result, the grouping algorithm for the panels occupies the majority of the workload in the hole-programming process. After the honeycomb panels in the 14 regions are perforated in the model, they are batch-converted into technical drawings (Figure 8) and sent to the manufacturer for large-scale production. After the production is completed, the panels are transported to the site for installation and testing. Following the completion of one cycle of perforation-production-installation for the first batch of panels, the subsequent 13 batches are constructed progressively using the same cycle. This is the most time-consuming and technically demanding core process in the façade development process.

From a purely technical perspective, in the construction process of highly customized complex curved façades, precise grooving, perforating, and joint interface design are relatively complex procedures. These procedures are also the most crucial steps for empowering similar engineering projects with

digital workflows. Their importance has been repeatedly demonstrated in research on designing and constructing highly customized architectural space frameworks and other practical projects [5]. For example, in this step, the selection and finalization of reference construction forms require a series of steps, such as case references, structural design, and program-assisted calculation. The calculation process is highly tense and requires a relatively high level of computer technology proficiency. Ideally, the construction form and the scheme design of the building envelope should be highly unified, and the implementation of the entire process relies on specialized digital teams' support.

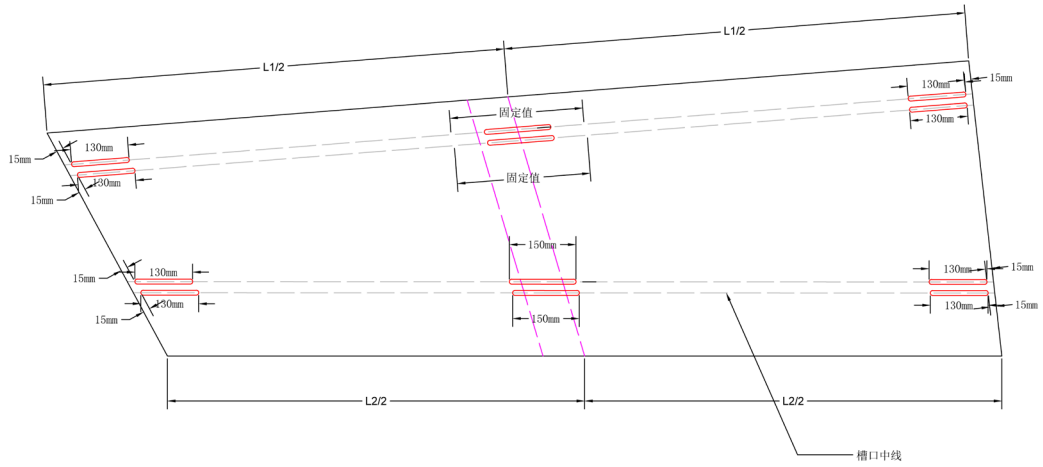


Figure 5. Drawing of façade panel with slots information

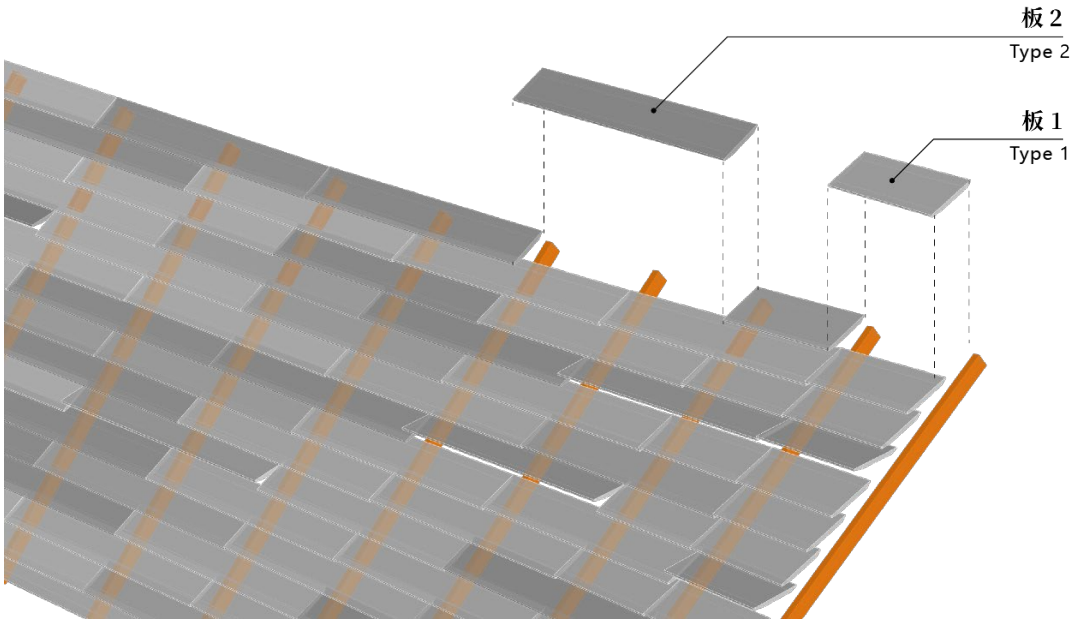


Figure 6. Purlin—panel matching.

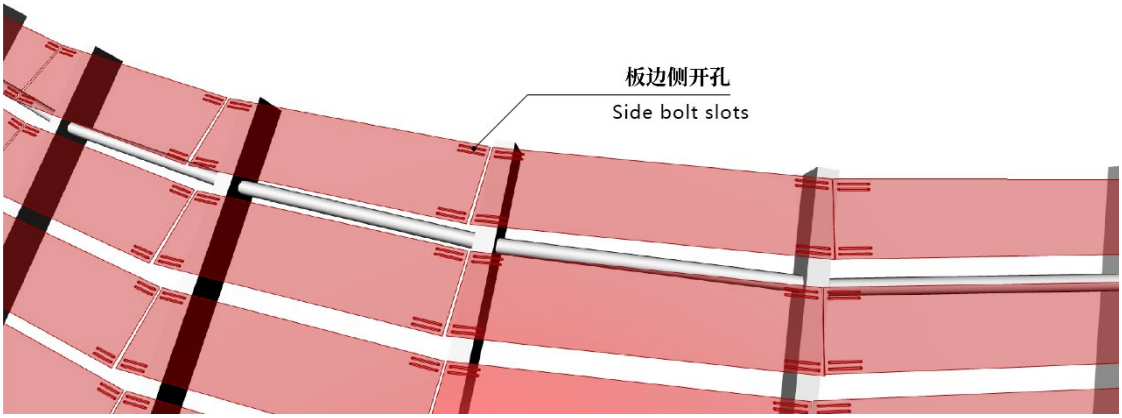


Figure 7. Purlin—slot matching.

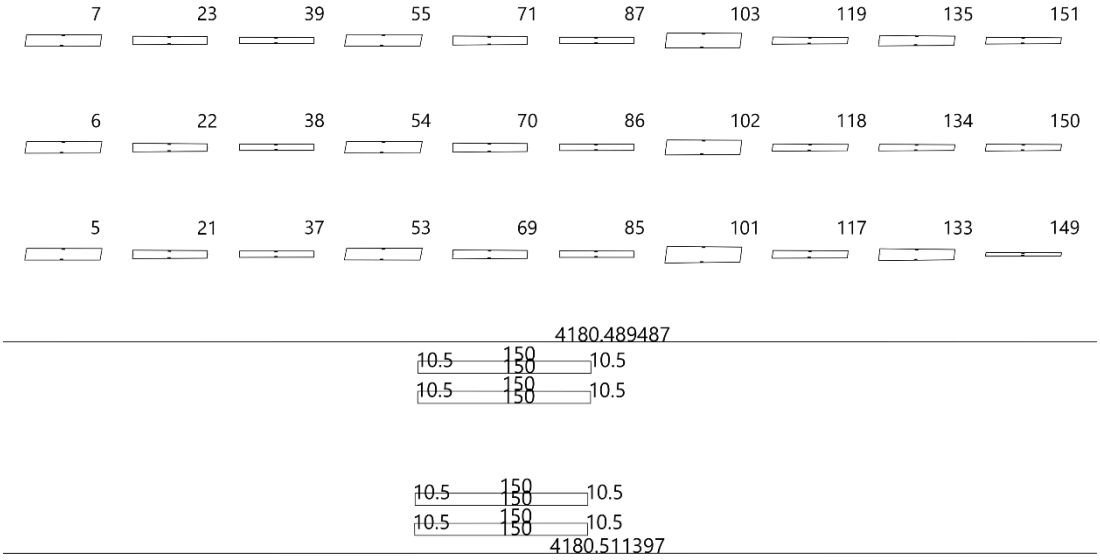


Figure 8. Drawings of flattened panels for digital fabrication.

3.2.2. Composition of angle steel, ear plates, and diagonal bracing

Based on the grouping algorithm from the previous step, precise positioning and dimensional data for components such as angle steel and ear plates can be further obtained. As a significant portion of the panel units in the primary area can reach a length of up to 4 meters, diagonal braces were used underneath the honeycomb panel to increase structural stability due to excessive weight caused by the length. Since the cross-sectional and projection dimensions of each panel are different, the hole positions for the side ear plates and diagonal braces gradually change as the curvature of the façade changes. Thus, the hole-punching task for the diagonal braces of the façade panels still needs to rely on the grouping algorithm.

According to structural calculations, panel units longer than 3 meters require additional diagonal braces (Figure 9). The intersection points between the diagonal braces and the panel units vary with the corresponding panel's angle, maintaining the diagonal braces' regular angle changes to meet the aesthetic requirements of the curved surface (Figure 10).

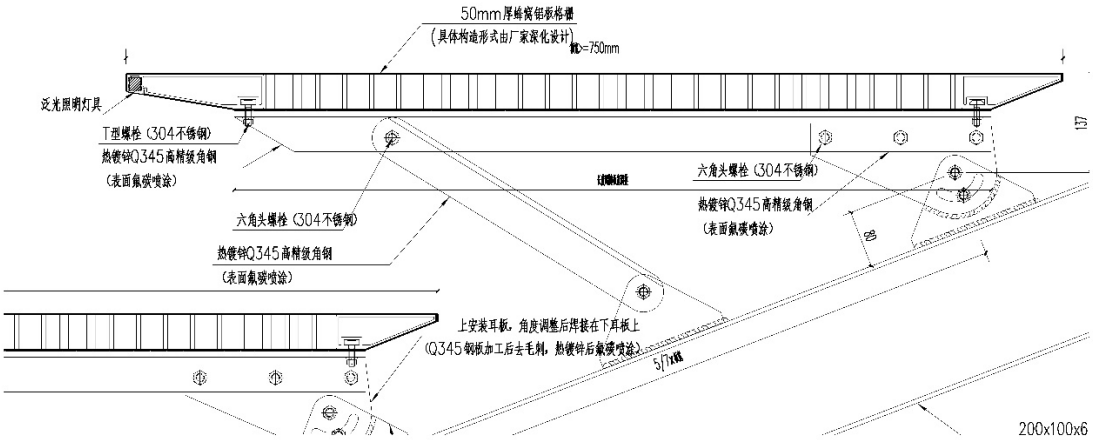


Figure 9. Detail drawing of panels with a length larger than 4m.

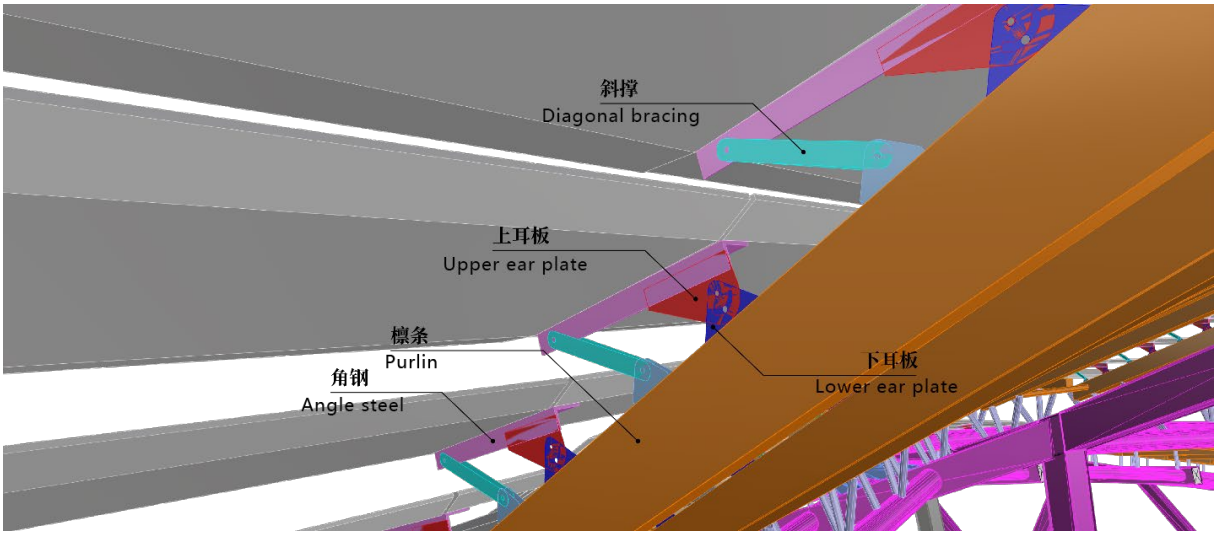


Figure 10. Purlin—panel connection.

3.2.3. Connection between purlins and the primary structure frame

Considering the precision of façade construction as a core requirement for ensuring project quality, during the positioning process, a large number of actual purlins still underwent corresponding displacement and angle adjustments based on the specific situation of the façade panel units, to ensure the highest smoothness of the gradual curvature jointly embodied by both. Adjustable-length connecting pieces were used as support between the purlins and the transverse round pipes of the steel structure through point-to-point distance measurement, ensuring that the connecting pieces were perpendicular to both the purlins and the round pipes to minimize material usage. Finally, length data tables were directly exported from the model as production references. In consideration of the support strength, an additional oblique strengthening connecting piece with an angle no less than 45 degrees was added next to each vertical connecting piece (Figure 11), and the total length of the connecting pieces was calculated based on the existing point data and angle calculation as a material preparation and post-settlement basis during the construction process.

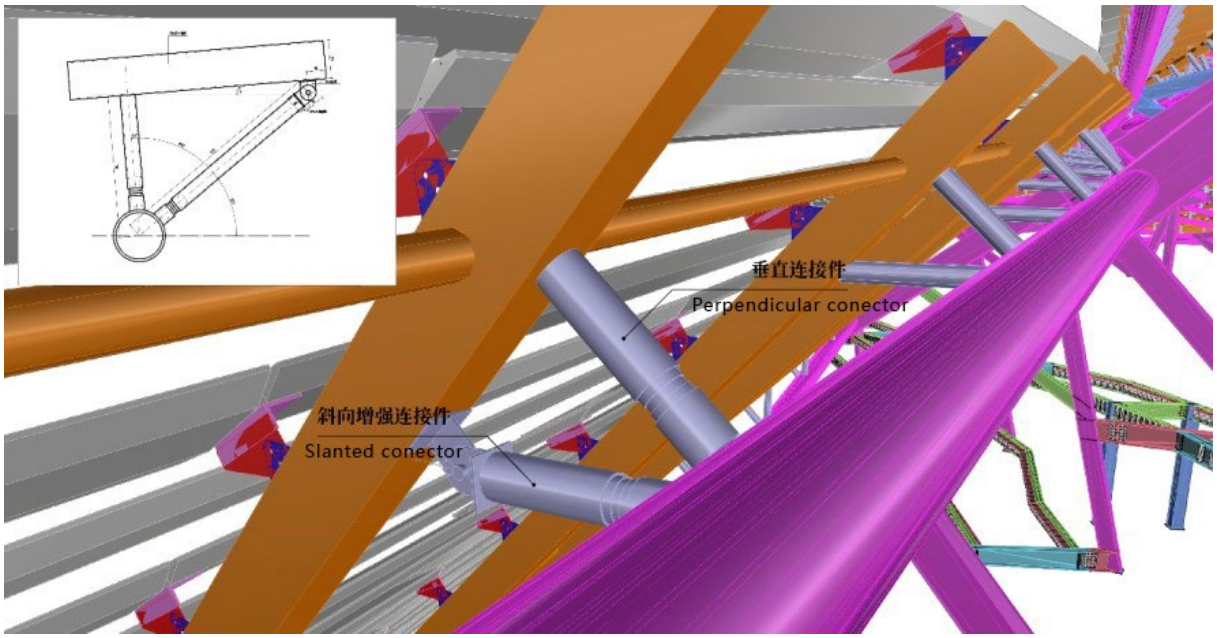


Figure 11. Purlin—main structure connection.

3.3. Development of construction data

With the completion of the algorithmic framework in the model, the development of unit-level data derived from collaboration has greatly facilitated the construction team during the actual construction process. This has truly achieved one-click generation and repeated extraction, simplifying the complex manual processes that require significant risk-taking and directly reducing them to basic operations such as coordinate positioning at a lower level. It has greatly improved construction efficiency and avoided construction risks. Additionally, using precise models and data as guidance for construction arrangements has transformed multiple single-threaded processes into multi-threaded parallel processes. This not only enhances project completion but also significantly optimizes project duration and cost, contributing the highest marginal benefit to the entire project. Construction data extracted in the later stages of the project include:

3.3.1. Batch processing dimensions for various construction components

These include angle irons with different lengths of unit plates, the identification numbers and lengths of purlins, and the length of diagonal braces. The application of automated processes in generating fabrication drawings can improve the productivity of construction processes by reducing unnecessary work and potential errors [6]. The key point of composing a detailed information model of the façade is to automate and batch-print all the fabrication drawings to be sent out to the manufacturer of the panels.

3.3.2. Extraction of coordinates for construction

These include all connector endpoint coordinates (Figure 12), the coordinates of the two endpoints of all purlins (Figure 13), the coordinates of the welding points for the upper and lower ear plates, the coordinates of the bolt-hole positions for the upper and lower ear plates, and so on.

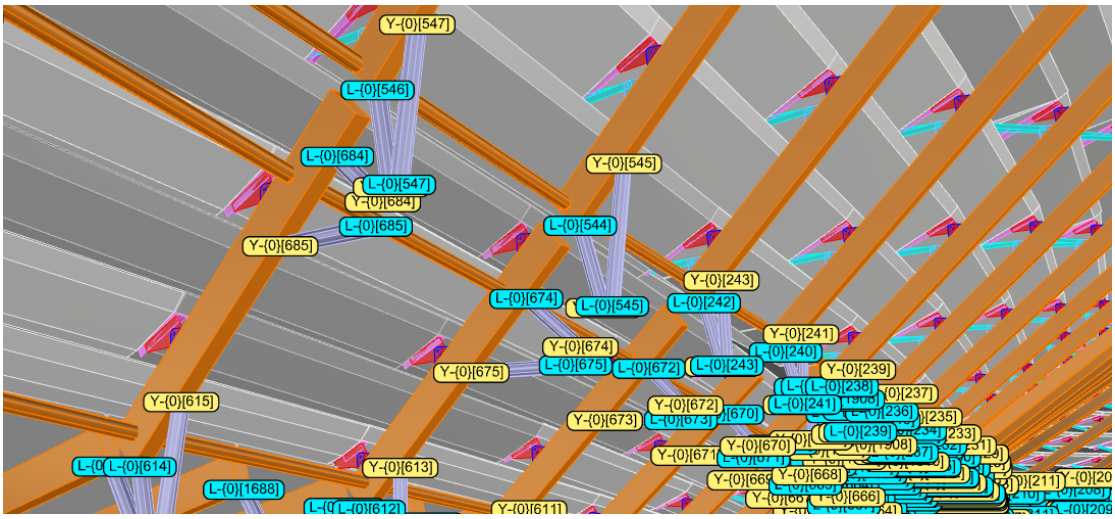


Figure 12. Endpoint coordinates and numbering of connectors.

	A	B	C	D	E	F	G	H	I	J	K	L	M
1	檩条定位点编号	X	Y	Z		檩条定位点编号	X	Y	Z		现圆管面与檩条间的距离	连接件	接圆管长度
2	LA-1	6566	-16860	8674		YA-1	6596	-16731	7974		700	150	550
3	LA-2	4432	-17129	8547		YA-2	4483	-17018	7808		739	150	589
4	LA-3	2243	-17105	8362		YA-3	2304	-17011	7642		720	150	570
5	LA-4	89	-16783	8135		YA-4	153	-16703	7484		651	150	501
6	LA-5	-1974	-16161	7890		YA-5	-1900	-16095	7338		552	150	402
7	LA-6	-3733	-14722	7732		YA-6	-3627	-14666	7159		573	150	423
8	LA-7	-5434	-13293	7549		YA-7	-5326	-13235	6982		567	150	417
9	LA-8	-7104	-11882	7347		YA-8	-7000	-11826	6807		540	150	390
10	LA-9	-8741	-10492	7134		YA-9	-8640	-10443	6635		499	150	349
11	LA-10	-8906	-10352	7113		YA-10	-8805	-10303	6615		498	150	348
12	LA-11	-10492	-9001	6899		YA-11	-10391	-8955	6414		485	150	335
13	LA-12	6987	-13324	9309		YA-12	7030	-13210	8647		662	150	512
14	LA-13	5077	-13132	9189		YA-13	5133	-13035	8530		659	150	509
15	LA-14	3192	-12626	9044		YA-14	3254	-12543	8425		619	150	469
16	LA-15	1401	-11809	8892		YA-15	1466	-11737	8337		555	150	405

Figure 13. Extracted coordinates data of purlins.

3.3.3. Verification of construction information

This includes verification of the coordinates of the ear plate after actual welding (Figure 14), verification of the coordinates and angles of the purlin placement, verification of the installation angle of the unit plate, and collision inspection of the unit plate.

	A	B	C	D	E	F	G	H	I	J	K	L	M	N	O	P	Q
1	左耳板									右耳板							
2	编号	高点			低点			备注		编号	高点			低点			备注
3		X	Y	Z	X	Y	Z				X	Y	Z	X	Y	Z	
4	2992-3004	模型中耳板悬浮于檩条之外，无法投影								3010	-21626.7	-48305.6	15017.57	-21631.3	-48305.1	14837.63	
5										3011	-21637.4	-48304.5	14599.96	-21642	-48304	14420.02	
6										3012	-21648.1	-48303.4	14182.35	-21652.7	-48302.9	14002.41	
7										3013	-21658.8	-48302.4	13764.75	-21663.4	-48301.8	13584.81	
8										3014	-21669.5	-48301.3	13347.14	-21674.1	-48300.7	13167.21	
9										3015	-21680.1	-48300.3	12929.54	-21684.8	-48299.6	12749.61	
10										3016	-21690.8	-48299.2	12511.95	-21695.4	-48298.5	12332.01	
11										3017	-21701.5	-48298.2	12094.35	-21706.1	-48297.5	11914.41	
12										3018	-21712.2	-48297.2	11676.75	-21716.8	-48296.4	11496.82	
13										3019	-21722.9	-48296.2	11259.16	-21727.5	-48295.3	11079.22	
14										3020	-21733.6	-48295.2	10841.57	-21738.2	-48294.3	10661.63	
15										3021	-21744.2	-48294.2	10423.98	-21748.9	-48293.3	10244.04	
16										3022	-21754.9	-48293.2	10006.39	-21759.5	-48292.2	9826.451	
17										3023	-21765.6	-48292.2	9588.802	-21770.2	-48291.2	9408.864	
18										3024	-21776.3	-48291.2	9171.215	-21780.9	-48290.2	8991.277	
19										3025	-21787	-48290.2	8753.63	低点超出檩条范围外			
20	3005	-21556.87	-49508.7	14986.75	-21560.4	-49525.6	14807.58			3026	-21552.3	-49577.4	14990.69	-21555.8	-49594.3	14811.51	
21	3006	-21564.93	-49553.2	14561.11	-21568.5	-49570.1	14381.93			3027	-21560.3	-49622.3	14565.07	-21563.8	-49639.2	14385.9	
22	3007	-21572.99	-49597.8	14135.46	-21576.5	-49614.5	13956.28			3028	-21568.3	-49667.1	14139.44	-21571.9	-49684.1	13960.28	

Figure 14. Extracted coordinates data of ear plates.

The installation positioning of the ear plate has always been a core issue for construction teams as it directly determines the accuracy of the positioning and installation of the façade panel. Before the involvement of the digital design development team, the construction team's method was to calculate the distance between each ear plate on the beam and the endpoint of the beam, and then weld them

together. They completed the ear plate welding of panels No. 504 to 597 and the corresponding trial installation work, but the installation error was very obvious. The digital team corrected the ear plate errors in the trial installation area by directly extracting and exporting the coordinate values of the ear plate relative to the overall construction origin of the project. This was used as construction guidance data to complete the positioning and welding work of all ear plates. According to on-site measurements, the accuracy error range between the distance measurement method and the direct coordinate positioning method is between 0 to 80mm.

3.3.4. Other information

This includes the total length of LED strips in the longitudinal direction of each unit panel, as well as the placement and length of segmented data and control cables, the calculation of the façade panel area, the positioning of the electrical box, and the routing of cables. These factors are all relevant to the project's design and implementation. In future similar projects, this set of information packages can be used for process mining to provide insight into improving design and construction quality and efficiency [7].

4. Result

According to the data collected (Figure 15) during the construction of Zone 1 (through manual labor) and Zone 9 (through digital process), beside an obvious improvement on installation accuracy, a projected 715% increase in construction efficiency and 483% decrease in construction duration is achieved.

	Construction Duration	Number of Panels	Efficiency	Efficiency Improvement	Total Construction Duration (projected)	Duration Improvement
Manual Process (Zone 1)	360 h	503	1.39 panles/h	715%	4279.9 h	483%
Digital Process (Zone 9)	80 h	652	8.15 panels/h		733.7 h	

Figure 15. Data collected during construction

5. Conclusion

The façade subproject of the Chongqing Center for Planning and Exhibition is a typical Building Information Modeling (BIM) project that empowers the entire process of complex projects with increased efficiency. In ideal situations, BIM models for such projects can be integrated with blockchain technology to establish a decentralized information network for parallel processing of building information [8]. However, due to the need for digital construction empowerment for the façade part with uniform height, the scheme design team and the structural design team need to cooperate in depth. Compared with ordinary BIM projects based on Revit or ArchiCAD BIM platforms, the information modeling technology and data usage hierarchy and difficulty involved in this project have increased significantly, so the digital platform used for design development of the entire façade part is Rhino3D and Grasshopper plugin. To ensure that the surface modeling information on the design end is retained to the maximum extent and extended to the end of the construction process, the digital team has developed a series of Grasshopper algorithm programs (Figure 16) based on the design and partition schemes to extract and deepen various façade information from different angles and degrees of operation.

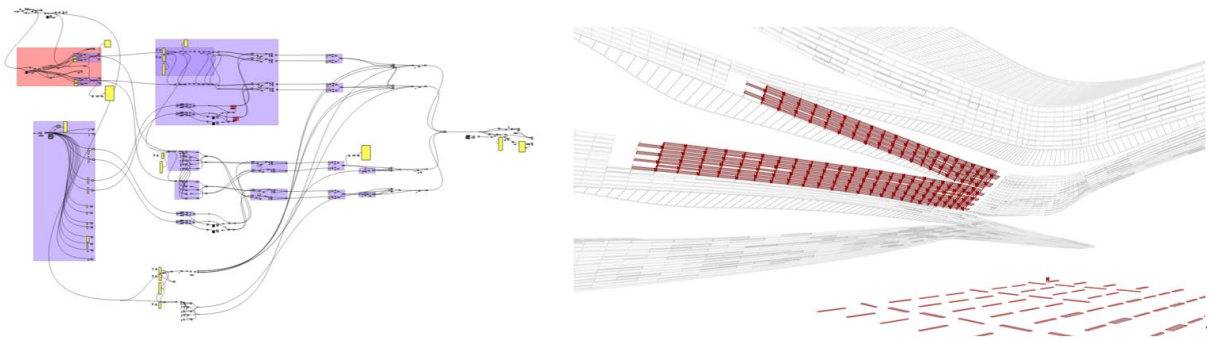


Figure 16. Grasshopper scripts for design and construction development.

Overall, the introduction of digital tools into the façade design and construction process has brought practical advantages, including breaking through the efficiency ceiling of manual construction, establishing a design and construction delivery system based on building information modeling, and greatly optimizing project duration and construction costs, enabling the entire construction process to be fully empowered and achieving a significant improvement in project completion.

Acknowledgments

This work is supported by the Joint Funds of the National Natural Science Foundation of China Key Project Grant (U1913603) and the Shanghai Municipal Science and Technology Major Project (2021SHZDX0100) and the Fundamental Research Funds for the Central Universities.

References

[1] Quim Moya, Oriol Pons, "Improving the design and production data flow of a complex curvilinear geometric Glass Reinforced Concrete façade," *Automation in Construction,* 38 (2014) 46–58

[2] Ming Zhang, Rui Xu, Haitao Wu, Jia Pan, Xiaowei Luo, "Human-robot collaboration for on-site construction," *Automation in Construction,* 150 (2023) 104812

[3] Khalid Amin, Grant Mills, Duncan Wilson, "Key functions in BIM-based AR platforms," *Automation in Construction,* 150 (2023) 104816

[4] Rui He, Mingkai Li, Vincent J.L. Gan, Jun Ma, "BIM-enabled computerized design and digital fabrication of industrialized buildings: A case study," *Journal of Cleaner Production,* 278 (2021) 123505

[5] Jingyang Liu , Yi-Chin Lee, Daniel Cardoso Llach. "Computational design and fabrication of highly customizable architectural space frames: Making a flat-cut Weaire-Phelan structure," *International Journal of Architectural Computing,* 2020-08-21:42-43.

[6] Min Deng, Yi Tan, Jyoti Singh, Ajay Joneja, Jack C.P. Cheng, "A BIM-based framework for automated generation of fabrication drawings for fac¸ade panels," *Computers in Industry,* 126 (2021) 103395

[7] Wen Gao, Shuai Lu, Xuanming Zhang, Qiushi He, Weixin Huang, Borong Lin, "Impact of 3D modeling behavior patterns on the creativity of sustainable building design through process mining," *Automation in Construction,* 150 (2023) 104804

[8] Timothy O. Olawumi, Daniel W.M. Chan, Stephen Ojo, Michael C.H. Yam, "Automating the modular construction process: A review of digital technologies and future directions with blockchain technology," *Journal of Building Engineering,* 46 (2022) 103720

IASS 2023
July 10–14 Melbourne
Integration of Design and Fabrication

Proceedings of the IASS Annual Symposium 2023
Integration of Design and Fabrication
10–14 July 2023, Melbourne, Australia
Y.M. Xie, J. Burry, T.U. Lee and J. Ma (eds.)

Generative design of isostatic ribbed slabs using anisotropic Reaction-Diffusion

Alessandro ZOMPARELLI[a], Roberto NABONI[a,*]

[a,*] CREATE -University of Southern Denmark
Campusvej 55, 5230 Odense, DK
ron@iti.sdu.dk

Abstract

Principal stresses and moments are increasingly used to design efficient structural geometries in concrete slabs and shells. These are typically obtained through Finite Element Analysis (FEA) packages and represented as vector fields with singularities, such as high convergence or divergence areas. Designing architectural structures interpreting these fields currently relies on laborious parametric modelling. This paper introduces a generative method for isostatic ribbed slab design, where the stiffening topology layout is found with an anisotropic Reaction-Diffusion system. Based on FEA for a given slab design, the system emergently finds structural patterns along the principal stress and moment fields, which can be easily tuned into rib stiffeners, controlling their density and thickness. This bio-inspired approach, associated with field compositing, allows us to streamline the accurate modelling of structural elements with appropriate geometrical and dimensional control, which considers fabrication constraints. The workflow is successfully applied to proof-of-concept ribbed concrete slab prototypes, successfully designed, built and tested using this novel method.

Keywords: reaction-diffusion, field-based modelling, ribbed slabs, isostatics, computational design

1. Introduction

Structural optimisation is of utmost importance in the age of decarbonisation of architecture. Computational means of design and fabrication support a progressive redefinition of building technology, which can be increasingly reconceived with bespoke elements of high structural - and, therefore, ecological - performance. Recent research has focused on studying new concepts per mass-reduction of horizontal structures, such as slab and beam elements, using combinations of computation-driven optimisation techniques with advances in digital fabrication [1,2,3]. However, the design optimisation of slab structures was already a topic of interest during the XX century. Still, it is rarely adopted in contemporary construction because of its increased costs when using traditional means of design and construction. Remarkable is the example from Pierluigi Nervi, who designed the wool-factory building “Lanificio Gatti” in 1951, featuring a reinforced concrete slab system with stiffening rib elements following the direction of primary and secondary principle moments [4]. This milestone project introduced a new language for material-efficient ribbed concrete slabs, which inspires contemporary research.

SDU CREATE demonstrated with a series of experiments the structural efficiency of a series of beams whose design for concrete 3D printing is parametrically developed based on the isostatic fields of principal moments and stresses [5,6]. The diffusion of FEA software integration into parametric modelling environments has made exploring such structures more accessible to designers without an advanced engineering background. However, existing software and workflows do not support a straightforward translation of structural analysis into usable isostatic paths and structural shapes, requiring laborious modelling procedures.

Copyright © 2023 by Alessandro ZOMPARELLI and Roberto NABONI, University of Southern Denmark. . Published in the Proceedings of the IASS Annual Symposium 2023 with permission.

In search of an alternative approach, we refer to observing natural structures, where geometrical stiffening of plates in bending can be found in species such as plant leaves and insect wings. One example is the Victoria leaf which adopts a two-way network of radiating ribs to enhance bending stiffness [7]. This and other natural pattern formations provide exciting role models for the optimisation of ribbed plates and suggest the possibility of linking the fields of biological morphogenesis with structural optimisation. Following this line of investigation, this paper describes a novel bio-inspired method for designing geometrically stiffened plate structures, adopting anisotropic Reaction-Diffusion (RD) to generate various structural patterns following the information obtained from vector fields of principal stresses and moments in a provided structure.

1.1 Background

The formation of structural patterns in Nature finds recurring similarities across species and scales, and it is still unexplained if those arise from similar self-organising behaviours [8]. The theory of Reaction-Diffusion, introduced in 1952 by Alan Turing [9], provides a universal model to explain pattern formation using simple reactions of two diffusible components. It generates various emerging patterns by manipulating a few diffusion and reaction parameters. Because of this property, RD has been recently used in mechanical engineering as a form-finding strategy to generate structural patterns [10,11]. In the work of [12], an anisotropic RD system that grows adaptively following provided tensor fields to generate 3D lattice structures is implemented.

Inspired by this approach, our work developed a custom RD system to interpret and react to vector fields of principal stress and moments obtained from shell-based FEA of structural plates subjected to bending forces. We combine this with structural, morphological and functional information layers, described with a set of 2D plots consisting of scalar and vector fields to automate the 3D modelling of geometrically stiffened structures.

2. Modelling approach

2.1 Reaction-Diffusion

RD is a computational model that generates emergent patterns closely resembling some of the ones found in animals´ skin and plants. According to Alan Turing's theory, these patterns can be generated by two reacting chemical substances spreading along a tissue at different speeds. The Gray-Scott mathematical model was developed from that assumption to simulate such a chemical reaction [13]. Since then, this was widely adopted to simulate the pattern formation using two differential equations that describe the variation in the concentrations of two substances, A and B, in a given time interval [14]. The chemical reaction between the two substances is controlled by the parameters F and k, representing respectively the *feed* and *kill* values. For the case of a bi-dimensional space, which is of interest to this article, the model is implemented by evaluating the values of the two chemicals, A and B, stored in the pixels of an image. The model´s diffusive behaviour is based on computing the Laplacian function that requires the evaluation of the neighbours' pixels to spread the concentration for the substances.

$$\frac{\partial A}{\partial t} = Diff_A \nabla^2 A - AB^2 + F(1 - A),$$
$$\frac{\partial B}{\partial t} = Diff_B \nabla^2 B + AB^2 - (F + k)B. \quad (1)$$

The variation of these few parameters produces a highly varied range of patterns, including continuous, closed cellular, maze-like networks and dotted configurations adapting to the conditions of the organism. Some of these patterns offer opportunities for generating geometrical stiffeners in complex structures.

2.2 Phase plot for isotropic Reaction-Diffusion

An RD phase plot is used to evaluate the pattern formations achieved by varying F and k parameters in an isotropic system (Figure 1). It is worth noticing how the gradual transition between phases is seamlessly processed locally, ensuring overall coherence and continuity. Since A and B substances generate nearly complementary values, the study of the pattern phase behaviour can be fairly observed in the sole substance A (Figure 1A). Here five phases can be identified according to the topological properties of the generated pattern: Z0 is mostly substance A without any relevant geometric features; Z1 is defined by dotted elements filling the space isotropically; Z2 has linear labyrinth-like elements with a directionality that is subject to the initial distribution of the substances; Z3 is similar to Z2 but exhibits a more robust network-like structure transitioning to negative spots on the lower part; Z4 does not exhibit any pattern. All phases show a slight change in scale parallel to their transition line, from a larger scale in the bottom-left corner to a finer scale towards the top-right corner. In addition, it is observed that the behaviour of the pattern is highly dynamic and unstable with low-value parameters and becomes slow and stable when adopting higher values. The perceivable colour gradient represents the dynamic behaviour obtained by overlaying three different states at 20 iterations of distance as *Red*, *Green* and *Blue* (RGB) channels. The pattern's scale changes by multiplying DiffA and DiffB with the same factor, preserving the same characteristics. This can be correlated to an input scalar field represented by a grayscale image (Figure 1B).

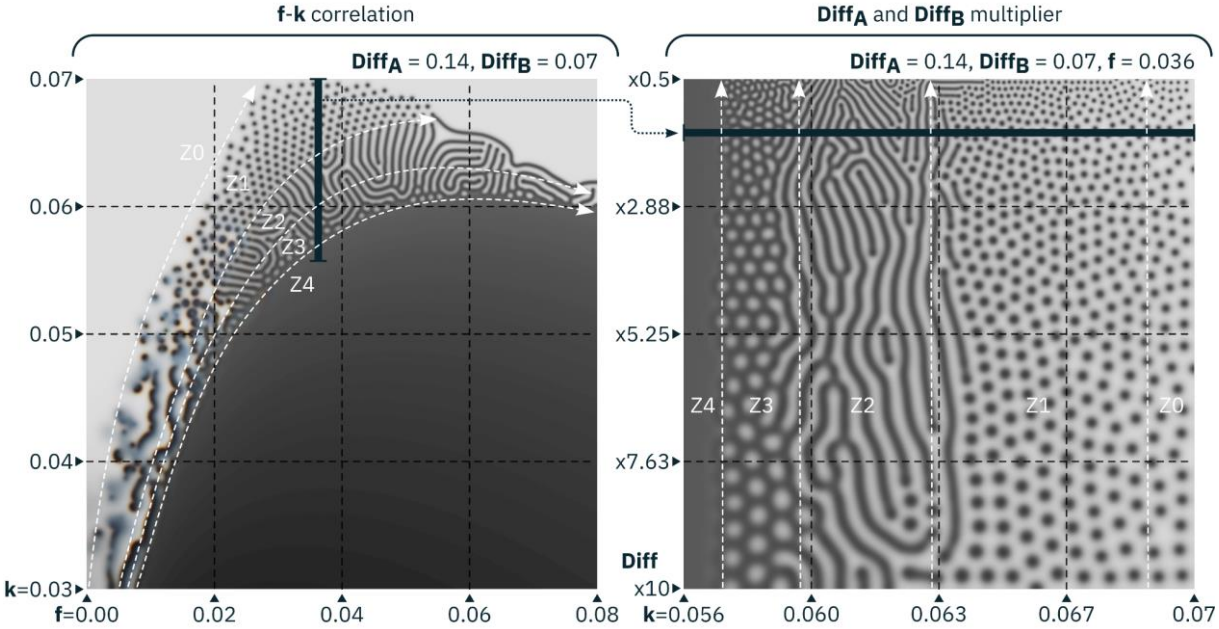


Figure 1A. Phase diagram for isotropic Gray-Scott model according to a variation of both f and k; 1B - Scale variation of the selected range of variation of the parameter k given a constant f value.

2.2 Anisotropic Reaction-Diffusion growth

In the model described above, the RD exhibits patterns with labyrinthine stripes features in Z2 and Z3, which cannot be controlled in their direction. The growth process primarily governs their orientation. To enable the control of these patterns´ direction and use them as structural patterns, it is necessary to introduce anisotropic conditions during the simulation to obtain tissue with varying diffusive behaviour

according to their direction. Provided a vector field, the diffusion model is controlled by the Laplacian function, which evaluates the neighbourhood in both *x* and *y*:

$$\nabla \cdot \nabla f = \nabla^2 f = \frac{\partial^2 f}{\partial x^2} + \frac{\partial^2 f}{\partial y^2} \tag{2}$$

An anisotropic behaviour is obtained along the main axis by reducing or increasing the derivative in one of the axes. To obtain this, a typical 4-neighbours cell was updated into an 8-neighbours model, towards which the Laplacian function is computed (Figure 2). The top row shows a Laplacian mask (or kernel) considering only 4-neighbours (Figure 2A). The numeric values represent the information weight for each pixel in determining the value of the Laplacian. While altering the proportions in x and y produces an anisotropic behaviour in the main axis (Figure 2B), it does not allow an anisotropic diffusion along any arbitrary direction (Figure 2C). The bottom row shows the 8-neighbours mask used for this work (Figure 2D). This approximates the diffusion along the main axis (Figure 2E) and towards any arbitrary direction (Figure 2F).

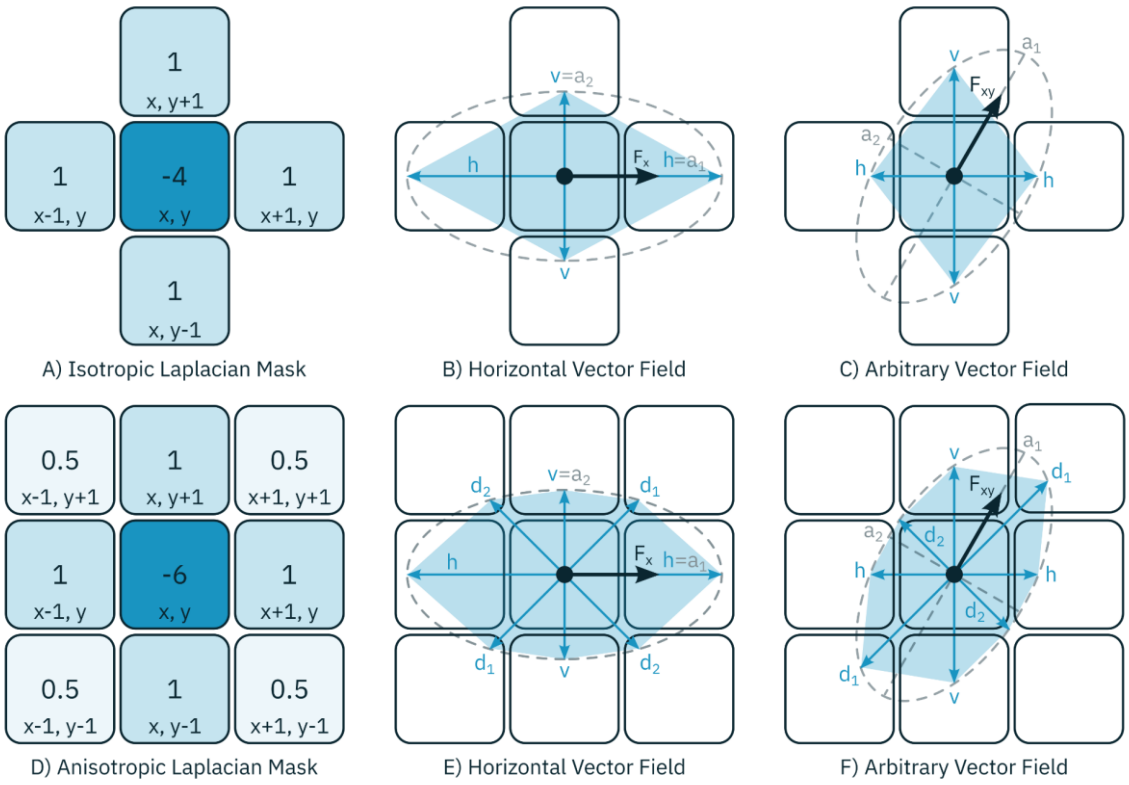


Figure 2. Comparison between 4-neighbours and 8-neighbours Laplacian masks in defining the anisotropic behaviour of diffusion

2.3 Controlled pattern generation

The intensity of the anisotropic behaviour can be controlled by turning off parameters a_1 and a_2, affecting the diffusion respectively in the parallel and perpendicular field direction. When $a_1=a_2$, a simple isotropic diffusion occurs (Figure 3A). When $a_1=1$ and $a_2=0$, the pattern exhibits anisotropy along the field

direction. When $a_1=0$ and $a_2=1$, the anisotropic behaviour is perpendicular to the direction of the vector field. When the proportion a_{A1}/a_{A2} for substance A is the same as a_{B1}/a_{B2} for substance B, the pattern has an isotropic distribution but is stretched in shape along the field direction (Figure 3B). A different behaviour occurs when $a_{A1}/a_{A2} \neq a_{B1}/a_{B2}$. For instance, if the behaviour of substance A is purely isotropic, then the pattern is not stretched but developed along the direction of the vector field (Figure 3C).

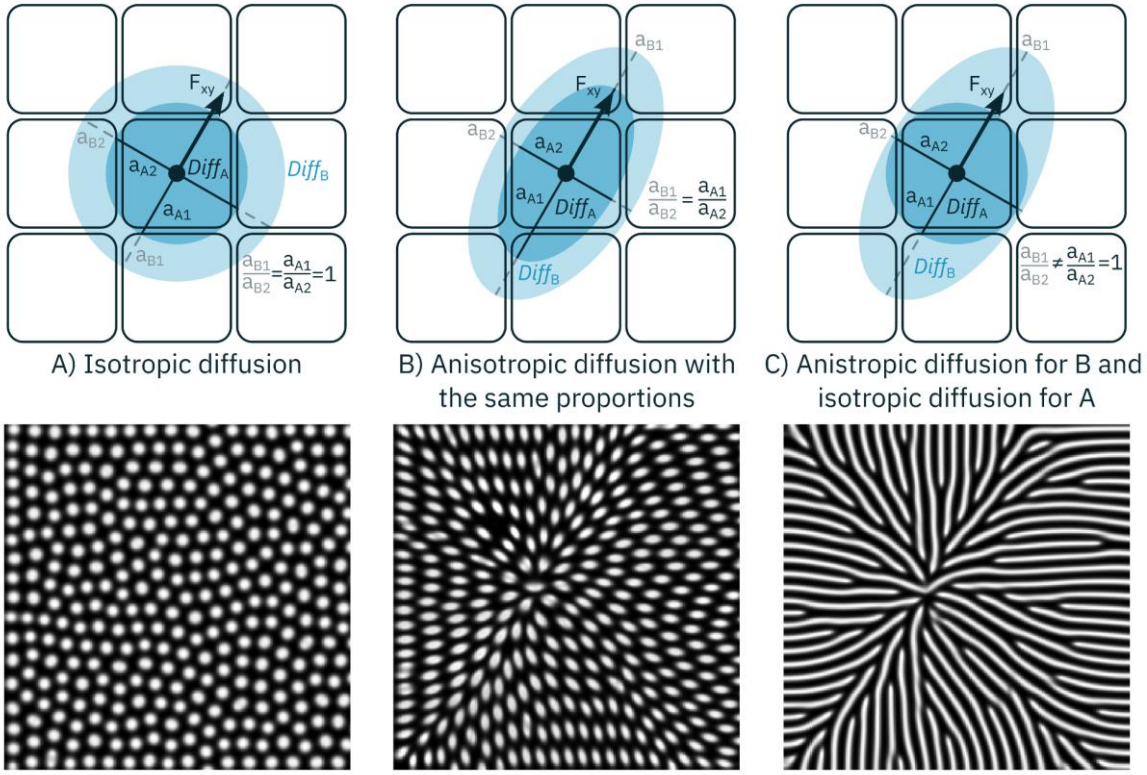


Figure 3A. Isotropic diffusion for the substances A and B.
Figure 3B. Anisotropic diffusion for both A and B.
Figure 3C. Isotropic diffusion for A and anisotropic diffusion for B

Figure 4 shows the behaviour of the anisotropic RD for a given vector field. The pattern is aligned to the vector field on the left while it follows the perpendicular direction on the right. Compared to the isotropic case, the pattern appears more stable, exhibiting uniform features for a broader range of f and k variation parameters. Similar phases can be observed compared to the isotropic case (Figure 1).

These patterns can be easily transformed into 3D geometry to obtain geometrical features with various structural properties. The bottom part of Figure 4 shows a few cases of surface thickening based on anisotropic RD patterns provided by a vector field. These ribbed geometries are obtained by directly transferring the value of substance A into a thickness height map. In addition, the patterns generated parallel to the vector field can be combined with those generated along the perpendicular direction (crossed patterns) to obtain a two-way ribbed layout.

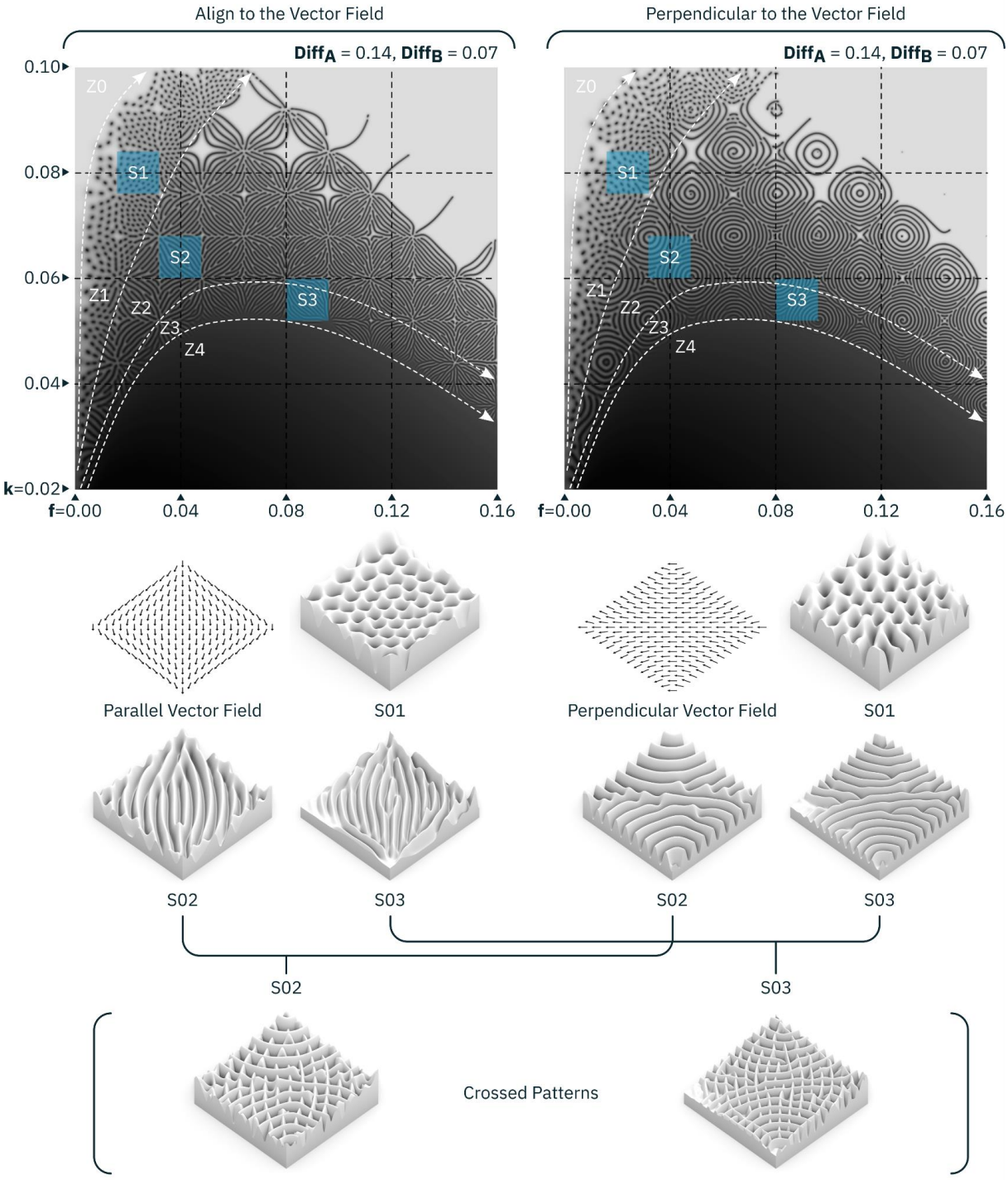


Figure 4. Phase diagrams for anisotropic RD. On the left side, the pattern is generated parallel to a given vector field. On the right, the pattern is generated in the perpendicular direction.
In the lower part, a set of displacement tiles is extrapolated to visualise the patterns in 3D. At the bottom, two crossed patterns for S02 and S03 are overlapped to obtain a two-way configuration.

3. Software implementation

Available RD implementations that allow an interactive tuning of parameters have been developed for graphic representation [15,16] and therefore lack integration with modelling software. To make this a tool for designers, the field-based anisotropic RD system described in this work has been implemented within Tissue, an open-source Blender add-on. In its current form, pixel-based and vertex-based modes are available. The pixel-based method was used in this work. It uses image textures as fields for A and B. The input vector field for controlling the anisotropic behaviour is an image where the channel *Red* and *Green* represent, respectively, the x and y components of the vector remapped from -1 and 1. Furthermore, additional grayscale images can be used as input to control the parameters F, k, scale, DiffA, DiffB, and Anisotropy. The vertex-based method processes the RD along an arbitrary mesh surface, using the Blender´s vertex groups as input fields to define height maps, where a value from 0 to 1 is assigned for every vertice. The vector field can be computed as a gradient function of a scalar field or by using the vector attributes.

4. Application case of isostatic path generation for ribbed slabs

The above-described method and implementation are deployed into a design-engineering computational pipeline, which is applied to proof-of-concept ribbed slab prototypes. Researchers and students developed these during SDU CREATE´s Summer School on Experimental Architecture in 2022. The following sections describe the modelling process and physical outcomes and illustrate a concrete application case for our method. The software pipeline encompasses the subsequent phases: (1) FEA-generation of scalar and vector structural fields; (2) generative design of isostatics patterns with RD; (3) Multi-field compositing of ribbed slabs.

The pipeline was applied onto two different slab cases of a rectangular shape, both measuring 20m x 10m, (RD-01) used four-point supports placed at the angles, with a slight offset from the perimeter; (RD-02) was based on two diagonal linear supports evenly placed in the longitudinal mid axes. Both elements were calculated with self-load and a distributed load equivalent to 6 kN/m^2. For this study, the prototypes were built in scale 1:10, and some construction details were tuned accordingly.

4.1 Modelling pipeline

A breakdown of the modelling pipeline blocks is described below:

(1A) Generation of structural fields - Starting from provided mesh shell elements representing the intended slab plan geometry, supports, loading conditions and material properties were applied into a linear FEA using Karamba for Grasshopper. The analysis includes primary and secondary principal moments, moment intensity, and sign information. Moment principals show the direction of the highest and lowest moment of inertia along the analysed surface.

(1B) Generation of fields maps - Through a custom exporter which translates mesh face properties into RGB colours, 2D maps were exported for the following steps of the design pipeline: (i) two maps of primary and secondary moment vectors directions, where the red (R) and (G) channels correspond to X and Y directions of the vectors; (ii) two grayscale scalar maps showing the absolute values of the moment intensities; (iii) two grayscale scalar maps outlining the sign of the principal moments, i.e. whether it is positive or negative.

(2) RD generation of isostatic structural patterns - In this phase, structural patterns for ribbed slabs were generated with the anisotropic RD system previously described, using the input fields from the preliminary FEA. Using a Graphical User Interface (GUI), designers controlled the pattern directionality according to the field of principal moments. They regulated the scaling of individual rib elements according to construction and fabrication constraints by scaling the pattern locally. The real-time behaviour of the RD simulation allowed us to preview results quickly and manually interact with its diffusion using Blender's brush tools to force the regeneration of critical parts, such as supports. In RD

Slab 01, the process was applied for both primary and secondary principal moments to generate a network of perpendicular ribs treated with two distinct scaling factors. In RD Slab 02, it was used to generate rib stiffeners only in the direction of the dominant principal moments, using local scale variations according to the moment intensity (Figure 5).

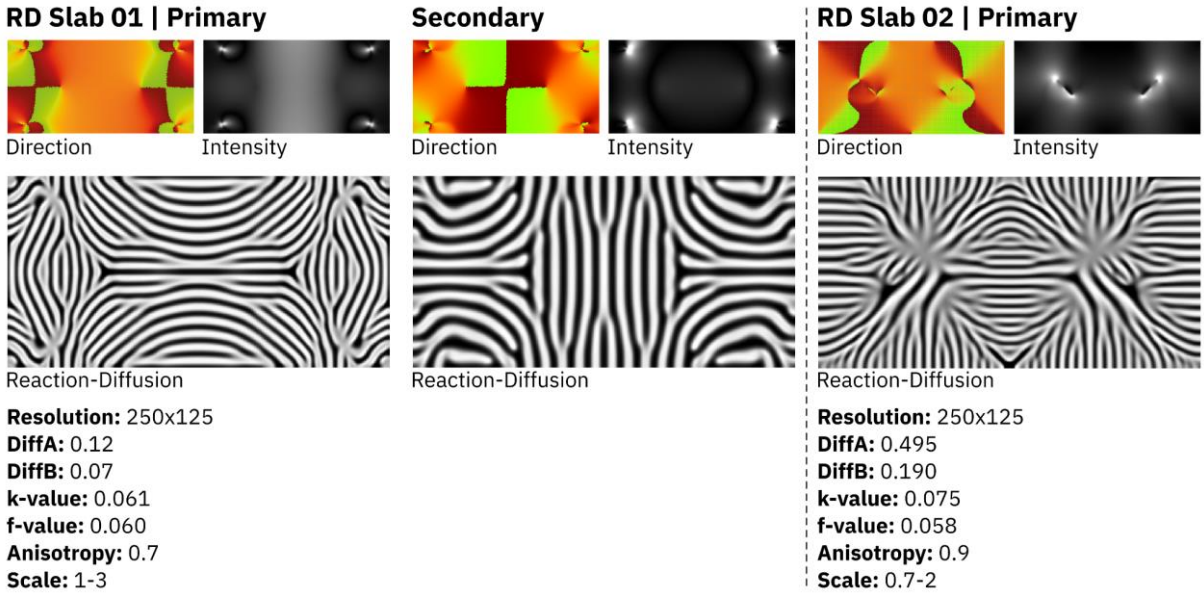


Figure 5. RD patterns were generated for the two slabs starting from the structural input fields. For RD Slab 01, both principal directions have been considered working with two scales for the primary and secondary directions. For RD Slab 02, a single rib orientation has been used, emphasising the scale varies according to the moment intensity.

(3A) Multi-field Compositing - In this phase, the three-dimensional geometry of ribbed slabs were obtained by combining the previously collected information layers. Scalar 2D maps representing design elements, structural data, and RD patterns were combined into a single height map with a compositing method for generating the slab geometry. The RD pattern was thickened to obtain ribbed elements that stiffen the tensional areas induced by the bending moment. The ribs´ cross-section shape was tuned mathematically through function curves according to the reinforcement rebar´s size and needed concrete cover. The ribs´ sectional height (H) for the primary ribs was parameterised according to the moment intensity (I) to obtain the required moment of inertia for any given moment value in the slab without the structural need for additional steel reinforcements. This is achieved with the following formulation *H=RD'*I*T*. For the case of RD Slab 01, a two-way ribbed slab, the secondary ribs´ sectional height was parameterised on a different layer. Afterwards, the information on the cross-section height for primary and secondary ribs was combined using the maximum value at every point of the slab: *h=max(h1,h2)*. The field-based compositing for the supports provided a mathematical control for the transition among the various slab parts (Figure 6).

(3B) Local Model Editing - The output geometries from the multi-field compositing were then analysed and prepared for fabrication. In this phase, additional geometric requirements can be introduced, for instance, to ensure integrated connection interfaces and construction details. Mesh sculpting tools are conveniently used to accommodate such needs and mitigate the transition between the generated ribbed geometries and the support areas.

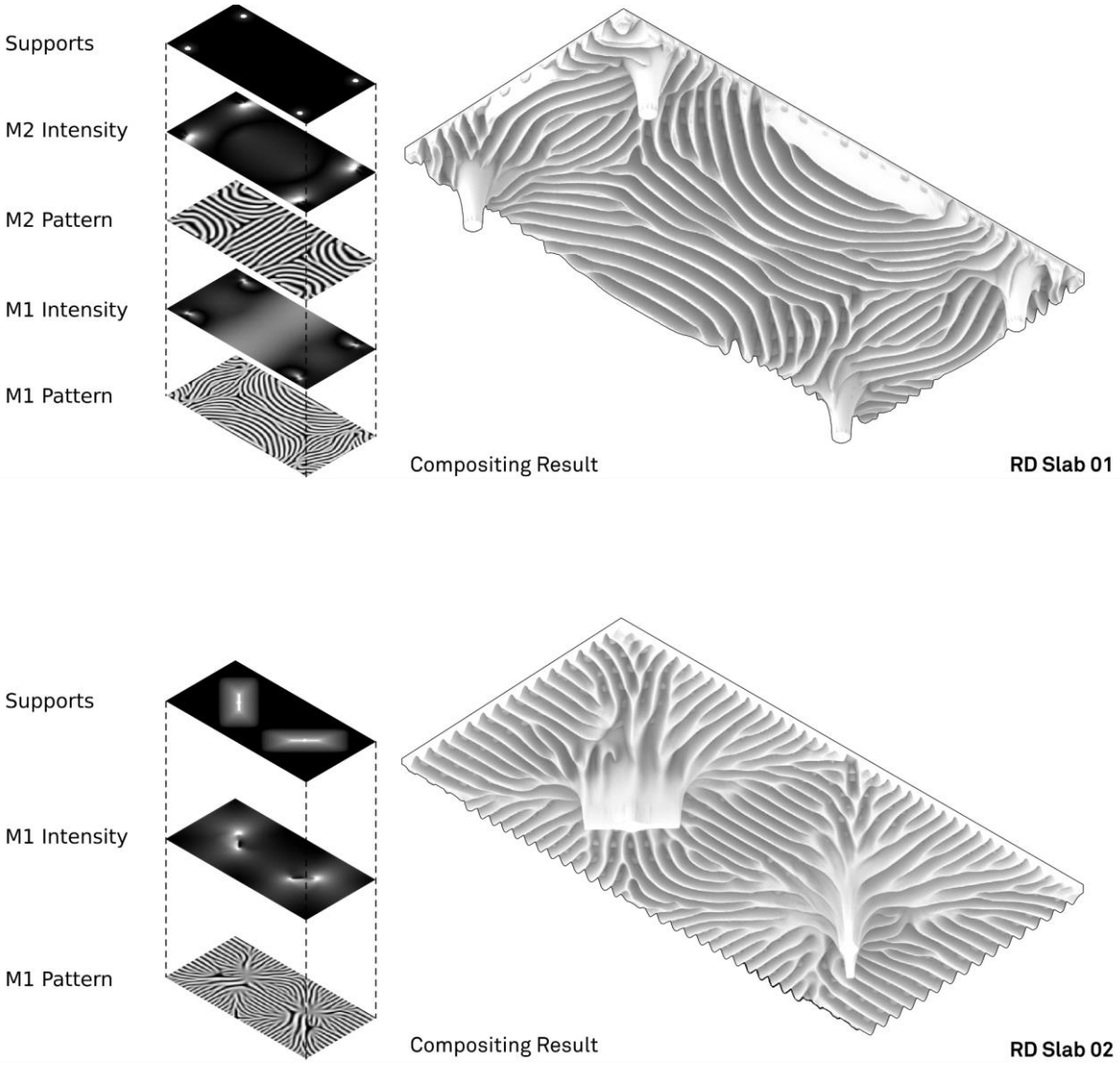


Figure 6. Multi-field Compositing process and generated 3D geometries for both slab prototypes.

5. Results

The RD-driven modelling pipeline for ribbed slab structures was successfully applied to the design and construction of two proofs-of-concept ribbed concrete slabs, realised in scale 1:10. These were fabricated through the use of 7-axis robotic milling of styrofoam moulds combined with Mixed Reality-assisted rebar bending, where Ultra-High-Performance Concrete (UHPC) was cast. A comprehensive overview of the fabrication process is provided in [17].

Two fully functional slab prototypes were built, verified using a non-linear FEA in Abaqus, and physically tested using non-destructive loading methods. The ribbed slabs confirmed their intended structural behaviour showing a bending high-stiffness despite their minimum thickness. The innovative design approach provides a new perspective from both computational and morphological viewpoints, resulting in a novel language for densely ribbed concrete slabs, virtually flexible to any boundary condition (Figure 7).

The presented RD pipeline allowed users to easily engage with the design of isostatic ribbed slabs, solving complex topological conditions in the path generation of the structural patterns without the need for establishing laborious parametric models. Designers could generate options using relatively intuitive tuning operations on the bi-dimensional RD patterns.

The use of the field-based anisotropic RD system proved to be particularly effective in the following:

(i) generating quickly structural patterns with a user-controlled scale where the rib stiffeners and their in-between spacing are semi-constant;

(ii) solving regions of largely variable proportions, where stress and moment principal vector fields quickly converge/diverge - often near supports. Our system generates seamless bifurcation and interactions that are coherent with the intended stiffening direction;

(iii) providing dimensional control in the individual ribs' width and height, particularly relevant in areas where stresses and support have a significant variation

(iv) providing opportunity for quick manual editing of unsatisfying configurations thanks to the interactive nature of the RD simulation.

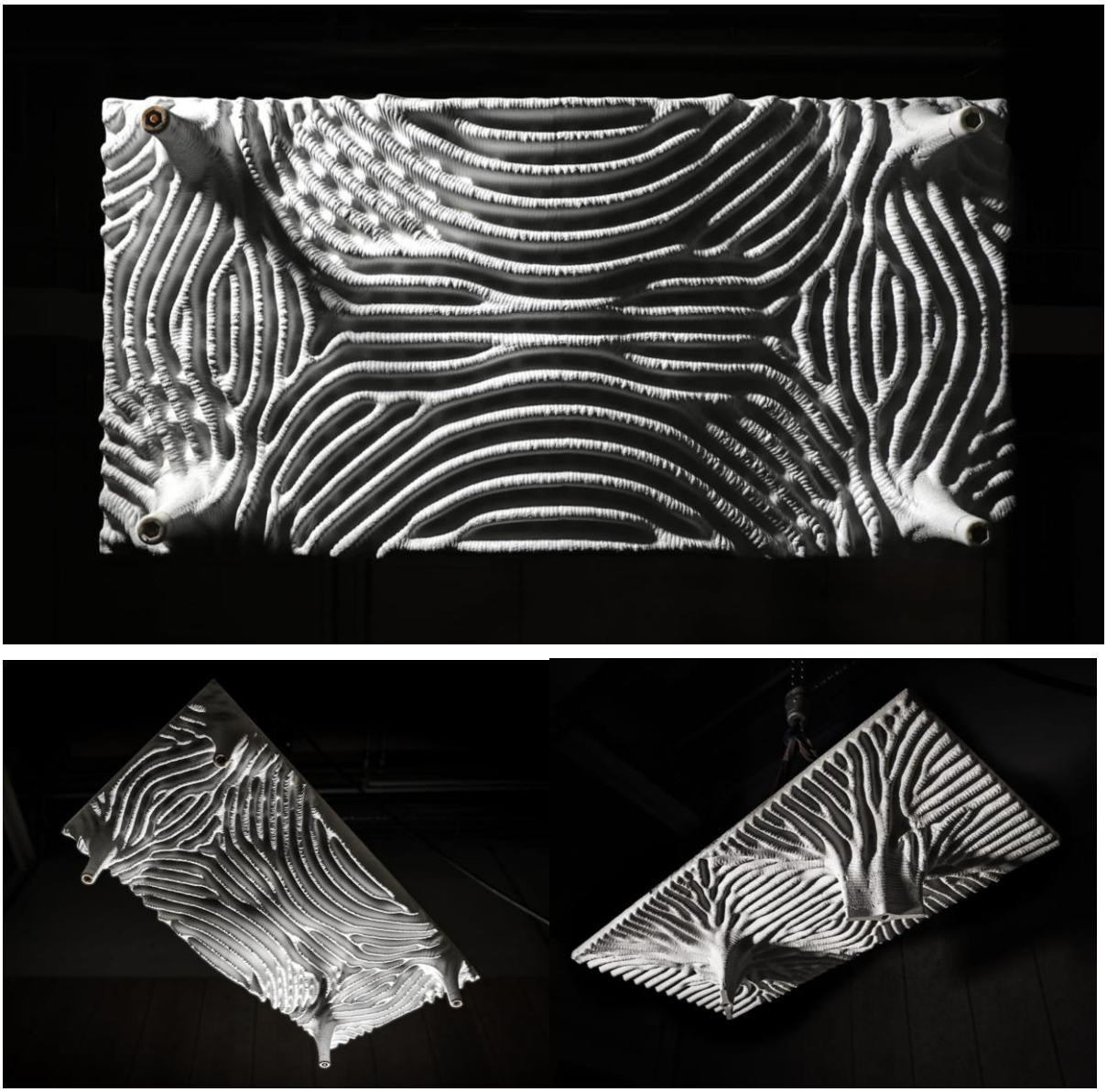


Figure 7. Pictures of the realised ribbed concrete slab prototypes.
RD Slab 01 (top and bottom left) and RD Slab 02.

6. Conclusion and future works

The paper discussed an unexplored development of anisotropic RD to generate ribbing layouts in structural plates subjected to bending. The approach successfully solves the geometrical and topological problems when exploring the design of isostatic ribbed slabs with different boundary conditions, offering a quick-to-use and interactive tool. Learning from this work, future upgrades of the current pipeline will focus on simplifying the user experience for non-advanced designers by introducing real-scale dimensional control of the patterns independently from simulation resolution and providing tunable presets for post-processing the stiffeners´ cross-section profile and relative dimensions. Furthermore, migrating the current implementation made in Numba to GPU computing will be considered to speed up the simulation. Future studies will extend the current 2D approach to the design of material-efficient 3D structures with a volumetric implementation of the RD system.

7. References

[1] A. Liew, D. López López, T. Van Mele and P. Block, "Design, fabrication and testing of a prototype, thin-vaulted, unreinforced concrete floor", *Engineering Structures,* vol. 137, pp. 323-335, 2017.

[2] A. Jipa, C. C. Barentin, G. Lydon, M. Rippmann, G. Chousou, M. Lomaglio, A. Schlueter, P. Block and B. Dillenburger, "3D-Printed Formwork for Integrated Funicular Concrete Slabs", in *Form and Force: Proceedings of the IASS Annual Symposium 2019,* Barcelona, Spain, October 7-10, 2019.

[3] A. Jipa, M. Bernhard, M. A. Meibodi and B. Dillenburger, "3D-Printed Stay-in-Place Formwork for Topologically Optimized Concrete Slabs." In *TxA Emerging Design + Technology*, San Antonio, Texas, USA, November 3-4, 2016, K. Bieg, Ed.

[4] A. B. Halpern, D. P. Billington and S. Adriaenssens, "The Ribbed Floor Slab Systems of Pier Luigi Nervi", in *Beyond the limits of man: Proceedings of the International Association for Shell and Spatial Structures (IASS) Symposium*, Wroclaw, Poland, September 23-27, 2013, J.B. Obrębski and R. Tarczewski, Eds.

[5] L. Breseghello and R. Naboni, "Toolpath-based Design for 3D Concrete Printing of Carbon-efficient Architectural Structures", in *Additive Manufacturing*, vol. 56, 2022.

[6] S. Gislason, S. Bruhn, L. Breseghello, B. Sen, G. Liu and R. Naboni, "Porous 3D printed concrete beams show an environmental promise: a cradle-to-grave comparative life cycle assessment", in *Clean Technologies and Environmental Policy*, vol. 24, pp. 639–2654, 2022.

[7] F. Box, A. Erlich, J. H. Guan and C. Thorogood, "Gigantic floating leaves occupy a large surface area at an economical material cost", *Science Advances*, vol. 8, 2022.

[8] A. N. Landge, B. M. Jordan, X. Diego and P. Müller, "Pattern formation mechanisms of self-organizing reaction-diffusion systems", *Developmental Biology*, vol. 460, pp. 2-11, 2020.

[9] A. M. Turing, "The Chemical Basis of Morphogenesis", *Philosophical Transactions of the Royal Society of London. Series B, Biological Sciences*, Vol. 237, No. 641, pp. 37-72, 1952.

[10] D. Wang, M. Abdalla, Z-P. Wang and Z. Su, "Streamline stiffener path optimization (SSPO) for embedded stiffener layout design of non-uniform curved grid-stiffened composite (NCGC) structures", *Computer Methods in Applied Mechanics and Engineering*, vol. 344, 2018.

[11] H. Li, M. Yu, P. Jolivet, J. Alexandersen, T. Kondoh, T. Hu, K. Furuta, K. Izui and S. Nishiwaki, "Reaction–diffusion equation driven topology optimization of high-resolution and feature-rich structures using unstructured meshes", *Advances in Engineering Software*, vol. 180, 2023.

[12] D-H. Garnier, M-P. Schmidt and D. Rohmer, "Growth of oriented orthotropic structures with reaction/diffusion", *Structural and Multidisciplinary Optimization*, vol. 65, 327, 2022.

[13] J. Pearson, "Complex patterns in a simple system", *Science*, vol. 261, pp. 189-192, 1993.

[14] A. Witkin and M. Kassy. Reaction–Diffusion Textures, in *Proceedings of the 18th Annual Conference on Computer Graphics and Interactive Techniques*, 1991.

[15] Pmneila, "Reaction diffusion system (Gray-Scott model)". http://pmneila.github.io/jsexp/grayscott/, 2012.

[16] R. Munafo, "Reaction-Diffusion by the Gray-Scott Model: Pearson's Parametrization". http://mrob.com/pub/comp/xmorphia/index.html, 2022.

[17] R. Naboni, A. Zomparelli, A. Kunic and L. Breseghello, "Design, robotic fabrication and augmented construction of low-carbon concrete slabs through field-based Reaction-Diffusion", in Architecture and design for Industry 4.0: theory and practice, Springer, 2023, M. Barberio et al., Eds.

Proceedings of the IASS Annual Symposium 2023
Integration of Design and Fabrication
10–14 July 2023, Melbourne, Australia
Y.M. Xie, J. Burry, T.U. Lee and J. Ma (eds.)

Guided irregular cement geometry stacking using real-time optimization and motion tracking

Alex ORSHOLITS[*], Ren IMAI[b], Hirotaka UJIOKA[b], Shimpei KOJIMA[b], Mika ARAKI[c], Yusuke OBUCHI[a], Jun SATO[b]

[a,*] The University of Tokyo, Graduate School of Engineering, Tokyo, Japan
alex-orsholits@g.ecc.u-tokyo.ac.jp

[b] The University of Tokyo, Graduate School of Frontier Sciences, Tokyo, Japan
[c] Kwansei Gakuin University, School of Architecture, Hyogo, Japan

Abstract

In the rapidly changing world of construction and architecture, reassessing standard fabrication practices has become paramount, as they have been slow to adapt to increasingly prototypical requirements. Confronted with the unpredictability of non-uniform materials and uncertain site conditions, there is an evident lack of tools able to adapt to variable conditions during construction. Is it therefore possible to augment human tactical sensibilities with computerized form optimization to overcome these challenges [1]? In this paper, we demonstrate a highly adaptable construction process implementing concepts of feedback-loop generative design, continuous structural safety analysis, cloud-based data management, real-time spatial data acquisition, and builder guidance. Our process is underpinned by four key developments: (1) the on-site production of randomized branched cement geometries by pouring into organic-shaped channels directly drawn in soil, (2) the development of a novel macro-scale aggregate structural model [2] capable of performing continuous data analysis, (3) the integration of VR motion-tracking hardware with custom accessories for human-assisted cooperative real-time data acquisition and user guidance, and (4) the implementation of a custom cloud-based data interlink and visualization system for comprehensive remote multi-site construction management. The result is a closed-loop system where motion tracking equipment supplies XYZ coordinates for each stacked cement piece to a structural model that optimizes the target prototype and generates the allowed building volumes, which are then conveyed as instructions via LED-equipped accessories worn by each builder.

Keywords: digital fabrication, generative design, structural optimization, human-assisted fabrication, Hangai Prize applicant

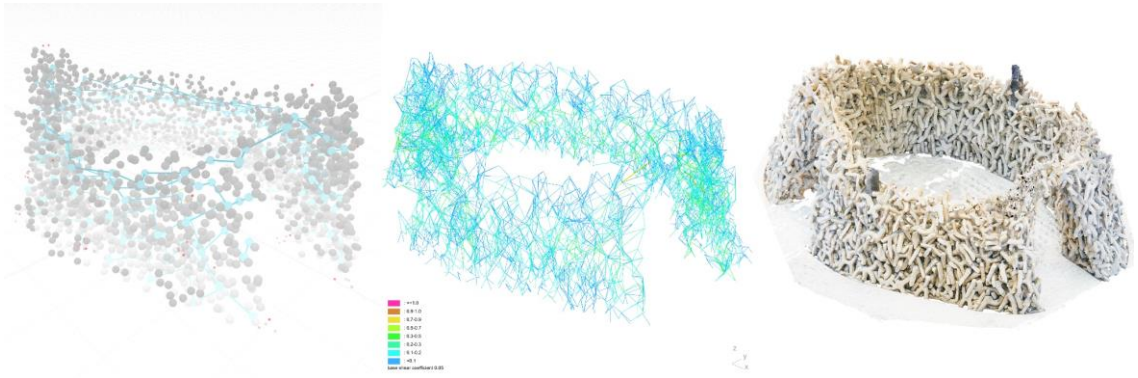


Figure 1. Perspective views of: (left) acquired point cloud data, (middle) calculated base shear coefficient, (right) 3D scan of constructed prototype of the Venice Biennale Architettura 2021 United Arab Emirates Pavilion.

Copyright © 2023 by Alex ORSHOLITS, Ren IMAI, Hirotaka UJIOKA, Shimpei KOJIMA, Mika ARAKI, Yusuke OBUCHI and Jun SATO. Published in the Proceedings of the IASS Annual Symposium 2023 with permission.

1. Introduction

This paper presents the development and application of an experimental construction process utilizing variable-form branched cement pieces derived from prescribed pouring guidelines, combined with a digitally guided assembly process. The pieces are stacked to achieve stability through friction from rough surfaces in direct contact while maintaining moderate porosity, as required by the client's design specifications. Balancing sufficient friction and maximizing voids between pieces is a challenging task due to the highly manual process of stacking pieces by hand.

During assembly, the builder exercises discretion in stacking pieces within the provided guidance volume, resulting in uneven stack density and shape deviations. Consequently, the final form remains unknown until completed. To ensure builder safety, fabrication guidance must be sequentially generated from structural analyses throughout the construction process.

The proposed construction method follows these operational steps:

i. Initial guidance is sent to the construction site, and pieces are stacked up to a certain stage.
ii. Stacked pieces are continuously scanned for position information.
iii. A point cloud derived from scanned pieces is merged with an automatically generated point cloud estimation of the completed structure, creating a structural model for static linear analysis (described in subsection 2.3)
iv. Structure safety is evaluated using the method described in subsection 2.4. If safe, the system proceeds to vi; if not, it proceeds to v.
v. Generate a new point cloud estimation of the completed structure and return to iii.
vi. Update the guidance volume and transmit the data to the construction site.

This paper comprises three sections: structural model development, construction system toolchain, and comments on the erected structures. The first section discusses the evaluation method for the construction system, covering construction material guidelines, material characteristic modelling, structural model schema, structural evaluation procedure, and optimization method. The second section details the hardware and software implementations, as well as the cloud-based construction visualization and management system. We conclude with an analysis of the erected prototypes and a commentary on the generated data for each structure.

2. Simplified modelling and evaluation of randomized branched cement geometries

With the rapid development of structural modelling in recent years, the precise analysis of complex geometries has been made possible. Nevertheless, structural analyses are commonly carried out prior to the construction phase and are based on given design characteristics where all variables can be exhaustively evaluated. Additionally, significant development costs are required to create new, high-precision material models. As such, it is extremely difficult to implement these conventional processes in unplanned construction situations. The structural evaluation method proposed in this paper is therefore based on the premise of ensuring continuous structural safety, which enables us to appropriately downscale the requisite analysis methods and simplify the overall material model. As a result, the evaluation of structural strength and structural optimization during construction can be performed nearly in real-time. We expect this novel process to not only serve as a solution for our specific fabrication research but also drive further technological developments in the construction industry.

2.1 Fabrication of randomized branched cement pieces

In an optimal scenario, builders would create construction materials on-site through a straightforward, freeform cement pouring process, producing randomized branched cement geometries. However, due to the potential for high variability in stacking ability of these geometries, we established a minimal guideline to maintain consistency between pieces without imposing excessive restrictions. We determined that each piece should have branches longer than 60 mm and a cross-sectional diameter of 50 to 80 mm. Although not indispensable, we also established a series of positive material shape characteristics to look for when pouring the randomized geometries.

The cement was mixed by weight with a ratio of 1.0:0.46:1.0 between water, mortar, and sand aggregate. In some cases, we tested an alternative cement type that replaced Portland cement with magnesium-based cement from desalination brine [3] which achieved comparable results. The cement was poured as a single object into organic-shaped channels drawn directly in soil near each construction site, and separators such as thin plywood were added to form the branch lengths according to our guidelines immediately after pouring, as illustrated in Figure 2.



Figure 2. Photographs of the material pouring process and diagrams of positive material characteristics.

2.2 Material modelling and analysis

To develop an effective material model and analysis method, we conducted a series of experiments to determine the structural properties of the randomized branched cement pieces. Test specimens were created by stacking six to eight fabricated pieces together and evaluating them through compression tests. The resulting load-deformation curve is shown in Figure 3. However, this approach has a limitation: it does not scale well with changes in material composition resulting from constructing in multiple locations using domestically poured cement. To account for these differences, compression tests must be conducted for each locally produced material.

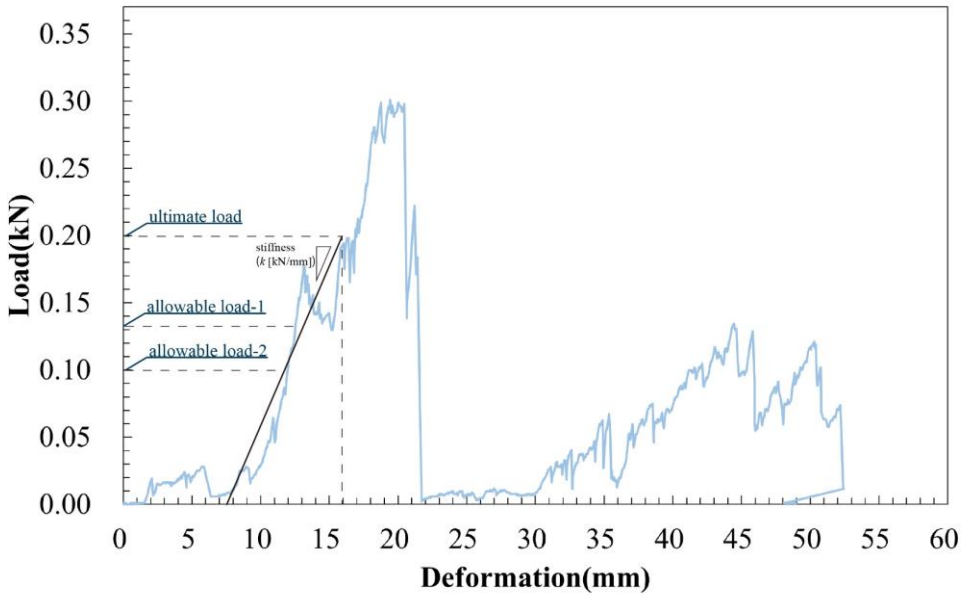


Figure 3. Load-deformation curve of material compression test

The analytical model is generated by representing the structure as a three-dimensional truss. Each piece's centre of gravity is represented as a node, and contacting pieces are connected by line elements of specific strength and stiffness, as illustrated in Figure 4, and further explained in Subsection 2.3. For the static linear stress analysis, we consider the maximum load and ultimate loads as follows: ultimate compression force N_{cu}, ultimate tension force N_{tu}, ultimate shear force Q_u, and ultimate bending moment M_u. Two load scenarios are examined: self-weight (Load-1) and self-weight plus horizontal load (Load-2, with a base shear coefficient of 0.05). The allowable stress is calculated from the ultimate load of the experiment:

$$\boldsymbol{Load-1}\text{: } [\mathrm{N_{ca1}}, \mathrm{N_{ta1}}, \mathrm{Q_{a1}}, \mathrm{M_{a1}}] = 1/2 \times [\mathrm{N_{cu}}, \mathrm{N_{tu}}, \mathrm{Q_u}, \mathrm{M_u}] \quad (1)$$

$$\boldsymbol{Load-2}\text{: } [\mathrm{N_{ca2}}, \mathrm{N_{ta2}}, \mathrm{Q_{a2}}, \mathrm{M_{a2}}] = 2/3 \times [\mathrm{N_{cu}}, \mathrm{N_{tu}}, \mathrm{Q_u}, \mathrm{M_u}] \quad (2)$$

The overall structure is designed to resist its own self-weight and horizontal force and is evaluated using allowable stress design.



Figure 4. Photograph of material compression test and truss modeling

2.3 General modelling scheme

To model the material stacking process, we developed a schema that generates a simplified representation of the structure based on a three-dimensional truss model. This schema comprises the following steps:

i. Populate a point cloud of nodes by acquiring the approximate centre of gravity of each stacked cement piece as a single point in 3D space.
ii. Set z-coordinates (height) less than 120mm to 0mm. This is to ensure that the first layer of cement pieces is placed on the ground plane.
iii. Classify nodes by XY-planes at z=n*H (for n=0 to N), where H is the vertical distance between planes.
iv. Link each node in the nth group to three nearest points in the n-1th group, if the distance is less than 400mm.

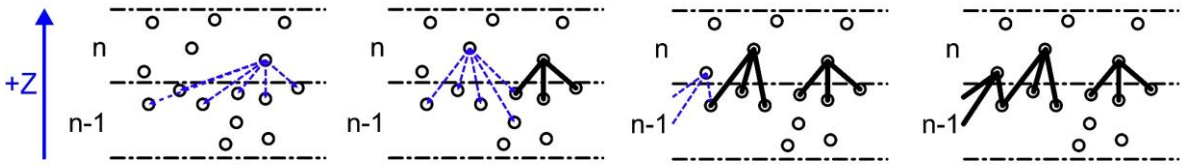


Figure 5. Section diagram of generating a three-dimensional truss.

Base parameters of the model, such as the vertical distance (H) between planes are established during mock-ups tests and adjusted according to the average size and shape of the cement pieces. This modelling schema, however, omits specific character information normally found in distinct-element modelling methods [4] such as points of contact between each piece and the shape of the piece itself. While necessary for a precise evaluation of the mechanical condition of each piece, this level of detail becomes insignificant in active construction site conditions, where pieces may break apart or shift positions. Furthermore, in the absence of reinforcement, such as rebar, cracking is not expected to significantly impact the structure's strength. While such cracking may initially cause load reductions, the load continues to increase subsequently, indicating the structure's resilience despite minor crack formation. Instead, the schema solely models the total number of stacked pieces and approximate contact density between them to ensure an adequate safety factor.

This contact density, defined as the number of truss links per unit volume, serves as a key robustness indicator of the structure's ability to withstand horizontal forces due to human contact and geometry displacements from significant material breakage. The greater the value, the more contacting frictional forces are expected. Additionally, the volume occupied by a piece per unit volume indicates the structure's ability to withstand its own weight.

The model considers two load scenarios: the long-term load due to the structure's weight (load 1) and the short-term horizontal load from human contact (load 2). We perform static linear analyses for each scenario and calculate the safety ratio (R) for each truss as a percentage of allowable stress:

$$R = max\{max\{N/N_{a1} + M/M_{a1}Q/Q_{a1}\}, max\{N/N_{a2} + M/M_{a2}Q/Q_{a2}\}\} \leq 1.0 \qquad (3)$$

N, M, and Q represent axial force, bending moment, and shear force in the truss member, respectively. N_a depends on whether N is compression (N_{ca}) or tension (N_{ta}). N_{a1}, M_{a1}, and Q_{a1} correspond to load scenario 1, while N_{a2}, M_{a2}, and Q_{a2} correspond to load scenario 2.

Static linear analysis offers near real-time calculation speed and sufficient insight into the overall safety of the structure. The simplification of the structure model is considered acceptable, based on realistic constraints on the overall shape of the structure, sufficient weight, small horizontal forces, and the absence of lifting or other problems. Analysis results are visualized by mapping safety ratios.

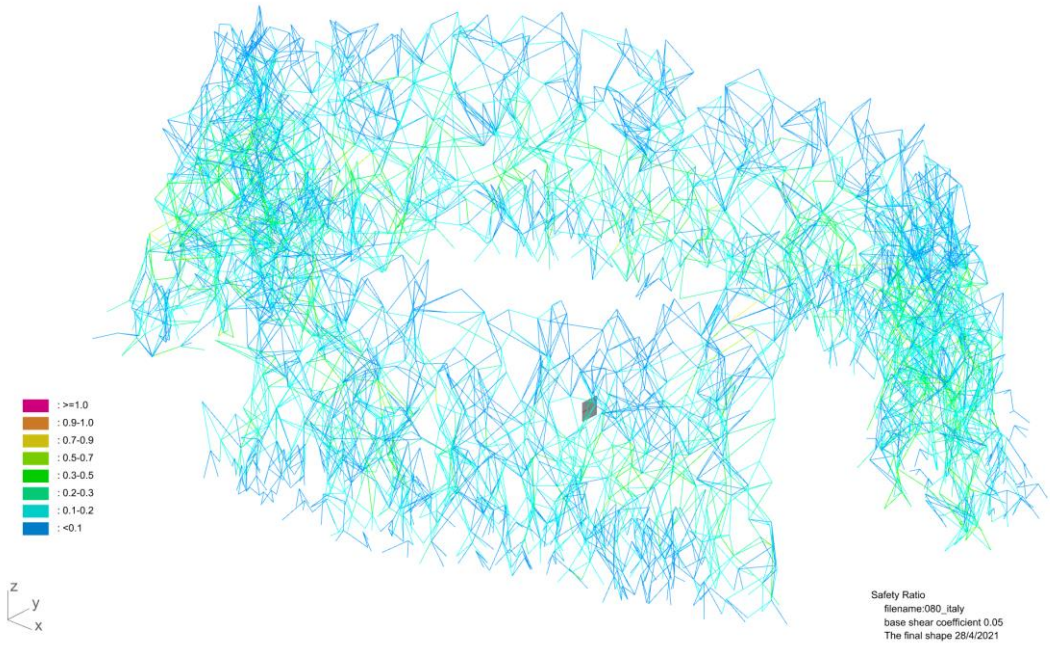


Figure 6. Analysis results mapped by safety ratio.

2.4 Real-time structural optimization and feedback during construction

During the construction phase, structural optimization is achieved by adjusting the target shape to minimize the highest calculated safety ratio value. The input variables of the optimization process consist of control points on multiple cross-section curves representing the target shape. By modifying the control points in the unconstructed volume, an optimized shape is continuously generated. The following automated operations are proposed for adjusting the target shape:

A. Deform the top of the cross-section curve horizontally (XY) by a certain distance in any direction.
B. Deform the top of the cross-section curve vertically downward (-Z) by a certain distance.

Operation A results in a more even weight distribution on the bottom of the structure by shaping the cross-section to resemble an isosceles triangle, reducing the load on lower pieces. Operation B reduces the number of stacked pieces, leading to an overall stress reduction. Utilizing these two operations, the structural optimization is performed using the following method:

i. Provide a target shape based on construction site conditions, and stack pieces up to a certain stage.
ii. Generate a truss model using already stacked pieces and randomly generated points in unconstructed areas. Perform static linear analyses and calculate the safety ratio. If structural issues arise, proceed to step iii; otherwise, skip to step v.
iii. Perform Operation A and return to step ii. If no solution is found before the peak cross-section curve reaches the middle of the base, move to step iv.
iv. Perform Operation B and return to step ii. If no solution is found before reaching the height of already stacked pieces, manually evaluate if it is safe to continue with the construction process.
v. Complete the optimization. If the construction is not finished, update the target shape and resume construction. Return to step i.

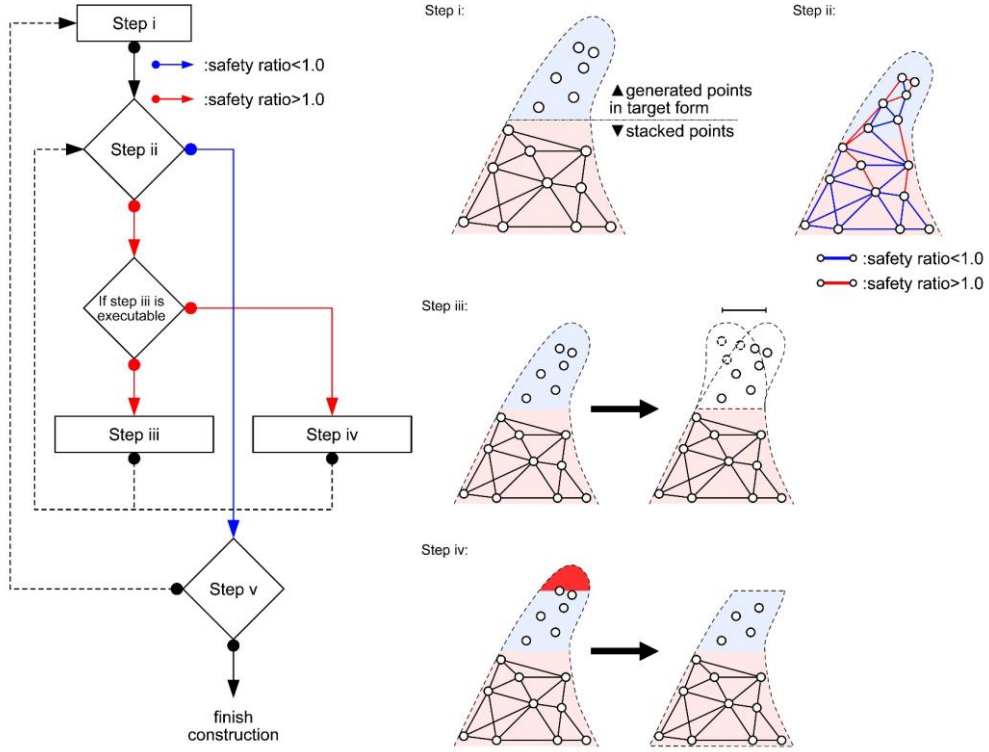


Figure 7. Optimization logic diagram along with sectional diagrams of each step.

3. Construction system toolchain

Deploying a digital fabrication system on a site that is completely inaccessible to project researchers and designers is challenging, especially without a dedicated assembly team that can be deployed in multiple construction locations. The fabrication system must therefore provide user guidance for piling and balancing randomized concrete shapes while also serving as a management platform to minimize inherent construction risks and hazards. By enabling real-time data interoperability, continuous collaboration among engineers, designers, managers, clients, and the general public is facilitated, ensuring a resilient construction system that can adapt to design changes while maintaining structural safety.

3.1 On-site hardware implementation

SteamVR [5] and its accompanying hardware, commonly used in industries such as digital fabrication, virtual production, and VR gaming, offer a cost-effective solution for acquiring precise 3D position and orientation data at around 50Hz [6]. However, challenges such as tracker occlusion, coordinate discrepancies between real and virtual environments, and long-term tracking system drift need to be addressed.

To mitigate tracker occlusion, an offset virtual origin is established using the local orientation of tracked devices. In the case of the VIVE controllers (deployed as point scanners), this virtual origin corresponds to the equipped pointer extension, positioning the virtual scan at -525 mm on the Y axis and 330 mm on the Z axis. For each builder, a VIVE tracker incorporating a blue LED and armband is mounted just before the elbow. An offset virtual origin is positioned at the palm of the user's hand. Some concessions had to be made in terms of positioning precision to ensure accessibility. The implemented offset factor is therefore based on the average forearm length of 269 mm [7].

Both coordinate parity and long-term tracking system drift are resolved by employing a continuously tracked world origin. The coordinates and orientations of all VIVE devices reference a base VIVE tracker representing world space and its corresponding rotation. This referential coordinate system creates a self-correcting tracked space resilient to external perturbations and ensures alignment between the physical environment and digital systems for structural analysis, visualization, and construction.



Figure 8. From left to right: reference origin tracker with 3D printed XY axis pointer, user guidance tracker with LED attachment, scanning controller with added pointer.

3.2 On-site software implementation

The on-site software implementation consists of straightforward tasks for users. Wherever the blue LED on the VIVE tracker lights up, stack up the cement material. After balancing a selection of pieces, scan each stacked piece by pointing at the centre of gravity position with the modified VIVE controller. These tasks are managed by a Unity Engine [8] application deployed on a gaming laptop. To process incoming guidance volumes, the application deserializes mesh data [9] and generates a collection of collision boxes using a volume-capable voxelization script [10]. Although this leads to a nominal loss of resolution, it allows real-time assessment of the user's virtual tracker position within the buildable area.

We developed a web app, accessible on a user's smartphone, to manage the scanning system within the Unity application. Users can select from three point types: Main points (centre of gravity of each concrete fragment), Blue points (tie points of the safety wire), and Red points (verification of virtual environment positioning and structural displacement evaluation). Selecting a scanning type generates a new session ID and forwards it to the Unity application.

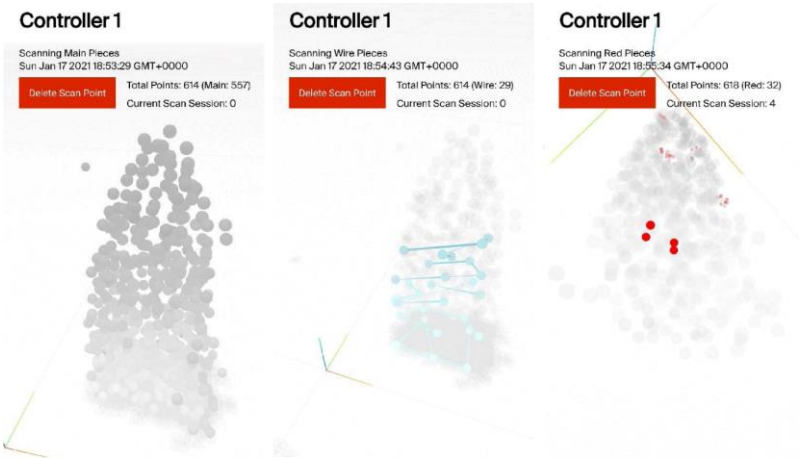


Figure 9. Screenshot depiction of mobile web app. From left to right: main scan points, blue points, red points.

Users can scan required points by actuating the trigger on the VIVE controller, while simultaneously monitoring the ongoing scan session on the web app. This app displays descriptive information such as the number of points scanned in the current session and the total number of points scanned throughout the fabrication process, along with a real-time 3D visualization of the generated point cloud. If a mistake occurs, the web app provides a delete button with immediate visual and audible feedback.

To complete a scan session, users tap the "Finish session" button within the web app. Sessions are automatically closed if a loss of connection occurs or if the web page is closed abruptly, ensuring a scanning lockout to prevent unforeseen scan points from appearing.

For each scanned point, the Unity application generates a JSON-compatible string containing the sessionID, controller actuated (to support multiple scanners), point type (command), individual pointID, point position in meters, and the layer (corresponding to the construction day). The format is as follows:


```
{"sessionID":"fdbc36c0-9125-11eb-bb11-fd31f66d0264","controller":"controller1",
"command":"red","pointID":"a9d4cbc6-fc9a-4d26-b8b6-f12afeb5d312",
"positionedPT":"(5.301707,-0.09540617,1.038687)","layer":"1"}
```


(4)

3.3 Cloud-based management and visualization deployment

We deployed a Raspberry Pi 4B single board computer [11] as a lightweight server to relay data between the construction site and the structural analysis system using Node-red flow-based JavaScript development platform [12]. The server manages three main components: real-time data sharing using websockets [13] and REST APIs [14], a RAM-based database with persistent backups utilizing Node-Red's 'Context Data' feature, and coordinate conversion of scan data between the right-handed (Z-up) coordinate system of Grasshopper, left-handed (Y-up) coordinate system of Unity Engine, and the right-handed (Y-up) coordinate system of ThreeJS [15]

To address potential misuse of equipment and incorrect data, resulting in a potentially dangerous construction environment, we created a real-time interactive visualization with ThreeJS, allowing all parties to monitor the construction and correct any miss-scans. The digital twin is accessible on various mobile devices from any location. On launch, the visualization interface fetches the latest database point cloud via the REST API and establishes a websocket connection for real-time updates. An optional live view of the on-site VIVE controller positions is available to minimize errors for the on-site users in charge of scanning the construction.

We integrated the Meta Quest 2 [16] and webXR capabilities for an immersive experience with true 3D depth perception, enhancing remote management and reducing the burden on users. Advanced locomotion options provide a more accurate assessment of the structure's 3D geometry, further reducing the chances of errors during remote management.

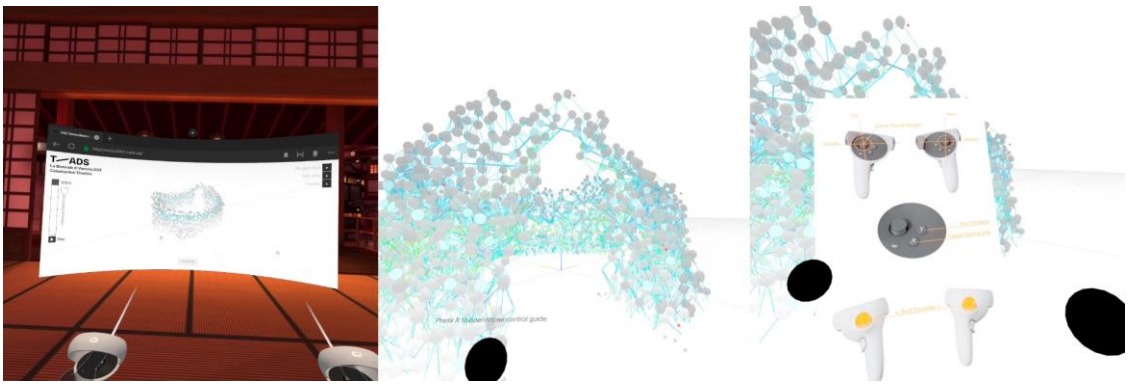


Figure 10. Screenshots of 3D visualization web app accessed via Meta Quest 2.

4. Comments on the constructed architectures

To evaluate our construction system, we erected three mock-ups with similar dimensions to test the structural model and scanning and guidance system. The first two mock-ups were towers (1.5m x 1m base, 2.7m height), and the third tested arching with a steel support frame. A large-scale pavilion (7m length, 5.2m width, 2.7m height) was constructed incorporating prior test elements. The second and third mock-ups and pavilion were remotely managed.

4.1 Standalone tower in Tokyo, Japan

Constructed in a local and controlled environment, the goal of this standalone tower was to achieve an approximate stack height of 2.8 meters. This was considered the structural limit of the material. Without guidance, previous tests achieved only 1.7m height due to tapering. With guidance, the planned height was achieved in a week. After achieving the target height, it was decided to continue stacking until overcompression. This led to collapse, but with controlled toppling.



Figure 11. From left to right: safety factor of 3D truss model, 3D scan of completed mock-up, 3D scan of collapsed mockup due to overcompression.

4.1 Construction tests in Dubai, UAE

Two prototypes were built in Dubai using a new team and domestically produced stacking material. The first prototype, a copy of the Tokyo tower, achieved the target 2.8m height in three days with minimal tapering. The second prototype tested arched stacking assisted by prefabricated steel arch frames. The arched structure was completed in two days.



Figure 12. From left to right: safety factor of 3D truss model (arch), photograph of completed arch, photograph of Tokyo tower analogue.

4.2 Large-scale pavilion construction in Venice, Italy

The structure's initial stacking area is an elliptical torus of an external length of 7 metres and width of 5.2 metres, and an internal length of 4.6 metres and width of 2.8 metres. In elevation, the pavilion gently varies in height between two peaks of a maximum of 2.8 metres and a minimum of 1.7 metres. Arched stacking from the Dubai mock-up was utilized for the two 2.2-metre-high openings that allow passage for people. The torus has a roughly triangular cross-section with the upper part slightly inclined inward. This inward portion is compressed by gravity from both sides, similar to a masonry dome structure. The pavilion took six days to construct utilizing a local construction team and two representatives from the Dubai team.

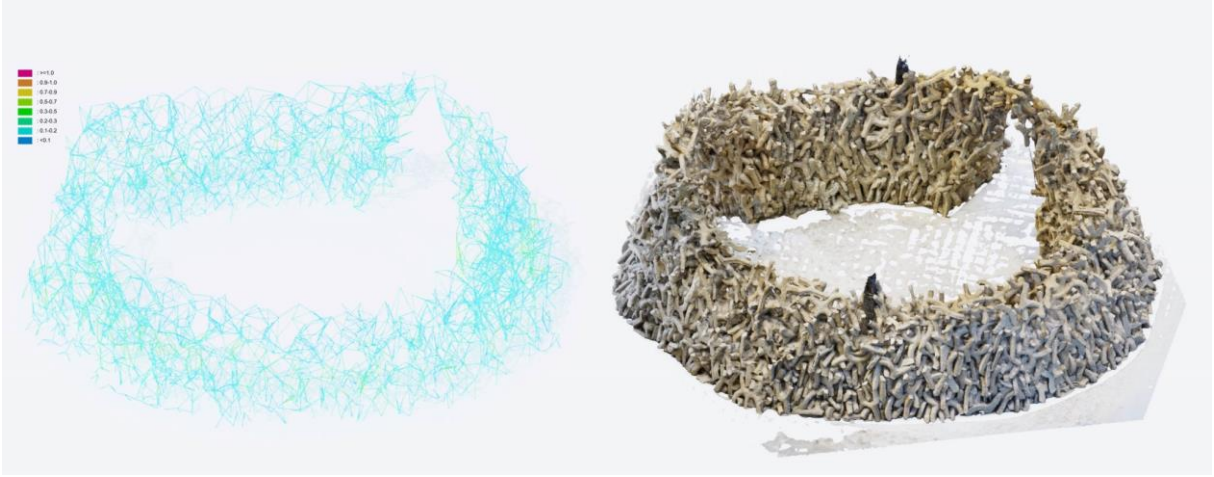


Figure 13. From left to right: safety factor of 3D truss model, 3D scan of completed pavilion.

We conducted a long-term creep evaluation of the structure via comparative photogrammetry analysis at the start of the exhibition and 6 months later near the end. This showed a 1.5 to 2 cm inward displacement on one of the facades. The cause of this displacement however remains inconclusive as we are unable to make a distinction between a slow movement and a single event.



Figure 14. Long-term creep analysis of overall pavilion

5. Conclusion

The paper demonstrates an innovative construction process both in terms of material modelling and construction site management. By adopting a simplified structural analysis method, we are able to rapidly model complex material interactions, thus ensuring near real-time analysis during construction. The practical applications of this system, as demonstrated through the construction of various mock-ups and a large-scale pavilion, attest to its effectiveness in diverse scenarios. Moreover, this approach also illustrated the relevance of a cloud-managed construction system for rapid and flexible deployment in multiple construction sites, enabling continuous collaboration among builders, engineers, designers, managers, clients, and the general public. As a result, we believe that adopting more responsive and adaptable construction processes can scale, allowing rapid adaptation while ensuring the safety of builders and users. Looking ahead, this construction system implementation offers promising opportunities for innovation in the industry by facilitating construction management, increasing efficiency, and accommodating a wide range of architectural designs.

References

[1] H. Yoshida, T. Igarashi, Y. Obuchi, Y. Takami, J. Sato, M. Araki, M. Miki, K. Nagata, K. Sakai, and S. Igarashi, "Architecture-scale human-assisted additive manufacturing," ACM Trans. Graph., vol. 34, no. 4, jul 2015. Available: https://doi.org/10.1145/2766951

[2] P. Aejmelaeus-Lindstr¨om, J. Willmann, S. Tibbits, F. Gramazio, and M. Kohler, "Jammed architectural structures: towards large-scale reversible construction," Granular Matter, vol. 18, no. 2, p. 28, Apr 2016. Available: https://doi.org/10.1007/s10035-016-0628-y

[3] N. Dung, R. Hay, A. Lesimple, K. Celik, and C. Un-luer, "Influence of co2 concentration on the performance of mgo cement mixes," Cement and Concrete Com-posites, vol. 115, p. 103826, 2021. Available: https://www.sciencedirect.com/science/article/pii/S0958946520303310

[4] K. Dierichs and A. Menges, "Simulation of aggregate structures in archi-tecture: Distinct-element modeling of synthetic non-convex granulates," in Advances in Architectural Geometry 2014, P. Block, J. Knippers, N. J. Mitra, and W. Wang, Eds. Cham: Springer International Publishing, 2015, pp. 1–13.

[5] V. Corporation, "Steamvr™ tracking," 2016. Available: partner.steamgames.com/vrlicensing

[6] M. Borges, A. Symington, B. Coltin, T. Smith, and R. Ventura, "Htc vive: Analysis and accuracy improvement," in 2018 IEEE/RSJ Interna-tional Conference on Intelligent Robots and Systems (IROS), 2018, pp. 2610–2615.

[7] G. Singh, A. Singla, and G. Virk, "Modeling and simulation of a passive lower-body mechanism for rehabilitation," 01 2016.

[8] U. Technologies, "Unity real-time development platform," 2005. Available: https://unity.com/

[9] J. Horikawa, "Meshreceivingunityclient," 2017. Available: https://github.com/jhorikawa/MeshReceivingUnityClient

[10] I. P. Studio, "Mesh voxelizer," 2019. Available: https://www.icepond.cyou/project/meshvoxelizer/

[11] T. R. P. Foundation, "Raspberry pi 4," 2019. Available: https://www.raspberrypi.com/products/raspberry-pi-4-model-b/

[12] IBM, "Node-red," 2013. Available: https://nodered.org/

[13] I. Trust, "The websocket protocol," 2011. Available: https://datatracker.ietf.org/doc/html/rfc6455

[14] RedHat, "What is a rest api?" 2020.Available: www.redhat.com/en/topics/api/what-is-a-rest-api

[15] threejs.org, "three.js," 2010. Available: https://threejs.org/

[16] M. Platforms, "Meta quest 2," 2020. Available: www.meta.com/jp/en/quest/products/quest-2/

Proceedings of the IASS Annual Symposium 2023
Integration of Design and Fabrication
10–14 July 2023, Melbourne, Australia
Y.M. Xie, J. Burry, T.U. Lee and J. Ma (eds.)

KNOTSHELL pavilion – Development of a low-tech approach for transferring complex digital data to building elements

Kristina Viktoria KRÖLL[*], Alec Bikramjit SINGH[a], Felipe RIOLA-PARADA[b]

[a,*] University of Wuppertal, Faculty of Architecture and Civil Engineering,
Pauluskirchstrasse 7, 42885 Wuppertal, Germany
kkroell@uni-wuppertal.de

[b] Bremen City University of Applied Sciences, Faculty of Architecture,
Civil and Environmental Engineering, Neustadtswall 30, 28199 Bremen, Germany

Abstract

In the article, the challenges associated with traditional timber lattice shells are discussed. Despite their high efficiency, their manufacturing requires significant expertise and assembly effort, making them difficult to enter the industry. The research explores alternative irregular lattice shells based on geodesic patterns, which are suitable for low-tech manufacturing and limited budgets. The paper focuses on the method of transferring complex digital data to building elements using a low-tech tool, explaining the design process for multilayer geodesic grid shells and discussing the advantages and challenges of this approach. Furthermore, the design principle with individual connections is explained in detail, followed by an explanation of the transfer of data from the design and construction process to the lattice shell. To facilitate this, a low-tech tool was developed from conventional available components, which transfers data on assembly to the construction elements. The article concludes with a report on the experiences of building an elastically bent lattice shell made of timber using this concept.

Keywords: lattice shell, digital fabrication process, timber construction, computational design, structural design, digital process chain, digital tool, man machine interface, low-tech approach

1. Introduction

1.1. Overview

The Chair of Structural Engineering and Building Construction deals with the topic of lattice shells in teaching and research within the framework of digital timber construction and novel wood technologies. The aim is to use digital tools and optimized planning processes to design, construct and build efficient and sustainable lightweight structures. In the related course, the students dealt with the static properties of shell structures and created their own designs with digital tools on the basis of these laws.

1.2. Motivation

The advent of computational tools in design and architecture has opened up areas of architectural geometry that now enable design, optimisation and fabrication for complex geometries. However, the optimised symbiosis of form and fabrication often requires exclusive multi-axis numerical control, which is not always accessible and usually very cost intensive. With the construction of the "In A Knotshell" pavilion, the aim is to show how manufacturing processes can be simplified with efficient, universal tools without sacrificing complexity. The main goal is to efficiently inform the building elements with the necessary data for handcrafting.

Copyright © 2023 by Kristina Viktoria KRÖLL, Alec Bikramjit SINGH and Felipe RIOLA-PARADA. Published in the Proceedings of the IASS Annual Symposium 2023 with permission.

1.3. Boundary conditions

The main constraints for the fabrication are a limited toolset (chopsaw, drill stand, drilling machine for slotted holes) and an overall low budget of 3000 € for materials and tools. Since multi-axis CAM was not available for the project at that time, the decision was made to use a low-tech approach. This meant that most of the manufacturing will be done by hand and the geometric complexity had to be broken down for humans.

For the remainder of the project, only structural elements that are planar in their initial state were considered. There was also a desire to realise a sophisticated geometric form that works with a grid without constant node spacing and with different meshes.



Figure 1. (a) The finished ‘Knotshell’ pavilion.

2. Concept design

2.1. Geometric description

The final geometry of the 'Knotshell' pavilion was developed using the shape of a torus. More precisely, it is a section of a torus that represents an anticlastic surface and is reminiscent of a hyperbolic paraboloid. The advantage of using a torus, however, is that the shape is easily reproducible from a simple set of parameters and additional offset surfaces can easily be derived.

The section of the torus with the ground plane leads to the fact that the support points are not lined up on two parallel lines. Consequently, the contact area with the ground is increased.

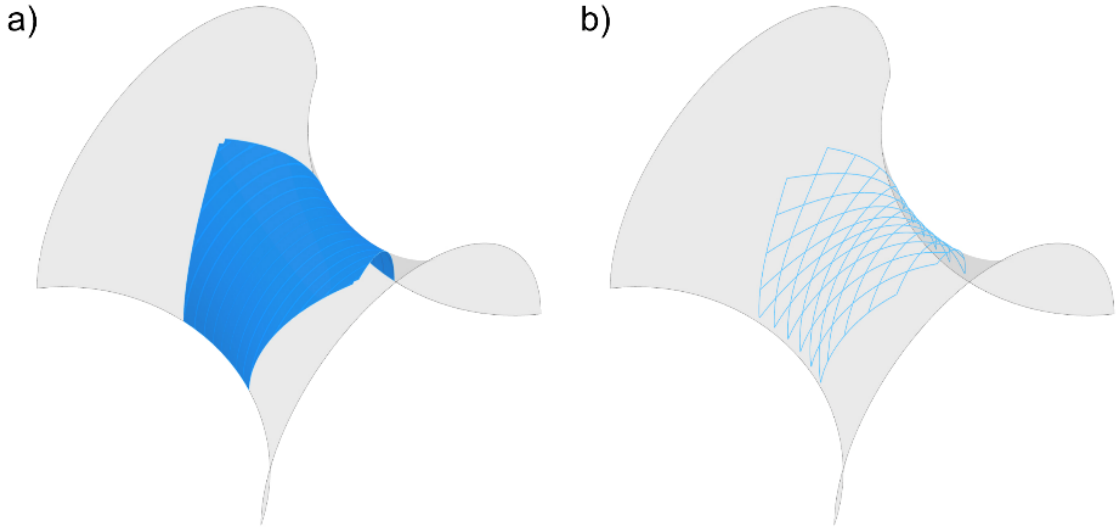


Figure 2. (a) The section of the torus as a basis for form-finding, (b) The geodesics based on the torus section.

2.2. Geodesic grid

The grid of the lattice shell consists of geodesics, the shortest path between two points in a surface. [1] Those two points are equal to the support points and are uniformly distributed on the boundary of the section. All intersection points of the geodesics will later be the points of the connections but with the addition that, strictly speaking, they lie on different offset surfaces. Overall, they form a distorted regular grid of quadrilaterals with smooth transitions due to the changing curvature and mirror symmetry.

For finding the geodesics the native Grasshopper algorithm was used.

2.3. Active bending and layering

The reason geodesics are chosen as grid lines is because they allow torsion and bending in the weak axis of the laths [2]. This is a requirement for the use of active bending, which significantly simplifies the fabrication process, because the geometry is encoded in 1D. A disadvantage though is that the bent state introduces pretension on the elements and therefore reduce their total load bearing capacity. The minimal bending radius has to be considered carefully in combination with the material thickness to preserve a certain amount of residual load capacity.

2.4. Software tools

The pavilion was designed and planned using digital tools such as 'Rhino' and the plug-in 'Grasshopper'. The structural analysis was done with the plug-in 'Karamba3D'[3] and the FEM software 'SCIA Engineer'. G-Code will be generated inside Grasshopper and executed via open software.

3. Conflicts and design strategies

The following describes the design factors on which the design, construction, choice of materials and choice of connections depended. It also describes what influence the decisions had on the development of the fabrication tool.

3.1. Complex geometry and fabrication

3.1.1. Design conflict

Building a lattice shell out of timber can be a demanding task that requires a high degree of pre-planning. This is mainly because such a structure consists of a multitude of laths, joints and nodes that must be precisely coordinated. In the construction of the Knotshell Pavilion, this was compounded by the fact that, due to its complex geometry, it has an alternating grid with different angles and nodes at different positions. Such a geometry can be very costly and time-consuming to produce.

3.1.2. Design strategy: Low-tech tool for fabrication process

In order not to compromise on the design of the lattice shell, it was decided to build a tool that allows the geometry data to be applied to the individual laths. This tool was developed from conventional components and simply guides a pen which conveys the information to the individual elements at the right place. With the precise definition of the geometric data, it becomes possible to manufacture the laths and joints and ensure that they have the required dimensions and tolerances.

3.2. Bended structure vs. planar fabrication

3.2.1. Design conflict

Making a curved support structure, such as that of the lattice shell of the "Knotshell" pavilion, from planar laths is a difficult task. Because of the restoring forces, any bending that is applied to the laths will result in the structure quickly losing its shape and stability.

Another reason for the difficulty of making a curved support structure is that the laths have to be bent in a continuous curve. This requires a high degree of precision and craftsmanship to ensure that the laths remain in the correct position and that there are no gaps or kinks.

3.2.2. Design strategy: Active bending

One possible solution to the problem of producing a curved supporting structure from planar material is the principle of active bending [2]. This is a technique in which the curved shape of the supporting structure is approximated by fixing elements in a bent state. Choosing the right fixture points the desired curve can be created [3].

In the design of the "Knotshell" pavilion, the individual elements were pre-curved using the active bending principle by precisely marking the nodes using the developed pen-plotter. The 3 layers have a minimal deviation in the position of the node points.

3.3. Flexible connections vs. achieving a fixed geometry

3.3.1. Design conflict

Due to the alternating grid, it was important to prefabricate the position of the nodes as accurately as possible in order not to have to compensate for too many inaccuracies in the overall construction of the shell. Therefore, it was decided not to use slotted holes for drilling. In some projects with lattice shells [7], slotted holes were chosen in order to be able to vary the structure afterwards. This had to be done because it was not possible to determine the exact nodes beforehand. We could not afford the inaccuracy caused by slotted holes in the project, as this would have made the fabrication on site much more

complex and it would hardly have been possible to erect the alternating grid as planned. So we were faced with the problem of making the nodes flexible only to the extent that the angles of the individual laths could change among themselves, but not the position of the nodes.

3.3.2. Design strategy: Exact determination of the nodes

With the low-tech tool developed, called a pen plotter, it is possible to determine the position of the nodes so precisely that it was possible to prefabricate segments. The prefabrication in turn made it possible to achieve an actively curved pre-curvature. This made it possible to dispense with further equipment on the construction site, such as a crane to lift the structure, as was the case with the truss shell of the Multihalle in Mannheim [8]. The actively pre-bent modules could only be joined together at the joints on site using a ladder and appropriate conventional tools.

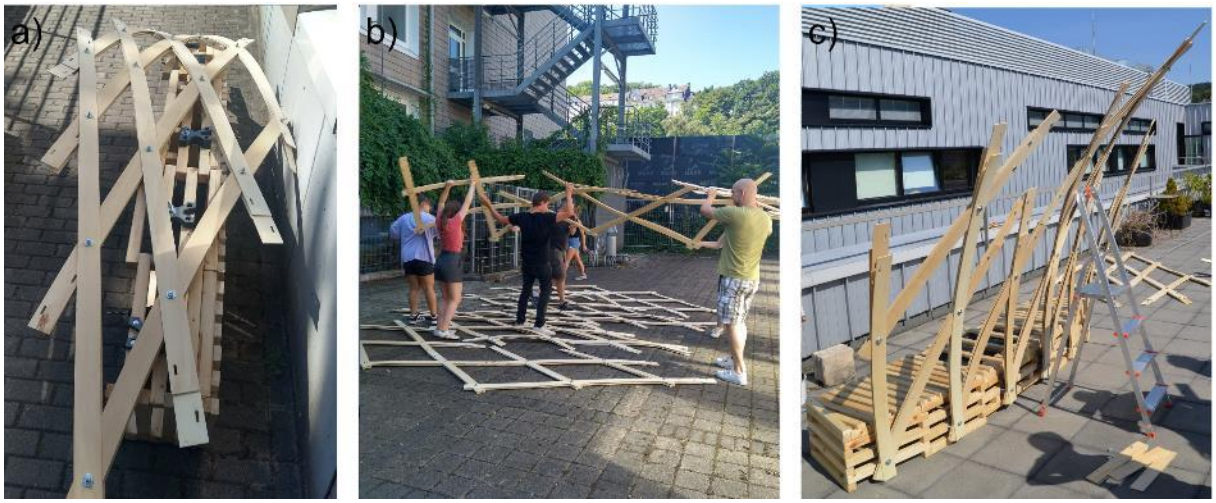


Figure 3. (a) a ready-assembled module for the lattice shell, (b) the planar assembly of the individual modules to test whether everything has been assembled correctly, (c) the installation of the first module in connection with the support module.

3.4. Erection process

3.4.1. Design conflict

The construction of timber lattice shells already reaches its limits on a small scale. At larger scales, the lack of a standardised and cost-efficient assembly method means that the technique has to be reinvented each time. Lattice shells are therefore only affordable for exceptional projects such as the Weald and Downland Museum or the Multihalle in Mannheim [7], where the costs and time required vary depending on the context. One reason for this is that the construction phase is an exceptional load case for an elastic timber lattice shell. This is due to high bending stresses caused by deformations during transport and erection, which also depend on the type of assembly and the shape and size of the shell. They have to be avoided where possible to prevent pre-damage and fractures.

In a review of elastic grid shells and their erection methods, Quinn and Gengnagel identify five viable means of elastic gridshell erection, which can be used in combination if needed. These include "pull up", "push up", "ease down", "inflate", and "by constraint"[9]. However, all of these methods require a grid that is made in the planar plane and is actively bent using these different strategies. These methods have the disadvantage that, on the one hand, they require a lot of space, since the planar development of the shell is usually much larger. In addition, the individual laths are subjected to alternating stresses during erection, which often lead to fractures [11]. This can make the building of complex geometries very costly. Those methods were not feasible for this project.

3.4.2. Design strategy: Prefabrication of bended structure

To avoid a costly erection process, a method of sequential construction was chosen. For this, the shell was divided into 6 modules which were prefabricated. This way, a substantial amount of pre-bending could be done in advance. In contrast to other [11] lattice shell projects, no breaks were recorded here.

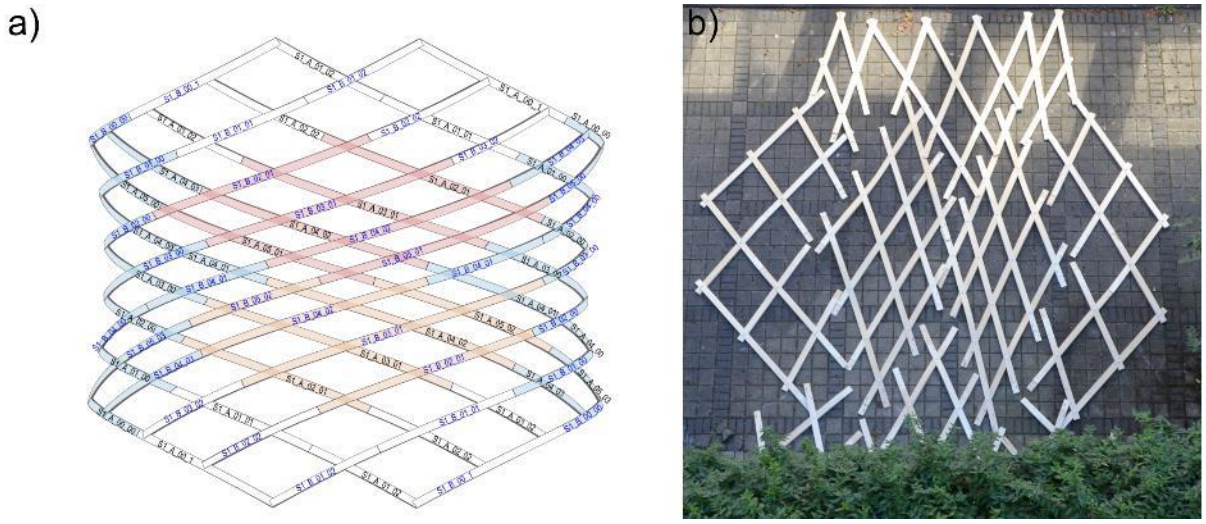


Figure 4. (a) top view with marking of the 6 modules needed for the assembly, (b) all completed modules are placed next to each other for inspection before erection.

4. Construction and joints

4.1. Material

For the active bending to work properly without breaking the laths, it was critical to carefully select the right material thickness. The choice was between plywood panels made of poplar (4 mm and 6 mm) and birch (6 mm). A reality check was the most practical approach, so breaking test were carried out with samples of the different wood panels. The minimum radius of curvature was of great interest here and as a result the 4 mm poplar plywood was picked, as it was better to go with a thinner material and use more layers. The plywood was delivered in panels measuring 2.5 m x 1.5 m. For an optimal usage of the material, the panels were cut into strips of 7.5 cm (20 pcs per panel). The length of 2.5 m was also optimal to match the size of the segments and modules. In total approx. 333 m of the strips were used (volume: 0.1 m^3, weight: 45 kg).

4.2. Nodes and layers

At the crossing points of the laths, the 3 layers of one direction are interlocked with the 3 layers of the other direction. They are connected with an M10 bolt, two washers and a nut. The connected laths can still be pushed together or apart in the plane and thus be stored in a more compressed way. However, since the geometries of the laths have already been adapted to the curved shape of the lattice shell and no slotted holes but ordinary holes are drilled according to the curved shape, they have a slight bend in the plane and are not as flexible as a lattice shell with slotted holes. At the nodes the layers meet and the 3 layers of one lath and the 3 layers of the other lath interlock. So at the nodes there are 6 layers on top of each other.

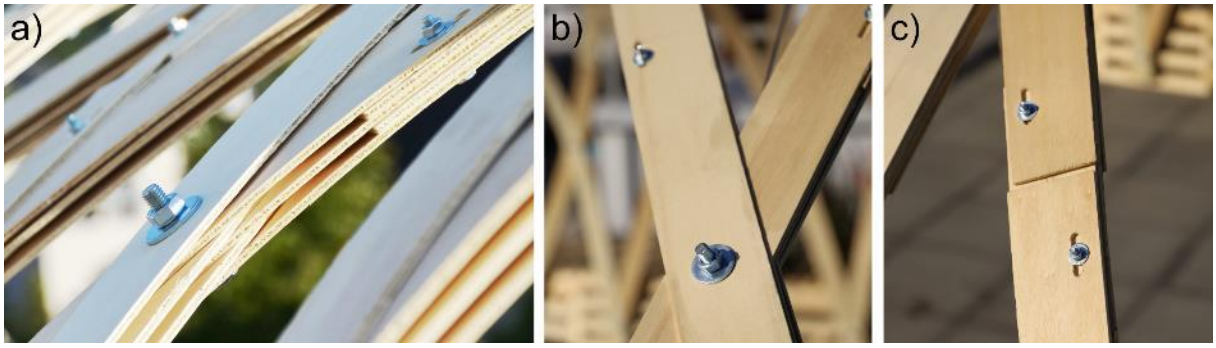


Figure 5. (a) Typical connection point, where all 6 layers of the laths are connected, (b) a node in the frontal view connected with a m6 screw, (c) a typical joint of the modules in the frontal view .

4.3. Joints between modules

The modules divide the shell into 6 segments, making it easier to erect on site. Therefore, a solution for the joint between the modules is mandatory. Overlapping the boards would result in a height offset in the individual layers and thus a change in the geometry of the lattice shell and all its elements. To prevent this, the boards in one layer are not overlapped but laid against each other. The cuts of the first and third layer are each on top of each other, while the cut of the second layer is shifted. This allows the 40 cm long connecting boards between the layers to be joined with only 3 screws instead of four. Due to the low loads of the lattice shell and the number of screws, M6 screws are used so that material and weight can be saved. In each layer, one of the meeting laths has two screws that firmly connect the connector against twisting, while the other lath is only fixed to the connector board by one screw. All 3 layers are connected by 3 screws and kept apart by the connecting pieces. To compensate for minor inaccuracies in the material, planning and machining of the boards, the laths are prepared with slotted holes at the predefined screw points. Any errors or small deviations in the lengths of the laths can thus be compensated for in this way.

4.4. Supports

The supports are special nodes (12 pcs in total) that are mounted to a bench on each side of the pavilion. They differ in shape and are also 3d-printed to connect to the structure at the correct spatial angle and height. The connection is also made with an M10 thread and nuts. The benches also serve as a foundation. As they support planters with soil, the benches have a certain weight and cannot be easily moved.

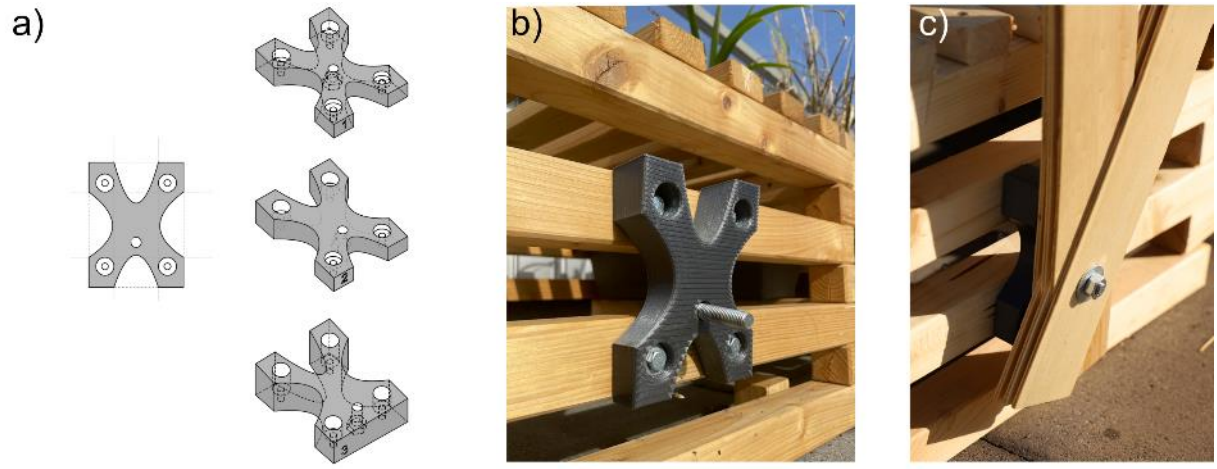


Figure 6. (a) axonometric representation of the typology-optimised support elements, (b) 3d printed support element for connecting the support to the lattice shell, (c) the finished assembly of a support node.

4.5. Bracing

The lattice shell is stiffened by a row of compression laths (red) in the longitudinal direction (= passage) on the vertex of the lattice shell. In transverse direction, two tension cables (blue) connected to the supports of the lattice shell take on this task.

4.5.1. Compression lath

Since the nodes of the lattice shell are only in a row on the vertex in the longitudinal direction, the compression laths are attached here. They fix the nodes on the vertex at the measured distances of the planning. The laths have pre-drilled holes at the appropriate distance and are placed on the nodes from above and screwed together. Due to the fixed distances, the lattice shell is contracted at the top and curves more upwards at the ends according to the planned shape.

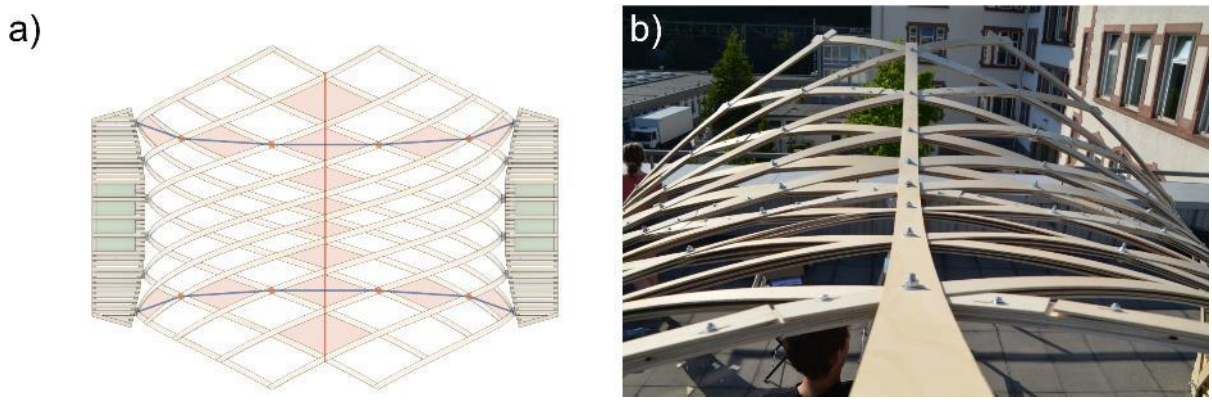


Figure 7. (a) elevation view of the bracing system, (b) view along the apex line (compression lath).

4.5.2. Tension ropes

To attach the tension ropes to the crossing points of the nodes, special clamps for fastening were developed and printed with a 3D printer. They consist of two flat discs that can be placed on top of each other and are attached to the screws of the crossing points. Two semicircular cut-outs on both discs allow the steel cable to pass through. When the nuts are tightened, the discs are pressed together. Small protrusions in the bushings prevent the rope from slipping through.

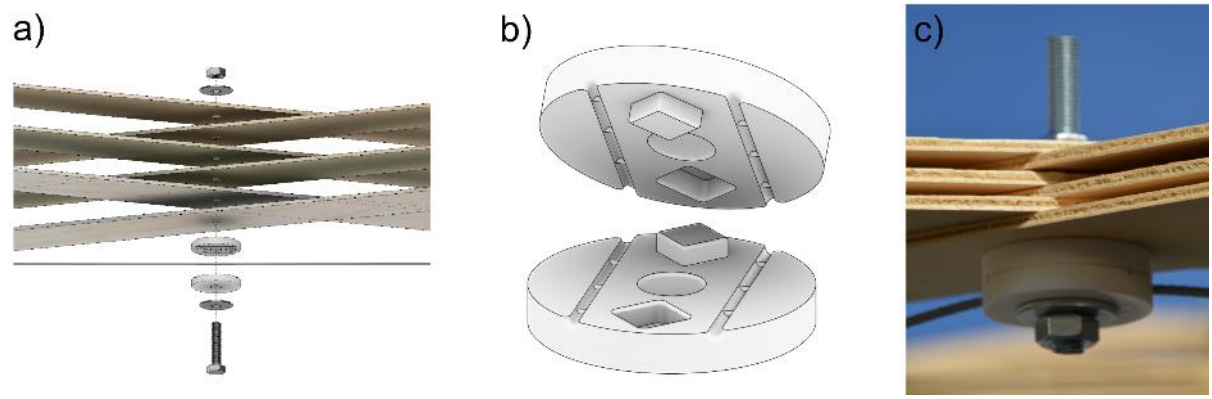


Figure 8. (a) exploded view of a node in connection with the 3d printed clamp for the tension rope, (b) axonometry of the clamp consisting of two discs with semicircular cut-outs for the steel cable. , (c) assembled node with the 3d printed clamp and steel cable.

5. Low-tech tool as interface

5.1. Fabrication approach and necessary data

The design decisions mentioned earlier reduce the complexity and the amount of fabrication data which has to be transferred to the wooden laths. All manufacturing steps will be executed by hand and need to be simple. Furthermore, all of the necessary information must be available at first glance and are directly tied to the component. These requirements led to the decision to use a custom large-format pen plotter. The plotter doesn't have to be built very sturdy, because there are little to no forces acting on the wooden laths in the process. The workflow is completely 2D and is comparable to laser cutting. The following information should be put on the components:

- Labelling/numbering of the laths
- Markers for drilling holes (both, connections and joints)
- Marker for cutting the lath to length

5.2. Customized low-tech tool: large format pen-plotter

The frame of the pen plotter was built from 2020 v-slot aluminium profiles. In combination with ball bearings and rubber wheels they also act as rails for the linear movement, so there is no need for expensive linear bearings. Movement is possible in 2 axes on a 500 x 3000 mm working space that is sufficient for labelling the laths. The frame is mounted on wooden base plates which in turn rest on 3 fixed tables. All connectors and mechanical parts are 3D-printed in FDM/FFF. 3 NEMA17 stepper motors drive the tool head via gears and timing belts. A small servo motor is responsible for lifting the pen, downward force during drawing is provided by a small spring. The controller is an Arduino Uno with a CNC shield. It is running the free GRBL firmware (GPLv3) which translates G-Code sent from a PC over a USB connection into movements. The cost of materials for the pen plotter is about 350 €.

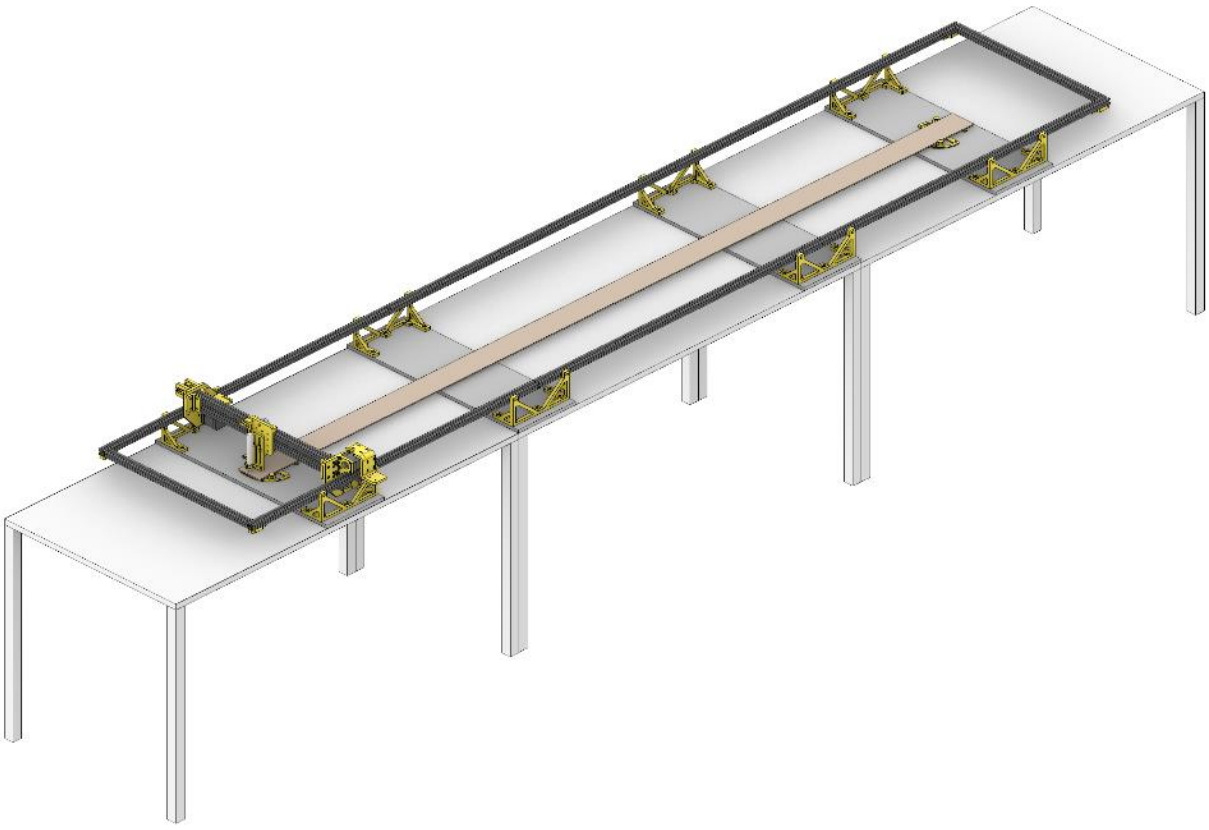


Figure 9. Isometric view of the custom large-format pen plotter.

5.3. Data transfer and conversion

The G-Code commands can be sent directly to the controller through a serial connection. For more precise control and manual commands, the open-source software 'Universal Gcode Sender' was used to load and execute the G-Code files. These are generated through a custom script in Grasshopper, which takes the previously generated drawings for each lath and translates them into movement commands. This also involves a quick optimization to minimize the amount of travel moves (= empty movements between the drawing of labels): The curves are sorted in ascending order according to the x-value of their starting point.

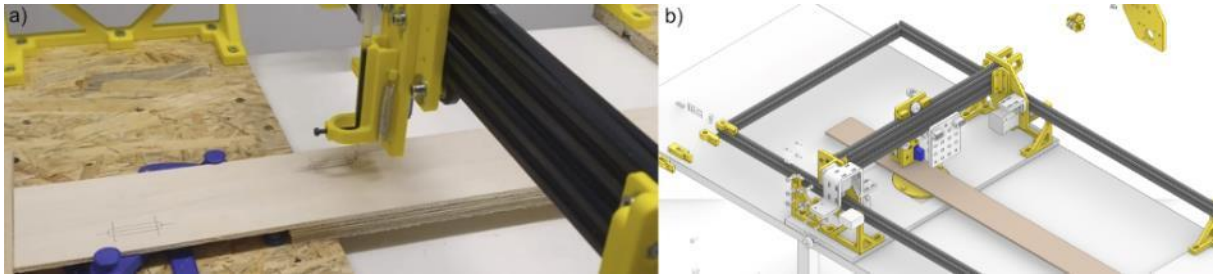


Figure 10. (a) developed pen-plotter in action, (b) exploded drawing of the pen plotter.

Each lath has a unique identifier which encodes its final location. It is readable and understandable for humans, at least it gives one a rough idea where the element is located in the structure. The labelling convention is as follows and is also used for the G-Code files:

S<layer>_<direction>_<row>_.gcode

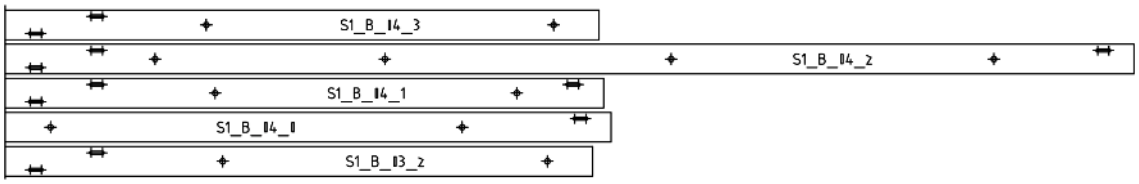


Figure 11. Automatically created drawings for the pen plotter.

5.4. Practical application and problems

The first practical problem to solve is the alignment of the laths in the machine. There was a total of 135 elements, which means that there is a substantial amount of manual interactions involved during the labelling process. Due to the manual cutting, the laths also vary slightly in width, so a conventional one-sided mechanical limit stop for positioning does not work for the y-axis. Instead a rotational spring bracket is used at both ends, which automatically centres the laths. Inaccuracies in the y-position while mounting the brackets are compensated for in the script by a one-time calibration. A deviation angle is measured and will be applied to all coordinates generated by the script. The best results for labelling were achieved by using regular pencils, which had to be exchanged and sharpened regularly. Gel pens or rollers were not suitable because of the rough and absorbent surface of the wood.

5.5. Full fabrication process

With the help of the pen plotter, the nodes and slotted holes as well as the cutting edge of the laths were drawn. The sticks were then cut to the correct length and the holes drilled accordingly with hand crafting tools in the following order:

1. Chop saw: cutting to length
2. Drill stand: drill the 10 mm holes for the connections
3. Drilling machine for slotted holes: prepare the slotted holes for the joints

All parts are then grouped together for the assembly of the modules.

6. Evaluation and conclusions

6.1. Overall precision of the fabrication process

The built result shows, that the achieved precision is sufficient to transfer the planned geometry into reality. When assembling the modules, the laths had to be bent in order to be able to push through the screws. The typical deviation in the distance between the holes related to the innermost and the outermost layer in one direction is about 4-6 mm.

The deviation between the planned and the built geometry was not determined, because the structural analysis was only limited to the active bending of individual laths and the minimal bending radius. The final geometry would deform under pretension and its own weight.

6.2. Time consumption and problems during assembly

It took two working days to label all laths. The machine time accounted for about half of the time (approx. 3-4 min per element), the rest was spent on manual activities (changing the laths, loading the files, changing/sharpening the pencils, keeping track of the parts).

The joints and support points were so precisely determined by the pen plotter that we were able to complete assembly of all modules within 2 hours.

The most difficult and time-consuming part during assembly was the screw joint between the modules. Originally, it was intended that the structure could be dismantled effortlessly if needed. The design of the joints originates from the decision to utilize active-bending to implement the geometry. Therefore, the butt joints must transmit bending moments and be stiff. Those requirements contradict each other to a certain extent and make it difficult to find an suitable solution.

The assembly of the whole structure on site took around 3 hours.

6.3. Disadvantages of the construction principle

A major disadvantage, which only became apparent in retrospect, was the very large overall surface area of the material (approx. 50 sqm) and the number of gaps that resulted from the layered structure. This makes it especially difficult to weatherproof the Knotshell pavilion. Moisture holds well in the gaps between the joints.

Acknowledgements

This template was adapted from the one used for IASS-IACM 2008 with modifications modelled after templates for recent IASS annual symposia.

The authors thank and acknowledge the support of the FABU (Association of Friends and Alumni of the University of Wuppertal) which founded the workshop and construction of the Knotshell-Pavillon.

References

[1] S. Adriaenssens, P. Block, D. Veenendaal and C. Williams, *Shell Structures for Architecture: Form Finding and Optimization*, Routledge, 2014.

[2] Y. Weinand, *Advanced Timber Structures: Architectural Designs and Digital Dimensioning*, Birkhäuser, 2017.

[3] C. Preisinger, "Linking Structure and Parametric Geometry," *Architectural Design*, vol. 83, no. 2, pp. 110–113, 2013.

[4] F. H. Günther, "Geodesic Winding of Minimal Surfaces: the architecture, structure and geometry of an irregular grid-shell pavilion assembled from thin plywood strips," in *IASS Annual Symposium 2020/21 & the 7th International Conference on Spatial Structures: Inspiring the Next Generation*, Guilford, United Kingdom, August 23–27, 2021, A. Behnejad, G. Parke and O. Samavati, Eds.

[5] B. Addis, K. Kurrer, W. Lorenz, *Physical models: Their historical and current use in civil and building engineering design*, Berlin: Ernst & Sohn, 2021.

[6] E.Adiel, C.Brandt-Olsen, J. Isaksson, I. Näslund, K. Olsson, E. Poulsen and C. Williams, "The design, fabrication and assembly of an asymptotic timber gridshell*"*. in *Form and Force: Proceedings of the IASS Annual Symposium 2019*, Barcelona, Spain, October 7–10, 2019, C. Lázaro, K. U. Bletzinger and E. Oñate, Eds.

[7] J. C. Chilton and G. Tang, Eds., *Timber gridshells: Architecture, structure and craft. London, New York: Routledge*, Taylor & Francis Group, 2017.

[8] J. Hennicke, F. Otto, E. Schauer, and T. Hasegawa, Eds., *Grid shells*. Stuttgart: Institute for Lightweight Structures, 1974.

[9] G. Quinn and C. Gengnagel, "A review of elastic grid shells, their erection methods and the potential use of pneumatic formwork," in *Mobile and Rapidly Assembled Structures IV*, N. de Temmerman and C. A. Brebbia, Eds.: WIT Transactions on The Built Environment, 2014, pp. 129–143.

[10] W. Nerdinger, Ed., *Frei Otto: Das Gesamtwerk : leicht bauen - natürlich gestalten*. Basel, Boston, Berlin: Birkhäuser, 2005.

[11] J. Cichocka, "INFRAME - design and construction of a sequentially erected elastic timber gridshell," MASSACHUSETTS INSTITUTE OF TECHNOLOGY, 2020.

IASS 2023
July 10–14 Melbourne
Integration of Design and Fabrication

Proceedings of the IASS Annual Symposium 2023
Integration of Design and Fabrication
10–14 July 2023, Melbourne, Australia
Y.M. Xie, J. Burry, T.U. Lee and J. Ma (eds.)

Morphogenesis method for thin metal plate with non-uniform stiffness distribution by applying auxetic mechanism

Hirotaka UJIOKA[a,*], Mika ARAKI[b], Kai MORINAGA[c], Masaaki IWAMOTO[d], Yuri IWATA[d], Akitoshi IWAMOTO[e], Miki KATSUKI[d], Hanano TANAKA[d]

[a,*] Graph Studio Inc.
u@graph-studio.net

[b] Kwansei Gakuin University
[c] The University of Tokyo
[d] Kyushu University
[e] Kanagawa University

Abstract

In recent years, computational methods have made it possible to design complex curved surfaces. Finding an easy and economical way to create desirable free-form surfaces is important for extending design possibilities. Based on a biomimetic approach, inspired by the mechanical force-induced morphological changes in floral development, this study developed a method for creating porous curved surfaces by applying auxetic structures. A free-form surface was obtained by suspending a thin metal plate with equilateral triangular repeated incisions under an equally distributed load. The form can be freely changed by changing the incision pattern. Material tensile tests were conducted to elucidate the mechanical properties, and it was observed that the material behaved elastically until the apex of the triangle buckled locally. After the load decreased, it gradually increased again up to the maximum load. The stiffness and strength depended on the length and angle of incisions. Based on the results, an incremental load analysis method was developed to find the form under a distributed load. The simulation was a geometric nonlinear analysis considering material nonlinearities. A mock-up was constructed to validate the simulation results. It is expected that the proposed method for creating free-form surfaces will be applied to various spatial structures in the future.

Keywords: auxetic mechanism, biomimicry, morphology, form finding, metal spatial structures, free-form surface, new fabrication method, floral development, Hangai Prize applicant

1. Introduction

In recent years, computational methods have made it possible to design complex curved surfaces. However, there are still few methods for manufacturing free-form surfaces, and in many cases, complex and uneconomical machining is required. Finding an easy and economical way to create desirable free-form surfaces is important for extending design possibilities.

During floral development in the floral meristem of plants, the tension distribution of epidermal cells becomes non-uniform, which is thought to be related to morphogenesis. Inspired by the cellular morphological changes of floral organs, this study developed a novel method for creating porous curved surfaces by exploiting the geometric properties of the auxetic mechanism [1] to create a non-uniform stiffness distribution in thin metal plates, and applying a load to the plates. Through the application of the geometric properties of the auxetic mechanism to thin metal sheet structures, this study developed a new method for the morphogenesis of free-form surfaces.

Copyright © 2023 by Hirotaka UJIOKA, Mika ARAKI, Kai MORINAGA, Masaaki IWAMOTO, Yuri IWATA, Akitoshi IWAMOTO, Miki KATSUKI and Hanano TANAKA. Published in the Proceedings of the IASS Annual Symposium 2023 with permission.

2. Morphogenesis system of floral meristem in plants.

Angiosperms have meristems, which produces organs at their tips. In most plants, a shoot apical meristem initially makes only leaves, which eventually transform into a floral meristem that forms flowers. The floral meristem continuously produces a dome-shaped floral primordium without floral organs (sepal, petal, stamen, and pistil). The floral organs, at first sepals, are subsequently initiated on the floral primordium in stages, and this process is called "floral development".

Typically, floral development is stable within a single species, and results in the formation of a uniform morphology of flowers in the species [2]. For example, in the plant *Arabidopsis thaliana*, four sepals are almost simultaneously initiated in every floral primordium, followed by four petals, six stamens, and one pistil to complete the floral development. The number of each floral organ is typically constant, and the arrangement of floral organs is stable. However, in the male flowers of the aquatic plant *Ceratophyllum demersum*, the number and arrangement of stamens vary with each flower, and various floral forms exist in the species [3], [4].

Morphological analysis suggests that, in the male flowers of *Ceratophyllum demersum*, the adaxial side of young floral primordium is pressed by a leaf primordium, and the mechanical forces between the two primordia suppress the initiation of floral organs (sepals) on the adaxial side [4], [5]. When the mechanical forces are released, different numbers of sepals are initiated depending on the degree of contact. It is hypothesized that various developmental patterns, from the early to the mid-stages of floral development, are caused by mechanical forces, leading to diverse floral morphology in the mature male flowers of *Ceratophyllum demersum*.

To verify this hypothesis experimentally, a previous study developed a novel experimental system to alter the floral morphology by artificially applying mechanical forces to the floral meristem of *Arabidopsis thaliana* [6]. In this experiment, a microdevice fitted to the shape of a young floral primordium was placed on the abaxial surface of another floral primordium and induced mechanical forces on it. The analysis of the results obtained by this experimental system revealed that the morphology or number of sepals occasionally changed at the site of contact (abaxial side) with the microdevice. This change in the floral development can be explained by considering the change of the stiffness distribution in the floral primordium at the abaxial side (Figure 1). Current studies are attempting to estimate changes in the stiffness distribution based on changes in the cell morphology and related gene expression in the floral meristem before and after the application of mechanical forces.

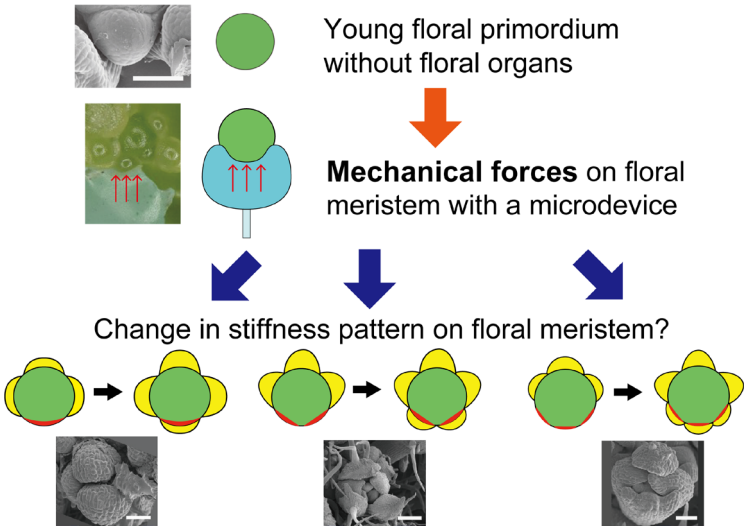


Figure 1. Morphological optimization in floral development: photos of floral primordia of *Arabidopsis thaliana* (scale bars = 50 μm).

3. Framework of metal plate structures applied with auxetic mechanism

3.1. Auxetic mechanism

Based on a biomimetic approach, it is expected that a new form-finding method, which can efficiently create complex three-dimensional shapes such as those of plant flowers can be developed by generating materials with non-uniform stiffness distribution [7], [8]. As a method for fabricating panels with non-uniform stiffness distribution, this thesis proposes the application of an auxetic pattern of incisions to thin sheets.

Auxesis is a property where material expands in a direction perpendicular to the direction of the force applied to stretch it. The material can be endowed with the auxetic property by creating a pattern of many periodic incisions on a flat surface, like Japanese paper cut-outs known as "*kirigami*". In this study, an auxetic pattern with repeating equilateral triangles was used (Figure 2). A surface material with non-uniform stiffness distribution can be created by making periodic random incisions with different angles on a thin metal plate, which is then suspended by an equally distributed load to obtain a free-form curved surface. By controlling the incision pattern, a free-form surface can be obtained after the suspension (Figure 3).

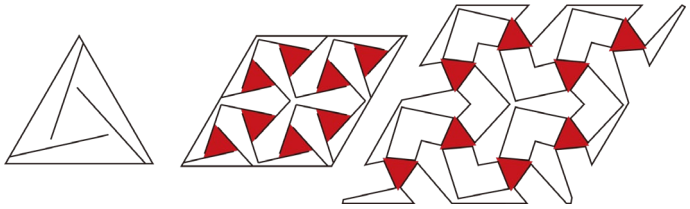


Figure 2. Auxetic mechanism: The process of expansion from left to right.



Figure 3. Image of a suspended form created by an auxetic pattern with various angles of incision (Kent paper model).

3.2. Paper model experiment

This study conducted a apaper model experiment to understand the correlation between the auxetic pattern and the curved surface shape after suspension. Four paper models with different patterns were prepared to observe the relationship between the incision angle (θ) and the sag after suspension (Figure 4), and it was found that the sag decreased as the angle (θ) increased.

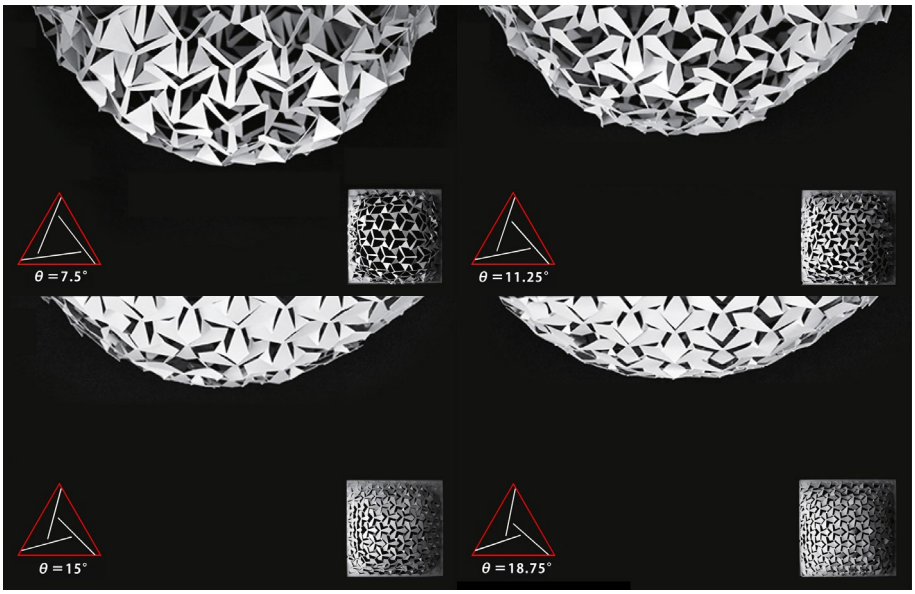


Figure 4. Paper model experiment: correlation between the incision angle (θ) and the suspended shape.

3.3. Framework of form finding method

A face material with non-uniform stiffness can be obtained by periodically arranging triangles with different incision angles. It is assumed that a free-form surface can be obtained by pulling down it with an equally distributed load. This study developed an algorithm to obtain an auxetic pattern from a given curved surface shape (target shape) using the Grasshopper visual programming language with the Kangaroo plug-in. The equilateral triangular unit that serves as the repetitive unit was conceptualised as three springs with equal stiffness (spring constants), and the springs of adjacent units were combined and converted into a wire model (Figure 5). First, a metal plate without incision was modeled as a triangular mesh, and geometric nonlinear analysis was performed by applying equally distributed loads to calculate the curved surface shape. Next, the convergence calculation was performed by varying the stiffness of each unit so that the difference between the obtained shape and the target shape was reduced (Figure6), and a stiffness distribution was obtained (Figure 7). Finally, the auxetic pattern was obtained by mapping the equilateral triangle units obtained from the stiffness distribution.

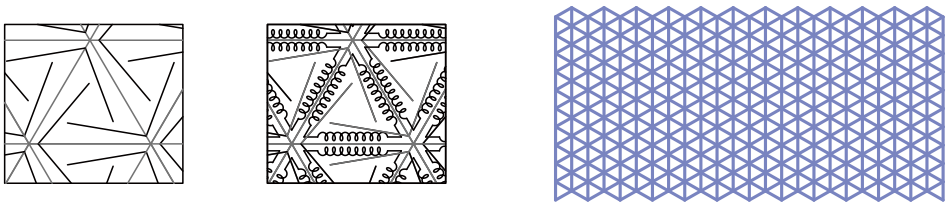


Figure 5. Replacement of wire model with spring and wire mesh model.

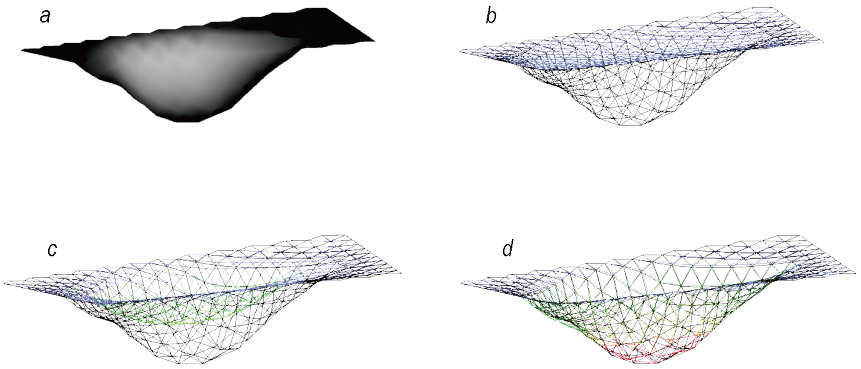


Figure 6. Convergence calculation: (a) target shape; (b) convergence calculation at step 0; (c) convergence calculation at step 1; (d) convergence calculation result.

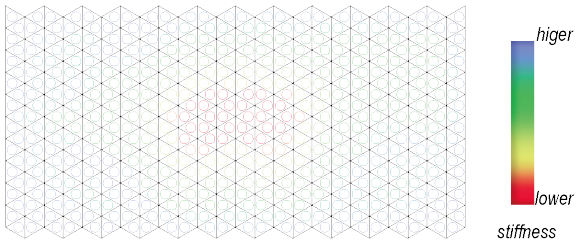


Figure 7. Stiffness mapping for target shape.

The results obtained by the paper model experiments suggest that the incision pattern changes the suspension shape and a framework for stiffness mapping that achieves the desired free-surface shape under an equally distributed loading was investigated.
Designing a free-form surface by introducing an incision pattern requires the detailed investigation of the actual incision pattern and mechanical properties. The geometric nonlinear analysis described in this section assumes that the material properties of the springs in the analysis models are linear elastic, and the quantitative relationship between the incision pattern and the stiffness in the actual material is unknown. It is thought that accurate calculations can be carried out by elucidating the relationship between the incision patterns and the stiffness and by considering nonlinear material properties.

4. Material properties of auxetic mechanism and application to design method

4.1. Material tensile experiment

Material tensile tests were conducted to elucidate the mechanical properties. A specimen with the geometry shown in the figure 8 was prepared by incising 1mm-thick stainless-steel plates of grade SUS304.

Figure 8 shows the shape of the tensile test specimen. The tensile test parameters are the remaining length after incision ($e = 5.0\text{mm}, 10.0\text{mm}$) and the incision angle ($\theta = 0°, 5°, 10°, 15°$). As shown in Figure 8(b), eight specimens were subjected to the tensile test.

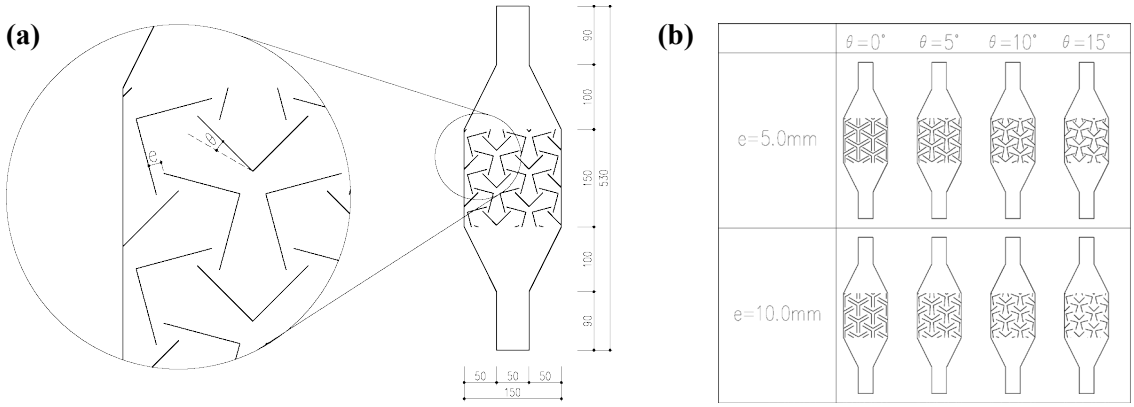


Figure 8. Tensile test specimens:(a) general diagram of the material tensile test specimen; (b) specimens subjected to tensile test.

The tensile tests were performed using an Amsler testing machine. Figure 9 shows the tensile test setup, and Figure 10(a) and (b) shows the load–deformation curves for each specimen, and the plot of the relationship between the vertical displacement of the Amsler head and the load during the tensile test. For the specimen with e=5mm and θ=0°, data were only available up to the point where the specimen was deformed to approximately 2/3 of its deformation at rupture due to a troubles with the testing machine.

The results reveal that, as the load increased, the equilateral triangle surrounded by the Y-shaped incision rotated while the incision opened. The material behaved elastically until the apex of the triangle buckled locally. After the load decreased, the load gradually increased again to show the maximum load, eventually leading to the fracture of the material. A trend was observed such that as the incision angle θ increased, the stiffness and the maximum load increased and the the extension after yielding decreased.



Figure 9. Material Tensile Test: The triangular pattern rotates, causing local buckling and out-of-plane distortion (left: e=5.0mm, θ=0°; right: e=5.0mm, θ=10°).

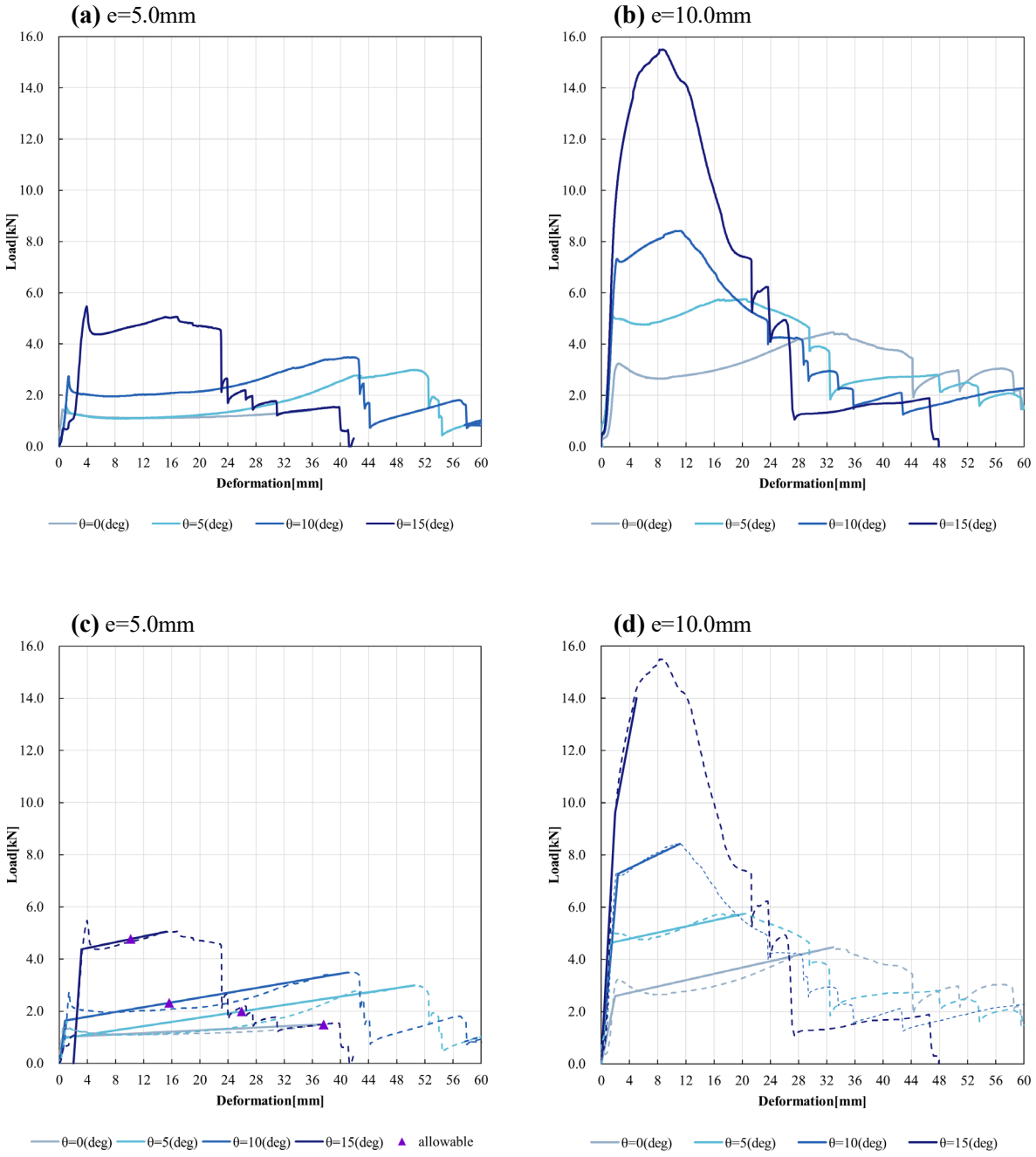


Figure 10. Experimental result and bi-linear model: (a) load–deformation curve (e=5.0mm), (b) load–deformation curve (e=10.0mm), (c) bi-linear model (e=5.0mm), and (d) bi-linear model(e=10.0mm).

4.2. Analysis method considering material properties of auxetic mechanism

Based on the experimental results, an incremental load analysis method was developed to find the form under a distributed load. The simulation was a geometric nonlinear analysis considering the material nonlinearities. The metal plate was mesh modelled with a bilinear model depending on the incision angle.

The bilinear model was created based on the load–deformation curves obtained from the tensile tests, as follows: the primary stiffness K_1 was approximated based on the stiffness obtained experimentally in the elastic range. It was assumed that, after yielding, it is assumed to the load increases linearly up to the maximum load, and the secondary stiffness K_2 is determined such that the integral values up to the maximum load point are equivalent. The intersection of the straight line between the elastic and plastic ranges is the yield point P_y (displacement δ_y), while the allowable stress P_a is the point corresponding to 2/3 of the maximum load P_2. Figure 11 shows the diagram of the bilinear modelling process and Figure 10(c) and (d) shows the actual load–deformation curve of the bilinear model obtained by the experiment.

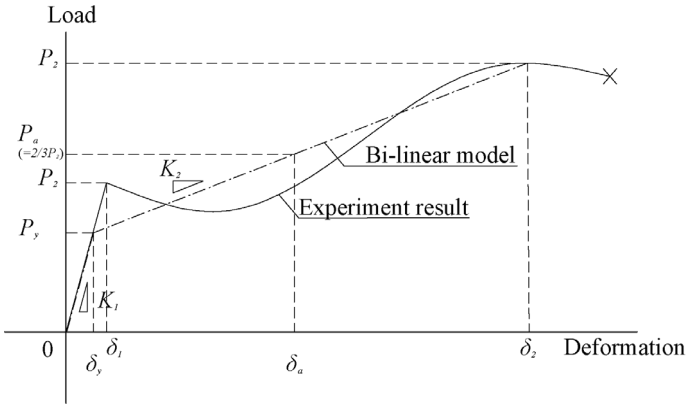


Figure 11. Diagram of bilinear modelling.

The load and deformation obtained from the tensile test were converted to the stress degree and strain, and the primary and secondary stiffness values were converted to the apparent Young's moduli E_1 and E_2.

$$\delta = \frac{P}{A}, \varepsilon = \frac{\delta}{L} \ (A = 150\text{mm}^2, L = 150\text{mm})$$
$$E = \frac{\Delta\delta}{\Delta\varepsilon}$$

In the incremental load analysis process, the curved surface shape is obtained by reducing the Young's modulus of a wire to the second-order stiffness once its tensile stress reaches the yield point. Assuming that the unloading stiffness is equal to the primary stiffness, the shape after unloading can be also obtained by geometric nonlinear analysis. It is assumed that similar auxetic patterns conform to the same bilinear model, and the Young's modulus and yield stress are equal to the experimental values.

An example of the application of the proposed analysis method is presented below. The analysis model is a stainless-steel panel with a thickness of 1.0 mm with an auxetic pattern incision; the effective width of the wires constituting the mesh is 50 mm.
The stiffness was mapped as shown in Figure 12(a), and Young's modulus is based on experimental results. The boundary conditions were fixed on four sides, and the proposed analysis method was applied for one cycle, that is, an equally distributed load of 9.8 kN/m^2 (1.0 tf/m^2) was applied and then removed. The load–deformation curves obtained by plotting the vertical displacements of the representative nodes A, B, and C (Figure 12(a)) on the horizontal axis, and the equally distributed load on the vertical axis

are shown in Figure 12(b). The deformation after applying the equally distributedload of 9.8 kN/m^2 (1.0 tf/m^2) and unloading is shown in Figure 12(c).

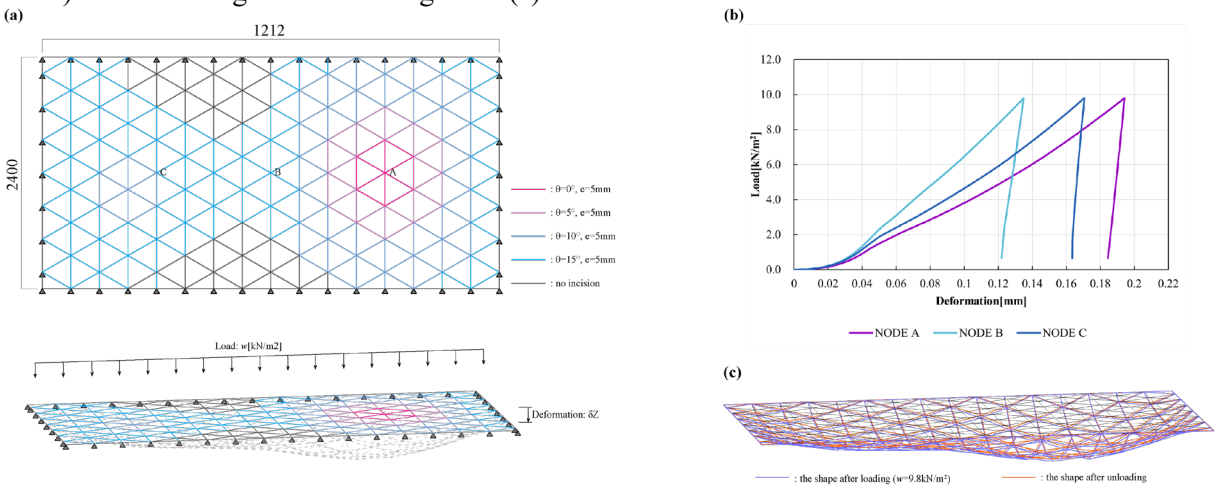


Figure 12. Example of analysis using proposed method: (a) analysis model diagram; (b) load–deformation curves for NODE A, B, and C; (c) deformation after loading and unloading.

4.3. Mock-up experiment

The roof surface of the mock-up consisted of two thin metal sheets with a width of 1.2 m and length of 2.4 m. The metal sheets were made of 1 mm-thick SUS2B stainless-steel, and different incision patterns were created on each sheet using laser processing. Side A has a uniform incision of 0°, and the side B has incisions of gradational angles in the range of 0° to 18.75°. These metal sheets were fastened to the four-way frame with bolts, and subsequently hung over a frame to form the roof. The overall shape of the mock-up is shown in Figure 13.

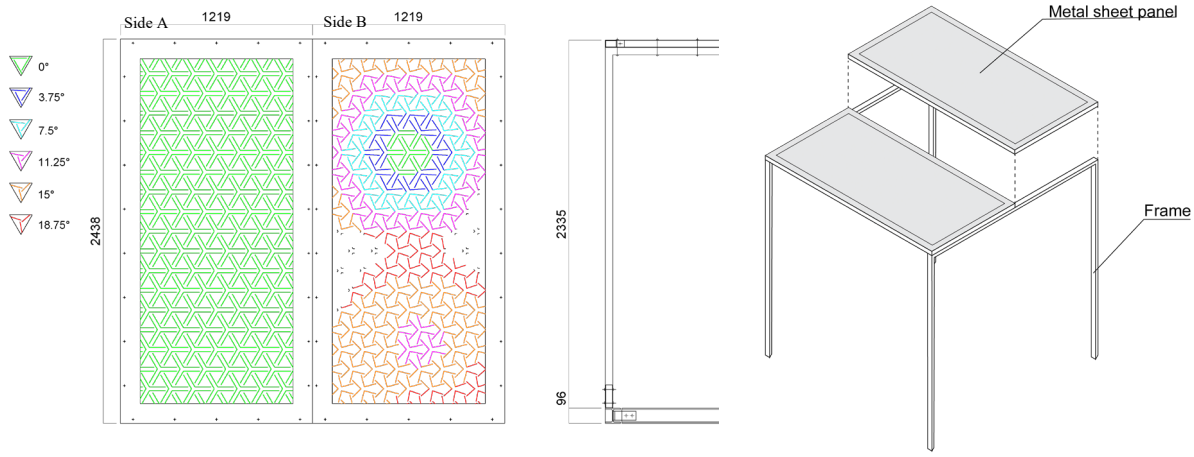


Figure 13. Overall shape of mock-up.

Loads of approximately 98 N (10 kgf) were applied by chain blocks installed at each loading point, and the values indicated by the spring weights attached to each loading point and the vertical displacements were recorded each time (Figures 14 and15). Figure 16 shows the final shape of the mock-up after loading.

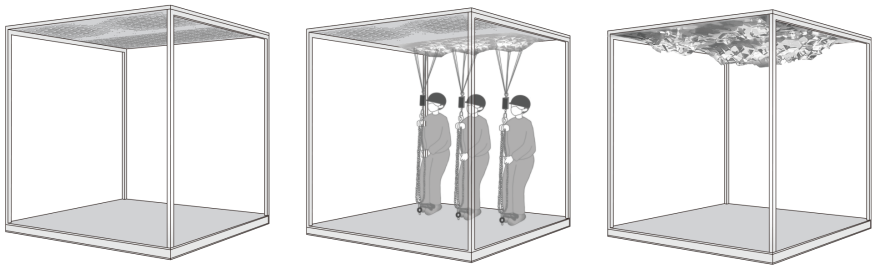


Figure 14. Diagram of mock-up loading and measurement process.



Figure 15. Mock-up: loading and measurement.



Figure 16. Mock-up after loading.

The analysis model and the results obtained using the procedure outlined in Section 4.2 are shown in Figure 17. The auxetic pattern is similar to the pattern of the material tensile test and the bilinear model obtained in this study was used. The incision angles in the mock-up patterns include angles that have not been experimentally verified. The analysis model maps the wires to stiffnesses values that are linearly complementary to the angles that have been tested, and that the stiffness is assumed to vary continuously with the incision angle.

The load-deformation curves and analytical results at each loading point of the mock-up are presented in Figure 17. The maximum displacement occurred at the loading point at the center of span for the uniform stiffness model, and at the loading point with the smallest incision angle for the non-uniform stiffness model; both exhibited the same trend as the analytical results.

For the uniform model, the error between the experimental and analytical displacement values after loading was 2.1%, 0.9%, and 2.1% for loading points 1, 2, and 3, respectively, and the error after unloading was 5.6%, 0.88%, and 7.8%, respectively.

For the non-uniform model, the errors between the experimental and analytical displacement values after loading was 13%, 5%, 5%, and 2.1%, respectively. The error after unloading was 6.3%, 4.4%, and 46%, respectively. The error after unloading was 6.3%, 4.4%, and 46%, respectively.

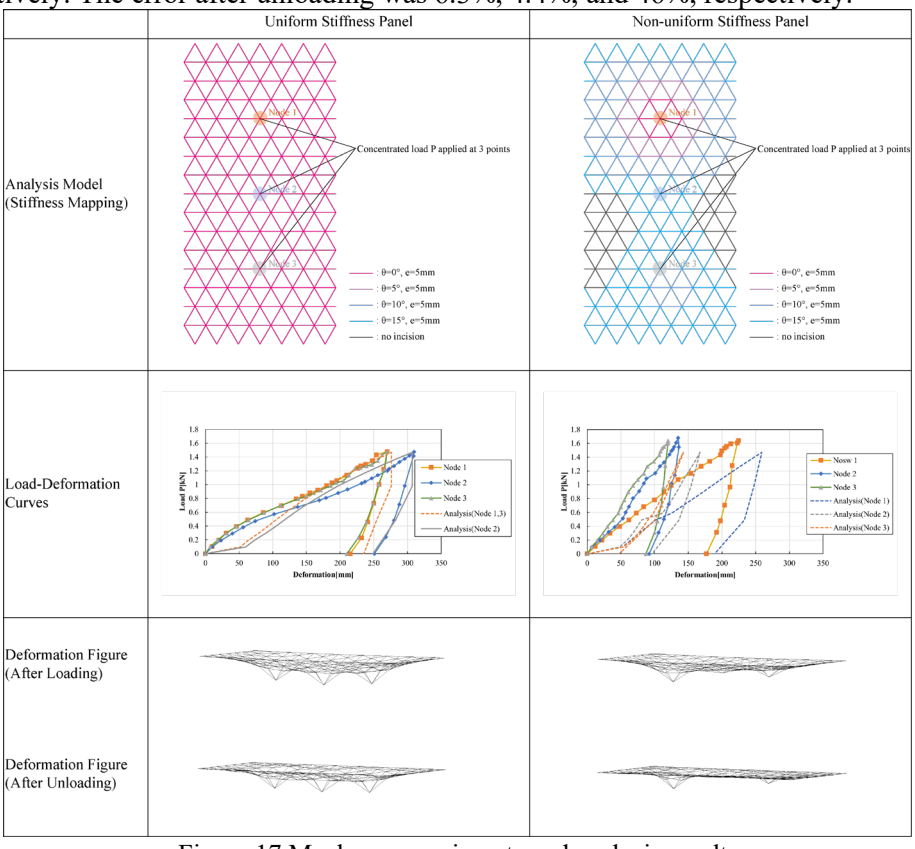


Figure 17 Mock-up experiments and analysis results

The following improvements can be made to the analysis:

1. The analytical model load was assumed to be at the center of each loading point, but in the mock-up, the load was distributed among three points within each loading point, so the surface shape obtained by the analysis was more deformation concentrated at the loading points compared with the actual mock-up.
2. All wire joint conditions were modeled as rigid for the convenience of solving large deformation problems, but modelling of the rigidity of the bolted joints may be considered.

3. More material tests should be conducted for more incision angles to investigate the relationship between incision angle and stiffness in detail.

5. Conclusion

This study found that a free form can be obtained by randomly distributing incision patterns. A mock-up was constructed to validate the simulation results. The research presented herein has potential for further development. For example, our innovative pavilion can be developed into spatial structures that adapt their form to control the heat radiation according to the climatic conditions at the structure's location. It is expected that the proposed method for creating free-form surfaces will be applied to various spatial structures in the future.

Acknowledgements

This work was supported by MEXT KAKENHI Grant Numbers 19H05358 (to A.I.) and 21H003759 (to A.I.). We thank Edanz (https://jp.edanz.com/ac) for editing a draft of this manuscript.

References

[1] M.Konaković-Luković, J.Panetta, K.Crane and M.Pauly, "Rapid deployment of curved surfaces via programmable auxetics," *ACM Transactions on Graphics,* vol. 37, Issue 4, 2018.

[2] L.P.Ronse De Craene, E.F.Smets, "Merosity in flowers: definition, origin, and taxonomic significance," *Plant Systematic Evolution* vol. 191, pp. 83–104,1994.

[3] P.K.Endress, "Evolutionary aspects of the floral structure in *Ceratophyllum*," *Plant Systematic Evolution* vol. S8, pp. 175–183, 1994.

[4] A.Iwamoto, A.Shimizu, and H.Ohba, "Floral development and phyllotactic variation in *Ceratophyllum demersum* (Ceratophyllaceae)," *American Journal of Botany,* vol. 90, pp. 1124–1130, 2003.

[5] A.Iwamoto, R.Izumidate, and L.P.Ronse De Craene, "Floral anatomy and vegetative development in *Ceratophyllum demersum* : A morphological picture of an "unsolved" plant," *American Journal of Botany,* vol.102, pp. 1578–1589, 2015.

[6] K.Bull–Hereñu, P.dos Santos, J.F.G. Toni, J.H.L.El Ottra, P.Thaowetsuwan, J.Jeiter, L.P.Ronse De Craene, and A.Iwamoto, "Mechanical forces in floral development," *Plants,* vol. 11, 661, 2022.

[7] A.Iwamoto, M.Iwamoto, M.Araki, "A Model of Membrane Structures with Non-uniform Stiffness Distribution: With Reference to Morphological Optimization in Flower Development," *Summaries of Technical Papers of Annual Meeting, Summaries of Design Works of Annual Meeting. Architectural Institute of Japan,* pp. 793-796, 2021.

[8] Y.Baranovskaya, M.Doerstelmann, M.Prado, A.Menges, "Knitflatable Architecture: Pneumatically Activated Preprogrammed Knitted Textiles," *eCAADe 34,* pp. 571-580, 2016.

IASS 2023
July 10–14 Melbourne
Integration of Design and Fabrication

Proceedings of the IASS Annual Symposium 2023
Integration of Design and Fabrication
10–14 July 2023, Melbourne, Australia
Y.M. Xie, J. Burry, T.U. Lee and J. Ma (eds.)

Nonlinear analysis of multi-scale coupling based on coordinated distributing method

Junjie YAO[a], Yanfeng ZHENG[a], Yaozhi LUO[a,*]

[a,*] College of Civil Engineering and Architecture, Zhejiang University
866 Yuhangtang Rd, Hangzhou 310058, P.R. China
luoyz@zju.edu.cn

Abstract

Multi-scale simulation is a widely used method for balancing the accuracy and cost of numerical simulations of structures. This technique allows designers to obtain both global characteristics and local information of structures simultaneously. In this paper, we propose a coordinated distributing multi-scale coupling method based on the Finite Particle Method. The method aims at deformable interfaces. We first describe the basic theory of coordinated distributing coupling. Next, we present a calculation process which includes the following steps: the calculated interface force is distributed to the secondary particles based on the force balance relationship; the displacements of the secondary particles are obtained by calculating the motion equation; and the motion of the major particle is calculated through applying the displacement coordination relationship. This method enables the coupling of beam-plane, beam-shell and beam-solid, while avoiding stress concentration on the coupling interface. Numerical tests have been conducted to validate the stability and reliability of the proposed method in dynamic nonlinear problems. The calculation results indicate that this method is effective for the multi-scale fine analysis of structures.

Keywords: finite particle method, coordinated distributing coupling method, major-secondary particle coupling system, displacement coordination relationship, force balance relationship

1. Introduction

Accuracy and efficiency are critical concerns in the numerical simulation of structures [1]. There are three primary modeling approaches: structural modeling, refined modeling, and multi-scale modeling. Structural modeling involves building a global simplified model of the structure using low-dimensional elements such as beam elements. However, this approach cannot reflect the mechanical properties and failure mechanisms of the structure due to the lack of local information [2]. Refined modeling involves building a detailed model to examine the local response of the structure using high-dimensional elements such as shell or solid elements [3]. However, the reduced element mesh size significantly increases the computational cost of the model by requiring an excessive number of nodes and elements [4]. Multi-scale modeling is a combination of structural and refined modeling. It involves building a simplified simulation of the entire structure with low-dimensional elements and a refined simulation of key parts with high-dimensional elements. This approach not only describes the overall response of the structure but also captures the local fine behavior, achieving a balance between accuracy and efficiency [5].

Unlike the Finite Element Method (FEM), the Finite Particle Method (FPM) is based on the Vector Form Intrinsic Finite Element Method and employs particle description and the concept of path unit to describe the deformation and motion of the continuum [6]. It calculates the pure deformation of an element by inverse motion, which has better stability in geometric nonlinearity. FPM has achieved excellent results in structural dynamic behavior [7, 8], fracture behavior [9, 10], mechanism motion behavior [11], contact and collision behavior [12], buckling and failure behavior [13, 14]. Recently, a

Copyright © 2023 by Junjie YAO, Yanfeng ZHENG and Yaozhi LUO. Published in the Proceedings of the IASS Annual Symposium 2023 with permission.

computational platform of FPM based on GPU parallel acceleration strategy had been developed [15]. FPM is suitable for solving complex structural nonlinear problems, and the coordinated distributing coupling proposed in this paper is based on this method.

The deformable interface method in the multi-point constraints (MPC) has been studied and improved by many current scholars. McCune [16] used Reissner bending and assumed stress distribution to construct constraint equations to achieve beam-solid and shell-solid coupling under geometric linear conditions. Yan [17] established a multi-scale deformable interface model for a single-branch beam using the stress equation for rectangular cross-sections. Wang [18] derived force and displacement constraint equations of the interface through the principle of virtual work and proposed a multi-scale constrained construction method applicable to geometric nonlinearity. However, most of these studies aiming at deformable interfaces are based on implicit finite element methods.

Multi-scale methods for explicit finite elements have also been investigated. Meguid [19] proposed a coupling method applicable to explicit finite elements based on the assumption of a rigid interface, but neglected the contribution of local bending moments and moments of inertia at the nodes of high-dimensional elements. Based on the concept of Vector Form Intrinsic Finite Element Method, Zheng [20] proposed a physical quantity transfer method and displacement constraints suitable for FPM multi-scale connections, and realized three types of connections: beam-solid, beam-shell, and shell-solid. However, the above studies have the limitation of planar assumptions and do not solve the stress concentration caused by rigid constraints.

In this paper, we propose a coordinated distributing multi-scale coupling method applicable to the explicit solution of FPM. The method adopts the concept of force distribution and displacement coordination to allow the coupling interface to deform. Firstly, the calculated interface force is distributed to the secondary particles according to the force balance relationship. Then, the displacements of the secondary particles are obtained through the motion equation. Finally, the motion of the major particle is calculated by applying the displacement coordination relationship.

In the following sections, we introduce the basic principle of FPM, followed by the principle of the coordinated distributing multi-scale coupling. Finally, we verify the effectiveness and stability of the method through several typical cases.

2. Basic principle of finite particle method

The basic principles of the FPM include particle description, path unit, deformation description, and motion control equations [6]. The particle description refers to the discretization of the geometry and spatial location of the structure using a finite number of particles as the smallest basic cell. The path unit is the time trajectory of the particle motion discretised into microsegments, and the properties of the structure represented by particles are kept constant within any path unit.

The deformation description mechanism is the core feature of FPM. The deformation increment of the solid micro-element in the path unit $(t \sim t + \Delta t)$ contains the rigid body displacement and pure deformation $(V_t \sim V_{t+\Delta t})$. FPM makes the particle undergo a virtual inverse motion to reach an intermediate form V_a to deduct the rigid body displacement, and treats the remaining part $(V_a - V_t)$ as pure deformation.

The motion equation of particle i follows the Newton's Second Law in each path unit, i.e.:

$$\boldsymbol{M}_i \ddot{\boldsymbol{x}}_i = \boldsymbol{F}_i^{ext} + \boldsymbol{F}_i^{int} \tag{1}$$

where $\boldsymbol{M}_i$ is the generalized mass matrix of particle i, $\ddot{\boldsymbol{x}}_i$ is the generalized acceleration vector of particle i, and $\boldsymbol{F}_i^{ext}$ and $\boldsymbol{F}_i^{int}$ are the generalized internal force and generalized external force on particle i, respectively. FPM uses an explicit central difference algorithm, and the displacement of the particle at

the moment $t + \Delta t$ is obtained from the increment of moment $t - \Delta t$ to moment t, and sub-steps are iterated continuously to complete the calculation of the whole progress.

3. Basic principle of coordinated distributing multi-scale coupling

In contrast to the rigid interface method, which treats the major-secondary particle system on the interface as a rigid body for calculation, the coordinated distributing coupling algorithm allows the system to deform relatively under the satisfaction of the displacement coordination relationship and force balance relationship in this paper. In this section, the displacement coordination and force balance relationship for the major-secondary particle system are described.

3.1. Major-secondary particle displacement coordination relationship

The major-secondary particle coupling system is defined in the multi-scale connection interface. The coupling of beam element and hexahedral solid elements is shown in Figure 1. In this paper, the particles in the interface are distinguished according to their dimensions, the beam particle in the low-dimensional element is defined as the Major particle, and the solid particle in the high-dimensional elements is defined as the secondary particle. The low-dimensional element and the high-dimensional element at the interface jointly characterize the motion and deformation of the connection interface.

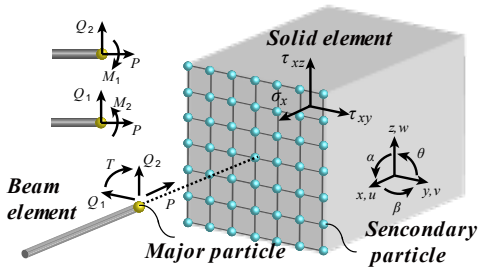


Figure 1. Major-secondary particle coupling system of beam-hexahedral solid

The linear displacement coordination relationship between the major and secondary particles can be expressed as:

$$f(\boldsymbol{x}_\alpha, \boldsymbol{x}_\beta) = \boldsymbol{x}_\alpha - \mathbf{C}\boldsymbol{x}_\beta = 0 \tag{2}$$

where $\mathbf{C}$ is the displacement coordination coefficient matrix of $6 \times 6n$, n is the number of secondary particles, $\boldsymbol{x}_\alpha$ is the 6×1 vector of major particle displacement, and $\boldsymbol{x}_\beta$ is the displacement vector consisting of $6n \times 1$ for each secondary particle. The form of imaginary displacement equation (2) , i.e.:

$$\delta f(\boldsymbol{x}_\alpha, \boldsymbol{x}_\beta) = \delta\boldsymbol{x}_\alpha - \mathbf{C}\delta\boldsymbol{x}_\beta = 0 \tag{3}$$

where $\delta\boldsymbol{x}_\alpha$ and $\delta\boldsymbol{x}_\beta$ are the imaginary displacement vectors for the major particle and secondary particle, respectively.

In large deformation problems, the coupling interface may rotate or produce non-negligible sectional deformation, and the displacement coordination coefficient matrix $\mathbf{C}$ is constantly changing between two adjacent path units, so the displacement coordination relationship is described nonlinearly, i.e.:

$$f(\boldsymbol{x}_\alpha, \boldsymbol{x}_\beta) = \boldsymbol{x}_\alpha - \mathbf{C}(\boldsymbol{x}_\beta)\boldsymbol{x}_\beta = 0 \tag{4}$$

Its imaginary displacement equation is expressed as:

$$\delta f(\boldsymbol{x}_\alpha, \boldsymbol{x}_\beta) = \delta\boldsymbol{x}_\alpha - \mathbf{C}^*(\boldsymbol{x}_\beta)\delta\boldsymbol{x}_\beta = 0 \tag{5}$$

$$\mathbf{C}^*(\boldsymbol{x}_\beta) = \frac{\partial \mathbf{C}(\boldsymbol{x}_\beta)}{\partial \boldsymbol{x}_\beta}\boldsymbol{x}_\beta + \mathbf{C}(\boldsymbol{x}_\beta) \tag{6}$$

where $\mathbf{C}^*(\boldsymbol{x}_\beta)$ is displacement incremental coordination matrix in the coupled interfaces.

3.2. Major-secondary particle force balance relationship

The force balance relationship between the major and secondary particles can be expressed as:

$$\boldsymbol{F}_\beta^I = -\mathbf{C}_f \boldsymbol{F}_\alpha^I \tag{7}$$

where $\boldsymbol{F}_\beta^I$ and $\boldsymbol{F}_\alpha^I$ are the vector of interface forces on the major particle and each secondary particle respectively, and $\mathbf{C}_f$ is the $6n \times 6$ force distribution matrix, which can be interpreted as the reverse of the interface forces on the major particle (i.e. $-\boldsymbol{F}_\alpha^I$) distributed to each secondary particle. the formulas for $\boldsymbol{F}_\alpha^I$, $\boldsymbol{F}_\beta^I$ are as follows:

$$\begin{aligned} \boldsymbol{F}_\alpha^I &= \mathbf{M}_\alpha \boldsymbol{a}_\alpha - \boldsymbol{F}_\alpha^e \\ \boldsymbol{F}_\beta^I &= \mathbf{M}_\beta \boldsymbol{a}_\beta - \boldsymbol{F}_\beta^e \end{aligned} \tag{8}$$

where $\mathbf{M}_\alpha, \mathbf{M}_\beta$ are the generalized mass matrixs of the major particle and the whole secondary particle set, $\boldsymbol{a}_\alpha$, $\boldsymbol{a}_\beta$ are the generalized acceleration vectors of the major particle and the whole secondary particle set; $\boldsymbol{F}_\alpha^e, \boldsymbol{F}_\beta^e$ are the element particle force vectors of the beam unit on the major particle and the element particle force vectors of all solid elements at the secondary particles, respectively. $\boldsymbol{F}_\alpha^e$ contains the axial force (P), the shear force in two directions (Q_1, Q_2), the torque (T) and the bending moment (M_1, M_2).

The force balance relationship between the major and secondary particles in implicit finite element method can be derived from the principle of virtual work [18]: the sum of the virtual work done by forces (stresses) of different types of elements in the interface should be equal to zero. For explicit dynamic calculations, the sum of the virtual work done by the forces (stresses) of different types of units in the interface should be equal to the work done by the unbalanced forces of the masses at the interface at the virtual displacement, i.e:

$$(\mathbf{M}_\alpha \boldsymbol{a}_\alpha - \boldsymbol{F}_\alpha^e)^T \delta \boldsymbol{x}_\alpha = -\left(\mathbf{M}_\beta \boldsymbol{a}_\beta - \boldsymbol{F}_\beta^e\right)^T \delta \boldsymbol{x}_\beta \tag{9}$$

Under the linear displacement constraint, substituting the displacement coordinated imaginary displacement in the form $\delta \boldsymbol{x}_\alpha = \mathbf{C}\delta \boldsymbol{x}_\beta$, and approximately removing $\delta \boldsymbol{x}_\beta$ as it applies to arbitrary imaginary displacements, we obtain:

$$\mathbf{M}_\beta \boldsymbol{a}_\beta - \boldsymbol{F}_\beta^e = -\mathbf{C}^T(\mathbf{M}_\alpha \boldsymbol{a}_\alpha - \boldsymbol{F}_\alpha^e) \tag{10}$$

Comparing equation (15) with equation (7), it can be seen that under the linear displacement constraint, the force distribution matrix $\mathbf{C}_f$ is a transpose of the displacement coordination matrix $\mathbf{C}$, i.e.:

$$\mathbf{C} = {\mathbf{C}_f}^T \tag{11}$$

Substituting $\delta \boldsymbol{x}_\alpha = \mathbf{C}^*(\boldsymbol{x}_\beta)\delta \boldsymbol{x}_\beta$, under the nonlinear displacement constraint and approximately removing $\delta \boldsymbol{x}_\beta$, the same can be obtained as:

$$\mathbf{C}^*(\boldsymbol{x}_\beta) = {\mathbf{C}_f}^T \tag{12}$$

The linear constraint is essentially a special case of the nonlinear displacement constraint, and the displacement incremental coordination matrix of Eq. (17) is degenerated to the displacement coordination matrix to obtain Eq. (16). It can be seen that there is a transposition relationship between

the force distribution matrix and the displacement increment coordination matrix for both linear and nonlinear constraints.

3.3. Force distribution for secondary particles

The interfacial forces can be assigned to each secondary particle based on the force balance relationship. The study of deformable interface method has proposed various ways to implement the interface force distribution, including temperature stress method [1], stiffness matrix method [18], and stress distribution weight method [16]. In this study, based on the local coordinate system $\boldsymbol{\Omega}$ of the coupled interface, the assumption that the components are independent of each other in the distribution of the interface force in the stress distribution weight method is adopted:

$$\mathbf{C}_{f_i} = [\boldsymbol{c}_{i,P} \;\; \boldsymbol{c}_{i,Q_1} \;\; \boldsymbol{c}_{i,Q_2} \;\; \boldsymbol{c}_{i,T} \;\; \boldsymbol{c}_{i,M_1} \;\; \boldsymbol{c}_{i,M_2}] \tag{13}$$

$$\mathbf{C}_f = [\mathbf{C}_{f_1} \;\; \mathbf{C}_{f_2} \;\; \mathbf{C}_{f_3} \;\; \cdots \;\; \mathbf{C}_{f_n}] \tag{14}$$

where $\boldsymbol{c}_{i,Y}$ denotes the vector of force distribution coefficients (6×1) from particle i under load component Y, corresponding to the six components of force distribution. According to equation (14), $\mathbf{C}_{f_i}$ of each secondary particle is integrated as the force distribution matrix $\mathbf{C}_f$.

3.4. Displacement solution for major particle

After obtaining the force assigned for the secondary particles, the displacement of the secondary particles and major particle can be solved. The displacement increments $\{d\widehat{\boldsymbol{u}}_{Si}, d\widehat{\boldsymbol{\theta}}_{Si}\}$ for secondary particles in the interface coordinate system can be obtained after the calculation by the central difference method of FPM. In order to solve the displacement of the major particle, it is assumed that the center of secondary-particle set is connected with the major particle by a rigid beam, and the displacement of the center of secondary-particle set is calculated according to the displacement increment of each secondary particle, and then the displacement of the major particle is solved according to the motion of the rigid beam.

Based on the transposition relation of equation (12), the force distribution matrix $\mathbf{C}_f$ is transformed into the displacement increment coordination matrix $\mathbf{C}^*$, and the displacement increments $\{d\widehat{\boldsymbol{u}}_C, d\widehat{\boldsymbol{\theta}}_C\}$ from the center of secondary-particle set in the interface coordinate system are calculated as follows:

$$\begin{bmatrix} d\widehat{\boldsymbol{u}}_C \\ d\widehat{\boldsymbol{\theta}}_C \end{bmatrix} = \mathbf{C}^* d\widehat{\boldsymbol{u}}_S = \sum_{i=1}^{n} \mathbf{C}_{f_i}^T \begin{bmatrix} d\widehat{\boldsymbol{u}}_{Si} \\ d\widehat{\boldsymbol{\theta}}_{Si} \end{bmatrix} \tag{15}$$

After obtaining the displacement $\{\boldsymbol{u}_{C,t+\Delta t}, \boldsymbol{\theta}_{C,t+\Delta t}\}$ from the center of secondary-particle set at the moment $t + \Delta t$, the displacement $\{\boldsymbol{u}_{M,t+\Delta t}, \boldsymbol{\theta}_{M,t+\Delta t}\}$ of the major particle at the moment $t + \Delta t$ can be solved according to the translation and rotation of the rigid beam:

$$\begin{aligned} \boldsymbol{u}_{M,t+\Delta t} &= \boldsymbol{u}_{C,t+\Delta t} + \boldsymbol{u}_{C,0} + \boldsymbol{d}_{M,t+\Delta t} - \boldsymbol{u}_{M,0} \\ \boldsymbol{\theta}_{M,t+\Delta t} &= \boldsymbol{\theta}_{C,t+\Delta t}\,, \boldsymbol{d}_{M,t+\Delta t} = \boldsymbol{R}\big(d\boldsymbol{\theta}_{C,t+\Delta t}\big)\boldsymbol{d}_{M,t} \end{aligned} \tag{16}$$

where $\boldsymbol{u}_{C,0}$ and $\boldsymbol{u}_{M,0}$ are the initial position vectors of the center of the secondary-particle set and major particle, respectively, $\boldsymbol{d}_{M,t}$ is the position vector of the major particle relative to the center of the secondary-particle set at time t, and $\boldsymbol{R}\big(d\boldsymbol{\theta}_{C,t+\Delta t}\big)$ is the three-dimensional rotation matrix.

Note that the interface coordinate system is updated by the rotation matrix $\boldsymbol{R}\big(d\boldsymbol{\theta}_{C,t+\Delta t}\big)$ between adjacent time steps, and the force assignment matrix $\mathbf{C}_f$ needs to be recalculated based on the position from the secondary particles in the new interface coordinate.

4. Numerical example analysis

4.1. Beam-plane element coupling

In order to verify the effectiveness of coordinated distributing coupling for beam-plane element connections, a rectangular cantilever beam as shown in Figure 2 is used as an analysis example (mm). The cantilever beam is unit thickness, using isotropic linear elastic material, $E = 2.1 \times 10^5$MPa, $v = 0.3$, $\rho = 7850\text{kg/m}^3$, and the free end is subjected to a vertical concentrated load F.

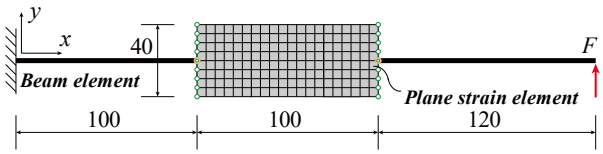
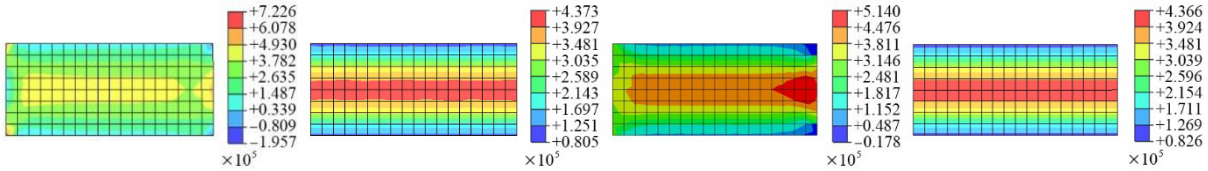


Figure 2. Coupling for beam-plane: geometric schematic

The time step is $\Delta t = 1 \times 10^{-6}$s. The stress distribution form of equation (17) is selected to build a coordinated distributing coupling model, and the fully refined model, FPM dynamic coupling model[20] and Abaqus distributing coupling model are established for comparison. The element number of fully refined model is 512, and the element number of the above three multi-scale models is 171.

$$\sigma_x = \frac{P}{A} + \frac{M_1 z}{I}, \tau_{xy} = \frac{3Q_2}{2A}\left(1 - \frac{4z^2}{h^2}\right) \tag{17}$$

where A is the interface area, I is the interface moment of section, z is the distance from the mass point in the interface to the central axis, and h is the interface height.



(a) (b) (c) (d)

Figure 3. Coupling for beam-plane: shear stress distribution of plane element under small deformation: (a) FPM dynamics coupling, (b) coordinated distributing coupling, (c) Abaqus distributing coupling and (d) fully refined

The shear stress distribution results of the plane strain element when the free end $F = 12\text{kN}$ (small deformation) for each method are shown in Figure 3. It should be noted that compared with the fully refined model, the multi-scale model lacks half of the elements participating in the stress weighting of the particles at the coupling interface. Therefore, in order to ensure the effectiveness of the comparison, the stress cloud plot comparison area starts from the second row of elements closest to the coupling interfaces. The FPM dynamic coupling model has obvious stress concentration at the corners; the Abaqus distributing coupling model changes uniformly in the middle, but the stress concentration still appears near the interfaces; the shear stress of this method is basically unchanged along the beam axis direction, it has the highest degree of agreement with the fully refined model, and the relative error of the maximum shear stress is 0.16%. The comparison verifies the applicability of the method in beam-plane element coupling under small deformation.

4.2. Beam-shell element coupling

In order to verify the effectiveness of the coordinated distributing coupling for the beam-shell element connection, a cantilever thin plate example is shown in Figure 4. The left end of the cantilever thin plate is fixed, the shell element is coupled with the beam element at the middle interface, and the other end is

subjected to concentrated force or bending moment (dimensions are in mm). Isotropic linear elastic material is used, $E = 120\text{MPa}$, $v = 0.3$, $\rho = 5000\text{kg/m}^3$, and the thickness of the sheet is 10mm.

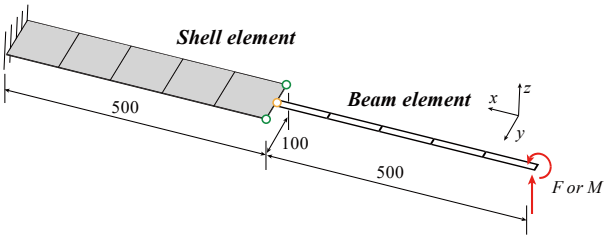
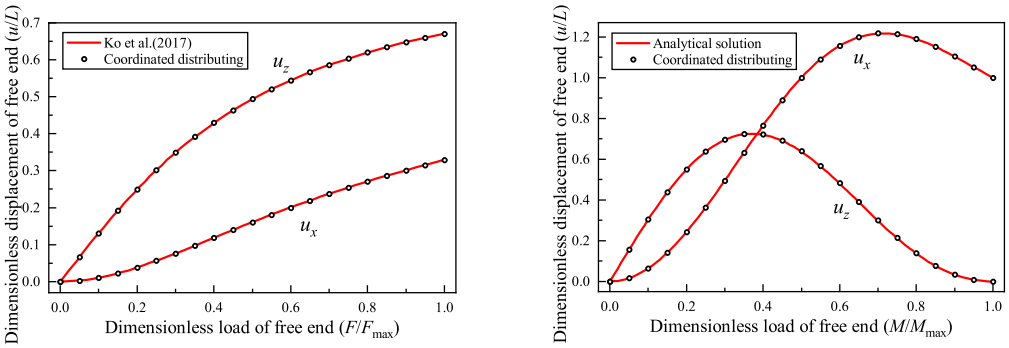


Figure 4. Coupling for beam-shell: geometric schematic

The model adopts FPM-S4 thin shell element, the time step $\Delta t = 3 \times 10^{-4}\text{s}$, and the force distribution matrix of the coupling part is calculated in the form of regular stress distribution. The maximum value of the vertical concentrated force F on the free end is set $F_{\max} = 4EI/L^2$; the maximum value of the concentrated moment M is set $M_{\max} = 2\pi EI/L$.



(a) (b)

Figure 5. Coupling for beam-shell: load displacement curve at the free end: (a) concentrated force along z axis and (b) concentrated moment in positive direction around y axis

The load-displacement curve of the free end under the vertical concentrated force is shown in Figure 5(a). It is in good agreement with the results of the fully shell model using MITC9 elements in literature [21], which verifies the effectiveness of the coupling method in beam-shell connection processing. The load-displacement curve of the free end under concentrated moment is shown in Figure 5(b). The matching effect with the analytical solution is also ideal, which further verifies that the method can effectively solve the connection problem of thin shells with large deformation.

4.3. Beam-solid element coupling

In order to verify the effectiveness of the coordinated distributing coupling for the beam-solid element connection, an example of a rectangular beam fixed at both ends (dimensions in mm) is used as shown in Figure 6, using isotropic linear elastic materials, $E = 2.1 \times 10^3\text{MPa}$, $v = 0.2$, $\rho = 7850\text{kg/m}^3$.

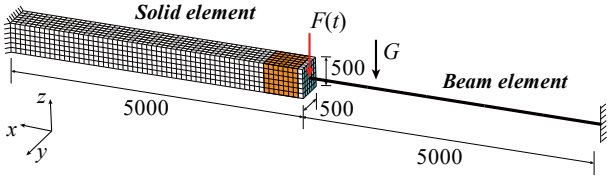
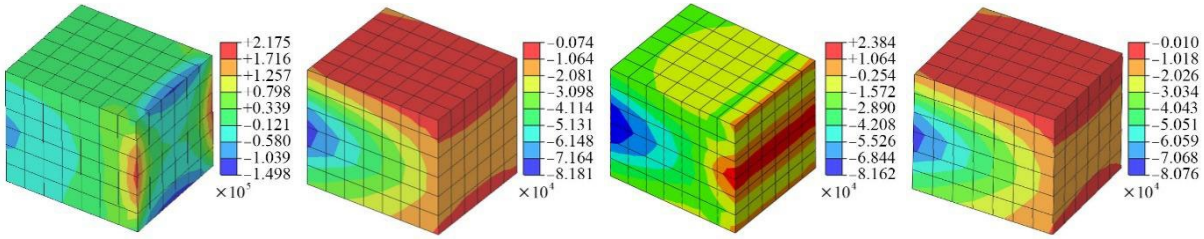


Figure 6. Coupling for beam-solid (bending): schematic

In order to consider the coupling effect of the method under the action of gravity, the gravity load is applied to the whole structure, the gravitational acceleration is taken as $9.8\text{kg} \cdot \text{m/s}^2$, the time step is

taken as $\Delta t = 1 \times 10^{-4}$s, the regular stress distribution form of equation (17) is chosen to establish the coordinated distributing multi-scale model. The fully refined model, the FPM dynamics coupling model and the Abaqus distributed coupling model are also developed for comparison. The element number of the fully refined model is 4320, and the element number of the multi-scale model is 2165.

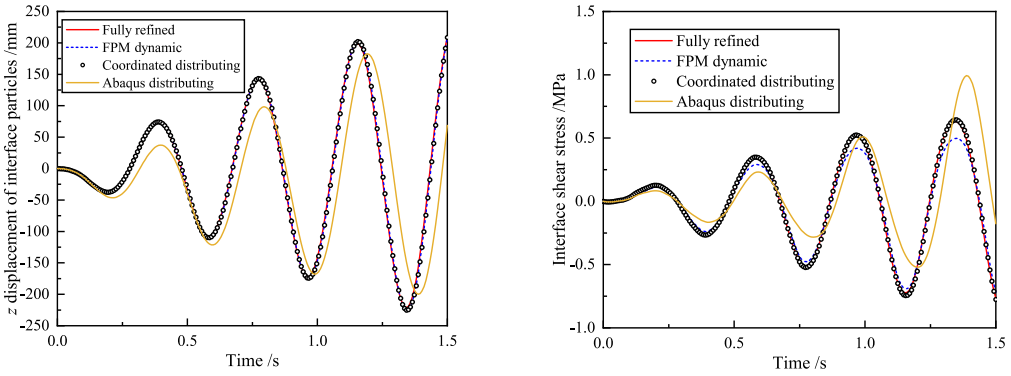


(a) (b) (c) (d)

Figure 7. Coupling for beam-solid (bending): shear stress distribution at the interface under gravity: (a) FPM dynamics coupling, (b) coordinated distributing coupling, (c) Abaqus distributing coupling and (d) fully refined

Figure 7 shows the results of shear stress distribution of solid elements at the coupling interface (the highlighted area in Figure 6). The FPM dynamic coupling has a significant stress concentration at the outer boundary of the interface; the Abaqus distributing coupling has the same problem at the top and bottom boundaries and the neutral axis position; the stress results of the coordinated distributing coupling have a parabolic distribution at the interface, and the values are closer to those of the fully refined model, with the relative error is 1.30%. This comparison indicates that the method is applicable in the case of beam-solid element coupling.

In order to verify the coupling effect of the method in dynamic problems, the gravity load is changed to a vertical time history load at the mid-span position, $F(t) = 5 \times 10^4 \sin(5\pi t)$N, and the mass damping coefficient $\alpha = 0.05$, the calculation time is 1.5s. The time-history curves of secondary particle displacement and shear stress at the interface are shown in.



(a) (b)

Figure 8. Coupling for beam-solid (bending): z displacement and shear stress curve at the interface particle under time history load: (a) z displacement curve, (b) shear stress curve

It is obvious to find that the natural frequency of the Abaqus distributing coupling model is significantly smaller than that of the fully refined model from Figure 8(a), and the displacement error is remarkable, because Abaqus distributing coupling method may weaken the coupling stiffness at the interface. The displacement results of the coordinated distributing coupling model and the FPM dynamic coupling model are in good agreement with the fully refined model. For the interface shear stress curve shown in Figure 8(b), the stress results of the Abaqus distributed coupling model are also significantly different from those of the fully refined model due to the small natural frequency; The errors on the peak values

are 20.87% and 2.92%, respectively, reflecting that the method has a higher accuracy advantage in the stress calculation of beam-solid coupled dynamic problems.

5. Conclusion

Based on the basic theory of the Finite Particle Method, this paper proposes a coordinated distributing coupling method for explicit solution to create the interaction between major particle and secondary particles. Compared with other multi-scale explicit methods, the deformability of interface is considered and the displacement coordination equation is adopted instead of the averaging process in the proposed method, and the conclusions are as follows:

(1) In static problems, compared with FPM dynamic coupling and Abaqus coupling, the stress results of the coordinated distributing coupling method are closest to the fully refined model, especially in the direction of the shear stress, the stress concentration problem caused by the sudden changes at the coupling interface is effectively solved.

(2) In dynamic problems, the displacements and stress results of the coordinated distributing coupling model are consistent with the fully refined model, especially in the interface shear stress of the beam-solid coupling, the error is still controlled within 3.0%, which is obviously less than those of FPM dynamic coupling model and Abaqus coupling model. The comparison reflects the high calculation accuracy of the method in dynamic problems.

The coordinated distributing coupling method proposed in this paper can be applied to multi-scale modeling of actual engineering, so as to obtain more accurate local information while grasping the overall characteristics of the structure. Further research will conduct an in-depth discussion on the development of coupling interface plasticity.

Acknowledgements

This research is based on the National Natural Science Foundation of China, No. 52238001. The authors would like to express the gratitude to the FPM general computing platform, which belongs to the Space Structure Research Center of Zhejiang University, for providing invaluable software support during this study.

References

[1] K. W. Shim, D. J. Monaghan and C. G. Armstrong. “Mixed dimensional coupling in finite element stress analysis,” *Engineering with Computers*, vol. 18, no. 3, pp. 241-252, 2002.

[2] W. Lu, Y. Cui and J. Teng. “Mixed-dimensional coupling method for box section member based on the optimal stress distribution pattern,” *Measurement*, vol. 131, pp. 277-287, 2019.

[3] Y. D. Zhang, X. W. Cheng, Y. Li and H. L. Sun. “A detailed numerical analysis for progressive collapse of concrete frame substructures strengthened with strips,” *Engineering Mechanics*, vol. 39, no. 12, pp. 151-164, 2022.

[4] Y. L. Ding, A. Q. Li, D. S. Du and T. Liu. “Multi-scale damage analysis for a steel box girder of a long-span cable-stayed bridge,” *Structure and Infrastructure Engineering*, vol. 6, no. 6, pp. 725-739, 2010.

[5] P. Mata, A. H. Barbat and S. Oller. “Two-scale approach for the nonlinear dynamic analysis of RC structures with local non-prismatic parts,” *Engineering Structures*, vol. 30, no. 12, pp. 3667-3680, 2008.

[6] Y. Z. Luo, Y. F. Zheng, C. Yang, et al. “Review of the finite particle method for complex behaviors of structures,” *Engineering Mechanics*, vol. 31, no. 8, pp. 1-7, 2014.

[7] Y. Yu, X. Xu and Y. Z. Luo. “Dynamic nonlinear analysis of structures based on finite particle method,” *Engineering Mechanics*, vol. 29, no. 6, pp. 63-69+84, 2012.

[8] X. H. Lin, Y. Z. Luo, J. Z. Tang, et al. "A fiber beam element for the finite particle method considering shear and torsion deformation," *Engineering Mechanics*, vol. 39, no. 5, pp. 34-43, 2022.

[9] Y. Yu and Y. Z. Luo. "Structural collapse analysis based on finite particle method I: basic approach," *Journal of Building Structures*, vol. 32, no. 11, pp. 17-26, 2011.

[10] J. Z. Tang, W. Wang, Y. F. Zheng, at el. "Interface failure and contact analysis based on parallelized finite particle method," *Engineering Mechanics*, vol. 38, no. 6, pp. 24-35, 2021.

[11] Y. F. Zheng, C. Yang, L. Liu, et al. "Dynamics analysis of planar mechanism with revolute joint clearance based on finite particle method," *Engineering Mechanics*, vol. 37, no. 3, pp. 8-17, 2020.

[12] W. Wang, Y. F. Zheng, J. Z. Tang, et al. "Parallel Algorithm for 2D Large Deformation Contact Problems Using the Finite Particle Method," *Computer Modeling in Engineering & Sciences*, vol. 129, no. 2, pp. 595-626, 2021.

[13] P. F. Zhang, Y. Z. Luo and C. Yang. "Buckling analysis of thin shell using the finite particle method," *Engineering Mechanics*, vol. 34, no. 2, pp. 12-20, 2017.

[14] C. Yang, Y. Z. Luo and Y. F. Zheng. "Large deformation analysis of orthotropic membranes using the finite particle method," *Engineering Mechanics*, vol. 36, no. 7, pp. 18-29, 2019.

[15] J. Z. Tang, Y. F. Zheng, C. Yang, et al. "Parallelized Implementation of the Finite Particle Method for Explicit Dynamics in GPU," *Computer Modeling in Engineering & Sciences*, vol. 122, no. 1, pp. 5-31, 2020.

[16] R. W. McCune, C. G. Armstrong and D. J. Robinson. "Mixed-dimensional coupling in finite element models," *International Journal for Numerical Methods in Engineering*, vol. 49, no. 6, pp. 725-750, 2000.

[17] F. Yan, W. Chen and Z. Lin. "Prediction of fatigue life of welded details in cable-stayed orthotropic steel deck bridges," *Engineering Structures*, vol. 127, pp. 344-358, 2016.

[18] F. Y. Wang, Y. L. Xu and W. L. Qu. "Mixed-dimensional finite element coupling for structural multi-scale simulation," *Finite Elements in Analysis and Design*, vol. 92, pp. 12-25, 2014.

[19] R. J. Ho, S. A. Meguid, Z. H. Zhu, R. G. Sauvé. "Consistent element coupling in nonlinear static and dynamic analyses using explicit solvers," *International Journal of Mechanics and Materials in Design*, vol. 6, no. 4, pp. 319-330, 2010.

[20] Y. F. Zheng and Y. Z. Luo. "Multi-scale fine analysis based on the finite particle method," *Engineering Mechanics*, vol. 33, no. 9, pp. 21-29, 2016.

[21] Y. Ko, P. S. Lee, K. J. Bathe. "A new MITC4+ shell element," *Computers & Structures*, vol. 182, pp. 404-418, 2017.

IASS 2023
July 10–14 Melbourne
Integration of Design and Fabrication

Proceedings of the IASS Annual Symposium 2023
Integration of Design and Fabrication
10–14 July 2023, Melbourne, Australia
Y.M. Xie, J. Burry, T.U. Lee and J. Ma (eds.)

Optical parametric component referencing for the facilitated prefabrication of timber wall elements

Felix SCHMIDT-KLEESPIES[a,*], Laurenz ANDRITZ[a], Cristoph DIJOUX[a], Alexander STAHR[a]

[a,*] Leipzig University of Applied Sciences,
04277 Leipzig, Karl-Liebknecht-Straße 132
felix.schmidt-kleespies@htwk-leipzig.de

Abstract

A guidance system for three-dimensionally accurate projections of timber frame construction elements was developed. Employing augmented reality (AR) glasses, interactive assembly instructions are projected onto the work environment of a timber construction company and integrated into their operational workflow. The purpose of this was to restructure the conventional assembly process utilising paper plans into a semi-digital, temporally relevant and accelerated process. The necessary geometry data was readily available and could be exported by current timber construction-specific CAD systems. The component information and layering sequence were configured for the glasses using an AR toolkit. Compared to preceding systems, the developed solution applies a successive relevant temporal filter as well as a fitting algorithm that refers to several localisation markers. Specifically developed software facilitates the levelling of the projection plane, measuring functions as well as approval and monitoring functions of individual components. According to practical trial runs of the assembly process, it was found that the project significantly improved the positioning of the individual timbers, the fastening of the sheeting and the insulation panels, while also reducing the extent of accumulative errors. Further development also managed to include non-conventional, free-form geometries. Tests revealed that the developed solution did not require any extensive training and its application could be considered intuitive.

Keywords: prefabricated timber structures, digital transformation, augmented reality, timber frame, design for manufacturing and assembly, precision, projection

1. Introduction

The duration of the manufacturing process of wooden panel elements strongly depends on the technical equipment of the respective timber construction company [1, 2]. The joint research project OptiPaRef (funded by the BMEL within the ZIM funding program 2021/2022) has therefore set itself the goal of increasing manufacturing efficiency and process reliability in the manual production of timber frame construction elements by making the low-investment technology of augmented reality (AR) usable for timber construction. To this end, the FLEX research group led by Prof. Dr.-Ing. Alexander Stahr has developed an assistance system for the holographic display of complex manufacturing information.

All relevant data is already defined by timber engineers; afterwards the information exchange takes place via a predefined interface from the CAD program [1]. The core idea of the project is to make the already existing planning data available to the carpenters in the workshop with the help of optical-parametric component referencing. To this end only the information required for the current work step is displayed and scaled directly in the carpenter's field of vision using AR glasses. At the same time, quality assurance in production is significantly simplified by the AR-based documentation of already placed elements.

Copyright © 2023 by Felix SCHMIDT-KLEESPIES, Laurenz ANDRITZ, Cristoph DIJOUX and Alexander STAHR. Published in the Proceedings of the IASS Annual Symposium 2023 with permission.

2. Timber element construction in the SME sector

Traditional timber frame construction is based on prefabrication of large building elements, which are only assembled at the construction site. Due to the multi-layered requirements (statics, thermal insulation, sound insulation, etc.), wood panel construction has a high complexity in its overall structure as well as in its individual elements [1]. This requires a considerable manufacturing effort, which must be implemented in a secure production process. Within the market sector, a strong price competition can be generated by few companies that are automating their manufacturing in portal processing machines. Such large-scale equipment requires considerable investment, which is not manageable for medium-sized companies [2], In general, large production facilities and machinery are not necessary for the manufacturing process. In Germany the large majority of timber construction companies is employing less than 20 employees, who are joining timber elements manually in their workshops [3].

Factory planning for the manual production of wood panel elements takes place digitally with the help of wood construction-specific, menu-driven CAD software. This software is capable of generating the plans for the assembly of the panel elements as well as the control data for numerically controlled joinery systems or nailing bridges. In the company of the project partner Holzbau Lepski, ready-tied lumber and wood-based panels (see Figure 1) have so far been laid out and joined in a manual process. The information from the digital planning is stored on printed plans and transferred and checked from these analogously. For marking out complex geometries or free-form shapes, such as those found in bat dormers, it is necessary to print dimensionally accurate copies of corresponding partial sections of the construction drawings and to arrange them over the work piece. This analogous intermediate step is very time-consuming.

An existing solution for the paperless transfer of assembly information are laser systems permanently installed above the work table, which project the component contours onto the work surface in two-dimensional projections. However, the projections do not offer the desired possibility of information retrieval and are associated with a location-bound assembly, from which the research project would like to free itself [4].



Figure 1. Person mounting a timber frame

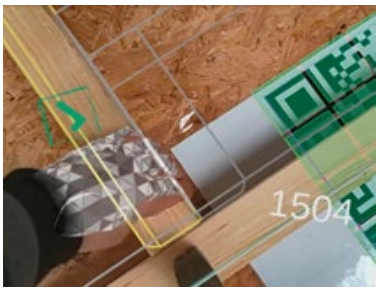


Figure 2. Positioning-outlines, localisation marker, release button and object ID

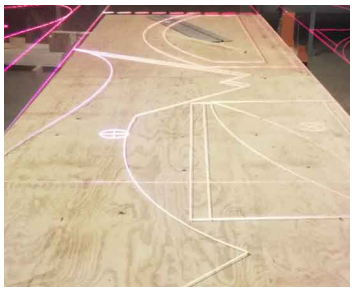


Figure 3. AR-Projection of free-form building parts onto LVL-boards

3. AR glasses instead of paper plans

In order to overcome these obstacles and to be able to offer an innovative, low-investment alternative, the project partners studied and further developed the application of AR glasses in the field of timber element construction [6, 7]. The overall goal was to extend the chain of digital planning data into the manufacturing process. The core of the work was therefore the description of a corresponding workflow and the development of interfaces, which ensure the availability of all information necessary for the assembly without time-consuming conversions.

This development was based on the HoloLens2 by Microsoft - AR glasses that use time-of-flight cameras to orient and locate themselves in space. With the help of a device-specific AR toolkit, special functionalities could be programmed to make the planning data already available in digital form directly

and intuitively available to the workers during the production of the panels. Based on this, an action-oriented information structure was developed, which is based on geometry projection.

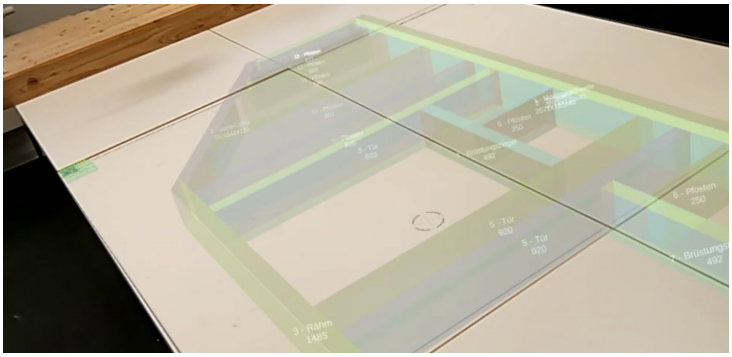


Figure 4. Geometry projection

In addition to the pure projection of target positions, a measuring tool was developed that processes information from the positions of a measuring marker (coordinates, lengths and angles) as well as an approval tool that enables paperless logging of the manufacturing process by means of gesture-controlled command input.

The multi-layered and written instructions that were initially envisaged proved not to be effective, as they severely restrict the worker's approach and his room for maneuver. Instead, the instructions are provided in purely geometric "information layers". Furthermore, it has proven useful to allow jumping back in the information sequences. This implies a shift from the term "instruction for action" to "possibility for action".

4. Setup and turning table

An element to be manufactured consists of a squared timber frame, which on both sides is clad with insulation, foils and boarding. This requires to turn the element. Due to the large dimensions, heavy weights and low stiffness of the unsheeted frame, a manual turning operation carries a high risk of damage or injury. Therefore, a butterfly turning table is used for this step, which consists of two adjacent assembly tables, a feeder table and a receiving table.



Figure 5. Butterfly turning table (feeder table)

The feeder table has a stop bar in the longitudinal direction and a clamping device in the transverse direction, by which the wooden frame is held in position. The individual parts of the wooden frame are positioned in it and joined together. This is followed by the planking and machining of the visible upper side of the frame with nailing or stapling machines; in addition, openings and holes can be cut in the planking.

Once the planking of one side is completed, the element is transferred to the receiving table by means of a hydraulically operated folding mechanism. To prevent collisions, the table has neither a stop nor a clamping device. These are not necessary for the dimensional stability of the element, as the frame is already connected. The second side can now be planked and machined here.



Figure 6. Sequence of butterfly turning table in action

5. Technical implementations

The FOLOGRAM toolkit (www.fologram.com) was used to control and program the HoloLens. FOLOGRAM is a mixed reality application that provides tools for processing 3D data and interpreting environmental data (e.g., QR markers, hands, spatial map, etc) on devices with autonomous location (e.g., smartphones, tablets, AR glasses). As its base, FOLOGRAM uses GRASSHOPPER, a node-based extension for parametric modeling under RHINOCEROS (www.rhino3d.com).

5.1. Precision of the Hololens

When switched on, the HoloLens generates a coordinate system from its current position. This means that the resulting coordinate system is unpredictable; however, the origin of the coordinate system can optionally be bound to a QR marker [4, 5]. From the sensor data, an environment model is created with respect to the coordinate system, the so-called spatial map, in which the HoloLens can locate itself. The spatial map is permanently updated. When changing the position of the glasses, minimal deviations in the assignment of the spatial map to the coordinate system occur due to the noise of the sensor data. This results in visible shifts and rotations of the coordinate system over time, the so-called drift. The longer and more widespread the movements, the more drift occurs [6, 7].

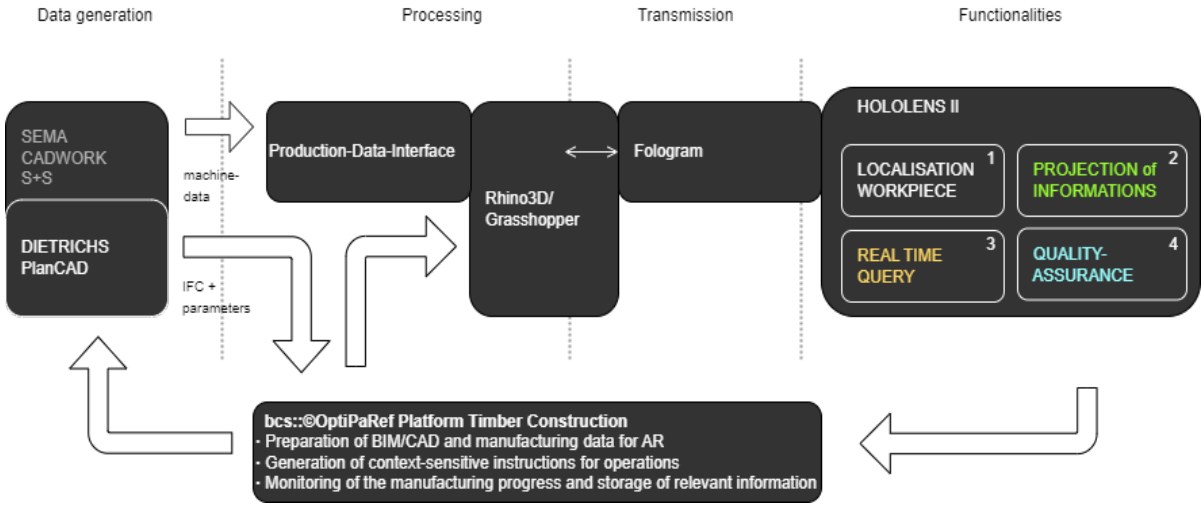


Figure 7. Data flow and required components

So the HoloLens-internal coordinate system is not suitable for millimeter-accurate positioning without a correction device (e.g. WLT tools for Unity) [8]. In addition, length measurements in space result in deviations of up to 1%. Measurements at different times result in different deviations. Therefore, precise position determination must be based on exactly defined reference points.

5.1.1 Positioning on the feeding table

Precisely measured, abrasion-resistant localization markers are attached to the feeding table, which are recognized by the HoloLens and matched with stored marker positions. Thus, the exact position and the scaling factor of the feeder table are unambiguous. Deviations from the target positions are displayed on a scale next to the marker. In this way, deviations caused by drift can be detected and corrected by re-reading the markers. The deviation of the projection to the physical components could be kept below 2mm over a length of the work table of 8 meters. This accuracy was considered sufficient for timber construction by project partner Lepski.



Figure 8. Abrasion-resistant localization markers

The markers are weighted in favor of the most recently read markers to account for the temporal effects of drift. To prevent all markers on the table from being covered by components, there are 2 markers placed on top of the stop bar at the end of the working area, which is usually never covered.

5.1.2. Positioning on the receiving table

After the turning process, the turned element rests in undetermined position on the receiving table. For integration into the digital workflow, however, its position must be precisely determined. This is achieved with the turning table markers that are placed on the corners of the turned element and read in. The lower corner closest to the stop bar of the feeder table defines the origin, the other corners define directions of the element. Since the four corners are oriented in different directions, the corresponding corner can be recognized from the marker orientation.

The positions of the markers on the receiving table are stored relative to the feeder table so that they can be removed again. This prevents the markers from being irreversibly buried under the plates mounted above them. To correct the drift, a marker could be read in at the encoder table.

5.1.3. Coordinate systems

The final positioning of the element takes place in relation to the clamping device integrated in the feeding table. The dimensionally accurate mapping of the element to be produced on the assembly tables requires the following coordinate spaces to be linked:

- HoloLens-internal (CS1), subject to drift
- CAD-related (CS2), origin of the geometry model
- Work tables (feeder and receiving table) (CS3), at a defined base point

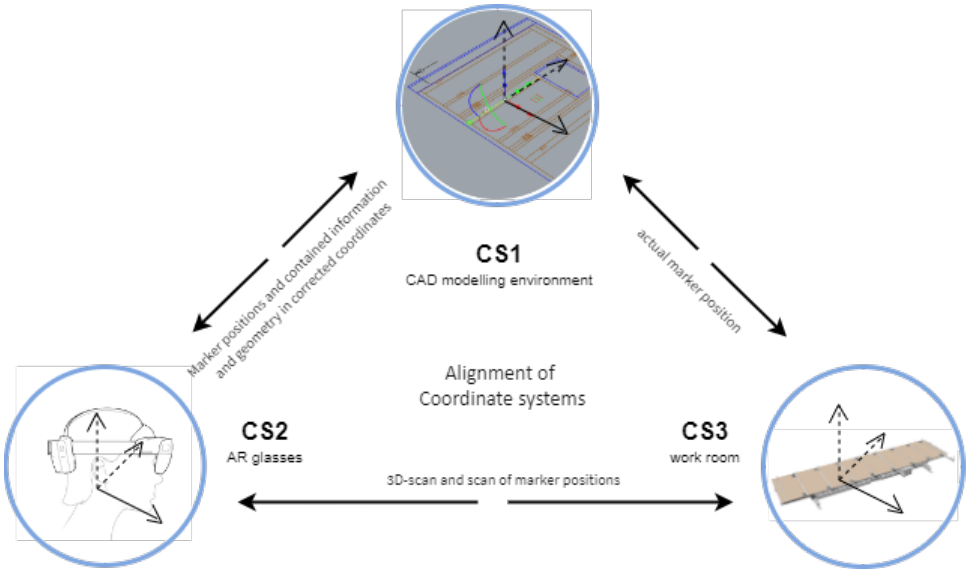


Figure 9. Relations between the coordinate

5.2. Interaction

The individual elements and functions that make up the system are shown below:

5.2.1. QR Marker Labels

A QR code ("Quick Response Code") is a two-dimensional barcode with integrated error correction, developed by the Japanese company Denso Wave in 1994. The HoloLens can determine the position of the markers in space as well as read out the information encoded in them. Depending on the strength of the error correction, even partially hidden markers can be read. The accuracy in determining the position of the markers varies with the environmental conditions (distance of the HoloLens to the marker, incidence of light, contrast). When observing a marker with the HoloLens, a wobbling of its image can be detected. This noise can be mitigated by calculating a mean value (median) from the last 25 marker positions determined.



Figure 10. Position marker, measure marker



Figure 11. Display of the user's hands

5.2.2. Control by hands

The HoloLens recognizes the user's hands and displays them in real time as a separate graphical element in the hologram. Coordinates can be extracted and processed from the geometry of the hand and the individual fingers, e.g. the position of the fingertip of a particular finger. If a fingertip comes close enough to a defined point, e.g. to the image of a control element, an action is triggered. To select an element, two fingertips are placed near the element in question.

5.2.3. Model Data

For the transfer of data from the element construction CAD program, an interface was casted which would fulfill the following requirements:

- universal, supported by as many CAD programs as possible
- complete, with all production-relevant information
- text-based for easier evaluation and, if necessary, extension

The WUP format from the Homag/Weinmann Company met all these requirements. It was especially developed for element construction systems. It is ASCII based and well documented.



Figure 12. 3D geometry of a bat dormer

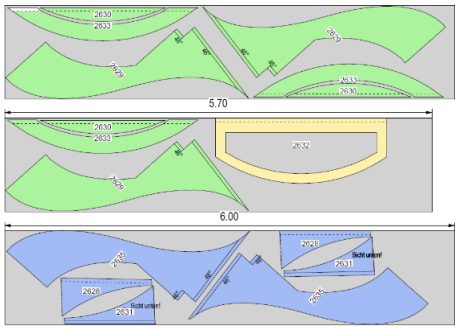


Figure 13. Placement of the curves within the measurements of the sheets

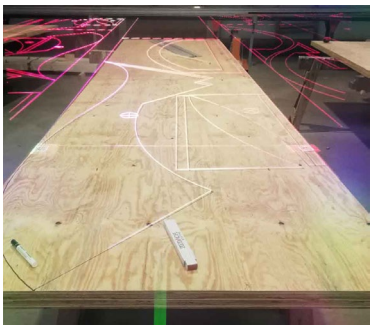


Figure 14. Projection of the outlines via AR device

In order to be able to use the positioning system for geometries other than wood-frame construction elements, a second projection interface was programmed which makes it possible to place any geometries from RHINOCEROS on the feeder table. It is designed only for tracing the outline of freeform geometries but not for interaction. For test purposes, the cut curves of a bat dormer were projected and drawn on raw boards (see Figure 14). The resulting measurements of the cut out building parts were all within the required range of precision.

6. Usage

6.1. Positioning and labeling

The original idea of displaying the element edges as lines along which the components can be aligned did not prove to be effective, since the line thickness must represent several millimeters for sufficient recognizability. Therefore, individual parts were broken down into their individual surfaces, which were colored differently. The component edges could thus be precisely positioned along the edges of the color transitions.



Figure 15. Coloured line display style



Figure 16. White line display style

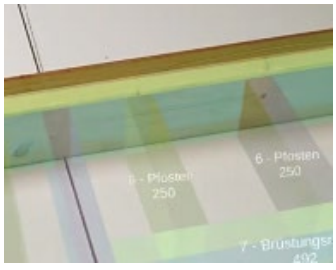


Figure 17. Surface display style

Since most of the individual parts have box geometry, 3 colors would be sufficient; i.e. one for each main plane. However, since there are also parts with oblique sections and individual parts connecting each other, 4 colors are used instead. Each part is randomly assigned 3 colors for the main planes and the fourth for slants. By using 4 colors, the probability that 2 coplanar faces of adjacent parts have the same color is reduced to 1:4. However, if situations arise where this is not sufficient, the random seed can be manually changed.

The component number and, if required, its designation are displayed to represent the individual part. It can be set whether the label is displayed only for the active part or for all parts. Machining operations are displayed with the values required by the operator, e.g. drilling diameter or setting values for the nailing machine.

6.2. Measuring

There is a separate QR marker for measuring lengths. It is placed at the point to be measured and read in with the HoloLens. As soon as the display has stabilized, a measuring point can be read in by touching the displayed measuring symbol with the hand (see Figure 18). By pressing the displayed reset symbol, the measuring points are reset and a new measurement can be performed. The quantity of read-in measuring points leads to different details:

- One measuring point shows the coordinates of the element origin (stop bar on clamping fixture).
- Two measuring points show the distance between these measuring points as well as the X, Y and Z distance in the coordinate system of the work table.
- Three measuring points show a triangle with distances and angles
- Four measuring points show a quadrilateral with distances and angles as well as the diagonal distances.



Figure 18. Measuring marker displaying set and reset-buttons

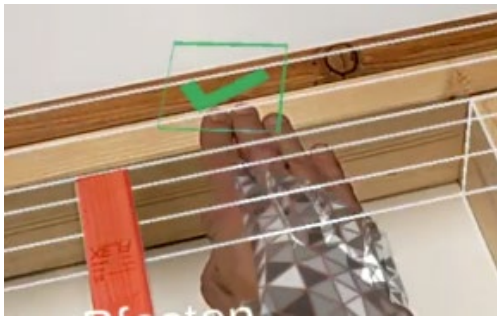


Figure 19. Selected element with approval button

6.3. Approval and documentation

After selecting a specific part with 2 fingers, it is highlighted and a detailed description is displayed. In addition, approval symbols are displayed, which can be activated with the hand. In this case the part gets documented in a text file. After the approval, only the outlines of the part are displayed and it can no longer be selected. The explicit selection of any part is intended to prevent individual parts or machining operations from being overlooked.

The text file with the documentation of the used parts also pilots the display of the parts to be processed. The work progress is laid out as follows:

- From the start of assembly, all parts of the wooden frame are displayed on the feeding table as long as at least one part of the frame is still not approved.
- Once the frame is finished, one side of the planking is displayed until the last part has been inserted or the last machining operation has been performed here as well.
- The element can now be turned. After the turning process, the position of the element on the receiving table must be read in with the turning table markers.
- Once the position of the element on the receiving table is determined, remaining machining operations and parts are displayed.
- After all parts and machining operations to be documented have been released, the element display hides and the next element can be loaded for machining.

6.4. Several HoloLenses

When using multiple HoloLenses, it must be taken into account that each HoloLens uses its own calibration as well as its own coordinate system. To work with the required precision, a separate FOLOGRAM computer must be set up for each HoloLens. If the text files that control the program progress are stored on a network drive that is accessible to all FOLOGRAM computers, they can be used simultaneously on the same element. This setup process could not be performed by the workers.

6.5. Ergonomics and practical use

In general, the use of the HoloLens was received with curiosity and positive feedback by the workers. The interactive control as well as the measuring and approval processes were immediately understood and applied. However, the setup process was found to be very complicated by the workers. The following peculiarities were documented:

1) Safety at Work: Particular hearing protection that can be worn together with the HoloLens is available for use in factory halls.

2) Power: The low battery power of the HoloLens was found to be problematic. However, this can be remedied with an additional battery worn on the body.

3) Robustness: When using tools with strong vibrations or large chip ejection, the HoloLens is irritated. In these cases, the contour to be produced was traced with a pen and then produced without HoloLens. After removing and putting away, the screen was occasionally forgotten to be folded up, after which the system was automatically put into sleep mode and then had to be restarted.

4) Wearing Comfort: For the duration of the test scenarios of a few hours, continued wearing of the HoloLens was not a problem. It was not tested how the wearing comfort develops during a whole day or over several days.

7. Evaluation of assembly times

To document the reduction in assembly time, 2 elements with similar dimensions and the same number of individual parts were manufactured by two workers; one in conventional manual joinery and the other with AR glasses. While the conventional paper plan guided assembly of a standard timberframe wall took 1,5h, the AR-projection based assembly of the identical wall took only 46 min from the moment of uploading the geometry until the wall was finished.

8. Results

After embedding abrasion-resistant QR markers into the surface of the worktable, the deviation of the projection to the physical components with an accuracy that was deemed to be sufficient for timber construction by the project partner Holzbau Lepski.

The intuitive approach proved to be successful during the test runs carried out. Test subjects who had no experience in using AR solutions were able to intuitively operate and use the developed system without extensive training periods. Short explanations were sufficient for the use of the measuring and approval tools as well as for the markers for the turning table. Only startup and setup of the AR glasses required extensive training.

Although the glasses are not technically mature at this point, time savings based on AR projections in the digital continuation of planning can already be demonstrated.

9. Future work

Recognition of components based on glued labels does not currently work because the markers required for recognition by the AR glasses do not fit on the slim surfaces of the wooden elements. In addition, the effort required to manually apply the labels (on multiple component sides) is not commensurate with the expected time savings. In a follow-up project, it would be recommended to investigate how a component marking generated with the help of numerically controlled joinery systems can be reliably read and recognized by the glasses. This way the correct placement of the marked component could be automatically identified. The development would result in additional quality control and further time savings. An additional increase in usability and simplification of the setup installation would be the renunciation of the proprietary software Grashopper and Fologram and to develop an open source app, which fulfills mentioned task steps.

References

[1] G. Horn, Holzbau Deutschland-Institut e.V., und Bund deutscher Zimmermeister, *Holzrahmenbau - Bewährtes Holzbau-System*, 6. Aufl. Köln: Rudolf Müller, 2021.

[2] T. Schauerte, F. Lindblad, und M. Flinkman, „Critical success factors determining economic health of firms producing wooden single-family houses.“, S. 12, 2017.

[3] R. Kabelitz-Ciré, „Lagebericht 2022 . Zimmerer/Holzbau“, Holzbau Deutschland, Mai 2022.

[4] Dorreneb, „Map physical spaces with HoloLens“, 13. Oktober 2022. https://learn.microsoft.com/en-us/hololens/hololens-spaces (zugegriffen 7. März 2023).

[5] K. Khoshelham, H. Tran, und D. Acharya, „Indoor Mapping Eyewear: Geometric Evaluation of Spatial Mapping Capability of Hololens“, *Int. Arch. Photogramm. Remote Sens. Spatial Inf. Sci.*, Bd. XLII-2/W13, S. 805–810, Juni 2019, doi: 10.5194/isprs-archives-XLII-2-W13-805-2019.

[6] V. Sardenberg, A. L. Rolim, und D. Digiandomenico, „The Hyphae House and the Paperless Worksite“, S. 12.

[7] R. Hughes, T. Osterlund, und N. M. Larsen, „Integrated design-for-manufacturing and AR-aided-assembly workflows for lightweight reciprocal frame timber structures“, *Constr Robot*, Bd. 5, Nr. 2, S. 147–157, Juni 2021, doi: 10.1007/s41693-020-00048-3.

[8] S. Teruggi und F. Fassi, „Mixed Reality Content Alignment in Monumental Environments“, *Remote Sensing and Spatial Information Sciences*, Bd. Volume XLIII-B2-2022 XXIV ISPRS Congress (2022 edition), Nr. The International Archives of the Photogrammetry, S. 8, 2022.

Proceedings of the IASS Annual Symposium 2023
Integration of Design and Fabrication
10–14 July 2023, Melbourne, Australia
Y.M. Xie, J. Burry, T.U. Lee and J. Ma (eds.)

Process simulation for enhancing self-supporting printability in 3D curvature-oriented clay form printing with an additional-axis base

Xuanyu LU[a,*], Yasushi IKEDA[a], Arastoo KHAJEHEE[a], Koki ITO[b]

[a,*] Department of Architecture, Graduate School of Engineering, The University of Tokyo
luxuanyu@g.ecc.u-tokyo.ac.jp

[b] Koki Ito, Graduate School of Media and Governance, Keio University

Abstract

3D printing technology has ushered in a new era for the construction industry. It offers a new approach to manufacturing complex geometrical structures with numerous advantages over traditional construction methods, significantly increasing the value of parametric shape design. Nevertheless, because of gravity, structures with overhang features need support structures during the printing process. This significantly limits their printability and reduces the freedom of parametric shape design. From previous studies [16], Curvature-orient printing with an Additional-axis base seems a new solution to enhance Self-support printing to make the overhanging objects without any support structures. Rotating the Additional-axis base can reduce the inclination of the printing paths to reduce the effects of gravity. However, there are still three main failure phenomena for self-support printed objects with curvature-orient printing: (1) Overhanging collapse, (2) Slipping off from the Additional-axis base, and (3) Global deformation. If these effects cannot be predicted, it is impossible to calculate the failure limitations to generate optimized printing actions to enhance Self-support printability in Curvature-orient printing. These failure causes depend on the material, mechanical factors, the shape of objects, and so on. Thus, the failure limitations are dynamic during the printing process. Therefore, developing the process simulation for Self-support printing seems promising. Some current previous studies have developed simulation tools for triaxial printing, but the potential of the process simulation for Self-support printing has not been explored so much. This paper proposes a process simulation tool for Self-support printability of 3D Curvature-orient printing with an Additional-axis base. The proposed tool was developed based on Shaun Wu's work [18]. This research tried to fabricate it into a simulation tool predicting the Self-support limitations of the printing process, adapting to diverse materials and shapes. Additionally, the user can optimize the printing actions based on these predictions to enhance Self-support printability. To make the proposed simulation closer to reality, the parameters in this simulation program were generated from previous studies and numerous physical printing experiments. Ultimately, actual validation was done to show the potential of this proposed tool. The Grasshopper file of this tool is made freely downloadable for educational and academic use.

Keywords: process simulation, FEA, additive manufacturing, 3D curvature-orient printing, self-support printability, additional-axis base, overhang feature

Copyright © 2023 by Xuanyu LU, Yasushi IKEDA, Arastoo KHAJEHEE and Koki ITO. Published in the Proceedings of the IASS Annual Symposium 2023 with permission.

1. Introduction

Additive Manufacturing (AM), first introduced by Pegna [1], has revolutionized the construction field, enabling customization and flexible mass production. Robot-assisted construction, as discussed by Nycz et al. [2], offers numerous advantages, including increased quality, reduced mistakes, and faster work cycles. This technology, known as 3D printing (3DP), involves an extrusion-based manufacturing process and has been used in various projects such as the design of a topology-optimized 3D-printed bridge by concrete printing [4], topology-optimized concrete components [5], and the concrete funicular spatial structure [6].

3D printing can produce mass-customized architectural components quickly, accurately, and cost-effectively, transforming traditional building forms. Despite the prevalence of square buildings and furniture, curved forms are more common in nature. Ancient human housing, such as the Huts of the Matakam people, utilized curved forms. With increasing urbanization, high-cost curved buildings have become less prevalent due to traditional construction technology limitations. 3D printing technology can overcome form limitations and reintroduce curved buildings to the mass market. In a collaborative project, parametric shape design was explored, focusing on the potential of 3D printing in producing complex shapes. The design process considers mechanical performance, environmental factors, and topography, resulting in unique and intricate shapes. Thus, 3D printing is an optimal approach for complex architectural designs. 3D printing technology, while faster and more accurate for complex forms, faces challenges with overhang features such as shells and roofs. Common solutions involve support structures [5, 6], which can be wasteful and limiting (See Fig.1). Alternative methods to reduce support volume [7–9] have become bottlenecks in efficiency, precision, and cost reduction.

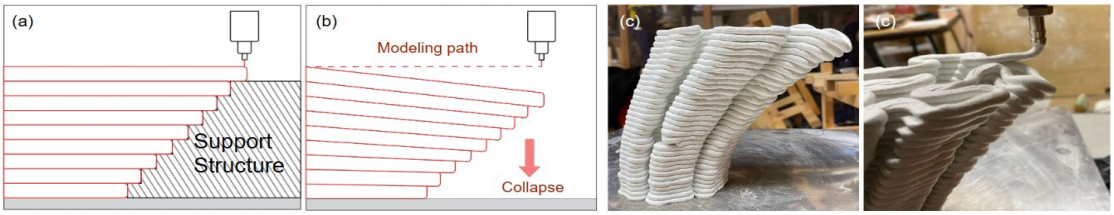


Figure 1. Self-support 3D printing in the triaxial printing way: (a) printing process with support structure, (b) printing process without support structure, (c) collapse occurring without support structure in triaxial printing.

Aiming to enhance self-supporting printability, the study takes advantage of Curvature-oriented printing with an Additional-axis base as an alternative to traditional triaxial printing [10, 11]. Curvature-oriented printing generates curved slicing layers, allowing greater kinematic freedom and smooth orientation adjustments during printing [12, 13]. This method supports new paths more effectively due to continuous extrusion direction changes based on curvature, enhancing self-supporting printability compared to triaxial printing. However, gravity-induced deformation remains an issue even with curvature-oriented printing and accelerated curing using a heat gun, as shown in Fig.2. This leads to increased global deformation and potential collapse.

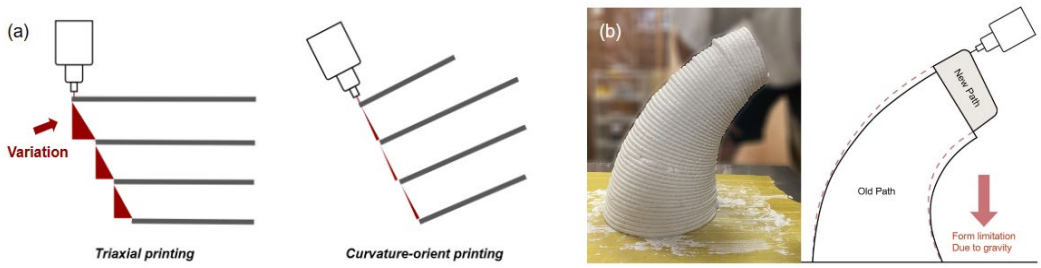


Figure 2. Curvature-oriented printing with an additional-axis base: (a) reduced path variations in curvature-oriented printing compared to triaxial printing, (b) global deformation occurring during the curvature-oriented printing process.

Gravity is inescapable, so I explored adjusting the printing path inclination to reduce gravity's effect by rotating the additional-axis base. The 3D curvature-oriented printing with an additional-axis base, consisting of a 6-axis robotic arm and a 2-axis base, was employed to improve Self-support printability of clay forms. Through numerous experiments, I identified three primary failure modes: (1) overhanging collapse, (2) slipping off the Additional-axis base, and (3) global deformation. Overhang collapse occurs when the printed model's shape isn't compatible with the printer's capabilities, causing global deformation and eventual collapse. Objects slip off the base because it rotates during printing without support structures to secure them, causing detachment if the object is too heavy or the base's inclination angle is too large. Global deformation arises from gravity, and if deformation isn't controlled within acceptable limits, accurate printing is impossible. Avoiding these failure modes and optimizing printing steps require understanding their boundaries during the printing process. Predicting these limitations is challenging due to their dynamic nature, relying on factors like shape and material properties. Developing a process simulation tool for curvature-oriented printing to enhance self-supporting printability appears promising (See Fig.3).

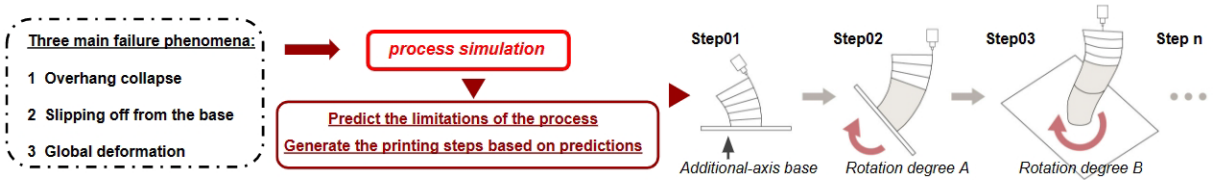


Figure 3. Objectives of the Process Simulation in Curvature-Oriented Printing with an Additional-Axis Base.

Some existing studies have developed simulation tools [14–16] for triaxial printing, but the potential of process simulation for self-supporting printing remains largely unexplored. In this paper, a process simulation tool was developed using Grasshopper (a visual programming language [17]) to predict self-supporting printing limitations and optimize printing steps to enhance Self-supporting printability of curvature-oriented printing with an additional-axis base. Global deformation simulation analysis was conducted using the Finite Element Analysis (FEA) software Karamba3D. Building on Shaun Wu's [18] study, my self-supporting global deformation simulation system was developed and was also created to predict overhang collapse and slipping off failure phenomena. All simulation analyses were combined into a process simulation system.

Although clay was used as the experimental material in this study, the proposed tool aims to predict a variety of materials and shapes. This paper thoroughly discusses the general methodology and simulation strategies for the three failure phenomena, and actual validations were performed to demonstrate the tool's potential. The proposed tool predicted the printing process of clay forms, generating optimal printing actions based on predictions and sending these actions to the self-supporting printing system. The Grasshopper file of this tool is freely downloadable for educational and academic use.

The paper's subsequent sections are organized as follows: Section 2 discusses the schematic overview of the general methodology, including numerical and validation methodologies. Section 3 presents the main simulation strategies for predicting the process limitations of the three failure phenomena. In Section 4, the actual validation results demonstrating the potential of the proposed process simulation tool for enhancing self-supporting printability are reported. Finally, Section 5 provides the conclusion and discussion.

2. General methodology

2.1. Numerical methodology

The proposed 4-step simulation system enhances self-support printability in curvature-oriented printing (Fig.4). It identifies three main failure phenomena from numerous experiments: (1) Overhanging collapse, (2) Slipping off from the Additional-axis base, and (3) Global deformation. The methodology predicts these limitations and generates printable paths and optimized actions. A robotic control system like FireFly [19] or Machina [22] sends these actions to the printing system. Step 1 predicts and optimizes printable paths. Step 2 predicts global deformation and organizes actions accordingly. Step 3 predicts slipping-off limitations based on step 2 actions. If slipping risks exist, actions are modified and re-analyzed in step 2; otherwise, the final optimized path is generated. In step 4, optimized actions are sent to the printing system to create objects. A changeable printing speed generation system is included to improve self-support printability, to be discussed later.

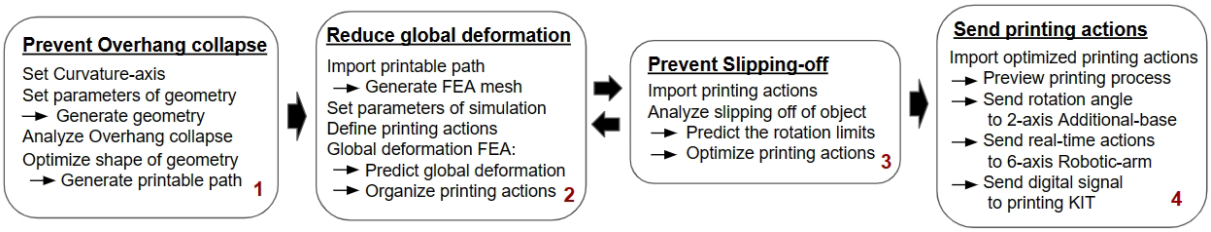


Figure 4. Overview of numerical methodology.

2.2. Validation methodology

The validation methodology involved testing various shapes, from simple curved cylinders to complex Liquid-rock geometries [23], demonstrating the potential of the proposed simulation tool and enabling parameter adjustments. Printing limitations depend on factors like material properties and mechanical performance. Paper-clay was chosen for its suitability, affordability, and ease of use, with a final density of 1.386 g/cm3. It was extruded using a StoneFlower Ceramic KIT [21], with signals sent from the KUKA Robot Controller (KRC) and an Arduino board. The curvature-oriented printing system includes a 6-axis robotic arm (KR6-16-20 from KUKA) and a 2-axis DIY additional-axis base. Robotic actions involve additional-axis base actions, robotic arm actions, and printing KIT switch signals. Additional-axis base actions were sent using FireFly [19], robotic arm actions via Machina [22], and printing KIT information was loaded into an external controller using Arduino programming. The controller, connected to the KRC, controls extrusion speed and receives switch signals using Machina. Fig.5 provides an overview of the validation methodology and the tools/connections for this printing system.

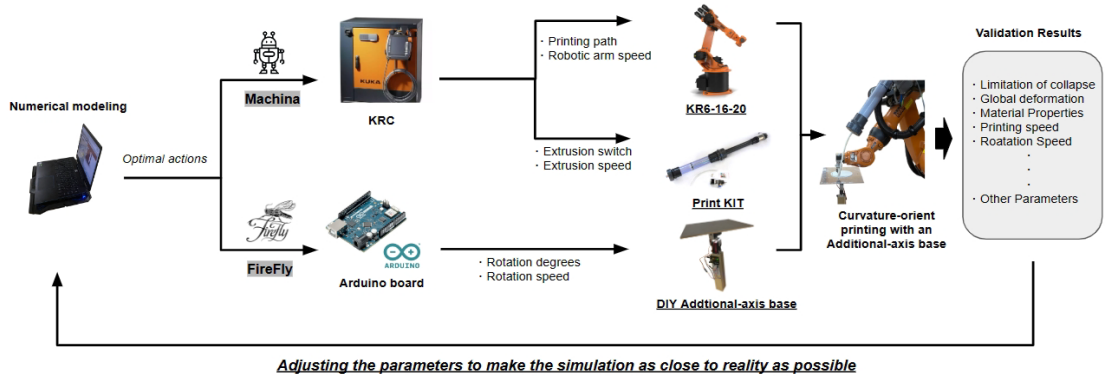


Figure 5. Overview of validation methodology.

3. Simulation Strategies

This section delves into the main simulation strategies of the proposed numerical methodology in the same order as the numerical methodology analysis: Overhanging collapse, Global deformation, and Slipping off. Additionally, a changeable printing speed generation system for enhancing self-support printability is discussed. An overview of the Grasshopper file and case examples of the proposed simulation results are presented at the end of this section. Numerous Grasshopper plugins, such as KUKA PRC, Machina, FireFly, Karamaba3D, as well as custom C# and Python scripts, were used to create the simulation system.

3.1. Overhanging collapse simulation strategy

The printable path generation is crucial as it directly affects printing results. Geometries have a Curvature-axis as a reference, and graphics along it form the geometry, varying in size and complexity. The simulation tool targets diverse shapes, but due to time constraints, two representative shapes were tested: Hollow curved geometries (simple) and Liquid-rock geometries (complex). Both have continuous, collision-free paths.The height range of the printing path is a crucial factor affecting print quality in Curvature-orient printing, as it constantly changes according to curvature and shape, unlike the constant value in triaxial printing. Incorrect path heights can lead to printing errors and, ultimately, overhanging object collapse. Using Self-support Liquid-rock geometry [23] as an example, the complex geometry generated through the Kangoo2 plugin from Grasshopper avoids path collision due to a 7mm nozzle diameter.

As shown in Fig.6(a), Layer 52 of the geometry is divided into 19 points (Ph0-18) with varying path heights (Ph). Through experimentation, a Ph range of 1.5 to 6.0 mm has been determined to result in successful printing. To prevent overhanging collapse, a function was developed to calculate the Ph range automatically, optimizing geometry shapes based on printable Ph values. As shown in Fig.6(b), the grey path is not printable due to its Ph range being outside the 1.5-6.0 mm limit. By adjusting the Curvature Axis, the geometry's shape changes, making the red path printable for the next FEA mesh generation.

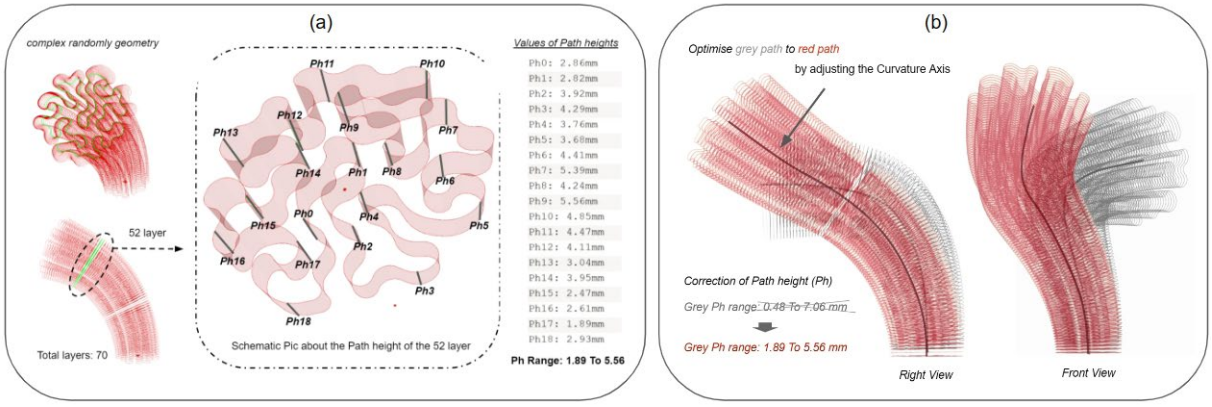


Figure 6. Overhanging Collapse Simulation Strategy: (a) automatic calculation of path heights, (b) Optimizing the shape of geometry based on calculation data to prevent overhanging collapse.

3.2. Simulation strategy for global deformation

Global deformation is a crucial reference for optimizing printing actions. However, it is dynamic during the printing process and depends on factors such as geometry shapes, and material properties. The mechanical performance prediction of global deformation in the 3D printing process follows the general methodology proposed by Shaun Wu [18]. A commercial FEA software, Karamba3D, was used for global deformation analysis through Grasshopper. In this study, a Self-support FEA system was developed to predict global deformation in the Curvature-orient printing process with an Additional-axis base.

3.2.1. FEA mesh generation for global deformation

Global deformation FEA requires an adapted mesh for the Self-support printing process. With the modified overhanging geometry shape and generated printable path from the previous strategy, a function was developed to automatically generate the FEA mesh. The mesh configuration is mainly based on six parameters (see Fig.7(a)): (1) Printing path, (2) Path width (***w***), (3) Path heights (***hi***) for analysis mesh, (4) Number of printed segments (ni) for each layer part, (5) Segment length (***ls***) in the direction tangential to the print path, (6) Perpendicular planes (***pi***) of each segment for the printing path. FEA mesh generation in this system requires inputting only the printing path and path width (***w***), while other parameters are automatically determined. A zero-thickness shell structure (see Fig.7(b)) was selected as the final FEA mesh, whose Values ***Phi*** of height are changeable, to accommodate Karamba3D's lack of volumetric element support. Only small global deformation needs to be calculated, so the Voxelization methodology[14][16] was not necessary for this simulation tool.

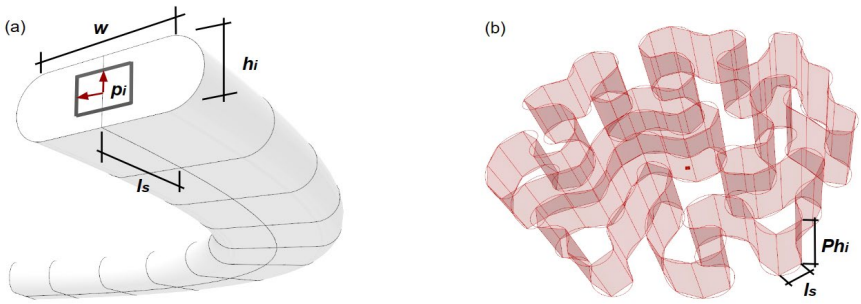


Figure 7. Printing Path Configuration: (a) general mesh configuration of the path, (b) a zero-thickness shell structure of the FEA path in Karamba3D.

3.2.2. FEA parameters setting for global deformation

To analyze global deformation limitations using FEA, material and mechanical parameters must be set. Most parameters were extracted from previous studies and adjusted through self-experiment validation.

FEA parameters setting:

1.	*Specific weight of material:*	*13.865*	*KN/m³*
2.	*Coefficient of thermal expansion:*	*5.6*	*1/C°*
3.	*Stiffness Module (t=min):*	*0.002 + 0.000013t*	*KN/m²*
4.	*Compressive Strength (t=min):*	*0.0015 + 0.000014t*	*KN/m²*
5.	*Curing parameters:*	*0.0056*	*KN/m²*
6.	*Rotation base degree A:*	*-90 ~ 90*	°
7.	*Rotation base degree B:*	*-90 ~ 90*	°

The material used was DAISO paper clay with a 35 ml water to 500 g clay ratio. The specific weight was determined through self-experiments, while the coefficient of thermal expansion is from Culbertson W. Ross's clay research [24]. The stiffness Module and Compressive Strength values were adapted from Xiyao Zheng's study [25] and adjusted with self-tests. A heat gun accelerated clay curing during printing, ensuring Self-support strength. Curing parameters were incorporated into Stiffness Module and Compressive Strength formulas. Other settings were based on Shaun Wu's study [18], and rotation degrees A&B were set according to the RDS5160 Torque Digital Robot Servo used for the DIY Additional-axis base.

3.2.3. FEA elements definition for global deformation

To reduce computational effort, the mesh model combines multiple printing paths into one layer for FEA (See Fig.8(a)). Elements in the mesh follow the FEA mesh generation method from Fig.7 and are affected only by gravity. Rotation force from the 2-axis Additional-axis base is ignored due to low speed and the heat gun's accelerated curing. The crucial setting in FEA elements definition is the changeable Supporting Points for the Self-support geometry, as the whole printed object undergoes dimensional rotation during simulation. The printing path is split into Old-path (no deformation analysis) and New-path (with deformation analysis). Supporting Points' position is determined automatically based on curing speed (5mm/s, according to the heat gun). The New-path, based on Supporting Points, is generated for deformation analysis (FEA). The Base path at the geometry's bottom predicts if the Self-support geometry slips off the Additional-axis base during rotation (Fig.8(b)). The simulation strategy for Slipping off will be elaborated later.

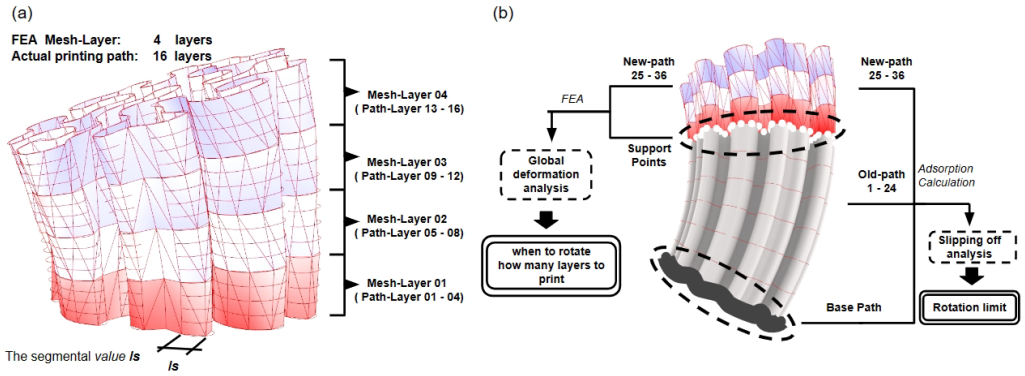


Figure 8. FEA elements definition for global deformation: (a) layer definition in FEA mesh, (b) defining Supporting Points between Old-paths and New-paths.

3.3. Simulation strategy for slipping-off

1. *Rotation base degree A:*	*-90 ~ 90*	°
2. *Extrusion speed of printing KIT:*	*0.35*	*g/s*
3. *Atmospheric pressure:*	*101,325*	*Pa*
4. *Security Factors:*	*0.029 ~ 0.021*	*(25° ~ 75°)*

This function aims to simulate Self-support 3D Curvature-orient printing clay with an Additional-axis base, making it crucial to predict if the Self-support geometry will slip off from the base during printing. Two causes for Slipping-off are: (1) object sliding on the base, and (2) object separating from the base. Experiments indicate that the primary cause is the latter: object separating from the base. Additionally, the Base path of the object and the surface of the Additional-base can form a vacuum-like condition, enabling the fixation of self-support geometries using air pressure instead of support structures. However, air pressure fixation has limitations. When the object's total weight exceeds the theoretical attraction value $\boldsymbol{w}$ (kg) or the Additional-axis base inclination is too large, the object's bottom will separate from the base (See Fig.9).



Figure 9. Slipping-off experiments: (a)(b) objects fixed on the base, (c)(d) objects slipping off from the base.

Fig.10 shows three main factors influencing the vacuum adsorption force's attraction value ***w***: object weight ***mg***, effective vacuum area ***A***, and rotation angle ***θ***. With known printing path length, machine speed, and extrusion speed, the object's weight ***mg*** (*Kg*) is calculated. Despite the DIY Additional-axis base's two-axis rotation, Rotation degreeA ***θa*** (See Fig.3) primarily affects tilting pressure. When calculating area ***A*** for pressure value ***P***, the actual printing path width is 5mm, not 7mm, due to bottom material evaporation and shrinkage. In calculating the Theoretical attraction value ***w***, multiply by the Security factor value ***F*** for better error tolerance, as the Base path bottom is not in a complete vacuum. The Security factor value ***F***, an empirical value from self-experiments, may need re-measurement if conditions change. If the final ***w*** value is greater than the object's ***mg***, the object meets Self-support conditions and won't slip off the base.

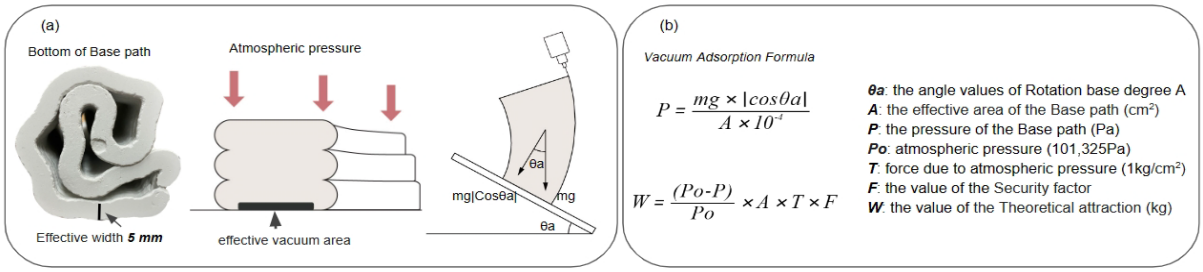


Figure 10. Vacuum adsorption calculation: (a) principle of vacuum adsorption during 3D printing, (b) formula and factors influencing vacuum adsorption during 3D printing.

3.4. Generation strategy for changeable printing speed

In the Self-support 3D printing system, path height values vary within the same layer (See Fig.6). To ensure a constant 7mm printed path width for different path heights, the robotic arm's speed is adjusted while maintaining a consistent extrusion speed (231 mm³/s), given the nozzle diameter is 7mm. Based on self-experiments, the printable path height range is 1.5-6.0mm, with corresponding robotic speeds of 720mm/min for 1.5mm height and 360mm/min for 6.0mm height (See Fig.11(a)). A comparison between objects printed with constant and changeable speeds is shown in Fig.11(b), demonstrating improved accuracy using changeable printing speeds. Changeable printing speeds (Ps) are generated based on path height (Ph) values. Using the printable Ph range (1.5-6.0mm) and the corresponding optimal robotic speed range (360-720 mm/min), the appropriate printing speeds are determined (See Fig.11(c)). These changeable printing speeds are inserted into the robotic action programming through the real-time robotic tool Machina [22]. The robot adjusts its speed based on variable path heights, ensuring the printed object is consistent with the analysis model and improving printing accuracy.

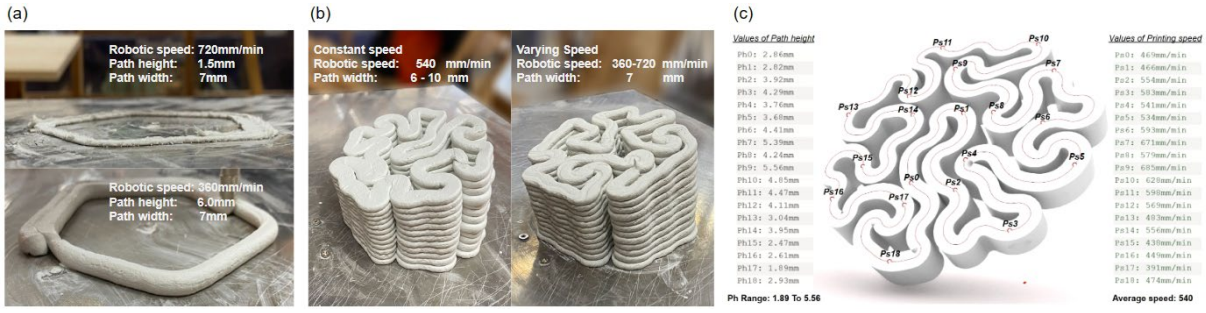


Figure 11. Changeable printing speeds: (a) the relationship between robotic speed and path height, (b) a comparison of objects printed with constant versus changeable speeds, and (c) a function for automatically generating optimized robotic speed according to various path heights.

3.5. The showcase of the Grasshopper file

Although the controller of the Printing KIT and DIY Additional-axis base requires hardware code programming in Arduino board, most of the programming is executed through Grasshopper [17]. (See

Fig.12&13) The Grasshopper file will be open-source and uploaded to GitHub. My YouTube video will explain the operation of the proposed tool and the steps of parameter adjustment. I hope this tool will be used and further developed by other researchers who are interested in Self-support 3D printing. Link of my video: https://www.youtube.com/watch?v=GJUpvVhbB4o&t=95s

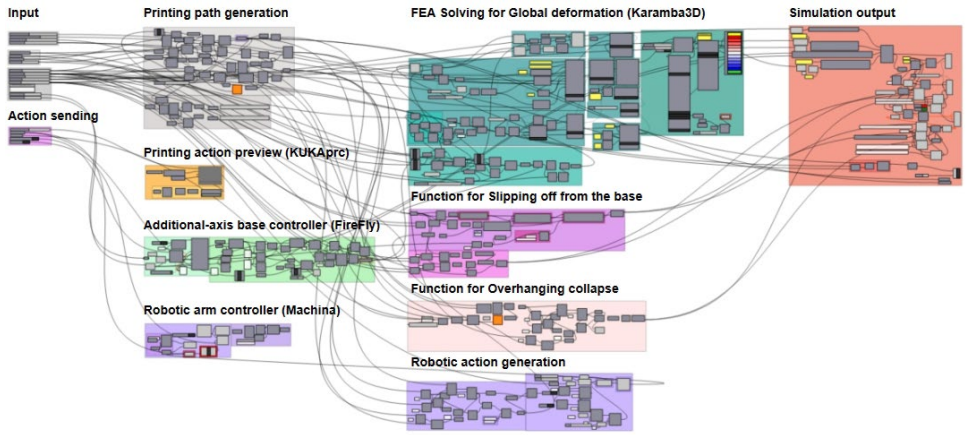


Figure 12. The overview of the Grasshopper file of the developed process simulation tool.

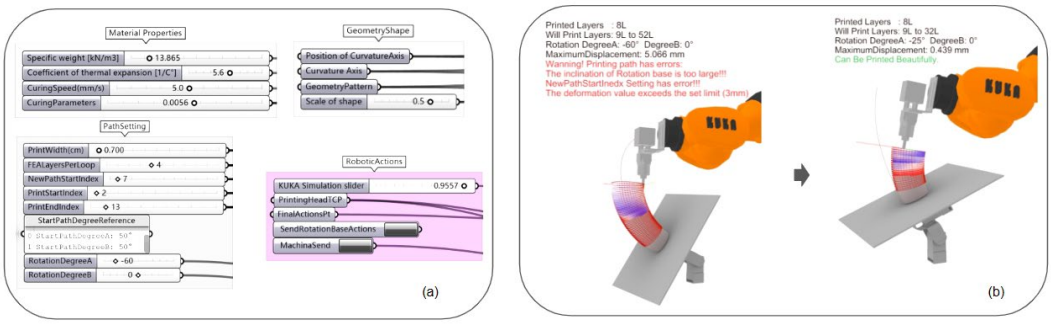


Figure 13. Process Simulation Showcase: (a) input factors for the process simulation system, (b) simulation results highlighting optimized printing actions to enhance self-supporting printability.

4. Validation

The validation phase involves two steps: (1) Training simulation - fine-tune parameters to align simulations with reality; (2) Potential validation - use the refined tool to optimize printing actions for two cases, print actual objects, and compare global deformation values between simulations and reality to verify the tool's effectiveness.

4.1. Training simulation

Building on Shaun Wu's work [18], this research focuses on simulating self-support limitations of 3D curvature-oriented printing with an additional-axis base. Adjustments are made based on self-experiments to closely match reality. First, predict self-support limitations of typical shapes and organize printing steps. Print the clay form step by step, following the simulation's steps. Set the same fixed observation view in both reality and simulation (See Fig.14), comparing the deformation value (*Dv*) of the global clay form. Measure the lowest and highest distance values from the top printing path to the additional-axis base to reduce errors. Finally, adjust simulation parameters based on global clay form comparisons until the process simulation closely resembles reality.

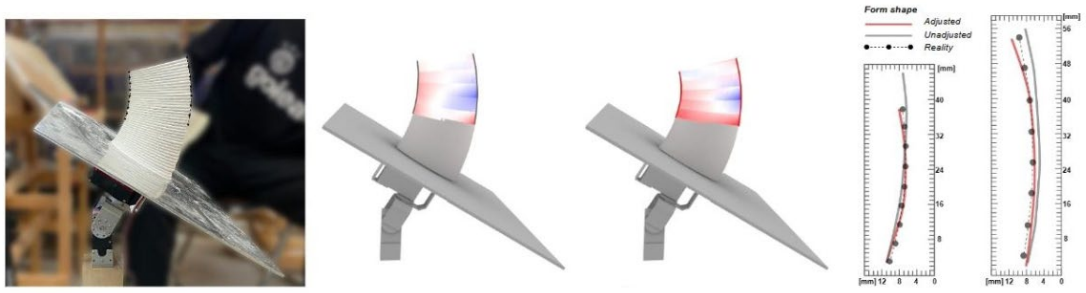


Figure 14. Parameters adjustment method: (a) The global self-support clay form in reality, (b) The simulation of self-support clay form with unadjusted parameters, (c) Comparing global deformation values to adjust parameters, making the simulation as close to reality as possible.

4.2. Potential validation

After adjusting parameters, the simulation results closely resemble reality. To verify the simulation tool's generalizability for diverse shapes, two self-support clay forms, Gradient polygon geometry (simple) and Liquid-rock geometry (complex), are used in the validation phase. The proposed tool predicts printing process limitations and generates optimized printing actions/steps. Actual clay objects are printed following these steps. A global *deformation limit* of 6mm is set. The differences between *Reality Dv*, *Simulation Dv*, and the *Deformation limit* are compared using line charts. If *Reality Dv* values remain below the *Deformation limit*, it suggests the tool can provide valuable predictions for self-support limitations, improving global clay form accuracy.

4.2.1. Gradient polygon geometry validation

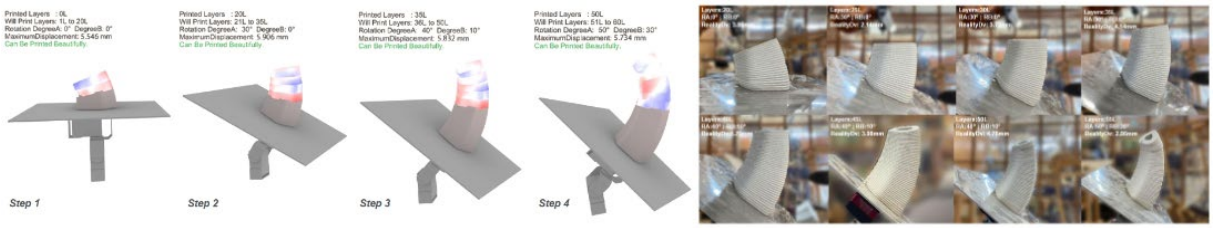
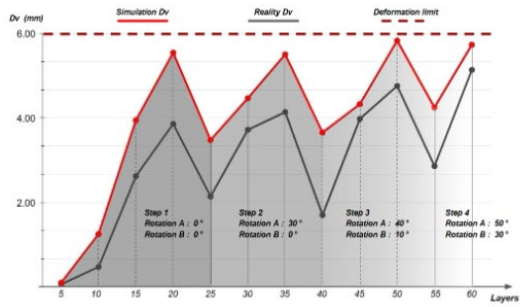


Figure 15. Optimized printing process for the gradient polygon geometry & actual deformation results during the Self-support Curvature-orient printing process.

Validation results show that *Reality Dv* for the gradient polygon geometry is controlled within 6mm, indicating improved global form accuracy using the proposed simulation tool's optimized printing process (See Table 1). While *Simulation Dv* overestimates global deformation compared to *Reality Dv*, the proposed tool still closely reflects the actual printing process, demonstrating its potential for predicting simple geometry printing processes.

Table 1. Comparing global deformation values of the gradient polygon geometry between reality and simulation.



layers	5	10	15	20	25	30	35	40	45	50	55	60
Reality Dv (mm)	0.06	0.48	2.62	3.86	2.14	3.72	4.14	1.70	3.98	4.76	2.86	5.14
Simulation Dv (mm)	0.092	1.246	3.944	5.546	3.476	4.468	5.506	3.654	4.326	5.832	4.248	5.734
Additional base angle (°)	DegreeA: 0 DegreeB: 0				DegreeA: 30 DegreeB: 0			DegreeA: 40 DegreeB: 10			DegreeA: 50 DegreeB: 30	

4.2.2. Liquid-rock geometry validation

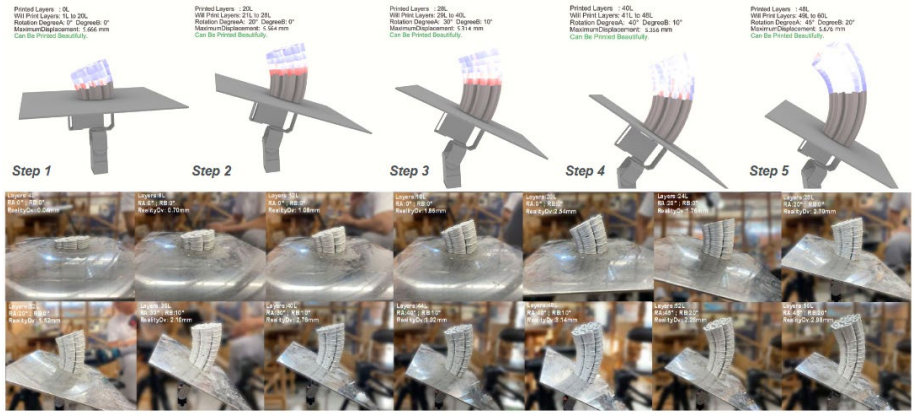
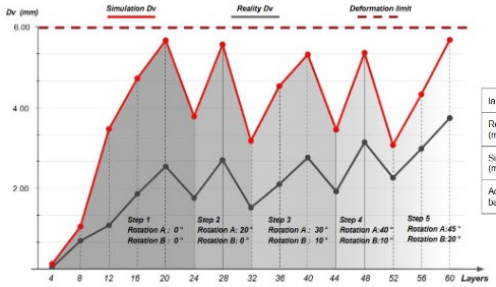


Figure 16. Optimized printing process for the liquid-rock geometry & actual deformation results.

In Table 2, Reality Dv for Liquid-rock geometry stays within 6mm, but the difference with *Simulation Dv* is greater than in Table 1. The discrepancy may result from the imperfect Curing rate setting. A heat gun accelerates clay curing, but curing is non-linear with printing time. Complex geometry has longer printing times, leading to more complex curing rates for the same layers compared to simpler geometries. Although the proposed tool improves Self-support printability for complex geometry, it can't accurately predict the printing process.

Table 2. Comparing global deformation values of the liquid-rock geometry between reality and simulation.



layers	4	8	12	16	20	24	28	32	36	40	44	48	52	56	60
Reality Dv (mm)	0.04	0.70	1.08	1.86	2.54	1.76	2.70	1.52	2.10	2.76	1.92	3.14	2.26	2.98	3.74
Simulation Dv (mm)	0.124	1.052	3.468	4.722	5.666	3.778	5.584	3.174	4.530	5.314	3.450	5.356	3.070	4.326	5.676
Additional base angle (°)	DegreeA: 0 DegreeB: 0					DegreeA: 20 DegreeB: 0		DegreeA: 30 DegreeB: 10			DegreeA: 40 DegreeB: 10			DegreeA: 45 DegreeB: 20	

5. Conclusion and discussion

This paper introduces a Grasshopper process simulation tool designed to predict dynamic Self-support limitations and optimize printing actions in Curvature-orient printing with an Additional-axis base. The tool offers a versatile technique for diverse forms and materials, enhancing parametric shape design value while analyzing dynamic printing limitations of Self-support geometries. The primary objective is to predict printing process limitations and improve Self-support printability, taking into account factors such as geometry, material properties, and mechanical factors. The study emphasizes global form printability, excluding internal form considerations. However, based on validation results, the current simulation tool struggles to accurately predict printing limitations for complex Self-support geometries. Future research should incorporate randomized changes in FEA mesh node positions to simulate imperfections during the actual printing process of complex geometries.

The author plans to apply the tool to 3DP concrete construction projects in future studies, optimizing parametric shape design and printing actual structures based on the tool's dynamic predictions. The proposed process simulation tool is freely available for educational and academic use and can be downloaded from the following website: https://github.com/XuanyuL/Process-simulation-for-Self-support-printability-of-3D-Curvature-orient-printing-clay-form-with-an-A/blob/main/Self-supportPrintingSimualtion.gh.

References

[1] J. Pegna, Exploratory investigation of solid freeform construction, Autom. Constr. 5 (1997) 427–437, https://doi.org/10.1016/S0926-5805(96)00166-5.

[2] H. Son, C. Kim, H. Kim, S.H. Han, M.K. Kim, Trend analysis of research and development on automation and robotics technology in the construction industry, KSCE J. Civ. Eng., 14 (2010), pp. 131-139, 10.1007/s12205-010-0131-7.

[3] R.A. Buswell, W.R. Leal de Silva, S.Z. Jones, J. Dirrenberger, 3D printing using concrete extrusion: a roadmap for research, Cem. Concr. Res. 112 (2018) 37–49.

[4] G. Vantyghem, W. De Corte, E. Shakour, O. Amir, 3D printing of a post-tensioned concrete girder designed by topology optimization, Autom. Constr., 112 (2020), p. 103084, 10.1016/j.autcon.2020.103084.

[5] Guo Yiyao, Luo Yang, Wang Sihan, Tan Ying Yi, Tracy, Kenneth, Robotic Fabrication of Topology Optimized Concrete Components With Reusable Formwork, Jeroen van Ameijde, the 27th CAADRIA Conference, Sydney, 9-15 April 2022, pp. 91-100.

[6] Hao WuHao, WuZiyan, LiXinjie ZhouShow, Digital Design and Fabrication of a 3D Concrete Printed Funicular Spatial Structure, Conference: The 27th International Conference on Computer-Aided Architectural Design Research in Asia (CAADRIA) 2022At: Sydney, AustraliaVolume: 2, 10.52842/conf.caadria.2022.2.071.

[7] J. Jiang, X.Xu, Support structures for additive manufacturing: a review, J.Manufact.Mater. Process.,2 (4) (2018), p. 64.

[8] J. Jiang, X. Xu, J. Stringer, Optimization of process planning for reducing material waste in extrusion based additive manufacturing, Robot. Comput. Integr. Manuf., 59 (2019), pp. 317-325

[9] J. Jiang, Y. Ma, Path planning strategies to optimize accuracy, quality, build time and material use in additive manufacturing: a review, Micromachines (Basel), 11 (7) (2020), p. 633.

[10] Yamin Li, Kai Tang, Dong He, Xiangyu Wang, Multi-Axis Support-Free Printing of Freeform Parts with Lattice Infill Structures, Computer-Aided Design, Volume 133, April 2021, 102986.

[11] Yamin Li, Dong He, Shangqin Yuan, Kai Tang, Jihong Zhu, Vector field-based curved layer slicing and path planning for multi-axis printing, Robotics and Computer-Integrated Manufacturing, Volume 77, October 2022, 102362.

[12] D. Coupek, J. Friedrich, D. Battran, O. Riedel, Reduction of support structures and building time by optimized path planning algorithms in multi-axis additive manufacturing, Procedia. Cirp., 67 (2018 Jan 1), pp. 221-226.

[13] S. Keating, N. Oxman, Compound fabrication: a multi-functional robotic platform for digital design and fabrication, Robot. Comput. Integr. Manuf., 29 (6) (2013), pp. 439-448.

[14] Gieljan Vantyghem, Ticho Ooms, Wouter De Corte, VoxelPrint: A Grasshopper plug-in for voxel-based numerical simulation of concrete printing, Automation in Construction, Volume 122, February 2021, 103469.

[15] A.S.J. Suiker, Mechanical performance of wall structures in 3D printing processes: theory, design tools and experiments, Int. J. Mech. Sci. 137 (2018) 145–170.

[16] Ticho Ooms, Gieljan Vantyghem, Ruben Van Coile, Wouter De Corte, A parametric modeling strategy for the numerical simulation of 3D concrete printing with complex geometries, Additive Manufacturing, Volume 38, February 2021, 101743.

[17] Grasshopper - Robert McNeel & Associates (n.d.), https://developer.rhino3d.com/guides/grasshopper.

[18] Shaun Wu, Buckling Simulation for 3D Printing in Fresh Concrete, Nov 2020 Journal/ Construction Printing Technology CPT 4.20 Page 34 - 37, Buckling Simulation for 3D Printing in Fresh Concrete

[19] Grasshopper plug-in for Rhino - Firefly, https://www.food4rhino.com/en/app/firefly.

[20] R.J.M. Wolfs, F.P.Bos, T.A.M. Salet, Early age mechanical behaviour of 3D printed concrete: Numerical modeling and experimental testing, Cement and Concrete Research, Volume 106, April 2018, Pages 103-106.

[21] The ceramic printing KIT products information of StoneFlower.

[22] Arastoo Khajjehee, Remote Collaborative Solution for Interactive Parametric Design and Digital Fabrication, Academic Year 2022, Page 91-114.

[23] Eftihis Efthimiou, Georg Grasser, Liquid rock - Agent based modeling for concrete printing, Advances in Architectural Geometry 2018, Pages 236-255.

[24] Culbertson W.Ross, THERMAL EXPANSION OF CLAY BUILDING BRICKS, Part of Journal of Research of the National Bureau of Standard, Volume 27, August 1941, Pages 21.

[25] Xiyao Zheng, Jun Wun, Early Strength Development of Soft Clay Stabilized by One-Part Ground Granulated Blast Furnace Slag and Fly Ash-Based Geopolymer, Frontiers in Materials 8. (April 2021), 10.3389/fmats.2021.616430.

[26] Calculation formula of vacuum adsorption force (from ULVAC), https://ulvac-kiko.com/ch/support/vac03_adsorption.html.

[27] KUKA|PRC - PARAMETRIC ROBOT CONTROL FOR GRASSHOPPER (by Robots in Architecture), https://www.food4rhino.com/en/app/kukaprc-parametric-robot-control-grasshopper.

IASS 2023
July 10–14 Melbourne
Integration of Design and Fabrication

Proceedings of the IASS Annual Symposium 2023
Integration of Design and Fabrication
10–14 July 2023, Melbourne, Australia
Y.M. Xie, J. Burry, T.U. Lee and J. Ma (eds.)

Sequential augmented assembly of interlocking timber elements for circular wood construction

Nima ZAHIRI[a,*]

[a,*] Department of Manufacturing and Civil Engineering, Faculty of Engineering
Norwegian University of Science and Technology
Beryll-bygget, 305, Gjøvik, Teknologivegen 22, 2815
nima.zahiri@ntnu.no

Abstract

Development of new timber construction techniques has mainly focused on the hybridization of wood with other materials to improve the bearing capacity through integration with steel plates and fasteners. Advantage of embodied carbon in wood constructions are often threated by the burning demolishing process, e.g., if the wood is incinerated at the end of buildings' life. To remedy this, reduction in joint complexity increases the reusability of building components such as beams, as in our case short linear timber element, for disassembly. To do so, a functioning demonstrator reflects on how innovative structures are realized through synthesizing of interlocking joinery, and how augmented-reality assembly could enable the circular economy in wood. Nevertheless, the structural applications of timber construction are ever expanding, and it is of the utmost importance to broaden this essential dimension of industry and develop novel and acquisitive value-added design with high-performance application. We employ a design-fabrication-construction strategy to fill the gap between designers or engineers with local practitioners and advance wood machinery. This leads us to a certain knowledge on digitalized process and fabrication before being deployed in non-experimental and industrial applications.

Keywords: timber structures, interlocking joinery, augmented construction, structural optimization

1. Introduction

Mass timber constructions rely on hybrid joineries, most of which may be statically interlocked, but extensively use secondary material such as steel connections or fasteners. "Steel accounts for about 4% of global energy use" [1, p. 10], whereas renewable material of wood is manufactured by the sun, and its sustainable nature gives considerable environmental advantages. "Historic wood construction in different parts of the globe widely used interlocking joints before metal connections." [2]

Moreover, "while these hybrid materials have opened new markets such as multi-story housing, separating the component materials of such products is not economically feasible, and the reduction of carbon emissions from timber are largely negated by the high emissions of secondary materials. Solid timber is much more readily reused, recycled, or consumed as a source of compost or energy." [3, p. 425]

Advantage of embodied carbon in wood constructions are often threated by the burning demolishing process, e.g., if the wood is incinerated at the end of the buildings' life. To remedy this, reduction in joint complexity or material variety results in a simpler process for separating the wood components. The use of one material enables the building to be completed with a single dominant trade, which reduces the cost. We seek three main objectives for this investigation.

1. Upward scaling: exploration of optimal aggregation of short linear elements for upward scaling of free-form structures.

Copyright © 2023 by Nima ZAHIRI. Published in the Proceedings of the IASS Annual Symposium 2023 with permission.

2. Only-timber: consistent reduction of material joint complexity by adhering to material monotony of processed timber, by the possibilities that digital fabrication brings forward.
3. Reusability: examining the ease of assembly and disassembly throughout augmented reality for an easy installation, dismantling and future reuse.

To do so, a functioning demonstrator, serving as a case study, reflects on how innovative structures are realized through synthesizing of simple joint geometry, and how digital twin through sequential augmented assembly could enable a circular economy in wood construction. This represents a circular approach to maximize the reusability of timber elements by developing a new concept for disassembly.

This leads us to a certain knowledge on digitalized process and fabrication before being deployed in non-experimental and industrial applications. Herein, the paradigm of lightweight construction is thus interpreted in a more profound and comprehensive way. This serves as an investigation upon some other similar projects for further high-rise endeavors.

2. Experiment: finding tolerances

Before recessing the demonstrator elements, it is crucial to understand the optimum offset volume of intersection for interlocking joints through a simple mockup test. (Figure 1) The offset depends on the type of wood and accuracy of the machine. The experiment involves testing different offsets, and then measuring the dimensions through a CT scanner.

2.1. Testing

A simple setup, shown in Figure 1, examines different offset values. (The offsets from right to left are 0, 0.2, 0.5, 1, and 2 mm) Surprisingly, the 0 mm offset fitted perfectly fine in the mockup experiment. While, in theory we need a small gap in pockets. To realize this behavior, having the accurate dimensions will give a better insight.

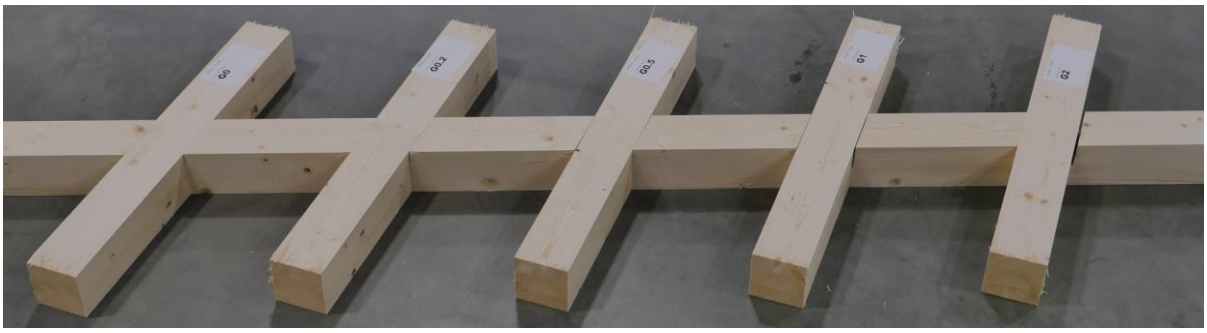


Figure 1. Mockup test for finding the tolerances.

2.2. Measuring

Industrial computed tomography (CT) scanning is used to inspect internal wood quality. In addition, our CT scanner can also be used for geometry measurements in line with a coordinate measuring machine. The CT scanner is part of MANULAB, the national manufacturing research infrastructure at NTNU.

The right image in Figure 2 shows a small, desired portion of the mockup sample in the scanner. As the dimensions indicate, the splinter tool of the Hundegger machine recesses slightly larger (approximately 80.06 mm) than the computer model. The cross section ought to be 80 mm, which is approximately 79.3 mm obtained from the planer machine. That is, the offset gap is 80.06 - 79.03 = 0.76 mm. The decision is to proceed with 0 mm offset in the computer design model.

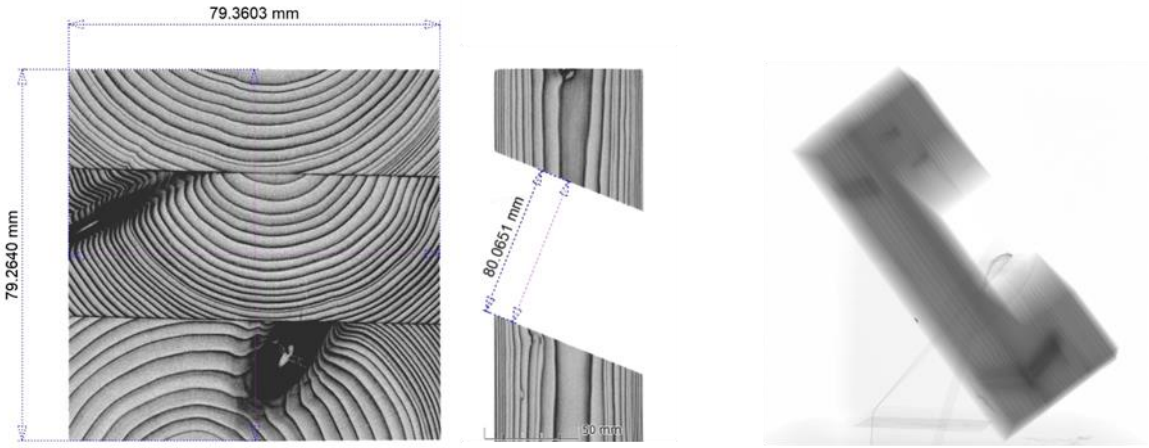


Figure 2. CT scanning

3. Demonstrator: design-fabrication-construction

The design-fabrication-construction strategy is employed to fill the gap between designers or engineers with local practitioners and advance wood machinery. According to Figure 3, the workflow could be fragmented into three recursive subsequences:

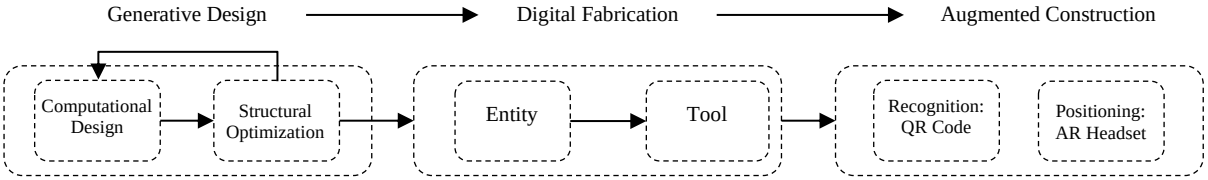


Figure 3. design-fabrication-construction diagram

In the following sub-chapters, each subsequence is investigated in an organized manner as Figure 3.

3.1. Generative design

In conventional design processes, "workflows are typically linear and have little opportunity for mutual informing or recursion between steps." [4, p. 93] However, we adhere to a recursive process, as illustrated in Figure 4, and embody integrative iterative sequences to overcome the limitation to a few, firmly established and recurring structural typologies.

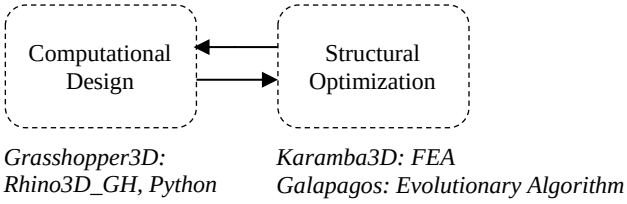


Figure 4. Generative design diagram

During the design process, the generative design plays a central role. "Evolutionary Algorithms, applying the biological principles of mutation, selection, and inheritance, reinterpret the parametric system that becomes the genome . . . and the architect's design goal becomes the fitness criteria." [5] It defines optimized solutions based on multiple variables and fitness criteria, exploring multi-objective genetic algorithms using Galapagos from Grasshopper for Design optimization.

A parametric model generates and examines different scenarios; n numbers of circles are stacked with the distance of z and variable radii between 0 and R with free rotation. To provide structural depth, the components are aggregated on two sets of circular configurations. (Figure 5)

The lines are then translated to timber beams and nodes are assigned as joints with translational and rotational stiffness. "The joint behavior is considered semi-rigid, or an intermediate between an idealized moment connection and an idealized pin connection." [6, p. 2] It creates a finite element model from given entities (points, beams, supports, loads, cross sections, materials), and calculates the deflections of a given model using first order theory for small deflections.

"The problem of high building design particularly concerns problems related to the limitation of horizontal displacements of the building and ensuring its spatial rigidity, proper foundation and resistance to dynamic wind action and seismic effects." [7, p. 2] So, the key design challenge associated with acting load is to minimize the horizontal displacement on the tip of the structure, while simultaneously optimizing the geometrical typology.

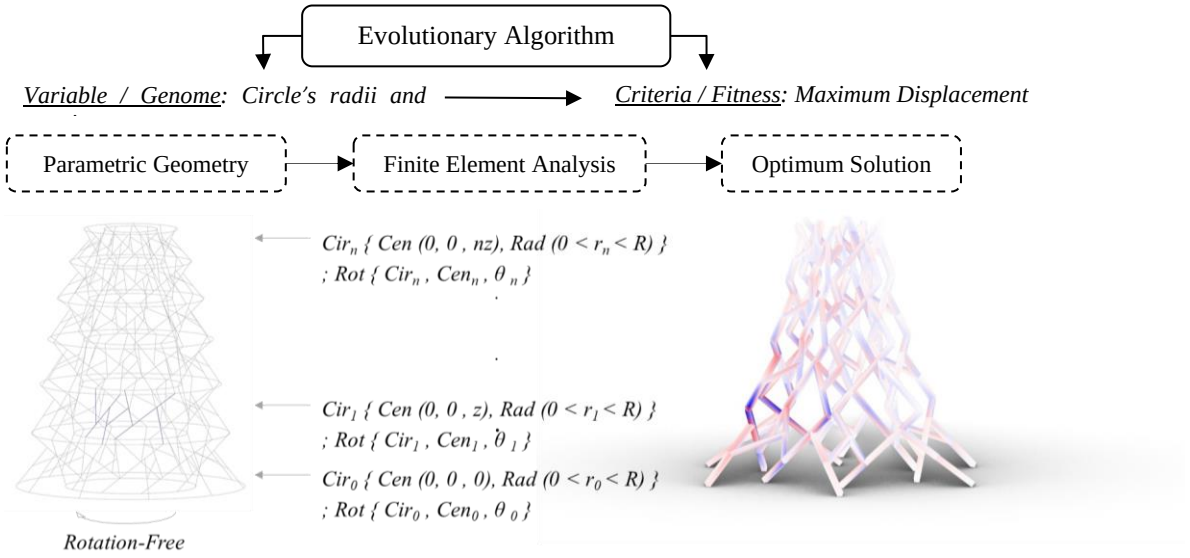


Figure 5. Evolutionary algorithm

3.1.1. Computational design

The classic orthogonal setup is shown in (Figure 6a). It is shown how the connections sit on which proportion of the length. In this arrangement each two interconnections are planar, so interlocking joints could relate to the half lap joint, "one of the most basic joint types that is formed by simply removing half the thickness of each component of a pair and fit into each other." [8, p. 566]



(a) (b) (c)

Figure 6. (a) Basic logic of components placed in a rectilinear array. (b) Placement of components in a non-orthogonal pattern (c) axial rotation for the highest volume of intersection.

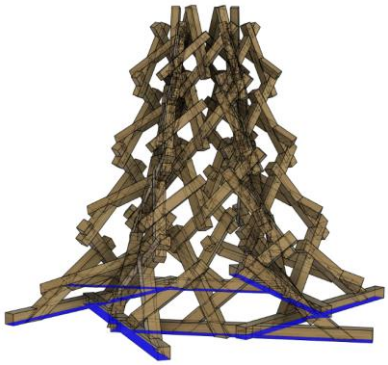
However, on a circular array, or non-orthogonal intersections, according to (Figure 6b), beams need to be slightly offset or rotated along their length axis to perform the highest volume of intersection solid. (Figure 6c) The aggregation of components has a repetitive pattern. These five beam types (named U, X, D, B, and C), as shown in Figure 7, embodies the whole structure.



Figure 7. Beam types

3.1.2. Structural analysis

In the previous section, multiple iterations investigated the optimum aggregation of short timber elements for upwards scaling. However, for more accurate finite element analysis, including contact surface tolerances in the interlocking joineries, nonlinear static analysis is employed in Autodesk Fusion 360 to guarantee that the stresses and displacements are in allowed boundaries. (Figure 8 and Figure 9) The outcome consists of 102 beams and 276 notches.



Density	1.38E-06 kg / mm^3
Young's Modulus	6890 MPa
Poisson's Ratio	0.34
Yield Strength	51.71 MPa
Ultimate Tensile Strength	51.71 MPa
Thermal Conductivity	1.7E-04 W / (mm C)
Thermal Expansion Coefficient	2.75E-05 / C
Specific Heat	1464 J / (kg C)

Figure 8. 3D model and material specification

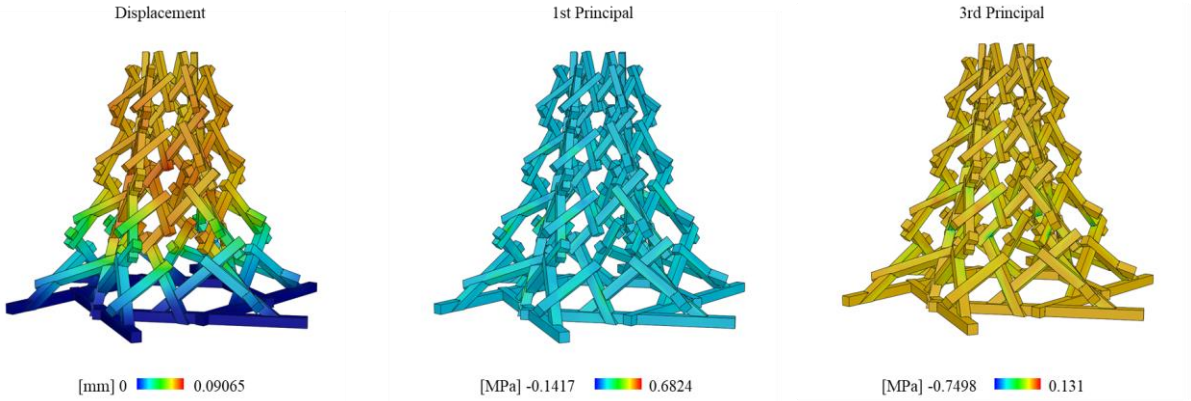


Figure 9. From left to right: displacement, 1st principal and 3rd principal theory.

3.2. Digital fabrication

New controlled timber-processing machine centers, such as Hundegger K2-Industry in this case, allow for the precise cut-outs with precision. The K2i sets a unique standard in performance and flexibility for industrial joinery. Unlike in mass timber construction which is mostly bounded to 90° or 180° angle cuts, we aim to study the use of conventional machines beyond their standard use and to reflect on contemporary fabrication technology for mass-customization.

First, the generated B-rep geometries in Rhino3D should be translated to information entities, using cadwork software to export .bvx format file. Then, it is possible to simulate our process and command the Hundegger with Cambium software. See the diagram in Figure 10.

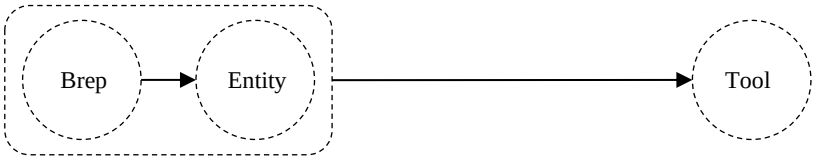


Figure 10. Fabrication diagram

3.2.1. Conversion

The cadwork software enables us to define all recessing across the beams and ending saw cuts as well. The defect parts could be found and checked. (Figure 11) The pocket connections are simple in terms of geometry, but complex in terms of the cutting plane. “The design of connections in timber structures is crucial to global structural performance.” [6, p. 1] In this respect, axial rotation to perform the highest volume of intersection is thus very efficient. These rectangular cross section beams could be intersected and subtracted simpler when they meet each other at almost right angles or when they receive perpendicular elements, otherwise specific rotation and positioning shall be maintained.

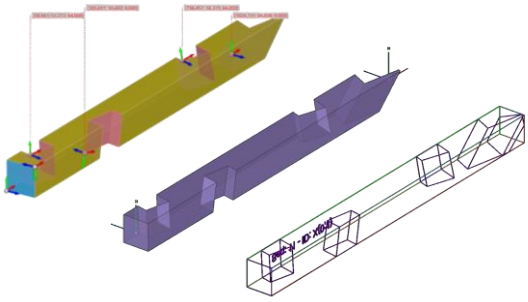


Figure 11. Conversion: from B-rep to .bvx format file, using cadwork

2.2.2. Fabrication

Wood is extensively machinable, brought by the opportunity to create precise operations, which converts this natural material to a digitalized one via interlocking joineries. Cambium simulation interface allows for checking the entire fabrication process in Hundegger K2i. Specific configuration of elements could be maintained, such as nesting the beams with the same cross-section. This hints us to purchase the optimum length and quantity of logs for each cross-section.

In fact, each floor or level has a different cross-section, which is indicated with color gradients, shown in Figure 12. The hierarchy of cross-section are 86, 80, 70, 60 millimeters, from bottom to top. Obviously, the lower levels have a greater cross-section to provide more structural stability. The reduced cross-sections of 86, 80, 70, and 60 mm are converted from 90 mm logs via planer machine.

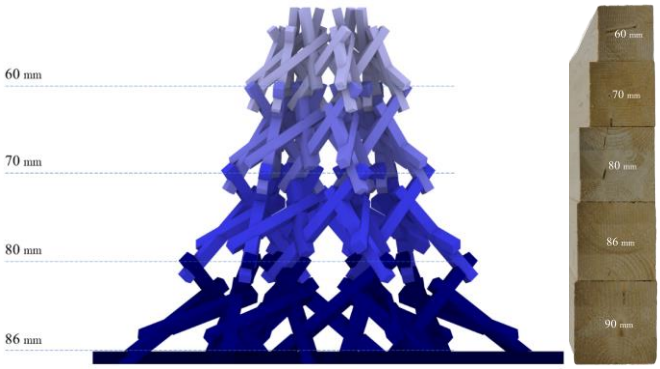


Figure 12. Hierarchy of cross-sections

The embedded tools in the planer machine take away from four sides of the logs, so the side dimensions are slightly different. To minimize this differentiation, the employed device is highly calibrated, and thus, the inaccuracy is very negligible. (Less than a millimeter) (Figure 13a) Then the output logs are transferred and automatically passed through on rails (Figure 13b) to the input of the Hundegger machine for recessing and saw cutting processes. (Figure 13c)



(a) (b) (c)

Figure 13. Chronological fabrication stages: (a) cross-section reductions with planer machine, (b) passing the logs automatically on rail to the Hundegger machine, and (c) process operation with Hundegger K2i

3.3. Augmented construction

Augmented construction facilitates the assembly-disassembly process via recognition and positioning of timber elements. This creates interactive and immersive augmented or mixed reality[1] presentations from existing 3D model. This interconnects the workflow from engineers (who makes the 3D model in computers) to constructors (who use the 3D model in augmented reality gadgets as fabrication instructions). While AR does not entirely eliminate 2D drafting, it can enhance the design process and improve communication between stakeholders or contractors by offering new ways to visualize and interact with construction designs. This section on augmentation has mostly focused on investigating the role of digital twins as an enabler for circular strategies. This strategy transits the construction from linear to circular process and bridges the gap between virtual 3D model and real construction.

As seen in Figure 14, for instance, an id: X beam has four front and back pockets every other interlocking connection. That means it cannot be assembled like a puzzle, but rather like bricks, it shall follow a sequential process, with an ability to reverse the process for disassembly, while keeping track of the status of elements. (Figure 15) The mixed reality serves as a reference to provide ease of assembly and disassembly.

[1] The difference between *augmented* and *mixed* terms derives from the ability to work in only the physical world or if the physical interactions have an impact in virtual mode.

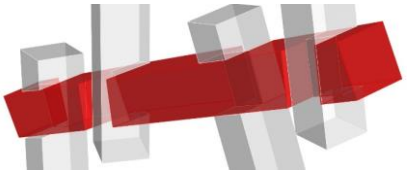


Figure 14. One element with front and back pockets every other interlocking connection

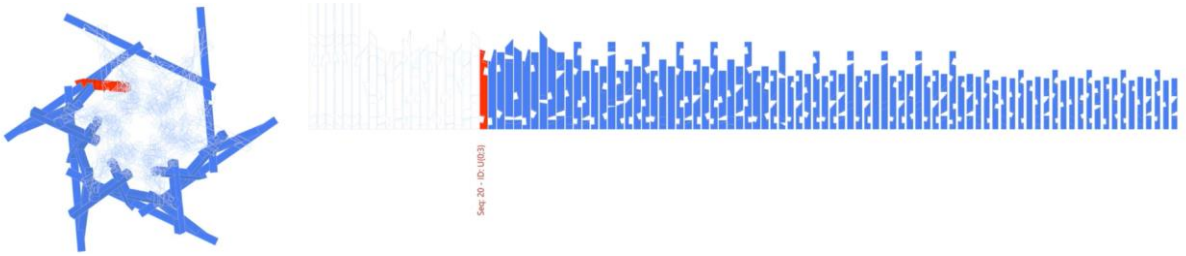


Figure 15. Sequential assembly

This starts with recognition or identification by scanning the QR code or Aruco marker and then follows up with positioning or placement using MS HoloLens 2 headset in augmented reality mode. (Figure 16)

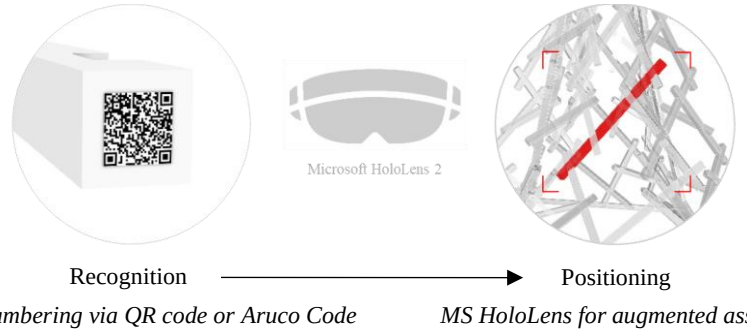


Figure 16. Two stages of assembly process; recognition via QR / Aruco and positioning via MS HL2

The Fologram software establishes an instant mixed reality experience between Rhino Grasshopper and the MS HL gadget. Geometry, layers, and grasshopper parameters can be edited in real time in Fologram to create powerful tools for design, communication, collaboration, and fabrication.

3.3.1. Recognition

The QR code or Aruco marker contains only a single number, which refers to the assembly sequence number. The QR code is printed on the main label along with all project information, using Cambium. (Figure 17a) However, since reading the Aruco marker is faster with installed Fologram in MS HoloLens 2, this has been used as well. A single Aruco marker is attached on the cross-section ends. (Figure 17b)



(a) (b)

Figure 17. (a) Main label, including project information and beam specification, printed along with a QR code. (b) Cross-section label, including single Aruco marker.

It is also possible to track a geometry via Aruco marker and save its location in Grasshopper. Then it becomes a digital twin model in which real-world interactions have a virtual reality impact in our computer interface.

Alternatively, we can identify the location of elements by using a customized menu with slider (Figure 18a), or we could toggle to another menu (Figure 18b) with next and previous button (Figure 18c), which could be used based on individual preference. This provides interactive instructions, presenting workers with visual arrows and cues, overlaid onto the physical environment to help them understand the assembly sequence.



(a) (b) (c)

Figure 18. (a) slider menu (b) toggle between menus (c) button menu

3.3.2. Positioning

It seems fair to report that the comfort and precision of HoloLens 2 is still questionable. The automatic placement is done by scanning a coordinate QR code, attached on the ground in the middle of the structure. Fologram fails to adequately orient it with the digital model, so some alignment is necessary. Nevertheless, the custom menu made by the author could effectively engage constructors with the virtual model to track the position and orientation of elements in real-time. (Figure 19)

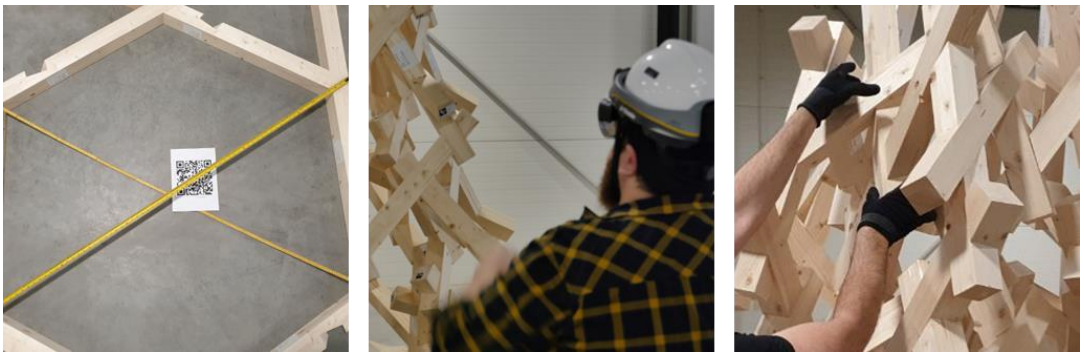


Figure 19. (a) coordinate placement; (b) collaboration; (c) manual-digital placement

As discussed, the assembly adheres to a sequential process, which is reversible. Figure 20 shows the assembly time lapse.



Figure 20. Sequential assembly of the structure

4. Discussion

Digital processes may allow for more complex and, if designed well, potentially performative high-rise structures. In this paper, we presented a tool-aware AR-assisted workflow which could be targeted for various timber systems e.g., CLT or hybrid floor decks in real construction. However, the experimental proposed structure employs short linear timber elements to create a mono-material structural system which is interconnected with interlocking joinery (Figure 21), since "structures made from linear elements required a large amount of material knowledge and technical skill to source and carve them, resulting in the emergence of extremely skilled craftsmen and a culture of wood fabrication". [9, p. 63] This leads us to a certain knowledge on the amount of computational design and digitalized fabrication before being deployed in non-experimental and industrial applications. As a further investigation upon some other similar projects, this research resulted in a functioning demonstrator which serves as a manifestation to unlock the possible futuristic trajectory in the evolving architectural typology of tall wood buildings.



Figure 21. Demonstrator

"The potential benefits of using joinery connections in mid-rise scale buildings are multifaceted. The elimination of metal joints could further drive down the embodied energy of structures. Using joinery connections may offer new implications in construction assembly speed of timber structures. Innovations in digital fabrication suggest that the cost of milling joinery could become competitive with that of fasteners . . ., [but the] analysis procedures for these unique wood-only joints are less standardized than those of metal connectors." [6, p. 1] "Their ecological and economic advantages make timber-only systems an interesting alternative for efficient and sustainable buildings." [3, p. 425] This helps us to realize how a single mono-material culture can inform all levels of performance from form to construction to disassembly.

5. Conclusion

This paper investigates the generative design of interlocking joinery timber construction and the potential implementation for upward scaling for future high-rise endeavors. The digital fabrication process incorporates automated manufacturing methods, but also from the construction sector point of view is still characterized by a high proportion of manual assemblies. The linked topic of disassembly is regarded as a vital factor of sustainability and long-term management of materials in use.

Figure 22 shows the general implication of design-production-construction approach.

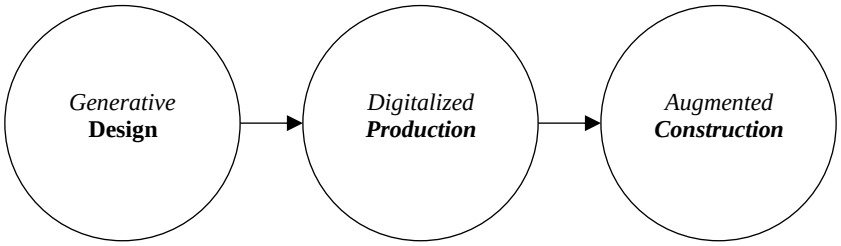


Figure 22. General implication of design-production-construction

To sum up, the whole process could be summarized according to Table 1.

Table 1. design-fabrication-construction process

Generative Design	1. *computational design* by parametric platform of Grasshopper inside Rhino3D. 2. *structural optimization*, utilizing a finite element model in Karamba3D
Digital Fabrication	1. *conversion* the B-rep geometries into legible entities, using cadwork. 2. *manufacturing* the element by Hundegger K2i, commanded by Cambium.
Augmented Construction	1. *recognition* by scanning the QR code / Aruco marker. 2. *positioning*, using augmented reality Microsoft HoloLens 2 headset.

The following conclusion are made:

- Simulation proves that shifting approach from orthogonal to free form twisted morphology possess better structural performance.
- Interlocking joinery is highly appreciated due to consistent reduction of joint complexity for ease of assembly and disassembly.
- Augmented construction, coupled by mixed reality, enables a digital twin mode for circular economy processes in wood construction.

This streamline construction process improves accuracy, reduces errors, enhances worker productivity, and expedites the assembly process for circular wood construction projects. The structural applications of timber construction are ever expanding, and it is of the utmost importance to broaden this essential dimension of industry and develop novel and acquisitive value-added design with high-performance application and fill the gap between engineers and local practitioners in complex design and construction. It is deliberately aimed to go beyond the framework of standard construction assumptions to excavate additional unusual aesthetic experiences, which are structurally more sensible, unfolded by wood.

Acknowledgements

This research was funded by the Department of Manufacturing and Civil Engineering (IVB) at Norwegian University of Science and Technology (NTNU). The fabrication is done in Innlandet Treindustri and Østlaft AS. I thank colleagues who provided insight, expertise, or practical knowledge that greatly assisted the research, although they may not agree with all the interpretations or conclusions of this paper.

References

[1] M. Green and J. Taggart, Tall Wood Buildings: Design, Construction and Performance, R. Stein, Ed., Basel: Birkhäuser Verlag GmbH, 2017, p. 177.

[2] G. Foliente, "History of Timber Construction," in *Wood Structures: A Global Forum on the Treatment, Conservation, and Repair of Cultural Heritage*, S. J. Kelley, Ed., West Conshohocken, ASTM International, 2000, pp. 3-22.

[3] O. Bucklin, H. Drexler, O. D. Krieg and A. Menges, "Integrated Solid Timber: A Multirequisite System for the Computational Design, Fabrication, and Construction of Versatile Building Envelopes," Mexico City, 2018.

[4] T. Svilans, M. Tamke, M. R. Thomsen, J. Runberger, K. Strehlke and M. Antemann, "New Workflows for Digital Timber," in *Digital Wood Design: Innovative Techniques of Representation in Architectural Design*, F. Bianconi and M. Filippucci, Eds., Switzerland, Springer, 2019, pp. 93-134.

[5] F. Bianconi and M. Filippucci, "WOOD, CAD AND AI: Digital Modelling as Place of Convergence of Natural and Artificial Intelligent to Design Timber Architecture," in *Digital Wood Design: Innovative Techniques of Representation in Architectural Design*, F. Bianconi and M. Filippucci, Eds., Switzerland, Springer, 2019, pp. 3-61.

[6] D. Fang and C. Mueller, "Joinery connections in timber frames: analytical and experimental explorations of structural behavior," MIT, Boston, USA, 2018.

[7] J. Szolomicki and H. Golasz-Szolomicka, "Technological Advances and Trends in Modern High-Rise Buildings," *MDPI Buildings,* vol. 9, no. 9, 2019.

[8] H. Chai, D. Marino, C. So and P. F. Yuan, "Design for Mass Customization: Robotic Realization of a Timber Tower with Interlocking Joints," Austin, Texas, 2019.

[9] D. Correa, O. D. Krieg and A. Meyboom, "Beyond Form Definition: Material Informed Digital Fabrication in Timber Construction," in *Digital Wood Design: Innovative Techniques of Representation in Architectural Design*, F. Bianconi and M. Filippucci, Eds., Switzerland, Springer, 2019, pp. 61-92.

[10] M. Hegger, V. Auch-Schwelk, M. Fuchs and T. Rosenkranz, Construction Materials Manual, eBook English Document ed., Basel/ Berlin/ Boston: Birkhäuser, 2006.

[11] K. E. Larsen and C. Schindler, "From Concept to Reality: Digital Systems in Architectural Design and Fabrication," *international journal of architectural computing,* vol. 6, no. 4, pp. 397-413, 2008.

[12] A. Gustavsson, M. Valtersson, C. Merschbrock and P. Johansson, "Exploring the utility of AR for quality inspections in timber-frame house production – A case study from Småland, Sweden," in *Conference CIB W78*, Luxembourg, 2021.

Proceedings of the IASS Annual Symposium 2023
Integration of Design and Fabrication
10–14 July 2023, Melbourne, Australia
Y.M. Xie, J. Burry, T.U. Lee and J. Ma (eds.)

Structural design and construction of a large building with a 3D '*circle truss*' and ETFE membrane roof

Idogawa TATSUYA*, Miyasaka TAISUKE[a], Ueda MASAHIRO[b], Komiya MASAYA[c], Kurata TAKASHI[c]

[a,*] Azusa Sekkei Co., Ltd.
3F, MFIP Haneda,10-11, Haneda Asahi-cho, Ohta-ku, Tokyo,144-0042, Japan
idogawa1161@azusasekkei.co.jp

[b] Taisei Corporation
[c] Nippon Steel Engineering Co., Ltd

Abstract

This paper describes the structural design and construction of a three-dimensionally curved '*circle truss*' and ETFE membrane roof, which is a key design element of the Haneda Airport (Tokyo International Airport) Terminal 2 expansion. First, the design conditions and constraints are discussed, explaining why such a structural system was adopted. Next, the construction and execution is described, including the use of BIM to manufacture the curved steel pipe members and unique solutions used to build the '*circle truss*'.

Keywords: EFTE, membrane roof, 3D curved truss, large space buildings

1. Project summary

The existing structure of Haneda Airport (Tokyo International Airport) Terminal 2 was completed in 2004. As this building was originally designed just for domestic operations and a significant increase in the number of flights was anticipated after as the scope expanded to international operations, a major terminal expansion plan was launched in 2016 with an anticipated opening date of April, 2020.

The design was conducted over a year and half from April 2016 to October 2017, with construction following over a 2.5 year period from October 2017 to March 2020. The enlarged terminal building features an international check-in lobby, duty-free shopping areas, airline lounges and government office areas, with the original 93,000m^2 total floor area enlarged by 65,000m^2 and separated by expansion joints into A, B and C zones. The new international check-in lobby in zone B (Figs. 1 and 2) required a large open space and long-span roof covering a 7,700m^2 plan area. This was achieved using a unique structural frame referred to as a "circle truss" and ETFE membrane. The circle truss is curved in three dimensions and is shown in Figs. 3 and 4. The membrane has three layers, including one opaque PTFE layer and two ETFE layers. This achieved a 1hr fire rating and blocks out strong sunlight, while giving the internal space the appearance of a general membrane roof.

2. Structural design challenges

A number of design challenges were overcome when designing and constructing the new roof, particularly with how it integrates with the existing structure, as shown in Fig.5.

1) The new structure is sandwiched between the existing terminal building and a viaduct, and had to span an existing common ditch. 2) The foundation used existing piles cast prior to designing the enlarged building. 3) The floor-to-floor height was limited to align with the existing building floors, while ducts and the baggage handling system had to fit within the structural depth, running through opening in the

Copyright © 2023 by Idogawa TATSUYA, Miyasaka TAISUKE, Ueda MASAHIRO, Komiya MASAYA and Kurata TAKASHI. Published in the Proceedings of the IASS Annual Symposium 2023 with permission.

truss beams. 4) The roof is supported by the existing building and foundations, and so it was imperative to minimize the roof self-weight. 5) The existing structure had to be locally retrofitted to integrate the expansion and support the increased loads.

Nevertheless, this paper primarily focuses on the roof structure.



Figure 1: Building outline

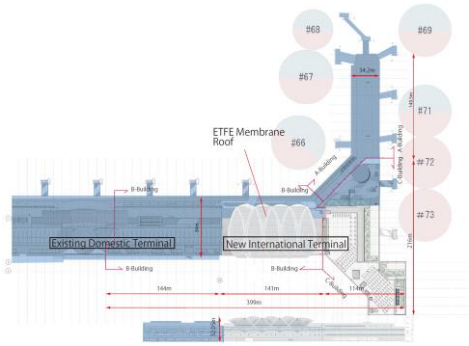


Figure 2: Plan



Figure 3: Construction of the circle truss

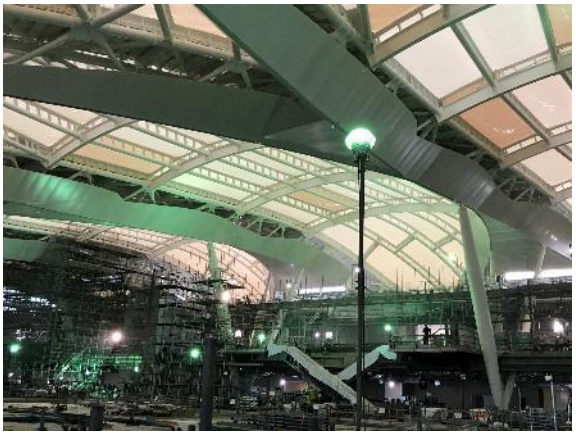


Figure 4: Construction of the check-in lobby

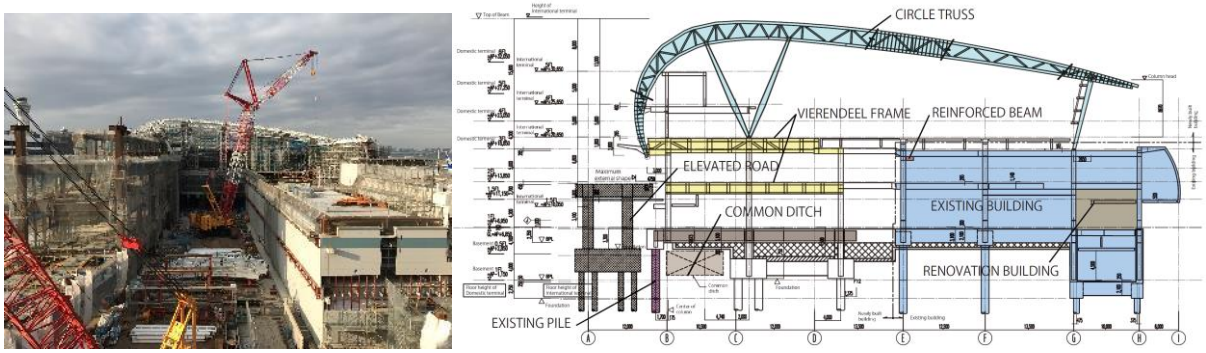


Figure 5: diagram of the structure plan

2.1 Structural design of the roof truss

The roof covers a 120m by 62m space, with a 59.5m main span (Fig.6). Additional loads imposed on the existing building were minimized by adopting lightweight roofing materials (ETFE) and by supporting the roof gravity load on the new structure as much as possible. This was achieved by

effectively cantilevering the roof from the new structure, with the far end supported by pinned-jointed struts so that bending moments are not transmitted to the existing structure.

Initial concept models created by the building designer with wire forming the roof frame are shown below. The circle truss concept is shown in Fig.7 and an alternative "triple beam" concept in Fig. 8. Both support about 65% of the roof gravity load on the columns of the new structure. However, time history analysis conducted during the final stage of design uncovered several vulnerabilities of the three beam concept in the event of a strong earthquake. The long direction of the existing structure experienced excessive deformations, the long roof chord members deformed about their weak axes like string of a guitar, while maximum vertical roof accelerations exceeded 4,000gal (40 m/s^2). The "circle truss" was instead adopted, as the three-dimensionally interlocking frame provided greater in-plane stiffness to the roof surface, reducing the earthquake demands on the existing structure.

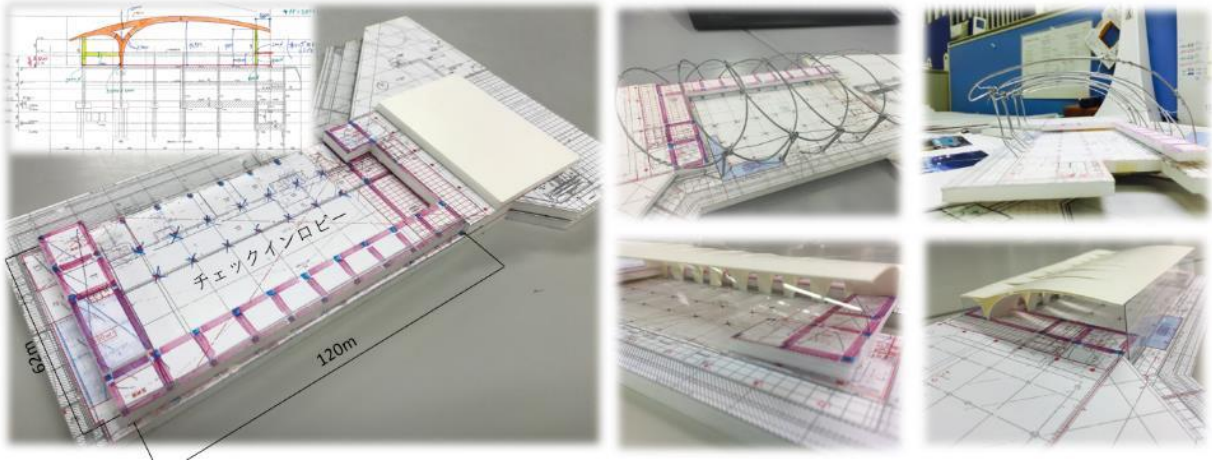


Figure 6: First sketch model of a large space building and the circle truss plan

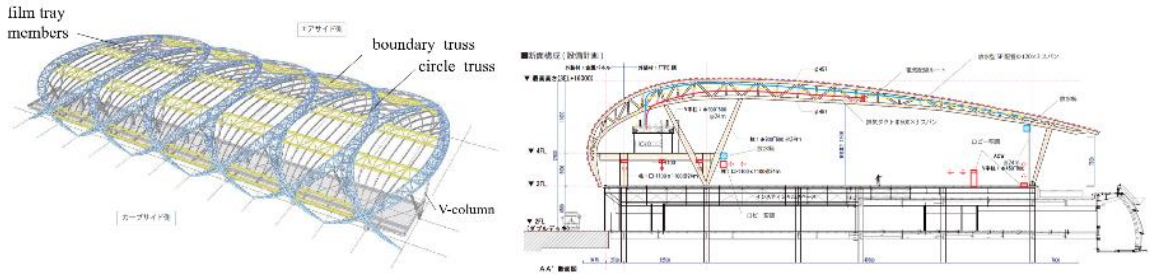


Figure 7: Circle truss concept

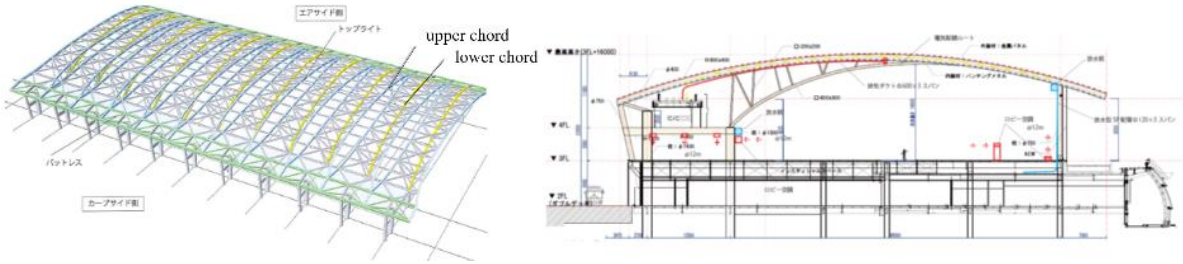


Figure 8: Three beam concept

2.2 Circle truss structure

The roof frame consists of five (later reduced to four) overlapping circles arranged in plan and then bent to arch over the check-in lobby and form one of the wall surfaces (Fig. 9). Each doubly-curved truss has two upper and one lower steel tube (STKR490, Φ400mm) chord. The internal clear height provides an open lobby space and maintains sightlines for the control tower, while the building height restriction ensures the airplane tails are visible from the control tower.

Three rows of boundary trusses were included in the longitudinal direction to brace and stiffen the circle truss. The primary columns of the three-pronged steel tubes taper down from φ900 to 600mm at the tip and are supported on cast steel plinth with ball joints. Although the curved steel tubes are clad, ring plate joints were adopted in preference to intersecting welded joints to simplify the fabrication and construction of the circle truss.

The circle truss was further optimized during the construction stage by eliminating a 12m half circle section of the roof and revising the truss members. First, the secondary beams were revised from box to tube sections, which are more effective in resisting torsion induced by the membrane tension. This permitted smaller sizes that reduced the roof self-weight and inertial earthquake forces. Next, the triangulated boundary trusses were changed to Vierendeel trusses, with fixed end beams connected into the secondary beams. These modifications reduced the roof frame steel tonnage from 230 to 200 kg/m^2 (Fig. 10). Note that this tonnage figure is highly conservative estimates, as it includes all steel (including secondary beams, fixings and columns) in the Tekla model, except for the curtain wall mullions, divided by the project plan area (even though the roof curves to form the land-side wall). A 3D printed model and final rendering of the roof structure are shown in Figs.11 and 12.

2.3 ETFE roof membrane

ETFE membrane was selected to minimize the roof weight. However, there are dimensional limitations when importing this material, and so the membrane framework was sized to have a width of less than 11m. The weight of the ETFE membrane and supporting steel members was about 70 kg/m^2, which is significantly lighter than the 100 kg/m^2 of conventional metal cladding. This reduction in imposed load further reduced the roof weight and influence on the existing building.

Although ETFE was codified for use in Japanese buildings in 2018, this material has low fire resistance and has difficulties satisfying domestic regulations for roofs to be fire rated. Therefore, a triple membrane was adopted that includes an inner flame-retardant PTFE layer with outer ETFE layers (Fig.13). The characteristic texture of the ETFE cushion gives a pleasing appearance, while the triple-layered composition helps to block the strong summer sunlight.

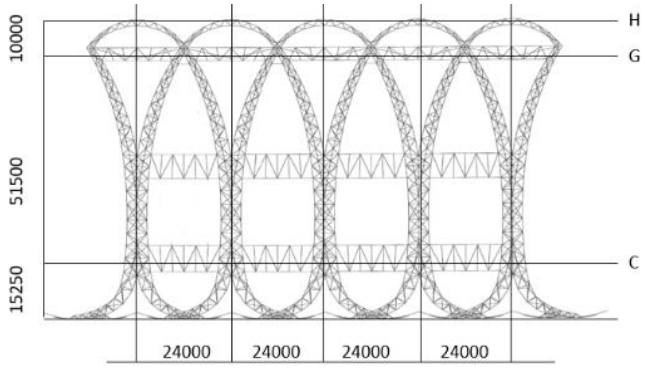


Figure 9: Original circle truss

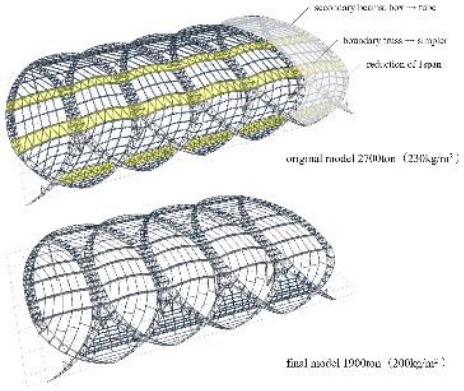


Figure 10: Optimized roof structure

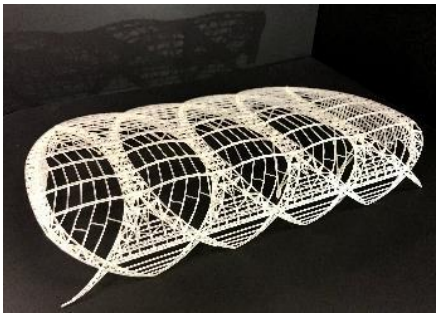


Figure 11: 3D printed model

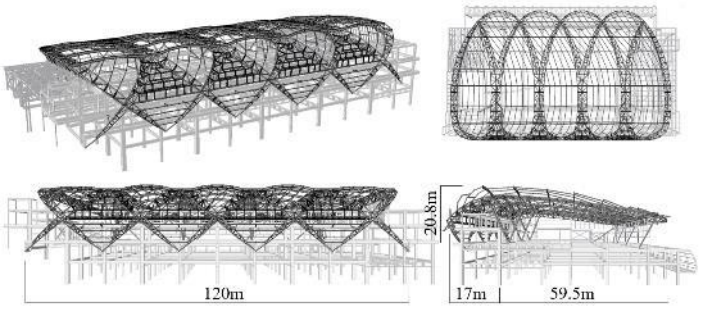


Figure 12: Roof rendering

2.4 Curtain wall

The check-in lobby airside face features a large glass curtain wall supported by V shaped columns and wind-resistant box beams (Fig.15). The columns are located outside of the glass and the 18m long box beams cantilever a further 1m, providing a clean glass surface and direct view of the airplanes from the check-in lobby. Vertical members were intentionally terminated above the floor level to further open the field of view, and instead were suspended from the top floor to help suppress vertical deformations. These were arranged in either an A- or V- shape, with the compression members ■-60×60mm square bars and the tension members φ-25mm circular bars (Fig.14). A 75mm clearance was provided to accommodate the vertical roof deflections and avoid damaging the glass.

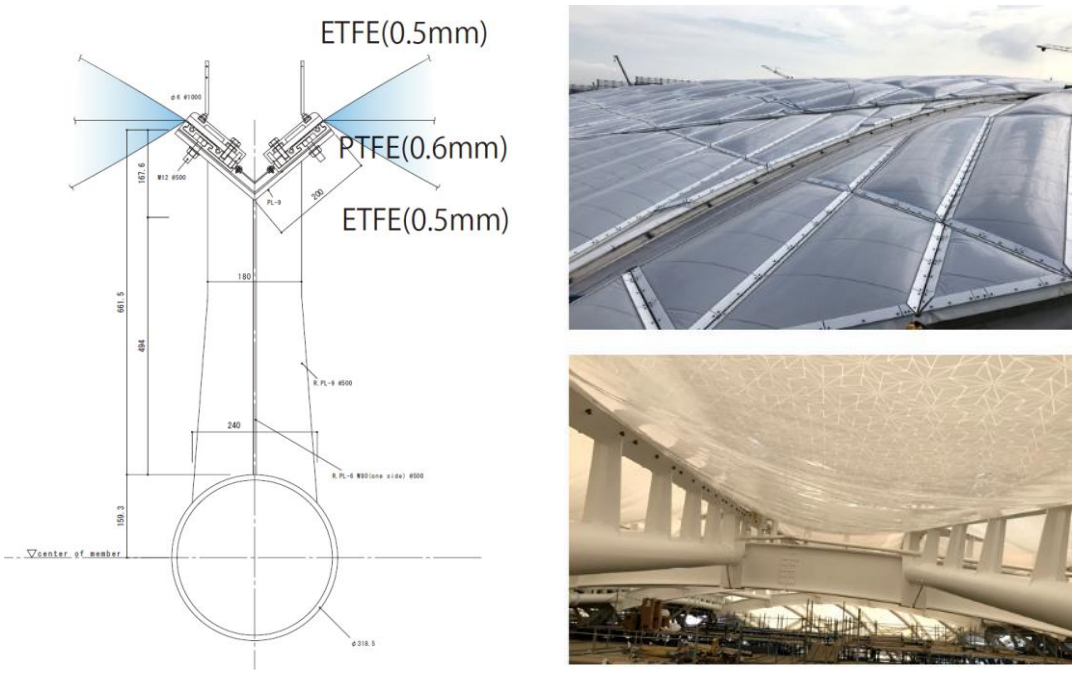


Figure 13: Triple-layered membrane detail and completed photos

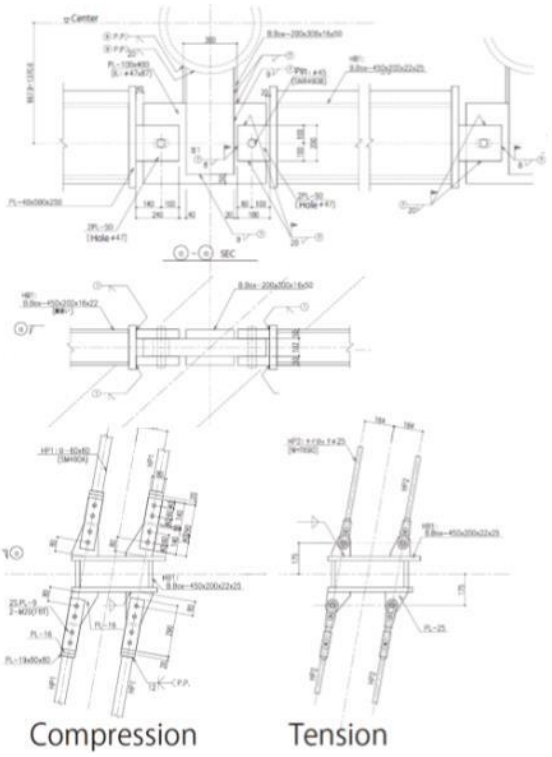


Figure 14: Wind-resistant beam details



Figure 15: Completed curtain wall

3. Fabrication plan/process

3.1. Geometry design for effective fabrication of circle truss

It is exceptionally challenging to accurately fabricate doubly-curved 3D trusses. While it is possible to bend pipe in two directions, that process would have exceeded the project's budget and construction schedule, given the limited number of suppliers with such specialized equipment. This situation was further compounded by the increased construction activity surrounding the Tokyo 2020 Olympics. This issue was avoided by rationalizing the circle truss geometry to achieve the double-curved global geometry from singly-curved individual pipes.

The solution was to combine and rotate multiple planar curves to approximately fit the complex original curve, as shown in Fig. 16. Each curve is circular with a different center and radius, and targets a different part of the 3D curve surface. These are then connected in a chain with tangent intersections, and were defined from three reference points to find the closest match the original curve. Further adjustments were made for ease of fabrication. Some points were defined up to 1m away from chord-diagonal intersections to provide straight segments at the connections, while the short elements at the circle truss intersections were straightened to minimize fabrication cost. Straight pipes were also used for the chord segments with large radius near the middle of the circle truss to minimize fabrication cost, as these near-flat segments still satisfied the architect's image and concept of the circle truss.

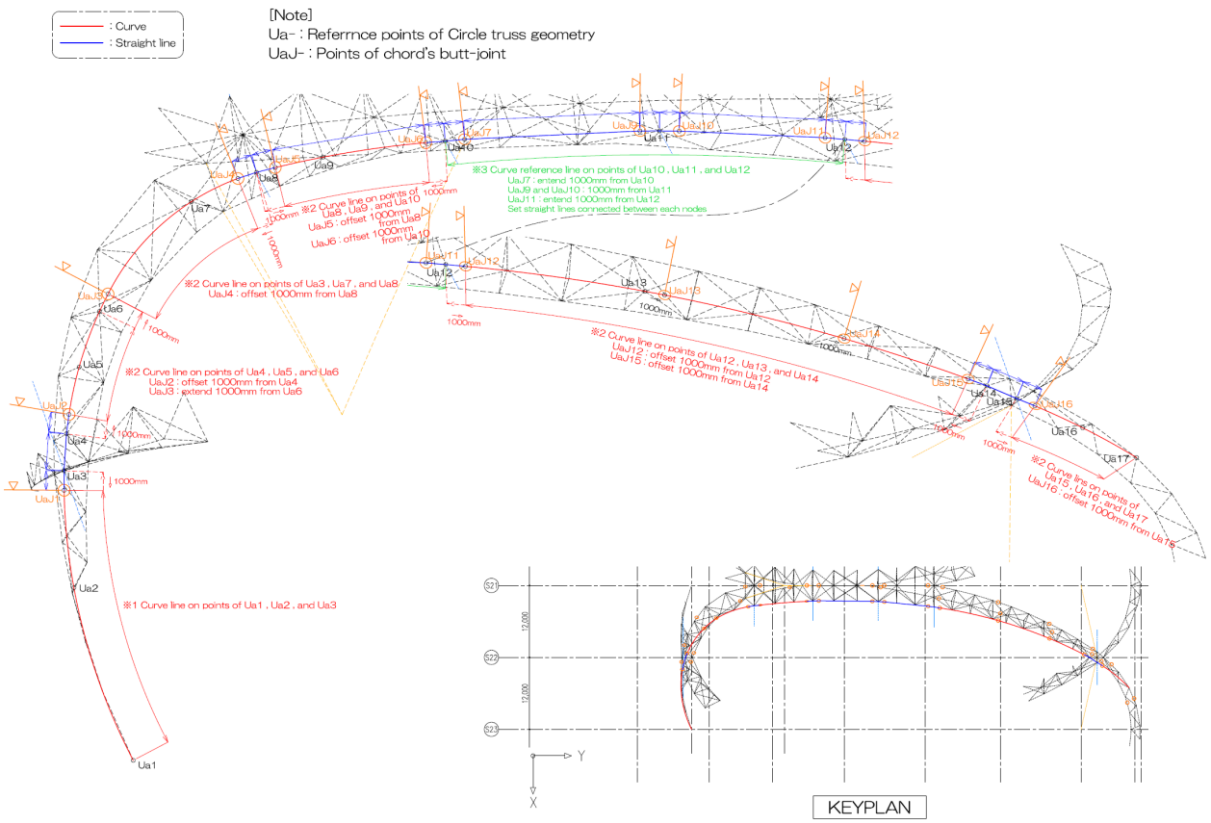


Figure 16: Geometric rationalization of the circle truss

3.2. Fabrication of roof structure

Preparing the shop drawings and fabricating the steel structure was expected to take a considerable amount of time due to the complexity of the roof structure and circle trusses. Therefore, a detailed 3D BIM model of the entire steel roof structure was modelled in Tekla Structures (Fig.17). This was used to visual and review the fabrication and on-site construction, including member clashes, transportation sub assemblage blocks, site welding access.

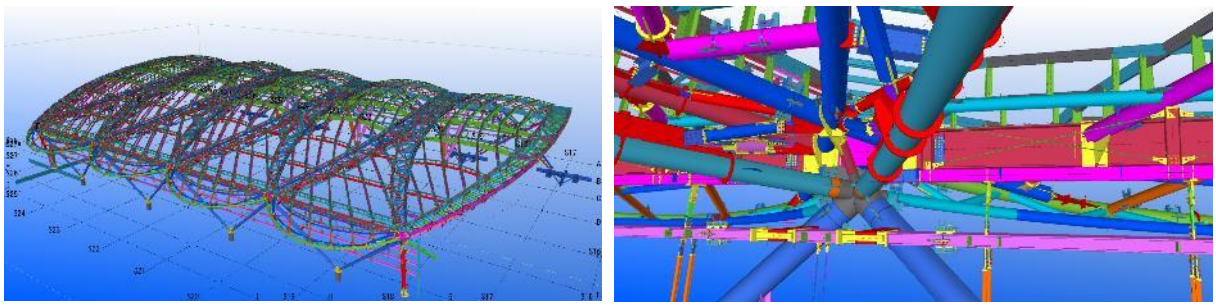


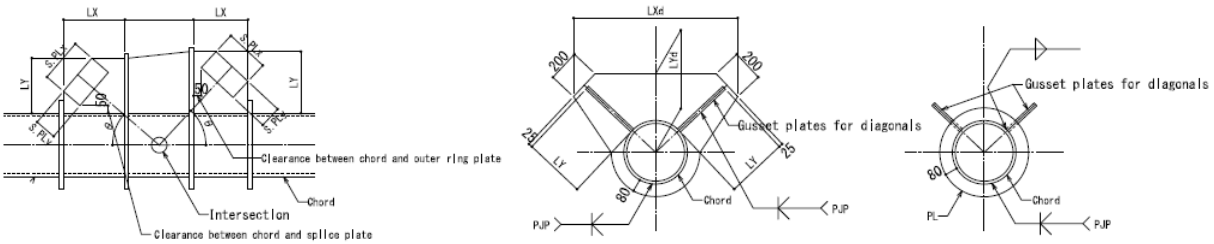
Figure 17: BIM model of roof structure

3.2.1 Circle truss connections

Representative connection details and fabrication photos of the circle truss are shown in Fig.18. The connections between the chords and diagonals consisted of outer ring plate reinforcement, gusset plates and slip-critical bolted connections to maximize onsite efficiency. The same type of connection was repeated throughout the roof structure, and were designed as follows:

- The shape and size of the gusset plates were determined from the clearance to the splice plates, ring plates and chords
- The joint design was automated, with only the weld lengths and sizes varied

However, several locations adopted prefabricated truss blocks, most notably the areas outside of the curtain wall. The diagonals within these blocks were factory welded to the chords. (Fig.18(c))



(a) Typical joint design



(b) Upper chords



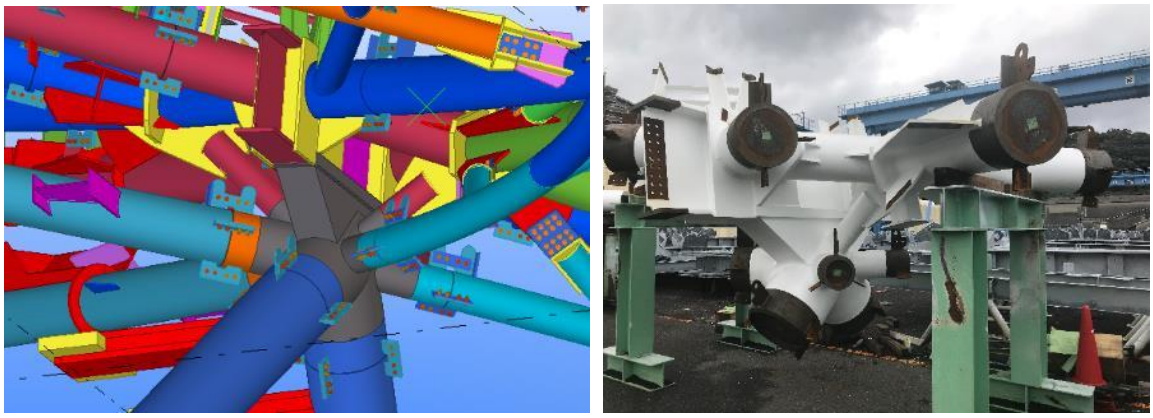
(c) Circle truss with welded joints

Figure 18: Fabrication of circle truss

3.2.2 Cast steel connections

Beams running along the top of the curtain wall have joints connecting more than ten members of upper chords, lower chords and diagonals. These complex joints are located in a narrow space, but must provide moment fixity to the top of the columns to ensure redundancy in the out-of-plane direction. Therefore, large cast steel nodes were used to achieve a compact and cost effective joint design, with each featuring eight branches and two beam stubs. (Fig. 19(a))

The pin joints at the base of the primary three-pronged columns were also fabricated from cast steel. These connect members at a narrow angle and needed to be compact to minimize the bending moments transmitted to the frame under the bearing. (Fig. 19(b))



(a) Beam connections at the top of the curtain wall



(b) Three-pronged column base connections

Figure 19: Construction photos of cast steel connections

4. Construction plan

The construction had to meet a number of challenging criteria (Fig. 20, 21).

1) Height was restricted by the Aviation Law. This limited the construction staging yard to a narrow area surrounded by the existing buildings, elevated roads and runway.
2) Ensuring accurate construction despite the complicated roof shape.
3) A tight construction schedule.
4) Ensuring safety in the event of an earthquake during construction.
5) Coordinating the temporary supports and scaffolding.

These challenges were met using several strategies (Fig.22, 23).

1) A 350-ton crawler crane was used to minimize the height of the heavy construction equipment.
2) An accurate shape was achieved by first assembling all roof components on the ground.
3) The construction timeline was shortened by conducting a partial jack down after completing all welds for the respective section, instead of waiting until the entire roof was installed.

4) The temporary supports were designed for construction-stage earthquakes. The Japanese Level 1, (serviceability earthquake) seismic hazard was adopted, with a 0.2 G elastic short period horizontal acceleration. The vertical load was amplified to 1.2 to account for destabilizing eccentricity.

5) The temporary supports and scaffolding were laid out using BIM and carefully checked for clashes with permanent and existing structure.

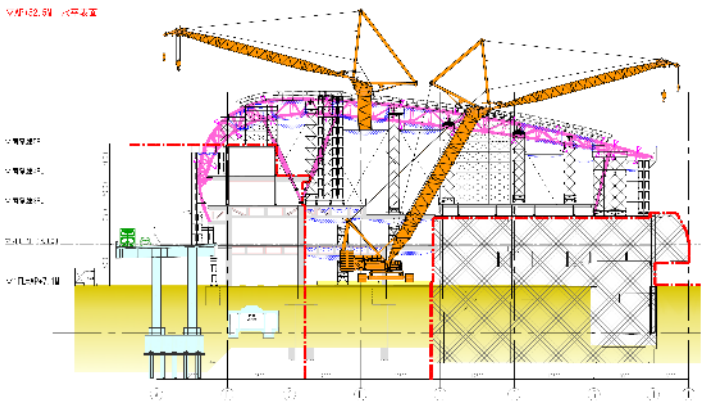


Figure 20: Construction plan



Figure 21: Surveying

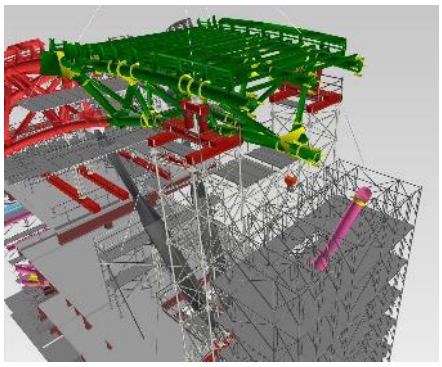


Figure 22: BIM modeling with scaffolding



Figure 23: Structural steel erection

4.1 Quality control

A survey was performed at chord positions that were pre-marked in the fabricator facility. About 5,000 coordinates were taken from the model to manage the accuracy of the temporary supports and construction. Although tight tolerances were specified, corrective action was only taken on site if deviations were anticipated to affect the subsequent section. Relatively large deviations were possible due to the jack down procedure, and so at these interfaces the level was compensated by raising the steel work 5 to 10 mm, or until it no longer interfered with welding.

4.2 Jack down

Jacking down was completed in 4 stages (Fig.24, 25), each corresponding to the welding and completion of a full circular truss. To add redundancy and improve accuracy, jacking down also waited until the adjacent circular truss was fully welded, but still supported. The second jack down stage is depicted in Fig. 24, with the previously lowered jacks in green, the jacks being lowered in purple and the completed welds indicated in orange.

Self-weight and construction stage deformations were analyzed and compensated in the roof geometry, and then closely monitored on site. As a point of comparison to the construction stage analysis, all monitored points with vertical deflections exceeding 50mm were compiled, and found to be 70% of the predicted displacements on average, with a 13% standard deviation. A maximum deflection of 60mm was recorded as the jack down loaded the self-weight into the roof structure, which compared favorably to the 58mm predicted displacement. This indicates that the partial jack down method offered accurate control of the roof geometry.

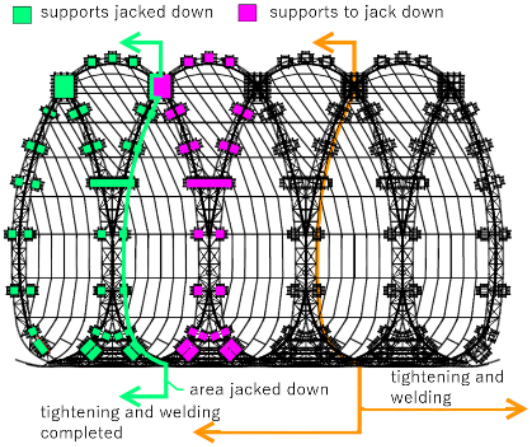


Figure 24: Second jack down stage



Figure 25: Hydraulic jack

4.3 Membrane roof installation

The roof membrane was separated into 318 units. On the steep land-side faces, sections were installed by hanging members from a Potain self-erecting situated on the elevated road (Fig.26, 27). However, none of the cranes could reach the steep air-side face, and so these membrane sections had to be manually transported and positioned. Since the membrane action of the ETFE cushions requires internal pressure, temporary blowers were activated immediately upon placing and until main blower was installed.



Figure 26: Installing the membrane roof



Figure 27: Lifting the membrane roof

5. Summary

This paper described the conception, structural design and construction of a unique “circle truss” roof as part of the Haneda Airport Terminal 2 expansion. This included the design process of the circle truss and triple-layer ETFE/PTFE membrane, integration with the existing building, and modifications implemented to reduce the cost. The use of BIM in the design and fabrication of the complicated steel structure was then described, followed by the membrane installation and partial jack down procedure. This challenging project was completed by clarifying and resolving unique challenges at each stage of the design, fabrication and construction with the entire project team (Fig. 28, 29).



Figure 28: Completed check-in-lobby



Figure 29: Completed exterior

Acknowledgement

We were only able to accomplish the design and construction over the four year period thanks to the cooperation of all involved, and special thanks to the Client, Prof. Toru Takeuchi of the Tokyo Institute of Technology for instruction during the design stage, cooperating design offices, airport employees who tolerate the expansion construction, and passengers flying through this airport.

We hope that this building warmly welcomes you in future.

Proceedings of the IASS Annual Symposium 2023
Integration of Design and Fabrication
10–14 July 2023, Melbourne, Australia
Y.M. Xie, J. Burry, T.U. Lee and J. Ma (eds.)

Towards upscaling membrane tensegrity shells: A design-to-fabrication workflow

Ying Yi TAN*, Kenneth J. TRACY[a], Christine YOGIAMAN[a]

* Singapore University of Technology and Design
8 Somapah Road Singapore 487372
yingyi_tan@sutd.edu.sg

[a] Singapore University of Technology and Design
8 Somapah Road Singapore 487372

Abstract

Membrane tensegrity shells use tensegrity structural principles to create self-supporting and wide-spanning spatial enclosures. These consist of a network of discrete struts pre-tensioning a single customised membrane surface, in place of multiple linear cables. While previous literature has documented the installation of occupiable pavilions, there are challenges in upscaling membrane tensegrity shells to be viable as larger outdoor shelters. Our research tackles these challenges in the ongoing development of an 8.0m span pavilion, entitled 'M-shell'. To achieve this, we implement our computational design-to-fabrication workflow consisting of four main phases: (a) determining optimal strut placement; (b) validating the model via finite element analysis (FEA); (c) extracting fabrication data; and (d) manufacturing and assembly. This paper documents the execution of this workflow for our half prototype 'M-shell' pavilion.

Keywords: membrane tensegrity shell, structural optimisation, design-to-fabrication

1. Introduction

Membrane Tensegrity Shells (MTS) are novel structural systems premised on the principles of tensegrity to create lightweight self-supported dome-like spatial enclosures. These systems consist of two main components: (i) a network of discontinuous discrete struts that act in compression and (ii) a large continuous membrane that acts in tension. The struts, arranged as crosses across the membrane, biaxially tension the elastic surface at localised areas. This interaction enables the formation of free-standing doubly curved envelopes. MTS also features several advantages over other conventional structural membrane systems, such as pole tents or frame-supported canopies. Specifically, these advantages include: (a) enabling large-spanning column-free enclosures to be created with a minimal number of linear elements, thereby minimising machining costs; (b) minimising their contact area on the ground by negating the need for tethering around its perimeter using cables; (c) relatively fast deployment with minimal skilled manpower in its set up.

MTS has been adopted as occupiable outdoor shelters with recent literature reporting several pavilion variations done by our team [1], [2] and Yang, et. al. [3], with the largest documented span achieved to date being the Bamboo Tensegrity Shell at 5.0m. While there is a potential for these shells to be viable as larger outdoor shelters, upscaling these systems poses several challenges. This is mainly due to the lack of understanding and formal engineering analysis of this non-trivial structural typology at larger scales. The complex interplay of tension and compression, coupled with the non-linear material

Copyright © 2023 by Ying Yi TAN, Kenneth J. TRACY and Christine YOGIAMAN. Published in the Proceedings of the IASS Annual Symposium 2023 with permission.

behaviour of the membrane and disconnected struts, makes modelling this system a challenging endeavour.

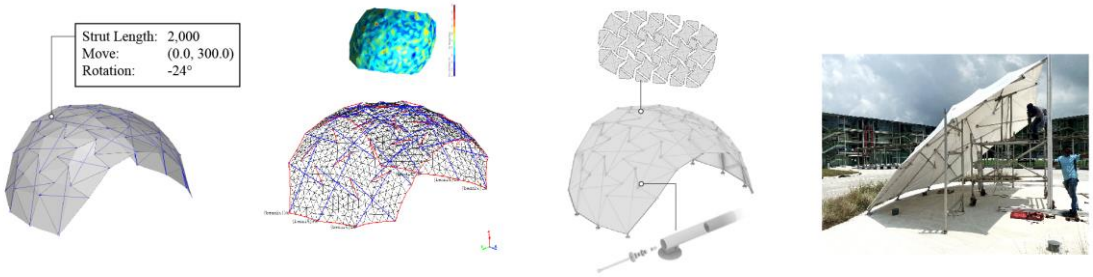
Moreover, there is a need to strike a balance between the mechanical properties of the struts and the membrane and their material weight. As there are no interim support elements, maintaining adequate pretension of the membrane is vital to create an 'inflated' dome geometry for the structure to be in structural equilibrium. This pretension also needs to be induced without causing the struts to buckle while ensuring that the struts do not excessively weigh down the membrane. Thus, making larger MTS structures would warrant stiffer components for both membrane and struts and possibly include other auxiliary support elements (e.g., internal cables) to achieve the required amount of stiffness in the system.

As such, upscaling MTS systems has to be addressed from both engineering and fabrication perspectives. This research tackles the challenge through an improved design-to-fabrication workflow for creating large scale MTS structures, specifically for making a half prototype that was partitioned from our intended 8.0m span structure, entitled the M-shell. This paper will document the various processes of this design-to-fabrication workflow. It will further share the challenges that we faced during the installation of this half prototype and suggest necessary improvements to address them. In short, the objectives for this paper are:

- To expand upon our computational design workflow by incorporating FEM analysis and design-to-fabrication scripts to obtain necessary fabrication data;
- To construct a half prototype pavilion to assess the viability of our fabricated components and assembly sequence.

2. Design-to-fabrication workflow

Our computational design-to-fabrication workflow consists of 4 phases: (A) Computational design of optimal strut mapping; (B) Validating using Finite Element Analysis (FEA); (C) Extracting fabrication data; (D) Manufacturing & assembly.



(a) Optimal Strut Mapping (b) Validating using FEA (c) Extracting Fabrication Data (d) Manufacturing & Assembly

Figure 1. Design-to-fabrication workflow in creating our 8.0m span membrane tensegrity pavilion.

This section is written with reference to the design and fabrication of our 1:1 scale half prototype. It is a segment of an asymmetrical arch that was derived from our full prototype of 18 crosses with a 45.3m^2 surface area coverage and mass of 345.6kg. The prototype is anchored to the ground at two edges with a total of 6 base footings. In this paper, the current prototype consists of 9 strut crosses, 2.6m average length, in a 3x3 configuration with 3 base footings. It also has a welded membrane with a surface area of 36.6m^2. Since it only has half its geometry, the exposed upper boundary condition was supported by a mobile scaffolding rig.

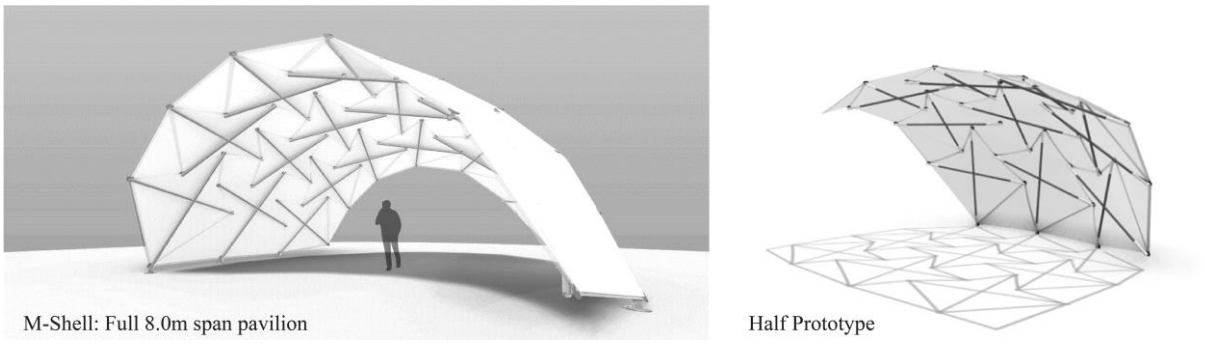


Figure 2. Renders of the full and half prototypes

2.1. Earlier prototyping using stiff components

Prior to executing this workflow on the half prototype, we created smaller 1:10 scale physical models to better understand the behaviour of the system as we were intending to use much stiffer elements compared to our previous iterations. Our models were made with cut-and-sewn ripstop fabric and aluminium tubes that were fitted onto the membrane using bolts and washers. This prototyping allowed us to decide on the elongation axis being the bias, 45 degrees of the warp/weft axis. Biaxially tensioning the membrane in the bias axis allowed the flat surface to deform into a curved surface with a grid of 2x2 strut crosses.

We later attempted this elongation strategy on a 1:1 scale strut cross made from two aluminium 6061 tubes that were pre-tensioning a polyester membrane laminated with a PVC coating. Thus, the pre-tensioning was decided to be up to 2.5% strain along the bias to ensure that the laminated membrane was adequately taut without causing either component type to yield.



Figure 3. 1:10 and 1:1 scaled models to determine the pre-tensioning strategy.

2.2. Computational design: Iterative conformal mapping

The computational design phase involves optimising the strut parameters to obtain an MTS geometry in structural equilibrium with minimal deviations from its intended geometry. The workflow includes a mix of procedures, namely strut mapping, conformal mapping, structural analysis, and optimisation. For more details and further application of this computational workflow, kindly refer to our recent published paper [4].

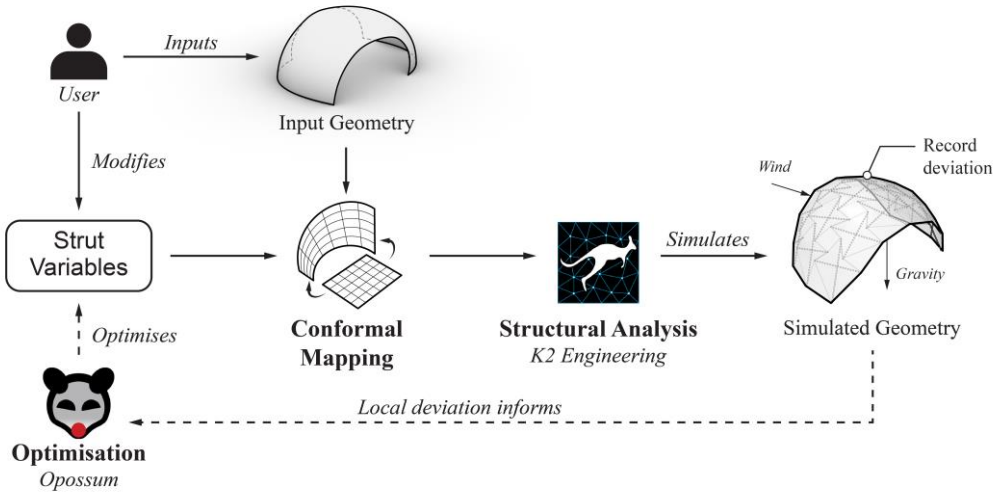


Figure 4. Computational design workflow.

Firstly, we input our intended shell geometry, as a mesh, into the Grasshopper script. The script generated a series of cross-like strut units in a grid-like formation based on the size of the mesh. Strut parameters, such as its position in x-/y-direction, average lengths, rotation, etc. can be adjusted to change the initial configuration of the struts. The script then implemented conformal mapping to mathematically position the struts onto the mesh faces while preserving their angles but changing their lengths [5]. This mapping ensures that the struts are always at 90 degrees regardless of their locations on the input mesh, which makes the struts pretension the membrane biaxially. Additionally, the struts with their endpoints closest to the bottom were extended so that these struts intersect the ground x-y plane. This ensures that the pavilion is always in contact with the ground. The script generates a Delaunay mesh from the end points of the struts to represent the membrane as a cable-net system.

Next, the script implements non-linear structural analysis on the newly created MTS digital model using the *K2Engineering* plug-in paired with *Kangaroo* [6]. The intention of this simulation is to give a sense of whether the given strut configuration is structurally feasible as a free-standing MTS system. The strut crosses were assigned as bar elements, specifically aluminium tubes, while the membrane was treated as a cable net with the interconnected mesh lines assigned as laminated polyester membrane material. These specifications can be found in Table 1. The strut endpoints at the ground plane (z = 0.0) were assigned as pinned supports that are free to rotate in any plane. Subsequently, the plug-in assigns gravitational and wind loads (20m/s in both x/y directions) to mimic the loading conditions in real life.

Table 1. Mechanical properties for the K2Engineering analysis

Type	Material	Cross-Section	Density	Young's Modulus	Pretension
Struts (Bar)	Aluminium 6061	Hollow Tube (50 x 45mm)	2720 kg/m³	68.9 GPa	N/A
Membrane (Cable Net)	PVC Laminated Polyester (700gsm)	Rectangular (50 x 0.78mm)	1.75 kg/m³	3.5 GPa	1000 N

Once the model converges, the deformation between each mesh face is extracted to quantify how much local deviation there is from the input mesh after loads have been applied. This compares the distance between the mesh faces between the simulated model and the input model. Both the average and maximum deviations will be fed into the optimiser in the next step.

The final step involves optimisation which uses the Opossum plug-in [7], a radial-based optimisation algorithm, that iteratively changes the strut parameters to obtain a structurally viable MTS structure with minimal local deviations from its input model. As Opossum runs, the Zombie Solver of Kangaroo is preferred to ensure that the simulated model has converged before it is assessed to generate new parameters for the next iteration.

2.3. FEA validation

While the computational design phase gives us an approximate digital model that is shown to be structurally viable, there is a need to validate this model using Finite Element Analysis (FEA). In this project, we worked with a local engineering firm that specialises in structural membranes, Multimedia Engineering, in the analysis of our pavilion. This analysis also takes into account building code regulations (Eurocode) in the modelling of the M-shell.

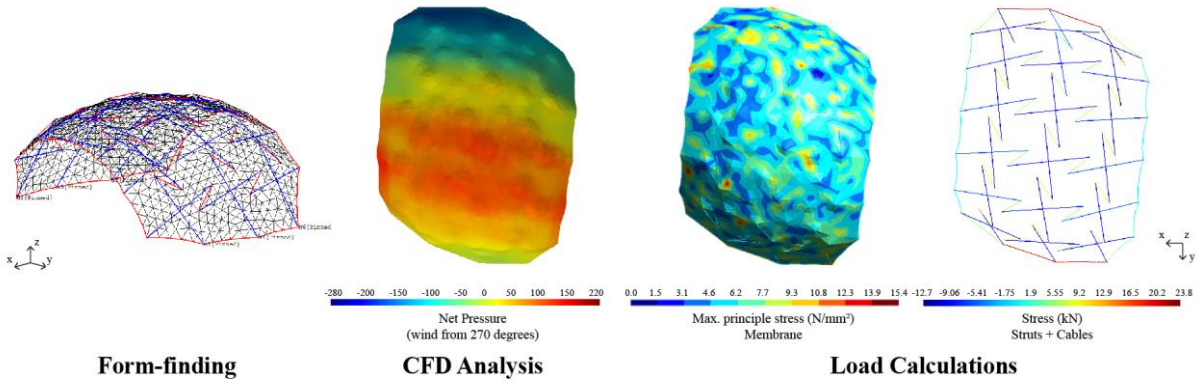


Figure 5. Structural analysis to validate the model.

Taking reference from our model, the engineering team performed a form-finding step to determine the natural shape of the MTS pavilion under its self-weight. This involved remeshing the Delaunay mesh to a finer resolution version and assigning the bases as pin support points. The form-finding step was carried out by changing the cross-section of the aluminium tube struts to ensure that the pavilion remains in structural equilibrium with no deflection from our given model. This converged model specified the aluminium tubes to be of 44.5mm diameter with a wall thickness of 6mm. Moreover, the form-finding step proposed the need for stainless steel wire rope cables at two main locations: (1) aligned along the perimeter edge of the membrane and (2) internally connecting the closest endpoints of the struts. These were 10mm diameter cables for the bottom-most perimeter edges and 6mm diameter cables for the internal connections and side perimeter edges respectively.

The next step involved a load analysis based on a combination of self-weight, rain load (0.1 kN/m2) and 8 different wind load scenarios (at 20m/s) using *Windas Tensinet*, a load incremental non-linear finite element analysis solver. Due to the asymmetrical geometry of the MTS pavilion, computational fluid dynamics (CFD) was performed initially to record the different amounts of pressure exerted across the membrane's surface before the non-linear finite element solver was used.

At each load scenario, deflections, stresses, and reaction forces from the support points were extracted from the pavilion. Stresses from the membrane, struts and cables were taken at the load scenarios where each component experienced maximum principal stresses. This data was assessed to determine whether these components were within their material limits. The assessment was inclusive of a 2.5 factor of safety for the membrane and 1.5 factor of safety for the struts and cables. Additionally, this load analysis helped us to determine the ideal orientation of the pavilion on the site to reduce the scenario of wind loading that will cause the maximum stress on the membrane.

2.4. Extraction of fabrication data

After the structure was validated, fabrication data of its constituent components were extracted from the model. These were categorised as data from the membrane, the struts and their end connectors, and the cables. The data was translated into working drawings which were used to communicate with fabrication specialists.

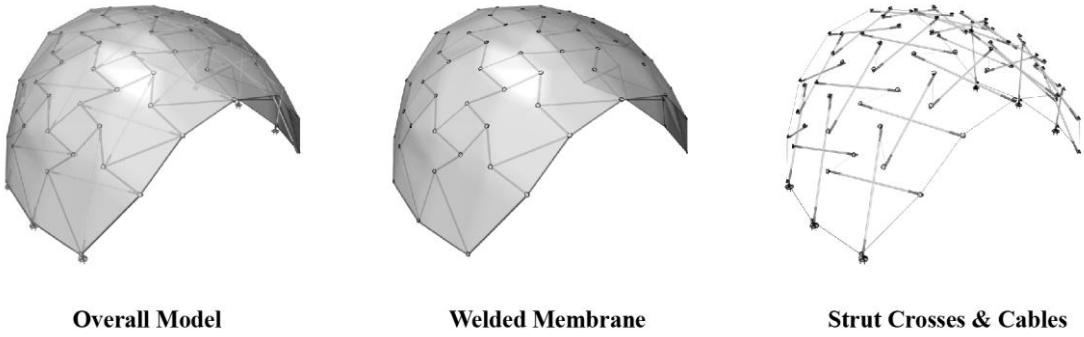


Figure 6. Various components of the M-shell.

2.4.1. Struts and connectors

To minimise buckling, each cross strut unit was modelled as an interconnected and in-plane component for the structural analysis steps. This property of the model was physically manifested by welding the tubes together to form an in-plane cross. Additional 6mm thick gussets were added at the intersection as triangular fins to further reduce the occurrence of buckling when the struts are pre-tensioning the membrane.

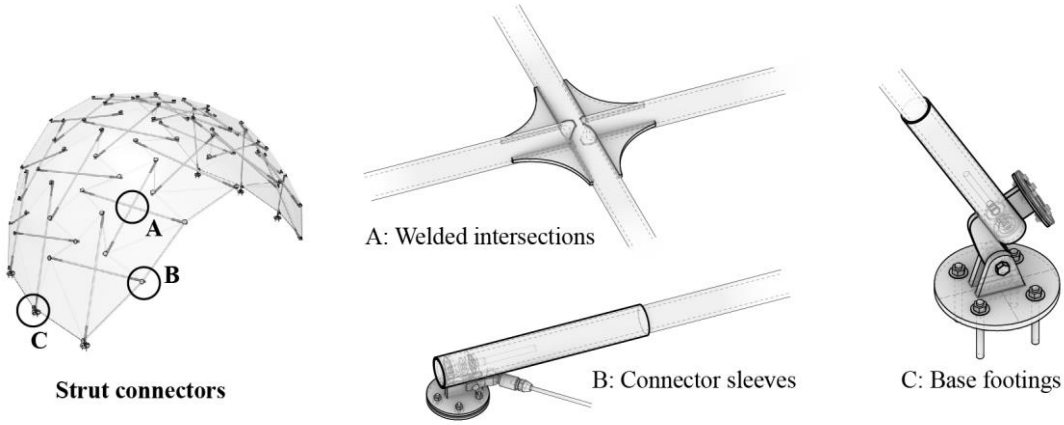


Figure 7. Various hardware connectors.

In addition to the struts, connector sleeves were also included to serve a dual function: (i) to connect the ends of the struts to the membrane, and (ii) to provide a way to mechanically elongate the struts to pretension the membrane. These aluminium connectors were designed as 350mm long tubes that were welded onto 4mm circular discs that could be bolted onto the membrane. The connector tubes were designed to be slightly larger than the strut tubes (50.8mm diameter with 2.8mm wall thickness) to house the ends of the crosses. These connectors also housed an extension mechanism where a hand drill with a hex adapter could be used to elongate the strut at each end.

As the connectors would interface the membrane at different angles, 100mm diameter circular discs were drawn at the end points of the struts in the digital model. This gave a reference surface to assess the number of different angles measured between the membrane mesh and the struts along the individual

planes of the struts' axes. These angles were all adjusted to be multiples of 5 degrees to standardise the connectors to a total of 5 variations of 90 to 115°, minimising the number of unique components needed to be made. This data was incorporated as a short vertical plate that was welded between the sleeve tube and the disc. 5 holes were also added to the discs to allow for the aluminium connector to be bolted onto the membrane.

The bases were also designed as 200mm diameter and 12.0mm thick aluminium discs that could be affixed onto the concrete slab of the site using anchor bolts. Each base had an aluminium fin mechanism that allowed the struts closest to the ground to rotate along their respective axes. This flexibility would provide room for adjustments during installation and allow for deflections to accommodate wind loads.

2.4.2. Membrane cutting patterns

The 3D membrane surface was segmented into cutting patterns for the fabricator, Advance Canvas, to cut and weld the pieces together. The segmentation of the membrane was based on the positions of the struts by creating and connecting lines between the closest neighbouring points. This led to the patches directly above the strut crosses adopting a star geometry; patches in between crosses adopting a diamond geometry; and patches along the perimeter having a triangle geometry. Due to the doubly curved nature of the membrane, each patch was made into a triangulated surface between the joined lines and later unrolled on the x-y plane. This created flattened 2D surfaces from the 3D mesh with minimal distortions.

Next, each patch was given an offset of 25mm from its perimeter edge as tabs for the welding of the seams. The tabs between neighbouring patches overlap and undergoes ultrasonic welding to connect the membrane pieces together. The 100mm diameter circular discs, used to interface with the aluminium hardware connectors, were added by laminating several layers directly on top of tabs added at these intersections. Furthermore, the seams along the perimeter were designated as wider 70mm and130mm offsets to accommodate the perimeter cables. These served as continuous channels to house the perimeter cables to further stiffen the membrane along its edges.

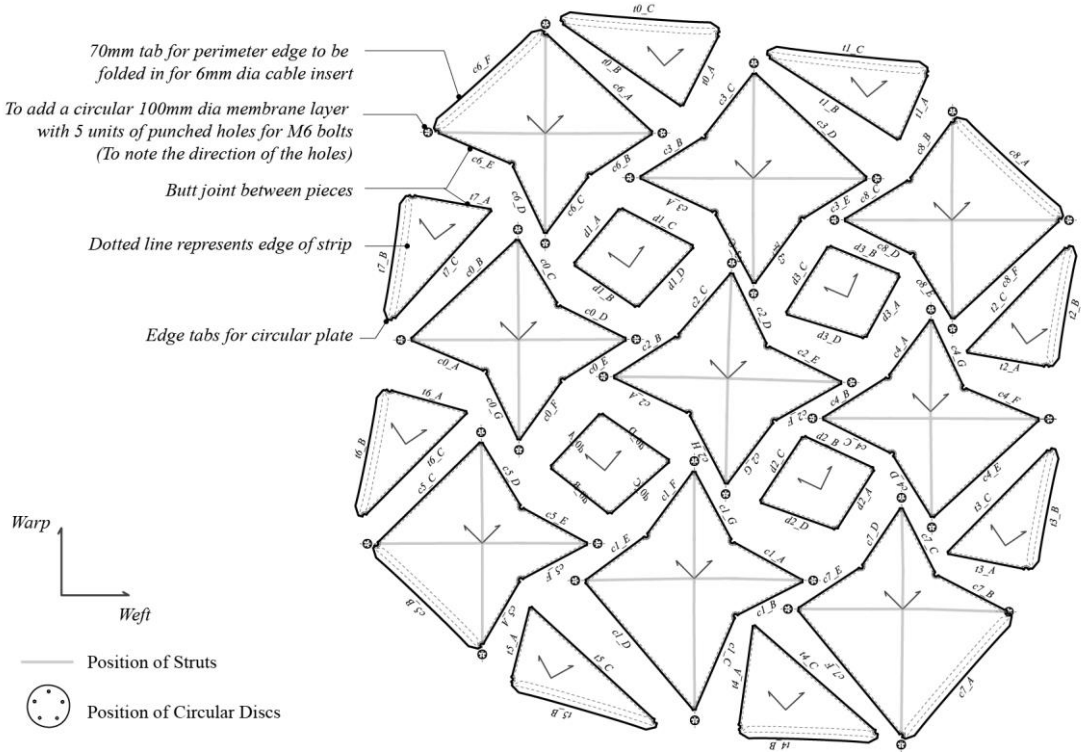


Figure 8. Cutting pattern of half prototype with 3x3 strut cross units.

2.4.3. Cables

Lastly, cable lengths were extracted from the model with consideration of the hardware dimensions (i.e., stud and turnbuckles). Internal connection cables were affixed onto the vertical plate of the connector and linked together using toggle end hardware. These allowed rotation in two axes, namely along and perpendicular to the length of the strut, to accommodate the different end points of the wire rope in 3D space. On the other hand, the perimeter cables were slotted through the perimeter channels of the membrane and their hardware was affixed onto special laser-cut pieces of the connectors.

3. Assembly and installation of the M-shell half prototype

The components were mass produced by multiple vendors and transported directly onto site. Before starting the assembly, the components were laid out and checked for their fit. Holes were also marked out on site and drilled into the concrete slab for the bases to be bolted onto the ground. The pavilion was then installed in the following sequence:

1. Fitting: The strut crosses were fitted onto the membrane by inserting the connector sleeves onto the struts and bolting them onto the membrane;

2. Flipping: A mobile scaffolding rig was brought to site and the un-tensioned membrane-strut assembly was flipped upwards using a pulley-rope system such that the assembly rests on the rig. This ensured that there was an empty space between the ground and the membrane to perform the next step;

3. Tensioning: The struts were elongated at every end using hand drills to their intended lengths to induce pretension within the membrane.

4. Repositioning: The tensioned membrane-strut assembly was hoisted up onto the scaffolding rig and shifted to the correct place. This involved aligning the end fins of the bottom most struts and locking them into the bases.



Figure 9. Assembly sequence.

3.1. Assessments and improvements

While the half prototype pavilion was able to be installed with relative success, we faced several challenges that led to the damage of the sleeve connectors and tearing of the membrane. We believe that these problems could stem from both the design of the components and our assembly sequence.

For the components, our extension mechanism needs to be improved to accommodate high torque drilling to prevent galling of the rivet nut of the extension mechanism. This led to jamming of the mechanism for certain sleeve connectors as the internal threads of the rivet nut were worn down by the drilling action. Thus, we are replacing the mechanism with lead screws which are more suited for high-speed applications. Additionally, the PVC membrane needs to be further reinforced with wider seams to resist tearing during installation. This has been implemented in cutting patterns of the final design of the full pavilion.

From the assembly sequence standpoint, we find that the membrane needs to be hoisted up to be in its final state as much as possible in step 2. We believe that this would minimise unnecessary overstretching of the membrane when elongating the crosses. This strategy would be implemented in the set up of the final pavilion by having the mobile scaffolding rig in the centre of the membrane-strut assembly. The rig would allow the propping up of the pavilion to be as curved as possible to target the final geometry of the intended pavilion.

4. Conclusion

In summary, this paper demonstrates a design-to-fabrication workflow for large-scale occupiable MTS pavilion using stiffer elements of aluminium tubes and a continuous welded polyester coated membrane. It showcased the design, analysis, and fabrication of half of the 8.0m span MTS pavilion which proves that these structures can be manufactured and assembled on a large scale.

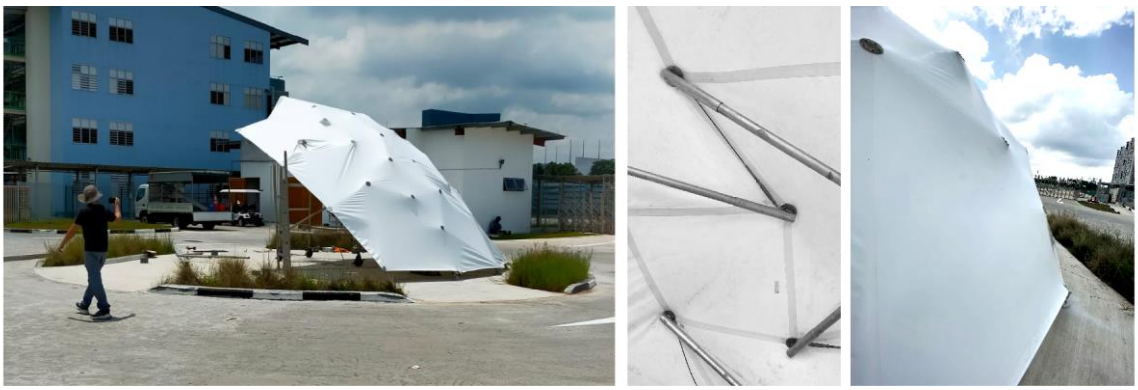


Figure 10. Half prototype with detail photos.

Currently, we are working towards making the full M-shell pavilion while making modifications to the design of the membrane and strut crosses. This would be assembled as the intended continuous arch that will serve as a self-supported outdoor shade pavilion. In the meantime, our team is also working with an engineering consultant to endorse this novel structural system with respect to the local building codes.

Acknowledgements

This research was supported and funded by the Decentralised GAP Funding project, Grant number: RGGAP20015, Tensile Ventures - Design Solutions for aesthetically unique, modular, quick assembly, event and recreation shelters. The authors would like to give their utmost gratitude to Dr. Phang (Multimedia Engineering), Mr. Larry Lim (Advance Canvas), Mr. Darren Mok (CutAnything) and Mr. Sam Vedanaigam (The Shelter Company), for their guidance and expert advice throughout this research. We also want to thank Chia Pei Zhi for copy-editing this paper and Sachin Gupta for developing the conformal mapping script. Lastly, we are grateful to Lance Macro Yu, Chung Zhi Xue, Lyvia Annabelle, Michelle Tan, Isaac Tan, Joy Liew, for assisting us as student helpers.

References

[1] S. S. Gupta *et al.*, "Prototyping knit tensegrity shells: a design-to-fabrication workflow," *SN Appl. Sci.*, vol. 2, no. 6, 2020, doi: 10.1007/s42452-020-2693-4.

[2] K. Tracy *et al.*, "Tensile Configurations Exploring Spatial Membrane Tensegrity Shell Structures," *Ubiquity Auton. - Pap. Proc. 39th Annu. Conf. Assoc. Comput. Aided Des. Archit. ACADIA 2019*, pp. 110–119, 2019.

[3] Z. Yang, K. Okumura, and K. Suehiro, "Simulation and Optimization Method of Tensegrity

Structure with Elastic Membrane as Tension Material BT - Proceedings of the 2019 DigitalFUTURES," 2020, pp. 3–16.

[4] L. M. Yu, Y. Y. Tan, S. S. Gupta, and K. J. Tracy, "Towards a Tool Kit for Membrane Tensegrity Shells: Exploring the relationship between struts and geometry," in *HUMAN-CENTRIC, Proceedings of the 28th International Conference of the Association for Computer-Aided Architectural Design Research in Asia (CAADRIA) 2023*, 2023.

[5] P. Song, C. -Wing Fu, P. Goswami, J. Zheng, N. J. Mitra, and D. Cohen-Or, "Reciprocal frame structures made easy," *ACM Trans. Graph.*, vol. 32, no. 4, 2013, doi: 10.1145/2461912.2461915.

[6] C. Brandt-Olsen, "K2Engineering," 2021. [Online]. Available: https://github.com/CecilieBrandt/K2Engineering. [Accessed: 31-Mar-2023].

[7] T. Wortmann, "Opossum," 2023. [Online]. Available: https://www.icd.uni-stuttgart.de/research/research-tools/opossum/. [Accessed: 31-Mar-2023].

IASS 2023
July 10–14 Melbourne
Integration of Design and Fabrication

Proceedings of the IASS Annual Symposium 2023
Integration of Design and Fabrication
10–14 July 2023, Melbourne, Australia
Y.M. Xie, J. Burry, T.U. Lee and J. Ma (eds.)

Xtect: a digital intelligence platform for off-site prefabricated construction

Jackie Leong Shong YONG[a,*], Wanyu HE[b], Lei GU[c], Peiwen LI[b], Ying WANG[b]

[a,*] Shenzhen XKool Technology Co., Ltd.
Xili Rd, Nanshan, Shenzhen, China, 518055
jackie@xkool.org

[b] Shenzhen XKool Technology Co., Ltd.
[c] China Construction Science and Industry Co., Ltd.

Abstract

The practice of off-site prefabricated construction dates back to the early 20th century. The advancement of information technology and the recent economic uncertainty may make this a new normal for the construction industry. The industry is composed of a number of players. Integrating information technology throughout the entire industry chain is essential. This will enable us to achieve the full potential of prefabricated construction in this large ecosystem, not just digitally but also intelligently. A cloud platform integrating artificial intelligence and cloud computing technology is presented in this paper and applied specifically to off-site prefabricated construction. AI generative modules shorten model creation and accelerate optimised solution finding, while cloud computing provides economical deployment with shared computing resources. In addition to global optimised prefabrication schemes generation in the investment or planning phase, this platform allows associative interaction between a standardised library and multiple disciplines and supports real-time spreadsheet calculation and IFC format export. These features facilitate further fabrication in the construction phase. With the use of a platform and factory production, off-site prefabricated construction has improved design efficiency and reduced loss in a hotel example project.

Keywords: construction industry, off-site construction, prefabricated construction, modular-integrated construction, BIM modelling, Xtect, global optimization, generative design

1. Off-site prefabricated construction

1.1. Introduction

As early as the 20th century, off-site prefabrication was practiced. In terms of design theory, we can see the emergence of this concept from Le Corbusier: “If houses were manufactured industrially, mass-produced like chassis, an aesthetic would be formed with surprising precision” [1]. As a matter of practice, the Sears Roebuck Company in the United States was able to transport prefabricated parts of buildings by rail to users before World War I, thus allowing the buyer to assemble the items on site [2]. Prefabricated semi-cylindrical buildings (Quonset huts), which had been imported from Britain, were used by American soldiers during the 1940s. Zachry Construction Company constructed a 21-story modular hotel in Texas at the end of the 1960s, which is currently known as the Hilton Palacio Del Rio Hotel [3]. Similarly, Kisho Kurokawa, one of the representatives of Metabolism in Japan, used prefabrication in the construction of the Nakagin Capsule Tower in the next decade, assembling all the prefabricated modules on site and anticipating their replacement if necessary.

Having a large carbon footprint, the construction industry has once again encouraged off-site prefabrication under the pressure of recent carbon emissions (in fact, the most critical factors during

Copyright © 2023 by Jackie Leong Shong YONG, Wanyu HE, Lei GU, Peiwen LI and Ying WANG. Published in the Proceedings of the IASS Annual Symposium 2023 with permission.

the epidemic were the high cost of manpower, building materials, and transportation). Recently, some countries and regions, including Singapore and China (including Hong Kong S.A.R.), have introduced proactive and incentive policies related to prefabricated construction, vigorously promoting the adoption of this green construction method. As opposed to conventional on-site construction methods, off-site prefabrication reduces carbon emissions during construction as well as upgrading the construction industry over time.

In general, off-site prefabrication can be divided into two categories: non-modular/volumetric prefabricated construction and modular/volumetric prefabricated construction [4]. The latter is also known as "Modular Integrated Construction" (MIC) [5].

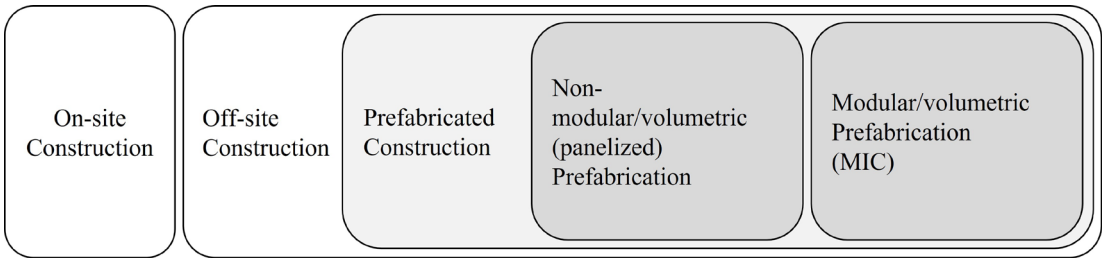


Figure 1. Concept of off-site prefabricated construction.

Non-modular/volumetric prefabrication refers to the fabrication of specific elements within a factory, such as walls, floors, stairs, decorative elements, etc. Alternatively, modular prefabricated construction involves the installation and assembly of various prefabricated components, including structures, mechanical, electrical, and plumbing components, as well as furniture and other components, in a single box-shaped unit. Depending on the degree of integration and the size of the unit, the unit can generally be divided into pods (smaller units with specific amenities, such as bathrooms) or modules (larger units with more comprehensive utilities). The modular units are transported to the construction site and linked and assembled to form the building units. Having completed the roof finishing and facade detail on site, the construction is basically complete and ready for review and delivery.

Off-site prefabricated construction also differs from conventional on-site construction in its design process. It adheres to the design principle "Design for Manufacture and Assembly" (DfMA), which stresses the need to take into consideration additional factors during the design process, such as factory manufacturing, logistics, and installation sequence. As a result, this mode of construction requires a higher level of design expertise. Designers must not only develop architectural designs, but also plan how they will be manufactured, transported, and assembled on site. As a result, the design stage schedule will also be extended [6].

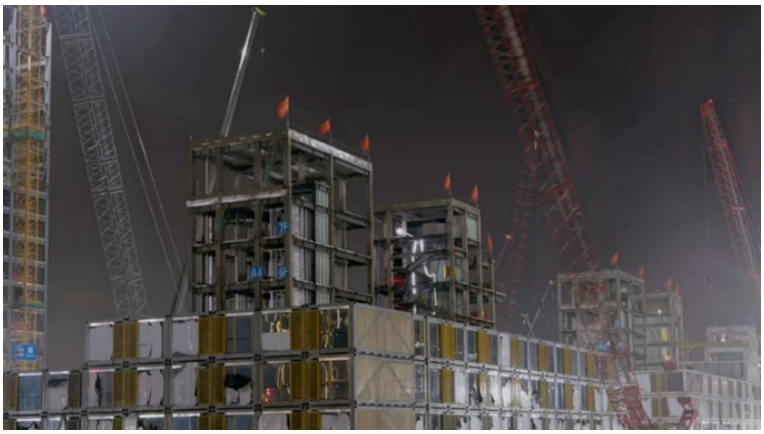


Figure 2. The assembly of prefabricated module on site [Courtesy of China Construction Science and Industry Co., Ltd].

1.2. Industry bottleneck

It is common for on-site construction to require outdoor work. Open working environments are susceptible to environmental factors such as rainfall, snowfall, high temperatures, and even less daylighting areas such as the Arctic Circle. The construction schedule on site is therefore difficult to control. Furthermore, due to the limited flexibility of the construction team to switch or relocate as the project changes, ensuring the quality of available labour is challenging. In addition to the scattering of the construction site management and the difficult conditions of the construction site, safety hazards are also present. There are often negative situations such as accidents during operations and large amounts of construction waste.

As off-site prefabricated construction is largely carried out in a controlled operating environment and standardized process flow, and even enjoys a more controllable procurement channel, it has the advantage of being less affected by the outdoor environment, providing a higher quality construction, and reducing emissions and waste during construction on-site [7]. The epidemic has made this method of construction a viable alternative for many projects such as temporary hospitals and affordable housing that require high construction standards and a controlled schedule [4]. However, there is still resistance to off-site prefabricated construction.

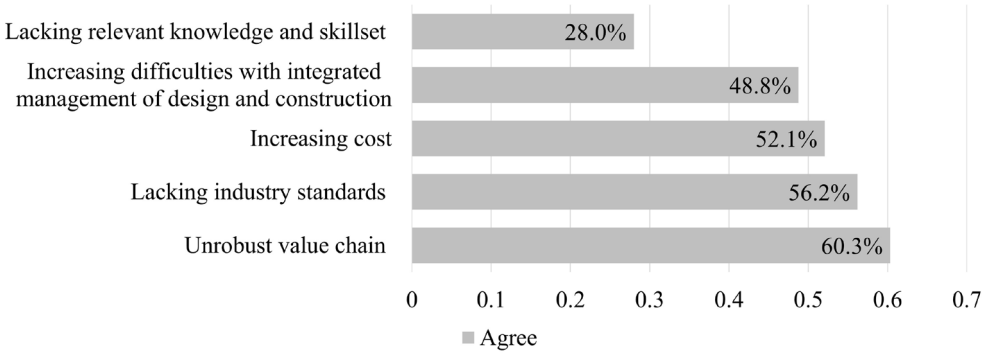


Figure 3. Examples of resistance to off-site prefabrication in China [8].

1.2.1 Supply

Prefabrication has not yet been fully adopted throughout the value chain, particularly upstream, where developers, designers and engineers, and suppliers of materials are involved. A common practice among designers is to produce a "modular key plan" after the architectural design, that is, without considering off-site fabrication processes at the outset of the design process. It is therefore difficult for developers to determine the feasibility of a project at the investment stage, such as calculating the cost and revenue. Due to the absence of geometric information in this phase, a calculation or compliance check is not possible. The recent turmoil in global politics and the economic situation, however, has also resulted in a lack of stability in the supply of building materials and parts, causing delays and affecting the completion of projects. Most on-site construction participants do not yet possess sufficient knowledge of this construction technique [9].

A lack of sound standards leads to a lack of unified standards for supervision and control throughout the entire project process. Developers, designers, and construction parties work independently. It is difficult to integrate and manage multiple terminals, and a strong prefabricated construction ecosystem cannot be established.

All of these factors contribute to the fact that the average cost of prefabricated construction is usually not lower than that of conventional construction, and is sometimes even higher. As an example, in modular prefabricated construction, each module is an independent box structure. If the module adopts a steel framework, the amount of steel used in modular prefabricated construction will be 1.5 to 2

times greater than that of traditional steel framework construction. In this regard, it is important to be able to estimate the amount to be procured and the costs involved.

1.2.2 Demand

As with any project, the owner generally has a variety of needs and objectives, and construction projects have different constraints and compliance requirements. It is no longer feasible to prefabricate off-site using traditional construction drawings or BIM models of LOD 200-300. In order to bridge the production and construction phases after design, off-site prefabricated construction requires a higher level of accuracy at the design stage, including the BIM model that reaches LOD400.

It may be possible to resolve the above problems through the "more combinations with fewer products" design approach [10]. The development of industrialized products requires not only a sound collaborative value chain, but also the ability to meet a wide range of market demands in order to attain economic scale. It is possible to achieve this by producing fewer types of parts, components, and modules to satisfy a larger market, thereby reducing unit costs. Furthermore, prefabricated modules can be used to construct some parts of a project to reduce construction time, whereas another part can be built with standardized components to suit individual needs. These different combinations of prefabricated components, modules, and on-site construction methods will result in a variety of possible solutions.

As a result, manual design adjustments for off-site prefabricated buildings and excavation of multi-combination design schemes will result in double the workload. The role of information technology in off-site prefabrication is therefore critical, as it contributes to finding a balance between standardization and individualization.

2. Digitalization and intelligence in construction

With information technology advancement and recent economic uncertainty, it may become a potential new normal for the construction industry [9]. The industry consists of multiple players. It is essential that information technology is deeply integrated throughout the entire industry chain. This will enable us to achieve the full potential of prefabricated construction in this large ecosystem, not just digitally but also intelligently.

2.1. Existing digitalization as basis: BIM

Industrialization of construction requires an integrated information platform covering the entire life cycle of construction projects. Information regarding the design, cost, and progress of all industry stakeholders must be coordinated simultaneously. In recent years, parts of the construction industry value chain have also adopted BIM for the purpose of interoperability of data.

Because prefabricated construction requires high levels of accuracy, it is a natural fit for BIM technology. By applying BIM to prefabricated construction at the investment or early design stage, one can not only evaluate the feasibility of prefabrication proposals early on but also estimate procurement or simulate construction more accurately. Although BIM requires a great deal of information processing, it remains essentially a manual modeling process. The prefabricated construction design stage brings more challenges for designers because they need to explore “more combinations with fewer products” and “multi-objective optimal solutions”.

However, the development of digital and intelligent information technology seems to bring a potentially effective solution to this problem, that is, the modeling process is simplified through intelligent computing, and computers can replace human beings to complete a large number of tedious repetitive labor and information processing tasks.

2.2. Integration of advanced information technology: AI and cloud computing

Using the AI generation, BIM model creation will be shortened and the search for optimal solutions will be accelerated. In the context of artificial intelligence-assisted architectural design, artificial intelligence does not refer to a specific algorithm or results from a training set, but rather to a series of intelligent systems which integrate multiple models that range from rule-based to data-driven models, including deep learning, machine learning, and operational research with computational optimization.

The cloud computing model offers a more economical deployment solution due to the sharing of computing resources. Using the cloud, not only is the requirement for local hardware reduced, but multiple terminals can collaborate simultaneously and efficiently.

2.3. The platform, Xtect

By integrating the aforementioned technologies, this article introduces a cloud platform designed specifically for off-site prefabricated construction: Xtect. It utilizes AI technology as well as cloud computing technology to simplify the production process of BIM models for prefabricated buildings, as well as its further construction.

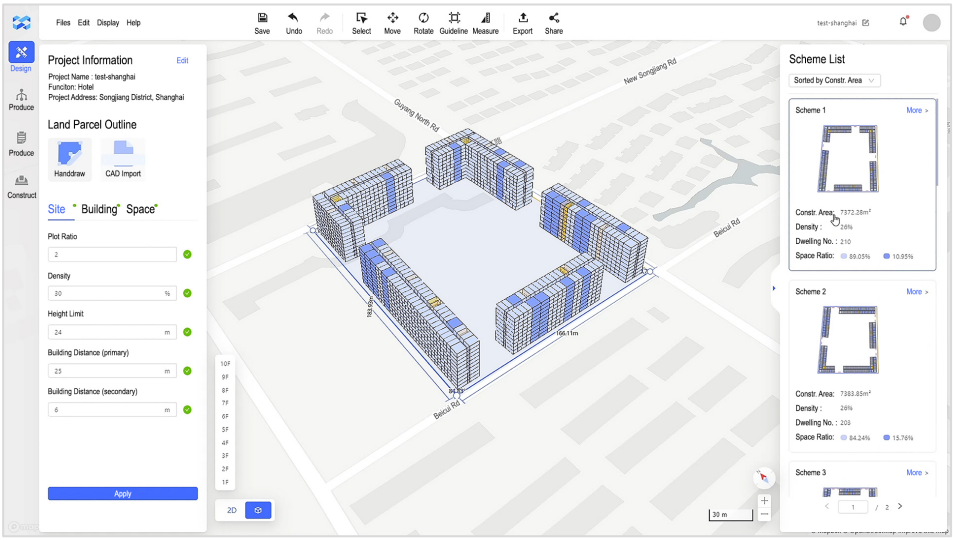


Figure 4. Screenshot of Xtect.

Three key features of the platform are as follows:

2.3.1. Generative design for multi-objectives

Due to the limitations of manual design, there are few comparative design alternatives to meet the project requirements, the design cycle is long, repeated communication is required, and it is difficult to reuse previous projects' design results in subsequent projects. In contrast, this platform performs multi-objective design optimisation and generates a number of design schemes that meet a project's goals and constraints by simply inputting some significant parameters. As a result, developers and designers are able to evaluate the feasibility of a project in advance based on the architectural form, parameters calculation, and compliance checking result of the generated scheme in the early stages.

Take for instance a modular prefabricated building project. Initially, the user sets up the configuration of the project. CAD files can be uploaded, or approximate geometric outlines can be drawn on the webpage to indicate the project's property line. Next, the user enters the project's goals, such as floor area ratio, building coverage, housing types ratio, etc. Afterwards, the user selects the appropriate module (housing or hotel) from the library and sets up the generation parameters to proceed with the layout and massing. The platform generates a number of modular prefabricated building schemes

based on the stated objectives and constraints, such as embedded compliance rules. A comparison is then possible between the generated proposals based on the parameters, allowing users to compare them side-by-side.

The module library described above stores the information about the module in a BIM-like data structure, which enables the library to be flexibly queried or adjusted according to the needs of various projects. The data structure of the modules consists of a number of parts that work together to facilitate the process of purchasing, production and installation. Additionally, some of the key components are based on associative design logic that may undergo certain variations depending on the requirements. By doing so, it can offer both standardization and customization to a certain degree of controllability, thereby making mass customization even more feasible.

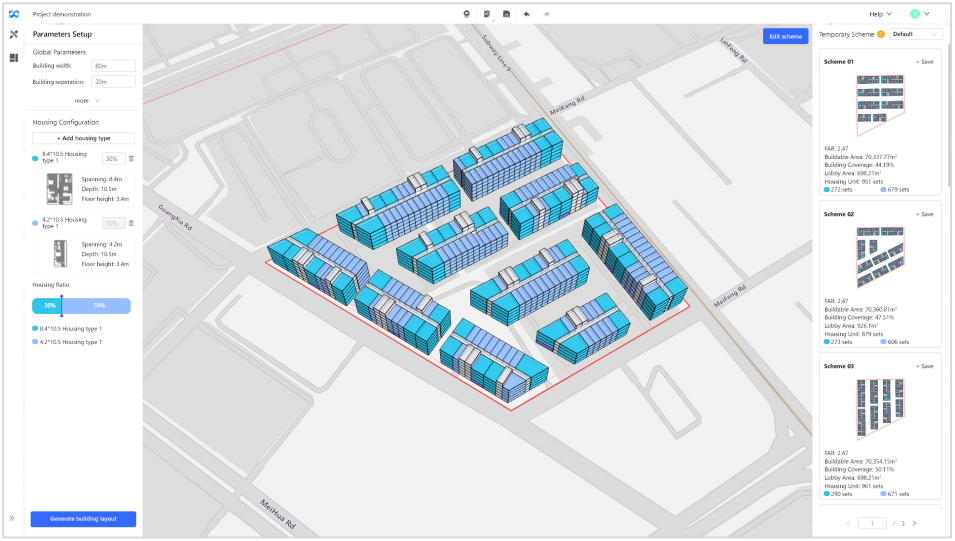


Figure 5. The layout schemes generated on Xtect.

To generate building layout schemes that are suitable for different actual projects, the "land division template" is employed initially. To accommodate different scenarios, project types, and land characteristics, this template is composed of several division rules and adaptive algorithm.

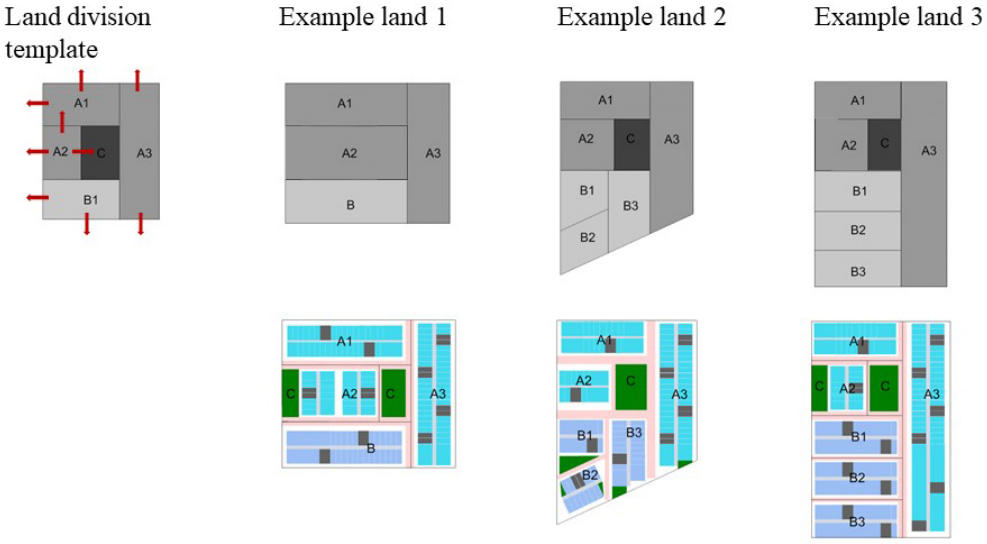


Figure 6. The adoptive application of the "land division template".

Please refer to Figure 6 as an example. The arrows indicate the possible direction of extension to suit various land scenarios. During template adjustment, the internal partitions of the template will undergo adaptive changes. If partitions such as A1, A2, A3, etc., are changed, the number of buildings and layout will also be altered. There are some divisions, such as B, that will be further subdivided in accordance with their size. Meanwhile, some divisions, such as C, represent public spaces such as parks or squares. A method such as the one described above can be used to turn a complex and difficult-to-solve building layout problem into a combination of labelled, modularized, and template-solvable problems.

2.3.2. Associative design of multi-disciplinary

Since prefabricated construction entails a closer relationship between design and production, it is imperative for various engineering disciplines to be integrated into the design process, which includes structural, MEP, and HVAC. The problem is that there are technical barriers between different disciplines. It is often the case that designers who control the whole must spend considerable energy and time coordinating between disciplines, which increases the difficulty of designing and the likelihood of inadequate consideration. Furthermore, it is inevitable to encounter situations where the design needs to be adjusted more or less during the process of developing the design scheme for prefabricated buildings. It is possible that a slight adjustment in one part of the situation may have an impact on the entire situation at this time. This will lead to the architectural design and engineering professions collaborating on a number of occasions.

The platform incorporates the architectural and engineering design logic of various disciplines and combines it with compliance audit logic in order to form associative design algorithms. With the integration of the associative generation algorithm of this platform, users are not only able to adjust the module size by modifying the parameters of the module building, but the change of size will also affect the relevant engineering professional components therein. For example, when the user adjusts the module layout by dragging the exterior wall, the algorithm will make linkage adjustments to the interior decoration, structure, and mechanical and electrical pipelines based on the new wall position, take into account avoidance, and update and transmit to the display interface.

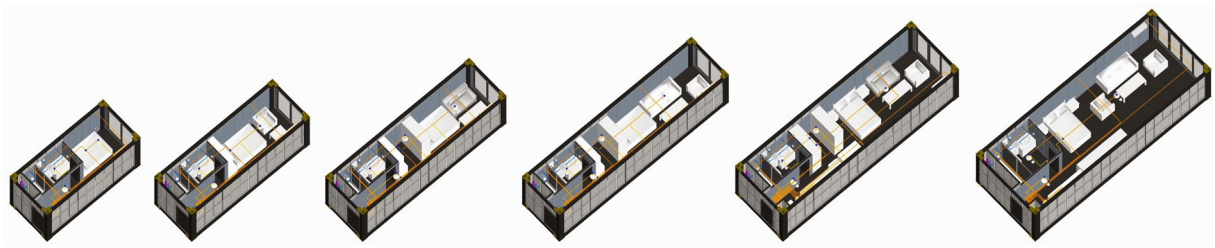


Figure 7. Component size and position changes due to module resizing on Xtect.

To achieve the aforementioned standardized and modularized interior layout scheme, the generation design for each module size is realised by a large number of structured data of modules with detailed interior information clustered into a controllable number of layout unit templates. To meet the interior customization requirements in projects with standardized methods, each unit template has a corresponding interior layout and configuration, which may include various engineering systems, furniture, and even the paving settings of modular panels.

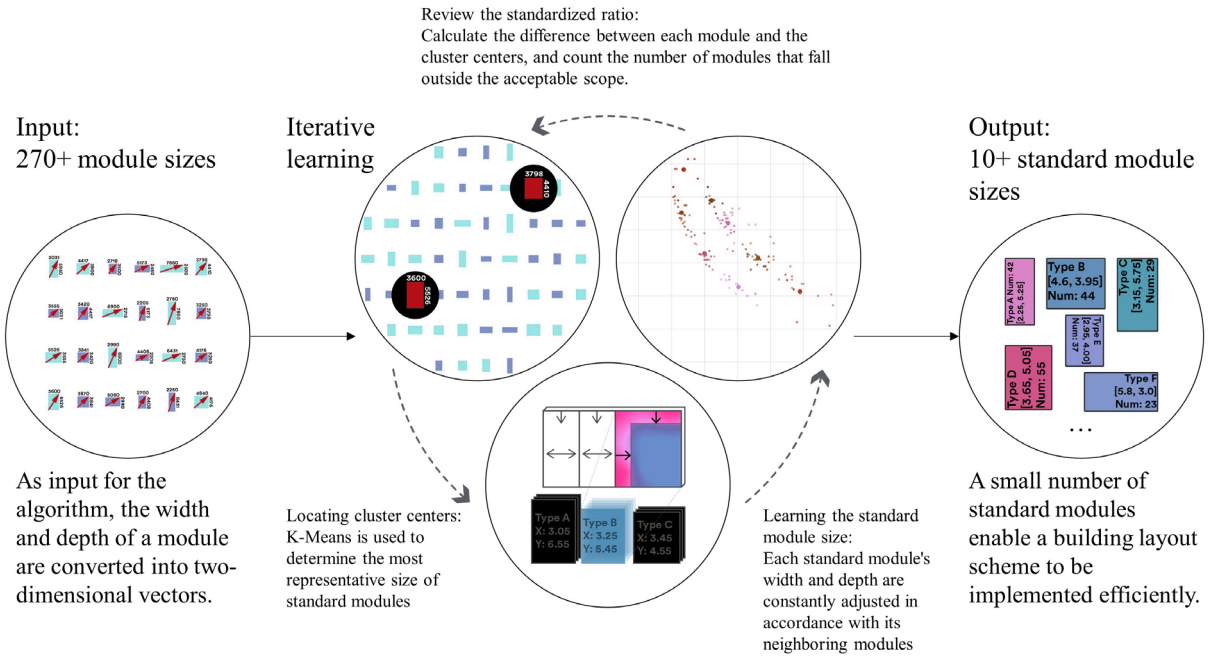


Figure 8. Iterative clustering and estimation of standard modules based on structured data.

Currently, this platform can support BIM models up to LOD400, so that the ceiling, hanging ribs, joists, air valves within the plumbing, and even some detailed components, such as screws, will be displayed simultaneously on the platform. Consequently, the designer's intuitive feeling is that when the building space is manually adjusted, the engineering professional components corresponding to the space can be adjusted automatically in real-time and reflected in the BIM model of the modular prefabricated building immediately.

2.3.3. Spreadsheet calculation and IFC format export

This platform generates a BIM model with semantic and attribute information, which acts as the connector for the various functions of the platform. Consequently, changes to the BIM model in different phases are transmitted through the entire platform. Through the reading of the model and the identification of components, the calculation module of the platform can automatically calculate various data statistics and indicators for the scheme. As a result of these standardized building components, several spreadsheets are automatically generated corresponding to the entire design in real time, containing information such as specs, quantity, price, etc. Additionally, users can choose to export the model in IFC format, so that they can edit and deepen the scheme in other BIM applications. In this way, real-time calculations greatly enhance the ability to control construction costs during the design phase, making it easier for the results of the design to be implemented during production and construction.

Technically, we have developed a centralized plan for the internal modeling algorithm and model storage structure, so that the front-end web rendering, 3D modeling, and IFC model generation can all use the same model storage structure. As a result, the model built by the algorithm engineer can be conveniently displayed on the front-end web page and verified and debugged in dedicated 3D modeling software. IFC format export is implemented using several SDKs and a core algorithm library. The SDKs correspond to applications that involve web page, 3D model, or IFC format generation, and the instructions of the core algorithm library can be converted into instructions for model generation under these applications.

3. Case study

This paper presents a case study of the platform in a hotel project in Shenzhen, in which China Construction Science and Industry Co., Ltd. (CSCEC) is the principal contractor.



Figure 9. Aerial rendering of the project

3.1. Module set up in library

In the module setup phase, the platform recognizes the uploaded components such as structures, interiors, and engineering. These recognized components later support associative regeneration with manual module adjustment. The regenerated modules can also be restored in the module library for future use. Meanwhile, the model depth of LOD400 allows for the calculation of the construction spreadsheet, which facilitates the efficient connection between the design, suppliers, and production ends. This reduces the grey area in cost estimation.



Figure 10. The various disciplinary components on Xtect.

3.2 Multi-objectives optimised design generation

The architectural design stage involves generating the layout based on the property boundary and the modules selected from the module library. Building setbacks and separations are met in the generated scheme in compliance with the local code requirements. The data for these several schemes can be viewed in real-time in the right display column to help the user select the scheme that best meets their requirements, such as comparing the economic parameters of various schemes.

As a result of scheme generation based on the module library, the basic information associated with the model is efficiently exported to the list of components required for the prefabricated hotel, and a

direct data interchange is established between design and production. In addition, each component will be assigned a unique ID, making it possible to inspect the model in a comprehensive manner and identify the problem in a timely manner. This ensures consistency in information for the site, building, module, and components, as well as future connections to production.

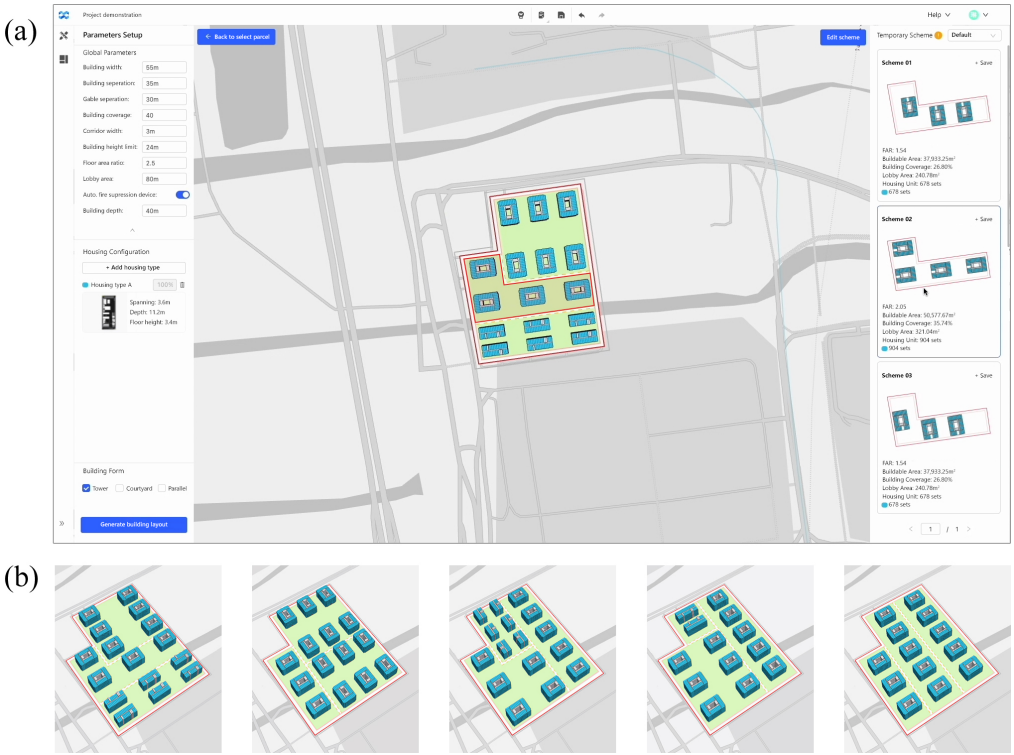


Figure 11. The development process of the building layout scheme for the case study on Xtect: (a) modular prefabricated building layout for a specific land parcel after land division, (b) overall building layout schemes on several land division strategies.

3.3. Prefabricated production

With the integration of this platform into the production line management system, it will be possible to order, monitor, and produce the components found in the designated scheme on the production line. For the construction of modules, CSCEC has developed an intelligent production line. This module production line is based on the concept of non-standard automation engineering equipment. The system utilizes high-precision servos, screw rods, and other structures, along with an automated control system, which improves the overall efficiency by more than 50%. Modules manufactured by it are variable in length, width, and height, covering more than 85% of the mainstream market's specifications and sizes.

Most of the work has been completed in the factory, so only the assembly of module and seam processing remains to be done on-site. As a result of the precision of the manufacturing process, the total size error can be controlled within 0-2 mm, and the module can be installed on-site within 20-30 minutes. As production volume increases, the cost of modular units processed at the later stage is often lower than that of modular units processed at the early stage, and a reduction in the construction schedule is achieved.

With the use of a platform and factory production, off-site prefabricated construction has improved design efficiency and reduced loss in this hotel project. Moreover, by using modular buildings, most of the on-site construction operations can be carried out in advance, thereby reducing more than 90% of the carbon dioxide emissions during the construction phase. It is also possible to reuse modular

units under certain circumstances. When turnover and reuse are taken into account, the overall carbon emissions of a building will be significantly reduced.

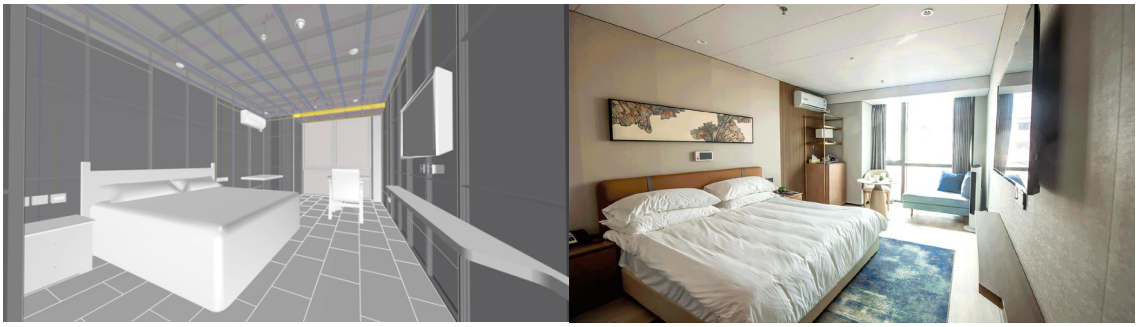


Figure 12. The before (BIM on the platform) and after (built) of hotel module.

4. Conclusion

As part of the general trend of reducing carbon emissions and reducing energy consumption, prefabricated off-site construction offers several benefits. Utilizing digital and intelligent technologies, it attempts to resolve the standardization-individualization conflict. Further research and development are needed to verify and deepen the research, as well as to explore the platform's application value in other regions. The platform can also be expanded to include other industrial value chains, such as building material supply management, project management, and green operations.

References

[1] L. Corbusier, *Toward an Architecture*, Los Angeles: Getty Research Institute, 2007.

[2] "Sears Mail Order Homes," Modular Today, [Online]. Available: https://www.modulartoday.com/searshomes.html. [Accessed Mar. 15, 2023].

[3] E. Wesselsky, "The Father Emil Wesselsky Collection - Construction of the Hilton Palacio del Rio (1967)," 1967. [Online]. Available: https://texasarchive.org/2012_01128. [Accessed Mar. 15, 2023].

[4] Modular Building Institute, "Permanent Modular Construction Reports," Modular Building Institute, Virginia, 2021.

[5] "Modular Integrated Construction," Buildings Department of Hong Kong SAR, December 23, 2022. [Online]. Available: https://www.bd.gov.hk/en/resources/codes-and-references/modular-integrated-construction/index.html. [Accessed Mar. 15, 2023].

[6] American Institute of Architects, "Design for Modular Construction: An Introduction for Architects," American Institute of Architects, Washington, 2019.

[7] N. Bertram, S. Fuchs, J. Mischke, P. Robert, G. Strube and J. Woetzel, "Modular construction: From projects to products," McKinsey & Company, 2019.

[8] Q. Huang and B. Song, *The Digitalized Comparative Study and Application of Industrialized Construction Mode*, Beijing: China Architecture & Building Press, 2023.

[9] M. J. Ribeirinho, J. Mischke, G. Strube, E. Sjödin, J. L. Blanco, R. Palter, J. Biörck, D. Rockhill and T. Andersson, “The next normal in construction: How disruption is reshaping the world’s largest ecosystem,” McKinsey & Company, 2020.

[10] The Ministry of Housing and Urban-Rural Development, “Notice of the Ministry of Housing and Urban-Rural Development on Printing and Distributing the "14th Five-Year" Construction Industry Development Plan,” January 1, 2022. [Online]. Available: http://www.gov.cn/zhengce/zhengceku/2022-01/27/5670687/files/12d50c613b344165afb21bc596a190fc.pdf. [Accessed Mar. 15, 2023].

Dynamic response of metal spatial structures

Active bending
Additive manufacturing/ 3D printing
Architectural geometry
Bamboo for sustainable construction and quality of life improvement
Bio-inspired structures and architecture
Bridge structures
Computational form-finding
Conceptual design
Concrete structures
Construction techniques
Deployable and inflatable structures
Design competition (WG21)
Digital modelling and fabrication
► **Dynamic response of metal spatial structures**
Dynamic response of other structures
Form-finding and structural optimisation of interlocking discrete assemblages
Graphical methods
Gridshell and lattice structures
Historical concrete shells
Historical structures
Lattice structures
Life-cycle design and assessment of structures
Metal gridshell structures, connections and stability
Methods and construction technologies for sustainable shell structures
Morphology and configuration processing
Next generation parametric design
Novel methods in modelling, optimisation and construction for reducing carbon footprint of continuous roof shells
Numerical methods for geometry, form-finding and optimisation of lightweight structures
Optimisation methods and applications
Origami
Other
Teaching design uncertainty: working with unknown qualities/quantities of new and re-claimed materials
Teaching of shell and spatial structures
Tensegrity systems and cable structures
Tension and membrane structures
Tension structures in the Asia-Pacific
Timber and bio-based structures
Topology optimisation
Traditional masonry structures and innovation
Transformable structures

IASS 2023
July 10–14 Melbourne
Integration of Design and Fabrication

Proceedings of the IASS Annual Symposium 2023
Integration of Design and Fabrication
10–14 July 2023, Melbourne, Australia
Y.M. Xie, J. Burry, T.U. Lee and J. Ma (eds.)

Collapse mechanism under strong earthquake and seismic design of single-layer aluminum alloy latticed shells

Jinzhi WU[a], Yu LIU[a], Guojun SUN[a,*], Jianhua ZHENG[a], Miao FENG[a], Yigang ZHANG[a], Jie HU[a], Yafang GU[a], Xianquan CHANG[a]

[a,*] Faculty of Architecture, Civil And Transportation Engineering, Beijing University of Technology
Beijing 100124, PR China
sunguojun@bjut.edu.cn

Abstract

Aluminum alloys have been increasingly used in civil engineering due to their favourable properties, such as high strength-to-weight ratio, high corrosion resistance, very good processability and recyclability. Many aluminium alloy single-layer latticed shells with span larger than 100m have been built in China over the past two decades. In order to study the seismic performance of aluminum alloy latticed shells, the material properties, the cyclic behaviour of H-section aluminium alloy members under axial and eccentric loads have been studied, and then two shaking table tests of a cylindrical and a spherical single-layer latticed shells have been carried out. The nodal displacement and acceleration and member forces of the shells were studied under frequent and rare earthquakes, when both models keep in elastic stage. And then, the collapse tests have been conducted to both model shells under severe earthquakes, and the whole collapse processes were studied. Finite element models have been established and verified to simulate the shaking table tests, and the seismic performance and the failure mechanism were studied. The results indicate that the aluminium alloy single-layer latticed shells have excellent seismic performance, but the lower elastic modulus leads to bigger displacements than that of steel shells, which should be considered thoroughly in the design of this kind of shells.

Keywords: aluminum alloy, single-layer latticed shell, shaking table test, collapse mechanism, seismic design

1. Introduction

Aluminum is the most abundant metallic element in the earth's crust. Aluminum alloys have many favourable properties, such as high strength-to-weight ratio, high corrosion resistance, and very good processability and recyclability[1]. And thus, there are more and more aluminium alloy single-layer latticed shells built in China over the past two decades, many of them have the spans larger than 100m[2]. There are many research on the static stability of single-layer latticed shells and found that the static stability behavior of aluminum alloy latticed shells is quite different from that of steel shells [3–6]. The seismic design of aluminum alloy latticed shells follows the code for steel latticed shells, but there are many differences between aluminum alloy and steel structures, such as different Young's Modulus of the materials, different member profiles and different connections.

The constitutive model of the aluminum alloy have been studied, and the parameters of Chaboche hybrid reinforcement model of aluminum alloy under cyclic load have been obtained[7],[8] , which are essential to the seismic response analysis of aluminium alloy structures. The hysteretic performance and failure modes of H-section members with different slenderness ratios under axial and eccentric cyclic loads have been studied [9],[10]. The mostly used joints in aluminum alloy latticed shells are gusset joints, the hysteretic performance and failure modes have been studied by experimental and analytical methods [11–14].

Copyright © 2023 by Jinzhi WU. Published in the Proceedings of the IASS Annual Symposium 2023 with permission.

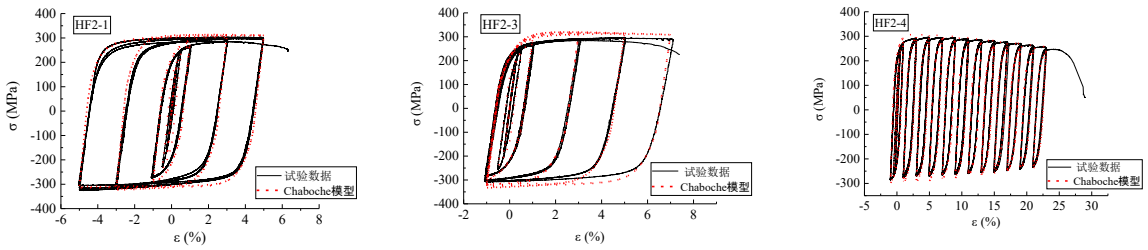
For the seismic performance of aluminum alloy latticed shells, Yu analyzed the seismic performance and failure mechanism of a single-layer cylindrical latticed shell using numerical analysis[15]. However, the only shaking table tests on aluminum alloy latticed shells were conducted by the Wu et al[16][17]. In this paper, based on the constitutive model of the aluminum alloy material, the hysteretic performance and failure modes of H-section members will be introduced. Based on the shaking table tests and numerical analysis, the seismic performance and collapse mechanism of a cylindrical latticed shell and a spherical latticed shell are studied and the seismic design of this kind of structure is suggested.

2. Hysteretic performance of H-section aluminium alloy members

2.1. Material property

To study the constitutive model of aluminum alloy, the material samples are taken from the flange and the web of the H-section members. The low cyclic loading test was completed on the QBS-300 dynamic and static universal material testing machine in the laboratory of Beijing University of Technology [9],[10]. The Chaboche hybrid strengthening model is used to describe the mechanical properties of aluminum alloy materials under cyclic loading, and the parameters of the model have been obtained. The comparison of the analytical and test values are shown in Figure 1. The hysteretic curve of the specimen obtained based on the Chaboche hybrid strengthening model is in good agreement with the experimental results, and the calibrated aluminum alloy material parameters have good accuracy, which can be applied to the seismic performance analysis of aluminum alloy energy dissipation components.

(a)



(b)

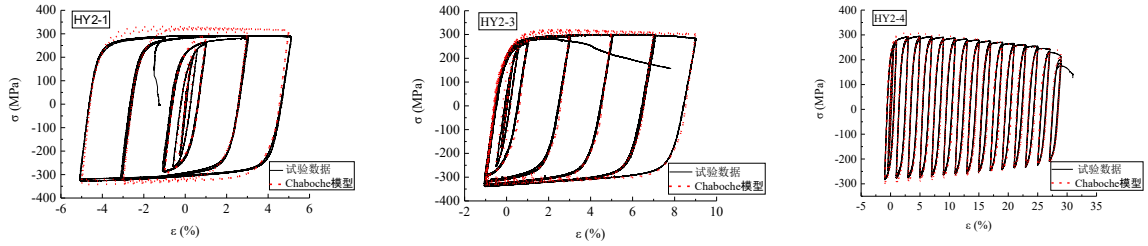


Figure 1. Stress-strain curve under cyclic loading: (a) specimen from the flange of H-section member, (b) specimen from the web of H-section member.

2.2. Performance of H-section members under axial and eccentric cyclic loads

H-section members are widely used for aluminium alloy latticed shell structures. Both the axial and eccentric cyclic loading test objects are three H-section 6061-T6 aluminium alloy members[9][10]. The section size of the members is H250mm×125mm×5mm×9mm, different lengths are used for different slenderness of the members. The load-displacement curves and the skeleton curves of the three axial loaded specimens are shown in Fig. 2. The load-displacement curves of the three eccentric loaded specimens are shown in Fig. 3, in which λ is the slenderness ratio of the. The comparison of failure modes between the FEM and experiment is shown in Fig 4 and 5.

(a) (b)

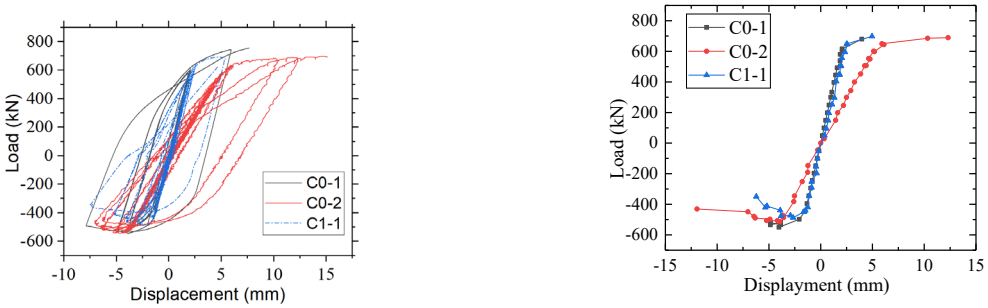


Figure 2. Load-displacement and skeleton curves of each axial loaded specimen: (a) Load-displacement curves of each specimen, (b) Skeleton curves of each specimen.

(a) (b) (c)

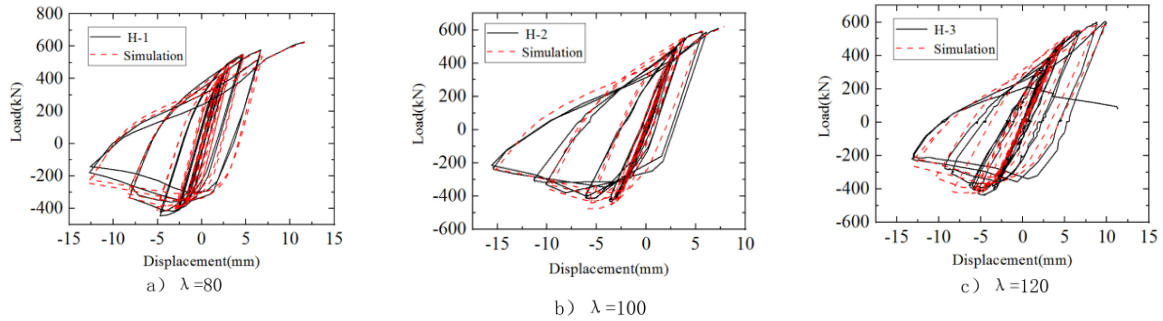


Figure 3. Load-displacement curves of each eccentric loaded specimen: (a)λ=80, (a)λ=100, (a)λ=120.

(a) (b)

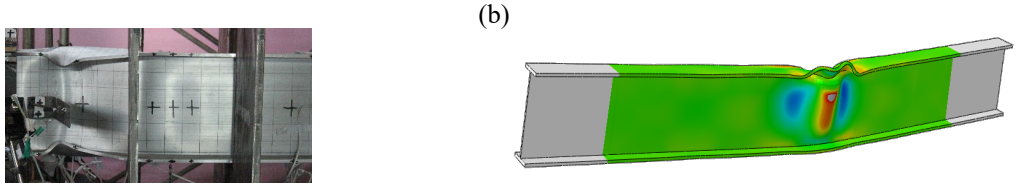


Figure 4. Failure mode of the axial loaded member with the slenderness ratio of 80: (a) test, (b) FE model.

(a) (b)

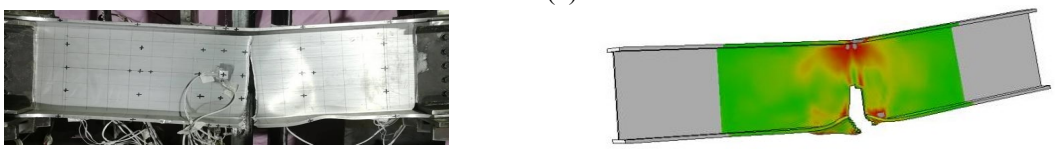


Figure 5. Failure mode of the eccentric loaded member with the slenderness ratio of 80: (a) test,(b) FE model.

For the axial loaded members, the load-displacement curves show that the members experiencing in-plane buckling with a small slenderness ratio have better seismic performance. Among them, the member with a smaller slenderness ratio and in-plane bending has a larger fracture load due to higher material utilization rate. After local buckling under compression, the stiffness of the member on the compression side reduces significantly, so the area of the hysteresis loop increases suddenly when most of the member reach plasticity, meaning that the energy dissipation of the members after local buckling

is more obviously reflected in the compression stage. Comparing the skeleton curve of members with different slenderness ratios, the bearing capacity degenerates more significantly with the increase of slenderness ratio. This means that limiting the slenderness ratio of members can improve the energy dissipation capacity of the structure, and this should be considered carefully in the seismic design of the latticed shells.

For the eccentric loaded members, with the same eccentricity, smaller the slenderness ratio leads to fuller the hysteresis curve of the members. The Skeleton curve shows that at the initial stage of increasing loading displacement amplitude, the tensile bearing capacity shows a strengthening trend, and the tensile bearing capacity with a large slenderness ratio is slightly lower. When the eccentricity is the same, the increase in the overall slenderness ratio decreases the energy dissipation capacity of the aluminium alloy member.

3. Shaking table tests of single-layer aluminum alloy latticed shells

3.1. Experimental models

The prototype structures used in the two tests is a 21.6m × 21.6m single-layer cylindrical latticed shell and a 60m span Kiewit-6 (K6) aluminum alloy single-layer spherical latticed shell. Referring to the similarity theory[18], the span and length of the cylindrical latticed shell model are both 3.6m, with a rise-span ratio of 1/4 and the length similarity ratio of 1/6, as shown in Fig. 6a. The spherical model is simplified to a spherical latticed shell with a span of 4.0 m and a rise-span ratio of 1/7, in which the length similarity ratio is 1/15, as shown in Fig. 6b[16][17]. The member sections are shown in Fig. 6. The pictures of the two test models are shown in Fig. 7.

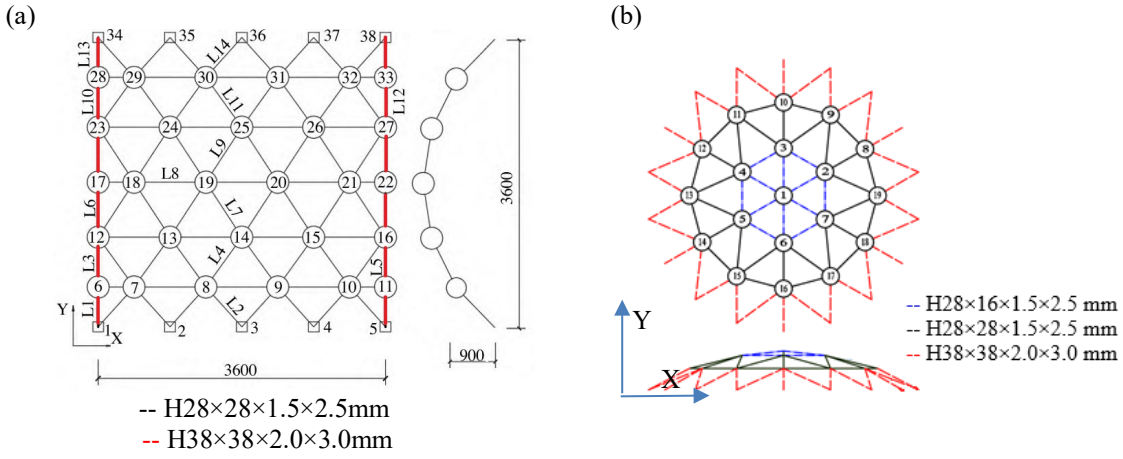


Figure 6. Layout of shell models and member sections (mm): (a) Cylindrical shell test model, (b) Spherical shell test model.

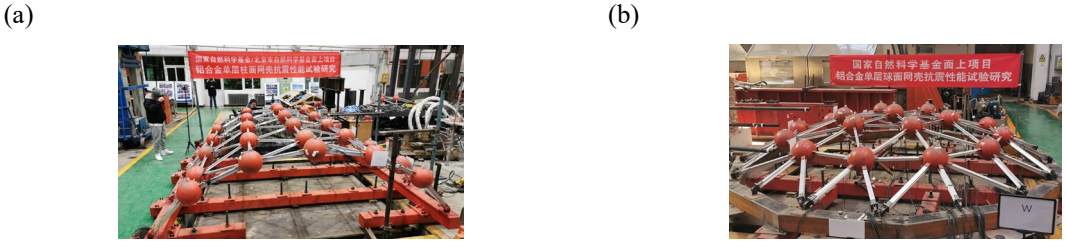


Figure 7. Pictures of shell models: (a) Cylindrical shell test model, (b) Spherical shell test model.

3.2. Distribution of measuring points

The displacement responses, acceleration responses and dynamic strain responses of the model are measured during the experiments (Fig. 8). The loads are applied to the models along Y-direction. The label AY6 is accelerometer of joint 6 along Y direction, and the other accelerometers are labelled in the same way. The label DZ1 is the displacement measuring point of joint 6 along Z direction.

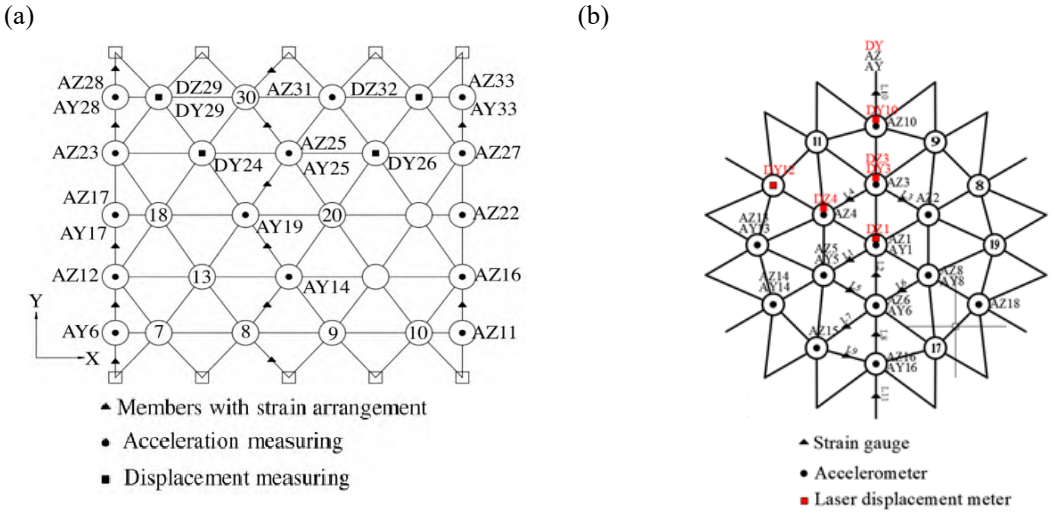


Figure 8. Arrangement of measuring points: (a) Spherical shell test model, (b) Cylindrical shell test model.

3.3. Experimental phenomena and results

3.3.1. Single-layer cylindrical latticed shell

The Taft, El Centro and CHY058 seismic waves are selected as the input ground motions for the cylindrical latticed shell along Y direction. The test is divided into three stages, i.e., elastic stage, elastoplastic stage and collapse stage.

Before the shaking table test, the first six natural frequencies of the model were tested, which are 2.20Hz, 5.37Hz, 6.34Hz, 9.03Hz, 9.77Hz and 11.71Hz respectively.

(1) Elastic stage test

The shell keeps in elastic stage when the peak ground acceleration (PGA) of the input waves less than 0.6g. The accelerations and displacements response are shown in Fig. 9. The maximum stress is 106Mpa, which appears at the end of L10, in which the bending stress is 98Mpa. This means that the bending moment is the main force for the members of the cylindrical shell subjected to horizontal lateral earthquakes.

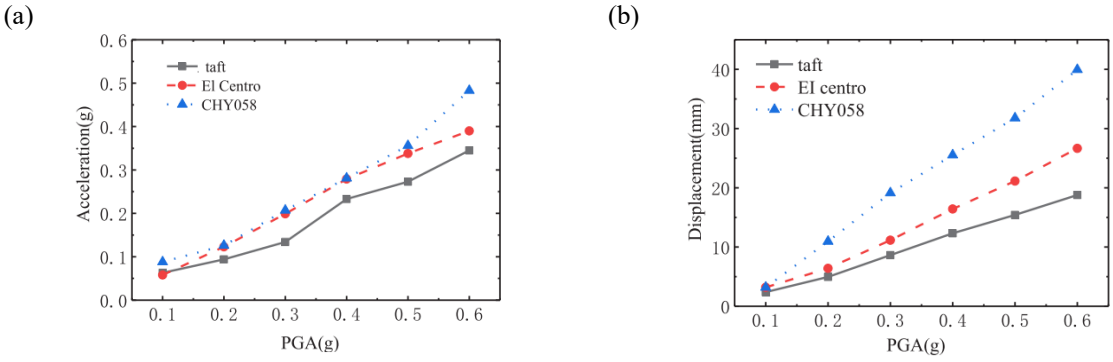


Figure 9. Responses of the cylindrical shell: (a) X-accelerations of joint 28, (b) Y-displacements of joint 29

(2) Elastoplastic stage test

The peak accelerations and displacements under Taft wave from 0.6g to 2.0g are shown in Fig. 10. It can be seen that the responses become nonlinear after the PGA of 1.8g. There are slightly plastic bending deformation on the flanges at the ends of member L3 and member L10. The maximum Y-displacement is 79mm at joint 24, equal to 1/11 pf the height of the shell. This means the displacement is too large for proper use of the roof.

(a) (b)

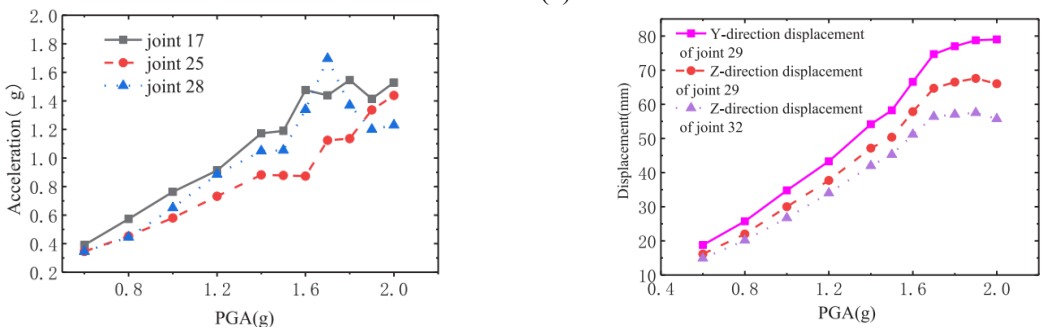


Figure 10. Responses of the cylindrical shell: (a) X-accelerations of joint 28, (b) Y-displacements of joint 29

(3) Collapse test

The CHY058 seismic wave leads to largest response to the shell. When the PGA reaches 0.9 g, the ends of member L10 breaks suddenly. The vertical displacement of joint 28 increases substantially, the slant members around it twist one after another, and a pit appears in a part of the latticed shell. As loading continues, the vertical displacement of the adjacent joints of joint 23 continues to increase, and the area of the pit further increases. Since the other member connected to joint 23 in the edge arch of the latticed shell breaks, the vertical displacement of joint 23 increases suddenly, and one side of the latticed shell collapses completely, as shown in Fig. 11.

(a) (b)

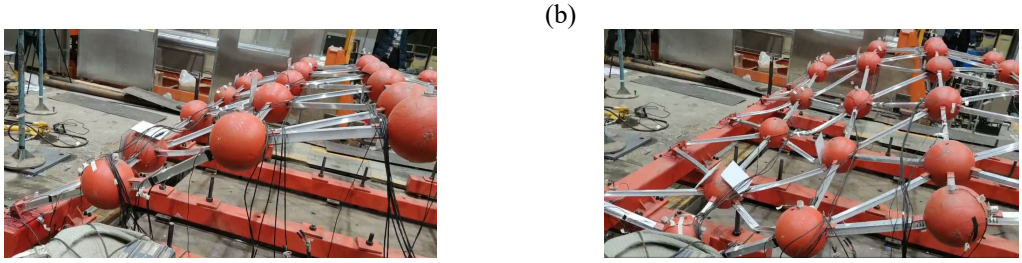


Figure 11. Collapse test of the cylindrical shell: (a) member broken, (b) Local collapsed

When the PGA is 2g, the displacement of the shaking table has reached its maximum limit. During the loading process, the maximum horizontal displacement of joint 29 is 79.06 mm, which is 1/45 of the model span. Besides, the vertical displacement is 62.02 mm, which is 1/53 of the model span (see Fig 9). When the PGA is 2.0 g, the proportion of members in the plastic stage is less than 5%, and the plastic development is concentrated in the four main stressed members at the edge arch of the latticed shell.

3.3.2. Single-layer spherical latticed shell

The Taft, El Centro and Manjil seismic waves are selected and applied to the model horizontally along Y direction. The test is divided into three stages, i.e., elastic stage, elastoplastic stage and collapse stage.

Before the shaking table test, the first six natural frequencies of the model were tested, which are 16.11Hz, 16.49 Hz, 16.60 Hz, 17.58 Hz, 18.07 Hz and 18.63 Hz respectively.

(1) Elastic stage test

The PGA of each seismic waves applied to the model increases from 0.1g to 0.6g by a step of 0.1g, during this stage all the members keep elastic. The acceleration and displacement responses of the latticed shell under Taft wave are shown in Fig. 12. It can be seen that the maximum acceleration is 1.5g, at joint 16 along Y direction. The vertical displacement of top joint is about 2.0mm, a very small value equal to 1/2000 of the span of the shell. The maximum stress is 42Mpa appearing on the member of the first top ring.

(2) Elastoplastic stage test

The peak accelerations and displacements under Taft wave from 0.7g to 2.0g are shown in Fig. 13. It can be seen that the responses increase nonlinearly, especially the displacement of joint 3, which increased greatly after the PGA of ground motion larger than 1.5g. The measures natural frequencies have also decreased than those of elastic stages. There are very slightly plastic bending deformation at the flanges of the ends of the outer members parallel to the Y direction. These mean the structure has entered the elastoplastic stage. But we have to say that this shell has have a very good seismic performance. The maximum vertical displacement under PGA of 2.0g is only 17mm, which is equal to 1/235 of the span.

(3) Collapse test

Because the shell is so 'strong' that there are only slightly plastic deformation under 2.0g. In order to study the how the latticed shell collapses under severe earthquake, some members of the shell are removed, as shown in Fig. 14.

(a) (b)

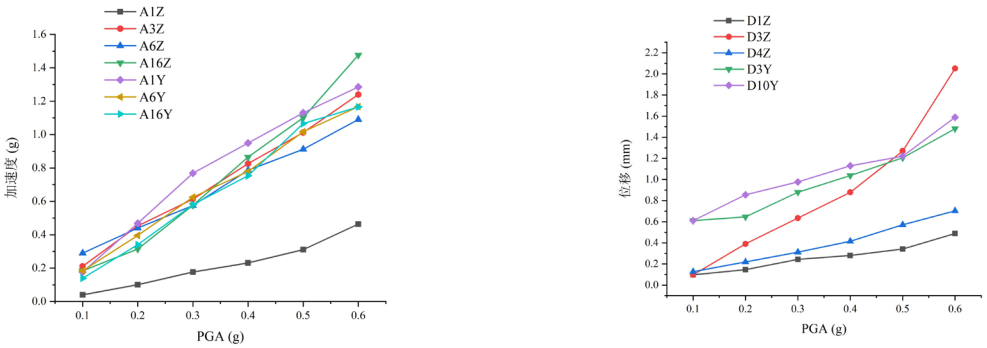


Figure 12. Seismic response of the shell in elastic stage under Taft wave: (a) Accelerations, (b) Displacements

(a) (b)

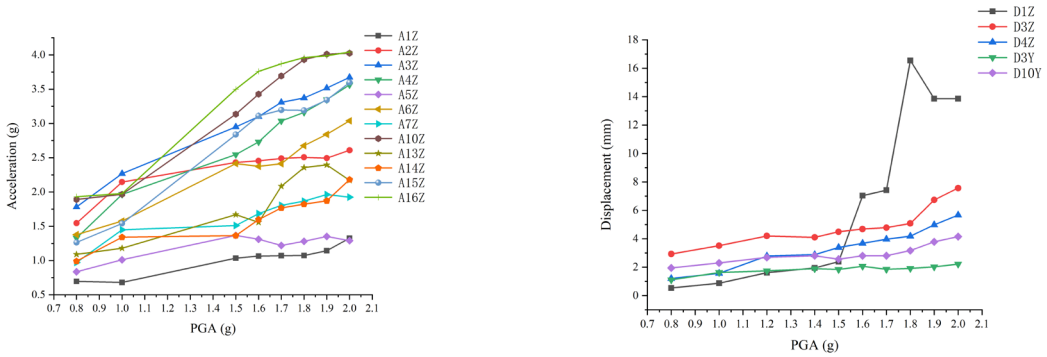


Figure 13. Seismic response of the shell in elastoplastic stage: (a) Accelerations, (b) Displacements

(a) (b)

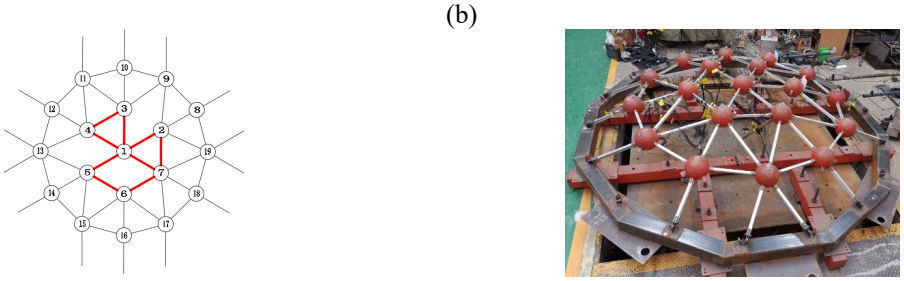


Figure 14. model with members removed for collapse test: (a) Plan, (b) model with members removed

The measured first natural frequency of the modified shell is 7.08Hz, and a sine wave with the frequency of 7.0Hz and PGA of 2.0g is applied to the model. Under the action of 2.0g ground motion, the lattice shell undergoes very significant deformation. Due to the instability of the top rib around the weak axis, the vertex torsion is caused, which in turn drives the six joints on the first ring to rotate; Under the combined action of axial force and weak axial bending moment, due to the significant difference in the moments of inertia between strong and weak axes and the cross-sectional form of the opening, a ring rod buckles in the plane of the shell, and the central flange of the rod is warped; Subsequently, the displacement of the vertex and the first ring joint diverged, causing the region to collapse. In view of the problem that H-shaped open sections are prone to buckling under compression and bending, it is recommended to pay attention to the slenderness ratio of the lattice shell members in engineering seismic design.

(a) (b)

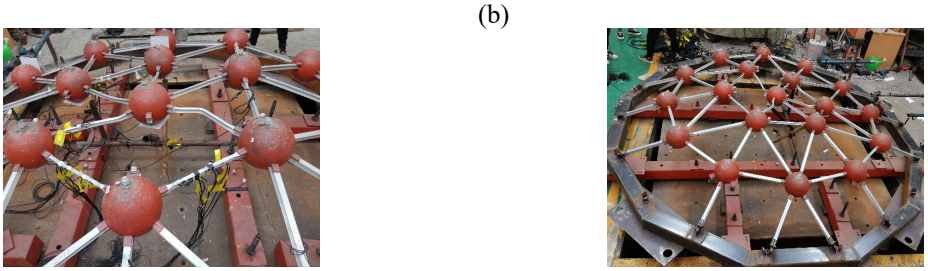


Figure 15. Collapse test of the shell: (a) member buckled, (b) Local collapsed

4. Numerical analysis of the seismic performance of single-layer aluminum alloy shells

4.1. FE model

A multi-scale modeling method combining the shell and beam element is adopted in ABAQUS software, the solid elements are used for connections . The constitutive parameters of the aluminum alloy material, considering the damage accumulation, are fitted by the material test, as shown in Fig. 15. The fitting of the stress-strain curves is compared with the material test data, as shown in Fig. 15b and 15c.

(a) (b) (c)

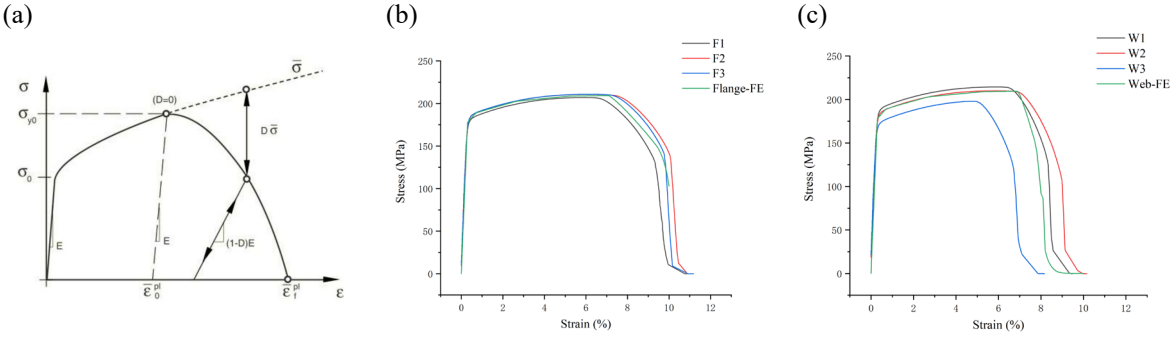


Figure 16. Numerical simulation of material test: (a) Stress-strain curve, (b) Flange sample, (c) Web samples.

Since the first ring in the latticed shell is the region with significant dynamic response, the radial members and ring members, here, are modeled using the shell element S4R. Moreover, the shear deformation beam element B31OS is applied to model the members except in the first ring, which considers the warpage of the open thin-walled cross-section. For steel ball joint, a discrete rigid body is used to simulate. In view of the tightness of the rivet connection, the connection between the members and the ball joint is regarded as a rigid one.

The shear deformation beam element B31OS is selected for component modeling. The joint sphere is modeled by a shell element, which is convenient for mesh generation and adopts a discrete rigid body simulation. The bearing connection is considered to be hinged. Rayleigh damping is implemented. According to the modal mass participation coefficient, the frequency and modal damping ratio of the first and fifth order are selected to calculate Rayleigh damping. The key members of the latticed shell model are L3, L5, L10, and L12. The material parameters and boundary conditions of the model are the same as those of the FE model based on the beam element. Only the above four members are modeled with the shell element.

4.2. Analysis of single-layer cylindrical latticed shell

The measured frequencies and mode shapes are in good agreement with the numerical results, with the maximum error is only 4%, as shown in Table 1.

Table 1. Frequencies and damping ratios of the latticed shell model

Order	1st	2nd	3rd	4th	5th	6th
Measured model frequency /Hz	2.20	5.37	6.34	9.03	9.77	11.71
Numerical model frequency/Hz	2.26	5.29	6.37	9.35	9.38	11.91

The displacement results of joint 29 of the latticed shell model in the severe earthquake stage obtained from the experiment and simulation are shown in Fig. 17a and 17b. Fig. 18 shows the comparison between the simulated and measured horizontal displacement of joint 26 and the stress of point 1-5. The results are in good agreement, and this means the FE model is accurate enough.

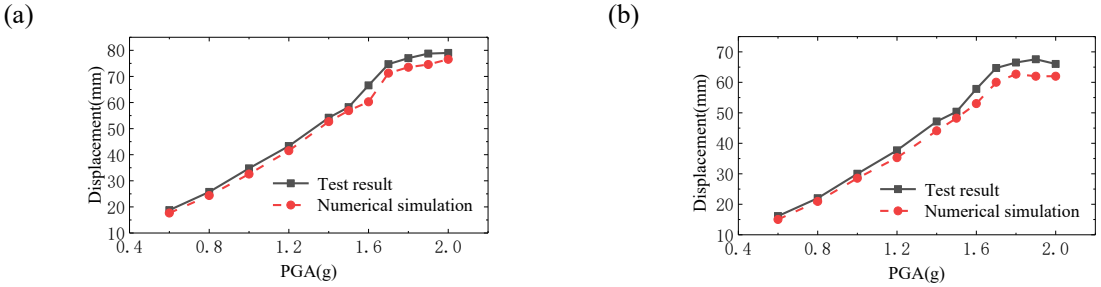


Figure 17. Displacement response comparison of joint 29: (a) Horizontal displacement of joint 29, (b) Vertical displacement

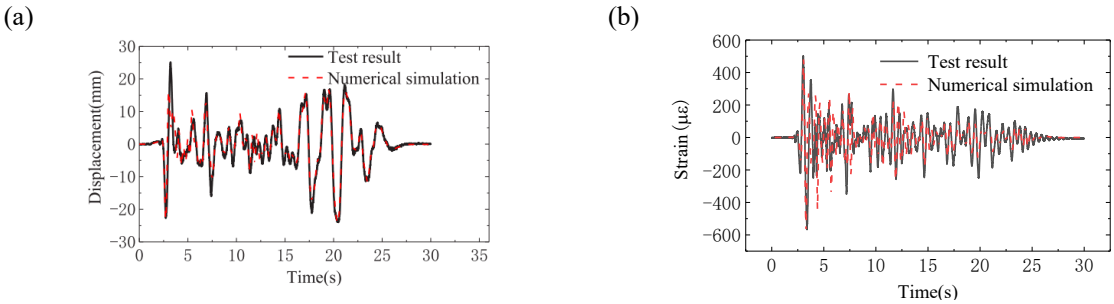


Figure 18. Time history response comparison: (a) Horizontal displacement of joint 26, (b) Strain of point 1-5.

Fig. 19 shows the calculation results of the FE model of the beam structure. The red line indicates that the member element has reached plasticity. The results show that the plastic development of the members is consistent with the test results. Before the first member broke and the lattice shell began to collapse, only four reinforcing members at the end of the lattice shell were monitored to enter plasticity, and the proportion of members entering plasticity was only 5% of all members. The rod with a relatively large cross-section undergoes end failure, while the rod with a smaller cross-section undergoes torsion failure. It is recommended to pay attention to the weakening of the member joint area and the influence of the member section on the member failure and the bearing capacity of the latticed shell during the seismic design of the latticed shell.

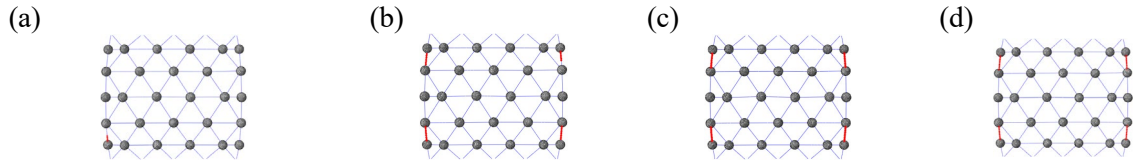


Figure 19. Plastic development: (a) PGA=1.3g, (b) PGA=1.4g, (c) PGA=1.6g, (d) PGA=2.0g。

4.3. Analysis of single-layer spherical latticed shell

The first six natural frequencies of the test and FE are listed in Table 2, the maximum error is about 2%.

Table 2. The first six order vibration frequencies of the test and FE

Order	1st	2nd	3rd	4th	5th	6th
Measured frequency (Hz)	16.11	16.49	16.60	17.58	18.07	18.63
Simulated frequency (Hz)	16.18	16.45	16.56	17.75	18.43	18.71

The displacement results of joint 3 in the elastoplastic stage, which are obtained from the experiment and simulation, are shown in Fig. 20a-b. Fig. 21a-b present four acceleration time-history comparison curves between numerical simulation and experiment under the Taft seismic ground motion with a PGA of 2.0g. Although the arrangement position of the accelerometers causes a measurement error, the simulated curves as well as the experimental curves are conforming in amplitude and shape, verifying the validity of the simulation method in the elastoplastic stage.

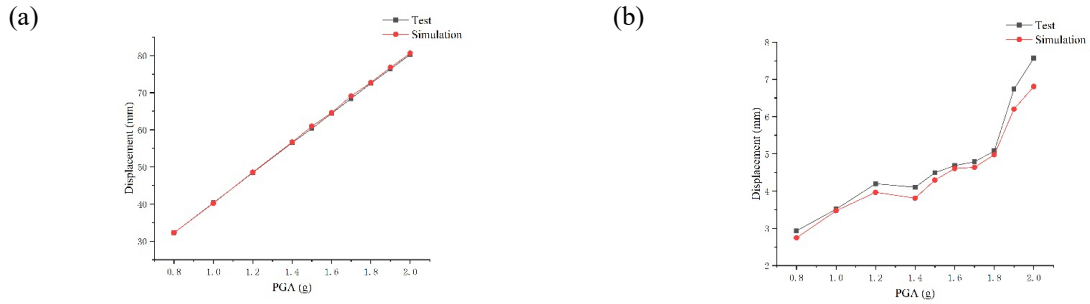


Figure 20. Displacement responses of Joint 3: (a) horizontal displacements, (b) vertical displacements.

(a) (b)

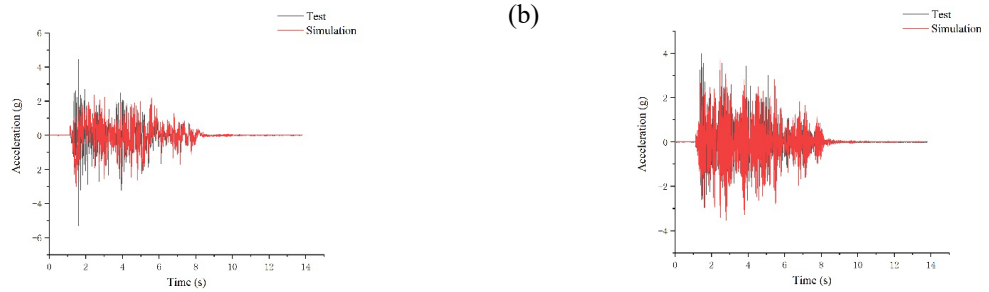


Figure 21. Acceleration measured and simulated of Joint 16: (a) horizontal acceleration, (b) vertical acceleration.

The time-history analysis in full load domain, is carried out on the FE model of test shell, whose plastic development process under the action of Taft seismic ground motion is listed, as shown in Fig. 22. The first ring of the latticed shell model is the region of plastic development.

(a) (b) (c) (d)

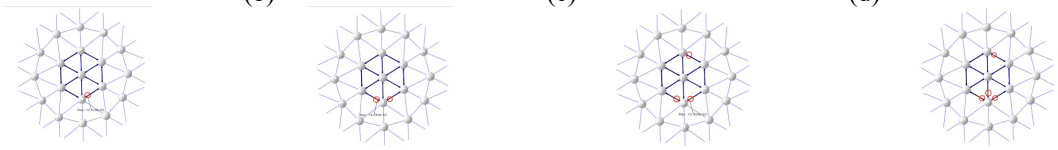


Figure 22. Plastic development process: (a) Taft-1.7g, (b) Taft-1.8g, (c) Taft-1.9g, (d) Taft-2.0g.

As can be seen from the figure, the deformation of the rod in the first ring of the model is the most obvious, manifested by the in-plane bending of the H-shaped rod and the in-plane rotation of the joint ball. Due to errors such as initial eccentricity and initial bending of the rod in the test model, the simulation results are inconsistent with the vertex rotation direction in the test phenomenon, but the plastic distribution and deformation of the simulation results are basically the same as those in the test.

(a) (b)

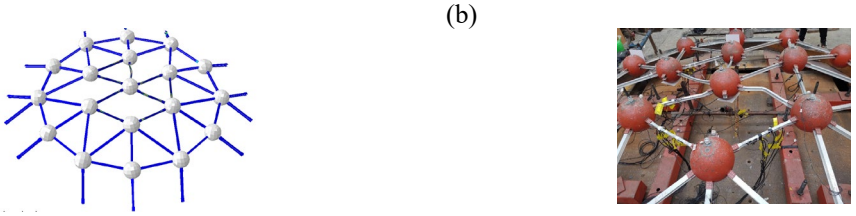


Figure 23. Failure mode comparison: (a) Finite element simulation, (b) Test model.

5. Conclusions

The seismic performance of single layer latticed shells was studied, especially the shaking table tests have been conducted. The following conclusions are drawn:

(1) The Chaboche hybrid strengthening model is reasonable to be used for the seismic analysis of aluminum alloy materials.

(2) The results of the shaking table tests indicates that aluminum alloy latticed shells have good seismic performance. But the displacement of the cylindrical shell is very big, due to the low Young's modulus.

(3) The multi-scale FE models are accurate enough to simulate the response of the shells, and the plastic development in the shells, and thus can be used to analyse the behaviour of the aluminum alloy latticed shells.

(4) the large displacement if the cylindrical shell suggested that besides the strength and stability of the structure, the displacement of the aluminum alloy cylindrical shells must be considered carefully during the design.

Acknowledgement

This work was sponsored by the National Natural Science Foundation of China (grant number 51778016) and Beijing Municipal Natural Science Foundation, China (grant number 8182006).

References

[1] E. Georgantzia, M. Gkantou, G. S. Kamaris, "Aluminium alloys as structural material: A review of research". *Engineering Structures*, vol. 227, pp. 1-16,2021.

[2] J. Wu, Z. Song, G. Sun, et al, "Development and Application of Aluminum Alloy Single-layer Latticed Shells," in *Creativity in Structural Design: Proceedings of the IASS Symposium 2018*, Boston, USA, July 16-20, 2018.

[3] Y. Hiyama, H. Takashima, T. Iijima, et al. "Buckling behaviour of aluminium ball jointed single layered reticular domes," *International journal of space structures.*,. vol. 15, pp. 81-94, 2000.

[4] H. Liu, Y. Ding, Z. Chen. "Static stability behavior of aluminum alloy single-layer spherical latticed shell structure with Temcor joints." *Thin-Walled Structures*., vol. 120, pp. 355-365, 2017.

[5] Z, Xiong, X, Guo, Y, Luo, et al. "Experimental and numerical studies on single-layer reticulated shells with aluminium alloy gusset joints," *Thin-Walled Structures*., vol 118, pp. 124-136, 2017.

[6] H. Ma., L. Yu, F. Fan, et al. "Mechanical performance of an improved semi-rigid joint system under bending and axial forces for aluminum single-layer reticulated shells," *Thin-Walled Structures*., vol. 142;pp. 322-339,2019.

[7] P. Xiang, M. Shi, L. Jia, et al. "Ultra-low cycle fatigue life of aluminum alloy and its prediction using monotonic tension test results," *Engineering Fracture Mechanics.*, vol. 186, pp. 449-465, 2017.

[8] P. Xiang, M. Shi, L. Jia , et al., "Constitutive Model of Aluminum under Variable-amplitude Cyclic Loading and Its Application to Buckling-Restrained Braces," *Journal of material in Civil Engineering.*, vol. 30, pp. 1-13, 2018.

[9] J. Wu, J. Zheng, G. Sun. "Experimental and numerical analyses on aluminium alloy H-section members under eccentric cyclic loading," *Thin-Walled Structures.*, vol. 162, pp. 1-20, 2021.

[10] J. Wu, J. Zheng, G. Sun and X. Chang, "Experimental and numerical analyses on axial cyclic behavior of H-section aluminium alloy members," *Structural Engineering and Mechanics.*, Vol. 81, pp. 11-28, 2022.

[11] X Guo, S Zhu, X Liu, et al. "Experimental study on hysteretic behavior of aluminum alloy gusset joints." *Thin-Walled Structures*., vol. 131, pp.883-901, 2018.

[12] Y. Wu, H. Liu, Z. Chen, et al. "Study on low-cycle fatigue performance of aluminum alloy temcor joints," *KSCE Journal of Civil Engineering*., vol. 24, pp. 195-207, 2020.

[13] Y. Y. Ma, H. H. Ma, S. Ren, et al. "Hysteretic behavior of a new assemble joint under out-of-plane bending: Experimental and numerical studies." *Journal of Constructional Steel Research.*, vol. 167, April 2020.

[14] J. Wu, Y. Li, G. Sun, S. Chen. "Experimental and numerical analyses of the hysteretic performance of an arched aluminium alloy gusset joint," *Thin-Walled Structures*, vol. 171, 108765, 2022

[15] Z. Yu, S. Zheng., C. Zheng. "Failure mechanism and seismic vulnerability of single-layer aluminum alloy cylindrical reticulated shells." Journal of Building Structures, vol. 41, pp. 17-24

[16] J. Wu, J. Zheng, G. Sun and M. Feng, "Shaking table test of the single-layer aluminum alloy cylindrical reticulated shell," *Thin-Walled Structures*, vol. 172, 108866, 2022

[17] J. Zheng, "Shaking table test of the single-layer aluminum alloy reticulated dome", 2022, Beijing University of Technology. [in Chinese]

[18] J. Yang, *Theory and Structural Model Test*, Wuhan University of Technology Press, 2005

Proceedings of the IASS Annual Symposium 2023
Integration of Design and Fabrication
10–14 July 2023, Melbourne, Australia
Y.M. Xie, J. Burry, T.U. Lee and J. Ma (eds.)

Influence of axial force on the dynamic response of the aluminum foam-filled 6082-T6 aluminum tube under lateral impact

Ximei ZHAI[a,*], Lingzhao MENG[b], Guangming CUI[b]

[a,*] Key Lab of Structures Dynamic Behavior and Control of the Ministry of Education
Harbin Institute of Technology, Harbin 150090, China
xmzhai@hit.edu.cn

[b] Key Lab of Smart Prevention and Mitigation of Civil Engineering Disasters of the Ministry of Industry and Information Technology, Harbin Institute of Technology, Harbin, 150090, China

Abstract

Recently, aluminum alloy circular tubes have been widely utilized in the field of the grid, latticed shell, tubular truss, and bridge for its advantages of high strength–mass ratio, excellent corrosion resistance, and great durability. To improve the impact resistant performance of these aluminum alloy components, aluminum foam is employed as energy absorption filler in this study. Moreover, it is worth noting that the aluminum tubes are usually subjected to axial loads and the impact direction is perpendicular to the axis of the tube in practical engineering applications. Therefore, an impact test system which can realize the coupling of the lateral impact and axial force is developed to investigate the dynamic response of the aluminum foam-filled aluminum tubes. The failure modes, impact force histories, displacement histories, energy absorption, and permanent deformation of the foam-filled tubes were obtained and compared with those of the empty tubes under the same impact loading. In addition, the finite element (FE) model was also established via the software ANSYS/LS-dyna and the accuracy of the FE method was verified against impact test results. Based on the FE method, the influence of the axial force on the dynamic behavior of the aluminum foam-filled composite tube was analysed by consideration of the direction of the axial force (tension or compression) and the axial compressive ratio. The results show that axial tension benefits the impact resistance of the tube while the impact resistance of the tube is reduced by applying the axial compression. Furthermore, the adverse effect of the axial compression was weakened when the aluminum foam was employed.

Keywords: aluminum foam-filled, thin-walled tube, lateral impact resistance, energy absorption, axial compressive ratio, numerical simulation

1. Introduction

Aluminum alloy structures have the advantages of light weight, beautiful appearance, corrosion resistance, good processability, and high recyclability. Therefore, aluminum alloy is more widely used in the construction fields such as large-span space structure and bridge structure these days. However, these aluminum alloy structures are at the risk of accidental impact, which seriously threatens personal safety, property safety, and even social stability. Aluminum foam, which has the advantages of low density, high porosity, and high energy absorption ability, is widely utilized as filler in the field of protective structure for the purpose of energy dissipation [1]. Thus, to improve the impact resistant performance of the aluminum alloy tube employed in the construction field, filling aluminum foam is an effective way without significantly increasing the self-weight of the component.

The energy absorption performance of the aluminum foam-filled aluminum tube subjected to lateral loadings and bending has been widely studied [2-4]. However, all the above existing research on

Copyright © 2023 by Ximei ZHAI, Lingzhao MENG and Guangming CUI. Published in the Proceedings of the IASS Annual Symposium 2023 with permission.

mechanical properties, dynamic response, and energy dissipation of thin-walled metal tubes filled with aluminum foam is limited in the crashworthy structure utilized in the automobile, aircraft and astronautic, and military engineering, etc. Nowadays, study on the impact resistance of aluminum tubes utilized in the field of civil engineering under lateral impact has been carried out [5], whereas, in practical engineering applications, aluminum alloy members are usually subjected to axial forces (axial stretching or compression), which are ignored in the impact tests. Moreover, some researches on the influence of the axial preload on the dynamic response of the mild steel tubes have been published [6-9]. Zeinoddini et al. [6] carried out the impact tests on the cold drawn steel tubes, and the axial force was applied to the pipe before impact as a preload. Both the experimental and numerical results indicated that the axial force had a significant influence on the response of the pipe under the impact. Zhang et al. [7-8] conducted lateral impact test research on Q235 steel tubes with circular hollow section under axial preloads. "three plastic-hinge modes" were observed and the empirical formula for predicting the relationship between the displacement and impact force is proposed. Cui et al. [9] studied the dynamic behavior of the axially pre-loaded high-strength steel circular tubes under the lateral impact loadings, and detailly discussed the effect of the impact energy, diameter-thickness ratio, axial compression ratio, axial force direction, and shape of the hammerhead. However, the lateral impact resistant performance of the aluminum foam-filled aluminum tubes with axial preload have not been studied. Hence, in order to fill the gap in related research, the dynamic response of an axially preloaded aluminum alloy composite member under lateral impact is investigated in this paper.

In this study, lateral impact tests on 8 axially preloaded tubes and 2 tubes without axial preload are carried out to explore the dynamic behavior of specimens under the combined loadings. The deformation modes, impact force–displacement histories of the specimens were also investigated. Subsequently, an FE model based on ANSYS/LS-DYNA is established to reproduce the entire response process of the specimen. Besides, the simulation results of the specimens were compared with the test results to verify the accuracy of the FE model, and then the parameter analysis was conducted to investigate the influences of direction of axial force and axial compression ratio on the impact response performance of the axially preloaded empty tubes and composite tubes.

2. Materials and specimens

6082-T6 aluminum alloy and closed-cell aluminum foam are employed in this study, and the corresponding engineering stress–engineering strain relationships of the materials utilized is obtained based on the tensile tests on the aluminum alloy coupons and the uniaxial compression tests on the aluminum foam, respectively. In addition, the stress–strain relationship of the 6082-T6 aluminum alloy is described by the modified Johnson-Cook constitutive formula as follows [10]:

$$\sigma_{\mathrm{y}} = \left(A + B\bar{\varepsilon}^{\,p^{n}} + \sum_{i=1}^{2} Q_i \left(1 - \exp\left(-C_i \bar{\varepsilon}^{\,p} \right) \right) \right) \tag{1}$$

where σ_{y} represents the true stress; $\bar{\varepsilon}^{\,p}$ represents the effective plastic strain; A, B, n, Q_1, C_1, Q_2, C_2 are the material parameters. Furthermore, the stress–strain relationship of the closed-cell aluminum foam can be calculated by the equation as follows [11]:

$$\sigma = \sigma_{\mathbf{P}} + \gamma \frac{\varepsilon}{\varepsilon_{\mathbf{D}}} + \alpha \ln\left(\frac{1}{1 - \left(\varepsilon / \varepsilon_{\mathbf{D}} \right)^{\beta}} \right) \tag{2}$$

where σ and ε represent the true stress and the true strain of the aluminum foam, respectively; σ_{p} represents the foam plateau stress; ε_{D} represents the foam true complete compaction strain, which is obtained by Eq. (3); α, β, and γ are the fitting parameters. The material parameters of the aluminum alloy and the aluminum foam are listed in Table 1.

$$\varepsilon_{\mathbf{D}} = 1 - \rho_{\mathbf{f}} / \rho_{\mathbf{Al}} \tag{3}$$

where ρ_{f} and ρ_{Al} represent the density of the aluminum foam and its base material, respectively.

Table 1. Material properties of 6082-T6 aluminum alloy and closed-cell aluminum foam.

6082-T6 aluminum alloy	E (GPa)	$\sigma_{0.2}$ (MPa)	σ_u (MPa)	e (%)
	68.3	321.7	350.1	12.97
	A	B	n	
	278.8	390.8	0.747	
	Q_1	C_1	Q_2	C_2
	22.63	7218.34	19.27	1386.39
Aluminum foam	ρ_f (kg/m^3)	E (MPa)		σ_p (MPa)
	271	128.5		2.06
	α	β		γ
	23.48	8		2.19

In the experimental study of this work, 10 specimens with axial preload are lateral impacted to investigate the dynamic performance of the empty tube and the composite tube under the combined axial compression/tension and lateral impact load. Besides, to obtain the dynamic response of the specimen with various parameters which include the direction of the axial force (tension or compression), axial compressive ratio, and impact energy, numerical studies are also carried out. The span of all the specimens is 900 mm, and the impact position is located at the mid span of the tube. A wedge hammer with a weight of 147 kg is utilized for all the tubes. The code of the specimens and the corresponding load condition are given in Table 2 and Table 3. The contents "ET" and "CT" in the first part of the codes represent the empty tube and composite tube, respectively. And the number "1" and "2" in the first part of the codes represent different section sizes of the aluminum tube, i.e., the specimens with number "1" have an outer diameter of 89 mm and a wall thickness of 4 mm, and the specimens with number "2" have an outer diameter of 89 mm and a wall thickness of 5 mm. The letters "C" and "T" in the second part of the codes represent the axial compressive preload and the axial tensile preload, respectively, while the number "0.2/0.4/0.6" indicates the ratio μ of the axial preload to the axial bearing capacity N (calculated by Eq. (4)) of the fully plastic section of the tube. Moreover, the number "4.8/6.8/9" in the last part of the code represents the initial impact velocity.

$$N = \frac{\pi D^2}{4} t\sigma_{0.2} \tag{4}$$

where D and t are the outer diameter and the wall thickness of the tube, respectively; $\sigma_{0.2}$ represents the yield stress of the aluminum alloy.

Table 2. Geometric parameters of specimens and test results.

Specimen	$D_0 \times t_0$ (mm × mm)	V_0 (m/s)	KE (J)	F_{max} (kN)	D_{max} (mm)	T (ms)
ET1-T0.4-4.8	89.32 × 4.16	4.760	1665.3	67.58	40.81	24.38
ET1-0-4.8	89.09 × 3.99	4.962	1809.7	56.35	43.72	24.19
ET1-C0.4-4.8	89.12 × 3.96	4.756	1662.5	52.57	47.83	26.81
CT1-C0.4-4.8	89.07 × 4.03	4.843	1723.9	60.83	44.66	24.26
ET2-T0.4-4.8	88.92 × 4.84	4.784	1682.2	71.86	34.69	20.49
ET2-0-4.8	88.80 × 4.89	4.882	1715.4	69.59	38.42	20.71
ET2-C0.4-4.8	88.93 × 4.91	4.831	1715.4	53.61	41.84	23.58
ET2-C0.4-6.8	88.98 × 4.90	6.722	3321.1	58.84	67.76	25.48
CT2-C0.4-4.8	88.72 × 4.91	4.808	1699.1	56.53	38.91	20.89
CT2-C0.4-6.8	88.93 × 4.99	6.805	3403.6	68.15	63.29	23.62

3. Experimental and numerical method

A drop hammer impact system is employed to carry out the local lateral impact tests on the aluminum foam tube, as shown in Fig. 1. The loading device can be divided into two parts: axial loading device

and lateral impact device. A 100 t jack is utilized for the axial preload, while a wedge drop hammer with a weight of 143 kg is applied for the lateral impact. It is worth to point out that the axial force may suddenly drop during the impact process, which is because that axial compression deformation of the tube occurs after the drop hammer contacts to the tube. Therefore, to provide a more stable axial load during the impact process, an energy accumulator is utilized. With regard to the boundary condition of the tube, fixed end is applied for one side of the tube, and a sliding boundary is applied for another side of the tube. Both the impact force and the static axial force are recorded by the load cell, as shown in Fig. 1. The sample frequency of the axial force and the impact force are set as 10^3 Hz and 10^5 Hz, respectively, because that the duration of the axial force was much longer than that of the impact force. Moreover, the whole impact process was recorded by a high-speed camera with a sample frequency of 3200 Hz.

A half finite element (FE) model is established based on the ANSYS/LS-dyna considering the computing efficiency. The modified Johnson-Cook model and the crushable foam model are respectively utilized to simulate the aluminum alloy and the aluminum foam in this FE model, and the corresponding material parameters are listed in Table 1. Considering the low-velocity impact is used for the drop hammer impact tests, the strain rate effect of the aluminum alloy and the aluminum foam is neglected in the numerical simulation. The rigid mat is employed for the other part of the FE model, including the holding device, the end plate, the wedge hammer head, and the counterweight. With regard to the aluminum alloy tube, shell element is employed, while solid element is used for the other part of the model. The mesh size of the aluminum foam tube wall is set as 2×10 m^2 and refined to 2×2 m^2 in the part of the composite tube which is near the impact position. Furthermore, the same densification area of the mesh size is applied for the aluminum foam, and the mesh size of the aluminum foam filler is determined as $10 \times 2 \times 2$ m^3 and refined to $2 \times 2 \times 2$ m^3. To simulate the fixed boudary of the side of the tube and the sliding boudary of the another side, the nodes of the holding device and the end plate are constrained. And the tied contact is utilized to simulate the contact between the tube wall and the end plate, while the surface to surface contact is employed to simulate the contact between the tube wall and the aluminum foam, the contact between the wedge hammer and the tube wall, the contact between the holding device and the tube wall.

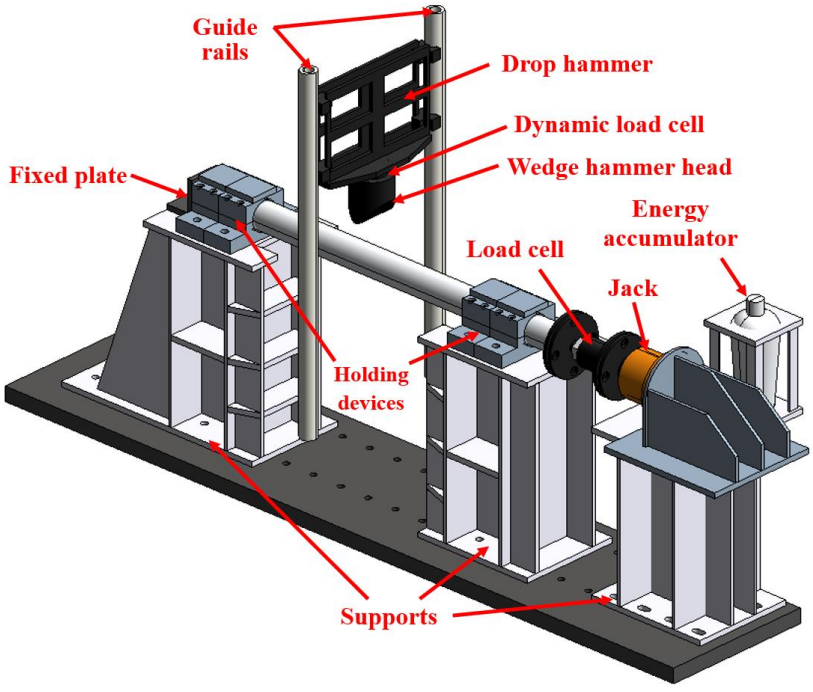


Figure 1. Test setup.

A two-step loading method is applied in the FE model to simulate the static axial load and the lateral impact loading. Firstly, the axial tension or compression is simulated via the implicit analysis module in ANSYS. The node coordinates and the stress state of the elements are recorded in a 'drelax' file for the next step. Secondly, the corresponding file is read in the explicit code ANSYS/LS-dyna the impact load is simulated by applying initial velocity to the drop hammer via the keyword *INITIAL_VELOCITY. Figure 3 shows the comparison of the permanent deformation of the specimens between the experimental and numerical results, and the comparison of the impact force–displacement curves between the experimental and numerical results is plotted in Fig. 4. In addition, the calculated average ratio of the FE results to the test results for F_{max} and D_{max} are 1.031 and 1.059, respectively Therefore, the numerical method proposed in this work can accurately predict the dynamic response of the composite tube under the combined load.

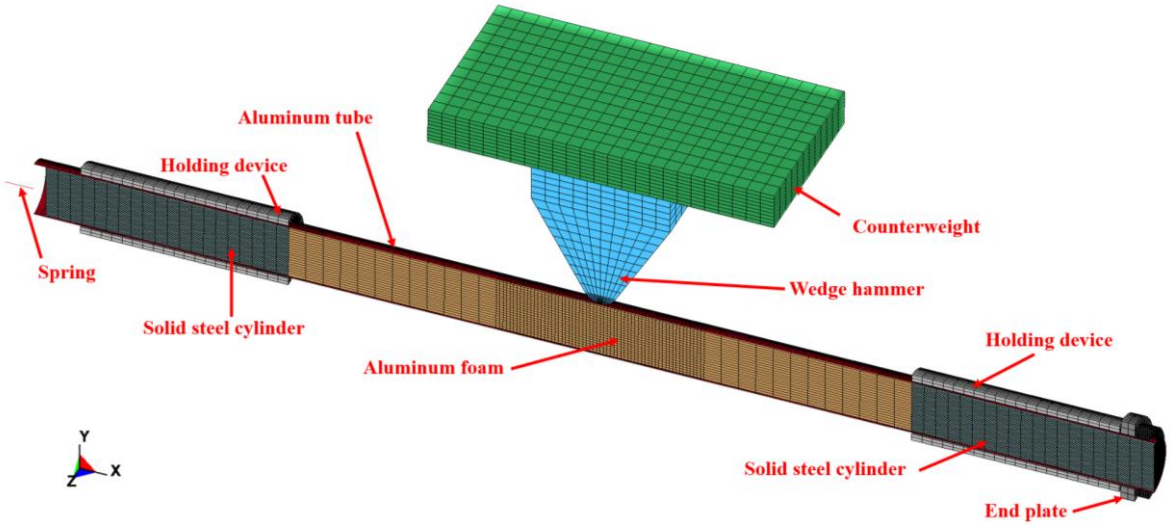


Figure 2. Half FE model.

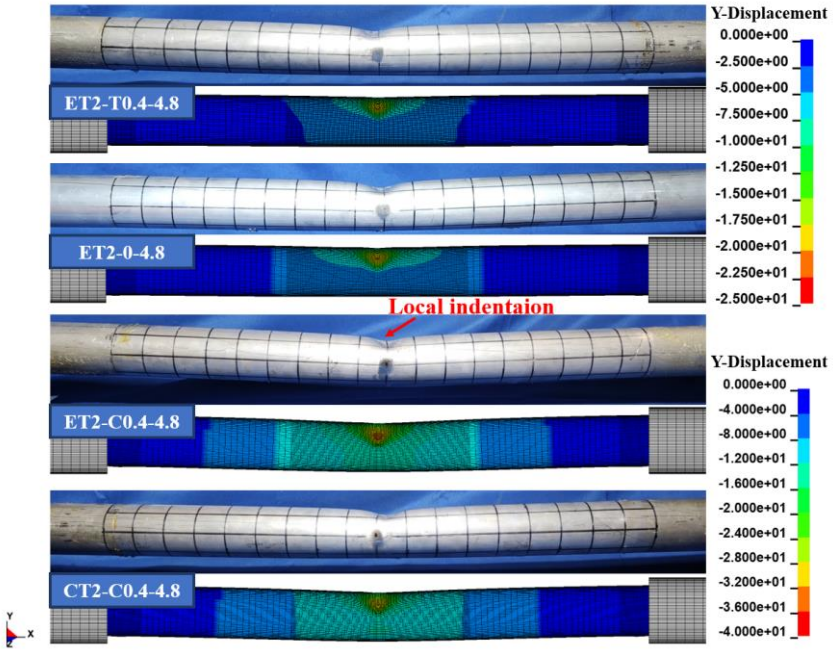


Figure 3. Permanent deformation of the specimens.

4. Influence of axial preloads on the dynamic behavior of the tubes

The permanent deformation of the tested tubes is shown in Fig. 3. It can be observed that the deformation of the tube is composed of the local indentation near the impact position and the global bending of the whole span of the tube. Moreover, the impact force–displacement of hammer head curves are recorded, as plotted in Fig. 4. The results show that the empty tube and the composite tube exhibit the similar impact process under the combined load. The impact force quickly rises at the beginning of the impact process, as well as the displacement of the hammer head is limit at this stage. At the following stage, the growth rate of the impact force–displacement of hammer head curve gradually decrease. When the velocity of the drop hammer reaches zero, the total initial kinetic energy (*KE*) of the hammer is transmitted to the tube, and then the elastic recovery of the tube occurs. The influence of different axial forces on the deformation is detailed discussed in the following subsection.

To investigate the effect of the direction of the axial force (tension or compression) and the axial compressive ratio on the dynamic response of the composite tube and the empty tube under the combined loadings, the parameters analysis is carried out by the numerical method. The results of the numerical study are given in Table 3. Besides, the response of the composite tube and the empty tube discussed in the following subsections are described as follows: the impact resistance of the composite tube and the empty tube can be compared by their maximum displacement $D_{\max}$ at the same impact energy; the depth of the permanent local indentation of the tube ΔD_{per} can be obtained by Eq. (5); the energy absorption ability of the composite tube and the empty tube is evaluated by integrating the impact force–displacement curves, while the integral interval is [0,40], as given in Eq. (6).

$$\Delta D_{\text{per}} = \left| D_{\text{h-per}} - D_{\text{b-per}} \right| \tag{5}$$

where $D_{\text{h-per}}$ and $D_{\text{b-per}}$ represent the permanent displacement of the top and the bottom point of the cross section at the impact position, respectively.

$$\text{EA}_{40\text{mm}} = \int_0^{40} F \text{d}\delta \tag{6}$$

where F and d represent the impact force and the corresponding displacement of the hammer head, respectively.

Table 3. Numerical results.

Specimen	V_0 (m/s)	*KE* (J)	F_{maxFE} (kN)	$\frac{F_{\text{maxFE}}}{F_{\max}}$	D_{maxFE} (mm)	$\frac{D_{\text{maxFE}}}{D_{\max}}$	ΔD_{perFE} (mm)	T_{FE} (ms)	$\text{EA}_{40\text{mmFE}}$ (J)
ET1-T0.4-4.8	4.760	1665.3	70.02	1.036	39.45	0.967	18.66	24.5	$D_{\text{maxFE}} < 40$ mm
ET1-0-4.8	4.962	1809.7	58.60	1.040	48.80	1.116	25.09	27.80	1337.5
ET1-C0.4-4.8	4.756	1662.5	48.87	0.930	52.52	1.098	28.44	28.62	1122.5
CT1-C0.4-4.8	4.843	1723.9	55.52	0.913	47.16	1.056	23.81	24.87	1393.0
ET2-T0.4-4.8	4.784	1682.2	77.83	1.083	35.52	1.024	17.31	21.25	$D_{\text{maxFE}} < 40$ mm
ET2-0-4.8	4.882	1715.4	69.82	1.003	40.61	1.057	21.14	22.80	1738.4
ET2-C0.4-4.8	4.831	1715.4	58.19	1.085	45.69	1.092	24.29	24.00	1465.5
ET2-C0.4-6.8	6.722	3321.1	62.42	1.061	73.01	1.077	34.29	27.37	1507.7
CT2-C0.4-4.8	4.808	1699.1	64.46	1.140	41.28	1.061	20.93	22.13	1699.9
CT2-C0.4-6.8	6.805	3403.6	69.48	1.020	66.18	1.046	29.36	24.50	1757.8
ET2-0-6.8	6.800	3398.6	87.40	-	60.82	-	28.72	24.00	1835.6
ET2-C0.2-6.8	6.800	3398.6	75.50	-	63.79	-	30.83	24.50	1766.3
ET2-C0.6-6.8	6.800	3398.6	49.81	-	90.88	-	38.17	33.12	1308.8
ET2-T0.4-6.8	6.800	3398.6	95.19	-	54.25	-	24.27	22.87	2155.4
CT2-0-6.8	6.800	3398.6	90.10	-	56.71	-	25.35	22.40	2084.4
CT2-C0.2-6.8	6.800	3398.6	80.86	-	59.01	-	27.15	22.62	2008.3
CT2-C0.6-6.8	6.800	3398.6	54.37	-	79.43	-	32.44	28.75	1514.2
CT2-T0.4-6.8	6.800	3398.6	100.27	-	50.17	-	20.59	21.12	2434.6

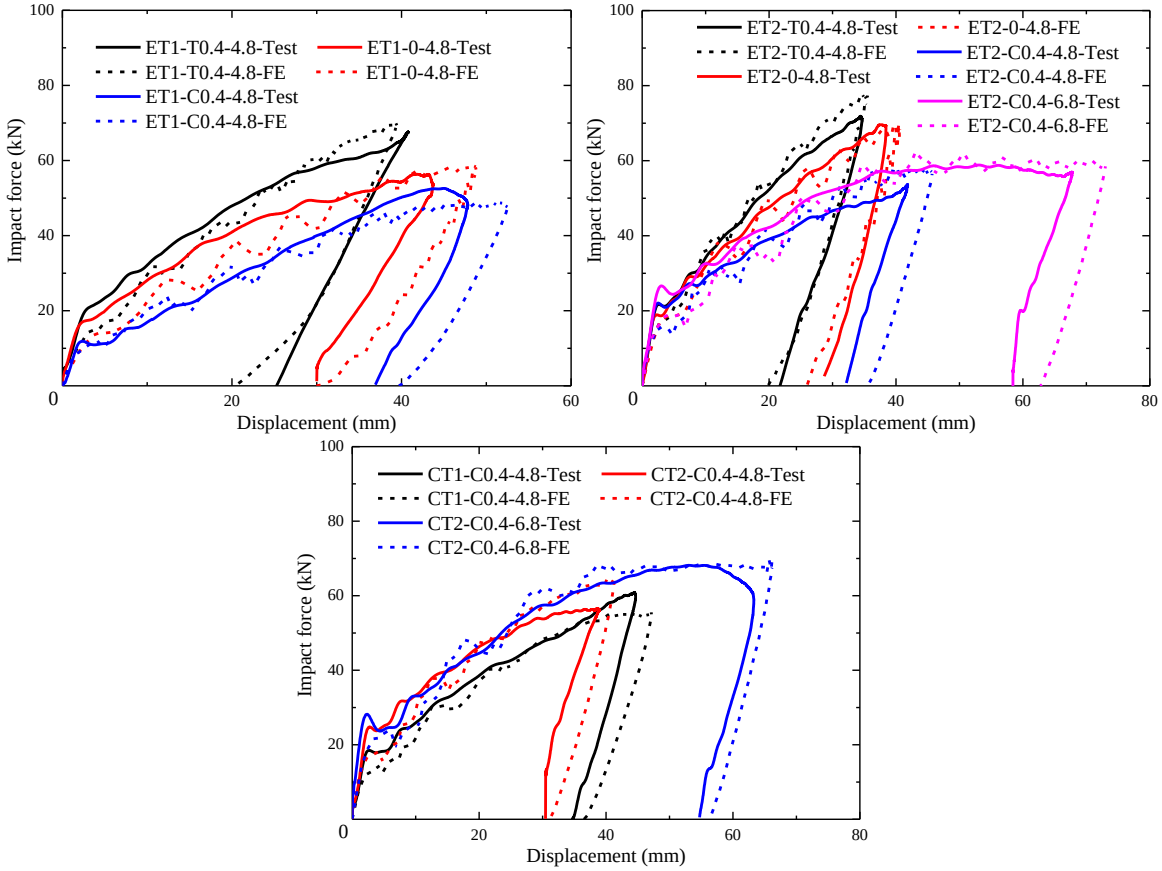


Figure 4. Comparison of the impact force–displacement curves between the experimental and numerical results.

4.1. Effect of the direction of the axial force

Both the axial tensile and axial compressive preloads are applied to the aluminum foam-filled tubes and the empty tubes before the beginning of the impact process in this discussion. In addition, the tubes without axial preload are also considered. All the tubes discussed in this subsection have the same section size, and the outer diameter and the wall thickness are 89 mm and 5 mm, respectively. The initial impact velocity of the hammer for all the tubes is set as 6.8 m/s. Furthermore, the ratio μ of the axial force to the axial bearing capacity N is 0.4 for the tubes with axial preload (T0.4 and C0.4 in Fig. 5 represent the axial tension and axial compression, respectively).

Figure 5 shows the comparison of the dynamic response of the composite tubes and the empty tubes with different axial force directions. It is observed that the influence law of the axial direction force on the behavior of the composite tube and that of the empty tube is similar. As shown in Fig. 5, the D_{max} of the composite tube increases from 56.71 mm to 66.18 mm when the axial force changes from 0 to C0.4, while the D_{max} decreases from 56.71mm to 50.17 mm when the axial force changes from 0 to T0.4. Therefore, it can be indicated that the axial tensile preload benefits the impact resistance of the tube while the impact resistance of the tube is reduced by applying the axial compression. Moreover, the depth of the local indentation is also improved by 15.8% (changed from 25.35 mm to 29.36 mm) after the axial compressive preload is applied, which leads to a more serious defect at the impact location, thereby further affecting the axial bearing capacity of the tube member after impact. The energy absorption EA_{40mm} of the composite tube decreases from 2434.6 J to 1757.8 J when the direction of the axial force changes from tensile to compressive, as shown in Fig. 5(c). In addition, the effect of the aluminum foam filler is also investigated, as plotted in Fig. 5. It can be found that filling the aluminum foam will reduce the deformation of the tube under the lateral impact loading, i.e., the reduction of D_{max}

and ΔD_{per} are 4.11 mm and 3.37 mm after the aluminum foam is filled when the axial preload is not applied. Moreover, the reduction of the deformation by filling the aluminum foam is more obvious when the axial compressive preload is applied, while little change in the reduction of the deformation is observed compared with the corresponding value of the tube without preload for the tubes which are axially tensile. In addition, the effect of filling aluminum foam into the empty tube on the EA_{40mm} is almost unchanged for the tubes with various axial preload.

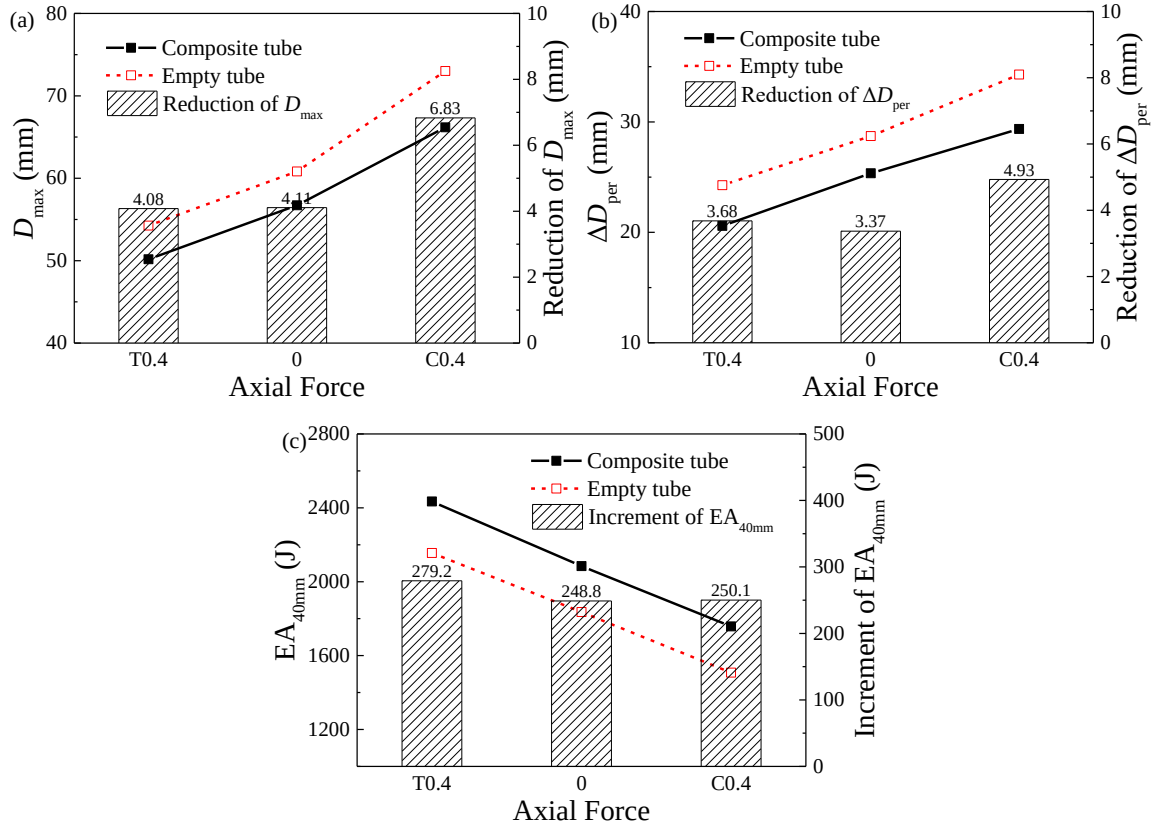


Figure 5. Effect of direction of the axial force on the dynamic response of the composite tube and the empty tube: (a) maximum displacement D_{max}, (b) permanent local indentation depth ΔD_{per}, and (c) energy absorption EA_{40mm}.

As shown in Fig. 6, the X-stress contours on the composite tube surface at the moment of impact completion are used to investigate the effect of the axial force on the residual stress. Compared with the axially tensile preloaded tube, the compression zone appears in the span and near the clamp for the tube subjected to axial compression preload. For all the tubes, the tensile stress concentration area mainly appears at the impact location. In addition, the tensile stress area of the tube under axial tension is larger than that of the tube under axial compression.

4.2. Effect of the axial compressive ratio

It is found in the above subsection that the combination of the axial compression and the lateral impact loading is the most unfavorable state, and the effect of filling aluminum foam on the axially tensile preloaded tube is close to that on the tube without axial preload. Thus, only the tubes which are axially compressive are discussed in this subsection. Three different axial compressive ratios (0.2/0.4/0.6) are employed to investigate the influence of the axial compressive ratio on the lateral impact resistance of the composite tube and the empty tube. All the tubes have an outer diameter of 89 mm and a wall thickness of 5 mm, and the initial impact velocity is 6.8 m/s.

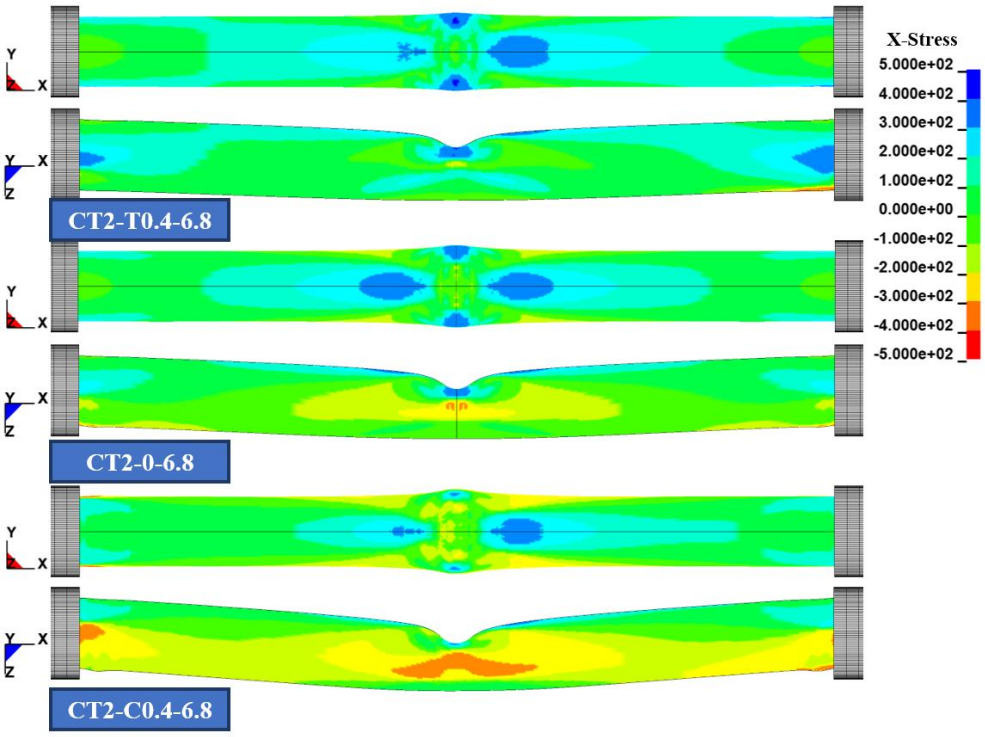


Figure 6. Contours of the residual stress of the composite tubes under different axial preloads.

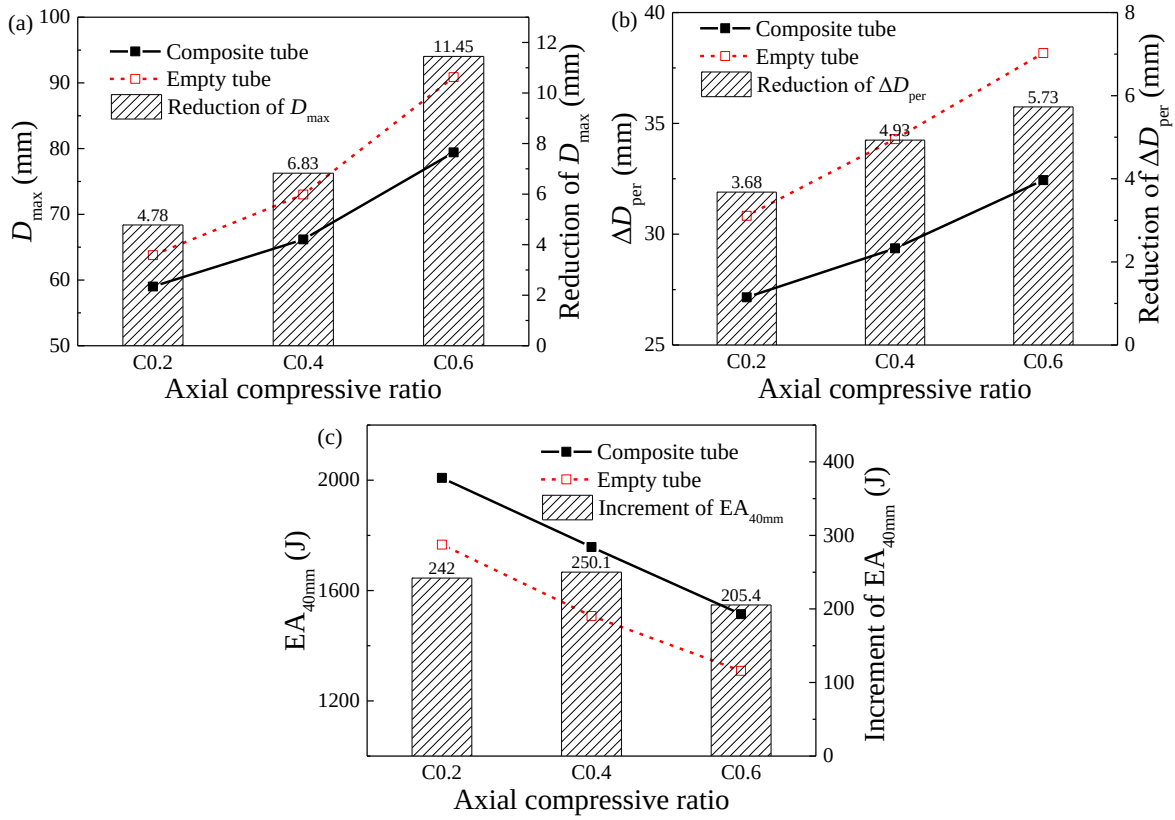


Figure 7. Effect of direction of the axial compressive ratio on the dynamic response of the composite tube and the empty tube: (a) maximum displacement D_{max}, (b) permanent local indentation depth ΔD_{per}, and (c) energy absorption EA_{40mm}.

As shown in Fig. 7(a) and 7(b), with the axial compressive ratio increases from 0.2 to 0.6, the maximum displacement D_{max} of the composite tube is improved by 34.6% (changes from 59.01 mm to 79.43 mm), and the local indentation depth ΔD_{per} is improved by 19.5% (changes from 27.15 mm to 32.44 mm). Furthermore, the influence by filling the aluminum foam into the empty tube also becomes more obvious with the increment of the axial compressive ratio, i.e., the reduction of D_{max} increases from 4.78 mm to 11.45 mm when the axial compressive ratio increases from 0.2 to 0.6, and the corresponding reduction of ΔD_{per} increases from 3.6 mm to 5.73 mm. The energy absorption EA_{40mm} of the tube decreases with the axial compressive ratio increases, which indicates that higher axial compressive preload will reduce the energy absorption of the tube subjected to lateral impact loadings.

In addition, as shown in Fig. 8, with the axial force changed from T0.4 to C0.6, the effective plastic strain of the tube wall with large deformation at the impact position significantly increases (the area of the dark red part increases). Furthermore, the filled aluminum foam shows an obvious influence on the plastic strain of the tube wall at the impact position, the value of the effective plastic strain decreases in the large deformation region of the tube wall, which can explain that filling the aluminum foam can inhibit the initiation and propagation of cracks near the impact region of the aluminum tube.

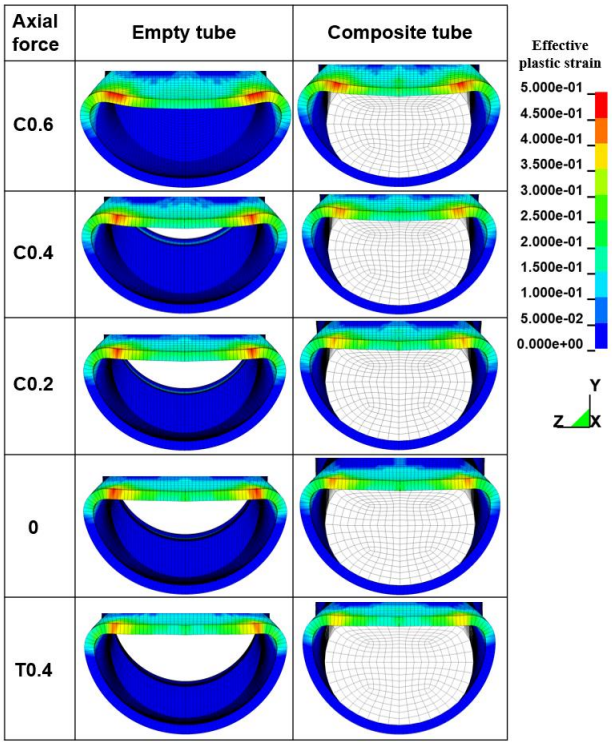


Figure 8. Contours of the plastic strain of the aluminum tube wall under different axial preloads.

5. Conclusion

In this work, the dynamic behavior of the axially preloaded empty aluminum tube and aluminum foam-filled composite tube were investigated by the experimental and numerical studies. The following observations and conclusions can be extracted from this study:

(1) The axially preloaded composite tube and the corresponding empty tube subjected to the lateral impact loading exhibit a combined deformation mode, including the local dent near the impact position and the global bending of the whole span of the tube.

(2) The maximum displacement of the tube D_{max} and the permanent local indentation depth ΔD_{per} decrease when the axial tensile preload is applied, indicating that the impact resistance performance of

the specimens with axial tension is improved. Instead, the axial compressive preload weakens the lateral impact resistance of the tube. Furthermore, filling aluminum foam can reduce the adverse effect of the axial compression force, i.e., both the D_{max} and ΔD_{per} decreases by filling aluminum foam into the empty tube.

(3) With regard to the axially compressive preloaded tube, its impact resistant performance decreases with the axial compression ratio increase, and the D_{max} and ΔD_{per} are improved by 34.6% and 19.5% with the axial compressive ratio increases from 0.2 to 0.6. Besides, the supporting effect of filled aluminum foam on the tube wall is more obvious with the increase of axial compression ratio.

(4) Compared with the empty tubes, aluminum foam-filled tubes exhibit better energy absorption capacity, whereas the improvement of energy absorption by filling aluminum foam is slightly affected by the direction of the axial preload and axial compression ratio.

Acknowledgements

The research presented in this paper is financially supported by the National Natural Science Foundation of China (Grant No: 51978208).

References

[1] Y. Wang, X. Zhai, J. Yan, W. Ying, W. Wang, "Experimental, numerical and analytical studies on the aluminum foam filled energy absorption connectors under impact loading," *Thin Wall Structures*, vol. 131, pp. 566-576, 2018.

[2] Z. Fan, J. Shen, G. Lu, D. Ruan, "Dynamic lateral crushing of empty and sandwich tubes," *International Journal of Impact Engineering*, vol. 53, pp. 3–16, 2013.

[3] J. Shen, G. Lu, D. Ruan, C. C. Seah, "Lateral plastic collapse of sandwich tubes with metal foam core," *International Journal of Mechanical Sciences*, vol. 91, pp. 99-109, 2015.

[4] Z. Li, Z. Zheng, J. Yu, L. Guo, "Crashworthiness of foam-filled thin-walled circular tubes under dynamic bending," *Materials & Design*, vol. 52, pp. 1058-1064, 2013.

[5] L. Meng, X. Zhai, Y. Wang, G. Cui, "Experimental study on dynamic response of 6082-T6 aluminum alloy circular tubes under lateral low-velocity impact loading," *International Journal of Impact Engineering*, vol. 166, pp. 104257, 2022.

[6] M. Zeinoddini, G. A. R. Parke, J. E. Harding, "Axially pre-loaded steel tubes subjected to lateral impacts: an experimental study," *International Journal of Impact Engineering*, vol. 27, pp. 669–690, 2002.

[7] R. Zhang, X. D. Zhi, F. Fan, "Plastic behavior of circular steel tubes subjected to low-velocity transverse impact," *International Journal of Impact Engineering*, vol. 114, pp. 1–19, 2018.

[8] X. D. Zhi, R. Zhang, F. Fan, et al., "Experimental study on axially preloaded circular steel tubes subjected to low-velocity transverse impact," *Thin Wall Structures*, vol. 130, pp. 161–175, 2018.

[9] G. Cui, X. Zhai, L. Meng, "Behavior of axially loaded high-strength steel circular hollow section tubes under low velocity lateral impact," *Thin Wall Structures*, vol. 185, pp. 110595, 2023

[10] LSTC, LS-DYNA *Keyword User's Manual, Livermore Software Technology Corporation*, California, America: Livermore; 2013.

[11] A. G. Hanssen, O. S. Hopperstad, M. Langseth, H. Ilstad, "Validation of constitutive models applicable to aluminium foams," *International Journal of Mechanical Sciences*, vol. 44(2), pp. 359-406, 2002.

IASS 2023
July 10–14 Melbourne
Integration of Design and Fabrication

Proceedings of the IASS Annual Symposium 2023
Integration of Design and Fabrication
10–14 July 2023, Melbourne, Australia
Y.M. Xie, J. Burry, T.U. Lee and J. Ma (eds.)

Mechanical properties of the curvature-consistent frictional pendulum isolation system and vibration control of spherical reticulated shell

Niyi LIANG[a], Xudong ZHI[a,*]

[a,*] School of Civil Engineering, Harbin Institute of Technology, Harbin, China
zhixudong@hit.edu.cn

Abstract

With the increasing demand for isolated long-span spatial structures, we proposed a type of curvature-consistent frictional pendulum isolation system that may induce notable seismic isolation effects in long-period and long-span spatial structures during rare earthquakes in this study. Taking the isolation system as the research object, a series of mechanical performance tests were carried out. The hysteretic characteristics and energy dissipation mechanism of the isolation system were analysed, and a refined numerical simulation method was established. The accuracy of the simulation method was verified by comparing the simulation results with experimental results. The isolation system was applied to a double-layer spherical reticulated shell structure, and the dynamic time history response of the structure was analysed. The results indicated that compared with classical friction pendulum bearings, according to the mechanical properties of the isolation system, the proposed curvature-consistent friction pendulum isolation system has excellent isolation performance and energy dissipation capacity, and the isolation system is more suitable for long-span structures. It has a good isolation effect for double-layer spherical reticulated shell structure, and the isolation effect is more effective when subjected to large earthquakes and rare earthquakes.

Keywords: curvature-consistent frictional pendulum isolation, double-layer spherical reticulated shell, mechanical performance tests, isolation performance, energy dissipation

1. Introduction

The classical friction pendulum bearing, a type of sliding isolation bearing, prolongs the natural vibration period of superstructures by adjusting the slider on the sliding surface of the chute, thereby weakening the seismic response of the structure under the action of external excitation. Considering the FPB characteristics of low sensitivity to seismic input frequency range, strong self-reset ability, and excellent isolation energy dissipation [1], it has become one of the most widely used and technologically mature isolation devices in the construction of buildings and bridges worldwide. Considering its mechanical properties, the FPB exhibits good hysteresis ability [2]. In previous studies, FPBs have typically been used in traditional multilayer and bridge structures [3-5], and the seismic response of structures is significantly reduced [6,7].

The isolation performance of the classical friction pendulum bearing is primarily determined by the friction coefficient and radius of curvature of the sliding surface. However, because the classical friction pendulum bearing is limited by its own size parameters, the seismic isolation effect of a structure with the characteristics of a long natural vibration period and encountering rare earthquakes is limited. Therefore, researchers have proposed some improved friction pendulum bearings [8-10]. If the curvature radius of the sliding surface or the number of sliding surfaces of the chute is increased to improve the isolation of a structure, the self-resetting ability of the isolation layer decreases, and the superposition of the residual displacement of the isolation layer affects the isolation performance of the classical

Copyright © 2023 by Niyi LIANG and Xudong ZHI. Published in the Proceedings of the IASS Annual Symposium 2023 with permission.

friction pendulum bearing. In this study, we developed a curvature-consistent frictional pendulum bearing (CC-FPB), which is suitable for long-span spatial structures. An isolation system composed of an annular array of CC-FPBs can afford sufficient seismic isolation and has short self-resetting time, as illustrated in Figure 1. Under static force, the outermost ring members of the upper shell structure primarily act to balance the outwards horizontal thrust of the structure. Conventional isolation bearings have low stiffness and thus reduce the horizontal restraint force of the outermost ring members. When the friction surface of the CC-FPB is mounted on a spherical surface with the same large radius of curvature as the friction surface, each slider of the CC-FPB is initially mounted at a certain angle. The sliders have a horizontally constraining effect on the superstructure, thereby causing the structure to slide on the spherical surface during strong earthquakes.

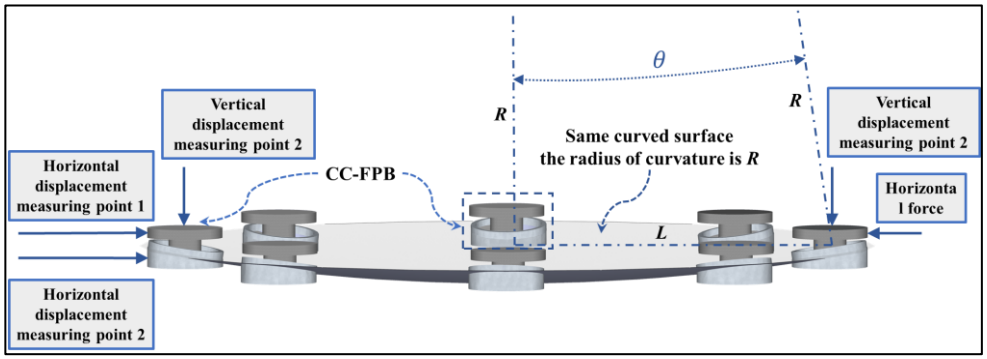


Figure 1. Arrangement of CC-FPBs.

The hysteresis curve of the CC-FPB was obtained by performing hysteresis tests and combining it with the theoretically deduced restoring force formula. The hysteresis characteristics and isolation energy dissipation mechanism were analysed. In addition, the variation of various mechanical performance indexes of the CC-FPB with loading conditions were characterized. To validate the accuracy of the hysteresis test and the feasibility of subsequent research, we developed a refined simulation method for 3D solid element modelling. According to the proposed refined simulation method, we applied CC-FPBs to a long-span spatial structure and analysed the seismic isolation effect and mechanism in the long-span spatial structure.

2. Hysteresis test of CC-FPB

In this study, a hysteresis test of a group of CC-FPBs was carried out to verify the hysteresis performance of the proposed bearing and to explore the variation of various mechanical performance indexes with vertical pressure, loading frequency, and displacement amplitude.

2.1. Test model design

The test model consisted of two CC-FPBs and a loading beam. The loading beam was used to connect the two CC-FPBs, and the loading beam was used to apply vertical pressure and caused loading displacement to the two CC-FPBs (Figure 2.). The total length of the loading beam was 3600 mm, and the loading beam was welded with the two CC-FPBs. The jack was located at the centre of the loading beam and moved and rotated with the loading beam. The jack moved when the loading beam moved along the direction of the actuator, and the pressure head rotated by 360° with the loading beam. The CC-FPBs were lifted by the ground beam to the horizontal position of the actuator. The height of the ground beam was 400 mm, and the height of the centre of the actuator was 1000 mm. The CC-FPB was fixed on the pedestal by using ground anchors that were separated by a distance of 1000 mm. The actuator and the loading beam were connected using a connector. The actuator was extended by half in the initial state to ensure normal reciprocation. During the test, different degrees of vertical pressures were applied through the jack, and various loading frequencies and displacements were applied through

the actuator. The overall test model is displayed in Figure 3. During the test, the lateral support ensured that the loading beam did not sway or twist.

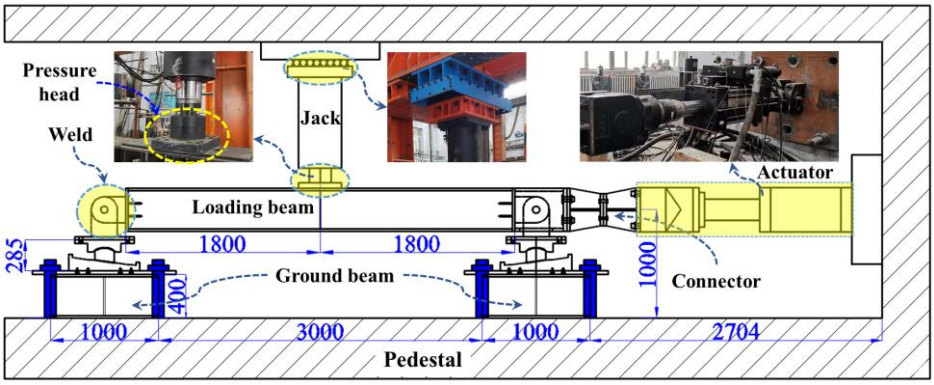


Figure 2. Test device diagram.

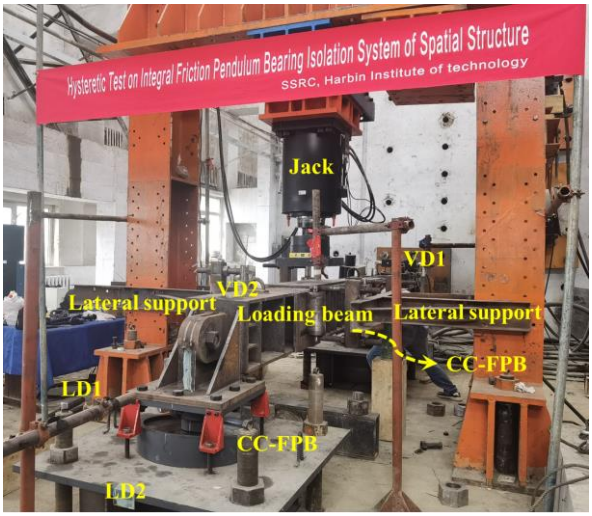


Figure 3. Overall test model.

Linear variable differential transformers (LVDT) were used to measure the horizontal and vertical displacements of the chute and cover plates of the CC-FPB. The layout positions are shown in Figure 4. To eliminate the slight displacement of the loading beam caused by the loosening of the ground anchors, the horizontal displacement of the cover plate and the ground beam were measured by horizontal displacement meters LD1 and LD2, respectively, and the vertical displacements of the left and right bearings were measured using vertical displacement meters VD1 and VD2, respectively.

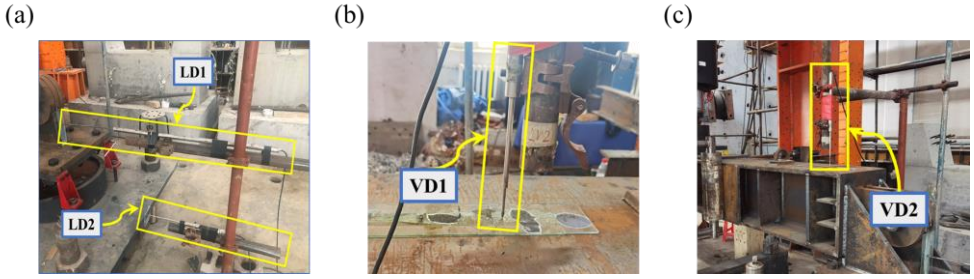


Figure 4. Location of the points of measurement: (a) LD1 and LD2, (b) VD1 and (c) VD2.

The loading system follows the sine wave loading, and the horizontal displacement was loaded according to Equations (1) and (2), respectively. The loading conditions are shown in Table 1, which is represented by vertical pressure-displacement amplitude-loading frequency.

$$d(t) = d_x \sin(2\pi f_0 t) \tag{1}$$

$$f_0 = v_0 / 2\pi d_x \tag{2}$$

Table 1. Loading conditions.

Number	Condition	Number	Condition	Number	Condition	Number	Condition
1	200-67-0.01	9	400-67-0.05	17	600-50-0.09	25	600-100-0.01
2	200-67-0.03	10	400-67-0.07	18	600-50-0.1	26	600-150-0.01
3	200-67-0.05	11	400-100-0.01	19	600-67-0.01	27	800-67-0.01
4	200-67-0.07	12	400-150-0.01	20	600-67-0.03	28	800-67-0.03
5	200-100-0.01	13	600-50-0.01	21	600-67-0.05	29	800-67-0.05
6	200-150-0.01	14	600-50-0.03	22	600-67-0.07	30	800-67-0.07

2.2. Hysteresis curve

The theoretical model of the bearing can be obtained according to the working principle of the CC-FPB (Figure 5), where K_{eff} denotes the equivalent stiffness, K_{fpb} denotes the swing stiffness, R denotes the radius of the curvature of the spherical surface, D denotes the horizontal displacement of the bearing, L denotes the offset distance of the slider, μ denotes the friction coefficient and G denotes the vertical gravitational force acting on the slider.

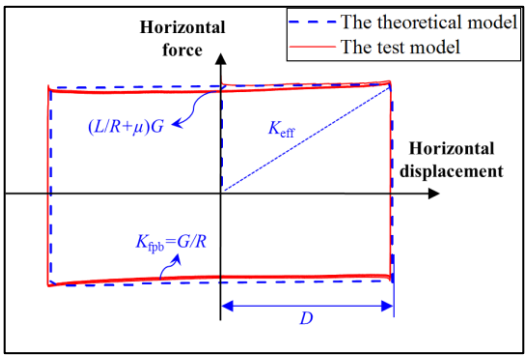


Figure 5. Theoretical model and experimental hysteresis curve.

3. Analysis of test results

The average cycle energy consumption (ACEC), average equivalent stiffness (AES), equivalent dynamic friction coefficient (EDFC), and equivalent damping ratio (EDR) were used as the main indexes to analyse the mechanical performance of the CC-FPB. The average value of the area enclosed by each hysteresis curve was the ACEC, the average value of the antilateral movement of each hysteresis curve was the AES, the EDFC was obtained by calculating the initial restoring force and vertical pressure, and the EDR was calculated according to the ACEC and AES. The mechanical performance indexes were normalised using Eq. (3).

$$V = \frac{x_i}{x_{\max i}} \tag{3}$$

where V is the normalised mechanical performance, x_i is the corresponding parameter value in Group, and $x_{max \cdot i}$ is the maximum parameter value under all working conditions in this group. Based on Eq. (3), the normalised ACEC is V_W, the normalised AES is V_K, the normalised EDFC is V_μ, and the normalised EDR is V_ζ.

3.1. Variations in mechanical performance indexes with vertical pressure

Considering the loading conditions listed in Table 2 as an example, the variation of various mechanical performance indexes with vertical pressure was studied, while the loading frequency and displacement amplitude remained constant

Table 2. Loading condition A.

	Group 1	Group 2	Group 3	Group 4
Loading frequency (Hz)	0.01	0.07	0.01	0.01
Displacement amplitude (mm)	67	67	100	150
Vertical pressure (kN)	200, 400, 600, 800	200, 400, 600, 800	200, 400, 600, 800	200, 400, 600, 800

The hysteresis curves obtained from the four groups of tests under loading condition A were processed, and the normalised mechanical performance indexes are shown in Figure 6. With an increase in vertical pressure, AES increased significantly, and the maximum increment was 60%; ACEC increased significantly, with a maximum value of 57%; EDFC decreased significantly, with a maximum decrease of 48%; and EDR changed little. In conclusion, the vertical pressure significantly influenced the isolation performance and energy dissipation capacity of the CC-FPB. The friction force of the slider was proportional to the vertical pressure, and the external force required for the slider to slide increased with the increase in the vertical pressure. Therefore, the equivalent stiffness and cycle energy consumption of the bearings increased. When the same excitation was applied, the isolation performance decreased with an increase in vertical pressure. Therefore, in the actual engineering isolation design, to ensure that the isolation bearing can give full play to its seismic isolation effect, it is necessary to consider setting a sufficient number of isolation bearings in the isolation layer to ensure that the vertical pressure acting on a single bearing will not affect the normal operation of the entire isolation system.

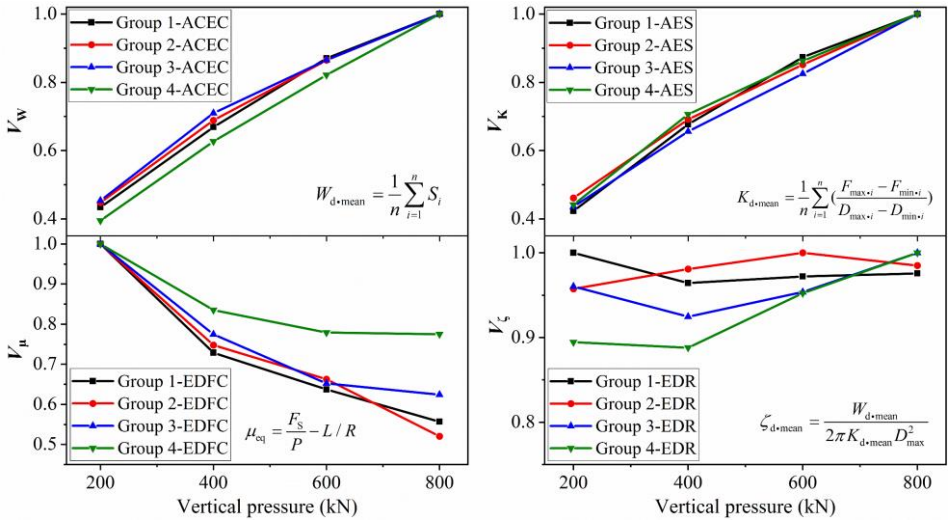


Figure 6. Variations in various mechanical indexes with vertical pressure.

3.2. Variations in mechanical performance indexes with loading frequency

Considering the loading conditions listed in Table 3 as an example, the variation of various mechanical performance indexes with loading frequency was studied, while the displacement amplitude and vertical pressure remained constant.

Table 3. Loading condition B.

	Group 1	Group 2	Group 3	Group 4
Displacement amplitude (mm)	67	67	50	67
Vertical pressure (kN)	200	400	600	800
Loading frequency (Hz)	0.01, 0.03, 0.05, 0.07	0.01, 0.03, 0.05, 0.07	0.01, 0.03, 0.05, 0.07, 0.09, 0.1	0.01, 0.03, 0.05, 0.07

The normalised mechanical performance indexes for loading condition B are shown in Figure 7. With the increase in loading frequency, the change in the AES was small, indicating that the isolation performance of the CC-FPB was less affected by the loading frequency. However, the ACEC increased significantly, with a maximum increase of 20%; EDFC increased, with a maximum increase of 21%; and EDR increased, with a maximum increase of 27%, indicating that the energy dissipation capacity of the CC-FPB increased with an increase in the loading frequency. When the input excitation frequency was high, the bearings had low sensitivity to the input frequency range and demonstrated a stable and excellent seismic isolation effect. Simultaneously, the energy dissipation capacity due to the friction between the slider and the sliding surface of the chute improved.

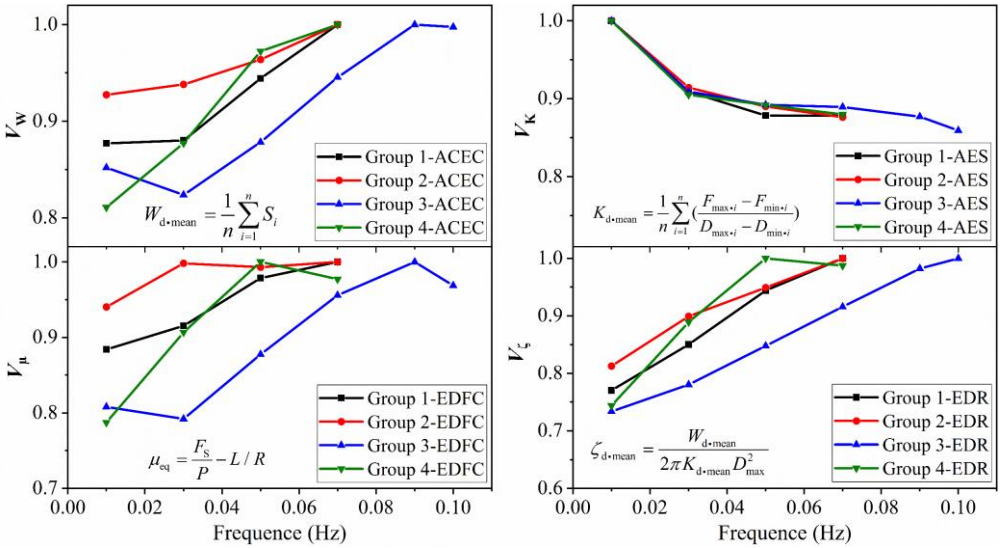


Figure 7. Variations in various mechanical indexes with loading frequency.

3.3. Variations in mechanical indexes with displacement amplitude

Considering the loading conditions listed in Table 4 as an example, the variation of various mechanical performance indexes with displacement amplitude was studied, while the vertical pressure and loading frequency remained constant.

Table 4. Loading condition C.

	Group 1	Group 2	Group 3	Group 4
Vertical pressure (kN)	200	400	600	800
Loading frequency (Hz)	0.01	0.01	0.01	0.01
Displacement amplitude (mm)	67, 100, 150	67, 100, 150	50, 67, 80, 100, 150	67, 100, 150

The normalised mechanical performance indexes under loading condition C are shown in Figure 8. With an increase in the displacement amplitude, AES decreased, and the maximum decrease was 59%; ACEC increased significantly, with a maximum increase of 68%; EDFC decreased by 16%, and EDR decreased by 19%. These results show that the isolation performance and energy dissipation capacity of the CC-FPB increased with an increase in the displacement amplitude. During a rare earthquake, the isolation layer of the isolation structure would produce a large displacement, the large displacement of the isolation layer would promote the large relative movement of the slider and chute, isolating most of the earthquake transmission to the superstructure and improving the amount of seismic energy consumed to overcome the friction.

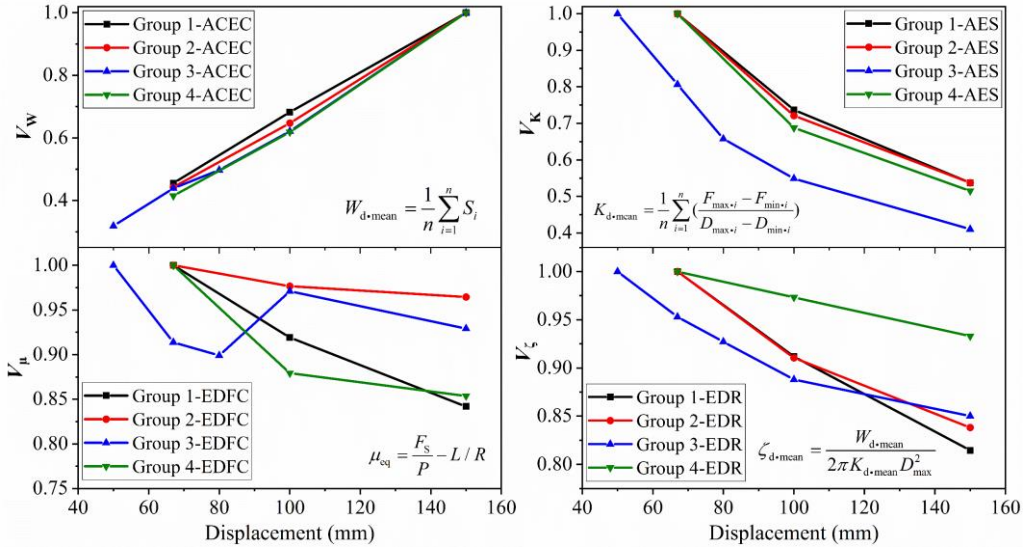


Figure 8. Variations in various mechanical indexes with displacement amplitude.

4. Refined numerical analysis model and test verification

The size of the numerical model was consistent with that of the test model, and the bearing and loading beams were modelled using solid elements. The entire model adopted eight-node hexahedral linear reduced integral elements (C3D8R), suitable for elastic-plastic analysis and contact analyses. The CC-FPB consists of two materials. The cover plate, slider, and chute are made of Q345 steel, and the PTFE plate is made of polytetrafluoroethylene (PTFE)-modified ultra-high-molecular-weight polyethylene. The two materials were assumed to be in an ideal linear elastic stage under all working conditions. The properties of the materials are listed in Table 5.

Table 5. Material property parameters.

Material	Q345	PTFE
Modulus of elasticity (MPa)	2.06E+5	1020
Poisson's ratio	0.3	0.4
Density (kg/m3)	7850	950

The chute was set as a fixed connection, and the upper load was applied at the midpoint of the loading beam to restore the test conditions. The loading beam was defined as a rigid body to improve the calculation efficiency. The hysteresis test model of the CC-FPB is illustrated in Figure 9. The refined simulation method described above was used to reproduce the numerical value of the hysteresis test with CC-FPB. ACEC and AES were calculated from the simulation results and compared with the test values (Table 6). The maximum error of the ACEC was only 5.1%, and the maximum error of the AES was only 7.05%, suggesting that the refined numerical simulation method is reasonably accurate.

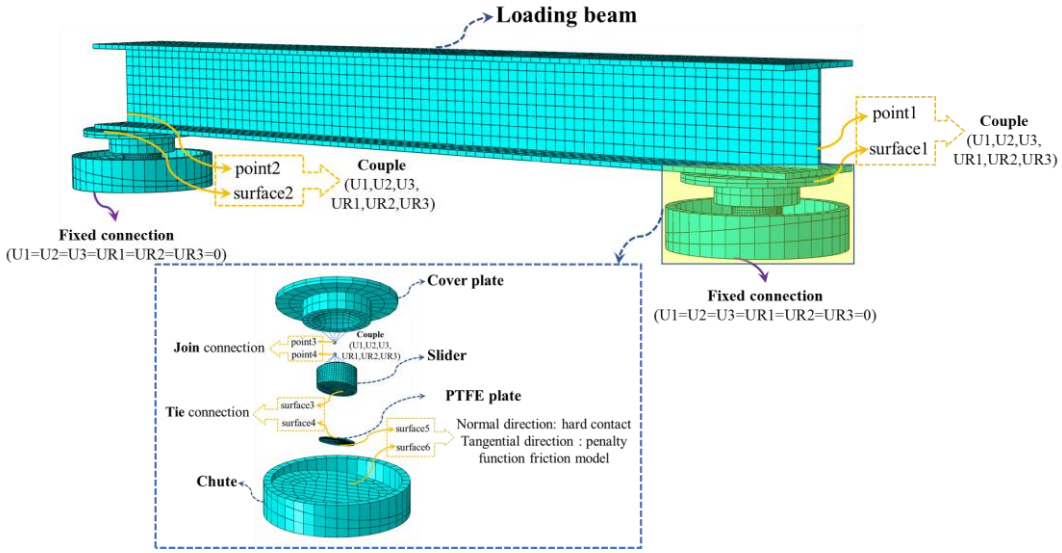


Figure 9. Hysteresis test model of CC-FPB.

Table 6. Test and simulated values.

Condition number	ACEC (kN•m)			AES (kN/m)		
	Test value	Simulated value	Error (%)	Test value	Simulated value	Error (%)
2	4103.982	4163.514	1.45	0.261	0.247	5.36
8	5574.463	5858.979	5.10	0.375	0.349	6.93
20	7195.711	7468.316	3.79	0.482	0.448	7.05
28	10081.54	9795.891	2.83	0.628	0.592	5.73

5. Isolation performance of double-layer spherical reticulated shell

For the common double-layer spherical reticulated shell structures in practical engineering, the isolation effect of the CC-FPB should be considered. In order to reasonably design the size of the member and avoid the problem of excessive slenderness ratio of the member, the structural member is designed with

multiple dimensions. The Truss element is selected as the bar element, and the rod connection method adopts hinge joint. The cross-sectional areas of the members are shown in Table 7. The non-isolated and the CC-FPB reticulated shell structure model are shown in Figure10.

Table 7. Cross-sectional area of the members.

Section type	Cross-sectional area (mm^2)				
	302	481	537	829	905

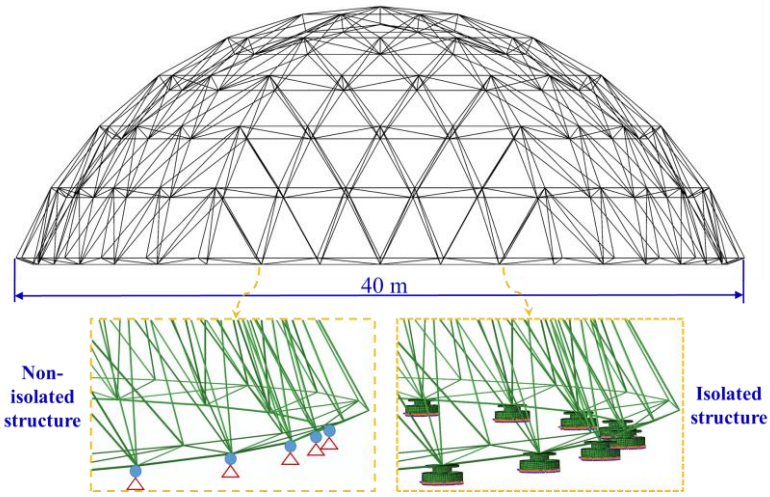


Figure 10. Numerical model boundary condition diagram.

The spectrum distributions of the non-isolated structure and the CC-FPB structure are shown in Figure 11. It is observed that CC-FPBs can also reduce the natural frequency of the double-layer spherical shell, and the natural frequency of the structure is reduced by 38 %, and the amplitude corresponding to the fundamental frequency is reduced by 93 %. At the same time, it is observed that the acceleration response and displacement response of the double-layer spherical reticulated shell structure with the CC-FPB isolation system are reduced by 27 % and 75 % respectively. The stress values of the structural members are significantly reduced, and the maximum stress values of the first layer members, second layer members, and connecting members of the double-layer spherical reticulated shell structure are reduced by 60%, 48%, and 55%, respectively.

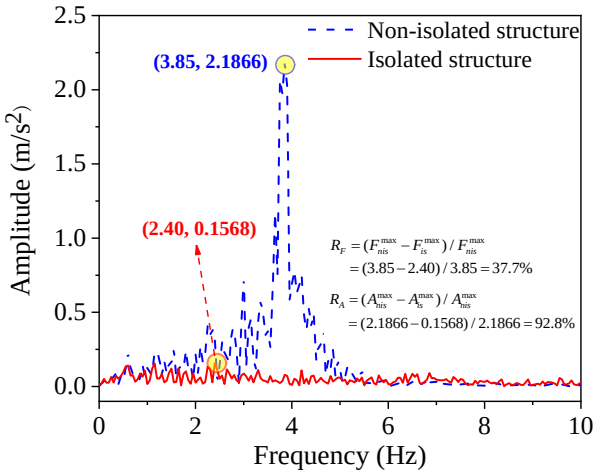


Figure 11. Spectrum distribution diagram.

6. Conclusion

In this study, a CC-FPB is proposed. Considering the bearing as the research object, a series of hysteresis tests and numerical simulations were carried out to obtain the isolation performance and energy dissipation capacity of the isolation system, and the variation of various mechanical performance indexes with external excitation. The seismic isolation effect of the isolation system was studied when applied to a double-layer spherical reticulated shell structure. The following conclusions can be drawn:

(1) The horizontal hysteresis curve of the CC-FPB was complete, and the CC-FPB exhibited high isolation performance and energy dissipation capacity. The isolation capacity of the CC-FPB decreases with an increase in vertical pressure. In an actual engineering isolation design, it is necessary to consider the number of isolation bearings in the isolation layer to ensure normal operation of the isolation system.

(2) The isolation performance of the CC-FPB has negligible effect on the loading frequency, whereas the energy dissipation capacity increased with the increase in loading frequency. When the higher frequency excitation was applied, the energy dissipation capacity due to the friction between the slider and the sliding surface of the chute improved.

(3) The isolation performance and energy dissipation capacity of the CC-FPB increased with the increase in loading displacement. Under the action of a large earthquake, the isolation layer produces a large relative displacement, which can isolate most of the earthquake transmission to the superstructure and increase the seismic energy consumed to overcome the friction.

(4) The refined simulation method of the bearing is proposed, and the bearing is applied to the double-layer spherical reticulated shell structure. the isolation effect of the double-layer spherical reticulated shell structure is better. The natural vibration period of the structure is effectively extended, and the fundamental frequency of the isolated structure is reduced by 93 %. At the same time, the dynamic response values of the structure are significantly reduced.

Acknowledgements

This research was conducted with financial support from the National Natural Science Foundation Innovation Research Group Project of China (Grant NO. 51921006) and High Performance Structural Engineering Innovation Research Team of Heilongjiang Province Head Goose Team (Grant NO. XNAUEA5640206920)

References

[1] Constantinou M, Mokha A and Reinhorn A, "Teflon Bearings in Base Isolation II: Modeling" *Journal of Structural Engineering,* vol. 116(2), pp. 455–474, 1990.

[2] Kumar M, Whittaker AS and Constantinou MC, "Characterizing friction in sliding isolation bearings" *Earthquake Engineering & Structural Dynamics,* vol. 44(9), pp. 1409–1425, 2015.

[3] Mokha A, Constantinou MC, Reinhorn AM and Zayas VA, "EXPERIMENTAL-STUDY OF FRICTION-PENDULUM ISOLATION SYSTEM" *Journal of Structural Engineering,* vol. 117(4), pp. 1201–1217, 1991.

[4] Eroz M and DesRoches R, "The influence of design parameters on the response of bridges seismically isolated with the Friction Pendulum System (FPS)" *Engineering Structures,* vol. 56, pp. 585–599, 2013.

[5] Castaldo P, Palazzo B and Della Vecchia P, "Seismic reliability of base-isolated structures with friction pendulum bearings" *Engineering Structures,* vol. 95, pp. 80–93, 2015.

[6] Gandelli E, De Domenico D, Dubini P, Besio M, Bruschi E and Quaglini V, "Influence of the breakaway friction on the seismic response of buildings isolated with curved surface sliders: Parametric study and design recommendations" *Structures,* vol. 27, pp. 788–812, 2020.

[7] Y. B. Peng, L. C. Ding, J. B. Chen, J. T. Liu and Roberto Villaverde, "Shaking Table Test of Seismic Isolated Structures with Sliding Hydromagnetic Bearings" *Journal of Structural Engineering*, vol. 146(9), pp. 04020174, 2020.

[8] C. S. Tsai, T. C. Chiang, B. J. Chen, "Finite element formulations and theoretical study for variable curvature friction pendulum system" *Engineering Structures*, vol. 25(14), pp. 1719–1730, 2003.

[9] C. S. Tsai, "Characterization and modeling of multiple friction pendulum isolation system with numerous sliding interfaces" *Earthquake Engineering & Structural Dynamics*, vol. 39, pp. 1463–1491, 2010.

[10] D. W. Kong, F. Fan, X. D. Zhi, " Seismic Performance of Single-Layer Lattice Shells with VF-FPB" *International Journal of Steel Structures*, vol. 14(4), pp. 901–911, 2014.

IASS 2023
July 10–14 Melbourne
Integration of Design and Fabrication

Proceedings of the IASS Annual Symposium 2023
Integration of Design and Fabrication
10–14 July 2023, Melbourne, Australia
Y.M. Xie, J. Burry, T.U. Lee and J. Ma (eds.)

Seismic force reduction factor evaluation for double-layered domes supported by single-story substructures

Yuki TERAZAWA[a,*], Haruna SHIJO[a], Deepshikha NAIR[a], Toru TAKEUCHI[a]

[a,*] Tokyo Institute of Technology, Department of Architecture and Building Engineering.
2-12-1, Ookayama, Meguro, Tokyo, Japan
terazawa.y.aa@m.titech.ac.jp

Abstract

Static elastic analysis procedures with seismic force reduction factor remain the cornerstone of seismic design practice even now because it is simple to use and does not require engineers to have an understanding of structural dynamics. However, particularly for metal spatial structures with complicated vibration characteristics, while code-based identical seismic force reduction factors (i.e. American R_μ or Japanese D_s) for specific seismic resisting systems are applied to the roof member design as it is in design practice, the actual (appropriate) force reduction factor has not been investigated yet in detail. Therefore, in this study, a series of nonlinear response history analyses (NLRHAs) for double-layered domes supported by single-story substructures were performed to investigate the effect of the roof span L of 60m to 150m, yielding story drift ratio θ_y, yielding base shear coefficient C_y of 0.3 to 0.6 and post-yielding stiffness ratio p of 0.01 to 0.5 on the seismic force reduction factor D_s and ductility ratio μ. According to the results, the D_s and μ mainly depend on the C_y and p, and are strongly affected by the resonance between the dome and substructure. Furthermore, a modified force reduction factor evaluation method considering the resonance was proposed and captured the NLRHA results more accurately compared with a conventional D_s evaluation method using an equivalent single-degree-of-freedom system.

Keywords: force reduction factor, seismic design, equivalent seismic load, dome, gridshell, buckling-restrained brace

1. Introduction

Static elastic analysis procedures with seismic force reduction factor [1], [2] remain the cornerstone of seismic design practice even now because it is simple to use and does not require engineers to have an understanding of structural dynamics. However, particularly for metal spatial structures with complicated vibration characteristics, while code-based identical seismic force reduction factors [3], [4] (i.e. American R_μ or Japanese D_s) for specific seismic resisting systems of multi-story buildings are applied to the roof member design as it is in design practice, the actual (appropriate) force reduction factor has not been investigated yet in detail. Therefore, in this study, a series of nonlinear response history analyses (NLRHAs) for double-layered domes supported by single-story substructures were performed to investigate the effect of the roof span L of 60m to 150m, yielding story drift ratio θ_y, yielding base shear coefficient C_y of 0.3 to 0.6, post-yielding stiffness ratio p of 0.01 to 0.5 on the seismic force reduction factor D_s and ductility ratio μ. Furthermore, a simple force reduction factor evaluation method considering the resonance between the dome and substructure was proposed. Finally, the static analyses with an equivalent seismic load[5] with the proposed D_s were compared to the NLRHA results.

Copyright © 2023 by Yuki TERAZAWA, Haruna SHIJO, Deepshikha NAIR and Toru TAKEUCHI. Published in the Proceedings of the IASS Annual Symposium 2023 with permission.

2. Overview of the numerical analysis

2.1. Target structure and numerical modelling

An overview of the numerical analysis is shown in Fig. 1. The target structure is a double-layered dome supported by a single-story substructure, and is modelled as a 3D roof structure with a simple shear spring simulating the elasto-plastic behaviour of the substructure, as shown in Fig. 1(b). The double-layered roof members are modeled as an equivalent single-layered roof member for simplicity. The member specification of the roof structures is listed in Table 1. As shown in Fig. 1(d), the parameters in this study are the roof span L of 60m to 150m, yielding story drift ratio θ_y, yielding base shear coefficient C_y of 0.3 to 0.6, post-yielding stiffness ratio p of 0.01 to 0.5. As shown in Table 2 summarizes the relationships between the parameters and the target seismic resisting systems, an American buckling-restrained braced frame (BRBF, θ_y = 1/750 rad. and p = 0.01~0.05), Japanese special moment resisting frame with BRB (SMRF+BRB, θ_y = 1/750 rad. and p = 0.20~0.50), special moment resisting frame (SMRF, θ_y = 1/150~1/100 rad. and p = 0.01~0.05), and the dual system of SMRF+other devices (SMRF', θ_y = 1/150~1/100 rad. and p = 0.20~0.50) are adopted for the substructure, and the effect of the type of seismic resisting system on the seismic response is investigated in detail. In the non-linear response history analysis (NLRHA), the Newmark method (β = 1/4) was used to calculate the incremental displacement, and the large displacement response (i.e., geometric nonlinearity) of the roof structures was considered. The Rayleigh-type proportional damping matrix calculated from the initial stiffness and mass matrix was adopted for NLRHA, and the first and second modal damping ratios were set to 2.0%. The predominant modes of the double-layered domes and response spectra of input ground motions are shown in Fig. 2. In the double-layered dome, an antisymmetric 1 wave mode O1 is the fundamental mode, and the fundamental period ratio R_T of the substructure to the roof was used in the later discussion. As shown in Fig. 2(b), three Japanese spectrally matched seismic waves are assigned. The design spectrum is adopted from the Japanese design base earthquake level where the peak base shear factor is 1.0.

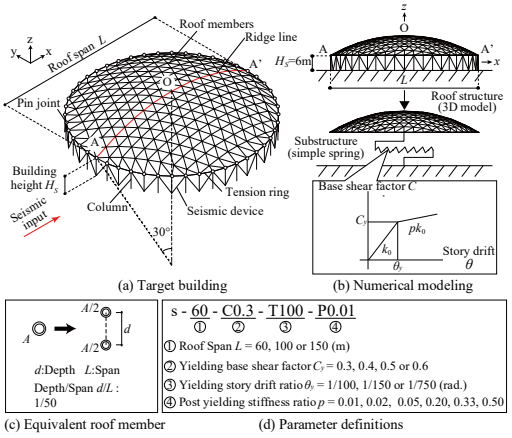


Figure 1. Numerical model.

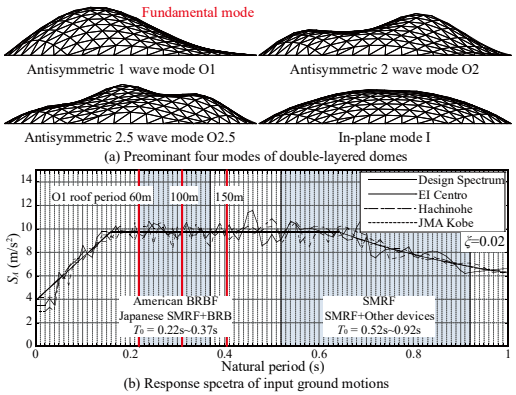


Figure 2. Predominant modes and input ground motions.

Table 1. Target seismic resisting systems.

C_y	θ_y (rad.)	Post-yielding stiffness ratio p = 1/(1+k_d/k_f)	
		0.01~0.05	0.20~0.50 (k_d/k_f=1.0~4.0)
0.3 ~ 0.6	1/750	American Buckling-restrained braced frame (BRBF) T_0=0.22s~0.37s, R_T=0.60~1.55	Japanese Special moment resisting frame with BRB (SMRF+BRB) T_0=0.22s~0.37s, R_T=0.60~1.55
	1/150	Special moment resisting frame (SMRF) T_0=0.52s~0.92s, R_T=1.37~4.09	Dual system of SMRF + other devices (SMRF') T_0=0.52s~0.92s, R_T=1.37~4.09
	1/100		

Table 2. Member specification of the roof structures.

	Roof span L (m)		
	60	100	150
Roof member	O-307.5×7.5	O-414.5×14.5	O-715.5×15.5
Tension ring	O-809.0×9.0	O-1020.0×10.0	O-2525.0×25.0

2.2. Conventional force reduction factor evaluation using equivalent SDOF system

Force reduction factor D_s can be theoretically evaluated by the structural dynamics of an equivalent single-degree-of-freedom (SDOF) system [6]. The schematic image of the evaluation procedure is shown in Fig. 3. Firstly, as shown in Figs. 2(a) and 2(b), a target structure is converted to an initial elasto-plastic SDOF system composed of the whole mass M_{eq}, the substructure's height H_s, and the substructure's stiffness K_s which is equal to $(M_{eq}C_y\mathrm{g})/(H_s\theta_y)$. The fundamental period T_0 is calculated by Eq. (1). As shown in Figs. 3(c) and 3(d), this elasto-plastic SDOF system is iteratively translated to the corresponding equivalent elastic SDOF system composed of the equivalent period T_{eq} and equivalent damping ratio ξ_{eq}, by Eq. (2) to Eq. (4). After the convergence, the force reduction factor D_s and ductility ratio μ are finally evaluated by Eq. (4) and Eq. (5). In Section 3, the theoretical D_s and μ are compared with the NLRHAs. Please note that D_s is equal to $1/R_\mu$ as shown in Eq. (5).

$$T_0 = \sqrt{\frac{\theta_y H_s}{C_y g}} \tag{1}$$

$$T_{eq} = \sqrt{\frac{\mu}{1-p+p\mu}}T_0 \tag{2}$$

$$\xi_{eq} = \xi_0 + \frac{2}{\pi\mu p}\ln\frac{1+p(\mu-1)}{\mu^p} \tag{3}$$

$$\mu = \left(\frac{S_A}{H_s\theta_y}\right)\left(\frac{T_0}{2\pi}\right)^2\sqrt{\frac{1+25\xi_0}{1+25\xi_{eq}}}\times\begin{cases}\dfrac{T_0}{T_{eq}}\dfrac{T_0+T_{eq}}{2T_{eq}T_0} & (T_{eq}<0.64)\\ \dfrac{T_0}{T_{eq}}\left\{\dfrac{T_0}{T_c}-\dfrac{(T_0/0.64-1)^2}{2(T_{eq}/0.64-1)}\right\} & (T_{eq}\geq 0.64, T_0<0.64)\\ \dfrac{T_0}{T_{eq}} & (T_0\geq 0.64)\end{cases} \tag{4}$$

$$D_s = \frac{1}{R_\mu} = \sqrt{\frac{1+25\xi_0}{1+25\xi_{eq}}}\times\begin{cases}\dfrac{T_{eq}}{T_0}\dfrac{T_0+T_{eq}}{2T_{eq}T_0} & (T_{eq}<0.64)\\ \dfrac{T_{eq}}{T_0}\left\{\dfrac{T_0}{0.64}-\dfrac{(T_0/0.64-1)^2}{2(T_{eq}/0.64-1)}\right\} & (T_{eq}\geq 0.64, T_0<0.64)\\ \dfrac{T_{eq}}{T_0} & (T_0\geq 0.64)\end{cases} \tag{5}$$

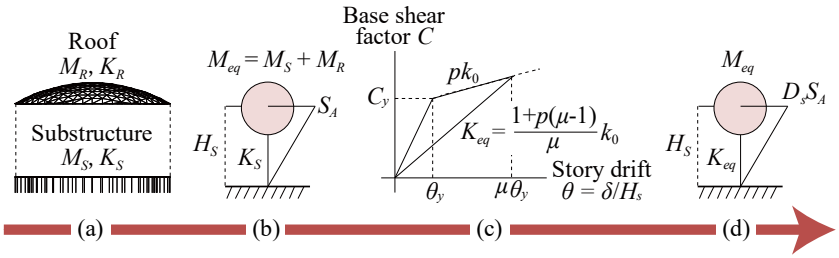


Figure 3. The procedure of the conventional force reduction factor evaluation using equivalent SDOF system.

3. Numerical analysis results

Numerical analysis results of the force reduction factor D_s and ductility ratio μ are shown in Fig. 4. The results are organized by the post-yielding stiffness ratio p, the yielding base shear ratio C_y, the roof span L and the types of seismic resisting systems which yields in the combination of yielding story drift ratio θ_y and p. The average values of NLRHA to three input ground motions are plotted as the marker ○, □, and △. The variation of NLRHA to three input ground motions is plotted as the error bars. Furthermore, the theoretical D_s and μ are also written as "SDOF." In general, the D_s and μ mainly depend on the C_y and p, and have a trade-off relationship where lower C_y and p result in better D_s for the dome design but worse μ for the substructure response, and higher C_y and p result in better μ for the substructure response but worse D_s for the dome design. A higher post-yielding stiffness ratio (p = 0.20~ 0.50) has a greater effect on the average D_s and μ. Furthermore, the type of seismic resisting system has a remarkable effect on the average and variation of D_s and μ. As shown in Fig. 4(a), American BRBF with lower C_y is the best choice for mitigating the seismic input to the roof structure although the story drift response of the substructure is non-negligible. As shown in Fig. 4(c), the D_s of SMRF well agreed with the C_y, and can be controlled by the selection of C_y. However, the story drift response is generally greater than that of BRBF. In contrast to American BRBF and SMRF, as shown in Fig. 4(b), Japanese SMRF+BRB with lower C_y and p contributes to reducing both the seismic input to the roof structure and the substructure's response. On the other hand, while the code specified single force reduction factor (e.g. the D_s of 0.25 for BRBF, SMRF, and SMRF+BRB in Japan) is used in design practice, but generally underestimates the actual value as shown in Figs. 4(a), 4(b) and 4(c). The simple D_s sheet is summarized in Table 3 based on the NLRHA results and can be used as the alternative force reduction factor for regular double-layered dome structures.

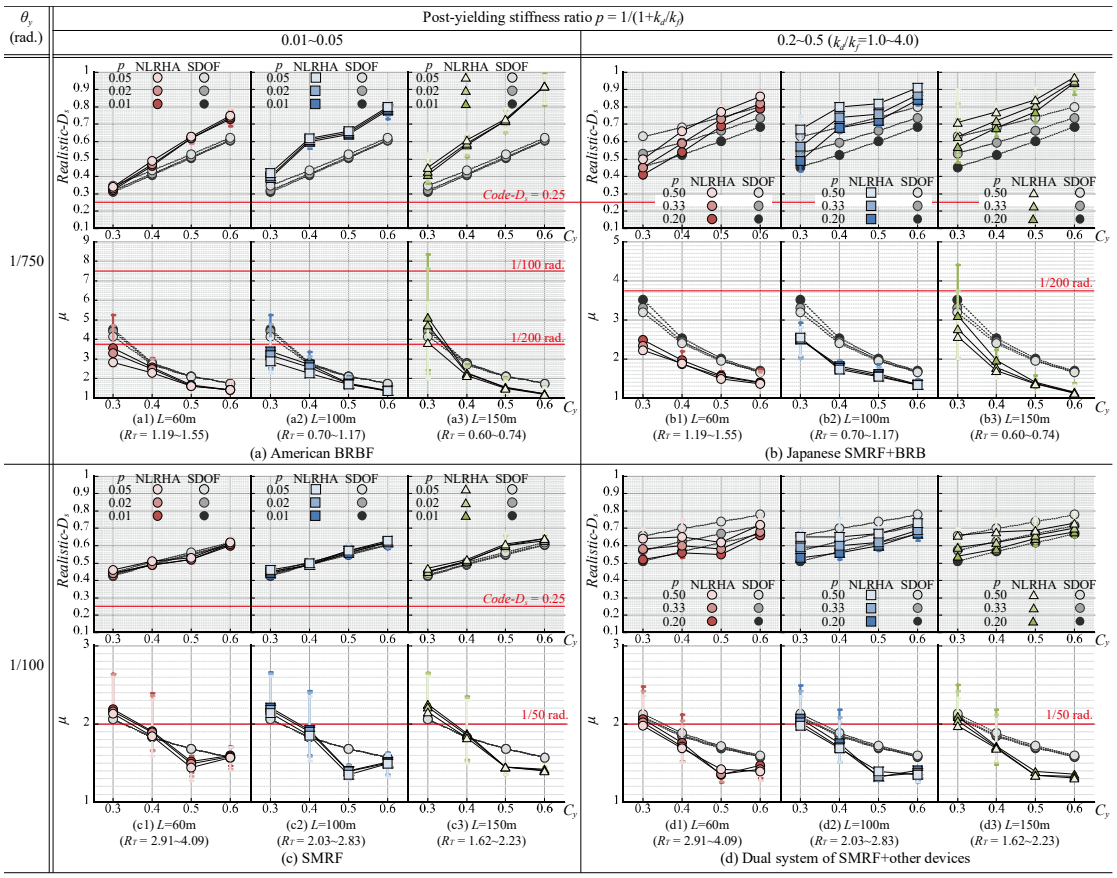


Figure 4. Numerical analysis results of the force reduction factor D_s and ductility ratio μ.

Table 3. Simple D_s sheet for the regular double-layer domes based on the numerical analysis results.

D_s (=1/R_u)		Post-yielding stiffness ratio p = 1/(1+k_d/k_f)					
θ_y	C_y	0.01	0.02	0.05	0.20 (k_d/k_f=4.0)	0.33 (k_d/k_f=2.0)	0.50 (k_d/k_f=1.0)
1/750	0.3	0.40	0.40	0.40	0.45	0.50	0.60
	0.4	0.50	0.50	0.50	0.60	0.70	0.70
	0.5	0.60	0.60	0.60	0.70	0.70	0.80
	0.6	0.70	0.70	0.70	0.80	0.80	0.90
1/150	0.3	0.35	0.35	0.35	0.40	0.45	0.50
	0.4	0.40	0.40	0.40	0.45	0.50	0.55
	0.5	0.50	0.50	0.50	0.60	0.60	0.70
	0.6	0.60	0.60	0.60	0.70	0.70	0.80
1/100	0.3	0.45	0.45	0.45	0.50	0.60	0.65
	0.4	0.50	0.50	0.50	0.55	0.60	0.65
	0.5	0.55	0.55	0.55	0.60	0.60	0.65
	0.6	0.60	0.60	0.60	0.65	0.70	0.70

The response reduction effects on the roof acceleration and roof member's force are shown in Figs. 5 and 6, respectively. These results are the average values of NLRHA to three input ground motions. As shown in Fig. 5, while the horizontal response acceleration decreases in proportion to the yielding base shear factor C_y, the vertical response slightly increases by about 1.5 m/s^2 in some cases of SMRF with longer fundamental substructure's period T_0. As shown in Fig. 6, the axial forces and bending moment of roof members generally decrease in proportion to the C_y. Remarkably, the post-yielding stiffness ratio p has less effect on the response reduction. As shown in Figs. 5(c1) and 6(c1), the slight increment of the vertical acceleration response does not affect the member forces.

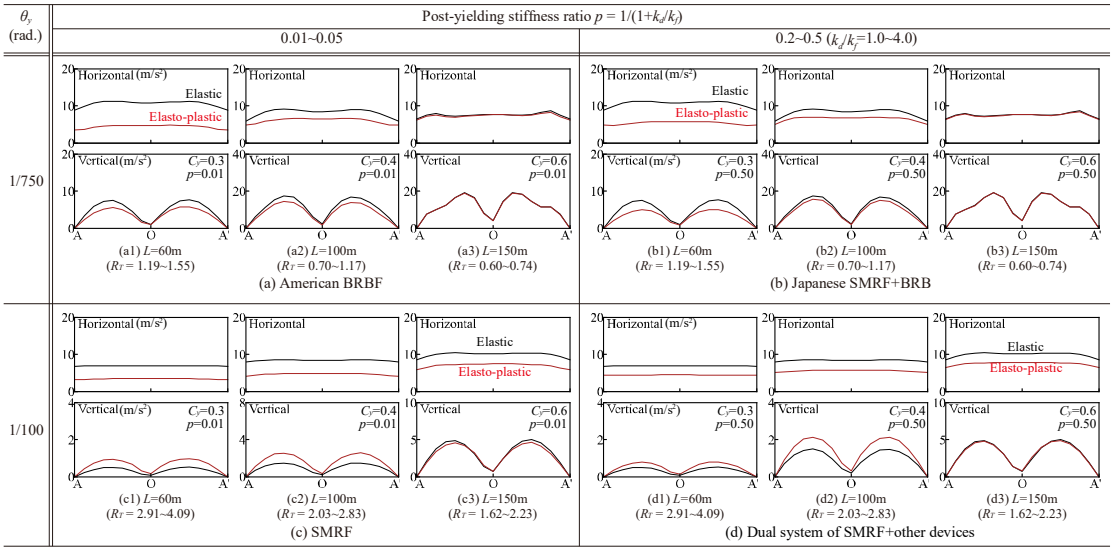


Figure 5. Response reduction effect on the roof acceleration.

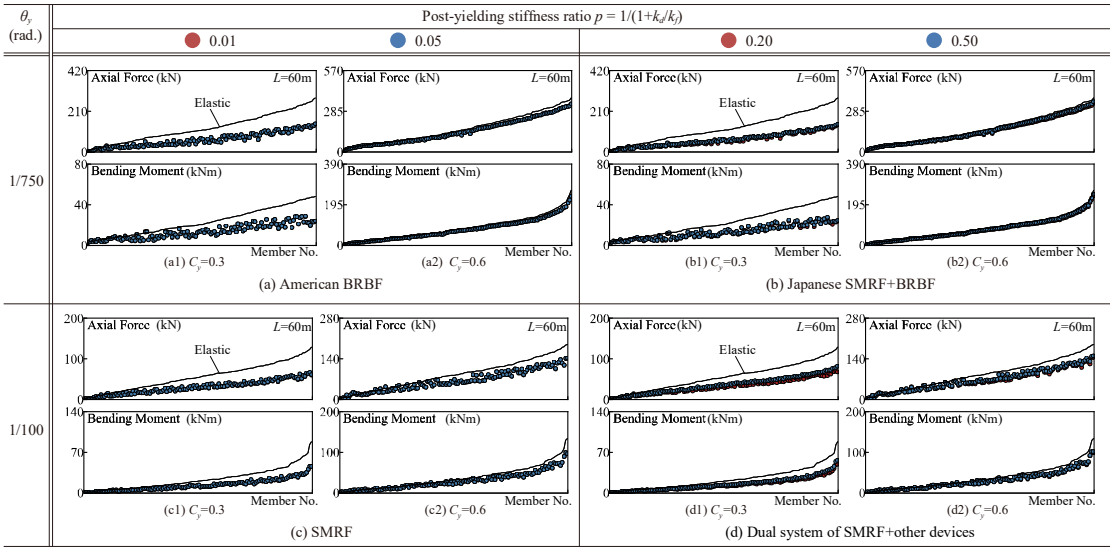


Figure 6. Response reduction effect on the member force of the dome structures.

4. Proposal of a simple force reduction factor evaluation method

As shown in Fig. 4, the equivalent linearization theory [6] of elasto-plastic SDOF systems qualitatively captures the NLRHA results of the partial 3D models. In other words, as shown in Eq. (1) to Eq. (5), the D_s and μ mainly depend on the θ_y, C_y, and p. However, as shown in Fig. 4, the theory significantly underestimated the D_s, particularly for American BRBF and Japanese SMRF + BRB. The relationships between the evaluation error and the fundamental period ratio R_T. are shown in Fig. 7. The relationships between the participation vector value β and the fundamental period ratio R_T. are shown in Fig. 8. As shown in Fig. 7(a), the evaluation error of D_s significantly increases as R_T is closed to 1.0 where the roof response is amplified by the resonance between the roof and substructures. As shown in Fig. 8, the substructure's participation vector value β_s similarly decreases, and have a large gap from the β_s of 1.0 assumed in the conventional theory, that is, the evaluation error of D_s is due to the non-consideration of the resonance effect.

The modified evaluation method was proposed. The schematic of the modified procedure is shown in Fig. 9. As shown in Fig. 9(b), a target building is firstly converted to a two-degree-of-freedom system considering the period ratio R_T between the roof O1 mode and substructure's fundamental mode and the effective mass ratio R_M. The substructure's participation vector value β_s is subsequently calculated by Eq. (6) and Eq. (7). While these equations are according to the theoretical eigenvalue analysis, the lower limit of 0.6 is defined in Eq. (6) based on the numerical results as shown in Fig. 8. In the modified procedure, the D_s and μ are evaluated by an elasto-plastic SDOF system where the acceleration spectrum value S_A is replaced with the $\beta_s S_A$. As shown in Fig. 10(a), the modified method accurately evaluates the D_s of NLRHAs. However, the evaluation error of μ has less improvement because of the large variation due to the input ground motions.

$$\beta_s = \max\left\{\frac{(1-C)+(1-C)^2 R_M}{1+(1-C)^2 R_M}, 0.6\right\} \tag{6}$$

$$C = \frac{\left\{\left(1+R_T^2\right)-\sqrt{\left(1+R_T^2\right)-4R_T^2\left(1+R_M^{-1}\right)}\right\}\left(1+R_M^{-1}\right)}{2R_T^2} \tag{7}$$

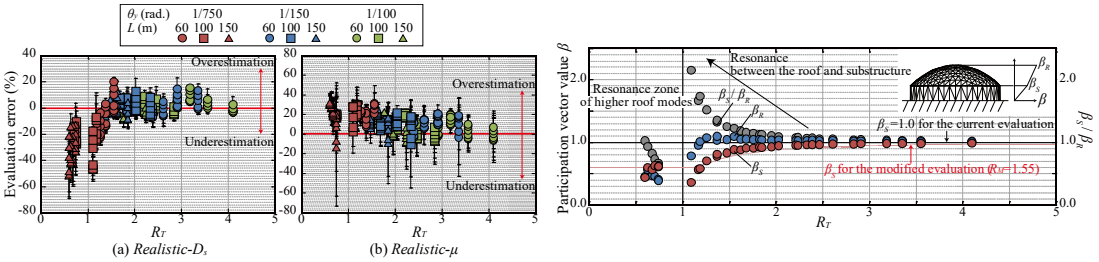


Figure 7. Evaluation error of the conventional method. Figure 8. Participation vector value – R_T relationships.

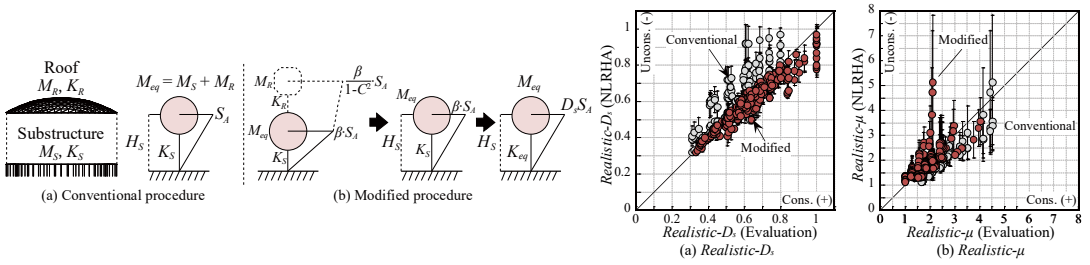


Figure 9. Modified evaluation procedure. Figure 10. Comparison between the evaluation and NLRHAs.

5. Static elastic analysis under the equivalent static seismic load with the proposed D_s

The seismic response computed by static elastic analysis under the equivalent static seismic load [5] with the proposed D_s was compared with that computed by NLRHA. The equivalent static seismic load is calculated by the product of the nodal mass and the distribution formula of roof acceleration. The horizontal and vertical distribution of roof acceleration is calculated by Eq. (8) and Eq. (9). This formula is based on the participation vector of the roof O1 mode shown in Fig. 2(a). The response amplification by the resonance between the roof and substructure is calculated by Eq. (10) to Eq. (13). The force reduction effect is considered by multiplying the D_s with S_A. The comparison of roof acceleration is shown in Fig. 11. The equivalent static seismic loads with the proposed D_s and the simple D_s listed in Table 3 are denoted as "Modified" and "D_s-table", respectively. The equivalent static seismic load captures the NLRHA results except for the cases where the vertical acceleration increases regardless of the D_s. The comparison of seismic response is shown in Fig. 12. The static elastic analysis with the proposed D_s has the same accuracy as the existing static elastic analysis for elastic substructures.

$$A_H(x,y) = D_s S_A \left\{ 1 + (F_H - 1)\cos\left(\pi \frac{\sqrt{x^2+y^2}}{L} \right) \right\} \tag{8}$$

$$A_V(x,y) = D_s S_A F_V \left(\frac{x}{\sqrt{x^2+y^2}} \right) \sin\left(2\pi \frac{\sqrt{x^2+y^2}}{L} \right) \tag{9}$$

$$F_H = \begin{cases} 1.5 & (0 < R_T \le 5/36) \\ \sqrt{5/(4R_T)} & (5/36 < R_T \le 5/4) \\ 1 & (5/4 < R_T) \end{cases} \tag{10}$$

$$F_V = \begin{cases} 3C_V\theta & (0 < R_T \le 5/16) \\ \sqrt{5/R_T - 1}\,C_V\theta & (5/16 < R_T \le 5) \\ 0 & (5 < R_T) \end{cases} \tag{11}$$

$$F_H' = \sqrt{F_H^2 + \left\{ (1-R_T^2)^2 + R_M^{-\theta} \right\}^{-1}} \tag{12}$$

$$F_V' = \sqrt{F_V^2 + \left\{ (1-R_T^2)^2 + R_M^{-1} \right\}^{-1}} \tag{13}$$

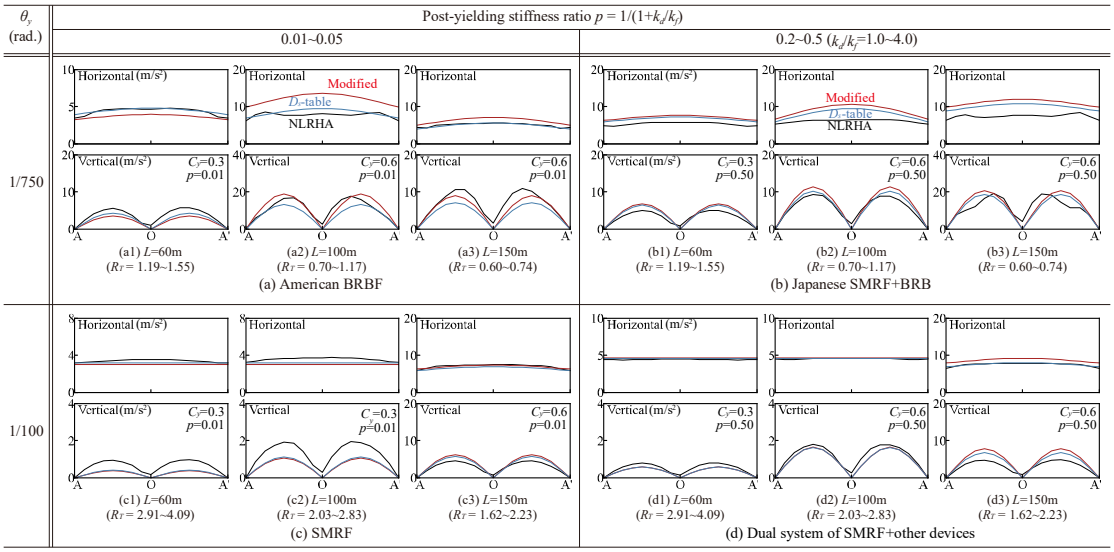


Figure 11. Comparison of roof acceleration between the equivalent static seismic load with Ds and the NLRHAs.

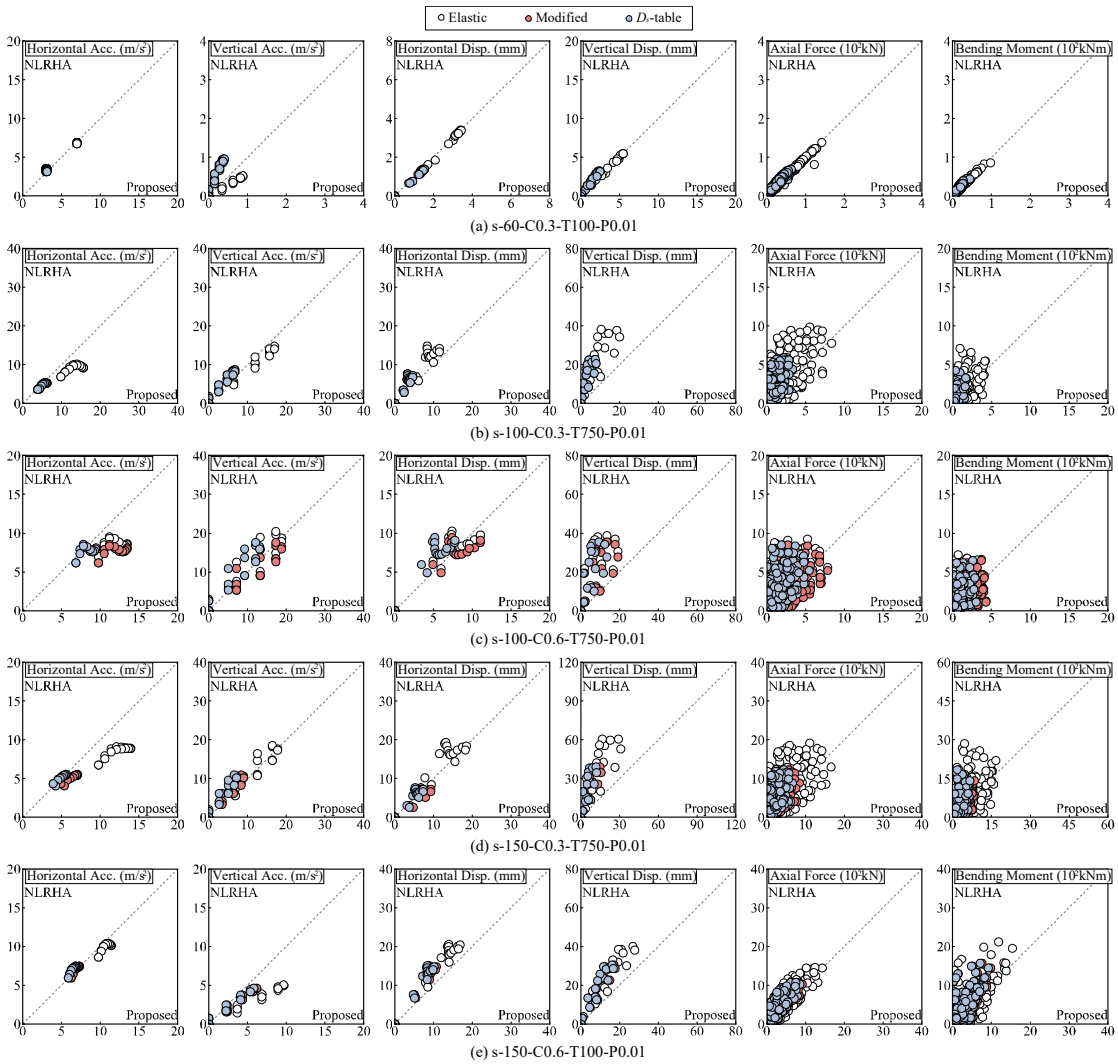


Figure 12. Comparison of seismic response between the static elastic analyses and the NLRHAs.

6. Conclusion

The following conclusions were obtained:

1) The force reduction factor D_s for the dome and ductility ratio μ mainly depends on the yielding base shear factor C_y and the post-yielding stiffness ratio p, and have a trade-off relation where lower C_y and p result in better D_s for the dome design but worse μ for the substructure response and higher C_y and p result in better μ for the substructure response but worse D_s for the dome design. Furthermore, the type of seismic resisting system has a remarkable effect on the D_s and μ. American BRBF with lower C_y is the best choice for mitigating the seismic input to the roof structure although the story drift response of the substructure is non-negligible. Japanese SMRF+BRB with lower C_y and p contributes to reducing both the seismic input to the roof structure and the substructure's response. The code-specified single force reduction factor (e.g. the D_s of 0.25 for BRBF, SMRF, and SMRF+BRB in Japan) is used in design practice, but generally underestimates the actual value.

2) The equivalent linearization theory [6] of elasto-plastic SDOF systems qualitatively captures the NLRHA results of the partial 3D models. However, the evaluation error of D_s significantly increases as the fundamental period ratio R_T is close to 1.0 where the roof response is amplified by the resonance between the roof and substructures. The substructure's participation vector value β_s similarly decreases, and have a large gap from the β_s of 1.0 assumed in the conventional theory, that is, the evaluation error of D_s is due to the non-consideration of the resonance effect.

3) The modified evaluation method of the D_s and μ was proposed, and accurately evaluates the D_s of NLRHAs. However, the evaluation error of μ has less improvement because of the large variation due to the input ground motions.

4) The static elastic analysis with the proposed D_s has the same accuracy as the NLRHA as the existing static elastic analysis for elastic substructures.

Acknowledgments

This work was supported by a research fund from the Japanese Society of Seismic Isolation (JSSI) and by a Grant-in-Aid from the Japan Society for the Promotion of Science Fellowships (No. 21H04581).

References

[1] A. Whitterker, G. Hart, C. Rojahn, "Seismic Response Modification Factors," *Journal of Structural Engineering*, ASCE, vol. 125(4), pp. 438-444, 1999.

[2] N. M. Newmark, W. J. Hall, *Earthquake spectra and design*, Eartquake Engineering Research Institute, 1982.

[3] C. Uang, "Establishing R (or R_W) and C_d factors for building sesimic provisions," *Journal of Structural Engineering*, ASCE, vol. 117(1), pp. 19-28, 1991.

[4] C. Uang, "Comparison of seismic force reduction factors used in U.S.A. and Japan," *Earthquake Engineering and Structural Dynamics*, vol. 20, pp. 389-397, 1991.

[5] D. Nair, Y. Terazawa, T. Takeuchi, "Equivalent static loads for double-layered domes supported by multistorey buckling-restrained braced frames," *International Journal of Space Structures*, vol. 37(4), pp. 227-260, 2022.

[6] K. Kasai, H. Ito, A. Watanabe, "Peak response prediction rule for a SDOF elasto-plastic system based on equivalent linearization technique," *Journal of Structural and Constructional Engineering (Transactions of AIJ)*, No. 571, pp. 53-62, 2003. (in Japanese)

IASS 2023
July 10–14 Melbourne
Integration of Design and Fabrication

Proceedings of the IASS Annual Symposium 2023
Integration of Design and Fabrication
10–14 July 2023, Melbourne, Australia
Y.M. Xie, J. Burry, T.U. Lee and J. Ma (eds.)

Seismic response modification factors of space structures in the horizontal and vertical directions

Mehdi POURSHA*, Karim ABEDI[a], Hamed JAFARZADEH[a],
Pouya HEIDARIAN[a], Ali ABDOLLAHI[a]

[a,*] Sahand University of Technology, Tabriz-Iran
poursha@sut.ac.ir

Abstract

The aim of this paper is to investigate the seismic behavior of space structures and extract the seismic response modification factors to answer the challenges faced by structural engineers to determine the effective seismic parameters of these types of structures. For this purpose, three types of space structures, including the single-layer diamatic dome (SLDD), double-layer diamatic dome (DLDD), and double-layer barrel vault (DLBV) with different span lengths, rise-to-span ratios, and length-to-span ratios are studied. The absence of a general criterion for determining the control point, target displacement, and logical load pattern in the pushover analysis of space structures is one of the important tips studied in this research. In all analyses, material and geometric nonlinearities were applied. First, these models were designed under the applied loads, based on valid regulations. Then, the nonlinear time history analyses were done by using three translational components of earthquake accelerograms to obtain the target displacement at the control node in both horizontal and vertical directions. Finally, by carrying out pushover analyses, the seismic response modification factors, including the behavior factor and the displacement amplification factor, for space structures in both horizontal and vertical directions were obtained.

Keywords: latticed space structures, seismic behavior of space structures, nonlinear analyses, seismic response modification factors

1. Introduction

Behavior factor of a structure includes the nonlinear performance and the hidden strength of the structure in the nonlinear phase. Thus, the required strength for the design is reduced. To obtain the behavior factor, the ductility factor, over-strength factor, and ductility reduction factor should be calculated. A small value of the behavior factor leads to the non-economic design, and its large values represent the acceptance of higher levels of nonlinear deformations in the structure. Therefore, determining this factor is of special importance [1]. Many investigations have been carried out on the seismic behavior of space structures. The 1995 Kobe and 2016 Kumamoto earthquakes showed that although these structures are safer than conventional structures, they cannot be considered safe. Moghaddam studied the seismic behavior of space structures and concluded that the seismic forces resulting from the dynamic analysis of space structures in the nonlinear region is much higher than conventional buildings. He recommended that the behavior factor, *R*, should be assumed as equal to 1.0 for determining the seismic forces in supports and nodal connections [2]. Takeuchi et al. reported buckling of the upper chord and diagonal members and fracture of the bolts of the longitudinal members connected to the bearing by the out-of-plan response of RC supporting frame which led to the falling of the members in space frame gymnasiums during the Kumamoto earthquake [3]. Khalili et al. studied the seismic response modification factors of single-layer barrel vaults and evaluated the effects of the rise-to-span ratio and the length of the structure on the seismic response modification factors. Also, they proposed equations to calculate the period, behavior factor, and displacement amplification factor of these structures [4]. It

Copyright © 2023 by Mehdi POURSHA, Karim ABEDI, Hamed JAFARZADEH, Pouya HEIDARIAN and Ali ABDOLLAHI. Published in the Proceedings of the IASS Annual Symposium 2023 with permission.

should be noted that there is no comprehensive research on space structures, and no general criterion has been given to determine the control point, target displacement, and logical load pattern in the pushover analysis for the calculation of the seismic response modification factors of this kind of space structures. On the other hand, no specific behavior factor has been proposed in the codes for the design of these structures, and this issue is a main challenge for designers. Therefore, the present study aims to comprehensively investigate the seismic behavior of space structures and extract their seismic response modification factors.

2. Definition of the seismic response modification factors

In this paper, the Uang's method has been used to obtain the seismic coefficients. The overall ductility factor of the structure is defined as the maximum lateral displacement (Δ_{max}) to the yield lateral displacement (Δ_y) [1]. To obtain the ductility reduction factor in terms of ductility factor, the equation presented by Newmark-Hall has been used [5], as shown in Table 1.

Table 1. Ductility reduction factor according to the Newmark-Hall method [5].

Ductility reduction factor (R_μ)	Period of Structure (T)
$R_\mu = 1$	$T < 0.05\ sec$
$R_\mu = \sqrt{2\mu - 1}$	$0.12\ sec < T < 0.5\ sec$
$R_\mu = \mu$	$T \geq 1\ sec$

The over-strength factor is defined as the ratio of the load corresponding to the ultimate yield strength of the structure during the formation of the failure mechanism (C_y), to the load corresponding to the formation of the first plastic hinge in the structure (C_s); but to take into account some factors such as the effect of non-structural elements and the difference between the nominal and actual yield stress of the material, the over-strength factor is multiplied by 1.155 [6]. The behavior factor of the structure is obtained by multiplying the ductility reduction factor in the over-strength factor. The displacement amplification factor is obtained by multiplying the ductility factor in the over-strength factor [1].

3. Configuration and property of the models

In this study, three types of space structures including the single-layer diamatic dome (SLDD) (Figure 1: a), double-layer diamatic dome (DLDD) (Figure 1: b), and double-layer barrel vault (DLBV) (Figure 1: c) with different span lengths, rise-to-span ratios, and length-to-span ratios are considered as the structural models. The configuration of all the models is done by the Formian software.

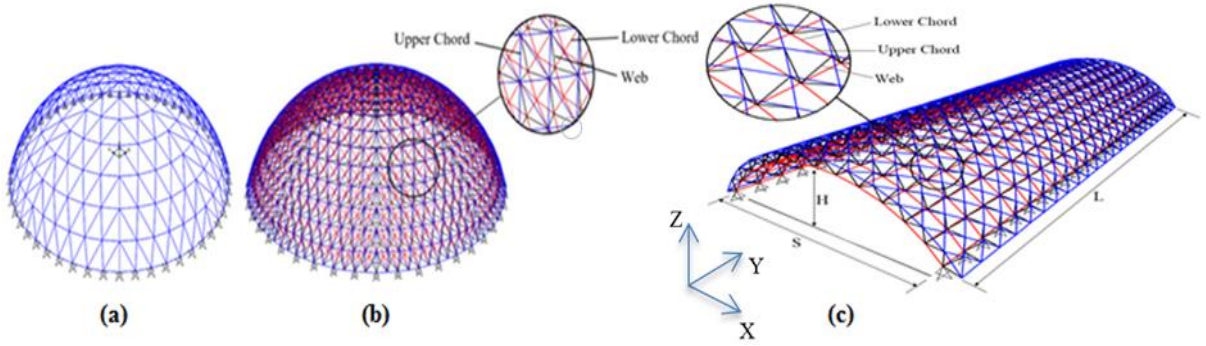


Figure 1. Configuration of the models studied in this research: SLDD (a), DLDD (b), DLBV (c).

3.1. Single-layer diamatic lattice domes

Single-layer Diamatic dome is one of the most widely used types of domes. Its feature betrays high stiffness and avoidance of accumulation of members in the crown of the dome. The length of the members is close to each other which results in a uniform structure and, as a result, a uniform stress distribution among the members. This type of domes includes a small number of members and nodes, which has a positive effect on reducing costs. In these models, pinned supports were used in the last ring. In this research, 12 models with span lengths of 30, 40, and 50 m and rise-to-span ratios of 1/7, 1/5, 1/3, and 1/2, which have different numbers of members, were used.

3.2. Double-layer diamatic lattice domes

In this research, double-layer diamatic domes have been studied with the rise-to-span ratios of 1/7, 1/5, 1/3, 1/2 and span lengths of 50, 65 and 80 meters which were formed based on Buckminster Fuller's icosahedron. An imprtant characteristic of double-layer diamatic domes is that they don't have element irregularity and cluttering problems in the crown of domes and are suitable for large spans due to their high rigidity. For models with span lengths of 50, 65, and 80 meters, the depth of the domes is equal to 1.25, 1.5, and 2 meters, and the frequency or in other words, the number of rings, is equal to 8, 10, and 12, respectively. The Nodal connections of members and support boundary conditions are pinned.

3.3. Double-layer lattice barrel vaults

Twelve models of double-layer barrel vaults are assumed. The span of the models is 50 meters in X direction, and the lengths are 50, 100 and 150 meters in Y direction with different rise-to-span ratios of 0.1, 0.2, 0.3, and 0.5. Due to better distribution of gravity forces on the supports, a square configuration for the bottom layer of the double-layer barrel vaults is considered. Also, the diagonal lattice is used for the top layer to increase the rigidity of the structures in the longitudinal direction.

4. Design of the models

The section of the members is tubular, and the steel grade used in the design of the structures is St-37 with mechanical properties given in Table 2.

Table 2. Mechanical properties of the material.

Density	Modulus of elasticity	Yield stress	Ultimate stress	Poisson's ratio
7850 kg/m^3	210 GN/m^2	240 MN/m^2	370 MN/m^2	0.3

Design loads including the dead, symmetric and asymmetric snow, wind, temperature, and earthquake loads were applied to all of the models according to the Iranian national building code (sixth volume) [7], the Iranian code of Practice for the skeletal steel space structures (Standard No. 400) [8], and the Iranian code of practice for the seismic resistant design of buildings (Standard No.2800, 4th edition) [9]. The SAP2000 software and AISC 360-16 code are used in the design process [10]. The spectral dynamic analysis was used for the design of structural models. In addition, site class *C* for DLDDs, *D* for SLDDs, and *E* for DLBVs were assumed [11]. It was assumed that the structures are located in a zone with a very high level of relative seismic hazard. Furthermore, the seismic effective mass is equal to dead load plus 20% of the snow load according to the Iranian seismic design code. Since the design spectrum is defined for a damping ratio of 5% according to the Iranian seismic design code, and the damping ratio of space structures is in the range of 1.5% to 2.5%, the design spectrum was multiplied by the damping modification factor (DMF) according to Eurocode 8 [12] as follows:

$$DMF = \sqrt{\frac{10}{5+\zeta}} = \sqrt{\frac{10}{5+2}} = 1.195 \quad (1)$$

5. Finite element modeling

In this study, the numerical analysis of space structures is investigated by using the ABAQUS finite element software. After the determination of loads and design of the structures by using the SAP2000 software, the models are transferred to the finite element software, to perform the nonlinear time history and pushover analyses. The geometrical and material nonlinearities are considered in these analyses. The elastoplastic and post-buckling behaviors are considered for tension and compression members respectively. In double-layer space structures, the initial imperfection is considered to be $0.001L$ in the middle of compression members. In the double-layer space structures, the member joints are considered pinned and the T3D2 truss element is used. In the single-layer domes, all connections are assumed to be rigid and the Timoshenko beam element (B31), which is in the form of two nodes, is used. In all analyses, the geometric and material nonlinearities are applied. The von-Mises yield level and Rayleigh damping are used as well. A sensitivity analysis for determining the number of elements is also performed to obtain the appropriate number of elements in the analyses. Given that the greater the number of elements, the more accurate the results obtained from the analyses; but the analyses will be time consuming. In this research, the number of elements selected for the finite element modeling of single-layer domes is equal to 5.

6. Verification of numerical modeling and time history analysis

To verify the accuracy of the finite element modeling in the current research, two studies were considered as follows:

6.1. Verification of modeling and buckling behavior of members

In this research, Parke's experimental model was investigated. This model is a double-layer flat grid with a square plan, 1800 mm length in the lower layer and 1400 mm in the upper layer and a height of 254.56 mm. In this model, three types of members are used, and the external load is applied in the vertical direction on the central node of the upper layer. The specifications of the members' materials in tension and compression are presented in Table 3.

Table 3. Characteristics and tensile and compressive behavior of the members [13].

Profile		T1		T5		T6	
Shape		Tubular		Tubular		Solid Circular	
Diameter (mm)		4.76		9.52		10	
Thickness (mm)		0.91		0.91		-	
Tension Material Behaviour	Young's Modules (MPa)	200.9×10^3		200.1×10^3		201.5×10^3	
	Poisson's Ratio	0.3		0.3		0.3	
	Yield Stress (MPa)	252.53		352.84		515.02	
	Plastic Range	Stress(MPa)	Strain	Stress(MPa)	Strain	Stress(MPa)	Strain
		253	0.00111	353	0.00113	515	0.00454
		265	0.01555	359	0.02386	524	0.00568
		316	0.02777	412	0.05227	531	0.01136
		328	0.05550	452	0.09659	546	0.3636
		354	0.10668	452	0.13295		
Compression Material Behaviour	Flexural Buckling Stress (MPa)	-		319		313	

Figures 3 and 4 showing the numerical results of the buckling behaviour of two compression members, T5 and T6 as well as the response of the structure in this research, respectively, indicate that they are close to the experimental results [13].

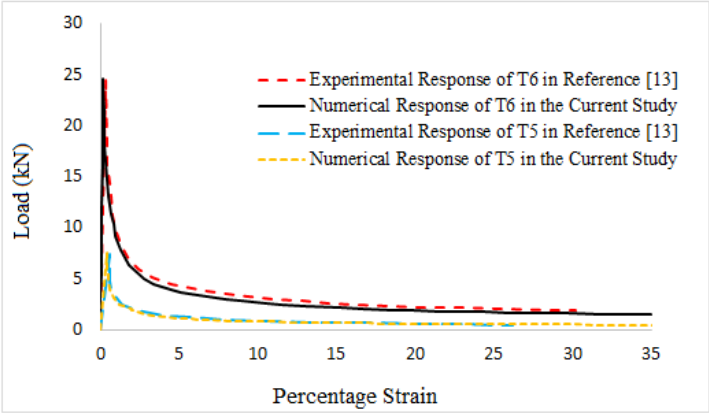


Figure 3. Buckling behaviour of two compression members T5 and T6 in the Parke's experimental response [13] and the current study.

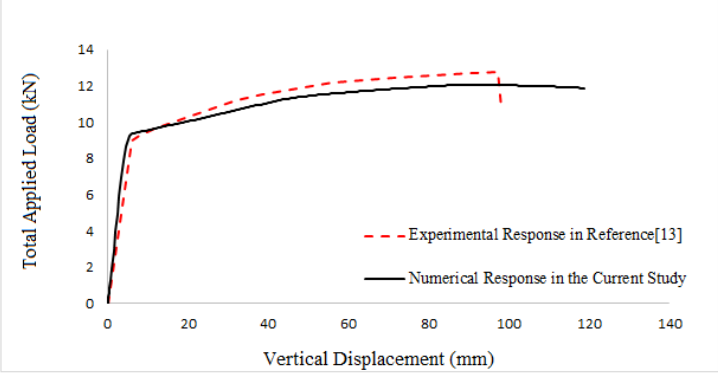


Figure 4. Load-displacement diagram of the experimental model [13] and the current study.

6.2. Verification of time history analysis

The second verification is related to the time history analysis of a single-layer diamatic dome under the El Centro ground motion. An experimental model with a span length of 23.4 m and a rise-to-span ratio of 0.5 was selected for this verification which has 1261 nodes and 3660 members. The mechanical characteristics of the materials are given in Table 4. Figure 5 shows the plan and the support conditions of the experimental model [14].

Table 4. Mechanical characteristics of the materials [14].

Cross-sectional type	Elastic modulus/GPa	Yield strength/MPa	Ultimate strength/MPa	Extensibility rate/%
Φ18 × 1	194.0	197.7	347.6	37.1
Φ23 × 1	189.2	200.5	408.1	37.3
Φ38 × 2	192.6	198.5	374.2	25.7
Φ63.5 × 3.5	200.0	235.0	375.0	26.0
Φ114 × 4	200.0	235.0	375.0	26.0

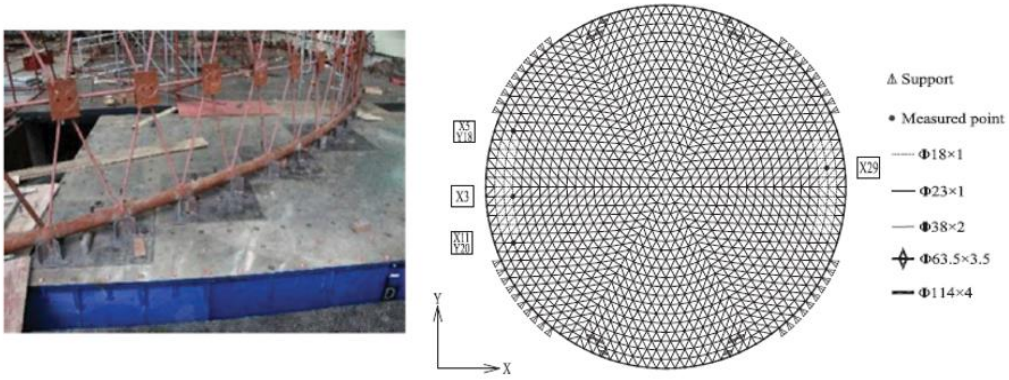


Figure 5. Plan and support conditions of the single-layer diamatic dome in Reference [14].

As shown in Figure 6, the displacement history obtained in the current study is in good agreement with that of the experimental study. Therefore, it was found that the finite element modeling is sufficiently reliable to be used in the current investigation.

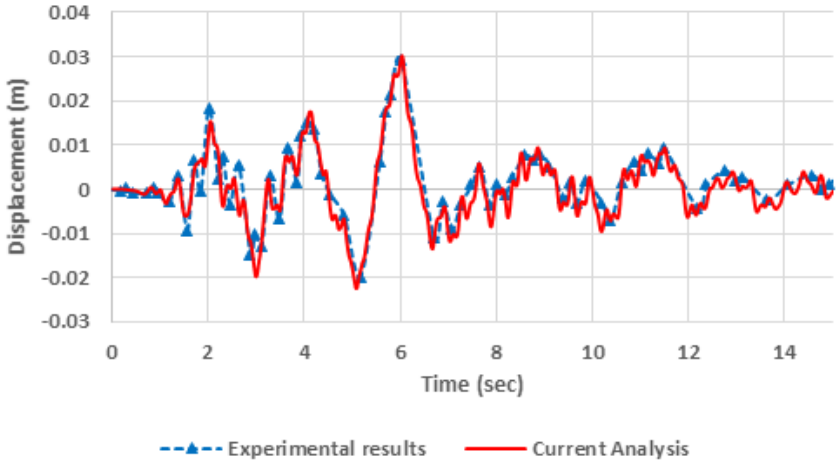


Figure 6. Displacement history of the single-layer diamatic dome obtained in the current study and Reference [14].

7. Nonlinear time history analysis

Time history analysis is the most accurate and reliable method of determining the forces and deformations of structures. In this study, a three-dimensional time history analysis is performed to determine the control point and the target displacement in the pushover analysis.

7.1. Selection and scaling the records

In the first step, 12 far-fault strong ground motions with a distance of more than 60 km and a magnitude upper than 6 are used to perform three-dimensional nonlinear dynamic time history analyses. The earthquake records were extracted from the PEER Ground Motion Database. The specification of the records for the three types of space structures are presented in Table 5. Scaling the horizontal components of ground motions is done using the FEMA P-750-2009 [15]. Also, according to a report presented by NEHRP and ATC for Engineering of Laboratory of National Institute of Standards and Technology (NIST GCR 11-917-15), the vertical component of ground motions is scaled by the same scaling factor used for the pair of horizontal components [16].

Table 5. The ground motion records used for the time-history analysis.

SLDD				DLDD				DLBV			
RSN	**Record**	**Rjb (Km)**	**Vs (m/s)**	**RSN**	**Record**	**Rjb (Km)**	**Vs (m/s)**	**RSN**	**Record**	**Rjb (Km)**	**Vs (m/s)**
12	Kern County	115	316	137	Tabas	120	378	1147	Kocaeli	68	175
92	San Fernando	68	348	304	Irpinia	64	496	1310	Chi-Chi	87	124
124	Friuli	102	356	32	Parkfield	63	494	1599	Duzce	188	175
140	Tabas	90	303	140	Kern County	81	515	2561	Chi-Chi	125	158
3599	Taiwan SMART	94	286	747	Loma Prieta	68	510	2718	Chi-Chi	61	172
792	Loma Prieta	68	362	928	Big Bear	64	564	2975	Chi-Chi	84	170
860	Landers	69	328	17	Southern Calif	73	494	3117	Chi-Chi	136	167
923	Big Bear-01	64	333	434	Borah Peak	100	446	5117	Chuetsu-oki	97	167
1783	Hector Mine	65	367	533	N Palm Spring	65	390	5536	Iwate	159	154
2727	Chi-Chi	76	247	76	San Fernando	109	441	6273	Tottori	165	148
3958	Tottori	89	367	1151	Kocaeli	180	468	6475	Niigata	196	143
6727	Niigata	104	291	1338	Chi-Chi	64	621	6601	Niigata	159	144

7.2. Determining the control point and target displacement

To determine the control point and target displacement, the history of displacements in the nodes under the effect of the relevant earthquake records is extracted; then, the absolute magnitude of all displacements is obtained, and their maximum amount is determined. Finally, the average of the absolute magnitude of the maximum displacements obtained under the earthquake records is calculated. The node that has the maximum displacement is selected as the control point, and the target displacement for the pushover analysis is considered to be equal to the maximum displacement obtained from the nonlinear time history analyses.

8. Pushover analysis

Due to the complexity and time-consuming nature of the time history analyses, a simpler and more practical method called the pushover analysis is used to determine the capacity of the structures and their seismic performance during an earthquake. This method is based on the static analysis so that the nonlinear behavior of materials is considered, and the structure is subjected to increasing static loads. In the second step, the pushover analysis is performed considering geometric and materials nonlinearities to obtain the force-displacement curve of the structures. According to FEMA-P695 [17], the pushover analysis is conducted under the gravity load combination of 1.05D+0.25L and static lateral forces. The lateral load applied to the structures is computed using the ASCE/SEI 41-06 [18] regulations that is equal to mΦ, where *m i*s the mass matrix, and Φ is the mode shape of the structure. It should be noted that the first mode of vibration of the structure in the horizontal direction was used to perform the pushover analysis in this direction. Also, to perform the pushover analysis in the vertical direction, the dominant mode, which has the largest effective modal participation mass ratio in the vertical direction, was used. For simplification, the capacity curve of the structure is approximated by a bilinear curve according to FEMA-356 [19].

9. Discussion of the results

The results of the nonlinear time history and pushover analyses in both horizontal and vertical directions are presented below.

9.1. Period of the models

The period of the dominant mode in the horizontal and vertical directions of the SLDDs, DLDDs, and DLBVs are shown in Figures 7, 8, and 9, respectively.

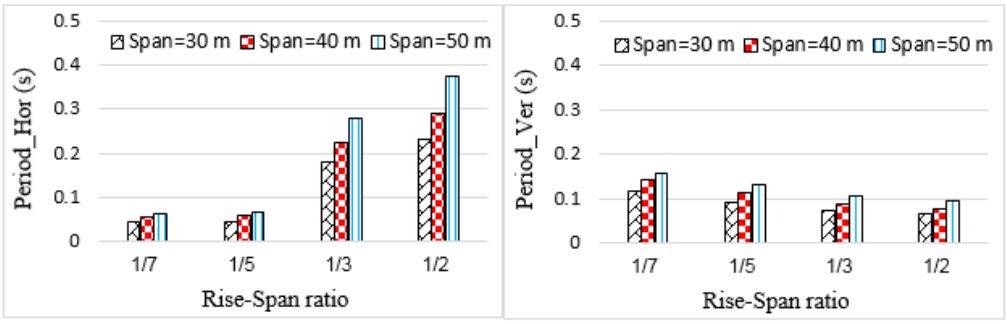


Figure 7. The period of the dominant mode in the horizontal and vertical directions of the SLDDs.

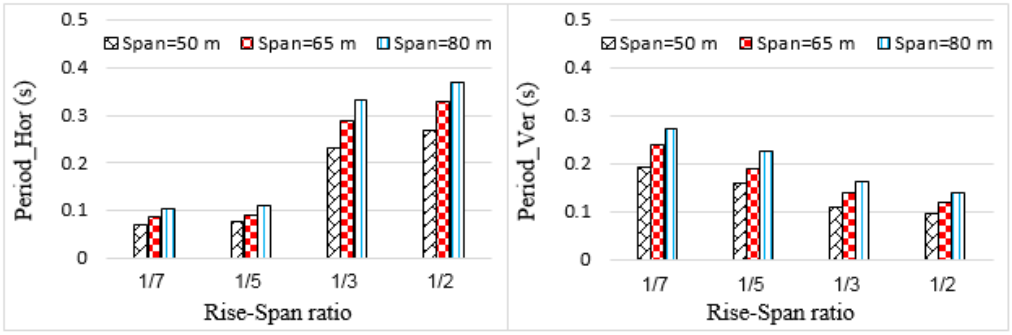


Figure 8. The period of the dominant mode in the horizontal and vertical directions of the DLDDs.

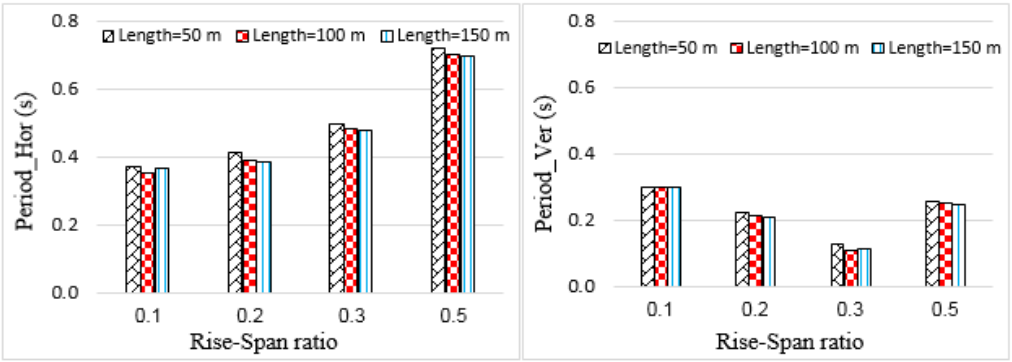


Figure 9. The period of the dominant mode in the horizontal, X, and vertical directions of the DLBVs.

9.2. Target displacement of the models

The target displacement in the horizontal and vertical directions of the SLDDs, DLDDs, and DLBVs are shown in Figures 10, 11, and 12, respectively. As shown in Figure 11, with the increase in the span length of the DLDDs, the target displacement increases in both horizontal and vertical directions. Also, with the growth of the rise-to-span ratio, the target displacement has an upward trend in the horizontal direction. Contrary to the expectation, due to the reduction of vertical stiffness of dome structures with a rise-to-span ratio of 1/5 compared to domes with a rise-to-span ratio of 1/7, the vertical displacement of these structures is less. The reason is that, in the design of the structures, the snow load pattern dominates, and the domes with the rise-to-span ratio of 1/7 are closer to the flat state than the domes with the rise-to-span ratio of 1/5. Therefore, the value of the slope coefficient, Cs, in the calculation of the snow load for the dome 1/7 is larger than the dome 1/5 at the height level of the control point. Consequently, during the time history analysis under earthquake records, the target displacement in the vertical direction of the dome 1/7 is less than that of the dome 1/5. The plastic hinges are first formed

in the members of a ring where the control point is determined in that ring. Also, the maximum horizontal displacement occurs near the center of mass of the domes.

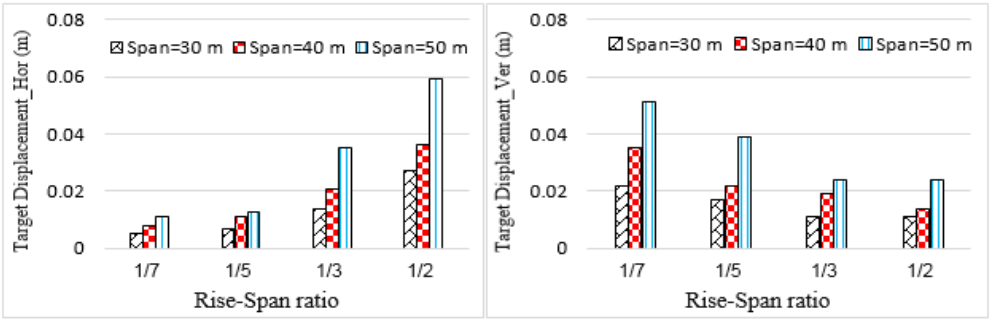


Figure 10. The target displacement in the horizontal and vertical directions of the SLDDs.

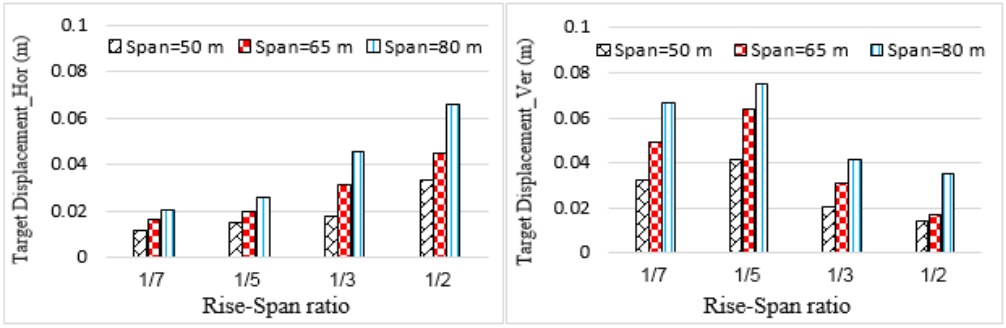


Figure 11. The target displacement in the horizontal and vertical directions of the DLDDs.

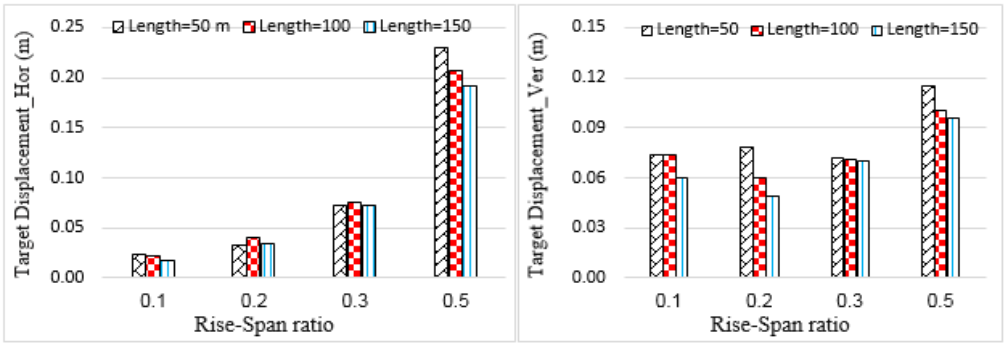


Figure 12. The target displacement in the horizontal, X, and vertical directions of the DLBVs.

9.3. Effective seismic parameters

The seismic response modification factors, obtained from the pushover analyses in the horizontal and vertical directions of the SLDDs, DLDDs, and DLBVs, are shown in Tables 6, 7, and 8, respectively. As seen in Table 6, the results illustrate that the behavior factor of SLDDs in the horizontal and vertical directions is in the range of 1.15-2.26 and 1.15-2.74, respectively. The behavior factor in the horizontal direction of the SLDDs with rise-to-span ratios of 1/7 to 1/3 for all the span lengths is equal to 1.15. Because these models remained in the elastic range in the horizontal direction, they should be designed considering a linear elastic behavior in this direction. For the models with a rise-to-span ratio greater than 1/3, if the span length is kept unchanged and the rise-to-span ratio increases, or if the rise-to-span ratio is kept constant and the span length increases, both the over-strength factor and the ductility reduction factor increase in the horizontal direction; thus, the behavior factor increases in the horizontal direction. If the span length is kept unchanged and the rise-to-span ratio increases, both the over-strength

factor and the ductility reduction factor decrease in the vertical direction; therefore, the behavior factor decreases in this direction. Also, the displacement amplification factor of SLDDs in the horizontal and vertical directions is in the range of 1.15-2.48 and 1.15-2.93, respectively.

Table 6. The seismic response modification factors in the horizontal and vertical directions of the SLDDs.

Models	Span length	30 m				40 m				50 m			
	Rise-to-span ratio	1/7	1/5	1/3	1/2	1/7	1/5	1/3	1/2	1/7	1/5	1/3	1/2
Horizontal Direction	μ	1	1	1	1.14	1	1	1	1.35	1	1	1	1.7
	$R\mu$	1	1	1	1.13	1	1	1	1.3	1	1	1	1.55
	Ω	1.15	1.15	1.15	1.16	1.15	1.15	1.15	1.44	1.15	1.15	1.15	1.46
	Behavior factor	1.15	1.15	1.15	1.31	1.15	1.15	1.15	1.88	1.15	1.15	1.15	2.26
	Displacement amplification factor	1.15	1.15	1.15	1.32	1.15	1.15	1.15	1.95	1.15	1.15	1.15	2.48
Vertical Direction	μ	1.29	1.05	1	1	1.33	1.28	1.07	1	1.55	1.48	1.47	1.21
	$R\mu$	1.25	1.03	1	1	1.29	1.23	1.03	1	1.45	1.4	1.32	1.12
	Ω	1.35	1.16	1.15	1.15	1.61	1.26	1.16	1.15	1.90	1.32	1.25	1.22
	Behavior factor	1.68	1.20	1.15	1.15	2.07	1.55	1.19	1.15	2.74	1.85	1.66	1.37
	Displacement amplification factor	1.73	1.22	1.15	1.15	2.14	1.62	1.23	1.15	2.93	1.96	1.85	1.47

Table 7. The seismic response modification factors in the horizontal and vertical directions of the DLDDs.

Models	Span length	50 m				65 m				80 m			
	Rise-to-span ratio	1/7	1/5	1/3	1/2	1/7	1/5	1/3	1/2	1/7	1/5	1/3	1/2
Horizontal Direction	μ	1	1	1.18	1.19	1	1	1.15	1.23	1	1	1.23	1.44
	$R\mu$	1	1	1.16	1.17	1	1	1.14	1.21	1	1	1.20	1.37
	Ω	1.15	1.15	1.28	1.34	1.15	1.15	1.29	1.34	1.15	1.15	1.27	1.31
	Behavior factor	1.15	1.15	1.49	1.57	1.15	1.15	1.47	1.62	1.15	1.15	1.53	1.79
	Displacement amplification factor	1.15	1.15	1.51	1.59	1.15	1.15	1.48	1.65	1.15	1.15	1.56	1.88
Vertical Direction	μ	1.67	2.30	1.89	1.24	1.39	2	2	1.29	1.44	1.90	1.66	1.68
	$R\mu$	1.53	1.90	1.60	1.14	1.34	1.73	1.74	1.26	1.37	1.67	1.53	1.54
	Ω	1.44	1.49	1.16	1.26	1.53	1.74	1.18	1.34	1.64	1.82	1.35	1.23
	Behavior factor	2.21	2.82	1.86	1.44	2.10	3	2	1.69	2.25	3.05	2.06	1.89
	Displacement amplification factor	2.41	3.42	2.20	1.56	2.14	3.49	2.37	1.74	2.36	3.46	2.25	2.07

Table 7 demonstrates that the value of ductility factor (μ), ductility reduction factor ($R\mu$) and overstrength factor (Ω) in the horizontal direction for structures with the rise-to-span ratio of 1/7, 1/5 and the entire span lengths of the domes are equal to unity and the structures are in the elastic range. Then, an upward trend is observed with the growth of the rise-to-span ratio. The value of the overstrength factor is almost constant with the growth of the span length of the domes. In other words, the rate of changes of the yield load level to the load level corresponding to the formation of the first plastic hinge is almost constant. In the vertical direction, the aforementioned coefficients increase for the rise-to-span ratio of 1.7 to 1.5, then decrease with the growth of the rise-to-span ratio which is affected by the target displacement. The behaviour factor increases with the growth of the rise-to-span ratio and the span length of the domes in the horizontal direction. In structures with the rise-to-span ratio of 1/7 and 1/5 and for the entire span lengths, based on the dominant period of these structures, which are near the acceleration-sensitive region, the value of the behaviour factor is equal to 1.15. This implies that these structures should designed in the elastic state. In the vertical direction, the maximum value of the behaviour factor belongs to the domes with the rise-to-span ratio of 1/5. In the structure with the rise-to-span ratio of 1/2 and the span length of 80 meters, the maximum value of displacement amplification factor reaches 1.88 in the horizontal direction. In the vertical direction, the value of this coefficient increases with the increase in the rise-to-span ratio until it reaches 1/5, and then it has a downward trend.

Table 8. The seismic response modification factors in the horizontal and vertical directions of the DLBVs.

Models	Length	50 m				100 m				150 m			
	Rise-to-span ratio	0.1	0.2	0.3	0.5	0.1	0.2	0.3	0.5	0.1	0.2	0.3	0.5
Horizontal Direction	μ	1	1	1	1.11	1	1	1	1.07	1	1	1	1
	$R\mu$	1	1	1	1.11	1	1	1	1.07	1	1	1	1
	Ω	1.15	1.15	1.15	1.18	1.15	1.15	1.15	1.16	1.15	1.15	1.15	1.15
	Behavior factor	1.15	1.15	1.15	1.32	1.15	1.15	1.15	1.24	1.15	1.15	1.15	1.15
	Displacement amplification factor	1.15	1.15	1.15	1.32	1.15	1.15	1.15	1.24	1.15	1.15	1.15	1.15
Vertical Direction	μ	1	1.25	1.87	2.68	1	1.03	1.93	2.75	1	1.04	1.82	2.25
	$R\mu$	1	1.22	1.54	2.09	1	1.03	1.43	2.12	1	1.04	1.53	1.87
	Ω	1.15	1.22	1.26	1.48	1.15	1.15	1.18	1.35	1.15	1.15	1.17	1.23
	Behavior factor	1.15	1.49	1.95	3.1	1.15	1.19	1.69	2.86	1.15	1.2	1.79	2.3
	Displacement amplification factor	1.15	1.52	2.37	3.99	1.15	1.19	2.28	3.7	1.15	1.2	2.14	2.78

According to Table 8, the behavior factor of the DLBVs in the horizontal and vertical directions is in the range of 1.15-1.32 and 1.15-3.1, respectively. In the horizontal direction, the behavior factor of the DLBVs with rise-to-span ratios of 0.1 to 0.3 for all the barrel vault lengths is equal to 1.155. So, these models remained in the elastic range, and they should be designed considering a linear elastic behavior in this direction. For the models with a rise-to-span ratio greater than 1/3, if the barrel vault length is kept unchanged and the rise-to-span ratio increases, or if the rise-to-span ratio is kept constant and the barrel vault length decreases, both the over-strength factor and the ductility reduction factor increase in the horizontal direction. So, the behavior factor increases in the horizontal direction. If the barrel vault length is kept unchanged and the rise-to-span ratio increases, both the over-strength factor and the ductility reduction factor increase in the vertical direction; therefore, the behavior factor increases in this direction. Also, the displacement amplification factor of the DLBVs in the horizontal and vertical directions is in the range of 1.15-1.32 and 1.15-3.99, respectively.

10. Conclusions

The present paper investigates the seismic behavior of three types of space structures called SLDDs, DLDDs, and DLBVs and extracts the seismic response modification factors. After the design of the structural models and performing the nonlinear time history and pushover analyses, the target displacement and the idealized force-displacement curve are extracted. Then, the behavior factor and displacement amplification factor are evaluated. The results illustrate that the models with a low rise-to-span ratio have elastic behavior in the horizontal direction, and by increasing the rise-to-span ratio, the ductility and behavior factor increase in the horizontal direction. The behavior factor in the vertical direction for the dome models decreases by increasing the rise-to-span ratio, but increases in the barrel vault models.

References

[1] C. Uang, "Establishing R (or Rw) and Cd Factors for Building Seismic Provisions," *Journal of Structural Engineering*, vol. 117, no. 1, pp. 19–28, Jan. 1991, doi: 10.1061/(asce)0733-9445(1991)117:1(19).

[2] H. A. Moghaddam, "Seismic behaviour of space structures," *International Journal of Space Structures*, vol. 15, no. 2, pp. 119–135, 2000, doi: 10.1260/0266351001495026.

[3] S. Inanaga, T. Takeuchi, Y. Terazawa, and R. Matsui, "Collapse analysis of space-frame gymnasiums damaged in 2016 Kumamoto earthquake," *Proceedings of the IASS Symposium 2018, Creativity in Structural Design*, MIT, Boston, USA, July 16-20, 2018, Caitlin Mueller, Sigrid Adriaenssens, Eds.

[4] R. Khalili, M. Poursha, and K. Abedi, "Behavior factor and displacement amplification factor

for the seismic design of single-layer barrel vaults," *Journal of Constructional Steel Research*, vol. 169, 2020, doi: 10.1016/j.jcsr.2020.105987.

[5] N. M. Newmark and W. J. Hall, "Earthquake Spectra and Design," *Earthquake Spectra*, vol. 1, no. 1, pp. 1–103, 1982.

[6] B. Ellingwood, T. V Galambos, and J. G. MacGregor, *Development of a probability based load criterion for American National Standard A58: Building code requirements for minimum design loads in buildings and other structures*, vol. 13. Department of Commerce, National Bureau of Standards, 1980.

[7] Iranian National Building code, Part 6,Loadings on structure, *Ministry of Housing and Research Center,* 2013.

[8] Iranian code of Practice for Skeletal Steel Space Structures: Standard No. 400, *Office of Deputy for Strategic Supervision Bureau of Technical Execution System*, 2010.

[9] Iranian Code of Practice for Seismic Resistance Design of Buildings: Standard No. 2800 (4th Edition), *Building and Housing Research Center*, 2015.

[10] AISC 360-16, "Specification for Structural Steel Buildings, an American National Standard," *American Institute of Steel Construction, Chicago*, p. 612, 2016.

[11] ASCE/SEI 7-16, "Minimum Design Loads and Associated Criteria for Buildings and Other Structures," *Am. Soc. Civ. Eng.*, 2002.

[12] Eurocode 8, "Design of Structures for Earthquake Resistance-part 1: General Rules, Seismic Actions and Rules for Buildings," *Brussels Eur. Comm. Stand.*, 2005.

[13] G. A. R. Parke, "The Behaviour of Space Trusses Incorporating Novel Compression Members," University of Surrey, 1988.

[14] L. Xu and J. Ye, "DEM Algorithm for Progressive Collapse Simulation of Single-Layer Reticulated Domes under Multi-Support Excitation," *Journal of Earthquake Engineering*, vol. 23, no. 1, pp. 18–45, 2019, doi: 10.1080/13632469.2017.1309606.

[15] FEMA, "NEHRP Recommended Seismic Provisions," *Fema P-750*, p. 406, 2009.

[16] NIST, "Selecting and Scaling Earthquake Ground Motions for Performing Response-History Analyses," pp. 1–256, 2011.

[17] FEMA P695, "Quantification of Building Seismic Performance Factors," *Fed. Emerg. Manag. Agency, Washington, DC*, 2009.

[18] ASCE/SEI 41-06, "Seismic Rehabilitation of Existing Buildings," *Am. Soc. Civ. Eng.*, 2007.

[19] FEMA 356, "Prestandard and Commentary for the Seismic Rehabilitation of Buildings," *Fed. Emerg. Manag. Agency, Washington, DC*, 2000.

IASS 2023
July 10–14 Melbourne
Integration of Design and Fabrication

Proceedings of the IASS Annual Symposium 2023
Integration of Design and Fabrication
10–14 July 2023, Melbourne, Australia
Y.M. Xie, J. Burry, T.U. Lee and J. Ma (eds.)

Study on finite element numerical simulation of seismic response of suspended-dome structure

Guojun SUN[a,*], Shuo XIAO[a], Xiongyan LI[a], Cong ZHANG[a], Jinzhi WU[a], Suduo XUE[a]

[a,*] Faculty of Architecture, Civil And Transportation Engineering, Beijing University of Technology, Beijing 100124
sunguojun@bjut.edu.cn

Abstract

Suspended-dome structures are widely used as a typical representative of spatial structures with large spans. While there have been many studies on the seismic performance of traditional spatial grid structures, such as reticulated shells, trusses, and arches, there are relatively few studies on the seismic performance of suspended-dome structures under strong seismic. This paper aims to investigate the mechanical response and failure mechanism of suspended-dome structures under strong seismic considering different bearing conditions. The results indicate that the displacement under the action of three-way hinged constraints is smaller than that of the radial release structure, and the failure mode of the suspended-dome structure under different support conditions during strong seismic is steel tie rod failure.

Keywords: suspended-dome structure, strong seismic action, seismic response, numerical simulation

1.Introdution

With the development of social economy and technology and the improvement of people 's living standards, people 's demand for large-span buildings is increasing, such as large stadiums, exhibition centers, station terminals, hangars, etc. The grid structure suitable for the construction of large space has become the preferred structural system. The research on the seismic performance of large-span spatial structure is an important basis for the progress of engineering disaster prevention and mitigation technology [1-2]. The suspended-dome structure has high mechanical performance and broad application prospects. Scholars at home and abroad have carried out a lot of research on reticulated shell structure and achieved rich results. However, there is no in-depth study on the strong seismic of suspended-dome structure, and its seismic performance needs further study.

In terms of reticulated shell structures, a large number of theoretical, experimental and large-scale numerical analysis studies have been carried out on the failure mechanism of steel reticulated shells under strong seismics at home and abroad. Shen et al [3] proposed a criterion for dynamic instability and strength failure of reticulated shell structures under strong seismics. Zhou et al [4] proposed the progressive collapse mode of ' double inclined rod fracture zone ' under the condition of strong seismic of cylindrical reticulated shell with longitudinal support. Li et al [4] analyzed the dynamic stability of-Kiewitt-8 single-layer spherical reticulated shell structure under seismic. Ma et al [5] studied the dynamic behavior and seismic design method of single-layer reticulated shells with semi-rigid connections. In the aspect of seismic performance of suspended-dome, domestic scholars mainly carried out relevant research on structural dynamic characteristics, dynamic stability and dynamic response time history analysis in combination with practical projects. Ding et al [6] analyzed the dynamic characteristics of the latticed shell string structure of the gymnasium roof of Anhui University. Cai et al [7] compared and analyzed the natural frequency and basic characteristics of suspended-dome with

Copyright © 2023 by Guojun SUN, Shuo XIAO, Xiongyan LI, Cong ZHANG, Jinzhi WU and Suduo XUE. Published in the Proceedings of the IASS Annual Symposium 2023 with permission.

different prestress levels and different upper single-layer reticulated shell sections. Wei et al [8] analyzed the dynamic characteristics and seismic response of the elliptical suspended-dome roof structure. Liu et al [9] summarized the effects of structural parameters, uniform load and the introduction of cables on the dynamic stability of suspended-dome structures under seismic loads. Gui et al [10] analyzed the dynamic stability of long-span suspended-dome structure. Li et al [11] studied the dynamic response of Kiewitt suspended-dome with large span and small rise-span ratio. Zhang et al [12] used bilinear constitutive model and strain-damage coupling constitutive model to analyze the whole process dynamic time history of an 8-point supported suspended-dome structure under different seismic accelerations. Based on 18 examples, Wang et al [13] studied the elastic-plastic response characteristics of suspended-dome under rare seismics. In the study of suspended-dome structures, Lu [14-16] conducted dynamic scale model tests to obtain the natural frequency and damping measurements of the structure. Zhao [17] investigated the seismic performance of suspended-dome structures with different lower supports using dynamic scale model tests and finite element numerical analysis. Wang [18] created a 1:20 scale model of the roof structure of Lanzhou Olympic Stadium to investigate the prestressed distribution characteristics and static characteristics of the ribbed small-rise-span ratio cantilever dome structure.

However, these studies have mainly focused on conventional seismic action and have not explored the effects of strong seismic action on the structure. The destructive impact of strong seismics, as demonstrated by the recent seismic in Turkey, highlights the importance of studying the behavior of structures under such conditions. Therefore, this paper aims to analyze the time-history response differences and failure modes of the suspended-dome structure under strong seismic action, taking into account various bearing conditions.

2. Engineering background and overview

The structure of Lanzhou Olympic Sports Center Gymnasium adopts a rib-ring and union-square combined single-layer reticulated shell for the roof, as shown in Figure 1. The chord-supported dome roof structure has the characteristics of large span, dense nodes, and complex seismic performance. Based on this, this paper chooses the chord-supported dome roof structure of Lanzhou Olympic Sports Center Gymnasium as the research object for dynamic characteristics, which is more representative and typical.

The structural parameters of Lanzhou Olympic Sports Center Gymnasium's chord-supported dome roof structure are a span of 94 meters and a rise of 8 meters. The seismic fortification intensity is 8 degrees, the design seismic basic acceleration is 0.2g, and the design seismic grouping is the third group. The site category is category II. The structure consists of an upper single-layer reticulated shell and a lower Levy-type cable support system, as shown in Figure 2. The permanent load value is 1.2 kN/m^2, and the live load value is 0.5 kN/m2. The upper reticulated shell is composed of 528 rods and 253 nodes. There are 12 central nodes where the 12 shell diameter rods intersect, forming a circular shape in plan view. The roof has a total of 7 rings of ring rods, and the outermost ring is divided into 48 equal parts by the diameter rods. The outer 4 rings have diagonal support rods to increase the overall stability of the structure. There are 24 evenly distributed supports along the outermost ring of the roof. The lower part is a Levy-type cable support system consisting of 5 rings of circular cables, 186 radial steel tension rods, and 90 vertical bracing rods. The prestressed value of the cable support system from the outer to the inner ring is 2800, 1300, 700, 350, 300 kN, respectively. Both the radial and ring rods are of box section while the diagonal support rods are of circular pipe section, all made of Q355B material. The cables are high-vanadium-plated tension cables, the radial steel tension rods are solid round rods of Q690D, and the vertical bracing rods are circular steel pipes of Q355B.



Figure 1. Details of Lanzhou Olympic Gymnasium



(a) Single-layer latticed shell (b) Cable-supported system

Figure 2. Structural roof details

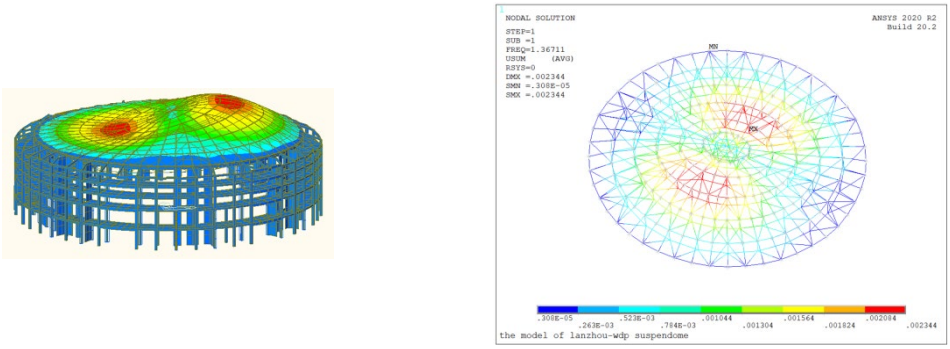
3. Strong seismic response analysis of suspended-dome structure

3.1. Model verification

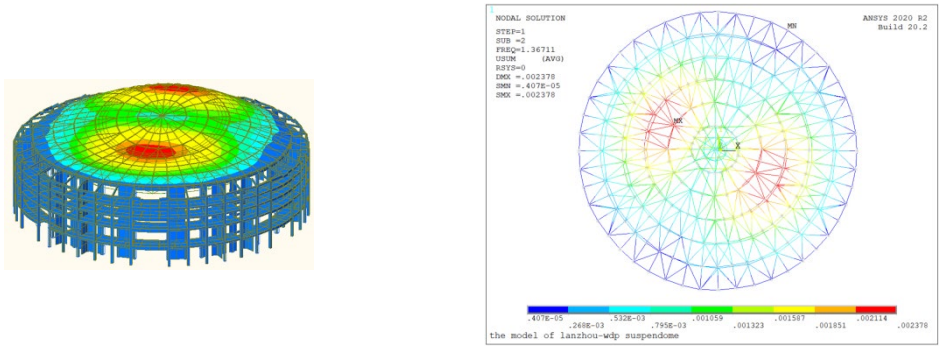
A finite element model was established using the large finite element software ANSYS. Firstly, the finite element model of the prototype structure was compared and analyzed with the modal analysis results of the design institute model to verify the correctness of the finite element model. As shown in Figure 3 and Table 1, the natural frequencies of the modal analysis can be well matched, proving that the built model can meet the actual requirements well. Then, time-history analysis under strong seismic action was carried out, and three-directional inputs were selected for analysis, with horizontal X and Y directions and vertical Z direction. The proportional selection of three-directional inputs was 1:0.85:0.65. The structure is located in Lanzhou, a rare seismic zone with a design intensity of 8 degrees. Considering two types of supports: three-way hinged constraints and radial release, seismic response analysis was performed under extremely rare seismics. The trend of member internal force and displacement changes of the structure under the extreme rare seismic action was obtained, and the time-history response variation law of the structure under different seismic waves such as TAFT wave, EL-Centro wave, and Beijing wave was obtained through time-history analysis. Combining the model with the on-site experimental situation and according to the symmetry of the structure, specific members were selected for analysis at appropriate positions in the finite element analysis model, as shown in Figure 4. The specific member selection situation was given in the form of "xa-b" with "x" as the test content code, "a" as the radial number (there are 48 radial member numbers in total as shown in Figure 4(a)), and "b" as the circumferential number (from inner to outer, there are 1-7 circles, and the vertex number of the net shell is 1-0).

Table 1 Natural frequency of prototype structure

Mode order	（Midas）/Hz	（ANSYS）/Hz
1	1.3301	1.3392
2	1.3330	1.3392
3	2.1955	2.3093

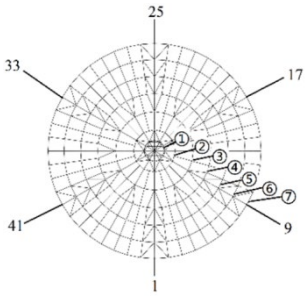


(a)First-order

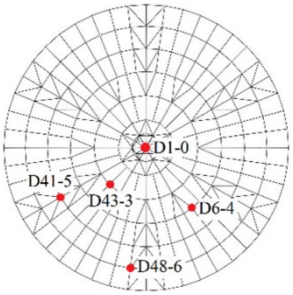


(b)Second-order

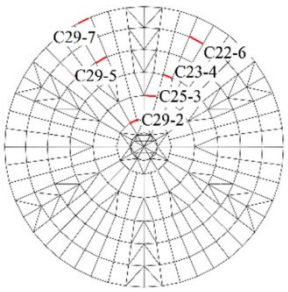
Figure 3. Comparison of natural frequencies



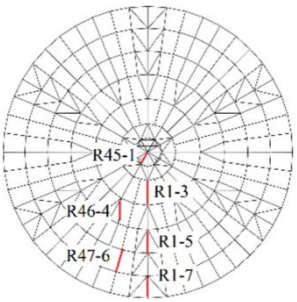
(a)Rod number



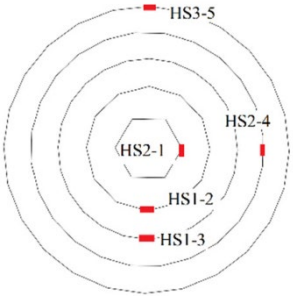
(b)displacement measuring point



(c)Ring rod number



(d)Radial rod number



(e)Ring cable rod number

Figure 4. Bar selection details

3.2. Seismic response analysis of structure under different bearing conditions

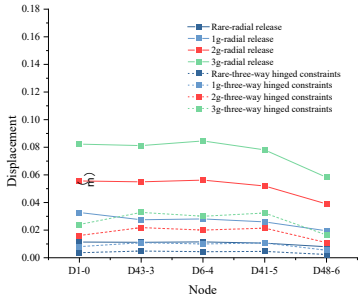
To investigate the effect of boundary support conditions on the seismic performance of suspended-dome structure, simplified models with boundary conditions of radial release and three-way hinged constraints were established using the numerical modeling method described in the previous section. A comparative analysis of the strong seismic mechanical performance of the suspended-dome structure under different support conditions was conducted.

3.2.1. Extremely rare seismics

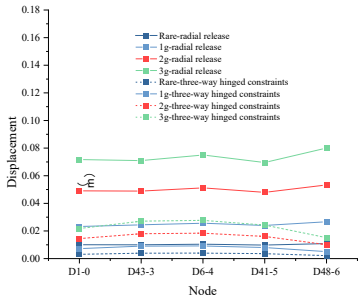
(1) Displacement

Fig. 5 to 7 show the peak horizontal and vertical displacements under different seismic waves and amplitudes. By comparing the displacements at different locations of the models with radial release and tri-axial hinge constraints, it is found that as the seismic waves and amplitudes increase, the vertical displacement of the suspended-dome structure with tri-axial constraints decreases significantly compared to that of the radial release.

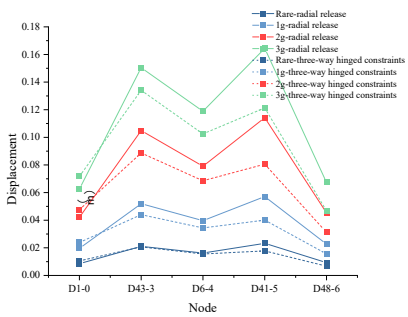
Under extremely rare seismic conditions, as the seismic waves increase, the displacement gradually increases, and the trend is consistent with that under rare seismic conditions, with a larger increase in the Z-direction displacement than in the horizontal displacement. As the seismic waves increase, the displacement at the middle position of the suspended-dome structure with tri-axial hinge constraints gradually increases, but it is still smaller than that of the radial release structure. The main reason for this is that the structure support cannot deform, and the seismic forces are mainly counteracted by the central structural members, resulting in smaller displacement.



(a) X-direction displacement

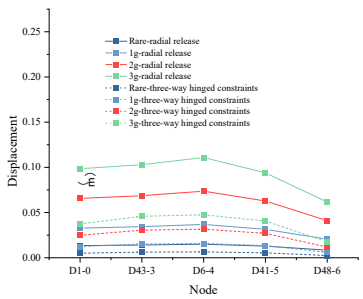


(b) Y-direction displacement

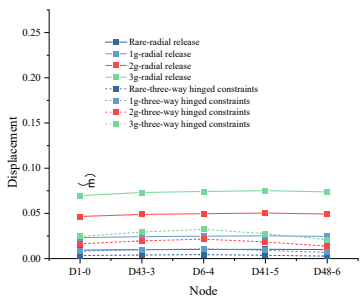


(c) Z-direction displacement

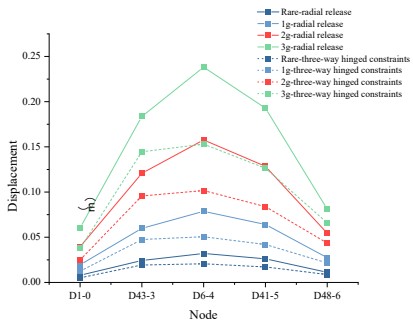
Figure 5. Peak displacement response of TAFT wave



(a) X-direction displacement

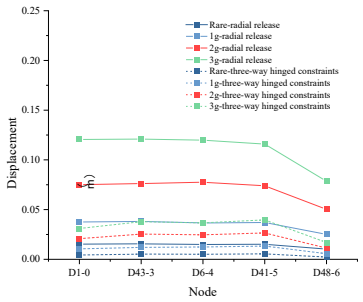


(b) Y-direction displacement

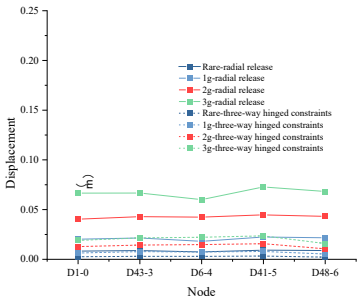


(c) Z-direction displacement

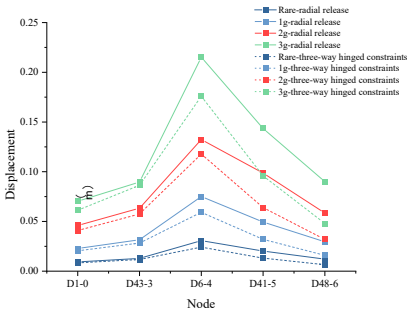
Figure 6. Peak displacement response of EL-Centro wave



(a) X-direction displacement



(b) Y-direction displacement



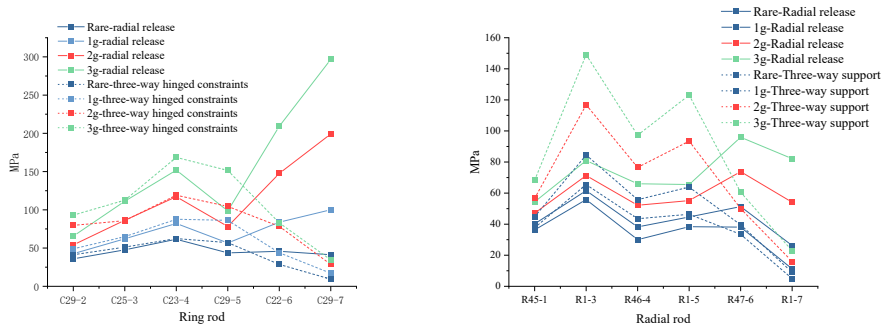
(c) Z-direction displacement

Figure 7. Peak displacement response of Beijing wave

(2) Internal force of structural members

Based on the analysis above, the structure is more sensitive to EL-Centro wave, so EL-Centro wave was selected for member force analysis. The variation of maximum member forces of the model under rare seismic and extremely rare seismic effects under different support conditions is shown in Figure 8. As shown in Figure 8, for different support conditions, the internal forces of the ring rod members C29-7 and C22-6 near the support in the three-axis constrained support structure are smaller than those of the middle circumferential members, which is significantly different from the variation trend of the radial release support structure. The main reason for this is that the deformation is restricted at the support, and the members at the support cannot generate large deformation, resulting in a decrease in internal forces. However, the seismic action is mainly offset by the members in the middle structure, resulting in internal forces larger than those of the middle members in the radial release structure. In addition, as the amplitude of the seismic wave increases, the internal forces of the ring rod members increase slower than those of the radial members. For cable members, under the three-way hinged constraints condition, the minimum cable force on the outer ring is significantly reduced compared with that of the radial release support, but slack is still observed in the inner ring cable.

Through Figure 8, it can be observed that the support has a significant influence on the internal forces of the members near the support position. The internal forces at the support will decrease, but there will be an increase in internal forces for the middle members of the structure. The internal forces of the structure will have significant differences under different support conditions, and the influence of support conditions on the structure should be considered in structural design.



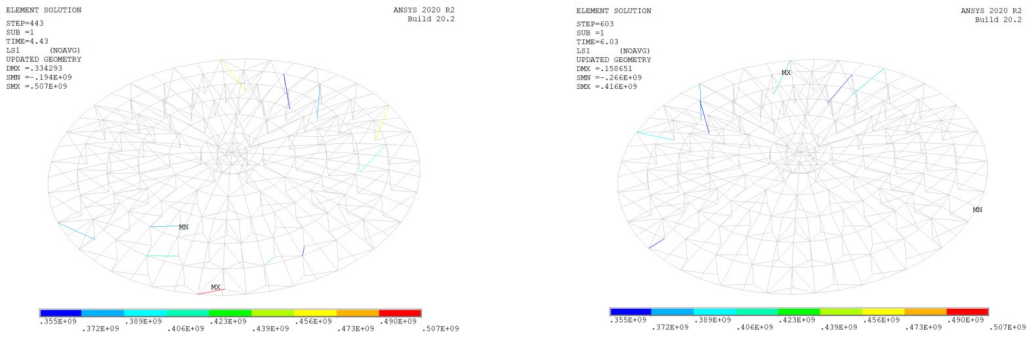
（a）Ring rod　　（b）Radial rod

Figure 8. Comparative analysis of peak internal force of components under different bearing conditions

3.3. Failure analysis of suspended-dome structure under strong seismic

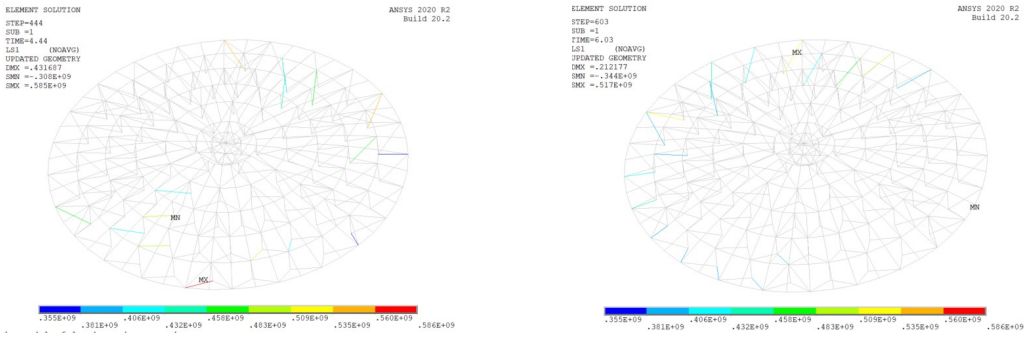
3.3.1. Radial release constraint support

The failure mode analysis of the suspended-dome structure under strong seismic action is studied in this section, as shown in Figures 9 to 12. Under seismic waves of 3g and above, the upper shell structure and cable of the structure did not enter the plastic state, but some of the steel tie rods entered plastic state under seismic action, and even some tie rods reached the ultimate load, so the suspended-dome structure is selected for failure analysis in this section. According to the existing Q355B material, its ultimate strength is 470MPa. Under the 3g seismic wave action, when the structure has the maximum downward displacement, the maximum stress of the steel tie rod component near the support reaches 490MPa, which reaches the ultimate load. When the structure has the maximum upward displacement, the steel tie rod near the support enters plastic state without reaching the ultimate load. With further increase in seismic action, the upper shell structure and cable of the structure still did not enter plastic state. When the structure had the peak displacement in the downward direction, the steel tie rod gradually developed plasticity from the outside to the inside, and when the peak displacement was in the upward direction, the trend was consistent with the downward direction and developed from the outside to the inside, but did not reach the ultimate load. For the suspended-dome structure, when the stiffness of the upper shell structure is large, the steel tie rod strength failure will occur in the structure, and attention should be paid to the design of the steel tie rod in the design process.



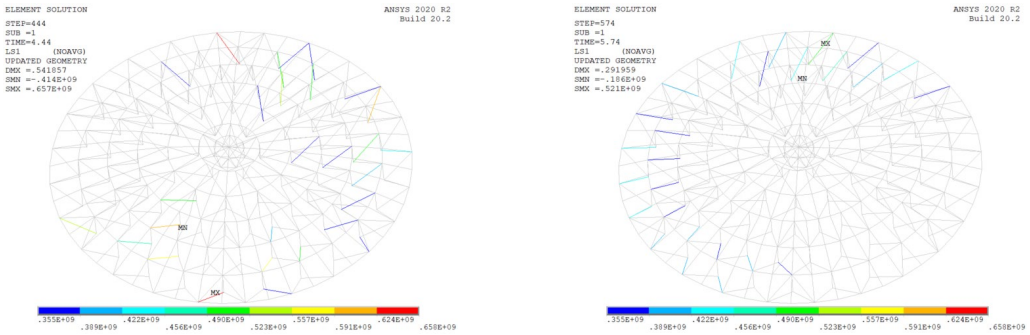
(a) Peak downward displacement　　(b) Peak upward displacement

Figure 9. 3g seismic wave plastic rod distribution



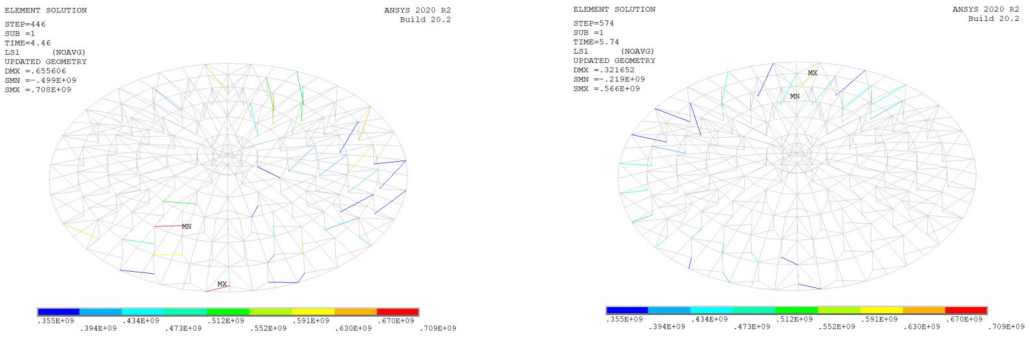
(a) Peak downward displacement (b) Peak upward displacement

Figure 10. 4g seismic wave plastic rod distribution



(a) Peak downward displacement (b) Peak upward displacement

Figure 11. 5g seismic wave plastic rod distribution



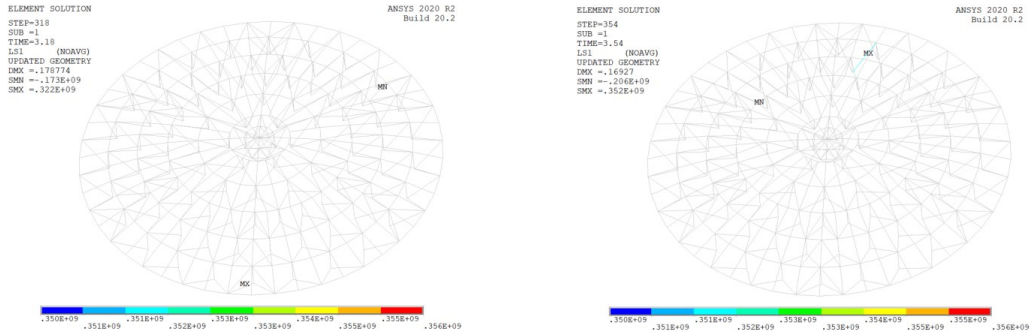
(a) Peak downward displacement (b) Peak upward displacement

Figure 12. 6g seismic wave plastic rod distribution

3.3.2. Three-way hinged constraints

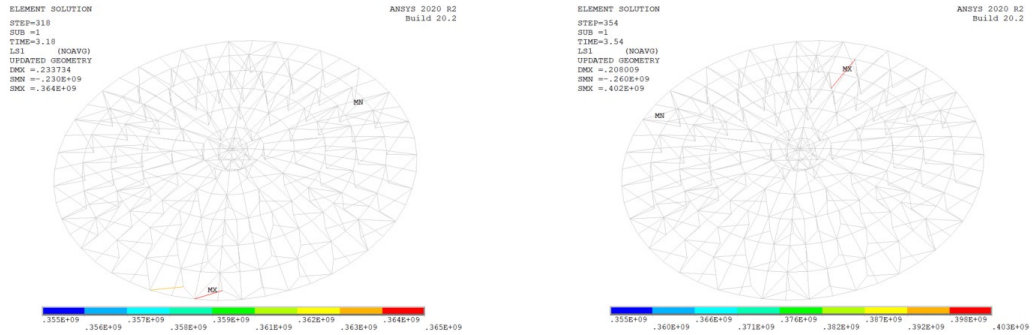
The failure mode analysis of the suspended-dome structure with three-way hinged constraints under strong seismic action was studied, as shown in Figure 13. Under seismic waves with an acceleration of 3g or more, the upper mesh shell structure and cables of the structure did not enter plastic deformation. However, some steel rods entered plastic deformation under seismic action, and compared with the radial release support, no rods in the structure reached the ultimate bearing capacity. According to the existing Q355B material, its ultimate strength is 470MPa. Under the downward maximum peak displacement of the structure under 3g seismic waves, the maximum stress of the steel rod component near the support reached 356MPa, and the rod entered plastic deformation. When the structure reached the upward maximum peak displacement, the steel rod near the support entered plastic deformation, but no rods reached the ultimate bearing capacity. When the seismic action was further increased, as shown

in Figures 14 to 16, the upper mesh shell structure and cables of the structure still did not enter plastic deformation. When the structure reached the downward peak displacement, the steel rods gradually developed plastic deformation from the outside to the inside, and when the structure reached the upward peak displacement, the trend was consistent with that when it reached the downward peak displacement, developing from the outside to the inside. When the acceleration reached 6g, the internal force of the rod reached the ultimate bearing capacity when the structure reached the upward peak displacement. For the suspended-dome structure with different supports, there are significant differences in its seismic performance and internal forces of the rods, but steel rod design should be carefully considered during the design process, as the steel rods of the suspended-dome structure will experience strength failure.



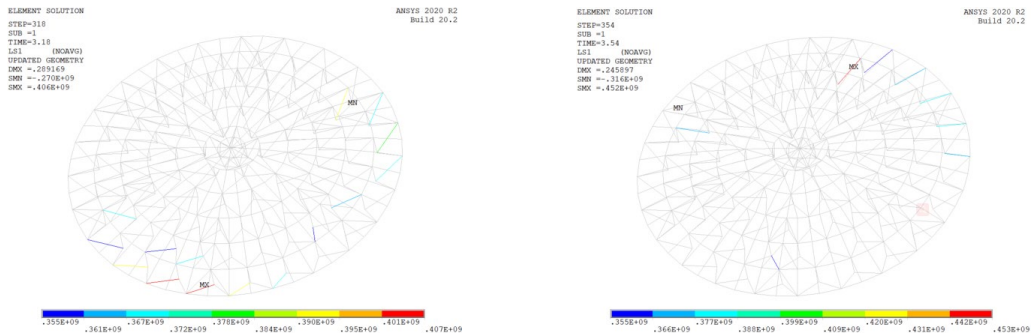
(a) Peak downward displacement (b) Peak upward displacement

Figure 13. 3g seismic wave plastic rod distribution



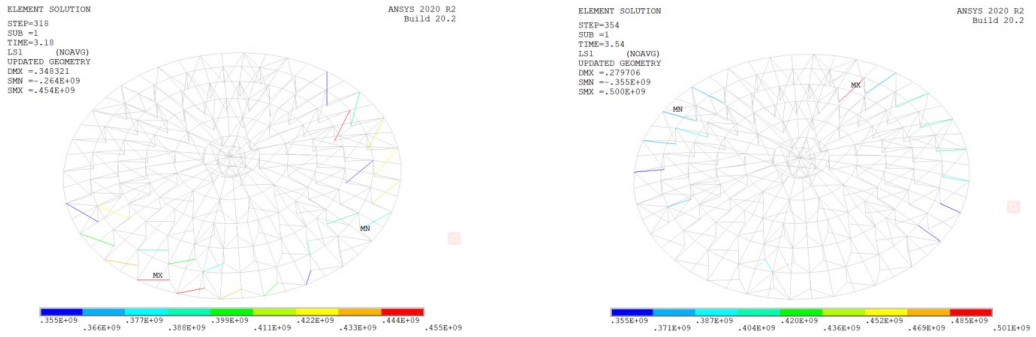
(a) Peak downward displacement (b) Peak upward displacement

Figure 14. 4g seismic wave plastic rod distribution



(a) Peak downward displacement (b) Peak upward displacement

Figure 15. 5g seismic wave plastic rod distribution



(a) Peak downward displacement (b) Peak upward displacement

Figure 16. 6g seismic wave plastic rod distribution

4.Conclusion

This article conducts a finite element numerical simulation analysis of the suspended-dome structure of the Lanzhou Olympic Sports Center under strong seismic conditions. The dynamic method is used to obtain the natural vibration characteristics of the structure, and then the time-domain response of the suspended-dome structure is obtained to analyze the impact of support conditions on the structure. Finally, an extremely rare seismic analysis is conducted to obtain the failure mode of the suspended-dome structure. The main conclusions are as follows:

(1) Under strong seismic conditions, there are significant differences in the internal force changes of the structure under three-way hinged constraints and radial release restrained supports. The internal forces of the members near the support under the t three-way hinged constraints are smaller than those under the radial release restrained support condition, but the internal forces of the members in the middle of the structure under the three-way hinged constraints are larger than those under the radial release restrained support condition. Additionally, the internal forces of the circumferential cable members near the support decrease significantly under seismic action.

(2) Under strong seismic conditions, the failure mode of the suspended-dome structure is strength failure. When the stiffness of the upper shell is high, the shell will not experience plastic deformation, but the lower steel cables will undergo plastic deformation, mainly in the steel cable members near the support. Therefore, the design should focus on the steel cable design.

Acknowledgement

This work was sponsored by the National Nature Science Foundation of China [grant number 51878013].

Reference

[1] Mamoru Kawaguchi, Masaru Abe, Tatsuo Hatato, et al. On a structural system “suspen-dome” system, Proceedings of IASS Symposium, Istanbul, 1993, pp: 523-530.

[2] Chen ZH. “Research Progress and Engineering Practice on Suspen-Dome Structure”. Progress in Steel Building Structures, vol. 13(5), pp. 11-20, 2011.

[3] Shen SZ, Zhi XD. Failure mechanism of reticular shells subjected to dynamic actions[J]. CHINA CIVIL ENGINEERING JOURNAL, 2005, (1):11-20.

[4] Zhou HT, Zhang YG, Wu JZ. Mechanism and pattern of progressive collapse of single-layer cylindrical latticed shell under severe seismic[J]. Spatial Structures, 2015, 21(01): 3-13+25.

[5Li YM, Hu K, Zhang WJ. Dynamic Stability of Single-layer Latticed Shells Considering Damage Accumulation Effect[J]. Journal of Hunan University (Natural Sciences), 2014, 41(06): 16-21.

[6] Huihuan Ma, Zhiwei Shan, Feng Fan. Dynamic behavior and seismic design method of a single-layer reticulated shell with semi-rigid joints [J]. Thin-Walled Structures, 2017, 119:544-557.

[7] Ding JM, Kong DD, He ZJ. Seismic response analysis of cable-strut-supported shell structure of Anhui University Gymnasium[J]. Building Structure, 2009, 39(01): 34-37+68.

[8] Cai JG, Feng J, Tu ZQ, et al. Prestress Design and Seismic Behavior of Suspended-dome[J]. Advanced Engineering Sciences, 2009, 41(04): 70-75.

[9] Wei DM, Peng ZH, Kong P. Investigation on seismic responses of a long-span suspen-dome structure under non-uniform seismic excitation[J]. Spatial Structures, 2012, 18(02): 14-20.

[10] Liu HJ, Han QH, Zhou QZ. Analysis on the dynamic stability of suspen-dome. Journal of Tianjin University of Technology, 2007, 23(2): 84-88.

[11] Gui GQ, Zeng FQ, Wang YE. Dynamic stability of large span suspend dome under seismic excitation[J]. Journal of Jinggangshan University (Natural Sciences Edition) , 2014, 35(01): 76-83.

[12] Li YM, Guo L, Zhang WJ. Dynamic stability of Kiewitt suspen dome with a hole under seismics[J]. Spatial Structures, 2011, 17(04): 16-22.

[13] Zhang R, Xiao N. Research on dynamic failure of suspended-dome structures under severe seismics[J]. Journal of Zhejiang University (Engineering Science), 2010, 44(06): 1185-1190+1219.

[14] Wang Q, Deng H. Analysis of elasto-plastic dynamic responses of suspendome under rare seismic[J]. Journal of Zhejiang University (Engineering Science), 2013, 47(11): 1889-1895.

[15] XUE S, LU Z, LI X, et al. Experimental and numerical investigations on the influence of center-hung scoreboard on dynamic characteristics of suspended-dome structure[J]. Journal of Building Engineering, 2022,57: 104787.

[16] LU Z, LI X, LIU R, et al. Shaking table experimental and numerical investigations on dynamic characteristics of suspended-dome structure[J]. Structures, 2022,40: 138-148.

[17] XUE S, ZHAO Z, LI X, et al. Shaking Table Test Research on the Influence of Center-Hung Scoreboard on Natural Vibration Characteristics and Seismic Response of Suspen-Dome Structures[J]. Buildings, 2022,12(8): 1231.

[18] XUE S, WANG Z, LI X, et al. Model test study on static performance of rib-patterned small rise-span ratio suspended-dome structure[J]. Structures, 2022,43: 1615-1628.

Dynamic response of other structures

Active bending
Additive manufacturing/ 3D printing
Architectural geometry
Bamboo for sustainable construction and quality of life improvement
Bio-inspired structures and architecture
Bridge structures
Computational form-finding
Conceptual design
Concrete structures
Construction techniques
Deployable and inflatable structures
Design competition (WG21)
Digital modelling and fabrication
Dynamic response of metal spatial structures
► **Dynamic response of other structures**
Form-finding and structural optimisation of interlocking discrete assemblages
Graphical methods
Gridshell and lattice structures
Historical concrete shells
Historical structures
Lattice structures
Life-cycle design and assessment of structures
Metal gridshell structures, connections and stability
Methods and construction technologies for sustainable shell structures
Morphology and configuration processing
Next generation parametric design
Novel methods in modelling, optimisation and construction for reducing carbon footprint of continuous roof shells
Numerical methods for geometry, form-finding and optimisation of lightweight structures
Optimisation methods and applications
Origami
Other
Teaching design uncertainty: working with unknown qualities/quantities of new and re-claimed materials
Teaching of shell and spatial structures
Tensegrity systems and cable structures
Tension and membrane structures
Tension structures in the Asia-Pacific
Timber and bio-based structures
Topology optimisation
Traditional masonry structures and innovation
Transformable structures

IASS 2023
July 10–14 Melbourne
Integration of Design and Fabrication

Proceedings of the IASS Annual Symposium 2023
Integration of Design and Fabrication
10–14 July 2023, Melbourne, Australia
Y.M. Xie, J. Burry, T.U. Lee and J. Ma (eds.)

Modal identifications of a scaling stratospheric airship in still air

Longlong CHEN[a], Wujun CHEN[*]

[*] Space Structures Research Center, Shanghai Jiao Tong University, Shanghai, 200240, China
cwj@sjtu.edu.cn

[a] Space Structures Research Center, Shanghai Jiao Tong University, Shanghai, 200240, China

Abstract

Mode is the most basic and important dynamic characteristic of a structure. Modal analysis is mainly used for dynamic property evaluation, vibration fault diagnosis, structural health monitoring, etc. For conventional rigid structures, modal testing and prediction methodology are well established and mature enough. However, for flexible inflatable membrane structures, the modal state is significantly influenced by the internal pressure and surrounding air, which makes the modal identifications more difficult. In this paper, a scaling stratospheric airship with a length of 2.48 m was used to study the dynamic mechanical properties of the airship envelope under different pressure. To obtain the overall vibration modes of the inflatable airship, the 3D laser vibrometers were arranged at four positions under each pressure condition, and the results were combined to obtain the global vibration mode diagram. It was found that the vibration mode distribution of the envelope was mainly breathing, and the frequency values of the first four modes indicated that the larger the internal pressure of the airship envelope, the greater the stiffness. This study realized the full-field modal testing and analysis of the flexible airship envelope. The measured data was reliable, which can provide experimental system support and test program reference for the dynamic characteristics of stratospheric airships as well as other inflatable membrane structures.

Keywords: stratospheric airship; inflatable membrane structures; dynamic analysis; modal identifications; full-field measurement

1. Introduction

As one of the most crucial and seminal dynamic characteristics for structural systems, modal analysis has been widely adopted across a broad spectrum of industries including aerospace, machinery, civil engineering, and the like. Essentially, modal analysis is to transform complex physical coordinates in vibration differential equations into uncoupled modal coordinates [1]. It is primarily used to investigate the natural frequencies and modal shapes of structures, thus providing support for vibration fault diagnosis, structural dynamic modifications, design optimization, and other related aspects in engineering. The modal identification of conventional rigid structures such as reinforced concrete and vehicles is a well-established and streamlined process, which is little affected by environmental factors. However, the modal characteristics of flexible membrane structures such as airships are substantially influenced by the ambient air and pressure [2]. The discrepancy between pure solid simulation results and experimental frequencies can reach up to 50% [3]. While the simulation of fluid fields and geometric nonlinearity is complex and demands considerable computational resources. To solve for the vibration properties of membrane structures in still air, various numerical simulation and experimental methods have been developed.

The representative numerical methods mainly include the added-mass method [4], acoustic-structure interaction (ASI) [5], and fluid-structure interaction (FSI) [6]. The added-mass method is a widely employed approach for analyzing the dynamics of flexible membranes or plates in fluid flow, which

Copyright © 2023 by Longlong CHEN and Wujun CHEN Published in the Proceedings of the IASS Annual Symposium 2023 with permission.

equivalently relates the kinetic energy of the fluid to added mass [7]. Chen et al. [8] derived the added mass of one-way tensioned membrane vibrating in the fluid domain. The results demonstrated that the added mass was related to the modal order. The ASI method considers the fluid domain as an acoustic medium, and the vibration energy is transferred through acoustic pressure [9]. Srivastava et al. [10] investigated the effect of internal gas filling on the dynamic response of inflatable torus using the ASI approach. The results showed that the air significantly altered the eigenfrequency value and vibration modes. The FSI method is a combination of computational fluid dynamics (CFD) and computational solid mechanics (CSM). It can solve the coupled modes of complex membrane structures with irregular shapes and accurately reflect the interaction between fluid motion and structural deformation [11]. Based on the FSI theory and potential fluid theory, Qiu et al. [12] established a theoretical model on the membrane structure and the air field interaction.

In addition to numerical simulation, experimental methods play an important role in modal analysis. Hu et al. [2] tested the modal behaviors of an inflated tube cantilever, and the targets were arranged on the front side of the tube. Zhang et al. [13] developed a method for simultaneously calculating the top and bottom Z-displacement of the hexagon air cushion. However, the research mentioned above mainly focused on flat films or part region of airships. To the best of the authors' knowledge, there have been no reports on three-dimensional full-field modal testing of inflatable membrane structures. Therefore, this paper aims at the full-field modal testing and analysis of a scaling airship envelope. The PSV-500-3D scanning vibrometer was employed to identify the airship modes under five loading cases. The modal testing principle and main process are clarified. And the experimental results of different pressure are thoroughly analyzed and compared.

2. Modal testing principle and process

2.1. Experimental principle

The vibration testing was conducted using the PSV-500-3D full-field scanning laser vibrometer from the German company Polytech, while the modal extraction was performed using the LMS modal analysis software from Siemens. To ensure the rationality and accuracy of the experiments, the elaboration on the measurement and modal identification principle is necessary.

2.1.1. vibration measurement principle

Polytec laser vibrometer utilizes laser Doppler interferometry technology, which is widely used in the fields of national defense and basic research. It mainly utilizes the optical Doppler principle [14] to measure the vibration magnitude of objects. Laser measurement has the advantages of non-contact, high measurement accuracy, large measurement dynamic range, and high spatial resolution. The laser emitted by the laser generator is divided into two beams of light through a lens. Beam 1 is the reference beam and beam 2 is reflected by the surface of the moving object. The Doppler signal proportional to the velocity of the moving object is generated by interference, and the time history signal of the velocity and displacement of the moving object can be obtained by frequency and phase demodulation.

2.1.2. Modal identification principle

Since the PSV-500-3D three-dimensional full-field scanning laser vibrometer is only a modal testing software and cannot directly perform post-processing analysis on each order mode. In order to calculate the modal assurance criterion (MAC) of each order vibration mode, the test results need to be imported into professional modal analysis software LMS. Fast Fourier Transform (FFT) is one of the most commonly used signal decomposition methods in LMS. The classical Fourier principle shows that any continuous measured time sequence or signal can be represented as an infinite superposition of sine wave signals with different frequencies. For computers, only discrete and finite-length data can be processed. Hence, the Discrete Fourier Transform (DFT) is more suitable for discrete signal transformation. And FFT is one fast algorithm of DFT to reduce computational complexity.

The MAC is used to measure the similarity between two modal vibration modes, which can be expressed as follows:

$$MAC_{ij} = \frac{\left|\varphi_i^T \varphi_j\right|^2}{(\varphi_i^T \varphi_i)(\varphi_j^T \varphi_j)} \tag{1}$$

where φ_i is the *i*th order vibration mode of one model, φ_j is the *j*th order vibration mode of another model, and *T* represents the conjugate transpose of the matrix.

2.2. Experimental process

2.2.1. The experimental airship layout

The illustration and experimental layout of the airship can be seen in Figure 1. The full length of the model is 2.48 m, and the maximum diameter is 0.548m. The airship membrane is URETEK-3216LV laminated fabric material, which is interwoven by warp and weft yarns.

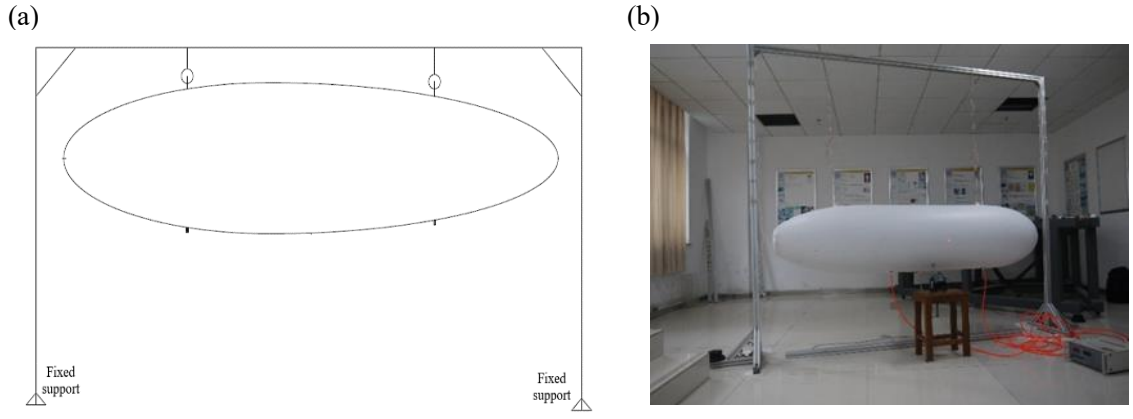


Figure 1. Layout of the airship envelope, (a) Illustration, (b) Experiment.

2.2.2. Testing system

The experimental system and equipment are shown in Figure 2, including a fixed frame, suspension connector, inflation and pressure control system, three-dimensional photogrammetry system and data acquisition system. The fixed support is an aluminium alloy profile with a height of 2.3 m and a width of 2.8 m. The inflation and pressure control system is independently developed by our laboratory. The measurement system uses the German PSV-500-3D Scanning Vibrometer full-field laser vibrometer, which includes a three-dimensional laser emitter, controller and test integration system, and the measurement error is less than 0.1%. All measurement data are digital signals stored in the host data management system, and the data acquisition is controlled by the PSV-500-3D software.

2.2.3. Experimental implementation

Five loading cases (2 kPa, 4 kPa, 6 kPa, 8 kPa and 10 kPa) were set to investigate the effect of pressure difference on the dynamic characteristics. For each case, the air pressure state, vibration mode and frequency, and modal assurance criterion of the airship were monitored or calculated. Measurement points (as shown in Figure 3) were firstly arranged and the modal shaker sweeping excitation was activated. Then the PSV-500-3D full-field scanning laser vibrometer was applied to measure the vibration modes and frequencies. To obtain the global vibration mode of the inflatable envelope, the laser vibrometer was arranged at four positions under each air pressure condition, and the four results were combined together to obtain the overall vibration mode contour.

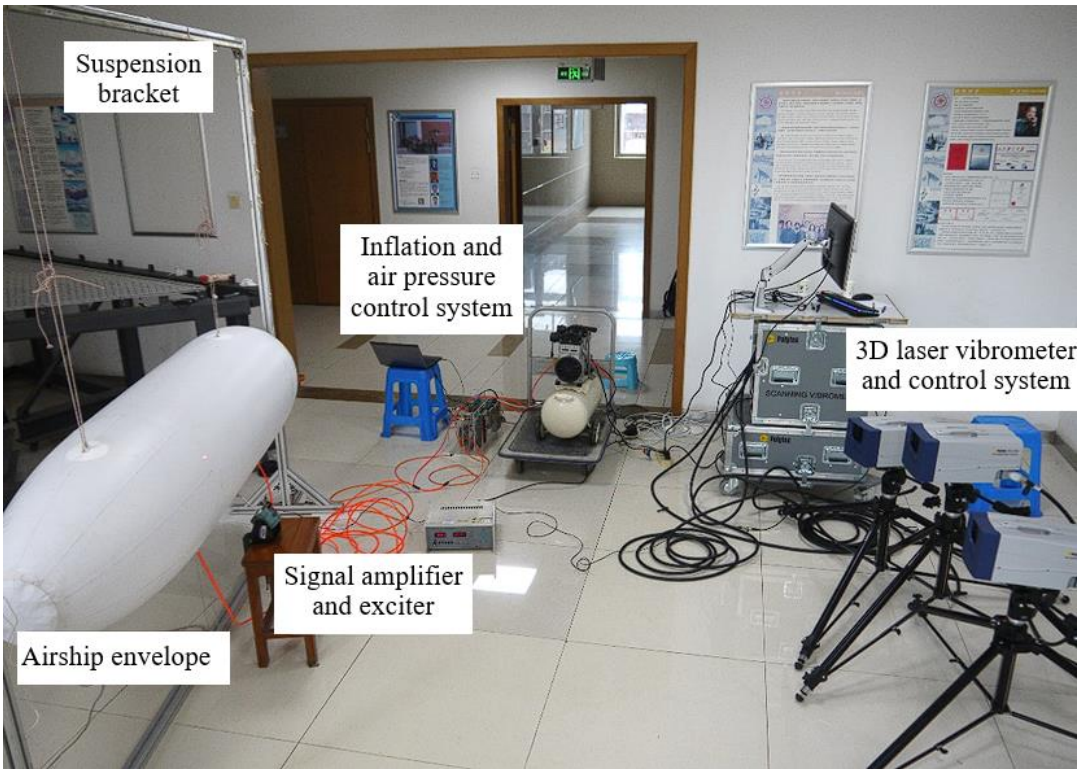


Figure 2. Modal testing system of the airship envelope.

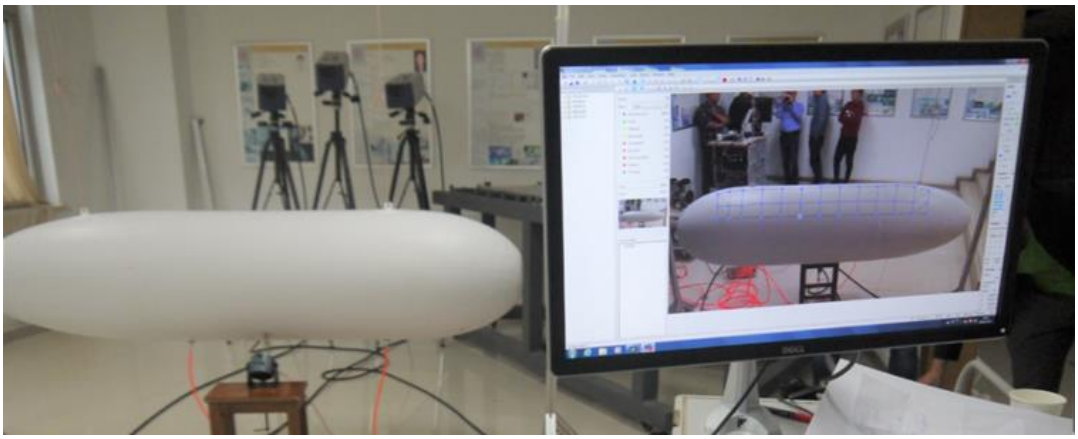


Figure 3. Measurement points arrangement of the envelope.

3. Results and comparisons

3.1. Results of 6 kPa pressure

The testing results of the airship envelope under the 6 kPa air pressure condition were chosen as representative for analysis. The full-field amplitude-frequency curve is shown in Figure 4. To measure the first four modes of the airship envelope, the frequency domain range was selected as 0~160Hz. Based on the figure, the rigid body modes of the airship envelope are concentrated in the range of 0~15 Hz, and the first main mode is about 50Hz, which meets the requirement that the rigid body vibration mode is less than one-third of the main mode frequency. Typical modes identified by LMS analysis software are shown in Table 1. The modal contours of the flexible airship under various pressure showed that the vibration modes are mainly breathing modes.

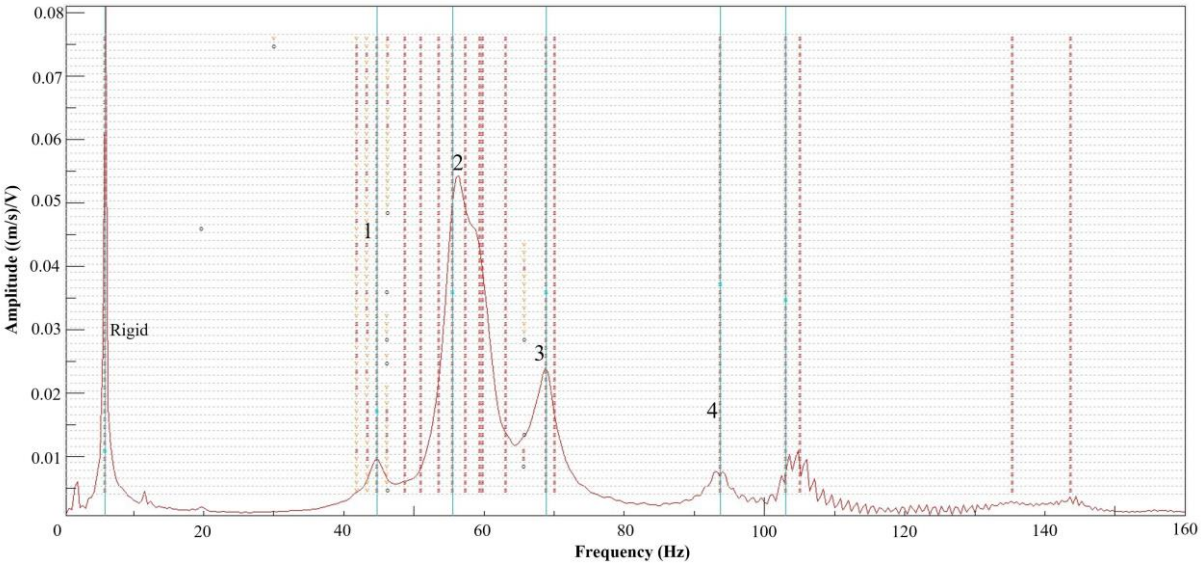
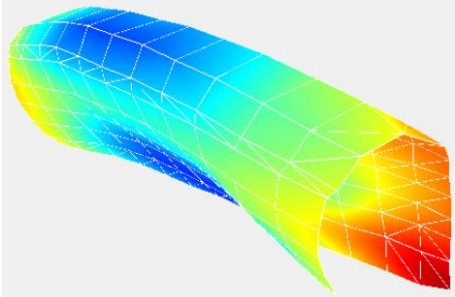
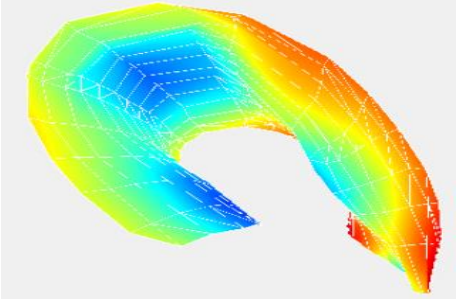
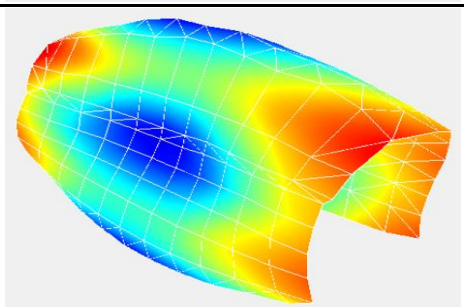
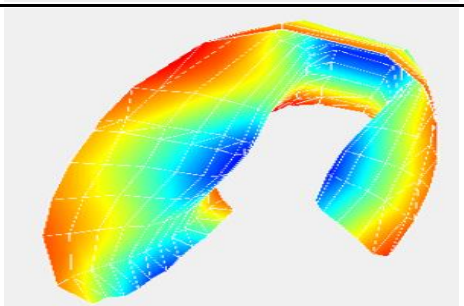
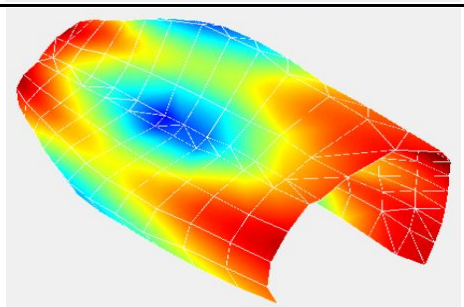
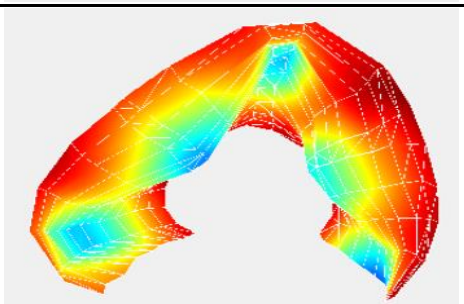
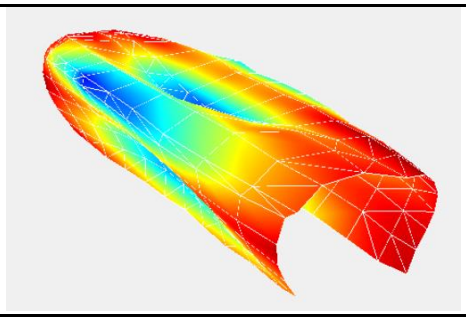
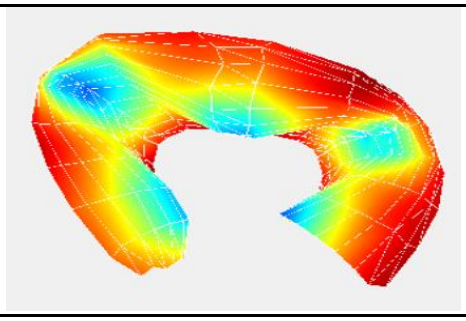


Figure 4. The amplitude-frequency curve identified by LMS.

Table 1. The vibration modes under 6 kPa pressure.

Modes /Hz	Side view	Perspective view
1st Mode /44.8		
2nd Mode /56.4		
3rd Mode /68.8		

4th Mode /93.2		

The modal assurance criterion under 6 kPa pressure are listed in Table 2. The coefficients on the main diagonal are all 100%, while the average value of the off-diagonal coefficients is 19.4%, indicating a high level of stability and reliability for the vibrating modes.

Table 2. The modal assurance criterion under 6 kPa pressure.

Modes	MAC values / %				
Rigid mode	100	17.279	0.083	0.39	1.392
Mode1	17.279	100	28.346	58.495	10.559
Mode2	0.083	28.346	100	36.004	26.468
Mode3	0.39	58.495	36.004	100	14.986
Mode4	1.392	10.559	26.468	14.986	100

3.2. Comparisons of different loading cases

The experimental results under different pressure conditions are graphed in Figure 5. It is evident that with the increase of internal pressure, the frequency values of the first four modes of the airship exhibit a rising trend. Moreover, this trend becomes more pronounced at higher internal pressure. The results demonstrated that the greater the internal pressure of the airship, the greater its stiffness.

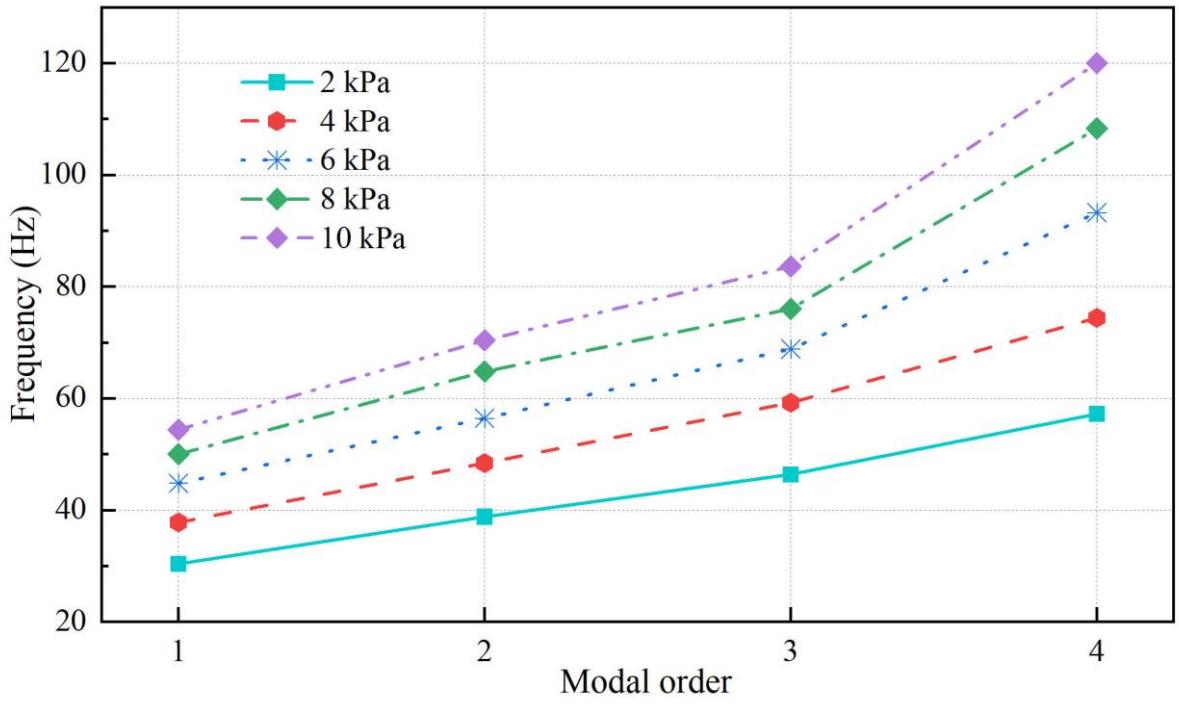


Figure 5. The frequencies of the airship under different pressure.

4. Conclusions

This paper presents a full-field vibration test and analysis system based on the PSV-500-3D Scanning Vibrometer, and the vibration characteristics of a scaling airship envelope under different pressure are investigated using the system. Specifically, the frequencies, vibration patterns and MAC values of the first four modes of the main envelope were analyzed under five pressure cases. The main conclusions can be drawn as follows:

(1) The rigid body vibration mode was less than 1/3 of the main modal frequency under each internal pressure condition, which indicated that the experimental results were credible. Besides, it showed that the boundary and excitation equipment were properly arranged and achieved the expected experimental objectives.

(2) The vibration mode distribution was primarily breathing, and the first four vibration modes were all breathing modes under five different pressure conditions.

(3) By comparing the frequencies under different pressure, it can be observed that as the internal pressure increases, the frequency values of the first four modes of the airship show an increasing trend. This indicates that the stiffness of the airship is positively correlated with the internal pressure.

This experimental research has established a good experimental foundation for testing and analyzing the modal behaviors of the flexible airship. The measured data is reliable, providing experimental support for the study of the dynamic properties of airships and other inflatable membrane structures.

Acknowledgements

Gifeng Gao and Yibei Zhang helped with the experiments and data analysis. The authors gratefully acknowledge with thanks all the help and other unmentioned ones.

References

[1] A. K. Chopra, *Dynamics of structures: theory and applications to earthquake engineering*, 5th ed. London: Person, 2016.

[2] Y. Hu, W. Chen, Y. Chen, D. Zhang, and Z. Qiu, "Modal behaviors and influencing factors analysis of inflated membrane structures," *Engineering Structures*, vol. 132, pp. 413-427, 2017, doi: 10.1016/j.engstruct.2016.11.037.

[3] Y. F. Chen, W. J. Chen, and Y. L. He, "Analysis and Test for the Space Different Thickness Film Structure in Still Air," *Advanced Materials Research,* vol. 671-674, pp. 611-617, 2013, doi: 10.4028/www.scientific.net/AMR.671-674.611.

[4] H. Minami, "Added mass of a membrane vibrating at finite amplitude," *Journal of Fluids and Structures*, vol. 12, no. 7, pp. 919-932, 1998, doi: 10.1006/jfls.1998.0175.

[5] X. Y. Cui, X. Hu, G. Wang, and G. Y. Li, "An accurate and efficient scheme for acoustic-structure interaction problems based on unstructured mesh," *Computer Methods in Applied Mechanics and Engineering*, vol. 317, pp. 1122-1145, 2017, doi: 10.1016/j.cma.2017.01.022.

[6] Y. Pan, M. Rao, Y. Zhou, S. Wang, and Y. Lin, "Research on vibration frequency of membrane structure considering fluid and structure interaction," *Journal of Building Structures,* vol. 40, no. 8, pp. 136-144, 2019, doi: 10.14006/j.jzjgxb.2018.0266.

[7] X. Wang, Y. Zhang, S.-s. Law, Q. Yang, and N. Yang, "Modeling of the added mass of air on ETFE cushions vibrating in still air," *Thin-Walled Structures,* vol. 174, 2022, doi: 10.1016/j.tws.2022.109170.

[8] Z. Chen, Y. Wu, and X. Sun, "Research on the added mass of open-type one-way tensioned membrane structure in uniform flow," *Journal of Wind Engineering and Industrial Aerodynamics*, vol. 137, pp. 69-77, 2015, doi: 10.1016/j.jweia.2014.12.004.

[9] S. Kukathasan and S. Pellegrino, "Vibration of prestressed membrane structures in air," presented at the 43rd AIAA/ASME/ASCE/AHS/ASC Structures, Structural Dynamics, and Materials Conference, 2002.

[10] A. Srivastava, B. K. Mishra, and S. C. Jain, "Effect of enclosed fluid on the dynamic response of inflated torus," *Journal of Sound and Vibration,* vol. 309, no. 1-2, pp. 320-329, 2008, doi: 10.1016/j.jsv.2007.01.019.

[11] T. Sussman and J. Sundqvist, "Fluid–structure interaction analysis with a subsonic potential-based fluid formulation," *Computers & Structures,* vol. 81, no. 8-11, pp. 949-962, 2003, doi: 10.1016/s0045-7949(02)00407-8.

[12] Z. Qiu, W. J. Chen, B. Zhao, C. Gao, and Z. Yu, "Wet modal analysis and experiment study on an airship envelop," *Journal of Vibration and Shock,* vol. 36, no. 12, pp. 61-67+82, 2017, doi: 10.13465/j.cnki.jvs.2017.12.011.

[13] Y. Zhang, B. Zhao, J. Hu, X. Mi, and W. Chen, "Modal measurement and identification of hexagonal air cushions," *Mechanical Systems and Signal Processing,* vol. 179, 2022, doi: 10.1016/j.ymssp.2022.109377.

[14] S. Zhao, S. Li, W. Guo, C. Zhang, and B. Cong, "Quantitative diagnosis method of beam defects based on laser Doppler non-contact random vibration measurement," *Measurement,* vol. 152, 2020, doi: 10.1016/j.measurement.2019.107271.

Form-finding and structural optimisation of interlocking discrete assemblages

Active bending
Additive manufacturing/ 3D printing
Architectural geometry
Bamboo for sustainable construction and quality of life improvement
Bio-inspired structures and architecture
Bridge structures
Computational form-finding
Conceptual design
Concrete structures
Construction techniques
Deployable and inflatable structures
Design competition (WG21)
Digital modelling and fabrication
Dynamic response of metal spatial structures
Dynamic response of other structures
► **Form-finding and structural optimisation of interlocking discrete assemblages**
Graphical methods
Gridshell and lattice structures
Historical concrete shells
Historical structures
Lattice structures
Life-cycle design and assessment of structures
Metal gridshell structures, connections and stability
Methods and construction technologies for sustainable shell structures
Morphology and configuration processing
Next generation parametric design
Novel methods in modelling, optimisation and construction for reducing carbon footprint of continuous roof shells
Numerical methods for geometry, form-finding and optimisation of lightweight structures
Optimisation methods and applications
Origami
Other
Teaching design uncertainty: working with unknown qualities/quantities of new and re-claimed materials
Teaching of shell and spatial structures
Tensegrity systems and cable structures
Tension and membrane structures
Tension structures in the Asia-Pacific
Timber and bio-based structures
Topology optimisation
Traditional masonry structures and innovation
Transformable structures

IASS 2023
July 10–14 Melbourne
Integration of Design and Fabrication

Proceedings of the IASS Annual Symposium 2023
Integration of Design and Fabrication
10–14 July 2023, Melbourne, Australia
Y.M. Xie, J. Burry, T.U. Lee and J. Ma (eds.)

Chain mail assembly: a new model of programmable modular structure

Nabila AFIF*, Gergana RUSENOVA[a], Charlie RANSCOMBE[a], Jane BURRY[a]

[a,*] School of Design and Architecture, Swinburne University of Technology
John Street, Hawthorn, Victoria, Australia 3122
nafif@swin.edu.au

Abstract

The paper explores a new type of programmable structural system that uses chain mail-like structures made of interlocking identical skeletal cubes. The programmable aspect of the system is defined as the ability of the initially planar modular assemblies to be reversibly constructed as distinctive self-supporting curved structures. The study focuses on an initially planar identical chain mail structure that was used to construct various curved structures by placing it in different placement orientations and erecting it in several steps of the same actuation procedure. The study found that various shapes of curved formations can be developed reversibly from the same planar structure. It also found the range of dimensional variations can be significantly increased by modifying the input of the orientation and actuation sequence parameters. Furthermore, it also found that by applying a local transformation only on a single row of interlocking modules at one end of the strip-like structure, an average of two-thirds of the modules in the configuration can be actuated to create a curved structure. Overall, this study provides a systematic investigation of the impact of applying a simple transformation mechanism on the overall behavior of the chain mail structure. The findings demonstrate the preliminary potential of chain mail structures as a new model of programmable modular structures, which could be useful in a variety of applications where flexibility, adaptability, and ease of construction are essential.

Keywords: programmable structure, interlocking assembly, adaptive structure, chain mail structure, form-finding

1. Introduction

1.1. Research interest surrounding chain mail structure

In simple terms, chain mail can be defined as an armour or protective garment formed of interlinked metal rings. In general, it is mostly known as a type of armour that was widely used by soldiers from the Middle to the early Renaissance era [1]. However, outside of the field of ballistic study, designers' and researchers' interest in chain mail-like material systems has developed quite rapidly in the last two decades [2]. This phenomenon is driven by the development of 3D printer fabrication technology and its increasingly widespread, easy and inexpensive use, which has triggered the emergence of a wealth of new design variations for chain mail-like material systems that were previously challenging to fabricate. As a result, the range of potential functionality of chain mail has been significantly expanded from wearable electronic devices [3], wearable medical support [4-6], and soft robotic components [7] to lunar mobility structures [8].

1.2. Chain mail material system for architectural application

Specifically in the architectural field, in the last ten years, there have been several publications that point out the potential implementation of a chain mail material system for an architectural application, for example, as an adaptive building skin [9, 10] and as transportable reconfigurable structures [4]. In both studies, as well as in some other studies which are not directly touching on the architectural field, the

Copyright © 2023 by Nabila AFIF, Gergana RUSENOVA, Charlie RANSCOMBE and Jane BURRY. Published in the Proceedings of the IASS Annual Symposium 2023 with permission.

concept of 'programmability' emerges through the abstraction of programmable-related design goals (such as being adaptive, customisable, and tunable products) [4, 6, 7, 9].

However, although chain mail adaption for an architectural scale holds exciting prospects, judging by the number of sources and depth of information published, there has been little progress in advancing this concept. Although several chain mail applications can indeed be found on built projects, for example, as an internal screen or an external building façade, in terms of design-led innovation, this is still relatively behind compared to other fields of science.

1.3. Identified problem

One recent study mentioned that despite the vast design space for a chain mail-like structures (geometrical interlocking assemblies), there is a lack of formalised design process to work with them, and the existing product development is largely dependent on intuition [11]. The importance of design method in architecture cannot be understated, especially when working with a new system [12]. However, there is currently a lack of explanation for the absence of research progress on chain mail-like structures for an intended application in an architectural context. Therefore, we consider the knowledge gap around chain mail material system adoption for architectural application to be due to the lack of a systematic design method.

2. Methodology

2.1. Research objective and scope

Aimed to advance the development of a chain mail material system for an architectural application, with emphasis on its potential programmability, we develop a body of research focusing on systematically exploring various design parameters and constraints tied to the development of a chain mail material system for architectural application. The objective of the programmability here is the ability of the initially planar modular assemblies to be reversibly constructed as distinctive self-supporting curved structures. The relevance of this system comes from the continuous need to improve efficiency in the construction of free-form architecture, which is strongly associated with highly-customized irregular curved geometries. Thus, it follows that the design of our chain mail module is limited to something that is made of simple and rigid identical modules in the form of a skeletal cube.

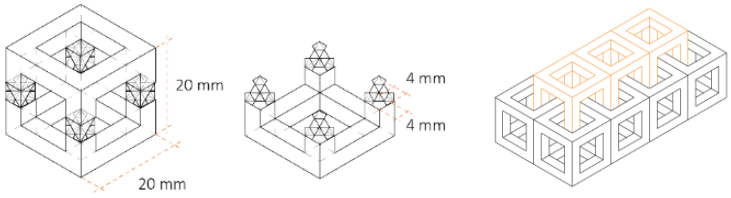
Based on a literature study and a series of pilot projects, we have discovered that one of the significant parameters in the design system is the transformation mechanism. In this context, the transformation mechanism defined as a series of conditions and processes that must be executed to 'actuate' certain sets of the desired physical behaviour of the chain mail structure (geometries) in accordance with a pre-arranged design program. Specifically, in this study, the scope of the transformation mechanism would be limited to examining the impact of two construction process-related parameters. These are the impact of structure orientation and structure actuation sequence on the chain mail structure's flexible shape-forming capacity and self-supporting capacity.

2.2. Prototype design

This specific study utilises only physical simulation on a small-scale physical model to identify the potential and limitations of programming the structure's physical behaviour through controlling the structure's boundary condition (specifically its pre-actuated placement orientation) and actuation sequence. The chain mail model was produced using a rapid prototyping method in the form of Fused Deposition Modelled (FDM) 3D prints using Polylactic Acid filament.

The chain mail physical model is in the form of a slender, strip-like assembly made of 3 rows of interlocked cubes sized 20 x 20 x 20 mm each, with a total length of 15 modules and a width of 2 modules in its basic, contracted state. Each chain mail module has two parts of an element with a 4 x 4 mm dimension of rectangular cross-section, as seen in Figure 1. Each of the elements is connected using

a 'kawai-tsugite' joint typically applied in timber constructions. These choices of dimension-to-thickness ratio and joint type are the result of another focused study on the same parent topic that is yet to be published.



(a) (b)

Figure 1. (a) Cube module dimension and (b) module assembly pattern used in this study.

The decision to use a small-scale, 3D printed prototype derives from the importance of this particular research in the larger systematic design study is to examine the relationship between placement orientation, actuation sequence, and flexible shape-forming capacity, which hypothetically is scale invariant. Additionally, self-supporting capacity is considered the most basic structural function that the structure should perform. Therefore, self-supporting capacity comes as a consequential significant parameter that can be observable regardless of the prototype scale and choice of material. It should be noted the design considerations for production and assembly of our chain mail structure are not within the scope of this paper.

2.3. Simulation procedure

2.3.1. Placement orientation

The first step of the simulation procedure begins with placing the structure in certain placement orientations. Here, there are six placement orientations that were applied, which were derived from two conditions, which are the structure's face placement and the structure's twisting.

As can be seen in Figure 1, the three rows of interlocking chain mail modules composing the test prototype form two levels of module stack. This stack can be placed with either the central row of modules (drawn in orange line in Figure 1b) facing up or facing down. Then, for any of the face placements, the structure can also be placed flat on the ground or the test base or can also be twisted to a certain degree of twisting, called by the term 'twist cycle' here. According to the number of faces in the cubic module, at least four stages of twist can be applied within one axis of rotation, as illustrated in Figure 2. Then, following the slender, strip-like proportion of the structure, intuitively, each twist can be initiated from either one or both ends of the structure.



(a) (b) (c) (d) (e)

Figure 2. End view representations of four types of that twisting cycles that can be applied sequentially to the structure: (a) no twisting, (b)1/4 cycle, (c) 1/2 cycle, (d) 3/4 cycle and (e) 1 full cycle.

Among the many combinations of placement orientation that can be generated, we applied six different types of input for the "structure orientation" parameter in this study, which are flat-up, flat-down, 1/2 cycle-up, 1/2 cycle-down, one cycle-up and one cycle-down orientation. The detailed definition and visualisation of each orientation type (illustrated with photos of the chain mail structure taken from above), are provided in Table 1.

Table 1. Six types of initial structure placement which act as the inputs for placement orientation parameter illustrated with photos of the chain mail structure taken from above.

No	Name	Definition	Visual information (top view)
1	Flat-up orientation	The central chain mail row is facing up without any twisting applies at both ends of the structure	
2	Flat-down orientation	The central chain mail row is facing down without any twisting applies at both ends of the structure	
3	1/2 cycle-up orientation	The central chain mail row is facing up with 1/2 cycle twisting applies at one end of the structure	
4	1/2 cycle-down orientation	The central chain mail row is facing down with 1/2 cycle twisting applies at one end of the structure	
5	One cycle-up orientation	The central chain mail row is facing up with 1 cycle twisting applies at one end of the structure	
6	One cycle-down orientation	The central chain mail row is facing down with 1 cycle twisting applies at one end of the structure	

2.3.1. Actuation method

Following the structure placement, the next step of the simulation procedure is to actuate the structure to transform it from a planar modular assembly into a reversibly constructed distinctive self-supporting curved structure. The actuation method that was used here is a mechanical actuation method that follows the general principle of installing designed instabilities that would create either temporary or permanent deformations in the structure [13]. The actuation method used in this study is made of only two simple step-procedure, such as rotating the last rows of the modules and then securing them to the base. The rotation is done in a 1/4 cycle intensity along the axis parallel to the structure's long side and in the opposite direction to where the structure span will be constructed, as seen in the illustration provided in Table 2.

While the actuation method is kept simple and identical in every simulation iteration, the actuation sequence can be customised as part of the programmable system's transformation mechanism. As with the structure's twisting, the structure's actuation process can also be initiated from either one or both ends of the structure. To examine the impact of actuation sequence in the curved structure's physical behaviour, four different types of actuation sequences were applied in each of the six simulation iterations (based on the number of different placement orientation types tested).

Technically, the four different sequences are part of a four step-procedure that is performed sequentially. However, for analysis purposes, according to the research objective, each step of the procedure will be analysed independently as a different type of actuation sequence. The detailed definition and visualisation of each actuation sequence type are provided in Table 2.

Table 2. Four types of structure actuation actions which act as the inputs for actuation sequence parameter illustrated with photos of the chain mail structure taken from the side.

No	Name	Definition	Visual information (side view)

1	First stage single end-actuation	The chain mail unit at the first end of the structure is rotated and secured. One curvature is formed.	
2	First stage double end-actuation	The first end of the structure is kept actuated, while the chain mail unit at the second end of the structure is rotated and secured. Two curvatures are formed.	
3	Second stage single end-actuation	The first end of the structure is deactuated (unsecured to let loose), while the second end of the structure is kept actuated. One curvature is formed.	
4	Second stage double end-actuation	The first end of the structure is re-actuated (re-rotated and re-secured), while the second end of the structure is kept actuated. Two curvatures are formed.	

2.4. Data capturing

Considering the initial stage of the study and its objective (to effectively explore and identify the potential and limitations of programming the structure's physical behaviour through a particular transformation mechanism for providing immediate feedback into the larger systematic method study under construction), a simple data capturing method via sequential photography is used. Two cameras were set at two different points to capture the simulation process simultaneously. One camera captured the simulation from the side view along the long axis of the structure and another camera captured it from the top view.

2.5. Data extraction, accuracy, and unit of measurement

This research employs a quantitative approach. Therefore, a form of quantifiable measurement is required from each set of data generated out of the simulation. At the same time, a photograph would always naturally create a perspective image which may contain a certain degree of distortion depending on the photo's field of view. Thus, to emphasize the concept of scale invariance and avoid misinterpretation related to the level of accuracy of dimensional measurement that can be extracted from a photograph, the dimension of one module itself will be used as the unit of measurement in this study.

Then, to improve the accuracy level in the data reading, a smaller grid of measurement is provided by dividing one module size by a factor of four. In the data analysis process, the measurement grid was overlaid on top of every photo. The point of origin is started above the upper line of the structure in its initial planar position to ensure that any measurable dimension from the photo is only the one created after the actuation action has been implemented.

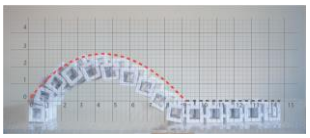
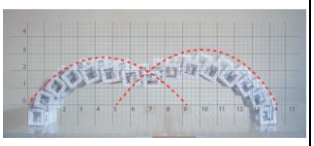
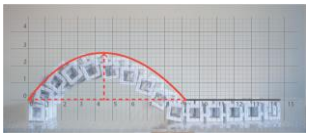
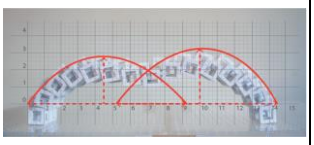
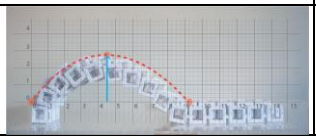
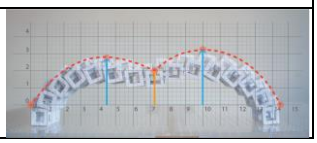
3. Data and discussion

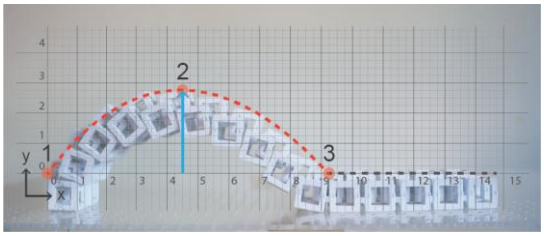
3.1. Evaluation points

In total, there were twenty-four unique sets of visual data that can be observed in this study. They are generated from simulations of chain mail structure placed in six different types of orientation and then actuated with four types of actuation sequence. Based on their striking physical characteristics, the curved structures resulting from the simulation can be categorised into two groups. The first group consists of simulations involving actuation sequences 1 and 3, where there is a single curvature identified within the curved structure, while the second group consists of simulations involving actuation sequences 2 and 4, where two curvatures are identified in each curved structure.

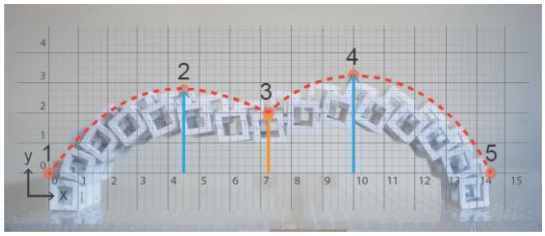
To enable a quantitative data analysis process, there must be quantifiable evaluation parameters that can be extracted from each group. To do this, a set of evaluation points is mapped throughout the structure's outer form, following the location of unique sections along the curvatures. Borrowing the concept of wave evaluation, some of the essential points of evaluation which can be identified in those structures are the curved lines' boundary (that are the start and end points), the crest or peak points, and the interference or intersection point. The procedure to identify the location of the mentioned Evaluation Points (EPs), the definition of each point, and visual information on their location in each simulation group are provided in Table 3, Table 4, and Figure 3.

Table 3. Three steps-procedure to identify the structure's evaluation points in each simulation

No	Definition	Visualization	
		Group 1: single end-actuated structure	Group 2: double end-actuated structure
1	Trace the outer form of the structure, differentiating parts that are impacted by the actuation process to form the curvature (marked by the red line), and parts that are not impacted (marked by the grey line).		
2	Focusing on the traced red line, use the line as a guideline to approximate the general shape of the curves and then check if the structures have been categorised within the correct group (based on the number of curvatures).		
3	Use the traced line as a guideline to approximate the location of several evaluation points and then extract their coordinates within the grid system.		



(a)



(b)

Figure 3. Different number and distribution of evaluation points for each of the simulation group: (a) Group 1 for curved structure with a single curvature and (b) Group 2 for curved structure with two intersecting curvatures

Table 4. Defintions for each evaluation point

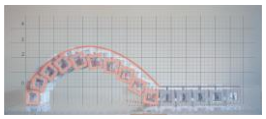
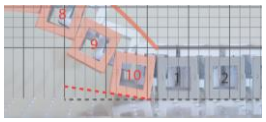
No	Name	Definition	Evaluation point (EP)	
			Group 1	Group 2
1	Start point	The position where the identified curved portion of the structure is started	1	1
2	Peak point	The highest point in the curved portion of the structure	2	2 and 4
3	Intersection point	The location where the two curvatures meet (happened only in the second group of simulation)	-	3

4	End point	The position where the identified curved portion of the structure is ended	3	5

3.2. Evaluation parameters

Based on the evaluation points mapped on each simulation data, at least three quantifiable sets of parameters can be evaluated to examine the shape-forming and self-supporting capacity of the structures. The definition, extraction method, result indication, and limitation of each evaluation parameter are described in Table 5.

Table 5. The definition, extraction method, result indication, and limitation of the three evaluation parameters

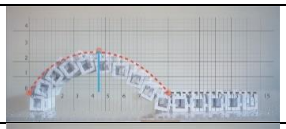
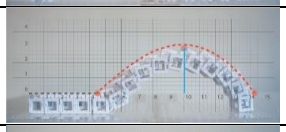
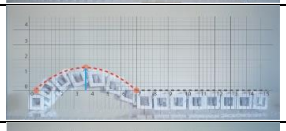
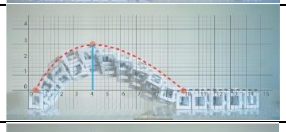
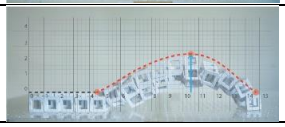
No and name	**1. Actuation reach**	**2. Curved structure's span and rise**	**3. Curved structure's regularity index**
Definition	Actuation reach is the count on the number of modules that can be actuated from one point of actuation, indicated by a rise on the module's base from the test platform/ground.	Span is the distance between the two endpoints of the curved structure, while rise is the height of the peak point of the curvature.	The regularity index is a value to indicate the profile of the curved structure, whether it is closer to a regular, half-circle-like curve with high vertical symmetry or if it is closer to an irregular, floppy curve.
Data extraction method	The regularity of the structure's design enables the count of actuated modules to be taken from only one of three rows of interlocking modules (the front row with the most visibility from the side photograph).  	The span can be measured by calculating the distance between the first and last EPs along the x-axis. **<u>Group 1:</u>** The rise is the distance between EP 2 and the origin axis along the y-axis. **<u>Group 2</u>**: For simplification, the rise is determined by averaging the distance between EP 2, 3, and 4 from the origin axis along the y-axis.	**<u>Group 1:</u>** **Span-to-rise ratio:** measured by dividing half of the span with the rise. *Result:* <1 = the sharper the curve is likely to be; 1 = the more likely the structure to have a more regular, half-circle-like profile; >1 = the flatter the curve is likely to be. **Peak point position:** subtracting half of the span with the distance of EP 2 to EP 1/EP 3. *Result:* in its absolute value form, the smaller the subtraction result is, the more likely the structure to have vertical line symmetry. **<u>Group 2:</u>** **Peak point similarity:** subtracting the height of EP 2 and EP 4 along the y-axis. **Peak point position:** subtracting half of the span with the distance of EP 3 to EP 1/EP 5. *Result:* for both factors, in their absolute value forms, the smaller the subtraction results, the more likely the structures will have vertical line symmetry.
Result indication	The larger amount of modules actuated, the more effective the structure's actuation mechanism, and the more significant the structure's flexible	The larger the curvature span and rise, the more effective the structure's actuation mechanism is and the larger the structure's flexible	Overall, the higher the structure's regularity, the greater the structure's self-supporting ability, as it does have many floppy proportions of its curved structure.

	shape-forming and self-supporting ability.	shape-forming and self-supporting ability.	
Current limitation	Although it is visually clear that each module is actuated with different intensities (indicated by its rotational angles), this parameter is not measured yet due to the potentially low precision measurement for small details caused by perspective distortion inherent in a photograph.	The current method of approximating the curvature's dimension is greatly simplified. Although together, span and height can generally indicate the overall dimension of the structure, it does not confirm the actual profile of the curve itself.	The current method of approximating the curved structure profile is greatly simplified, especially because they left out some sections between the evaluation points.

3.3. Simulation data

Table 6 and Table 7 below are the simulation data for Group 1 and Group 2, respectively, along with the measurement of all the identifiable evaluation parameters.

Table 6. The result of simulation for Group 1. Note values are factors of a single module.

Orientation /actiuation type	Visual information	Evaluation points coordinate (x,y)			Evaluation parameter (in module)				
					1	2		3	
		1	2	3	No. of actuated modules (1st row)	Curved structure span	Peak point rise	Span to rise ratio	Peak point position
Flat-up/1 and 3		(0, 0)	(4.5, 2.75)	(9.25, 0)	10	9,25	2,75	1,68	0,13
		(4.5, 0)	(10, 3)	(14.5, 0)	10	10	3	1,67	0,50
Flat-down/1 and 3		(0.5, 0)	(3.75, 1.5)	(7, 0)	7	6,5	1,5	2,17	0,00
		(5.25, 0)	(10.75, 2.25)	(14.75, 0)	10	9,5	2,25	2,11	0,75
1/2 cycle-up/1 and 3		(0.5, 0)	(4.25, 3)	(10, 0)	10	9,5	3	1,58	1,00
		(4.5, 0)	(10.5, 2.5)	(14.75, 0)	10	10,25	2,5	2,05	0,88

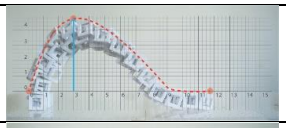
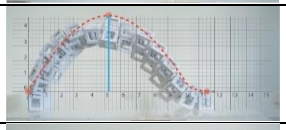
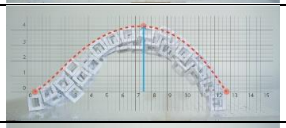
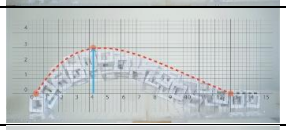
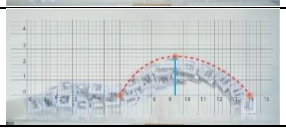
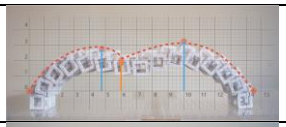
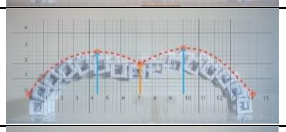
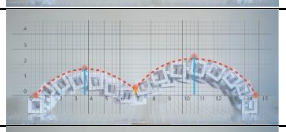
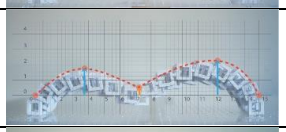
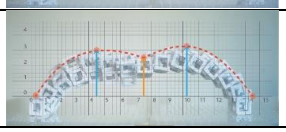
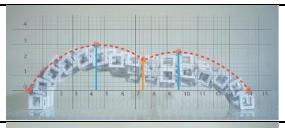
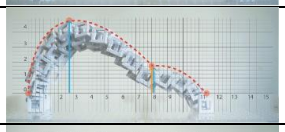
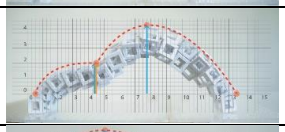
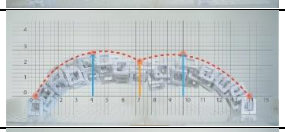
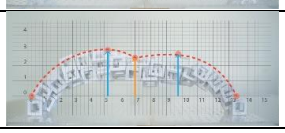
1/2 cycle-down/1 and 3		(0, 0)	(3, 4.75)	(11.75, 0)	15	11,75	4,75	1,24	2,88
		(2, 0)	(9.25, 4.25)	(13.75, 0)	13	11,75	4,25	1,38	1,38
1 cycle-up/1 and 3		(0, 0)	(5.25, 5)	(11.5, 0)	14	11,5	5	1,15	0,50
		(0.5, 0)	(7.5, 4.25)	(12.75, 0)	15	12,25	4,25	1,44	0,88
1 cycle-down/1 and 3		(0, 0)	(4.25, 3)	(13, 0)	13	13	3	2,17	2,25
		(6, 0)	(9.5, 2.5)	(14.25, 0)	9	8,25	2,5	1,65	0,63

Table 7. The result of simulation for Group 2. Note values are factors of a single module.

Orientation/actuation type	Visual information	Evaluation points coordinate (x,y)					m				
							1	2		3	
		1	2	3	4	5	No. of actuated modules (1st row)	Curved structure span	Averaged peak point rise	Peak points similarity	Peak point position
Flat-up/2 and 4		(0, 0)	(4.5, 2.75)	(7.25, 2)	(10, 3.25)	(14.5, 0)	15	14,5	2,67	0,5	0,00
		(0, 0)	(4.5, 2.75)	(7.25, 2)	(10, 3)	(14.5, 0)	15	14,5	2,58	0,25	0,00
Flat-down/2 and 4		(0, 0)	(3.75, 2.75)	(7, 1.75)	(10.75, 2.5)	(14.75, 0)	15	14,75	2,33	0,25	0,38
		(0.5, 0)	(3.75, 1.75)	(7.25, 0.5)	(12.25, 2.25)	(15, 0)	15	14,5	1,50	0,5	0,50
1/2 cycle-up/2 and 4		(0.5, 0)	(4.5, 3)	(7.5, 2.5)	(10.25, 3.25)	(14.5, 0)	15	14	2,92	0,25	0,00

		(0, 0)	(4.5, 3)	(7.5, 2)	(9.75, 2.5)	(14.25, 0)	15	14,25	2,50	0,5	0,38
1/2 cycle-down/2 and 4		(0, 0)	(2.75, 4.75)	(8, 1.75)	(8, 1.75)	(11.5, 0)	15	11,5	2,75	3	2,25
		(0.5, 0)	(4.5, 2)	(4.5, 2)	(7.75, 4.5)	(13.5, 0)	15	13	2,83	2,5	2,50
1 cycle-up2 and 4		(0, 0)	(5, 5.25)	-	-	(11.25, 0)	15	11,25	5,25	0	0,38
		(0, 0)	(3.75, 4.25)	(5.5, 3.75)	(6.75, 4.25)	(12, 0)	15	12	4,08	0	0,50
1 cycle-down2 and 4		(0.5, 0)	(4.25, 2.75)	(7.25, 2.25)	(10, 2.75)	(14.25, 0)	15	13,75	2,58	0	0,13
		(0.25 ,0)	(5.25, 3)	(7, 2.5)	(9.75, 2.75)	(13.5, 0)	15	13,25	2,75	0,25	0,13

3.4. Discussion

Referring back to the focus of the study, to examine the impact of two construction process-related parameters, such as "structure orientation" and "structure actuation sequence", on the chain mail structure's flexible shape-forming and self-supporting capacity, there are two findings that can be observed out of the data presented in Table 6 and Table 7.

Firstly, various shapes of curved formations can be developed reversibly from the same planar structure. This claim is evidenced by the presence of at least two categories of structures (Group 1 for structures with a single curvature and Group 2 for structures with double curvatures) that can be actuated from the same test prototype, even when the structure is put in the same pre-actuated orientation.

Furthermore, there were more variations that were generated within each group of structures parallel with the increasing number of orientation variations applied for each actuation sequence in this study. These variations can be quantified by the different ranges of structure span and rise. For the span, the range of structure span in Group 1 is significantly larger than that of Group 2, with the longest span up to 100% and only approximately 31% greater than the shortest span in the first and second groups of data, respectively. As for the rise, the range is relatively close between the two groups, with the highest rise being around 3,16 and 3,5 times greater than the shortest rise in the first and second groups of data, respectively.

Moreover, an additional sub-finding observable from this exercise that supports the main argument is that the actuation sequence plays a significant role in determining the final shape of the structure. This claim is evidenced by the different readings of evaluation parameter results, for example, in the curved structure's rise and span between structures generated with actuation type 1 and 3, and type 2 and 4, albeit the structures being made of the same test prototype which was also positioned in identical orientations. These findings confirm the importance of considering not only geometrical-related factors

(such as the structure design) but also the construction process-related factor (such as the actuation sequence) in the systematic method of designing chain mail as a programmable structure.

Secondly, aside from the shape-forming capacity, there is another important finding related to the self-supporting ability of the structure. The result of the simulations has shown that the self-supporting formations can be erected effectively by applying local transformation on only a small area of the structure. This is evidenced by, for example, the number of modules impacted for each actuation sequence. The most apparent evidence is illustrated within the first group of structures, where the actuation sequence is only initiated from one end of the strip-like prototype. For each of the simulations within this group, the number of modules that are impacted by the action and thus raised to the curved structure is predominantly more than 50% of the total number of the modules. The smallest number in the actuation range is 47%, with some simulations managed to transform up to 100% modules in the configuration with just a single actuation action.

4. Conclusion and future study

4.1. Conclusion

Concluding, this paper has presented a systematic study examining the impact of two construction process-related parameters, such as structure orientation and structure actuation sequence, on a chain mail structure's flexible shape-forming capacity and self-supporting capacity. In relation to the first dependent variable, the result of the study has shown that by applying only a simple transformation mechanism a single planar chain mail structure can be programmed to create a self-supporting curved structure with a relatively large range of span and height. Furthermore, by modifying the input of the orientation and actuation sequence parameters, the range of the dimensional variation of the structures can be enlarged significantly. Then, regarding the second dependent variable, the study has demonstrated the effectiveness of the designed actuation sequence in constructing the curved structure as a local transformation applied in a single row of modules which can impact an average of 76% of the modules in the configuration. These findings have demonstrated the preliminary potential of chain mail structure to be developed as a new model of programmable modular structure for constructing irregular, curved, free-form structures effectively.

4.2. Future study

Developed as a part of a body of research on the systematic design of programmable chain mail structure, the results from this study have been fed back into the project to aid with the next stage of research development. Some of the topics for the subsequent studies that will be developed out of this research include a study on the integrity of the curved structure when subjected to local transformation post-actuation and also a study on the scaling up of the test prototype to examine the scale invariant-ability of the research subject and method.

References

[1] E. Wood, D. Edge, and A. Williams, "A note on the construction and metallurgy of mail armour exhibited in The Wallace Collection," *Acta Militaria Mediaevalia IX*, pp. 203-229, 2013.

[2] G. A. Bingham, "The generation of 3D data for rapid manufactured textiles," Doctor of Philosophy, Mechanical engineering, Loughborough University, Loughborough, 2007. [Online]. Available: https://repository.lboro.ac.uk/articles/thesis/The_generation_of_3D_data_for_rapid_manufactured_textiles/9519899. [Accessed: 28 January 2023].

[3] J. Engel and C. Liu, "Creation of a metallic micromachined chain mail fabric," (in English), *Journal of Micromechanics and Microengineering*, vol. 17, no. 3, pp. 551-556, 2007, Art no. 018, doi: 10.1088/0960-1317/17/3/018.

[4] Y. Wang, L. Li, D. Hofmann, J. E. Andrade, and C. Daraio, "Structured fabrics with tunable mechanical properties," *Nature*, vol. 596, no. 7871, pp. 238-243, 2021/08/01 2021, doi: 10.1038/s41586-021-03698-7.

[5] V. Ricotta, R. I. Campbell, T. Ingrassia, and V. Nigrelli, "Generative Design for Additively Manufactured Textiles in Orthopaedic Applications," in *Lecture Notes in Mechanical Engineering*, L. Roucoules, M. Paredes, B. Eynard, P. Morer Camo, and C. Rizzi, Eds., 2021: Springer Science and Business Media Deutschland GmbH, pp. 241-248, doi: 10.1007/978-3-030-70566-4_39.

[6] A. R. Ploszajski, R. Jackson, M. Ransley, and M. Miodownik, "4D Printing of Magnetically Functionalized Chainmail for Exoskeletal Biomedical Applications," *MRS Advances*, vol. 4, no. 23, pp. 1361-1366, 2019, doi: 10.1557/adv.2019.154.

[7] M. Ransley, P. Smitham, and M. Miodownik, "Active chainmail fabrics for soft robotic applications," in *Smart Materials and Structures* vol. 26, ed: IOP Publishing, 2017, p. 08LT02.

[8] P. Radziszewski *et al.*, "iRings - Development of a wheel prototype concept for lunar mobility," (in English), *Can Aeronaut Space J*, vol. 57, no. 1, pp. 1-11, 2011, doi: 10.5589/q11-003.

[9] A. Borhani and N. Kalantar, "Material Active Geometry - Constituting Programmable Materials for Responsive Building Skins," presented at the Education and Research in Computer Aided Architectural Design in Europe (eCAADe) Conference, Oulu, 2016.

[10] A. Borhani and N. Kalantar, "The emergence of a new material culture: forging unprecedented alliances between design and engineering," in *18th International Conference on Engineering and Product Design Education (E&PDE)*, Aalborg Univ, Aalborg, DENMARK, Sep 08-09 2016, GLASGOW: Design Soc, in E&Pde, 2016, pp. 417-422. [Online]. Available: <Go to ISI>://WOS:000387927800067. [Online]. Available: <Go to ISI>://WOS:000387927800067

[11] Y. Estrin, V. R. Krishnamurthy, and E. Akleman, "Design of architectured materials based on topological and geometrical interlocking," *Journal of Materials Research and Technology*, vol. 15, pp. 1165-1178, 2021/11/01/ 2021, doi: https://doi.org/10.1016/j.jmrt.2021.08.064.

[12] S. Ahlquist and A. Menges, "Introduction: Computational design thinking," in *Computational Design Thinking*, A. Menges and S. Ahlquist Eds. Chichester, UK: John Wiley & Sons, 2011, ch. 1, pp. 10-29.

[13] X. Xia, C. M. Spadaccini, and J. R. Greer, "Responsive materials architected in space and time," *Nature Reviews Materials*, 2022/06/20 2022, doi: 10.1038/s41578-022-00450-z.

IASS 2023
July 10–14 Melbourne
Integration of Design and Fabrication

Proceedings of the IASS Annual Symposium 2023
Integration of Design and Fabrication
10–14 July 2023, Melbourne, Australia
Y.M. Xie, J. Burry, T.U. Lee and J. Ma (eds.)

Double-curved plate components in configurable systems

Ahmed SOLIMAN[a,b,*], Ellen LEEMANS[a], Lars DE LAET[a], Niels DE TEMMERMAN[a]

[*] Department of Architectural Engineering (ARCH),
Department of Mechanics of Materials and Constructions (MEMC),
Vrije Universiteit Brussel (VUB), 1050 Elsene, Belgium
ahsolima@vub.be

[a] Vrije Universiteit Brussel, Department of Architectural Engineering (ARCH)
[b] Vrije Universiteit Brussel, Department of Mechanics of Materials and Constructions (MEMC)

Abstract

The current climate changes call for sustainable development in many sectors, and the temporary structures sector is on this list. Temporary structures primarily define spaces and regulate the voids between permanent constructions, but they can be designed for disassembly as a way to reuse the same materials in different applications. This could further expand the flexibility of the systems to be rapidly assembled and disassembled, rebuilt in different configurations, and to be easily transported from one place to another. While deployable systems that deal with plate components like folded plates or curved surfaces face many challenges and complexity in articulating viable structural solutions, the paper focuses on designing double-curved plate modular components to fit together within a transformable system. The plates component are to be adjustable into different spacial configurations. The paper presents two main case studies that investigated double-curved plate components in a framework of developing the project ReciPlyDome [1]. The first case study used adjustable plate slits, in which the plate curvature can be controlled through adjustable slit surface connections. The second case study used double-layered bending-active plates, in which the components consist of two connected bending-active plates. In Addition, the paper discusses possible configurations of those two modules in structural sets based on polyhedral geometries or different surface tesselations. The resulting temporary systems can be reconfigured in different shapes and sizes using the same components, and are demountable systems with reversible dry connections. The paper also explores transformable kit-of-parts systems through digital and physical models and undergoes design and structural analysis using visual coding software.

Keywords: transformability, modularity, prefabrication, configurable, plates, temporary structures

1. Introduction

Over the last few years, the effects of climate change on the environment have become increasingly clear to people. There is an urgent need for more to be done to address this issue, leading to action being taken in a variety of fields to move towards a more sustainable future. Despite this, there is still much to be done. In the construction and building sector, there is a focus on creating sustainable strategies for permanent architecture, but less attention is given to the in-between, temporary structures that are found in all outdoor spaces. When walking around European cities, these temporary structures can be seen everywhere, ranging from street markets to festivals and parades. Even though the function of those temporary systems is only short-term, the use of materials and the reuse of the whole systems are permanent.

Copyright © 2023 by Ahmed SOLIMAN, Ellen LEEMANS, Lars De LAET and Niels De TEMMERMAN. Published in the Proceedings of the IASS Annual Symposium 2023 with permission.

Temporary structures are those which are built to serve a specific purpose for a limited amount of time and then be taken apart. Some of these structures are designed to be used only once and their materials are either recycled or discarded. Examples of these could include event stages, exhibition pavilions, and decorative installations. On the other hand, this research approaches temporary structures as systems that are designed for disassembly with reversible connections and can be taken apart, relocated, and reassembled. Demountable structures provide great potential for creating a reconfigurable system that can be modified by rearranging its components.

Architectural engineering from VUB has been striving to create reversible systems. This effort was furthered when the ReciPlyDome [1], created in collaboration with the Royal Danish Academy of Fine Arts (KADK) in Copenhagen, demonstrated the potential of combining active bending double-layered reciprocal beams into a demountable structure. Although the ReciPlyDome has enabled the possibility of creating a demountable structure where every element is self-stabilized and works within the system, further development of the skeleton result is needed in order to provide a cover and a more enclosed space. To that end, two Master's theses were developed to investigate the potential of utilizing double-curved plate components to allow more covering areas in the system. These two research are represented as two case studies in this paper. The first case study simplified the double-layered beam system into single beams within reciprocal perpendicular cross-sections, then coupled the system with double-curved configurable plates for cladding. The second case study investigates plate bending-active elements instead of beams which reveals the potential of constructing a multifunctional system that offers coverage while preserving its structural qualities. "Figure 1" shows the different approaches of the case studies to tackle the cladding feature in the system.

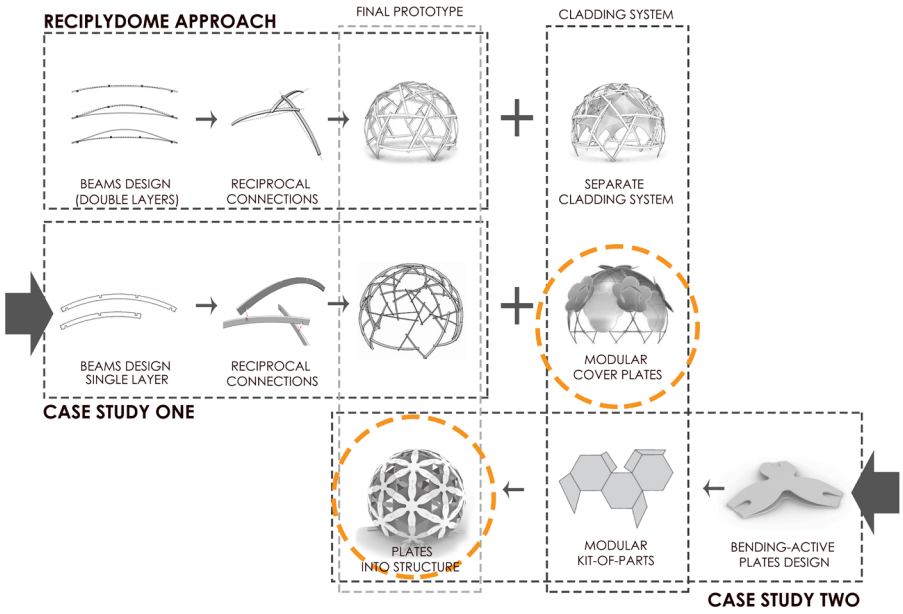


Figure 1. Different approaches of the case studies

2. Case study one

2.1. Design

After studying and reflecting on the ReciPlyDome, this research investigates the cover for a developed version of the dome. By replacing the double-layered beam system with single beams, It merges the knowledge of double-curved plates with the insights acquired during the testing and development of the skeleton system of the new modular beams.

The double-curved plates were simply created through slits designed into a flat plate surface, by creating a slit in the radius of a circular form, two overlapping ends can be used to form a conical shape "Figure 2". This action will cause the radius of the circle to decrease while creating a new double-curved cone with increased height. The same methodology was tested with different shapes and configurations and resulted in a library of shapes that can correlate with the regular polygons on 3D polyhedral geometries.

By selecting the appropriate module types from those variables, a fully enclosed lid for the dome can be made efficiently. During the design of these modules, the attachment to the dome and the joints between the modules were examined. In addition, the ideal materials for these modules were explored since the previously tested wooden modules did not seem to be suitable.

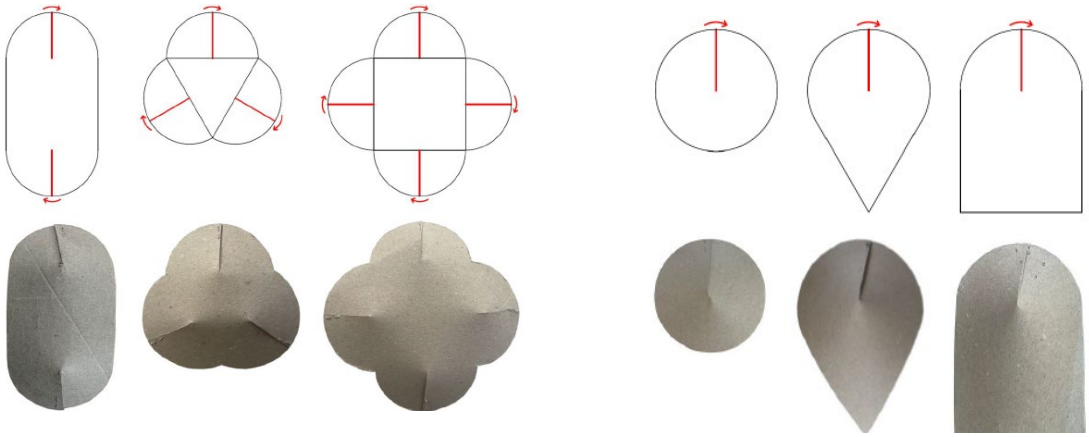


Figure 2. Different alterations of modular double-curved units

In order to create a covering for the ReciPlyDome, the double curved plates are placed on top of the grid of beams in different configurations. The dome consists of multiple equilateral triangles and pentagons which can be used as a central part around which semi-circles are placed to form optimized modules respectively. "Figure 3" shows the cover configuration on a scaled model using two types of double-curved units. The units were used to provide a semi to full covering state for the dome.



Figure 3. Scaled model of the ReciPlyDome after the addition of different levels of coverage.

The modular system allows the creation of two options for covering the dome: the first, which provides shading with a semi-enclosed surface, connects the corners of the central piece and the triangles and pentagons in the dome "Figure 4". The second creates an overlap between the triangle and pentagon surfaces to provide a fully covered option. Alternating the panels can create a more dynamic and open outlook "Figure 5", The cutting pattern can also be optimized in terms of material. By making the cutting boundaries straighter, less material is wasted and an even better cover is achieved.

Additionally, The panels of both the triangular and pentagonal plates have incisions that allow them to overlap and create the desired curvature. The incision is finished with a circular cutout, which not only makes it easier to overlap with thicker materials but also serves as an ideal connection point.

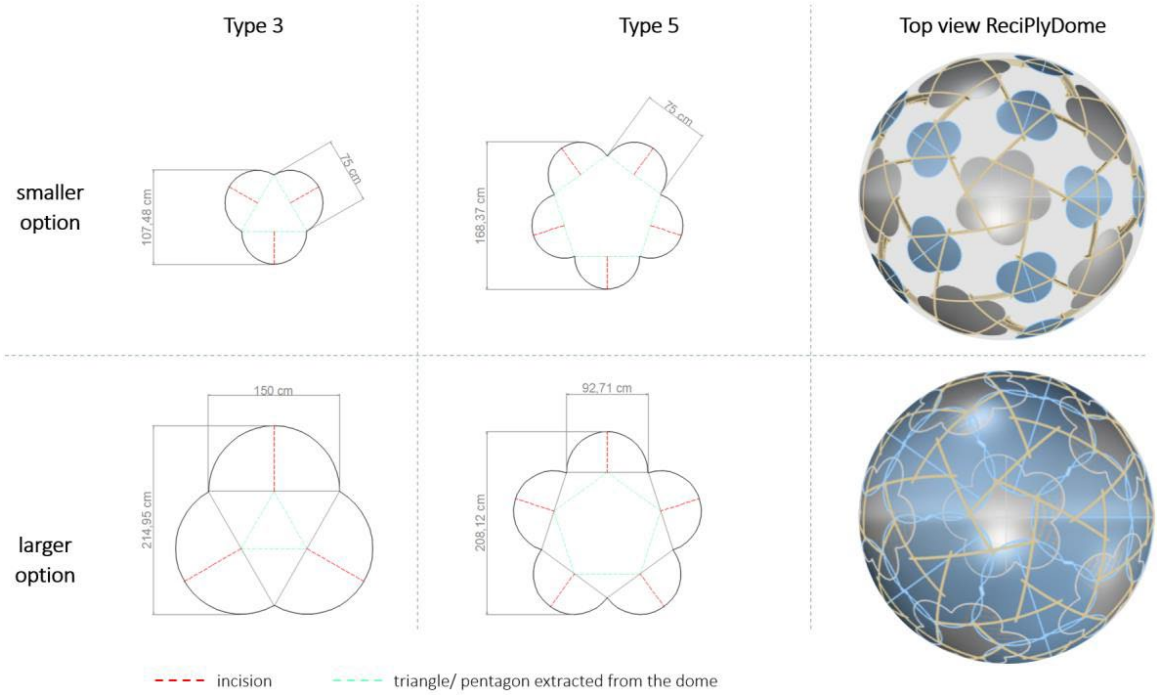


Figure 4. Cover for the ReciPlyDome, obtained by combining different modules and creating variations of the shading percentage within the space.

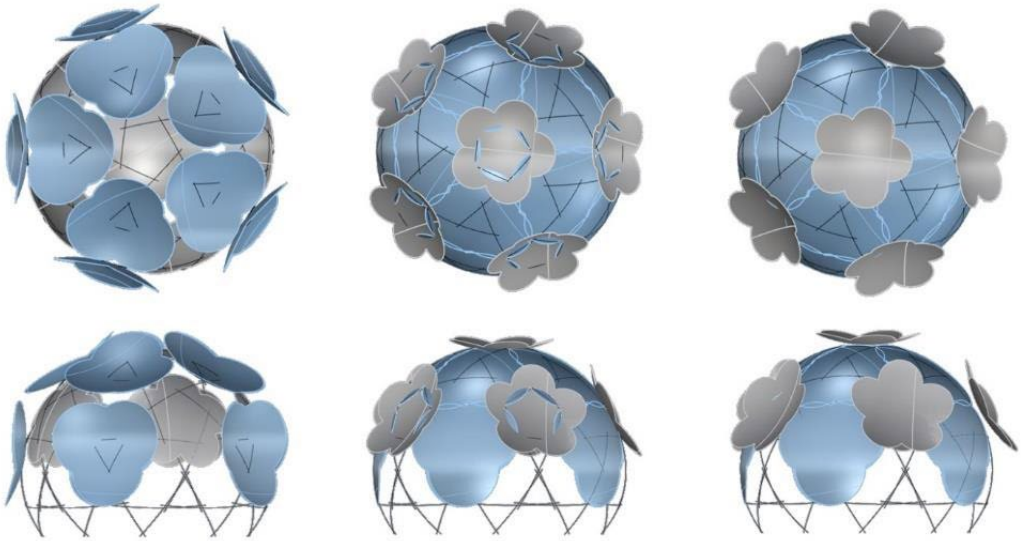


Figure 5. Alternating the panels by flipping part/all of them result in a different shape and shade configurations

2.2. Materiality

In order to choose the best material, some comparative analysis was conducted on the petal-shaped modules, Several materials were tested using physical models to define the future possibilities of scaling up the cover modules. Polypropylene, Polycarbonate, and Aluminium were chosen for their elastic flexibility to strength properties "Figure 6".



Figure 6. Models of one panel of Type 5 in polycarbonate, polypropylene and aluminium on scale 1:4.

Table 1. Summary of the results of the material study on scale 1:4 for the materials polycarbonate, polypropylene and aluminium.

	POLYCARBONATE	**POLYPROPYLENE**	**ALUMINIUM**
TRANSMITTANCE	transparent	translucent	opaque
THICKNESS	1mm	1mm	0.5mm
FLEXIBILITY	Stiff	Flexible	Very stiff
MAINTENANCE	Dirt is easily visible	Low	Can corrode
WEIGHT RATIO	1	1	2

This analysis suggests that either the polypropylene foil or the aluminium module may be the best material for the dome's coverage. The polypropylene foil will provide a peek into the interior when a light is illuminated from within, while the aluminium can create an attractive reflection of the environment. Additionally, a variety of colors can be chosen for the polypropylene to suit the occasion. When considering the outdoor elements, polypropylene is a more flexible material that can withstand heavy wind loads, while the aluminium panel is 1.6 times heavier than the polypropylene panel, meaning that a heavier primary structure may need to be installed to support it. Ultimately, the best material will depend on the desired outcome and environmental conditions.

3. Second Case Study:

3.1. Design

Despite the large amount of research that has been conducted on active-bending structures over the years, the advent of digital tools has opened up new opportunities to explore further the potential of these structures. However, few projects have merged the concepts of bending-active and demountable transformable systems together. This case study examines the potential for combining these two concepts and the flexibility and adaptiveness that such a combination could generate. It intertwin the double-layering of **bending-active plates** within a reconfigurable kit-of-parts system based on polyhedral geometries.

The plates based their shape on regular polygons to allow connectivity within uniform grids. The grid system determines the location of the joints and thus the connection points of the component. As depicted in "Figure 7", the joint connections (blue dots) serve as the basis of the component when applied to a regular n-sided polygon (e.g. triangle, square, pentagon, hexagon, heptagon). The number of supports will be equal to the number of sides of the polygon. In addition, the load distribution of the component plate is defined by the apothem line (from the center of the polygon to the midpoint of sides). Consequently, Using "form conversion" design process [2], the form-finding of the unit is constrained by the different constraints, the position of the support points, the load distribution along the apothem line in addition to the material properties (especially plastic deformation), and local stresses.

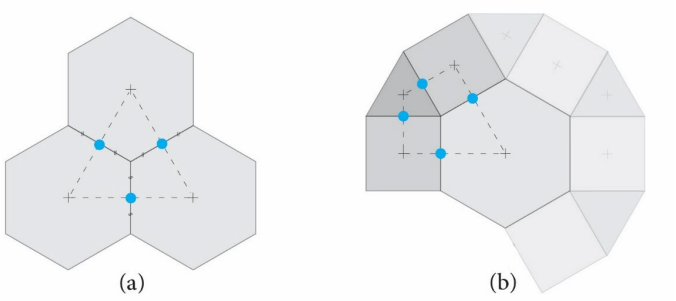


Figure 7. Application of joint positioning method with (a) Similar geometries (b) different sets of geometries in a tessellation.

The plates are then theoretically bent to create a convex multi-curved surface with maintaining the support points intact. A conversation between the form and the material's characteristics, with the boundaries determined by the material's behavior under tension. The surface being bent causes different stresses in material fibers. Removing the stress area of the material from the surface releases the rest of the surface fibers from the encompassing stress, resulting in spaces between the material's strips on the surface, and into the "star" shape with n-Fins.

The same methods were used to build the modular unit of the project based on n-gons. By fixing the location of the supports and the boundaries of the component, the desired shape was specified. After considering the minimum shape requirements and the elastic deformation of the material, the final form of the top layer was determined. Removing the areas of stress between the fins during bending "Figure 8", enabled the fins to bend independently in different directions.

The shape of the various versions of the components was parametrically designed, evaluated, and adjusted in response to the simulated stress. Plywood materials were assumed as the primary calculated properties in this paper. A slight alteration in the material used should lead to a modified shape. Different bases for the components (other regular polygon-based) will result in different variations of the unit.

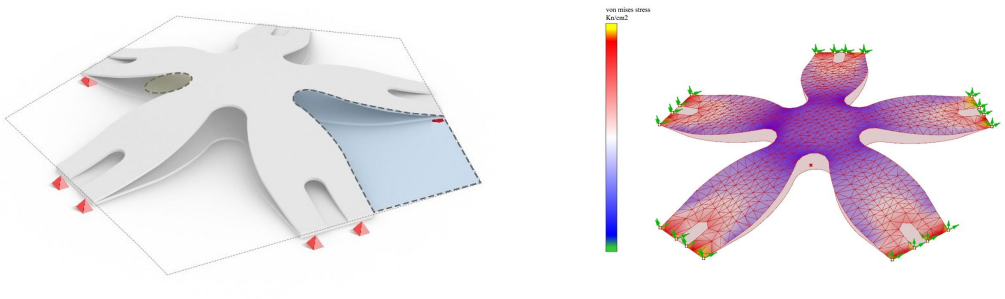


Figure 8. Simulated von mises stress, Pentagon-based component. The areas with dotted boundaries show the Simulated stress, Pentagon-based component.



(a) (b)

Figure 9. ReciPlyDome three main beam component [1] (b) Concept development, Double layering in plates within Regular triangle based component design.

The fundamental principles of the ReciPlyDome served as the basis for the design of the proposed modular unit. This technique is characterized by the use of two layers of components of different lengths that are pre-curved and connected to create self-restraint and structural rigidity. The ICD/ITKE 2010 research pavilion [3] applied a similar technique that utilized two layers of adjoining strips. In addition, Lienhard [3] conducted structural studies concerning the double layering of active-bending components. This research builds upon this concept by applying it to a transformable system. A comparison of ReciPlyDome's "beam" component design and the new "plate" component design can be seen in “Figure 9”. The form was parametrically simulated with Grasshopper scripting to allow for expanded exploration possibilities “Figure 11”. This algorithmic process creates components with adjustable proportions, determined by parameters such as the curvature, width, thickness of the stripe, size of the component, and most importantly, the base shape of the unit.

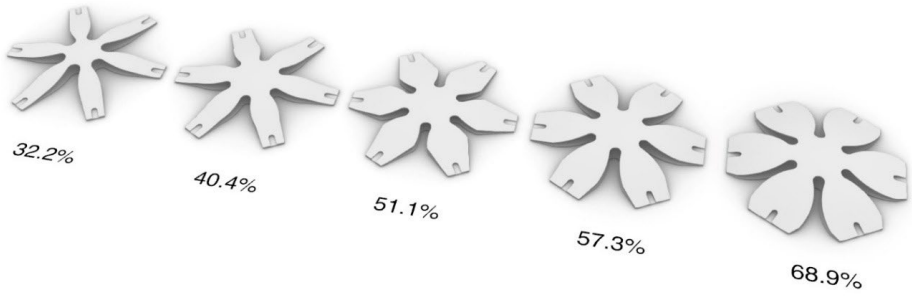


Figure 10. The percentage of solid area to the total area of the base hexagon outline.

In addition, Altering the proportions of the component within its structural limits can create a new ratio between the solid and voided areas. An example of this is illustrated in "Figure 10", which demonstrates the change in the solid area of a hexagon-based component from approximately 70% to 32% of the total area of the hexagon outline. This additional solid area will create a self-shading effect within the space.

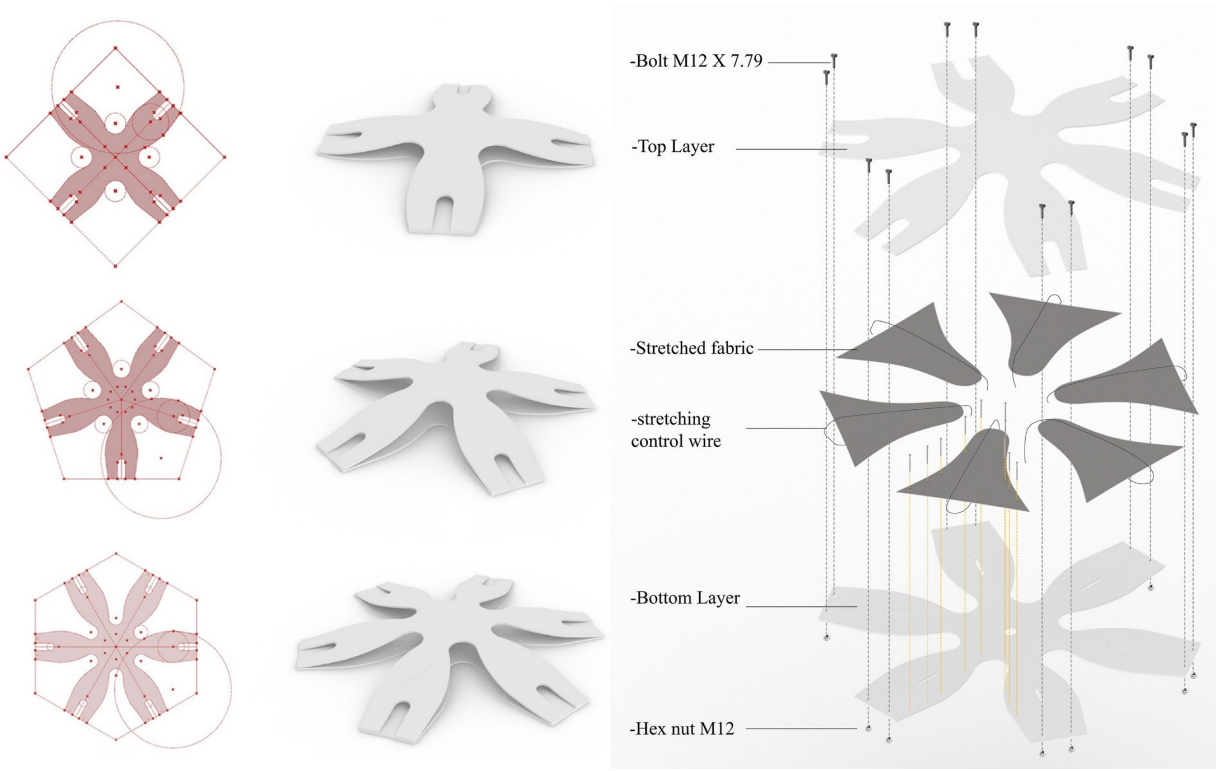


Figure 11. Different variations of the unit based on n-gons geometries, and exploded view of a hexagon-based component with the internal shading system.

The impeded shading system can be customized to accommodate various applications by extending the fabric between fins to cover the voids in the full geometry and attaching it with zippers "Figure 11&Figure 12". This creates a completely sealed system. However, the amount of fabric needed to cover the voids will vary depending on the application, Therefore, the impeded shading system can be effectively used in most applications but will need to be customized and tailored to provide a completely sealed shading system within each case.

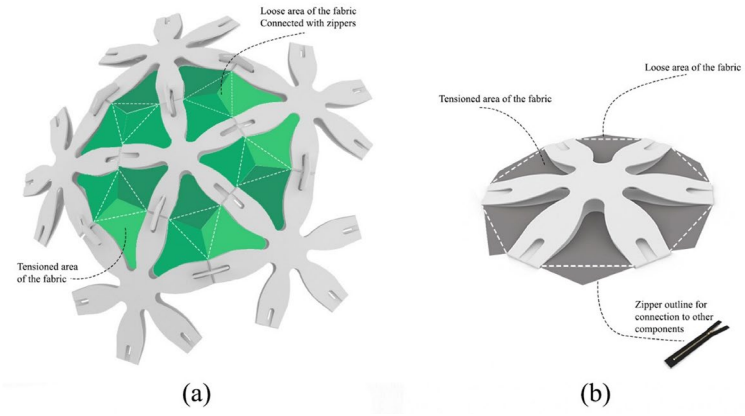


Figure 12. (a) Fully sealed solution for the impeded shading system, (b) Extended shading system of one component.

3.2. Joints:

The design of the joint component is a major challenge as it must be reversible and simple to assemble in order to provide the flexibility needed in a transformable system. Moreover, it is critical in forming the structural integrity of the overall system. In the proposed system, the most important responsibility of the joint is to set the dihedral angles between components in order to achieve the desired shape. For example, the dihedral angle between components in a cube is 90 degrees whereas in an icosahedron it is 138.18 degrees. This difference in shape requires different angles for the joint to create the desired shape. This necessitated the development of two types of joints: the Fixed Joint (FJ) and the Hinged Joint (HJ) in order to facilitate the reconfiguration of the system and maintain its transformability. This paper illustrates the Fixed joint that is used and tested during the fabrication process "Figure 13".

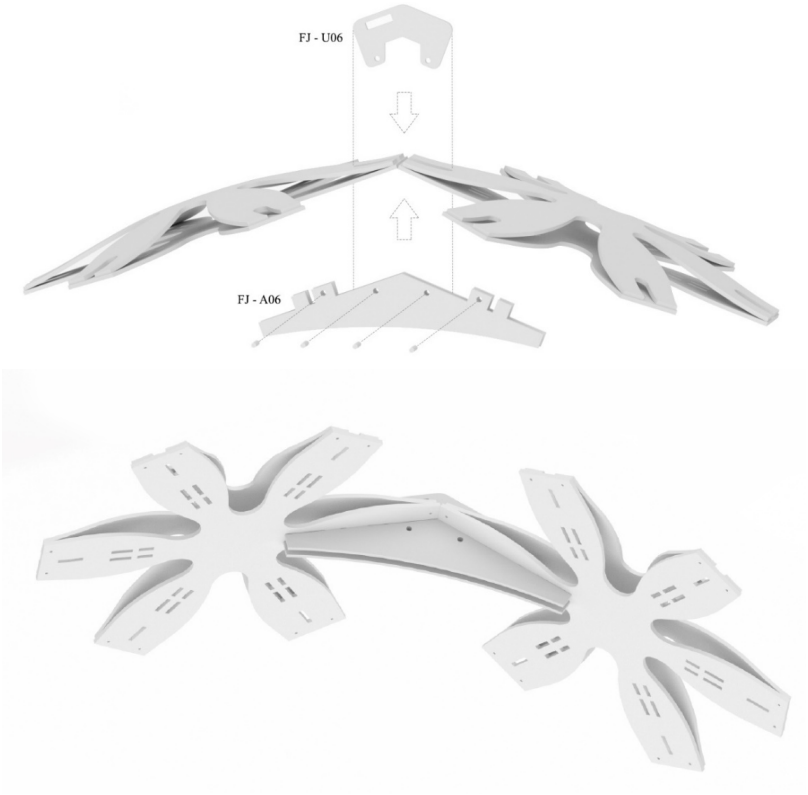


Figure 13 – Fixed joint with two Hexagon-based units

The angular unit of the (FJ) is composed of wooden plates connected with spacers in between to form a lintel. This unit is affixed to the main components with a reversible mortise and tenon connection. The second part of the joint (FJ-U) is then slotted inside the two layers of the lower unit (FJ-A) to provide more stability and a secure angle. Moreover, to reinforce the connection, four "wooden keys" are used to fasten the two components. This technique provides a viable, reversible locking mechanism.

3.3. Polyhedral geometric applications

The research explored the potential for application to various families of geometries. In order to apply the system to different applications, the main idea is to substitute each regular face with a modular component and link all the components with the joints on the right dihedral angle joints. As a result, equilateral shapes such as platonic and Archimedean solids are well-suited to be simple applications for the system due to their symmetrical nature within a complex appearance. "Figure 14" shows an exploration of the possible application based on Archimedean solids.

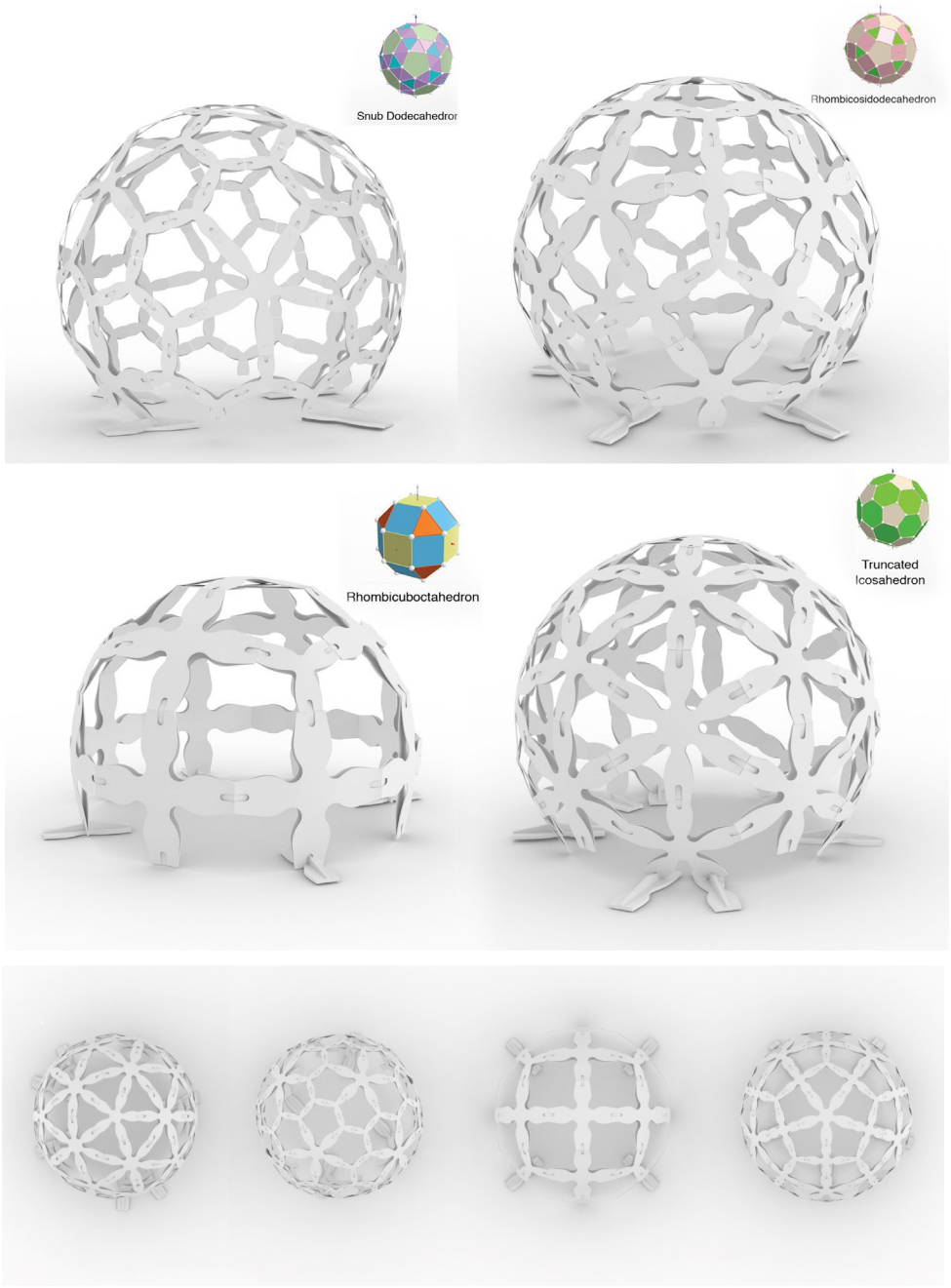


Figure 14 - 3D View of the application of the system on a Rhombicosidodecahedron, Rhombicuboctahedron, Truncated icosahedron and snub dodecahedron base form.

3.4. Truncated icosahedron prototyping

For proof of concept, a Truncated icosahedron-based physical prototype was fabricated for testing. The components were analyzed using different sizes and materials to investigate the response of the materials when subjected to external loads. “Figure 15” shows scaled 4mm MDf modular components of two laser cut layers. The components were put together based on the truncated icosahedron planes to create the full dome “Figure 16”.



Figure 15. MDF physical model, Hexagon-based component

The objective of the design is to enhance structural resilience against external loads through the use of bending-active double layering. To validate this concept, physical tests were conducted on different cases to conceptually (not numerically) test the behavior of materials under loads. “Figure 17” shows the increase of stiffness in comparison to the same load being applied to a flat plate of the same component. Further structural analysis should be done to map the exact structural effect.

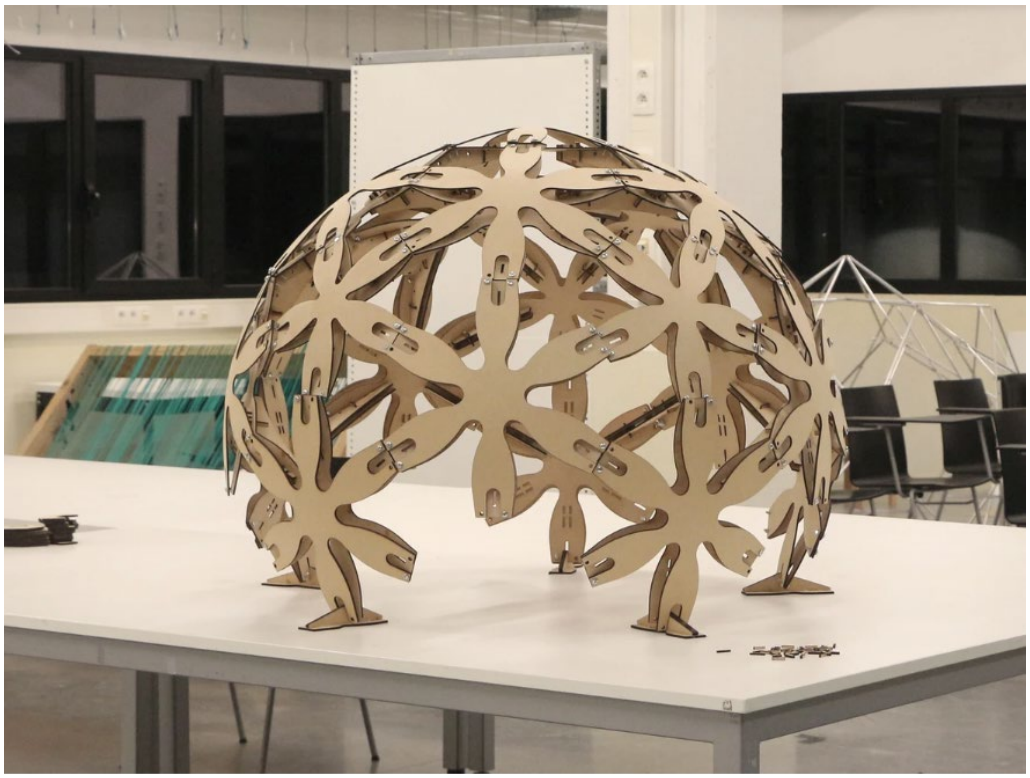


Figure 16. Application to truncated icosahedron base form- scale 1:4.



(a) (b)

Figure 17. (a) One layer of the component under stress, (b) Double-layer components in bending-active state.

4. Conclusion

This paper proposed two alternatives for a rapidly assembled temporary structure based on double curved plates. Both case studies created a systematic methodology that is developed to connect configurable components into different variations. The final structures allowed a responsive use for the user, giving the user the ability to alter the covering ratio and add the shading systems. These kit-of-parts methods encourage the efficient use of the materials for different applications and seasons. However, throughout the research, Two major conclusions were apparent; The complications of the plate-based systems mostly come down to the connection systems. While the double-curved plates generally have a lot of potential and areas for improvement and exploration for new systems. Demountable systems still need to focus on the innovation within the connection systems that can result in structural strength. Additionally, the research focused on analyzing and testing the detailing of a limited amount of possible variations. While those variations showed significant potential. more research could be done into testing and experimenting with different configurations within free-form-based shapes. It is important to point out the crucial impact of the scale size of the samples. Scaling up the samples will be limited by the thickness of the plates and the material properties of the units, potentially restricting the final geometric space of the structure. Further research may be required to gain a deeper understanding of how the units behave on a larger scale.

Visual story: (case study two): https://youtu.be/w2GxYpVNqng

Acknowledgment: The authors would like to express their sincere gratitude to Dr. ir. arch. Stijn Brancart whose valuable work on the ReciPlyDome formed the foundation of this research.

References

1. Brancart, S., et al., *Rapidly Assembled Reciprocal Systems with Bending-active Components: The Reciplydome Project. Journal of the International Association for Shell and Spatial Structures, 2019. 60: p. 65-77.*
2. *La Magna, R., S. Schle*icher, and J. Knippers, *Advances in Architectural Geometry 2015 - Bending-Active Plates: Form and Structure*. 2016.
3. Lienhard, J., *Bending-active structures : form-finding strategies using elastic deformation in static and kinetic systems and the structural potentials therein*. 2014.

Graphical methods

Active bending
Additive manufacturing/ 3D printing
Architectural geometry
Bamboo for sustainable construction and quality of life improvement
Bio-inspired structures and architecture
Bridge structures
Computational form-finding
Conceptual design
Concrete structures
Construction techniques
Deployable and inflatable structures
Design competition (WG21)
Digital modelling and fabrication
Dynamic response of metal spatial structures
Dynamic response of other structures
Form-finding and structural optimisation of interlocking discrete assemblages
► Graphical methods
Gridshell and lattice structures
Historical concrete shells
Historical structures
Lattice structures
Life-cycle design and assessment of structures
Metal gridshell structures, connections and stability
Methods and construction technologies for sustainable shell structures
Morphology and configuration processing
Next generation parametric design
Novel methods in modelling, optimisation and construction for reducing carbon footprint of continuous roof shells
Numerical methods for geometry, form-finding and optimisation of lightweight structures
Optimisation methods and applications
Origami
Other
Teaching design uncertainty: working with unknown qualities/quantities of new and re-claimed materials
Teaching of shell and spatial structures
Tensegrity systems and cable structures
Tension and membrane structures
Tension structures in the Asia-Pacific
Timber and bio-based structures
Topology optimisation
Traditional masonry structures and innovation
Transformable structures

Proceedings of the IASS Annual Symposium 2023
Integration of Design and Fabrication
10–14 July 2023, Melbourne, Australia
Y.M. Xie, J. Burry, T.U. Lee and J. Ma (eds.)

3D auxetic materials designed with algebraic polyhedral graphic statics

Yao LU[a,*], Márton HABLICSEK[b], Abdolhamid AKBARZADEH[c], Masoud AKBARZADEH[a,d]

[a,*] Polyhedral Structures Laboratory, Weitzman School of Design, University of Pennsylvania, Philadelphia, USA Pennovation Center, 3401 Grays Ferry Ave. Philadelphia, PA, 19146
yaolu61@upenn.edu

[b] Department of Mathematics, Leiden University, Leiden, Netherlands
[c] Department of Mechanical Engineering, McGill University, Montreal, Canada
[d] General Robotic, Automation, Sensing and Perception (GRASP) Lab, School of Engineering and Applied Science, University of Pennsylvania, Philadelphia, USA

Abstract

Auxetic materials show unusual reaction behaviors under uni-axial compression or tension forces. For instance, they contract perpendicular to the load direction under an applied compressive force and expand under tension. Their unique behavior has been harnessed in the fields of sensors, medical instruments, sportswear, aerospace devices, etc. As a continuation of the previous research that proposes to use algebraic 2D graphic static for the design of 2D auxetic metamaterials, this paper presents a novel approach to designing 3D auxetic metamaterials using an algebraic formulation of polyhedral reciprocal diagrams (PGS), resulting in concave geometric configurations that are shared by many auxetic materials. The proposed method offers two approaches for generating these concave configurations: modifying a convex polyhedral framework using geometric transformations or constructing a concave polyhedral framework directly using the algebraic formulation of PGS. The validity of the proposed method is demonstrated by testing two models using the finite element method, which clearly shows a negative Poisson's ratio.

Keywords: auxetic materials, negative Poisson's ratio, three-dimensional graphic statics, algebraic graphic statics, reciprocal polyhedral diagrams

1. Introduction

Auxetic metamaterials show unusual reaction behaviors under uni-axial compression or tension forces. They contract perpendicular to the load direction under an applied compressive force and expand under tension. This unique behavior, namely negative Poisson's ratio, has found its way to be applied to various fields such as sensors, medical instruments, sportswear, aerospace devices, etc [1]. Reid et al. [2][3] stated that this behavior heavily depends on internal concave cellular geometries. Existing methods for designing auxetic materials are mostly empirical, meaning that people usually sculpt the configuration based on experiences as well as intuitions.

A previous research project aims to provide a more systematic approach to designing 2D auxetic materials using algebraic 2D graphic statics (A2DGS) [4]. Focusing on the geometric formulation, the algebraic method has shown its ability to create a variety of 2D auxetic patterns. This paper intends to extend this design method to three dimensions through the algebraic formulation of polyhedron-based 3D graphic statics (3DGS), also called polyhedral graphic statics (PGS) [5], hoping to provide a tool and help the science, design, and engineering communities investigate and develop new auxetic metamaterials with ease.

Copyright © 2023 by Yao LU, Márton HABLICSEK, Abdolhamid AKBARZADEH and Masoud AKBARZADEH. Published in the Proceedings of the IASS Annual Symposium 2023 with permission.

1.1. Related work

1.1.1. Current design approaches of auxetic materials

Auxetic behaviors exist in both natural and man-made materials. Within the scope of man-made materials, there are various types of geometrical configurations, including re-entrant models [6–10], rotating polygonal models [11–14], chiral models [15–19], crumpled sheets models [20, 21], perforated sheets models [22–24], random network models [2, 3], etc. Among those different geometrical configurations, some are periodic cellular, and others are irregular and disordered. The discoveries and reports of new auxetic models usually lack a general guideline. Reid et al. [2][3] observed that the concave geometric configuration is a common characteristic of the auxetic metamaterials, upon which a computational algorithm was developed to generate random network-based patterns with negative Poisson's ratio.

1.1.2. Algebraic formulation of graphic statics and its application in auxetic materials

Graphic statics is a geometric form-finding tool based on reciprocal form and force diagrams. Hablicsek and Akbarzadeh [4] found the algebraic formulation of 2DGS convenient in tuning the global configuration of form diagrams based on the geometric degrees of freedom (GDoF), which can be used to create 2D auxetic patterns. The polyhedral nature of PGS makes it a great tool for creating cellular geometries. The algebraic formulation for PGS has also been formulated by Hablicsek et al. [25], Akbarzadeh and Hablicsek [26, 27], and Lu et al. [28] proposed an improved formulation with comprehensive edge length and vertex location controls for the polyhedral reciprocal diagrams, providing a handy tool for generating 3D cellular geometries with concave configurations.

1.2. Problem statement and objectives

As stated above, the previous explorations and discoveries of auxetic metamaterials are case specific. Some explorations have provided a systematic approach in 2D. By extending the approach developed for 2D materials to 3D, this paper aims to propose a new design method that can create more complex and sophisticated geometries with concave configurations that exhibit negative Poisson's ratio. One of the major challenges in this approach is ensuring that the resulting configurations are truly concave without any entangling and self-intersecting, which is addressed by exploiting the power of the enhanced algebraic formulation of PGS.

2. Method

In the context of PGS, a form diagram is usually generated given an input force diagram. There are two existing implementations of PGS, an iterative approach based on nodal operations [29], and an algebraic approach based on the mathematical essence of the form and force reciprocity [25–28]. The iterative approach is limited solution space due to the geometrical restrictions introduced by the iterative algorithm, which makes it difficult to create concave cellular geometries. Focused on the more abstract mathematical relationships, the algebraic method has a greatly extended solution space that enables the flexible exploration of the GDoF, making it easier to generate geometries with concave cells. This section is based on the enhanced algebraic formulation with comprehensive edge length and vertex position control that has been extensively described by Lu et al. [28]. Since only the edge length control is used in this paper, this formulation can be simplified as a system of non-homogeneous constrained linear equilibrium equations written as follows:

$$\mathbf{Mq} = \mathbf{t}. \tag{1}$$

Here **q** is a vector that contains all edge lengths in the form diagram, and the matrix **M** is named the constrained equilibrium matrix, obtained by vertically stacking the equilibrium matrix **A** and the edge constraint matrix **B**:

$$\mathbf{M} = \begin{pmatrix} \mathbf{A} \\ \mathbf{B} \end{pmatrix}. \tag{2}$$

Matrix **A** contains the reciprocal constraints for the form and force diagram, and matrix **B** represents which edges are constrained. The column vector **t** is obtained by vertically stacking the zero vector and the vector **l**, which encodes the target lengths of the constrained edges. Each solution of **q** represents a set of edge lengths of the form diagram that satisfy all equilibrium requirements and constraints, and it can be used to construct the form diagram.

There are two ways that this algebraic formulation can be used to find a form with concave configurations. First, it can start from a convex configuration and modify the strut lengths based on the GDoF to turn certain cells into concave. Alternatively, the concave configuration can be generated directly from a force diagram with concave cells, which is not supported by the iterative approach as the form diagram can become entangled during the solving process and therefore cannot converge.

2.1. Concave configuration turned from convex configuration through GDoF

When a force diagram only contains convex cells, it usually leads to a form diagram with a convex configuration. However, not all form diagrams can be turned into concave without entangling and self-intersecting. For those that can be turned, there is a common characteristic that they all contain a group of edges with common directions. By assigning proper negative edge lengths to those edges, each cell can be turned concave without creating any self-intersection (Figure 1).

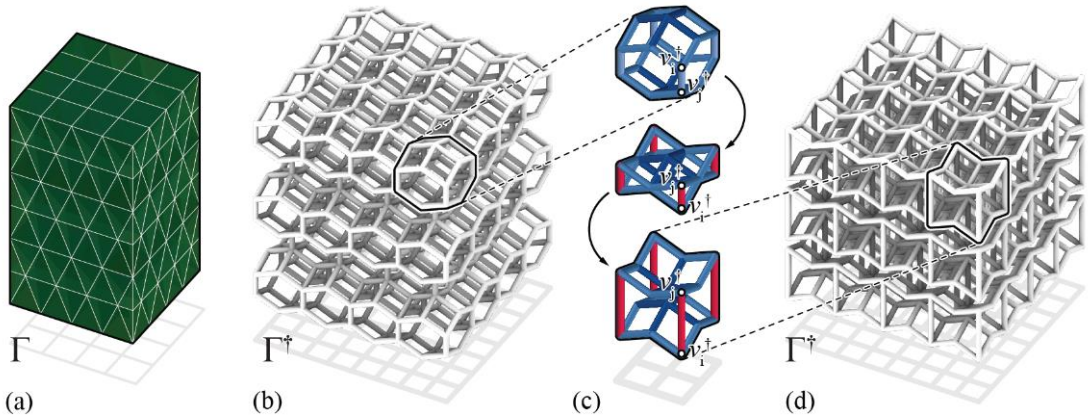


Figure 1. A simple example that shows a geometry with a convex configuration can be turned concave by assigning negative edge lengths to the parallel edges. (a) An input force diagram, (b) a form diagram with a convex configuration, (c) Negative edge lengths are assigned to the edges that share directions, and (d) the modified form with a concave configuration.

2.2. Concave configuration directly generated from negative force cells

Thanks to the flexibility of mathematical abstraction, all solutions that satisfy the reciprocal relationship can be freely accessed without being limited by geometrical restrictions. Therefore, a force diagram with concave cells can be accepted by the algebraic approach without any issue. The resulting form diagram will directly have a concave configuration (Figure 2). In this case, there is no need to go through the edge length modification process as described in Section 2.1.

3. Verification of the auxetic behavior

After having the geometries with concave configuration generated from Section 2, the finite element method (FEM) is used to verify their auxetic behavior. The specimens are modeled with a footprint of 50 mm by 50 mm, and all edges are materialized as 1.2 mm diameter struts using a linear elastic material. The bottom vertices are fixed in *z*-direction, and a total vertical force of 10 kN is distributed to

all top vertices. The simulation results are shown in Figure 3. The deformation clearly shows those two specimens manifest negative Poisson's ration under vertical loads.

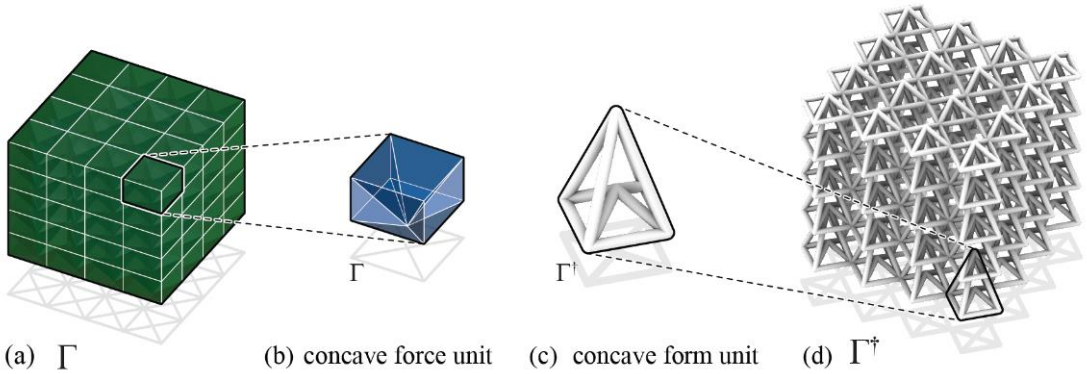


Figure 2. A form geometry with a concave configuration can be generated directly from a force diagram with concave cells. (a) The input force diagram that contains concave cells, (b) a highlighted concave unit of the force diagram, (c) a highlighted concave unit of the form, (d) The form geometry with a concave configuration

The Finite Element Method (FEM) used to simulate the mechanical behavior of materials is computationally intensive and can be time-consuming to set up and run. As an alternative, matrix kinematic analysis can be used to quickly assess the kinematic response to applied loads [30]. This analysis method treats the geometry as a pin-jointed, inextensible framework and ignores its material properties, focusing only on the kinematic behaviors. This lightweight analysis method allows for qualitative and rapid evaluations, making it suitable for fast design iterations and explorations.

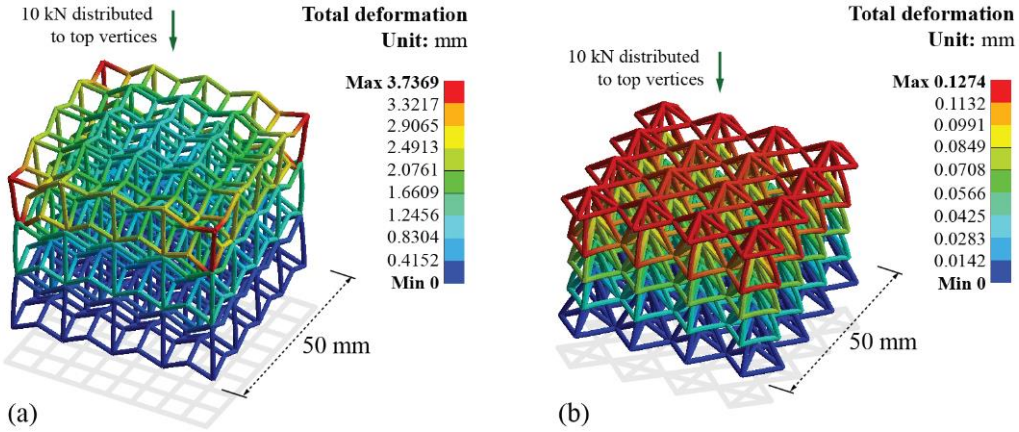


Figure 3. The auxetic behaviors of the two form geometries are verified using FEM. The displacements clearly show negative Poisson's ratios.

4. Conclusion

This paper presents a novel approach to designing 3D auxetic metamaterials using an algebraic formulation of PGS, resulting in concave geometric configurations that are shared by many auxetic materials. The proposed method offers two approaches for generating these concave configurations. The first approach involves starting with a convex polyhedral framework and modifying it using geometric transformations to create a concave configuration. The second approach involves constructing a concave polyhedral framework directly using the algebraic formulation of PGS. Two models are tested using the finite element method, and the results clearly show a negative Poisson's ratio, proving the validity of the proposed method.

By expanding the current design toolset with this novel systematic approach, this research has the potential to drive innovation in various industries. Moreover, this research opens new possibilities for creating materials with unique mechanical properties that can be tailored to specific applications. This has the potential to revolutionize various fields of engineering, from materials science to civil and mechanical engineering, by enabling the development of materials with unprecedented mechanical properties and performance.

Acknowledgments

This research is funded by the National Science Foundation CAREER Award (NSF CAREER-CMMI 1944691) and the National Science Foundation Future Eco Manufacturing Research Grant (NSF FMRG-CMMI 2037097) to Masoud Akbarzadeh.

References

[1] X. Ren, R. Das, P. Tran, T. D. Ngo, and Y. M. Xie, "Auxetic metamaterials and structures: a review," *Smart Materials and Structures*, vol. 27, no. 2, p. 023001, Feb 2018.

[2] D. R. Reid, N. Pashine, J. M. Wozniak, H. M. Jaeger, A. J. Liu, S. R. Nagel, and J. J. de Pablo, "Auxetic metamaterials from disordered networks," *Proceedings of the National Academy of Sciences*, vol. 115, no. 7, p. E1384–E1390, Feb 2018.

[3] D. R Reid, N. Pashine, A. S Bowen, S. R Nagel, and J. J. d. Pablo, "Ideal isotropic auxetic networks from random networks," *Soft Matter*, vol. 15, no. 40, p. 8084–8091, 2019.

[4] M. Hablicsek and M. Akbarzadeh, "Structural form-finding of auxetic materials using graphic statics," in *Proceedings of IASS Symposium and Spatial Structures Conference 2020/21, Inspiring the next generation*, Guildford, UK, August 23-27 2021.

[5] M. Akbarzadeh, "3d graphic statics using reciprocal polyhedral diagrams," Ph.D. dissertation, ETH Zurich, Zurich, Switzerland, 2016.

[6] L. J. Gibson, M. F. Ashby, G. S. Schajer, and C. I. Robertson, "The mechanics of two-dimensional cellular materials," *Proceedings of the Royal Society of London. A. Mathematical and Physical Sciences*, vol. 382, no. 1782, p. 25–42, Jan 1997.

[7] L. J. Gibson and M. F. Ashby, *Cellular Solids: Structure and Properties*, 2nd ed., ser. Cambridge Solid State Science Series. Cambridge: Cambridge University Press, 1997.

[8] S. Hengsbach and A. D. Lantada, "Direct laser writing of auxetic structures: present capabilities and challenges," *Smart Materials and Structures*, vol. 23, no. 8, p. 085033, Jul 2014.

[9] M.-H. Fu, Y. Chen, and L.-L. Hu, "A novel auxetic honeycomb with enhanced in-plane stiffness and buckling strength," *Composite Structures*, vol. 160, p. 574–585, Jan 2017.

[10] Y. Wang, L. Wang, Z.-d. Ma, and T. Wang, "Parametric analysis of a cylindrical negative poisson's ratio structure," *Smart Materials and Structures*, vol. 25, no. 3, p. 035038, Feb 2016.

[11] J. N. Grima and K. E. Evans, "Auxetic behavior from rotating squares," *Journal of Materials Science Letters*, vol. 19, no. 17, p. 1563–1565, Sep 2000.

[12] J. N. Grima and K. E. Evans, "Auxetic behavior from rotating triangles," *Journal of Materials Science*, vol. 41, no. 10, p. 3193–3196, May 2006.

[13] G. J. N, A. Andrew, and E. K. E, "Negative poisson's ratios from rotating rectangles," *CMST*, vol. 10, no. 2, p. 137–145, 2004.

[14] J. N. Grima, P.-S. Farrugia, R. Gatt, and D. Attard, "On the auxetic properties of rotating rhombi and parallelograms: A preliminary investigation," *physica status solidi (b)*, vol. 245, no. 3, p. 521–529, 2008.

[15] R. Lakes, "Deformation mechanisms in negative Poisson's ratio materials: structural aspects," *Journal of Materials Science*, vol. 26, no. 9, p. 2287–2292, May 1991.

[16] D. Prall and R. S. Lakes, "Properties of a chiral honeycomb with a poisson's ratio of — 1," *International Journal of Mechanical Sciences*, vol. 39, no. 3, p. 305–314, Mar 1997.

[17] J. N. Grima, R. Gatt, and P.-S. Farrugia, "On the properties of auxetic meta-tetrarchical structures," *physica status solidi (b)*, vol. 245, no. 3, p. 511–520, 2008.

[18] R. Gatt, D. Attard, P.-S. Farrugia, K. M. Azzopardi, L. Mizzi, J.-P. Brincat, and J. N. Grima, "A realistic generic model for anti-tetrachiral systems," *physica status solidi (b)*, vol. 250, no. 10, p. 2012–2019, 2013.

[19] R. Gatt, J. P. Brincat, K. M. Azzopardi, L. Mizzi, and J. N. Grima, "On the effect of the mode of connection between the node and the ligaments in anti-tetrachiral systems," *Advanced Engineering Materials*, vol. 17, no. 2, p. 189–198, 2015.

[20] K. Alderson, A. Alderson, N. Ravirala, V. Simkins, and P. Davies, "Manufacture and characterisation of thin flat and curved auxetic foam sheets," *physica status solidi (b)*, vol. 249, no. 7, p. 1315–1321, 2012.

[21] Z. Zhang, H. Hu, S. Liu, and B. Xu, "Study of an auxetic structure made of tubes and corrugated sheets," *physica status solidi (b)*, vol. 250, no. 10, p. 1996–2001, 2013.

[22] J. N. Grima and R. Gatt, "Perforated sheets exhibiting negative poisson's ratios," *Advanced Engineering Materials*, vol. 12, no. 6, p. 460–464, 2010.

[23] J. N. Grima, R. Gatt, B. Ellul, and E. Chetcuti, "Auxetic behaviour in non-crystalline materials having star or triangular shaped perforations," *Journal of Non-Crystalline Solids*, vol. 356, no. 37, p. 1980–1987, Aug 2010.

[24] J. N. Grima, L. Mizzi, K. M. Azzopardi, and R. Gatt, "Auxetic perforated mechanical metamaterials with randomly oriented cuts," *Advanced Materials*, vol. 28, no. 2, p. 385–389, 2016.

[25] M. Hablicsek, M. Akbarzadeh, and Y. Guo, "Algebraic 3d graphic statics: Reciprocal constructions," *Computer-Aided Design*, vol. 108, p. 30–41, Mar 2019.

[26] M. Akbarzadeh and M. Hablicsek, "Geometric degrees of freedom and non-conventional spatial structural forms," in *Impact: Design With All Senses*, C. Gengnagel, O. Baverel, J. Burry, M. Ramsgaard Thomsen, and S. Weinzierl, Eds. Cham: Springer International Publishing, 2020, p. 3–17.

[27] M. Akbarzadeh and M. Hablicsek, "Algebraic 3d graphic statics: Constrained areas," *Computer-Aided Design*, vol. 141, p. 103068, Dec 2021.

[28] Y. Lu, M. Hablicsek, and M. Akbarzadeh, "Algebraic 3d graphic statics with edge and vertex constraints: A comprehensive approach to extending the solution space for polyhedral form-finding," *Computer-Aided Design*, In peer-review.

[29] A. Nejur and M. Akbarzadeh, "Polyframe, efficient computation for 3d graphic statics," *Computer-Aided Design*, vol. 134, p. 103003, May 2021.

[30] Y. Lu, H. Chai, and M. Akbarzadeh, "Towards a novel form-finding method using matrix analysis: exploiting nodal displacements of pin-jointed frameworks," in *Proceedings of the International Association for Shell and Spatial Structures (IASS) Symposium 2023*, T. L. J. M. Y.M. Xie, J. Burry, Ed., Melbourne, Australia, July Submitted to IASS 2023.

IASS 2023
July 10–14 Melbourne
Integration of Design and Fabrication

Proceedings of the IASS Annual Symposium 2023
Integration of Design and Fabrication
10–14 July 2023, Melbourne, Australia
Y.M. Xie, J. Burry, T.U. Lee and J. Ma (eds.)

The extended affine method for form finding of a spoke wheel system in light of graphic statics: part 2

Hiroki TAMAI[a,*]

[a,*] Nikken Sekkei
Chiyoda-ku Tokyo
tamai.hiroki@nikken.jp

Abstract

This paper provides an alternative proof for the proposition that the ring shapes of a spoke wheel system, having equal and uniform magnitude of forces in the compression and tension rings and equal forces in the radial cables, as well as minimizing the sum of the squared segment lengths, approach to a cycloid if the number of divisions increases infinitely. The proof is rendered in the dual space expressed by the Airy stress force polyhedra. The optimality condition about the minimum sum in terms of x and y coordinates in the form diagram can be translated in terms of only z* coordinates of the force polyhedra, and the recursive expression represents a polyline inscribing to the trajectory of a rotating regular n-polygon.

Keywords: graphic statics, spoke wheel structure, graphic form finding, dual Airy stress polyhedra, optimization, cycloid

1. Introduction

The form finding of a spoke wheel roof structure is a highly nonlinear problem as it requires simultaneously determining the geometry of tension ring and radial cables, flying struts, and compression ring as well as ensuring prestressed self-equilibrium such that there are only axial forces. While such difficulty lies in the general form of the problem, the affine method was developed for non-computational approaches and has been applied by Schlaich Bergermann und Partner since their early spoke wheel roof structures [1]. However, the original affine concept was, in fact, developed only on concentric arcs, patched smoothly, such as a three-centered arc (aka korbborgen). Therefore, applications were limited to symmetric circular or elliptic shapes.

The author extended the concept of the affine spoke wheel roof system for converting more arbitrary closed convex curves to self-stressed equilibrium geometry. Two graphical constructions were demonstrated to apply this concept. In the first construction method, by laying out identical isosceles, as many as the axis number, adjacent to each other along the legs, the geometry of radial cables is defined by the legs. Then by cutting them out with two polygons, all segments of which are set parallel to the bases of the isosceles, tension and compression rings are defined. (Figure 1 top). In the alternative construction method, an arbitrary closed convex curve can be directly converted to a segmented compression ring by translating the edges of a regular polygon to the points of tangency on the given curve. Then the tension ring is generated by offsetting the compression ring inward by an equal distance. The radial cables are defined by connecting the corresponding vertices of the polygonal rings. (Figure 1 bottom).

In both constructions, the polygons for the compression and tension rings are convex and the inner angles all become equal, but the side lengths may not be equal. The distances between the compression

Copyright © 2023 by Hiroki TAMAI. Published in the Proceedings of the IASS Annual Symposium 2023 with permission.

and tension polygons are set to be all equal. Note, however, that the two polygons are not similar to each other in general. Thus, the tension and compression rings cannot be scaled to one another.

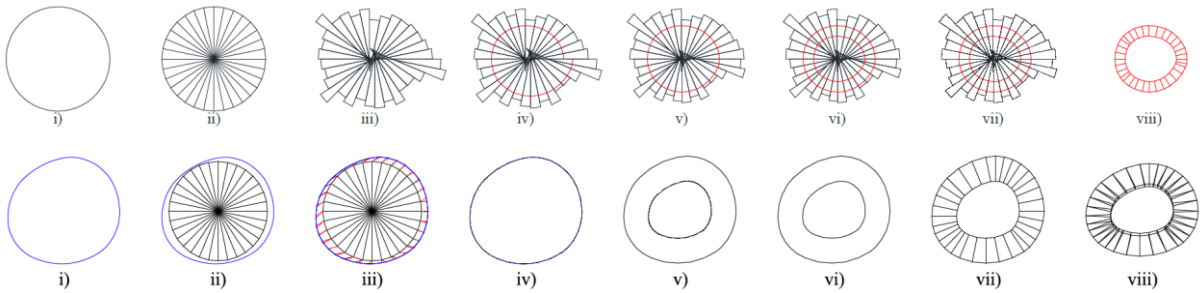


Figure 1. Graphical form finding of a spoke wheel roof system with an arbitrary shape [3]

The structural advantages of the spoke wheel structure generated by the extended affine concept are that the magnitude of the forces in the compression and tension rings can be made equal and uniform all around, and the forces in the radial cables are all equal [3]. Of course, this also means that the level of material utilization is well balanced over the structure, and more notably that the differential cable forces over clamping nodes are all zero in theory for the prestressed self-equilibrium state. Consequently, they are nearly zero under the dead load condition, so the size of the clamps can be made smaller than otherwise.

The author demonstrated determinate and indeterminate applications of the extended affine concept for non-circular shape constraints [3]. These include how to control the total length of the compression ring by minimizing the sum of the squared segmented lengths, as well as how to control the uniformity of the polygonal curve of the ring by minimizing the variance of the segmented lengths. The in-depth study revealed the unexpected relationship between the two sets of geometry; Any polygonal ring with the minimum variance of the segment lengths can be generated as an involute of the polygonal ring with the minimum sum of squared segment lengths with the same number of divisions (Figure 2). In other words, the polygonal ring with the minimum sum of squared segment lengths is the evolute of the other. The study also found that the limit curve of the evolute polygonal curve was a cycloid (Figure 3). Mathematical explanations on these propositions were given later by the author [4].

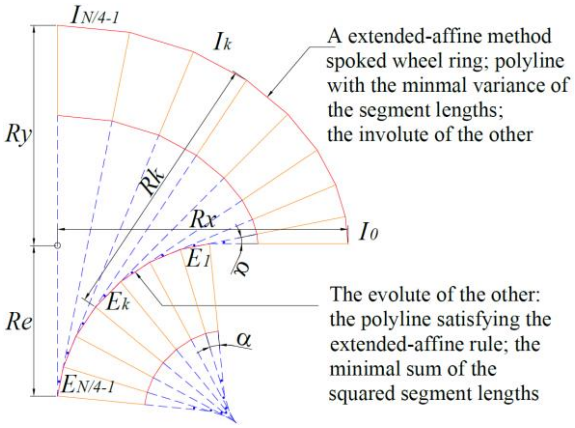


Figure 2. Involute and evolute polylines

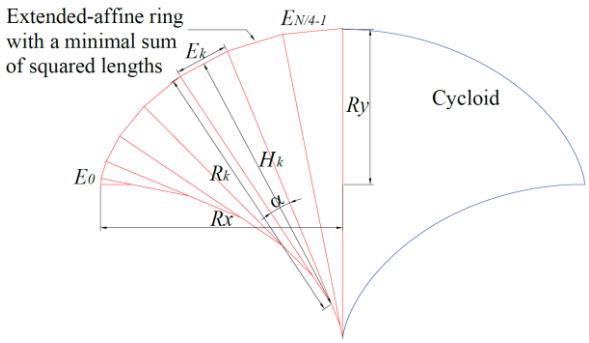
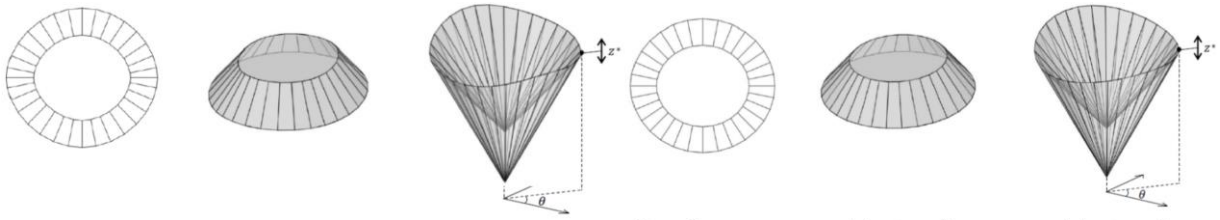


Figure 3. Extended-affine ring and cycloid

The previous paper re-examined the above-mentioned geometric findings in light of graphic statics [5]. The starting point of the study was the fact that the force diagram is unique, though scalable, for all spoke wheel geometry that can be generated by the extended affine concept within the same topology.

The dual discrete Airy stress polyhedra, defined by Cremona's mapping rule [6], of the two special groups of spoke wheel systems, one with the minimum sum of the squared lengths and the other with the minimum variance of the lengths, were investigated in order to find relevant connections between them as found in the forms. The z* coordinates of them are of great interest since only this distinguishes the forms from each other. The limit shapes of the two discrete Airy stress polyhedra were derived based on the knowledge that the limit polygonal curve of the evolute is a cycloid, and found in quite simple expressions of trigonometry.



a) minimum sum of squared ring segments (evolute) b) minimum variance of ring segments (involute)

Figure 4. Form diagram, Airy stress form polyhedron and Airy stress force polyhedron

However, despite the remarkable relation in the forms of evolute and involute found in their form diagrams, the equivalent relation has not been thoroughly revealed and therefore not visualized in the dual force polyhedra. The trigonometric function defining the parts of the Airy stress force polyhedron neither reversely led to any alternative derivation of a cycloid yet nor revealed the connection to the optimality conditions of the form diagrams.

As a part of reflection on the questions above, this paper attempts to provide an alternative proof for the proposition that the limit curve of extended affine spoke wheel ring geometry with the minimum sum of squared segment lengths approaches a cycloid.

2. Notes on terms

This section adds a few notes on the specific terms used in this paper since they may sometimes lack mathematical correctness for the sake of readability.

spoke wheel system (or structure): Although the study concerns roof structures with a spoke wheel system that usually has two layers of radial cables stretched by flying struts, in this paper the word *spoke wheel system* is in most cases used to refer to the 2-dimensional projection of the system or simply a planer spoke wheel structure. The validity of the following discussion is not affected as far as it concerns the in-plane self-equilibrium state by prestressing.

Affine method, affine concept or affine spoke wheel: The word affine is not used with the exact mathematical definition in this paper. Rather it only refers to the method reported by Bergermann [1]. In his paper, the term was used to describe the non-computational form finding method of spoke wheel systems by setting equal angles for the inner tension and outer compression rings in relation to each radial cable in the form of a circular and a three-centered-arc also known as korbbogen.

Involute polyline (polygonal curve, or polygon): An involute polyline is defined as a polygonal curve inscribed in the involute curve of a polyline (evolute) at the points where the rotational radius of the involute changes corresponding to passing the vertices of the polyline (evolute).

Evolute polyline (polygonal curve, or polygon): An evolute polyline appears as a special case of evolute where the centers of the curvature of the involute jumps, corresponding to the step change of the rotational radius. The polyline connecting the discrete locus is referred to as an *evolute polyline* in general, or an *evolute polygon* if it is closed.

3. Proposition

From the two propositions on equilibrium geometry of spoke wheel structures, addressed by the author [4], the one relevant to this paper is rewritten as below.

Proposition on the limit curve of ring geometry of extended affine spoke wheel system with minimum squared lengths:

Let a polyline be a part of the ring geometry of a spoke wheel system determined by the extended affine rules. Suppose it is symmetric and the set of segments is selected to minimize the sum of the squared segment lengths, then a series of polylines can be defined in terms of the number of segments. The limit curve of the series with an infinitely large number of segments is a cycloid. (Figure 3)

4. Proof by dual polyhedra

The dual force polyhedron is used for an alternative proof for the proposition that the limit curve of extended affine spoke wheel ring geometry with a minimum sum of squared segment lengths approaches a cycloid. The outline of the proof is as follows;

1. Express the optimality condition for the minimum sum of squared lengths in terms of z* coordinates of the force polyhedra.

2. Identify the geometry that satisfies the condition.

3. Unroll the geometry to the rotating regular polygon along a line

4. Increase the edge number of the polygon infinitely, and let a circle represent the limit geometry of the n-polygon.

4.1. Calculation of the ring form diagram in dual problem using Airy stress force polyhedron

The difficulty to obtain the form diagram (x, y) lies in the fact that it is defined implicitly by the optimal condition of the minimum sum squared length in the form of a Lagrangian function that includes the geometric boundary condition as follows.

$$L_{\substack{(x_k, y_k, \lambda_i) \\ k=1\ldots n/2, i=1\ldots 4,}} = \sum_{k=1}^{n/2}\{(x_k - x_{k-1})^2 + (y_k - y_{k-1})^2\} + \lambda_1(x_0 - 1) + \lambda_2(y_0 - 0) + \lambda_3\big(x_k - (-1)\big) + \lambda_4(y_k - 0) \quad (1)$$

Eq.(1) does not include any of the constraints between nodes imposed by the extended affine rules. It should be noted that the variables of the equation use nodal coordinates rather than the lengths unlike the equations presented in the author's other paper, which is integrated by the extended affine rule's constraints [4].

Let us think of solving this minimization problem in Cremona's dual space (x^*, y^*, z^*) rather than the primal space of (x, y, z) because we know about the force diagram better than the form diagram. That is, at this point we do not know x_k and y_k but we do know x^*_k and y^*_k due to the common nature of the extended affine spoke wheel system that the two-dimensional force diagram is always a regular n-polygon.

In Cremona's dual Airy stress polyhedra for the force diagram, the adjacent two vertices (x^*_k, y^*_k, z^*_k) and (x^*_{k+1}, y^*_{k+1}, z^*_{k+1}) and the corresponding apex (x^*_O, y^*_O, z^*_O) of the polyhedra are on the same plane defined by $z^* = y_k\, x^* - x_k\, y^* + z_k$; in other words, the plane's normal vector is (y_k, $-x_k$, -1) and the z*-intercept is z_k.

$$\begin{Bmatrix} x^*_O & y^*_O & 1 \\ x^*_k & y^*_k & 1 \\ x^*_{k+1} & y^*_{k+1} & 1 \end{Bmatrix} \begin{pmatrix} y_k \\ -x_k \\ z_k \end{pmatrix} = \begin{pmatrix} z^*_O \\ z^*_k \\ z^*_{k+1} \end{pmatrix} \quad (2)$$

where (x^*_O, y^*_O, z^*_O) is selected as the origin (0, 0, 0). Now recall that the force diagram is a regular n-polygon and it is rotated clockwise by 90 degrees plus π/n by Cremona's mapping rule. The radius of the vertices can be assumed to be unity without losing the generality. Thus, the force diagram is expressed as below.

$$\begin{aligned}(x^*_k, y^*_k) &= \left(cos\left(\frac{2\pi}{n}k - \frac{\pi}{2} - \frac{\pi}{n}\right), sin\left(\frac{2\pi}{n}k - \frac{\pi}{2} - \frac{\pi}{n}\right)\right) \\ &= \left(sin\frac{(2k-1)\pi}{n}, -cos\frac{(2k-1)\pi}{n}\right)\end{aligned} \tag{3}$$

Plug Eq. 3 into Eq. 2 and solve for x_k and y_k. Then x_k and y_k for k = 1 to n/2 can be expressed only with z^*_k as independent variables as below.

$$\begin{aligned}x_k &= \csc\left(\frac{2\pi}{n}\right)\left(\ sin\left(\frac{(1+2k)\pi}{n}\right)z^*_k + sin\left(\frac{(1-2k)\pi}{n}\right)z^*_{k+1}\right) \\ y_k &= \csc\left(\frac{2\pi}{n}\right)\left(-cos\left(\frac{(1+2k)\pi}{n}\right)z^*_k + cos\left(\frac{(1-2k)\pi}{n}\right)z^*_{k+1}\right)\end{aligned} \tag{4}$$

Substituting Eq.(4) to Eq.(1), the Lagrangian is rewritten in terms of z^*_k instead of (x_k, y_k) as Eq. (5). It is interesting to see how the expression of the squared lengths is simplified by z^*_k.

$$\begin{aligned}L_{k=1\ldots n/2, i=1\ldots 4,}(z^*_k, \lambda_i) &= \csc\left(\frac{2\pi}{n}\right)^2 \sum_{k=1}^{n/2}\left(z^*_{k-1} - 2cos\left(\frac{2\pi}{n}\right)z^*_k + z^*_{k+1}\right)^2 \\ &+ \frac{1}{2}\lambda_1\left(-2 + \sec\left(\frac{\pi}{n}\right)(z^*_0 + z^*_1)\right) + \frac{1}{2}\lambda_2\left(2 - \sec\left(\frac{\pi}{n}\right)\left(z^*_{n/2} + z^*_{n/2+1}\right)\right) \\ &+ \frac{1}{2}\lambda_3\csc\left(\frac{\pi}{n}\right)(-z^*_0 + z^*_1) + \frac{1}{2}\lambda_4\csc\left(\frac{\pi}{n}\right)\left(z^*_{n/2} - z^*_{n/2+1}\right)\end{aligned} \tag{5}$$

Now the minimization problem is defined as

$$arg\min_{z^*_k, \lambda_i \in R} L_{k=1\ldots n/2, i=1\ldots 4}(z^*_k, \lambda_i) \tag{6}$$

by the Lagrangian of the objective function and the boundary conditions. The necessary conditions for optimality are

$$\frac{\partial L(z^*_k, \lambda_i)}{\partial z^*_j} = 0 \quad \text{for } j = 0\ldots\frac{n}{2} + 1 \tag{7}$$

$$\frac{\partial L(z^*_k, \lambda_i)}{\partial \lambda_j} = 0 \quad \text{for } j = 1\ldots 4. \tag{8}$$

Note that the total number of variables is n/2+5 since the indexed variables are from z^*_0 to $z^*_{n/2+1}$, and there are four Lagrange multipliers. The four variables, z^*_0, z^*_1, $z^*_{n/2}$ and $z^*_{n/2+1}$, can be solvable from the four equations in Eq (8), while other variables including λ_i for i = 1~4 are dependent sequentially.

Among them, let us take a general part that does not include λ_i, which is expressed as below.

$$\frac{\partial L(z^*_k, \lambda_i)}{\partial z^*_j} = 2\left(l_{j-1} - 2cos\left(\frac{2\pi}{n}\right)l_j + l_{j+1}\right) = 0 \quad \text{for } j = 2\ldots\frac{n}{2} - 1, \tag{9}$$

where l_k is defined, referring to Eq. (5), as

$$l_k = z^*_{k-1} - 2cos\left(\frac{2\pi}{n}\right)z^*_k + z^*_{k+1} \tag{10}$$

and it is the length of the k-th segment in the form diagram scaled by $\sin\left(\frac{2\pi}{n}\right)^2$. It is interesting to see that the optimal condition in terms of the segment lengths in the form diagram and the segment length in terms of z* have the same expression.

The optimality conditions can be rewritten in a recurrence sequence as

$$l_{j+1} = 2cos\left(\frac{2\pi}{n}\right) l_j - l_{j-1} \quad \text{for } j = 2\ldots\frac{n}{2} - 1, \tag{11}$$

or by De Moivre's formula,

$$l_k = sin\left(\frac{2\pi}{n}k + \frac{\pi}{n}\right)\frac{l_0}{sin\frac{\pi}{n}} \quad \text{for } k = 0\ldots\frac{n}{2} - 1. \tag{12}$$

These two expressions identify the geometry in different manners.

4.2. The geometry satisfying the optimality condition

Lemma: Suppose the two identical regular polygons with m (=n/2 for the sake of convenience) vertexes connected to each other at the corresponding vertexes, translate one of them by the edge length parallel to a major diagonal passing the centroid, and rotate by 2 π /m radian. Then the lengths of the skewed edges connecting the vertexes satisfy the condition described by Eq.(11) or Eq.(12). See edges in Figure 5, lengths of which are denoted by l_0, l_1 (*or* l_{k-1}), l_k, l_{k+1}, and so on.

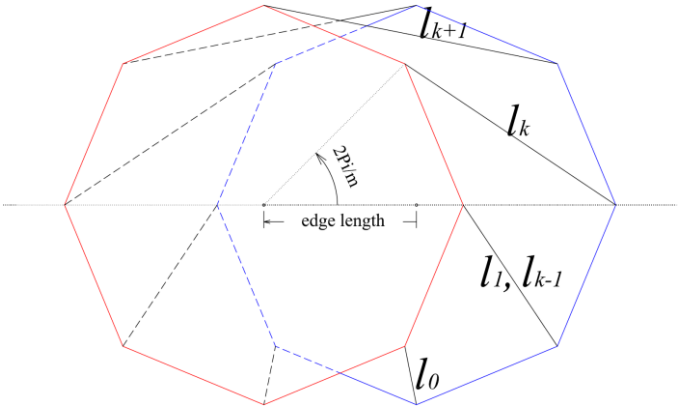


Figure 5. Series of segments satisfying the optimality condition

4.2.1. Proof for Eq.(11)

Point A in a) and point A' in b) of Figure 6 are both defined by the above-mentioned translated polygons in green and blue, relative to the ones in red, and the parallelograms sharing the edges with the polygons. Although they are determined differently, it is evident that they are in the same position within the base (red) polygon. Find the identical parallelograms in a) and b), two edges of which are shared with red polygons. Since points A and A' are found to be identical, the edges AV and A'V' are both equal to l_k from the other parallelograms composed with AV or A'V'. In c) of Figure 6, a) and b) are laid over with the common red polygon. The isosceles A (=A')VV' with the base angle a equal to 2 π /n (= π /m) self-evidently illustrates the recurrence relation in Eq.(11).

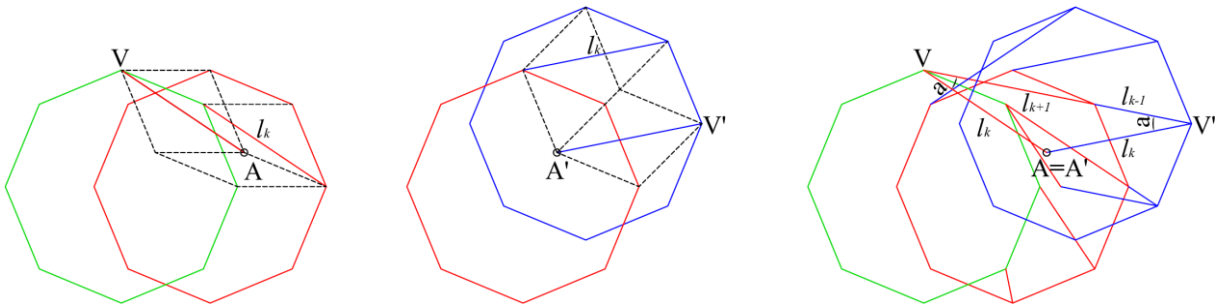


Figure 6. Series of segment lengths expressed by the recursive relation of adjacent segments

4.2.1. Proof for Eq.(12)

By using the angle $a_0 = 2\pi/n$ (for an octagon, $a_0 = 2\pi/(2m) = \pi/8$) and $a_k = 2\pi/n + 2\pi k/m$ in Figure 7, Eq.(12) can be rewritten as

$$l_k = \sin\left(\frac{a_k}{2}\right)\frac{l_0}{\sin\frac{a_0}{2}} = 2l_e\sin\left(\frac{a_k}{2}\right) \quad \text{for } k = 0\ldots\frac{n}{2}-1 \tag{13}$$

where l_e denotes the edge length of the regular polygon. Figure 7 evidently illustrates that Eq.(13), thus Eq.(12) is met.

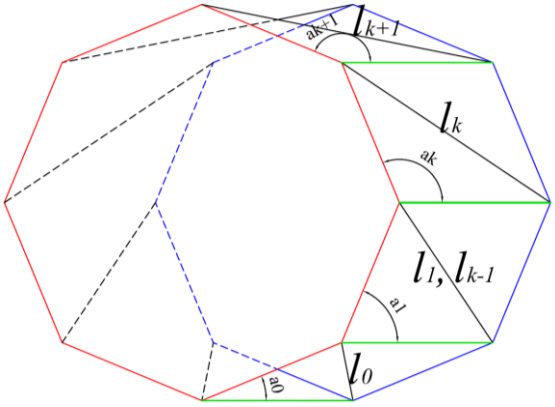


Figure 7. Series of segment length expressed by an arithmetic sequence of angles

4.3. Unroll the geometry to the rotating regular polygon along a line

Now unroll the m-sided polygon along a line, such that m+1 identical m-sided polygons are positioned with equal spacing, that is equal to the edge length, and connect vertexes in the same manner as constructed in Figure 5, but between the adjacent polygons in one stroke. As shown in Figure 8, this results in an extended affine polyline inscribing the trajectory of a vertex of the rotating regular polygon with m (=n/2) sides. (These results can be confirmed by numerical calculations from various approaches.)

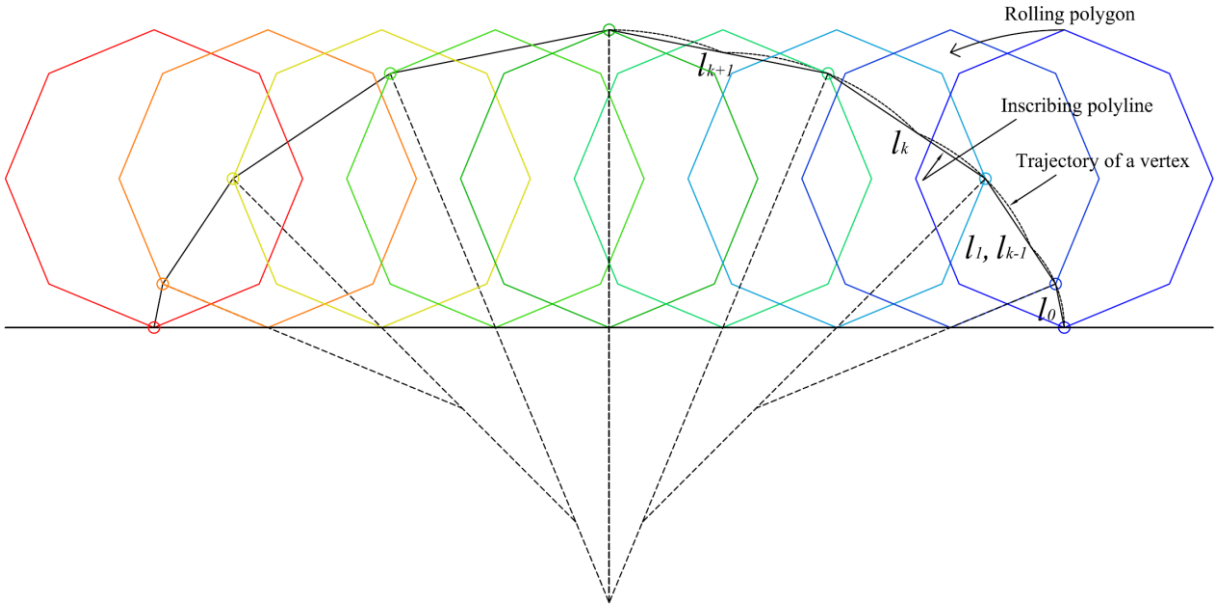


Figure 8. Extended affine spoke wheel ring with minimum squared lengths shown as polyline inscribing the trajectory of a rotating regular polygon

4.4. The limit curve

Noticing that a circle is the limit curve of regular polygons with the side numbers infinitely increased, the trajectory and the inscribing polyline, which minimizes the sum of squared lengths, should approach a cycloid. This completes the proof.

5. Concluding remarks

An alternative proof based on dual polyhedra is provided to the proposition that the limit curve of extended affine spoke wheel ring geometry with a minimum sum of squared segment lengths approaches a cycloid. The proof neither requires any sophisticated trigonometric identities, nor solution of linear algebra including the boundary conditions. Therefore, it is more directly associated with the optimality condition and yields a more illustrative understanding. Since the proof provided in this paper retains the representation of the length in the form diagram, it is also possible that the proof steps 4.3 and 4.4 can be integrated with the other formulation with lengths as unknown variables [4].

Applying the dual polyhedron shows advantages in reducing the number of variables while satisfying the geometric constraints by the extended affine rules implicitly but very easily. However, the meanings of z* coordinates are neither clarified nor play a significant role in the proof steps. The geometric lengths of the segments remain relevant although the dual space used in the proof is a force polyhedron. It should be addressed with further study whether or not the problem can be converted to a purely dual problem including conversion of the minimization to possibly maximization.

Although the proposition concerned in this paper is a very special case of choosing a ring shape under the extended affine concept, it is of great interest from the aspect of graphic statics, or in other words from mechanical and mathematical aspects, because it relates a type of force diagram that makes great sense in structural performance to a form diagram (or part of it) that is well known in mathematics and physics, through a filter of optimization. The first question is if this is purely a coincidence or more than that. If not more, in fact, the intriguing relation has been proved more directly and graphically by applying graphic statics, particularly Airy stress polyhedra of both diagrams, than by the geometric approach alone. It may not be always the case that the dual problem or mixed problem like this case makes the problem simpler or more understandable. Nonetheless, the study has indicated that the duality leads to a new solution approach to form and force problems, i.e. form finding, of spoke wheel systems. Suppose there are some geometric constraints to satisfy for an extended affine spoke wheel system; rewrite them only with z^* coordinates of the vertexes of the undulated regular polygon. Then form finding is reduced to solve for z^*s instead of nodal coordinates xs and ys.

The other questions raised in the introduction, such as the translation of the evolute-involute relation of two form diagrams into force diagrams or the meaning of the trigonometric curve of the z* beyond just the conversion by Cremona's duality mapping rule, have not been successfully answered or thoroughly investigated yet. Again, it is not necessarily certain if these questions are even meaningful, but yet they remain fascinating for some as there seem to be hints to develop new aspects of form finding of spoke wheel structures.

Acknowledgments

The author is grateful to Nikken Sekkei Ltd. for its support for this research and publication.

References

[1] R. Bergermann, K. Göppert, "Das Speichenrad – Ein Konstruktionsprinzip für weitgespannte Dachkonstruktionen", Stahlbau 69, 2000, Heft 8.

[2] K. Göppert, K. Stockhusen, T. Moschner, "Estadio Jornalista Mario Filho, Rio de Janeiro", *Stahlbau* 83, 2014, Heft 6.

[3] H. Tamai, "On a family of equilibrium geometry of a spoke-wheel structure: Geometric approach to form finding of a spoke wheel system", Creativity in Structural Design: Proceedings of the IASS Annual Symposium 2018, Boston, USA, July 16-20, 2018.

[4] H. Tamai, "Geometric approach to form finding of a spoke wheel system: Mathematical explanations", in *Form and Force,*:*Proceedings of the IASS Annual Symposium 2019 – Structural Membranes 2019*, Barcelona, Spain, October 7 – 10, 2019, C. Lázaro, K.-U. Bletzinger, E. Oñate Eds.

[5] H. Tamai, K. Takahashi, "The extended affine method for form finding of a spoke wheel system in light of graphic statics", Proceedings of the IASS 2022 Symposium affiliated with APCS 2022 conference, Innovation · Sustainability · Legacy 19 – 22 September 2022, Beijing, China

[6] L. Cremona, Graphical statics: Two treatises on the Graphical Calculus and Reciprocal Figures in Graphical Statics. Clarendon Press, 1890.

IASS 2023
July 10–14 Melbourne
Integration of Design and Fabrication

Proceedings of the IASS Annual Symposium 2023
Integration of Design and Fabrication
10–14 July 2023, Melbourne, Australia
Y.M. Xie, J. Burry, T.U. Lee and J. Ma (eds.)

Towards homological methods in graphic statics

Zoe COOPERBAND[a,*], Robert GHRIST[a,b]

[*] Department of Electrical and Systems Engineering
University of Pennsylvania, 200 S. 33rd St., Philadelphia, PA, USA
zcoop@seas.upenn.edu

[a] Department of Electrical and Systems Engineering, University of Pennsylvania
[b] Department of Mathematics, University of Pennsylvania

Abstract

Recent developments in applied algebraic topology can simplify and extend results in graphic statics – the analysis of equilibrium forces, dual diagrams, and more. The techniques introduced here are inspired by recent developments in cellular cosheaves and their homology. While the general theory has a few technical prerequisites (including homology and exact sequences), an elementary introduction based on little more than linear algebra is possible. A few classical results, such as Maxwell's Rule and 2D graphic statics duality, are quickly derived from core ideas in algebraic topology. Contributions include: (1) a reformulation of statics and planar graphic statics in terms of cosheaves and their homology; (2) a new proof of Maxwell's Rule in arbitrary dimensions using Euler characteristic; and (3) derivation of a novel relationship between mechanisms of the form diagram and obstructions to the generation of force diagrams. This last contribution presages deeper results beyond planar graphic statics.

Keywords: graphic statics, graphical methods, Maxwell's rule, sheaf theory, cosheaves, cellular sheaves, algebraic topology, homology, Euler characteristic

1. Introduction

Applied topology is a branch of contemporary applied mathematics that uses algebraic topology as a toolset in applications [1]. Some prominent examples from the past two decades include the use of topological tools in data analysis [2], neuroscience [3], sensor networks [4], and signal processing [5].

One of the more recent and exciting developments in applied topology is the establishment and implementation of *cellular sheaf theory*. Building on the classical and powerful sheaf theory of the 1950s-60s [6], cellular sheaves (and dual *cosheaves*) provide a locally finite and inherently computation-friendly toolset which matured in the thesis of Curry [7]. These tools have been used in network coding [8], pursuit and evasion games [9], distributed optimization [10], opinion dynamics [11], scene analysis [12], and extending spectral graph theory [13].

In this introduction we use cellular cosheaves to characterize the static behavior of trusses. Following a classical history [14], [15], advances in the late 20th century [16]–[18] laid foundations for homological methods in static analysis. Algebraic foundations for the mechanical properties of two dimensional graphic statics has been further developed since [19]–[21]. Additional great strides have been made in algebraic descriptions of 3D polyhedral graphic statics [22]–[24]. Our contributions via cellular cosheaves extend these threads.

2. Cellular cosheaves

In the simplest possible setting, cosheaves are algebraic structures attached to a *network* (or graph of vertices and edges) and comprised of *vector spaces* and *linear transformations*.

Copyright © 2023 by Zoe COOPERBAND and Robert GHRIST. Published in the Proceedings of the IASS Annual Symposium 2023 with permission.

2.1. A general construction

Let $X = (V, E)$ denote a graph with vertex set V and (undirected) edge set E, with each edge connecting distinct vertices. A *cosheaf* $\mathcal{F}$ on X associates to each vertex $v \in V$ and each edge $e \in E$ a finite dimensional vector space $\mathcal{F}_v$ ($\mathcal{F}_e$ respectively). These vector spaces – called *stalks* – can be thought of as *local data*, and they can vary from vertex to vertex and edge to edge. The cosheaf consists not only of the underlying graph along with the stalks, but also linear transformations connecting the stalks where edges and vertices meet. For each incident edge-vertex pair $e \trianglerighteq v$, the cosheaf contains a linear transformation $\mathcal{F}_{e \trianglerighteq v}: \mathcal{F}_e \to \mathcal{F}_v$ from data over e to data over v. In all examples in this introduction, the vector spaces have explicit bases, and the maps $\mathcal{F}_{e \trianglerighteq v}$ are matrices. One thinks of these *cosheaf matrices* as being programmable: they define the constraints of the cosheaf stalk data.

Example 1: For any graph X, the unit *constant cosheaf* $\mathcal{I}_X$ has a 1-dimensional vector space as every stalk with all cosheaf matrices the identity. For a fixed (not necessarily 1-dimensional) vector space V, the V-constant cosheaf V_X has a copy of V on each vertex and edge, connected by identity matrices.

Example 2: Consider single-variable *polynomial splines* over a graph. These splines over edges are degree $\leq m$ polynomials in a single variable, meeting at vertices with global smoothness class C^r (r times continuously differentiable). Consider the cosheaf $\mathcal{K}$ with edge stalks consisting of P_m, the vector space of degree $\leq m$ polynomials. The vertex stalks are quotient vector spaces P_m/I^{r+1}, where I^{r+1} is the subspace of polynomials which vanish at the vertex with complementary degree at least $r + 1$. The matrices $\mathcal{K}_{e \trianglerighteq v}$ are quotient projections $P_m \to P_m/I^{r+1}$. Further exposition may be found in [25].

Our definitions have focused on the case where the base space is an undirected network. Extension to (regular) higher dimensional cell complexes is straightforward [7], with stalks attached to higher dimensional cells and corresponding cosheaf matrices.

2.2 The force cosheaf

Our central object of study is the *force cosheaf* – a means of tracking force vectors across a truss. Fix a graph $X = (V, E)$ modelling a mechanical truss built from axial geometric members E pinned at their ends with free-rotational joints V. Assume that X is realized in Euclidean space $\mathbb{R}^n$ (with $n = 2,3$ being typical) by an assignment $p: V \to \mathbb{R}^n$ (that embeds edges linearly). The force cosheaf $\mathcal{F} = \mathcal{F}(X, p)$ for this realization of X has vertex stalks $\mathcal{F}_v$ all equal to $\mathbb{R}^n$, encoding the static loads at the joints. The edge stalks $\mathcal{F}_e \cong \mathbb{R}$ encode a stress along the member: positive or negative for tension or compression respectively. For each edge e connecting joints u and v, the matrices $\mathcal{F}_{e \trianglerighteq u}: \mathcal{F}_e \to \mathcal{F}_u$ and $\mathcal{F}_{e \trianglerighteq v}: \mathcal{F}_e \to \mathcal{F}_v$ send the basis vector of $\mathcal{F}_e$ to the vectors $p(u) - p(v) \in \mathcal{F}_u$ and $p(v) - p(u) \in \mathcal{F}_v$ respectively. A sketch of the force cosheaf is pictured on the right in Figure 1.

The force cosheaf contains within it all the data from which statics and graphic statics unfolds. What reveals degrees of freedom and equilibrium is the classical algebraic-topological tool called *homology*.

3. Homology

Given a graph, one often considers its global topological properties such as the number of its connected components or independent cycles. These intuitive properties generalize greatly to homology – the algebraic study of *"holes."* Cosheaves, as introduced above, appear as mere containers of data; deeper meaning follows from considering their homology.

3.1 Classical cellular homology

We begin by describing a simple, classical instance of homology. In the case of $X = (V, E)$ a graph, one defines the vector spaces $C_0 = C_0X$ and $C_1 = C_1X$ with basis the formal set of vertices and edges respectively. Counting the number of edges and vertices we have $\dim C_0 = |V|$ and $\dim C_1 = |E|$. One may then define the *oriented incidence matrix* $\partial: C_1 \to C_0$ with respect to an arbitrary orientation given to edges. This matrix sends a basis edge e to the linear combination of vertices $\partial e = u - v$, respecting

this orientation. The null space, or *kernel* of this matrix $H_1X = \ker \partial$ has basis of oriented cycles in X, where multiplication by -1 changes the orientation of the cycle. The quotient vector space $H_0X = C_0/\operatorname{im}\partial$ of C_0 by the image of the oriented incidence matrix is known as the *cokernel* (isomorphic to the left null space of ∂); it has basis of connected components of X.

This graph construction generalizes to X a higher dimensional cell complex with more specialized language. The vector space $C_k = C_kX$ is known as the space of *k-chains*, linear combinations of formal k-cells (with arbitrary orientation). These vector spaces assemble into a sequence called a *chain complex* by means of *boundary matrices* $\partial\colon C_k \to C_{k-1}$ which send a basis k-cell σ to the linear combination of boundary $(k-1)$-cells $\partial\sigma = \sum \pm\tau$, where the sign comes from compatibility of orientation [26]. Composed boundary matrices are the zero matrix, with $\partial_k \circ \partial_{k+1} = 0$.

The crucial definition is this. The (cellular) *homology* of X, HX, is a collection of vector spaces $H_k = H_kX$. This k^{th} homology of X is defined to be the quotient vector space $H_kX = \ker \partial_k \,/\, \operatorname{im}\partial_{k+1}$: kernels mod images, or equivalence classes of collections of k-cells with vanishing boundary, modulo distributions that are the boundary of a higher dimensional chain. The dimensions of the homologies, $\beta_k = \dim H_kX$, are known as the *Betti numbers* of X. In general, β_0 gives the number of connected components of X, and higher Betti numbers count the number of different dimensional holes within X (in a graph, cycles are 1-dimensional holes). Homology is invariant with respect to the arbitrary orientation of cells and any homotopy (think: controlled deformation) of the space X.

3.2 Cosheaf homology

Homology extends to cosheaves. Let $\mathcal{F}$ be a cosheaf over a graph $X = (V, E)$. The space of cosheaf *0-chains* $C_0 = C_0\mathcal{F} = \bigoplus_v \mathcal{F}_v$ is the product vector space bundling data over all vertices, and the space of *1-chains* $C_1 = C_1\mathcal{F} = \bigoplus_e \mathcal{F}_e$ is the corresponding amalgamation of vector data over all edges. A vector in C_0 (or C_1) is interpreted as a distribution of data over vertices (or edges). The *cosheaf boundary matrix* $\partial\colon C_1 \to C_0$ acts on a 1-chain $\xi = (\xi_e)$ yielding a 0-chain $\partial\xi$ whose value on a vertex v is given by

$$(\partial\xi)_v = \sum_{e_i \triangleright v} \pm\mathcal{F}_{e_i \triangleright v}\left(\xi_{e_i}\right) \tag{1}$$

where the sign is informed by an arbitrary choice of orientation and the sum is over all edges incident to v. Summations of the form (1) occur over all vertices, utilizing cosheaf matrices $\mathcal{F}_{e_i \triangleright v_j}$ to transform a distribution of data over edges to data over vertices. One imagines the vertices communicating and pulling data from their neighbor edges. For a cosheaf over a n-dimensional cell complex, the boundary matrix extends to a sequence of linear transformations $\partial_k\colon C_k \to C_{k-1}$, the entire sequence being collected into a chain complex $C\mathcal{F} = (C_k, \partial_k)$, with $\partial_k = 0$ when $k \leq 0$ or $k > n$.

The *homology* of the cosheaf, $H\mathcal{F}$, is the collection of vector spaces $H_k = H_k\mathcal{F}$, where $H_k\mathcal{F} = \ker \partial_k \,/\, \operatorname{im}\partial_{k+1}$. This is kernels mod images, just as in (classical) cellular homology. The difference between cellular homology and cosheaf homology is in the difference of data of the chain complex CX or $C\mathcal{F}$ - the process of taking homology is afterwards identical.

Examples: Recall the examples in Section 2.1.

1. The cellular homology of a network X is the same as the homology of the unit constant cosheaf $\mathcal{I}_X$ over it. Here, $H\mathcal{I}_X \cong HX$ and so the homology is the same as the cellular case. The Betti numbers of $\mathcal{I}_X$ count connected components and independent cycles of X. For a general constant cosheaf V_X, this has homology isomorphic to m copies of HX, where $m = \dim V$.
2. The space of splines over a polygonal cycle is isomorphic to $H_1\mathcal{K}$, the 1st homology of the spline cosheaf of Example 2. This is a simple example of more general results on splines [25].

These examples hint at the role that homology plays in classifying solutions of constrained systems.

3.3 Force cosheaf homology

What does the homology of the force cosheaf entail? At the physical level, each truss joint combines the axial forces along incident members. In the mathematical model, this is precisely what the force cosheaf boundary matrix describes. Given a 1-chain – a choice of axial force along all members – the boundary matrix $\partial: C_1\mathcal{F} \to C_0\mathcal{F}$, otherwise known as the *equilibrium matrix* [27], evaluates a distribution of net forces at all joints. This is significant: *the homology of the force cosheaf, $H\mathcal{F}$, characterizes equilibrium-stresses and configurations of the mechanism.* The details are worth emphasizing:

1. The 1-dimensional homology $H_1\mathcal{F} = \ker \partial$ consists of all stress distributions that keep the structure in static equilibrium (zero net force at each joint). The dimension of this null space (the 1st Betti number $\beta_1 = \dim H_1\mathcal{F}$) records the number of dimensions of *self-stress*.
2. The 0-dimensional homology, $H_0\mathcal{F} = C_0\mathcal{F}/\text{im } \partial$, records distributions of forces at joints which cannot impart forces to edges. This space of un-resistible forces is interpretable as the space of constrained *degrees of freedom* of vertices of X, including global translations, rotations, and mechanisms [19]. Under these infinitesimal motions, edge lengths would remain constant.

A sample graph X with non-zero self-stress is provided in Figure 1. As is common in a well-constructed cosheaf, homology characterizes/classifies properties of the global system. With these tools, nontrivial inferences can be made in a unified fashion.

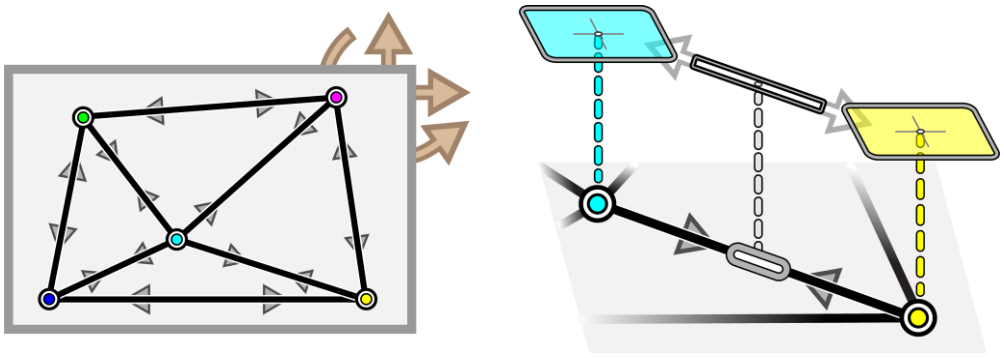


Figure 1. The force cosheaf $\mathcal{F}$ over the graph (left) has cosheaf boundary matrix of size 10 by 8 with nullity 1. The homology of $\mathcal{F}$ characterizes the self-stress over edges and three degrees of freedom (two translational and one rotational of the entire structure). A local view of $\mathcal{F}$ is highlighted (right), with the cosheaf matrices mapping edge stalks to vertex stalks "above" the graph.

4. Euler, Maxwell, & Betti

Maxwell's Rule [14] is the classic condition for a frame structure to be isostatic. The modern form for 3D trusses is given in [27]:

$$3|V| - |E| = 6 + |M| - |S|, \tag{2}$$

where $|M|$ is the number of linkage mechanisms, $|S|$ is the number of self-stresses, $|V|$ is the number of vertices of the truss, and $|E|$ is the number of its edges. The prevalence of differences (especially in the number of vertices and edges) is a clue that this is related to *Euler characteristic*.

Recall that elementary topological fact that for a finite polyhedral *spherical* surface X with $|V|$ vertices, $|E|$ edges, and $|F|$ faces, the Euler characteristic $\chi(X) = |V| - |E| + |F|$ equals $+2$, independent of how the spherical surface is discretized. The reason for this is an elementary but fundamental result. For a finite collection of finite-dimensional vector spaces $C = \{C_k\}$, its Euler characteristic

$$\chi(C) = \sum_k (-1)^k \dim C_k \tag{3}$$

is likewise finite and agrees with the classical formula that counts vertices, edges, and faces. This is formulated as an alternating sum of Betti numbers by the following classical result:

Lemma 1: [26] *The Euler characteristic of a chain complex $C = (C_k)$ and its homology H agree:*

$$\chi(C) = \chi(H) = \sum_k (-1)^k \beta_k \,, \tag{4}$$

This is why for a triangulated spherical surface $\chi = 2$, since its homology satisfies $\beta_0 = \beta_2 = 1$ and $\beta_1 = 0$. The proof of Lemma 1 is neither more nor less than the rank-nullity theorem from linear algebra, suitably generalized. Indeed, a single linear transformation $A: U \to V$ *is* an elementary chain complex where $C_1 = U$ and $C_0 = V$. Taking homology, one recovers the rank-nullity theorem as a special case.

We reinterpret Maxwell's Rule as coming from a chain complex and its homology: in this case, the force cosheaf $\mathcal{F}$. For a structure in n-D, its Euclidean group of translations and rotations in n-D has dimension $\binom{n+1}{2} = \frac{1}{2}n(n+1)$. With this, Lemma 1 applied to the force cosheaf $\mathcal{F}$ in n-D yields

$$n|V| - |E| = \dim C_0 - \dim C_1 = \dim H_0 - \dim H_1 = \binom{n+1}{2} + |M| - |S|. \tag{5}$$

This is the Maxwell Rule in dimension n, giving equation (2) when $n = 3$.

5. Boundary conditions

Trusses are outfitted with external loadings and reaction forces in practice. The statics of these trusses are characterized by *relative homology*, meaning homology relative to an external structure. This requires some additional theoretical tools.

5.1 Cosheaf maps and quotients

For two cosheaves $\mathcal{F}$ and $\mathcal{G}$ over a graph $X = (V, E)$, a *cosheaf map* $\phi: \mathcal{F} \to \mathcal{G}$ is comprised of stalk-wise linear maps $\phi_x: \mathcal{F}_x \to \mathcal{G}_x$ for x ranging over every cell of X. In addition, the cosheaf map must respect the cosheaf matrices of $\mathcal{F}$ and $\mathcal{G}$: the equations $\phi_v \circ \mathcal{F}_{e \triangleright v} = \mathcal{G}_{e \triangleright v} \circ \phi_e$ must hold.

It may be the case that the data of cosheaf $\mathcal{F}$ can be considered as a subset of the data of $\mathcal{G}$. In this special case, $\phi: \mathcal{F} \hookrightarrow \mathcal{G}$ is an *inclusion* of the stalks of $\mathcal{F}$ into the stalks of $\mathcal{G}$, and one can think of $\mathcal{F}$ as lying "inside" $\mathcal{G}$. To model the data in $\mathcal{G}$ not captured by $\mathcal{F}$, one builds the *quotient cosheaf* $\mathcal{G}/\mathcal{F}$ with stalks of quotient vector spaces $(\mathcal{G}/\mathcal{F})_x = \mathcal{G}_x/\mathcal{F}_x$, with x ranging over all cells. One can think of the cosheaf $\mathcal{G}/\mathcal{F}$ as encoding the *orthogonal compliment* to $\mathcal{F}$ inside of $\mathcal{G}$, satisfying the isomorphism of cosheaves $\mathcal{F} \oplus \mathcal{G}/\mathcal{F} \cong \mathcal{G}$ (comprised of vector space isomorphisms between stalks). Here, the data of $\mathcal{G}$ is subdivided into its constituent components parallel and orthogonal to $\mathcal{F}$. This construction will help with modelling external forces on a truss.

5.2 External loadings

We model external forces on a truss somewhat differently from other authors [19], [21], [27], considering boundary conditions as residing on an exterior truss abstracting the origin of the boundary loads. This exterior truss loosely set to be a loop around the structure: the intention of this is to model the loaded truss of interest as a sub-truss of a larger structure. The benefits of this approach are a clear differentiation between loaded vertices and unloaded vertices, as well as a homological formulation of equilibrium stresses. This is specifically important in simple 2D graphic statics, where loads are only applied on the exterior of a loaded truss.

Suppose that $Y = (V_Y, E_Y)$ (the exterior truss loop) is a closed subgraph of $X = (V, E)$ (the extended original truss with *boundary conditions*) as in Figure 2. For the force cosheaf $\mathcal{F} = \mathcal{F}_X$ with domain over X, the cosheaf $\mathcal{F}_Y$ has stalks identical to those of $\mathcal{F}_X$ for vertices and edges in Y and zero stalks

elsewhere. It is straightforward to define the inclusion cosheaf map $\iota: \mathcal{F}_Y \hookrightarrow \mathcal{F}_X$, with stalk-wise linear maps the identity matrix over cells of Y and the zero matrix over $X - Y$. The ensuing quotient cosheaf $\mathcal{F}_{X-Y} \coloneqq \mathcal{F}_X/\mathcal{F}_Y$ has support strictly on the set $X - Y$ (which is topologically an open disk). Some edges $\{e_l, e_r\}$ of $X - Y$ have an open end in Y - these are *loaded edges* and *reaction edges* of $X - Y$. These edges represent lines of action of forces transferred between Y and $X - Y$.

The quotient cosheaf $\mathcal{F}_{X-Y}$ models the static behavior of the original truss $X - Y$ with respect to the space of peripheral boundary conditions Y. The *relative homology* $H_1\mathcal{F}_{X-Y}$ of this cosheaf characterizes the full space of *equilibrium stresses*, including internal self-stresses as well as external equilibrium loadings from edges $\{e_l, e_r\}$ (ignorant of whether Y could deliver these forces or not). Here, the truss $X - Y$ is blind to the statics of Y and liberally permits any possible loading through edges $\{e_l, e_r\}$. Our next goal is to relate the homologies of the force cosheaves $\mathcal{F}_X, \mathcal{F}_Y$, and $\mathcal{F}_{X-Y}$ with varying domains.

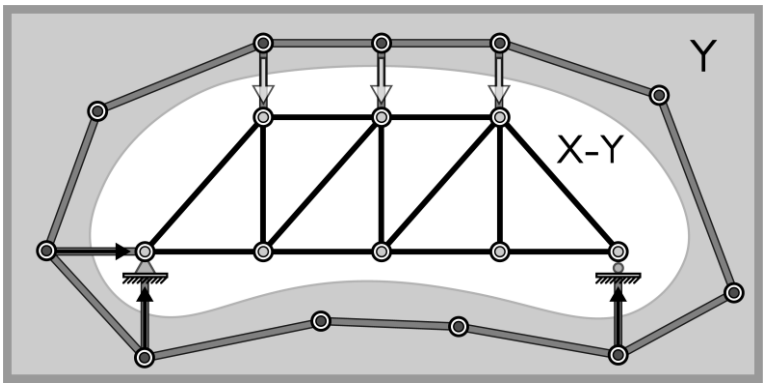


Figure 2. Boundary conditions in the form of loading and reaction forces are modeled as edges connecting the truss to an external loop Y.

5.3 Exact sequences

Exactness is a criterion of sequences of vector spaces and linear transformations that compactly characterizes a myriad of relationships between. Such a sequence of vector spaces

$$\ldots \to V_3 \to V_2 \to V_1 \to V_0 \to V_{-1} \ldots \tag{6}$$

is said to be *exact* if the image of every incoming transformation is equal to the kernel of the outgoing transformation at every vector space. That is, the homology of the sequence (6) completely vanishes. In the special case that (6) is non-zero only at the central three terms, there is an isomorphism of vector spaces $V_1 \cong V_0 \oplus V_2$ where $V_0 \cong V_1/V_2$; this can be worked out using properties of exactness [26].

It is a fact that any triple of cosheaves of the form $\mathcal{F} \hookrightarrow \mathcal{G} \to \mathcal{G}/\mathcal{F}$, where the first cosheaf map is an inclusion and the second is a quotient projection, induces a *long exact sequence* in homology

$$\ldots \to H_{k+1}\mathcal{G}/\mathcal{F} \to H_k\mathcal{F} \to H_k\mathcal{G} \to H_k\mathcal{G}/\mathcal{F} \to H_{k-1}\mathcal{F} \to \cdots, \tag{7}$$

derived from the corresponding exact sequence of cosheaf chain complexes [7]. True to its name, sequence (7) is an exact sequence of vector spaces and is a core feature of *homological algebra*.

Applying this to the externally loaded force cosheaf $\mathcal{F}_Y \hookrightarrow \mathcal{F}_X \to \mathcal{F}_{X-Y}$, where $\mathcal{F}_{X-Y} = \mathcal{F}_X/\mathcal{F}_Y$, one has

$$0 \to H_1\mathcal{F}_X \to H_1\mathcal{F}_{X-Y} \to H_0\mathcal{F}_Y \to H_0\mathcal{F}_X \to H_0\mathcal{F}_{X-Y} \to 0 \tag{8}$$

where $H_1\mathcal{F}_Y = 0$ (because Y is assumed to be a loop with no self-stress) and all higher-homology terms vanish. This sequence collates the following elements:

1. The 1st homology $H_1\mathcal{F}_X$ is the vector space of *internal self*-stresses of X.

2. The relative 1st homology $H_1\mathcal{F}_{X-Y}$ is the total space of equilibrium stresses including those from boundary conditions.
3. The 0th homology $H_0\mathcal{F}_Y$ is the space of degrees of freedom of the frontier Y.
4. The 0th homology $H_0\mathcal{F}_X$ captures degrees of freedom of X (potentially including those of Y).
5. The 0th homology $H_0\mathcal{F}_{X-Y}$ is the space of *constrained degrees of freedom* of $X - Y$ with respect to the various loadings and reactions restricting said freedom.

Exactness of (8) means that there are constraints tying together sequential terms. For example, the statement that *"every self-stress is an equilibrium stress with zero loading"* is equivalent to exactness of (8) at $H_1\mathcal{F}_X$ (the transformation $H_1\mathcal{F}_X \to H_1\mathcal{F}_{X-Y}$ is injective). Exactness at $H_1\mathcal{F}_{X-Y}$ has the interpretation: *"every equilibrium stress of a loaded structure is a sum of internal self-stresses and those resulting from outside forces"*. These outside forces are generated by instabilities in Y that, in the larger structure X, "push" and "pull" on $X - Y$. Similar statements may be made about the remaining terms.

6. Planar graphic statics

Maxwell's seminal paper [14] made the astute observation that force vectors within members of a static truss combine to form a *reciprocal diagram* topologically dual to the primal (see Figure 3 for examples). Various aspects of 2D duality have been studied, such as the planarity condition [21] or kinematic properties [19], [20]. Here we develop the root of the duality in its substantial form and extend to new territory.

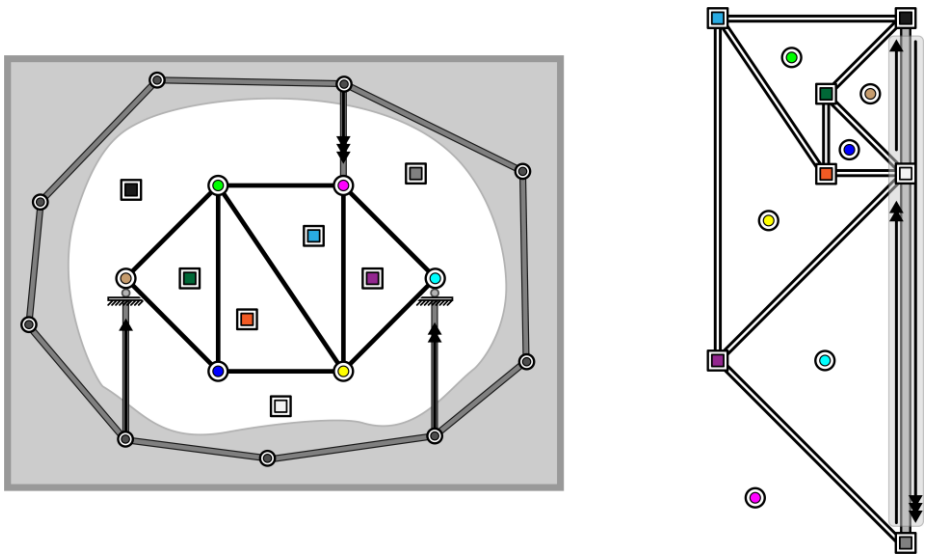


Figure 3. An example of graphic statics with boundary conditions is pictured. A form diagram is subject to external loads (left), with a single degree of equilibrium. A representative force diagram (a combined free body diagram) is drawn (right), with edge lengths equal to the load over the primal edge. Equilibrium of forces on the left is equivalent to dual face cells on the right being closed. The grey exterior (*cf.* Figure 2) on the left is dualized to the interior of the vertical degenerate triangle on the far right.

We focus on finite *planar graphs* with straight, non-overlapping edges. For a particular realization of a planar graph in the plane, the polyhedral regions interior to minimal cycles are *face cells*. Introducing these face cells extends a planar graph to a two-dimensional *cell complex*. Including the exterior which extends to infinity as one additional face yields a cell complex with the topology of the sphere $\mathbb{S}^2$. We remind the reader that although this cell complex $X = (V, E, F)$ has spherical topology, it remains realized in the flat plane by an assignment $p: V \to \mathbb{R}^2$. This is called a *form diagram*.

It is natural to extend our definitions of cosheaves over the plane as a 2D cell complex. The force cosheaf $\mathcal{F}$ over this spherical cell complex $X = (V, E, F)$ is an extension of that over its graph (V, E): the stalks over all face cells are set to zero (0-dimensional vector spaces) with zero-matrices from face stalks to incident edge stalks. There is more to the story, based on how this force cosheaf is situated in the plane.

6.1 The position cosheaf

While the force cosheaf $\mathcal{F}$ describes the compatibility of forces over the truss, it is a natural question what the complementary data to forces are in the plane. Namely, since edge stalks $\mathcal{F}_e$ contain force information *parallel* to edges, what data structure describes information *perpendicular* to edges? This question naturally leads to its *complimentary cosheaf*, the quotient of the constant cosheaf $\mathbb{R}^2_X$ by $\mathcal{F}$. The reason for considering the constant cosheaf here is that it encompasses the *ambient space* of the plane. Stalks of $\mathbb{R}^2_X$ are akin to the tangent space: copies of $\mathbb{R}^2$ allocated to each location in the plane, stitched together by identity matrices.

There is an inclusion map $\phi\colon \mathcal{F} \hookrightarrow \mathbb{R}^2_X$ of cosheaves which we now describe. The force cosheaf has no edge stalks so ϕ_f is the zero matrix over faces. By ϕ_e over edges, the vector $\mathcal{F}_e \cong \mathbb{R}$ is sent to the vector $p(u) - p(v)$, the position of the edge endpoints. Over vertices, stalks of $\mathcal{F}$ and $\mathbb{R}^2_X$ are both copies of $\mathbb{R}^2$, so it is valid to let ϕ_v be the identity linear transformation. It is straightforward to check that ϕ is a valid cosheaf map by this construction.

The quotient cosheaf $\mathcal{G} \coloneqq \mathbb{R}^2_X/\mathcal{F}$, called the *position cosheaf*, is the complementary data structure we desire. Over faces, this cosheaf has face stalks $\mathcal{G}_f \cong \mathbb{R}^2$ encoding *positions* (to be detailed momentarily). There is trivial data over vertices, with $\mathcal{G}_v = 0$. The edge stalks $\mathcal{G}_e = \mathbb{R}^2/\mathcal{F}_e$ represent the linear subspace perpendicular to the thrust of e in the plane. The non-trivial cosheaf matrices $\mathcal{G}_{f \rhd e}$ are projection matrices $P_{e^\perp}$, projecting from the face stalk $\mathcal{G}_f$ onto the perpendicular space $\mathcal{G}_e$.

Recall the *Poincaré dual* cell complex to $X = (V, E, F)$ is the cell complex $\tilde{X} = (\tilde{F}, \tilde{E}, \tilde{V})$ where faces are converted to dual vertices, edges to dual edges, and vertices to dual faces [26]. In this way, the cell structure is dualized to an alternative cell structure on the sphere $\mathbb{S}^2$. We note that $\tilde{X}$ is merely the topological dual to X as of now; the geometric bearing of cells of $\tilde{X}$ is informed by homology classes of the position cosheaf.

Face stalks of $\mathcal{G}$ encode the positions of the *dual vertices* of $\tilde{X}$ in $\tilde{F}$. Namely, $\mathcal{G}_f \cong \mathbb{R}^2$ may be considered as the space of possible positions for the dual vertex $\tilde{f}$ in the plane. With this identification, the homology space $H_2\mathcal{G}$ consists of these realizations of dual vertices subject to constraints along edges. For every edge bounded by faces $e \lhd f_1, f_2$, there is the corresponding dual incidence $\tilde{e} \rhd \widetilde{f_1}, \widetilde{f_2}$ and dual restraint. For ξ to be a homology element of $H_2\mathcal{G}$ it must be the case that

$$\mathcal{G}_{f_1 \rhd e}(\xi_{f_1}) = \mathcal{G}_{f_2 \rhd e}(\xi_{f_2}) \tag{9}$$

or equivalently that

$$P_{e^\perp}\left(\xi_{f_1} - \xi_{f_2}\right) = 0. \tag{10}$$

In other words, the difference between ξ_{f_1} and ξ_{f_2} along the perpendicular direction to e is zero – and so *any difference between these two positions lies along the linear subspace to edge* e. This means that the difference in positions of dual vertices $\widetilde{f_1}, \widetilde{f_2}$ is parallel to edge e as determined by ξ. Moreover, every parallel dual realization $\xi\colon \tilde{F} \to \mathbb{R}^2$ is a homology class of $H_2\mathcal{G}$ as this condition is descriptive. A parallel dual graph to that of Figure 1 is pictured in Figure 4.

In conclusion, the vector space $H_2\mathcal{G}$ of the position cosheaf encodes *all possible parallel realizations* of the dual cell complex $\tilde{X}$ in the plane. These realizations of $\tilde{X}$ are called *force diagrams*.

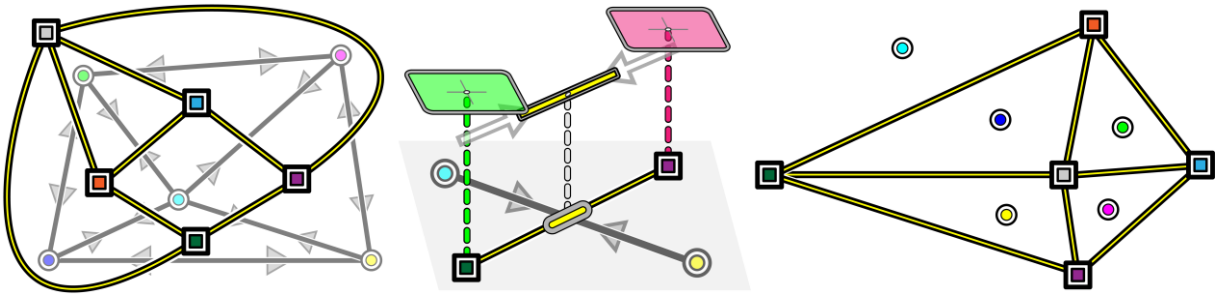


Figure 4. The topological dual to the form diagram of Figure 1 is pictured (left), with its geometry realized (right). A local view of the position cosheaf $\mathcal{G}$ is highlighted (center), with cosheaf matrices mapping face stalks to edge stalks. A generator of $H_2\mathcal{G}$ provides the geometric coordinates to dual vertices on the right, characterizing a force diagram. This parallel dual realization may be derived from the self-stress of the form diagram via the graphic statics of Theorem 1.

6.2 Dual trusses

We arrive at the heart of 2D graphic statics. While the classical history of form and force diagram duality reaches back over a century and a half [14], cosheaves permit an efficient modern reformulation. The cosheaf triple $\mathcal{F} \hookrightarrow \mathbb{R}^2_X \to \mathcal{G}$ leads to a long exact sequence as per sequence (7):

$$... \to H_2\mathcal{F} \to H_2\mathbb{R}^2_X \to H_2\mathcal{G} \to H_1\mathcal{F} \to H_1\mathbb{R}^2_X \to H_1\mathcal{G} \to H_0\mathcal{F} \to H_0\mathbb{R}^2_X \to H_0\mathcal{G} \to 0 \tag{11}$$

The force cosheaf has zero-stalks over faces, so $H_2\mathcal{F} \cong 0$. The constant cosheaf has homology $H_2\mathbb{R}^2_X \cong \mathbb{R}^2$, $H_1\mathbb{R}^2_X \cong 0$, and $H_0\mathbb{R}^2_X \cong \mathbb{R}^2$, matching Betti numbers of the underlying sphere (multiplied by two, see example 1, Section 3.2). These computations simplify and split the exact sequence (11) into two:

$$0 \to \mathbb{R}^2 \to H_2\mathcal{G} \to H_1\mathcal{F} \to 0 \tag{12}$$

$$0 \to H_1\mathcal{G} \to H_0\mathcal{F} \to \mathbb{R}^2 \to 0 \tag{13}$$

The first exact sequence (18) *is* the establishment of 2D graphic statics. The space $\mathbb{R}^2$ corresponds to *global translations* of dual realizations of $\tilde{X}$ in $H_2\mathcal{G}$: these are global shifts of all dual vertices by the same translation vector. The linear transformation $H_2\mathcal{G} \to H_1\mathcal{F}$ takes the pointwise difference between dual coordinates and converts them to force values within a self-stress.

Theorem 1: [14], [17] *Over a truss X realized in $\mathbb{R}^2$, there is a bijective correspondence between self-stresses of X and parallel dual realizations of $\tilde{X}$ in $\mathbb{R}^2$ up to global translation.*

This is the isomorphism of vector spaces

$$H_1\mathcal{F} \cong H_2\mathcal{G}/\mathbb{R}^2 \tag{14}$$

following exact sequence (12). The ease of writing this equation conceals the underlying linear relationships at play. The force within each edge of a self-stress is equivalent to the distance between dual nodes in the corresponding force diagram. A benefit of the abstraction presented here is the readily generalization of isolated graphic statics to graphic statics with boundary conditions – the isomorphism of vector spaces

$$H_1\mathcal{F}_{X-Y} \cong H_2\mathcal{G}_{X-Y}/\mathbb{R}^2. \tag{15}$$

As $X - Y$ (Figure 2) has the topology of an open disk, its dual counterpart $\tilde{X} - \tilde{Y}$ has the topology of a closed disk. Equation (15) then is the statement that equilibrium stresses over a structure with boundary forces are equivalent to parallel realizations of the dual disk $\tilde{X} - \tilde{Y}$, up to global translation. An example is pictured in Figure 3.

Isomorphism (15) relies on $X - Y$ having $\beta_1 = 0$ so the constant cosheaf homology $H_1\mathbb{R}^2_X$ vanishes. If this requirement is exempted it is still possible to formulate graphic statics, such as the case of *internally applied loadings* where loads are applied within the structure (and holes inserted into $X - Y$). In this case, exact sequence (11) does not split into the two sequences (12) and (13) so more care is required.

There are numerous applications and extensions of the abstract formulation here. With care, the boundary loop Y can generalized to empower *relative graphic statics*. One can consider *partial* form diagrams $X - Y$ of a larger truss and rigorously compute consequent *partial* force diagrams $\tilde{X} - \tilde{Y}$. The relations to the whole are given by sequences analogous to (8).

6.3 Impossible rotations of the dual

The second exact sequence (13) also has meaning, although the homology $H_1\mathcal{G}$ is difficult to interpret. This space consists of *impossible dual edge rotations* in the sense that edges of any parallel dual realization of $\tilde{X}$ cannot possibly rotate in the specified manner (even if edges are permitted to freely extend or contract axially). These edge rotations *obstruct* dual realizations. Just as mechanisms of a truss are not resistible by truss members, these rotations are *not realizable* by nodal positions. In fact, rotations of truss members under mechanism or global rotation *are* impossible edge rotations on dual force diagrams. Only the space $\mathbb{R}^2$ of global translations of X does not rotate edges; the isomorphism

$$\mathbb{R}^2 \cong H_0\mathcal{F}/H_1\mathcal{G} \tag{16}$$

of vector spaces following exact sequence (13) certifies this. This relationship is novel.

Theorem 2: *The system of edge rotations from any mechanism or global rotation of a truss X in $\mathbb{R}^2$ are impossible to satisfy on any force diagram $\tilde{X}$ in $\mathbb{R}^2$, even permitting dual edges in $\tilde{X}$ to freely extend axially.*

Note that dual edges have their rotations flipped when realized in tension versus compression (see Figure 5). The symmetry of sequences (12) and (13) suggests this theorem is as fundamental as Theorem 1. Indeed, if rotation values are converted to stress values along edges (with clockwise rotation converted to compression, and counterclockwise to tension for instance), they form a self-stress of the dual $\tilde{X}$. This is *graph reciprocity*, the mirroring of the force and form diagrams [19], [20].

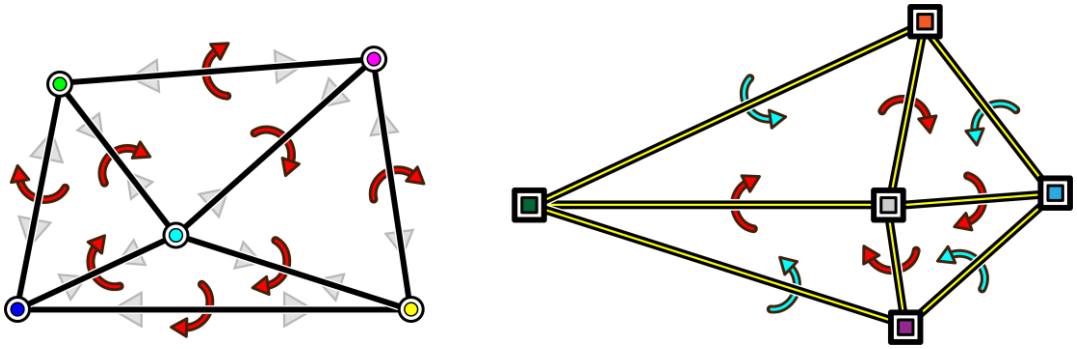


Figure 5. The form diagram of Figure 1 is globally rotated clockwise (left), inducing edge rotations. In a force diagram (right), dual edges have their rotations flipped when the primal edge is in tension. Even allowing dual edges to extend or contract, it is impossible to simultaneously rotate the internal four dual edges clockwise and rotate the external four dual edges counterclockwise. This illustrates Theorem 2; the single dimension of global rotation of the form diagram corresponds to the dimension of impossible dual edge rotations of force diagrams.

If the nodes of a truss are fixed connections instead of pinned, free-rotational connections, then impossible edge rotations are equivalent to states of *self-shear* of the structure. In this setting,

perpendicular shear forces are applied along each member instead of parallel axial forces. These self-shear forces are in equilibrium, with zero net force at nodes.

One central application of graphic statics is in *form finding*, where a force diagram is manipulated to find efficient geometry for the primal truss. In this context, a repositioning of dual nodes of a force diagram $\tilde{X}$ (not necessarily parallel) may be considered as an element of $C_2\mathcal{G}$. Its boundary $\partial\xi$ is a possible system of rotations of dual edges, and therefore, it is in the zero class of $H_1\mathcal{G}$. By sequence (13), this system of rotations (with rotations flipped over edges in tension) lies in the zero class of $H_0\mathcal{F}$. This force assignment to vertices of X is free of any translational, rotational, or mechanical components. Consequently, any preimage in $C_1\mathcal{F}$ of such an element of $C_0\mathcal{F}$ is a (not necessarily conservative) edge force assignment of X. This outlines a method of translating between *general* dual coordinates and *general* force assignments of force and form diagrams.

7. Beyond the plane

There are numerous potential extensions of the cosheaf-based graphic statics presented here.

One clear path is the extension of the well-known 3D polyhedral theory by Maxwell [14], [15] and Cremona [28], among others. Self-stresses of a cell complex X in the plane are in bijective correspondence to a family of three-dimensional *lifted polyhedra* that project vertically onto X. As 2D reciprocal graphic statics is very much linked to plane liftings of the truss [17] with a correspondence that is homological in nature [18], one can build a cosheaf adaptation.

Recalling Example 2 on polynomial splines, there is potential to integrate splines with *linear shape functions* utilized in structural engineering. For a beam in bending, the deflection, moment, and shear quantities all may be approximated by polynomials. At ends, beams are connected and restrained by C^r differentiability conditions - equivalent to compatibility conditions of spline cosheaves. More generally, the *finite element method* deconstructs complex shapes into simplified constituent components. It may be fruitful to investigate the homological properties of equilibrium equations in these models.

Finally, as presented in Sections 2 and 3, the force cosheaf $\mathcal{F}$ makes sense in dimension 3 and above. Indeed, the derivation of the Maxwell Rule (2) here given is no more difficult in n-D than in 2-D. To what extent, then, can the framework of cosheaves be integrated with recent breakthroughs in 3D polyhedral graphic statics [22]–[24]?

With 3-dimensional cells, the complexity between relationships of equilibrium spaces increases dramatically. While a single cosheaf map initiated 2D graphic statics in Section 6, higher dimensional graphic statics requires *filtrations* (or increasing sequences) of cosheaves, the analysis of which prompts the use of *spectral sequences*, a far-reaching generalization of the cosheaf long exact sequence (7).

Acknowledgements

The authors appreciate insightful discussions with J. Hansen, M. Akbarzadeh, M. Hablicsek, E. Saliklis, and D. Lee. This work is supported by the Air Force Office of Scientific Research under award number FA9550-21-1-0334.

References

[1] R. Ghrist, *Elementary Applied Topology ed 1.0*. Createspace, 2014.
[2] R. Ghrist, "Barcodes: the persistent topology of data," *Bulletin of the American Mathematical Society*, vol. 45, no. 1, pp. 61–75, 2008.
[3] A. E. Sizemore, J. E. Phillips-Cremins, R. Ghrist, and D. S. Bassett, "The importance of the whole: topological data analysis for the network neuroscientist," *Network Neuroscience*, vol. 3, no. 3, pp. 656–673, 2019.
[4] V. De Silva, R. Ghrist, and others, "Homological sensor networks," *Notices of the American mathematical society*, vol. 54, no. 1, 2007.

[5] M. Robinson, *Topological Signal Processing*, vol. 81. Springer, 2014.
[6] G. E. Bredon, *Sheaf Theory*. Springer New York, 1997.
[7] J. Curry, "Sheaves, Cosheaves and Applications," University of Pennsylvania, 2013.
[8] R. Ghrist and Y. Hiraoka, "Network codings and sheaf cohomology," *IEICE Proceedings Series*, vol. 45, no. A4L-C3, 2011.
[9] R. Ghrist and S. Krishnan, "Positive Alexander duality for pursuit and evasion," 2017.
[10] J. Hansen and R. Ghrist, "Distributed optimization with sheaf homological constraints," in *2019 57th annual allerton conference on communication, control, and computing (allerton)*, 2019, pp. 565–571.
[11] J. Hansen and R. Ghrist, "Opinion dynamics on discourse sheaves," *SIAM Journal on Applied Mathematics*, vol. 81, no. 5, pp. 2033–2060, 2021.
[12] H. Crapo, "Applications of geometric homology," in *French Workshop on Geometry and Robotics*, Springer, 1988, pp. 213–224. doi: 10.1007/3-540-51683-2_32.
[13] J. Hansen and R. Ghrist, "Toward a spectral theory of cellular sheaves," *Journal of Applied and Computational Topology*, vol. 3, no. 4, pp. 315–358, 2019.
[14] J. C. Maxwell, "XLV. On reciprocal figures and diagrams of forces," *The London, Edinburgh, and Dublin Philosophical Magazine and Journal of Science*, vol. 27, no. 182, pp. 250–261, 1864, doi: 10.1080/14786446408643663.
[15] J. C. Maxwell, "I.—On Reciprocal Figures, Frames, and Diagrams of Forces," *Transactions of the Royal Society of Edinburgh*, vol. 26, no. 1, pp. 1–40, 1870, doi: 10.1017/S0080456800026351.
[16] W. Whiteley, "Motions and Stresses of Projected Polyhedra," *Structural Topology*, vol. 7, no. June, pp. 13–38, 1982.
[17] H. Crapo and W. Whiteley, "Plane self stresses and projected polyhedra I : The Basic Pattern," *Structural Topology*, vol. 20, 1993.
[18] J. E. Hopcroft and P. J. Kahn, "A paradigm for robust geometric algorithms," *Algorithmica*, vol. 7, no. 1–6, pp. 339–380, 1992, doi: 10.1007/BF01758769.
[19] T. Mitchell, W. Baker, A. McRobie, and A. Mazurek, "Mechanisms and states of self-stress of planar trusses using graphic statics, part I: The fundamental theorem of linear algebra and the Airy stress function," *International Journal of Space Structures*, vol. 31, no. 2–4, pp. 85–101, 2016, doi: 10.1177/0266351116660790.
[20] A. McRobie, W. Baker, T. Mitchell, and M. Konstantatou, "Mechanisms and states of self-stress of planar trusses using graphic statics, part II: Applications and extensions," *International Journal of Space Structures*, vol. 31, no. 2–4, pp. 102–111, 2016, doi: 10.1177/0266351116660791.
[21] T. V. Mele and P. Block, "Algebraic graph statics," *CAD Computer Aided Design*, vol. 53, pp. 104–116, 2014, doi: 10.1016/j.cad.2014.04.004.
[22] M. Akbarzadeh, "3D Graphical Statics Using Reciprocal Polyhedral Diagrams," 2016. doi: 10.3929/ethz-a-010782581.
[23] M. Hablicsek, M. Akbarzadeh, and Y. Guo, "Algebraic 3D graphic statics: Reciprocal constructions," *CAD Computer Aided Design*, vol. 108, pp. 30–41, 2019, doi: 10.1016/j.cad.2018.08.003.
[24] M. Konstantatou, P. D'Acunto, and A. McRobie, "Polarities in structural analysis and design: n-dimensional graphic statics and structural transformations," *International Journal of Solids and Structures*, vol. 152, pp. 272–293, 2018.
[25] L. J. Billera, "Homology of smooth splines: generic triangulations and a conjecture of Strang," *Transactions of the american Mathematical Society*, vol. 310, no. 1, pp. 325–340, 1988.
[26] A. Hatcher, *Algebraic Topology*. Cambridge University Press, 2002.
[27] C. R. Calladine, "Buckminster Fuller's 'Tensegrity' structures and Clerk Maxwell's rules for the construction of stiff frames," *International Journal of Solids and Structures*, vol. 14, no. 2, pp. 161–172, 1978, doi: 10.1016/0020-7683(78)90052-5.
[28] L. Cremona, *Le figure reciproche nella statica grafica*. Tipografia di G. Bernardoni, 1872.

Gridshell and lattice structures

Active bending
Additive manufacturing/ 3D printing
Architectural geometry
Bamboo for sustainable construction and quality of life improvement
Bio-inspired structures and architecture
Bridge structures
Computational form-finding
Conceptual design
Concrete structures
Construction techniques
Deployable and inflatable structures
Design competition (WG21)
Digital modelling and fabrication
Dynamic response of metal spatial structures
Dynamic response of other structures
Form-finding and structural optimisation of interlocking discrete assemblages
Graphical methods
► Gridshell and lattice structures
Historical concrete shells
Historical structures
Lattice structures
Life-cycle design and assessment of structures
Metal gridshell structures, connections and stability
Methods and construction technologies for sustainable shell structures
Morphology and configuration processing
Next generation parametric design
Novel methods in modelling, optimisation and construction for reducing carbon footprint of continuous roof shells
Numerical methods for geometry, form-finding and optimisation of lightweight structures
Optimisation methods and applications
Origami
Other
Teaching design uncertainty: working with unknown qualities/quantities of new and re-claimed materials
Teaching of shell and spatial structures
Tensegrity systems and cable structures
Tension and membrane structures
Tension structures in the Asia-Pacific
Timber and bio-based structures
Topology optimisation
Traditional masonry structures and innovation
Transformable structures

IASS 2023
July 10–14 Melbourne
Integration of Design and Fabrication

Proceedings of the IASS Annual Symposium 2023
Integration of Design and Fabrication
10–14 July 2023, Melbourne, Australia
Y.M. Xie, J. Burry, T.U. Lee and J. Ma (eds.)

Design and construction of the ReciPlyDome, a lightweight modular reciprocal dome

Ellen LEEMANS[a,*], Ahmed SOLIMAN[a,b], Stijn BRANCART[a], Niels DE TEMMERMAN[b], Lars DE LAET[b]

[a,*] Department of Architectural Engineering (ARCH),
Vrije Universiteit Brussel (VUB), 1050 Elsene, Belgium
ellen.leemans@vub.be

[b] Department of Mechanics of Materials and Constructions (MEMC), Vrije Universiteit Brussel
[c] Faculty of Architecture and the Built Environment
Delft University of Technology (TU Delft), 2628 BL Delft, The Netherlands

Abstract

In the event sector, where there is a search for architectural constructions with an innovative morphology, reuse is key to strive towards more sustainable events. Designing modular structures and detailing them for easy disassembly and re-assembly is an ideal way to encourage and facilitate reuse. This way a longer lifespan is assured for the used components. However, temporary (event) structures are often hard to assemble, which can compromise their reusability. The difficulties of assembly are usually induced by the morphology of the modules or by using certain types of connections. Therefore these structures require optimization in terms of assembly while remaining resource efficient. The main objective of this research is to reimagine a developed structure, the ReciPlyDome, and optimize it in terms of assembly. The ReciPlyDome is a reciprocal dome structure based on a rhombic triacontahedron, whereby all elements are identical (except for the five elements that touch the ground). During the assembly phase of the first version of the ReciPlyDome, torsion in the components appeared to hinder efficient construction. To eliminate this, the dome was reviewed, which led to the development of a new connection system and an improved shape for the beams. A new full-scale version of the dome has been built, showing the positive effect of the improved connection system and the optimised beam position. In-situ measurements were made after construction, illustrating good correspondence between the digital and built model. Further research will focus on the covering of this modular reciprocal dome for outdoor use.

Keywords: optimization, modularity, prefabrication, material efficiency, prototyping

Copyright © 2023 by Ellen LEEMANS, Ahmed SOLIMAN, Stijn BRANCART, Niels De TEMMERMAN and Lars De LAET. Published in the Proceedings of the IASS Annual Symposium 2023 with permission.

1. Introduction

As events only last for a couple of days or maybe a few months, their structures are usually designed for short-term use. Afterwards, they are thrown away and generate about 20.4 kg/m² waste per year [1]. For events in France, except for travel and accommodation, the carbon emissions related to space design and production are the largest, reaching up to about 55% of all emissions for the average events [2]. To resolve this, reuse is key. A study of Catalan covered trade fairs has proven that when 75% of stands are reusable, the waste generation is 3.5 times lower than when none of the structures are reusable. In these cases, gluing all parts of the structure together was the main factor making them non-reusable. Since the useful life of the stands are on average 4.3 days, changing the connection systems to make the overall structure reusable could already significantly prolong the life of these stands [1]. Thus, in these type of structures reuse can mainly be obtained through providing an easy assembly and disassembly phase. Additionally, designing the structures to be easily compacted allows for a smoother transportation.

Modularity can play an important role to provide this easy assembly and disassembly. Because of the standardization of the used elements, modularity often helps to simplify the process. This standardization often even makes place for flexibility to create several designs with the same 'module', as in the case of the ReciPlyDome.

The ReciPlyDome, a reciprocal plywood dome, is a structure designed and prototyped by VUB researchers Stijn Brancart, Lars De Laet and Niels De Temmerman and by Olga Popovic Larsen of the Royal Danish Academy of Fine Arts, School of Architecture, Design and Conservation. Its identical elements are composed of two beams, with different lengths, connected at the ends. This not only allows pre-tensioning of each module but also increases the cross-sectional thickness, both elements that lead to a higher overall stiffness [3]. Only at the bases , the elements have a shorter length to provide a stable connection to the ground. In total four type of beams were designed which allow to create six different structures. Although its modularity already increases the easy for assembly, the torsion that occurred during this phase makes it still challenging. Therefore, some optimizations are needed.



Figure 1. The assembled ReciPlyDome, version 1.

2. Rethinking the structure

To eliminate the torsion occurring during the assembly phase, a stress-free alternative was required. This is obtained through rotating the beams by 90 degrees.

However, when rotating these beams, the current connection method would result in eccentricities (Figure 3 (a)). Therefore, incisions were provided on the places of the eccentricities, which also helped fixing the beams (Figure 3 (b)). Another result of the rotation is that the beams needed to be cut out in a curved shape to obtain the same curvature in a stress-free manner (Figure 3 (b)). The curvature of these beams was optimized to obtain a material efficient cutting pattern. Additionally, the elements were reduced to a single layer beam.

This version of the dome was tested with a model, obtained through laser cutting the required beams (Figure 2). The incisions were made slightly bigger to allow for some movement during the assembly of the model. However, this resulted in the structure falling apart halfway through the assembly. Therefore some locking around the connection points was needed to secure the structure. Furthermore, using these incisions would also create weak spots in the elements, causing them to rupture over time.

A solution to these weak points could be to increase the beam height, however it was opted not to do so as this would not be material efficient. Therefore it was decided to eliminate the incisions and create a connection system. (Figure 3 (c)).



Figure 2. Model of ReciPlyDome with incissions to eliminate eccentricities and fix the structure.

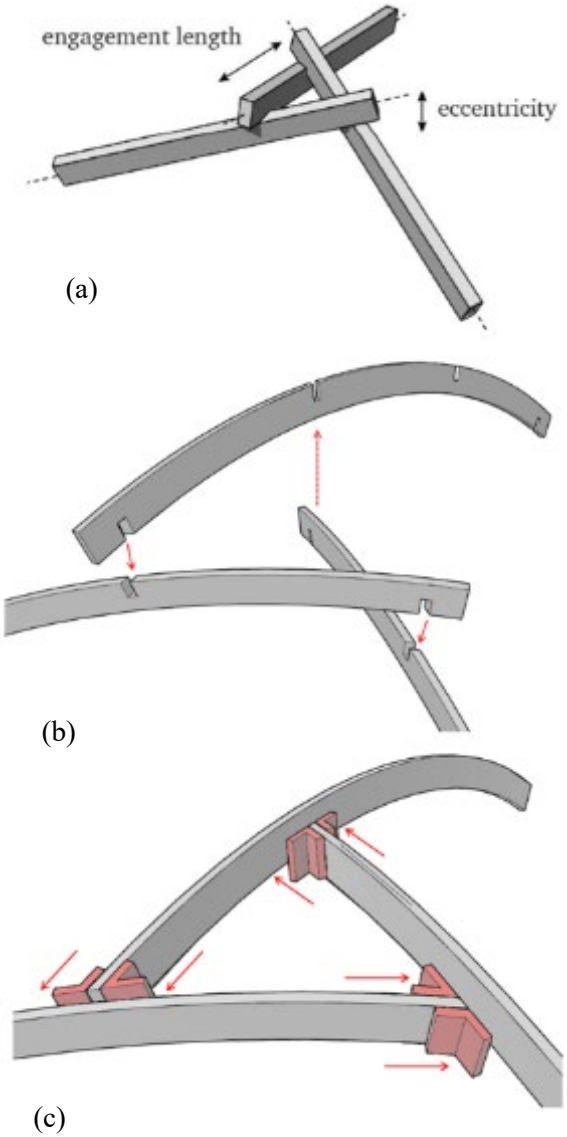


Figure 3. Rethinking the structure. (a) eccentricities occur due to rotation, [3] (b)incisions are provided to eliminate eccentricities, (c) addition of connection system for most ideal assembly.

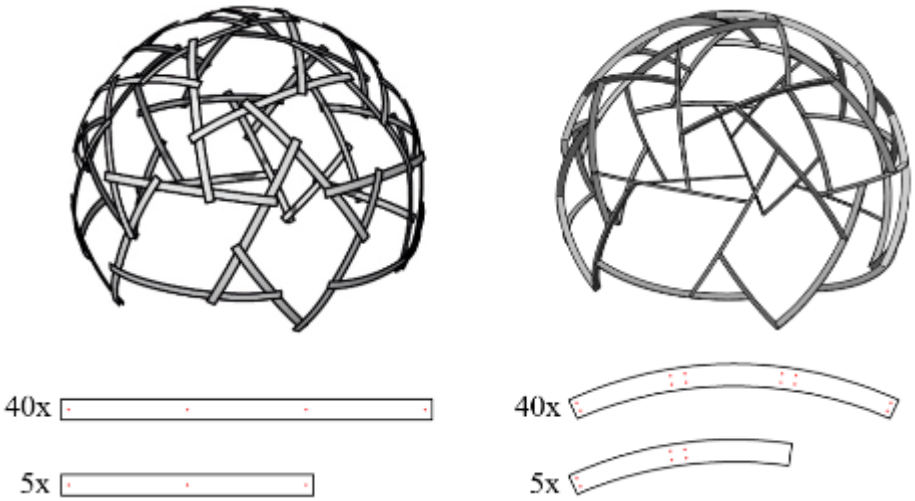


Figure 4. (a) 3D model of the original single-layered ReciPlyDome and the needed elements (source), (b) 3D model of a new version of the ReciPlyDome, whereby the elements are rotated over 90°, resulting in curved beams.

3. Connection system

3.1. Model scale

To connect the unstrained curved beams with each other, without creating cut-outs, a connection system was designed. With this system the beams were able to lean on each other in a reciprocal manner (Figure 5). It also allowed for sidewards movements to facilitate the assembly.

In total, three different type of connectors were designed, two for connecting the beams to each other and a third to connect them to the ground. Within the first-mentioned, a distinction was made based on the geometries that can be found in the dome. When looking closely, it can be seen that the dome consists of rhombuses and equilateral triangles and pentagons. The connection system was thus based on the corners of these equilateral triangles and pentagons, resulting in respectively a 'Type 60°' connector and a 'Type 108°' connector.

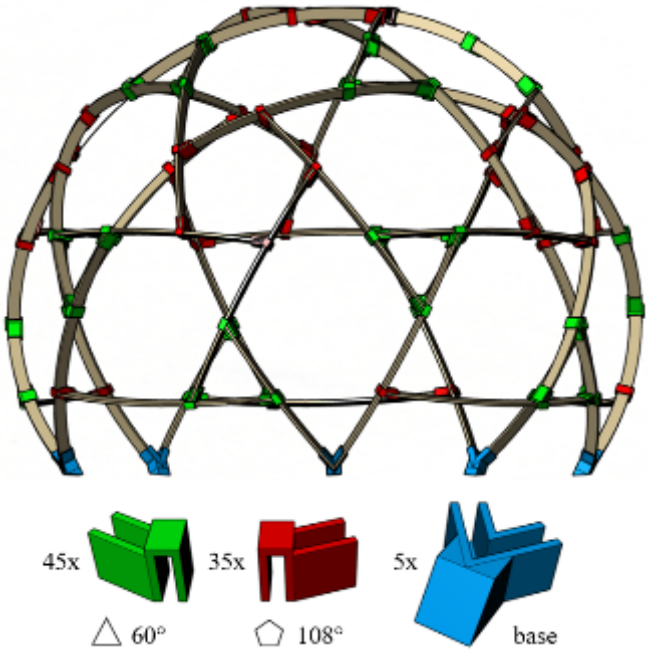


Figure 5. Connection system for the unstrained version of the ReciPlyDome with curved beams, consisting of three types: Type 60° for the triangles, Type 108° for the pentagons and Type base for a connection to the ground.

To test this connection system, 3D models were made and 3D printed. The design allowed for the Type 60° end Type 108° to be easily slid over the beams, while the adjacent beam can lean on the side of the connector (Figure 6).

To connect the dome to the ground, a base type was designed where two beams come together under an angle of 60°. By incorporating this angle in the connection piece, the base was able to touch the ground on a stable flat side (Figure 7).



Figure 6. The (a) Type 60° and (b) Type108° connection system, which can be respectively used to create (a) triangles and (b) pentagons.



Figure 7. The Type Base connection system, to provide a stable connection between the lower beams and the ground.

3.2. Prototype scale

To translate this connection system to the prototype scale, some alterations had to be made. First, to make the system more efficient in terms of material use and fabrication, the design was simplified. The first result of this was a connection system consisting of a pre-drilled 2 mm U-shaped steel plate welded onto a another pre-drilled 2 mm steel plate. However, since it still included a lot of operations, cutting out the right shape, drilling, folding and welding, it was simplified even more.

The next version consisted of two 2 mm L-shaped stainless steel plates of 60° and 120° for the Type 60° connector and 108° and 72° of the Type 108° connector (Figure 10). However, although equilateral triangles and pentagons are used in the dome, there corners turned out to be slightly different. Due to the three dimensional spherical shape of the structure, the connection angles



Figure 8. First version of the connection system Type 60° on prototype scale.

are turned inwards as can be seen in Figure 9. Therefore more correct angles would be 60.77° and 119.23° for the Type 60° connectors and 70.18° and 109.85° for the Type 108° connectors.

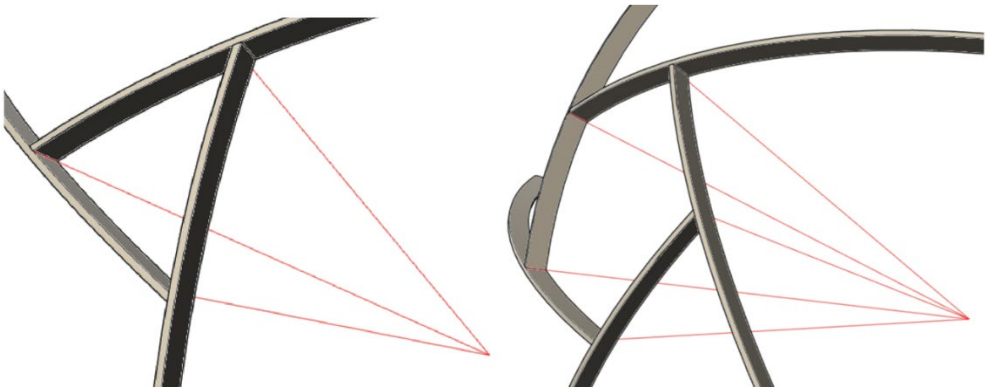


Figure 9. Inclined connection angles due to the sperical shape of the structure.

Another change was elongating the holes in the steel plates on the side that would be connected at one third of the beam length (Figure 10). This allows for some flexibility during assembly, but still sufficient stiffness once fully assembled. Lastly, some smaller holes were added onto the plates to allow a future cladding system.



(a) (b)

Figure 10. Second version of the connection system (a) Type 60° and (b) Type 108° on prototype scale.

4. Assembly

4.1. Assembly of the model

For a smooth assembly of the scale model, the laser-cut beams were prepared by attaching the 3D printed connection pieces to the end of each beam. As can be seen in Figure 11, each beam contains a Type 60° connector on one side and a Type 108° connector on the other side. Only for the five beams at the base the Type 108° connector was exchanged for a Base connector. By subsequently attaching the connectors at one third of the beam length, triangles can be created from the Type 60° connectors and pentagons from the Type 108° connectors (Figure 12).

Compared to the earlier model with incisions, this version allowed an easier assembly thanks to the connection system. Additionally, the structure was more secure, whereas the previous version started to fall apart halfway through the assembly. Therefore the connection system allowed for an overall stiffer structure.

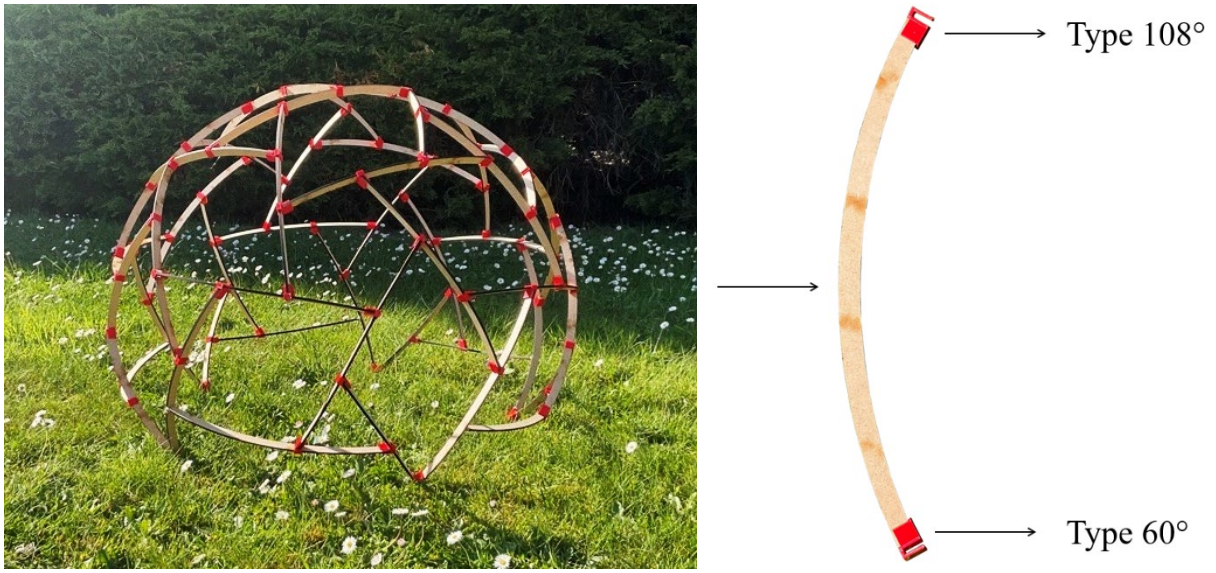
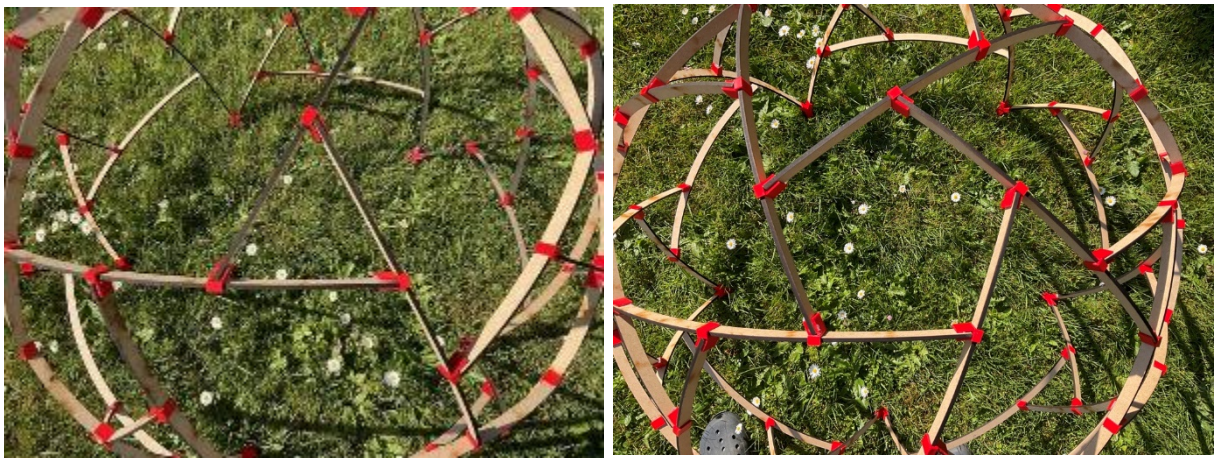


Figure 12. Assembly of the scale model of the rethought ReciPlyDome with modular beams and connection pieces of Type 60°, Type 108° and Base.



(a) (b)

Figure 11. (a) Triangles and (b) pentagons formed by respectively the Type 60° and Type 108° connectors.

4.2. Assembly of the first prototype

The first connectors made for the prototype were obtained through drilling holes through 2mm steel plates, folding the steel plates and finally welding the required edges together. Afterwards a coating was applied to achieve a homogeneous look and protect the connectors from corrosion. The final result were three Type 60° connectors.



Figure 13. First prototype for the Type 60° connection system.

The plywood beams for the prototype were manufactured with the aid of a jigsaw. However, due to the curved shape of the beams, a lot of plate material was wasted. Therefore options to repurpose the leftover materials should be explored.

For the assembly, the beams were prepared in a similar manner as the scale model. At the end of each beam a Type 60° connector was attached. Next, the beams were connected to each other by attaching the connector at one third of the beam. This connection system allowed for a torsion- and stress-free assembly of a triangular fragment of the dome.

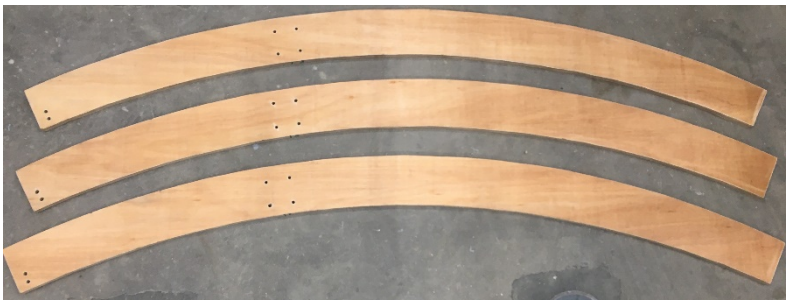


Figure 14. First prototype for the single-layer curved beams.



Figure 15. The prototype of the Type 60° connection system connected to the beams.



Figure 16. Assembly of a triangular fragment of the dome with the first prototypes of the Type 60° connection system and single-layer curved beams.

4.3. Assembly of the second prototype

To make the connection system more material efficient and easier to fabricate, a second version was developed. The beams were already prepared by connecting the adapted Type 60° and Type 108° connection system, now consisting of L-shaped plates, respectively to each side of the beam. Thereafter six pentagons were made by connecting each time five beams with each other through the Type 108° connectors. The central pentagon was then attached to a lift, whereafter the other pentagons could be attached to this central pentagon by raising and lowering the lift. Lastly the remaining beams were attached from top to bottom.

The two beams forming a base of the structure are connected with the L-shaped plate bended over 70.18°, which is part of the Type 108° connection system. To fix it to the ground a U-shaped anchor was used. During future research a better connection to the floor will be developed.

From this assembly it was concluded that the torsion present in the ReciPlyDome with the double-layered beams was eliminated. However the assembly process might still be optimized in the future by working out a smoother plan such as a beam per beam top to bottom assembly starting from the central pentagon, as during the tested assembly process the attachment of the pentagons to each other was still challenging due to their size.



Figure 17. Assembly of the full scale prototype of the second version of the ReciPlyDome.



Figure 18. The assembled ReciPlyDome, version 2

5. Conclusion

While working towards reusable temporary structures, the ReciPlyDome was reviewed to obtain a smoother assembly and disassembly process. To achieve this goal, the torsion present in the assembly process needed to be eliminated. This was mainly achieved by rotating the beams by 90° degrees and reducing them to a single-layered module. However, to obtain the same curvature the beams are cut out in a curved manner, which results in some material losses.

Next to the rotation of the beams, a new connection system was developed that also contributes in the elimination of torsion and a smooth assembly due to the margins provided by the slotted holes. A connection system to fix the dome to the ground still needs to be developed. In future research it will be reviewed if these excess pieces of wood created by the curved shape of the beams can be used in the design for the base connection pieces of the dome.

The hands-on approach during this research allowed for accurate insights in the performance of the developed concepts. Additionally, the prefabrication of the beams and the connection system contributed to an overall smoother assembly. However, for future use a more fluent assembly plan will be designed.

The next step in this research is to conduct both a physical as a digital structural analysis to asses the optimisations. Additionally, a cladding system will be designed to provide more comfort in outdoor usage of the structure.

Acknowledgements

This research was partially supported by the VUB IOF Funding for a Proof of Concept.

References

[1] M. Núñez, R. García-Lozano, P. Boquera, X. Gabarrell and J. Rieradevall, “Temporary structures as a generator of waste in covered trade fairs,” *Waste Management,* 2009.

[2] Net Zero Carbon Events, “A Net Zero Roadmap for the Events Industry,” 2022.

[3] S. Brancart, O. Popovic Larsen, L. De Laet and N. De Temmerman, "Rapidly assembled reciprocal systems with bending-active components: The ReciPlyDome project.," *Journal of the International Association for Shell and Spatial Structures,* pp. 1-13, 2019.

IASS 2023
July 10–14 Melbourne
Integration of Design and Fabrication

Proceedings of the IASS Annual Symposium 2023
Integration of Design and Fabrication
10–14 July 2023, Melbourne, Australia
Y.M. Xie, J. Burry, T.U. Lee and J. Ma (eds.)

Development of the design of the new Sydney Football Stadium

Alex EDWARDS[a,*], Tristram CARFRAE[a], Andrew JOHNSON[a]

[a,*] Arup,
Level 5, 151 Clarence Street, Sydney, NSW
Alex.edwards@arup.com

Abstract

The original Sydney Football Stadium (SFS), completed in 1988, was demolished to make way for a new stadium that opened in 2022. This paper outlines the early stages of the engineering design work for the roof structure. The roof of the stadium is a PTFE fabric covered form-found grid shell structure that is light and elegant. Arup developed a reference design for the project, supported the winning architect in the design competition and worked with that architect to develop the project though an early contractor involvement phase. Following a design and construct tender process, the contract was awarded to a different contractor and the design was then completed by the new contractor's (John Holland) team. Arup were engaged by the Client to continue our involvement and peer review the contractor's design finalisation.

Keywords: stadium, form finding, fabric roof, grid shell



Figure 1. Image of the completed new Sydney Football Stadium

Copyright © 2023 by ARUP. Published in the Proceedings of the IASS Annual Symposium 2023 with permission.

1. **Introduction**

The original Sydney Football Stadium (SFS) [1], completed in 1988, was demolished to make way for a new stadium that opened in 2022. The roof of the new stadium is twice as efficient as its predecessor, and twice the size. Structurally, it is an evolution of AAMI Park in Melbourne and Adelaide Oval with a dash of Suncorp from Brisbane.

A great many recent stadium roofs have used some variant of opposing cable nets using one or two perimeter compression rings and one or two inner tension ring(s). All owe their pedigree to Schlaich Bergermann Partner's original at Stuttgart in 1993. While using high strength tensile steel cables is very efficient, could a well-proportioned single layer tension/compression structure be similarly efficient?

The height constraints for the new SFS hinted that a single layer shell configuration of some sort might be an attractive proposition. The new stadium had to remain low around the eaves, especially along the northern side adjacent to housing in Paddington, and there was an overall height limit for the entire development (similar to the original) which was too low to accommodate a Pantheon style "dome with a hole". So the design team decided to trade the upper seating in the corners for the ability to more directly support the roof from the stand itself (as Suncorp) [2].

Borrowing Antoni Gaudi's hanging chain approach, albeit in a digital form, we inverted the roof and form-found the funicular grid shell shape hanging from the perimeter and the corners of the lower stand. The diagrid roof uses deeper members in the arching radial direction to facilitate erection on a bay-by-bay basis.

The Arup team developed the roof, through design development, including the fabric, steelwork connections and indicative construction sequencing, which was then finalised, documented and constructed by the John Holland design and construct team.

The finest contemporary stadiums integrate into the fabric of the communities they serve, taking on the dual roles of both entertainment destination and iconic city landmarks. This innovative, sophisticated, multi-purpose building is aesthetically pleasing, environmentally sensitive, and maintains a high degree of future flexibility.

2. Site history

The original Sydney football stadium was opened in 1988 and served as the major stadium for rectangular pitch events in NSW. The design was innovative, however the stadium only offered weather protection to 25,000 of the possible 40,000 spectators and was lacking in modern spectator amenities. Arup were involved in numerous investigations in the 2000's to extend the existing roof, increase seating capacity, add a full retractable roof, or to create a larger stadium on an adjacent site [3].

In 2017 the NSW government committed to demolishing the existing stadium and replacing it with a contemporary facility on roughly the same site that addressed the shortcomings of the existing stadium and provide a new world class stadium for sporting fans to enjoy.

3. Reference design

In early 2018 Arup were engaged to provide technical input into the brief for a new stadium to be built on the site of the existing stadium. It was intended that the new stadium be at least 45,000 seats over 3 tiers and provide a modern, iconic world class rectangular pitch facility that could be utilized both for sporting and entertainment events. The stadium was to be integrated with the Moore Park precinct, and in particular, with the Sydney Cricket Ground (SCG) to the south, allowing ease of concurrent events and sharing of facilities to optimize operation, performance, spectator enjoyment, and player satisfaction.

The technical brief required the stadium to be best in class internationally and required as a minimum full compliance with international design criteria as set by FIFA and World Rugby. It was intended that

the roof covers a minimum of 100% of the seating, on the basis of a vertical drip line, and provide adequate rigging provision for all modern sporting activities and entertainment events as could be reasonably expected to be held at the venue.

As part of that work Arup developed a range of structural options for the roof form including tension rings, truss arrangements, cantilevers and shell options.

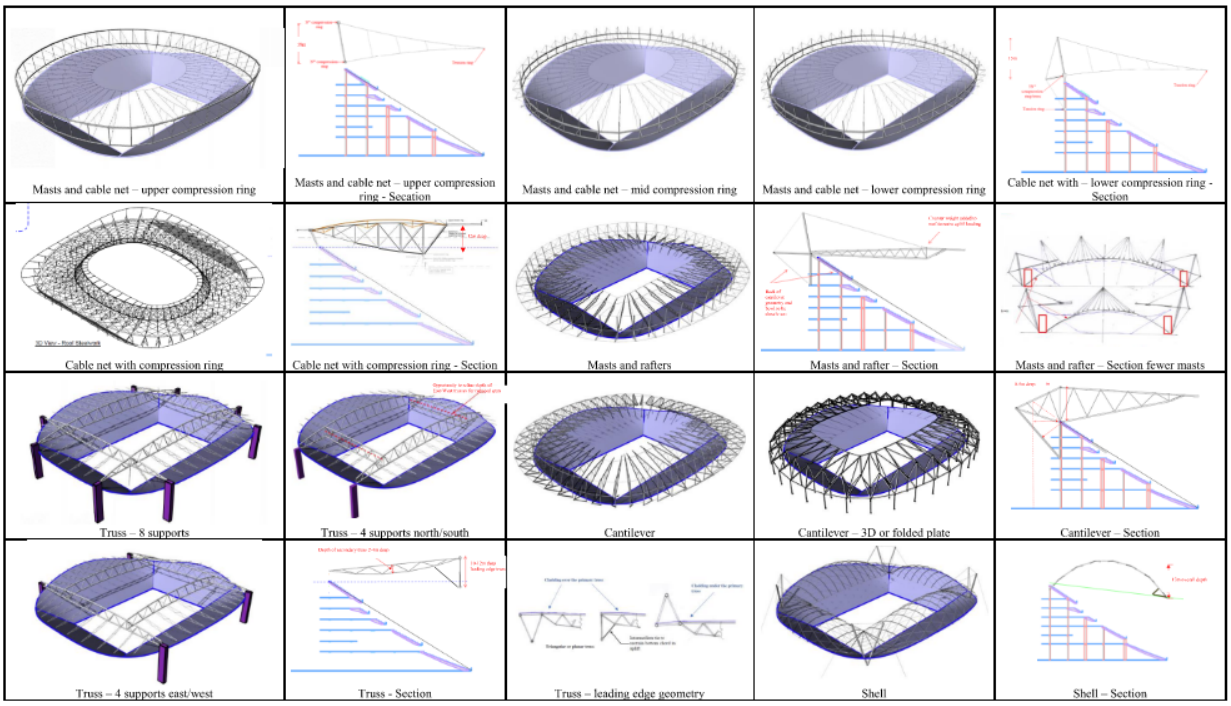


Figure 2. A subset of the stadium geometry forms developed for the reference design. The shell option ultimately used is a development of the lower right.

4. Design competition

In late 2018 an architectural design competition was held for the roof, façade and public realm. Arup supported COX architecture through the design competition. The design was geometrically constrained by:

- a height plane that limited the overall height of the roof to similar to the existing stadium;
- a requirement that every seat have visibility of the scoreboard; &
- that all the seats have roof coverage, vertically.

The design also needed to be low in scale at the north so as not to dominate the adjacent residential areas. The design developed utilized the corners of the seating bowl for the primary support of the roof while maximizing the clear span to provide uninterrupted views for the spectators from every seat.

The resulting roof form was a grid shell supported by a tension ring that is propped off the rear of the seating bowl. The inner edge of the shell is supported by 4 arches, roughly following the geometry of the pitch. The shell and the arch have been digitally form-found. This has the following consequences:

- The arches are not planar but are 3-dimensional space curves that respond to the applied loads from the shell onto to the arch. This means that though the steelwork looks like a truss the axial force is concentrated into only one of the chord members;

- The arches can be adjusted in height by adjusting the tension used in the form finding, such that the resultant lateral thrusts from the two (2) arches into the derrick (refer Figure 3) structure remain aligned with the derrick plan geometry;
- The lateral thrusts of the arches combined with the vertical loads of the roof mean that the line of action extends through the concrete abutment structure continuously to foundation level, eliminating vertical eccentricity in the abutment and alleviating the need for tension piles.

The design competition proposed two material choices for the roof, the first being a timber hybrid roof where the diagonal "radial" members of the shell were 600 deep glulam timber elements and the shell circumferential hoops being steel. An all-steel option was also presented.

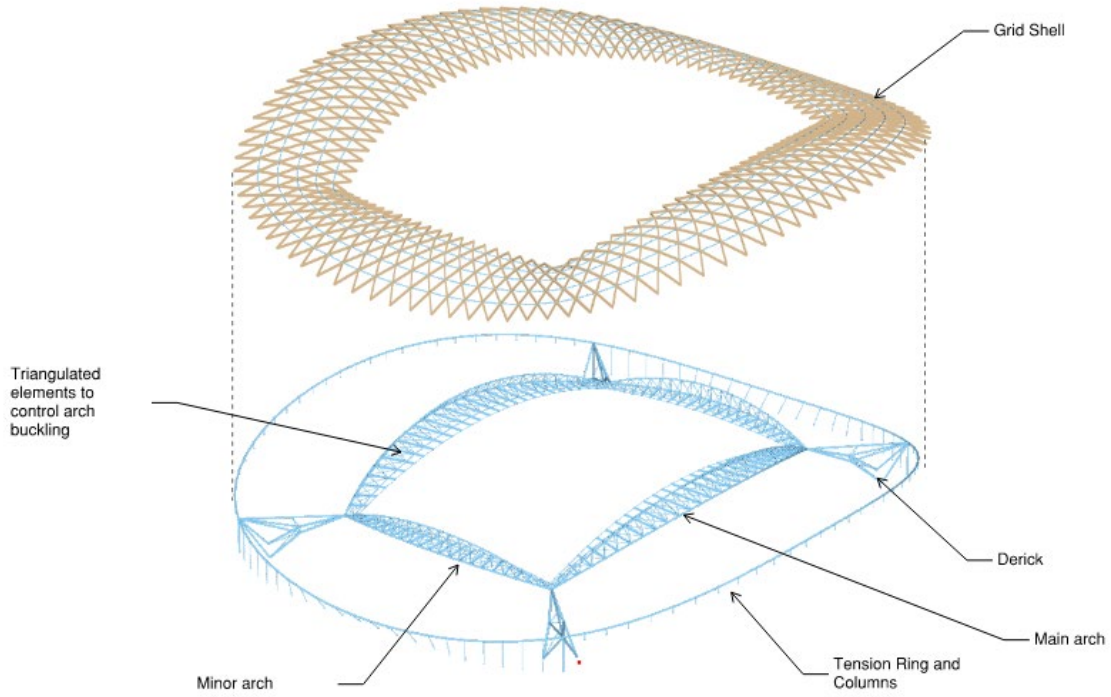


Figure 3. Key components of the roof structure.

5. Design development

Following the design competition a period of design development was undertaken with the involvement of a contractor to develop pricing and design options on an Early Contractor Involvement (ECI) basis. Arup were engaged to develop the design of the roof through this period as subconsultant to the architects. Early on in this process it became apparent that while the design principles were set, there was still considerable need to explore bowl geometries, sightlines and roof curvatures while remaining within the limiting height plane.

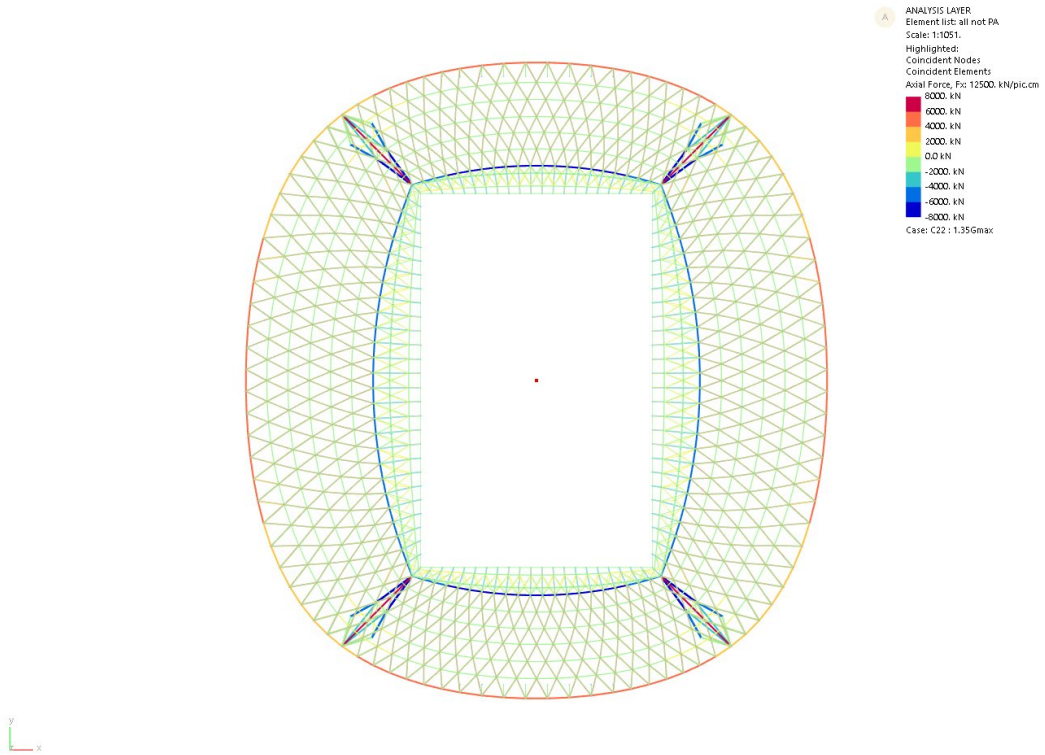


Figure 4. Axial Force in the roof members under gravity loads. Note the compression in the single arching member showing that this portion of the roof is acting as an arch rather than as a truss.

A fully automated digital workflow was developed in conjunction with the architects to allow for the rapid investigation of geometries. The workflow used Grasshopper and Rhino for the geometry, Oasys GSA for the structural analysis, and utilized GHData files for the transfer of information between the architects and engineers. The general process was:

- The architects provided the geometry of the rear line of the bowl, the front rows of seats, bowl structural grid, the arch/derick intersection height - a key driver of the sightlines, and the maximum allowed height plane for the roof;
- Arup developed an initial roof geometry form those generating constraints that represented an approximate starting point for the form finding;
- GeometryGym was used to export the initial structural geometry to GSA where a form-finding analysis was run to determine the shape of the shell and arches. The Grasshopper script could take parameters for how much curvature was allowed in the shell part of the roof and how much in the arches. Greater curvatures generally mean better structural performance but at the expense of an overall height of the roof, thus one of the key decisions was how the curvature should be distributed rather than the absolute amount. The relative curvatures of the major and minor arches was tuned so that the reaction into the corner supports was aligned at a 45-degree angle (this angle was set by planning and sightlines, recognising that this is not the most efficient resultant thrust angle for the rectangular roof footprint);
- This form-found geometry was taken back into grasshopper and the full model of the roof developed - including the front eyebrow steelwork and the bracing members to provide stability for the arch;
- This full model geometry was exported again to GSA via geometry gym and an iterative member sizing routine used to determine optimum member sizes; &

- A GHdata file was sent back to the architects that included key splines and locations for them to automatically position sports lighting, scoreboards and access walkways.

This process allowed for the rapid investigation of alternative bowl geometries and roof sizes through this stage of the project.

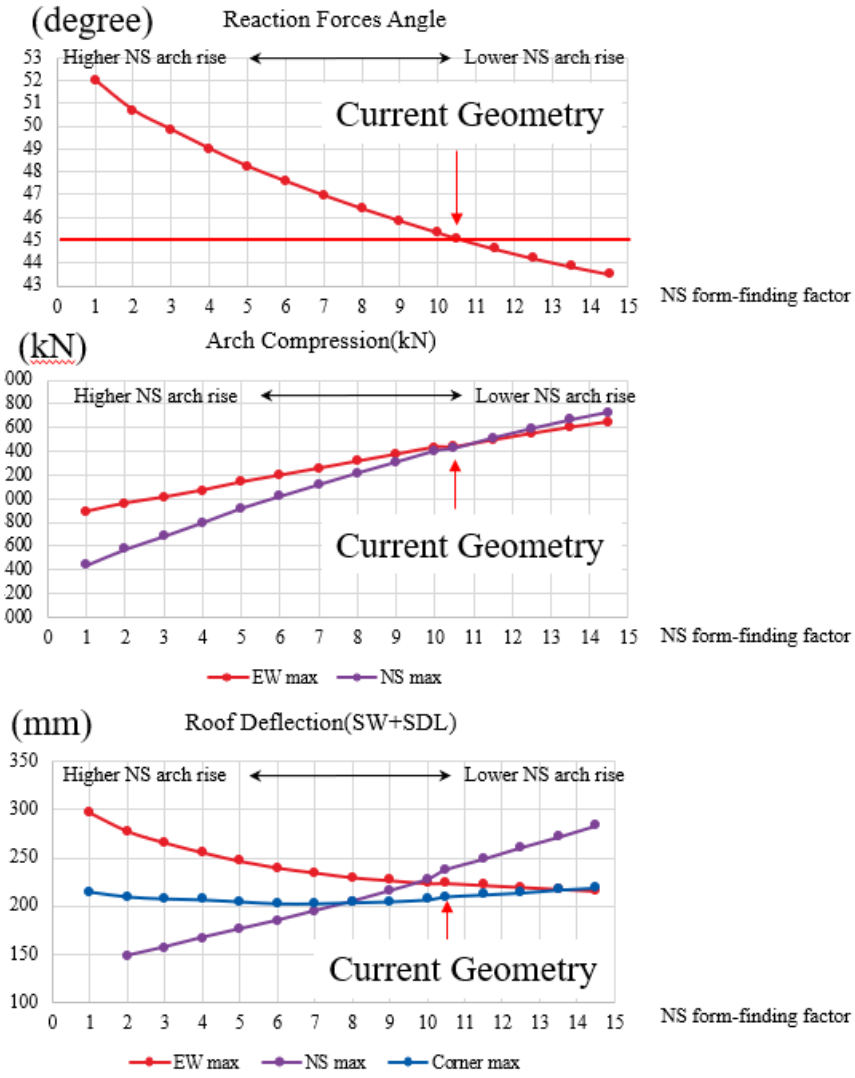


Figure 5. Graphs showing the geometry investigations. These graphs show how balancing the height of the north, south-and east west arches of the roof affect the angle of the reaction force into the derrick, the arch compression, and the roof deflections.

The two options for member material were progressed in parallel during this stage of the project. One of the key risks identified by the ECI contractor was the timber connections. Arup addressed this in two ways, initially by providing three options for each type of connection based on the 75th, 95th and 100th percentile design forces. Quite often designers, especially when time is limited, will only document the worst case and this causes concern to contractors and clients. By having automated model results we were able to produce three designs relatively quickly demonstrating that whilst there were some members with high forces, the vast majority of the of the connections were relatively easy to construct.

The other method was to concentrate the complexity into only part of the system, while making the rest of the system less complex. Glulam is most cost effective when the members are straight. The shell geometry requires a curved member to follow the overall shape as well as a twist to follow the local surface normal. The solution developed was to utilize straight timber elements orientated to normal to the shell at the member mid-point, with a steel node where the twist and the facet could be taken by profile cutting a single plate. To connect the timber to the steel onsite, a connection type similar to that used for furniture was proposed. Steel bars were threaded into a solid steel cross rods in holes in the timber. This portion is similar to that used with great success by the designers of the Nelson Airport terminal [5], and Arup previously at the Royal Agricultural Society at Homebush.

The ECI contractor had a strong preference to remove risk form the project and considered the timber likely to have substantial program and cost uncertainty. With the project timeframe being tight and the budget stretched, the decision was made to focus attention on the full steel option and not progress the timber design any further. The steel option was further developed as described in the sections below.

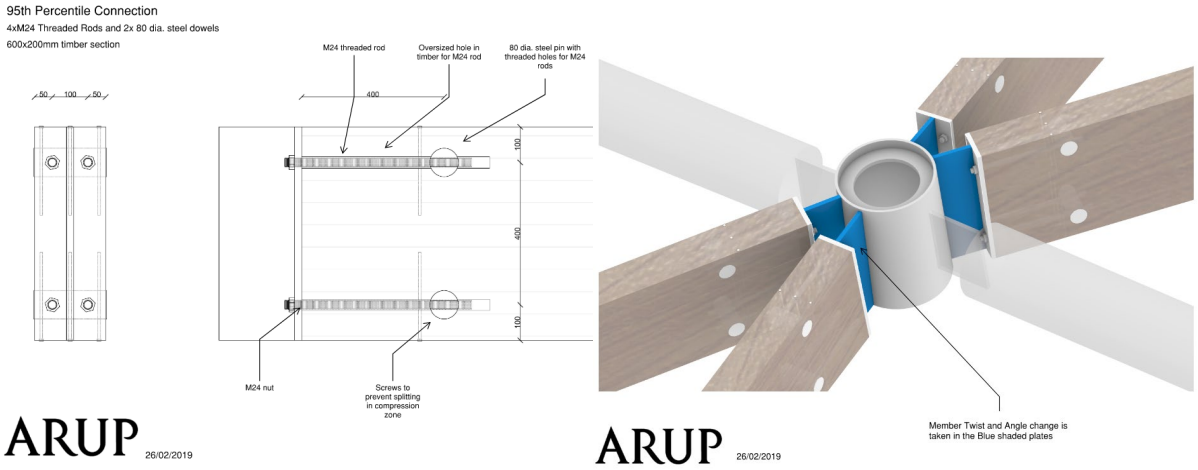


Figure 6. Timber connection design option. The highlighted blue plate was cut in a trapezoidal shape with 1 curved edge to accommodate required twist and facet angle particular to this location. The circular node is made from a section of 457 dia CHS with 2 internal stiffeners.

6. Wind tunnel analysis

A 1:300 scale model of the Stadium was tested in the CPP boundary layer wind tunnel in Sydney. The top and bottom surfaces of the stadium roof were instrumented with a total of 310 pressure taps and the time-history pressures recorded for 36 cardinal directions. The 310 pressure tap results were mapped to 64 load patches for application onto the structural analysis model.

The full time-history data from the wind tunnel was processed to determine the critical load cases for consideration in the structural design. A unit load was applied in the structural analysis model to each of 64 load patches in turn. The design action at a point of interest was extracted for each of the patch loads and multiplied component wise by the pressure from the wind tunnel time-history and summed - thus a time history of the design action of interest could be created. The time-histories for each direction were broken into wind-storm events of approximately 10 minutes at full scale and the worst design action for each wind-storm event calculated. The median of the worst 5 design wind-storms was extracted as a load pattern and used in the structural analysis. This process was automated using scripts for convenience as the total number of time steps exceeded two million.

The choice of which design action to maximize or minimize was made using an understanding of the behavior of the structure. Finding the extremes of axial force in the arching members was an obvious

area of interest, however shell and arch structures are susceptible to out-of-balance loads and lateral deflection was used as a proxy to find the cases that caused the worst pattern load in the structure. These load distributions used for the structural analysis for member sizing. A selection of images showing the various design actions and the resulting wind load patterns are shown below in Figure 7.

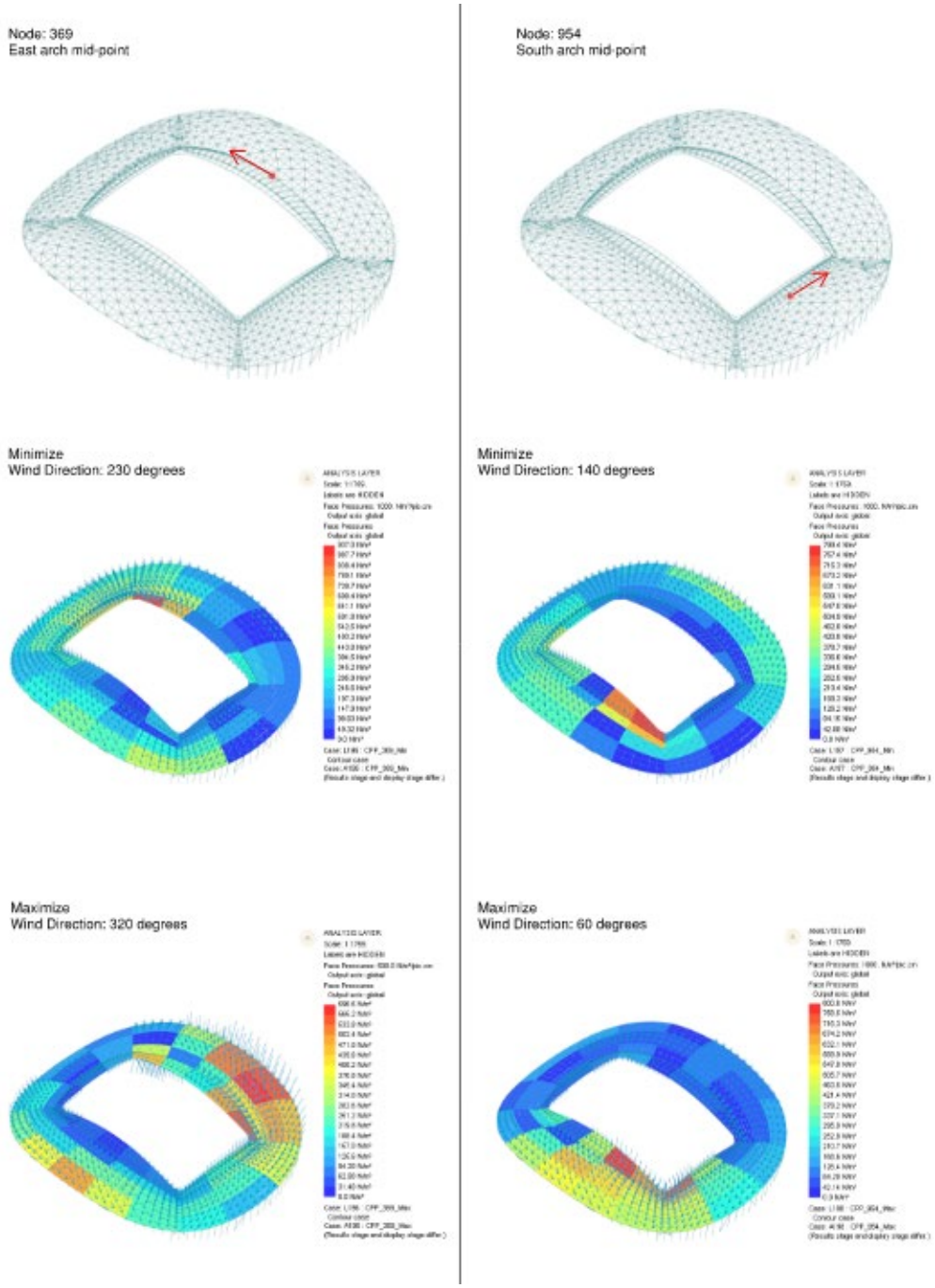


Figure 7. Extracted patterns of wind load from the wind tunnel time-history. These cases represent cases that generate the maximum lateral displacement on the major and minor arches and were used to determine the most adverse out-of-balance load for the strength design of the arches. Colours show pressure magnitude and arrows show the direction.



Figure 8. Stadium model in the wind tunnel showing modelling of surrounding buildings.

7. Construction sequence analysis

Construction of the roof was given careful consideration both in conceiving the roof concept and developing the design. This allowed us to demonstrate a functional construction sequence, and to quantify the effects of construction sequence on the material quantities. The original competition entry envisioned the arches being constructed on towers at six (6) locations with sections of the shell being lifted into place between the tension ring and the arches. This construction methodology meant that the only temporary support that the roof needed during construction was very close to the pitch, having minimal impact on the construction and fit-out of the stadium bowl below.

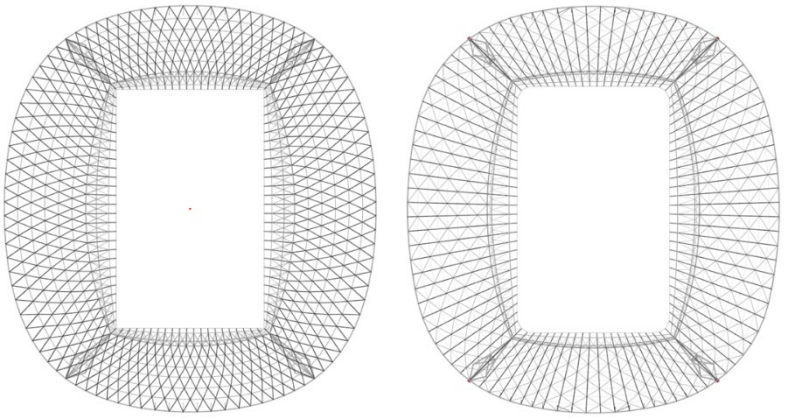


Figure 9. The competition geometry left, compared with the developed geometry right. The change allows pairs of shell members to be lifted into place as a unit and then infill lacing between units installed.

The spiral nature of the shell geometry meant that ideal size of element to be lifted was relatively large, with approximately six lifts on each of the long sides of the stadium. By rotating the grid of the shell by 30 degrees compared to the competition scheme and using a temporary tension tie, sections of the shell roof consisting of only two ribs and one bay of lacing were stable and could be lifted into place.

Construction of the roof could proceed in two directions to speed installation with the weight of the roof supported by the towers. The base case envisioned that the roof would remain on the towers until the structure was complete, though options were investigated to allow early de-propping of the roof, this case needing some temporary ties in the arches and more careful management of tolerance and deflections. Ultimately the construction sequence developed by the contractor and their team followed that developed during this stage.

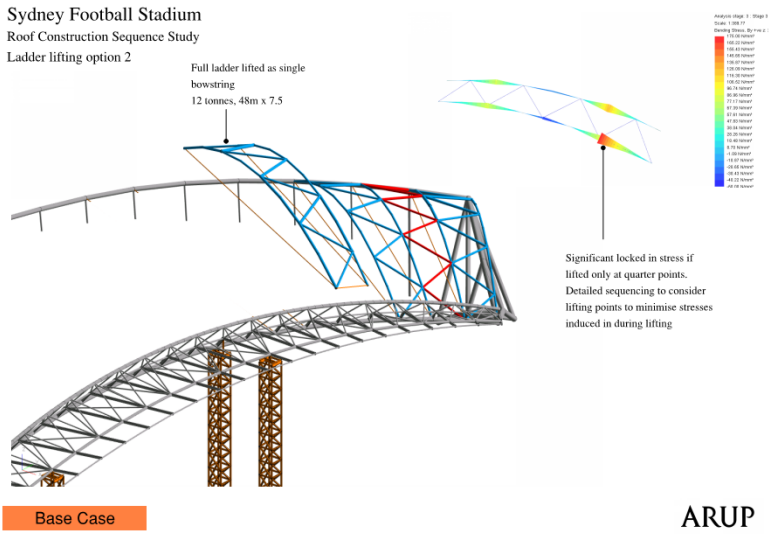


Figure 10. Extracts from the construction sequence sketch pack showing lifting and erection of the shell elements.



Figure 11. Construction stage image showing support of towers at discrete locations and the installation of temporary ties to the shell members.

8. Designing for robustness

The client brief had a specific robustness requirement - the removal of any one element was not to lead to disproportionate collapse of the roof. This procedure is documented in BV2 of the Australian National Construction Code.

Initial investigations of the analysis model indicated that it was difficult to determine which elements to remove and investigate further and so the process was automated and all elements were considered. One structural element was removed at a time and the impact on maximum member stresses in the remaining members and resulting change in loading at support points considered. In all approximately 5000 analysis models were generated. To minimize the run-time several techniques were used including running the models on several computers in parallel, as individual analyses were independent, and initially using elastic material properties for faster analysis time to find cases where the structure remained elastic following element removal. Once removal of a particular element was identified as needing further investigation the analysis was re-run with material non-linearity to allow redistribution of the load into surrounding areas.

The analysis indicated that there were a few elements where increasing the size was needed to meet the elements removal requirement, but overall, this increase in tonnage was only about 48t or 4% or the total roof weight.

9. Fabric design

Preliminary analysis of the fabric membrane was undertaken to confirm the structural performance of the membrane, as well as to inform the structural design of the roof. One of the key issues was the spacing of the supporting rafters in the primary structure. A larger primary rib spacing leads to fewer steel connections and so increasing the spacing as much as possible lead to a more economic outcome. The automated workflow used for the primary structure design was extended to form-find and analyse the fabric so that multiple options could be considered. Clashing of the fabric with the primary structure of the roof under wind loading cases was also considered.

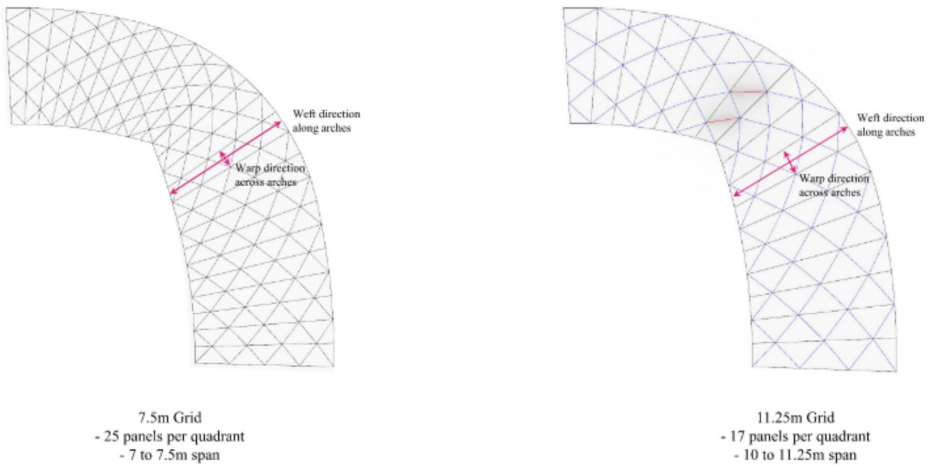


Figure 12. Images of the fabric analysis models showing 2 grid options under consideration.

Also of interest was ponding of water on the fabric membrane. Areas of possible ponding were identified by looking at the vertical height contours of the fabric surface and identifying areas where they formed closed loops. The geometry was checked for both the at-rest condition and extremes of primary structure and fabric deflection to ensure adequate drainage under all conditions.

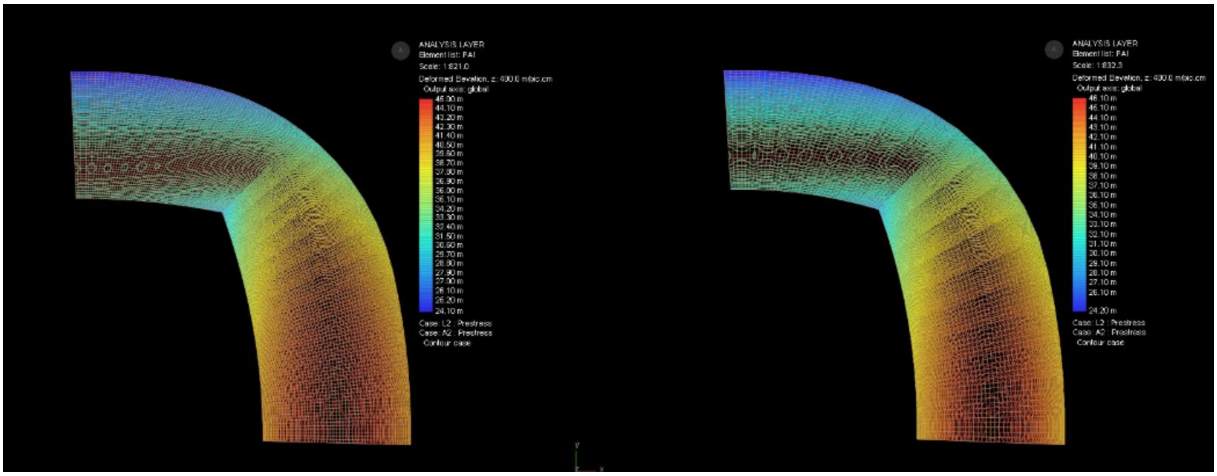


Figure 13. Vertical height contours of the form-found fabric membrane used to detect possible areas of ponding.

10. Post tender

In late 2019 the NSW government awarded the design and construction contract to John Holland group to complete the design and construction of the stadium. Arup were retained by the client to peer review the design as it progressed while the contractor engaged a team of Engineers including Aurecon and Schlaich Bergermann und Partner to continue working with COX and carry out the detailed design and documentation of the roof. That almost all the design principles mentioned in this paper have survived the design and construction process is a testament to the whole team's skill and dedication. The end result is a structurally generated stadium roof that is elegant, efficient and wonderful.

References

[1] T. Carfrae; "The structure of stadia – from exoskeletons to haute couture," Australian Journal of Structural Engineering, vol. 6 issue 3, pp. 169-180 2006

[2] I. Ainsworth; "Suncorp Stadium Redevelopment." Australian Structural Engineering Conference Sydney, N.S.W.: Engineers Australia, 2005.

[3] S. Finlayson; "The Undeniable Benefits of Parametrics: A Stadium-Design Case Study" Autodesk University(Conference) Las Vegas, 2016

[4] P. Thompson, B.Thomas, T. Carfrae; "Sydney Football Stadium", Arup Journal, Issue 1 1989

[5] E. Novak, S. Zondag, S. Berry, S. Hardy, "Nelson Airport's new terminal – overview of the design of a large-span engineered timber specialist building" . NZ Journal of Forestry, November 2018, Vol. 63, No. 3

IASS 2023
July 10–14 Melbourne
Integration of Design and Fabrication

Proceedings of the IASS Annual Symposium 2023
Integration of Design and Fabrication
10–14 July 2023, Melbourne, Australia
Y.M. Xie, J. Burry, T.U. Lee and J. Ma (eds.)

FreeGrid: a benchmark on design and optimisation of free-edge gridshells

Luca BRUNO[a,*], Paolo CIGNONI[b], Stefano GABRIELE[c], Ernesto GRANDE[d], Maura IMBIMBO[e], Francesco LACCONE[b], Francesco MARMO[f], Elena MELE[f], Lorenzo RAFFAELE[a], Valentina TOMEI[e], Fiammetta VENUTI[a]

[a,*] Politecnico di Torino,
Viale Mattioli 39, 10126 Torino, Italy
freegrid@ctanet.it

[b] Institute of Information Science and Technologies, National Research Council of Italy, Italy
[c] Università degli studi Roma Tre, Italy
[d] Università degli studi Guglielmo Marconi, Italy
[e] Università degli studi di Cassino e del Lazio Meridionale, Italy
[f] Università degli studi di Napoli Federico II, Italy

Abstract

FreeGrid is meant to offer a common benchmark to test and compare different approaches to the design and optimization of steel gridshells, from man-based heuristic design to AI-based one. FreeGrid sets three design baseline problems: a barrel vault, a paraboloidal dome, and a hyperbolic paraboloid, having their spring line partially not constrained (free-edge) and subjected to symmetric and asymmetric load conditions. Participants are called to modify the baseline gridshell(s) in order to improve their structural performances, buildability, and sustainability, all three of them weighted in a single, bulk quantitative performance metric. Participants shall comply with a limited number of design constraints, while any other design solution is allowed. Baseline setups, performance metrics and design constraints will be fully detailed in technical specifications made publicly available. The full data of the baseline structures will be offered to participants according to an Open Data policy, together with postprocessing utilities intended to align the procedure to obtain the performance metrics. The FreeGrid benchmark will be launched within the IASS Symposium 2023 in Melbourne.

Keywords: freeGrid, benchmark, steel gridshell, free-edge, conceptual design, optimisation

1. Introduction

FreeGrid is a benchmark on design and optimization of gridshells (Fig. 1) conceived by the Authors of the present paper as members of its Steering Committee, advised by an international Scientific Committee. FreeGrid moves from seven general problem statements, and towards the related goals, as briefly listed in the following.

i. The activity in Structural Engineering in general, and about gridshell as well, is increasingly polarized between mechanical modelling and analysis versus design practice and applications [1]. FreeGrid is intended to bridge these two approaches. It proposes a genuine design problem, and targets the rigorous quantitative comparison of the solutions and their performances.

ii. The design and optimization of gridshells as form-resistant discrete structures is intrinsically a multidisciplinary activity jointly carried out by experts in mathematics, computer graphics, mechanics,

Copyright © 2023 by Luca BRUNO, Paolo CIGNONI, Stefano GABRIELE, Ernesto GRANDE, Maura IMBIMBO, Francesco LACCONE, Francesco MARMO, Elena MELE, Lorenzo RAFFAELE, Valentina TOMEI and Fiammetta VENUTI. Published in the Proceedings of the IASS Annual Symposium 2023 with permission.

structural engineering, architecture, designers and builders. FreeGrid aims at gathering competences and input from all the above fields around a common design problem.

iii. Artificial Intelligence (AI) is among the most recent generalized trends in contemporary science, and in structural engineering as well [2]. FreeGrid is meant to offer a common benchmark to comparatively test the readiness of different approaches to the conceptual design of form-resistant structures, from the classical man-based heuristic design, to the optimization approach in its different forms (e.g. gradient-based, topological, genetic-algorithm-based), to the AI-assisted design methods (e.g. artificial neural networks, machine learning).

iv. Horizontal spring line and/or perfect infinitely rigid constraints only seldom occur in built gridshells. Usually and more and more frequently, gridshells include edges free of constraints eventually bounded by stiffening members [3]. Conversely, the structural performances of free-edge gridshells and their design proposals are scarcely treated in scientific systematic studies. FreeGrid aims at filling the gap between the design practice and the scientific literature in this field by adopting free-edge gridshells as case studies.

v. Design is a holistic activity accounting for multiple goals [4]. FreeGrid calls for the holistic improvement of structural, buildability, and sustainability performances. Multiple, even if not necessarily exhaustive, design goals and related performance metrics are defined.

vi. Benchmarking best practices require that *studies and related results are reproducible* [5]. FreeGrid sets mandatory requirements to participants intended to secure the full description of (a) the geometrical and mechanical features of the design solutions, (b) the methods adopted for design/optimization/assessment, (c) the obtained results. FreeGrid adopts an Open Data policy applied to preprocessing and postprocessing files offered by the organizers and/or required to participants.

vii. The *fair comparative evaluation* of contributions in benchmarks on structural design and optimization is recognised as a challenging issue [5]. FreeGrid precisely and analytically adopts objective, purely quantitative performance metrics that do not need a posteriori assessment.



Figure 1. Logo of the FreeGrid benchmark

The present paper articulately describes in what follows the way in which FreeGrid plans to achieve the above goals. For a better understanding, the terminology used in the present paper and in the benchmark is summarized in Table 1.

Table 1. Main terminology adopted in the paper

entity	**geometry**	**Structure / construction**	**mathematical model**	**Subscript, total number**
0D	vertex	joint	node	*j, N*
1D	edge / line / arc	member	element	*i, M*
2D single entity	face	panel	---	*f, F*
2D overall entity	mesh	grid	discretization	

2. Baseline gridshells

FreeGrid considers three types of gridshells (Fig. 2): a barrel vault, a paraboloidal dome, and a hyperbolic paraboloid, with simple, double gaussian positive, and double gaussian negative curvature, respectively. By 'Background Gridshells' we refer to gridshells fully hinged along their boundaries, while by 'Design Baseline Gridshells' (DBGs) we refer to gridshells having their spring line partially not constrained along what is called a 'free-edge' [3]. Although imperfections play a role in gridshell design and optimization [6], for the sake of clarity DBGs are free from any kind of imperfections induced by constraints, load conditions, mechanical properties, or geometrical features.

2.1. Geometrical setups

The main geometrical features of the DBGs are shown in Figure 2.

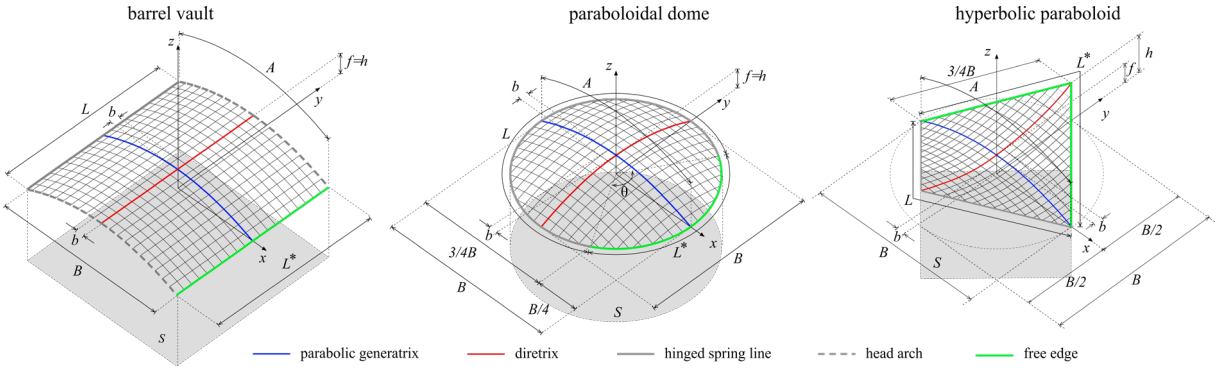
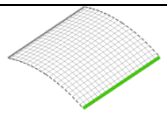
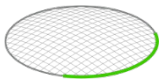
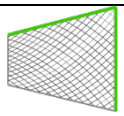


Figure 2. FreeGrid DBGs: barrel vault, paraboloidal dome, hyperbolic paraboloid

All the DBGs share the same parabolic generatrix, whose equation is included in Table 2.

Table 2. Geometrical features of the DBGs

			
Generatrix equation	$z = -\frac{x^2}{2B} + f, \quad D = \left\{-\frac{B}{2} \le x \le \frac{B}{2}\right\}$ $A = \frac{B}{4}\sqrt{5} + B \cdot ln\left(\frac{1+\sqrt{5}}{2}\right)$		
Directrix equation	$z = f,$ $D = \left\{-\frac{B}{2} \le y \le \frac{B}{2}, x = 0\right\}$	$z = -\frac{y^2}{2B} + f,$ $D = \left\{-\frac{B}{2} \le y \le \frac{B}{2}, x = 0\right\}$	$z = \frac{y^2}{2B} + f,$ $D = \left\{-\frac{B}{2} \le y \le \frac{B}{2}, x = 0\right\}$
f	$B/8$		
h	$B/8$	$B/8$	$B/4$
L	A	$\frac{2}{3}\pi B$	$3/2B$
L^*	L	$L/2$	L
S	BL	$\pi B^2/4$	$\pi B^2/2$
b	$A/20$		

The generatrix span B =30 m is adopted as reference length, and $f = B/8$ is its rise. The horizontal plane $z = 0$ is referenced in the following as 'horizontal reference plane'. The generatrix arc length A accommodates 20 edges with constant length b. The directrix is split with the same step b. Therefore, all DBGs are discrete translational surfaces, whose resulting mesh is homogeneous, and made by planar square faces, except for boundary ones that are obtained by intersection with the horizontal reference plane. The other main geometrical features of the DBGs are: $\boldsymbol{h}$ is the maximum height above the horizontal reference plane; the lengths $\boldsymbol{L}$ and $\boldsymbol{L}^*$ of the spring line and free-edge respectively refer to their continuous counterpart; the surface extent $\boldsymbol{S}$ corresponds to the area encircled by the projection of the continuous spring line, free-edge and head arches, if any, on the horizontal reference plane.

2.2. Structural setups

2.2.1. Structural members

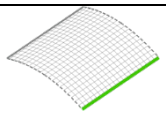
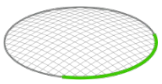
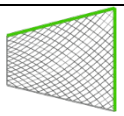
All the structural members of the DBGs are made of steel with a bilinear elastic-perfect plastic constitutive law. Table 3 summarizes the adopted material properties.

Table 3. Material properties of the structural members in the DBGs

Steel grade	density	Young's modulus	Poisson's ratio	yield strength
S355	ρ = 7850 kg/m^3	E = 2.1e+5 MPa	v = 0.3	f_y = 355 MPa

Structural members have circular hollow cross-section and are not subjected to initial prestressing in all the DBGs. The structural members of a single DBG have the same cross section. The cross-section dimensions differ among the DBGs (Table 4), in order to ensure their homogeneous mechanical performances.

Table 4. Cross-section dimensions of the structural members in the DBGs

			
Section type (type, diameter, thickness [mm])	O/139.7/14.2	O/101.6/10	O/101.6/10
Area [mm^2]	5596	2876	2876
Inertia [mm^4]	11157936	3052611	3052611

2.2.2. Structural constraints

External constraints at the structural joints along the spring lines L are perfect hinges, except for the head arches of the barrel vault, along which only z- and x-wise joint displacements are constrained in order to avoid non-linear stiffening induced by the y-wise members. All the internal structural joints are rigid. The structural joints along the free-edge length L^* are not constrained.

2.2.3. Load Conditions

The design solutions shall be evaluated with reference to two Load Conditions (LC$_k$, k =1:2). Both LCs are simplified and exploratory, intended to assess structural performances under ideal and controlled working conditions. Nevertheless, their moduli have the same order of magnitude of standardized design loads on gridshells. They are sketched in Figure 3 in terms of piecewise uniform loads for the sake of clarity.

The first Load Condition (LC_1) cumulates the distributed self-weight of the structural members and the point loads $Q_{1,j} = (q_1 + q_2)s_j$ applied to all the structural joints, where s_j is the projection on the horizontal plane of the tributary area of the j-th structural joint, q_1 is the uniform distributed load that mimics the permanent weight-like load of a glass cladding, and q_2 is the uniform distributed load that mimics the live snow-like load.

The second Load Condition (LC_2) mimics not only the effects of non-uniform vertical loads, but also the ones of wind-induced loads or other horizontal loads. LC_2 cumulates the distributed self-weight of the structural members, the point loads $Q_{2,1,j} = q_1 s_j$, where q_1 is the uniform distributed load as described above, and the point loads $Q_{2,2,j} = q_2 s_j$, where q_2 is the piecewise uniform distributed load as described above, and it is applied on the surface with $x \geq 0$ (barrel vault and parabolic dome) and $y \geq 0$ (hyperbolic paraboloid).

Structural performances at Ultimate Limit States (ULS) are evaluated by setting $q_1 = 600\ \mathrm{N/m^2}$ and $q_2 = 1200\ \mathrm{N/m^2}$, while the ones at Serviceability Limit States (SLS) are assessed under $q_1 = 400\ \mathrm{N/m^2}$ and $q_2 = 800\ \mathrm{N/m^2}$.

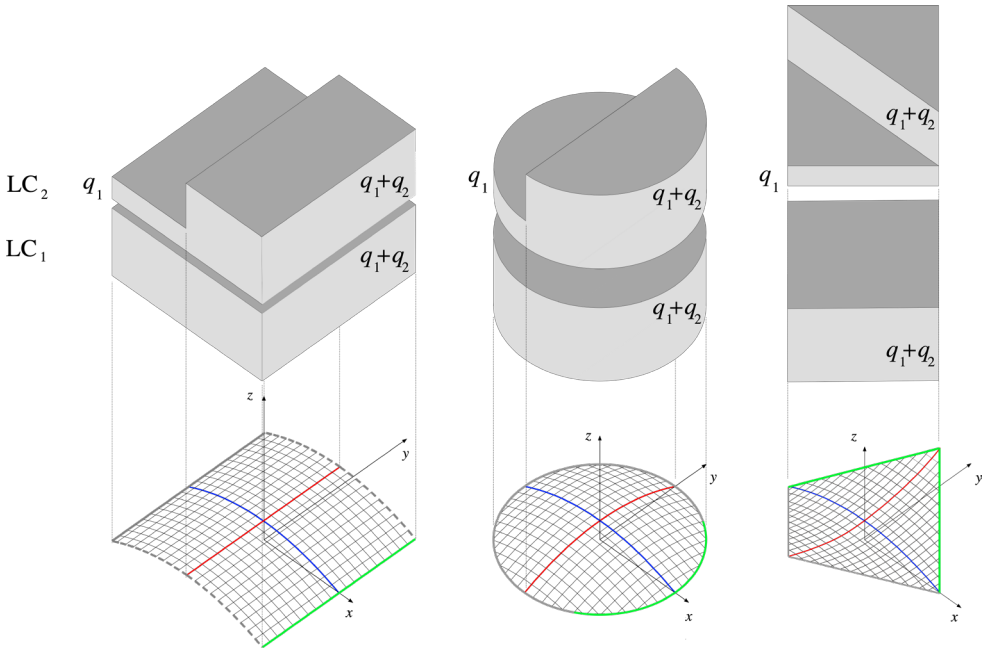


Figure 3. FreeGrid Load Conditions

3. Design goals and performance metrics

Participants to the benchmark are called to modify the above DBG(s), and conceive the Design Solution Gridshell(s) (DSG) in order to achieve seven selected Design Goals (DGs) in a genuine holistic perspective.

The whole performance assessment of each DSG develops in three conceptual steps (Fig. 4). First, each DG is expressed through a quantitative metric to be increased (↑) or decreased (↓), and made dimensionless with respect to the corresponding metric of the DBG (subscript 0). Second, DGs are grouped into three performance categories, covering the structural response (subscript *s*), the buildability (subscript *b*) and the sustainability (subscript *su*) of the DSG(s). Correspondingly, the single DG metrics are clustered into partial performance metrics P_k ($k = s, b, su$). Finally, a bulk performance metric P is obtained as linear combination of the above partial ones.

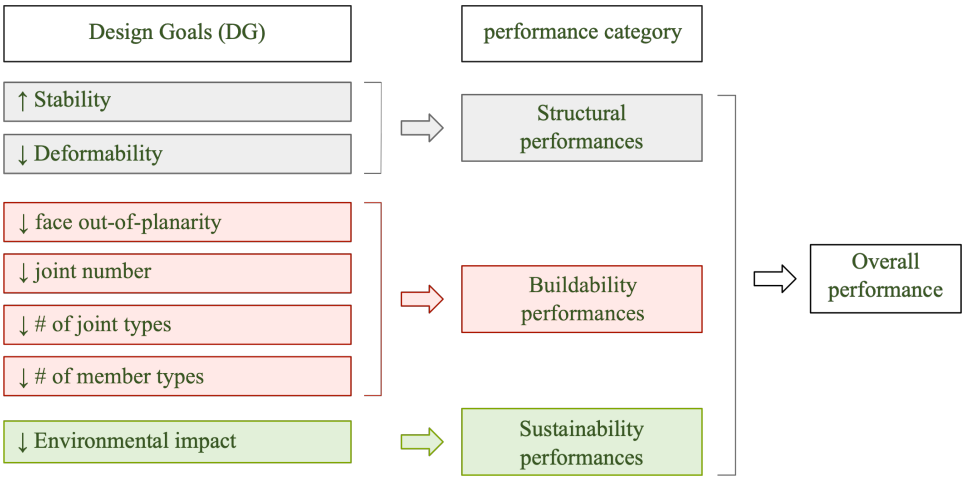


Figure 4. Performance assessment framework

3.1. Structural goals and metrics

Gridshells are form-resistant structures, and the design and optimization of their shape traditionally mainly focus on their mechanical performances, e.g. [7][8][9]. As a result, they are as efficient as exposed to instability and deformability issues [10] at ULS and SLS, respectively.

Stability (ULS). The adopted DG quantitative metric to be increased is the critical Load Factor $\widehat{LF}$, with reference to both LC_1 and LC_2 defined in subsect. 2.2.3. $\widehat{LF}$ accounts for global, local and member instability, and/or member plasticization [11][12][13]. The adopted lower limit value is $\widehat{LF}_l = 1$.

Deformability (SLS). The adopted DG quantitative metric to be decreased is the modulus of the maximum joint vertical displacement $|\hat{\delta}_z|$ over the whole gridshell, under LC_1 and LC_2 load conditions. The adopted upper limit value is $\hat{\delta}_{z,l} = B/200$.

The structural performance metric is averaged over the Load Conditions LC_k (k =1:2) and is defined as

$$P_s = \frac{\sum_{k=1}^{2} \frac{\widehat{LF}_k}{\widehat{LF}_{k,0}} \Big/ \frac{|\hat{\delta}_{z,k}|}{|\hat{\delta}_{z,k,0}|}}{2}. \quad (1)$$

Under the setup conditions specified in Sect. 2, the background gridshells fulfil the selected structural requirements at both ULS and SLS, while the DBGs do not.

3.2. Buildability goals and metrics

To the authors' best knowledge, buildability performances (also known as 'fabrication-aware design') are not thoroughly and unanimously defined in literature, in spite of their paramount design role and recent excellent proposals [14][15][16]. As such, the selected DGs, the related metrics and the resulting partial metric are intended to be an intentionally not all-encompassing, although rigorous, buildability performance model. In particular, the selected buildability DGs only refer to the geometry of 2D gridshell panels coincident with the face, 1D line-like structural members coincident with edges, and 0D joints at vertices. Hence, in a truly conceptual design perspective, the adopted DGs do not include issues related to the panel-face offset and to the joint 3D manufacturing (e.g. kinks at joints, edge offset [15]).

Face out-of-planarity. Face planarity is the most widespread and traditionally considered construction constraint for double curvature gridshells (e.g. [17][18]). Indeed, planar faces accommodate cheaper flat panels that are significantly less expensive than moulded or cold bent doubly curved panels. The adopted

DG quantitative metric $\overline{\Delta}$ to be decreased is the average, computed over the whole gridshell, of the modulus of the mean distances of the face vertices from the best fitting plane divided by the face semiperimeter [19][20].

Joint number. The number of structural joints largely affects the overall cost and buildability [21]. The adopted DG quantitative metric to be decreased is the cardinality of the structural joints $\#(N)$.

Uniformity of structural joints. The DG is aimed at shortening the joints chart, but also affecting the gridshell aesthetics. In what follows the joint type results from its valence v and the relative angles θ between converging members [22]. The adopted DG quantitative metric to be decreased is the cardinality of the joint type $\#(J)$.

Uniformity of structural members. The DG is aimed at shortening the members chart, but also affecting the gridshell aesthetics. In what follows the member type results from its length and cross section. The corresponding DG quantitative metrics to be decreased are the standard deviation of members length $\tilde{l}$ [14][23] and the cardinality of the members cross-sections $\#(C)$.

The buildability performance metric results from the average of the DG metrics as

$$P_b = \frac{1}{\frac{1}{5}\left[\frac{1+\bar{\Delta}}{1+\bar{\Delta}_0} + \frac{\#(N)}{\#(N_0)} + \frac{\#(J)}{\#(J_0)} + \frac{1+\tilde{l}}{1+\tilde{l}_0} + \frac{\#(C)}{\#(C_0)}\right]}. \quad (2)$$

3.3. Sustainability goals and metrics

Weight reduction is the traditional, widespread and largely emphasized design objective for structures in general, and for lightweight ones in particular, gridshells included, e.g. [24]. In a Life Cycle Assessment perspective, steel weight reduction is rephrased in the reduction of the gridshell embodied carbon that depends on the steel weight and grade, and on the type of sections of the structural members [25][26]. The adopted corresponding DG quantitative metric to be decreased is $W = \sum_{i=1}^{M} g_i \cdot l_i \cdot \alpha_i$, where the summation over the *M* structural members includes the weight per unit length g, the length l of the *i*-th member, and a correction coefficient α that depends on the steel grade and the type of member cross section, and that is normalized with respect to hollow sections made of S235.

The sustainability performance metric reads as

$$P_{su} = \frac{1}{\frac{W}{W_0}}. \quad (3)$$

3.4. Bulk performance metric

A bulk performance metric *P* results from the three partial performance metrics above

$$P = \gamma_s \cdot P_s + \gamma_b \cdot P_b + \gamma_{su} \cdot P_{su} \quad (4)$$

where $\gamma_s, \gamma_b, \gamma_{su}$ are partial weighting factors constrained by $\gamma_s + \gamma_b + \gamma_{su} = 1$, so that $P_0 = 1$. In the FreeGrid benchmark, the partial weighting factors are uniformly set equal to $\gamma_s = \gamma_b = \gamma_{su} = 1/3$ in order to offer to the participants a common term of reference. In a broader perspective, designers are in charge to discuss the overall performance of DSG(s) by setting other values of the partial weighting factors.

Being *P* a sortable performance metric, the ranking of the DSG issued from the benchmark for each DBG does not depend to a subjective and *a posteriori* assessment.

4. Design constraints

DSGs shall fulfil the following Geometrical (GC) and Mechanical (MC) Constraints. They are listed in the following by making general reference to a design solution with generic shape and structural features:

GC.1. the single-layer gridshell structural type cannot be changed, i.e. the mesh is 2-manifold, that is non-manifold vertices and edges are not permitted [27];
GC.2. the position, shape and length of the continuous spring line and of the head arches (for barrel vault only) cannot be modified;
GC.3. the gridshell spans along the x and y directions B_x and B_y, respectively, shall not be shorter than 30 m, being B_x and B_y generally defined as the maximum span free of external constraints;
GC.4. the extent of the projection of the overall gridshell surface on the horizontal reference plane shall be no smaller than $S - 0.05S$;
GC.5. the rise shall be kept equal to f=B/8, being f generally defined as the distance between the horizontal reference plane and the horizontal tangent plane to the shell surface having the minimum height;
GC.6. the height h shall be not longer than B /4, being h generally defined as the distance between the horizontal reference plane and the horizontal plane passing through the shell vertex having the maximum height;
GC.7. geometrical vertices and structural joints cannot lie below the horizontal reference plane;
MC.1. along the spring line L, x-, y- and z-displacements of all the structural joints resulting from mesh generation shall be externally constrained (perfect hinges);
MC.2. along the head arches (barrel vault), x- and z-displacements of all the structural joints resulting from mesh generation shall be externally constrained;
MC.3. additional structural external constraints are not allowed anywhere;
MC.4. the structural members shall have commercial cross sections;
MC.5. the structural material shall be steel.

Whichever design parameter can be varied if not explicitly excluded above, for instance geometry (e.g. overall shape of the gridshell, node position, grid density and topology), number and properties of the structural members (cross section, length), number and type of the structural joints, steel grade, prestressing magnitude, et cetera.

5. Design approaches and performance assessment methods

Whatever approach to design and optimization is welcome, for instance man-based heuristic design, AI-based design (e.g. neural networks, machine learning), gradient-based or topological optimization, physical scale model-based, models based on continuous analogy, et cetera.

Any kind of structural models can be used by the participants during the design/optimization (e.g. Reduced Order Models, surrogate models, simplified models such as linear static or buckling analysis).

Final structural performance assessment of the retained DSG(s) shall be carried out by a Geometrically and Materially Nonlinear Analysis (GMNA).

6. Requirements for participants

The method adopted for the performance assessment of the retained DSG(s) shall be well documented in order to guarantee the *reproducibility* of the results, and the *comparability* among them.

In order to reduce the model uncertainties, the following specifications about the Finite Element Model and the numerical solver used in GMNA are given:

- Finite Elements shall be 3D beam elements based on Timoshenko model, with cubic shape function;
- The Distributed Plasticity (DP) approach [28] shall be adopted, with nonlinear behaviour modelled along the element and over the element cross section;

- each structural member should be preferably discretised by 4 Finite Elements of equal length, in order to account for member buckling;
- the load control path-following procedure shall be applied within the analysis. The load step magnitude shall be set equal to 1/1000 the magnitude of the load condition LC_i;
- the iterative convergence shall be accomplished at each load step by means of the standard Newton-Raphson method, with a tolerance set equal to 5e-3 in terms of weighted residuals of the variables.

To pursue reproducibility and comparability, data about DSG, design approaches, performance assessment tools, and results shall be provided by the participants as Open Data. The complete set of requested data is detailed in the FreeGrid Technical Specifications.

In order to guarantee *comparability*, participants are strongly advised to precisely specify for each proposed design solution each single Design Goal metric, partial performance metrics, and bulk performance metric.

In order to allow *reproducibility*, participants are warmly encouraged to precisely specify for each proposed design solution: (i) *data on DSG*, i.e. geometrical and structural features; (ii) *data on models*, i.e. adopted design approach (e.g. heuristic approach, optimization algorithm(s), AI technique), name and version of the Finite Element code(s) and details about the Finite Element Model used for performance assessment; (iii) *main output* of the structural performance assessment.

Open Access automatic tools will be made available in order to assist participants in checking the fulfilment of the design constraints during the conceptual design, and in the calculation of buildability performance metrics during the final assessment.

The above information shall be delivered by participants in the form of data uploaded on the FreeGrid web site, technical report/white paper sent to the FreeGrid Steering Committee, or published scientific paper.

7. Outlook and conclusion

The FreeGrid benchmark is launched at the IASS 2023 Annual Symposium in Melbourne. The benchmark technical specifications are made available at the FreeGrid website (https://sites.google.com/view/freegrid). A position paper will discuss in deep the mechanical behaviour of the background and design baseline gridshells, in order to provide to participants stimuli for design solutions.

In itinere special sessions will be possibly organized in the following years at international conferences. The benchmark first milestone is tentatively set within the IASS Annual Symposium 2026, when the FreeGrid ArcelorMittal Steligence Awards will be remitted according to given specific regulation to the young author(s) of the most performing design solution for each type of DGS, together with an additional award remitted to the author(s) who will deal with all the three DGS and obtain the highest performances in average.

Acknowledgements

The Authors gratefully acknowledge the support of the Italian Council for Steel Structures (CTA, https://www.collegiotecniciacciaio.it), the umbrella of the International Association for Shell and Spatial Structures (IASS, https://iass-structures.org), and the partnership with ArcelorMittal Steligence (https://steligence.arcelormittal.com). The Authors thank Riccardo Zanon and Marina D'Antimo (ArcelorMittal Steligence) for the stimulating insight and fruitful discussion about steel gridshell sustainability. The Authors warmly thank Yi Min ‘Mike’ Xie and Jane Burry, Co-Chairs of the IASS

annual Symposium 2023, and its Organizing Committee for hosting the launch of the benchmark within the event.

References

[1] I. Paya-Zaforteza and M.E.M. Garlock, "Structural Engineering Heroes and Their Inspirational Journey", *Structural Engineering International*, vol. 31(4), pp. 584-597, 2021.

[2] H. Salehi and R. Burgueño, "Emerging artificial intelligence methods in structural engineering", *Engineering Structures*, vol. 171, pp. 170-189, 2018.

[3] F. Venuti and L. Bruno, "Influence of in-plane and out-of-plane stiffness on the stability of free-edge gridshells: A parametric analysis", *Thin-Walled Structures*, vol. 131, pp. 755–768, 2018.

[4] R.Q. Feng, L. Zhang and J.M. Ge, "Multi-objective morphology optimization of free-form cable-braced grid shells", *International Journal of Steel Structures*, vol.15(3), pp. 681-691, 2015.

[5] O. Sigmund, "On benchmarking and good scientific practise in topology optimization", *Structural and Multidisciplinary Optimization*, vol. 65(11), pp. 315, 2022.

[6] V. Tomei, E. Grande and M. Imbimbo, "Influence of geometric imperfections on the efficacy of optimization approaches for grid-shells", *Engineering Structures*, vol. 228, pp. 111502, 2021.

[7] E. Vouga, M. Höbinger, J. Wallner and H. Pottmann, "Design of self-supporting surfaces", *ACM Transactions on Graphics*, vol. 31(4), art. no. 87, 2012.

[8] L. Mourad, J. Bleyer, R. Mesnil, J. Nseir, K. Sab and W. Raphael, "Topology optimization of load-bearing capacity", *Structural and Multidisciplinary Optimization*, vol. 64(3), pp. 1367 – 1383, 2021.

[9] F. Laccone, L. Malomo, M.Froli, P. Cignoni, N. Pietroni, "Automatic Design of Cable-Tensioned Glass Shells", *Computer Graphics Forum*, vol. 39.1, pp. 260-273, 2020.

[10] D. Tonelli, N. Pietroni, E. Puppo, M. Froli, P. Cignoni, G. Amendola and R. Scopigno, "Stability of Statics Aware Voronoi Grid-Shells", *Engineering Structures*, vol. 116, pp. 70-82, 2016.

[11] T. Bulenda and J. Knippers, "Stability of grid shells", *Computers and Structures*, vol. 79(12), pp. 1161–74, 2001.

[12] M. Mohammadi, K. Abedi and N. Taghizadieh, Stability analysis of single-layer barrel vault space structures. *International Journal of Space Structures*, vol. 7(4), pp. 203-218, 2012.

[13] J. Yan, F. Qin, Z. Cao, F. Fan and Y. Mo, Mechanism of coupled instability of single-layer reticulated domes, *Engineering Structures*, vol. 114, pp. 158-170, 2016.

[14] R. Mesnil, C. Douthe, O. Bavarel, B. Léger, J.F. Caron, "Isogonal moulding surfaces: A family of shapes for high node congruence in free-form structures", *Automation in Construction*, Vol. 59, pp. 38-47, 2015.

[15] X. Tellier, C. Douthe, L. Hauswirth, O. Baverel, "Caravel meshes: A new geometrical strategy to rationalize curved envelopes", *Structures,* vol. 28, pp. 1210-1228, 2020.

[16] V. Tomei, M. Imbimbo and E. Mele, "Optimization of structural patterns for tall buildings: the case of diagrid", *Engineering Structures*, vol. 171, pp. 280-297, 2018.

[17] J. Schlaich and H. Schober, "Glass roof for the Hippo House at the Berlin Zoo". *Structural Engineering International*, vol. 7(4), pp. 252–254, 1997.

[18] R. Mesnil, C. Douthe, C. Richter and O. Bavarel, "Fabrication-aware shape parametrisation for the structural optimisation of shell structures", *Engineering Structures*, vol. 176, pp. 569 – 5841, 2018.

[19] C. Tang, X. Sun, A. Gomes, J. Wallner, and H. Pottmann, "Form-finding with polyhedral meshes made simple", *ACM Transactions on Graphics*, vol. 33(4), pp. 70:1–70:9, 2014.

[20] N. Pietroni, D. Tonelli, E. Puppo, M. Froli, R. Scopigno and P. Cignoni, "Statics Aware Grid Shells", *Computer Graphics Forum*, vol. 34(2), pp. 627-641, 2015.

[21] H. Seifi, A.R. Javan, S. Xu, Y. Zhao, Y.M. Xie, "Design optimization and additive manufacturing of nodes in gridshell structures", *Engineering Structures*, vol. 160, pp. 161-170, 2018.

[22] Y. Liu, T.U. Lee, A. Koronaki, N. Pietroni and Y.M. Xie, "Reducing the number of different nodes in space frame structures through clustering and optimization", *Engineering Structures*, vol. 284 (116016), 2023.

[23] F. Otto, "*IL10: Gitterschalen - Grid Shelss*", Institut für Leichte Flächentragwerke, Stuttgart, 1974.

[24] M. Kilian, D. Pellis, J. Wallner and H. Pottmann, "Material-minimizing forms and structures", *ACM Transactions on Graphics*, vol. 36 (6), art. no. a173, 2017.

[25] O. P. Gibbons, J. J. Orr, C. Archer-Jones, W. Arnold, D. Green, "*How to calculate embodied carbon*" (2nd ed.), The Institution of Structural Engineers, London, UK, 2022.

[26] R. Stroetmann, "High Strength Steel for Improvement of Sustainability", in *Proceedings of Eurosteel 2011*, Budapest, Hungary, August 31 - September 2, 2011.

[27] L.W. Tu, "*An Introduction to Manifolds"* (2nd ed.), New York: Springer, 2011.

[28] F.F. Taucer, E. Spacone, F.C. Filippou, "*A Fiber Beam-Column Element for Seismic Response Analysis of Reinforced Concrete Structures*", Report No. UCB/EERC-91/17, Earthquake Engineering Research Center College of Engineering University of California, Berkeley, 1991.

IASS 2023
July 10–14 Melbourne
Integration of Design and Fabrication

Proceedings of the IASS Annual Symposium 2023
Integration of Design and Fabrication
10–14 July 2023, Melbourne, Australia
Y.M. Xie, J. Burry, T.U. Lee and J. Ma (eds.)

Simultaneous stress-aligned and flat-panel-aligned grids on mixed tension-compression membrane shells

Masaaki MIKI[*], Toby MITCHELL[a]

[*] The University of Tokyo, Tokyo, Japan
masaakim@g.ecc.u-tokyo.ac.jp

[a] Skidmore, Owings, and Merrill, Chicago, USA
toby.mitchell@som.com

Abstract

Our recent paper, "Interactive exploration of tension-compression mixed shells" [1], discusses the topic of the form-finding of shell structures in which both compression and tension are present and proposes a novel numerical approach that can iteratively refine the problem until a solution is found. This is achieved by regarding two surfaces—a shell and a stress function—as unknown functions, and then iterating until equilibrium is satisfied. This new approach allows us to explore a new frontier. In that paper, we propose that these shells can be used as an initial design step for discrete grid shells. This study takes up this task by using an equation presented in [1] to trace out a special set of curves on an equilibrium pair of continuum shell and stress function surfaces. This unique set of curves is both conjugate and funicular; that is, it is aligned with a grid on the shell that is locally flat-paneled, and it is in axial force equilibrium as a grid shell with no bending in the grid members under the applied load. In this paper, we propose an algorithm to trace these simultaneously stress- and flat-panel-aligned curves on equilibrium shell–stress function pairs. We test the method on several analytical examples, and then move to general form-found shells. The conditions of existence of the curve networks are not trivial, and we need to modify the method of [1] to add a constraint that guarantees that the curve networks exist on form-found shells. After modifying the method, we present several different complex examples of the resulting curve networks.

Keywords: airy stress functions, form-finding, tension-compression mixed shells, variable projection method, hyperbolic boundary problems, bilinear tensor least squares problems, conjugate curve networks, funicular grid shells

1. Introduction

In 2015, an Airy stress function-based form-finding method that does not rely on triangulated mesh surfaces but directly calculates smooth and continuous NURBS surfaces was presented [5]. The method requires the Airy stress function to be convex everywhere and can only compute a pure-compression shell. In 2022, we presented a novel computational approach that enables us to execute a form-finding analysis of shells that can balance with a mixed tension-compression stress state [1]. Although a similar method was previously proposed by Yu-Chou et al. [2], we pointed out that in tension-compression mixed cases, it is very likely that the equilibrium equation does not provide any solution in general. Our new method deals with this issue by refining the stress function as well as the shell, so that both the shell and stress function are iterated until the problem converges to an equilibrium solution. To solve the problem, Yu-Chou et al. [2] selected a simple alternating approach (ALT). However, a comparison presented by Elden et al. [4] reports that, while ALT is not guaranteed to converge or the rate of convergence is extremely low, the variable projection (called VP or VarPro; we call it VP in this paper)

Copyright © 2023 by Masaaki MIKI and Toby MITCHELL. Published in the Proceedings of the IASS Annual Symposium 2023 with permission.

can solve the problem with sufficient accuracy. Hence, we concluded that VP is more suitable to solve this problem. Although the computational cost of VP is extremely high, we successfully accelerated the computation using modern Nvidia GPUs and the Cuda toolkit library. With the successful solutions obtained by executing the proposed method, we concluded that the well-posed problems form a vast solution space that is comparatively far less well-studied than the case of all-compression or all-tension surface structures.

This new method has significant merits from both aesthetic and technical viewpoints. The shells, classically derived with pure compression, are now extended to include tension-compression mixed regions, and overhanging anticlastic surfaces are now possible. Furthermore, from a technical viewpoint, because the solutions are represented by NURBS surfaces, continuous curvature and stress tensors can be computed everywhere on the surface.

Helmut Pottmann's research group has published an extensive body of surface structure shape optimization techniques that rely on mesh surfaces. One study [3] presented a method to obtain a net that is simultaneously conjugate and funicular by tracing the eigenvectors of a generalized eigenvalue problem in terms of the Hessians of the shell and stress function. Thus, a net that can support load with no bending action and that also has all planar quad faces can be easily computed. Although Helmut Pottmann's research group applied this idea to discretized mesh surfaces, here, we directly compute the eigenvectors on the obtained NURBS surfaces and perform a curve tracing algorithm to obtain nets that provide simultaneously stress- and flat-panel-aligned curve networks.

2. A net that is simultaneously conjugate and funicular

In shell form-finding, the stress field is often described using an Airy stress function. In this study, we consider two functions $z(x, y)$ and $\phi(x, y)$ that represent the shape of the shell and the stress function, respectively. In the following, the shell has units of length, and the stress function has units of force times length. The equilibrium of the shell in the vertical direction is given by the Pucher equation

$$\frac{\partial^2\varphi}{\partial x^2}\frac{\partial^2 z}{\partial y^2} - 2\frac{\partial^2\varphi}{\partial x\,\partial y}\frac{\partial^2 z}{\partial x\,\partial y} + \frac{\partial^2 z}{\partial y^2}\frac{\partial^2\varphi}{\partial x^2} = p \tag{1}$$

For zero-shear stresses and flat panels (conjugate curves) to be aligned on a membrane shell, we must have

$$\begin{aligned}\frac{\partial^2 z}{\partial u\,\partial v} &= 0\\ \frac{\partial^2\varphi}{\partial u\,\partial v} &= 0\end{aligned} \tag{2}$$

where *u* and *v* are some sets of curvilinear coordinates on the projected *x*-*y* plane, which do not need to be orthogonal. The first condition gives panel flatness via vanishing of the off-diagonal curvature tensor entry, while the second condition yields zero shear in the *u* and *v* directions, which is required if bending is to be avoided along the *u* and *v* curves.

Given $z(x, y)$ and $\phi(x, y)$, we want to solve for the specific *u* and *v* that satisfy (2). It is easier to solve in terms of coordinates that we already know, for example, *x* and *y*. Using the chain rule, we can write

$$\frac{\partial^2 z}{\partial u\,\partial v} = \frac{\partial^2 z}{\partial x^2}\frac{\partial x}{\partial u}\frac{\partial x}{\partial v} + \frac{\partial^2 z}{\partial x\,\partial y}\frac{\partial x}{\partial v}\frac{\partial y}{\partial u} + \frac{\partial^2 z}{\partial x\,\partial y}\frac{\partial x}{\partial u}\frac{\partial y}{\partial v} + \frac{\partial^2 z}{\partial y^2}\frac{\partial y}{\partial u}\frac{\partial y}{\partial v}$$

$$= \begin{bmatrix}\frac{\partial x}{\partial u} & \frac{\partial y}{\partial u}\end{bmatrix}\begin{bmatrix}\frac{\partial^2 z}{\partial x^2} & \frac{\partial^2 z}{\partial x\,\partial y}\\ \frac{\partial^2 z}{\partial x\,\partial y} & \frac{\partial^2 z}{\partial y^2}\end{bmatrix}\begin{bmatrix}\frac{\partial x}{\partial v}\\ \frac{\partial y}{\partial v}\end{bmatrix} = 0 \tag{3}$$

Therefore, by treating the *u* and *v* derivatives of *x* and *y* as unknown vectors, the problem of finding the stress- and panel-aligned coordinate curves reduces to

$$\begin{aligned} v_1^T[\nabla^2 z]v_2 &= 0 \\ v_1^T[\nabla^2 \varphi]v_2 &= 0 \end{aligned} \tag{4}$$

where the bracketed terms are the Hessians of the shell and the stress function, that is,

$$[\nabla^2 z] = \begin{bmatrix} \frac{\partial^2 z}{\partial x^2} & \frac{\partial^2 z}{\partial x \partial y} \\ \frac{\partial^2 z}{\partial x \partial y} & \frac{\partial^2 z}{\partial y^2} \end{bmatrix}, [\nabla^2 \varphi] = \begin{bmatrix} \frac{\partial^2 \phi}{\partial x^2} & \frac{\partial^2 \phi}{\partial x \partial y} \\ \frac{\partial^2 \phi}{\partial x \partial y} & \frac{\partial^2 \phi}{\partial y^2} \end{bmatrix} \tag{5}$$

and where

$$v_1 = \begin{bmatrix} \frac{\partial x}{\partial u} \\ \frac{\partial y}{\partial u} \end{bmatrix}, v_2 = \begin{bmatrix} \frac{\partial x}{\partial v} \\ \frac{\partial y}{\partial v} \end{bmatrix} \tag{6}$$

are the tangent vectors of the *u* and *v* coordinate curves. Solving the two simultaneous Eqs. (4) is equivalent to solving the generalized eigenvalue problem

$$[\nabla^2 z]v = \lambda[\nabla^2 \varphi]v. \tag{7}$$

Eq. (7) was first presented in [3].

The eigenvalues of (6) are given by

$$\lambda^2 \left(\frac{\partial^2 \varphi}{\partial x^2} \times \frac{\partial^2 \varphi}{\partial y^2} - \left(\frac{\partial^2 \varphi}{\partial x \, \partial y} \right)^2 \right) - \lambda \left(\frac{\partial^2 \varphi}{\partial x^2} \times \frac{\partial^2 z}{\partial y^2} - 2 \times \frac{\partial^2 \varphi}{\partial x \, \partial y} \times \frac{\partial^2 z}{\partial x \, \partial y} + \frac{\partial^2 \varphi}{\partial y^2} \times \frac{\partial^2 z}{\partial x^2} \right) + \left(\frac{\partial^2 z}{\partial x^2} \frac{\partial^2 z}{\partial y^2} - \left(\frac{\partial^2 z}{\partial x \, \partial y} \right)^2 \right) = 0 \tag{8}$$

However, we can recognize the middle term as the left-hand side of Eq. (1), and the other terms as determinants of the Hessians, so that Eq. (8) becomes

$$\lambda^2 \det(\nabla^2 \varphi) - \lambda p + \det(\nabla^2 z) = 0. \tag{9}$$

Note that the determinants of the Hessians (called the "isotropic Gaussian curvatures" in [3]) are related to the (ordinary Euclidean) Gaussian curvatures of the shell and stress function. In particular, the sign of the determinants is the same as the sign of the Gaussian curvatures.

It follows that

$$\lambda = \frac{p \pm \sqrt{p^2 - 4\det(\nabla^2 \varphi)\det(\nabla^2 z)}}{2\det(\nabla^2 \varphi)}. \tag{10}$$

From elementary linear algebra, we know that Eq. (7) has real eigenvalues if $\det(\nabla^2 \varphi) > 0$ and $\det(\nabla^2 z) > 0$, since both matrices are then symmetric positive definite. Also, the cases in which $\det(\nabla^2 \varphi) > 0$ and $\det(\nabla^2 z) < 0$ or $\det(\nabla^2 \varphi) < 0$ and $\det(\nabla^2 z) > 0$ clearly have a real discriminant. The only case in which we must pay special attention is when both determinants are negative. In those cases, the solution discriminant must be checked, that is,

$$p^2 \geq 4\det(\nabla^2 \varphi)\det(\nabla^2 z) \tag{11}$$

must be examined to determine whether the inequality is satisfied.

An interesting special case is the "self-Airy" case [8], where $z(x,y)=\phi(x,y)$. In this case,

$$p^2=\left(2\frac{\partial^2 z}{\partial x^2}\times\frac{\partial^2 z}{\partial y^2}-2\times\left(\frac{\partial^2 z}{\partial x\,\partial y}\right)^2\right)^2=4\left(\frac{\partial^2 z}{\partial x^2}\frac{\partial^2 z}{\partial y^2}-\left(\frac{\partial^2 z}{\partial x\,\partial y}\right)^2\right)^2=4\det(\nabla^2 z)\det(\nabla^2 z), \tag{12}$$

that is, the self-Airy case corresponds to the equality case of (11). In this case, the eigenvalues of (7) are not distinct, so the eigenvectors of (7) can be chosen in any conjugate directions, with stress-alignment guaranteed for any choice.

3. Curve tracing algorithm

The procedure to trace the stress- and flat-panel-aligned curves given by (7) is as follows.

When a NURBS surface is represented by three functions $x(u^1,u^2), y(u^1,u^2)$, and $z(u^1,u^2)$, where (u^1,u^2) are the isocurve parameters of the NURBS surface, we compute

$$\bar{g}_1=\begin{bmatrix}\frac{\partial x}{\partial u^1} & \frac{\partial y}{\partial u^1}\end{bmatrix}^T, \bar{g}_2=\begin{bmatrix}\frac{\partial x}{\partial u^2} & \frac{\partial y}{\partial u^2}\end{bmatrix}^T, \tag{13}$$

which are the basis vectors projected onto the *x*-*y* plane. We also compute the second derivatives as

$$\bar{h}_{11}=\begin{bmatrix}\frac{\partial^2 x}{\partial (u^1)^2} & \frac{\partial^2 y}{\partial (u^1)^2}\end{bmatrix}^T, \bar{h}_{12}=\begin{bmatrix}\frac{\partial^2 x}{\partial u^1\,\partial u^2} & \frac{\partial^2 y}{\partial u^1\,\partial u^2}\end{bmatrix}^T, \bar{h}_{22}=\begin{bmatrix}\frac{\partial^2 x}{\partial (u^2)^2} & \frac{\partial^2 y}{\partial (u^2)^2}\end{bmatrix}^T, \tag{14}$$

which are also projected onto the *x*-*y* plane. Using these, we compute the first fundamental form by $\bar{g}_{ij}=\bar{g}_i\cdot\bar{g}_j$ and $\bar{g}^{ij}=\left(\bar{g}_{ij}\right)^{-1}$. The dual basis vectors can then be computed as $\bar{g}^i=\bar{g}^{ij}\bar{g}_j$. With these, Christoffel's symbols of the second kind are computed by $\overline{\Gamma}^k_{ij}=\bar{h}_{ij}\cdot\bar{g}^k$, and we finally compute the Hessian on the curvilinear coordinates in terms of the second covariant derivative as

$$\nabla^2 z=z|_{ij}=\frac{\partial^2 z}{\partial u^i\,\partial u^j}-\overline{\Gamma}^k_{ij}\frac{\partial z}{\partial u^k}. \tag{15}$$

Although it is possible to solve the generalized eigenvalue problem in curvilinear coordinates directly using the laws of raising and lowering indices, we extract its components in the *x*-*y* coordinates via

$$z|_{\alpha\beta}=z|_{ij}\left(e_\alpha\cdot\bar{g}^i\right)\left(e_\beta\cdot\bar{g}^j\right), \tag{16}$$

where $e_1=[1,0]^T$ and $e_2=[0,1]^T$.

Following this procedure, for a set of two surfaces: the Airy function $[x(u^1,u^2), y(u^1,u^2), \phi(u^1,u^2)]^T$ and the shell $[x(u^1,u^2), y(u^1,u^2), z(u^1,u^2)]^T$, with $x(u^1,u^2)$ and $y(u^1,u^2)$ in common between them, we obtain two Hessians $\nabla^2\phi$ and $\nabla^2 z$. By setting those two matrices to the first and second matrices in the generalized eigenvalue problem defined in Eq. (7), we obtain two normalized directions v_1 and v_2, that is, we obtain the eigenvectors (6). To trace the stress-aligned conjugate curve network in the initial step, given an initial point p_0, we select the initial velocity vector from $v_1,-v_1,v_2,-v_2$ and set it to the velocity vector v_0. Except in the initial step, the angles between the previous v_0 and $v_1,-v_1,v_2,-v_2$ are checked, and the one that gives the smallest angle is chosen as the new velocity v_0. With a sufficiently small step size dt, we then generate a point series by repeating:

$$p_{t+1}=p_t+v_0\mathrm{dt}. \tag{17}$$

Given that the level of approximation is not very high, termination of the point generation is recommended when even the smallest angle exceeds a predefined threshold (e.g., we used 0.6 in radians as the threshold in our code).

4. Simple cases in which analytical solutions can be hand-calculated

There are relatively simple tension-compression mixed cases in which analytical solutions can be derived by hand. We use these solutions to demonstrate the results of tracing the stress-aligned conjugate curve network.

4.1. Equilibrium equation in curvilinear coordinates

In curvilinear coordinates described with $\{r, \theta\}$ (not limited to polar coordinates for the time being), Eq. (1) becomes:

$$\left(\frac{\partial^2 z}{\partial r \partial r} - \Gamma^r_{rr}\frac{\partial z}{\partial r} - \Gamma^\theta_{rr}\frac{\partial z}{\partial \theta}\right)\left(\frac{\partial^2 \phi}{\partial \theta \partial \theta} - \Gamma^r_{\theta\theta}\frac{\partial \phi}{\partial r} - \Gamma^\theta_{\theta\theta}\frac{\partial \phi}{\partial \theta}\right) - 2\left(\frac{\partial^2 z}{\partial r \partial \theta} - \Gamma^r_{r\theta}\frac{\partial z}{\partial r} - \Gamma^\theta_{r\theta}\frac{\partial z}{\partial \theta}\right)\left(\frac{\partial^2 \phi}{\partial r \partial \theta} - \Gamma^r_{r\theta}\frac{\partial \phi}{\partial r} - \Gamma^\theta_{r\theta}\frac{\partial \phi}{\partial \theta}\right) + \left(\frac{\partial^2 z}{\partial \theta \partial \theta} - \Gamma^r_{\theta\theta}\frac{\partial z}{\partial r} - \Gamma^\theta_{\theta\theta}\frac{\partial z}{\partial \theta}\right)\left(\frac{\partial^2 \phi}{\partial r \partial r} - \Gamma^r_{rr}\frac{\partial \phi}{\partial r} - \Gamma^\theta_{rr}\frac{\partial \phi}{\partial \theta}\right) = \det g\, p, \quad (18)$$

where Γ^k_{ij} is the Christoffel's symbols of the second kind. In polar coordinates, it is known that $\Gamma^r_{\theta\theta} = -r$, $\Gamma^\theta_{r\theta} = \Gamma^\theta_{\theta r} = \frac{1}{r}$, $\det g = r^2$, and all others are zero. Hence, in polar coordinates, we obtain:

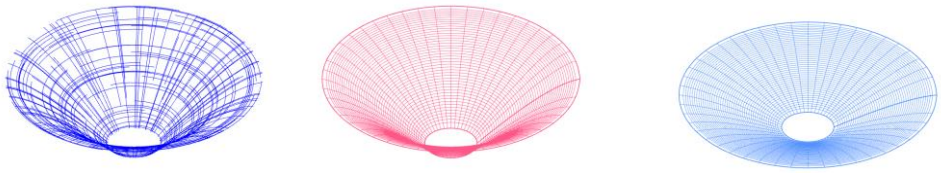
$$\left(\frac{\partial^2 z}{\partial r \partial r}\right)\left(\frac{\partial^2 \phi}{\partial \theta \partial \theta} + r\frac{\partial \phi}{\partial r}\right) - 2\left(\frac{\partial^2 z}{\partial r \partial \theta} - \frac{1}{r}\frac{\partial z}{\partial \theta}\right)\left(\frac{\partial^2 \phi}{\partial r \partial \theta} - \frac{1}{r}\frac{\partial \phi}{\partial \theta}\right) + \left(\frac{\partial^2 z}{\partial \theta \partial \theta} + r\frac{\partial z}{\partial r}\right)\left(\frac{\partial^2 \phi}{\partial r \partial r}\right) = r^2 p. \quad (19)$$

4.2. A simple self-Airy example

If the stress surface and the shell are given by the same functions, there is no need to solve the generalized eigenvalue problem, because any conjugate directions are already stress-aligned (since the eigenvalues of (7) are not distinct). An analytical solution can be obtained by introducing an assumption that the shell and the stress are the same except for the scaling factor and that they are both surfaces of revolution, that is, $z = f(r), \phi = Af(r)$. In this case, an analytical solution can be obtained [6] as

$$z(r) = \frac{1}{2\sqrt{2A}}\left(r\sqrt{B^2 - r^2} + \arcsin(r)\right), \quad (20)$$

where A and B are the integration coefficients. Figure 1 shows the solutions and the traced curvature lines when $A = 0.5, B = 1,$ and $0.2 < r < 1$.



(a) (b) (c)

Figure 1. (a) Curvature lines traced using the algorithm described above, (b) shell surface, and (c) stress surface.

4.3. Monkey saddle ($z = r\cos 3\theta$)

An example of a shell-stress function pair that does *not* admit real eigenvalues of (7) anywhere on the surface was discussed in [8] as

$$z = r\cos 3\theta\,, \phi = r\sin 3\theta. \quad (21)$$

This is a self-stressed surface, with no external loads applied (roughly similar to a cable net or tensile fabric membrane, but with tension and compression both present). Both determinants are negative (and in fact identical, since ϕ is just a rotated copy of z). The lack of any real eigenvalues of (7) then follows from the fact that p is zero in (11). This solution shows that it is possible for large areas of a shell to have *no* solutions to the eigenvalue problem (7).

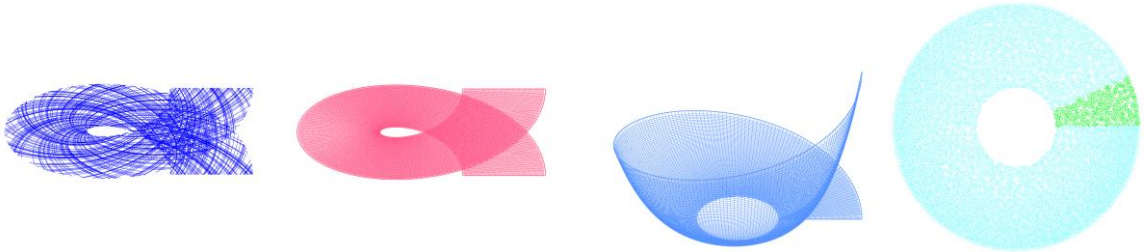
Note that it is not generally true that self-stressed surfaces do not have real eigenvalues in (7). This example is unusual in that it has tension and compression both present in the self-stress state. For a pure compression or pure tension self-stress state, the shell will be negatively curved while the stress function will be positively curved, so that the product of determinants in (11) is positive and therefore the surface will have real eigenvalues even with no applied load present.

4.4. Helicoid

A pair of helicoidal shell and stress surfaces that partially yields negative Gaussian curvatures was derived in [7] as

$$z = \frac{h}{2\pi}\theta, \phi = -p\frac{\pi r^4 \theta}{3h} \tag{22}$$

where h is the total height of a full $2 * \pi$ turn. This is an interesting example because there is a region where both surfaces give negative Gaussian curvatures (in the range $\theta < \sqrt{3}/4$), and yet a stress-aligned conjugate net exists in that region, because Eq. (11) is satisfied everywhere. Figure 2 shows the surfaces, the stress-aligned conjugate net obtained by using the algorithm described above, and the region where the two surfaces give negative Gaussian curvature.



(a) (b) (c) (d)

Figure 2. (a) A stress-aligned conjugate net, (b) shell surface, and (c) stress surface. (d) The region where both surfaces give negative Gaussian curvatures (green).

This example shows that real eigenvalues can indeed be found for fairly general shell-stress function pairs with negative-negative regions: this class of solutions is *not* restricted to a trivially small set. Between this example and the previous example, we can see that the condition for stress- and flat-panel-aligned curves to exist is neither trivially satisfied nor trivially restrictive. It is not necessarily possible to find sets of curves that are simultaneously stress- and flat-panel-aligned on any given surface, but the class of such solutions is still rich enough to be worth exploring. This exploration can be done by using shell form-finding, and in fact, we can impose the constraint (7) on shell form-finding results to ensure that solutions exist.

5. Mixed tension-compression shell form-finding

In this section, we briefly summarize the novel tension-compression mixed-shell form-finding method that we have proposed. Readers interested in the full technical details can navigate to [1].

If ϕ is given in equation (1), then the equation becomes

$$A\frac{\partial^2 z}{\partial x \partial x} - B\frac{\partial^2 z}{\partial x \partial y} + C\frac{\partial^2 z}{\partial y \partial y} = p, \tag{23}$$

where the terms A, B, and C are given functions of x and y over the surface.

In a tension-compression mixed case, this second-order partial differential equation becomes hyperbolic, or hyperbolic-elliptic mixed, and it is known that a compatible set of boundary conditions must be sought first before solving the problem; otherwise, the problem becomes ill-posed. In general, finding a compatible set of boundary conditions is a challenge, and thus, this type of problem is considered

notoriously difficult to solve. This is very different from pure-compression cases, which make the problem elliptic and thus provide solutions regardless of what kind of boundary conditions are given.

Although the problem is very likely ill-posed when the coefficients are chosen freely, a preliminary study conducted by the authors and C. J. K. Williams's research group from Chalmers University of Technology [6] strongly suggests that combinations of the coefficients that make the hyperbolic problem provide a solution do exist. The basic idea of our method is that instead of attempting to solve a problem that can easily become ill-posed, we solve a parameter identification problem to find a set of coefficients that makes the equilibrium equation well-posed. To this end, we simply regard both z and ϕ as unknown functions. If we do so, the problem is described with two unknown functions versus one condition, which expands a unique solution that may not exist to a vast solution space.

By defining the residual of Eq. (1) by

$$r(\phi, z) = \frac{\partial^2 \varphi}{\partial x^2}\frac{\partial^2 z}{\partial y^2} - 2\frac{\partial^2 \varphi}{\partial x\,\partial y}\frac{\partial^2 z}{\partial x\,\partial y} + \frac{\partial^2 z}{\partial y^2}\frac{\partial^2 \varphi}{\partial x^2} - p, \tag{24}$$

the problem can be approximately solved by solving a least squares problem defined by

$$\int r(\phi, z)^2 \ \mathrm{d}\bar{a} + \int b_\phi(\phi)^2 \mathrm{d}\bar{l} + \int b_z(z)^2 \mathrm{d}\bar{l} \to \min,$$

where b_ϕ and b_z are additional residual functions of the stress function and shell boundary conditions respectively, evaluated and integrated on the projected boundary curves $\bar{l}$. Note that the projected boundary curves are the same between the shell and stress function, so it is not necessary to distinguish the domain over which these terms are integrated. When ϕ and z are represented with NURBS basis functions, this least squares minimization problem results in a bilinear tensor least squares (BTLS) problem [4]. Considering either the shell or the stress function to be given (called "pinning" in [1]), we obtain two partial linear least squares problems, defined as:

$$\int r(\phi, \bar{z})^2 \ \mathrm{d}\bar{a} + \int b_\phi(\phi)^2 \mathrm{d}\bar{l} \to \min, \tag{25}$$

$$\int r(\bar{\phi}, z)^2 \ \mathrm{d}\bar{a} + \int b_z(z)^2 \mathrm{d}\bar{l} \to \min, \tag{26}$$

where $\bar{\cdot}$ was put above ϕ or z when it is "pinned". Hence, the basic strategy for solving this type of problem is to find a solution that simultaneously satisfies both partial problems. The ALT method is a simple approach that alternately solves two problems. As mentioned earlier, we reported that VP works better than ALT. The computational results presented in [1] are showcased in Figure 3. Figure 4 also shows the 3D prints of an obtained pair.

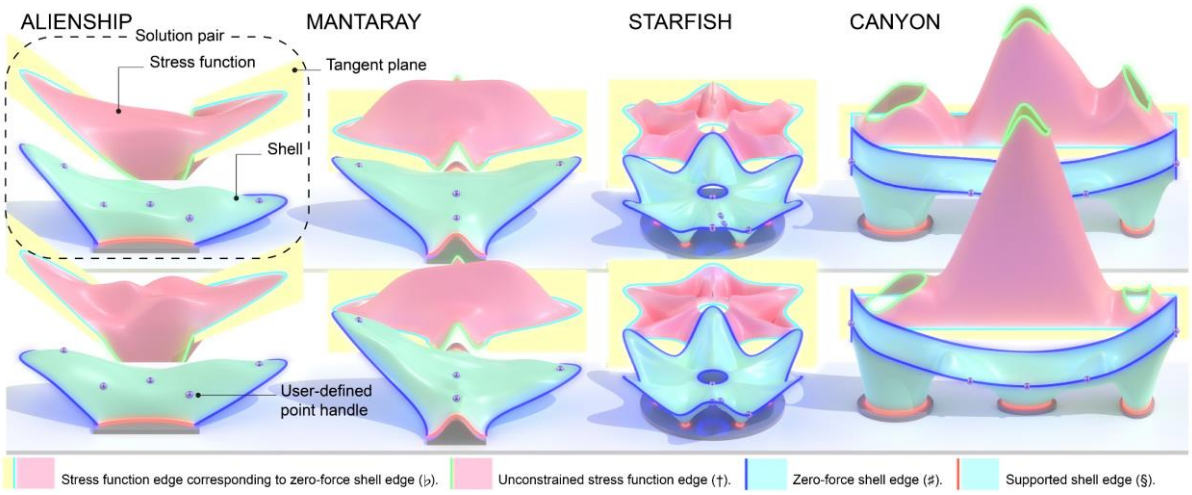


Figure. 3. Pairs of stress functions and shells obtained using the proposed method.



Figure 4. Above: A tension-compression mixed shell whose shape was computed using the proposed method. Below: An Airy stress function was used to compute the shell floating above, which was also an optimization result obtained by the proposed method.

5.1. Inequality constraints for existence of stress- and flat-panel-aligned curve networks

Examining curve-traced results on several general mixed tension-compression shells made it clear that regions where (11) is *not* satisfied will often be present on form-found shells. Even though equilibrium holds everywhere on the shells, regions where no real eigenvalues exist are often found, sometimes extending over large regions of the surface. Therefore, for the method of [1] to be suitable for stress- and flat-panel-aligned curve tracing, it is necessary to modify it by *imposing* equation (11) as an inequality constraint on the form-finding algorithm.

To incorporate Eq. (11) into our computational framework, we extended the original method in a way that it can also solve inequality constraints. We do this via a penalty method approach. We add a least squares term defined as $w * (f)^2$ to the method, where w is a penalty coefficient, and where $f = p^2 - 4\det(\nabla^2\varphi)\det(\nabla^2 z)$ is the inequality constraint term. In each step, the inequality constraints are checked to determine if $f \geq 0$, and the penalty coefficient is set to a constant non-zero number if the condition is violated and to 0 when it is satisfied.

This activate-deactivate process makes the computation far less efficient than with no inequality constraints and thus longer computation times were needed. However, we were able to obtain interesting and useful results. As a byproduct, this extension enabled us to limit the Gaussian curvatures of the two surfaces to certain ranges.

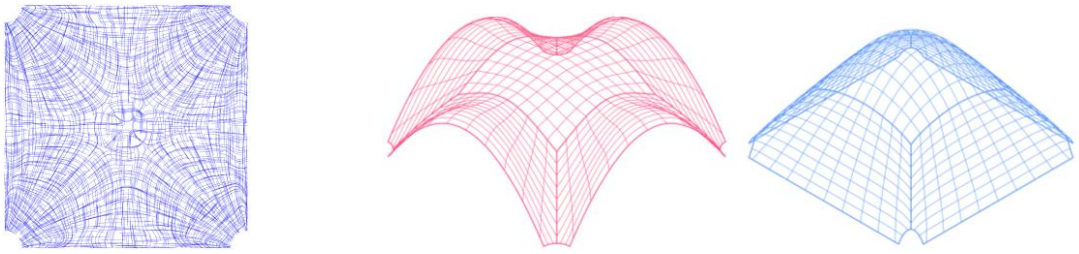
As is typical for penalty methods in general, the choice of the penalty coefficient w affects the accuracy of the results. A penalty coefficient that is too low leads to violation of the constraint, that is, the surface will still have imaginary eigenvalues. Conversely, a penalty coefficient that is too high can result in an ill-conditioned problem. Our penalty values were chosen by trial and error, and tended to result in sufficient constraint enforcement at the cost of less accurate iteration convergence (around 1e-4 in the L2 norm of the residual vector when the inequality constraint is active versus 1e-6 or less for the original, unconstrained method).

6. Curve tracing on NURBS surfaces

Now that it is possible to incorporate inequality constraints into our method, we show several examples of our curve-tracing method, in order of increasing difficulty of solution.

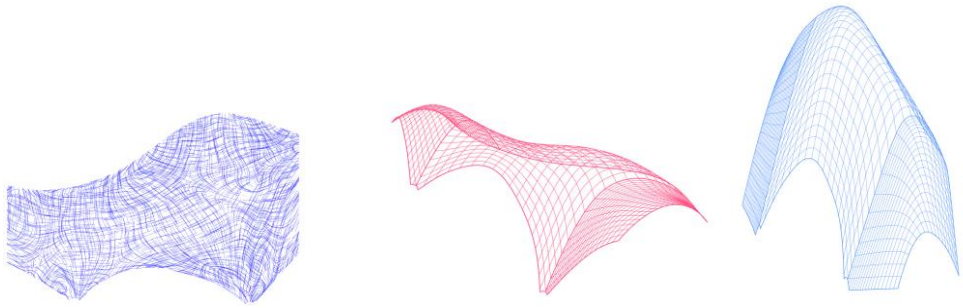
6.1. All-compression examples

Figures 5–6 (b) and (c) show the successful form-finding results of pure compression cases, and Figures 5–6 (a) show stress-aligned conjugate curve networks obtained by the curve tracing algorithm. In pure compression cases, the generalized eigenvalue problem always gives solutions; thus, there is no need to ensure that Eq. (11) is satisfied.



(a) (b) (c)

Figure 5. (a) A stress-aligned conjugate net obtained by our algorithm, (b) a shell obtained by limiting the Gaussian curvature to greater than -2, and (c) a stress function obtained by limiting the Gaussian curvature to greater than 0.

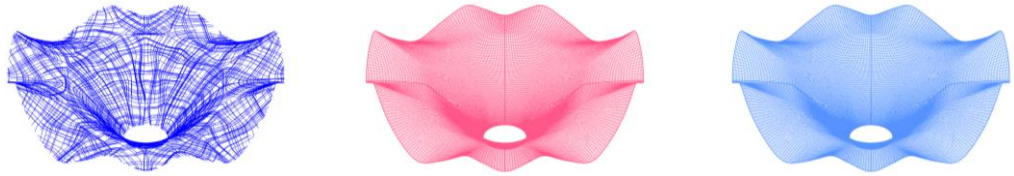


(a) (b) (c)

Figure 6. (a) A stress-aligned conjugate net obtained by our algorithm, (b) a shell obtained by limiting the Gaussian curvature to greater than -1, and (c) a stress function obtained by limiting the Gaussian curvature to greater than 0.

6.2. Non-trivial self airy example

Using the proposed method, by setting $\phi = z$, a non-trivial self-Airy case can be computed. Figure 7 shows the two surfaces obtained by the proposed method. Similar to example 4.2, the conjugate curves are chosen to be the lines of curvature for this example; since Eq. (7) does not give distinct eigenvalues in the case of self-Airy shells, we can select a preferred conjugate network at will.



(a) (b) (c)

Figure 7. (a) Curvature lines of the two surfaces, (b) shell surface, and (c) stress surface.

6.3. General mixed tension-compression examples

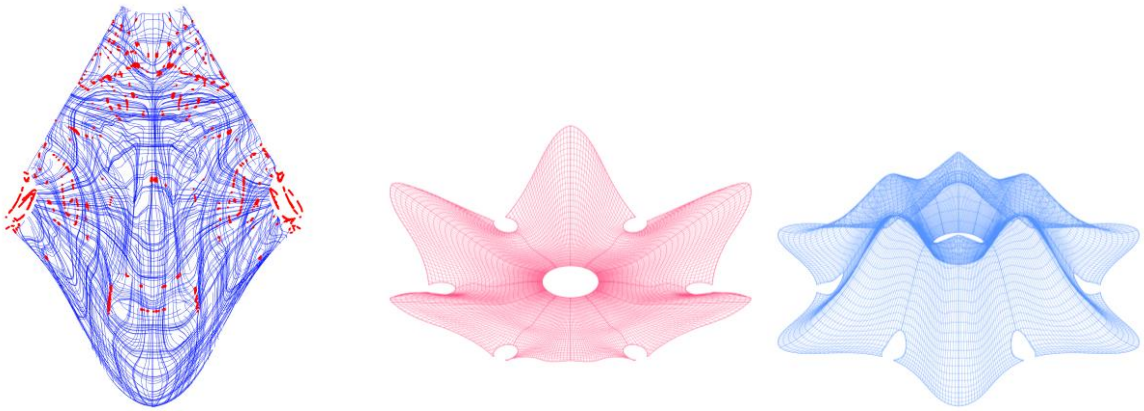
Two typical tension-compression mixed examples, obtained using the approach explained in Section 5 were also studied. The results are shown in Figures 8 and 9. Unlike the previous examples, Eq. (11) must be ensured by activating an inequality term. The actual inequality we used was $0.23p^2 \geq \det(\nabla^2\varphi)\det(\nabla^2 z)$ with an expectation that slightly narrower range can wipe out regions where the discriminant is not satisfied. In Figures 8–9 (a), the spots where the discriminant is violated are shown with red dots, and as shown in the figures, they disappear outside of a few isolated areas. The stress-aligned conjugate curve networks obtained using our tracing algorithm are also shown. Because the

inequality terms make the computation less efficient, we started with a smaller weight coefficient and increased it every 1000 steps. Obtain the solutions shown in figures 8 and 9 took more than 3000 steps.



(a) (b) (c)

Figure 8. (a) A stress-aligned conjugate net obtained by our algorithm, (b) a T/C shell, and (c) a stress function used to compute (b).



(a) (b) (c)

Figure 9. (a) A stress-aligned conjugate net obtained by our algorithm, (b) a T/C shell, and (c) a stress function used to compute (b).

7. Conclusions

We can solve a generalized eigenvalue problem to find a stress-aligned conjugate net. However, the generalized eigenvalue problem may not provide any solution in the regions where both surfaces give negative Gaussian curvatures. We have derived an inequality condition that ensures that the generalized eigenvalue problem provides a solution, and have extended the novel computational approach presented in [1] so that the method can simultaneously solve inequality constraints. As a result, a pair of shell and stress surfaces on which stress-aligned conjugate curves exist almost everywhere can be obtained by our proposed method, even when both surfaces give negative Gaussian curvature zones.

8. Future work

Although the form-found inequality-constrained mixed tension-compression shells of Figure 8 and Figure 9 are in equilibrium (to within 1e-4 in the L2 norm of the residual), and though they have real eigenvalues almost everywhere, the results, though correct within these limits, appear visually /

aesthetically rough. There are three potential reasons for this, all of which we intend to resolve in future work.

First, in the case of mixed tension-compression shells, the surfaces themselves can be quite complex in shape while still being in equilibrium and having real eigenvalues. This is a consequence of the much richer / more complex space of solutions available in the general mixed elliptic-parabolic-hyperbolic space of equilibrium shell shapes. Though corrugated / rippled solutions are valid from an equilibrium perspective, it is aesthetically desirable to smooth the solutions to remove ripples (while still satisfying equilibrium). Smoothed surface solutions will also naturally have less topologically and geometrically complicated stress- and flat-panel-aligned curve networks. Therefore, adding smoothing / filtering terms to the form-finding method of [1] is a key topic for future work.

Second, as noted in section 5.1, the penalty method used to enforce the inequality constraint (11) in the form-found shell results can lead to loss of accuracy. This numerical error may be partly responsible for the ripples of the solutions, in addition to the physical complexity of the solution space itself. Consequently, we plan on moving to more accurate inequality constraint enforcement technique in future work, such as the augmented Lagrangian method.

Finally, we note that the BTLS numerical solution method used in [1] and in this paper may have reached its limits when used to enforce the constraint (11). Specifically, the BTLS method is designed around bilinear problems specifically, while the constraint (11) is not bilinear. Although the results in this paper nonetheless achieve a sufficient level of accuracy for initial shape exploration and form-finding, higher accuracy may not be achievable without moving to a more general nonlinear equation-solving method.

Acknowledgements

The research was partially supported by the Nohmura Foundation, which is a funding body founded by the Taiyo Kogyo Corporation.

References

[1] M. Miki and T. Mitchell, Interactive exploration of tension-compression mixed shells. ACM Transactions on Graphics (TOG), Vol. 41, Issue 6, Article 263, (December 2022).
[2] C. Yu-Chou, and A. Borgart, A form-finding method for membrane shells with radial basis functions. Engineering Structures, Vol. 251, p.113514, (2022).
[3] E. Vouga, M. Höbinger, J. Wallner, and H. Pottmann, Design of self-supporting surfaces. ACM Transactions on Graphics (TOG), Vol. 31, Issue 4, Article 87, (July 2012).
[4] L. Eldén, and S. Ahmadi-Asl, Solving bilinear tensor least squares problems and application to Hammerstein identification. Numerical Linear Algebra with Applications, Vol. 26, Issue 2, p.e2226, (2019).
[5] M. Miki, T. Igarashi, and P. Block, Parametric self-supporting surfaces via direct computation of airy stress functions. ACM Transactions on Graphics (TOG), 34(4), pp.1-12, (2015).
[6] M. Miki, E. Adiels, W. Baker, T. Mitchell, A. Sehlström, and C. J. K. Williams, Form-finding of shells containing both tension and compression using the Airy stress function. International Journal of Space Structures, Vol. 37, Issue 4, pp.261-282, (2022).
[7] P. Csonka, P, Theory and practice of membrane shells. Akadémiai Kiadó (1987)
[8] C. Millar, T. Mitchell, A. Mazurek, A. Chhabra, A. Beghini, J. Clelland, A. McRobie, and W. Baker, On designing plane-faced funicular gridshells. International Journal of Space Structures, Vol. 38, Issue 1, pp. 40-63, (2023).

IASS 2023
July 10–14 Melbourne
Integration of Design and Fabrication

Proceedings of the IASS Annual Symposium 2023
Integration of Design and Fabrication
10–14 July 2023, Melbourne, Australia
Y.M. Xie, J. Burry, T.U. Lee and J. Ma (eds.)

Sydney's Central Station upgrade – design modularity and heritage enhancement in the renewal of the Grand and Northern Concourse

Michael CHERNYAVSKY[a,*], Amy CLARK[a]

[a,*] Aurecon Australasia
michael.chernyavsky@aurecongroup.com

Abstract

The Central Station Metro Works will deliver the most significant upgrades to Central Railway Station in decades, comprising an integral part of the NSW Government's Sydney Metro City & Southwest project. As the only underground station to be erected integrally within a live station environment, prioritisation of 'design for manufacture and assembly' (herein DfMA) and heritage interfaces, whilst minimising disruption to 270,000 daily commuters (pre-COVID), were the fundamental design drivers. This paper focuses on the heritage enhancement and DfMA approach championed in delivering the Grand & Northern Concourse Intercity cantilever slab and centrepiece canopy roof. The Intercity cantilever slab serves as a surface-level confluence point linking the new metro to suburban and Intercity platforms. The statement ~10-metre exposed-concrete cantilever features an organic double-curvature form and optimised reinforcement arrangement amidst a latticework of building services. Oversailing the Intercity cantilever slab and tracing the sandstone façade line of the heritage Sydney Terminal Building is the centrepiece canopy roof. The design of the steel-framed 40-metre-spanning propped cantilever was modularised, prefabricated, and preassembled, including services, fixtures, and finishes. This paper explores how a DfMA and user-centric approach to structural design and construction made viable 'open-heart surgery' within Australia's busiest railway interchange.

Keywords: case study, modular, preassembled, DfMA, sustainability, heritage, metro, railway, steel spatial structure

1. Introduction

1.1. Project scope

Sydney Metro is Australia's biggest rail infrastructure investment and will revolutionise the way our community navigates the city. By 2030, Sydney will have four metro lines, with forty-six stations and 113 kilometres of standalone metro rail. Sydney Metro City & Southwest will extend the Metro Northwest Line from the northern suburb of Chatswood to Bankstown in the city's south-west.

As part of the Central Station Metro Works (herein CSM), Laing O'Rourke, with its design and architecture partners, will deliver the most significant upgrades to Central Station in decades, comprising of an integral part of the NSW Government's Sydney Metro City & Southwest project. As the only underground metro station to be erected integrally within a live station environment, maintaining the operability of the railway interchange, and minimising disruption to commuters, was paramount. The scope of structural works includes the excavation and construction of the Sydney Metro platforms beneath existing platforms 13, 14, and 15 [1 & 4], the new 19-metre wide Central Walk concourse from a new entrance on Chalmers Street [3], escalators directly to suburban platforms 16 – 23, and a revitalisation of the Grand and Northern Concourse (herein GNC) entrance on Eddy Avenue [2]. This

Copyright © 2023 by Michael CHERNYAVSKY and Amy CLARK. Published in the Proceedings of the IASS Annual Symposium 2023 with permission.

paper focuses on the heritage enhancement and DfMA approach championed in delivering the GNC Intercity cantilever slab and centrepiece canopy roof.

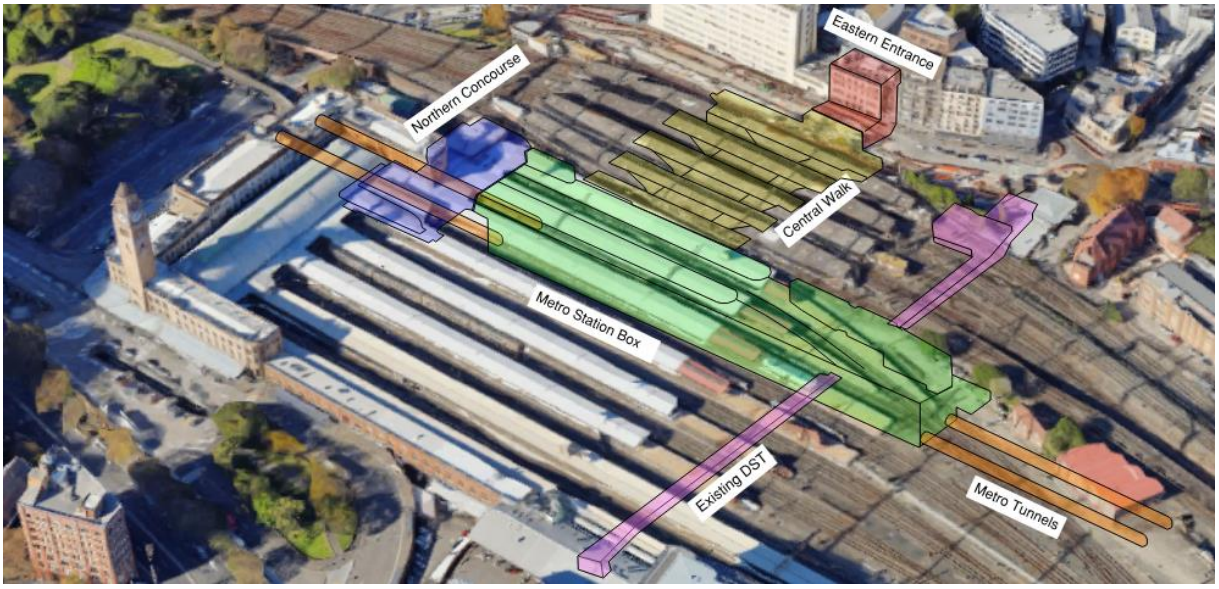


Figure 1. Project Scope, Annotated Aerial Site Photograph.

1.2. Heritage and site-specific constraints

The Central Station railway site is a state landmark, containing the original Sydney Railway Company grant, on which the first station and yards were opened in 1855. The heritage significance of the site, coupled with its complicated history of seemingly ad hoc developments and constrained inner-city location, demanded a sensitive and cross-disciplinary design approach. Furthermore, as a major infrastructure development, the project required a 120-year design life.

The GNC faced numerous constraints that required careful consideration in its design and construction. The most significant constraint was that the GNC needed to be constructed whilst the primary access to seven railway platforms remained operational. Furthermore, the GNC is situated over one of the most highly utilised commuter pathways within Australia's busiest railway station. It was not possible to have full public closure of the area during normal operation of the station for construction without any adverse impact to commuters. Therefore, designing for staged construction, speed of assembly, minimal temporary works and 'just-in-time' delivery was paramount.

The GNC is nestled between multiple new and heritage structures on all sides, each requiring careful consideration to ensure a seamless interface was achieved. It was essential to align the in-situ tree-head columns, precast colonnade, and, consequently, the primary canopy rafters with the existing and new Intercity and suburban platforms. The design also needed to facilitate an important view to the historic Central Station Clock Tower, which holds significant cultural and architectural value and was not previously visible from within this space.

Ensuring the safety of commuters and workers during the construction phase was a critical priority. In order to minimise disruption to the 270,000 daily commuters, the station needed to be handed over in a safe and secure condition after each night or weekend possession, ready for the daily influx of commuters. The workers had to navigate complex construction and installation tasks while adhering to strict safety protocols amidst time pressures and, at times, in conditions of high wind, rain, darkness, and extremes in temperature. Unlike construction within a vacant site, the weekend possessions and night works required considerable planning and the team needed to adapt to the changing conditions.

Managing tolerances in a precast, modular, or pre-assembled system is a meticulous task, particularly when it interfaces with in-situ concrete construction. On one hand, construction tolerances must be considered to enable site flexibility, while on the other hand, they must ensure the correct alignment and erection of the structure within acceptable tolerances. This balancing act demands accurate planning, precision in execution, and a comprehensive understanding of the construction process to avoid the need for major corrections and to ensure a successful outcome.

Considering its location and function, the structural elements of the GNC were required to withstand potential blast or train derailment loads. This constraint necessitated the careful consideration of various factors during the design process, such as the incorporation of redundant or stiffer elements, alternate structural load paths, and redistribution of loads post-yielding in these extreme scenarios. The challenge was to develop a design that not only met the functional requirements but also ensure a high level of safety and resilience for both the commuters and the surrounding infrastructure.

The steel canopy structure needed to be designed for disassembly and future extendibility, allowing for potential modifications or expansions in the future, embracing circular economy principles and reducing the risk of a premature end-of-life scenario. The constrained working area for pre-assembly of formwork or modules was another challenge, with the only available space being over the construction of the metro station box – a logistically complex area. Access to the site was limited to the Sydney Yard Access Bridge, which imposed spatial and weight constraints on the transportation of materials and equipment, necessitating careful planning, coordination, and, where possible, 'just-in-time' delivery to avoid any complications during the construction process.

1.3. Nature of the design

At the north entrance to Australia's busiest active railway interchange is the Northern Concourse, a new urban room positioned immediately to the south of Vernon's Grand Concourse. The Northern Concourse provides access between Eddy Plaza, the existing Intercity platforms, and the new metro platforms.

The scope of the works to the Northern Concourse includes the following;

- A new steel canopy roof, with glass walls enclosing the room,
- A new precast column colonnade at the intercity platform level to support the canopy,
- A new suspended concourse comprised of in-situ concrete at intercity platform level,
- A refurbished concourse at street level, which is largely supported on ground, and
- Associated sub-floor structures, retaining walls, and foundations.



Figure 2. Grand & Northern Concourse, Architectural Sectional Render.

Prioritisation of 'design for manufacture and assembly,' through modularity, was at the heart of the team's approach to delivering the complex structural designs and staging for the steel canopy roof, precast colonnade, and in-situ concrete Intercity concourse.

2. Intercity cantilever & tree-head columns

The statement ~10-metre, exposed-concrete cantilever at Intercity platform level features an organic double-curvature form and optimised reinforcement arrangement amidst a latticework of building services. The structural design team collaborated closely with the architectural and building services consultants to rationalise the organic form, minimising the extent of double-curvature geometries, which accommodated simpler modular reinforcement and formwork arrangements. This modular approach was further implemented in the rationalisation of the post-tensioning arrangement amidst a latticework of service pits and cast-in conduits. The cantilever formwork was comprised of plywood contours digitally fabricated using a Computer Numerically Controlled (CNC) router, while bespoke fibreglass moulds were fabricated to achieve the 'tree-head' form of the underlying supporting columns.

2.1. Modularisation of an organic architectural vision

The architectural vision for the Grand and Northern Concourse was to establish a world class entrance to the new metro station as an iconic urban room, which serves as a confluence point linking the new metro to suburban and Intercity platforms. The reference design for the Intercity cantilever, as shown on the left in Figure 3, met the functional requirement to improve pedestrian connections through the introduction of an Intercity level concourse. However, this design limited the aspirational performance of the lower concourse level as it obscured visibility of the canopy roof, restricted natural lighting, and introduced an underlying column grid that complicated wayfinding. The winning tender design proposed a cantilevered Intercity concourse, which achieved a column-free lower concourse level flooded with natural lighting. The monolithic cantilever is comprised of exposed concrete formed in an organic, curvilinear geometry and is supported on underlying 'tree-head' columns, so called due to the truncated conical form of their capital.

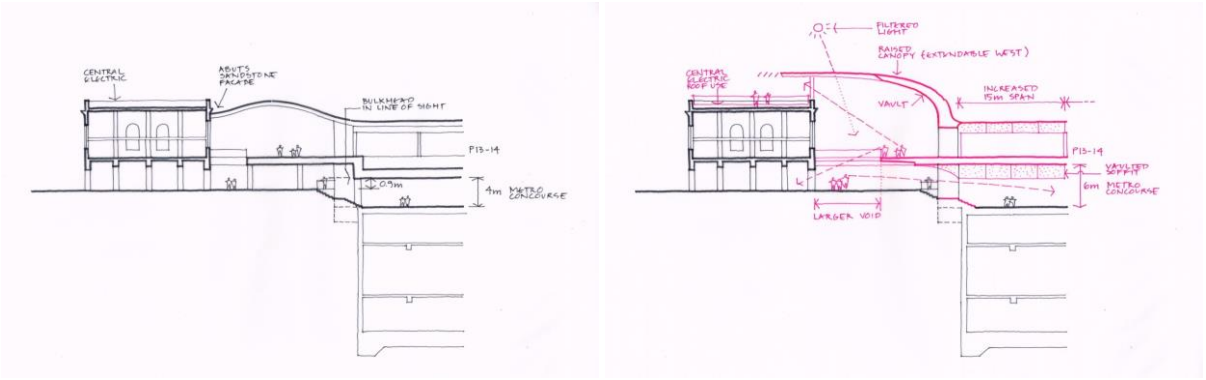


Figure 3. (Left) Reference Design Scheme and (Right) Winning Tender Design in Section.

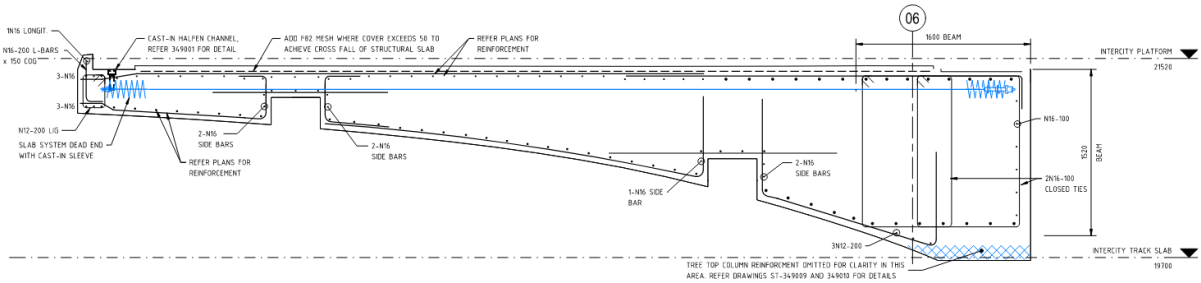


Figure 4. Typical Intercity Cantilever Profile in Section.

Early architectural designs of the statement cantilever were of highly multifarious geometries, with double-curvature forms generated extensively throughout the Intercity level. This variable geometry was highly impractical for structural design, fabrication, and construction. The structural design team

collaborated closely with the architectural consultants to rationalise the organic form, minimising the extent of double-curvature geometries to achieve the single curvature profile as denoted in Figure 4.

2.2. Description of the structural design

The cantilevered balcony protrudes approximately ten metres beyond the underlying tree-head columns and extends approximately 35 m along its leading edge in the east-west direction. The cantilever is supported by a 1230 mm deep beam running along the southern perimeter of the urban room and by two 2350 mm deep track edges beams running along gridlines G and J either side of the lift voids for north-south gridline locations). The cantilever is ultimately supported by two tree-head columns, located at gridlines G and J, and by the eastern and western curvilinear retaining walls.

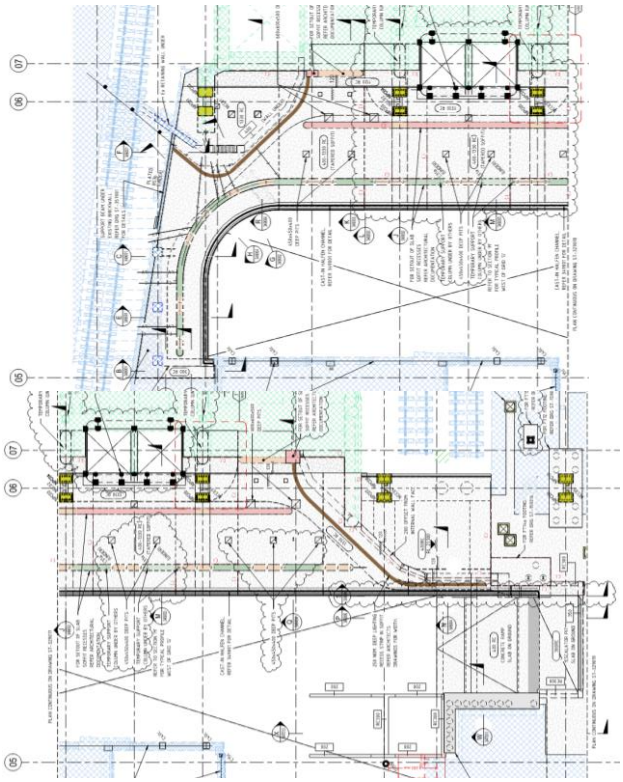


Figure 5. (Left) Eastern and (Right) Western Intercity Cantilever in Plan.

At gridlines G and J, the canopy colonnade is offset northward of the underlying tree-head columns by approximately 1.2 metres. This required a transfer structure, which was achieved by extending the track edge beams below the canopy colonnade in a tapered manner in alignment with the architectural intent.

The track edge beams were post-tensioned using multistrand tendons, which extend to a construction joint located approximately 2,000 mm south of the cantilever's leading edge. The cantilever was post-tensioned using monostrand 'flat duct' tendons, which generally extend between the cantilever's leading edge and the metro station box located to the south of gridline 7. Post-tensioning tendons have been arranged to minimise the differential displacements along the exposed perimeter of the cantilever by locally permitting and restricting deflection. Post-tensioning anchorages were concealed under the finishes using shallow pans to achieve the mass concrete architectural vision. Tendons have been extended into the platform level slab, where appropriate.

The Intercity cantilever has been modelled and analysed using finite element plate analysis in the CSi Bentley SAFE and Strand7 software packages. Linear, non-linear, and transient dynamic analyses were undertaken to assess performance against short and long-term functional criteria and construction staging requirements. Displacement studies have been carried out to consider the sensitivity of the

structural configuration to the placement of post-tensioning tendons, rotational stiffness of supporting columns and walls, geotechnical springs, and variability in material properties, such as creep and Young's modulus, in order to achieve an imperceptible leading-edge displacement. Furthermore, the design observed the prescriptive post-disaster recovery and protective design performance criteria, including consideration of alternate load paths and load redistribution in post-yielding scenarios.

2.3. Buildings services interfaces

Further to the organic architectural geometries, the design was complicated through the introduction of a series of recesses in the curved soffit, which would house lighting, electrical, and fire protection services. Services reticulations made in the cantilever soffit to accommodate sprinklers, lighting, and communications (PA) are located in two slots running parallel to the cantilevered edge. These lighting slots are visible within Figure 4 as the two recesses in the cantilever soffit. The slot nearest the leading edge is alternately 30 mm and 250 mm deep, with the key structural strength aligning with the shallow recess. The southern slot is consistently 250 mm. To accommodate the maintenance replacement strategy for the sprinkler pipes, concrete-encased pipes were placed inside conduits with clearances safeguarded to ensure straight lengths of pipe could be fed through. Along the southern edge, lighting and communications conduits are fed through the cantilever via services pits located at regular intervals throughout the cantilevered slab, which are 600 mm long x 600 mm wide, and extend to a depth of 500 mm below the top of the slab. The structural design team collaborated closely with the services consultants to design a modularised recess and pit arrangement to simplify conventional reinforcement and post-tensioning layouts, whereby post-tensioning ducts were 'bundled' either side of pits. The cross-disciplinary approach to design and prioritisation of stakeholder requirements balanced the technical design criteria and constructability constraints without compromising the architectural vision.

2.4. Temporary works & construction staging

2.4.1. Formwork & bespoke moulds for double curvature zones

While the geometry of the Intercity cantilever was rationalised to achieve a single-curvature profile, the tree-head columns and change in cantilever spanning direction required localised double-curvature forms. The cantilever is comprised of architecturally exposed concrete with a required formwork class of 2CX. Digital fabrication enabled construction of the bespoke geometries in alignment with the architectural vision.

At the eastern end of the Intercity level, the cantilever spanning direction changes from north-south to east-west as it wraps around the perimeter of the void. This creates a zone of double curvature where the single curvature profile of the cantilever in section wrapped around the circumference of the void in plan. The formwork in this zone was comprised of plywood contours digitally fabricated using a Computer Numerically Controlled (CNC) router, as shown in Figure 6. Each formwork component was physically numbered within the desired form for easy identification on site. The Intercity cantilever formwork was supported on a temporary flat deck.





Figure 6. Intercity Cantilever (Left) Double Curvature Formwork by Peri Formwork and (Right) Reinforcement.

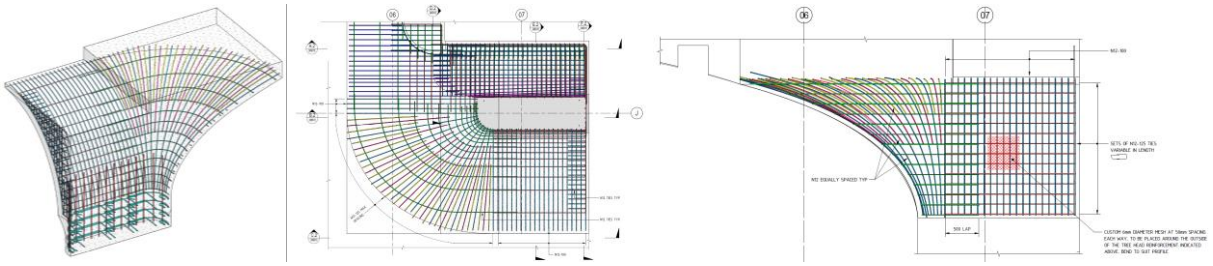


Figure 7. Tree-Head Column Reinforcement (Left) Isometric, (Middle) Plan, and (Right) Section.

For the underlying supporting columns, bespoke fibreglass moulds were fabricated to achieve the 'tree-head' form, as shown in Figure 8. The reinforcement latticework utilised easily workable 12 mm diameter low density grade D250N reinforcement to achieve the required forms, as shown in Figure 7.

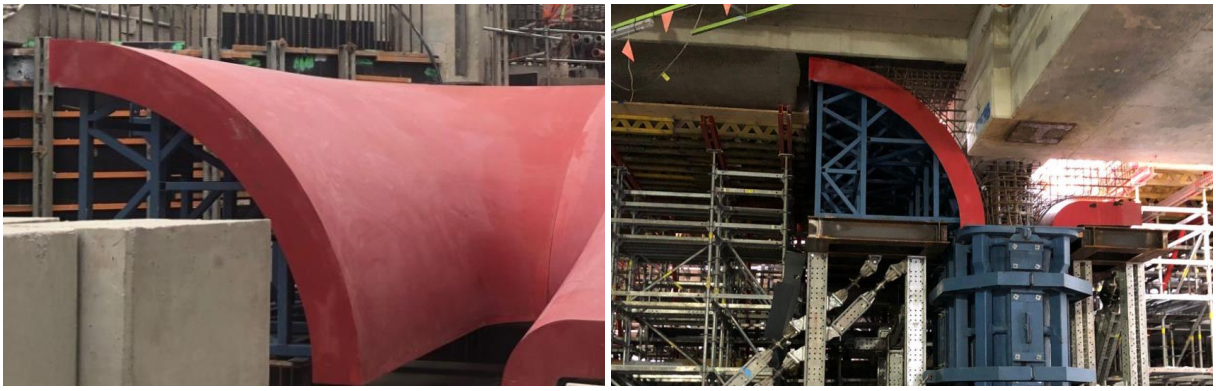


Figure 8. Tree-Head Column (Left) Moulds by Shapeshift and (Right) Temporary Works by Peri Formwork.

2.4.2. Construction staging within a live station environment

The station was to remain operational throughout construction, which required the Intercity cantilever to be designed to be poured in eleven discrete stages. This was largely driven by access requirements for stressing cables and staging regarding demolition of the existing lift and reinstation of the new lift. The staged construction of the Intercity cantilever took place over a period of over twelve months. In order to achieve a consistent colour across the multiple pours, the aggregate required for all pours was stored in the batching factory throughout the construction period.

2.4.2. As-built structural condition

The as-built condition of the Intercity cantilever structure is depicted in Figure 9, in which the cantilever soffit is viewed from street level looking towards the east in the left image and west in the right image.

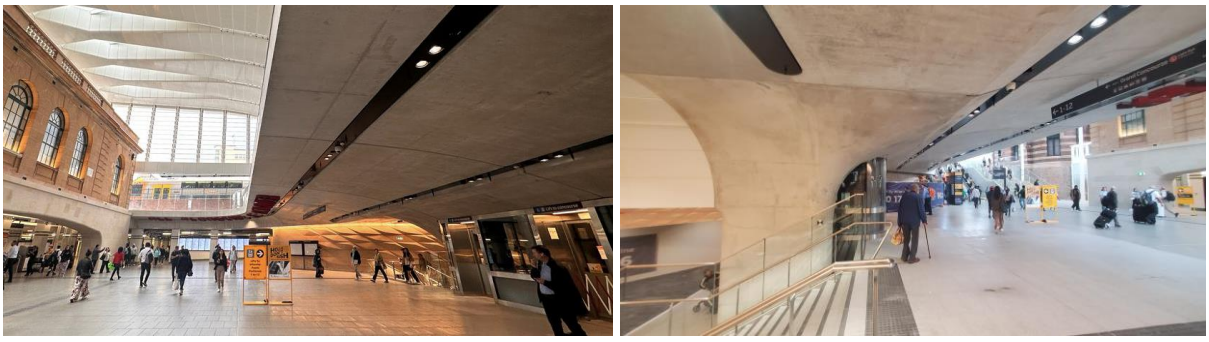
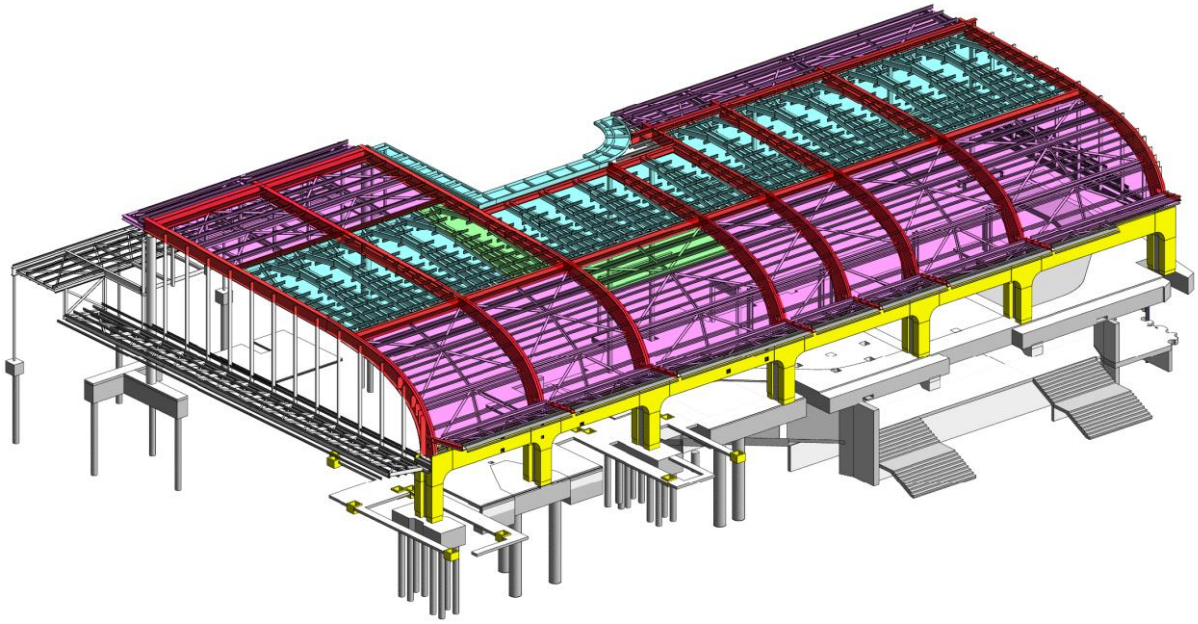


Figure 9. Intercity Cantilever Soffit (Left) Leading Edge and (Right) Tree-Head Columns.

3. Steel canopy roof

The northern concourse canopy roof is approximately 40 metres wide, 80 metres long, and 16 metres high. The propped cantilever steel structure features a curved aluminium outer cladding and 21 large kite-shaped skylights, which admit daylight into the new concourse, helping to create a clear, orienting space adjoining disparate parts of the station. The ceiling is a curved and discretised 30% porous aluminium cladding. The canopy consists of a primary frame of open section curved rafters and circular hollow section (CHS) columns. The secondary structure was modularised into fifty-eight preassembled and fully fitted out modules with all services and most of the soffit cladding installed off-site, weighing up to 9.2 tonnes. The structural system was optimised for speed in on-site assembly and was erected within a live station environment that remained functional during all stages of erection.

The roof is supported on its southern edge by a reinforced precast concrete colonnade sway frame above the platform level. The north edge is supported on tall, slender steel CHS columns. A portion of the canopy is supported by a steel transfer structure atop the heritage Central Electric Building. This transfer structure ensured that any loads from the canopy were able to be accommodated by the existing structure without the need for strengthening works. The steel roof is fully braced with all lateral loads resolved at the precast colonnade sway frame on the southern edge. The colonnade provides a fixed support to the main rafters, reducing deflections and creating improved efficiency.



Red indicates primary steelwork assembled on-site during night-time possessions. **Pink**, **blue**, and **green** indicate bays preassembled off-site.

Figure 10. Northern Concourse Structure, Primary Steelwork and Preassembled Modules.

3.1 Efficient construction through prefabricated modular construction

The 330-tonne northern concourse canopy is a grand and iconic structure that needed to be almost entirely erected within a staggered four-week period. To accomplish this, the design team developed an approach focused on optimising preassembled modules for rapid assembly. Through the use of Prefabricated Prefinished Volumetric Construction (herein PPVC), the team facilitated off-site assembly of the steelwork, glazing, cladding, fixtures, and services for the for the majority of the canopy.

Each of the 58 preassemblies were designed to incorporate only four simple connections to the primary steelwork. These connections were engineered to only have between two and four bolts, significantly reducing the time required working at height with over 90% of all steel connections undertaken off-site. This design consideration not only heightened the safety of the construction personnel but also

accelerated the erection process, ensuring minimal disruption to the station's daily operations. The prefabricated canopy roof was designed with an emphasis on disassembly and future extendibility, a forward-thinking approach that aligns with circular economy principles. The potential of this approach is evidenced in the full scale off-site pre-erection in *Figure 13*. The design and detailing of the canopy structure ensured it could be modified or expanded as needed in the future, ensuring its adaptability to changing requirements and conditions. By incorporating these concepts, the project team mitigated the risk of premature end-of-life scenarios and contributed to a more sustainable construction process. This is particularly critical for a canopy roof that is designed for an extensive 120-year design life.

Each component of the structure, including the preassembled modules had to be stable individually during lifting and after installation in their partly erected state. This was crucial as the station needed to be handed over in a safe and secure condition after each night or weekend possession, ready for the daily influx of commuters. This was achieved through designing bracing for each pre-assembled bay, which formed part of the global bracing solution when all the panels were installed but also provided stability during lifting. This was particularly critical for the large and delicate 14-metre-long, 2.5-metre-wide skylight modules, which had the glazing installed prior to lifting. A design approach was undertaken to improve the strength of the primary framing to reduce the amount of temporary works required and to ensure the part-erected structures were stable. Each of the fully modularised and pre-assembled steel framed panels required additional edge members, bracing, and strengthening of the primary structure, but enabled stable liftable pre-assembled modules, weighing up to 9.2 tonnes, that could be installed in under one hour on-site.

By adopting PPVC and off-site assembly, this project facilitated rapid on-site erection during the three weekend possessions of 48-hour periods available and the short night work sessions of 3-hour periods. During these times, the contractor, Laing O'Rourke and fabricator, Alfabs, had access to the required work areas while ensuring safe passage for commuters through alternative routes. This approach demonstrates the potential of integrating design and fabrication to overcome complex constraints in large-scale infrastructure projects.



Prior to Installation – January 2020 **Erection** – 5 September 2020 **Erection** – 12 September 2020

Figure 11. Aerial Photos Illustrating the Rapid On-site Erection of Northern Concourse Canopy.

In total, the northern concourse canopy was largely erected in just 250 hours of construction time on-site and has now become a world class ‘front door’ to the new metro station.

3.2 Creating a visually uniform appearance with a constrained primary structure

Through computational design techniques, the structural design and installation solution achieved regularly spaced skylights and a monolithic soffit appearance despite the irregular spacing of existing structures and, hence, the primary structure, which was typically spaced between 10 and 13 metres.



Figure 12. (Left) Preassembled Skylight Module, (Middle) Photograph of Canopy, (Right) Clock Tower.

The design process optimised several parameters, including the skylight width, the total number of skylights, the spacing between each glazed panel, and the distances between each secondary steel structure, all while striving to attain the largest possible skylight area. By determining the optimal combination of these parameters, it was possible to create twenty-one standard preassembled skylight modules with consistent spacing, resulting in a visually cohesive and harmonious architectural form for the skylights and soffits. The Rectangular Hollow Section (herein RHS) mullions and glazed louvers also frame an important view to the historic Central Station Clock Tower, which holds significant cultural and architectural value.

3.3 Balancing site flexibility and precise site assembly

Striking the right balance between installation, preassembly and fabrication tolerances was a critical aspect of designing and detailing the canopy structure. Insufficient tolerances could lead to challenges in installing the structure without locking in forces or displacements, while excessive tolerances might result in components shifting and moving during installation, making it difficult to accurately position the steelwork and potentially leading to delays and disruption associated with re-alignment or future modules potentially not ‘fitting’.

The primary structure, standing approximately sixteen meters above the ground, was considerably flexible. This characteristic enabled many of the modules to forego slotted connections or packing, which could otherwise have increased the risk of installing the steelwork out of tolerance. Therefore, in many instances the decision was made that the tolerances of standard bolt holes of simple connections would be sufficient and preferable for maintaining the required balance. For rigid connections where the structure was less flexible, slotted or oversized holes were introduced to provide an installation position tolerance of approximately ±15 mm. This strategy was put to the test during the pre-erection stage when the entire roof was assembled at the Alfabs Group workshop in Kurri Kurri (refer Figure 13 below). The pre-erection process served as a crucial validation of the design and detailing approach, confirming that the canopy could be successfully installed on-site within a staggered four-week period while maintaining the desired balance between tolerances.



Figure 13. Canopy Full Scale Pre-Erection at Alfabs Group's Workshop.

4. Precast concrete colonnade

The exposed precast colonnade supports the northern concourse canopy structure and the terminating overhead wires of the trains. Its alignment follows the existing platforms with columns at irregular spacings of up to thirteen metres and is approximately 80 metres in length and 5.4 metres in height. The colonnade also accommodates two full cable trays of services from the roof through to the Intercity cantilever slab and incorporates integral wayfinding signage. The columns provide a rigid support to the primary beams of the northern concourse canopy. They are a highly expressed, class 2CX concrete arch portal, which emulates some of the curves that are expressed throughout the historic station.

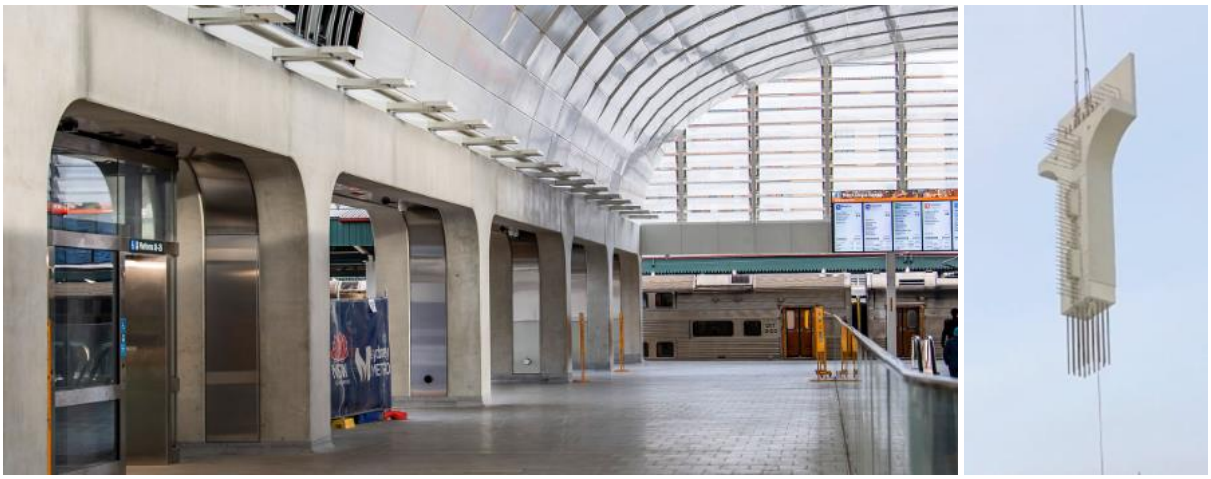


Figure 14. Precast Colonnade, (Left) Photo from East End of Intercity Cantilever Slab and (Right) Column Lift.

The precast colonnade was constructed within a staggered 32-hour period with minimal formwork and temporary works to ensure the station remained functional throughout construction. It also required sufficient tolerances between all precast elements and stitched steel reinforcement for rigid connections into the Intercity cantilever slab, under and between each segment. The discretisation of the precast elements was specifically designed for transportation and crane lifting limitations. The design effectively addressed crane and transport restrictions while achieving the goal of constructing the colonnade in just a few days, without reliance on temporary works beyond those required for positioning. Corrugated steel ducts were employed for reinforcement continuity, tolerance, and anchorage in both precast-to-precast connections and precast-to-in-situ footing connections. The structure was discretised and detailed such that there was a seating for each and every precast element and that it would be stable in the temporary state prior to the in-situ stitch pours. The in-situ pour of the beams were formed using 30 mm thick glass reinforced concrete (GRC), which could span prop-free and achieve the required 120-year design life. These in-situ concrete pours provided the necessary continuity for the structure to

behave monolithically, ultimately delivering an efficient and rapid construction solution for the precast colonnade with minimal disruption to the station's operation.

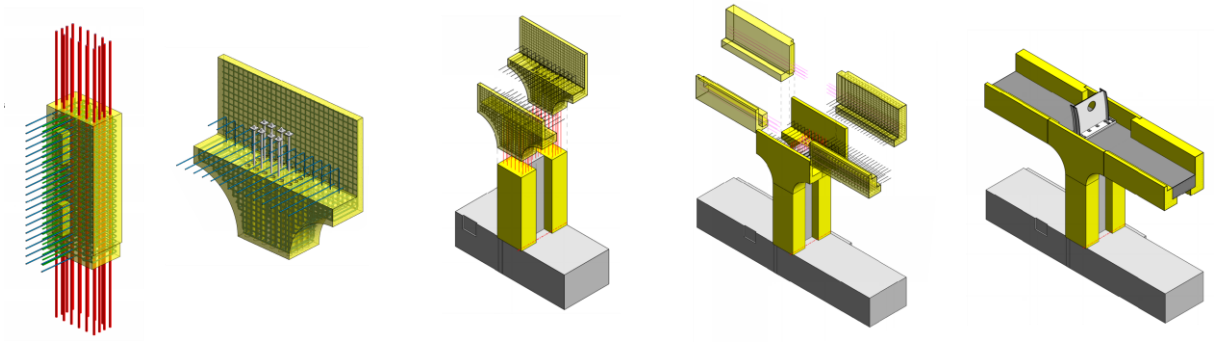


Figure 15. Installation Sequence of the Precast Colonnade.

5. Conclusion

As part of Central Station Metro Works, Laing O'Rourke, with its design and architecture partners, will deliver the most significant upgrades to Central Station in decades, comprising an integral part of the NSW Government's Sydney Metro City & Southwest project. The new Intercity cantilever slab serves as a surface-level confluence point linking the new metro to suburban and Intercity platforms. The statement ~10-metre exposed-concrete cantilever features an organic double-curvature form and optimised reinforcement arrangement amidst a latticework of building services. The cantilever formwork comprises plywood contours digitally fabricated using a Computer Numerically Controlled (CNC) router, while bespoke fibreglass moulds were fabricated to achieve the 'tree-head' form of the underlying supporting columns. Oversailing the Intercity cantilever slab and tracing the sandstone façade line of the heritage Sydney Terminal Building is the centrepiece canopy roof. The prefabricated, steel-framed propped cantilever spans 40-metres from precast colonnades towards the newly underpinned Central Electric Building. The DfMA approach and minimisation of on-site works ensured that Central's busiest commuter railway remained functional throughout the weekend possessions allotted to erection of the canopy and colonnade structures. These works have been likened to 'open-heart surgery' within Australia's busiest railway interchange.



Figure 16. Grand & Northern Concourse, (Left) Architectural Perspective Render and (Right) Site Photograph.

Central Walk and the new escalators from platforms 16 – 23 opened in April 2023 with the new metro platforms becoming operational once Sydney Metro City & Southwest services commence in 2024.

Acknowledgements

The authors wish to make acknowledgement of Sydney Metro and Transport for New South Wales for undertaking Australia's largest public transport project, of which Central Station Metro Works forms an

integral part. Together with principal contractor, Laing O'Rourke, and ultimate client, Sydney Metro, Aurecon delivered the detailed design for the new and upgraded rail infrastructure comprising the Central Station Metro Works, in partnership with GHD and Atkins. In particular, the authors wish to thank Laing O'Rourke's Aston Williams, Channari Penh, Edward Labinski, Huw Griffiths, Lachlan McMaster, and Martin Bibb for their support and expertise during the design and construction phases of the project. Woods Bagot, John McAslan + Partners, and GHD delivered the architectural design.

References

[1] J. Turley, A. Clark, and M. Chernyavsky, "Sydney's Central Station upgrade – Top-down construction of the Metro Station Box," *Informit*, pp. 260 – 269, 2022.

[2] M. Chernyavsky and A. Clark, "Sydney's Central Station upgrade – Design modularity and heritage-enhancement in the renewal of the Grand and Northern Concourse," *Informit*, pp. 312 – 324, 2022.

[3] M. Liang, K. Kamalarasa, K. Su, and M. Wiltshire, "Sydney metro central station project – central walk temporary track slab and underground support structures," *Informit*, pp. 301 – 3011, 2022.

[4] P. Gadagi, J. Turley, W. Deng, and T. Lavorato, "Devonshire Street Tunnel Underpinning – an Innovative Approach," in *State of the Art and Practice in Geotechnical Engineering: Proceedings of Geo-Congress 2022 hosted by the ASCE Geo-Institute*, Charlotte, North Carolina, March 20 – 23, 2022.

Historical concrete shells

Active bending
Additive manufacturing/ 3D printing
Architectural geometry
Bamboo for sustainable construction and quality of life improvement
Bio-inspired structures and architecture
Bridge structures
Computational form-finding
Conceptual design
Concrete structures
Construction techniques
Deployable and inflatable structures
Design competition (WG21)
Digital modelling and fabrication
Dynamic response of metal spatial structures
Dynamic response of other structures
Form-finding and structural optimisation of interlocking discrete assemblages
Graphical methods
Gridshell and lattice structures
► **Historical concrete shells**
Historical structures
Lattice structures
Life-cycle design and assessment of structures
Metal gridshell structures, connections and stability
Methods and construction technologies for sustainable shell structures
Morphology and configuration processing
Next generation parametric design
Novel methods in modelling, optimisation and construction for reducing carbon footprint of continuous roof shells
Numerical methods for geometry, form-finding and optimisation of lightweight structures
Optimisation methods and applications
Origami
Other
Teaching design uncertainty: working with unknown qualities/quantities of new and re-claimed materials
Teaching of shell and spatial structures
Tensegrity systems and cable structures
Tension and membrane structures
Tension structures in the Asia-Pacific
Timber and bio-based structures
Topology optimisation
Traditional masonry structures and innovation
Transformable structures

IASS 2023
July 10–14 Melbourne
Integration of Design and Fabrication

Proceedings of the IASS Annual Symposium 2023
Integration of Design and Fabrication
10–14 July 2023, Melbourne, Australia
Y.M. Xie, J. Burry, T.U. Lee and J. Ma (eds.)

Digital tools and technologies in the preservation of historic concrete shells

Marisela MENDOZA[a,*], Mariana ESPONDA[b], Albero MUCIÑO-VÉLEZ[c], Alejandro LEAL-MENEGUS[c], Juan I. DEL CUETO RUIZ-FUNES[c], Nohema C. RUIZ-GÓMEZ[c]

[a,*] Nottingham Trent University, UK.
marisela.mendoza@ntu.ac.uk

[b] Carleton University, Canada.
[c] Universidad Nacional Autónoma de México.

Abstract

Awareness in the preservation and conservation of 20th Century architectural heritage in Mexico and particularly that of historic concrete shells have increased in the last decades. In a paper presented and published in the IASS2022 [1] the authors of this paper identified the main preservation challenges and opportunities that such heritage assets face locally and globally within the contexts of cultural heritage, circular economy, sustainability, and climate change. Building upon these findings, this paper will focus on the technology advancements related to digital tools and Non-Destructive Testing (NDT) and their potential to complement traditional methods in the assessment, documentation, and intervention of heritage buildings. To exemplify this, two research studies investigating different methodologies to evaluate the quality of reinforced concrete will be presented in this paper. These studies aimed to explore and advance the use of digital technology and NDT to assess the current state of the iconic Cosmic Rays Pavilion shell built by the architect Félix Candela in 1951. The Cosmic Rays Pavilion holds a significant architectural heritage value as it represents Candela's step-in stone to further develop some of the most ingenious and elegant 20th Century hypar shells worldwide and it is also part of the UNESCO heritage site of Ciudad Universitaria in Mexico City. The first study, a digital documentation workflow, was caried out by Sepideh Rajabzadeh from Carleton Immersive Media Studio (CIMS) and Mariana Esponda from Azrieli School of Architecture, Carleton Canada in 2019. This study was carried out to explore the use of emerging digital technologies to document and analyse if the Cosmic Rays Pavilion shell had suffered any damages after the 2017 earthquake. The second case study, conducted in 2022 by Dr. Alberto Muciño and Dr. Alejandro Leal, researchers at the Faculty of Architecture at Universidad Nacional Autónoma de México used NDT (ultrasonic pulse velocity (UPV) and sclerometer test) to assess the current condition of the shell's concrete. Both studies were also supported by traditional survey tools and methods. The analysis of these two studies will discuss the potential of using emerging digital and other NDT technologies as complementary tools to support a more efficient and sustainable preservation of 20th Century historic concrete shells.

Keywords: Félix Candela, historic concrete shells, preservation, conservation, sustainability, circular economy, digital technology, non-destructive testing

1. Introduction

During the mid-half of the 20th Century fast and significant developments in science and technology supported digital advancements such as digital media (software, digital images, digital video, digital data and database and electronic documents) which use has gradually grown for heritage buildings surveying and 3D modelling, thus resulting in new research methods and protocols. Since the 1970s

Copyright © 2023 by Marisela MENDOZA, Mariana ESPONDA, Albero MUCIÑO-VÉLEZ, Alejandro LEAL-MENEGUS, Juan I. DEL CUETO RUIZ-FUNES and Nohema C. RUIZ-GÓMEZ. Published in the Proceedings of the IASS Annual Symposium 2023 with permission.

disciplines like archaeology started exploring the use of laser scanning, photogrammetry, advanced software for modelling, data analysis and computer-based visualization which is now recognised as an effective research method to assess heritage assets [2]. At the outset digital technologies were promoted as economic and time saving tools, recently they have also been identified as enablers of sustainability as they can reduce the use of materials, natural resources, and energy. As stated by the Unite Nations, digital advancement can support and accelerate achievement of each of the 17 Sustainable Development Goals [3]. However, the challenge in the field of heritage preservation remains in producing bespoke research methods and protocols adequate for each socio-cultural, economic, and geographic context. Furthermore, the use of digital technologies promotes circular economy in the field of built-heritage preservation in how we assess, document, and promote value in collaboration with stakeholders and the wider community. Digital technologies can also support to maintain and increase the functional, economic, and socio-cultural value of built-heritage assets for as long as possible. Heritage-built assets should be maintained and managed to support their reuse, re-adaptation and recycle, assisted using available digital technology.

Scientific and technological advancements have also supported the development of the Non-destructive evaluation (NDE) or Non-destructive tests (NDT) which are used to inspect, evaluate, or test constructive systems and materials' irregularities without causing damages or alterations to the serviceability of the analyzed structures [4]. The purpose of NDT is to assess the quality and integrity of structures' materials or assemblies without compromising their intended structural and functional performance. However, it is important to mention that some non-destructive testing methods can include invasive actions on the structure.

Whilst NDT methods have emerged as a response to detect and prevent structural damage and have been mainly driven by economics and safety, they also present circular economy advantages and they can be enablers of sustainability. As stated in the 'Guide to sustainability criteria in the conservation and restoration of immovable cultural heritage' [5] the use of NDTs can support saving materials resources by developing primary physical and/or mechanical properties analysis of structural components which can facilitate a minimal intervention in the cultural asset with the use of minimal resources. Furthermore, non-invasive NDTs can safeguard the structural integrity of the cultural asset during testing thus extending its value and serviceability. Some of the most common NDTs are sonic, ultrasonic, georadar, dynamic, sclerometers, thermography, etc. Some of the semi-destructive tests are the carried out by means of penetrometers, resistographs, flat jack tests, etc.

The methodology of NDTs for historic concrete shells is complex as it requires a multidisciplinary approach. As stated by Shull [6], a successful NDT must start with a good idea of what is that intended to be found which requires a conscientious knowledge of the geometry and construction methos of reinforced concrete shells as well as the physical and mechanical properties of reinforced concrete. A basic knowledge of how the various NDT methods work is essential to choose a method or a combination of methods. Furthermore, competent knowledge of the use, advantages, and limitations of the existing technology and for the particular case of reinforced concrete shells and their context is important 'we must be aware of the actual sensitivity of the equipment relative to the environment in which it is used' [7]. Also, competent knowledge of regulations and guidelines for the assessment and intervention of historic buildings for a specific context is required. It is important to mention that some of the most common non-destructive testing methods include invasive actions, which for the specific characteristics of thin shell reinforced concrete structures may not be the most appropriate. Shull [8], lists five levels to choosing an appropriate NDT method for a specific application:

1.- Understanding the physical nature of the material property or discontinuity to be inspected.

2.- Understanding the underlying physical process that govern NDT methods

3. Understanding the physical nature of the interaction of the probing field (or material) with the test material

4.- Understanding the potential and limitations of available technology

5. Considering economic, environmental, regulatory, and other factors.

To maximize the effectiveness of any NDT methods, it is paramount to have a good knowledge of the materials' properties and any potential issues/anomalies we are looking for such as voids, cracks, delamination, coating thickness, etc.

Through the application of NDTs it is possible to minimize the uncertainty of conventional primary assessments which by and large tend to result in unnecessary invasive interventions to heritage buildings. Furthermore, the non-destructive and non-invasive characteristic of some NDTs can safeguard the structural integrity and functionality of the cultural asset. As stated by Damazo [9] the use of NDTs can support a more effective decision-making process regarding the reuse, repair, repurpose or demolition and recycling of existing concrete structures. Furthermore, NDTs can be used prior to minimise the impact of any required destructive testing thus complementing it and making it more effective. Some of these destructive testing techniques include carbonation analysis, petrographic analysis, compression test, adhesion of the surface layers of the concrete (pull-of), moisture and density concrete test and coring [10]. The various efforts and interest of the international community of conservation experts to promote the implementation and application of NDT to concrete heritage are evident in the publications of the Getty Conservation Institute: *Conservation Principles for Concrete of Cultural Significance published in 2021* [11] and the Cadiz Document: *InnovaConcrete Guidelines for Conservation of Concrete Heritage,* ICOMOS published in 2021 [12]. It is also important to note that assessment of concrete structures through digital technology and NDTs are not substitute of traditional field research but are complementary.

2. Digital documentation and NDT of the Cosmic Rays Pavilion

2.1. The Cosmic Rays Pavilion, 20th century historic concrete shell

The Cosmic Rays Pavilion, located on the north-east of Ciudad Universitaria's campus in México City belongs to the complex of buildings that made up the original architectural scheme of Ciudad Universitaria built from 1950 to 1954, and listed as a UNESCO World Heritage Site in 2007. The Cosmic Rays Pavilion was one of the three pavilions (Van der Graaf Pavilion and the Gravitation Pavilion) that were built to support the innovative research activities of the Institute of Nuclear Physics at Unversidad Autonoma de Mexico new campus.

In 1951 Félix Candela worked in collaboration with the architect Jorge González Reyna, chief architect for the Institute of Nuclear Physics, to design and build a thin-shell reinforced concrete structure which had to comply with a thickness specification of approximately 16mm thick [13] to allow the pass through of cosmic radiation whilst providing a robust and secure shelter for the expensive and sensitive equipment. The final constructed roof "figure 1" was comprised of two saddle-shaped shells with a thickness of 5/8" (16 mm) at the crown increasing to 1½" (37mm) at the base [14]. Since this was Candela's first commissioned hyperbolic paraboloid (hypar) shell, he took further precaution against buckling and included three supporting arches (31 centimeters deep each) concealed under the shell and spaced at 5 metres. It is worth to note that due to the innovative nature in the construction field of reinforced concrete shells at that time, it was common for shell builders to advanced their knowledge through trial and error and experimentations on site which means that in some cases the current available construction drawings do not match with the final constructed shell. This poses a particular challenge when dealing with the conservation of heritage buildings and in these cases, NDT and digital technology can be very useful to corroborate construction drawings and assess the condition of a heritage building. The archival study and survey conducted by Cordero et al [15] demonstrated that all three stiffening arches had been designed, drawn, and built of equal height without considering that the lateral arches were short of height to meet the initially designed shell. Therefore, the shell's geometry was slightly

modified on site to resolve this anomaly, thus altering the final shape of the shell and in turn not matching with the existing construction drawings.



Figure 1. Cosmic Rays Pavilion, Ciudad Universitaria Mexico. Image: M.Mendoza, 2018.

The Cosmic Rays Pavilion is recognized for its historical associations and architectural values. Félix Candela was known to be one of the most innovative architects of the 20th Century specialised in thin shell reinforced concrete structures. With the Cosmic Rays Pavilion, Candela sparked international attention at the beginning of the 1950s and paved way for his practice to be further explored. Candela´s concrete shells are an important contribution Mexican modern architecture. Candela's ingenious use of the hyperbolic paraboloid geometry allowed the development of some of the most elegant thin shell concretes structures of the 20th Century while also achieving economic and structural design efficiency. Candela's hypar thin shell structures are also exemplary as they explored the synergy between form, function, and the inherent qualities of reinforced concrete to create very thin shells (thickness of as little as 15mm) thus minimizing the use of concrete and reducing carbon footprint.

2.2. Digital documentation workflow of the Cosmic Rays Pavilion concrete shell

In May 2019 Professor Mariana Esponda from Azrieli School of Architecture organized a student internship programme which included an in-depth research study and documentation of the Cosmic Rays Pavilion after the earthquake of September 2017. In collaboration with Sepideh Rajabzadeh, student leader from Carleton Immersive Media Studio (CIMS), develop the first digital documentation workflow for Candela's Cosmic Rays Pavilion. This research project was supported by The *New Paradigm New Tools for Architectural Heritage in Canada* (NPNT) research program and funded by the Social Sciences and Humanities Research Council of Canada (SSHRC). This documentation was undertaken to better understand the pavilion's structure, its evolution, and to assess if it had suffer any damages from the 2017 earthquake.

Followed by a traditional survey, material catalogue, condition assessment, and placement of targets markers on the pavilion, the Carleton team conducted a digital documentation of the pavilion using the CIMS workflow protocol "figure 2".



Figure 2. Photogrammetry workflow in Agisoft Photosan by CIMS, 2019.

Documentation began with the capture of exterior photogrammetry images using digital single-lens reflex (DSLR) cameras. Interior photogrammetric elevation photos were subsequently taken and combined in Agisoft Photoscan to create a point cloud, and which was then processed into a point cloud model. Exterior photogrammetry was also created using photos from the DSLR cameras and a drone. This equipment allowed assisted the data collection from the shell extrados, the site, and all exterior angles. The two-point clouds were then brought into Revit and combined manually. Since the interior walls were painted plain white without any noticeable texture, the team used more than usual number of targets to increase accuracy "figure 3".



Figure 3. Student from Carleton University collecting interior photogrammetry data of the pavilion using a handheld DSLR camera. Image: M. Esponda.

To ensure data was completed and accurate before traveling back to Canada, it was important to do a quality check of the photogrammetric models, data, and elevation photos using Bentley Context Capture and Adobe Photoshop as in Rajabzadeh et al [16]. The Cosmic Rays Pavilion was modeled in Revit using the point cloud model developed from the photogrammetric data attained on site and with Professor Esponda's supervision. This detailed point cloud allowed for an extremely high level of accuracy in modeling the Heritage Building Information Model (HBIM). The 2D drawings and 3D point cloud data were carried out at the CIMS Lab, Ottawa, Canada. By creating sections through point cloud at regular intervals, building elements could be modeled and adjusted to the point cloud within millimetres of accuracy. This method of modeling was particularly useful for the unique hypar roof structure and ultimately led to further discoveries, as in Esponda *et al*. [17]. The cross-reference between the collected data and observations recorded on site during the visit allowed to gain a more in-depth understanding of the endogenous and exogenous factors that have contributed to the current damages of the shell. Furthermore, the team developed a specific 'Statement of Significance' for the Cosmic Rays Pavilion including its important relationship with Ciudad Universitaria's main campus, which is listed as a UNESCO World Heritage Site, as in Esponda *et al* [18].

The preliminary objective for the project was to produce two sets of drawings from the existing pavilion using two methods: traditional and digital documentation. The two sets of drawings were then overlaid and compared with the original construction drawings by Candela and with the survey drawings developed by Cordero. This study helped to ratify Cordero´s initial findings to demonstrate that the dimensions of the shell had been modified during construction "figure 4" Rajabzadeh [19]. This comparative analysis demonstrated that compared to traditional survey techniques the use of contemporary digital technologies can provide significant advantages such as ease of access, speed in data collection and measurements´ accuracy.

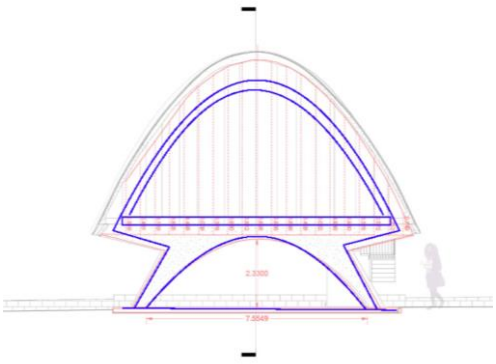


Figure 4. Comparison between 2D drawings by CIMS (grey), Cordero (red) and Candela's original construction drawing (blue). Image: S. Rajabzadeh (CIMS Lab).

Considering the three most significant earthquakes that have shook Mexico City (1985, 1999 and 2017) another aim of this research project was to identify any structural changes on the pavilion. While the team did not identify any damages to the building which could have been cause of seismic activity, the comparison between the digital model and the original construction drawings revealed that changes and deterioration observed in the building are mainly of anthropic nature as well as moisture penetration. These were identified and recorded during the site observations, including plaster stains, spalling, flacking, profile detachments, concrete spalling, and exposed rebar at the bottom of the shell's base. Corrosion of exposed reinforcement was also observed on one of the ground level arches supporting the shell and which requires prompt repair to avoid any further deterioration that may compromise the integrity of the structure, as illustrated in "figure 5" and further discussed in Esponda et al [20].

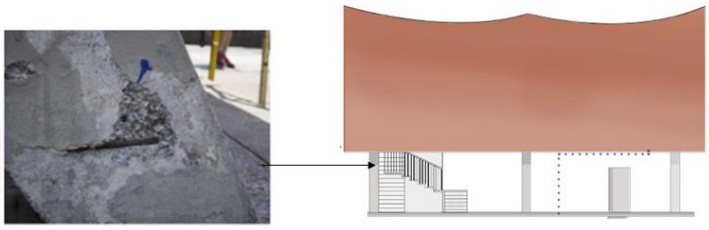


Figure 5. Condition assessment of the Cosmic Rays Pavilion. Image: Carleton Team, 2019.

One of the most significant findings through the analysis of the HBIM digital model by Rajabzadeh and in combination with the analysis of archival drawings was a significant surface-thickness difference between the intrados and extrados of the shell, showing a thicker surface on the extrados of the shell. This prompted further analysis of archival images of the pavilion in combination with the digital model. Moreover, the team lead by Dr. Esponda discovered a slight deviation in the curvature of the structure over time. Deeper analysis and an interview with relevant staff from the States Management and Conservation Directive, UNAM (Dirección General de Obras y Conservación, UNAM) corroborated the team's initial hypothesis to explain these anomalies. It was found that asphalt waterproofing layers had been gradually applied throughout the years without proper removal and cleaning of all previous waterproofing material thus adding thickness to the shell. Furthermore, there are no detailed maintenance or intervention reports which could provide information regarding the timeline, materials and methods applied to waterproof the shell or any other intervention as in Rajabzadeh et.al [21] and Mendoza et.al [22]. It is worth to note that this could not have been detected by solely relying on traditional documentation techniques. There were some valuable lessons learnt in using digital technology to document and assess the CRP and which arose from the fact that the main strategy was to rely on point-to-point correspondences for the software to merge the interior and the exterior point clouds. Later, it was understood that there was a lack of redundancy in the process. Although there were

thorough hand measurements taken by the team, no ground control points were collected to stitch the pictures together and which should have collected as precautionary measure in case of software failure.

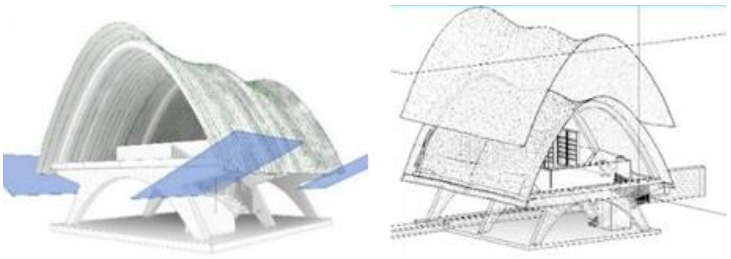


Figure 6. Exploded axonometric from Revit model to analyse the waterproof membrane and the concrete shell. Image: Rajabzadeh, 2019.

Despite the missing control points, the small size of the shell allowed for the interior and exterior point cloud data sets to be compiled manually. The target points were accurate to allow for a comprehensive point cloud data set of the pavilion to be created using photogrammetry. However, it is worth mentioning that for larger projects, collecting ground control points is necessary "figure 6" Rajabzadeh et.al [23]. It is also important to mention that while the use of a laser scanner could have produced a point cloud relatively faster, this was not accessible to the team at that time as they are a more expensive technology than DSLR cameras and drones as mentioned by Rajabzadeh et al [24].

Using photogrammetry technique assisted a faster visual assessment to identify which part of the building required immediate attention. Other advantages of the photogrammetry using DSLR versus laser scanners is its affordability and file size, files used in photogrammetry are considerably smaller than those obtained with a laser scanner, and which require more powerful computers to handle and more digital storage. Photogrammetry can be as accurate as laser scanner data collection, they both record the exact texture, condition, and circumstances of the sites. However, unlike laser scanners, DSLR cameras do not have an integrated GSP to collect control points and as a result it is more challenging to merge the two sets of data (interior and exterior) together. Another important lesson learnt was the consideration of lighting conditions for which it is best to record all data in one setting, as different lighting conditions (particularly daylight changes) can make it hard for the software to stich the pictures together. Although not always possible, it is best practice to remove all furniture and occupants from the space to be analysed to minimize the obstacles that restrict access to data collection.

Whilst using laser scanners and/or photogrammetry to assess heritage buildings are optimum as they use non-invasive and non-destructive techniques, they have a significant limitation as they are restricted to only record surfaces seen by the eye without being able to penetrate the surface to assess other physical or mechanical conditions of structural components. However, this limitation can be overcome by complementing laser scanner and photogrammetry assessments with other NDTs such as sonic, ultrasonic, georadar, dynamic, sclerometers, thermography, etc. One of the main advantages of using laser scanner and/or photogrammetry assessments for heritage buildings is that they apply non-invasive and non-destructive techniques protecting the integrity and value of the cultural asset.

2.3. Non-destructive testing of the Cosmic Rays Pavilion concrete shell

In 2022 Dr. Alberto Muciño and Dr. Alejandro Leal carried out a study to assess the current condition of the CRP's reinforced concrete using NDTs. This study was also presented at the Candela-Isler-Mütter Symposium, ETH, Zurich, Switzerland, 2022. The main reason for using the NDTs in this study was to comply with the specific assessment protocols required for heritage buildings such as the CRP. Two different NDTs were used in combination to maximise the reliability of results. The NDT methos used were the rebar location using the Proceq Profometer 200, combined with the surface hardness method

using a Proceq SilverSchmidt 8200 Tipo L. The guidelines used for the application and interpretation for the standard rebound were ASTM C805/C805M-13A y NMX-C. -192-ONNCCE-2018. To determine the correlation between resistance and rebound index it was necessary to build a control sample to be tested under simple axial compression and correlate the obtained resistances with the detected rebound index.

The project started with literature review analysing material from the archive: Archivo de Arquitectos Mexicanos, including architectural and construction drawings. This was followed by identifying and cleaning the testing areas (ideally, areas to be analysed with NDT should be identified in collaboration with the authorities in charge of safeguarding the cultural asset). For the purposes of this study square sections of (1000 mm X 1000mm were identified and labelled according to their north, south, east, and west orientation "figure 7". Once the areas of study were identified their surface was cleaned and any paint coating was removed to avoid any distortion of the sclerometer test readings of concrete carbonation.



Figure 7. Process of cleaning and preparation of the area where NDT was conducted. Image: A. Muciño.

It was relatively fast to obtain readings and data using NDTs. Overall, the study took three months and most of the time required was to clean and prepare the surfaces and set the scaffolding to take the instruments readings. However, the obtained results showed that to enhance the reliability of the study, the obtained data needs to be compared with results from control samples analysed in the laboratory and against existing literature.

It is important to mention that NDTs do not necessarily replace destructive ones but complement them. Non-destructive techniques can identify specific areas of a heritage building which may require further investigation and potential destructive testing to obtain samples to be analysed in the laboratory. The Mexican Construction Technical Standards for reinforced concrete structures acknowledges the use of destructive and non-destructive techniques to assess the quality of concrete structures or elements [25]. However, these standards have not yet established specific guidelines, protocols, methods, or criteria to use this technology for heritage buildings. Current building regulations need to be updated to provide adequate guidance and regulate the assessment and intervention of reinforced concrete heritage buildings. Such updates can assist professionals dealing with historic buildings and who may not be experts in conservation [26]. This is of particular interest if the construction sector wants to promote and advance the reuse and re-purpose of historic buildings as circular economy and sustainability strategies.

One of the main limitations of the study was that only the intrados of the concrete shell was analysed. To arrive at more reliable and holistic results of the integrity of the structure, testing of the extrados of the shell is needed not least because exposed to weather conditions, it is most prone to deterioration. The analysis carried out from the central and lateral testing on the shell's intrados showed a flacking in the shell's concrete. Furthermore, the sclerometer results showed that the resistance of the concrete is not optimum, and which shows that an adequate maintenance protocol and technique to keep the

concrete in the best possible conditions is needed. One of the important findings of this study was that the final built shell was thicker than what is cited in Faber's book, and which will support to rectify and advance existing literature.

After the non-destructive testing of February-March 2022, it became clear that the building needs further study, expanding the examination area to include not only the shells (upper structure), but also the slab and arches (lower structure). In addition, after collecting all the data it was evident that a bespoke protocol is needed at the outset of the assessment with a holistic approach to incorporate other complementary digital technology and to include other experts in the field.

3. Conclusion: submission of contributions

This paper presented the available technology (non-invasive and non-destructive) most used for the assessment of heritage buildings. The two studies presented in the paper aimed to develop a methodology to evaluate the concrete conditions of reinforced concrete shells using traditional and digital technology. The paper discussed the challenges and opportunities in the use of this technology for historic concrete shells such as the Cosmic Rays 20th Century historic concrete shells. The use of digital technology and other NDTs have the advantage of facilitating more holistic and accurate assessment of heritage buildings whilst maintaining their functional and structural integrity value. It is also important to note that the field research that complemented both studies was very valuable to make an initial visual assessment of the structure and materials' conditions such as concrete deterioration. Moreover, the use of the images collected and archived were crucial to better understand the complex geometry of the CRP and to ensure that it correlated with the data given by the digital tools.

One of the main limitations of the study relates to the NDTs. While it was possible to confirm the rebar location against available construction drawings it was not possible to identify and assess any potential corrosion. Furthermore, the surface hardness analysis of the shell's concrete was only applied to a designated area of the intrados and results may differ from those that could have been obtained from testing other intrados and extrados areas. Furthermore, another important aspect to consider as a limitation is the lack of archival information related to the shell's concrete mixture as well as the material and methods applied in the various waterproofing layers, and which have increased the thickness of the shell.

The analysis of these two preliminary and exploratory studies have prompted the authors of this paper to develop a third study in which traditional methods, digital media and NDTs will be carried out simultaneously to develop a more holistic protocol and approach as this paper demonstrated that they are complementary of each other and important when assessing heritage buildings. Furthermore, the paper has also discussed the potential of digital technology and other NDT techniques to support circular economy and sustainability strategies as they can reduce the use of materials, natural resources and energy and they can also safeguard the buildings structural integrity thus extending their heritage value and use.

In the last decade, concrete conservation research is progressing to find better solutions and to develop strategies to retain their cultural significance (aesthetic and technological) as well as to carefully assess modern concrete structures. Based on this process, the initial studies that we have done since 2018 in the Cosmic Rays Pavilion will allow us to identify key current issues on the concrete hyper, to understand how to assess the main damage, inherent environmental features and future threats, to recognize the main important challenges (socio-cultural, technical, economic, and sustainable) and to develop which best practice will be the most appropriate in conserving/intervening the concrete shells in Mexico.

We have based our thorough evaluation of the CPR following the Conservation Principles for Concrete Getty Conservation Institute [27] with the future intention of developing a sustainable conservation strategy and to create an inventory of other concrete shells built by Félix Candela and other architects

and shell builders in Mexico. We anticipate that the findings of this and future research will be of value to other researchers and practitioners around the world dealing with the conservation of 20th Century historic concrete shells as hitherto there is not consensus on the tools and methods on how to approach the conservation of 20th Century historic concrete shells. Future research will aim to consolidate and establish a protocol addressing the best conservation practices specific to the concrete shells built in Mexico and which could potentially inform the research and conservation of other concrete shells around the world. Some of the next steps will be to evaluate workmanship, maintenance records, materials deterioration (environmental characteristics and aggressiveness to concrete considering the specific context of Mexico City such as pollution levels, CO2 and other contaminants, exposure to sun, winds, rain), preliminary testing, structural evaluation and monitoring. Finally, future research can also include the us of the HBIM for seismic analysis and anticipate any damage scenarios and propose risk management strategies.

Acknowledgements

The authors of this paper would like to thank Sepideh Rajabzadeh, as the Carleton student team leader for all the data, images and 3D modelling, as well as other Carleton students that participated in the study. Part of this research was funded by New Paradigm New Tools internship at Carleton Immersive Media Studio (CIMS), P.I. Professor Stephen Fai, supported by the Social Sciences and Humanities Research Council of Canada (SSHRC) and the International Research Seed Grant (IRSG). As well as the support by the stakeholder Mtro. Julio Valencia Navarro (UNAM) all UNAM students and researchers that collaborated with Dr. Alberto Muciño and Dr. Alejandro Leal to carry out the NDT of the Cosmic Rays Pavilion project.

References

[1] M. Mendoza. M. Esponda, J.I. Del Cueto Ruiz-Funes, A. López & N. C. Ruiz-Gómez. "Félix Candela's architectural heritage at the intersection of sustainable development," in: *Innovation, Sustainability and Legacy: Proceedings of the IASS Annual Symposium 2022 and the13th Asian-Pacific Conference on Shell and Spatial Structures*, Beijing, China, September 19-22, 2022, S. Xue, J. Wu and G. Sun, Eds.

[2] S. Brusaporci, *Digital Innovations in Architectural Heritage Conservation: Emerging Research and Opportunities.* IGI Global, 2017.

[3] The Impact of digital technologies, United Naations Digital Library, 2020. Last access March 2023. Available at: file:///C:/Users/sbe3mendom/Downloads/un75newtechnologies.pdf

[4] ASNT American Society for Nondestructive Testing. Introduction to Nondestructive Testing, 2021. Available at: https://asnt.org/MajorSiteSections/About/Introduction_to_Nondestructive_Testing.aspx

[5] J. A. A. Campanero, et al., "Guide to sustainability criteria in the conservation and restoration of immovable cultural heritage", Sustainability in Cultural Heritage, Comunidad de Madri, General Directorate for Cultural Heritage, 2022. [Online]. Available: http://www.madrid.org/bvirtual/BVCM050606.pdf [Accessed February. 10, 2023].

[6] P. Shull, *Nondestructive Evaluation: Theory, Techniques and Applications.* New York: Marcel Dekker, Inc, 2002.

[7] P. Shull, *Nondestructive Evaluation: Theory, Techniques and Applications.* New York: Marcel Dekker, Inc, 2002.

[8] P. Shull, *Nondestructive Evaluation: Theory, Techniques and Applications.* New York: Marcel Dekker, Inc, 2002.

[9] J. Damazo Juárez, "Pruebas No Destructivas del Concreto. Las Estructuras no son eternas," in: *Construcción y Tecnología*, 2006, p.48-54.

[10] IMCYC Instituto Mexicano del Cemento y del Concreto. IMCYC Gerencia Técnica. Retrieved in January 2023, from https://www.imcyc.com/gerencia-tecnica/index.php/laboratorio-de-concreto.

[11] S. Macdonald and A. P. Arato Gonçalves, *Conservation Principles for Concrete of Cultural Significance, Principles*. Los Angeles: Getty Conservation Institute.2020. [Online]. Available: http://hdl.handle.net/10020/gci_pubs/conservation_principles_concrete [Accessed February. 11, 2023].

[12] G. Harboe, et al, *The Cádiz Document: InnovaConcrete Guidelines for Conservation of Concrete Heritage*. Project Report. ICOMOS International, 2021. [Online]. Available: https://openarchive.icomos.org/id/eprint/2578/1/CadizDocument-ICOMOS-InnovaConcrete-2021.pdf [Accessed February. 11, 2023].

[13] C. Faber, *Candela: The Shell Builder,* London: The Architectural Press, 1963.

[14] K. Kelly, M. Garlock and D.P. Billington, *Cosmic Rays Laboratory. Félix Candela: Engineer, Builder, Structural Artist.* Yale University Press, 2008.

[15] L. G. Cordero Espinosa, "Pavellón de Rayos Cósmicos: pasado, presente y futuro," Undergraduate tesis. (2019). National Autonomous University of Mexico, Mexico, 2019.

[16] S. Rajabzadeh, M. Esponda, L. Cordero, "Photogrammetry, HBIM and Damage Analysis of Cosmic Rays Pavilion for rising awareness to its cultural heritage," in: *CIPA 28th Symposium,Tsinghua University, Beijing, China*, August 28- September 1, 2021.

[17] M. Esponda, J. Babe, M. Hanna, S. Rajabzadeh, M. Grandmont, M. *México DSA: Conservation of World Heritage Sites in Mexico*. Azrieli School of Architecture & Urbanism, Ottawa, Carleton University, 2021.

[18] M. Esponda, J. Babe, M. Hanna, S. Rajabzadeh, M. Grandmont, M. *México DSA: Conservation of World Heritage Sites in Mexico*. Azrieli School of Architecture & Urbanism, Ottawa, Carleton University, 2021.

[19] S. Rajabzadeh, M. Esponda, L. Cordero, "Photogrammetry, HBIM and Damage Analysis of Cosmic Rays Pavilion for rising awareness to its cultural heritage," in: *CIPA 28th Symposium,Tsinghua University, Beijing, China*, August 28- September 1, 2021.

[20] M. Esponda, J. Babe, M. Hanna, S. Rajabzadeh, M. Grandmont, M. *México DSA: Conservation of World Heritage Sites in Mexico*. Azrieli School of Architecture & Urbanism, Ottawa, Carleton University, 2021.

[21] S. Rajabzadeh, M. Esponda, L. Cordero, "Photogrammetry, HBIM and Damage Analysis of Cosmic Rays Pavilion for rising awareness to its cultural heritage," in: *CIPA 28th Symposium,Tsinghua University, Beijing, China*, August 28- September 1, 2021.

[22] M. Mendoza. M. Esponda, J.I. Del Cueto Ruiz-Funes, A. López & N. C. Ruiz-Gómez. "Félix Candela's architectural heritage at the intersection of sustainable development," in: *Innovation, Sustainability and Legacy: Proceedings of the IASS Annual Symposium 2022 and the13th Asian-Pacific Conference on Shell and Spatial Structures*, Beijing, China, September 19-22, 2022, S. Xue, J. Wu and G. Sun, Eds.

[23] S. Rajabzadeh, M. Esponda, L. Cordero, "Photogrammetry, HBIM and Damage Analysis of Cosmic Rays Pavilion for rising awareness to its cultural heritage," in: *CIPA 28th Symposium,Tsinghua University, Beijing, China*, August 28- September 1, 2021.

[24] S. Rajabzadeh, M. Esponda, L. Cordero, "Photogrammetry, HBIM and Damage Analysis of Cosmic Rays Pavilion for rising awareness to its cultural heritage," in: *CIPA 28th Symposium,Tsinghua University, Beijing, China*, August 28- September 1, 2021.

[25] Secretaria de Obras y Servicios. (2021, Julio 20). Normas Técnicas Complementarias para Diseño y Construcción de Estructuras de Concreto con Comentarios. Gaceta Oficial de la Ciudad de

México. Retrieved from: http://www3.contraloriadf.gob.mx/prontuario/resources/normatividad/69247.pdf

[26] H.Heinemann. *Historic Concrete from Concrete Repair to Concrete Conservation.* Universitat Dortmund, 2013.

[27] S. McDonald, A.P. Arato Goncalvez. *Conservation Principles for Concrete of Cultural Significance*. Getty Conservation Institute, Los Angeles. 2020

IASS 2023
July 10–14 Melbourne
Integration of Design and Fabrication

Proceedings of the IASS Annual Symposium 2023
Integration of Design and Fabrication
10–14 July 2023, Melbourne, Australia
Y.M. Xie, J. Burry, T.U. Lee and J. Ma (eds.)

Naiju community center by Shoei Yoh: pioneering computational architecture applying origami geometry and bamboo formwork

Masaaki IWAMOTO[a,*], Tomo INOUE[a], Shoichi NAKAMOTO[b], Nicole GARDNER[c], M. Hank HAEUSLER[c]

[a,*] Faculty of Design, Kyushu University
iwamoto@design.kyushu-u.ac.jp

[b] Shigeru Aoki Architects and Associates
[c] The University of New South Wales

Abstract

This paper aims to clarify the linkages between various actors in the pioneering period of computational design by elaborating on the design and construction history of the Naiju Community Center, a complex free-form shell structure built in Fukuoka in 1994, designed by Japanese Architect Shoei Yoh (1940-). Yoh envisioned an undulated roof that resembles the moment a handkerchief is picked up. Early in the design process, he collaborated with Professor Gengo Matsui of Waseda University to study a woven bamboo dome, and eventually, decided to apply bamboo as the formwork of a concrete shell. The form was studied with computational models, then physical models were created using origami geometry, from which the coordinates of the surface were determined. For the structure, local engineer Kusaba Motoshige collaborated with Yoichi Minagawa of Kagoshima University, who analyzed the stresses in the shell using Finite Element Method. To design the formwork, Yoh referred to the properties of bamboo identified by Matsui's laboratory at Waseda University. Regarding the construction, the villagers worked together to weave a square bamboo net 22 meters per side. This net was lifted by a crane and formed a complex surface. The historical importance of the building lies in how the computationally-designed complex surface was constructed; not as a building on screen but as an actual structure. The key was the application of origami geometry, flexible bamboo formwork, the collaboration of experts, and construction with local participation.

Keywords: Shoei Yoh, Gengo Matsui, computational design, concrete shells, bamboo formwork, origami, form finding, local participation, historical structures

1. Introduction

In recent years, there has been growing momentum, both in Japan and abroad, to re-evaluate Shoei Yoh (1940-) as a pioneer of contemporary timber structures and as a pioneer of digital design [1]. As for timber, the Oguni Dome (1988), Japan's first large-scale timber structure, won the JIA 25-year award in 2018 and was also featured in the web media of the Architectural Institute of Japan in 2019 [2]. As for the digital, Yoh's projects such as Galaxy Toyama (1992), a pioneering architecture using parametric methods, were highlighted in the exhibition 'Archaeology of the Digital' at the Canadian Centre for Architecture in 2013 [3], while the exhibition 'Revisiting Shoei Yoh', which reassessed the digital design of Yoh, was held at the Australian Design Centre in 2021 [4]. The subject of this paper, the Naiju Community Center, is also a highly original work unlike any other of its time.

The Naiju Community Center (Figure 1) is a community center and nursery school built in 1994 in Chikuho Town (now Iizuka City), Fukuoka Prefecture, with an organic, three-dimensional curved concrete shell as its distinctive architectural feature. Yoh used origami geometry for its form-finding,

Copyright © 2023 by Masaaki IWAMOTO, Tomo INOUE, Shoichi NAKAMOTO, Nicole GARDNER and M. Hank HAEUSLER. Published in the Proceedings of the IASS Annual Symposium 2023 with permission.

while his collaborators made full use of computational structural analysis. They also developed an ingenious construction method, using bamboo as formwork to create the complex curved surface. In order to explore the origins of today's architectural trend of integrating natural materials and computation, this paper provides a detailed historical study of the design and construction process of this building.

The research methodology of this paper is based on the analysis of a newly developed 'Shoei Yoh Archive' at Kyushu University and Shoei Yoh fonds at Canadian Centre for Architecture; primary interviews with Shoei Yoh and his collaborators (conducted in 2018-2021); and field surveys of Yoh's works in Kyushu region. These sources are utilized to achieve detailed insights into the development of the Naiju Community Center, a pioneering application of computational approaches to the innovative use of the bamboo-formwork concrete shell. To supplement the above primary sources, archival journal and magazine articles from the 1980s and 1990s are examined. These sources of data are triangulated and used to generate new historical insights into this missing part of Japan's architectural heritage.



Figure 1. Naiju Community Center, current status. Photo by Yashiro Photo Office, 2020.

2. Design process of Naiju Community Center

2.1. Bamboo as a building material

The design of the Naiju Community Center began in May 1993 at the request of Tatsuo Yoshinaga, the Mayor of Chikuho Town at the time. From the very beginning of the design, Yoh wanted to use bamboo as a building material. Yoh wrote in 1994; "The starting point for the Naiju Community Center was the idea of using bamboo, inspired by the bamboo shoot cannery in Chikuho Town" [5]. The origin of his inspiration for using bamboo can be pointed to the Yukinogawa Bridge (figure 2a), a bamboo-reinforced concrete structure in Oguni Town, Kumamoto Prefecture. Yoh came to know about this bridge when he was involved in a series of projects in Oguni Town in the late 1980s. He then designed Japan's first legal bamboo structures, the Bamboo Dome and the Tensegrity Shelter, at the 1989 Asian-Pacific Exposition in Fukuoka (figure 2b) [6]. This bamboo dome was realized in collaboration with the Gengo Matsui

Laboratory of Waseda University, which conducted structural experiments on bamboo. The application of bamboo as a building material in the Naiju Community Center can be considered as an extension of these efforts.

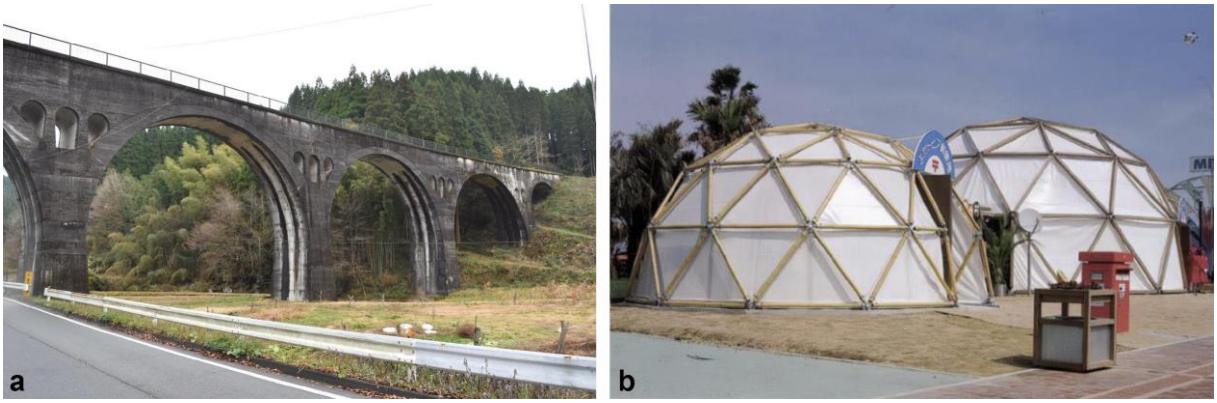


Figure 2. Earlier examples of the use of bamboo as a building material in Kyushu. (a) Yukinogawa Bridge, Kuamoto, ca,1939. Photo by the author. (b) Bamboo Dome at Asian-Pacific Exposition, Fukuoka, 1989. Image from Shoei Yoh Archive.

For Naiju, Yoh envisioned an undulated roof that resembles the moment a handkerchief is picked up, based on his design philosophy, 'in response to natural phenomena' [7]. To realize this form with bamboo, Yoh asked Professor Gengo Matsui to study its geometry and feasibility. Matsui proposed a dome-shaped structure made of woven bamboo net and conducted photoelastic experiments (figure 3). However, the local structural designer of the project, Motoshige Kusaba, was concerned about deformation due to external forces. Therefore, Yoh abandoned the use of bamboo as a structural material and instead conceived a concrete shell structure using bamboo netting as a formwork.

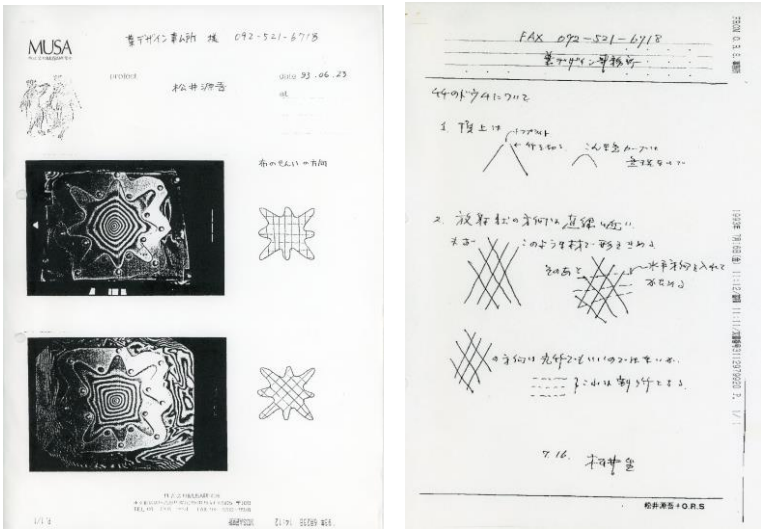


Figure 3. Fax sent from Gengo Matsui laboratory to Yoh Design Office. Materials from Shoei Yoh Archive. Left: Results of photoelastic experiments with different orientations of the bamboo framework, 23 June 1993. Right: sketch by Gengo Matsui on the shape of the dome top and the bamboo weave, 16 July 1993.

2.2. Form finding with physical models and origami geometry

In the initial design phase, the form of the building was studied mainly through model making. The first model was made using mesh blind fabric samples (Figure 4a). The model was made by placing a stick on cardboard as a base, placing the fabric on top of the stick, and then fixing its perimeter to the base with pins. This method of model-making is similar to the actual construction process of the building. Next, a model was produced using the same mesh fabric, with FRP coated over it. This model was used in the presentation to the town mayor, based on which the early 3D model and renderings of the project were likely produced (Figure 4b).

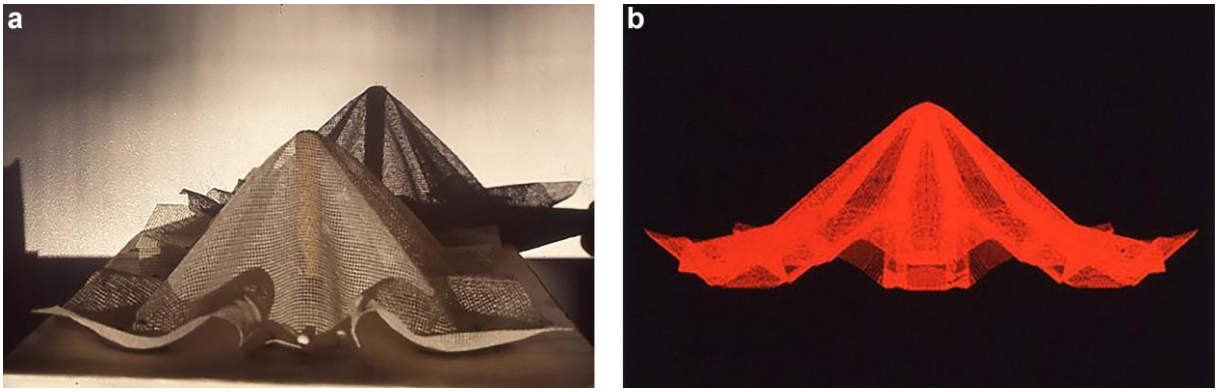


Figure 4. Physical model and rendering of Naiju Community Center at the basic design phase. Materials from Shoei Yoh Archive. (a) Photograph of the model in the basic design phase, 1993. (b) Rendering in the basic design phase, printed on paper, 1993.

After the first proposal was approved by the town, Yoh Design Office began detailed design work. To carry out structural analysis, it was necessary to know the coordinates of each part of the roof. For this, physical models were created using origami geometry (Figure 5a), from which the height of each part of the building, the position of the folds, and the height of the openings were examined, then the coordinates of the curved surface were identified based on the origami development diagram. Through studies using origami models, a major design change was made to add a skylight to the top of the building, otherwise, it would not have been possible to create a complex curved surface by folding a single square paper (Figure 5b).

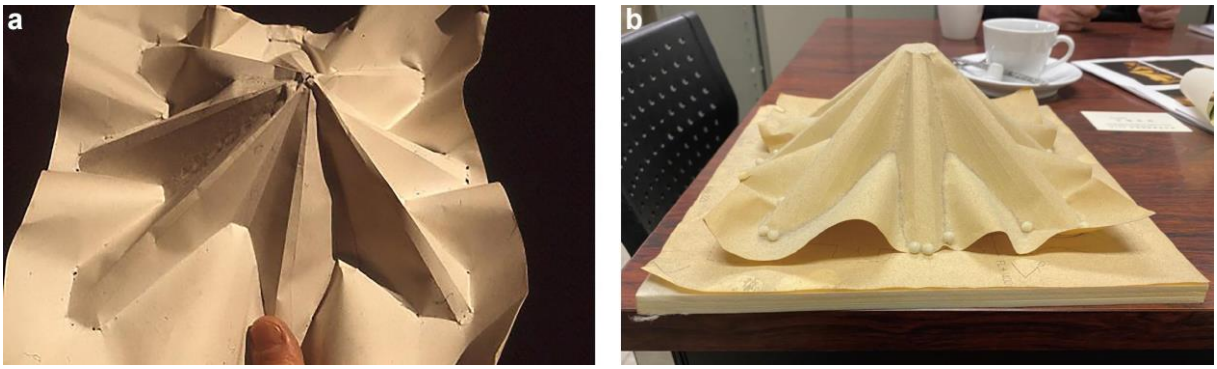


Figure 5. Origami models of Naiju Community Center. Materials from Shoei Yoh Archive. (a) Photograph of the origami model in the detailed design phase, 1993. (b) Photograph of the origami model stored in the office of Motoshige Kusaba, the structural designer of the project.

2.3. Structural design

The structural design of the Naiju Community Center was carried out in collaboration with several structural engineers. As mentioned earlier, Prof. Gengo Matsui, who had collaborated with Yoh to design Bamboo Dome at the Asian-Pacific Expo, was involved in the initial conceptual stage, after which Motoshige Kusaba, an engineer who had communicated with both Yoh and Matsui, took over the overall structural design. Kusaba asked advice from Ikuo Tokuhiro, his mentor since his student days, regarding the structural analysis of the complex concrete shell, and Tokuhiro introduced him to Yoichi Minagawa, who was researching concrete shell structures at Kagoshima University at the time.

Based on the coordinates provided by Yoh design office in late July 1993, Minagawa modeled a 150 mm thick concrete shell and carried out a structural analysis using Finite Element Analysis Method (FEM). First, the structural model was divided into quarters, then a quarter was divided into 248 elements and 148 nodes, and analyzed in two cases: fixed loads and horizontal forces (Figure 6a, 6b). The results of the analysis were delivered in late September, upon which Minagawa and Kusaba calculated the concrete cross-sections and reinforcement arrangements. Reinforcement drawings were drawn using a development diagram of the origami model (Figure 6c).

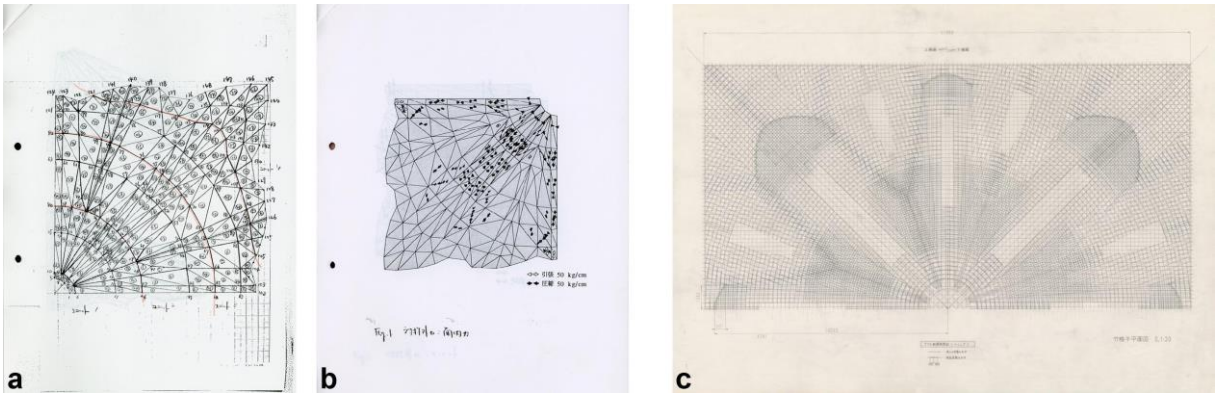


Figure 6. Structural design of Naiju Community Center. (a), (b): Fax sent from Yoichi Minagawa to Yoh Design Office, 1993. Materials from Shoei Yoh Archive. (c) Reinforcement drawing, collection of Canadian Centre for Architecture, Montreal, ARCH402299

3. Construction process of Naiju Community Center

3.1. Building by local people and local materials

Three rounds of bidding were conducted to determine the contractor for the Naiju Community Center. Two bids, one from a local general contractor and the other from a major general contractor in Japan, were unsuccessful. These general contractors assumed that the concrete shell formwork would be made by conventional methods, rather than the bamboo formwork specified by Yoh Design Office, and therefore their estimates were much higher than the budget. Thus, Yoh proposed that a third bidding round be held with local carpenters, which attracted five companies in the region. A local carpenter, Isao Kawakami, was ultimately selected as the successful bidder. Yoh explained his intention to ask a local carpenter to be the builder: “If you ask a local carpenter, the skills will remain (in the region). [...] The fact that the building was built by local people using local materials gives the community a sense of pride." [8] In response to Yoh's expectation, Isao Kawakami undertook an in-depth and thorough preparation for the construction that included making models and mock-ups on site to understand the complexities of the design (Figure 7).



Figure 7. Photograph of model and mock-up made by Carpenter Isao Kawakami. Materials from Shoei Yoh Archive. (a) On-site meeting around the model made by Kawakami, 1994. (b) Mock-up for testing concrete casting, 1994.

The details of the bamboo formwork were discussed around April 1994. First, it was decided to split the bamboo into eight strips. Next, two options for making the net were considered: bolting all the intersections of bamboo or weaving the split bamboos together (Figure 8a). Consequently, the idea of weaving bamboo was selected to reduce the amount of bolts. A 22m wide square net was composed of split bamboo, each approximately 5 m long, overlapped by 300 mm, and fixed with three bolts. The strength of the bamboo formwork was evaluated using data from structural experiments conducted by Gengo Matsui laboratory when designing the Bamboo Dome for the Asian-Pacific Expo.

On the initiative of Yoh Design Office, local people participated in the work of weaving the bamboo net. Yoh said: 'The work of weaving bamboo and constructing the formwork was done by the local people. We tried to leave traces of their hands, or rather the traces of everyone's sweat work''. [9] The collaborative process of weaving bamboo was a participatory design method. The work was carried out over a two-week period from the end of April to the beginning of May 1994, taking advantage of a Japanese public holiday period. Forty-six local residents, including junior and senior high school students, participated in the process (Figure 8b).



Figure 8. Bamboo net as formwork. Materials from Shoei Yoh Archive. (a) Mock-up of bamboo net with all intersections bolted together (not applied), 1994. (b) Local people weaving bamboo nets, 1994.

3.2. Forming a three-dimensional curved surface

The woven bamboo net was lifted by crane on 19 May 1994 and covered over a temporary support post erected at the center of the foundation (Figure 9). The temporary posts were made of steel, with a circular ring on its top to correspond with the design of the skylight, and steel cables were stretched from this ring to points on the foundations as guides to fix the perimeter of the netting in place.



Figure 9. Lifting bamboo net by crane, 19 May 1994. Materials from Shoei Yoh Archive. (a) Lifting bamboo net by crane. (b) Bamboo net on the temporary post. (c) Temporary post and steel cables.

After the bamboo net had been lifted onto the temporary post, the forming of the bamboo formwork began. The first step was to fix the bamboo formwork to the foundations. Next, supports were produced using timbers and steel pipe scaffolding. The bamboo net was only used to define the shape and does not carry the structure. This means that the shoring had to be inserted into the netting and withstand the load of the concrete. The forming work and shoring took place over a period of one month, from the end of May to the end of June (Figure 10).

In parallel with the construction of these supports, the temporary support post at the center of the building was jacked up. The temporary post was built lower than the maximum height on the design drawings and was gradually jacked up as the fabrication of the shoring and forming of the curved surfaces progressed. The intention of the jacking up was to tension the bamboo net and to pin and straighten the ridges to withstand the compressive forces of the shell. The jacking-up was carried out twice during the forming process, raising the post by approximately 60 mm from its initial position.



Figure 10. Forming process. Materials from Shoei Yoh Archive. (a) Lifting bamboo net by crane. (b) Bamboo net on the temporary post. (c) Temporary post and steel cables.

3.3. Concrete works

After the bamboo formwork had been formed and the shoring installed, the curved surfaces were sheeted, sprayed with urethane foam and rebar was placed according to the structural drawings (figure 11).



Figure 11. Roof works. Materials from Shoei Yoh Archive. (a) Sheeting work, July 1994. (b) Urethane foam spraying, August 1994 (c) Rebar placement, August 1994. Areas marked with red lines are single reinforcement, as they mainly transmit compressive forces.

For the concrete casting, advice was provided by Takao Yonemitsu of Ando Construction, who had worked with Yoh on previous projects such as the Glass Station (1993). Yonemitsu suggested that the concrete be poured in several stages, with the lower section, including the outer folds, being poured in the first stage. The intention was to stabilize the bamboo formwork and prevent overall deformation, to provide a scaffold for the upper concrete pour, and to prevent the central section from lifting. This suggestion was accepted, and the concrete was placed in five separate stages between 8 and 26 September 1994 (Figure 12). The fresh concrete used for casting was extremely hard with a slump value of 4-5 cm. In addition, reinforcing steel fibers, Dramix, were mixed into the fresh concrete to increase the cracking strength. After the pouring was completed at the end of September, the concrete roof was left to harden for two weeks. The steel temporary post was removed on 14 October. There was concern that the rooftop would drop under its own weight when the temporary post was removed, but measurements showed almost no change in height.

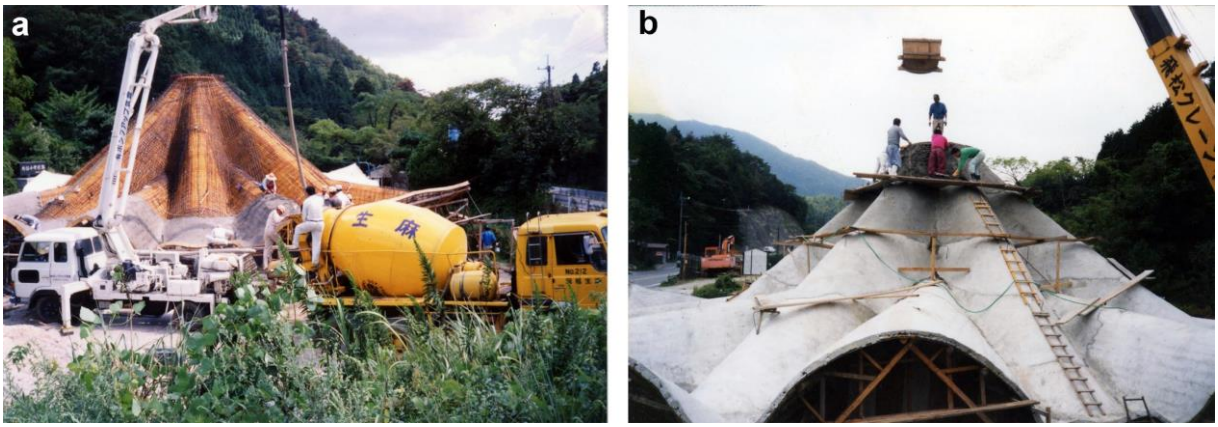


Figure 12. Concrete works. Materials from Shoei Yoh Archive. (a) First concrete placement, 8 September 1994. (b) Fifth (last) concrete placement, 26 September 1994. Fresh concrete was placed by hand in the box suspended by a crane. The fresh concrete was too hard to be placed using a pump truck.

3.3. Completion and after

Interior work began in mid-October; the roof was waterproofed in November and Naiju Community Center was completed in mid-December 1994 (Figure 13). Its inauguration ceremony was held on 12 December, at which children from the Naiju Nursery School, which will move to the Community Center, sang songs and performed in an ensemble. Mayor Nagayoshi expressed his hope that the new building would be "a catalyst for community revitalization" [10]. Naiju Community Center was thus welcomed by the town, but unfortunately, it was forced to close temporarily in 2001 due to the river pollution in the neighborhood. And it was closed in 2007 due to a decline in the number of users caused by depopulation. In 2023, Naiju Community Center still stands empty and quiet in the mountains.



Figure 13. Naiju Community Center nearing completion. Materials from Shoei Yoh Archive.

4. Conclusion and discussion

The design and construction process of Naiju Community Center was extremely advanced and unparalleled in its time and is unique and creative even from today's perspective, some 30 years after its construction. The study reveals that the unique idea of a free-form concrete shell using bamboo formwork was realized in collaboration with talented structural engineers Gengo Matsui, Motoshige Kusaba, Ikuo Tokuhiro, and Yoichi Minagawa. It is important to note that the origami models acted as a conceptual bridge between these structural engineers and architects, defining the geometry and coordinates of the surface, and therefore enabling computational analysis of its structure. This fact shows that physical models played an essential role in the pioneering days of computational design.

In terms of construction, despite the complexity and difficulty of the work, Yoh insisted on local craftsmen and community participation. Building by local people and local materials - this was the secret of success for regional architecture, which Yoh arrived at through his experience of designing timber structures in Oguni Town, Kumamoto. Naiju Community Center was realized by mobilizing the experience and connections that Yoh had cultivated in his design activities until then. In a sense, it proved to be the culmination of Shoei Yoh's architectural achievements.

Acknowledgments

The authors would like to thank Mr. Shoei Yoh, Mr. Motoshige Kusaba, Mr. Isao Kawakami, Mr. Toyohiro Kawakami, Mr. Hiroyuki Yageta and Mr. Takao Yonemitsu for their cooperation in the interviews. We also thank Iizuka City for giving us the opportunity to research the building in detail. A part of this research work is the result of a grant by JSPS KAKENHI Grant Number JP21K14334.

References

[1] S. Hawken and M, Iwamoto, “The Pioneering Computational Architecture of Shoei Yoh: A Study of the Avant Garde Timber Space Frame Structures of Oguni, Kumamoto,” 16th Docomomo International Conference Proceedings, pp. 622-631, 2021.

[2] Architectural Works Subcommittee, Architectural Institute of Japan, "Architectural Review: Shoei Yoh [Oguni Dome] - Exploring the origins of contemporary timber architecture and computational design in Japan," Kenchiku Touron, No.34, 2019

[3] G. Lynn et al, *Archaeology of the Digital*, CCA and Sternberg Press, 2013.

[4] N. Gardner, M. H. Haeusler, J. Barton, K. Dunn, T. Huang, M. Iwamoto and T. Inoue, "Developing a workflow for a browser-based 3Dmodel environment to create an immersive digital archive,” CAADRIA 2022, 2022.

[5] S. Yoh, "Naiju Community Center and Nursery School," Nikkei Architecture, 19 June 1995 issue, pp. 68-71, 1995.

[6] S. Yoh, "Bamboo Shelter and Post Postal Pavilion," Shinkenchiku, Vol.64, No.5, pp. 226-227, 1989.

[7] S. Yoh, Shoei Yoh: *In Response to Natural Phenomena*, L'Arcaedizioni , 1997.

[8] S. Yoh, "Naiju Community Center and Nursery School," Nikkei Architecture, 19 June 1995 issue, pp. 68-71, 1995.

[9] Ibid.

[10] Article of Nishinihon Shinbun (newspaper), 13 December 1994 issue, p.18, 1994.

Proceedings of the IASS Annual Symposium 2023
Integration of Design and Fabrication
10–14 July 2023, Melbourne, Australia
Y.M. Xie, J. Burry, T.U. Lee and J. Ma (eds.)

Translucent concrete shells in Ecuador

Mauricio LUZURIAGA*

* Universidad San Francisco de Quito
mluzuriaga@usfq.edu.ec

Abstract

In 1954, Felix Candela produced one of his most striking projects, the High Life Textile Factory in Coyoacán, Mexico City, built with his recognized inverted hyperbolic paraboloid umbrellas. Its uniqueness came from the way natural light filtered into the factory hall. Glass bricks embedded in concrete membranes allowed for light to flood the space below. Thin shells pierced with glass bricks are scarce however beautiful. From 1950 to 1960, *hormigón translúcido* or translucent concrete thin shells were produced in several Caribbean and South American countries. This paper hypothesizes that, contrary to experiences elsewhere, translucent concrete shells appeared in meaningful numbers with compelling aesthetic and constructive solutions in Ecuador. After a brief review of international and national examples, the study centers itself in works designed and build by architect Gilberto Gatto Sobral at Universidad Central del Ecuador in the capital City of Quito. The research encompassed an investigation never attempted before. Primary sources, entailing site visits, study of construction archives, and interviews were done to document the development of translucent concrete shells, an unheard-of feature in the history of Modern Architecture in Ecuador.

Keywords: translucent, concrete shell, glass brick, elliptic paraboloid, catenary vault, hyperbolic paraboloid, low-rise barrel vault, Gilberto Gatto Sobral

1. Introduction

Reinforced concrete system, patented by Françoise Hennebique and refined by Auguste Perret, initially leaned towards the production of straight porticoes. Impressive concrete shells appeared with hangars in Avord (1916) and Orly (1923) by Eugène Freyssinet. Transgressing the predominance of *angle droit* by Le Corbusier, the *Sao Francisco de Assis* church (1943) in Pampulha, Belo Horizonte-Brazil by Oscar Niemeyer, introduced sensuality to concrete shell structures. Similarly, diverging from the generalizing decree of universal applicability claimed the International Style of Phillip Johnson and Henry-Russell Hitchcock, "influential sectors of the modern movement around 1950 were ready to rebel against rectangular rectitude [through] the application of new thinking techniques to curvilinear structures" [1]. The Turin Exhibition Hall (1951) by Pier Luigi Nervi, also helped to lay foundations for the arrival of shells in the mid-20th century, such as the Kresge Auditorium (1955) by Eero Saarinen (Fig. 1), and the CNIT (1958) by Nicolas Esquillan. Organic shells were gaining notoriety to the point that Le Corbusier himself studied them at the Phillips Pavilion in 1958. However, the work of Spanish architect Félix Candela in Mexico was responsible for spreading the word worldwide. Candela was recognized for creating the thinnest existing reinforced concrete shell, for the Cosmic Ray Pavilion (1951) at the National University of Mexico in Mexico City. In 1958 Candela produced his masterpiece, Los Manantiales Restaurant.

Architectural Forum magazine baptized Candela as the *Wizard of the Shells* at the height of his unconventional production that predicted revolutionary possibilities for new architecture [2]. Candela's production, based on thin concrete shells, lasted twenty brilliant years. The inverted hyperbolic paraboloid (hypar) or inverted umbrella was used largely to roof markets, industrial sheds, and

Copyright © 2023 by Mauricio LUZURIAGA. Published in the Proceedings of the IASS Annual Symposium 2023 with permission.

warehouses. An inverted umbrella typically consists of a laminar shroud formed by four tympans. Each tympan is a hypar –a few centimeters thick– generated by two horizontal ridges at the edge and two opposite ridges descending to a lower vertex. The four hypars together are supported by a single central column inside which a rainwater downspout runs downward. A beautiful example of inverted umbrellas by Candela is the Coyoacán Market (1955) in México City (Fig. 2).

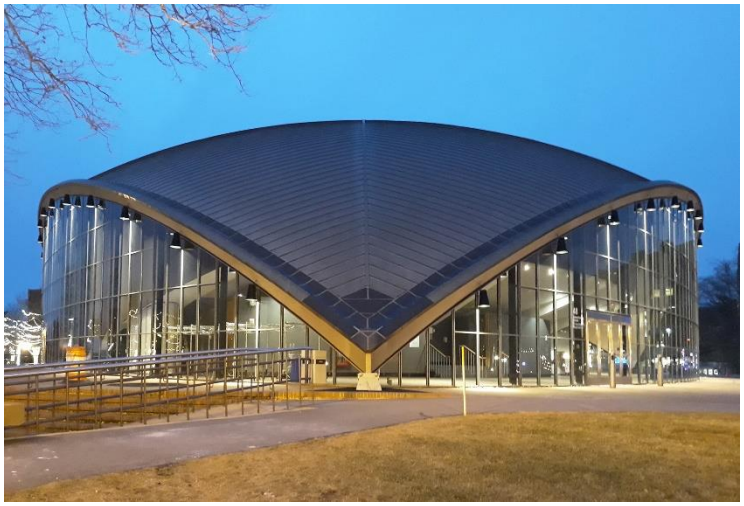



Figure 1: Kresge Auditorium (1955), MIT, Cambridge, Massachusetts-USA. Photo by the author, 2020. Figure 2: Coyoacán Market (1955), Mexico. Photo by the author, 2010. appropriate].

Hypar inverted umbrellas were replicated everywhere for its apparent ease of construction and economic feasibility –elements needed were: barely trained hands as workforce, available construction materials such as cement, sand, aggregates, water, wood poles and boards for simple scaffoldings, straight planks for falsework, reinforcing steel bars placed upon falsework. Once concrete was poured and cured, scaffolding was decentered and falsework removed producing a highly efficient double-curvature membrane.

2. Thin *shells* combined with glass bricks

One block North from the Coyoacán Market, Candela built the *High Life Textile Factory* (1954-1955). Unlike the market, at the factory he made an experiment –the utilization of glass bricks embedded in the shells to bring natural day light down to the factory hall. A revolutionary aesthetic emerged. The factory roof includes twelve identical hypars, 11.10 x 12-meter each, in a 3 x 4 layout. Since the umbrellas are tilted, they form rows of connecting hypars in one direction. Consequently, a continuous horizontal opening is created between rows and a sawtooth roof profile turns out. The horizontal openings are glazed with clear glass window bands. Most of the membranes were punctured with square *blocks de vidrio* –as they are called in Mexico– or glass bricks at a rate of 4.5 units/m^2 (Fig. 3). The result was a luminous space "as if there were no roof at all. But this brilliant mosaic provoked such heat and insulation problems that it was never repeated [3]" (Fig. 4).

International publication exposure for the *High Life Factory* started with an early article at *Informes de la Construcción* in 1956 [4]. Then it was featured in 1957 in a canonic book by Eduardo Torroja [5] where he predicted that these types of structural elements opened "a wealth of possibilities of all genres that […] are still kept hidden." In 1958 it was featured in an article titled Engineering of Excitement at The Architectural Review [6]. Six years later, the factory was included in the 1963 book *Candela/The Shell builder* by Colin Faber [7], followed by the German and Spanish versions of 1965 and 1970. The factory was renamed Cavalier Fashion Group but is now permanently closed. The building was put for sale, hopefully waiting for a buyer interested in its renovation and protection.



Figure 3: High Life Textile Factory, Coyoacán, 1954-1955. Photo: from *Candela und seine Schalen*, 1965. p. 124. Figure 4: High Life Textile Factory, as it looked in 2019. Photo: by the author.

Inventor Thaddeus Hyatt is credited with the creation of *Hyatt Patent Lights* [8], that consisted of round glass lenses, set into cast iron sidewalks, in 1845. Thus, glass bricks have been in used for a considerable time. Preceding the factory, glass blocks puncturing thin shells and slabs were visible in projects in several countries. In 1951, Max Borges Jr., purportedly used punctured shells (Fig. 5) at the dazzling conical segment shells covering the stage floor of *Arcos de Cristal*, a portion of Cabaret Tropicana in Havana, Cuba [9]. There are some examples in Caracas-Venezuela such as the *Santa María* building (1951) (Fig. 6), by engineer Arturo Luján with two spherical caps, one with a diameter of 8-meters and the smaller of 5.3-meters [10], or *Casa Sindical* auditorium (1954), by architect Henrique García Maldonado with one cap of 6-meters in diameter [11]. All these feature round glass bricks to flood with light helicoidal staircases, and hall spaces. A much larger case is found at *Banco de Descuento (1954)* in Guayaquil-Ecuador, designed by Karl Kohn. Its impressive dome has a diameter of 14 meters, covering a hall, staircase and balconies for what is now *Biblioteca de las Artes* or Library for the Arts (Fig. 7).

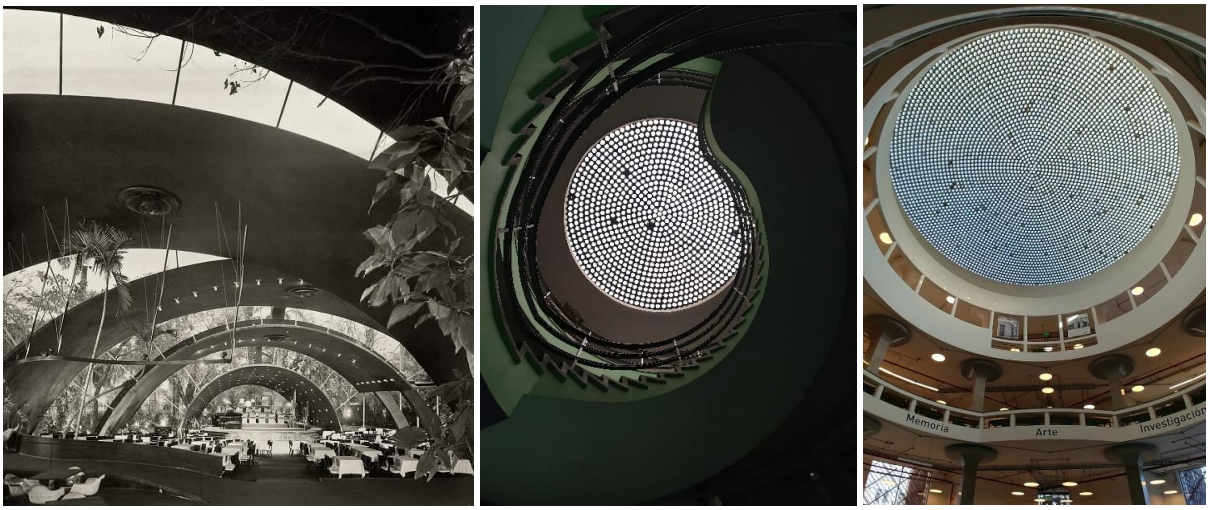


Figure 5: Tropicana Club Glass Arches, 1951. Havana-Cuba Photo: Muñis for Progressive Architecture. Figure 6: *Edificio Santa María*, 1951. Caracas-Venezuela. Photo: Lilia Tellez, 2022. Figure 7. Banco de Descuento, 1954. Guayaquil-Ecuador. Photo: Luis Paredes, 2019.

Another project with glass pierced hypars was built decades later at *Miller Bajo* car workshop (1977) in Las Palmas de Gran Canaria-Spain, a project by Luis López Díaz. There, "the lighting of the car workshop is done by means of 20 x 20 x 5-cm glass moldings, embedded in the central membranes and isolated from them with butyl sheets [12]. Yet, this paper concentrates on cases of thin shells pierced by glass blocks –translucent concrete– designed by one of the most important figures of Ecuadorian Modernity.

3. Gilberto Gatto Sobral (1910-1978) at *Universidad Central del Ecuador* (UCE)

Uruguayan architect Gilberto Gatto Sobral was invited by his fellow compatriot Guillermo Jones Odriozola to join him to develop several important commissions in Quito-Ecuador. He landed in the country in 1942 where he settled for the rest of his prolific life. In view of Jones departure from the country –due to ill health conditions– Gatto was appointed to bring to terms various of Jones' projects, such as the *Plan Ordenador de Quito* and the creation of the School of Architecture –commissioned by UCE authorities. Gatto was then chosen to start a Master Plan for *Ciudad Universitaria* (1947), which became his most achieved master piece. Facing times of professional uncertainty, he dared to bring Ecuadorian architecture into Modernity with an unmistakable architectural voice that gained the respect from local architectural colleagues. His academia-learnt rationalism, applied to the novel university campus, started with a coherent display of buildings adapted to a challenging topography. *Ciudad Universitaria* was the first large modern urban-architectural enterprise undertaken in the country [13]. It should be noted that *Ciudad Universitaria* in Quito began its construction just three years after *Ciudad Universitaria* in Caracas-Venezuela (1944), and two years before *Ciudad Universitaria de México* (1949), now *Universidad Nacional Autónoma de México*.

Gatto put in practice an "imaginative employment of reinforced concrete, (…) use of natural stones, brick, marble, including translucent glass blocks" [14]. He designed and built the first thin shell in the country for the Main Hall of the Central Administration building [15]. For the following years he proceeded to design various other expressive double curvature structures that work through form. Gatto, implemented a variety of translucent concrete shells at the School of Law; at the Institute for Materials y Static Testing; at the School of Agronomic and Veterinary Sciences; and at the School of Economy Library –presented herein as case studies in chronological order.

3.1 School of law –*Facultad de Jurisprudencia* (1952-1955)

The expression *hormigón translúcido* or translucent concrete was utilized for the first time on cross-section drawings for the main hall of the School of Law. Although this was just Gatto's second building at UCE campus, he experimented with glass brick shells as skylights to illuminate three different locations: the main hall which is also the *Paraninfo Che Guevara* auditorium foyer (Figs. 8 & 9), on top of a stairwell and above the school library. Unfortunately, the later skylight was condemned years ago because of humidity problems, and was not available for viewing.



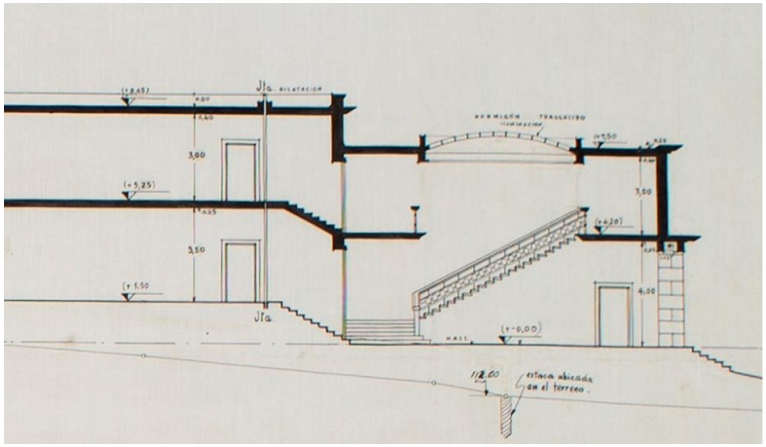


Figure 8: School of Law main hall and auditorium foyer. Photo by the author, 2023. Figure 9: Cross-section of main hall. Courtesy of *Fondo Documental de Arquitectura* UCE. Code FDA-FP-DP-JR-AR-006.

The hall translucent shell is a 5.9 x 5.9-meter elliptic paraboloid profusely pierced by glass bricks –1369 units were utilized at a rate of 39 units/m^2 (Fig. 10). The shell above the stairwell has more ample distancing between glass brick units. –only 224 glass bricks were utilized, using a combined pattern, at a rate of 7.5 units/m^2. Gatto proved that natural light effect can be balanced depending on where and how the translucent concrete was employed –very dense at the hall, and more separated at the stairwell (Fig. 11).



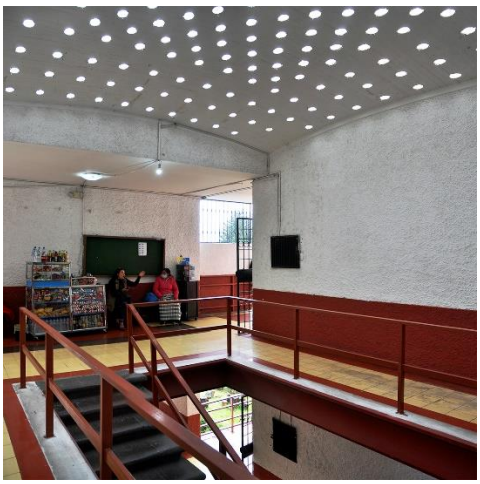


Figure 10: Close up of glass bricks above main hall/foyer. Figure 11: School of Law stairwell. Photos by the author, 2023.

3.2 Institute for materials & static testing –*Instituto de Ensayo de Materiales y Estática* (1955-1958)

Gatto made a structural study along the lines of the Freyssinet and Nervi arched vaults, but also owing references to the Central Garage for National Public Assistance (1931) in Montevideo-Uruguay, designed by his university mentor Julio Vilamajó. The main engine room is a large catenary nave with 16 inverted concrete beams that protrude 25 centimeters from the extrados. 11-cm hexagonal tiles by *Ceramica Vaccari* from Ponzano Magra-Italy were used for exterior waterproofing. The inverted catenary rests on buttresses set 2.80 meters apart, rises 12.40 meters at the vertex and clears a free span

of 21 meters (Fig. 12). The shells are 6.5 centimeters thick with double steel armor. The UCE structure was calculated by engineer Eduardo Narvaez.





Figure 12: Institute for Materials and Static Testing, interior showing prefabricated skylight panels. Figure 13: Closeup of prefabricate skylight panel. 41 glass blocks are inserted in each frame. Photos by the author, 2022.

At the summit of the vault, three rows of 1.4 x 1.4-meter prefabricated skylight panels allow for mid-morning-to-midday light filter to the interior –avoiding afternoon sun (Figs. 13-14). Specifications call for "translucent concrete with *Cristales DIA*" glass blocks. Each round glass brick measures ⌀13-cm at the top, ⌀15-cm at the bottom, and is 65-mm thick, matching the slab thickness. At that time, newspapers and professional journals showed advertisements by AMSON promoting glass bricks made in Belgium (Fig. 15). Projects at UCE possibly used glass bricks acquired from local construction material importers.

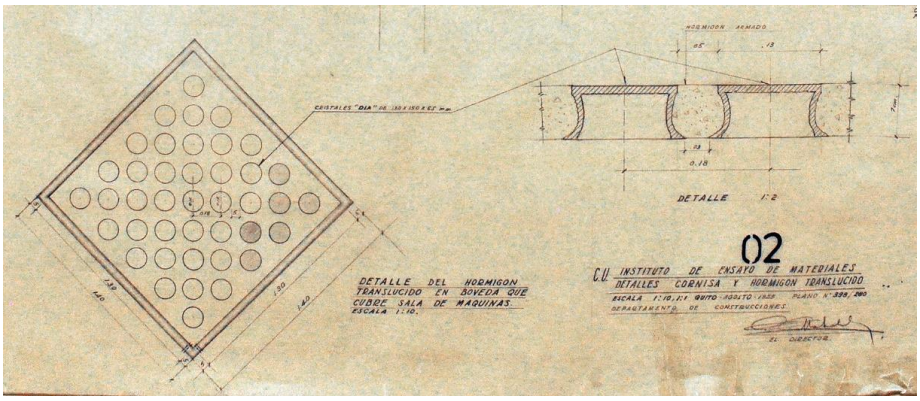


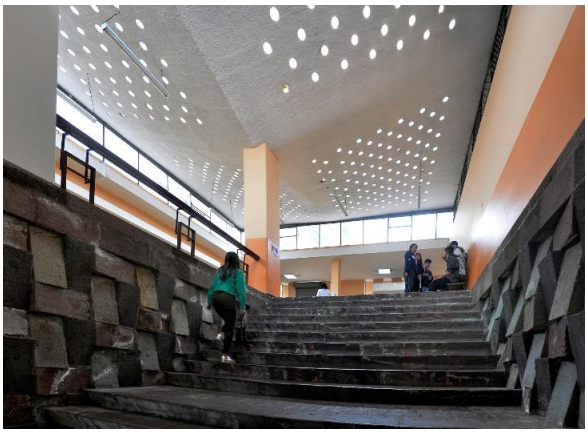


Figure 14: Translucent concrete detail. Courtesy of Physical Plant UCE. Figure 15: Belgian glass brick ad. From: Sociedad de Ingenieros y Arquitectos de Pichincha (SIAP) journal, no.8, march 1959:51.

3.3 School of agronomy and veterinary sciences –*Facultad de Ciencias Agronómicas y Veterinarias* (1959)

Gatto utilized glass bricks in 9 x 10-meter hypars for this building's main hall, gathering spaces and stairwells. He must have resorted to the 1956 *Informes de la Construcción* article for reference because other High Life Factory publications came into circulation only after this work began. He rose the level of inverted umbrellas higher than the surrounding walls to reveal their self-supporting nature. The expressive power, inherent to double curvature surfaces, was accentuated by the alignment of light dots that reaffirmed the generatrixes of the hypars, and thanks to natural light that, filtered by the cylindrical bricks, virtuously enhanced their spatial quality (Fig. 16). Seen from below, the lower surface of the

slabs was sprayed with mortar before being whitewashed and painted white, hiding the trace of wood falsework. It should be considered that, Quito is a city in the Andes mountain range, and the university campus is settled on the eastern slope of the Pichincha volcano. The temperature of the city in the fifties of the last century used to be mild. Regulating the temperature at selected spaces was achieved by translucent concrete as mechanism to obtain heat gain in tall and wide spaces of the building. Detail drawings specify the "Placement diagram of Paris-type, ϕ140 mm x 40 mm glass brick. (180 total units in this area)" (Fig. 17). However, only 111 units were actually placed on each tympan in a staggered pattern. Then, each hypar has 444 glass bricks placed at an average of 5 units/m^2.



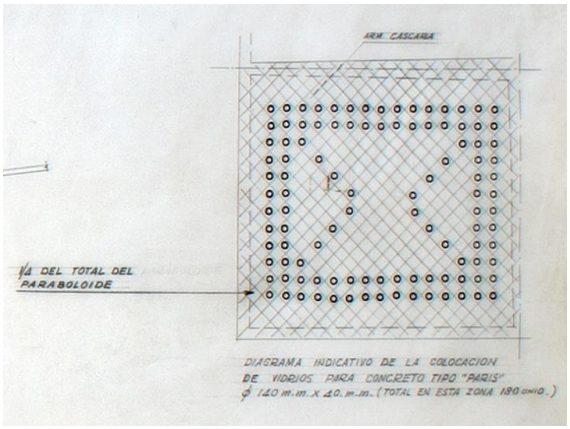


Figure 16: School of Agronomy and Veterinary Sciences Main Hall. Photo by the author, 2023. Figure 17: Glass brick placement diagram. Courtesy of *Fondo Documental de Arquitectura* UCE. Code FDA-FP-DP-AGVT-ES-304.

Thanks to a site visit to UCE campus facilities, a large stock of wooden crates containing unused glass bricks were found in a maintenance warehouse. These glass bricks are exactly as prescribed –ϕ140 mm x 40 mm, labeled *Val S$^{t.}$ Lambert—Belgique*. Its clarity is superb and enhanced by 12 bumps that act as lenses to multiply the incidence of light downwards (Fig. 18). A visual inspection showed that the membranes are bent at the corners, but are otherwise in good shape. Unlike the High Life factory in Mexico, sixty-six years after being built, these 'translucent concrete' hypars remain almost intact with only a small number of glass brick units damaged (Fig. 19).

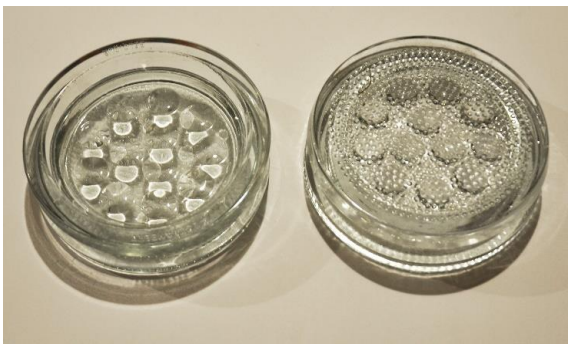




Figure 18: *Val S$^{t.}$ Lambert* Belgian glass bricks upside-down and upright. Figure 19: School of Agronomy and Veterinary Sciences hypars visited. Photos by the author, 2023.

3.4 School of economy sciences –*Facultad de Ciencias Económicas* (1957-1959)

Four long low-rise barrel vault with sloping ends skylights are placed above the lecture hall and one additional barrel vault illuminates the book shelves' area at the School of Economy Library (Fig. 20). Different from previously considered cases, this location is not meant to illuminate circulation areas but a place for longer periods of stay –such as this lecture hall. Arguably, Gatto intended to create a space that improved study performance. Large sun-lit translucent shells, mimic the broad source of the bright sky with less glare. According to Lisa Heschong [16], contrary to artificial lighting, natural light with its varying intensity and full spectrum of colors –that change as sun rises and sets– have positive impact on people. Gatto explored these natural lighting options to trigger physical and mental sensations under this particular UCE library roof. By bringing bright natural light, he was looking for positive impact on improved task performance, health, and desired physiological and emotional responses.

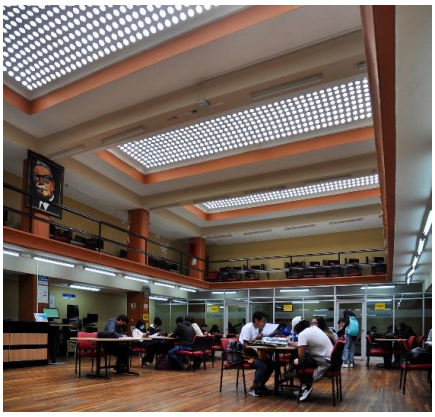
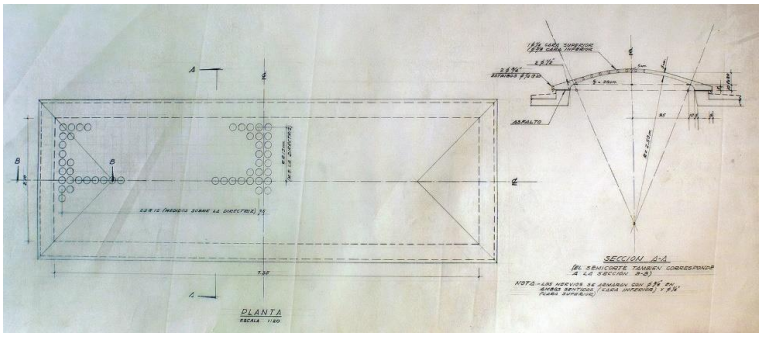




Figure 20: Soft/homogeneous natural light at School of Economy library lecture hall. Figure 21: Library low-rise barrel vaults with formed ends skylights seen from above. Photos by the author, 2023.

Each translucent low-rise barrel vault measures 2.10 x 7.35-meters and is traced with a 2.5-meter radius (Fig. 22), flooding the 5.2-meters high lecture hall below with homogeneous and soft lighting (Fig. 23). Each skylight has 585 glass bricks placed at 38 units/m^2.



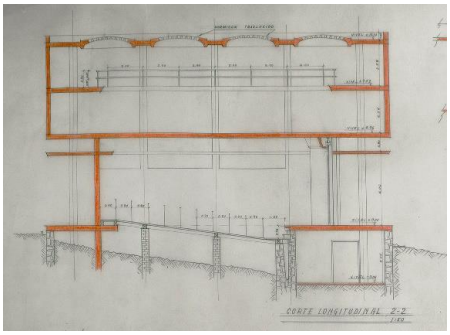


Figure 22: Glass brick placement and low-rise barrel vault geometry. Courtesy of *Fondo Documental de Arquitectura* UCE. Code FDA-FP-DP-EC-ES-015. Figure 23: Cross Section thru lecture hall. Courtesy of *Fondo Documental de Arquitectura* UCE. Code FDA-FP-DP-EC-ES-020.

4. Conclusion: submission of contributions

Use of translucent concrete shells punctured by glass bricks can be traced to Cuba, Venezuela, Mexico, Spain, and Ecuador, among other countries. Publications featuring the Hight Life factory in Coyoacán,

Mexico City may have informed the works of architect Gilberto Gatto Sobral at *Ciudad Universitaria* in Quito-Ecuador. Gatto left a legacy of fascinating cases of sky-lit translucent concrete shells in multiple formal, functional and structural configurations: elliptic paraboloids, catenary shells, hyperbolic paraboloids, and low-rise barrel vaults. Furthermore, he explored these natural lighting options as mechanisms to control air temperature and to trigger positive sensations on people using educational spaces. Studying these elements of Ecuadorian Modern identity will provide us with instruments to reinforce awareness on their patrimonial values and character.

Acknowledgements

Recognitions are given to PhD. Juan Ignacio del Cueto in Mexico D. C., México on information regarding High Life Factory; architect-engineer Ángel Álvarez in La Habana-Cuba on information concerning Arcos de Cristal; architect Orlando Marín in Caracas-Venezuela on information about Santa María and Casa Sindical projects; architects Marcelo Amores, Maritza Balcazar, Edwin Benalcazar, Marco Salazar, and engineer Luz Juinia at various Universidad Central del Ecuador departments. Thanks to photographers: Lilia Tellez in Caracas-Venezuela and Luis Paredes in Guayaquil-Ecuador.

References

[1] Banham, Reyner. *Age of the Masters*. p. 43. Blume, London: Architectural Press, 1975.

[2] Holmes, Burton H. & Creighton, Thomas H. Can A Man Be Architect, Engineer, Builder? *Progressive Architecture* 40(2), p. 140-141. New York: Reinhold, 1959.

[3] Garlock, Maria E. & Billington, David P. *Félix Candela. Engineer, Builder, Structural Artist.* Princeton University Art Museum & Yale University Press. New Heaven and London, 2009.

[4] Hormigón, material noble de hoy. *Informes de la Construcción* vol 4, no. 86. December 1956.

[5] Torroja, Eduardo. Razón y ser de los tipos estructurales. *Textos Universitarios* 13. Revised 3rd edition, 2007. 1st reprint. 2010, p. 121. Madrid: Doce Calles, 1957.

[6] Boyd, Robin. Engineering of excitement. *The architectural Review*, 124 no. 742, p. 294-308. London. November 1958.

[7] Faber, Colin. *Candela / The Shell builder*, p. 114. New York: Reinhold, 1963.

[8] Architectural Glass Patent Index. https://glassian.org/Prism/Patent/4266/page1.html. Obtained 29 march 2023.

[9] Thin-shell concrete vaults. Night Club: Havana, Cuba. *Progressive Architecture*, no. 6, p. 108. June 1954. The placement of the stage was relocated to the opposite end of the arches. Ángel Álvarez in conversation with the author, 24 March 2023.

[10] Delgado, Daniel, Rodriguez, Denisse & Tarlano, Onella. *Develando arquitectura "anónima" de la modernidad caraqueña. Edificio Santa María, parroquia Catedral.* Academic essay directed by Marín, Orlando. Departamento de Diseño, Arquitectura y Artes Plásticas, Universidad Simón Bolívar. March 2023.

[11] Calvo, Azier & Vera, Henrique. ¿Sabía usted...? *Boletín Contacto Fundación Arquitectura y Ciudad*, no. 74. 29 April 2018.

[12] López Díaz, Luis. Talleres de automóviles en Miller Bajo, Las Palmas de Gran Canaria, España. *Informes de la Construcción*, vol. 30, no. 290, p. 45-53, May1977.

[13] *Anales*. Universidad Central del Ecuador. Various issues.

[14] Maldonado, Carlos. La obra del arquitecto Gilberto Gatto Sobral en la arquitectura del Ecuador. *Arquitectura y Sociedad.* No. 6. Facultad de Arquitectura y Urbanismo. Universidad Central del Ecuador: Quito, p. 69-74. June 1986.

[15] Luzuriaga, Mauricio. El paraboloide hiperbólico de concreto armado en Ecuador. DAYA, *Diseño, Arte y Arquitectura*, no. 8, p. 233-256. 2020.

[16] Heschong, Lisa. *Visual delight in Architecture*. 1st edition. Routledge, 2021.

Historical structures

Active bending
Additive manufacturing/ 3D printing
Architectural geometry
Bamboo for sustainable construction and quality of life improvement
Bio-inspired structures and architecture
Bridge structures
Computational form-finding
Conceptual design
Concrete structures
Construction techniques
Deployable and inflatable structures
Design competition (WG21)
Digital modelling and fabrication
Dynamic response of metal spatial structures
Dynamic response of other structures
Form-finding and structural optimisation of interlocking discrete assemblages
Graphical methods
Gridshell and lattice structures
Historical concrete shells
► **Historical structures**
Lattice structures
Life-cycle design and assessment of structures
Metal gridshell structures, connections and stability
Methods and construction technologies for sustainable shell structures
Morphology and configuration processing
Next generation parametric design
Novel methods in modelling, optimisation and construction for reducing carbon footprint of continuous roof shells
Numerical methods for geometry, form-finding and optimisation of lightweight structures
Optimisation methods and applications
Origami
Other
Teaching design uncertainty: working with unknown qualities/quantities of new and re-claimed materials
Teaching of shell and spatial structures
Tensegrity systems and cable structures
Tension and membrane structures
Tension structures in the Asia-Pacific
Timber and bio-based structures
Topology optimisation
Traditional masonry structures and innovation
Transformable structures

IASS 2023
July 10–14 Melbourne
Integration of Design and Fabrication

Proceedings of the IASS Annual Symposium 2023
Integration of Design and Fabrication
10–14 July 2023, Melbourne, Australia
Y.M. Xie, J. Burry, T.U. Lee and J. Ma (eds.)

Pier Luigi Nervi ‘s arch in E’42

Satoru KIMURA[a,*], Toshiaki KIMURA[b], Yosuke KOMIYAMA[c]

[a,*] Department of Urban Design, Faculty of Science and Engineering, Ritsumeikan University.
k-satoru@fc.ritsumei.ac.jp

[b] Graduate School of Design and Architecture, Nagoya City University
[c] Department of Architecture and Architectural Engineering, Kyoto University

Abstract

Pier Luigi Nervi was an engineer who contributed to the development of construction technology for reinforced concrete in Italy. The engineer is developing Hennebique and Monie system in Italy. Changes in the construction between the two system are due to the inadequate use of reinforcing bars and woods as a formwork, and a new construction technique called a prefabricated construction method has been used later. On the other hand, Nervi is engaged in the design of the pavilion of the World Exposition which was scheduled to be held in Rome in 1942, that is “Esposizione Universale Roma”. In this thesis I will deal specifically with “Arch of Emperor” in the EUR area. Its basic design is done by Adalberto Libera(1903-1963). Nervi is examining the structure and creating construction drawings. An arch of 200 meters in wide and 100 meters in height is considered. The arch is studied with concrete only without reinforcing bars. How did Nervi try to use a concrete as a structure of an arch in the state that he can not use steel bars? In addition, we will analyze a construction system which was considered at the time of construction in this paper. Then Nervi uses ferro-cement for his works after the world war II. Before the system, Nervi tried a plain concrete and a ferro-cement. While building resources cannot be used freely, the historical significance of making a monument of a huge arch with plain concrete is discussed in this thesis. Also this paper clarifies the process leading to Nervi’s ferro-cement construction in post-war.

Keywords: Pier Luigi Nervi, arch, EUR’42, reinforced concrete, reverse engineering, Adalberto Libera

1. Introduction

EUR 42 was an event scheduled for 1942 and was supposed to be a good experimental site for the expression of Italian fascist architecture (Fig. 1). Fascist architecture can be seen as a fusion of rationalist architecture with ancient Roman style in this paper, but it was actually built at the Livera conference hall (Fig. 2) and Mr. B's Colosseum (Fig. 3). However, the plan for the World's Fair in Rome was not limited to that, and a huge number of proposals were made centering on the main gate called the arch of the empire. Livera and Nervi are involved in the arch. The arch was also treated as a symbol of peace as "Pax Romana"[1]. In this paper, I would like to focus on the arch and consider the understanding of ancient Roman architecture by Nervi and Livera. From the viewpoint of research, the shape of the arch and the construction method. Furthermore, I would like to reassess the significance of this arch in EUR '42 (Fig. 4).

Research interests are Nervi's books and magazine articles, and Livera's memos. The method is to sort out each claim and compare what Nervi and Livera were looking for. By considering the results, we will clarify the significance of Nervi's claim and its ideas to the EUR plan. Previous studies include C.Greco[2], G. Neri[3], and R.Bologna[4], but none of them consider the significance of the arch of the empire. This study reassesses EUR'42 from the analysis of the arch. Nervi is also said to have been critical of the fascist regime after the war. However, until just before the end of World War II, he was

Copyright © 2023 by Satoru KIMURA, Toshiaki KIMURA and Yosuke KOMIYAMA. Published in the Proceedings of the IASS Annual Symposium 2023 with permission.

involved in a project that could be called a symbol of the fascist system, and this research provides an opportunity to learn about Nervi's thinking at the time.

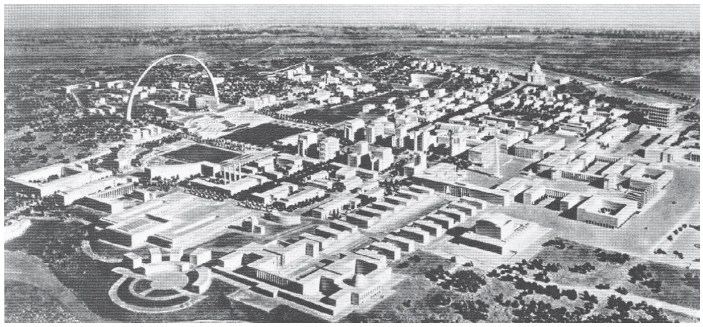


Figure 1. Overall image of the E'42 plan

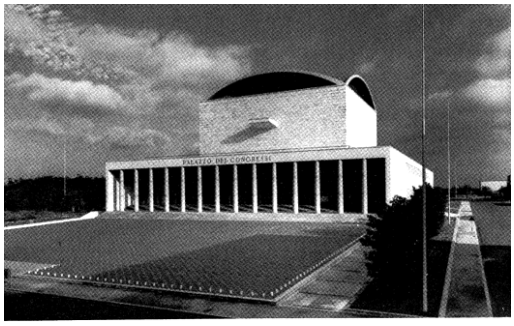


Figure 2. EUR conference hall



Figure 3. EUR Civilization Hall

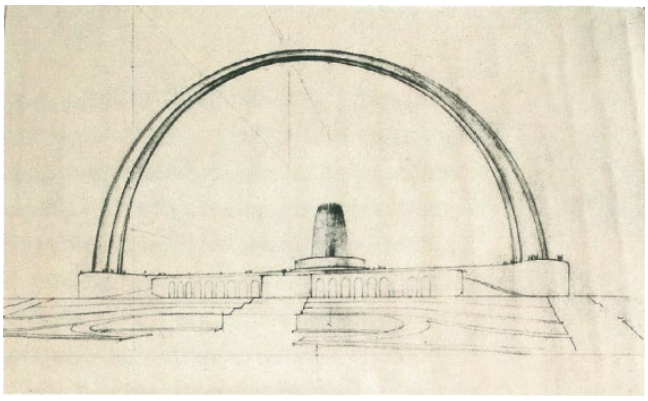
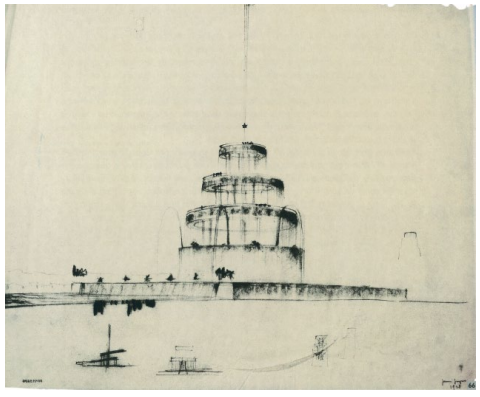


Figure 4. Sketch of the imperial arch

2. Nervi's involvement in the EUR'42 project

As I said in the background, Nervi is involved in three plans centered on the arch of the empire(Fig.5, Fig.6, Fig.7). Looking at those proposals, a parabolic arch is used. In the arch of the empire, a semi-circular arch was pro-posed by Libera, but since Nervi took the initiative in designing the three plans described here, Nervi's intention is directly expressed. A parabola is clearly more effective than a semicircle in terms of building a large roof, but Nervi is planning a large parabolic roof in RC.





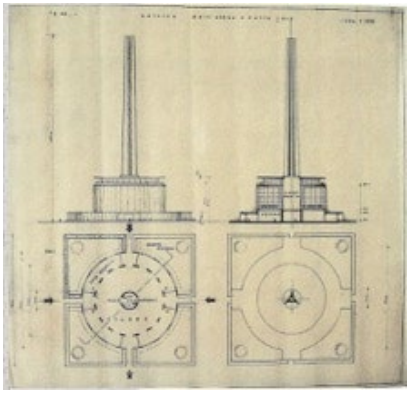


Figure 5 (left). Perspective(A) of pavilion with water and light

Figure 6 (center). Perspective(B) of same Project

Figure 7 (right). Perspective(C) of same project

It is being considered in the Pavilion B plan planned for EUR'42 (Fig. 8). On the other hand, Plan B was a circular plane with a diameter of 70 m, and the same size as the above-mentioned circular hangar was examined (Fig. 9). In the hangar plan, the roof support member provided in the center of the circle has a rigid frame structure, while in the B plan, the arch is extended. In addition, in the hangar plan, the center of the plane was the warehouse, while in the center of the B plan, an external space is provided, and some improvements can be seen.

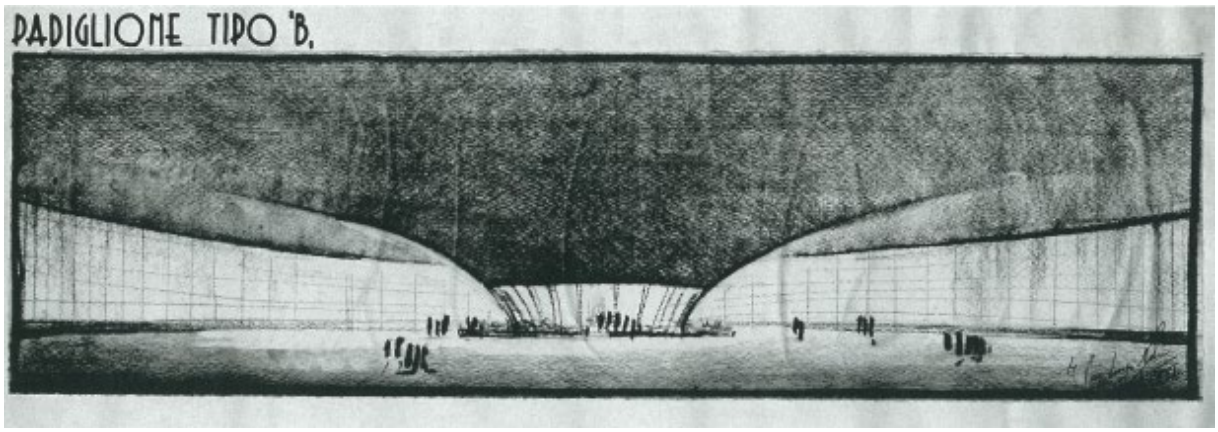


Figure 8. Perspective for pavilion of exhibition hall

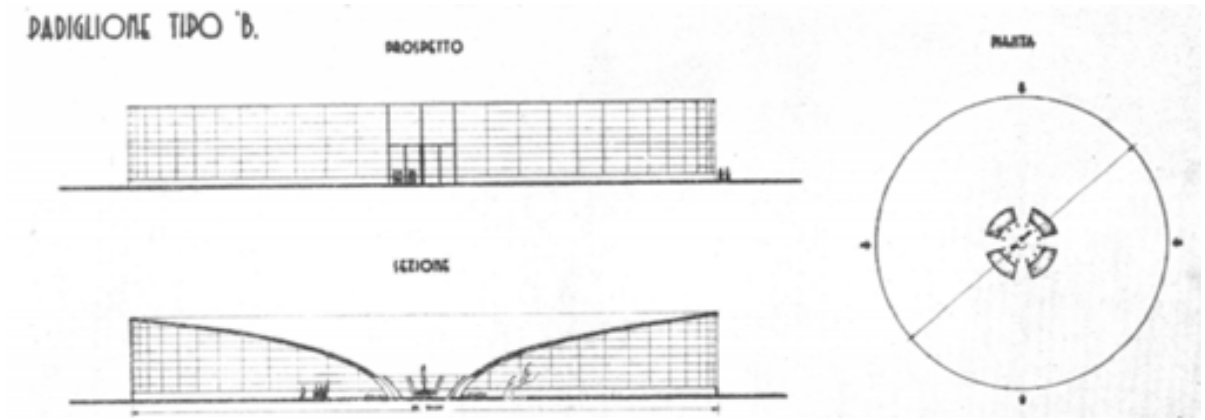


Figure 9. Elevation and plan for pavilion of exhibition hall

3. Remarks on the shape of the arch

If you look at the memorandum about Livera's arch (Fig. 10), you can see that five things are written * 3. They are (1) the cross section of the axis that constitutes the arch is elliptical, (2) the major axis of the ellipse is 1.5 times the minor axis, and (3) the lengths of the base, middle, and top. It was the length of the axis and the minor axis, (4) the radius of the arch, the dimensions of the inscribed and circumscribed circles, and (5) the height of the base. It should be noted that the arch looks like an elevation, and although the arch's cross section in the lateral direction is elliptical, the entire elevation is a perfect circle with a radius of 100 m.

EUR was selected as the new city of Rome as the main venue of the Expo, and Livera has left an actual work called the EUR conference hall. The conference hall used flat and elevation symmetry and colonnades at the entrance. On the other hand, it can be said that the arch of the empire was trying to express fascist architecture with a semicircular arch instead of a parabola as a form. Nervi also made the following criticisms while designing the implementation of the arch designed by Libera. Beyond all

relations to stable facts, the unnaturalness of this form, due to the abstract ideas formed in advance in the designer's mind, gave all the works non-concrete features [5].

This shape" in the quote is exactly the arch of the empire. Nervi also points out that Livera's arch proposal emphasizes morphology over structural safety.

“In special and exceptional cases, it is a characteristic that can be a sensory element (...), but there is no doubt that it has a completely unpleasant appearance [6]”

While criticizing the elevation in this way, he has left a detailed view (Fig.11). From this, it can be seen that there was another form that Nervi should aim for. Also in his own book, Nervi also discusses the example of an ideal bridge, comparing the two bridges. “A quick observation of these two bridge schemes reveals that voluntary obedience to static laws is a condition of aesthetic success(Fig.12&Fig.13). Type A is statically unhappy and aesthetically unhappy” (Fig.12). As the quote suggests, Nervi has a negative opinion about the shape of the bridge using a perfect circle, while the parabolic shape is ideal.



Figure 10. Libera’s sketches and notes on the arch of empire

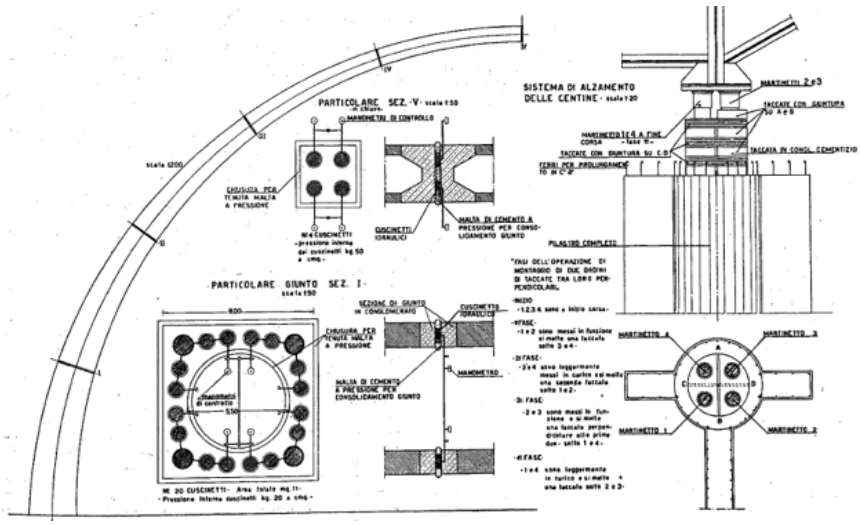


Figure 11. Detail of connects of same arch

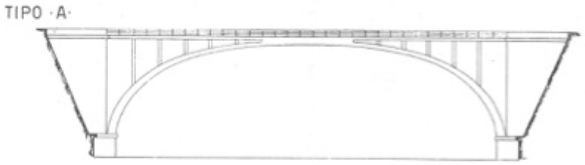


Figure 12. Type A of an ideal bridge

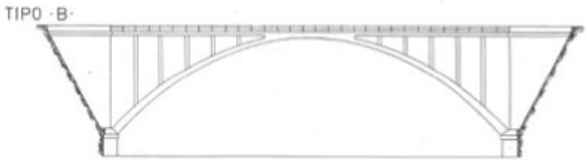


Figure13. Type B of an ideal bridge

4. Consideration

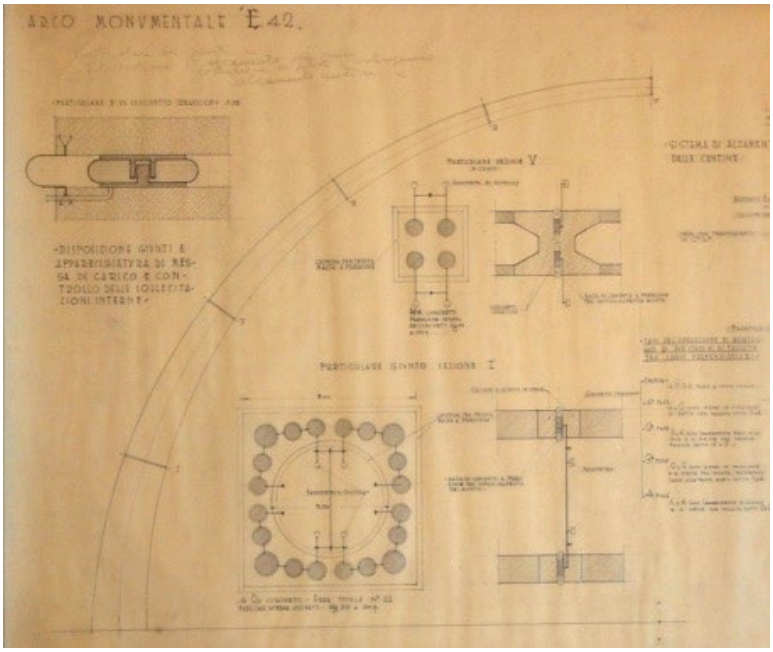
Here, based on the contents of the previous chapter, we will consider three points: form, material, and history. First, Nervi unilaterally criticized Livera's empire arch proposal for form, but there is something in common between the two. They are about the size of the arch and the materials that make it up. The size of the arch is a perfect circle with a radius of 100 m, and even if you look at other sketches and drawings, there are no plans for different dimensions or ellipses, so the two people agreed on this size and form.

It is probable that an agreement was reached on the use of Roman concrete as the material to be constructed. In addition to Livera and Nervi's proposals, other architects' proposals for aluminum and iron were also being considered [6]. In response to that proposal, the two may have been conducting a

more detailed examination of the construction of unreinforced concrete. Also, it may have been trying to form the style of ancient Rome at that time.

Next, regarding materials and construction methods, Nervi is studying for construction (Fig. 14). We tried to form an integral arch with unreinforced concrete by dividing half of the semicircular arch into five and providing ribs at each connection. The cross section of the arch is a perfect circle.In addition, Nervi has commissioned an experiment on a scale model in collaboration with Professor Oberti of the Polytechnic University of Milan (Guido Oberti, date of birth unknown) (Fig. 15). It has been confirmed that collapse does not occur due to wind pressure or its own weight [7]. As they were considered, it was really aimed at construction.

From here, we will consider how Livera and Nervi perceived rationalist and fascist architecture. The results are shown in Table 1. Livera used symmetry and low rise arches in rationalist architecture such as the EUR conference hall. On the other hand, for fascist architecture, the symmetry is similar, but a semicircular arch is assumed. Furthermore, regarding materials, it was considered desirable to use RC and steel frames as rationalist architecture. And, as fascist architecture, he probably thought that unreinforced concrete, which is Roman concrete, was suitable.



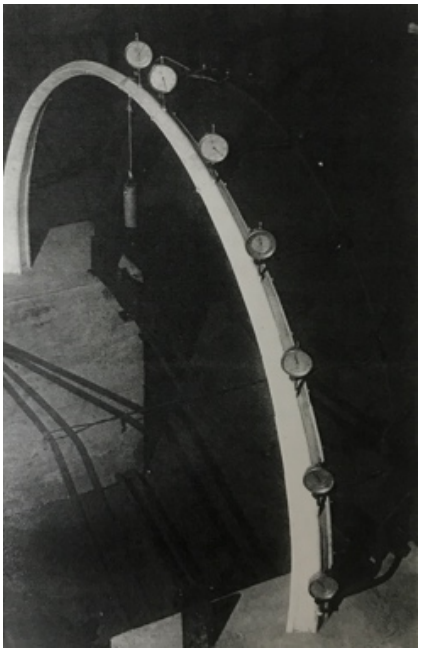


Figure 14 (right). Detailed view of the empire arch by Nervi (in CSAC)
Figure 15 (left). Obertis Structural Experiments on the Arch of the Empire .

5. Conclusion

Nervi wanted to build a parabolic arch rather than a semi-circular arch, while considering the detailed view of the semi-circular arch proposed by Libera as an empire arch. This is because Nervi prefers something that is structurally rational and highly workable, rather than a symbolic one that represents the authority of the ancient Roman Empire.

Nervi is also considering inheriting traditional construction methods for its arches. He is being considered for construction without rebar, and it is believed that he replaced Roman concrete with the construction method of the time. In that sense, it can be said that Nervi sought his own method of form and construction, with reference to what was used in the ancient Roman Empire. Livera planned to quote the ancient arches as they were, but Nervi did not. In other projects in EUR, shell shapes in RC were

considered, and it seems that they were looking for a shape as RC instead of a semicircular arch as a stone.

Furthermore, in the examination of the construction method, it is closer to the Monier type construction method instead of the Hennebique type, showing the sprouting of postwar ferro-cement. Construction with unreinforced concrete, which does not even have a main bar or band bar, has the same idea as the postwar Nervi system in that ribs are provided and the structure is segmented. In the future, I would like to consider the significance of Nervi's ferro-cement architectural works.

Acknowledgements

I have browsed the original drawings at the Parma University Library (Centro Studi e Archivio della Comunicazione, CSAC). In addition, MAXXI provided drawings and photographic data. I would like to express my gratitude.

References

[1] Giorgio Ciucci, “Gli architetti e il fascismo Architettura e città 1922-1944, Einaudi, 1989.

[2] G. Claudio, “Pier Luigi Nervi. Dai Primi Brevetti al Palazzo delle Esposizioni di Torino 1917-1948”, Quart, Luzern, 2008.

[3] Gabriele Neri,” Capolavori in miniature. Pier Luigi Nervi e la modellazione strutturale, Mendrisio Academu Press, 2014.

[4] R. Gargian and A. Bologna, “The rhetoric of Pier Luigi Nervi. Concrete and ferrocement forms”, EPFL Press, pp.26-67, 2016.

[5] Pier Luigi Nervi: Un arco monumentale in conglome-rato non armato, Casabella, n.176, 1942.8.

[6] Pier Luigi Nervi: La tecnica ed i nuovi orientamenti es-tetici, Atti del convegno di Ingegneria dell’anno XVIII, Sindacato fascista ingegneri di Milano, 1939, pp.1-4.

[7] Ibid., pp.43-45(G.Neri).

IASS 2023 July 10–14 Melbourne Integration of Design and Fabrication

Proceedings of the IASS Annual Symposium 2023
Integration of Design and Fabrication
10–14 July 2023, Melbourne, Australia
Y.M. Xie, J. Burry, T.U. Lee and J. Ma (eds.)

The hybrid statics by Heinz Hossdorf – interaction between physical models, material and the first computers

Baris WENZEL[*], Eberhard MÖLLER[*], Benjamin SCHMID[a], Christiane WEBER[a]

[*] Faculty of Architecture and Engineering, Karlsruhe University of Applied Sciences
baris.wenzel@h-ka.de

[a] Construction History, Universität Innsbruck

Abstract

Heinz Hossdorf (1925-2006) was an exceptional engineer. His research and work included very different fields, such as small-scale physical model tests, electronics, structural engineering, architecture, computer applications, three-dimensional CAD (ITS-10), revolutionary calculation methods such as the Finite Element Method, and the development of new materials [1]. For Heinz Hossdorf, model statics was well on the way to overcoming its conventional cumbersomeness through the sensible integration of electronic calculating machines as process computers in the test sequence and to increasing the reliability of the experimentally recorded data to perfection through the use of modern measurement technology. The reinterpretation of the measured values into statements of interest to the engineer, which was associated with laborious calculation processes, was easily mastered by the computer [2]. This paper gives an overview of the wide range of hybrid statics, which Heinz Hossdorf used to achieve technological progress in the field of civil engineering. The materials used and the measurement methods will be analysed, and the question of what influence they had on the planning of the structures will be answered.

Keywords: physical models, FEM, concrete shells, computer statics, new material, electronics.

1. Introduction

Since ancient times, scale models have been used to study physical processes in the real world, to understand the laws of nature, and to make them usable for humans. At the end of the 15th century, Leonardo da Vinci used physical models to study the bending behaviour of elastic beams with different spans. Later, in the 20th century, physical models were indispensable for civil engineers and architects to check the load-bearing capacity of unconventional and innovative structures [3].

Heinz Hossdorf used physical models from the beginning to check his theoretical assumptions for constructive designs. What distinguished him from other civil engineers of his time is that in 1967 he was one of the first to use the computer to automate the whole process of testing physical models. In the 1980s, his lab developed a 3D modelling program that accessed a central model, automatically generated its plans and views, and managed masses in a database [1]. This so-called ITS-CAD system is what is nowadays called BIM.

2. The engineer Heinz Hossdorf

Heinz Hossdorf (Fig. 1.) was born in Wiesbaden (Germany) and grew up in Basel (Switzerland). Hossdorf began his civil engineering studies in 1946 at the Federal Institute of Technology (ETH) in Zurich and, after his intermediate diploma, completed an internship at a shipyard near Antwerp (Belgium). He finally continued his studies at the TU Aachen in 1950, but at the same time began working as a structural engineer at the Rudolf Hascha engineering office in Basel, so he didn't finish his

Copyright © 2023 by Baris WENZEL, Eberhard MÖLLER, Benjamin SCHMID and Christiane WEBER. Published in the Proceedings of the IASS Annual Symposium 2023 with permission.

studies and soon worked full-time there. Already during his time as an employee in the engineering office, Hossdorf felt the cooperation with architects fruitful and his interest in designing his own constructions was awakened. Hossdorf finally founded his own engineering office in 1953, seeking constructive solutions in harmony with the new technological working methods, building materials and construction processes. Therefore, he opened his own private laboratory for experimental statics in Reinach (Switzerland) in 1957 to introduce the tools of the second half of the 20th century's electrical revolution into civil engineering and enhance model statics technologically. In combination with new technologies, experimental statics was to become a modern contemporary medium for structural design and planning. This was also to be achieved through numerous contacts at a national and international level with people and institutions in the field of model statics. His laboratory became internationally renowned for combining physical models with the possibilities of using new electronic computers in engineering, called hybrid statics. In 1966, his laboratory moved to a new building in Basel, where Hossdorf, in addition to his projects as a civil engineer in collaboration with architects, increasingly conducted modelling studies for external colleagues. He also gave lectures on model testing at the ETH Zurich between 1967 and 1969. At the same time, he prepared his book “Modellstatik” (Model Statics), which was published in 1971 [4].

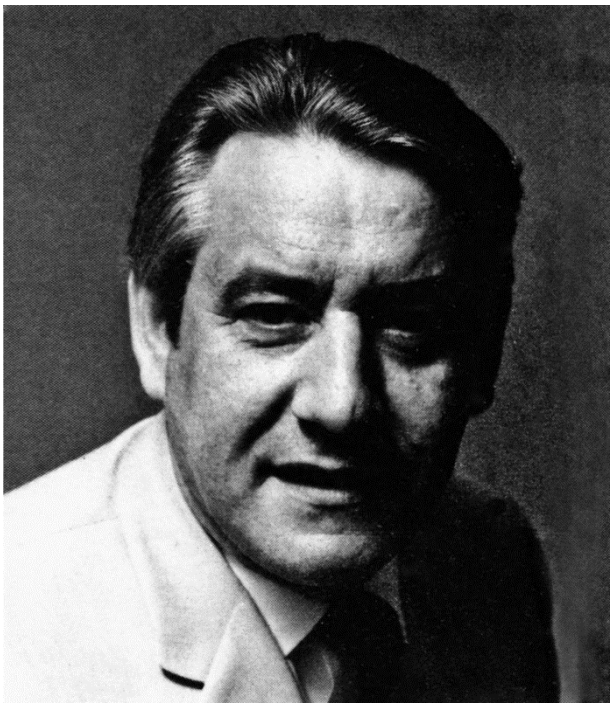


Figure 1. Portrait of Heinz Hossdorf (Bauverlag BV GmbH) [6].

In his publication “Modellstatik”, which Hossdorf understood as a textbook, he further emphasised integrating electronic data processing into physical model tests, in addition to the classical model statics. He was convinced that this was an opportunity to establish the method of model statics, which in his opinion, was not always taken seriously by his engineering colleagues as a fully adequate and practicable tool. The book presents the purpose of model statics, different types of applications and the historical development at the beginning. This is followed by separate chapters on the theoretical principles and the experimental techniques, where the possibilities of materials, experimental set-ups, measurement techniques, etc., are explained. The fourth chapter deals with the computer in model statics and shows the contemporary and possible uses of hybrid statics. In the end, a chapter entitled “Documentation” contains examples from all over the world of projects that have been investigated with the help of experimental model tests. The diverse examples are intended to provide an instructive reflection of engineers' possible applications and ingenuity. Most of the information and documentation on these

model tests was requested by Hossdorf himself directly from the persons involved. Hossdorf benefited from his effective international network of persons and institutions in the field of model statics. Among the institutions and persons requested were the Laboratorio Nacional de Engenharia Civil in Lisbon (Portugal), the University of Southampton (United Kingdom), the Istituto Sperimentale Modelli e Strutture in Bergamo (Italy), the Laboratorio Central in Madrid (Spain), the University of Tokyo (Japan) and the Polish engineer Waclaw Zalewsky, all of whom were known to him personally and perhaps even in close contact [5].

Convinced of the potential of digital object modelling, his laboratory concentrated on this topic and the development of corresponding software from 1974 onwards, so no experimental model tests were carried out there anymore. The laboratory eventually became CAD-Systems AG, which, in addition to development and research, also carried out the first training courses on CAD-Systems in Switzerland. After various holdings and financial difficulties, the company had to be abandoned in 1983. In 1984 Hossdorf emigrated to Madrid and continued consultancy work there, e.g. for Expo 92 in Seville. Hossdorf returned to ETH Zurich in 1996-1997 as a guest professor at the architecture department [4].

Hossdorf became known, among other things, for his shell structures, as he was born at a time when shell construction and prestressing technology were gaining importance. The physical parameters limited the design freedom for shell structures, and theoretical principles were only available for simple, regular geometries. For this reason, only a few architects were concerned with shell construction, but at this time, a number of structurally designing engineers emerged, including Heinz Isler, Pier Luigi Nervi, Eduardo Torroja, Felix Candela and Eladio Dieste, in addition to Heinz Hossdorf. Due to the lack of analytical principles and as the computer technology was not fully developed, Hossdorf resorted to model statics. He carried out load tests on scaled models and determined forces, deformations and strains, allowing him to deduce stress curves in the model and the actual structure. Increasingly, he also used the computer to evaluate and present the measurement results and recognised its potential early on. Ahead of his time, Hossdorf failed to find the financial and human resources to develop a practical CAD system or finite element calculation programs on virtual models, which are now part of the engineer's routine [6].

3. The laboratory for experimental statics

The central tasks of Hossdorf's laboratory were research and development of modelling techniques, as well as the practical application of model statics, especially for external projects for architectural and engineering offices. In this function, the laboratory was a popular excursion destination for students and teaching staff. The laboratory consisted of a mechanical and electronic workshop (Fig. 2) and an experimental laboratory. In the workshop, the models for the experiments were built, and new modelling techniques were developed. The experimental laboratory was equipped with mechanical experimental technology, electronic measuring equipment and a computer. Some circuits were designed there to control the experimental technology using a computer so that specific load cases could be carried out under computer control. The experimental laboratory also had a robust floor on which the models were tested. Results could be output as classical computer printouts or in graphical representations utilising specially developed programmes. Hossdorf saw the success of the application of model statics in the international use of the method, as in England, Germany or, especially emphasised by Hossdorf, at Cornell University in the USA. Hossdorf expressed the following basic idea concerning model statics in an interview: “It is our concern to simply see the truth. Man often tends to prefer to believe in a theoretical line of thought which flatters him rather than to want to find out the bitter truth through experiment [7].”



Figure 2. Workshop of Heinz Harsdorf's laboratory (Walter Grunder) [4].

4. Personal and institutional networks

One of Hossdorf's closest confidants was Kilian Weiss, who was employed as a student assistant in Hossdorf's laboratory during the 1958 semester break. After finishing his studies, Weiss was permanently employed in Hossdorf's office in 1963 and took care of the day-to-day business there. Weiss took over the duties in the office and became a partner in the renamed Hossdorf and Weiss engineering office in 1972 until Hossdorf left the office in 1978 so that he could devote himself entirely to the development of CAD systems. Nevertheless, the two kept in touch until Hossdorf's death. Even before leaving his office, Weiss had taken over many tasks so that Hossdorf could concentrate on working on the models and further developing hybrid statics, although the office naturally benefited from their application. In the laboratory, Léon Beuret, as head, took care of the ongoing processes and also disburdened Hossdorf. Beuret also further developed, for example, tensioning devices for strength models made of prestressed micro-concrete. In addition to the model tests, manual calculations were carried out for individual details, to check the results internally for plausibility. Hossdorf and his staff were in close contact with other model test facilities, such as the laboratory of José Antonio Torroja in Madrid, but an external check of the test results was hardly possible. The architects' trust in Hossdorf and his methods were decisive for many projects; only in this way could a constructively holistic design be developed together. This trust was always crucial to Hossdorf, who preferred creative collaboration over a bottle of red wine to the daily office routine so that statics and construction could become part of the architecture [8].

His close relationship with Spain was established as early as 1954 after Hossdorf published an article on a possible solution for the construction of the third Devil's Bridge as part of the Gotthard Road as a prestressed structure made of purely natural stone in the "Schweizerische Bauzeitung". The construction principle proposed by Hossdorf aroused the interest of Eduardo Torroja and his Instituto de la Construcción y del Cemento, so initial contacts were made with Spain, and a meeting with Eduardo Torroja followed. Eduardo Torroja's statics analysis method using physical models inspired Hossdorf, and he benefited from Eduardo Torroja's reputation and existing network. A close friendship also developed with Eduardo's son, José Antonio Torroja. This friendship even led so far that after the end of the physical model tests in Hossdorf's laboratory in 1978, a large part of the equipment was taken over by the Faculty of Civil Engineering at the Technical University of Barcelona, which was just being established, under the direction of José Antonio Torroja. The transfer and correct use of the equipment was accompanied by Hossdorf himself, thus ensuring the transfer of knowledge. In Barcelona, the method was mainly used in teaching and was part of the curriculum at least until the 2000s. A couple of engineers, together with Hossdorf and José Antonio Torroja, founded the company Digitec AG in 1974, which set itself the task of rationalising engineering work with the help of computer programmes [4].

From his office and laboratory practice, Hossdorf established many, often fruitful, contacts with architects and firms with whom he could realise several projects over longer periods. These contacts often gave Hossdorf great freedom in his constructive solutions, including, for example, the architects Otto and Walter Senn, Hans Beck and Heinrich Baur, Vischer Architects and Felix Schwarz and Rolf Gutmann. As Hossdorf increasingly concentrated on software development, he also sought contact with corresponding experts, which also led to contact and friendship with the physicist and computer scientist Peter Dietz, who was able to provide further help, especially in questions of process control [4].

5. What is hybrid statics?

Hybrid statics was used in Heinz's laboratory in the 1970s to calculate complex structures or to check previously made calculations. The experimental setup in which a computer is integrated into symbiosis with a physical test and measurement facility to form a monolithic technical unit, Hossdorf called hybrid statics. At that time, Heinz Hossdorf was of the opinion that the computer, by tailoring the computational processes to finite element analysis, would be particularly useful in elastic beam statics for plane structures that had been difficult to capture until then. He was critical of the computer's penetration into other areas of structural analysis. He saw the increased computation time from the third power of unknowns in the inversion of matrices and the size of the computers of the time as the limiting factors. He nevertheless predicted the great potential of computers, but only in a symbiotic relationship with the physical measurement model. This symbiotic relationship makes use of the strengths of both components. The computer is in a dialogue with the physical model [2]. The control and regulating devices, which are attached to the model, send analogue data to the computer, which converts these in fractions of millionths of seconds into numerical values, and vice versa, also gives them to the models. The computer is able to make controlled decisions based on the results of complex data analysis in fractions of a second.

Hossdorf describes the computer as a mindless, oversized athlete, capable of indefatigable patience to perform arithmetic operations at high speed and to repeat them any number of times. The physical model has inherently complementary properties. As a material world component, the model knows basically everything (Fig. 3). The physical reality is, by nature, its own. Only it has no language to communicate its experiences to us.

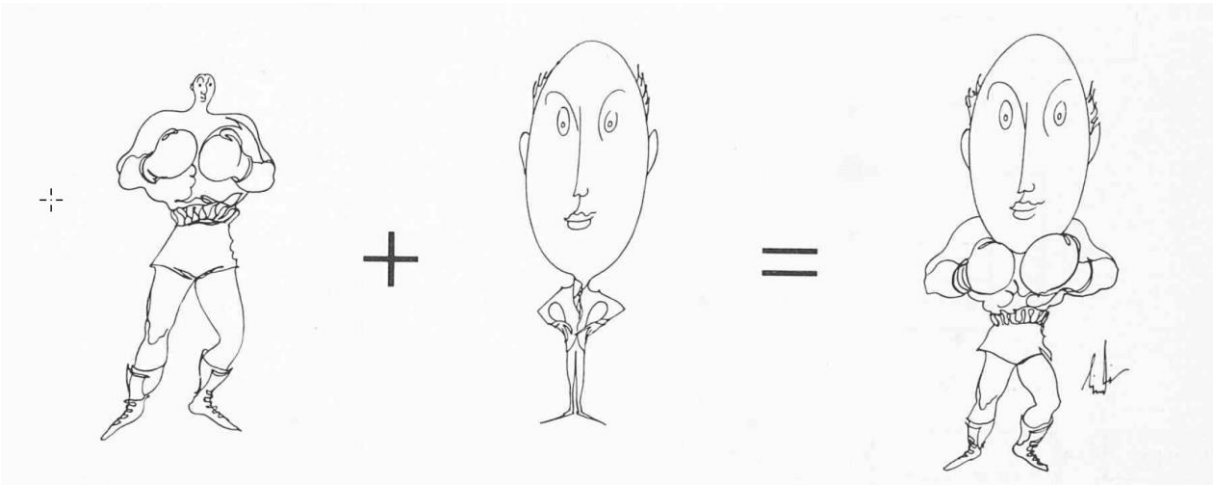


Figure 3. "Hybrid statics – the optimal symbiosis between the workaholic but mindless digital computer and the omniscient but mute analogue model." (Caricature of the well-known illustrator Lindi in an article in the Schweizerische Bauzeitung. 1965) [5].

The whole process of carrying out a hybrid model experiment on a physical measurement model may be described as follows: In the first step, the model is produced. This is often made up of thousands of individual parts, some of which have been specially manufactured and assembled by hand onto an individually tailored test frame, sometimes over days or weeks. After the first part, which is already very time-consuming, has been completed, measuring sensors must be attached. Some of these are also custom-made. This is followed by the load test. For the load test, multiple weights, whose distribution is calculated and each of which is weighed, are attached to the model at a great expense of time. This leads to the fact that one tries to simulate as few load cases as possible. Simultaneously, the measurement is made, which is also very time-consuming, which leads to the tendency to keep the number as small as possible. After the monitored deformations and forces, the evaluation follows. This also must be done manually and consumes additional time. Hossdorf tried to save time and material in the first step, so a modular substructure was made in his laboratory, where the different measuring instruments were mounted [4]. For more or less plane structures, a program-controlled loading device (Fig. 4) was used for the first time in Heinz Hossdorf's laboratory. With this experimental equipment, many of the negative factors from the previous paragraph can be eliminated. This loading carriage can approach any model coordinate with 0.1 mm accuracy. The load can be chosen arbitrarily and applied as often as required. Time-consuming weighing and application of weights are eliminated. For a medium-sized bridge, 100 measuring points can quickly accumulate. With 100 load positions, 10,000 measured values are available. However, it can also run into the hundreds of thousands. Thanks to the computer, the evaluation of these data and the conversion into data that the engineer can use can be done in a few minutes and not in days or weeks, as was previously the case. The read-out values are stored on punch cards. So the inevitable human errors in reading, transmitting and calculating the values are eliminated. Temperature differences or changed bridge voltages can be avoided by calibration measurements as often as required. A xy recorder connected to the system graphically recorded the data on paper [5].

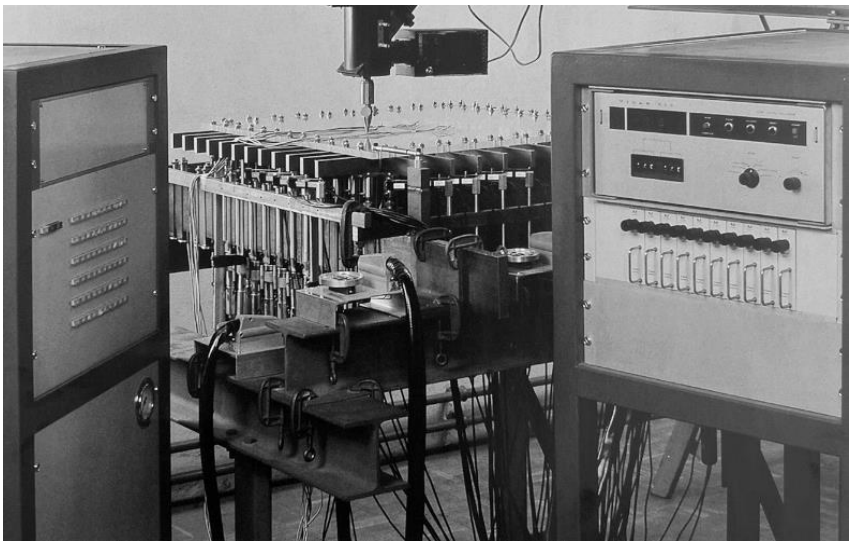


Figure 4. Automatic device for the loading of mostly planar structures [4].

6. Material use

If, as a layman, you see the acrylic resin measuring models, you probably ask yourself why the measuring model was cast from acrylic while the later structure is to be made from reinforced concrete. Of course, the most accurate analogy would be a model made of the same material as the later structure. To understand the use of materials in the models, it is necessary to understand a little about their properties and the principles of the theory of elasticity. The theory of elasticity presupposes a homogeneous continuum, which will be difficult to find in real building materials. Attempts were made to build models from similar rheological materials with similar Young's modulus. The prerequisite was knowledge of the stress-strain diagram and Poisson's ratio, which is the effect of the error effect from the deviation of the transverse contraction coefficient. Also crucial in this context are the principles of Hook's law, which states that the strain depends linearly on the acting force.

Hossdorf saw major problems using micro-concrete since many factors, such as water content and aggregates, can influence the properties. The so-called scale effect also makes micro-concrete a rather poorly suited modelling material. An example of this is the altered proportions of a component's edge and cut surface. The relationship becomes apparent when the area-volume ratio is considered. The area increases quadratically while the volume increases cubically. These differences in the proportion of surface area and interior are neglected in the engineer's usual design methods. Still, in smaller models, they may well carry more weight and must be considered accordingly. “The larger the test specimen compared to the individual “grain”, the smaller the scatter of the measured values. For example, the usual test specimens for concrete have a linear expansion of only about ten times that of the largest individual grain. It would be inconceivable here to reduce the size of the test specimens even further if one wanted to speak at all of a statistical mean value for the interaction of the overall structure. For the same reason, it is impossible to make small models of concrete without at the same time reducing its fine structure [9].” Hossdorf considered acrylic resin a good model building material to simulate concrete elements. Besides the material characteristics, he also saw many advantages in preparing and conducting the elastic tests with acrylic resin. It was easy to process and quickly formed into the desired shape. It is transparent, making it easy to see the weak points in the joints. And it was easier to accurately position the strain gauges on top of each other, which made the measurements more accurate [1]. Since the density of the plastic is much lower than that of concrete, the lack of weight had to be weighted down with weights distributed as evenly as possible to compensate [5].

For his experiments, Heinz Hossdorf did not rely solely on the available materials [5]. In his opinion, there was no perfect material for his model experiments, so he tried to develop more suitable materials

on his own. To do this, he examined various materials, such as plastics, and mixed them with additives such as araldite and aluminium powder [1].

Table 1. Overview of hybrid models tested in Heinz Hossdorf's laboratory. This table is only an excerpt and does not claim to be complete.

Building	**Location**	**Tests**	**Material**	**Year**
University Library	Basel, Switzerland	Elastic tests	Acrylic resin	Appx. 1964
Building system Eurogas	e.g. Genf, Luzern, Switzerland	Probably elastic tests	Epoxy resin	Appx. 1969
High-rise building	Coventry,UK	Probably elastic tests	Acrylic resin	No data found
Support bracket, National Westminster Tower	London, UK	Probably elastic tests	Acrylic resin	Appx. 1977
House Vischer	Basel, Switzerland	Deflection and strain measurement	Timber	Appx.1960
Central warehouse Konsumvereine	Wangen, Switzerland	Probably hydraulic loading	Micro-concrete	Appx. 1959
Pavillon Expo 64	Lausanne, Switzerland / 1965 demolished	Probably elastic tests	Glass-fibre reinforced polyester	Appx. 1962
Municipal theater	Basel, Switzerland	Elastic tests	Acrylic resin	Appx. 1968
Mushroom 1	Maybe Basel, Switzerland	Elastic tests	Acryl resin	Appx. 1968
Bruder-Klaus Church	St. Gallen, Switzerland	Hydraulic loading	Micro-concrete	Appx. 1957-1958
Rudolf Steiner School	Basel, Switzerland	Elastic tests	Acrylic resin	No data found
Auditorium Maximum of the University of Hamburg	Hamburg, Germany	Elastic tests	Acrylic resin	1956
Highrise Sandoz AG Bau 503	Basel, Switzerland	Natural frequency	Acrylic plastic (trade name: Plexiglas)	Appx. 1969
High rise M.G.B	Zürich, Switzerland	Horizontal forces	Acrylic plastic (trade name: Plexiglas)	Appx. 1968

7. Example of a hybrid test

Today the 183 m high building, the second tallest in central London, is called Tower 42. It was built from 1971 to 1979 according to plans by the office of the Swiss-British architect Richard Sieffert as the headquarters of the National Westminster Bank and completed in 1980. The structural principle is a reinforced concrete core clamped into the foundation, from which reinforced concrete brackets cantilever at different heights up to 42 m. Before constructing the physical model, a statics model was calculated by computer. However, since the bracing and cantilevers make it a geometrically complex structure difficult to understand, the commissioned engineers Pell, Frischmann and Partners decided to use Hossdorf's laboratory to conduct a model test that would help to understand the data from the computer analysis [4]. The 1:50 scale acrylic resin model (Fig. 5) was fitted with 200 strain gauges whose output was stored on magnetic tape. This data provided the input for analysis software on a main-frame computer [1]. The data obtained in the experiments were thus digitally preserved, and the results were still reproducible even if the model was lost. Today, over 40 years later, models are predominantly used digitally and no longer hybrid.

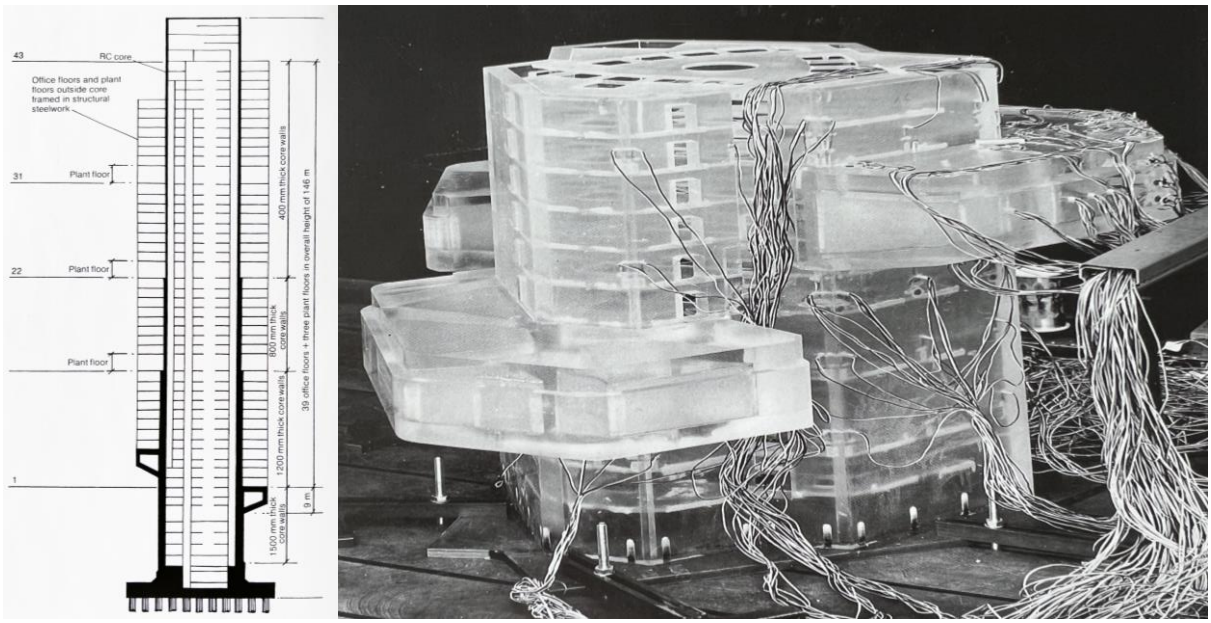


Figure 5. Section and acrylic model of the National Westminster Bank building [4].

8. Comparison of hybrid model and FEM

A comparison of the hybrid models with today's FEM programmes would be very interesting, but is difficult due to several factors. First of all, the data situation has to be mentioned, especially the results obtained by means of the hybrid models. In the sources, mostly only methods and the static system itself are described. Calculated results were only found in graphical tables Hossdorf himself devotes only one page in his nearly 300-page autobiographical work to the comparison of classical computer statics vs hybrid statics [4]. Next, data quality and contextualisation must be considered. The available results, as in Fig. 6, only make it possible to read approximate values. Besides the line width, it remains open where exactly the value indicated by the triangle lies. The most important missing links are the applied load as well as the exact place where it was applied to.

The fact that it is comparatively difficult to obtain data may have to do with the fact that in Switzerland it is not necessary for engineers to record the calculation for buildings being constructed. The authors are currently trying to find contemporary witnesses in order to locate documents that would make it possible to carry out an extensive comparison.

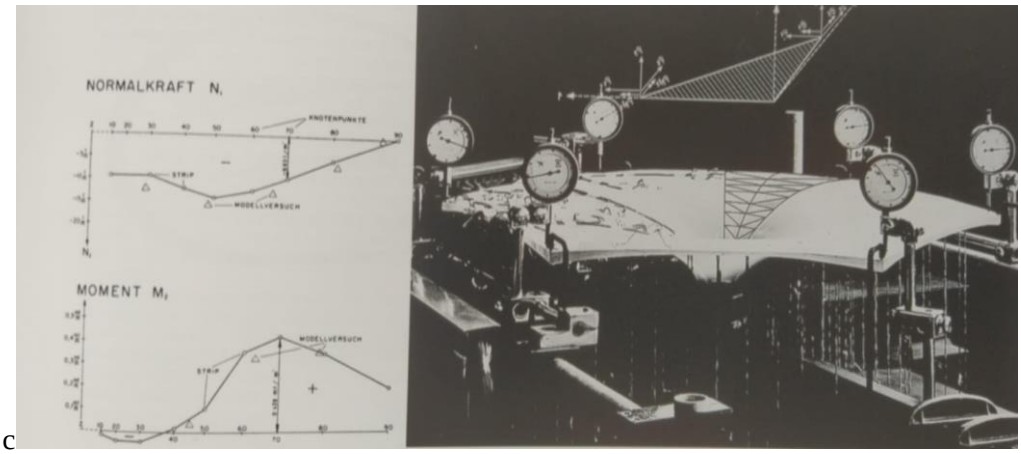


Figure 6. Vergleich Ergebnisse FEM des Strip Programmes und physisches Modell[4].

9. Conclusion and outlook

Hossdorf recognised the potential of the computer as a tool but also as a communication medium very early, which is why he tried to make the use of physical models economical and improve them by optimising their production and measurement technology while at the same time, he wanted to enable the use of virtual models. Hossdorf finally abandoned the physical models altogether which could be a reason that the authors know nothing about the whereabouts of Heinz Hossdorf's models. Since many of the models were tested to the point of destruction or were no longer of importance, and the test facility was dissolved, we must assume that there are, unfortunately, no surviving specimens left.

It is, therefore, all the more important to document the great treasure of knowledge contained in the surveyed witnesses of model testing and to make it available to the public. In order to generate the greatest possible benefit from the surviving physical models found, our results are to be made available to the public as far as possible. This is done within the framework of an ongoing research project, “Last Witnesses”, funded by the German Research Foundation (DFG). For this purpose, an open database is generated, which is fed not only with basic data such as the name of the model, the model scale, the engineer(s), the institute or company, the date of the model, the origin of the model, the current location of the model with contact details, the dimensions of the model, the materials of the model, the description of the model, the location of the project, the date of the start and completion of the project but also with the recorded data of the models and the material stored in archives such as photos, plans and calculations (Fig. 6). However, less common data are also available, such as point clouds and textured polygon meshes. These were acquired in the course of a retro-digitization of still-existing objects and are to be processed into a common web format and made accessible on a homepage within the framework of the research data infrastructure for objects (NFDI4Objects).

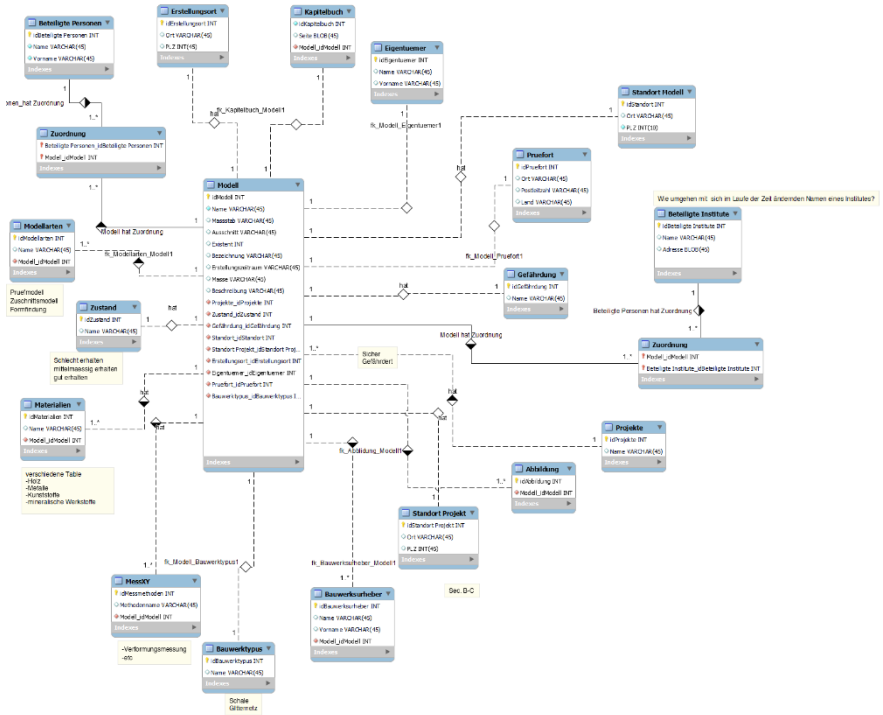


Figure 6. Entity relationship diagram for the database (Baris Wenzel)

References

[1] P. Cassinello, “Heinz Hossdorf: his contribution to the development of physical model testing” in *Physical Models. Their historical and current use in civil and building engineering design*, B. Addis, Ed. Berlin: Wiley Ernst & Sohn, 2020, pp. 551-568.

[2] H. Hossdorf, "Structural Models and Design", *IABSE congress report*, vol. 9, pp. 263-277, 1972.

[3] B. Addis, Ed., *Physical Models. Their historical and current use in civil and building engineering design*, Berlin: Wiley Ernst & Sohn, 2020.

[4] H. Hossdorf, P. Dietz, and J. A. Torroja, *Heinz Hossdorf – Das Erlebnis Ingenieur zu sein*, Basel: Birkhäuser, 2003.

[5] H. Hossdorf, *Modellstatik*, Gütersloh: Bauverlag, 1971.

[6] H. Schnetzer, "Sprunghafter Pionier", *TEC21*, vol. 140, pp. 26-27, 2014.

[7] s.n., "Die Anwendung der Modelltechnik in der Statik: ein Gespräch mit Ingenieur Heinz Hossdrof", *Das Werk: Architektur und Kunst*, vol. 59, pp. 454-455, 1972.

[8] T. Ekwall, "Die Modelle wurden extern kaum geprüft", *TEC21*, vol. 140, pp. 32-35, 2014

[9] H. Hossdorf, "Modellversuchstechnik des entwerfenden Bauingenieurs" *Schweizerische Bauzeitung*, vol. 81, pp. 277-283, April 1963. [Online]. Available: http://doi.org/10.5169/seals-66775 [Accessed March. 07, 2023]

Lattice structures

Active bending
Additive manufacturing/ 3D printing
Architectural geometry
Bamboo for sustainable construction and quality of life improvement
Bio-inspired structures and architecture
Bridge structures
Computational form-finding
Conceptual design
Concrete structures
Construction techniques
Deployable and inflatable structures
Design competition (WG21)
Digital modelling and fabrication
Dynamic response of metal spatial structures
Dynamic response of other structures
Form-finding and structural optimisation of interlocking discrete assemblages
Graphical methods
Gridshell and lattice structures
Historical concrete shells
Historical structures
► **Lattice structures**
Life-cycle design and assessment of structures
Metal gridshell structures, connections and stability
Methods and construction technologies for sustainable shell structures
Morphology and configuration processing
Next generation parametric design
Novel methods in modelling, optimisation and construction for reducing carbon footprint of continuous roof shells
Numerical methods for geometry, form-finding and optimisation of lightweight structures
Optimisation methods and applications
Origami
Other
Teaching design uncertainty: working with unknown qualities/quantities of new and re-claimed materials
Teaching of shell and spatial structures
Tensegrity systems and cable structures
Tension and membrane structures
Tension structures in the Asia-Pacific
Timber and bio-based structures
Topology optimisation
Traditional masonry structures and innovation
Transformable structures

Proceedings of the IASS Annual Symposium 2023
Integration of Design and Fabrication
10–14 July 2023, Melbourne, Australia
Y.M. Xie, J. Burry, T.U. Lee and J. Ma (eds.)

Structural design of a public library with lamella shell roof

Yoshiharu KANEBAKO[a,*], Yasuhiro MOCHIZUKI[a]

[a,*] Kanebako Structural Engineers
3-12-14, Nishigotanda, Shinagawa-ku, Tokyo, Japan
kanebako@kanebako-se.co.jp

Abstract

Structural design of a public library with single-layered lamella shell roof is introduced in this paper. The building is 76 meters by 66.5 meters in planer size, with four floors and one basement floor. There are a large reading room through the ground floor to the third floor, which is continuously connected by step-floors and slopes. The large reading room named “Great Hall” is covered with flat roof, which is supported with dome shaped lamella shell structure. The planer shape of lamella dome is ellipse. The members of dome structure are arranged diagonally in two directions to form a diamond-shaped grid. Since there are no circular members, the dome doesn’t have the properties of a triangular grid dome, and is closer to the stress state of arch. The members are jointed with pin-joint because the joint details would be simple, and vertical members are arranged at the intersections of the diamond-shaped grid and connected to the bending rigid members of the flat roof. The elastic buckling strength of the roof structure has 8 times strength as design load.

Keywords: metal spatial structure, lamella shell, lattice shell, buckling strength of dome structure

1. Introduction

Structural design of a public library with single-layered lamella shell roof is introduced in this paper. The building is 76 meters by 66.5 meters in plain size, with four floors and one basement floor. There are a large reading room named “Great Hall” through the ground floor to the third floor, which is continuously connected by step-floors and slopes, and has circular grid. The basement floor was used for closed stacks, and the structural grid is rectangular. The grid of upper ground floor is different from the basement floor, and it is an important issue of this structural design. The most important issue is a structural design of roof covering the Great Hall.



Figure 1. Outer View.

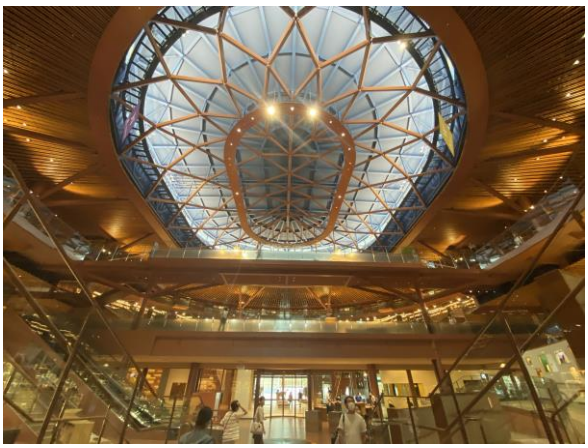


Figure 2. Inner View of Reading Room.

Copyright © 2023 by Yoshiharu KANEBAKO and Yasuhiro MOCHIZUKI. Published in the Proceedings of the IASS Annual Symposium 2023 with permission.

2. Structure of the building

Figure 4 shows the structural section of the building. A base-isolated structure was adopted to enhance seismic safety and to maintain its function as a library after an earthquake. The basement floor is a rigid-frame structure with seismic resistant walls, and the beam of the ground floor is used with steel reinforced concrete and steel. While the structural frame has a rectangular grid for the basement floor, the structure of the upper floor is used a steel rigid frame with an elliptical grid. Therefore, the structural grid is not matched as the grid of the basement in some areas, and steel columns are placed on the steel beams of the ground level. Because the rigidity of the steel frame upper the ground level is not sufficient to act as isolation structure, the concrete confined steel pipe columns (CFT column) are arranged at the perimeter. Stair-stepped steel beams and stepped slabs are used for floors and slopes.



Figure 3. Inner View of Great Hall.

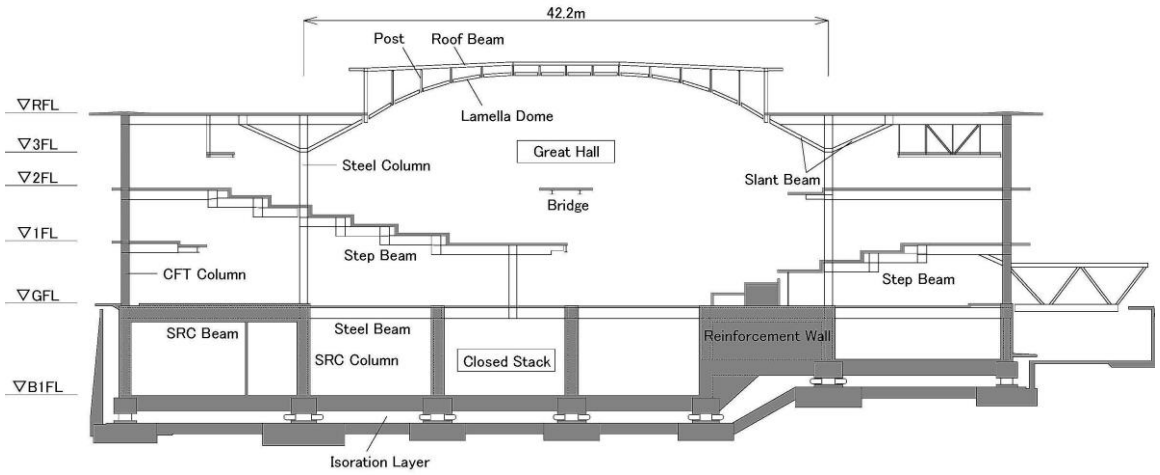
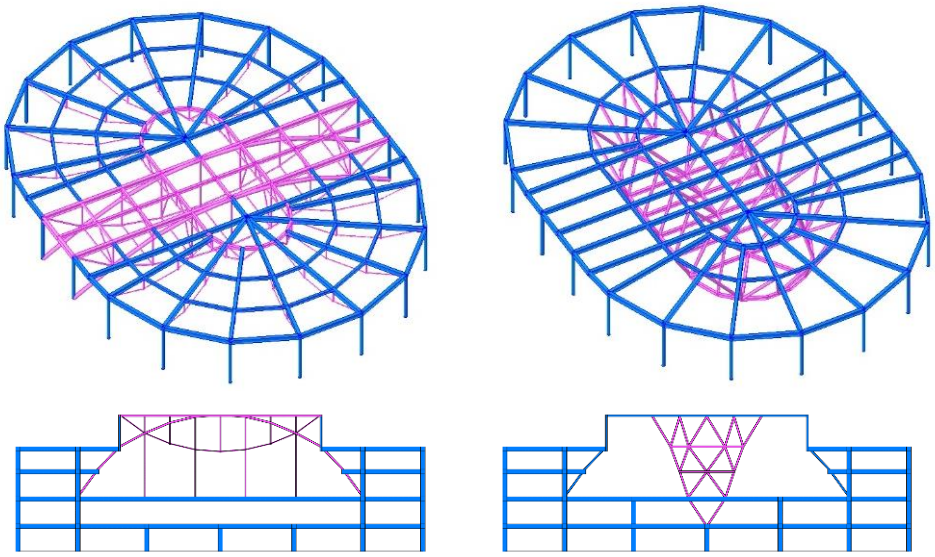


Figure 4. Structural Section.

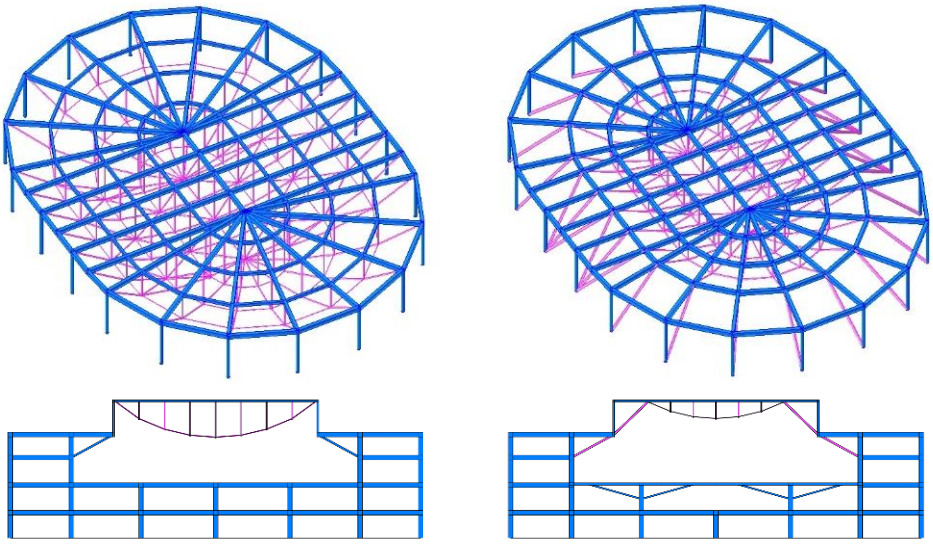
3. Structural System of the roof

3.1 Structure design process of the roof structure

Various types of structure for the roof of the reading room were considered in the schematic design phase. The plan of the room was rectangle in shape, and the center of the roof should rise in an elliptical shape. The elliptical dome is 42.2 meters by 34.2 meters in planer size A bridge across the room was required to be placed in the center of the room. Various ideas for the bridge and the roof structure were considered. Figure 5 shows several combined ideas for the bridge and roof structure. At first, we considered to use the central bridge as a keel structure to support the roof shown in figure A) or B).



A) Bridge: Suspen-arch, Roof: BSS B) Bridge: Tree shape structure, Roof: Simple beam



C) Roof: BSS D) Roof: BSS and slant Coolum

Figure 5. Structural Ideas of the Bridge and the Roof.

For the roof structure, beam string structures (BSS), truss structures and tree shape structures were considered. A truss structure and a beam string structure don't cause horizontal reaction; therefore, it is easy to be supported by the under structure. In this case the center of the roof is convex downward. However, sufficient height in the center of the room was required from an architect aspect. The structure like a dome and an arch were studied to satisfy the architectural request.

The final structural idea is shown Figure 6, which is an irregular single-layer lamella dome with a diamond-shaped grid of members arranged diagonally in two directions in an elliptical plane, topped by the roof support structure. The ratio of rise-span is 6.5 as shortage direction and 8.9 as longitude direction. The feature of this grid is not existing circumferential members, so it does not have the properties of a triangular grid dome (shell). It is closer to the stress state as a collection of arches (Figure 7). The arrangement and size of members were determined by manual design based numerical analysis.

To simplify the joint details, the members are connected used pin-joints. In this case, it is unstable against unbalanced vertical and horizontal loads, so post members are provided at the intersections of the diamond-shaped grid and connected to the bending rigid members of the top roof. It is important to deal of the thrust in this structure. It is efficient to arrange the arch members down to the floor level to transfer the axial force, but this was not possible due to the architectural plan. Therefore, the arches are supported by columns, and diagonals members are placed at the opposite side of the column for axial to transfer axial force to the roof (Figure 8). The thrust is resisted by the ring-like restraint effect of the surrounding roof slab.

3.2 Member Shape and Joint Detail

The feature of this structure is that many members are existed and jointed with various angles at the intersection point. Therefore, a universal joint system was required. Steel pipe is the most effective member for axial force, but when bolt joints are used, gusset plates must be used at the end of members, and may breaks visually continuity of the member (Fig.9A). If T-shaped members or angle shaped members are used back-to-back, and are fastened with bolts directly to gusset plates, visual continuity can be maintained (Fig.9B). But bolts at the joints will be visible. An original detail was proposed for this project. The angle members were assembled with the corners facing outward, and were attached the plates on the inside of the members at the both ends. When they were bolted to the gusset plates (Fig.9C), the continuity of members were realized used this method (Fig.10). The size of angle section member

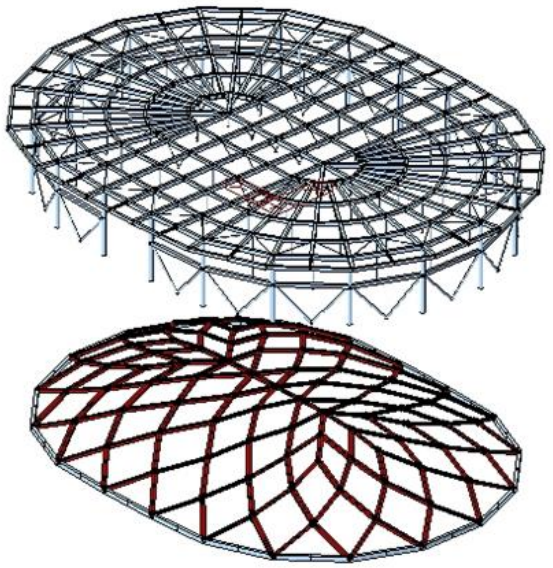


Figure 6. Structural Ideas of the Roof.

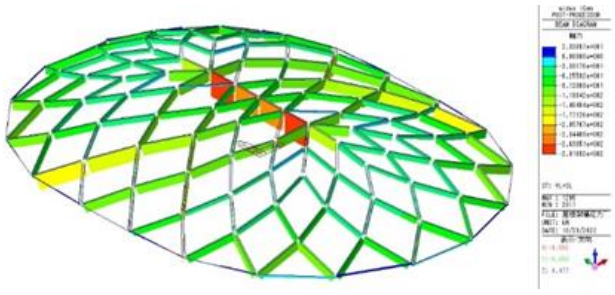


Figure 7. Stess Analysis Result of the vertical load.

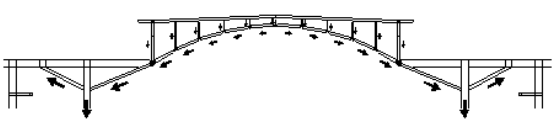
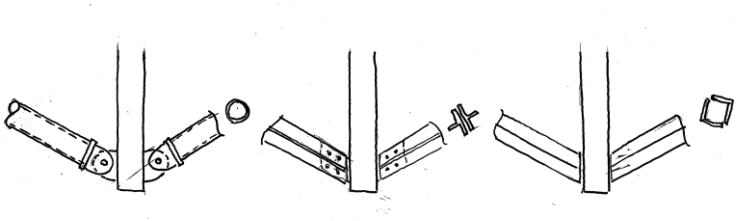


Figure 8. Stress Flow.

is 150 mm x 150 mm. Since the gusset plates are attached to members at various angles, the plates were welded to vertical steel post members. The ends of the members were chipped on one side when they were joined (Fig.11), and a cover plate was welded after the bolts were fastened (Fig.12). After completion, the members are distinctive box-shaped with emphasized edges. The members of rooftop are H-shaped beams.

4. Buckling Strength Evaluation of the Roof

The site is height snowfall area, and the amount of snow depth for design is 215 cm depth. Buckling load evaluation of the roof was important for this project. The buckling strength is dominated by the



A) Pipe B) T Shaped C) Angle

Figure 9. Diference of joint shape.



Figure10. Continuity of Members.



Figure11. Before Bolt Fasteing.

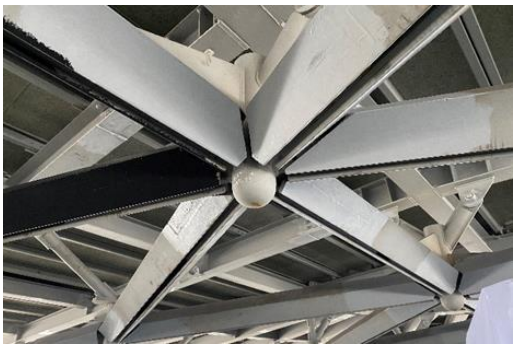


Figure12. After Bolt Fasteing.

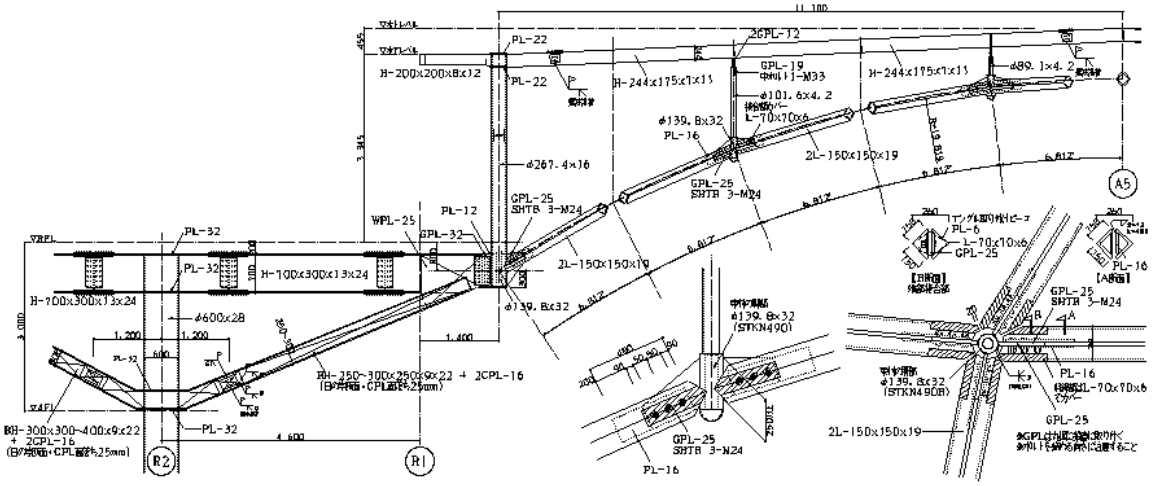


Figure13. Structural Detail Lamella Dome and Roof.

minimum amount of member buckling strength and shell-like buckling strength. The member buckling strength is calculated using buckling length of each member. The shell-like buckling strength is investigated by the method included Report of Activity of IASS WG8[1)]. Firstly, elastic buckling analysis was performed. When the generalized slenderness ratio λ_c is defined Eq. (1), the buckling strength of axial member is defined Eq. (2), (3) by the design code for allowable stress design of steel structure defined by AIJ.

$$\lambda_c = \sqrt{N_y / N_{cr}^{el}} \tag{1}$$

N_y: yield force, N_{cr}^{el}: elastic buckling load

$$\text{for } \lambda_c \leq 1.29 \qquad N_{cr} = \left(1 - 0.24{\lambda_c}^2\right)/\left(1 + 4{\lambda_c}^2/15\right) N_y \tag{2}$$

$$\text{for } \lambda_c \geq 1.29 \qquad N_{cr} = 1/\left(1.2{\lambda_c}^2\right) N_y \tag{3}$$

The buckling strength depend on the rotational stiffness of the joint and the bending stiffness of the roof beam. The joint is assumed pin connection in this structure; therefore, the top roof beam is important element to enhance buckling strength (Figure 14). Figure 15 shows the first buckling mode. The buckling mode is not individual member buckling of lamella dome but the anti-symmetry mode of the arch. The amount of the elastic buckling load was confirmed to be about 8 times that of the vertical design load. The generalized slenderness ratio λ_c defined Eq. (1) is 0.769, and the value of N_{cr}/N_y is 0.741. On the other hand, the value of N_{cr}/N_y for the buckling strength depended on the member buckling is 0.313. As a result, the buckling strength depends on the member buckling, and the safety factor is 0.59 for the buckling against vertical load.

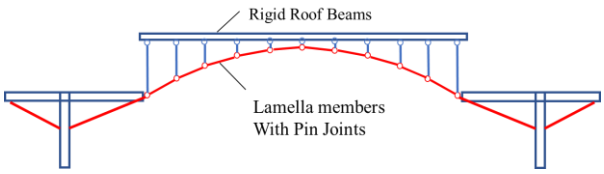


Figure 14. Relation Lamella Members and Beams.

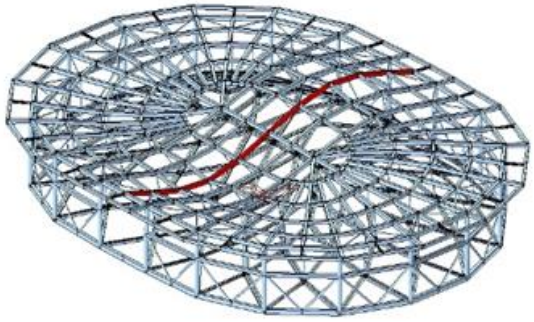


Figure 15. 1st Buckling Mode.

5. Conclusion

A structural design of a distinctive roof with single-layered lamella shell is introduced in this paper. Lamella dome structure without circumferential member acts like arch, and its joints are used pin joint. It is important for this project to handle the thrust force and to enhance buckling strength of pin-jointed arches with the flat roof beams. Distinctive feature of structure was realized by using combination of angle members.

References

[1] IASS WG8 (Chair: Shiro Kato), "Guide to Buckling Load Evaluaton of Metal Reticulated Roof Structurees": *Report of Activity of IASS WG8*, 2014.

IASS 2023
July 10–14 Melbourne
Integration of Design and Fabrication

Proceedings of the IASS Annual Symposium 2023
Integration of Design and Fabrication
10-14 July 2023, Melbourne, Australia
Y.M. Xie, J. Burry, T.U. Lee and J. Ma (eds.)

Structural optimization of lattice shells with geometric nonlinearity using machine learning

Yuma YABUUCHI*, Shinnosuke FUJITA[a]

[a,*] The University of Kitakyushu
Hibikino, Wakamatsu-ku, Kitakyushu, Fukuoka 808-0135, Japan
d2mbb021@eng.kitakyu-u.ac.jp

Abstract

In this paper, prediction models of the nonlinear buckling load calculated by the geometric nonlinear analysis are constructed by supervised learning for lattice shells composed of steel pipes. Then, structural optimization was performed using the obtained prediction models. Specifically, shell shapes with high nonlinear buckling loads are generated in realistic computational time by solving optimization prob-lems in which nonlinear buckling load calculations are replaced by the obtained prediction models. The effectiveness of the proposed method is verified through several numerical examples.

Keywords: lattice shell, form finding, machine learning, geometric nonlinearity

1. Introduction

In recent years, with advances in analytical techniques, optimization methods have been introduced into the field of architectural engineering, and there has been many studies of obtaining optimal shell shapes, cross-sections, or topologies with high structural rationality [1-3].Since most of those previous studies are intended for use in the early stages of structural design, structural performances are usually evaluated only in the linear elastic range. However, shell structures can be affected by geometric nonlin-earity, so optimization that takes structural performances only in the linear elastic range as the objective functions is not necessarily optimized for actual structural performances. Although the computational morphogenesis proposed in previous studies has usually complex and free form, such structure requires large computational cost to carry out geometric nonlinear analysis. Therefore, if the structural behaviour in the linear-range diverges from that of nonlinear-range, it may be necessary to modify the structural form obtained by the previous optimization methods considering only linear range through repeated trial and error with huge computational time. It is difficult to directly consider the geometric nonlinearity in the process of computational morphogenesis due to the problem of computational cost. On the other hand, machine learning, a type of artificial intelligence, has been applied to structural optimization in recent years to shorten optimization time and reduce computational cost [4-5].

Therefore, in this study, a prediction model of geometric nonlinearity is constructed using machine learn-ing, and the geometric nonlinear analysis that is repeatedly performed in the structural optimization pro-cess is replaced by this prediction model in order to solve the computational time problem and extend the structural optimization methods to the nonlinear range.

2. Method for creating analytical models

The nodal cordinates of shell structures are discretized by a B-spline surface with $(I+1)\times(J+1)$ control point nets. The vector of x-,y- and z-coordinates of each control point is denoted by q_x, q_y and q_z as follows:

Copyright © 2023 by Shinnosuke FUJITA and Yuma YABUUCHI. Published in the Proceedings of the IASS Annual Symposium 2023 with permission.

$$\begin{aligned}
\boldsymbol{q}_x &= \begin{bmatrix} q_{x,00} & \cdots & q_{x,0J} & \cdots & q_{x,I0} & \cdots & q_{x,IJ} \end{bmatrix}^\top \\
\boldsymbol{q}_y &= \begin{bmatrix} q_{y,00} & \cdots & q_{y,0J} & \cdots & q_{y,I0} & \cdots & q_{y,IJ} \end{bmatrix}^\top \\
\boldsymbol{q}_z &= \begin{bmatrix} q_{z,00} & \cdots & q_{z,0J} & \cdots & q_{z,I0} & \cdots & q_{z,IJ} \end{bmatrix}^\top
\end{aligned} \tag{1}$$

If the number of nodes is n, the nodal coordinate vector r is expressed as follows:

$$\begin{aligned}
\boldsymbol{r} &= \begin{bmatrix} \boldsymbol{x} & \boldsymbol{y} & \boldsymbol{z} \end{bmatrix} \\
\boldsymbol{x} &= \begin{bmatrix} x_1 & \cdots & x_n \end{bmatrix}^\top \\
\boldsymbol{y} &= \begin{bmatrix} y_1 & \cdots & y_n \end{bmatrix}^\top \\
\boldsymbol{z} &= \begin{bmatrix} z_1 & \cdots & z_n \end{bmatrix}^\top
\end{aligned} \tag{2}$$

Is this case, the nodal coordinates are discretized as follows:

$$\begin{aligned}
x_k &= \sum_{i=0}^{I} \sum_{j=0}^{J} q_{x,ij} \boldsymbol{B}_{i,N}(u_k) \boldsymbol{B}_{j,M}(v_k) \qquad (k = 1, \cdots, n) \\
y_k &= \sum_{i=0}^{I} \sum_{j=0}^{J} q_{y,ij} \boldsymbol{B}_{i,N}(u_k) \boldsymbol{B}_{j,M}(v_k) \qquad (k = 1, \cdots, n) \\
z_k &= \sum_{i=0}^{I} \sum_{j=0}^{J} q_{z,ij} \boldsymbol{B}_{i,N}(u_k) \boldsymbol{B}_{j,M}(v_k) \qquad (k = 1, \cdots, n)
\end{aligned} \tag{3}$$

where, u_k and v_k is the parameter corresponding to the nodal coordinate of the $k-$th node. $B_{i,N}(u)$ and $B_{j,M}(v)$ are the B-spline basis functions. N and M are the orders of the functions.

3. Prediction methods using machine learning

Neural network that is a type of machine learning is used to predict nonlinear buckling load factor of shell structures. A neural network is a computational graph made by connecting differentiable transformations, as shown in Fig. 1, and consists of three layers an input layer, an middle layer, and an output layer. In Fig. 1, the nodes represented by circles contain numerical values, and the vertical set of these nodes in called a layer. The first layer represents the input variables for prediction, and is called the input layer.

As shown in Fig. 1, when the relationship between input vector and output vector are nonlinear, it is necessary to transform the output vector to the input vector in the middle layer nodes. The function to perform this transformation is called an activation function, and in this paper, we use an activation function called Reacted Linear Unit (ReLU) [6].The ReLU is a function as shown in Fig. 2, and is represented by the following equation:

$$\mathrm{ReLU}(a) = \begin{cases} a & \text{if}(a \geq 0) \\ 0 & \text{else} \end{cases} \tag{4}$$

ReLU is a function that always outputs 0 when the input is negative and outputs the same value as the input value when the input is positive. By repeating the above calculation until the output layer node becomes 1. the predicted value y can be obtained.

When the number of learning data is N, the neural network determines the parameter vector W obtained by the following equation:

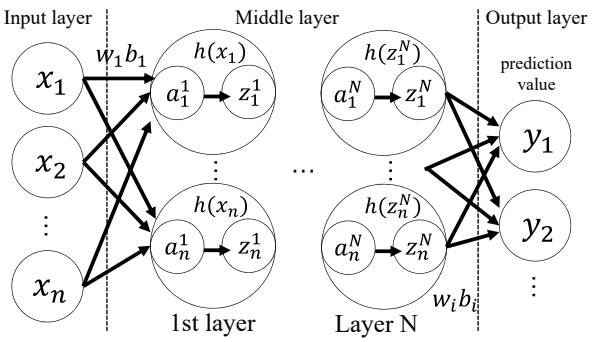


Figure 1: Neural Network calculation flow

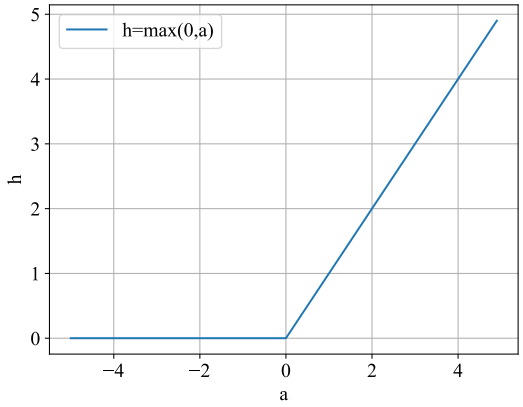


Figure 2: ReLU

$$\underset{\boldsymbol{W}}{\text{minimize}} \quad \text{MSE} = \sum_{n=1}^{N} (t_n - y_n)^2 \tag{5}$$

$$\boldsymbol{y} = \begin{bmatrix} y_1 & \dots & y_n \end{bmatrix}$$
$$\boldsymbol{t} = \begin{bmatrix} t_1 & \dots & t_n \end{bmatrix}$$

N : Number of data
W : Parameter vector
$\boldsymbol{y}$: Prediction value vector
$\boldsymbol{t}$: Target value vector

By inputting the obtained parameter vectors and the input variables of the prediction model, the predictions of the prediction model can be obtained.

Neural networks are built using Keras [7], a high-level neural network library written in Python that can be run on TensorFlow [8].

4. Prediction model building

In this paper, nonlinear buckling load facotor is considered as the objective function for geometric nonlinearity. The nonlinear buckling load factor, which is repeatedly required during shape optimization, is predicted by a neural network. The calculation of the nonlinear buckling load factor takes into account the initial shape imperfections corresponding to the linear first buckling mode obtained from linear buck-ling analysis. First, linear buckling analysis is performed on lattice shells created by randomly placing control point *z*-coordinates. Then, initial shape imperfections based on the first-order buckling mode are applied to those shells with an amplitude of 1/1000 of the span. Subsequently, a geometric nonlinear analysis is repeatly performed on those shells with initial shape imperfection to generate training data.

The nonlinear buckling load factor is calculated by incremental analysis based on the arc-length increment method. Linear buckling analysis and geometric nonlinear analysis are performed using Opensees [9].

5. Formulation of optimization problems

In this paper, four multi-objective optimization problems are considered in problems (6) to (9). In these optimization problems, the nonlinear buckling load factor is maximized under volume constraints, in addition to minimizing the linear elastic strain energy, as is often carried out in conventional optimization approach. To examine the correlation between the nonlinearity of the equilibrium path and the prediction accuracy, (the prediction values of) the nonlinear buckling load factor are defined as $\lambda^{\mathrm{p}}_{1/100}$, $\lambda^{\mathrm{p}}_{1/50}$, $\lambda^{\mathrm{p}}_{1/25}$, and $\lambda^{\mathrm{p}}_{1/20}$ for displacements up to 1/100, 1/50, 1/25, and /20 of the span, respectively, which are the objective functions for problems (6) to (9). An overview of how nonlinear buckling load factor are defined and an example of a load-displacement curve for a geometry in the learning model are shown in Fig.3 and Fig.4. In this study, λ^{p} is defined as the load factor at the point when the tangential stiffness turns negative, but if no buckling point exists within the specified displacement range, λ^{p} is defined as the load factor at the point when the maximum specified displacement is reached. Therefore, note that in cases with small displacement reference ranges, such as $\lambda^{\mathrm{p}}_{1/100}$, the structure may not yet have buckled. Optimization calculations are performed using MIDACO [10], a multi-objective optimization solver that uses ant colony optimization, a type of heuristic method.

$$\begin{aligned} &\underset{\boldsymbol{q}_z}{\text{minimize}} && \begin{cases} -\lambda^{\mathrm{p}}_{1/100} \\ f \end{cases} \\ &\text{subject to} && \begin{cases} V \leq \overline{V} \\ -5.0 \leq \boldsymbol{q}_z \leq 20.0 \end{cases} \end{aligned} \tag{6}$$

$$\begin{aligned} &\underset{\boldsymbol{q}_z}{\text{minimize}} && \begin{cases} -\lambda^{\mathrm{p}}_{1/50} \\ f \end{cases} \\ &\text{subject to} && \begin{cases} V \leq \overline{V} \\ -5.0 \leq \boldsymbol{q}_z \leq 20.0 \end{cases} \end{aligned} \tag{7}$$

$$\begin{aligned} &\underset{\boldsymbol{q}_z}{\text{minimize}} && \begin{cases} -\lambda^{\mathrm{p}}_{1/25} \\ f \end{cases} \\ &\text{subject to} && \begin{cases} V \leq \overline{V} \\ -5.0 \leq \boldsymbol{q}_z \leq 20.0 \end{cases} \end{aligned} \tag{8}$$

$$\begin{aligned} &\underset{\boldsymbol{q}_z}{\text{minimize}} && \begin{cases} -\lambda^{\mathrm{p}}_{1/20} \\ f \end{cases} \\ &\text{subject to} && \begin{cases} V \leq \overline{V} \\ -5.0 \leq \boldsymbol{q}_z \leq 20.0 \end{cases} \end{aligned} \tag{9}$$

$\lambda^{\mathrm{p}}_{1/100}$: Predicted maximum nonlinear buckling load factor in the range up to span × 1/100 deformation
$\lambda^{\mathrm{p}}_{1/50}$: Predicted maximum nonlinear buckling load factor in the range up to span × 1/50 deformation
$\lambda^{\mathrm{p}}_{1/25}$: Predicted maximum nonlinear buckling load factor in the range up to span × 1/25 deformation
$\lambda^{\mathrm{p}}_{1/20}$: Predicted maximum nonlinear buckling load factor in the range up to span ×1/20 deformation
f : Linear elastic strain energy[kNm]
$\boldsymbol{q_z}$: z-coordinate vector of control point[m]
V : Total volume of the lattice shell[m^3]
$\overline{V}$: Upper limit of the total volume of the lattice shell[m^3]

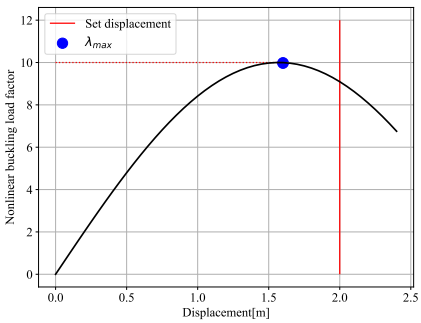


Figure 3: Difinition of load factor

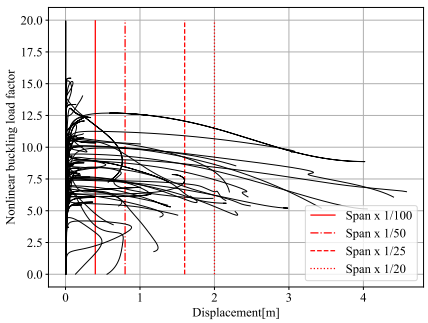
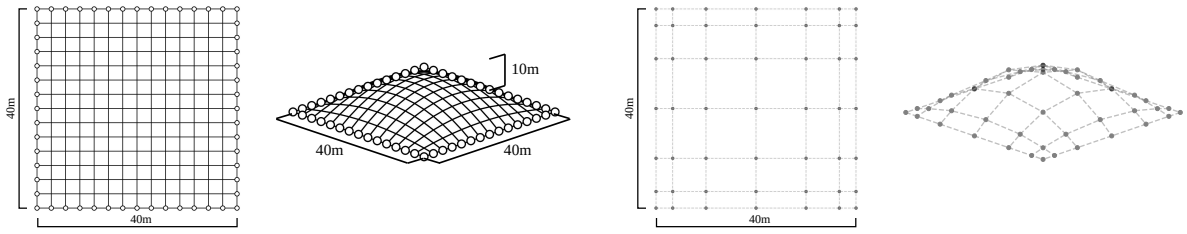


Figure 4: Example of a Load-Displacement curve for a learning model

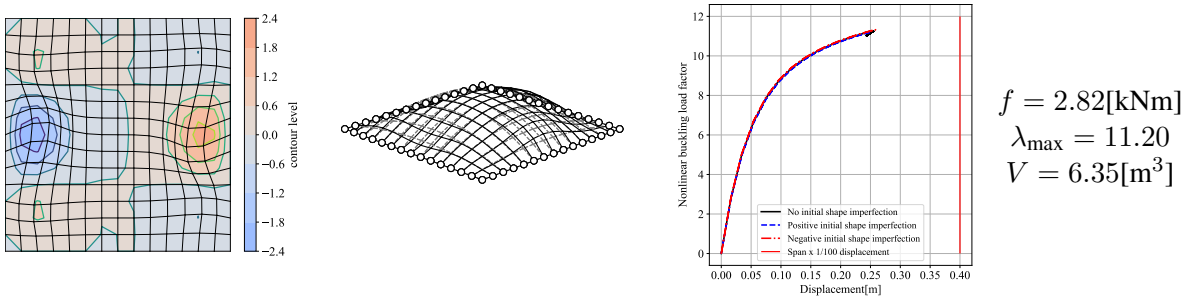
6. Numerical examples

For numerical examples, the lattice shells with pin support all around shown in Fig. 5 is considered as an analytical model. The analytical model consists of a 15×15 grid with a square plane of 40 m on a side and a rise of 10 m. The shape is discretized by a 3rd-order B-spline surface with 7×7 grid control net. The cross section of all members are steel pipes with an external diameter of 267.4 mm and a thickness of 6.0 mm. For each member, the unit weight, Young's modulus, and Poisson's ratio are set to 77kN/m^3, 205GPa, and 0.3, respectively. Symmetry is taken into account in this study, with the z-coordinate vector of control point in the one-fourth region as design variables and the other z-coordinate vector of control point determined dependently from symmetry. The condition for stopping the optimization calculation by MIDACO is when the calculation time reaches 12 hours. Computation was carried out on 4.20GHz Intel i7-7700K processor with 64GB RAM.



(a) Shell shape (b) Control points

Figure 5: Initial model



(a) Linear first-order buckling mode for initial model (b) Load-Displacement curve

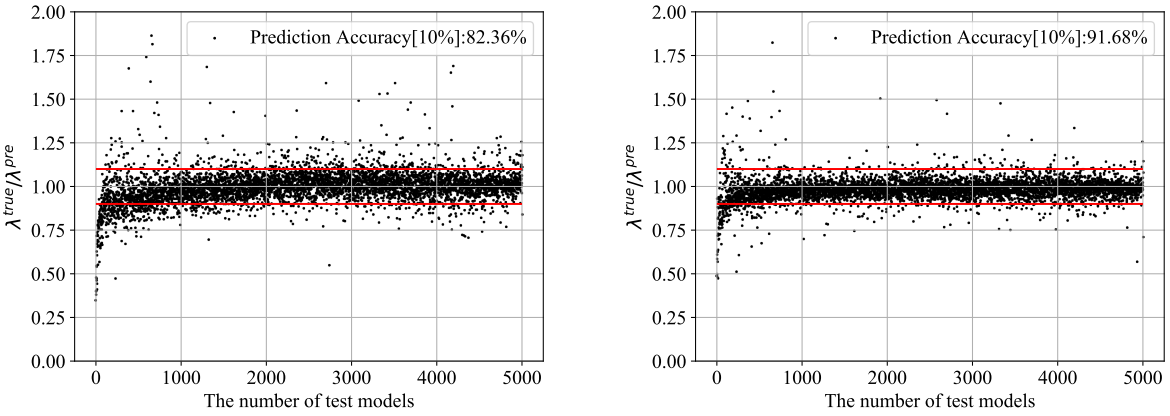
Figure 6: Mechanical performance of initial model

7. Machanical performance to be predicted

In this study, the nonlinear buckling load factor $\lambda^{p}_{1/100}$, $\lambda^{p}_{1/50}$, $\lambda^{p}_{1/25}$ and $\lambda^{p}_{1/20}$ is predicted by the neu-ral network. First, 90,000 learning models and 5,000 test models with randomized control point z-coordinates of the analytical model in Fig. 5 are prepared while one-fourth symmetry condition is maintained. The prediction accuracy of the prediction model is evaluated by the 5,000 test models. Prediction accuracy in this study refers to the ratio of the true value λ^{true} divided by the predicted value λ^{p} that falls within the range $0.9 \leq \lambda^{true}/\lambda^{p} \leq 1.1$. Adam [11] is used as the optimizer to solve the Eq. (5), and its learning rate is set to 0.0001. Hyperparameters are validated using a total of 4 combinations; 5 middle layers; 32 and 64 batch sizes; and 100 and 200 epochs. Create a prediction model using the hyperparam-eters with the lowest MAE for the test model.
The accuracy of the prediction model through 5,000 test models are shown in Table. 1 and Fig. 7. The results of the training showed that the hyperparameters with 5-layers, 32 batch size, and 200 epochs had the highest prediction accuracy for $\lambda^{p}_{1/50}$, $\lambda^{p}_{1/25}$ and $\lambda^{p}_{1/20}$, 5-layers, 32 batch size, and 100 epochs for $\lambda^{p}_{1/100}$, respectively. Fig. 7 shows that the prediction accuracy is more than 80 % for any output function, and the predicted value for the true value is generally within 1.0.

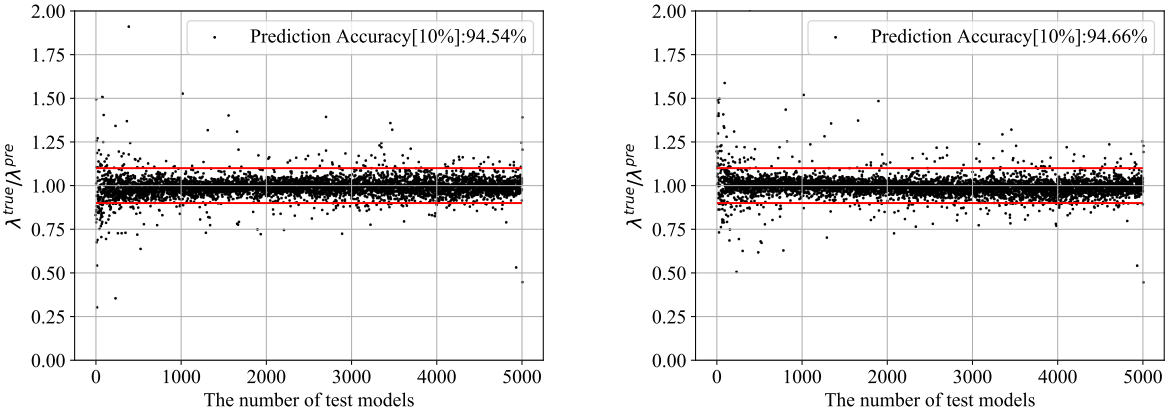
Table 1: Prediction accuracy table

Output function	Epochs	Batch size	$\lambda^{true}/\lambda^{p}$[%]
$\lambda^{p}_{1/100}$	100	32	82.36
		64	69.45
	200	32	81.24
		64	79.74
$\lambda^{p}_{1/50}$	100	32	83.18
		64	90.40
	200	32	91.68
		64	91.06
$\lambda^{p}_{1/25}$	100	32	91.28
		64	93.32
	200	32	94.54
		64	93.30
$\lambda^{p}_{1/20}$	100	32	92.44
		64	93.42
	200	32	94.12
		64	94.66



(a) $\lambda^{\mathrm{p}}_{1/100}$

(b) $\lambda^{\mathrm{p}}_{1/50}$



(c) $\lambda^{\mathrm{p}}_{1/25}$

(d) $\lambda^{\mathrm{p}}_{1/20}$

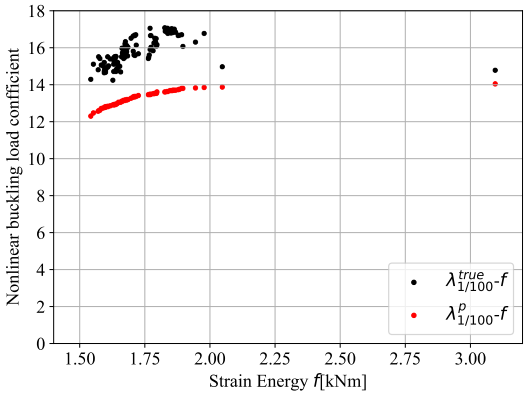
Figure 7: Prediction accuracy for machine learning

8. Shape optimization result

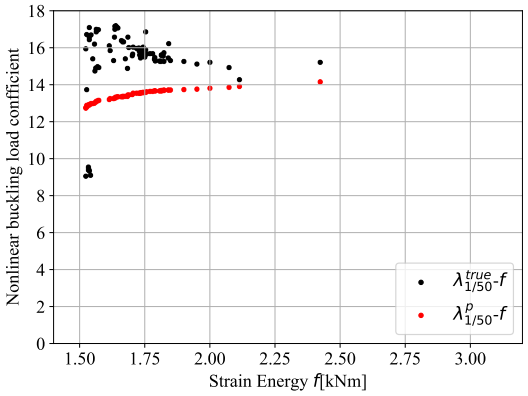
The pareto front of the multi-objective optimization results from problem (6) to (9) is shown in Fig. 8. The figure shown the pareto front of λ^{p}-f at optimization, together with λ^{true}-f for which a geometric nonlinear analysis was performed on the pareto front solution. From the figure, prediction value tend to be underestimated relative to true value.

The form with minimum strain energy and maximum true nonlinear buckling load factor in the pareto front is shown in Fig. 10 to Fig. 13. As a comparison, the shape with single objective optimization of strain energy is shown in Fig. 14.

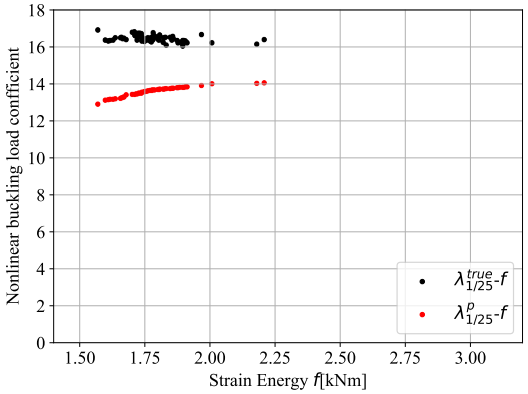
Fig. 8 shows a summary of the pareto front for true values and strain energy. The figure shows that the true values and strain energy are generally in a trade-off relationship, with the true nonlinear buckling load factor being at most about 1.5 times higher than the initial shape.



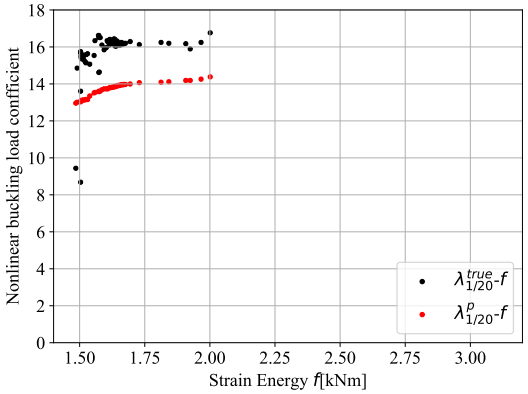
(a) Pareto front with $\lambda^{\mathrm{p}}_{1/100}$-$f$ and $\lambda^{\mathrm{true}}_{1/100}$-$f$



(b) Pareto front with $\lambda^{\mathrm{p}}_{1/50}$-$f$ and $\lambda^{\mathrm{true}}_{1/50}$-$f$



(c) Pareto front with $\lambda^{\mathrm{p}}_{1/25}$-$f$ and $\lambda^{\mathrm{true}}_{1/25}$-$f$



(d) Pareto front with $\lambda^{\mathrm{p}}_{1/20}$-$f$ and $\lambda^{\mathrm{true}}_{1/20}$-$f$

Figure 8: Pareto front from problem (6) to problem (9)

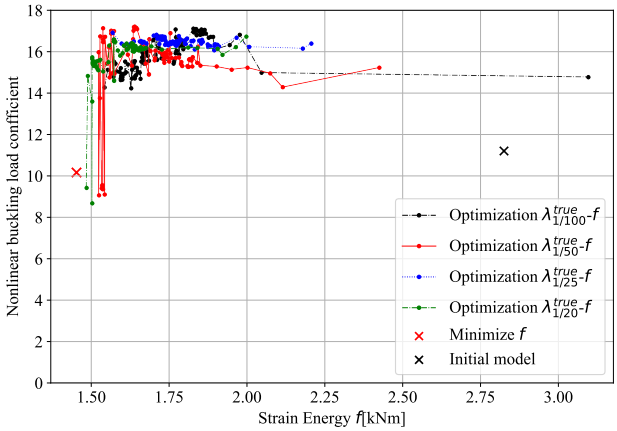
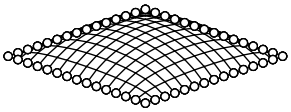
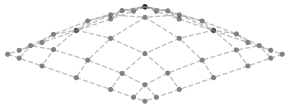


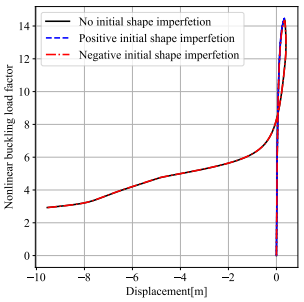
Figure 9: Summary of pareto front in λ^{true}-f



(a) Shell shape

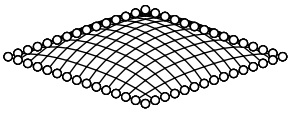


(b) Control points

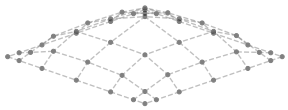


(c) Mechanical performance Min f

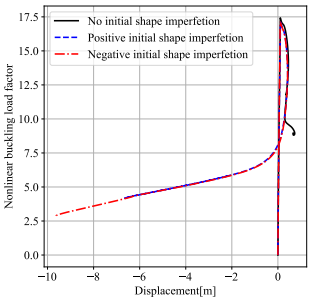
$f = 1.54[\mathrm{kNm}]$
$\lambda^{\mathrm{p}}_{1/100} = 12.34$
$\lambda^{\mathrm{true}}_{1/100} = 14.30$
$V = 6.35[\mathrm{m}^3]$



(d) Shell shape



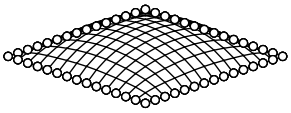
(e) Control points



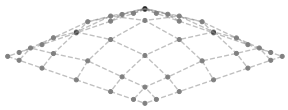
(f) Mechanical performance Max λ^{true}

$f = 1.82[\mathrm{kNm}]$
$\lambda^{\mathrm{p}}_{1/100} = 13.60$
$\lambda^{\mathrm{true}}_{1/100} = 17.09$
$V = 6.35[\mathrm{m}^3]$

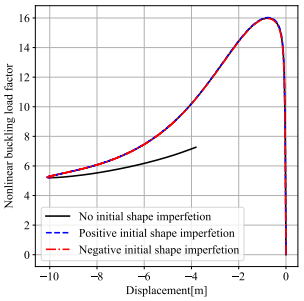
Figure 10: Optimized shape when problem (6) is solved



(a) Shell shape

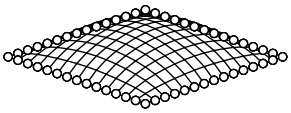


(b) Control points

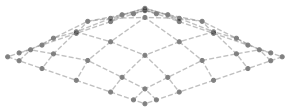


(c) Mechanical performance Min f

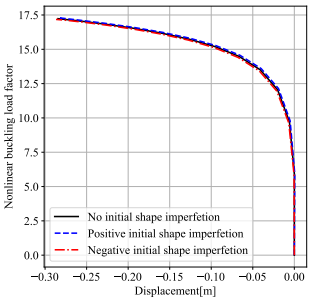
$f = 1.52[\mathrm{kNm}]$
$\lambda^{\mathrm{p}}_{1/50} = 12.76$
$\lambda^{\mathrm{true}}_{1/50} = 15.95$
$V = 6.35[\mathrm{m}^3]$



(d) Shell shape



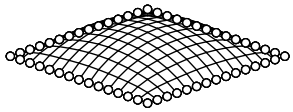
(e) Control points

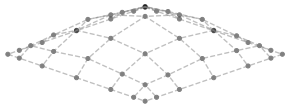


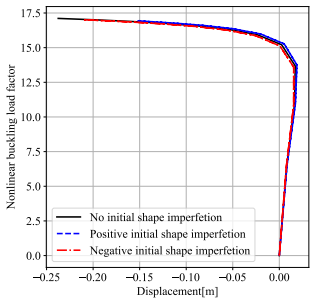
(f) Mechanical performance Max λ^{true}

$f = 1.64[\mathrm{kNm}]$
$\lambda^{\mathrm{p}}_{1/50} = 13.32$
$\lambda^{\mathrm{true}}_{1/50} = 17.17$
$V = 6.35[\mathrm{m}^3]$

Figure 11: Optimized shape when problem (7) is solved



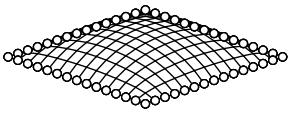




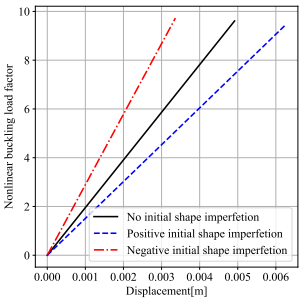
$f = 1.57[\mathrm{kNm}]$
$\lambda^{\mathrm{p}}_{1/25} = 12.93$
$\lambda^{\mathrm{true}}_{1/25} = 16.93$
$V = 6.35[\mathrm{m}^3]$

(a) Shell shape (b) Control points (c) Mechanical performance

Figure 12: Optimized shape when problem (8) is solved

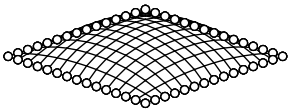


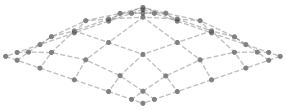


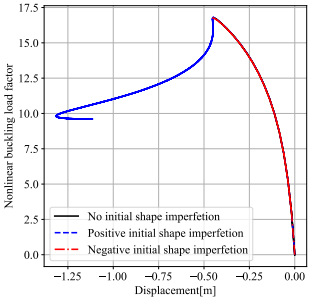


$f = 1.48[\mathrm{kNm}]$
$\lambda^{\mathrm{p}}_{1/20} = 12.96$
$\lambda^{\mathrm{true}}_{1/20} = 9.46$
$V = 6.35[\mathrm{m}^3]$

(a) Shell shape (b) Control points (c) Mechanical performance Min f



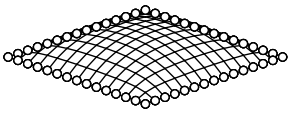


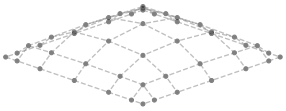


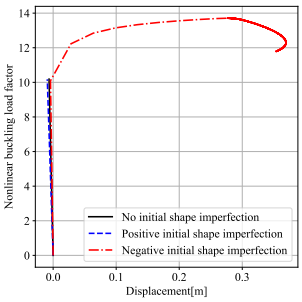
$f = 1.99[\mathrm{kNm}]$
$\lambda^{\mathrm{p}}_{1/20} = 14.35$
$\lambda^{\mathrm{true}}_{1/20} = 16.73$
$V = 6.35[\mathrm{m}^3]$

(d) Shell shape (e) Control points (f) Mechanical performance Max λ^{true}

Figure 13: Optimized shape when problem (9) is solved







$f = 1.45[\mathrm{kNm}]$
$\lambda_{\max} = 10.17$
$V = 6.35[\mathrm{m}^3]$

(a) Shell shape (b) Control points (c) Mechanical performance Min f

Figure 14: Minimize strain energy f model

9. Conclusion

In this paper, the nonlinear buckling load factor and shape optimization using the prediction model. The results showed that the predicted values during optimization were underestimated relative to the true values, but there was generally a trade-off relationship between the strain energy of the pareto front and the nonlinear buckling load factor. Thus, shape optimization that accounts for geometric nonlinearity can be achieved by using machine learning. However, further study is needed as it takes a great deal of time to create a learning model.

Acknowledgement

This work was partially supported by JSPS KAKENHI 22K04416.

[1] E. Ramm and G. Mehlhorn : On shape finding methods and ultimate load analyses of reinforced concrete shells, *Eng.Struct*, Vol. 13, pp. 178–198, 1991

[2] S. Fujita and M. Ohsaki : Shape optimization of shells considering strain energy and algebraic invariants of parametric surface , *J. Struct. Constr. Eng. AIJ*, Vol. 74, No. 639, pp. 857–863, 2009 (in Japanese)

[3] G. Mirra and A. Pungnale : Comparison between human-defined and ai-generated design spaces for the optimisation of shell structures, *Structures*, Vol. 34, pp. 2950–2961, 2021

[4] H.Zheng and N.Akbarzadeh V.Moosavi : Machine learning assisted evaluations in structural design and construction, *Automation in Construction 119,103346*, 2020

[5] Y. Moritomo and S. Fujita : Predicting the structural behavior of geometrical nonlinearity of shell structures by machine learning , *Proceedings of the IASS Annual Symposium 2020/21 and the 7th International Conference on Spatial Structures*, 2021.8

[6] S. Weidman : Deep learning from scrath: Building with python from first principles. , *Oreilly Associates Inc.*, 2019/9

[7] François Chollet, et al. : Keras, *https://keras.io*, 2015

[8] Martín Abadi, Paul Barham, Jianmin Chen, Zhifeng Chen, Andy Davis, Jeffrey Dean, Matthieu Devin, Sanjay Ghemawat, Geoffrey Irving, Michael Isard, et al. : Tensorflow: A system for large-scale machine learning, *Proceedings of the 12th USENIX conference on Operating Systems Design and Implementation*, 2016

[9] M. Zhu, F. McKenna, and M. H. Scott : OpenSeesPy: Python library for the OpenSees finite element framework, *SoftwareX*, Vol. 7, pp. 6–11, 2018

[10] M. Schlueter, J. A. Egea, and J. R. Banga : Extended ant colony optimization for non-convex mixed integer nonlinear programming, *Computers & Operations Research*, Vol. 36, No. 7, pp. 2217–2229, 2008.8

[11] Jimmy Lei Ba Diederik P. Kingma : Adam: A method for stochastic optimization, *3rd International Conference on Learning Representations, ICLR2015*, 2015

Life-cycle design and assessment of structures

Active bending
Additive manufacturing/ 3D printing
Architectural geometry
Bamboo for sustainable construction and quality of life improvement
Bio-inspired structures and architecture
Bridge structures
Computational form-finding
Conceptual design
Concrete structures
Construction techniques
Deployable and inflatable structures
Design competition (WG21)
Digital modelling and fabrication
Dynamic response of metal spatial structures
Dynamic response of other structures
Form-finding and structural optimisation of interlocking discrete assemblages
Graphical methods
Gridshell and lattice structures
Historical concrete shells
Historical structures
Lattice structures
► **Life-cycle design and assessment of structures**
Metal gridshell structures, connections and stability
Methods and construction technologies for sustainable shell structures
Morphology and configuration processing
Next generation parametric design
Novel methods in modelling, optimisation and construction for reducing carbon footprint of continuous roof shells
Numerical methods for geometry, form-finding and optimisation of lightweight structures
Optimisation methods and applications
Origami
Other
Teaching design uncertainty: working with unknown qualities/quantities of new and re-claimed materials
Teaching of shell and spatial structures
Tensegrity systems and cable structures
Tension and membrane structures
Tension structures in the Asia-Pacific
Timber and bio-based structures
Topology optimisation
Traditional masonry structures and innovation
Transformable structures

IASS 2023
July 10–14 Melbourne
Integration of Design and Fabrication

Proceedings of the IASS Annual Symposium 2023
Integration of Design and Fabrication
10–14 July 2023, Melbourne, Australia
Y.M. Xie, J. Burry, T.U. Lee and J. Ma (eds.)

Algorithmic investigation of structural system utility for urban development reusing existing foundations

Kiley FEICKERT[a,*], Caitlin T. MUELLER[a]

[a,*] Massachusetts Institute of Technology
77 Massachusetts Avenue, Cambridge, MA 02139, USA
feickert@mit.edu

Abstract

In a context of simultaneous rising global temperatures and increasing urban density, the need to build additional floor area while reducing the building sector's environmental impact is extremely pressing. Reusing existing structural elements, such as the foundations, presents an opportunity to significantly reduce the carbon emissions associated with constructing a building. This paper presents and deploys a method that demonstrates how designing different superstructures, constrained by the capacity of an existing foundation, leads to different utility. The impact of occupancy, materiality, and efficient structural design on potential floor area is demonstrated, which can vary up to 90 percent, for an office, for example. The impact of these combinations on embodied carbon is also demonstrated, as well as the fact that materiality does not preclude carbon competitive solutions if they are designed efficiently.

Keywords: design for reuse, superstructure design, foundations, embodied carbon, urban development, algorithmic design

1. Introduction

The building stock is expected to increase by over 40% in the U.S. over the next 30 years, due to population and gross domestic product growth [1]. At the same time, current processes required to construct buildings, including material extraction and manufacturing, contribute over 10% of global carbon emissions, annually (often called embodied carbon) [2]. Structural materials, such as concrete and steel, have the ability to last up to 200 years if properly maintained [3] and also embody the majority of a buildings' carbon [1]. This suggests that existing structural elements have the capacity to be reused, to limit the carbon emitted while constructing new buildings.

1.1. Motivation

Despite this potential, the average lifespan of buildings is about one-third of that timeframe in North America [4], [5] and much less in other locations such as South Korea and China [6]. In a study of over 200 building demolitions, nearly 90% were motivated by three criteria: 1) urban redevelopment due to (market driven) changing land values, 2) a lack of maintenance of non-structural elements leading to an undesirable physical condition, and 3) a lack of suitability for current needs (relating to program and building services) [5]. In the case that a building needs to be replaced, or if a site is redeveloped to increase density, foundations have the potential to be reused.

This paper presents and deploys a method to quantify the potential floor area and the resulting embodied carbon for various construction systems, utilizing an existing foundation (Section 2), following a review of relevant literature (Section 1.2). Four floor systems are studied (See Figure 1): 1) flat reinforced concrete (RC) two-way floor with RC frame, 2) shape-optimized one-way RC floor with RC frame, 3) composite steel deck and RC floor (steel deck) with steel frame, and 4) cross-laminated timber (CLT) floor with timber glulam frame. Where applicable, these systems are designed for three program

Copyright © 2023 by Kiley FEICKERT and Caitlin T. MUELLER. Published in the Proceedings of the IASS Annual Symposium 2023 with permission.

(occupancy) types: 1) multifamily residential, 2) office, and 3) light manufacturing. This study demonstrates and discusses how designing different superstructures, constrained by the capacity of an existing foundation, leads to different utility. The total floor area is evaluated, as well as the normalized embodied carbon and normalized structural mass for the respective combinations (Section 3).

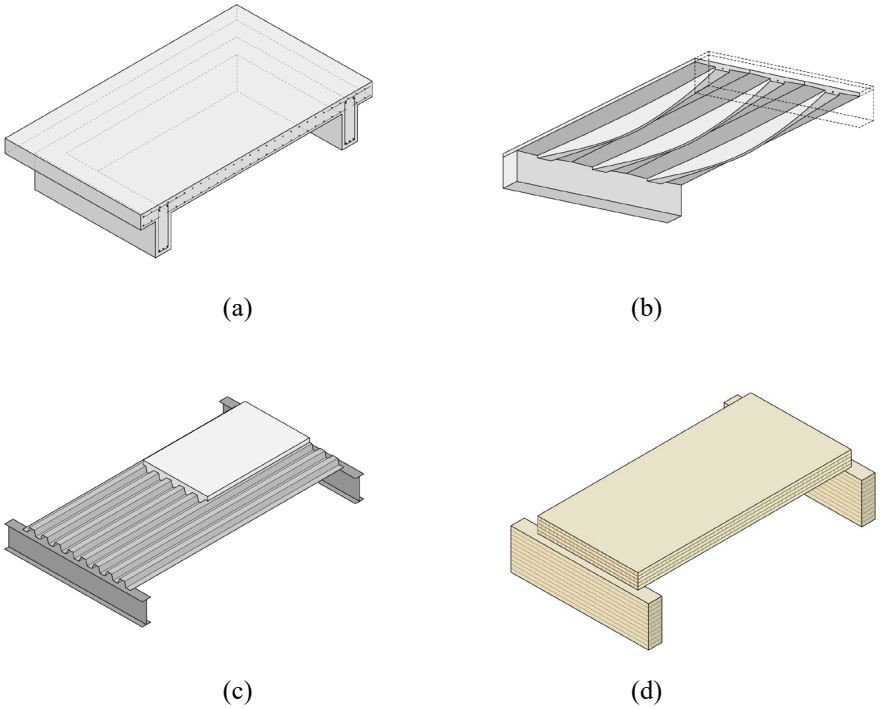


Figure 1. Superstructures being evaluated include: (a) Flat reinforced concrete (RC) two-way floor with RC frame, (b) Shape-optimized RC floor with RC frame [image adapted from Ismail and Mueller [7]], (c) Composite steel deck and RC floor with steel frame, and (c) One-way CLT floor with timber glulam frame

1.2. State of the art

Increasing the longevity of structural elements has the potential to significantly reduce resource demand and emissions. For example, in the United States, increasing longevity of cement-based materials between 1900 to 2015 by 50% could have led to 14% less greenhouse gas emissions [8]. One opportunity to reduce resource consumption in construction is to reuse existing foundations, which are both resource intensive and extremely difficult to remove, particularly in congested urban sites [9].

An example of a building that utilized this approach is 1 Triton Square in London. Originally designed by Arup in 1995, the building was refurbished by Arup in 2021. Primary structural elements, including the foundations and parts of the existing superstructure were maintained, supporting a roof addition and floor infill. The refurbishment saved an estimated 35,000 tons of concrete, 840 tons of reinforcing steel, and 340 tons of structural steel, with the foundation reuse accounting for 25% of the total saving [10]. Using global average embodied carbon coefficients (See Sec. 2.3), the savings from the foundations alone can be estimated at 1.9 million kg CO_2e. The added cost saving (43%) and speed of construction (30% faster) were also noted (Arup, 2023).

Another approach to reducing carbon emissions is to efficiently allocate structural material only where it is necessary. Significant research has been developed by architects and engineers demonstrating the material savings that can be achieved for reinforced concrete floors [7][11][12]. This approach demonstrates that there is room for improvement in reducing the embodied carbon of business-as-usual structural systems across all common material systems.

2. Methodology

To evaluate the embodied carbon impact and utility of reusing existing foundations to support various structural systems, the following methodology is used (See Figure 2).

2.1. Conceptual overview

An existing foundation with a known capacity per column is assumed to be located on a site for re-development. Four gravity load-resisting structural systems -- 1) Flat RC two-way slab with RC frame, 2) Shape-optimized one-way RC slab with RC frame, 3) composite steel deck and RC floor (steel deck) with steel frame, and 4) cross-laminated timber (CLT) floor with timber glulam frame -- are designed for multifamily residential, office, and light manufacturing program using physics-based calculations. This paper references the 2018 International Building Code [13] with the code considerations outlined in Table 1.

Once the superstructures are designed, the systems are evaluated to determine the total floor area that can be built in the respective materials for a given foundation capacity. At the same time, structural material quantities (SMQs) are quantified and used to compare normalized structural mass and to calculate the relative embodied carbon (kg CO_2e/m^2) of each design to compare their environmental impact. Different combinations of occupancy, superstructure materiality, and foundation capacity are evaluated.

2.2. Superstructure design

Design of the superstructure begins with the floors. The one-way spanning steel deck and CLT floors are the most constrained elements in their systems, due to the number of prefabricated parts used in their construction. Design of the structural frame follows, as secondary beam spacing is dictated by the allowable span of the floor system and sizing is based on floor loading. The method presented simulates the design process of a practicing structural engineer using existing construction systems, and accounts for the minimum material necessary to satisfy the design loads and applicable building codes outlined in Table 1. Sound transmission, including impact, is not considered.

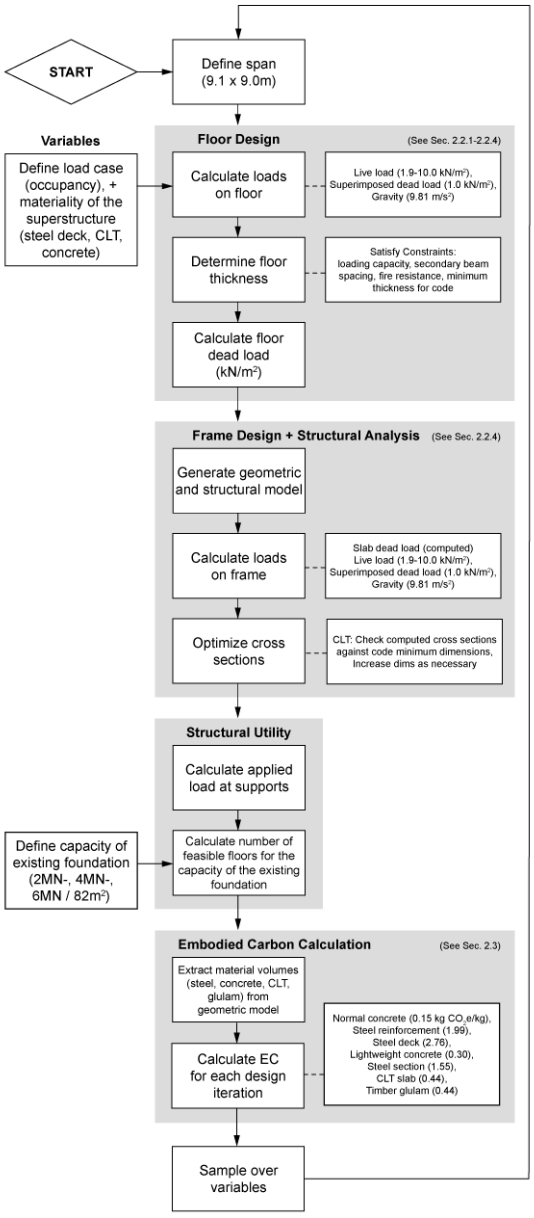


Figure 2. Methodology to evaluate the embodied carbon impact and utility of reusing existing foundations to support various structural systems

For all of the materials being evaluated, the floors are designed for a typical office bay, 9.1 x 9.0m (See Table 4), as office buildings have a shorter lifespan on average when compared to other occupancy types [6]. For all combinations, the roof and its supporting beams are not included in the analysis.

Table 1. Design loads by occupancy and materiality of structural system for superstructure design *2018 IBC [13]

Floor system	**Program**	**Occupancy** (Ch. 3*)	**Construction classification** (Ch. 6*)	**Fire resistance** (Table 601*)	**Uniform live load** (Table 1607.1*) (kN/m^2)	**Superimposed dead load** (kN/m^2)
RC two-way flat slab	Residential (multifamily)	Group R-2	Type I-B	2 Hr. - Structural frame 2 Hr. – Floor separation	1.9	1
	Office	Group B			2.4	1
	Manufacturing (light)	Group F-2			6	1
RC one-way shape optimized slab	Residential (multifamily)	Group R-2	Type I-B	2 Hr. - Structural frame 2 Hr. – Floor separation	1.9	1
	Office	Group B			2.4	1
	Manufacturing (light)	Group F-2			6	1
Steel deck	Residential (multifamily)	Group R-2	Type I-B	2 Hr. - Structural frame 2 Hr. – Floor separation	1.9	1
	Office	Group B			2.4	1
	Manufacturing (light)	Group F-2			6	1
CLT	Residential (multifamily)	Group R-2	Type IV	HT – min dimensions per Table 2304.11* (See Table 2)	1.9	1
	Office	Group B			2.4	1
	Manufacturing (light)	Group F-2			**Exceeds capacity**	-

2.2.1. Flat reinforced concrete floor design

A two-way spanning RC slab (non-prestressed) is designed using typical normal weight concrete and reinforcing steel (See Table 5 for material properties). The slab thickness and area of steel is calculated to satisfy ACI 318-19: Building Code Requirements for Structural Concrete [14] using first principles. The RC floor and frame design workflow used in this paper was developed by Sory, Lyu, and Mueller [15] [16]. The resulting dead load for all floors is noted in Table 3.

2.2.2. Shape-optimized reinforced concrete floor design

A one-way spanning shape-optimized slab is designed to satisfy code [14] using the constrained optimization method developed by Ismail and Mueller [7]. This method reduces structural material where it is not required to reduce the slabs overall mass and embodied carbon. Designs are optimized for each for the loading conditions outlined in Table 1.

2.2.3. Steel deck floor design

The one-way spanning steel deck is designed following technical guidance from Vulcraft [17]. To satisfy the superimposed dead load and required fire resistance, a total composite floor depth of 15.88 cm, deck type 3VLI22 (the lightest allowable deck), and lightweight concrete is selected. For the bay size being studied (9.1x9.0m), secondary beams are spaced at 3m (3 span) to satisfy the 3.5m maximum unshored

clear span. This build up is typical of North American construction, and results in a ULL capacity of 46.1 kN/m^2, far exceeding the necessary capacity.

2.2.4. CLT floor design

The one-way spanning CLT floors are designed following technical guidance from Nordic [18] and checked against the minimum dimensions prescribed by code. To satisfy the design loads outlined in Table 1, the minimum dimensions outlined in Table 2, and the minimum material, secondary beams are spaced at 4.5m and a double-span 105-3s floor slab [18] is selected. This floor has a thickness of 10.5cm, satisfying code; however, the fire-resistance rating from the manufacturers is only 30 minutes, compared to 120 minutes for the steel deck floor. Due to the significant discrepancy, a double-span 175-5s floor slab [18] is also studied, which has a thickness of 17.5cm and a fire-resistance rating of 120 minutes. The CLT floors are not designed for light manufacturing occupancy, as the live load exceeds the allowable capacity of the material.

Table 2. Minimum dimensions of heavy timber structural members from Table 2304.11, 2018 IBC due to fire requirements [13]

Element	**Minimum width** (cm)	**Minimum depth** (cm)
Columns	17.1	21.0
Beams, girders	12.7	26.7
Floors	-	10.2

2.2.4. Structural frame design

Following the floor design and secondary beam spacing, the structural frames are designed to satisfy the loads described in Table 1 and Table 3, as well as the minimum dimensions from Table 2 for the timber glulam frame. The overall configuration of the frame is described in Table 4.

Table 3. Calculated floor dead load by materiality of structural system for structural frame design

Floor system: total thickness	**Occupancy**	**Floor dead load** (kN/m^2)	**Frame dead load**
RC two-way flat slab: 27.2 cm	Residential	11.94	Computed automatically
	Office	12.74	
	Light manufacturing	18.50	
RC one-way shape optimized slab: varies	Residential	5.15	
	Office	5.16	
	Light manufacturing	12.17	
Steel deck (7.6 cm) with lightweight structural concrete: 15.88 cm	Residential, Office, Light manufacturing	2.17	
CLT: 10.5 cm	Residential, Office	0.53	
CLT: 17.5 cm	Residential, Office	0.88	

Table 4: Configuration used for structural frame design

Primary span (m)	**Secondary span** (m)	**Column height** (m)	**Secondary beam spacing** (m)		**Primary bays** (#)	**Secondary bays** (#)
			Steel frame	**Timber frame**		
9.1	9.0	4.0	3.0	4.5	2	5

Karamba3D is used to efficiently select the cross-sections of the structural frame for the configurations being studied. Beams and girders are designed for a deflection limit of 3.8cm (span/240) for all materials and constrained to a depth of 110cm for the concrete and glulam frame to fairly compare the depth against that of steel sections. The allowable beam depth is increased to 133cm for the glulam frame when the building reaches 26-35 floors, as a depth of 110cm is not sufficient.

Glulam member widths are extracted from Table 3.7, Standard Net Finished Widths for Structural Glued Laminated Timber and depths increase in increments of 38mm, the standard lamination thickness of typical softwood species, according to APA – The Engineered Wood Association [19]. The members are checked against the minimum dimensions prescribed by code (Table 2), and the minimum allowable cross-section is selected.

For steel and timber frames, column dimensions are sized to increase material efficiency and reduce in cross-sectional area for each floor, due to the discretized nature of these systems. For the RC frame, uniform column dimensions are designed for the largest required cross-section for every five floors, due to the desired continuity of the material.

Once the frame members are efficiently sized, the number of floors for each material system is sampled (up to 35 floors), tracking the total structural mass, the maximum reaction forces at the column locations and the structural material quantities. The number of floors that can be built for each system for a maximum reaction force of 2-, 4-, and 6 MN/82m^2 tributary area is reported as well as the structural material quantites for the respective designs.

2.3. Embodied carbon comparison of RC, steel, and timber superstructures

Structural material quantities (SMQs) are tracked during the design of the superstructures discussed in Section 2.2. These material quantities are extracted and multiplied by their respective density and embodied carbon coefficient (ECC) (See Table 5) to determine the environmental impact of the designs. The ECCs represent the amount of carbon (CO_2e) emitted during LCA Stages A1-A3 (cradle to gate) according to EN 15978:2001. World average ECCs are used from the Inventory of Carbon and Energy (ICE database) [20], due to the reliability of these values [21]. For materials not included in the ICE database (structural lightweight concrete), the global average value is used from the Embodied Carbon in Construction Calculator (EC3) tool [22]. Carbon storage is not considered for timber elements, due to the range in values present in the literature.

Table 5. Material properties for structural design and embodied carbon calculations. ECCs are from the ICE database* [20], unless otherwise noted** [22].

Floor system	**Material**	**Embodied carbon coefficient*** (kg CO2e/kg)	**Density** (kg/m^3)	**Strength** (Mpa)
RC	Concrete (normal)	0.15	2400	slab, beam: 34.5 column: 55.1
	Steel reinforcement	1.99	7850	415
Steel deck	Steel deck (hot dip galvanized)	2.76	7850	
	Concrete (lightweight, structural)	0.30**	1762	
	Steel mesh (reinforcement)	1.99	7850	
	Steel section	1.55	7850	
CLT	CLT floor	0.44	513	
	Timber glulam	0.44	513	

Embodied carbon and structural mass are normalized by square meter of built floor area and reported against the total number of floors that can be constructed, for comparison.

3. Results

The total number of floors that can be supported by an existing foundation with a capacity of 2MN, 4MN and 6MN/82m^2 and the normalized embodied carbon (EC) is shown in Figure 3 for flat concrete, shape-optimized concrete, steel and timber superstructures designed for residential, office, and light manufacturing occupancies (where applicable).

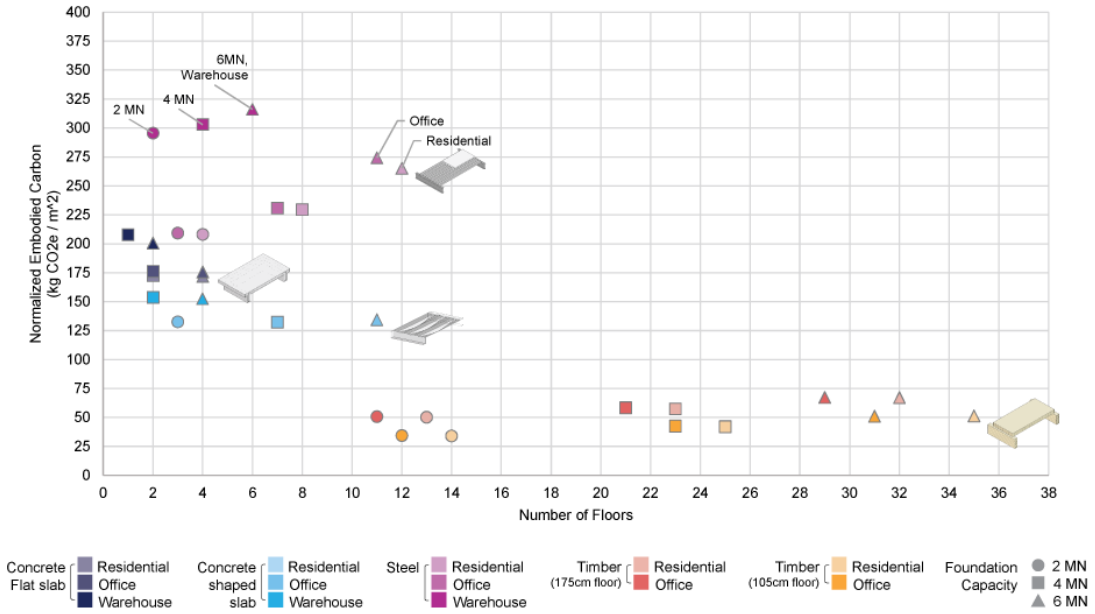


Figure 3. Normalized embodied carbon and allowable number of floors for flat concrete, shape-optimized concrete, steel, and timber structures designed for a foundation capacity of 2-, 4-, and 6MN/82m^2 tributary area

As one might expect, the normalized embodied carbon for the timber superstructures is significantly lower than the steel and concrete superstructures, supporting the same loads. This can be attributed to the low normalized structural mass as well as the low embodied carbon coefficient for glulam and CLT. The normalized EC values for the flat concrete structures are around 10-25% lower than those of the steel structures due to the relative carbon intensity of steel sections as well as the increased cement content (and resulting EC) from using lightweight structural concrete for the floors. It should be noted that for the flat concrete system, the additional mass precludes it from achieving a factored column load of 2MN for the tributary area studied. However, the shape-optimized RC floor (designed for office loading) saves around 60% of the embodied carbon from the steel system for the same load and can achieve the number of floors.

As the live load increases from residential program to warehouse program, the quantity of structural material required to support the additional live load leads to a significant increase in embodied carbon for the business-as-usual steel and flat RC systems. For example, a steel residential and office building designed for a 4MN foundation can reach 8 and 7 floors, respectively, for 230 kg CO_2e/m^2. For the same foundation capacity, a steel warehouse can reach 4 floors, for 303 kg CO_2e/m^2. By utilizing material efficient systems in these scenarios, a significant amount of carbon can be saved.

For the two CLT slabs studied, intuitively, the normalized EC increases, and the number of achievable floors decreases for the 175cm thick CLT floor from the 105cm thick CLT floor. However, the additional thickness doesn't significantly alter the utility of the 175cm system, compared to the 105cm system, while providing significantly higher fire resistance (120min compared to 30min).

The normalized structural mass relative to the normalized embodied carbon values for the same designs are shown in Figure 4.

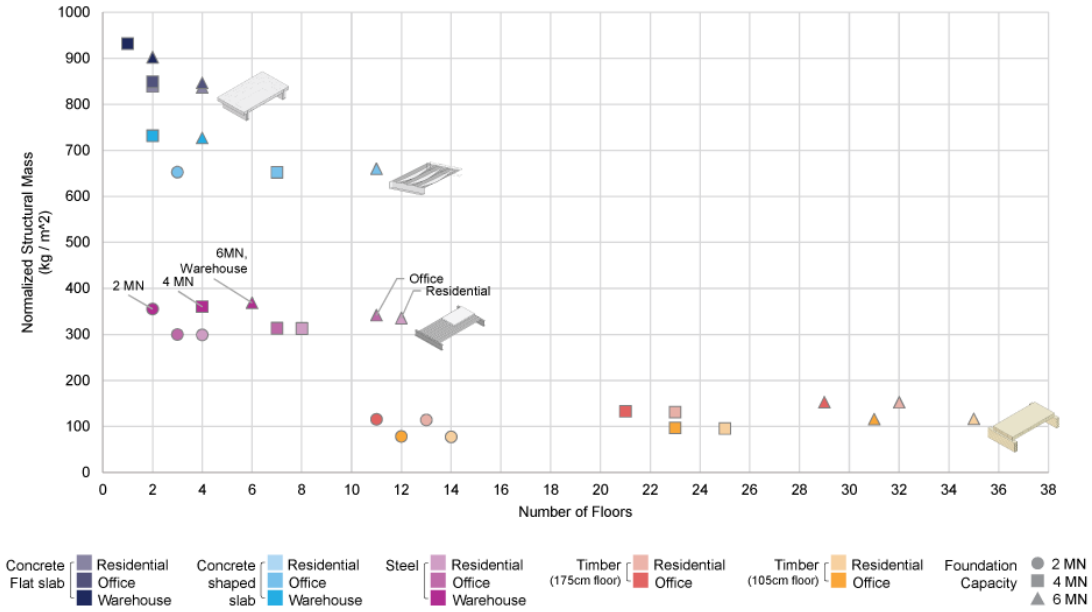


Figure 4. Normalized structural mass for concrete, steel, and timber structures designed for a foundation capacity of 2-, 4-, and 6MN/82m^2 tributary area

CLT floors have a significantly lower normalized structural mass (kg/m^2) than typical steel deck and RC floors (See Table 6). This contributes to the ability to build more floors in timber for the same maximum column load, all things remaining equal. For lower allowable column loads (4MN/82m^2) one can build three times the number of residential floors in timber compared to steel and shape-optimized RC floors, and twelve times the number of flat RC floors. However, if a more material efficient steel system is developed, the normalized mass may bring it closer to the timber systems shown here.

The total mass of the flat concrete system is significant, at three times the values for steel and nine times the values for timber. A shape-optimized RC slab brings this total mass down by one-third. If the shape-optimized RC floor is compared to a one-way flat RC floor, this shift could be even more significant.

The normalized structural mass and normalized embodied carbon for an office designed for a foundation with a capacity of 4MN is compared for each structural system in Table 6.

Table 6. Structural system utility for an office designed for an existing foundation with a 4MN capacity

Floor system: number of floors	**Max applied column load** (MN)	**Total floor area** (m^2)	**Structural Mass** (kg)	**Normalized structural mass** (kg/m^2)	**Total embodied carbon** (kg CO_2e)	**Normalized embodied carbon** (kg CO_2e/m^2)
RC flat: 2	3.78	1,638	1,575,900	962	335,090	207
RC shape-optimized: 7	3.95	5,733	36,99,063	652	750,824	132
Steel deck: 7	3.63	5,733	1,797,200	313	1,322,500	231
CLT, 10.5cm: 23	3.96	18,837	1,820,500	97	801,014	43
CLT, 17.5cm: 21	3.88	17,199	2,280,500	133	1,003,400	58

Normalized mass quantities are closely aligned to previous bottom-up structural design for the steel and timber systems [23] [24], however, the flat RC system is roughly double that of the same studies. This may be attributed to the fact that the studies referenced utilize one-way ribbed slabs for a 9m span, reducing the material volumes for the floors themselves as well as the beams required for 2-way systems. The normalized mass quantities for the flat RC system are more closely aligned (albeit slightly lower) with the median value in the top-down analysis of 59 concrete buildings conducted by De Wolf *et al.* [25]. While this paper doesn't include the structural material quantity of the lateral load resisting system, it is assumed that a comparison is still warranted given the low rise of the structures considered.

However, the shape-optimized RC floor becomes more competitive when evaluating the tradeoffs of this system compared to the others. For example, although the normalized mass is double that of the steel system and six times that of the timber system, the normalized embodied carbon is almost half of the steel system. Additionally, the shaped RC system is designed for warehouse loading, which is not possible in the timber system.

A summary of the normalized structural mass and normalized embodied carbon for all the design combinations are shown in Figure 5.

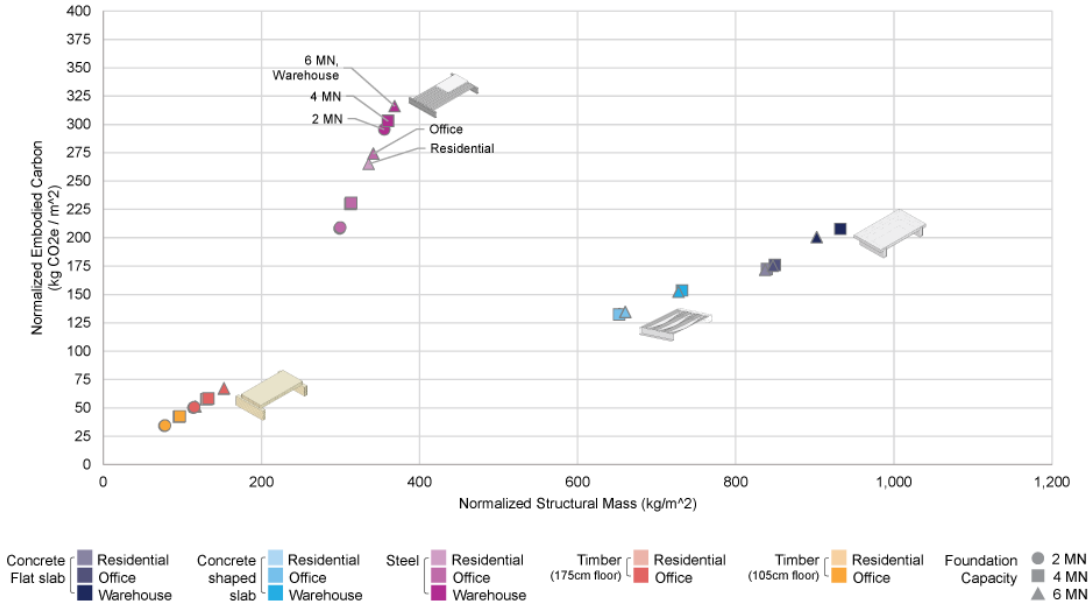


Figure 5. Normalized embodied carbon and normalized structural mass for concrete, steel, and timber structures designed for a foundation capacity of 2-, 4-, and 6MN/82m^2 tributary area

4. Conclusion: Summary of contributions and potential impact

This paper aims to encourage reuse of existing structural materials to limit carbon emissions associated with new construction. Acknowledging the fact that urban redevelopment often necessitates building a new superstructure, the utility of existing foundations is determined for flat concrete, shape-optimized concrete, steel, and timber structural systems to evaluate the environmental impact and total allowable floor area of the respective systems, if a new superstructure is warranted.

The utility of the timber systems is best exemplified in Figure 3, both in terms of applicability and limitations. Compared to a steel system, one can build three times the number of floors in timber for only two-thirds of the total embodied carbon. However, as high live loads cannot be supported by CLT floors, their use is limited to occupancies such as residential and office. CLT also incurs a cost premium over reinforced concrete for the same span and faces limited supply volumes [26]. The trade-offs

between the various systems warrant further exploration, especially when CLT floors are not possible due to loading, cost, or material sourcing limitations.

Business-as-usual steel and flat slab concrete systems are both massive and can have a high environmental price. However, shape-optimizing these systems can have a significant impact on their applicability, allowing them to be more competitive when evaluating the tradeoffs against the other systems. For example, although the normalized mass of the shape-optimized RC floor is more than both the steel and timber systems, the normalized embodied carbon is almost half of the steel system. Additionally, the shaped RC system is designed for warehouse loading, which is not possible in timber.

4.1. Limitations and future work

In this paper, lateral load-resisting systems are not included in the structural material quantities. It is assumed that lateral stiffness is not the controlling factor for the concrete and steel designs sampled [23]. However, the additional height of the timber structures may necessitate the inclusion of the lateral systems in the overall EC evaluation.

Additionally, in terms of total carbon emissions, whole life carbon emissions (beyond LCA stage A3) and the thermal performance of the structural materials is not accounted for. Thermal mass of the concrete and steel systems has the potential to improve operational performance of a building during use, which requires further study.

Lastly, the majority of the systems studied in this paper, with the exception of the shape-optimized RC floors, are indicative of business-as-usual construction methods, which often sacrifice material efficiency for speed of construction. There is potential to reduce the structural material quantities of these systems by utilizing efficient geometry, which may bring the respective designs closer to one another for both normalized mass and EC. Significant work has been done in this area for reinforced concrete floors, however an opportunity exists to reduce the mass and embodied carbon of traditional steel deck systems. Using less material intensive and lower cost systems is particularly relevant where timber is not readily available, or the cost premium precludes it from being used.

4.2. Concluding remark

In a context of simultaneous increasing global temperatures and increasing urban density, the need to provide additional floor area while reducing the AEC sector's environmental impact is extremely pressing. By reusing existing building foundations, significant carbon savings can be achieved. Additionally, understanding the constraints of these elements and designing a superstructure that maximizes their utility will be key in achieving this objective. The method presented in this paper aims to encourage designers and engineers to minimize the embodied carbon associated with urban development by rethinking business-as-usual construction methods and demonstrating the utility of various superstructure designs constrained by reusing existing foundations.

Acknowledgements

The authors would like to thank Mohamed A. Ismail, Leilah Sory, and Yiwei (Lucy) Lyu for their contributions to the structural design workflows for the reinforced concrete structural floors and frames.

Funding for this research was provided in part by the Homer A. Burnell (1928) Presidential Fellowship, Massachusetts Institute of Technology.

References

[1] J. H. Arehart, F. Pomponi, B. D'Amico, and W. V. Srubar, "Structural material demand and associated embodied carbon emissions of the United States building stock: 2020–2100," *Resources, Conservation and Recycling*, vol. 186, p. 106583, Nov. 2022, doi: 10.1016/j.resconrec.2022.106583.

[2] M. Adams, V. Burrows, and S. Richardson, "Bringing Embodied Carbon Upfront: Coordinated action for the building and construction sector to tackle embodied carbon," World Green Building Council, Sep. 2019.

[3] J. Rissman *et al.*, "Technologies and policies to decarbonize global industry: Review and assessment of mitigation drivers through 2070," *Applied Energy*, vol. 266, p. 114848, May 2020, doi: 10.1016/j.apenergy.2020.114848.

[4] C. B. Aktas and M. M. Bilec, "Impact of lifetime on US residential building LCA results," *international journal of life cycle assessment*, vol. 17, no. 3, pp. 337–349, Jan. 2012, doi: 10.1007/s11367-011-0363-x.

[5] J. O'Connor, "Survey on actual service lives for North American buildings," presented at the Woodframe Housing Durability and Disaster Issues Conference, Las Vegas, Nevada, Las Vegas, Nevada: Madison, WI: Forest Products Society, Oct. 2004.

[6] R. Andersen and K. Negendahl, "Lifespan prediction of existing building typologies," *Journal of Building Engineering*, vol. 65, p. 105696, Apr. 2023, doi: 10.1016/j.jobe.2022.105696.

[7] M. Ismail and C. Mueller, "Minimizing embodied energy of reinforced concrete floor systems in developing countries through shape optimization," *Engineering Structures*, vol. 246, p. 112955, Nov. 2021, doi: 10.1016/j.engstruct.2021.112955.

[8] S. A. Miller, "The role of cement service-life on the efficient use of resources," *Environ. Res. Lett.*, vol. 15, no. 2, p. 024004, Feb. 2020, doi: 10.1088/1748-9326/ab639d.

[9] T. Chapman, B. Marsh, and A. Foster, "Foundations for the future," *Proceedings of ICE Civil Engineering*, pp. 36–41, Feb. 2001.

[10] H. Tayler, "A short guide to reusing foundations," *STRUCT ENG*, vol. 98, no. 11, pp. 20–23, Nov. 2020, doi: 10.56330/GYPR7761.

[11] W. Hawkins, J. Orr, T. Ibell, and P. Shepherd, "A design methodology to reduce the embodied carbon of concrete buildings using thin-shell floors," *Engineering Structures*, vol. 207, p. 110195, Mar. 2020, doi: 10.1016/j.engstruct.2020.110195.

[12] D. L. López, D. Veenendaal, M. Akbarzadeh, and P. Block, "Prototype of an ultra-thin, concrete vaulted floor system," p. 8, 2014.

[13] International Code Council, "2018 International Building Code (IBC)," International Code Council, Inc., 2018.

[14] American Concrete Institute, "Building Code Requirements for Structural Concrete (ACI 318-19)," ACI Standard, ANSI Standard ACI 318-19, 2022.

[15] L. Sory, "Towards Integrated Building Archetypes for Enhanced Urban Modeling of Embodied and Operational Carbon," Massachusetts Institute of Technology, In preparation.

[16] Y. (Lucy) Lyu, "Building Early Stage Embodied and Operational Analysis Through Neural Network Surrogate Models," Massachusetts Institute of Technology, In preparation.

[17] Vulcraft, "Vulcraft: Composite deck with composite stud tables," USA, 2010.

[18] Nordic, "Mass Timber Construction: Nordic X-Lam Technical Guide," USA, Technical Guide NS-GT6, Apr. 2022.

[19] APA - The Engineered Wood Association, *Standard Specification for Structural Glued Laminated Timber of Softwood Species*. 2020.

[20] C. Jones and G. Hammond, "Inventory of Carbon & Energy (ICE)." 2019. Accessed: Jul. 12, 2019. [Online]. Available: http://www.circularecology.com/ice-database-faqs.html

[21] A. M. Moncaster and J.-Y. Song, "A comparative review of existing data and methodologies for calculating embodied energy and carbon of buildings," *International Journal of Sustainable*

Building Technology and Urban Development, vol. 3, no. 1, pp. 26–36, Mar. 2012, doi: 10.1080/2093761X.2012.673915.

[22] C-Change Labs, "Embodied Carbon in Construction Calculator (EC3) Tool." Building Transparency, Aug. 11, 2021. Accessed: Aug. 11, 2021. [Online]. Available: https://buildingtransparency.org/ec3

[23] B. D'Amico and F. Pomponi, "On mass quantities of gravity frames in building structures," *Journal of Building Engineering*, vol. 31, p. 101426, Sep. 2020, doi: 10.1016/j.jobe.2020.101426.

[24] J. Hart, B. D'Amico, and F. Pomponi, "Whole-life embodied carbon in multistory buildings: Steel, concrete and timber structures," *Journal of Industrial Ecology*, vol. 25, no. 2: Material Efficiency for Climate Change Mitigation, pp. 249–537, 2021.

[25] C. De Wolf, F. Yang, D. Cox, A. Charlson, A. Seif Hattan, and J. Ochsendorf, "Material quantities and embodied carbon dioxide in structures," *Engineering Sustainability*, vol. 169, no. 4, p. 12, Aug. 2016.

[26] P. D. Kremer and L. Ritchie, "Understanding Costs and Identifying Value in Mass Timber Construction: Calculating the 'Total Cost of Project' (TCP)," *Mass Timber Construction Journal*, vol. 1, 2018.

[27] K. Feickert and C. T. Mueller, "Thin shell foundations: Quantification of embodied carbon reduction through materially efficient geometry," Under review.

IASS 2023
July 10–14 Melbourne
Integration of Design and Fabrication

Proceedings of the IASS Annual Symposium 2023
Integration of Design and Fabrication
10–14 July 2023, Melbourne, Australia
Y.M. Xie, J. Burry, T.U. Lee and J. Ma (eds.)

Aurecon buildings carbon sketcher: A cross-disciplinary webtool for carbon neutral building design

Max G. MARSCHALL[a,*], Jack WALKER[a], Daniel FITZMAURICE[a], Hamed SEIFI[a], Cindy LAM[a], Nathan PALAIRET[a], Darcy CREIGHTON[a], Qisi ZHENG[a], James ALLISON[a], Tristan MORGAN[a], Pablo SEPULVEDA[a], Matthew AUSTIN[a]

*Aurecon
8/850 Collins Street, Docklands VIC 3006, Australia
Max.Marschall@aurecongroup.com

Abstract

A lot of the most consequential building design decisions are locked in during the early-design phase. However, lifecycle assessments are commonly conducted later in the planning phases where the analysis has limited potential to meaningfully affect the design. It would be ideal to front-load this analysis into the early-design phase, however, this is challenging since project information at this stage is limited and the design process is fast-paced. This paper addresses this challenge by creating a user-friendly webtool for indicative lifecycle assessments to be used during the concept design phase. Existing research has resulted either in sophisticated software with maximised functionality but limited practicality for early design or point solutions that often lack the interdisciplinary approach necessary to achieve truly sustainable outcomes. This tool is novel in that it addresses both embodied and operational emissions, and both the main structural and façade elements, while considering the margin of error associated with early-stage assessments and reaching carbon neutrality. It does so as a web-based tool that provides integrated access to expertise through a highly accessible interface with near real-time feedback. A unique contribution of the tool is a design automation algorithm that auto-sizes structural members based on a first-principles approach.

Keywords: parametric design, user-friendly, lifecycle assessment, carbon neutrality, embodied carbon, operational carbon, agile development, energy modelling, environmental flows, concept design

1. Introduction

Over the past decades, sustainable building design has focused mainly on operational emissions, that is, those associated with the day-to-day running of the building. With increasing progress on the energy-efficiency of HVAC systems and high-performance facades, as well as the increasing decarbonisation of energy grids, the significance of embodied emissions associated with the manufacture and transport of building materials has risen. Sustainable building design should therefore consider lifecycle assessments (LCA). In other words, estimating both operational and embodied carbon emissions.

Some of the most impactful building design decisions are made in the early project stages [1]-[3]. At this point, engineering analysis is commonly limited, while architects are left to make many design decisions based on tacit knowledge rather than data-driven insights. It is difficult to significantly change the design after a town planning permit has been lodged, since this process solidifies design expectations with legal and financial ramifications should the initial design have to be reworked. The issue here is that the town planning permit tends to lock in the structural system and overall envelope design, both of which are the greatest contributors to lifecycle emissions [4].

Copyright © 2023 by Max G. MARSCHALL, Jack WALKER, Daniel FITZMAURICE, Hamed SEIFI, Cindy LAM, Nathan PALEIRET, Darcy CREIGHTON, Qisi ZHENG, James ALLISON, Tristan MORGAN, Pablo SEPULVEDA and Matthew AUSTIN. Published in the Proceedings of the IASS Annual Symposium 2023 with permission.

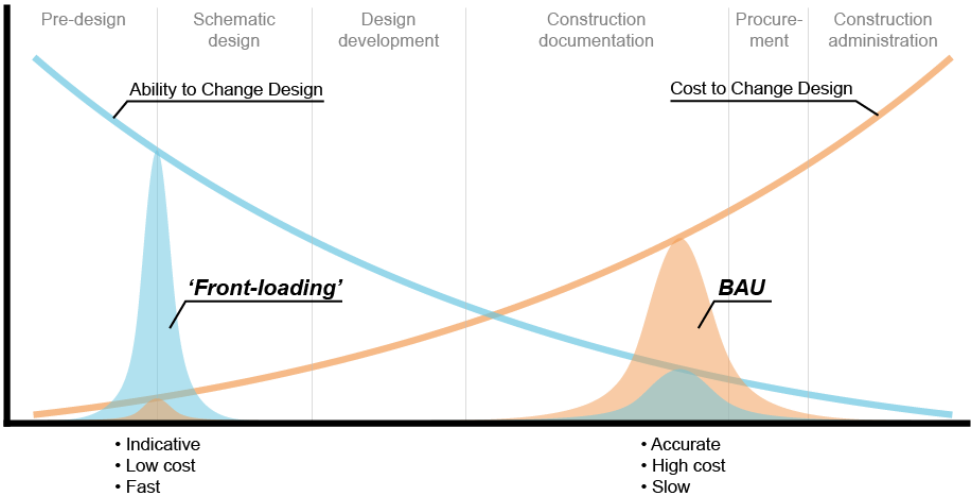


Figure 1. A "MacLeamey" curve as it applies to LCAs. (Adapted from [5])

LCAs are commonly only conducted in the late planning phases. This is a problem as design changes become increasingly costly as the project proceeds, hence the analyses have limited potential to meaningfully affect the design (Figure 1). Sustainable building design could be facilitated by 'front-loading' LCAs into the early design phase, but this is challenging since project information at this stage is limited and the design process iterative and fast-paced. This is a common dilemma that plagues all aspects of early design and is one that computational designers typically seek to alleviate by developing algorithms to automate processes and decrease the effort needed to conduct analyses, or by using new types of tools and visualisation techniques to enhance design processes, or sometimes even by developing custom software. Compared to other contexts, conducting LCAs for buildings is more challenging due to the long lifespans of buildings, their complexity, and the multiplicity of stakeholders involved throughout their design and operation [6]. Any effort to conduct these kinds of analyses in the early-design stage must be accompanied by an understanding that the results will necessarily be indicative rather than accurate calculations. These intrinsic error margins should not become a roadblock to considering sustainable design from the project outset; the uncertainties just need to be expressed clearly and quantified where possible [7].

While several academics have proposed various theoretical frameworks (e.g., [8], [9]) to tackle the challenges in conducting early design LCAs, there are now also numerous consultancies that have developed digital tools for use in practice. This is an emerging field with direct potential impacts on the sector with the largest contribution to worldwide emissions [4] and therefore warrants deeper research attention. An analysis of the currently available tools shows a diversity in terms of the approaches and methodologies followed, the types of user input they require, the scope of carbon-related design tasks and disciplines considered, and the solution maturity. A lot of the existing tools appear to be in the beta phase of their development (e.g., [10]-[13]) which demonstrates that this is an emerging field in the industry. Some tools are specifically intended for browsing existing material emissions databases and therefore require an existing geometry model (e.g., [10], [12], [14], [15]), while others allow the user to input top-level geometric data (e.g., building width and length, etc.) and the tool then auto-sizes all building elements to estimate material volumes (e.g., [11], [13], [16]-[20]). Tools tend to focus on a specific discipline, typically producing an informed estimate either of the embodied carbon of the structure or the façade; a search conducted by the authors did not reveal an early design tool within this space that considered operational carbon.

There appears to be a gap in research to create a tool that:

- Holistically estimates emissions across all major contributors

- Assesses embodied carbon of the structure and façade as well as operational carbon
- Auto-sizes structural elements in the early design stage where a sophisticated geometric model (e.g., a reliable Revit model) may not be available for determining material quantities
- Allows exploring the interdependencies between upfront façade emissions versus lifecycle emissions through operational energy consumption

2. A cross-disciplinary tool

2.1. Aim

The aim of this research was to create a user-friendly design tool for conducting indicative, early-design stage LCAs and allowing a broad user group to compare design options holistically, for the goal of reducing lifecycle emissions in building design. A focus of this tool was to enable user groups beyond sustainability experts to make informed decisions and communicate these to clients, while establishing a technological framework that retained flexibility for individual domain specialists to maintain and update algorithms and calculations.

2.2. Requirements

To achieve their aim, the authors developed a webtool called *Aurecon Buildings Carbon sketcher* (ABCs). The name was chosen deliberately to indicate the specific intent for using it to design buildings rather than other asset types. 'Sketcher' intends to signal to the user that it is aimed at producing indicative estimates in schematic design, thereby distinguishing itself from other tools that conduct specific calculations to determine accurate results for compliance purposes in the later stages.

To fulfil the purposes of an early stage LCA tool, the authors gathered the following requirements from key stakeholders and domain experts within their home organisation to be addressed by the tool:

- Consider the 'big-ticket items' in terms of lifecycle emissions and reaching carbon neutrality that can be assessed with information levels available in early design. In other words, consider operational emissions from energy use as well as embodied emissions for the main structural and façade elements, but exclude items that are unknown in the early design stage and have a lesser impact on carbon emissions, like interior finishes and furniture.
- Make the tool accessible for a wide stakeholder group by minimising dependencies and user knowledge of third-party software, and without requiring users to install specialist software environments on their local computer hardware.
- Build it in a modular way from several domain-specific modules that can be maintained over time by subject matter experts from different disciplines.
- Design the tool in a way that caters to about 95% of Aurecon building projects in terms of allowable geometric complexity and building usages.
- Design the tool for a user group consisting of environmentally sustainable design (ESD) consultants, mechanical, structural, and façade engineers.
- Assume the user does not have a detailed geometric model when using the tool. That is, the tool should auto-size structural elements based on the overall building massing.
- Develop ways to communicate to the user that the estimates generated by the tool are indicative and convey a margin of error.

In essence, the overarching requirement for the development of the tool was to enable interdisciplinary design exploration to generate holistic low emission strategies in the early building design stage.

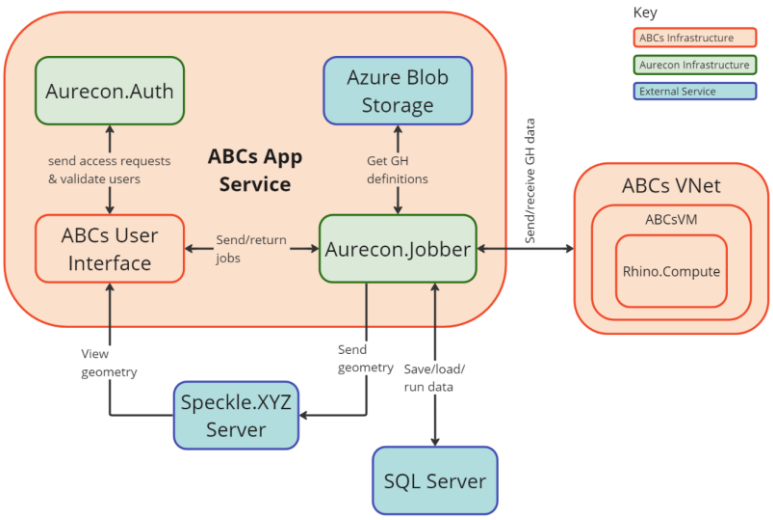


Figure 2. Overall software architecture and Grasshopper definitions contained within ABCs.

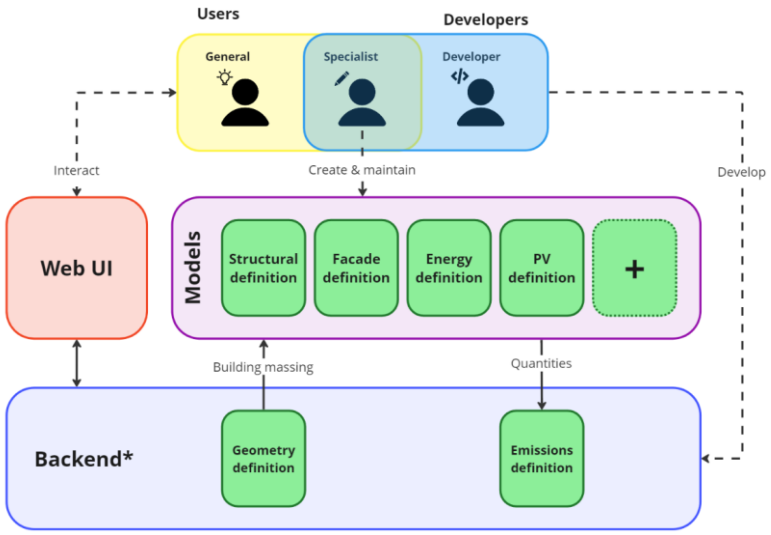


Figure 3. Developing, maintaining, and interacting with the tool. *See Figure 2

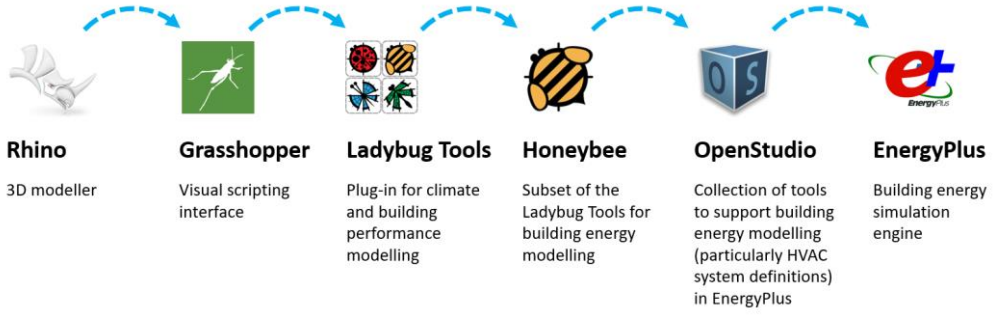


Figure 4. Software used for energy simulations.

2.3. Software architecture

ABCs consists of several Grasshopper definitions that run within Rhino.Compute. The definitions are provided inputs from a browser-based application built on the Blazor framework that uploads the results through a REST API hosted in the cloud. The Blazor application utilizes Speckle to provide the to the user an interactive 3D viewer with metadata. The Telerik for Blazor package is used to provide interactive web elements for the user to input design parameters, and to generate charts that the user can interact with to interrogate the results (Figure 2).

The development of ABCs was a joint effort between software engineers developing the "backend" of the tool, and domain experts creating calculation models (Figure 3). This includes a Grasshopper definition to create the building massing geometries (see Section 2.5), and one for applying the appropriate emissions factors to the corresponding building material and energy quantities (see Section 2.10). There are several domain-specific Grasshopper definitions that cover calculations relation to different disciplines impacting lifecycle emissions: structural element sizing (see Section 2.6), facade element sizing (see Section 2.7), energy modelling (see Section 2.8 and Figure 4), and on-site energy generation modelling (see Section 2.9). These Grasshopper definitions were created and are being maintained and extended by domain experts within the organisation who have appropriate computational design skillsets.

2.4. UI/UX

ABCs was designed to have a highly accessible and easy-to-use user interface and user experience (UI/UX), enabling a broad user group extending beyond computational designers, sustainability experts, and engineers. Rather than automating an existing process [21], the webtool proposes novel affordances that democratise and demystify the relationship between early-stage design decisions and emissions. In doing so, the webtool not only provides key insights to impact design, but also clearly illustrates relationships and sensitivities, supporting users to further develop their understanding of LCA and ESD.

During development, the authors conducted frequent demonstrations of ABCs' UI/UX design to collect feedback from subject matter experts. This helped design a highly accessible and easy-to-use tool. For example, the team discovered that one of the main roadblocks preventing from people using an earlier version of ABCs was that it had been built purely as a Grasshopper tool. As a result, ABCs was built as a webtool that does not require any installations or specialised domain knowledge to use. It has a job management system in which the user can create '*projects*'; each project can have several '*studies*', and each study can have several design '*options*' to be compared in a dashboard view side-by-side (Figure 5). Clicking on a design option from a study page brings up the main UI (Figure 7).

The main UI consists of two columns: user inputs on the left and result visualisations on the right. The columns are sub-divided into logical sections that clearly differentiate between different disciplines; input sections including 'Building', 'Structure', 'Façade', 'Shading', 'Materials', and 'Operation', and output sections including 'Geometry', 'Embodied Carbon', 'Operational Carbon', and 'Carbon Neutrality'. The interface does not freeze while waiting for simulation results to be produced; instead, the visualisation sections that are awaiting data are blurred out until the results become available while the user can keep navigating the UI. It includes an interactive Speckle 3D viewer displaying the structural, façade, and PV panel geometries.

The UI/UX was designed to convey the inherent uncertainties in early-stage LCA analysis. This was done by including a welcome page, guided tour, and documentation that describe the intent, assumptions, and limitations of the tool. Result data is expressed in round numbers so as not to convey a false sense of accuracy [7]. As described in Section 2.10, embodied carbon is calculated using 'high', 'medium', and 'low' scenarios that are displayed side-by-side in the UI for the user to consider the variance of environmental impact across different materials.

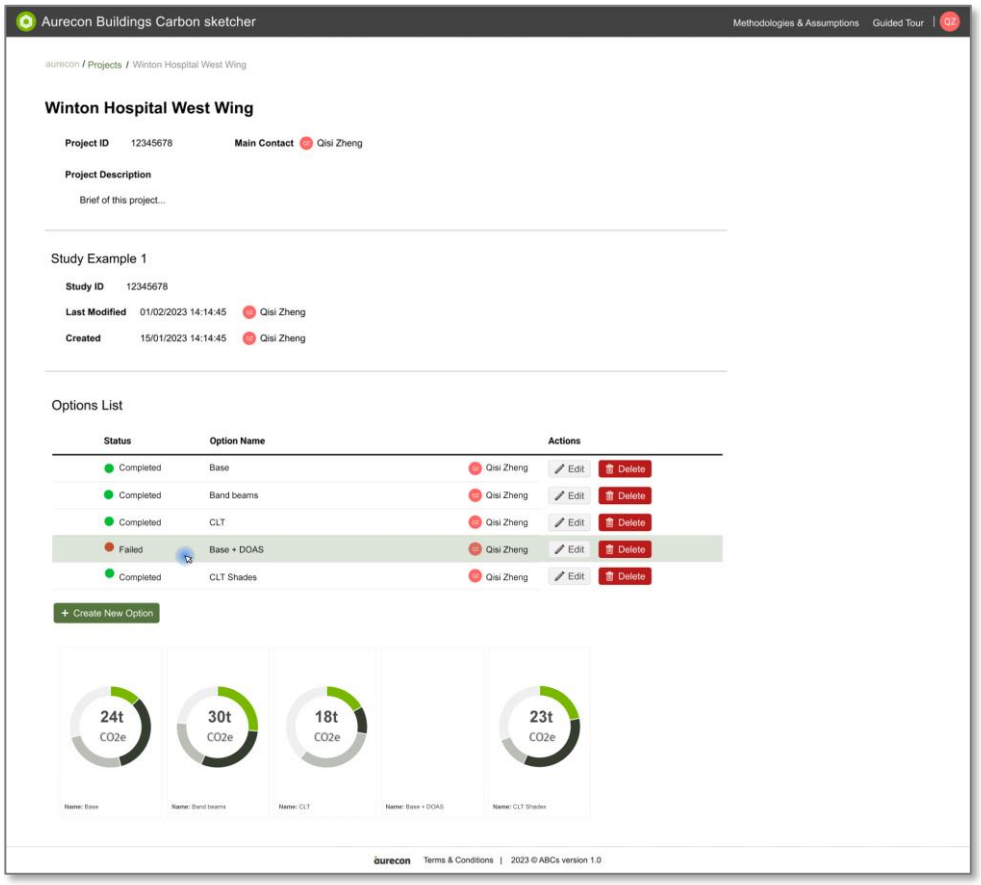


Figure 5. ABCs' "Study" viewer to compare design options at a top level.

2.5. Geometry definition

The first Grasshopper definition to execute within an ABCs run is one that generates the overall building massing as a closed polysurface. Users have three options to describe the building shape (Figure 6): for box-shaped buildings they can enter purely numeric parameters, for buildings that can be described as a vertical extrusion of an irregular footprint the user can upload a polyline defining the footprint, and for more complex building shapes they can directly upload a closed polysurface.

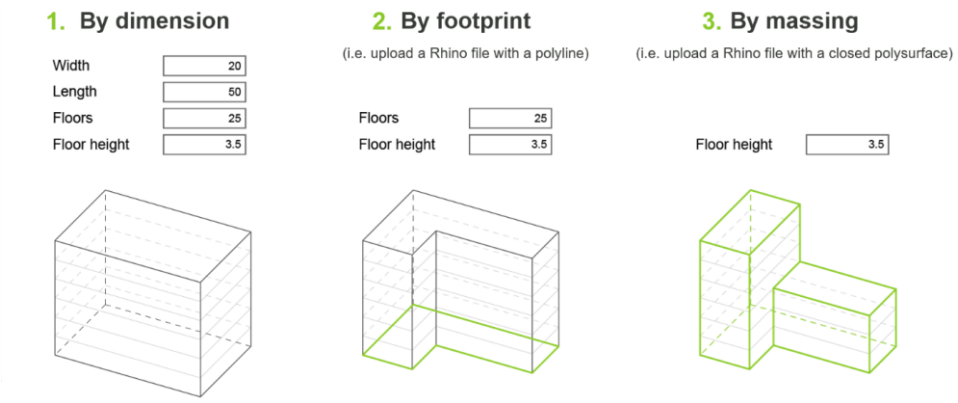


Figure 6. The 3 options to describe building shapes in ABCs.

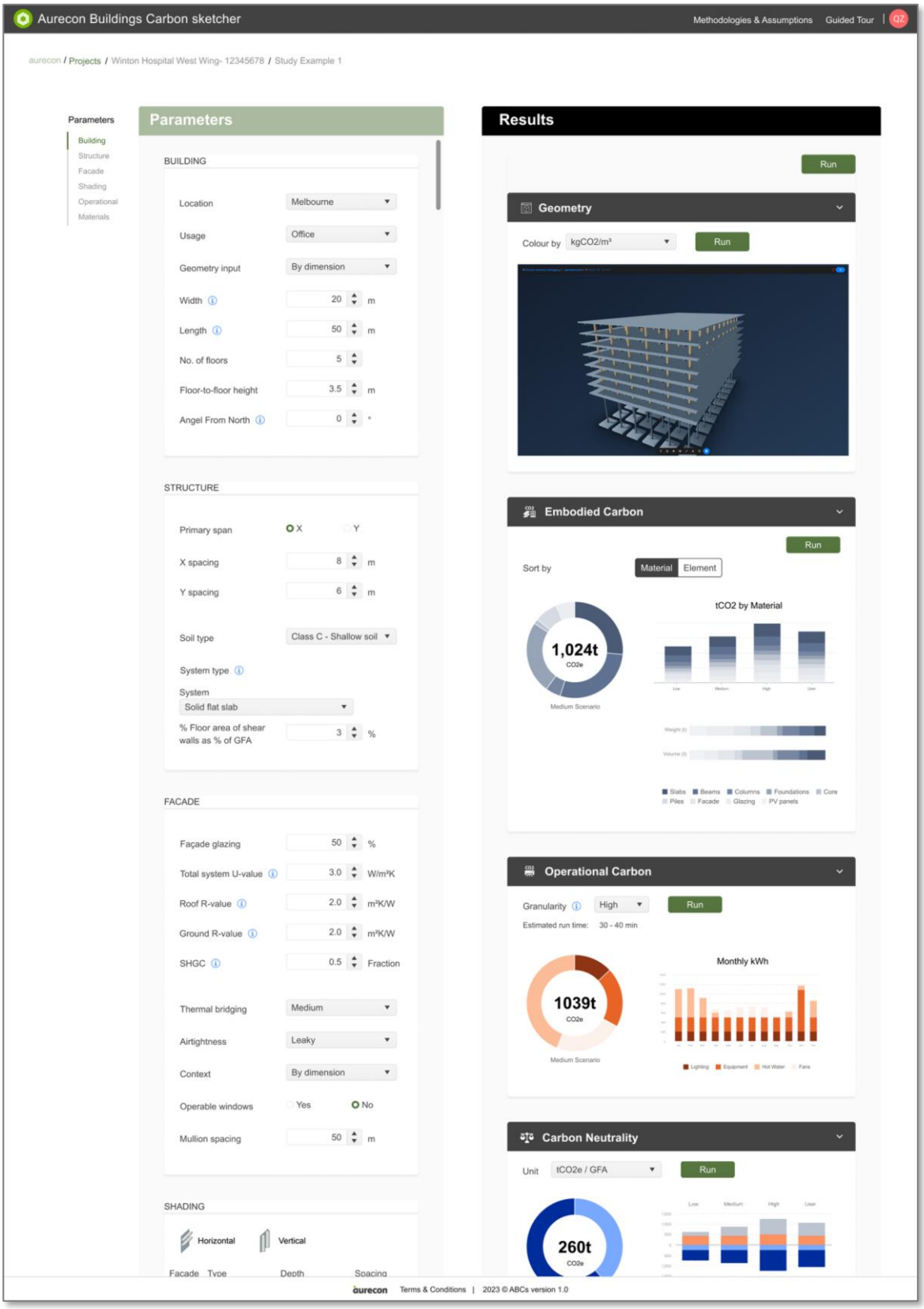


Figure 7. ABCs web UI. Each parameter panel reflects a Grasshopper definition executed with Rhino.Compute.

2.6. Structural definition

A particular contribution of the tool is a design automation definition that auto-sizes structural members based on a "first-principles" approach. That is, based on the building shape and user inputs it determines the applicable loads and slab thicknesses using basic formulas and look-up tables from various standards and supplier catalogues. Once the slab geometries are generated, it applies a similar approach to the beams, then the columns, and lastly the foundations and shear walls. The resulting geometries are sent to the Speckle viewer for visualisation in the web UI; the material quantities are sent to the Emissions definition (see Section 2.10) to calculate embodied carbon.

2.7. Façade definition

ABCs includes a simplified façade embodied carbon calculation that takes several user inputs to generate an estimate of various material volumes for a curtain wall façade (aluminium, glass, and rockwool) and sends these results to the Emissions definition. The curtain wall framing elements are sized using preliminary wind load calculations following building Australian standards. Mullions are sized assuming a simply supported condition, comparing the calculated deflection to an assumed deflection limit. To satisfy the resulting minimum required second moment of inertia (I-value), the definition selects a mullion and transom profile from a set of typical off-the-shelf products. ABCs allows considering vertical and horizontal aluminium shading fins by allowing users to define their spacing and depth for each cardinal direction. All extrusions are assumed to have a wall thickness of 3 mm which is common for curtain wall façades. The insulation, spandrel, and glass material volumes are calculated based on the user's window-to-wall ratio and thermal performance input.

2.8. Energy definition

This definition runs an energy simulation using Ladybug Tools and EnergyPlus, and outputs the estimated annual operational energy consumption data to the Emissions definition (see Section 2.10). It also generates a wireframe of the façade to be visualised in the web UI.

The building mass is segmented into floors and thermal zones, band windows are applied (assuming a curtain wall façade), and shading elements are added as 2D surfaces based on the respective user inputs. User-defined thermal envelope properties are passed into the construction definitions. Thermal bridges are considered by applying a degradation of the thermal properties of these constructions as per the methodology used in the LBT2PH plug-in for Grasshopper. ABCs allows users to choose one of several building usages, based on which ABCs sets a default list of heat load assumptions. ABCs also allows users to pick from several HVAC templates. Finally, the user can pick a trade-off between accuracy and speed by means of a 'granularity' setting that modifies several of the simulation parameters and geometry creation processes (see Figure 8).

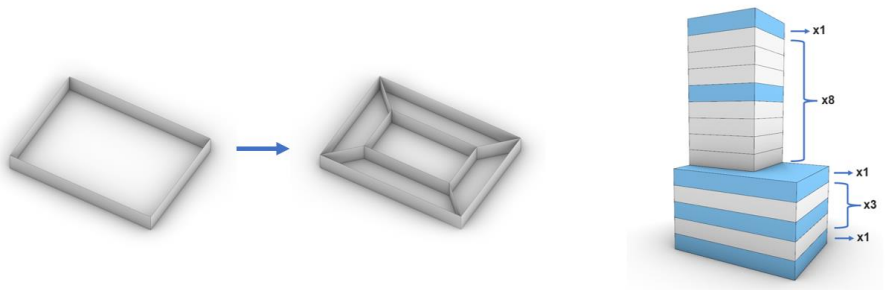


Figure 8. Examples of energy modelling simplifications. Left: ABCs allows either considering each floor as a single thermal zone, or as a core and several perimeter zones. Right: Only unique floors are considered.

2.9. Photovoltaic definition

This definition isolates all roof surfaces, populates them with PV panels and runs a simplified calculation of energy generation using Ladybug Tools. It assumes common panel dimensions, tilt angles, spacings and capacities. The annual, cumulative incident solar radiation on the panels is determined using the Ladybug Tools, the results of which are scaled by an assumed panel efficiency to estimate energy generation. It sends the energy results to the Emissions script (see Section 2.10) and the PV panel geometries back to the web UI for visualisation in the geometry viewer.

2.10. Emissions definition

This script collects all material and energy consumption quantities calculated in the other definitions and applies carbon factors to estimate lifecycle emissions. Given the tool's intent to be used in early design, the authors limited the tool's scope to the lifecycle assessment (LCA) phases A1 (raw materials supply), A2 (transport), and A3 (manufacturing) for the embodied carbon calculation, and phase B6 (operational energy) for the operational carbon calculation. All units are given in weight (kg or t) of equivalent carbon dioxide (CO_2e).

To give the user an idea of the variance in embodied carbon within different material types, the ABCs results section shows "High", "Medium", and "Low" scenarios. The corresponding embodied carbon values were determined by selecting representative products from various suppliers' environmental product declarations (EPDs). To estimate the operational energy emissions, ABCs multiplies the annual energy outputs from the Energy definition (see Section 2.8) by the carbon intensity of the electrical grid of the region of the selected project location. ABCs considers the targets set by the governments of the different regions across Australia and New Zealand to decarbonise their grids by increasing renewable energy sources in future. While it is not guaranteed that these targets will be met, the authors deemed this scenario more suitable than assuming that the current energy mixes will not change in future, which would lead ABCs to convey the false impression that reducing embodied carbon has little impact over the building lifecycle. The purpose of ABCs is to generate insights by comparing options; not to conduct a precise LCA which would be impractical in early design.

The "Carbon Neutrality" section of the web UI simply shows the how much of the lifecycle emissions can be offset by on-site energy generation through PV panels, and therefore what the remaining difference is that would need to be offset by other means in order to reach carbon neutrality.

3. Reflections

Our analysis led to several general insights and lessons learnt regarding the development of early-design lifecycle assessment tools. These are described in the following sub-sections.

3.1. Design strategy vs. design

The current use of lifecycle analysis in building design is limited to the late stages of the design process, where the results of the assessments have limited potential to meaningfully impact the design. Early design assessments have the potential to be much more valuable, however at this stage the design process is fast-paced and information limited. Adopting parametric modelling for lifecycle assessments in early design can create opportunities to explore design options more comprehensively and generate insights. Importantly, however, the designer must understand that the purpose of these design investigations cannot be to obtain a fully accurate and reliable prediction of actual lifecycle emissions. Instead, the value lies in generating insights that can inform an overall design strategy rather than a finalised solution.

3.2. Carbon reduction is a group effort

Many current solutions for carbon reduction in building design are point solutions targeting a specific discipline. However, truly sustainable and low-carbon design tends to be the result of holistic design strategies and cross-disciplinary optimisation. Introducing a design feature that is low-carbon for one

discipline may cause a detriment to another discipline. For example, while introducing shading fins might reduce operational cooling energy emissions, these fins tend to be constructed from aluminium that is so high in embodied carbon that it might not pay off over the building lifecycle. Therefore, any tool developed to address this issue should consider a cross-disciplinary approach.

3.3. Flexibility vs. accuracy

While the previous insight suggests increasing the complexity of a tool to address LCA in early design, there is an important trade-off that developers should consider: the usability and extensibility of the tool on the one hand, and on the other hand, attempting to optimise the tool's accuracy by increasing the complexity of the tool's parameters and calculations. Through the development process of ABCs, the authors have found that the former often outweighs the latter. That is, it is recommended to focus on developing the tool to allow for interdisciplinary considerations and co-development, to produce a flexible tool that allows developing design strategies and creating insights, rather than hyper-focusing on a precision that is unrealistic to achieve given the nature of early design.

3.4. Build tools that can grow

ABCs' software architecture allows for a novel approach to maintenance, future development, and governance. Firstly, ABCs implements each discipline specific embodied-carbon definition as a stand-alone algorithm that obeys a designed schema. The advantage of this is that the platform becomes easily extendable with new models to produce increasingly accurate predictions as other disciplines develop strategies for calculating carbon. The extendibility of the platform can be achieved with minimal developer engagement meaning that extensions are not only easy to implement but allows for anyone with a low level of programming knowledge to contribute to the software. This becomes increasingly important as individuals with a high level of specific disciplinary knowledge do not always have high-level programming experience. This allows for a simplicity in engaging and working with collaborators and maintain disciplinary definitions. Secondly, disciplinary specialists have a degree of ownership and responsibility over their contribution to the software platform. This includes changing and updating the model, maintenance, and testing for accuracy. The value of such a distinct set up is that the individuals with the knowledge to produce and check the outputs of the algorithms are the individuals producing the algorithm.

Thus, the governance and ownership of the tool allows for individual actors to contribute to carbon reduction in whatever way they can. Although the definitions produced to give carbon results for ABCs are not necessarily novel, the capacity to allow these disparate disciplinary definitions to conglomerate into a more *inclusive* and *complete* calculation is. Rather than having to engage a series of disciplines and depend upon their time and hardware, ABCs provides access to this expertise in a real-time, dynamic environment using modern web-development frameworks and remote computing to make this analysis as accessible as possible.

4. Conclusion

Reducing both up-front and operational emissions in the built environment has become increasingly crucial, as it accounts for a significant portion of global emissions. However, the industry faces a complex challenge due to a variety of factors. Firstly, operational emissions depend on local conditions, such as climate, site characteristics, and the emission intensity per kWh of the regional power grid. Secondly, in a global economy, the up-front emissions for the same material can vary greatly. Lastly, the technical and interdisciplinary expertise required to define a low-emission building can be overwhelming.

Without an interdisciplinary approach and a tool that considers the specificities of each project, it is difficult to develop a low-carbon strategy that properly considers the project context. By focusing on major carbon contributors and understanding the interdependencies between different fields, the tool

proposed by the authors within the current research aims to establish a solid foundation in the early design stage for low-emission buildings.

The research led to several more general conclusions on developing early-design lifecycle assessment tools. For example, their purpose should likely be to inform a design strategy rather than a finalised design; developers should accept that the results will be indicative and design a user interface that illustrates margins of error. Most development decisions will be related to finding an acceptable trade-off between flexibility and accuracy. Importantly, carbon footprint reduction is best tackled as an interdisciplinary design practice.

5. Future research

The authors seek to deepen the research in future by considering the following factors:

- Increase functionality and options: For example, include other façade and structural system types, and the embodied carbon of services.
- Revised carbon factors: Replace the current indicative carbon factors by ones based on an extensive data analysis of large LCA databases; also include other emissions metrics.
- Benchmarking: The ability to get an LCA "score" for a given design option (e.g., using [22])
- Cost: Considering the cost impact of different design features.
- Machine learning: ABCs logs all design options ever simulated by its users. Once a sizable database has been generated, the authors intend to use it to generate new insights and conduct predictive modelling to decrease simulation times
- Horizontal extension: The authors intend to create variations of tools like ABCs but geared toward other markets and asset types. The way that ABCs has been developed (see Section 2.3) specifically facilitates reuse and extension of this kind

References

[1] E. O. Cofaigh, E. Fitzgerald, R. Alcock, A. McNicholl, V. Peltonen, A. Marucco, *A green Vitruvius: principles and practice of sustainable architectural design*. London: James & James (Science Publishers) Ltd, 1999.

[2] P. Ellis, P. Torcellini, D. Crawley, "Energy design plugin: an EnergyPlus plugin for sketchup," Berkeley: IBPSA-USA SimBuild Conference; 2008.

[3] S. Kotaji, A. Schuurmans, S. Edwards, "Life-cycle assessment in building and construction: a state-of-the-art report of SETAC-Europe." Brussels: Society of Environmental Toxicology & Chemist; 2003

[4] T. Abergel, B. Dean, and J. Dulac, "Towards a zero-emission, efficient, and resilient buildings and construction sector: Global Status Report 2017," UN Environment and International Energy Agency: Paris, France, 22.

[5] D. Davis. "MacLeamey." Daniel Davis. https://www.danieldavis.com/macleamy/ (accessed April 14, 2023)

[6] M. M. Khasreen, P. Monkiz, P. F. G. Banfill, and G. F. Menzies, "Life-Cycle Assessment and the Environmental Impact of Buildings: A Review" *Sustainability* 1, no. 3: 674-701, 2009.

[7] A. Hollberg et al., "Review of visualising LCA results in the design process of buildings," *Building and Environment*, vol. 190, March 2021.

[8] F. Shadram and J. Mukkavaara. "An integrated BIM-based framework for the optimization of the trade-off between embodied and operational energy." *Energy and Buildings* 158 (2018): 1189-1205.

[9] J. Basbagill et al. "Application of life-cycle assessment to early stage building design for reduced embodied environmental impacts." *Building and Environment* 60 (2013): 81-92.

[10] Arup. “A Carbon Tool.” https://act.speckle.arup.com/assessment (accessed April 14, 2023)

[11] Sasaki. “Carbon Conscience.” https://carbon-conscience.web.app/ (accessed April 14, 2023)

[12] Building Transparency. “tallyCAT beta.” https://www.buildingtransparency.org/tally/tallycat/ (accessed April 14, 2023)

[13] Bollinger+Grohmann. “B+G Structural Web Tool beta.” https://structural-webapp.vercel.app/ (accessed April 14, 2023)

[14] Thornton Tomasetti. “Beacon.” https://www.thorntontomasetti.com/capability/beacon (accessed April 14, 2023)

[15] One Click LCA. “Calculate your environmental impacts in minutes.” One Click LCA. https://www.oneclicklca.com/ (accessed April 14, 2023)

[16] Ramboll. “Fenix tuo rakennesuunnittelun tulevaisuuden tähän päivään.” Ramboll. https://c.ramboll.com/fi/fenix-by-ramboll (accessed April 14, 2023)

[17] Thornton Tomasetti. “Asterisk*.” Asterisk alpha. https://asterisk.thorntontomasetti.com/ (accessed April 14, 2023)

[18] J. Helal, “Towards a comprehensive framework for integrating embodied environmental flow assessment into the structural design of tall buildings,” Ph.D. dissertation, The University of Melbourne, Melbourne, VIC, Australia, 2021.

[19] Akt II. “Carbon.AKT.” akt II. https://www.akt-uk.com/latest/akt-carbon-calculator/ (accessed April 14, 2023)

[20] Payette. “Kaleidoscope: Embodied Carbon Design Tool.” https://www.payette.com/kaleidoscope/ (accessed April 14, 2023)

[21] R. E. Susskind and D Susskind, “The Future of the Professions: How Technology Will Transform the Work of Human Experts”. Oxford University Press, 2017, p. 111.

[22] K. Simonen, R. R. Droguett, L. Strain, and E. McDade, “Embodied carbon benchmark study: LCA for low carbon construction”. University of Washington. 2017

IASS 2023
July 10–14 Melbourne
Integration of Design and Fabrication

Proceedings of the IASS Annual Symposium 2023
Integration of Design and Fabrication
10–14 July 2023, Melbourne, Australia
Y.M. Xie, J. Burry, T.U. Lee and J. Ma (eds.)

Autarkic office boat

Arno D.C. PRONK*

* Eindhoven University of Technology
Vertigo 9.35 Postbus 513 5600 MB EINDHOVEN
a.d.c.pronk@tue.nl

Abstract

The autarkic office boat accommodates a small office with about 10 to 15 employees. The office has a total area of 120m2 divided over 2 floors, both of which are 60m2 in size (5.6m wide, 11m long). It is possible to choose your own office setup. In addition, there is meeting room with an area of 25 M2 and an archive room. The roof of the boat is curved and has photovoltaic cells. The archive is located at the bottom of the office boat with a limited floor height. The size of the archive is 15m2. Other areas in the boat are a reception, the toilets, a pantry and an installation room. For the realization of this design we tried to realize the following objectives: Autarkic, Environmental friendly, Reliable Attractive and Affordable. With this project we would demonstrate an example to show that it is possible to combine high environmental requirements, and an attractive affordable space.

Keywords: autarkic, office boat, energy, eco-friendly

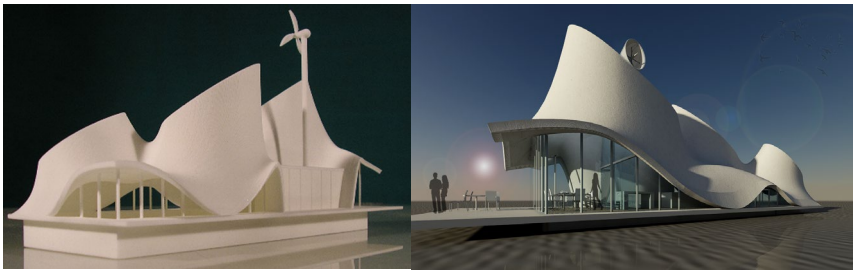


Figure 1 and 2. Design for an autarkic office boat

1 Starting points

With the realization of this room, we started with the following objectives:

1 Autarkic

2 Environmentally friendly C2C

3 Reliable

4 Attractive design

5 Affordable

With this autarkic office boat we have strived for an optimal combination of these objectives. With this project wants to show that it is possible to combine high environmental requirements with an attractive design and affordable space.

1.1 Installation concept

The installation concept is based on three pillars:

1. energy generation
2. energy storage
3. energy consumption

By efficiently combining these three pillars with the situation, use and architecture, the aim is to achieve an optimal and affordable installation [2].

Copyright © 2023 by Arno D.C. PRONK. Published in the Proceedings of the IASS Annual Symposium 2023 with permission.

1.2 Energy generation

On the water, depending on the situation, there is soon 40% - 60% more wind than in the built environment. Due to the economical installation and the relatively large supply of wind, the size of the wind turbine can be limited. When there is no wind, the office boat is supplied with energy by the PV cells that are directed at the sun at an angle of 36 degrees. The ratio between wind and solar energy is on average 60% - 40%. A fully electric solution was chosen because it has the highest efficiency with the best price/quality ratio.

1.3 Energy storage

The principle is based on the storage of heat/cold. This storage is equipped with PCM panels (Phase Changing Materials). The storage with the PCMs provides heat storage in the winter and cold storage in the summer. The buffer makes it possible to significantly reduce the power to be reduced. For example, a heat pump of only 2.3 kW is sufficient. In the event of a large supply of energy by wind turbine and/or PV cells, the cold/heat buffers will first be filled. Storage of energy in batteries will take place to a limited extent; surplus energy can be made available to the grid. The extraction of energy from the grid will only take place if too little energy is generated over a longer period of time and the accumulated buffers have been used. Such a situation can occur in the winter months, for example in case of fog in combination with a frost period, as a result of which there is no energy generation, combined with high consumption.

1.4 Energy consumption

The energy consumption of the office boat will be limited as much as possible by ensuring a low surface, good insulation, heat recovery, energy efficient devices, using buffers and offering a local 48 VDC electricity grid in addition to the usual 230 VAC electricity grid.

2 Technical solutions

2.1 Ventilation, heating and cooling

A modern office anno 2011 must be sustainably heated and cooled. The heating and cooling of the office boat are tailored to the Dutch climate. The climate in the Dutch winter situation is characterized by two situations:

• A very cold non-cloudy day with relatively much sunshine (diffuse and direct) and a lot of nocturnal radiance.

• A cold cloudy day with relatively little sunshine, mainly diffuse solar radiation, but less nocturnal radiance.

In the summer, the design is tailored to a period with a lot of sun with high temperatures. The architecture of the boat allows for smaller openings and overhangs on the south and larger openings on the north, limiting the cooling load. Furthermore, the high spaces of the *cones* act as natural storage that can be used as a heat or cold buffer depending on the weather forecast.

2.2 PCM

The abbreviation "PCM" stands for the Phase change material. The PCM is used for the melting and solidification of material. At this phase transition, a lot of energy is absorbed or released. Converting a material from solid to liquid costs 80 times more energy than heating the same amount of material 1°C. The phase transition material consists of paraffin or saline solutions. The phase transition can be set to a predetermined temperature, e.g. 18°C or 40°C. This makes it possible to buffer a large amount of energy at a given temperature. If the room temperature is higher than the melting temperature, the PCM underfloor heating cools the room until all pcm has melted. If the room temperature is lower than the melting temperature, the PCM underfloor heating heats the room until all the PCM is solidified. This process takes place without the need to use moving parts such as compressors, heating pumps or similar

installations. A 10 mm thick PCM-panel has the heat-accumulating capacity of a 300 mm thick concrete slab. By using this heat-accumulating capacity, it is possible to reduce the installed power for the office boat by 50%. This can be achieved by anticipating the desired temperature in the living areas in combination with the weather forecast, for example in the summer night cooling and in the winter night heating. (In doing so, cheap and widely available energy is used in the winter night of the electricity grid) This building installation concept has been translated into affordable system concepts, as described in the scientific journal *Bau Bionik* (O.A. University of Saarbrücken)

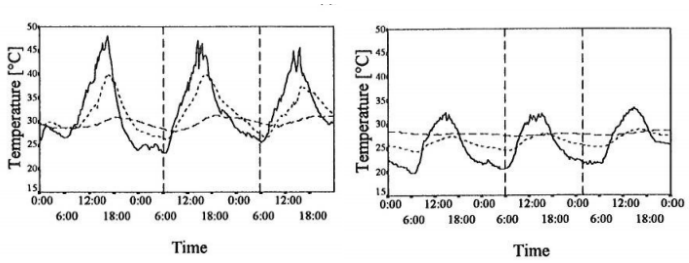


Figure 3. Temperature graphs

Measurement results free field

Dense line = outside temperature

Dotted line = Temperature in the semipermeable membrane

Dashed line = Measuring temperature in the conditioned room

The graph shows the dampening effect of PCMs in combination with anticipatory floor cooling and heating in the office boat. An additional advantage of the application of PCM floor heating and cooling is that particularly high insulation values are superfluous, resulting in less material use and a manageable investment.

2.3 Air-water electric heat pump

The application of PCMs is combined with the application of a new generation air-water electric heat pump as well. The required pump has a thermal capacity of only 2.3 kilowatts. This is half of the required power. (It can be compared to a refrigerator whose condenser is used to heat in winter and to cool in summer.) For hot water production, instead of a flow-through device, such as a combi boiler, an indirectly heated hot water boiler is chosen. This is connected to the electric air-water heat pump and a heat recovery of the heat from waste water.

2.4 Electricity

The summer is characterized by many sun and heigh temperatures. In winter the temperatures are low but there is more wind. We will use electricity in the winter months mainly from the wind and during the summer mainly from photovoltaic solar cells. A hybrid combination between Pv-cells and an urban wind turbine (UWT) will be a better solution than only using PV cells or UWTs. Even if the low efficiency of UWTs is taken into account, a hybrid combination remains the best solution in the Netherlands. We have opted for a hybrid solution in which 60% of the energy is supplied by wind turbines and the remaining 40% by PV cells. This combination delivers an average of 14 kWh (e) / summer day and 21 kWh (e) / winter day.

For the electrical installation we opt for direct current (DC) at 48 Volts, because DC has many advantages compared to alternating current AC. For example, DC motors are more efficient and DC does not suffer from electricity, which means that AC grids are oversized. Furthermore, solar panels, fuel cells and wind turbines all supply DC. In conventional situations, these are all converted into the

usual 230 volt AC. The conversion from DC to AC occurs some loss. To avoid the loss it is better to chouse for DC. Due to the lower voltage we need thicker cables. By choosing 48 Volt DC, the efficiency improves by 20%, so we have to install fewer solar cells and can choose a smaller wind turbine with less nuisance for surrounding neighbors. Nowadays, electrical appliances can be purchased in various places that operate on 24 or 48 VDC. We split the electricity distribution into 24 VDC (measurement and control installation), 48 VDC (mechanical installation) and 230 VDC (external energy demand).

The office boat must be able to bridge a cycle of 1 day. To bridge the requested period, we assume the worst situation for our system: a cloudy, windless winter day. Then the energy demand is the highest, while the energy production is the smallest. The energy that is needed is provided by a collection of batteries with a capacity for this day. If the weather forecast predicts a second day with the same weather type, the buffers will be replenished by using night power from the electricity grid. Such a situation will occur several times a year. Sizing the buffers over a period of several days is possible but requires disproportionate investments in batteries, PV cells and UWTs. In addition, night power is available and the Netherlands has a good electricity grid. We assume that the boat is used 6 days a week for a period of 12 hours per day. From 8 a.m. to 8 p.m.

The dimensioning of the installation complies with the applicable Dutch and European standards. For the dimensioning of the design, the performance criteria are derived from the following current standards:

- The Dutch Building Decree.
- The Dutch and European standard NEN-EN 15251, criteria for indoor conditions including thermal, air quality, light and sound.
- The heating capacity is calculated according to the Dutch and European standard NEN-EN 12831, heating systems in buildings, method for calculating the design heat load.
- The cooling load is calculated according to the Dutch standard NEN 5067, the cooling load calculation of a room.
- The electrical installation must comply with the Dutch standard NEN 1010.

3.Installations

3.1. Introduction

The design of the installations is based on the following innovations:

- It is an orientation-dependent design to prevent an excessive cooling load. Contrary to what has been propagated so far with regard to zero energy houses or passive housing: 'use passive solar heat on the south façade as much as possible', this does not apply to offices. Due to the internal heat production, cooling in offices is a much bigger problem than heating.
- The office is not only ventilated and heated but also sustainably cooled. Anno 2022 this is desirable for thermal comfort. By responding to this need, residents will be prevented from purchasing an energy-consuming electric air conditioner themselves in the future.
- Part of the office is conditioned by PCM underfloor heating and cooling.
- Furthermore, the office boat is equipped with a new generation of reversible electric air-water heat pump of 2.3 Kilowatts. This is only possible in combination with PCM underfloor heating and cooling.
- It is an 'all electrical solution' in which new calculation rules have been developed to achieve an ideal hybrid electricity production.

- Out of efficiency, it was decided to apply a local 48 VDC electricity grid. This leads to an efficient improvement of 20 percent compared to a 230 VAC electricity grid. By massively realizing the switch in the Netherlands from the current 230 VAC grid to local 48 VDC electricity grids, it would be fairly easy to achieve these environmental objectives.
- The excessively thick insulation packages of up to 30 to 40 centimeters, as is also proclaimed for zero energy houses and passive housing, are superfluous in the given design. Here, only optimal insulation is provided.

We have strived for a simple thought-out and robust installation concept. By equipping the office boat with 60m^2, 10 mm thick PCM underfloor heating and cooling panels, the installation can be greatly simplified without having to compromise on comfort. This allows us to offer a solution that is both affordable and robust.

3.2. The mechanical installation

3.2.1 Room ventilation

The ventilation installation must ensure a healthy indoor climate. In addition, we do not want to lose energy as a result of ventilation. That is why an HR-WTW unit is used.

Total net floor area 103.8[m^2]Including the overflows we round this off to 116[m^2]

According to the Building Decree, the minimum ventilation flow rate is 0.7[ltr/(s.m^2)]=2.5[m^3/(h.m^2)].

The size of the HR-HR-WTW unit then challenges 116 [m^2]*2.5[m^3/(h.m^2)]=rounded 290[m^3/h].

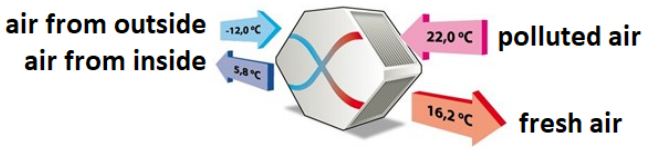


Figure 4. WTW unit

3.2.2 Space heating and cooling

On the basis of the international standard NEN-EN 15251, Criteria for indoor conditions including thermal, air quality, light and sound, a thermal comfort performance Roman II is chosen. This concerns an adaptive indoor temperature of at least 20 degrees Celsius at an outside temperature of -10 degrees Celsius and an operative indoor temperature of 26 degrees Celsius at an outside temperature of +30 degrees Celsius.

In the office boat, the offices and kitchen are covered with innovative PCM underfloor heating (a patented Dutch invention) while the other rooms are covered with conventional underfloor heating.

3.2.3. Warmwater production

The average drinking water consumption of a four-room house is 280 liters per day. For an office, this is much lower. That is why we explicitly opt for an indirectly fired hot water boiler of 160 liters. The hot water supply is provided with a water-saving tap and heat recovery from the waste water. The 160 liter boiler is connected to the 2.3 Kilowatt innovative air water electric heat pump.

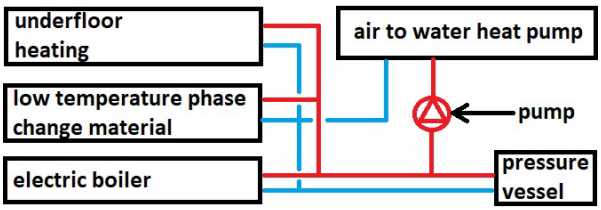


Figure 5. Installation scheme

3.2.6. Electrical installation

When comparing alternating current (AC) and direct current (DC), the following stands out:

• A brushless DC motor is more efficient and easier to control than an AC motor. The smaller fans, pumps and compressors are already equipped with DC motors as standard. The return improvement is approximately 15%. Motors are equipped with transformers and rectifiers for the conversion of 230 VAC or 300 VAC from the grid to the required DC voltage of the motor for example 24 or 48 VDC. The loss factor for this is approximately 5% to 10%, which largely cancels out the efficiency improvement of the engine.

• Photovoltaic solar cells, fuel cells and wind turbines equipped with synchronous DC generators produce 'automatically' DC electricity. Nowadays this 12 or 24 or 48 VDC is still converted to 230 or 300 VAC by means of transformers and invertors. The loss amounts to approximately 5% to 10%.

• Alternating current and ac grids have another thing called 'reactive power'. Due to capacitive and inductive action, the current 'runs in front of or behind the voltage', so that the maximum power is not available. Because of this reactive power, an AC network must be oversized. This 'loss' is indicated by a cosine phi of 0.85. On the other hand, DC grids must be equipped with batteries that also have a loss factor of 10%.

• Because the voltages of DC grids are lower than for AC networks, the cable thicknesses increase and it is necessary to switch from a 'central box network' to a 'star network' with direct power supplies of all components. Furthermore, only local networks are applicable. Electricity grids as Thomas Edison already proposed and made around the turn of the century from the 19th to the 20th century.

The efficiency improvement that occurs by opting for a local 48 VDC grid instead of a 230 VAC is then: η_accu-η_motor η_gelijk η_cos φ η_invertor=0.9-0.9*0.95*0.85*0.95≈21[%].

Furthermore, in 2010 computers can already be purchased on PV solar energy. With the latest development of integrated computers on solar energy through PV cells is an interesting development because it combines all the advantages of direct current. Nevertheless, we opt for a split electricity distribution in the boat, namely:

• 48 [VDC] for the mechanical engineer installation.

• 24 [VDC] for the measurement and control system and

• 230 [VAC] for white and brown goods.

It is also striking that the electricity consumption of a one person household is approximately 60% of a four-person household. So the dimensioning of the sustainable electricity supply depends on the occupancy rate of the office boot. Nevertheless, we opt for a decentralized electricity production per office boat consisting of:

• A UWT power of 4.5[kW]

• 12[m^2] PV cells.

This combination produces 14[(kWh(e))/day] under summer conditions and 21[(kWh(e))/day] under winter conditions. This fits the electricity demand of a four-person family. This hybrid combination forms a self-regulating electricity production unit.

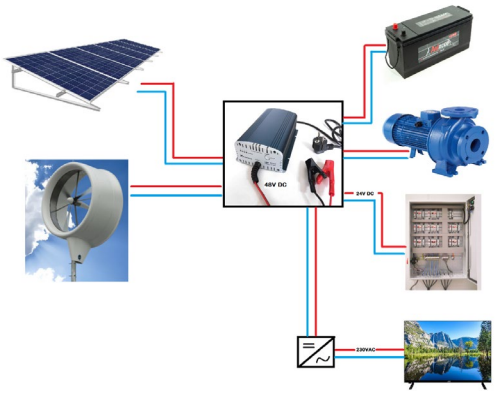


Figure 6. Electrical installation

3.2.7 Red un dance, risk and robustness

The installation must bridge a time period of 7 days! What does this mean?

The worst design day is: A cloudy, not too cold winter day with windless weather. Then the largest electricity demand occurs and the electricity production is the smallest.

The wind turbines are stationary. The maximum electricity production through PV cells is then 12*0.11*(90*16)/π=0.60 [(kWh(e))/d] while the electricity demand is 21[(kWh(e))/d].

Under the condition that the clouds and the windless weather persist for 7 days (this is in principle an unrealistic assumption) and the office is occupied with 4.0 people during these days, the PCM buffer will also be completely discharged. This results in a daily storage capacity of: (21,000-600)/48=425[Ah/d]. This time 7 days and that is 7*425≈3.000[Ah]

In the calculations we have assumed 12 m2 of PV cells. Due to the robustness of the design, we assumed an area of 20 m2.

3.2.8. Operation of installations

3.2.8.1. Mechanical engineering installation

• The ventilation installation. A natural air supply through pressure-controlled outside air grilles and a mechanical air exhaust fan executed as a variable volume system. Air flow rate 290[m^3/h]

Operation: It draws air in outside and carries air inside In the Heat Recovery installation (WTW), the heat is exchanged between these two streams with the indoor air transferring the heat to the incoming outside air.

Energy consumption: 0.9 [kWh/d]

Maintenance: The filters must be changed every 6 months

• The conventional space heating. all other rooms are equipped with conventional underfloor heating and cooling approximately 60[m^2] with a heating capacity of 40[W/m^2] total 2.4[kW]

Operation: The air that runs along the radiator is heated by the radiator. The air rises and the room passes through a pressure difference.

• The innovative space heating. The office and meeting rooms are equipped with an innovative PCM underfloor heating and cooling also approximately 60[m^2] with a heating capacity of also 40[W/m^2] total 2.4[kW]

Operation: PCM stands for phase changing materials, these materials change from solid to liquid at a certain temperature. For this transition, the material needs a lot of energy, which is achieved because the outside temperature rises. If the outside temperature drops again, the material will transfer its heat back to its surroundings.

• Hot water production. An indirectly fired hot water boiler of 160[ltr]

Operation: The central heating water of the boiler flows through a heat exchanger in the boiler and thereby indirectly heats the water in the boiler. As a result, a very high hot water yield can be achieved.

The heat and cold production. A new generation of reversible electric air water

heat pump with a heating capacity of 2.4[kW]

Operation: The heat is extracted from the outside air, this heat is released to the water circuit of the office boat. This heat is brought to temperature together with an indirectly fired hot water boiler for heating.

Energy consumption: for heating is = 6,5[kWh/d]

Maintenance: cleaning 1 time a year.

3.2.4. Water production

Water for the flushing of toilet is obtained by collecting rainwater. In case of a shortage of rainwater, surface water can be absorbed. Drinking water is obtained by connecting to the water network or bunkering water in a water tank. In every port, water can be obtained from a bunker boat.

3.2.5. Cleaning waste water

For the cleaning of the waste water, we opt for the direct cleaning of the waste water by a pre-treatment in a skeptical tank by means of an anaerobic pre-cleaning and a after switched aerobic after cleaning, so that the cleaned waste water can be discharged into a central swimming pool and from there can flow to the surface water. A separate cleaning of the pool water with chlorine is therefore no longer necessary. See the diagram below.

3.2.6. Drinkwater and wastewater production

• Helophyte filter

Operation: The helophyte filter is a filter where the bacteria in the reeds purify the water. This way of filtering removes a lot of waste from the water, but it is not yet enough to be used as drinking water. It can be used to discharge it to the surface water or as a flush of water in the toilet.

Maintenance: check the pipes 1 time a year, mow the green 1 time every 2 years in the spring.

• Sceptic tank

Operation: In the septic tank, the waste water from the toilet enters a tank, in this tank one part settles and another part floats on the water. The sludge that lies on the bottom digests by a slow process with bacteria. Not all matter is digested, which is why it still has to be emptied every so often.

Maintenance: Some chemicals should not be in the septic tank. Such as bleach, unblocking agents, strong descaling agents, alkaline agents, medicines, oils, cooking fat, pesticides and paint.

Furthermore, it must be emptied every 5 years by a sewer cleaning company.

• Fat separator

Operation: Grease traps are mandatory for catering establishments, snack bars, butchers, bakers, etc.

In the grease trap, the waste water comes from the shower, sink, kitchen and washing machine. The water gets in here and vertical bulkheads ensure that the water stops, the fat therefore floats above. The water can then be discharged back to the helophyte filter.

Maintenance: With a floating layer of 16cm of fat, it can be emptied.

• Pumps and pressure vessels in the system:

Operation: The pumps and pressure vessels ensure in the water pipe system that the water is pumped around and that it can expand at high temperatures.

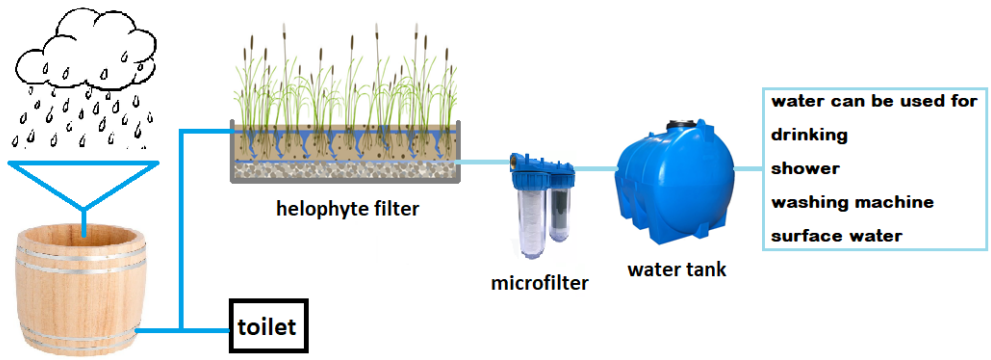


Figure 7. Cleaning waste water

4. Material

The office boat is constructed from sustainable materials.

4.1 How can sustainability be measured?

Daniël Tulp's [1] graduation report (The possibilities for the Cradle to Cradle concept in Dutch housing APR 2009 4416) explains how he arrived at the scores of the various materials. These have been taken up in this report. The concept of sustainability is also described here[3].

4.2 Inventory of which building materials / parts are needed for the boat

• Mezzanine floor (European oak or poplars)

• Insulation (sheep's wool, hemp, expanded stool or flax insulation)

• Glass (HR+)

• The characteristic shell construction is made of composite based on flax and cork which is processed with a natural resin.

• Floor covering/laminate

• Finishing/stucco/tiles

• Construction boat itself (concrete box)

As an alternative to the concrete barge , a standbarge or pontoon can be taken for the office boat. This is filled with a light and durable filling material such as blast furnace slag.

4.3. NIBE waste scenario

The NIBE [4] waste scenarios (Netherlands Institute of Building Biology & Ecology) give a picture of the current recycling practice, but do not have the potential that the materials have in the future in the field of recycling. Therefore, they are an important indicator, but will need to be supported by other data. The NIBE waste scenarios are based on discard scenarios used in the eco-quantum 2.0 from 2002 (developed by founding build research).

Table 1. Nibe waste scenario

material	specification	reuse	recycling	burning	dumping	material	specification	reuse	recycling	burning	dumping
finishing	sticks to debris	0	0	0	100	copper	plates and tubes	0	95	0	5
finishing	sticks to wood, plastic ar	0	0	100	0	copper	power lines	0	85	5	10
aluminum	profile plates tubes	0	94	3	3	plastics	waste	0	0	80	20
concrete	elements bricks	0	99	0	1	plastics other	profile plates tubes	0	5	85	10
concrete	0% rubble granulate	0	99	0	1	lead	slabs	0	95	0	5
concrete	20% rubble granulate	0	99	0	1	metals	waste	0	90	5	5
concrete	100% rubble granulate	0	99	0	1	metals other	conneting	0	90	5	5
bitumen	roofing material	0	5	90	5	organic	waste	0	0	85	15
aerated concrete	elements blocks	0	99	0	1	organic other	insulation	0	0	95	5
elastomers	roofing material	0	5	85	10	plate material clean	large parts	0	10	85	5
elastomers	roofing material	0	5	85	10	plate material dirty	large parts	0	0	95	5
polystyrene	insulation	0	5	90	5	polyolefins	tubes foils	0	5	85	5
fine ceramic	plumbing	5	80	0	15	debris	waste	0	0	10	90
gypsum	plates blocks	0	5	0	95	pvc	profiles	0	80	10	10
glass	flat glass	0	70	0	30	pvc	tubes	0	70	20	10
glass foam	insulation	0	10	5	85	pvc	roofing material	0	5	85	10
glass wool	insulation	0	10	5	85	shells	earthwork	0	90	0	10
gravel	ballast	99	0	0	1	steel light	profiles plates tubes	0	95	0	5
coarse ceramic	stones and tiles	0	99	0	1	steel heavy	beams	50	45	0	5
wood clean	beams and plates	5	10	80	5	stone wool	insulation	0	10	5	85
wood clean	waste	0	0	85	10	full core	cladding	0	20	75	5
wood dirty	waste	0	0	90	10	xps	insulation	0	5	90	5
wood dirty	panted	0	0	95	5	sand	earthwork	95	0	0	5
limestone	elements and bloks	0	99	0	1	zinc	profiles plates tubes	0	95	0	5

4. 4. Possibilities to apply C2C materials

Wood fiberboard

This product is made without the addition of binders and is therefore completely biodegradable. Wood fiberboards are boards of waste wood that are made into insulation boards by a process of fiberization under humid conditions and without added binders or adhesives, making the material suitable for composting. The nature plus quality mark has been awarded to this product, which offers a certain guarantee for the low environmental impact. Further study of this German quality mark could provide more insight, but has not been included in the research of D. Tulp.

Oak parts (93.8%)

European oak is a very hard softwood that, due to its long service life and because it can be used untreated as façade cladding, has a very favorable score in the c2c instrument. But due to the scarcity and price almost no longer used as façade material. Oak wood is harvested in forests and not in plantations.

Sheep wool insulation (63.2%)

Due to the use of pesticides in herding sheep, biodegradability may be a problem. After the use of the sheep wool, based on the NIBE waste scenario we assume that 5% will be dumped and 95% will be burned. According to NIBE, the sheep wool insulation blankets have the lowest environmental load of all insulation materials. It has a thermal conductivity coefficient of 0.0412 W/mK, which means that a thickness of about 105mm is required for an Rc value of 3m²K/W.

However, the sheep wool insulation material are often treated with pesticides against mold formation. However, this stands in the way of biodegradability and affects the social and ecological aspects.

Expanded cork insulation (77.8%)

Expanded cork insulation is biodegradable and no artificial means are added for fire safety and mold prevention. Based on the NIBE waste scenario 5% dumping, 95% burning.

The cork, which comes from sustainably managed forests, can be harvested from a tree for around 10 years, after which the cork is taken into an autoclave. This increases the resistance to biological degradation and no additional resources need to be fed to it. The product is still susceptible to rot in the long run, so it is believed to be biodegradable.

Flax (insulation) (76.4%)

Flax (insulation) is biodegradable if binders based on organic products are used. When growing flax, it is possible that pesticides are used to protect the harvest. These products are inferior to biodegradability and social and ecological aspects. Growing the crop in monocultures is not conducive to biodiversity and, if scaled up, can disadvantage the food supply.

Organic cultivation does not use chemical pesticides and will therefore have less or no influence on biodegradability and social and ecological aspects. Synthetic resins are used as a binder, but also on the basis of an organic product.

NIBE waste scenario 5% dumped, 95% burning

HR Glass (85.4%)

Glass can be recycled into a similar product provided that no films or material coatings are mixed in it.

In the NIBE publication, glass is not assessed as a separate material. The only clue given is an exterior door made of HR++ glass in an aluminum frame, which also includes the pillars and sills. Therefore, for the absence of toxicity, the emission profile from the GPR Building database was used. Pure glass can be recycled, but glass with metal coatings, foil or reinforcement will have to be dumped or burned.

Aluminum(68.1%)

Aluminum is one of the materials in which it is technically possible to produce the same product in the next cycle. The properties of aluminum (homogeneous, mono-material, no alloy, low melting temperature) make it extremely suitable for recycling without loss of quality. When anodizing aluminum, a protective oxide layer is applied to the aluminum with the help of an electrolysis. This makes no difference to recycling

NIBE waste scenario 5% dumped, 5% burned, 90% recycling

Anhydrite cast screed (41.0%)

The material becomes contaminated additives and physical mixing with these substances and possibly the interfaces of other products ensures that only inferior recycling is possible. Anhydrite is hydrated gypsum (CaSo4) that was already used as a binder during the construction of the Egyptian pyramids.

NIBE waste scenario 5% dumped and 95% recycling.

4.5 lifecycle costing

Table 2. Lifecycle costing

material	realisation	Price, euro	live span	transport	demolition	dumping	recycling	burning	Score
loam stone	inside walls	48/m2	75	+	21,35/m2	1%	99%		92%
loam plaster	finishing	8,12/L	25	+	+	1%	99%		82%
straw loam stone	inside walls	0,69/stone		+	+	1%	99%		
robinia wood	structure/finishing	1910/m3	>25	+/-	+/-	5%	10%	85%	88%
oak	structure/finishing	4290/m3	>25	+/-	+/-	5%	10%	85%	94%
poplars	structure/finishing	2100/m3	>25	+	+/-				
expanded cork insulation	insulation	31,20/m2	75	-	-	5%		95%	78%
coconut fiber board	insulation	14/m2	75	-	-	5%		95%	78%
episis	insulation	16,3/m2		+	-				
woodfiber insulation	insulation	15,45/m2		+	-	5%		95%	
sheep wool insulation	insulation	20,35/m2	75	+	-	5%		95%	63%
flax insulation	insulation	14,04/m2	75	+	compost	5%		95%	76%
stucco paint	finishing		25	+	+	1%	99%		
waterproof loam plaster	finishing	6/kg	25	+	+	1%	99%		
loam plaster	finishing		25	+	+	1%	99%		
HR glass	glass	42/m2	20	+	+/-				85%
anhydrite floor	finishing			+	+/-				41%
elastomers	roofing material	9,95/m2	50	-	+/-	10%	85%	5%	41%
aluminium	roof trim	3/m1		-	+/-	5%	5%	90%	68%

References

[1] Tulp, Daniël (June 2009) B The possibilities for the Cradle to Cradle concept in Dutch housing. NL-4416 BWK

[2] Ramesh, T., Prakash, R., & Shukla, K. K. (2010). Life cycle energy analysis of buildings: An overview. *Energy and buildings*, *42*(10), 1592-1600.

[3] Geldermans, R. J. (2016). Design for change and circularity–accommodating circular material & product flows in construction. *Energy Procedia*, *96*, 301-311.

Internet

[4] NIBE (Netherlands Institute of Building Biology & Ecology) http://www.nibe.org/

http://nl.wikipedia.org/wiki/Levenscyclusanalyse

http://nl.wikipedia.org/wiki/Life_cycle_costing

http://www.groenebouwmaterialen.nl/a-9402180/leemstenen/procrea-leem-elementen-25-x-25-x-10-cm-pallet-met-80-stuks-5-2-m2

http://www.glasdiscount.nl/Zonwerend.htm

http://www.af.nl/voorraad/massief/eiken/prijslijst.html

http://www.duboshop.nl/index.php?item=vlasisolatie-pl040--in-pak-van-12-platen--per-pak&action=article&aid=144&lang=NL

Proceedings of the IASS Annual Symposium 2023
Integration of Design and Fabrication
10–14 July 2023, Melbourne, Australia
Y.M. Xie, J. Burry, T.U. Lee and J. Ma (eds.)

Designing structures from reused steel: A cost-effective carbon mitigation strategy

Juliana BERGLUND-BROWN[*], John OCHSENDORF[a]

[a,*] Massachusetts Institute of Technology
MIT Room 5-418, 77 Massachusetts Ave, Cambridge, MA 02139 USA
jbbrown@mit.edu

Abstract

New structures can be designed from existing steel elements at lower cost and with dramatically lower carbon emissions when compared to conventional steel structures. This paper establishes more certainty about the supply of steel elements, quantifies potential carbon and cost savings, and identifies the variables that most impact such savings to better enable designing steel frames. This work first outlines why reusing gravity beams and columns is particularly advantageous via a state-of-the-art overview of the steel value-chain. Next, a high-level material flow analysis is conducted for three of the largest steel-producing markets globally, indicating that the quantity of the existing steel heavy section scrap covers 140% of the demand for imports of steel. A partial LCA utilizing a comparative cut-off method is then performed coupled with a cost estimation, which demonstrates a potential for around an 87% reduction in carbon emissions from steel reuse instead of recycling. Based on the findings of the partial LCA, a factor analysis is performed with both a stochastic sampling and nine real building projects to identify the variables impacting carbon cost associated with reuse. Structural weight was found to have the largest impact on reuse emissions, followed by number of elements, and then transportation distance. This paper then proposes strategies for practitioners to deploy reused elements in their designs.

Keywords: salvaged materials, uncertainty, life-cycle design, steel, unknown material quantities, circular economy, reuse of structural components, gravity beams and columns, structural design, Hangai prize applicant

1. Introduction

In today's steel value chain, heavy section steel is extracted from buildings and stockyards, remelted with other steel sources, reformed, and remanufactured to create new heavy sections and other products. Figure 1(a) depicts structural steel elements sold to scrap collectors and remelted before the end of their usable life. An alternative to remelting viable heavy section steel is element reuse. Figure 1(b) demonstrates a recent example where 83 metric tons of steel from an existing project were dismantled, stored, refurbished, and reused to construct a new building.

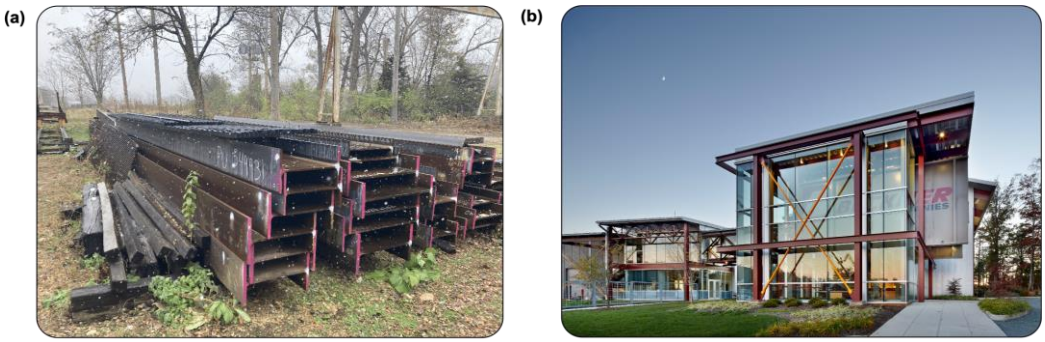


Figure 1. (a) Surplus steel destined for a scrap yard. (b) 83 tons of salvaged steel (in red) used in a new facility [1]

Copyright © 2023 by Juliana BERGLUND-BROWN and John OCHSENDORF. Published in the Proceedings of the IASS Annual Symposium 2023 with permission.

The structural system typically accounts for 50-60% of embodied carbon, and the majority of buildings are demolished before the end of their maximum usable life [2, 3]. The climate crisis demands an acute transformation of the way we source and design the built environment. Reducing the carbon of structural systems will markedly reduce the overall environmental impact of the construction sector and help meet IPCC 2050 goals [4]. One strategic pathway to reduce the embodied carbon in structures is to incorporate reuse of salvaged materials into the structural design process [5].

This paper focuses on gravity beams and columns, due to their loading conditions and structural weight in buildings. The paper clarifies the opportunity for steel reuse in three ways: 1) Characterizing steel component demand with reused building stock supply (scrap market/percentage of whole building components); 2) Establishing the cost and carbon savings potential of component reuse; and 3) Understanding the variables and factors that most affect the cost and carbon savings potential of component reuse of structural frames.

1.1 Reuse of structural steel elements

Steel building structures typically have the highest embodied carbon impacts when compared to masonry, wood, concrete, and reinforced concrete projects [6]. Reuse of steel elements in buildings has been identified as a strategy to cut industrial emissions [7]. Steel structures often have a far shorter service life than its capacity allows [3]. Reusing structural steel gravity elements bypasses the recycling step that is standard practice in most steel supply chains; circumventing the recycling process of steel components leads to the avoidance of high energy costs and carbon impacts, in addition to alleviating new pressures on the steel supply chain [8]. Today's structural steel supply chain is experiencing high carbon impacts, increased demand and growing impacts of more copper contamination in structural steel supply chains [9, 10].

While designing with salvaged structural steel is a beneficial alternative for structural engineers to reduce embodied carbon in the built environment, there are still many barriers that inhibit designing with reused gravity elements in buildings at scale. Uncertainty surrounding element availability and opportunity cost are two of the largest concerns about implementing reuse [11].

1.1.1 Existing use cases

The reuse of structural elements has existed as a building practice since antiquity. Steel reuse specifically has become increasingly present in recent building projects. The steel depicted in Figure 1(b) was obtained from both a 58-foot-long truss bridge, and 15-foot steel plate girders used in a collegiate stadium [1]. Steel tubes have been reused as load bearing elements in Colorado and London [12, 13]. Additional analyses have demonstrated how to utilize used transmission line towers as space trusses [14]. Several projects, such as Holbein Gardens in the UK, reuse structural frames [15].

2. State of the art

Figure 2 details the structural steel industry's current best practices for steel making, wherein structural steel is taken as scrap from demolished buildings or surplus in stockyards, recycled, melted down, mixed with other scrap, reformed into heavy sections, fabricated, and then erected on a new project. This figure does not detail additional inputs to the system such as heavy-section imports. Additionally, throughout the supply chain, surplus steel returns to scrap before being used structurally. The use of salvaged steel prior to remelting would modify this value chain.

2.1 Understanding the steel reuse value chain

Despite avoiding steel waste via recycling, current literature indicates emissions reduction targets set by the IPCC will not be met with current "best steel-making practices" alone, and limited research highlights potential for Circular Economy independence in the U.S. steel sector [18].

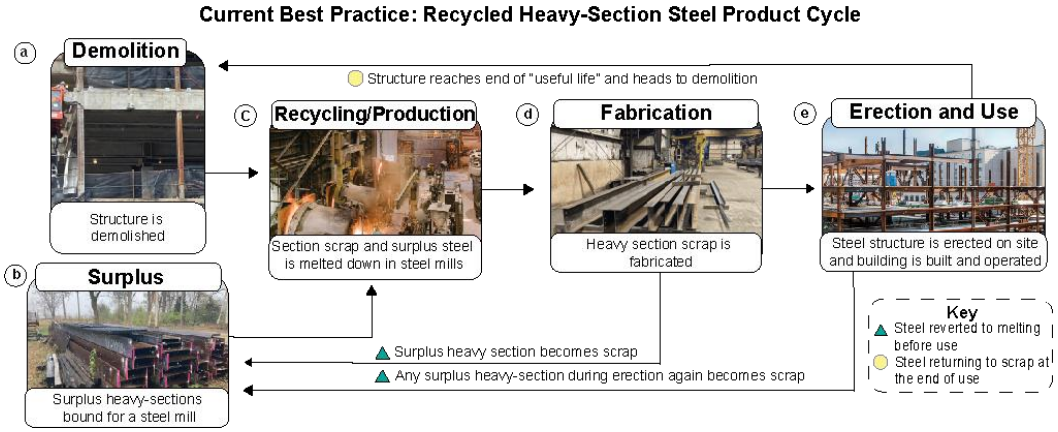


Figure 2. Current Best Practices for Steel Making. (a) Steel structural demolition (b) Surplus, unused steel sold for scrap(c)Recycling and Production [16] (d) Fabrication facility (e) Erection and Use Phase [17]

2.1.1 Material flow analysis and demand projections in literature

A commonly identified barrier to steel reuse is the lack of understanding about supply and demand of structural steel [11, 19]. Existing literature anticipates global steel consumption will grow [9] but does not estimate demand for heavy section steel specifically. Additional literature identifies other factors affecting steel supply including copper contamination in steel recycling [10].

High level Material Flow Analyses (MFAs) have been conducted for global and local steel supply chains that identify end-use sectors for steel and identify steel losses associated with melting scrap steel [18, 20, 21]. Material efficiency is also discussed in the context of strategies to reduce demand. Additionally, doubling product lifespan is noted to halve life-cycle steel demand and initial energy input [20]. While structural steel is discussed through the lens of end-use sectors, a more specific MFA understanding the specifics of structural steel elements availability has yet to be realized.

2.2 Opportunity cost and carbon savings of reuse

Estimates of the carbon emissions of reused steel have been achieved primarily through case study analyses conducting a whole building LCA of a specific building project, or by utilizing hypothetical geometries that compare traditional building design to design for reuse. Three papers specifically estimate the embodied carbon associated with structural steel reuse, whereas other work has estimated reuse savings from other material types, discussed further in [14, 22, 23, 24]. Existing Environmental Product Declarations (EPDs) also calculate Embodied Carbon Coefficient (ECC) values for recycled and reused structural steel. This paper estimates new embodied carbon values and compares them to the literature values.

Like carbon estimations, the cost of specific building projects with reused elements are compared with traditional structures. Under certain conditions, steel reuse demonstrated cost savings [25]. Another paper found steel reuse to cost minimally more than traditional construction but exhibited much larger risk [22].

2.3 Variables impacting carbon of reuse

While aforementioned literature estimates emissions, little is known about the high-level supply chain and design factors that influence the emissions associated with reuse. Various works analyze performance criteria including procurement risk, construction techniques, environmental impacts and project costs, structural performance, topology optimization influence on reuse rates, and geometry [22,

23, 26]. Such works primarily understand reuse through the lens of reuse rate, instead of its general impact on cost and carbon implications, which is analyzed here.

3. Understanding supply and demand

Having a robust understanding of the nature of available and projected heavy section scrap stock helps designers discern what elements are available for reuse in their building projects. This section seeks to characterize steel recycling trends in four steel producing markets. It also seeks to understand the current state of heavy-section scrap availability, production and demand in the US.

3.1 Methodology

Understanding the distinction between recycling and reuse is essential for comprehending the potential benefits of reuse. Recycling steel is enabled by the use of an Electric Arc Furnace (EAF). The two global primary methods for new steel production are the use of Blast Oxygen Furnaces (BOF) and EAF. Prevalence of EAFs in different markets enables overall recycling rates (defined in section 3.1.1). 3.2.1 breaks down the BOF and EAF utilization in four of the ten largest steel producing markets, their subsequent reuse rates, and the implications they have for reuse.

A Material Flow Analysis (MFA) aggregates units of physical data pertaining to the extraction, production, transformation, consumption, recycling, and disposal of materials [27]. A high-level MFA for new and scrap steel heavy sections is carried out in this analysis that focuses specifically on the inputs (imports), outputs (exports), production of new steel, and supply of scrap steel in the United States (US). This MFA therefore takes the form of an abbreviated physical input-output analysis for new and scrap heavy-section steel. Similarities across like steel value chains allow the primary takeaways from the US high-level MFA to be applied to additional markets with similar steel value chains.

3.1.1 Variables for analysis and data sources

The component of the material flow analysis focused on process flows for four markets: Japan, US, Germany, Brazil. These markets were selected out of the top ten crude steel producers because they spanned four continents and represent disparate steel ecosystems. The EAF and BOF breakdown represent the amount of steel produced with each process defined above. More specific to structural steel, the MFA primarily focused on total heavy new heavy section consumed, and total heavy section scrap generated. Data for the high-level material flows in section 3.2. came from two public data sources: the World Steel Association and the US Geological Survey [28, 29, 30].

3.2. Results and discussion

3.2.1 Characterizing market processes and abbreviated material flow analysis

Japan, USA, Germany, and Brazil are all within the top ten Steel Producers globally. China produces ten times the amount of steel as Japan. China produces around 90% of steel in a BOF. The US, also a top producer, has a robust EAF system, with a 93% recycling rate for structural steel [31]. Brazil, Japan, and Germany all utilize predominately BOFs.

While section 3.2.1 made the United States' EAF ecosystem clear, an important aspect of understanding reuse potential is characterizing scrap supply and new element demand. Figure 3(bi) demonstrates inputs, outputs, and demand of new structural steel shapes, and figure 3(bii) demonstrates inputs, outputs, and steel structural shape scrap generation. The data points depicted also include fabricated shapes. Figure 3(b) demonstrates that the total domestic structural scrap quantity could displace the number of new shapes we import by over twofold. The total generation of scrap is less than the consumption of new structural steel sections. That being said, the quantity of generated scrap is around 80% of the quantity of consumed new steel structural sections, including imports. Further analysis is needed to determine actual displacement potential on a granular level.

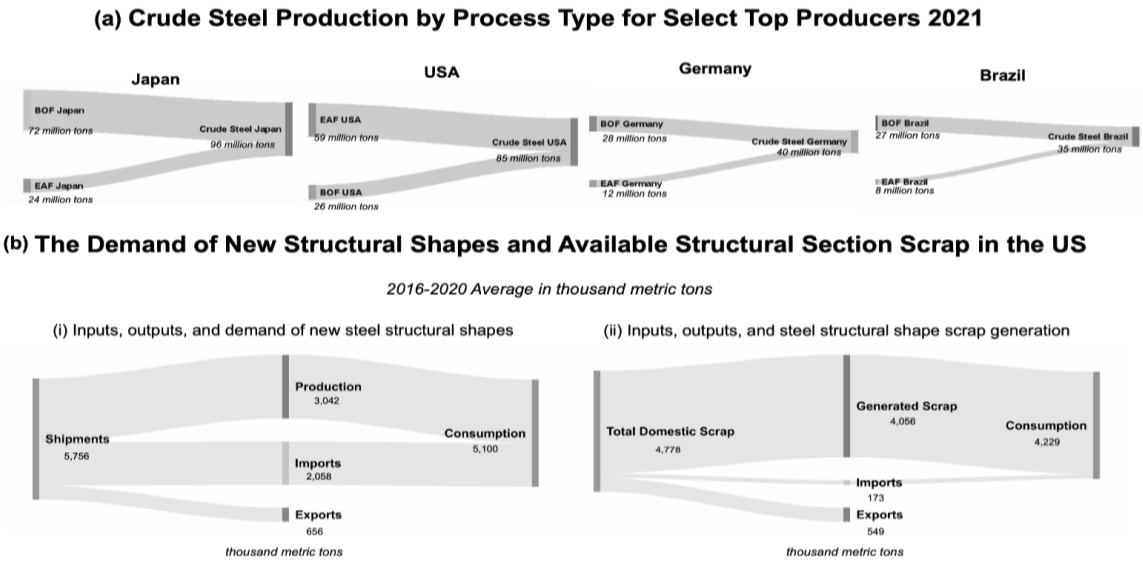


Figure 3.(a) Characterizing steel production processes in different markets for Electric Arc Furnace (EAF) and Blast Oxygen Furnace (BOF) [28] (b) Understanding supply and demand in the US Structural Steel Ecosystem [29, 30].

4. Opportunity cost and carbon savings

Quantifying the magnitude of potential savings is an essential part of the case for reused frame structures. This section explores the potential carbon and cost savings associated with reuse.

4.1 Methodology

4.1.1 Environmental impact assessment

One challenge of evaluating the potential for reuse is how to compare carbon emissions between reuse and recycling to ensure a like-to-like comparison. There are numerous methods for calculating the carbon emissions of reused structural steel elements. The methods mentioned in literature are characterized in Table 1.

Table 1. Different Methodologies for Reuse Impact Assessment in Literature

Methodology	Governing body	Summary	Consideration of Whole Building LCA	Consideration of future reuse potential (Reusability, multiple use cycles)	How many Lifecycles considered?	Production/Demolition Impacts distributed across multiple life cycles?	Sources
Module D, 100:0, "Cut-off Method"	European EN15'804, ISO14040	Places all production impacts in the first use cycle	Y	Y	>2	N	De Wolf 2021 [32], Vares et al 2019 [22], Kupfer et al 2022[23], Brutting et al 2019 [14]
Module D, 0:100, "End of Life Method"	European EN15'804, ISO14040	Places all production impacts in the last use cycle	Y	Y	>2	N	De Wolf 2021 [32], Vares et al 2019 [22], Kupfer et al 2022 [23]
Distributed Allocation	PAS-2050, BSI	Impacts of production, demolition divided across all lifecycles	Y	Y	>2	Y	De Wolf 2021 [32], Vares et al 2019 [22], Kupfer et al 2022[23], Brutting et al 2019 [14]
Market- Based Approach	European Commission 2012	Only A:100-A is analyzed (Cradle to gate)	N	N	2	N	Vares et al 2019 [22]
Modular-Based Approach	CEN	Modules A--C, Module D shows benefits beyond the system boundary	Y	N	2	N	Vares et al 2019 [22]
Comparative LCA	N/A	Only the difference (like displaced scrap)	N	N	2	N	Yeung et al 2016 [24]

One of the primary distinguishing characteristics of the methodologies is the consideration of a whole building LCA. Most methodologies consider at least Module A(A1-A3) of a building LCA. Another differing characteristic of the possible methodologies covers how many total building life cycles the analysis considers. All the LCA methods enable the consideration of more than two life cycles,

including the first use lifecycle, second, and third. The boundary conditions are demonstrated in Table 1. This is like the Cut off approach in that demolition impacts are accounted for in Module A, but differs as the end-of-life impacts after the second life cycles are not considered.

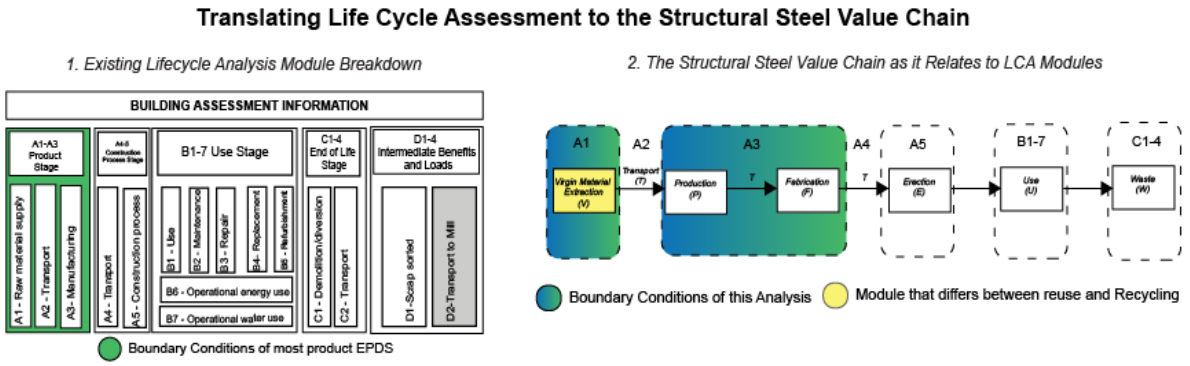


Figure 4. Translating Life Cycle Assessment to the Structural Steel Value Chain [33]

This analysis implements a comparative, cut-off method LCA approach. The LCA used in this analysis sets the boundary conditions spanning the end of the first use lifecycle (Modules C3-4& D1-4) to the beginning of the second use cycle (A1-A3). As demonstrated in Figure 4., the module that differs between reuse and recycling is A1. In the reuse scenario, this analysis places the deconstruction impacts in Modules C3-4 & D1-4 from the previous use cycle into A1 of the new use cycle. In other words, the "Raw Material Supply" for reused structures are just the deconstruction processes and transportation associated with demolition. This was also done for several other EPDs and reuse case studies [14, 23].

This breakdown is depicted in Figure 4. The latter approach will also aid the factor analysis explored in section 5. Additionally, the carbon coefficients for each approach are also compared with the carbon coefficients and factors found in literature exploring other methods of reused elements. The calculations and methods are outlined in Table. The Reuse LCA is also compared against reuse values found in existing heavy section EPDs produced by AISC and the ICE database, and an existing reuse EPD [34, 35, 36]. Additional literature where these methods were utilized, and more carbon estimation methodologies can be found in [37].

$$\Sigma\, Total\ Emissions_{Salvaged} = m_{elements}(Ecc_{cutting}) + m_{elements}(Ecc_{hoisting}) + m_{elements}(Ecc_{grinding}) + m_{elements}(Ecc_{transport}) + m_{elements}(m_{elements}) \quad (1)$$

$$\Sigma\, Total\ Emissions_{Recycled} = m_{elements}(Ecc_{EAF}) + m_{elements}(Ecc_{transport}) + m_{elements}(Ecc_{fabrication}) \quad (2)$$

The partial LCA conducted in this paper includes an inventory, and a subsequent Environmental Impact Assessment. The first step in the IA was to determine which subprocesses to include in phase A1 for reuse. Existing literature has identified several subprocesses associated with deconstruction, including the two utilized in this paper: hoisting and cutting. These subprocesses are evident in equation 1, which demonstrates the equations used for reuse. The A2 value for this paper was determined by averaging transportation coefficients defined by the GHG protocol, and an initial distance of 70 km, as that is the distance utilized in existing EPDs. The GHG protocol and transportation coefficients are better defined in [37]. The A3 value for this paper LCA was obtained from existing recycled steel EPDs in order to conduct a like-to-like comparison. Equation 2 details the processes included in these calculations. Exact energy consumption values used in this LCA are outlined in [37].

4.1.2 Cost estimation

There are three primary methods of estimating cost values in literature: stakeholder interviews, case study costing, and utilizing existing cost databases. Stakeholder interviews obtain specific cost

estimates, often via surveying [38]. Several analyses have estimated construction cost differences from the deconstruction of a specific building. This analysis utilizes RSMeans data to estimate a cost differential between recycled and reused steel. RSMeans is a database containing ~92,000 validated line items for construction cost data [39]. The equations used for cost comparison estimation of recycled structures versus reused structures can be found in equations (3) and (4). Given that this is a comparative cost estimation, only the cost premiums of building deconstruction and labor are considered, along with hard material costs of salvaged and recycled steel.

$$\Sigma\, Costs_{Recycled} = m_{elements}(C_{Material\,Steel}) \quad (3)$$

$$\Sigma\, Costs_{Salvaged} = m_{elements}(C_{Material\,Steel}) + m_{elements}(P_{DecProct}) + m_{elements}(P_{DecLabor}) \quad (4)$$

4.2 Results and discussion

4.1.1 Environmental impact assessment

Figure 7(a) demonstrates the comparison of carbon coefficients for reused steel in literature, EPDs, and the LCA conducted in this paper. All values have boundary conditions from A1-A3. The result of this paper's LCA is a carbon coefficient for reuse of 0.255 kg co2/kg. This can be compared with the literature average for reused steel, which is 0.267 kg co2/kg steel. The only known public EPD for steel reuse detailed the carbon coefficient as 0.045 kg co2/kg steel. Figure 4.6 compares these values with literature and EPD values for recycled steel. This comparison demonstrates an average of an 87% reduction in emissions from reusing steel versus recycling steel. These coefficients are further employed in section 5.

The results of this analysis make a compelling argument for reuse; significant reductions in carbon can be achieved by reusing structural steel versus recycling. While the existing reuse EPD demonstrated lower emissions on average than the literature and this paper's LCA, all three reuse values demonstrate lower carbon than recycled steel. The EPD for recycled steel also demonstrated lower carbon values, making the delta attributed to reuse only minimally lower than literature LCAs. This is likely due to the nature of EPDs, wherein the material supplier often produces the EPD. Notwithstanding, all values reflect a potential for carbon savings and reuse.

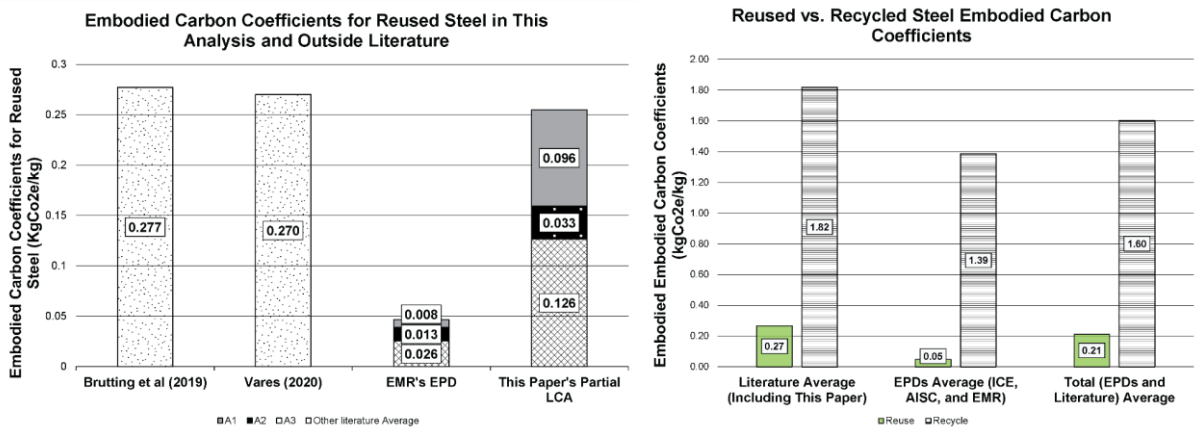


Figure 7. Embodied Carbon Coefficients for Reused Steel from This analysis and outside literature

4.2.2 Cost estimation

Based on calculations governed by equations (3) and (4), the material costs associated with reused material, deconstruction, and the labor premium for reuse sum to $538/ton of salvaged steel. In contrast, raw material costs for new steel are around $4635/ton of a new steel section. This indicates dramatic cost savings potential from reuse based on the delta between new and salvaged material costs. This

analysis is limited in that it only considers material, deconstruction, and labor costs. The calculations do not account for storage and additional refurbishment costs. Additionally, travel and gasoline costs were not considered in this calculation. Material costs are incredibly volatile, and future exploration is needed for line-by-line cost estimating, forecasting, and risk assessment.

5. Variables impacting carbon of reuse

It is evident from section 4 that several variables impact the emissions associated with reuse. The question of which variables most impact carbon emissions is addressed in this section. Predominantly, the most significant variables emerge from the inventory analysis, which accounted for both process and quantity values. Such variables are examined in this chapter and include: travel distances, structural weight, and the number of elements in a project.

5.1 Methodology

5.1.1 Stochastic sampling

Given limited data availability, the factor analysis required a random sampling method varying the number of elements, structural weight, and transportation distance to create a sample of 500 data points. In order to isolate one variable, averages of the building projects used in section 5.1.2 were utilized for the other data points not being sampled. The averages were ~800 kilometers, ~5,500 kg of steel, and ~2,500 elements. The random sampling of the number of elements varied from 50 to 5,000 elements, 1,500 to 10,000 kg for structural weight, and 3 to 1,600 km for transportation distances. These ranges were selected based on thinking surrounding the typical design of a structural steel bay, in addition to typical travel distances of the steel to different projects.

5.1.2 Real building projects

While the stochastic sampling reveals trends in how building characteristics could impact emissions associated with reuse, much can be learned about applying the ECCs to real building projects, such as general understanding about carbon per area of a reused steel structure, a known industry metric that is beneficial when comparing reuse to other sustainable building methods [6]. To carry out this analysis, the Steel Solutions Center at AISC provided data for nine real projects depicted in Figure 9(a) [40]. The Steel Solutions Center provided information about framing plans, location, element sizes, areas, and element types. Across all nine projects there was a range of ~600 to 4800 km, ~30 to 3000 metric tons, and 70 to 4000 elements.

5.2 Results and discussion

5.2.1 Stochastic sampling

Figure 8(a) indicates recycling is impacted more by structural weight than reuse. The analysis demonstrates significantly more emissions are produced as structural weight increases. Reuse has minimally more emissions as structural weight increases, depicted in 8(a). Transportation also impacts emissions minorly when compared to structural weight. The large gap in Figure 8(b) can be attributed to the process difference between melting and scrap. The slope in 8(b) is the same across process types because the method for transportation emissions used the same factor. The recycling method is not impacted by the number of elements in this analysis, only reuse. Element number showed a minimal increase as the number of elements changed, though the rate of change was minimal when compared to distance and structural weight. This indicates there is less concern pertaining to refurbishment, cutting, and selective deconstruction of materials regarding carbon emissions. The factor analysis indicates that the structural weight associated with recycling plays the largest role in emissions reduction.

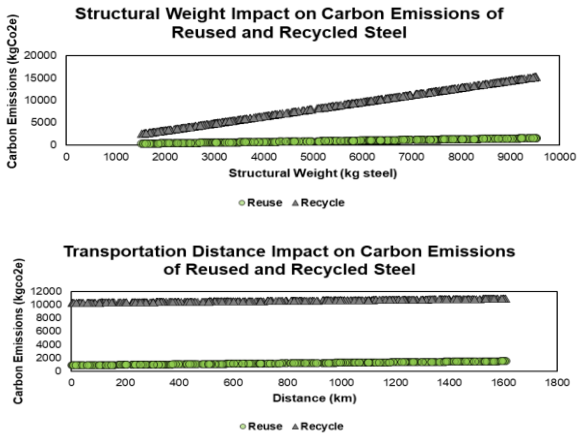


Figure 8. Estimating Emissions of Reused and Recycled Steel: (a) Structural Weight (Transport distance of 800 km) (b) Transportation Distance (Average structural weight of 5.5 tons of steel, 2,500 elements).

5.2.2 Real building projects

All building projects exhibited lower emissions when reused steel carbon coefficients were applied. There was a direct, linear correlation between more weight and more emissions (evident in Figure 9), whereas there was not an entirely linear relationship when the number of elements varied. The average carbon for reused building structures was 98.4 kg CO2e/M^2, whereas an average of 119.4 kg CO2e/M^2 was presented for recycled steel structural systems. Reused steel ranged from 15.9-459.1 kg CO2e/M^2 for reuse and 54.8-476 kg CO2e/M^2 for recycling. This indicated an average 23% reduction in GWP (emissions per square meter) by using reused steel. This delta differs from reductions outlined in section 4.2.2. likely due to the higher transportation distances (average of ~2,580 km) instead of 73 km which was used to calculate a comparable reused steel EPD. Additionally, understanding carbon in relation to floor area leads to greater variability in GWP than in a generalized ECC because of individual project differences. The carbon values for each project Figure 9 also depicts a literature benchmark for business-as–usual steel buildings that have been databased, with a GWP ranging from approximately 250 to 600 kg CO2e/M^2. This benchmark is higher than the ranges for reused and recycled steel for all projects but one, likely due to the benchmark's inclusion of the entire structural system

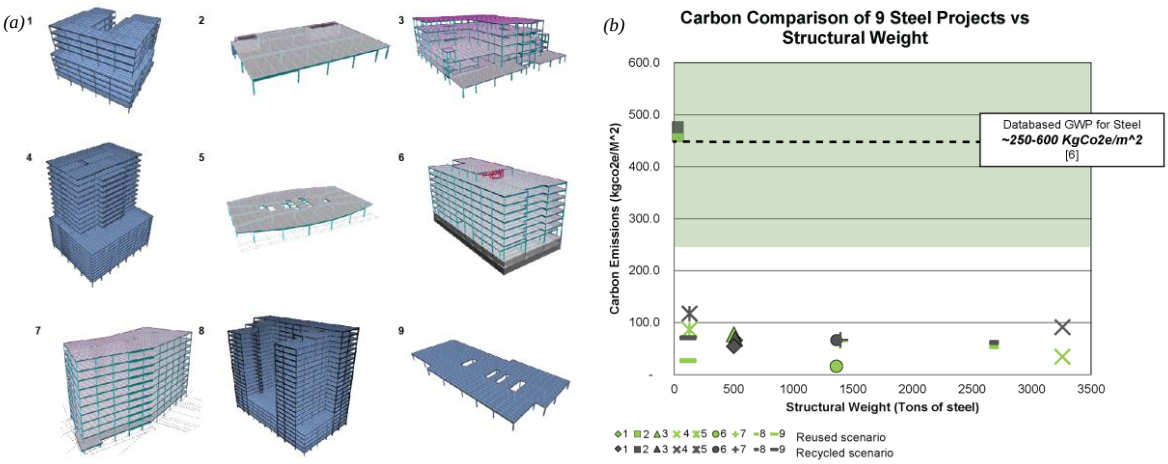


Figure 9. (a) Nine steel structures obtained from the Steel Solutions Center (project identifiers not included)(b) Comparison of 9 Steel Projects

6. Conclusions

This paper has three primary takeaways regarding the reuse of gravity beams and columns in buildings: 1. There is existing supply potential for utilizing structural section scrap in markets where the EAF recycling system is robust; 2. Across literature, industry EPDs, and an additional LCA, reused steel has lower carbon emissions than recycled steel and lower material costs; 3. Structural weight most demonstrably influences emissions associated with structural system steel reuse.

More specifically, this preliminary analysis indicates available scrap could meet most of the scrap demand in markets with a large presence of EAF. Further analysis is needed at a more detailed level for each market. There is potential for 87% greenhouse gas emissions reduction by using reused steel. Structural weight had the largest impact on reuse emissions. Across all variable changes, reuse still had lower emissions than recycling, and recycled steel is impacted much greater by structural weight than reused elements. Given the results of this analysis, layout complexity, quantity, and carbon impacts of refurbishment are less of a concern for structural designers when compared to the impacts of recycled steel. Figure 10 presents the future best practice for reuse, one where heavy section scrap is deconstructed from an existing building, refurbished, and reused in a new structure. By adopting this practice, structural designers could aid in decoupling structural steel design from additional carbon and cost implications associated with reprocessing.

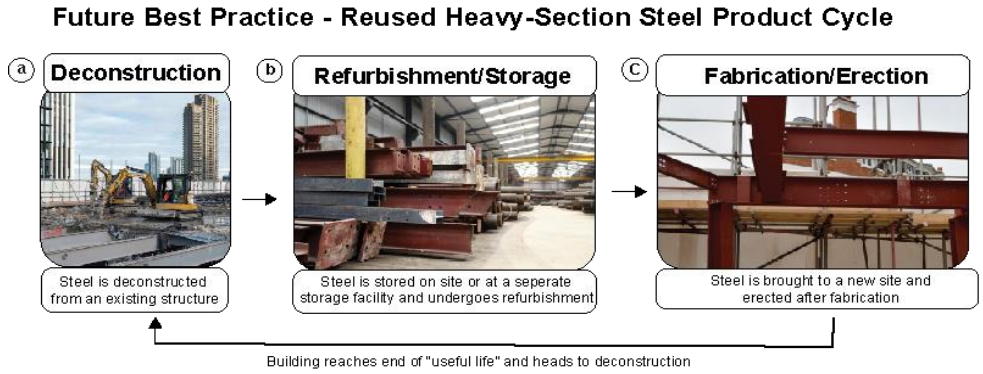


Figure 10. Future Best Practice: Reused Heavy-section Product Cycle. (a) Elements are deconstructed from a building. (b) Elements are refurbished and stored. (c) Elements are fabricated and erected on a new site [15].

7. Acknowledgments

This work would not have been possible without funding support from the National Science Foundation Graduate Research Fellowship Program. Thanks to the MIT Climate and Sustainability Consoritum. The authors are grateful to the AISC Steel Solutions Center for providing data for Section 5 of this project.

References

[1] C. Posey and M. Hoeft "Past in Service of the Future." *Structure Magazine*. https://www.structuremag.org/?p=1140 (accessed Mar. 28, 2023).

[2] S. C. Kaethner and J. A. Burridge, "Embodied CO2 of structural frames," *Structural Engineer*, vol. 90, pp. 33–40, May 2012.

[3] J. O'connor, "Survey on actual service lives for North American buildings," 2004. Accessed: May 11, 2023. [Online]. Available: https://www.semanticscholar.org/paper/Survey-on-actual-service-lives-for-North-American-O'connor/fafdf361e1bd3fa4b5f69359d2436e0784022f7c

[4] "Global Warming of 1.5 ◦C —." https://www.ipcc.ch/sr15/ (accessed Mar. 30, 2023).

[5] M. D. Webster, Ed., *Structural Materials and Global Climate*. American Society of Civil Engineers, 2017. doi: 10.1061/9780784414934.

[6] C. De Wolf, F. Yang, D. Cox, A. Charlson, A. S. Hattan, and J. Ochsendorf, "Material quantities and embodied carbon dioxide in structures," *Proceedings of the Institution of Civil Engineers - Engineering Sustainability*, vol. 169, no. 4, pp. 150–161, Aug. 2016, doi: 10.1680/ensu.15.00033.

[7] D. R. Cooper, A. C. H. Skelton, M. C. Moynihan, and J. M. Allwood, "Component level strategies for exploiting the lifespan of steel in products," *Resources, Conservation and Recycling*, vol. 84, pp. 24–34, Mar. 2014.

[8] D.R. Cooper, and T. G. Gutowski. "The Environmental Impacts of Reuse: A Review." *Journal of Industrial Ecology* 21, no. 1 (2017): 38–56.

[9] B. J. van Ruijven, D. P. van Vuuren, W. Boskaljon, M. L. Neelis, D. Saygin, and M. K. Patel, "Long-term model-based projections of energy use and CO2 emissions from the global steel and cement industries," *Resources, Conservation and Recycling*, vol. 112, pp. 15–36, Sep. 2016.

[10] K. E. Daehn, A. Cabrera Serrenho, and J. M. Allwood, "How Will Copper Contamination Constrain Future Global Steel Recycling?," *Environ. Sci. Technol.*, vol. 51, no. 11, pp. 6599–6606, Jun. 2017.

[11] C. F. Dunant, M. P. Drewniok, M. Sansom, S. Corbey, J. M. Allwood, and J. M. Cullen, "Real and perceived barriers to steel reuse across the UK construction value chain," *Resources, Conservation and Recycling*, vol. 126, pp. 118–131, Nov. 2017.

[12] A. Guggemos and S. Franklin, "Greening Steel Construction," 2011. https://lsc-pagepro.mydigitalpublication.com/article/Greening+Steel+Construction/705908/67487/article.html (accessed Apr. 25, 2023).

[13] "Brent Cross Town Substation," *IF_DO — Architecture & Design*. https://www.ifdo.co (accessed Mar. 28, 2023).

[14] J. Brütting, J. Desruelle, G. Senatore, and C. Fivet, "Design of Truss Structures Through Reuse," *Structures*, vol. 18, pp. 128–137, Apr. 2019.

[15] R. Mills, "Holbein Gardens: delivering a low-carbon structure with reclaimed steel - The Institution of Structural Engineers," Mar. 01, 2023. https://www.istructe.org/journal/volumes/volume-101-(2023)/issue-3/holbein-gardens-low-carbon-reclaimed-steel/ (accessed Apr. 25, 2023).

[16] S. Frizell, "Nucor Corp: Go Inside an American Steel Mill | Time," Oct. 30, 2014. https://time.com/3502128/nucor-corp-steel-mill/ (accessed Mar. 30, 2023).

[17] "Modern Steel Construction." https://www.aisc.org/modernsteel/ (accessed Mar. 15, 2023).

[18] D. R. Cooper, N. A. Ryan, K. Syndergaard, and Y. Zhu, "The potential for material circularity and independence in the U.S. steel sector," *Journal of Industrial Ecology*, vol. 24, no. 4, pp. 748–762, 2020.

[19] D. Densley Tingley, S. Cooper, and J. Cullen, "Understanding and overcoming the barriers to structural steel reuse, a UK perspective," *Journal of Cleaner Production*, vol. 148, pp. 642–652, Apr. 2017, doi: 10.1016/j.jclepro.2017.02.006.

[20] M. Cullen, J. M. Allwood, and M. D. Bambach, "Mapping the Global Flow of Steel: From Steelmaking to End-Use Goods," *Environ. Sci. Technol.*, vol. 46, no. 24, pp. 13048–13055, Dec. 2012.

[21] D. R. Cooper, A. C. H. Skelton, M. C. Moynihan, and J. M. Allwood, "Component level strategies for exploiting the lifespan of steel in products," *Resources, Conservation and Recycling*, vol. 84, pp. 24–34, Mar. 2014, doi: 10.1016/j.resconrec.2013.11.014.

[22] S. Vares, P. Hradil, M. Sansom, and V. Ungureanu, "Economic potential and environmental impacts of reused steel structures," *Structure and Infrastructure Engineering*, vol. 16, no. 4, pp. 750–761, Apr. 2020.

[23] C. Küpfer, M. Bastien-Masse, and C. Fivet, "Reuse of concrete components in new construction projects: Critical review of 77 circular precedents," *Journal of Cleaner Production*, vol. 383, p. 135235, Jan. 2023.

[24] J. Yeung, S. Walbridge, C. Haas, and R. Saari, "Understanding the total life cycle cost implications of reusing structural steel," *Environment Systems and Decisions*, vol. 37, pp. 101–120, 2017.

[25] C. F. Dunant, M. P. Drewniok, M. Sansom, S. Corbey, J. M. Cullen, and J. M. Allwood, "Options to make steel reuse profitable: An analysis of cost and risk distribution across the UK construction value chain," *Journal of Cleaner Production*, vol. 183, pp. 102–111, May 2018.

[26] J. Yeung, S. Walbridge, and C. Haas, "The role of geometric characterization in supporting structural steel reuse decisions," *Resources, Conservation and Recycling*, vol. 104, pp. 120–130, Nov. 2015.

[27] P. Ferrão and J. E. Fernández, *Sustainable Urban Metabolism*. The MIT Press, 2013. doi: 10.7551/mitpress/8617.001.0001.

[28] "World Steel in Figures 2022," *worldsteel.org*. https://worldsteel.org/steel-topics/statistics/world-steel-in-figures-2022/ (accessed Feb. 08, 2023).

[29] "Iron and Steel Statistics and Information | U.S. Geological Survey." https://www.usgs.gov/centers/national-minerals-information-center/iron-and-steel-statistics-and-information (accessed Feb. 08, 2023).

[30] "Iron and Steel Scrap Statistics and Information | U.S. Geological Survey." https://www.usgs.gov/centers/national-minerals-information-center/iron-and-steel-scrap-statistics-and-information (accessed Feb. 08, 2023).

[31] "Structural Steel Sustainability | American Institute of Steel Construction." https://www.aisc.org/why-steel/sustainability/ (accessed May 17, 2023).

[32] C. De Wolf, E. Hoxha, and C. Fivet, "Comparison of environmental assessment methods when reusing building components: A case study," *Sustainable Cities and Society*, vol. 61, p. 102322, Jun. 2020.

[33] BS EN 15978:2011 Sustainability of construction works. Assessment of environmental performance of buildings. Calculation method - European Standards." https://www.en-standard.eu/bs-en-15978-2011-sustainability-of-construction-works-assessment-of-environmental-performance-of-buildings-calculation-method/ (accessed Mar. 31, 2023).

[34] "Environmental Product Declarations | American Institute of Steel Construction." https://www.aisc.org/why-steel/resources/leed-v4/ (accessed Mar. 30, 2023).

[35] "Embodied Carbon Footprint Database," *Circular Ecology*. https://circularecology.com/embodied-carbon-footprint-database.html (accessed Mar. 31, 2023).

[36] "EMR Reusable Steel EPD Declaration | EMR Metal Recycling Reimagined." https://uk.emrgroup.com/what-we-do/our-specialist-areas/emr-reusable-steel-edp-2023 (accessed Mar. 30, 2023).

[37] J. Berglund-Brown, "Structural Steel Reuse as a Cost-Effective Carbon Mitigation Strategy." Master 's Thesis. *Massachusetts Institute of Technology.* June 2023.

[38] C. F. Dunant, M. P. Drewniok, M. Sansom, S. Corbey, J. M. Allwood, and J. M. Cullen, "Real and perceived barriers to steel reuse across the UK construction value chain," *Resources, Conservation and Recycling*, vol. 126, pp. 118–131, Nov. 2017.

[39] "2022 Building Construction Costs Book." https://www.rsmeans.com/products/books/2023-cost-data-books/2022-building-construction-costs-book (accessed Mar. 31, 2023).

[40] "Steel Solutions Center | American Institute of Steel Construction." https://www.aisc.org/steel-solutions-center/ (accessed Mar. 31, 2023).

IASS 2023 July 10–14 Melbourne Integration of Design and Fabrication

Proceedings of the IASS Annual Symposium 2023
Integration of Design and Fabrication
10–14 July 2023, Melbourne, Australia
Y.M. Xie, J. Burry, T.U. Lee and J. Ma (eds.)

Interactive design with optimum matchmaking of reused structural elements – a software implementation

Jonas WARMUTH[a,*], Jan BRÜTTING[b], Corentin FIVET[a]

[a,*] Structural Xploration Lab, Ecole Polytechnique Fédérale de Lausanne (EPFL), Fribourg, Switzerland
Passage du Cardinal 13B, CH-1700 Fribourg
jonas.warmuth@epfl.ch

[b] schlaich bergermann partner, Stuttgart, Germany

Abstract

Structural systems are a significant contributor to buildings' embodied carbon and reusing structural elements in new load-bearing applications is one strategy to reduce this impact. However, integrating this approach into existing design workflows without affecting design freedom is challenging. New computational tools like Phoenix3D, a plugin for Grasshopper within the Rhino3D environment, are intended to help master this task. This paper extends current research developments of Phoenix3D by integrating the tool into a more flexible multi-objective optimization framework. Hence, the outcomes obtained from Phoenix3D are employed as an objective function in the optimization workflow. This enables designers to move from a mere assignment operation on a predetermined structural system to a more comprehensive approach, wherein alternative design options are thoroughly investigated. Two case studies are conducted here to showcase this extension's effectiveness: (1) a theoretical study that compares generated designs with established typologies; and (2) a real-world application of the proposed tool to design a façade system using only reclaimed steel elements. Results show that adequate design solutions are found in real-time and interactively for the same stock of reused structural elements. Not only does Phoenix3D turn component reuse constraints into new circular design opportunities, but it also reduces the detrimental environmental impact of a structure and therefore allows the establishment of a more sustainable building culture.

Keywords: computational design, interactive design, optimization, reuse, circular design

1. Introduction

The construction industry is responsible for substantial global greenhouse gas emissions, resource exploitation, and waste generation [1]. To mitigate these adverse effects and decrease the detrimental environmental impact (DEI) of constructed buildings, one possible solution is to adopt a circular economy approach, which involves reusing structural components to construct new buildings.

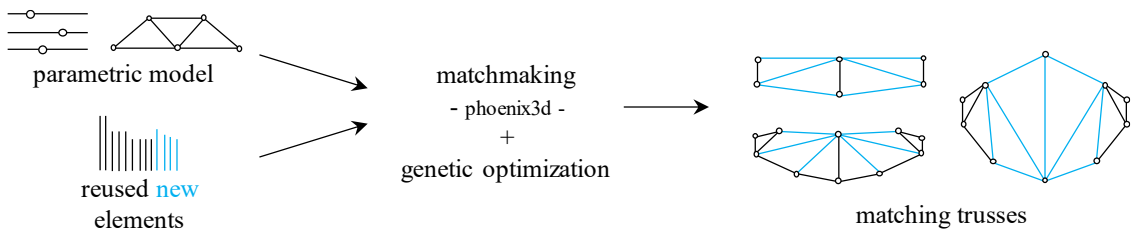


Figure 1. Matchmaking of truss structures for a given stock of reused and new elements

Copyright © 2023 by Jonas WARMUTH, Jan BRÜTTING and Corentin FIVET. Published in the Proceedings of the IASS Annual Symposium 2023 with permission.

With a few exceptional cases, this approach is not commonly used in current building practices. One of the reasons for this is that reusing structural components demands an inversion of the conventional design approach, as the synthesis of a structural system (including topology and geometry) must comply with the geometric and static characteristics of the available elements. As a result, this leads to challenges in the regular construction process. One solution to this issue is using computational tools that assist architects and engineers when designing from a fixed inventory of elements. An early approach of such computational tools was presented by Fujitani and Fujii [2], who optimized plane frames of fixed topology subject to given elements of known length and cross-section. Kim and Kim [3] used genetic algorithms to optimize embodied carbon, weight, and cost of frame structures made from a stock of reclaimed elements. Bukauskas et al. [4] developed a strategy based on heuristics to form-fit a supply of wood logs to statically-determinate trusses. Brütting et al. [5] presented structural optimization techniques based on mixed integer linear programming (MILP) to design truss and frame structures from reclaimed steel elements. Huang et al. [6] employed the Hungarian Algorithm to design wooden geodesic domes from a stock of elements. Additionally, they briefly compare various algorithmic formulations for reuse-driven design in computational tools. In previous work, Warmuth et al. [7] introduced the computational tool **Phoenix3D** which optimally assigns reclaimed and new elements from a given stock to target truss designs. This tool was built upon a MILP formulation and was later extended with a Best-Fit heuristic to accelerate result generation.

To further open up the design possibilities of stock-constrained design, this paper introduces an extended method to generate design alternatives when working with a given stock of elements. Rather than solely assigning stock elements to a pre-defined structural system, this method enables interactive design with the available stock components. The method's general workflow is depicted in Figure 1. The input consists of a parametric model and a stock of both reclaimed and new elements, which are fed into an optimization framework. This framework utilizes a combination of Phoenix3D and genetic optimization algorithms to modify the parametric model and to optimally assign stock elements to the design. As a final step, the framework produces several truss structures that make optimal use of available stock elements. Section 2 elaborates on the algorithms of Phoenix3D and the genetic optimization process. Furthermore, Section 3 features a theoretical case study that compares generated structures with established typologies and a real-world project that illustrates the practicality of this framework.

2. Method

2.1 Phoenix3D

Phoenix3D is an open-source tool to design optimum truss structures made from a stock of new and reclaimed elements. In the tool, the assignment of stock elements to a design brief is formulated as a discrete optimization problem.

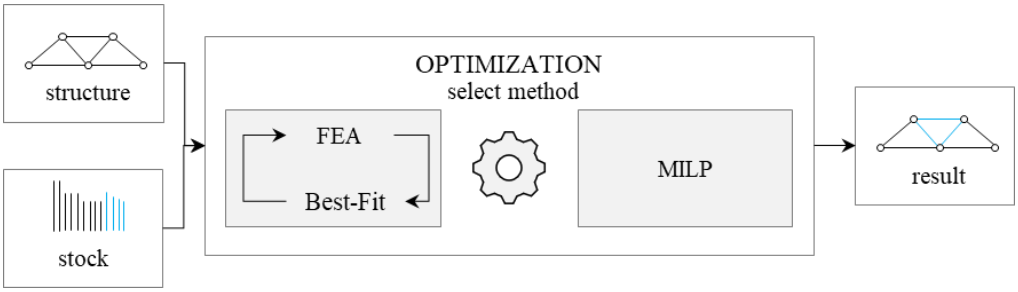


Figure 2. Workflow of Phoenix3D

It is implemented by the authors based on previous research in the field [6]. The core of Phoenix3D is molded by two optimization algorithms: (1) a MILP formulation that delivers globally optimal results

but is computationally expensive, and (2) a Best-Fit heuristic combined with a linear-elastic finite element analysis (FEA) of first order that delivers just close-to-optimal results but in real-time and with low computational costs. The objective function is to minimize DEI, computed by a Life-Cycle-Assessment (LCA). Details for the implementation of the optimization algorithms as well as the LCA, can be found in [7, 8]. The workflow of the tool is illustrated on Figure 2. An initial structure serves as input to which reusable stock elements are assigned, as well as newly-manufactured elements. Subsequently, users can select which of the two optimization algorithms should be employed to assign the stock elements to the structure optimally. As a result, the structure with the assigned stock elements is displayed, including statistics about the run optimization. Among these are the DEI in $kgCO_2eq$ and the cut-off waste in kg. Cut-off waste occurs when reclaimed elements from the stock must be cut to fit a target position in the intended design. In general, it is worthwhile to minimize the amount of cutoff waste and employ reclaimed elements as they are to enable an additional cycle of repurposing.

2.2 Global optimization framework

As outlined in Section 1, the proposed framework employs a genetic optimization algorithm to produce trusses that match a given stock of reclaimed elements. The overall workflow is illustrated on Figure 3, which starts with the definition of a parametric model. For the case study in Section 3.1, the parameters, i.e. the design variables, include the number of bays, the direction of diagonals, and the nodal coordinates of the design brief. A stock of reclaimed and new elements is provided, all made of steel S235. Furthermore, various circular cross-sections are available, with both reclaimed and new elements ranging from diameters of 10 mm to 100 mm with steps of 10 mm in between. For each cross-section of reclaimed elements, six pieces of length 3.0 m are available.

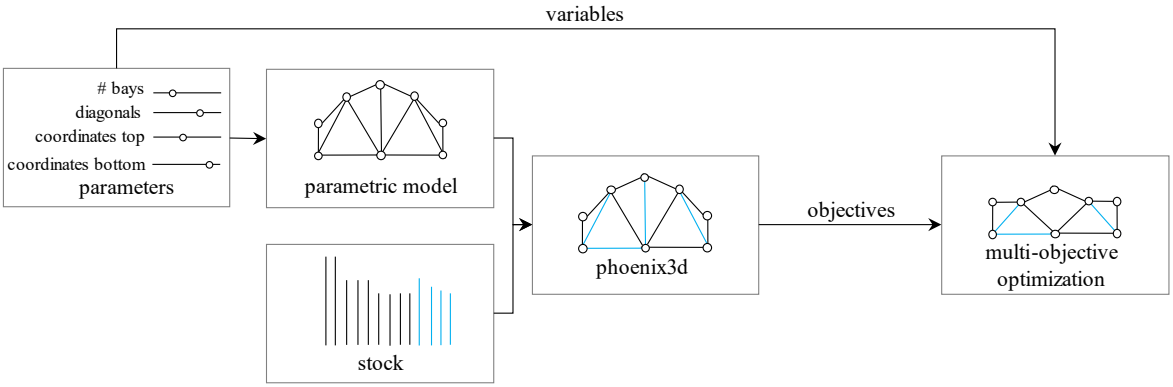


Figure 3. Workflow of the presented framework

Despite Phoenix3D's ability to optimally assign stock elements to an already specified structure, modifying the topology and geometry of the design brief opens up the solution space by allowing the design to adjust to the characteristics of the reclaimed elements from the stock. Since the model is parametric, this can also be regarded as an optimization problem where the model's parameters serve as design variables, and the calculation of DEI and cut-off waste in Phoenix3D act as objective functions to be minimized. Wallacei [9], an evolutionary optimization and analytic engine for Rhino/Grasshopper [10], is the primary tool for this overarching optimization.

3. Case studies

3.1 Theoretical case study

The theoretical case study setup is illustrated on Figure 4. The design boundaries in which the parametric truss is generated are presented on Figure 4a. To simulate a loading scenario, a line load of 15 kN/m is assumed, and the self-weight of each bar is applied at its respective end nodes. In addition, Figure 4b

displays a benchmarking truss optimized by employing the Best-Fit heuristic to minimize DEI solely. Three well-known truss typologies, a Warren truss, a Pratt truss, and a Howe truss, are shown in Figure 4c. The corresponding metrics for these trusses, such as their DEI in $kgCO_2eq$ and their cut-off waste in kg, are given in Table 1.

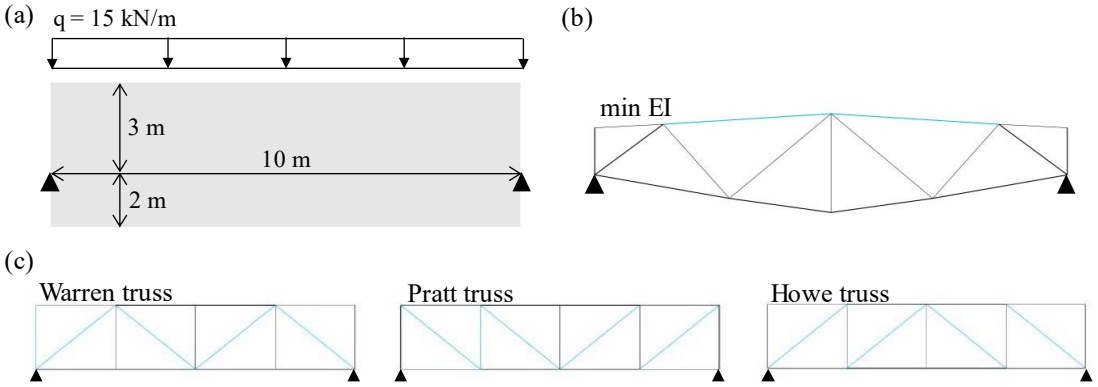


Figure 4. Matchmaking of well-known trusses with optimal trusses for minimization of DEI

Table 1. Results for the trusses from Figure 4

	min DEI	Pratt truss	Howe truss	Warren truss	(5a)	(5b)	(5c)	(5d)
DEI [$kgCO_2eq$]	41	83	67	70	55	46	44	43
Cut-off [kg]	8	27	18	17	0	1	2	4

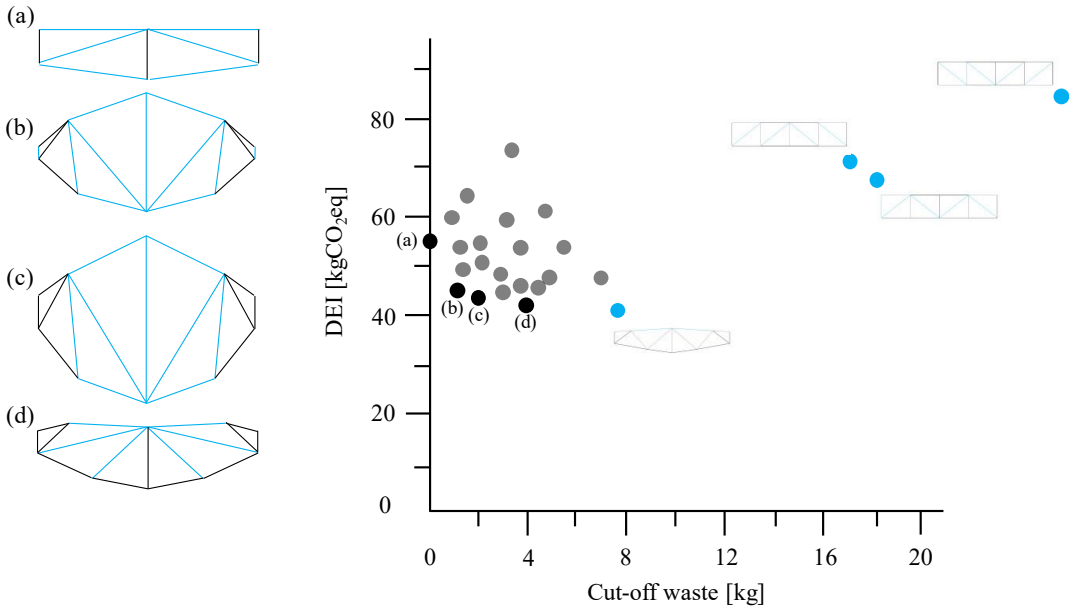


Figure 5. Pareto front with selected samples subject to the minimization of DEI and cut-off waste

Table 1 shows that the benchmark DEI is 41 $kgCO_2eq$, which results in a cut-off waste of 8 kg. The three truss structures have DEI values ranging from 67 $kgCO_2eq$ to 83 $kgCO_2eq$ and also generate significant amounts of cut-off waste, ranging from 17 kg to 27 kg. The goal of the optimization is to generate truss structures that are more suitable for the given stock, with the ability to reduce cut-off waste and ideally outperform the three standard trusses in Figure 4c in terms of DEI. Therefore, a multi-objective optimization is set up for two objective functions: minimizing DEI and cut-off waste. Selected results from the multi-objective optimization are presented on Figure 5. The Pareto front of the optimization is represented by black dots, non-optimal solutions by grey dots, and the trusses in Figure 4 by blue dots. The four Pareto-optimal solutions (Figure 5a-d) are displayed to the left of the graph. As shown in Table 1, all generated trusses have a significantly lower DEI than the three trusses in Figure 4c, ranging from 43 kgCO2eq to 55 kgCO2eq. Moreover, their cut-off waste ranges from 0 kg to 4 kg, indicating that the identified solutions are more suitable for the stock than the initial truss structures.

3.2 Façade Primeo Energie Kosmos

The real-world project presented in the following involves designing and constructing the façade for the Primeo Energie Kosmos in Münchenstein, Switzerland. The design intent was to obtain a tree-like façade structure of complex geometry. Reclaimed steel elements from obsolete electric masts were to be used, which had already been dismantled and inventoried.. The available stock contains 1’361 linear elements with a total length of 4’329 m ranging from 1.4 m to 6.2 m. Figure 6 shows a scatter diagram of the in total 125 different stock element groups.

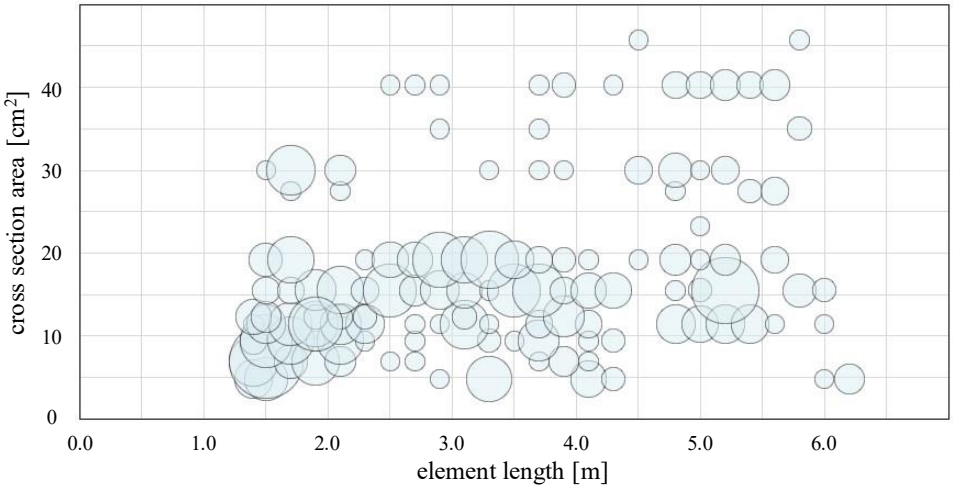


Figure 6. Stock composition

Most elements are either circular hollow sections or L-sections, an excerpt of which is pictured on the top left of Figure 7. In the following step, the available inventory was imported into Phoenix3D to be used for the assignment optimization. After applying the method described in Section 2, a range of design variations was generated; the eventually selected one is shown at the bottom left of Figure 7. Following several iterations, the final solution was established. An added advantage of working in the Rhino/Grasshopper environment was that detailed component drawings could be generated

automatically, which could be directly delivered to the steel fabricator. The construction of the façade was completed in fall of 2022, Figure 7.



Figure 7. Realized facade system based on the proposed method

4. Conclusion

This paper introduced an extended framework for the reuse-driven design of structural systems based on the parametric design tool Phoenix3D for Rhino/Grasshopper in combination with a genetic multi-objective optimization algorithm. A theoretical case study has been developed to generate different design alternatives from one stock of structural elements. Moreover, the framework was used to design a real-world application, the façade of the Primeo Energie Kosmos in Münchenstein, Switzerland.

Regarding design flexibility, future investigations will further expand the range of applicability to frame structures. Moreover, the developed Best-Fit heuristic will be improved to generate more accurate results when compared with a MILP-based implementation. This allows for more real-world applications and emphasizes integrating reuse strategies into conventional structural design workflows.

References

[1] J. M. Allwood and J. M. Cullen, "Sustainable materials: with both eyes open," in *UIT Cambridge*, Cambridge, UK, 2012.

[2] Y. Fujitani and D. Fujii, "Optimum structural design of steel plane frame under the limited stocks of members," in *Proceedings of the RILEM/CIB/ISO International Symposium, Integrated Life-Cycle Design of Materials and Structures*, Helsinki, 2000, pp. 198–202.

[3] S. Kim and S.-A. Kim, "Design optimization of noise barrier tunnels through component reuse: Minimization of costs and CO2 emissions using multi-objective genetic algorithm," *J. Clean. Prod.*, vol. 298, p. 126697, May 2021, doi: 10.1016/j.jclepro.2021.126697.

[4] A. Bukauskas, P. Shepherd, P. Walker, B. Sharma, and J. Bregulla, "Form-Fitting Strategies for Diversity-Tolerant Design," Sep. 2017.

[5] J. Brütting, J. Desruelle, G. Senatore, and C. Fivet, "Design of Truss Structures Through Reuse," *Structures*, vol. 18, pp. 128–137, 2019, doi: 10.1016/j.istruc.2018.11.006.
[6] J. F. G. Brütting, "Optimum design of low environmental impact structures through component reuse," Ph.D., EPFL, Lausanne, 2020. doi: 10.5075/epfl-thesis-8448.
[7] J. Warmuth, J. Brütting, and C. Fivet, "Computational Tool for Stock-Constrained Design of Structures," in *Proceedings of the IASS Annual Symposium 2020/21 and the 7th International Conference on Spatial Structures*, Guilford, UK, 2021. [Online]. Available: https://infoscience.epfl.ch/record/287984
[8] J. Brütting, C. Vandervaeren, G. Senatore, N. De Temmerman, and C. Fivet, "Environmental impact minimization of reticular structures made of reused and new elements through Life Cycle Assessment and Mixed-Integer Linear Programming," *Energy Build.*, vol. 215, 2020, doi: 10.1016/j.enbuild.2020.109827.
[9] "Wallacei." 2021. [Online]. Available: https://www.wallacei.com/
[10] D. Rutten, "Grasshopper 3D." Robert McNeel & Associates, 2021. [Online]. Available: https://www.grasshopper3d.com/

IASS 2023
July 10–14 Melbourne
Integration of Design and Fabrication

Proceedings of the IASS Annual Symposium 2023
Integration of Design and Fabrication
10–14 July 2023, Melbourne, Australia
Y.M. Xie, J. Burry, T.U. Lee and J. Ma (eds.)

Long-term strength prediction model for structural glass

Siyi YI*, Suwen CHEN[a,b], Roberto BALLARINI[c]

* College of Civil Engineering, Tongji University, Shanghai, China
1810720@tongji.edu.cn

[a] State Key Laboratory for Disaster Reduction in Civil Engineering, Tongji University, Shanghai, China

[b] College of Civil Engineering, Tongji University, Shanghai, China

[c] Department of Civil and Environmental Engineering, Cullen College of Engineering, University of Houston, Houston, TX, USA

Abstract

The ever-increasing use of glass in load-bearing applications has led to concern about the effects of sustained loads on its strength. Ample experimental data is available on short-term strength of various types of glass. However, the short-term strength cannot be used directly in the design of structural components because the nominal strength decreases with time as a result of environmentally-assisted subcritical crack propagation. The load duration factor has been introduced to account for the dependence of strength on sustained loading, but a more comprehensive understanding of long-term strength is needed to guarantee the reliability of glass structures. This paper proposes a strength-prediction model based on stress corrosion theory to account for the effects of temperature, humidity and loading rate on crack growth parameters. An empirical power-law function is used for two types of stress histories: constant stress (life-time service condition) and constant stress rate (laboratory test condition). The relationships between applied constant stresses and lifetime, applied stress and stress/strain rate, and the proposed load duration factor are analyzed and quantified. The results of the model are validated using a large set of available data for various load durations and are compared with international standards. The results demonstrate that the proposed model provides accurate predictions of the long-term strength of structural glass.

Keywords: structural glass, long-term strength, load duration factor, life-time service condition, laboratory tests condition

1. Introduction

The use of glass in architecture has a long history, from its use in traditional windows to modern glass curtain walls. Because of its versatility and transparency, glass has become a major building material, second only to concrete and steel. In recent years, there has been an ever-increasing use of glass in load-bearing structures such as beams, columns, and stairs. However, its use has increased despite insufficient understanding of its long-term strength, a critical factor in the design of load-bearing structures. Laboratory testing (mostly constant stress rate, as shown in Figure 1(a)) provides short-term strength values that are useful for estimating the initial nominal resistance of a glass component, but they may not accurately reflect the long-term behaviour under sustained loading (constant stress, as shown in Figure 1(b)).

Glass, a nominally elastic-brittle material, contains large numbers of microcracks on the surface introduced by manufacturing and processing. When subjected to tensile stress and exposed to atmospheric environments, these microcracks propagate subcritically as a result of a chemical reaction between glass and water molecules. The subcritical extension under sustained load is referred to as static

Copyright © 2023 by Siyi YI, Suwen CHEN and Roberto BALLARINI. Published in the Proceedings of the IASS Annual Symposium 2023 with permission.

fatigue, or stress corrosion. If one or more of the surface cracks extend to critical lengths, the structural component can fail catastrophically. Therefore, the apparent (nominal) long-term strength of glass is lower than the short-term strength that is typically measured in the laboratory. Numerous studies have been conducted on time-dependence of glass strength using lifetime tests, in which the constant load is applied and time-to-failure is measured. The results have consistently shown that the glass strength decreases with increasing service life.

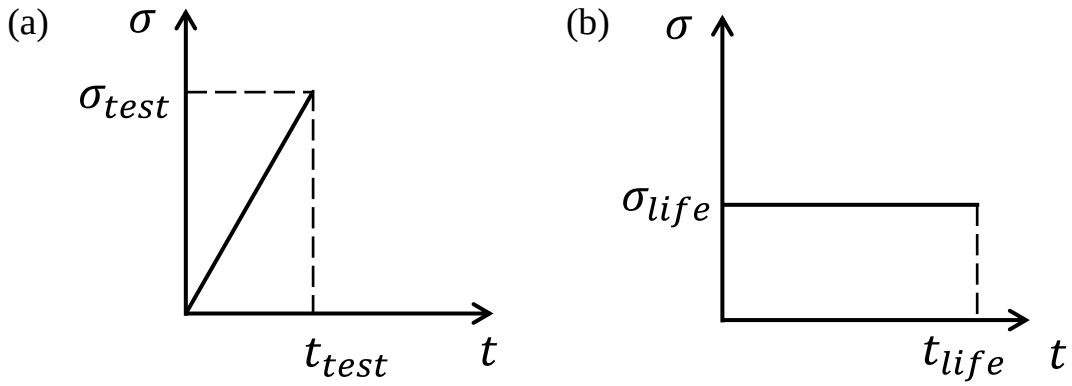


Figure 1. Two different stress histories: (a) stress history under laboratory tests condition (constant stress rate), (b) stress history under life-time service condition (constant stress).

The load duration factor k_{mod} has been introduced to consider the influence of subcritical crack propagation on glass strength, and is widely used in various standards. k_{mod} is defined as the ratio of long-term strength to short-term strength. The short-term strength is obtained by testing a certain number of specimens and performing a statistical analysis of data. The characteristic bending strength of soda-lime-silica glass is specified as f_k = 45 Mpa in EN 572-1[1]. Figure 2 presents the different methods used to determine k_{mod} in various standards. When the design lifetime is known, European [2], American [3], Australian [4] and Italian [5] standards provide formulas for calculating k_{mod}. When the designe lifetime is unknown, Chinese [6] and Australian [4] standards offer values of k_{mod} for corresponding lifetimes. However, as shown in Figure 2, the Chinese standard sets a very conservative k_{mod} value of 0.3 for design lifetimes greated than 10 minutes. Moreover, the formulas for calculating k_{mod} in other standards do not account for the effects of stress history and environment, and therefore may lead to unsafe designs.

To address this gap in knowledge, a novel approach is presented here to assess the long-term strength of structural glass through laboratory tests. Drawing from stress corrosion theory, an empirical power-law function is introduced to characterize subcritical crack propagation that quantifies the effects of temperature, humidity, and loading rate on crack growth parameters. The effectiveness and reliability of the model is demonstrated through a comparison of its results with international standards and available data.

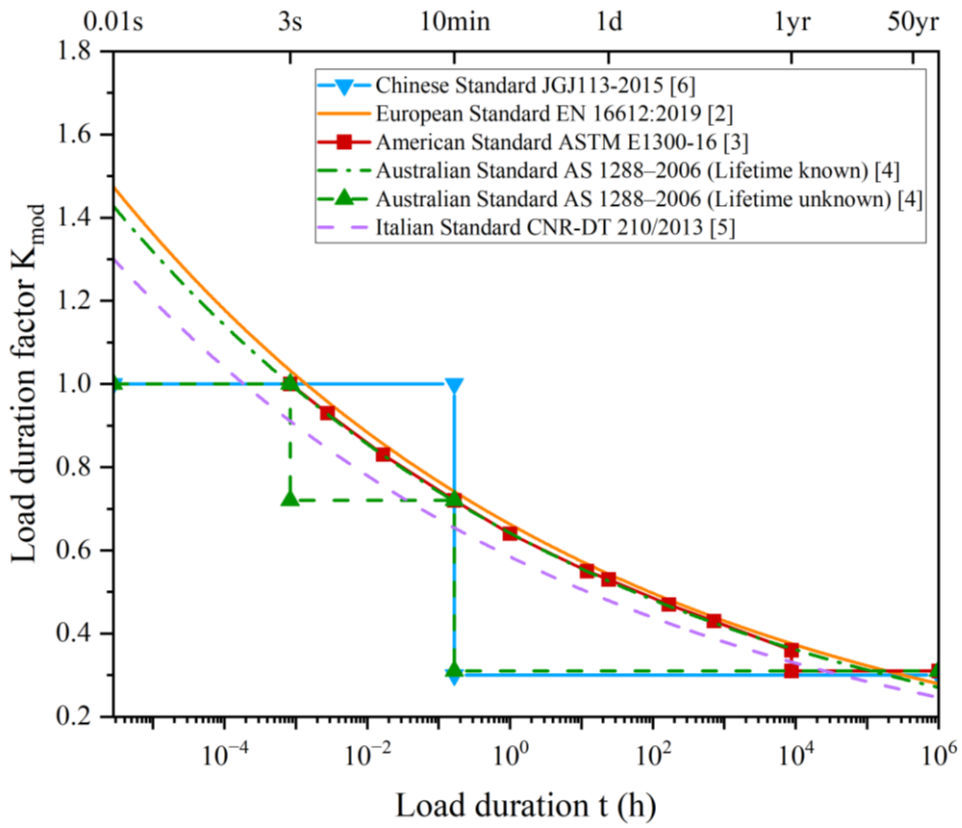


Figure 2. The determine methods of k_{mod} from different standards

2. Subcritical crack propagation

Glass is essentially an elastic and perfectly brittle material. Therefore, the cracks that are inevitably introduced on its surface by the manufacturing process and processing procedures can be modelled using Linear Elastic Fracture Mechanics (LEFM). LEFM assumes that a crack subjected to pure tension (Mode-I) will extend when the stress intensity factor K_{I} (a parameter that depends on the loading and crack length, or possibly another characteristic dimensión of the specimen) reaches the critical value K_{IC} (the fracture toughness). Under load-control the crack will propagate catastrophically when $K_{\mathrm{I}} = K_{\mathrm{IC}}$. However, it is also posible for a crack to propagate subcritically at values of K_{I} less than K_{IC} if the glass is exposed to a humid environment. This because the applied stress combines with a chemical reaction between the glass and water molecules to break the bonds along the crack front, thus effectively increasing the crack size. The crack velocity associated with this static fatigue (or stress corrosion) phenomena is determined by the stress intensity factor.

2.1. Relationship between crack velocity and stress intensity

Figure 3 illustrates the relationship between crack velocity v and K_{I} for a typical glass. When K_{I} exceeds the threshold K_{th}, the crack will begin to grow subcritically at a rate that depends on K_{I} (region I). In region II the crack velocity v is affected by relative humidity, but is independent of K_{I}. The velocity in region III returns to K_{I}-dependence and can be as fast as 0.001 ~ 1 m/s. When K_{I} reaches K_{IC}, the glass element fails catastrophically. In general, for the design of glass load-bearing structures which will withstand long-term loads, the mechanical behaviour of glass in region I is of interest.

For the case of brittle materials, an empirical power-law function[7] is usually used to describe the relationship between crack velocity and stress intensity in region I:

$$v = \frac{da}{dt} = v_0 \left(\frac{K_I}{K_{IC}}\right)^n \tag{1}$$

where v_0 and n are the linear and exponential crack velocity parameters, respectively. On the logarithmic scale (Figure 3), v_0 represents the ordinate of K_{IC} and n is the slope.

Here it suffices to summarize the fracture mechanics of two-dimensional configurations (plane stress or plane strain) under pure tension. As such, the crack front (a line) reduces to a crack tip (a point). The stress intensity factor K_{I} is usually written as:

$$K_I = Y\sigma\sqrt{\pi a} \tag{2}$$

where Y is the geometry factor, σ is the tensile stress perpendicular to the crack plane, and a is the crack depth.

Combining Equations (1) and (2), with the assumption of constant n and negligible K_{th}, leads to:

$$\int_{a_i}^{a_f} a^{-\frac{n}{2}} da = \frac{v_0 (Y\sqrt{\pi})^n}{{K_{IC}}^n} \int_0^{t_f} (\sigma(t))^n \, dt \tag{3}$$

where a_i is the initial crack depth, and a_f is the crack depth at failure, t_f is the time-to-failure.

In Chapter 3, Equation (3) is utilized to derive the crack resistances for two different stress histories. By considering the effects of temperature, humidity and loading rate, we will establish a relationship between these two crack resistances, enabling us to assess the long-term strength of glass based on the short-term strength obtained from laboratory tests.

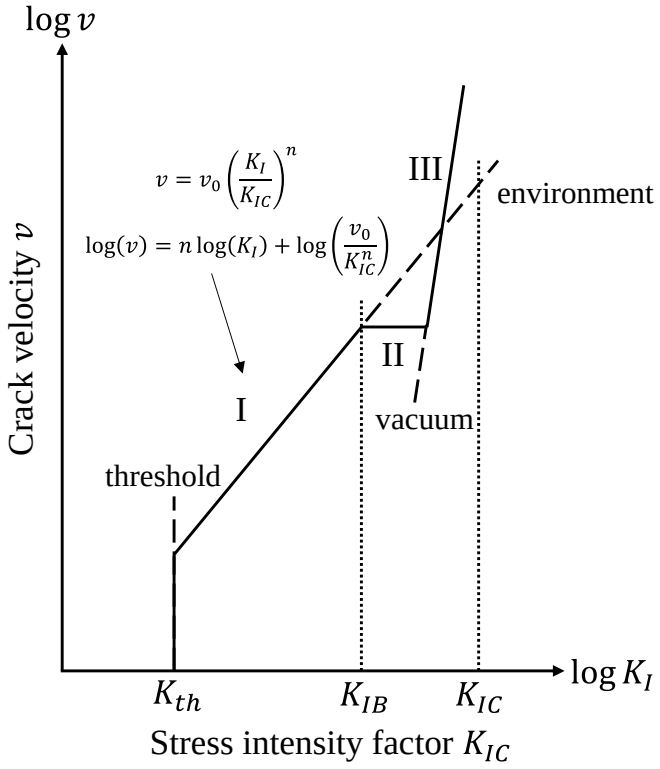


Figure 3. Relationship between crack velocity and stress intensity factor for glass

2.2. Quantification of the model parameters

To establish the relationship between life-time service condition and laboratory tests condition, it is crucial to analyse the effects of environment factors and stress history as well as to quantify the model parameters.

2.2.1. Geometry factor

Generally, the geometry factor Y is dependence of the crack geometry, the crack depth, the stress field applied and the geometry of glass element. However, the crack depth is too small in comparison with the thickness of glass element, so the dependence of the geometry of crack is the most significant. And it is assumed that Y is constant during the crack propagation. For surface cracks away from edge, Y = 1.12[8, 9] is commonly taken. For edge cracks caused by processing, it is reasonable to simplify as half-penny or quarter-circle cracks, and Y =0.722[8-10].

2.2.2. Fracture toughness

Fracture toughness K_{IC} is regarded as a material constant, which is only dependence of material itself (for example, the chemical composition of the material). Table 1 lists experimentally measured K_{IC}, and shows that K_{IC} = 0.75 MPa·m$^{0.5}$ is a reasonable assumption for soda lime silica glass in all applications.

Table 1. An overview of experimentally measured K_{IC} for soda lime silica glass

Source	K_{IC} (MPa·m$^{0.5}$)
Wiederhorn[11]	0.82
Atkins and Mai[12]	0.78
Gehrke et al. [13]	0.78
Mencek[14]	0.72~0.82
Ullner[15]	0.76

2.2.3. Crack velocity parameters

Crack velocity parameters v_0 and n are both affected by the temperature and humidity of the ambient environment. v_0 is also influenced by loading rate. Increases in temperature and humidity accelerate the chemical reactions between glass and water molecules, and in turn increase v_0 and decrease n [11, 16, 17]. Haldimann[8] established a linear crack velocity – stress rate relation based on experimental data, as depicted in Figure 4. On a double logarithmic scale, v_0 exhibits an approximately linear relationship with stress rate. For the typical loading stress rate of 2 MPa/s used in many laboratory test standards, v_0 is approximately 10 μm/s. By performing a linear fit (R^2=0.89) on the data points in Figure 4, the value of v_0 can be calculated for different loading stress rates $\dot{\sigma}$:

$$\log v_0 = -0.56 \log \dot{\sigma} + 1.27 \tag{4}$$

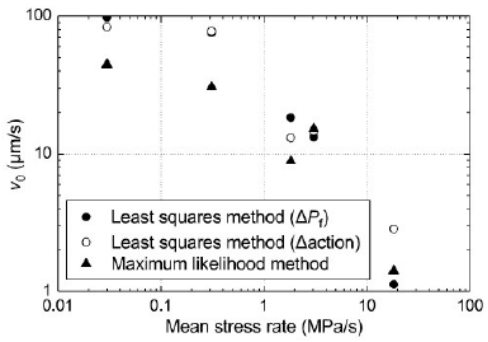


Figure 4. Curve of v_0 in relation to stress rate[8]

An overview of proposed v-K_I relations is shown in Figure 5, with the corresponding v_0 and n shown in the legend. The experimentally measured n is in the range of 14.77 ~ 21.5, and it is generally accepted that the use of n =16 [8-10, 18] is reasonable and conservative for most environmental conditions. The experimentally measured v_0 varies greatly due to its dependence on loading stress rate. However, with comprehensive consideration of environment and loading conditions, a reasonable range of 4.5~8.2mm/s can be used for load-bearing glass components. Haldimann[8] suggested that for general applications, v_0 = 6mm/s may be used as a conservative assumption; for glass elements that are permanently immersed in water, a higher value of e.g. v_0 = 30 mm/s might be required.

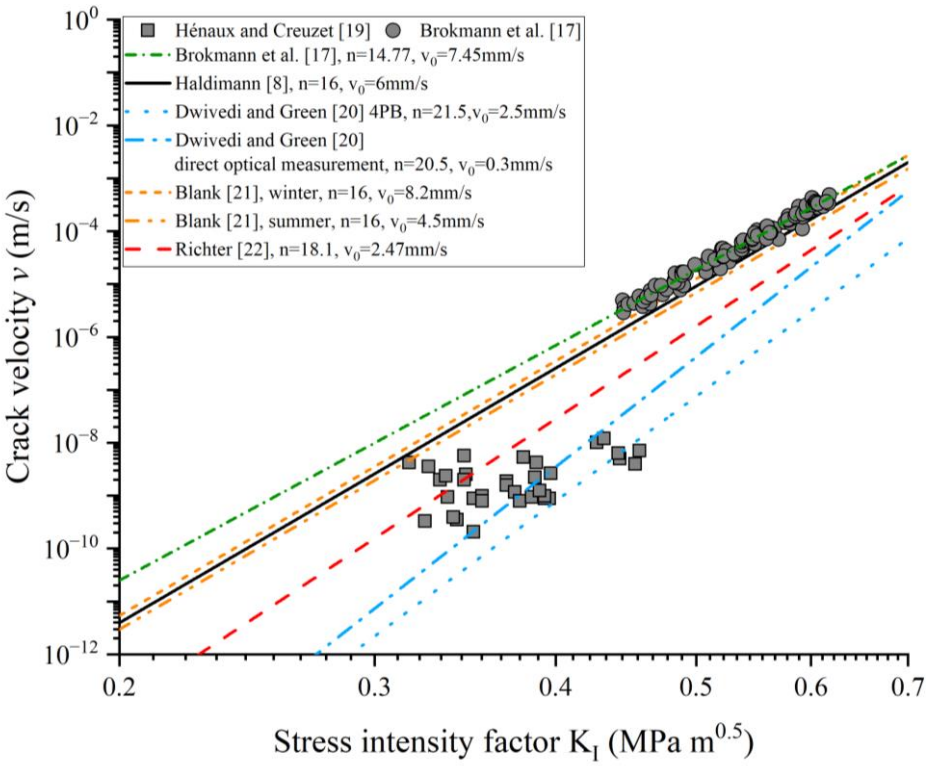


Figure 5. An overview of the v-K_I relations and crack growth data

3. Crack resistances under two different stress histories and the interrelationships

Equation (3) is now utilized to derive the crack resistances for two stress histories, and the relation between them will be established based on the parameter quantification in Chapter 2.

3.1. Laboratory tests condition (constant stress rate)

In laboratory tests the applied stress typically increases linearly with time. That is, the loading stress rate $\dot{\sigma}$ is constant, so that $\sigma(t) = \dot{\sigma}t$, as illustrated in Figure 1(a). Equation (3) becomes:

$$\int_{a_i}^{a_{test}} a^{-\frac{n}{2}} da = \frac{v_0 (Y\sqrt{\pi})^n}{{K_{IC}}^n} \int_0^{t_{test}} (\dot{\sigma}t)^n \, dt \tag{5}$$

with a_{test} defined as the crack depth at failure. Assume n to be constant and integrate Equation (5), yields

$$\frac{2}{n-2}\left({a_i}^{\frac{2-n}{2}} - {a_{test}}^{\frac{2-n}{2}} \right) = \frac{v_0 (Y\sqrt{\pi})^n}{{K_{IC}}^n} \cdot \frac{{\sigma_{test}}^{n+1}}{(n+1)\dot{\sigma}} \tag{6}$$

When the time-to-failure is more than 0.01s, the size of the critical crack at the end of the test can be assumed to be much higher the initial size [9]. Thus, the interrelationship between applied stresses of two identical cracks under identical conditions, loaded at different constant sstress rates $\dot{\sigma}_1$ and $\dot{\sigma}_2$, is obtained:

$$\frac{\sigma_1}{\sigma_2} = \left(\frac{\dot{\sigma}_1 v_{02}}{\dot{\sigma}_2 v_{01}}\right)^{1/(n+1)} \tag{7}$$

When under the standard stress rate of $\dot{\sigma_0} = 2$ MPa/s, the linear crack velocity parameter v_{00} =0.01mm/s. And values of v_0 for different loading stress rates $\dot{\sigma}$ can be calculated by Equation (4). Thus, the interrelationship between applied stresses of two identical cracks under identical conditions, loaded at standard and other constant stress rates $\dot{\sigma}_0$ and $\dot{\sigma}_1$, is obtained:

$$\frac{\sigma_1}{\sigma_{\dot{\sigma}_0}} = \left(\frac{\dot{\sigma}_1 v_{00}}{\dot{\sigma}_0 v_{01}}\right)^{1/(n+1)} \tag{8}$$

Equation (8) can also be expressed by strain rate, $\dot{\varepsilon}_0$ =2.86×10^{-5} s^{-1} ($\dot{\sigma_0}$ =2 MPa/s for elastic modulus E= 70 GPa[1]):

$$\frac{\sigma_1}{\sigma_{\dot{\varepsilon}_0}} = \left(\frac{\dot{\varepsilon}_1 v_{00}}{\dot{\varepsilon}_0 v_{01}}\right)^{1/(n+1)} \tag{9}$$

3.2. Life-time service condition (constant stress)

In the case of life-time service condition, the applied stress is commonly constant, $\sigma(t) = \sigma_{life}$, as illustrated in Figure 1(b). Equation (3) can be expressed as:

$$\int_{a_i}^{a_{life}} a^{-\frac{n}{2}} da = \frac{v_0 \left(Y\sqrt{\pi}\right)^n}{{K_{IC}}^n} \int_0^{t_{life}} {\sigma_{life}}^n \, dt \tag{10}$$

with a_{life} being the crack depth at failure under life-time service condition. Assume n to be constant and integrate Equation (10) to obtain

$$\frac{2}{n-2}\left(a_i^{\frac{2-n}{2}} - a_{life}^{\frac{2-n}{2}}\right) = \frac{v_0 \left(Y\sqrt{\pi}\right)^n}{{K_{IC}}^n} \sigma_{life}^n t_{life} \tag{11}$$

When the time-to-failure is greater than 0.01s, the interrelationship between applied constant stresses and lifetimes of two identical cracks under identical conditions is also obtained:

$$\frac{\sigma_1}{\sigma_2} = \left(\frac{t_2}{t_1}\right)^{1/n} \tag{12}$$

Thus, the applied constant stresses under different lifetimes can be normalised to a relative applied stress σ_{t_0}:

$$\frac{\sigma_1}{\sigma_{t_0}} = \left(\frac{t_0}{t_1}\right)^{1/n} \tag{13}$$

There are different values of t_0 used in standards and researches, e.g., 0.67s [5], 1s [8], 3s [3, 4, 8], 5s [1] and 60s [8, 18].

3.3. Assessing the long-term strength through laboratory tests

Assume the exponential crack velocity parameter n to be constant (n =16) for both laboratory tests condition and life-time service condition, and the linear crack velocity parameters are v_{0t} and v_{0l} respectively. For two identical cracks, the interrelationship between strength under laboratory tests condition σ_{test} and life-time service condition σ_{life} can be obtained:

$$\frac{\sigma_{life}}{\sigma_{test}} = \left(\frac{v_{0t}\sigma_{test}}{v_{0l}(n+1)t\,\dot{\sigma}}\right)^{1/n} \tag{14}$$

For convenient application, the long-term strength σ_{life} can be assessed through short-term strength obtained from standard laboratory tests ($\dot{\sigma} = \dot{\sigma}_0$ =2 MPa/s), and $v_{0t} = v_{00}$ =0.01mm/s. In the case of life-time service condition, v_{0l} = 6mm/s. The value of σ_{test} can be adopted as the characteristic bending strength f_k = 45 MPa, which is specified in EN 572-1[1]. Thus, the modified load duration factor k_{mod} can be obtained:

$$k_{mod} = \frac{\sigma_{life}}{f_k} = \left(\frac{f_k}{600(n+1)t\dot{\sigma}_0}\right)^{1/n} \tag{15}$$

4. Comparison of the model predictions with test data

A large number of laboratory strength tests have been conducted on glass using various methods such as three-point bending, four-point bending, coaxial double ring bending and uniaxial tensile tests. The tests data have been collected in [23]. Those tests are conducted under different constant stress rates. Remarkably, all the test data align with Equation (9) quite well, which considers the influence of stress rate on linear crack velocity parameters v_0, as demonstrated in Figure 6(a).

A significant amount of lifetime test data has also been gathered in [23] where the applied constant load and time-to-failure are recorded. This type of test closely simulates the life-time service condition and the specimen is typically loaded by dead-weight or through universal testing machine. Notably, all the data fit Equation (13) very well, as shown in Figure 6(b). Here t_0=1s is selected.

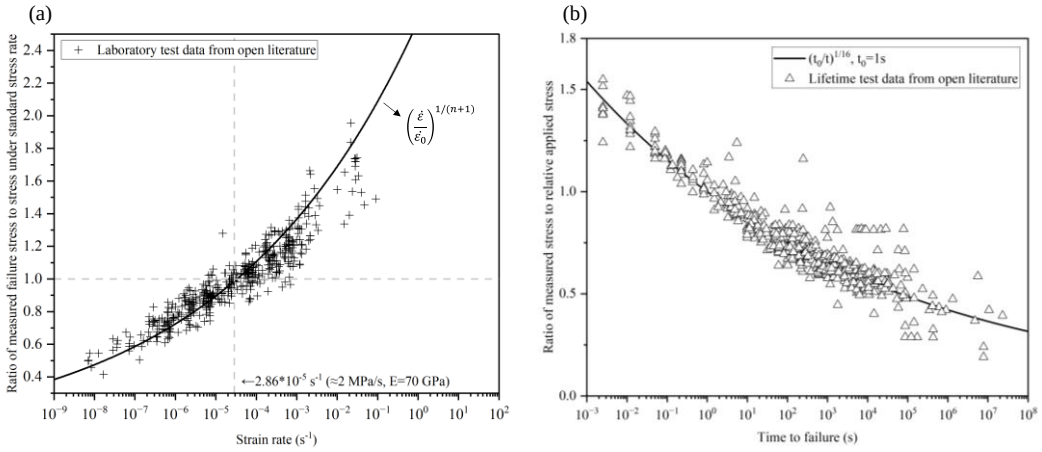


Figure 6. Comparisons of (a) Equation (9) and (b) Equation (13) with test data.

The lifetime test data are also compared with the proposed load duration factor k_{mod}, as shown in Figure 7. It can be observed that almost all the lifetime test data are above the proposed model. Most international standards use Equation (13) with different values of t_0 to assess the long-term strength, which may lead to unsafe design. This indicates that the proposed k_{mod} is safe enough to predict the long-term strength of glass through short-term strength obtained from standard laboratory tests.

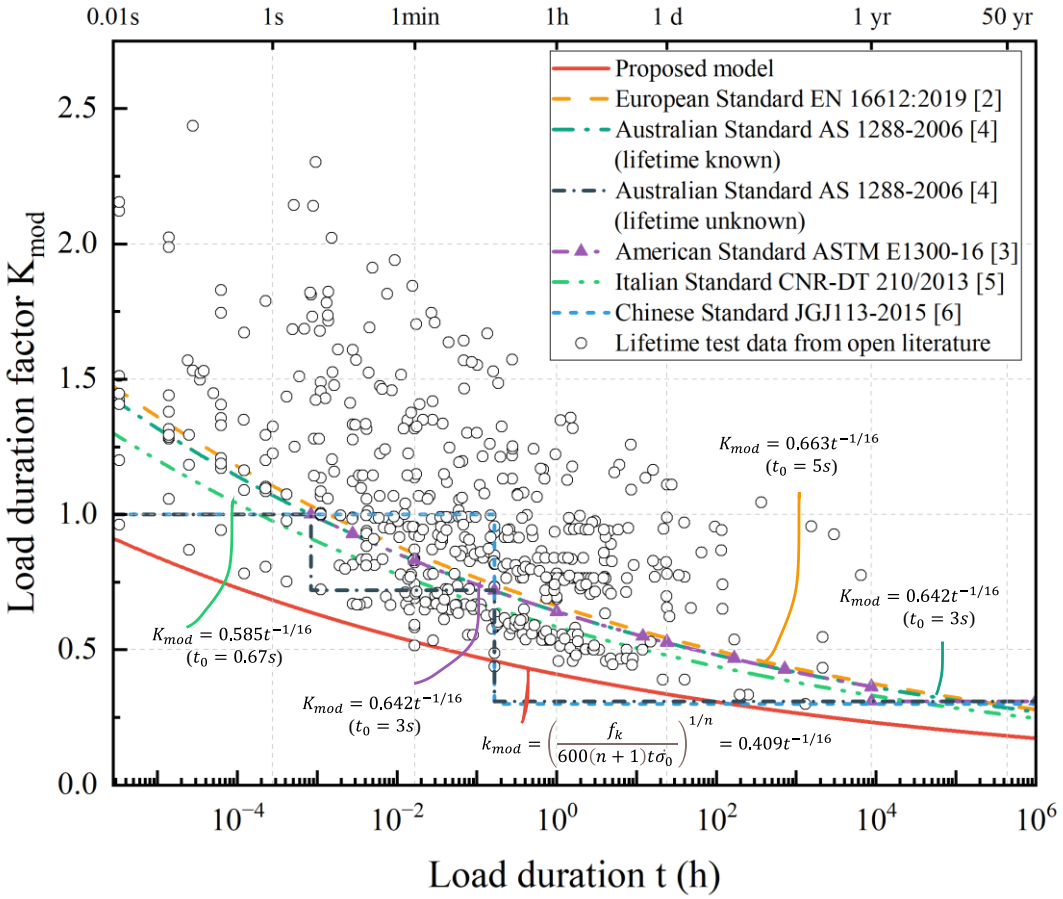


Figure 7. Comparison of proposed k_{mod} with test data

5. Conclusions

This paper proposes a predictive model for the long-term strength of structural glass that relies on short-term strength data obtained from laboratory tests. The model is motivated by the limitations of existing methods for determining the load duration factor k_{mod} from international standards. This paper addresses these limitations by developing a modified k_{mod} that considers and quantifies the influences of environment and stress rate on crack velocity parameters. The proposed model is verified against a large data set of laboratory test data for various load durations, and the results are compared to the international standards. It is demonstrated that the proposed model is more capable of converting short-term strength under different stress/strain rates, normalise the applied constant stresses under different lifetimes to the relative applied stress, and predict the long-term strength through short-term strength obtained from laboratory tests. It is concluded that the proposed model provides a safe and reliable method for assessing the long-term strength of structural glass, and offers promise improving design of load-bearing glass structures.

Acknowledgements

We would like to thank Dr. Xing Chen for the time spent in discussion and all the useful suggestions.

References

[1] *Glass in building–Basic soda-lime silicate glass products–Part 1: Definitions and general physical and mechanical properties*, EN 572-1, 2016.

[2] *Glass in Building-Determination of the Lateral Load Resistance of Glass Panes by Calculation*, EN 16612: 2019, 2019.

[3] *Standard Practice for Determining Load Resistance of Glass in Buildings*, ASTM E1300-16, 2016.

[4] *Glass in Buildings: Selection and Installation*, AS 1288-2006, 2006.

[5] *Istruzioni per la progettazione, l'esecuzione e il controllo di costruzioni con elementi strutturali in vetro*, CNR-DT-210, 2012.

[6] *Technical Regulations for Architectural Glass Application*, JGJ113-2015, 2015.

[7] G. Evans, "A general approach for the statistical analysis of multiaxial fracture," *Journal of the American Ceramic Society*, vol. 61, no. 7-8, pp. 302-308, 1978.

[8] M. Haldimann, "Fractures strength of structural glass elements-analytical and numerical modeling, testing and design." Ph. D. dissertation, Ecole polytechnique federale de Lausanne, 2006.

[9] G. Pisano, "The statistical characterization of glass strength: from the micro-to the macro-mechanical response," Ph. D. dissertation, Università degli Studi di Parma, 2018.

[10] M. Porter, "Aspects of structural design with glass," Ph. D. dissertation, University of Oxford, 2001.

[11] S. M. Wiederhorn. "Influence of water vapor on crack propagation in soda-lime glass." *Journal of the American Ceramic Society*, vol. 50, no.8, pp. 407-414, 1967.

[12] A. G. Atkins and Y. W. Mai, Elastic and plastic fracture: metals, polymers, ceramics, composites, biological materials, Chichester, England/New York, Ellis Horwood, Ltd./John Wiley and Sons, 1985.

[13] E. Gehrke, C. Ullner, and M. Hähnert, "Effect of corrosive media on crack growth of model glasses and commercial silicate glasses," *Glastechnische Berichte*, vol. 63, no. 9, pp. 255-265, 1990.

[14] J. Mencek, Strength and fracture of glass and ceramics, Amsterdam: Elsevier, 1992.

[15] C. Ullner, "Untersuchungen zum Festigkeitsverhalten von Kalk-Natronsilicatglas nach mechanisher Vorsch adigung durch Korundberieselung," BAM, Berlin, Germany, Tech. Rep. 1993.

[16] S. M. Wiederhorn and L. H. Bolz, "Stress corrosion and static fatigue of glass," *Journal of the American ceramic society*, vol. 53, no. 10, pp. 543-548, 1970.

[17] C. Brokmann, S. Kolling, J. Schneider, "Subcritical crack growth parameters in glass as a function of environmental conditions," *Glass Structures & Engineering*, vol. 6, no. 1, pp. 89-101, 2021.

[18] M. J. Meyland, J. H. Nielsen, and C. Kocer, "Tensile behaviour of soda-lime-silica glass and the significance of load duration–A literature review," *Journal of Building Engineering*, vol. 44: 102966, 2021.

[19] S. Hénaux and F. Creuzet, "Kinetic fracture of glass at the nanometer scale," *Journal of materials science letters*, vol. 16, no. 12, pp. 1008-1011, 1997.

[20] P. J. Dwivedi and D. J. Green, "Determination of subcritical crack growth parameters by in situ observation of indentation cracks," *Journal of the American Ceramic Society*, vol. 78, no. 8, pp. 2122-2128, 1995.

[21] K. Blank, "Dickenbemessung von vierseitig gelagerten rechteckigen Glasscheiben unter gleichförmiger Flächenlast," Forschungsbericht des Instituts für Konstruktiven Glasbau, Gelsenkirchen, Germany, Tech. Rep. 1993.

[22] H. Richter, "Experimentelle Untersuchungen zur Rißausbreitung in Spiegelglas im Geschwindigkeitsbereich 10E-3 bis 5*10E3 mm/s," Ph. D. dissertation, Inst. für Festkörpermechanik der Fraunhofer-Ges., 1974.

[23] M. J. Meyland, J. H. Nielsen, and C. Kocer, "Datasets: Tensile behaviour of soda-lime-silica glass and the significance of load duration-A literature review." DTU Data, Technical University of Denmark, 2021.

IASS 2023
July 10–14 Melbourne
Integration of Design and Fabrication

Proceedings of the IASS Annual Symposium 2023
Integration of Design and Fabrication
10–14 July 2023, Melbourne, Australia
Y.M. Xie, J. Burry, T.U. Lee and J. Ma (eds.)

Neural ODE-based data-driven approach for prediction of the creep behaviour of steel cables

Weijia ZHANG[a,b,*], Xingfei YUAN[c], Lei YUAN[a,b], Yi-Qing NI[a,b], Su-Mei WANG[a,b]

[*] Research Institute for Sustainable Urban Development, The Hong Kong Polytechnic University
Z Block, The Hong Kong Polytechnic University, Hung Hom, Kowloon, Hong Kong SAR
wei-jia.zhang@connect.polyu.hk

[a] Department of Civil and Environmental Engineering, The Hong Kong Polytechnic University
[b] National Rail Transit Electrification and Automation Engineering Technology Research Center (Hong Kong Branch), The Hong Kong Polytechnic University
[c] College of Civil Engineering and Architecture, Zhejiang University

Abstract

Creep exists in the prestressed cables in spatial structures such as cable nets and cable domes. The occurrence of creep in structural elements leads to stress relaxation, resulting in a degradation of global stiffness or even failure of the entire structure. Therefore, it is critical to accurately predict the creep behaviour of structural members such as steel cables in structural design and assessment. To investigate this issue, this paper compares two methods for precisely predicting long-term creep behaviour in steel cables: a physical model based on viscoelastic theory and a neural ordinary differential equation (ODE)-based data-driven approach. Neural ODE is a powerful machine learning tool for governing equation discovery or approximation. Different from other neural network-based methods, Neural ODE learns the changing trend from measured data by approximating the derivative of the input-to-output transform rather than abstractly seeking the underlying relation between input and output, which enables it to generate a more accurate prediction. Furthermore, Neural ODE can not only learn the creep constitutive equation, but also flexibly integrate other physical information such as the diameters of cables into the model, which shows the evolutionary capability of the model. Based on the experimental data of a long-term creep test in previous research, prediction performance of both methods will be compared in this study. The Neural ODE framework possesses several advantages compared to the physical model method for directly fitting the creep constitutive equation: Firstly, the creep prediction of Neural ODE will be more accurate because it learns the changing trend of the data, while the accuracy of physical model is based on the assumed form of the constitutive equation and quantity of measurement data; Secondly, Neural ODE framework is more general because various parameters of steel cables can be considered and integrated into the framework.

Keywords: neural ODE, machine learning, creep behaviour, steel cables, cable structures, structural assessment

1. Introduction

Steel cables are a fundamental component of many engineering structures, ranging from bridges and towers to cranes and suspension systems. The long-term creep and stress relaxation behaviours of steel cables under tension have considerable implications for the reliability and safety of these structures. Accurate predictions of the creep deformation of steel cables are, therefore, a prerequisite for improving the design of these structures [1, 2].

Creep and stress relaxation are two important phenomena that are exhibited by viscoelastic materials. In general, creep and stress relaxation are different manifestations of the same mechanism under different conditions [3]. Creep is a particularly important concern for steel cables that are subject to

Copyright © 2023 by Weijia ZHANG, Xingfei YUAN, Lei YUAN, Yi-Qing NI and Su-Mei WANG. Published in the Proceedings of the IASS Annual Symposium 2023 with permission.

sustained tension. Over time, the length of a steel cable can increase significantly due to creep deformation, which can result in a loss of tension, reduced structural performance, and even failure. The precise nature of the creep deformation can depend on a range of factors, including the magnitude and duration of the applied load, and the composition and microstructure of the material itself. Stress relaxation, on the other hand, can also have significant implications for the long-term behaviour of steel cables. If a steel cable is stretched to a certain length and then held in that position, the stress on the cable will gradually decrease over time. This decrease in stress can result in reduced structural performance and can contribute to the potential for failure of the structure as a whole.

Given the importance of creep and stress relaxation in determining the long-term behaviour of steel cables, it is crucial to develop accurate methods for predicting these phenomena [4, 5]. By doing so, engineers and designers can make more informed decisions about the structural integrity of their designs and can take steps to mitigate the potential for failure over time. Different branches of neural networks are used to predict structural creep. For example, artificial neural networks [6] and recurrent neural networks [7] are used to predict creep behaviour in masonry structures. Convolutional neural networks are used to model creep and shrinkage in concrete structures [8]. However, there lacks studies on creep prediction of steel cables using machine learning methods.

In this research paper, two different methods are introduced to predict the long-term creep behaviour of steel cables: a physical model [4] based on viscoelastic theory [3] and a machine learning approach known as Neural Ordinary Differential Equation (Neural ODE) [9]. The physical model is a well-established method that describes the time-dependent behaviour of materials under stress by considering the inherent viscoelastic properties of the material. On the other hand, Neural ODE is a recent development in the field of machine learning, which has shown great promise in learning dynamic systems [9, 10].

The main objective of this study is to compare and evaluate the performance of these two methods in predicting the creep deformation of steel cables. We will use experimental data from previous studies [5] to calibrate and validate our models. Additionally, we will discuss the potential of combining these two methods to enhance the accuracy and efficiency of the prediction process.

The results of this study will provide valuable insights into the long-term behaviour of steel cables under tension and may help to improve the safety and reliability of engineering structures that rely on steel cable components.

2. Methodology

In this section, we will discuss two ways to describe the time-dependent creep constitutive model. The first method is physical model based on viscoelastic theory, which is commonly used. The second method is a data-driven machine learning method called Neural ODE.

Both methods can be utilized to describe the creep behaviour of steel cables by extrapolating from the limited data obtained within a short period of time. The aim of learning the creep constitutive equation is to predict the long-term creep behaviour of these steel cables in order to accurately evaluate the structural performance, with particular regard to the creep effect; this is important due to the difficulty of obtaining measurement data. To assess their effectiveness in fulfilling this purpose, the predictive performance of both methods will be evaluated in the subsequent section.

2.1. Physical model

The application of a physical model rooted in viscoelastic theory is well-suited for establishing the nonlinear relationship between the strain and stress exerted upon steel cables due to the creep effect. The construction of typical models embodying the principles of viscoelastic theory incorporates both ideal elastic elements and viscous elements, i.e. the springs and the dashpots. The relationship between stress and strain can be represented by Eq. (1) and Eq. (2) for springs and dashpots, respectively.

$$\sigma = E\varepsilon \tag{1}$$

$$\sigma = \eta \frac{d\varepsilon}{dt} = \eta\dot{\varepsilon} \tag{2}$$

Complex models, such as the Maxwell model and Kelvin model, may be constructed to describe the creep property of diverse viscoelastic materials by integrating multiple basic elements in either a parallel or series configuration. A typical Kelvin chain model is shown in Figure 1. The constitutive model of this Kelvin chain model is succinctly conveyed by the differential equation expressed as Eq. (3):

$$\sigma + p_1\dot{\sigma} + p_2\ddot{\sigma} + \cdots + p_n\sigma^{(n)} = q_0\varepsilon + q_1\dot{\varepsilon} + q_2\ddot{\varepsilon} + \cdots + q_n\varepsilon^{(n)} \tag{3}$$

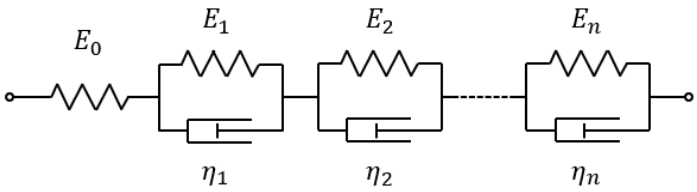


Figure 1. A general Kelvin chain model

By applying Laplace transformation to Eq. (3), it gives the relationship between total strain and applied constant stress:

$$\varepsilon(t) = \frac{\sigma_0}{E_0} + \sigma_0 \sum_{i=1}^{n} \frac{1}{E_i}\left(1 - e^{-\frac{t}{\tau_i}}\right) = \varepsilon_e + \varepsilon_{cr}(t) \tag{4}$$

Then, the expression of the total creep strain can be derived as:

$$\varepsilon_{cr}(t) = \sigma_0 \sum_{i=1}^{n} \frac{1}{E_i}\left(1 - e^{-\frac{t}{\tau_i}}\right) = \sum_{i=1}^{n} \phi_i\left(1 - e^{-\frac{t}{\tau_i}}\right) \tag{5}$$

It should be noted that Eq. (5) is derived from a Kelvin model with three basic unit, which is a parallel combination of a spring and a dashpot. The values of the relevant parameters are obtained through measurement data and may vary depending on the specific model chosen and the quantity of data available, potentially impeding the accuracy of predictions derived through this formulation. Careful attention to parameter selection and model choice is therefore paramount in ensuring the reliability and validity of results obtained from this approach.

2.2. Neural Ordinary Differential Equation (Neural ODE)

Neural ODE has raised significant attention in recent years for it provides a new insight into the relation between neural networks and differential equations. Neural ODE is a variant of Residual Networks (ResNets) [11]. In ResNets, the states of a system can be expressed by hidden layers of neural networks. The state of layer *t*+1 can be obtained from the state of layer *t* through a function $f(\cdot)$:

$$h_{t+1} = h_t + f(h_t) \tag{6}$$

This process can be regarded as a numerical integration with a time step $\Delta t = 1$:

$$h_{t+1} = h_t + f(h_t)\Delta t \tag{7}$$

By taking the limit of Δt to approach zero, Eq. (7) can be transformed from a discrete form into a continuous ordinary differential equation with respect to time *t*:

$$\lim_{\Delta t \to 0} \frac{h_{t+1} - h_t}{\Delta t} = \frac{dh(t)}{dt} = f(h(t), t) \tag{8}$$

The differentiable function $f(\cdot)$ is the derivative of the hidden state $h(t)$, which can be parameterized by deep neural networks (DNNs) as $f(h(t), t, \theta)$. θ represent the trainable parameters, i.e. weights and biases, in the DNNs. It is the core idea of Neural ODE that modelling a dynamic system using DNNs in the format of an initial value problem of an ODE:

$$\dot{h}(t) = f(h(t), t, \theta) \qquad h(t_0) = h_0 \tag{9}$$

As a powerful function approximator, DNNs can learn the derivative, i.e. the dynamics, of the states of the concerned system from data. To train the DNNs, the loss function can be constructed by:

$$L_{total} = \sum_{i=1}^{n_m} \left| h(t_0) + \int_{t_0}^{t_i} f(h(t), t, \theta) dt - u_m(t_i) \right|^2 \tag{10}$$

By minimizing the loss function, the parameters of the DNNs can be optimized and updated during the training process. At the same time, the DNNs will be finally trained as a surrogate model of the time derivative of $h(t)$.

Neural networks such as artificial neural networks [6] have been applied to predict creep by learning the creep itself. In this study, however, we try the newly emerged Neural ODE framework. The advantage of Neural ODE is its superior curve-fitting accuracy provided by the key idea of Neural ODE, which is to learn the underlying dynamics of the system rather than learn the structural response itself. On the other hand, Neural ODE is a data-driven method, which means it learns the dynamics from data. Thus, the effectiveness of learning and the accuracy of prediction highly depend on the quality of the data.

3. Creep constitutive model

In this section, we present an evaluation of the predictive accuracy of two methods, previously discussed. The evaluation process includes two steps, whereby the measurement data is obtained from a long-term creep test. In the first step, we use the measurement data of 2,000 hours to model the creep constitutive equation derived from viscoelastic theory and train the DNN-based Neural ODE model. In the second step, the fitted physical model and learned Neural ODE model will be used to predict the creep behaviour of 9,000 hours, and their performance will then be assessed.

3.1. Physical model

To fit the time-creep strain curve depicted in Figure 2, a Kelvin chain model comprising one spring and three spring-dashpot units was selected. The elastic behaviour is represented by the spring, while the viscoelastic behaviour is mimicked by the three units. The scatter chart in Figure 3(a) illustrates the time-creep strain relationship. It is worth noting that only 2,000 hours of data was employed to establish the model, while the remaining data was utilized to evaluate the predictive performance. The resulting creep constitutive model can be adequately fitted and expressed as follows:

$$\varepsilon_{cr}(t) = \sum_{i=1}^{3} \phi_i \left(1 - e^{-\frac{t}{\tau_i}}\right) \tag{11}$$

in which, $\phi_1 = 1.41 \times 10^{-2}$, $\phi_2 = -1.39 \times 10^{-2}$, $\phi_3 = 1.17 \times 10^{-4}$, $\tau_1 = 2.17 \times 10^{1}$, $\tau_2 = 2.15 \times 10^{1}$, $\tau_3 = 7.98 \times 10^{2}$. Figure 3(b) presents a comparison between the fitted curve and measured data. Additionally, Figure 3(b) illustrates the prediction obtained from the physical model concerning time-creep behaviour over the interval between 2,000 and 9,000 hours. The physical model exhibits a reasonable agreement with the available data, albeit portraying a tendency towards horizontal progression, which means it cannot predict the changing tendency of the curve well. The relative error at *t*=9,000 h is 7.23%, and the average error of prediction is 4.17%.

The limited suitability of the physical model for prediction, despite being appropriate for modelling the time period of the available data, is attributed to uncertainty in the selection of model components and

the quantity of data utilized. The accuracy of the model is dependent on the amount and quality of the data used. In situations where data is inadequate, the model may fail to capture the complete trajectory of data fluctuations, thereby affecting the reliability of predictions.

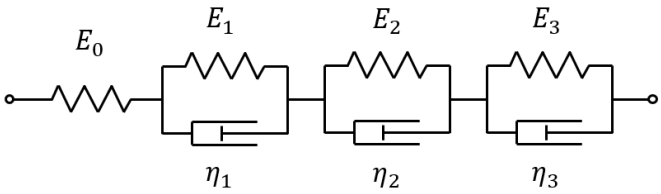
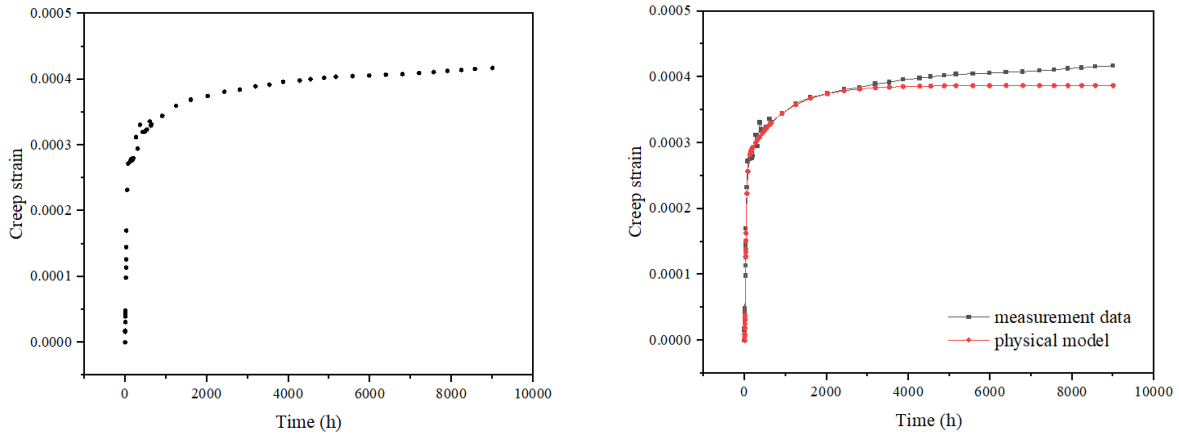


Figure 2. The Kelvin chain model with one spring and three units



(a) Time-creep strain curve of creep test (b) Comparison of measured data and physical model

Figure 3. The time-creep strain relation

3.2. Neural ODE

The implementation of Neural ODE for learning the creep constitutive equation from limited data will be detailed in this subsection.

First, a DNN was designed to serve as the primary component of the Neural ODE framework. The DNN features two hidden layers, each of which comprises 40 neurons. Given that the DNN's architecture exerts a significant influence on the learning process, trials were undertaken to optimize this feature. Various choices exist for the activation function [12], including ReLU, Sigmoid, and Tanh. In this study, we utilized Tanh, which performs the nonlinear transformation for every hidden layer. The inputs of the DNN are the time variable, *t*. If additional factors such as the steel cable's diameter and stress level are considered, the DNN easily accommodates other inputs accordingly. The outputs of the DNN will be the derivative $f(t)$. In contrast to other machine learning methods, the DNN in the Neural ODE framework learns the derivative of the time-creep strain curve, which represents the fundamental dynamics of the creep effect, as opposed to merely the curve itself. The transformation through the DNN can be represented explicitly as follows:

$$y_i = \sigma(W_i \cdot x_{i-1} + B_i), \qquad 1 \le i \le n \tag{12}$$

in which, x_{i-1} and y_i are the input and output of *i*th layer, respectively; W_i and B_i are matrices for weights and biases; σ is the nonlinear activation function.

To construct the loss function, an ODE solver is required to compute the integral term in Eq. (10). The ODE solver can be built based on numerical integration methods such as Runge-Kutta method and Gaussian quadrature. Chen [9] proposed an adjoint sensitivity method-based ODE solver, which can significantly reduce the memory cost. Then, the total loss function can be computed by:

$$L_{total} = \sum_{i=1}^{n_m} |h(t_0) + ODESolver(f(t), t_0, t_i, \theta) - u_m(t_i)|^2 \quad (13)$$

After calculating the total loss, the DNN can be trained to learn the derivative $f(t)$ during the training process. The training of a DNN involves the use of two critical algorithms, forward propagation and backpropagation. Forward propagation performs the critical function of taking an input and proceeding through the neural system to generate an output. On the other hand, backpropagation computes the gradient of the loss function concerning each neuron in the network. This gradient is then utilized to update the weights and biases of the network via an optimizer method such as SGD, L-BFGS, Adam, or RMSprop, among others. For this study, Adam will be employed to train the model, with a fixed learning rate of 0.01. Training will be stopped once the model reaches a certain iteration number or when the loss value has become stable. The learned derivative of the data will be leveraged to make predictions, and the overall Neural ODE framework is displayed in Figure 4, with the image depicting the convergence of the total loss throughout the training phase shown in Figure 5.

The prediction in the entire time period is shown in Figure 6. The relative error at *t*=9,000 h is 2.90%, which is smaller than that of physical model (7.23%). The average error of prediction is 2.19%, and it is also better than physical model (4.17%). This result shows the ability of Neural ODE in learning time-dependent behaviour and generating accurate long-term predictions.

3.3. Comparison of the physical model and Neural ODE model

The observation from Figure 3(b) and Figure 6 reveals that the physical model and Neural ODE model effectively fit the measurement data until 2,000 hours. However, the Neural ODE model outperforms the physical model in terms of predictive performance. It is worth mentioning that both models have potential areas of improvement.

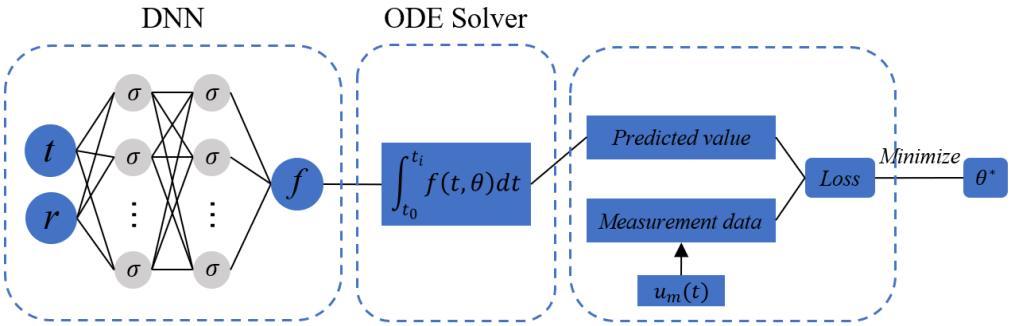


Figure 4. The Neural ODE framework

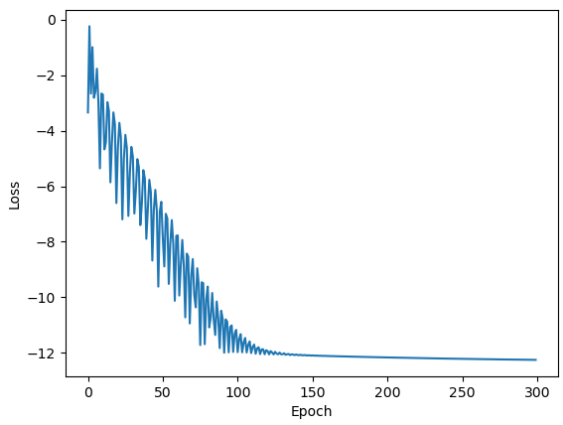


Figure 5. The training loss curve

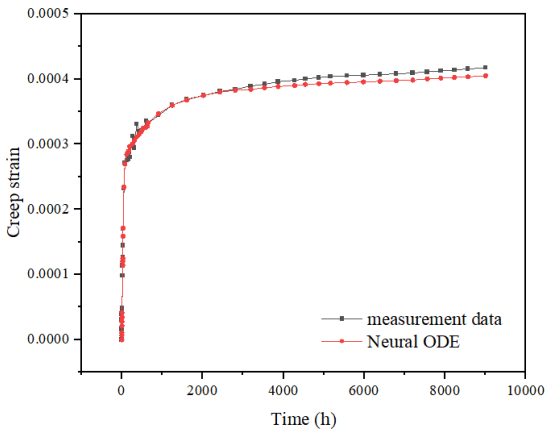


Figure 6. Comparison of time-creep strain curves

4. Conclusion and discussion

The accurate prediction of creep behaviour in steel cables is crucial for the structural design and assessment of spatial structures such as cable nets and cable domes. This paper presents a preliminary study on creep behaviour prediction. Two methods including physical model based on viscoelastic theory and a Neural Ordinary Differential Equation (Neural ODE)-based data-driven approach are investigated and compared.

Compared to the physical model method that derive the theoretical creep constitutive equation from viscoelastic theory and fit the equation directly, Neural ODE possesses several advantages such as more accurate prediction through learning the changing trend of the data, which is the underlying dynamics of the creep behaviour, and being more general by considering different parameters of steel cables. The results show that Neural ODE owns good extrapolation capability and is suitable to learn time-dependent properties and dynamics of structural systems.

In addition, the performance of Neural ODE can still be further improved. For example, Neural ODE is a data-driven approach, whose prediction accurate highly relies on the quantity and quality of the measurement data. However, the measurement data is sparse, and even hard to get in many cases. Therefore, prior physical knowledge like the theoretical creep constitutive equation can be integrated to facilitate computation and enhance the accuracy in the future work.

Acknowledgements

The work presented in this paper was supported by National Key R&D Program of China (2017YFC0806100) and the National Natural Science Foundation of China (Grant No. 51878600). The authors would also like to appreciate the funding support by a grant from the Research Grants Council (RGC) of the Hong Kong SAR, China (Grant No. PolyU 152308/22E), a grant from the National Natural Science Foundation of China (Grant No. U1934209), and a funding from the Innovation and Technology Commission of Hong Kong SAR Government to the Hong Kong Branch of National Rail Transit Electrification and Automation Engineering Technology Research Center (Grant No. K-BBY1).

References

[1] S. Kmet and M. Mojdis, "Time-dependent analysis of prestressed cable nets," *Journal of Structural Engineering*, vol. 142(7), 04016033, 2016.

[2] S. Youakim and V.M. Karbhari, "A Simplified Method for Prediction of Long term Prestress Loss in Post-Tensioned Concrete Bridges," University of California, San Diego, 2006.

[3] W. N. Findley, J. S. Lai, and K. Onaran, *Creep and Relaxation of Nonlinear Viscoelastic Materials with an Introduction to Linear Viscoelasticity*, North Holland Publishing Co., Amsterdam, 1976.

[4] W. Zhang, X. Yuan, L. Yang, and M. Deng, "Research on creep constitutive model of steel cables," *Construction and Building Materials*, vol. 246(20), 118481, 2020.

[5] W. Zhang, X. Yuan, C. Chen, and L. Yan, "Finite element analysis of steel wire ropes considering creep and analysis of influencing factors of creep," *Engineering Structures*, vol. 229, 111665, 2021.

[6] M. M. R. Taha, A. Noureldin, N. El-Sheimy, and N. G. Shrive, "Artificial neural networks for predicting creep with an example application to structural masonry," *Canadian Journal of Civil Engineering*, vol. 30(3), 523-532, 2003.

[7] A. El-Shafie, A. Noureldin, M. R. Taha, A. Hussain, and H. Basri, "Performance enhancement for masonry creep predicting model using recurrent neural networks," *Engineering Intelligent Systems for Electrical Engineering and Communications*, vol. 17(1), 29-38, 2009.

[8] J. Zhu and Y. Wang, "Convolutional neural networks for predicting creep and shrinkage of concrete," *Construction and Building Materials*, vol. 306, 124868, 2021.

[9] R. T. Q. Chen, Y. Rubanova, J. Bettencourt, and D. Duvenaud, "Neural Ordinary Differential Equations," in *32nd Conference on Neural Information Processing Systems* (*NeurIPS 2018*), Montréal, Canada, 2018.

[10] V. M. M. Alvarez, R. Rosca, and C. G. Fălcutescu, "DyNODE: Neural Ordinary Differential Equations for Dynamics Modeling in Continuous Control," arXiv preprint arXiv:2009.04278, 2020.

[11] K. He, X. Zhang, S. Ren, and J. Sun, "Deep residual learning for image recognition," in *Proceedings of the IEEE conference on computer vision and pattern recognition*, pp. 770–778, 2016.

[12] L. Sun, H. Gao, S. Pan, J. X. Wang, "Surrogate modeling for fluid flows based on physics-constrained deep learning without simulation data," *Computer Methods in Applied Mechanics and Engineering*, vol. 361, 112732, 2020.

IASS 2023
July 10–14 Melbourne
Integration of Design and Fabrication

Proceedings of the IASS Annual Symposium 2023
Integration of Design and Fabrication
10–14 July 2023, Melbourne, Australia
Y.M. Xie, J. Burry, T.U. Lee and J. Ma (eds.)

Optimal sensor placement of large-span spatial structures based on sensitivity analysis

Yiqun WANG[a], Yaozhi LUO[a,*]

[a,*] College of Civil Engineering and Architecture, Zhejiang University
866 Yuhangtang Rd, Hangzhou 310058, P.R. China
luoyz@zju.edu.cn

Abstract

Large-span spatial structures are widely used as public facilities. In order to ensure the safety and durability of the structures and protect the lives and property of the occupants, it is necessary to monitor the health of large-span spatial structures. Sensor placement is important for structural health monitoring. Since large-span spatial structures have complex shapes and a large number of members and nodes, research on optimal sensor placement can effectively address many problems associated with excessive and inappropriate placement. The sensors placed effectively should be sensitive to changes of the structural condition, which can provide enough information. In this paper, a novel method of sensitivity analysis based on the static characteristics of large-span spatial structures is proposed. The key members that are sensitive to load changes and govern the structural mechanical property are identified by the method to arrange sensors. This sensitivity analysis method was applied in the Ouhai Olympic Centre Stadium to place stress sensors. The monitoring data successfully reflects the condition changes of the structure during construction and ensured structural safety, showing the effectiveness of the method.

Keywords: large-scale spatial structure, structure health monitoring, optimal sensor placement, sensitivity analysis

1. Introduction

Large-scale spatial structures are widely used in public facilities such as airports, railway stations, and stadiums, but the potential safety risks cannot be ignored [1]. To ensure the safety of structures and provide early warning of potential risks, structural health monitoring (SHM) systems are widely used. The optimal sensor placement (OSP) method is one of the key parts in the design of an SHM system. Due to constraints such as site conditions and economic conditions, only a relatively small number of sensors can be placed in limited locations [2]. Therefore, sensor placement has a significant impact on the effectiveness of monitoring data collection.

Many methods have been proposed for OSP. Some dynamic characteristic-based methods include the modal assurance criterion-based method [3], the effective independence method [4], the kinetic energy method [5], and the singular value decomposition method [6]. By analyzing different data features in the dynamic response information collected by sensors, changes in structural health due to damage or degradation can be obtained. Some static characteristic-based methods based on strength [7], sensitivity [8], energy [9], redundancy [10], and susceptibility [11] analysis have also been proposed. By placing sensors on key members, their properties can be analyzed in time to obtain the stress state of the whole structure and provide early warning.

The OSP should be based on the stress properties features of structures, consider the key processes of different construction methods, and the mechanical properties of different structural members. Large-scale spatial structures have various structural systems, complex construction methods, and different kinds of members [7]. The response of a structure is mostly through static stress and deformation, and

Copyright © 2023 by Yiqun WANG and Yaozhi LUO. Published in the Proceedings of the IASS Annual Symposium 2023 with permission.

the effect of the structure varies under different loads. In addition, large-scale spatial structures are super-stationary and have a high degree of redundancy. The "domino effect" may be triggered when some key members with high sensitivity fail, resulting in the successive buckling of the members arranged in parallel or bearing the same directional load, eventually leading to the destruction of the whole structure [12]. For this reason, strain monitoring based on static characteristics is necessary for large-scale spatial structures. In this paper, the OSP is carried out from structural static characteristics, and a sensitivity-based analysis method is introduced. The members with obvious stress changes under load changes were first selected by load sensitivity analysis, and self-sensitivity analysis was further carried out to select the key members with high influence on the structural stress state during damage. The sensors are placed according to the selected key members. This method is used to design the sensor placement scheme of the Ouhai Olympic Centre Stadium. Based on the collected real-time data, the stress conditions of the key members are promptly analyzed and the safety status of the structure is evaluated.

2. Sensitivity analysis method

2.1. Load sensitivity analysis

The structural load sensitivity analysis is based on the member load sensitivity analysis, which concerns the relationship between load changes and member response. During its operational life, a large-scale spatial structure is subjected to various environmental factors such as snow load, wind load, and temperature effect. The response of different members will vary under the influence of different variable loads, this response is represented by stress and nodal deformation.

Under linear conditions, when a particular type of load is applied, the greater the change in a member's stress, the more sensitive the member is to that type of load. A member whose stress changes significantly with the change in load is defined as being sensitive to that type of load.

The load sensitivity I_{Li} of a member is defined as follows:

$$I_{Li} = \frac{SZ_i}{SZ_{max}} \tag{1}$$

$$SZ_i = \left|\gamma_{wind} S_{wind,i} + \gamma_{snow} S_{snow,i} + \gamma_{temp} S_{temp,i} \cdots\cdots\right| \tag{2}$$

Where SZ_i is the comprehensive load sensitivity coefficient of member i; $SZ_{\max}$ is the maximum value in SZ_i; $S_{wind,i}$, $S_{snow,i}$, $S_{temp,i}$ is the load sensitivity coefficient of wind load, snow load or temperature effect of member i; γ_{wind}, γ_{snow}, γ_{temp} is the load influence weight coefficient, the highest is 1 and the lowest is 0.

Since the probability of occurrence of different environmental loads is different and the magnitude is a random variable. To facilitate the comparison and calculation between different environmental loads, it is necessary to define the probability of occurrence and the range of values of environmental loads. The definition of the sensitivity of a member to a certain type of load is proposed as follows: if the wind load (snow load, temperature effect) on the structure changes from the design value of 50 years to the design value of 100 years, the amount of stress change Δs_i in the member is the sensitivity coefficient of the member to this load. The calculation formula is as follows:

$$S_i = \Delta s_i = s_{i100} - s_{i50} \tag{3}$$

Where s_{i100}, s_{i50} is the stress of a member i under a certain type of load taking the design value of 100 years and 50 years; the type of load can be wind load, snow load, temperature effect, and others.

2.2. Self-sensitivity analysis

The structural self-sensitivity analysis is based on the member self-sensitivity analysis, which concerns the relationship between member damage and structural mechanical property. The component self-sensitivity is the degree of effect on the safety evaluation index of structures when member damage occurs. The current simulation of member damage is performed by weakening the cross-sectional area of the member [13], and this method is also used here to simulate the effects of member damage on the structure.

Structural displacement and member stress are controlling factors in structural design, these two factors can be used as response indicators to consider the effects on the structure after member damage [14]. Since the change in these two factors after the damage is positively correlated [15], either one of them is analyzed as a response index with the same results. The maximum change in structural displacement is used here as the output parameter.

The self-sensitivity I_{Si} of a member is defined as follows:

$$I_{Si} = \frac{R_i}{R_{max}} \tag{4}$$

$$R_i = \left| \Delta_{max}(i) \right| \tag{5}$$

Where R_i is the maximum response of the structure after the section weakening of member i; $R_{\max}$ is the maximum value in R_i; $\Delta_{max}(i)$ is the maximum displacement change of the structure before and after the section weakening of the member.

3. Optimal sensor placement based on sensitivity analysis

A square flat grid structure is used as an example for sensitivity analysis and selecting key members with high sensitivity for sensor placement. The grid plan size is 30m*30m, with a thickness of 3m, the number of grids in both directions is 10, and each side of the grid is 3m, as shown in Figure 1.

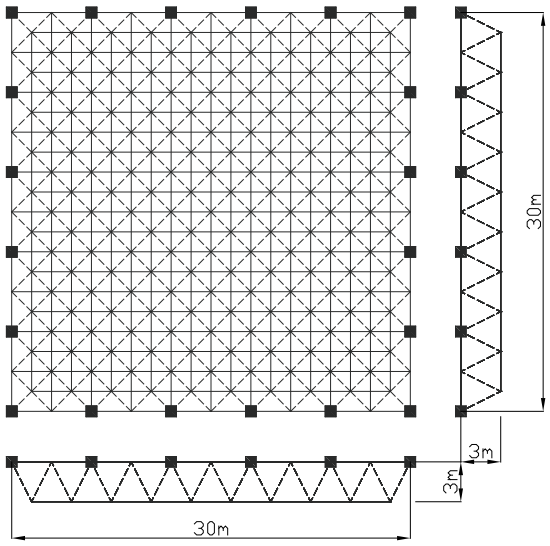


Figure 1. Square flat grid structure

The load sensitivity analysis was carried out on the calculated model and the values taken for the load and weight coefficients are shown in Table 1. The load sensitivity of each member is calculated and sorted. The results of the calculation are shown in Figure 2. The members with the top 15% of the load

sensitivity orders are selected and shown in Figure 3. The minimum load sensitivity of these members is close to 0.8.

Table 1. Load and weight coefficients

		Dead load	Liveload	Wind load	Download	Temperature effect
Load	50 years	0.3 kN/m2	0.5 kN/m2	0.45 kN/m2	0.45 kN/m2	-20℃~+30℃
	100 years			0.5 kN/m2	0.5 kN/m2	-22℃~+32℃
Weight coefficients				0.4	0.4	0.2

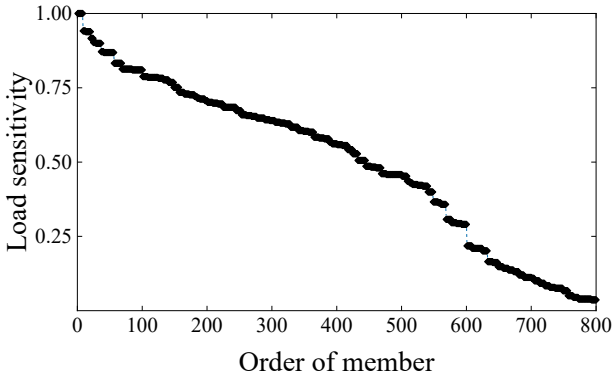


Figure 2. Load sensitivity distribution

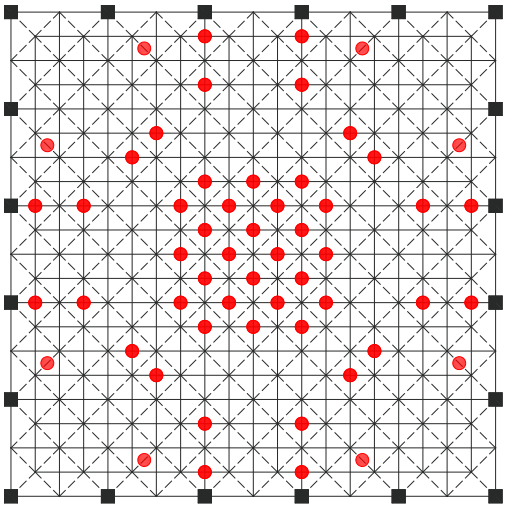


Figure 3. Diagram of the members to be selected

The members selected by the load sensitivity analysis are subjected to the self-sensitivity analysis. The cross-sections of these members are weakened by 50%. The self-sensitivity of each member is calculated and sorted. The results of the calculation are shown in Figure 4. The members with the top 20% of the self-sensitivity orders are selected and shown in Figure 5. These members are the key members with high comprehensive sensitivity, sensors should be placed on them.

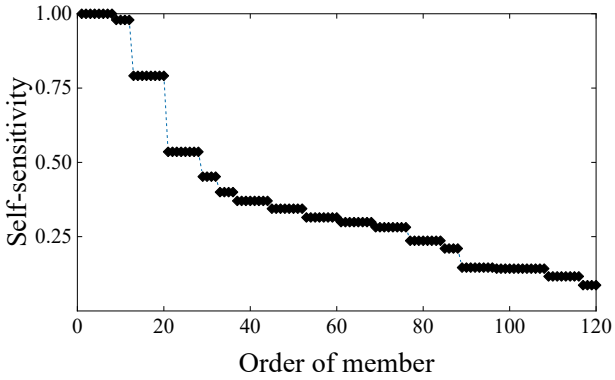


Figure 4. Self-sensitivity distribution

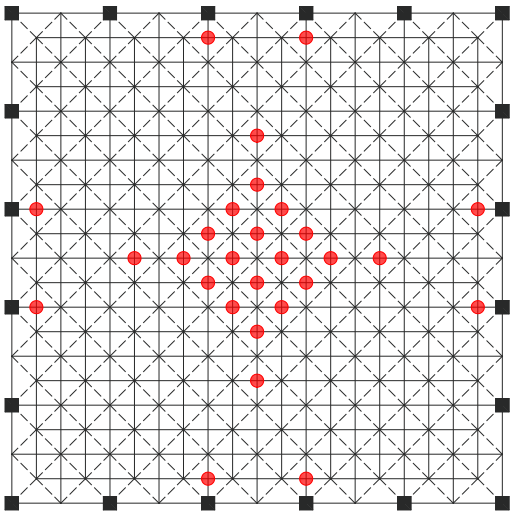


Figure 5. Diagram of the key members

4. Application on the Ouhai Olympic Centre Stadium

The Ouhai Olympic Centre Stadium is one of the competition venues for the Hangzhou 2022 Asian Games. The roof of the stadium is crescent-shaped, with an outer circle radius of approximately 223m and an inner circle radius of approximately 176m. The structure is supported by concrete columns on the outside of the grandstand and tubular steel columns on the perimeter. As the structure has a large span and a special shape, the mechanical properties and construction program of the station are very complicated. To monitor the structural condition and ensure safety, the SHM system is applied at the beginning of the structural construction. The sensitivity analysis based on the actual forces on the structure was carried out for the sensor placement, as shown in Figure 6.

The key elements of the structure were selected through sensitivity analysis, and the sensors placed on these elements monitored the construction process of the structure in real-time. The constraints of the structure will change during the unloading process, and the stress of the structural members will change simultaneously. Figure 7 shows the monitoring data from the sensors during the unloading stage of the structure, and the construction period is from September 14 to September 20, 2021. Stress 1 and stress 2 represent the stress on the two symmetrical surfaces, and the deviation of stress 1 and stress 2 indicates the bending moment of the member.

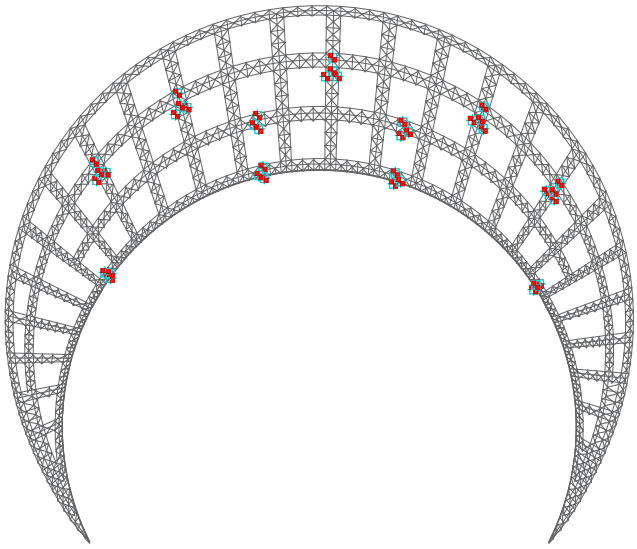


Figure 6. Sensor placement

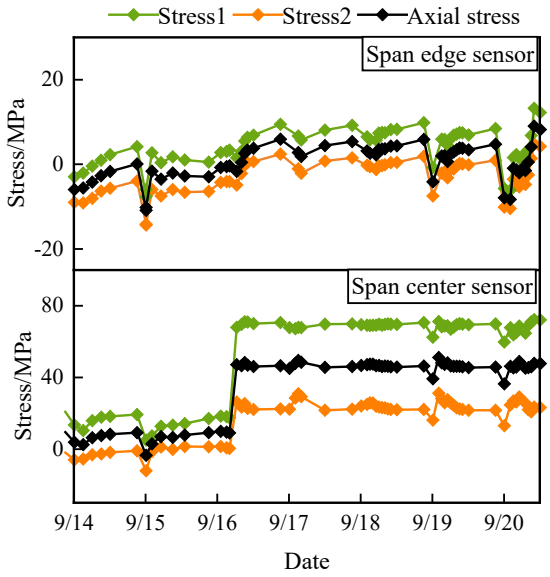


Figure 7. Monitoring data during the unloading stage

The monitoring data shows that the sensors in the span of the structure have a more obvious stress increase during the unloading stage, while the sensors at the edge of the structure have minor stress fluctuations. The stress values are within the allowable stress range of the steel. The monitoring data from the sensors successfully provided critical information during the unloading of the structure.

4. Conclusion

In this study, we propose a novel sensitivity analysis method based on structural static characteristics, which is used to guide the OSP. By calculating the sensitivity index, the method can identify the key members with significant stress change under load change and high influence on the structural mechanical property during their damage for sensor placement. The method is applied to place sensors in the Ouhai Olympic Sports Center stadium, the monitoring data shows that the sensors can reflect the stress of the whole structure and have a high sensitivity to changes in the structural state.

Acknowledgements

This work was supported by National Key R&D Program of China (2021YFF0501001), Zhejiang Provincial Key Research and Development Program (Grant No. 2021C03154), and the National Natural Science Foundation of China (Grant No. 51878235).

References

[1] J. Agarwal, D. Blockley, and N. Woodman, "Vulnerability of structural systems," *Structural Safety,* vol. 25, no. 3, 2003.

[2] D. S. Bayard, F. Y. Hadaegh, and D. R. Meldrum, "Optimal experiment design for identification of large space structures," *Automatica,* vol. 24, no. 3, pp. 357-364, 1988.

[3] Y.-T. Chung and J. D. Moore, "On-orbit sensor placement and system identification of space station with limited instrumentations," in *Proceedings of the International Modal Analysis Conference*, 1993, pp. 41-41: SEM Society for Experimental Mechanics Inc.

[4] C. Stephan, "Sensor placement for modal identification," *Mechanical Systems and Signal Processing,* vol. 27, 2011.

[5] G. Heo, M. L. Wang, and D. Satpathi, "Optimal transducer placement for health monitoring of long span bridge," *Soil Dynamics and Earthquake Engineering,* vol. 16, no. 7, 1997.

[6] E. Tongco and D. Meldrum, "Optimal sensor placement of large flexible space structures," *Journal of Guidance Control and Dynamics,* vol. 19, no. 4, pp. 961-963, 1971.

[7] M. R. E. and B. A. T., *Structural Reliability Analysis and Prediction*. John Wiley & Sons Ltd, p. 2017.

[8] J. T. Pinto, D. I. Blockley, and N. J. Woodman, "The risk of vulnerable failure," *Structural Safety,* vol. 24, no. 2, 2002.

[9] X. Wu, D. I. Blockley, and N. J. Woodman, "VULNERABILITY OF STRUCTURAL SYSTEMS PART 1: RINGS AND CLUSTERS," *Civil Engineering and Environmental Systems,* vol. 10, no. 4, 1993.

[10] A. W. Beeby, "Safety of structures, and a new approach to robustness," *structural engineer,* 1999.

[11] P. C. Pandey, "Structural Sensitivity as a Measure of Redundancy," *Journal of Structural Engineering,* vol. 123, no. 3, 1997.

[12] A. A. Mufti, "Structural Health Monitoring of Innovative Canadian Civil Engineering Structures," *Structural Health Monitoring,* vol. 1, no. 1, 2002.

[13] Y. Zhang, S. Pang, and Y. Wang, "Orthogonal arrays obtained by generalized Hadamard product," *Discrete Mathematics,* vol. 238, no. 1, 2001.

[14] E. Rafajlowicz, "Optimal experiment design for identification of linear distributed-parameter systems: Frequency domain approach," *IEEE Transactions on Automatic Control,* vol. 28, no. 7, pp. 806-808, 2003.

[15] J. Chen, Y. Peng, and X. Zhao, "FEM Simulation and Field Monitoring of Depropping Procedure of a Large-Span Single-Layer Latticed Shell," *International Journal of Space Structures,* vol. 26, no. 1, 2011.

IASS 2023 July 10–14 Melbourne Integration of Design and Fabrication

Proceedings of the IASS Annual Symposium 2023
Integration of Design and Fabrication
10–14 July 2023, Melbourne, Australia
Y.M. Xie, J. Burry, T.U. Lee and J. Ma (eds.)

Predicting embodied carbon of building structure types through machine learning.

Sandie Kate FENTON[a,b,*], Klaas DE RYCKE[a,*], Lars DE LAET[b]

[*] Bollinger + Grohmann S.A.R.L., 15 rue Eugène Varlin, 75010 Paris
sandie-kate.fenton@etu.u-cergy.fr

[a] Ecole nationale supérieure d'architecture Versailles
[b] Vrij Universiteit Brussel

Abstract

The building industry is responsible for 38% of total global energy-related CO2 emissions. In the previous years, policies have focused on reducing operational energy, and embodied emissions have become most significant contributors to the total greenhouse gas (GHG) emissions of buildings. Structural systems almost always constitute the largest source of embodied carbon in buildings and largest emissions occur during the production stage. However, embodied CO2 values are strongly influenced by material provenance, and their magnitude varies greatly between countries [1]. Databases gathering information on GHG emissions are therefore essential to improve our understanding of current emissions (baseline), targeted emissions (budget) and to make recommendations from their analysis for the future (benchmarks). The digitalization of the building industry has facilitated the introduction of carbon footprint assessment tools in the structural engineering practice [2]. Choosing appropriate structures in a given project can greatly reduce material consumption and material waste. However, methods to efficiently assess GHG emissions of such structures are lacking. Moreover, they are rarely computed at early design stages, when changes with highest impact are made, but quantitative volumetric and material information – 'hard' features - are still unavailable [3]. This research uses machine learning models and investigates strategies to predict the GHG emissions of buildings with two structure typologies, massive structures and frame structures, using descriptive data available in competition briefs - "soft" features. It proposes a methodology to obtain accurate predictions, despite limited data available for the learning. The methodology is tested on the Embodied Carbon of European Buildings EUCB-D database, describing the embodied GHG emissions of buildings. Results prove the potential of the methodology, and motivate its further developments into a tool for data-driven low carbon structural design. Moreover, results identify the importance of soft-features and suggests ways of assembling efficient databases describing building structures, in order to improve the understanding of their environmental impact.

Keywords: structural design, greenhouse gas emissions, machine learning, structures, sustainable architecture, feature analysis, Hangai Prize

1. Introduction

The building sector accounts for 38% of total global energy-related CO2 emissions [4]. Greenhouse gas (GHG) emissions of buildings include Embodied Emissions (EE) and Operational Emissions (OE). EE correspond to GHGs emitted during the production of a material, including mining, manufacturing, transportation, installation, maintenance and disposal. OE correspond to GHGs emitted during the operational phase of a building, including energy consumption tasks such as heating, ventilation and lighting. To help reduce GHG emissions, tools, policies and certification bodies can be developed [5].

Copyright © 2023 by Sandie Kate FENTON, Klaas DE RYCKE and Lars DE LAET. Published in the Proceedings of the IASS Annual Symposium 2023 with permission.

In the previous years, policies have focused on reducing operational energy [6]. They have resulted in the regulation of energy consumption on new buildings and have motivated the renovation of old buildings for increased energetic performance. They have also led to the development of "green" building certificates such as LEED or BREEAM [7]. As a result, operational emissions have dropped in buildings and are expected to be reduced to near zero in the future. EE in buildings have become therefore become increasingly significant contributors to total GHG emissions [8].

Tools for computing building GHG emissions are numerous. Tables, such as the Structural Carbon tool, allow to estimate the amount of carbon at different design stages, based on materials and volumes used [2]. Parametric tools, such as the grasshopper plug-in One Click LCA [9], are directly linked to building geometries, and are updated as the design materials and volumetry change. The different tools help identify GHG emissions hotspots and help communicate about impacts of design on these emissions. Unfortunately, since using these tools is often highly time-intensive, they are run at late stages of the design, when data is fixed, and little effective changes can be made. Moreover, architects and engineers have a limited control and visibility on the emissions of their projects since GHG emissions assessments are often performed by environmental offices [10].

Many research projects have worked on developing new GHG emissions evaluation tools. Studies making use of data from existing buildings include the use of value engineering principles to integrate embodied carbon reduction strategies in building design [11], the use of linear regression to predict GHG emissions of buildings from main building materials and structural forms [12], the use of statistical and probabilistic principles to evaluate GHG emissions from main materials and quantities [13] and the use of analytical principles to evaluate the impact of structural forms on GHG emissions in high-rise buildings [14]. Studies making use of data from generated buildings include the use of data visualization techniques to explore thousands of parametrically generated architectural alternatives[15], or the use of visualization frameworks to explore multi-dimensional intuitive design spaces without requiring any underlying parameterization [16].

2. Problem statement

GHG emissions are usually computed from "hard" features, by summing all emissions associated to materials with given volumes. Since precise building materials and geometries are often unavailable at early design stages, GHG emission computation tools are used later in the design process. Unfortunately, this means less changes can be made to the design and costs of making changes are high.

This research aims to "sum" GHG emissions associated to building properties in order to evaluate building emissions. These properties, called "soft" features in the scope of this work, include quantitative features such as gross floor area, and qualitative features such as structure type [17]. They are already available in design briefs meaning emissions can be assessed early on. Rather than computed, EE are predicted by first gathering data describing many buildings, then building tools to model this data and learning to progressively predict the content, as displayed in Figure 1. To reach this goal, the underlying modelling and predictive methodology makes use of multiple machine learning techniques. To facilitate model interpretability and understand feature impacts, regressions models are preferred to black-box models.

GHG emission values vary strongly depending on the assessment boundaries and the hypothesis set. To be applicable to any country or context, the methodology developed in this research can be tailored to any database containing a list of buildings for which both soft features and associated EE emissions are provided. To allow working despite the little data available, data and features used for the training are made efficient. Redundant and uncorrelated elements are removed during data processing and feature processing steps. The resulting "soft-feature approach" aims to provide a real-time carbon assessment tool, available at early design stages and accessible to practitioners. The research builds on previous work from the authors, in which the methodology was introduced and developed [18]. In this paper, we

test and discuss its performance for the assessment of GHG emissions of building with two types of structures, massive structures and frame structures.

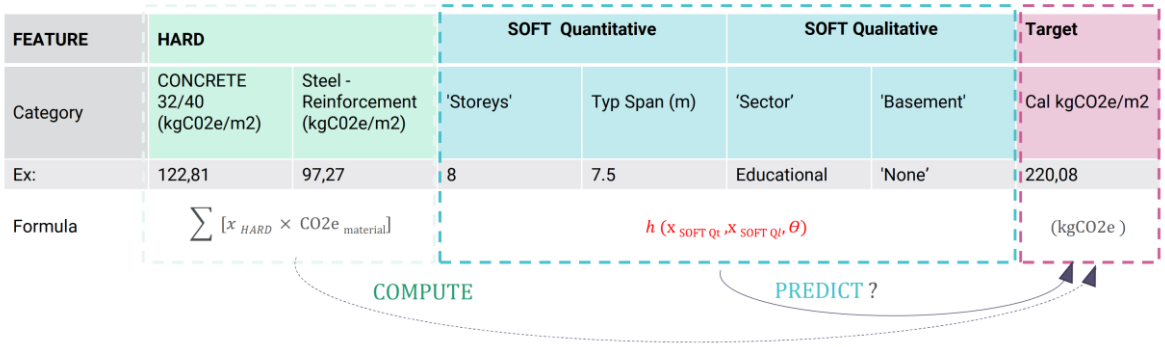


Figure 1: Soft Feature Approach – Rather than computed from ”hard” features, EEs are predicted by first gathering ”soft” features describing many buildings, then building tools to model this data and learning to predict the target values.

3. Data

The database used for the learning models lists 625 buildings, and provides 16 soft features (quantitative and qualitative) and their computed true GHG embodied emissions expressed in kgCO2e/m². Values, ranging between 100 and 1800 kgCO2e/m2 , include Ground, Structure, Envelope, and Internal Services and Appliances. Learning features are provided in Table 1. Data was extracted from the Embodied Carbon of European Buildings database, a public repository on Embodied and Whole Life Carbon. Data was assembled and verified as part of the ”Towards embodied carbon benchmarks for buildings in Europe” project [19] funded by the Laudes Foundation, and performed in collaboration between Ramboll, Aalborg University Build and KU Leuven [20].

Table 1: 16 Soft features are extracted from the Embodied Carbon of European Buildings database - The 625 buildings in the database are used to train and test prediction algorithms and evaluate the methodology.

FEATURE NAME	Range of values
Gross_Floor_Area [m2]	65 - 79000
Use type	Non residential / Residential
Use_Subtype	Hospital and health, Mixed Use, Office, Retail and restaurant , school and daycare, Technology and Science / Single Family, Multi family house, Row house, semi-detached , Hotel and resort
Site Country	Austria, Germany, United Kingdom, Finland, Belgium, Germany, France, Switzerland
Completion Year	2015-2019, 2020-Today
QTO Type	As-built measurement, Conceptual Design, Detailed design
Building area interval	0-5000, 5001-10000, 10001-15000, 15001-20000, 20001-25000, 25001-30000, 30001-35000, 35001-40000, 40001-45000, 45001-50000, 50001-55000, 55001-60000
Users_Total [-]	2-1800
Structure	Frame Concrete, Frame Concrete-Wood, Frame steel, Frame Wood/ Massive brick, Massive Concrete, Massive Wood
Roof	Flat roof / Gable or Saddle Roof / Single Pitched Roof / Other
Energy_Class_Country	1-2-3/A-A+-B/2015-2020
Energy_Class_General	New standard, existing standard, New advanced
Main_Material	Ceramics, Concrete reinforced, Concrete w/o reinforcement, Stone Timber / Metals, Earth, Other
Second_Material	Cement mortar plaster, Ceramics, Concrete reinforced, Concrete w/o reinforcement, Stone, Stone wool, Timber, Steel, Earth, Other, Gypsum
Lifespan	14, 25, 50, 60, 80,100
Life cycle scopes	ABCD, ABC,
Life cycle scope handling D	not in scope, separately considered, substracted,
GHG_sum_em_m2	100 - 1800

4. Method

The goal is to build a predictive algorithm that can accurately estimate a building's GHG emissions based on a set of features matching a training database. The methodology followed is divided into 4 training steps: data processing, feature processing, model processing and blender processing, described in Figure 2. *Data processing* consists in converting input data into a format that can be read by training algorithms. *Feature processing* consists in reducing the size of the training data to be more effective, by extracting impactful feature subsets with selectors. *Model processing* consists in using the data and training regression models to map feature subsets to the target values. In supervised learning, regression models are used to model data with continuous target values. Regression methods are composed of a hypothesis function, that maps input data to a function, and error functions, that evaluate how close the points predicted with this function are to the true points [21]. Many types of regression methods can be built by varying the mathematical formulation of the hypothesis and error. They are always a function of x, the value of input features, and theta, the weights associated to the features or transformations of the features. For each regression, the goal is to find the best weights (θ), that minimize the error and allow to best predict the target footprints with input soft features (x_i) [17] . *Blender processing* consists in using the best trained models and training "meta" regression models to map predictions from these individual models, to a blended prediction with higher robustness and accuracy.

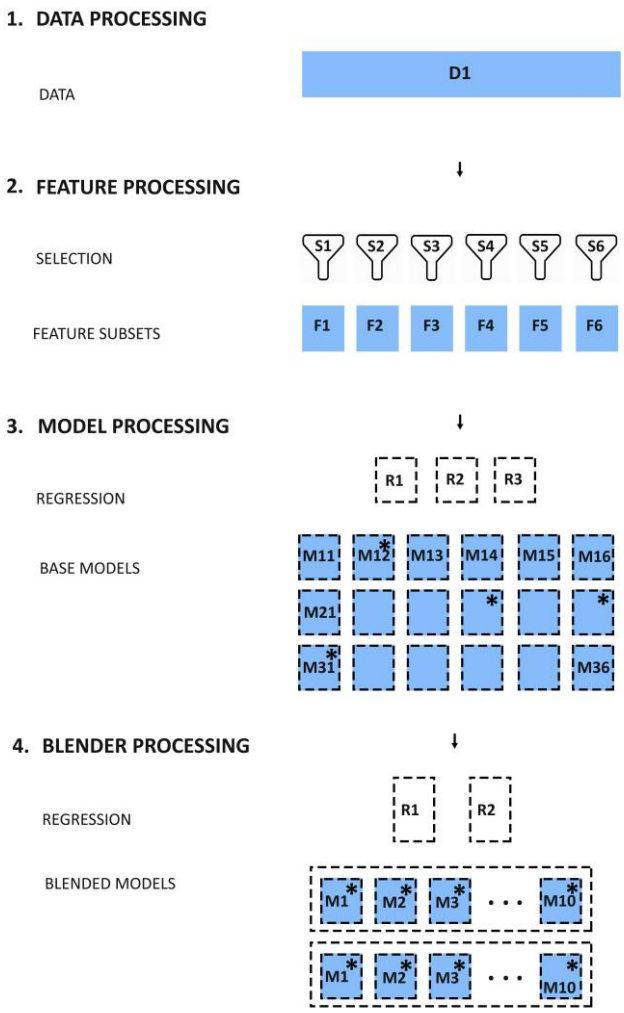


Figure 2 : The methodology followed is divided into 4 training steps: data processing, feature processing, model processing and blender processing.

Different metrics can be used to assess prediction results. This research uses four evaluation metrics : the coefficient of determination R^2 , the mean squared error MSE, the predictive accuracy PA and the residual plot. MSE evaluates the performance based on the squared distance between true and predicted values, it ranges between 0 and $+\infty$. R^2 evaluates the performance based on the variability of the predicted value around the mean. It penalizes models that always predict average values, regardless of input data, and ranges between 1 and $-\infty$. PA is the percentage of accurate predictions that fall within a 15% threshold of the true value, it ranges between 100 and 0 %. The difference between true and predicted values are called residuals. Residual plots should present a random distribution, be normally distributed and centered around zero.

In order to evaluate a model's performance, two conditions must be met : training and testing must be done on two separate data sets, and the training and testing steps must be repeated 10 times in order to retrieve mean and standard deviation of the scoring metrics after 10 runs. Results used in this research are retrieved from nested cross validation, a data partitioning scheme that meets these two conditions. All results described below are averaged over 10 training runs.

5. Results

A base model is composed of a set of features and a regression algorithm. Model processing consists in feeding feature subsets to regression algorithm, calibrating their weights and hyperparameters, and selecting the best predictive models amongst them. This research compares 18 models made from the combinations of 6 feature subsets (pearson filter, spearman filter, gradient boosting regressor, decision

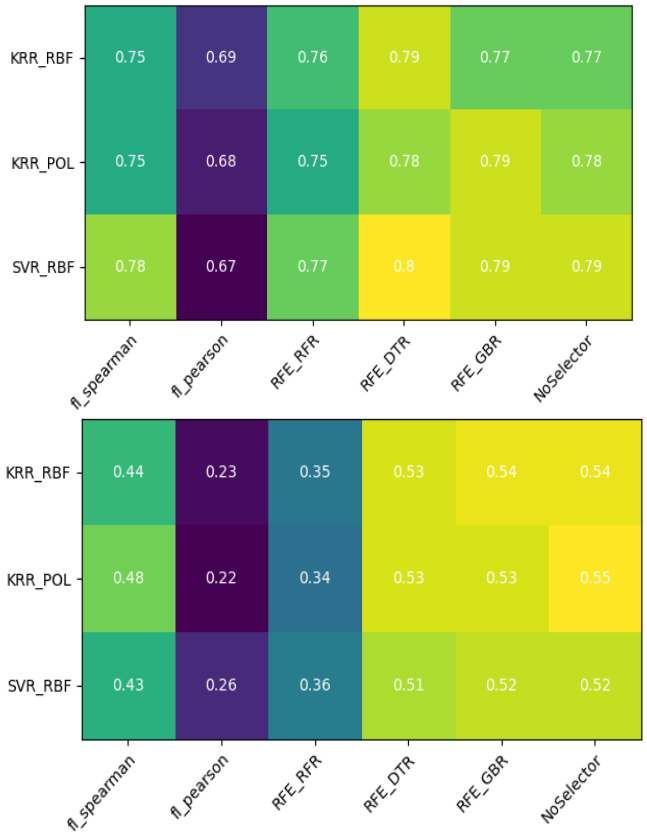


Figure 3: Prediction results for the 18 learning models, made from 3 regression algorithms trained on 6 feature subsets. Prediction accuracies (top) are similar, ranging between 67 and 80 %. R^2 values on testing (bottom) range between 0.22 and 0.55.

tree regressor, random forest regressor, no selector) and 3 regression algorithms (support vector regressions with radial basis function, kernel ridge regression with radial basis function, kernel ridge regression with polynomial kernel). The prediction accuracies and R^2 values for the 18 models are displayed in Figure 3. The 10 models with the highest R^2 values on testing are used as base models for the blender models.

A blender model is composed of a set of trained base models and a regression algorithm. Blender processing consists in feeding base models to regression algorithm and calibrating weights and hyperparameters accordingly. This research compares 2 blender models (linear ridge regression and support vector regression) made from the blending of 10 base models. The evaluation metrics of the 10 best base models and the 2 blender models are compared in Table 2. Evaluation metrics are similar amongst base models, with prediction accuracies PA ranging between 75 and 80 %. Blender models have higher evaluation metrics than base models, with a PA increase of 9 % for SVR RBF and 12 % for LR Ridge. Moreover, they have a higher R^2 score on testing, a lower MSE on testing, lower residual means and residual variance. The residual distributions for the two blender models are displayed in Figure 4. Both graphs present a Gaussian centered distribution with residual values comprised between -200 to +200 $kgCO2e/m^2$.

Table 2: Prediction results for 10 best base models and 2 blender models - an average PA of 78% is reached with base models, 87% with LR Ridge Blender and 91 % with SVR RBF Blender.

		Train R^2	Test R^2	Test MSE	Test PA	Residual Mean	Residual Variance
A	**KRR_RBF_RFE_DTR (Best model)**	0,81	0,53	7254,66	79%	59,01	7124,11
	KRR_RBF_RFE_GBR	0,81	0,54	7106,93	77%	57,61	6915,35
	KRR_RBF_NoSelector	0,81	0,54	7186,27	77%	57,59	6981,21
	KRR_POL_fl_spearman	0,76	0,48	7948,54	75%	62,32	7741,74
	KRR_POL_RFE_DTR	0,81	0,53	7289,64	78%	59,16	7135,94
	KRR_POL_RFE_GBR	0,80	0,53	7246,18	79%	58,67	7089,44
	KRR_POL_NoSelector	0,82	0,55	6988,98	78%	57,98	6825,98
	SVR_RBF_RFE_DTR	0,83	0,51	7590,96	80%	58,01	7462,02
	SVR_RBF_RFE_GBR	0,83	0,52	7466,85	79%	58,27	7344,20
	SVR_RBF_NoSelector	0,83	0,52	7391,28	79%	58,06	7270,52
B	**Base model (Average)**	0,81	0,52	7347,03	78%	58,67	7189,05
C	**LR RIDGE Blender model**	0,66	0,68	3349,28	87%	43,42	3056,36
D	**SVR RBF Blender model**	0,70	0,72	3064,27	91%	39,55	2959,99
	C - A	-0,15	0,15	-3905,38	9%	-15,60	-4067,75
	C - B	-0,15	0,16	-3997,75	9%	-15,25	-4132,69
	D - A	-0,11	0,19	-4190,39	12%	-19,46	-4164,12
	D - B	-0,11	0,19	-4282,76	13%	-19,12	-4229,06

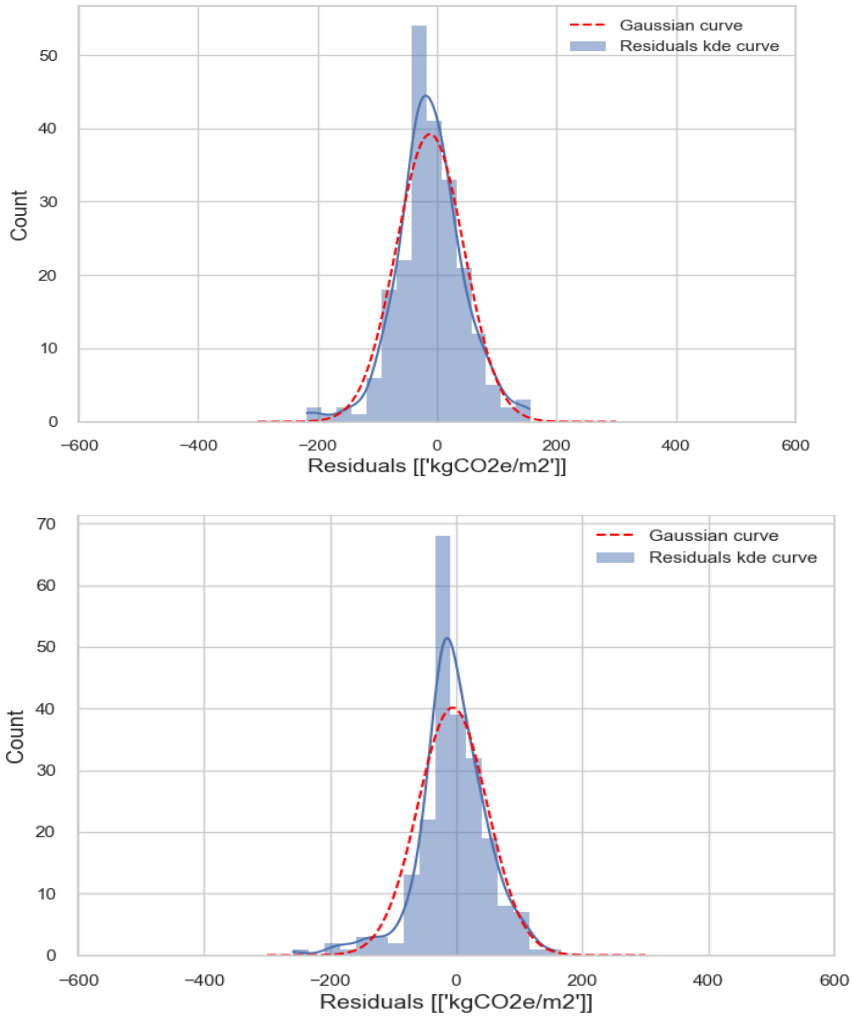


Figure 4: Residual distribution for blender models, LR RIDGE (top) and SVR RBF (bottom) - graphs present a Gaussian centered distribution of residuals, proving the predictive capacity of the methodology.

6. Application

With this methodology, trained models can be implemented into GHG emission prediction tools. One can simply input a building's soft features and receive the predicted emissions as output. In Table 3, the GHG emissions of a building are predicted with the trained KRR RBF base model.

Output values can be interpreted using explanation tools, such as SHAP, SHapley Additive exPlanations. SHAP quantifies the magnitude and direction of a feature's effect on a prediction. On Figure 5, the SHAP waterfall plot provides an explanation of the value predicted with the KRR RBF model. On the plot, features are ranked in descending order of importance. Each row shows the positive (red) or negative (blue) contribution of a feature. The sum of these contributions explains the difference between the predicted output ($f(x) = 491.92$ kg CO_2e/m^2), and the expected output ($E[f(x)] = 624.46$ kg CO_2e/m^2) corresponding to the average of the learning dataset. The QTO type, "Conceptual Design" (-81.01 kg CO_2e/m^2), the structure type, "frame wood" (-66.99 kg CO_2e/m^2), and the second material type, "Timber, wood" (-54.06 kg CO_2e/m^2), are the three main features that help reduce GHG emissions of the building, compared to an average project. Although these values are still very preliminary, and explanations must be further investigated, the potential of providing real-time detailed explanations to help reduce GHG emissions, and pointing out impactful features is great.

Table 3: GHG emissions of an example building, predicted with the trained KRR RBF base model, using the listed soft features

FEATURE	INPUT VALUES
Gross_Floor_Area [m2]	200
Use type	Residential
Use_Subtype	Single Family
Site Country	France
Completion Year	2015-2019
QTO Type	Conceptual Design
Building area innterval	0-5000
Users_Total [-]	4
Structure	Frame Wood
Roof	Gable or Saddle Roof
Energy_Class_Country	A
Energy_Class_General	New standard
Main_Material	Timber, wood
Second_Material	Timber, wood
Lifespan	50
Life cycle scopes	ABC
Life cycle scope handling D	not in scope
TARGET	OUTPUT VALUES
GHG_sum_em_m2 [kgCO2e/m²]	491.92

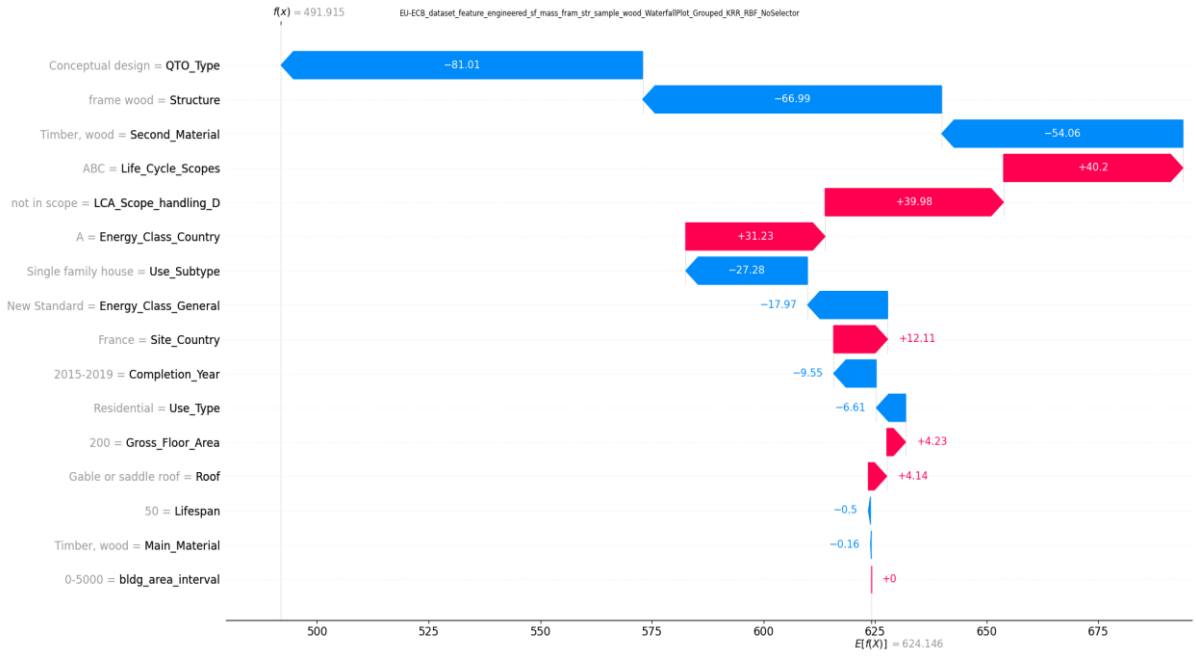


Figure 5 : SHAP explanation quantifies the magnitude and direction of a feature's effect on a prediction. This SHAP waterfall plot explains predictions made with the trained KRR RBF base model for the building studied in Table X.

7. Conclusion

In this research we further developed the "soft feature approach", a methodology for predicting embodied GHG emissions of buildings at early design stages, using building features rather than materials and volumes. With the heterogeneity of data available, and the high variability of GHG emission values, the methodology has been made adaptable to any database, containing a list of buildings features and associated GHG emissions. For the prediction, basic regression models are used in order to facilitate the explainability of results. Despite limited training data available, feature selection, nested cross-validation and model blending help ensure the robustness of the predictions.

18 base models were trained and compared. The 10 best base models were selected and fed into two blender models. The combined data processing, feature processing and model processing steps lead to a GHG emission prediction accuracy of 78 %, and blender processing rose the number to 91 %. All trained models presented a gaussian distribution of residuals centered around 0, indicating they were working and confirming the potential of the presented methodology. This motivated the investigation of the prediction values themselves. Although results are still preliminary, explanation models using SHAP values identified "QTO type", "structure type" and "second material type", as the three main levers to reduce GHG emissions on a given building. Next steps will focus on these explanation methods, aiming to enable the "soft feature approach" to provide real-time predictions as well as tailored recommendations and explanations about GHG emissions of buildings. Finally, and since learning models are only as good as the data they are trained on, a focus will also be set on acquiring more learning data, and motivating companies to archive and share their data in a systematic way.

References

[1] X. Le Den *et al.*, "Towards embodied carbon benchmarks for buildings in Europe - #3 Defining budget-based targets," 2022, [Online]. Available: https://doi.org/10.5281/zenodo.6397514.

[2] O. P. Gibbons and J. J. Orr, *How to calculate Embodied Carbon*. 2020.

[3] C. Herrmann, W. Dewulf, M. Hauschild, A. Kaluza, S. Kara, and S. Skerlos, "Life cycle engineering of lightweight structures," *CIRP Ann.*, vol. 67, no. 2, pp. 651–672, 2018, doi: 10.1016/j.cirp.2018.05.008.

[4] UN Environment Programme, "2020 Global Status Report for Buildings and Construction," *Glob. Status Rep.*, pp. 20–24, 2020, [Online]. Available: www.iea.org.

[5] U. Eichhorst, D. Bongardt, Novikova, and Victoria, "Compendium on greenhouse gas baselines and monitoring," p. 65, 2017.

[6] EU, "Directive (EU) 2018/2001 of the European Parliament and of the Council of 11 December 2018 on the promotion of the use of energy from renewable sources (recast)," *Off. J. Eur. Union*, vol. 2018, no. L 328, pp. 82–209, 2018.

[7] A. Pomponi, Francesco and Moncaster, "Scrutinising embodied carbon in buildings : The next performance gap made manifest," *Renew. Sustain. Energy Rev.*, vol. 81, no. 2, pp. 2431–2442, 2018, doi: 10.1016/j.rser.2017.06.049.

[8] M. Röck *et al.*, "Embodied GHG emissions of buildings – The hidden challenge for e ff ective climate change mitigation ☆," *Appl. Energy*, vol. 258, no. June 2019, p. 114107, 2020, doi: 10.1016/j.apenergy.2019.114107.

[9] D. Apellániz, P. Pasanen, and C. Gengnagel, "A Holistic and Parametric Approach for Life Cycle Assessment in the Early Design Stages," *Symp. Simul. Archit. Des. 2021*, 2021, [Online]. Available: https://www.oneclicklca.com/wp-content/uploads/2021/05/SimAUD-2021-Camera_Ready-LCA_early_design_stages.pdf.

[10] D. Vuarnoz, E. Hoxha, J. Nembrini, T. Jusselme, and S. Cozza, "Assessing the gap between a normative and a reality-based model of building LCA," *J. Build. Eng.*, vol. 31, no. March, p. 101454, 2020, doi: 10.1016/j.jobe.2020.101454.

[11] M. Robati, P. Oldfield, A. A. Nezhad, D. G. Carmichael, and A. Kuru, "Carbon value engineering: A framework for integrating embodied carbon and cost reduction strategies in building design," *Build. Environ.*, vol. 192, no. October 2020, p. 107620, 2021, doi: 10.1016/j.buildenv.2021.107620.

[12] Y. Cang, L. Yang, Z. Luo, and N. Zhang, "Prediction of embodied carbon emissions from residential buildings with different structural forms," *Sustain. Cities Soc.*, vol. 54, no. December 2019, p. 101946, 2020, doi: 10.1016/j.scs.2019.101946.

[13] G. Kang, T. Kim, Y. W. Kim, H. Cho, and K. I. Kang, "Statistical analysis of embodied carbon emission for building construction," *Energy Build.*, vol. 105, no. January 2021, pp. 326–333, 2015, doi: 10.1016/j.enbuild.2015.07.058.

[14] V. J. L. Gan, C. M. Chan, K. T. Tse, I. M. C. Lo, and J. C. P. Cheng, "A comparative analysis of embodied carbon in high-rise buildings regarding different design parameters," *J. Clean. Prod.*, vol. 161, pp. 663–675, 2017, doi: 10.1016/j.jclepro.2017.05.156.

[15] T. B. P. Jusselme, *PhD Thesis: Data-driven method for low-carbon building design at early stages*. Lausanne: Ecole Polytechnique Fédérale de Lausanne, 2020.

[16] C. M. Ashley J. Hartwell, Eamon Whalen, Bryan Ong, "Visualization of Design Data in the Wild: Interactive Evaluation and Exploration of Combined Performance and Geometric Data," in *Design Computing and Cognition'22*, 2023.

[17] S. K. Fenton, "Strategies for data-driven low carbon structural design," 2022.

[18] S. K. Fenton, K. D. E. Rycke, A. Munteanu, and N. Deligiannis, "Strategies for data-driven low carbon structural design.," in *IASS 2022 Symposium*, 2022, no. September, pp. 1–12.

[19] M. Röck *et al.*, "Towards embodied carbon benchmarks for buildings in Europe - #1 Facing the data challenge," 2022, doi: https://doi.org/10.5281/zenodo.6120522.

[20] M. Röck *et al.*, "Towards embodied carbon benchmarks for buildings in Europe," 2022, doi: https://doi.org/10.5281/zenodo.6120522.

[21] C. M. Bishop, *Pattern Recognition and Machine Learning*, Springer. 2011.

Proceedings of the IASS Annual Symposium 2023
Integration of Design and Fabrication
10–14 July 2023, Melbourne, Australia
Y.M. Xie, J. Burry, T.U. Lee and J. Ma (eds.)

Probability-based life cycle carbon emission assessment for space grid structures

Jianzhou YOU[a,b], Xian XU[a,b,*]

[a,*] Space Structures Research Center, Zhejiang University, China
xianxu@zju.edu.cn

[b] Space Structures Key Laboratory of Zhejiang Province, Hangzhou, China

Abstract

The construction industry takes up a significant part of global carbon emissions and other environmental impacts, and thus accurate calculation and evaluation of the life cycle carbon emissions of structures are important for low carbon-oriented structural design. Current studies often ignore the emission of repair and replacement in the use phase. The omission of in-service impacts increases the uncertainty of the results and might lead to wrong judgments. This paper proposes a probability-based method to calculate the structure carbon emissions generated by the repair and replacement during the life cycle. Based on probabilistic risk assessment, the proposed method is divided into four parts: load hazard analysis, structural response estimation, damage assessment, and loss analysis. An orthogonal pyramid space grid structure is used as a case study to evaluate its life cycle carbon emissions. The effects of different load distribution models on its life cycle carbon emissions are discussed. It is found that carbon emissions from repair and replacement due to loads with high variability should be considered in the design of low carbon-oriented structures. This study provides a useful reference for carbon emission assessment.

Keywords: life cycle assessment, probability, carbon emission, space grid structure

1. Introduction

Global warming caused by greenhouse gas (GHG) emissions has become the focus of attention around the world. Many governments aim to achieve the targets of the Paris Agreement [1] by limiting and reducing carbon emissions. The building sector is responsible for a significant proportion of carbon emissions across the world. For example, the building sector in China consumed the most energy and accounted for 51.3% of the total carbon emissions in 2018 [2]. As the largest contributor to building carbon emissions, the operational phase has received much attention. In recent years, there has been a great growth of energy saving and emission reduction measures in the building operation phase [3, 4]. In this context, the carbon emissions beyond the operational phase of buildings, known as embodied carbon emissions, account for an increasing proportion of the total [5]. As a result, the embodied carbon emissions of buildings are currently key to addressing emissions from the building sector.

The carbon emissions of building structures make up the majority of the embodied carbon emissions [6], and scientifically evaluating the life cycle carbon emissions of building structures is the key to the lower carbon-oriented design of structures. Life cycle assessment (LCA) is an approach that can be used to assess whole life environmental impact of products or processes. It analyzes the inflow of material and energy processes and the outflow of environmental impacts during the entire lifespan. For the carbon emission assessment, there are three conventional methods: the process-based method (P-LCA) [7], the input-output analysis-based method (I-O LCA) [8], and the hybrid LCA method [9].

P-LCA calculates carbon emissions from the top down using process activity data and emission factors based on the numerous production processes in the life cycle of a building. I-O LCA converts the

Copyright © 2023 by Jianzhou YOU and Xian XU. Published in the Proceedings of the IASS Annual Symposium 2023 with permission.

monetary value to carbon emissions, and based on the value-based economic input-output table, carbon emissions can be calculated by evaluating economic activities. Considering the strengths and weaknesses of the above methods, the hybrid LCA is regarded as a potential alternative. According to the ways of data combination, hybrid LCA can be divided into tiered hybrid (TH), IO-based hybrid (IOH) [10], and integrated hybrid (IH) methods. Case studies on the hybrid LCA of building carbon emissions mainly focused on the TH method, due to its clear concept and low computational effort [11].

By using the above LCA approach, many recent studies have focused on the carbon emissions assessment and lower carbon-oriented design of structures. Kumanayake et al. [12] assessed the embodied carbon of a commercial office building in Sri Lanka, confirming that reinforced concrete and clay bricks are the major carbon-emitting materials. Hart et al. [13] conducted a systematic comparison of the carbon emissions of steel, concrete, and wood structures. Gan et al. [14] investigated the carbon emissions of different structural forms of high-rise buildings. Su et al. [15] analyzed the energy consumption and carbon emissions of three steel structure residential cases.

It should be noted that most of the existing studies focus on the carbon emissions from the production and construction phases. The carbon emissions from repair and replacement are ignored by assuming that the service life is equal to the design life. However, Francart et al. [16] indicated that service life can significantly affect LCA results and maintenance and replacement processes may be important for some materials.

In recent years, studies of structural seismic damage have developed rapidly due to the huge human casualties and economic losses caused by seismic hazards[17]. The Performance-Based Earthquake Engineering (PBEE) methodology, takes into account the relationship between structural seismic damage and loss and various uncertainties [18]. The PBEE provided useful information regarding the importance of probabilistic seismic assessment, and there are studies [19-21] evaluating the economic losses and environmental impacts of seismic hazards. It should be noted that, when the loads are greater than the resistance, the structure or member will be damaged, and the seismic hazards are one of the 'loads' during the design life. Therefore, the probability of damage to a structure can be calculated by the probabilistic risk assessment method proposed by PBEE, and thus the carbon emissions can be assessed.

Based on the probabilistic risk assessment method, this paper proposes a method to calculate the structure carbon emissions generated by the repair and replacement during life cycle. An orthogonal pyramid space grid structure is used as a case study to evaluate its life cycle carbon emissions. The effects of different load distribution models on its life cycle carbon emissions are discussed. Instead of previous studies, the proposed method provides a new perspective and a useful reference for life cycle carbon emission assessment.

2. Methodology

2.1. System boundary

The first step in LCA is to determine the system boundary. The life cycle of a building involves a variety of processes, from the extraction of raw materials to recycling. According to EN 15978 [22], the life cycle of a building is divided into the product stage, construction process stage, use stage, and end-of-life stage. The recovery and reuse of building materials after demolition are not within the life cycle boundary, as shown in Figure 1. The life cycle carbon emissions of a structure are the main component of the life cycle embodied carbon emissions of the building, and the scope of its life cycle includes A1-C4, but not B6-B7. Normally, structure elements are not allowed to be replaced within the design life, therefore many studies ignored the carbon emissions in the B3 and B5 phases.

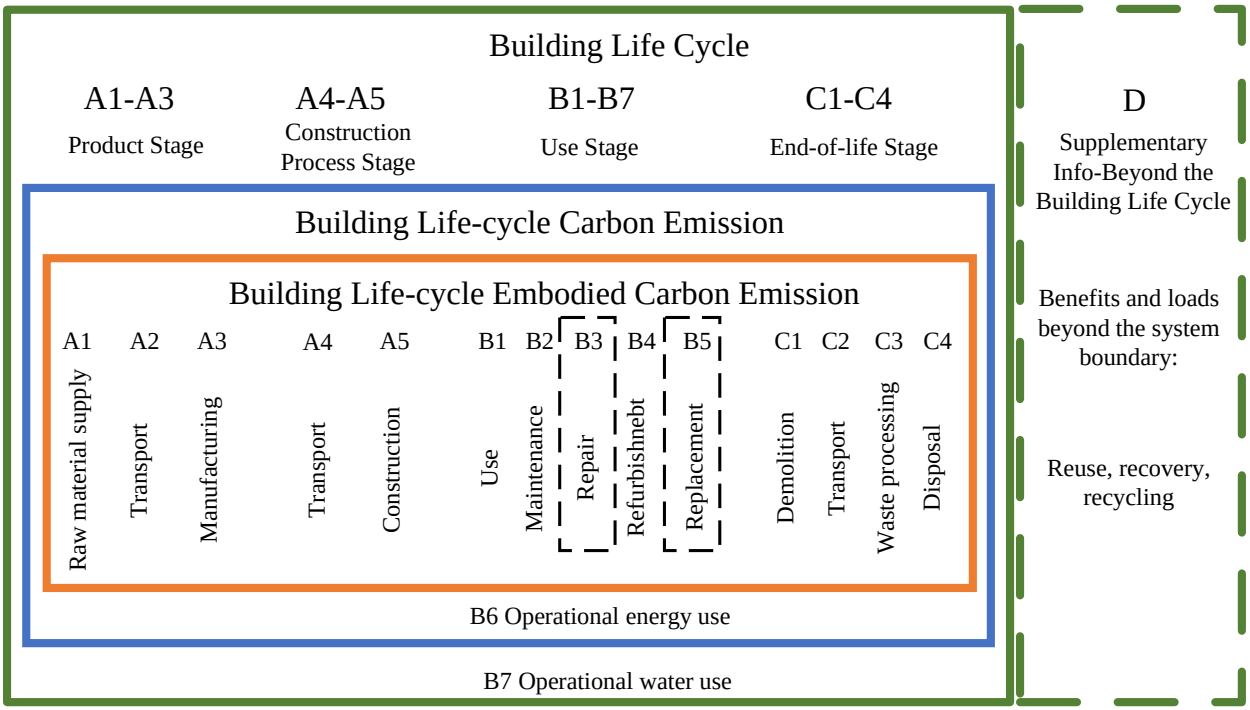


Figure 1. Building life cycle according to EN 15978

2.2. Method for carbon emission assessment

2.2.1. Process-based method

The basic concept of process-based method can be expressed as:

$$E_{pro} = \sum_{i=1}^{n} (EF_i \cdot Q_i) \tag{1}$$

where E_{pro} is the life-cycle carbon emissions, EF_i and Q_i are the carbon emission factor and activity data of production process i, respectively.

Because of the numerous production processes, a comprehensive database for emission factors is necessary for accurately calculating carbon emissions. Besides, the process-based method typically involves truncation of the system boundary, which introduces errors to the calculations.

2.2.2. Input-output analysis

The input-output analysis is commonly used to calculate the carbon emissions of sectors in an economic system. According to carbon emission input-output table [23], the carbon emissions of sector j can be calculated as:

$$E_{IO,j} = C_j \cdot \varsigma_j \tag{2}$$

where C_j and ς_j are the value of products and embodied carbon emission intensity of sector j.

When using input-output analysis to calculate structure carbon emissions, the result is inaccurate due to the use of average data instead of individual.

2.2.3. Tiered hybrid method

By combining the two methods described above, the basic concept of the TH method can be expressed as:

$$E_{TH} = E_{pro}^{m} + E_{IO}^{n} = \sum_{i=1}^{m}(EF_i \cdot Q_i) + \sum_{j=1}^{n}(C_j \cdot \varsigma_j) \tag{3}$$

Note that combining process and input-output data remains a highly manual and time-consuming process, Crawford et al. [24] proposed a path exchange method and established emission factors database of common building materials EPiC [25], thus the E_{TH} can be calculated as:

$$E_{TH} = \sum_{i=1}^{m+n}(EF_i^{EPiC} \cdot Q_i) \tag{4}$$

where EF_i^{EPiC} is the hybrid emission factor for process i in EPiC.

2.3. Probability-based assessment method

When calculating carbon emissions for phases B3 and B5 using above method, the Q_i or ς_i of repair and replacement is uncertain. Therefore, it is necessary to calculate the structure damage under load based on probability. Referring to the PBEE method, the damage calculation can be divided into four steps: load hazard analysis, structural response estimation, damage assessment, and loss analysis.

The purpose of load hazard analysis is to assess the probability of the load occurrence. The probability distribution functions of typical loads are assumed based on statistical analysis, for example, constant loads are assumed to be normally distributed, live loads to be extreme value I distributed, and seismic hazard to be Poisson distributed.

Structural response estimation is to calculate the response of a structure under different load magnitudes by elastoplastic analysis, select the response (displacement, stress, strain, etc.) of the structure or member as engineering demand parameters (EDPs), and determine the relationship between load and EDPs.

The damage assessment aims to calculate the conditional probability that the load demand S_d (generalized load) exceeds the structural resistance S_c (generalized resistance) under a given load. Considering the uncertainty of S_d and S_c, usually both are assumed to follow a logarithmic normal distribution, thus the fragility function of the structure can be expressed as:

$$P\left[\frac{S_d}{S_c} \geq 1\right] = 1 - \Phi\left(\frac{\ln(1) - \lambda}{\zeta}\right) = \Phi\left(\frac{\lambda}{\zeta}\right) \tag{5}$$

Where λ is the mean value of $\ln(S_d/S_c)$, ζ is the standard deviation of $\ln(S_d/S_c)$, $\Phi(\cdot)$ is the normal cumulative distribution function.

Based on the EDPs, structural damage is classified into different damage states (DS). After that, the probability that the structure exceeds the DS_i under a specific load can be expressed as:

$$P[DS > DS_i \,|\, Load] = \int_{EDP} P[DS_i \,|\, EDP] \cdot p[EDP \,|\, Load] \cdot dEDP \tag{6}$$

Where $P[DS_i \,|\, EDP]$ shows the probability of the DS_i on condition of the EDP, and $p\left[EDP \,|\, Load\right]$ denotes the probability density of the EDP for the load.

Based on the fragility analysis, the probability of DS_i under a given load can be obtained from Eq. (7):

$$P\left[DS = DS_i \middle| Load\right] = \begin{cases} 1 - P\left[DS > DS_1 \middle| Load\right], i = 0 \\ P\left[DS > DS_i \middle| Load\right] - P\left[DS > DS_{i+1} \middle| Load\right], 1 \le i \le n-1 \\ P\left[DS > DS_i \middle| Load\right], i = n \end{cases} \tag{7}$$

Loss analysis is to specify repair strategies for different damage states and calculate the carbon emissions of the m th repair strategy $E(DV_m|DS)$ using Eq. (1) to Eq. (4).

As a result, the carbon emissions from the B3 and B5 phases of the structure can be expressed as:

$$E_R = \sum_m \int_{Load} E(DV_m|DS) P(DS = DS_i|Load) \cdot dp(Load) \tag{8}$$

The life cycle carbon emission of the structure can be calculated by Eq. (9):

$$E_T = E_P + E_C + E_R + E_M + E_E \tag{9}$$

Where E_T is the life cycle carbon emission, E_P is the carbon emission from production stage, E_C is the carbon emission from construction process stage, E_M is the carbon emission from maintenance process, E_E is the carbon emission from end-of-life stage. However, this paper mainly focuses on the calculation of E_R, the E_C, E_M, and E_E are ignoring. Therefore the E_T can be expressed as:

$$E_T = E_P + E_R \tag{10}$$

3. Case study

3.1. Structure design

Consider an orthogonal pyramid space grid (OPSG) structure with a square plan of 30 m × 30 m, as shown in Figure 2. The size and height of the grid are 5 m and 3 m, and the supports are arranged at intervals around the top chord elements. The structure is made of Q235 steel and the design load is a uniform load of 1.3 kN/m^2, which is assumed to be loaded on the top chord joints. According to China Technical Specification for Space Frame Structures (JGJ7-2010) [26] and the Standard for Design of Steel Structures (GB50017-2017) [27], the elements are made of round steel pipe, and the cross-sections are designed according to the full stress principle. Figure 3 shows the design results of the OPSG, noting that the line widths represent the size of the element cross sections.

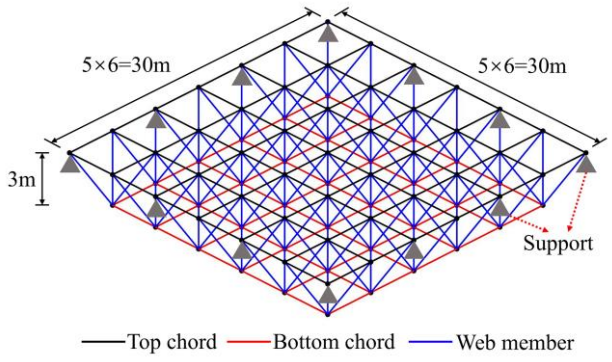


Figure 2. Schematic diagram of OPSG structure

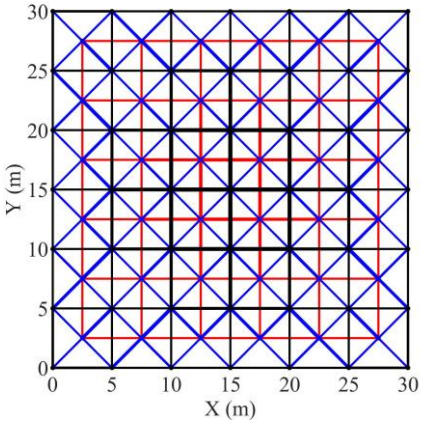


Figure 3. Section design result of the OPSG

3.2. Fragility analysis

Consider the load as a uniform load and perform elastic-plastic analysis on the structure. When the yield strength is 235 MPa and the elastic modulus is 206 Gpa, the curve of the maximum joint displacement versus load is shown in Figure 4. The ratio of tangential stiffness to initial stiffness (K_t/K_0) is taken to be EDP [28], and the variation of EDP with load is shown in Figure 5. The damage state of the OPSG structure can be divided into four stages [29], and the EDP corresponding to each damage stage is defined as shown in Table 1.

According to the uncertainty of yield strength and modulus of elasticity of the structural material (Table 2), multiple elastoplastic analyses were performed by Monte Carlo sampling. After that, the λ and ζ of Eq.(4) for each damage state were obtained statistically, as shown in Table 3.

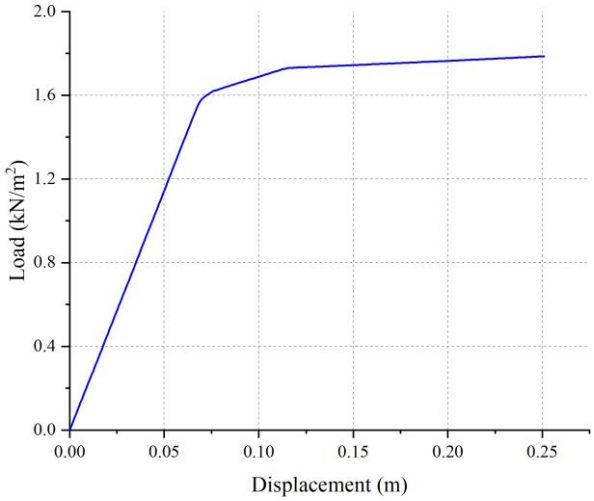


Figure 4. Load-displacement curve

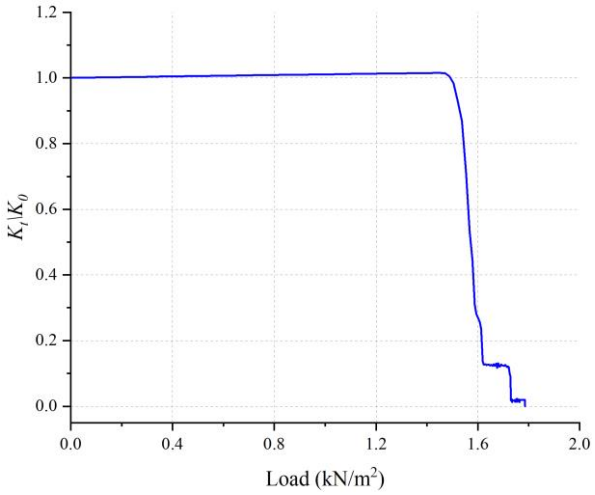


Figure 5. EDP (K_t/K_0)-load curve

Table 1. Damage state classification of OPSG structure

Damage state	Discriminatory boundaries	EPD (K_t/K_0)
DS0 Undamage	Before structure enters plasticity	≥ 1
DS1 Slight damage	Structure enter plasticity and before the stiffness decreases significantly	≤ 0.5
DS2 Moderate damage	Stiffness significantly reduced and before stabilization	≤ 0.25
DS3 Extensive damage	After structural stiffness stabilization and before structural failure	≤ 0.1
DS4 Complete damage	After structural failure	> 0.1

Table 2. Probabilistic models of structural parameters

Structure parameters	Distribution Model	Standard value	μ	CV
Yield strength f_y /Mpa	Normal	235	270	0.08
Elastic modulus E /10^5Mpa	Normal	2.06	2.06	0.03

Table 3. Statistical parameters of $\ln(S_d/S_c)$ in fragility analysis

Statistical parameters	DS1	DS2	DS3	DS4
λ	0.503	0.557	0.579	0.640
ζ	0.0928	0.0929	0.0916	0.0936

Based on Eq. (4) to Eq. (6), the fragility curves and damage probability curves of the OPSG structure are shown in Figure 5 and Figure 6.

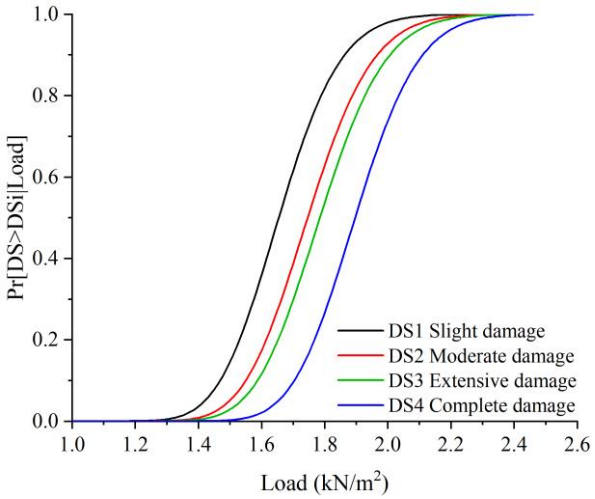


Figure 5. Fragility curves of the OPSG

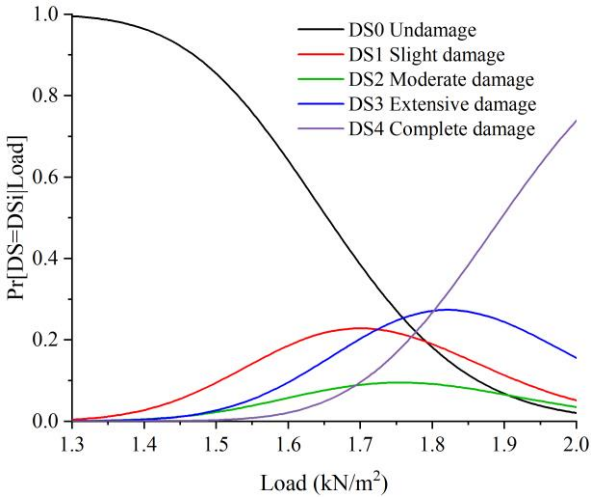


Figure 6. Damage probability curves of the OPSG

3.3. Carbon emission assessment

According to the design result, the self-weight of the OPSG structure is 6081.04 kg, and the EF^{EPiC} of the steel pipe is 3.5kg/kgCO_2e. Using Eq. (4), the carbon emissions of product stage E_P are 21283.6 kgCO_2e. Note the E_P calculated above do not include the emissions of joints, as these are not the focus of this paper. Since the same EF^{EPiC} is used for different sizes of steel pipes in EPiC, the carbon emissions of the structure are linearly related to the steel consumption, thus the carbon emission variation in the processing of different sizes of steel pipes is ignored.

Based on the damage probability curves, repair and replacement strategies for different damage states need to be determined and then the E_R can be calculated. However, there are no comprehensive repair and replacement strategies for space grid structures. In this paper, the carbon emissions from repairing and replacing slight damage are assumed to be 30% of E_P, 60% for moderate damage, 80% for extensive damage, and 100% for complete damage.

When the load follows normal distribution $N(1,0.2)$, the E_R of the structure are 36.23 kgCO_2e and the E_R of each damage stage are shown in Table 4. It should be emphasized that fragility is an inherent property of the structure once the design is completed. Hence the distribution of loads has a greater effect on E_R.

Assuming the uniform load is normal and extreme value I distribution, the mean value is 1.0 to 1.3, and the coefficient of variation is 0.05 to 0.3. The carbon emissions under different load distributions are calculated. Figure 7 shows the ratio of E_R to E_P with different load distributions. As can be seen, the carbon emissions from repair and replacement increase rapidly as the coefficient of variation increases. While E_R also increase with the mean value of the load, existing design methods (e.g. the partial factor

method) have ensured that the probability of failure of the structure is within acceptable limits and the corresponding E_R are small. However, the E_R caused by loads with large coefficients of variation are not ignorable. Although the probability of failure of the structure has been verified, the E_R are large once the damage occurs under such loads.

Table 4. Carbon emissions of repair and replacement for each damage state

Damage state	DS1	DS2	DS3	DS4
E_R (kg/CO_2e)	15.14	6.72	11.46	2.91

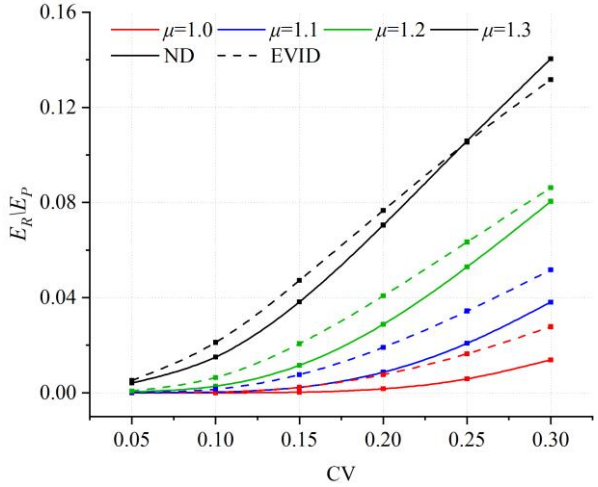


Figure 7. E_R/E_P for different load distributions

4. Conclusion

This paper proposes a probability-based method to calculate the structure carbon emissions generated by the repair and replacement during life cycle, which are always neglected in previous studies. Based on probabilistic risk assessment, the proposed method is divided into four parts: load hazard analysis, structural response estimation, damage assessment, and loss analysis. An orthogonal pyramid space grid structure is designed as a case study to evaluate its life cycle carbon emissions. By assuming that the loads are normally and log-normally distributed with varying coefficients of variation, the effects of different load distribution models on its life cycle carbon emissions are discussed. The results show that the carbon emissions from structural repair and replacement is proportional to the coefficient of variation of the load distribution. The carbon emissions from repair and replacement due to loads with high variability should be considered in the design of low-carbon structures. Overall, this study provides insight into the carbon emission assessment of structures and provides a systematic repair and replacement carbon emission calculation method.

Acknowledgments

This work was funded by the National Natural Science Foundation of China (Grant Nos. 52108182 and 52178175) and the Center for Balance Architecture, Zhejiang University.

References

[1] C. Schleussner, G. Ganti, J. Rogelj, and M. J. Gidden, "An emission pathway classification reflecting the Paris Agreement climate objectives," *Communications Earth & Environment*, vol. 3,

2022-6-17 2022.

[2] China Association of Building Efficiency, "China Building Energy Research Report 2020" (in Chinese), 2020. Available from: https://www.cabee.org/site/content/24021.html

[3] S. Attia, J. Kurnitski, P. Kosiński, A. Borodiņecs, Z. Deme Belafi, K. István, H. Krstić, M. Moldovan, I. Visa, N. Mihailov, B. Evstatiev, K. Banionis, M. Čekon, S. Vilčeková, K. Struhala, R. Brzoň, and O. Laurent, "Overview and future challenges of nearly zero-energy building (nZEB) design in Eastern Europe," *Energy and Buildings,* vol. 267, p. 112165, 2022.

[4] H. X. Li, Y. Chen, M. Gül, H. Yu, and M. Al-Hussein, "Energy performance and the discrepancy of multiple NetZero Energy Homes (NZEHs) in cold regions," *Journal of Cleaner Production,* vol. 172, pp. 106-118, 2018.

[5] M. Röck, M. R. M. Saade, M. Balouktsi, F. N. Rasmussen, H. Birgisdottir, R. Frischknecht, G. Habert, T. Lützkendorf, and A. Passer, "Embodied GHG emissions of buildings – The hidden challenge for effective climate change mitigation," *Applied Energy,* vol. 258, p. 114107, 2020.

[6] C. De Wolf, F. Yang, D. Cox, A. Charlson, A. S. Hattan, and J. Ochsendorf, "Material quantities and embodied carbon dioxide in structures," *Proceedings of the Institution of Civil Engineers - Engineering Sustainability,* vol. 169, pp. 150-161, 2016.

[7] S. Roh and S. Tae, "An integrated assessment system for managing life cycle CO2 emissions of a building," *Renewable and Sustainable Energy Reviews,* vol. 73, pp. 265-275, 2017.

[8] G. Q. Chen and Z. M. Chen, "Carbon emissions and resources use by Chinese economy 2007: A 135-sector inventory and input – output embodiment," *Communications in Nonlinear Science and Numerical Simulation,* vol. 15, pp. 3647-3732, 2010.

[9] A. Stephan, R. H. Crawford and P. Bontinck, "A model for streamlining and automating path exchange hybrid life cycle assessment," *The International Journal of Life Cycle Assessment,* vol. 24, pp. 237-252, 2019.

[10] S. Suh and G. Huppes, "Methods for Life Cycle Inventory of a product," *Journal of Cleaner Production,* vol. 13, pp. 687-697, 2005.

[11] X. Xu, J. You, Y. Wang, and Y. Luo, "Analysis and assessment of life-cycle carbon emissions of space frame structures," *Journal of Cleaner Production,* vol. 385, p. 135521, 2023.

[12] R. Kumanayake, H. Luo and N. Paulusz, "Assessment of material related embodied carbon of an office building in Sri Lanka," *Energy and Buildings,* vol. 166, pp. 250-257, 2018.

[13] J. Hart, B. D'Amico and F. Pomponi, "Whole‐life embodied carbon in multistory buildings: Steel, concrete and timber structures," *Journal of Industrial Ecology,* vol. 25, pp. 403-418, 2021.

[14] V. J. L. Gan, C. M. Chan, K. T. Tse, I. M. C. Lo, and J. C. P. Cheng, "A comparative analysis of embodied carbon in high-rise buildings regarding different design parameters," *Journal of Cleaner Production,* vol. 161, pp. 663-675, 2017.

[15] X. Su and X. Zhang, "A detailed analysis of the embodied energy and carbon emissions of steel-construction residential buildings in China," *Energy and Buildings,* vol. 119, pp. 323-330, 2016.

[16] N. Francart, T. Widström and T. Malmqvist, "Influence of methodological choices on maintenance and replacement in building LCA," *The International Journal of Life Cycle Assessment,* 2021-11-1 2021.

[17] A. Nouri, P. Asadi and M. Taheriyoun, "Life-Cycle Cost Analysis of Seismic Designed RC Frames Including Environmental and Social Costs," *Journal of earthquake engineering : JEE,* vol. 26, pp. 5958-5977, 2022-1-1 2022.

[18] A. Athanasiou, M. Dakour, S. Pejmanfar, L. Tirca, and T. Stathopoulos, "Multihazard Performance-Based Assessment Framework for Multistory Steel Buildings," *Journal of Structural Engineering-ASCE,* 2022.

[19] B. Gencturk, K. Hossain and S. Lahourpour, "Life cycle sustainability assessment of RC buildings in seismic regions," *Engineering Structures,* vol. 110, pp. 347-362, 2016.

[20] K. A. Hossain and B. Gencturk, "Life-Cycle Environmental Impact Assessment of Reinforced Concrete Buildings Subjected to Natural Hazards," *Journal of Architectural Engineering-ASCE,* vol. 22, 2016.

[21] E. Romano, L. Cascini, M. D'Aniello, F. Portioli, and R. Landolfo, "A simplified multi-performance approach to life-cycle assessment of steel structures," *Structures,* vol. 27, pp. 371-382, 2020.

[22] B. S. Institute, "Sustainability of Construction Works—Assessment of Environmental Performance of Buildings—Calculation Method," in *BS EN 15978:2011* London, UK, 2011.

[23] X. Zhang and F. Wang, "Assessment of embodied carbon emissions for building construction in China: Comparative case studies using alternative methods," *Energy and Buildings,* vol. 130, pp. 330-340, 2016.

[24] R. H. Crawford, P. Bontinck, A. Stephan, and T. Wiedmann, "Towards an Automated Approach for Compiling Hybrid Life Cycle Inventories," *Procedia Engineering,* vol. 180, pp. 157-166, 2017.

[25] R. H. Crawford, A. Stephan and F. Prideaux, "Environmental Performance in Construction (EPiC) Database," Melbourne: The University of Melbourne, 2019.

[26] "Technical Specification for Space frame Structures," *JGJ7-2010*: China Construction Industry Press, 2010.

[27] "Standard for design of steel structures," *GB 50017-2017*: China Construction Industry Press, 2017.

[28] J. Li, " The vulnerability analysis of roof-isolated large-span space truss structure based on IDA" (in Chinese) (M.Ph.thesis), Guangzhou University, 2020.

[29] X. Zhi, J. Gong, and F. Fan, " Research on the seismic fragility of orthogonal pyramid space grid " *Journal of Harbin Institute of Technology,* vol. 49, pp. 32-38, 2017.

Metal gridshell structures, connections and stability

Active bending
Additive manufacturing/ 3D printing
Architectural geometry
Bamboo for sustainable construction and quality of life improvement
Bio-inspired structures and architecture
Bridge structures
Computational form-finding
Conceptual design
Concrete structures
Construction techniques
Deployable and inflatable structures
Design competition (WG21)
Digital modelling and fabrication
Dynamic response of metal spatial structures
Dynamic response of other structures
Form-finding and structural optimisation of interlocking discrete assemblages
Graphical methods
Gridshell and lattice structures
Historical concrete shells
Historical structures
Lattice structures
Life-cycle design and assessment of structures
► Metal gridshell structures, connections and stability
Methods and construction technologies for sustainable shell structures
Morphology and configuration processing
Next generation parametric design
Novel methods in modelling, optimisation and construction for reducing carbon footprint of continuous roof shells
Numerical methods for geometry, form-finding and optimisation of lightweight structures
Optimisation methods and applications
Origami
Other
Teaching design uncertainty: working with unknown qualities/quantities of new and re-claimed materials
Teaching of shell and spatial structures
Tensegrity systems and cable structures
Tension and membrane structures
Tension structures in the Asia-Pacific
Timber and bio-based structures
Topology optimisation
Traditional masonry structures and innovation
Transformable structures

Proceedings of the IASS Annual Symposium 2023
Integration of Design and Fabrication
10–14 July 2023, Melbourne, Australia
Y.M. Xie, J. Burry, T.U. Lee and J. Ma (eds.)

Design and construction of two tree-columns supported gridshells in Canberra

Catherine POIRRIEZ*, Yacine BOUZIDA*

* Passage Projects
14A Sago Street, 059015 Singapore
cp@passage-projects.com

Abstract

Canberra centre is an existing commercial development in Canberra, comprising retail spaces, restaurants and cinema. The development is divided into several buildings, each of the buildings being separated by street crossings accessible by cars. In order to bring back a sense of unity in the shopping centre, make the restaurants attractive again and improve the customers experience, it was decided to close to traffic one of the streets separating the buildings. The newly pedestrian Scott's crossing street has been covered by two new steel and ETFE canopies, providing an elegant space protected from the rain for the pedestrians. Although complex, the geometry of the canopies was generated to fully take into account buildability – all the steel members were translated in a language of single radii, comprehensible for the steel fabricator. As the shopping centre would remain in use during the steelworks installation, bolted connections have been designed to simplify installation without impacting the sizes of the members, which were designed to be as small as possible. The resulting structure is an elegant lightweight structure providing protection from the rain, reviving an underused part of the shopping centre and bringing pride to the adjacent shop owners.

Keywords: metal spatial structures, buckling, optimization, ETFE, buildability



Figure 1. Overall view of one of the Scott's crossing canopies [Vector Foiltec]

1. Introduction

Canberra centre is an existing commercial development in Canberra, comprising retail spaces, restaurants and cinema. The development is divided into several buildings, each of the buildings being separated by street crossings accessible by cars. In order to bring back a sense of unity in the shopping centre, make the restaurants attractive again and improve the customers experience, it was decided to close to traffic one of the streets separating the buildings. The newly pedestrian Scott's crossing street

Copyright © 2023 by Catherine POIRRIEZ and Yacine BOUZIDA. Published in the Proceedings of the IASS Annual Symposium 2023 with permission.

has been covered by two new steel and ETFE canopies, providing an elegant space protected from the rain for the pedestrians.

The Scott's crossing canopies are steel canopies supporting ETFE cushions and surrounded by buildings on 3 sides each. The canopies are supported by 4 tree columns each. The structure is composed of 9 curved main arches spaced at about 2.8m and spanning diagonally between the edge beam and straight transversal beams spanning between the arches and providing restraints to the arches. The east canopy is about 19mx19m in plan and 12m high, the west canopy is about 24mx15m in plan and 15m high. Plan view and section of each canopy is shown in Figures 2 and 3.

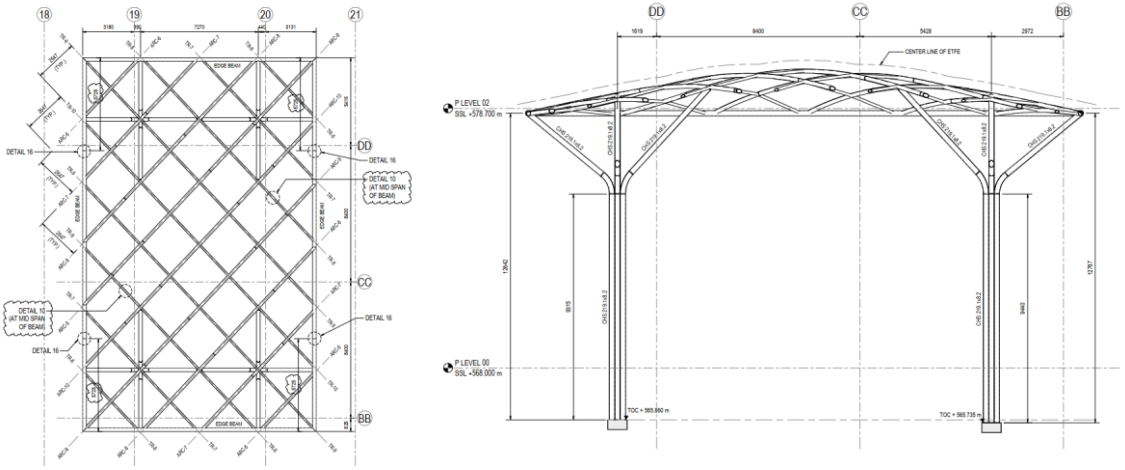


Figure 2. West Canopy plan view and section [Passage Projects]

The fabrication and installation of the steel occurred between July 2022 to October 2022 while the installation of the ETFE occurred between October 2022 to December 2022.

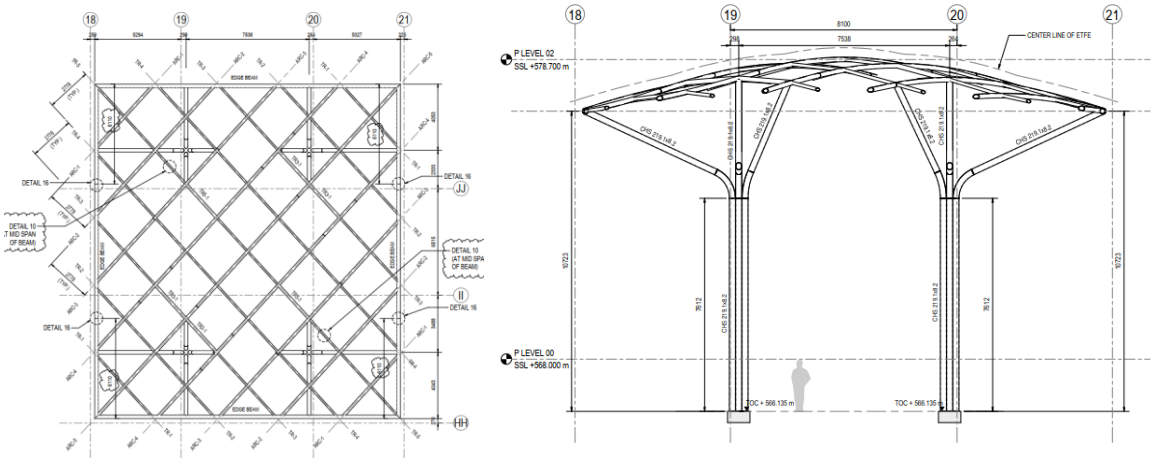


Figure 3. East Canopy plan view and section [Passage Projects]

2. Basis of design

The steel structure has been designed following Australian code AS1170-0 [1], AS1170-1 [2], AS1170-2 [3] and AS4100:2020 [4]. The next sections present the loadings applied to the structure.

2.1. General Loadings

2.1.1. Dead Loads and Live Loads

The roof should be able to withstand the self-weight of the steel, the weight of the ETFE and aluminium, about 10 kg/m2 and the weight of services running on the structure, estimated to 25 kg/m^2. The Live Loads correspond to maintenance loadings. The Live Loads applied are 25kg/m^2 on the whole roof surface.

2.1.2. Wind Loads

A wind tunnel test has been carried out for the roof. The pressures obtained for the roof steel structure design vary between 0.75 kPa to -0.73 kPa.

2.1.3. Temperature Loads

The variations of temperature of the steel structure are mainly caused by the heat from the sun during the day and the colder temperatures of the night. The construction temperature is assumed to be 20ºC, so the temperature differentials considered for the design are +42ºC/-30ºC.

2.1.3. Seismic Loads

Following Australian code AS1170-4 [5], the canopies structures fall in Earthquake category 2. A simplified design approach of equivalent lateral force can be used. The lateral force to be applied on the structure is equivalent to 0.14Wi where Wi is the seismic weight of the structure, including the dead loads of the structure. The seismic loads were not governing the design.

2.1.4. Load combinations

The load combinations considered for the design are shown in Table 1:

Table 1: ULS Load Combinations

LC1	1.2(SW+DL)+1.5LL+0.9T
LC2	1.2(SW+DL)+1.5WL+0.9T
LC3	0.9(SW+DL)+1.5WL+0.9T
LC4	1.0(SW+DL)+1.0E

3. Geometry Rationalization and setting out

3.1. Structure setting out

To avoid the need to use costly nodes for the ETFE aluminium extrusions and costly ETFE cushions, the ETFE cushions are not diamond shaped cushions but are long strips spanning between arches, as shown in Figure 4. The setting out between the main arches supporting the cushions and the transversal beams providing restraints to the arches was carefully studied in order to avoid any clash between the transversal beams and the cushion belly.

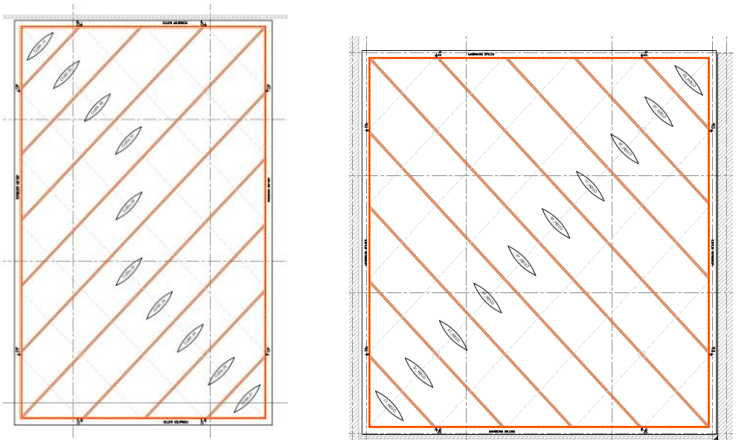


Figure 4. Canopies ETFE cushions layout [Vector Foiltec]

Several options have been considered in the design, as shown in Figure 5. The first option consists in keeping the arches and the transversal beams at the same level and using high Tee brackets to elevate the ETFE cushions from the structure to avoid any clash. The second option consists in offsetting the transversal beams down compared to the arches, giving 3 layers in the structure, a first layer for the ETFE, a second layer for the arches and a third layer for the transversal beams. The third option consists in offsetting the transversal beams up and supporting the ETFE cushions from the transversal beams.

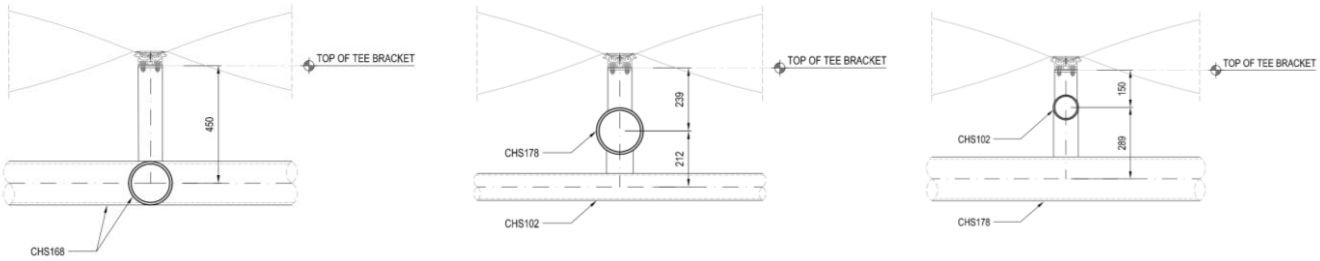


Figure 5. Beams setting out options considered in the design [Passage Projects]

The option adopted in the design was option 1, as it enabled to run services above the arches through the Tee brackets, effectively hiding the services from the public view. Tee brackets height and shape have been optimised to achieve an elegant look of the canopy, as shown in Figure 6.

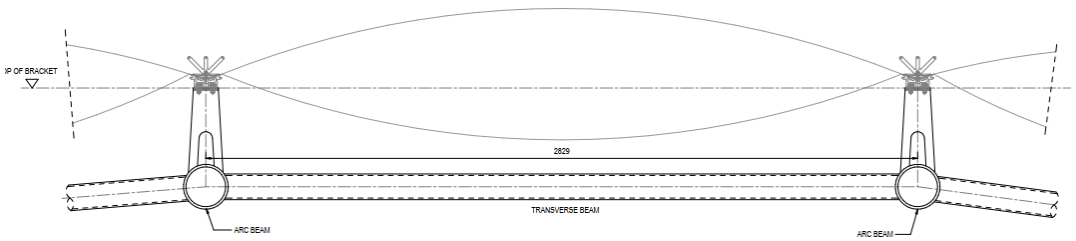


Figure 6. Section through arches and ETFE cushions [Passage Projects]

3.2. Geometry rationalisation

The initial geometry generated by the architects consisted in freeform curved arches and transversal beams. Without further rationalisation, the structure would have been difficult to fabricate.

The arches geometry has been translated in a language of single radii, ie arcs, comprehensible for the steel fabricator. The canopies are mirrored diagonally so there are only 5 different arches on each canopy. Each arch is decomposed into a maximum of 1 radii each of minimum 5m long, except for one arch which has been decomposed into 4 radii, which simplified the fabrication.

As seen in Figure 7, the deviation from the architect original design is maximum 100mm, which was acceptable from an aesthetic point of view.

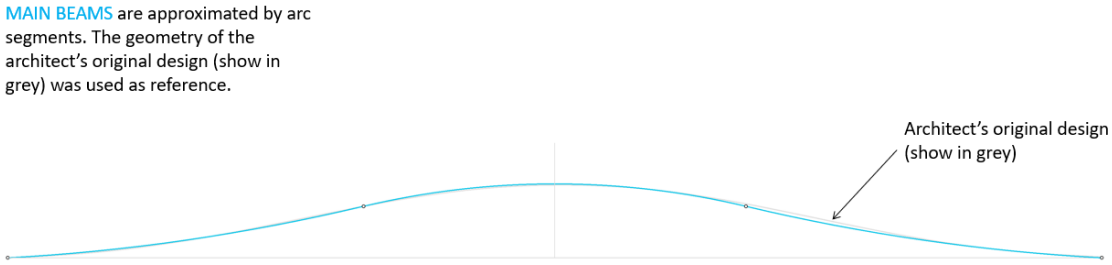


Figure 7. Approximation of arches into arcs with slight deviation from the architect's geometry [Passage Projects]

The transversal beams were proposed to be straight between arches to simplify the fabrication. Straightening the transversal beams also enabled to reduce the tee bracket height.

4. Structural analysis

4.1. Stability and supporting conditions

The Scott's crossing canopies are supported by 4 tree columns each. The tree columns are fixed to the concrete. Surrounded by existing buildings, the canopies could not rely on horizontal restraints to the existing façade. As a result, lateral and torsional sway buckling had to be accounted for in the structural design in addition to the arches buckling.

The stability of the roof is checked in two steps: the global stability of the structure and the local stability of the members.

The global stability of the structure is checked following AS4100 Annex E [4]. A Linear buckling analysis, also called Eigenvalue analysis is carried out.

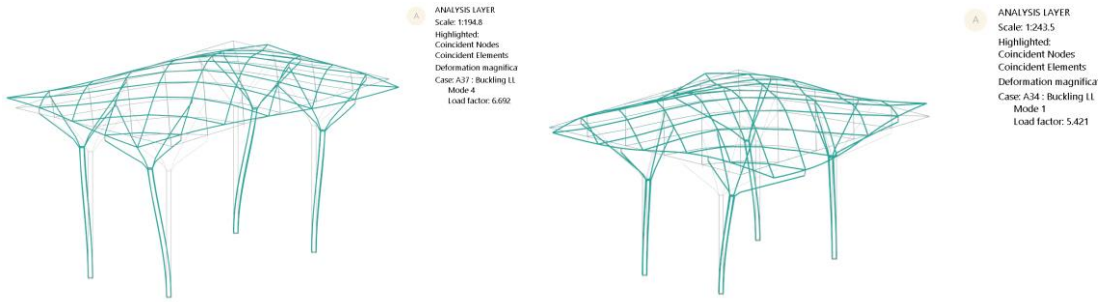


Figure 8: Structure first buckling mode – Critical Load Factor = 5.4 [Passage Projects]

The first buckling mode can be seen in Figure 8. The structures are highly sensitive to lateral and torsional sway buckling, with the first buckling modes having a critical load factor of around 5.4.

As per AS4100 [4], a structure of buckling factor smaller than 10 will be highly sensitive to second-order effects. As a result, if any global buckling mode is found with a buckling factor lower than 10, a Geometrically non-linear elastic analysis with imperfections included is performed. Global imperfections are included in the model using the deformed shape of the global buckling modes with a buckling factor lower than 10 one at a time. A non-linear buckling analysis was also performed to confirm the buckling modes from the Eigenvalue analysis.

The local imperfections and local stability of the members are taken into account in the checks for buckling resistance of members following AS4100 [4] – as an addition to the imperfections taken into account in the GNIA, for conservative design.

4.2. Bolted connections

As the shopping centre would remain in use during the steelworks installation, no welding was allowed on site. Bolted connections have been carefully placed to facilitate transport and installation without impacting the sizes of the members.

The connections of the arches to the edge beams consist in a stump welded to the edge beam and connected to the arch through and end plate connection, as seen in Figure 9.

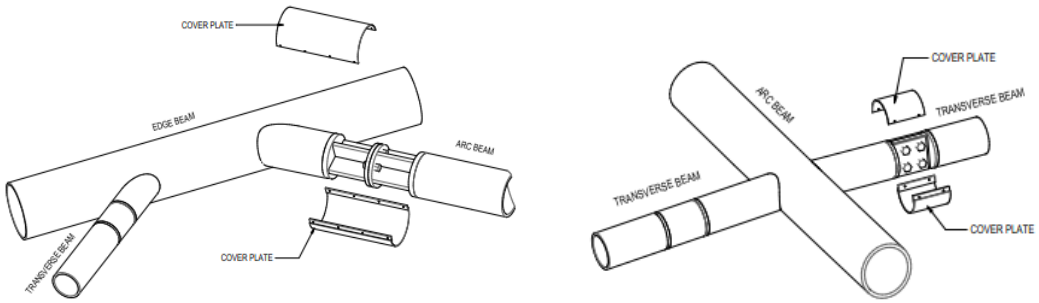


Figure 9: Bolted connections [Passage Projects]



Figure 10: Canopy view during construction with various bolted connections [Passage Projects]

The connections of the transversal beams to the arches consist in a stump welded to the arch and connected to the transversal beam through a 4-bolts fin plate connection, as shown in Figure 9. The connection can transfer moment in the major axis direction of the transverse beam to provide stiffness to the canopy. The connection is considered as a pin or semi-rigid connection with low stiffness in the minor axis direction of the transversal beam. This release condition has been considered in the analysis model to ensure that the adequate stiffness of the arch-transversal beam system has been taken into account in the buckling analysis. Figure 10 shows the various bolted connections in the structure during installation.

All bolted connections have been covered by cover plates once installation has been completed, almost invisibles to the visitors.

4.3. Final design summary

The main arches support the ETFE cushions. They are circular hollow sections of diameter 168mm. The arches transfer the forces to the edge beams through compression and bending. The edge beams are circular hollow sections of diameter 219mm. The transversal beams beams provide a restraint against out-of-plane and lateral-torsional buckling to the arches. They are circular hollow sections of diameter 114mm. The columns transfer all forces to the ground, they are formed of 4 branches of circular hollow sections of diameter 219mm joining into a 4-column trunk to the baseplate.



Figure 11. Overall view of the two Scott's crossing canopies during construction [Passage Projects]

5. Conclusion

As a conclusion, the resulting structure is an elegant lightweight structure providing protection from the rain, reviving an underused part of the shopping centre and bringing pride to the adjacent shop owners. Careful consideration in the design enabled to avoid connecting to the adjacent buildings with complex existing facades. Bolted connections enabled to allow construction without welding on site accommodating the intricate site conditions of a building under use.

Acknowledgements

The authors would like to thank all the parties of Scott's Crossing ETFE canopoies: Bloc, Vector Foiltec, HDM.

References

[1] AS1170-0: Australian/New Zealand Standard – Structural design actions, Part 0: General principles.

[2] AS1170-1: Australian/New Zealand Standard – Structural design actions, Part 1: Permanent, imposed and other actions.

[3] AS1170-2: Australian/New Zealand Standard – Structural design actions, Part 2: Wind actions.

[4] AS4100-2020: Australian Standard – Steel structures.

[5] AS1170-4: Australian Standard – Structural design actions, Part 4: Earthquake actions in Australia.

IASS 2023
July 10–14 Melbourne
Integration of Design and Fabrication

Proceedings of the IASS Annual Symposium 2023
Integration of Design and Fabrication
10–14 July 2023, Melbourne, Australia
Y.M. Xie, J. Burry, T.U. Lee and J. Ma (eds.)

Grid shell for Hamad Airport expansion in Doha

David CABALLERO[a,*], Mikel MONASTERIO[a], Oscar BATUECAS[a], Josu GOÑI[a], Gabriel RUIZ[b], Jose Miguel RICO[b]

[a,*] LANIK I, S.A., Mundaiz 8, 20012, San Sebastián, Spain
jgoni@lanik.com

[b] School of Architecture, University of the Basque Country (UPV/EHU)
Plaza Oñati 2, 20018, San Sebastián, Spain

Abstract

The new expansion of Hamad Airport in Doha includes a very big atrium covered by a glazed grid shell of 14052 m² surface. The intention was to create a very big organic space with the perception of being in an openair garden. The scope of Lanik in this project included geometrical design, calculation, fabrication, and installation of the metallic grid shell structure. One of the main challenges during the design process was to define the boundary connections to the buildings providing enough bracing to avoid too low natural frequencies, but at the same time, allowing enough relative displacement and elasticity between the structure and the buildings to avoid excessive efforts due to thermal and deformational effects. The design and fabrication were integrated by means of Lanik's GOOSE software. This paper explains the design, engineering, parametric fabrication, and assembly of the structure. In January, 2023, the airport is operative and the atrium ready for being used by the travelers.

Keywords: realization, airport, funnel, grid shell, parametric fabrication, parametric design

1. Introduction

This paper describes the envelope from a structural point of view, since this is the scope of Lanik in the project. Lanik was awarded for the redesign, reengineering, fabrication and assembly supervision of the structure. The client of Lanik in this project was Glassline, who contracted the whole envelope package and installed the glass.

This project has been challenging for Lanik, first because of its size, 14.000 m² of free form surface to be covered by glass. The original triangular mesh was optimizable in terms of size and mainly angulations between members. The dynamic analysis was critical to define the right way to connect the upper side of the structure to the surrounding buildings, and finally, GOOSE software was use for the first time for the CSL single layer System meaning a huge advantage in terms of fabrication engineering performance and efficiency, integrating design and fabrication in the same software. These aspects of the project are developed along the paper.

Copyright © 2023 by David CABALLERO, Mikel MONASTERIO, Oscar BATUECAS, Josu GOÑI, Gabriel RUIZ and Jose Miguel RICO. Published in the Proceedings of the IASS Annual Symposium 2023 with permission.

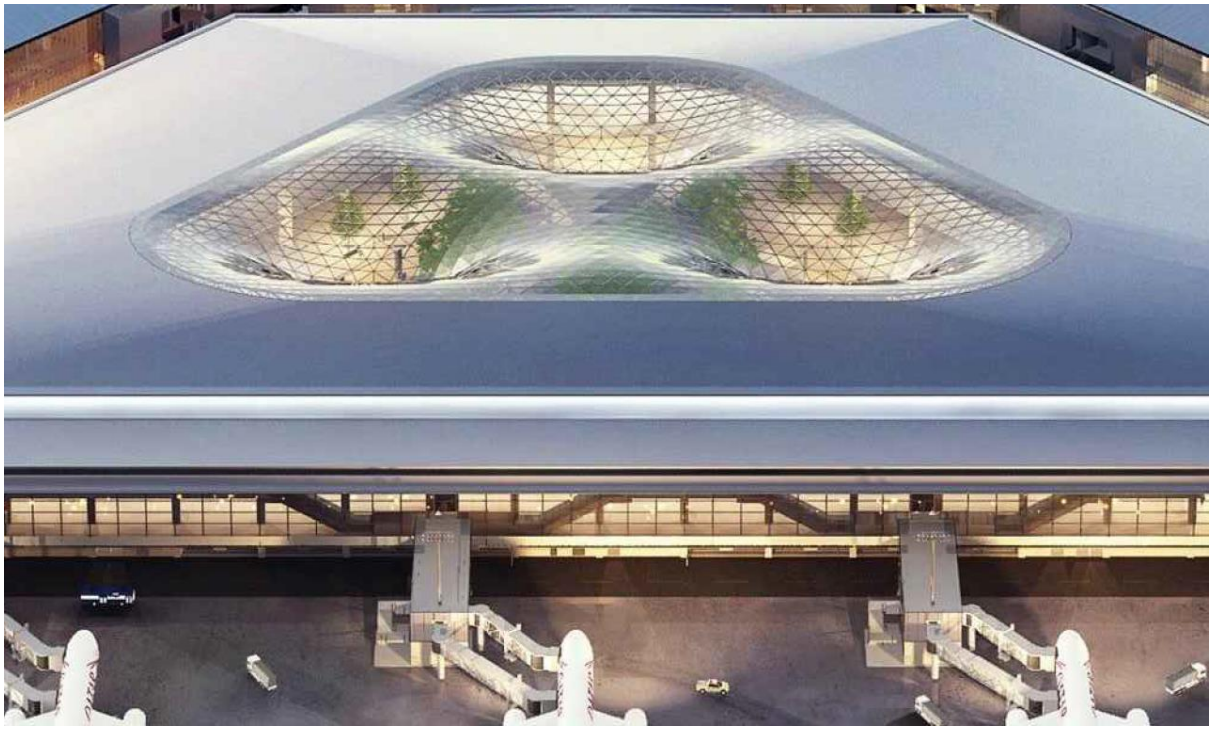


Figure 1: Render of the general aspect of the project

2. Project description

2.1. Geometry

The global dimensions of the structure are 175m long, 94m width and 29m high. The main characteristic is the structural configuration based on a double curvature surface with three funnels with structural purposes that introduce stiffness out of the plane because of the double curvature, drain the water, and work as supporting columns in collaboration with the perimetral supports.

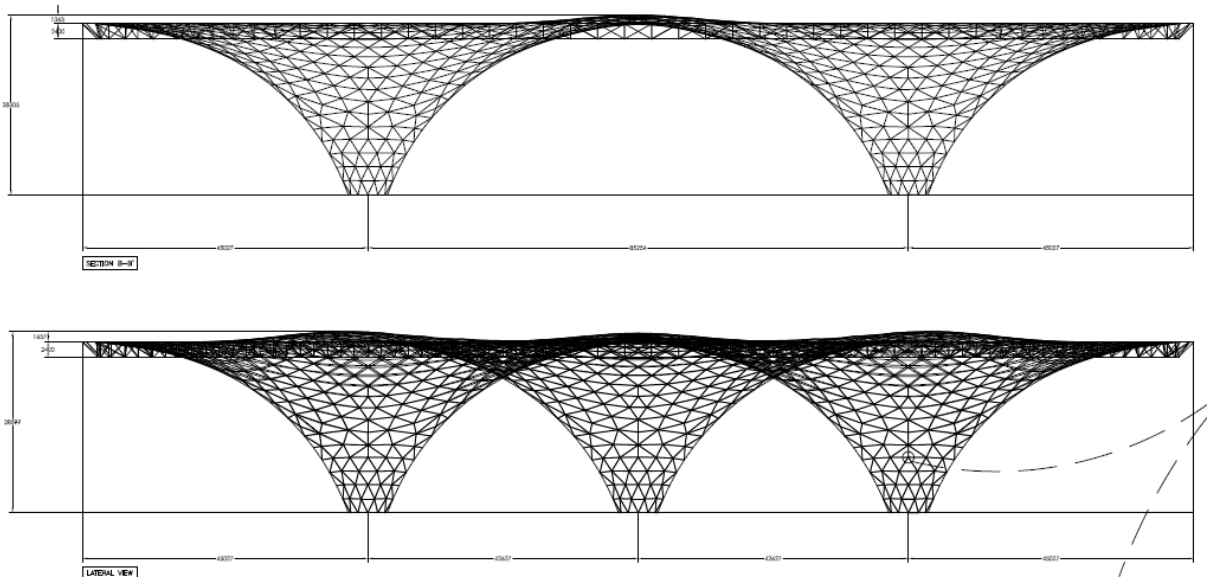


Figure 2: Front and lateral views

2.2. Mesh optimization

The generatrix surface was an input coming from the architectural design. In a previous phase, before Lanik being involved in the project, there was a triangular grid design for the envelope. The polygonal discretization of the funnels was based on local partitions producing the geometry shown in Figure 3.

(a) (b)

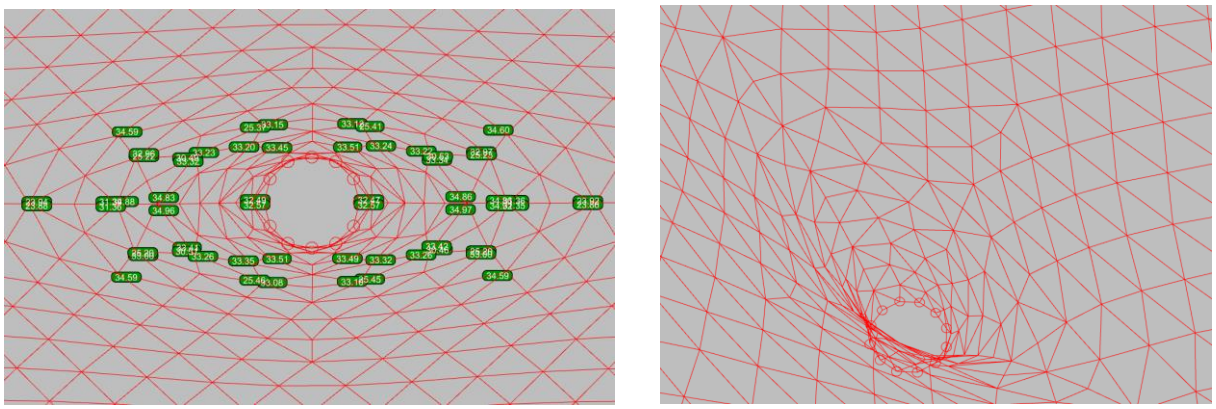


Figure 3: original mesh of funnel with many singularities and bad angles: (a) Angles under 35º, (b) Perspective

This triangular mesh had many discontinuities and very bad angles creating interferences and need for big nodes. After many redesign phases using Rhino and grasshopper tools, the mesh was smoothed, rationalized and as a result, size of elements, angulations and aesthetic was significantly improved.

(a) (b)

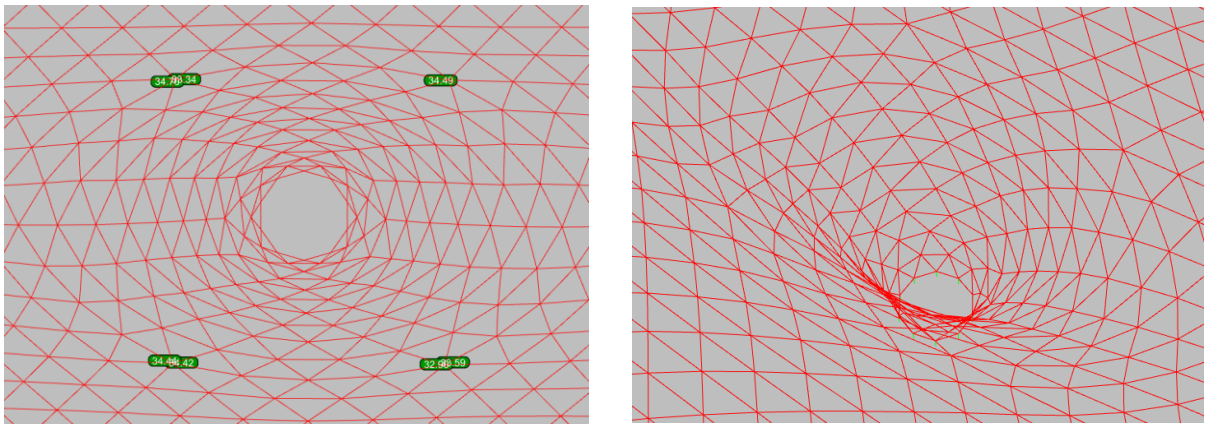


Figure 4: optimized mesh with smoother angles and les singularities: (a) Angles under 35º, (b) Perspective

In figure 4 it can be checked that the amount of angles under 35º (used as reference for reasonable limit to avboid too big nodes) decreases very significantly with the new mesh. This change was approved by the architect and the property, and became the basis for the design and calculation of the structure.

2.3. Constructive system

The single layer structure is composed by RHS (Rectangular Hollow Section) profiles connected to each other by CSL structural system. This system is based on some truncated hollow nodes to which the bar are fixed by means of bolts

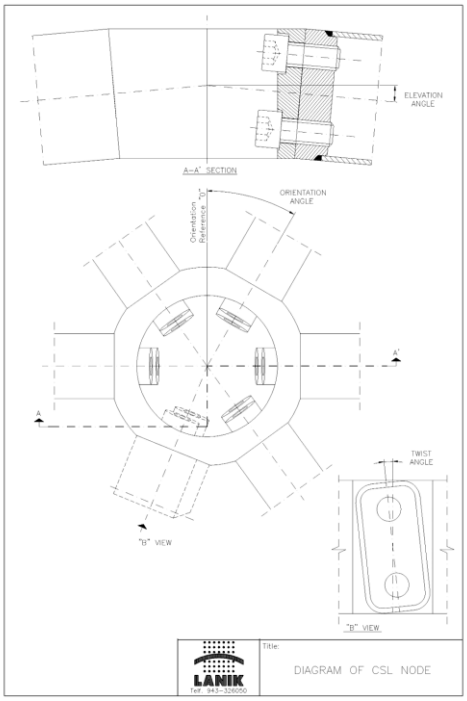


Figure 5: CSL system sketch



Figure 6: CSL System general aspect

All angulations can be solved by the system and the connection allows for bending moment transmission in the main axis.

3. Boundary conditions and dynamic analysis

The first calculations of the structure before Lanik was involved in the project were based on the assumption that the boundary upper perimeter was supported only vertically by means of sliding supports. This way, all the horizontal loads where transmited to the basement trough the funnels and no horizontal reaction needed to be transmited to the upper side of the surroundin buldings.

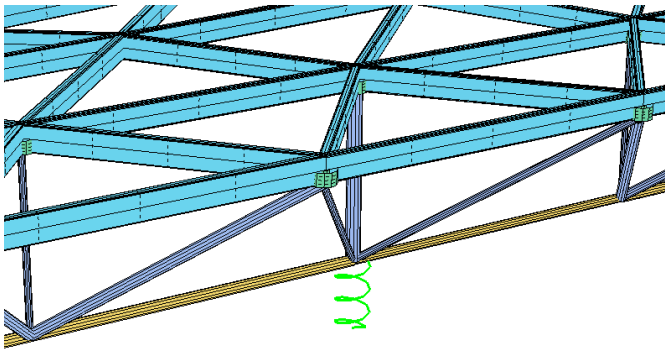


Figure 7: Top horizontally sliding supports

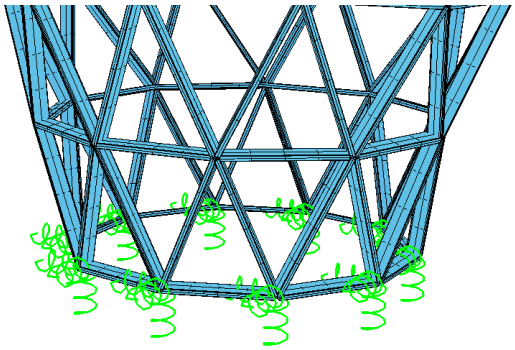


Figure 8: bottom fixed pin supports

This support configuration promotes a big horizontal elasticity of the whole system since the embedding connection of the funnels and the funnels themselves are responsible to retain horizontally the upper part of the structure.

This lack of horizontal stiffness combined with an enormous amount of mass in the upper side (structure + glass) lead on very low frequency of the first vibration modes. In fact, the first vibration modes for this configuration are translational activating mass in X and Y directions as can be shown in table 1.

Table 1. Natural vibration frequencies and activate masses without horizontal retention in upper supports

Modal masses - activated mass

No.	LC	frequency [Hertz]	effective modal Mass X[t]	Y[t]	Z[t]	factor X[%]	Y[%]	Z[%]	activated mass [%]*
1	500	0.527	3	398	0	0.15	18.41	0.00	21.12714
2	501	0.559	1	1252	0	0.05	57.94	0.00	24.43589
3	502	0.791	1325	0	0	61.32	0.00	0.00	23.44008
4	503	1.095	0	7	3	0.00	0.32	0.14	15.77187
5	504	1.144	1	0	0	0.05	0.00	0.00	14.83568
6	505	1.172	0	3	0	0.00	0.12	0.00	7.20517
7	506	1.242	11	0	0	0.52	0.00	0.00	12.96900
8	507	1.283	0	3	9	0.00	0.14	0.42	13.24051
9	508	1.330	14	0	0	0.63	0.00	0.00	8.65561
10	509	1.405	0	6	48	0.02	0.28	2.20	11.15456
11	510	1.442	5	0	1	0.21	0.02	0.06	7.78489
12	511	1.471	0	9	121	0.00	0.42	5.59	8.16760
13	512	1.521	9	6	22	0.43	0.27	1.03	7.34113
14	513	1.537	10	3	7	0.48	0.12	0.32	11.64638
15	514	1.700	0	0	4	0.02	0.02	0.17	6.91177
		sum	1381	1687	214	63.88	78.05	9.92	
	System activ		2161	2161	2161				

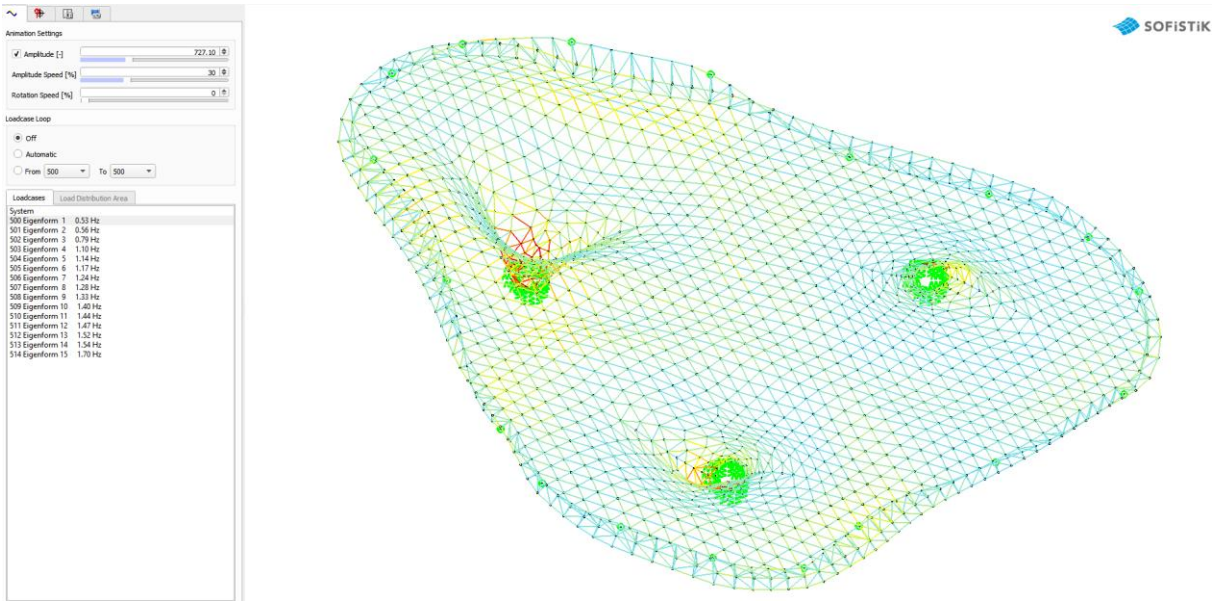


Figure 9: Deformation of the structure with the first natural vibration mode of 0.53 Hz (translational)

This very low frequencies supposed a big risk of resonance response under alternate wind loads and because of this reason the supporting configuration needed to be changed. In the other hand, the surrounding buildings where already designed and executed without taking into consideration reactions of the grid shell.

It took more than 65 attempts of supporting configurations with different combinations of sliding, retained in only one or two directions, elastic, and friction simulations etc. to achieve to a final configuration of top support which allowed to enough stiffness to avoid low frequency vibration modes, but at the same time did not transmit too big and undesirable reactions to the surrounding buildings.

Table 2. Natural vibration frequencies and activate masses with new upper horizontal retention configuration

Modal masses - activated mass

No.	LC	frequency [Hertz]	effective modal Mass X[t]	Y[t]	Z[t]	factor X[%]	Y[%]	Z[%]	activated mass [%]*
1	550	1.345	0	39	3	0.02	1.76	0.15	5.54651
2	551	1.417	288	1	0	12.86	0.03	0.00	6.78225
3	552	1.472	15	3	0	0.66	0.13	0.00	6.23585
4	553	1.501	2	310	15	0.09	13.88	0.68	5.96661
5	554	1.540	1	25	15	0.04	1.13	0.65	8.86717
6	555	1.585	23	4	2	1.04	0.16	0.08	6.61563
7	556	1.632	0	146	14	0.00	6.54	0.65	6.03695
8	557	1.774	82	0	1	3.67	0.01	0.04	9.34539
9	558	1.848	0	122	47	0.02	5.44	2.11	10.27756
10	559	1.947	38	4	17	1.72	0.17	0.77	4.75098
		sum	450	654	115	20.12	29.22	5.13	
		System activ	2236	2236	2236				

The first natural frequency with this new configuration is 1.34 Hz, which is quite high, and therefore, no dynamic analysis against wind load is needed anymore.

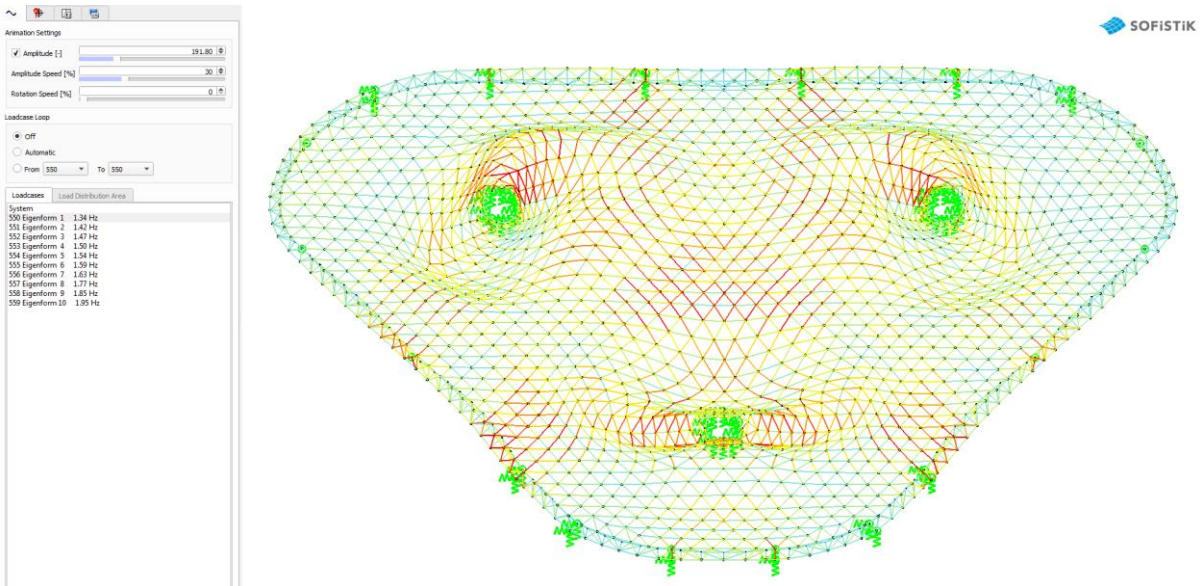


Figure 10: Deformation of the structure with the first natural vibration mode of 1.34 Hz

4. Integration of design and fabrication

This project has been developed using LANIK's automatic tool for grid shell design, calculation and fabrication engineering. This tool is called GOOSE and is a complete self-made software environment which allows for geometrical design with Rhino-grasshopper, calculation pre-processing inside Rhino, direct use of Sofistik non-linear engine from goose Rhino plugin (automatic resizing), automatic 3D solid and parametrical fabrication engineering inside Rhino, and assembly phases definition in Rhino for its simulation in Sofistik. Databases are directly edited via goose web application.

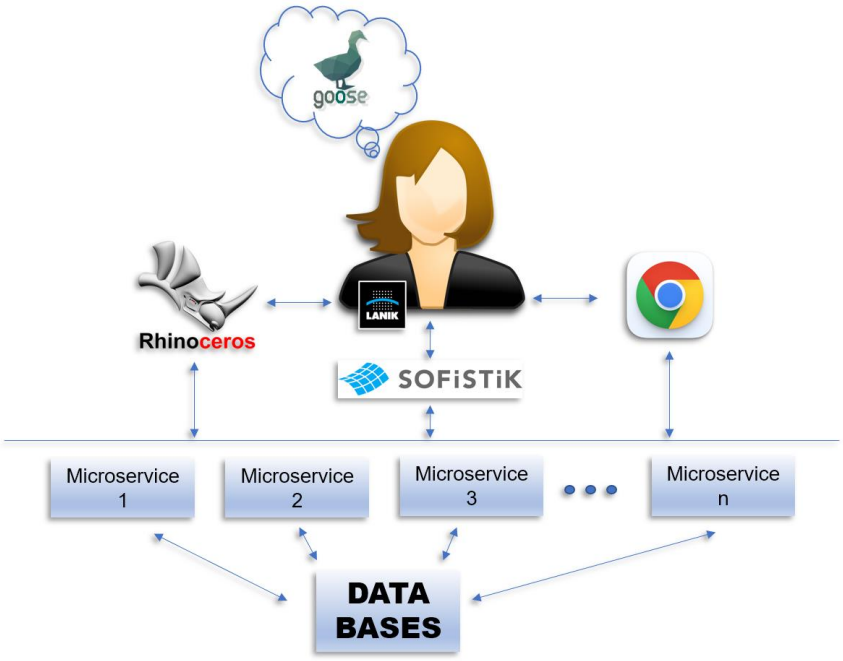


Figure 11: GOOSE environment graphic description

As some examples of the tools that includes GOOSE, the next image shows Calculation model preprocessing inside Rhino by means of GOOSE:

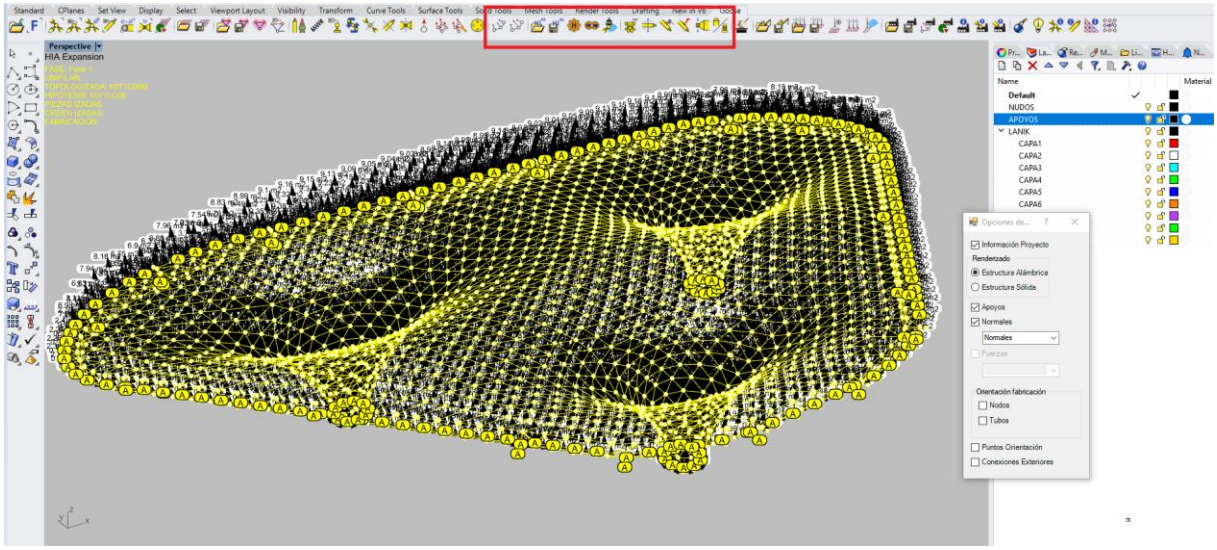


Figure 12: GOOSE Rhino plugin calculation model pre-processing

The calculation model can be launched automatically in Sofistik and GOOSE is able to interact directly with the database of Sofistik and extract from the calculation model all information needed for structural sizing of beams and connection bolts.

Regarding fabrication engineering, the next images show fabrication parametric design where nodes are automatically generated to solve interferences using standard node sizes:

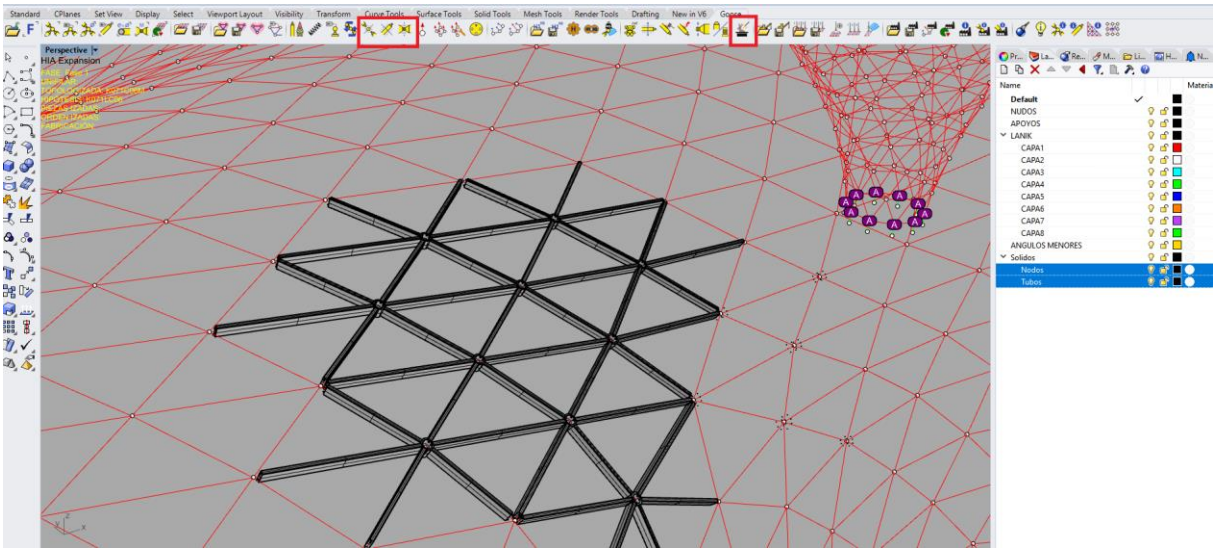


Figure 13: GOOSE Rhino plugin node automatic generation

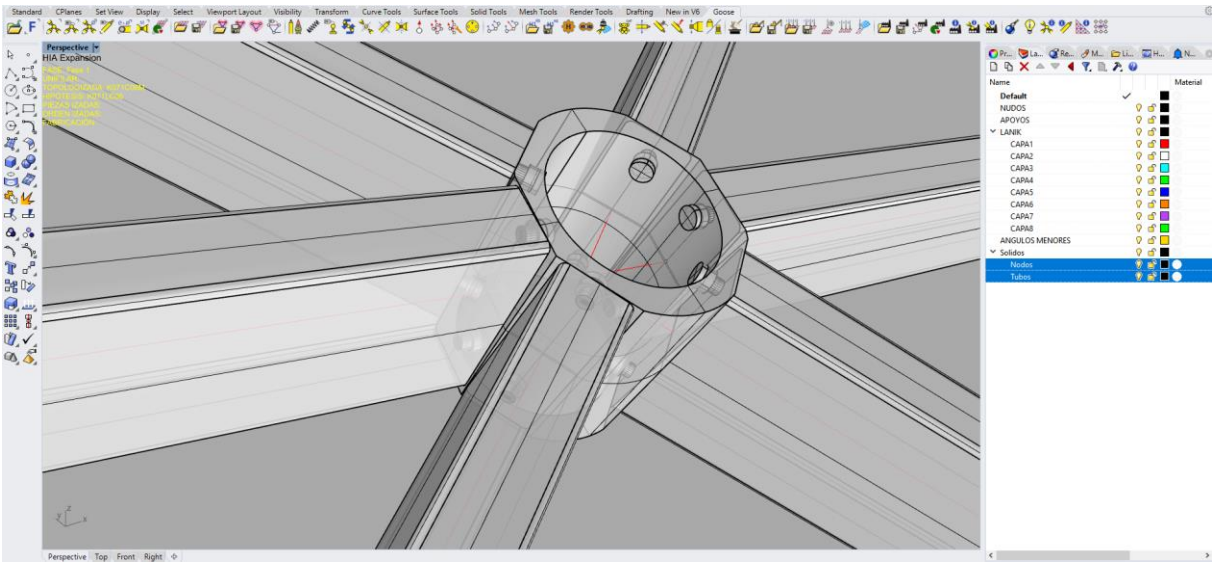


Figure 14: GOOSE Rhino plugin node automatic generation

5. Final aspect

The aesthetic result can be seen in the following pictures:



Figure 15: inside view



Figure 16: Inside view



Figure 23: Inside view of the lower part of the funnels

References

[1] J. Goñi and L. Irisarri, "Elastic-plastic behaviour of the SLO node for the second order calculation of the safety factor against global buckling in single layer structure", *IASS Symposium*, Wroclaw, Poland, 2013.

[2] L. Irisarri, J. Martínez and J. Goñi, "Past, present and future of the space frame Market: LANIK experience", *IASS Symposium*, Valencia, Spain, 2009

IASS 2023
July 10–14 Melbourne
Integration of Design and Fabrication

Proceedings of the IASS Annual Symposium 2023
Integration of Design and Fabrication
10–14 July 2023, Melbourne, Australia
Y.M. Xie, J. Burry, T.U. Lee and J. Ma (eds.)

Plastic buckling test of axially compressed aluminium latticed cylinders formed by 3D-printer

Tetsuo YAMASHITA*, Kohki UCHIDA[a]

* School of Architecture, Kogakuin University
tetsuo_y@cc.kogakuin.ac.jp

[a] Graduate School of Engineering, Kogakuin University

Abstract

Tubelike latticed cylindrical shells have come to be used as building column or tower. For the use as building columns, not only buckling strength but also post-buckling deformation capacity is sometimes required especially in earthquake-prone region. An experimental study was conducted to observe buckling and post-buckling behaviour of axially compressed latticed cylinder made of aluminium alloy. Two test bodies were fabricated using 3D-printer. Axially symmetric (elephant leg) buckling occurred in the test. However, the shell geometry had some considerable deviation from the anticipated flawless cylinder. 3D-scaned data of the test bodies were measured and analysed in the Grasshopper to specify the deviation and an FE models including the specified imperfection were constructed. The newly devised method to specify the initially distorted geometry is highlighted in the paper. The buckling behavior was traced using the FE models. The plastic buckling load is also evaluated by comparing to calculation based on the column-bucking concept using the generalized slenderness.

Keywords: latticed cylindrical shell, buckling, aluminium, 3D-printer, elephant leg buckling, experiment, 3D-scan

1. Introduction

Latticed cylindrical shells have been used to form airplane bodies because of good efficiency [1]. So far, buckling of latticed cylinders have been studied especially in the aircraft field and several experimental studies using various materials have been conducted. Chen et al calculated energy absorption on aluminium latticed cylinders for impact load using FE, and conducted axially loading test of 3D-printed ABS latticed cylinders for the validation of numerical analysis [2]. Kim[3] and Fan[4] also conducted axial compression test of latticed cylinders made of composite material. Graciano formed metal latticed cylinder with expanded metal sheet and conducted axial compression test focusing deformability [5]. However, though the load-deformation curves are shown in these papers, information on the test bodies such as geometric imperfection, dimension or nonlinear properties of material is not sufficiently described and the buckling strength is not evaluated at all.

On the other hand, in the architectural field, the use as building column or tower is becoming popular today (Figure 1). As such building structure, not only sufficient strength but also deformable capacity in the post-buckling path is sometimes required especially in earthquake-prone region. For understanding strong nonlinear phenomenon like buckling of metal shells, both experimental and analytical studies are required. However, experiments on large-scaled metal latticed shells consisting of members and joints, which have been carried out in the field of building construction [6,7], require a large amount of money and large-scaled facilities. Easier and cheaper experimental method is needed.

Copyright © 2023 by Tetsuo YAMASHITA and Kohki UCHIDA. Published in the Proceedings of the IASS Annual Symposium 2023 with permission.

To propose an easier and cheaper method on buckling test of metal latticed structures, the authors carried out buckling test of 3D-printed aluminium latticed cylinders that were axially loaded to buckle. This paper :

1) describes a buckling test carried out on two latticed cylinders, composed of hexagonal and triangular grid. The diameter, height and thickness were approximately 160mm, 100mm and 2mm, respectively.

2) demonstrates a method to build an FE model of the test bodies composed of beam elements, where the actual nodal coordinates were specified from the 3D-scanned data using functions of grasshopper. The FE models contained actual geometric imperfection and variation of member section.

3) reports the follow-up FE analysis. The maximum strength is also evaluated in accordance with a method proposed by the AIJ recommendation in which the generalized slenderness is used [8].

2. 3D-printed latticed cylinders

2.1. Anticipated geometry

Figure 1 illustrates the designed dimensions for the input of 3D-printer and the definition of the layer. Two latticed cylinders, composed of regular hexagon (called hereafter “Cylinder 1”) and equilateral triangle (“Cylinder 2”), were fabricated. The thickness and width of the anticipated member section in the two latticed cylinders were 2mm x 3mm and 2mm x 2mm, respectively. 16 and 20 were the number of circumferential division. To fix the upper and lower boundary, continuous 8mm bands were installed.

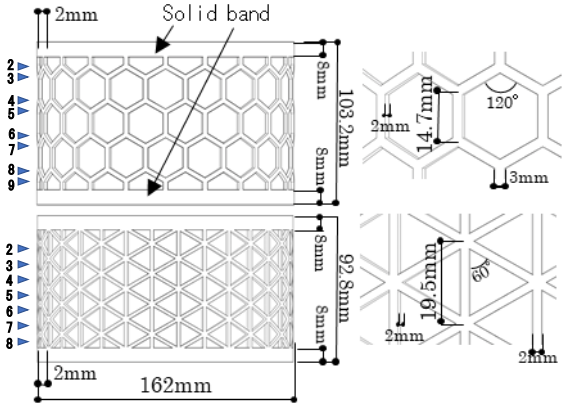


Figure 1. Designed geometry

2.2. Material

Aluminum alloy (AlSi10Mg) powder was used for the additive manufacturing. After completion of the 3D-printing, annealing was provided to improve ductility. Figure 2 illustrates the stress-strain diagrams. The tensile specimens were manufactured simultaneously to the latticed cylinders, where the direction of additive manufacturing was the same as the cylindrical axis. Despite annealing, the fracture strain was only up to 6%, approx. Table 1 contains approximated function of the s-s curves for the FE nonlinear analysis, in which the n-th power hardening law was assumed. In the S-S curve of the aluminium alloy, clear yield point cannot be not specified so that 0.2%-offset strength is used to determine the yield point.



Figure 2. Stress-strain diagram

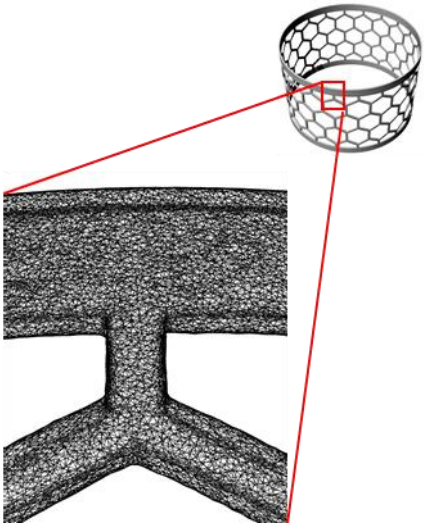
2.3 3D-scan of test bodies

The 3D-printed two-test bodies are shown in Figure 3(a). These were 3D-scanned to specify the actual geometry. The 3D-scanner can measure with the resolution of 85 μ m. The scanned geometry was output as a meshed surface data (Figure 3(b)). The meshed surface was not smoothed.





(a) Test bodies made of aluminum alloy



(b) 3D-scanned data

Figure 3. 3Dprinted cylinderical shells

2.4 Finding nodal points and geometry of latticed cylinders

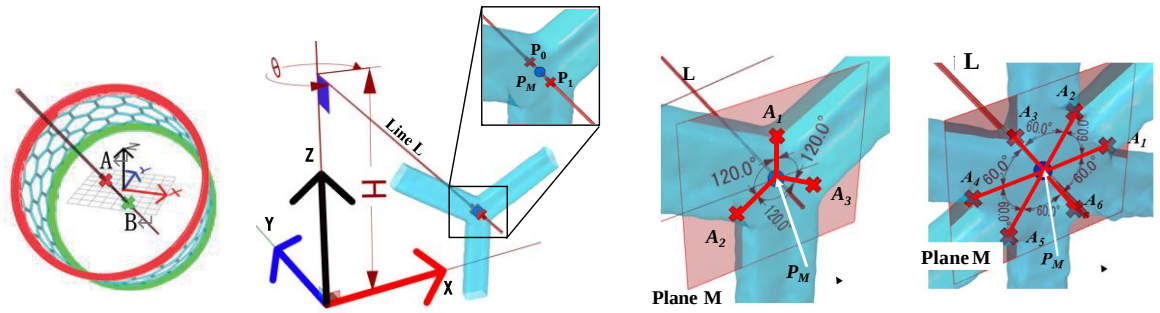
To construct a FE model composed of linear beam elements, the nodal points, connecting the elements, had to be specified from the scanned surface. To specify the nodal coordinates, the cylindrical axis, corresponding to the Z-axis of the Cartesian coordinate, had to be established.

Several previous researches [9 for example] demonstrates how to determine the cylindrical axis from many 3D points (dots) distributing to a cylindrical shape. However, these methods are not applicable so that a method using Galapagos, a component of Rhino+Grasshopper, was developed to specify the axis. The procedure on the Grasshopper is described as follows:

1) A temporary cylindrical axis is set as the line AB, between the centers of the top (A) and bottom (B) rigid belts (Figure 4(a)). Coordinate of A or B is determined as the average of the coordinates of vertices of the mesh within the belt. The Z axis corresponds to the cylindrical axis.

2) A line (*L*) perpendicular to the Z axis (=the cylindrical axis) is drawn which penetrates the nodal joints. The penetrating points on the inner and outer surfaces, and the midpoints between them are denoted as P_0, P_1 and P_M (Figure 4(b)) . The Z coordinate of the starting point of line L on the Z axis and the angle between the X axis and line L are denoted as H and θ.

3) Let *M* be the plane that contains P_M and is perpendicular to line *L*. For Cylinder 1, set a straight line parallel to the Z-axis on plane *M*, and let *A1* be the nearest intersection with the scanned surface. Next, set two straight lines forming an angle of 120° with this straight line on *M*, and set the intersection points with the scanned surface as *A2* and *A3*(Figure 4(c)). For Cylinder 2, set 6 straight lines starting from P_M on the plane *M* at 60° intervals, and set the intersection points with the scanned surface as *A1* to *A6*(Figure 4(d)).



(a) Temporary axis

(b) Penetration of L to scanned surface

(c) Intersection of radiating lines to scanned surface

(d)

Figure 4. Extract nodal points from 3D-scanned surface

4) Next, determine the coordinates of the nodal point P_M. Let J be the variance of the distance between P_M and A_i ($P_M A_i$).

$$J = \sum_{i=1}^{n} \left(P_M A_i - \overline{P_M A} \right)^2 \rightarrow \min \tag{1}$$

in which n is 3 for Cylinder 1 and 6 for Cylinder 2. $\overline{P_M A}$ is the average of $P_M A_i$. Using Galapagos (a Grasshopper plug-in, for optimization by GA), H and θ minimizing J are determined together with the coordinates of P_M. In the optimization, the points of A_i move depending on the location of P_M. This sequence of operations is performed for all nodes.

5) Determine the center of all the nodal points, specified by the step 4). Let the distance between the center O (x_o,y_o,z_o) and the i-th nodal points P_{Mi} be d_i. By minimizing the variance of d_i L, the coordinates of the center O are determined as step 4).

$$L = \sum_{i=1}^{N} \left(d_i - \overline{d_i} \right)^2 \rightarrow \min \tag{2}$$

in which N is the number of nodes. $\overline{d_i}$ is the average of d_i.

6) The latticed cylinder is subjected to further small rotation around the determined center O, to find more appropriate cylinderical axis for the initially distorted cylinder. Let α and β be the rotation about the X and Y axes, respectively. The rotated nodal coordinates are calculated by Eq.(3).

$$\left\{ \overline{x_i} \right\} = \left[R_y(\beta) \right] \left[R_x(\alpha) \right] \left\{ x_i \right\} \tag{3}$$

where $\left\{ \overline{x_i} \right\}$ and $\{x_i\}$ are the rotated and original i-th nodal coordinates. $[R_y(\beta)]$ and $[R_x(\alpha)]$ are the linear rotation matrix about Y and X axes, respectively. Then, a circle that approximates the projected nodal points to XY plane is determined by least square method.

$$\left(\overline{x_i} - a \right)^2 + \left(\overline{y_i} - b \right)^2 = {r_m}^2 \tag{4}$$

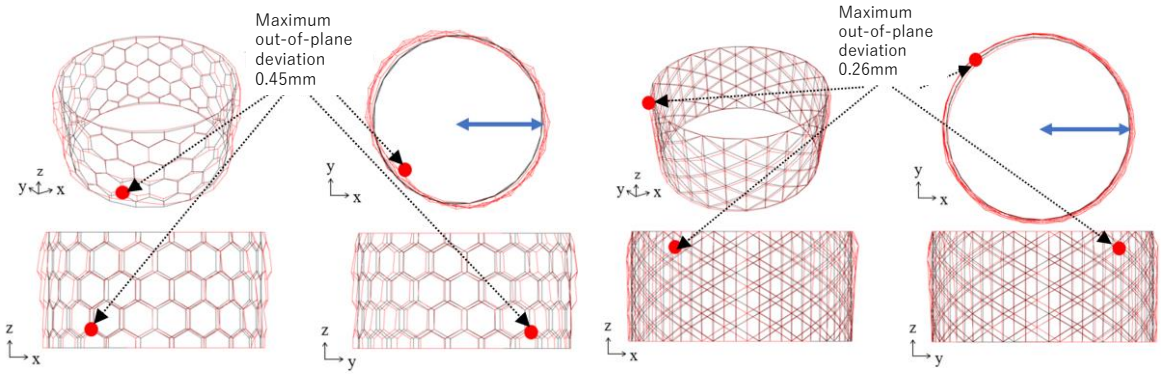
where a,b and r_m are the center and radius of the circle. Then the approximation error Q is defined by Eq.(5).

$$Q = \sum_{i=1}^{N} \left(\sqrt{(x_i - a)^2 + (y_i - b)^2} - r_m \right) \rightarrow \min \tag{5}$$

All the variables in Eq.(5) depend on α and β. Q is minimized changing α and β using Galapagos and then the Z axis is the most appropriate cylindrical axis. The origin have to be moved to $\{a,b,0\}$.

2.5 Out-of-plane imperfection

In Figure 5, the initially distorted geometry, specified applying the aforementioned procedure, is drawn by the red lines where the deviation is 20 times enlarged.



(Cylinder 1) (Cylinder 2)

Figure 5. Specified geometry including initial imperfection

The out-of-plane imperfection of the latticed cylinders was finally specified based on the optimized coordinate system for α and β. The out-of-plane deviation at the i-th node from the perfect cylinder is calculated using Eq.(6).

$$\delta_i = \sqrt{x_i^2 + y_i^2} - r_m \tag{6}$$

In Cylinder 1, the specified maximum out-of-plane deviation δ_{max} and radius r_m were 0.45mm and 80.15mm. δ_{max} was 0.56% of r_m. In Cylinder 2, these were 0.26mm and 79.22mm. δ_{max} was 0.33% of r_m.

2.6 Member section

The width and thickness of the member section (Figure 6) were also measured in the 3D-scanned data. Table 1 contains the dimensions. With respect to Cylinder 1, the fabrication dimensions were generally 10% less than the anticipated, while the width of the diagonal member in Cylinder 2 was 17% larger. The fabrication error on thickness was larger than that on width.

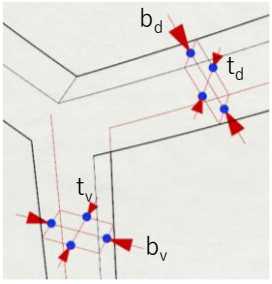


Figure 6. Width(b) and thickness(t) of diagonal(d) and vertical (v) member

Table 1 Section dimensions

				Designed dimension (mm)	Average (mm)	Fabricated/ Design	Maximum (mm)	Minimum (mm)	C.O.V
Cylinder 1	Vertical member	Width	b_v	3.00	2.74	0.91	2.82	2.66	0.015
		Thickness	t_v	2.00	1.74	0.87	1.83	1.68	0.016
	Diagonal member	Width	b_d	3.00	2.89	0.96	3.20	2.56	0.029
		Thickness	t_d	2.00	1.73	0.87	1.81	1.69	0.014
Cylinder 2	Vertical member	Width	b_v	2.00	1.98	0.99	2.32	1.89	0.044
		Thickness	t_v	2.00	1.58	0.79	1.69	1.53	0.018
	Diagonal member	Width	b_d	2.00	2.33	1.17	3.70	2.10	0.117
		Thickness	t_d	2.00	1.57	0.79	1.74	1.50	0.021

3. Bucking test

3.1 Setup

Figure 7 overviews the axial compression test setup. Mechanical displacement gauge was used to measure axial shrinkage, while nodal 3D displacement was measured using a non-contact 3D measurement system (VENUS3D Nobby-Tech. Ltd.). The applied load was monitored by the load-cell installed at the jackhead. Axial load was statically given by forced axial deformation (1.3mm/min).

Spherical washer was not installed between the jackhead and the test body to avoid instability in largely deformed state.

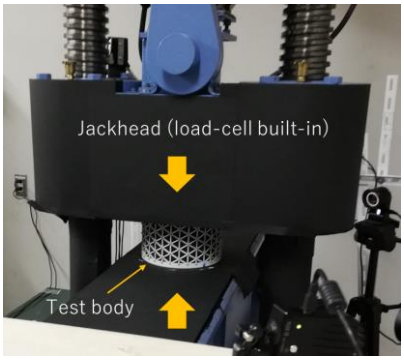
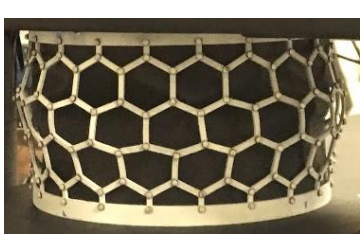


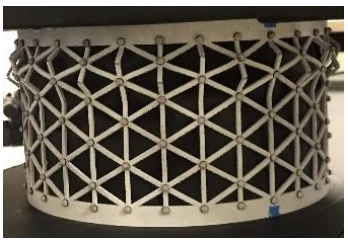
Figure 7 Test setup

3.2 Cylinder 1

Figure 8(a) shows the deformed test bodies. In Cylinder 1, axially symmetric deformation was observed where the out-of-plane deformation was maximum at the 5-6th layers. The load-deformation curve is illustrated in Figure 9(a), in which the axial shrinkage of the latticed portion is for the horizontal axis. The shrinkage was measured by the aforementioned 3D system.

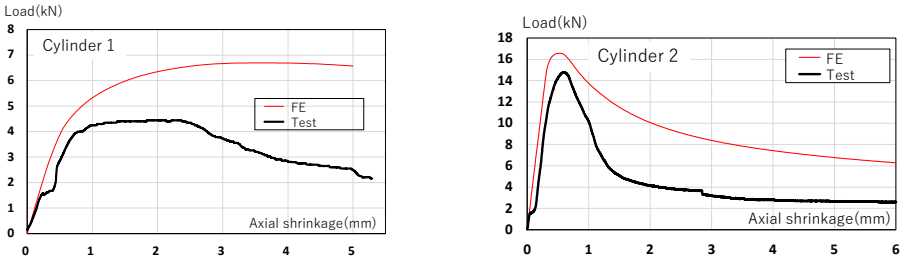


(a) Cylinder 1



(b) Cylinder 2

Figure 8 Observed buckling



(a) Cylinder 1 (b) Cylinder 2

Figure 9 Load-deformation curve (Test vs. FE)

As shown in the graph, the buckling behaviour was extremely nonlinear. Since hexagonal grid structures are bending-dominated, crack due to in-plane bending was observed at the shrinkage of about 1mm as illustrated in Figure 10. The load-deformation curve becomes flat during the shrinkage of 0.8～2.3mm.

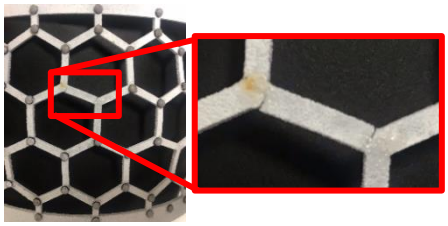
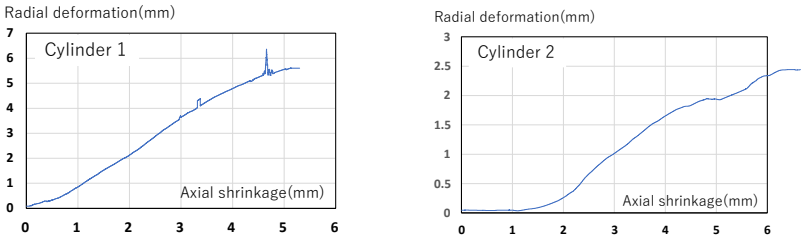


Figure 10 Crack due to in-plane bending

In spite of the strong nonlinearity, compatibility between axial and out-of-plane radial deformations was almost linear. The radial deformation gradually increased from the early stage (Figure 11(a)).



(a) Cylinder 1 (b) Cylinder 2

Figure 11 Axial vs radial deformation

3.3 Cylinder 2

As shown in Figure 8(b), the upper portion locally and extremely deformed, so-called “elephant-leg” buckling. The load-deflection curve is greatly different from that of Cylinder 1, where rapid degradation after the peak is observed in Figure 9(b).

Out-of-plane radial deformation was very small until the peak of axial strength, but it was remarkably developed in the post-buckling behavior after the peak (Figure 11(b)). The buckling wavelength was about 1.5 times of the member length. Severe crack on the buckled member was also observed in the post-buckling behavior.

4. Follow-up FE analysis

4.1 FE model

MSC-Marc[10] was used for geometrically and materially nonlinear FE analysis. Two kinds of FE model for a test body were constructed. These models are composed of linear beam-column elements. One (called Model_0, hereafter) is a latticed cylinder without geometric imperfection and scattering of section dimension. The radius was r_m, determined from the 3D-scanned data. Single member section of which the dimension was the average of the measured dimension indicated in Table 1. Another model (called Model_1) was a digital-twin of the test body, the FE model that imitated the actual geometry including imperfection and variable member section, which has been described in the previous section.

The top boundary of the latticed cylinders was completely fixed. For the bottom boundary, only displacement along the cylindrical generatrix was free and other D.O.F.s were fixed. Displacement control to the bottom boundary, similarly to the experiment, was given.

The stress and strain curves already shown in Figure 2 were used. One member was divided into 20 beam-column elements where shear deformation was considered.

4.2 Test and FE results

Figure 9 superposes two load-deformation curves, the test and FE results. The FE results is higher especially on Cylinder 1, where the maximum load is 1.6 times that of the test. This discrepancy of strength was guessed to be caused by the aforementioned crack observed in the test, which was out of consideration in the FE analysis. Figure 12 illustrates the increase of bending strain of a cracked vertical member, calculated in the FE analysis. The bending strain exceeds the failure strain when the axial shrinkage reaches 1.2mm. It can be related to that the load-deformation curve becomes flat after the shrinkage of about 1mm.

A better agreement is found for Cylinder 2. This is because the fracture occurs at the very large deformed state in the post-buckling path, and not near the maximum strength.

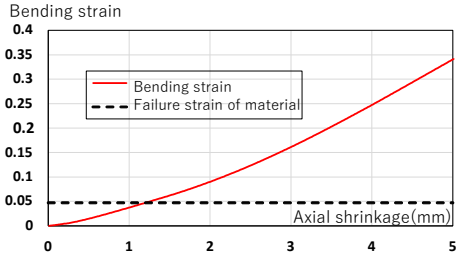


Figure 12 Strain due to in-plane bending

4.3 Eigenvalue analysis

Figure 13 illustrates the buckling modes and loads of Model 0 and 1 for each cylinder, obtained using the linear eigenvalue buckling analysis.

For Cylinder 1, the 1st linear buckling load of Model 1 (with geometric imperfection and variation of section properties) is 20.01kN, larger than 17.16kN of Model 0 (without imperfection). For Cylinder 2, 44.8kN of Model 1 is less than 50.0kN of Model 2. Generally, these buckling loads up to 5th are close.

The observed collapse deformation in the test was axially symmetric “elephant-leg-like” shape. However, except Model 0 of Cylinder 2, the buckling modes have circumferential buckling waves. In plastic buckling affected by material nonlinearity, a mode similar to the first-order linear buckling mode does not necessarily occur.

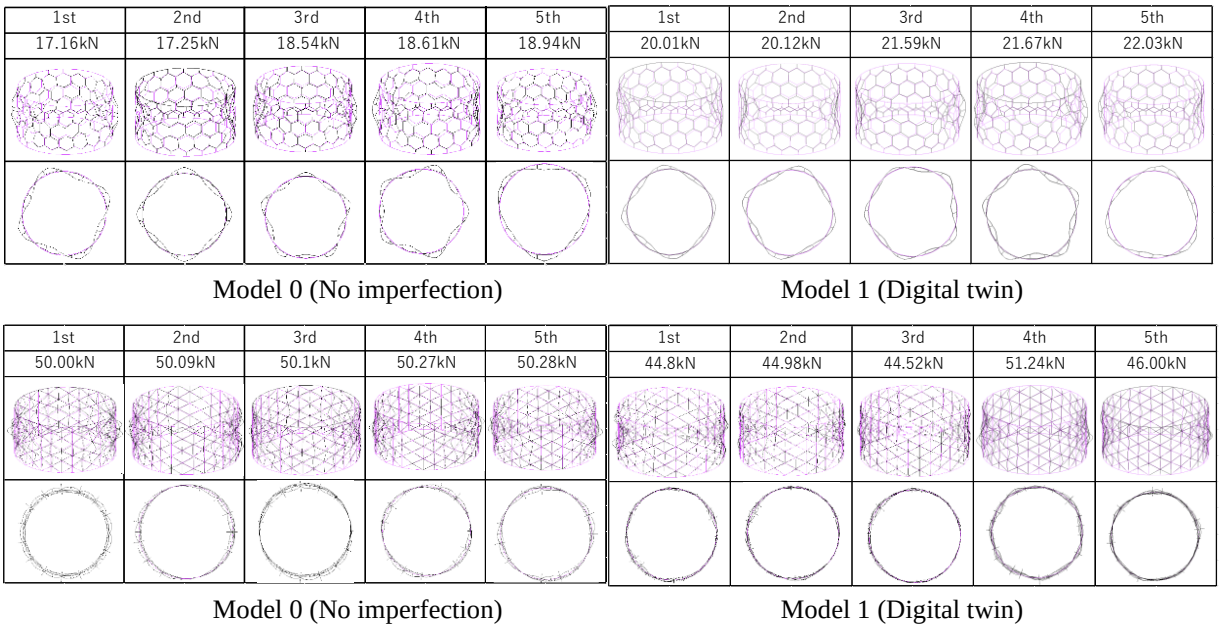


Figure 13 Linear buckling eigenmodes

4.4 Ultimate strength evaluation using generalized slenderness

The AIJ recommendation [8] provides a general concept to evaluate ultimate buckling strength of metal latticed shells. A formula to estimate ultimate buckling strength (P_{cr}) is given by Eq.(7).

$$\frac{P_{cr}}{P^{pl}} = \begin{cases} \dfrac{1-0.24\Lambda_s^2}{1+\dfrac{4}{15}\Lambda_s^2} & \left(\Lambda_s \le \dfrac{1}{\sqrt{0.6}}\right) \\ \dfrac{9}{13\Lambda_s^2} & \left(\Lambda_s > \dfrac{1}{\sqrt{0.6}}\right) \end{cases} \tag{7}$$

where P_{pl} is the yield strength obtained using so-called "pushover" analysis in which only material nonlinearity is taken into account in calculation. Λ_s is the generalized slenderness, defined by Eq.(8)

$$\Lambda_s = \sqrt{\frac{P_{pl}}{P_{cr}^{el}}} \tag{8}$$

$P_{cr}{}^{el}$ is the elastic nonlinear buckling load obtained geometric nonlinear incremental analysis, where yield is out of consideration. However, in the case of cylinderical shells subjected to axial compression, static nonlinear analysis applying Rik's arc-length method often becomes unstable especially in the post-buckling path. Thus a quasi-dynamic transient analysis [11] was employed to obtain $P_{cr}{}^{el}$, in which mass-proportional damping was used and the damping factor h_1=0.5. Figure 14 illustrates two kinds of load-deformation curves drawn by elastic nonlinear and "pushover" analysis.

The ultimate strength in the two tests fall in the vicinity of the estimation curve (Figure 15). However, the strength of Cylinder 1 might be much higher if bending crack did not occur.

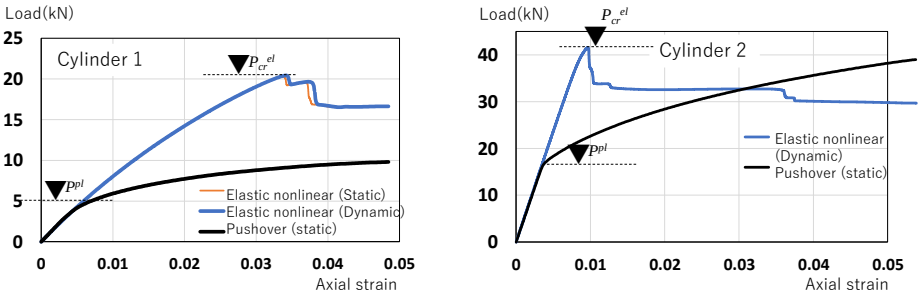


Figure 14 Elastic nonlinear and "pushover" analysis

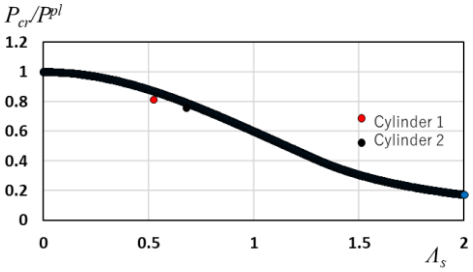


Figure 15 Ultimate strength evaluation using column-bucking concept

5. Conclusion

Two aluminium latticed cylinders were fabricated by 3D-printer with annealing to increasing ductility. One was composed of hexagonal and another was triangular grid. The cylinders were 3D-scaned and a methodology to specify the actual geometry, using Grasshopper, has been proposed in this paper.

The out-of-plane radial deviation in the 3D-printed geometry were 0.56 and 0.33 % of the specified radius for Cylinders 1 and 2, respectively. The variation in the section dimension was about 10% less than the anticipated.

Axially symmetric buckling was observed in both tests. The buckling wavelength of Cylinder 1 was longer than that of Cylinder 2 where localized "elephant-leg-like" protruding was observed. This is different from the 1st linear buckling eigenmode. Due to low ductility of the material, severe crack occurred, which reduced the strength especially in Cylinder 1.

The maximum load obtained in the follow-up FE analysis was larger than the test results, especially on Cylinder 1. This is guessed to be due to crack caused by in-plane bending in hexagonal lattice. The maximum strength was also evaluated by comparing to the calculation by the AIJ method using the generalized slenderness. The plotted strength is quite near the estimation curve.

Acknowledgements

This work was supported by JSPS KAKENHI Grant Number 18K04440.

References

[1] Vasiliev, Barynin, Rasin: Anisogrid lattice structures –survey of development and application, *Composite Structures*, No54, pp.361-370, 2001

[2] Chen, Zhang, Du, Zhoud, Liu, Guo, Li, Fang: Dynamic crushing behavior and energy absorption of graded lattice cylindrical structure under axial impact load, *Thin-Walled Structures*, Vol.127, pp.333-343, 2018.6

[3] Kim: Fabrication and testing of composite isogrid stiffened cylinder, *Composite Structures* Vol.45, pp.1-6, 1999

[4] Fan, Fang, Chen, Dai, Yang: Manufacturing and testing of a CFRC sandwich cylinder with Kagome cores, *Composites Science and Technology*, Vol.69, pp.2695-2700, 2009

[5] Graciano, Martı´nez, Smith: Experimental investigation on the axial collapse of expanded metal tubes, *Thin-Walled Structures*, Vol.47, pp.953–961, 2009

[6] Takashi Ueki,Yasuo Matsue,Shiro Kato,Seishi Yamada : Loading test and elastoplastic buckling load of unit single layer latticed domes, Journal of Struct Constr.Engng, AIJ,No.452, 1991 (in Japanese)

[7] Kenichi Sugizaki, Shigeru Kohmura and Yasuhiko Hangai :Experimental study on structural behavior of an aluminum single−layer lattice shell, Struct . Constr.Eng. AIJ , No.480, pp.113−122, 1996 (in Japanese)

[8] AIJ：*AIJ recommendation for design of latticed shell roof structures*, 2016 (in Japanese)

[9] Tetsuji Konno, Kouichi Konno, Column form extraction and shaft estimation using point cloud by 3D measurement: trial reconstruction of the south gate, outer fence of Shiwajo, Papers and proceedings of Japan Society for Archaeological Information, Vol.4, pp.17-24, 2007(in Japanese)

[10] MSC Software Inc.Marc 2017 Volume A Theory and User Information, 2017

[11] T.Yamashita and K.Kageyama, “Buckling and post-buckling behavior of axially compressed elastic latticed cylinders”, *Proceedings of the IASS2018 Boston* (full paper in CD), 2018.7

IASS 2023
July 10–14 Melbourne
Integration of Design and Fabrication

Proceedings of the IASS Annual Symposium 2023
Integration of Design and Fabrication
10–14 July 2023, Melbourne, Australia
Y.M. Xie, J. Burry, T.U. Lee and J. Ma (eds.)

State-of-the-art review of initial imperfection field simulation methods for single-layer gridshells

Shaojun ZHU[a,*], Qiang ZENG[a], Xu YANG[b], Chenyu WU[a]

[a,*] College of Civil Engineering, Tongji University
No. 1239 Siping Road, Yangpu District, 200092 Shanghai
zhushaojun@tongji.edu.cn

[b] Shanghai Construction No.4 (Group) Co., Ltd.

Abstract

The safety of single-layer reticulated shells depends largely on their buckling capacity, on which the initial geometric imperfections of joint deviations generated during the installation of the structure have a significant impact. By reviewing existing simulation methods on the initial geometric imperfection field of single-layer gridshells, it is concluded that existing stochastic, deterministic, and semi-stochastic simulation methods are all with deficiencies, and it is impossible to determine the real probability model of the buckling capacity of single-layer gridshells. This study proposes an initial imperfection field simulation method considering fabrication constraints, with reasonable basic assumptions and controllable computational costs, providing a scientific basis for improving the stability analysis method for single-layer gridshells and a theoretical foundation for the analysis of stability reliability.

Keywords: single-layer reticulated shells, initial geometric imperfection, simulation methods, buckling capacity

1. Introduction

Due to the advantages of small self-weight, excellent load-bearing performance, and strong individuality, single-layer gridshells (SLGs) have been widely used in China since the 1950s [1]. With the development of social economy and modern aesthetics, SLGs with larger spans and made of different materials have also become landmark buildings in various regions in recent years.

SLGs and continuous thin-shell structures share similarities in that they both resist external loads through internal forces within the shell plane, with the axial forces in the members being predominant [2]. To meet the requirements for clear height and drainage in the lower space, the shape of the shell is often designed as an arch to induce axial compression in the members. The load-bearing capacity of thin, flexible or long, slender compression structures is generally controlled by stability, and the global stability of the SLGs must be considered during its design. When the global stability of an SLG is lost, most joints will significantly deviate from their initial equilibrium positions, resulting in large-scale depressions or bulges on the shell surface and a loss of load-bearing capacity, ultimately leading to collapse and failure [3]. Thus, it is evident that the analysis of the global stability of an SLG exhibits strong non-linear characteristics.

All structural systems inevitably have initial imperfections, such as material, geometric, and physical imperfections, which can alter the stability of the perfect structure at its critical equilibrium point and significantly affect its load-bearing capacity [3]. In practical engineering, these initial imperfections are further classified according to their location and impact range as member imperfections, joint imperfections, and global structural imperfections [4].

Copyright © 2023 by Shaojun ZHU, Qiang ZENG, Xu YANG and *Chenyu WU. Published in the Proceedings of the IASS Annual Symposium 2023 with permission.*

Member imperfections mainly include geometric imperfections and residual stress imperfections. Geometric imperfections refer to the global or local deformation of components, such as initial bending [5−7], initial eccentricity [8], irreversible deformation, and section deformation. However, the component factory and site acceptance can easily eliminate these imperfections. Moreover, previous studies [7] have shown that the weakening effect of initial bending on the global stability and load-bearing capacity of a shell structure is less than 5% when meeting the acceptance standards.

Joint imperfections vary depending on the type of joint. For welded joints, common imperfections include weld cracks, incomplete penetration, and slag inclusion [9], while for bolted connections, common problems include looseness, fracture, and insufficient tightening. Similarly, these joint imperfections can be avoided by improving construction quality and increasing inspection frequency.

Global structural imperfections include random installation deviations of the designed surface shape, non-uniform structural settlement, and global tilting. Among these, the random installation deviation of the surface shape, which refers to the random initial deviation between the actual and design joint positions, is a significant factor that cannot be effectively avoided. Besides, this issue also has a major impact on the buckling capacity of SLGs [10−12]. Additionally, the evolution of the buckling capacity of SLGs under random initial geometric imperfections exhibits highly non-linear characteristics [13].

Currently, the modeling methods for the initial imperfection field of SLGs can be classified into four categories: field measurement, stochastic simulation, deterministic simulation, and semi-stochastic search. Field measurement primarily utilizes modern techniques (such as 3D scanning and optical measurement) to measure the precise values of the initial imperfections of the structure, but this method cannot be applied in the structural design phase. In this paper, we investigate the research status and development trends of three modeling methods for initial imperfection fields that can be used in the structural design phase and summarize the existing problems.

2. Stochastic simulation method

Since construction errors in SLGs are often random, their initial imperfections should also follow a stochastic distribution [2]. Therefore, a probabilistic simulation approach based on random search and probability theory is more suitable for evaluating the non-linear buckling capacity of imperfect gridshells [14]. Existing stochastic simulation methods mainly include the random imperfection method and the random field method.

2.1. Random imperfection method

The random imperfection method [2] (also known as the random imperfection modal method) assumes that the joint deviation amount $\Delta\mathbf{P}$ of an SLG, caused by random construction errors, follows a truncated normal distribution in the x, y, and z directions [15], and is mutually independent, can be expressed as

$$\begin{cases} \Delta\mathbf{P}_i = \left(\mathrm{d}x_i, \mathrm{d}y_i, \mathrm{d}z_i\right)^{\mathrm{T}} \\ \mathrm{d}x_i \sim N_{\mathrm{t}}\left(0, \sigma^2\right) \\ \mathrm{d}y_i \sim N_{\mathrm{t}}\left(0, \sigma^2\right) \\ \mathrm{d}z_i \sim N_{\mathrm{t}}\left(0, \sigma^2\right) \end{cases} \tag{1}$$

in which $\mathrm{d}x_i$, $\mathrm{d}y_i$, and $\mathrm{d}z_i$ represent the initial deviation of the ith joint (i = 1, 2, ..., n) in the x, y, and z directions, respectively. $N_{\mathrm{t}}(0, \sigma^2)$ denotes a truncated normal distribution with a mean of 0 and a variable range of $[-2\sigma, 2\sigma]$. Figure 1(a) shows the results of 10,000 samplings according to Eq. (1), which indicates that the generated joint deviations fall within a cube with a side length of 4σ. In Ref. [2], this method was applied to introduce 50 random initial imperfections in the gridshell experiment conducted

by Hu *et al*. [16]. The obtained average non-linear buckling capacity matched well with the experimental results.

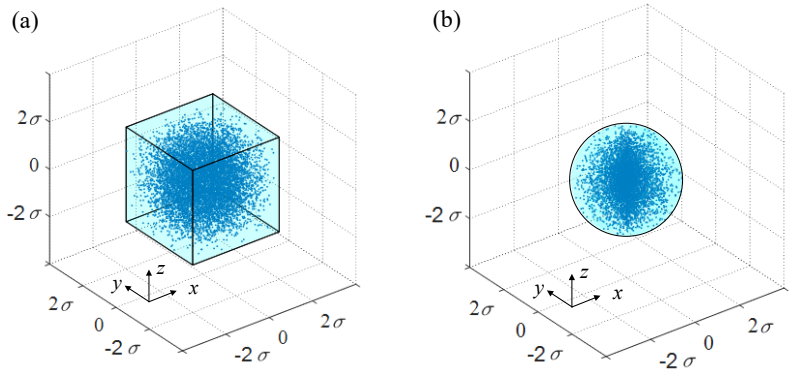


Figure 1. Sampling results of joint deviation of random imperfection method: (a) The method in reference [2], (b) The method in reference [18].

However, existing codes [17] often specify limits for the resultant deviation amplitude of joints $\|\Delta\mathbf{P}_i\|$:

$$\|\Delta\mathbf{P}_i\| = \sqrt{\mathrm{d}x_i^2 + \mathrm{d}y_i^2 + \mathrm{d}z_i^2} \le R_{\max} \tag{2}$$

where $R_{\max}$ is the limit value of the combined deviation of the joint. Thus, Sun [18] pointed out that the actual feasible domain of the initial deviation of each joint should be a sphere, and each directional component is calculated based on spherical coordinates:

$$\begin{cases} \mathrm{d}x_i = K_i \sin\gamma_i \cos\alpha_i \\ \mathrm{d}y_i = K_i \sin\gamma_i \sin\alpha_i \\ \mathrm{d}z_i = K_i \cos\gamma_i \end{cases} \tag{3}$$

in which K_i represents the amplitude of the resultant deviation amplitude of the ith joint, while γ_i (α_i) represents the angle between the bias direction (projection direction) and the positive direction of the local coordinate axis, as defined in Figure 2. According to reference [18], K_i should follow a truncated normal distribution, while γ_i and α_i should follow a uniform distribution U:

$$\begin{cases} K_i \sim N_{\mathrm{t}}\left(0, \sigma^2\right) \\ \gamma_i \sim U\left(0, 2\pi\right) \\ \alpha_i \sim U\left(0, 2\pi\right) \end{cases} \tag{4}$$

Unfortunately, this method is also unable to simulate actual joint deviation accurately. Figure 1(b) shows the 10,000 samples generated using Eqs. (3) and (4), indicating that although the feasible domain has been changed from a cube to a sphere, the generated joint deviations are significantly concentrated along the z-axis. This is because the spherical coordinate sampling method employed in Eqs. (3) and (4) cannot consider the non-uniform distribution of the spherical volume along the z-axis direction. Furthermore, from Eq. (3), it can be seen that although the maximum amplitude of each directional component is K_i, theoretically, the necessary condition for $\mathrm{d}x_i$ ($\mathrm{d}y_i$) to take the maximum amplitude is for $\sin\gamma_i$ and $\cos\alpha_i$ (or $\sin\gamma_i$ and $\sin\alpha_i$) to simultaneously take their amplitudes, while the necessary condition for $\mathrm{d}z_i$ is for $\cos\gamma_i$ to take the amplitude only.

On the other hand, Chen *et al*. [19] pointed out that the initial deviations between joints should be coupled due to the presence of members. Specifically, the fabrication errors in member length are generally on the order of millimeters [17, 20]. Considering the joint initial deviations independently will

lead to a significant deviation between the member length of the imperfect structure and its design length. If such deviations occur during the construction process, significant initial stress will appear in the member, and some members may enter the plastic state. Therefore, the initial deviations of the joints in the actual initial imperfection distribution are not independent random variables [21]. In order to consider the influence of member length on the coupling relationship between the initial deviations of joints, Du *et al*. [20] and Li *et al*. [22] proposed a stochastic imperfection method to simulate the initial deviations of joints under different member length deviations by heating and cooling the members. The methods proposed in Refs. [20, 22] also introduced the initial stress caused by member length deviation but did not discuss the specific magnitude of this initial stress or the reasonableness of the generated initial deviation amplitudes.

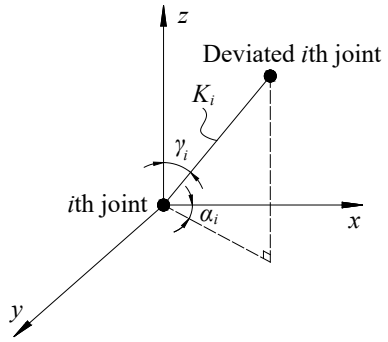


Figure 2. Spherical coordinate system parameters.

2.2. Random field method

To address the shortcomings of the random imperfection method, Chen *et al*. [19] and Liu *et al*. [23] proposed that the initial imperfections of SLGs can be regarded as a weakly homogeneous random field $B(\mathbf{P})$ with mean μ and variance σ^2, where $\mathbf{P} = (\mathbf{P}_1, \mathbf{P}_2, \ldots, \mathbf{P}_n)$ is the three-dimensional coordinate matrix of the gridshell joints, and $\mathbf{P}_i = (x_i, y_i, z_i)^{\mathrm{T}}$ is the three-dimensional coordinate vector of the ith joint. Assuming that the lengths of the grid shell members are equal, Ref. [19], based on experimental data, proposed that the correlation coefficient ρ_{ij} at the positions of the ith and jth joints in the random field $B(\mathbf{P})$ can be further assumed to exponentially decay with the minimum number of members S_{ij} between two joints, i.e.,

$$\rho_{ij} = \sqrt{\mathrm{e}^{-S_{ij}}} \tag{5}$$

Therefore, the correlation of initial deviations between joints caused by the topology of the gridshell can be considered through the covariance matrix $\mathbf{C}$:

$$\mathbf{C} = \left(c_{ij}\right)_{n\times n} \tag{6}$$

where c_{ij} is the covariance between the positions of joint i and j, calculated according to the following formula:

$$c_{ij} = \rho_{ij}\sigma^2 \tag{7}$$

Cholesky decomposition of $\mathbf{C}$:

$$\mathbf{C} = \mathbf{L}\mathbf{L}^{\mathrm{T}} \tag{8}$$

where $\mathbf{L}$ is the lower triangular matrix obtained by Cholesky decomposition. To determine the actual initial displacements of the joints, Chen *et al*. [19] assumed that the directions of the initial displacements were all in the outward direction of the shell plane. That is, each joint had an initial

displacement along the straight line of its normal vector. The vector of the magnitude of the initial displacement **r** is calculated as follows:

$$\mathbf{r} = \left(\left\|\Delta\mathbf{P}_1\right\|, \left\|\Delta\mathbf{P}_2\right\|, \ldots, \left\|\Delta\mathbf{P}_n\right\|\right)^{\mathrm{T}} = \mathbf{L}\boldsymbol{\kappa} + \boldsymbol{\mu} \tag{9}$$

where $\boldsymbol{\kappa} = (K_1, K_2, \ldots, K_n)^{\mathrm{T}}$ T is the magnitude vector of the resultant deviation of the joints subject to the standard normal distribution, $\boldsymbol{\mu} = (\mu)_{n\times 1}$ is the mean vector of random field $B(\mathbf{P})$.

Based on numerical examples of Kiewitt-type single-layer spherical gridshells, Ref. [19] compared the stochastic field method with the stochastic imperfection method and pointed out that the imperfect structure obtained by the former has significantly smaller non-linear buckling capacity variability.

3. Deterministic simulation method

The computational cost of stochastic simulation methods is generally high. Deterministic simulation methods rely on physical concepts and introduce displacement trends during structural buckling as the *most unfavorable initial imperfection distribution pattern*. These displacement trends include both non-linear and linear buckling modes. For clarity, Figure 3 presents an example of the load-displacement curve for a typical SLG under vertical loading, where Λ is the load coefficient, δ is the resultant displacement of the critical joint at buckling, and point *A* represents the first critical point of the structure.

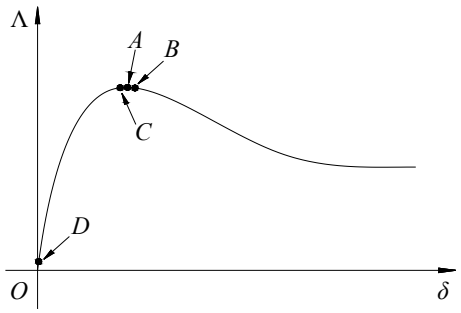


Figure 3. Example of the load-displacement curve of a typical perfect SLG.

3.1. Consistent imperfection modal method

In 1992, Chen and Shen [24] proposed that the displacement trend at the first critical point of the load-displacement curve of SLGs (i.e., the non-linear buckling mode) could be a possible *most unfavorable initial imperfection distribution pattern*. The non-linear buckling mode can be calculated based on the displacement difference before and after structural buckling (points *A* and *B* in Figure 3) or through linear buckling analysis approximation before the critical point (point *C* in Figure 3). Based on the computational results of a single-layer spherical gridshell example, Ref. [24] indicated that the non-linear buckling capacity of the imperfect structure introduced by this method was consistent with the lowest value obtained by the random imperfection method under the same amplitude. However, the authors did not provide specific methods for determining the imperfection amplitude in the paper, nor did they discuss the practicality of the imperfection distribution.

Cao [25] pointed out the high cost of solving non-linear buckling modes. Therefore, the lowest-order linear buckling mode of the structure near its initial state (point *D* in Figure 3) can be used as the initial imperfection distribution pattern. Ref. [25] termed this method the *eigenmode imperfection method* and indicated that it also falls within the category of the *consistent imperfection modal method*. Numerical results show that the consistent imperfection modal method can provide a non-linear buckling capacity of imperfect structures extremely close to those obtained by the traditional eigenmode imperfection method under the same amplitude.

Fan *et al*. [26] and Xiong *et al*. [27], based on the eigenmode imperfection method, conducted numerical analyses on the non-linear buckling capacity of Kiewitt-type single-layer steel and aluminum alloy

gridshells with different imperfection amplitudes. They pointed out that when the imperfection amplitude is greater than $L/300$ (where L is the span), the non-linear buckling capacity of the structure will not be further reduced. Therefore, it is suggested in Refs. [26, 27] that when analyzing the non-linear buckling capacity of imperfect SLGs using the lowest-order linear buckling mode, the imperfection amplitude should be conservatively taken as $L/300$.

3.2. *N*-order eigenmode imperfection method

Based on numerical analysis, Cai *et al*. [28] pointed out that the lowest-order linear buckling mode is not necessarily the *most unfavorable initial imperfection distribution pattern* for Kiewitt-type grid shells with relatively large height-to-span ratios, and the corresponding imperfect structure has lower stability reliability. Considering that the eigenvalues (i.e., linear buckling coefficients) corresponding to the linear buckling modes of SLGs are quite dense, Ref. [28] suggests that the first N linear buckling modes of an SLG should be used to simulate the initial imperfection distribution patterns to obtain N non-linear buckling capacities of the imperfect structures. The minimum value among them should be taken to evaluate the non-linear buckling capacity of the structure. By comparing the results obtained by the N-order eigenmode imperfection method and the random imperfection method, Ref. [28] believes that the stability reliability of the imperfect structure obtained by the N-order eigenmode imperfection method can meet the requirements of actual engineering under the same imperfection amplitude when N is 20.

However, many scholars have questioned the rationality and effectiveness of deterministic simulation methods. Liu *et al*. [29] and Cai *et al*. [30] pointed out that the imperfection amplitude $L/300$ determined in Ref. [26] is significantly larger than the limit value $L/1500$ specified in the code [17] for local surface depressions of gridshells. It is worth mentioning that since this amplitude is significantly larger, the length of the structural members of the imperfect structure will also differ significantly from their design length, and the simulated initial imperfection is non-realistic, i.e., the initial imperfection cannot occur in actual engineering. Bruno *et al*. [31] used the eigenmode imperfection method to conduct numerical analysis on a meridian gridshell. The results showed that different linear buckling modes of different orders (as initial imperfection patterns) would induce lower non-linear buckling capacities of the structure under different amplitudes, indicating that a single linear buckling mode cannot represent the most unfavorable initial imperfection distribution pattern. This conclusion is consistent with the analysis results of Huang and Zhao [32] on small gridshells. In addition, when a specific-order linear buckling mode is used as the initial imperfection pattern, the non-linear buckling capacity of the imperfect structure does not monotonically decrease with the increase of the imperfection amplitude. Zhu *et al*. [13] pointed out that the mathematical essence of the linear buckling mode is the eigenvector, so the positive and negative linear buckling modes can be separately applied as initial imperfections to the perfect structure, and numerical analysis results show that there can be significant differences in the non-linear buckling mode and buckling capacity of the two imperfect structures. Therefore, Ref. [13] pointed out that the imperfection pattern has a significant impact on the non-linear buckling performance and explored the impact of different-order positive and negative linear buckling modes on the imperfection pattern and non-linear buckling capacity based on supervised learning methods.

4. Semi-random search method

4.1. Heuristic search method

From a theoretical perspective, there exists a highly non-linear relationship between the design parameters of a structure and its non-linear buckling capacity. Although various meta-models or surrogate models (such as response surface approximation and Kriging interpolation [33]) can approximate the structural response as a function of the design parameters, their ability to handle highly non-linear problems is limited. Therefore, some scholars regard *finding the most unfavorable initial imperfection* as an optimization problem to directly establish the relationship between the initial imperfection parameters (unknown variables) and the non-linear buckling capacity (objective function):

$$\begin{cases} \text{find} & \Delta\mathbf{P} \\ \text{min.} & \Lambda \\ \text{s.t.} & g\left(\Delta\mathbf{P}\right) \le 0 \end{cases} \tag{10}$$

where $\Delta\mathbf{P} = (\Delta\mathbf{P}_1, \Delta\mathbf{P}_2, \ldots, \Delta\mathbf{P}_n)^{\mathrm{T}}$ denotes the initial deviation matrix of three-dimensional coordinates at each joint of an SLG; n is the total number of joints; $g(\Delta\mathbf{P}) \le 0$ represents the constraint that the initial deviation of three-dimensional coordinates at each joint must satisfy.

Luo *et al*. [34], Karmi and Kani [35] utilized particle swarm optimization and genetic algorithm, respectively, to solve the optimization problem, and the results showed that these heuristic algorithms could provide lower non-linear buckling capacity than deterministic simulation methods and random imperfection method under a certain amount of computation.

However, it should be noted that the numerical examples used to verify the proposed algorithms in Ref. [34] are SLGs with few joints. Although heuristic algorithms have global search capabilities, their computational cost will significantly increase with the problem size, and there is a problem of premature convergence to local optimums [36]. Moreover, heuristic algorithms are generally based on intuitive experience and lack mathematical foundations such as convergence theory and complexity evaluation systems [37]. Therefore, heuristic algorithms are generally used to provide feasible solutions for complex problems at an acceptable computational cost but cannot guarantee that the obtained solution is the global optimum.

4.2. Stochastic imperfection modal superposition method

Liu *et al*. [38] considered the influence of higher-order linear buckling modes on the non-linear buckling capacity of structures. They indicated that the actual imperfection distribution pattern of the structure: $\Delta\mathbf{P}' = \left(\Delta\mathbf{P}_1', \Delta\mathbf{P}_2', \ldots, \Delta\mathbf{P}_n'\right)^{\mathrm{T}}$ can be represented as a random linear combination of linear buckling modes:

$$\begin{cases} \Delta\mathbf{P}' = \sum_{j=1}^{m} r_j \boldsymbol{\varphi}_j \\ r_j \sim U\left(-1,1\right) \end{cases} \tag{11}$$

where m is the order of linear buckling modes involved in the combination, r_j is the participation coefficient of the jth (j = 1, 2, ..., m) linear buckling mode, $\boldsymbol{\varphi}_j = (\mathbf{u}_{j,1}, \mathbf{u}_{j,2}, \ldots, \mathbf{u}_{j,n})^{\mathrm{T}}$ is the jth linear buckling mode of the perfect SLG, $\mathbf{u}_{j,i} = (\Delta x_{j,i}, \Delta y_{j,i}, \Delta z_{j,i})$ is the three-dimensional displacement vector of the ith joint under the jth mode, and $U(-1, 1)$ is a uniform distribution on the interval [−1, 1]. The actual imperfection distribution $\Delta\mathbf{P}$ can be calculated by adjusting the amplitude of $\Delta\mathbf{P}'$, i.e.,

$$\Delta\mathbf{P} = \frac{R_{\max}\Delta\mathbf{P}'}{\max\limits_{i}\left\|\Delta\mathbf{P}_i'\right\|} \tag{12}$$

Based on numerical examples of hexagonal single-layer flat gridshells, it has been verified that the stochastic imperfection modal superposition method can achieve a lower non-linear buckling capacity compared to the random imperfection method and the eigenmode imperfection method. Therefore, the reference [38] argued that the stochastic imperfection modal superposition method could provide the *worst initial imperfection* of the structure.

Similarly, Zhao *et al*. [39] combined the consistent imperfection modal method and the random imperfection method, decomposed the random initial imperfections of the structure based on the theory of random fields, and projected them onto the standard orthogonal basis of the structural linear buckling modes. Lu and Zhang [40] proposed a method for determining the worst initial imperfection of single-layer spherical gridshells based on the convex model, where the initial imperfection is also expressed as

a linear combination of the first *N*-order linear buckling modes. Through the analysis of a Kiewitt SLG example, Refs. [39] and [40] indicated that the proposed methods could give the *worst initial imperfection* at a lower computational cost.

However, the probability distribution of the non-linear buckling capacity of the imperfect structures obtained by the above methods has not been provided, and the basic assumptions of the random imperfection method used for verification are problematic (see section 2.1), making it difficult to determine the true probability characteristics of the analysis results and to ensure that the obtained imperfection is the *worst initial imperfection*. At the same time, the number of linear buckling modes *m* involved in the combination, and the specific modes combined will significantly affect the calculation results, and artificially adjusting these parameters will lead to a significant increase in workload and computational cost.

5. Initial imperfection field simulation method considering fabrication constraints

To solve the problems existing in the above methods, we propose a simple and efficient method to generate stochastic initial geometric imperfections for SLGs considering fabrication constraints by abstracting the gridshell into an equivalent particle-spring-particle system, and introducing non-linear heuristically perturbed virtual interaction forces, as shown in Figure 4.

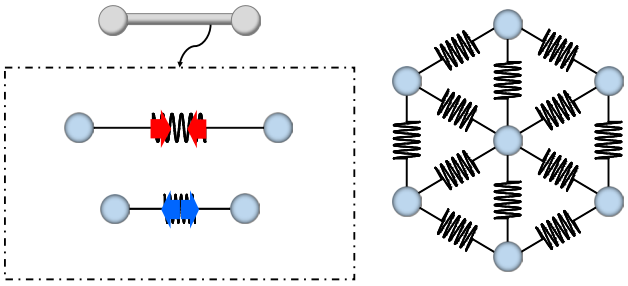


Figure 4. Illustration of the proposed method. (a) Virtual interaction forces. (b) Equivalent system.

To address the unrealistic distribution of random joints, the method assumes that the magnitude of the resultant joint deviation obeys $N_t(\mu, \sigma^2)$, while its components obey the uniform distribution. Specifically, the following procedures are used for generating the independent stochastic 3D joint deviations:

S1 Generate a unit uniformly-distributed direction vector for the *i*th joint $\mathbf{n}_i$ as

$$\begin{cases} \mathrm{d}x_i \sim U(-1,1) \\ \mathrm{d}y_i \sim U(-1,1) \\ \mathrm{d}z_i \sim U(-1,1) \\ \mathbf{n}_i = \dfrac{1}{\sqrt{\mathrm{d}x_i^2 + \mathrm{d}y_i^2 + \mathrm{d}z_i^2}} (\mathrm{d}x_i, \mathrm{d}y_i, \mathrm{d}z_i) \end{cases} \tag{13}$$

where $U(-1, 1)$ is the uniform distribution with an interval of $[-1, 1]$;

S2 Sample the amplitude of the resultant joint deviation of the *i*th joint m_i according to the truncated normal distribution as

$$m_i \sim N_t(\mu, \sigma^2) \tag{14}$$

S3 Calculate the actual joint deviation of the *i*th joint $\Delta\mathbf{P}_i$ as

$$\Delta \mathbf{P}_i = m_i \mathbf{n}_i \tag{15}$$

Considering the fabrication constraints of SLGs, we introduce virtual intercation forces (VIFs) to modify the unrealistic initial geometric imperfections pattern. The stiffness of the *j*th virtual non-linear spring K_j, corresponding to the *j*th member in the structure, can be expressed as

$$K_j = \frac{k_c}{l_{j,0} - \left| l_{j,0} - l_j \right|} \tag{16}$$

where $l_{j,0}$ and l_j are the design and actual lengths of the *j*th member, respectively; k_c is the dimensionless constant stiffness factor. This way, the VIF of the spring at the *j*th member F_j can be calculated as

$$F_j = K_j \left(l_j - l_{j,0} \right) \tag{17}$$

The complex topological relationship in SLGs can be implicitly considered by calculating the resultant virtual force at each joint as

$$\mathbf{T}_i = \sum_{j \in \Pi_i} \mathbf{F}_j \tag{18}$$

where $\mathbf{T}_i$ is the resultant virtual force vector at the *i*th joint; Π_i is the set of members connected to the *i*th joint; $\mathbf{F}_j$ is the virtual force vector of the spring at the *j*th member. Note that the magnitude of $\mathbf{F}_j$ is F_j, and its direction is along with the *j*th member.

In the proposed method, the joint coordinates in the equilibrium state are updated using the forward Euler method [41]. The joint coordinates **P** are assumed to be dependent on an artificial concept of time *t*. Furthermore, the proposed method introduced a perturbation VIF based on the firefly algorithm [42] in iterative equation expressed as

$$\mathbf{P}_i^{(k'+1)} = \mathbf{P}_i^{(k')} + \beta_i^{(k')} \Delta t \mathbf{T}\left[\mathbf{P}_i^{(k')} \right] + \alpha_i \Delta \mathbf{P}_i' \tag{19}$$

Denote $t_k = k\Delta t$ as the artificial time at the equilibrium state, in which Δt is the artificial time step and k is the iteration step. $\mathbf{P}^{(k)}$ is the joint coordinate matrix at the kth iteration step, $k' = 0, 1, 2, \ldots, k-1$. $\mathbf{P}_i^{(k'+1)}$ is the coordinates of the *i*th joint at the (k'+1)th step. Furthermore, the random time step factor of the *i*th joint at the k'th iteration step is expressed as $\beta_i^{(k')}$, which obeys $U(0, 1)$; α_i is the perturbation factor of the *i*th joint; $\Delta \mathbf{P}_i'$ is a random joint deviation vector.

To illustrate the effectiveness of the above method, 1,000 stochastic IGIs are generated for a Kiewitt-6 (K6) steel SLG using the initial imperfection field simulation method considering fabrication constraints. Its parameters are described as follows:

1) Span: L = 40 m;
2) Height-to-span ratio: f/L =1/4;
3) Number of rings: m = 8;
4) Joint system: welded spherical joints;
5) Support condition: pinned supports located at the joints along the periphery, i.e., the stochastic joint deviations are only introduced to the 169 internal joints.

The histograms of the resultant joint deviations $\|\Delta \mathbf{P}_i\|$ and the length deviations of the members Δl_j in the 1,000 stochastic IGIs generated by the above methods are shown in Figure 5.

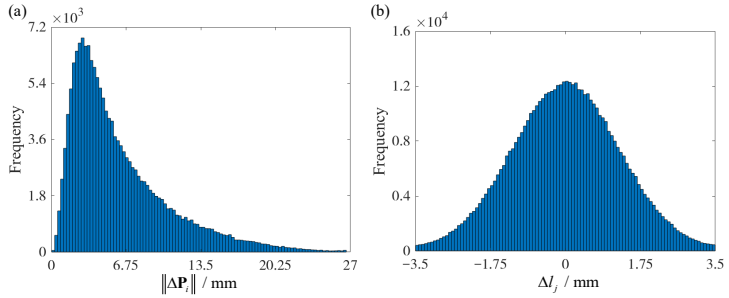


Figure 5. Distributions of 1,000 stochastic IGIs. (a) distributions of $||\Delta\mathbf{P}_i||$. (b) distributions of Δl_j.

As depicted in Figure 5, the distribution of $||\Delta\mathbf{P}_i||$ generated by the initial imperfection field simulation method considering fabrication constraints exhibits a high degree of concentration. It is also notable that the distribution of $||\Delta\mathbf{P}_i||$ generated by this method is the densest, around 2.800 mm. The amplitude of the joint deviation is taken as L/1,500 (i.e., 26.6 mm). Meanwhile, the distribution of Δl_j generated by this method is approximate to normal distribution. Manufacturing error is taken as 3.5 mm; obviously, $|\Delta l_j|$ of all members in the IGIs generated by the above method can strictly satisfy the manufacturing error constraint.

6. Conclusion

1) The random imperfection method suffers from an inherent lack of rationality in sampling the initial deviations of single joints and ignores the influence of the topology of the shell structure on the coupling relationship of the initial deviations of each joint. As this method may generate non-actual initial imperfections, although previous studies have shown good agreement between the non-linear buckling capacity values obtained and experimental results, it cannot be directly used statistically to determine the probability model of the actual buckling capacity or stability reliability;

2) The random field method considers the influence of the topology of the shell structure on the coupling relationship of the initial deviations of joints by making fundamental assumptions, thereby reducing the search range of the random imperfection method and lowering the discreteness of the obtained non-linear buckling capacity. However, this method does not directly consider the constraint effect of the topology of the shell structure. It completely ignores the initial deviation component of the joints in the plane of the shell structure while also including many simplified calculation assumptions. Therefore, although the random field method has certain theoretical significance, the probability model of the non-linear buckling capacity of the shell structure determined using this method is still not accurate;

3) The deterministic simulation method can provide a relatively conservative estimation of the non-linear buckling capacity of a structure based on physical background with lower computational costs. However, the simulated initial imperfections are not actual, and the introduced imperfection amplitude is significantly larger than the construction acceptance limit. Thus, this method cannot determine the probability characteristics of the obtained buckling capacity in the real probability distribution and cannot accurately determine the stability reliability of the structure;

4) The semi-stochastic search method can obtain the initial imperfections corresponding to relatively low non-linear buckling capacity at a certain computational cost but cannot determine the probability characteristics of the obtained non-linear buckling capacity.

5) A stochastic geometric initial imperfection simulation method that takes into account the coupling relationship between the initial geometric deviation of joints and the fabrication constraints of the structure (i.e., the influence of member lengths) is proposed. Theoretically, it has an acceptable computational cost for practical engineering applications. This method will provide a scientific

basis for improving the global stability analysis method for SLGs and a theoretical foundation for analyzing their stability reliability.

References

[1] Dong S, Yao J, "The future and prospects of reticulated shell structures," *Spatial Structures*, 1994, 1(1): 3-10. (in Chinese)
[2] Shen S, Chen X, *Stability of Reticulated Shell Structures*, Beijing: China Science Publishing& Media Ltd, 1999. (in Chinese)
[3] Luo Y, Han Q, Li H, *Stability of Steel Structures-The Theory and Implement*, Beijing: China Communications Press, 2010. (in Chinese)
[4] Yang X, Luo Y, Liu J, *et al*., "Research progress on damage detection and simulation methods for existing grid structures," *Progress in Steel Building Structures*, 2021, 23(2): 1-13+21. (in Chinese)
[5] Zhang T, *Refined analysis on dynamic performance and damage assessment of single-layer spherical reticulated dome under strong earthquake*, Tianjin: Tianjin University, 2018. (in Chinese)
[6] Xiao Y, Li H, "Effect of member curvature on load-carrying capacity of single-layer cylindrical reticulated shell with semi-rigid joint," *Progress in Steel Building Structures*, 2020, 22(1): 69-77. (in Chinese)
[7] Fan F, Yan J, Cao Z, "Stability of single-layer reticulated domes with initial imperfection to members," *Journal of Southeast University (Natural Science)*, 2009, 39(S2): 158-164. (in Chinese)
[8] Jiang S, Li H, Long T, "Stability of single-layer three-way reticulated barrel vaults considering global geometric imperfection, member imperfection and eccentricity," *Engineering Mechanics*, 2022, 39(2): 178-188. (in Chinese)
[9] Liu Y, *Mechanical behavior of joints and its influence on stability and progressive collapse resistance of single layer latticed shells*, Tianjin: Tianjin University, 2018. (in Chinese)
[10] Li Z, "Effects of initial geometrical imperfections on dynamic stability of reticulated shell structures," *China Civil Engineering Journal*, 2002, 35(1): 11-14+24. (in Chinese)
[11] Tang G, Wang F, Wu J, "Stability analysis of long-span single-layer latticed domes with stochastic geometric imperfections," *Steel Construction*, 2008, 23(5): 1-6. (in Chinese)
[12] Li H, Wang C, Xiao Y, "Effect of random nodal deviation and member eccentricity on load-carrying capacity of single-layer dome," *Journal of Building Structures*, 2020, 41(2): 134-141. (in Chinese)
[13] Zhu S, Ohsaki M, and Guo X, "Prediction of non-linear buckling load of imperfect reticulated shell using modified consistent imperfection and machine learning," *Engineering Structures*, 2021, 226: 111374.
[14] Ikeda K and Ohsaki M, "Generalized sensitivity and probabilistic analysis of buckling loads of structures," *International Journal of Non-Linear Mechanics*, 2007, 42(5): 733-743.
[15] Tang G, Li D, Zhao C, Zhao H, "Statistical regulation and parameter study on initial geometrical imperfections of spatial structures based on measured data," *Building Structure*, 2008, 38(2): 74-78. (in Chinese)
[16] Hu X, Qin X, Li L, Zhong Z, Li G, Hu G, "Experimental study on stability of domed reticulated shells," *Proceedings of the Fourth Academic Exchange Conference on Space Structures (Volume 2)*, Chengdu: Space Structures Committee of China Civil Engineering Society Bridge and Structure Engineering Society, 1988: 465-470. (in Chinese)
[17] Ministry of Housing and Urban-Rural Development of the People's Republic of China, "Technical specification for space frame structures," JGJ7-2010, 2010. (in Chinese)
[18] Sun Y, *Stability analysis and bearing capacity prediction of K6 aluminum alloy reticulated shell with random defects*, Xi'an: Xi'an University of Architecture and Technology, 2021. (in Chinese)
[19] Chen G, Zhang H, Rasmussen K J R, and Fan F, "Modeling geometric imperfections for reticulated shell structures using random field theory," *Engineering Structures*, 2016, 126: 481-489.

[20] Du X, Yan Y, Yan P, Liu W, Cheng X, "Length deviation tests on structural members of space latticed structures," *Spatial Structures*, 2016, 22(2): 44-49+87. (in Chinese)
[21] Liu J, Luo Y, Zhang Y, "Correlation of the geometric imperfection of Kiewit single-layer latticed spherical shell," *Journal of Tianjin University* (*Science and Technology*), 2020, 53(5): 535-541. (in Chinese)
[22] Li H, Xiao Y, Xiong H, Zhang K, "Effect of random member length error on load-carrying capacity of K6 single-layer reticulated dome," *Spatial Structures*, 2019, 25(3): 30-37. (in Chinese)
[23] Liu Y, Cui X, Li Y, Hong H, "Reliability analysis of stability of latticed shell structure considering initial geometric imperfections," *China Civil Engineering Journal*, 2021, 54(7): 12-23. (in Chinese)
[24] Chen X, Shen S, "Load-displacement process and imperfection analysis of single-layer geodesic domes," *Journal of Building Structures*, 1992, 13(3): 11-18. (in Chinese)
[25] Cao Z, *Elastic-plastic stability of reticulated shells*, Harbin: Harbin Institute of Technology, 2007. (in Chinese)
[26] Fan F, Cao Z, and Shen S, "Elasto-plastic stability of single-layer reticulated shells," *Thin-Walled Structures*, 2010, 48(10-11): 827-836.
[27] Xiong Z, Guo X, Luo Y, and Zhu S, "Elasto-plastic stability of single-layer reticulated shells with aluminium alloy gusset joints," *Thin-Walled Structures*, 2017, 115: 163-175.
[28] Cai J, He S, Jiang Z, Liu Q, Zhang Y, "Investigation on stability analysis method of single layer latticed shells," *Engineering Mechanics*, 2015, 32(7): 103-110. (in Chinese)
[29] Liu X, Zhang A, Ge J, Wang L, Qi Z, "Study on the influence of construction deviation random distribution on the integral stability of suspend-dome," *Journal of Building Structures*, 2007, 28(6): 76-82. (in Chinese)
[30] Cai J, He S, Jiang Z, Zhang Y, Liu Q, "Investigation on maximum value of initial geometric imperfection in stability analysis of single-layer reticulated shells," *Journal of Building Structures*, 2015, 36(6): 86-92. (in Chinese)
[31] Bruno L, Sassone M, and Venuti F, "Effects of the equivalent geometric nodal imperfections on the stability of single layer grid shells," *Engineering Structures*, 2016, 112: 184-199.
[32] Huang W, Zhao H, "Determination of the critical loads of single layer lattice domes with stochastic geometrical imperfections," *Spatial Structures*, 1994, 1(2): 26-32. (in Chinese)
[33] Wang G and Shan S, "Review of metamodeling techniques in support of engineering design optimization," *Journal of Mechanical Design*, 2007, 129(4): 370-380.
[34] Luo L, He W, and Zhang X, "PSO-based approach for buckling analysis of shell structures with geometric imperfections," *Mathematical Problems in Engineering*, 2019, 2019: 4073919.
[35] Karimi H and Kani I M, "Finding the worst imperfection pattern in shallow lattice domes using genetic algorithms," *Journal of Building Engineering*, 2019, 23: 107-113.
[36] Gao H, Feng B, Zhu L, "Reviews of the meta-heuristic algorithms for TSP," *Control and Decision*, 2006, 21(3): 241-247. (in Chinese)
[37] Cong M, Wang L, "Survey on the theory of meta-heuristic algorithms," *Chinese High Technology Letters*, 2003, 13(5): 105-110. (in Chinese)
[38] Liu H, Luo Y, Yang L, Zhang W, "Stochastic imperfection mode superposition method for stability analysis of single-layer lattice domes," *Journal of Tongji University (Natural Science)*, 2012, 40(9): 1294-1299. (in Chinese)
[39] Zhao H, Xu Y, Bai G, "Influence of stochastic imperfection field on performance of latticed shell structures," *Spatial Structures*, 2011, 17(4): 23-27. (in Chinese)
[40] Lu J, Zhang Q, "Convex and probabilistic models of uncertainties in initial geometric imperfections of latticed shells," *Engineering Mechanics*, 2013, 30(7): 100-104+12. (in Chinese)
[41] Persson P, Strang G, "A simple mesh generator in MATLAB," *SIAM Review*, 2006, 46(2).
[42] Yang X, "Firefly algorithm, stochastic test functions and design optimization," *Int. J. Bio. Inspired Com*, 2010, 2(2): 78–84.

Methods and construction technologies for sustainable shell structures

---

Active bending
Additive manufacturing/ 3D printing
Architectural geometry
Bamboo for sustainable construction and quality of life improvement
Bio-inspired structures and architecture
Bridge structures
Computational form-finding
Conceptual design
Concrete structures
Construction techniques
Deployable and inflatable structures
Design competition (WG21)
Digital modelling and fabrication
Dynamic response of metal spatial structures
Dynamic response of other structures
Form-finding and structural optimisation of interlocking discrete assemblages
Graphical methods
Gridshell and lattice structures
Historical concrete shells
Historical structures
Lattice structures
Life-cycle design and assessment of structures
Metal gridshell structures, connections and stability
► **Methods and construction technologies for sustainable shell structures**
Morphology and configuration processing
Next generation parametric design
Novel methods in modelling, optimisation and construction for reducing carbon footprint of continuous roof shells
Numerical methods for geometry, form-finding and optimisation of lightweight structures
Optimisation methods and applications
Origami
Other
Teaching design uncertainty: working with unknown qualities/quantities of new and re-claimed materials
Teaching of shell and spatial structures
Tensegrity systems and cable structures
Tension and membrane structures
Tension structures in the Asia-Pacific
Timber and bio-based structures
Topology optimisation
Traditional masonry structures and innovation
Transformable structures

IASS 2023
July 10–14 Melbourne
Integration of Design and Fabrication

Proceedings of the IASS Annual Symposium 2023
Integration of Design and Fabrication
10–14 July 2023, Melbourne, Australia
Y.M. Xie, J. Burry, T.U. Lee and J. Ma (eds.)

Bio-based composite spatial shell structures

Mostafa AKBARI[a,*], Farzaneh OGHAZIAN[c], Ji Yoon BAE[d], Felecia DAVIS[c], Laia MOGAS-SOLDEVILA[d], Masoud AKBARZADEH[a,b]

[a,*] Polyhedral Structures Laboratory, Weitzman School of Design, University of Pennsylvania, Philadelphia, USA
Pennovation Center, 3401 Grays Ferry Ave. Philadelphia, PA, 19146
akbariae@design.upenn.edu

[b] General Robotic, Automation, Sensing and Perception (GRASP) Lab, School of Engineering and Applied Science, University of Pennsylvania, Philadelphia, USA
[c] Computational Textile Lab, College of Arts and Architecture, Penn State University, PA, 16801, USA
[d] DumoLab Research, Department of Architecture, Weitzman School of Design, University of Pennsylvania, Philadelphia, PA, 19146, USA
M.Akbari and F.Oghazian contributed equally to this work.

Abstract

This research investigates the possibility of fabricating shell-based cellular structures using knitting techniques. Shellular Funicular Structures are two-manifold single-layer structures that can be designed in the context of graphic statics. These are efficient compression/tension-only structures that have been designed for a certain boundary condition. Although the shellular funicular structures are efficient geometries in transferring the forces, the fabrication process is challenging due to the geometric complexity of the structure. Since Shellular structures comprise a single surface, they are suitable candidates to be fabricated using knitting technique, a method by which yarn is manipulated to create a textile or fabric. Using knitting approach, one can fabricate shellular structures with minimum production waste in which the knit can work as a formwork for actual structure or act as a composite structure combined with bio-based resin. This research proposes a workflow to fabricate shellular structures using knitting that can be scaled up for industrial purposes. In this process, the designed shellular structures are divided into multiple sections that can be unrolled into planar geometries. These geometries are optimized based on the elastic forces in the knitted network and knitted and sewn to make a topologically complex geometry of the shellular systems. After assembling the knitted parts and applying external forces at the boundaries, the final configuration of the structural form in tension is achieved. Then this form is impregnated with custom bio-resin blends from chitosan, sodium alginate, and silk fibroin to stiffen the soft knit structures into a compressed system. Although this method is an efficient fabrication technique for constructing shellular structures, it needs to be translated into an optimized method of cutting, knitting, and sewing with respect to the complexity of the shellular geometry. As a proof of concept of the proposed workflow, a mesoscale shellular structure is fabricated.

Keywords: shellular funicular structures, graphic statics, knitting, biocomposite structures

1. Introduction

The following section is divided into three primary sections. The initial section introduces a collection of spatial shell geometries known as shellular funicular structures, designed within the framework of graphic statics. The subsequent section discusses knitting structures and the historical progression of knitting techniques used in the development of shell structures. Lastly, the third section delves into

Copyright © 2023 by Mostafa AKBARI, Farzaneh OGHAZIAN, Ji Yoon BAE, Felecia DAVIS, Laia MOGAS-SOLDEVILA and Masoud AKBARZADEH. Published in the Proceedings of the IASS Annual Symposium 2023 with permission.



Figure 1. Biomaterial-based Stiffening of the knitting samples

composite structures of fabric or knitting, which are subsequently solidified using synthetic or biological compunds.

1.1. Shellular funicular structures

Shell structures are thin, curved plate structures that transfer forces through compression, tension, and shear stresses that act within the surface plane. These structures have numerous applications in science, design, and construction [1–3]. As a category of cellular structures, shell cellular (shellular) structures consist of continuous, smooth-curved shells. The geometry of these structures involves a surface with minimal material, known as a minimal surface [4]. The geometry of these surfaces, found in nature such as soap films, has inspired architects and engineers to design lightweight structures [5]. At each point on the minimal surface geometry, the mean curvature ($H = k_1 \quad k_2$) is zero, and the Gaussian curvature ($G = k_1 \quad k_2 < 0$, considering k_1 and k_2 as the principal curvatures of the surface) is negative [6]. Due to their high surface-to-volume ratio and unique morphology, shells with these surfaces' geometry exhibit superior mechanical performance compared to other cellular structures, such as strut-based cellular structures [7–9].

Utilizing graphic statics as a method for structural design, designers can create structures using reciprocal diagrams while controlling the flow of force within the structure and the external loading scenario [10–14]. Polyhedral graphic statics (PGS), an extension of two-dimensional graphic statics (2DGS), enables the user to design axially-loaded structures in 3D, in which no bending occurs [15–17]. The form and force diagrams provide a clear relation between the geometry and the equilibrium of a 3-dimensional node (Figure 2a). In this technique, the form diagram (denoted by Γ) represents the reaction forces combined with the geometry of the structure while each force diagram (denoted by $\Gamma^{\dagger}$) explains the equilibrium of forces. Each strut member e_i in the form diagram is perpendicular to its corresponding face $f_i^{\dagger}$ in the force diagram. In this technique, each vertex$v_i^{\dagger}$, edge $e_i^{\dagger}$, face $f_i^{\dagger}$, and cell $c_i^{\dagger}$ in the force diagram corresponds to a cell c_i, face f_i, edge e_i, and vertex v_i in the form diagram [15]. In this technique, the magnitude of the force in each strut member is proportional to the area of the corresponding face in the force diagram. By applying different subdivisions to a force diagram, various cellular strut-based structures in equilibrium can be designed (Figure 2a-d). Adding thickness to each edge of the form diagram proportional to the area of its corresponding face results in a strut-based cellular funicular structure.

The process of increasing the number of subdivisions in the force diagram leads to a form diagram with

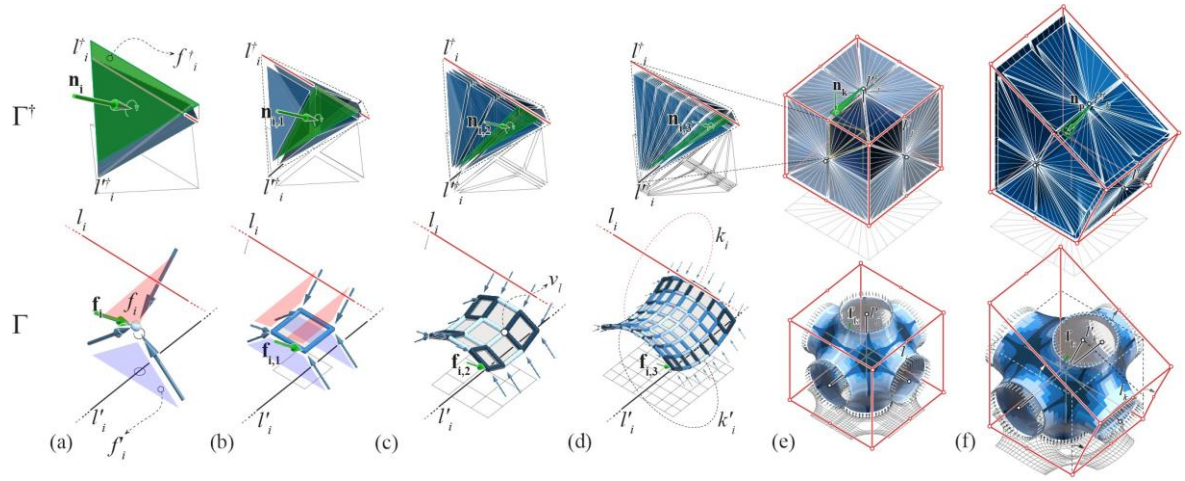


Figure 2. Iterative subdivision of a tetrahedron as a force diagram approximates a discrete surface with anticlastic curvature (a-d) as the form diagram. Using this subdivision between specific labyrinth graphs, one can design a shellular funicular structure (e) and use the labyrinths as control handles to manipulate the structure (f).

smaller edges and distributed forces in the members (Figure 2a-d). This procedure can eventually result in edges with near-zero length, approximating a surface as a form diagram. Polyhedral Graphic Statics (PGS) employs specific subdivision techniques to approximate surfaces with anticlastic or synclastic curvatures as form diagrams [9]. Figure 2a depicts a tetrahedron as a force diagram corresponding to a node in equilibrium with two upward and two downward forces as a form diagram (a node with an anticlastic curvature). This tetrahedron is produced by connecting the endpoints of the two skew lines $l_i^{\dagger}$ and $l_i'^{\dagger}$. Dividing these lines into equal segments and establishing a tetrahedron between every two skew segments from each line subdivides the force diagram into multiple tetrahedrons, resulting in a discrete anticlastic surface as a form diagram (Figure 2a-d) [9, 18]. This subdivision method is referred to as the *anticlastic subdivision*. These lines ($l_i^{\dagger}$ and $l_i'^{\dagger}$) serve as subdivision axes in the force diagram and curvature axes in the form diagram (Figure **??**d). These lines constitute two connectivity graphs known as *labyrinths*, which connect two segregated regions divided by the anticlastic surface in between [19]. By employing the *anticlastic subdivision* technique, one can design an anticlastic polyhedral surface, called a Shellular Funicular Structure (SFS) [20]. The labyrinths serve as subdivision axes in the form diagram and control handles in the force diagram, simplifying the design process and manipulation of the SFSs form-finding technique [18].

1.2. Knitting Structures

Historically, textiles have been a primary material used to develop fully tensioned structural systems. Knitted textiles, one of the many types of textiles, are created by producing loops with a continuous yarn and pulling that yarn through previously formed loops to create new ones. The resulting loops, or stitches, can be manipulated to form different stitch structures depending on the movement of the yarn. The structure of a knitted fabric is determined by the shaping of stitches, the manipulation of yarns, and the type of knitting machine used to create it. Knitted textiles have unique properties that make them suitable for developing complex and 3D shapes due to their multi-directional, heterogeneous and anisotropic characteristic [21]. Knitted textiles have been used in developing tension structures [22–25],

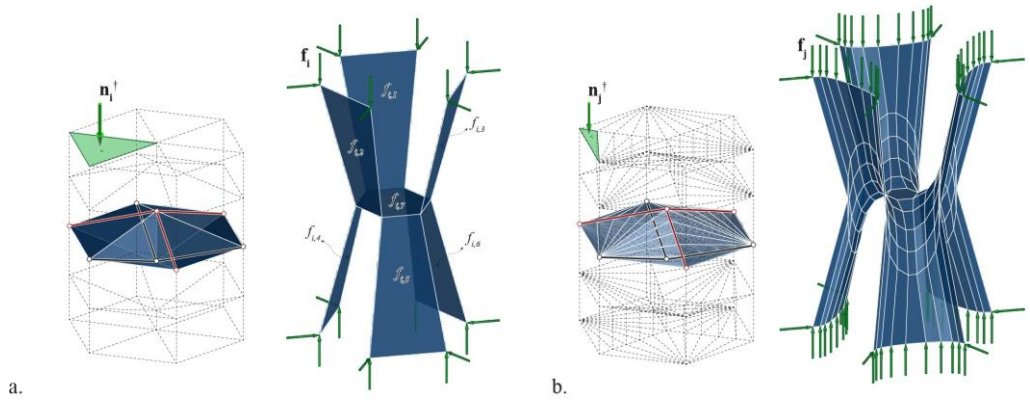


Figure 3. Designing a low-resolution (a) and high-resolution (b) of the force and form diagram of a shellular structure.

as well as in connection with concrete as a formwork system [26–28].

1.3. Biocomposite structures

Materials such as silk, shell, chitin, cellulose, or bone present internal hierarchical configurations that confer stiffness, flexibility, and buckling resistance unmatched by man-made materials [29, 30]. Recent research in chemical and biomedical engineering has derived new synthesis methods to extract these materials from the natural structures they produce such as insect cocoons or shrimp shells [31, 32], and reverse-engineer them as water-based raw biopolymers to make new structures such as drug delivery micro-devices, tissue scaffolds, resolvable electronics, small object casts, and natural adhesives [33, 34] that are not only biocompatible to the human body but also able to be naturally decomposed. As in nature some of these materials perform as bio-resins binding together minerals and proteins into organism structures, we explore here if they could substitute toxic man-made synthetic resin compounds that are widely used as stiffeners of woven fiber structures (i.e epoxy, vinylester, or polyester resins used on carbon fiber, fiberglass, and aramid fiber). In this work we used simple polysaccharides and proteins extracted from shrimp shells, algae cell walls, and silk cocoons, because of their biodegradability, strength, and flexibility properties, their compatibility with natural fibers of wool, cotton, and linen that compose our knits, and their proven ability to be precisely distributed in large additive manufacturing platforms as developed in our previous work [35, 36].

1.4. Problem statement and objectives

Shellular funicular structures are highly efficient structures designed for a specific boundary condition. However, their fabrication process can be challenging due to their geometric complexity. Shellular structures, consisting of a single surface, are suitable for fabrication using the knitting technique, a process used to manipulate yarn to create fabric. Knitting can minimize production waste while serving as a formwork or composite structure, when combined with bio-based resin. This study proposes a workflow to fabricate shellular structures using knitting and scale them up for industrial purposes. The process involves dividing the designed shellular structures into sections that can be unrolled into planar geometries. These geometries are optimized based on the elastic forces in the knitted network and stitched together to form a topologically complex shellular system. After assembling the knitted parts, external forces are applied to achieve the final configuration of the structural form in tension. The form is then impregnated

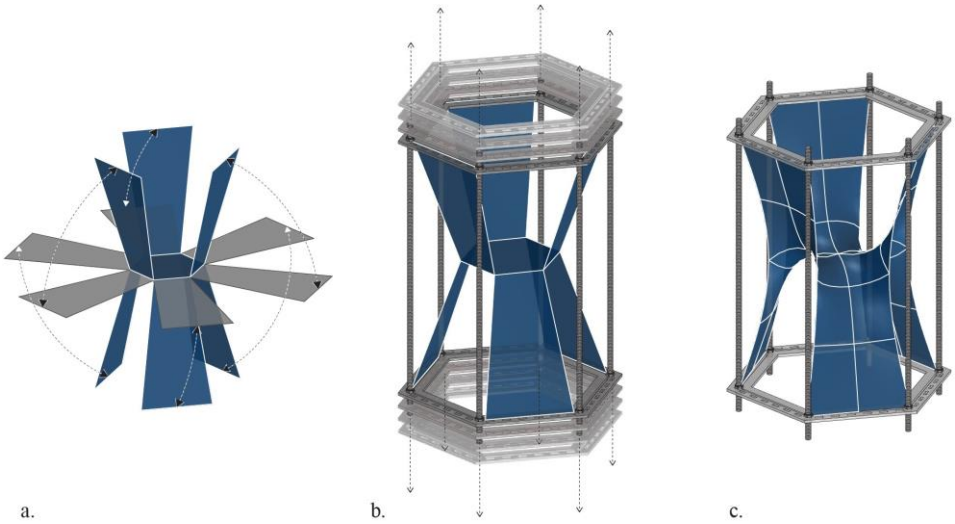


Figure 4. Unrolling the low-resolution shellular structure (a), and holding it using a jig (b). Turning the screws in the jig controls the height of the knit structure, assuring that the structure is in tension (c).

with custom bio-resin blends made from chitosan, sodium alginate, and silk fibroin to stiffen the soft knit structures into a compressed system. Although this method is efficient, an optimized method for cutting, knitting, and sewing must be developed to match the complexity of the shellular geometry. To demonstrate the proposed workflow's viability, a mesoscale shellular structure has been fabricated as a proof of concept.

2. Methodology

In this section, first, the process of designing a shallular structure for specific boundary conditions has been explained. In the next sections, this structure will be knitted and impregnated using bio-based materials. In the next section the knitting process will be explained through three different trials. In the last section, the biomaterial-based stiffening through different impregnation technique will be explained.

2.1. Shellular structural design

In order to develop a form for the structure in tension, shellular method in the context of graphic statics have been used [20, 37]. A rectangular prism (h:25 cm, w,l:20 cm) has been considered. Figure 3a displays the force diagram (left) corresponding to a structure comprising 30 edges, 7 faces, and 24 reaction forces. It is worth mentioning that the labyrinths graphs have been marked with black and red in the force diagram. Faces in the form diagram corresponding to these graphs have been removed in order to result in a 2-manifold structure [9]. To generate the form diagram, after designing the labyrinth graphs, a tetrahedron has been constructed for each pair of labyrinths (red and black labyrinths that are in a skew position together). This force diagram results in a low-resolution shellular funicular structure. The shellular structure with the higher resolution has a smoother surface along with a higher number of faces. In order to increase the smoothness of the structure, each labyrinth edge is subdivided into smaller segments, and a tetrahedron has been constructed between smaller edges in the force diagram (Figure 3b). In fact, each tetrahedron in Figure 3a is subdivided into 25 tetrahedrons in order to result in the force diagram in Figure 3b. This force diagram corresponds to a smooth form diagram, representing a shellular funicular structure.

In order to construct the geometry out of knitting, one needs to unroll the shellular structure to the *XY plane*. Due to the ease of unrolling the first form diagram prior to smoothing, the authors made the de-

cision to unroll the form diagram consisting of seven faces. In this process, faces $f_{i,1}$, $f_{i,2}$, $f_{i,3}$, $f_{i,4}$, $f_{i,5}$, $f_{i,6}$ (Figure 3a), have been rotated along one of their edges in order to unroll the whole structure (Figure 4a). Using an elastic material for constructing this structure and tensioning it would result in a smooth structure, approximating the form diagram in Figure 3b. To apply tension to the structure, a jig comprising two flat panels and 6 screws have been constructed (Figure 4a). The screws will give the user the possibility to control the height of the structure, assuring that the whole knitting structure is in tension (Figure 4b).

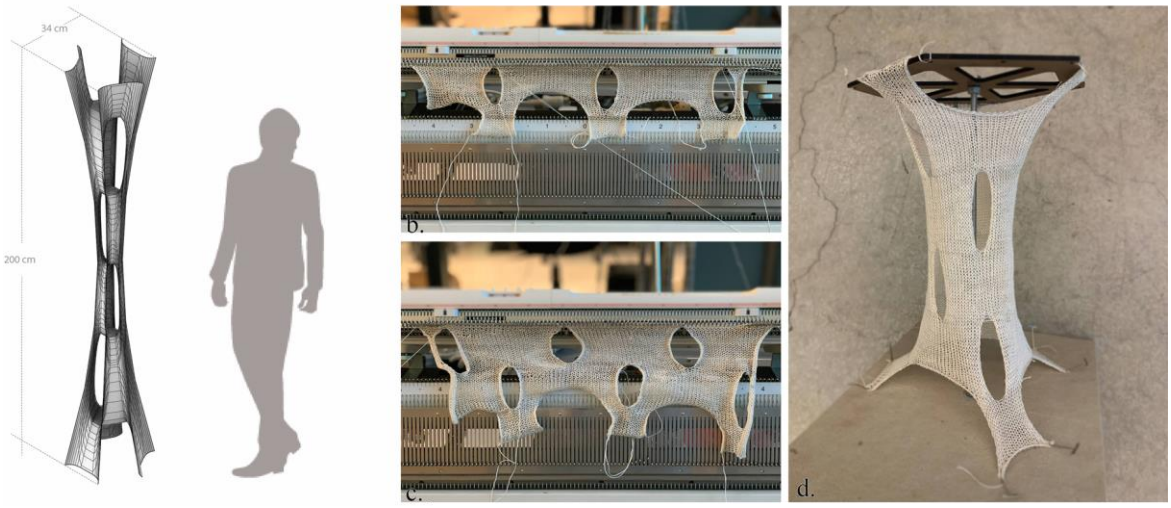


Figure 5. Trial1, The geometry of a shellular funicular structure (a), the knitting fabrication of a shell (b,c), and the tensioned model of it (d).

2.2. Knitting technology

The knitting process design for the shellular knit structure involves a series of trials aimed at achieving a seamless surface. The initial trial involved making a planar surface with holes, with the goal of making the entire surface seamless. However, the first attempt did not result in a shellular structure. For the second trial, a rough representation of the overall form was used, which was then unrolled as a seamless flat shape. The stitches were then generated over this flat shape and knitted. The knitted unrolled seamless flat shape was then sewn together to give an overall shape to the knitted textile. The rough 3D knitted structure was then tensioned to obtain a smooth tensioned structure. However, the model did not precisely replicate the digital model. Therefore, in the next step, efforts were made to increase the accuracy of the initial shape that should be knitted to achieve the final shape. At this stage, the focus was on only a portion of the overall form.

2.2.1. Trial 1

In the initial attempt, the focus was on creating a planar surface with holes (Figure 5). The aim of this trial was to knit the exterior skin first, and then add the interior planar surfaces. However, in this method, the exterior and interior surfaces were not connected and required more sewing to achieve the desired 3D shellular shape. This approach proved to be less efficient and required more effort and time to achieve the desired result. Therefore, further trials were conducted to explore alternative methods to create the shellular structure more efficiently and with fewer seams.

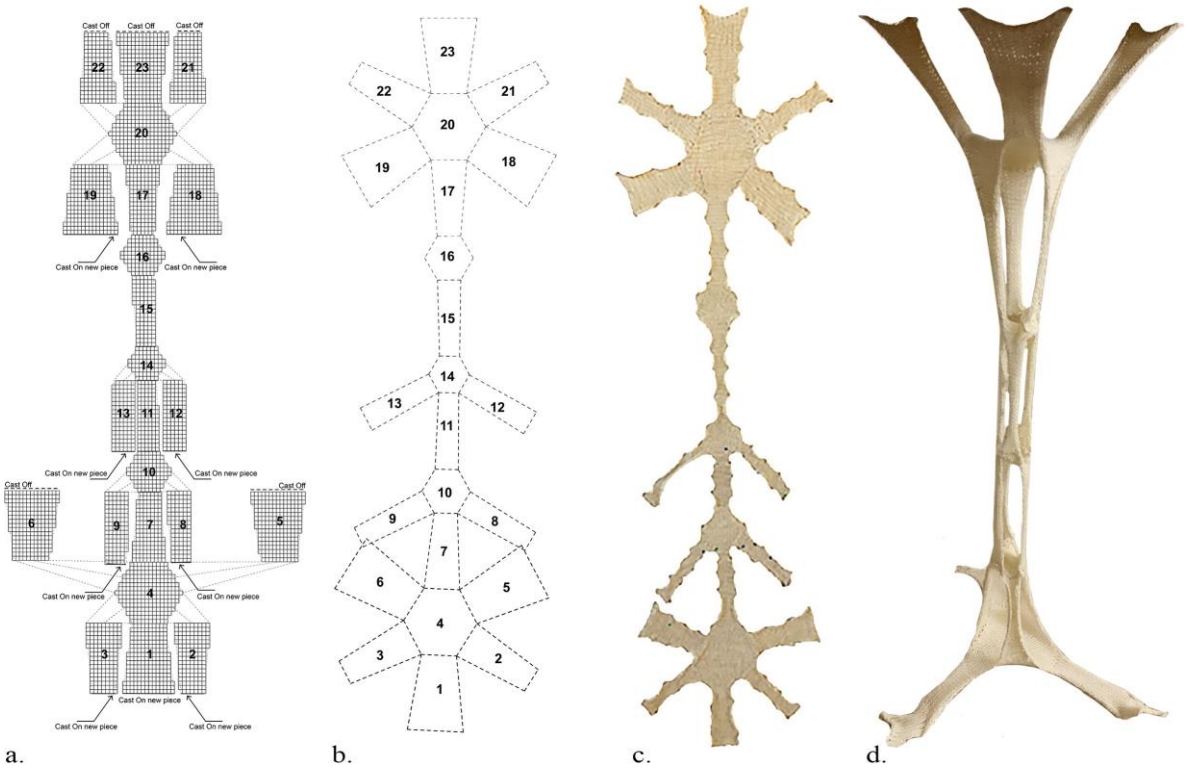


Figure 6. Trial 2, Sequence of knitting (a), distribution of stitches (b), knitted form pattern (c), and the knitted structure in tension.

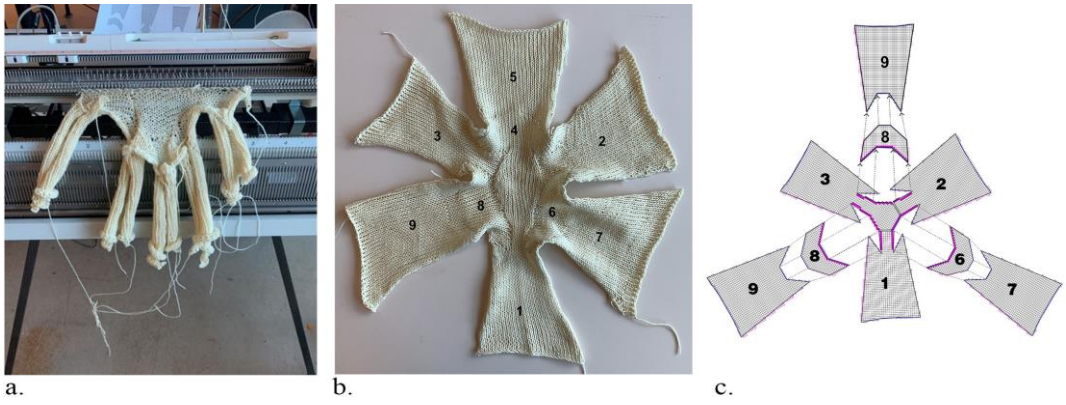


Figure 7. Trial3, sequence of knitting for the main alternative.

2.2.2. Trial 2

In the second trial, the authors aimed to improve the seamless feature of the shellular knit structure. To achieve this, the whole structure (Figure 5left) was unrolled and a single connection between the hexagons in the middle of the structure was ensured. The process involved creating a seamless flat shape and generating the stitches over this flat shape. The objective was to create pieces with the knitting direction pointing towards the center of the hexagon. This was considered crucial as the direction of knitting plays a significant role in determining the behavior and performance of the textile. It was important to achieve a consistent behavior throughout the entire structure. Therefore, special attention was given to the direction of knitting during the fabrication process to ensure a more uniform and reliable behavior of the knitted textile. In addition, by ensuring a consistent knitting direction, the

overall aesthetics of the structure were also improved, resulting in a more visually appealing end product. Figure 6 show the pro- cess of the knitting and after knitting the whole structure, in which the legs were sewn to the hexagon to obtain a rough 3D shape. This figure includes the unrolled diagram, distribution of the stitches, sequence of the knitting of different parts of the model, and the knit model in tension. By following this sequence, the authors were able to create a knitted shape that was more closely aligned with the digital model.

2.2.3. Trial 3

In order to achieve a higher degree of accuracy, the structure that is explained in section 2.1 is knitted. This structure is a portion of the structure displayed in Figure 5left, which is magnified in order to result in a more accurate model. The boundary shapes of this piece were then generated using a more precise digital model, and the stitches were generated accordingly. This approach aimed to improve the accuracy and consistency of the knitted structure, resulting in a more reliable and efficient end product.

2.3. Biomaterial-based stiffening

Biomaterials used as bio-resins here are chitosan from shrimp shells, sodium alginate from algae cell walls, and Fibroin protein from silk cocoons. Silk Fibroin solution was produced by Canon Virginia Inc. Chitosan (medium molecular weight at 85% deacetylation) was purchased from TidalVision Inc. Acetic acid, glycerol, and sodium alginate were purchased from Sigma-Aldrich (USA). Fibroin aqueous solutions at 7%w/v combined with sodium alginate at $4.5\%w/v$ as well as Chitosan at 4%w/v in 3%w/v acetic acid in gel solution are both blends used as homogeneous stiffeners throughout all knit samples (Figure 9). A blend of silk Fibroin at 7%w/v combined with sodium alginate at $4.5\%w/v$, natural coloring, and glycerol is used to additively manufacture targeted stiffening. To impregnate these blends onto knitted forms, casting and printing methods are used. Casting is based on spatula distribution of pre-measured biomaterial quantities according to surface area and knit thickness. Printing is performed with our exiting custom platform [35, 38]: a 3-axis computer numerically controlled (CNC) system with a 1x1m print bed that positions a pneumatic extrusion system in space. Toolpaths are designed in Rhinoceros3D® computer-aided design software and machine instructions are translated into custom Gcode via *C#* scripts. Positioning instructions are interpreted and sent via Serial Port JSON Server to the 3-axis CNC system. Extrusion machine instructions are sent via Serial Port to a dispense valve controller and precision valve using a $1.5mm$ inner diameter nozzle at 10PSI and receiving materials from 100PSI pressured reservoirs.

3. Results

The authors commenced their study by conducting experiments on stiffened knitted pieces composed of linen, wool, or cotton, as illustrated in Figure 9. Each of these materials was knitted in sparse and dense versions. The linen pieces were impregnated with Chitosan or Chitosan + Fibroin (Figure 9 S.01 - S.03). The wool pieces were impregnated with Fibroin + Alginate or Chitosan + Fibroin (Figure 9 S.04 - S.06). Lastly, the cotton pieces were impregnated with chitosan (Figure 9 S.07 - S.08). All specimens were subjected to loading after impregnation, and their loading capacity is presented in Figure 9. Based on the experimental results, the primary knitted structure shown in Figure 7 was homogeneously stiffened

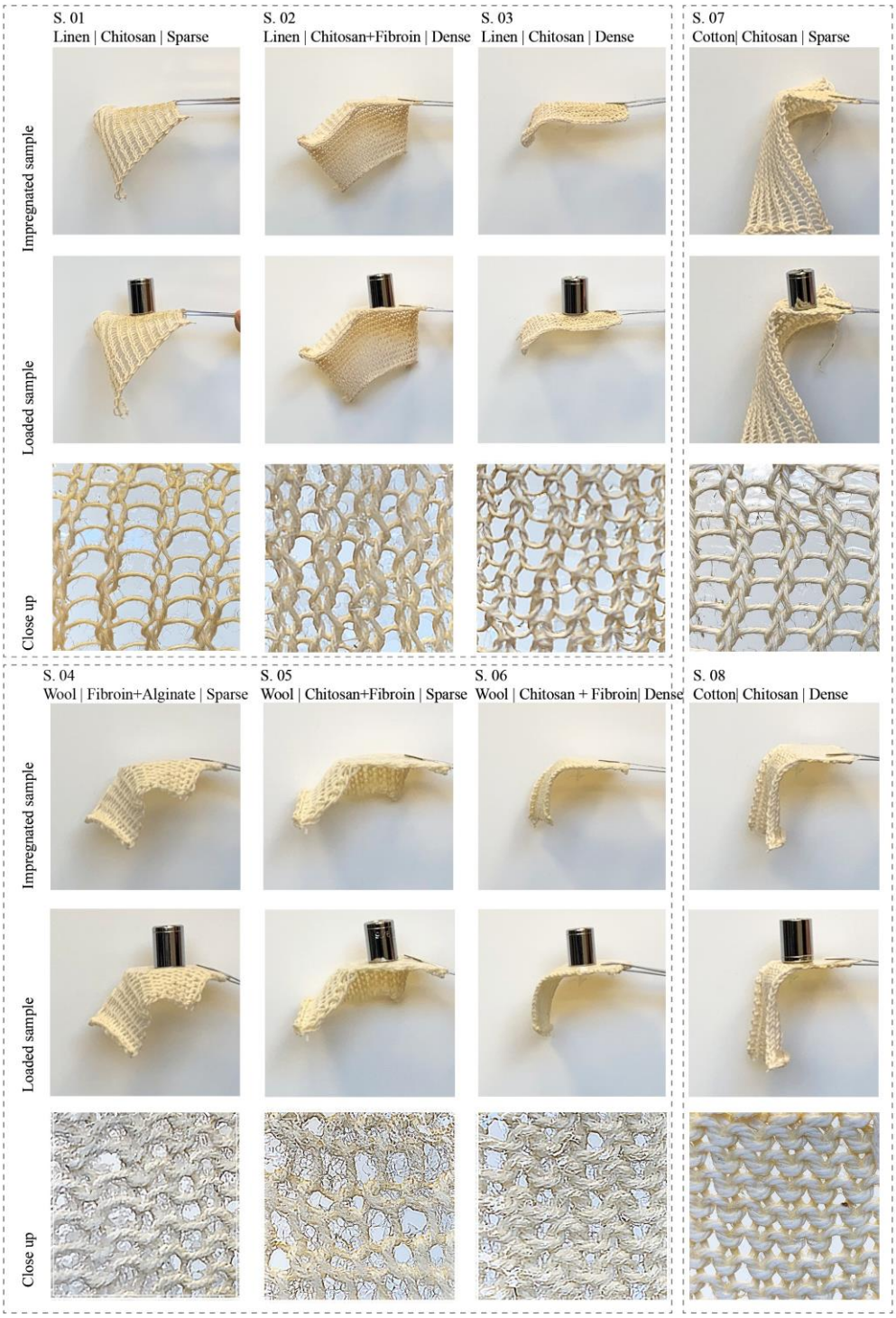


Figure 8. Biomaterial-based Stiffening of the knitting samples, in this experiments only half of the knit is impregnated in order to compare the stiffness of the rigid part with the part that is draped.

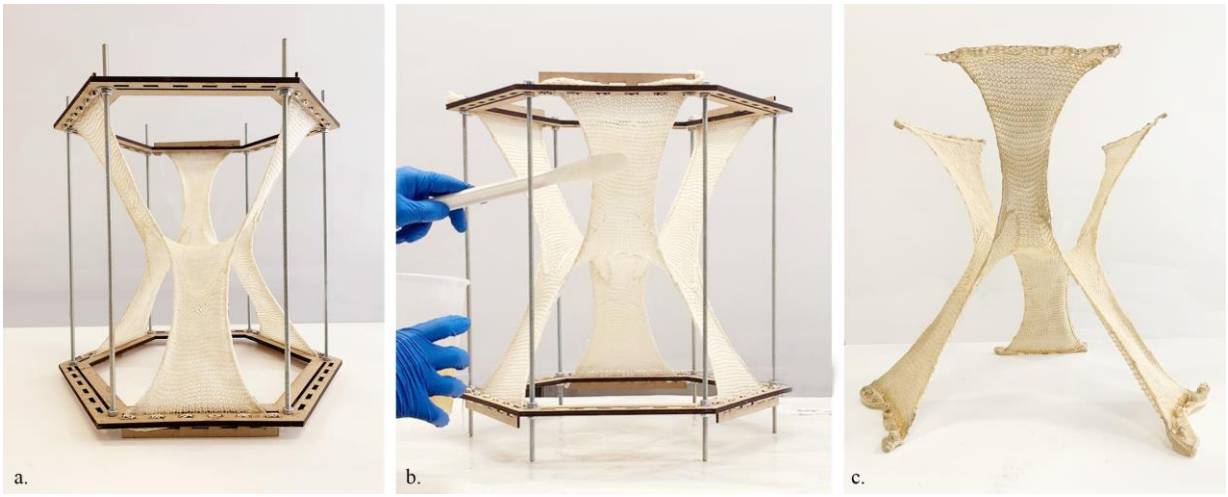


Figure 9. Biomaterial-based homogeneous stiffening of a knit structure: applying tension to the sample on the jig (a), impregnating the sample (b), and final structure after drying (c).

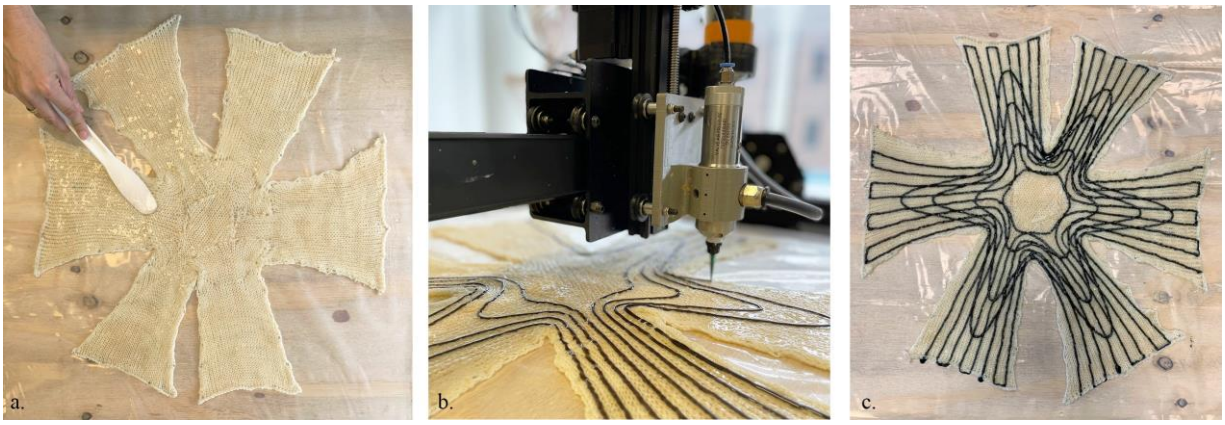


Figure 10. Biomaterial-based targeted stiffening; by impregnating the whole structure with a homogeneous Chitosan base layer (a), then printing a Fibroin-based stiffening toolpath on top (b), resulting in fully impregnated piece with expected differential behaviour (c).

by impregnating sparse wool knit with a blend of Chitosan + Fibroin (silk fibroin at 7%*w/v* combined with chitosan at 4%*w/v*) in the subsequent stage, and the model was held under tension in the jig. After one day, the dried model was loaded and its structural capacity was evaluated. In the final stage, targeted heterogeneous stiffening was performed the same knitted model in Figure 7, a base impregnation of Chitosan (at 4%*w/v*) was followed by an additively manufactured layer of Fibroin + Alginate blend (using in this case silk fibroin at 7%*w/v* combined with sodium alginate at 4.5%*w/v*, natural coloring, and glycerol to optimize the blend for our printing technology). Given that the smooth version of the model in Figure 3a is depicted in Figure 3b, the pattern of the smooth model has been applied and projected onto the model prior to smoothing. In fact the pattern that is printed on the model displays the force flow of the smooth version of the model. This pattern would increase the material in places that we need, improving the structural capacity of the system. Figure 11 displays the process of global stiffening (with a clear Chitosan gel) and local targeted stiffening of this specimen (with black silk fibroin blend). In this process a 3-axis computer numerically controlled (CNC) system with a 1x1m print bed has been

used to print the pattern on top of the knitted piece. Final experimental results display that both global and local impregnation of the knitted structures results in a stiff structure with specific structural capacity. It is noteworthy that the structure depicted in Figures 7 requires an identical boundary condition to the one it has been designed for, to attain adequate structural capacity. Consequently, several tension ties are necessary at the top and bottom of the structure to reinforce it.

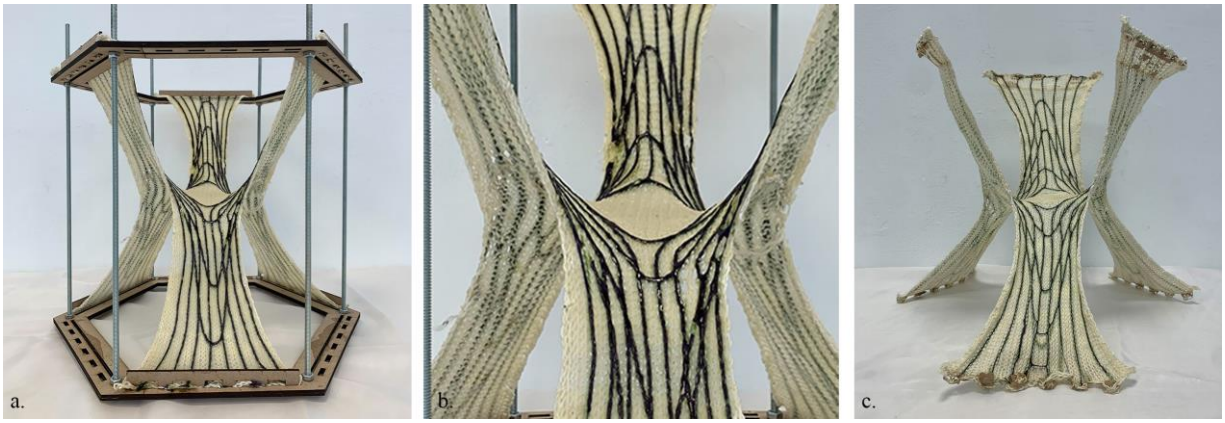


Figure 11. Biomaterial-based targeted stiffening.

4. Conclusion and future work

This research investigated the possibility of fabricating shell-based cellular structures using knitting techniques. The research proposed a workflow to fabricate shellular structures using knitting that can be scaled up for industrial purposes. In this process, the designed shellular structures are divided into multiple sections that can be unrolled into planar geometries. These geometries are optimized based on the elastic forces in the knitted network and knitted and sewn to make a topologically complex geometry of the shellular systems. After assembling the knitted parts and applying external forces at the boundaries, the final configuration of the structural form in tension is achieved. Then this form is impregnated with custom bio-resin blends from chitosan, sodium alginate, and silk fibroin to stiffen the soft-knit structures into a compressed system. In forthcoming research, it is crucial to concentrate on numerically assessing the structural efficacy of each structural specimen and contrasting it with experimental testing. Furthermore, it is imperative to concentrate on structures with greater dimensions, whose structural efficacy must be examined under actual loads.

Acknowledgement

This research was funded by the National Science Foundation CAREER Award (NSF CAREER-1944691 CMMI) and the National Science Foundation Future Eco Manufacturing Research Grant (NSF, FMRG-CMMI 2037097) to M. Akbarzadeh.

References

[1] T. Teng, M. Jia, and J. E. Sabin, “The designing of epithelial cell inspired-brick inmasonry shell system,” 2020.

[2] T. Teng and J. Sabin, “The design and 4d printing of epithelial cell-inspired programmable surface geometry,” 2021.

[3] S. Adriaenssens, P. Block, D. Veenendaal, and C. Williams, *Shell structures for architecture: form finding and optimization*. Routledge, 2014.

[4] W. Meeks III and J. Pe´rez, "The classical theory of minimal surfaces," *Bulletin of the American Mathematical Society*, vol. 48, no. 3, pp. 325–407, 2011.

[5] B. Burkhardt, "Natural structures-the research of frei otto in natural sciences," *International journal of space structures*, vol. 31, no. 1, pp. 9–15, 2016.

[6] D. Hilbert and S. Cohn-Vossen, *Geometry and the Imagination*, vol. 87. American Mathematical Soc., 2021.

[7] S. C. Han, J. W. Lee, and K. Kang, "A new type of low density material: Shellular," *Advanced Materials*, vol. 27, no. 37, pp. 5506–5511, 2015.

[8] S. C. Han, J. M. Choi, G. Liu, and K. Kang, "A microscopic shell structure with schwarz's d-surface," *Scientific reports*, vol. 7, no. 1, pp. 1–8, 2017.

[9] M. AKBARI, M. AKBARZADEH, and M. BOLHASSANI, "From polyhedral to anticlastic funicular spatial structures," in *Proceedings of IASS Symposium*, 2019.

[10] J. C. Maxwell, "On Reciprocal Figures and Diagrams of Forces," *Philosophical Magazine Series 4*, vol. 27, no. 182, pp. 250–261, 1864.

[11] W. J. M. Rankine, "Principle of the Equilibrium of Polyhedral Frames," *Philosophical Magazine Series 4*, vol. 27, no. 180, p. 92, 1864.

[12] L. L. Beghini, J. Carrion, A. Beghini, A. Mazurek, and W. F. Baker, "Structural Optimization Using Graphic Statics," *Structural and Multidisciplinary Optimization*, vol. 49, no. 3, pp. 351–366, 2013.

[13] L. Cremona, *Graphical Statics: Two Treatises on the Graphical Calculus and Reciprocal Figures in Graphical Statics. Translated by Thomas Hudson Beare*. Oxford: Clarendon Press, 1890.

[14] K. Culmann, *Die Graphische Statik*. Zürich: Verlag Meyer und Zeller, 1864.

[15] M. Akbarzadeh, *3D Graphic Statics Using Reciprocal Polyhedral Diagrams*. PhD thesis, ETH Zurich, Zurich, Switzerland, 2016.

[16] Y. Lu, M. Cregan, P. Chhadeh, A. Seyedahmadian, M. Bolhassani, J. Schneider, J. Yost, and M. Akbarzadeh, "All glass, compression-dominant polyhedral bridge prototype: form-finding and fabrication," in *Proceedings of IASS Symposium and Spatial Structures Conference 2020/21, Inspiring the next generation*, (Guildford, UK), August 23-27 2021.

[17] H. Chai and M. Akbarzadeh, "Web-based Interactive Polyhedral Graphics Statics Platform," in *Proceedings of the IASS Annual Symposium 2020/21*, (Surrey,UK), 2021.

[18] M. Akbari, A. Mirabolghasemi, H. Akbarzadeh, and M. Akbarzadeh, "Geometry-based structural form-finding to design architected cellular solids," in *Symposium on Computational Fabrication*, pp. 1–11, 2020.

[19] W. Fischer and E. Koch, "Genera of minimal balance surfaces," *Acta Crystallographica Section A: Foundations of Crystallography*, vol. 45, no. 10, pp. 726–732, 1989.

[20] M. Akbari, A. Mirabolghasemi, M. Bolhassani, A. Akbarzadeh, and M. Akbarzadeh, "Strut-based cellular to shellular funicular materials," *Advanced Functional Materials*, p. 2109725, 2022.

[21] C. L. McKnelly, *Knitting behavior: a material-centric design process*. PhD thesis, Massachusetts Institute of Technology, 2015.

[22] R. La Magna, V. Fragkia, R. Noe¨l, Y. Šinke, M. Tamke, P. La¨ngst, J. Lienhard, and M. Thomsen, "Isoropia: an encompassing approach for the design, analysis and form-finding of bending-active textile hybrids," 07 2018.

[23] M. R. Thomsen, M. Tamke, A. Karmon, J. Underwood, C. Gengnagel, N. Stranghöner, and J. Uhle-

mann, "Knit as bespoke material practice for architecture," in *Acadia 2016*, pp. 280–289, ACADIA, 2016.

[24] J. E. Sabin, "mythread pavilion: generative fabrication in knitting processes," in *ACADIA*, vol. 13, pp. 347–354, 2013.

[25] J. E. Sabin, J. Hilla, D. Pranger, C. Binkley, and J. Bilotti, "Embedded architecture: Ada, driven by humans, powered by ai," *Fabricate 2020*, pp. 246–255, 2020.

[26] A. Pal, W. L. Chan, Y. Y. Tan, P. Z. Chia, and K. J. Tracy, "Knit concrete formwork," in *Proceedings of the 25th CAADRIA Conference*, vol. 1, pp. 213–22, 2020.

[27] M. Popescu, L. Reiter, A. Liew, T. Van Mele, R. J. Flatt, and P. Block, "Building in concrete with an ultra-lightweight knitted stay-in-place formwork: prototype of a concrete shell bridge," in *Structures*, vol. 14, pp. 322–332, Elsevier, 2018.

[28] M. Popescu, M. Rippmann, A. Liew, L. Reiter, R. J. Flatt, T. Van Mele, and P. Block, "Structural design, digital fabrication and construction of the cable-net and knitted formwork of the knitcandela concrete shell," in *Structures*, vol. 31, pp. 1287–1299, Elsevier, 2021.

[29] J. Vincent, *Structural biomaterials*. Princeton University Press, 2012.

[30] M. A. Meyers, J. Mckittrick, and P.-Y. Chen, "Structural Biological Materials: Critical Mechanics-Materials Connections," *Science*, vol. 335, pp. 199–204, jan 2012.

[31] J. G. Fernandez and D. E. Ingber, "Bioinspired chitinous material solutions for environmental sustainability and medicine," *Advanced Functional Materials*, vol. 23, no. 36, pp. 4454–4466, 2013.

[32] F. G. Omenetto and D. L. Kaplan, "New opportunities for an ancient material.," *Science (New York, N.Y.)*, vol. 329, no. 5991, pp. 528–531, 2010.

[33] G. Guidetti, L. D'Amone, T. Kim, G. Matzeu, L. Mogas-Soldevila, B. Napier, N. Ostrovsky-Snider, J. Roshko, E. Ruggeri, and F. G. Omenetto, "Silk materials at the convergence of science, sustainability, healthcare, and technology," *Applied Physics Reviews*, vol. 9, p. 011302, mar 2022.

[34] J. G. Fernandez and D. E. Ingber, "Manufacturing of large-scale functional objects using biodegradable chitosan bioplastic," *Macromolecular Materials and Engineering*, vol. 299, no. 8, 2014.

[35] L. Mogas-Soldevila, G. Matzeu, M. L. Presti, and F. Omenetto, "Additively manufactured leather-like silk protein materials," *Materials Design*, vol. 203, p. 109631, 2021.

[36] L. Mogas-Soldevila, J. Duro-Royo, and N. Oxman, "Water-Based Robotic Fabrication: Large-Scale Additive Manufacturing of Functionally Graded Hydrogel Composites via Multichamber Extrusion," *3D Printing and Additive Manufacturing*, vol. 1, pp. 141–151, sep 2014.

[37] M. Akbari and M. Akbarzadeh, "Continuous approximation of shellular funicular structures," in *Proceedings of IASS 2022 symposium affiliated with APCS 2022 conference*, (Beijing, China), September 19-22 2022.

[38] G. Ho, V. Kubusˇova´, C. Irabien, V. Li, A. Weinstein, S. Chawla, D. Yeung, A. Mershin, K. Zolotovsky, and L. Mogas-Soldevila, "Multiscale design of cell-free biologically active architectural structures," *Frontiers in Bioengineering and Biotechnology*, vol. 11, 2023.

IASS 2023
July 10–14 Melbourne
Integration of Design and Fabrication

Proceedings of the IASS Annual Symposium 2023
Integration of Design and Fabrication
10–14 July 2023, Melbourne, Australia
Y.M. Xie, J. Burry, T.U. Lee and J. Ma (eds.)

New carbon paradigm: applications of carbon composite materials in the building industry

Shengdan YANG*

* Tsinghua University, Academy of Arts and Design. Visiting student at MIT architecture subsidized by China Scholarship Council
Sheng223@mit.edu

Abstract

Compared with metal, glass, wood and most other building materials, carbon composite materials offer a new paradigm by enabling the production of building components with complex shapes. As a construction material for shells, composite materials have outstanding structural and mechanical properties, such as light weight, high strength, high stiffness, fatigue resistance, strong durability, and corrosion resistance. They provide architects and engineers with new possibilities for design and construction modes. This paper reviews previous literature on composite fabrication and discusses its application in shells and structures. The structural properties and fabrication methods of composite materials are studied, and digital design technologies are discussed. An evaluation index system is offered for sustainability of composite projects from the perspectives of ecology, society, and economy. This paper offers a material perspective into shell and structural design and proposes the wider use of composite materials in urban environments.

Keywords: carbon composites, mechanical property, structural design, building industry, overview

1. Introduction

For more than 160 years, industrialized production and construction have reshaped the human living mode [1]. With urban expansion and population growth, the challenges brought by the climate crisis are becoming increasingly obvious. We need to rethink construction materials and technologies to improve the resilience and climate adaptability of human settlements. Many landscape architects and urban planners have attempted to mitigate climate change through the allocation of green space and vegetation, which absorbs CO_2 (carbon dioxide) from the atmosphere. However, the CO_2 emitted using various hard construction materials may exceed the CO_2 absorbed by green plants, so that the ecological benefits brought by greening cannot offset the energy cost of these traditional materials [2]. In addition, the buildings contribute to almost one third of the global greenhouse gas emissions annually, making it one of the primary sources of the greenhouse effect [3].

"Carbon footprint" refers to the total greenhouse gas emissions directly or indirectly caused by buildings from the material production, building construction, and use until the end of the life cycle of the materials [4]. The annual CO_2 emissions from the manufacturing of building materials are 18629 tons, of which the manufacturing of concrete and cement is the main cause of CO_2 emissions, accounting for 46% of the total CO_2 emissions of building materials [5]. Figure 1 shows the CO_2 emissions per functional unit of timber, aggregate, asphalt, steel, and concrete [2]. To mitigate the impact of greenhouse gas emissions and global warming, it is necessary to minimize energy consumption and CO_2 emissions at all stages of human settlements planning, to reduce the negative effects of the construction industry [6,7]. Thus, sustainability has been the key issue in architectural design, and "nature positive development" can help mitigate climate change and foster energy-saving effects [8, 9]. In 2014, the Intergovernmental Panel on Climate Change (IPCC) proposed measures to reduce building energy consumption and greenhouse gas emissions. Low-energy and low-carbon building materials are used to

Copyright © 2023 by Shengdan YANG. Published in the Proceedings of the IASS Annual Symposium 2023 with permission.

improve the durability of building components and the efficiency of water supply, cooking, lighting, electrical equipment and heating and cooling systems [10].

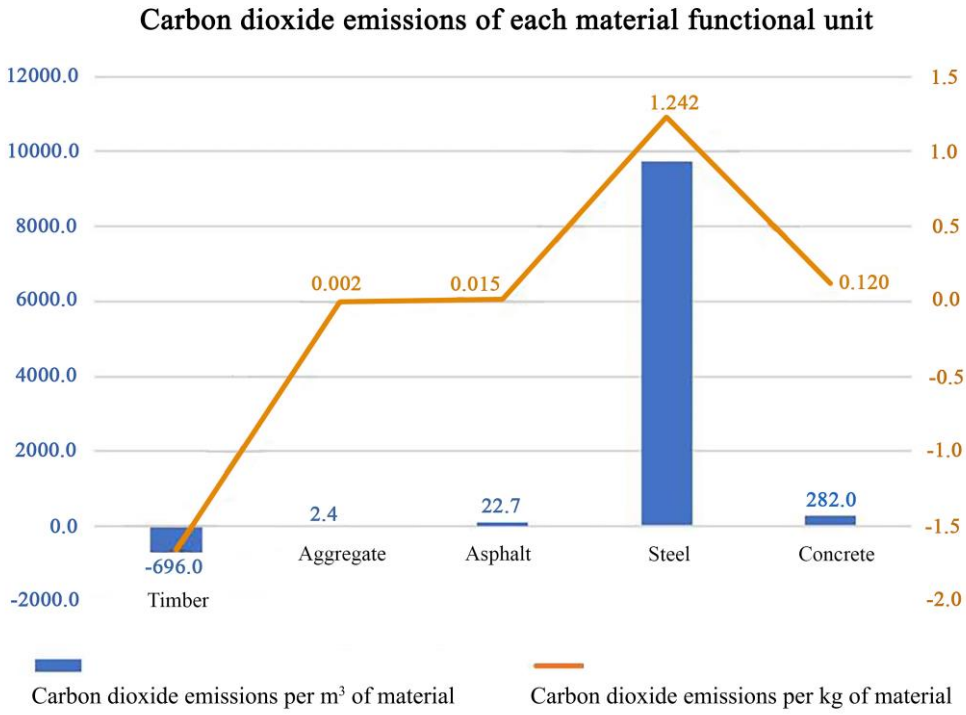


Figure 1. Data of CO_2 emissions of each material functional unit.

Source: K. O'Connor, C. Pocock, M. R. Barthelmeh and S. Davis (2011).

In the process of architecture and landscape construction, the use of building materials is the main factor that determines its impact on the environment [2]. Nanotechnologies and novel forms of materials including carbon composites, new alloys, ceramics, and metal assist in the innovative architectonics in modern architecture [11]. Considering the possible environmental impact caused by the doubling of the buildings and infrastructure in 2050, Goulthorpe (2019) put forward a new carbon material approach, which suggests using carbon-based building materials derived from methane pyrolysis for civilizational scale construction [12]. New forms of carbon materials are applied to the facade and structure of buildings to replace concrete, cement, steel, copper, aluminium, and other traditional building materials with high energy consumption. Goulthorpe (2019) advocates that this kind of material can be applied not only in residential houses, but also in other buildings and landscape infrastructure in urban environments, including bridges, parks, and irrigation systems. As a lightweight material, carbon composite has outstanding structural and mechanical properties, which can be used to build lightweight structures with beautiful shapes to achieve sustainable design goals. Just like the revolutionary impact of the steel structures on modern buildings in the 19th century [13], carbon materials have great application potential, which can promote innovation in architectural design concepts.

This paper gives an overview of the application of carbon composite materials in architectural design, and the framework of this review can be divided into three sections: 1) analysing the energy-saving characteristics of carbon composite materials compared to other construction materials; 2) discussing the properties and forms of carbon composite materials; and 3) investigating the fabrication and design methods of carbon composite materials. The objective of this paper is to summarize the main advantages of carbon composite materials in buildings and illustrate their potential for wider applications as a new paradigm for construction.

2. Research methods

A search for previous literature on the use of composite materials in the building industry was conducted on Web of Science, with four criteria: 1) the crossing keywords of "carbon composites" and "building design"; 2) publication year: 2013 to 2023; 3) language: English; 4) document type: article or book chapter. As the search result, 612 papers were found on Web of Science and VosViewer was used to analyse the co-occurrence of keywords from 2013 to 2023, with the minimum number of keywords co-occurrence as five. Figure 2 shows hot spots of "composites", "performance", "design", "carbon", "graphene" and "nanocomposites", and judging from the colours of keywords and their linking lines, most keywords fell in the time range from 2016 to 2020. The citation sources of the papers under this topic were also analysed (Figure 3). Then, we selected papers that are most relevant to our work and categorized them into the three sections defined in the introduction.

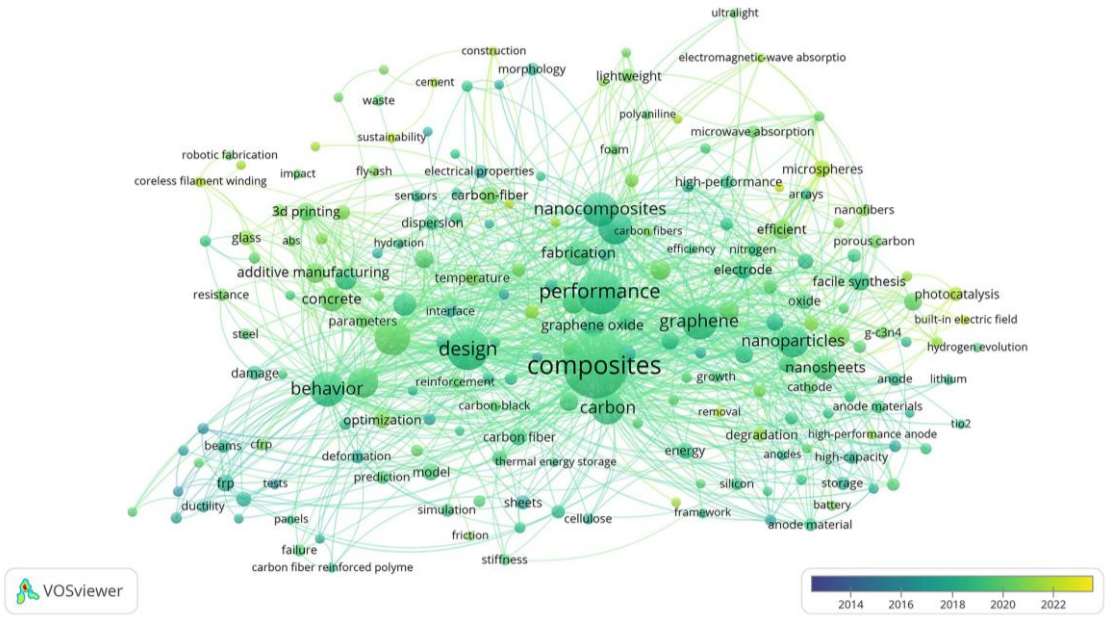


Figure 2. Co-occurrence of keywords on VosViewer (from 2013 to 2023)

Source: Author.

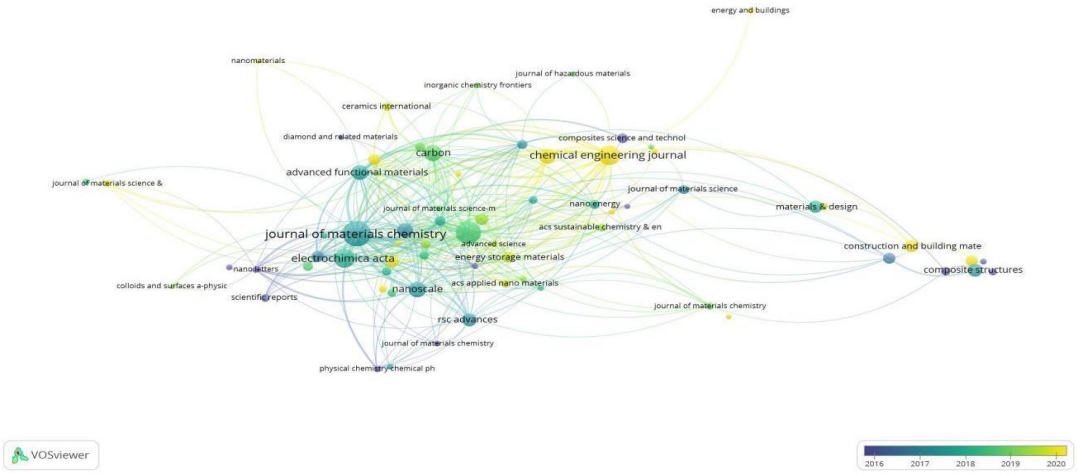


Figure 3. Citation sources (from 2016 to 2020)

Source: Author.

3. Properties and forms

3.1. *Energy-saving characteristics of carbon composite materials*

3.1.1. Reducing the overall mass of the construction materials

Embodied energy refers to the energy of all materials used in buildings and technical installations, as well as the energy generated during the construction and renovation of buildings [14]. The magnitude of the embodied energy of materials is affected by factors such as the difficulty of developing natural resources, the properties of raw materials, material preparation and processing technology, and the distance between materials and building sites [15]. In the process of preparing and using carbon composite materials, the energy in hydrocarbons (oil/natural gas /coal) stored in nature is converted into the embodied energy of the materials [16]. Although carbon composite materials have higher embodied energy compared with concrete, steel, metal, wood, ceramics, and other building materials, they have a lower specific weight and require less energy to achieve the same tensile strength, so they are more material-saving. How to offset the high embodied energy through the energy-saving effect of carbon composite materials poses a challenge in material manufacturing and deserves further inquiry [17].

3.1.2. Recyclability

There are two ways of recycling carbon composites: physical recycling and chemical recycling [17]. In physical recycling, after the construction is completed, the materials are removed and recycled, and the fiber-reinforced polymer is cut and ground into small elements for use in new composite materials. The other is the chemical method, which decomposes the composite materials and dissolves the matrix through heating or chemical treatment [17]. The fibers and resins obtained by pyrolysis, fluidized bed combustion, chemical and enzyme circulation have little mechanical damage, and these materials can be used to form new composites [18].

3.1.3. Life cycle assessment

Life cycle assessment uses quantitative indicators to measure the impact of materials on the environment throughout their life cycle [14]. For buildings, the system shown in Figure 4 describes the energy required to maintain the structural and functional integrity of the building throughout its life cycle, including the extraction of raw materials, the manufacture of building components, the transportation and placement of building materials, the installation of building components, the operation of building equipment, and the energy consumed by disassembly, disposal, and recycling after the end of functional use. Building materials are a very important factor, and various elements should be integrated to consider the energy input and output at all stages of the life cycle [19].

The initial embodied energy of building materials can account for a considerable proportion of the energy cost of a building, ranging from as low as 13% to as high as 50% [16]. The specific proportion is related to the scale, purpose, material type, operation efficiency and service life of the building, as well as the local climate and resources [14]. Compared with traditional building materials with high energy consumption, the embodied energy of high-performance building materials accounts for a larger proportion of the total energy cost of buildings. These materials can improve the use efficiency of buildings, to reduce the energy consumed by buildings in the operation and maintenance stage and control the total energy cost over the whole life cycle [17].

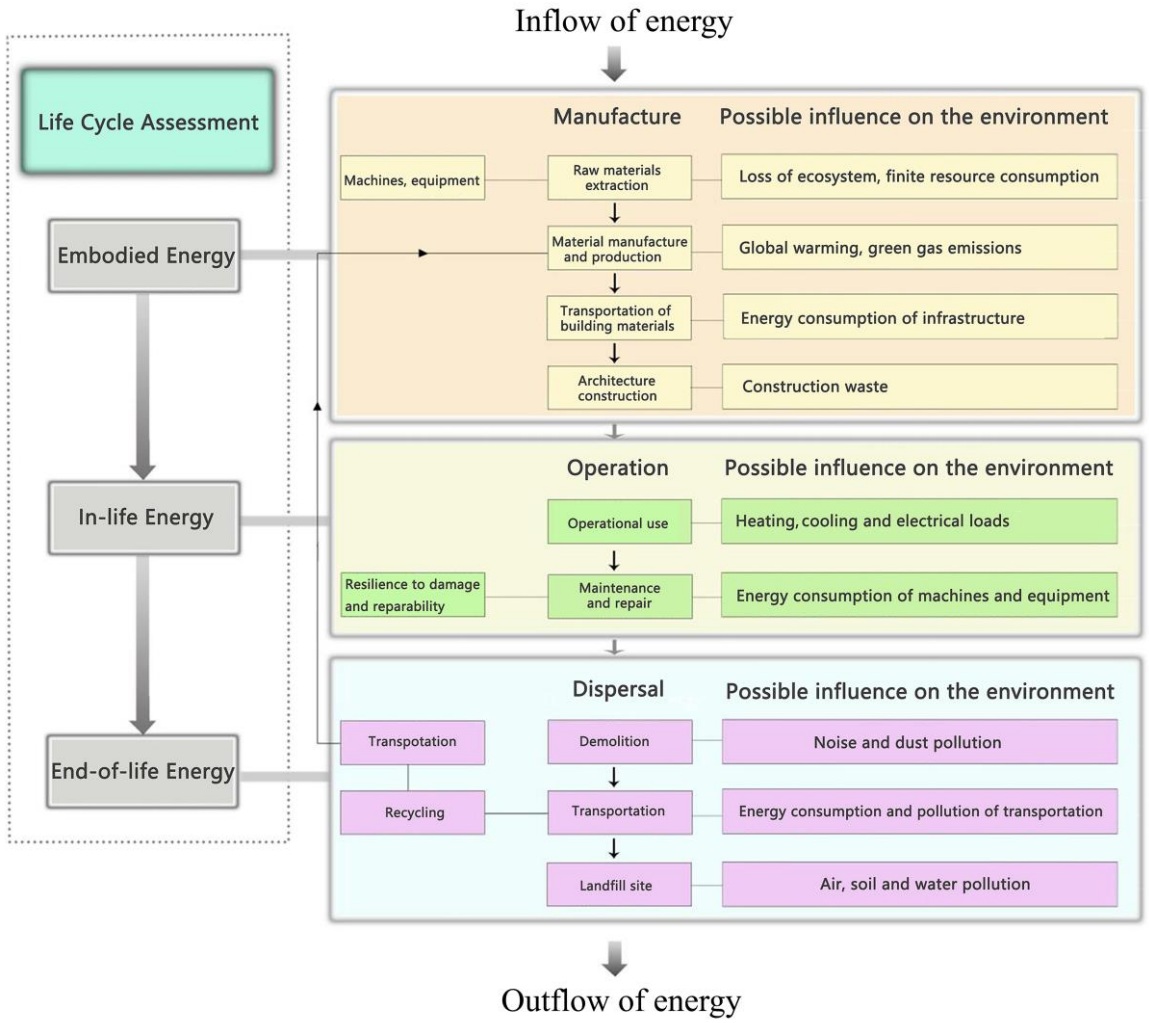


Figure 4. Life Cycle Assessment.

Source: Q. Truong (2020).

3.2. *Mechanical and structural properties*

3.2.1. High specific strength

The specific strength, also known as the strength/weight ratio, is the ratio of the tensile strength of materials to the apparent density of materials and is also an important index affecting the use efficiency of materials [17]. The specific strength of carbon fiber is 2457 NM/ kg [20]. Due to the special composition and connection between carbon fiber and resin matrix, the specific strength of carbon fiber composites is much greater than that of wood, concrete, steel bars and aluminium alloys. Generally, when comparing the strength of materials with the same thickness and size, the weight of fiber reinforced polymers (FRP) composites is one-seventh of that of steel and one half of that of aluminium [17]. In the appropriate interface, structure, and equipment of the building, replacing concrete, cement, metal, and other materials with lightweight, low-energy, high-strength carbon fiber composites will effectively reduce the total use of building materials and the energy contained therein, and make the building lighter and stronger [21]. When carbon fiber composites are used in long-span structures, the self-weight of the structure can be greatly reduced. For example, the self-weight of the whole carbon fiber roof of Jobs Theater is only 80t, which can be constructed by integral hoisting [22].

3.2.2. High durability

Carbon composites are corrosion-resistant and easy to maintain and clean [23]. This material has a variety of connection methods including bolting, and the light weight makes it easier to disassemble and assemble [24]. Due to the exceptional durability of the materials, the service life of the building is long, and the purpose of saving materials is achieved [17]. Considering the multitude, redundancy, and open-ended control of fiber reinforced polymers (FRP), the structures show higher resilience to geometrical errors at the local site and could return to stable state [25].

3.3. *Different forms*

The carbon composite forms discussed in the literature can be classified into several types: fibers, matrices, foams, sheets, fabrics, tapes, and carbon nanotubes, etc. FRP composite materials have three main characteristics: textile parametric variability, self-organization, and resilience, and can be built into linear elements and surface elements, enabling elegant architectural expression [25]. The CFRP sheets and fabrics are structural applications and manufacturing composite parts for aerospace, automotive, marine and sports industries. The CFRP bars, tapes, and strips are commonly used for reinforcement, repairs or strengthening applications [17].

4. Fabrication methods and design possibilities

4.1. *Carbon composites and related digital design and manufacturing tools*

Burry and Burry (2010) review 46 exemplary projects in computational design and delineate the interconnection between mathematical principles and parametric language in architectural forms [26]. Compared with metal, glass, wood and most other building materials, carbon composites can form and produce building components with complex shapes and improve the overall structural efficiency by increasing the structural spans. Through parametric design, intelligent construction and robotic manufacturing, new morphological logic can be obtained, and nonlinear components can be manufactured. Thus, architects will have wider design possibilities.

At present, carbon fiber weaving and 3D printing have created new manufacturing processes. For example, the technology of manufacturing continuous fiber composites with three-dimensional lithography 3D printing technology [27] can achieve high technical efficiency. The biomimetic design research conducted by Menges and Knippers (2015) has investigated the fiber tectonics in biological structures and transferred the fibrous morphology into architectural components, forming tectonic articulation in structural design [28]. The shape of the ITKE Research Pavilion has been compared to that of spider webs, and its fabrication process entails the assemblage of glass fiber shell and carbon fiber rovings. Supported by the Institute for Computational Design (ICD) and the Institute of Building Structures and Structural Design (ITKE) at the University of Stuttgart, the biomimetic shape forming research based on fiber composites integrates the computation, simulation and fabrication skills and exploits the structural and morphological potential in the inner shapes of nature. The tectonic philosophy behind this series of projects renders the fibrous composites as active and adaptive agents of shape formation rather than passive substances. Lee and Xie (2021) helped define the curve design parameters in the architectural forms and classified the elastic-ruled surfaces into five types: planar form, tabular or closed strip form, open surface, self-intersected and connected surface [25].

4.2. *Building components for energy conservation and environmental protection*

Carbon composites have outstanding mechanical structural properties and can be used to manufacture building components. In addition, they also have heat insulation, waterproofing and other properties. They can be used to build the envelope and equipment of residential or other light building structures, including wallboards, shells, roofs, doors and windows, structural systems and so on [17]. New material

manufacturing forms have been developed based on carbon fiber composites, including board structure, window frame, carbon solar skin, carbon nanotube structure, LED lamps and carbon nanotube lighting, carbon foam materials, etc. These materials show the application potential of carbon fiber composites, offering a variety of material characteristics for the construction of multi-functional "all carbon housing" [12]. For example, the roof of the penthouse called "Bankside Paramorph" next to the tower of Tate Modern apartments in London is composed of 16 light carbon fiber sheets, and the glass is assembled on the structural components [29]. The low thermal conductivity, opacity and vivid structural aesthetics of these plates make the shell of the attic roof innovative in structure and function. Similarly, Startink systems is also developing a modular composite system for building low-cost, energy-saving houses. The system connects a series of composite plates by bolts to realize rapid assembly. This design concept can provide more economical and environmentally friendly housing in developing countries and provide permanent or temporary housing [30].

4.3. *Reinforcement of ancient wooden buildings*

Carbon fiber composites can not only be used to build lightweight structures, but also to strengthen the main structure of bridges and historical buildings [31]. The Chinese ancient architectural heritage is a valuable resource that needs to be developed. Carbon fiber composites can be used for the restoration of ancient buildings in characteristic cultural sites, strengthening beams, columns, purlins, arches, and other wooden components [32]. Compared with wood, carbon fiber composites have the advantages of fire prevention, water resistance, chemical corrosion resistance, light weight, and good flexibility [33]. Properly combined with the wooden structures, they can help express cultural themes in regional landscape design. Meanwhile, this choice of material can greatly save natural wood and reduce damage to the environment.

5. Discussion

5.1. *Challenges*

Admittedly, carbon composites are not perfect choices for all construction applications, and as a result, the architects should take the following limitations of composite materials into consideration: 1) low thermal mass [34]; 2) high rigidity and stiffness [35]; 3) in-plane and through-thickness properties [36]; 4) structured randomness [25]; 5) complicated failure mechanism [34]; 6) influence of human factors [37]; 7) fire performance limitations [38]; 8) high cost [35]. For example, during the design and manufacturing process, despite the organized design principles, complexity still arises from the structured randomness and the internal configuration [25].

5.2. *Index framework for sustainability*

According to Truong (2020), architecture design is closely related to social, humanistic, ecological, and economic aspects of urban life. Therefore, the evaluation system for the sustainability of architecture and landscape should be composed of ecological, social, and economic considerations, among which the ecological benefits outweigh the others. Table 1 shows the index system for the sustainability of carbon composites, which embodies three aspects of sustainability, six levels of values, and 19 design goals for the projects [17]. The advantages and disadvantages of building projects can be assessed within the parameters in this table, and the related concerns can also be addressed.

Table 1. Sustainability evaluation index framework.

Sustainability	Evaluation	Design goals
Ecological	Basic properties of materials	Carbon footprint Life cycle Embodied energy Durability
	Energy consumption	Recycling and reuse of resources and materials Electric and thermal energy consumption Energy performance
Social	Climatic adaptability	Carbon dioxide emissions reduction Rainwater recycling Efficient use of solar energy
	Cultural impacts	Modern and regional expression Technical and aesthetic values Environmental behavior and psychology
Economic	Production	Promote workforce and skills development Support economic activities
	Mutual benefit	Efficient use of land and space Convenience of services and goods Fair financing environment Promoting physical and mental health of the general public

Source: Q. Truong (2020).

6. Conclusions

In the context of "all carbon", designers should not only pay attention to the forms, structures, and technologies of buildings, but also endow them with characteristics such as stability, toughness, sustainability, and eco-friendliness. Within the overall goal of consuming less energy and spending less on materials, carbon composites exemplify more sustainable construction materials. Carbon composite materials provide architects and engineers with new choices, open new design and construction pathways, and offer great potential for urban progress. The carbon material paradigm requires interdisciplinary collaboration and bridges the technical gaps between material production, fabrication, and design. The carbon composites will create new tectonics and expressions in architectural design and with its noticeable potential in forms, structures, and sustainable properties, could be developed and applied to larger-scale urban residential environments.

Acknowledgements

The author acknowledges the support from Robert A. Irwin at the MIT Writing and Communication Center.

Conflicts of interest

None.

References

[1] J. Rees, "Industrialization and urbanization in the United States, 1880–1929," *In Oxford Research Encyclopedia of American History*, 2016.

[2] K. O'Connor, C. Pocock, M. R. Barthelmeh and S. Davis, "Carbon and environmental profiling of hard landscape materials," *LEaP Research Report*, vol. 222011, 2011.

[3] A. Kong, H. Kang, S. He, N. Li and W. Wang, "Study on the Carbon Emissions in the Whole Construction Process of Prefabricated Floor Slab," *Applied Science*, vol. 10, no. 7, pp. 2326, 2020.

[4] A. E. Fenner, C. J. Kibert, J. Woo, S. Morque, M. Razkenari, H. Hakim and X. Lu, "The carbon footprint of buildings: A review of methodologies and applications," *Renewable and Sustainable Energy Reviews*, vol. 94, pp. 1142-1152, 2018.

[5] S. K. R. Jyosyula, S. Surana and S. Raju, "Role of lightweight materials of construction on carbon dioxide emission of a reinforced concrete building," *Materials Today*, vol. 27, pp. 984–990, 2020.

[6] L. Huang, G. Krigsvoll, F. Johansen, Y. Liu and X. Zhang, "Carbon emission of global construction sector," *Renewable and Sustainable Energy Reviews*, vol. 81, pp.1906-1916, 2018.

[7] A. Mardiana and S. Riffat, "Building energy consumption and carbon dioxide emissions: Threat to climate change," *Journal of Earth Science & Climatic Change*, S3, pp. 1, 2015.

[8] J. Birkeland, "Nature Positive: Interrogating Sustainable Design Frameworks for Their Potential to Deliver Eco-Positive Outcomes," *Urban Science*, vol. 6, pp. 35, 2022.

[9] H. Locke, J. Rockström, P. Bakker, M. Bapna, M. Gough, J. Hilty, M. Lambertini, J. Morris, P. Polman and C. M. Rodriguez, "A Nature-positive World: The Global Goal for Nature," 2021.

[10] Adopted, I. P. C. C, "Climate change 2014 synthesis report," IPCC: Geneva, Szwitzerland, 2014.

[11] N. V. Kasyanov, "The evolution of architectural morphogenesis at the beginning of XXI century in the context of scientific advances," Procedia Engineering, vol. 1, no. 153, pp. 266-270, 2016.

[12] M. Goulthorpe, "A New Carbon Ontology: Hydrocarbons as Benign Material Resource for Civilizational-Scale Building," *In APS March Meeting Abstracts*, vol. 2019, pp. F34-001, 2019.

[13] Yergün, Uzay, and Banu Çelebioğlu, "Steel Frame Construction Technology in Ottoman Architecture and 'Metro Khan'," *In Advanced Materials Research*, vol. 133, pp. 131-135, Trans Tech Publications Ltd, 2010.

[14] L. F. Cabeza, L. Rincón, V. Vilariño, G. Pérez and A. Castell, "Life cycle assessment (LCA) and life cycle energy analysis (LCEA) of buildings and the building sector: A review," *Renewable and Sustainable Energy Reviews*, vol. 29, pp. 394–416, 2014.

[15] L. F. Cabeza, C. Barreneche, L. Miró, J. M. Morera, E. Bartolí and A. I. Fernández, "Low carbon and low embodied energy materials in buildings: A review," *Renewable and Sustainable Energy Reviews*, vol. 23, pp. 536-542, 2013.

[16] V. Smil, *Making the Modern World: Materials and Dematerialization*, Chichester, West Sussex, United Kingdom: John Wiley & Sons, 2014.

[17] Q. Truong, *Composite Architecture: Building and Design with Carbon Fiber and FRPs*, Basel: Birkhauser Architecture, 2020.

[18] A. Zaara and A. Eylem, "Sustainable and Green Manufacturing Options of Fiber Reinforced Composites," Department of Mechanical Engineering at Wichita State University. Presented at CAMX 2018, Dallas, 2018.

[19] C. K. Chau, T. M. Leung and W. Y. Ng, "A review on life cycle assessment, life cycle energy assessment and life cycle carbon emissions assessment on buildings," *Applied energy*, vol. 1, no. 143, pp. 395-413, 2015.

[20] Y. Hayashi, Y. Chiba, H. Inoue, M. Hada and T. Nishikawa, "A review of dry spun carbon nanotube yarns and their potential applications in energy and mechanical devices," *Journal of Fiber Science and Technology*, Vol. 76, no. 2, pp. 72-78, 2020.

[21] Y. Hao, C. Shi, Z. Bi, Z. Lai, A. She and W. Yao, "Recent Advances in Properties and Applications of Carbon Fiber-Reinforced Smart Cement-Based Composites," *Materials*, vol. 16, no.7, pp. 2552, 2023.

[22] Y. Liu, "Suggestions on Improving the Seismic Performance of Portuguese Old 'Pombalino' Buildings," *In IOP Conference Series: Earth and Environmental Science*, IOP Publishing, Vol. 768, No. 1, pp. 012067, 2021.

[23] M. Qiao, G. Ji, Y. Lu and B. Zhang, "Sustainable corrosion-resistant superhydrophobic composite coating with strengthened robustness," *Journal of Industrial and Engineering Chemistry,* vol. 121, pp. 215-227, 2023.

[24] Z. Dawei, Z. Qi, F. Xiaoguang and Z. Shengdun, "Review on joining process of carbon fiber-reinforced polymer and metal: methods and joining process," *Rare Metal Materials and Engineering,* vol. 47, no. 12, pp. 3686-3696, 2018.

[25] A. Blonder, "FM-FRP: new materiality in FRP as architectured matter with textile attributes," *Architectural Science Review,* vol. 64, pp. 478-489, 2021.

[26] J. Burry and M.Burry, *The new mathematics of architecture,* Londres: Thames & Hudson, 2010.

[27] Y. Sano, R. Matsuzaki, M. Ueda, A. Todoroki and Y. Hirano, "3D printing of discontinuous and continuousfibre composites usingstereolithography," *Additive Manufacturing,* vol. 24, pp. 521–527, 2018.

[28] A. Menges and J. Knippers, "Fibrous tectonics," *Architectural Design,* vol. 85, no. 5, pp. 40-47, 2015.

[29] C. Calderon and R. Noble, " Beyond modelling: Avant-garde Computer Techniques in Residential Buildings," 2005.

[30] D. Kendall, "Building the future with FRP composites," *Reinforced Plastics,* vol. 51, no. 5, pp. 26-33, 2007.

[31] L. E. Yongtaeg, P. A. Junho, H. O. Seonguk and K. I. Seunghun, "A study of bond of structural timber and carbon fiber reinforced polymer plate," *Materials Science,* vol. 21, no. 04, pp. 563-567, 2015.

[32] Z. M. Bie and Y. R. LU, "The application of carbon Fiber composite in the protection design of wooden frame of ancient buildings," *Plastics Science and Technology,* vol. 07, pp. 137-140, 2020.

[33] G. Yang, M. Park and S. J. Park, "Recent progresses of fabrication and characterization of fibers-reinforced composites: A review*," Composites communications,* vol. 13, pp. 34-42, 2019.

[34] P. F. Liu, J. K. Chu, Y. L. Liu and J. Y. Zheng, "A study on the failure mechanisms of carbon fiber/epoxy composite laminates using acoustic emission," *Materials & Design,* vol. 01, no. 37, pp. 228-235, 2012.

[35] M. N. Gururaja and A. H. Rao, "A review on recent applications and future prospectus of hybrid composites," *International Journal of Soft Computing and Engineering,* vol. 01, no. 06, pp. 353-355, 2012.

[36] R. Gerlach, C. R. Siviour, J. Wiegand and N. Petrinic, "In-plane and through-thickness properties, failure modes, damage and delamination in 3D woven carbon fibre composites subjected to impact loading," *Composites Science and Technology,* vol. 72, no. 03, pp. 397-411, 2012.

[37] R. Gerlach, C. R. Siviour, J. Wiegand and N. Petrinic, "In-plane and through-thickness properties, failure modes, damage and delamination in 3D woven carbon fibre composites subjected to impact loading," *Composites Science and Technology,* vol. 72, no. 03, pp. 397-411, 2012.

[38] F. Yang, "Fire-retardant carbon-fiber-reinforced thermoset composites," *In Novel fire retardant polymers and composite materials,* Woodhead Publishing, pp. 271-293, 2017.

IASS 2023
July 10–14 Melbourne
Integration of Design and Fabrication

Proceedings of the IASS Annual Symposium 2023
Integration of Design and Fabrication
10–14 July 2023, Melbourne, Australia
Y.M. Xie, J. Burry, T.U. Lee and J. Ma (eds.)

Textile steel - experimental investigations of textile fabrication processes for steel shell and lattice structures

Vincent WITT[*], Pascal KNOPF[*], Erik ZANETTI[a], Baris WENZEL[a], Moritz DÖRSTELMANN[a]

[*] KIT-Faculty of Architecture
baris.wenzel@kit.edu

[a] Digital Design and Fabrication (DDF) - Karlsruhe Institute of Technology (KIT) Englerstraße 7, 76131 Karlsruhe, Germany

Abstract

Global steel production amounts to around 2 billion tons per year [1]. Half of the world's annual production of steel is used in the construction of buildings and infrastructure [2]. Steel is a material that can be recycled without loss of properties, a huge potential for urban mining and the circular economy, yet, the demand for new steel is higher than the offer of secondary raw material. Lightweight structures are saving material and can therefore help to reduce the extraction of materials through the primary route and optimise the use of secondary raw material, which can be extracted through urban mining [3].At the intersection of research and teaching, the paper examines the formation of concepts, starting from an understanding of materials and fabrication technologies and going forward to questioning and rethinking existing methods with strong focuses on computational design and digital fabrication processes that enable novel concepts for circular economy in construction. By applying fabrication concepts from textile technology, a series of steel structures were re-conceptualized, redesigned and prototyped. The material distribution was locally tailored, based on the interplay between geometry and structural behaviour. Several prototypes were built to validate the overall approach, and in a next step, recycled secondary building materials could be used.

Keywords: optimization, digital fabrication, form finding, steel, textile, metal, membrane structures, weaving, structural membrane

1. Introduction

Steel is a material that can be recycled without loss of properties, a huge potential for urban mining and the circular economy. Yet, the demand for new steel is higher than the offer of secondary raw material. The construction industry accounts for 50% of global steel production and consumes more than 3 billion tonnes of raw materials [3]. Steel is therefore a perfect case study for the implementation of circular material cycles in construction. Based on the principles of the technical cycle as described in the concept of circular economy by the Ellen MacArthur Foundation, the aim should be to avoid the extraction of materials through the primary route and focus instead on the use of secondary raw material, which can be extracted through urban mining. However, the recycled products must use the material more efficiently: recycling a conventional steel component into a multitude of components with locally tailored material distribution, while delivering the same function and strength as those created by traditional methods, could enable the industry to meet growing global demand. While steel is traditionally thought of as a heavy and rigid material, the availability of thin sections, wires and yarns allows a level of flexibility and adaptability which bigger profiles do not offer. The use of these materials enables it to be processed in a textile way, but still allows for the combination with established steel working processes such as cutting and welding. In this scenario, digital design and fabrication processes

Copyright © 2023 by Vincent WITT, Pascal KNOPF, Erik ZANETTI, Baris WENZEL and Moritz DÖRSTELMANN. Published in the Proceedings of the IASS Annual Symposium 2023 with permission.

could enable the shift from the serial production of identical parts to the custom production of material-optimised components.

At the intersection of research and teaching, the combination of fabrication concepts from textile technology and concepts of resource-efficient steel components were investigated. Experimental prototypes made of steel wire and yarn, focusing on hands-on explorations and concept models were created.

2. Research and teaching method

The course explored a variety of concepts through a design-through-making approach. Starting from an understanding of materiality and existing technology, students then developed initial concepts through exploratory prototypes and realised three final proof of concept models through full-scale prototyping. Guided through three development phases, the course investigated processes, techniques and material properties in an initial phase to provide students with the technical foundations for the seminar. The second phase entailed the development of exploratory small scale prototypes to iteratively refine a novel digital design and fabrication concept for material-efficient steel components. The third phase of the seminar focused on validation of the developed concepts through physical prototypes on a 1:1 scale, while showcasing its architectural implications.

3. Phase 01 - initial investigations

Students investigated a varied range of textile processes and digital fabrication techniques, in search for manufacturing and processing techniques that enable resource-efficient, functional arrangements, utilizing material properties and mechanical techniques for steel. This created a reliable repertoire of knowledge on which the following development phases could base upon. This phase was complemented by skill-building tutorials for digital design tools to aid the concept specific design tool development. In all examined textile fabrication techniques variations in weaving, braiding or knitting patterns can be used to create 3-dimensional spatial structures.

3.1 Textile steel fabrication techniques

Weaving is the process of interlacing two sets of thread, yarn or sometimes other materials to create textile sheets. There are different variations of weaving techniques, but the basic principle is the same: There are threads that are pre-tensioned parallel to each other, the "wefts", and threads that run orthogonally to them, the "warps". By passing the warp threads, which are contained by the "loom", alternately over and under the weft threads, a textile can be created. Special warp knitting machines can produce "spacer fabrics" that create connections between two or more layers of flat fabric, or even create a honeycomb structure in cross section (as implemented by the Belgian company "3D Weaving"). Braiding is the process of intertwining three or more strands of flexible material in a specific pattern to form a three dimensional structure. Unlike weaving, braiding in its purest form requires no equipment other than the material itself, on an industrial scale automated braiding machines are widely established (e.g. braiding machines by HERZOG GmbH) [4]. Knitting is the process of making interlocking loops of yarn or thread using two or more knitting needles. The loops are created by pulling a loop of yarn through an existing loop, then pulling a new loop through the previous loop, and so on, creating a series of interlocking loops. On an industrial scale there are two main types of knitting: flat bed and circular knitting. By varying the knitting pattern locally, the textile can be brought into a three dimensional shape later (as implemented by Zaha Hadid Architects and ETH Zurich) [5].

3.2 Steel joining techniques

During the seminar, the students have explored various fastening techniques with a focus on interlocking techniques that do not require fasteners and are suitable for thin sections rather than sheet material.

Therefore, techniques such as riveting, nailing and screwing were not considered. Instead methods that do not need any additional heat or adhesives such as clinching and interlocking, as well as methods that uses heat like welding, brazing and soldering, were explored. For the development of digital fabrication concepts it was important to focus on steel joining methods which can be implemented using industrial robots. This allows complex 3d structures to be produced with millimetre precision. As such, traditional methods like welding and bending can be used and incorporated in form of robotic WAAM(Wire Arc Additive Manufacturing) or robotic wire bending [6][7][8].

3.3 Material behaviour

Keeping the different properties of steel in mind, several options had been considered. Each has different characteristics to suit specific applications. In most cases, iron is either combined with other materials such as carbon, chromium and nickel to form an alloy, or coated with zinc or oxidised to form a protective layer against corrosion. Typically, the dead weight of the structure is a small fraction of the applied load or generated forces. Lightweight structures often use light and high strength materials as well as advanced technologies for their design and construction. Many shapes are pre-stressed, resulting in double-curved shapes that require special cutting patterns and care during erection. Typical lightweight structures include cable, membrane, shell and folded structures as well as space grids, braced vaults and domes, arched, stayed and trussed systems. For the purpose of the seminar such structural principles and typologies were investigated regarding their potential as textile steel structures and building components.

4. Phase 02 - development of initial concepts

Exploratory prototypes were manufactured as small experiments to gain insights into materials, systems and structures as well as test key assumptions, strengths and weaknesses of the concepts. Produced in rapid iteration, this helped to formulate further research questions and address them in the next evolution, but also narrowed the investigations through research-based decision making.

4.1 Knitted steel

Aiming to produce building elements utilising steel and knitting techniques, required the conceptualization of a process starting with form finding, extraction of 2d knitting information which has the three dimensional shape inscribed, a forming phase in which the knitted structure is tensioned and a solidification step in which the tensile structure assumes bending stiff properties. Different options for the solidification of the structure were explored. Using the custom knitted steel membrane as integrated concrete rebar and formwork provides a stiffening effect that allows the structure to resist bending forces as commonly used in construction. Through experimentation, it was determined that spaced layers of fabric were beneficial to build thickness on the structure, allowing concrete poured onto the mesh to adhere more effectively. Another method of transforming a tensile network into a bending stiff shell structure is to use local spot welding or brazing to join the steel wires together at specific points or along the entire curve network length to create a stiff structure. Such a knitted steel membrane could therefore be conceptualized as a precursor for a subsequent robotic WAAM process. To fabricate the building elements, a form-giving strategy was devised, and an external frame was employed to put the knitted meshes of steel under tension, enabling tension-based doubly curved membrane geometries to be created(Fig.1).

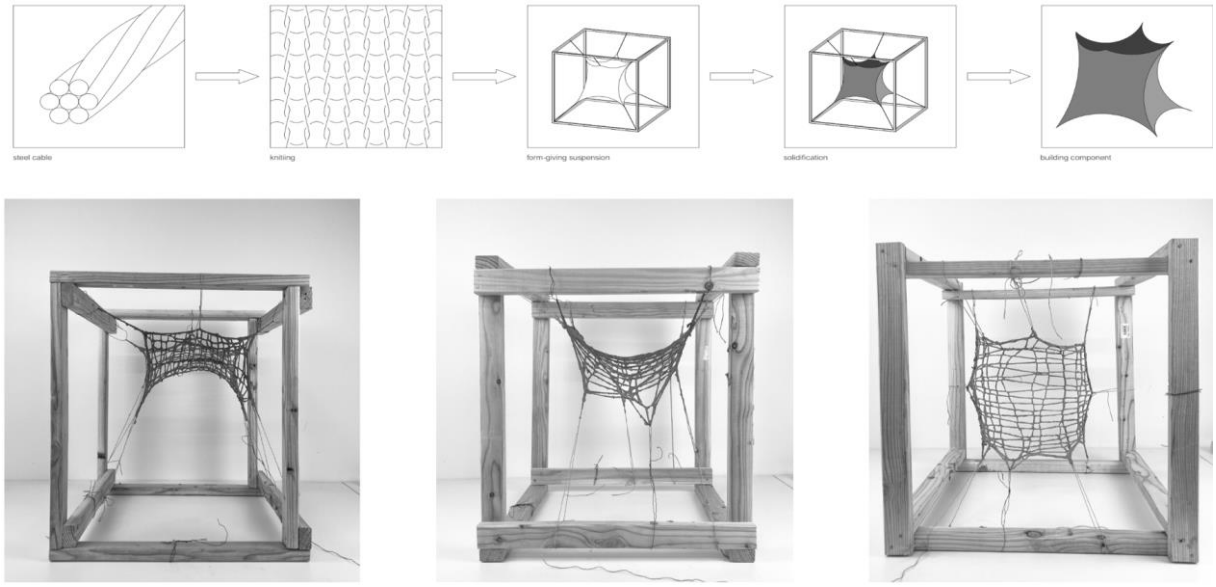


Figure 1. Production concept of steel knitting and first prototypes [Graphics and photo by authors].

4.2 Woven wall

The envisioned spatial weaving concept allows for a three dimensional interconnected network of steel cables to be spanned between a set of initial steel pipes. For building elements like floor slabs or wall segments, several hexagon patterns were subsequently merged into each other. These could either be lined up in a flat manner to develop slab like ceiling or wall components, or be spatially arranged into more complex geometrical configurations. The basic wire layout could be reinforced by subsequent locally differentiated reinforcement layers to provide differentiated structural capacity. Sleeves around the threaded rods separate the levels from each other and reduce the density of the structure as well as reduce the buckling length of the threaded rod. Vertical braces are woven in to provide additional stability (Fig.2).

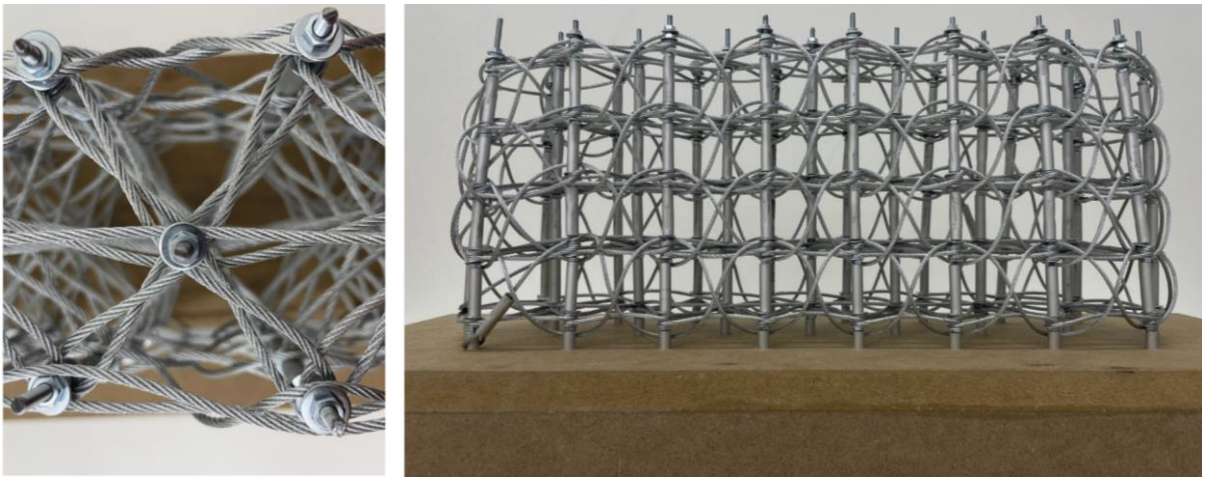


Figure 2. First prototype of steelweaving [Photos by authors].

4.3 Braided column

This fabrication concept utilises threaded rods which are intertwined by steel wire or cables through a braiding process. The steel cable is wound around rods to form connecting points, forming very fine mini-members of a spatial truss which is bracing the main parallel aligned members. The diagonally connected inner webbing supports the column and reduces the buckling length. Through the centre of the structure more cables tie the individual rods together to cope with the pressure forces resulting from vertical loads. These continuous wires represent the stiffening of the structure. The intertwined rods and wires are subsequently soldered and could conceptually be robotically spot welded to form load transferring nodes (Fig.3). Although locally consisting of weak members and connections the high resolution and redundancy of the structure could form a robust load bearing component.

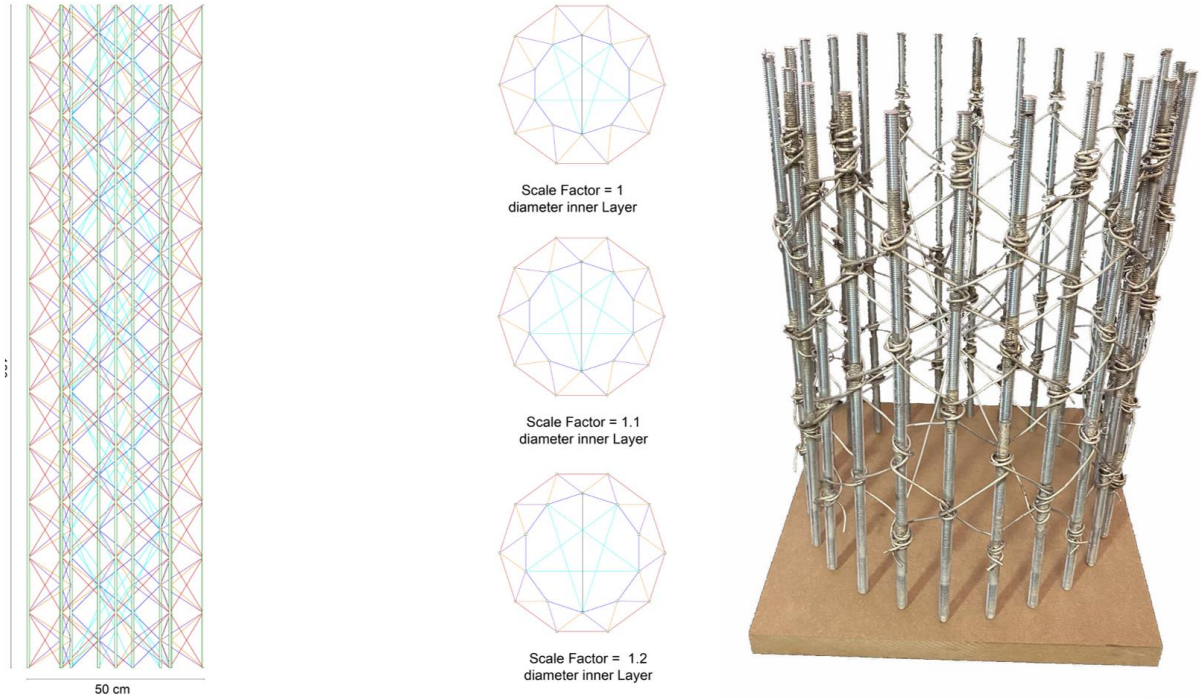


Figure 3. Production concept of steel braiding and first prototype [Graphics and photo by authors].

4.4 Metal distance weaving

Distance weaving is a fairly novel concept which is able to form multiple interconnected layers of fabric at once. Metal screen weaving on the other hand is practised for many decades and well understood. The concept aims to alter the manufacturing process of metal screen weaving in such a way that a rigid metal distance weave can be produced on an industrial scale. In a first prototype weaving pattern, the weaving process itself as well as the appropriate metal gauges were explored (Fig.4). The development of a process specific parametric design tool allowed to explore several different variations in thickness, patterns, as well as shapes of the structure. Through specific bending of the metal wefts of the 2nd prototype it was possible to prove the concept of inscribing curvature into the piece. This opened up the potential to inscribe information about the components global geometry into local machine bending instructions. Being able to form curved shapes opens up a wide range of possibilities from thin free standing walls to quick industrial production of mesh moulds for construction. Through the inscription of local deviation of material distribution, it is possible to tailor the structure to the specific application and load while using as little material as possible.

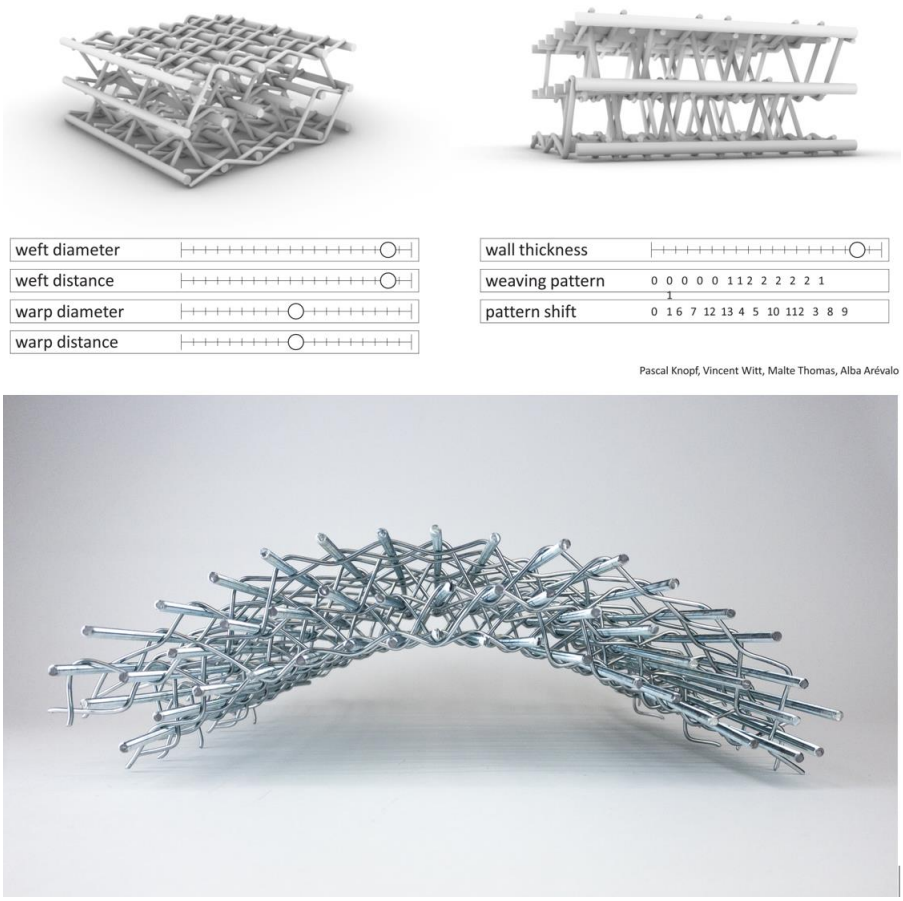


Figure 4. Production concept of steel distance weaving and first prototype [Graphics and photo by authors].

5. Phase 03 -1:1 scale explorative prototyping

The research of the third phase was driven by the bottom-up concept developments of the second phase process focused explorations and aimed at their translation into material-efficient building components based on simple structural models. Within the limited scope of a selected building element (e.g. column, façade panel etc.), each group carried out early qualitative design explorations for loading conditions to inform the material layout in high resolution and cross reference them for potential differentiation with the textile techniques investigated thus far. This resulted in three physical 1:1 scale, handcrafted prototypes, made of steel wire in varying gauges and yarn utilizing and scaling the techniques explored in the previous phases. Furthermore, the models were soldered, welded and galvanized(Fig.5) to provide structurally stable components. The final prototypes serve as a proof of concept at the intersection of research and teaching and validate the architectural potential.



Figure 5. Hot dip bath galvanisation of the final 1:1 prototypes [Photo by Daniel Fischer].

5.1 Braiding steel

Braiding techniques emerged as a concept from phase two to be explored further to interconnect paired rigid, straight, load-bearing braid strands with flexible strands to reduce the buckling distance of the load-bearing strands. The concept aims to explore an idea for lightweight, high-efficiency column structures using digital fabrication. The structure consists of vertical steel rods, which create its main skeleton; steel cables were braided between the rods to form the lattice structure. The diagonals, created by winding the cables around the rods, are digitally designed in continuous paths from the bottom to the top, an important aspect considering later potential for its implementation in a fully digitally controlled textile braiding process. The structural concept of the column has been extended through a double layered rod structure with local buckling bracing and a second layer was introduced within the inner core where cables create a secondary web to further strengthen the column. The entire structure was galvanised by immersion in a zinc bath to fix the braided structure in place and to provide a layer of adhesion and slip resistance at the interface between the rigid rods and the flexible steel cables. In a next step, the concept could be adapted to slab applications such as roof trusses or ceiling structures by modifying the manufacturing setup, which is currently conceptualized for circular linear construction members.

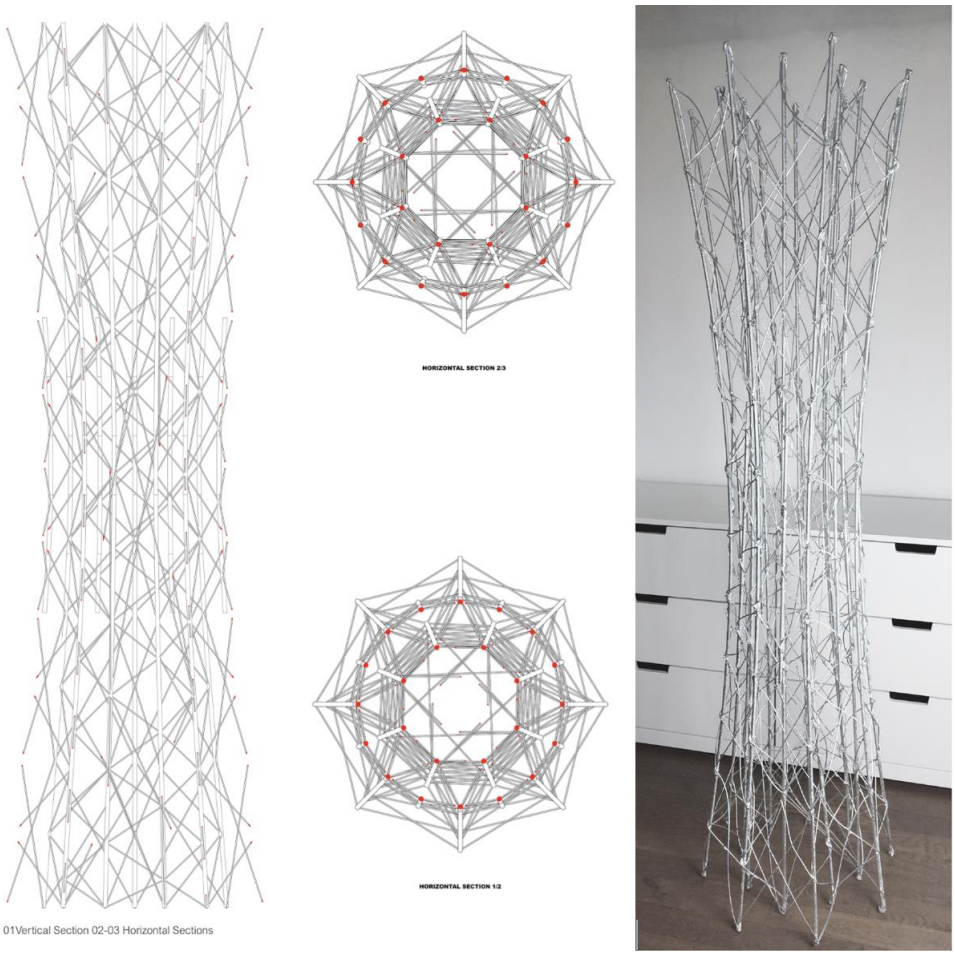


Figure 6. Production concept of steel braiding and second prototype [Graphics and photo by authors].

5.2 Weaving steel

The second 1:1 prototype resulting from phase three continued the exploration of industrial weaving techniques and applied them to steel components to create structures that are based on mechanical interlocking, thus enabling the structure to be fully dismantled after use and creating a closed material cycle. The process is derived from the looms used in the industrial manufacturing of woven textiles (Fig.7).

By adjusting parameters of the structure through the parametric design tool according to the differentiated requirements, such as structural load, the desired shape was found. The adaptable parameters are: weft and warp diameter, distance between wefts and warps, bending patterns as well as bending pattern shift. These parameters are derived from the global design of the geometry. Conversely, the specific sequence of wire bending instructions to the machine inscribes the global geometry and especially curvature into the produced part. Through varying these parameters, a high degree of local differentiation of the resulting properties of the structure is achieved resulting in a variety of possible geometries (Fig.2). The wefts and warps only form a connection through mechanical interlocking, thus enabling the structure to be reused or remanufactured. Other than as rebar the structure can serve as installation walls, facade elements, partitioning walls as well as plant racks or lattices. The manufacturing technique that was developed for the concept could become an industrial alternative for rebar installation, which usually requires great amounts of manual labour.

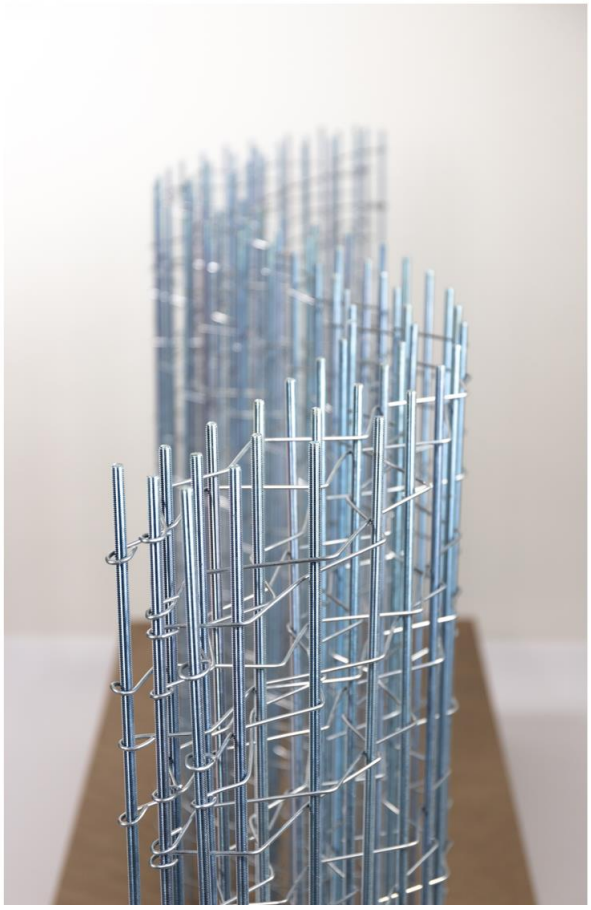


Figure 7. Final 1:1 prototype of weaved steel wall [Photo by the authors].

5.3 Knitting steel

The third 1:1 prototype resulting from phase three built on knitting techniques in combination with thin steel cables to create facade elements that are locally differentiated for shading and aesthetics, as well as material distribution. The concept is based on knitting a 2D mesh and using an external framework to suspend it. In this way, it is possible to navigate the textile repertoire of form found membranes as doubly curved lightweight structures. The form found membrane geometry enables the forming process during fabrication and provides structural performance as shell action in its final bending stiff configuration.

Different knitting technique patterns were investigated through the initial exploratory prototypes. By reducing the knitting patterns to three basic principles it was possible to create a pattern that offers great variation in terms of density and resolution but also enables ease of production. Different options for the solidification of the structure were explored in phase two. The 1:1 mock up realized in phase three utilized zinc dip bath galvanization to locally stiffen and bind the steel cables together. As an outlook this process could be replaced with a robotic WAAM process to locally thicken and stiffen the spatial metal network.

Digital tools were utilised as form-finding workflow for the concept. In particular, a physics simulation was used to adapt the behaviour and the final shape of the membrane according to potential positions of integrated building component connection details and tailored density of the knit. This also allowed to gain an understanding of the required fabrication bed size for potential future automated flat knit fabrication and varied density distribution to form the membrane.

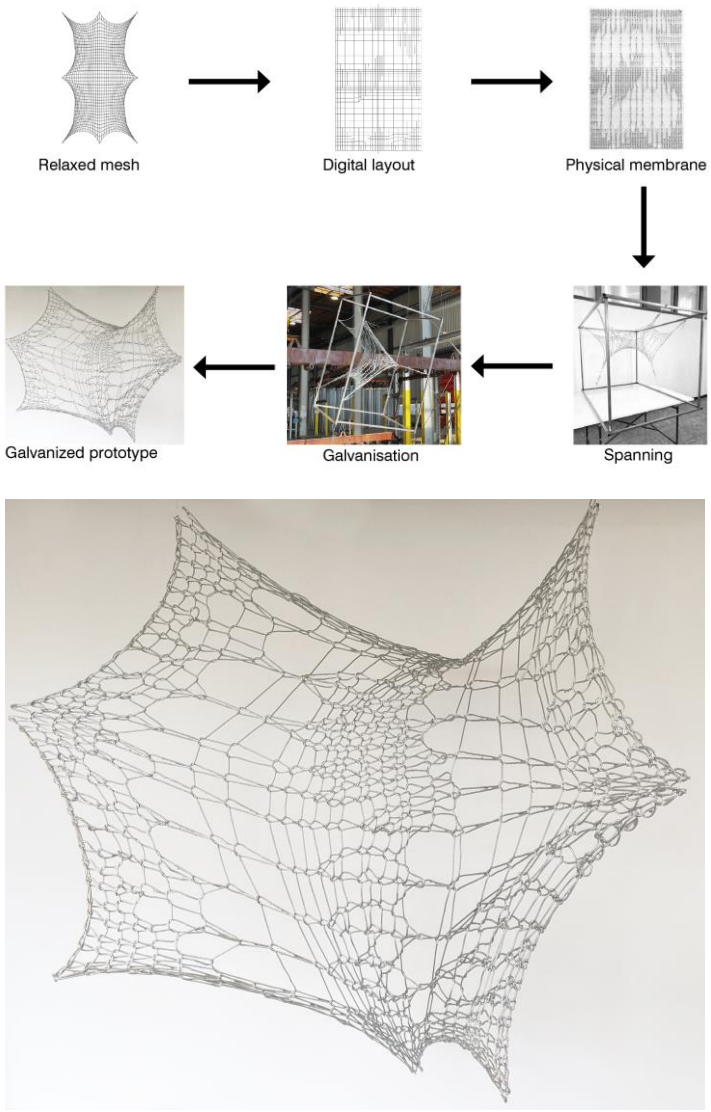


Figure 8. Production process of steel knitting and final prototype [Graphics and Photo by the authors].

5. Conclusion and outlook

We were able to show that through digital design workflows, a critical review of textile manufacturing techniques as well as a gained understanding of the interplay of steel and textile processes it is possible to generate new concepts for building technologies out of steel which offer the ability of local differentiation while reducing the amount of material used. Two of the three explored concepts make use of zinc galvanisation to stiffen the structure, through this process the recyclability of the resulting structures is impaired. Further development of the concepts should include processes to replace the zinc galvanization in order to keep the products mono-material structures. The seminar project revealed several design and fabrication related research questions as starting points for future research endeavours into digital circular construction concepts for steel structures.

6. Acknowledgements

The presented work is based on the seminar “Textile steel” taught by the Professorship Digital Design and Fabrication at the Faculty of Architecture at Karlsruhe Institute of Technology in the winter term 2021/2022.

Students:

Alba Arévalo Castro, Alexander Wurm, Clement Potier, Felix Booz, Joshua Wacker, Malte Thomas, Nils Bachert, Pascal Knopf, Thomas Bichel, Vincent Witt

Teaching team:

Erik Zanetti, Eszter Renata Olah, Moritz Dörstelmann

References

[1] Statista Research Department, “World crude steel production 2021,” Statista, April, 12, 2022. [Online]. Available: https://www.statista.com/statistics/267264/world-crude-steel-production/ [Accessed Dec. 19, 2022].

[2] M. C. Moynihan and J. M. Allwood, “The Flow of Steel into the Construction Sector,” Resources, Conservation and Recycling, vol. 68 pp. 88–95, November 2012. Available: https://doi.org/10.1016/j.resconrec.2012.08.009 [Accessed Dec. 19, 2022].

[3] Ellen MacArthur Foundation, “Circular economy principle: Circulate products and materials,” Ellen MacArthur Foundation. (n.d.). [Online]. Available: https://ellenmacarthurfoundation.org/circulate-products-and-materials [Accessed Dec. 21, 2022].

[4] Herzog, J. (n.d.). Homepage. Retrieved March 30, 2023, from https://herzog-online.com/

[5] M. Popescu u. a., „Structural design, digital fabrication and construction of the cable-net and knitted formwork of the KnitCandela concrete shell“, Structures, Bd. 31, März 2020, doi: 10.1016/j.istruc.2020.02.013.

[6] W. Mcgee, D. Pigram, und M. P. Kaczynski, „Robotic reticulations A method for the integration of multi-axis fabrication processes with algorithmic form-finding techniques“, S. 295–304, Jan. 2012.

[7] K. Dörfler et al., “Mobile robotic fabrication beyond factory conditions: case study Mesh Mould wall of the DFAB HOUSE”, Constr Robot, vol. 3, no. 1, pp. 53–67, Dec. 2019, Available: https://doi.org/10.1007/s41693-019-00020-w. [Accessed Feb. 03, 2023].

[8] H. Hamann u. a., „Flora robotica -- An Architectural System Combining Living Natural Plants and Distributed Robots“, Sep. 2017.

Morphology and configuration processing

Active bending
Additive manufacturing/ 3D printing
Architectural geometry
Bamboo for sustainable construction and quality of life improvement
Bio-inspired structures and architecture
Bridge structures
Computational form-finding
Conceptual design
Concrete structures
Construction techniques
Deployable and inflatable structures
Design competition (WG21)
Digital modelling and fabrication
Dynamic response of metal spatial structures
Dynamic response of other structures
Form-finding and structural optimisation of interlocking discrete assemblages
Graphical methods
Gridshell and lattice structures
Historical concrete shells
Historical structures
Lattice structures
Life-cycle design and assessment of structures
Metal gridshell structures, connections and stability
Methods and construction technologies for sustainable shell structures
► Morphology and configuration processing
Next generation parametric design
Novel methods in modelling, optimisation and construction for reducing carbon footprint of continuous roof shells
Numerical methods for geometry, form-finding and optimisation of lightweight structures
Optimisation methods and applications
Origami
Other
Teaching design uncertainty: working with unknown qualities/quantities of new and re-claimed materials
Teaching of shell and spatial structures
Tensegrity systems and cable structures
Tension and membrane structures
Tension structures in the Asia-Pacific
Timber and bio-based structures
Topology optimisation
Traditional masonry structures and innovation
Transformable structures

IASS 2023
July 10–14 Melbourne
Integration of Design and Fabrication

Proceedings of the IASS Annual Symposium 2023
Integration of Design and Fabrication
10–14 July 2023, Melbourne, Australia
Y.M. Xie, J. Burry, T.U. Lee and J. Ma (eds.)

Multi-modal transportation hub: 'Fill-material-free' technology for a marine-air-land terminal

Michael BURT*, Yehiel ROSENFELD[a]

* Architecture Technion, Israel Institute of Technology, Haifa 32000, Israel
matburt@netvision.net.il

[a] National Building Research Institute
Technion, Israel Institute of Technology, Haifa 32000, Israel
roseny@technion.ac.il

Abstract

'Multi-Modal Transportation Hub' terminals are a growing stark necessity, especially in mega port-cities. Transportation infrastructures, within port-city Metropolitan areas are in rising conflict, mostly concerning eco-environmental and economic (real-estate) values, while robbing the cities of their sea-frontage. A conceptual approach with supporting technologies are suggested: Development (in deep waters) of a combined marine-air-land terminal, as a 'Multi-Modal Transportation Hub'. It has to be compact, multi-layered, with shared work-service-storage infrastructures, with flight decks above the dock piers below, and connected by bridge avenues to the city and its hinterland beyond. A marine development 'fill material free' technology is suggested, with 'Permeable Sponge Breakwaters', 'Modular Tub Platforms' and 'Infinite Polyhedra Lattice' space frames. All the technology constituents were widely researched and analyzed, all with positive results and economically attractive.

Keywords: marine environment, transportation hub, multi-modal, compact, fill material free, space frames

1. Introduction

The human habitat is continuing to expand and devour greater space and land area resources, and that for multiple self-evident reasons:

- Worldwide population growth and the resulting evolution of mega-metropolitan urban areas, some with tens of millions of residents, mostly sprawling along the coastal lake-sea-ocean expanses of the globe.
- A continuously growing area-space consumption per-capita, as a manifestation of the basic human desire to raise its standard of living.
- A growing area-space consumption for public community services of education-culture-recreation-work and commercial conglomerates.
- A growing demand for mobility and the resulting explosive growth of land, air, marine transportation infrastructures, with the growing volumes-tonnage of shipped materials and merchandise, and their storage and trans-shipment.

All these happen in alarmingly growing proximity to the urban clientele, with a dramatic rise in the level of eco-environmental conflicts and costs, sky-rocketing real-estate land values, and perpetual rise of pressure on our free time, cost of living and well-being at large. Sometimes, as in the case of urban marine port terminals, the infrastructures are robbing the city of its sea-frontage and clogging the downtown land transportation to a state of paralysis. It turns out that all expertly statistic forecasting

Copyright © 2023 by Michael BURT and Yehiel ROSENFELD. Published in the Proceedings of the IASS Annual Symposium 2023 with permission.

are promising ever-continuing (doubling-tripling) growth within the foreseeable future, of land-space consumption and the resulting deterioration.
Eventually, we come to realize that land-space resources, especially those in close proximity to our urban environments, are most critically limited and expendable. We have to re-evaluate and re-think the way we manipulate space employment-usage within the context of our evolving future habitat.

Some development design paradigms were considered, and none of them appears to be as promising as the 'expansion into the marine environment' option.

2. Conceptual principles of the evolving design paradigm

Most of the attention in this paper is focused on the infrastructures, and in particular – transportation infrastructures. At the core of the issue, it is not just the land–space scarcity and its manipulation, but also the growing global public sensitivity and concern over the eco-environmental sustainability prospects, and whenever the marine development option is raised, the emergent 'Fill Material Based' design paradigm comes under ever-growing criticism, even to a point of its total rejection.

This double feature of land–space manipulation for effective economization of its exploitation, and the drastic reduction of dredged-excavated-mined fill-materials, to a point of 'Fill Material Free' conception, have to be the main-stay of the evolving design paradigm of expansion into the marine environment.

The conceptual principles of the evolving design paradigm of the Transportation Infrastructures in the Marine Environment are suggested to be the following:

a. Infrastructures have to be relocated-developed in deeper waters, leaving the coastal areas and the urban frontage for (mostly) social and recreational activities.
b. Infrastructures have to strive for much more compact development and employment of land and space, thus promoting multi-level (below and above the water level) design and sprawl.
c. Functionally interrelating and complementary transportation infrastructures have to be spatially combined-intertwined synergetically together, as much as possible and viable.
d. Every possible ingenuity and design orchestration has to strive and enable 'Fill Material Free' development, with no dredged, excavated or mined materials from nature, involved.
e. All production-assembly-construction processes must be realized in highly industrialized coastal (on the water line) plants and sea-transported to their sites of function.

The suggested comprehensive design paradigm should be termed as the 'Multi-Modal Transportation Hub'. It is a compact, multi-level combined Marine-Air-Land transportation terminal, utilizing for its realization a 'Fill Material Free' Technology.

2.1. "Fill Material Free" technology

The constituents of the "Fill Material Free" technology (Fig.1) may be summarized as follows:

2.1.1. Permeable sponge breakwaters (P.S.B.)

Of a highly periodic-modular continuous hyperbolic geometry, realized-executed as thin reinforced concrete (and/or metal, and/or composite, and/or other) Shell structure (Fig.2). A range of geometries was considered with a preference of the cubic sponge surface (hyperbolic continuous space partition between two dual cubic networks) [1]; [6]. Small scale experiments showed that 80% of the wave energy was absorbed, just 10% was reflected and 10%, infiltrating through. The dimensions will be dictated by a thorough analysis of the wave conditions, bathymetry and foundation considerations of the site and the demands on the standard of the water protection behind.

2.1.2. "Modular tub platforms" (M.T.P.)

From reinforced concrete or steel (volumetric) structure, to perform as reclaimed buildable land infrastructure, capable of carrying-supporting high-rise building structures, piers, interior (below water-level) storage volumes (Fig.4), all depending on the platforms interior depth characteristics [8]. The dimensional design of the platform, the size and depth of its modules and the structural design of its walls, floor space frames and piers, will be determined by its specific functional utilization mode.

The P.S.B. structures may reach to a hundred meters in width (in Mediterranean Conditions), up to 20 meters below sea level, and overall cross section of up to 2500 sqm, and still, the overall volume of the P.S.B. Shell structure amounts to just 3÷5% of the conventional breakwater's only. The M.T.P. structures may reach to 2500 sqm per each module's area and assembled into 15÷30 modular units mega-platforms, of 35.000÷75.000 sqm each (Fig.5). The P.S.B. and the M.T.P. modular structures will be fabricated and assembled in a coastal industrial plant, as floatable structures, sea-transported-dragged to their location sites (Fig.3) and founded on a worked out sea-bed, or pile supported, or moored-anchored, as may be required by the local bathymetric-geological conditions and functional characteristics.

2.1.3. Infinite polyhedral lattice (I.P.L.) space frames

From steel tubes-profiles, to construct large span upper mega-platforms (Fig.6). The I.P.L.'s six-layered space truss geometry conforms with the uniform hexavalent vertex configuration of the $3^3.4.3.4$ infinite polyhedrons [2]. It is 'just stable' and, with an edge length of a, with a very low projected density of 9,9593 a/a^2, slightly less than that of the double-layered octatruss (with 10,3923 a/a^2) and structural depth which is five times greater (!). [3]; [4]; [5]. Comparatively, it is a 'light weight' structure, with high-bearing capacity and rigidity, reaching to spans of hundreds of meters and being highly cost-effective. These I.P.L space trusses can support flight and plane parking decks, large span 'bridge avenues' and large functional work and storage platforms. It's six (or more) layered low-strut-density interior spaces may be utilized for a large variety of functions and (vehicular) transportation modes.

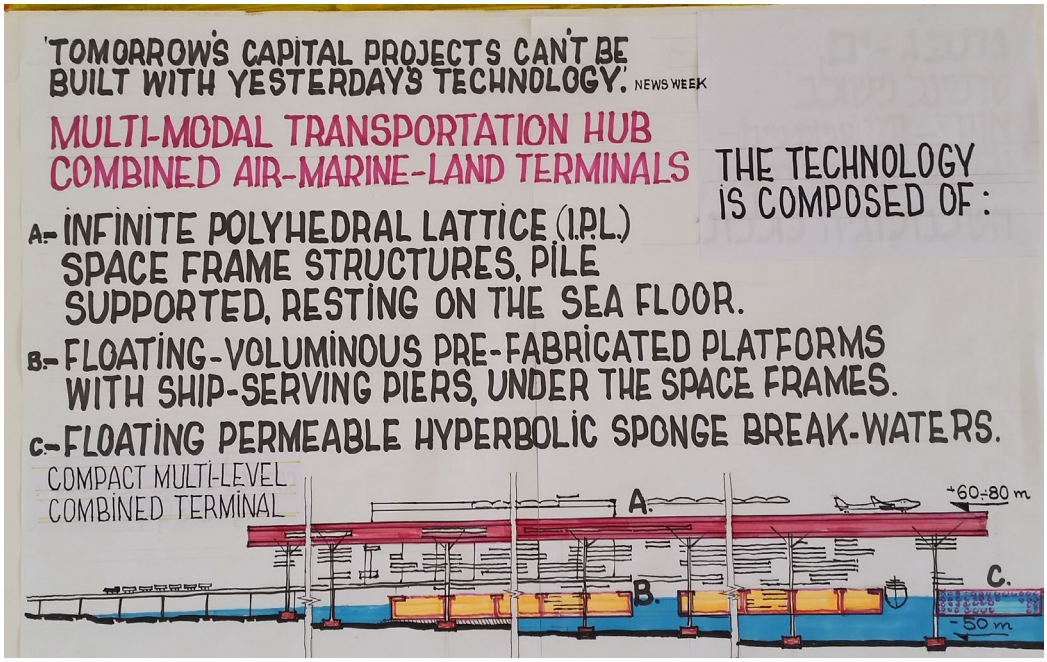


Figure 1. The technology constituents of the combined marine-air-land transportation terminal

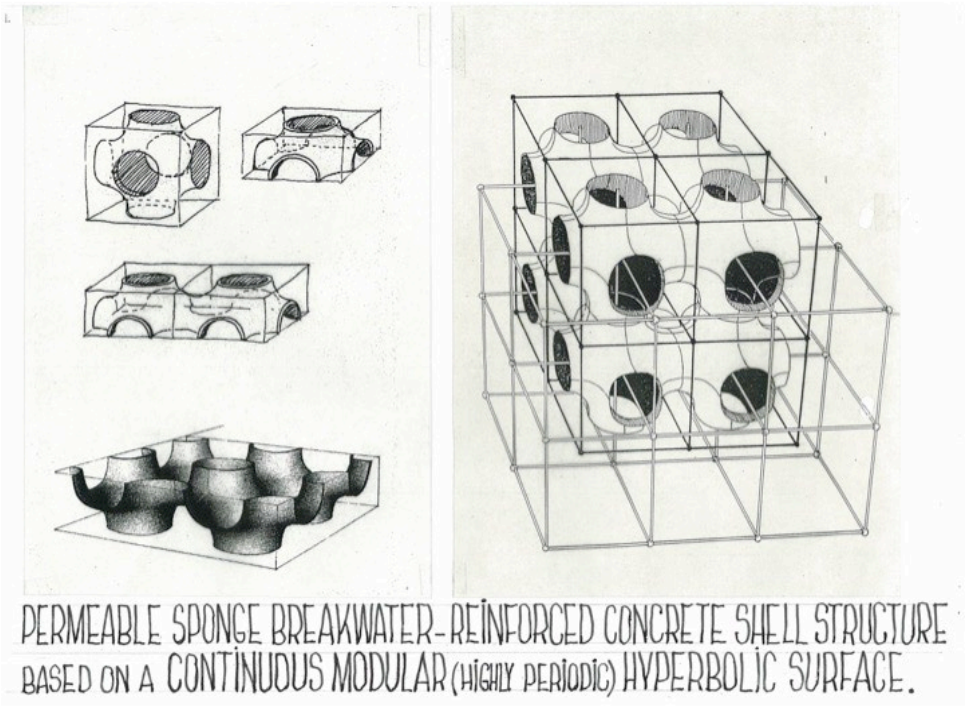


Figure 2 (left). Modular hyperbolic (cubic) shell structure, to be employed as 'Permeable Sponge Breakwater'.

Figure 3 (right). Modular floating mega-block, sea transported to its site of function.

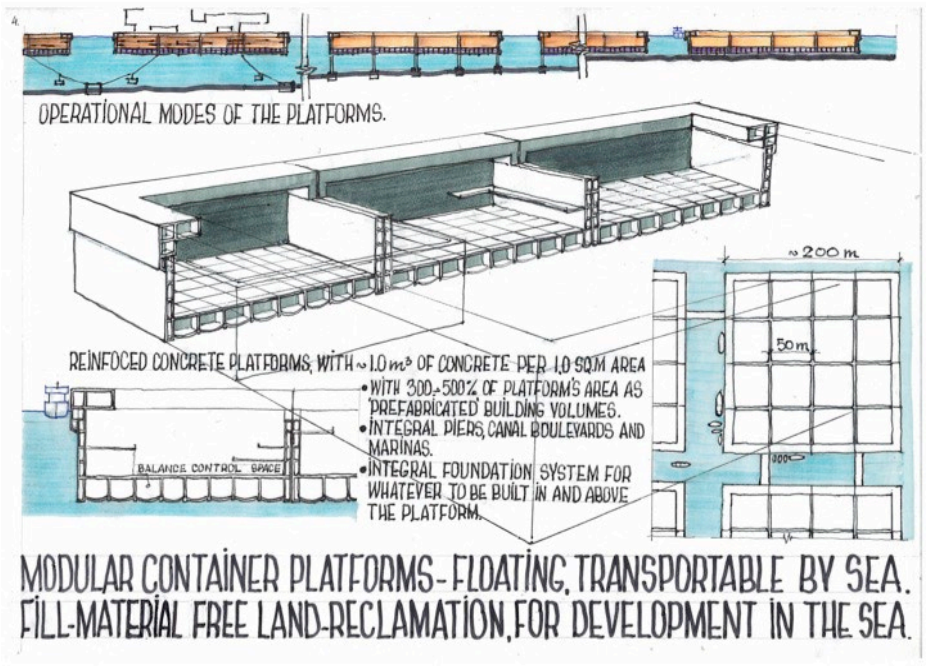


Figure 4. 'Modular Tub Platform' reinforced concrete structure.

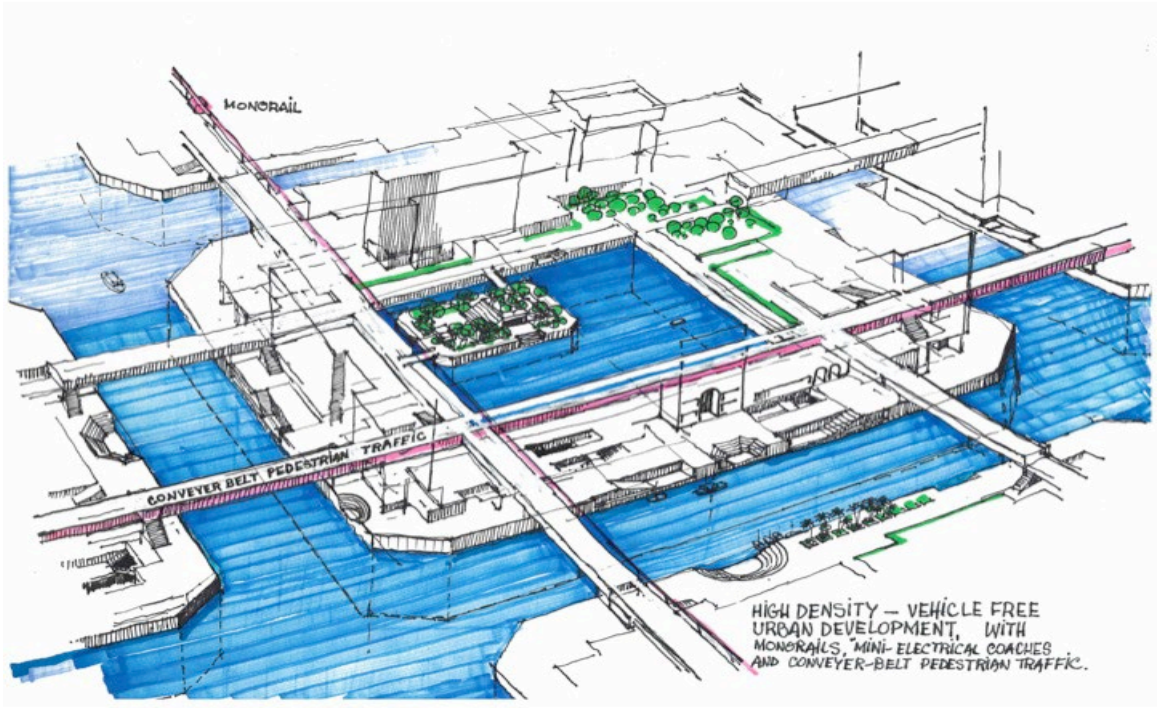


Figure 5. 'Modular Tub Platforms', assembled into mega-platforms, and the generated channel system.

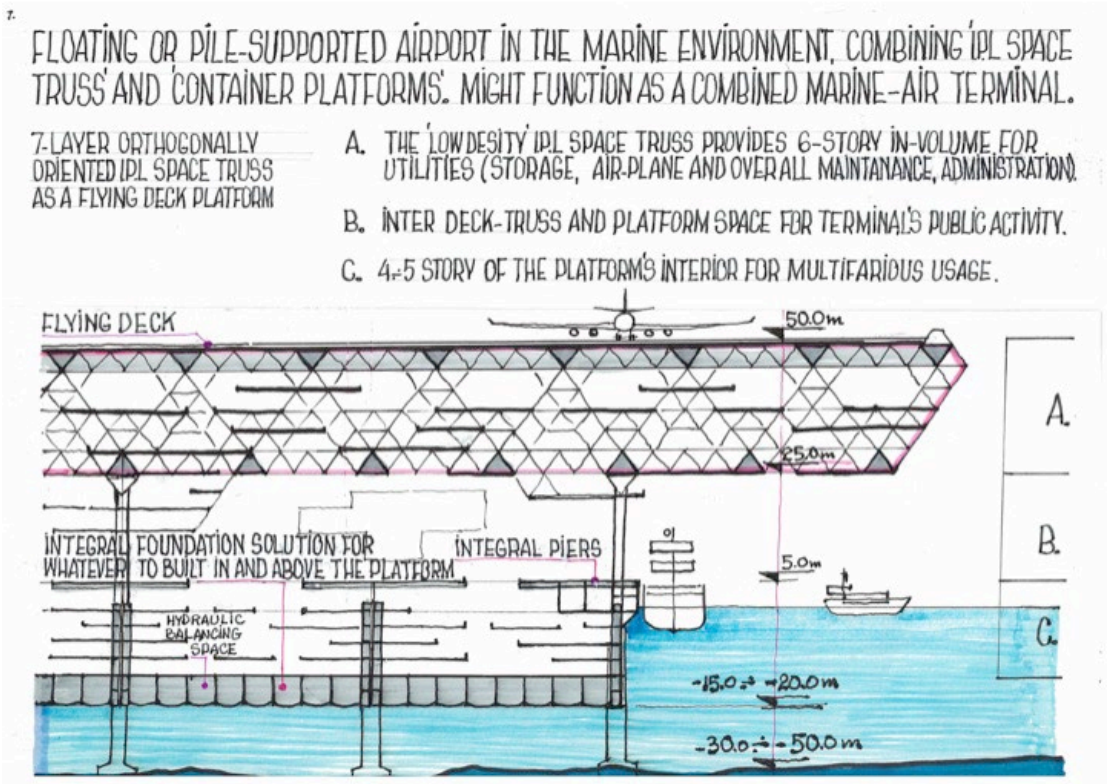


Figure 6. I.P.L Space Frame as an elevated mega-platform, supported on a Tub-platform, to perform as a combined working space.

The I.P.L. space truss concept (Burt-1969) was analyzed by many (P. Kneen, Y.Tene, H. Sanchez of 'Mero' in Wŭrzburg and M. Frances), all with converging positive results., [9] Within the protected water zone, the tub-platforms arrangement allows for a generation-realization of docking piers for large sea vessels and integrated interior multi-functional channel system for interior transportation, ferries-boat-yacht marinas, 'blue boulevards' of public recreation, when in an urban context utilization.
The channel system's area may amount to more than 50% of the reclaimed artificial island's area, thus contributing dramatically to it's cost-effectiveness and speed of its realization [8].

3. The multi-modal transportation hub

The combined Marine-Air-Land Terminal, with a marine deep-water port for mega-carriers, and the required piers and storage volumes within the platform's interior, with the elevated flight decks of 80÷100m above sea level, on I.P.L. (large span space truss) mega-platforms, starts to take shape (Fig.7).

The sea port infrastructures and the flight deck runway I.P.L. platforms, carried by the M.T.P.'s and protected by the P.S.B.'s, with all servicing and storage and the multi-layered working spaces, are connected with the coastal urban fabric and beyond by 'bridge avenues', carrying the vehicular-rail-conveyer transportation infra structures, mostly above the urban fabric. These 'bridge avenues', while 'above and through' the city, may assume the role and appearance of high-grade living-working spaces with green sky promenades (Fig.8).

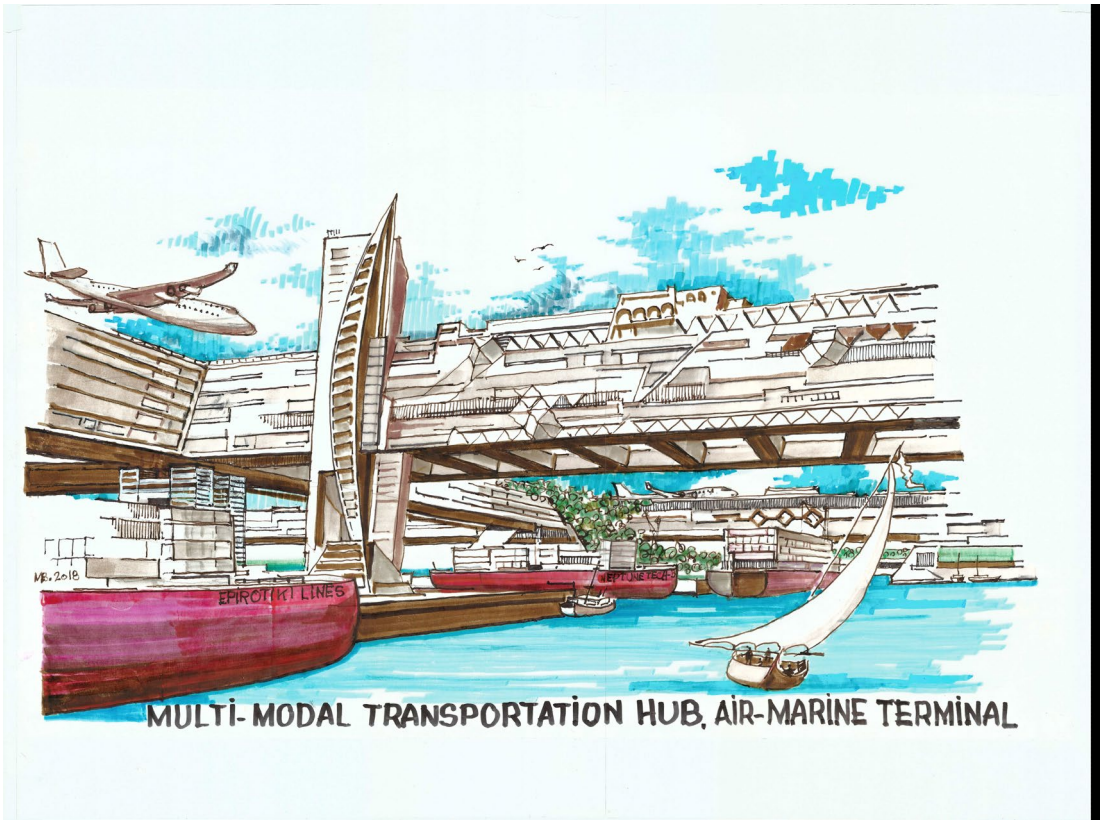


Figure 7. 'Multi Modal Transportation Hub', a combined marine-air-land terminal.

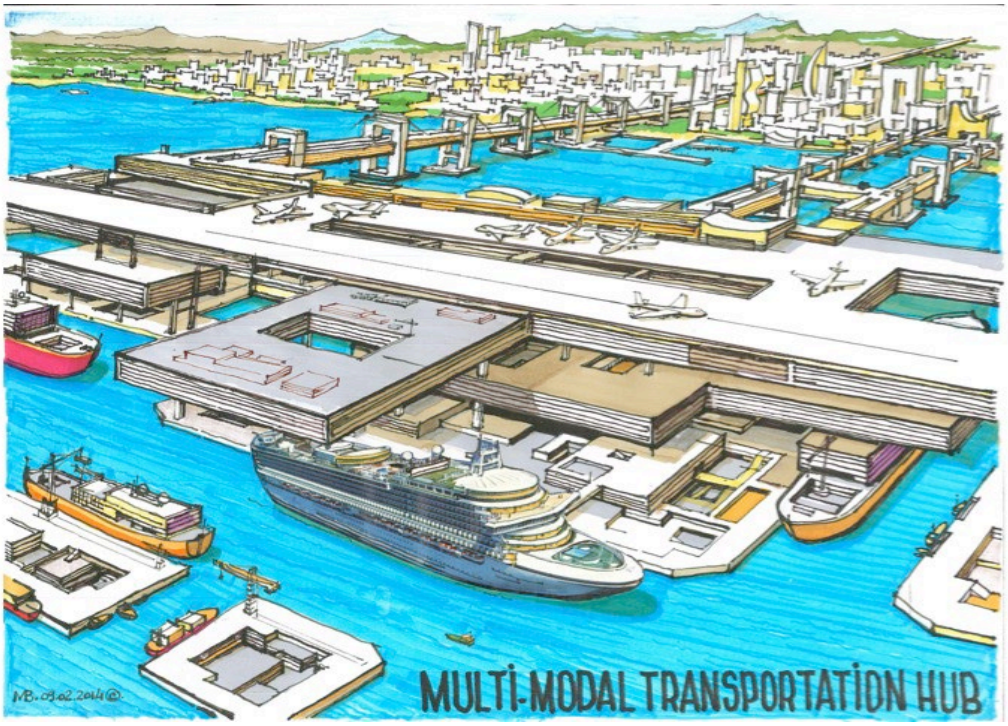


Figure 8. 'Multi Modal Transportation Hub', vis-a-vis the costal urban environment

The whole complex agglomeration of the combined 'multi-modal transportation hub' is very economical in terms of consumed area-volume-space and its realization time, that are just a fraction of the 'conventional approach' figures. The construction process is solved for stage-completion, expansion (with the time), rearrangement and relocation, if and when desired, into deeper waters or even to alternative sites, which is practically unimaginable with the conventional 'Fill Material Based' methods.

4. Conclusion

In view of the expected dramatic growth of transportation infrastructures, their spread, volume and cost, and the growing friction (environmental pollution and damage) with the land locked urban habitat, an alternative design paradigm is required, that is considerably more compact in terms of consumed space, employed servicing interaction, communication energy and time.

All that might be promoted and achieved by turning the various transportation terminals into one intertwined synergetic functioning conglomerate: the 'Multi-Modal Transportation Hub', with the Marine-Air-Land terminals sharing space, manpower, servicing and managerial infrastructures. This functional conglomerate, served by 'bridge avenues' for contacting the coastal city and beyond, enables a development venture into deeper waters (with 'fill material free' design approach and technology) thus relieving the pressure on the city sea-frontage, real-estate costs and the eco-environmental conditions.

All that may be achieved basically with the employment of existing fabrication-construction

- realization technology.

What is basically required is a critical state of mind that is receptive to a novel planning-design paradigm.

"Lets be the architects of the future and not its victims" (R. Buckminster Fuller)

References

[1] M. Burt, 'Spatial Arrangement and Polyhedra with Curved Surfaces and Their Architectural Application'. Technion, I.I.T publication, Israel, 1966.

[2] A. Wachman, M. Burt and M. Kleinman, 'Infinite Polyhedra', Technion, I.I.T publication, Israel, 1974; 2005.

[3] M. Burt, 'Low Density Space Frames, Based on Regular Infinite Polyhedra', proceedings, IASS symposium, Osaka, 1986.

[4] M. Burt, 'I.P.L. Plate Space Frames, Space Structures Journal G.B, 1987.

[5] M. Frances, 'Interactive Development of structural – Morphological Solutions for Space Frames, Based on Infinite Polyhedral Lattices (I.P.L.) DSc Thesis, Technion, I.I.T. Israel. 1990.

[6] M. Burt, 'An Experiments Study of Wave Transmission Through a Permeable Breakwater', prepared for M. Burt by N. Drimer, CAMERI-Coastal and Marine Engineering Research Institute, Technion, I.I.T Israel, 1999.

[7] M. Burt, 'Polyhedral Sponge Structure-New Imagery and Inspiration for Innovative Space Structures'. IASS-APCS, Beijing, 2006.

[8] M. Burt, 'The Israeli Marine Option, The Blue Avenue Vision'. Technion, I.I.T. publication, Israel. 2013.

[9] Burt, M. and Rosenfeld, Y. (2014), Permeable sponge breakwater shell structure, IASS – SLTE, Symposium, Brasilia, 2014.

[10] Burt, M. and Rosenfeld, Y. (2015), 'Fill Material Free' Marine Development Paradigm, Structural Engineering World Congress (SEWC), Singapore, 2015.

[11] Burt, M. and Rosenfeld, Y. (2017), Urban and Infrastructures Marine Development Based on 'Fill Material Free' Technology, IASS Symposium, Hamburg, 2017.

Next generation parametric design

Active bending
Additive manufacturing/ 3D printing
Architectural geometry
Bamboo for sustainable construction and quality of life improvement
Bio-inspired structures and architecture
Bridge structures
Computational form-finding
Conceptual design
Concrete structures
Construction techniques
Deployable and inflatable structures
Design competition (WG21)
Digital modelling and fabrication
Dynamic response of metal spatial structures
Dynamic response of other structures
Form-finding and structural optimisation of interlocking discrete assemblages
Graphical methods
Gridshell and lattice structures
Historical concrete shells
Historical structures
Lattice structures
Life-cycle design and assessment of structures
Metal gridshell structures, connections and stability
Methods and construction technologies for sustainable shell structures
Morphology and configuration processing
► **Next generation parametric design**
Novel methods in modelling, optimisation and construction for reducing carbon footprint of continuous roof shells
Numerical methods for geometry, form-finding and optimisation of lightweight structures
Optimisation methods and applications
Origami
Other
Teaching design uncertainty: working with unknown qualities/quantities of new and re-claimed materials
Teaching of shell and spatial structures
Tensegrity systems and cable structures
Tension and membrane structures
Tension structures in the Asia-Pacific
Timber and bio-based structures
Topology optimisation
Traditional masonry structures and innovation
Transformable structures

IASS 2023
July 10–14 Melbourne
Integration of Design and Fabrication

Proceedings of the IASS Annual Symposium 2023
Integration of Design and Fabrication
10–14 July 2023, Melbourne, Australia
Y.M. Xie, J. Burry, T.U. Lee and J. Ma (eds.)

Design workflows for a complex urban steel artwork

Sascha BOHNENBERGER-FEHR[a,*], Matthew TAM[a], Csaba BÖHM[a], Gergely PILLMANN[a], Ven IYER[a], Chris FOX[b], Tommaso PAGANI[b]

[a,*] Bollinger+Grohmann
sbohnenberger@bollinger-grohmann.com

[b] Studio Chris Fox

Abstract

Computational design is now ubiquitous in building practice having led to integrative, yet robust digital workflows [1]. In a culture of highly interdisciplinary collaboration, information transfer, data management and communication are critical for the successful completion of a built project. Architects, engineers, and contractors are now able to communicate in a more common language, however contrary to industry demand, software does not often natively communicate to the same degree. To deliver optimal results a multi-faceted tool environment [2] often ad-hoc solutions coupled with open-source tools provide much needed link to connect communication, processes, and people [3].This paper presents a one such case study of a design and construction of a landmark urban artwork located in Sydney, Australia. A sprawling steel structure populated with modulated zinc panelling and biophilic green wall elements is fluently wrapped around three concrete ventilation towers each 40m tall. With a total tonnage of approximately 170t of steel a close coordination with all parties involved is paramount. The project represents a challenging yet effective design workflow for this large-scale structure. The paper concludes with assessing emerging interoperability platforms and the presented workflow that allow for fruitful collaboration in design environments in a data driven setup.

Keywords: parametric framework, Grasshopper, geometric form finding, structural optimization, artist-engineer collaboration, BIM, Karamba3D, Dlubal RFEM

1. Introduction

A landmark urban structure emerges from a new parkland in the inner west suburbs of Sydney, Australia. This integrated landscaped artwork envelopes three concrete monoliths which reflect the history of the site: transformed from once vibrant ecosystems with mudflats and mangrove forests to industrial maritime and rail yards [4]. These concrete structures function as ventilation stacks for the Rozelle Interchange, a new underground motorway as part of Sydney's WestConnex major urban infrastructure project. The aim of the artwork is to help transform the vast infrastructure project into a habitat for urban biodiversity, whilst integrating into the surrounding parklands. Additionally, it allows for maintenance of the concrete outlet, and the air monitoring and sampling ports that are located at the elevated sampling platforms.

The artwork has been designed by Studio Chris Fox in close collaboration with structural engineers Bollinger+Grohmann. The cylindrical towers each have their various dimensions, providing challenges and opportunities for the new artwork design, having been previously designed, engineered and already undergoing construction. The three ventilation towers stand at 40-42m high with a diameter of 9.8-13.8m and were all constructed in in-situ reinforced concrete.

Copyright © 2023 by Sascha BOHNENBERGER-FEHR, Matthew TAM, Csaba BÖHM, Gergely PILLMANN, Ven IYER, Chris FOX and Tommaso PAGANI. Published in the Proceedings of the IASS Annual Symposium 2023 with permission.

The artwork encompasses a main steel framework of columns and beams that follow a radial spacing around each outlet. The columns are fixed onto the top slab of the cut and cover structure with mechanical anchors. The framing is laterally pinned back to the outlets with beams and the platform structure. Platforms at a height of 33m surround each outlet with stairs integrated in the interstitial space between the concrete and the framing. Bridging elements connect the three tower frames to form one coherent structure. A series of rope-like elements twist and weave around the entire structure. Figure 1 depicts the main structural elements of the artwork. Finally, modulated zinc panelling and biophilic green wall modules are distributed across the framework to create a porous and dynamic façade treatment (Fig.2).

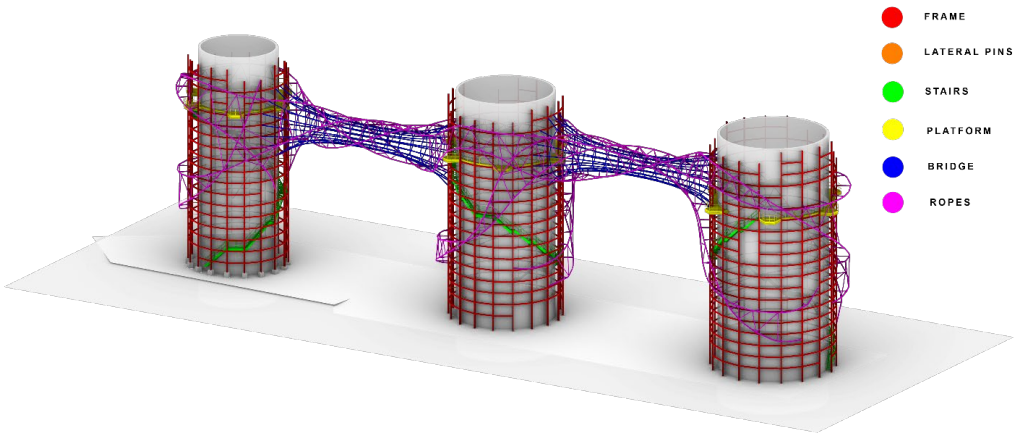


Figure 1. Main structural elements of the artwork

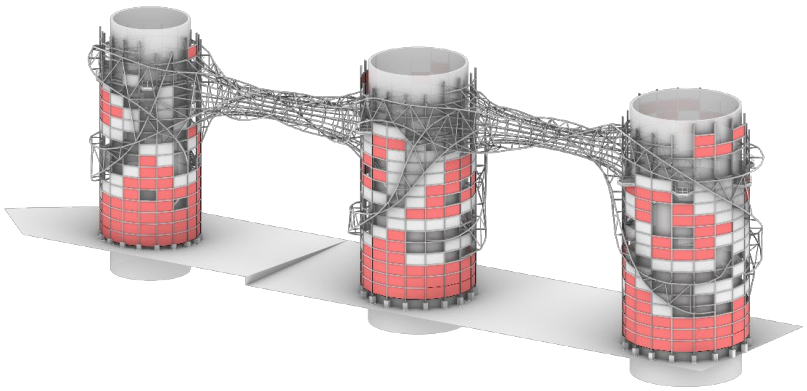


Figure 2. Zinc cladding (red) and green wall components.

This paper will present in three main sections the integrated design procedure of this artwork. We will look at how workflows were established to provide effective collaboration between artist and engineers. Optimisation techniques were explored to not only create more efficient structures but implemented to streamline fabrication and construction methods. Finally structural processes and challenges will be presented.

2. Integrated workflows

2.1. Teams and tools

In order to tackle such complex art/architectural design projects at large scales, there are many different actors involved at multiple stages of the project. Numerous consultants additional to the core artist and structural engineering team were engaged such as the lead contractor, the workshop planners, the steel fabricators and those responsible for vertical landscape design. It was also essential to consider a 'Design for Manufacture and Assembly' (DfMA) approach, where fabrication and assembly were seriously taken into account in the early design phases to avoid unexpected delays and costs later on [5].

When working in the field of Design Technology, a multi-faceted tool environment delivers optimal results [2]. An open and adaptive yet robust digital workflow needs to be established from the beginning to ensure clear communication between all stakeholders [6]. Such workflows and tools provided a much-needed link to connect communication, processes, and people [3].

2.2. Central data hub

A "Common Data Environment" follows the principle of interoperability where common data is shared using information management and transferable file formats [6]. All changes from the architectural model, structural analysis, façade engineering, MEP and other consultants are held centrally in this shared environment for coordination. Each discipline operates within their own individual software environment and typically additional work is required to translate this data to other specialists who work with different software platforms. A central data hub should allow for the exchange of data seamless throughout the various software packages as well as an interface to manage this geometry and data [7]. The implementation of a central data hub platform ensures a fully integrated digital workflow (Fig. 3).

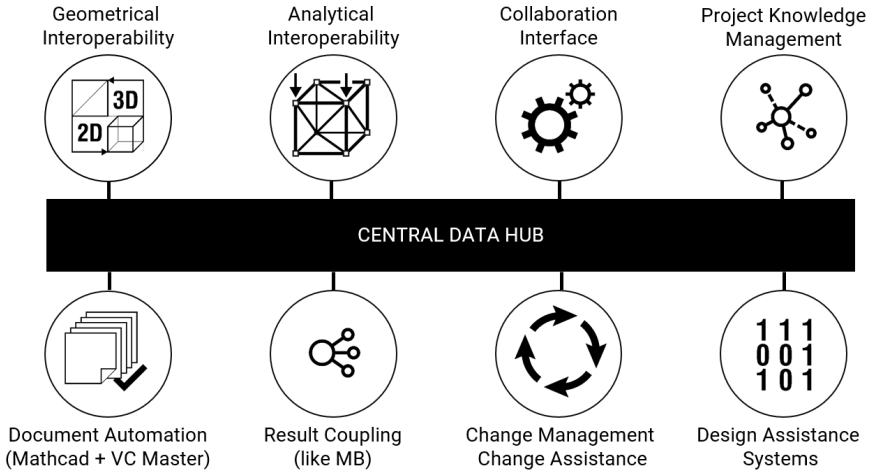


Figure 3. An example of an integrated central data hub.

Demand from the AEC industry has resulted in the emergence of several interoperability and CDE platforms such as Speckle [8], BHOM [9], 3D Repo [10], Konstru [11] and Conveyor [12]. Such platforms enable users to seamlessly communicate within different software environments. Speckle and BHOM offer a broader spectrum of support in an open-source framework; Konstru is especially tailored for engineering workflows and 3D Repo and Conveyor are directed towards the BIM environment.

2.3. Rhino as a central data hub

After assessing the multiple tools available in the aforementioned section, the team decided to opt for a more ad hoc approach by using Rhino as the main coordination model to feed into multiple software platforms, in essence a central data hub. The implementation of Grasshopper, Rhino.Inside [13] and an accessible Rhino3D/Grasshopper API has extended the interoperability functions of Rhino3D, allowing for translation of data at ease. The design and engineering team have had a long-time collaboration where model data was transferred in the interface of Rhino3D on smaller projects, it also seemed appropriate to implement it on this context. However careful control and management of the data was important for a successful workflow in such a large-scale project.

The implementation of Rhino3D as a central data hub platform was used in multiple phases of the project, for communication and exchange within the design/engineering team, as well as in the construction/documentation team. Often consultants work in a very manual process where models are created from scratch in each individual software environment [14]. This can potentially lead to data being lost on the way, as well as lost resources. All data in Rhino3D can be easily accessible, is easy to interrogate and check, making the entire process much easier. Typically used for its geometrical prowess, Rhino3D also offers the ability to assign attributes to all its objects. Attributes were critical to communicate with the entire team specific information about all objects in the model (Fig. 4). They also enabled for information from the model data to be easily transferred from the central Rhino3D model into multiple software platforms and vice versa.

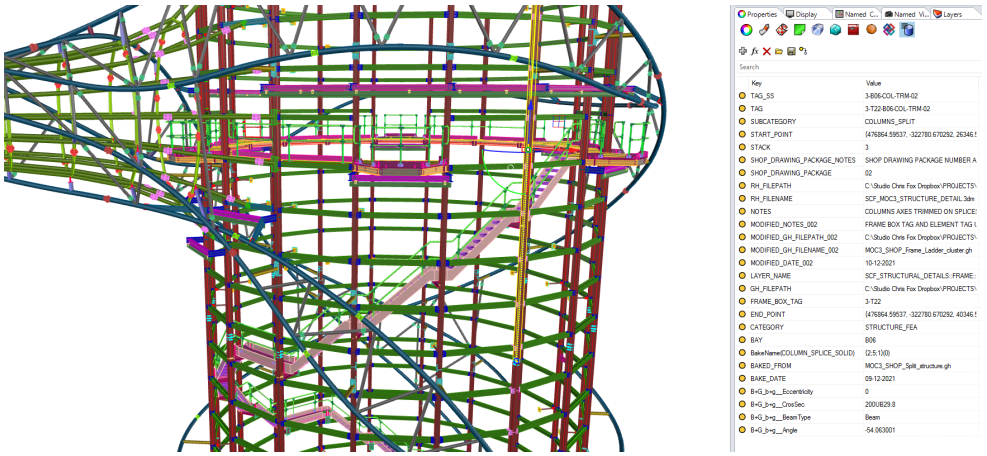


Figure 4. Rhino attributes.

The design team worked primarily in Rhino3D and Grasshopper to develop the complex geometry. Engineers worked with Karamba3d and RFEM to perform analyses of the structural model. Detailed analyses for the development of the steel connections were performed with IDEA Statica. Communication with the client and contract or was through a centralised Revit and Navisworks model taken from Rhino3D. GeometryGym and Rhino.Inside Revit were implemented to translate this data. Tekla Structures was finally used by the fabrication and construction team for detailed workshop planning of all the steel framing. Coordination of the models was managed by the core design/engineering team to ensure all parties involved received the most accurate and relevant data (Fig. 5).

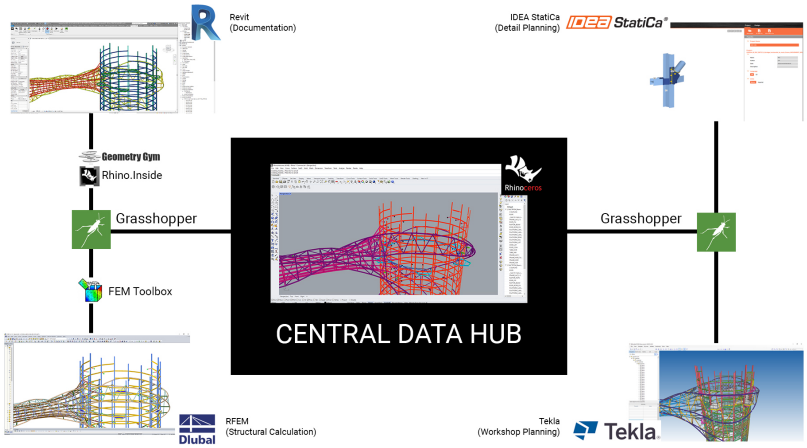


Figure 5. Coordination through a central data hub.

3. Geometry – optimisation & development

3.1. Steel vine elements

The rope geometry formed a crucial component of the overall design of the project. Wrapping the repetitive steel framing are twisted rope elements that weave and connect all components of the structure together. The freeform geometry was optimized (Fig.6) to potentially reduce the number of unique elements: their lengths and bending radii as well as its deviation to the original starting geometry (Fig. 7 & 8). Rigid beams were used to tie back the rope geometry to the main frame, whose position were also governed by optimisation algorithm. The computational logic was designed to be flexible to be adaptable for future design changes or external design parameters such as lateral connection positions and constructability. Overall, the geometry could be optimised and rebuilt into arc modules that can be easily rolled and fabricated.

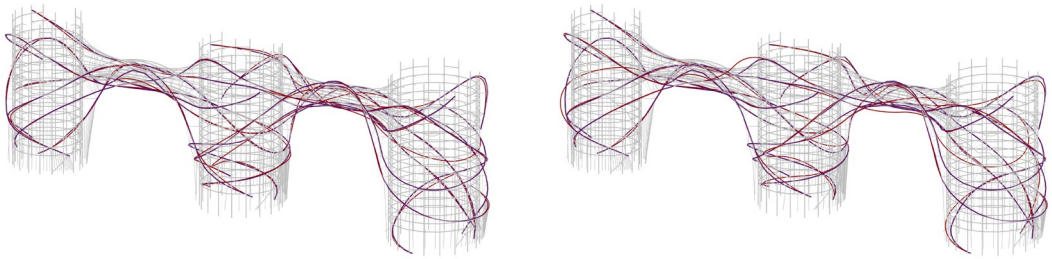


Figure 6. Iterations during the optimisation procedure showing the original (purple) and new (red).

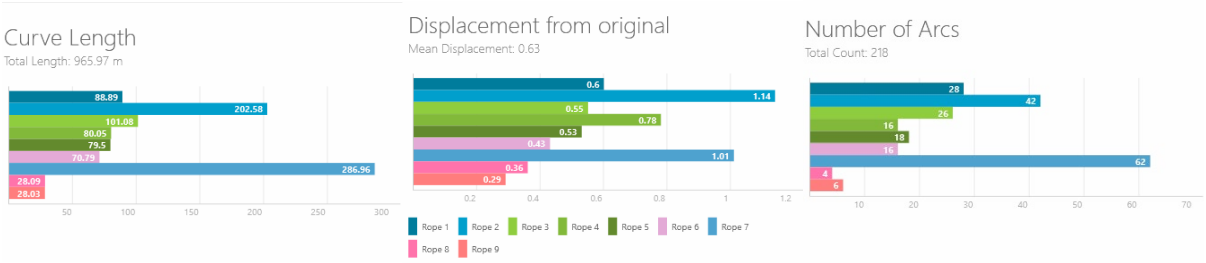


Figure 7. Parameters for the evaluation of the optimisation process.

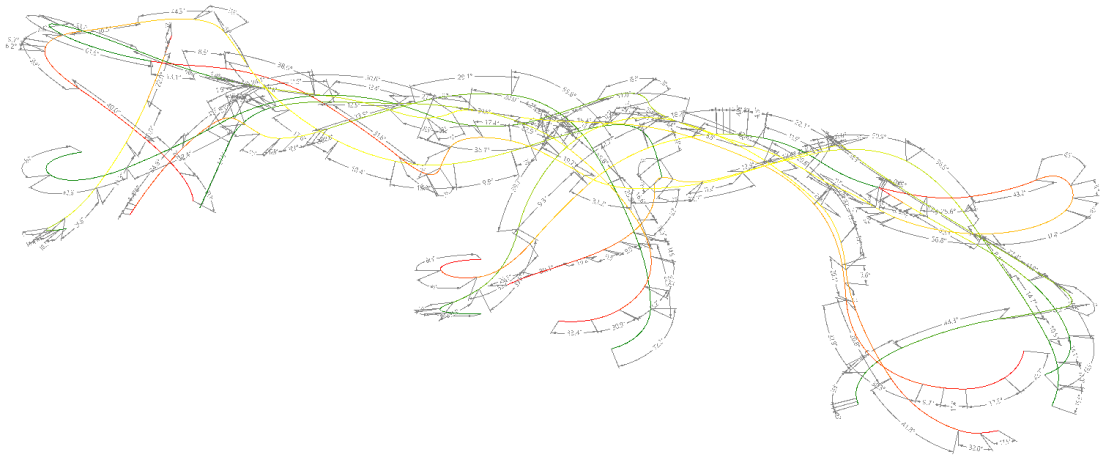


Figure 8. Overview of the steel vines showing the arc segment lengths and radii.

3.2. Stitching elements

To stabilise the rope geometry, prevent them from buckling and to maintain minimal cross section profiles, it was necessary to introduce stitching truss elements. Due to the complexity of the geometry and the multitude on options that are available to the stitching elements, an optimization algorithm was introduced to define the best positions, the number of elements at one single node and to limit the angles regarding constructability (Fig. 9). The stitching elements with the least performance were also then postprocessed and culled to achieve an optimised structural performance.

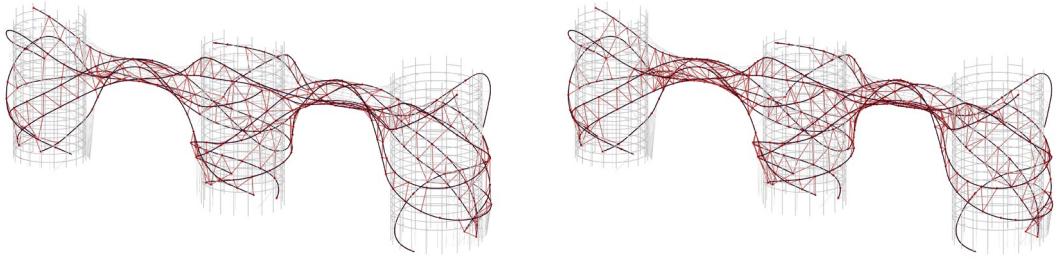


Figure 9. Overview of the steel vines showing the arc segment lengths and radii.

4. Structural model

4.1. Steel vines

The rope geometry was an integral component in the wholistic performance of the structure. They were not only a major architectural design feature, but also provided required global stability for the bridging elements. Figure 10 shows the impact on the overall structure should the steel vines and all there incorporated adjacent elements such as diagonals and pin locations be removed. Elements would start to become over-utilised and thus require much larger cross sections in order to resist all loading scenarios.

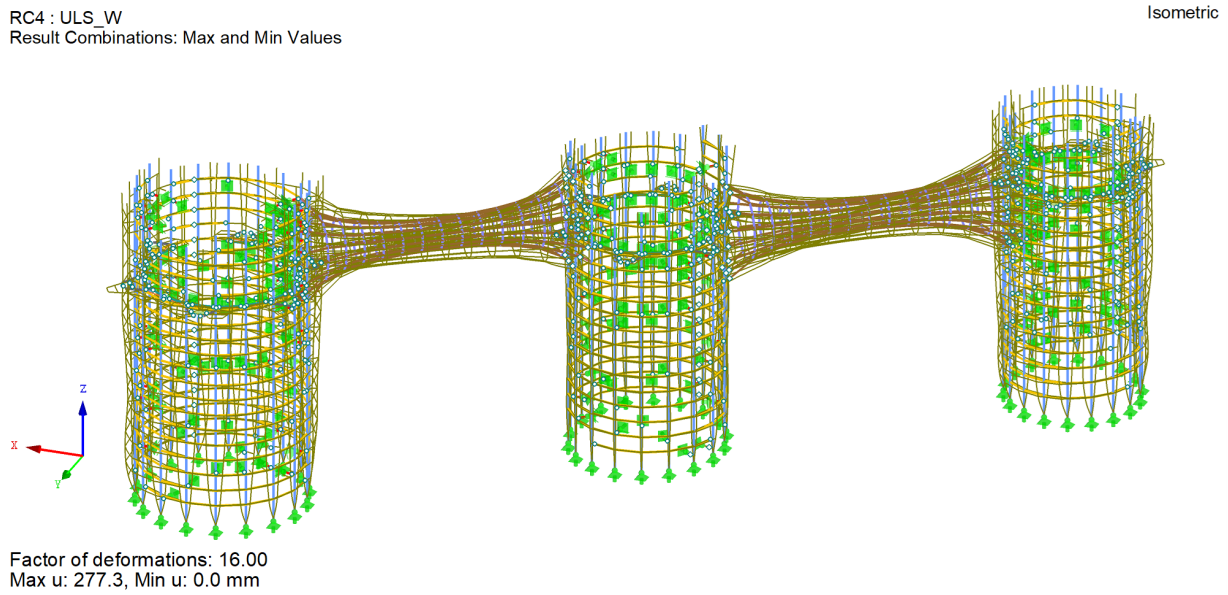


Figure 10. Impact of removing the freeform rope elements in the structure.

4.2. Joints

To allow for movement due to temperature changes (a temperature difference "ΔT" of maximum 50 was determined) and lateral deformations, it was critical to introduce movement joints in the connection between the bridging elements and the main frame, similar to bridge supports. In a similar manner, joints were also used in the rope geometry (Fig. 11). A mixture of pinned connections and physical gaps were applied for the steel vines. This was not only crucial to mitigate effects of deformations but aid in the fabrication and assembly process. Collaboration with the steel fabricators ensured that a balance between welded connections, pin connections and physical gaps were met.

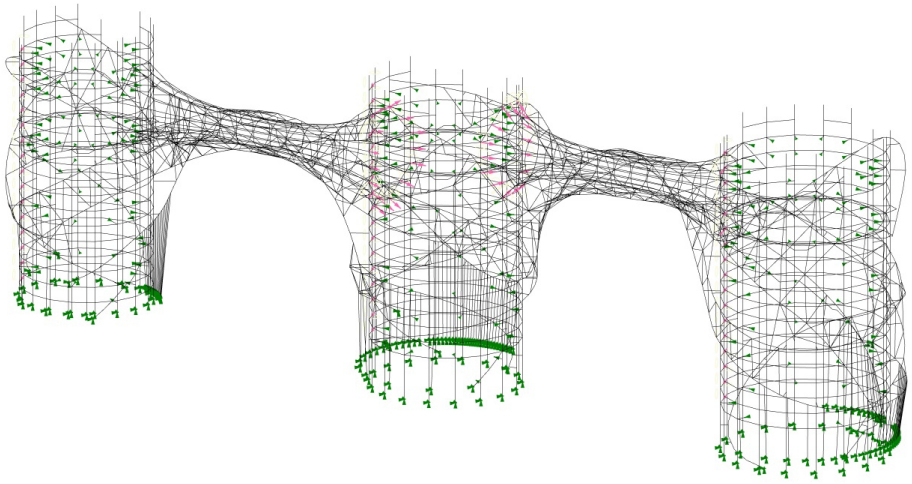


Figure 11. Positions of the movement joints in the overall structure.

4.3. Lateral pins

The vertical loads from the steel framing structure including the façade cladding and green wall elements are supported by the roof slab of the exhaust vent building below. To provide lateral support to resist wind loads and dynamic effects due to seismic loading for the steel framing, beams span from the frame and are pinned to the concrete stack. Beams in the platform and stair framing also contribute to the global lateral stability of the steel framing structure. The concrete structure had been designed with a specific load capacity and it was critical to evaluate the impact each anchoring element had on it. The developed workflow allowed for quick implementation of geometric updates and to extract the reaction forces at all the supports (Fig.12).

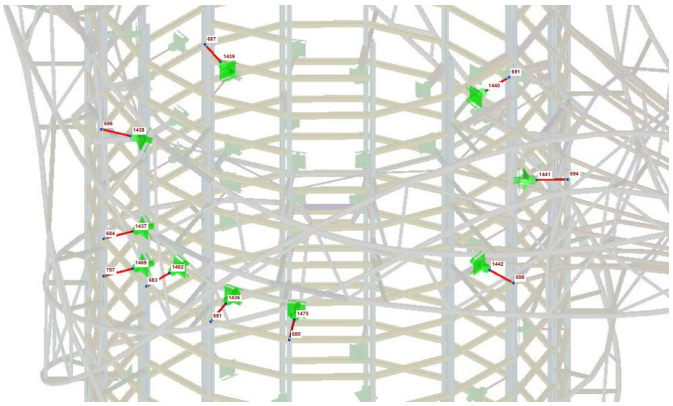


Figure 12. 3d structural model showing reaction forces at the supports on the concrete stack.

Optimisation algorithms (Fig. 13) were introduced to reduce the overall number of lateral pins and internal bracing elements to reduce dead load of the structure and the reaction forces onto the concrete outlet. Coordination with engineers of the ventilation structure were critical to ensure the maximum allowances of anchor forces that can be induced into the concrete stacks and the concrete roof.

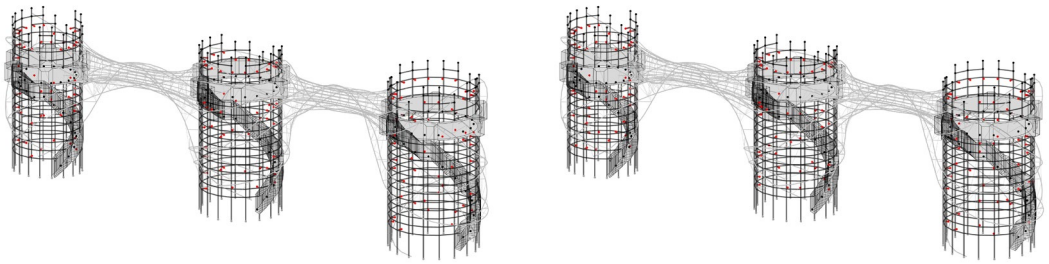


Figure 13. Iterations of the lateral pins.

5. Conclusion & reflection

The digital workflow from the early engagement in the concept phase was kept and improved thoroughly throughout the project until the implementation of the shop drawing process. The established central data hub platform was a crucial tool for communicating design decisions among the involved consultants and designers. The central data hub model was the 'master' template and served also as a control mechanism to check the 3D Tekla model, Revit models, the FEA models and the Rhino3D design files.

The project is currently under construction and is expected to be finished by the end of April / early May. Overall, the team had a little over one year of planning and one and a half years for shop drawing preparation and installation. During the shop drawing phase, the coordination and optimisation in regards of the buildability of the structures was intensified. Due to the early implementation of the DfMA process, many details could easily be adopted. Further to that, the high level of detail that was implemented in the design phase resulted in a very precise fabrication of the elements that did not need any mayor adjustment on site.

This paper discussed the utilisation of Rhino3D as a centralised "master" environment. The integration of open source and third-party plug-ins made it possible to design, exchange, control and coordinate the project over a multitude of software platforms. The presented work outlines the possibilities to effectively work on large scale projects in a "Common Data Environment".

References

[1] M.R. Thomsen and M. Tamke, "Introduction", *Design Transactions*, pp. 8-13, 2020.

[2] D. Holzer, *The BIM Manager's Handbook*, Wiley, 2016.

[3] R. Deutsch, *Superusers: Design Technology Specialists and the Future of Practice,* Routledge, 2019.

[4] Studio Chris Fox, "Rozelle Interchange", *Studio Chris Fox* [Online] https://www.studiochrisfox.com/projects/rozelle-interchange [Accessed 13/3/2023].

[5] M. Andreasen, S. Kahler, T. Lund and K. Swift, *Design for Assembly*, Springer-Verlag, 1988.

[6] The Institution of Structural Engineers, "Building a digital workflow in practice", *The Institution of Structural Engineers*, https://www.istructe.org/resources/guidance/building-digital-workflow-practice/ [Accessed 25/1/2023].

[7] P. Poinet, D. Stefanescu and E. Papadonikolaki, "Collaborative Workflows and Version Control Through Open-Source and Distributed Common Data Environment", *18th International Conference on Computing in Civil and Building Engineering (ICCCBE),* 2020.

[8] Speckle, https://speckle.systems (2023) [Accessed 14/2/2023].

[9] BHOM, "The Building and Habitats object Model", https://bhom.xyz/ [Online] (2022) [Accessed 14/2/2023].

[10] 3d Repo, [Online] https://3drepo.com/ (2022) [Accessed 14/2/2023].

[11] Konstru, [Online] https://konstru.com/ (2023) [Accessed 14/2/2023].

[12] Proving Ground, "Conveyor", [Online] https://provingground.io/tools/conveyor/ (2023) [Accessed 14/2/2023].

[13] Rhino3D, "Rhino.Inside Revit", [Online] https://www.rhino3d.com/inside/revit/ (2023) [Accessed 14/2/2023].

[14] M. Day, "Improving structural workflows", *AEC Magazine* [Online] https://aecmag.com/structural-engineering/improving-structural-workflows/ (23 Nov. 2020) [Accessed 25/1/2023].

IASS 2023
July 10–14 Melbourne
Integration of Design and Fabrication

Proceedings of the IASS Annual Symposium 2023
Integration of Design and Fabrication
10–14 July 2023, Melbourne, Australia
Y.M. Xie, J. Burry, T.U. Lee and J. Ma (eds.)

Form finding and structural analysis of free-form shells with specified horizontal projected stress distribution

Taku NAKAJIMA[a,*], Makoto OHSAKI[a]

[a,*] Department of Architecture and Architectural Engineering, Kyoto University
Kyoto-Daigaku Katsura, Nishikyo, Kyoto 615-8540, Japan
nakajima.taku.22x@st.kyoto-u.ac.jp

Abstract

This paper presents a form finding method for free-form shells that specifies the distribution of stresses projected onto the horizontal plane. The vertical coordinate of the shell surface is defined as a graph surface with respect to the horizontal coordinates. The shape of the shell is given as a solution to the vertical equilibrium equations of the surface heights at the grid points discretized by the finite difference method. The equilibrium shape is found by sequentially solving the linear system of equations. We specify the shear stress distribution that satisfies horizontal equilibrium to generate various shell shapes with a region of negative Gaussian curvature and a free boundary. Finite element analysis is carried out to investigate the effect of elastic deformation on the stress distribution due to material properties such as out-of-plane bending deformation and transverse strain that are dependent on Poisson's ratio. We compare the ratio of the membrane strain energy and the bending strain energy of the shell to demonstrate that the proposed method generates shell shapes that resist external loads through membrane action.

Keywords: free-form shell, form finding, horizontal projected stress, concrete shell, finite element analysis

1. Introduction

Shell structure is described by three-dimensional curved surface in which one dimension is significantly smaller compared to the other two [1], and its mechanical performance is highly correlated with geometry of the surface. It resists external loads primarily through membrane stresses. Recently, there has been renewed interest in form finding of spatial structures based on graphic statics. Thrust network analysis (TNA) is one of the methods based on graphic statics. Block and Ochsendorf [2] demonstrated that TNA can express the relationship between in-plane forces and funicular shell geometry as discrete reciprocal diagrams.

Free-form shells are complex-shaped shell structures compared to classical geometrical shells such as cylinders and spheres. The geometry of free-form shells is often described by non-uniform rational B-spline (NURBS) surfaces. When the vertical coordinate of the shell surface is defined as a graph surface with respect to the horizontal coordinates, Pucher's formulation [3] describes the equilibrium of membrane stresses on the shell with horizontal projected stresses, which can be expressed using Airy stress function. Various methods have been proposed for shape design of shells modelled as NURBS surfaces by utilizing the framework of Airy stress function. Miki *et al.* [4] developed a method to generate shell surface geometry modelled with NURBS surfaces using Airy stress function for the horizontal projected stress under gravity load. Xia *et al.* [5] suggested a method to design funicular shells by using NURBS and isogeometric analysis. Miki and Mitchell [6] extended the method by Miki *et al.* [4] to design tension-compression mixed shells by interactively searching for pairs of shell geometry and stress function that satisfy the equilibrium equations. Chiang and Borgart [7] proposed an approximation method employing radial basis functions to represent shapes and stress functions of shells

Copyright © 2023 by Taku NAKAJIMA and Makoto OHSAKI. Published in the Proceedings of the IASS Annual Symposium 2023 with permission.

and solve the equilibrium equations converted into a least-squares problem. The stress function is a powerful tool that automatically gives stress distribution that satisfies the horizontal equilibrium equations and obtains the shell shape in a reciprocal relationship with the stress function. However, higher-order derivatives are required for the NURBS basis functions, making it difficult to solve the differential equations analytically. In addition, parametric representation limits the class of possible shapes.

In contrast, non-parametric design methods that do not use parametric surfaces have been proposed. Sakai and Ohsaki [8] proposed a non-parametric design method for funicular shells under gravity load. The method enables designers to control the horizontal reaction forces on the boundaries, and accordingly, the influence on the substructure. Takeoka *et al*. [9] extended the method of Ref. [8] to shells with curved boundaries. Olivieri *et al*. [10] proposed a non-parametric method to design purely compressed shells by constraining the Airy stress function to be concave.

This paper extends the method in Ref. [9] and presents a non-parametric form finding method for continuous shell structures with specified horizontal projected stress distribution. The vertical coordinate of the shell surface is defined as a graph surface with respect to the horizontal coordinates and discretized by the finite difference method. The horizontal projected stresses are assigned to satisfy the horizontal equilibrium equations. The shell shape is given as a solution to the vertical equilibrium equations with respect to the surface heights at grid points. To generate various shell shapes, the shear stress distribution is described as a function of horizontal coordinates. Numerical examples show that the proposed method obtains various shapes with a region of negative Gaussian curvature and free boundaries where no reaction forces exist. Furthermore, finite element (FE) analysis is carried out to investigate the effect of elastic deformation on the stress distribution due to material properties such as out-of-plane bending deformation and transverse strain depending on Poisson's ratio. We compare the ratio of the membrane strain energy and the bending strain energy of the shell to show that the proposed method generates shell shapes that resist external loads through membrane action. Furthermore, the effect of the edge beams at the free boundary on the mechanical performance is discussed through FE analysis.

2. Equilibrium equations and discretization

Consider a shell structure described as a graph surface on the *xy* horizontal plane. The vertical *z*-coordinate of the surface *h* is defined as a function $h(x,y)$ of *x* and *y*.

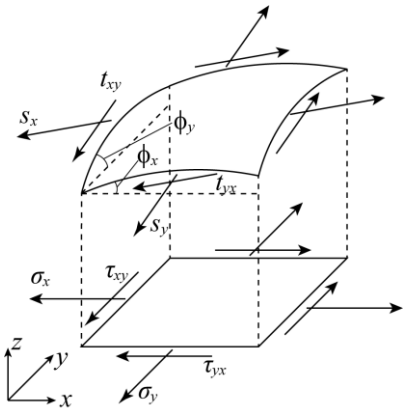


Figure 1. Definition of stresses and angles

A curved surface element is defined with respect to the planes parallel to *xz*- and *yz*-planes, respectively. The stress components on the element are shown in Fig. 1. Based on Pucher's formulation, the equilibrium between the membrane stresses and external loads is expressed using their projected components on the horizontal plane. Note that in-plane forces per unit length of the shell section are

referred to as *stresses* for simplicity. The membrane theory of shells is applied and bending moment and out-of-plane shear forces are not considered.

Let s_x and s_y be the in-plane normal stresses along the sections on the planes parallel to the *yz*- and *xz*-planes, respectively. They are the stresses in the tangent plane of the shell. t_{xy} and t_{yx} denote the in-plane shear stresses along the sections on the planes parallel to the *yz*- and *xz*- planes, respectively. The vectors corresponding to s_x, s_y and t_{xy} (= t_{yx}) are projected onto the *xy*-plane to generate the vectors of σ_x, σ_y, τ_{xy} and τ_{yx}, respectively. Horizontal projected stresses σ_x, σ_y, τ_{xy} and τ_{yx} are stresses per unit length of the horizontal plane. ϕ_x and ϕ_y denote the angles between the horizontal *xy*-plane and the curves obtained by cutting the surface with planes parallel to the *xz*- and *yz*-plane, respectively. s_x, s_y, t_{xy} (= t_{yx}), σ_x, σ_y and τ_{xy} (=τ_{yx}) satisfy the following equations.

$$\sigma_x = s_x \frac{\cos\phi_x}{\cos\phi_y}, \quad \sigma_y = s_y \frac{\cos\phi_y}{\cos\phi_x}, \quad \tau_{xy} = t_{xy} \tag{1}$$

The relationship between *h* and *x*, *y* can be written as

$$\frac{\partial h}{\partial x} = \tan\phi_x, \qquad \frac{\partial h}{\partial y} = \tan\phi_y \tag{2}$$

The horizontal equilibrium equation can be expressed as

$$\frac{\partial \sigma_x}{\partial x} + \frac{\partial \tau_{xy}}{\partial y} = 0, \qquad \frac{\partial \tau_{xy}}{\partial x} + \frac{\partial \sigma_y}{\partial y} = 0 \tag{3}$$

Integrating Eq. (3) with respect to *x* and *y*, respectively, σ_x and σ_y can be defined using τ_{xy} as

$$\sigma_x = -\int\left(\frac{\partial \tau_{xy}}{\partial y}\right)dx + C_x(y), \quad \sigma_y = -\int\left(\frac{\partial \tau_{xy}}{\partial x}\right)dy + C_y(x) \tag{4}$$

where $C_x(y)$ and $C_y(x)$ are arbitrary functions of *y* and *x*, respectively. If the shear stress τ_{xy} is given as a function of horizontal coordinates (*x*,*y*), the normal stresses σ_x and σ_y are defined as the sum of the functions of the shear stress and the arbitrary functions $C_x(y)$ and $C_y(x)$, respectively, according to Eq. (4). To satisfy the horizontal equilibrium equations, the functions $C_x(y)$ and $C_y(x)$ must be constant in the *x* and *y* directions, respectively. On the other hand, they can be defined independently and uncorrelated with the other horizontal projected stresses. The normal stresses σ_x and σ_y are correlated with the magnitude of the shell curvature and the shear stress τ_{xy} is correlated with the direction of the principal curvature of the shell, respectively. Therefore, the shell shape can be controlled by varying these stresses.

The vertical equilibrium equation is expressed as a second-order partial differential equation as

$$\sigma_x \frac{\partial^2 h}{\partial x^2} + 2\tau_{xy} \frac{\partial^2 h}{\partial x \partial y} + \sigma_y \frac{\partial^2 h}{\partial y^2} = f \tag{5}$$

where *f* is self-weight per unit horizontal projected area of the shell that is expressed by the following equation using the mass density ρ, the acceleration of gravity *g* and the uniform shell thickness *t*:

$$f = -\rho g t \sqrt{1 + \left(\frac{\partial h}{\partial x}\right)^2 + \left(\frac{\partial h}{\partial y}\right)^2} \tag{6}$$

In this paper, the *x* and *y* coordinates of the graph surface are defined by the mapping from parameter space $(u,v) \in [0,1]^2$, respectively, as $x(u,v)$ and $y(u,v)$ to generate surfaces with curved boundaries. The differential coefficients of *u* and *v* with respect to *x* and *y* are denoted by *a*, *b*, *c*, and *d* for simplicity.

The finite difference method discretises the vertical equilibrium equation. Consider an $N \times N$ uniformly spaced grid in the (u,v) parameter space. The grid point is indicated by (i, j) $(i, j = 1, \cdots, N+1)$ and the sizes of grid in u- and v- directions are δu and δv, respectively. Eq. (5) is discretized with the z-coordinate of the grid point $h_{i,j}$ using the central finite difference method :

$$\begin{aligned}
&\left(a^2\sigma_x + 2ac\tau_{xy} + c^2\sigma_y\right)\frac{h_{i+1,j} - 2h_{i,j} + h_{i-1,j}}{(\delta u)^2} \\
&+2\left[ab\sigma_x + (ad+bc)\tau_{xy} + cd\sigma_y\right]\frac{h_{i+1,j+1} - h_{i+1,j-1} - h_{i-1,j+1} + h_{i-1,j-1}}{4\delta u\delta v}z \\
&+\left(b^2\sigma_x + 2bd\tau_{xy} + d^2\sigma_y\right)\frac{h_{i,j+1} - 2h_{i,j} + h_{i,j-1}}{(\delta v)^2} \\
&+\left[\left(a\frac{\partial a}{\partial u} + b\frac{\partial a}{\partial v}\right)\sigma_x + 2\left(a\frac{\partial c}{\partial u} + b\frac{\partial c}{\partial v}\right)\tau_{xy} + \left(c\frac{\partial c}{\partial u} + d\frac{\partial c}{\partial v}\right)\sigma_y\right]\frac{h_{i+1,j} - h_{i-1,j}}{2\delta u} \\
&+\left[\left(a\frac{\partial b}{\partial u} + b\frac{\partial b}{\partial v}\right)\sigma_x + 2\left(a\frac{\partial d}{\partial u} + b\frac{\partial d}{\partial v}\right)\tau_{xy} + \left(c\frac{\partial d}{\partial u} + d\frac{\partial d}{\partial v}\right)\sigma_y\right]\frac{h_{i,j+1} - h_{i,j-1}}{2\delta v} = f_{i,j}
\end{aligned} \tag{7}$$

The right-hand side of Eq. (7) $f_{i,j}$ is computed as

$$f_{i,j} = -\rho g t\sqrt{1+\left(a^2+c^2\right)\left(\frac{h_{i+1,j} - h_{i-1,j}}{2\delta u}\right)^2 + 2(ab+cd)\frac{\left(h_{i+1,j} - h_{i-1,j}\right)\left(h_{i,j+1} - h_{i,j-1}\right)}{4\delta u\delta v} + \left(b^2+d^2\right)\left(\frac{h_{i,j+1} - h_{i,j-1}}{2\delta v}\right)^2} \tag{8}$$

See Ref. [9] for details. Takeoka *et al.* [9] solved Eq. (7) using the successive over-relaxation (SOR) method to derive the shell shape. In this study, the solution of Eq. (7) is found by sequentially solving linear system of equations [11]. If the right sides $f_{i,j}$ are constants, Eq. (7) can be regarded as a linear system with respect to the z-coordinates $h_{i,j}$ of the grid points. The shell shape is obtained by deriving Eq. (7) at all free grid points, fixing the right-hand sides $f_{i,j}$ to the current shape, and solving them as a linear system of equations. We have verified that the method converges with lower computational cost than the SOR method [11]. The procedure is summarized as follows.

1. Define horizontal projected geometries and horizontal projected stresses of a shell.
2. Solve the linear system of the equilibrium equation (7) to obtain the z-coordinates $h_{i,j}$ assuming that the right-hand side $f_{i,j}$ of the equation is a constant value $-\rho g t$.
3. Calculate $f_{i,j}$ from Eq. (8) based on the shell shape obtained in the previous iteration step.
4. Substitute the obtained $f_{i,j}$ into the right-hand side of Eq. (7) and solve it as a linear system of equations for $h_{i,j}$ to update the shell shape.
5. Calculate e, the sum of the changes in $h_{i,j}$ at each grid point, by the following equation. The superscript (l) indicates the iteration counter.

$$e = \sum_{i=1}^{N+1}\sum_{j=1}^{N+1}\left|h_{i,j}{}^{(l+1)} - h_{i,j}{}^{(l)}\right| \tag{9}$$

6. Return to Step 3 if e is greater than or equal to the specified positive small value ξ.
7. Output the solution $h_{i,j}$ for the shell shape and terminate the iteration.

The relationship between the specified horizontal projected stress distribution and the shell shape is discussed using Mohr's stress circle. The principal stress σ_1, σ_2 ($\sigma_1 \geq \sigma_2$) of the horizontal projected stress can be written as follows.

$$\sigma_1, \sigma_2 = \frac{\sigma_x + \sigma_y}{2} \pm \sqrt{\left(\frac{\sigma_x - \sigma_y}{2}\right)^2 + {\tau_{xy}}^2} \tag{10}$$

The angle θ between the direction of the principal stress σ_1 and the *x*-axis is expressed as

$$\theta = \tan^{-1}\left(\frac{\sigma_1 - \sigma_x}{\tau_{xy}}\right) \tag{11}$$

The relationship between the larger principal stress, which is simply called *principal stress* below, and the stress σ_x, σ_y and τ_{xy} is shown in Fig. 2 using Mohr's stress circle. The vertical equilibrium Eq. (5) is a second-order partial differential equation. For the coefficients σ_x, σ_y and τ_{xy} of the equation, the partial differential equation is elliptic when $\sigma_x\sigma_y - {\tau_{xy}}^2 > 0$ and hyperbolic when $\sigma_x\sigma_y - {\tau_{xy}}^2 < 0$. It is known to be difficult to obtain a solution when the equilibrium equation is hyperbolic [6].

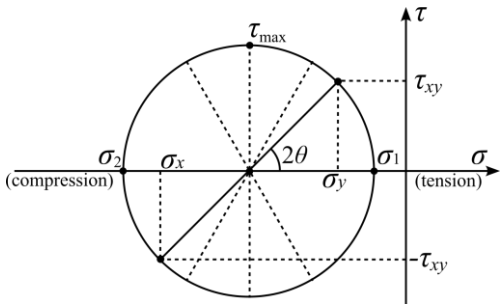


Figure 2. Mohr's Circle

3. Numerical examples

In this section, various shell shapes with different horizontal projected stress distributions are generated using the proposed method and their mechanical performances are investigated utilizing FE analysis. Note that the equilibrium surface shape depends only on the ratio of the projected stresses to the self-weight ρgt per unit projected area. Therefore, for simplicity, the units are omitted in the process of form finding and ρgt is set to 1. The Bernstein basis polynomials are used for defining the (*x*,*y*)-coordinates by the parameters $(u,v) \in [0,1]^2$. The number of grids in the parameter space is $N = 30$. The value of ξ for convergence of e is 1×10^{-10}. The form finding program is created using Python, and the linear system of the vertical equilibrium equations is solved using the Python library Numpy. OpenSeesPy [12], a Python interpreter of the FE-analysis software OpenSees, is used for linear static analysis. The shell surface is modelled utilizing the quadrilateral isoparametric shell element (ShellMITC4), which considers out-of-plane bending and shear deformations.

First, the relationship between the specified shear stress distribution and the shell shape is discussed using Models 1a–1f with rectangular boundaries and Models 2a–2f with curved boundaries. Next, the method is also applied to Model 3 with free boundary where vertical reaction forces do not exist. Finally, FE analyses are carried out for Models 1a, 1f, 2f and 3 to confirm their mechanical performance.

3.1. Form finding

We consider the following models with parameterized (*x*,*y*)-coordinates using the Bernstein polynomials:

Model 1a–1f, 3 : $x = 2u - 1, \quad y = 2v - 1$

Model 2a–2f : $x = -(2u-1)(2v^2 - 2v - 1), \quad y = (2u^2 - 2u + 1)(2v - 1)$

Models 1a–1f and 3 have square plans and Models 2a–2f have curved boundaries. The specified horizontal projected stresses are shown in Table 1. The forms found for Models 1 and 2 are investigated to reveal the influence of the shear stress distribution on the shell shape. The shell shapes and the directions of the principal curvature line of Models 1a–1e and 2a–2e are shown in Fig. 3. The red circles in the figures of shell shapes indicate the fixed boundaries. Only the *z*-coordinates of the diagonal view

Table 1. Specified horizontal projected stress

Model	σ_x	σ_y	τ_{xy} $(=\tau_{yx})$
1a–1e, 2a–2e	Defined by Mohr's stress circle. (σ_1=–0.2, σ_2 =–1.8, $\tau_{\max}$ =0.9 and θ={0, π/6, π/4, π/3,π/2})		
1f, 2f	$-\frac{1}{2}\left\{\frac{1}{2}(x+1)^2+1\right\}$	$-\frac{1}{2}\left\{\frac{1}{2}(y-1)^2+1\right\}$	$\frac{1}{2}\{(x+1)(y-1)+1\}$
3	$0.5(-x-1)$	–1	$0.5y$

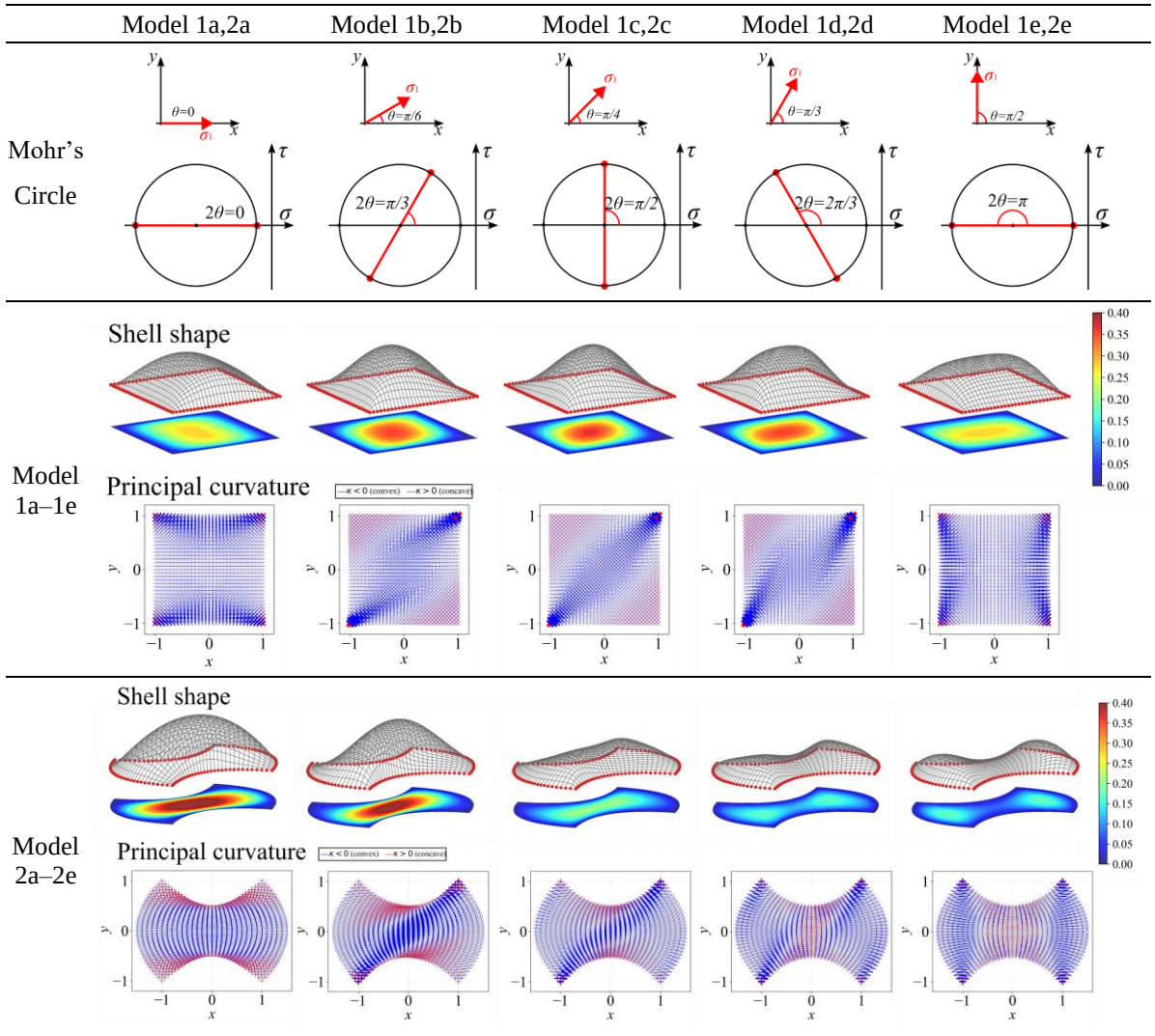


Figure 3. Shell shape and distribution of principal curvature of Model 1a–1e and 2a–2e

are scaled to 2.0 times the *x*- and *y*-coordinates. The directions of the principal curvature κ of the surface are shown as blue lines when the surface is convex ($\kappa < 0$) and red lines when it is concave ($\kappa > 0$). The thickness of the principal curvature line is proportional to the magnitude of the curvature, and the legends in the figure indicate the thickness of the line for curvature $\kappa = \pm 1$. The thick blue lines indicating the direction of smaller principal curvature are oriented orthogonally to the direction of the principal stresses. Model 2 has the highest rise when the principal stress direction is $\theta = 0$ (model 2a) due to the large span in the *x*-direction. It can also be seen that some shells contain regions of negative Gaussian curvature, where the product of the two principal curvatures is negative. These figures show that there is a correlation between the principal stress direction of the specified horizontal projected stress and the principal curvature direction characterising the shell shapes. The designer can control the curvature of the surface by specifying the principal stress direction of the horizontal projected stress.

Figure 4 shows the shell shapes and distributions of principal curvatures of Models 1f and 2f. The shear stress is defined as a function of (*x*,*y*)-coordinates. Asymmetric shell shapes are obtained by specifying asymmetric horizontal projected stress distribution.

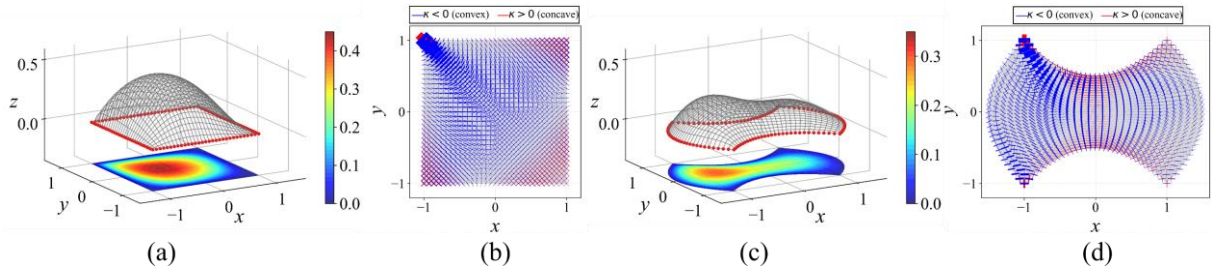


Figure 4. Shell shapes and distributions of principal curvature: (a) Model 1f, (b) Model 2f

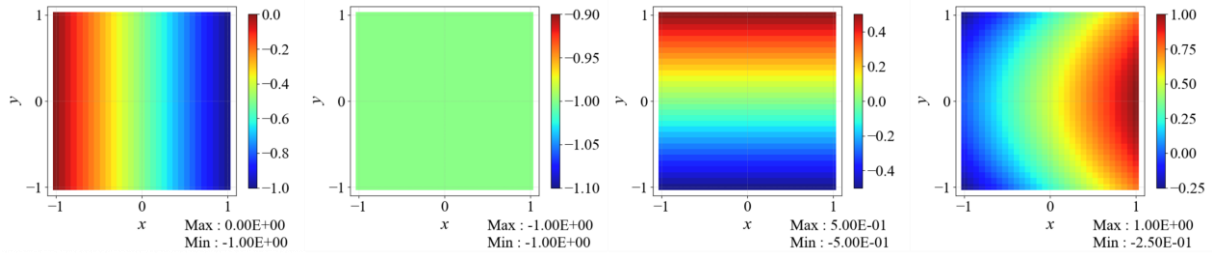


Figure 5. Horizontal projected stress distribution of Model 3: (a) σ_x, (b) σ_y, (c) τ_{xy}, (d) $\left(\sigma_x \sigma_y - {\tau_{xy}}^2\right)$

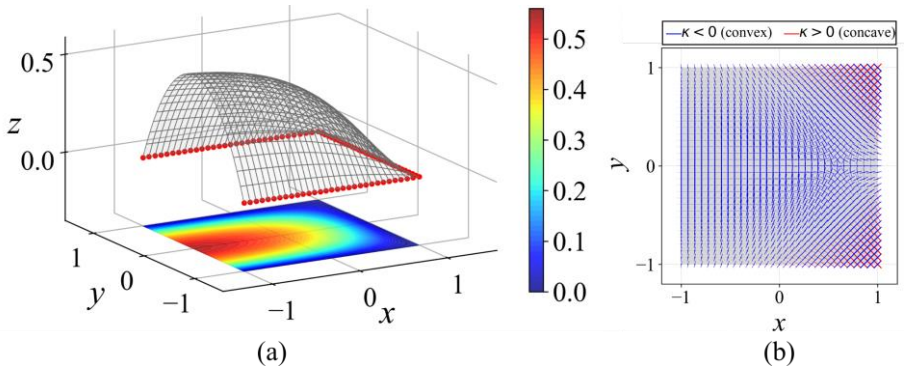


Figure 6. Model 3: (a) shell shape, (b) distribution of principal curvature

Model 3 has free boundary at $x = -1$, and the *z*-coordinates of along the free boundary are considered as variables in the shape design. The normal stresses σ_x at $x = -1$ are specified to be 0. The horizontal projected stress distribution and the corresponding shell shape are shown in Figs. 5 and 6, respectively. Note that s_y and t_{xy} are not 0 at the free boundary. These stresses can be transferred to the supports by the axial forces of beams if edge beams are arranged. Model 3 has areas where the equilibrium equations are hyperbolic as shown in Fig. 5(d). The results indicate that shell shape with hyperbolic region can be successfully obtained for this specific model, which has a free boundary and a small hyperbolic region.

3.2. Finite element analysis

FE analyses are performed for Models 1a, 1f, 2f and 3 to account for elastic deformation, including out-of-plane bending deformation and transverse strain due to Poisson's ratio; thus, units are considered for length and force. For the coordinates (*x*, *y*, *h*) of a graph surface in the form finding method, the respective coordinate values are scaled as (αx, αy, αh) (m) using the coefficient α in FE analysis. In the following examples, α is set to 10 and the scaling gives, for example, the span is 20 (m) and the rise is 2.80 (m) for Model 1a. The shell thickness and vertical distributed load are t = 0.1 (m) and $\rho g t$ = 2.4 (kN/m^2), respectively. The shells are assumed to be composed of concrete material with Young's modulus E = 20.0 (GPa) and Poisson's ratio $\nu = 0.2$. The horizontal projected stress $\sigma_x = -1.8$ in the form finding method for Model 1a corresponds to the horizontal projected stress $\sigma_x = -43.2$ (kN/m) in the FE analysis. To study the differences in shell properties with and without edge beams placed at the free boundary, FE analyses are carried out for Model 3a without edge beams at the free boundary and Model 3b with edge beams. The edge beam is assumed to have a rectangular section with the width 0.3 (m) and the height 0.6 (m).

Figure 7 shows the horizontal projected stress distribution of Model 1a obtained from the FE analysis. Focusing on the stresses at the boundary that correspond to the horizontal reaction forces, the result for Model 1a demonstrates that the stresses at the middle of the boundary closely approach the specified horizontal projected stress σ_x of 43.2 (kN/m). However, the stress falls below the specified value at the boundary near the corner. The maximum vertical displacement and the strain energy of each model are listed in Table 2, and Fig. 8 shows the distribution of the vertical displacement. The maximum displacement of Models 1a, 1f and 2f are less than 0.05% of the shell span length. More than 90% of the strain energy is due to membrane action (in-plane stress). For Model 3b, the effect of the edge beams transferring the load by axial forces reduces the vertical deformation to approximately 25% of that of Model 3a. The results of these FE analyses confirm that the shell shapes that resist external loads through membrane action have been successfully found.

Table 2. Summary of FE analysis

Model	Max. displacement (mm)	Strain energy (Nm) (Ratio (%))		
		Membrane	Bending	Total
1a	0.57	121.5 (95.4)	5.8 (0.8)	127.3 (100.0)
1f	0.43	77.3 (97.4)	2.1 (2.6)	79.4 (100.0)
2f	0.96	79.8 (93.9)	5.2 (6.1)	85.0 (100.0)
3a	1.93	101.9 (96.0)	4.3 (4.0)	106.2 (100.0)
3b	0.46	91.8 (98.6)	1.3 (1.4)	93.1 (100.0)

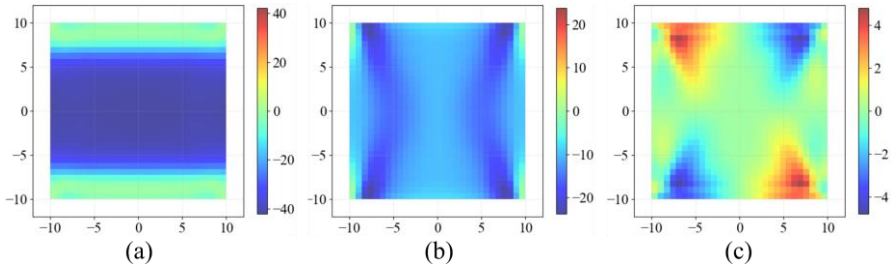


Figure 7. The projected stress distribution of model 1 obtained by FE analysis (kN/m): (a) σ_x, (b) σ_y, (c) τ_{xy}

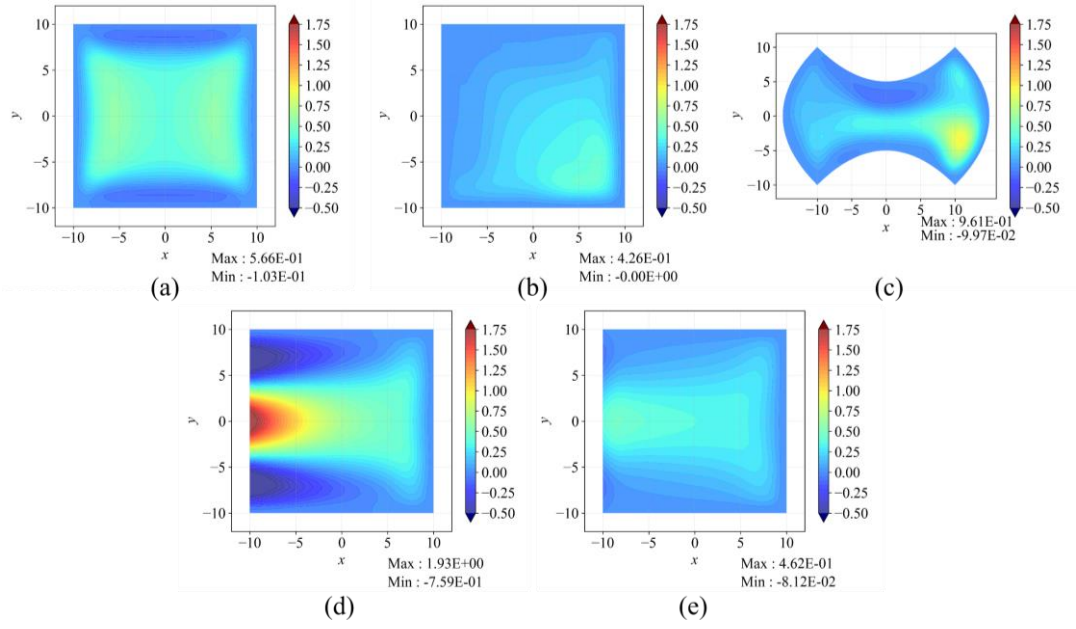


Figure 8. Distribution of vertical displacement (mm): (a) Model 1a, (b) Model 1f, (c) Model 2f, (d) Model 3a, (e) Model 3b

4. Conclusions

This study has shown a form finding method for free-form shells specifying the distribution of stresses projected onto the horizontal plane. The shell shape is obtained as a solution to the vertical equilibrium equations of the surface heights at the grid points discretized by the finite difference method. Our research has shown that various shell shapes can be generated by varying the shear stress and a shell shape with free boundaries. We conducted FE analyses to investigate the effect of elastic deformation

due to material properties on the mechanical performance of shells. These analyses confirmed that the obtained shell shapes by the proposed method resist external loads through membrane action. Conditions for obtaining solutions for shells with hyperbolic regions have not yet been clearly obtained, which is a subject of future study.

Acknowledgements

This research is partially supported by JST CREST No. JPMJCR1911.

References

[1] Adriaenssens S., Block P., Veenendaal D., Williams C. (Eds.), *Shell structures for architecture: form finding and optimization*, Routledge, 2014.

[2] P. Block and J. Ochsendorf, "Thrust network analysis: a new methodology for three-dimensional equilibrium," *J. Int. Assoc. shell Spat. Struct.*, vol. 48, no. 3, pp. 167–173, 2007.

[3] W. Flügge, *Stresses in Shells*, 2nd. ed., Springer-Verlag, 1973.

[4] M. Miki, T. Igarashi, and P. Block, "Parametric self-supporting surfaces via direct computation of airy stress functions," *ACM Transactions on Graphics*, vol. 34, no. 4, Jul. 2015.

[5] Y. Xia, A. Mantzaflaris, B. Jüttler, H. Pan, P. Hu, and W. Wang, "Design of self-supporting surfaces with isogeometric analysis," *Comput. Methods in Appl. Mech. Eng.*, vol. 353, pp. 328–347, Aug. 2019.

[6] M. Miki and T. Mitchell, "Interactive Exploration of Tension-Compression Mixed Shells," *ACM Trans. Graph.*, vol. 41, no. 6, Nov. 2022.

[7] Y. C. Chiang and A. Borgart, "A form-finding method for membrane shells with radial basis functions," *Eng. Struct.*, vol. 251, p. 113514, Jan. 2022.

[8] Y. Sakai and M. Ohsaki, "Non-parametric shape design method of free-form shells using membrane stresses projected onto horizontal plane," *AIJ J. Technol. Des.*, vol. 27, no. 66, pp. 1098–1103, Jun. 2021. (in Japanese)

[9] R. Takeoka, M. Ohsaki, and Y. Sakai, "Non-parametric design of free-form shells with curved boundaries and specified reaction forces," *Engineering Structures*, vol. 255, pp. 113892, Mar. 2022.

[10] C. Olivieri, M. Angelillo, A. Gesualdo, A. Iannuzzo, and A. Fortunato, "Parametric design of purely compressed shells," *Mech. Mater.*, vol. 155, p. 103782, Apr. 2021.

[11] T. Nakajima, M. Ohsaki, "Form finding of free-form shells with specified horizontal projected stress distribution," *J. Struct. Constr. Eng.* (*Trans. AIJ*), accepted for publication. (in Japanese)

[12] M. Zhu, F. McKenna, and M. H. Scott, "OpenSeesPy: Python library for the OpenSees finite element framework," *SoftwareX*, vol. 7, pp. 6–11, Jan. 2018.

IASS 2023
July 10–14 Melbourne
Integration of Design and Fabrication

Proceedings of the IASS Annual Symposium 2023
Integration of Design and Fabrication
10–14 July 2023, Melbourne, Australia
Y.M. Xie, J. Burry, T.U. Lee and J. Ma (eds.)

Isogeometric deep learning framework to predict the structural performance of free-form surfaces

Kazuki HAYASHI[*], Makoto OHSAKI[a]

[a,*] Kyoto University
Kyotodaigaku-katsura, Nishikyo, Kyoto 615-8540, Japan
hayashi.kazuki@archi.kyoto-u.ac.jp

Abstract

To capture complex structural properties of free-form surfaces, geometric deep learning approaches, which can encode geometric properties of data, have been proposed regarding mesh models as graphs: a specific type of data consisting of nodes and edges. However, the connectivity of graphs becomes complex as the resolution of finite elements increases, which causes a huge computational load in training the geometric deep learning model. Recently, as an alternative to the finite element method (FEM), an increasing number of studies have focused on isogeometric analysis, which maintains the smoothness of the surface by utilizing parametric representation. In this research, by combining isogeometric analysis and geometric deep learning, a new machine learning method is developed for free-form structures that consistently perform surface representation, structural analysis, and machine learning to capture the latent information of free-form structures. This study utilizes hierarchical graphs to represent the structural model; the connectivity of patches is represented by a graph, where its nodes is associated with another subgraph representing the shape and connectivity of the control polygon. The proposed workflow will be applied to predict the maximum displacement of free-form shell structures, which requires a large computational load when using the conventional FEM. Since the proposed method uses only the control points of the surface and does not require surface discretization, more precise structural properties and behavior can be captured at a lower computational cost.

Keywords: shells, free-form structures, machine learning, geometric deep learning, isogeometric analysis, hierarchical graph neural networks, discrete representation

1. Introduction

As computer-aided design spreads to architects and engineers, free-form surfaces have become a popular choice to create dynamic, organic, and visually attractive shapes. Although it is possible to intuitively manipulate the shape of a free-form surface by manipulating control polygons, the shape needs to be converted into a polyhedron with finite small elements to analyze its structural performance using a finite element method (FEM). Moreover, a well-known dilemma in FEM is that the finer the element resolution, the higher the accuracy of structural analysis results, but the greater the computational load.

In recent years, many attempts have been made to introduce machine learning to reduce the computational load of numerical analyses. One of the most famous applications is physics-informed neural networks (PINNs) [1], where neural networks approximate solutions to partial differential equations governing the laws of physics over the predetermined domain. However, the performance of regular PINNs can be ensured only on a single geometry, and they need to be re-trained when the domain or the boundary conditions are changed; this suggests that regular PINNs cannot fully take into account the geometrical information of the various regions.

Copyright © 2023 by Kazuki HAYASHI and Makoto OHSAKI. Published in the Proceedings of the IASS Annual Symposium 2023 with permission.

Geometric deep learning is a field that explicitly considers the geometric property of data in the machine learning model [2]. It has become increasingly popular, as it enables the analysis and manipulation of complex geometric data, such as meshes, graphs, and point clouds, in a more efficient and accurate way. Geometric deep learning represents the input geometry as a graph, where nodes represent individual elements and edges represent the connections between them. By analyzing the data using geometric deep learning techniques, it is possible to accurately predict stress distribution [3,4], displacements [5], and dynamic particle behavior [6].

In addition to geometric deep learning, hierarchical deep learning is a method that explicitly considers the hierarchical structure of data and machine learning models, and has the strong potential to enhance the prediction performance of the machine learning model. The work by Marvouniotis and Chang [7] is one of the earliest examples of introducing hierarchy into machine learning models. Saha et al. [8] utilized a hierarchical neural network architecture to capture stress concentration and solve multiscale problems.

Considering both geometric and hierarchical aspects in deep learning may improve the prediction accuracy of the machine learning models. Fortunato et al. [9] introduced a hierarchical approach to process mesh data with two different resolutions, and the trained machine learning model successfully predicted a Kármán vortex street, one of the typical fluid behaviors, on a very coarse mesh at high accuracy.

Regular FEM, geometric deep learning, and hierarchical deep learning methods are developed on a discrete basis. On the other hand, isogeometric analysis (IGA) [10] is based on the concept of isogeometric modeling of smooth shapes, which uses the same mathematical expressions, e.g., Bézier, B-spline, and NURBS, to describe both the structural geometry and the shape functions used for numerical analysis. This approach allows for more seamless integration between the design and analysis phases, as the same mathematical functions can be used for both tasks without the need for re-meshing. IGA also offers several advantages over traditional finite element analysis, including improved accuracy, smoother results, and more efficient computation. IGA is expected to be applicable to new parametric forms of surfaces consisting of limited favorable classes of surface patches such as piecewise constant Gaussian/mean curvature surfaces [11].

This study attempts to seamlessly perform free-form shape modeling, structural analysis, and machine learning to capture the structural performance by combining geometric deep learning, hierarchical deep learning, and IGA techniques. We use Bézier surfaces and Bézier curves to represent the shape of concrete shells and their ribs, respectively. The control net is not only a discrete representation of the surface shape, but can also be regarded as graph-structured data, making it posible to use existing machine learning methods for graphs. In the numerical examples, the machine learning model trained by the proposed framework predicts the displacement distribution of the structure with 93.3% accuracy in a logarithmic scale.

2. Hierarchical graph representation of ribbed shell structures

2.1. Hierarchical graph representation of a Bézier surface with multiple patches

In this research, we use Bézier surfaces, which are a relatively simple free-form surface representation uniquely defined by the position information of the control net. For a Bézier surface with order $n_\mathrm{u} \times n_\mathrm{v}$, the position of the point on the surface is calculated by the following formula by specifying the parameters $u, v \in [0,1]$ on the surface

$$\mathbf{p}(u,v) = \sum_{i=0}^{n_\mathrm{u}} \sum_{j=0}^{n_\mathrm{v}} B_i^{n_\mathrm{u}}(u) B_j^{n_\mathrm{v}}(v)\, \mathbf{R}_{ij} \tag{1}$$

where $B_i^{n_\mathrm{u}}(u)$ and $B_j^{n_\mathrm{v}}(v)$ are the Bernstein basis polynomials, and $\mathbf{R}_{ij}$ is a position vector of the control point indexed by (i,j).

In almost all practical cases, it is necessary to design the shell shapes with multiple patches, because the tensor product expression of parameters of a single patch is not suitable for representing complex shapes. Multiple-patch representation is also beneficial when considering constructability; the surface shape can be simply reinforced with ribs along the patch connection to stiffen the shell structure.

One of the highlights of this research lies in representing multiple-patch surfaces using hierarchical graphs. Figure 1 shows an example of the hierarchical graph representation. Here, the parent graph represents the connectivity of patches. Each node in the parent graph corresponds to a patch, and each edge represents G0 continuity between the patches. A child graph branches from a parent node, and the nodes and edges of the child graph represent the control nets of the patch surface.

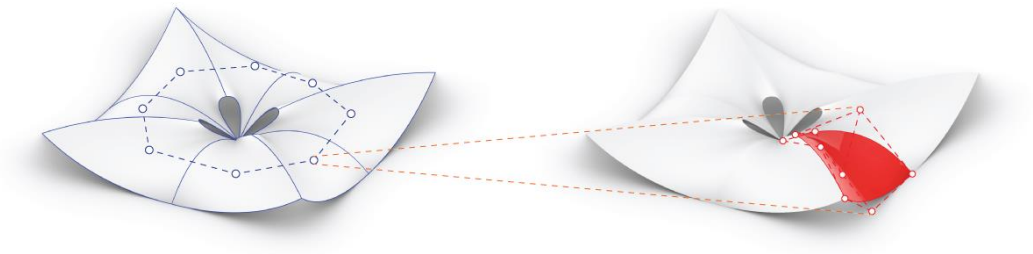


Figure 1. Hierarchical graph representation of a multiple-patch Bézier surface.

2.2. Extraction of node and global features over a single graph

To handle graph data with arbitrary connectivity in geometric deep learning, graph neural networks are the most popular machine learning model. Among various graph neural network models, Edge-Conditioned Convolution (ECC) [12] is introduced to extract node features, because it is one of the representative methods to handle both node and edge inputs.

This paragraph briefly summarizes the ECC method. Suppose there are n_n nodes and n_m edges in a graph. Let $\mathbf{X}_0(i) \in \mathbb{R}^{n_\mathrm{v}}$ denote the input of node i and $\mathbf{L}(j,i) \in \mathbb{R}^{n_\mathrm{w}}$ denote the input of edge (i,j). If node i is connected to a set of nodes $N(i)$, the node feature $\mathbf{X}_l(i)$ $(l \geq 0) \in \mathbb{R}^{d_l}$ is updated to $\mathbf{X}_{l+1}(i) \in \mathbb{R}^{d_{l+1}}$ as follows:

$$\mathbf{X}_{l+1}(i) = \frac{1}{|N(i)|} \sum_{j \in N(i)} F_l(\mathbf{L}(j,i); \mathbf{w}_l)\mathbf{X}_l(j) + \mathbf{b}_l \tag{2}$$

where $\mathbf{w}_l \in \mathbb{R}^{(d_{l+1} \times d_l) \times s}$ and $\mathbf{b}_l \in \mathbb{R}^{d_l}$ are the trainable parameters, and $F^l \colon \mathbb{R}^s \mapsto \mathbb{R}^{d_{l+1} \times d_l}$ is a filter generating network parametrized by $\mathbf{w}_l$. Except that $d_0 = n_\mathrm{v}$, the feature dimension d_l $(l \geq 1)$ can take an arbitrary positive integer. By repeating this convolution, the node features can capture the property of neighborhood nodes and edges.

This study modifies the ECC method to further consider self-node and global features. In addition to the node and edge input matrices, the proposed method requires another input vector $\mathbf{G}_l \in \mathbb{R}^{n_\mathrm{g}}$, which inform the machine learning model of the global information about the entire graph. The modified convolution operation is formulated as

$$\mathbf{X}_{l+1}(i) = \mathbf{H}_{l+1}^1(i) + \mathbf{H}_{l+1}^2(i) + \mathbf{H}_{l+1}^3(i) \tag{3a}$$

$$\mathbf{H}_{l+1}^1(i) = \varphi\left(F_{l,1}\left(\mathbf{X}_l(i); \mathbf{w}_{l,1}, \mathbf{b}_{l,1}\right)\right) \tag{3b}$$

$$\mathbf{H}_{l+1}^{2}(i) = \frac{1}{|N(i)|} \sum_{j \in N(i)} \varphi\left(F_{l,2}\left(\mathbf{L}(j,i); \mathbf{w}_{l,2}, \mathbf{b}_{l,2}\right)\right) \mathbf{X}_l(j) \tag{3c}$$

$$\mathbf{H}_{l+1}^{3}(i) = \varphi\left(F_{l,3}\left(\mathbf{G}_l; \mathbf{w}_{l,3}, \mathbf{b}_{l,3}\right)\right) \tag{3d}$$

where φ is the Leaky ReLU activation function, and $F_{l,1}$, $F_{l,2}$, and $F_{l,3}$ are filter generating networks parametrized by $(\mathbf{w}_{l,1}, \mathbf{b}_{l,1})$, $(\mathbf{w}_{l,2}, \mathbf{b}_{l,2})$, and $(\mathbf{w}_{l,3}, \mathbf{b}_{l,3})$, respectively. From each operation, $\mathbf{H}_l^1$, $\mathbf{H}_l^2$, and $\mathbf{H}_l^3$ are regarded as features encapsulated into a node considering the self-node, neighbor nodes and edges, and whole graph, respecrively.

The node feature matrix can be expressed in a matrix form $\widetilde{\mathbf{X}}_l \in \mathbb{R}^{n_\mathrm{n} \times n_\mathrm{v}}$, whose rows contains the feature of each node. Once the updated node feature matrix $\widetilde{\mathbf{X}}_{l+1} \in \mathbb{R}^{n_\mathrm{n} \times n_\mathrm{v}}$ are obtained, the global feature vector $\mathbf{G}_l$ can also be updated to $\mathbf{G}_{l+1}$ using a variant of the soft attention mechanism [13] modified by the PyTorch geometric library [14] as

$$\mathbf{G}_{l+1} = \sum_{i=1}^{n_\mathrm{n}} \mathrm{softmax}\left(F_{l,4}\left(\widetilde{\mathbf{X}}_{l+1}; \mathbf{w}_{l,4}, \mathbf{b}_{l,4}\right)\right) \odot F_{l,5}\left(\widetilde{\mathbf{X}}_{l+1}; \mathbf{w}_{l,5}, \mathbf{b}_{l,5}\right) \tag{4}$$

where $\Sigma_{i=1}^{n_\mathrm{n}}$ indicates column-wise summation, "softmax" is a softmax function over the matrix rows, and $\odot$ indicates element-wise multiplication. Similar to Eq. (3), Eq. (4) introduces neural networks $F_{l,4}$ and $F_{l,5}$.

2.3. Extraction of node and global features over a single graph

This study further augments the graph embedding method in Sec. 2.2 to handle hierarchical graph data. Figure 2 illustrates the two types of graphs on the surface; one is a parent graph representing the patch connectivity; the other is a child graph representing the control net connectivity of each patch. Tables 1 and 2 describe the node and edge inputs of the parent graph, and Tables 3 and 4 describe the inputs of the child graphs. Although any number of inputs can be given with any definition for $\mathbf{X}_0$ and $\mathbf{L}$ we carefully defined these inputs such that the machine learning model can accurately capture the geometrical and struructural information on the surface.

Table 1. Node input definition $\mathbf{X}_0(i)$ of the parent graph.

index	description
1	Maximum difference of *x*-coordinate in the control net
2	Maximum difference of *y*-coordinate in the control net
3	Maximum difference of *z*-coordinate in the control net

Table 2. Edge input definition $\mathbf{L}(j,i)$ of the parent graph.

index	description
1	1 (constant)

Table 3. Node input definition $\mathbf{X}_0(i)$ of the child graph.

index	description
1	*u*-coordinate of the closest point on the patch
2	*v*-coordinate of the closest point on the patch
3	1 if supported, 0 otherwise
4	Normalized *x*-coordinate in the control net
5	Normalized *y*-coordinate in the control net
6	Normalized *z*-coordinate in the control net

Table 4. Edge input definition $\mathbf{L}(j,i)$ of the child graph.

index	description
1	1 if beam, 0 otherwise

In the proposed method, the graph embedding operations Eqs. (3) and (4) are alternately repeated for the child graphs and the parent graph. That is, the global feature of the child graph becomes the node feature of the parent graph, and vice versa. This way, the node feature of child graph can capture not only the local-scale information about the control net but also global-scale information about the patch after several iterations. In this study, the number of repetitions is two.

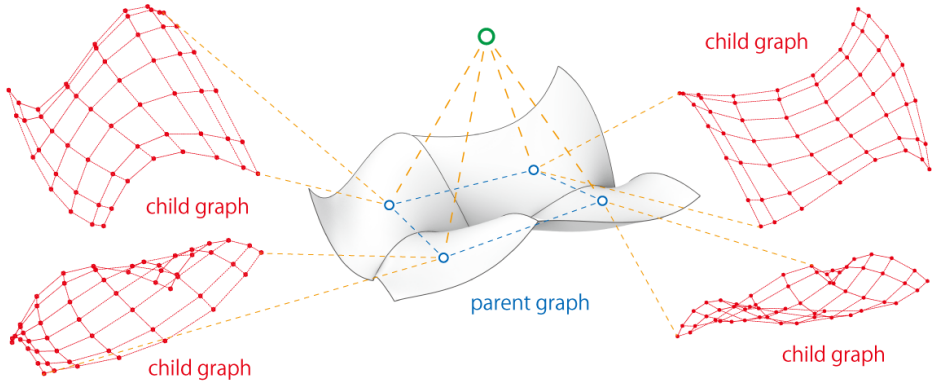


Figure 2. Classification of two types of graphs in the multiple-patch Bézier surface: parent and child graphs.

2.4. Prediction of responses at the nodes

Let d_{r} denote the intermediate feature dimension in predicting the nodal responses. After obtaining the node features $\widetilde{\mathbf{X}}_2 \in \mathbb{R}^{n_{\mathrm{n}} \times d_2}$ in the child graphs, the prediction of response value $\mathbf{r}_{\mathrm{pred}} \in \mathbb{R}^{n_{\mathrm{n}}}$ is computed as follows:

$$\mathbf{r}_{\mathrm{pred}} = \mathrm{Sigmoid}\left(F_{\mathrm{r},1}\left(\varphi\left(F_{\mathrm{r},2}\left(\widetilde{\mathbf{X}}_2; \mathbf{w}_{\mathrm{r},2}, \mathbf{b}_{\mathrm{r},2}\right)\right); \mathbf{w}_{\mathrm{r},1}, \mathbf{b}_{\mathrm{r},1}\right)\right) \tag{5}$$

where $F_{\mathrm{r},1}: \mathbb{R}^{d_{\mathrm{r}}} \mapsto \mathbb{R}$ and $F_{\mathrm{r},2}: \mathbb{R}^{d_2} \mapsto \mathbb{R}^{d_{\mathrm{r}}}$ are the neural network layer parametrized by $(\mathbf{w}_{\mathrm{r},1}, \mathbf{b}_{\mathrm{r},1})$ and $(\mathbf{w}_{\mathrm{r},2}, \mathbf{b}_{\mathrm{r},2})$, respectively. Equation (5) can be interpreted as the process of converting the node feature of size d_2 into another feature vector with size d_{r} and then into a scalar value. Note that the output is scaled by the Sigmoid function into (0,1) to facilitate the training.

3. Numerical example

3.1. Surface modeling

In this study, the shell shape is composed of $n_{\mathrm{u}} \times n_{\mathrm{v}}$ grid Bézier patches, where n_{u} and n_{v} take 2 or 3 randomly; i.e., the orders of the patch can be either quadratic or cubic in its two directions. For example, if the order of the patch is determined as quadratic in one direction and cubic in the other direction, the patch shape is defined by a control net composed of $3 \times 4 = 12$ control points. Once the patch topology is determined this way, the overall surface shape is determined by the order of the patch surfaces and the location of control points. In order to generate various shapes, the positions of control points are randomly generated as follows. The *x* and *y* coordinates are determined by a uniform distribution so that there is a space within 5 to 7.5 meters between adjacent control points. The *z* coordinate is determined by a uniform distribution of between 0 to 5.0 meters.

The shell material is assumed to be the default concrete property of Kiwi!3D [15], which is an isogeometric analysis plug-in for the numerical modeling tool Grasshopper: Young's modulus 35000 N/mm^2, zero Poisson's ratio, and the strength 25 N/mm^2. The shell thickness shall be 200 mm. The rib material is assumed to be Kiwi!3D's default steel property: Young's modulus 210000 N/mm^2, zero Poisson's ratio, and the strength 235 N/mm^2.

The four corners in each Bézier patch are fixed in translation, while their rotation is unconstrained. The surface is subject to a downward surface load of 10 kN/m^2. For simplicity, the self-weight of concrete and steel is not included in the loading condition.

To accurately compute the displacement distributions, the surface orders are increased by increasing the control points while maintaining the original shape. In the following, the refined control nets are utilized to express the child graphs. In order for the machine learning model to learn on various surfaces, surface generation is performed 5000 times based on the rules explained above.

3.2. Structural analysis

For the surfaces randomly generated in the previous section, The displacement distribution is computed using Kiwi!3D. In Kiwi!3D, we implemented geometric nonlinear analysis to obtain the displacements closer to the actual behavior.

Structural analysis results by Kiwi!3D are generated in a text format summarizing displacements and stresses at Gauss integration points. After reading the text data, the displacement values of the closest Gauss point are assigned to each control point. This way, all the control points are associated with unique displacement values, which become the target value to be predicted. This process is repeated for all the 5000 surface shapes, and the target values are stocked and used for machine learning in the next section.

3.3. Machine learning

The displacements have a large variance among 5000 configurations and even within a single configuration. In order to normalize the displacement to be predicted, the response value r_{true} is normalized to $\tilde{r}_{\mathrm{true}}$ by the following equation:

$$\tilde{r}_{\mathrm{true}} = \frac{\log(r_{\mathrm{true}}) - \min(\log(r_{\mathrm{true}}))}{\max(\log(r_{\mathrm{true}})) - \min(\log(r_{\mathrm{true}}))} \tag{6}$$

Figure 3 shows the distributions of displacements sorted in the increasing order in the training data before and after the normalization. As seen in Fig. 3, the target values are distributed relatively evenly in the range [0, 1] by normalization described in Eq. (6).

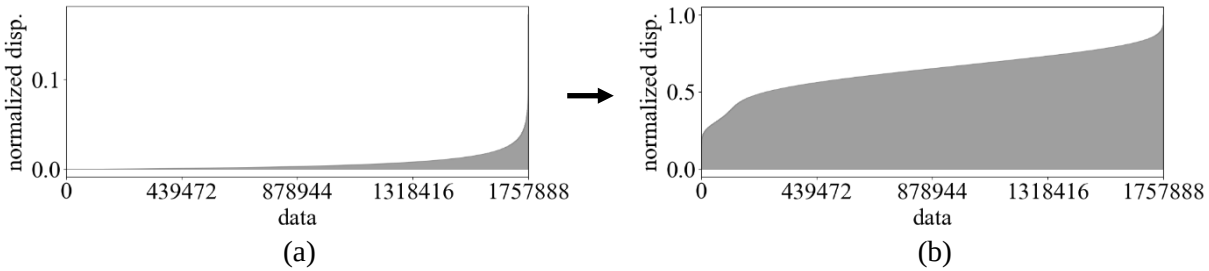


Figure 3. Distribution of displacements in the training data. (a): original displacements. (b): normalized displacements.

Structural analysis results corresponding to randomly-sampled 4500 configurations, which are 90% of the total training data, are used for training, and the remaining 500 configurations are used as test data for performance verification of the machine learning model. Suppose a unit learning process using all the training data is regarded as one epoch. This process repeats for 500 epochs in this example.

The following is the settings to train the machine learning model. The trainable parameters are initialized with a normal distribution with zero mean and 0.05 variance. The mean squared error (MSE) is adopted as the loss function to be minimized. Adam [16] is used as the tuning method of trainable parameters, and the initial learning rate is set to 0.001. The batch size is fixed to 32.

It took 55 minutes to finish the 500-epoch training with the 12th Gen Intel(R) Core(TM) i9-12900K@3.19 GHz CPU and the NVIDIA GeForce RTX 3090 GPU. Figure 4 describes the history of average MSE losses for training data and test data. Both train and test losses have deceased almost monotonically; however, the train and test losses are slightly separated as learning progresses in the second half of learning. This suggests that increasing the training epochs may merely result in overfitting, and the machine learning model will no longer be able to improve its generalization performance.

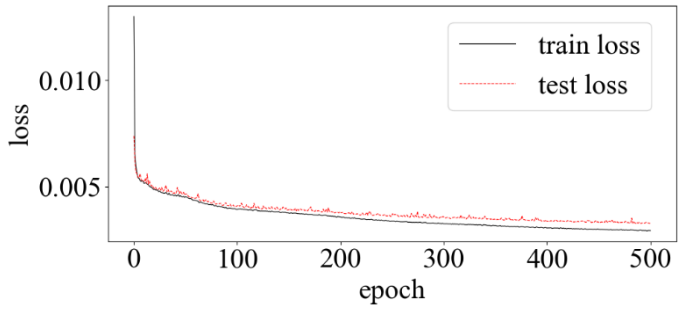


Figure 4. History of average MSE losses for training data (train loss) and test data (test loss).

Figure 5 shows the history of explained variance score, which is a prediction accuracy metric. Although the prediction accuracy improves as the learning process progresses, the score peaks at 93.3% after 491 epochs. Considering that the best possible score is 1.0 and the target value $\tilde{r}_{\mathrm{true}}$ is logarithmically scaled, this prediction accuracy is insufficient to be used as a practical predictor bypassing the structural analysis.

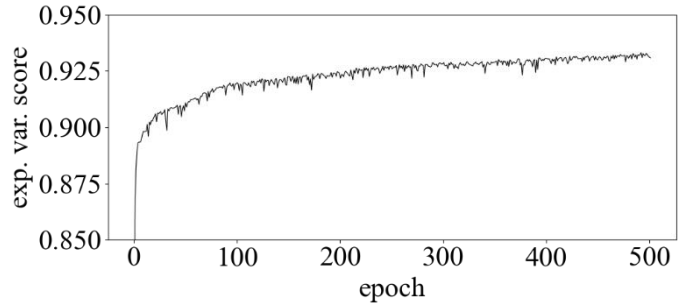
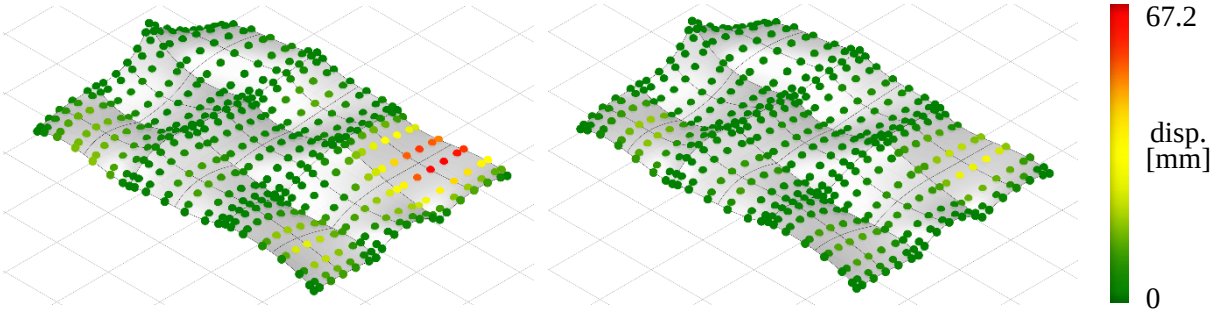


Figure 5. Explained variance score for the set of test data.

Figure 6 illustrates the difference between the true and predicted displacement distributions for a 3 × 3-patch structure. Note that this structural model has not been included in the training material. The maximum true displacement is 67.2 mm, while the maximum predicted displacement is 29.5 mm. Although the trained machine learning model cannot accurately estimate the magnitude of the displacement, it succeeds in simulating the true deformation mode in Fig. 6.



(a) (b)

Figure 6. Difference between the true displacement distribution (a) and the predicted distribution (b).

4. Conclusion

We proposed an isogeometric deep learning framework that combines geometric deep learning, hierarchical deep learning, and IGA techniques. This framework is specially designed to predict the displacements of free-form surfaces with piecewise smooth properties. To represent the structural shape composed of concrete shells ribbed by steel beams at the edges, two-level hierarchical graphs are introduced, in which the upper-level graph represents the connectivity of patch surfaces, and the lower-level graph represents the connectivity of control nets. By consistently using this representation for shape modeling, structural analysis, and machine learning, the proposed framework succeeded in completely avoiding re-meshing, which has been the cause of numerical errors and workload.

The development of isogeometric deep learning framework is still in the preliminary phase, and there are several limitations in the proposed method. The first limitation is the dilemma regarding surface order; higher order surfaces are necessary to accurately interpolate the displacement distribution; meanwhile, increasing the surface order makes the machine learning problem more difficult and computationally intensive. Second, this research dealt with only Bézier curves and surfaces. In order for the proposed method to handle NURBS, which are more general free-form surface representations, it is necessary to improve the data representation to include knot vectors. Third, the prediction accuracy of the current model has peaked at 93.3% in a logarithmic scale. In order to use the trained model as a surrogate model that does not require structural analysis, further improvement of the prediction accuracy is required.

Acknowledgements

This research is supported by JSPS Grant-in-Aid for Young Scientists (Start-up) No. JP21K20461 and JST CREST Grant No. JPMJCR1911.

References

[1] M. Raissi, P. Perdikaris and Karniadakis, “Physics-informed neural networks: A deep learning framework for solving forward and inverse problems involving nonlinear partial differential equations”, *Journal of Computational Physics*, vol. 378, pp. 686-707, 2019.

[2] W. Cao, Z. Yan, Z. He and Z. He, "A Comprehensive Survey on Geometric Deep Learning," in *IEEE Access*, vol. 8, pp. 35929-35949, 2020.

[3] N. N. Vlassis, R. Ma and W. Sun, “Geometric deep learning for computational mechanics Part I: anisotropic hyperelasticity”, *Computer Methods in Applied Mechanics and Engineering*, vol. 371, no. 1, 2020.

[4] V. Krokos, S. Bordas and P. Kerfriden, "A graph-based probabilistic geometric deep learning framework with online physics-based corrections to predict the criticality of defects in porous materials", *arXiv*, no. 2205.06562, 2022.

[5] I. Y. Ha, L. Hansen, M. Wilms and M. P. Heinrich, "Geometric deep learning and heatmap prediction for large deformation registration of abdominal and thoracic CT", in *Medical Imaging with Deep Learning (MIDL)*, London, UK, July 8-10, 2019.

[6] A. Sanchez-Gonzalez, J. Godwin, T. Pfaff, R. Ying, J. Leskovec and P. W. Battaglia, "Learning to simulate complex physics with graph networks," in *the 37th International Conference on Machine Learning (ICML'20)*, no. 784, pp. 8459-8468, 2020.

[7] M. L. Mavrovouniotis and S. Chang, "Hierarchical neural networks," *Computers Chemical Engineering*, vol. 16, issue 4, pp. 347-369, 1992.

[8] S. Saha, Z. Gan, L. Cheng, J. Gao, O. L. Kafka, X. Xie, H. Li, M. Tajdari, H. A. Kim, W. K. Liu, "Hierarchical Deep Learning Neural Network (HiDeNN): An artificial intelligence (AI) framework for computational science and engineering," *Computer Methods in Applied Mechanics and Engineering*, vol. 373, 2021.

[9] M. Fortunato, T. Pfaff, P. Wirnsberger and A. Pritzel, "MultiScale MeshGraphNets", in *ICML 2022 AI for Science Workshop*, Baltimore, USA, July 22-23, 2022.

[10] J. A. Cottrell, T. J. R. Hughes and Y. Bazilevs, *Isogeometric Analysis: Toward Integration of CAD and FEA*, WILEY, 2009.

[11] K. Hayashi, Y. Jikumaru, M. Ohsaki, T. Kagaya and Y. Yokosuka, "Mean curvature flow for generating discrete surfaces with piecewise constant mean curvatures", *Computer Aided Geometric Design*, vol. 101, no. 102169, 2023.

[12] M. Simonovsky and N. Komodakis, "Dynamic edge-conditioned filters in convolutional neural networks on graphs", in *2017 IEEE Conference on Computer Vision and Pattern Recognition (CVPR)*, Honolulu, USA, July 21-26, 2017.

[13] P. Veličković, G. Cucurull, A. Casanova, A. Romero, P. Liò and Y. Bengio, "Graph attention networks", in *6th International Conference on Learning Representations (ICLR2018)*, Vancouver, BC, Canada, April 30-May 3, 2018.

[14] M. Fey and J. E. Lenssen, "Fast Graph Representation Learning with PyTorch Geometric", in *ICLR Workshop on Representation Learning on Graphs and Manifolds*, New Orleans, LA, USA, May 6, 2019.

[15] I. N. Tsiptsis, "Kiwi!3D meshfree, isogeometric FE analysis integrated in CAD", in *Advances in Architectural Geometry (AAG)*, Gothenburg, Sweden, September 22-25, 2018.

[16] D. P. Kingma and J. Ba, "Adam: A method for stochastic optimization," *arXiv*, no. 1412.6980, 2014.

IASS 2023
July 10–14 Melbourne
Integration of Design and Fabrication

Proceedings of the IASS Annual Symposium 2023
Integration of Design and Fabrication
10–14 July 2023, Melbourne, Australia
Y.M. Xie, J. Burry, T.U. Lee and J. Ma (eds.)

Using augmented reality for interactive value engineering of structural steel connections

Yuyu WANG[a], Vitor S. BOTTAZZI[b], Joseph M. GATTAS[a,*]

[a,*] School of Civil Engineering, University of Queensland
Brisbane, 4067, Queensland, Australia
j.gattas@uq.edu.au

[b] Watkins Steel Pty Ltd, 106 Depot St Banyo, Queensland, Australia

Abstract

The detailing of structural steel connections in routine building design has a high reliance on the use of standardised connection arrangements. These arrangements, specified by national industry organisations or in-house as typical details, are formulated to incorporate structural, cost, and sustainability efficiency as well as constructability best practice. This integration of multiple knowledge bases, as well as the sophisticated design checks and detailing rules required for connection design, can make the underlying rationale for component selection difficult to intuit for junior structural engineers. This paper explores the use of Augmented Reality (AR) tools for the interactive design exploration and value engineering of structural steel connections. Connection component descriptions and structural design data is stored and accessed from a 'component-set' connection database. The database is connected to a parametric model of the connection in Rhino/Grasshopper, with model visualisation and interactivity then enabled via the Fologram mixed reality plug-in. Using a HoloLens 2 or mobile device, users are able to intuitively explore the real-time design variations of connection component alternatives. This tool is thus able to improve collaboration and understanding between designers and fabricators, toward the co-design of more efficient steel connections and structures.

Keywords: augmented reality, set-based parametric design, design automation, structural engineering, steel connection detailing

1. Introduction

The detailed design and documentation of structural steel connections is seen as a specialised and time-consuming task. Initial connection descriptions are normally specified by the structural engineer, based on connected member sizing and transmitted design load requirements. During coordination with fabricators and site erectors, connections will then be iteratively redesigned to improve the economy and efficiency of building manufacture and construction [1]. To reduce the level of required redesign, engineers often utilise standardised connection arrangements, which are specified by national industry bodies or from project precedent, to describe connection arrangements which are known to already achieve structural, cost, and sustainability efficiency, as well as constructability best practice [2].

Standardised connection design information is available to engineers through a range of physical or computational design support tools, including for example design look-up tables, parametric structural design tools (e.g. spreadsheet or code), and integrated structural design and analysis software (e.g. commercial software which may support BIM integration) [3]. These tools encapsulate sophisticated design checks, detailing rules, and permissible component arrangements, allowing users to quickly specify or compare connection options. However, for junior or inexperienced structural engineers, the

Copyright © 2023 by Yuyu WANG, Vitor S. BOTTAZZI and Joseph M. GATTAS. Published in the Proceedings of the IASS Annual Symposium 2023 with permission.

underlying rationale for component selection can be difficult to intuit, particularly as related to material vs labour cost efficiency and offsite vs onsite productivity differentials.

The aim of this paper is to provide users with an intuitive perception on the variation of connection designs, via 3D visualisation and real-time interaction with a mixed-reality connection model. This is proposed to enable improved designer evaluation and selection of valid and efficient connection component arrangements. A 'component-set' connection database is proposed to store connection component descriptions and structural design data. The database data is then accessed and connected to a Rhino/Grasshopper parametric model, enabling visualisation and interactivity of the connection models. With a HoloLens headset or smart devices, users can have an immersive 3D experience and intuitive exploration of real-time design variations of connection component alternatives.

2. Background

2.1. Component-set connection representation

A wide range of steel connection types are physically constructed from a relatively small range of constituent components. For example, a common simple connection typically consists of steel sections, bolts, welds, or plates as shown in Fig.1.

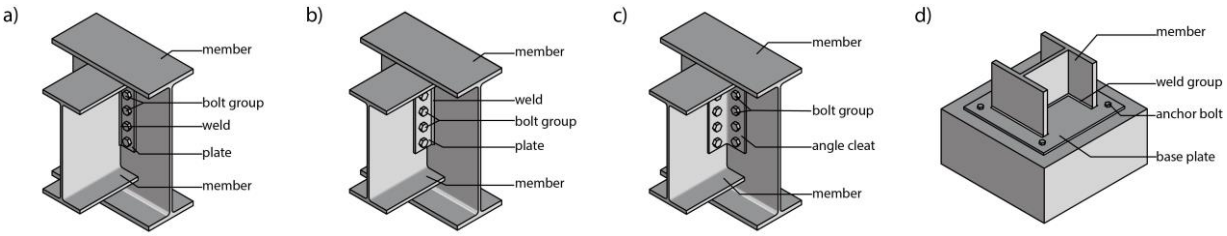


Figure 1. Simple steel connections with assembled components. Connection types: (a) flexible end plate, (b) web side plate, (c) angle cleat and (d) pinned base plate connection.

This component-based connection representation is commonly standardised in Building Information Model (BIM). It utilises Industry Foundation Class (IFC) data schema following an object-oriented modelling approach to store building information into entities with inheritance hierarchy [4]. This allows for a steel connection to be represented as an aggregation from individual component objects [5]. The geometric and non-geometric attributes and properties associated with the connections are all organised and integrated on a component object basis [6]. Relationships between the connection object with its component objects and other objects remains hierarchical. The component-based connection model has also been applied in simulation and analysis of structural behaviour. For example, the analytical connection modelling methods originally defined in the Eurocode 3 'Component Method' [7] and in component-based finite element modelling (CBFEM) for numerical analysis [8]. These procedures consider a connection as a set of discrete components, modelled as springs or rigid links to determine connection stiffness or rigidity [9, 10].

Some precedent research has formulated feasible component-based design process for steel connections [11-13]. In these frameworks, a connection is modelled from a hierarchical sub-component definition. The relevant design methods and parameters are encapsulated within each component object. Although the component-based representation is well established in BIM-enabled structural design tools, this design process is rarely utilised in the contemporary structural design tools. Rather, these usually require sequential input of discrete parameters for design capacity evaluation, without managing the relationships and hierarchy between components and connection structures.

2.2. Set-based parametric method in structural design

Due to the characteristics of internal design models within prevailing structural design tools, engineers predominately follow a point-based design (PBD) method. This involves progressive modification of the design variables of a single design option through consecutive deign steps, until a solution is satisfied [14]. Premature convergence in this design methods restricts the design space, resulting in a feasible but suboptimal design [15]. Low information availability during the early design phase may also cause high uncertainty and require repetitive rework, reducing time and cost efficiency [16].

As an alternative approach, set-based design (SBD) is based on concurrent and delayed decision-making. Its initial concept has been attributed to Toyota, known as 'second Toyota paradox', for improving car product development [17]. Design space exploration starts with sets of designs with feasible range; set size is progressively narrowed down based on input design constraints and criteria, until finally converging on a single solution [18]. This design approach is beneficial in solving contemporary and complex design and optimisation problems, especially in lean product development [19]. Its application in structural design problem is found primarily in reinforced-concrete design [20-22]. The SBD method has been used to assess and optimise the safety, cost or material efficiency, and environmental impact of sets of reinforced-concrete structures with varying design parameters (e.g. structural geometry, member sizes, rebar details, et cetera). However, its application to aspects of steel structure design is limited.

2.3 AR support tools for structural design and construction

The growing maturity and development of AR technology and devices have resulted in their widespread adoption in Architecture, Engineering, and Construction (AEC) industries, particularly in the areas of education, design, planning, manufacturing, and construction [23, 24]. AR is an advanced visualisation technique that seamlessly integrates virtual content, such as 3D models, video, and text, into the real world [25]. By superimposing the virtual object onto the physical environment, users can perceive an enhanced reality with coexisting virtual and physical objects [24]. AR is also noted as a vital technology for Industry 4.0, which for the steel industry aims to achieve the automation and digitisation of the entire production process to improve energy efficiency, productivity, quality, and flexibility of production customisation [26]. AR is suggested to apply steel manufacture and construction for workplace operator training and virtual assistance with assembly, maintenance, and inspection tasks [27].

AR has also been shown to be highly valuable and versatile when integrated with structural design and analysis processes. Researchers have developed interactive AR tools for educational purposes, to support students or junior engineers in understating intuitive design features and real-time simulation of structural behaviour [23, 28]. Wen et al. utilised cloud-based AR to superimpose virtual 3D BIM model of steel connection sculptures onto paper-based drawings, to assess the effectiveness of AR in helping student understand complex 2D drawing [25]. Dib and Adamo proposed an interactive learning environment to assist student to visualise stress, deformation, and failure on a virtual connection model, overlaid on a physical model by applying force [29]. Luo and Mojica Cabico developed an AR-based learning tool for bridge construction, that can superimpose a bridge model with load transfer path and highlighted elements on images [30]. Ilgu developed an AR application that allows users to adjust input load to observe structural behaviour of a physical building under certain loading condition [31]. Quinn et al. proposed an AR prototype which users can interact with visually augmented physical structure model and observe a real-time variation of internal load and deflection caused by applied forces [32, 33]. Abdullah, Kassim and Sanusi conducted an experiment to evaluate the effectiveness of AR application in enhancing students' understanding of steel architectural constructions [34]

3. Methodology

The aim of this study is to present an AR model for interactive design exploration and value engineering of structural steel connections. The proposed model is illustrated in Fig. 2 and comprises four processes, detailed further in the following subsections:

1) *Steel Connection Database:* Precalculated detailed design information of many connection alternatives and their assembled components.
2) *User Connection/Component Selection*: Interactive interface for user selection of connection and/or component arrangements, for indexing and deserialisation of database record.
3) *Geometric and Semantic Modelling*: A 3D parametric model of connection geometry, with accompanying textual and diagrammatic annotations of connection failure mechanisms.
4) *AR Visualisation and Interactivity*: a life-sized virtual connection model in mixed reality environment, with clickable buttons for failure mode observation and component selection.

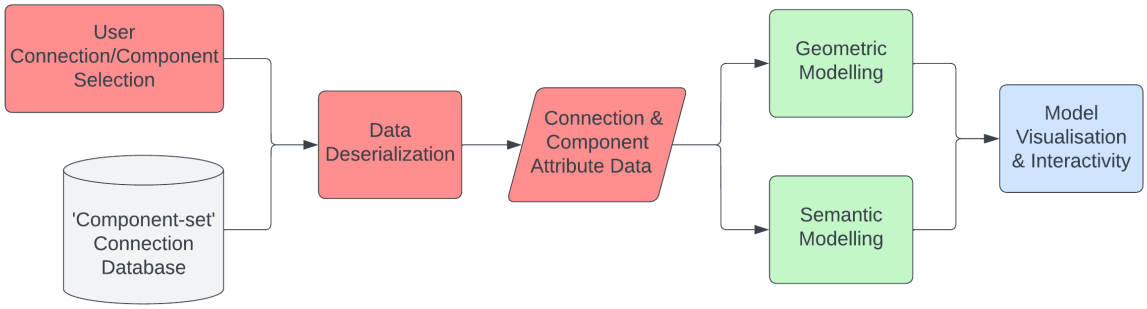


Figure 2. Modelling process of interactive AR steel connection in Rhino/Grasshopper.

3.1 Steel connection database

In prior research, the authors developed a ‘component-set’ steel connection design database for concise description and reusability of connection design data. Database information is generated from the integration of a component-based connection design model and a set-based parametric design method.

The component-based connection design model allows a connection to be represented as hierarchical aggregation of different class types, including component classes, component group classes, and connection classes as illustrated in Fig. 3. Component classes (e.g. bolts, welds, plates) encapsule the defined attributes and design methods for single component types, including designation, sizes, material properties, and capacities. Component group classes (e.g. bolt groups) aggregate component objects with additional attributes and methods to specify component groupings that are frequently used. Connection classes are constructed by aggregating component and component group objects. Connection objects can then invoke attributes and methods of their constituent components to perform detailed checks and component capacity calculations.

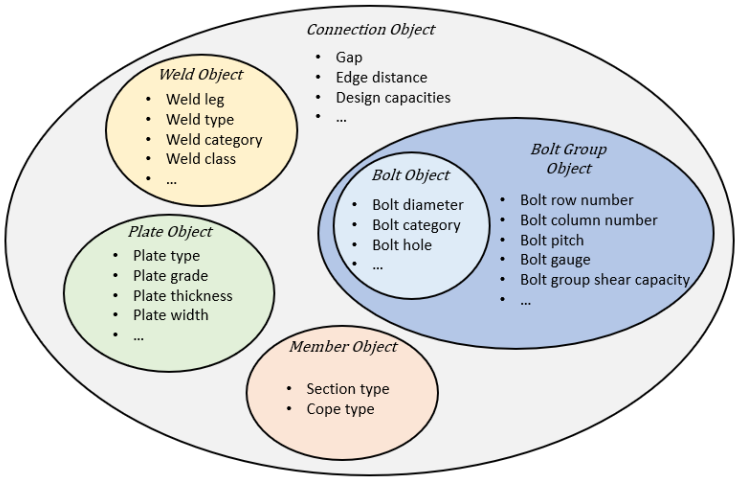


Figure 3. Data structure of a connection object and its constituent component objects.

Extending from the component-based connection design model, a set-based parametric design method is integrated to allow the highly flexible and concise generation of component, component group, and connection objects from set operations. Component and component group object sets are first generated from design parameters corresponding to standard Australian component sizes, types, and construction practice. Connection design parameter sets are then generated as the Cartesian Product of component objects with additional component arrangement parameters, that is as any potential combination of standard components. A set of connection design objects that contain full design data can be generated from their defined connection class accordingly.

In generating connections from the mass-combination of any potential component, a large number of invalid and/or inefficient connection designs are created. Here, validity of connection objects is self-evaluated based on the detailing checks implemented in the connection class, and efficiency is evaluated based on material consumption. For the present purpose of interactive design exploration, we preserved these invalid options in the generated data collection such that they can be 'discovered' by users and interrogated to understand the invalid or limiting conditions. The final collection of component and connection objects forms the steel connection database, containing all geometric, material, and structural capacity data in a structured JSON data format.

3.2 User component/connection selection

Interactive user engagement with the steel connection design database is facilitated via two input methods: 1) users select a connection record directly; or 2) users select connection sub-components, which are then aggregated to find a corresponding unique connection record. The first method allows a user to iterate directly over standardised (valid and efficient) design options, whereas the second method allows a user to explore the influence of component selection on connection validity/invalidity and efficiency/inefficiency.

From provided user input, a unique name-key index is used to retrieve the specified objects (connection and/or components) from the connection database. The returned data is in a serialised JSON format; this is deserialised to expose object attribute data for subsequent modelling steps. For the first input method, connection attribute data includes containing components, which can be used to retrieve and deserialise related component objects from the database, Fig. 4.

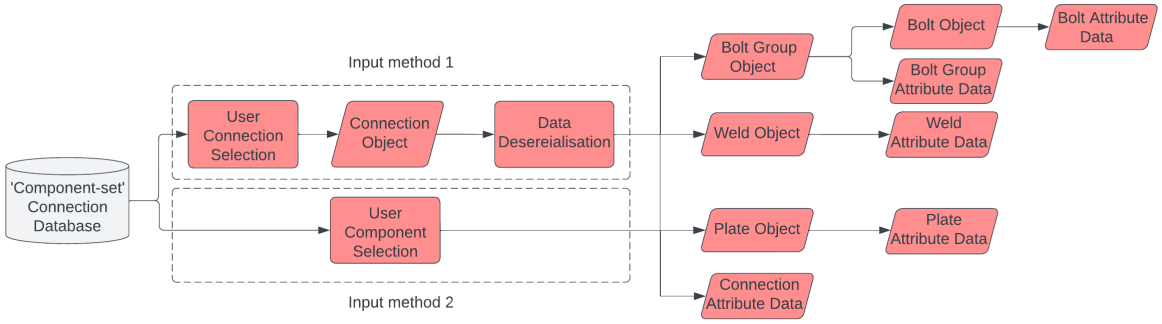


Figure 4. Deserialisation process of connection database data.

3.3 Geometric and semantic modelling

Parametric models for connection geometry were constructed for detailed connection visualisation, also adopting a component-based approach. For bolt components, detailed geometries containing thread and nut features were created first as static CAD meshes and parametrically referenced via bolt attribute data. Remaining components, including bolt group, weld, plate, and section were modelled as separate parametric geometries (closed Breps), instanced by geometric attribute data extracted from the component objects. Connection attribute data was then used to spatially arrange components, which were finally joined to create a 3D connection geometry.

Alongside the geometric model, we developed a semantic model to support user visualisation and interrogation of structural design features of a specified connection. Semantic design information includes the display of component design capacities, component failure modes, and governing design capacity. Capacity information is presented as floating text and input from the connection and component attribute data. Failure mode information is presented as geometric annotations (arrows and coloured surfaces) in the corresponding failure region.

3.4 Visualization and interactivity of virtual connection model

Final supporting processes were implemented to support the visualisation and interactivity of the virtual connection model in a mixed reality. For model visualisation, three ArUco marker trackers [35], detectable via AR device from their actual positions in physical three-dimensional space, were provided as virtual model inputs. The orientation and position of markers was evaluated in a virtual model to determine a central location point, orientation direction, and length scale for the virtual model to be displayed as actual size when viewed in the mixed environment. Two methods of model interactivity were implemented to support user interrogation of i) structural performance calculations and ii) connection design exploration. For structural performance interrogation, spherical buttons were placed next to each design capacity description in the semantic model. This were established as clickable triggers in the AR interface, such that selection of a particular capacity would display the corresponding failure region annotation. For connection design exploration, buttons were created to allow users interacting with component sizes. Simplified annotations would then state whether a connection was valid/invalid and efficient/inefficient, relative to the standardised connections. Users can inspect the connection geometry to find the source of invalid detailing condition and review the semantic information to find the source of design inefficiencies (for example, oversized components).

4. Implementation and result

4.1 Model implementation

The steel connection database was implemented in Python 3.10.4 for a ‘Flexible End Plate’ (FEP) beam-to-column or beam-to-beam connection type, Fig. 1a. The connection design space $\mathbb{C}^{FEP}$ was generated from the Cartesian Product of the component object sets specified in Table 1, with the expression defined

in Equation 1. The connection object set thus contains 8832 connection designs, of which 117 are the standardised connection details recommended by the Australia Steel Institute [36]

$$\mathbb{C}^{FEP} = \mathbb{B} \times \mathbb{W} \times \mathbb{P} \times \mathbb{M} \times \mathbb{A}_1 \times \mathbb{A}_2 \quad (1)$$

Remaining processes were implemented in Rhino/Grasshopper. Three Grasshopper plug-ins, jSwan, GeomGym, and Fologram, were used for database deserialisation, geometric modelling, and AR interactivity, respectively [37-39]. The integrated Grasshopper model is illustrated in Fig 5. The connection database collections are provided as input files and red, green, and blue regions correspond to the user component/connection selection, geometric/semantic modelling, and AR visualisation/interactivity processes as described previously.

Table 1. Component object sets for FEP connection CPs.

Component	Design Parameters		Design Parameters/Object Sets	
	Name	Unit	Values	#
Bolt Group $\mathbb{B}$	bolt	N/A	{M20 8.8/S TI}	(1)
	rows	mm	{2, 3, 4, 5, 6, 7, 8, 9}	(8)
	columns	mm	{2}	(1)
	pitch	mm	{70}	(1)
	gauge	mm	{90, 140}	(2)
Weld $\mathbb{W}$	leg thickness	mm	{6, 8}	(2)
	type	N/A	{CFW}	(1)
	category	N/A	{SP}	(1)
	class	N/A	{E49XX}	(1)
Plate $\mathbb{P}$	type	N/A	{Plate GR250}	(1)
	width	mm	{150, 200}	(2)
	thickness	mm	{10}	(1)
Member $\mathbb{M}$	type	N/A	{200UB→610UB}	(23)
	cope	N/A	{O, SWC, DWC}	(3)
Spacing 1 $\mathbb{A}_1$	gap	N/A	{70, 100}	(2)
Spacing 2 $\mathbb{A}_2$	edge distance	N/A	{35}	(1)

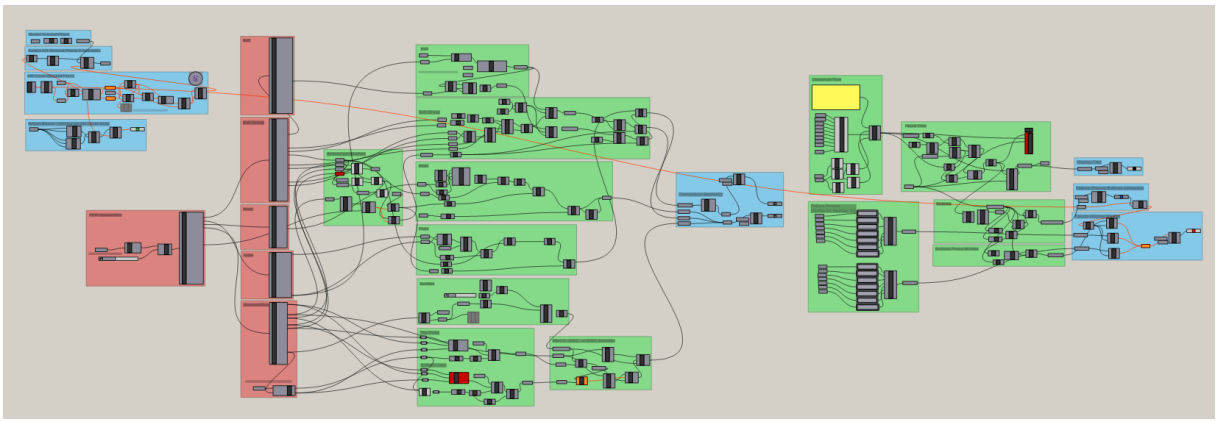


Figure 5. Grasshopper script for AR connection model construction.

The Fologram Grasshopper provides the visualisation and interaction of the virtual connection model with Microsoft HoloLens headsets or mobile devices installed with the accompanying 'Fologram' program. Users first need to connect the AR devices to access 'Fologram' mixed reality environment and AR interface by scanning a QR code. Three ArUco markers, placed in orthogonal direction on a ground plane, are then detected as reference points for virtual model display. By detecting the markers sequentially with an AR device, the coordinates of the markers' location are input into the parametric model with the orientations of markers solved in Grasshopper. A green box is placed onto the markers denoting the marker has been detected correctly (Fig. 6a). The central point, orientation direction, and length scale of the virtual model are determined from the distance and vectors derived from the three coordinates. The virtual connection model is then superimposed in the mixed environment at life-sized scale.

4.2 Model interaction

After placing the virtual connection model in a mixed reality, users can easily implement the two proposed input and interaction methods to observe the structural performance and evaluate the validity and efficiency of various connection designs. For the first method, user browse standard connection designs by selecting key-name index of a specific connection. Users click on the spherical buttons in the AR interface to switch the display of failure modes under each load capacity. The failure region is highlighted on the component part with an arrow, facilitating inspection from all angles (Fig. 6b).

a) b)

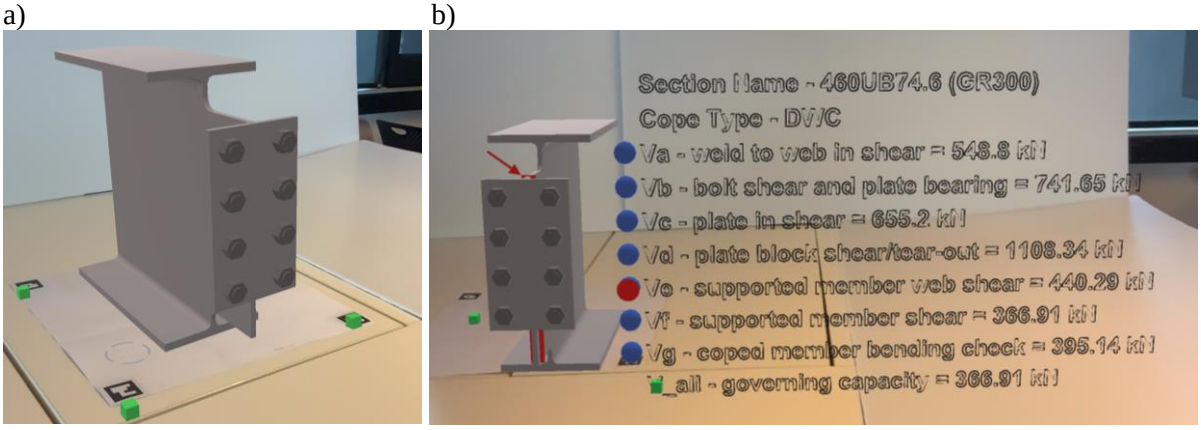


Figure 6. Virtual connection model. a) Detected ArUco markers. b) Failure region and structural capacity annotations.

With the second method, users are able to customise a connection design with specific size and arrangement of components by selecting options from dropdown lists. Textual annotations are displayed by the side of connection model denoting the validity and efficiency of the connection relative to standardised designs. User can then examine and compare the geometric characteristics of assembled components, in order to identify the origin of invalid detailing conditions and understand potential causes of structural inefficiencies. For example, Fig. 7a illustrates an example of a standardised connection design for a 460UB82.1 section. It incorporates a 150 mm wide plate and ten M20 bolts arranged in two columns, with a bolt gauge of 90 millimetres separating each bolt. An inefficient design has an increased plate width (Fig. 7b), which adds to connection weight without increasing the governing design capacity. An invalid design (Fig. 7c) selects an overly-large bolt group, which violates detailing requirements for both minimum bolt-to-plate edge distance and maximum plate-to-section depth ratio.

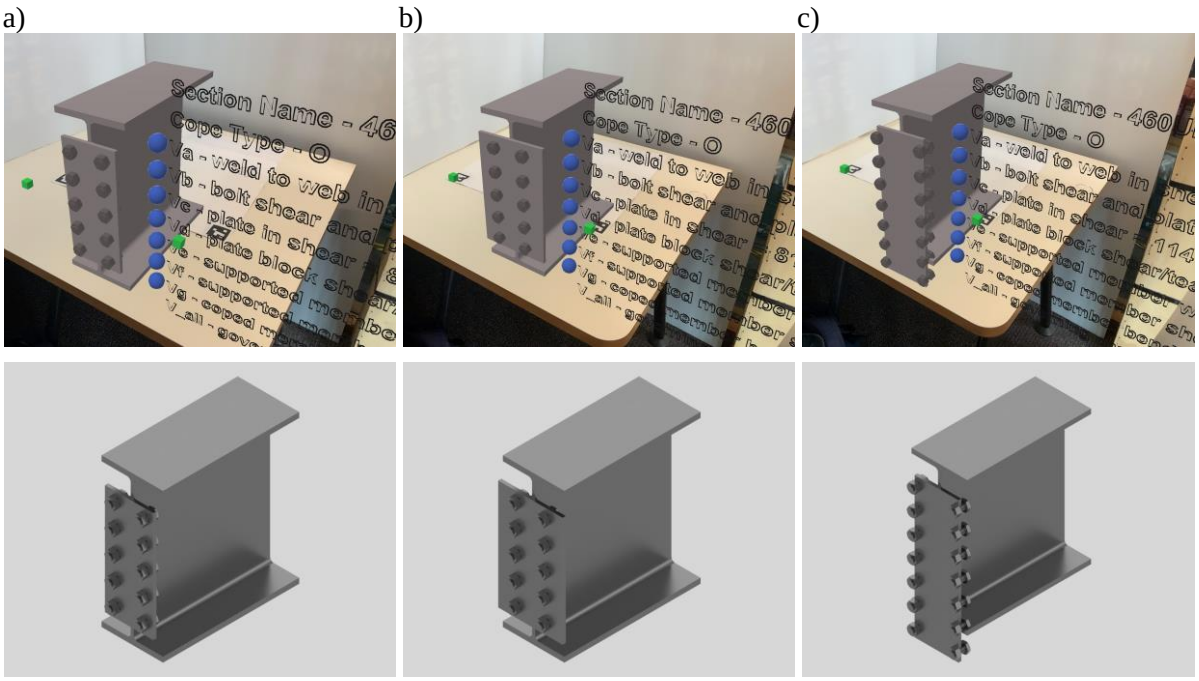


Figure 7. Virtual connection model with user defined component selection for a) standardised, b) inefficient; and c) invalid connection designs. Top row: virtual model in mixed reality, bottom row: Rhino rendered model.

5. Conclusion

This paper presents a parametric virtual 3D steel connection model linked to a connection database that contains many 'ready-to-use' designs. By leveraging the immersive environment and interactivity created by AR tools, users can evaluate various connection designs in real-time via inspection of connection geometric details and semantic information. This parametric AR model is highly valuable for educational purposes and value engineering, as it enables junior engineers to develop a more intuitive understanding of the influence of component selection on validity and efficiency of connection design, as well as the structural performance of steel connections.

For future development, the connection design database will incorporate process-based fabrication cost for connections. Both designers and fabricators will then be able to evaluate the cost variations among different connection design alternatives and make design improvement. The semantic model annotations could also be extended to support guided user exploration toward the cost-efficient standardised connections. The design database can also be expanded with broader range of design information, encompassing different types of structural members and building materials (e.g. steel open sections, steel hollow sections, cold-formed structural steel, timber, and reinforced concrete). Furthermore, by utilising AR tools, users can capture real-world structural elements and their surroundings from the real world and understand the impact of design modifications on structural performance or behaviour in video form through visually augmented physical objects.

Acknowledgements

The authors would like to thank Dr Peter Key and Mr John Gardner from the Australian Steel Institute for supporting information provided for research development.

References

[1] J. V. Abi O. Aghayere, *Structural Steel Design*, 3 ed. Mercury Learning and Information, 2020.

[2] K. A. Cowie, "PRE-ENGINEERED STANDARDIZED INDUSTRY STRUCTURAL STEELWORK CONNECTIONS - A NEW ZEALAND PERSPECTIVE," presented at the Connections in Steel Structures, Boston, Massachusetts, USA, 2016.

[3] E. Duong, A. Darras, R. G. Driver, M. Essa, and A. Imanpour, "Applications of Artificial Intelligence Techniques for Optimization of Structural Steel Connections," in *Proceedings of the Canadian Society of Civil Engineering Annual Conference 2021*, Singapore, S. Walbridge *et al.*, Eds., 2022// 2022: Springer Singapore, pp. 273-285.

[4] C. Eastman, P. Teicholz, R. Sacks, and G. Lee, *BIM Handbook: A Guide to Building Information Modeling for Owners, Designers, Engineers, Contractors, and Facility Managers*. Newark: John Wiley & Sons, Incorporated, 2018.

[5] S. I. Park, J. Park, B.-G. Kim, and S.-H. Lee, "Improving Applicability for Information Model of an IFC-Based Steel Bridge in the Design Phase Using Functional Meanings of Bridge Components," *Applied Sciences*, vol. 8, no. 12, p. 2531, 2018. [Online]. Available: https://www.mdpi.com/2076-3417/8/12/2531.

[6] S. Cursi, L. Martinelli, N. Paraciani, F. Calcerano, and E. Gigliarelli, "Linking external knowledge to heritage BIM," *Automation in construction*, vol. 141, p. 104444, 2022, doi: 10.1016/j.autcon.2022.104444.

[7] J.-P. Jaspart, K. Weynand, G. H. Couchman, and A. M. G. o. Coelho, "Design of joints in steel structures : Eurocode 3, Design of steel structures, part 1-8 : Design of joints," 2017.

[8] L. Šabatka, F. Wald, J. Kabeláč, D. Kolaja, and M. Pospíšil, "Structural Analysis and Design of Steel Connections Using Component-Based Finite Element Model," *Journal of Civil Engineering and Architecture*, vol. 9, 08/28 2015, doi: 10.17265/1934-7359/2015.08.002.

[9] A. A. Del Savio, D. A. Nethercot, P. C. G. S. Vellasco, S. A. L. Andrade, and L. F. Martha, "Generalised component-based model for beam-to-column connections including axial versus moment interaction," *Journal of Constructional Steel Research*, vol. 65, no. 8-9, pp. 1876-1895, 2009-08-01 2009, doi: 10.1016/j.jcsr.2009.02.011.

[10] C. Liu, K. H. Tan, and T. C. Fung, "Component-based steel beam–column connections modelling for dynamic progressive collapse analysis," *Journal of constructional steel research*, vol. 107, pp. 24-36, 2015, doi: 10.1016/j.jcsr.2015.01.001.

[11] Y. Paek and H. Adeli, "Structural design language for coupled knowledge-based systems," *Advances in Engineering Software (1978)*, vol. 12, no. 4, pp. 154-166, 1990/10/01/ 1990, doi: https://doi.org/10.1016/0141-1195(90)90001-M.

[12] Z. Nouas, "A Knowledge-Based System for the Design of Hybrid Connections in Structural Steelwork," Ph.D., The University of Manchester (United Kingdom), England, 30169280, 1993.

[13] G. E. Willemse, "Object-oriented steel connection design framework," Stellenbosch University, 2004.

[14] J. K. Liker, D. K. Sobek, A. C. Ward, and J. J. Cristiano, "Involving suppliers in product development in the United States and Japan: evidence for set-based concurrent engineering," *IEEE Transactions on Engineering Management*, vol. 43, no. 2, pp. 165-178, 1996, doi: 10.1109/17.509982.

[15] D. J. Singer, N. Doerry, and M. E. Buckley, "What Is Set-Based Design?," *Naval engineers journal*, vol. 121, no. 4, pp. 31-43, 2009, doi: 10.1111/j.1559-3584.2009.00226.x.

[16] S. Dullen, D. Verma, M. Blackburn, and C. Whitcomb, "Survey on set-based design (SBD) quantitative methods," *Systems Engineering*, vol. 24, no. 5, pp. 269-292, 2021.

[17] A. Ward, J. K. Liker, J. J. Cristiano, and D. K. Sobek II, "The second Toyota paradox: How delaying decisions can make better cars faster," *MIT Sloan Management Review*, 1995.

[18] B. Toche, R. Pellerin, and C. Fortin, "Set-based design: a review and new directions," *Design Science*, vol. 6, p. e18, 2020, Art no. e18, doi: 10.1017/dsj.2020.16.

[19] D. Raudberget, "Practical applications of set-based concurrent engineering in industry," *Journal of Mechanical Engineering*, vol. 56, no. 11, pp. 685-695, 2010.

[20] K. Parrish, J. M. Wong, I. D. Tommelein, and B. Stojadinovic, "Value propositions for set-based design of reinforced concrete structures," in *16th Annual Conference of the International Group for Lean Construction, IGLC16*, 2008, pp. 495-506.
[21] S.-I. Lee, J.-S. Bae, and Y. S. Cho, "Efficiency analysis of Set-based Design with structural building information modeling (S-BIM) on high-rise building structures," *Automation in construction*, vol. 23, pp. 20-32, 2012.
[22] R. Rempling, A. Mathern, D. T. Ramos, and S. L. Fernández, "Automatic structural design by a set-based parametric design method," *Automation in Construction*, vol. 108, p. 102936, 2019.
[23] A. Z. Kolaei, E. Hedayati, M. Khanzadi, and G. G. Amiri, "Challenges and opportunities of augmented reality during the construction phase," *Automation in Construction*, vol. 143, p. 104586, 2022/11/01/ 2022, doi: https://doi.org/10.1016/j.autcon.2022.104586.
[24] Y. Turkan, R. Radkowski, A. Karabulut-Ilgu, A. H. Behzadan, and A. Chen, "Mobile augmented reality for teaching structural analysis," *Advanced Engineering Informatics*, vol. 34, pp. 90-100, 2017/10/01/ 2017, doi: https://doi.org/10.1016/j.aei.2017.09.005.
[25] J. Wen, M. Gheisari, S. Jain, Y. Zhang, and R. E. Minchin, "Using Cloud-Based Augmented Reality to 3D-Enable the 2D Drawings of AISC Steel Sculpture: A Plan-Reading Educational Experiment," *Journal of Civil Engineering Education*, vol. 147, no. 3, p. 04021006, 2021, doi: 10.1061/(asce)ei.2643-9115.0000046.
[26] R. Miśkiewicz and R. Wolniak, "Practical Application of the Industry 4.0 Concept in a Steel Company," *Sustainability*, vol. 12, no. 14, p. 5776, 2020. [Online]. Available: https://www.mdpi.com/2071-1050/12/14/5776.
[27] E. Marino, L. Barbieri, B. Colacino, A. K. Fleri, and F. Bruno, "An Augmented Reality inspection tool to support workers in Industry 4.0 environments," *Computers in Industry*, vol. 127, p. 103412, 2021/05/01/ 2021, doi: https://doi.org/10.1016/j.compind.2021.103412.
[28] W. Li, A. Y. C. Nee, and S. K. Ong, "A State-of-the-Art Review of Augmented Reality in Engineering Analysis and Simulation," *Multimodal Technologies and Interaction*, vol. 1, no. 3, p. 17, 2017. [Online]. Available: https://www.mdpi.com/2414-4088/1/3/17.
[29] H. N. Dib and N. Adamo, "An augmented reality environment for students' learning of steel connection behavior," in *Computing in Civil Engineering 2017*, 2017, pp. 51-58.
[30] X. Luo and C. D. Mojica Cabico, "Development and evaluation of an augmented reality learning tool for construction engineering education," in *Construction Research Congress 2018*, 2018, pp. 149-159.
[31] A. K. Ilgu *et al.*, "Board 62: Usability of a mobile augmented reality application to teach structural analysis," in *2018 ASEE Annual Conference & Exposition*, 2018.
[32] G. Quinn, A. Galeazzi, and C. Gengnagel, "Augmented and virtual reality structures," in *Proceedings of IASS Annual Symposia*, 2017, vol. 2017, no. 9: International Association for Shell and Spatial Structures (IASS), pp. 1-8.
[33] G. Quinn *et al.*, "Calibrated and interactive modelling of form-active hybrid structures," in *Proceedings of iass annual symposia*, 2016, vol. 2016, no. 16: International Association for Shell and Spatial Structures (IASS), pp. 1-9.
[34] F. Abdullah, M. H. B. Kassim, and A. Sanusi, "Go Virtual: Exploring Augmented Reality Application in Representation of Steel Architectural Construction for the Enhancement of Architecture Education," *Advanced Science Letters*, vol. 23, pp. 804-808, 02/01 2017, doi: 10.1166/asl.2017.7449.
[35] S. Garrido-Jurado, R. Muñoz-Salinas, F. J. Madrid-Cuevas, and M. J. Marín-Jiménez, "Automatic generation and detection of highly reliable fiducial markers under occlusion," *Pattern Recognition*, vol. 47, no. 6, pp. 2280-2292, 2014/06/01/ 2014, doi: https://doi.org/10.1016/j.patcog.2014.01.005.
[36] T. J. Hogan and S. A. Munter, *Connection design guide 4: Flexible end plate connections*. 2007.
[37] "jSwan." https://www.food4rhino.com/en/app/jswan (accessed 10/03/2023.
[38] "Geometry Gym." https://geometrygym.wordpress.com/ (accessed 10/03/2023.

[39] "Fologram." https://www.food4rhino.com/en/app/fologram (accessed 10/03/2023.

IASS 2023
July 10–14 Melbourne
Integration of Design and Fabrication

Proceedings of the IASS Annual Symposium 2023
Integration of Design and Fabrication
10–14 July 2023, Melbourne, Australia
Y.M. Xie, J. Burry, T.U. Lee and J. Ma (eds.)

Using data-rich objects in geometric parametric modelling

Lennert LOOS*

* Katholieke Universiteit Leuven
lennert.loos@kuleuven.be

Abstract

Earlier research by the author investigated how using data visualisations could be helpful to structural designers. The research implicitly showed that the versatile handling, management and manipulation of data is important in order to fully exploit the benefits of parametric design. This paper presents the development of *Inkbeagle Data*, a new Grasshopper3d plugin that aims to facilitate data management in parametric modelling. The paper discusses how the use of data-rich objects can help make it easier to work with geometric objects and the custom data associated with them. The implementation of the plugin is explained, as well as its user interface, and a small example of its use in practical applications in the field of structural design is given.

Keywords: computational design, data management, parametric design

1. Introduction

The use of data visualisations to gain specific insights during the structural design process has been extensively researched by the author [1-3]. The research observed the typical workflows and processes of the structural designer and identified some of the problems they face. One of the main problems appeared to be the difficulty of comparing design alternatives with the commonly used finite element analysis tools. However, comparison is an important part of the design process as it allows an understanding of how design solutions are behaving and performing in a relative way. These commonly used analysis tools are well-suited for understanding the structural behaviour of a single design, dimensioning the members of the structure, and performing the regular code checks. However, they do not necessarily guide designers to better designs, nor do they allow the structural behaviour and performance of different design options to be compared.

Based on this practical observation and the fact that a huge amount of structural data (model, loads and results) is contained in the finite element models that engineers use during design, data visualisation has been proposed and investigated earlier as a way to facilitate an informed structural design process by digesting the data more efficiently. This previous research evaluated data visualisation as a way to present complex data sets from finite element models in a compact but meaningful way. With visual representations of the data from multiple structural design alternatives at hand, the structural designer is assisted in an informed structural design process and is better able to understand the influence of certain design parameters on the structural behaviour of complex structures.

To be meaningful and informative to the designer's problem, the right visualisation should be chosen or developed by the designer. Therefore, to facilitate informed decision-making, the choice of data and how to visualise it must therefore lie with the designer. The research provoked an approach that forces designers to create and develop graphs themselves that are meaningful to the current state of the design process and the corresponding questions and interests. When designing structures in practice, the questions and interests are often very different and context-specific. For this reason, case-dependent approaches (in this case visualisations) need to be used. The research implicitly showed the need to be able to handle all structural data easily. Irrespective of the specific topic of data visualisation for

Copyright © 2023 by Lennert LOOS. Published in the Proceedings of the IASS Annual Symposium 2023 with permission.

structural design, the need to handle data in a versatile way is a general theme and concern in modern digital design processes, according to the author's experience in professional design offices.

This paper discusses a new Grasshopper plugin that has been developed to allow the use of data-rich objects in a parametric design environment. Object-oriented elements in parametric design will be discussed briefly. Furthermore, the implementation of the plugin is explained, as well as its user interface and a small example showing its use for practical applications in the field of structural design. Finally, an evaluation of the implementation is carried out to point out the strengths and weaknesses of the developed plugin and the use of data-rich objects within the Grasshopper3d environment.

2. Problem statement and background

The idea of working with data-rich objects in a geometric parametric design environment such as Grasshopper was initiated by the need to handle structural data more easily for the assembly of graphs in earlier research, but also originates from practical needs in a professional design office, as observed and experienced by the author.

2.1. Parametric design environments and its application in practice

Parametric and computational design approaches are widely used in architectural and structural design practices. All kinds of software, scripts, algorithms and tools are provided by the community, often even open source. In architecture and structural design practice, the last decade has seen a move away from text-based programming in computational design towards the use of visual programming and coding with tools like Grasshopper [4] or Dynamo [5]. One of the reasons for this is the reduced effort required to learn visual programming languages compared to textual programming [6]. Another reason is the speed with which designers can set up scripts to perform tasks. In addition, it can be argued that many architects and engineers in design practices do not have the skills or time to become proficient in developing custom software and algorithms through textual coding. It is important to note that this makes designers often reliant on other people's implementations and third party software; as a result, there is a risk that this software may not accurately meet their needs [7].

From personal experience as a structural designer, the author observed that Grasshopper3d in particular is used for all sorts of tasks by both engineers and architects. Although this parametric design environment has its main focus on parametric geometry, the tasks for which this tool is used in practice are not limited to this purpose. Beside generating and manipulating geometries, the parametric design environment of Grasshopper3d seems to be a well-suited framework for analysing structural models [8], preliminary form-finding of structures [9], quickly performing geometrical operations, executing small geometric and numerical checks on designs [10], importing, manipulating and exporting data and/or geometries [11], or even working with remote databases [12].

In other words, when working on structural projects, Grasshopper3d is often not used to create fully parameterised models from A to Z, but rather as a very versatile tool for a series of small, different and unrelated operations. This allows the designer to stay within a single digital design environment without having to switch between different interfaces which requires frequently exporting and importing data. Often the geometry (possibly with attributes) is saved as a Rhino3d file, which serves both as a starting point for new parametric scripts and as a snapshot of the current state of the design.

2.2. Data and BIM

Parametric design is almost exclusively geometry driven and therefore has an inherent focus on modelling [14]. Working with related data is not impossible, but rather cumbersome in current implementations of popular parametric design environments. However, working freely with data in parametric interfaces is crucial if we are to make informed design decisions in a conscious way. Indeed, preliminary analyses and checks based on numerical data are regularly performed when working with parametric models at different stages of the design process.

Data in digital architectural and structural design is often referred to as Building Information Modelling (BIM). The structure of current BIM software may lack support for the actual design process and is generally used to document a more finished design [13]. BIM has however important and useful features that can be of value in any design phase, such as a structured model with clear semantic information, user-defined properties and data values, spatial relationships between elements, etc. Greater similarity between parametric design and BIM approaches is desirable, but not easy to achieve [13-14].

2.3. Expressing the needs for a more object-oriented parametric design

To maximise the potential of parametric and computational tools in the digital design process, data-rich parametric design environments will be essential. A BIM or object-oriented approach that supports the actual design process could serve these needs well [13]. In order to make informed decisions, to react to design data, e.g. from analyses, and to make use of (associated) data, versatile and flexible but simple tools are needed that can be easily integrated into existing design approaches and practices [7]. Convenient data management is of utmost importance for understanding and digesting the data/results/information generated during design.

As visual programming languages such as Grasshopper3d are often used by computational designers with limited textual programming skills, the parametric design environment should allow working with data without relying on textual programming. In addition, the author's experience has shown that parametric modelling is also used in practice as a way to perform small operations (geometric parametric modelling, import and export, data processing) quickly. For this reason too, the implementation of data-rich objects in parametric design must be closely aligned with the existing parametric design environment.

Recently there has been the robust development of BHoM (Buildings and Habitats object Model) [15]. BHoM aims to standardise the data and functionality that are used in the architecture, engineering and construction industry. It proposes a central Object Model, which is a schema, therefore BHoM's main focus and value lies in interoperability between software tools by sharing the same schema, the central common language. Although it shows a lot of potential to also work in a more object-oriented way in parametric design environments, it does not actually support design processes and tasks that computational designers do on a daily basis within parametric design environments.

Performing basic operations such as selecting, sorting, evaluating and modifying objects should be an inseparable part of parametric geometric design. These types of operations are relatively easy to perform in database environments (for instance BIM interfaces) and using textual programming. In parametric design environments such as Grasshopper3d, however, it becomes very tedious to set up without the use of third-party plugins. In the following paragraphs, the new *Inkbeagle Data* plugin [18] for Grasshopper3d is introduced and discussed. It allows the creation of objects from named keys and corresponding values, including basic data types (textual and numerical) as well as geometry. This implementation can be seen as an attempt to facilitate object-oriented parametric design within the Grasshopper interface.

3. Implementation and user interface

This section describes the implementation of *Inkbeagle Data* [18], a custom plugin written in C# developed for Grasshopper3d. *Inkbeagle Data* allows to assemble data keys and corresponding values into an *InkObject* on which basic operations such as list filtering, evaluating expressions and list sorting can be performed, fully based on Grasshopper's native data types. Furthermore various methods are included to import and export the InkObjects as a file to and from Grasshopper.

3.1. Implementation

The *Inkbeagle Data* plugin is based on the idea of the *Objectify* plugin [16]. However, the implementation of *Inkbeagle Data* takes the basic idea a step further by the operations that can be performed on the *InkObjects* and the methods for exporting and importing.

The main logic of an *InkObject* follows the idea of a dictionary that stores key-value pairs in no particular order. The key is of type *string*, while the corresponding value is of type *IGH_Goo*, the base interface for all data inside Grasshopper. Any data type that inherits from the *IGH_Goo* type can be used as data for the *InkObject* assembly: e.g. *GH_Curve, GH_Colour, GH_Integer, GH_Line, GH_String…* As a result, any supported data type can be assembled into an *InkObject*. Additionally, information about the "bakability" and "visibility" of the geometric values is included and can be set.

Grasshopper uses the *GH_InkObject* class as the GH-wrapper for *InkObjects* and is derived from *GH_GeometricGoo<InkObject>*, *IGH_PreviewData*, *IGH_BakeAwareData* and *GH_ISerializable*. As a result, the *InkObjects* are fully serialisable and their geometric values are bakable in Rhino3d. Since *GH_InkObjects* are derived from the abstract class *GH_GeometricGoo*, *InkObject*s can contain *InkObjects* themselves; in other words *InkObjects* can be nested.

Since the implementation as described above does not allow to store a list of *IGH_Goo* objects as a value in the *InkObject*, it is possible to wrap a *List<IGH_Goo>* in a custom class *GH_InkList* derived from *GH_GeometricGoo*. This way lists can be packed, stored in an *InkObject* and unpacked later.

In the following paragraphs, the most important features of the plugin are shown.

3.2. User interface (UI)

3.2.1. Constructing and deconstructing InkObjects

The *Construct InkObject* and *Deconstruct InkObject* components (Figure 1) allow *InkObjects* with named keys and corresponding values to respectively be assembled and to be separated into its different values.

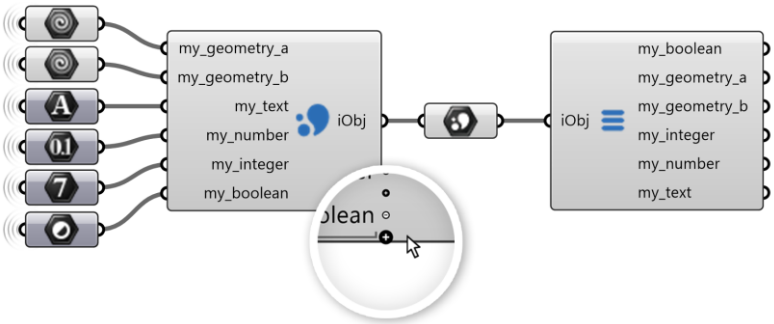


Figure 1. The components used to construct and deconstruct *InkObjects*.

Inkbeagle Data's implementation aims to provide a seamless user experience by closely following the native Grasshopper UI. To achieve this, the component for constructing an *InkObject* is implemented as a variable parameter component, allowing dynamic input and output parameters to be created at runtime (adding or removing input parameters). The key name can be set by right-clicking on the input parameter label. This makes the plugin's UI similar to native Grasshopper components, ensuring that users can easily integrate the plugin into their existing workflows.

An *InkObject* is created with data attached to each named key. Adding lists of data to the *Construct InkObject* component, creates a list of *InkObjects* with all the individual data items from the input lists

attached to the corresponding named keys. If lists of different lengths are used for different keys, the component will be solved according to Grasshopper's default solving routine. Also when data trees are used, the default Grasshopper logic is maintained.

3.2.2. Working with InkObjects

The following components (Figure 2) can be used to work with associated data in *InkObjects*: *Add Key*, *Modify Value*, *Remove Key* and *Get Value*. The functionalities of these components are considered as self-explanatory.

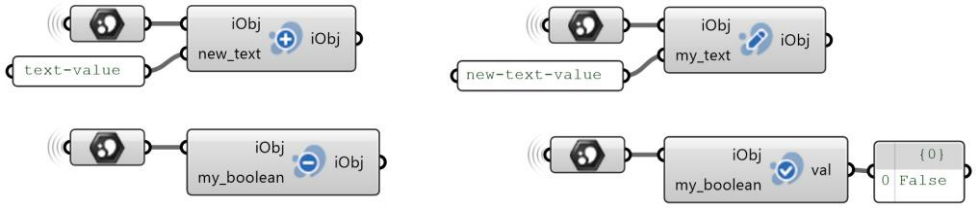


Figure 2. The components that allow to add new key-value pairs (Add Key), modify the value of key-value pairs (Modify Value), remove key-value pairs (Remove Key), get the values of key-value pairs by the textual key (Get Value).

The UI of these components aims to be as consistent as possible with Grasshopper's default UI. For example, the values of multiple keys can be retrieved by adding and selecting multiple existing keys as input parameters from the right-click parameter menu (Figure 3). A similar UI is provided for the other components that are listed in Figure 3.

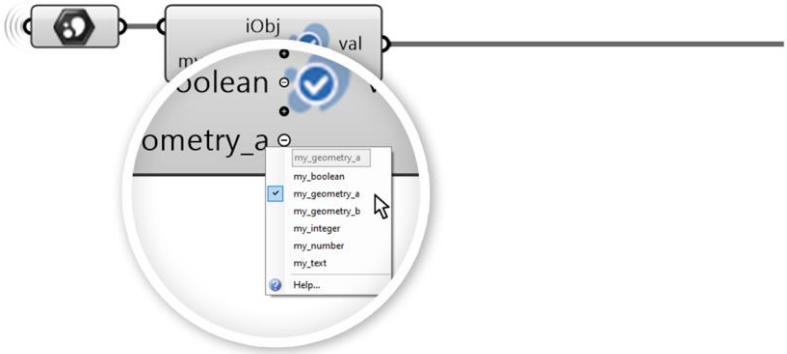


Figure 3. Compact UI for adding and selecting key-value pairs, similar to Grasshopper's default UI.

3.2.3. Operations

In order to perform operations on (lists of) *InkObjects*, a few helpful components have been developed: *Evaluate*, *Filter*, *Sort by Key* and *Search by Value*, each with a specific purpose.

The *Evaluate* component (Figure 4) allows to execute basic expressions with the same syntax as used for the native Grasshopper components *Expression* and *Evaluate*. The *Evaluate* component can be used to solve expression syntax and return numeric or string values as the result or to perform conditional evaluations which will return a boolean value. The key names of the *InkObjects* are directly used as

parameters in the expression to be evaluated. If for instance an *InkObject* contains numerical values in certain keys (*key_a*, *key_b*, *key_c*), the following logical and numerical expressions can be constructed:

- `key_a > (key_b - key_c)` logical expression
- `key_a / (key_b^3 * sqrt(key_c))` numerical expression

If one wants to filter a list of *InkObjects* based on a logical expression, the *Filter* component (Figure 4) can be used. It has similar functionality to Grasshopper's native *Dispatch* component, but the logical expression can be expressed based on the named keys of the *InkObjects*.

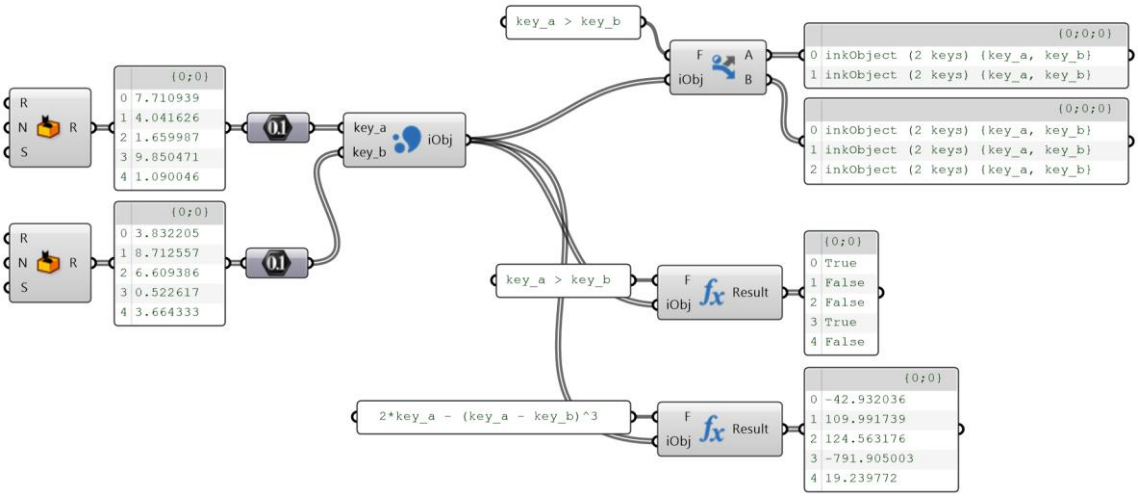


Figure 4. The use of components that allow to execute expressions and filter a list of *InkObjects*.

The *Sort by Key* component (Figure 5) sorts a list of *InkObjects* based on the value of a specified key, while the *Search by Value* component (Figure 5) allows users to search for *InkObjects* with specific key values.

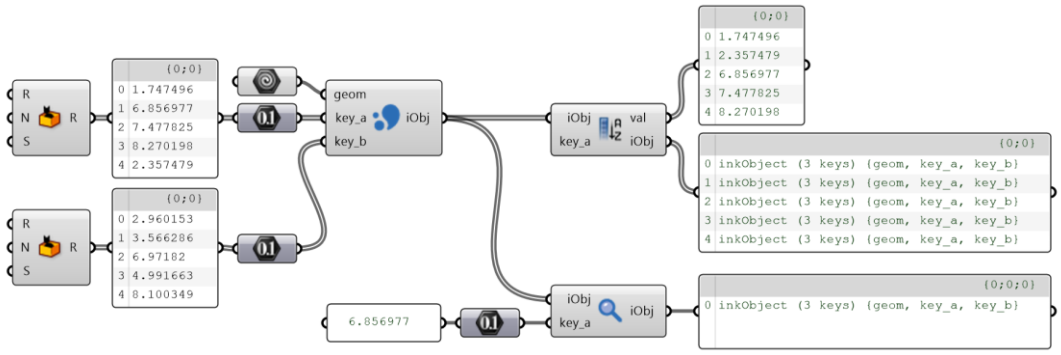


Figure 5. The use of the components that allow to sort a list of *InkObjects* and to search for *InkObjects* in a list that have a specific value assigned to a certain key. Note that it is important that the correct type must be used to look up certain values: the string "6.856977" is casted to a *GH_Number* first. Searching by the string value would not return any *InkObjects*.

3.2.4. Export-Import

A series of components have been developed to facilitate exporting and importing *InkObjects*. The user is able to *Bake* one or more *InkObjects* as geometries in Rhino3d with textual or numerical attributes, based on the non-geometric key-value pairs of the *InkObject*. Geometries with attributes can be referenced from Rhino3d back into Grasshopper3d as well, where the attributes will become textual or numerical key-value pairs of the *InkObject*. The *Serialize* component allows to save a data tree of *InkObjects* as a binary file. This way one is able to work with data and Grasshopper geometries between various files. A binary file containing the serialised data and geometry can be deserialized into the Grasshopper3d environment. To conclude, *InkObjects* containing basic data type values (textual or numerical) can be exported to *csv*, *xml* or *json* data files and imported from data files in corresponding format.

4. Practical use cases

In practice, the author uses the developed plugin mostly to work more efficiently with data and FEA results within a parametric design context.

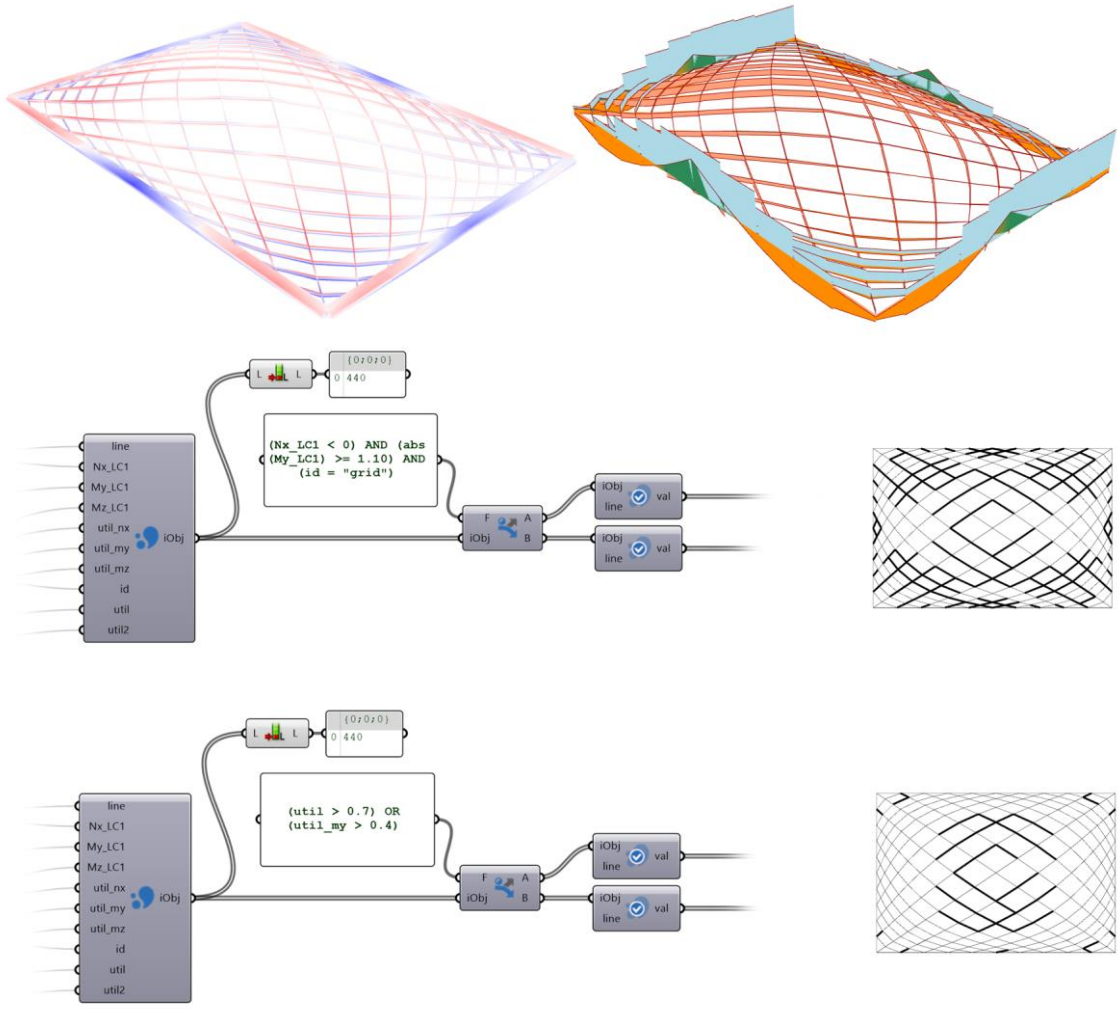


Figure 6. The beam elements are filtered based on the following more complex logical expressions:
Expression 1: `(Nx_LC1 < 0) AND (abs(My_LC1) >= 1.10) AND (id = "grid")`
Expression 2: `(util > 0.7) OR (util_my > 0.4)`

When using for instance Karamba3d [8], all result data is available in the parametric environment and can now be attached to structural geometries and processed further, without leaving the design interface. For instance, the plugin can be used to filter structural elements based on the structural results. This way the behavioural characteristics of the structural elements can be identified more easily. Figure 6 illustrates this with a small example.

Inkbeagle Data makes filtering of objects/elements more easy. This provides users with the capability to effectively manage and digest large volumes of structural results without leaving the parametric design environment. In the example shown above, more complex logical expressions are used to filter structural elements based on their *internal forces*, *utilisation* and *type*. These values are retrieved from the Karamba3d plugin and assigned to line elements, representing each beam. The key names such as *Nx_LC1* or *util_my* can be chosen freely, according to the needs of the structural designer.

Another example where the author used *Inkbeagle Data* is to prepare the definition of the pretension loadcase for a SOFiSTiK finite element model. The form-found geometry of a pretensioned cable structure is baked in Rhino3d as snapshot of the project's current design state. The baked geometry contains User Attributes with information such as the form-found force (F), E-modulus (E), cable id (cable_id), cross-sectional area (E), etc.

When the line objects in Rhino3d are referenced in Grasshopper3d, the User Attributes can be attached to the geometry as *InkObjects* with the help of the *Inkbeagle Data* plugin (Figure 7). Based on the data values, the shortening of each cable can easily be calculated with the help of the *Evaluate* component and added as a key "shortening" to the *InkObjects*. The *Evaluate* component is then used once more to format a specific string with variables, to match the desired SOFiSTiK Teddy syntax.

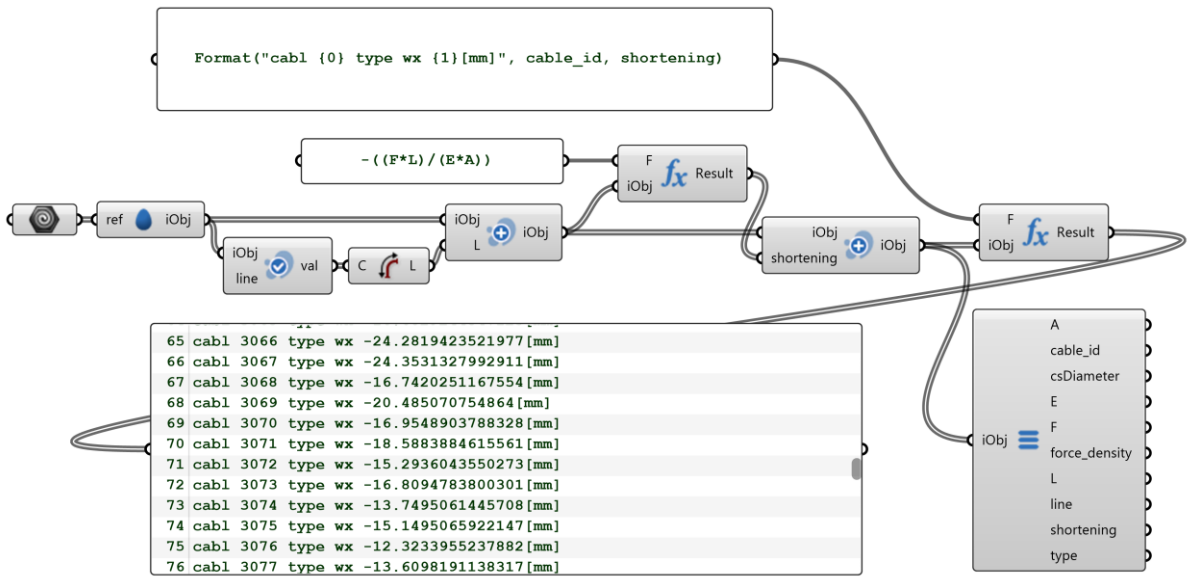


Figure 7. Without too much effort the pretension load can be formatted as a shortening of the cables in the desired SOFiSTiK Teddy syntax, without the need to do this data processing in another computational environment.

5. Discussion and conclusion

Based on the author's observations and experiences of how Grasshopper3d is used in practice and that the parametric framework is used for all kinds of tasks of different nature became clear from the practical use cases. The presented cases show that a more object-oriented approach in parametric modelling has some direct benefits for the workflow of architects and structural designers, especially when it comes to supporting daily custom operations with data and geometries. This was the main reason for the development of the plugin.

The idea of combining all kinds of Grasshopper3d data types into one "object" seems to be reasonable as an approach. However, there is no such thing as a free lunch. The goal of supporting all possible data types implies using the *IGH_Goo* type for the values of the object. While this has many advantages such as the ability to work with Grasshopper3d's expression syntax, it also has drawbacks. For example the *Sort by Key* component must first check that all values corresponding to the given key are in fact numeric. Other operations like casting of types can also reduce the performance of the implementation. However, for sorting, evaluating expressions, looking up *InkObjects* from a list of manageable size (up to about 50 000), the implementation seems to be competitive with a native Grasshopper3d solution performing the same task.

Although nesting of *InkObjects* is possible, the current implementation is very much geared towards a flat application. In fact, it is not possible to retrieve the values of nested *InkObjects* using the plugin's components alone; instead, custom scripting is required. Also, the evaluation of the expression syntax is not applicable to nested values either. It may be worth investigating thoroughly to what extent such features are feasible without compromising on the UI which should remain as similar as possible to the native Grasshopper3d UI and its user experience. The workaround method of using *InkLists* may be helpful in some cases, but a more general approach is desirable.

While the plugin was being developed, Grasshopper 2.0 [17] had not yet been released. This second major release of Grasshopper3d comes with the support for so-called metadata. This means that meta values can be attached to any regular value, similar to the assembly of *InkObjects*. This provides the ability to associate certain values with their main value, but also offers a way to control in more detail how Grasshopper handles data. This particular feature is an important one in the development of parametric design environments and may even suggest that object-oriented approaches are essential to the future development of visual programming and parametric design interfaces.

7. References

[1] L. Loos, Structural Design by means of Data Visualisation , 2019.

[2] K. Verbeeck, L. Loos, L. De Laet, "How to re-open the black box in the structural design of complex geometries" in Proceedings of the International Conference on Structures and Architecture, Guimaraes, 2016.

[3] L. Loos, L. De Laet, "A Structurally Informed Design Process by Real-time Data Visualisations" in Proceedings of ECAADE 2018: Computing for a Better Tomorrow, 2018.

[4] Robert McNeel & Associates, Grasshopper, https://www.grasshopper3d.com, 2007.

[5] Autodesk, Dynamo, https://www.dynamobim.org, 2011.

[6] G. Celani, C. Eduardo Verzola Vaz, "CAD scripting and visual programming languages for implementing computational design concepts: a comparison from a pedagogical point of view" in International Journal of Architectural Computing 10 (2012).

[7] N. C. Brown, V. Jusiega, C. T. Mueller, "Implementing data-driven parametric building design with a flexible toolbox" in Automation in Construction 118 (2020).

[8] C. Preisinger, Karamba3d, https://www.karamba3d.com, 2014.

[9] D. Piker, Kangaroo Physics, https://www.food4rhino.com/app/kangaroo-physics, 2011.

[10] M. Pryor, Pufferfish, https://www.food4rhino.com/app/pufferfish, 2021.

[11] Thornton Tomasetti - Core Studio, TT Toolbox, https://www.food4rhino.com/app/tt-toolbox, 2013.

[12] N. Miller, Slingshot!, https://www.food4rhino.com/app/slingshot, 2012.

[13] J. Coenders, "Parametric and associative design as a strategy for conceptual and delivery to BIM" in Proceedings of the International Association for Shell and Spatial Structures (IASS) Symposium, Valencia, Spain, 2009.

[14] S. Boeykens, "Bridging building information modeling and parametric design" in eWork and eBusiness in Architecture, Engineering and Construction, Taylor & Francis Group, London, 2012.

[15] BHoM, https://bhom.xyz/documentation/, 2018

[16] Ranjeeth Mahankali, Objectify, https://www.food4rhino.com/app/objectify, 2019.

[17] Robert McNeel & Associates, Grasshopper 2.0, https://discourse.mcneel.com/t/grasshopper-2-alpha-available-for-testing/, 2022.

[18] L. Loos, Inkbeagle.io, https://www.inkbeagle.io, 2021.

Novel methods in modelling, optimisation and construction for reducing carbon footprint of continuous roof shells

---

Active bending
Additive manufacturing/ 3D printing
Architectural geometry
Bamboo for sustainable construction and quality of life improvement
Bio-inspired structures and architecture
Bridge structures
Computational form-finding
Conceptual design
Concrete structures
Construction techniques
Deployable and inflatable structures
Design competition (WG21)
Digital modelling and fabrication
Dynamic response of metal spatial structures
Dynamic response of other structures
Form-finding and structural optimisation of interlocking discrete assemblages
Graphical methods
Gridshell and lattice structures
Historical concrete shells
Historical structures
Lattice structures
Life-cycle design and assessment of structures
Metal gridshell structures, connections and stability
Methods and construction technologies for sustainable shell structures
Morphology and configuration processing
Next generation parametric design
► Novel methods in modelling, optimisation and construction for reducing carbon footprint of continuous roof shells
Numerical methods for geometry, form-finding and optimisation of lightweight structures
Optimisation methods and applications
Origami
Other
Teaching design uncertainty: working with unknown qualities/quantities of new and re-claimed materials
Teaching of shell and spatial structures
Tensegrity systems and cable structures
Tension and membrane structures
Tension structures in the Asia-Pacific
Timber and bio-based structures
Topology optimisation
Traditional masonry structures and innovation
Transformable structures

IASS 2023
July 10–14 Melbourne
Integration of Design and Fabrication

Proceedings of the IASS Annual Symposium 2023
Integration of Design and Fabrication
10–14 July 2023, Melbourne, Australia
Y.M. Xie, J. Burry, T.U. Lee and J. Ma (eds.)

Isogeometric refinement for shells' shape optimization

Gloria Rita ARGENTO[a], Enzo MARINO[b], Valerio VARANO[a], Stefano GABRIELE[a,*]

[a,*] Department of Architecture, Roma Tre University, Rome, Italy
stefano.gabriele@uniroma3.it

[b] Department of Civil and Environmental Engineering, University of Florence, Florence, Italy

Abstract

In a previous work the classical funicularity definition for shell structures has been extended to the so called Relaxed Funicularity (R-Funicularity). A parameter called generalized eccentricity has been used for this purpose, following that a shell is R-Funicular when the generalized eccentricity on each shell's point doesn't exceed an admissibility limit. A shells' shape optimization process aiming at finding R-Funicular analytical shells, previously developed by some of the authors, is here modified at the geometry definition level by describing the shells' shape with spline surfaces and using the coordinates of the control polygon vertices as optimization variables. Compared to existing works in which this approach was used, here an isogeometric (IG) refinement is applied in order to improve the local control of the shape in the optimization process. In fact, an advantage of this approach is that, since it introduces new vertices in the control polygon, the number of optimization variables becomes tunable. Namely, starting with the lowest number used to generate the initial geometry, the additional vertices can possibly be entered as new variables whenever a more accurate local control of the surface is needed. We present significant numerical examples.

Keywords: shape optimization, NURBS, generalized eccentricity, R-funicularity, isogeometric refinement

1. Introduction

Funicular shell structures are characterized by a shape that follows the flow of forces and are ideally able to bear the design load without introducing bending. As a result, they pursue a full exploitation of the resistant cross section and a minimum waste of material. Thus, funicular shells are an example of efficiency and many form finding techniques have been developed in order to find the "right" shape in accordance with the applied load [1].

Nevertheless, when shell structures have a non negligible bending stiffness and/or the boundary conditions are not properly assigned, a funicular behaviour is not possible and bending arises. In order to take into account this occurrence and quantify the actual funicular behaviour of shells, a method based on Relaxed Funicularity (R-Funicularity) has been developed in [2]; the parameter used to quantify the funicularity is the generalized eccentricity. In these cases, the amount of bending moments exploited by a shell to resist applied loads can be reduced by means of a shape optimization process, i.e. an inverse problem properly formulated to minimize an objective function somehow measuring the shell's bending moments. The minimization is pursued by updating some shell geometric features, i.e. variables, that are admitted to vary within a range. The goal of bending moments reduction is usually approached by minimizing the strain energy [3, 4, 5]; other objectives of shape optimization can be, for example, the minimization of the weight, the stress levelling [3, 4] or the minimization of displacements [6].

In [7] a shells' shape optimization process aimed at finding a shape that minimizes the generalized eccentricity extrema, i.e. an as much as possible R-Funicular shell, has been developed. Considered the

Copyright © 2023 by Gloria Rita ARGENTO, Enzo MARINO, Valerio VARANO and Stefano GABRIELE. Published in the Proceedings of the IASS Annual Symposium 2023 with permission.

strict link between geometry and mechanical behaviour of shells, the description of the first strongly influences the solution quality and the computational time. Similarly to what proposed, for example, in [5, 6], when an R-Funicular shell has been sought, the shape has been described by means of an analytical function [8], in some cases obtained by a linear combination of analytical functions [7, 9] and a finite element analysis has been performed.

In this work we propose a modification at the geometry definition level of the shape optimization process shown in [8] by introducing the shell's surface description by means of B-spline surfaces [10]. Compared to existing works in which this approach was used (see, for example, [5, 11]), here an isogeometric (IG) refinement is applied in order to improve the local control of the shape in the optimization process. In fact, an advantage of this approach is that, since it introduces new vertices in the control polygon, the number of optimization variables becomes tunable. This feature is exploited by performing a shape optimization where, starting with the lowest number used to generate the initial geometry, all or some of the additional vertices are then entered as new variables whenever a more accurate local control of the surface is needed. A similar approach has been employed in [12], where, in order to expand the feasible design space, a refinement of the initial geometry has been performed.

After a brief description of the concepts of R-Funicularity and generalized eccentricity $e(\alpha)$, we discuss the optimization strategy with a major focus on the geometry description. Two effective numerical examples are then proposed and the conclusions are drawn.

2. Generalized eccentricity and R-funicularity

The generalized eccentricity measure and its use to define the R-Funicularity concept are briefly introduced in this section. For a complete discussion, please refer to [2].

Let us consider a point P belonging to the surface S, endowed with its orthonormal basis $\boldsymbol{a}_1, \boldsymbol{a}_2, \boldsymbol{a}_3$, and a generic direction of the tangent plane represented by the unit vector $\boldsymbol{u} = (cos\theta, sin\theta)$ (Fig. 1).

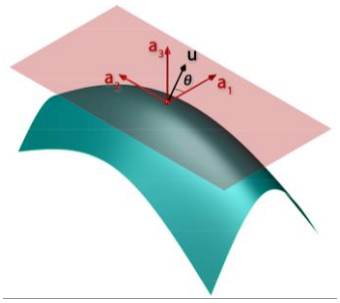


Figure 1. Local orthonormal basis on P belonging to the surface S.

The local tensors $\boldsymbol{N}$ and $\boldsymbol{M}$, respectively associated with the membrane forces and the bending moments, can be evaluated in each point P:

$$\boldsymbol{N} = \begin{pmatrix} N_{11} & N_{12} \\ N_{12} & N_{22} \end{pmatrix}, \quad \boldsymbol{M} = \begin{pmatrix} M_{11} & M_{12} \\ M_{12} & M_{22} \end{pmatrix} \tag{1a, b}$$

Then, $N(\theta) = \boldsymbol{u}^T \boldsymbol{N} \boldsymbol{u}$ and $M(\theta) = \boldsymbol{u}^T \boldsymbol{M} \boldsymbol{u}$ are, respectively, the generalized membrane force acting along $\boldsymbol{u}$ and the generalized bending moment acting in the plane $(\boldsymbol{u}, \boldsymbol{a}_3)$. Using the multiple-angle and the power-reduction trigonometric formulae and setting $\alpha = 2\theta$, it has been possible to write the following explicit form for Eq. $N(\theta)$ and $M(\theta)$:

$$\begin{aligned} N(\alpha) &= \bar{N} + \hat{N} cos\alpha + N_{12} sin\alpha \\ M(\alpha) &= \bar{M} + \hat{M} cos\alpha + M_{12} sin\alpha \end{aligned} \tag{2}$$

where $\overline{N} = \frac{N_{11}+N_{22}}{2}$, $\widehat{N} = \frac{N_{11}-N_{22}}{2}$, $\overline{M} = \frac{M_{11}+M_{22}}{2}$, $\widehat{M} = \frac{M_{11}-M_{22}}{2}$. Then, the generalized eccentricity is defined as the ratio:

$$e(\alpha) = \frac{M(\alpha)}{N(\alpha)} \tag{3}$$

Eq. 2 is the equation of a parametric curve in the plane $(N, M) \in \mathbb{R}^2$, that is an ellipse when $\alpha \in [0,\ 2\pi]$, called *ellipse of eccentricity* or *Relaxed Funicularity (RF) ellipse* (Fig. 2).

It is well known that a surface structure is funicular, for a given load, if the condition (4) is verified.

$$M(\alpha) = 0 \quad \forall\ \alpha \tag{4}$$

The actual behaviour exhibited by shells with non negligible thickness shows that the nullity of bending internal forces is an ideal that never verifies. The aim of R-Funicularity is to define a criteria to consider a structure funicular in a relaxed manner even if Eq. 4 is not respected, when $e(\alpha)$ belongs to an admissible range set as $[-\lambda h,\ \lambda h]$, where h is the thickness of the surface and $\lambda \in \left[0,\ {}^{1}/_{2}\right]$ an admissibility coefficient that depends on the applications.

In the light of above, the Relaxed Funicularity (RF) is defined as follow: "a shell is R-Funicular if, $e(\alpha) \in [-\lambda h,\ \lambda h]\ \forall\ \alpha \in [0,\ 2\pi]$, for each point of the surface". In practice the problem of the R-Funicularity is that of verifying:

$$\left[min\big(e(\alpha)\big),\ max\big(e(\alpha)\big)\right] \subset [-\lambda h,\ \lambda h] \tag{5}$$

For completeness, we show the graphical representation of $e(\alpha)$ in the (N, M) plane. More details about its use are given in [2].

Considered the definitions below, the generalized eccentricity is the Rayleigh quotient: $e(\theta) = \frac{\boldsymbol{u^T M u}}{\boldsymbol{u^T N u}}$, and the maximum and minimum eccentricities (e_{max}, e_{min}) are found by solving the associated eigenvalue problem:

$$(\boldsymbol{M} - e\boldsymbol{N})\ \boldsymbol{u} = 0 \tag{6}$$

The solution of (6) depends on the algebraic conditioning of $\boldsymbol{M}$ and $\boldsymbol{N}$ and has been discussed in [2]. It gives the local extrema e_{max} and e_{min}, shown in the equation (17) of [2].

The global extrema of the eccentricities can be finally evaluated as follows:

$$min\big(e(\alpha)\big), max\big(e(\alpha)\big) = \begin{cases} -\infty, +\infty & if\ \det(N) < 0 \\ e_{min}, e_{max} & if\ \det(N) \geq 0 \end{cases} \tag{7}$$

The angles $\varphi_{max} = \text{atan}\ (e_{max})$ and $\varphi_{min} = \text{atan}\ (e_{min})$ in Fig. 2 have been used to define the functional to be minimized with the aim of improving the shells' mechanical behaviour.

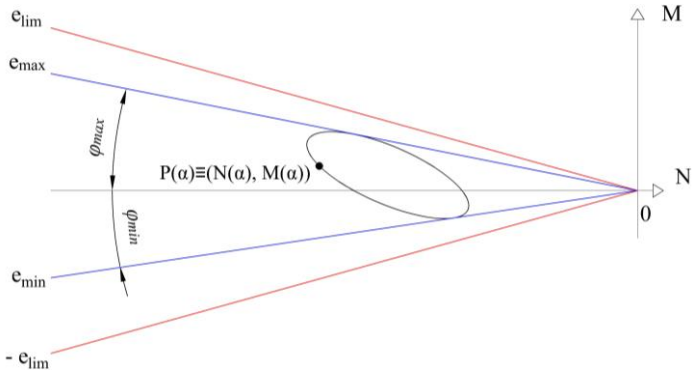


Figure 2. RF ellipse with eccentricity extrema e_{max} and e_{min}, eccentricity limits e_{lim} and $-e_{lim}$, respectively equal to the slope of the upper and lower blue and red lines and eccentricity angles φ_{max}, φ_{min}

3. Shells' shape optimization for R-funicularity

The main goal of the shells' shape optimization process proposed in [7] is to obtain a shape for the shell to be R-Funicular as much as possible and is pursued by minimizing the generalized eccentricity extrema e_{max} and e_{min} all over the shell. Here the procedure is modified at the geometry definition level. Aiming at a wider design freedom, the shell shape is now described with B-spline surfaces and an isogeometric refinement is applied and exploited to obtain a major local control of the shape.

3.1. Modelling of geometry and isogeometric refinement

The shell geometry has been modelled by means of a non-rational B-splines surface, obtained by fixing a bidirectional net of control points $\mathbf{P}_{i,j}$, two knots vectors $\mathbf{U} = \{0, \dots, 0, u_{p+1}, \dots, u_{r-p-1}, 1, \dots, 1\}$ and $\mathbf{V} = \{0, \dots, 0, v_{q+1}, \dots, v_{r-q-1}, 1, \dots, 1\}$ and the products of the two univariate B-spline functions of degree p and q, $N_{i,p}(u)$ and $N_{j,q}(v)$:

$$\mathbf{S}(u,v) = \sum_{i=0}^{n} \sum_{j=0}^{m} N_{i,p}(u) N_{j,q}(v) \mathbf{P}_{i,j} \tag{8}$$

The vectors **U** and **V** contain, respectively, $r+1$ and $s+1$ knots, being:

$$r = n + p + 1 \qquad s = m + q + 1 \tag{9a,b}$$

The surface resulting from (8) is then manipulated by performing the isogeometric *h*-refinement that consists in the well-known algorithm of knots insertion. This type of refinement has multiple uses, among which: evaluating points and derivatives on curves and surfaces, subdividing curves and surfaces, adding control points in order to increase flexibility in shape control [10].

In order to understand the effect of knot insertion, let us consider a B-spline curve $\mathbf{C} = \sum_{i=0}^{n} N_{i,p}(u)\mathbf{P}_i$ defined on $\mathbf{U} = \{\mathrm{u}_0, \dots, \mathrm{u}_m\}$, whose vector space is $\mathcal{V}_U$. If we insert $\bar{u} \in [u_k, u_{k+1})$ into U we obtain the new vector $\bar{\mathbf{U}} = \{\bar{u}_0 = u_0, \dots, \bar{u}_k = u_k, \dots, \bar{u}_{k+1} = \bar{u}, \bar{u}_{k+2} = u_{k+1}, \dots, \bar{u}_{m+1} = u_m\}$, whose vector space $\mathcal{V}_{\bar{\mathrm{U}}}$ has dimension $\dim(\mathcal{V}_{\bar{\mathrm{U}}}) = \dim(\mathcal{V}_U) + 1$ and, since $\mathcal{V}_U \subset \mathcal{V}_{\bar{\mathrm{U}}}$, it is possible to represent **C** on $\bar{\mathbf{U}}$:

$$\mathbf{C}(\mathrm{u}) = \sum_{i=0}^{n+1} \bar{N}_{i,p}(u) \mathbf{Q}_i \tag{10}$$

where $\mathbf{Q}_i$ are the new control points that can be obtained by exploiting the following equality:

$$\sum_{i=0}^{n} N_{i,p}(u)\mathbf{P}_i = \sum_{i=0}^{n+1} \bar{N}_{i,p}(u)\mathbf{Q}_i \tag{11}$$

and the property according to which in a given knot span $[u_j, u_{j+1})$, at most $p+1$ $N_{i,p}$ are nonzero. Omitting the intermediate mathematical steps, that can be found in [10] together with an exhaustive treatment of the topic, the new control points (Fig. 3) are:

$$\mathbf{Q_i} = \alpha_i \mathbf{P}_i + (1-\alpha_i)\mathbf{P}_{i-1} \tag{12}$$

where

$$\alpha_i = \begin{cases} 1 & i \le k-p \\ \dfrac{\bar{u}-u_i}{u_{i+p}-u_i} & k-p+1 \le i \le k \\ 0 & i \ge k+1 \end{cases}$$

and k is an index that locates the inserted knots in the vector $\bar{\mathbf{U}}$.

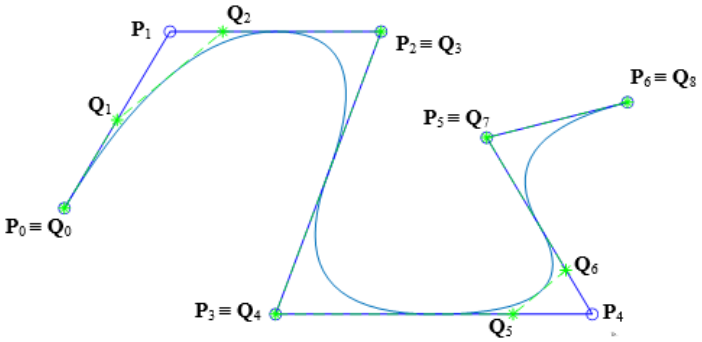


Figure 3. Effect of knots insertion into a quadratic curve. Blue, solid line: control polygon before knot insertion; green, dashed line: control polygon after inserting $u = 0.1$ and $u = 0.7$ into $\mathbf{U} = \{0\ 0\ 0\ 0.2\ 0.4\ 0.6\ 0.8\ 1\ 1\ 1\}$.

In this specific case, basis functions of degree 2 have been employed. Initially, a net of 3×5 control points and the following knots vectors $\mathbf{U} = \{0\ 0\ 0\ 1\ 1\ 1\}$ and $\mathbf{V} = \{0\ 0\ 0\ 1/3\ 2/3\ 1\ 1\ 1\}$ have been considered. **U** and **V** contain, respectively 6 and 8 knots, accordingly to the equations (9a,b). The resulting shape and the control net are depicted in Figure 4.

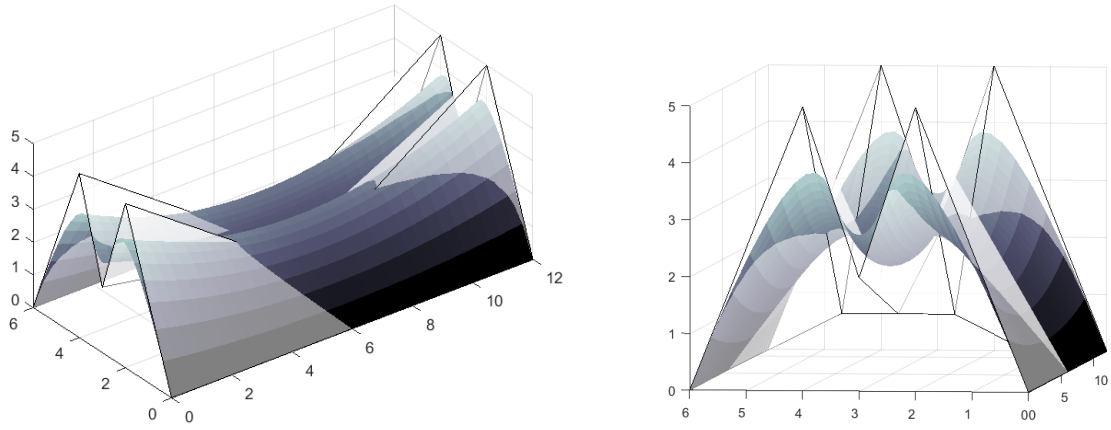


Figure 4. Starting shape and control net

The positions of the 9 inner control points (Fig. 5) have been updated in the optimization process by varying 4 different coefficients, each multiplying the z-coordinates of the points marked with the same colour in Figure 5; the black ones are maintained fixed. Thus, each control point admitted to vary is

defined as $\boldsymbol{P}_i \equiv (x_i, y_i, z_i c_i)$, where c_i are the optimization variables. The variables of the starting shape, denoted as c_{oi} are equal to 1.

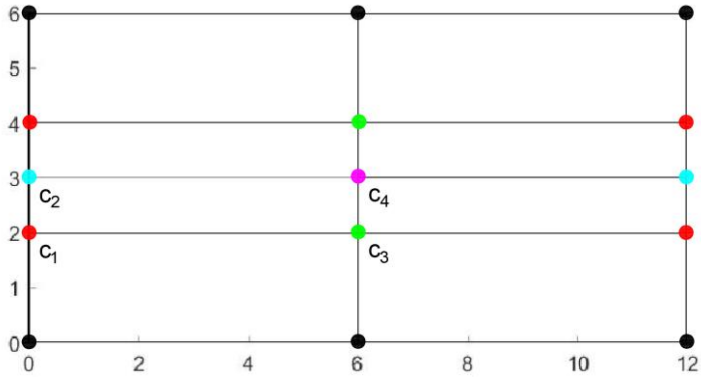


Figure 5. Plane view of the initial control net. Black dots: control points maintained fixed in the optimization process; Coloured dots: control points updated in the optimization process.

The two knot vectors $\mathbf{U_1} = \{1/3 \;\; 2/3\}$ and $\mathbf{V_1} = \{1/6 \;\; 1/2 \;\; 5/6\}$ have been inserted, respectively into **U** and **V**, obtaining the new control net shown in Figure 6.

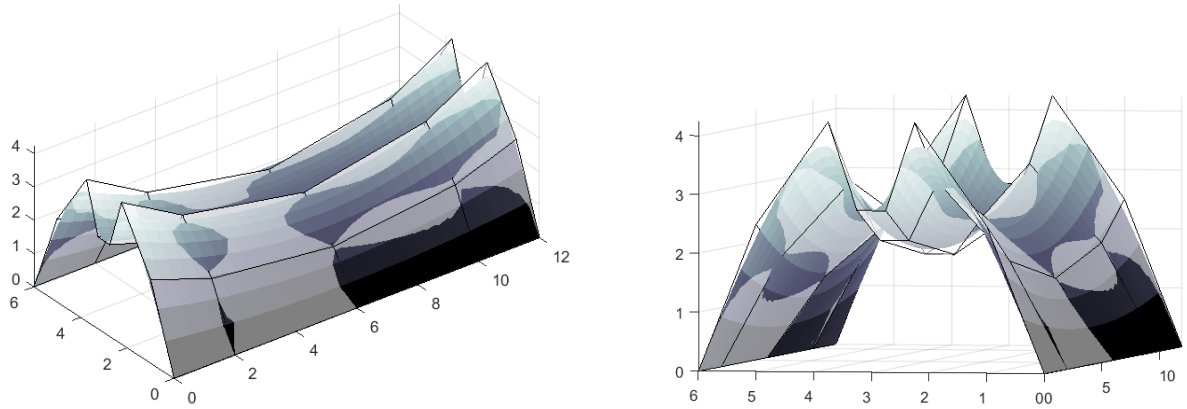


Figure 6. Starting shape and new control net

Also in this case, the positions of the 30 inner control points (Fig. 7) have been updated in the optimization process by varying 9 different coefficients, each multiplying the z-coordinates of the points marked with the same colour in Figure 7; the black ones are maintained fixed. The coordinates of the control points are defined analogously to the previous case.

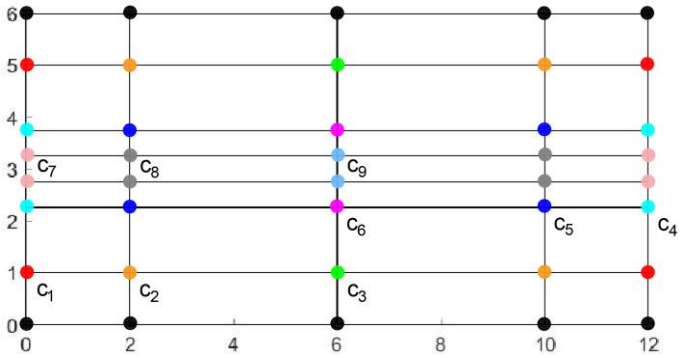


Figure 7. Plane view of the refined control net. Black dots: control points maintained fixed in the optimization process; Coloured dots: control points updated in the optimization process.

3.2. Optimization strategy

The shape optimization process is illustrated in Figure 8. Firstly, a few general definitions should be provided: shell material, eccentricity limits and boundary conditions. The initial geometry is the B-spline surface described in §3.1 and shown in Figure 4, properly discretized to build a Finite Element (FE) model. In the following step a linear static analysis of the structure subject to the self-weight load and an in plan uniform vertical load of 5 kN/m^2 is performed and the internal moments and forces are stored for each *i-th* area element of the model. The minimum and maximum eccentricities of each *i-th* element are computed by using bending moments normalized with respect to the shell thickness and collected in the vectors $\boldsymbol{e}_{0,min}, \boldsymbol{e}_{0,max}$ respectively. In addition, the eigenvalues $\lambda_{1,i}$ and $\lambda_{2,i}$ of the tensor $\boldsymbol{N}_i$ (Eq. 1a) are evaluated and used to check if the ellipse of eccentricity of the *i-th* element crosses the M axis, that is $\lambda_{1,i}$ and $\lambda_{2,i}$ have different signs. Then, the values of eccentricity extrema $e_{min,\bar{\imath}} = 10000$ and $e_{max,\bar{\imath}} = 10000$ are imposed to the $\bar{\imath}$th areas with discordant eigenvalues. The eccentricities ~~vectors~~ that result from these computations, $\boldsymbol{e}_{min}, \boldsymbol{e}_{max}$, are used to evaluate the objective function to be minimized. If convergence is reached the process stops, otherwise the shape is updated by moving the position of the control points $\boldsymbol{P}$ or $\boldsymbol{Q}$ and the procedure is repeated until convergence.

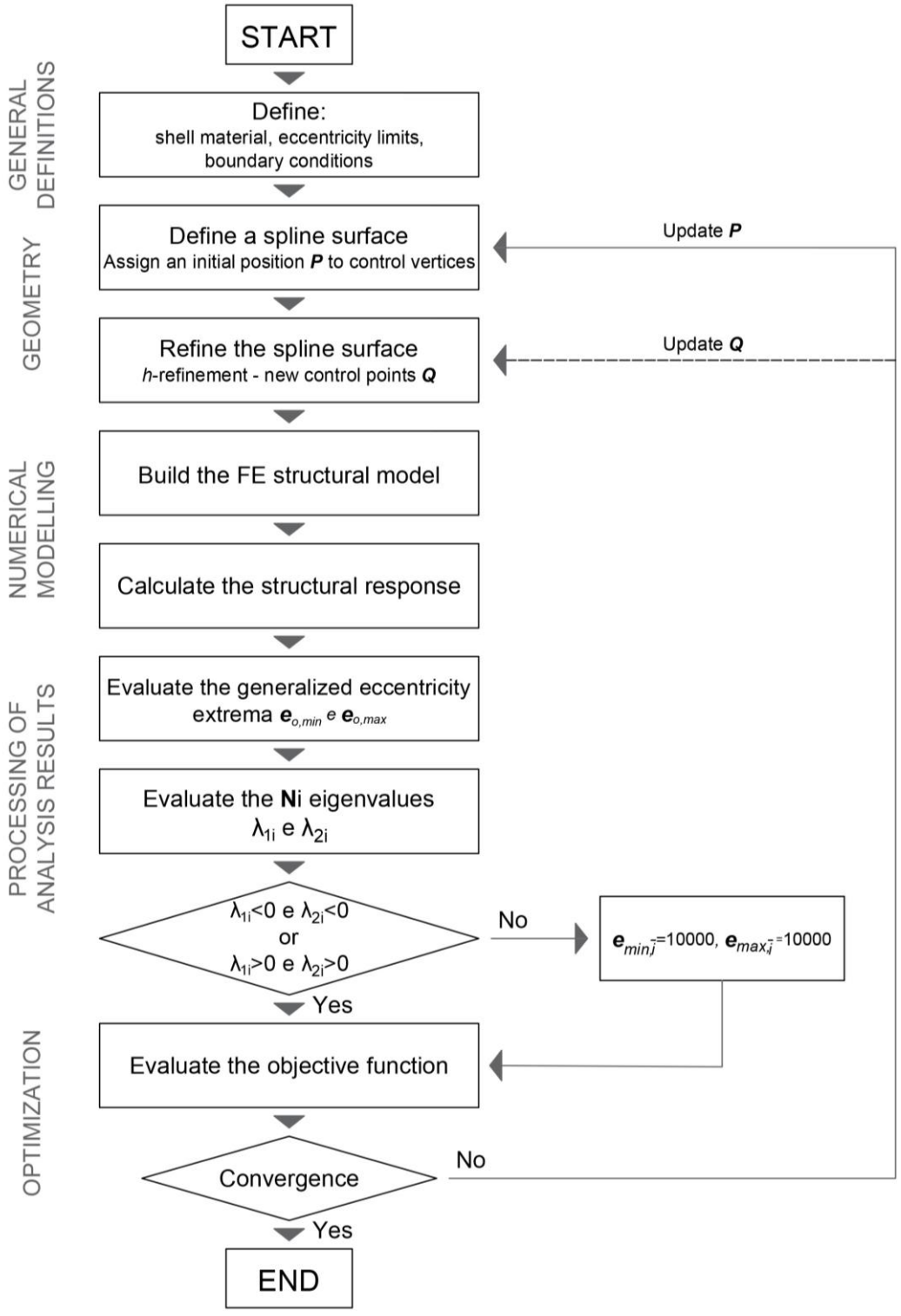


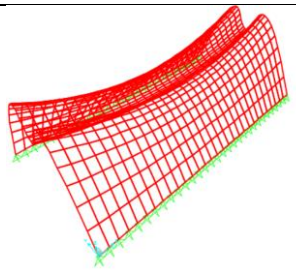
Figure 8. Overview of the shape optimization process

Defining $\varphi_{M,i} = \max\left(\left|\varphi_{max,i}\right|, \left|\varphi_{min,i}\right|\right)$, where $i = 1, \ldots, N$, being N the number of shell elements in the FE model, the objective function is defined as the root mean square of $\varphi_{M,i}$:

$$f_{obj} = \sqrt{\frac{\sum_i \varphi_{M,i}^2}{N}}$$

In Table 1, the optimization settings are summarized:

Table 1. Optimization settings

Parameter	**Value/Description**
Shell thickness h	0.1 m
Material	Concrete: $w = 25\ \frac{kN}{m^3};\ E = 3 \times 10^7\ \frac{kN}{m^2}$
Admissible eccentricity	$e_{adm} = h\,\lambda$ with $\lambda = 1/6$ or $e_{adm} = \lambda$ when bending moments normalized with respect to h are used (middle third rule)
Starting shape	Non-rational B-spline surface. Control points multipliers: $c_{oi} = 1$
Mesh Boundary conditions Shell formulation	 Quadrangular mesh; pinned x edges; shell-thin element formulation.
Objective function	$f_{obj} = \sqrt{\frac{\sum_i \varphi_{M,i}^2}{N}}$
Software	MATLAB (scripts for evaluation of eccentricities, optimization, shape update) SAP2000 (FE solver)
Optimization algorithm	Sequential quadratic programming (SQP): find local minimum of constrained nonlinear multivariable function
Variables constraints	$0.01 \leq c_i \leq 2$

4. Results and conclusions

The shape optimization results are expressed in terms of shape variation and eccentricity distribution. As shown in Figure 9, left, the starting shell is mostly non R-Funicular, being the eccentricity extrema larger than e_{adm} and the value of the objective function $f_{obj} = 1.28$.

The image in the centre of Figure 9 shows the results obtained by means of the first shape optimization, where only 4 variables were updated to modify the control net and, consequently, the shell's shape. The optimization variables, starting from $c_{o1} = c_{o2} = c_{o3} = c_{o4} = 1$, turn $c_1 = 0.1, c_2 = 0.16, c_3 = 0.24, c_4 = 0.12$ after optimization. A notable improvement of the shell funicular behaviour has been obtained, especially in the central areas of the shell, also proved by the objective function that reaches the value $f_{obj} = 0.42$.

The right image (Fig. 9) shows the results obtained by performing the shape optimization after knots insertion. Also in this case, the starting variables have been fixed to 1, the parameters after shape optimization are:

$c_1 = 0.59, c_2 = 0.53\ c_3 = 0.39\ c_4 = 0.57, c_5 = 0.49, c_6 = 0.33, c_7 = 0.91, c_8 = 0.76, c_9 = 0.47.$

It can be observed that the increased local control and thus the major number of optimization parameters obtained by knot insertion allowed to obtain a shell mostly R-Funicular. The objective function, starting from 1.28, reduces to 0.32.

According to R-Funicularity, a good shell has been obtained in both examples. Nevertheless, by comparing the shapes and the eccentricity distribution, it can be stated that enriching the initial geometry description by means of IG refinement allowed for a better shape adjustment, also confirmed by the initial and the final f_{obj} in the two proposed cases. The objective function, in fact, providing the root mean square of the eccentricity angles (Fig. 2), gives a summary measure of how much the shell behaviour differs from the R-Funicular one, which is immediately evident by comparing the values assumed by f_{obj} before and after the optimization with $\mathrm{atan}(e_{adm}) = 0.165$.

In the light of above, we believe that this approach could be useful when the accuracy of the shape local control should be modulated according to design and computational demands. Further studies about this approach could be devoted to observing the objective function trend as the number of optimization variables increase, in order to state whether if there is a threshold number over which the function no longer decreases.

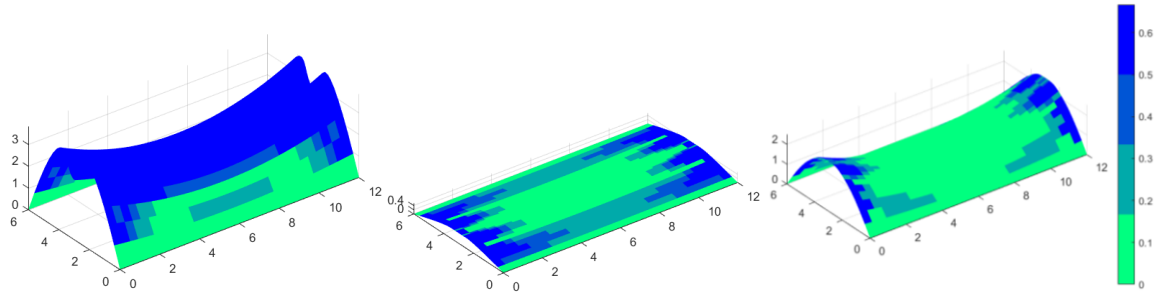


Figure 9. Shells' shape and eccentricity distribution. The colorbar represents the values of the $e_{M,i} = max\,(|e_{max,i}|, |e_{min,i}|)$ that increases going from green to blue, the latter meaning that the eccentricity falls out of the cross section. The shell is R-Funicular in the light green areas. Left: before optimization, $f_{obj} = 1.28$; centre: after optimization with 4 variables, $f_{obj} = 0.42$; right: after optimization with 9 variables, $f_{obj} = 0.32$.

References

[1] S. Adriaenssens, P. Block, D. Veenendaal and C. Williams (eds), *Shell Structures for Architecture: Form Finding and Optimization*, Routledge, 2014.

[2] S. Gabriele, V. Varano, G. Tomasello and D. Alfonsi, "R-Funicularity of form found shell structures", *Engineering Structures*, vol. 157, pp. 157-169, 2018.

[3] E. Ramm, K.-U. Bletzinger and R. Reitinger, "Shape optimization of shell structures", *Revue Européenne des Éléments Finis*, vol. 2(3), pp. 377-398, 1993.

[4] A. Tomás and P. Martí,"Shape and size optimization of concrete shells", *Engineering Structures*, vol. 32, pp. 1650 - 1658, 2010.

[5] E. Marino, L. Salvatori, M. Orlando and C. Borri, "Two shape parametrizations for structural optimization of triangular shells", *Computers & Structures*, vol. 166, pp. 1–10, 2016.

[6] S.I. Robles and N.F. Ortega, "Study of volumetric displacements of shells", *Journal of the International Association for Shell and Spatial Structures*, vol. 42(137), pp. 139-147, 2001.

[7] G. R. Argento, F. Marmo, V. Varano and S. Gabriele, "Shells' shape optimization based on R-Funicularity" in *Proceedings of the IASS Annual Symposium 2020/21 and the 7th International Conference on Spatial Structures – Inspiring the Next Generation*, Guildford, UK, 23 – 27 August 2021, S.A. Behnejad, G.A.R. Parke and O.A. Samavati (eds.), pp. 2548-2556, 2021.

[8] G. R. Argento, S. Gabriele and V. Varano, "Different uses of the generalized eccentricity for shells' shape optimization: a comparison" in *Proceedings of the IASS 2022 Symposium affiliated with APCS 2022 conference – Innovation, Sustainability and Legacy*, Beijing, China, September 19 – 22, 2022, Su-duo Xue, Jin-zhi Wu and Guo-jun Sun, Eds.

[9] G.R. Argento, S. Gabriele, F. Marmo and V. Varano, "Exploring the use of R-Funicularity in shells' shape optimization", *IWSS2020 – 1st Italian Workshop on Shell and Spatial Structures*, Web Meeting, 25 – 26 June 2020

[10] L. Piegl and W. Tiller, *The NURBS Book*, Springer Berlin, Heidelberg, 2012.

[11] K.-U. Bletzinger and E. Ramm, "Form finding of shells by structural optimization", *Engineering with Computers*, 1993

[12] A. P. Nagy, S. T. IJsselmuiden and M. M. Abdalla, Isogeometric design of anisotropic shells: Optimal form and material distribution, *Comput. Methods Appl. Mech. Engrg*., vol. 264, pp. 145-162, 2013.

IASS 2023 July 10–14 Melbourne Integration of Design and Fabrication

Proceedings of the IASS Annual Symposium 2023
Integration of Design and Fabrication
10–14 July 2023, Melbourne, Australia
Y.M. Xie, J. Burry, T.U. Lee and J. Ma (eds.)

Leaned brick shells with Mexican quoins and steel edges

Juan Gerardo OLIVA[*], Marcos Javier ONTIVEROS[a]

[a,*] Universidad Nacional Autónoma de México, Faculty of Architecture, Lightweight Structures Laboratory
jgos@unam.mx

Abstract

The Lightweight Structures Laboratory – LSL constructed the experimental pavilion PabUNAM at the Faculty of Architecture in the Universidad Nacional Autónoma de México – UNAM. The LSL Research Group aims to demonstrate that bricks are still in force for conceiving, designing, and constructing continuous shells with a complex geometry, which shape may vary beyond the traditional geometric forms. The Mexican Technique, "leaned bricks," is practiced in many areas of central Mexico to construct shells and was applied to build this pavilion. The so-called quoins *("cuñas"* in Spanish) are the most used burnt bricks, with 20 X 10 X 5 cm dimensions. No falsework is necessary. Oliva et al [1 and 2]. The designers used the parametric program Rhino Vault_2 developed by the Block Research Group. Besides bricks, steel profiles fix all shell edges. The LSL Research Group constructed the pavilion on top of a layer of volcanic stones in the main yard of the Faculty of Architecture and developed a foundation system consisting of five curved horizontal steel supports with variable curvature and length. There are four openings surrounding the pavilion and another one inside. These openings are arches with uneven curvature. Building these arches with steel profiles was one of the challenges to overcome during the design process. One professional vault worker ("*bovedero"* in Spanish) and eight Architecture and Civil Engineering students constructed the pavilion in 4 weeks.

Keywords: continuous shells, complex geometry, form-finding, burnt bricks, sustainability

1. Introduction

Research groups at various universities worldwide develop proposals to build continuous roof shells. In addition, these groups are developing new modeling, optimization, and construction methods to improve the design and construction process and reduce the carbon footprint. Among these groups, the universities of Stuttgart in Germany, the ETH of Switzerland, and the universities of Princeton and MIT in the USA stand out. The proposals developed can be grouped into two procedures. The first one explores the construction of continuous shells by discretizing the surface, in which the stereotomy of each piece is controlled. Examples of this trend are the shells of the research group headed by Jan Knippers (Vuga Vault) at the University of Stuttgart and the vaults led by Phillipe Block (Armadillo Vault) of the ETH research group. The second group explores the construction of continuous shells through a small module, as is the case of brick, which is assembled based on various courses. Alfonso Ramírez Ponce's vaults in Figure 1 are examples of these cases [3].

In this paper, the LSL Research Group proposes constructing complex geometries with burnt bricks manufactured in Mexico. Since more than 10.000 years ago, ancient constructions have been built with bricks in many regions worldwide. Burnt bricks are environment-friendly, recyclable, and fire-resistant. In central Mexico, many brick shells have been constructed in different locations applying the "leaning bricks vaults technique." Oliva et al. [1 and 4]. Using this technique, no falsework is required, and conventional materials such as reinforced concrete can be strongly diminished, which turns into an excellent opportunity for reducing the footprint of continuous roof shells.

Copyright © 2023 by Juan Gerardo OLIVA and Marcos Javier ONTIVEROS. Published in the Proceedings of the IASS Annual Symposium 2023 with permission.

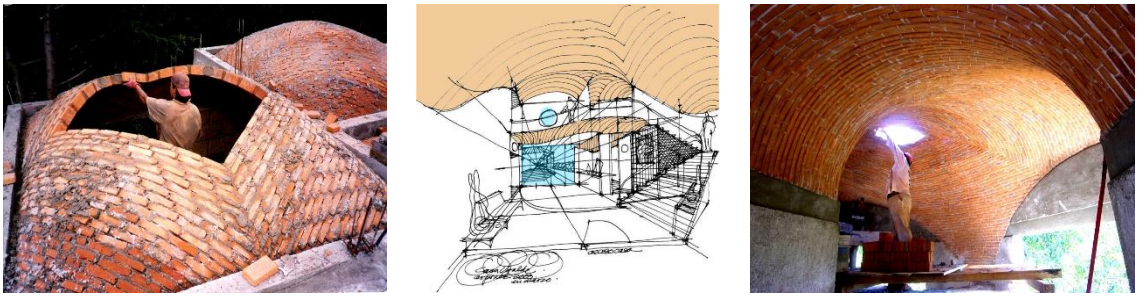


Figure 1: Alfonso Ramirez Ponce's shells: a) Mexican vault, b) Project sketch, c) Mexican house.

2. Project PabUNAM

The LSL Research Group designed and constructed the PabUNAM, See Fig. 2, A burnt brick pavilion focussed on demonstrating that today bricks are still in force to build continuous roof shells with conventional and nonconventional geometries.



Figure 2: The experimental pavilion PabUNAM

The PabUNAM is a leaned brick shell designed and constructed with Mexican quoins and steel edges. It was conceived and designed as an opened pavilion in the main yard of the Faculty of Architecture at the UNAM as a sporadic gathering place for the students and Professors. See Fig. 3. More than ten enthusiastic students and five Professors of the faculties of Architecture and Engineering were involved during the design and construction process.



Figure 3: Students building the experimental pavilion PabUNAM

The UNAM central campus was built from 1949 to 1952. In 2007, UNESCO declared it a World Heritage Site. Therefore, modifying or constructing any new building inside this area is forbidden. The UNAM permitted the LSL Research Group to build the PabUNAM on a volcanic stone floor, but they were warned to avoid sinking or damaging the stones. This experimental pavilion will be dismantled at the end of this year. The construction of this experimental prototype turned into an excellent opportunity for the students to learn the leaned brick technique. Nevertheless, it was necessary to hire the services

of a specialist brick-vault worker who oversaw the building process and whose skills and experience, combined with the researchers' theoretical knowledge, were essential to construct the pavilion successfully and adequately.

2.1. Form-finding process.

The LSL Research Group conceived a prototype of leaned brick with complex geometry. The shells combine synclastic and anticlastic curved surfaces. The aims were to explore their construction feasibility and offer new possibilities to architects and engineers for designing vaults with continuous brick surfaces. A first proposal arose with the bachelor's thesis of the student Rodolfo Rodríguez Muñoz. His proposal was used to build a 1:5 scale model. The purpose of the model was to deliver guidelines and tips for the PabUNAM future construction process. The full-scale prototype would later be made with the Mexican quoins measuring 20 cm X 10 cm X 5 cm. This brick is the most used material to build vaults in central Mexico. An enthusiastic group of students manufactured ca. 7,000 small bricks on a 1:5 scale whose dimensions are 4 cm X 2 cm X 1 cm. Unfortunately, the budget available for the final prototype construction was scarce. Therefore, it was necessary to reduce the pavilion dimensions.



Figure 4: Students manufacturing the small quoins and building the PabUNAM model on a scale of 1:5: a) Brick manufacturing, b) Gide structure, c, and d) Model in progress.

The LSL Research Group determined the form of the shells with the digital tool RhinoVault2 developed by the Block Research Group – BRG, using the TNA algorithm to emulate a hanging Net mechanical behavior.

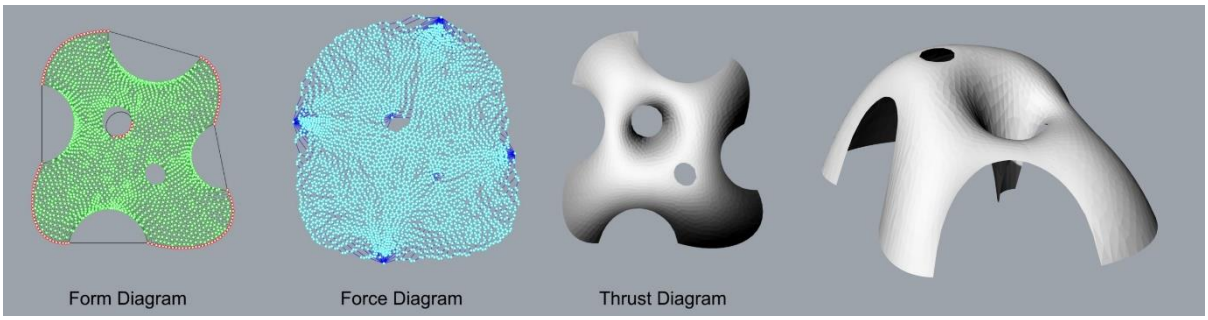


Figure 5: Applying RhinoVault2

The fundamental principle of design and execution of the leaned brick technique is that it must be built with concave curved courses in the shape of an arch, supported at its ends and on the previous lower layer, thereby making possible the absence of falsework.

Subsequently, the following practical conditions come out:

- It is built from the bottom up.

- The line of action of the gravity vector, located at the mass centroid of each brick, must intersect the support face of the previous course.
- It is built with small bricks (of low mass) that remain stable in their position even before the joint mortar has set.
- Straight courses with a convex curvature are unacceptable.

Considering these previous requirements, it was possible to determine the initial RhinoVault design parameters to fix the final shape of the PabUNAM.



Figure 6: PabUNAM model on a scale of 1:5

The LSL Research Group used a timber grid to control the shape of the vaults. This procedure helped the students to fix the small quoins in the correct position. However, some students were more sensible than others in adequately improving the quoins' location. Often, it was necessary to dismantle some brick courses of the surface and reconstruct it again. Finally, the model was completed; however, several uneven parts arose on the continuous surface of the vaults.

The model construction delivered the following teaching:

- The proper continuous curved surface depends on the vault worker's skills. Therefore, hiring an experienced worker to build leaned brick vaults was indispensable.

- Traditional methods like active-bending tubes or timber grids to control the complex geometry are insufficient. For example, a grid with timber panels inside the vaults would disturb the building process of the brick-vault worker. Therefore, developing and applying other, more efficient control methods and techniques was essential.

To overcome the first issue, the vault worker Ignacio Dorantes Gómez, called "Nachín," was hired to construct the PabUNAM. Nachín lives and works in the Hidalgo State, 300 km from Mexico City. The building process lasted four weeks, and several students helped without any break, except for the weekends. There was an exciting and fruitful collaboration between Nachín and the LSL Research Group.

On the other side, to control the complex geometry in the second issue, the five steel edges on the borders of the vaults and the four steel edges on the floor turned into the best guides. Some temporary timber panels and PVC tubes also helped Nachín control the curvature of the proper vaults. In addition, the augmented reality digital tool "Fologram" allowed the vault workers and supervisors to review frequently the vault's curvature. Just twice it was necessary to dismantle a few brick courses and reconstruct them again to improve the proper shape.

2.2. Steel edges

As described, each brick course in a leaned brick vault must be supported at its ends, usually with reinforced concrete elements. The PabUNAM's support elements are steel edges manufactured with 76.2 mm X 4.8 mm plates. The volcanic stones on the yard surface were used as fundament, where four curved profiles were fixed with 9.5 mm high-strength steel rods stuck 12 cm between the joints of the stones.

The four entrances to the vault and the opening in the central support are arches that do not lie on a plane, and that turn around in space. Therefore, the four steel edges were manufactured, joining two flat screed bars with diagonal plates to fix and control the variable angle between the bars. To fulfill the form of this complex geometry, the designers delivered the blacksmith the printed cutting patterns on a scale of 1:1. This procedure was a great help at the workshop. Besides, during the erection process of these arches, a topographic team overviewed the proper geometry continuously.

Besides guides, these arches supported the dead weight of the first vault segments before they were all joined at the upper parts of the vaults. To fix the final position of all arches, they were propped up with 3.8 mm PTR poles, which were removed at the end of the building process.



Figure 7: Steel arches at the four entrances and the central support.

The form-finding process emulating funicular nets required several optimization steps modifying the location and the curvature parameters of the supports, tessellations, and nets density, as well as the high proportions or the vertical deformation vector. The aim was to validate all technical, economic, and manufacturing possibilities. A particular case was how to control the geometry of the arches at the openings, which should be manufactured with traditional standard methods. RhinoVault was a beneficial tool for finding the equilibrium between the funicular form and opening arches. The directrix of the edge arches was obtained from the final network. This directrix was the intersection axis of the steel edges.



Figure 8: Geometric control whit Fologram, mixed reality viewer device

3. Conclusion

The LSL Research Group presented in this paper the entire design and construction process of the experimental pavilion PabUNAM. This pavilion was built applying the Mexican leaned quoins technique. The aim was to demonstrate that bricks are still in force today to make continuous roof shells with complex geometries and that using this technique helps reduce the carbon footprint.

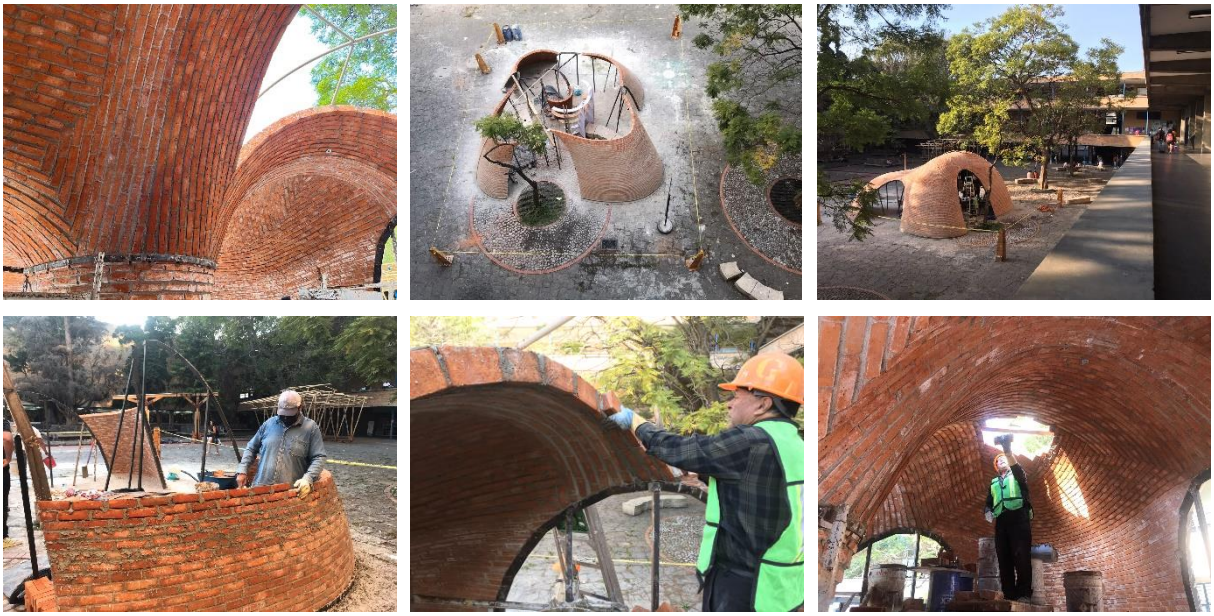


Figure 9: Construction process of the experimental pavilion PabUNAM.

Acknowledgments

The authors would like to thank the collaboration of Alfonso Ramírez Ponce, Ramón Abud Ramírez, Susana Ezeta Genis, Carlos Zetina Gargollo, Alejandro Gómez Aguirre – AXIAL, Alejandro Marambio Castillo – LATE, Rodrigo Schiordia López and all the students who helped to design and construct the experimental pavilion PabUNAM. The Faculty of Architecture-UNAM and the General Issues Department for Academic Personnel DGAPA-UNAM sponsored this research project through the Program PAPIIT IG 400620.

References

[1] J.G. Oliva, S. Ezeta, R. Abud, R. Rodríguez and M. Cruz “Brick vaults for rural housing in Mexico,” *in Innovation-Sustainability-Legacy: Proceedings of the IASS Annual Symposium 2022 affiliated with APCS 2022 Conference*, Beijing, China, September 19-22, 2022,

[2] J.G. Oliva, M. Trujillo, H. Guerrero (2019) "Sustainable lightweight structures constructed with bamboo, paperboard, bricks, nylon and textile membrane with jute fibers," *International Symposium IASS 2019 and Structural Membranes 2019*, Barcelona, Spain. 2019, C. Lázaro, K. U. Bletzinger and E. Oñate, Eds.

[3] A. Ramírez (2014), “Curvas de suspiro y barro,” *in Tecnología: Una contribución sistémica de acción reflexión y análisis*, Facultad de Arquitectura, Universidad Nacional Autónoma de México, Mexico. 2014

[4] J.G. Oliva, M. Trujillo, A. Ramírez, A. Hernández, and M.J. Ontiveros. "Sustainable materials applicable to the construction of housing for vulnerable groups.” *Proceedings of the International Association for Shell and Spatial Structures (IASS) Symposium*, Hamburg, 2017

Numerical methods for geometry, form-finding and optimisation of lightweight structures

---

Active bending
Additive manufacturing/ 3D printing
Architectural geometry
Bamboo for sustainable construction and quality of life improvement
Bio-inspired structures and architecture
Bridge structures
Computational form-finding
Conceptual design
Concrete structures
Construction techniques
Deployable and inflatable structures
Design competition (WG21)
Digital modelling and fabrication
Dynamic response of metal spatial structures
Dynamic response of other structures
Form-finding and structural optimisation of interlocking discrete assemblages
Graphical methods
Gridshell and lattice structures
Historical concrete shells
Historical structures
Lattice structures
Life-cycle design and assessment of structures
Metal gridshell structures, connections and stability
Methods and construction technologies for sustainable shell structures
Morphology and configuration processing
Next generation parametric design
Novel methods in modelling, optimisation and construction for reducing carbon footprint of continuous roof shells
► **Numerical methods for geometry, form-finding and optimisation of lightweight structures**
Optimisation methods and applications
Origami
Other
Teaching design uncertainty: working with unknown qualities/quantities of new and re-claimed materials
Teaching of shell and spatial structures
Tensegrity systems and cable structures
Tension and membrane structures
Tension structures in the Asia-Pacific
Timber and bio-based structures
Topology optimisation
Traditional masonry structures and innovation
Transformable structures

IASS 2023
July 10–14 Melbourne
Integration of Design and Fabrication

Proceedings of the IASS Annual Symposium 2023
Integration of Design and Fabrication
10–14 July 2023, Melbourne, Australia
Y.M. Xie, J. Burry, T.U. Lee and J. Ma (eds.)

A novel generatively designed and additively fabricated ankle-foot orthosis

Ryan BLAKIS[a,*], Peter DABNICHKI[b], Mladenko KAJTAZ[a]

[a,*] Centre for Additive Manufacturing, School of Engineering, RMIT University, Melbourne, Australia
P.O. Box 71, Bundoora, VIC 3083, Melbourne, Australia
ryan.blakis@student.rmit.edu.au

[b] School of Engineering, RMIT University, Bundoora, Australia

Abstract

An ankle-foot orthosis (AFO) is an external mechanical device that is prescribed to patients that require assistance to control or support their ankle-foot complex. Traditionally, AFOs are designed and fabricated manually using resource-intensive methods that may restrict design outcomes. Additive manufacturing (AM) presents an exciting opportunity to radically streamline and improve AFO design by enabling fabrication of more complex designs. However, despite the ability to produce optimised topology with AM, traditional designs are often retained, missing out on the numerous benefits of AM. Although desired, the expanded design freedom of AM presents a new challenge to AFO designers, who have only been educated to develop solutions within the scope of the traditional manufacturing method using basic design tools. Instead of few design parameters to adjust, the potential design choices are now infinite. Therefore, although AM can produce an optimised topology, there is a lack of knowledge of its application in this context. This paper features a design methodology that leverages generative design and shape optimisation to produce an AFO with reduced mass whilst maintaining the fundamental mechanical behaviour of the traditionally fabricated device. The enabler driving the iterations of digital design is a high-fidelity computational model within the commercial finite element package – Abaqus, which facilitated improved representations of loading and boundary conditions and a comprehensive material model. The final outcome of this study was an optimised digital AFO design that is 30% lighter and suitable for fabrication with HP multi-jet fusion (MJF).

Keywords: generative design, additive manufacturing, ankle-foot orthosis, finite element analysis, multi-jet fusion

1. Introduction

An ankle-foot orthosis (AFO) is an external mechanical device that is prescribed to both children and adults that require assistance to control or support their ankle-foot complex [1]. AFOs aim to improve dysfunctional gait patterns typically caused by neuromuscular disorders [2], by mechanically providing passive support at the patient's ankle-foot complex to improve stability and ambulation [3-5]. Traditionally, bespoke passive AFOs are designed and fabricated manually, with manufacture utilising a vacuum thermoforming method whereby a sheet of heated thermoplastic, typically polypropylene, is shaped by draping it over a plaster mould [6]. To achieve a patient specific fit and necessary therapeutic correction, the mould is derived from a patient plaster cast, which is taken and modified prior to draping by a clinician. The mechanical performance and therapeutic corrections are controlled by the material, AFO thickness, the trimline that describes the anatomy coverage of the shell, and the geometry of the patient's morphology [7].

Due to manufacturing constraints, clinicians are required to select and modify the most suitable AFO design from a range of templates, characterised by their mechanical properties. Solid AFOs (SAFO) are

Copyright © 2023 by Ryan BLAKIS, Peter DABNICHKI and Mladenko KAJTAZ. Published in the Proceedings of the IASS Annual Symposium 2023 with permission.

a type of AFO that aim to block movement throughout gait in all three anatomical planes of motion. A considerable challenge for this design is limiting dorsiflexion movement at the ankle during the second rocker of gait to a maximum of 2-3°. This requires a high level of stiffness around the ankle joint in the sagittal plane, known as the ankle stiffness. This is characterised by the AFO angle-moment relationship reported in Newton-meters per degree of ankle rotation (Nm/°) [8]. The clinician aims to achieve a desired level of ankle stiffness through the AFO design parameters that are within their control, which are the material thickness and trimline.

A continual challenge for clinicians is reliably predicting the ankle stiffness of an AFO design prior to manufacture [9]. Prediction is impossible with classical methods or handbook formulae due to the complexities related to the material properties, geometries, and loading & boundary conditions [10]. To address this, the research community has made numerous attempts to develop methods for objective AFO ankle stiffness prediction prior to manufacture with computational techniques like finite element analysis (FEA), and evaluation post manufacture via bench-testing with custom fixtures or functional analysis [11]. Despite its importance, the ankle stiffness of bespoke AFOs are rarely predicted or measured outside of research studies. This appears to be due to the lack of in-clinic characterisation equipment, and the inability to precisely manufacture designs with desired mechanical properties. This is because the traditional manufacturing method, although a straightforward process, is difficult to control. The most considerable challenge is shell thinning, whereby the initial constant material thickness of the shell reduces unpredictably during the draping process. This is observed predominately around the ankle region, which is the area having the greatest influence over ankle stiffness. This issue is compounded further by the manual marking and cutting of the trimline, which often relies on good judgement by the clinician and tends to be subject to human error.

Despite the majority of orthotic & prosthetic clinics still employing the traditional manufacturing method, a transition to alternative design and manufacturing methods have been explored for some time now [12]. Of particular interest is additive manufacturing (AM). AM is attractive because it significantly eases design constraints by enabling the manufacture of more complex geometry whilst eliminating manual workflows that both limit design outcomes and prohibit manufacturing consistency. Crucially, it can ensure the desired shape and functional characteristics established in design are realised with consistency [13]. For more than a decade, researchers have increasingly investigated AM produced AFOs, with feasibility studies determining that AM AFOs can have at least equivalent performance to their traditionally manufactured counterparts [2, 14, 15]. Whilst AM is beginning to be successfully implemented by some clinics, both research and commercial outputs do not appear to have fully exploited the extended capabilities that are available to the designer. Instead of innovative designs, those reflective of traditional designs with slightly modified topology have instead been produced with AM. The expanded design freedom creates and demands more design decision, which present a new challenge to clinicians. With AM, instead of only selecting the constant material thickness and the trimline, the potential design choices are infinite. Therefore, although additive manufacturing can produce optimised topology, there is a lack of design tools and knowledge for application of AM in this context.

To address this gap, we propose a novel design method for the generation of an AFO design with optimised topology for AM, without compromising the fundamental mechanical behaviour of a benchmarked traditional device. This paper describes the developed method, which utilises generative design to inform the optimal placement and distribution of material for a parametric design that is subsequently refined with shape optimisation to achieve the desired behaviour. This is illustrated using a case-study, to produce a patient-specific lightweighted SAFO that was optimised for fabrication via HP multi-jet fusion (MJF) polyamide-11 (PA11).

2. Method

The design method proposed in this research was developed on two key ideas: (i) leveraging generative design to inspire novel topology potentially inconceivable by a designer in isolation, and (ii) utilising shape optimisation coupled with high-fidelity prediction models to achieved desired mechanical behaviour. The developed method includes the following three distinct steps: traditional design for benchmarking only, generative design, and shape optimisation. These are visually presented with key sub-steps in Figure 1.

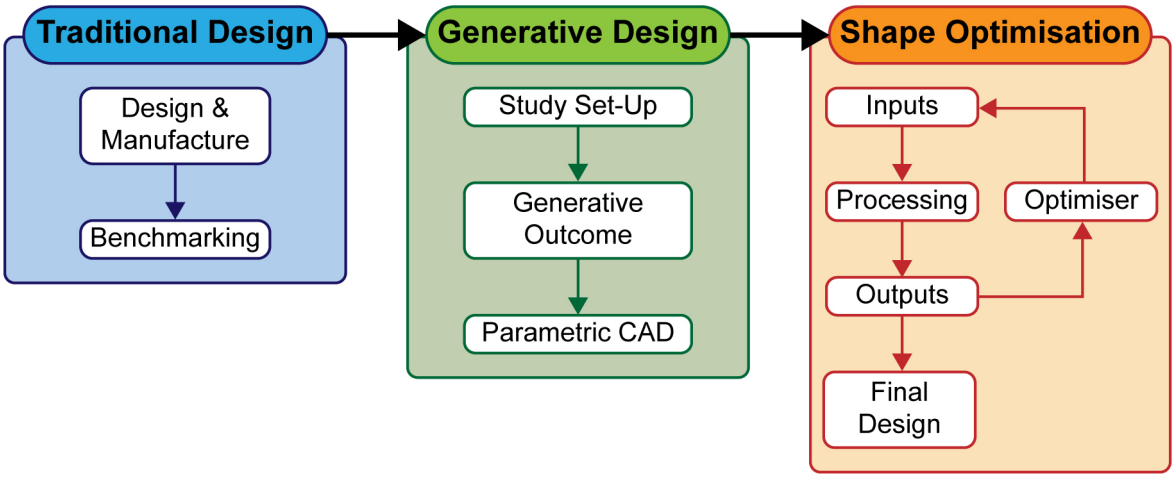


Figure 1. Flowchart representing the key steps and sub-steps of the proposed design method.

2.1. Traditional design

Clinical experts were consulted to design and manufacture a patient specific traditional AFO. The manufactured AFO was used to benchmark physical and mechanical properties. Physical measurements were taken to obtain its mass, average thickness, and trimline details. Computer aided design (CAD) was used to generate the AFO geometry for computational evaluation in FEA. The FEA prediction model was developed to characterise the mechanical behaviour of interest during the defined phase of gait.

2.2. Generative design

Generative design was employed to produce novel optimised topology. Although similar to topology optimisation, used to generate a single lightweight design from a defined design space, generative design is a design exploration process whereby a number of potential optimal designs are generated in an evolutionary way from a set of system requirements [16]. A generative design study was established with the necessary components and key sub-components outlined in Figure 2.(a). The generative study was conducted in an iterative manner, whereby study parameters were modified until a satisfactory outcome was generated. The final generative outcome (Figure 2.(b)) was used to create a parametric design to be refined via shape optimisation (Figure 3).

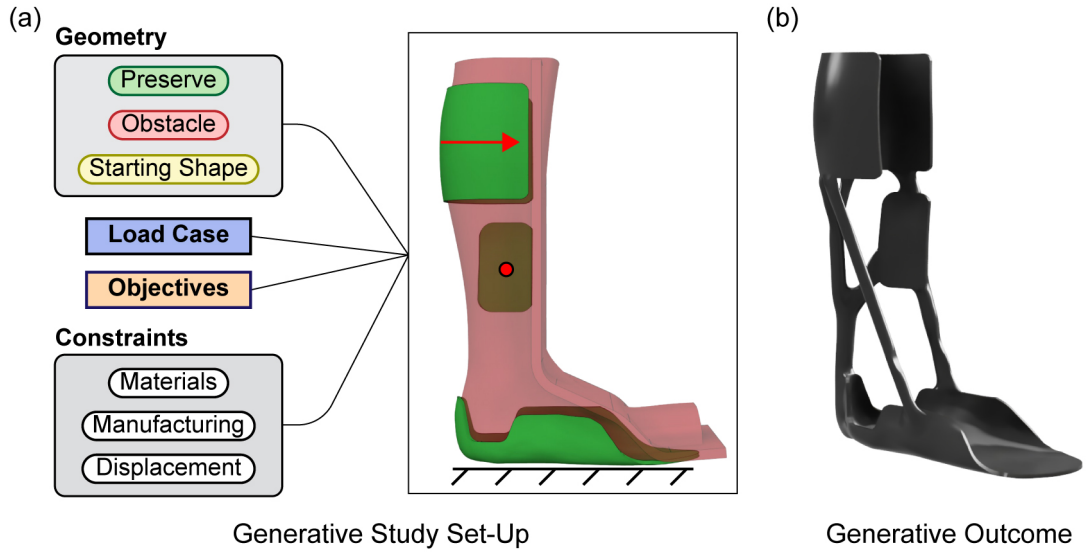


Figure 2. Generative study: (a) generative study set-up with key sub-steps, (b) final generative outcome.

2.3. Shape optimisation

Shape optimisation was conducted on the parametric design based on the generative outcome. This leveraged high fidelity computational FEA models to evaluate the performance of different parameter combinations to meet the constraints and objectives by coupling the FEA evaluation model with an optimisation engine. The applied design search method featured three distinct sections which are common in a typical optimisation problem: input, processing, and constraints & objectives. The inputs consisted of constant and variable parameters that were associated with the parametric design. The processing section consisted of two distinctive parts which were differentiated by their functionality. These were geometry creation (employing CAD) and design evaluation (employing FEA). The results were then assessed for feasibility by the constraints and ranked by the objectives. The optimiser then generated a new set of values for the variable input parameters and repeated the process for the set number of iterations. The workflow can be seen in Figure 3.

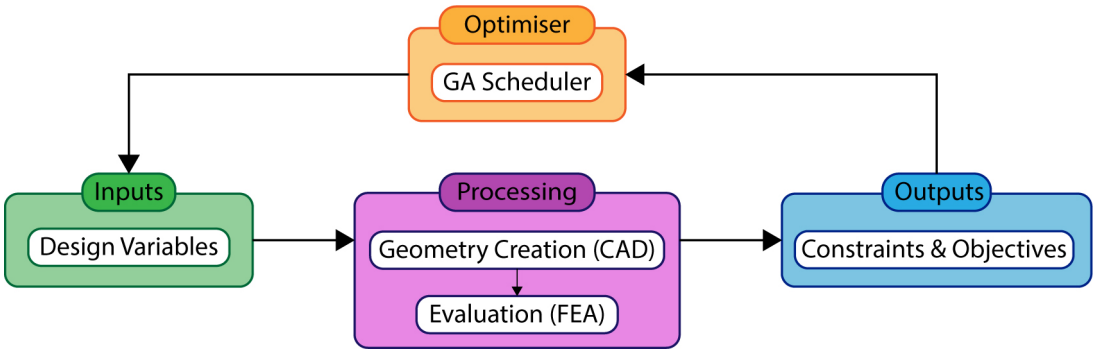


Figure 3. Shape optimisation flowchart with key sub-steps.

3. Traditional design

In collaboration with clinical experts, a traditional SAFO was designed and manufactured for a healthy male patient with the aim of achieving sufficient rigidity at the ankle in the sagittal plane to limit dorsiflexion during the second rocker to 2-3°. Despite the adult patient in this study being non-pathological, a slight foot valgus (rolling in of the foot) was observed and corrected during casting. The SAFO was made from a sheet of 6mm thick polypropylene, with a conservative trimline described as beginning approximately 2cm below the fibula head, passing slightly anterior to the tip of the malleoli,

and leaving the sides of the toes and head of the metatarsus completely clear. Representations of these design parameters can be seen in Figure 4.(a).

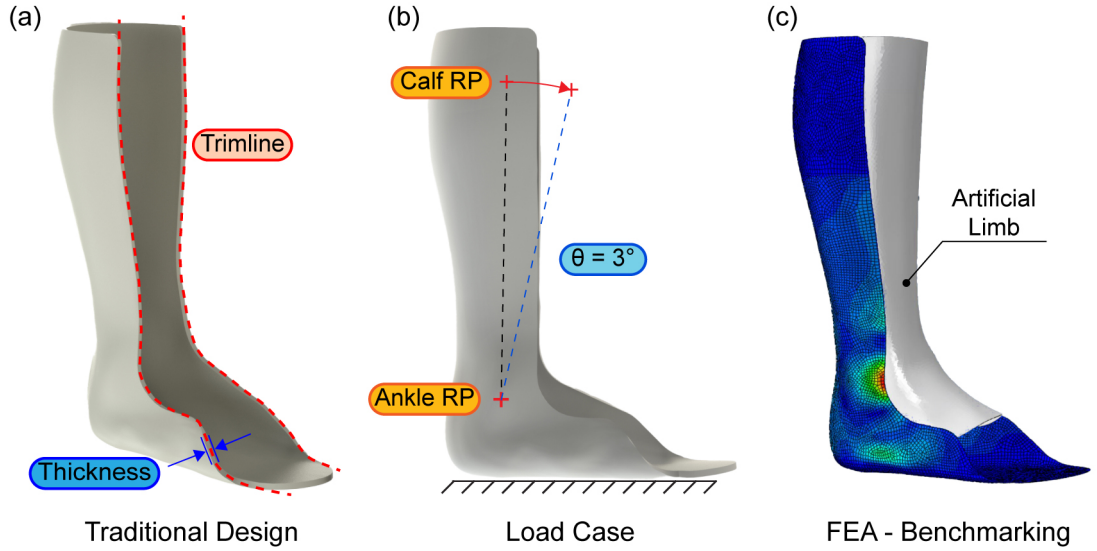


Figure 4. Traditional design: (a) traditional AFO with design parameters, (b) second rocker FEA load case, (c) FEA benchmarking of traditional AFO design.

3.1. Benchmarking

The final fabricated SAFO had a mass of 491g without straps. Finite element analysis was used to characterise the ankle stiffness using a load case reflective of the second rocker during gait adapted from Lelapi et al. (2019) [13] and Schrank et al. (2013) [17]. The static analysis was conducted using the commercial FEA software ABAQUS CAE from Dassault Systemes [18]. The geometry of the traditional SAFO was generated as a surface externally using the commercial CAD software SolidWorks, also from Dassault Systemes [19], using a method inspired by Dal Maso & Cosmi (2019) [1]. In the evaluation model, the SAFO geometry was modelled as a 3D deformable shell. The material properties for polypropylene were obtained from the literature [20], and defined as linear, elastic and isotropic, with a Young's Modulus of 1000MPa and Poisson's Ratio as 0.35. The constant thickness of 4.8mm was obtained by measuring along the trimline of the physical SAFO in the ankle region and averaging the values. A static general load step was created, and nonlinear geometry (nlgeom) enabled. The load case as seen in Figure 4.(b) fixed the underside of the foot plate in all 6 degrees of freedom (DOF) with an appropriate boundary condition, whilst rotation about the virtual ankle joint was enforced at the calf reference point. This reference point was connected to the ankle reference point via a revolute connector. The calf reference point was linked to a partitioned section of the internal surface of the SAFO that represented the calf cuff by a kinematic coupling. In this study, additional geometry representing a partial artificial limb was modelled as a 3D discrete rigid shell to combat excessive buckling in the SAFO shell. This geometry was connected to the calf reference point via a rigid body constraint. Contact between the SAFO and limb was defined as frictionless. All geometry was meshed using the free meshing technique and quad-dominate element shape with shell elements S4R and S3. A mesh sensitivity study was conducted until the peak stress converged within 2%, resulting in an element seed size of 3mm. Two loading conditions were considered. The first applied a concentrated force of 100N in the negative Y-direction at the cuff reference point to induce rotation about the ankle axis so ankle stiffness could be calculated. The second applied an enforced rotation boundary condition to achieve 3° dorsiflexion, which was used to evaluate the maximum stress over the articulation expected during use. The stress distribution typical of the deformed traditional SAFO can be seen in Figure 4.(c).

4. Generative design

Generative design was employed to inspire novel topology that both varied from the traditional AFO design philosophy and was potentially inconceivable by a human designer. To perform this task, the generative design workbench within Fusion 360 from Autodesk [21] was employed.

4.1. Generative study set-up

4.1.1. Objectives

The objective was set to maximise stiffness whilst aiming for a target mass off 375g or less.

4.1.2. Geometry

Included as preserved geometry bodies (Figure 2.(a) green) were the calf cuff, the independent valgus correction patch, and the footplate which included valgus correction contacts. These bodies were excluded from the optimisation envelope but incorporated into the final shape of the design. The patient's limb and an additional body were defined as obstacle geometry bodies (Figure 2.(a) red) and represented spaces material could not be placed. Defining the leg as only obstacle geometry is insufficient as it leads to geometry that is not compatible with footwear or clothing.

4.1.3. Load case

The load case described in *3.1.* was modelled as closely as allowable within the Fusion 360 generative environment. A concentrated force of 100N was applied to the calf cuff to induce dorsiflexion rotation, whilst the underside of the footplate was fixed. To account for the resistance of the patient's limb on the valgus correction patch, a concentrated force was applied normal to its surface. The magnitude of this force was estimated to be substantially lower than that acting on the calf cuff. Thus, a magnitude of 25N (a quarter of the calf cuff force) was deemed to be sufficient. The load case can be seen in Figure 2.(a).

4.1.4 Constraints

PA11 – Nylon-HP 11-30 was selected as the study material from the in-built material library, and the manufacturing method was set to unrestricted, placing no manufacturing constraints on the generative solver. A local displacement limit of 6mm was placed on the calf cuff in the direction of its applied force and 3mm on the valgus correction patch in the direction of its assigned force. These limits were enforced to provide bounds of acceptable displacement for the desired rigidity.

4.2. Generative outcome

The resulting topology was an organic scaffold that in retrospect was quite intuitive, visible in Figure 2.(b). Due to the directness of the scaffold paths between preserve geometries, the structure is less conformal with the patient anatomy than the traditional shell design. This outcome revealed several large areas of the traditional shell design from where material could be removed, and areas where additional material would add value.

4.3. Parametric CAD model

The generative outcome was translated into a parametric design with a conformal surface that was scaffold like. The conformal surface was partitioned into the following regions: cuff, valgus correction patch, footplate, and lateral and medial halves. The geometry and thickness of the cuff, valgus correction patch, and footplate remained the same as the geometry used in the generative studies. For the rest of the model, parametric sketches driven by input parameters were used to produce trimming surfaces to remove sections of the surface to approximate the material distribution as suggested by the generative outcome. The medial sketch had a total of five modifiable parameters whilst the lateral sketches had six. The shape of the lateral sketch outlines can be seen in Figure 5.(b), with grey surfaces representing original geometry, and yellow and blue surfaces those for shape optimisation.

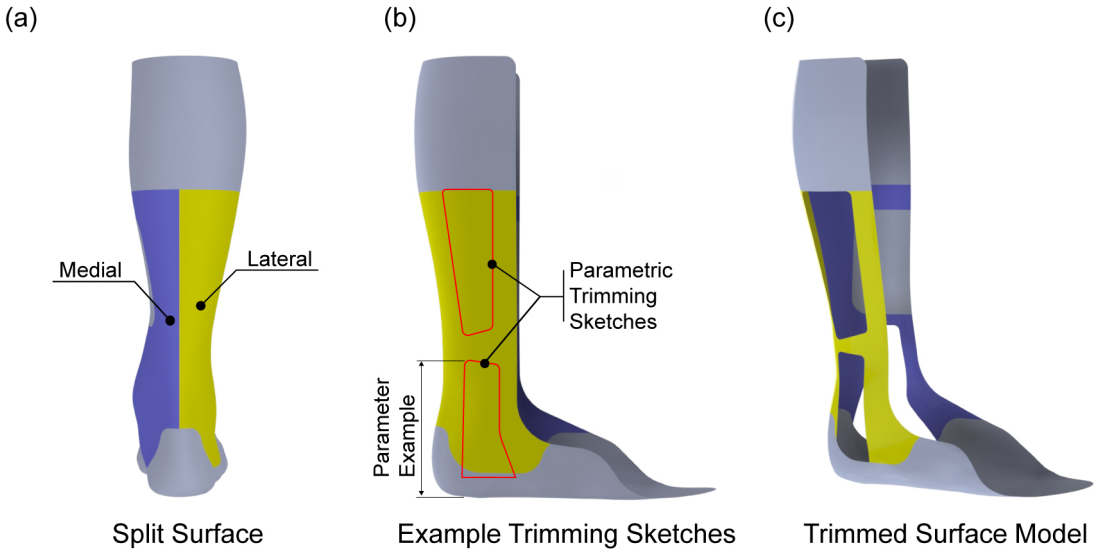


Figure 5. Parametric design: (a) rear view of parametric surface model, (b) examples of lateral trimming sketches, (c) trimmed parametric AFO design.

5. Shape optimisation

Shape optimisation, as outlined in *2.3.*, was performed on the parametric design to achieve the desired mechanical properties of the SAFO. Shape optimisation was conducted in the commercial optimisation software package modeFRONTIER provided by ESTECO [22]. Implementation in modeFRONTIER can be seen in Figure 6.

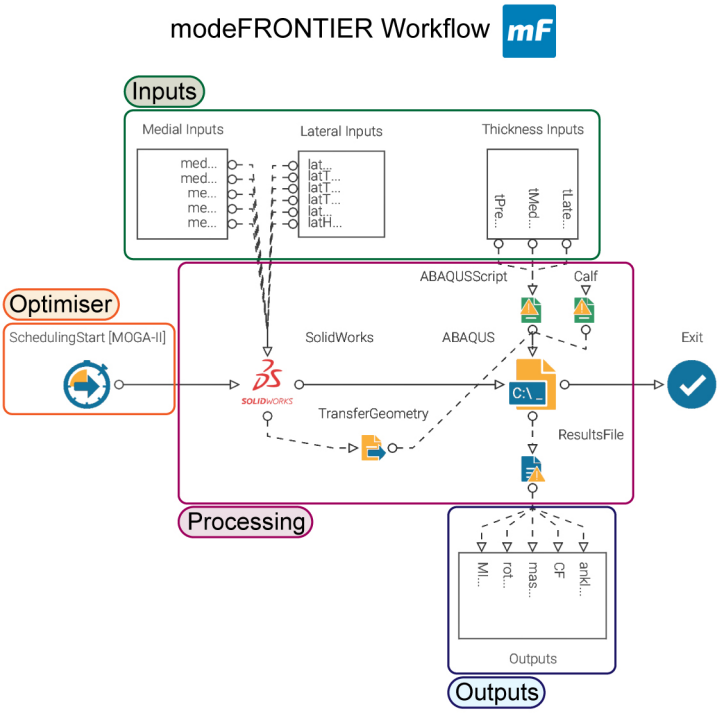


Figure 6. Implementation of shape optimisation in modeFRONTIER with key sub-systems outlined.

5.1. Input parameters

The parametric design used in this study had 14 parameters, 13 of which were variables. The variable parameters were defined as discrete and continuous, with a range (lower and upper value) and step size defined for each parameter. Table 1. presents three example input parameters and their respective properties.

Table 1. Example input parameters for shape optimisation.

Name	Association	Type	Lower (mm)	Upper (mm)	Step Size (mm)
medTrimline1	Medial	Discrete ordered	10	40	1
tMedialGeo	Thickness	Discrete ordered	5	12	0.5
tPreserveGeo	Thickness	Constant	3	3	-

5.2. Processing

The SolidWorks node was used in modeFRONTIER with the parametric design embedded within. The design input parameters were linked to the equations in the part file which directly modified trimming sketch parameters. Once the design was updated, the surface model was exported as a STEP file and transferred to the FEA environment.

A Python script was developed to automatically generate and run the FEA model described in *3.1.* to characterise the ankle stiffness and evaluate the stress-strain response. The script allowed the input parameters to make appropriate model modifications such as shell thicknesses. The material was modelled with the ABAQUS native elastic-plastic combined hardening (EPC) model as reported by Kajtaz & Lee [23]. The Python script was also used to analyse and report the FEA results.

5.3. Constraints & objectives

Three constraints and two objectives were defined to evaluate design feasibility and rank performance of feasible outcomes. The first constraint was the average ankle stiffness, which had a target value of 14Nm/° and a tolerance of ±0.5Nm/°. The second constraint was the upper limit of the mass of the SAFO, which was 375g and calculated directly using the volume of a design concept and the material density of HP-MJF PA11. The third constraint was the upper limit of the peak mises stress, which was defined as 30MPa. The limiting stress was based on the stress-strain response of HP-MJF PA11, which becomes substantially nonlinear beyond this magnitude. The first objective was mass minimisation, and the second objective was peak stress minimisation.

5.4. Optimisation scheduler

The defined objectives in this study were conflicting, thus, a suitable optimiser was required that was capable of finding a compromise and producing a Pareto Front. In this study, the multi-objective genetic algorithm (MOGA-II) was employed due to the reported performance equivalence with well-tested evolutionary multi-objective methods such as NSGA-II [24] and its ability to handle the ankle stiffness constraint tolerance. The algorithm was set to self-initialising and 500 evaluations. After approximately 200 evaluations, the optimisation schedular was regularly producing parameter sets for feasible designs. Once this occurred, the majority of the designs populated a small area between 345 and 365g. This area is magnified and highlighted in the red box in Figure 7.a).

5.5. Final design

The selected optimal design was the lightest feasible solution on the Pareto Front. It was generated during shape optimisation on the 204th evaluation. With a mass of 345.5g, the selected design was 30%

lighter than the benchmarked device, which had a mass of 491g. A render of the final design is presented in Figure 7.b).

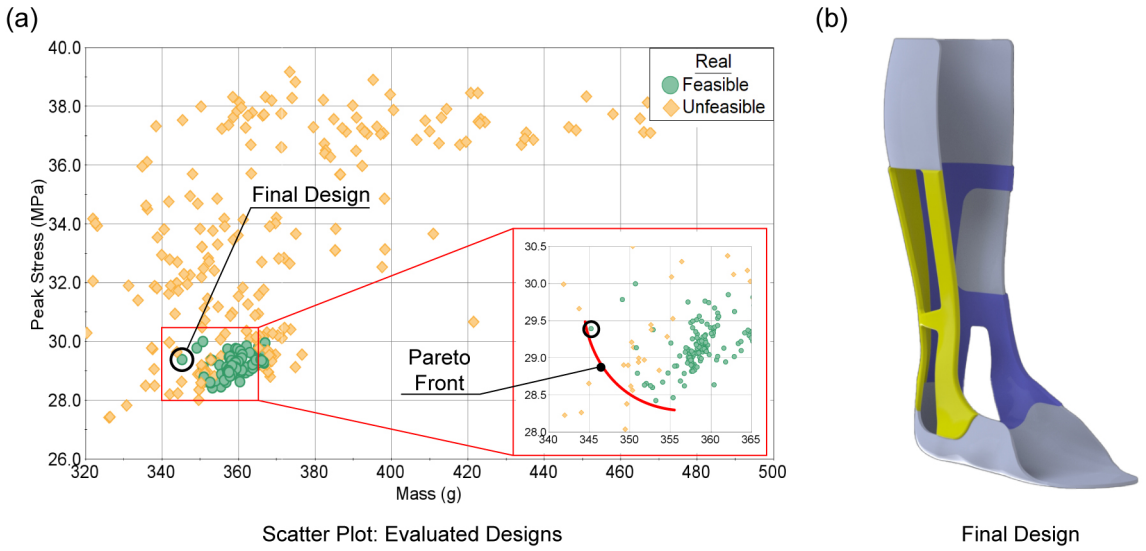


Figure 7. Shape optimisation outcomes: (a) scatter plot of peak stress and mass for evaluated designs, (b) final shape optimised AFO design render.

6. Conclusions

The design method proposed in this research leverages generative design and shape optimisation to produce novel AFO designs for additive manufacture with reduced mass whilst maintaining the fundamental mechanical behaviour of the traditionally fabricated device. The design method deploys two concepts: (i) leveraging generative design to inspire novel topology potentially inconceivable by a designer in isolation, and (ii) utilising shape optimisation coupled with high-fidelity prediction models to achieve desired mechanical behaviour. As demonstrated in this paper, the proposed method has capabilities to:

- yield an accurate and lightweight solution that satisfies the benchmarked mechanical performance requirement
- leverage generative design to provide patient and load-case specific insight into optimal material placement and distribution that may not be obvious to a designer in isolation
- speed up design refinement through automatic and intelligent shape optimisation

The proposed design method was successfully applied to a case study which demonstrated its effectiveness by generating a final design that was 30% lighter than the traditionally manufactured benchmarked device. This study is considered as a valuable starting point for further exploration of the benefits that can be obtained through the implementation of computational design tools for design of AFOs for additive manufacture.

Acknowledgements

The authors would like to acknowledge Rod Lawlor and Simon Lalor from the Royal Children's Hospital in Melbourne for providing the traditional SAFO used for benchmarking in this research.

References

[1] A. Dal Maso and F. Cosmi, "3D-printed ankle-foot orthosis: a design method," *Materials Today: Proceedings,* vol. 12, pp. 252-261, 2019, doi: 10.1016/j.matpr.2019.03.122.

[2] E. Wojciechowski *et al.*, "Feasibility of designing, manufacturing and delivering 3D printed ankle-foot orthoses: a systematic review," *J Foot Ankle Res,* vol. 12, p. 11, 2019, doi: 10.1186/s13047-019-0321-6.

[3] K. Pongpipatpaiboon *et al.*, "The impact of ankle–foot orthoses on toe clearance strategy in hemiparetic gait: a cross-sectional study," *Journal of NeuroEngineering and Rehabilitation,* vol. 15, no. 1, p. 41, 2018/05/23 2018, doi: 10.1186/s12984-018-0382-y.

[4] A. Shih, D. W. Park, Y.-Y. Yang, R. Chisena, and D. Wu, "Cloud-based Design and Additive Manufacturing of Custom Orthoses," *Procedia CIRP,* vol. 63, pp. 156-160, 2017, doi: 10.1016/j.procir.2017.03.355.

[5] C. Morris, R. Bowers, K. Ross, P. Stevens, and D. Phillips, "Orthotic management of cerebral palsy: recommendations from a consensus conference," *NeuroRehabilitation,* vol. 28, no. 1, pp. 37-46, 2011, doi: 10.3233/NRE-2011-0630.

[6] D. D. Zou *et al.*, "Experimental and computational analysis of composite ankle-foot orthosis," (in English), *Journal of Rehabilitation Research and Development,* vol. 51, no. 10, pp. 1525-1535, 2014 2014.

[7] G. Rogati, P. Caravaggi, and A. Leardini, "Design principles, manufacturing and evaluation techniques of custom dynamic ankle-foot orthoses: a review study," *Journal of Foot and Ankle Research,* vol. 15, no. 1, p. 38, 2022/05/19 2022, doi: 10.1186/s13047-022-00547-2.

[8] D. J. J. Bregman, A. Rozumalski, D. Koops, V. de Groot, M. Schwartz, and J. Harlaar, "A new method for evaluating ankle foot orthosis characteristics: BRUCE," *Gait & Posture,* vol. 30, no. 2, pp. 144-149, 2009/08/01/ 2009, doi: https://doi.org/10.1016/j.gaitpost.2009.05.012.

[9] D. Teixeira, J. Milho, M. S. Carvalho, and M. A. R. Loja, "Ankle Foot Orthosis (AFO) stiffness design for mitigation of ankle inversion injury," in *2019 IEEE 6th Portuguese Meeting on Bioengineering (ENBENG)*, 22-23 Feb. 2019 2019, pp. 1-4, doi: 10.1109/ENBENG.2019.8692490.

[10] D. Leone, S. Diemente, and M. Lopez-Isa, "Structural stability prediction for thermoplastic ankle-foot orthoses," ed: IEEE, 1991, pp. 231-232.

[11] T. P. Kobayashi, A. K. L. P. Leung, and S. W. P. Hutchins, "Techniques to measure rigidity of ankle-foot orthosis: A review," (in English), *Journal of Rehabilitation Research and Development,* vol. 48, no. 5, pp. 565-76, 2011.

[12] S. Telfer, J. Pallari, J. Munguia, K. Dalgarno, M. McGeough, and J. Woodburn, "Embracing additive manufacture: implications for foot and ankle orthosis design," *BMC Musculoskeletal Disorders,* vol. 13, no. 1, p. 84, 2012/05/29 2012, doi: 10.1186/1471-2474-13-84.

[13] A. Ielapi *et al.*, "A validated computational framework to evaluate the stiffness of 3D printed ankle foot orthoses," *Comput Methods Biomech Biomed Engin,* vol. 22, no. 8, pp. 880-887, Jun 2019, doi: 10.1080/10255842.2019.1601712.

[14] Z. Liu, P. Zhang, M. Yan, Y. M. Xie, and G. Z. Huang, "Additive manufacturing of specific ankle-foot orthoses for persons after stroke: A preliminary study based on gait analysis data," *Math Biosci Eng,* vol. 16, no. 6, pp. 8134-8143, Sep 9 2019, doi: 10.3934/mbe.2019410.

[15] V. Creylman, L. Muraru, J. Pallari, H. Vertommen, and L. Peeraer, "Gait assessment during the initial fitting of customized selective laser sintering ankle foot orthoses in subjects with drop foot," *Prosthet Orthot Int,* vol. 37, no. 2, pp. 132-8, Apr 2013, doi: 10.1177/0309364612451269.

[16] J. Pelovitz. "Generative Design Versus Topology Optimization." 3DHEALS. https://medium.com/healthcare-3d-printing-stories/generative-design-versus-topology-optimization-ed549dbf19b4 (accessed 23/02/2023, 2023).

[17] E. S. Schrank, L. Hitch, K. Wallace, R. Moore, and S. J. Stanhope, "Assessment of a Virtual Functional Prototyping Process for the Rapid Manufacture of Passive-Dynamic Ankle-Foot

Orthoses," *Journal of Biomechanical Engineering,* vol. 135, no. 10, 2013, doi: 10.1115/1.4024825.
[18] Dassault Systèmes Simulia Corp. (2021), "Abaqus (Version 2021)," ed: Dassault Systèmes.
[19] Dassault Systèmes SolidWorks Corp. (2021), "SolidWorks (Version 2020 - 2021)," ed: Dassault Systèmes,.
[20] S. Syngellakis, M. A. Arnold, and H. Rassoulian, "Assessment of the non-linear behaviour of plastic ankle foot orthoses by the finite element method," (in eng), *Proc Inst Mech Eng H,* vol. 214, no. 5, pp. 527-39, 2000, doi: 10.1243/0954411001535561.
[21] Autodesk Inc. (2023), "Fusion 360 (Version 2023)," ed: Autodesk Inc. .
[22] ESTECO SpA (2021), "modeFRONTIER (Version 2021)," ed: ESTECO SpA.
[23] M. L. Kajtaz, K.P.M., "Finite element modelling of additive-manufactured polyamide-11," presented at the In Proceedings of the 13th International Conference on the Mechanical Behaviour of Materials 2019, Melbourne, Australia, 2019.
[24] E. Rigoni and S. Poles, "NBI and MOGA-II, two complementary algorithms for Multi-Objective optimizations," 01/01 2005.

IASS 2023
July 10–14 Melbourne
Integration of Design and Fabrication

Proceedings of the IASS Annual Symposium 2023
Integration of Design and Fabrication
10–14 July 2023, Melbourne, Australia
Y.M. Xie, J. Burry, T.U. Lee and J. Ma (eds.)

An efficient shape optimisation algorithm for gridshells based on node shifting

Chao DING[a], Zhen WANG[a], Yang ZHAO[b,*], Huiping TANG[a], Yi Min XIE[c]

[*] Space Structures Research Centre, Zhejiang University, Hangzhou, 310058, China
ceyzhao@zju.edu.cn

[a] Advanced Materials Additive Manufacturing Innovation Research Centre, Hangzhou City University, Hangzhou, 310015, China
[b] School of Civil Engineering, Shaoxing University, Shaoxing, 312000, China
[c] Centre for Innovative Structures and Materials, School of Engineering, RMIT University, Melbourne, 3001, Australia

Abstract

In this paper, a novel and efficient shape optimisation algorithm for gridshells, especially for cantilevering structures, is proposed based on the evolutionary node shifting method, where the nodal positions are iteratively updated to minimise the structural compliance. The sensitivity numbers for both structural compliance and volume against nodal shifting are explicitly derived. The surface smoothness is significantly improved by the introduction of the distributed load filter scheme, where the negative sensitivity numbers are applied to each node as the fictitious external load to ensure both the smoothness of surfaces and the sustained reduction of structural compliance at each iteration. A much more stable and faster convergence is achieved compared to the conventional nodal shifting methods. The numerical example of a rectangular gridshell is presented to demonstrate the effectiveness and the efficiency of the proposed algorithm.

Keywords: gridshells, shape optimisation, node shifting, distributed load filter

1. Introduction

The widely application of free-form gridshells results in an increasing demand for robust and efficient shape design methodologies connecting architectural intent and mechanical performance. Early form-finding works mainly relied on the physical experiments [1,2] and their computational simulations [3–5]. Many form finding techniques have been developed for the last four decades, such as the force density method [6–8], the thrust network analysis method [9] and the dynamic equilibrium methods [10–12]. Although being successfully applied for decades, conventional form-finding methodologies and their extensions based on the physical experiments are limited to shape generation of structures in pure tension or compression, and would fail in the cases where bending moments cannot be eliminated such as cantilevering shells or the cases with the objectives not related to stress conditions such as the buckling capacity maximization problems. Therefore, the shape design for such structures should turn to more generalized shape optimisation approaches [13–17]. However, due to the strong nonlinearity and massive variables for shape optimisation problems, the optimisation algorithms often pay for a high computational cost and lead to jagged surfaces when applied in large span structures.

In this paper, a novel and efficient shape optimisation algorithm based on the evolutionary node shifting method is proposed for gridshells especially those with cantilevering parts. The nodal coordinates are chosen as the design variables and are iteratively updated to minimize the structural compliance under a volume constraint. In order to smooth the jagged surfaces caused by the non-smooth gradient fields, fictitious distributed forces based on the sensitivity analysis are applied as a filter scheme to construct

Copyright © 2023 by Chao DING, Zhen WANG, Yang ZHAO, Huiping TANG and Yi Min XIE. Published in the Proceedings of the IASS Annual Symposium 2023 with permission.

the configurations instead of the sensitivity numbers. The example of a cantilevering rectangular gridshell is presented to demonstrate the effectiveness and the efficiency of the proposed algorithm.

2. The evolutionary node shifting method

The evolutionary node shifting method is a recently developed non-parametric shape optimisation approach for grid structures, in which nodal positions are iteratively updated according to the sensitivity information of the objective functions based on the gradient method [17–20]. Due to the non-smooth gradient fields, it may fall into premature convergence with jagged surfaces when applied in large span structures, thus extra smoothing procedure is required for optimal solutions [21–23]. However, the smoothing procedure generally follows the geometry principles, which means nodal shifting determined by the smoothing filter is independent of mechanical properties and may be opposite to the physical objectives, therefore leading to an oscillation around the optimal solution, i.e. unstable convergence. Thousands of iterations are required for the final convergence, making the method quite time-consuming. This article aims to develop a more efficient and smoother shape updating scheme to alleviate the oscillated convergence.

2.1. Objective function and sensitivity analysis

This article mainly concerns the general shape optimisation problems of maximizing structural stiffness under the volume constraint, which is equivalent to minimise the structural compliance. It is noteworthy that the algorithm can also be extended for other objectives based on similar principles. The objective of compliance minimization can be formulated as

$$\text{Minimise} \quad C = \frac{1}{2}\boldsymbol{f}^{\mathrm{T}}\boldsymbol{u}(\boldsymbol{x},\boldsymbol{y},\boldsymbol{z}) \tag{1a}$$

$$\text{Subject to} \quad V \le V^{*} \tag{1b}$$

where C indicates the mean compliance. $\boldsymbol{F}$ is the external load vector, and $\boldsymbol{u}$ is the unknown nodal displacement vector which is related to structural shapes. $\boldsymbol{x}$, $\boldsymbol{y}$ and $\boldsymbol{z}$ represent the vectors of design variables, namely x-, y-, z-coordinates of the free nodes. V and V^{*} denote the actual and constraint volume of the structure respectively.

The sensitivity analysis can be carried out using the adjoint method [22], by which the differentiation of the objective function with respect to design variables is explicit derived as

$$\frac{\partial C}{\partial x_i} = -\frac{1}{2}\boldsymbol{u}^{\mathrm{T}}\frac{\partial \boldsymbol{K}}{\partial x_i}\boldsymbol{u}, \quad \frac{\partial C}{\partial y_i} = -\frac{1}{2}\boldsymbol{u}^{\mathrm{T}}\frac{\partial \boldsymbol{K}}{\partial y_i}\boldsymbol{u}, \quad \frac{\partial C}{\partial z_i} = -\frac{1}{2}\boldsymbol{u}^{\mathrm{T}}\frac{\partial \boldsymbol{K}}{\partial z_i}\boldsymbol{u} \tag{2}$$

where the subscript i represents the ith node. $\boldsymbol{K}$ represents the global stiffness matrix. Since the position of the ith node only affects the stiffness of the beam elements connected to it, the sensitivity number for node i can be discretized as the summation of all the related elements as

$$\boldsymbol{S}_i^{c} = \left\{\frac{\partial C}{\partial x_i}, \frac{\partial C}{\partial y_i}, \frac{\partial C}{\partial z_i}\right\} = \left\{-\sum_e \frac{1}{2}\boldsymbol{u}_e^{\mathrm{T}}\frac{\partial \boldsymbol{k}_e}{\partial x_i}\boldsymbol{u}_e, -\sum_e \frac{1}{2}\boldsymbol{u}_e^{\mathrm{T}}\frac{\partial \boldsymbol{k}_e}{\partial y_i}\boldsymbol{u}_e, -\sum_e \frac{1}{2}\boldsymbol{u}_e^{\mathrm{T}}\frac{\partial \boldsymbol{k}_e}{\partial z_i}\boldsymbol{u}_e\right\} \tag{3}$$

where S^{c}_i indicates the sensitivity number for node i. $\boldsymbol{k}_e$ and $\boldsymbol{u}_e$ represent the stiffness matrix and the displacement vector of the eth element connected to node i in the global coordinate system respectively.

The structural shape may not be optimal when the structural volume reaches the limitation if only the compliance sensitivity numbers are involved, as they are independent with material consumptions. Thus, a volume adjustment subroutine of Eq. (1b) should be introduced in the updating process. The sensitivity of structural volume against the nodal shifting is derived as

$$\boldsymbol{S}_i^{v} = \left\{\frac{\partial V}{\partial x_i}, \frac{\partial V}{\partial y_i}, \frac{\partial V}{\partial z_i}\right\} = \left\{\sum_e \frac{\partial A_e l_e}{\partial x_i}, \sum_e \frac{\partial A_e l_e}{\partial y_i}, \sum_e \frac{\partial A_e l_e}{\partial z_i}\right\} = \left\{\sum_e A_e \frac{x_i - x_j}{l_e}, \sum_e A_e \frac{y_i - y_j}{l_e}, \sum_e A_e \frac{z_i - z_j}{l_e}\right\} \tag{4}$$

where A_e and l_e denote the cross-sectional area and the current length of element e respectively.

2.2. Shape updating scheme

As the sensitivity numbers reflect the influence on the structural compliance against nodal movements, nodes with larger sensitivity numbers are regarded as more important and supposed to be updated in priority. Thus, the conventional evolutionary node shifting method finds the optimal nodal movements in proportion to the normalized sensitivity numbers based on the gradient method. The shape updating procedure follows the strategy as

$$\boldsymbol{L}^{k+1} = \boldsymbol{L}^{k} + \alpha l_{\min} \left\{ -\boldsymbol{S}_i^{c} \right\}^{k}_{\text{normalized}} + \beta l_{\min} \left\{ -\boldsymbol{S}_i^{v} \right\}^{k}_{\text{normalized}} \tag{5}$$

in which $\boldsymbol{L}^{k+1}$ and $\boldsymbol{L}^{k}$ indicate the nodal coordinates in the current and the past iterations, the superscript k indicates the kth iteration. $l_{\min}$ represents the minimum length among all the beams. α is the step size for each iteration and is suggested not to exceed 5% for a stable convergence. β corresponds to the volume adjustment factor, which can be obtained by the bisection method between 0 and 0.5. The subscript of normalized means the normalization of the sensitivity matrix as,

$$\left\{ -\boldsymbol{S}_i \right\}_{\text{normalized}} = \left\{ -\boldsymbol{S}_i \right\} / \max\left(\text{abs}\left\{ -\boldsymbol{S}_i \right\} \right) \tag{6}$$

The volume adjustment subroutine is performed once the structural volume exceeds the constraint. It has also been verified effective for smoothing jagged edges as nodes tend to gather in the same plane with the surrounding connected nodes to decrease the structural volume, hence helps generate smooth surfaces. Although the volume subroutine gives the rectification for shape updating scheme by a perturbation at each step, it may force the nodes to move in the direction against compliance sensitivities, which is opposite to the objective. The interaction between the two subroutines results in an oscillation of the updating scheme and therefore leads to a slow convergence with thousands of iterations. Thus, it is essential to smooth the jagged surfaces caused by the non-smooth gradient field at each step to alleviate the oscillation after reaching the volume limitation. Although Wang *et al.* [23] introduced a double filter scheme for irregular edges, the surfaces are partially smoothed due to a limited filter radius, thus a high computation cost is still required. Considering that structures deformed smoothly under distributed load, instead of sensitivity numbers, fictitious distributed forces are introduced in this article to determine the nodal movements for maintaining the smoothness at each iteration. The shape updating scheme of Eq. (5) is then modified as

$$\boldsymbol{L}^{k+1} = \boldsymbol{L}^{k} + \alpha l_{\min} \left\{ \Delta x_i, \Delta y_i, \Delta z_i \right\}^{k}_{\text{normalized}} + \beta l_{\min} \left\{ -S_i^{v} \right\}^{k}_{\text{normalized}} \tag{7}$$

in which Δx_i, Δy_i and Δz_i indicate the nodal displacements of node i in the x-, y- and z-direction under the fictitious distributed load, and can be evaluated from the equilibrium equation of the shape updating analysis,

$$\boldsymbol{u}_{op} = \left\{ \Delta x_i, \Delta y_i, \Delta z_i, \Delta \theta_{xi}, \Delta \theta_{yi}, \Delta \theta_{zi} \right\}^{\mathrm{T}} = \boldsymbol{f}_{op} / \boldsymbol{K}_{op} \tag{8}$$

where $\boldsymbol{u}_{op}$ represents the structural deformations composed of nodal displacements and rotations with respect to x-, y- and z-axis under the fictitious distributed load $\boldsymbol{f}_{op}$, and $\boldsymbol{K}_{op}$ corresponds to the global stiffness matrix with respect to the shape updating analysis, which depends on the architectural intents and only differs in a few corresponding elements with $\boldsymbol{K}$ according to the boundary condition changes, thus no extra numerical modelling procedure is needed for the reconstruction of global stiffness matrix.

As nodal updating movements at each iteration are in proportion to the nodal displacements under the fictitious distributed load, the change for the compliance at each iteration is estimated as

$$\Delta C \approx \gamma \sum \left(\frac{\partial C}{\partial x_i} \Delta x_i + \frac{\partial C}{\partial y_i} \Delta y_i + \frac{\partial C}{\partial z_i} \Delta z_i \right) = \gamma \sum \left\{ \frac{\partial C}{\partial x_i}, \frac{\partial C}{\partial y_i}, \frac{\partial C}{\partial z_i} \right\} \cdot \left\{ \Delta x_i, \Delta y_i, \Delta z_i \right\}^{\mathrm{T}} \tag{9}$$

where γ is the positive factor related to step size. It can be extended in the form of structural deformations according to Eq. (8) as

$$\begin{aligned} \Delta C &\approx \gamma \sum \left\{ \frac{\partial C}{\partial x_i}, \frac{\partial C}{\partial y_i}, \frac{\partial C}{\partial z_i}, 0, 0, 0 \right\} \cdot \left\{ \Delta x_i, \Delta y_i, \Delta z_i, \Delta \theta_i, \Delta \beta_i, \Delta \gamma_i \right\}^{\mathrm{T}} \\ &= \gamma \left\{ \boldsymbol{S}_i^c, 0, 0, 0 \right\} \cdot \boldsymbol{u}_{op} = \gamma \left\{ \boldsymbol{S}_i^c, 0, 0, 0 \right\} \cdot \boldsymbol{K}_{op}^{-1} \cdot \boldsymbol{f}_{op} \end{aligned} \tag{10}$$

In order to keep the compliance declining at each iteration, the fictitious distributed forces are defined as the negative compliance sensitivities,

$$\boldsymbol{f}_{op} = \left\{ -\boldsymbol{S}_i^c, 0, 0, 0 \right\}^{\mathrm{T}} = \left\{ -\frac{\partial C}{\partial x_i}, -\frac{\partial C}{\partial y_i}, -\frac{\partial C}{\partial z_i}, 0, 0, 0 \right\} \tag{11}$$

which means that the negative sensitivities are applied as distributed load to each free node along the *x*-, *y*-, *z*-direction respectively to erect the structures. Consequently, the compliance change for nodal shifting becomes

$$\Delta C \approx -\gamma \, \boldsymbol{f}_{op}^{\mathrm{T}} \boldsymbol{K}_{op}^{-1} \boldsymbol{f}_{op} < 0 \tag{12}$$

As the stiffness matrix is positive definite for stable structures, Eq. (12) is guaranteed negative, which gives a sustained reduction for the structural compliance during the optimisation process, meanwhile the smoothness of updated surfaces at each step is significantly improved as structures tend to deform uniformly under distributed load. In fact, the strategy of introducing distributed load instead of sensitivity numbers makes all the nodes deformed interactively, as sensitivities in the form of nodal load would also result in a change for other nodes rather than the loading node only, which can be regarded as a filter scheme over all the free nodes. Considering that the models for sensitivity and shape updating analysis are the same, the non-smooth gradient fields are offset by the dual operation, makes it more effective than the previous filter schemes.

2.3. Optimisation procedure

The proposed shape updating scheme determines the nodal shifting at each iteration in a much smoother or in other words a more efficient way by the fictitious distributed load filter. The distributed forces based on sensitivity numbers are applied to evolutionarily erect the stiffest structural shape. The optimisation procedure is illustrated as follows:

1. Define the initial conditions, including the starting grid model, the boundary conditions and the architectural constraints.
2. Perform the finite element analysis (FEA) for the nodal displacements under external load. The global stiffness matrix corresponding to the current shape is constructed at this step.
3. Evaluate the sensitivity numbers according to Eq. (3), then assign them to the distributed load for the following shape updating analysis as Eq. (11).
4. Revise the global stiffness matrix with respect to architectural constraints, then perform the shape updating analysis for the nodal displacements by Eq. (8).
5. Update the nodal coordinates according to Eq. (7), where the step size α is defined adaptive in this article for more stable convergence, by endowing with 5% when under the volume constraint and 5‰ otherwise. Evaluate the current structural volume, perform the volume adjustment scheme if necessary, otherwise continue step 2 to 5 until the convergence criterion referring to the literature [24] is satisfied:

$$\left| \frac{\sum_{m=1}^{M} \left(C^{k-m+1} - C^{k-M-m+1} \right)}{\sum_{m=1}^{M} C^{k-m+1}} \right| \leq \tau_1 \tag{14a}$$

$$\left| \frac{V^k - V^*}{V^*} \right| \leq \tau_2 \tag{14b}$$

where τ_1 and τ_2 are the convergence tolerances with respect to the structural compliance and volume, and is defined 10^{-3} and 10^{-5} respectively for the numerical examples in Section 3. $M = 10$ is applied in this article for a stable convergence of at least 20 iterations.

It is noteworthy that although an extra shape updating analysis is required for the proposed algorithm, the computational time for each iteration only increased limitedly with regard to the matrix calculation in Eq. (8). There is no need to reconstruct the global stiffness matrix for shape updating analysis as it can be easily obtained by revising the corresponding elements of $\boldsymbol{K}$, which is already known in the compliance analysis. Furthermore, if the boundary conditions for shape updating analysis remain the same with the compliance analysis, the inverse global stiffness matrix can be applied directly to the updating analysis for multiplication, which is much faster than matrix division. Although the computational time slightly increased at each iteration, it is worthy to do so if the recursive steps are reduced more. In fact, as the distributed load filter offers a much smoother and more efficient way for nodal shifting, the non-smooth gradient fields are significantly alleviated, thus leading to a remarkable reduction in recursive steps with a more stable convergence.

3. Numerical example

The numerical example of a cantilevering rectangular gridshell is presented in this section to verify the effectiveness of the proposed algorithm. The node shifting methods proposed in the literature [22,23] are also applied as comparison to demonstrate the advantage of the fictitious distributed load filter. For simplicity, the non-unit parameters are used, as the material is defined with an elastic modulus and a shearing modulus both of 1. All the beam elements are endowed with a uniform square cross section of 20×20. The initial model and the boundary conditions are shown in Fig. 1. A vertical point load of $F = 1$ is applied to the cantilevering corner, which makes the conventional form-finding techniques for tension- or compression-only structures inapplicable as non-negligible bending moments are generated for the beam elements. The target volume is defined as 110% of the initial flat shell, and the *z*-coordinates of all the free nodes except the ones on the four red sidelines are defined as the design variables, as shown in Fig. 1(b). The optimisation procedure is implemented in MATLAB and run on a PC with 16 GB RAM and 2.10 GHz Intel Core i7 processor.

The sensitivity numbers would be zero for the initial fat shell as it stays at a stagnation state, where the nodes moving upward or downward bring the same effect on the structural compliance symmetrically, thus an initial perturbation is needed for this special state, but not necessary in other cases where nodes are not all in the same horizontal plane. It has been verified that the perturbation in proportion to the initial structural deformation gives a more stable and stiffer solution [23], therefore the same perturbation scheme is applied in this article. To further improve the computational efficiency, all the nodes are constrained at *x*- and *y*-direction in the shape updating analysis as they are not design variables. The optimised shape generated by different filter schemes are shown in Fig. 2(a)-(c). The compliance and volume histories are given in Fig. 2(d).

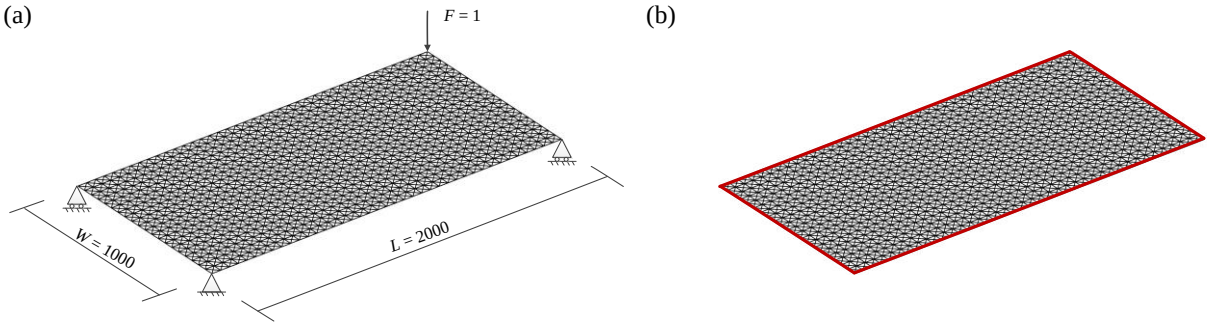


Figure 1. The initial model and boundary conditions for (a) compliance analysis and (b) shape updating analysis.

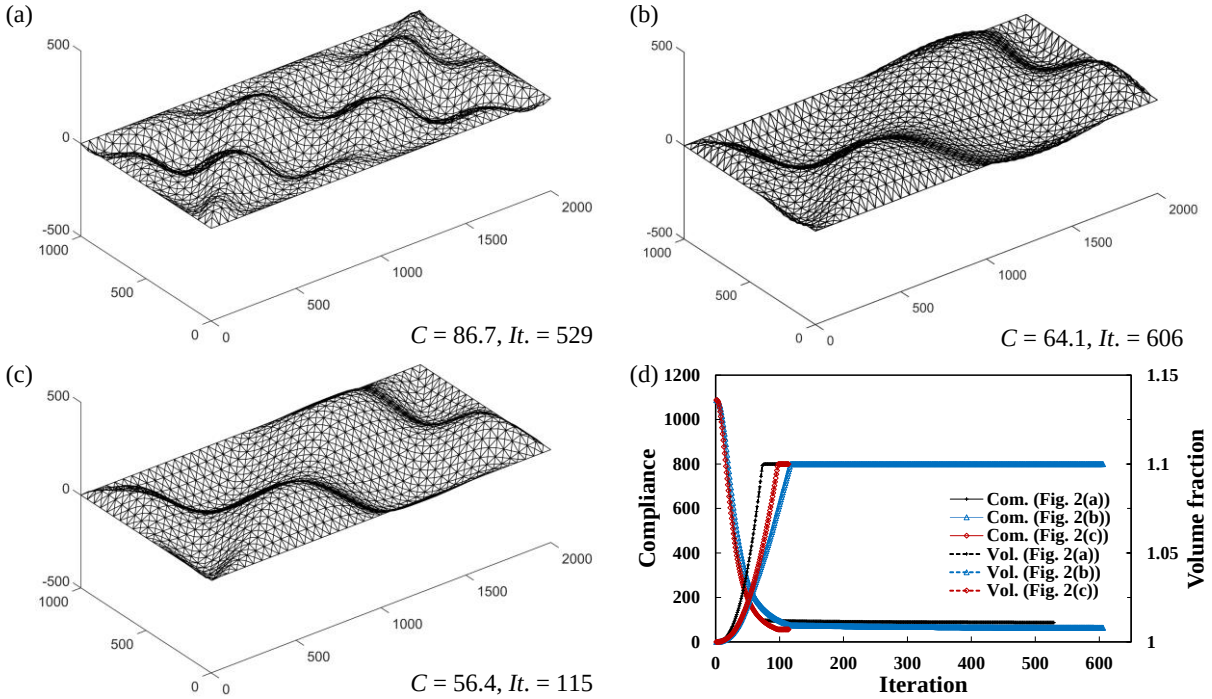


Figure 2. The optimised shapes generated by the evolutionary node shifting method: (a) without filter [22], (b) with the double filter scheme [23], (c) with the distributed load filter scheme, and (d) evolutionary histories for structural compliance and volume.

The optimised shape obtained by the distributed load filter is similar to the one by the double-filter, but with smoother surface and lower compliance, while the model without any filter obviously falls into premature convergence. The contradiction between compliance and volume adjustment subroutines leads to a very slow nodal shifting towards the optimal positions, which makes the compliance vary very little at each step and finally leads to a premature convergence for the first two models. As nodes are still moving towards the optimal positions slowly, a stricter convergence criterion is needed to allow further optimisation for the compared methods. Fig. 3 shows the further optimised shapes for the models in Fig. 2(a) and (b) with respect to the same compliance level of the new method. The final optimised shapes are similar to the one or its inverse form in Fig. 2(c), but with far more iterations. The shape updating scheme with fictitious distributed load filter only takes 115 steps for the optimal shape while the other two strategies need more than 5,000 steps. Although the double filter scheme alleviates the non-smooth gradient field compared to the conventional node shifting method without any filter, it cannot avoid the contradiction between the compliance and volume adjustment scheme as it only gives local smoothness within the filter radius, massive iterations are still required after reaching the volume limitation. The in-process optimised shapes when reaching the volume constraint with respect to the three approaches are shown in Fig. 4, where obvious jagged surfaces are observed for the first two

shapes while the nearly optimal shape is already obtained by the proposed method. The nodal movements determined by the sensitivity numbers only ensure the decline of structural compliance, but not by the most efficient way, thus premature shapes are generated when the structural volume reaches the limitation. A sustained perturbation by the volume adjustment subroutine is needed for the revision of nodal shifting scheme, but this strategy could result in a ponderous evolutionary process. The new proposed approach avoids the trouble by shifting the nodes in a smoother and more efficient way at each step, a nearly optimal shape is generated when the volume limitation is reached, thus no more perturbation is needed. The time consumptions for the three methods are listed in Table 1. It is shown that even though the average computing time for each step is increased due to the updating analysis, the new algorithm with distributed load filter saves more than 97% time in total.

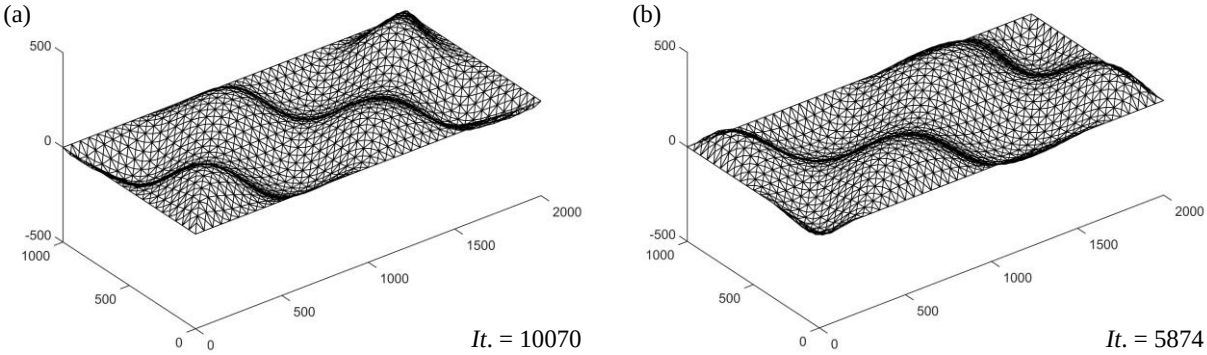


Figure 3. The further optimised shapes (a) without filter, (b) with the double filter scheme.

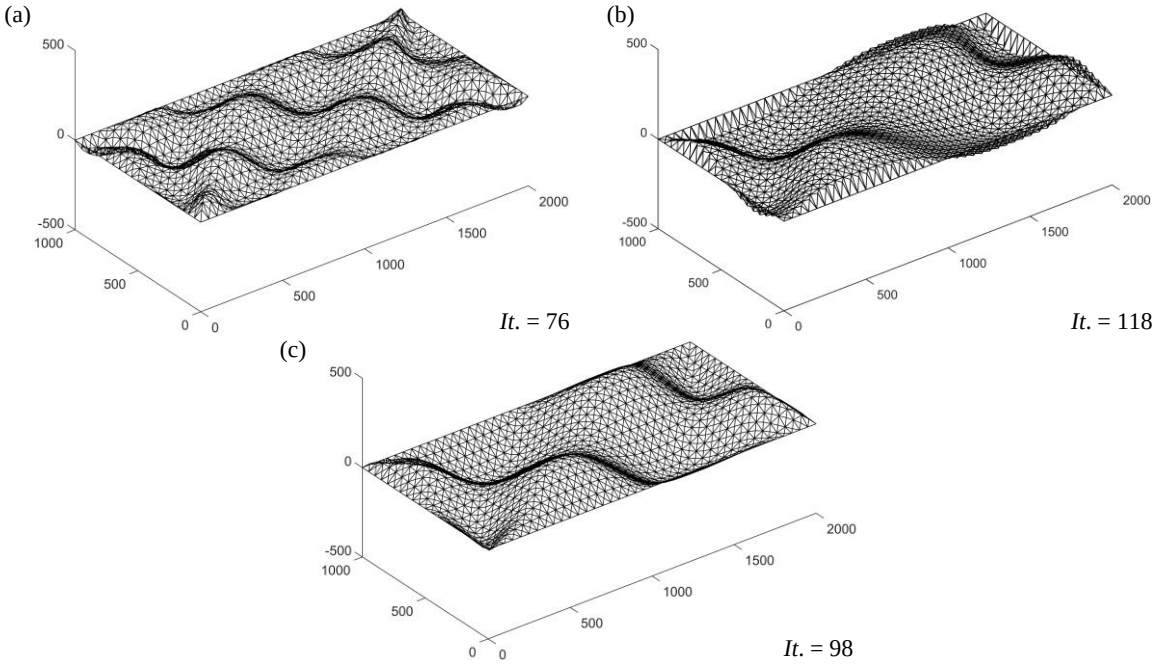


Figure 4. The in-process optimised shapes when reaching the volume constraint (a) without filter, (b) with the double filter scheme and (c) with the distributed load filter scheme.

Table 1. Time consumptions for the same compliance level with different strategies.

Strategy	Compliance	Total iterations	Time for each iteration	Total time consumption
without filter	56.4	10070	3.03s	30522.6s
double filter		5874	3.72s	21860.4s
distributed load filter		115	5.88s	676.7s

4. Conclusion

The shape optimisation algorithm proposed in this study offers a more efficient and robust computational designing tool for freeform gridshells, especially those with non-negligible bending moments where the conventional form-finding methodologies would fail. Nodal coordinates are treated as design variables without any extra parameterisation. A smoother and more efficient shape updating scheme by introducing the distributed load filter is proposed. The negative sensitivity numbers are applied to each node as the fictitious external load to ensure both the smoothness of surfaces and the sustained reduction of structural compliance at each step. With the nodes shifting interactively under external load, the distributed load filter scheme acts as a global filter over all the free nodes based on structural mechanic properties, thus significantly alleviates the non-smooth gradient field caused by the structural nonlinear effect. A much more stable and faster convergence is achieved compared to the conventional nodal shifting methods. The numerical example indicates that although the average computing time for each iteration is increased with the shape updating analysis, the proposed method can save more than 97% computational time overall due to a significant drop in the iteration number, which makes it applicable for large span structures with complex curvatures. As the method is developed from general mechanical principles, it is possible to be extended in the future to more general fields such as maximising the buckling load or being combined with concurrent size and topology optimisation.

References

[1] I. Liddell, "Frei Otto and the development of gridshells," *Case Studies in Structural Engineering*, vol. 4, pp. 39–49, 2015.

[2] H. Isler, "Concrete shells derived from experimental shapes," *Structural Engineering International*, vol. 4, no. 3, pp. 142–147, 1994.

[3] E. Ramm and G. Mehlhorn, "On shape finding methods and ultimate load analyses of reinforced concrete shells," *Engineering Structures*, vol. 13, no. 2, pp. 178–198, 1991.

[4] K.-U. Bletzinger and E. Ramm, "Structural optimization and form finding of light weight structures," *Computers & Structures*, vol. 79, pp. 2053–2062, 2001.

[5] I. Vizotto, "Computational generation of free-form shells in architectural design and civil engineering," *Automation in Construction*, vol. 19, no. 8, pp. 1087–1105, 2010.

[6] H. -J. Schek, "The force density method for form finding and computation of general networks," *Computer Methods in Applied Mechanics and Engineering*, vol. 3, no. 1, pp. 115–134, 1974.

[7] J. Y. Zhang and M. Ohsaki, "Adaptive force density method for form-finding problem of tensegrity structures," *International Journal of Solids and Structures*, vol. 43, no. 18–19, pp. 5658–5673, 2006

[8] M. Miki and K. Kawaguchi, "Extended force density method for formfinding of tension structures," *Journal of the International Association for Shell and Spatial Structures*, vol. 51, no. 4, pp. 291–303, 2010.

[9] P. Block and J. Ochsendorf, "Thrust network analysis: a new methodology for three-dimensional equilibrium," *Journal of the International Association for Shell and Spatial Structures*, vol. 48, no. 3, pp. 1–8, 2007.

[10] S. Adriaenssens and M. Barnes, "Tensegrity spline beam and grid shell structures," *Engineering Structures*, vol. 23, no. 1, pp. 29–36, 2001.

[11] J. Rombouts, G. Lombaert, L. D. Laet and M. Schevenels, "On the equivalence of dynamic relaxation and the Newton-Raphson method," *International Journal for Numerical Methods in Engineering*, vol. 113, no. 9, pp. 1531–1539, 2017.

[12] A. Liew, T. V. Mele and P. Block, "Vectorised graphics processing unit accelerated dynamic relaxation for bar and beam elements," *Structures*, vol. 8, pp. 111–120, 2016.

[13] A. Jarraya, F. Dammak, S. Abid and M. Haddar, "Shape and thickness optimization performance of a beam structure by sequential quadratic programming method," *Journal of Failure Analysis and Prevention*, vol. 7, no. 1, pp. 50–55, 2007.

[14] J. Cui, Y. Zheng, M. Ohsaki, and Y. Luo, "Shape optimization of piecewise developable free-form grid surface using plate components," *Engineering Structures*, vol. 245, 2021.

[15] L. Gil and A. Andreu, "Shape and cross-section optimisation of a truss structure," *Computers & Structures*, vol. 79, pp. 681–698, 2001.

[16] P. Chen and M. Kawaguchi, "Optimization for maximum buckling load of a lattice space frame with nonlinear sensitivity analysis," *International Journal of Space Structures*, vol. 21, no. 2, pp. 111–118, 2016.

[17] D. Wang, W. H. Zhang and J. S. Jiang, "Truss shape optimization with multiple displacement constraints," *Computer Methods in Applied Mechanics and Engineering*, vol. 191, pp. 3597–3612, 2002.

[18] D. Wang, "Optimal shape design of a frame structure for minimization of maximum bending moment," *Engineering Structures*, vol. 29, no. 8, pp. 1824–1832, 2007.

[19] C. Cui and B. Jiang, "A morphogenesis method for shape optimization of framed structures subject to spatial constraints," *Engineering Structures*, vol. 77, pp. 109–118, 2014.

[20] X. Zhang, Y. M. Xie and S. Zhou, "A nodal-based evolutionary optimization algorithm for frame structures," *Computer-Aided Civil and Infrastructure Engineering*, vol. 38, no. 3, pp. 288–306, 2022.

[21] X. Li, Y. Wu, F. Wan, G. Lin, "A computational morphogenesis method for free form structures by adjusting key points on surfaces". In *Future Visions: Proceedings of the IASS Annual Symposium 2015*, Amsterdam, Netherlands, August 7–10, 2015.

[22] C. Ding, H. Seifi, S. Dong and Y. M. Xie, "A new node-shifting method for shape optimization of reticulated spatial structures," *Engineering Structures*, vol. 152, pp. 727–735, 2017.

[23] H. Wang, Z. Chen, G. Wen, G. Ji and Y. Min Xie, "A robust node-shifting method for shape optimization of irregular gridshell structures," *Structures*, vol. 34, pp. 666–677, 2021.

[24] X. Huang and Y. M. Xie, *Evolutionary Topology Optimization of Continuum Structures: Methods and Applications*, John Wiley & Sons, 2010.

IASS 2023
July 10–14 Melbourne
Integration of Design and Fabrication

Proceedings of the IASS Annual Symposium 2023
Integration of Design and Fabrication
10–14 July 2023, Melbourne, Australia
Y.M. Xie, J. Burry, T.U. Lee and J. Ma (eds.)

Designing the West Gate Tunnel portals: Façade geometry and structure

Benjamin COOP[a,*], Andre PEREIRA[b], Hieu TRAN[b], Dwayne VAN HALEWIJN[b], Richard WHITFIELD[b], Manning THOMSON[b], Atreyu DE LACY[b]

[a,*] Taylor Thomson Whitting (TTW)
benjamin.coop@ttw.com.au

[b] Taylor Thomson Whitting (TTW)

Abstract

The West Gate Tunnel Project in Melbourne, a toll road alternative to the West Gate Bridge, includes decorative entrance and exit exhaust vent structures designed by Wood Marsh Architecture. This paper examines the design process of the Northern and Southern vents undertaken by Taylor Thomson Whitting, specifically surrounding the aluminium façade and supporting structural steel. The design process focused on panelising the freeform façade and optimising the supporting structure. A distorted grid in the surface envelope's UV space was used to ensure a continuous flow between the timber portal and aluminium structures topologies. Further geometric optimisation employed k-means clustering to minimise discrepancies in connection lengths and member bend radii. The structural design process was automated using C# libraries and Grasshopper scripts, in conjunction with FEA models, AS4100 design checks, and an optimisation framework inspired by bone mechanobiology research. Computational design methods implemented on the project allowed for rapid and precise structural feedback, prompting informed decision-making among stakeholders regarding geometric changes impacting architectural intent and structural design.

Keywords: architectural geometry; bio-inspired structures; construction engineering; digital modelling and fabrication, metal structures, connections and stability; parametric design; numerical methods for geometry; form-finding and optimisation of lightweight structures; Hangai prize applicant

1. Introduction

The West Gate Tunnel Project aims to provide a crucial alternative to the West Gate Bridge, resulting in faster and safer commutes while redirecting a significant number of trucks away from residential areas. The project is composed of three major elements: a tunnel structure, an elevated roadway section, and an upgraded segment of the West Gate Freeway. At each of the three entrances/exits to the tunnel, there exists an architectural timber and aluminium structure that serves as a decorative feature and, in the case of the two largest structures, housing the tunnel's ventilation systems within the aluminium portion of the design.

The vent structures are formed from a double layered structural steel system supporting a triangulated aluminium facade with expressed diamond panalisation. The largest of the two vent structures, the Northern portal, is located adjacent to Yarraville Gardens on Whitehall Street, measuring 136 meters long, 38 meters wide, and 46 meters high (Figure *1*).

Copyright © 2023 by Benjamin COOP, Andre PEREIRA, Hieu TRAN, Dwayne VAN HALEWIJN, Manning THOMSON and Atreyu DE LACY. Published in the Proceedings of the IASS Annual Symposium 2023 with permission.

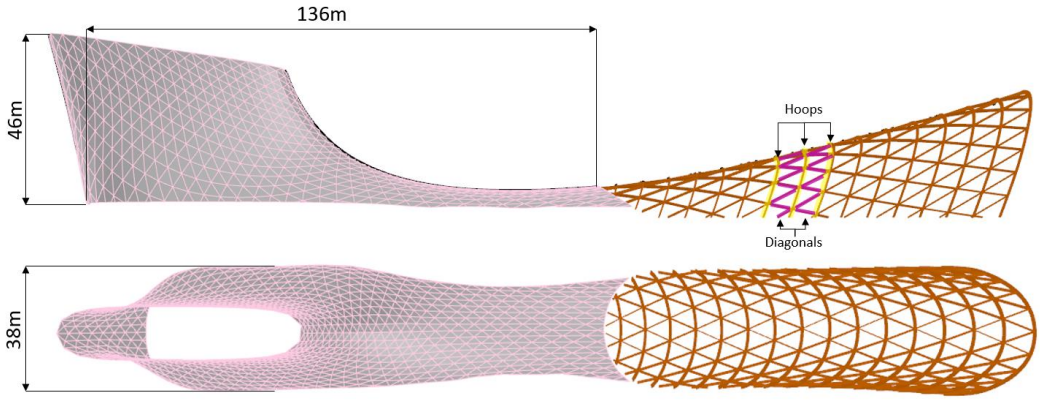


Figure 1. North portal composed of timber structure and vent structure. Vent aluminium cladding dimensions shown along with timber architectural subdivision of hoops (yellow) and diagonals (purple).

Taylor Thomson Whitting (TTW) was engaged by the managing contractor for the tunnel project, CPBJH Consortium, to develop the structural design and façade engineering for the aluminium vent structures of both the Northern and Southern outbound vents. The design approach adopted took into account various constraints, including structural design standards, durability, transportation, fabrication, erection, and maintenance. However, this paper focuses solely on the generation of the geometry and topology of the aluminium panels, as well as the façade design and the structural optimisation work carried out to design the vent structures support system.

This paper is organised into three main sections. Section 2 describes the geometry work carried out to unify the vent structures with their paired architectural timber structures [1]. Section 3 details the façade optimisation carried out, and Section 4 explores the structural optimisation targets and processes of the façade support system.

2. Geometry

One of the aesthetic aspects deemed of high importance to the architect's vision was achieving a seamless transition between the timber gridshell topology and the vent aluminium cladding. To accomplish this, a geometric constraint was to the match nodal locations and member tangency at the transition between the two zones. The timber gridshell was designed to a parallel hoop scheme with infill diagonal members in between each hoop as seen in Figure *1* and a changing its geometry was not within the scope of works for this project. An additional complexity of this task was that both vent structure surfaces are asymmetrical, unlike the timber structures that were designed with a central symmetry plane, as seen in Figure *2*.

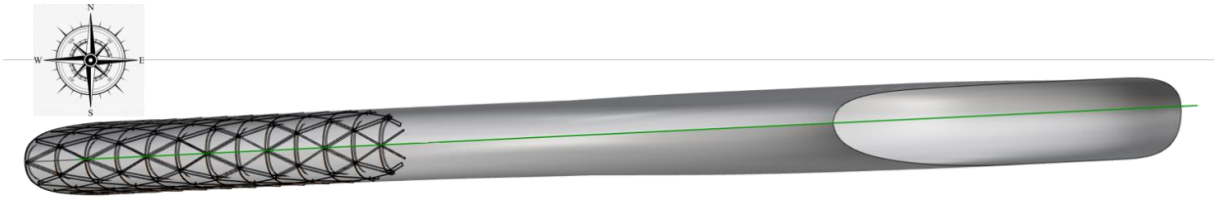


Figure 2. Plan view of the Southern Outbound portal, with Wood Marsh envelope surface shown in grey and architectural timber structure symmetry plane in green.

2.1 Methods

The first step in developing the panelisation geometry was to perform minor alterations to the original Wood Marsh envelope surface to avoid clashes within the structure. This process involved offsetting the surface inward to the estimated maximum offset of the internal structural steel system, analysing the

new offset surface for clashes and then rebuilding the original surface control points accordingly to prevent these clashes. The rebuilt surface went through multiple iterations to avoid external road sway envelopes as well as to blend the changed control points such that the differences between the original and modified sock surface were as subtle as possible. Once a suitable initial surface was produced, the panelisation process could proceed, following the process described in the subsections below.

2.1.1 General panel logic

There was a degree of common logic shared between both the north and south vent structures. Both structures used two sets of reference curves to form the panels of the façade. The first set of curves were generated from cutting planes of changing orientation starting oriented parallel to the timber hoops and finishing aligned with the outlet plane. The intersect of these planes with the envelope surface created the first set of curves nominated Plane Set Curves (PSC's). By using these PSC's as the diagonal of the panels we allow node planarity and avoid the timber hoop direction to be visually expressed in the panels. To ensure a smooth and even transition from the timber topology to the rest of the geometry, a transition zone was imposed where the first planes in the plane set were aligned with the timber parallel hoop direction. This process is illustrated in Figure *3*.

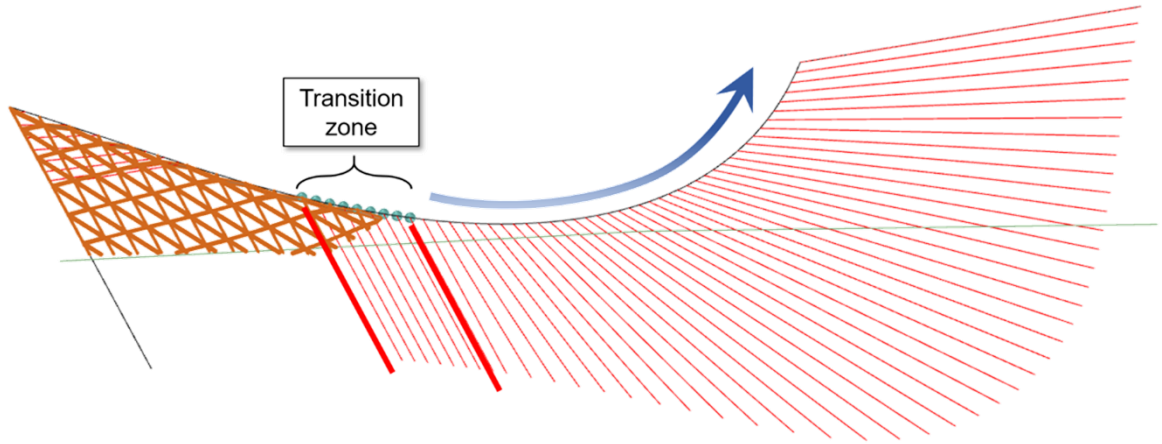


Figure 3. A transition zone is used to seamlessly transition from the architectural timber parallel hoop planes to the outlet vent cap plane at the top of the structure generating the Panel Set Curves (PSC's).

The second set of curves used to define a grid differed for the two portals. The Southern portal utilised logintudinal iso-curves whilst the Northern portal used a distorted UV grid both described below.

2.1.2 South portal specific panel logic

The Southern portal utilised longitudinal iso-curves as shown in Figure *4*. The iso-curves are set to start at equidistant points along the top outlet boundary. The intersection point of the PSC and iso-curves are then used as corner nodes for each diamond in the final panelisation.

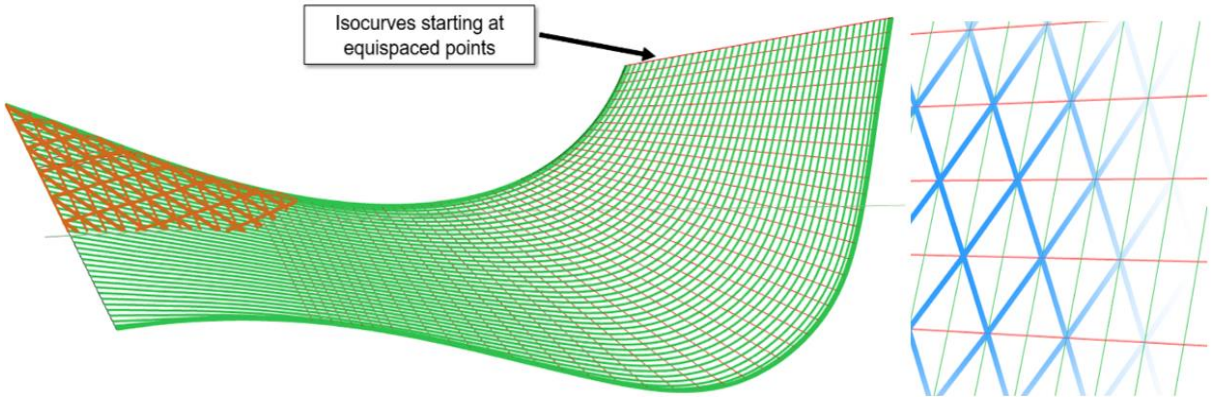


Figure 4. Panels are expressed from grid generated using the plane set curves (in red) and a set of surface iso-curves (in green). (a) Isocurves are generated starting at equispaced points along the outlet boundary. (b) Panels (in blue) are created from the intersection between planes and iso-curves.

These steps, however, do not guarantee a consistent transition between the timber and vent topologies. This is due to the shallower profile of the envelope surface close to the timber gridshell and start of the vent regions. It is noticeable in Figure *4* that the iso-curves are closer when the surface constricts, making the panels narrower than required for a smooth transition in the topologies. A simple strategy to address this is to adjust the surface depth, stretching the cladding panels up to the point they approximately match the timber topology in terms of node location and edge tangency. This is illustrated in Figure *5*.

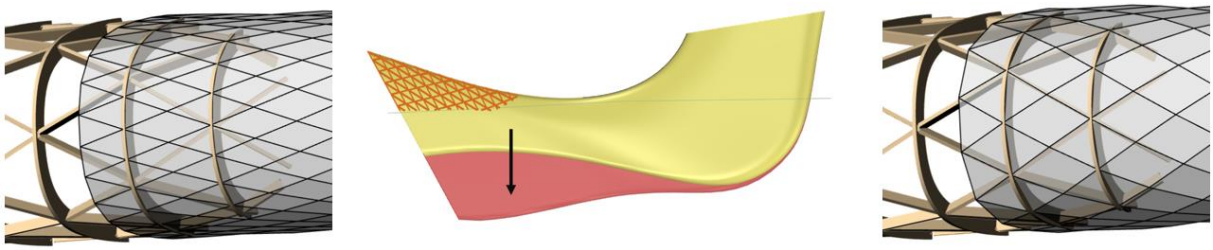


Figure 5. Accomplishing a smooth transition between timber gridshell topology and cladding panels. (1.) Transition between timber and cladding is not consistent (2.) The original surface (yellow) can be stretched to adjust the distance between iso-curves and, consequently, (3.) modify the panel proportions to match the timber gridshell topology.

2.1.3 North portal specific panel logic

Whilst the estimation of the best fit longitudinal iso-curves based on a modified surface was sufficient to seamlessly blend the timber members and vent panels on the Southern portal, on the Northern portal, the varying pattern densities between the two structures prevented the use of this technique. Figure *6* shows a superposition of the timber topology and the longitudinal iso-curves of the envelope surface, where this misalignment is evident.

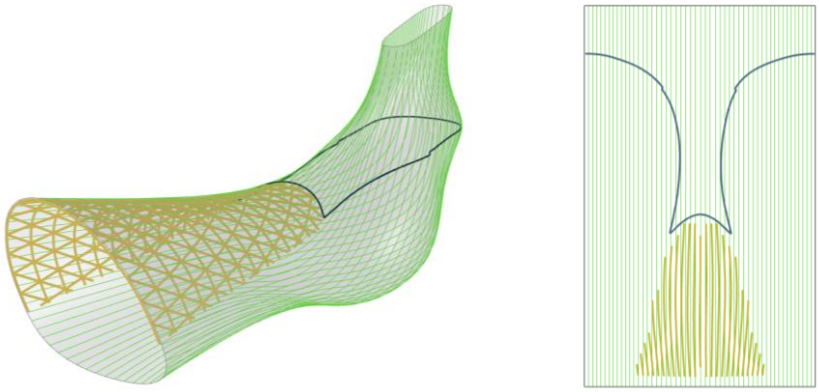


Figure 6. Misalignment between longitudinal iso-curves (in green) and timber gridshell reference curves (in yellow) for the North Portal (left) in 3D and (right) in UV mapping coordinates.

To improve continuity between the two geometries, a new set of longitudinal iso-curves was created in UV mapping coordinates, which maintained panel aesthetics around the vent region and gradually transitioned to the pattern of the timber portal. These curves were modelled as B-splines, starting "vertically" at the top in the UV space (the vent region), and matching the direction and curvature of the timber reference curves. The process of creating these curves is illustrated in Figure *7*.

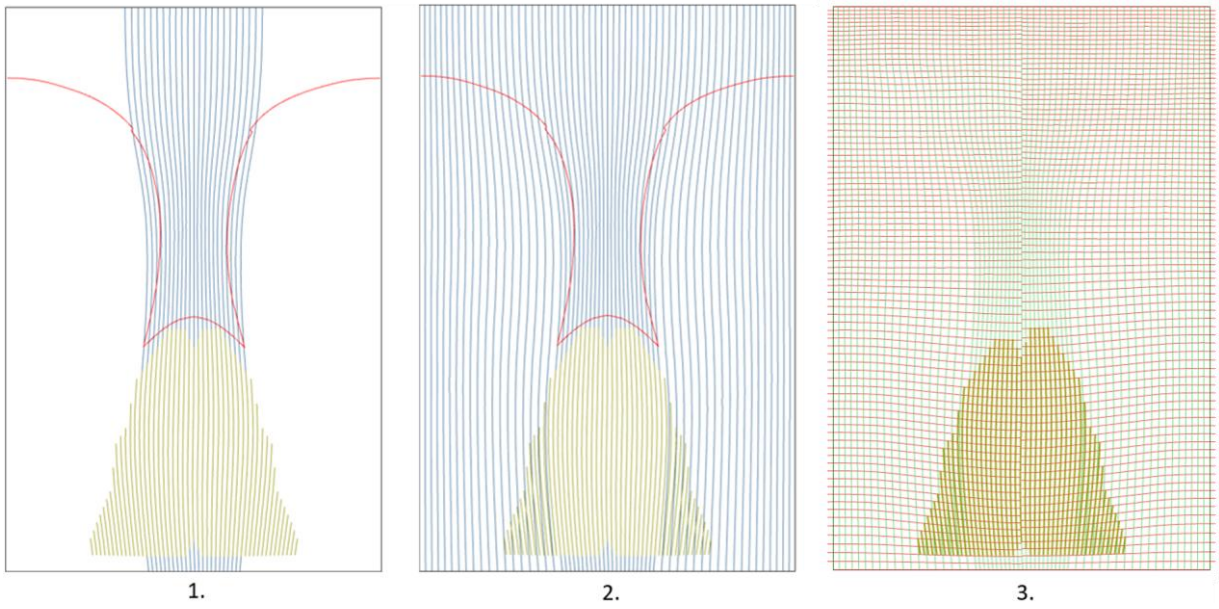


Figure 7. Development of North Portal panelisation curve sets. (1.) Develop internal spline curves between existing timber curves and vertical curves at exhaust. (2.) Tween curves to edge of UV coordinates (3.) Finalise grid with the placement of PSC's (in red).

2.2 Results

By varying the frequency of iso-curves in each curve set that generated the panelisation grid in the section above, the number of panels could be increased or decreased to accommodate varying shape parameters. Several iterations of different panel division options were produced with the aim of minimising the number of panels with edge lengths greater than 6.5m (an additional geometric constraint discussed in Section 3), while also minimising the total number of panels. The final subdivisions seen in Figure *8* had a small number of panels that exceeded the maximum edge length parameter; however, the façade team was confident that a unique solution could be found for these zones at a lower cost than

the fabrication and construction costs associated with further subdividing the panels of the structure to produce smaller panels.

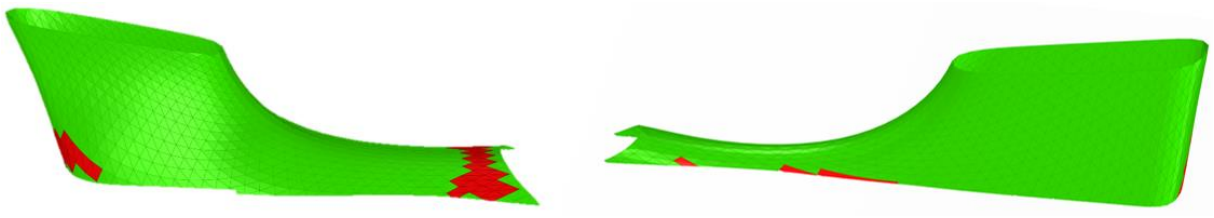


Figure 8. Panel compliance to maximum 6.5m edge. North Portal 94% compliant (Left) South Portal 99.3% compliant (Right)

3. Façade

A key architectural constraint of the project, as described in Section 0 of this paper, was to maintain the timber gridshell topology across into the vent structure. This geometry called for expressed joints around non-planar diamond panels with diagonal lengths up to 6.5m. The 6.5m edge length limitation was a direct result of the panel system described in this section. Aluminium extrusions are used under each panel, and feedback from the market suggested that by limiting the extrusion length to this value, we would increase the number of companies that could compete for the fabrication of the façade. Significant effort was made to simplify these expressed diamonds into planar triangular panels with minimal material wastage.

3.1 Method

Early feedback from builders indicated that the best aluminium source for the façade would be coils of aluminium instead of sourcing metal sheets. The standard maximum width available for aluminium coils is 1500mm, with thickness ranging from 0.6mm to 3mm. To avoid curving the aluminium to fit the non-planar diamond shapes, each panel was divided into a pair of triangles. A study was conducted to assess the visual impacts of dividing the diamonds along either the U or V gridlines as specified in Section 2 It was determined that dividing the panels in the longitudinal direction, or "Iso" as shown in Figure *9* was most appropriate for maintaining the architectural intent of the structure.

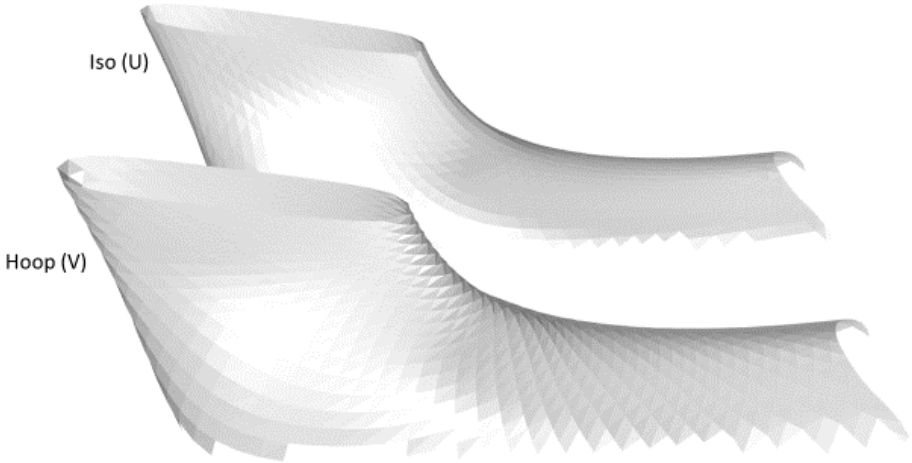


Figure 9. Comparison of alternative iso-curve subdivisions of diamond panels

With a maximum edge length of 6.5m each planar triangle panel still required multiple strips of aluminium. In order to minimise wastage, strips of aluminium were placed from the leading edge of a triangle at their full width of 1500mm. By starting the placement of the strips from a straight factory edge tolerance, issues were minimised compared to using a cut edge where a slight angle difference

could cause a cumulative misalignment with the addition of subsequent panels panel. It is for this reason that the panels on each triangle do not align with one another as the leading edge is on opposite sides of the diamonds (right-hand side for the top triangle and left-hand side for the bottom triangle in Figure *10*).

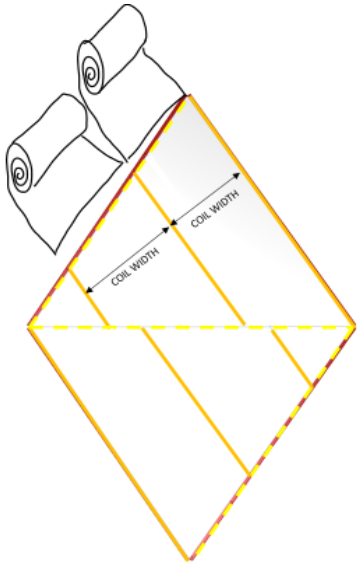


Figure 10. Panel strip layout, yellow dotted lines represent cuts whilst orange solid lines represent factory straight edges.

In addition to having an aluminium extrusion running under each panel edge to provide a surface to fasten to, additional stiffeners were required to reduce panel deflections. These framing members were structurally optimised by grouping panels based on similar surface area and then designing the stiffener elements to withstand the maximum wind load experienced by all panels in the group.

In some cases, we observed large panels in areas of high wind loads, which required substantial stiffening. In order to avoid a high density of stiffeners in these locations, we adjusted the panelisation of the aluminium facade (following the approach detailed in Section 2 of this paper) to reduce the affected panel areas. The final façade system can be seen in Figure 11.

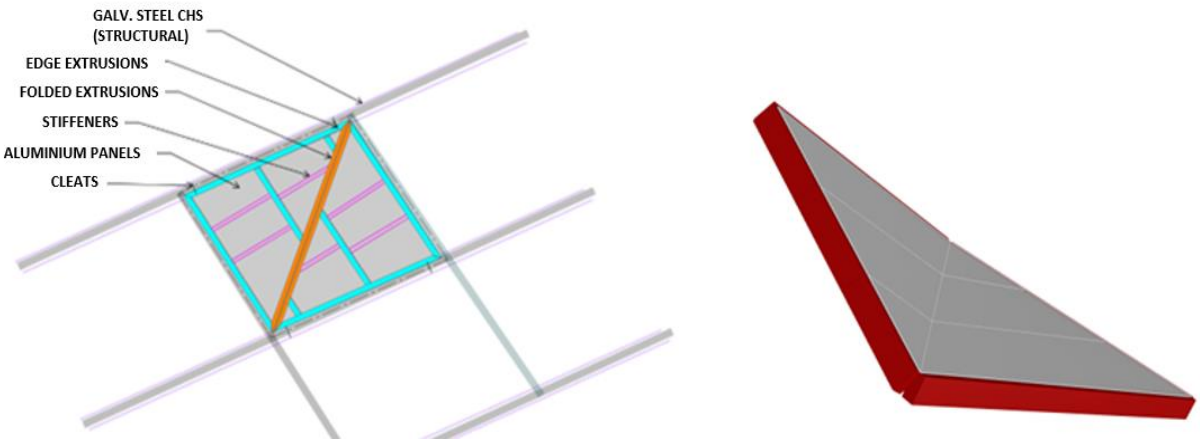


Figure 11. Façade Panel Setout.

3.2 Results

The final panel count across the structures came to 1785 triangular panels on the Northern portal and 1644 on the Southern. With an average panel area of 5m^2 and 5.67m^2, respectively, this resulted in the bulk of panels being comprised of three aluminium coil strips as displayed in Figure *12* which portrays the final structures appearance with exaggerated seams between the coil strips.

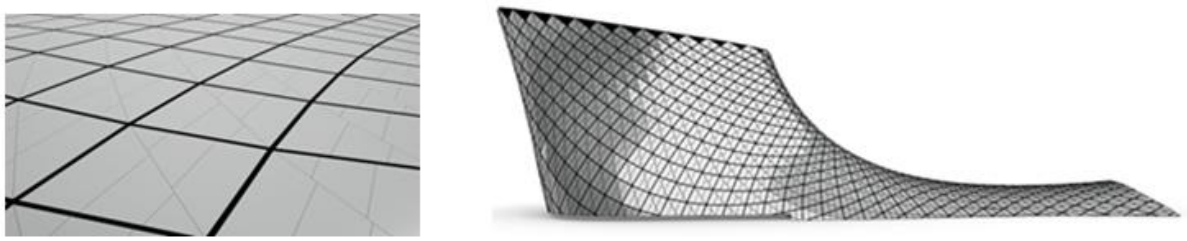


Figure 12. Final panelisation with exaggerated panel seams.

4. Structure

The façade support system consists of two layers of steel structure. The primary members shown as red in Figure are offset inwards from the yellow secondaries, this allows the secondary members to run continuously. The secondary members provide the structure to which the aluminium façade support extrusions described in Section 0 will connect. The resulting load path is as follows; the aluminium extrusions distribute the load to the secondary structure at the vertices of the triangular panels. The secondary structure runs continuously over columns and arches which will pick up the load and distribute it either into the core through brace members or directly down to the footings in the case of the arches. This scheme seeks to improve structural efficiency by providing continuity of steelwork members where possible, rationalising the number of arc radii required and utilising stock member lengths where possible to simplify fabrication.

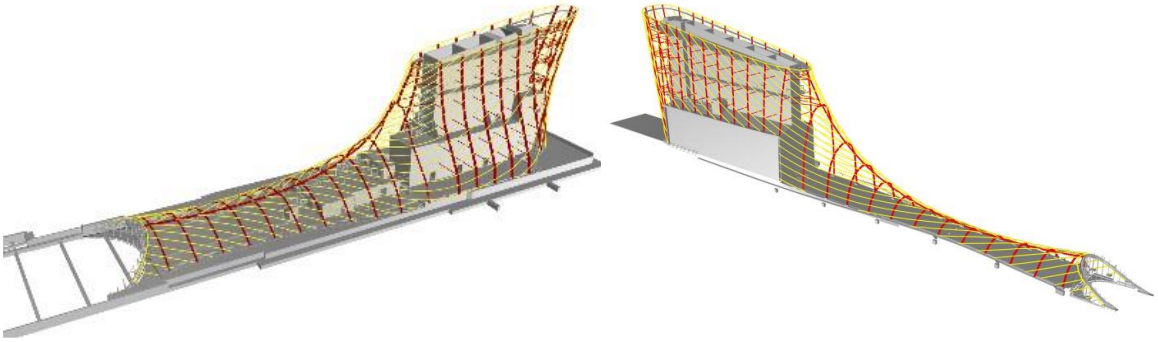


Figure 13. Façade Support System.

4.1 Method

The entirety of the structural design process, from generating of the geometry to analysing of the steel to AS 4100, was automated to accommodate sudden geometric changes driven by both changing architectural requirements and functional constraints such as access walkways and traffic sway envelopes. This was achieved by developing multiple Grasshopper scripts for the project, so that a change at any stage of design could be quickly filtered through a series of parametric models to provide near immediate feedback on the structural implications such a change would have.

4.1.1 Geometric optimisation

Geometry optimisation was a major component of the project. Beyond the initial architectural geometry rework described in Section 0, TTW further manipulated the geometry to improve structural efficiency by maximising the continuity of steelwork members, utilising stock member lengths where possible to simplify fabrication, rationalising the number of arc radii required and minimising the variation between support members and facade.

Segment rationalisation attempted to maximise the number of secondary CHS members that were of stock lengths 9 or 12m. This was achieved by alternating the "bays" of the structure between ladder bays with segments at stock length and filler bays of variable length in between, as shown in Figure . This process had the added benefit of aiding the construction sequencing, as the ladder bays could be built in liftable segments and then once positioned with temporary bracing, the infill members could complete the structure.

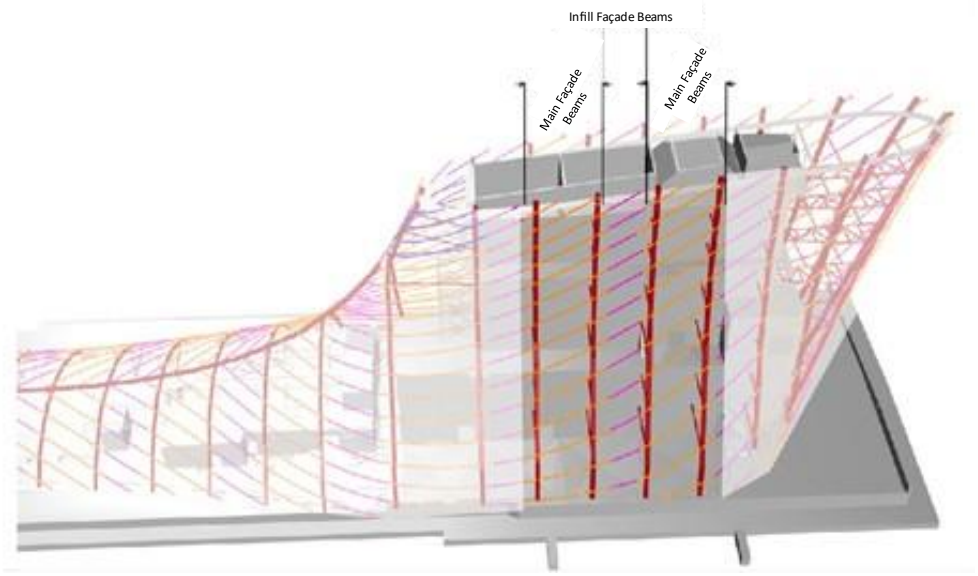


Figure 14. Alternated Main (Orange) and Infill (Purple) Bays.

The secondary steelwork of the structure follows the longitudinal iso-curves of the "sock surface" described in Section 0 of this paper (in the case of the Northern portal, the adjusted curves were used instead). These members have a varying curvature across their length, so simple segmentation would result in nearly all secondary structural members needing to be bent to different radii. This represents not only an enormous cost in terms of fabrication but also a complication on-site as each member would be unique, resulting in the need for more micromanagement of materials during construction. A k-means clustering algorithm was applied to the different bend radii across each the Northern and Southern portals to minimise the number of these unique bend radii. The centroid of each cluster was set as the radius of the grouped members.

After simplifying the secondary members across the structure, the original mesh had no consistent connection length to the new secondary members. Again, having unique connection lengths across the structure would result in high fabrication costs and increased complexity in the construction phase. As such, another clustering process was undertaken to minimise the number of unique connection lengths across the structure, rebuilding the panel mesh out from the secondary members at these clustered offsets.

Utilising stock lengths has a secondary benefit for fabrication, as stock CHS members come prepped with bevelled ends for butt welding.

The combined effects of clustering both the secondary steel bend radii and connection lengths caused variations in the final mesh position that represented the vent structure panel location. As such, the impacts of both clustering algorithms had to be evaluated for deviation from architectural intent and egress outside of allowable construction envelopes.

4.1.2 Structural optimisation

Structural optimisation of the varying geometric concepts outlined above was undertaken using a combination of Strand7 for finite element analysis and in-house steel design Grasshopper modules. Strand7 interoperability was achieved by TTW's in-house Grasshopper plugin called Kookaburra. The optimisation process aimed to satisfy structural requirements while minimising total steel volume.

The iterative Grasshopper/Strand7 script (shown in Figure and simplified in 16) either increased or decreased member sizes based on their compliance within predefined criteria. A member with a strength utilisation ratio greater than 0.9 would increase in section size whilst those under 0.7 would decrease in size (limited to a preselected range of sizes of a given section type). The range in utilisation between 0.7 and 0.9 was considered a 'lazy zone', and members within that range would not change in size. Although a simple approach, this method of redistributing steel volume around the structure is inspired by the mechanoadaptation process of bones. More specifically, it was inspired by the mechanostat hypothesis where bone formation accumulates in areas of high stress and bone resorption in areas of low stress [2].

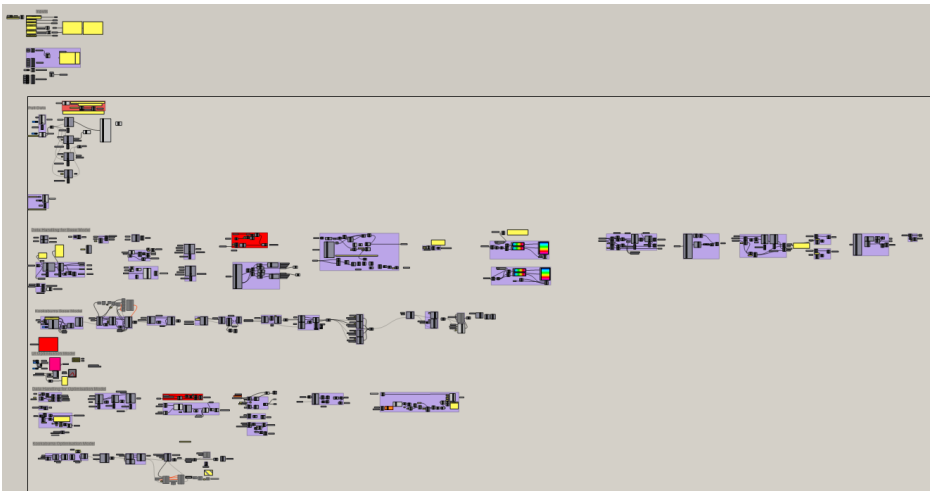


Figure 15. Grasshopper Optimisation Script.

Members in the structure were grouped such that each group was optimised to have a single section work for all its members. This was to ensure that the number of unique section profiles used on the project did not become too high.

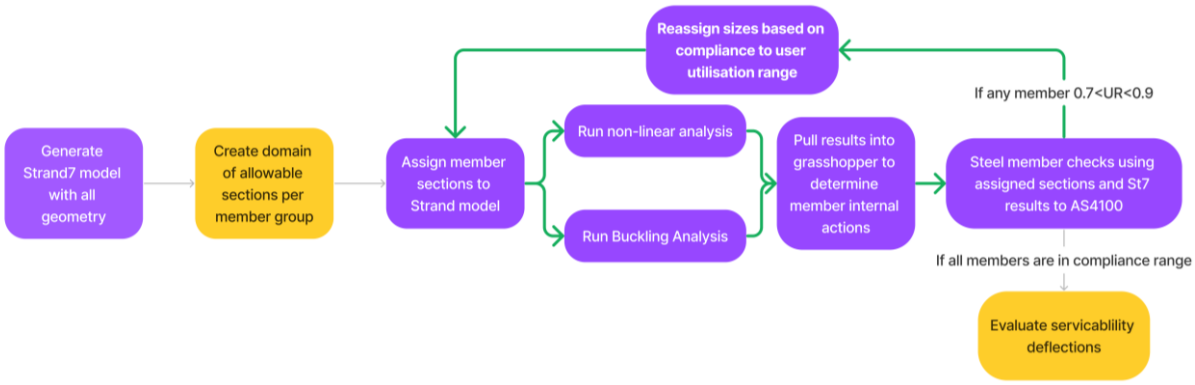


Figure 16. Flowchart of the optimisation process. Automatic Tasks (Purple), Manual Tasks (Yellow), Optimisation Loop (Green Arrows).

4.2 Results

4.2.1 Segment length rationalization

For the Northern portal 64% of secondary steel members were of standard stock length whilst for the Southern Outbound portal the number rose to 67%. The distribution of these members in the Northern structure is shown in Figure .

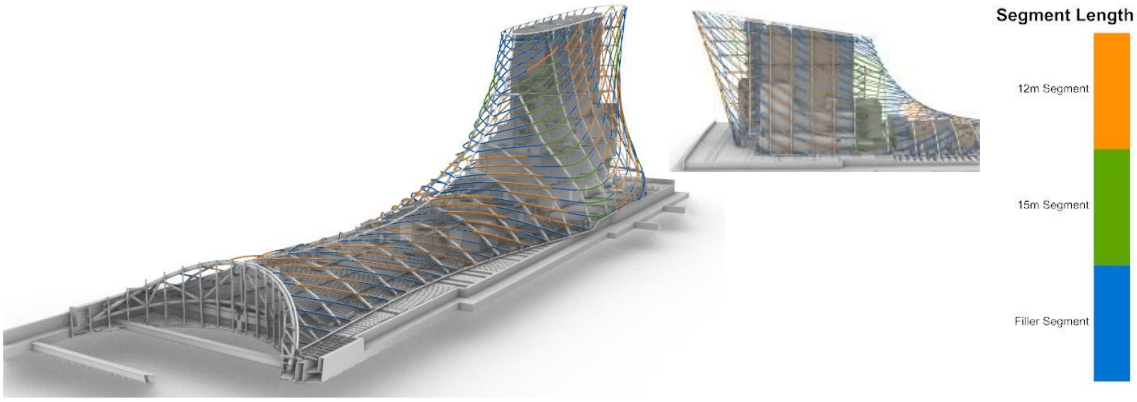


Figure 17. North Vent Secondary Segment Length Distribution (15m segments chosen for a common member length across the largest arch gap, not as a common stock length)

4.2.2 Segment radii rationalization and connection length

Both structures targeted 10 unique bend radii along with utilising straight members to best fit the original architectural intent of the vent surface. The distribution of these bend radii sets for the Northern structure are displayed in Figure *13*.

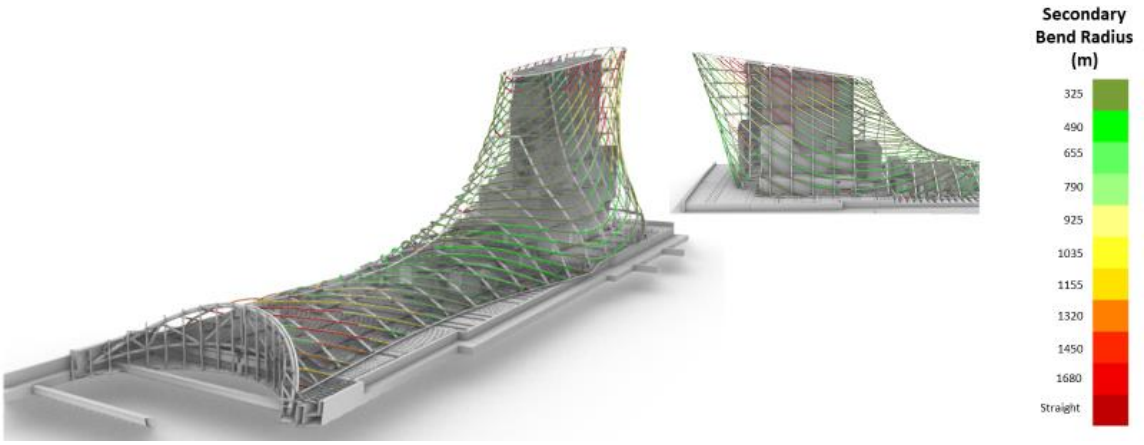


Figure 13. North Vent Secondary Bend Radius Distribution.

In combination with these clustered bend radii, it was determined that a grouping of 5 unique connection lengths on the Northern and 10 on the Southern structure between the façade panels and secondary steel work, allowed for the preservation of architectural intent in the façade.

4.2.3 Structural optimisation

For the purpose of project confidentiality, the exact tonnage of the structure is not provided in this paper. However, it is worth noting that the optimisation process undertaken by TTW reduced the structural steel tonnage of the structures (exclusive of connection details) on average between the two structures to 60% of the original design prior to our engagement on the project.

5. Conclusion

Overall, the West Gate Tunnel Project vent structures showcase the benefits of integrating digital modelling and optimisation techniques into the design and construction process of complex architectural structures. By utilising computational processes, the project was able to achieve significant efficiencies in design and construction that would have been difficult to achieve using traditional engineering methods. As the use of computational processes in engineering continues to grow, it is likely that more complex and innovative structures will be able to be designed and built in a more streamlined and cost-effective manner.

Acknowledgements

The authors express our heartfelt thanks and appreciation to the entire West Gate Tunnel team for their exceptional collaboration and support throughout the project. We extend special thanks to Dean Anderson, Hii King, and John Haralabakos from CPBJHJV, as well as Armin Voelske, Moshe Chong, and Roger Wood from Wood Marsh, for their invaluable contributions to the project. Their expertise, dedication, and hard work played a vital role in bringing the project to fruition, and we greatly appreciate their guidance throughout the process.

References

[1] Pereira A., Coop B., Zelenkin D., Whitfield R. and Berry K. "Designing the West Gate Tunnel portals: Timber Gridshells." in *Integration of Design and Fabrication: Proceedings of the IASS Annual Symposium 2023*, Melbourne, Australia, July 10-14, 2023.

[2] Frost, Harold M. "Bone's mechanostat: a 2003 update." *The Anatomical record part a: discoveries in molecular, cellular, and evolutionary biology: an official publication of the American association of anatomists*, 275, no. 2, pp. 1081-1101, 2003.

IASS 2023 July 10–14 Melbourne Integration of Design and Fabrication

Proceedings of the IASS Annual Symposium 2023
Integration of Design and Fabrication
10–14 July 2023, Melbourne, Australia
Y.M. Xie, J. Burry, T.U. Lee and J. Ma (eds.)

Multi-objective optimization of the large telescope structure under temperature loading

Hiroaki KAWAMURA[a,*], Ayame USUI[d], Chihiro IMAMURA[b], Akio TANIGUCHI[b], Kohei SHINTANI[c], Takayuki YAMADA[c], Yoichi TAMURA[b], Toshiaki KIMURA[d]

[a,*] Graduate School of Design and Architecture, Nagoya City University
Kita-Chikusa, Chikusa-ku, Nagoya, Japan
kawamura@sda.nagoya-cu.ac.jp

[b] Graduate Scheel of Science, Nagoya University
[c] Graduate Scheel of Mechanical Engineering, University of Tokyo
[d] Graduate School of Design and Architecture, Nagoya City University

Abstract

A new 50 m class single dish telescope, the Large Submillimeter Telescope (LST), is planned. From the view of construction, it is essential to reduce the weight of the antenna mounts because LST will be constructed at high altitudes. Furthermore, despite the large-scale structure, the deformation needs to be kept to a minimal value (e.g., 1/100 mm order) required for light collection performance. Additionally, it is necessary to consider the effects of temperature changes and wind loads in addition to deformation due to their weight because such large telescopes are installed outside, and long periods are needed for the observation. A novel structural design approach is required to realize a backup structure because it is tough to achieve with the conventional design approach. This study proposed a new multi-objective optimization for such large telescope structures by extending to previous papers. In addition to the total mass, the surface accuracy of the primary reflector, which is expressed by root-mean-square (RMS) of deformation subjected to vertical and thermal load for the normal direction of the reflector, is assigned as the objective function. The shape of the primary reflector is evaluated by considering homologous structures. Its focus point can vary through optimization to obtain the optimal shape. The effectiveness of the proposed method is discussed through numerical examples.

Keywords: large submillimeter telescope, multi-objective optimization, space structure

1. Introduction

In an effort to increase the diameter of submillimeter telescopes to meet the scientific need for deep space exploration, the construction of a 50-m diameter Large Submillimeter Telescope (LST) is planned as shown in Figure 1 (a) [1]. Because the Large Submillimeter Telescope requires high sensitivity and high-resolution optical performance, the support structure of the mirror surface must be lightweight and highly rigid. In addition, homologous deformation performance [2, 3], in which the mirror surface maintains a rotating paraboloidal plane after deformation under various loading conditions, is required for optical performance. The present paper describes a numerical method to design the LST structure using topology optimization considering its design requirements.

The large aperture of submillimeter-wave telescopes is a necessary performance required to achieve a large light-gathering area and high resolution. The telescope's primary mirror is required to have a high mirror surface accuracy (e.g., less than 45 μm), and as the mirror surface becomes larger, the primary mirror must maintain that accuracy in a variety of observation postures. Figure 1 shows a conceptual diagram of the LST. The surface accuracy of the primary mirror is important to collect electromagnetic

Copyright © 2023 by Hiroaki KAWAMURA. Published in the Proceedings of the IASS Annual Symposium 2023 with permission.

waves from deep space with high accuracy. Therefore, the backup structure supporting the primary mirror must have high rigidity. For example, the allowable deformation of an ordinary large building is about 1/300 of its span, but if this is applied to a 50-m class large telescope, the maximum deflection would be 50 m/300 = 167 mm, and the mirror surface accuracy requirement cannot be satisfied using ordinary building structure design methods. However, the mass of the structure generally increases as the rigidity of the primary mirror increases. Requirement-1). Therefore, an optimal design that satisfies both rigidity and mass performance is necessary. Although there are some examples of optimal design for improving the accuracy of the mirror surface in engineering telescopes with relatively small apertures as shown in Figure 1 (b) [4], there are few studies on large radio telescopes with apertures in the 50-m class.

This study proposed a new multi-objective optimization for such large telescope structures by extending to previous papers. We aim to obtain the configuration of the large-scale buck-up structure such as the LST plan by using the proposed method.

(a) (b)

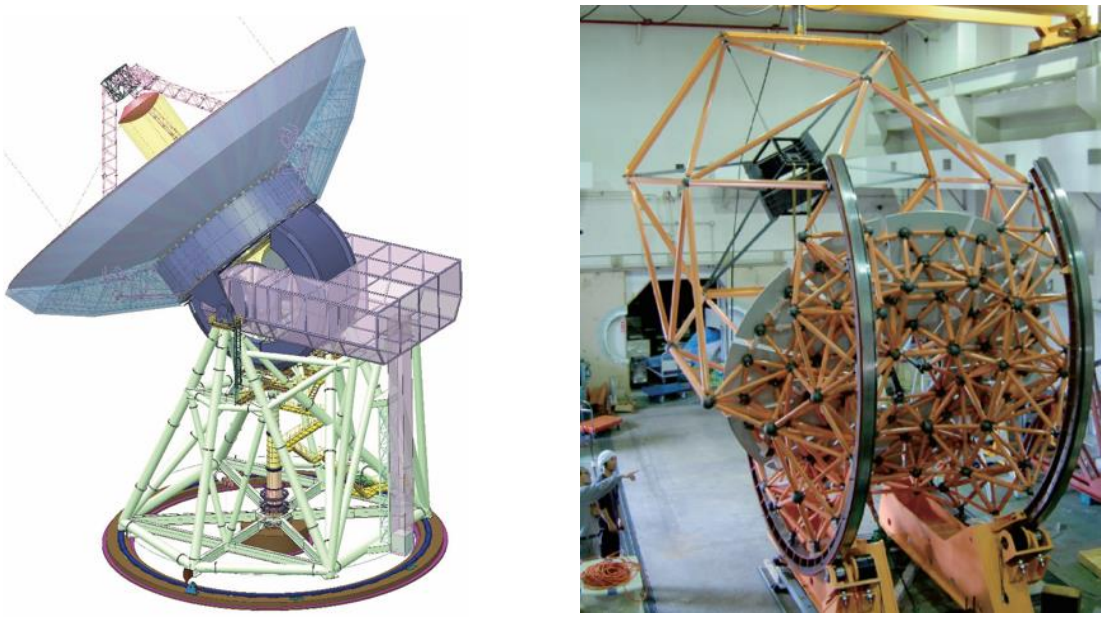


Figure 1. Examples of telescopes; (a) conceptual figure of LST [1], (b) heuristic-optimized buck-up structure for 4 m class telescope [2]

2. Problem formulation

2.1. Structural optimization considering homologous deformation.

Figure 2 illustrates a cross-section image of a paraboloid antenna. The surface of the primary reflector is deformed by mechanical or thermal loadings. The design domain of LST backup structure Ω is the supporting structure that consists of truss elements with the cross-sectional area as design variables $\boldsymbol{x} = (x_1, x_2, \dots, x_n)$. Cross-sectional area $\boldsymbol{x}$ is considered about the selection from the material list $\boldsymbol{a}$ which consists of m kinds of materials for each truss element. The solution set $\mathcal{D}$ is expressed by $\mathcal{D} = \{\boldsymbol{x} \in \boldsymbol{a} \mid \boldsymbol{a} = (a_1, a_2, \dots, a_m) \in \mathbb{R}^{n \times m}\}$. The displacement vector $\boldsymbol{u}$ of the supporting structure are obtained by solving the equilibrium equation as follows:

$$\boldsymbol{K}(\boldsymbol{x})\boldsymbol{u} = \boldsymbol{f} \tag{1}$$

where, the global stiffness matrix is $\boldsymbol{K}(\boldsymbol{x}) = \sum_{i=1}^{n} \boldsymbol{K}_i(x_i)$, with the element stiffness matrix $\boldsymbol{K}_i(x_i)$. Furthermore, the homologous deformation $h = h(\boldsymbol{u})$ is defined as follows:

$$h(\boldsymbol{u}) = \int_{\Gamma_D} (\boldsymbol{u}(\boldsymbol{x}) - \overline{\boldsymbol{u}}) \cdot (\boldsymbol{u}(\boldsymbol{x}) - \overline{\boldsymbol{u}})\, d\Gamma_D \tag{2}$$

where, $\overline{\boldsymbol{u}} \in \mathbb{R}$ is the pre-described deformation vector which can be defined as follows:

$$\overline{\boldsymbol{u}} = S(\boldsymbol{c}, \boldsymbol{p}) - S_0 \tag{3}$$

where $S(\boldsymbol{c}, \boldsymbol{p})$ is the paraboloid function with given vertex coordinate $c = \{x_c, y_c, z_c\}^T$ and focus $\boldsymbol{p}$. S_0 is the surface of the undeformed primary reflector. Paraboloid parameters $\boldsymbol{c}$ and $\boldsymbol{p}$ are given as follows:

$$\boldsymbol{c}, \boldsymbol{p} = \min_{\boldsymbol{c} \in \mathbb{R}^3, p \in \mathbb{R}} \int_{\Gamma_D} (\boldsymbol{u}(\boldsymbol{x}) + S_0 - S(\boldsymbol{c}, \boldsymbol{p})) \cdot (\boldsymbol{u}(\boldsymbol{x}) + S_0 - S(\boldsymbol{c}, \boldsymbol{p}))\, d\Gamma_D \tag{4}$$

Using the homologous deformation $h_\varphi(\boldsymbol{u}, t, \boldsymbol{b})$ with loading condition t on the boundary Γ_t and body force $\boldsymbol{b} = \boldsymbol{b}(\boldsymbol{x})$ in the design domain Ω, we defined an objective function as follows:

$$J_\varphi = \int_t \boldsymbol{w}_\varphi(t) \cdot h_\varphi(\boldsymbol{u}, t, \boldsymbol{b}) dt \tag{5}$$

where, $\varphi \in [\varphi_{min}, \varphi_{max}]$ is the elevation angle of the reflector and $w_\varphi(t)$ is weight function to the loading condition t at the elevation angle. For constraint functions, the stress $i \in \{1, \dots, m\}$ of truss element are constrained as follows:

$$J_{t,i}(\boldsymbol{x}) = \prod_{j}^{i} \sigma_{t,j} - c_i \leq 0 \tag{6}$$

where, c_i is constraint value of the elemental stress of element i and $\sigma_{t,i}$ is elemental stress of the i-th truss element under loading condition t. The optimization problem to minimize the objective function Eq. (4) while satisfying subjective functions Eq. (5) can be described as follows:

$$\min_{\boldsymbol{x} \in X} \{J_\varphi(\boldsymbol{u}) \mid J_{t,i}(\boldsymbol{x}) \leq 0, i \in \{1, \dots, m\}, \boldsymbol{K}(\boldsymbol{x})\boldsymbol{u} = \boldsymbol{f}_t\} \tag{7}$$

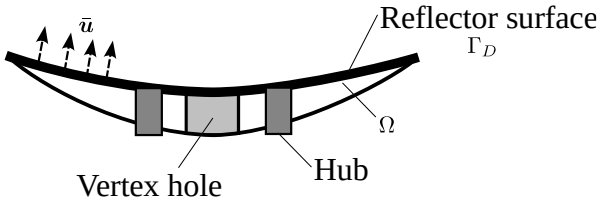


Figure 2. Illustration of a cross-section of paraboloid antenna

3. Numerical examples

3.1. Configurations of the test model

We conduct the optimization for the test model to validate the effectiveness of the proposed method. Figure 3 represents the initial model with the isometric view. Figure 3 (b) and (c) show the cross-section diagram of the ground structure at *y*=0. The diameter of the reflector dish is 50 m, and the two-layered truss structure supports the reflector. The truss structure is constrained by the rigid ring, called Hub, with 12 m diameter. In this figure, the white marker indicates nodes of the truss structure, and the black marker indicates fixed nodes to Hub.

Figure 4 shows the top view of the ground structure. The colour of each element indicates the group of elements. Note that there are 232 element groups in this model. Each element has the same cross-section property in the same element groups. Table 1 shows loading cases for the structural optimization problem. There are three cases, two kinds of mechanical loading and thermal loading.

Table 1 shows optimization parameters for the diameters of each truss member. DEAP, which is the python library for the genetic algorithm is adopted for the optimizer [5]. NSGA-II is adopted for the selection algorithm for multi-objective optimization [6]. OpenSees is used to obtain the displacement for computing the homologous deformation performance of each solution [7]. Table 2 shows loading conditions for multi-objective optimization. Table 3 shows the diameters of pipes for each truss member group. The tube cross-section is selected from fifteen standard sizes based of the JIS G3444, which is carbon steel pipes for general structural purposes STK400.

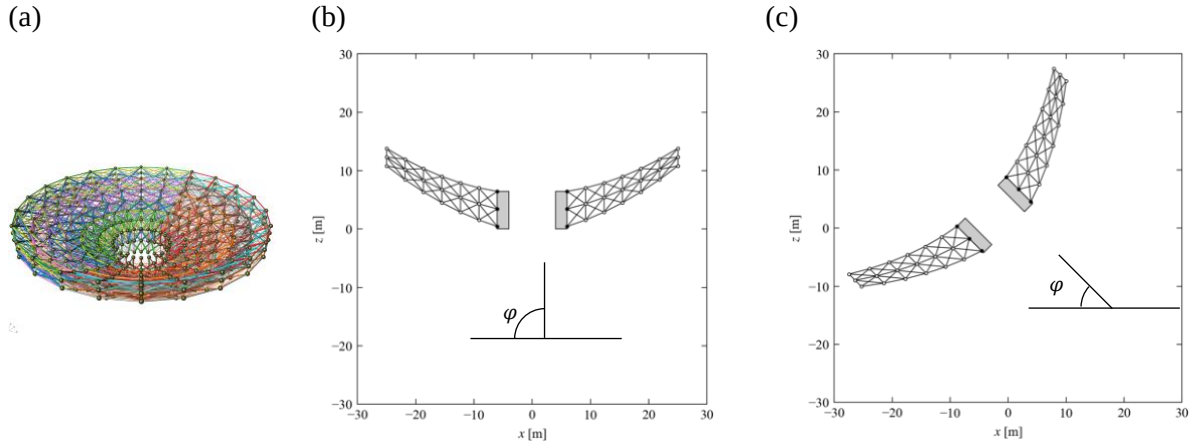


Figure 3. Initial ground structure: (a) perspective view, (b) cross-section at *y*=0 with elevation angle $\varphi = 90°$, (c) cross-section at $y = 0$ with elevation angle $\varphi = 45°$

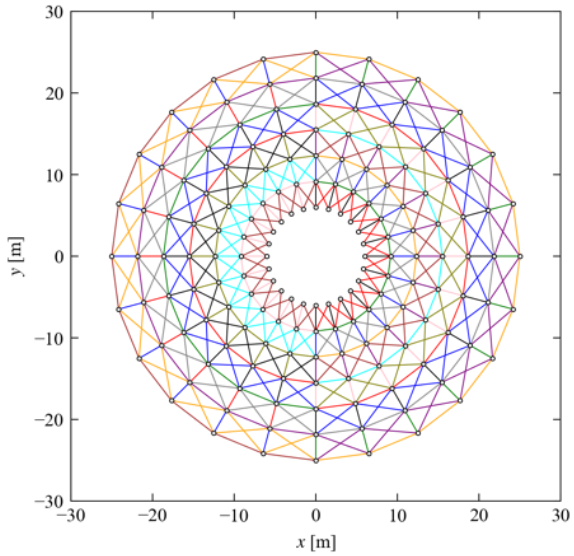


Figure 4. Top view of ground structure colored by element groups

Table 1. Optimization parameters

Number of individuals	500
Number of generations	500
Type of crossover	Two-point crossover
Crossover rate	0.7
Mutation rate	0.1
Selection algorithm	NSGA-II

Table 2. loading conditions

#	Elevation φ	Loading condition
1	90 deg.	Dead load 200 kg/m2
2	30 deg.	Dead load 200 kg/m2
3	90 deg.	Thermal +30 K

Table 3. Pipes for truss members

ID	Outside diameter (mm)	Thickness (mm)	Cross-sectional area (mm^2)	ID	Outside diameter (mm)	Thickness (mm)	Cross-sectional area (mm^2)
1	9.0	1.7	5.5	9	114.3	3.5	1035.7
2	34.0	2.3	90.3	10	139.8	3.5	1551.4
3	42.7	2.3	143.4	11	165.2	4.5	2165.3
4	48.6	2.3	186.3	12	190.7	5.3	2885.0
5	60.5	2.3	289.6	13	216.3	4.5	3716.6
6	76.3	2.8	460.8	14	267.4	6.0	5678.5
7	89.1	3.2	628.5	15	318.5	6.0	8061.1
8	101.6	3.2	818.2				

3.2. Numerical results and discussion

Figure 5 shows the convergence history of objective functions. In this case, the objective function of the thermal loading condition shows earlier convergence than in other loading cases. Figure 6 shows the distribution of the non-inferior solutions according to the value of the objective functions. The objective function in the dead loading with elevation angle $\varphi = 90$ has a wider range distribution than in other loading conditions.

Figure 7 shows the configuration of truss elements in obtained solutions. Each element color indicates axial stress (red: tension, blue: compression). In the case of the elevation angle $\varphi = 30$, truss elements in the lower part (marked as "A" in Figure 7(b)) are thicker than the upper part (marked as "B"). It indicates that this result is effective for improving the homologous deformation performance in the angled loading condition.

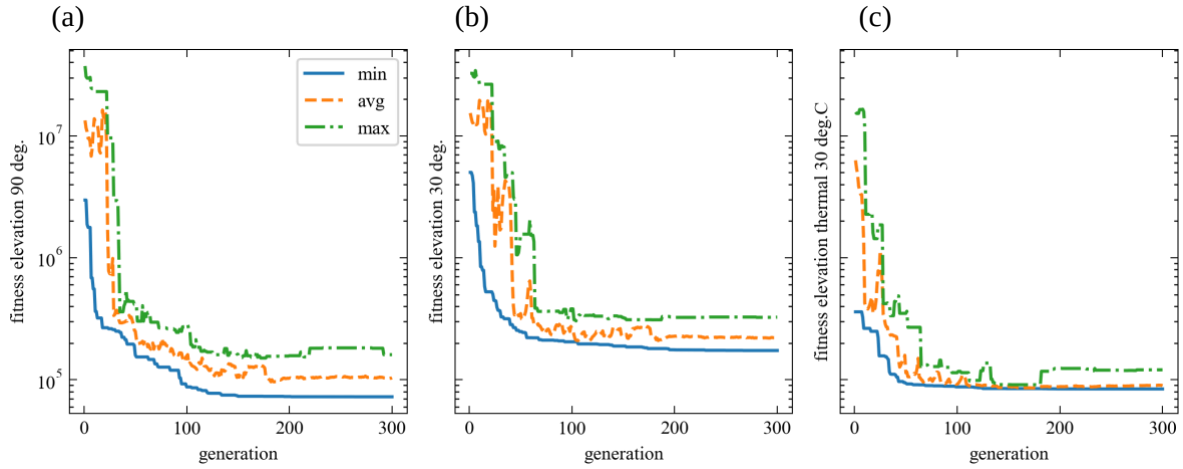


Figure 5. convergence histories of objective functions under each loading conditions: (a) dead loading with elevation angle $\varphi = 90$, (b) dead loading with elevation angle $\varphi = 30$, (c) thermal loading with 30 K.

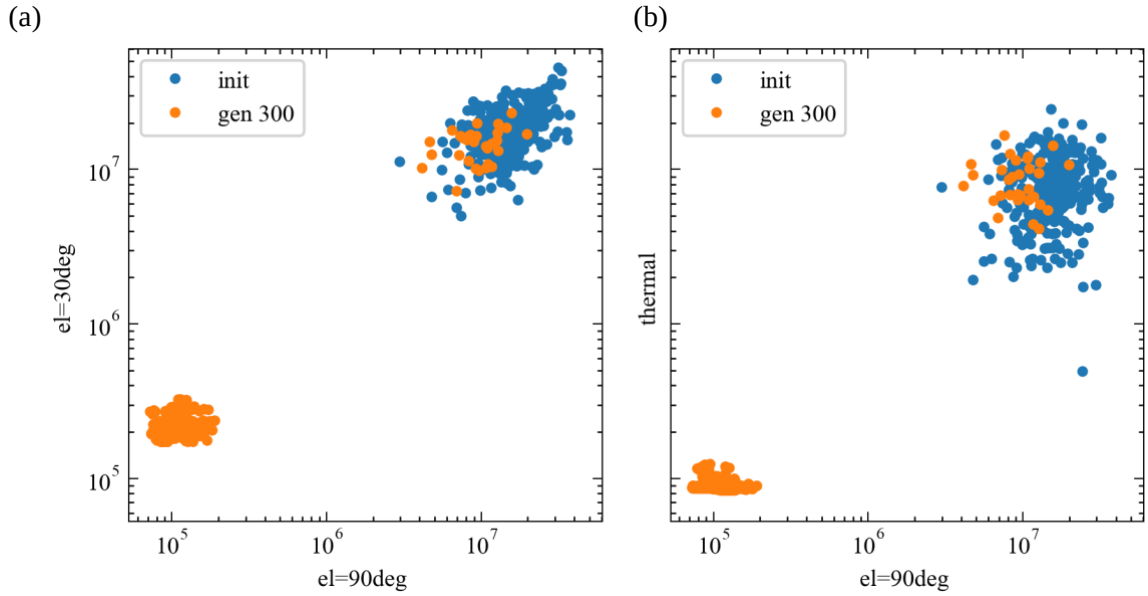
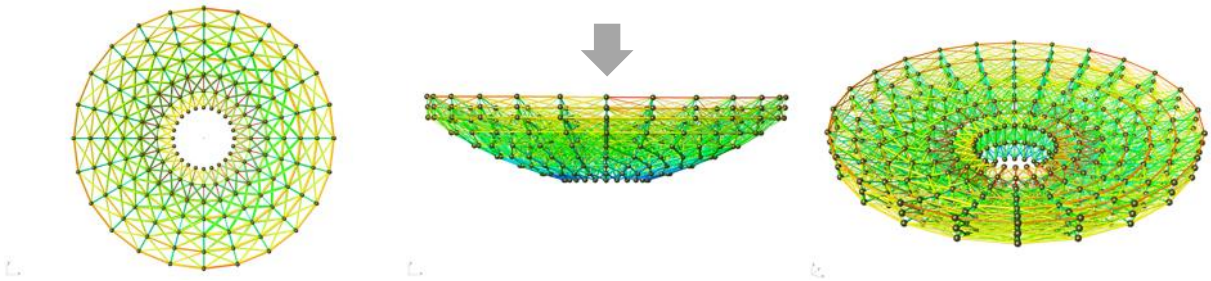
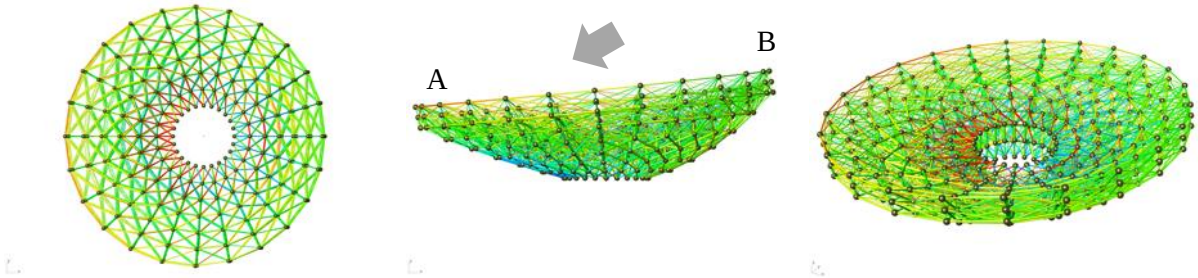


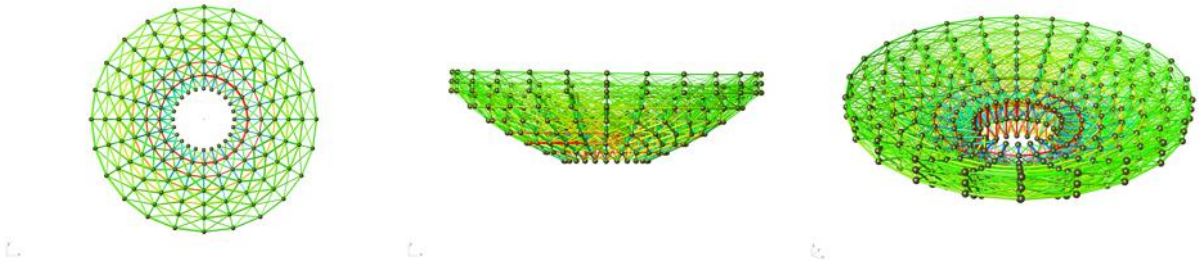
Figure 6. comparison of distribution of objective function values



(a) Under dead loading with elevation angle $\varphi = 30$



(b) Under dead loading with elevation angle $\varphi = 90$



(c) under thermal loading condition

Figure 7. obtained solution with element stress contours (deformation scale 1:200). Arrows indicate direction of gravity.

4. Conclusion: submission of contributions

This paper describes a multi-objective optimization method of the backup structure of the Large Scale Telescope (LST). In this paper, the new objective functions are proposed for each elevation angle of the dish with not only mechanical but also thermal loading conditions. Obtained solutions have reasonable element configurations for several loading conditions.

References

[1] R. Kawabe, K. Kohno, Y. Tamura, T. Takekoshi, T. Oshima, and S. Ishii, "New 50-m-class single-dish telescope; Large Submillimeter Telescope (LST)" *Proceedings of SPIE*, vol. 9906, 2016. https://doi.org/10.1117/12.2232202

[2] S. V. Hoerner, Homologous Deformation of Tiltable Telescope, Proceedings of the American Society of Civil Engineers, Journal of the Structural Division, 93 (5), 1967

[3] Y., Hangai, Shape Analysis of Structures, Theoretical and Applied Mechanics, vol. 39,

Proceedings of 39th Japan National Congress for Applied Mechanics, Ed. JNCTAM, Science Council of Japan, University of Tokyo Press, 1990.

[4] M. Kunda, M. Kurita, and H. Ohmori, "Computational Morphogenesis of Truss Structures – Application to Telescope Structure –", *Journal of the International Association for Shell and Spatial Structures*, Vol. 53, 1, 171, pp. 49-56 (8), 2012.

[5] Fortin, F.-A. et al., DEAP: Evolutionary algorithms made easy. *Journal of Machine Learning Research*, 13, p.2171–2175, 2012.

[6] Deb, K., Pratap, A., Agarwal, S., and Meyarivan, T. "A fast and elitist multiobjective genetic algorithm: NSGA-II," *IEEE Transactions on Evolutionary Computation* **6**, No. 2, 182-197, 2002, DOI: 10.1109/4235.996017.

[7] https://opensees.berkeley.edu

IASS 2023 July 10–14 Melbourne Integration of Design and Fabrication

Proceedings of the IASS Annual Symposium 2023
Integration of Design and Fabrication
10–14 July 2023, Melbourne, Australia
Y.M. Xie, J. Burry, T.U. Lee and J. Ma (eds.)

Nonparametric shape optimization of piecewise developable surfaces for maximum stiffness using discrete differential geometry

Makoto OHSAKI[*], Kentaro HAYAKAWA[a], Jingyao ZHANG[a]

[a,*] Department of Architecture and Architectural Engineering, Kyoto University
Kyoto-Daigaku Katsura, Nishikyo, Kyoto 615-8540, Japan
ohsaki@archi.kyoto-u.ac.jp

Abstract

A shape optimization method of curved surfaces is presented for the limited class of surface, namely, piecewise developable surfaces. The surfaces are generated using the nonparametric method proposed by the authors based on the formulations of discrete differential geometry, and the locations of selected points on the surface are optimized for minimizing the compliance that is a measure of flexibility of the structure. The developability of the polyhedral surface with triangular mesh is defined using the discretized Gauss map at each vertex; i.e., the area of local Gauss map vanishes for a developable surface. The heights of the specified points are optimized using simulated annealing which is classified as a heuristic algorithm based on local search. Responses to static loads are evaluated using finite element analysis with quadrilateral elements. It is shown in the numerical examples, that various optimal shapes in view of structural performance and constructional cost can be generated using the proposed method by limiting the surface class to the piecewise developable surface.

Keywords: developable surface, discrete differential geometry, Gauss map, shape optimization

1. Introduction

One of the drawbacks for designing a free-form shell surface is that it requires large cost for construction. For example, it is difficult to manufacture formworks for a doubly curved concrete shell. The construction cost can be significantly reduced if the surface is designed as an assembly of developable surface patches [1], because the surface or the formwork can be generated by simply bending a plate. Furthermore, for latticed shells, straight beams can be used in the direction of the ruling of a developable surface that is classified as a ruled surface [2]. Another aspect of designing free-form surfaces is that structural performances are evaluated using finite element analysis after discretization into a polyhedral surface. Therefore, it is desirable to use discretized model and formulations throughout the process of design, analysis, and optimization.

In this paper, we utilize the formulations of discrete differental geometry for structural optimization of piecewise smooth shell surfaces consisting of a limited class of desirable property; namely, piecewise developable surfaces. The developable surface patches are generate using the nonparametric meshless approach proposed by the authors [3]. The stiffness of shell surface is maximized by minimizing the total strain energy under the specified loads using a heuristic search method called simulated annealing (SA).

2. Meshless approach to design of piecewise developable surface

In this section, we briefly summarize the shape generation method proposed in Ref. [3] for completeness of paper.

Copyright © 2023 by Makoto OHSAKI, Kentaro HAYAKAWA and Jingyao ZHANG. Published in the Proceedings of the IASS Annual Symposium 2023 with permission.

Consider a surface with grid points as shown in Fig. 1, where the dashed grid lines are drawn for convenience of visualizing the surface. The auxiliary edges are generated for defining the discretized form of Gauss map that is a unit sphere consisting of unit normal vectors. For example, point A in Fig. 2 is connected to eight neighborhood points by the red dotted auxiliary edges. By generating the auxiliary edges at other grid points, the surface as shown in Fig. 3 is generated from the grid points in Fig. 1.

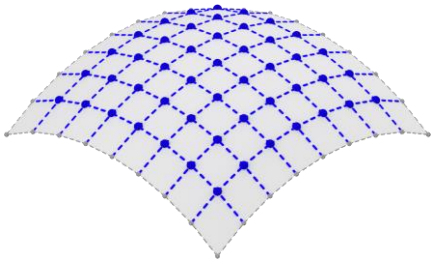


Figure 1. Surface with grid points

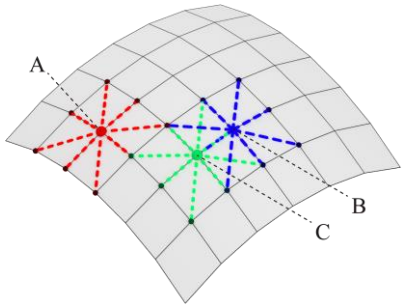


Figure 2. Grid points A, B, C and auxiliary edges connecting to their neighborhood points

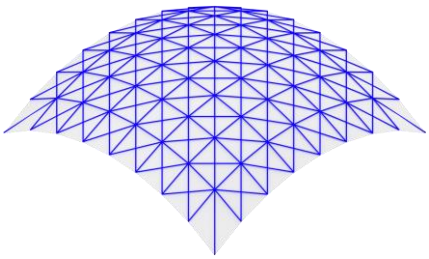


Figure 3. Grid points and auxiliary edges on a curved surface

The condition for developability of surface is formulated by the vanishing area of the Gauss map [3]. Here, the normal vector at a grid point is defined as the average of the unit normal vectors of the adjacent faces defined by the auxiliary edges. The area of local Gauss map is computed without any mesh discretization. Let $\mathbf{q}_1,\ldots,\mathbf{q}_{m_i}$ denote the location vectors of m_i points, which are simply denoted by points $1,\ldots,m_i$, in the neighborhood of point *i*, for which the location vector is denoted by $\mathbf{p}_i$, as shown in Fig. 2. Auxiliary edges are drawn between $\mathbf{p}_i$ and $\mathbf{q}_1,\ldots,\mathbf{q}_{m_i}$ which are denoted by edges $1,\ldots,m_i$.

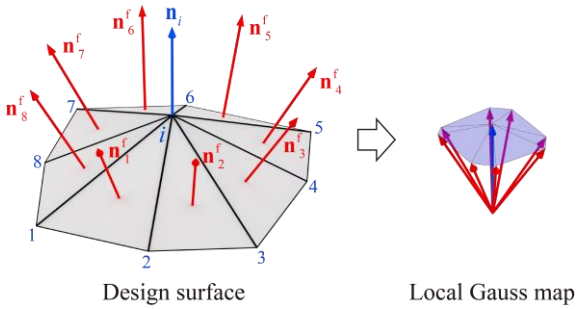


Figure 4. Local Gauss map at a point on a surface

The unit normal vector of the region between edges *j* and $j+1$, denoted by $\mathbf{n}_j^{\mathrm{f}}$, is computed as

$$\mathbf{n}_j^{\mathrm{f}} = \frac{\hat{\mathbf{n}}_j^{\mathrm{f}}}{\left\|\hat{\mathbf{n}}_j^{\mathrm{f}}\right\|},\ \hat{\mathbf{n}}_j^{\mathrm{f}} = (\mathbf{q}_j - \mathbf{p}_i)\times(\mathbf{q}_{j+1} - \mathbf{p}_i),\ \ (j = 1,\ldots,m_i) \tag{1}$$

Then the unit normal vector $\mathbf{n}_i$ at point i is computed as the average of the unit normal vectors of the surrounding regions as

$$\mathbf{n}_i = \frac{\hat{\mathbf{n}}_i}{\|\hat{\mathbf{n}}_i\|}, \quad \hat{\mathbf{n}}_i = \frac{1}{m_i}\sum_{j=1}^{m_i} \mathbf{n}_j^{\mathrm{f}} \tag{2}$$

The unit normal vector at a grid point, indicated with blue in the left figure of Fig. 4, is computed from those of the regions indicated with red defined by the locations of the neighborhood points. The normal vectors are translated to have the same origin to generate the local Gauss map as shown in the right figure of Fig. 4. The *area of local Gauss map* is to be reduced to zero to obtain a developable surface. It is easily seen that the local Gauss map degenerates to a point if the surface is locally planar, and the area vanishes for a cylindrical surface. It should be noted here that the area of local Gauss map vanishes also for a conical surface, if the points are appropriately located along a ruling of the surface.

The area A_i of local Gauss map in the neighborhood of point i is computed as

$$A_i = \sum_{j=1}^{m_i} a_{ij}, \quad a_{ij} = \frac{1}{2}\|\mathbf{v}_{ij}\|, \quad \mathbf{v}_{ij} = (\mathbf{n}_j^{\mathrm{f}} - \mathbf{n}_i) \times (\mathbf{n}_{j+1}^{\mathrm{f}} - \mathbf{n}_i) \tag{3}$$

Let I denote the set of indices of the interior grid points at which the area of local Gauss map is to be computed. The vector of variables $\mathbf{x}$ consists of the coordinates of grid points that are to be varied. To prevent divergence of gradients of a_{ij} in the vicinity of optimal solutions obtained using a gradient based method, the square area of the local Gauss map is to be minimized, and the optimization problem is formulated as

$$\begin{aligned} &\text{Minimize} \quad F(\mathbf{x}) = \sum_{i \in I} \sum_{j=1}^{m_i} (a_{ij})^2 \\ &\text{subject to} \quad \mathbf{x} \in \chi \end{aligned} \tag{4}$$

where χ is the feasible region of $\mathbf{x}$ defined by its upper and lower bounds. Note that some selected points are excluded from the set I to obtain piecewise approximately developable surfaces with specified locations of points on the internal boundary of patches.

3. Shape optimization of piecewise developable surface

Stiffness of the piecewise developable surface generated using the method in Sec. 2 is maximized by minimizing the total strain energy against static loads. The quadrilateral mesh is generated from the grid points, and static responses are evaluated by the finite element analysis. The design variable vector $\boldsymbol{\xi}$ consists of the coordinates of some grid points that are to be specified in the form-finding problem in Sec. 2. Hence, the vector $\mathbf{x}$ in Eq. (4) is considered as function of $\boldsymbol{\xi}$ and denoted by $\mathbf{x}(\boldsymbol{\xi})$.

The shell is pin-supported at the boundary, and the static loads are calculated from the self-weight proportional to the covering area of each grid point. Let M denote the number of grid points. The load and displacement vectors at point i $(i = 1, \ldots, M)$ are denoted by $\mathbf{p}_i \in \mathbb{R}^3$ and $\mathbf{d}_i \in \mathbb{R}^3$, respectively. The optimization problem is formulated as

$$\begin{aligned} &\text{Minimize} \quad S(\boldsymbol{\xi}) = \frac{1}{2}\sum_{i=1}^{M} \mathbf{p}_i^{\mathrm{T}}(\xi)\mathbf{d}_i(\xi) \\ &\text{subject to} \quad \mathbf{x}(\boldsymbol{\xi}) = \underset{\mathbf{x} \in \chi}{\operatorname{argmin}} F(\mathbf{x}), \quad z \in \zeta \end{aligned} \tag{5}$$

where ζ is the feasible region of $\mathbf{z}$ defined by its upper and lower bounds. Figure 5 shows the process

of solving Problem (5) using SA. At each step of SA, Problem (4) is solved for $\boldsymbol{\xi}$ using a gradient based algorithm, and the structural response is evaluated to update the solution.

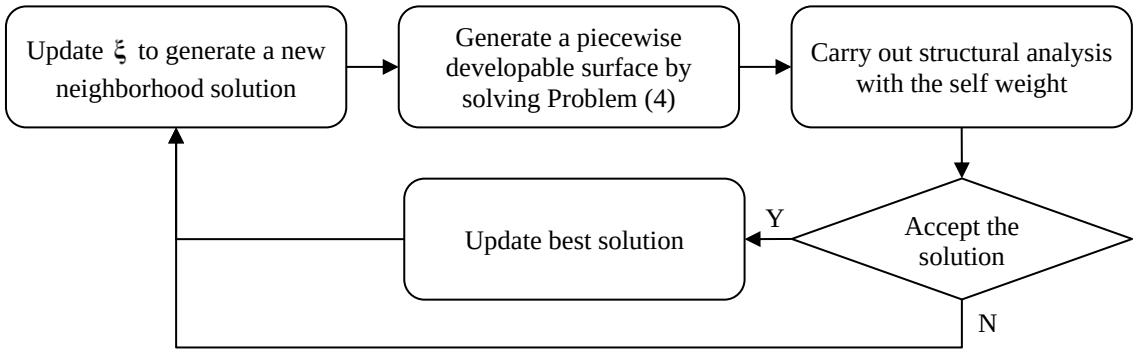
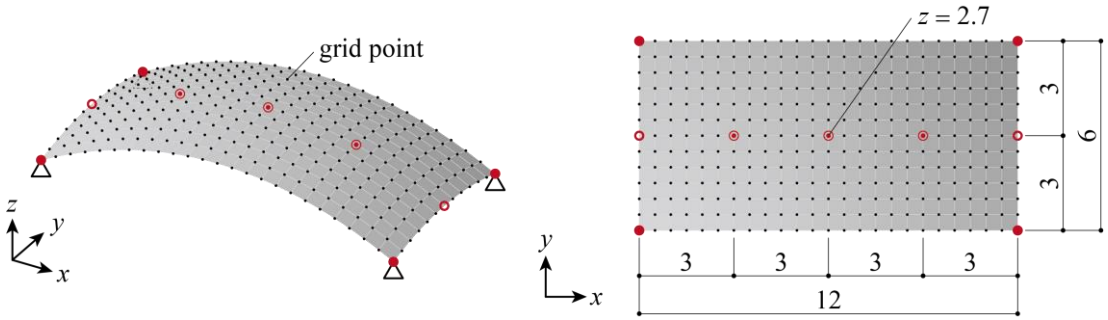


Figure 5. Procedure at an iterative step of SA



fixed in the generation of a piecewise developable surface

area of Gauss map is ignored in the generation of a piecewise developable surface

z-coordinate is updated in SA (variable in SA)

pin-supported in the structural analysis

Figure 6. Initial arrangement of grid points

4. Examples

Optimal shapes are found from the initial shape in Fig. 6. The red internal grid points are excluded from calculation of the area of Gauss map in $F(\mathbf{x})$ of Problem (4) to generate internal boundaries of developable surface patches. The variables in Problem (4) are the *z*-coordinates of the points without marks in Fig. 6. Problem (4) is solved using SNOPT ver. 7 [5] implemented in pyOpt [6]. The lower and upper bounds of the *z*-coordinates at each grid point are $z_0 - 5$ and $z_0 + 12$, respectively, where z_0 is the value at the initial shape in Fig. 6. Note that symmetry of the model is not considered here.

The boundary condition for structural analysis is given as shown in Fig. 7. Young's modulus and Poisson's ratio of the material are 2.0×10^7 kN/m^2 and 0.2, respectively, and the load is given as 1.0×10^3 kN/m^2. The size of shell on the plane is 12×6 m, and the thickness is 0.1 m. Dual-annealing [7] implemented in SciPy is used for solving the structural optimization problem (5). The maximum number of temperature reduction steps is 200, and neighborhood search is carried out 10 times at each temperature; i.e., the total number of analysis is 2000. Local search is not used, and the default values are used for other parameters. The lower and upper bounds of the variable *z*-coordinates are $z_0 - 1$ and $z_0 + 1$, respectively, for the structural optimization.

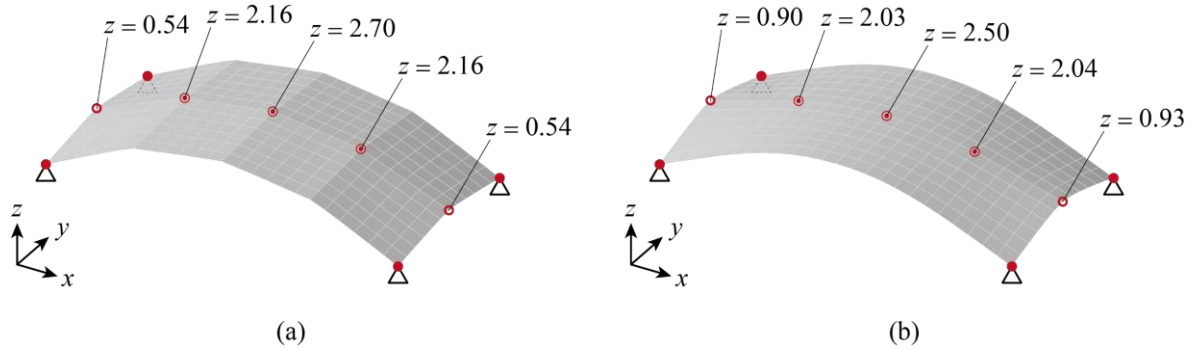


Figure 7. Piecewise developable surfaces (regular grid points are not displayed); (a) initial surface before structural optimization, (b) optimal surface

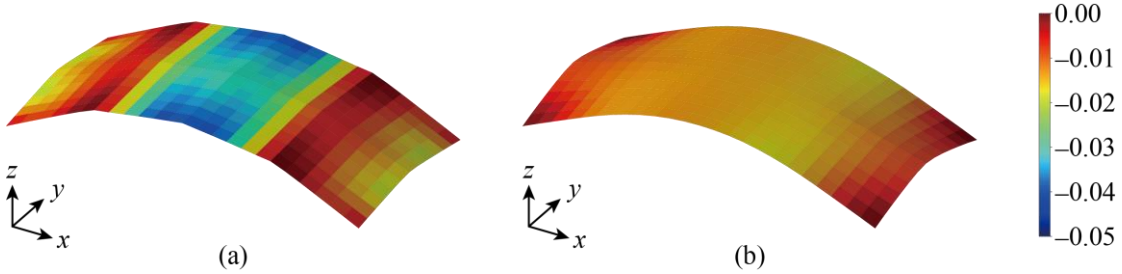


Figure 8. Displacement in *z*-direction (m); (a) initial surface, (b) optimal surface

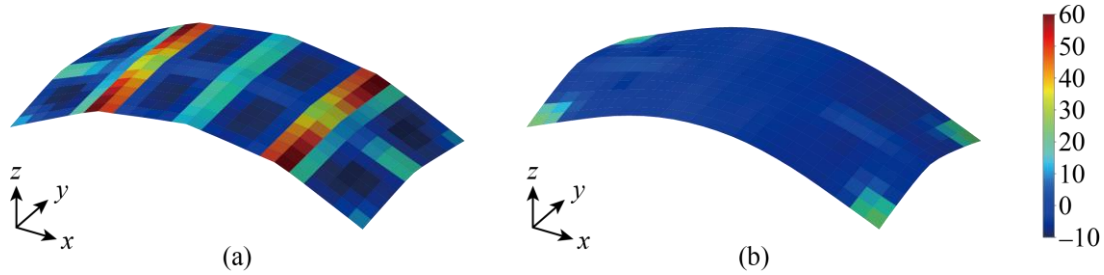


Figure 9. Maximum bending stress (kN); (a) initial surface, (b) optimal surface

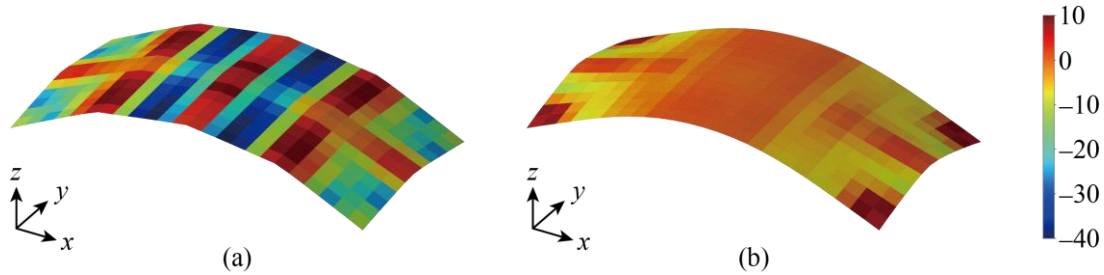


Figure 10. Minimum bending stress (kN); (a) initial surface, (b) optimal surface

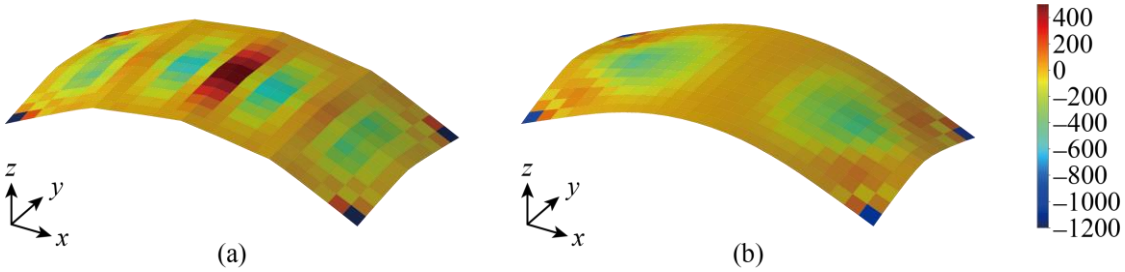


Figure 11. Maximum in-plane stress (kN/m); (a) initial surface, (b) optimal surface

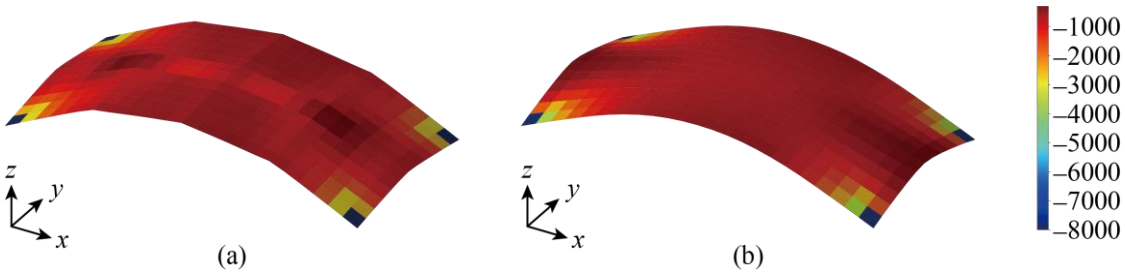


Figure 12. Minimum in-plane stress (kN/m); (a) initial surface, (b) optimal surface

Figures 7 shows the initial and optimal shapes of Problem (5). It can be seen that the initial surface consists of eight planar patches, while the optimal surface has a smooth cylindrical patch around the center and two ridges near the boundary. The height of the shell is slightly reduced at the center and increased at the exterior boundary. The total strain energy decreases from 66.91 to 47.09 (kNm) as a result of optimization. The nodal displacement in z-direction is shown in Fig. 8, and we can see that the magnitude of the displacement is reduced in the optimal shape. It can also be seen that, in the optimal shape, the distribution of displacement is smoother than in the initial shape. Figures 9–12 show the contour of the maximum bending moment, minimum bending stress, maximum in-plane stress, and minimum in-plane stress, respectively, evaluated as force per unit length of section. The overall trend is that the magnitude of stress is smaller in the optimal shape. Since the initial shape has the significant ridges, stress concentration occurs and the magnitude of the stress tends to be large around the ridges. On the other hand, the optimal shape has the smoother distribution of stress, while the stress slightly concentrates at the ridges near the boundary.

5. Conclusions

A shape optimization method has been proposed for shells consisting of piecewise developable surface, which is generated by using a meshless approach for minimizing the sum of squares of areas of local Gauss map. The locations of some selected points are regarsed as fixed in the process of generating the piecewise developable surface, and they are considered as design variables of the structural optimization problem for minimizing the toral strain energy, which is solved using the SA. It has been shown in the numerical examples that various mechanically efficient surface can be generated by limiting the surface class to the piecewise developable surface that is efficient also in view of construction cost.

Acknowledgements

This research is partially supported by JST CREST No. JPMJCR1911.

References

[1] J. Cui and M. Ohsaki, “Shape design of curved surface of membrane structure using developable surface,” *J. Int. Assoc. Shell. Spatial Struct.*, Vol. 59, No. 3, pp. 199-214, 2018.

[2] S, Fujita, M. Ohsaki and K. Seki, Shape optimization of latticed shells consisting of ruled surface, Proc. IASS Symposium 2016, Tokyo, Int. Assoc. Shell and Spatial Struct., Paper No. CS6M-1251, 2016.

[3] K. Hayakawa, M. Ohsaki and J. Y. Zhang, "Meshless non-parametric shape design of piecewise approximately developable surfaces using discretized local Gauss map," *J. Int. Assoc. Shell Spatial. Struct.*, published online. DOI: https://doi.org/10.20898/j.iass.2022.023

[4] O. Stein, E. Grinspun and K. Crane, "Developability of triangle meshes," *ACM Transactions on Graphics*, Vol. 37, No. 4, Article 77, 2018.

[5] P. E. Gill, W. Murray and M. A. Saunders, "SNOPT: An SQP algorithm for large-scale constrained optimization," *SIAM J. Optim*., vol. 12, No. 4, pp. 979-1006, 2002.

[6] pyOpt Documentation, Release 1.2, http://www.pyopt.org/

[7] Y. Xiang, D.Y. Sun, W. Fan, and X.G. Gong. "Generalized simulated annealing algorithm and its application to the thomson model," *Physics Letters A*, vol. 233, pp. 216-220, 1997.

Proceedings of the IASS Annual Symposium 2023
Integration of Design and Fabrication
10–14 July 2023, Melbourne, Australia
Y.M. Xie, J. Burry, T.U. Lee and J. Ma (eds.)

Sizing optimization of free-form lattice shells using deep deterministic policy gradient and graph convolutional networks

Chi-tathon KUPWIWAT[a,*], Kazuki HAYASHI[a], Makoto OHSAKI[a]

[a,*] Kyoto University
Kyoto 615-8540, Japan
kupwiwat.chitathon.73c@st.kyoto-u.ac.jp

Abstract

This paper proposes a method for sizing optimization of free-form lattice shells using a Deep Deterministic Policy Gradient (DDPG) agent with Graph Convolutional Networks (GCNs). The problem aims to minimize the volume of the structure by choosing sizes of structural members where the objective function is the total structural volume subjected to the stress constraints of the members. DDPG is a type of reinforcement learning (RL) that trains an agent to accomplish tasks using reward signal. This method represents a latticed shell structure as a graph and utilizes neural networks and GCNs as an agent. In each optimization step, the nodes and elements in lattice shells are represented as a graph by node and adjacency matrices which contain structural information on the current structure. The agent observes the structure through these matrices and chooses the elements to reduce the size. The agent receives a reward computed from the reduction of the structural volume and the maximum stress to be constrained. Results show that the GCN-DDPG agent can learn to minimize the structural volume. It can be applied to large free-form lattice shells using a small computational cost and has competitive performance compared to the genetic algorithm and simulated annealing.

Keywords: sizing optimization, lattice shell, machine learning, reinforcement learning, deep deterministic policy gradient, graph convolutional networks

1. Introduction

Structural optimization is a procedure that aims to obtain the best structures determined by design variables where the structural performance is evaluated by the objective function and constraints. Sizing optimization is a class of structural optimization that aims to find suitable sizes of structural components. For discrete structures such as trusses and frames, the sizing optimization can provide solutions with the smallest amount of structural material. In this type of structure, the sizes of the structural elements and the total structural volume are usually selected as the design variables and the objective function, respectively. Since the optimized structures must withstand the loads, the constraints should be assigned for the responses such as stress and displacement.

The choice of design variables also affects how the optimization methods are to be used since the availability of the gradients of the objective and constraint functions depends on the type of the design variables. In continuum structures such as concrete beams and shells, the mathematical programming methods can be utilized if the structures can have continuous geometrical dimensions and the gradient of the objective and constraint functions with respect to the design variables (i.e., size or sections) can be computed. However, in discrete structures, the sizes of structural elements are often chosen from available structural sections from the manufacturers, making it difficult to obtain the gradient of the functions. The sizing optimization problem of trusses and frames can be defined as a combinatorial optimization problem and solved using heuristic methods such as genetic algorithm (GA) and simulated

Copyright © 2023 by Chi-tathon KUPWIWAT, Kazuki HAYASHI and Makoto OHSAKI. Published in the Proceedings of the IASS Annual Symposium 2023 with permission.

annealing (SA) without the gradient of the objective function. In general, heuristic methods randomly generate solutions and improve them based on some rules. Hence multiple trials of optimization are required to find the best solution.

Machine learning (ML) is a method to train or instruct computational models to do given tasks. In recent years, ML approaches have been shown to be effective for many engineering problems. ML can be classified into three classes, including supervised learning, where the data-label pairs are initially provided for the training; unsupervised learning, where the data without a label is provided; and reinforcement learning (RL), where the data-label pairs are not initially provided but gradually collected during the training. Note that suitable ML models depend on the data type to be processed; for example, the neural networks [1] are applicable to the tabular data, and the convolutional neural networks [2] are suitable for processing image data. In recent years, the RL approach has been applied to structural optimization together with representing the structure as graph data. Hayashi and Ohsaki [3] proposed a graph embedding and RL agent method to optimize the structural volume of the planar truss. Zhu et al. [4] proposed an RL agent that generated the initial ground structures for topology optimization of trusses. Kupwiwat et al. [5–7] proposed RL agents for topology optimization of grid shells, topology optimization of building frames, and geometry optimization of latticed shells. It should be noted that RL methods in these researches are more computationally efficient than benchmark heuristic methods.

This paper proposes a method of sizing optimization of lattice shell for minimizing the structural volume under stress constraint using a type of RL named deep deterministic policy gradient (DDPG) [8] and graph convolutional networks (GCNs) [9]. DDPG is effective when multiple design variables are to be modified simultaneously because it reduces the number of optimization steps and computational cost. Furthermore, the GCN allows the DDPG agent to observe the whole structure and modify the sizes of all structural elements. The proposed method sequentially reduces the indices of structural element sizes of the elements until it violates the stress constraint or reaches the maximum computational step. The rest of the paper is organized as follows: Section 2 outlines the optimization problem. Section 3 introduces the concept of RL, DDPG, and GCNs. Section 4 explains the proposed optimization method. Section 5 shows numerical examples of the proposed method against the GA and SA. The summary of this paper is indicated in Section 6.

2. Objective function of the sizing optimization of lattice shells

The objective function is to minimize the structural volume of the lattice shell subjected to external loads under stress constraints. Let $c_i \in \{0,1,\dots,n_c\}$, $\mathbf{c}$, and l_i denote predetermined indices of cross-sectional properties, a vector that represents all indices of cross-sectional properties in the structure, and lengths of structural element i, respectively. The structural volume V of a lattice shell, which has n lattice elements, is derived from the sectional areas $H(c_i)$ and the lengths l_i as follows:

$$V(\mathbf{c}) = \sum_{i=1}^{n} H(c_i) l_i \tag{1}$$

In this paper, the lattice elements are three-dimensional beam elements with 12 degrees of freedom (DoFs). The internal stress can be obtained from the local displacement of each element after solving the stiffness equation (i.e., structural analysis) $\mathbf{p} = \mathbf{K}\mathbf{u}$ where $\mathbf{p}$, $\mathbf{K}$, and $\mathbf{u}$ are the nodal load vector, the global stiffness matrix, and the global displacement vector, respectively. The ratio of internal stress to the yield stress σ_i of an element i is computed similarly to Lagaros et al. [10] as follows:

$$\sigma_i = \begin{cases} \frac{|\sigma_x|}{\bar{\sigma}_x} + \frac{|\sigma_y|}{\bar{\sigma}_y} + \frac{|\sigma_z|}{\bar{\sigma}_z} & : \ \frac{|\sigma_x|}{\bar{\sigma}_x} \leq 0.15 \\ \frac{|\sigma_x|}{0.6\bar{\sigma}_x} + \frac{|\sigma_y|}{\bar{\sigma}_y} + \frac{|\sigma_z|}{\bar{\sigma}_z} & : \ \frac{|\sigma_x|}{\bar{\sigma}_x} > 0.15 \end{cases} \tag{2}$$

where σ_x, σ_y, and σ_z are the axial stress, maximum stress due to the bending moment in the local y axis, and in the local z axis, respectively, and $\bar{\sigma}_x$, $\bar{\sigma}_y$, and $\bar{\sigma}_z$ denote their upper bounds.

The optimization problem of lattice shell to minimize the structural volume is formulated as follows:

$$\begin{aligned} \text{minimize} \quad & V(\mathbf{c}) && \text{(3a)} \\ \text{subject to} \quad & \sigma_{\max} \leq 1 && \text{(3b)} \\ & c_i \in \{0,1,\dots,n_c\} && \text{(3c)} \end{aligned}$$

where $\boldsymbol{\sigma}_{\mathbf{max}}$ denotes the largest ratio of internal stress to the yield stress among the structural elements.

3. DDPG agent with GCN

This research proposes a method to utilize an RL agent to solve the sizing optimization of lattice shells. RL is a type of ML that trains an agent to accomplish a given task through interaction within an environment. Components of RL are a policy function to determine action, a reward signal to evaluate the outcome from the action, and a value function to estimate future rewards [11]. The interaction between an agent and the environment is modeled using Markov decision process (MDP). Figure 1 illustrates the MDP in this research. In a discrete timestep t, the agent observes the state S_t which is the graph representation of the current structural configuration shown in Figure 1(a). The agent uses its policy function to determine the action A_t to reduce the cross-sectional indices of elements illustrated in Figure 1(b). The sizes of structural members are modified and structural responses are computed. The agent obtains a reward R_{t+1} based on the changed structure shown in Figure 1(c) and proceeds to the next timestep.

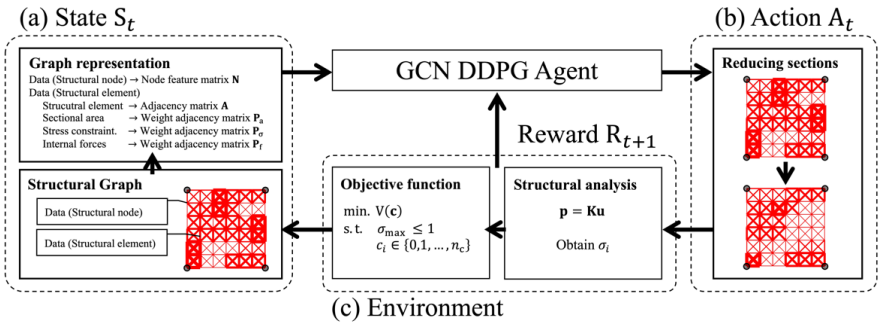


Figure 1. Propose MDP for sizing optimization of lattice shells.

DDPG is a type of RL that can take multiple actions simultaneously in an MDP, which can reduce the number of steps in the optimization and the cost of structural analyses. The DDPG agent has a policy function $\boldsymbol{\pi}_{\theta_1}$ (*actor network*) to determine the probability of taking action i, denoted by $\mathrm{P}(\mathrm{A}_t^i|\mathrm{S}_t)$, in a state S_t and a value function Q_{θ_2} (*critic network*) to predict the reward obtained by executing action i in a state S_t, defined as follows:

$$\boldsymbol{\pi}_{\theta_1}(\mathrm{S}_t) = \mathrm{P}(\mathrm{A}_t^i|\mathrm{S}_t) \quad \text{(4a)}$$

$$\mathrm{Q}_{\theta_2}\left(\mathrm{S}_t, \boldsymbol{\pi}_{\theta_1}(\mathrm{S}_t)\right) = \sum_{v=1}^{\infty} \gamma^{v-1} \mathrm{R}_{t+v} \quad \text{(4b)}$$

where $\gamma \in [0,1)$ is a discount factor that is proportionate to the importance of future rewards. θ_1 and θ_2 are trainable parameters that are adjusted during the training.

Both functions of the DDPG agent are trained using training data gradually collected from the MDP as $\{\mathrm{S}_t, \mathrm{A}_t, \mathrm{R}_{t+1}, \mathrm{S}_{t+1}\}$ and stored in a *replay buffer*. The value function is trained to predict the accumulated rewards to be obtained, and the policy function is trained to maximize the obtained reward using the prediction of the value function. For training surrogate policy and value functions, the *tau update* method [12] is utilized to stabilize the training, in which their weight parameters are updated using a value τ

($\tau \ll 1$) at every tau update interval. The training algorithm of DDPG, where $\mathcal{L}(y, \hat{y})$ signifies a loss function between the correct value y and a predicted value $\hat{y}$, is as follows:

DDPG algorithm

1. Sample n_{batch} training data $\{S_t, A_t, R_{t+1}, S_{t+1}\}$ from the stored replay buffer and aggregate them into a set of vectors $\{\mathbf{S}_t, \mathbf{A}_t, \mathbf{R}_{t+1}, \mathbf{S}_{t+1}\}$.
2. Update the parameters as follows:

$\boldsymbol{\pi}'_{\theta'_1}(\mathbf{S}_t) = \widehat{\mathbf{A}}_t$

$\boldsymbol{\pi}_{\theta_1}(\mathbf{S}_{t+1}) = \widehat{\mathbf{A}}_{t+1}$

$Q'_{\theta'_2}(\mathbf{S}_t, \mathbf{A}_t) = \widehat{\mathbf{Q}}_t$

$Q_{\theta_2}(\mathbf{S}_{t+1}, \widehat{\mathbf{A}}_{t+1}) = \mathbf{Q}_{t+1}$

$\nabla Q'_{\theta'_2} = \nabla_{\theta'_2} Q'_{\theta'_2}(\mathbf{S}_t, \mathbf{A}_t) \nabla_{\widehat{\mathbf{Q}}_t} \mathcal{L}(\mathbf{R}_{t+1} + \mathbf{Q}_{t+1}, \widehat{\mathbf{Q}}_t)$

$\nabla J'_{\theta'_1} = -\mathbb{E}\left[\nabla_{\theta'_1} \boldsymbol{\pi}'_{\theta'_1}(\mathbf{S}_t) \nabla_{\widehat{\mathbf{A}}_t} Q'_{\theta'_2}(\mathbf{S}_t, \widehat{\mathbf{A}}_t)|_{\widehat{\mathbf{A}}_t = \boldsymbol{\pi}'_{\theta'_1}(\mathbf{S}_t)}\right]$

Update $\boldsymbol{\theta}'_2$ in $Q'_{\theta'_2}$ using $\nabla Q'_{\theta'_2}$

Update $\boldsymbol{\theta}'_1$ in $\boldsymbol{\pi}'_{\theta'_1}$ using $\nabla J'_{\theta'_1}$

If *tau update* interval is reached:

$\boldsymbol{\theta}_1 = (1-\tau)\boldsymbol{\theta}_1 + \tau \boldsymbol{\theta}'_1$

$\boldsymbol{\theta}_2 = (1-\tau)\boldsymbol{\theta}_2 + \tau \boldsymbol{\theta}'_2$

In this paper, Adam [13] optimizer is utilized to find the optimal weights of the agent (i.e., training), and Ornstein-Uhlenbeck noise is added to the output of the policy function to activate the exploration of the DDPG agent.

The DDPG agent is built from GCNs which can compute graph signals (i.e., action) from graph representation of the structure (i.e., state). The computation of GCN is explained in this section. A graph that has n nodes with g features per node can be represented using a node feature matrix $\mathbf{N} \in \mathbb{R}^{n \times g}$, an adjacency matrix $\mathbf{A} \in \mathbb{R}^{n \times n}$, a degree matrix $\mathbf{D} \in \mathbb{R}^{n \times n}$, and a weighted adjacency matrix $\mathbf{P} \in \mathbb{R}^{n \times n}$, containing information of features in each node, nodal connections, numbers of connections of the node, and weights of nodal connections, respectively. Node signal $\mathbf{N}' \in \mathbb{R}^{n \times h}$ is computed from the summation of the features of nodes and their adjacent nodes, where h denotes the dimension of embedding space, using a GCN unit (i.e., *layer*) as follows:

$$\mathbf{N}' = \mu(\boldsymbol{\Phi}\mathbf{N}\mathbf{w}) \tag{5}$$

where $\mu(\cdot)$ and $\mathbf{w}$ are a non-linear activation function and parameterized weights in the GCN layer, respectively. $\boldsymbol{\Phi}$ denotes either a weighted adjacency matrix $\mathbf{P}$ or a normalized form of adjacency matrix $\widetilde{\mathbf{A}} = \mathbf{D}^{-1/2}[\mathbf{A} + \mathbf{I}]\mathbf{D}^{-1/2}$ where $\mathbf{I} \in \mathbb{R}^{n \times n}$ is the identity matrix, and $\mathbf{D}^{-1/2}$ is the inverse of the matrix $\mathbf{D}^{1/2}$ satisfying $\mathbf{D}^{1/2}\mathbf{D}^{1/2} = \mathbf{D}$. Note that GCN layers can be stacked to construct a computation model. When stacked, the next layer can take the embedded node signal $\mathbf{N}'$ of the previous layer as one of the inputs.

4. DDPG and GCN for sizing optimization of lattice shells

This section explains the graph representation of the structure for the state data, the computational parts of the DDPG agent, the action interpreted from the output of the agent, the reward, and the proposed optimization algorithm.

4.1. State

The state consists of graph representations of the structure using node feature matrix $\mathbf{N}$, adjacency matrix $\mathbf{A}$, weighted adjacency matrix of sectional area $\mathbf{P}_a$, weighted adjacency matrix of stress ratio $\mathbf{P}_\sigma$, and weighted adjacency matrix of internal forces $\mathbf{P}_f$, whose entries are shown in Tables 1 and 2. Note that all values in Tables 1 and 2 are normalized using the min-max normalization method.

Table 1. Entries in node feature matrix **N**.

$n_{i,1}$	x-coordinate of node i
$n_{i,2}$	y-coordinate of node i
$n_{i,3}$	z-coordinate of node i
$n_{i,4}$	1 if the node has fixed support, else 0
$n_{i,5}$	1 if the node has no support, else 0

Table 2. Entries in adjacency and weighted adjacency matrices **A**, $\mathbf{P}_\mathrm{a}$, $\mathbf{P}_\sigma$, and $\mathbf{P}_\mathrm{f}$.

$a_{i,j}$	1 if there is an element connecting nodes i and j else 0
$p_{a\,i,j}$	Cross-sectional area of an element if there is an element connecting nodes i and j else 0
$p_{\sigma\,i,j}$	Ratio of internal stress to the yield stress of an element if there is an element connecting nodes i and j else 0
$p_{f\,i,j}$	Ratio of the summation of internal bending forces in y and z axes (f_y, f_z) to the axial force (f_x) of an element if there is an element connecting nodes i and j else 0 where $p_{f\,i,j} = (\lvert f_y\rvert + \lvert f_z\rvert)/(1 + \lvert f_x\rvert)$

4.2. Agent

The agent consists of a policy function **π** that computes the action and a value function **Q** that computes the expected reward (Q-value). These functions are made of GCN layers with activation function $\mathrm{ReLU}(\cdot) = \max(0,\cdot)$, GCN layers with activation function $\mathrm{Sigmoid}(\cdot) = 1/(1+\mathrm{e}^{-(\cdot)})$, global sum pooling (GSP) operation, and a two hidden layers neural network $\mathrm{f_{NN}}$ represented as follows:

$$\mathrm{ReLU}(\mathbf{M}_1, \mathbf{M}_2) = \mathrm{ReLU}(\mathbf{M}_1\mathbf{M}_2\mathbf{w}) \tag{6a}$$

$$\mathrm{Sigmoid}(\mathbf{M}_1, \mathbf{M}_2) = \mathrm{Sigmoid}(\mathbf{M}_1\mathbf{M}_2\mathbf{w}) \tag{6b}$$

$$\mathrm{GSP}(\mathbf{M}_3 \in \mathbb{R}^{n\times g}) = \left[\sum_{i=1}^{n} \mathbf{m}_{3\,i,1} \quad \cdots \quad \sum_{i=1}^{n} \mathbf{m}_{3\,i,\mathrm{g}}\right] \in \mathbb{R}^{1\times g} \tag{6c}$$

$$\mathrm{f_{NN}}(\mathbf{M}_4) = \mathbf{w}_3\left(\mathrm{ReLU}\left(\mathbf{w}_2\left(\mathrm{ReLU}\left(\mathbf{w}_1{\mathbf{M}_4}^{\mathrm{T}} + \mathbf{b}_1\right)\right) + \mathbf{b}_2\right)\right) + \mathbf{b}_3 \tag{6d}$$

Where $(\cdot)^{\mathrm{T}}$ denotes the transpose of a matrix, $\mathbf{M}_1$ denotes a node feature matrix or a node embedding matrix. $\mathbf{M}_2$ denotes an adjacency matrix or a weighted adjacency matrix. $\mathbf{M}_3$ denotes a matrix to be changed into a one-dimensional vector. $\mathbf{M}_4$ denotes a one-dimensional vector. $\mathbf{w}_{i\in\{1,2,3\}}$ and $\mathbf{b}_{i\in\{1,2,3\}}$ denote internal weight and bias matrices in each neural network layer, respectively. The values of **w**, $\mathbf{w}_{i\in\{1,2,3\}}$ and $\mathbf{b}_{i\in\{1,2,3\}}$ are adjusted during the training phase.

Table 3 shows the inputs, computations, and outputs of the policy function (left column) and the value function (right column), where ⊙ denotes the element-wise multiplication.

Table 3. Inputs, computations, and outputs of the policy and value functions.

policy function	value function
input: **N**, **A**, $\mathbf{P}_\mathrm{a}$, $\mathbf{P}_\sigma$, $\mathbf{P}_\mathrm{f}$	input: **N**, **A**, $\mathbf{P}_\mathrm{a}$, $\mathbf{P}_\sigma$, $\mathbf{P}_\mathrm{f}$, **π**
computation: step 1: $\mathbf{X}_{1.1} = \mathrm{ReLU}(\mathrm{ReLU}(\mathbf{N}, \mathbf{P}_\mathrm{a}), \mathbf{P}_\mathrm{a})$ $\mathbf{X}_{1.2} = \mathrm{ReLU}(\mathrm{ReLU}(\mathbf{N}, \mathbf{P}_\sigma), \mathbf{P}_\sigma)$ $\mathbf{X}_{1.3} = \mathrm{ReLU}(\mathrm{ReLU}(\mathbf{N}, \mathbf{P}_\mathrm{f}), \mathbf{P}_\mathrm{f})$ step 2: $\mathbf{X}_2 = \mathbf{X}_{1.1} + \mathbf{X}_{1.2} + \mathbf{X}_{1.3}$ step 3: $\boldsymbol{\pi} = \mathrm{Sigmoid}(\mathrm{ReLU}(\mathbf{X}_2, \mathbf{P}_\sigma), \mathbf{A})$	computation: step 1: $\mathbf{X}_{1.1} = \mathrm{ReLU}(\mathrm{ReLU}(\mathbf{N}, \mathbf{P}_\mathrm{a}), \mathbf{P}_\mathrm{a})$ $\mathbf{X}_{1.2} = \mathrm{ReLU}(\mathrm{ReLU}(\mathbf{N}, \mathbf{P}_\sigma), \mathbf{P}_\sigma)$ $\mathbf{X}_{1.3} = \mathrm{ReLU}(\mathrm{ReLU}(\mathbf{N}, \mathbf{P}_\mathrm{f}), \mathbf{P}_\mathrm{f})$ step 2: $\mathbf{A}^* = (\boldsymbol{\pi}\cdot\boldsymbol{\pi}^{\mathrm{T}})\odot\mathbf{A}/100$ $\mathbf{X}_2 = \mathrm{ReLU}(\mathrm{ReLU}(\boldsymbol{\pi}, \mathbf{A}^*), \mathbf{A}^*)$ step 3: $\mathbf{X}_3 = \mathbf{X}_{1.1} + \mathbf{X}_{1.2} + \mathbf{X}_{1.3} + \mathbf{X}_2$ step 4: $\mathbf{X}_4 = \mathrm{ReLU}(\mathbf{X}_3, \mathbf{A})$ step 5: $\mathbf{X}_5 = \mathrm{GSP}(\mathbf{X}_4)$ step 6: $\mathrm{Q} = \mathrm{f_{NN}}(\mathbf{X}_5)$
output: $\boldsymbol{\pi} \in \mathbb{R}^{n\times 100}$	output: $\mathrm{Q} \in \mathbb{R}^{1\times 1}$

4.3. Action

The agent determines to reduce the section size of multiple elements simultaneously. Each size index c_i of an element i that connects nodes p and q is determined using an action interpreted from the output of the policy function $\boldsymbol{\pi}$ as

$$c_i = \begin{cases} c_i = \min(0, c_i - 1) & : \sum_{u=1}^{100} \boldsymbol{\pi}_{p,u} \boldsymbol{\pi}_{q,u} > \varphi_1 \\ c_i = c_i & : \sum_{u=1}^{100} \boldsymbol{\pi}_{p,u} \boldsymbol{\pi}_{q,u} \leq \varphi_1 \end{cases} \tag{7}$$

where φ_1 = 0.3 in the following examples.

4.4. Reward

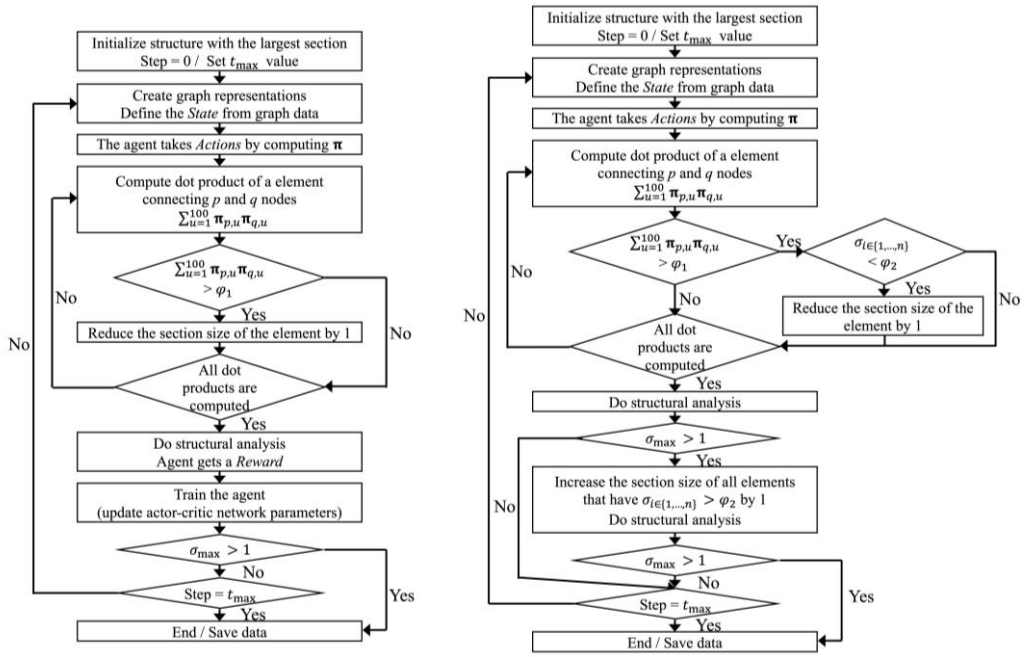
The reward signal R_{t+1} that the agent obtains after modifying the structure by the action A_t in a state S_t in an optimization step t is computed from the change of the structural volume (i.e., the objective function) as follows:

$$\mathrm{R}_{t+1} = \begin{cases} (V_t - V_{t+1})/V_0 & : \quad \sigma_{\max} \leq 1 \\ -1 & : \quad \sigma_{\max} > 1 \text{ or } t = t_{\max} \end{cases} \tag{8}$$

where V_t and V_0 are the value of the objective function at step t and the initial step, respectively. $t_{\max}$ is the maximum step of the optimization.

4.5. Optimization method

In each optimization step, the DDPG agent made from GCN layers observes the graph representation of the structure. The agent chooses elements, reduces their section sizes and obtains the reward computed from the volume reduction of the structure. The optimization ends when any structural element violates the stress constraint or the number of optimization steps reaches $t_{\max}$.



(a) (b)

Figure 2. Flowcharts of the algorithm: (a) training phase, (b) test phase.

The agent is trained to optimize the structure to obtain high rewards in the training phase and applied to other structures in the test phase. Note that in the test phase, the agent cannot perform actions onto the element that has a ratio of internal stress to the yield stress larger than φ_2. If the modified structure violates the constraint, all elements with the ratio of internal stress larger than φ_2 will increase their section indices by one. Flowcharts of proposed algorithms in the training and test phases are shown in Figures 2(a) and (b), respectively.

5. Numerical examples

5.1. General experiment setting and structural properties

Frame elements used in this experiment have round hollow sections selected from Table 4 and have Young's modulus of 205 kN/mm^2. $\bar{\sigma}_x$, $\bar{\sigma}_y$, and $\bar{\sigma}_z$ are set as 235/1.5 N/mm^2, 0.66×235/1.5 N/mm^2, and 0.66×235/1.5 N/mm^2, respectively. Dimension of the embedding space h in all GCN layers is set to 300 and each layer in NN in Eq. (6d) has 300 cells.

Table 4. Frame section list.

section No.	diameter (mm)	thickness (mm)	area (cm^2)	2nd moment of area (cm^4)
0	21.7	2.0	1.238	0.607
1	34.0	2.3	2.291	2.890
2	42.7	3.2	3.971	7.800
3	48.6	3.2	4.564	11.80
4	60.5	4.0	7.100	28.50
5	76.3	4.0	9.085	59.50

5.2. Training phase

The agent is trained to optimize 6 different lattice shells illustrated in Figures 3(a)–(f) and shown in Table 5 which are subjected to different nodal loads applied to all nodes guaranteeing that the structures with the largest sections do not violate the constraints and those with the smallest sections violate the constraints. The ability of the agent to improve its policy is evaluated every 10 times (*episodes*) of training using the same 6×6-grid lattice shells in Figure 3(g) subjected to a downward load of 1kN at all nodes. Adam optimizer adjusts the trainable parameters in surrogate policy and value functions with learning rates of 10^{-6} and 10^{-5}, respectively. τ is set to 0.05 to update weights in surrogate functions to the online function every 100 steps. $t_{\max}$ of the episode for training and episode for evaluation are set to 50 and 100, respectively.

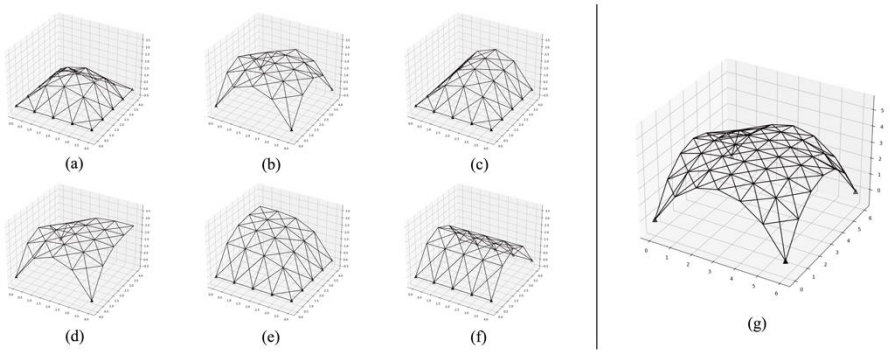


Figure 3. Structures used for training the agent: (a) S 1, (b) S 2, (c) S 3, (d) S 4, (e) S 5, (f) S 6, (g) structure used for evaluating the improvement of the trained agent.

Table 5. Structures for training.

	S 1	S 2	S 3	S 4	S 5	S 6
grid size	4×4	4×4	4×4	4×4	4×4	4×4
grid span (m.)	1	1	1	1	1	1
downward load (kN.)	25	5	10	0.5	0.2	15

Figure 4 shows variations of accumulated reward obtained in each evaluation episode where the thick red line indicates the moving average of the reward at every 20 episodes of evaluation. The total number of structural analyses in this phase is 25849. It is seen from this figure that the agent can improve its policy function to obtain a high reward to minimize the structural volume. Note again that the agent is evaluated using a structure that is different from the training data, indicating the applicability of the agent to unseen problems which will be further investigated in the test phase.

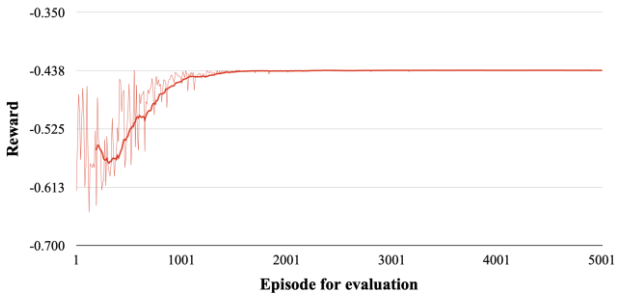


Figure 4. Variations of accumulated reward.

5.3. Test phase

The trained agent with the weights saved at the 5000th episode of the training phase is utilized for optimizing larger lattice shells shown in Table 6 ten times. In this phase, Structure A has fixed supports at the corners, Structure B has fixed supports at the corners with an irregular shape, and Structure C has fixed supports at the perimeter nodes as shown in Figures 5, 6, and 7, respectively. φ_2 is set to 0.6. Solutions from the proposed RL are compared to the result obtained by GA and SA using python libraries named DEAP [14] and SciPy [15], respectively. In GA, each gene is encoded as an integer in the list $\{0, 1, \ldots, 5\}$ to represent the sectional index of each element with numbers of the population and generation set as 100 and 10, respectively. In SA, the design parameters are the same as those of GA with a maximum number of structural analyses set as 1000. In both SA and GA, ten trials using different random seeds are implemented to minimize the penalty function $\phi(\mathbf{c})$ defined as follows:

$$\phi(\mathbf{c}) = \frac{V(\mathbf{c})}{V_0} + \sum_{i=1}^{n} w_c(\max[0, |\sigma_i| - 1])^2 \tag{9}$$

where V_0 is the total structural volume of the structure where all elements have the largest indices of cross-sectional properties, n is the number of elements in the structure, and w_c is the weight for the constraint set as 50.

Table 6. Structures for test.

	Structure A	Structure B	Structure C
grid size	10×10	20×20	20×20
grid span (m)	1	1	1
downward load (N)	200	5	300
Number of elements	420	1640	1184
$t_{\max}$	100	200	200

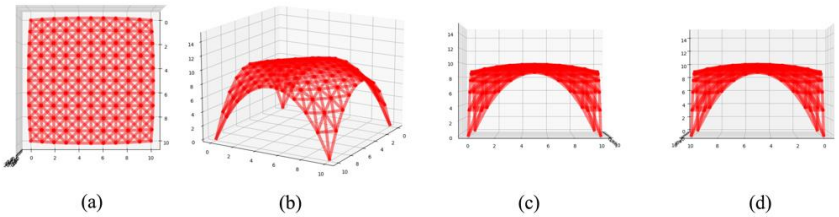


Figure 5. Structure A: (a) plan, (b) isometric, (c) elevation 1, (d) elevation 2.

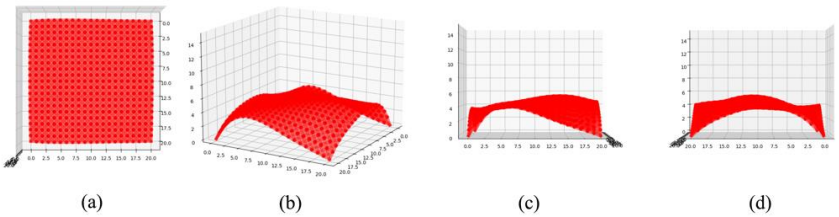


Figure 6. Structure B: (a) plan, (b) isometric, (c) elevation 1, (d) elevation 2.

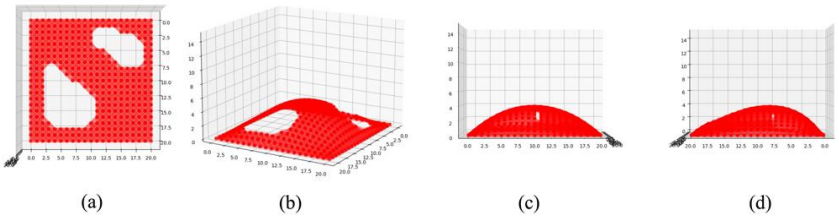


Figure 7. Structure C: (a) plan, (b) isometric, (c) elevation 1, (d) elevation 2.

The performance of RL, GA, and SA are measured using the volume reduction of the optimized structure computed as

$$\text{volume reduction} = (V_0 - V_*)/V_0 \tag{10}$$

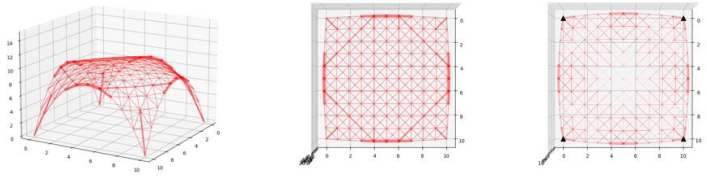
where V_* is the final volume of the structure.

Table 7 shows the minimum (min), the mean, the maximum (max), and the standard deviation (std) of the volume reductions and the number of structural analyses for RL, GA, and SA. In every structure, the RL agent achieved better volume reductions than those obtained by GA and SA. The standard deviations of results from RL are also low compared to those of GA and SA. These results confirms stable performance of the proposed RL.

Table 7. Test result: volume reduction (%).

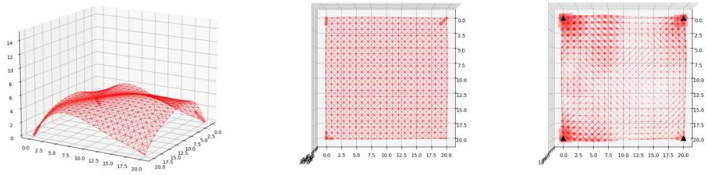
	structure	min	mean	max	std	analyses(times)
RL	A	82.06	82.36	82.53	0.15	2000
	B	86.00	86.07	86.12	0.03	4000
	C	84.57	84.69	84.75	0.05	4000
GA	A	0.00	22.86	39.35	19.69	10000
	B	82.25	82.74	83.20	0.37	10000
	C	73.29	73.97	74.67	0.49	10000
SA	A	0.00	34.46	70.34	36.33	10000
	B	68.08	68.34	68.60	0.19	10000
	C	0.00	60.97	68.08	21.42	10000

Figures 8–10 show the best results of each structure obtained by RL. The subfigures (a) and (b) show the isometric and plan views of the final structure where the line thickness indicates the index of cross-sectional properties of the element. The subfigure (c) shows the plan view of the initial structure where the line thickness indicates the stress ratio of the element. In these figures, the solutions obtained by RL generally have elements with large sections where the initial stress ratio is large.



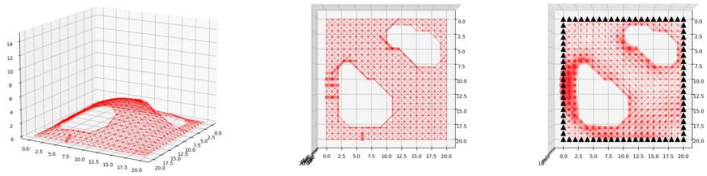
(a) (b) (c)

Figure 8. Structure A: (a) final isometry, (b) final plan, (c) initial stress ratio.



(a) (b) (c)

Figure 9. Structure B: (a) final isometry, (b) final plan, (c) initial stress ratio.



(a) (b) (c)

Figure 10. Structure C: (a) final isometry, (b) final plan, (c) initial stress ratio.

4. Conclusion

This paper presents a method for sizing optimization of free-form lattice shells to minimize the structural volume under the stress constraints using DDPG and GCN. The DDPG agent observes the structure represented as a graph and reduces the sectional index of each structural element. First, the agent is trained to minimize the structural volume, where the improvement of the agent is measured using the reward obtained from the volume reduction. Note that the agent is trained using small structures and evaluated using a structure with a different configuration. The ability of the agent to optimize different structures is also verified in the test phase where the agent is not further trained and the results obtained by the RL agent are compared to those obtained by GA and SA.

The numerical result shows that the proposed method can obtain superior solutions than GA and SA for all test cases using different free-from lattice shells. The trained RL agent also has a more stable performance than GA and SA while utilizing smaller computational costs than those algorithms. However, it should be noted that the proposed method requires some computational cost during the training phase but utilizes a small computational cost during the test phase. Therefore, the benefit of the proposed method in the aspect of computational efficiency becomes large when the agent is applied to many problems.

In this paper, the lattice shell consists of only three-dimensional beam elements, and the lists of the structural section are the same in both the training and test phases. However, in practice, the types of

structural elements and sectional lists could be varied. Therefore, further investigation on the applicability of the trained agent is needed for the cases using different lists of structural sections and different types of structural elements, such as both three-dimensional beam and truss systems.

Acknowledgements

A part of this research has been supported by Japan ministry of education, culture, sports, science and technology (MEXT) scholarship [grant number 180136] and Japan society for the promotion of science (JSPS) KAKENHI [grant numbers JP 20H04467, JP 21K20461].

References

[1] F. Rosenblatt, "The perceptron: a probabilistic model for information storage and organization in the brain," *Psycological Review,* vol. 65, no. 6, pp. 386–408, 1958.

[2] Y. LeCun, L. Jackel, et al., "Comparison of learning algorithms for handwritten digit recognition," in *Proceedings of international conference on artificial neural networks,* vol. 10, no. 1, 1995.

[3] K. Hayashi and M. Ohsaki, "Reinforcement learning and graph embedding for binary truss topology optimization under stress and displacement constraints," *Frontiers in Built Environment,* vol. 6, pp. 59, 2021.

[4] S. Zhu, M. Ohsaki, K. Hayashi and X. Guo, "Machine-specified ground structures for topology optimization of binary trusses using graph embedding policy network," *Advances in Engineering Software,* vol. 159, pp. 103032, 2021.

[5] C. Kupwiwat, K. Hayashi and M. Ohsaki, "Deep deterministic policy gradient and graph convolutional network for bracing direction optimization of grid shells," *Frontiers in Built Environment,* vol. 8, pp. 899072, 2022.

[6] C. Kupwiwat, Y. Iwagoe, K. Hayashi and M. Ohsaki, "Deep deterministic policy gradient and graph convolutional network for topology optimization of braced steel frames," *Structural Engineering B, Architectural Institute of Japan,* vol. 69B, 2023.

[7] C. Kupwiwat, K. Hayashi and M. Ohsaki, "Deep deterministic policy gradient and graph attention network for geometry optimization of latticed shells," *Applied Intelligence,* 2023.

[8] T. P. Lillicrap, J. J. Hunt, et al., "Continuous control with deep reinforcement learning," in *International conference on learning representations,* Poster, 2016.

[9] T. N. Kipf and M. Welling, "Semi-supervised classification with graph convolutional networks," in *Proceedings of the 5th international conference on learning representations,* pp. 1-14, 2017.

[10] N. D. Lagaros, M. Papadrakakis and V. Plevris, "Multiobjective optimization of space structures under static and seismic loading conditions," in *Evolutionary multiobjective optimization,* A. Abraham, L. Jain, R. Goldberg, Ed. London: Springer, 2005, pp. 273-300.

[11] R. S. Sutton and G. B. Andrew, *Reinforcement learning, an introduction*. Cambridge: The MIT Press, 2018.

[12] T. Haarnoja, A. Zhou, P. Abbeel and S. Levine, "Soft actor-critic: off policy maximum entropy deep reinforcement learning with a stochastic actor," in *Proceedings of international conference on machine learnings,* pp. 1861-1870, 2018.

[13] D. Kingma and J. Ba, "Adam: a method for stochastic optimization," in *Proceedings of international conference on learning representations,* pp. 1-15, 2015.

[14] F. A. Fortin, F. M. De Rainville, et al., "DEAP: Evolutionary algorithms," *Journal of Machine Learning Research,* vol. 13, pp. 2171-2175, 2012.

[15] P. Virtanen, R. Gommers, et al., "SciPy 1.0: fundamental algorithms for scientific computing in Python," *Nature Methods,* vol. 17, no. 3, pp. 261-272, 2020.

IASS 2023
July 10–14 Melbourne
Integration of Design and Fabrication

Proceedings of the IASS Annual Symposiu2023
Integration of Design and Fabrication
10–14 July 2023, Melbourne, Australia
Y.M. Xie, J. Burry, T.U. Lee and J. Ma (eds.)

Study on quasi-static compression performance of honeycomb structures with negative Poisson's ratio

Yiyi ZHOU[a], Jiabin SONG[a], Amardeep SINGH[*], Dan JIANG[b]

[*] School of Civil Engineering & Architecture, Changzhou Institute of Technology
Changzhou 213032, China
adsingh@tongji.edu.cn, er.singh.amardeep@gmail.com

[a] School of Mechanics and Material Hohai University, Nanjing 210000, China
[b] College of Civil Engineering, Nanjing Tech University, Nanjing 211800, China

Abstract

To examine the quasi-static compression performance of a honeycomb structure with a negative Poisson's ratio, this paper employs finite element analysis software, Abaqus, and utilizes stainless steel property data for numerical simulation analysis of the honeycomb structure with a negative Poisson's ratio. Concurrently, through a comparison of honeycomb structures with zero and positive Poisson's ratios, the mechanical and energy dissipation properties of negative Poisson's ratio honeycomb structures are investigated under varying length-thickness ratios and cell configurations. Key parameters such as nominal stress-strain, platform stress, energy absorption capacity, specific energy absorption, and Poisson's ratio are considered in the study.

Keywords: re-entrant honeycomb, quasi-static compression, large deformation, energy absorption, stainless steel

1. Introduction

Honeycomb structures, characterized by their porous composition and regular hexagonal arrangement, boast low density and high strength. Consequently, they exhibit superior strength-to-weight and rigidity-to-weight ratios compared to solid structures of the same type[1, 2]. The buckling of cell walls effectively distributes compression forces across each cellular unit, resulting in a stable structure with excellent compressive deformation capabilities and energy dissipation performance. These features make honeycomb structures ideal for use as protective components in aerospace [1, 2], transportation [3, 4], construction [5, 6], and other protective fields.

In recent years, reentrant hexagonal honeycomb structures have been extensively studied due to their unique negative Poisson's ratio characteristics. This innovation significantly enhances the in-plane compression performance of honeycombs [7, 8] and effectively addresses their anisotropy, where in-plane compression performance is inferior to that of out-of-plane. Initially, Poisson's ratio was a mechanical parameter applicable only under elastic conditions, so early research on reentrant hexagonal honeycomb structures was primarily focused on the elastic range [11, 12]. However, recent studies have explored the potential of negative Poisson's ratio performance in metal materials like brass and aluminum alloy to improve energy dissipation performance in structures. For example, Ruan et al. [13] examined the in-plane fracture behavior of aluminum honeycombs in two directions, considering the effects of wall thickness and impact velocity on local deformation modes and plateau stress. They also derived an empirical formula to calculate the stress of aluminum honeycomb plateaus at high impact velocities. Yasuki et al. [14] developed an offset deformable barrier model with aluminum honeycomb

Copyright © 2023 by Yiyi ZHOU, Jiabin SONG, Amardeep SINGH and Dan JIANG. Published in the Proceedings of the IASS Annual Symposium 2023 with permission.

for vehicle collision simulations, while Li et al. [15] investigated the energy absorption capacity of two types of concave hexagonal honeycomb structures made from brass with negative Poisson's ratio. Stainless steel, possessing exceptional physical and mechanical properties, can better replicate the plastic buckling failure mechanism of honeycomb structures under impact [16]. Realizing a negative Poisson's ratio effect in steel honeycomb structures under large deformations has promising applications.The advent of 3D printing technology has provided advanced techniques for manufacturing stainless steel honeycomb structures. Xi et al. [17] introduced a new asymmetric rotatable concave hexagonal honeycomb structure made from stainless steel via 3D printing, based on the symmetrical concave hexagonal honeycomb structure with a negative Poisson's ratio. They demonstrated that adjusting the honeycomb structure's rotation improved its energy absorption performance. Zhou et al. [18] used 3D printing to create 316L stainless steel concave hexagonal honeycomb samples with varying length-to-thickness ratios and cell types. They studied the deformation process and associated mechanical parameters (e.g., Poisson's ratio, failure mode, plateau stress, and energy absorption capacity) under three distinct energy inputs. The results showed that negative Poisson's ratio honeycomb samples had higher plateau stress and specific absorption energy than traditional honeycomb specimens. This paper investigates negative Poisson's ratio honeycombs using material property data from 3D-printed 316L stainless steel.

To examine the quasi-static compression performance of negative Poisson's ratio honeycomb structures, finite element analysis software Abaqus was employed for numerical simulation analysis. By comparing zero and positive Poisson's ratio honeycomb structures, this study explored the mechanical properties and energy dissipation capabilities of negative Poisson's ratio honeycomb structures with different length-to-thickness ratios and cell configurations. Key parameters such as nominal stress-strain, plateau stress, energy absorption capacity, specific energy absorption, and Poisson's ratio were analyzed.

2. Specimen design

In this study, four hexagonal honeycomb samples were designed, including two negative Poisson's ratio structures (A0.6 and A1.0), one positive Poisson's ratio structure (H0.6), and one zero Poisson's ratio structure (Z0.6)[1]. To maintain uniform horizontal size, height, and cell count for each specimen, the hypotenuse length for every element type was set at 10mm [2]. The horizontal side length for the negative Poisson's ratio element was 20mm, and the angle between the horizontal side and the hypotenuse was 60°[3]. For the zero Poisson's ratio element, the horizontal side length was 15mm, with angles of 120° and 60° between the horizontal side and the hypotenuse[4].

Each Poisson's ratio honeycomb specimen had cell wall thicknesses of 0.6mm and 1.0mm [5]. Consequently, the ratio of hypotenuse length to thickness for each specimen was 50/3 and 10 [6]. Every specimen contained five elements along both vertical and horizontal directions, resulting in identical external dimensions for all specimens: 140x86.6x50mm [7]. The specific geometric parameters for specimens with different Poisson's ratio elements are depicted in the accompanying figure[8].

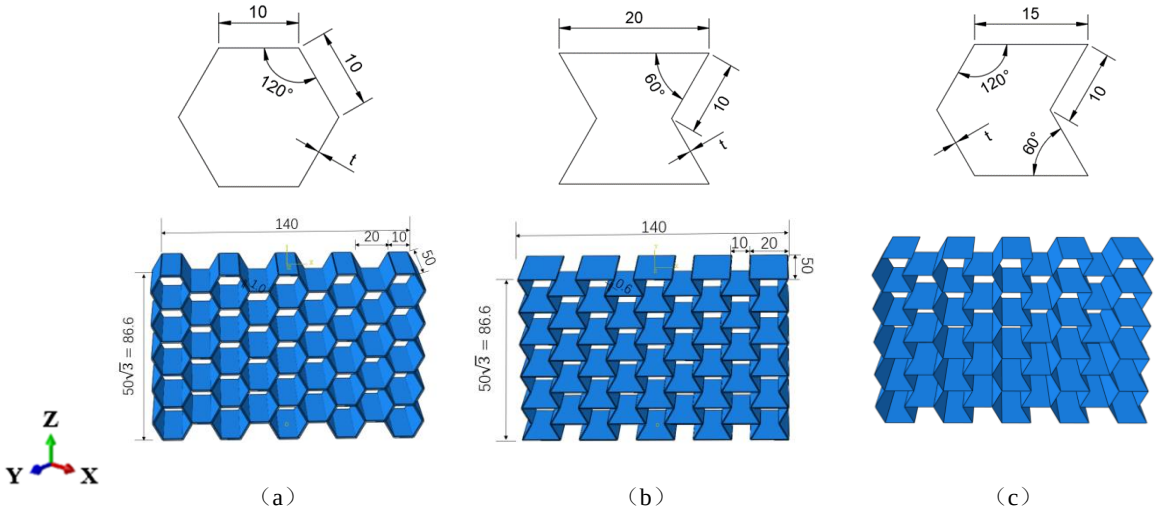


Fig. 7 Specimen model (a) positive Poisson's ratio, (b) negative Poisson's ratio, (c) zero Poisson's ratio

3. Finite element simulation

In this study, the ABAQUS explicit module is employed to investigate the quasi-static compression performance of various Poisson ratios. The model utilizes the S4R element for grid partitioning. Convergence studies indicate that the optimal mesh size is 2 mm. In the simulation, the sample is positioned on the bottom plate, and fixed constraints are applied to it. The material used is 316L stainless steel, with material parameters as follows: elastic modulus E of 200 GPa, density of 7.81 kg/m3, and Poisson ratio of 0.30. Key parameters of the Johnson-Cook model for this material are established based on material property test data by Zhou [18], as displayed in Table 5. In the analysis, the top surface of the honeycomb model and the bottom surface of the panel are set to face-to-face contact, while the remainder employs a self-contact algorithm. A tangential friction coefficient of 0.30 is assigned. The specimen is compressed in the Y direction, and a displacement load equivalent to 80% of the model's height is applied, meaning the panel's displacement is set to 70 mm. Additionally, the panel's displacement in the X and Z directions, as well as all directional angles, are restricted.

Table 5 Parameters of Johnson-Cook model.

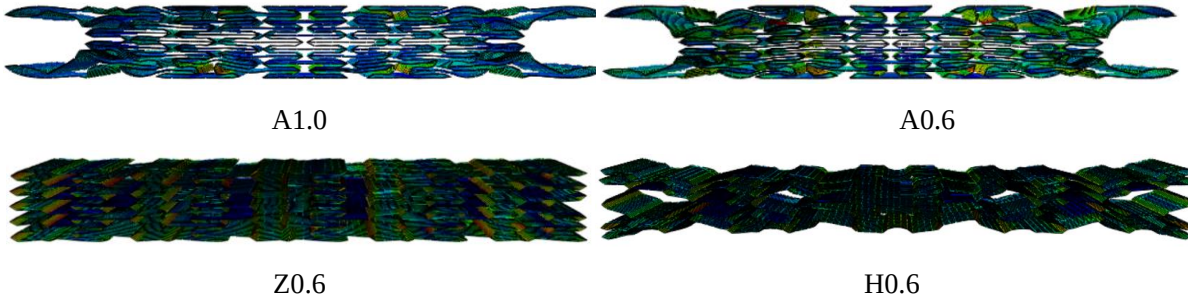
A (MPa)	*B* (MPa)	*N*	*C*
400	1047	0.7043	0.1

4. Simulation result

4.1 Deformation mode

The finite element simulation's compression results are displayed in the figure. A nominal strain of 0.8 is observed, which refers to the relative deformation between a sample's upper and lower edges, divided by its initial height. Post-compression, honeycomb structures with a negative Poisson's ratio achieve the dense stage under the same nominal strain, whereas those with zero or positive Poisson's ratios do not enter this stage.

Furthermore, during deformation, negative Poisson's ratio honeycomb specimens exhibit prominent cell wall aggregation and curve inward, leading to a significant negative Poisson's ratio effect. In contrast, positive Poisson's ratio honeycomb structures typically expand laterally, while zero Poisson's ratio specimens demonstrate neither noticeable expansion nor contraction.



A1.0 A0.6

Z0.6 H0.6

4.2 Nominal stress and strain

The nominal stress is the transient force during compression divided by the external cross-sectional area of the specimen. By analyzing the nominal stress and strain, the elastic limit stress, compaction stress and corresponding strain values are obtained. Platform stress [19, 20] can be calculated by Equation (1) :

$$\sigma_p = \frac{1}{\varepsilon_d - \varepsilon_{cr}} \int_{\varepsilon_{cr}}^{\varepsilon_d} \sigma(\varepsilon) d\varepsilon \quad (1)$$

where σ_p is the plateau stress, $\sigma(\varepsilon)$ is the nominal stress varying with the nominal strain, ε_{cr} is the nominal strain corresponding to the elastic limit stress and ε_d is the maximum strain value before the material is compacted, and according to the literature [20], ε_d is calculated by Eq. (2):

$$\frac{d}{d\varepsilon}\left[\frac{1}{\sigma(\varepsilon)} \int_0^{\varepsilon} \sigma(\varepsilon)\, d\varepsilon\right]|_{\varepsilon=\varepsilon_d} = 0 \quad (2)$$

The nominal stress-strain curves of the four specimens can be divided into elastic stage, platform stage and compaction stage, showing the typical characteristics of honeycomb energy absorption structure. Table 3 provides complete nominal stress and strain data.

Table 3 Compaction stress and strain of test results.

Specimen	Stress			Strain		
	Ultimate elastic stress (MPa)	Plateau stress (MPa)	Compaction stress (MPa)	Ultimate elastic strain	Compaction strain	Final strain
A 1.0	4.798	4.563	6.734	0.020	0.618	0.8
A 0.6	1.537	1.404	2.012	0.036	0.649	0.8
H 0.6	1.631	1.544	NA	0.028	NA	0.8
Z0.6	1.499	1.359	NA	0.027	NA	0.8

Table 4 Energy absorption of experimental results.

Specimen	Total energy absorption			Volumetric energy absorption (J/cm³)			Specific energy absorption (J/g)		
	Energy absorption in elastic stage (J)	Energy absorption in plateau stage (J)	Total Energy absorption (J)	In elastic stage	In Plateau stage	In Total	In Elastic stage	In Plateau stage	In Total
A 1.0	41.482	1651.301	4654.042	0.068	2.792	7.677	0.053	2.170	5.967
A 0.6	22.191	526.043	998.758	0.037	0.904	1.648	0.047	1.171	2.134
H 0.6	19.423	NA	747.660	0.032	NA	1.233	0.0555	NA	2.130
Z0.6	14.374	NA	657.289	0.024	NA	1.084	0.035	NA	1.603

4.3 Energy absorption

The energy absorption capacity is of great importance for the auxetic structures under the impact loading, where energy absorption efficiency is an important index. According to the literature, it can be calculated by Eq. (6):

$$\beta(\varepsilon) = \frac{\int_0^{\varepsilon} \sigma(\varepsilon)\mathrm{d}\varepsilon}{\sigma(\varepsilon)} \tag{6}$$

where $\beta(\varepsilon)$ represents the energy absorption capacity and is defined as the ratio of the energy absorbed under the given nominal strain to the corresponding nominal stress. The nominal stress-strain curve and energy absorption efficiency curve are combined in Fig. 5.

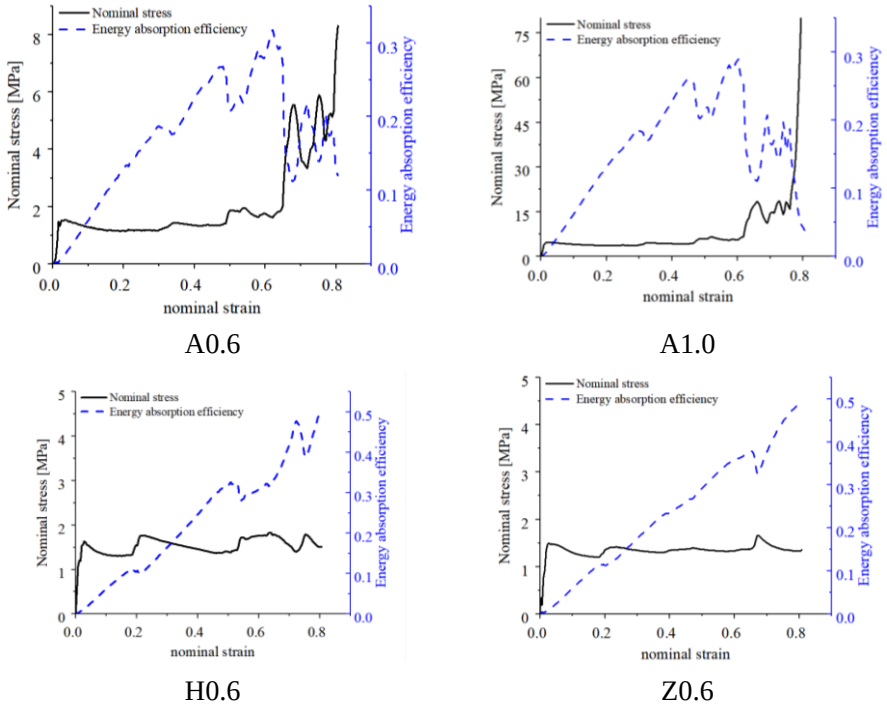
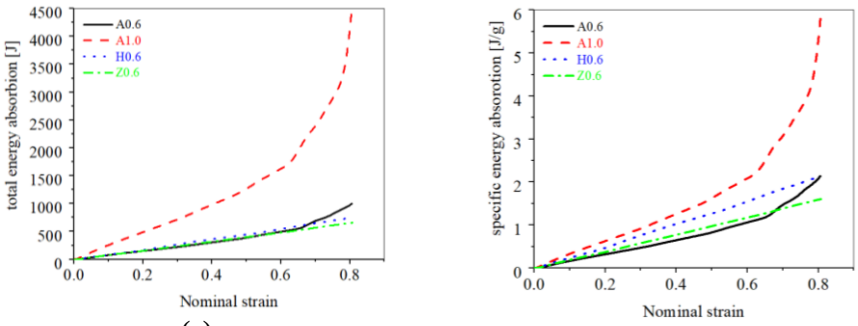


Fig. 5 Nominal stress-strain curves and energy absorption efficiency curves of A0.6, A1.0, H0.6, Z0.6.

The total energy absorbing E_{TEA} in the impact process was calculated by the transient force and the measured displacement as shown in Fig. 6(a). The energy absorbed in different deformation stages were obtained by the elastic limit stress, compaction stress and corresponding strain values given in Table 4. In order to accurately describe energy absorption of the specimen, specific energy absorption, E_{SEA} [31, 39], in Fig. 6(b), defined as energy absorption per unit mass, is computed by the following formula:

$$E_{SEA} = \frac{E_{TEA}}{Q} \tag{7}$$

where Q is the mass of the specimen.



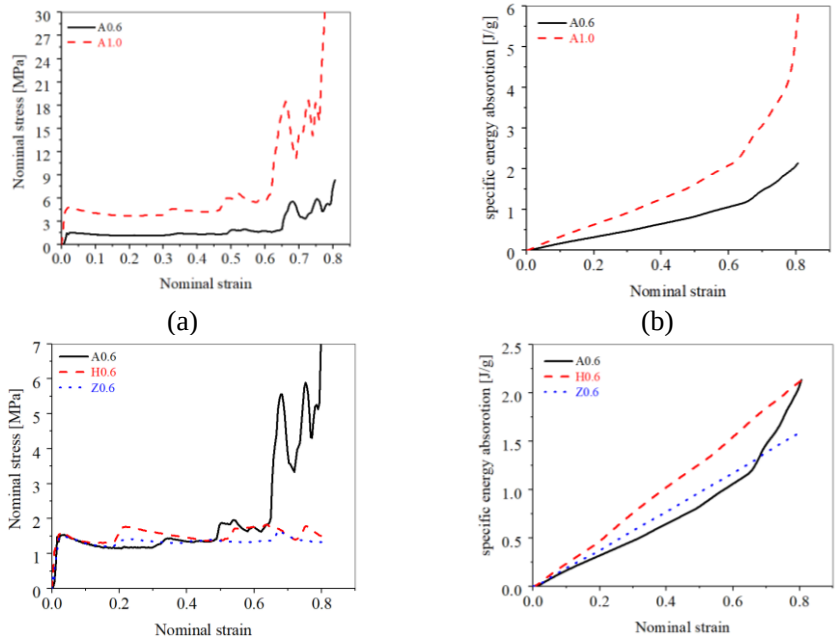
(a) (b)

Fig. 6 Energy absorption versus nominal strain curves (a) Total energy absorption, (b) Volumetric energy absorption

5. Discussion

5.1 Cellular configuration

In comparison with the test outcomes for A0.6, H0.6, and Z0.6 under identical strain conditions, only the honeycomb featuring a negative Poisson's ratio initially transitions into the dense phase due to structural aggregation. This is in line with the traits of materials exhibiting negative Poisson's ratios. The area enclosed by the nominal stress-strain curve signifies the energy absorption attributes, as illustrated in Figure 9(a). There is minimal disparity in the peak stress and plateau stress among components with differing Poisson's ratios. However, as depicted in Figure 9 and Table 4, components with negative Poisson's ratios notably absorb more energy, whereas those with zero Poisson's ratios exhibit the weakest energy absorption. Despite this, the mass of components with negative Poisson ratios is greater than that of other Poisson ratio components, resulting in lower specific energy absorption during the initial phase.



(a) (b)

(c) (d)

Fig. 9 Stress-strain curves and specific energy absorption of specimens with different width/thickness ratios and cell configurations

5.2 Side length-to-thickness ratio

The specimen thicknesses in this research were 1.0 and 0.6, while the ratios of side length to thickness on the inclined side were 10 and 50/3, respectively. Based on the experimental findings, specimens with varying side length-to-thickness ratios demonstrated distinct performance characteristics. A comparison of test results for specimens A0.6 and A1.0 reveals that under the same strain, specimen A1.0, with a larger width-to-thickness ratio, exhibits significantly higher energy absorption than specimen A0.6. Additionally, its stress-strain curve and specific energy absorption surpass those of specimens with smaller width-to-thickness ratios. Consequently, it can be inferred that specimens with greater width/thickness ratios possess superior mechanical properties and energy absorption capabilities. Furthermore, the stress-strain curve trends for A1.0 and A0.6 are nearly identical, suggesting that the width/thickness ratio has minimal impact on the deformation mode of specimens

5.3 Poisson's ratio

As a typical auxetic structure, the Poisson's ratio of specimens is an important parameter, and it can be evaluated using the following formula:

$$v = -\frac{\varepsilon_x}{\varepsilon_y} \tag{9}$$

where ε_x is the transverse nominal strain and ε_y is the nominal vertical stain. The change process of Poisson's ratio was calculated by recording the position data of key points.

According to the Poisson's ratio and nominal vertical strain curve in FIG. 10, the Poisson's ratio of the test piece with negative Poisson's ratio is always in the negative range, and the Poisson's ratio decreases rapidly in the elastic stage of the specimen, gradually increases in the platform stage, and becomes stable in the dense stage. The convex specimen showed a completely different trend, that is, in the compression process, its Poisson's ratio first increased rapidly and then gradually decreased, and its Poisson's ratio was always in a positive range. The Poisson ratio of the zero Poisson ratio test piece always hovers around 0.That's exactly what theory would expect.

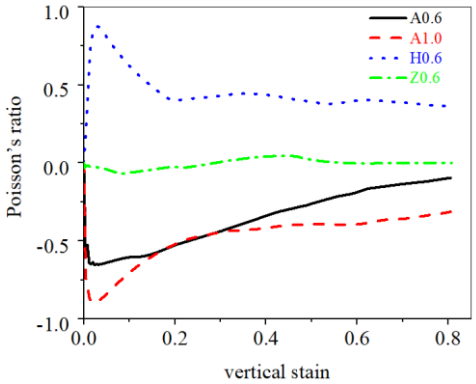


Fig. 10 Poisson's ratio curves of four specimens

6. Conclusion

(1) The deformation of 3D-printed stainless steel auxetic honeycomb structures under quasi-static compression is investigated using numerical analysis. Based on the simulation outcomes, the following conclusions can be drawn:

(2) The deformation process of honeycomb structures with a negative Poisson's ratio can be categorized into three distinct stages: elastic, plateau, and compaction. Owing to their negative Poisson's ratio properties, only auxetic specimens reach the compaction stage under the same strain.

(3) As the width-to-thickness ratio increases, both the mechanical attributes and energy absorption capabilities of the honeycomb structure see significant improvement under identical strain.

(4) Comparatively, the energy absorption potential of structures with a negative Poisson's ratio is greater than those with positive or zero Poisson's ratios. In contrast, structures with a zero Poisson's ratio exhibit the lowest energy absorption capacity.

Reference

[1] Ryan S, Schaefer F, Destefanis R, Lambert M. A ballistic limit equation for hypervelocity impacts on composite honeycomb sandwich panel satellite structures. Advances In Space Research. 2008;41(7):1152-66.

[2] Arunkumar MP, Pitchaimani J, Gangadharan KV, Babu MCL. Influence of nature of core on vibro acoustic behavior of sandwich aerospace structures. Aerospace Science And Technology. 2016;56:155-67.

[3] Mohammadiha O, Beheshti H, Aboutalebi FH. Multi-objective optimisation of functionally graded honeycomb filled crash boxes under oblique impact loading. International Journal Of Crashworthiness. 2015;20(1):44-59.

[4] Wang JF, Shi CY, Yang N, Sun HN, Liu YQ, Song BY. Strength, stiffness, and panel peeling strength of carbon fiber-reinforced composite sandwich structures with aluminum honeycomb cores for vehicle body. Composite Structures. 2018;184:1189-96.

[5] Lai CM, Hokoi S. Thermal performance of an aluminum honeycomb wallboard incorporating microencapsulated PCM. Energy And Buildings. 2014;73:37-47.

[6] Garrido M, Madeira JFA, Proenca M, Correia JR. Multi-objective optimization of pultruded composite sandwich panels for building floor rehabilitation. Construction And Building Materials. 2019;198:465-78.

[7] Hou XH, Deng ZC, Zhang K. Dynamic Crushing Strength Analysis of Auxetic Honeycombs. Acta Mechanica Solida Sinica. 2016;29(5):490-501.

[8] Hu LL, Zhou MZ, Deng H. Dynamic crushing response of auxetic honeycombs under large deformation: Theoretical analysis and numerical simulation. Thin-Walled Structures. 2018;131:373-84.

[9] Masters IG, Evans KE. Models for the elastic deformation of honeycombs. Composite Structures. 1996;35(4):403-22.

[10] Lee JH, Choi JB, Choi K. Application of homogenization FEM analysis to regular and re-entrant honeycomb structures. Journal Of Materials Science. 1996;31(15):4105-10.

[11] Scarpa F, Panayiotou P, Tomlinson G. Numerical and experimental uniaxial loading on in-plane auxetic honeycombs. Journal Of Strain Analysis for Engineering Design. 2000;35(5):383-8.

[12] Grima JN, Ellul B, Attard D, Gatt R, Attard M. Composites with needle-like inclusions exhibiting negative thermal expansion: A preliminary investigation. Composites Science and Technology. 2010;70:2248-52.

[13] Ruan D, Lu G, Wang B, Yu TX. In-plane dynamic crushing of honeycombs - a finite element study. International Journal Of Impact Engineering. 2003;28(2):161-82.

[14] Yasuki T, Kojima S. Application of aluminium honeycomb model using shell elements to offset deformable barrier model. International Journal Of Crashworthiness. 2009;14(5):449-56.

[15] Li D, Yin JH, Dong L, Lakes RS. Strong re-entrant cellular structures with negative Poisson's ratio. Journal Of Materials Science. 2018;53(5):3493-9.

[16] Harris JA and McShane GJ. Impact response of metallic stacked origami cellular materials. International Journal of Impact Engineering. 2021;147:103730.

[17] Xi HF, Xu JC, Cen SD, Huang SQ. Energy Absorption Characteristics of a Novel Asymmetric and Rotatable Re-entrant Honeycomb Structure. Acta Mechanica Solida Sinica. 2021;34(4):550-60.

[18] Zhou YY, Li YF, Jiang D, Chen Y, Xie YM, Jia LJ. In-plane impact behavior of 3D-printed auxetic stainless honeycombs. Engineering Structures. 2022;266:15.

[19] Li Z, Gao Q, Yang S, Wang L, Tang J. Comparative study of the in-plane uniaxial and biaxial crushing of hexagonal, re-entrant, and mixed honeycombs. Journal of Sandwich Structure & Material. 2019;21:1991-2013.

[20] Fan X, Yin X, Tao Y, Chen M, Fang D. Mechanical behavior and energy absorption of graded honeycomb materials under out-of-plane dynamic compression. Acta Mechanica Solida Sinica. 2015;36:114-22.

Proceedings of the IASS Annual Symposium 2023
Integration of Design and Fabrication
10–14 July 2023, Melbourne, Australia
Y.M. Xie, J. Burry, T.U. Lee and J. Ma (eds.)

Tailoring Poisson's ratio of bending-active mechanical metamaterials with periodic and nonperiodic pentagonal grids

Yusuke SAKAI*

* Sony Computer Science Laboratories, Inc., Kyoto Laboratory
13-1 Hontorocho, Shimogyo, Kyoto 600-8086, Japan
Yusuke.C.Sakai@sony.com

Abstract

This study proposes a shape design method for a bending-active mechanical metamaterial composed of a three-dimensional pentagonal grid with a tailorable Poisson's ratio. The specific shape of the proposed grid is derived from a dual geometry of rotating rigid squares. Slender flexible beams with rectangle cross-sections are used for components of structural units, and the connections between members are rigid. To explore the values of Poisson's ratio for in-plane deformation of the proposed grid, we parametrically alter the shape of a structural unit and the bending stiffness of a member. Shape parameters are defined as positions of connections, cross-sectional height and width of a member, and the ratio determining the convexity and concavity of a pentagonal grid. Based on geometric frustration, a nonperiodic pentagonal grid can also be designed. In numerical examples, we investigate the mechanical properties for in-plane and out-of-plane deformations of grids by carrying out finite element analysis. A wide range of Poisson's ratios ranging from –5 to 5 is observed. Moreover, we investigate the relationships between the distribution of Poisson's ratio of an initial pentagonal grid and that of discrete Gaussian curvature on nodes of a curved surface obtained by out-of-plane deformation.

Keywords: three-dimensional pentagonal grid, auxetic structures, bending-active gridshells, Poisson's ratio, geometrical frustration

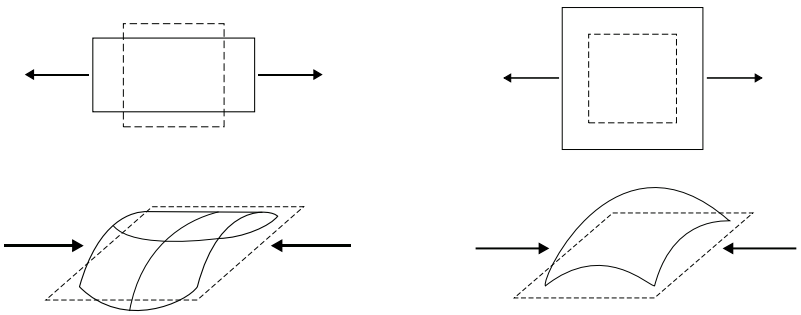
1. Introduction

Active bending is a key technique in designing architectural roofs and spatial structures that are lightweight and efficient in material use [1]. By replacing traditional construction methods such as masonry and latticed shell with active bending, construction time and cost can be reduced. The use of computational design tools and fabrication technologies has greatly facilitated the design and construction of a bending-active structure. There have been a lot of studies and works on bending-active (elastic) gridshells composed of flexible beams [2]. We can obtain various curved surfaces by elastically deforming an initial flat grid. The obtained surface is dependent on the geometrical shape of a grid [3]. It is, therefore, an important challenge to develop a new type of initial flat grid for generating a more complex free-form surface that is difficult to achieve using the existing quadrilateral grid.

The burgeoning developments of mechanical metamaterials have opened a new era of designing a wide range of engineering applications because of their exotic mechanical properties that conventional structures and materials in nature are unachievable [4, 5]. Auxetic structures, which are a class of mechanical metamaterials that exhibit a negative Poisson's ratio, expand or shrink transversely under uniaxial tension or compression, respectively. Figure 1 compares the deformed shapes of conventional and auxetic structures. The unconventional deformation behavior of auxetic structures is caused by specific internal structural units, including reentrant polygons, chiral geometries, and rotating rigid polygons [6]. Naboni *et al*. [7] and La Magna and Knippers [8] applied a few types of auxetic units to

Copyright © 2023 by Yusuke SAKAI. Published in the Proceedings of the IASS Annual Symposium 2023 with permission.

design an initial flat grid of a bending-active gridshell for easily obtaining a dome-like shape that is difficult to be deformed from a conventional structure with a positive Poisson's ratio [9]. Sakai and Ohsaki [10] proposed an initial flat grid composed of nonperiodic and/or hybrid auxetic units based on reentrant honeycomb and reentrant quadrilateral. It enables us to obtain a more complex free-form surface than that with uniform and periodic units. The prior works indicate that a bending-active gridshell with auxetic property is to be an efficient structural system for constructing a spatial structure; however, few types of internal structural units have been investigated. There has still been a challenge to expanding the range of attainable mechanical properties of auxetic bending-active structures with simple and tunable geometrical properties.



(a) (b)

Figure 1. Comparison of relationships between Poisson's ratios and deformation behaviors. Initial and deformed shapes are represented by dotted and solid lines, respectively. In-plane and out-of-plane deformations are shown in the upper and lower figures, respectively.: (a) conventional structure with positive Poisson's ratio, (b) auxetic structure.

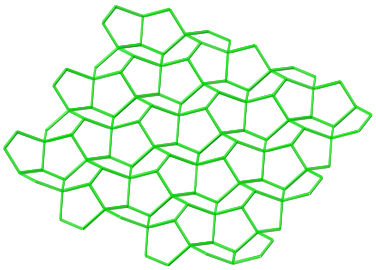


Figure 2. Geometrical configuration of penta-graphene composed of multiple periodic three-dimensional pentagons. Carbon atoms at the intersections are connected by three or four carbon bonds (green line). In numerical simulations in Refs [11, 12], the bending stiffness is not assumed, because the size of carbon allotrope is micro-scale.

In this study, we present a new bending-active mechanical metamaterial based on a three-dimensional pentagonal grid. Previous research has found penta-graphene, a carbon allotrope based on the specific three-dimensional pentagonal configuration composed of carbon atoms and bonds, using numerical simulation in 2015 [11]. Figure 2 shows the geometrical configuration of penta-graphene, which notably exhibits a negative Poisson's ratio. Additionally, artificial carbon material based on a three-dimensional pentagonal configuration is proposed by numerical simulation, and its geometrical configuration and in-plane Poisson's ratio can be parametrically designed [12]. The prior works investigated micro-scale material; therefore, the bending deformation of a beam is neglected. By contrast, our mechanical metamaterial is composed of rigid nodes and bending flexible beams connecting them. The anisotropy of bending stiffness of a beam is used for exploring the mechanical properties of pentagonal grids. By performing finite element analysis, we investigate the relationships between the shape parameters and the mechanical properties: Poisson's ratio for in-plane deformation and discrete Gaussian curvatures at nodes on a curved surface obtained by out-of-plane deformation. Furthermore, we design a nonperiodic

pentagonal grid inspired by the concept of geometric frustration. The proposed design method allows us to obtain a complex shape of a curved surface combined with positive and negative Gaussian curvatures. In numerical example, we tailor the distribution of Poisson's ratio by altering the shape parameters for designing a curved surface with a desirable distribution of discrete Gaussian curvatures.

2. Shape design of a three-dimensional pentagonal grid

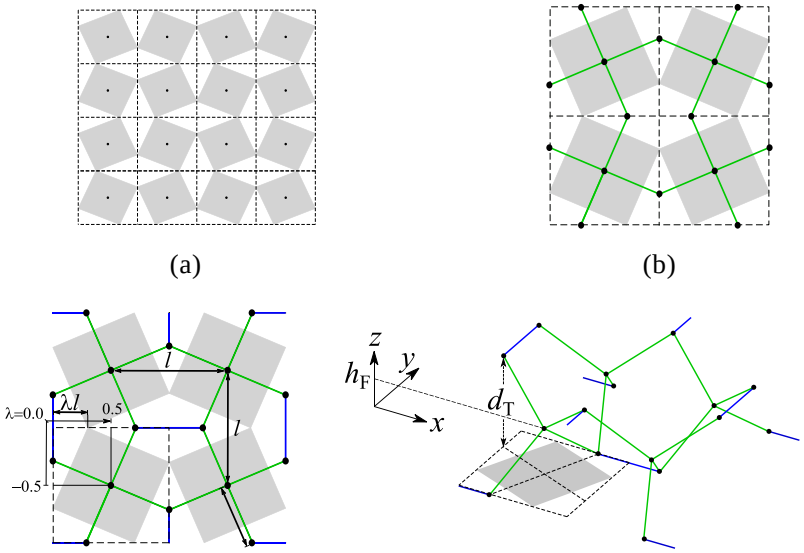


Figure 3. Design workflow of generating a geometrical configuration of a three-dimensional pentagonal grid: (a) rigid rotating squares (grey) and the square grid (dotted line), (b) dual geometry of rigid rotating squares represented as the edges (green) connecting vertices (circular marks), (c) planar pentagonal grid constructed by additional edges (blue) connecting three-valent vertices, and shape parameters λ and l, (d) three-dimensional pentagonal grid in *xyz*-coordinate system obtained by translating the vertices along *z*-direction.

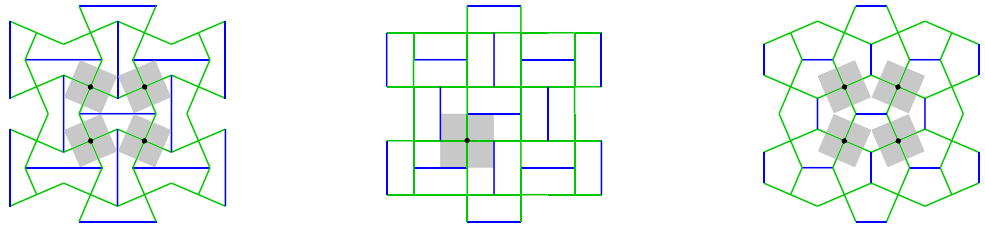


Figure 4. Geometrical shapes of planar pentagonal grid designed by three different tilting ratios λ: (a) $\lambda = -0.3$, (b) $\lambda = 0.0$, (c) $\lambda = 0.3$.

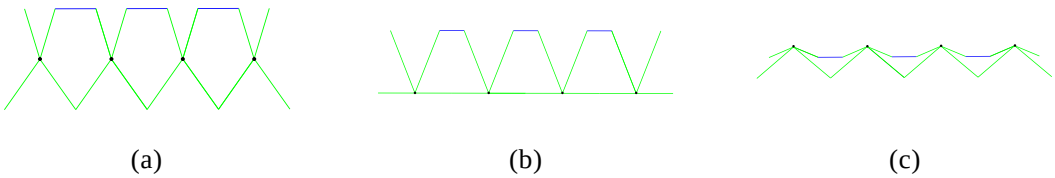


Figure 5. Geometrical shapes of three-dimensional pentagonal grids projected onto *yz*-plane: (a) $d_T = 0.5$ and $h_F = 0.0$, (b) $d_T = 0.3$ and $h_F = -0.3$, (c) $d_T = 0.1$ and $h_F = 0.2$.

A geometrical shape of three-dimensional pentagonal grid is designed based on the dual geometry of rotating rigid squares. Figure 3 shows the design workflow of generating a geometrical shape of the

proposed metamaterial. As illustrated in Fig. 3(a), rotating rigid squares (grey) are arranged in a square grid (dotted lines). Figure 3(b) shows the dual geometry of rotating rigid squares, which is a discrete frame with edges (green) and vertices (circular marks). We can obtain a planar pentagonal grid by constructing additional edges (blue) connecting three-valent vertices, as shown in Fig. 3(c). Tilting ratio of a rotating rigid square and the distance between the centers of neighbouring squares are denoted as λ and l, respectively. A planar pentagonal grid is parametrically determined by tuning the value of λ, ranging from –0.5 to 0.5, as shown in Fig. 4. Figure 3(d) shows the geometrical shape of a three-dimensional pentagonal grid in *xyz*-coordinate system. Let h_F and d_T denote the *z*-directional coordinate of the four-valent vertices and the distance in *z*-direction between edges connecting three-valent vertices along *x*- and *y*-axis, respectively. We show, in Fig. 5, examples of three-dimensional pentagonal grids with different values of h_F and d_T projected onto *yz*-plane.

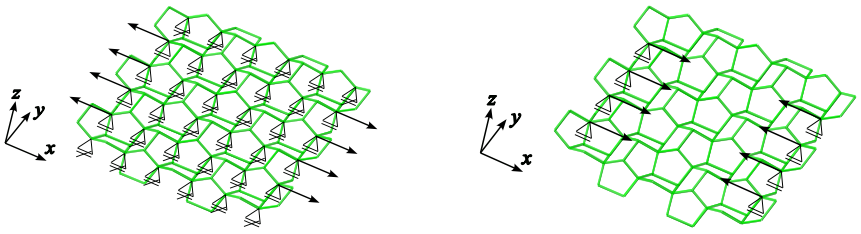
3. Mechanical properties of three-dimensional pentagonal grid

To investigate the static mechanical properties of a three-dimensional pentagonal grid, we carry out nonlinear structural analysis by finite element method. Edges are modelled as bending flexible beams that have a uniform rectangular cross-section. Vertices intersecting the edges are assumed to be elastic connections without any kinematical joints. The width and height of cross-section of all members are denoted as t_b (m) and t_h (m), respectively. The vertices are assumed as rigid nodes intersecting beams with no hinge-joints. Let E, and k_{in} and k_{out} represent Young's modulus of the material, and in-plane and out-of-plane bending stiffness, respectively. We define the bending stiffness ratio as

$$\frac{k_{out}}{k_{in}} = \frac{Et_b t_h^3}{12} \Big/ \frac{Et_h t_b^3}{12} = \left(\frac{t_h}{t_b}\right)^2 . \tag{1}$$

In the following examples, the material has Young's modulus E = 25 GPa, Poisson's ratio 0.221, and yielding stress 433 MPa. We use Abaqus Ver. 2022 for quasi-static deformation analysis [13].

3.1. Poisson's ratio for in-plane deformation



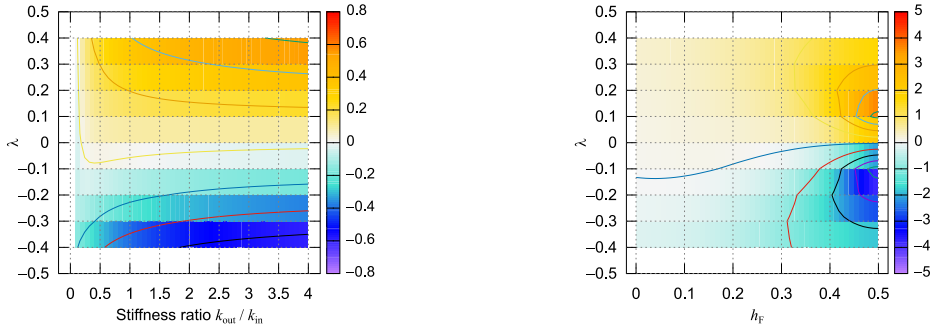
(a) (b)

Figure 6. Roller-supports (triangular marks) and forced displacements (arrows) for in-plane and out-of-plane deformation of three-dimensional pentagonal grids: (a) in-plane deformation, (b) out-of-plane deformation.

Figure 6 shows the boundary conditions for investigation of in-plane Poisson's ratio of the three-dimensional pentagonal grid under elastic small strain range. All four-valent nodes are roller-supported on *xy*-plane. The outer connections arranged along *y*-direction are supported by roller that can move along *x*-direction. Forced displacements 0.1% of the size in *x*-direction of the structure are given at the outer supports as shown with arrows in Fig. 6(b). We compute the Poisson's ratio as the signed ratio of *y*-directional (lateral) strain to *x*-directional (axial) one, which are obtained from displacements of the outer four-valent nodes except those of the corners. In the following examples, the three-dimensional pentagonal grids have 6×6 structural units, and the distance between four-valent nodes is set as $l = 1/\sqrt{2}$. Table 1 shows the values of shape parameters for Cases 1 and 2.

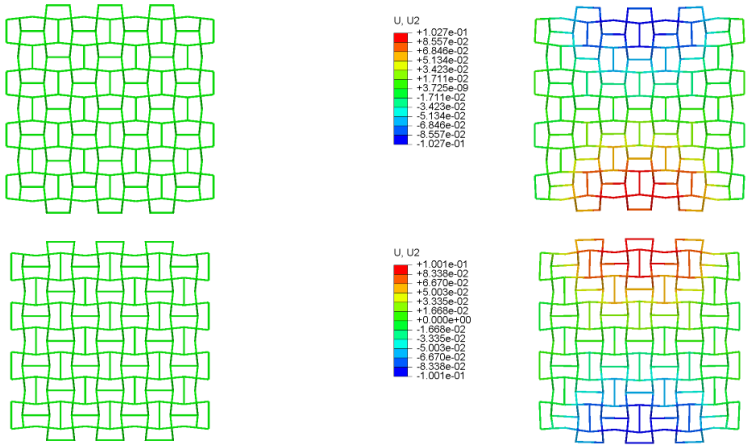
Table 1. Values of shape parameters for Cases 1 and 2.

	h_F	d_T	t_b	t_h
Case 1	0.0	0.3	0.05	–
Case 2	–	0.5	0.05	0.05



(a) (b)

Figure 7. In-plane Poisson's ratio (contour) of the proposed metamaterials specified as $\lambda \in \{-0.4, -0.3, \ldots, 0.4\}$ under elastic small tension: (a) bending stiffness ratios are changed in the range $0.08 \leq k_{out}/k_{in} \leq 4.0$, (b) height of the four-valent vertices are changed in the range of $0.0 \leq h_F \leq 0.5$.



(a) (b)

Figure 8. Comparison of in-plane deformations of three-dimensional pentagonal grids with positive and negative Poisson's ratios in the upper and lower figures, respectively: (a) initial shape, (b) deformed shape projected onto *xy*-plane with contour of *y*-directional displacement.

Figure 7 shows the relationships between the in-plane Poisson's ratio and tunable shape parameters. The contours in the figure represent the values of Poisson's ratio for in-plane deformation, while the tilting ratio is specified as $\lambda \in \{-0.4, -0.3, \ldots, 0.4\}$. In Fig. 7(a), the bending stiffness ratio is varied in the range of $0.08 \leq k_{out}/k_{in} \leq 4.0$ by increasing the cross-sectional height t_h by 0.08 m with a constant cross-sectional width $t_b = 0.05$, in Case 1. For Case 2, as shown in Fig. 7(b), we alter the values of h_F, ranging from 0.0 to 0.5, while setting $d_T = 0.5$.

As seen in both Figs. 7(a) and (b), the sign of Poisson's ratio is dependent on the shape parameter λ, because the convexity and concavity of structural units are determined by λ. In Case 1, as explained in Fig. 7(a), the absolute values of in-plane Poisson's ratio gradually increase by designing the members with a larger bending stiffness ratio. When the bending stiffness ratio is sufficiently small, an auxetic structure composed of convex pentagonal grids with $\lambda > 0$ is obtained. This result is not common, since a convex geometrical shape rarely exhibits a negative Poisson's ratio. In Case 2, as shown in Fig. 7(b), we can obtain a specific metamaterial with various values of Poisson's ratio ranging from –5 to 5. The pentagonal grids designed with shape parameters close to $|\lambda| = 0.1$ and $h_F = 0.5$ exhibit the maximum and minimum values of Poisson's ratio.

Figure 8 compares the deformed shapes of three-dimensional pentagonal grids with positive and negative Poisson's ratio under the same boundary conditions as illustrated in Fig. 6(a). Forced displacements 1% of the size of the grid in *x*-direction are given at the roller-supports. Figures 8(a) and (b) are initial and deformed shapes with contour of *y*-directional displacement of the grids, respectively. In the upper figure, the grid with a positive Poisson's ratio shrinks in the transverse direction; in the lower figure, the grid with a negative Poisson's ratio stretches. It is verified that a sign of Poisson's ratio of the pentagonal grids can be parametrically tuned.

3.2. Deformed shape and discrete Gaussian curvature of a curved surface

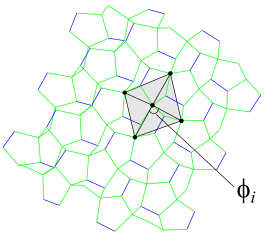
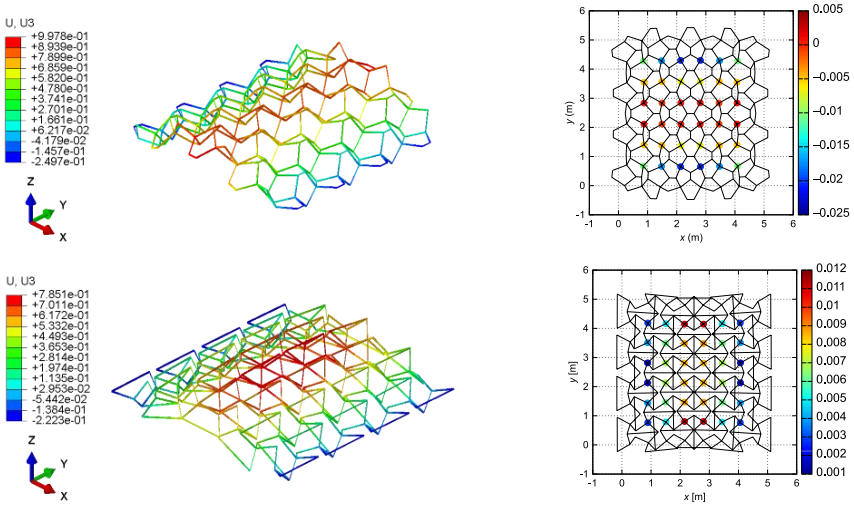


Figure 9. Quadrangular cone (grey) corresponding to a four-valent node on a surface, which is composed of four triangles for computing angle defect.



(a) (b)

Figure 10. Comparison of curved surfaces obtained by out-of-plane deformation from initial grids. The grids with positive and negative Poisson's ratios are shown in the upper and lower figures, respectively.: (a) deformed shapes with contour of *z*-directional displacement, (b) distribution of discrete Gaussian curvatures at nodes.

By carrying out large-deformation analysis, we investigate the deformed shape of a curved surface obtained from an initial grid. Loading parameter τ is linearly increased from 0.0 to 2.0 with the maximum time increment 1.0×10^{-2}. In the period $0.0 \leq \tau \leq 1.0$, upward artificial load equal to self-weight is applied to all members for avoiding the numerical difficulties due to bifurcation buckling. In the latter period from 1.0 to 2.0, we give the forced displacements at the supports along *x*-direction while applying downward artificial load equal to self-weight, and a shape of curved surface is obtained finally. As illustrated in Fig. 6(b), roller-supports that can move along *x*-direction and forced displacements given at roller-supports are represented by triangular marks and arrows, respectively.

To compute the discrete Gaussian curvature, we generate a quadrangular cone at a four-valent node on a polyhedral discrete surface, as outlined in Ref. [10]. To discretize a curved surface, we use triangulation, as illustrated in Fig. 9. Discrete Gaussian curvature can be computed as angle defect

$$2\pi - \sum_{i}^{4} \phi_i , \tag{2}$$

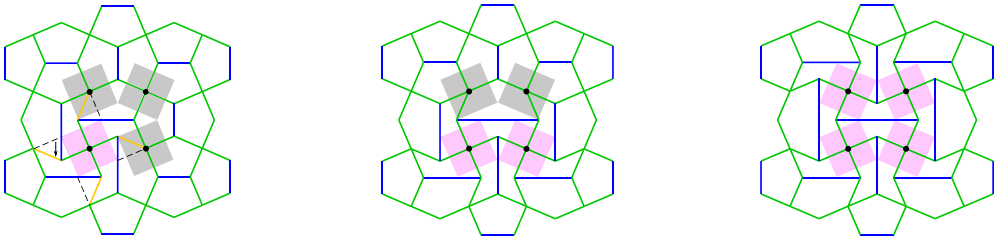
where ϕ_i ($i \in \{1, 2, 3, 4\}$) represents an internal angle of the *i*th triangle incident at a four-valent node.

Figure 10 compares the curved surfaces deformed from initial grids with positive and negative Poisson's ratios in the upper and lower figures, respectively. Figures 10(a) and (b) show a curved surface with contour of *z*-directional displacement and a distribution of discrete Gaussian curvature at four-valent nodes, respectively. A saddle shape is generated by out-of-plane deformation of the grid with a positive Poisson's ratio. As seen in the upper figure in Fig. 10(b), negative values of discrete Gaussian curvature are mainly distributed on a curved surface. By contrast, a dome-like shape is obtained, as shown in the lower figures, by largely deforming the pentagonal grid with negative Poisson's ratio. All values of discrete Gaussian curvatures at nodes except those on the boundaries are larger than 0. The results are consistent with the relationships between the sign of Poisson's ratio and that of Gaussian curvature based on plate theory [9].

4. Nonperiodic three-dimensional pentagonal grids

In terms of ease of design and fabrication, structural units consisting of mechanical metamaterials have usually periodic shapes. In this section, we present a nonperiodic three-dimensional pentagonal grid with both positive and negative Poisson's ratios. This extraordinary mechanical property can lead to generate a more complex free-form surface.

4.1. Shape design method based on the concept of geometrical frustration



(a) (b) (c)

Figure 11. Nonperiodic three-dimensional pentagonal grids generated by introducing inverted structural units based on the frustrated rotating rigid squares (pink): (a) pentagonal grid composed of 4×4 structural units with an inverted unit and modified members (yellow) connecting units, (b) pentagonal grid with two inverted units, (c) pentagonal grid with four inverted units.

Based on the concept of geometrical frustration, which is an incompatible physical phenomenon or system due to its geometrical property [14], we design a nonperiodic three-dimensional pentagonal grid by assigning inverted structural units to the original periodic grid. Figure 11 shows several examples of

nonperiodic grids projected onto *xy*-plane. Frustrated rotating rigid squares, represented by pink square, are designed by inverting the sign of tilting ratio λ, and the corresponding inverted structural units are obtained. We delete the members represented by dotted lines and add the members represented by yellow segments, as shown in Fig. 11(a). Figures 11(b) and (c) are examples of nonperiodic grids with two and four inverted structural units, respectively. By inverting clustered structural units neighboring each other, we can design a nonperiodic pentagonal grid with multiple regions exhibiting different signs of Poisson's ratio.

4.2. Mechanical properties of nonperiodic grids under in-plane and out-of-plane deformations

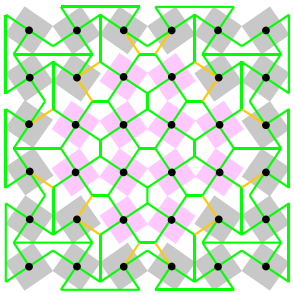
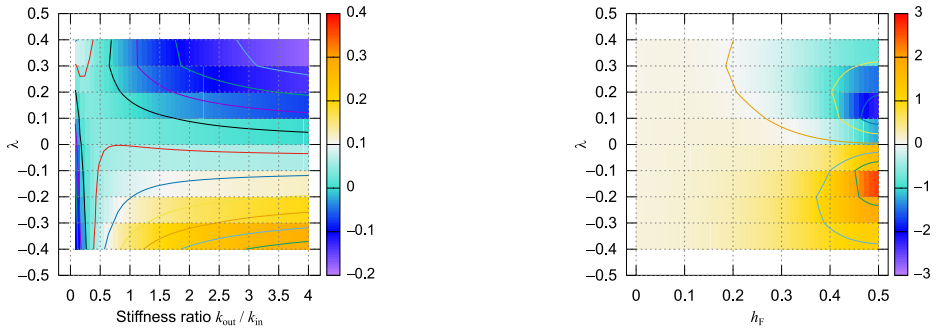


Figure 12. Example of a planar shape of the nonperiodic pentagonal grid used for the investigation of in-plane Poisson's ratio. Twelve inverted structural units are assigned to the center region of the original grid composed of 6×6 structural units.

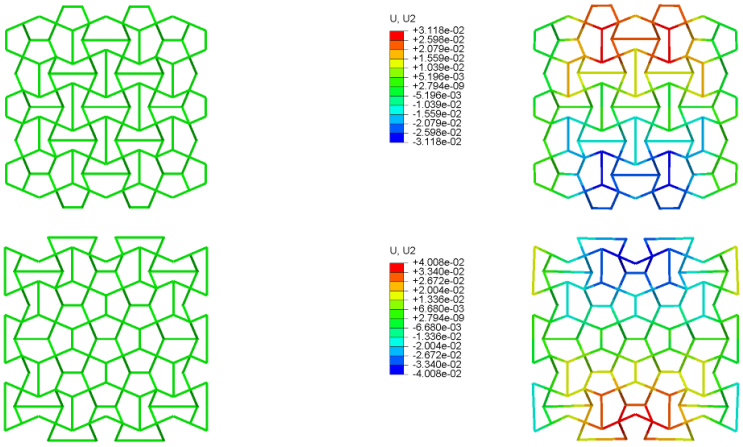


(a) (b)

Figure 13. In-plane Poisson's ratio (contour) of nonperiodic three-dimensional pentagonal grids specified as $\lambda \in \{-0.4, -0.3, \ldots, 0.4\}$ under elastic small tension: (a) bending stiffness ratios are varied in the range of $0.08 \leq k_{out}/k_{in} \leq 4.0$, (b) height of the four-valent vertices are changed in the range of $0.0 \leq h_F \leq 0.5$.

Nonperiodic three-dimensional pentagonal grids are generated to investigate their in-plane and out-of-plane mechanical properties. To compare the mechanical properties of periodic and nonperiodic pentagonal grids, the same in-plane deformation analyses are performed as detailed in Sec. 3.1. The geometrical shapes of nonperiodic pentagonal grids are designed by assigning twelve inverted units to the center region of the original periodic grid composed of 6×6 structural units, as illustrated in Fig. 12.

It is apparent from the results in Fig. 13 that the sign of Poisson's ratio tends to be negative and positive when λ is positive and negative, respectively. These results are different from those of the original periodic grids, as shown in Fig. 7. It seems possible that these results may be due to the arrangement of inverted structural units.

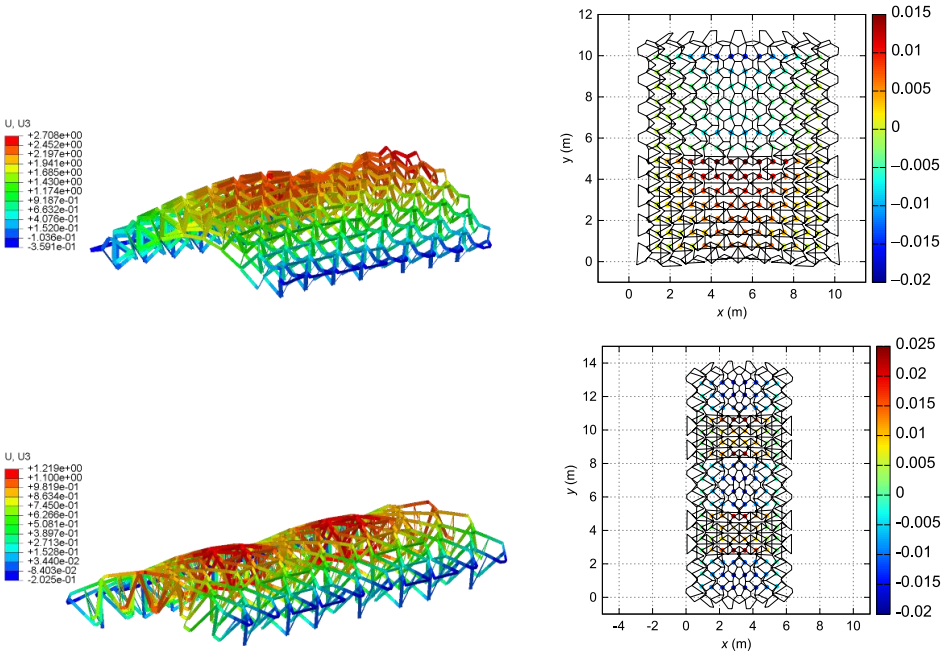


(a) (b)

Figure 14. Comparison of in-plane deformations of nonperiodic pentagonal grids with positive and negative Poisson's ratios in the upper and lower figures, respectively: (a) initial shape, (b) deformed shape projected onto *xy*-plane with contour of *y*-directional displacement.

Table 2. Values of shape parameters for Cases 3 and 4.

	Num. of units	λ	h_F	d_T	t_b	t_h
Case 3	16×16	0.35	0.3	0.5	0.02	0.15
Case 4	10×20	0.4	0.5	0.5	0.02	0.10



(a) (b)

Figure 15. Curved surfaces deformed from nonperiodic pentagonal grids: (a) deformed shapes with contour of *z*-directional displacement, (b) distributions of discrete Gaussian curvatures at four-valent nodes.

Figure 14 shows the in-plane deformation behaviors of 6×6 nonperiodic pentagonal grids with twelve inverted units. The tilting ratios of initial shapes of the original periodic grids in the upper and lower figures are $\lambda = 0.3$ and -0.3, respectively. The contour represents *y*-directional displacement of members. The inverted structural units assigned to the center region of the original grid affect deformation behaviors for both examples, because the deformed shapes in the upper and lower figures are similar to those of the structures with negative and positive Poisson's ratios, respectively.

Furthermore, a curved surface composed of nonperiodic pentagonal grid is obtained by performing large-deformation analysis, as detailed in Sec. 3.2. This section presents several numerical examples and distributions of discrete Gaussian curvature at four-valent nodes. Table 2 provides the shape parameters for designing the initial shapes of 16×16 and 10×20 nonperiodic pentagonal grids in Cases 3 and 4, respectively. Figure 15 shows the obtained surfaces with contour of *z*-directional displacements of members and distributions of discrete Gaussian curvatures.

In Case 3, we obtain a curved surface combined with dome-like shapes and saddle shapes, which are deformed from the nonperiodic pentagonal grid with negative and positive Poisson's ratios, respectively. The upper figure in Fig. 15(b) illustrates the distribution of positive and negative values of discrete Gaussian curvature on the two regions exhibiting negative and positive Poisson's ratios, respectively. Similarly, a curved surface in Case 4 has a more complex shape composed of dome-like and saddle shapes distributed alternately. The sign of discrete Gaussian curvatures is also dependent on the corresponding regions, as shown in the lower figure in Fig. 15(b). The results presented in this section demonstrate that designing a nonperiodic pentagonal grid allows for the generation of a desirable distribution of the sign of Poisson's ratio and Gaussian curvature.

5. Conclusions

This paper introduces a new class of bending-active mechanical metamaterials based on a three-dimensional pentagonal grid inspired by penta-graphene. The values of Poisson's ratio for in-plane deformation of the proposed metamaterial can be tailored in a broad range.

We present a design method for a geometrical shape of the pentagonal grid derived from a dual geometry of rotating rigid squares. The cross-sectional sizes t_h and t_b of a bending flexible beam are utilized as parameters for exploring the values of Poisson's ratio, because these parameters determine the bending stiffness of a beam, which plays an important role of designing a bending-active structure. As seen in Fig. 7(b), the *z*-directional coordinate of four-valent node significantly affect the absolute value of Poisson's ratio. To measure qualitatively the convexity and concavity at four-valent nodes on a curved surface, the values of discrete Gaussian curvature are computed as angle defect. Dome-like and saddle shapes are obtained from the three-dimensional pentagonal grids with negative and positive Poisson's ratios, respectively.

Based on the concept of geometrical frustration, a nonperiodic pentagonal grid can be easily designed. We can obtain a desirable distribution of the sign of Poisson's ratio by assigning inverted structural units to the original periodic grids. It is verified, in the numerical examples, that our method enables us to generate a curved surface with multiple regions exhibiting positive and negative Gaussian curvatures. Three-dimensional pentagonal grid can be a superior structural system for constructing various free-form surfaces deformed from initial grids.

References

[1] J. Lienhard, H. Alpermann, C. Gengnagel and J. Knippers, "Active bending, a review on structures where bending is used as a self-formation process," vol. 28, pp. 187–196, 2013.

[2] M. Leyral, S. Ebode, P. Guerold and C. Berthou, "Elastica project: dynamic relaxation for post-formed elastic gridshells," in *Inspiring the Next Generation: Proceedings of the IASS Annual*

Symposium 2020/21 and the 7th International Conference on Spatial Structures, Guilford, UK, August 23–27, 2021, S. A. Behnejad, G. A. R. Parke and O. A. Samavati, Eds.

[3] M. H. S. Tabari, F. Khojastehmehr and G. H. Filz, "Parametric thinking for decision-making in elastic gridshell design," in *Innovation Sustainability Legacy: Proceedings of the IASS Annual Symposium 2022 affiliated with APCS 2022 conference*, Beijing, China, September 19–22, 2022, S. Xue, J. Wu and G. Sun, Eds.

[4] X. Ren, R. Das, P. Tran, T. D. Ngo and Y. M. Xie, "Auxetic metamaterials and structures: a review," Smart Materials and Structures, vol. 27, 023001, 2018.

[5] E. Barchiesi, M. Spagnuolo and L. Placidi, "Mechanical metamaterials: a state of the art," Mathematics and Mechanics of Solids, vol. 24, pp. 212–234, 2019.

[6] K. K. Saxena, R. Das and E. P. Calius, "Three decades of auxetics research – Materials with negative Poisson's ratio: A review," Advanced Engineering Materials, vol. 18, pp. 1847–1870, 2016.

[7] R. Naboni, S. Sartori and L. Mirante, "Adaptive-curvature structures with auxetic materials, " Advanced Materials Research, vol. 1149, pp. 53–63, 2018.

[8] R. La Magna and J. Knippers, "Tailoring the bending behaviour of material patterns for the induction of double curvature," Humanizing Digital Reality, pp. 441–452, 2018.

[9] K. E. Evans, "The design of doubly curved sandwich panels with honeycomb cores," Composite Structures, vol. 17, pp. 95–111, 1991.

[10] Y. Sakai and M. Ohsaki, "Parametric study of non-periodic and hybrid auxetic bending-active gridshells," Journal of the International Association for Shell and Spatial structures, vol. 61, pp. 275–284, 2020.

[11] S. Zhang, J. Zhou, Q. Wang, X. Chen, Y. Kawazoe and P. Jena, "Penta-graphene: A new carbon allotrope," Proceedings of the National Academy of Sciences, vol. 112, pp. 2372–2377, 2015.

[12] Winczewski S, Rybicki J. Negative Poisson's ratio from pentagons: A new auxetic structure combining three different auxetic mechanisms, Computational Materials Science, vol. 201, 110914, 2022.

[13] Systémes Dassault. Abaqus User's Manual Ver. 2022, 2022.

[14] R. Moessner and A. P. Ramirez, "Geometrical frustration," Physics Today, vol. 59, pp. 24–29, 2006.

IASS 2023
July 10–14 Melbourne
Integration of Design and Fabrication

Proceedings of the IASS Annual Symposium 2023
Integration of Design and Fabrication
10–14 July 2023, Melbourne, Australia
Y.M. Xie, J. Burry, T.U. Lee and J. Ma (eds.)

Towards a novel form-finding approach using matrix analysis: exploiting nodal displacements of pin-jointed frameworks

Yao LU[*], Hua CHAI[a], Masoud AKBARZADEH[b]

[a,*] Polyhedral Structures Laboratory, Weitzman School of Design
University of Pennsylvania, Philadelphia, USA
Pennovation Center, 3401 Grays Ferry Ave. Philadelphia, PA, 19146
yaolu61@upenn.edu

[b] General Robotic, Automation, Sensing and Perception (GRASP) Lab, School of Engineering and Applied Science, University of Pennsylvania, Philadelphia, USA

Abstract

This paper presents a simple method to calculate nodal displacements of kinematically indeterminate pin- jointed frameworks using matrix analysis, aiming to facilitate the early-stage design and analysis of space frames. This method can also inform a novel funicular form-finding approach by iteratively accumulating nodal displacements until reaching a new state of equilibrium. This method assumes that the framework is massless and inextensional, and requires only minimal inputs such as the frame geometry, support locations, and force vectors. The method intends to provide fast and preliminary engineering insights into the kinematic behavior of the framework, like identifying critical locations and suggesting new forms that best fit the force vectors. The proposed method can be a useful tool for designers in the early stages of design, providing them with quick and intuitive displacement results to inform design iterations. By using this method, designers can bridge the gap between early-stage designs and in-depth engineering rationalizations. The results can be used to identify potential problems or limitations in the design and suggest improvements or modifications to optimize the design. This method has been implemented as part of a Grasshopper® plug-in that is freely available for designers to explore. Several case studies are also demonstrated to show how this method can facilitate early-stage space frame designs.

Keywords: funicular form-finding, matrix analysis, kinetic indeterminacy, multi-layer space frame

1. Introduction

Space frames are commonly used in the engineering world at various scales due to their lightweight and high efficiency. Usually, the initial form-finding and schematic design requires the participation of experienced engineers with structural intuition and knowledge of structural analysis and material properties. The geometry-based structural design method based on 2D and 3D reciprocal diagrams developed since the 19th century [1–12], namely 2D/3D graphic statics (GS), allows designers without limited knowledge in the engineering field to create, manipulate, and analyze structural forms while knowing the internal force distributions. However, those preliminary structural forms are usually kinematically unstable and are generated solely based on the design loads, which only represent the equilibrium for this specific load case. That is, when the applied loads are different from the design loads, the structural form may have deflections. To ensure their safety and reliability in real-world scenarios with more complex boundary conditions and material properties, it is crucial for professionals to carefully examine and evaluate them using more rigorous engineering methods such as finite element analysis (FEA) before moving into de- sign development. The design process often requires multiple

Copyright © 2023 by Yao LU, Hua CHAI and Masoud AKBARZADEH. Published in the Proceedings of the IASS Annual Symposium 2023 with permission.

iterations, and designers usually need to take the evaluation and analysis results to inform and adjust the forms.

There is a gap between the geometric-based form-finding process and the more sophisticated engineering rationalization. To bridge this gap, this paper proposes matrix analysis methods as an intermediate stage, which can provide designers with engineering insights while maintaining clarity and simplicity. During the matrix analysis, a structural form is simplified and abstracted as an easy-to-analyze pin-jointed inextensional framework, and its equilibrium matrix and kinematic matrix (also called compatibility matrix) can be constructed. Although space frames are often made with rigid joints, the behavior of a pin-jointed frame with the same configuration could be a good indicator and estimate of the performance of real engineering structures. By using matrix analysis methods, designers can obtain a wealth of static and kinematic information that cannot be abstracted from the conventional formulation without considerable effort [13]. It allows for a better understanding of the structure's behavior under different load cases and empowers designers to make informed decisions throughout the design process.

Focused on the kinematic aspect of matrix analysis, this paper proposes a way to calculate the nodal displacements using minimal inputs, which can then be exploited to inform a novel approach for form-finding, aiming to facilitate the early-stage design of space frames. Nodal displacements serve as an intuitive indicator and can be used for spotting critical locations for a specific load case. Moreover, the deformed configuration often represents a more appropriate form for this load case, suggesting an approach for form-finding and modification.

1.1. Related work

1.1.1. Matrix analysis on the static and kinematic indeterminacies of pin-jointed frameworks

Matrix analysis is found convenient in organizing calculations in engineering fields such as aerospace, civil, and mechanical engineering. With a focus on pin-jointed frameworks, Calladine [14], Pellegrino and Calladine [15] formulated an algorithm that evaluates the static and kinematic indeterminacies in a rapid manner by determining the rank of equilibrium and kinematic matrices and the bases of its four linear-algebraic vector subspaces. Specifically, it offers complete details of any states of self-stress and modes of inextensional deformation that a framework may possess. Lu et al. [16] adapted this method from bars to faces and applied it to the design of multi-layer sheet-based funicular structures by ensuring all mechanisms are restrained. Pellegrino [17] later presented a matrix algorithm that analyzes the mechanisms and nodal displacements of a pre-stressed network upon change of loads, which leads to a new deformed configuration and can be used for form-finding. This algorithm requires the input of material properties such as Young's modulus and cross-sectional areas of each bar.

1.1.2. Methods for calculating nodal displacements and the corresponding form-finding approaches

Existing form-finding methods of space frames based on nodal displacements can be categorized into three main clusters [18], including geometric matrix methods [19, 20], stiffness matrix methods [21], and dynamic relaxation methods [22, 23]. Geometric stiffness methods are material-independent, with only a geometric stiffness that relates the forces to the length of the edge members. Stiffness matrix methods are based on the standard elastic and geometric stiffness matrices. Both geometric and stiffness matrix methods find the equilibrium by reducing unbalanced forces. Dynamic relaxation methods, on the other hand, calculate the velocity and acceleration for each time increment, until the structure becomes static due to artificial damping. A variety of inputs need to be prepared to use such methods. For stiffness matrix methods, the elastic properties need to be provided to set up the tangent stiffness matrix. For the geometric matrix methods, a prescribed set of force densities together with the applied forces need to be provided in order to find a form. The dynamic relaxation methods also require elastic properties and masses to calculate the physical movements.

1.2. Problem statement and objectives

As stated above, an intermediate stage is desired to bridge the gap between geometric-based form-finding and engineering rationalization. Analysis of equilibrium matrix and kinematic matrix is a great candidate as it can provide a wealth of static and kinematic information without much effort, maintaining simplicity and clarity for early-stage design iterations. However, for more detailed information such as nodal displacements, it still needs to assign material-related parameters to the framework in order to carry out calculations. This paper aims to provide a simple method for calculating nodal displacements that requires minimal input such as the structural form and force vectors on the nodes, hoping to assist preliminary space frame designs and enrich the available toolset. In other words, this method can qualitatively analyze the nodal displacements given a user-defined framework with support conditions. The results can be used in the following ways:

- Display the tendency of nodal displacements if the applied force vectors cannot be balanced.
- Identify critical locations with large displacements.
- Accumulate the displacements incrementally, serving as an accurate kinematic simulation tool.
- Iteratively reverse and accumulate the displacements towards a different state of equilibrium, suggesting a new form that better fits this load case.

2. Method

The construction of the equilibrium matrix and kinematic matrix follows the convention established by Pellegrino and Calladine [15]. The framework is described as b bars (or edges) pin-jointed by j nodes (or vertices) with k supported dimensions, each supported dimension defined as constrained movement along one direction. Two kinematic variables and two static variables are considered, they are displacements of the vertices assembled in a $[3j-k \times 1]$ vector $\mathbf{d}$; elongation coefficients of the edges assembled in a $[b \times 1]$ vector $\mathbf{e}$, each entry defined as $e_i \times l_i$ where e_i is the elongation of the i-th edge, l_i is the edge length; external forces on the vertices assembled in a $[3j-k \times 1]$ vector $\mathbf{f}$; and tension densities in the edges assembled in the $[b \times 1]$ vector $\mathbf{t}$, each entry defined as t_i/l_i where t_i is the tension of the i-th edge. The elongation coefficients and tension densities can be easily turned to the actual elongations and tensions as the edge lengths are known. All forces applied to each node must be in equilibrium, written as

$$\mathbf{A} \cdot \mathbf{t} = \mathbf{f}, \tag{1}$$

where $\mathbf{A}$ is the $[3j-k \times b]$ equilibrium matrix. And all extensions in the edges must be compatible with the nodal displacements, written as

$$\mathbf{B} \cdot \mathbf{d} = \mathbf{e}, \tag{2}$$

where $\mathbf{B}$ is the $[b \times 3j-k]$ kinematic matrix, or compatibility matrix. It's easy to prove by the principle of virtual work that the equilibrium matrix and kinematic matrix are the transposes of each other [14]

$$\mathbf{B} = \mathbf{A}^{\mathbf{T}}. \tag{3}$$

2.2. Calculation of unbalanced forces

Eq.1 is helpful in terms of calculating the forces in the edges given $\mathbf{f}$. However, not all $\mathbf{f} \in \mathrm{R}^{3j-k}$ can be in equilibrium when $\mathbf{f}$ lies in the column space of the equilibrium matrix $\mathbf{A}$. Otherwise, mechanisms (pin-joints) will be activated when it lies in the left null space of $\mathbf{A}$. In such cases, if the framework has

no mass, then the least squares solution of $\mathbf{t}$, denoted as $\hat{\mathbf{t}}$, can be used to estimate the edge forces, calculated as

$$\hat{\mathbf{t}} = (\mathbf{A}^{\mathbf{T}}\mathbf{A})^{-1}\mathbf{A}^{\mathbf{T}}\mathbf{f} \tag{4}$$

when $\mathbf{A}$ has a full rank. If not, $\hat{\mathbf{t}}$ can be calculated as

$$\hat{\mathbf{t}} = \mathbf{A}^{+}\mathbf{f}, \tag{5}$$

where $\mathbf{A}^{+}$ denotes the Moore-Penrose Inverse of $\mathbf{A}$. The principle of least action can provide some evidence for it. The action S of the framework is defined as the integral of the Lagrangian L between time t_1 and time t_2, written as

$$S = \int_{t_1}^{t_2} L(t)dt \tag{6}$$

where L is the difference of the kinetic energy T and potential energy V.

$$L = T - V \tag{7}$$

For the framework, it's assumed as particles connected by massless bars. Let the mass of each particle be m, then T and V can be written as

$$T = \frac{1}{2}\sum_{a=1}^{3j-k} mv_a^2 \tag{8}$$

$$V = \sum_{i=1}^{j-k_z} mgz_i \tag{9}$$

where v_a is the velocity of the particles along each 3D Euclidean axis, z_i denotes the z-coordinate the the i-th particle, and k_z denotes the number of nodes that have their z-coordinate constrained.

Since the whole system is not in equilibrium, the velocity v_a will be determined by the summation of all external forces and all axial forces in the edge members, namely residual forces or unbalanced forces and assembled in a $3j$ - k vector $\mathbf{f_r}$, written as

$$\mathbf{f_r} = \mathbf{f} - \mathbf{A}\hat{\mathbf{t}} \tag{10}$$

where external forces $\mathbf{f}$ and equilibrium matrix $\mathbf{B}$ are known. Then the Lagrangian of the middle point is used to approximate the Lagrangian for the small time interval dt. The vertex velocities, assembled in a $3j$ - k vector $\mathbf{v}$ can be written as

$$\underset{\mathbf{t}\in\mathbb{R}^e}{\text{minimize}}\ \mathbf{L} = \mathbf{T} - \mathbf{V} = \frac{1}{2}\sum_{a=1}^{3j-k} mv_a^2 - \sum_{i=1}^{j-k_z} mgz_i = \frac{dt^2}{8m}\mathbf{f_r^2} - \sum_{i=1}^{j-k_z} mgz_i. \tag{12}$$

When the masses of the vertex particles are infinitely small, then the kinetic energy in the Lagrangian becomes dominant:

$$\underset{\mathbf{t}\in\mathbb{R}^e}{\text{minimize}}\ \mathbf{L} = \frac{dt^2}{8m}\mathbf{f_r^2}. \tag{13}$$

which is equivalent to solving for the least square solution $\hat{\mathbf{t}}$ of Eq. 1, proving that the residual forces $\mathbf{f_r}$ can be calculated by Eq. 10. When the frame is kinematically determinate, the kinematic indeterminacy *m* equals zero:

$$m = 3j - k - r_{\mathbf{A}} = 0, \tag{14}$$

where the rank of **A** is denoted as $r_{\mathbf{A}}$. This shows **A** has a full rank and Eq.1 has a solution. In this case, the unbalanced forces will be zero.

2.3. Transforming unbalanced forces to nodal displacements

As mentioned by Pellegrino [17], any infinitesimal inextensional displacement from the original configuration, while leaving the prestress unchanged, results in unbalanced loads of magnitude proportional to the size of the displacement. This is also true in our case when restress does not exist. That means the nodal displacements in the inextensional mode can be directly represented as the residual forces $\mathbf{f_r}$ multiplied by a user-specified scale factor ξ

$$\mathbf{d} = \xi \mathbf{f_r}. \tag{15}$$

This can be proved using Eq. 2

$$\mathbf{Bd} = \xi \mathbf{B} \mathbf{f_r}. \tag{16}$$

Substitute $\mathbf{f_r}$ using Eq.10,

$$\mathbf{Bd} = \xi \mathbf{B}(\mathbf{f} - \mathbf{A}\hat{\mathbf{t}}). \tag{17}$$

Then substitute $\hat{\mathbf{t}}$ using Eq.4, and substitute **B** using Eq.3,

$$\mathbf{Bd} = \xi \mathbf{A^T}(\mathbf{f} - \mathbf{A}(\mathbf{A^T A})^{-1}\mathbf{A^T f}) = \xi(\mathbf{A^T f} - \mathbf{A^T A}(\mathbf{A^T A})^{-1}\mathbf{A^T f}) = \xi(\mathbf{A^T f} - \mathbf{A^T f}) = \mathbf{0}, \tag{18}$$

which shows zero edge elongation coefficients, meaning that the nodal displacements are under inextensional mode. That is, there won't be any edge elongation during the displacement, and the result can be a good estimation of the behavior of pin-jointed rigid bars. Note that the above calculations are based on the small displacement theory. The displacement results are accurate when $\xi\mathbf{f_r}$ is small. Otherwise, matrices **A** and **B** are no longer valid and need to be updated.

2.4. Accumulation of the small displacements

Given the applied force vectors are unchanged and always attached to the nodes, the small displacements can be incrementally accumulated until the frame reaches a new form where all applied force vectors can be balanced and there is no force residual. This process simulates the more accurate kinematic behavior of the frame in response to the applied forces. Note that matrices **A** and **B** need to be updated after each step. The updated equilibrium matrix and kinematic matrix are denoted as $\mathbf{A'}$ and $\mathbf{B'}$, respectively. Again, when $\xi\mathbf{f_r}$ is small the displacements are accurate at each step and the change of edge lengths is negligible. The Moore-Penrose Inverse can be used again to determine whether the applied forces are all balanced. The deformed frame reaches a stable state only when Eq.19 holds:

$$\mathbf{f} = \mathbf{A'A'^{+}f}. \tag{19}$$

2.5. Accumulation of the reversed displacement: towards a novel form-finding approach

Instead of deforming along the displacement direction, the frame can also deform opposite to the displacement direction at each step, acting like a pre-deformation to counteract the displacements. This iterative operation is the same as the process described in Section 2.4, except that the displacements applied to the frame are reversed at each step. After reaching a new state of equilibrium, the new frame geometry will represent a new form that fits the applied load. The computational pipeline of those processes is illustrated in Figure 1.

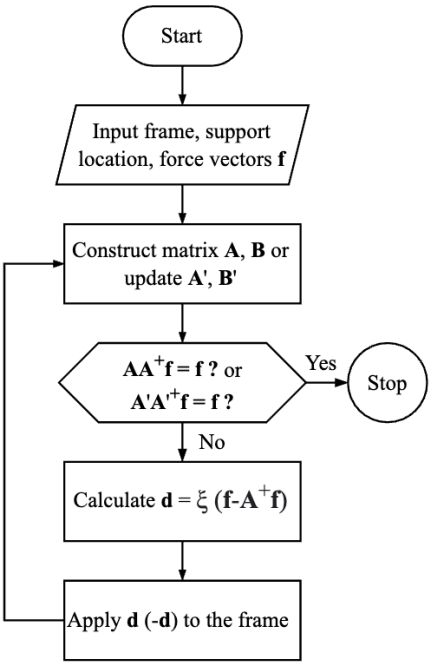


Figure 1. The computational flowchart of incremental accumulation of the (reversed) displacements.

3. Case study

The above-mentioned process has been implemented and included as part of a Grasshopper® plug-in named PolyFrame 2 [24]. The matrix computations are supported by Numpy.NET [25], a .NET binding of the scientific computing library Numpy [26]. With the help of this implementation, several studies are created to demonstrate the possible use cases.

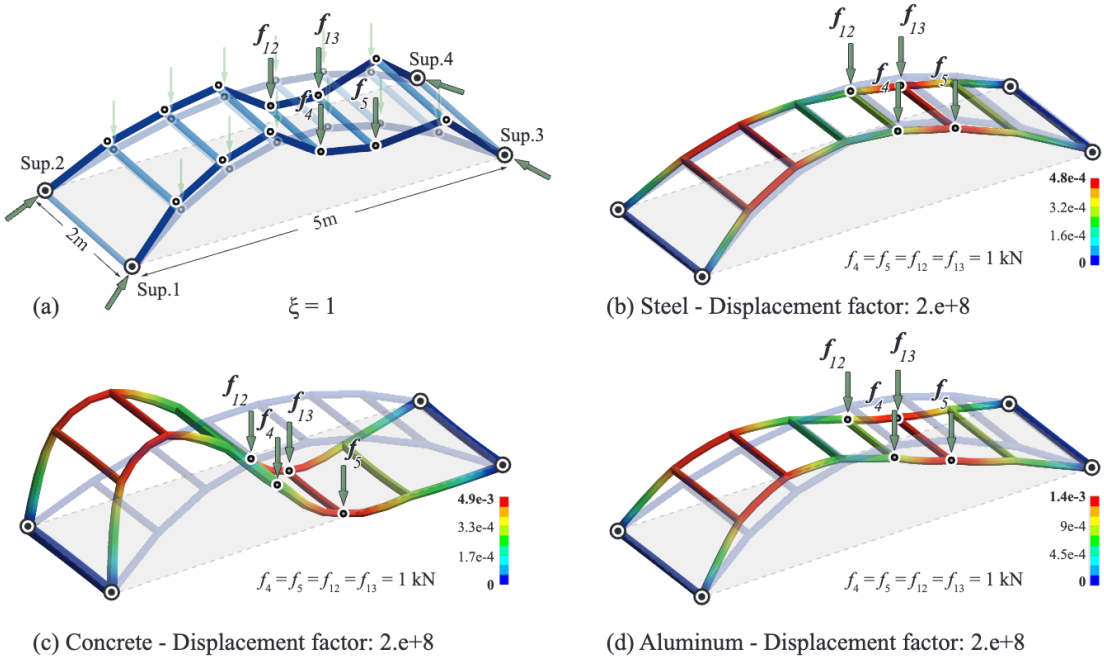


Figure 2. Compare the nodal displacement result with FEA.

3.1. Deformation estimation

Although this proposed method for calculating displacements is based on many assumptions such as massless frame, frictionless pin-joint, and rigid edge, the result can still represent a qualitative estimation of the real behavior of a structure. Figure 2 shows the comparison of analysis results between this proposed method and the finite element method (FEM). For the FEM, three different materials are simulated. The results manifest clear relevance between the simple nodal displacement results and the more rigorous FEM results.

3.2. Simulate the kinematic behavior or find a new form

Figure 3 shows the incremental accumulation of the nodal displacements from an initial flat grid network. In each step, if the displacements are applied to the previous state of the frame, the result will be a kinematic simulation in response to the external forces (Figure 3a); otherwise, the result will show a new form that better fits the applied forces (Figure 3b, 4).

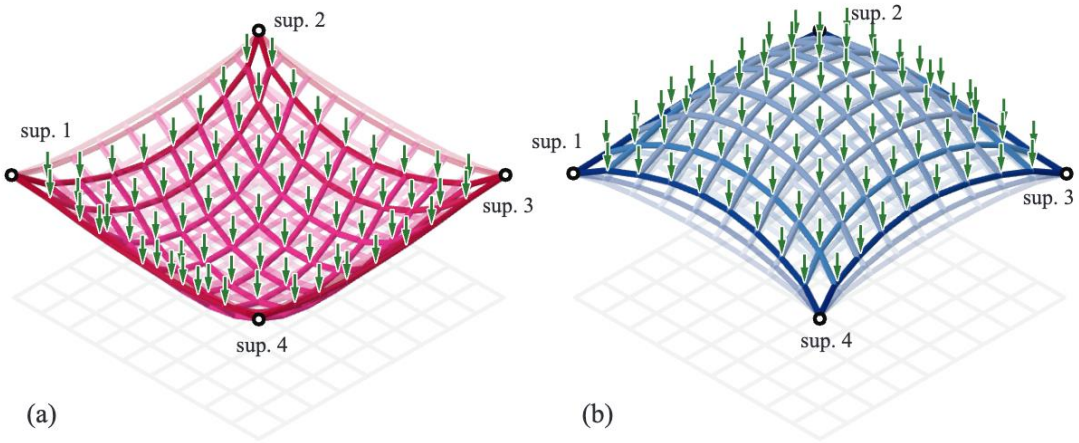


Figure 3. (a) The nodal displacements are iteratively applied to the frame, (b) The reverse of the nodal displacements are iteratively applied to the frame.

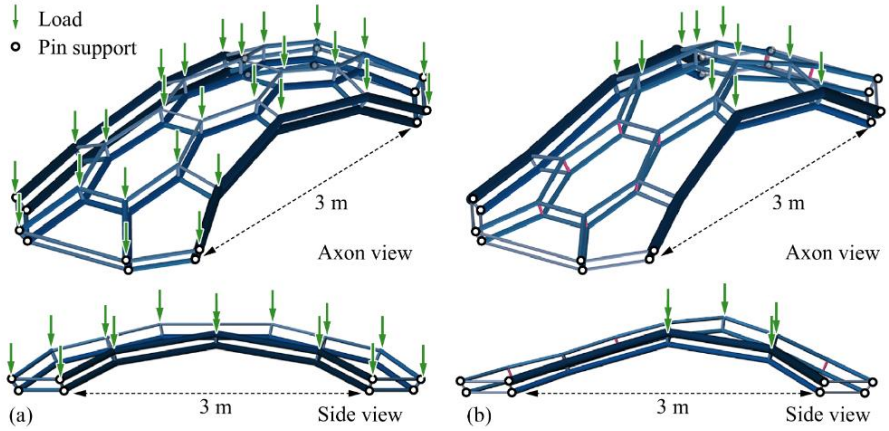


Figure 4. By applying the reverse of the asymmetrical forces, a new bridge geometry can be found that better fits the new load case.

4. Conclusion

This paper presents a simple method to calculate nodal displacements of a pin-jointed framework under a group of force vectors using matrix analysis. This method assumes that the framework is massless and inextensional, and requires only minimal inputs such as the frame geometry, support locations, and force vectors. The method intends to provide fast and preliminary engineering insights into the kinematic behavior of the framework, like identifying critical locations and suggesting new forms that best fit the force vectors. The proposed method can be a useful tool for designers in the early stages of design, providing them with quick and intuitive displacement results to inform design iterations. By using this method, designers can bridge the gap between early-stage designs and in-depth engineering rationalizations. The results can be used to identify potential problems or limitations in the design and suggest improvements or modifications to optimize the design. This method has been implemented as a software tool that is freely available for designers to explore. Several case studies are also demonstrated to show how this method can facilitate early-stage space frame designs.

In summary, the proposed method enriches the toolset for designing space frames, allowing designers to make informed decisions based on preliminary engineering analysis, and saving time and resources in the design iteration process.

Acknowledgements

This research is funded by the National Science Foundation CAREER Award (NSF CAREER-CMMI 1944691) and the National Science Foundation Future Eco Manufacturing Research Grant (NSF FMRG-CMMI 2037097) to Masoud Akbarzadeh.

References

[1] W. J. M. Rankine, "Principle of the Equilibrium of Polyhedral Frames," *Philosophical Magazine Series 4*, vol. 27, no. 180, p. 92, 1864.

[2] J. C. Maxwell, "On Reciprocal Figures and Diagrams of Forces," *Philosophical Magazine Series 4*, vol. 27, no. 182, pp. 250–261, 1864.

[3] K. Culmann, *Die Graphische Statik*. Zürich: Verlag Meyer und Zeller, 1864.

[4] R. H. Bow, *Economics of construction in relation to framed structures*. London: Spon, 1873.

[5] L. Cremona, *Graphical Statics: Two Treatises on the Graphical Calculus and Reciprocal Figures in Graphical Statics. Translated by Thomas Hudson Beare*. Oxford: Clarendon Press, 1890.

[6] W. S. Wolfe, *Graphical Analysis: A Text Book on Graphic Statics*. New York: McGraw-Hill Book Co. Inc., 1921.

[7] P. D'Acunto, J.-P. Jasienski, P. O. Ohlbrock, C. Fivet, J. Schwartz, and D. Zastavni, "Vector-based 3d graphic statics: A framework for the design of spatial structures based on the relation between form and forces," *International Journal of Solids and Structures*, vol. 167, p. 58–70, Aug 2019.

[8] M. Akbarzadeh, "3d graphic statics using reciprocal polyhedral diagrams," Ph.D. dissertation, ETH Zurich, Zurich, Switzerland, 2016.

[9] J. Lee, "Computational design framework for 3d graphic statics," Doctoral Thesis, ETH Zurich, 2018, accepted: 2019-03-14T06:19:28Z. [Online]. Available: https://www.research-collection.ethz.ch/handle/20.500.11850/331210

[10] A. McRobie, "Rankine reciprocals with zero bars," *Preprint*, 2017.

[11] A. McRobie, "The geometry of structural equilibrium," *Royal Society Open Science*, vol. 4, no. 3, 2017.

[12] A. Mcrobie, "Graphic analysis of 3d frames: Clifford algebra and rankine incompleteness," in *Proceedings of IASS Annual Symposia*, vol. 2017, Sep 2017, p. 1–10.

[13] S. Pellegrino, "Mechanics of kinematically indeterminate structures." Thesis, University of Cambridge, Nov 1986, accepted: 2015-09-16T14:37:56Z. [Online]. Available: https://www.repository.cam.ac.uk/handle/1810/250895

[14] C. R. Calladine, "Buckminster fuller's "tensegrity" structures and clerk maxwell's rules for the construction of stiff frames," *International Journal of Solids and Structures*, vol. 14, no. 2, p. 161–172, Jan 1978.

[15] S. Pellegrino and C. R. Calladine, "Matrix analysis of statically and kinematically indeterminate frameworks," *International Journal of Solids and Structures*, vol. 22, no. 4, pp. 409–428, 1986.

[16] Y. Lu, T. Alsalem, and M. Akbarzadeh, "A method for designing multi-layer sheet-based lightweight funicular structures," *Journal of the International Association for Shell and Spatial Structures*, vol. 63, no. 4, p. 252–262, Dec 2022.

[17] S. Pellegrino, "Analysis of prestressed mechanisms," *International Journal of Solids and Structures*, vol. 26, no. 12, p. 1329–1350, Jan 1990.

[18] D. Veenendaal and P. Block, "An overview and comparison of structural form finding methods for general networks," *International Journal of Solids and Structures*, vol. 49, no. 26, p. 3741–3753, Dec 2012.

[19] H. J. Schek, "The force density method for form finding and computation of general networks," *Computer Methods in Applied Mechanics and Engineering*, vol. 3, no. 1, p. 115–134, Jan 1974.

[20] G. Aboul-Nasr and S. A. Mourad, "An extended force density method for form finding of constrained cable nets," *Case Studies in Structural Engineering*, vol. 3, p. 19–32, Jun 2015.

[21] J. H. Argyris, T. Angelopoulos, and B. Bichat, "A general method for the shape finding of lightweight tension structures," *Computer Methods in Applied Mechanics and Engineering*, vol. 3, no. 1, p. 135–149, Jan 1974.

[22] M. R. Barnes, "Form finding and analysis of tension structures by dynamic relaxation," *International Journal of Space Structures*, vol. 14, no. 2, p. 89–104, Jun 1999.

[23] A. Kilian and J. Ochsendorf, "Particle-spring systems for structural form finding," *Journal of the International Association for Shell and Spatial Structures*, vol. 46, p. 77–84, Aug 2005.

[24] PSL, "PolyFrame 2," https://www.food4rhino.com/app/polyframe-2, March 2023. [Online]. Available: https://www.food4rhino.com/app/polyframe-2

[25] Dec 2022. [Online]. Available: https://github.com/SciSharp/Numpy.NET

[26] C. R. Harris, K. J. Millman, S. J. van der Walt, R. Gommers, P. Virtanen, D. Cournapeau, E. Wieser, J. Taylor, S. Berg, N. J. Smith, R. Kern, M. Picus, S. Hoyer, M. H. van Kerkwijk, M. Brett, A. Haldane, J. F. del R´ıo, M. Wiebe, P. Peterson, P. Ge´rard-Marchant, K. Sheppard, T. Reddy, W. Weckesser, H. Abbasi, C. Gohlke, and T. E. Oliphant, "Array programming with NumPy," *Nature*, vol. 585, no. 7825, pp. 357–362, Sep. 2020. [Online]. Available: https://doi.org/10.1038/s41586-020-2649-2

Optimisation methods and applications

Active bending
Additive manufacturing/ 3D printing
Architectural geometry
Bamboo for sustainable construction and quality of life improvement
Bio-inspired structures and architecture
Bridge structures
Computational form-finding
Conceptual design
Concrete structures
Construction techniques
Deployable and inflatable structures
Design competition (WG21)
Digital modelling and fabrication
Dynamic response of metal spatial structures
Dynamic response of other structures
Form-finding and structural optimisation of interlocking discrete assemblages
Graphical methods
Gridshell and lattice structures
Historical concrete shells
Historical structures
Lattice structures
Life-cycle design and assessment of structures
Metal gridshell structures, connections and stability
Methods and construction technologies for sustainable shell structures
Morphology and configuration processing
Next generation parametric design
Novel methods in modelling, optimisation and construction for reducing carbon footprint of continuous roof shells
Numerical methods for geometry, form-finding and optimisation of lightweight structures
► **Optimisation methods and applications**
Origami
Other
Teaching design uncertainty: working with unknown qualities/quantities of new and re-claimed materials
Teaching of shell and spatial structures
Tensegrity systems and cable structures
Tension and membrane structures
Tension structures in the Asia-Pacific
Timber and bio-based structures
Topology optimisation
Traditional masonry structures and innovation
Transformable structures

IASS 2023
July 10–14 Melbourne
Integration of Design and Fabrication

Proceedings of the IASS Annual Symposium 2023
Integration of Design and Fabrication
10–14 July 2023, Melbourne, Australia
Y.M. Xie, J. Burry, T.U. Lee and J. Ma (eds.)

A study on the binary harmony search algorithms for an optimal design of the truss system

Hyeonju HA[a], Sudeok SHON[b,*], Seungjae LEE[a]

[b,*] School of Industrial Design & Architectural Engineering
Korea University of Education and Technology
sdshon@koreatech.ac.kr

[a] Department of Architectural Engineering, Korea University of Education and Technology

Abstract

The Harmony Search (HS) algorithm, inspired by the process of tuning musical instruments, is widely used in optimizing various fields due to its simplicity and ease of use. The Binary Harmony Search (BHS) algorithm was developed to enhance search techniques in binary number optimization problems such as the knapsack problem of the decimal-based HS algorithm. In the development of BHS, it was discovered that the role of the pitch-adjust rate (PAR) operator could be improved by addressing the issue of the mutation operator. However, the success of binary-based algorithms in more complex problems heavily depends on how the PAR operator is defined. To address this issue, this study compared the characteristics of the algorithm according to the PAR operator with the decimal-based HS and bit-based algorithms and analyzed the results.

Keywords: optimization, harmony search, binary number, benchmark function, plane truss, minimum weight

1. Introduction

The term "metaheuristic" was first used in the 1980s to describe an optimization algorithm designed to find an optimal solution [1]. In the 2000s, several metaheuristic algorithms, including Particle Swarm Optimization, Ant Colony Optimization, and Harmony Search Algorithm, were developed for optimization problems. The Harmony Search (HS) algorithm is a metaheuristic algorithm that imitates the process of musical improvisation to find harmony through the combination of musical notes. It was introduced by Geem [2] in 2001. The Harmony Memory (HM) is created by selecting notes from musical instruments with a probability to achieve better harmonies. The size of the Harmony Memory Size (HMS) affects the convergence speed and precision in the search process. The HS algorithm is a stochastic search algorithm that employs a probabilistic approach to finding an optimal solution. The HS algorithm consists of several critical parameters. To find an optimal solution for the fitness function $f(x)$ subject to decision variables x_i $(i = 1,2, \dots, n)$ where n is the dimension of the problem, the Harmony Memory (HM) needs to be initialized. A new harmony is generated by the Harmony Memory Consideration Rule (HMCR) and Pitch Adjustment Rule (PAR), denoted as x_i' . HMCR is the probability of selecting a value from the HM when generating a new harmony and typically takes a value between 0.7 to 0.95. PAR controls the amount of random perturbation introduced in the selected values when generating a new harmony and usually takes a value between 0.1 to 0.5 [1]. The tune can be adjusted depending on the width of the b_w. After generating a new harmony, the Harmony Memory is updated, and the same process is repeated until the stopping criterion is met. The best harmony stored in HM is used to find the optimal solution. Figure 1 illustrates the process of the HS algorithm.

Copyright © 2023 by HyeonJu HA. Published in the Proceedings of the IASS Annual Symposium 2023 with permission.

The Harmony Search (HS) algorithm is a well-known metaheuristic optimization algorithm that is primarily used for decimal-based optimization problems. However, the application of the HS algorithm to binary-coded problems is an emerging field of research. The Binary Harmony Search (BHS) algorithm was first introduced by Geem [2] to solve a water pump switching problem. Since then, various modifications to the BHS algorithm have been proposed to enhance its performance. Kong et al. [3] introduced the Hybrid BHS Algorithm, which adapts the search mechanism of the Ant System. Additionally, Ling et al. [4] proposed an Adaptive BHS Algorithm. The BHS algorithm was developed to improve search techniques in binary number optimization problems, such as the knapsack problem of the decimal-based HS algorithm. It has been widely applied in various fields, including architecture engineering, where it has been used to optimize truss topology and member sizing[5][6]. It is important to note that the optimal values of the HMCR and PAR parameters in the BHS algorithm may vary depending on the characteristics of the specific binary optimization problem being solved. Ongoing research and development in the field of metaheuristics are essential for the continued advancement of optimization algorithms. As mentioned in the abstract, the binary HS operator is more complicated to find a good solution. Thus, we will create the binary HAS according to the HMCR and PAR skills.

2. Binary search algorithm

The Binary Harmony Search (BHS) algorithm is a variant of the Harmony Search (HS) algorithm, which is a population-based optimization algorithm that aims to find the optimal solution through a musical improvisation process. The BHS algorithm builds upon the HS algorithm by using a binary coding process for decision variables to solve binary optimization problems, where the variables take on only two values (0 or 1). This extension allows the BHS algorithm to efficiently explore and exploit the solution space of binary optimization problems. The BHS algorithm has demonstrated its effectiveness in solving a wide range of binary optimization problems.

2.1. Binary harmony search (BHS) algorithm

Pseudo code of a classic Harmony Search Algorithm

```
procedure CLASSIC HS ALGORITHM
    t ← 0
    Initialize HMS, HMCR, PAR, BW
    Initialize HM
    while t < t_max (or ε_tol) do
        t ← t + 1;
        Calculate HMCR, PAR
        Initialize candidate x^new
        for j=1:ndim do
            if r <HMCR then
                Select x_j^new ∈ HM
                if r <PAR then
                    Adjust x_j^new using BW
                end if
            else
                Generate x_j^new
            end if
            Put x_j^new into x^new
        end for
        Evaluate x^new
        Update HM
    end while
    Output results
end procedure
```

Figure 1. Pseudo Code of a Classic Harmony Search (HS) Algorithm

To compare the Harmony Search (HS) algorithm and the Binary Harmony Search (BHS) algorithm, the pseudo-code for each algorithm is provided in Figure 1 and Figure 2. It should be noted that the HS algorithm is based on decimal arithmetic, while the BHS algorithm employs binary arithmetic. Two types of the BHS algorithm are proposed in this section for further investigation. This comparison is essential to determine the effectiveness of the BHS algorithm and to evaluate the impact of binary arithmetic on the optimization process. By providing the pseudo-code for both algorithms, it is possible

to gain a better understanding of the differences between the two and to analyze their performance in solving optimization problems.

Pseudo code of a binary-coded HSearch Algorithm (Type A)

```
procedure BINARY-CODED HS ALGORITHM (A)
    t ← 0
    Initialize HMS, HMCR, PAR, BW
    Initialize HM_b using random bits
    Decode and evaluate HM_b
    while t < t_max (or ε < ε_tol) do
        t ← t + 1;
        Calculate HMCR, PAR
        Initialize candidate B^new
        for j=1:ndim do
            if r <HMCR then
                Select j-th variable bits b_j^new ∈ HM_b
                if r <PAR then
                    Calculate rBW
                    Set mutation point m
                    Mutate b_j^new(m) (0 ← 1 or 1 ← 0)
                end if
            else
                Generate b_j^new
            end if
            Put b_j^new into B^new
        end for
        Decode and evaluate B^new
        Update HM_b
    end while
    Output results
end procedure
```

(a) Type A

Pseudo code of a binary-coded HS Algorithm (Type B)

```
procedure BINARY-CODED HS ALGORITHM (B)
    t ← 0
    Initialize HMS, HMCR, PAR, BW
    Initialize HM_b using random bits
    Decode and evaluate HM_b
    while t < t_max (or ε < ε_tol) do
        t ← t + 1;
        Calculate HMCR, PAR
        Initialize candidate B^new
        for j=1:nbit do
            if r <HMCR then
                Select b_j^new ∈ HM_b
                if r <PAR then
                    Mutate b_j^new (0 ← 1 or 1 ← 0)
                end if
            else
                Generate b_j^new
            end if
            Put b_j^new into B^new
        end for
        Decode and evaluate B^new
        Update HM_b
    end while
    Output results
end procedure
```

(b) Type B

Figure 2. Pseudo-Code of a Binary-coded Harmony Search (BHS) Algorithm

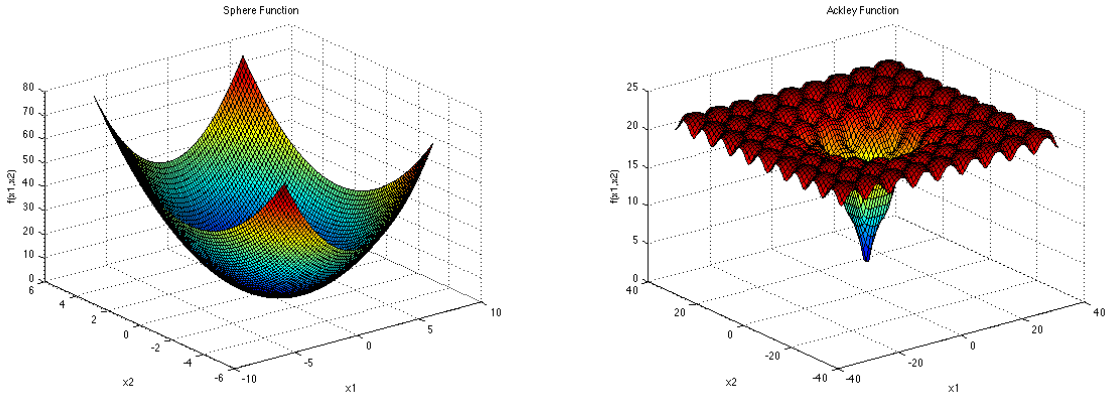
To handle the binary value problem, we can consider two types of binary HS operators. One is, as Figure 2(a), binary HS based on decimal asymmetric. And the other, as Figure 2(b), is based on the binary value. In this work, we compare these types of operators.

2.2. Benchmark function

This section utilized the Harmony Search (HS) and Binary Harmony Search (BHS) algorithms to optimize a benchmark function and find the optimal solution. The benchmark function was constructed based on two mathematical models: the Sphere (1) and Ackley (2) functions, which are commonly used benchmark functions in optimization studies due to their simplicity and effectiveness in evaluating algorithm performance. Figure 3 displays the graphs of each benchmark function. The Sphere function represents a convex quadratic function with a single minimum, while the Ackley function represents a non-convex function with multiple local minima. The study aimed to compare the performance of the HS and BHS algorithms in finding the global minimum of the benchmark function. We compared how well the BHS algorithm and the HS algorithm work to see if using binary code for solutions is effective.

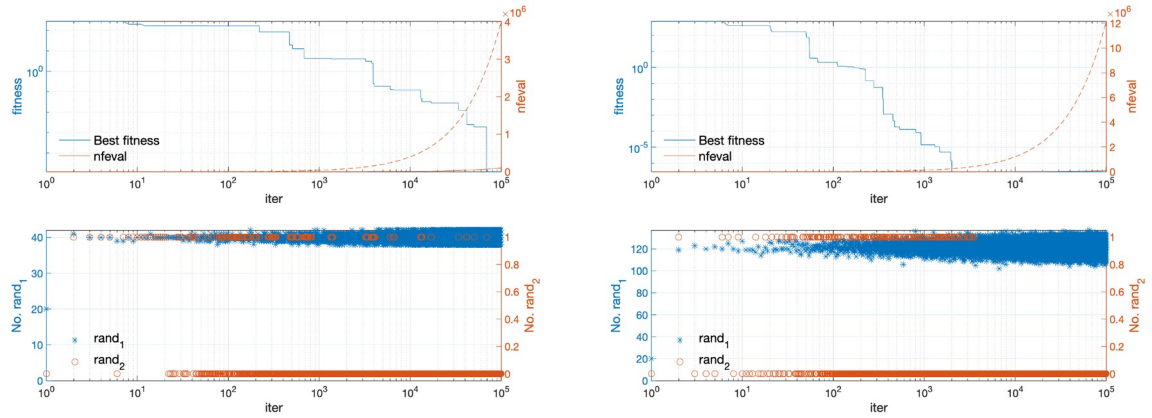
$$f(x) = \sum_{i=1}^{n} x_i^2 \tag{1}$$

$$f(x) = -ae^{\left(-b\sqrt{\frac{1}{d}\sum_{i=1}^{n} x_i^2}\right)} - e^{\left(\frac{1}{d}\sqrt{\cos(cx_i)}\right)} + a + e^1 \tag{2}$$



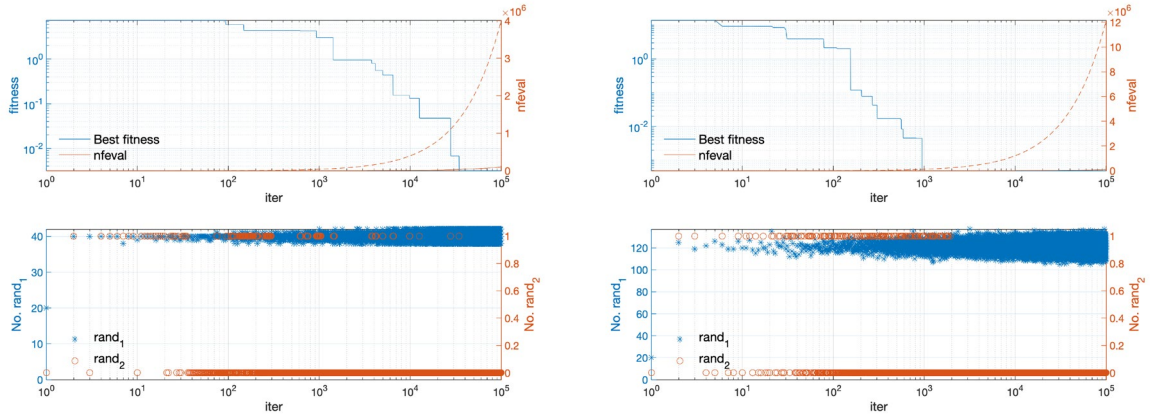
(a) Sphere Function (b) Ackley Function

Figure 3. Graph of Benchmark Function



(a) Type A considering fixed b_w (b) Type B

Figure 4. Result of Sphere Function



(a) Type A considering fixed b_w (b) Type B

Figure 5. Result of Ackley Function

Figures 4 and 5 illustrate the results of the study, where (a), (b), and (c) demonstrate the results of type A and (d) represents the type B. In particular, (a) displays the result when b_w was not considered, (b)

shows the result when a fixed b_w was used, and (c) illustrates the result when b_w was decreased. The graph shows that as the amount of increasing generation, the optimal solution converges. By storing candidates in the harmony memory, it can be seen that Type B has excellent convergence performance. Type B has three times the amount of random generator than Type A, but its convergence performance is excellent.

3. Three bar truss optimization problem

As an illustrative example, the present study addresses the optimal design problem of a truss structure comprising three members is in Figure 6. The objective of this investigation is to optimize the performance of the truss by minimizing the weight of the structure while satisfying the design constraints. To this end, a set of benchmark functions were utilized to evaluate the convergence rate of the optimization algorithm. Figure 4 show the truss structure with three members [14], where the cross-sectional areas of member 1 and member 3 are held constant. The optimization problem is formulated with the objective function (3), in which x_1 and x_2 are the design variables representing the cross-sectional areas of members 1 and 3, respectively. The values of x_1 and x_2 are adjusted to optimize the weight of the structure. Figure 7 shows the analysis results using the BHS operator.

$$f(x_1, x_2) = 2\sqrt{2}x_1 + x_2 \tag{3}$$

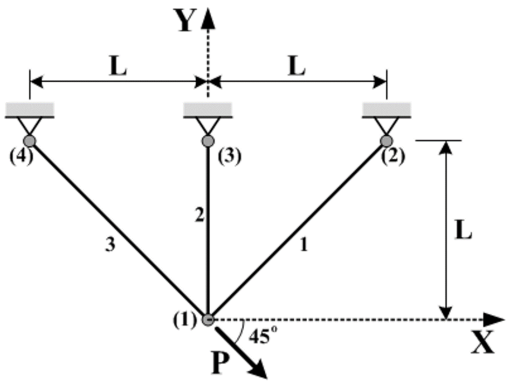
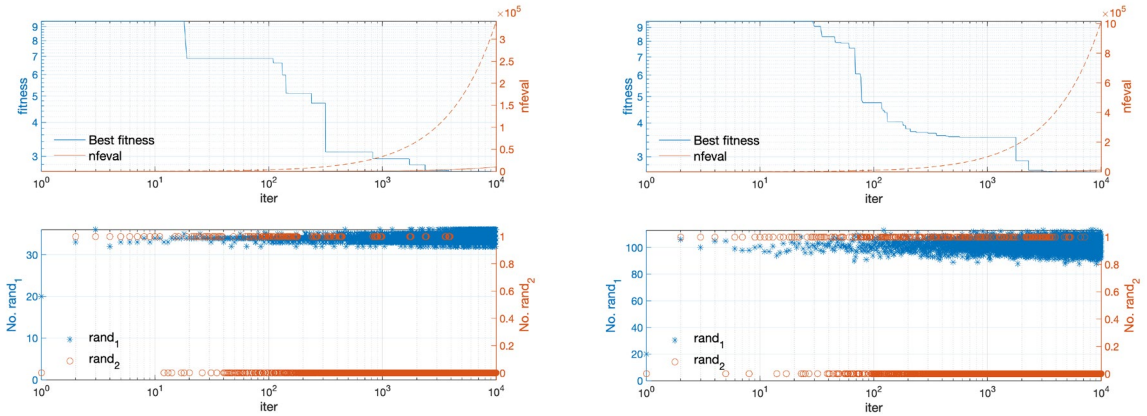


Figure 6. Three-Member Truss



(a) Type A considering fixed b_w (b) Type B

Figure 7. Result of Three Bar Truss Optimization using BHS Algorithm

4. Conclusion: submission of contributions

This work investigated the characteristic of the Binary Harmony Search (BHS) algorithm according to HS operator skill. Through experiments to benchmark function, we check the performance of the operator. Type A has a smaller number of random numbers than Type B, but Type B has better convergence performance than Type A. The results of this study indicate that the BHS algorithm is an effective method for addressing binary optimization problems and may have broad applications in various fields.

Acknowledgements

This research was supported by Basic Science Research Program through the National Research Foundation of Korea (NRF) funded by the Ministry of Science and ICT (NRF-2019R1A2C2010693).

References

[1] Y.K. Kim, "Metahueristics," Chonnam National University Press, 2017.

[2] Z.W. Geem, "Harmony search in water pump switching problem," in: *L. Wang, K. Chen, Y. Ong (Eds.), Advances in Natural Computation*, Springer Berlin, Heidelberg, pp. 751–760, 2005.

[3] X. Kong, L. Gao, H. Ouyang and S. Li, "A simplified binary harmony search algorithm for large scale 0–1 knapsack problems," Expert Systems with Applications, vol. 42, pp. 5337-5355, 2015.

[4] L. Wang, R. Yang, Y. Xu, Q. Niu, P. M. Pardalos and M. Fei, "An improved adaptive binary Harmony Search algorithm," *Information Sciences,* vol. 232, pp. 58–87, 2013.

[5] S. Shon and S. Lee, " Structural optimization of planar truss using quantum-inspired evolution algorithm," Journal of Korea Institute of Safety Inspection, vol. 18(4), pp. 1-9, 2014.

[6] S. Shon and S. Lee, "Development of Quantum-inspired Harmony Search Algorithm for Minimum Weight Design of Truss Structures," Journal of the Architectural Institute of Korea, Structures & Construction, vol. 31(10), pp. 39-46, 2015.

[7] Kong, X., Gao, L., Ouyang, H., & Li, S., "A simplified binary harmony search algorithm for large scale 0–1 knapsack problems," Expert Systems with Applications, vol. 42(12), pp.5337-5355, 2015.

[8] Askarzadeh, A., & Rashedi, E., "Harmony search algorithm: Basic concepts and engineering applications," In Intelligent Systems: Concepts, Methodologies, Tools, and Applications, pp. 1-30, IGI Global, 2018.

[9] Al-Betar, M. A., Awadallah, M. A., Khader, A. T., & Abdalkareem, Z. A., "Island-based harmony search for optimization problems," Expert Systems with Applications, vol. 42(4), pp. 2026-2035, 2015.

[10] Geem, Z. W., "Novel derivative of harmony search algorithm for discrete design variables," Applied mathematics and computation, vol. 199(1), pp. 223-230, 2008.

[11] Geem, Z. W., Kim, J. H., & Loganathan, G. V., "A new heuristic optimization algorithm: harmony search. simulation," vol. 76(2), pp. 60-68, 2001.

[12] Geem, Z. W., & Sim, K. B., "Parameter-setting-free harmony search algorithm," Applied Mathematics and Computation, vol. 217(8), pp. 3881-3889, 2010.

[13] Lee, D., W., Developing Quantum-based HS Algorithm and Optimization the Weight of Truss Structures, issertation, Korea University of Technology and Education, 2022.

[14] Seong, H., "Introduction to Optimal Design," Gold Publishing, pp.20-21, 2005.

Proceedings of the IASS Annual Symposium 2023
Integration of Design and Fabrication
10–14 July 2023, Melbourne, Australia
Y.M. Xie, J. Burry, T.U. Lee and J. Ma (eds.)

Applications of shape-optimised cold-formed steel cross-sections in roof purlin and wall stud construction

Ziqi ZHAO[a,*], Zichen WEI[a], Hong GUAN[a], Bin WANG[b], Huiyue QIAO[a]

[a,*] School of Engineering and Built Environment, Griffith University, QLD 4222, Australia
ziqi.zhao@griffithuni.edu.au

[b] Xstructe Consulting, QLD 4109, Australia

Abstract

Cold-formed steel (CFS) members are widely used in low-to-medium rise light steel building construction due to their lightweight, fabrication versatility and low production costs. Optimising the conventional CFS (CCFS) members for enhanced load-bearing capacity and less material consumption will lead to efficient and economical construction solutions. This study presents two applications of (i) an optimised folded-flange lipped channel sections for roof purlins and (ii) an optimised folded-flange "*Sigma*" sections for wall studs. The aim of this study is to minimise the cross-sectional areas of the individual shape-optimised CFS sections with the same load-bearing capacity as the corresponding CCFS ones for these applications. The optimisation process for each application results in five shape-optimised sections having 100%, 80%, 60%, 40% and 20% of the cross-sectional area of the CCFS section. The elastic buckling analyses of all the optimised CFS sections are conducted using *CUFSM* software based on the Finite Strip Method (FSM), and the obtained buckling stresses are used to determine the nominal capacity of each optimised CFS sections using the Direct Strength Method (DSM). The area-capacity curves for the five shape-optimised sections indicate that the cross-sectional areas of the optimal CFS cross-sections for a roof purlin and a wall stud are 89.2% and 52.7% of the CCFS area, respectively. Furthermore, a finite element analysis of the obtained optimal cross-sections is conducted in *Strand7* to validate the reliability of the optimisation process.

Keywords: cold-formed steel (CFS), shape-optimised sections, optimal cross-sectional area, load-bearing capacity, finite element analysis

1. Introduction

Cold-formed steel (CFS) is a kind of semi-finished or finished product made from rolled or pressed thin-walled coiled or flat bars without any heat treatment. Due to the high strength-to-weight ratio, dimensional stability, flexibility in cross-sectional profiles, and ease of fabrication and transportation, CFS is considered a more cost-effective construction material being widely used in low-to-medium rise light steel buildings and modular construction [1,2]. Conventional cold-formed steel (CCFS) members are mainly available in *Cee*, *Zed* and *Sigma* profiles with or without local stiffeners (Figure 1). They are commonly used as flexural members of structural frames for specific applications such as roof purlins, girts and wall studs [3] (Figure 2(a)). Due to its thin-walled nature, the strength and efficiency of a CFS cross-section are usually governed by a combination of three basic modes of buckling, viz. local, distortional and global buckling, which are closely related to the shape of the CFS section [4]. The Direct Strength Method (DSM) [5], by integrating the computational stability analysis into the design process, can be used to determine the capacity of members accounting for these three buckling modes. DSM is based on the elastic buckling analysis and has the advantage of dealing with the entire section of the CFS member rather than on individual elements [6].

Copyright © 2023 by Ziqi ZHAO, Zichen WEI, Hong GUAN, Bin WANG and Huiyue QIAO. Published in the Proceedings of the IASS Annual Symposium 2023 with permission.

Optimisation of CCFS members can increase load-bearing capacity and reduce material consumption. Such an enhancement at the component level can also increase the overall capacity of the CFS frame system [7]. In general, the optimisation of CFS members can be divided into two categories: (i) shape optimisation, where the profile of the cross-section is changed to obtain an innovative shape [4,8,9], or (ii) size optimisation, where the optimal dimensions of the cross-section with a predefined shape can be obtained [10,11]. The study presented in this paper is focused on the size optimisation process for two shape-optimised sections (SOCFS) applied to roof purlins and wall studs, with the aim of minimising the cross-sectional areas of the individual SOCFS section with the same load-carrying capacity as the corresponding CCFS ones for these applications. The elastic buckling analyses of all the optimised CFS sections are conducted using *CUFSM* software based on the Finite Strip Method (FSM) [12], and the obtained buckling stresses are used to determine the nominal capacity of each optimised CFS member by DSM. Furthermore, a finite element analysis of the obtained optimal members is also conducted to validate the reliability of the optimisation process.



(a) (b) (c)

Figure 1. Conventional CFS sections with or without stiffeners, (a) "*Cee*", (b) "*Zed*", and (c) "*Sigma*".

2. Structural models

Two structural models are considered to investigate the optimisation problem: (i) a 2,100*mm* span, simply supported roof purlin subjected to a nominal bending moment M_b, with a shape-optimised folded-flange lipped channel section (Figure 2(b)), and (ii) a 2,400*mm* length, simply supported wall stud subject to an axial compressive load N_c, with a shape-optimised folded-flange "*Sigma*" section (Figure 2(c)).

The reference SOCFS cross-sections (Figures 3(b) and 4(b)), produced by Wang et.al [1], were optimised from the unconstrained simply-supported CFS beams. The previously developed augmented Lagrangian Genetic Algorithm (GA) [11] was used as a "self-shape" optimisation algorithm to find the new cross-section, which aims for minimising the cross-sectional area subject to an inequality penalty function (Eq. (1)) on a uniform bending moment M^* and a compressive axial load N^*.

$$\frac{N^*}{\phi_c N_c} + \frac{M^*}{\phi_b M_b} \leq 1 \tag{1}$$

where ϕ_c and ϕ_b are the capacity reduction factors, taken as 1.0 [13].

In this algorithm, GA serves as the search algorithm by using the cross-over operator and mutation operator to generate superior offsprings, the Augmented Lagrangian (AL) method is combined as a powerful tool to avoid the ill-conditioned process by controlling the penalty factors to remain finite [14]. The fitness function suitable for GA and AL was determined as Eq. (2) and Eq. (3), respectively.

$$f(GA) = \frac{A_s}{A_{ref}} + \alpha\{\max[0, (\frac{N^*}{\phi_c N_c} + \frac{M^*}{\phi_b M_b} - 1)]\} \tag{2}$$

In Eq. (2), A_s is the cross-sectional area of the optimised cross-section, A_{ref} is the reference area of similar value to the optimised cross-sectional area, and α is a penalty factor [1].

$$f(AL) = \frac{A_s}{A_{ref}} + \frac{1}{2}\{\gamma + [\max(0, (\frac{N^*}{\phi_c N_c} + \frac{M^*}{\phi_b M_b} - 1) + \mu)]^2\} \quad (3)$$

In Eq. (3), γ is the penalty function coefficient, and μ is the real parameter to the penalty function [1].

The optimised folded-flange lipped channel section was obtained from the CCFS *Cee* section without stiffeners (Figure 3(a)), which can be characterised as a four-element (① to ④) per half cross-section type, in Figure 3(b), for the roof purlin model. The optimised folded-flange "*Sigma*" section was obtained from the CCFS *Cee* section with stiffeners (Figure 4(a)), in which the eight elements (① to ⑧) per half cross-section is the fittest to the wall stud model (Figure 4(b)).

The CCFS *Cee* cross-sections with and without stiffeners considered in this study were chosen from the design manuals *Rondo* [15]and *LYSAGHT* [16], respectively. The area of a cross section can be simply determined by multiplying its thickness by its perimeter. Note that the area and the thickness of the initial SOCFS (e.g. Figure 3(b)) are the same as those of the CCFS (e.g. Figure 3(a)). Note also that the aspect ratio remains the same for CCFS and SOCFS. Thereafter, the total length of all the elements in an individual SOCFS can be derived. Then the length of each element that forms the cross-section can be mathematically calculated based on the element's orientation [1]. Since the aspect ratio and the thickness of the cross-section remain constant, reducing the length of each element in the initial SOCFS (e.g. Figure 3(b)) with the same proportion can result in a correspondingly reduced cross-sectional area of the subsequent SOCFS (e.g. Figures 3(c) to (f)). In this study, the cross-sectional area of the SOCFS is gradually reduced to 80%, 60%, 40% and 20% of the CCFS section (A_{CS}), for both roof purlin and wall stud members.

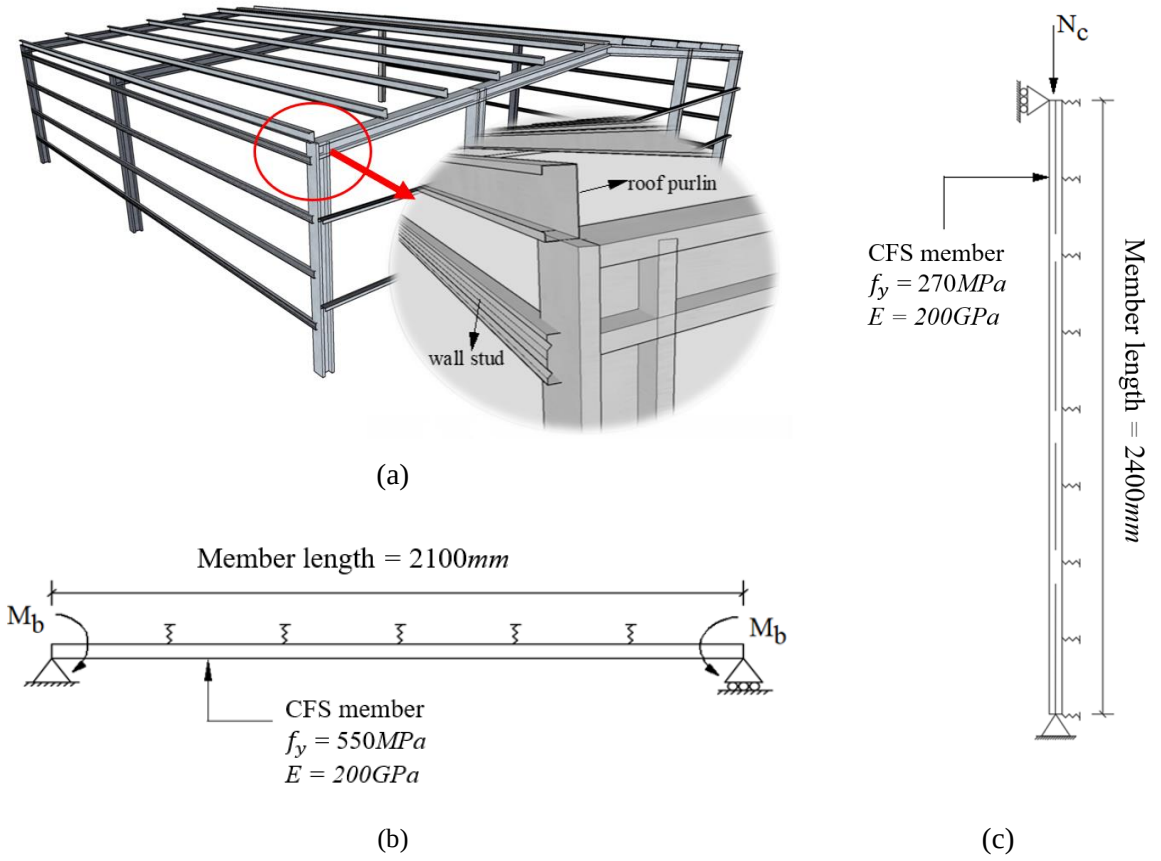
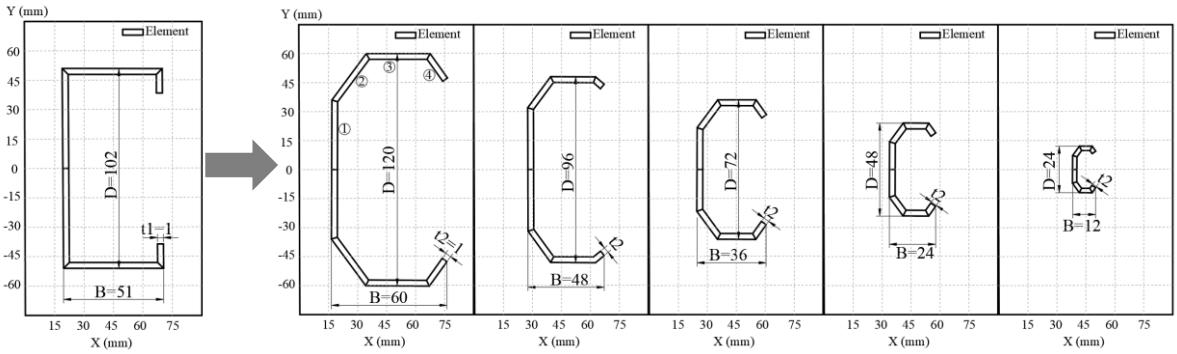
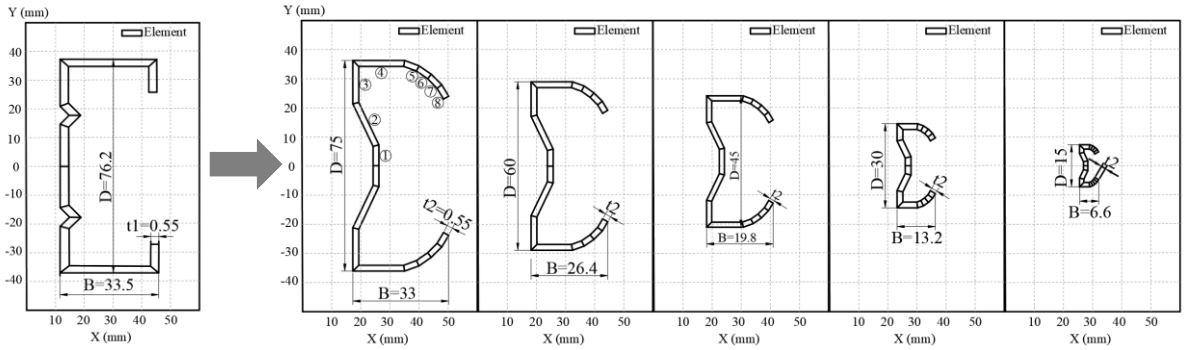


Figure 2. Structural models for the optimisation problem: (a) structural frames, (b) roof purlin and (c) wall stud.



(a) A_{CS} (b) 100%A_{CS} (c) 80%A_{CS} (d) 60%A_{CS} (e) 40%A_{CS} (f) 20%A_{CS}

Figure 3. Dimensions of CCFS and shape-optimised cross-sections for roof purlin cross-section.



(a) A_{CS} (b) 100%A_{CS} (c) 80%A_{CS} (d) 60%A_{CS} (e) 40%A_{CS} (f) 20%A_{CS}

Figure 4. Dimensions of CCFS and shape-optimised cross-sections for wall stud cross-section.

3. Numerical analysis

3.1. Elastic buckling analysis

Elastic buckling analysis is a technique for determining the buckling loads and deformed shapes when a structure becomes buckled and unstable. It allows to obtain the buckling stress f_o under the corresponding buckling modes, which can subsequently be used to determine the bearing capacity of the CFS cross-sections. In this study, the elastic buckling analyses were carried out using the software *CUFSM*, which was developed based on the Finite Strip Method (FSM) and can provide a quick analysis to obtain the buckling load factors by entering the basic parameters, such as the element coordinates, dimension and thickness, and the expected loads of the CFS sections. The obtained buckling load factors are expressed as the ratio of the elastic buckling stress f_o to the steel yield stress f_y. The principles for distinguishing and determining the three buckling load factors, viz. f_{oe}/f_y (global buckling), f_{ol}/f_y (local buckling) and f_{od}/f_y (distortional buckling), are described in detail in Section 4.2. Table 1 and Table 2 list the obtained local (f_{ol}/f_y) and distortional (f_{od}/f_y) load factors for each cross-section of the roof purlin and wall stud members. The buckling stresses f_{ol} and f_{od} can then be determined which are also given in Tables 1 and 2.

3.2. Bearing behaviour

The Direct Strength Method (DSM) was used in this study to calculate the bearing capacity of all cross-sections. It is based on AS/NZS 4600 [13] and employs the strength curves on the entire CFS member rather than the isolated cross-sectional elements [17]. The DSM allows the calculation of the nominal bearing capacities under local, distortional and global buckling modes by using the corresponding buckling stresses and the design bearing capacity is determined as the minimum of these three values. In this study, the design bending moment applied to the roof purlin structural model can be determined as

$$M_b = \min (M_{bl}, M_{bd}, M_{be}) \tag{4}$$

where M_{bl}, M_{bd}, and M_{be} are the nominal bending capacities for local, distortional, and global buckling modes, respectively.

Similarly, the design axial compressive load applied to the wall stud structural model was expressed as

$$N_c = \min (N_{cl}, N_{cd}, N_{ce}) \tag{5}$$

where N_{cl}, N_{cd}, and N_{ce} are the nominal axial compressive capacities for local, distortional, and global buckling modes, respectively.

The calculated M_b and N_c for the roof purlin and wall stud cross-sections are also summarised in Table 1 and Table 2, respectively.

4. Results and discussion

4.1. Optimal cross-sectional area

According to Table 1 and Table 2, the piecewise linear area-capacity curves for the five SOCFSs can be plotted for the roof purlin and the wall stud structural models, respectively, in Figures 5(a) and (b). It can be seen that the initial SOCFS with a cross-sectional area of $100\%A_{CS}$ (e.g. point B1 in Figure 5(a)) has a greater bearing capacity than the CCFS (e.g. point A1 in Figure 5(a)) for both roof purlin and wall stud sections, which validates the shape optimisation outcomes that the SOCSF has a higher strength than that of the corresponding CCFS with the same cross-sectional size [1]. By drawing a horizontal line from the CCFS point (e.g. point A1), an intersection point with the plotted area-capacity curve, denoted as a blue triangle in the diagram, was obtained indicating that the optimal SOCFS has the same load carrying capacity as the CCFS. Given the linear relation between every two adjacent SOCFS points on the area-capacity curve, the cross-sectional areas of the optimal SOCFSs for the roof purlin and wall stud sections can be determined by linear interpolation.

Specifically, for the roof purlin member, the optimal SOCFS point in Figure 5(a) falls between points B1 and C1, on a linear line which can be expressed as

$$y = 0.0214x\text{-}1.65 \tag{6}$$

where x is the cross-sectional area and y is the bending moment capacity.

By substituting the same bending moment capacity of 2.72 *kNm* as the CCFS into Eq. (6), the optimal cross-sectional area of the roof purlin member is determined to be $204.2mm^2$, which is only $89.2\%A_{CS}$.

Similarly, the optimal SOCFS point for the wall stud member falls between points D2 and E2 in Figure 5(b), also on a linear line which can be expressed as

$$y = 0.1646x+3.1872 \tag{7}$$

where x is the cross-sectional area and y is the axial compressive capacity.

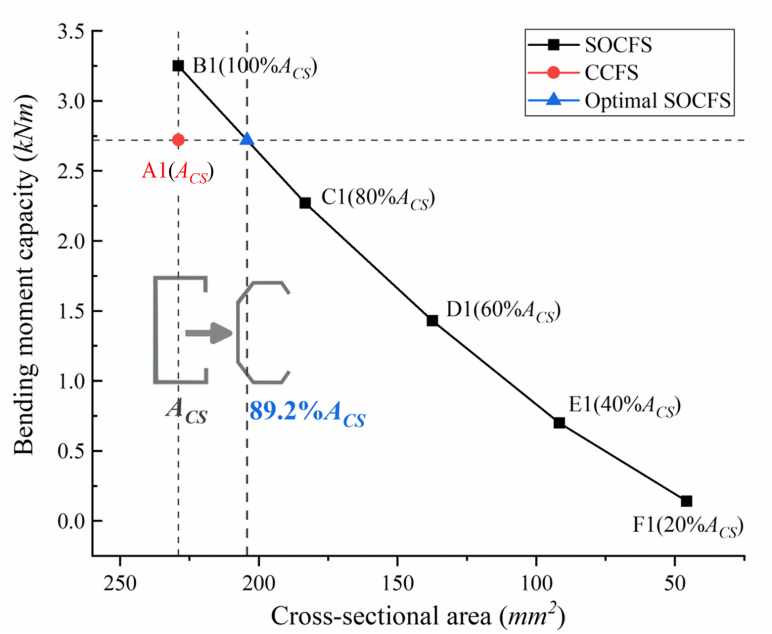
Taking the same axial compressive capacities of the SOCFS and CCFS of 10.73kN, the optimal cross-sectional area of the wall stud member can be calculated using Eq. (7) as 45.85mm^2, which is only 52.7%A_{CS}.

Table 1. Results of elastic buckling analysis and DSM for roof purlin cross-sections.

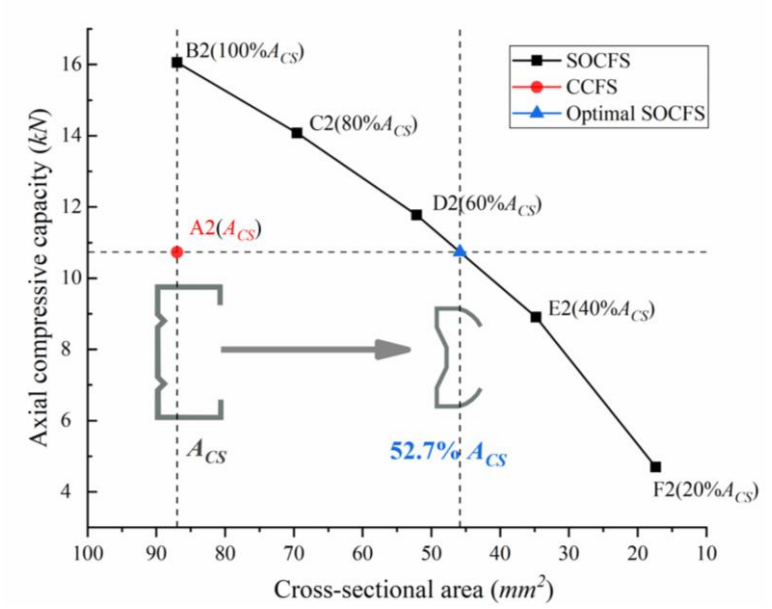
Cross-section naming	Cross-section area (mm^2)	Load factors		Steel yield stress	Buckling stress		Design bending moment M_b (kNm)
		f_{ol}/f_y	f_{od}/f_y	f_y (MPa)	f_{ol} (MPa)	f_{od} (MPa)	
A1 (A_{CS})	229	0.60	0.56	550	330.0	308.0	2.72
B1 (100%A_{CS})	229	1.21	0.77	550	665.5	423.5	3.25
C1 (80%A_{CS})	183.2	1.89	0.98	550	1039.5	539.0	2.27
D1 (60%A_{CS})	137.4	3.37	1.37	550	1853.3	753.3	1.43
E1 (40%A_{CS})	91.6	7.32	-	550	4026.0	-	0.7
F1 (20%A_{CS})	45.8	-	4.84	550	-	2662.0	0.14

Table 2. Results of elastic buckling analysis and DSM for wall stud cross-sections

Cross-section naming	Cross-section area (mm^2)	Load factors		Steel yield stress	Buckling stress		Design axial compressive load N_c (kN)
		f_{ol}/f_y	f_{od}/f_y	f_y (MPa)	f_{ol} (MPa)	f_{od} (MPa)	
A2 (A_{CS})	86.99	0.91	0.34	270	244.54	92.61	10.73
B2 (100%A_{CS})	86.99	2.96	0.80	270	799.47	216.27	16.06
C2 (80%A_{CS})	69.52	4.56	1.00	270	1231.2	270.0	14.08
D2 (60%A_{CS})	52.15	7.86	3.08	270	2122.2	831.6	11.77
E2 (40%A_{CS})	34.76	-	1.78	270	-	480.6	8.91
F2 (20%A_{CS})	17.39	-	4.88	270	-	1317.6	4.69



(a)



(b)

Figure 5. Area-capacity curves for (a) roof purlin and (b) wall stud.

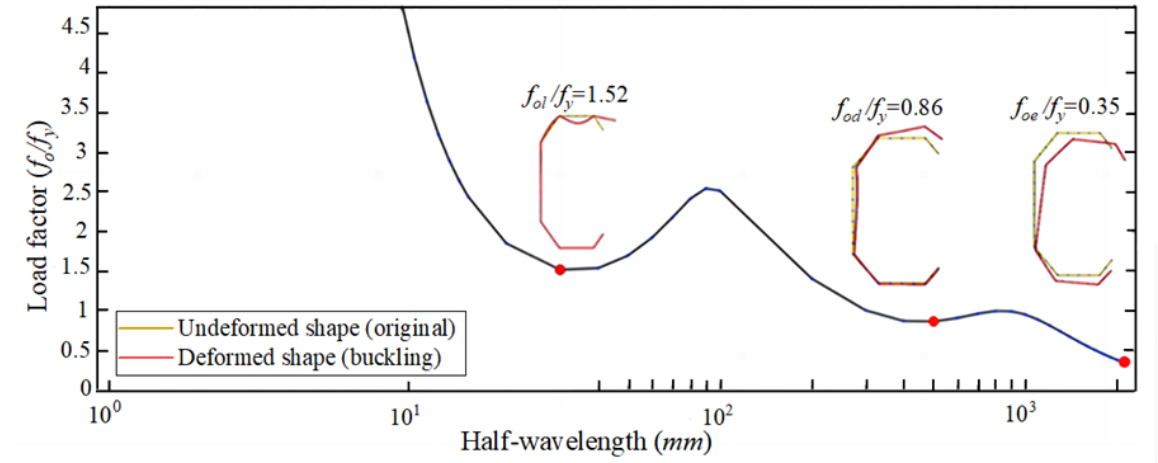
4.2. Validation of CUFSM results using finite element analysis

In order to verify the accuracy of the optimal SOCFSs for the roof purlin and wall stud members as described above, a finite strip analysis in *CUFSM* and a finite element analysis in *Strand7* were performed. Note that the elastic local and distortional buckling modes cannot be distinctly identified in *Strand7*. Therefore, this validation study only focused on the global buckling mode which is readily obtainable in *Strand7* and *CUFSM*.

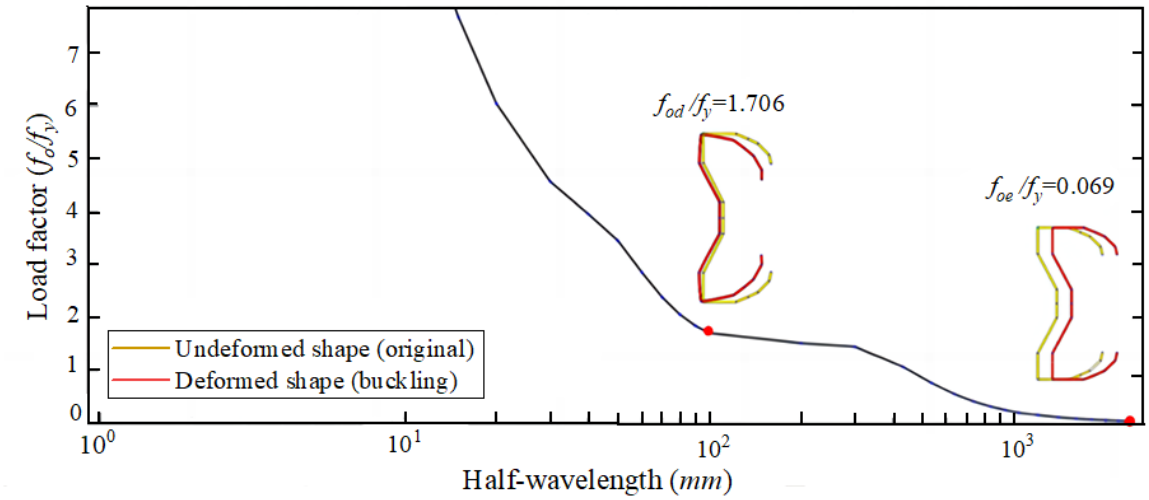
For the individual optimal roof purlin and wall stud sections, the buckling load factor (f_o/f_y) versus the half-wavelength (1/2 sine wave) from *CUFSM* is shown in Figure 6 in the form of the "signature curve". Ideally, each signature curve contains two local minima, the first one of which is usually considered to be the local buckling load factor (f_{ol}/f_y), and the second is the distortional buckling load factor (f_{od}/f_y) [12]. In the case where only one local minimum exists on this curve (Figure 6(b)), Gilbert et al. [4] suggested that if the buckling occurs at a half-wavelength being less than the perimeter length of the cross-section, this single minimum is regarded as the local buckling load factor; otherwise, it is deemed as distortional. Due to the simply-supported boundary condition, the global buckling generally exists at the end of the member, as shown in the elastic buckling analysis. Thus, the global buckling load factor (f_{oe}/f_y) is usually obtained when the half-wavelength equals the member length. Based on the above descriptions, the local, distortional, and global buckling modes for the optimal roof purlin cross-section can be clearly identified in Figure 6(a). However, no local buckling was identified on the signature curve for the optimal wall stud cross-section (Figure 6(b)), but only distortional and global buckling modes were distinguished.

The global buckling analysis in *Strand7* for the optimal roof purlin section resulted in a load factor equalling 0.48*MPa*, which is slightly higher that the corresponding *CUFSM* value of 0.35*MPa* (Figure 6(a)). Similarly, the load factor for the optimal wall stud section is 0.082*MPa* from *Strand7*, also slightly higher than the *CUFSM* value of 0.069*MPa* (Figure 6(b)). The disparity in the predicted load factors from the two analysis methods is due to the different ways they simulate the members, i.e., finite element versus finite strip. Nevertheless, such a discrepancy can be considered acceptable.

Figure 7 and Figure 8 show the *Strand7* initial shape and the corresponding deformed shape under the global buckling mode for the optimal roof purlin and wall stud structural models, respectively. The global buckling deformation of the roof purlin model is an apparent tilt of the whole CFS section (Figure 7(b)), while the deformation of the wall stud model is primarily a lateral movement of the web along the *x*-axis (Figure 8(b)). Compared to the global buckled shapes obtained from *CUFSM* as shown in Figure 6, the deformed shapes from *Strand7* are rather consistent. Therefore, the buckling analysis results of the optimal cross-sections obtained from *CUFSM* are well validated by *Strand 7*.

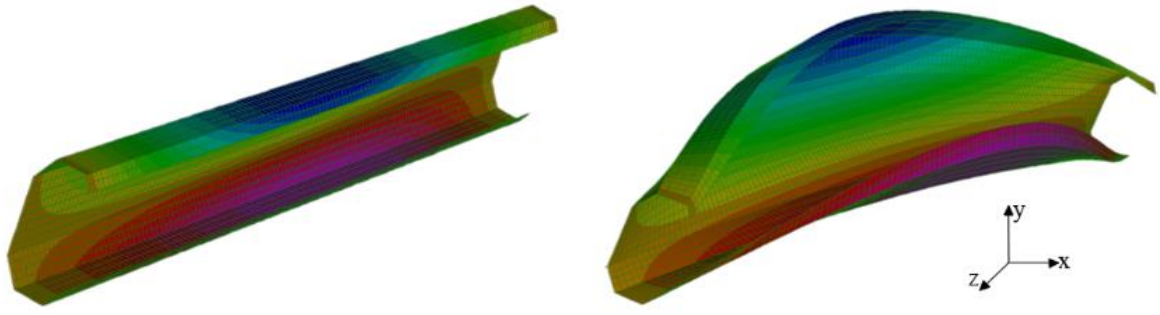


(a)



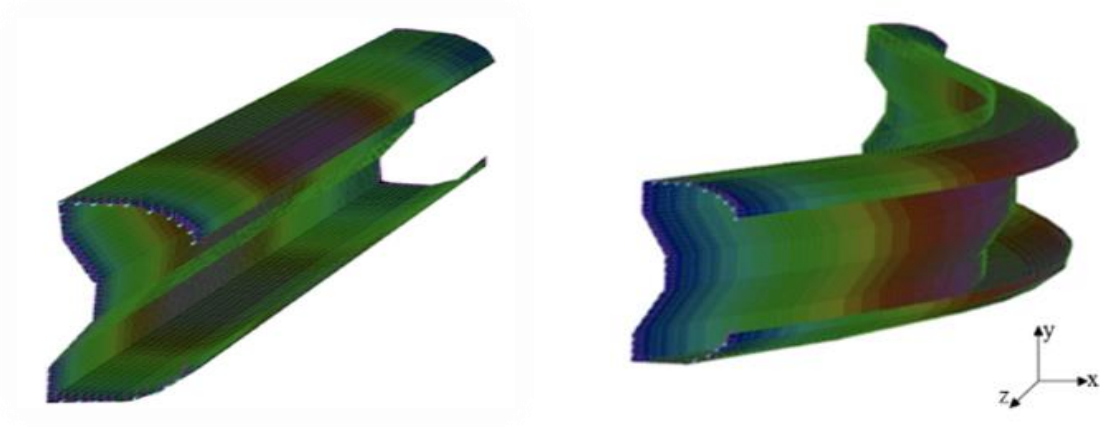
(b)

Figure 6. Elastic buckling analysis of optimal SOCFSs for (a) roof purlin and (b) wall stud.



(a) (b)

Figure 7. Deformed shape of the optimal roof purlin structural model in *Strand7*, (a) initial 3D model, and (b) global buckling mode.



(a) (b)

Figure 8. Deformed shape of the optimal wall stud structural model in *Strand7*, (a) initial 3D model, and (b) global buckling mode.

5. Conclusion

This paper presents the size optimisation process of the individual shape-optimised cold-formed steel sections (SOCFSs) for roof purlin and wall stud structural models. For each model, a series of elastic buckling analyses and bearing capacity calculations were carried out using *CUFSM* and DSM, leading to an optimal SOCFS with a reduced cross-sectional area whilst maintaining the same load bearing capacity as the equivalent conventional CFS (CCFS). The cross-sectional areas of the optimal roof purlin and wall stud members are found to be 89.2% and 52.7% of that of the corresponding CCFS, respectively. Finite element analyses were also performed in *Strand7* on the two structural models with the optimal cross-sections, which verified the accuracy of the entire size optimisation process for SOCFSs using the finite strip method in *CUFSM*.

References

[1] B. Wang, G. L. Bosco, B. P. Gilbert, H. Guan, and L. H. Teh, "Unconstrained shape optimisation of singly-symmetric and open cold-formed steel beams and beam-columns," *Thin-Walled Structures*, vol. 104, pp. 54-61, 2016.

[2] B. W. Schafer, "Cold-formed steel structures around the world," *Steel Construction*, vol. 4, no. 3, pp. 141-149, 2011

[3] P. Gatheeshgar, K. Poologanathan, S. Gunalan, B. Nagaratnam, K. D. Tsavdaridis, and J. Ye, "Structural behaviour of optimized cold-formed steel beams," *Steel Construction*, vol. 13, no. 4, pp. 294-304, 2020.

[4] B. P. Gilbert, T. J.-M. Savoyat, and L. H. Teh, "Self-shape optimisation application: Optimisation of cold-formed steel columns," *Thin-walled structures*, vol. 60, pp. 173-184, 2012.

[5] *Direct Strength Method Design Guide*, American Iron and Steel Institute, 2006

[6] B. W. Schafer, "The direct strength method of cold-formed steel member design," *Journal of constructional steel research*, vol. 64, no. 7-8, pp. 766-778, 2008.

[7] D. T. Phan, S. M. Mojtabaei, I. Hajirasouliha, J. Ye, and J. B. Lim, "Coupled element and structural level optimisation framework for cold-formed steel frames," *Journal of Constructional Steel Research*, vol. 168, p. 105867, 2020.

[8] M. Moharrami, A. Louhghalam, and M. Tootkaboni, "Optimal folding of cold formed steel cross sections under compression," *Thin-Walled Structures*, vol. 76, pp. 145-156, 2014.

[9] V. M. Guimaraes, B. P. Gilbert, N. Talebian, and B. Wang, “Shape optimisation of singly-symmetric cold-formed steel purlins,” *Thin-Walled Structures*, vol. 161, 2021.

[10] J. Lee, S.-M. Kim, and H. S. Park, "Optimum design of cold-formed steel columns by using micro genetic algorithms," *Thin-Walled Structures*, vol. 44, no. 9, pp. 952-960, 2006.

[11] B. P. Gilbert, L. H. Teh, and H. Guan, "Self-shape optimisation principles: Optimisation of section capacity for thin-walled profiles," *Thin-Walled Structures*, vol. 60, pp. 194-204, 2012.

[12] B. W. Schafer and S. Adany, "Buckling analysis of cold-formed steel members using CUFSM: conventional and constrained finite strip methods," in *Eighteenth international specialty conference on cold-formed steel structures*, 2006: Citeseer, pp. 39-54.

[13] *AS/NZS 4600: Cold-formed steel structures*, Standards Australia, 2005.

[14] B. Wang, B. P. Gilbert, H. Guan, and L. H. Teh, "Shape optimisation of manufacturable and usable cold-formed steel singly-symmetric and open columns," *Thin-Walled Structures*, vol. 109, pp. 271-284, 2016.

[15] Rondo Buliding Service Pty Ltd, *Rondo STEEL STUD Framing Systems Installation Manual. 2008.*

[16] BlueScope Steel Limited, *LYSAGHT Zeds and Cees Users Guide. 2017.*.

[17] B. W. Schafer and T. Pekoz, "Direct strength prediction of cold-formed steel members using numerical elastic buckling solutions," 1998.

IASS 2023
July 10–14 Melbourne
Integration of Design and Fabrication

Proceedings of the IASS Annual Symposium 2023
Integration of Design and Fabrication
10–14 July 2023, Melbourne, Australia
Y.M. Xie, J. Burry, T.U. Lee and J. Ma (eds.)

Design space exploration of shell structures using quality diversity algorithms

Konstantinos SFIKAS[a,*], Antonios LIAPIS[a], Joel HILMERSSON[b], Jeg DUDLEY[b], Edoardo TIBUZZI[b], Georgios N. YANNAKAKIS[a]

[a,*] Institute of Digital Games, University of Malta
konstantinos.sfikas@um.edu.mt

[b] AKT II

Abstract

Computer-aided optimization algorithms in structural engineering have historically focused on the *structural performance* of generated forms, often resulting in the selection of a single 'optimal' solution. However, *diversity* of generated solutions is desirable when those solutions are shown to a human user to choose from. Quality-Diversity (QD) search is an emerging field of Evolutionary Computation which can automate the exploration of the solution space in engineering problems. QD algorithms, such as MAP-Elites, operate by maintaining and expanding an archive of diverse solutions, optimising for quality in local niches of a multidimensional design space. The generated archive of solutions can help engineers gain a better overview of the solution space, illuminating which designs are possible and their trade-offs. In this paper we apply Quality Diversity search to the problem of designing shell structures. Since the design of shell structures comes with physical constraints, we leverage a constrained optimization variant of the MAP-Elites algorithm, FI-MAP-Elites. We implement our proposed methodology within the Rhino/Grasshopper environment and use the Karamba Finite Element Analysis solver for all structural engineering calculations. We test our method on case studies of parametric models of shell structures that feature varying complexity. Our experiments investigate the algorithm's ability to illuminate the solution space and generate feasible and high-quality solutions.

Keywords: evolutionary algorithm, evolutionary computation, quality diversity, optimisation, multi objective optimisation, conceptual design, shell structures, spatial structures

1. Introduction

A frequently encountered problem within the AEC industry is the design of efficient shell structures. Such structures–in which architectural form is inextricably linked to structural behaviour and performance–require a close collaboration between architect, structural engineer and other AEC consultants to find a shape that is acceptable to all parties and their separate demands. Historically, many of these shells were conceived as form-active structures, and thus their final shape was ascertained through form-finding techniques–first physically [1],[2], then digitally [3]. These digital simulations are remarkably flexible, and able to incorporate a range of physical input constraints, such as ensuring structural efficiency (e.g. axial loading only) or geometric rationalisation (e.g. avoiding panel warp). However, for a single set of inputs (materials, loading and support conditions) form-finding algorithms only generate a singular solution, rather than a range of potential solutions. As such, it can be difficult for the designer to evaluate potential trade-offs between the desired criteria and propose new weightings of them.

Copyright © 2023 by Konstantinos SFIKAS, Antonios LIAPIS, Joel HILMERSSON, Jeg DUDLEY, Edoardo TIBUZZI and Georgios N. YANNAKAKIS. Published in the Proceedings of the IASS Annual Symposium 2023 with permission.

We see similar limitations in evolutionary computation (EC) algorithms, such as Divide-and-Conquer or Hill-Climbing. These algorithms are Single Objective Optimisation (SOO) approaches, and as such they too suffer from a difficulty in weighting and combining output values to achieve a well-balanced fitness evaluation for the variants. More sophisticated EC approaches include Multi Objective Optimisation (MOO) or Pareto optimisation algorithms, such as SPEA-2 and HypE. These MOO algorithms have been implemented in AEC digital design toolkits for several years now [4],[5], and allow substantially more detailed exploration of the solution space.

Quality Diversity (QD) search is a family of EC algorithms that simultaneously maintain the quality and diversity of solutions [6] by rewarding *divergence* of the population according to some ad-hoc measure of difference between the actual artefacts rather than the genotypic information. *Quality* can be a secondary objective to this divergence [7], act as a constraint on minimal quality [8], or as a survival criterion between similar artefacts [9]. Algorithms such as MAP-Elites can illuminate the search space, maintaining and evolving in parallel different solutions in different behavioural niches (i.e. with similar design characteristics orthogonal to quality). MAP-Elites and its variants has been a popular algorithm for problems where the "optimal solution" is subjective, such as evolutionary art [10] and game content generation [11].

This paper presents a constrained variant of the MAP-Elites algorithm for QD search and tests it in a set of shell structure optimization tasks ranging from simple to complex. While shell structure optimization has received attention in the past through evolutionary approaches [12], here we propose a QD method that explicitly produces a large archive of potential solutions and visualizes their trade-offs. The FI-MAP-Elites algorithm, proposed here, leverages two archives evolving in parallel: one archive of solutions that fail a constraint on maximum allowed displacement, and another archive of solutions that satisfy this constraint and search for optimal elastic energy of the structure. The algorithm is integrated into Grasshopper and allows engineers to specify the structure of possible solutions and the dimensions towards which FI-MAP-Elites should explore. Comparisons against a baseline SOO algorithm available in Grasshopper show that the proposed constrained QD search algorithm produces far more diverse solutions, while SOO typically converges towards a single type of solution. This paper, therefore, argues that QD search algorithms that illuminate the solution space and show trade-offs between different designs will help engineers interface with the subjectivity of the AEC design process.

2. General methodology for constrained quality diversity search

Feasible-Infeasible Multidimensional Archives of Phenotypic Elites (FI-MAP-Elites) is a hybrid of the MAP-Elites [11] and the FI-2Pop GA [13] algorithms. Its main goal is to combine the illumination capabilities of the former with the constraint-solving capabilities of the latter. Its operation is controlled by the following hyperparameters that are problem-specific: **(1) Representation:** refers to how the algorithm stores the artefacts in a compact genotype [14]. **(2) Initialization:** refers to how the initial population is formed. In many cases initialization of the genotype is as simple as generating a random list of numbers. More complex representations, however, may require a more elaborate scripted initialization [15]. **(3) Variation:** refers to the genetic operators applied while evolution is carried out to produce offspring from selected individuals. While traditional EC operators include recombination and mutation [16], FI-MAP-Elites only uses mutation of one individual. **(4) Infeasible fitness (F_i):** measures how many constraints are failed by the solution and to which degree. The infeasible population aims to minimise the distance to feasibility; to convert this into a maximisation task, we consider that an infeasible fitness below a threshold (usually $F_i < 1$) means that the individual is *infeasible* (i.e. at least one constraint is not satisfied). Ad-hoc heuristics are designed per constraint and added together to form the infeasible fitness score. **(5) Feasible fitness (F_f):** is a problem-specific measure of the desirable property of the final artefact. Feasible fitness is only calculated if the individual is feasible, as failed constraints in some problems render calculating the feasible fitness impossible [17]. **(6) Behaviour characterizations (BCs):** refer to quantifiable characteristics of the artefact. BCs are orthogonal to

quality and artefacts of both high and low BC scores should be desirable. These BCs define the dimensions of exploration and diversity and should be of interest to the designer. While most MAP-Elites implementations use two BCs, the algorithm can operate with any number of BCs but this may impact the computational cost of evolutionary search.

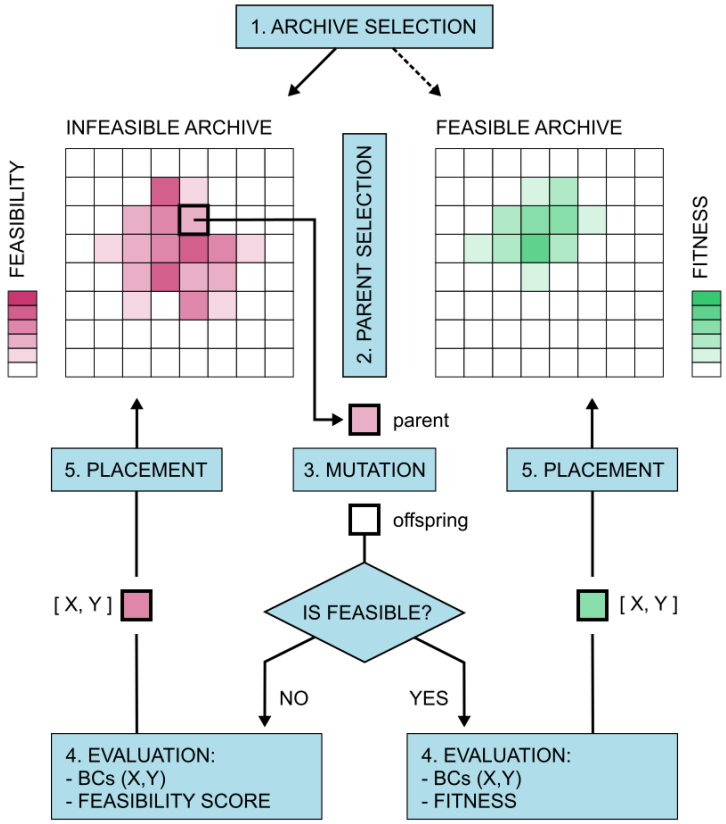


Figure 1. Functional diagram showcasing the operation of the FI-MAP-Elites algorithm, for two BCs.

The FI-MAP-Elites [15] algorithm, visualised in Fig. 1, maintains two separate archives for feasible and infeasible solutions, organised in an n-dimensional grid based on the problem's BCs. Each grid cell contains a single elite with specific BC values. An initial population seeds the archives according to feasibility. The algorithm randomly selects an individual, mutates and evaluates it, and places it in the proper archive and cell based on feasibility and BCs. Offspring replace current elites if their fitness is higher. Through repeated iterations, the algorithm fills the archives with solutions that approach locally maximum fitness, providing a diverse set of fit and feasible solutions for users.

3. Applied methodology & experiment protocol

To efficiently test FI-MAP-Elites in shell structure design tasks, a series of parametric shell models were defined in Rhino's visual programming interface, Grasshopper, based on SubDivision (SubD) surfaces. SubD surfaces have the advantage of being derived from a low polygon control mesh that is easy to manipulate through adjustment of its vertices (control points). This gives them geometric flexibility and makes them suitable for representing a wide range of forms. Furthermore, the resulting surfaces are generated through iterative Catmull-Clark subdivisions [18] of the input mesh which guarantees a smooth, continuous curvature. SubD-based approaches have been successfully utilised by AKT II on a series of built and unrealised projects over the last decade [19],[20].

3.1. Algorithmic parameters

Based on Section 2, there are several problem-specific hyperparameters to the algorithm. We elaborate the parameters for the shell use case here.

- **Representation:** The parametric shell model is manually defined by the designer in Rhino/Grasshopper [21]. This includes a definition of a SubD surface, several constraints on its control points' variability, as well as a number of control parameters that affect the points' movement along specified vectors. Any point on the SubD control polygon selected as a *support* by the designer is defined as 'creased' to ensure that the point that is constrained exists on the smooth shape. The genetic algorithm only stores (and manipulates) the values of the control parameters.
- **Initialization:** When initialising the population for evolution, control parameters are assigned a random value within a designer-specified value range.
- **Variation:** Variation occurs solely through the mutation operator that iterates over all the control parameters defined in the model and changes their values according to two parameters: *Max Step Size* (i.e. the maximum distortion allowed per mutation step) and *Mutation Rate* (i.e. the probability that this control parameter will be changed).
- **Infeasible fitness:** The only constraint in this use case is an upper limit on displacement (d), i.e. the distance between the point in the original model and the deformed model. The upper limit on displacement is specified by the designer (C_d). Equation (1) calculates the infeasible fitness for this problem (F_i), which is bound in the value range of [0,1] and feasible individuals always have $F_i = 1$.

$$F_i = \begin{cases} \frac{C_d}{d} & \text{, if } d > C_d \\ 1 & \text{, if } d \leq C_d \end{cases} \tag{1}$$

- **Feasible fitness:** For feasible individuals, quality is ascertained based on the total elastic energy (U) of the structure. The value for U measures how much energy is stored in the structure based on its elastic deformation. The feasible fitness (F_f), as shown in shown in Equation (2), is bound in the value range of [0,1] with higher values being preferred (lower elastic energy). FI-MAP-Elites calculates F_f only for individuals that satisfy the constraints ($d \leq C_d$); the score of $F_f = 0$ for infeasible individuals is calculated only for the baseline single-objective algorithm in the experiments of this paper.

$$F_f = \begin{cases} 0 & \text{, if } d > C_d \\ \frac{1}{1+U} & \text{, if } d \leq C_d \end{cases} \tag{2}$$

- **Behaviour characterizations (BCs):** Two formulas based on control point coordinates are explored as BCs in this work: (1) *Edge Point Coordinate Average*, as the average coordinate value of a set of parametric points on a series of edges in the SubD geometry (either X, Y, or Z, determined by the user); (2) *Edge Point Coordinates Deviation*, calculated as the difference between the average value and the coordinate (X, Y, or Z, determined by the user) of each point on a series of edges in the SubD geometry, divided by the number of points.

3.2. Rhino implementation

In order to apply FI-MAP-Elites to structural engineering problems, we exploit the parametric design capabilities of the Rhino/Grasshopper design environment. Within this environment, we developed a set of components which allow the structural engineer to (1) define the structural parametric model, (2) select the algorithmic parameters and (3) run the FI-MAP-Elites algorithm and generate an optimised (in terms of quality and diversity) set of variations of the parametric model.

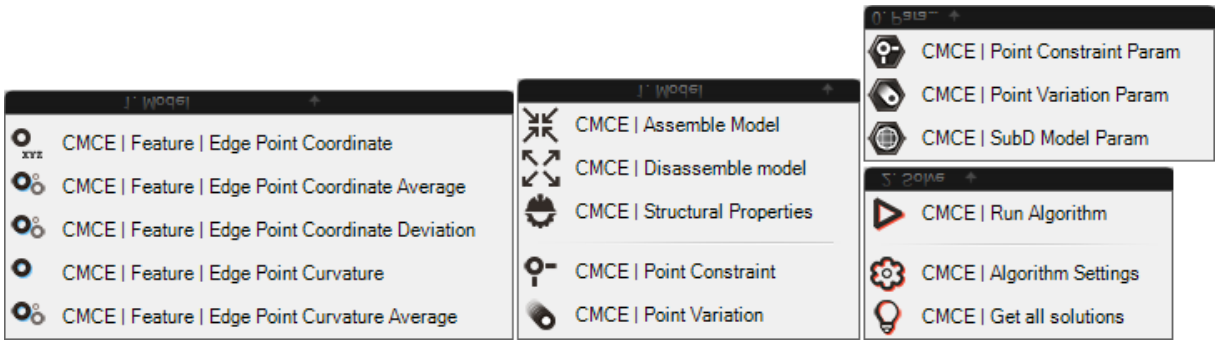


Figure 2. Grasshopper toolbars for the FI-MAP-Elites implementation of shell design.

Customization of the algorithm is done through parameters (on the point constraints, its variation range, and parameters of the SubD model) and through details on the physics model and BC characterizations (see Fig. 2 for a summary of the components available). The solver toolbars provide the settings and components to run the process, along with tools to retrieve results. The components can be combined to produce a pipeline to initialise and evaluate solutions.

As soon as the algorithm's operation is over, a Grasshopper component outputs the data of all elites in both archives, as well as their positions on the archive's grid (based on their BCs). Each one of the generated variations includes various meta-information, including: (1) its Karamba [22] model, (2) its Rhino geometry, (3) its genome (parameter values), (4) its elastic energy and (5) its BC scores. Based on these outputs, the archive's contents can be visualised in Rhino's viewport, in a customised manner. Fig. 6. illustrates an example of such a visualisation of the feasible archive, which includes a visual (by vertex colours) indication of the parametric model's fitness.

3.3. Hyperparameters and baseline algorithms

For all experiments with FI-MAP-Elites in this paper, we use an initial population of 100 random individuals, a mutation rate of 50% and mutation step of 20%, a grid of elites of 16 by 16 (BC1 by BC2) for both feasible and infeasible archives, and results are collected after 50,000 evaluations.

As a baseline to test the performance of FI-MAP-Elites, we use a single-objective optimizer (SOO) of the Galapagos library within Grasshopper. This simple algorithm aims to maximise a single-objective fitness (F_b) computed as the average of the infeasible and feasible fitness; see Eq. (3). Therefore, it overlooks diversity dimensions but tackles constrained optimization.

$$F_b = \frac{1}{2}(F_i + F_f) \tag{3}$$

The evolutionary solver of the Galapagos optimizer within Grasshopper is used for this baseline, with the following settings: a *population* of 256 individuals, an *initial boost* of 1 (the initial population size is 256), an *elitism* of 5% (the 13 fittest individuals are retained across generations) and an *inbreeding rate* of 50% (slightly favours the selection of similar parents during crossover). The population evolves for a number of generations resulting in a comparable number of evaluations as FI-MAP-Elites. We collect solutions from the final population on the last generation to derive SOO performance metrics.

3.4. Hypothesis and performance metrics

Our hypotheses in the experiments described in Chapter 5 can be summarised as follows:

- The two-population approach of FI-MAP Elites will discover more feasible solutions faster.
- Evolution will focus on the feasible population earlier and lead to higher quality solutions in FI-MAP-Elites compared to single-population approaches.
- As a QD algorithm the variety of solutions (in terms of the chosen BCs) will be higher.

- It is expected that more high-quality solutions that are structurally different will emerge from the QD search process that favours local competition within the same behavioural niche.

Following the literature in QD search [9], we evaluate the following metrics: (1) **maximum performance**, as the lowest elastic energy (U_{min}) score and lowest displacement (d_{min}) among feasible individuals of the SOO population or the feasible archive, (b) **coverage**, as the ratio of all cells in the feature map occupied by feasible solutions[1], (3) **QD score**, as the sum of feasible fitness scores among all elites in the feasible archive (of feasible individuals in the SOO population). The maximum performance assesses whether at least one solution is well-performing, while coverage assesses whether a large behavioural variety of solutions is found. Finally, the QD score assesses a combination of the above, with higher scores achieved when the algorithm produces many behaviourally diverse individuals of high quality. In addition, we measure the **fitness deviation** (σ_U and σ_d) as the standard deviation in terms of the elastic energy and displacement (respectively) of all feasible solutions. This measure captures the uniformity of designs when exploring along different BCs.

Moreover, we assess constraint satisfaction and constraint optimization performance through the following metrics: (1) **feasible ratio**, as the ratio of solutions that satisfy all constraints against all solutions in the final population(s); (2) **infeasible coverage**, as the ratio of all possible cells in the feature map that are occupied by infeasible solutions (i.e. the infeasible archive for FI-MAP-Elites).

4. Results

To evaluate the proposed algorithm's performance, we use three different test cases: two variants of a simple test case, and a complex test case comparable to real-world engineering problems.

4.1. Simple test case

Fig. 3 shows the parametric surface model of the simple test case, based on a square SubD surface subdivided into 9 patches and 16 points. The algorithm varies the height of each point in order to optimise the shape. Each point is given a variability in Z-direction from 0 to 5, which is represented by the green arrows at each control point.

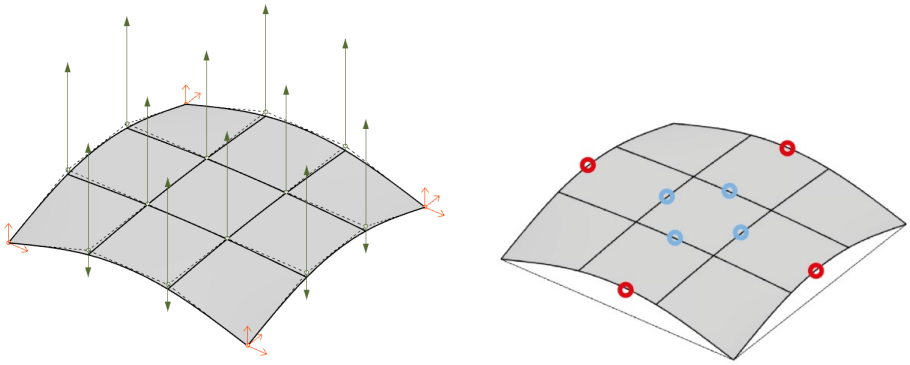


Figure 3: The simple test case with the square base, with the height variability range (left), and the BCs calculated based on the average height of the centre points (blue dots in right image) and height difference between arches (red dots in right image).

Diversity dimensions (BCs) focus on two target areas, namely the central region and the arches (blue and red dots, respectively in Fig. 3). BC1 is taken as the average Z coordinate of the edges of the central face, to capture the height at the middle of the shell. BC2 is the Z coordinate deviation between the midpoints of the side arches, in order to capture asymmetric aspects of an otherwise symmetrical problem. High performing solutions for this form are largely known beforehand, so these two case

[1] For the SOO baseline, all solutions are processed and only feasible ones are placed on the feasible feature map along the two BCs of FI-MAP-Elites (with only the fittest solution retained in each cell).

studies act as benchmarks to ensure that the solutions provided by the QD algorithm are as expected. Based on preliminary experiments, the value ranges for each BC were specified by the structural engineers at BC1$\in$[0,1.3] and BC2$\in$[0.5,3.5], forming the design space that QD should illuminate.

Experiments conducted with this structure assume a base of 16m by 16m, made of grade C16/20 concrete, and a thickness of 7cm, a mesh resolution of 2 subdivisions, and applied loads of 2kN/m^2. For the FI-MAP-Elites hyperparameters, we use an initial population of 100 random individuals, a mutation rate of 50% and mutation step of 20%, a grid of elites of 16 by 16 (BC1 by BC2) for both feasible and infeasible archives, and a total of 50,000 iterations of parent selection. The upper threshold for displacement (C_d) is set to 5cm.

We test two versions of this simple test case (Case 1 and Case 2). In both cases an identical input geometry is used, but they are given two different support constraints. Case 1 has all translations (X, Y, Z) constrained at the four corner points, while Case 2 has the X direction free. This means that Case 1 can transfer horizontal forces in two directions to the supports, while Case 2 can only transfer the horizontal forces in one direction. This should force the same patch into two different structural behaviours, thereby rendering different resulting shapes in the two maps.

Table 1. **Simple Test Case**: Comparing the final archive of QD with the final population of SOO, for Case 1 and Case 2. Results are averaged across 10 experiment repetitions. Error signifies a confidence interval of 95%.

	Case 1		**Case 2**	
	FI-MAP-Elites	**SOO**	**FI-MAP-Elites**	**SOO**
Feasible Coverage	94.3% ± 2.1%	0.6% ± 0.3%	88.9% ± 0.6%	0.7% ± 0.1%
Feasible QD-Score	110.37 ± 1.20	1.12 ± 0.51	75.32 ± 0.91	0.44 ± 0.11
Feasible U_{min}	0.38 ± 0.00	0. ma34 ± 0.01	0.72 ± 0.02	3.01 ± 0.74
Feasible σ_U	1.16 ± 0.08	0.00 ± 0.00	1.82 ± 0.04	0.02 ± 0.01
Feasible d_{min}	0.37 ± 0.04	0.13 ± 0.02	0.44 ± 0.06	2.08 ± 0.35
Feasible σ_d	0.62 ± 0.03	0.03 ± 0.01	0.76 ± 0.02	0.03 ± 0.01
Feasible Ratio	48.5% ± 0.6%	100.0% ± 0.0%	47.1% ± 0.2%	100.0% ± 0.0%
Infeasible Coverage	100.0% ± 0.0%	0.0% ± 0.0%	99.8% ± 0.3%	0.0% ± 0.0%

Table 1 shows the different performance metrics (see Section 3.4) for both Case 1 and Case 2. Results are averaged from 10 independent runs of both FI-MAP-Elites and SOO per case. A first observation for both cases is that the final SOO population contains exclusively feasible individuals, and those individuals have almost identical scores in elastic energy among them (very low σ_U). Moreover, based on the very low coverage when these solutions are mapped in the FI-MAP-Elites feature map, the solutions are geometrically very similar. Unsurprisingly, FI-MAP-Elites is designed to explore the BCs specified by the designer and reaches very high scores in both feasible and infeasible coverage. Case 2 seems to be more challenging for EC to optimise, as evidenced by the much higher elastic energy in the best solution for both SOO and FI-MAP-Elites. While for Case 1 the SOO manages to converge towards a solution with a U score lower than the best U score found in FI-MAP-Elites, this is not true in Case 2. We presume that SOO converges early to a *local optimum* and does not explore the search space enough in order to find a better solution. The QD algorithm unsurprisingly does explore along the BCs and thus finds (many) better solutions. However, both the lower coverage and lower QD-score of FI-MAP-Elites in Case 2 compared to Case 1 shows that the freedom of changing the corner points' coordinates makes the problem more difficult.

Fig. 4 shows how the feature map of some indicative runs of FI-MAP-Elites differ between Case 1 and Case 2. It is evident that better solutions (with lower elastic energy) can be found in different parts of the design space (for these BCs), thus indicating different trade-offs between geometric designs. It can be seen that the change in support conditions leads to different solutions for each location in the map,

as the shapes with the lowest fitness go from two-directional compression shells in Case 1 to single-span shell topologies in Case 2. This can be seen as the fittest individuals in Case 1 are the ones with a high middle height, regardless of symmetry, whereas in Case 2 the fittest solutions have moved to the spots with high single-axis symmetry (barrel vault forms) and two-axis symmetric solutions are not observed. Moreover, in Case 2 we also see a different class of fit individuals in the middle of the map as the lower middle height of these shells allows them to develop some synclastic curvature, which further increases stiffness.

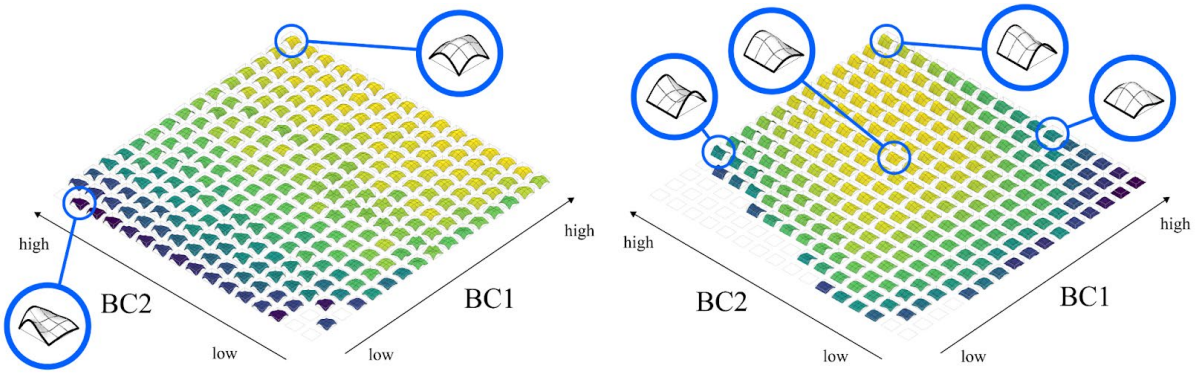


Figure 4: Indicative archives of feasible solutions from a single run of FI-MAP-Elites for Test Case 1 (left) and Test Case 2 (right), collected after 50,000 evaluations. Yellow shapes have higher feasible fitness.

4.2. Complex test case

The complex case study focuses on a more detailed four-arch vault shell which is initially mirror symmetrical in the XZ and YZ planes (as seen in Fig. 5). This form comprises 16 patches, and has 29 control points adjusted by the optimisation algorithms. The shell has a base boundary of 20m by 10m, is formed in grade C16/20 concrete with a thickness of 10cm, a mesh resolution of 3 subdivisions, and only self-weight (no applied loads). The upper threshold for displacement (C_d) is set to 6cm.

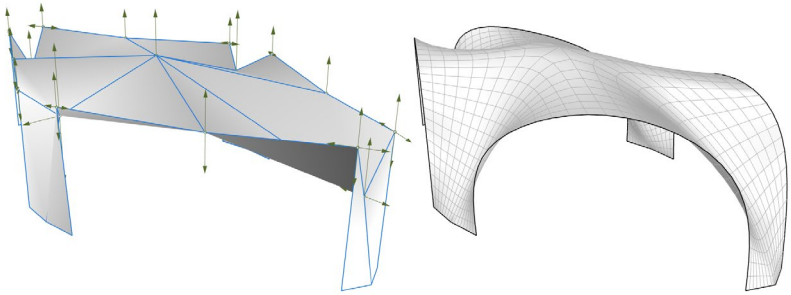


Figure 5: Inputs for complex case study: control mesh and control point variation vectors (left, vectors in green), and resulting smoothed mesh that is structurally analysed (right).

Diversity is defined using two *Edge Point Coordinates Deviation* BCs: BC1 is the Z coordinate deviation between midpoints of the four external arches, BC2 is the Z coordinate deviation between midpoints of the four axial iso-curves that meet at the centre of the vault. The problem-specific value ranges for the BCs in this case are found through trial and error at BC1$\in$[0,1.0] and BC2$\in$[0,1.15].

Table 3 shows the performance metrics on the complex test case, averaged from 8 independent runs. The increased complexity of this test case impacts the feasible coverage of the FI-MAP-Elites approach. However, more than half of the examined domain has been covered with feasible solutions in this approach (64%). On the other hand, the SOO's feasible coverage remains at a very low value, suggesting that solutions discovered in SOO are very similar to each other in every run. Furthermore, the feasible population discovered by the QD approach exhibited better performance in terms of both elastic energy

and displacement, in comparison to SOO. This observation is aligned with the general notion that diversification in evolutionary approaches is a means of achieving better fitness.

Table 3. **Complex Test Case**: Comparing the final archive of QD with the last population of SOO. Error signifies a confidence interval of 95%. Displacement (d) is reported in centimetres.

	FI-MAP-Elites	SOO
Feasible Coverage	66.9% ± 1.5%	0.8% ± 0.3%
Feasible QD-Score	110.66 ± 2.18	1.46 ± 0.56
Feasible U_{min}	0.34 ± 0.01	0.45 ± 0.02
Feasible σ_U	0.21 ± 0.02	0.01 ± 0.00
Feasible d_{min}	0.15 ± 0.01	0.27 ± 0.02
Feasible σ_d	0.11 ± 0.01	0.01 ± 0.00
Feasible Ratio	49.5% ± 0.4%	100.0% ± 0.0%
Infeasible Coverage	68.3% ± 1.7%	0.0% ± 0.0%

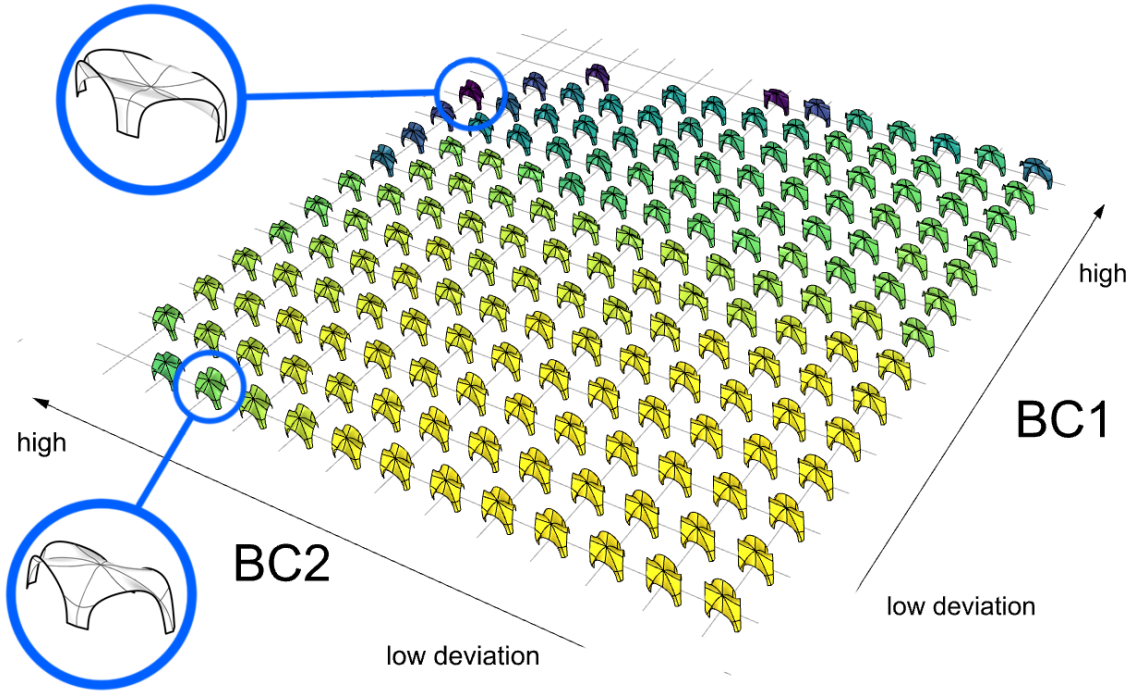


Figure 6: Visualisation of all feasible solutions found in a single run of the FI-MAP-Elites algorithm on the Complex Test Case. Meshes in yellow have a higher fitness (i.e. lower elastic energy). All feasible designs are found in the first 13 by 14 cells (BC1 by BC2) of the feature map; empty cells beyond this range are omitted.

As seen in Fig. 6, the fittest solutions are concentrated in regions of low deviation for both sets of control points. Furthermore, we observe a clear gradient that starts from this point and diminishes the further away we move from it. This observation is aligned with an engineering intuition that more symmetric solutions will exhibit better structural properties. Despite this fact, it is worth noting that all presented solutions are feasible and locally optimised, rendering them potential candidates for further investigation.

Finally, Fig. 7 visualises the best individual solutions found by FI-MAP-Elites and SOO approaches, for a detailed examination. In these examples the QD algorithm found a lower deformation solution than the SOO. The QD optimal solution has sharper curvature at the two supports [20] in the short-span axis but achieves a shallower angle into the two long-axis supports. As these results suggest, the best range

of solutions for high-dimensional problems like this can often not be easily intuited by the engineer, unlike the simple test cases.

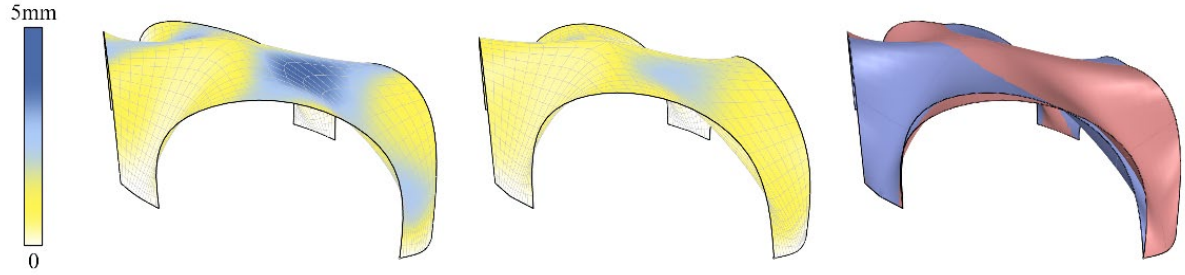


Figure 7: Best solution found by the SOO (left) and by FI-MAP-Elites (middle), with blue regions representing high displacement. Both solutions overlaid (right) with blue colour for FI-MAP-Elites and red colour for SOO, to highlight their difference.

5. Discussion

This paper introduces a constrained Quality-Diversity evolutionary approach in structural engineering and tests it on the problem of designing shell surfaces. Unlike traditional evolutionary optimization, which converges towards similar solutions, our method produces many diverse solutions and improves them throughout evolution. It uses a two-population approach to explore the design space efficiently and discover feasible solutions. It produces many individuals, with a high coverage of the design space of geometric properties specified by the designer. The produced visualisation of all possible layouts can provide important feedback to engineers and inspire future iterations. As shown in some use-case example shell structures, this approach can offer many good alternatives for an engineer to choose from, compared to the single design produced by single-objective evolution.

The experiment setup included three test cases: two variants of a simple problem and a more complex problem closer to the real-world structural engineering problems encountered by AKT II [19],[20]. We compared the output of FI-MAP-Elites against designs collected from a traditional single-objective optimization (SOO) method available to all engineers through the Galapagos optimizer (in Rhino/Grasshopper). While the objective function included both the design goal and the constraints, through a form of fitness penalty typical in constrained optimization [17], other evolutionary approaches may perform differently. For instance, a two-population approach such as FI-2pop GA is expected to find feasible individuals even in the complex case study, where SOO struggled. Moreover, traditional genetic diversity preservation mechanisms such as the Fitness Uniform Selection Strategy [23] could also lead to more diverse results. Finally, a multi-objective approach [24] where the BCs are used as objectives alongside the SOO objective function (F_b) may lead to a more diverse population. On the other hand, since the best solutions were found at specific BC coordinates, sometimes with low BC scores, optimising towards high BCs may not lead to any improvements at a higher computation cost. Such more complex baselines will be explored in future work, where more complex structural engineering problems will be tested with FI-MAP-Elites.

Results of FI-MAP-Elites as a method of illuminating the design space and generating many good alternatives is promising for the structural engineering test cases, including the complex one which is close to real-world problems faced by professionals. However, there are many other problems within the AEC domain that could benefit from FI-MAP-Elites and could be explored in future work. Preliminary studies in illuminating the space of stick models for structural engineers with FI-MAP-Elites [25] have shown that the method is valuable for simple test cases but does not scale for more complex problems due to the additional burden on designers to define the entire range of allowed designs. FI-MAP-Elites has also been tested for MEP engineering towards designing ventilation shafts

[25], operating under strict design spaces provided by the designers; this allows designers to ensure that solutions satisfy their ad-hoc constraints but limits the potential of QD search to provide truly surprising solutions to the designers. Beyond testing FI-MAP-Elites in other engineering tasks, a more ambitious avenue for future work is testing the output of the algorithm (e.g. the feature maps of Fig. 4) in real-world, everyday workflows of a professional setting and their applicability as inspiration for engineers, for communicating between disciplines (e.g. showing a feature map of alternatives to other AEC stakeholders, such as architects), and for communicating with clients. This ambitious direction of inquiry would shed more light on the potential of Quality-Diversity search and the improvements needed to the algorithm, visualisation, explainability [26], and tools (e.g. Rhino plugin).

6. Conclusions

This paper presented a novel approach to structural engineering, testing a new algorithm that takes advantage of recent advances in constrained optimization and quality-diversity (QD) evolutionary search. The method shows promise in both simple and complex test cases and can produce a range of geometrically diverse high-quality solutions, which can be beneficial during conceptualization stages and when exploring alternatives with different stakeholders. The algorithm is integrated into the Grasshopper visual programming environment within Rhino, which makes it both easily accessible and customizable by engineers, and also provides tools to intuitively visualise and inspect all generated solutions. Compared to a traditional single-objective optimization method currently available in Rhino, our constrained QD approach can find feasible solutions more easily and produce far more viable alternatives, compared with a single optimum that the single-objective approach converges to. Future work will explore converting FI-MAP-Elites into a plugin available for everyone via online repositories (e.g. food4rhino.com) and assessing its applicability further in everyday structural engineering workflows.

Acknowledgements

The research leading to these results has received funding from the European Union H2020 Horizon Programme (2014-2020) under grant agreement 952002, project PrismArch: Virtual reality aided design blending cross-disciplinary aspects of architecture in a multi-simulation environment. Konstantinos Sfikas is supported by the European Union's H2020 research and innovation programme (Grant Agreement No. 951911).

References

[1] F. Otto and B. Rasch, *Finding Form: Towards an Architecture of the Minimal*, Axel Menges 1996.

[2] M. Burry, *The Expiatory Church of the Sagrada Famíli*a, Phaidon Press 1993.

[3] D. Piker, "Kangaroo: Form Finding with Computational Physics", in *Architectural Design*, vol. 83 no. 2, 2013.

[4] R. Vierlinger, "Multi Objective Design Interface", Master's Thesis, TU Wien, 2013.

[5] M. Kyropoulou, "Shading Design for Outdoor Learning in Warm and Hot Climates Using Evolutionary Computation: A Case Study In Houston TX," in *Proceedings of the Annual Modeling and Simulation Conference (ANNSIM)*, 2022, pp. 682–693.

[6] J. K. Pugh, L. B. Soros, and K. O. Stanley, "Quality Diversity: A New Frontier for Evolutionary Computation," *Frontiers in Robotics and AI*, vol. 3, 2016.

[7] J. Lehman, and K. O. Stanley, "Evolving a Diversity of Virtual Creatures through Novelty Search and Local Competition," in *Proceedings of the Annual Conference on Genetic and Evolutionary Computation*, 2011.

[8] A. Liapis, G. N. Yannakakis, and J. Togelius, "Constrained Novelty Search: A Study on Game Content Generation," *Evolutionary computation*, vol. 23, no. 1, pp. 101–129, 2015.

[9] J.-B. Mouret, and J. Clune, “Illuminating search spaces by mapping elites,” *arXiv preprint 1504.04909*, 2015.

[10] M. C. Fontaine, and S. Nikolaidis, “Differentiable Quality Diversity,” *arXiv preprint 2106.03894*, 2021.

[11] D. Gravina, A. Khalifa, A. Liapis, J. Togelius and G. N. Yannakakis, "Procedural Content Generation through Quality-Diversity," in *Proceedings of the IEEE Conference on Games*, 2019.

[12] C. Cui, H. Ohmori and M. Sasaki, “Computational morphogenesis of 3D structures by extended ESO method." *Journal of the International Association for Shell and Spatial Structures 44.1*, 2003.

[13] S. O. Kimbrough, G. J. Koehler, M. Lu, and D. H. Wood, “On a Feasible–Infeasible Two-Population (FI-2Pop) genetic algorithm for constrained optimization: Distance tracing and no free lunch,” *European journal of operational research*, vol. 190, no. 2, pp. 310–327, 2008.

[14] K. O. Stanley and R. Miikkulainen, “A Taxonomy for Artificial Embryogeny,” *Artificial life*, vol. 9, no. 2, pp. 93–130, 2003.

[15] K. Sfikas, A. Liapis, and G. N. Yannakakis, “A General-Purpose Expressive Algorithm for Room-Based Environments,” in *Proceedings of the 17th International Conference on the Foundations of Digital Games,* 2022.

[16] K. De Jong, “Evolutionary Computation: A Unified Approach,” in *Proceedings of the Conference [23]Companion on Genetic and Evolutionary Computation*, 2012, pp. 737–750.

[17] A. Coello Coello, “Theoretical and numerical constraint-handling techniques used with evolutionary algorithms: a survey of the state of the art,” 2002, *Computer Methods in Applied Mechanics and Engineering* 191(11-12):1245-1287.

[18] E. Catmull and J. Clark, “Recursively Generated B-Spline Surfaces on Arbitrary Topological Meshes,” in *Seminal Graphics: Pioneering Efforts That Shaped the Field*, Association for Computing Machinery, 1998, pp. 183–188.

[19] P. Schumacher, “The Congeniality of Architecture and Engineering”, in *Shell Structures for Architecture: Form Finding and Optimization*, Routledge 2014.

[20] J. Janssen and R. Parker, “Hybrid Shells”, in *Design Engineering Refocused*, Wiley 2017, H. Kara and D. Bosia, Eds.

[21] http://www.rhino3d.com

[22] http://www.karamba3d.com

[23] M. Hutter, “Fitness uniform selection to preserve genetic diversity,” in *Proceedings of the 2002 Congress on Evolutionary Computation*. pp. 783–788.

[24] K. Deb, A. Pratap, S. Agarwal, and T. Meyarivan, “A fast and elitist multiobjective genetic algorithm: NSGA-II,” *IEEE Transactions on Evolutionary Computation*, vol. 6, no. 2, pp. 182–197, 2002.

[25] K. Sfikas, A. Liapis, G. N. Yannakakis and J. Hilmersson, “Final revised version of parametric space of design, algorithms for AI assisted editing/design in VR, and algorithms for designer modelling”, Technical Report, https://prismarch-h2020.eu/download/497.

[26] J. Zhu, A. Liapis, S. Risi, R. Bidarra and G. M. Youngblood: “Explainable AI for Designers: A Human-Centered Perspective on Mixed-Initiative Co-Creation,” in *Proceedings of the IEEE Conference on Computational Intelligence and Games*, 2018.

IASS 2023
July 10–14 Melbourne
Integration of Design and Fabrication

Proceedings of the IASS Annual Symposium 2023
Integration of Design and Fabrication
10–14 July 2023, Melbourne, Australia
Y.M. Xie, J. Burry, T.U. Lee and J. Ma (eds.)

Development of 3D mathematical models for tendon layout optimization by strain energy minimization

Hanna DOMNICK[a,*], Juan Pablo OSMAN-LETELIER[b]

[a,*] KLÄHNE BUNG Ingenieure
Behrenstraße 29, 10117 Berlin
hanna.domnick@gmail.com

[b] schlaich bergermann partner (sbp)

Abstract

Applying prestress to concrete structures makes it possible to redirect forces, thus increasing their efficiency by optimizing their structural behaviour and durability. This paper proposes an efficient and practical tendon optimization method that allows engineers to find an optimal tendon layout in spatial beamlike structures. It is based on the minimization of strain energy, while also taking geometrical boundary conditions into consideration. The constrained optimization problem is solved using approaches from variational calculus, including the Rayleigh-Ritz method and Lagrange multipliers. The consideration of practical boundary conditions and the precise polynomial solution reduce post-processing and facilitate an easy implementation of the method in the structural design process. Numerical examples that apply the method to thin-walled beamlike structures demonstrate its flexible applicability for both simple and complex systems with a variety of support conditions and design constraints. The proposed method is efficient, flexible, and accurate, thus improving the tendon layout optimization process with respect to past approaches and equipping structural engineers with a powerful, yet user-friendly tool for designing more sustainable and lightweight concrete structures.

Keywords: prestressed concrete, post-tensioned concrete, structural optimization, tendon layout optimization, strain energy minimization, folded slabs, concrete shells, thin-walled structures, Hangai Prize applicant

1 Introduction

Reducing the amount of concrete in structures is indispensable in order to contribute to more sustainable construction, since concrete production is an extremely resource-intensive process. Optimizing the structures' geometry according to the principle of *form follows force* leads to slenderer and filigree structures such as folded slabs or shells. Moreover, using the concept of prestress makes it possible to optimize the structural behaviour and durability of concrete structures. As the effect of prestress depends heavily on the tendon, finding an optimal tendon layout is a crucial step in the design process. Conventional methods for the design of an optimal tendon layout require engineering experience and frequently the use of complex methodologies, thus making it difficult to apply them in practice.

Most previous studies on optimizing tendon layouts minimize the costs or material usage in simple beams with two-dimensional tendon layouts. In early papers by Kirsch [1] the tendon was optimized using linear programming. Subsequent studies used projected Lagrangian algorithms, among others, to optimize several objectives such as minimum cost, weight, or initial camber simultaneously [2]. An energy-based optimization method was proposed by Eurviriyanukul and Askes [3] who optimized the tendon layout by minimizing the residual of the configurational forces in simple and continuous beams. Avelino et al. [4] and Hymans et al. [5] used topology optimization and gradient-based optimization methods to optimize spatial tendon layouts in concrete slabs. They showed that the optimization of

Copyright © 2023 by Hanna DOMNICK and Juan Pablo OSMAN-LETELIER. Published in the Proceedings of the IASS Annual Symposium 2023 with permission.

structural behaviour also results in a reduction of costs. Their approaches have recently been developed further by Zelickman and Amir [6], [7] by using B-splines in order to gain more freedom with respect to the tendon layout and reduce post-processing. Whilst those studies successfully optimize the tendon layout, the methods all include elaborate iterations and FE analysis. Moreover, extensive post-processing is required to obtain tendon layouts that comply with practical boundary conditions such as continuity above supports.

The method proposed in this paper contributes to solving the problems mentioned above. The authors of this work developed a method to optimize tendon layouts based on the minimization of strain energy at the Technical University of Berlin [8]. Minimizing the strain energy minimizes the deflection and maximizes the stiffness, therefore allowing for the design of slenderer and more efficient structures. By considering geometrical boundary conditions during the optimization, post-processing is reduced and the efficiency of the structural design process increased.

The model for a prestressed spatial beamlike thin-walled structure and the resulting internal forces are visualized in Figure 1 and Figure 2. The tendon layout is defined by its eccentricity to the centroid of the beam described by the three-dimensional curve $\boldsymbol{r}: \mathbb{R} \to \mathbb{R}^3, t \mapsto \boldsymbol{r}(t)$. It is assumed that deformation resulting from prestressing is not restrained (statically determinate), which means that the secondary effects of prestressing thus do not need to be taken into account. Note that the subsequent addition of static constraints still allows statically indeterminate systems to be achieved. The global stress resulting from prestress is then given by:

$$\sigma_P(x,z) = \frac{N_P(x)}{A} + \frac{M_P(x)}{I} z \tag{1}$$

Where $N_P(x)$ is the axial force in the structure's cross section due to prestressing and $M_P(x)$ is the bending moment about the y-axis resulting from prestressing.

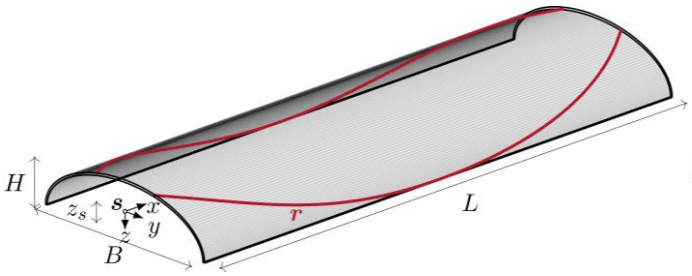


Figure 1 Model for a prestressed beamlike spatial structure

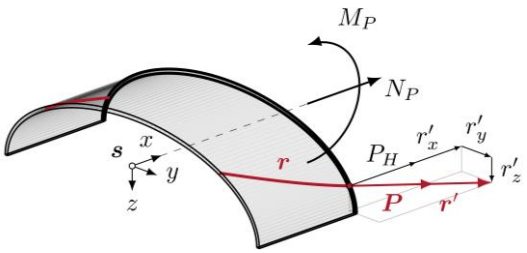


Figure 2 Internal forces due to prestress

2 Tendon layout optimization as a constrained optimization problem

The energy required to deform a prestressed body depends on the structure's geometry, material, and external loads, as well as the tendon layout. Hence, minimizing the strain energy reduces the deflection and optimizes the tendon layout for the structure and loads being considered. The objective of the optimization problem considered in this paper is thus as follows:

The tendon layout is considered optimal if the vertical deflection under a certain external load is zero, i.e., the strain energy is zero.

The optimization problem is characterized as follows:

Variable	Tendon layout
Objective function	Strain energy
Constraints	Geometrical boundary conditions
Method	Rayleigh-Ritz method with Lagrange multipliers
Solution	Polynomial

2.1 Objective function derivation

Strain energy is the potential energy stored in a body as a result of its deformation by external loads. For a beam with isotropic elastic materials, the strain energy from axial and bending stresses σ_x (assuming $\sigma_y = \tau_{xy} = \tau_{yx} = 0$) is defined as:

$$\Pi_i = \frac{1}{2E} \int_V \sigma_x^2 \, dV \tag{2}$$

The strain energy in a prestressed beam depends on the elasticity modulus E and the stress resulting from external loads and prestress. Here only normal stresses resulting from bending moments due to external loads M_E and prestress M_P are considered, as they are responsible for the vertical deflection of a beam.

$$\sigma_x = \sigma_E + \sigma_P = \frac{M_E \, z}{I} + \frac{M_P \, z}{I} \tag{3}$$

Assuming a constant cross section and substituting σ_x from equation (3), equation (2) thus yields:

$$\Pi_i = \frac{1}{2E} \int_V \sigma_x^2 \, dV = \frac{1}{2EI^2} \int_H \int_B \int_L (M_E + M_P)^2 \, dx \, dy \, z^2 \, dz \tag{4}$$

As shown by Osman-Letelier [8] minimizing the strain energy in equation (4) leads to the following expression, stating that the strain energy is minimized by minimizing the integral of the squared sum of moments over the beam length.

$$\Pi_i = 0 \Rightarrow \min \Pi_i \equiv \min \overbrace{\int_L \overbrace{(M_E + M_P)^2}^{\mathcal{H}} \, dx}^{\mathcal{J}_P} \tag{5}$$

This term is called J_P and serves as the objective function for the proposed optimization method.

$$\mathcal{J}_P = \int_L \mathcal{H} \, dx = \int_L (M_E + M_P)^2 \, dx \rightarrow \min \tag{6}$$

M_E depends on external loads and the system considered while M_P depends on the tendon layout.

2.2 Solution with the Euler-Lagrange equation

In analogy to differential calculus, which addresses the change of a function that depends on a scalar variable, the change of a functional that depends on a function, is addressed by variational calculus. To find an optimal tendon layout, a function $\boldsymbol{r}(t)\colon \mathbb{R} \rightarrow \mathbb{R}^3 \, , t \mapsto \boldsymbol{r}(t)$ that extremizes the objective function

$$\mathcal{J}_P\colon \mathbb{R}^3 \rightarrow \mathbb{R}, \boldsymbol{r}(t) \mapsto \int_{t_1}^{t_2} \mathcal{H}\big(t, \boldsymbol{r}(t), \boldsymbol{r}'(t)\big) \, dt, \tag{7}$$

with $\mathcal{H}\colon \mathbb{R}^3 \rightarrow \mathbb{R}, \boldsymbol{r}(t) \mapsto \mathcal{H}\big(t, \boldsymbol{r}(t), \boldsymbol{r}'(t)\big)$ depending on the unknown function $\boldsymbol{r}$ and its derivative $\boldsymbol{r}'$, can be found by solving the Euler-Lagrange equation:

$$\delta \mathcal{J}_P = 0 \Leftrightarrow \frac{d}{dt} \frac{\partial \mathcal{H}}{\partial \boldsymbol{r}'} - \frac{\partial \mathcal{H}}{\partial \boldsymbol{r}} = 0 \tag{8}$$

As demonstrated by Osman-Letelier [8] optimizing the tendon layout by using the Euler-Lagrange equation leads to highly complex non-linear differential equations, which could not be solved. The design space is thus restricted by applying the Rayleigh-Ritz method.

2.3 Design space

The design space of the curve $\boldsymbol{r}$ is restricted in two ways in order to ensure that the tendon is located inside the structure's cross section and to reduce the complexity of the optimization problem. Table 1

shows various cases of tendon layouts in beamlike structures. To ensure that the tendon is located inside the concrete, the placement of the tendon needs to be constrained to the possibly curved neutral surface of the thin-walled structures cross section. Consider the curve $\boldsymbol{r}$ and surface $\boldsymbol{S}$:

$$\boldsymbol{r}(t) = \begin{bmatrix} r_x(t) \\ r_y(t) \\ r_z(t) \end{bmatrix} \tag{9}$$

$$\boldsymbol{S}(u,v) = \begin{bmatrix} u \\ f_y(u,v) \\ f_z(u,v) \end{bmatrix} \tag{10}$$

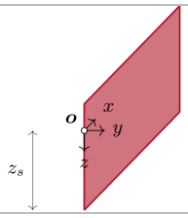
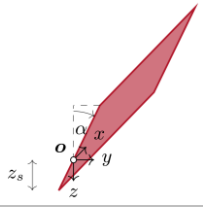
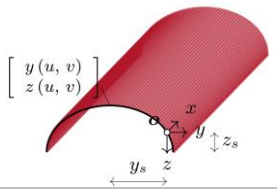
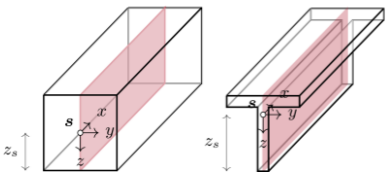
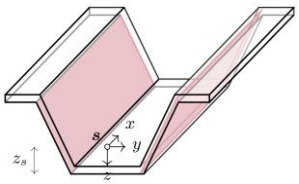
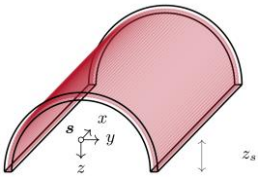
The curve $\boldsymbol{r}$ lies on the surface $\boldsymbol{S}$ between t_1 and t_2 if their minimal distance vanishes for all $t \in [t_1, t_2]$.

$$\boldsymbol{r} \subset \boldsymbol{S} \iff \forall\, t \in [t_1, t_2]\ \exists\, (u,v) \in \mathbb{R}^2 \mid 0 = \boldsymbol{r}(t) - \boldsymbol{S}(u,v) \tag{11}$$

In order to restrict the tendon to the cross section, $\boldsymbol{r}$ is projected onto $\boldsymbol{S}$, so that the following statement, which is derived from equation (11), applies:

$$\begin{bmatrix} r_x(t) \\ r_y(t) \\ r_z(t) \end{bmatrix} = \begin{bmatrix} u \\ f_y(u,v) \\ f_z(u,v) \end{bmatrix} \tag{12}$$

Table 1 Parametrized surfaces for spatial tendon layouts with examples

	Planar tendon layouts	Spatial tendon layouts in planar surfaces	Spatial tendon layouts in curved surfaces
Surface			
Example	Simple beams 	Folded slab 	Cylindrical shell 

A second restriction of the design space is introduced in order to reduce the complexity of the equations by applying the Rayleigh-Ritz method. Instead of searching for entirely unknown functions for the components of $\boldsymbol{r}$, an approximation $\tilde{\boldsymbol{r}}$ that satisfies

$$\lim_{n\to\infty} \tilde{\boldsymbol{r}} = \boldsymbol{r} \tag{13}$$

and depends on the coefficients $\boldsymbol{a} \in \mathbb{R}^n$ as well as on the shape functions $\boldsymbol{\phi} \in \mathbb{R}^n$ is defined as follows:

$$\tilde{\boldsymbol{r}}\colon \mathbb{R} \to \mathbb{R}^3, x \mapsto \boldsymbol{r}(\boldsymbol{a}^T\boldsymbol{\phi}) = r\left(\sum_{i=1}^{n} a_i \phi_i(x)\right) \tag{14}$$

In this paper a polynomial approach has been chosen, thus restricting the design space to polynomials which are described by the shape functions

$$\phi_i = x^{i-1} \tag{15}$$

Combining both design space restrictions by substituting

$$u = t = x \tag{16}$$

$$v = \boldsymbol{a}^T \boldsymbol{\phi}(x) \tag{17}$$

in equation (12), the approximation of a spatial tendon layout that is restricted to a surface that is described by the functions $f_y(u, v)$ and $f_z(u, v)$ is defined by:

$$\tilde{\boldsymbol{r}}(\boldsymbol{a}, x) = \begin{bmatrix} r_x \\ r_y \\ r_z \end{bmatrix} = \begin{bmatrix} x \\ f_y\big(x, \boldsymbol{a}^T \boldsymbol{\phi}(x)\big) \\ f_z\big(x, \boldsymbol{a}^T \boldsymbol{\phi}(x)\big) \end{bmatrix} \tag{18}$$

The curve $\boldsymbol{r}$ in equation (9) consists of three entirely unknown functions, whereas the approximated curve $\tilde{\boldsymbol{r}}$ in equation (18) contains one unknown polynomial that depends on the scalar coefficients $\boldsymbol{a}$. Hence, replacing $\boldsymbol{r}$ with its approximation $\tilde{\boldsymbol{r}}$ results in the objective function $\mathcal{J}_P$ being dependent on the unknown scalar coefficients $\boldsymbol{a}$ instead of on an unknown three-dimensional function $\boldsymbol{r}$.

$$\mathcal{J}_\mathrm{P}\colon \mathbb{R}^3 \to \mathbb{R}, \boldsymbol{a} \mapsto \int_{x_1}^{x_2} \mathcal{H}\big(x, \tilde{\boldsymbol{r}}(\boldsymbol{a}, x), \tilde{\boldsymbol{r}}'(\boldsymbol{a}, x)\big)\, dx = \int_{x_1}^{x_2} \mathcal{H}(\boldsymbol{a}, x)\, dx \tag{19}$$

This restriction of the design space reduces the complexity of the equations and the processing time.

2.4 Constraints

To eliminate extensive post-processing and obtain realistic tendon layouts, practical boundary conditions such as continuity above supports, tendon curvature, concrete cover depth, or anchor positions should be fulfilled. Consider the boundary conditions $\boldsymbol{g}\colon \mathbb{R}^n \to \mathbb{R}^m, \boldsymbol{a} \mapsto g(\boldsymbol{a})$. By introducing the Lagrange multipliers $\boldsymbol{\lambda} \in \mathbb{R}^m$, the Lagrange function $\mathcal{L} \in \mathbb{R}$ is defined

$$\mathcal{L}(\boldsymbol{a}) = \mathcal{J}_P(\boldsymbol{a}) + \boldsymbol{\lambda} \cdot \boldsymbol{g}(\boldsymbol{a}) \tag{20}$$

and the constrained optimization problem can be solved by minimizing the Lagrange function

$$\mathcal{L} \to \min \Rightarrow \nabla \mathcal{L} = \boldsymbol{0} \tag{21}$$

2.5 Summary

The complete constrained optimization problem for spatial tendon layouts is defined as follows:

Minimize $\boldsymbol{r}$	$\mathcal{J}_P$	subject to	$\boldsymbol{g} = \boldsymbol{0}$

The solution algorithm is described as follows:

Find	$\tilde{\boldsymbol{r}} \in \mathbb{R}^3$	with	$\lim_{n\to\infty}(\tilde{\boldsymbol{r}}) = \boldsymbol{r}$
by solving	$\nabla \mathcal{L} = \boldsymbol{0}$	for	$\boldsymbol{a} \in \mathbb{R}^n$
		with	$\mathcal{L}(\boldsymbol{a}) = \mathcal{J}_P(\boldsymbol{a}) + \boldsymbol{\lambda} \cdot \boldsymbol{g}(\boldsymbol{a})$
			$\mathcal{J}_P = \int_L \big(M_E(x) + M_P(\boldsymbol{a}, x)\big)^2\, dx$
			$\tilde{\boldsymbol{r}}(\boldsymbol{a}, x) = \begin{bmatrix} \tilde{r}_x \\ \tilde{r}_y \\ \tilde{r}_z \end{bmatrix} = \begin{bmatrix} x \\ f_y\big(x, \boldsymbol{a}^T \boldsymbol{\phi}(x)\big) \\ f_z\big(x, \boldsymbol{a}^T \boldsymbol{\phi}(x)\big) \end{bmatrix}$
			$\phi_i(x) = x^{i-1}$

3 Study cases

3.1 Optimization of planar tendon layouts in simple beams

The optimization of planar tendon layouts can be described by a simplified formulation of the optimization problem, as they are a special case of spatial tendon layouts. In a simple beam with a constant rectangular cross section, the tendon lies on the XZ plane. The tendon layout is defined by its vertical eccentricity to the x-axis $r_z \in \mathbb{R}$, with $r_x = x$ and $r_y = 0$. In order to define $\boldsymbol{r}$, we solely need to find the term r_z. Hence, the optimization problem and solving algorithm for planar tendon layouts is simplified as follows:

Minimize r_z	$\mathcal{J}_P$	subject to	$\boldsymbol{g} = \boldsymbol{0}$
Find	$\tilde{r}_z \in \mathbb{R}$	with	$\lim_{n\to\infty}(\tilde{r}_z) = r_z$
by solving	$\nabla\mathcal{L} = \boldsymbol{0}$	for	$\boldsymbol{a} \in \mathbb{R}^n$
		with	$\mathcal{L}(\boldsymbol{a}) = \mathcal{J}_P(\boldsymbol{a}) + \boldsymbol{\lambda} \cdot \boldsymbol{g}(\boldsymbol{a})$
			$\mathcal{J}_P(\boldsymbol{a}) = \int_L \left(M_E(x) + M_P(\boldsymbol{a}, x)\right)^2 dx$
			$\tilde{r}_z(\boldsymbol{a}, x) = \boldsymbol{a}^T \boldsymbol{\phi}(x),\ \phi_i(x) = x^{i-1}$

As the tendon is located on the XZ plane, the resulting moment is calculated as follows:

$$M_P(x) = -P_H(x)\, r_z(x) = -P \frac{r_z}{\sqrt{1 + r_z'^2}} \tag{22}$$

Numerical examples for the optimization of planar tendon layouts are presented by Osman-Letelier [8].

3.2 Optimization of spatial tendon layouts in folded slabs

To validate the proposed optimization method, three numerical examples of spatial tendon layouts in folded slabs as shown in Figure 3 and Figure 4 are presented. The results are obtained by implementing the algorithm described in section 2.5 in MATLAB (©MathWorks, Version R2020b). The built-in functions *vpaintegral* and *vpasolve* are used to solve the integral $\mathcal{J}_P$ and the system of equations $\nabla\mathcal{L} = \boldsymbol{0}$.



Figure 3 Prestressed folded slab [9]

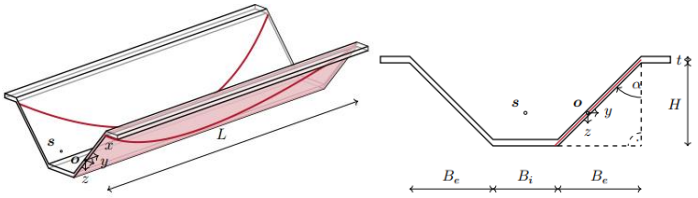


Figure 4 Model of a folded slab

The tilted plane of a folded slab as in Figure 4 is described by the functions $f_y = -\tan(\alpha)\, v$ and $f_z = v$. With equations (16), (17), and (18), that leads to the following approximation for the tendon:

$$\tilde{\boldsymbol{r}}(x) = \begin{bmatrix} u \\ f_y \\ f_z \end{bmatrix} = \begin{bmatrix} u \\ -\tan(\alpha)\, v \\ v \end{bmatrix} = \begin{bmatrix} x \\ -\tan(\alpha)\, \boldsymbol{a}^T \boldsymbol{\phi}(x) \\ \boldsymbol{a}^T \boldsymbol{\phi}(x) \end{bmatrix} \tag{23}$$

In this paper, only the moment about the y-axis is considered. It is assumed that the tendons are arranged symmetrically along the y-axis, so that no moment occurs about the z-axis.

$$M_{P,y}(x) = -P_H(x)\, r_z(x) = -P \frac{r_x'\, r_z}{\sqrt{r_x'^2 + r_y'^2 + r_z'^2}} \tag{24}$$

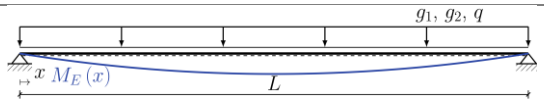
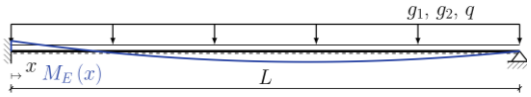
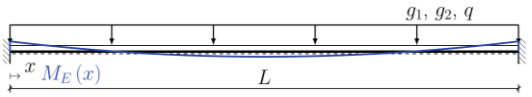
The additional term $r_y'^2$ in the denominator of equation (24) compared to equation (22) reduces the moment resulting from the change in the tendon's horizontal eccentricity. In the context of this paper, this effect will be called geometrical loss. Geometrical losses occur for the change in vertical ($= r_z'$) as well as in horizontal ($= r_y'$) eccentricity.

A quasi-permanent load combination of uniformly distributed loads composed of self-weight g_1, additional dead loads g_2, and live loads q is considered. At the time of prestressing, the beams under self-weight g_1 are simply supported (statically determinate), while the additional dead and live loads are applied to the system in its final state, which might be statically indeterminate. Applying prestress while the system is statically determinate and subsequently adding static constrains to achieve statically indeterminate systems is commonly seen in precast concrete elements. Under this assumption, indirect moments from prestressing do not need to be taken into account.

For all the beams considered, the following parameters concerning geometry, loading, and degree of the polynomial are defined: $L = 20\,m$, $H = 4\,m$, $B_i = 3\,m$, $B_e = 0{,}5\,m$, $\alpha = \pi/4$, $g_1 = 3\,kN/m$, $g_2 = 4\,kN/m$, $q = 2\,kN/m$, $n = 15$.

Three different static systems are considered: simply supported beam (SSB), beam fixed at one end (BFOE), and beam fixed at both ends (BFBE). The beams considered might represent a singular field of a continuous beam. To ensure a continuous geometry of the tendon above the supports, a constraint $\boldsymbol{g}$ is defined in such way that that the tendon arrives at the end of the fixed supports horizontally. To fully utilize the vertical space available, an optimal prestressing force P is chosen for each beam.

Table 2 Static systems of study cases

	System	Constraints
Simply supported beam (SSB)		$g \coloneqq \emptyset$
Beam fixed at one end (BFOE)		$g \coloneqq r'(0) = 0$
Beam fixed at both ends (BFBE)		$\boldsymbol{g} \coloneqq \begin{bmatrix} r'(0) \\ r'(L) \end{bmatrix} = \mathbf{0}$

The quality of the optimized tendon layout is evaluated by the achieved minimal value of the objective function $\mathcal{J}_P$. Moreover, the effectiveness of the optimized tendon layout is compared to two alternative approaches for the design of tendon layouts. First, a simplified solution that ignores the gradient of the tendon ($r_i'(x) \approx 0$ for slender beams) is introduced:

$$\boldsymbol{r}_{simp}(x) = \begin{bmatrix} x \\ f_y(x) \\ M_E(x)/P \end{bmatrix} \tag{25}$$

Second, the tendon layout r_{xz}, which is optimized without considering geometrical losses, is introduced. Instead of using the definition of $\tilde{\boldsymbol{r}}$ in equation (23) and considering the decrease in the tendon's effectivity due to its horizontal eccentricity during the optimization process, the tendon is optimized according to the simplified algorithm in section 3.1 and projected horizontally onto the tilted plane of the folded slab afterwards.

$$r_{xz}(x) = \begin{bmatrix} x \\ f_y(x) \\ \boldsymbol{a}^T \boldsymbol{\phi}(x) \end{bmatrix} \tag{26}$$

3.2.1 Simply supported beam (SSB)

The static system of a simply supported beam (SSB) at the time of prestressing does not differ from its system in the final state. Thus, the moment $M_E(x)$ due to the loads g_1, g_2, and q in the final state is:

$$M_E(x) = M_{SSB}(g_1 + g_2 + q) = \frac{1}{2}\,(g_1 + g_2 + q)\,x\,(L - x) \tag{27}$$

Figure 5 shows the optimized tendon layout considering a prestressing force of $P = 294\,kN$. The objective function has been minimized to a value of $\mathcal{J}_P = 1{,}917 \cdot 10^{-7}\,(kN\,m)^2 m$.

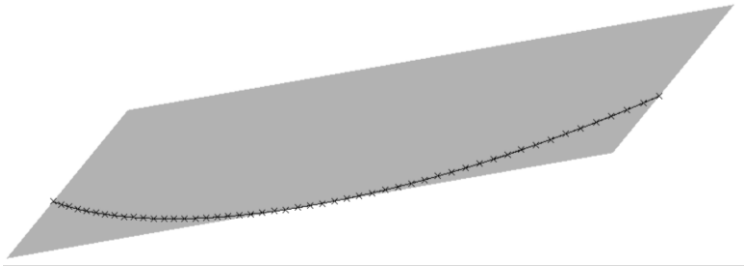


Figure 5 Optimized spatial tendon layout in a simply supported beam (SSB)

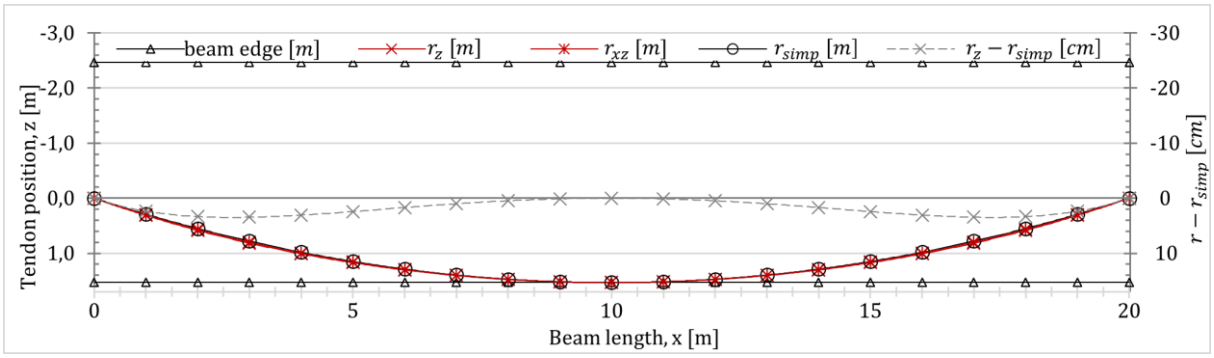


Figure 6 Vertical component r_z of the optimized spatial tendon layout in a simply supported beam (SSB), with and without considering geometrical losses in comparison to the simplified approach

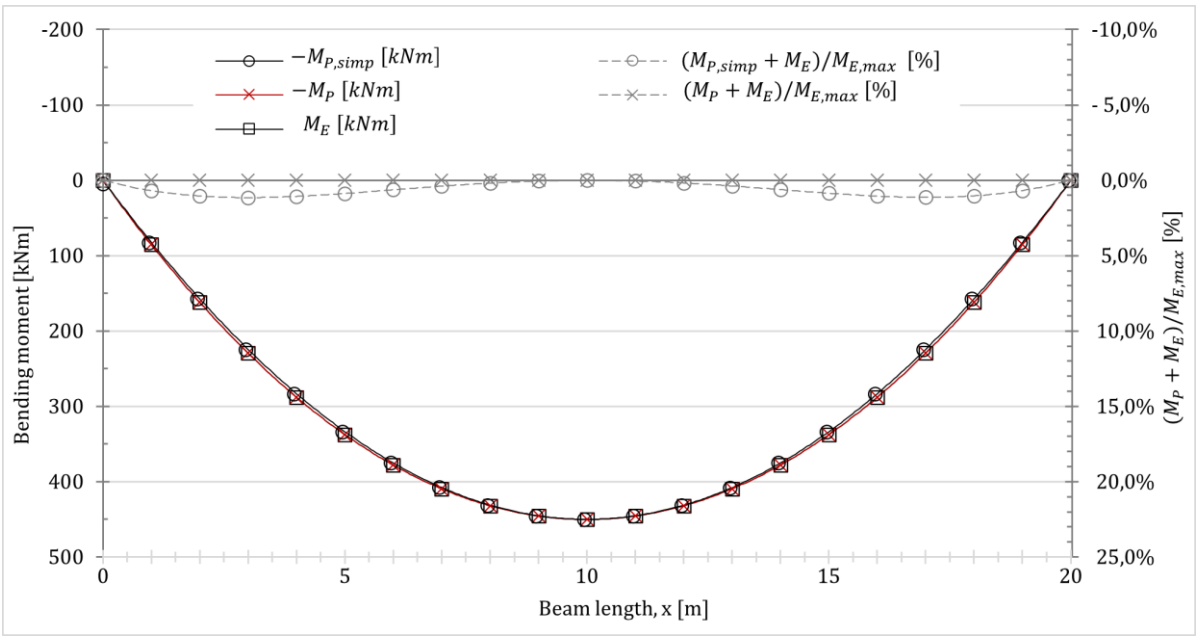


Figure 7 Bending moments due to external loads and prestress in a simply supported beam (SSB)

3.2.2 Beam fixed at one end (BFOE)

The static system of a beam fixed at one end (BFOE) at the time of prestressing is an SSB. Only in the final state is the system of a BFOE valid. Thus, the moment $M_E(x)$ resulting from the loads g_1, g_2, and q in the final state is:

$$M_E(x) = M_{SSB}(g_1) + M_{BFOE}(g_2 + q) = \frac{1}{2}\, g_1\, x\, (L - x) - \frac{1}{2}(g_2 + q)\left(x^2 - \frac{5}{4}\, L\, x + \frac{1}{4}\, L^2\right) \qquad (28)$$

Figure 8 shows the optimized tendon layout considering a prestressing force of $P = 204\ kN$. The objective function has been minimized to a value of $\mathcal{J}_P = 6{,}859 \cdot 10^0\ (kN\ m)^2 m$.

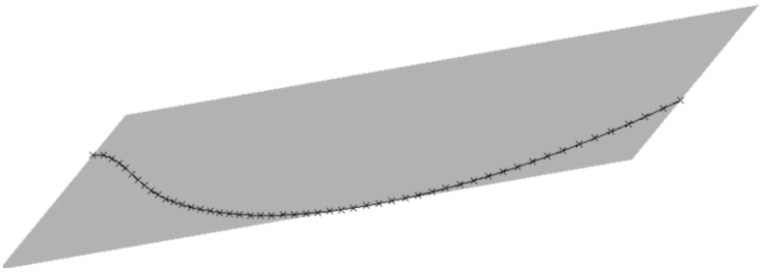


Figure 8 Optimized spatial tendon layout in a beam fixed at one end (BFOE)

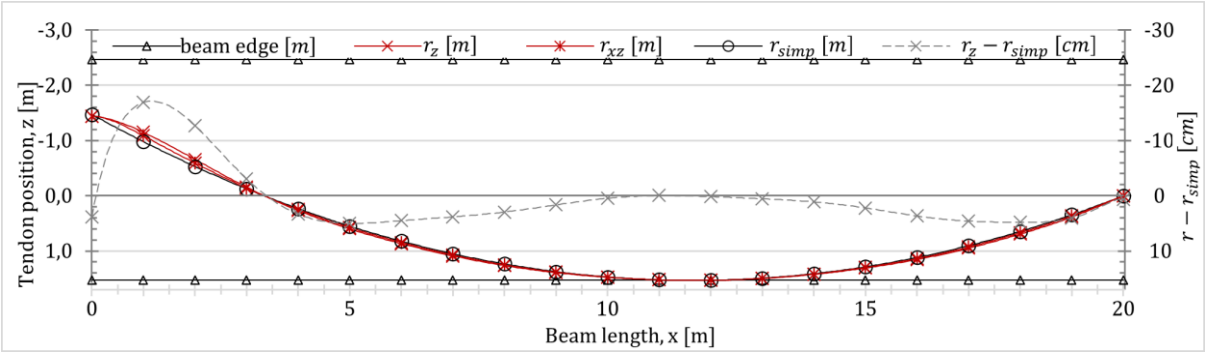


Figure 9 Vertical component r_z of the optimized spatial tendon layout in a beam fixed at one end (BFOE), with and without considering geometrical losses in comparison to the simplified approach

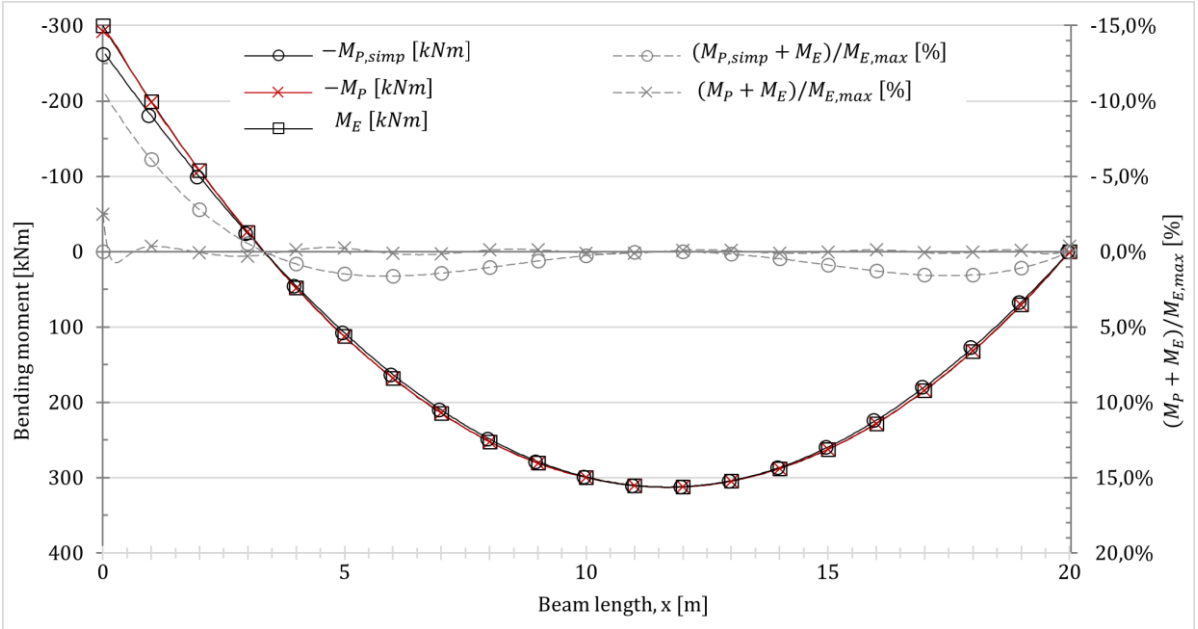


Figure 10 Bending moments due to external loads and prestress in a beam fixed at one end (BFOE)

3.2.3 Beam fixed at both ends (BFBE)

In the case of a beam fixed at both ends (BFBE), the static system at the time of prestressing is an SSB. The system of a BFBE applies in the final state. The moment $M_E(x)$ resulting from the loads g_1, g_2, and q in the final state is thus:

$$M_E(x) = M_{SSB}(g_1) + M_{BFBE}(g_2 + q) = \frac{1}{2}\, g_1\, x\, (L - x) - \frac{1}{2}(g_2 + q)\left(x^2 - L\, x + \frac{1}{6}\, L^2\right) \qquad (29)$$

Figure 11 shows the optimized tendon layout, considering a prestressing force of $P = 193\, kN$. The objective function has been minimized to a value of $\mathcal{J}_P = 1{,}387 \cdot 10^1\ (kN\ m)^2 m$.

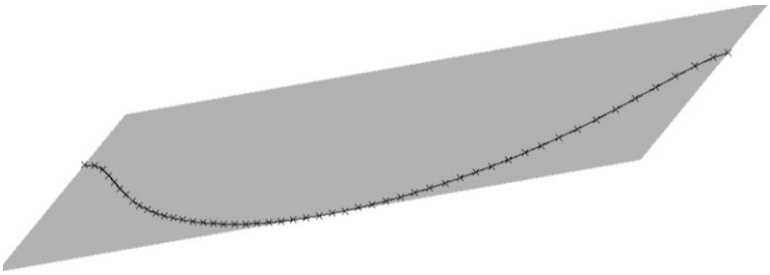


Figure 11 Optimized spatial tendon layout in a beam fixed at both ends (BFBE)

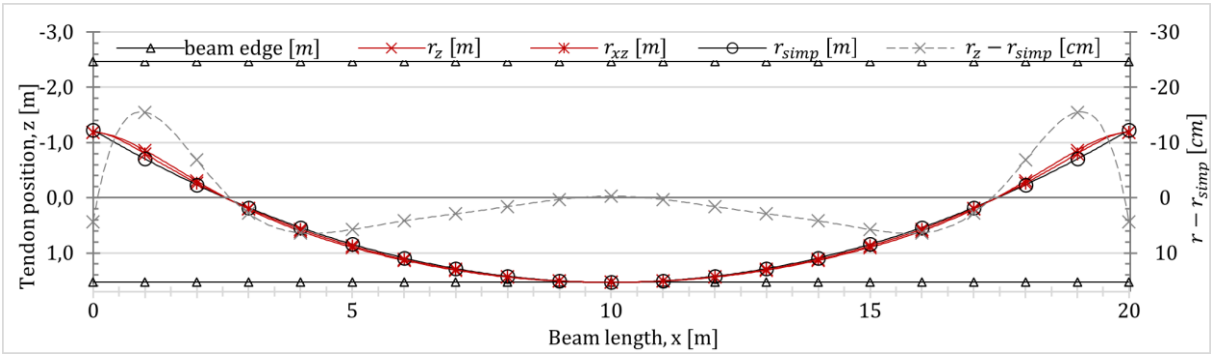


Figure 12 Vertical component r_z of the optimized spatial tendon layout in a beam fixed at both ends (BFBE), with and without considering geometrical losses in comparison to the simplified approach

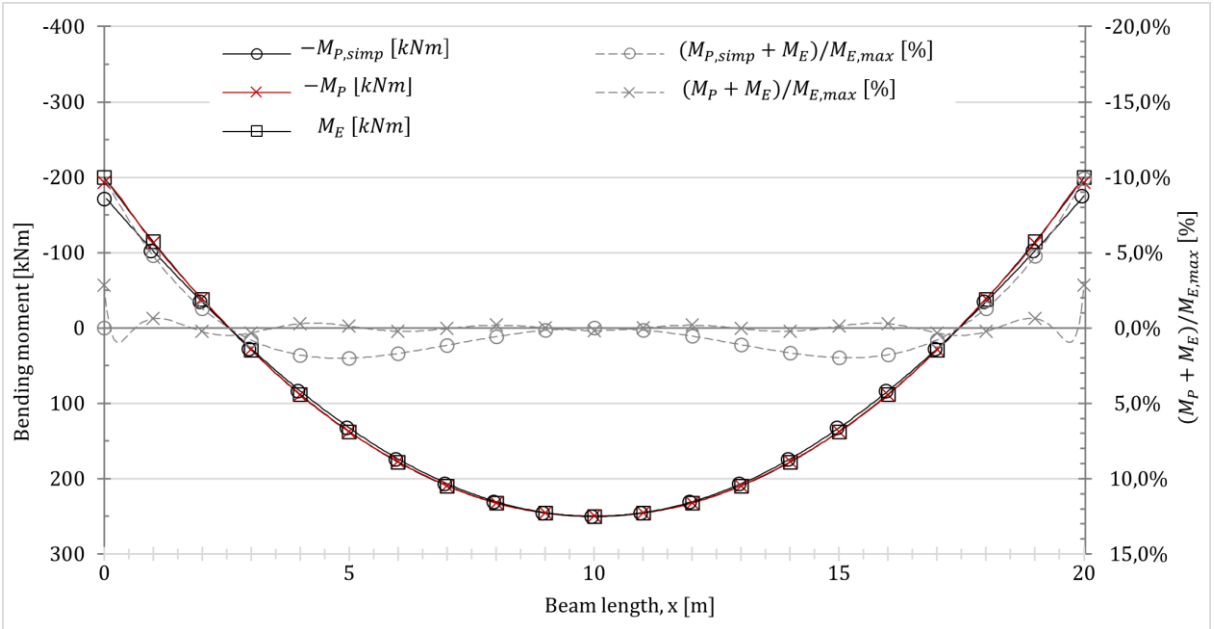


Figure 13 Bending moments due to external loads and prestress in a beam fixed at both ends (BFBE)

3.2.4 Analysis and comparison of the results

The z-components of the optimized tendon layouts in Figure 6, Figure 9, and Figure 12 show that the geometrical boundary condition of arriving horizontally at the fixed support was satisfied in every case. For an SSB, the simplified approach already results in very good compensation of the external moments. The improvement of the optimization is almost invisible in Figure 7. Figure 10 and Figure 13, by contrast, show for a BFOE and a BFBE that 99 % of the moment due to external loads M_E was compensated by the moment induced by the optimized tendon layout M_P, while the moment induced by a tendon designed with the simplified approach (see equation (25)) $M_{P,simp}$ compensates only up to 90%. As expected, the improvement is particularly visible in regions where there is a steep slope close to the fixed supports, where the geometrical loss due to the gradient of the vertical eccentricity r_z' is highest.

The comparison of the optimized tendon layout r_z to r_{xz} (see equation (26)) demonstrates the influence of the decrease in the tendon's effectiveness due to its horizontal eccentricity. The consideration and compensation of the change in horizontal eccentricity r_y' leads to an increase in vertical eccentricity r_z of the optimized tendon in comparison to r_{xz}. This demonstrates that it is necessary to consider the horizontal placement during the optimization process, instead of projecting the tendon onto the desired surface afterwards.

The achieved values of the objective function $\mathcal{J}_P$ differ between the three examples. The lowest value of $\mathcal{J}_P = 1{,}917 \cdot 10^{-7}\ (kN\,m)^2 m$ was achieved for the SSB, while for the BFBE a minimal value of $\mathcal{J}_P = 1{,}387 \cdot 10^{1}\ (kN\,m)^2 m$ was achieved. This demonstrates that with the same degree of the polynomial, the quality of the solution obtained for an SSB without constraints is higher than for a BFBE with two constraints. In order to satisfy the additional constraints during the optimization, additional turning points in the tendon layouts are necessary, requiring a higher degree of the polynomial.

3.3 Optimization of spatial tendon layouts in shells

To demonstrate the flexibility and potential of the proposed optimization method, the geometrical model of spatial tendon layouts is applied to a shell as shown in Figure 14 and Figure 15.



Figure 14 Prestressed cylindrical shell [10]

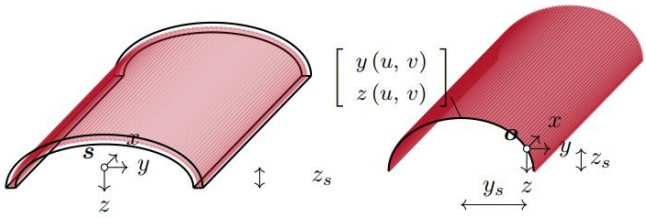


Figure 15 Geometric model of shells

The curved surface of an elliptical shell is described by $f_y = R\cos(v) - y_s$ and $f_z = -R\sin(v) - z_s$. With equations (16), (17), and (18), that leads to the following approximation for the tendon:

$$\tilde{\boldsymbol{r}}(x) = \begin{bmatrix} u \\ f_y \\ f_z \end{bmatrix} = \begin{bmatrix} u \\ a\,R\cos(v) - y_s \\ -R\sin(v) - z_s \end{bmatrix} = \begin{bmatrix} x \\ a\,R\cos\left(\boldsymbol{a}^T\boldsymbol{\phi}(x)\right) - y_s \\ -R\sin\left(\boldsymbol{a}^T\boldsymbol{\phi}(x)\right) - z_s \end{bmatrix} \tag{30}$$

More in-depth examinations of local effects that influence the mechanics and structural behaviour of shells need to be conducted based on the geometrical model for tendons in shells.

4 Conclusions and outlook

This paper proposed a novel method for optimizing tendon layouts in spatial structures. The optimized tendon counteracts the deflection of beamlike spatial structures resulting from external loads, while complying with practical boundary conditions. It is defined as a three-dimensional curve that is restricted

to the cross section of the thin-walled spatial concrete structure. The examples presented here provide evidence of the effectiveness and flexibility of the approach.

The proposed method employs analytical solving and approximation techniques rather relying on elaborate iterations. Incorporating design space restrictions immensely reduces the complexity of the solving algorithm, resulting in a significant reduction in processing time. The solution obtained is fully defined by a precise polynomial that takes into account any desired geometrical boundary conditions. This approach greatly facilitates easy implementation of the method and more efficient structural design.

The formulation of the objective function also allows for varying loads or the consideration of prestress losses during the optimization process. Notably, the geometrical model of a spatial tendon was successfully applied to a shell, which shows the potential for the proposed method to be applied to a wide range of spatial structures. Further examinations should nonetheless be conducted in order to examine if tendon layouts in more complex structures with non-prismatic cross sections or multidimensional stresses can be optimized by basing the objective function on stresses instead of bending moments. Additionally, the secondary effects of prestress in statically indeterminate systems should be examined to determine how they can be taken into account during the optimization process.

In conclusion, the proposed optimization method for tendon layouts in spatial structures represents a significant advancement in the field of structural engineering. Its flexibility, efficiency, and accuracy make it a powerful tool for designing more sustainable and lightweight concrete structures.

References

[1] U. Kirsch, "Optimum design of prestressed beams," *Computers & Structures*, vol. 2, no. 4, pp. 573-83, 1972.

[2] Z. Lounis and M. Z. Cohn, "Multiobjective Optimization of Prestressed Concrete Structures," *Journal of Structural Engineering*, vol. 119, no. 3, pp. 794-808, 1993.

[3] S. Eurviriyanukul and H. Askes, "The equilibration of configurational forces in the tendon layout optimisation of pre-stressed concrete beams," *Computers & Structures*, vol. 88, no. 23-24, pp. 1412-18, 2010.

[4] R. Avelino, D. Shook, A. Beghini, E. Long and M. Sarkisian, "Efficient flat-slab post-tensioning layouts guided by Topology Optimization," *Proceedings of IASS Annual Symposia*, no. 3, 2018.

[5] M. Hymans, M. Sarkisian, E. Long, F. Mola and D. Shook, "Optimization of post-tensioned concrete floor slabs," *Proceedings of IASS Annual Symposia*, no. 3, 2018.

[6] Y. Zelickman and O. Amir, "Layout optimization of post-tensioned cables in concrete slabs," *Structural and Multidisciplinary Optimization*, vol. 63, no. 4, pp. 1951-74, 2021.

[7] Y. Zelickman and O. Amir, "Optimization of post-tensioned concrete slabs for minimum cost," *Engineering Structures*, vol. 159, p. 114132, 2022.

[8] J. P. Osman-Letelier, "Investigation on Structural Behaviour of Prestressed Thin-Walled Concrete Structures," unpublished doctoral dissertation, Technical University Berlin, Berlin, 2023.

[9] J. P. Osman Letelier, A. Hückler and M. Schlaich, "Dünnwandige Fertigteile aus vorgespanntem Carbonbeton," *Beton- und Stahlbetonbau*, vol. 116, no. 10, pp. 786-97, 2021.

[10] R. Anderson, "The Kimbell Art Museum by Louis Kahn in Texas," [Online]. Available: https://archeyes.com/kimbell-art-museum-louis-kahn. [Accessed 17 September 2021].

IASS 2023
July 10–14 Melbourne
Integration of Design and Fabrication

Proceedings of the IASS Annual Symposium 2023
Integration of Design and Fabrication
10–14 July 2023, Melbourne, Australia
Y.M. Xie, J. Burry, T.U. Lee and J. Ma (eds.)

Enhancing interactivity in structural optimisation through reinforcement learning: an application on shell structures

Gabriele MIRRA[a], Alberto PUGNALE[a,*]

[a,*] Faculty of Architecture, Building and Planning, The University of Melbourne
Glyn Davis Building (133), The University of Melbourne, Masson Rd, Parkville VIC 3010, Australia
alberto.pugnale@unimelb.edu.au

Abstract

This paper describes a novel approach to structural optimisation based on learning design strategies rather than searching for optimal solutions. In the proposed approach, an AI agent is trained through Reinforcement Learning (RL) to explore a 3D modelling environment and iteratively morph a flat NURBS surface into a doubly-curved shell structure. At each iteration of the 3D modelling process, the agent computes the maximum structural displacement through FEM analysis: it learns to select modelling actions through this feedback and progressively improves the performance of the input surface. Unlike current applications of RL in structural design, where the AI agent generates design options by recombining a predefined set of design variables, our approach aims to create structural forms through the interaction of a designer and an AI agent within a 3D modelling environment. An application illustrates that our agent can interpret a preliminary structural form defined by a designer and iteratively transform such a form to improve its structural performance. The trained agent can hence transform the geometry and improve the structural performance of any open surface that features a square footprint and is defined through a sequence of modelling commands. Preliminary results suggest that this AI agent can be used for the development of more interactive tools for structural design and optimisation.

Keywords: computational methods, artificial intelligence, reinforcement learning, concrete shells, structural optimisation, computer-aided design, interactive design

1. Introduction

In 1995, John Fraser wrote that "space, structure and form are the traditional outward expressions of an architectural concept which has developed in the mind of the architect" and that "architectural concepts are expressed as generative rules so that their evolution may be accelerated and tested. […] Computer models are used to simulate the development of prototypical forms which are then evaluated on the basis of their performance in a simulated environment." Regarding the role of computers in the creative/generative process of architectural form, Frazer stated that they are "slaves of infinite power and patience" and "are not without their dangers. If used unimaginatively, they have a tendency to: dull critical faculties, induce a false sense of having optimised a design which may be fundamentally ill conceived" [1]. On the one hand, these statements lucidly explain how aware Frazer was of the limits of using optimisation algorithms as an integral part of the architectural design process. On the other hand, these sentences denote an unbridgeable gap in the interface between humans and machines – a separation and a consequent interruption of the workflow between the conception and implementation of design ideas that still exists today every time one formulates the invariants and design variables of a parametric model for optimisation purposes.

Contrary to what one might intuitively think, computational and performance-oriented design workflows based on classical parametric modelling and optimisation algorithms disrupt rather than support the spontaneous and mostly unconscious human process of synthesis: what we generally refer

Copyright © 2023 by Gabriele MIRRA and Alberto PUGNALE. Published in the Proceedings of the IASS Annual Symposium 2023 with permission.

to as the holistic creation of an architectural idea. Human designers do not need an explicit and analytic definition of design spaces to be able to explore and test formal solutions within such spaces. Expert designers rarely constrain themselves to search for creative design solutions within a single design space. The processes of human thoughts are complex and flow more like a river than follow a set of instructions. The emergence of unexpected architectural forms through optimisation is, therefore, a clear illusion because it is always an expert designer to call the shots throughout the process [2]. Mutsuro Sasaki wrote that structural forms designed through optimisation are mutable, fluid and organic and can hence be called *flux structures*, but he also described in his book how critical it is that architects and engineers collaborate throughout the optimisation process to create such fluid structural ideas [3].

The problem does not lie in the workflow or efficiency of the tools used: the problem is the interface between human thought processes and the internal functioning of computer programs.

To an extent, this might explain why it is easier for architecture students to learn structural design strategies based on physical form-finding models: the workflow presents fewer interface issues, allowing young designers to synthesise ideas entirely within the analogue domain. Unfortunately, classical form-finding is not plague-free and has many other limits that might impact human creativity, such as the impossibility of generating non-optimal structural forms or simulating more than one physical phenomenon at a time [4].

We believe there is a better way to approach structural optimisation through Reinforcement Learning (RL), and we quantify 'better' as enhanced interactivity between human designers and computers. The paper illustrates this approach, which allows designers to conceive, model, morph, and explore structural forms in a CAD environment without requiring an analytic problem formulation, as is the case for classical optimisation processes. Section 2 briefly introduces RL applied to structural design and highlights the differences between RL and other machine learning algorithms for structural optimisation. Section 3 describes how we conceived our RL application as the definition of a *design game*. It also provides details on the AI agent training and evaluation. Section 4 focuses on the key aspect of this paper: interactivity between a human designer and the AI agent. In the concluding section, we reflect on the limits and potential of our application, noting that, in this field, innovation is achieved through a series of small results. Such results do not provide readers with tools that are readily available to use in practice. However, they aim to indicate a path to follow, whose originality can be better understood if read in parallel with a more theoretical article on optimisation, creativity and AI that we published in 2022 [5].

2. Reinforcement learning in structural design

Artificial intelligence (AI) has become increasingly popular in structural design and optimisation, with many approaches focusing on prediction tasks. For instance, AI has widely been used to predict the behaviour of structures based on large datasets. In a previously published work, we demonstrated that generative models based on AI, such as Variational Autoencoders (VAE) have advantages over traditional methods based on parametric modelling in structural optimisation applications [6]. We also used generative models to synthesise new structural forms by recombining features extracted from existing design precedents [7]. These approaches have something in common: they all rely on large amounts of data. In contrast, AI models trained through RL do not require datasets and can be applied to a broader range of problems, particularly those where data is scarce or unavailable.

RL relies on the Markov Decision Process (MDP), a mathematical framework that formalises decision-making problems as the interaction between an agent that takes actions and an environment in which such actions are performed. An MDP unfolds as a sequential process: at each iteration of the decision process, the agent performs an action, which modifies the subsequent state of the environment, and collects a reward, i.e. positive or negative feedback that indicates whether the agent is moving towards or away from its goal.

In structural optimisation, the agent may represent a designer, whereas the environment can be a digital representation of a preliminary structural form. The objective of the decision-making problem can be to adjust the design to improve its structural performance. To achieve this objective, the agent needs to learn a strategy or *policy* to select actions, in this case, local adjustments of the structural form, that lead to a structural improvement. In the real world, an expert designer would already know the best course of action to produce a structurally sound design option. Conversely, an AI agent cannot rely on an existing body of knowledge: it needs to acquire such knowledge from experience.

RL can be used to teach an AI agent how to discriminate between actions and select only those that lead to a successful outcome. The objective of the training process is to learn a function that for each state of the environment, e.g. any partially defined structural form, returns the action which leads, in expectation, to the highest possible structural improvement. A popular approach computer scientists use consists of modelling the agent as an Artificial Neural Network (ANN) and training such a model to perform the mapping between state observations and actions.

RL has historically been applied to teach AI agents how to play video games [8] and control robots [9]. In the design fields, RL has instead been applied for optimisation and has thus been tested as an alternative to other computational techniques for performance-driven design.

Mandow et al. [10] described an application of RL for the spatial planning of single-family dwellings. The application was aimed at optimising such performance requirements as habitability and energy consumption and was based on a previous work by Ruiz-Montiel et al. [11], which only considered functional requirements. In that study, the researchers used a representation scheme based on shape grammar, in which actions corresponded to the selection of a design rule from a predefined set. The agent was trained to find any sequence of rules that produced an optimal planning solution.

Similar performance-driven approaches have been used to address such engineering design problems as the optimisation of combustion systems for coal-fired boilers [12], traffic flow optimisation [13], and waterflooding optimisation [14]. In these applications, the agent observed simplified representations of the state space – i.e., feature vectors representing design attributes – and performed actions that involved the adjustment of predefined variables. Yonekura and Hattori [15] used a different representation of the state space for turbo-machinery optimisation. In that case, the state space was represented by coloured contour images of pressures around an airfoil – therefore pixels rather than features – although the action space was still described by a limited set of design variables.

Hayashi and Ohsaki [16] used RL in structural design for the optimisation of 2D steel frame structures of buildings under static loads, where each structure was parametrised by a set of design variables. They also tested RL for 2D topology optimisation, where the representation of each structure was a connectivity graph [17]. RL has also been applied to optimise the design of truss structures for a set of boundary conditions [18, 19].

All the applications described above were successful because of the suitability of treating performance-driven design as an RL problem. Like other optimisation approaches, RL frameworks allow design problems to be formalised in terms of design variables – or design rules – and objectives.

The main difference between RL and other machine learning algorithms for structural optimisation, such as GAs, is that the former can be used to train an AI agent to learn an optimisation strategy. In other words, an agent trained with RL can solve an infinite number of optimisation problems by finding optimal or sub-optimal solutions for previously unseen boundary conditions. Conversely, each optimisation run with a GA requires the statement of a fixed set of boundary conditions. GAs can learn the best action to take – i.e., how to update the design variables – albeit only for those specific initial conditions, which means that the algorithm cannot reuse the experience acquired during each optimisation run to solve analogous problems.

Another characteristic of RL algorithms is that they can effectively learn decision-making strategies by exploring large action spaces. Although this creates an opportunity to enhance the capabilities of computational tools, in terms of design exploration, this feature has not been fully harnessed in current applications, which involve defining small action spaces consisting of a limited number of design variables. Such spaces are designed to ensure that the agent always produces solutions that satisfy a given set of design constraints, thereby minimising the time spent evaluating unfeasible design options. However, like other optimisation approaches, this prevents the agent from exploring solutions that lie outside the solution space considered by the designer.

A computational model that learns to optimise structural forms should explore large action spaces, just as humans do. Through the exploration of large action spaces, the agent is expected to gain sufficient knowledge to assist designers during the development of a preliminary structural design proposition, where such a proposition can be freely modelled in a CAD environment without the need to select a limited set of variables for the construction of a design space.

The following sections describe how an AI agent that interacts with a 3D modelling environment can be trained to learn sequences of actions or commands that maximise the structural performance of a preliminary design proposition. They also present an AI-CAD interface whereby the trained agent can interpret the 3D modelling actions taken by a designer and suggest additional actions to improve the performance of the design.

3. An AI agent for structural optimisation in CAD

Unlike conventional approaches for structural optimisation, which explore local adjustments of a single predefined design, the application described here involved training an AI agent to learn a design strategy that transformed any input design – constructed by moving the control points of a square surface – into a structurally sound design option. The agent developed this strategy by balancing the randomness involved in the action selection process with the maximisation of a structural performance reward.

3.1. The design game

The application required developing a *design game*, i.e. a simulation in which the AI agent could generate and assess the performance of a shell structure. During the game, the agent received feedback in the form of a reward based on how well the design performed according to a specified criterion. The *design game* comprised: (1) a 3D modelling environment, which allowed the agent to observe and manipulate 3D geometries, (2) a procedure that converted a 3D form produced by the agent into a structural model, and (3) a FEM solver that analysed a structural model to inform the agent about its structural performance.

The agent collected information about a specific state of the 3D modelling environment as a 2D image, hereafter referred to as ‘canvas’, whereas it performed 3D modelling actions by selecting points on a discrete 2D grid named ‘canvas grid’. The canvas grid consisted of an 8 × 8 matrix of values, representing the z-coordinates of 8 × 8 equally spaced control points used to construct a degree 7 NURBS surface. Given a canvas grid configuration, the environment first generated the NURBS surface (Figure 1, stage 1) and then sampled 16 × 16 points from such a surface to produce the canvas observation (Figure 1, stages 2-3). The canvas observation stored information about the height of the NURBS surface at the sampled point locations, which could therefore be visualised as a depth map. Height information was normalised from [-8, 8] to [0,1] so that the flat surface generated from a canvas grid initialised with zeros was rendered in the canvas observation space as a solid mid-grey image (v = 0.5). Moreover, any point z-coordinate outside the [-8, 8] range was clipped to keep the NURBS surface within a 20 × 20 × 16 3D volume. For instance, if the z-coordinate of a NURBS surface sample point was equal to 10, it was clipped to the upper bound of 8 and rendered in the canvas observation space as a white pixel (v = 1).

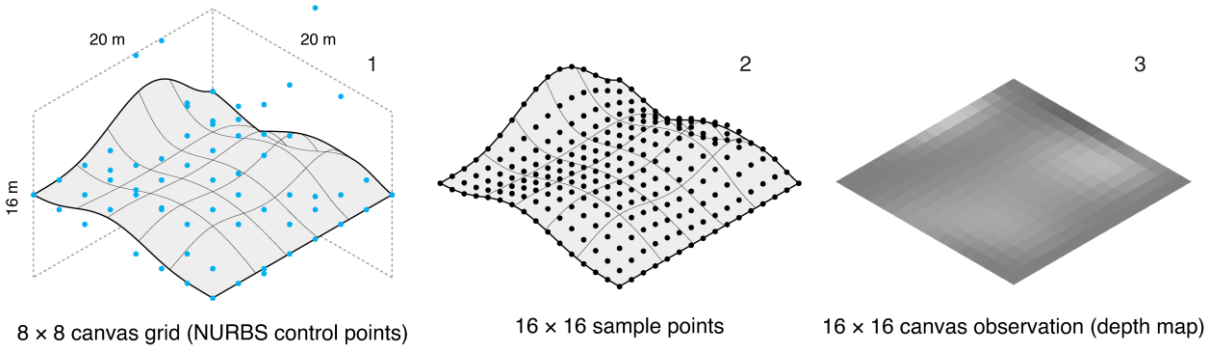


Figure 1. The three stages used to convert the canvas grid into the canvas observation space.

A design action modified the state of the canvas grid by updating one of its values, i.e. changing the z-coordinate of one control point. The agent selected a control point and applied a translation vector to perform this action, meaning it had to perform a sequence of sub-actions. The first sub-action was selecting a vector location point (*P*) from the 8 × 8 available control points. Having chosen a control point, the agent first decided on the vector direction *(d)*, which could be either -1 or 1, and then on the vector length (*l*), i.e., to what extent the control point had to be moved along the z-axis. The vector length was defined as an array of 10 values, where each value represented a 1-step increment in the [0,10] range. A design action was therefore characterised by a tuple of three elements (*P*, *d*, *l*) of (64, 2, 10) sizes.

After the agent performed the complete sequence of sub-actions described above, the environment updated the z-coordinate of a control point, generated a new NURBS surface, and produced a new canvas observation. Figure 2 shows a sequence of three actions performed by the agent in the canvas grid and the canvas observation space.

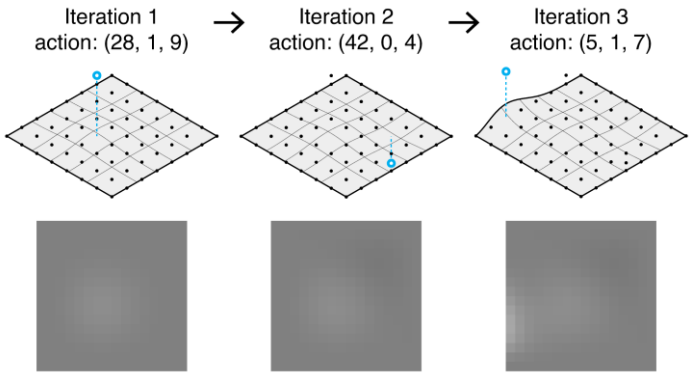


Figure 2. Sequence of three design actions performed in the environment development for the shell design application. At the top: drawing instructions in the canvas grid; at the bottom: canvas observations constructed from the canvas grid.

The structural model for FEM analysis was constructed from the data stored in the canvas observations. A 16 ×16 point grid spaced by 1.3 m in the x and y directions was first built to produce a 20 × 20 m shell footprint. Then the unnormalised height values of the canvas observations were assigned – in the [-8, 8] m range – to the z-coordinates of the point grid. Finally, a NURBS surface was interpolated from the resulting 3D point grid and transformed into a triangulated mesh, ready for the mechanical properties to be assigned.

All the mesh faces were converted into shell elements, and 5 cm thick C35/45 material concrete was assigned. The mesh corners were used as fixed support nodes, whereas a uniformly distributed gravity

load of 2 kN/m^2 was applied to the shell elements. The structural reward R_{str} was computed from the maximum displacement of the shell as follows:

$$R_{str} = 11 - min\left\{1, \frac{d}{m}\right\} \times 10 \quad (1)$$

with $m = 500$

where: d is the maximum displacement of a shell structure designed by the agent, and m is a positive margin representing the maximum allowed displacement.

Figure 3 shows the structural model of a shell structure constructed from a canvas observation, according to the abovementioned process.

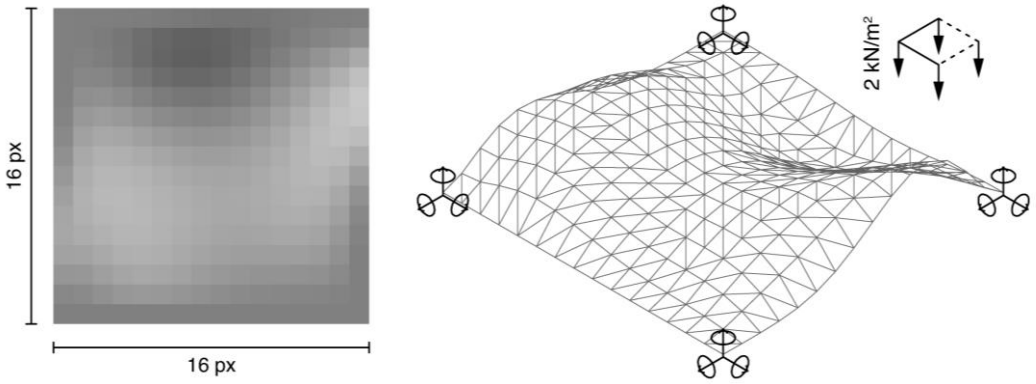


Figure 3. Conversion of a shell structure representation from the observation space (on the left) to a geometrical and mechanical model for FEM analysis (on the right).

3.2. Training and evaluation

The AI agent was modelled with an ANN – called policy network – and trained using an RL approach named Policy Gradients (PG). The training process works as follows: the agent takes a canvas observation as input and outputs a probability distribution p over actions. Then, it selects a modelling action with probability p, performs such an action in the environment and collects a structural reward. The scope of the training process is to compute a probability distribution that leads to the selection of actions producing increasingly higher structural rewards for every canvas observation.

PG can be implemented using different algorithms. The one used here is a variant of the REINFORCE algorithm called advantage actor-critic (A2C) [20]. The first author of this paper adapted the model architecture and training process from a previous work by Ganin, et al. [21]. Details about the network architecture can be found in Mirra [22]. The policy network was used to generate sequences of actions and, therefore, full design episodes and to produce the loss terms necessary for the training process.

Figure 4 illustrates how the agent interacted with the environment to produce shell design options. The episode length was set to 20 iterations, during which the agent observed the shell geometry – as a depth map – and decided how to modify it to improve the structural performance. At the end of an episode, the structural rewards, R_{str} were transformed into 1-step reward increments as follows:

$$R_{t(step)} = R_t - R_{t-1} \quad (2)$$

This reward redistribution allowed the agent to observe how much reward it received after performing an action compared to what it had achieved in the previous time step. In the context of the shell design task, this reward represents to what extent a design action contributed to reducing the maximum displacement of the shell.

As Ganin, et al. [21] suggested, an entropy loss term was included in the definition of the PG standard loss terms. This term penalised the agent for shrinking the probability distribution of each sub-action too soon, i.e., it introduced a degree of randomness into the action selection process by increasing the smoothness of the probability distributions.

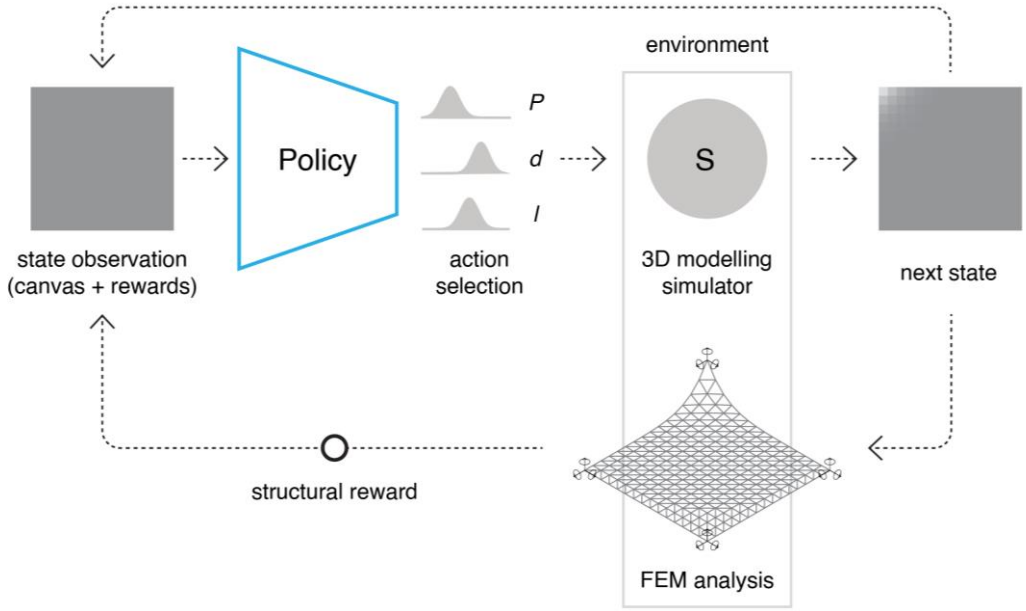


Figure 4. Interaction of the policy network with a 3D modelling simulator.

The agent was trained for 25,000 episodes, using a learning rate of 1e-4. Figure 5 (at the top) shows the structural reward collected by the agent at the end state, averaged for groups of 50 consecutive episodes. In contrast, Figure 5 (at the bottom) illustrates the canvas observation and corresponding NURBS surface at the end of some episodes produced during the training process. The reward graph in Figure 5 demonstrates that, by e_{50} = 100, the agent had already converged to a good-performing policy, achieving a reward of over 9. The trend slightly increased over the next episodes and peaked at 9.5, around e_{50} = 350. The end states in Figure 5 reveal that, between e = 250 and e = 5000, corresponding to e_{50} = 100, the agent learned to move most of the control points upwards, thereby producing depth maps with an average grey value $v > 0.5$, which led to progressively more convex surfaces. The agent also developed partially concave surfaces in e = 15,000 and e = 17,500 by either moving the internal control points to different heights or those on the edges to create openings.

The training process results demonstrate that the agent learned to solve the design task in the early iterations. However, it never reached a higher average reward than 9.5. This result was expected, considering the definition of the loss terms. Since the agent was trained to minimise the entropy of each sub-action probability distribution, it tended to produce variations of sub-optimal solutions rather than converging on a single optimal one.

The training process was further validated through a design generation task. The agent was run for 1000 episodes, and the rewards collected at the end state were plotted onto the histogram shown in Figure 6 (on the left). Since the agent always produced solutions with a score higher than 5, and most of the solutions fall into the three last bars of the graph, this test suggests that the agent successfully learnt to morph a flat surface into a performative shell structure.

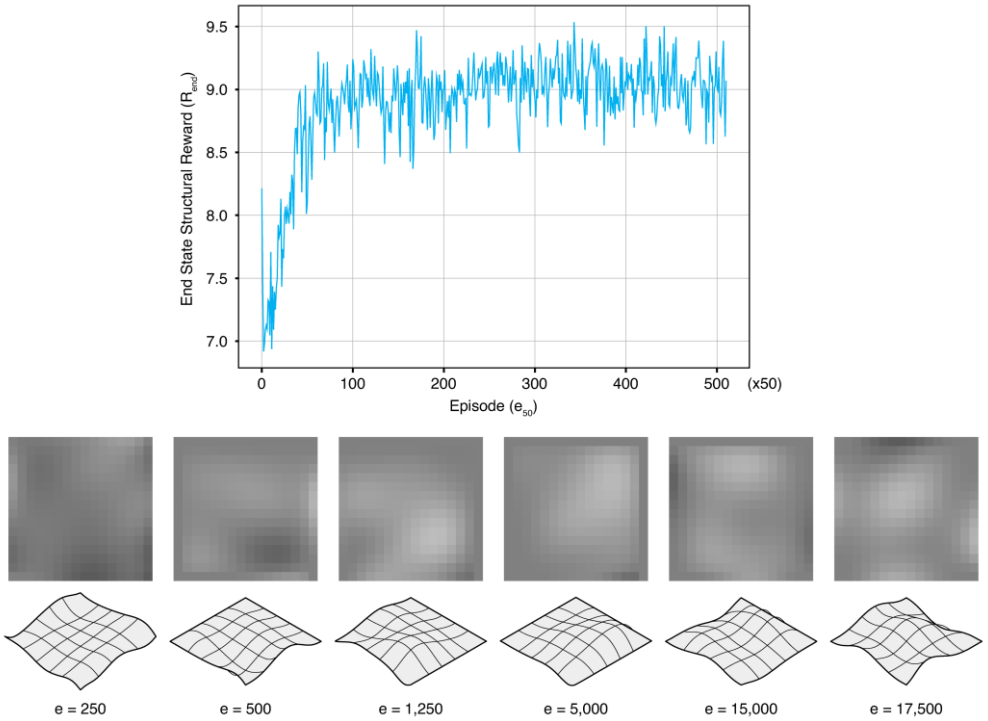


Figure 5. Results from the training process. At the top: trend of the structural rewards at the end-state averaged for groups of 50 consecutive episodes; at the bottom: End states achieved by the agent during the key stages of the training process visualised as depth maps (canvas observation format) and NURBS surfaces.

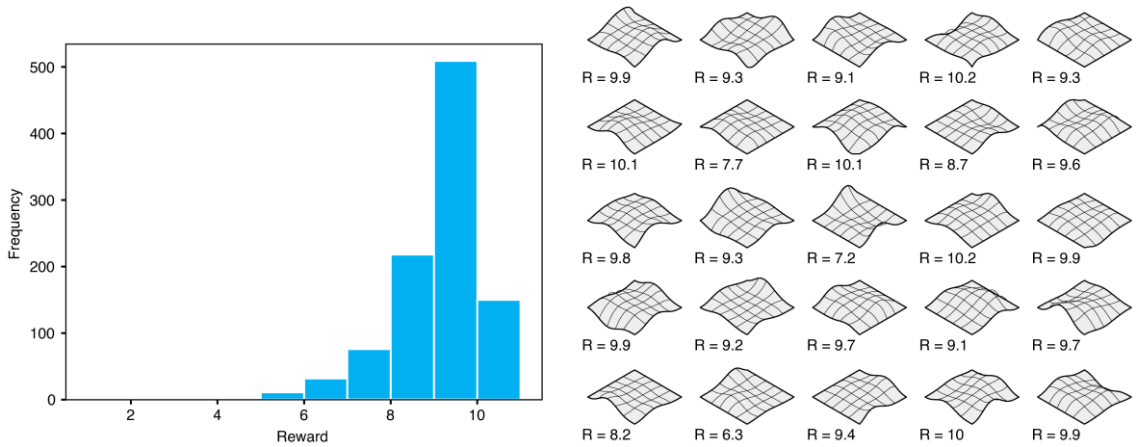


Figure 6. Results of the design generation task. On the left: distribution of the structural rewards collected by the agent at the end of the 1000 episodes; on the right: some of the shell design options generated by the agent at the end of the 1000 episodes.

Figure 6 (on the right) illustrates 25 solutions generated by the agent during the design generation task. Most of these shell structures are shallow and characterised by one or more openings, which is one of the strategies that the agent developed towards the end of the training process. The analysis of the mean structural reward per iteration collected by the agent at the end of the 1000 episodes of the design generation task (Figure 7, on the left) shows how the agent applied this strategy after training. The agent exploited all 20 available actions to progressively increase the performance of the flat surface used as input. Moreover, the trend of the 1-step structural reward can be seen to increment (Figure 7, on the

right), thus demonstrating that the agent performed the most valuable actions within the first five iterations and spent the remaining iterations refining the design. This, in turn, led to increasingly minor structural improvements.

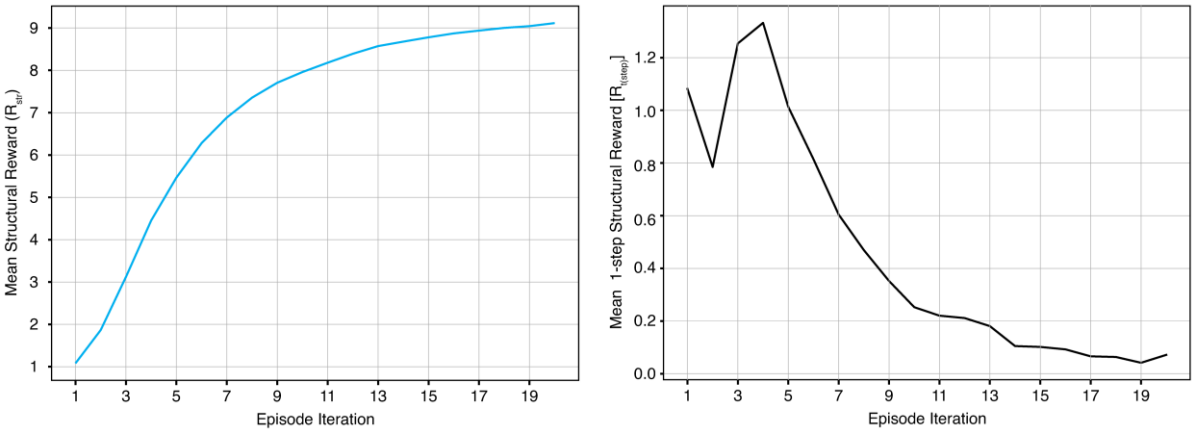


Figure 7. Detailed analysis of the average rewards collected by the agent during the 1000 episodes of the design generation task. On the left: mean structural reward for each episode iteration; on the right: mean 1-step structural reward increments for each episode iteration.

4. Interaction with the AI agent

A design completion test was used to assess how the agent could interact with a designer through CAD software and to what extent it could use the knowledge acquired during the training process to support the exploration of design options.

An AI-CAD interface was implemented in *Grasshopper* for *Rhinoceros 3D* to manage the exchange of information between the agent and the designer. Communication occurred through the specification of 3D modelling instructions, or commands, in the same format used for the training process. Therefore, a designer could transform a flat surface by moving the control points in the z-direction. Each time a control point was moved, the action was recorded and converted into a tuple (P, d, l) (see Section 3.1). After N transformations, the sequence of actions was sent to the agent, which then completed the design by performing additional actions (Figure 8).

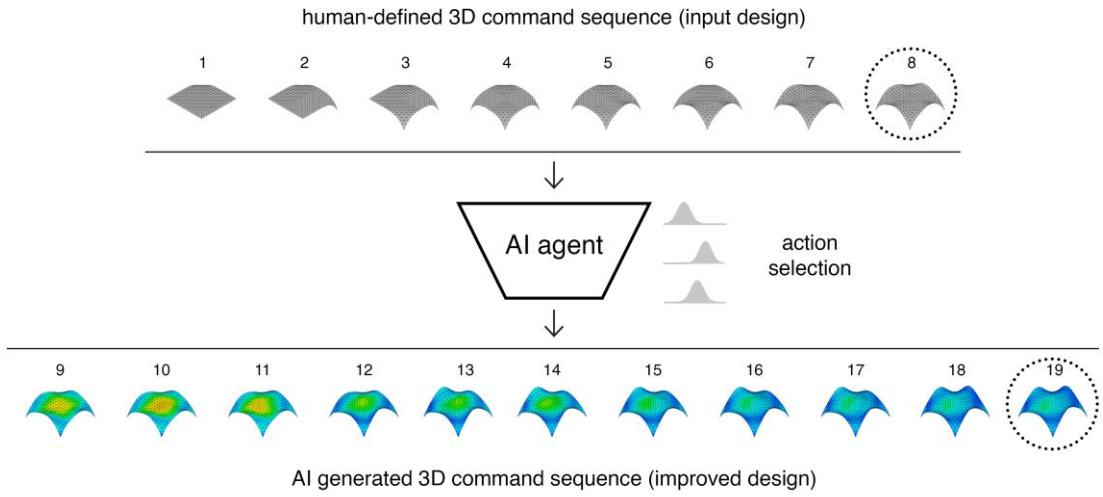


Figure 8. Human-AI interaction workflow for the structural optimisation of shell structures based on the exchange of 3D modelling commands.

Figure 9 shows three forms used as input and a set of outputs (a to e) produced by the agent after completing the 3D modelling sequence. The three forms reproduce a preliminary design for (1) a dome, i.e., a shell with four openings and two symmetry axes, (2) a barrel vault, and (3) an anticlastic shell.

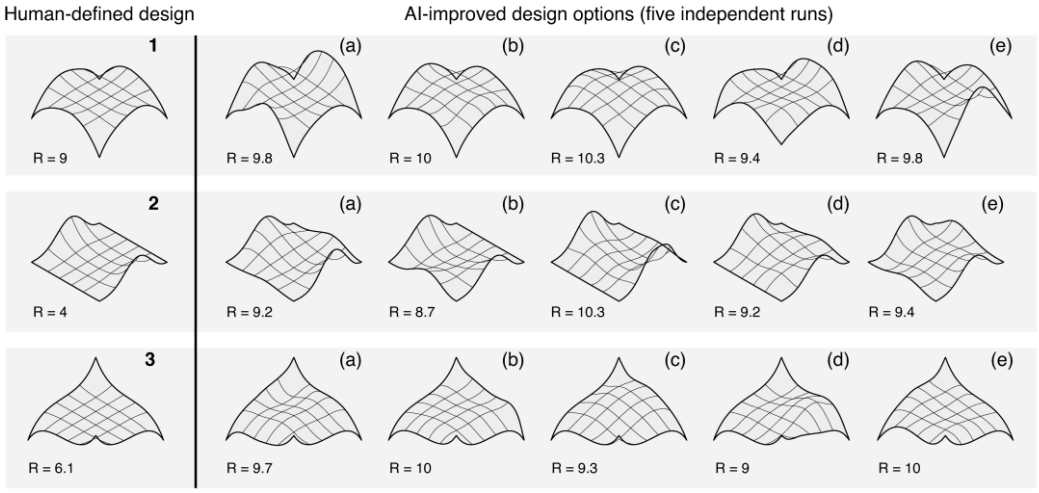


Figure 9. The three input shell designs used for the design completion task and the set of design options (a-e) generated by the agent at the 20th iteration.

Input design 1 (Figure 9, at the top) was constructed from a sequence of 8 modelling actions: the four control points at the corners of the surface were moved downwards, whereas the four control points at the centre of each edge were moved upwards. The resulting form achieved a structural reward of 9. The sequence was sent to the agent five times to produce five different design options. The agent processed the input sequence and performed additional actions until iteration 20. Overall, the five solutions produced by the agent preserved the main features of the form generated using the input sequence, i.e., a shell with four support points and four openings, but improved its structural performance. The agent completed the sequence by either increasing the height of the openings (solutions a, d, and e) or moving the internal control points (solutions b and c).

Input design 2 (Figure 9, in the centre) was generated from a sequence of four modelling actions. The control points in the centre of two opposite edges of the flat surface were moved upwards. There were four modelling actions because each point had to be moved twice: the maximum value of the sub-action l (vector length) did not allow sufficiently tall openings to be produced by a single modelling action. In this case, the agent was also able to improve the structural performance, but the main features of the input design were not preserved. The agent introduced at least one another opening for all the solutions, except for solution c, by moving the external control points.

Input design 3 (Figure 9, at the bottom) was also constructed from a sequence of four actions. The two control points at the end of each diagonal of the flat surface were moved upwards and downwards. The agent completed the design by mainly moving the internal control points, which produced high-scoring solutions while preserving the main features of the input design.

The test illustrates that a designer can interact with the agent by specifying a sequence of 3D modelling commands. The agent could produce more than one solution for each input, allowing multiple design options to be evaluated. This behaviour is possible because the agent did not output a single action for each state observation, but rather a probability distribution for selecting actions that maximised the reward. This can be seen as a way of steering a structural optimisation process towards design options with desirable features, such as the position of support points and openings. By interpreting an input form – resulting from a sequence of modelling actions – defined by a designer, the agent produced a design option that maximised the structural performance reward. It did this by adjusting the input design, thus simulating a process of form improvement.

5. Discussion and conclusions

The application described in this paper illustrates a novel manner of approaching structural design through AI, whose originality lies in a level of human-machine interactivity that cannot be seen in classical computational models for structural form-finding and optimisation. Our approach is not based on the definition of a design space like other optimisation procedures and, therefore, it is intrinsically more interactive and aims to open a research path for future AI applications.

It is worth noting that the test considered in this paper does not provide sufficient evidence that a trained AI agent can recognise specific structural performance issues in each input configuration and respond accordingly. It might have consistently applied the same strategy, which may have worked equally well regardless of the input sequence. In fact, due to the high degree of the NURBS surface, with which the agent interacted, moving the control points only generated a local deformation, thus producing flat regions in the centre of the input shell. Increasing the curvature in the centre is always expected to increase the structural performance of the shell, which might explain why the agent managed to produce high-scoring solutions consistently.

Another issue of the application described is that a designer must provide the 3D modelling commands by following the definition of the action space used for training the agent: this is a clear limit for the designer's freedom and flow of thoughts, particularly during the early design stages. With the current application settings, a designer cannot just produce a preliminary shell design using any geometric transformations the CAD software allows. For instance, they cannot move the control points in a direction other than z or exceed the maximum vector length per iteration. Furthermore, any input design must be provided as instructions that transform a flat surface since the agent always took this configuration as the initial state.

Future developments of this specific application should focus on providing the AI agent with examples of structural typologies to narrow down the search process and improve the quality of the feedback to the designer.

References

[1] J. H. Frazer, *An Evolutionary Architecture*. Architectural Association, 1995.

[2] A. Pugnale, T. Méndez Echenagucia, and M. Sassone, "Computational Morphogenesis: Design of freeform surfaces". in *Shell Structures for Architecture: Form Finding and Optimization*, S. Adriaenssens, P. Block, D. Veenendaal, and C. Williams (Eds.): Taylor & Francis, pp. 225-236, 2014.

[3] M. Sasaki, "Flux Structure", Toto Publishers, 2005.

[4] H. Kloft, "Logic and Form: From Isler Shells to Nonstandard Structures", *Journal of the International Association for Shell and Spatial Structures,* vol. 52:3, pp. 191-199, 2011.

[5] G. Mirra and A. Pugnale, "Expertise, playfulness and analogical reasoning: three strategies to train Artificial Intelligence for design applications", *Architecture, Structures and Construction,* vol. 2:1, pp. 111-127, 2022.

[6] G. Mirra and A. Pugnale, "Comparison Between Human-Defined and AI-Generated Design Spaces for the Optimisation of Shell Structures", *Structures,* vol. 34, pp. 2950-2961, 2021.

[7] G. Mirra and A. Pugnale, "Exploring a Design Space Of Shell and Tensile Structures Generated by AI from Historical Precedents", *Journal of the International Association for Shell and Spatial Structures,* vol. 63:3, pp. 172-188, 2022.

[8] V. Mnih *et al.*, "Playing Atari with Deep Reinforcement Learning", *arXiv:1312.5602v1 [cs.LG],* 2013.

[9] J. Ibarz, J. Tan, C. Finn, M. Kalakrishnan, P. Pastor, and S. Levine, "How to train your robot with deep reinforcement learning: lessons we have learned", *Journal of Robotics Research,* vol. 40:4-5, pp. 698-721, 2021.

[10] L. Mandow, J. L. Pérez-de-la-Cruz, A. B. Rodríguez-Gavilán, and M. Ruiz-Montiel, "Architectural planning with shape grammars and reinforcement learning: Habitability and energy efficiency", *Engineering Applications of Artificial Intelligence,* vol. 96, 2020.

[11] M. Ruiz-Montiel, J. Boned, J. Gavilanes, E. Jiménez, L. Mandow, and J.-L. Pérez-de-la-Cruz, "Design with shape grammars and reinforcement learning", *Advanced Engineering Informatics,* vol. 27:2, pp. 230-245, 2013.

[12] Y. Cheng, Y. Huang, B. Pang, and W. Zhang, "ThermalNet: A deep reinforcement learning-based combustion optimization system for coal-fired boiler", *Engineering Applications of Artificial Intelligence,* vol. 74, pp. 303-311, 2018.

[13] E. Walraven, M. T. J. Spaan, and B. Bakker, "Traffic flow optimization: A reinforcement learning approach", *Engineering Applications of Artificial Intelligence,* vol. 52, pp. 203-212, 2016.

[14] F. Hourfar, H. J. Bidgoly, B. Moshiri, K. Salahshoor, and A. Elkamel, "A reinforcement learning approach for waterflooding optimization in petroleum reservoirs", *Engineering Applications of Artificial Intelligence,* vol. 77, pp. 98-116, 2019.

[15] K. Yonekura and H. Hattori, "Framework for design optimization using deep reinforcement learning", *Structural and Multidisciplinary Optimization,* vol. 60:4, pp. 1709-1713, 2019.

[16] K. Hayashi and M. Ohsaki, "Reinforcement learning for optimum design of a plane frame under static loads", *Engineering with Computers,* vol. 37:3, pp. 1999-2011, 2021.

[17] K. Hayashi and M. Ohsaki, "Reinforcement Learning and Graph Embedding for Binary Truss Topology Optimization Under Stress and Displacement Constraints", *Frontiers in Built Environment,* vol. 6:59, 2020.

[18] M. E. Ororbia and G. P. Warn, "Design Synthesis Through a Markov Decision Process and Reinforcement Learning Framework", *Journal of Computing and Information Science in Engineering,* vol. 22:2, 2021.

[19] J. Seo and R. K. Kapania, "Development of an Artificial Intelligence System to Design of Structures using Reinforcement Learning: Proof of Concept", in *AIAA Scitech 2021 Forum*, Virtual Event, 2021.

[20] R. S. Sutton and A. G. Barto, *Reinforcement Learning: An Introduction*. Cambridge, MA: The MIT Press, 2018.

[21] Y. Ganin, T. Kulkarni, I. Babuschkin, S. M. A. Eslami, and O. Vinyals, "Synthesizing Programs for Images using Reinforced Adversarial Learning", *arXiv:1804.01118,* 2018.

[22] G. Mirra, "Expertise, playfulness, analogical reasoning: Three learning mechanisms to train Artificial Intelligence for design applications," PhD Thesis, Faculty of Architecture, Building and Planning, The University of Melbourne, 2022 (available at: http://hdl.handle.net/11343/326111).

IASS 2023
July 10–14 Melbourne
Integration of Design and Fabrication

Proceedings of the IASS Annual Symposium 2023
Integration of Design and Fabrication
10–14 July 2023, Melbourne, Australia
Y.M. Xie, J. Burry, T.U. Lee and J. Ma (eds.)

Functionally graded CharCrete slabs for embodied carbon optimisation in architecture

Nikol KIROVA*, Jane BURRY[a], Areti MARKOPOULOU[a], Mehrnoush LATIFI[a]

* Institute for Advanced Architecture of Catalonia, Advanced Architecture, Barcelona, Spain
Nikol.kirova@iaac.net

[a] Swinburne University of Technology School of Design in the Faculty of Health Arts and Design

Abstract

This research paper presents a computational method for designing architectural elements using functionally graded cementitious materials, with the aim of reducing embodied carbon and mass. Functionally graded materials, commonly found in nature, are materials that have a graded variation in their composition or properties, which can be tailored to specific structural requirements [8]. In this case, the material used is CharCrete, a cementitious material that includes biochar, a type of carbon-sequestering material made from biomass. The CharCrete material system includes five grades with varying quantities of biochar that attain a range of structural performances and carbon footprint. Topology optimization is used in architectural design to reduce the material while optimising the structural performance and is a common approach for designing geometrically complex structures. However, topological optimization is typically more suited to homogeneous material systems [20]. In contrast, the method proposed in this research additionally transfers complexity to the material allocation instead of, solely, to the geometry, and is specifically tailored to heterogeneous material systems. The finite element analysis (FEA) method is used to optimise the distribution of different grades of CharCrete according to structural requirements. By maximising the use of carbon-negative biochar in the CharCrete, the method aims to minimise embodied carbon and mass while maintaining structural integrity. The method is implemented using FEA within the Grasshopper environment with the Karamba3D plug-in, and multi-objective optimization is used to find the optimal material grade allocation on a case study of flat and vaulted slabs. The results are compared to homogeneously distributed standard concrete. The research results show that the developed computational method is effective in generating carbon-offsetting digital designs while maintaining structural integrity. The research suggests that optimisation techniques and generative design methods can be integrated into architectural design to address the challenge of decarbonisation from a material perspective.

Keywords: functionally graded concrete, bio-inspired design, vaulted slab, optimisation, carbon sink, biochar, charcrete, embodied carbon, decarbonisation

1. Introduction

The view that most carbon is produced during the "life" of a building, and only 11% of the total carbon was embodied is shifting as research from 2017 suggests that the gravity and time sensitivity of embodied carbon in the building sector has been significantly underestimated. Although our contemporary practices and policies primarily focus on reducing the energy consumption of buildings to lower the CO_2 emissions during their operation, the biggest challenge lies in decreasing the embodied carbon of the building industry.

In terms of computational design different approaches responding to the challenge of embodied carbon reduction have been explored. The accessibility to computational tools has empowered designers and

Copyright © 2023 by Nikol KIROVA, Jane BURRY, Areti MARKOPOULOU and Mehrnoush LATIFI. Published in the Proceedings of the IASS Annual Symposium 2023 with permission.

architects to generate data driven solutions for the build environment that have the potential to generate designs with optimised embodied carbon considering both material and geometry.

From the material side, the interest towards performance optimisation has resulted in the rise of applications for highly engineered multi-materials in various domains, such as the automobile, aeronautics, and energy industries. In the field of architecture this knowledge has been translated in development of structurally optimised composited. Developing new structural materials often involves trade-offs, especially with traditional design and fabrication methods that result in homogeneous materials with uniform composition, even though many real-world applications require heterogeneous materials. There is an opportunity to tailor the local properties of the material to meet specific requirements by optimising the composition and architecture in specific regions.

The mechanical performance of structural materials can be improved by designing higher strength in regions that are under higher stress. This method allows materials to have region-specific properties by combining varying degrees of heterogeneity or gradients. The term "gradient" refers to the non-uniform nature of materials instead of strict homogeneity. Creating variable properties or functionally graded materials (FGMs) offers a promising solution to meet the demands for emerging applications of materials. Furthermore, as the research on FGMs is gaining traction, it is important to include the environmental considerations as part of their optimisation criteria.

Reinforced concrete, as the most used construction material, offers versatility, resilience, and cost-efficiency due to its composite nature. However, the environmental impact, particularly in terms of embodied carbon and resource depletion, has become a major concern in new construction. To address this issue, the concrete industry is evolving to incorporate more sustainable construction methods, material compositions, and design solutions. With its composite nature and the ability to design mixtures with varying properties, concrete is an ideal candidate for exploration in optimization not only in geometric design but also in graded material allocation.

FGMs have been researched extensively with an engineering approach towards material reduction. Although there is a connection between the reduction in material mass and the reduction of the environmental impact, the link between the two is not always apparent. The research on FGMs until now has never been purely focused on reducing environmental impact or embodied carbon, in particular. This research gap has been addressed through the incorporation of biochar, a carbon-negative material, into the cementitious material family. The result of this research is the development of CharCrete, a net embodied carbon-optimized cementitious material system with various grades.

The paper discusses the development of a computational method which informs the allocation and distribution of various graded of CharCrete developed in the prior stages of the research. High quantities of biochar in the material mixture led to a decrease in mechanical properties but increased carbon sequestration and therefore lowered embodied carbon. Functionally grading the quantity of biochar in CharCrete composites results in a lower carbon footprint without compromising the structural properties of building elements.

2. Background

Currently, there is little research on how to inform the graded material composition within from a design perspective when focusing on embodied carbon and structural performance of cementitious composites. From a structural engineering perspective there are studies and sophisticated finite element analysis tools that would allow for simulation graded materials, however they are often inaccessible to architects and designers.

Providing a workflow which allows the optimisation of material allocation of a range of grades of cementitious materials within building elements, such as slabs, in a computational environment which is commonly used in the design practice, opens up the possibility for informed conceptual designs of building elements with reduced embodied carbon without compromised structural performance. The

biggest challenge addressed by the research is determining the optimal distribution of materials and properties within the structure to achieve the desired gradation layout.

2.1. Functionally graded materials

Functionally graded materials (FGMs) are a type of composite material that possess unique properties due to their gradual transition between two or more constituents. This results in variations in composition and structure, leading to improved durability and mechanical performance when compared to laminated composites. The concept of FGMs has been inspired by the naturally occurring heterogeneities found in high-performance biological materials, which have evolved over time to optimize their strength and functionality.

In nature, soft-to-hard variations and thermal gradings are common in the composition and structure of materials. Some examples of functionally graded natural materials include human and animal bones, human skin, horse hooves, bamboo stems, tree bark, and palm tree stems. These materials exhibit a range of density and composition throughout the cross-section, resulting in maximized strength with minimized density.

The principles of FGMs have been extensively studied in aerospace and alloy engineering since the 1980s [20], [15]. However, there has been a recent wave of research on how to translate these principles from material science to architecture and design. FGMs offer a novel method of material optimization that could link mechanical performance to environmental impact, potentially resulting in a new aesthetic expression. Although architecture and design tend to be slow in adopting new technologies compared to aerospace engineering, efforts have resulted in the development and application of pioneering multi-material design and fabrication tools, albeit to a limited extent [6], [9].

In her 2010 doctoral thesis, Neri Oxman discusses the significance of materials engineered with spatial gradients in composition and structure, which have applications in a variety of design disciplines. Oxman's work serves as a foundation for exploring the use of FGMs in architectural design, where digital fabrication is inspired by nature and driven by maximal performance with minimal resources through local material property variation.

Due to its applicability to an architectural scale, research on Functionally Graded Concrete (FGC) has gained traction. FGC can be classified into two categories: layered and continuously graded. Layered FGC can be manufactured by casting, which does not require complex fabrication.

Researchers at the University of Stuttgart have pursued collaborative research on the topic of FGC following the development of variable-density graded concrete by Oxman and her team at MIT. In particular, the Institute for Lightweight Structures and Conceptual Design (ILEK) have consistently pursued the development of FGCs however the work focuses on the development of continuous grading through robotic deposition of a foaming agent [1], [12]-[13].

Researchers at Concrete Infrastructure Research Group (CIRG) at the University of Cambridge have identified the potential to obtain FGC through a "Fresh-to-fresh" method of casting that leads to well-bonded graded materials and does not require robotic set-up. Their studies reveal a relationship between system stability, geometry, and material parameters. Both vertical and horizontal casting present challenges however there are clear guidelines published on how to work with this method of graded casting [5], [31] – [33]. The work developed by CIRG is proving that the use of functionally graded layered cementitious composites can be used to optimise the material allocation and reduce the need for cement in the regions of the structural element and has been demonstrated through a case study of a functionally graded concrete beam [34]. However, there is no defined workflow that can be used to inform the material allocation and simulate the correlation between embodied carbon and mechanical performance of graded elements.

2.2. Computing graded materials

Three main obstacles that must be identified when designing with FGMs, including the inaccessibility of scientific information, limitations in design software, and the gradient extent of digitally fused materials [9]. While computational methods such as voxel editing, finite elements, and particle systems allow for multi-materiality that is spatially varied, they do not consider material behaviour, which is of central value to the design process. To attribute gradients based on physical properties, simulations must be used to allow for the gradients to be computationally calculated. This enables the designer to evaluate any relevant design projects through comprehensive design theory or criteria, rather than relying solely on aesthetics with conventional design processes.

Recent studies have demonstrated the effectiveness of Topology Optimization (TO), Voxel-Based Methods (VBM), and Finite Element Methods (FEM) in designing with FGMs [14], [16]. Kaijima's work, for instance, combined structural optimization with design aesthetics by using von Mises stress as the initial design input and carefully shaping the resulting streamlines. These methods provide designers with different levels of control over the final design.

TO is typically used to minimize the mass of a design object given external loading, boundary conditions, and constraints. Various algorithms have been developed for TO to determine the material distribution within a given design domain, though it is typically applied to isotropic or homogeneous materials. However, with some adjustments, it is possible to use TO to inform variable structural distribution on a predetermined volumetric model. In contrast, VBM allows for more design geometry freedom and the creation of graded structures with heterogeneous material properties, but this approach can be computationally intensive.

The field of computational design methods for FGMs is rapidly evolving, providing ample opportunity for further development and refinement. These methods facilitate an efficient workflow for generative design, streamlining the process and making it easier to achieve desired outcomes. Although significant progress has already been made, there is still much potential for further improvement. State-of-the-art methods provide a good understanding of the tools that can be used to generate and evaluate elements with FGMs, including simulation, optimization, and analysis tools. These methods have the potential to revolutionize the design and use of FGMs across a wide range of applications, from construction and architecture to aerospace and beyond. With technology advancing and new computational methods emerging, the possibilities for innovative and sustainable design solutions with FGMs are endless.

3. Methodology

In this research, a case study approach is taken to investigate the performance of Functionally Graded CharCrete slabs with varying geometries and curvatures. The aim of the research is to examine the potential of functionally grading CharCrete to optimize material allocation based on structural loads and reduce the embodied carbon of concrete structures.

Floor slabs are selected as the case study due to their significant contribution to the total structural mass and the availability of opportunities for material optimization. Nine conditions are examined, with varying spans ranging from 2.5 to 7.5 meters and curvatures from flat to doubly curved. The computational workflow is developed using Rhino's Grasshopper with the Karamba3D structural analysis library. The study is conducted in three phases.

In the first phase, the nine conditions are tested using standard concrete, lightweight concrete, and the designed CharCrete mixtures. This is done with homogeneous material distribution to establish a comparative baseline.

In the second phase, a duo-material grading approach is tested, with all possible combinations of three CharCrete grades (25/75, 50/50, 75/25) to determine the most effective combination for reducing embodied carbon and optimizing structural performance.

In the third phase, all three grades of CharCrete are graded to determine the optimal proportions for reducing embodied carbon and optimizing structural performance. Two proportions are tested: 25/25/50 and 50/25/25 of BCM20, BCM40, and BCM50 respectively.

The study is conducted with fixed thickness for each geometry, and the mass, utilization, and embodied carbon of each morphology are recorded. Based on this, potential optimization possibilities are identified. The fixed proportions and thickness limit the optimization possibilities. At the final stage of the study, the nine conditions are examined using the multi-objective optimization solver Wallacei. The genes of the optimization are the partitioning and thickness, and the objectives are mass, displacement, and embodied carbon reduction. The focus is on the utilization domain related to compressive performance.

The computational workflow developed in this study allows for further optimization of slabs in terms of conceptual design. It enables designers and architects to extract data on environmental performance and test geometries with different structural conditions, spans, and curvatures.

Overall, the methodology presented in this study aims to provide a comprehensive analysis of the potential of Functionally Graded CharCrete for optimizing material allocation and reducing the embodied carbon of concrete structures.

3.1. CharCrete Grades

For the purpose of this research, CharCrete is referred to type of cementitious mortar which incorporates biochar, a carbon sequestering material which is produced during the pyrolysis of agricultural and forest management waste. As part of a larger research the author has developed a range of grades of CharCrete with a varying quantity biochar, resulting in a range of mechanical properties and embodied carbon [22]. In this paper three grades of CharCrete are examined in more detail in functionally graded material composition. The three grades BCM20, BCM40 and BCM50 are tested in a laboratory and have the compressive strength of 34MPa, 15MPa and 7MPa respectively. The results obtained by the material tests are computed in the computational environment of Rhino's Grasshopper and more specifically for the Karamba3D structural analysis plug-in (Figure 1.). This method allows for generating custom materials with big degree of freedom. Additionally, the embodied carbon of each mixture is added to their digital material data repository.

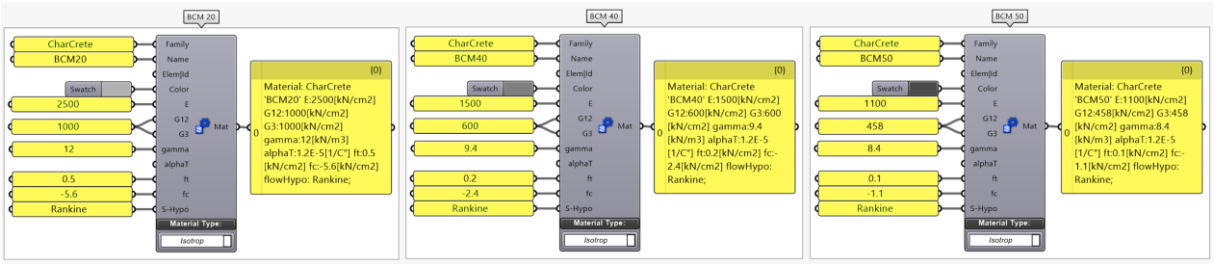


Figure 1. Material specification of the three grades of designed CharCrete mixtures examined in the research, with 20, 40 and 50 percent biochar concentration (left to right).

3.2. Computational Workflow

Computational design tools, such as Rhino's Grasshopper, offer infinite possibilities, limited only by the designer's imagination and skill. Through data-driven designs and complex optimisation processes, these tools are reshaping not only the design process but also the performance of the resulting geometries. The increasing accessibility of incorporating structural analysis, material optimisation, generative design, and performance data is transforming the role of architects and designers. New solutions to global environmental challenges can be proposed by adapting computational and data-driven design tools.

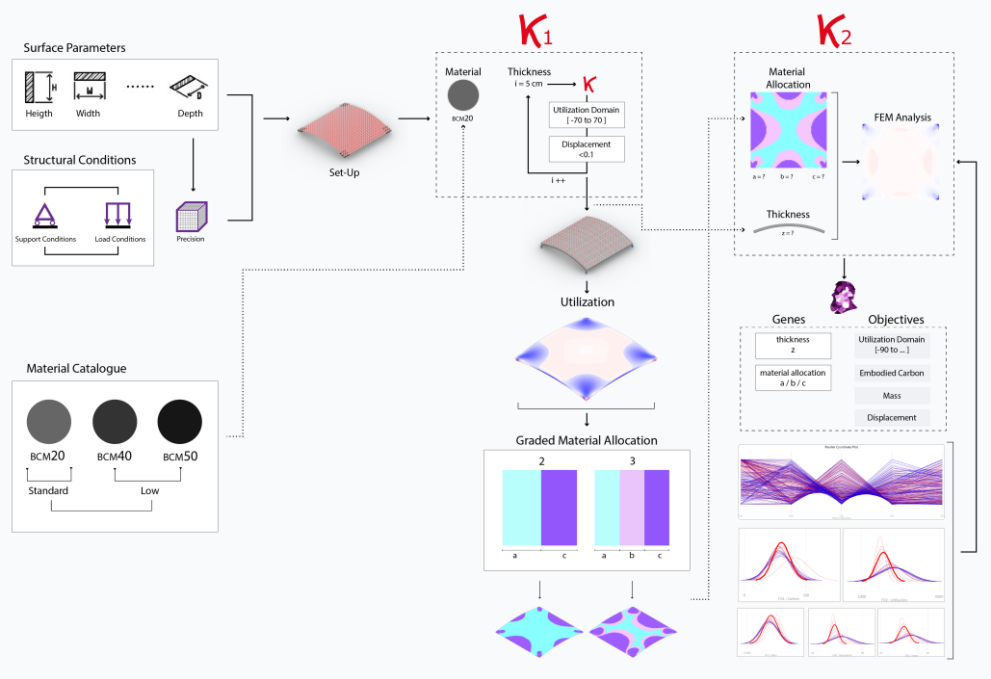


Figure 2. Computational design workflow for optimisation of functionally grading building elements.

This paper discusses the first iteration of a computational design method for generating optimised functionally graded slabs. In particular, the Karamba3D structural analysis plug-in is used to inform and test the impact the material allocations have on the structural performance. The Wallacei multi-objective solver is used to further optimise the slabs with respect to embodied carbon.

The main contribution of this computational workflow is the translation of a topologically optimised model with multi-material allocation, into a finite element model (FEM) that can be structurally tested in Karamba3D. This allows for the encoding of various BCC mixtures and their properties into the FEM mesh. Initially, a geometry is defined based on its surface parameters, including width, height, depth, or any other deformations. With this method, free-form geometries can also be used as inputs. The structural conditions, including supports and loads, are also defined, and the mesh resolution is set. The mesh resolution plays a crucial role and must follow a rule of thumb. In the first explorations, a lower resolution can be used to decrease the computing time. However, later, the resolution can be increased to improve accuracy.

The first stage of optimisation takes the input geometry and conditions, as well as the BCM20 material, which, according to material tests, meets structural regulations for cementitious materials used in building elements. Following that, the initial thickness of the shell is defined through an iterative process where the utilisation and displacement serve as criteria, allowing us to achieve optimal thickness for the geometry.

Through this process, the input that allows us to define the graded material allocation becomes crucial. Various types of inputs were tested, including user input attractor points, utilisation, stress and strain per node and stress lines defined through Karamba3D. The utilization calculations per node are selected as a method for obtaining the material allocation with the graded distribution. Following that, the number of grades that would be associated with the geometry can be tested, as well as the different proportions in proximity to the stress lines that they would take. As this whole process is done parametrically, those can afterwards be used as parameters for optimisation in a multi-objective optimisation engine.

The second stage allows for the material allocation, as well as the initial thickness, to be tested through Karamba3D structural analysis. This enables us to structurally test the heterogeneous or graded material

allocation on the initial geometry. Following that, the utilisation, and the formation of this structural analysis, together with the embodied carbon calculation as well as the mass calculation, can be used as inputs within a multi-objective optimisation solver; in this case, Wallacei was utilised. For the optimisation, the parameters were set to be thickness, as well as the material partitioning, and the objectives are to minimise the compression utilisation domain, the embodied carbon and the overall mass of the element. The computational workflow is graphically represented in the figure bellow (Figure 2.).

4. Data collection

The material combinations and allocations examined on the flat, singly curved and doubly curved slabs with dimensions 2.5 by 2.5 meters and 5 by 5 meters are represented in Figure 3. and the 5 by 7.5 meters in Figure 4. By comparing the homogeneous and graded possibilities of material allocation, the method allows to make informed decisions and optimise the slabs.

The different geometries are examined separately. In terms of utilization all flat floor slabs with span of 2.5 by 2.5 meters are underutilized allowing for weaker material and for the purpose of the study the optimal material is identified based on minimal embodied carbon to be homogeneous BCM50 (Figure 5). Furthermore, flat slabs with the medium span of 5meters can be attained when a dual material composition is used. Comparing the utilization and the embodied carbon, the medium span of 5 by 5 meters slabs would have the optimal condition of 50% BCM20 and 50% BCM40 material distribution as represented in Figure 3.

Studies conducted at ILEK on 5-meter span flat floor slab where graded optimisation was achieved by adding a foaming agent showed mass reduction by 43% and 62% [12]- [13]. Similarly, the CharCrete graded approach allow for 43% mass reduction but additionally it allows for a net negative embodied carbon value.

The singly curved slabs use the strength through geometry method which is allows for further reduction in thickness from 20cm to 15cm. Small and medium slabs with dual material exhibit sufficient performance in terms of both utilization and embodied carbon. The medium span with 20% BCM20 and 75% BCM40 is the most optimised in the study of singly curved slabs. The singly curved large span slabs have better utilization in comparison to the flat slabs however the utilisation values still go above 100 which indicated failure (Figure 5).

Finally, the doubly curved slabs are studied, and their structural performance is superior to the flat and singly curved slabs. When examining the doubly curved slabs all spans can be achieved with some material conditions. The double material allocation in the proportion of 25% BCM 20 and 75% BCM 40 is optimal in all the geometrical studies. However, there is room for further improvement when the thickness and material partitioning are examined further.

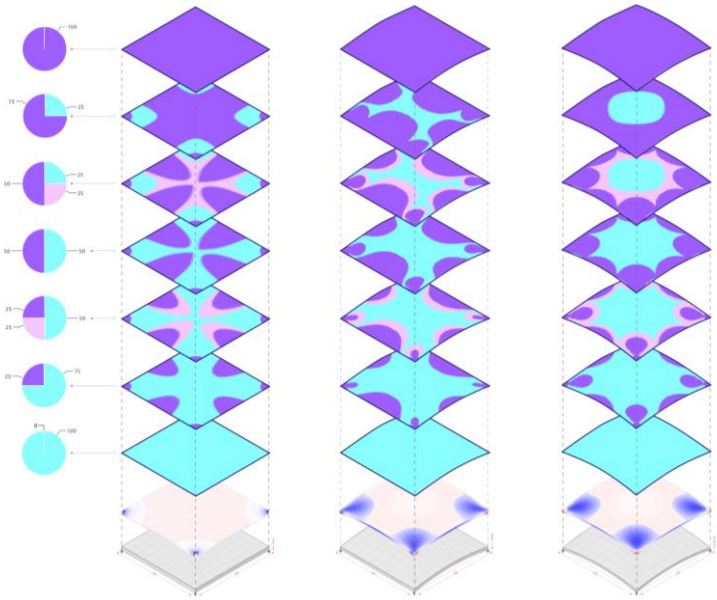


Figure 3. Slab case study with dimensions 2.5x2.5 and 5x5 meters with three geometrical variations: flat, singly curved and doubly curved (from left to right). The range of material conditions examined in the study derived by the utilization of the elements are presented with various quantities of graded – from 1 to 3 grades.

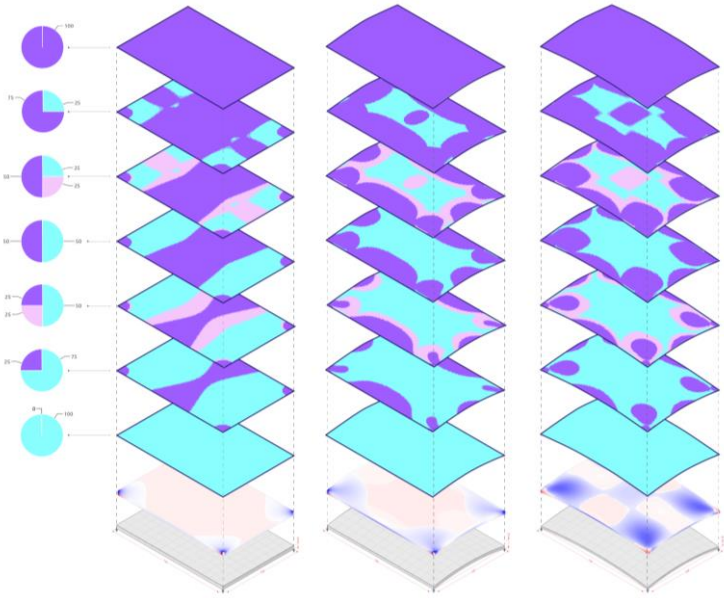


Figure 4. Slab case study with dimensions 7.5x5 meters with three geometrical variation: flat, singly curved and doubly curved (from left to right). The range of material conditions examined in the study derived by the utilization of the elements are presented with various quantities of graded – from 1 to 3 grades.

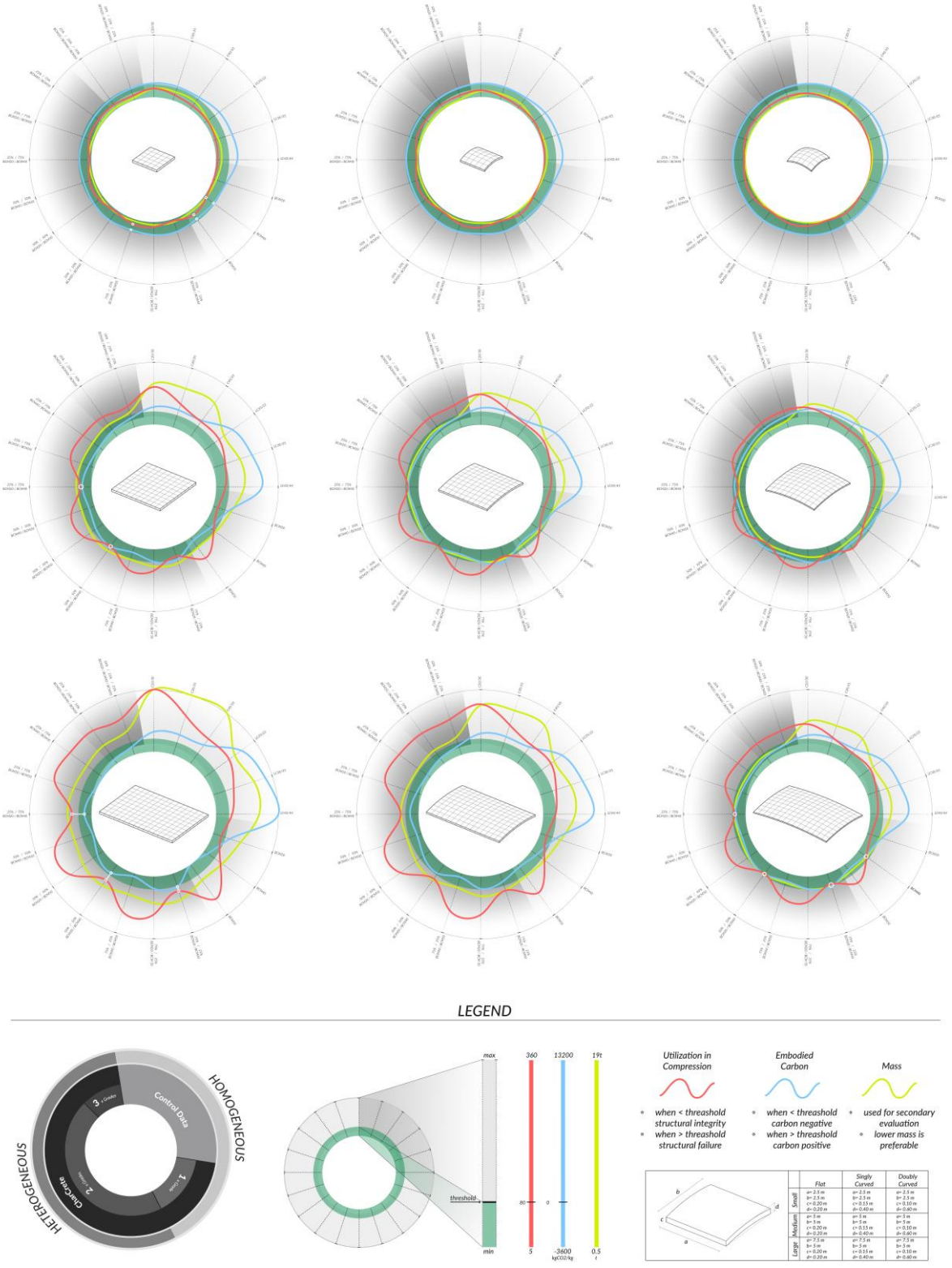


Figure 5. Remapped data of utilisation in compression (red), embodied carbon (blue) and mass (yellow) for all slab case studies.

The optimisation with Wallacei allows for vast numbers of conditions to be examined and analysed. Based on a study on the large span flat slabs, it was demonstrated that a range of possible slabs with span of 5 by 7.5 meters can be generated (Figure 6.). The study shows that graded material allocation cab be beneficial in reducing the embodied carbon without compromising structural integrity, however the work is only developed in a conceptual stage and further studies have to be conducted.

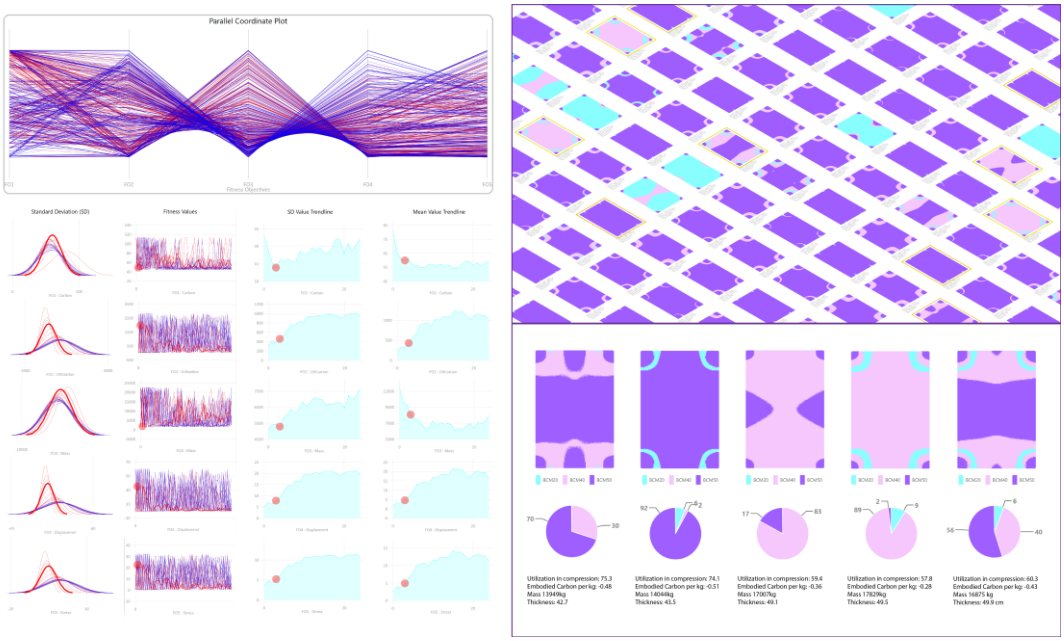


Figure 6. Flat slab case study with dimensions 7.5x5 meters optimised in terms of material allocation and thickness. The example shows the range of genes and optimisation criteria as well as a pool of slabs with ranging material allocation and a selection of five possible conceptual slabs generated using the optimisation method.

5. Conclusion

In conclusion, this paper introduces a computational workflow for informing and simulating performance graded slabs with various spans and geometrical typologies. This workflow is based on a finite element analysis conducted with the Karamba3D structural simulation plug-in within the Grasshopper environment. The method allows for the generation of conceptual digital models with graded material allocation, enabling designers and architects to incorporate environmental considerations into the design process with respect to embodied carbon. The method is tested with a CharCrete material system, which is part of a larger research project aimed at developing elements with negative embodied carbon due to the carbon sequestering nature of biochar.

The paper also highlights future directions for the method, including the case study of a load-bearing wall and testing the method with tensile strength mixtures that include fibres. As the material catalogue is enriched and developed further, the computational method will be developed to incorporate more material variations and optimization parameters. The main contribution of the research presented in this paper is the computational method and the generated data on graded slabs. The demonstration of the CharCrete material system as a case study for carbon-optimized building elements also highlights the potential for this method to impact the design of sustainable building elements. Overall, the presented computational workflow offers a promising approach for designers and architects to incorporate sustainability considerations into the design process of building elements by addressing the composition and allocation of heterogeneous material systems.

References

[1] Ahmed, Z.Y., Bos, F.P., van Brunschot, M.C.A.J., Salet, T.A.M., 2020. On-demand additive manufacturing of functionally graded concrete. Virtual Phys Prototyp 15, 194–210. https://doi.org/10.1080/17452759.2019.1709009

[2] Aylie, H., Gan, B.S., As'ad, S., Pratama, M.M.A., 2015. Parametric study of the load carrying capacity of functionally graded concrete of flexural members. International Journal of Engineering and Technology Innovation 5, 233–241.

[3] Bajaj, K., Shrivastava, Y., Dhoke, P., 2013. Experimental Study of Functionally Graded Beam with Fly Ash. Journal of The Institution of Engineers (India): Series A 94, 219–227. https://doi.org/10.1007/s40030-014-0057-z

[4] Baracchini, P., Kromm, F.X., Guillebaud, C., Wargnier, H., 2020. Multi-material design: architecture and components simultaneous selection. J Mater Sci 55, 9436–9447. https://doi.org/10.1007/s10853-020-04778-1

[5] Brault, A., Lees, J.M., 2020. Wet casting of multiple mix horizontally layered concrete elements. Constr Build Mater 247. https://doi.org/10.1016/j.conbuildmat.2020.118514

[6] Chmielewski, M., Pietrzak, K., 2016. Metal-ceramic functionally graded materials - Manufacturing, characterization, application. Bulletin of the Polish Academy of Sciences: Technical Sciences 64, 151–160. https://doi.org/10.1515/bpasts-2016-0017

[7] El-Galy, I.M., Saleh, B.I., Ahmed, M.H., 2019. Functionally graded materials classifications and development trends from industrial point of view. SN Appl Sci. https://doi.org/10.1007/s42452-019-1413-4

[8] G. Torelli, M. G. Fernández, J. M. Lees, "Functionally graded concrete: Design objectives, production techniques and analysis methods for layered and continuously graded elements," *Construction and Building Materials*, 2020.

[9] Grigoriadis, K., 2014. Mixed Matters: The Problems of Designing with Multi-materials. https://doi.org/10.13140/RG.2.1.4259.1448

[10] Güler, O., Varol, T., 2020. Fabrication of Functionally Graded Metal and Ceramic Powders Synthesized by Electroless Deposition, in: Advanced Surface Coating Techniques for Modern Industrial Applications. pp. 150–187. https://doi.org/10.4018/978-1-7998-4870-7.ch007

[11] Han, A.L., Gan, B.S., Kristiawan, S., Trtnh, T.H., 2016. The behavior of functionally graded concrete and the prospect of material optimization. CESB 2016 - Central Europe Towards Sustainable Building 2016: Innovations for Sustainable Future 1092–1098.

[12] Herrmann, M., Sobek, W., 2015. Development of Weight-Optimised, Functionally Graded Precast Slabs.

[13] Herrmann, M., Sobek, W., 2017. Functionally graded concrete: Numerical design methods and experimental tests of mass-optimized structural components. Structural Concrete 18, 54–66. https://doi.org/10.1002/suco.201600011

[14] Kaijima, S., Tan, Y.Y., Lee, T.L., 2017. Functionally graded architectural detailing using multi-material additive manufacturing. CAADRIA 2017 - 22nd International Conference on Computer-Aided Architectural Design Research in Asia: Protocols, Flows and Glitches 427–436.

[15] Klang, K., Bauer, G., Toader, N., Lauer, C., Termin, K., Schmier, S., Kovaleva, D., Haase, W., Berthold, C., Nickel, K.G., Speck, T., Sobek, W., 2016. Plants and animals as source of inspiration for energy dissipation in load bearing systems and facades. Biomimetic Research for Architecture and Building Construction 109–133.

[16] Li, Y., Feng, Z., Hao, L., Huang, L., Xin, C., Wang, Y., Bilotti, E., Essa, K., Zhang, H., Li, Z., Yan, F., Peijs, T., 2020. A Review on Functionally Graded Materials and Structures via Additive Manufacturing: From Multi-Scale Design to Versatile Functional Properties. Adv Mater Technol 5. https://doi.org/10.1002/admt.201900981

[17] Liu, X., Shapiro, V., 2016. Sample-based design of functionally graded material structures. Proceedings of the ASME Design Engineering Technical Conference 2A-2016, 1–15. https://doi.org/10.1115/DETC2016-60431

[18] Maier, M., Lees, J., 2022. Interlayer fracture behaviour of functionally layered concrete. Eng Fract Mech 271. https://doi.org/10.1016/j.engfracmech.2022.108672
[19] Mirzaali, M.J., Herranz de la Nava, A., Gunashekar, D., Nouri-Goushki, M., Veeger, R.P.E., Grossman, Q., Angeloni, L., Ghatkesar, M.K., Fratila-Apachitei, L.E., Ruffoni, D., Doubrovski, E.L., Zadpoor, A.A., 2020. Mechanics of bioinspired functionally graded soft-hard composites made by multi-material 3D printing. Compos Struct 237. https://doi.org/10.1016/j.compstruct.2020.111867
[20] Miyamoto, Y., Kaysser, W.A., Rabin, B.H., Kawasaki, A., Ford, R.G., 1999. Functionally Graded Materials: Design, Processing and Applications, Initial Reports of the Deep Sea Drilling Project, 28. https://doi.org/10.2973/dsdp.proc.28.101.1975
[21] N. Aage, O. Amir, A. Clausen, L. Hadar, D. Maier, A. Søndergaard, "Advanced Topology Optimization Methods for Conceptual Architectural Design," *Advances in Architectural Geometry*, 2014.
[22] N. Kirova, A. Markopoulou, J. Burry, Lafiti, "A study on carbon-neutral biochar-cementitious composites," *Design for Climate Adaptation - Proceedings of the World Congress of Architects*, 2023.
[23] Naghibdehi, M.G., Naghipour, M., Rabiee, M., 2015. Behaviour of functionally graded reinforced-concrete beams under cyclic loading. Gradjevinar 67, 427–439. https://doi.org/10.14256/JCE.1124.2014
[24] Oxman, N., 2010. Structuring Materiality: Design Fabrication of Heterogeneous Materials. Architectural Design, Special Issue: The New Structuralism: Design, Engineering and Architectural Technologies 80, 78–85.
[25] Oxman, N., 2011. Variable property rapid prototyping: Inspired by nature, where form is characterized by heterogeneous compositions, the paper presents a novel approach to layered manufacturing entitled variable property rapid prototyping. Virtual Phys Prototyp 6, 3–31. https://doi.org/10.1080/17452759.2011.558588
[26] Oxman, N., 2012. Programming Matter. Architectural Design, Material Computation: Higher Integration in Morphogenetic Design Architectural Design 82, 88–95.
[27] Oxman, N., Keating, S., Tsai, E., 2011. Functionally Graded Rapid Prototyping.
[28] Rahin, A., 2022. Bartlett architecture students fuse glass and metal to create innovative building skin, designboom. Available at: https://www.designboom.com/design/bartlett-school-of-architecture-students-fusion-glass-metal-building-skin-bpro-show-09-17-2019/ (Accessed: February 10, 2023).
[29] Shiota, I., Miyamoto, Y., 1996. Functionally graded materials 1996, in: Proceedings of the 4th International Symposium on Functionally Graded Materials.
[30] Toader, T.-N., Haase, W., Sobek, W., 2018. Energy Absorption in Functionally Graded Concrete Under Compression. Absorpţia De Energie În Betonul Cu Gradient De Densitate Supus La Compresiune. 68, 9–23.
[31] Torelli, G., Fernández, M.G., Lees, J.M., 2020. Functionally graded concrete: Design objectives, production techniques and analysis methods for layered and continuously graded elements. Constr Build Mater 242. https://doi.org/10.1016/j.conbuildmat.2020.118040
[32] Torelli, G., Lees, J.M., 2019. Fresh state stability of vertical layers of concrete. Cem Concr Res 120, 227–243. https://doi.org/10.1016/j.cemconres.2019.03.006
[33] Torelli, G., Lees, J.M., 2020. Interface bond strength of lightweight low-cement functionally layered concrete elements. Constr Build Mater 249. https://doi.org/10.1016/j.conbuildmat.2020.118614
[34] Win, M., Mak, T., Lees, J.M., 2022. Carbon reduction and strength enhancement in functionally graded reinforced concrete beams. https://doi.org/10.17863/CAM.9
[35] Wiscombe, T., 2012. Beyond assemblies: System convergence and multi-materiality. Bioinspir Biomim 7. https://doi.org/10.1088/1748-3182/7/1/015001

IASS 2023
July 10–14 Melbourne
Integration of Design and Fabrication

Proceedings of the IASS Annual Symposium 2023
Integration of Design and Fabrication
10-14 July 2023, Melbourne, Australia
Y.M. Xie, J. Burry, T.U. Lee and J. Ma (eds.)

Global topology optimization of lattice shell considering constructability dependent on connection relationships of members

Naoto OKUZONO*, Shinnosuke FUJITA*

* The University of Kitakyushu
1-1 Hibikino, Wakamatsu-ku, Kitakyushu, Fukuoka 808-0135, Japan
d2mbb004@eng.kitakyu-u.ac.jp

Abstract

In general, it is known that the topology optimization problem of steel structures can be formulated as a mixed-integer second order cone programming problem (MISOCP), when the compliance is minimized and the cross-section of each member is chosen from a set of predetermined candidates. On the other hand, real-world building structures should be considered not only structural performance such as compliance but also constructability. Hense, previous studies have demonstrated the effectiveness of the topology optimization method formulated as MISOCP which are considered constructability like the number of nodes and joint angles [1] [2].However, the analytical model of these studies is two-dimensional steel structures and constructability of obtained solutions cannot be evaluated only by them. Therefore, in this paper, the conventional MISOCP method is extended to 3D lattice shells. Additionally, a new constraint on the connection relationships between members that affect welding difficulty and cost is considered.

Keywords: lattice shell, topology optimization, constructability, global optimal solution, misocp

1. Introduction

It takes a lot of effort to find an optimal design by considering the shape and the section-type distribution of steel structures simultaneously using only the designer's experience and intuition. In previous studies, many methods for rational structural design have been proposed by solving the optimization problem for minimizing compliance. One of them is known that the topology optimization problem of steel structures can be formulated as MISOCP, when the compliance is minimized and the cross-section of each member is selected from a set of predetermined candidates [3] [4]. However, real-world steel structures are required not only high structural performance but also constructability. Consequently, a topology optimization method formulated as MISOCP which is considered the number of nodes and joint angles as indices for evaluating constructability was proposed [1] [2], nevertheless the analytical model of these studies is two-dimensional steel structures.Therefore, in this study, the topology optimization method in which structural rationality and constructability are simultaneously considered is applied to a three-dimensional lattice shell, and the effectiveness of that method is verified.

However, constructability cannot be evaluated only by the number of nodes and joint angles, which have been considered in previous studies. For example, Welding is an essential process in construction phase for steel structures and the number of members at each node have a significant impact on the difficulty of welding. Therefore, in this study, in order to prevent the concentration of members at each node, a new constraint that limits the number of members connected to each node is considered in the previous optimization method.

Copyright © 2023 by Naoto OKUZONO and Shinnosuke FUJITA. Published in the Proceedings of the IASS Annual Symposium 2023 with permission.

In this paper, a three-dimensional lattice shell is used as the analytical model and the topology optimization by MISOCP with a constraint on connection relationships of members to consider not only structural performance but also constructability simultaneously. Furthermore, the topology optimization is performed not only proposed constraint but also various constraints on constructability considered in previous studies, such as upper bounds for the number of nodes and lower bounds for joint angles of members are simultaneously considered.

2. Formulation of MISOCP

2.1. Minimizing compliance of lattice shells

$$\text{minimize} \quad \sum_{e=1}^{m}\sum_{l=1}^{6} 2w_{el} \tag{1a}$$

$$\text{subject to} \quad w_{e1} + a_e \geq \left\| \begin{pmatrix} w_{e1} - a_e \\ q_{e1}\sqrt{\dfrac{2l_e}{E}} \end{pmatrix} \right\|, \quad e = 1, \ldots, m \tag{1b}$$

$$w_{e2} + J_e \geq \left\| \begin{pmatrix} w_{e2} - J_e \\ q_{e2}\sqrt{\dfrac{2l_e}{\bar{G}}} \end{pmatrix} \right\|, \quad e = 1, \ldots, m \tag{1c}$$

$$w_{e3} + I_{ze} \geq \left\| \begin{pmatrix} w_{e3} - I_{ze} \\ q_{e3}\sqrt{\dfrac{6l_e}{E}} \end{pmatrix} \right\|, \quad e = 1, \ldots, m \tag{1d}$$

$$w_{e4} + I_{ze} \geq \left\| \begin{pmatrix} w_{e4} - I_{ze} \\ q_{e4}\sqrt{\dfrac{2l_e}{E}} \end{pmatrix} \right\|, \quad e = 1, \ldots, m \tag{1e}$$

$$w_{e5} + I_{ye} \geq \left\| \begin{pmatrix} w_{e5} - I_{ye} \\ q_{e5}\sqrt{\dfrac{6l_e}{E}} \end{pmatrix} \right\|, \quad e = 1, \ldots, m \tag{1f}$$

$$w_{e6} + I_{ye} \geq \left\| \begin{pmatrix} w_{e6} - I_{ye} \\ q_{e6}\sqrt{\dfrac{2l_e}{E}} \end{pmatrix} \right\|, \quad e = 1, \ldots, m \tag{1g}$$

$$\boldsymbol{p} = \sum_{e=1}^{m}\sum_{l=1}^{6} q_{el}\boldsymbol{b}_{el} \tag{1h}$$

$$\sum_{e=1}^{m} l_e a_e \leq \bar{V} \tag{1i}$$

$$a_e = \sum_{j=1}^{r} \bar{a}_j t_{ej}, \quad e = 1, \ldots, m \tag{1j}$$

$$I_{ye} = \sum_{j=1}^{r} \bar{I}_{yj} t_{ej}, \quad e = 1, \ldots, m \tag{1k}$$

$$I_{ze} = \sum_{j=1}^{r} \bar{I}_{zj} t_{ej}, \quad e = 1, \ldots, m \tag{1l}$$

$$J_e = \sum_{j=1}^{r} \bar{J}_j t_{ej}, \quad e = 1, \ldots, m \tag{1m}$$

$$\sum_{j=1}^{r} t_{ej} \leq 1, \quad e = 1, \cdots, m \tag{1n}$$

$$t_{ej} \in \{0, 1\}, \quad e = 1, \ldots, m \quad j = 1, \ldots, r \tag{1o}$$

In this paper, a lattice shell with n nodes, m elements, and D degrees of freedom for node displacement is optimized by MISOCP. According to the previous study [4], for the structural model of a lattice shell

with external nodal load $\boldsymbol{p} \in \mathbb{R}^D$, the topology optimization problem for minimizing compliance in which the optimal sections are selected from the list of the combinations of the member cross-section performances can be formulated as problem (1).

In problem (1), E, a_e, I_{ye}, I_{ze}, J_e and l_e are Young's modulus, section area, cross-sectional secondary moment of Y and Z-axis, torsional constant, and length of e-th member, respectively.

$\{(\bar{a}_1, \bar{I}_{y1}, \bar{I}_{z1}, \bar{J}_1), \cdots, (\bar{a}_r, \bar{I}_{yr}, \bar{I}_{zr}, \bar{J}_r)\}$ is the list of the combination of the member cross-section performances and t_{ej} is a 0-1 variable for selection of member section from the list. The design variable of problem (1) is t_{ej}, q_{el} and w_{el}. In the global optimal solution, $q_{e1}, q_{e2}, q_{e3}, q_{e4}, q_{e5}$ and q_{e6} are internal forces about axial, share, and bending, respectively and $\sum_{e=1}^{m}\sum_{l=1}^{6} 2w_{el}$ is consistent with compliance.

2.2. The constraint on intersection of members

Intersecting members, or even if not intersecting, overlapping cross sections, is not acceptable when considering actual construction. In this study, members that intersect in the plane are treated as intersecting members to avoid proximity or overlap of members when considering cross sections, even though the members do not intersect as lines in three-dimensional space. Pairs of member indexes of intersection of members is expressed as follows:

$$(C_{11}, C_{12}), \cdots (C_{x1}, C_{x2}) \tag{2}$$

where, x is the number of pairs of intersection of members. Then, intersection of members can be avoided by adding the constraint Eq. (3) to the problem (1):

$$\sum_{j=1}^{r} t_{\alpha j} + \sum_{j=1}^{r} t_{\beta j} \leq 1, \qquad \begin{array}{l} \alpha = C_{k1}, \quad \beta = C_{k2} \\ k = 1, \ldots, x \end{array} \tag{3}$$

2.3. The upper limit constraint on the number of nodes

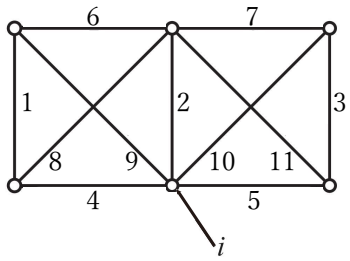


Figure 1: Node i and its surrounding members

Next, the upper limit constraint on the number of nodes is added to the problem (1). First of all, a set of indexes of members connected to node i is defined as $S(i) \subseteq \{1, \cdots, m\} (i = 1, \cdots, n)$ (In the example of Fig. 1, $S(i) = \{2, 4, 5, 9, 10\}$). Subsequently, the variable z_i is defined as follows:

$$z_i = \sum_{e \in S(i)} a_e, \quad i = 1, \cdots, n \tag{4}$$

For node i, the 0-1 variable $s_i \in \{0, 1\}$ is used to indicate the existence of that node. If setting the minimum length in the analytical model to $l_{\min}$, the following equation always holds under the upper volume constraint:

$$\sum_{e=1}^{m} a_e \leq \frac{\bar{V}}{l_{\min}} \tag{5}$$

Therefore, the relationship between s_i and z_i can be written as follows (where $0 \leq z_i$ is trivial):

$$0 \leq z_i \leq \frac{\bar{V}}{l_{\min}} \cdot s_i, \quad i = 1, \cdots, n \tag{6}$$

Also, the constraint on the number of nodes can be written as follows:

$$\sum_{i=1}^{n} s_i \leq \bar{n} \tag{7}$$

where, $\bar{n}$ is the upper limit value of the number of nodes.

2.4. The lower limit constraint on the joint angle

In order to prevent the members from connecting at extremely sharp angle, a constraint such that all joint angles are larger than or equal to the lower limit value $\bar{\theta}$ are considered. In this paper, pairs of member indexes connected at an angle less than $\bar{\theta}$ is expressed as follows:

$$(D_{11}, D_{12}), \cdots (D_{y1}, D_{y2}) \tag{8}$$

where, y is the number of pairs of members connected at an angle less than $\bar{\theta}$. Sharp connection can be avoided by adding the following constraint to the problem (1):

$$\sum_{j=1}^{r} t_{\alpha' j} + \sum_{j=1}^{r} t_{\beta' j} \leq 1, \qquad \begin{array}{l} \alpha' = D_{k'1}, \quad \beta' = D_{k'2} \\ k' = 1, \ldots, y \end{array} \tag{9}$$

2.5. The upper limit constraint on connection relationships of members

Welding is an essential process in steel construction and the number of members connected to each joint has a significant impact on the difficulty of welding. In order to consider constructability dependent on connection relationships of members, the following constraint which limit the number of members connected to each node is additionally considered to the problem (1):

$$\sum_{e \in S(i)} \sum_{j=1}^{r} t_{ej} \leq \bar{j} \quad i = 1, \ldots, n \tag{10}$$

where, $\bar{j}$ is the upper limit of the number of members connected to each node.

Finally, the following constraints are added to the problem (1):

$$\sum_{j=1}^{r} t_{\alpha j} + \sum_{j=1}^{r} t_{\beta j} \leq 1, \qquad \begin{matrix} \alpha = C_{k1}, \quad \beta = C_{k2} \\ k = 1, \ldots, x \end{matrix} \tag{11a}$$

$$z_i = \sum_{e \in S(i)} a_e, \quad i = 1, \ldots, n \tag{11b}$$

$$0 \leq z_i \leq \frac{\bar{V}}{l_{\min}} \cdot s_i, \quad i = 1, \cdots, n \tag{11c}$$

$$\sum_{i=1}^{n} s_i \leq \bar{n} \tag{11d}$$

$$\sum_{j=1}^{r} t_{\alpha' j} + \sum_{j=1}^{r} t_{\beta' j} \leq 1, \qquad \begin{matrix} \alpha' = D_{k'1}, \quad \beta' = D_{k'2} \\ k' = 1, \ldots, y \end{matrix} \tag{11e}$$

$$\sum_{e \in S(i)} \sum_{j=1}^{r} t_{ej} \leq \bar{j} \quad i = 1, \ldots, n \tag{11f}$$

2.6. Introducing the penalty function

When optimization is performed under the above constraints and there is margin for the volume constraint, it is possible to obtain multiple global optimal solutions with different volume.For example, when optimization is performed with $\bar{j} = 3$ for a anaiytical model in Fig. 2, there exist global optimal solutions with the same compliance as shown in Fig. 2. In that case, it is desirable to select the solution of (a) which has the smallest volume.

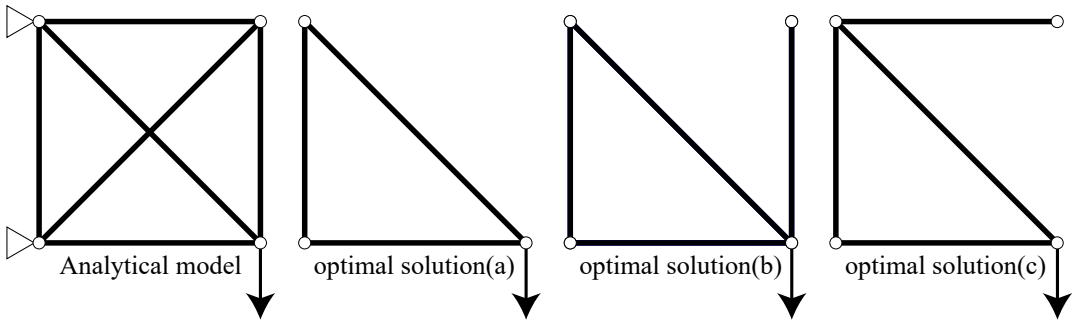


Figure 2: Examples of multiple global optimal solutions

In this study, to remove solutions other than the best solution in advance, the penalty functions are imposed to the volume by adding βV to the objective function using sufficiently small positive constant value β.

Therefore, in the optimal problem (1), the objective function is changed as follows:

$$\sum_{e=1}^{m} \sum_{l=1}^{6} 2 w_{el} + \beta V \tag{12}$$

3. Numerical examples

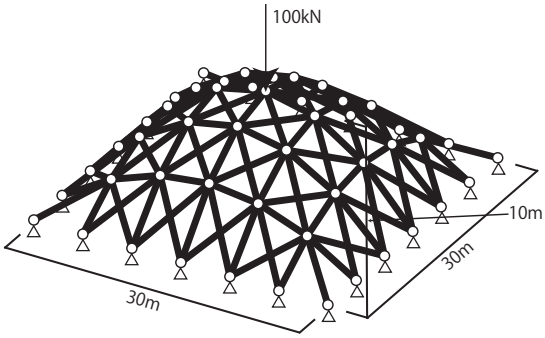


Figure 3: Analytical model

Table 1: The list of cross-sections (steel pipe)

j	1	2	3
outer diameter [mm]	216.3	216.3	216.3
width [mm]	4.5	7.0	12.7
$\bar{a}$ [$\times 10^{-3}$m^2]	2.99	4.60	8.12
$\bar{I}_y, \bar{I}_z$ [$\times 10^{-5}$m^4]	1.68	2.52	4.23
$\bar{J}$ [$\times 10^{-5}$m^4]	3.36	5.05	8.45

The optimization problem, where constraints Eq. (11a) to Eq. (11f) are additionally considered in the problem (1), is applied to the following analytical model with concentrated load shown in Fig. 3. In each numerical examples, Young's modulus and Poison's ratio are set to E=205[GPa] and $\nu = 0.3$, respectively. Member cross-sections are selected from the given list (Tab. 1). All joints are rigidly connected and boundary conditions are pinned support in circumference. The upper volume limits are set to $\bar{V}$=3.5[m^3]. In addition, in order to obtain the more realistic optimal solution, the number of design variables is reduced by considering the symmetry and analyzing the quarter region of its design area. We used PICOS ver. 1. 2. 0 [5], a Python interface to diverse optimization solvers. MOSEK ver. 8.0 [6] was used as the optimization solver. Computation was carried out on Intel (R) Core (TM) i7-1165G7@2.80GHz with 16GB RAM.

The optimal topologies are shown in Figs. 4. Changes in compliance were compared while optimization for various constraints on the maximum number of members to be connected to each node, the number of nodes, and the lower limit of joint angles. Fig.4 (a) shows the optimal solution obtained by solving a pure compliance minimization problem without any restrictions on the number of nodes, joint angles, or the number of members connected to each node. It can be confirmed that the volume constraint is satisfied and a high concentrartion of members at the load point, so this optimal solution is not always an appropriate design solution when considering constructability. Since the maximum number of members connected to each node is 8 in this optimal solution, optimization with member connectivity limit constraint of $\bar{j} \leq 7$ is iteratively carried out, the results of which are shown in Figs.4 (b) to (d), respectively. Since the optimal solution cannot be obtained with $\bar{j} = 3$ for half a day, the analysis is terminated. In each case, optimization with joint angle constraint is performed for the case where a frame including a joint smaller than $\bar{\theta} = 40^\circ$ is obtained, the result of which are shown in Figs. 4 (e) to (h). Furthermore, optimization with node constraint is performed for the topology in Fig. 4 (f) is obtained, the results of which are shown in Figs. 4 (i) to (o). In this paper, since optimization is considered the symmetry, optimization while reducing $\bar{n}$ by 4 from 41 to match the number of nodes. Since the optimal solution cannot be obtained with $\bar{n} = 9$ for half a day, the analysis is terminated. Mechanical quantity and computational time of global optimal solutions are shown in Tab. 2.

It can be confirmed from the optimization result that no intersecting members exist in each optimal solution because of the constraint Eq. (3). Any topologies can be confirmed that the solutions have a margin in volume constraint. Hense, in the case of this analytical model, any members that do not contribute to the stiffness may be used. However, these members are removed in optimal solutions due to the effect of the penalty functions about the volume.

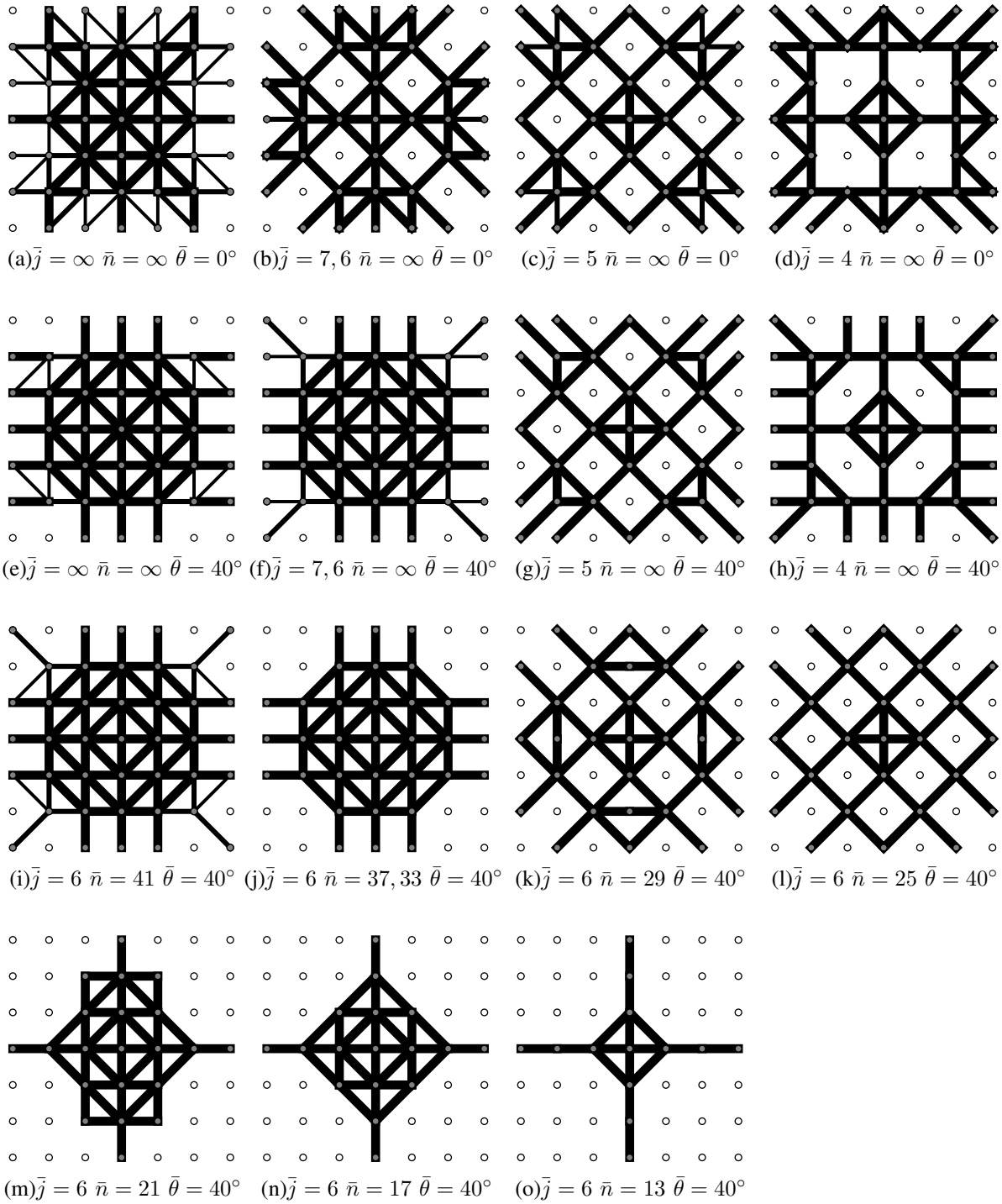


Figure 4: Global optimal solutions

Table 2: Mechanical quantity and computational time of global optimal solutions

※ a: $\bar{j} = 7$, b: $\bar{j} = 6$, c: $\bar{n} = 37$, d: $\bar{n} = 33$

	(a)	(b)	(c)	(d)	(e)	(f)	(g)	(h)	(i)	(j)	(k)	(l)	(m)	(n)	(o)
Compliance [kJ]	0.148	0.242	0.268	0.555	0.150	0.263	0.273	0.978	0.263	0.263	0.274	0.275	1.524	1.845	4.942
Volume [m^3]	3.493	3.465	3.086	3.070	3.495	3.448	2.869	2.635	3.470	3.040	2.560	2.272	2.001	1.649	0.834
Maximum number of members connected to each node	8	6	5	4	8	6	5	4	6	6	5	5	6	6	4
Number of nodes	45	37	33	37	41	45	33	41	41	33	29	25	21	17	13
Minimum joint angle [°]	33.78	33.78	37.43	35.57	40.40	40.40	42.06	40.40	42.08	42.45	46.35	46.35	42.44	42.86	46.35
Computational time [s]	163.1	157.1[a] 77.81[b]	83.54	388.2	7.722	508.5[a] 209.5[b]	55.21	2093	176.6	264.8[c] 619.2[d]	303.1	314.6	96.20	29.27	136.1

As the constraints on the number of nodes or connection relationships of members becomes stricter, the feasible region becomes narrower, and it has an impact on computational time. As a result, in the case of $\bar{j} = 3$ or $\bar{n} = 9$, optimal solutions cannot be obatained in realistic time. According to Fig. 4 (b), optimal solution with maximum number of members connected to each node is 7 does not exist. From Tab. 2, it can be confirmed that compliance and connection relationships of members are in a trade-off relationship with each other. However, the amount of increase is unequal. Optimal solutions in Figs. 4 (i) to (o) show that there is no correlation between the number of nodes and the maximum number of members connected to each node.

4. Conclusion

In this paper, a new topology optimization approach with MISOCP that takes into account connection relationships of members is applied to the three-dimentional lattice shell. In addition, the proposed constraint were combined with the constraints on the number of nodes and joint angles used in previous studies and the variation of the objective function values are compared to account for differences in the range of the constraints.

Acknowledgement

This work was partially supported by JSPS KAKENHI 22K04416.

References

[1] S. Fujita and Y. Kanno : Global Topology Optimization of Structural Frames with Upper Bounds for Member Lengths and Number of Joint -A Mixed-Integer Second-Order Cone Programming Approach- , *Journal of Structural and Construction Engineering (Transactions of AIJ)*, Vol. 83, No. 745, pp. 451–458, 2018 (in Japanese)

[2] S. Fujita and Y. Kanno : Global Topology Optimization of Structural Frames Considering Constructability, *IASS 2018 Annual Symposium* Boston, USA, 2018

[3] Y. Kanno : Mixed-Integer Second-Order Cone Programming for Global Optimization of Compliance of Frame Structure with Discrete Design Variables, *Structural and Multidisciplinaly Optimization*, Vol. 54, pp. 301–316, 2016

[4] S. Fujita and Y. Kanno : Topology Optimization of Three-dimensional Frame Structures Using Mixed-integer Second-order Cone Programming , *Journal of Structural and Construction Engineering (Transactions of AIJ)*, Vol. 82, No. 732, pp. 193–201, 2017 (in Japanese)

[5] G. Sagnol : *PICOS : A Python Interface for Conic Optimization Solvers*. https://yalmip.github.io/tutorial/bigmandconvexhulls (Accessed March 2023)

[6] E. D. Andersen, C. Roos, and T. Terlaky : On Implementing a Primal-Dual Interior-Point Method for Conic Quadratic Optimization, *Matheatical Programming*, Vol. 95, pp. 249–277, 2003

IASS 2023
July 10–14 Melbourne
Integration of Design and Fabrication

Proceedings of the IASS Annual Symposium 2023
Integration of Design and Fabrication
10–14 July 2023, Melbourne, Australia
Y.M. Xie, J. Burry, T.U. Lee and J. Ma (eds.)

Interactive gradient-decent optimization method for timber column-slab structures

Keerthana UDAYKUMAR[a,*], Luis OROZCO[b], Anna KRTSCHIL[c],
Achim MENGES[b,d], Jan KNIPPERS[c,d]

[a,*] ITECH Master's Program, University of Stuttgart, Keplerstrasse 11, 70174, Stuttgart, Germany
u.keerthana@gmail.com

[b] ICD Institute for Computational Design and Construction, University of Stuttgart, Germany
[c] ITKE Institute of Building Structures and Structural Design, University of Stuttgart, Germany
[d] IntCDC Cluster of Excellence Integrative Computational Design and Construction and Construction for Architecture, University of Stuttgart, Germany

Abstract

This paper proposes an interactive computational approach for designing the layout of timber column-slab structures in a material-saving and structural-performance aware manner. The generated column slab layout meets the serviceability limit state deflection criteria by integrating gradient-based optimization within an agent system approach. This was achieved by extending the ABxM framework with an interactive design framework termed Timber Column Slab (TCS) solver. This solver is underpinned by three data structures: Firstly, an agent system representing a column-slab system for layout exploration. The finite element (FE) model that computes the slab's nodal displacements, which enables rapid serviceability checks at each agent-system update in a real-time loop. With the TCS extension, the agent-based model uses the numerical analysis results to refine the decision of the adaptive agents. The real-time interaction built within the agent-based model is responsible for the live user guidance and design software integration. The proposed methodology has been built with multiple scientific stacks and encapsulated into an open-source framework in a C# environment. The developed method is tested on a wide range of real building floor plans of different scales and typologies, demonstrating how effective it is compared to previous efforts.

Keywords: agent systems, optimisation, interactive design, timber-structures, column-slab system, conceptual-design

1. Introduction

According to the Ellen MacArthur Foundation's guidelines [1] for designing for circularity the early design phase plays a key role in the process and is critical for making maximum changes for environmentally responsive design. While conceptual structural design and rapid analysis tools have been extensively explored for spatial structures, column-slab structures have not, despite being a widely used structural system [2]. Determining irregular support location layouts is particularly challenging as they have a direct influence on the structural material quantities, future adaptability, and architectural appearance [2],[3]. From a material perspective, timber structures pose the biggest challenge in terms of slab stiffness distribution and design due to their anisotropic nature [4]. Currently, few computational tools or techniques aid in designing timber structures in the early-design stage. This study aims to address these knowledge gaps by exploring an interactive optimization technique. The ability of agent systems to make adaptive decisions in changing environments, integrated with serviceability checks at each design iteration, is explored. Ultimately, the proposed method aims to allow architects to make

Copyright © 2023 by Keerthana UDAYKUMAR, Luis OROZCO, Anna KRTSCHIL, Achim MENGES and Jan KNIPPERS. Published in the Proceedings of the IASS Annual Symposium 2023 with permission.

informed decisions while considering structural constraints for column-slab systems from the early stages of design.

2. State of the art

This research lies at the intersection of design space exploration techniques, conceptual structural design, and architectural design. In the following paragraphs, we will discuss the most relevant studies focusing on the design of column-slab systems, the application of agent systems in structural design, and research on design interaction and guidance.

2.1. Agent systems in architectural design

The advantage of agent-based modelling is having adaptive agents make decisions in a changing environment. Groenewolt et al. [5] successfully applied agent-based modelling (ABM) to the design of segmented shells using a hierarchy of geometric rules to meet specific fabrication and structural requirements. Scheurer [6] simulated irregular column layouts using specific architectural objectives as behaviours to simulate a self-organizing model. Schwinn [7] demonstrates the computational pipeline of a complex segmented timber shell structure using an agent-based approach, optimizing material use and structural stability. Orozco et al. [8] also investigate the application of a multi-agent system in generating design layouts for multi-story timber structures. However, while previous methods achieved rapid interaction and geometric rule-based simulation, the end results are not informed by structural analysis inferences. Groenewolt et al. [5] discuss the interoperability of structural analysis, but this requires pausing the simulation and exporting the results to external software. In contrast, this research presents a method for computing slab deflection checks in real-time.

2.2. Design exploration for column-slab systems

Muresan et al. [3] investigated the design space of modular slab systems with discrete stiffness distribution and irregular column layout through a stochastic approach. Although stochastic approaches present the possibility of generating a large design space, navigating the large datasets they produce becomes challenging, particularly for complex cases. Meng et al.[2] adopt an optimization method to determine optimal support locations in the roof-column structural system. While optimization techniques present a robust approach to identify optimal solutions, they are typically time intensive and depend on accurate and reliable input data, which can be challenging to frame for the early design stages.

3. Method

The following section elaborates on the theoretical basis of an interactive design method that combines gradient-based optimization with ABM. The operation of the ABxM framework [9] is described, which is essential to understanding the agent system design and the proposed TCS extension. Figure 1 illustrates the various components and operations of TCS. By utilizing this method, column-slab layouts can be explored while accommodating various architectural design constraints in real-time. The agent system tracks and adjusts to the slab's changing structural behaviour. The aim of this method is to address the limitations outlined in the previous section by providing designers with an interactive, structurally compliant solver.

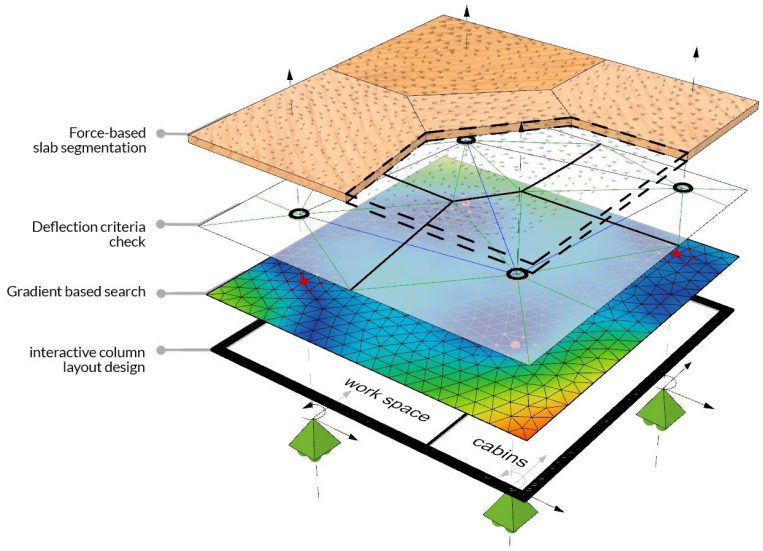


Figure 1. Diagram illustrating various components of the proposed TCS method.

3.1. The ABxM framework

ABM is a simulation technique that includes autonomous decision-making entities called agents. Behaviours that are applied to the agents determine how they interact with the environment and with each other. Schwinn [10] explain techniques to represent building components as agent systems, allowing architects to test and refine their designs in an interactive manner with multiple constrains. The ABxM framework provides an open platform for experimenting with agent-based models in an architectural setting by consolidating previous developments on the topic [5] [10], [11]. It comprises data structures for agents, environments, behaviours, and different data structures for agent systems based on their representation. The cartesian agent system is adopted for the TCS solver.

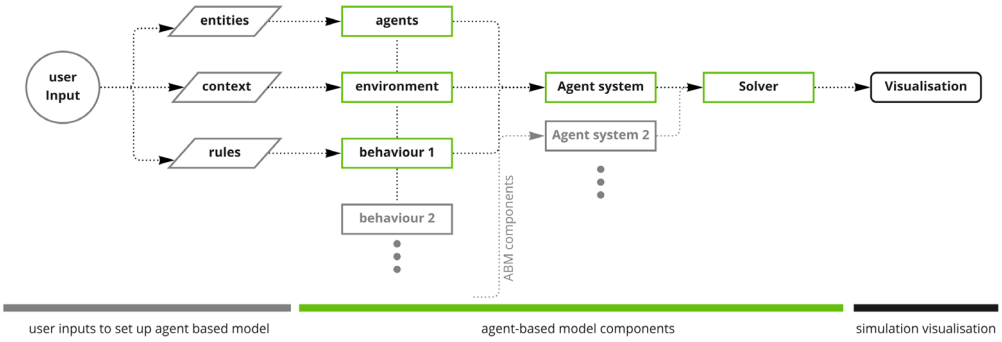


Figure 2. Figure illustrating the workflow of the components of an agent system based on the set up of the ABxM framework [9].

3.2. Agent model definition

For the given context of slab-column systems, the agents represent columns and their environment the slab. The goal of the agents is to converge to a column-layout configuration that minimizes the slab nodal deflection while accounting for designer intent. The primary input from the user is the floorplan layout 2D geometry. This geometry is used to generate the environment mesh. The initial location of the agents is also derived from this input geometry: they are evenly distributed along the exterior boundary of the environment.

The behaviours aim to guide the agents to configurations that minimize the slab nodal displacements. A backend slab displacement solver is a key feature of the TCS extension, which is elaborated in *Section 3.3.*

3.2.1. Serviceability checks

After computing nodal displacement, a static deflection check is carried out to verify if the atypical column arrangement satisfies the deflection standards. The process of determining a measurable serviceable check for irregular slabs and column layouts can be difficult. The first step involves performing a Delaunay triangulation, followed by extracting two types of lengths between the field and the cantilever to express the serviceability criteria, which is the minimum length ratio between them. To derive the serviceability limit checks, the Delaunay triangulation is performed using the irregular column positions. The length of the first edge of the triangulation marks the first length, while each column is measured from its vertex to the floor or the boundary of its respective Voronoi cell. This computation is integrated into the structural analysis package of the TCS solver and is activated at the conclusion of the agent system loop (figure 3).

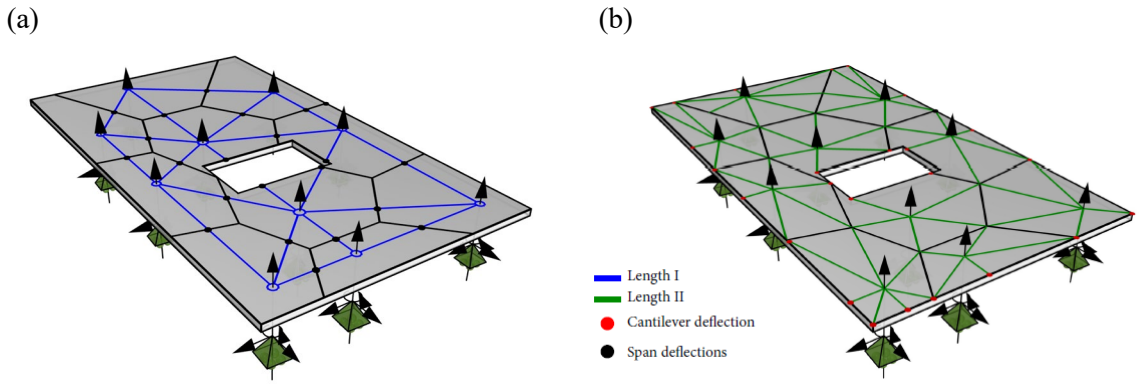


Figure 3. Diagram illustrating serviceability deflection check criteria for floor slabs with cut-outs.

3.2.2. Penalty function for material volume

A penalty feature is introduced to discourage the agent from searching for solutions that will increase the slab material volume. Through the penalty feature, column layout configurations that do not satisfy the SLS deflection criteria are avoided, or if they require higher slab densities. The slab volume is a function f(x) that should be minimised. To navigate away from the positions that cause unfavourable results, a penalty weight "r." is added to the agents when the constraint is not met for certain column configurations. The penalty formulation is explained through the equation below.

$$penality = r * \max(0, f(x) - fmax) \quad (1)$$

Here penalty is the weight that is added to the agent when the constraint is not met and "r" is the penalty weight factor. *f(x)* is the slab material volume function that needs to be minimized *fmax* is the maximum allowed slab volume. max(0, f(x) - f_max) is the maximum of 0 and the difference between the slab volume and the maximum allowed volume. This ensures that the penalty is only applied when the constraint is violated.

3.2.3. Interactivity

There are two types of interaction features, firstly dynamic interaction allows the user to redistribute the column locations while the solver is still converging. By triggering a nodal displacement recalculation, this method immediately updates the positions of the entire network of column agents. Meanwhile, the static interaction feature allows users to save specific design options and revert old iterations. A saved

design option's data structure is preserved in a history class, and the data is serialised into its constituent data structure for instant re-editing.

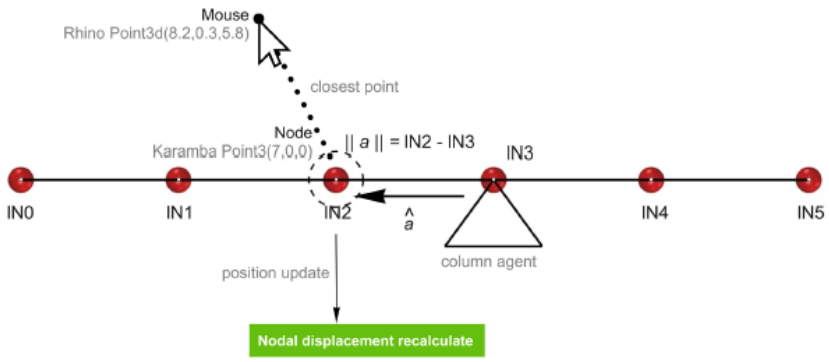


Figure 4. figure illustrating the logic behind the live mouse interaction feature in the context of a beam-column set up.

3.3. Extension to the ABxM framework

The TCS solver utilizes the core data structure of a cartesian system from the ABxM framework, which includes classes defining the agent, agent system, behaviour, and environment attributes. However, TCS extends this inherited structure in three important ways. Firstly, the slab environment is capable of storing not only the geometry data but also the FEA results in each node of the slab. This is achieved by modelling the slab geometry as a finite element model and using a backend FEA package built with the Karamba3D application programming interface [12] to calculate the nodal displacements. The result is a network of nodal positions and displacements of the slab, represented in a dictionary that serves as the environment for agent interaction. Secondly, the agent system includes a behaviour based on gradient-based optimization, which determines the column agent's position coordinates relative to the slab environment and references the neighbouring nodal displacements to compute the agent's updated position vector with the weight of the penalty feature added. Lastly, the TCS recursive solver is a key feature that triggers the environment class to recompute the nodal displacements at the end of each agent system loop until the deflection criteria is met. A broad overview of the data structure is illustrated in figure 5 and figure 6.

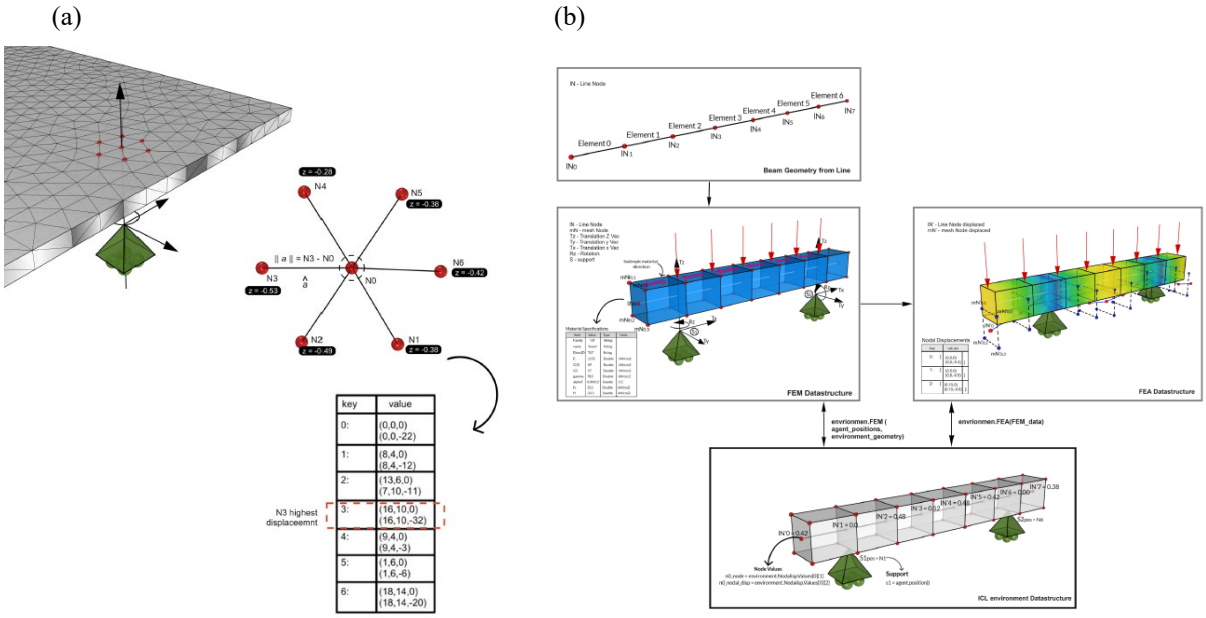


Figure 5. Diagram illustrating the backend communication between the FE analysis to Agent system pipeline of the TCS solver (a) slab-column set up (b) beam-column setup.

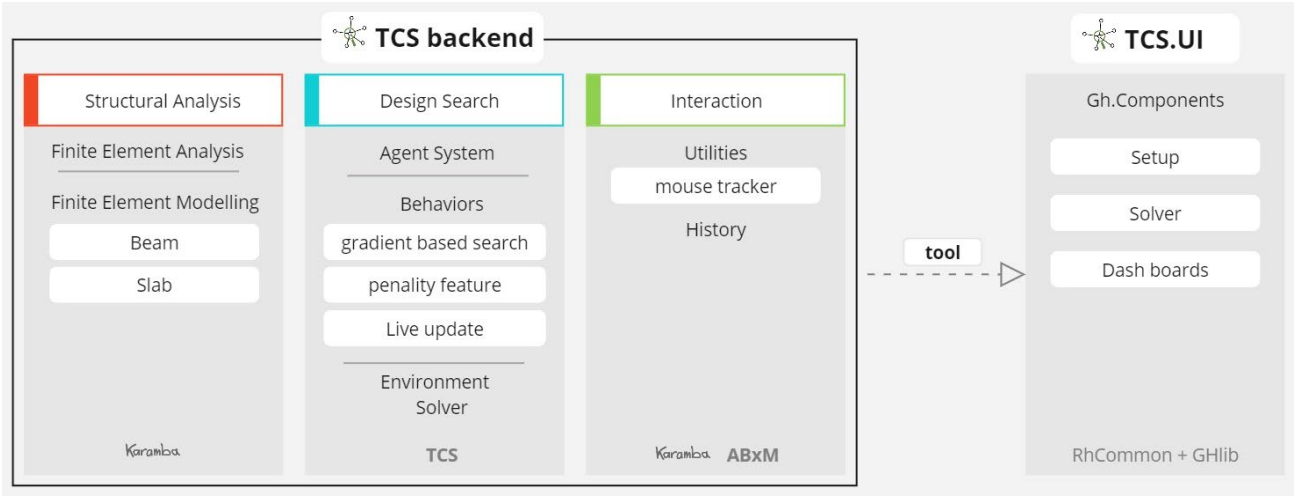


Figure 6. Diagram illustrating the data structure and algorithms of the TCS framework, its dependencies, and user interface.

4. Development: examples

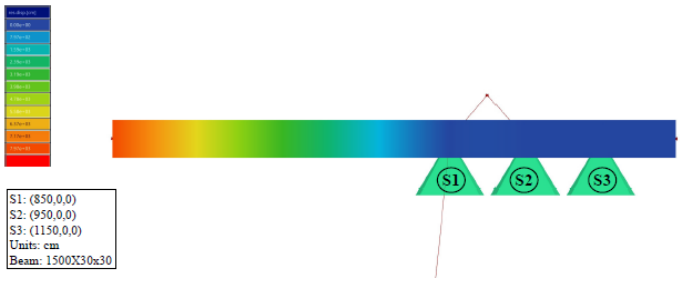
In this section, the effectiveness of the TCS solver is evaluated through three design case studies. The first case study involves a simple beam-column problem, followed by solving for a floor slab outline, and finally addressing a floor plan with multiple architectural constraints.

4.1. Beam-column problem

To evaluate the modelling capabilities and applicability of the TCS solver, a beam-column system is chosen as a prototype problem. The system comprises a 12m span beam element subject to both live and gravitational loads, with the aim of determining the positions of the column supports to meet the deflection criteria. The minimum required user input for the simulation is the beam width. Initially, the

column count starts at every 5m, and during simulation, the number of column agents is adjusted based on the deflection check and the penalty feature that aims to limit the material volume of the beam. The ultimate goal is to identify the optimal location for the column supports through simulation. The mouse tracking feature enables real-time movement of column agents, and the user interface (UI) for history tracking and solver prompts is implemented in the Rhino environment.

(a)



(b)

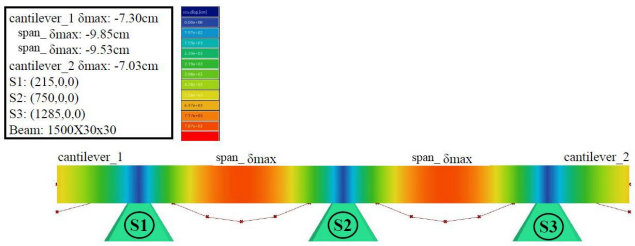


Figure 6. Output of a simple beam-column problem set up (a) start position of column agents on beam (b) result of converged simulation using the TCS solver.

4.2. Solving for floor slab boundary

This section presents a design case study utilizing the TCS solver. The study utilizes the Tamedia Building designed by Shigeru Ban Architects [13] as a real-life building design scenario to test the solver's efficacy. To ensure accurate testing, an actual building design was chosen over a theoretical layout. The solver is first tested to converge the column layout with only a floor layout boundary input. A young's modulus of 1155 KN/cm2 is uniformly applied to all elements. Anisotropic material characteristics are also modelled with the engineered timber grain direction considered along the XY axis. At the beginning of the simulation, the slab is set to a uniform thickness of 35 cm, and the Slab volume penalty results in a thickness reduction. The number of columns is computed based on the slab floor area and the minimum span between columns. The start positions of the column agents, their position at iteration 46, and the final converged solution are illustrated in Figure 6(a).

The live update behaviours tested previously on beam-column problems are then applied to the Tamedia case study. Figure 6(b) demonstrates the three steps of user interaction. Selecting a group of columns and holding down shift + left mouse button aligns the columns in a straight path, and when the column position is updated, the entire network updates. Furthermore, any column can be selected, dragged, or updated, prompting the entire column network to update the nodal displacement values.

4.2. Solving for floor slab with multiple architectural constrains

This section of the paper discusses the testing of a solver for floor plans with multiple cut-outs, which are common in architectural design for introducing atriums, building services, etc. The solver is tested

on the ground floor layout of the Hungarian house of music building designed by Sou Fujimoto architects, which features multiple cut-outs. A finite element (FE) model is computed with void features, which defines the search space of the column agents. For this test, 24 columns are considered, and an orthotropic material definition is used with a Young's modulus of 210 GPa and a tensile strength of 860 MPa.

In the preliminary stages of design, it is often necessary to identify areas with wide spans, and one useful feature is the no-column zone. This allows users to specify regions where columns should not be placed to achieve a wide span. Once these zones are marked, agents are prohibited from occupying nodal positions on the slab within the zone and are included for deflection checks. The FE model's mesh vertices closest to the boundary of the no-column zone marked by the user are highlighted and assigned a Boolean attribute value of "false". The agent system stores this attribute and verifies its status prior to calculating a new position. Figure 7 depicts a screenshot of the simulation at three different stages.

(a) (b)

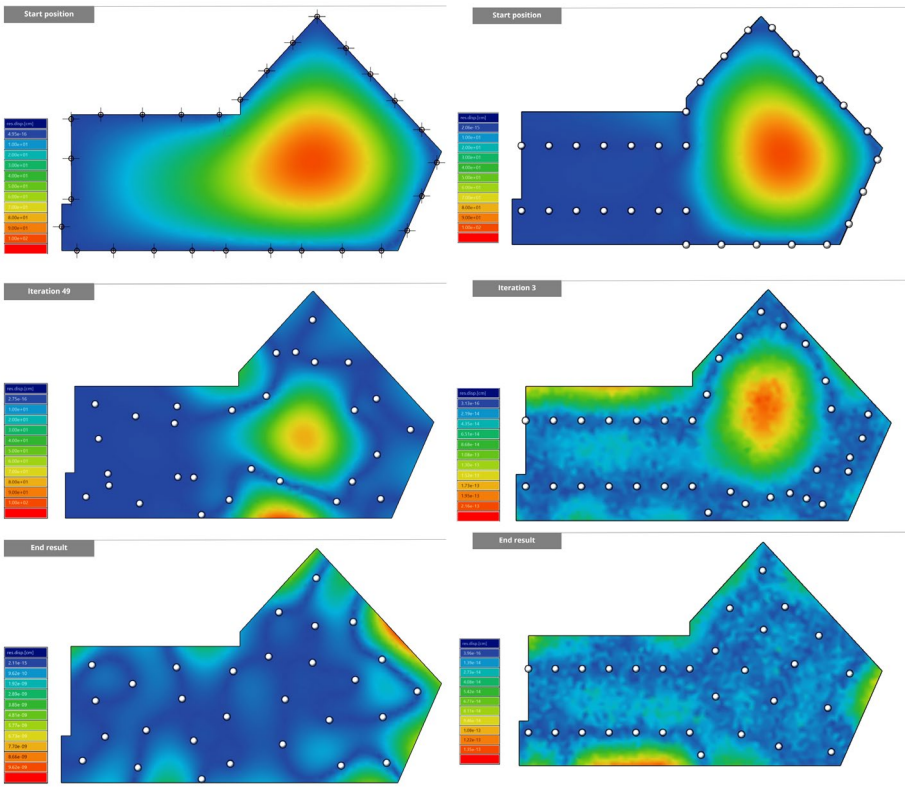


Figure 7. Output of simulation from TCS (a) solving for floor-slab boundary (b) solving floor-slab boundary with existing columns. Tamedia building case study [13].

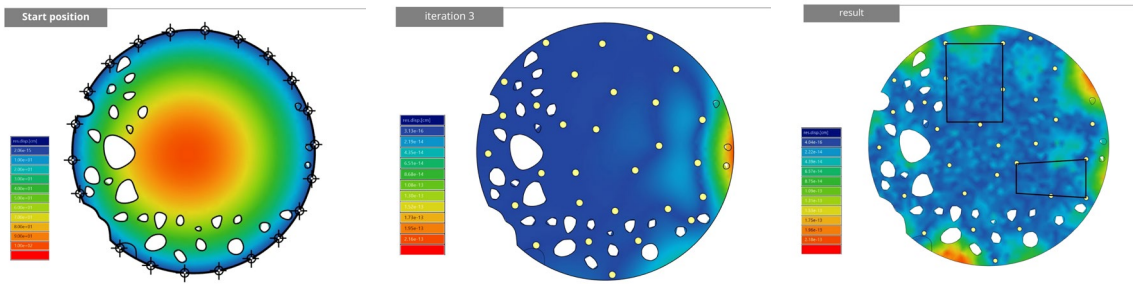


Figure 8. Output of simulation from TCS solving floor-slab boundary with multiple architectural constrains. Hungary house of music building as Case study.

```
using TCS.Core.Utilities;
using TCS.Core.Environment;
using TCS.Core.StructuralModelling;
using TCS.Core.AgentBehaviors;
using TCS.Core.AgentSystem;
using TCS.Core.TCSsolver;

// Compute start positions
Mesh3 kSlabMesh = iEnvironmentSrfGeo.Convert();
SlabInitializeAgents initializeAgents = new SlabInitializeAgents(iNcolumns, iEnvironmentGeo, iEnvironmentSrfGeo);
initializeAgents.ComputeColumnStartPosSlab();
List<Point3d> agentStartPositions = initializeAgents.ColumnStartPos;

// Compute nodal displacements of the environment & define TCSslabcartesianEnvironment
TCSslabCartesianEnvironment environment = new TCSslabCartesianEnvironment(StartPositions, iEnvironmentGeoPoints, kSlabMesh, iLoads, iMaterial);
environment.Execute();
Dictionary<int, List<Point3d>> startNodalDisplacements = environment.NodalDisplacement;

// Define behaviour
SlabMaxDisplacementBehavior maxDispBehavior = new SlabMaxDisplacementBehavior(iEnvironmentSrfGeo);
maxDispBehavior.StartNodalDisplacemenets = startNodalDisplacements;
List<BehaviorBase> agentBehaviors = new List<BehaviorBase>();
agentBehaviors.Add(maxDispBehavior);

// Define cartesian agents
List<CartesianAgent> cartesianAgents = new List<CartesianAgent>();
foreach(Point3d pt in agentStartPositions)
{
   CartesianAgent agent = new CartesianAgent(pt, agentBehaviors);
   cartesianAgents.Add(agent);
}

// Define agent system
List<AgentSystemBase> casSystems = new List<AgentSystemBase>();
TCSslabCartesianAgentSystem csSystem = new TCSslabCartesianAgentSystem(cartesianAgents, environment);
```

```
casSystems.Add(csSystem);

// Solver
SlabSolver testSlabSolver = new SlabSolver(casSystems);
testSlabSolver.AgentSystems = casSystems;
testSlabSolver.TCSslabSolverExecute();

// Output
oAgentStartPos = agentStartPositions;
oStartNodalDisplacement = startNodalDisplacements;
oMaxDispBehavior = maxDispBehavior;
oCartesianAgents = cartesianAgents;
```

Figure 9. C# code using the TCS framework to model example illustrated in figure7(a).

6. Discussion

This paper studied an interactive optimization technique to assist architects in the early design stage by providing guidance on structural and material quantities. The agent-based approach simplifies the computational pipeline by enabling live interaction, analysis, and solver guidance for the user. By incorporating gradient-based optimization as a behavior within the agent system, the search space results are improved compared to a pure geometric rule-based approach. The presented case studies demonstrate that the method generates layouts that fulfill the serviceability limit state deflection criteria for varying floor boundaries, area, and design requirements. The TCS framework and grasshopper plugin consolidate the study's developments and are available as open-source tools.

6.1. Limitations

The study presented in this paper has certain limitations and requires additional development to confirm the validity of results, particularly for large layouts. A significant lag in interaction speed was observed for large floor plan areas or layouts with multiple design constraints. While it is theoretically feasible to add multiple constraints to the current method, this may result in a black-box model with uncertain cause-and-effect relationships and outcomes. Additionally, a performance benchmark is necessary to quantify the tool's limitations and performance areas.

6.2. Outlook

Based on the study and its findings, integrating the workflow with performance algorithms to accelerate computation time, particularly for complex tasks, would be a valuable area to explore. Additionally, processing reuse material information in the (FE) model, which differs from standard factory process materials, has the potential to expand the tool's capabilities. Further research into detailed environmental considerations and modelling behaviour to introduce life-cycle-assessment-based constraints is also recommended.

6.3. Conclusion

The interactive optimization technique adopted in this study has the potential to make agent-based modelling more accessible to designers and simplify the design process by taking into account various technical constraints, such as structural performance and material quantities. The ultimate goal is to improve transparency and make the optimization process more interactive for the conceptual design stage.

Acknowledgements

The master thesis was conducted within the scope of the Integrative Technologies and Architectural Design Research M.Sc. program (ITECH) at the University of Stuttgart, under the guidance of the Institute of Building Structures and Structural Design (itke) and the Institute of Computational Design and Construction (ICD).

References

[1] A. Ratum, A. Sachari, and D. Wahjudi, "A Review on Circular Design Guideliness by Ideo and Ellen Macarthur Foundation," *Inst. Seni Budaya Indones.*, vol. 1, no. 1, pp. 61–70, 2019.

[2] X. Meng, T. U. Lee, Y. Xiong, X. Huang, and Y. M. Xie, "Optimizing support locations in the roof–column structural system," *Appl. Sci.*, vol. 11, no. 6, 2021, doi: 10.3390/app11062775.

[3] A. Mureşan, J. Brütting, D. Redaelli, and C. Fivet, "Design space of modular slab systems with discrete stiffness distribution and irregular column layout," *Proc. IASS Annu. Symp.*, vol. 2018, no. 3, pp. 1–8, 2018.

[4] J. Walker and J. Norman, "Designing timber buildings for longevity," no. December, pp. 56–59, 2021.

[5] A. Groenewolt, T. Schwinn, L. Nguyen, and A. Menges, *An interactive agent-based framework for materialization-informed architectural design*, vol. 12, no. 2. Springer US, 2018.

[6] F. Scheurer, "Computer Aided Architectural Design Futures 2005," *Comput. Aided Archit. Des. Futur. 2005*, no. January 2005, 2005, doi: 10.1007/1-4020-3698-1.

[7] T. Schwinn, "Landesgartenschau Exhibition Hall," in *Advancing Wood Architecture : A Computational Approach*, A. Menges, T. Schwinn, and O. D. Krieg, Eds. New York: Routledge, 2016, pp. 111–124.

[8] L. Orozco *et al.*, "Design Methods for Variable Density, Multi-Directional Composite Timber Slab Systems for Multi-Storey," in *Proceedings of the 39th eCAADe Conference*, 2021, vol. 1, pp. 303–312, [Online]. Available: http://papers.cumincad.org/cgi-bin/works/paper/ecaade2021_284.

[9] L. Nguyen, T. Schwinn, A. Groenewolt, M. Maierhofer, M. B. Zorn, D. Stieler, L. Siriwardena, F. Kannenberg, and "ABxM.Core: The Core Libraries of the ABxM Framework," DaRUS, 2022. [Online]. Available: https://doi.org/10.18419/darus-2994.

[10] T. Schwinn, "A systematic approach for developing agent-based architectural design models of segmented shells : towards autonomously learned goal-oriented agent behaviors," Institute for Computational Design and Construction, University of Stuttgart, Stuttgart, 2021.

[11] T. S. A. Menges, *A systematic approach for developing agent-based architectural design models of segmented shells*. .

[12] C. Preisinger and M. Heimrath, "Karamba - A toolkit for parametric structural design," *Struct. Eng. Int. J. Int. Assoc. Bridg. Struct. Eng.*, vol. 24, no. 2, pp. 217–221, 2014, doi: 10.2749/101686614X13830790993483.

[13] S. Ban, "Shigeru Ban Architects," *http://www.shigerubanarchitects.com/works/2013_tamedia-office-building/index.html*, 2013. http://www.shigerubanarchitects.com/works/2013_tamedia-office-building/index.html.

Proceedings of the IASS Annual Symposium 2023
Integration of Design and Fabrication
10–14 July 2023, Melbourne, Australia
Y.M. Xie, J. Burry, T.U. Lee and J. Ma (eds.)

Optimization of corrugation direction on corrugated shells

Kenji YAMAMOTO*, Kentarou DOI[a]

* Department of Architecture and Building Engineering, Tokai University
kyamamoto@tokai-u.jp

[a] Former Graduate Student of Tokai University

Abstract

The folded plate structure is a type of structure that enhances bending stiffness and strength by folding a flat plate. When a flat plate is corrugated, the in-plane stiffness and bending stiffness increase in the corrugation transverse direction, but the in-plane stiffness in the corrugation direction is extremely small because it behaves like a spring. Therefore, when using corrugated shell surfaces to enhance structural performance, it is important to consider the arrangement of the corrugations based on the direction of the forces acting on them. This paper investigates the optimal corrugation directions of corrugated shells using an optimization method. The finite element method with triangular shell elements is used for the structural analysis of corrugated shells. However, instead of directly discretizing the surface of corrugated shell, we approximate it as an anisotropic shell and used its constitutive law in the analysis. The objective of the optimization is to minimize the strain energy under self-weight, and the corrugation direction of each finite element is considered as design variable. The quasi-Newton method is used as the optimization method. We apply this method to two models with different boundary conditions, cylindrical shells and EP shells.

Keywords: cross section optimization, anisotropic plate, corrugated plate, Quasi-Newton method, form-finding analysis

1. Introduction

Thin-walled plates, while having low bending stiffness and bending strength, can be structurally enhanced by utilizing geometric effects. One such effect can be achieved through the folded-plate structure, in which a flat plate is repeatedly folded to add thickness and resist bending moments. Another approach is the shell structure, where forces are channeled in the in-plane directions by providing curvature in two directions to thin-walled plates. This reduces the occurrence of bending moments by distributing the forces throughout the structure. On the other hand, in nature, there are forms that have both of these structural forms in a composite manner. Shells, from which the term "shell structure" is derived, often have a shell surface that is rippled in small increments. CNIT La Defense, built in 1959, is an RC shell structure with a triangular plan and a span of 206 m. The shell surface is given additional stiffness by corrugating. Turin Exhibition Building [1] is a vaulted shell structure designed by Pier Luigi Nervi and built in 1948. The shell surface is precast and has many holes for light, but the overall proportions are corrugated.

In this paper, we define the direction in which the shell surface is corrugated as the "corrugation direction," and the direction perpendicular to it as the "transverse direction", as illustrated in Figure 1. When a flat plate is corrugated, the in-plane stiffness and bending stiffness increase in the corrugation direction, but the in-plane stiffness in the transverse direction is extremely small because it meanders like a spring. On the other hand, shell structures have curvature in two main directions, which mainly provides in-plane resistance to external forces. If corrugated plates are applied to the shell curvature, it may be structurally disadvantageous depending on the direction of the corrugations. When shell surfaces

Copyright © 2023 by Kenji YAMAMOTO, Kentarou DOI. Published in the Proceedings of the IASS Annual Symposium 2023 with permission.

are corrugated to enhance structural performance, an appropriate arrangement of corrugations should be considered depending on the direction of the forces.

This study investigates the optimal corrugation direction of corrugated shells using optimization methods. The objective function is the strain energy under self-weight, and the corrugation direction of each shell element, which is discretized by the finite element method, is used as the design variable. Mathematical programming is employed as the optimization method.

Previous studies similar to the present paper include Refs. [2], [3]. P. Winslow et al. [2] optimized the intersection angle and orientation of the rods in a two-way grid shell; they analyzed the shell as a continuum shell using the equivalent stiffness of the two-way grid and used heuristics as the optimization method. Y. Matsumura et al. [3] used mathematical programming to optimize the material orientation of shells made of orthotropic anisotropic materials.

T. Michels et al. [4] have generated corrugated cylindrical shells with high resistance to earthquakes by arranging the thrust lines of the arch, which are simultaneously subjected to vertical and horizontal loads, continuously in the girder direction, and have investigated the optimal corrugated shape.

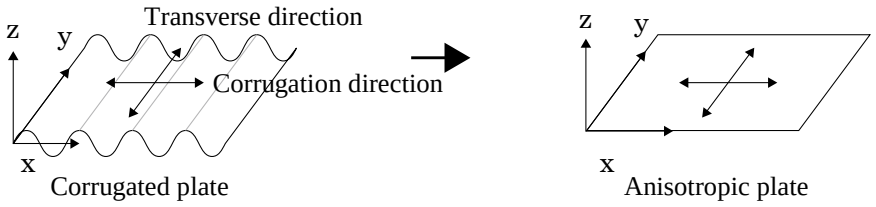


Figure 1. Replacement of corrugated plate with anisotropic flat plate

2. Optimization method

2.1. Equivalent stiffness of corrugated plate

The finite element method with triangular shell elements is used for the structural analysis of the corrugated shell. However, instead of discretizing the corrugated shell surface directly, the corrugated plate is approximated as an anisotropic flat plate in this study (Figure 1), and the following constitutive law of an anisotropic flat plate is applied.

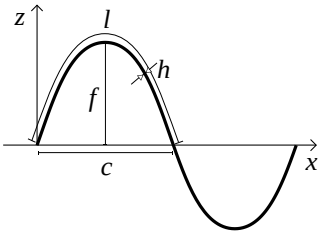
$$\begin{Bmatrix} \bar{N}_x \\ \bar{N}_y \\ \bar{N}_{xy} \end{Bmatrix} = \begin{bmatrix} \bar{A}_{11} & \bar{A}_{12} & 0 \\ \bar{A}_{12} & \bar{A}_{22} & 0 \\ 0 & 0 & \bar{A}_{66} \end{bmatrix} \begin{Bmatrix} \bar{\varepsilon}_x \\ \bar{\varepsilon}_y \\ \bar{\varepsilon}_{xy} \end{Bmatrix}, \quad \begin{Bmatrix} \bar{M}_x \\ \bar{M}_y \\ \bar{M}_{xy} \end{Bmatrix} = \begin{bmatrix} \bar{D}_{11} & \bar{D}_{12} & 0 \\ \bar{D}_{12} & \bar{D}_{22} & 0 \\ 0 & 0 & \bar{D}_{66} \end{bmatrix} \begin{Bmatrix} \bar{\kappa}_x \\ \bar{\kappa}_y \\ \bar{\kappa}_{xy} \end{Bmatrix} \quad (1), (2)$$

where $\bar{\varepsilon}_x$, $\bar{\varepsilon}_y$ and $\bar{\varepsilon}_{xy}$ are the in-plane strains in the mid-plane of the anisotropic plate, and $\bar{\kappa}_x$, $\bar{\kappa}_y$ and $\bar{\kappa}_{xy}$ are the curvatures. $\bar{N}_x$, $\bar{N}_y$, and $\bar{N}_{xy}$ are membrane force components, and $\bar{M}_x$, $\bar{M}_y$, and $\bar{M}_{xy}$ are moment components. Y.Xia et al. [5] derived the equivalent stiffness of an anisotropic flat plate for corrugated plates under the condition that the strain energy is equivalent. They derived a general-purpose constitutive law without limiting the shape of corrugation, but in this study, the shape of corrugation is sinusoidal as shown in Figure 2. In this case, following their formulation, we obtain the following equation.

$$\bar{A}_{11} = \frac{2ch^2}{h^2 I_1 + 12 I_2} \frac{Eh}{1-\nu^2}, \quad \bar{A}_{12} = \nu \bar{A}_{11}, \quad \bar{A}_{22} = \nu^2 \bar{A}_{11} + \frac{l}{c} Eh, \quad \bar{A}_{66} = \frac{c}{l} \frac{Eh}{2(1+\nu)}$$

$$\bar{D}_{11}=\frac{c}{l}\frac{Eh^3}{12(1-\nu^2)},\quad \bar{D}_{12}=\nu\bar{D}_{11},\quad \bar{D}_{22}=\frac{1}{2c}\left(I_2\frac{Eh}{(1-\nu^2)}+I_1\frac{Eh^3}{12(1-\nu^2)}\right),\quad \bar{D}_{66}=\frac{l}{c}\frac{Eh^3}{24(1+\nu)} \tag{3}$$

where E is Young's modulus, ν is Poisson's ratio, and $I_1=\int_s\left(\frac{dx}{ds}\right)ds$, $I_2=\int_s z^2 ds$. s is the coordinate along the corrugation curve.



$$z=f\sin\frac{\pi x}{c}$$

c : Half period of corrugation
f : Hight of corrugation
l : Lengh of corrugation
h : Plate thickness

Figure 2. Geometry of corrugated plate

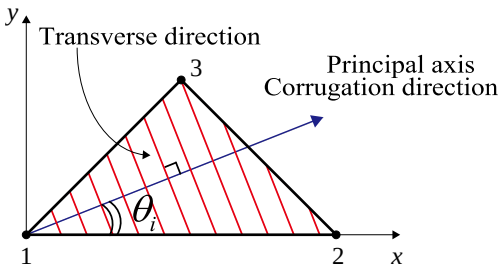
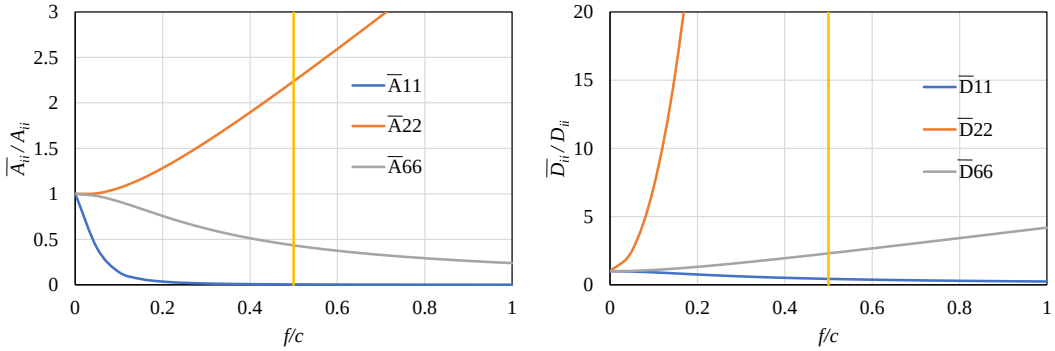


Figure 4. Triangular shell element



(a) In-plane stiffness (b) Out-of-plane stiffness

Figure 3. Equivalent stiffness

The in-plane stiffness of the equivalent stiffness in Eq. (3) is shown in Figure 3(a). The corrugation is represented by the plate thickness h=0.1 m, the half period of the corrugation c=0.5 m, Poisson's ratio ν=0.17, and the stiffness variation is expressed with the corrugation height f as a parameter. The horizontal axis is the ratio of the corrugation half period to the corrugation height, and the vertical axis is the ratio to the stiffness of the isotropic flat plate. Similarly, the out-of-plane stiffness is shown in Figure 3(b).

Figure 3(a) shows that $\bar{A}_{11}$ (in the transverse direction) decreases significantly with increasing corrugation height, while $\bar{A}_{22}$ (in the corrugation direction) increases. $\bar{A}_{66}$ decreases slowly. Figure 3(b) shows that $\bar{D}_{11}$ (in the transverse direction) decreases slowly as the corrugation height increases, while $\bar{D}_{22}$ (in the corrugation direction) increases sharply. $\bar{D}_{66}$ increases slowly. The corrugation height in this paper is f=0.25m, which is indicated by straight yellow lines in Figure 3.

Next, the treatment of the above constitutive law in the finite element method is described. Let θ_i denote the angle between the local x-coordinate of element i of the triangular shell element and the principal axis (transverse direction) of the corrugated plate (see Figure 4).

Since the constitutive law of the element involves a coordinate transformation in the angle θ_i, it can be expressed as follows.

$$\mathbf{D} = \mathbf{H}^T \mathbf{D}_0 \mathbf{H} \tag{4}$$

where

$$\mathbf{H} = \begin{bmatrix} \cos^2\theta_i & \sin^2\theta_i & \sin\theta_i\cos\theta_i \\ \sin^2\theta_i & \cos^2\theta_i & -\sin\theta_i\cos\theta_i \\ -2\sin\theta_i\cos\theta_i & 2\sin\theta_i\cos\theta_i & \cos^2\theta_i - \sin^2\theta_i \end{bmatrix} \tag{5}$$

and $\mathbf{D}_0$ is the stress-strain matrix of Eq. (1) or Eq. (2).

2.2. Formulation of optimization problem

The objective function is the strain energy of the shell under the self-weight.

$$U(\boldsymbol{\theta}) = \frac{1}{2}\sum_{i=1}^{M} \mathbf{d}_i{}^T \mathbf{k}_i(\theta_i)\mathbf{d}_i \tag{6}$$

where $\boldsymbol{\theta} = [\theta_1, ...\theta_M]^T$ is the principal axis angles of all elements, $\mathbf{d}_i$ is the displacement vector of the nodes comprising element *i*, and $\mathbf{k}_i(\theta_i)$ is the element stiffness matrix. *M* represents the number of elements. Eq. (6) is an unconstrained nonlinear programming problem, and the quasi-Newton method is used as the optimization technique. By partial differentiation of the above equation by θ_i, we obtain the following optimality condition.

$$\frac{\partial U(\boldsymbol{\theta})}{\partial \theta_i} = -\frac{1}{2}\mathbf{d}_i{}^T \frac{\partial \mathbf{k}_i}{\partial \theta_i}\mathbf{d}_i = 0, \quad (i = 1, \cdots, M) \tag{7}$$

The quasi-Newton method is used to find $\boldsymbol{\theta}$ satisfying the above equation. The element stiffness matrix $\mathbf{k}_i$ can be expressed as

$$\mathbf{k}_i = \int_S \mathbf{B}^T \mathbf{D}\mathbf{B} dS \tag{8}$$

where $\mathbf{B}$ is the strain-node displacement matrix and *S* is the element area. Therefore, $\partial\mathbf{k}_i / \partial\theta_i$ can be expressed as

$$\frac{\partial \mathbf{k}_i}{\partial \theta_i} = \int_S \mathbf{B}^T \frac{\partial \mathbf{D}}{\partial \theta_i}\mathbf{B} dS, \quad \frac{\partial \mathbf{D}}{\partial \theta_i} = \frac{\partial \mathbf{H}^T}{\partial \theta_i}\mathbf{D}_0\mathbf{H} + \mathbf{H}^T\mathbf{D}_0\frac{\partial \mathbf{H}}{\partial \theta_i}$$

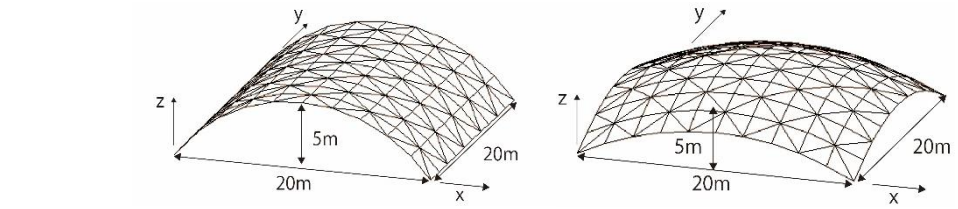
$$\frac{\partial \mathbf{H}}{\partial \theta_i} = \begin{bmatrix} -2\sin\theta_i\cos\theta_i & 2\sin\theta_i\cos\theta_i & \cos^2\theta_i - \sin^2\theta_i \\ 2\sin\theta_i\cos\theta_i & -2\sin\theta_i\cos\theta_i & -\cos^2\theta_i + \sin^2\theta_i \\ -2(\cos^2\theta_i - \sin^2\theta_i) & 2(\cos^2\theta_i - \sin^2\theta_i) & -4\sin\theta_i\cos\theta_i \end{bmatrix}$$

3. Numerical example

3.1. Analysis models

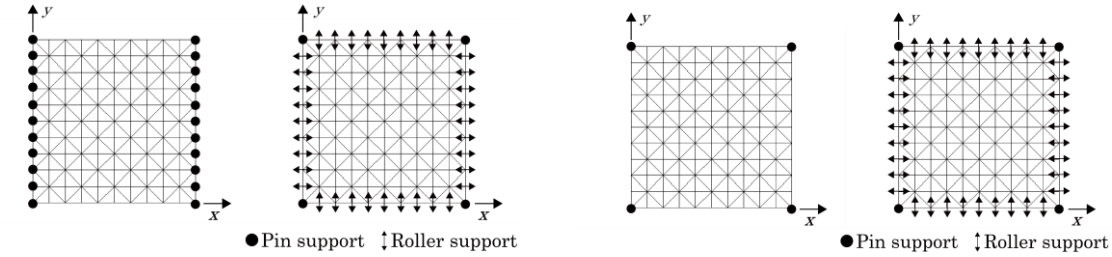
There are multiple analysis models, each with the geometry of a cylindrical shell or an EP shell, respectively. Both geometries have dimensions of 20 meters in span in the x-direction, 20 meters in span in the y-direction, and a 5-meter rise (as shown in Figure 5). The dimensions of the corrugated plate are defined as corrugation half period *c*=0.5 m, corrugation height *f*=0.25 m (corrugation length *l*=0.731 m), and plate thickness *t*=0.1 m. Since RC is assumed as the material, Young's modulus is $E = 2.1\times10^4$ N/mm^2, Poisson's ratio ν = 0.17, and unit volume weight ρ= 24 kN/m^3. The load is self-weight and thus a distributed load of $\omega = \rho hl / c$ unit area is given by equivalent nodal forces. For each type of shell,

there are two support conditions: 2-edge pin support and roller support for cylindrical shells, and 4-point pin support and roller support for EP shells, as illustrated in Figure 6. Therefore, a total of four models are optimized.



(a) Cylindrical shell (b)EP shell

Figure 5. Analysis models



(a1) 2-edge pin support (a2) roller support (b1) 4-point pin support (b2) roller support

(a) Cyrindrical shell (b) EP shell

Figure 6. Support conditions

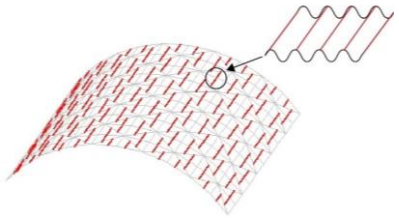


Figure 7. Graphical representation of corrugations:
the red line on each element represents the transverse direction of the corrugation.

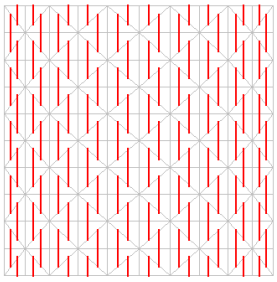
3.2. Optimization results

3.2.1. Results of 2-edge pinned cylindrical shell

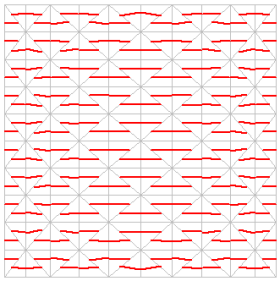
The initial solution and the optimal solution for the 2-edge pinned cylindrical shell are shown in Figure 8 and Figure 9, respectively. The red lines in Figure (a) represent the corrugation transverse direction of each element, as in Figure 7. The transverse direction in the initial solution was given in the *y*-direction, but in the optimal solution it is changed by 90 degree, toward the supported boundary.

Figure (b) is a membrane force diagram, where the magnitude of the membrane force in the principal stress direction is represented by the length of the line. The maximum value is also entered in the figure. Comparing Figure 8(b) and Figure 9(b), there is no change in the membrane force distribution. Figure (c) shows a bending moment diagram in the same way. The initial solution in Figure 8(c) shows that the bending moment for each element occurs in two directions, while the bending moment for the optimal solution in Figure 9(c) occurs mainly in one direction and in the same direction as the corrugation pattern in Figure 9(a). Note that these membrane forces and bending moments are the resultant stresses when the corrugated plate is considered an anisotropic flat plate.

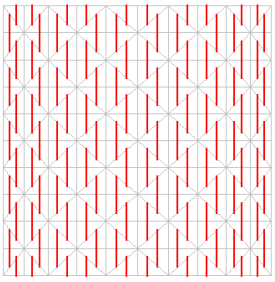
Figure (d) is a deformation diagram, showing the deformation due to the self-weight magnified 100 times. The deformation of the optimal solution is small compared to the initial solution.



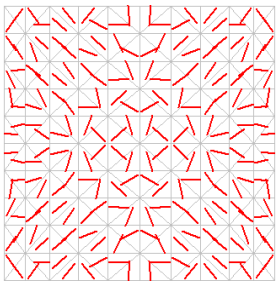
$U = 11.8$kNm
(a)Corrugation pattern



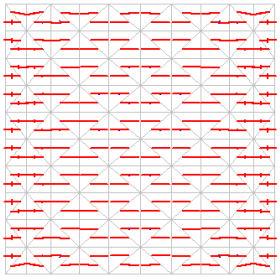
$U = 0.19$kNm
(a)Corrugation pattern



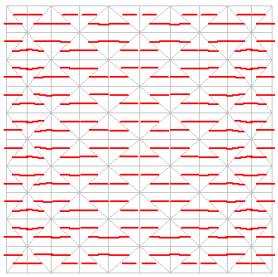
$U = 4.07$kNm
(a)Corrugation pattern



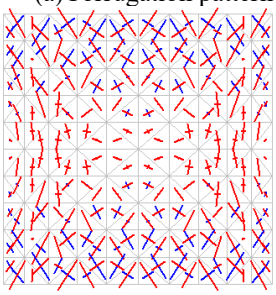
$U = 0.60$kNm
(a)Corrugation pattern



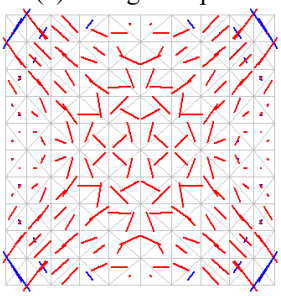
Max:52.8kN/m
(b)Membrane force diagram



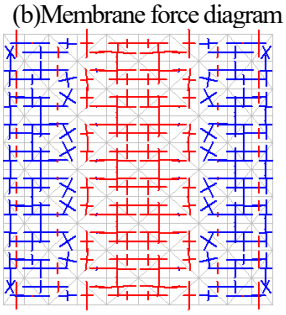
Max:58.1kN/m
(b)Membrane force diagram



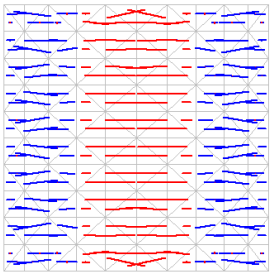
Max: 146.9kN/m
(b)Membrane force diagram



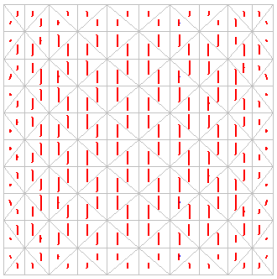
Max:168.1kN/m
(b)Membrane force diagram



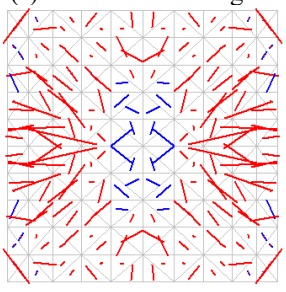
Max:4.86kN-m/m
(c)Bending moment diagram



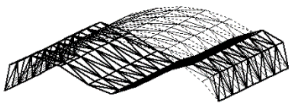
Max:5.20kN-m/m
(c)Bending moment diagram



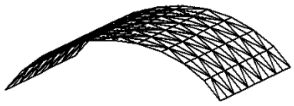
Max:16.2kN-m/m
(c)Bending moment diagram



Max:12.1kN-m/m
(c)Bending moment diagram



Max:0.048m
(d)Deformation diagram(x100)



Max:0.00082m
(d)Deformation diagram(x100)



Max:0.0104m
(d)Deformation diagram(x100)



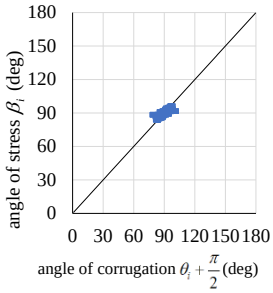
Max:0.00151m
(d)Deformation diagram(x100)

Figure 8. Initial solution (Cylindrical shell, 2-edge pin)

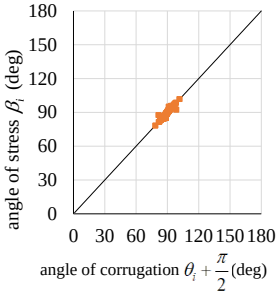
Figure 9. Optimal solution (Cylindrical shell, 2-edge pin)

Figure 11. Initial solution (Cylindrical shell, roller)

Figure 12. Optimal solution (Cylindrical shell, roller)

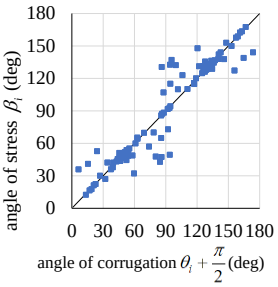


(a) Membrane force

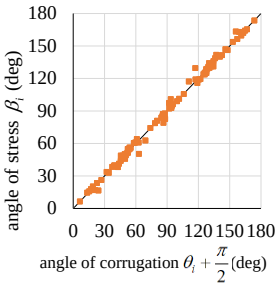


(b) Bending moment

Figure 10. Relation between corrugation orientation angle and principal stress angle (Cylindrical shell, 2-edge pin)

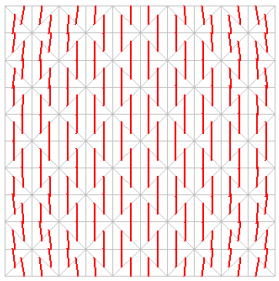


(a) Membrane force



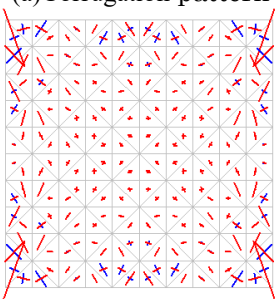
(b) Bending moment

Figure 13. Relation between corrugation orientation angle and principal stress angle (Cylindrical shell, roller)



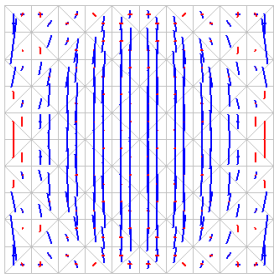
$U = 15.7$kNm

(a)Corrugation pattern



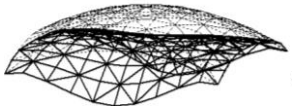
Max:709.1kN/m

(b)Membrane force diagram



Max:39.02kN-m/m

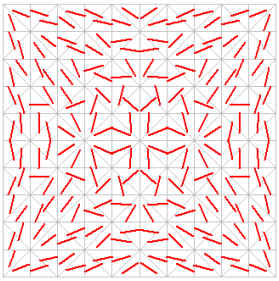
(c)Bending moment diagram



Max:0.0508m

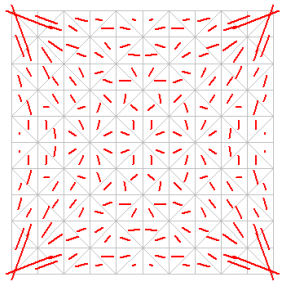
(d)Deformation diagram(x100)

Figure 14. Initial solution (EP shell, 4-point pin)



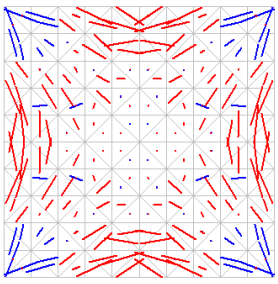
$U = 1.09$kNm

(a)Corrugation pattern



Max:405.9kN/m

(b)Membrane force diagram



Max:10.4kN-m/m

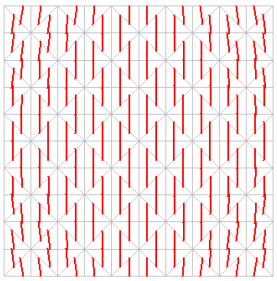
(c)Bending moment diagram



Max:0.00284m

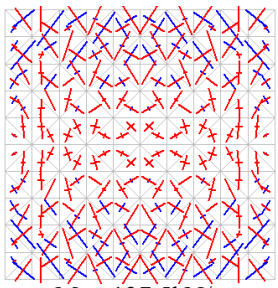
(d)Deformation diagram(x100)

Figure 15. Optimal solution (EP shell, 4-point pin)



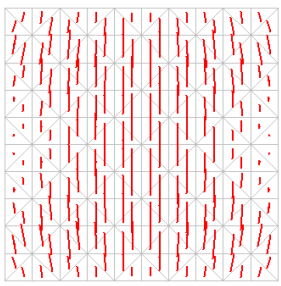
$U = 3.48$kNm

(a)Corrugation pattern



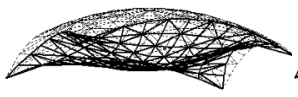
Max:137.5kN/m

(b)Membrane force diagram



Max:17.1kN-m/m

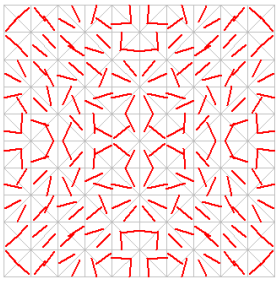
(c)Bending moment diagram



Max:0.0102m

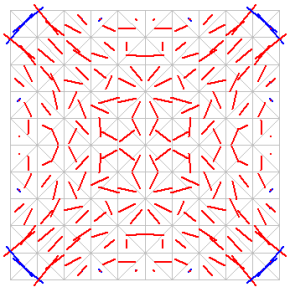
(d)Deformation diagram(x100)

Figure 17. Initial solution (EP shell, roller)



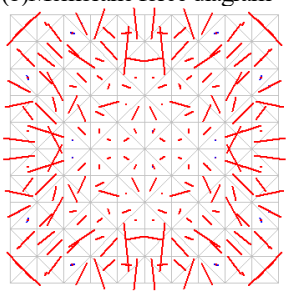
$U = 0.51$kNm

(a)Corrugation pattern



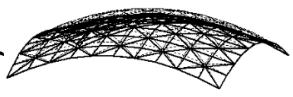
Max:175.3kN/m

(b)Membrane force diagram



Max:5.72kN-m/m

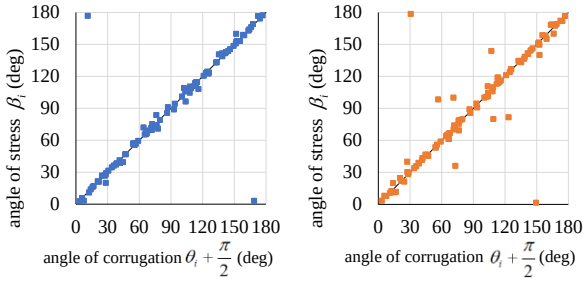
(c)Bending moment diagram



Max:0.00106m

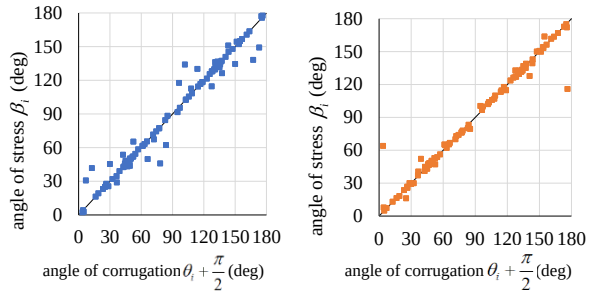
(d)Deformation diagram(x100)

Figure 18. Optimal solution (EP shell, roller)



(a) Membrane force (b) Bending moment

Figure 16. Relation between corrugation orientation angle and principal stress angle (EP shell, 4-point pin)



(a) Membrane force (b) Bending moment

Figure 19. Relation between corrugation orientation angle and principal stress angle (EP shell, roller)

Figure 10(a) plots the orientation angle of the corrugation $\theta_i + \frac{\pi}{2}$ (the transverse direction) for each element on the horizontal axis and the angle of the principal membrane force on the vertical axis for the optimal solution. The figure shows that the orientation angle of the corrugation and the angle of the membrane force are almost identical. Figure 10(b) similarly plots the orientation angle of the corrugation versus the angle of the principal bending moment. In this case, too, the two are almost identical.

3.2.2. Results of roller-supported cylindrical shell

The results of the roller-supported EP shell are shown in Figures 11 and 12. The corrugation transverse direction in the initial solution of Figure 11(a) was given in the *y*-direction, but in the optimal solution of Figure 12(a) it is oriented towards the outer boundary and irregularly oriented near the center, In the initial solution of Figure 11(b), the membrane force for each element occurs in two directions, but in the optimal solution of Figure 12(b), it occurs in one direction. In Figure 11(c), the bending moment occurs mainly in the *y*-direction, while in the optimal solution of Figure 12(c), the bending moment occurs in a direction similar to the membrane force in Figure 12(b). Near the center of the shell, the bending moment is small. Figure 13 shows that the orientation angles of the corrugation tend to coincide with the angles of the principal stresses.

3.2.3. Results of 4-point pinned EP shell

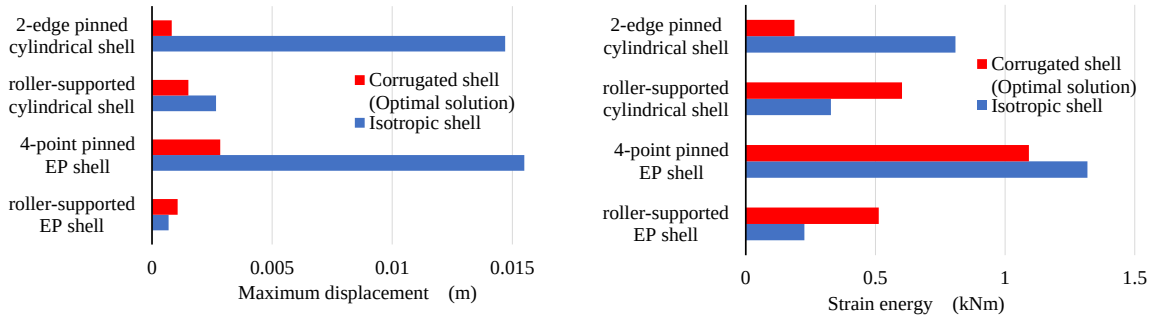
The results of the 4-point pinned EP shell are shown in Figures 14 and 15. Figure 14(a) shows that the corrugation pattern is oriented toward the support points and irregularly oriented near the center. In the initial solution of Figure 14(b), the membrane force for each element occurs in two directions, but in the optimal solution of Figure 15(b), it occurs in one direction. In Figure 14(c), the bending moment occurs mainly in the *y*-direction, while in the optimal solution of Figure 15(c), the bending moment occurs in a direction similar to the membrane force in Figure 15(b). Near the center of the shell, the bending moment is small. Figure 16 shows that the orientation angles of the corrugation tend to coincide with the angles of the principal stresses.

3.2.4. Results of roller-supported cylindrical shell

The results of the roller-supported EP shell are shown in Figures 17 and 18. The corrugation pattern of the optimal solution is oriented toward the boundary and irregularly oriented near the center. The results are very similar to those of the roller-supported cylindrical shell. Figure 19 still shows that the orientation angles of the corrugation tend to coincide with the angles of the principal stresses.

3.3. Comparison with isotropic shells

In order to observe the mechanical effects of corrugated shell surfaces, we compared the mechanical properties of optimal solutions obtained in the previous sections with those of normal shells of uniform thickness. The shells were separately analyzed by replacing the constitutive laws in equations (1) and (2) with the constitutive laws of isotropic flat plates. A comparison of the maximum displacement under self-weight is shown in Figure 20(a), and a comparison of strain energy is shown in Figure 20(b). The red bars represent corrugated shells, and the blue bars represent isotropic shells. The figures show that the values for corrugated shells are generally smaller than those for isotropic shells, but in the two cases of roller support, the strain energy of the corrugated shell is larger. This is due to the greater weight of the corrugated plate shell than the isotropic shell. For shells with free edges, the effect of corrugation is significant because they are more susceptible to bending and the membrane force flow is limited. On the other hand, shells with fully supported boundaries have a large shell effect, so the effect of corrugation is eliminated.



(a) Maxmum displacement (b) Strain energy

Figure 20. Comparison of corrugated and isotropic shells

4. Conclusion

In this paper, we investigate the optimal corrugation directions of corrugated shells. The corrugations on the shell surface are modeled as anisotropic materials, and the corrugation direction of each element is used as a design variable for optimization using the quasi-Newton method. Our results show that:

(1) The proposed optimization method yielded corrugation directions for corrugated shells with low strain energy under self-weight. The optimal solution tended to produce membrane forces and bending moments in only one direction over the entire region of the shell for both models, and the corrugation transverse direction tends to coincide with the direction of the principal stresses.

(2) We compare the mechanical properties of corrugated shells obtained by optimization and normal isotropic shells. The comparison of displacement and strain energy confirms the effect of applying corrugated shells. Depending on the support conditions, the strain energy may be lower for the normal shell due to the increase in self-weight caused by the corrugated surface.

The optimal solutions obtained in this paper may be difficult to realize as an actual structure because the corrugation direction changes abruptly in some places, resulting in almost perpendicular corrugation at adjacent elements. For this reason, we also propose a method to represent a smooth corrugation pattern by using contour lines of polynomial functions [6].

References

[1] P. L. Nervi “Structures”, *McGraw-Hill book*, 1956.

[2] P. Winslow, S. Pellegrino and S. B. Sharma, “Mapping two-way grids onto free-form surfaces”, *Journal of the International Association for Shell and Spatial Structures*, Vol. 49, No.2, pp. 123-130, 2008.

[3] Y. Muramatsu, M. Shimoda, “Optimization approach for designing free-orientation of orthotropic materials of a shell structure”, *Transactions of the JSME*, Vol83, No851, pp.1-15, 2017. (in Japanese)

[4] T. Michiels, S. Adriaenssens, and M. Dejong, “Form finding of corrugated shell structures for seismic design and validation using non-linear pushover analysis”, *Engineering Structures*, 181, pp.362-373, 2019.

[5] Y. Xia, M. I. Friswell and E. I. Saavedra Flores, “Equivalent models of corrugated panels”, *International Journal of Solids and Structures*, 49, pp.1453–1462, 2012.

[6] K. Doi and K. Yamamoto, “Optimization of corrugation pattern on corrugated shells using contour lines of polynomial functions”, *Proceedings of the School of Engineering of Tokai University*, Vol.61, No.1, pp.29-36, 2021. (in Japanese)

Proceedings of the IASS Annual Symposium 2023
Integration of Design and Fabrication
10–14 July 2023, Melbourne, Australia
Y.M. Xie, J. Burry, T.U. Lee and J. Ma (eds.)

Performance-based fire protection design and practical application of large-space aluminum alloy structure

Yuanwen OUYANG[a,b],Yufeng JIAO[b,*], Zhiqiang LI[b] , Xiaowei LIU[b]

[a] Shanghai Jianke Aluminum Structure Engineering Research Institute
[b,*] Shanghai Tongzheng Construction Technology Group Co., Ltd
jiaoyufeng@tal-china.com

Abstract

The use of aluminium alloys in the construction industry is becoming increasingly popular owing to their favourable mechanical properties such as high strength-to-weight ratio, excellent corrosion resistance, appealing appearance, good recyclability and ease of fabrication. However, a substantial number of studies have shown that high temperature will significantly reduce the strength and elastic modulus of aluminum alloys. Thus, investigations on the structural behaviour of aluminium alloy structures in fire disaster are necessary and significant.This paper presents a review of recent studies on the structural behaviour and performance-based design of aluminium alloy structures exposed to fire. Then, based on cases of some practical aluminum alloy large-span projects in China, such as Pixian Gymnasium, Zhangshu Sports Center, Expo Cultural Park Exhibition Greenhouse and other projects, the performance-based design and passive fire protection methods of large-span aluminum alloy structures are studied. The main contents are as follows: First, the fire smoke analysis model provided in NFPA92B and NFPA 204 is used to calculate the air temperature at different heights above the central axis of the flame. Then the fire dynamics simulation software FDS is used to simulate and analyze the fire development and smoke spread in the building. Through numerical simulation, the deformation and temperature field distribution of members of aluminum alloy structure under fire are obtained. The results show that FDS technology can accurately predict the non-uniform distribution of smoke temperature field in large space buildings. This study will enrich the fire resistance theory of large space aluminum alloy structures and provide reference for fire risk assessment of such large space buildings.

Keywords: performance-based fire resistance, large-space aluminum alloy structure, fire dynamic simulation, smoke temperature field

1.Introduction

Due to the increasingly large scale and complex structure of modern space buildings, the fire resistance performance of different structure will produce different mechanical performances and failure modes under various fire source locations, fire scale, structural parameters, and load conditions. In addition, the development and application of new material and technology has made the requirements for building fire protection increasingly personalized, and fire safety research of spatial structure have encountered many new challenges[1-2]. Traditional fire safety analysis methods cannot meet the design requirements of this new type of building, and performance-based design is the best way to solve the problem[3-4].

The performance-based fire resistance design method is to simulate and calculate the overall performance of the structure under real fire temperature rise, and determine the best fire protection

Copyright © 2023 by Yuanwen OUYANG, Yufeng JIAO, Zhiqiang LI and Xiaowei LIU. Published in the Proceedings of the IASS Annual Symposium 2023 with permission.

design scheme to achieve minimum fire economic losses and personal safety.Firstly, it is necessary to determine the overall safety goals, including performance-based goals and performance-based standards. Then reasonable fire scenario is defined. By selecting appropriate calculation formulas and method, a simulation model that conforms to the fire characteristics of the building is established to analyze the possible fire source location ,the spread and diffusion of fire smoke, the working conditions of fire-fighting facilities, personnel evacuation and escape behavior. Performance based fire resistance analysis is complex and uncertain, posing high requirements for designers.

Since 2000, China has established a "Fire Safety Engineering Working Group", which is responsible for collecting and analyzing relevant foreign data, proposing a development plan for China's fire safety engineering standards, organizing the formulation of performance-based design standards, promoting research in fire science, establishing performance-based evaluation methods, and establishing relevant database. In 2004, Tianjin Fire Science and Technology Research Institute of MEM, Sichuan Fire Science and Technology Research Institute and the State Key Laboratory of Fire Science of the University of Science and Technology of China jointly completed the Technical Guidelines for performance-based fire protection design of buildings, which is the first complete performance-based fire protection guidelines in China and has established a relatively complete performance-based fire protection design method and system.

With rapid economic development in the past 20 years, China has gradually established a method system that meets the domestic engineering needs: establishing fire safety analysis models and evaluation methods suitable for high-rise buildings, atrium buildings, and densely populated large space buildings [5-6]; A quantitative analysis model suitable for engineering application were established by combining field, area, and network. The reliability of the mathematical model was verified by combining simulation results with physical experiments; Study on personnel evacuation path planning and design was conducted to obtain status data such as spatial location information, complex perception ability, cognitive ability of personnel as well as evacuation facilities and fire environment [7-9]; The dynamic analysis model of personnel evacuation was established by using situational experiment and isometric graph methods, and the simulation software was completed on this basis; In addition, preliminary studies have been conducted on deterministic criteria, including fire ignition, fire development, limiting fire spread, life safety criteria, and safety factors.

At present, a large number of fire protection design cases of large-span space structures based on fire safety engineering methods have been accumulated, including the checking calculation of fire resistance bearing capacity of roof structures and components, thermal coupling simulation analysis and fire protection design, but most of them were concentrated on steel structures, and the fire resistance design methods of aluminum alloy structures were less involved. Aluminum alloy structures are favored by architects because of their low density, corrosion resistance and strong metal texture. A single-layer aluminum alloy reticulated shell has been increasingly used as a roof supporting structure in public buildings. Yet, the performance-based analysis of aluminum alloy structures is still relatively isolated from the respective fields of fire science and structural engineering, and the high-temperature stress of aluminum alloy structures is still in the initial research stage. The effects of smoke and temperature under fire are not yet uniform. The risk level changes of aluminum alloy structures and issues such as the route and time of personnel escape have not been considered and evaluated in the same environment. Therefore, the overall safety problem of aluminum alloy structures under fire cannot be well solved, the systematic characteristics of building fires cannot be revealed, and the interrelationships between various fire actions and influencing factors cannot be reflected as a whole. Moreover, the actual engineering situation is very different, and the models and methods related to fire development and spread, smoke flow, personnel safety evacuation and structural fire resistance analysis still require a lot of in-depth research.

Based on typical well-known domestic aluminum alloy large-span structural engineering cases, the mechanical properties and overall structural stability of aluminum alloy large-span roofs under fire was

analyzed. The performance-based fire protection design method was proposed and safety performance evaluation under fire was conducted. The project cases in this paper provide reference for the construction of large and complex buildings and engineering application of new technology and materials.

2. Case Study on Fire Resistance of Long Span Aluminum Alloy Reticulated Shell Structures

2.1. Pixian Gymnasium

2.1.1. Project Overview

Pixian Gymnasium is located in Pixian County, Chengdu City, Sichuan Province. It consists of a comprehensive gymnasium and an indoor swimming pool, with the roof of the two gymnasiums connected into one. An irregular hyperbolic aluminum alloy single layer reticulated shell with a span of 65.5 m was adopted.

2.1.2. Basic parameters

According to the European Code for Fire Protection Design of Aluminum Alloys, 170 ℃ was selected as the criterion for determining the failure temperature of aluminum alloys. The air temperature rise formula for large space buildings provided in the Technical Code for Fire Protection of Steel Structures of Buildings (CECS 200:2006) was selected as the air temperature rise curve. The fire smoke analysis models provided in NFPA 92B and NFPA 204 were used to calculate the airflow temperatures at different heights above the central axis of the flame, and compared with the critical failure temperature of aluminum alloy structures to determine the range of protection for aluminum alloy structures.

Fire source 1 is located on the ground of the competition hall area (at an elevation of 0 m), with a fire scale of 8.0 MW； Fire source 2 is located on the ground of the swimming pool site (at an elevation of 0 m), with a fire scale of 2.5 MW; Fast t^2 fire model was used for fire growth curve. The temperature of the airflow at different heights is shown in Table 1 and Table 2.

Table 1. Analysis of air flow temperature on axis of fire source one (8.0MW).

Height	Smoke temperature riseΔT（℃）	Average temperature of smoke T_m（℃）	Temperature of Smoke plume T_c（℃）	Temperature considering a safety factor of 1.2（℃）
11.0m	62.9	88.9	171.6	205.9
12.0m	57.7	83.7	152.0	182.4
13.0m	53.2	79.2	136.2	163.4
14.0m	49.4	75.4	123.4	148.1
15.0m	46.1	72.1	112.8	135.4

Table 2. Analysis of air flow temperature on axis of fire source two (2.5MW).

Height	Smoke temperature riseΔT（℃）	Average temperature of smoke T_m（℃）	Temperature of Smoke plume T_c（℃）	Temperature considering a safety factor of 1.2（℃）
6.0m	81.7	107.7	210.2	252.2
7.0m	70.0	96.0	168.4	202.1
8.0m	61.3	87.3	140.0	168.0
9.0m	54.5	80.5	119.7	143.6
10.0m	49.0	75.0	104.6	125.5

It can be seen from table 1 that the airflow temperature on the plume axis of the fire source one at a distance of 13m above fire source one is 163.4℃ (considering a safety factor of 1.2), which is lower than the critical temperature determination criterion of 170℃; From table 2, it can be seen that the airflow temperature on the plume axis of the fire source 2 at a distance of 8m above the fire surface is 168℃ (considering a safety factor of 1.2), which is below that of the critical temperature determination criterion of 170℃; Therefore, it is possible to determine the range of fire protection for the aluminum alloy structure of the gymnasium: the aluminum alloy structure within a range of 13m above the ground of the gymnasium competition venue in the case of fire source 1 should be protected; Aluminum alloy structures within 8m above the ground of the swimming pool competition venue in the case of fire source 2 should be protected.

2.1.3. Numerical simulation model

Due to the low melting point of aluminum alloys, temperature has a significant impact on the material and mechanical properties of aluminum alloys. As temperature increases, the material properties of aluminum alloys will undergo significant changes. In the finite element model, it is necessary to consider the changes in material properties at high temperatures. Considering that the highest point of the stand at 15.65m is the closest to the vertical distance of the reticulated shell and there are combustibles here, the fire source is set on the stand at 15.65m height, as shown in Figure 1.

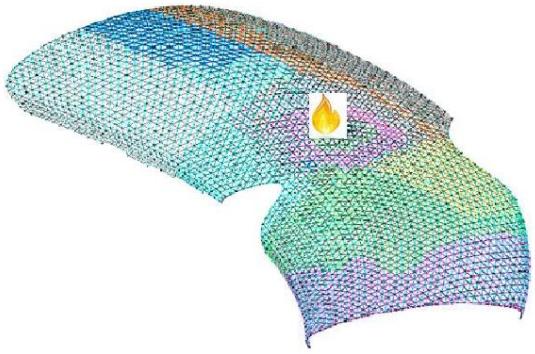


Figure 1. Finite Element Model and Fire Source Location.

2.1.4. Results analysis

Figure 2 shows the temperature field distribution of aluminum alloy structural members. It can be seen that the yield strength of aluminum alloy materials decreases with increasing temperature. When the temperature is around 150 ℃, there will be a significant decline of yield strength, and at 350 ℃, the

downward trend tends to be gentle. When the temperature reaches 500 ℃, aluminum alloy materials have lost their bearing capacity. When the calculation time is 1200s, the maximum temperature at the center of the fire source is 282 ℃. At this time, the yield strength of the rod decreases significantly, and corresponding fire protection measures must be taken.

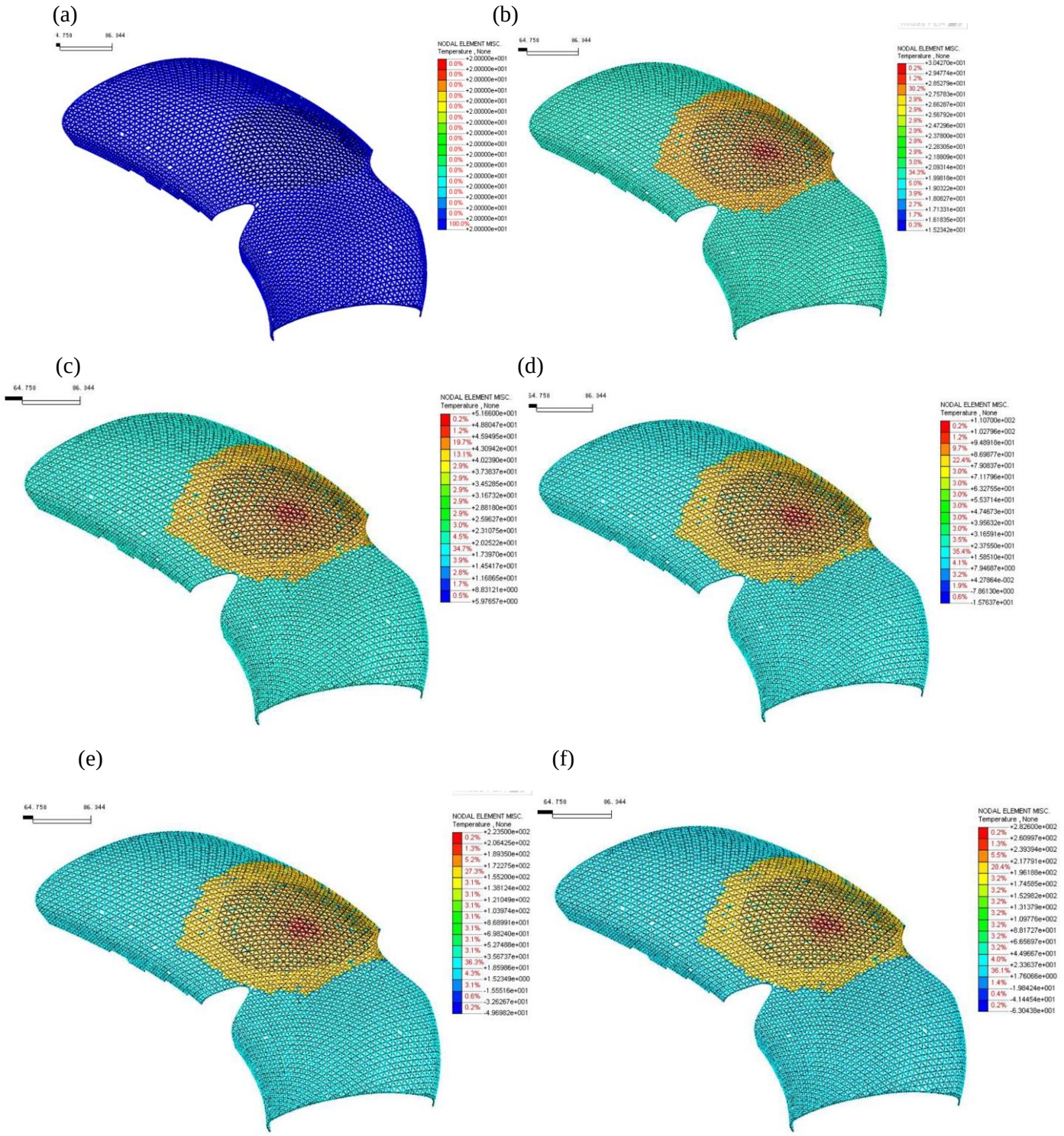


Figure 2. Temperature Field Distribution of Aluminum Alloy Structural Members: (a) 0s (b) 200s(c) 400s (d) 600s(e) 800s (f) 1200s

Figure 3 shows the deformation development of reticulated shell structures under fire. According to the simulation, it can be seen that with the increasing distance from the fire source, the deformation of aluminum alloy structural members gradually decreases, and the deformation above the fire source has exceeded 500mm.This is caused by the material properties of aluminum alloys. As fires continue, aluminum alloys continuously absorb the temperature of hot air through convection and radiation, ultimately leading to a continuous rise in the temperature of the members. The elastic modulus of aluminum alloys is inversely proportional to temperature, and is almost zero at 500 ℃.

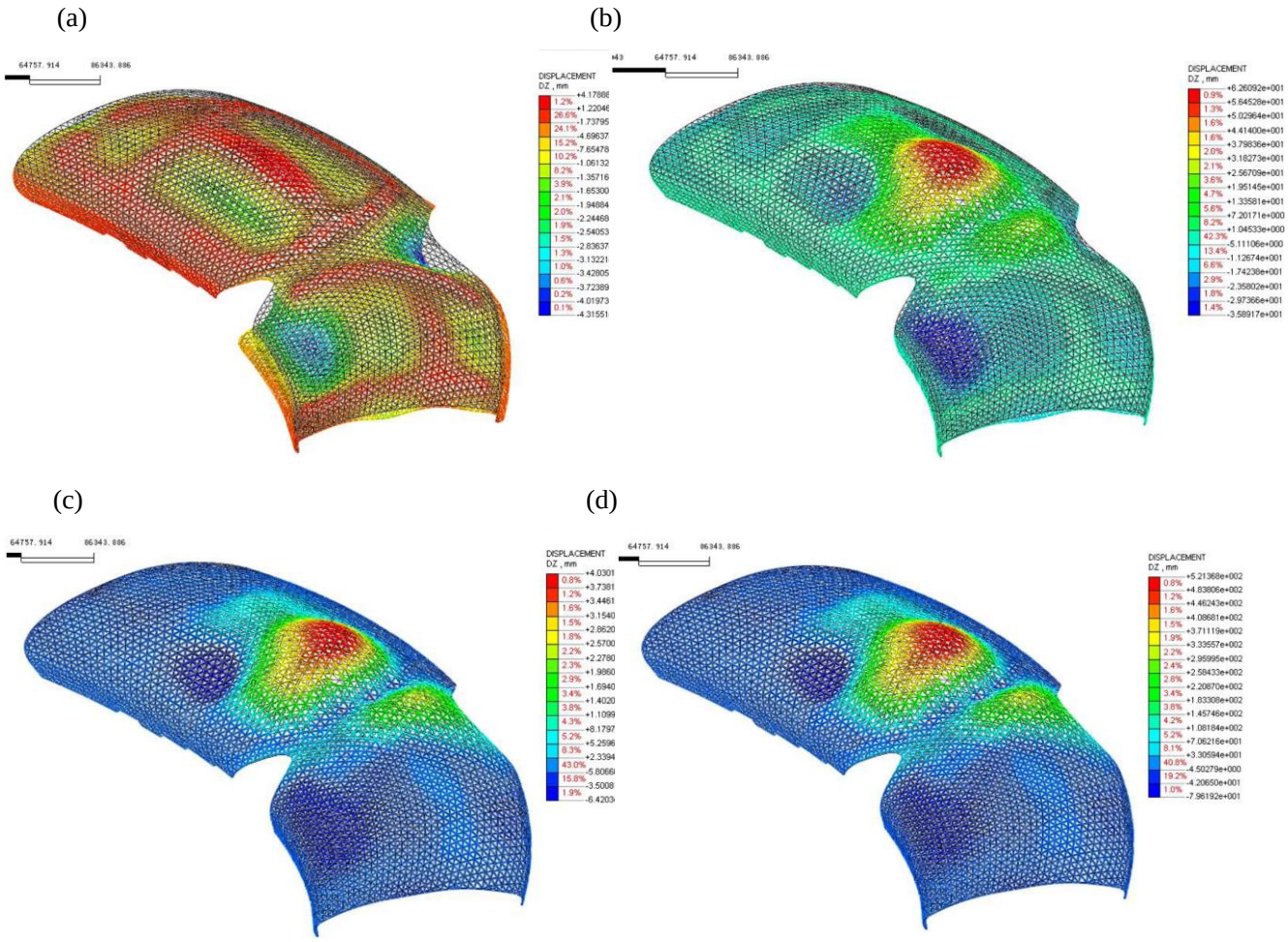


Figure 3. Deformation diagram of reticulated shell structure under fire: (a) 0s (b) 400s (c) 800s (d) 1200s

From the above analysis, it can be seen that under the most unfavorable design fire scenario, aluminum alloy roof structures without fire protection cannot meet the fire resistance bearing capacity requirements, and fire protection measures should be taken for aluminum alloys. Currently, effective water spray systems are commonly used for fire prevention measures of aluminum alloy structures. In addition, the aluminum alloy structure can be separated from the functional area by building a fireproof partition to block the conduction of heat flow under fire. Moreover, there are no fireproof coating products suitable for aluminum alloy on the market. After comprehensive consideration, it is proposed to use a water spray system and masonry fire barriers to protect the aluminum alloy structure in this project.

2.2. Expo Cultural Park Exhibition Greenhouse

2.2.1. Project Overview

Expo Cultural Park Exhibition Greenhouse includes four venues, and outdoor overhead corridors are set at a height of 5.5m between the aboveground buildings P2, P3, and P4. Steel columns are used as vertical load-bearing members. The roof is a string reticulated structure with special-shaped top chord， in which the top chord is made of aluminum alloy structure, the bottom chord is made of coated sealing cable, and the rest of the members of the structure are of steel structure, as shown in Figure 4.

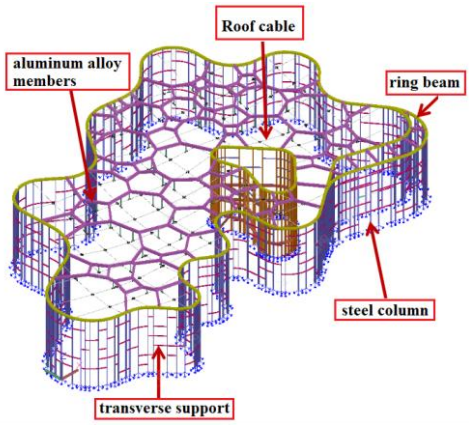


Figure 4. Structural diagram

2.2.2. Fire smoke simulation

The fire smoke model of P2, P3 and P4 venues was established by using Pyrosim software, as is shown in Figure 5. The grid size of the model was 0.5m×0.5m×0.5m, and the ambient temperature was 20°C. The fire simulation software FDS was used for numerical simulation.

(a) (b) (c)

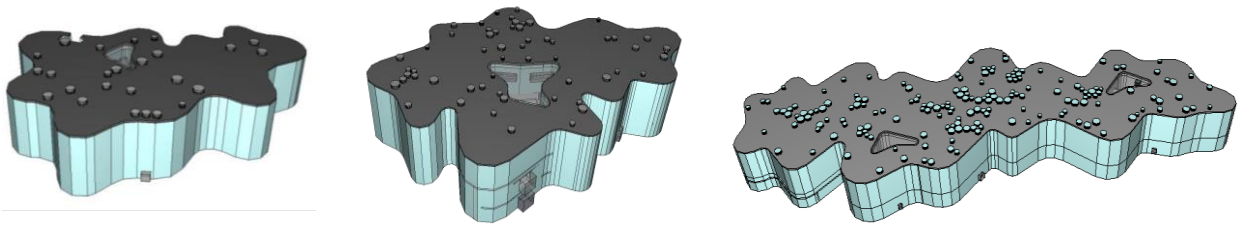


Figure 5. Fire Smoke Model: (a) P2 (b) P3 (c) P4

(a) (b)

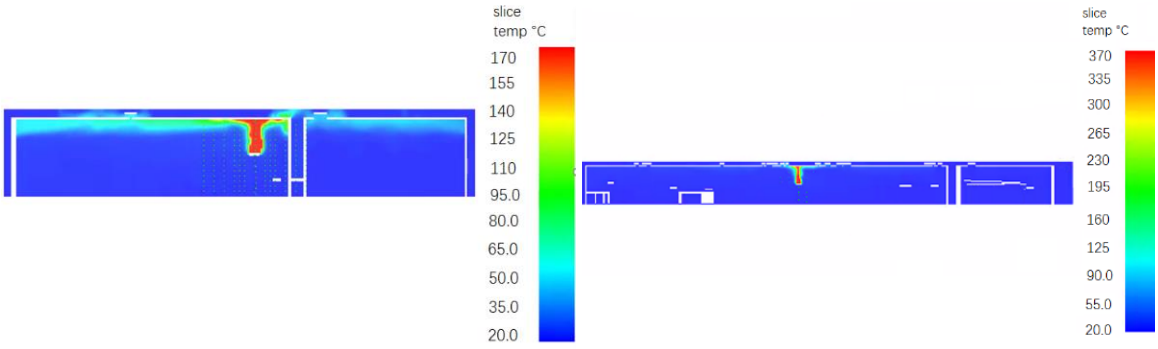


Figure 6. Profile temperature map: (a) Fire Scenario 2 (b) Fire Scenario 8

Figure 6 shows the sectional temperature map under two typical fire scenarios. Fire Scenario 2 (The fire resource is located at the 7.5m elevation of P2, with a fire scale of 11.0MW): Due to the high elevation of the fire source and the impact of fire smoke, the temperature near the aluminum alloy roof directly above the fire source is the highest, up to 170 ℃. The temperature near the aluminum alloy roof in the area far away from the fire source is relatively low, about 40-60 ℃.Fire Scenario 8 (The fire resource is located at the 7.0m elevation of P4, with a fire scale of 11.0MW): The temperature near the aluminum alloy roof directly above the fire source is relatively high, about 370 ℃. The temperature in other areas is relatively low.

2.2.3 Fire resistance bearing capacity analysis

Midas Building software was used to analyze the fire resistance performance of the structure. Based on the fire temperature rise calculation results, temperature action was applied to the components affected by the fire.Load combinations were performed based on the temperature distribution of components, and the stress results of the roof structure under the most unfavorable load combinations for each fire scenario are obtained through calculation, as shown in Figure 7.Fire Scenario 4 ： The fire resource is located at entrance area of P3, with a fire scale of 8.0MW； Fire Scenario 9： The fire resource is located a the 8.9m elevation of P4, with a fire scale of 8.0MW.

(a) (b)

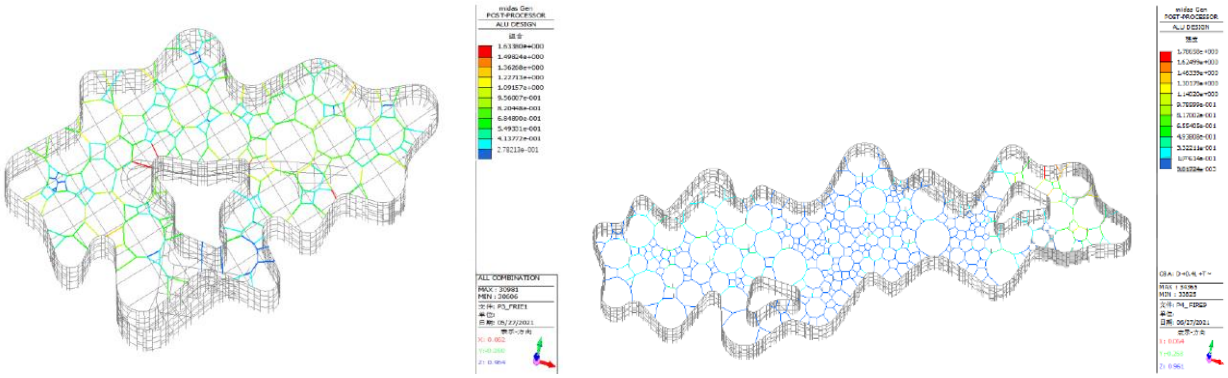


Figure 7. Stress diagram of aluminum alloy components: (a) Fire Scenario 4 (b) Fire Scenario 9

2.3 Zhangshu Sports Center

2.3.1. Project Overview

Zhangshu Sports Center Gymnasium is located in Zhangshu City, with reinforced concrete as its main structure and aluminum alloy single layer reticulated shell structure system as its roof. The size of the roof is an ellipse with a long axis of about 130m and a short axis of nearly 100m. The building elevation at the highest point of the roof is 26.000m. The design fire resistance rating is Grade I.The architectural expression chart is shown in Figure 8.

2.3.2. Fire smoke model

The fire dynamics simulation software FDS was used to simulate the fire development and smoke spread in the building. Since FDS can only build rectangular models , Therefore, the curved parts in this building were handled by using fold lines instead of curved lines. Figure 9 shows the model schematic.



Figure 8. Architectural expression chart

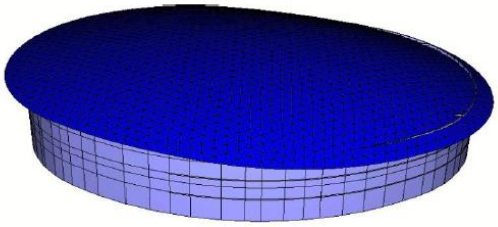


Figure 9. FDS model

The non-uniform grid division method is used to divide the grid: the grid size in the area near the fire source is 0.25m×0.25m×0.25m, and in other areas is 0.5m×0.5m×0.5m. Considering the places with more combustible materials, higher fire hazard and closer to the metal structure of the building, a total of four fire source were selectedas, shown in Figure10 .

(a) (b) (c)

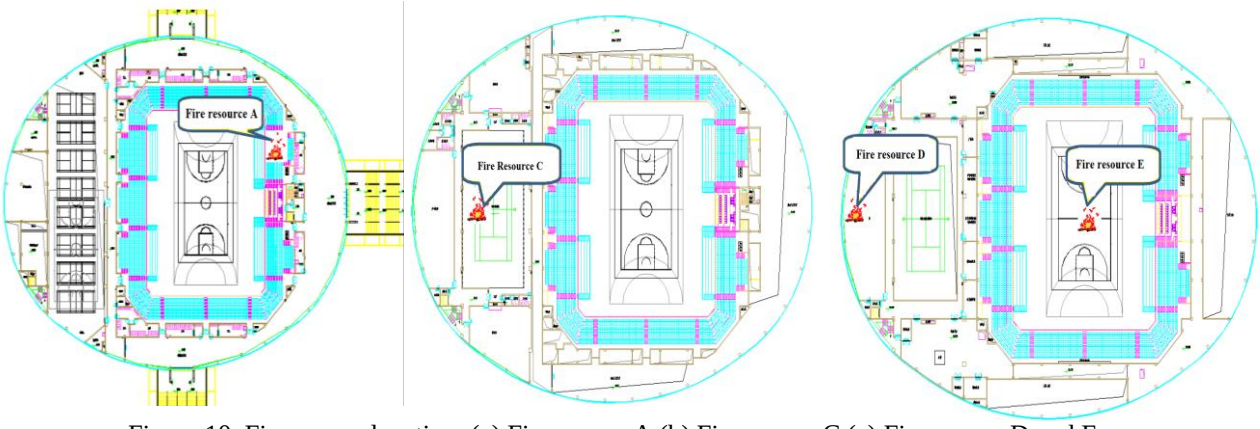


Figure 10. Fire source location: (a) Fire source A (b) Fire source C (c) Fire source D and E

2.3.2. Calculation results and analysis

Fire scenario A :The fire source is located in the stadium auditorium, and the minimum height from the fire source to the roof is 15.1m. The fire growth coefficient is 0.0244kW/s^2. Both the automatic fire extinguishing system and the smoke exhaust system have failed, and the maximum heat release rate of the fire is 2.2 MW. It can be seen from Figure 11 and Figure 12 that after a fire occurs, the fire smoke rises to the ceiling in the form of an axisymmetric smoke plume, which will gather, spread, and descend under the ceiling. Within 30 minutes of the simulation time, the maximum temperature of flue gas at the metal roof structure above the fire source in the fire area is about 68 ℃.

(a) (b) (c)

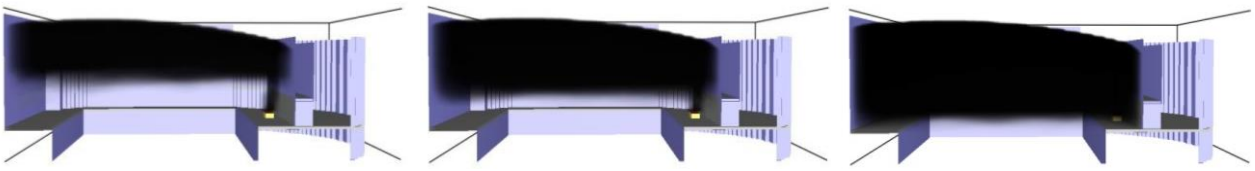


Figure 11. Smoke spread development diagram of fire scenario A:(a) t=600s (b) t=900s (c) t=1800s

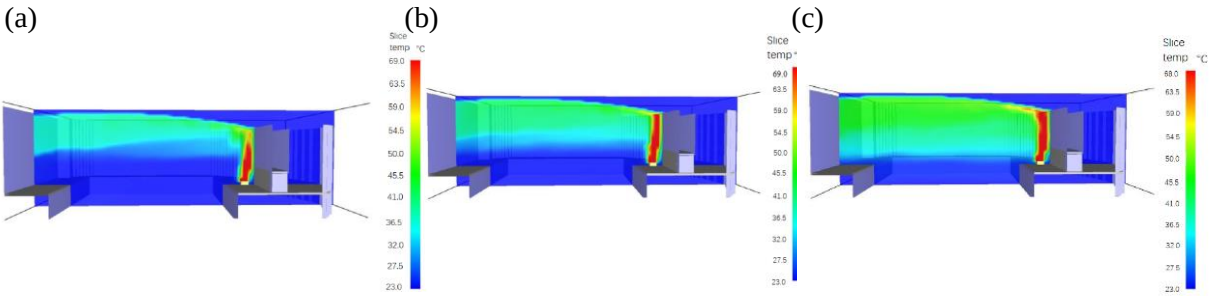


Figure 12.Fire development process and temperature distribution of fire scenario A:(a) t=600s (b) t=900s (c) t=1800s

Fire scenario C :The fire source is located in the gymnasium tennis training hall, and the minimum height from the fire source to the roof is 13.0m. The fire growth coefficient is 0.04689kW/s^2. Both the automatic fire extinguishing system and the smoke exhaust system have failed, and the maximum heat release rate of the fire is 3.5 MW. The simulation analysis results show within 30 minutes of the simulation time, the maximum temperature of flue gas at the metal roof structure above the fire source in the fire area is about 108 ℃.

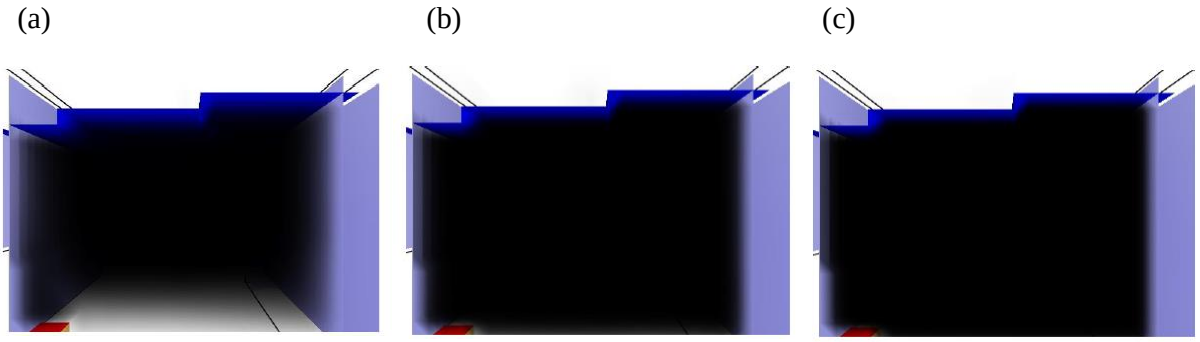


Figure 13. Smoke spread development diagram of fire scenario C:(a) t=400s (b) t=900s (c) t=1800

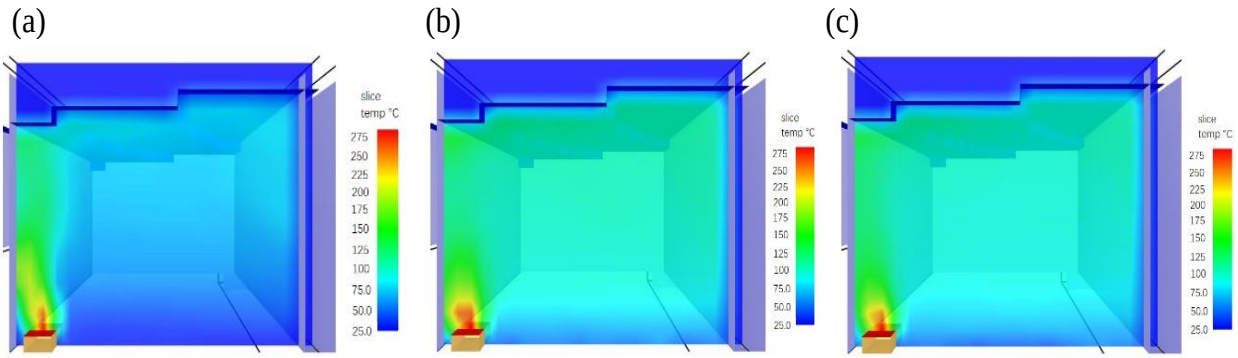


Figure 14.Temperature distribution of fire scenario C:(a) t=400s (b) t=900s (c) t=1800s

Fire scenario D :The fire source is located in the gym on the third floor of the gymnasium, and the minimum height from the fire source to the roof is 5.6m. The fire growth coefficient is 0.04689kW/s^2. Both the automatic fire extinguishing system and the smoke exhaust system have failed, and the maximum heat release rate of the fire is 3.5 MW. The simulation analysis results show within 30 minutes of the simulation time, the maximum temperature of flue gas at the metal roof structure above the fire source in the fire area is about 260 ℃.

(a) (b) (c)

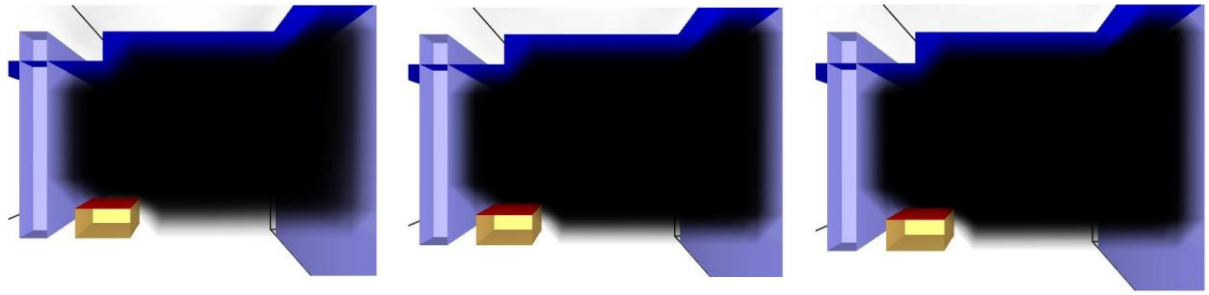


Figure 15. Smoke spread development diagram of fire scenario D:(a) t=400s (b) t=900s (c) t=1800

(a) (b) (c)

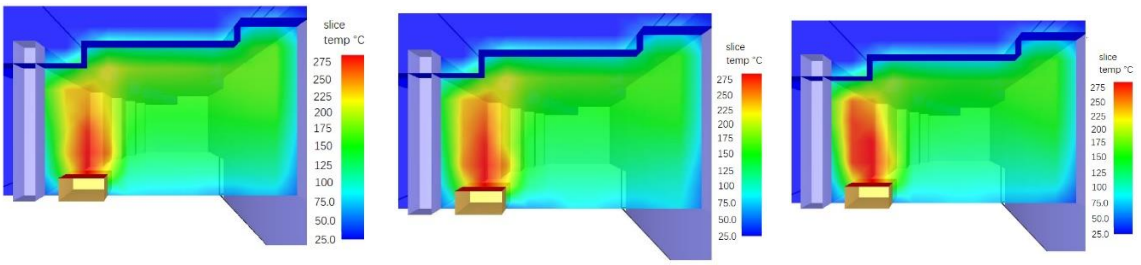


Figure 16.Temperature distribution of fire scenario D:(a) t=400s (b) t=900s (c) t=1800s

Fire scenario E : The fire source is located in the center of the competition venue on the first floor of the stadium, and the minimum height from the fire source to the roof is 25.5m. The fire growth coefficient is 0.04689kW/s^2. Both the automatic fire extinguishing system and the smoke exhaust system have failed, and the maximum heat release rate of the fire is 8.0 MW. The simulation analysis results show within 30 minutes of the simulation time, the maximum temperature of flue gas at the metal roof structure above the fire source in the fire area is about 83 ℃.

(a) (b) (c)

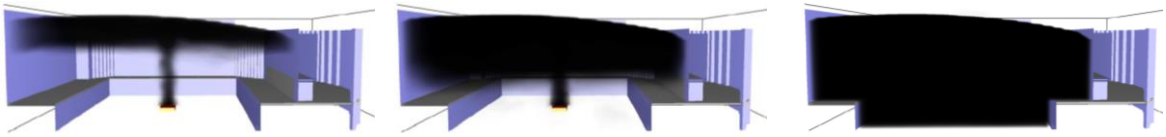


Figure 17. Smoke spread development diagram of fire scenario E:(a) t=300s (b) t=600s (c) t=1800s

(a) (b) (c)

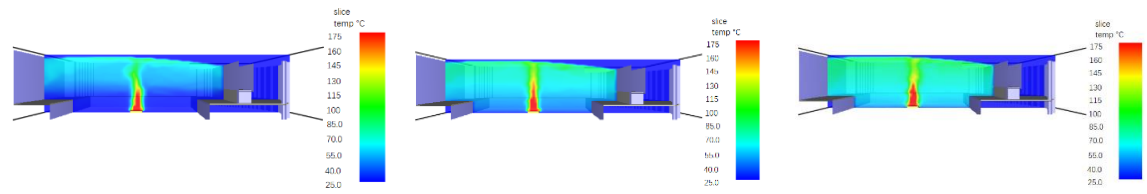


Figure 18.Temperature distribution of fire scenario D:(a) t=400s (b) t=900s (c) t=1800s

Only in the case of fire scenario D, that is, when fire occurs in the gym on the third floor of the gymnasium, the maximum temperature of the smoke layer near the roof exceeds 150 ℃, and the remaining areas are less than 150 ℃. Therefore, the fire protection area of the aluminum alloy roof structure can be determined.

3. Conclusion

The results show that FDS technology can accurately predict the non-uniform distribution of smoke temperature field in large space buildings. At present, China has made significant progress in research on performance-based fire protection design and evaluation, but basic scientific research on fire is still relatively weak and engineering practices are few. There are still many technical difficulties and application skills to be further studied. The fire resistance design cases of aluminum alloy large span structures provided in this paper will enrich the fire resistance theory and provide useful references for practical engineering applications such as fire protection design of complex structures, fire rescue, and fire risk assessment.

References

[1] Y.Liang, Z.P.NI, F.FAN,et al, "Current status analysis of fire protection design system of long-span spatial structures," Fire Science and Technology, vol. 37, pp1178-1180, 2018.
[2] Z.P.NI, "Innovation and practice of building fire protection design," Fire Science and Technology, vol, 42, pp51-54, 2023.
[3] J.Y.Shi, S.Sun, W.L.Liu, et al, " Study of performance-based fire resistance design methodology for large space structures," China Civil Engineering Journal, vol.44, pp69-78, 2011.
[4] Y.J.Shi, Y.Bai, W.Q.Wang, "Studies on performance-based fire resisting design method for large space structures," Spatial Structures,vol.11, pp16-20, 2005.
[5] Y.X.Lei, "People evacuation and rescue analysis of large connercial complex," Fire Science and Technology, vol. 35, pp524-527, 2016
[6] S.C.Lu, Z.P.NI, X.Liu, et al, "Discussion on fire safety management of large commercial complex ," Fire Science and Technology, vol. 38, pp1752-1755, 2019.
[7] C.Y.Yuan，K.Wang，H.Y.Chen, et al, "Research on evacuation efficiency of high-rise building in case of fires considering incentive mechanism," China Safety Science Journal, vol.30, pp79-85, 2020.
[8] H.Q.Tang, "Research on risk monitoring of evacuation in high-rise buildings fire. Fire Science and Technology," vol. 37, pp844-846, 2018.
[9] L.J.Zhang, J.C.Liu, S.B.Tan, "Multi-objective Planning of Personnel Evacuation Route in Complex Building Fire," Journal of Northeastern University(Natural Science), vol.41, pp761-766, 2020.

IASS 2023
July 10–14 Melbourne
Integration of Design and Fabrication

Proceedings of the IASS Annual Symposium 2023
Integration of Design and Fabrication
10–14 July 2023, Melbourne, Australia
Y.M. Xie, J. Burry, T.U. Lee and J. Ma (eds.)

Shape optimization of hyperellipsoid long-span structures using modified height adjustment method

Yuqing QU[a], Zhuang GUO[a], Zhenhui LI[a], Xiao LAI[a], Zheng HE[a,*]

[a,*] Department of Civil Engineering, Dalian University of Technology, Dalian, China
No. 2 Linggong Road, High-tech District, Dalian, China
Email: hezheng@dlut.edu.cn

Abstract

This paper presents a modification on the height adjustment method (HAM) proposed by Cui and Yan for the shape optimization hyperellipsoid shells. In the modified HAM, all the joints of a shell of concern are always maintained to be located in hyperellipsoid surface during the optimization process. The sensitivity of total strain energy with respect to joint height originally provided by HAM is converted into that with respect to the control parameters of hyperellipsoid shells. The implementation of the modified HAM invovles the construction of hyperellipsoid surface, finite element (FE) analysis and the optimal solution. The sensitivity and FE analysis parts, and its efficiency of the modified HAM is demonstrated by a case study. In addition, the computerized implementation of the shape optimizaiton using the modified HAM with D-SAP is proved to be sucessful.

Keywords: hyperellipsoid shell, shape optimization, height adjustment method, sensitivity, strain energy

1. Introduction

Compared with other common types of shells, hyperellipsoid shells possess a larger number of variations in geometrical configuration by changing its control parameters, being potentially capable of satisfy the needs from various designers. In view of the close relation of shells between structural performance and geometrical configuration, the shape optimization of hyperellipsoid shells needs to be carried out from the physical aspect to satisfy the requirement on structural performance, with full utilization of material.

In nowadays, numerical approaches have been extensively explored to perform shape optimization of curved long-span shells due to their desirable adaptability and robustness. On the basis of finite element method, Espath et al. [1] used the non uniform rational B spline (NURBS) description and automatic differentiation in the shape optimization of shells. Hassani et al. [2] introduced NURBS curve in the shape optimization of general curved surfaces with the solid isotropic microstructure with penalization (SIMP) method. The shape optimization process is to maximize structural efficiency or the degree of stress uniformity [3], as an optimization objective, by finding the relationship between geometrical configuration and internal force distribution of long-span shells, with some design limits (span, the minimum and maximum height, etc.), boundary conditions (support locations) and primary load cases of concern. However, in some cases, it is not easy to achieve expected structural efficiency by changing geometrical configuration of shells only via the adjustment of parameters involved. To overcome this issue, Cui and Yan [4] proposed the free form-based height adjustment method (HAM) to determine the curved surfaces of shells directly without any constraints from shape parameters. In HAM, the structural efficiency of a shell of concern is reflected by the total strain energy of its all joints which can be adjusted by their heights directly. From the physical aspect, the maximum efficiency is believed to be reached when the total strain energy is minimized. The solution flexibility and shape adaptability of HAM makes it more promising for the shape optimization of long-span shells structures.

Copyright © 2023 by Yuqing QU, Zhuang GUO, Zhenhui LI, Xiao LAI and Zheng HE. Published in the Proceedings of the IASS Annual Symposium 2023 with permission.

As for free-form shells, discrete structural components consist of their surfaces [5]. In HAM, the spatial correlation mechanism among joints is neglected. However, in the case of the shape optimization of hyperellipsoid shells, HAM is not acceptable for as the variation in stiffness of adjacent joints caused by height change of a joint in these shells is not neglibible. As mentioned by Barr [6], some constraints from other aspects need to be concerned when hyperellipsoid shells are converted into a mathematical model for shape optimization. The main purpose of this paper is to modify HAM to keep all the joints always located in the surface described by a hyperellipsoid equation in the process of shape optimization. In the modified HAM presented herein, the sensitivity of total strain energy with respect to joint height originally proposed by Cui and Yan [4] is converted into that with respect to the control parameters of hyperellipsoid shells. The modified HAM is successfully integrated into an finite element (FE) analytical platform, i.e. D-SAP [7], for both the sensitivity and FE analysis parts, and its efficiency is demonstrated by a subsequent case study.

2. Problem formulation

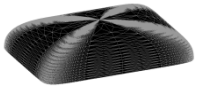
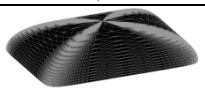
2.1. Design variables

The surface of hyperellipsoid shells can be mathematically expressed by the following [8]:

$$\left(\left| \frac{x}{r_x} \right|^{\frac{2}{e}} + \left| \frac{y}{r_y} \right|^{\frac{2}{e}} \right)^{\frac{e}{n}} + \left| \frac{z}{r_z} \right|^{\frac{2}{n}} = 1 \tag{1}$$

where r_x, r_y and r_z are the polar radii in the *x*-, *y*- and *z*-axis, respectively; *n* and *e* are the two parameters, controlling the squareness of a concerned shell in the *z*-axis and *x*-*y* plane, respectively.

Table 1. Hyperellipsoids with different control parameters of *n* and *e*

 *n*=0.2, *e*=0.2	 *n*=0.8, *e*=0.2	 *n*=1.0, *e*=0.2	 *n*=2.0, *e*=0.2	 *n*=3.0, *e*=0.2
 *n*=0.2, *e*=0.8	 *n*=0.8, *e*=0.8	 *n*=1.0, *e*=0.8	 *n*=2.0, *e*=0.8	 *n*=3.0, *e*=0.8
 *n*=0.2, *e*=1.0	 *n*=0.8, *e*=1.0	 *n*=1.0, *e*=1.0	 *n*=2.0, *e*=1.0	 *n*=3.0, *e*=1.0

Different combinations of the parameters of *n* and *e*, can yield a variety of geometrical shapes, as shown in Table 1. Table 1 indicates that Eq. (1) can cover nearly all regular polyhedrons and can realize smooth transition of shells between different patterns. It can be also seen that the parameter, *n*, controls mainly the roundness of hyperellipsoid shells while the parameter, *e*, affects the plumpness primarily. During the process of shape optimization using modified HAM (to be discussed later) or HAM, for the sake of simplicity, the *x*- and *y*-coordinates of any joint remain fixed while its height, *z*, is under adjustment. In design practice, the polar radii, r_x, r_y and r_z which are mostly dominated by function requirement are relatively fixed and they are assumed to be constant in the shape optimization process. Thus, only the parameters of *n* and *e* are the design variables in the optimization.

2.2. Optimization objectives

The structural efficiency of a shell of concern can be described by its stiffness and the amount of material used. As strain energy can well reflect both the two aspects via the relationship between stress level and material amount, it is employed as an indicator in the shape optimization problem. Smaller strain energy indicates larger ability to resist external loads and larger deformability. From the physical standpoint, a shell which has the minimum strain energy is believed to be most "shape resisting" efficient [4]. According to the discussion above, the total strain energy of a hyperellipsoid shell of concern $C(\mathbf{Z})$ can be expressed as the function of the heights of all joints invovled, i.e.

$$C(\mathbf{Z}) \rightarrow \text{minimum} \tag{2}$$

where $\mathbf{Z}$ is the vector of heights of all joints.

2.3. Constraints

According to Chinese technical specification for spatial grid structure [9], the deflection of a single-story lattice shell under gravity load should be controlled within $L/400$ (L is span). In the shape optimization of hyperellipsoid shells, this limit could be also used for control stiffness demand where l is taken as the shorter span. Thus, the constraint of the optimization problem is expressed as

$$\begin{cases} \mathbf{S} \subset \mathbf{\Omega}_0 \\ \delta_{\max} \le \delta_0 \end{cases} \tag{3}$$

where $\mathbf{S}$ is the function of joint heights with respect to the parameters of a hyperellipsoid shell of concern; $\mathbf{\Omega}_0$ is allowable design space; $\delta_{\max}$ is the maximum deflection; δ_0 is the code-specified deflection limit, i.e. $L/400$.

3. Optimization algorithm and implementation

3.1. Structural sensitivity matrix

The boundary well-adapted triangular shell elements are used in the shape optimization. For analytical simplicity, the rotational degrees of freedom (DOFs) of the elements are assumed to be not affected by the rotation caused by the variation of heights in adjacent elements [10].

The construction of structural sensitivity matrix depends on that of structural stiffness matrix. According to Tabarrok and Qin [11], the stiffness matrix of the r-th triangular shell element $\mathbf{K}^{sr}$ is expressed as

$$\mathbf{K}^{sr} = \begin{bmatrix} \mathbf{K}^{mr} & 0 & 0 \\ 0 & \mathbf{K}^{br} & 0 \\ 0 & 0 & 0 \end{bmatrix} \tag{4}$$

where $\mathbf{K}^{mr}$ and $\mathbf{K}^{br}$ are the membrane matrix and plate matrix of the r-th triangular shell element, respectively, determined by

$$\mathbf{K}^{mr} = \iint (\mathbf{B}^{mr})^{\mathrm{T}} \mathbf{D}^{mr} \mathbf{B}^{mr} t \mathrm{d}x\mathrm{d}y \tag{5a}$$

$$\mathbf{K}^{br} = \iint (\mathbf{B}^{br})^{\mathrm{T}} \mathbf{D}^{br} \mathbf{B}^{br} t \mathrm{d}x\mathrm{d}y \tag{5b}$$

where $\mathbf{B}^{mr}$ and $\mathbf{B}^{mr}$ are the strain matrices of the membrane part and plate part of the r-th triangular shell element, respectively; $\mathbf{D}^{mr}$ and $\mathbf{D}^{mr}$ are the elasticity matrices of the membrane part and plate part of the r-th triangular shell element, respectively.

The structural stiffness matrix $\mathbf{K}^s$ can be constructed by the summation of all element matrices $\mathbf{K}^{sr}$ over r_{max} with the coordinate transformation. By structural stiffness matrix $\mathbf{K}^s$, the structural sensitivity matrix with respect to the height of the i-th joint $\mathbf{dK}^s{}_i$ can be generated by the following:

$$\mathbf{dK}^s{}_i = \frac{\partial \mathbf{K}^s}{\partial z_i} = \begin{array}{c} \\ 1 \\ 2 \\ \vdots \\ i \\ \vdots \\ i_{\max} \end{array} \begin{array}{c} \begin{array}{cccccc} 1 & 2 & \cdots & i & \cdots & i_{\max} \end{array} \\ \begin{bmatrix} 0 & 0 & \cdots & \mathbf{dK}^s{}_{1i} & \cdots & 0 \\ 0 & 0 & \cdots & \mathbf{dK}^s{}_{2i} & \cdots & 0 \\ \vdots & \vdots & & \vdots & & \vdots \\ \mathbf{dK}^s{}_{i1} & \mathbf{dK}^s{}_{i2} & \cdots & \mathbf{dK}^s{}_{ii} & \cdots & \mathbf{dK}^s{}_{ii_{\max}} \\ \vdots & \vdots & & \vdots & & \vdots \\ 0 & 0 & \cdots & \mathbf{dK}^s{}_{i_{\max}i} & \cdots & 0 \end{bmatrix} \end{array} \tag{6}$$

where i_{max} is the number of joints.

Similary, the structural sensitivity matrix $\mathbf{dK}^s$ is also obtained by the summation of all element matrices $\mathbf{dK}^{sr}$ over r_{max} with the coordinate transformation, determined by

$$\mathbf{dK}^{sr} = \mathbf{dK}^{sr}{}_1 + \mathbf{dK}^{sr}{}_2 + \mathbf{dK}^{sr}{}_3 \tag{7a}$$

$$\mathbf{dK}^{sr}{}_l = \frac{\partial \mathbf{K}^{sr}}{\partial z_l^r} \qquad (l=1, 2, 3) \tag{7b}$$

where $z^r{}_l$ is the height of the r-th element at the l-node (l=1, 2, 3).

3.2. Height adjustment method

As proposed by Cui and Yan [4], HAM is used to optimize the shape of a shell via the adjustment of the heights of its joints in order to minimize their total strain energy. The strain energy of a shell is determined by solving the following static equilibrium equations under gravity loads:

$$\mathbf{K}^s\mathbf{U}=\mathbf{P} \tag{8}$$

where $\mathbf{U}$ is the displacement vector of a shell of concern; $\mathbf{P}$ is equivalent load vector. It is noteworthy that, in the shape optimization using HAM, the dead loads applied on joints may be variable as a result of changing joint heights (or element volume). As service loads are dependent only on projected area, they are constant during entire optimization process.

Differentiating equation (8) for both sides with respect to the height of the i-th joint z_i can yield

$$\frac{\partial \mathbf{K}^s}{\partial z_i}\mathbf{U} + \mathbf{K}^s\frac{\partial \mathbf{U}}{\partial z_i} = \frac{\partial \mathbf{P}}{\partial z_i} \tag{9}$$

If the variation in load vector $\mathbf{P}$ during optimization can be ignored for analytical convenience, equation (9) can be simplified as the following:

$$\frac{\partial \mathbf{K}^s}{\partial z_i}\mathbf{U} + \mathbf{K}^s\frac{\partial \mathbf{U}}{\partial z_i} = 0 \rightarrow \frac{\partial \mathbf{U}}{\partial z_i} = -(\mathbf{K}^s)^{-1}\frac{\partial \mathbf{K}^s}{\partial z_i}\mathbf{U} \tag{10}$$

The total strain energy, C, is determined by

$$C=\frac{1}{2}\mathbf{PU} \tag{11}$$

The sensitivity of C with respect to the i-th joint height z_i, i.e. α_i, can be determined further as follows without the consideration of the variation in load vector during optimization,

$$\alpha_i = \frac{\partial C}{\partial z_i} = \frac{1}{2}\frac{\partial \mathbf{P}^{\mathrm{T}}}{\partial z_i}\mathbf{U} + \frac{1}{2}\mathbf{P}^{\mathrm{T}}\frac{\partial \mathbf{U}}{\partial z_i} = \frac{1}{2}(\mathbf{K}^{\mathrm{s}}\mathbf{U})^{\mathrm{T}}\frac{\partial \mathbf{U}}{\partial z_i} = \frac{1}{2}\mathbf{U}^{\mathrm{T}}(\mathbf{K}^{\mathrm{s}})^{\mathrm{T}}\frac{\partial \mathbf{U}}{\partial z_i} \tag{12}$$

Substituting the partial derivative $\partial\mathbf{U}/\partial z_i$ in equation (10) into equation (12) leads to the following with the use of symmetry of stiffness matrix:

$$\alpha_i = \frac{\partial C}{\partial z_i} = -\frac{1}{2}\mathbf{U}^{\mathrm{T}}(\mathbf{K}^{\mathrm{s}})^{\mathrm{T}}(\mathbf{K}^{\mathrm{s}})^{-1}\frac{\partial \mathbf{K}^{\mathrm{s}}}{\partial z_i}\mathbf{U} = -\frac{1}{2}\mathbf{U}^{\mathrm{T}}\mathbf{K}^{\mathrm{s}}(\mathbf{K}^{\mathrm{s}})^{-1}\frac{\partial \mathbf{K}^{\mathrm{s}}}{\partial z_i}\mathbf{U} = -\frac{1}{2}\mathbf{U}^{\mathrm{T}}\frac{\partial \mathbf{K}^{\mathrm{s}}}{\partial z_i}\mathbf{U} \tag{13}$$

In HAM, the adjustment of the height at the ith-joint Δz_i is calculated by

$$\Delta z_i = -\frac{\partial C}{\partial z_i}\Delta = -\alpha_i\Delta \tag{14}$$

where Δ is an empirical positive parameter. It is suggested to be $1/5\alpha^0{}_{\max}$ by Cui and Yan [4] where $\alpha^0{}_{\max}$ is the maximum sensitivity at the first iteration step of all joints.

With the adjustment of joint heights of equation (16), the total structural strain energy is changed as

$$C(\mathbf{Z}+\Delta\mathbf{Z}) = C(\mathbf{Z}) - \sum_{i=1}^{i_{\max}}\alpha_i^2\Delta \tag{15}$$

With the adjustment above, the height of the ith-joint at the (k+1) iteration step, i.e. z_i^{k+1},

$$z_i^{k+1} = z_i^k - \alpha_i^k\Delta \tag{16}$$

3.3. Modified height adjustment method

To maintain all the joints during the shape optimization process using HAM to be always located on the surface of a hyperellipsoid described by equation 1. With this combination, HAM needs to be modified to reflect the sensitivities of structural strain energy C to the two parameters n and e, i.e. α_{ni} and α_{ei}, by the following two partial derivatives:

$$\alpha_{\mathrm{n}i} = \frac{\partial C}{\partial n_i} = \frac{\partial C}{\partial z_i}\frac{\partial z_i}{\partial n_i} = -\frac{1}{2}\mathbf{U}^{\mathrm{T}}\frac{\partial \mathbf{K}^{\mathrm{s}}}{\partial z_i}\mathbf{U}\frac{\partial z_i}{\partial n_i} \tag{17a}$$

$$\alpha_{\mathrm{e}i} = \frac{\partial C}{\partial e_i} = \frac{\partial C}{\partial z_i}\frac{\partial z_i}{\partial e_i} = -\frac{1}{2}\mathbf{U}^{\mathrm{T}}\frac{\partial \mathbf{K}^{\mathrm{s}}}{\partial z_i}\mathbf{U}\frac{\partial z_i}{\partial e_i} \tag{17b}$$

where

$$\frac{\partial z_i}{\partial n_i} = \frac{-e_i\cdot r_{\mathrm{z}}\cdot\left[\left(\frac{x_i}{r_{\mathrm{x}}}\right)^{2/e_i}+\left(\frac{y_i}{r_{\mathrm{y}}}\right)^{2/e_i}\right]^{e_i/n_i}\cdot\ln\left[\left(\frac{x_i}{r_{\mathrm{x}}}\right)^{2/e_i}+\left(\frac{y_i}{r_{\mathrm{y}}}\right)^{2/e_i}\right]}{2\cdot\left(\frac{z_i}{r_{\mathrm{z}}}\right)^{2/n_i}\cdot\ln\left(\frac{z_i}{r_{\mathrm{z}}}\right)} \tag{18a}$$

$$\frac{\partial z_i}{\partial e_i} = \frac{n_i r_{\mathrm{z}}^{2/n_i}\left[\left(\frac{x_i}{r_{\mathrm{x}}}\right)^{2/e_i}+\left(\frac{y_i}{r_{\mathrm{y}}}\right)^{2/e_i}\right]^{e_i/n_i}\left[\left(\frac{x_i}{r_{\mathrm{x}}}\right)^{2/e_i}\ln\left(\frac{x_i}{r_{\mathrm{x}}}\right)+\left(\frac{y_i}{r_{\mathrm{y}}}\right)^{2/e_i}\ln\left(\frac{y_i}{r_{\mathrm{y}}}\right)\right]\ln\left[\left(\frac{x_i}{r_{\mathrm{x}}}\right)^{2/e_i}+\left(\frac{y_i}{r_{\mathrm{y}}}\right)^{2/e_i}\right]}{z_i^{1/n-1}e_i^{\,2}} \tag{18b}$$

Where x_i and y_i are the x- and y-axis coordinates of the ith-joint, respectively.

With the replacement of α_i in equation (14) with α_{ni} and α_{ei} respectively, the adjustment of the parameters of n and e can be determined similarly by

$$\Delta n_i = -\frac{\partial C}{\partial z_i}\frac{\partial z_i}{\partial n_i}\Delta = -\alpha_{ni}\Delta_n \tag{19a}$$

$$\Delta e_i = -\frac{\partial C}{\partial z_i}\frac{\partial z_i}{\partial e_i}\Delta = -\alpha_{ei}\Delta_e \tag{19b}$$

where the positive parameters of Δ_n and Δ_e can be evaluated as $1/5\alpha_n{}^0{}_{max}$ and $1/5\alpha_e{}^0{}_{max}$, respectively, which $\alpha_n{}^0{}_{max}$ and $\alpha_e{}^0{}_{max}$ are the corresponding maximum sensitivities at the first iteration step of all joints.

After the adjustment at the (k+1) iteration step, the updated two shape control parameters become

$$e_i^{k+1} = e_i^k - \alpha_{ei}{}^k \Delta e_i \tag{20a}$$

$$n_i^{k+1} = n_i^k - \alpha_{ni}{}^k \Delta n_i \tag{20b}$$

The corresponding vectors of $\Delta\mathbf{e}$, $\Delta\mathbf{n}$, $\mathbf{e}$, $\mathbf{n}$, $\boldsymbol{\alpha}_e$ and $\boldsymbol{\alpha}_n$ of all joints can be described by

$$\Delta\mathbf{e} = \{\Delta e_1, \Delta e_2, \Delta e_3, ..., \Delta e_{i\max}\}^T \tag{21a}$$

$$\Delta\mathbf{n} = \{\Delta n_1, \Delta n_2, \Delta n_3, ..., \Delta n_{i\max}\}^T \tag{21b}$$

$$\mathbf{e} = \{e_1, e_2, e_3, ..., e_{i\max}\}^T \tag{21c}$$

$$\mathbf{n} = \{n_1, n_2, n_3, ..., n_{i\max}\}^T \tag{21d}$$

$$\boldsymbol{\alpha}_e = \{\alpha_{e1}, \alpha_{e2}, \alpha_{e3}, ..., \alpha_{e,i\max}\}^T \tag{21e}$$

$$\boldsymbol{\alpha}_n = \{\alpha_{n1}, \alpha_{n2}, \alpha_{n3}, ..., \alpha_{n,i\max}\}^T \tag{21f}$$

If convergence tolerance is satisfied during the optimization process, the averaged values of $\mathbf{e}$ and $\mathbf{n}$ of all joints at the (k+1) iteration step can be taken as final optimal ones, i.e.

$$e^k = \frac{\sum_{i=1}^{i_{max}} e_i^k}{i_{max}} \tag{22a}$$

$$n^k = \frac{\sum_{i=1}^{i_{max}} n_i^k}{i_{max}} \tag{22b}$$

In modified HAM, the total structural strain energy is updated as follows after the adjustment in each iteration step,

$$C(\mathbf{Z} + \Delta\mathbf{Z}) = C(\mathbf{Z}) - \sum_{i=1}^{i_{max}} \alpha_{ni}^2 \Delta_n - \sum_{i=1}^{i_{max}} \alpha_{ei}^2 \Delta_e \tag{23}$$

It is noteworthy that such update is performed one parameter after another, not simultaneously. And, in most cases, the sensitivity of total strain energy varies with the location of a joint of concern, i.e. not uniform, during the height adjustment process.

3.4. Computerized implementation

The shape optimization of a hyperellipsoid shell using the modified HAM invovles three primary steps, i.e. the construction of surface of hyperellipsoid, structural finite element analysis and optimal solution process. In the first step, it is neccessary to determine the coordinates of some key joints for the modeling

of hyperellipsoid surface and then to generate an optimal gird through the grid independence test in ANAYS®. In the second, the coordinates of all joints of a hyperellipsoid shell are transferred to a finite element analysis program, i.e. D-SAP used herein (as described later), for the determination of structural stiffness $\mathbf{K}^s$ and its sensitivity with respect to each joint height $\mathbf{dK}^s_i=\partial\mathbf{K}^s/\partial z_i$ by equation (6). Then, the sensitivity of total strain energy with respect to each joint height α_i is calculated by equation (13) and further to the parameters of n and e of all joints α_{ni} and α_{ei} by equation (17). In the third step, the modified HAM is performed using MATLAB®. The partial derivatives of joint height with respect to the parameters of n and e $\partial z_i/\partial n_i$ and $\partial z_i/\partial e_i$ is determined using equation (18). With these partial derivatives, equation (19) is applied to calculated the adjustment of the parameters of n and e Δn_i and Δe_i of all joints. The shape parameters n_i^{k+1} and e_i^{k+1} are then updated by equation (20) after the (k+1) iteration step. Such iteration is terminated if the following condition is satisfied with a specified tolerance:

$$\alpha_{\mathrm{n}\max}^{k} \text{ and } \alpha_{\mathrm{e}\max}^{k} \to 0 \tag{24}$$

The determination process of the sensitivity of structural stiffness matrix with respect to each joint height $\mathbf{dK}^s_i=\partial\mathbf{K}^s/\partial z_i$ is implemented into the finite element analytical platform D-SAP (Fu et al. 2015). Fig. 1 illustrates the basic framework of the platform using C++ object-oriented language. The information of earthquake wave, constraints and nodal coordinates are stored in the **Load** module, **Constraint** module and **Node3d** module, respectively. The **Analysis** module is used to generate some vectors and matrices, e.g. effective earthquake force vector, **q**, quasi-static load vector, **b**, stiffness matrix, **K**, quasi-static stiffness matrix, **Ḱ**, displacement vector, **u**. The **FullSystem** module yields unbalanced force vectors and the matrices of stiffness, damping and mass for each analytical time step. The **Solver** module is used to solve the generalized quasi-static equation, $\mathbf{\acute{K}\Delta u=\Delta b}$, to obtain $\Delta\mathbf{u}$ and other related response quantities. The updated response vectors are used to update stiffness matrices and restoring force vectors by the **FullSystem** module. The **Record** module and **Load** module are used to output analytical results and to define load cases for analysis, respectively. $\mathbf{K}_e$ and $\mathbf{K}_{sec}$ are the element stiffness matrix and section stiffness matrix, respectively; $\mathbf{f}_e$ and $\mathbf{f}_{sec}$ are the element restoring force vector and section restoring force vector, respectively; E is the Young's modulus of material.

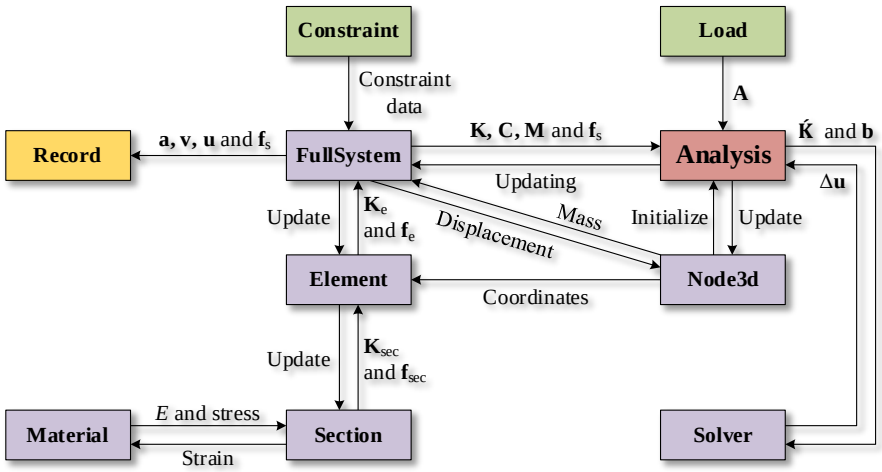


Figure 1. D-SAP analaytical platform [7].

The implemenation involves two parts. The first part is to integrate the triangular shell element into D-SAP and to store the element stiffness matrix and structural stiffness matrix. The second is to generate the sensitivity matrix $\mathbf{dK}^s_i$ with the interaction with the modified HAM program in MATLAB®. As a large number of elements are involved, as discussed in the case study, in the generation of structural

stiffness matrix and sensitivity matrix, narrow-band storage technique is used when they are transferred from D-SAP to MATLAB® for the minimization of storage space.

4. Case study

4.1. Basic information

A case hyperellipsoid steel shell shown in figure. 2(a) has the polar radii of r_x=105.963 m, r_y=71.663 m and r_z=42.335 m which are set as constants in the shape optimization. The parameters of n and e for the shell before the optimization are n=e=0.909. The total surface area of the shell before optimization is 33915.871 m^2. The modulus of elasticity of 206 GPa, Poisson's ratio of 0.30 and material density of 2.55 kg/m^3 are used. For the sake of stiffness determination, the thickness of the shell is assumed to be constant at t=300 mm throughout the optimization process, having the dead load of g=2.355 kN/m^2. The construction and maintenance live load is taken as q=0.7 kN/m^2. The gravity load applied the shell is calculated by G=g+0.5q. The peripheral joints of the shell are pin-connected with the rigid supports which are fixed on the foundation. The deflection limit of L/400 (shorter span herein), i.e. 0.36 m, is used as the constraint in the optimization.

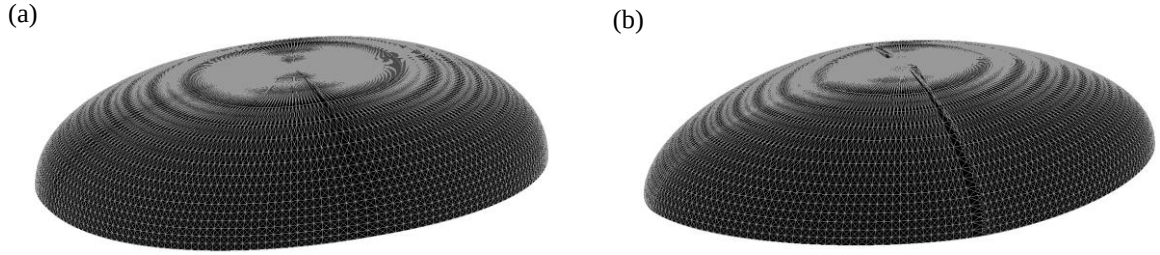


Figure 2. A hyperellipsoid shell: (a) before optimization, (b) after optimization.

4.2. Grid independence test

As the discretization process with finite elements is involved, a grid indepence test needs to be carried out before the shape optimization. Figure 3 shows the variation of the top displacement of the shell with the increase of grid numbers. As the number of elements increases, the top displacement increases but at a slowing rate and converges at 0.0561 m, exhibiting an optimal number around 4×10^4. In the case of the triangular shell elements used herein, the final grid has 40,568 elements.

4.3. Shape optimization

Figure 4 shows the relative variation of total strain energy $\gamma=(C^k-C^{k-1})/C^k$ of the shell in the optimization. As iteration proceeds, γ decreases at a slowing rate and converge at 21.2% in the 78th iteration step, with the parameters of n=1.020 and e=1.140. An increase of 12.2% in n and an increase of 25.4% in e are obtained. Equation (25) shows the mathematical expressions of the shell before and after the shape optimization, i.e.

$$\left(\frac{x}{105.9625}\right)^{2.2}+\left(\frac{y}{71.6625}\right)^{2.2}+\left(\frac{z}{45.2025}\right)^{2.2}=1 \tag{25a}$$

$$\left(\left|\frac{x}{105.9625}\right|^{1.961}+\left|\frac{y}{71.6625}\right|^{1.961}\right)^{0.895}+\left|\frac{z}{45.2025}\right|^{1.754}=1 \tag{26b}$$

Figure 2(b) illustrate the configuration of the shell after the optimization, from which it can be seen that the curvature of the optimized shell becomes smaller than the initial shell. From the aspect of structural design, the optimized shell is structurally more efficient and stable. However, it must be pointed out that,

in the shape optimization concerned herein, the constraint from architectural design is not included.The optimized shell may not be desirable from the functionality standpoing. If more constraints are addressed, the modified HAM needs to be developed further.

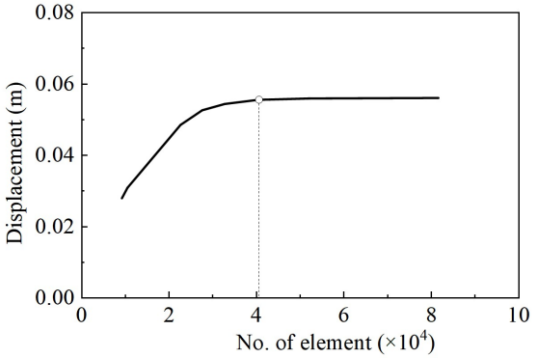


Figure 3. Grid independence test result.

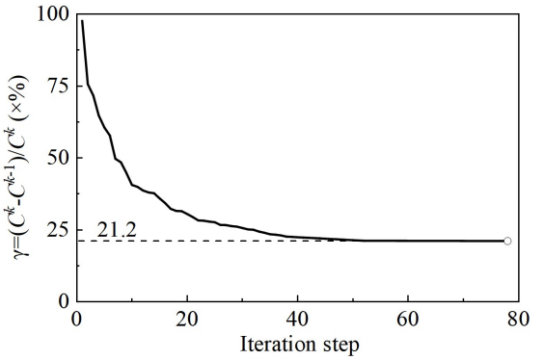


Figure 4. Convergence of total strain energy.

5. Conclusion

In this paper, HAM proposed by Cui and Yan (2006) is modified to perform the shape optimization for hyperellipsoid shells, the following observations can be reached:

(1) The modified HAM can maintain all the joints of a shell of concern during the shape optimization, where the sensitivity of total strain energy to joint height is converted into that to the two control parameters of hyperellipsoid shells. As the mathematicla expression of hyperellipsoid shells can cover nearly all regular polyhedrons and describe the transition of shells between different patterns, the modified HAM developed herein can be applied for more general purposes.

(2) The computerized implementation of the shape optimizaiton using the modified HAM invovlves three steps, i.e. the construction of hyperellipsoid surface in ANAYS®, finite element analysis using D-SAP and the optimal solution with the modified HAM in MATLAB®. Three different platforms interact well with each other. To minimize the storage space in MATLAB®, the narrow-band storage technique is applied for the transfer of structural stiffness matrix and sensitivity matrix from D-SAP.

(3) As indicated by the case study, using the modified HAM can achieve more structural efficiency. A substantial efficiency is achieved by the shape optimization, showing a decrease of 78.8% in total strain energy. The corresponding two control parameters of n and e are increased up to 12.2% and 25.4%, respectively after the optimization. It is noteworhty that a grid independence test needs to be conducted prior to the shape optimization.

(4) The design constraint included in this paper only account for stiffness demand via a code-specified deflection limit of L/400. By this constraint, the structural efficiency of the case shell is increased substantially. It must be acknowledged that the constraint from architectural design also needs to be seriously addressed. The optimized case shell may not be desirable from the functionality aspect. The modified HAM needs to be developed further when more constraints are included.

Acknowledgements

This research was financially supported by the Fundamental Research Funds for the Central Universities (Grant No. DUT19GJ208).

References

[1] C. Y. Cui and H. Yan. “A morphosis technique for curved-surface structures of arbitrry geometries —Height adjusting method and its engineering applications,” *China Civil Engineering Journal*, vol. 12, pp. 1-6, 2006.(in Chinese)

[2] L. F. R. Espath, R.V. Linn and A. M. Awruch, "Shape optimization of shell structures based on NURBS description using automatic differentiation," *International Journal for Numerical Methods in Engineering*, vol. 88, pp. 613-636, 2011.
[3] B. Hassani, S. M. Tavakkoli and Ghasemnejad H., "Simultaneous shape and topology optimization of shell structures Struct," *Structural and Multidisciplinary Optimization*, vol. 48(1), pp. 221-233, 2013.
[4] R. F. Coelho, T. Tysmans and E. Verwimp. "Form finding and structural optimization," *Structural and Multidisciplinary Optimization*, vol. 49, pp. 1037-1046, 2014.
[5] A. Berk and H. Giles, "Quadrilateral panelization of freeform surface structures," *Automation in Construction*, vol. 76, pp. 36-44, 2017.
[6] A. H. Barr, "Super quadrics and angle-preserving transformations," *Institute of Electrical and Electronics Engineers Comput Graphics and Applications*, vol. 1(1), pp. 11-23, 1981.
[7] S. J. Fu, Z. He, Z. Q. Li, X. Tu and Q. Tao. "Shared memory parallel computing procedures for nonlinear dynamic analysis of high-rise buildings," in *Proceedings of the Second International Conference on Performance-based and Life-cycle Structural Engineering*, Brisbane, Australia, December 9-11, 2015, Dilum Fernando, Jin-Guang Teng and Jose L Torero.
[8] P. Bourke, "Superellipse and superellipsoid: A geometric primitive for computer aided design," 1990.
[9] "Technical Specification for Spatial Grid Structure, JGJ7-2010," *China Architecture and Building Press, Beijing*, China, 2010. (in Chinese)
[10] L. S. Lauren, B. Alessandro, F. B. William and H. P. Glaucio. "Topology optimization for braced frames: Combining continuum and beam/column elements," *Engineering Structures*, vol. 37, pp. 106-124, 2011.
[11] B. Tabarrok and Z. Qin, "Nonlinear analysis of tension structures," *Computers and Structures*, vol. 45(5-6), pp. 973-984, 1992.

IASS 2023
July 10–14 Melbourne
Integration of Design and Fabrication

Proceedings of the IASS Annual Symposium 2023
Integration of Design and Fabrication
10–14 July 2023, Melbourne, Australia
Y.M. Xie, J. Burry, T.U. Lee and J. Ma (eds.)

Slimline floor an invention by Pronk and Lichtenberg

Arno D.C. PRONK[a,*], Elke MERGNY[b]

[a,*] Eindhoven University of Technology
a.d.c.pronk@tue.nl

[b] Delta GC Design Office

Abstract

The Slimline floor system is a light prefab floor construction that can be combined with all main supporting structures, allows large spans, functions as a structural disc and delivers very good performance in terms of acoustics and fire. This paper summarizes the state of the art concerning the use of this type of structure and shows an example of modelling on ABAQUS.

Keywords: autarkic, office boat, energy, eco-friendly

1. Introduction

A striking design or specific wishes of clients sometimes require constructive solutions that go beyond the traditionally applied construction techniques alone. As a structural engineer, it is nice to be able to rely on a proven and widely applied structural floor system that makes it possible to meet the most exceptional questions. The Slimline floor system offers a light prefab floor construction that can be combined with all main supporting structures, allows large spans, functions as a structural disc and delivers very good performance in terms of acoustics and fire. A slimline floor makes it possible to realize floor elements with a span up to 16 meters. With this floor it is possible to combine the installations with the structure of the slimline floor. The benefits of this floor are less structural height and reduction of the weight of the floor. It is even possible to change the function of parts of the building in the long term, for example from office function to residential or care function. At the end of the life of the building, the residual value is maximum. The Slimline floor elements are demountable and can be used to realize new buildings. This floor was invented and developed by Arno Pronk and Jos Lichtenberg [1] [2]. The application of this floor is up to now very successful within the Netherlands.

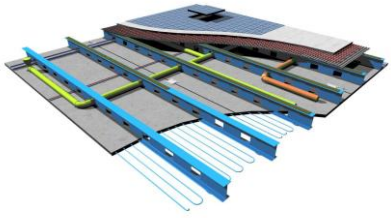


Figure 1. Render of slimline floor.



Figure 2. Picture of slimline floor.

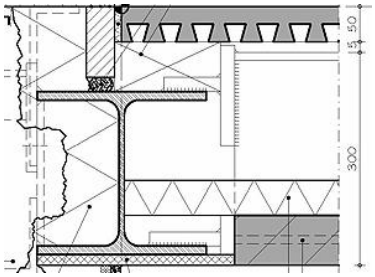


Figure 3. Drawing of detail.

Copyright © 2023 by Arno D.C. PRONK and Elke MERGNY. Published in the Proceedings of the IASS Annual Symposium 2023 with permission.

2. Buildings realised with the slimeline floor

The Slimline flooring system has been used in a wide range of buildings in high-rise, non-residential and residential buildings. Rijswijk (ZH) is home to the new office of the largest international organisation in the Netherlands, the European Patent Office. The 27-story office building of 85,000 square meters offers space for 1,950 employees in two main structures: New Main, the main building, and New Hinge, a lower part that includes the company restaurant, an atrium with courtyard and hearing rooms. In New Main, the storey floors, including the technical floor with a greater load, were equipped with the Slimline floor system. Flexibility has been one of the spearheads for this 107 meter high, 156 meter long 24.7 meter wide creation of the renowned architectural firms Ateliers Jean Nouvel (Paris) and Dam & Partners Architects (Amsterdam). All installations of the building are integrated into the Slimline floor and ceiling system with hollow installation space, so that spaces can be flexibly filled in. In addition, the Slimline floor system offered the solution to realize more floors and workplaces within the maximum building height and within such a slim design. The new EPO building combines contemporary architecture with a modern, state-of-the-art infrastructure. According to architect Diederik Dam, it is the tallest and thinnest construction in steel and glass in Europe. The main building is constructed of more than 10,000 tons of steel, making the building the largest steel construction in this quality in the Netherlands. A total of 100,000 m2 of glass was used in the building. The building consortium opted for a steel construction because of its relatively low weight, the modular character that allows construction to be built quickly and relatively quietly and the greater flexibility that the material offers in the layout of rooms. The Slimline floor system also contributes to the slim appearance, the low weight of the construction and the permanent adaptability." This building embodies the drive for innovation that benefits European citizens and the competitiveness of the European economy. This work by Jean Nouvel and Diederik Dam is more than just an impressive landmark in the skyline of The Hague and an economic boost for the region [7]. It is also a sign of our appreciation for the long-standing relationship with the Netherlands," said EPO President Benoît Battistelli. "This extraordinary building provides an environmentally friendly and sustainable workplace for our staff here and it is to the credit of all the people who have worked so hard to bring it about. We are convinced that the new office is also a harbinger of a new era, for our employees in the Netherlands and for the users of the European patent system. It is part of our efforts to modernise the EPO so that we can deliver state-of-the-art services with ever higher quality."A lot of interesting buildings have been realized with slime line floors. Below you will find the three most interesting and price winning projects.

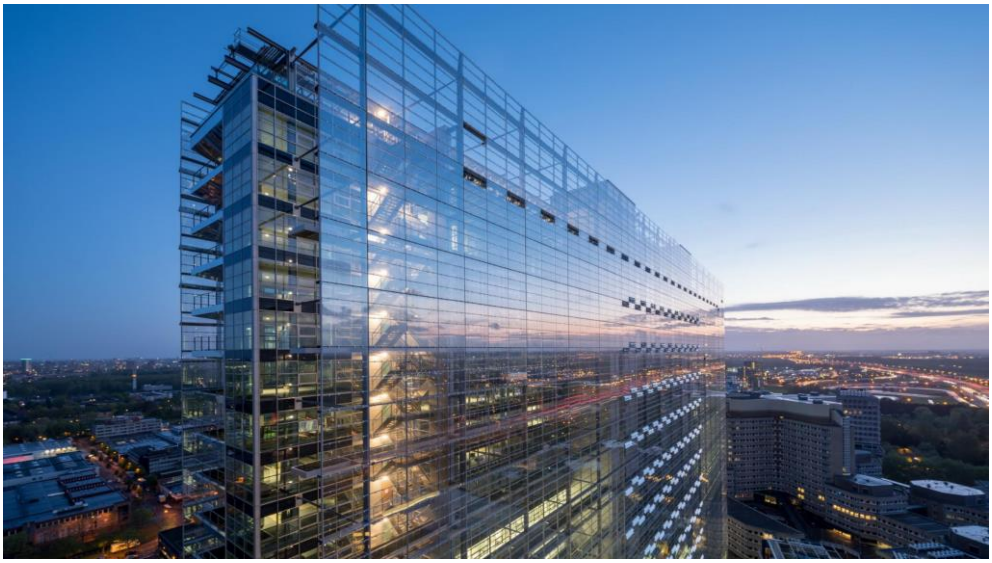


Figure 4. European patent office by Architect Jean Nouvel.

The eye-catcher of the Noord-IJ Oever is the unique Kraanspoor project. Architect Trude Hooykaas designed a 3-storey building with more than 10,000 m² of unique workspace with a beautiful view over the IJ. The aim was to integrate old and new and to maintain the atmosphere of the historic Kraanspoor. The result is a floating, transparent building above the existing structure, so that the former crane track is visible from the inside and there is a maximum view of the surroundings.

Kraanspoor is not only a spectacular, but also a green building. For example, the water from the IJ is used in the summer for cooling and in the winter for heating, ventilation takes place through openings in the floor and there are breeding grounds for wild birds.

Kraanspoor was awarded several prizes, including the National Steel Award 2008, the Glass Award 2008, MIPIM 2008 Green Building Award + Special Jury Award and the Urban Landscape Institute Global Award of Excellence [6].

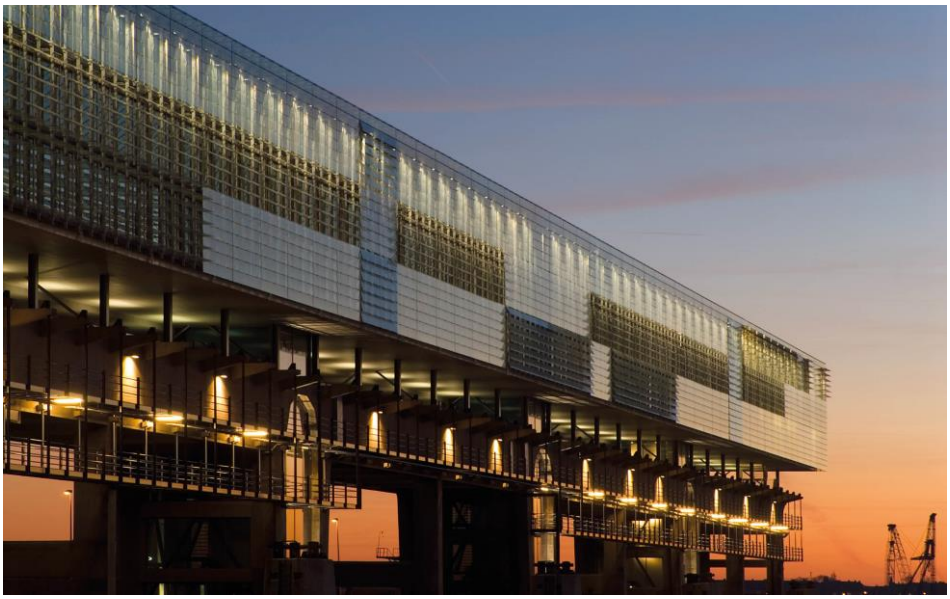


Figure 5. Kraanspoor by OTH Architecten.

The 'residential sculpture' Crystal Court is located at this relatively small location: 36 stacked luxury villas with beautiful wooden facades. In 2010, the project was awarded for the New Construction Award [8].

The houses are stacked in four loosely connected tree structures, in such a way that there is a lot of space in between and the footprint on the ground is kept as small as possible. Despite the compact buildings, many open spaces with views have been created in this way and the complex fits in well with the park-like environment. Due to the high density, 'continuity of the open space' is an important aspect of the design. This creates an interaction between the stacked volumes, the green environment and the open space.

Due to the way of stacking, all are different in typology, design and approach. They all have optimal views, privacy and sunlight. Most have several terraces with a view of the winter garden and the surrounding area.

Due to the high density, 'open space' is an important aspect of the design. This creates an interaction between the stacked volumes, the green environment and the open space.

Due to the way of stacking, all are different in typology, design and approach. They all have optimal views, privacy and sunlight. Most have several terraces with a view of the winter garden and the surrounding area. Both the main entrance and the entrance to the parking garage and the shared facilities

are located in the collective atrium. In the form of a water garden with fish and native plants, the park continues almost seamlessly into the atrium.



Figure 6. Crystal Court by Tangram architects.

3. Construction method

A Slimline floor offers great amount of freedom and great opportunities for large open, freely arranged spaces. Because the installation space is not filled with concrete, the own weight of the total floor package is relatively low, resulting in a weight reduction of 50% compared to traditional systems. In combination with the advantage that installations at Slimline are placed in the floor and therefore not in a suspended ceiling, it is possible to design main supporting structures with lighter foundations.

Building with Slimlinefloors means prefab, dry, fast and a stamp-free construction. In this way, the contractor cold realize the building in a shorter time. This also leads to an integral saving on construction costs. Due to the integration of ceiling, installation space and top floor, Slimline saves between 40 and 50 cm height per floor compared to other systems. This leads to a saving of 15% on the gross floor height. With Slimline, seven floors can therefore be realized at the same building height compared to six with other construction techniques. Slimline also offers excellent properties in terms of acoustics and comfort.

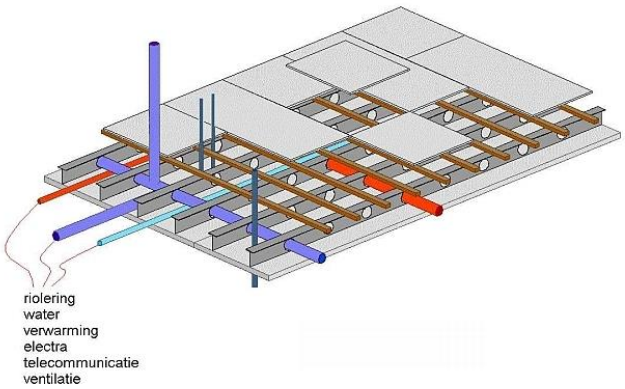


Figure 7. by A. Pronk.

4. Fire safety

The slimline floor has a good fire resistance determined by TNO Brand/Efectis in accordance with NEN6067:1997. With regard to the separating function (WBDBO) of more than 145 minutes for both the criteria of flame density involved in the seal, thermal insulation involved in the temperature and collapse (structural safety), Slimline can be used as a home-separating floor in a residential care or apartment complex. This floor delivers a good performance in terms of fire safety [9].

5. Details

On the steel profiles of the Slimline floor elements, different types of top floors with different possibilities for the accessibility of the installation space can be placed, such as a dovetail cast floor or a computer tile floor. The acoustic decoupling is achieved with a rubber granulate on the beams. Thanks to the two-tier construction with the acoustically decoupled floating screed on 15 mm rubber granulate, sound insulation values of Iluc and Ico > 10dB are achieved in both laboratory tests and practical measurements. Slimline can be used as a home-separating floor in a residential care or apartment complex. The Slimline floor system makes it possible to adjust installations, layouts and even the building function without structural interventions, so that the (rental) yield - and therefore the building value - can continue to be maximized with minimal costs.

Slimline extends the economic life of buildings. Because installations do not collapse and remain permanently accessible in the hollow floor, layouts can easily be determined and changed to measure, different rooms can be easily combined or separated, and the installation technology can easily be maintained or adapted to the latest state of the art and changing user requirements. Slimline makes building faster and easier. Because Slimline uses self-supporting prefab elements, submersible is not necessary. In addition, the installed floor elements are directly walkable, so that the installation of installations and the dismantling can start immediately, without affecting the other work. This makes it possible to slide several construction phases together, resulting in significant savings on construction costs and construction time. In addition, savings are possible on the foundation due to the lower weight and on expensive building components such as facades as a result of the slimmer floor package. In general, this leads to better preparation of the construction process and an increase in the number of building installations. The Slimline floor system enables quick and easy construction with prefabricated floor elements in an outrigger-free and dry process. Building installations are easily and permanently accessible in the hollow floor instead of suspended from the ceiling. The floor elements are interconnected into a constructive disc by welding coupling plates and (in the case of larger spans) tipping strips to be welded into the work. Usually, a (welding) connection is also made with the main supporting structure. Thanks to this stamp-free and completely dry process, up to 1,000 m2 of floor field can be realized per day. With an average total floor package weight of 300-350 kg/m2, it is in many cases possible to carry out the foundation lighter than with traditional floor systems. If desired, it is possible to include prefab climate pipes in the ceiling shell in order to easily realize ceiling cooling or heating. Layouts and facilities can be determined far into the construction process and, with the right facilities, remain adaptable or easy to maintain even after delivery.

6. FEM modeling

Numerical simulation is established using ABAQUS software [3]. The model is a common slimline floor that has the following characteristics. The beams are IPE 300 cellular beams. They are spaced 1.2 m apart and their span is 8.4 m. The steel grade considered is S355. The concrete slab is a 70 mm thick slab with a welded wire mesh made of bars of 16 mm in diameter and spaced 150 mm in both directions. The concrete class is C30. The steel grade of the reinforcement is BS500.

A floor element is composed of 2 beams and a slab element of 2.4m in length. The model considers four floor elements that lay on HEB 700 beams (length = 9.6m) that are supported by four HEB 300 columns (heigh = 3.5 m). In addition to the self-weight of the structural elements, a dead load G of 1.5 kN/m² and a live load Q of 4.5 kN/m² are applied with USL (1.35G+1.5G) and SLS (1.0G+0.3Q) combinations.

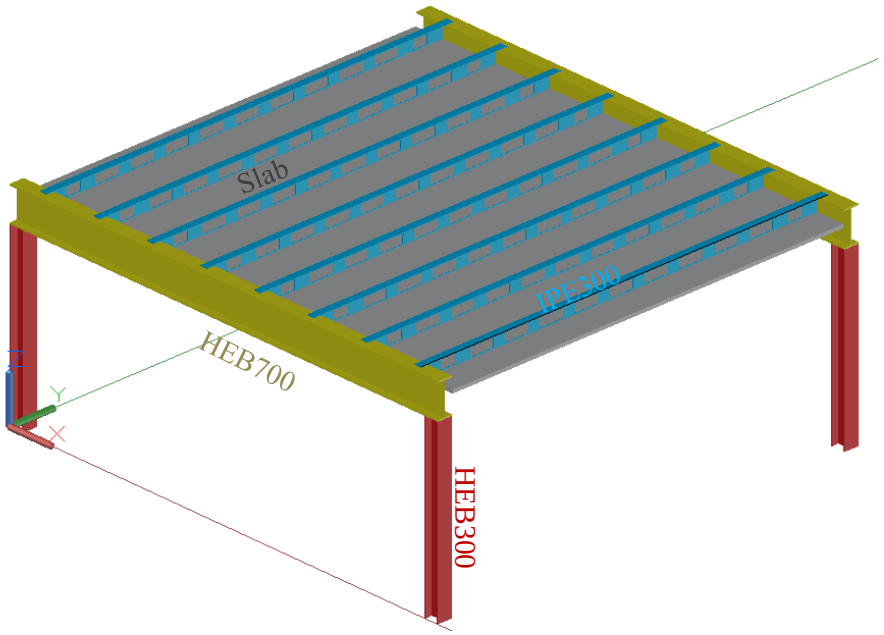


Figure 8. Model of the slimline floor.

The columns, the beams and the slab are modelled in 3D and are meshed with linear brick elements. Steel beams and columns are rigidly connected to each other. The columns are hinged to their supports. The connection between the IPE 300 beams and the concrete slab is not complete. A coefficient of tangential friction of 0.7 is considered between the two. Rebars are 1D elements and are meshed with truss elements. The bars are connected to the slab by the "embedded algorithm". This method allows a group of elements (rebars) to be constrained to the kinetic boundary conditions in "host" elements (slab).

The mechanical properties of steel and concrete are given by Eurocode 2 [4] and 3 [5]. Elastic-perfectly plastic [4] curve is considered for steel. Damage plasticity model [3] is used for concrete. The model considers the degradation of the elastic stiffness induced by plastic straining both in tension and compression.

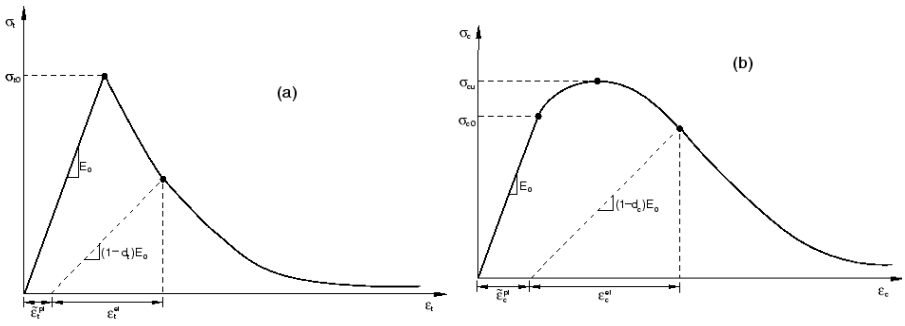


Figure 9. Mechanical model of concrete, tension (a) compression (b) [3].

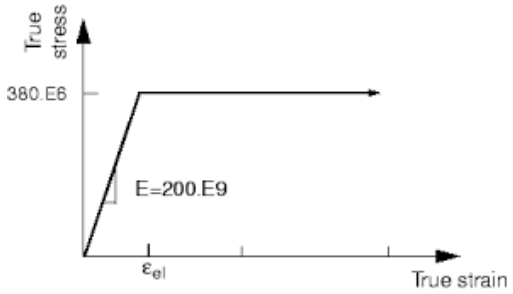


Figure 10. Mechanical model of steel [3].

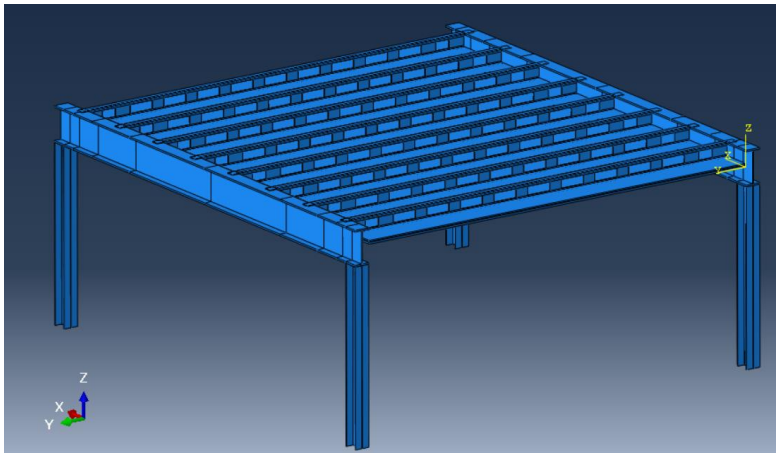


Figure 11. Model of the slimline floor in ABAQUS.

Figure , Fig 13 and Figure 14 show the stresses in the IPE 300 and the slab under the ULS combination. IPE 300 beams are in bending with stresses that do not exceed the strength limits of steel (355 MPa). The material remains in the elastic phase. The slab is subjected to tensile stresses largely taken up by the reinforcement. The stresses in the bars are below the design strength limit of steel (500 MPa / 1.15 = 435 MPa).

Figure 15 shows the vertical displacements when the floor is under the SLS combination. The displacement is limited to 2.26 cm, that is lower to the span of the beam divided by 250.

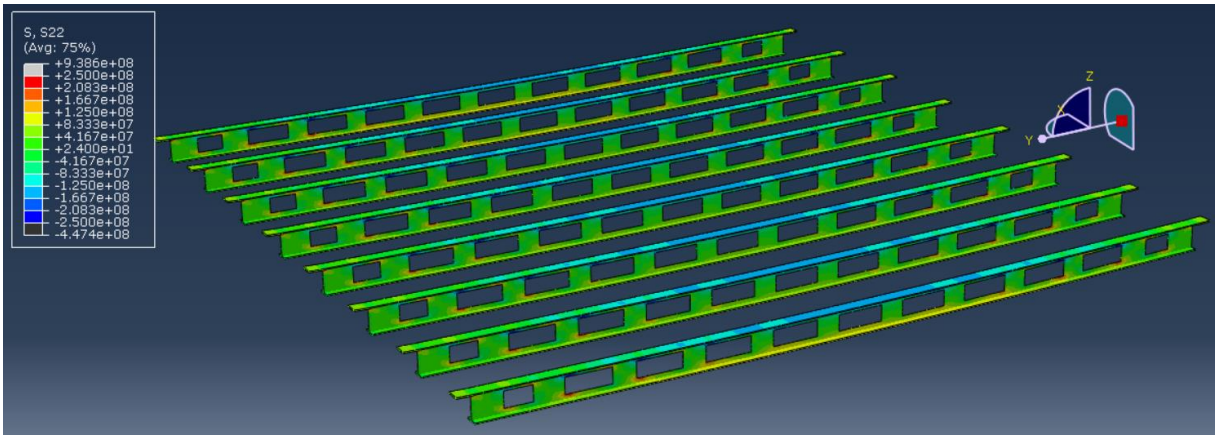


Figure 12. Stresses in y-direction in the beams IPE 300 (ULS combination) in N/m².

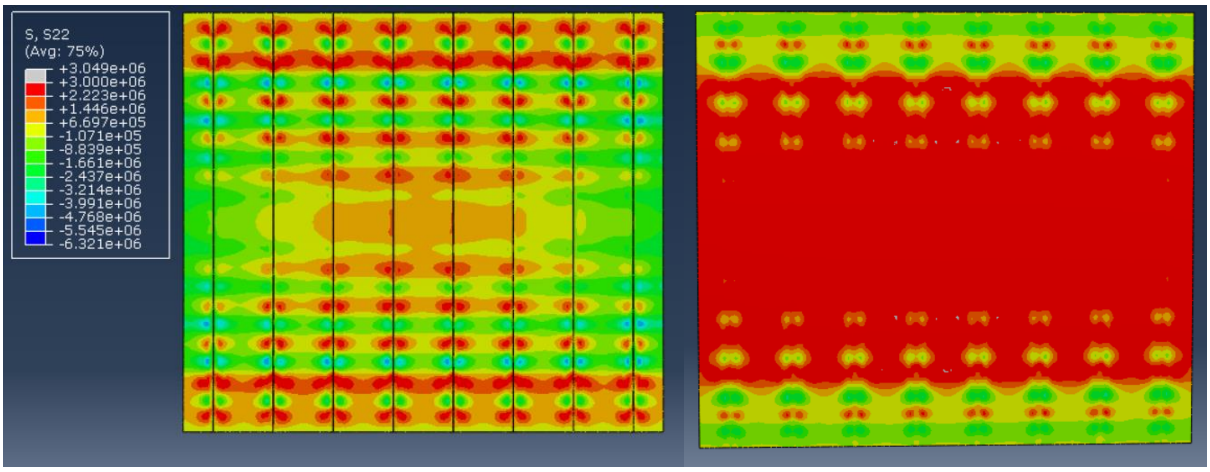


Fig 13. Stresses in y-direction in the slab (top and bottom) (ULS combination) in N/m².

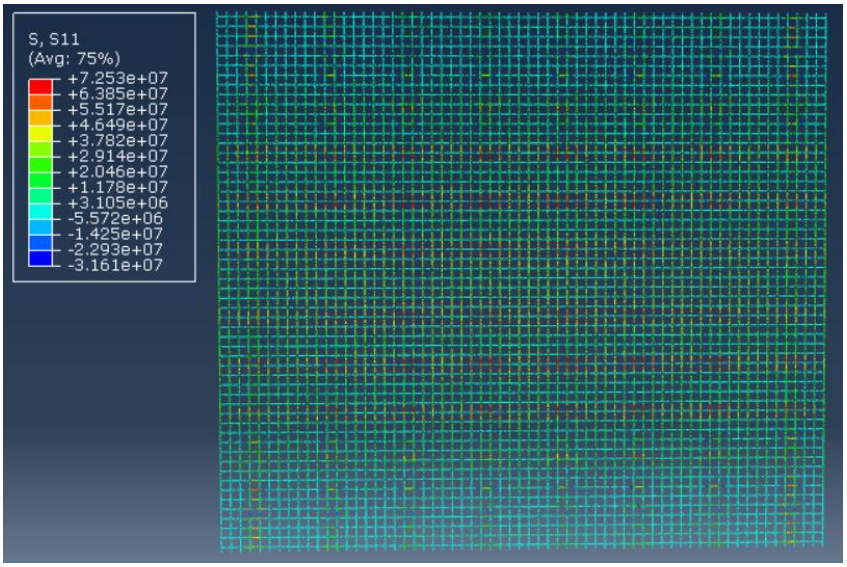


Figure 14. Stresses in the reinforcement (ULS combination) in N/m².

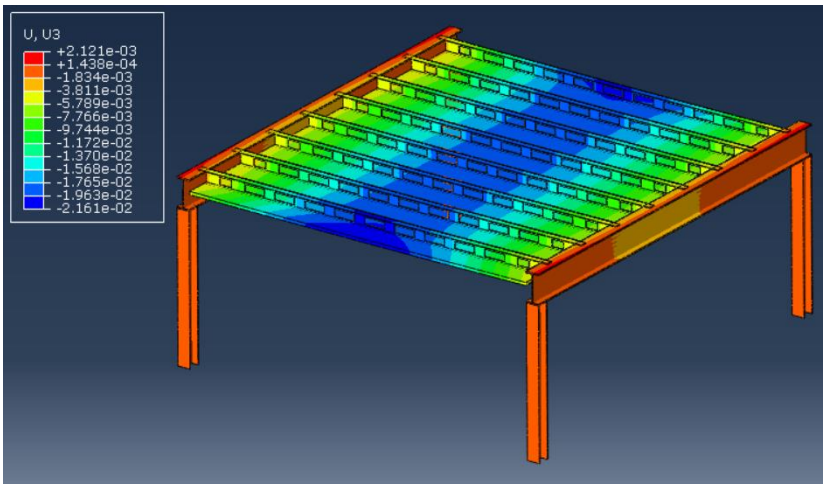


Figure 15. Vertical deflections (SLS combination) in m.

7. Conclusion

Based on this paper this slimline floor is a new innovation that is successful in the Netherlands. The benefits are: large span, better fire resistance, more freedom with installations, integration of the installation within the construction, less height. With this floor you will have more storeys within a building without the slimline floor. Floor modelling is easy and can be done in commercial finite element software's. It would be interesting to promote this type of floor also in other countries.

References

[1] Pronk Lichtenberg (1998-04-02) WO1998013560A1An assembly comprising a plate-shaped floor member, an assembly comprising at least two spaced-apart sections and at least one floor member extending between said sections, as well as a floor member and a section suitable for such assemblies.

[2] Pronk Lichtenberg (2000-07-14) NL1011011C1Flooring plate for multistory building has sandwich construction with layers of different materials.

[3] Smith, M., ABAQUS/Standard User's Manual, Version 6.9, 2009, Dassault Systèmes Simulia Corp, United States.

[4] 1993-1-1, BS EN. "Eurocode 3: Design of steel structures Part 1-1: General rules." 2005

[5] 1992-1-1, BS EN. "Eurocode 2: Design of concrete structures - Part 1-1: General rules and rules for buildings." 2004

[6] Casciani, S. (2008). WORKING ON THE DOCKS-With its" 270 metres of concrete silence", the Kraanspoor wharf in Amsterdam-Noord turned out to be the ideal base for a megastructure-office-DESIGN: OTH ONTWERPGROEP TRUDE HOOYKAAS BV. Domus, (913), 120.

[7] Nouvel, J. (2017). Oficina Europea de Patentes, Rijswijk (Holanda): Primer premio. AV proyectos, (79), 20-21.

[8] Kompier, V. (2009). Amsterdam versus Berlin: Paradoxes of the Luxury Apartment Market. DASH| Delft Architectural Studies on Housing, (02), 16-27.

[9] Newman, G. M. (1995). Fire resistance of slim floor beams. Journal of Constructional Steel Research, 33(1-2), 87-100.

Proceedings of the IASS Annual Symposium 2023
Integration of Design and Fabrication
10–14 July 2023, Melbourne, Australia
Y.M. Xie, J. Burry, T.U. Lee and J. Ma (eds.)

Stress reduction effect by changing the upper and lower surfaces near the boundary of a spherical shell

Shigehiro MOROOKA[a,*], Shouhei OHYAMA[b]

[a,*] School of Architecture and Urban Planning, Tokai University
morooka@tokai-u.jp
[b] RISE Structural Design (Former Graduate Student, Tokai University)

Abstract

Spherical domes and cylindrical roofs have been used for decades to cover large spaces due to their easy construction. By simply using a rope of a fixed length, the curvature of these structures can be maintained, and the outline can be drawn in 3D space. However, when the rises of these structures were high, large bending moments occurred at their boundaries, causing the domes made of stone or other materials that could not withstand the tension to crack. To prevent this, the plates were modified by thickening them or adding tension rings at the boundaries. This paper examines a method to modify the geometry near the boundary of a spherical shell to produce only beneficial compressive stresses. To simplify the modification of the shape, a shell of revolution was modelled using axisymmetric elements. The change in the normal direction of the upper and lower surfaces near the boundary was expressed as a quadratic function passing through the midpoint of the change value and the change at the boundary. We have also examined what kind of objective function would suit the purpose of this paper, as well as the shell shape and stress intensity distribution. We have also evaluated how much the stress intensity can be reduced by the shell opening angle and the range of change.

Keywords: spherical shell, shape optimization, thickness, stress in latitude and longitude direction, near the boundary, radius of curvature

1. Introduction

Spherical domes and cylindrical roofs have been used to cover large spaces due to their simple construction process, which involves drawing an outline in a 3D space with a rope of a fixed length [1]. However, when the rises of these structures were high, large bending moments occurred at the boundaries of these structures. To address this, some domes have been reconstructed with thicker boundaries or tension rings to strengthen them against any cracks that may occur after construction. Additionally, the shape of these structures has been optimized by hand, taking into account the materials used, such as stone and concrete, which are strong in compression but weak in tension. The optimal shape is one that does not produce tensile stress and has low compressive stress.

By the way, a calculation example revealed that even for a spherical dome, a slight change in its curvature could significantly reduce the bending moment [2]. Since a minor alteration of the shape could lead to a considerable decrease in the degree of stress, we decided to explore the possibility of creating a spherical dome that is easy to build and cost-effective, as fewer types of formworks would need to be prepared if the degree of stress can be dramatically decreased by merely changing the shape towards the boundary of the spherical shell.

Figure 1 shows an example of the boundary of an old shell structure [3]. Through slight modifications near the boundary, this shell has been able to withstand earthquakes and remain in existence. The aim of this study is to find a shape that has a beneficial stress distribution over the entire spherical dome

Copyright © 2023 by Shigehiro MOROOKA and Shouhei OHYAMA. Published in the Proceedings of the IASS Annual Symposium 2023 with permission.

surface (with no tensile stress and low compressive stress) and to evaluate its degree of benefit by changing the position of the upper and lower surfaces of the spherical dome in a certain area from the boundary.

In this paper, the finite element method and optimization techniques are employed to obtain such geometry. Firstly, an overview of the analytical model is presented, followed by an analysis of the objective function which can be used to attain an advantageous shape. Subsequently, the objective function is utilized to examine the effect of changing the shape of the upper and lower surfaces near the shell boundary to reduce the stress level and its shape.

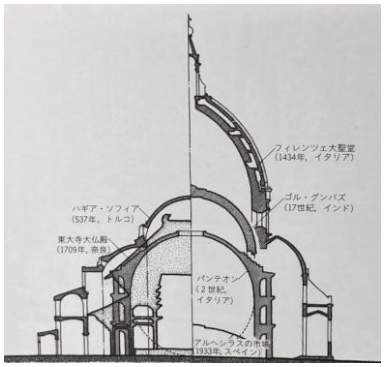


Figure 1. Example of the boundary of an old shell structure [3].

2. Outline of analysis model

The purpose of this study is to investigate how much stress can be reduced by modifying the shape of a spherical dome around its boundary, while keeping most of the dome's shape intact. Figure 2 provides an overview of the numerical analysis model used. To simplify the geometry modification, the rotational spherical shell was modeled with axisymmetric elements.

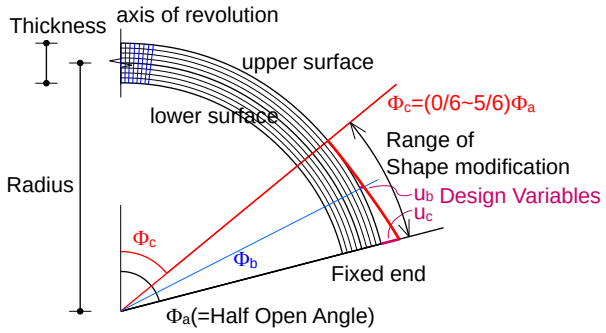


Figure 2. Numerical analysis model

The shape of the modified surface close to the shell boundary, from Φc to Φa in this figure, was expressed as a quadratic function, as shown in Figure 2. This was to avoid having too many design variables which could lead to a local solution. The finite elements were equally divided in the thickness and latitudinal directions to calculate the stress, and the range of shape modification was set to 6 types, from 0/6 to 5/6 of the half-opening angle Φa to the boundary. The quadratic function was obtained from two normal displacements at the Φb (midpoint of Φa and Φc) and Φc points, along with two conditions (normal displacement 0 and slope 0) that ensure a smooth transition to the original shell at Φc.

As a result, there are two design variables when movement is limited to either the upper or lower surface and four when movement is allowed on both. We considered using separate quadratic functions for the upper and lower surfaces to obtain a solution that intersects them, but this was not achieved even without any constraints. This angle, Φc, is referred to as the start angle of shape modification.

3. Examination of objective function

Since a suitable objective function for shape modification was not known, several objective functions were investigated. This chapter then examines the resulting stress distribution. It is noteworthy that all the convergence calculations presented in this chapter were done using the steepest descent method.

3.1. Bending moment minimization

First, we sought to minimize the maximum bending moment. In the prescribed study[1], the appropriate curvature was obtained by bending moment minimization. However, in the analytical model of this study, the boundary became like a pin. In the model with constant plate thickness, we were able to reduce the bending moment value by changing the curvature, thus causing the solution to converge. On the other hand, when we allowed the plate thickness to vary, the objective function became unsuitable. This was because the boundary became thin and pin-like, reducing the bending moment but increasing the stress intensity.

3.2. Minimizing the maximum stress

Next, we minimized the maximum vertical stress intensity in the latitudinal direction. Since the vertical stress varies linearly in the cross-section, we only evaluated the values at the upper and lower surfaces of the shell, which are the edges of the cross-section. From now on, we will refer to the vertical stresses in the latitudinal direction at node *i* on the upper and lower surfaces of the shell as σ_i^{upper} and σ_i^{lower}, respectively, and the maximum and average values as $\sigma_{\text{max}}^{\text{upper}}$, etc., using the subscript max and ave, respectively. The objective function a in this section is as follows.

$$a = \max.(\sigma_{\text{max}}^{\text{upper}}, \sigma_{\text{max}}^{\text{lower}}) \tag{1}$$

The signed value of tensile stress is being minimized as much as possible, with the positive value being reduced to a minimum.

3.2.1. Analysis model and analysis conditions

Table 1 shows an analytical model. Nine models were solved with three different surface patterns (upper surface only, lower surface only, and both surfaces) and three different thickness change start angles Φc, with the shell half-opening angle Φa set at 90°. Equal-distributed loads in the vertical direction were applied, and the amount of movement in one step of the design variable for the steepest descent method was set to *t*/100.

Table 1. Analysis model and conditions

Radius of neutral plane of initial shape (R) [mm]	5000
Initial thickness (t) [mm]	50
Number of divisions in the open angle direction	900
Number of divisions in the direction of plate thickness	10
Boundary condition	Fixed end
External Force	10N/mm² in vertical direction
Surface to be reshaped	moving both surfaces, upper surface only, lower surface only
Half Open Angle (Φa)	90
Shape change start angle(Φc)	75, 81, 85

3.2.2. Change in stress distribution

Figure 3 shows the distribution of vertical stress in the latitudinal direction when the upper and lower surfaces of the shell are changed, with the starting angle of each shape change indicated. Solid lines

represent stress levels on the upper surface, while dotted lines represent those on the lower surface. The tensile stress level is reduced, but not completely eliminated, and in some cases the compressive stress level even increases. This suggests that this is not a suitable objective function for determining the dome shape, which is typically made of compressed material.

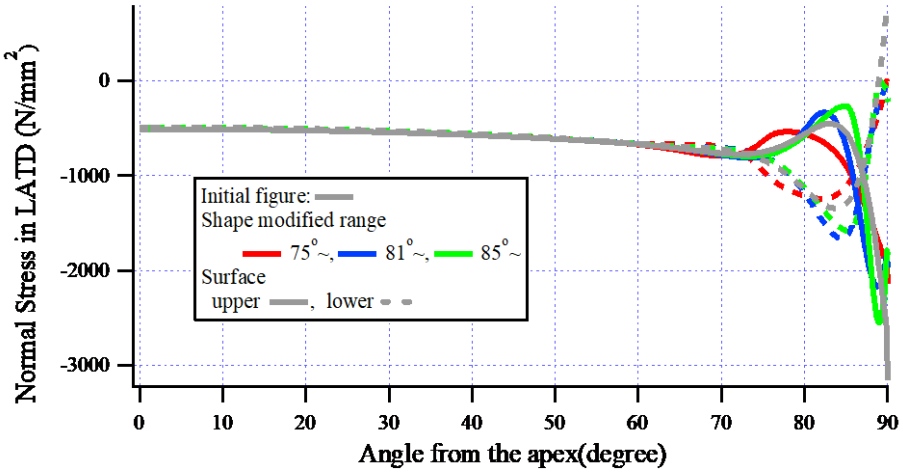


Figure 3. Stress distributions (Minimizing maximum stress)

3.3. Minimizing the sum of the squares of the differences from the mean of the stress levels

As our objective function, we considered the sum of the squares of the differences between the mean vertical stress levels on the upper and lower surfaces of the shell in the latitudinal direction. For the case of changes in the upper and lower surfaces, we used the following equation.

$$a = \sum (\sigma_i^{\text{upper}} - \sigma_{\text{ave.}}^{\text{upper}})^2 + \sum (\sigma_i^{\text{lower}} - \sigma_{\text{ave.}}^{\text{lower}})^2 \tag{2}$$

Note that the analytical model is the same as in the previous section.

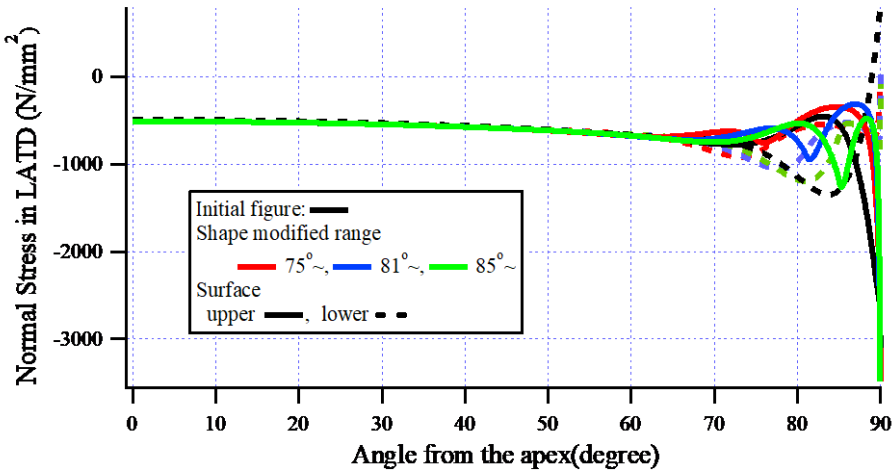


Figure 4. Stress distributions (Minimizing variance)

As Figure 4 illustrates, the stress distribution shows that, similarly to what was observed in the previous section, the tensile stress level is decreased but not eliminated, while in some situations, the compressive stress level increases. This suggests that using the maximum stress level as the objective function is not

suitable for producing dome shapes, which are generally made from compressed materials.

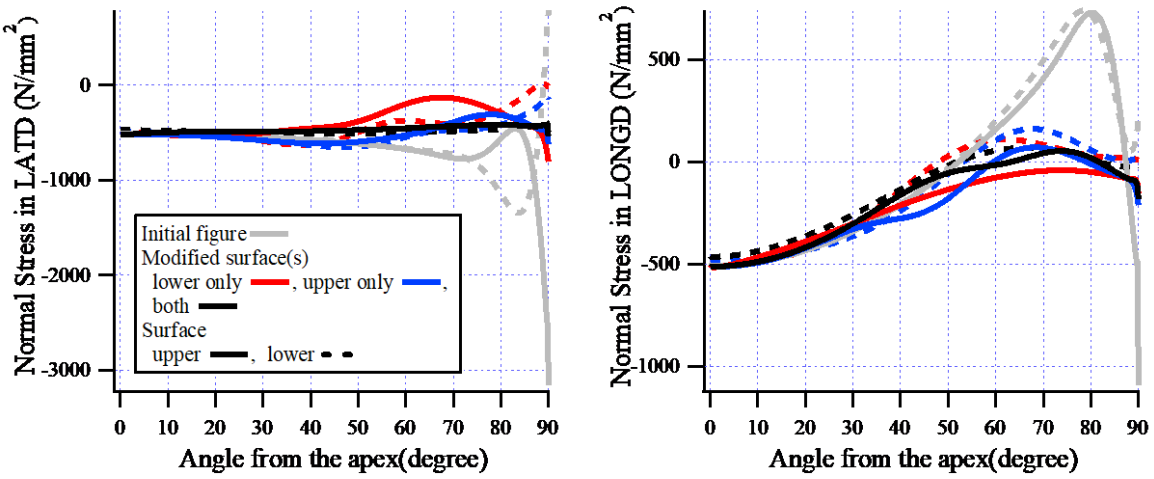
3.4. Minimizing the sum of squares of the difference between the maximum and minimum stress values

In the previous two sections, our aim was to minimize tensile stress and reduce compressive stress as much as possible. However, tensile stress still occurred in both cases. To address this issue, we considered combining the two objective functions and solving the problem as a minimization problem with an objective function of the sum of squares of the differences from the mean of the stress levels and a constraint that the maximum stress level should be less than or equal to zero (i.e., compressive stress level). But, instead, we decided to try a different approach: if the difference between the maximum and minimum stress levels is small, it may lead to a uniform compressive stress level throughout the entire structure. The equation is expressed as follows.

$$a = (\sigma_{\text{max.}}^{\text{upper}} - \sigma_{\text{min.}}^{\text{upper}})^2 + (\sigma_{\text{max.}}^{\text{lower}} - \sigma_{\text{min.}}^{\text{lower}})^2 \tag{3}$$

In the preceding two sections, we only modified the boundary area, resulting in various shape solutions, but it was difficult to determine if they were correct. Therefore, we hypothesized that optimizing the entire shell would result in a suspension surface, and set the shape change start angle Φc to the vertex (0°) in this section.

The distribution of the latitudinal vertical stress intensity at convergence is shown in Figure 5(a). It displays the values for the initial geometry and three geometries change surface patterns. The stress distributions after convergence of each shape change surface pattern show no tensile stress in any case, and particularly for the upper and lower surface changes, the vertical stress values are almost constant over the entire surface of the shell, confirming the effectiveness of the objective function.



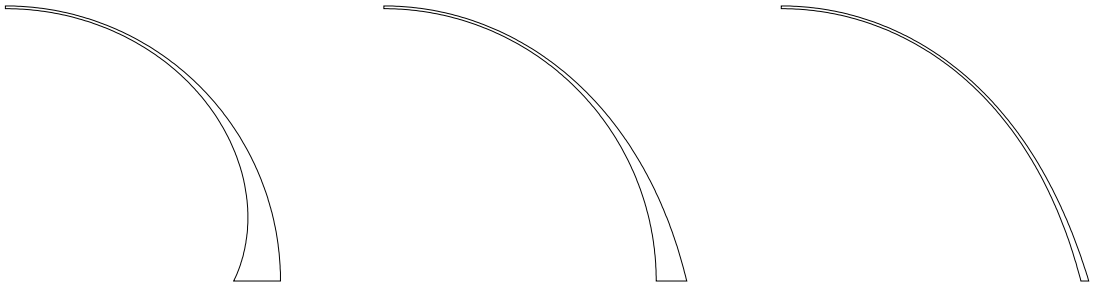
(a) in latitudinal direction (b) in longitudinal direction

Figure 5. The difference in stress distribution due to the modified surface

Figure 5(b) illustrates the distribution of the longitudinal stress. Despite the fact that the objective function is composed of latitudinal stresses, normal stresses in LONGD have also decreased.

Figures 6(a)-(c) depict the shapes of the three shape-changing surface patterns at convergence. The shape change surface pattern with the most reduced objective function is the upper and lower surface change, and as can be seen in Figure6 (c), its shape resembles a suspension surface with a bulging

boundary, which is similar to Wilhelm Flügge's isostrength shell [4].



(a) lower surface only (b) upper surface only (c) both of surfaces

Figure 6. Convergent solution (H.O.A.=90º)

3.5. Summary

In this chapter, we considered several objective functions and performed convergence calculations. As a result, we found that the shell shape in the fully compressed state can be obtained by using the sum of squares of the differences between the maximum and minimum values on the upper and lower surfaces of the shell as the objective function.

4. Effect of stress reduction by changing the shape of the shell boundary

In the previous chapter, we investigated the objective functions for obtaining the stress state of an ideal shell. In this chapter, we examine how changing the geometry of the shell boundary can reduce the stress state, which was the original objective. Table 2 presents the analytical model and conditions. As the initial shape, we take a spherical shell with half-open angles of 60°, 75°, and 90°, and we investigate the convergent solutions for six different shape modification ranges. If the shape change start angle is 0°, this means that the whole surface of the shell is changed (as seen in the previous section), whereas if it is 5/6, only 1/6 of the area around the shell boundary is modified.

Table 2. Analysis model and conditions

Span (mm)	10000
Radius of neutral plane of initial shape R (mm)	5000
Initial thickness t (mm)	50
Number of divisions in the open angle direction	900
Number of divisions in the direction of plate thickness	10
Boundary condition	Fixed end
External Force	Dead Load
Surface to be reshaped	moving both surfaces
Half Open Angle (Φa)	60, 75, 90º
Modified range	from 0/6, 1/6, … 5/6 of Φa
Number of initial shapes	100
Range of initial irregularities given to design variables	$-0.5t \sim +0.5t$

4.1 Rethinking of optimization methods

In the previous chapter, the optimization method of steepest descent was used to examine the objective functions, but due to the high computational load, the quasi-Newton method was explored in this chapter. As seen in Figure 7, when the number of initial shapes is 50 for the steepest descent method

and 100 for the quasi-Newtonian method, the convergence solutions for the maximum and minimum stress levels are distributed. The initial shapes were created by assigning values for the design variables ub and uc in the range of plus or minus 0.5 times the plate thickness. The linear line crossing the zero point in the graph indicates the equal value of max. stress (horizontal axis) and min. stress (vertical axis). Solutions that are near this line and closer to the zero point are more desirable, and are represented by circles (steepest descent) or X marks (quasi-Newton). The amount of movement of the design variable in the steepest descent method varies from t/10 to t/5120 depending on the convergence calculation times, while the quasi-Newton method involves a linear exploration routine of the solution. Although the steepest descent method has a smaller initial value dependence, the number of convergence calculations is much smaller for the quasi-Newtonian method. Therefore, this chapter discusses the solution with the smallest objective function value among the solutions obtained by the quasi-Newton method, as this is what we aim to achieve.

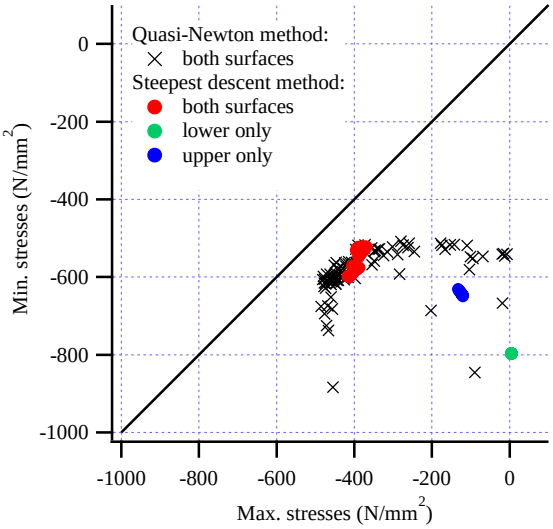
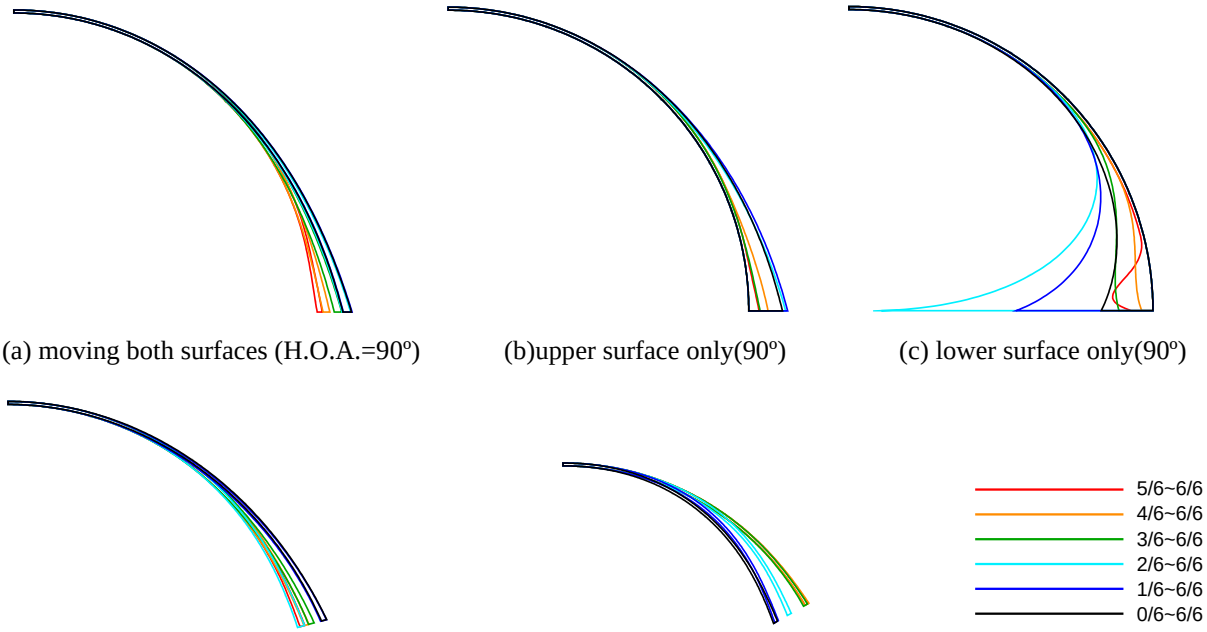


Figure 7. Differences in max/min values due to convergence methods

4.2. differences in optimum shape due to differences in the range of change

4.2.1. Shape change

The solutions with the smallest objective function values, obtained from the initial shape with a half-opening angle of 90 degrees, are presented in Figures 8(a)-(c). The six colors in the figure indicate the various degree of shape modification. In (a), where the shape is modified on the upper and lower surfaces, the shape is modified with almost no change in thickness, while the other two solutions, where only one of the surfaces is modified, show a distorted shape. The FEM model used in the calculations was equally divided in the thickness and latitudinal directions, respectively, in order to obtain an element aspect ratio of 1:1. However, as the plate thickness increased during the calculation process, the element aspect ratio became more than 100 times that of the elongated element division, resulting in an incorrect stress intensity distribution. To address this issue, the elements in the thickness direction should be divided in proportion to the thickness. As this paper is focused on the determination of the optimum shape obtained by changing only the boundary, the results of the upper and lower surface changes from the initial shapes with half-opening angles of 60 and 75 degrees are presented in Figures 8 (d) and (e).



(a) moving both surfaces (H.O.A.=90º) (b)upper surface only(90º) (c) lower surface only(90º)

(d) moving both surfaces (H.O.A.=75º) (e) moving both surfaces (60º)

Figure 8. Convergent Shapes

4.2.2. Distribution of radius of curvature and plate thickness

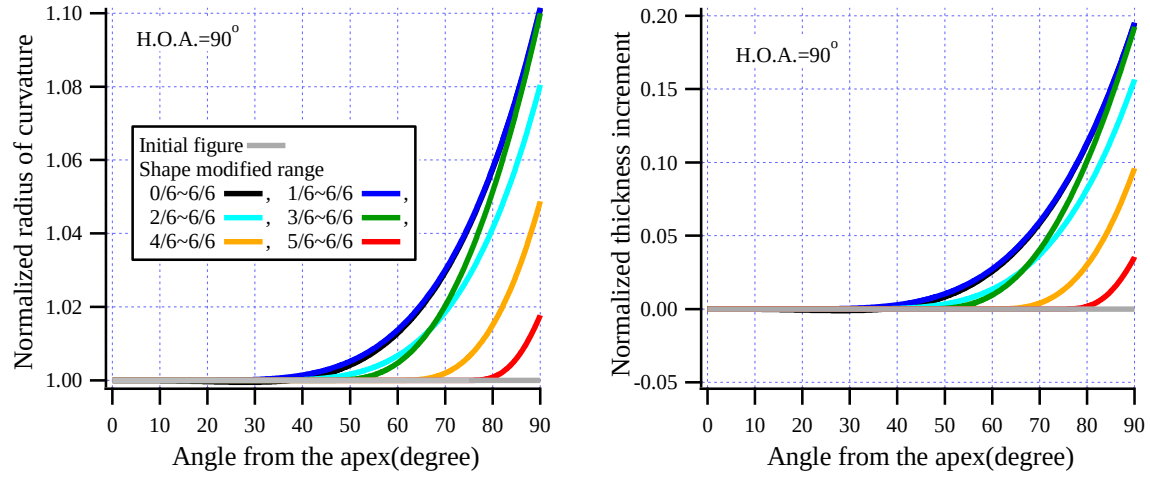
The shapes were roughly shown above. To see the details of the differences in shape change, Figure 9 displays the distribution of the radius of curvature in the latitudinal direction and the incremental thickness of the obtained shape. Since the aim is to observe the ratio of changes, each is normalized by the initial radius of curvature (i.e. the radius R of the spherical shell) and the initial plate thickness.

Outside the shape modification range, the radius of curvature is constant due to the initial shape being a spherical shell, however, at the boundary of the shape modification range, a larger radius of curvature is effective in reducing the stress level. It is also beneficial to adjust the plate thickness toward the boundary in the direction of increasing thickness.

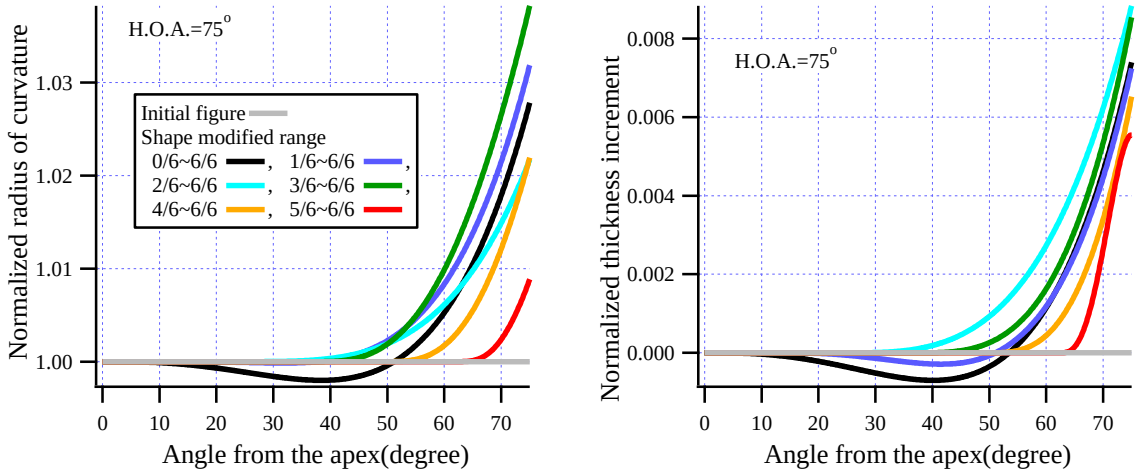
4.2.3. Stress distribution and stress reduction effects

Figure 10 shows the stress degree distributions in the latitudinal and longitudinal directions, where the smallest objective function value of the optimal solution for each modification range was obtained. The stress intensity distribution for the spherical shell is also given in the graph as a gray line. It can be seen that no tensile stress level occurs in the latitudinal direction for all cases, and that the stress in the latitudinal direction is almost constant, particularly for 90° and 75°, but not for 60°. As for the longitudinal direction, the stresses are generally decreased, although some tensile stresses remain in some cases. The initial spherical shell of 60° does not generate tensile stress in LATD, which is why the convergent solution in the 60° case is different from those in other cases.

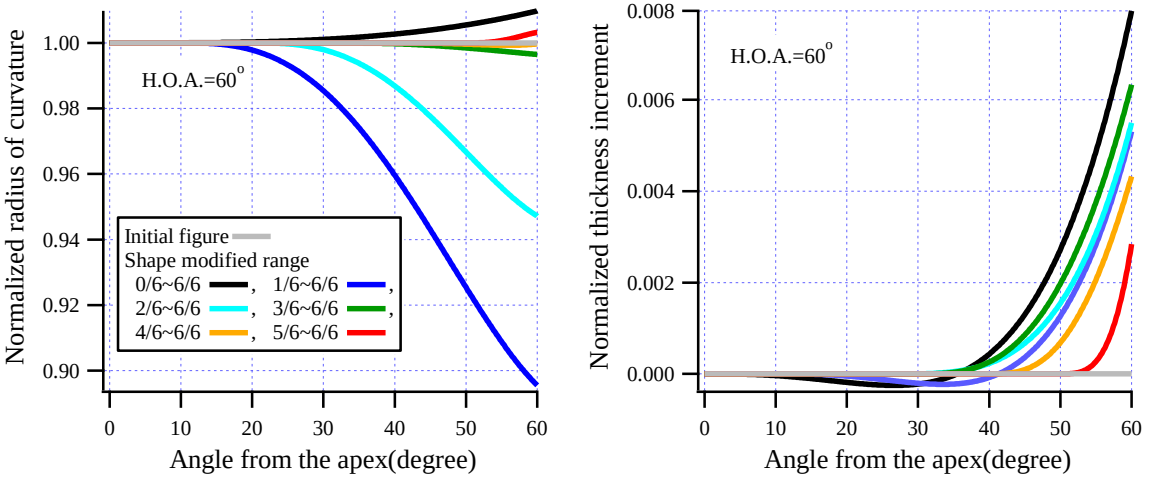
As shown in Figure 11, the compressive stress level is reduced by approximately 30% when the half-opening angle is 90°, 40% when it is 75°, and 60% when it is 60°. This suggests that even just a small change in shape near the boundary is enough to significantly reduce the stress level.



(a) H.O.A.=90°

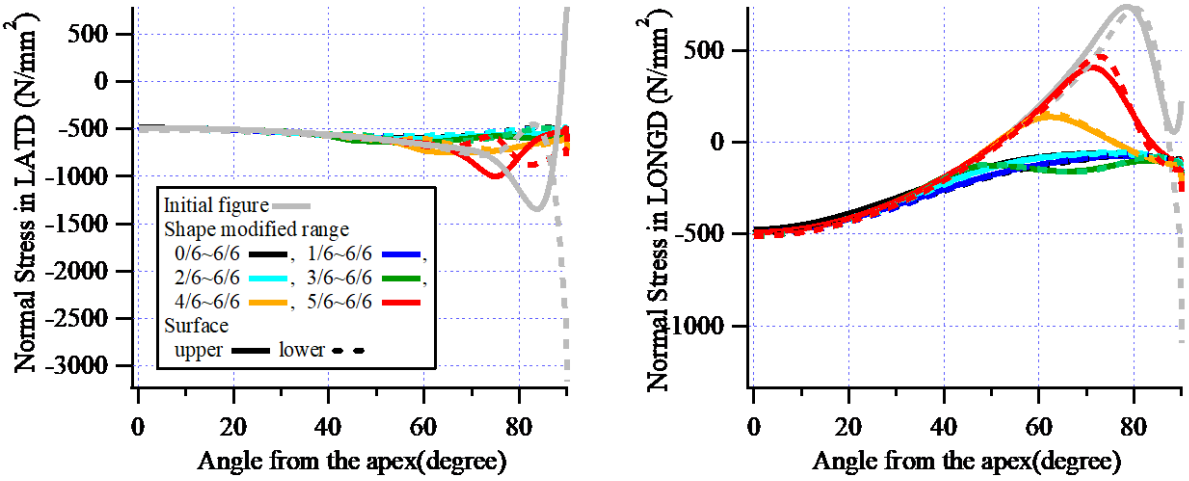


(b) H.O.A.=75°

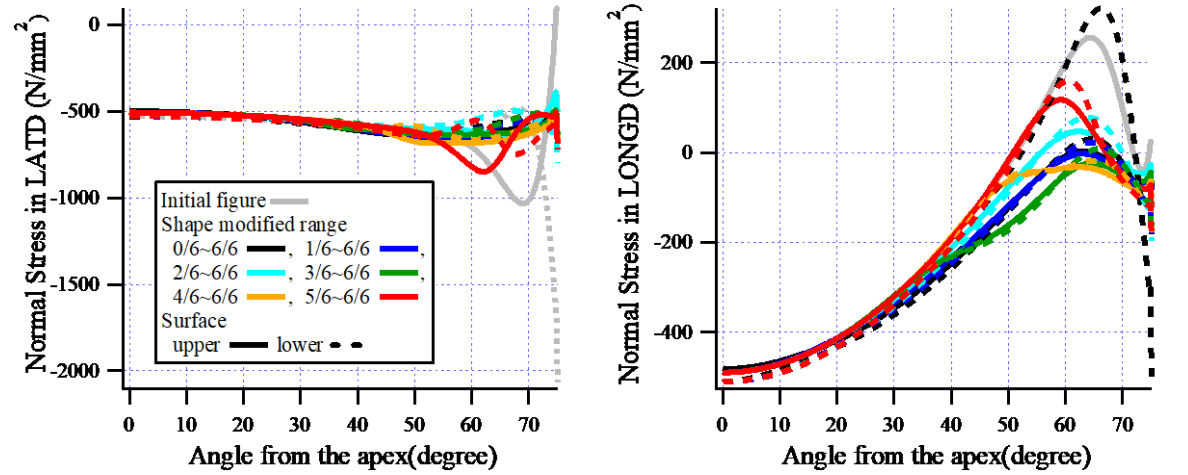


(c) H.O.A.=60°

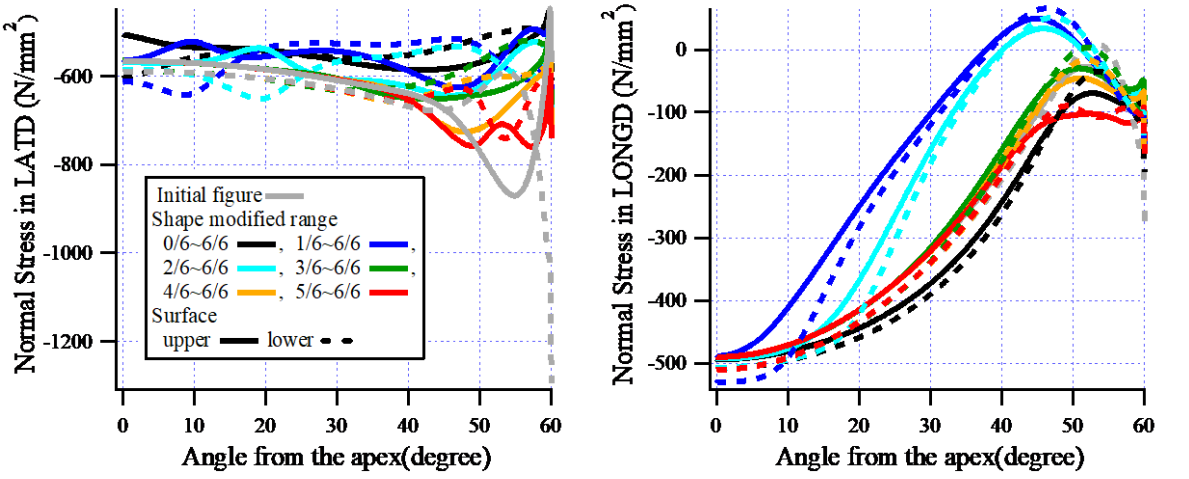
Figure 9. Distribution of radius of curvature and thickness in latitudinal direction



(a) H.O.A.=90°



(b) H.O.A.=75°



(c) H.O.A.=60°

Figure 10. Normal Stress Distibution in LATD and in LONGD

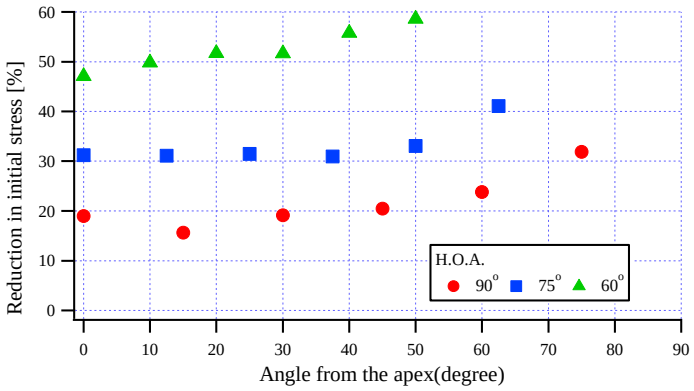


Figure 11. Stress Reduction Effects

5. Conclusion

In conclusion, this study suggests that the optimization of a part of the shape rather than the entire shape could reduce the stress level and improve the workability, and the spherical shell was taken as the initial shape because the curvature of a spherical shell is constant and common formwork can be used if as much area as possible is left as a spherical shell.

The following is a summary of the findings obtained within the scope of the study.

(a) For shell structures expected to be under compression, optimizing the geometry can be effectively achieved by taking the difference between the maximum and minimum stress levels on the upper and lower surfaces of the shell and the sum of their squares as the objective function.

(b) This is because the stress level at the top of the shell remains a constant compressive stress level, and the shape can be modified to get closer to this value.

(c) As a result, the entire surface of the shell takes on a suspension-like shape with thicker boundaries, similar to that of an isostatic shell

(d) Furthermore, by making changes only in the vicinity of the boundary, it is possible to reduce the tensile stress level to some degree in the longitudinal direction.

(e) The shape to reduce stress will have a larger radius of curvature near the boundary and a thicker plate.

Although the method in this paper is intended to leave the spherical shell as much as possible and simplify the construction, complex formwork is required at the boundaries where the curvature is varied. Therefore, in order to prioritize workability, we are currently researching a shape in which the curvature of the inner and outer surfaces of the shell is constant for each, and we hope to publish our results in the near future.

References

[1] Lloyd Kahn: SHELTER, (Supervised by Kazuhiro Tamai (Japanese version)), 2001 (in Japanese)

[2] Hiroshi OHMORI and Kenji YAMAMOTO: Shape optimization of Space structures for specified stress distribution Part 1 Application for shell structures, J. Struct. Constr. Eng., AIJ, No. 496, 67-73, Jun, 1997 (in Japanese)

[3] Mamoru KAWAGUCHI et al.: The Mechanics of Architectural Structures: Flow of Forces and Shapes (Picture Book of Architecture), 2nd edition, Jun, 2014 (in Japanese)

[4] Wilhelm Flügge: Stresses in Shells, Springer-Verlog,1966

IASS 2023
July 10–14 Melbourne
Integration of Design and Fabrication

Proceedings of the IASS Annual Symposium 2023
Integration of Design and Fabrication
10–14 July 2023, Melbourne, Australia
Y.M. Xie, J. Burry, T.U. Lee and J. Ma (eds.)

Study on the influence of structural optimization techniques on architectural design, with a focus on topology optimization methods

Bunji IZUMI[*], Anders RØNNQUIST[a], Bendik MANUM[b]

[b,*] Department of Architecture and Technology,
Norwegian University of Science and Technology
bunji.izumi@ntnu.no

[a] Department of Structural Engineering,
Norwegian University of Science and Technology

Abstract

Structural optimization in its modern definition emerged in the 1960s, and various optimization methods have been proposed to date. Structural optimization plays an important role in modern structural design. It can reduce the consumption of materials while maintaining the structural performance of buildings. Structural optimization can also be considered as a potential means to make architecture more attractive, beyond the change of shape as a by-product of minimizing materials and costs. The author's research group investigated what structural optimization methods were proposed during the decade 2012-2021 and found that topology optimization is important with respect to its impact on architectural design. As an extension of this work, this study focuses on the application of such structural optimization methods to architectural design. In order to evaluate the impact of structural optimization in architectural design as objectively as possible, the content of a major architectural online magazine was investigated. Among the projects, we further investigated whether and how structural optimization methods were applied and provide an analysis and discussion of the results.

Keywords: structural optimization, topology optimization, conceptual design, architecture and engineering, web-scraping, architectural magazines

1. Introduction

In last year's presentation [1], a literature survey was conducted using a systematic mapping approach on academic journals to find out what structural optimization methods have been proposed in the last decade.

The results showed that topology optimization is an optimization method for the layout of components and therefore has a high impact on the appearance of architecture, but the number of such methods is not very large. In addition, the number of real projects was very marginal (Figure 1), even though this was an expected result. This indicates that, due to the survey of literature in academic journals, it was not possible to assess to what extent and how structural optimization methods have an impact on the appearance of architecture in practice. This does not necessarily mean that structural optimization has no effect on the state of architecture.

Copyright © 2023 by Bunji IZUMI, Anders RØNNQUIST and Bendik MANUM. Published in the Proceedings of the IASS Annual Symposium 2023 with permission.

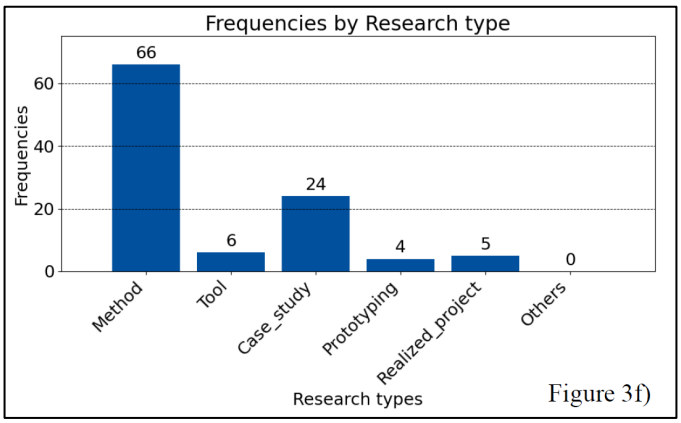


Figure 1. Frequencies by research type [1]

So, what information should be examined to better reveal the actual application of structural optimization? We initially tried to extract projects with structural optimization from architectural awards, but we considered that this would not gather much information. In the end, the authors focused on the architectural media. The information in the media is generally regarded as cobbled together, although it shows the results of editors' selection. However, the authors decided to turn to this option because it contains information that can be analysed in one way, such as attempts worth reporting and information on awards received.

In summary, the following points are sought to be clarified in this report. Research questions:

- What is the number and percentage of projects that allegedly used structural optimization within the last 10 years? In particular, how many of these projects used topological optimization?
- If the above numbers are found to be insufficient, what could be the reasons?
  Are there any unrecognised barriers in performing structural optimization methods, in particular topology optimization?

Limitation of research is as follows. This is the first attempt to use this methodology and relies on datasets from specific websites, as detailed in the Methodology in the next section. Hence, it is expected that different results will be obtained when different data sets are used. This report is therefore not intended to be a complete description of the situation, but rather a preliminary report on the validity of the data analysis methodology. It would also be meaningful to investigate the application of structural optimization in fields other than architecture (e.g. aerospace engineering), but the scope of the present study was to confirm its application in architecture and excluded these fields from the scope of the study.

2. Methodology

2.1. Web scraping

In this study, the main web-based architectural news sites were first selected. News sites often have a search window, but it is rare to be able to search by multiple criteria, such as the year the article was published, whether it contains an optimization statement, etc. Also, some articles contain not only articles on architectural projects, but also articles focusing on architectural education and architects, and articles on peripheral topics such as interior design and product information, etc. The articles also contain articles on other topics, which need to be removed.

In order to do this efficiently, we adopted the web-scraping method, which includes the retrieval of data by a human operator, but in this paper, we refer to a method that automates the process through programming.

2.2. Ethical issues

There are several important points that need special attention when carrying out web scraping. The following section presents the points to note, and the responses taken in this study.

Firstly, it can be accessed significantly faster than a physical human manually going to the information, as the information is accessed by automated methods through programming. However, accessing one site at a high frequency and retrieving information may slow down the response of the site and make it impossible to continue the service. Therefore, it should be noted that this may be regarded as an attack on the site by the site operator. It is recognised that there is no common understanding of how much is considered high frequency, as it depends on the capacity of each site. Here, we have referred to a number of previous cases and other examples, and generally referred to the fact that many sites advise that the site should not be accessed more than once every 1-3 seconds, and in this study, the setting was set to open more than 2 seconds from one access to the next.

Secondly, the usage and access range permitted by the site operators. It is common for major sites to have a "robots.txt" file in the top directory, which states which types of automated visitors are prohibited from accessing which range of directories. This study was conducted with strict adherence to this range. The "Terms of Use" and similar items are located on the website. These often state that unauthorised scrape is prohibited. In this study, sites that explicitly state in the "Terms of Use" base that scrape is prohibited were excluded from the scope of the search.

The last step is the use of the information obtained. Caution should be exercised mainly with regard to personal information such as e-mail addresses. In this study, the scope of information analysis was limited to the range in which the text was written, so that the possibility of personal information being included was reduced. Also, care was taken to ensure that the results obtained were used statistically. However, the resulting projects were analysed because they are in the field of building projects, which cannot be anonymous, and because of the extent to which they are accessible to the public.

2.3. Methods

From the main architectural media, the following two conditions were used to determine which ones were included in the study. One is that there must be no description in the robots.txt file prohibiting automatic access, and the other is that if a 'terms of use' is explicitly stated, it must be judged from its content that it does not prohibit automatic access. Dezeen (hereafter the website) was identified as one of the few websites that fit both criteria.

For the purpose of understanding the current situation, data were taken from web pages published between 2013 and 2022. In order to limit the population of articles, only articles with the tag 'Architecture' were obtained for the website. For the acquisition of information, parsing and analysis, the existing open-source libraries in Python 3, requests and beautifulsoup, were used. The data was acquired in March 2023.

The search key is as follows:

- the tags of the article include “Architecture”.

- whether the body text includes both “structur*” and “optimi*” (with “*” as wild cards).

Systematic approach, inspired by the work of Petersen et. al. [3], is employed to sort out projects identified as they are potentially related to structural optimizations. The including and excluding criteria are as follows:

(Inclusion rules)

- Articles on the website published between the periods 2013-2022 (10 years)
- The description of optimization of the structure of buildings or pedestrian bridges is found in the body text.

- The term “optim*” (with “*” as wild cards, such as optimisation, optimization, optimizing, …) is directly associated with its method.

(Exclusion rules)

- Not a design of new construction (ex. “diagnosis”, “inspection”, or “retrofit”)
- The term “optim*” is not related to structure.
- The term “optim*” is used without referring to particular methods (ex. “optimal shape”, “optimal solution” with no supporting information on methods) in the text.

The selected articles are further investigated according to the items in Table 1. Items excluded in this report are also shown but with striking lines. This is to align with the previous study [1]. In the case of items where a particular item was not readable, an "Unspecified" entry was made to distinguish it from "Others".

Table 1. Investigated items.

1. Category of optimization	Topology, Shape, Size, Unspecified, Others
2. Material	Steel, Timber, Concrete, Composite, Unspecified, Others
~~3. Objective~~	~~Stiffness, Stress, Strain energy, Weight Mass, Cost, Carbon and GHG Emissions, Vibration, Energy, Others~~
~~4. Num. of objectives~~	~~Single Objective Optimization (SOO), Multi-objective optimization (MOO)~~
5. Building type	Multistory, Spatial, Pedestrian bridge, Unspecified, Others
~~6. Type of research~~	~~Methodology, Tool, Case study, Prototyping, Realized project, Others~~
7. Application area	Entire building, Part of building, Building element, Material, Unspecified, Others

3. Result

3.1. Systematic search

The actual procedure of the search is shown in Figure 2. Number shown in the bold letter in the figure shows the remaining articles at each step. The search took place in March 2023. The total number of the articles found in the website was 36683, where the tag “Architecture” was given to 14672 articles (40.0%). The search key presented in the Section 2.3 identified 257 articles as potentially relevant articles. Manual screening was carried out to exclude irrelevant papers according to the rule also presented in the Section 2.3. The 23 relevant articles [5-27] were analyzed according to the predetermined as Table 1. The share of the articles describing on structural optimization was 0.16% against all the articles found under the “Architecture” tag.

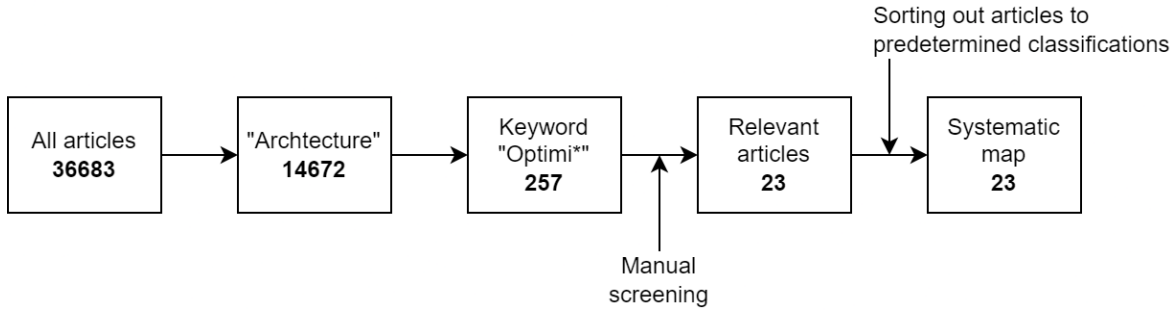


Figure 2. Procedure of systematic search

3.2. Analyses of the result

Results are shown in Figure 3. Figure 3a) shows that the most frequent structural optimization category is shape optimization (n=13) followed by topology optimization (n=5) [12, 16, 17, 21, 23]. There were no articles that showed sizing optimization in an explicit manner. Figure 3b) shows the result according to the building materials. Among the three major materials of steel, timber, concrete, no significant differences in number were observed. The others included carbon fiber, brick, aluminum, and silkworm. Figure 3c) shows the result according to the building typologies. Applications to spatial structures were the most frequent (n=12), followed by multistory type (n=3) and by pedestrian bridge (n=1). Figure 3d) shows the application areas. Application to the entire building was the most frequent (n=12) followed by building element (n=5) and part of the building (n=4).

Then, observations were further made by combining two sets of classifications. All the six combinations are presented in Figure 4. Figure 4a) shows that shape optimization is employed irrelevant of the material. Figure 4b) shows that shape optimization of spatial structure was the largest in number, whereas figure 4c) shows that from the material point of view, timber is used most frequently. Figures 4d) to 4f) shows the results from the application areas' point of view. Figure 4d) shows the shape optimization for entire building is the largest in number, and Figure 4f) shows that spatial structure for entire building is the largest in number.

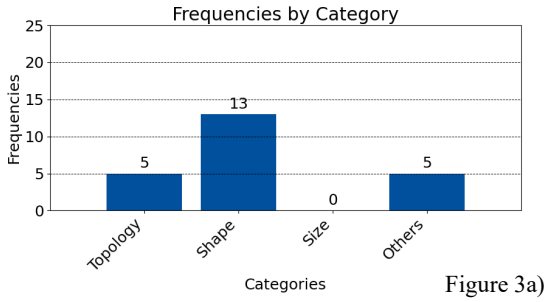


Figure 3a)

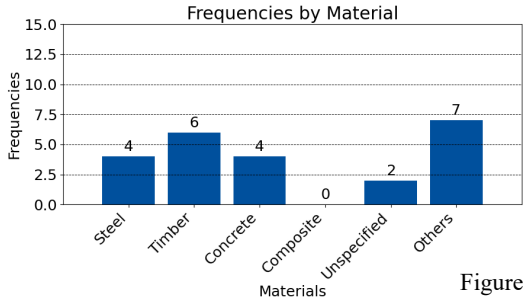


Figure 3b)

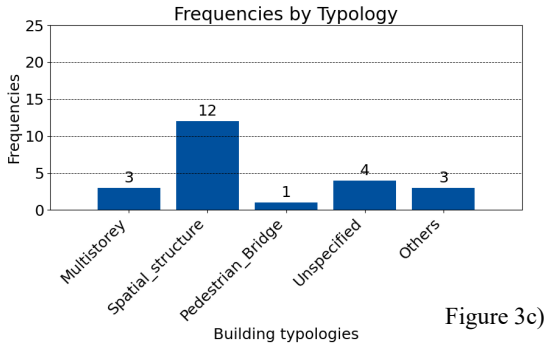


Figure 3c)

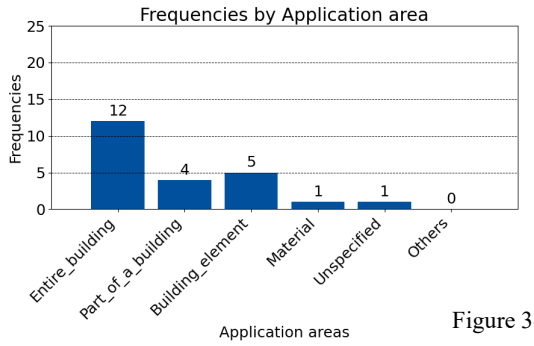


Figure 3d)

Figure 3. Result of systematic search

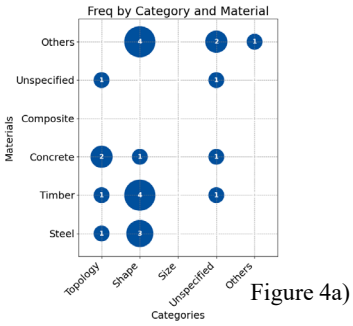


Figure 4a)

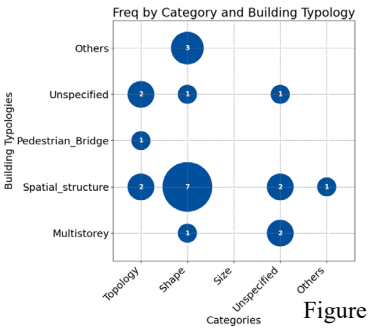


Figure 4b)

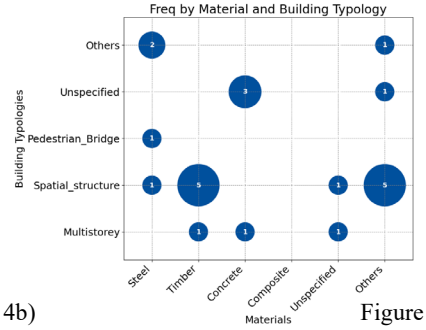


Figure 4c)

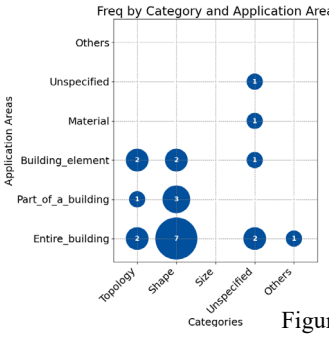


Figure 4d)

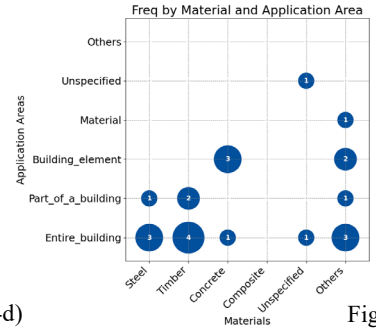


Figure 4e)

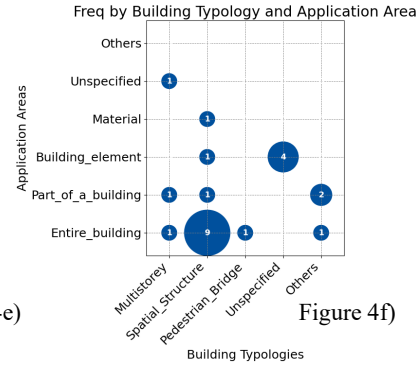


Figure 4f)

Figure 4. Interaction of the two classifications

4. Discussion

According to the results of the previous section, in the last decade, the 23 projects described structural optimization of buildings, of which only five were limited to topology optimization. Although topology optimization shares still non-negligible number of cases among the cases that addressed structural optimization, they are negligibly small cases if the entire population of "Architecture" tag (n=14762) is considered. This section therefore looks at the reasons for this.

According to Bendsøe [4], structural optimization is classified into three types: topology, shape and size. Of these, size is often implemented as a function in structural analysis programmes, and the algorithms that have been widely used in the past are relatively easy to use, so the actual frequency of use is likely to be greater than the number of cases, but the use of these is unlikely to have an impact on the architectural concept However, it is assumed that there is no need to advertise it in the media as it has little impact on the architectural concept and is not necessarily a new approach in terms of structure.

What was observed in large numbers this time was shape optimization. These suggest that with the increasing popularity of parametric design, it is becoming possible to create many variations of form with the same architectural concept in top-runner projects. On the other hand, there are fewer applications of topology optimization. Of particular note was the breakdown of these five projects: three were from university research institutes [12, 16, 23], one was a university student project [16], and one

was a firm with an architecture and engineering department [21]. More detailed research is needed here, but here are some hypotheses.

- Influence of topology optimization on form is too high on behalf of structure to be successfully applied to the architectural projects in collaboration with architects. This may also relate to the decision-making process in architectural design. Applying topology optimization to the entire architectural design, for example, where the architect formulates a concept with respect to form and the engineer assists in realising it, would be difficult due to the high degree of influence on the form of topology optimization. Conversely, the five topology optimization projects found in this study appear to have been examples of design processes where the application of topology optimization was the purpose of the project in the first place, or where the in-house engineer was influencing the architectural concept.
- The geometry obtained by topology optimization is usually optimized for the flow of forces, which makes it more difficult to fabricate members. Although there is software that takes into account fabrication constraints, such as Altair OptiStruct[28] or Autodesk Fusion 360[29], they are mainly placed in the context of additive manufacturing in the mechanical engineering field, and no software was found that takes into account joints, constant cross-sections of elements, etc., as in architecture. These would require programme development by specialists and are still at a stage where they would be difficult to apply in general. Put another way, when it comes to building parts of a certain scale or larger, the hurdle for structural application may be lowered, since the members will be segmented in any case, whether the geometry is special or not.

These are points that were considered suggestive when this study was conducted and cannot be anything concluding. Further research, e.g. interviews with visiting major architectural and structural design firms, would be necessary to prove these points, but are outside the scope of this study.

Limitation of this report includes the following. Dezeen is a web-based general design magazine that includes Architecture with significant rate (40% of the articles are tagged as “Architecture”). That said, it is not meant for the place to address engineering concepts with technical terms. Therefore, there is a chance that the word such as topology optimization has been rephrased to more plain words, that could have made it difficult to keep track of the structural optimization. On the other hand, it was not possible for the authors to find specialized magazines that allowed access to such a huge amount of data without special contracts.

5. Summary

This report supplements the authors’ previous report and an attempt was made to further clarify the status of the application of structural optimization to building projects. Many researchers are currently developing methods for structural optimization, but along with the methods, it is also important in its own right to create a situation where they can be used in real projects (e.g. design methods and software development to facilitate them).

We recognise that structural optimization techniques should be used not only to optimize the quantity of material, but also to enrich architecture. This means that structural optimization has both architectural and structural engineering aspects, and it is important to approach it from both fields.

References

[1] B. Izumi, N. Labonnote, A. Rønnquist, B. Manum, “A systematic mapping study of the optimization methods of structures in architectural design,” in *Innovation·Sustainability·Legacy: Proceedings of the IASS Annual Symposium 2022*, Beijing, China, September 19–22, 2022

[2] B. Izumi, “xml2csv” https://github.com/bunjii/StructuralToolBox, 2023

[3] Bendsøe, M.P., Sigmund, O. “Topology Optimisation”. Springer, Berlin, Heidelberg, 2004.

[4] Petersen, K., Feldt, R., Mujtaba, S., and Mattssson, M. 'Systematic Mapping Studies in Software Engineering'. *Proceedings of the 12th international conference on Evaluation and Assessment in Software Engineering*, 2008.

[5] Dezeen, "Studio RAP completes "first robotically fabricated building in the Netherlands" https://www.dezeen.com/2015/11/20/studio-rap-skilledin-office-first-robotically-fabricated-building-netherlands-innovation-dock-rotterdam/, Searched on 31. Mar. 2023

[6] Dezeen, "Landesgartenschau Exhibition Hall is a plywood pavilion made by robots" https://www.dezeen.com/2014/06/24/landesgartenschau-exhibition-hall-at-university-of-stuttgart-robot-prefabricated-plywood/, Searched on 31. Mar. 2023

[7] Dezeen, "Research Pavilion by ICD and ITKE" https://www.dezeen.com/2013/03/05/research-pavilion-by-icd-and-itke/, Searched on 31. Mar. 2023

[8] Dezeen, "DUS Architects builds 3D-printed micro home in Amsterdam" https://www.dezeen.com/2016/08/30/dus-architects-3d-printed-micro-home-amsterdam-cabin-bathtub/, Searched on 31. Mar. 2023

[9] Dezeen, "ETH Zurich casts intricate metal facade in a 3D-printed mould" https://www.dezeen.com/2018/06/22/eth-zurich-metal-facade-3d-printing-mould-technology/, Searched on 31. Mar. 2023

[10] Dezeen, "Zaha Hadid's D'Leedon complex in Singapore features towers with petal-shaped plans" https://www.dezeen.com/2016/04/20/zaha-hadid-architects-dleedon-complex-apartments-skyscrapers-towers-singapore/, Searched on 31. Mar. 2023

[11] Dezeen, "SOM debuts "world's largest 3D-printed polymer building" designed for off-grid living" https://www.dezeen.com/2016/01/25/additive-manufacturing-integrated-energy-3d-printed-structure-som/, Searched on 31. Mar. 2023

[12] Dezeen, "ETH Zurich combines 3D printing and casting to make more efficient concrete structures" https://www.dezeen.com/2020/07/02/eth-zurich-3d-printing-concrete-casting-fast-complexity/, Searched on 31. Mar. 2023

[13] Dezeen, "3XN unveils visuals of high-rise office complex for London" https://www.dezeen.com/2020/10/01/3xn-high-rise-office-complex-london-architecture/, Searched on 31. Mar. 2023

[14] Dezeen, "Sydney Opera VIP area table 2016 by Emily Leung" https://www.dezeen.com/2020/12/23/landscape-industrial-design-unsw-sydney-school-show/, Searched on 31. Mar. 2023

[15] Dezeen, "Archi-Union references calligraphy in curving tiled roof of Inkstone House cultural centre" https://www.dezeen.com/2019/06/05/inkstone-house-cultural-centre-archi-union-architects-calligraphy/, Searched on 31. Mar. 2023

[16] Dezeen, "Two robotic fabrication methods entwine to make Tongji University bridge" https://www.dezeen.com/2019/11/29/robotic-fabricated-hybrid-bridge-technology/, Searched on 31. Mar. 2023

[17] Dezeen, "Deconstruction / Reconstruction : An analysis of architecture through the lens of Structural Optimisation" https://www.dezeen.com/2021/08/06/national-university-singapore-architecture-student-show/, Searched on 31. Mar. 2023

[18] Dezeen, "Blast Studio 3D prints column from mycelium to make "architecture that could feed people"" https://www.dezeen.com/2022/01/18/blast-studio-tree-column-mycelium-design/, Searched on 31. Mar. 2023

[19] Dezeen, "Armadillo Vault is a pioneering stone structure that supports itself without any glue" https://www.dezeen.com/2016/05/31/armadillo-vault-block-research-group-eth-zurich-beyond-the-bending-limestone-structure-without-glue-venice-architecture-biennale-2016/, Searched on 31. Mar. 2023

[20] Dezeen, "Volvo Pure Tension Pavilion that charges an electric car by Synthesis Design + Architecture" https://www.dezeen.com/2013/11/14/volvo-pure-tension-pavilion-charges-an-electric-car-by-synthesis-design-architecture/, Searched on 31. Mar. 2023

[21] Dezeen, "SOM weaves small wood pieces into SPLAM pavilion at Chicago Architecture Biennial" https://www.dezeen.com/2021/10/01/som-splam-pavilion-chicago-architecture-biennial-2021/, Searched on 31. Mar. 2023

[22] Dezeen, "Höweler + Yoon creates canopy of folded metal plates for urban park in Phoenix" https://www.dezeen.com/2015/08/18/howeler-yoon-shadow-play-canopy-folded-metal-plates-urban-park-phoenix-arizona-pavilion/, Searched on 31. Mar. 2023

[23] Dezeen, “ETH Zurich develops formwork from 3D-printed foam to slash concrete use in buildings" https://www.dezeen.com/2022/01/10/foamwork-eth-zurich-concrete-casting/, Searched on 31. Mar. 2023

[24] Dezeen, “Silkworms and robot work together to weave Silk Pavilion" https://www.dezeen.com/2013/06/03/silkworms-and-robot-work-together-to-weave-silk-pavilion/, Searched on 31. Mar. 2023

[25] Dezeen, “New concrete vaulted floor suggests path to cutting carbon emissions" https://www.dezeen.com/2022/03/04/concrete-vaulted-floor-suggests-path-to-cutting-carbon-emissions/, Searched on 31. Mar. 2023

[26] Dezeen, “Invisible Studio unveils timber shelter "made with many hands" at Westonbirt arboretum" https://www.dezeen.com/2022/08/01/invisible-studio-timber-shelter-westonbirt-arboretum/, Searched on 31. Mar. 2023

[27] Dezeen, “Mass-timber structure in Chicago to be "tallest timber-made building" in the city since Great Fire" https://www.dezeen.com/2022/08/10/hpa-southport-avenue-mass-timber-chicago/, Searched on 31. Mar. 2023

[28] Altair, “Altair OptiStruct”. 2022. Retrieved from: https://www.altair.se/optistruct/

[29] Autodesk, “Fusion 360” version 2.0. Retrieved from: https://www.autodesk.com/products/fusion-360/

Proceedings of the IASS Annual Symposium 2023
Integration of Design and Fabrication
10–14 July 2023, Melbourne, Australia
Y.M. Xie, J. Burry, T.U. Lee and J. Ma (eds.)

The stability of laminated glass plate during anticlastic cold bending

Xiaohan HAO[a,*], Suwen CHEN[b,c]

[a,*] College of civil engineering, Tongji University
Siping Road, Shanghai, China
1572559611@qq.com

[b] State Key Laboratory for Disaster Reduction in Civil Engineering
[c] College of civil engineering, Tongji University

Abstract

Anticlastic glass surface is an important form for free-form glass facades. The traditional hot bending method can realize arbitrary curvature, but requires a pre-formed mold. Cold bending realizes anticlastic surface by loading at the corners of the plate, which is more adaptive and economic. The instability phenomena of monolithic glass plates in cold bending process are then summarized, and the instability modes of monolithic glass plates are defined clearly. In this paper, detailed FEM models simulating cold bending process of laminated glass plates are established and validated against existing experimental results. The effects of different supporting conditions, laminate compositions, width-thickness ratios are investigated to explore the cold bending properties of laminated glass plates. Bifurcation instability is identified to be the only control condition for both monolithic and laminated glass plates. The instability mechanisms of laminated glass are discussed. A bidirectional compression area in the center of the plate is observed to dominate instability, but the compression area changes from bidirectional to unidirectional for laminated glass with larger width-thickness ratio and PVB thickness-glass thickness ratio.

Keywords: anticlastic cold bending, stability, laminated glass, support condition, laminate composition, width-thickness ratio, free form facades

1. Introduction

The free form glass facades require curved glass elements, and double curved glass, particularly anticlastic glass, which is difficult to produce. The traditional hot bending method can realize desired curvature, but requires a pre-formed mold. Cold bending is an alternative technique for producing anticlastic glass plates. During this process, concentrated forces are applied to one or two corners of the glass plate while the other corners are fixed (Figure 1), the curvature is induced by the elastic deformation of glass under out-of-plane load, making the process more flexible [1-3].

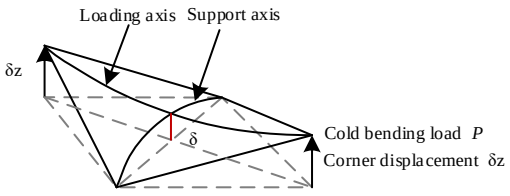


Figure 1. Anticlastic cold bending

Copyright © 2023 by Xiaohan HAO and Suwen CHEN. Published in the Proceedings of the IASS Annual Symposium 2023 with permission.

In general, the failure of glass plates during cold bending is primarily determined by instability rather than strength. Researches on the stability of anticlastic cold bending mainly focus on discriminating instability phenomena, predicating instability and analyzing influencing factors. Staaks and van [4] discovered that the deformation of glass plate concentrates in one diagonal during cold bending, resulting in asymmetric configuration. This configuration is commonly used by scholars as a symbol of instability, and influencing factors have been studied through testing and Finite Element Method (FEM) analysis. The cold bending force and corner displacement at instability point can be affected by the size of the glass plate, and there is a linear relationship between the cold bending corner displacement at the instability point and the thickness of the glass plate [5-9]. The configuration of cold bending instability can be affected by the types of bearing conditions. Generally, point support has better deformation capacity compared with frame support [5, 6, 9]. Deformation from gravity cannot be ignored when the plates are placed horizontally [5, 7, 9, 10]. Initial defect makes the stability of plate worse [5]. Datsiou defined the asymmetric configuration as the change of deformation mode, and then divided the cold bending instability modes into 3 types: the change of deformation mode, global snap-through instability and cold bending distortion, and attempted to establish a unified failure controlling condition [7, 10]. Actually the global snap-through is a normal curvature change under gravity which is not regarded as instability in this paper. Some tests have demonstrated that laminated glass, especially laminated thin glass, has superior cold forming capacity [6, 11]. The influence of aspect ratios [6] and support conditions [6, 11] have been explored, and a variety of support conditions have been proposed for cold bending laminated glass. However, there's no further analysis focusing on the instability mechanism of laminated glass. Galuppi proposed a bidirectional cylindrical model [12] and enhanced effective torsion thickness method [13] to study the instability of point supported glass elements during cold bending.

In a word, previous research has identified the changes in deformation mode and the cold bending distortion during the cold bending process. Support conditions, initial shape under gravity, initial imperfection, geometric dimensions and lamination may change the instability phenomena of glass plates. However, the controlling condition of cold forming and the instability modes have not been clearly identified for both monolithic and laminated glass plates, and the influences of support conditions, laminate compositions, width-thickness ratios need further analysis.

To address these issues and systematically study the stability of glass plates during anticlastic cold bending, this paper firstly summarizes the instability phenomena observed from literature analysis, and explores the instability modes, then studies the influences of support conditions, laminate compositions and width-thickness ratios on cold bending stability employing the FEM method. The instability mechanisms of laminated glass are discussed based on the results of parameters analysis.

2. Cold bending instability of monolithic glass plate

2.1. Cold bending process

Monolithic glass can be used as the basis for the stability analysis of laminated glass, Figure 7 illustrates the instability phenomena during the cold bending process for monolithic glass plates [7, 10]. For monolithic glass without the influence of gravity (Figure 2a), the deflection at the plate centre changes linearly with the cold bending corner displacement in the early stage of cold bending, with the loading axis and supporting axis bending in opposite directions (Figure 2b), resulting in a symmetric configuration that resembles a saddle surface. However, in the late stage of cold bending, the deflection at the centre of the plate changes nonlinearly with the cold bending corner displacement, and the out-of-plane deformation concentrates on one diagonal while the deformation of the other diagonal is small (Figure 2c), resulting in an asymmetric configuration. Subsequently, the bending direction in the middle of one diagonal reverses, and the curvature at the central area of the plate changes from anticlastic to sinclastic (Figure 2d).

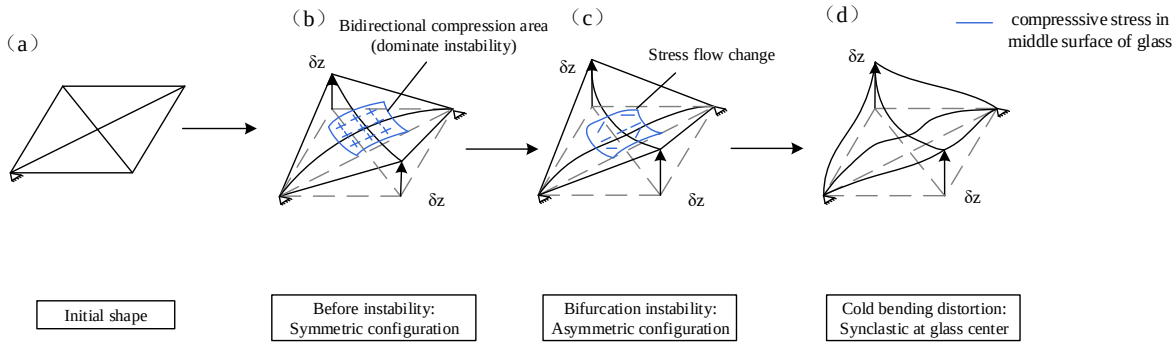


Figure 2. Cold bending process:(a) initial shape, (b) ideal cold bending, (c) bifurcation instability, (d) cold bending distortion.

2.2. Bifurcation instability

During anticlastic cold bending of glass plates, there are tensile stress at the edge of the glass plate and compression stress in both diagonal directions in the middle surface of the glass plate in addition to the bending stress (Figure 3). The collapse of the bi-directional compression area leads to the bifurcation instability, after which the out-of-plane displacement concentrates on one diagonal (Figure 2c).

The point at which the *P-δ* curve changes nonlinearly is known as instability point. Before the instability point, the disturbance force P_0 is applied at the centre of glass plate (Figure 4a), and the disturbance force changes nonlinearly with the deflection at the centre of glass plate (Figure 5b), which indicates the cold-formed plate with negative Gaussian curvature has stable load bearing capacity. Applying disturbance P_0 at the centre of glass plate after the instability point (Figure 4b), the snap through of disturbance force is obvious with the deflection at the centre of glass plate (Figure 5a, b), which means the cold-formed plate is unstable and not suitable for further cold bending. The occurrence of "snap through" confirms the presence of multiple equilibrium paths after the bifurcation point.

(a) (b)

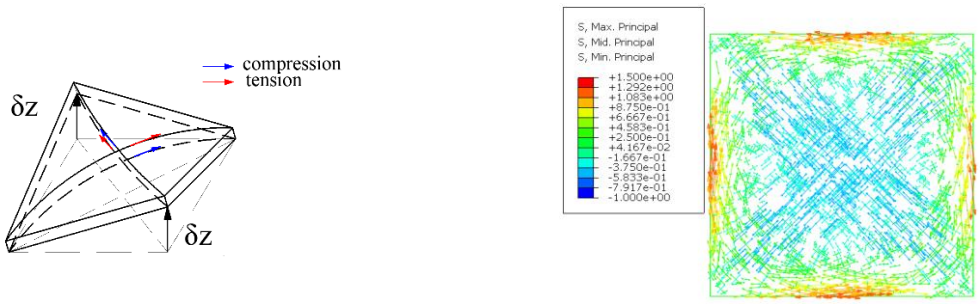


Figure 3. The stress of glass plates before bifurcation instability: (a) the schematic stress on the upper and bottom surfaces of the glass plate, (b) the membrane stress in the middle surface of glass plate.

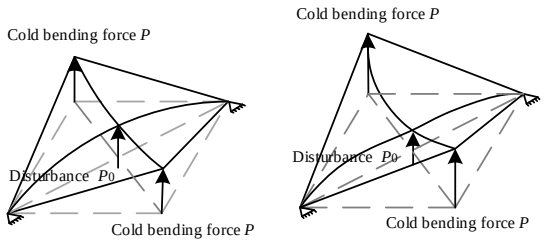


Figure 4. Apply disturbance P_0 before or after the bifurcation instability

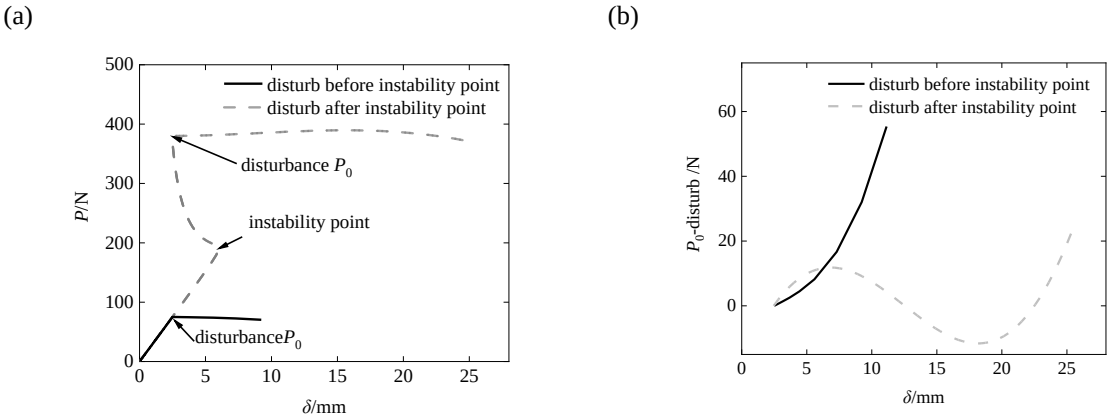


Figure 5. Response to disturbance force before or after instability: (a) P-δ curve (b) P_0-δ curve

2.3. Cold bending distortion

After the bifurcation instability point, the compression stress in the middle surface of glass concentrates on the diagonal with smaller deflection in asymmetric configuration (Figure 2c). As a result, the centre part of this diagonal may buckle, resulting in the changing from anticlastic to synclastic at the centre of plate (Figure 2d). This phenomenon is called cold bending distortion.

Since the cold bending distortion occurs after the bifurcation instability phenomena, monolithic glass takes the bifurcation instability as the controlling condition for cold bending.

3. Finite element model and validation

3.1. Model building

To capture the instability point during the cold forming process, finite element models are developed using ABAQUS software with static Riks step. The material properties of glass and steel are simplified into elastic, and the corresponding parameters are presented inTable 1. The Ogden hyperelastic material model is adopted to model PVB and silicon. Glass and steel are modelled with C3D20R solid elements, while silicon and PVB are modelled with C3D20RH hybrid elements. The size of mesh is set at 12.5×12.5 mm. The glass, silicon, PVB, and steel are divided into two, two, three, and two layers across the thickness, respectively (Figure 6. The finite element models).

Table 1. The property of materials

Material	Elastic modulus/ MPa	Poisson ratio
Glass	70000	0.22
Steel	210000	0.3
Silicon	Related parameters adopted in Ogden hyperelastic model : μ1=0.4145MP, α1=4.8962, D=0.09720.4	
PVB	Related parameters adopted in Ogden hyperelastic model : μ1=0.71938MP, α1=1.92245, D=0	

The constraints used in this study restrict only the out-of-plane displacements at the corners of glass plate while allowing for in-plane displacements and rotations, as shown in Figure 6. For frame support, 20×40 mm steel frames are bonded to the four sides of the glass plate with 12 mm silicone adhesive. The steel frames are not connected at the corners to enhance deformation capacity during the cold forming process. The silicone-to-glass, silicone-to-steel, and PVB-to-glass connections are assumed to be tie, not considering the debonding. Displacement loading scheme is applied, with loadings applied to the steel frames for frame support, and directly to the glass corners for the roller point support.

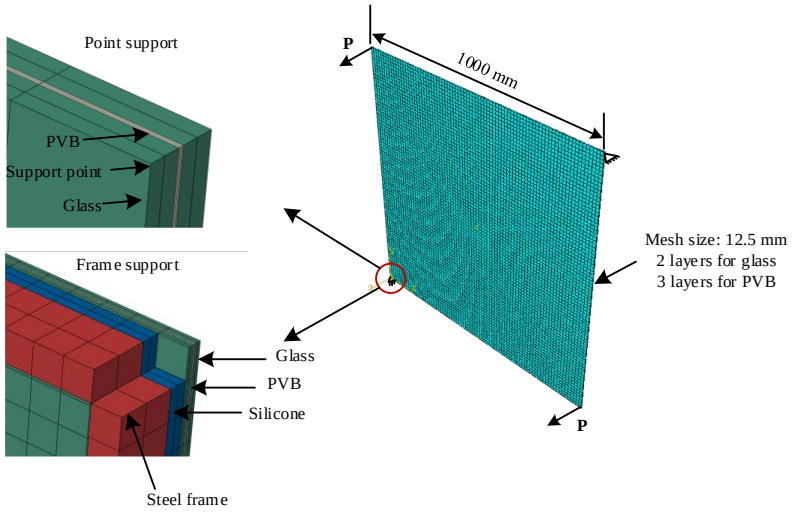


Figure 6. The finite element models

3.2. Model Verification

Caprili's test [11] utilized a linear bonding steel-to-glass connection, which was made up of a tubular stainless steel frame, laminated glass plate (5 mm glass+1.52 mm PVB+5 mm glass) and SIKA MT adhesive (average thickness equal to 6.0 mm). Loads are applied to the corner of stainless steel frame. The finite element models with frame support are modified according to Caprili's test (Figure 7). The relationship between the cold bending load and the corner loading displacement from the test and FEM analysis are illustrated in Figure 8.

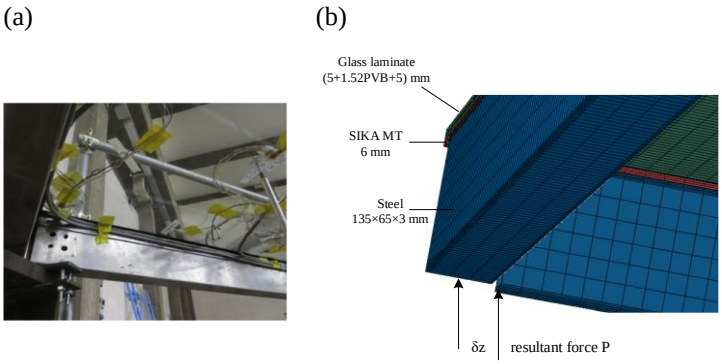


Figure 7. Cold bending laminated glass plate with frame support: (a) Caprili's test[11], (b) Finite element model.

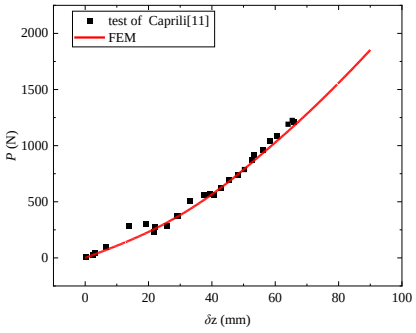


Figure 8. Verification with Caprili's test with frame support

Thierry [6] clamps the laminated glass plate at four points (Figure 9), and the cold bending load is applied by raising one of the four constraints. The deflections at the plate center (δ) and at the middle of glass edge(δ') from the test and FEM analysis are illustrated in Figure 10.

Figure 8 and Figure 10 shows that the deflection and cold bending force from the FEM analyses are in good agreement with the test results, which verifies the effectiveness of the built finite element model.

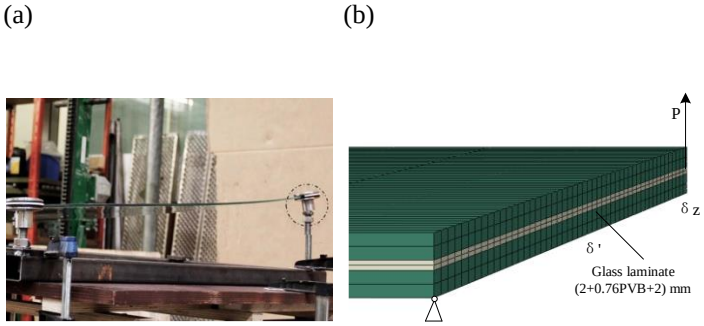


Figure 9. Cold bending laminated thin glass plate with point support : (a) Thierry's test[6], (b) Finite element model.

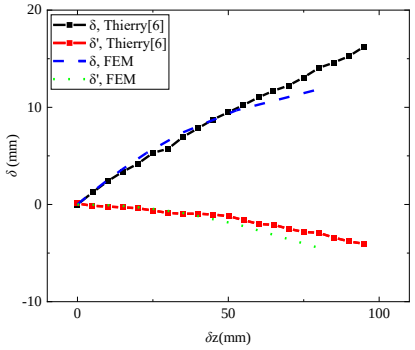


Figure 10. Verification with Thierry's test with point support

4. Parametric analyses

The validated finite element models are used to simulate the cold bending process. When the plate's centre deflection changes nonlinearly, the plate loses its symmetry, indicating that bifurcation instability has occurred.

4.1. The analysis of influencing factors

The influence of support conditions, laminate compositions and width-thickness ratios on cold bending stability is analyzed. The scopes of influencing factors are showed in Table 2.

Hidden frame and point-supported glass curtain walls have better transparency compared to exposed frame glass curtain walls. Moreover, mechanical point supports can avoid perforating the glass surface. Therefore, mechanical point supports and hidden frame supports are considered in cold bending process. Only the degree for out-of-plane displacement is constrained, while other degrees for the in-plane displacements and rotations are free to move for both mechanical point supports and hidden frame supports. The mechanical point support in this constraint conditions is referred to as roller point support. Both monolithic and laminated glass plates are considered with roller point and hidden frame supports (Table 2).

The glass plates used for cold bending are generally not thick, and PVB interlayers are preferred over SGP in cold bending due to their better flexibility. As a result, laminates with 2-10 mm glass and 0.76 mm, 1.52mm or 2.28 mm PVB interlayers are commonly used in cold-forming. 1000×1000 mm square laminated glass plates are used to explore the influence of the relative thickness of glass and PVB in laminates. The influences of laminate compositions are explored by controlling glass thickness, PVB thickness and laminate thickness as constants respectively (Table 2).

Then, the width-glass thickness ratio is taken as the variable, and the glass thickness-PVB thickness ratio is assumed to be constant to exclude the influence of laminate compositions. The widths of glass laminates range from 600 mm to 3000 mm, and the thicknesses of glass range from 2 to 10 mm, so the width-thickness ratios range from 60 to 1500 (Table 2).

Table 2. The influencing factors and the scope

Influencing factors	Support conditions	Glass thickness/ mm	PVB thickness/ mm	Width/ mm
Support conditions	Roller point, Hidden frame	5		1000
		4	1.52	
Laminate compositions	Roller point	5		1000
		3, 3.5, 4, 4.5, 5, 6, 8, 10	1.52	
		2, 2.5, 3, 3.5, 4, 5, 6, 8	0.76	
		5	0.76, 1, 1.2, 1.52, 2.28	
		4	1.52	
		4.2	1.12	
		4.5	0.52	
Width-thickness ratios	Roller point	2	0.76	600, 800, 1000, 1200, 1500, 2000, 3000
		4	1.52	600, 1000, 2000, 3000
		10	3.8	600,1000 ,3000

4.2. The influence of support conditions

Bifurcation instability phenomena are observed for both roller point and hidden frame support conditions and the instability configurations after bifurcation point are showed in Figure 11(a), (b). For monolithic glass, the centre deflection of glass plate before bifurcation instability is found to be similar under both roller point and hidden frame support conditions. However, for laminated glass, the bifurcation point occurs later in the case of roller point support compared to frame support (Figure 11c), but the edge of glass remains linear under frame support which makes it easier for tessellation (Figure 11a, b).

In general, both roller point and hidden frame support conditions can be used as support conditions for cold forming. In the following part of this paper, roller point support is considered for simplification.

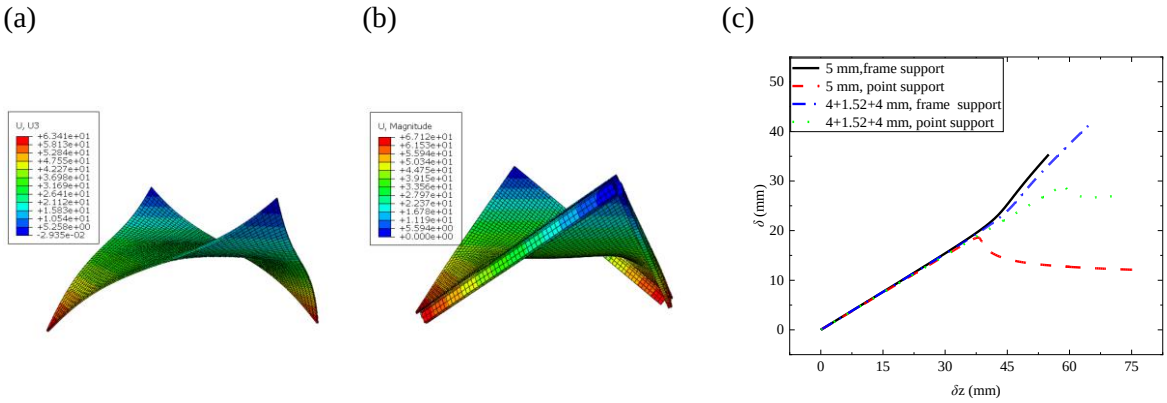


Figure 11 Cold bending under different bearing conditions : (a) instability configuration under roller point support, (b) instability configuration under hidden frame support, (c) δ-δz curve during cold bending process.

4.3. The influence of the laminate composition

The cold bending load and corner displacement at bifurcation instability are recorded as $F_{buckling}$ and $\delta z_{buckling}$, respectively. The relationship of $\delta z_{buckling}$ and t_{glass}/t_{PVB} for different laminate compositions are showed in Figure 12. The $\delta z_{buckling}$ for 5mm monolithic glass plate is also illustrated for comparison. Obviously, laminated glass plates have better deformation capacity compared with monolithic glass plates. Thicker interlayer or thinner glass results in smaller corner displacement at the instability point. (Figure 12).

Bifurcation instabilities always occur during cold bending process for different laminate compositions, which can be detected through the nonlinearity of the deflections at the centre of glass plates. It can also be seen that there are two types of configurations before bifurcation instability (Figure 13). In type 1, laminated glass plates can maintain nearly hyperbolic paraboloid before bifurcation instability, while in type 2, the deflection at the centre of laminated glass plate becomes flat, and the edges of glass plate cannot maintain straight. The configuration before bifurcation instability trends to type 1 with a larger glass thickness-PVB thickness ratio, while the configuration trends to type 2 with a smaller glass thickness-PVB thickness ratio.

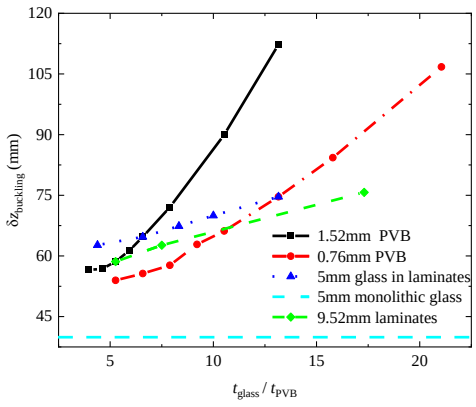


Figure 12. The relationship between $\delta z_{buckling}$ and t_{glass}/t_{PVB}

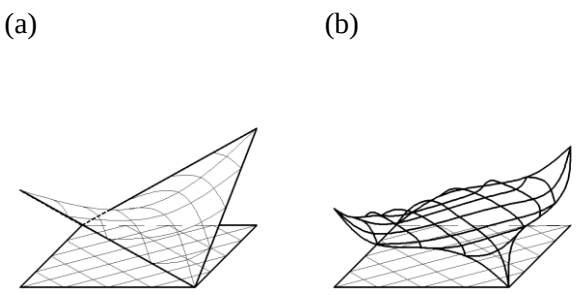


Figure 13. Cold bending configuration before bifurcation instability: (a) Type 1, (b) Type 2.

4.4. The influence of the width-thickness ratio

To eliminate the influence of scale factor, the ratio of $\delta z_{buckling}/t_{glass}$ is used as the dependent variable. Figure 14 presents the relationship between $\delta z_{buckling}/t_{glass}$ and $B/t_{glass.}$ The corner displacements at the bifurcation instability initially increase and then decrease with increasing width-glass thickness ratios. The configurations before bifurcation instability show that, when the width-thickness ratio get larger, the deformation mode tends towards type 2 (Figure 13b) before bifurcation instability.

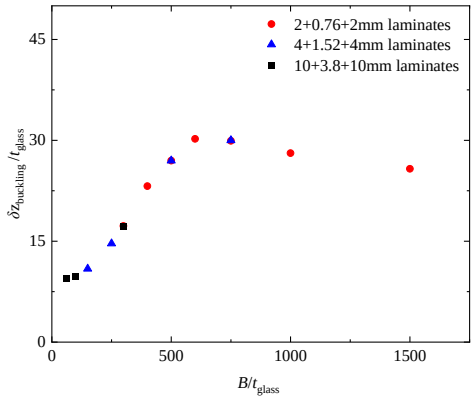


Figure 14. The relationship between $\delta z_{buckling}/t_{glass}$ and B/t_{glass}

4.5. Cold bending instability of laminated glass plate

The parameters analysis indicates that bifurcation instability is the dominant control condition for both monolithic and laminated glass plates. Different from monolithic glass, there are two types of configurations for laminated glass plates before bifurcation instability (Figure 13), which are defined as type 1 and type 2 in section 4.3. This section takes two examples illustrating these two configurations.

For type 1, laminated glass plate with laminate composition of 5mm+0.76mm+5mm and size of 800 mm×800 mm is selected for illustraion. Figure 15 presents the deflection and stress distribution of this example during cold bending process. The stress is the superposition of bending stress and membrane stress. The middle surfaces of both top and bottom glass plates in laminates are compressed in two diagonal directions during cold bending process, but the compressive stress distribution differs along two diagonals due to the influence of monolithic bending. The instability is caused by the collapse of the bi-directional compression area at the centre of plate (Figure 15f). There exists tensile stress in the middle surface of glass in laminates after bifurcation instability (Figure 15g).

For type 2, 1000 mm×1000 mm× (2mm+0.76mm+2mm) laminate is selected for illustraion. Figure 16 presents the deflection and stress distribution of this example during cold bending process. The layerd bending stress and membrane compressive stress are minimal, while the monolithic bending stress is evident compared to the stress distribution in type 1. Therefore, the mid-surface of the glass will always be tensile in one diagonal (Figure 16d). Different from monolithic glass, the cold bending deformation is larger before bifurcation instability because of the disappearance of the bi-directional compression zone in middle surface of the glass, then the edge of plate cannot maintain straight before bifurcation instability. However, the plate is still self-balanced and has stable bearing capacity before bifurcation instability.

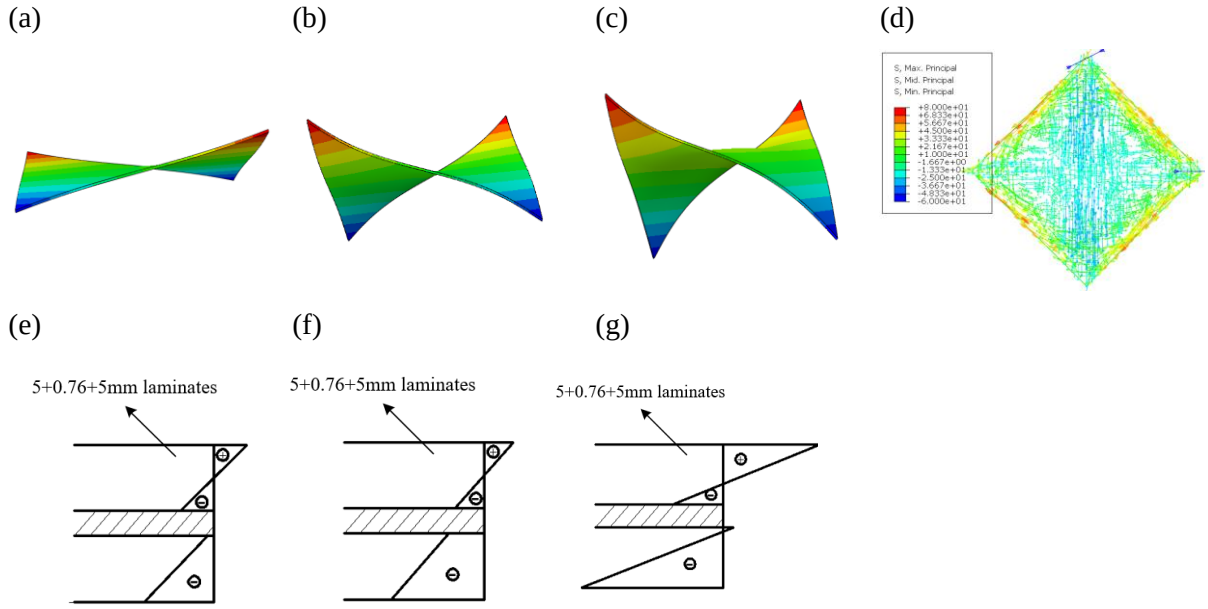


Figure 15. The deflection and stress distribution of (5mm+0.76mm+5mm) × 800 mm×800 mm laminate : (a) the deformation before bifurcation instability, (b) the deformation at bifurcation instability, (c) the deformation after bifurcation instability, (d) bi-directional compression stress at the middle surface of glass in laminate, (e) the stress distribution across the thickness before bifurcation instability, (f) the stress distribution across the thickness at bifurcation instability, (g) the stress distribution across the thickness after bifurcation instability.

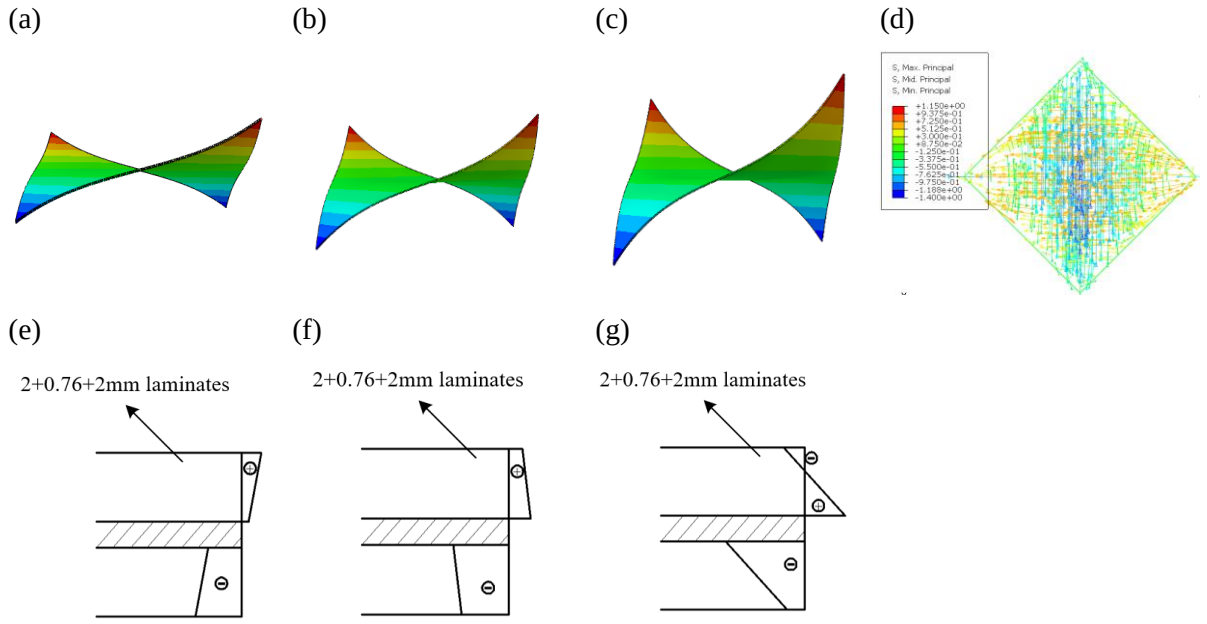


Figure 16. The deflection and stress distribution (2mm+0.76mm+2mm) × 1000 mm×1000 mm laminate: (a) the deformation before bifurcation instability, (b) the deformation at bifurcation instability, (c) the deformation after bifurcation instability, (d) compression and tension stress at the middle surface of glass in laminate.(e) the stress distribution across the thickness before bifurcation instability, (f) the stress distribution across the thickness at bifurcation instability, (g) the stress distribution across the thickness after bifurcation instability.

5. Summary and outlook

In this paper, the instability phenomena are summarized and instability modes are defined for monolith glass plate. The finite element models of laminated glass plates undergoing cold bending are established and verified, and then followed by parametic analyses. Finally, the cold bending instability of laminated glass plates are analyzed. Analysis results are summarized as follows:

(1) Two types of instability modes may occur during the cold bending of monolithic glass plates: bifurcation instability and cold bending distortion. The bifurcation instability is caused by the collapse of bidirectional compression area in the center of the glass plate. Cold bending distortion occurs after the bifurcation instability.

(2) Bifurcation instability is identified to be the only control condition for both monolithic and laminated glass plates.

(3) Laminated glass plate has better stability compared to monolithic glass plate due to the existence of the interlayer, and there are two types of configurations before bifurcation instability in laminated glass plates. The instability is caused by the collapsed of bi-directional compression area for type 1, while unidirectional compression area for type 2.

(4) Both hidden frame and roller point supports are suitable for cold bending. The compositions of laminated glass plates and width-thickness ratios influence the cold bending configurations before bifurcation instability and cold bending corner displacements at the bifurcation instability $\delta z_{buckling}$.

However, there are still some issues need further analysis in this research. Standards for controlling anticlastic cold bending need to be proposed for monolithic and laminated glass plates. A unified standard is possible with the introduction of equivalent torsion stiffness. Moreover, it's necessary to clarify the boundary between the two types of cold bending configurations before bifurcation instability for laminated glass plates.

References

[1] M.Eekhout , W. Lockefeer and D. Staaks, "Design and Build of a Warped Tram Station," in *Challenging Glass 2 – Conference on Architectural and Structural Applications of Glass*. 2010.

[2] M.Eekhout, and S. Niderehe, "The Cold Bent Glass Roof of the Victoria &Albert Museum, London," in *Challenging Glass 2 – Conference on Architectural and Structural Applications of Glass*. 2010.

[3] J.U.Neugebauer, "Applications for Curved Glass in Buildings," *Journal of Facade Design and Engineering*, vol. 2, pp. 67-83, 2014.

[4] F.van Herwijnen, D. Staaks and M. Eekhout, "Cold Bent Glass Sheets in Façade Structures," *SEI Discussion*, vol. 2, 2004.

[5] M.Benjamin, "Cold-Bent Glass Structures," 2015, Ecole Polytechnique Federale De Lausanne-Icom.

[6] T.Mainil, "Exploratory investigation on the cold bending of thin glass," 2015, Gent.

[7] K.C.Datsiou and M. Overend, "The mechanical response of cold bent monolithic glass plates during the bending process," *Engineering Structures*, 117: pp. 575-590, 2016.

[8] A.Spagnoli, R.Brighenti, M.Biancospino, M.Rossi, R.Roncella, "Geometrically non-linear bending of plates: Implications in curved building façades," *Construction and Building Materials*, 214, pp: 698 – 708, 2019.

[9] A.Bensend, "Maximizing the Twist of Cold Formed Glazing," in *Challenging Glass 5-Conference on Architectural and Structural Applications of Glass*. 2016.

[10] K.Datsiou, "Design and Performance of Cold Bent Glass," Cambridge, 2017.

[11] S.Caprili, N. Mussini and W. Salvatore, "An innovative solution for hybrid steel-glass self-bearing modular systems," *Journal of Constructional Steel Research*, Vol.130, pp: 159 – 176, 2017.

[12] L. Galuppi, S. Massimiani and G. Royer-Carfagni, "Buckling phenomena in double curved cold-bent glass,"

International Journal of Non-linear Mechanics, Vol.64, pp: 70-84. 2014.
[13] L Galuppia. and G. Royer-Carfagni, "Enhanced Effective Thickness for laminated glass beams and plates under torsion," *Engineering Structures*, Vol.206, 2020.

Proceedings of the IASS Annual Symposium 2023
Integration of Design and Fabrication
10–14 July 2023, Melbourne, Australia
Y.M. Xie, J. Burry, T.U. Lee and J. Ma (eds.)

Topology optimisation of free-form shells for architectural applications

Jiaming MA[a], Hongjia LU[a], Ting-Uei LEE[a], Zhonggao CHEN[b], Yi Min XIE[a,*]

[a,*] Centre for Innovative Structures and Materials, School of Engineering
RMIT University, Melbourne, 3001, Australia
mike.xie@rmit.edu.au

[b] School of Architecture, Yantai University, Yantai, 264005, China

Abstract

Free-form shells have been increasingly used in architectural applications owing to their aesthetically pleasing appearances and large span-to-weight ratios. Recently, topology optimisation techniques have been extended to shell structures, aiming to achieve innovative designs of free-form shells with improved material efficiency. However, despite its potential, the utilisation of existing topology optimisation techniques in the real-world architectural design of shells remains rare. This paper presents various strategies for optimising free-form shells that may be useful for architectural applications. First, we show that the ribs of shells can be optimised into free-form layouts with improved stiffness. Second, we demonstrate that topology optimisation can be combined with funicular form-finding techniques to generate diverse designs with high structural performance. Third, we illustrate how to combine surface tessellation and periodic constraints to achieve shell designs for cost-effective construction using repeated components. Finally, we present a new method that can optimise free-form shells with Voronoi patterns to facilitate aesthetic expression and functional design for architects. The presented strategies are useful for designing high-performance and innovative free-form shells for architectural applications.

Keywords: form finding, topology optimisation, shells, architectural design

1. Introduction

Shell structures are characterised by thin and curved forms that can span large spaces with minimal material. Due to their ability to utilise materials efficiently and provide aesthetic appeal, shell structures are commonly used in the construction of roofs, domes and other types of architectural structures. Despite their advantages, designing and constructing shell structures can be challenging due to their complex geometry [1]. It is generally difficult to find an optimised form of a shell structure that can sustain specific loads and boundary conditions, while also meeting aesthetical and functional requirements. Thus, there is a demand for innovative approaches that can effectively address these challenges and enable the seamless integration of shell structures in architectural design.

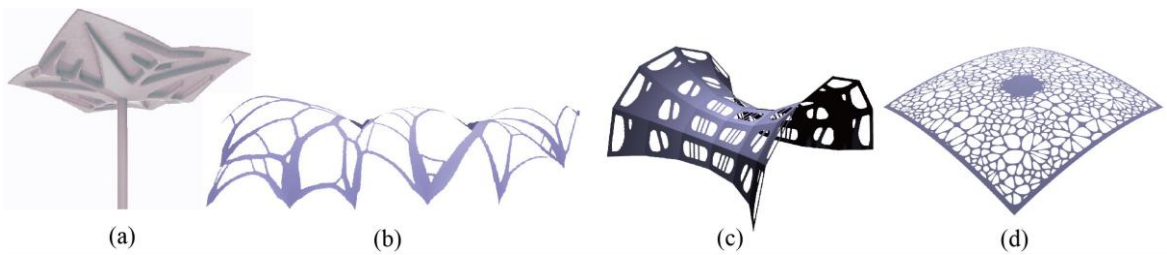


Figure 1. Topology optimisation of (a) a ribbed shell, (b) a funicular shell, (c) a tessellated shell designed with a periodic constraint and (d) a Voronoi-patterned shell.

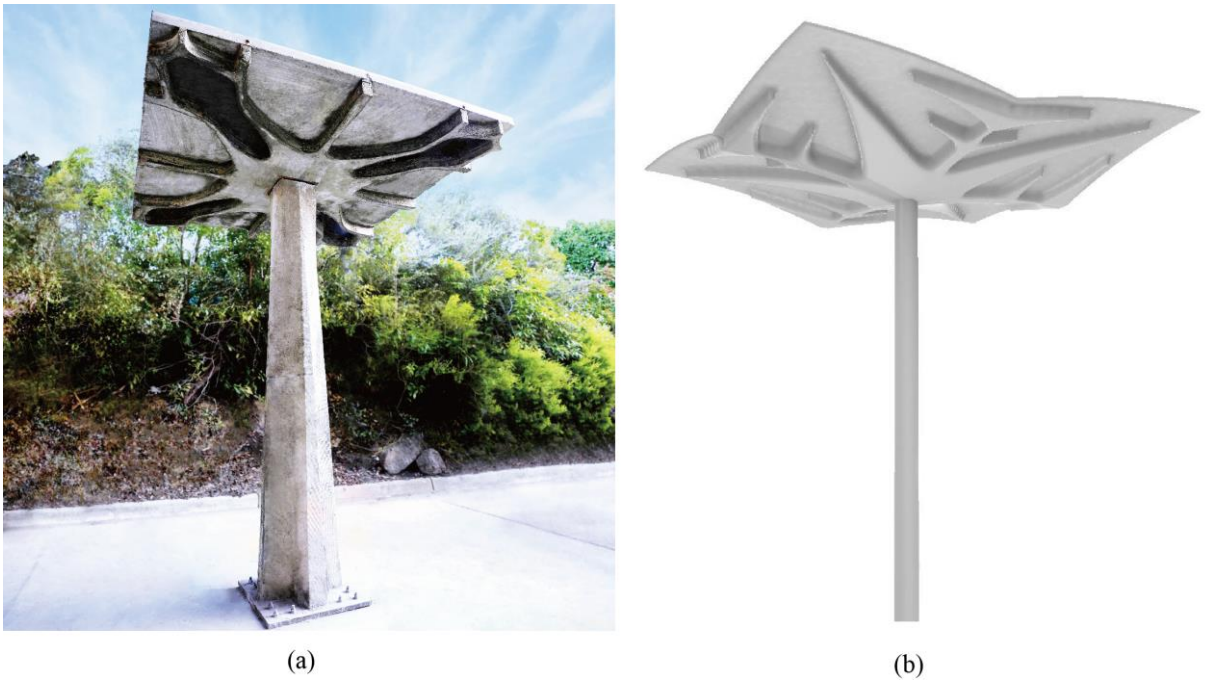
Copyright © 2023 by Jiaming MA, Hongjia LU, Ting-Uei LEE, Zhonggao CHEN and Yi Min XIE. Published in the Proceedings of the IASS Annual Symposium 2023 with permission.

Topology optimisation can generate highly efficient and structurally sound designs that are difficult or impossible to achieve through traditional design methods [2]. This technique can be used to produce a wide range of optimised structures, including civil, mechanical and aerospace structures in engineering and to simulate optimised structures in nature [3]. Topology optimisation typically begins with a given design domain, which is then subjected to a set of loads and boundary constraints. Through a series of iterations, the material distribution is adjusted until the most efficient design is found. Several different methods have been developed for topology optimisation in the past few decades, including the Solid Isotropic Material with Penalisation (SIMP) method [4], the Evolutionary Structural Optimisation (ESO) method [5], the Bi-directional Evolutionary Structural Optimisation (BESO) method [6], the Level-set method (LSM) [7] and the Moving Morphable Component (MMC) method [8]. Among these, the SIMP and BESO methods are particularly popular in designing visually striking and highly efficient buildings and bridges, owing to their simplicity and robustness [9].

Despite the increasing use of topology optimisation by architects, its real-world applications on shells are still limited due to a dearth of guidelines and pioneering precedents. This paper aims to classify different topology optimisation strategies for architectural shell design, as shown in Figure 1, and demonstrate how they can be applied to produce more useful and innovative results to meet architectural design requirements. The remainder of the paper is structured as follows: Section 2 demonstrates the optimisation of free-form ribs for floors and shells. Section 3 illustrates that by combining topology optimisation with funicular form-finding techniques, a variety of designs can be generated with exceptional structural performance. Section 4 illustrates how to combine surface tessellation and periodic constraints to achieve shell designs for cost-effective fabrication. Section 5 introduces a novel algorithm that can optimise free-form shells with Voronoi patterns. Section 6 summarises the key points discussed and identifies potential areas for further study.

2. Optimising free-form ribs for shells

For shells in buildings, *beams* are often used as stiffened ribs to improve stiffness. Traditional techniques typically produce over-designed ribs for shells, resulting in excessive material usage. Recently, computer-aided methods have been created to facilitate the design of rib layouts; nevertheless, they still rely on the conventional experience of ribbed shell designs. To discard the traditional shape restrictions on the ribs and improve their stiffness contribution, we have developed a topology optimisation technique capable of producing free-form and high-performance ribbed shells. Figure 2(a) shows a ribbed shell designed with the proposed optimisation technique [10]. In this example, we optimise and compare the stiffness of our ribbed shell with that of a famous design in architecture. Our result shows a 26.3% increase in terms of structural stiffness with the same amount of material. Additionally, we demonstrate that using a hybrid digital approach to mould fabrication is feasible and sustainable for constructing free-form ribbed shells. The developed technique is also applicable to the design of curved ribbed shells [11], as shown in Figure 2(b).



(a) (b)

Figure 2. (a) A topologically optimised and digitally constructed ribbed slab (slab dimensions: 2.2 m × 2.2 m; column height: 2.5 m). Image reproduced from [10]. (b) A topologically optimised curved ribbed shell. Image reproduced from [11].

3. Optimising free-form shells in funicular forms

In traditional shell design processes, the curvature form of a shell is typically prescribed. A curved shell can be modified by manually adjusting its curvature through trial and error, which is time-consuming and could result in low performance. Here, we show how topology optimisation can be combined with funicular form-finding techniques to generate diverse and efficient shell designs for a real building project. Figure 3(a) shows the floor plan of a building proposed by our industry collaborators, including 11 pillars and 12 walls below the roof. By configuring different support locations on the pillars and walls, distinctly different roof shells in funicular forms can be obtained using the commercial software Kangaroo (Version 2.42) [12]. The left-hand side of Figures 3(b–d) shows three examples of the resulting funicular roofs. Subsequently, topology optimisation can be performed on the three distinctive funicular shells to generate diverse roof designs with exceptional structural performance. The right-hand side of Figures 3(b–d) shows the optimised topology using BESO under gravity [13]. Note that funicular form-finding techniques usually generate shells with different amounts of material under different boundary conditions; thus, the volume constraint in topology optimisation shall be chosen accordingly by the designer, considering the functions, aesthetics and material usage factors. In the cases of Figures 3(b–d), the target volume fractions of topology optimisation are 30%, 63% and 63%, respectively. This case testifies that by simply combining topology and curvature optimisation techniques, diverse shell designs possessing unique curved shapes and optimised topologies can be generated on a single floor plan.

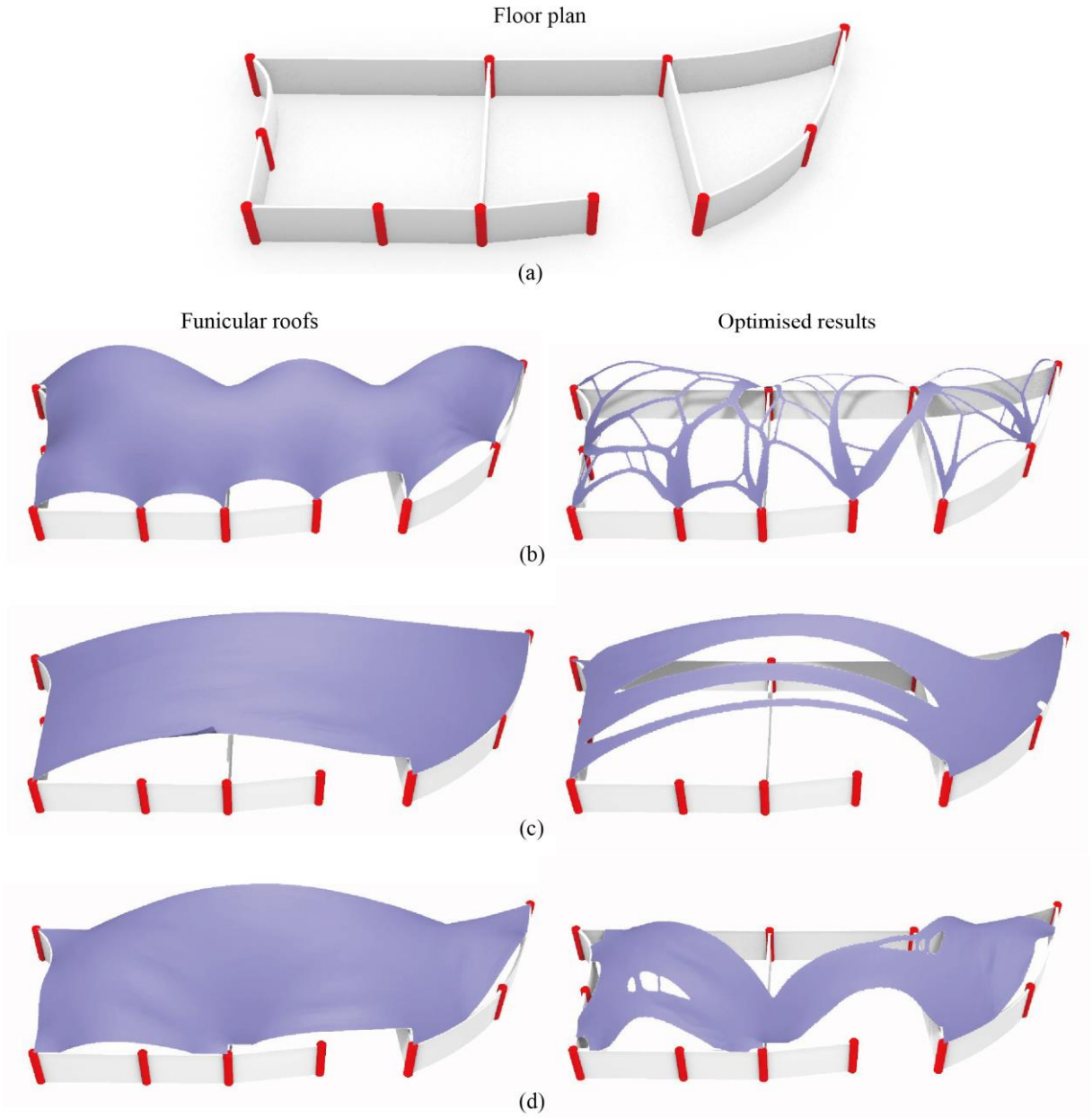


Figure 3. Funicular shells with different support locations and their topology-optimised designs: (a) floor plan, (b) a shell supported purely by columns, (c) a shell supported at the two ends and (d) a shell supported by columns and partially selected walls.

4. Optimising free-form shells with surface tessellation and periodic constraint

The fabrication of shell structures, especially with complex curvatures, is often difficult to perform accurately and within budget in real projects. One of the simple approaches to overcoming this challenge is to tessellate a curved shell with planar panels. Using this method, the general form of the shell can be maintained while the fabrication turns from a 3D problem into a 2D one, which is simpler and less expensive. Furthermore, several techniques have been proposed recently that can reduce the category of panels for shell tessellation [14, 15]. Figure 4 shows a symmetrical curved shell tessellated into multiple planar panels. Note that all the panels at the same axial position have the same shape. In this case, the shell in Figure 4(a) can be fabricated by using only three different categories of planar panels, as shown in Figure 4(b), which can reduce the fabrication costs enormously.

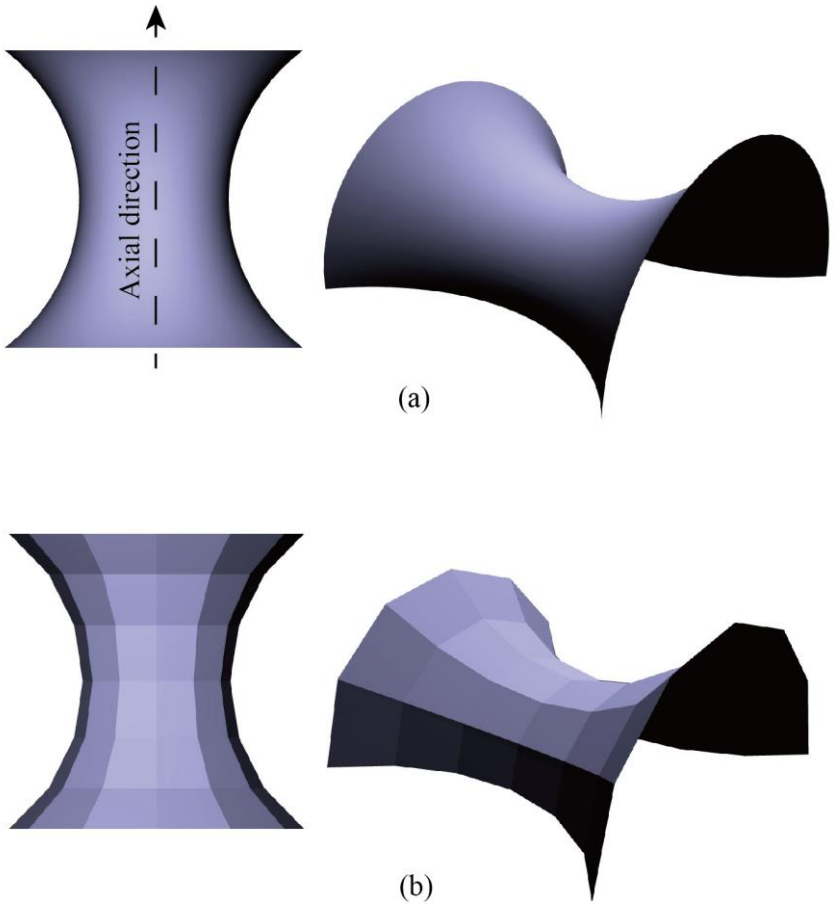


Figure 4. A free-form shell in its (a) curved form and (b) tessellated form.

Nevertheless, since panels within the same category are located at different positions of the shell and thus bear different loads, those panels will have distinctively different internal geometries after topology optimisation. Figure 5(a) shows an optimised design of the shell in Figure 4(b) under gravity using BESO. Non-design solid edges are applied to each panel to improve structural integrity and connectivity. To fabricate the whole shell structure, nine different panel categories are required, which are shown in different colours alongside the structure. Hence, the advantage of using category-reduced tessellation has disappeared. To overcome this setback, periodic constraints can be incorporated into topology optimisation, so that panels in the same category will have the same topology [16]. For example, a simple periodic constraint can be achieved by averaging the sensitivities of panels in the same category during the optimisation process. Figure 5(b) shows the optimised result after applying the period constraint. The panel category number is reduced from nine to three, which has great cost-saving benefits if the shell is to be built using casting. Meanwhile, the compliance is only increased slightly by 13%. Although the combination of category-reduced tessellation and periodic-constrained optimisation sounds trivial, it may significantly reduce the difficulty and costs of fabricating a free-form shell structure and hence would be useful for designers.

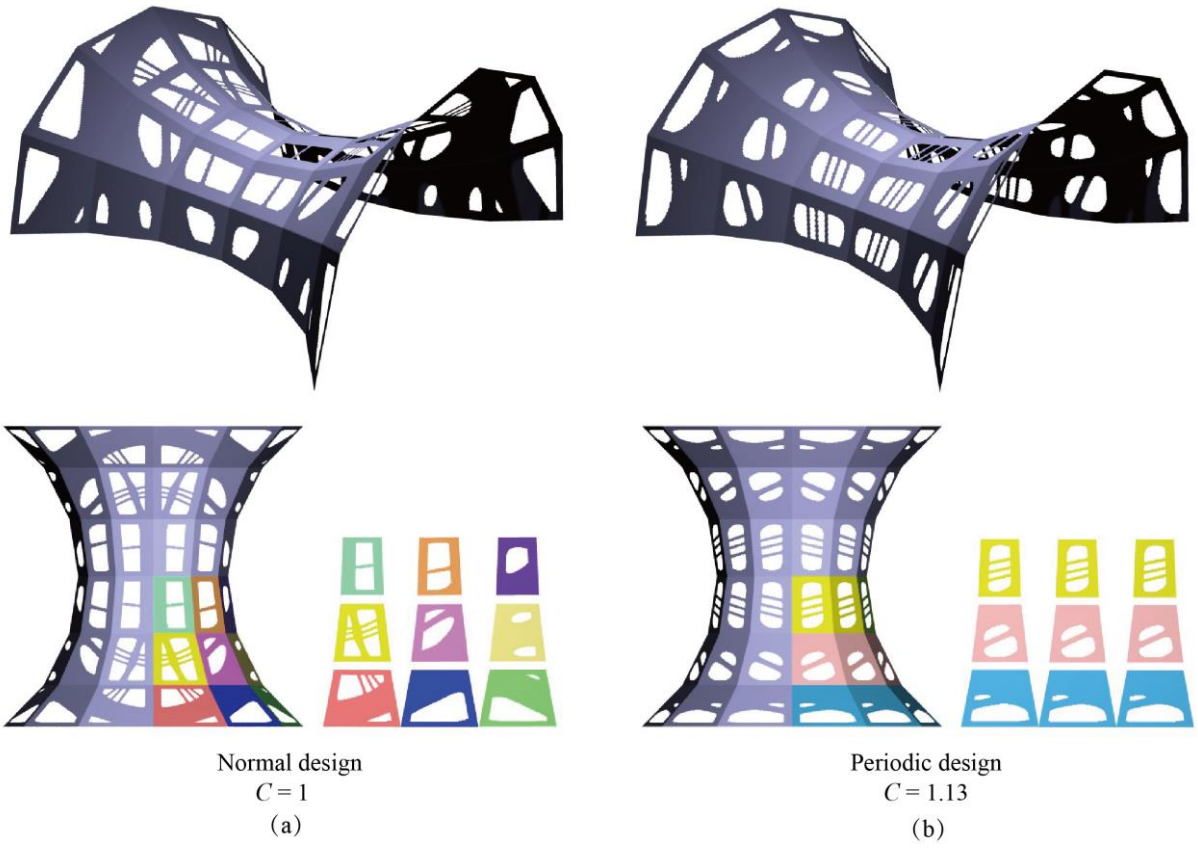


Figure 5. Topology-optimised roof with surface tessellation: (a) without periodic constraint and (b) with periodic constraint.

5. Optimising free-form shells with Voronoi patterns

Although optimising the curvature and topology of shells can maximise their structural performance, the results can be less readily accepted by architects due to their low aesthetic and functional values in architectural practice. In particular, large open spaces in the optimised results usually cannot satisfy buildings' functional requirements, and the unique solutions from traditional topology optimisation often lack artistic expression. To surmount this obstacle, multiple schemes have been proposed in topology optimisation for architecture applications, for instance, diverse and competitive design strategies [17, 18] and local volume constraints [19]. Apart from the existing methods, we advocate that customised design patterns can be integrated with topology-optimised results. Here, we develop a new method to integrate topology-optimised shells with the Voronoi pattern.

The workflow of the proposed method is demonstrated through a shell example as shown in Figure 6. By taking the advantage of symmetry, topology optimisation is performed on a quarter of the shell (i.e., Figure 6(a)) using the SIMP method. Figure 6(b) displays the boundary conditions of the optimisation setting as well as the resulting optimised structure at a 30% volume constraint. Then, by discretising the shell into multiple cells and generating seeds based on the average density of each cell from the optimised result, 3D Voronoi polyhedrons can be developed and projected onto the original shell surface, as indicated in Figures 6(c, d). As can be seen, more seeds are generated in the darker regions of the optimised result; consequently, the Voronoi polyhedrons become denser in those areas to eliminate large cavities. To further improve the organic appearance of the design, randomness can be introduced to the seeds' coordinates. Afterwards, the width of the structural members can be adjusted to precisely control the volume of the final structure. Figures 6(e, f) show the final shell in a quarter and a full model. Spline curves are implemented to smooth the Voronoi pattern. In this case, the solid region

from the optimised results and the non-design domain near the edges are reserved to improve the functionality and aesthetics of the shell. The large open cavities in the topology-optimised design, which is less practical in building applications, are eliminated.

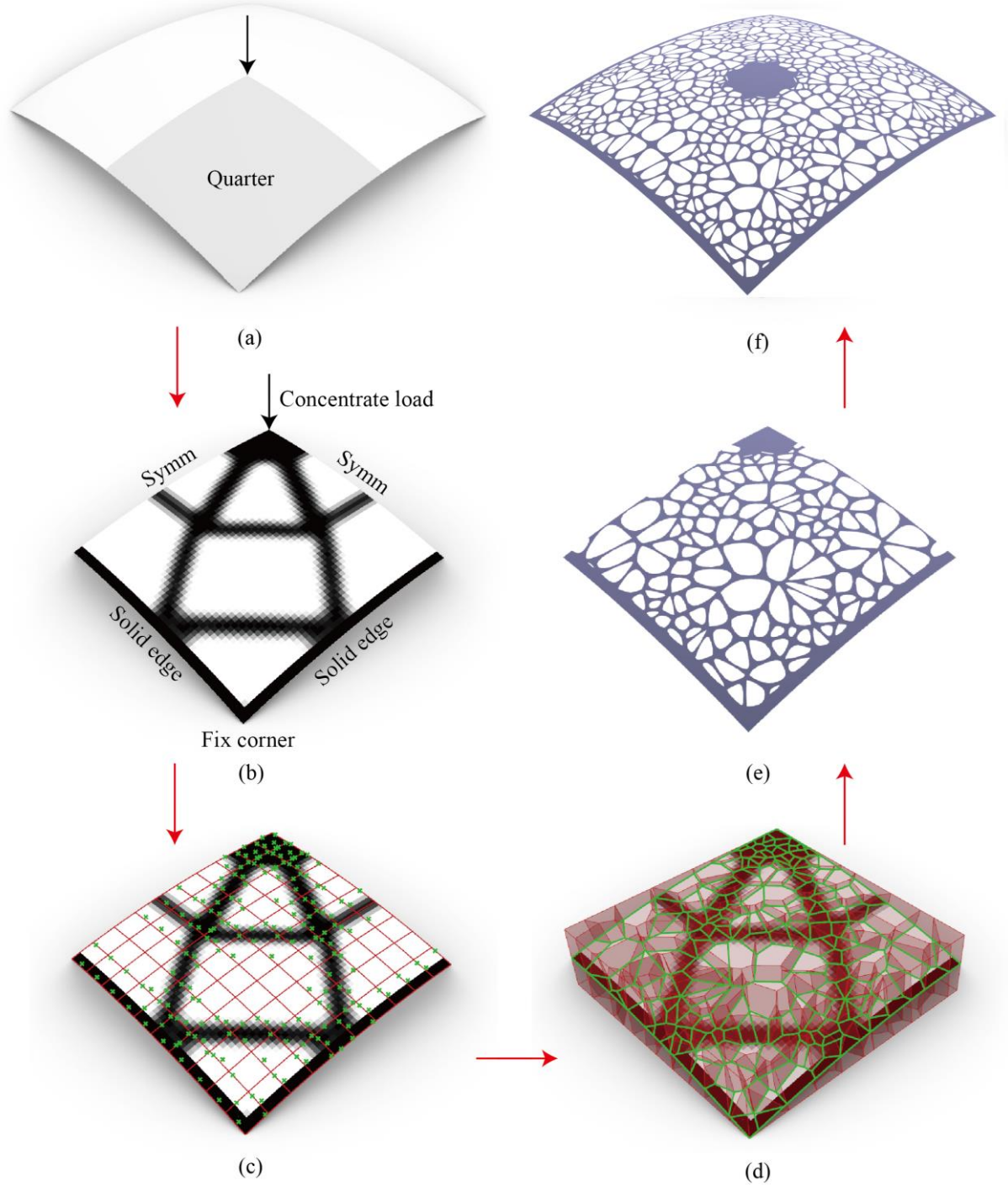


Figure 6. Shell design with topology-optimised Voronoi patterns: (a) initial shell model subjected to a concentrated load; (b) boundary conditions and the topology-optimised result of the quarter shell; (c) discretised shell, with seeds generated in each cell based on the average density; (d) project 3D Voronoi polyhedrons to the original shell; (e) final optimised design of the quarter shell in Voronoi pattern; (f) final shell design.

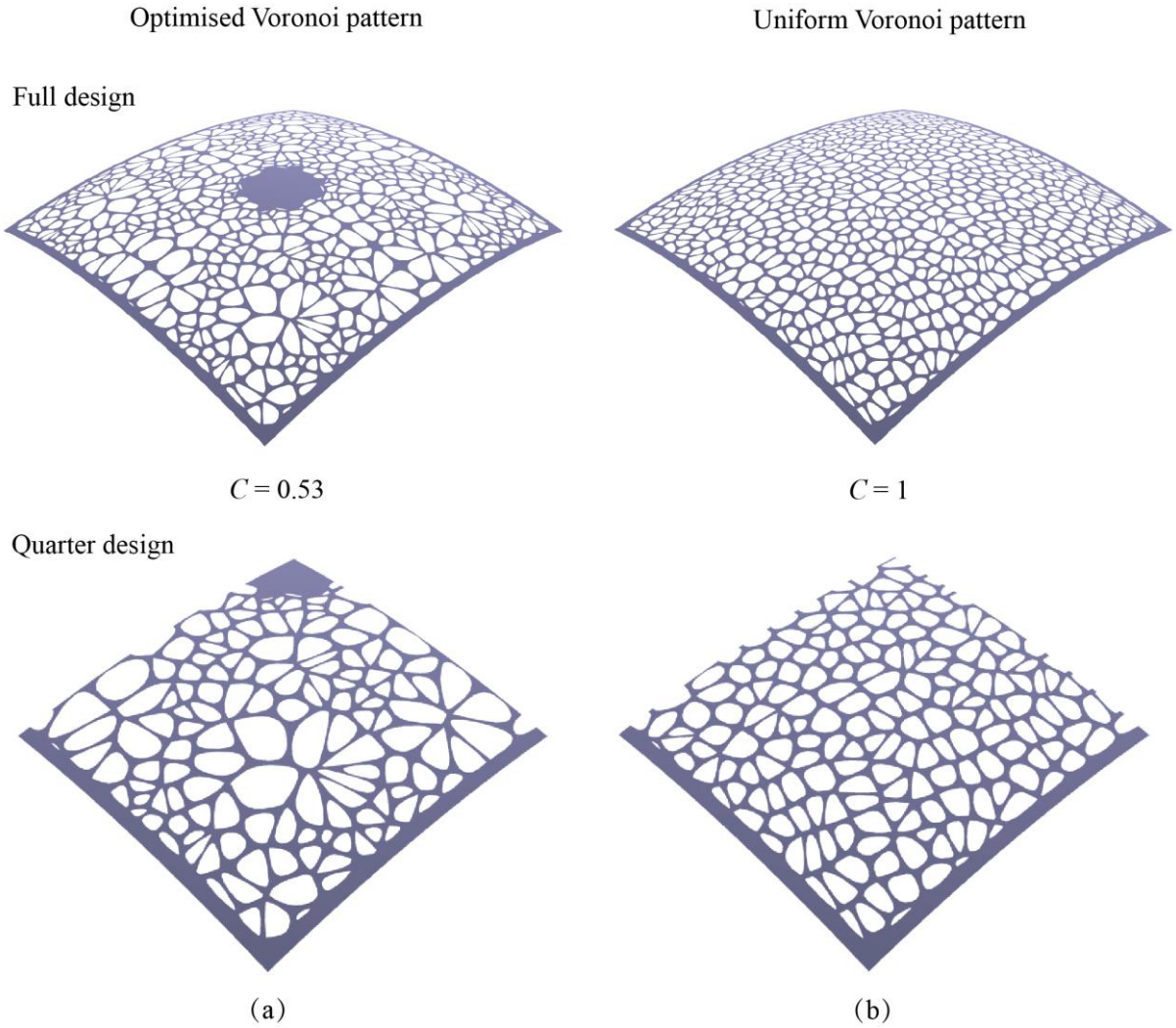


Figure 7. Shell design in Voronoi patterns (a) with topology optimisation and (b) without optimisation. *C* denotes normalised structure compliance.

To demonstrate the improvement of structural performance by generating Voronoi patterns based on topology-optimised results, we present and compare the Voronoi-patterned shell undergone topology optimisation against the one without having it. Figure 7(a) shows the optimised design from Figure 6, which has more materials and smaller cavities allocated to the darker regions of the topology-optimised result. In comparison, a shell with a uniformly distributed Voronoi pattern is generated with the same material volume. The non-design domains of the solid edges are also reserved. By performing finite element analysis on both designs, the normalised structural compliances of the optimised shell and the non-optimised shell are obtained as 0.53 and 1, respectively. Therefore, the structural stiffness of the optimised shell has increased by 88.7% compared to that of the non-optimised shell. In addition to the Voronoi pattern, other customised patterns developed by architects also hold the potential to be combined with topology optimisation to generate aesthetically pleasing and functionally satisfying shells.

6. Concluding remarks

In this paper, we have demonstrated several effective topology optimisation strategies for free-form shells for architectural applications. We reveal that topology optimisation can be used to generate structurally efficient and aesthetically pleasing designs for both the ribs and the surfaces of shells. By

extension, we show that curvature optimisation techniques and tessellation techniques can be combined effectively with topology optimisation to achieve diverse and cost-friendly designs for shells, respectively. Furthermore, we show that customised design patterns, such as the Voronoi pattern, can be integrated with topology optimisation to reflect the aesthetic and functional considerations of architects and engineers in shell design. The strategies presented in this paper are generally applicable to commonly used topology optimisation techniques and are expected to facilitate real-world applications of topology optimisation in architectural shell design projects.

Acknowledgments

This project is supported by the Australian Research Council (FL190100014). The authors are grateful to many collaborators for their contribution to the ideas and results reported in this paper. The authors are also grateful to Dr Ding Wen 'Nic' Bao, Felicetti Pty Ltd and Leeton Pointon Architects + Interiors Pty Ltd for their collaboration on the building project reported in Section 3.

References

[1] K. K. Choong, M. M. Yussof and J. Y. R. Liew, *Recent Advances in Analysis, Design and Construction of Shell and Spatial Structures in the Asia-Pacific Region*, Taylor & Francis Group, 2019.

[2] J. Ma, Z. Li, Z.-L. Zhao and Y. M. Xie, "Creating novel furniture through topology optimization and advanced manufacturing," *Rapid Prototyping Journal*, vol. 27, pp. 1749–1758, 2021.

[3] J. Ma, Z.-L. Zhao, S. Lin and Y. M. Xie, "Topology of leaf veins: Experimental observation and computational morphogenesis," *Journal of the Mechanical Behavior of Biomedical Materials*, vol. 123, 104788, 2021.

[4] O. Sigmund, "A 99 line topology optimization code written in Matlab," *Structural and Multidisciplinary Optimization*, vol. 21, pp. 120–127, 2001.

[5] Y. M. Xie and G. P. Steven, "A simple evolutionary procedure for structural optimization," *Computers & Structures*, vol. 49, pp. 885–896, 1993.

[6] X. Huang and Y. M. Xie, *Evolutionary Topology Optimization of Continuum Structures Methods and Applications*, John Wiley & Sons, 2010.

[7] Z. C. Zhuang, Y. M. Xie and S. W. Zhou, "A reaction diffusion-based level set method using body-fitted mesh for structural topology optimization," *Computer Methods in Applied Mechanics and Engineering*, vol. 381, 113829, 2021.

[8] X. Guo, W. Zhang and W. Zhong, "Doing topology optimization explicitly and geometrically—A new moving morphable components based framework," *Journal of Applied Mechanics*, vol. 81, 081009, 2014.

[9] Y. M. Xie, "Generalized topology optimization for architectural design," *Architectural Intelligence*, vol. 1, 2, 2022.

[10] J. Ma, M. Gomaa, D. W. Bao, A. Rezaee Javan and Y. M. Xie, "PrintNervi – Design and construction of a ribbed floor system in the digital era," *Journal of the International Association for Shell and Spatial Structures*, vol. 63, pp. 241–251, 2022.

[11] J. Ma, Y. He, Z.-L. Zhao, and Y. M. Xie, "Topology optimization of ribbed slabs and shells," *Engineering Structures*, vol. 277, 115454, 2023.

[12] D. Piker. "Kangaroo physics." *food4Rhino.com*. Available: https://www.food4rhino.com/en/app/kangaroo-physics#:~:text=Kangaroo%20is%20a%20Live%20Physics,included%20with%20the%20latest%20d ownload. [accessed Feb. 02, 2023].

[13] X. Yan, D. W. Bao, K. Cai, Y. F. Zhou and Y. M. Xie, "A new form-finding method for shell structures based on BESO algorithm," *Proceedings of the IASS Annual Symposium* 2019, Barcelona, Spain, October 7–10, 2019, C. Lázaro, K. U. Bletzinger and E. Oñate, Eds.

[14] Y. Liu, T.-U. Lee, A. Rezaee Javan and Y. M. Xie, "Extending Goldberg's method to parametrize and control the geometry of Goldberg polyhedra," *Royal Society Open Science*, vol. 9, 220675, 2022.

[15] T.-U. Lee, Y. Liu and Y. M. Xie, "Dividing a sphere hierarchically into a large number of spherical pentagons using equal area or equal length optimization," *Computer-Aided Design*, vol. 148, 103259, 2022.

[16] Y. M. Xie, Z. H. Zuo, X. Huang and J. H. Rong, "Convergence of topological patterns of optimal periodic structures under multiple scales," *Structural and Multidisciplinary Optimization*, vol. 46, pp. 41–50, 2012.

[17] Q. Cai, L. W. He, Y. M. Xie, R. Q. Feng and J. Ma, "Simple and effective strategies to generate diverse designs for truss structures," *Structures*, vol. 32, pp. 268–278, 2021.

[18] Y. He, K. Cai, Z.-L. Zhao, and Y. M. Xie, "Stochastic approaches to generating diverse and competitive structural designs in topology optimization," *Finite Elements in Analysis and Design*, vol. 173, 2020.

[19] X. Yan, Y. Xiong, D. W. Bao, Y. M. Xie and X. Peng, "A multi-volume constraint approach to diverse form designs from topology optimization," *Engineering Structures*, vol. 279, 115525, 2023.

Origami

Active bending
Additive manufacturing/ 3D printing
Architectural geometry
Bamboo for sustainable construction and quality of life improvement
Bio-inspired structures and architecture
Bridge structures
Computational form-finding
Conceptual design
Concrete structures
Construction techniques
Deployable and inflatable structures
Design competition (WG21)
Digital modelling and fabrication
Dynamic response of metal spatial structures
Dynamic response of other structures
Form-finding and structural optimisation of interlocking discrete assemblages
Graphical methods
Gridshell and lattice structures
Historical concrete shells
Historical structures
Lattice structures
Life-cycle design and assessment of structures
Metal gridshell structures, connections and stability
Methods and construction technologies for sustainable shell structures
Morphology and configuration processing
Next generation parametric design
Novel methods in modelling, optimisation and construction for reducing carbon footprint of continuous roof shells
Numerical methods for geometry, form-finding and optimisation of lightweight structures
Optimisation methods and applications
► **Origami**
Other
Teaching design uncertainty: working with unknown qualities/quantities of new and re-claimed materials
Teaching of shell and spatial structures
Tensegrity systems and cable structures
Tension and membrane structures
Tension structures in the Asia-Pacific
Timber and bio-based structures
Topology optimisation
Traditional masonry structures and innovation
Transformable structures

Proceedings of the IASS Annual Symposium 2023
Integration of Design and Fabrication
10–14 July 2023, Melbourne, Australia
Y.M. Xie, J. Burry, T.U. Lee and J. Ma (eds.)

Analysis of bending behaviour in simple flexible honeycomb cores with tetradecagonal cells

Chisaki KITAJIMA*, Kazuya SAITO[a], Taiju YONEDA[a], Hiroshi OKUBO[b], Kaoru SUEHIRO[c]

* Graduate School of Human-Environment Studies, Kyushu University, Fukuoka, Japan
kitajima.chisaki.218@s.kyushu-u.ac.jp

[a] Faculty of Design, Kyushu University
[b] Nissan Motor Corporation
[c] Faculty of Human-Environment Studies, Kyushu University

Abstract

Honeycomb core sandwich panels can achieve light weight, sufficient rigidity, and strength and are used in various engineering applications, including aircraft, space craft, and architecture. However, the formability of standard hexagonal honeycomb cores is low because they deform into an anticlastic shape during bending. Therefore, several special honeycomb cores with good curved surface moldability, such as flex and OX cores, have been proposed. Researchers have also proposed techniques for directly producing 3D honeycomb cores. However, these special honeycomb cores have poorer mechanical properties than the standard hexagonal honeycomb cores. In addition, their complex shapes increase manufacturing costs. Herein, we propose a simple and flexible honeycomb core with tetragonal cells. The characteristics of the proposed flexible honeycomb cores are (1) excellent mechanical properties owing to their cylindrical-like cell shape and (2) ease of manufacturing. In this study, the deformation of cells was analyzed using an algorithmic design tool by assuming that each facet deforms only on the edges and diagonals. Our results demonstrate that the tetradecagonal honeycomb cores realize curvature on the panels due to minute strains on the cell walls.

Keywords: honeycomb, structural design, form-finding, optimization, origami, kirigami, Hangai Prize applicant

1. Introduction

Honeycomb core sandwich panels exhibit excellent mechanical properties, including high specific strength and rigidity. This structure has been investigated primarily for applications in the aerospace

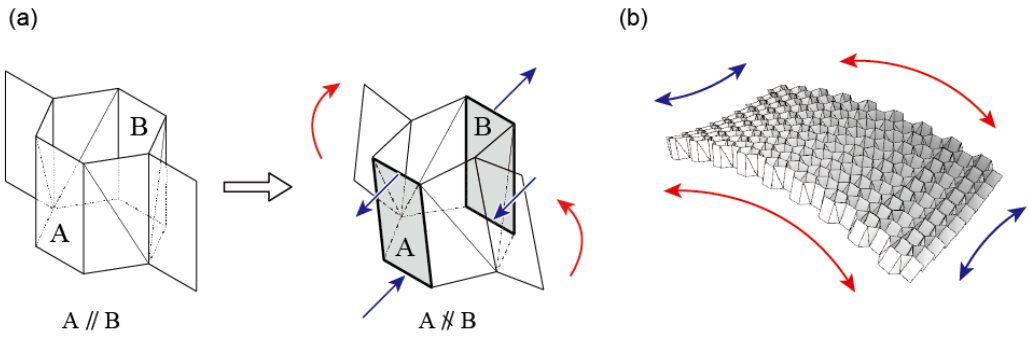


Figure 1. Bending regular hexagonal honeycomb core:
(a) honeycomb cell, (b) honeycomb panel.

Copyright © 2023 by Chisaki KITAJIMA, Kazuya SAITO, Taiju YONEDA, Hiroshi OKUBO and Kaoru SUEHIRO. Published in the Proceedings of the IASS Annual Symposium 2023 with permission.

industry. In addition, this lightweight structural material works as an engineering solution in architecture, for example, for constructing roofs and doors. However, the formability of a regular hexagonal cell is limited because segments A and B cannot remain parallel when forced into a curved state, as shown in Figure 1(a). Therefore, the curvature of the cores results in anticlastic behavior (Figure 1(b)).

Consequently, flexible honeycomb cores composed of special cells, such as Flex or OX cores, have been developed to form monoclastic or synclastic shapes [1]. However, these cores are more expensive than regular honeycomb cores owing to their more complex manufacturing processes. We previously demonstrated the process of manufacturing from a flat sheet using origami technology [2][5]. Although this method enables the manufacture of an arbitrary cross-sectional core, the stiffness of the core is reduced because the cell walls do not stand perpendicular to the curved surfaces. In this study, we demonstrate that flexible honeycomb cores composed of tetragonal cells exhibit excellent formability and high stiffness. The cores are manufactured using simple crease patterns and origami technology. Furthermore, simulations of the rigid folding model using an algorithm-based design tool illustrated the relationship between the shape parameters and the formability of the honeycomb cores.

The remainder of this paper is organized as follows. The second subsection describes the manufacturing method of tetradecagonal cells using origami technology and the mechanism to follow curved surfaces. The third subsection illustrates the design method of the cell shape using an algorithm-based design tool and details of the simulation when the cell is forced into a curved state. The fourth subsection establishes the relationship between the formability and shape parameters of the cell based on the simulations. Finally, the fifth subsection presents the conclusions and outlook of the study.

2. Tetradecagonal cells honeycomb core

2.1. Crease patterns of flexible honeycomb

In a previous study, we proposed a honeycomb core with a combination of tetragonal and hexagonal cells, as shown in Figure 2(a). This type of cell exhibits synclastic behavior without any reduction in the mechanical properties, as the segments stand perpendicular to the curved surfaces [6]. However, it requires complex manufacturing processes owing to non-orthogonal crease patterns. Therefore, we proposed an improved cell shape for easy production, as shown in Figure 2(b). This newly proposed honeycomb core has tetradecagonal cells folded from the crease patterns with only parallel or orthogonal crease lines (Figure 2(b)). This method enabled the manufacture of flexible honeycomb cores with excellent formability using simple crease patterns.

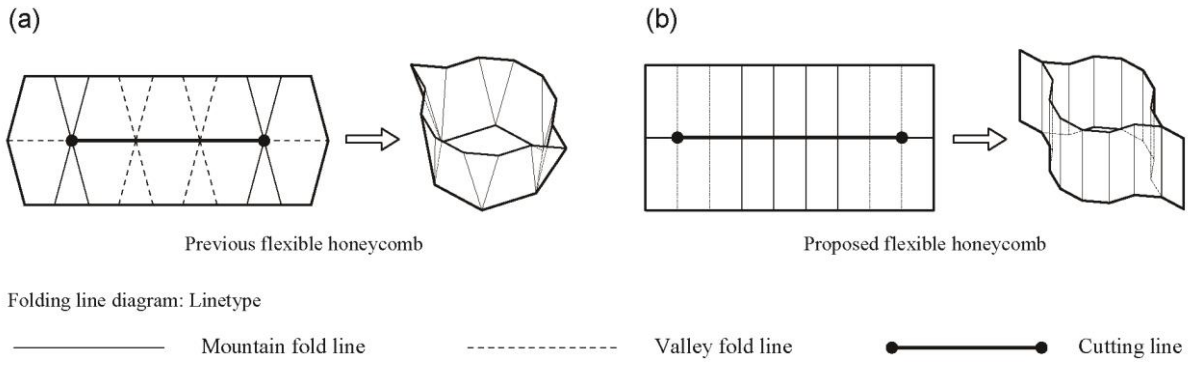


Figure 2. Crease pattern from the flexible honeycomb:
(a) Previous model, (b) Proposed model

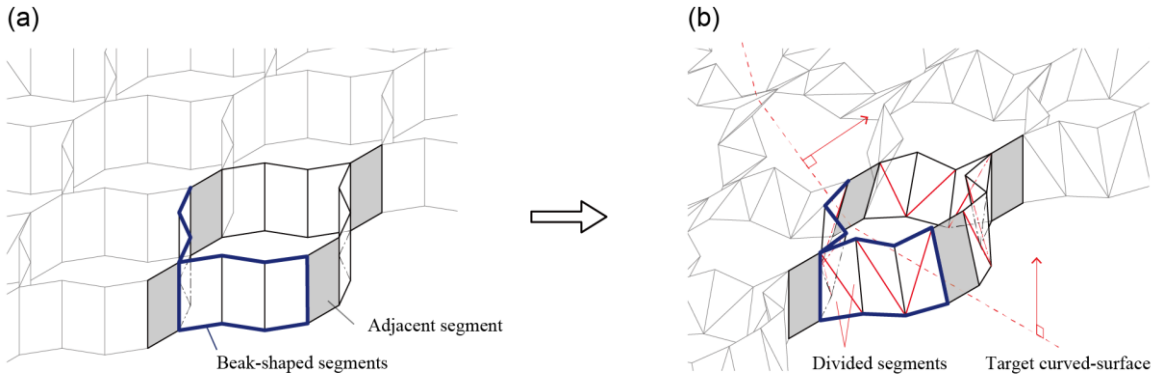


Figure 3. Proposed honeycomb core deformation:
(a) before deformation, (b) after deformation into curved-surface.

2.2. Mechanism to follow curved-surfaces in tetradecagonal honeycomb core

The tetradecagonal cells used in the present study had beak-shaped segments. When the core is forced to curve, the beak-shaped segments are divided into triangular components using diagonal lines [7]. This resulted in opening and closing of the beak-shaped segments opened and closed, causing the contorted segments to form a curved surface (Figure 3).

The cells stood perpendicular to the curved surface and retained their strength.

3. Simulation using of the rigid folding model

In this study, numerical simulations were performed to determine the effects of the geometric parameters of a tetragonal cell on the bending properties of a honeycomb core. Finite element analysis (FEA) is generally required to analyze the deformation of a cell when a honeycomb core panel is subjected to bending [8]. However, the FEA of a cell structure, such as a honeycomb structure, is time consuming because of the large number of elements.

Therefore, we propose a method to obtain the relationship between the curvature of the panel and the deformation of the cell diagrammatically by applying a rigid folding simulation. Our approach is based on the assumption that cell deformation can be accomplished using the crease line and diagonal folding

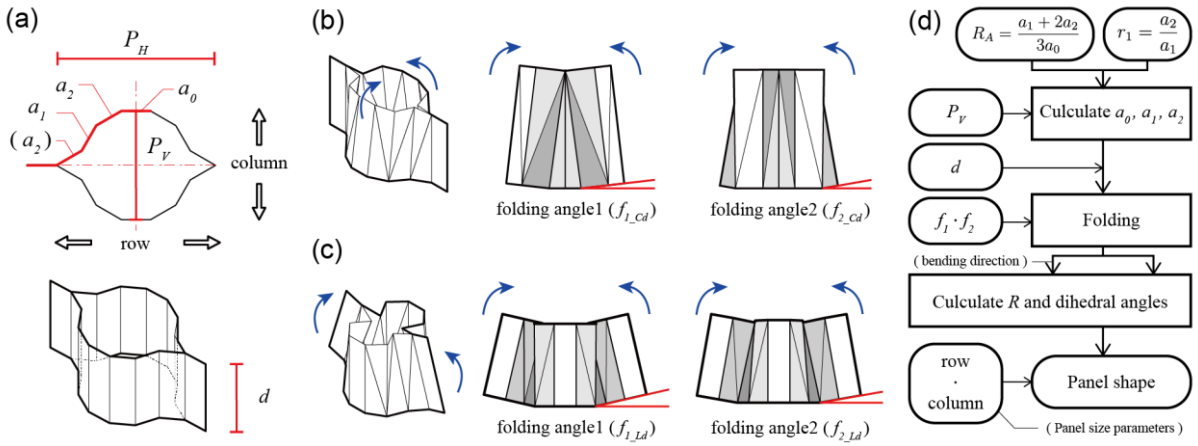


Figure 4. The shape parameters of honeycomb core and the flowchart of the algorithm:
(a) parameters of cell shape, (b) Crosswise folding angles,
(c) Lengthwise folding angles, (d) modeling and simulation flowchart.

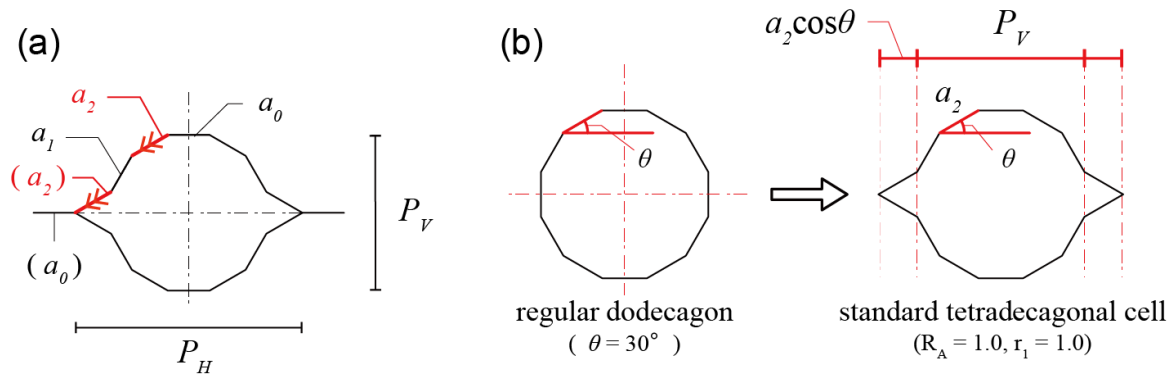


Figure 5. Parameters of cross section in tetradecagonal cell
(a) parallel pairs of lines, (b) standard cell parameter.

angle of each rectangular segment. We simulated a rigid folding model of tetragonal cells with Rhino 7.0 (Robert McNeel & Associates) and Grasshopper [9], an algorithm-based design tool, to investigate the formability of the cells when bent into a monoclastic surface. Figure 3 illustrates the cell shape and flowchart.

The unit cell deformation was calculated using the following process: First, we define the cross-sectional shape of the unit tetradecagonal cell, as shown in Figure 4. The parameters P_V, R_A, and r_1 are set to model the cell size and shape. The edges of a tetrahedron can be represented by three parameters, a_0, a_1, and a_2, based on the symmetry of the cells (Figure 4(a)). Two parameters, R_A and r_1, representing these relationships, were defined to represent the geometry. When the cell outline coincides with a regular dodecagon, R_A=r_1=1.. In this regard, a_0 represents the edge length of the segment adjacent to the next cell, a_1 is the length of the connection to the beaked-shaped segment, and a_2 is the length of the beaked-shaped segment. R_A corresponds to the ratio of triple a_0 to the sum of a_1 and a_2 and r_1 signifies the ratio of a_1 to a_2.

P_H denotes cell length based on a regular dodecagon. It can be calculated using P_V and a_2 as follows:

$$P_H = P_V + 2\,a_2 \cos\theta \tag{1}$$

Second, the coordinates of the original vertices are determined from P_V, R_A, and r_1 (Figure 5(a)). Using the symmetry of the honeycomb core, P1-P2 and P3-P4 were assumed to be parallel. Third, the coordinates of the three-dimensional vertices were sequentially calculated from the lengths of edges a_0, a_1, a_2 and the thickness d of the core panel (Figure 5(b)). Segments 0 and 7 remained parallel to adjacent

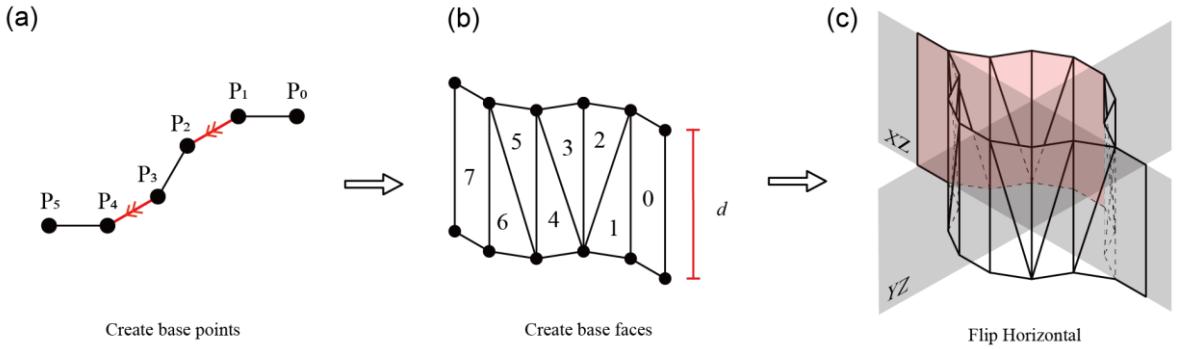


Figure 6. The process of modeling cell:
(a) the original vertices from PV, RA, and r1, (b) the three-dimensional vertex,
(c) inverting the symmetric part of the cell on the XZ,YZ planes.

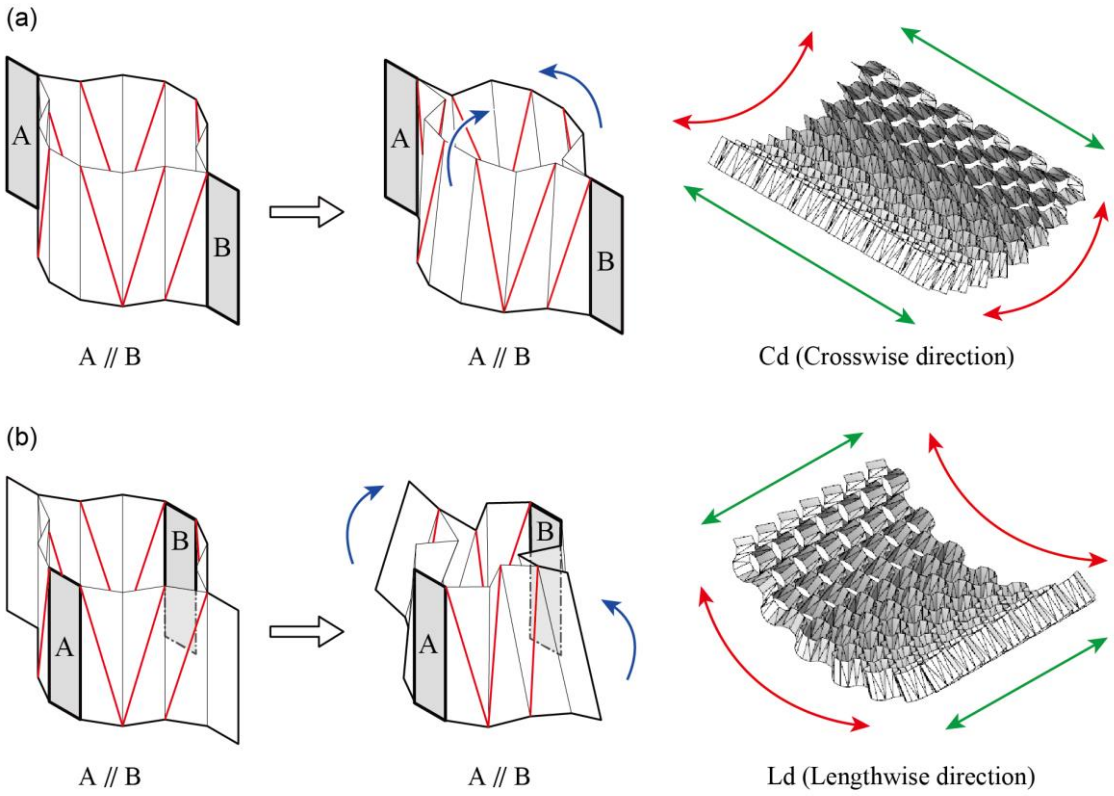


Figure 7. Bending the tetradecagonal honeycomb core:
(a) Crosswise direction, (b) Lengthwise direction.

cells following the bending direction. In addition, the twisting of the cell was attributed to the rigid body deformation as a diagonal fold. Furthermore, the symmetric part of the cell was inverted through its center on the XZ and YZ planes (Figure 5(c)).

In a rigid-fold unit cell with diagonals, if cells A and B are constrained in parallel, the positions of the other vertices can be determined graphically using the values of f_1 and f_2 (Figure 3). Thus, a computational algorithm was developed within the Grasshopper framework to ascertain the shape of the cell and the curvature of the panel. Finally, the cell was bent in the crosswise and lengthwise directions (Cd and Ld) by independent parameters of the folding angle (f_1 and f_2) to a cylindrical panel (Figure 6).

4. Curvature radius and dihedral angle analysis

The radius of curvature, R is the distance from the base of the segment to the adjacent cell to the intersection of the extension lines on the segments (Figure 7).

For simplicity, we assume that the spring constant of each hinge is directly proportional to the length of the fold line, and that the elastic energy stored in the fold line is proportional to the variation in the spring constant and the square of the fold line. Accordingly, we define the generalized energy using the following equation:

$$E = \sum_{i=0}^{4} l_i \cdot \Delta\theta_i^2 \tag{2}$$

We simulated the energy generated within the crease line when the curvature was specified for various models possessing distinct geometrical parameters, and found a combination that could generate a large curvature with less energy and high formability.

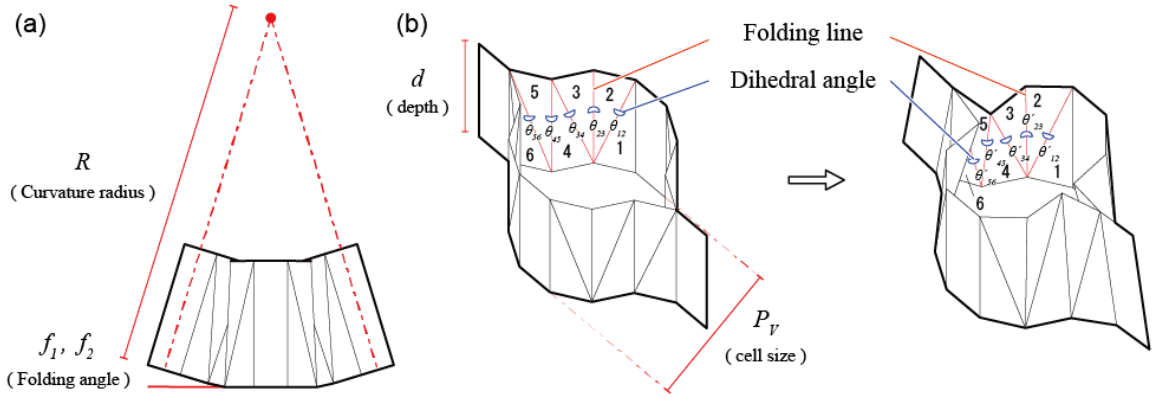


Figure 8. The parameters used to calculate the bending energy:
(a) Curvature radius, (b) Folding lines and dihedral angles.

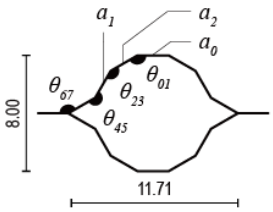
In this simulation, the cell parameters were P_V = 8.0 (mm) and d = 4.0 (mm). The values of *1/R* and *E* with the various combinations of R_A and r_1 were compared. The combinations of R_A and r_1 used in the simulations are listed in Table 1 below.

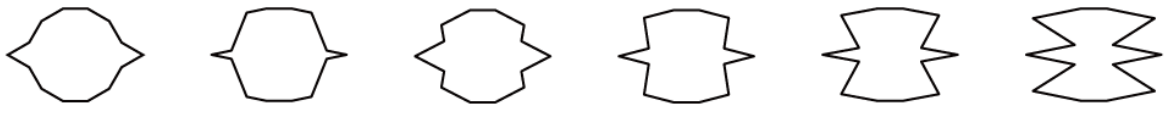
As f_1 and f_2 are independent variables that determine the curvature of the panel, multiple possible combinations exist for a particular curvature. The calculations utilized the values of f_1 and f_2 that yielded the minimum energy.

The value of f_{1_min} which minimizes *E* at a certain radius of curvature *R*, is calculated first since the deformation with the smallest energy is reasonable. The continuous variation in f_2 at f_{1_min} indicates the correlation between *1/R* and *E*.

Table 1. The shape parameters used in the simulation.

		r_1 = 1.0, R_A = 1.0	r_1 = 0.5, R_A = 1.1	r_1 = 2.0, R_A = 1.1	r_1 = 1.0, R_A = 1.25	r_1 = 1.0, R_A = 1.5	r_1 = 1.0, R_A = 2.0
(mm)	a_0	2.14	2.14	2.14	2.14	2.14	2.14
	a_1	2.14	3.54	1.41	2.68	3.22	4.29
	a_2	2.14	1.77	2.83	2.68	3.22	4.29
(deg)	θ_{01}	150	168.3	152.6	165.4	169.5	168.6
	θ_{23}	150	123.7	107.7	96.0	72.0	43.9
	θ_{45}	210	236.3	252.3	264.0	288.0	316.1
	θ_{67}	150	168.3	152.6	165.4	169.5	168.6





① r_1 = 1.0, R_A = 1.0 ② r_1 = 0.5, R_A = 1.1 ③ r_1 = 2.0, R_A = 1.1 ④ r_1 = 1.0, R_A = 1.25 ⑤ r_1 = 1.0, R_A = 1.5 ⑥ r_1 = 1.0, R_A = 2.0

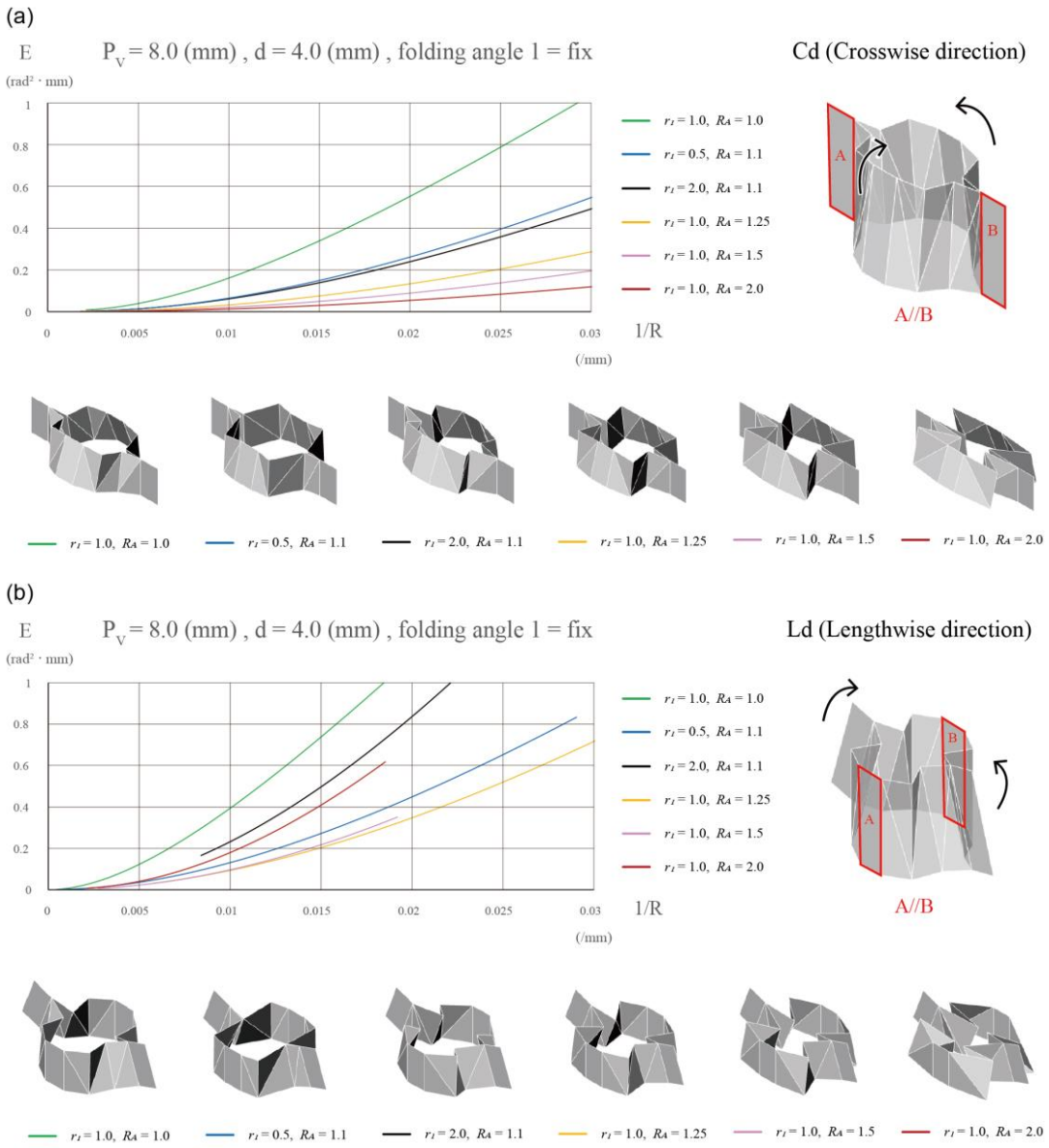


Figure 9. Calculation of *1/R* and *E*: (a) Crosswise direction, (b) Lengthwise direction.

Cd: Increasing R_A significantly improved formability. For r_1, the formability is improved by large values of R_A; however, the difference is nearly 15 times larger than that for the model with a large R_A.

Ld: As with Cd, the formability improved when R_A increased, but decreased when R_A exceeded 1.5.

Although other mechanical properties such as compressive strength should be considered when determining the actual parameters, the proposed method allows for the selection of a cell shape with high formability under the given conditions.

5. Conclusion

This study demonstrates simple manufacturable tetradecagonal cores using origami technology. The core was simulated using Grasshopper, an algorithm-based design tool. This rigid folding simulation

revealed the main formability parameters in each bending direction on cylindrical surfaces. The results demonstrate that increasing the R_A parameter leads to improved formability in the deformation of Cd. However, the formability of the deformation for Ld is improved if R_A is close to a certain value.

These findings indicated the possibility of designing a cell with high formability in each bending direction. In particular, this enabled the optimization of the value of R_A in the deformation of Ld. In addition, the value of r1 represents a trade-off between Cd and Ld, and the cell shape can be optimized depending on the curved surface.

6. Outlook

In this study, we have only described the main cell parameters of formability in unidirectional bending along cylindrical surfaces and have not yet evaluated the formability in bidirectional bending, such as synclastic surfaces. The effect of strain on the segment and variations in stiffness along the folding line are not considered in the simulation. It is anticipated that these effects can be disregarded due to the small deformation. However, we are preparing a further experimental validation with paper-made honeycomb cores. In addition, further verification is required to evaluate the mechanical properties of the structural material upon changes in cell parameters.

Acknowledgements

This research was supported by Nissan Motor Co., Ltd. JST FOREST (Grant Number JPMJFR203E4), and JST SPRING (Grant Number JPMJSP2136). We would like to thank Editage (www.editage.com) for English language editing.

References

[1] Tom Bitzer, *Honeycomb Techonology: Materials, Design, Manufacturing, Applications and Testing*, Chapman & Hall, 1997.

[2] Kazuya Saito, Sergio Pellegrino and Taketoshi Nojima, “Manufacture of Arbitrary Cross-Section Composite Honeycomb Cores Based on Origami Techniques”, *Journal of Mechanical Design*, Vol.136, No.5, 051011-(1-9), 2014.

[3] Lijun Wang, Kazuya Saito, You Gotou and Yoji Okabe, “Design and fabrication of aluminum honeycomb structures based on origami technology”, *Journal of Sandwich Structures and Materials*, Vol.21, No.4, pp.1224-1242, 2017.

[4] Rupert Maleczek, Kazuya Saito, “Deployable Honeycomb Structures”, *Origami 7: Proceedings from the seventh meeting of Origami, Science, Mathematics and Education*, Oxford, pp. 877-892, September 2018

[5] Kazuya Saito, Fabio Agnese, and Fabrizio Scarpa “A Cellular Kirigami Morphing Wingbox Concept”, *Journal of Intelligent Material Systems and Structures*, Vol.22, No.9, pp. 935-944, August 2011

[6] Nissan Motor Corporation, Hiroshi OKUBO, Honeycomb core, P2022-139017A in Japanese, 2022.9.26

[7] Rupert Maleczek, Gregoire Loriot de Rouvray, and Clemens Preisinger, “Linear Double Folded Stripes”, *IASS Symposium 2011*, Amsterdem, August 2015

[8] Evgueni T. Filipova, K. Liu, Tomohiro Tachi, Mark Schenk, and G.H. Paulino, “Bar and hinge models for scalable analysis of origami”, *International Journal of Solids and Structures*, Vol.124, pp. 26-45, June 2017

[9] McNeel, R. *Grasshopper* (2014). https://www.grasshopper3d.com/. Accessed 31 March 2023

Proceedings of the IASS Annual Symposium 2023
Integration of Design and Fabrication
10–14 July 2023, Melbourne, Australia
Y.M. Xie, J. Burry, T.U. Lee and J. Ma (eds.)

Bridging the gap – A study on foldable tubular bridges

Rupert MALECZEK[a,*], Kiumars SHARIFMOGHADDAM[b], Georg NAWRATIL[b], Clemens PREISINGER[c]

[a,*] i.sd / structure and design / department of design / university of Innsbruck
Technikerstraße 21c, UG Süd, 6020 Innsbruck, Austria
rupert.maleczek@uibk.ac.at

[b] Institute of Discrete Mathematics and Geometry & Center for Geometry and Computational Design, TU Wien
[c] Institute of Architecture / University of Applied Arts Vienna

Abstract

Recent investigations on foldable structures and particularly foldable tubes, raise the question if they can be advantageous for the construction of bridge-like beams. Transporting a flat packed structure on site and deploying it there, instead of bringing or constructing the structure on site will have a positive impact on the grey energy. Although a straight beam shows a better performance than a folded one with identical cross-section, the energy saved in transportation might justify the effort. In order to be able to answer this complex question, many steps and investigations need to be done. This paper will answer some questions concerning foldable structures and their geometry-related structural performance. During the ongoing research on T-hedral tubes, the authors developed a strategy to generate flat-foldable tubular beams, on which this particular investigation is based. For the paper at hand a set of these beams, with different cross-sections and variable amount of folds will be compared with respect to their structural performance. The study will focus on their geometry without exact detailing of the hinges or the material thickness. With the help of a parametric model a generic solver [1] and a FEM-module [2] the authors developed a method that evaluates the beams based on their weight after optimisation, in final unfolded state as well as in different configurations during unfolding.

Keywords: structural origami, folding, computational design, bridge building

1. Introduction

Recent advancements in the field of technical folding and structural origami have led to numerous innovative approaches for various applications. The development and investigation of new folding systems [3][4], along with experiments on a larger scale, have led to the assumption that large scale folding [5] could become more influential in the building industry.

Although new folding algorithms are often presented with freeform shell geometries, the building industry has often higher interest in simple beams or slabs. Elements that can be unfolded on site are often related to disaster relief. One interesting example in this context is the foldable bridge by Ario et al. [6]. Foldable plates structures of rigid material that can be folded on site, are not yet known to be implemented in the building industry.

During the research on foldable polyhedral tubes of the T-hedral type [7] the authors developed two variations of a flat foldable structure, that have a high potential for a beam-like application, as they can be transported in a small package and unfolded on site to their final configuration. Starting from the feasibility of foldable models with only one degree-of-freedom (1-DoF), the investigation towards realisation requires a validation of different folding concepts concerning their stiffness in relation to

Copyright © 2023 by Rupert MALECZEK, Kiumars SHARIFMOGHADDAM, Georg NAWRATIL and Clemens PREISINGER. Published in the Proceedings of the IASS Annual Symposium 2023 with permission.

their global geometry. In this paper a folded structure is evaluated through its mass after an optimisation process, that reduces the cross-sections of each element in the structure to be as light as possible. Doing so, we can evaluate the global geometry by its weight after optimisation. If certain boundary conditions as e.g. a fixed span are introduced, an algorithm can search for the lightest geometry, and therefore find the best variant.

As geometric and mechanical constraints allow for different geometric solutions, the authors developed a parametric set-up for their particular systems, in order to find optima within the corresponding solution space. After discussing the chosen geometric constraints, the paper focuses on the evaluation of a series of optimisations, to find the best shape for a 20-meter spanning bridge beam.

2. T-hedral tubes

We aim to design a transformable bridge that exploits the potential offered by polyhedral tubes composed of planar quads (PQ) connected by rotary joints. PQ-meshes in the combinatorics of a square grid with cylindrical topology are generically rigid, but certain geometries allow for a 1-parametric change of the dihedral angles without any deformation of the PQ-panels. This rigid-folding of the whole tubular structure can be controlled by a single actuated rotary joint. Beside this 1-DoF flexion, which can be used for a compact (even flat) folding for transportation, additional properties like a lightweight construction, make these structures suitable to be utilized in kinetic architecture and, in general, transformable design. A close look at the literature [7] on rigid-foldable tubular structures, composed of planar quads where each interior vertex has valence four, reveals that most of the known examples belong to the class of *T-hedral tubes*, which can be generated as follows:

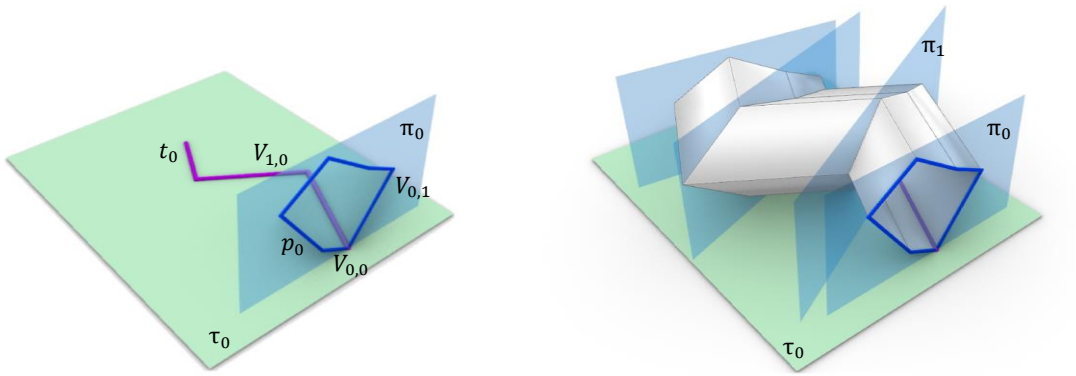


Figure 1. Construction of a T-hedral tube

We start with a planar, closed polygon p_0 located in the plane π_0 and a planar polygon t_0 whose carrier plane is denoted by τ_0 (Figure 1). Moreover, p_0 and t_0 have a common vertex $V_{0,0}$ and the planes π_0 and τ_0 are intersecting orthogonally. The remaining vertices of t_0 and p_0 are denoted by $V_{i,0}$ and $V_{0,j}$, respectively, with $i = 1, \dots, I-1$ and $j = 1, \dots, J-1$. Through each vertex $V_{i,0}$ of t_0 there is a plane π_i orthogonal to the *base plane* τ_0. By a parallel projection of p_{i-1} into the plane π_i along the direction of the polygon edge $V_{i-1,0}V_{i,0}$ of t_0, we obtain the planar polygon $p_i \in \pi_i$. Under this projection the vertices $V_{i-1,j}$ are mapped to $V_{i,j}$. Iteration of this process (for $i = 1, .., I-1$) generates the vertices of the tubular quad-mesh, which has planar trapezoidal faces as the sides $V_{i-1,j-1}V_{i,j-1}$ and $V_{i-1,j}V_{i,j}$ of every quad are parallel. Note that the letter T, stands for trapezoidal, in the nomenclature T-hedral tube. In order that the resulting tube is rigid-foldable the planar closed polygon p_0 has to meet the *loop closure condition* for which we refer to Theorem 3.1 of [7].

It is well-known [8] that T-hedral tubes reach their flexion limits as soon as either a PQ-loop gets completely flat (Figure 2a) or a PQ-strip gets parallel to the base plane (Figure 2c). In the latter case the tube can also transition from one working mode to another. As a consequence, the T-hedral tube can only flex back in such a bifurcation configuration, but the PQ-strip can flip to the opposite side (Figures

2b and 2d). Therefore, this property is also known under the notion of switching [9].

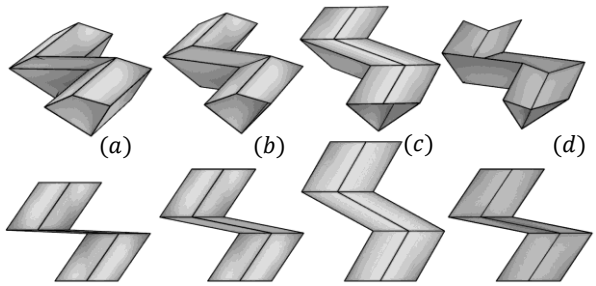


Figure 2. Illustration of the flexion limits (a,c) and working modes (b,d) on basis of a T-hedral tube with deltoidal cross-section in perspective (top) and top views (bottom)

2.1. Specifications for the bridge design

To keep the bridge design as simple as possible, we restrict to T-hedral tubes with a quadrilateral cross-section (Figure 3). It can easily be seen that in this case the above-mentioned loop closure condition is only fulfilled if and only if p_0 is

1. a parallelogram,
2. a deltoid with a symmetry line orthogonal to the base plane τ_0,
3. an anti-parallelogram with a symmetry line parallel to the base plane τ_0.

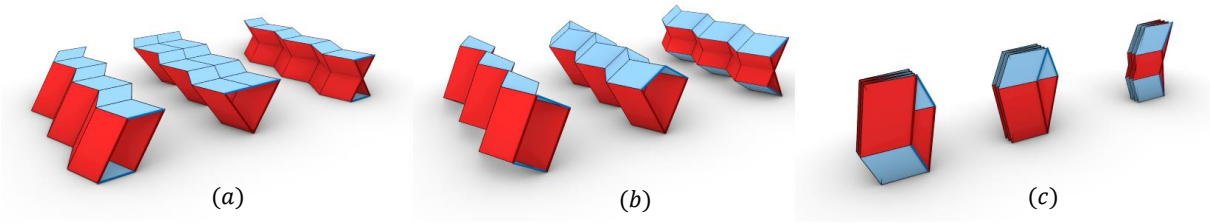


Figure 3. T-hedral tubes with all types of possible quadrilateral cross-sections; parallelogram (left), deltoid (center) and anti-parallelogram (right). (a) unfolded up to the flexion limit, (b) half-folded and (c) flat-folded

In fact, we only deal with cross-sections of cases 1 and 2, because case 3 results in self-intersections for tubular shell models. In addition, we require a repetitive structure of the tubes to ease and cheapen their manufacturing, which yields to the assumption that t_0 is a regular zig-zag. In order to meet our last request of flat-foldability, the planes π_i have to be angle bisectors of t_0 according to [9]. As a consequence, all planes π_i are parallel to the plane π_0 implying T-hedral tubes of the so-called *translational type* (as these tubes are generated by a pure translation from p_0 along t_0).

One can also compose T-hedral tubes by connecting them at PQ-strips in a way that the resulting structure is still rigid-foldable. One can distinguish the following two types of this face-sharing coupling of T-hedral tubes of the translational type [7]. One can put two such tubes together in a way that the corresponding base planes are

- **parallel/identical:** This so-called *aligned-coupling* can easily be constructed by merging two closed polygons p_0^+ and p_0^-, which both fulfil the loop closure condition and share (parts of) a common edge, to a single polygon p_0.
- **not parallel/identical:** This so-called *zipper-coupling* can be achieved by starting with the face-sharing PQ-strip, which has to be a discrete cylinder for the translational type, and chose two base planes in a way that their line of intersection is orthogonal to the cylinder rulings. Note that during the rigid-folding of the zipper tubes the angle enclosed by the base planes changes as illustrated in Figure 7.

Based on these fundamental properties of T-hedral tubes and their couplings, we proceed to explain the

ideas behind the proposed two bridge designs.

2.2. Proposed two bridge designs

Our goal is to achieve a flat bridge deck in the final unfolded state of the structure, which requires to be a flexion limit of at least one involved tube; i.e. the base plane of this tube has to be horizontal. However, as previously mentioned, this is also a bifurcation configuration and it is necessary to prevent the bridge from flexing back (under load). Our focus is on finding purely geometric solutions for blocking the bridge in the final unfolded state.

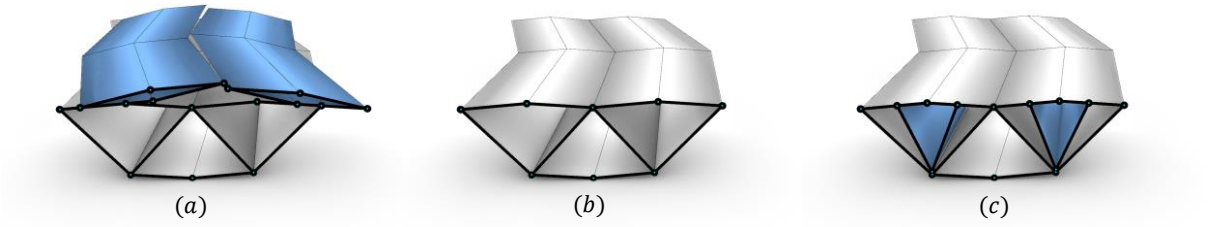


Figure 4. A zig-zag unit of the core structure (b), the zipper-tube solution (a) and the nested deltoid solution (c) close to their final unfolded state

Both presented solutions have the same core structure, which consists of three aligned-coupled deltoidal tubes (see Figure 4b). Note that such an arrangement was also used by Schenk and Guest [10] to construct self-locking metamaterial.

- **Nested deltoid solution**: In this case the bifurcation is prevented by two inner deltoidal tubes, which are aligned-coupled to the outer deltoidal tubes even along two PQ-strips, which is possible due to symmetry (see Figure 4c).
- **Zipper-tube solution**: We zipper-couple two rhombic tubes to the left and right deltoidal tubes of the core structure in a way that in the final unfolded state the rhombic tubes are flat and cover (even extend) the bridge deck (see Figure 4a).

Finally, it should be noted that a flat-foldable bridge structure constructed from zipper-coupled tubes was also presented in Figure 6 of [11]. But neither its deck is flat nor the blocking of the bridge in its finale state was discussed. The latter can for example be achieved by fixing the cross-sections at the bridge end-points to two plates as done in [12]. Moreover, a flat covering of zipper-tubular structures can be obtained by using the concept of smooth sheet attachments [13].

3. Potential application as a bridge

As described above, the T-hedral tubes offer interesting behaviour and potential for the building industry as they can be prefabricated in a controlled environment, transported and unfolded into their final spatial configuration on site. For this investigation the two different approaches were analysed for their performance under load, self-weight and their behaviour during the unfolding process, using the FEM-Tool Karamba3D [2] in combination with Galapagos [1] in the Rhino/Grasshopper environment. The authors decided to reduce complexity in this early investigation, and neglected therefore known problems and questions in relation to hinge detailing, material thickness, actuation or materiality.

3.1. Structural analysis of the geometries

If folding on site for a bridge should become a potential application two related questions need to be answered: What is the best geometry for the bridge in its final configuration, and what is the best geometry for the unfolding process. In the presented case, the authors also wanted to investigate if rather a nested or the zipper version of the bridge has a better structural performance.

To compare the two options the authors used the FEM-Solver Karamba3D and its ability to optimize cross-sections with given parameters as e.g. maximum admissible deformation. In the presented case

the deflection limit is set to span/300 in accordance to European building codes. As a result, the mass of the structure is optimized. This serves as a performance indicator for comparing design alternatives. The lighter the result the better the geometry. For reducing computational effort, the structures were not analysed as shell structures, but as spatial truss assemblies with the truss-members being aligned to the foldlines and placed as cross bracing thereby modelling the in-plane stiffness of the PQ-panels.

For an investigation on the geometry modelled via shell finite elements, the approach would have been to assign the same weight to the different bridge geometries by controlling the shell thickness and then compare the maximum deflection of the alternative structures. As the folded geometries have in the folded state several layers in the same plane, meshing becomes difficult and slow, resulting in inaccurate structural calculation results. Especially the zipper tube has a high level of complexity, that will be addressed in future investigations.

To have comparable results the bridge spans were defined to be 20 meters having a fixed deck width of 6 meters. The supports were allowed to freely rotate being movable in the bridge's axial direction at one end-point. As truss material hardwood D30 was chosen. The truss-members to be optimised were chosen from a set of cross-sections ranging from 10 to 50 cm edge lengths in 5 cm steps.

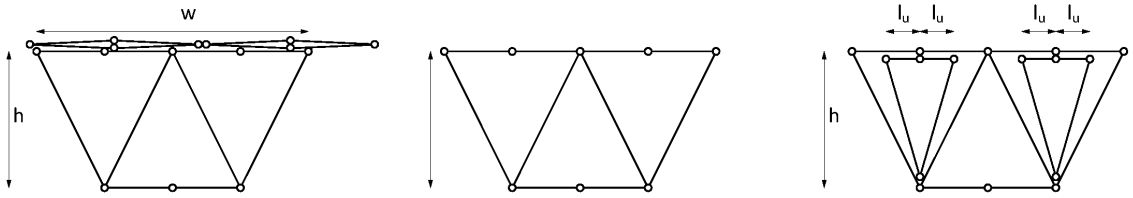


Figure 5. Concept sketch of the variable parameters in section of the zipper tube (left) and the nested solution (right) in its final folded state

The design-alternatives of the bridge had different design parameters that were optimised using Galapagos. As shown in Figure 5, the zipper bridge was variable in the bridge height h, the number of undulations n, the amplitude a of the undulations in x-direction, and the width w of the core structure. The nested bridge was variable in the bridge height h, the number of undulations n, the amplitude a of the undulations in x-direction, and the upper length l_u of the inner deltoid in relation to the total length.



Figure 6. Concept sketch of the two bridge concepts the zipper tube (left) and the nested solution (right) in its final folded state

The structures were optimised for different load cases and in different folding states. The bridges in final state where optimised under self-weight and for a live load of 6kN/m² on the bridge deck. During the (un)folding process the structures were only optimised for self-weight. It was assumed that the bridge would not be folded as a cantilever, but rather as a simply supported beam. This can be achieved with cranes on each side.

3.2. Optimisation results

As the cross-section optimisation in combination with the Galapagos solver necessitates long computation times the maximum amount of undulations was limited to four, and the deviation was limited to the range 0.25 to 7.5 meters, with a step size of 0.25 meters.

Under live load both solutions converge to the maximum allowed height of the system that was limited to two meters, having a maximum number of 4 undulations, using the minimum allowed deviation of 0.25 meters. The ten best results of both geometries have heights in the upper bound of the height domain and feature the maximum number of undulations. The high number of undulations is linked to the reduction of buckling lengths of the truss members, that result in better structural performance. The nested bridge is 1.4 tons heavier, and therefore less performative under live load as compared to the zipper geometry (cf. Table 1 and Figure 8).

Table 1. The best results of the two systems under live load

live load : 6 kN / m2	NESTED BRIDGE									
	1	*2*	*3*	*4*	*5*	*6*	*7*	*8*	*9*	*10*
FinalStateHeight [m]	2.0	1.9	1.8	2.0	2.0	1.9	1.9	1.9	1.8	1.8
lu	0,25	0,25	0,25	0,33	0,08	0,33	0,17	0,08	0,33	0,08
a - amplitude [m]	0,25	0,25	0,25	0,25	0,25	0,25	0,25	0,25	0,25	0,25
n - undulation	4	4	4	4	4	4	4	4	4	4
Mass [kg]	**10748**	**10789**	**10838**	**10845**	**10889**	**10896**	**10913**	**10918**	**10949**	**10987**

live load : 6 kN / m2	ZIPPER BRIDGE									
	1	*2*	*3*	*4*	*5*	*6*	*7*	*8*	*9*	*10*
FinalStateHeight [m]	2.0	2	1,9	2	1,9	1,9	2	1,9	1.9	2,0
w - width [m]	4,1	4	4	4,2	4,1	4,2	3,7	3,9	4,3	3,6
a - amplitude [m]	0,25	0,25	0,25	0,25	0,25	0,25	0,25	0,25	0,25	0,25
n - undulation	4	4	4	4	4	4	4	4	4	4
Mass [kg]	**9367**	**9399**	**9431**	**9461**	**9466**	**9566**	**9571**	**9580**	**9590**	**9592**

Under self-weight the total mass difference between the best results of the nested and zipper variant remains constant. Similar to the calculation with live load the mass difference amounts to 1.4 tons. Both systems tend towards the lower end of the possible predefined height range. The number of undulations switches from 4 to 2, but the amplitude is kept at the absolute minimum allowed (cf. Table 2).

Table 2. The best results of the two systems under self-weight

self-weight	NESTED BRIDGE									
	1	*2*	*3*	*4*	*5*	*6*	*7*	*8*	*9*	*10*
FinalStateHeight [m]	1	1	1	1.0	1.8	1.3	1.3	1.8	1.3	1.4
lu	0,08	0,17	0,25	0,17	0,25	0,75	0,83	0,33	0,50	0,58
a - amplitude [m]	0,25	0,25	0,25	0,25	0,5	0,25	0,25	0,75	0,75	0,5
n - undulation	2	2	2	2	2	2	2	2	2	2
Mass [kg]	**7183**	**7197**	**7214**	**7442**	**7463**	**7502**	**7526**	**7547**	**7551**	**7561**

self-weight	ZIPPER BRIDGE									
	1	*2*	*3*	*4*	*5*	*6*	*7*	*8*	*9*	*10*
FinalStateHeight [m]	1,2	1	1,3	2	1,5	1,5	2	1.5	1.9	1,7
w - width [m]	2	2	2,5	2,1	2,7	2,6	2,3	2,5	2,3	2,7
a - amplitude [m]	0,25	0,25	0,25	0,25	0,25	0,25	0,25	0,25	0,25	0,25
n - undulation	2	2	2	2	2	2	2	2	2	2
Mass [kg]	**5806**	**5806**	**5903**	**5904**	**5905**	**5908**	**5912**	**5912**	**5916**	**5917**

According to the intended eraction method of unfolding of the structure on site, one investigation was focusing on the optimisation with regards to the series of folding states. As different configurations feature different speeds of folding and unfolding, the folding ratio is defined to be between 0 and 1, where 1 corresponds to the fully unfolded state, and 0 to the fully folded package that has a total

thickness of 1.5 meters. This number constitutes an estimation, since material thickness and hinge detailing will probably not allow for smaller package sizes.

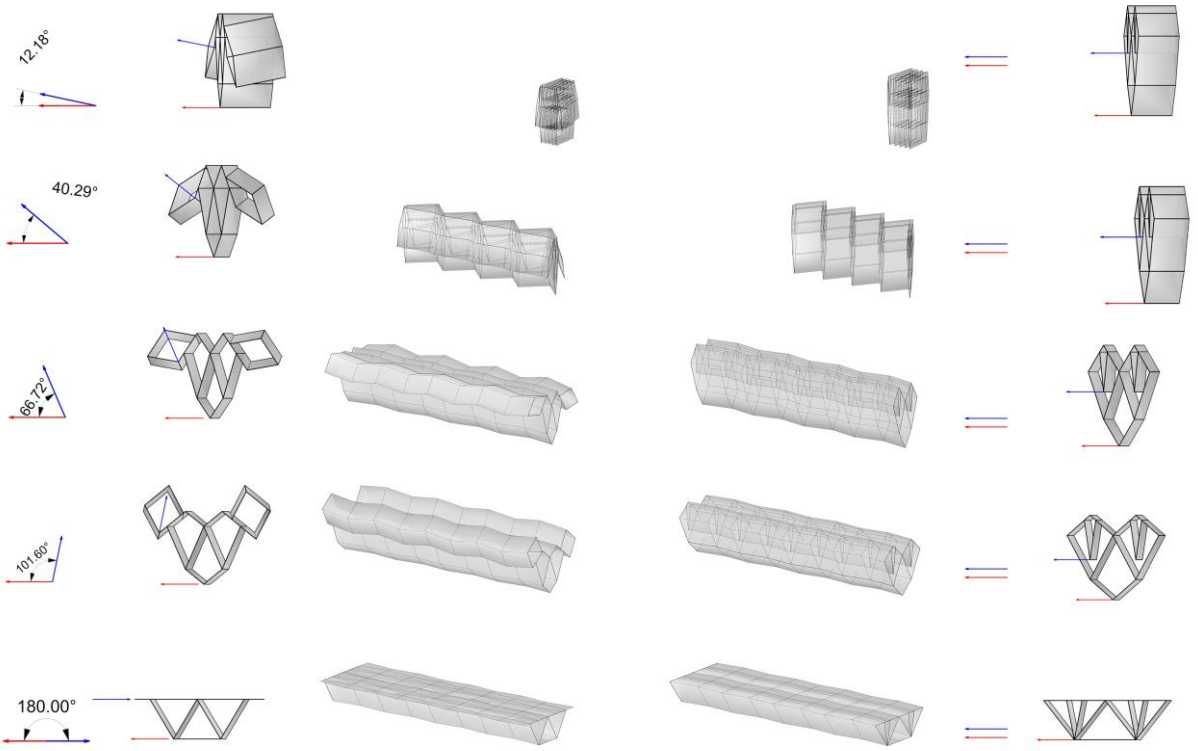


Figure 7. The unfolding sequence from top to bottom of the zipper bridge (left) and the nested bridge (right) with the correspondent angles of the deltoid's base planes. From top to bottom the configurations correspond to the folding ratios 0, 0.25, 0.5, 0.75 and 1.

The folding sequence was split into 4 steps: 0.75, 0.50, 0.25 and 0, respectively. As the entire system is rigidly foldable, the position of each planar quad is exactly defined. Each step has been optimised as a single state, with the endpoints being simply supported.

The results show (cf. Tables 3 and 4), that for the motion states the structural height converges towards the lowest third of the allowable range, whereas for the three best results the optimised height takes on the minimum height possible. The number of undulations is in almost all cases two, its amplitude being 0.25 for most variants. The total mass of both structures is similar and ranges from 7350 kg to 8650 kg. The extreme undulation in the smallest possible folded state leads to an increase in weight for both structures. While the nested bridge has a similar weight in all states, the zipper bridge features a weight increase of 1/3 compared to the case of only self-weight applied. As the folded package represents the transportation case, the latter results are not considered to govern the actual design. For transportation and placement on site necessitate additional manipulation tools which depend on the available technical means.

Table 3. The best results of the nested bridge during motion states

self-weight [0.75]	NESTED BRIDGE									
	1	*2*	*3*	*4*	*5*	*6*	*7*	*8*	*9*	*10*
FinalStateHeight	1	1	1	1	1,1	1,1	1	1,1	1,1	1,2
inner lu	0,8	0,8	0,8	0,8	0,8	0,8	0,8	0,8	0,8	0,8
Deviation	0,25	0,33333	0,41667	0,5	0,25	0,33333	0,58333	0,41667	0,5	0,25
n-undulation	2	2	2	2	2	2	2	2	2	2
Mass	**7352,49**	**7330,07**	**7337,11**	**7346,39**	**7351,18**	**7355,35**	**7357,74**	**7361,95**	**7370,8**	**7378,36**
self-weight [0.50]	NESTED BRIDGE									
	1	*2*	*3*	*4*	*5*	*6*	*7*	*8*	*9*	*10*
FinalStateHeight	1	1.1	1.0	1.2	1.0	1	1.2	1.1	1.1	1.0
inner lu	0,1	0,1	0,2	0,1	0,2	0,1	0,2	0,2	0,1	0,2
Deviation	0,25	0,5	0,25	0,25	0,25	0,5	0,25	0,25	0,5	0,5
n-undulation	2	2	2	2	2	2	2	2	2	2
Mass	**7379**	**7405**	**7406**	**7433**	**7438**	**7444**	**7463**	**7466**	**7468**	**7470**
self-weight [0.25]	NESTED BRIDGE									
	1	*2*	*3*	*4*	*5*	*6*	*7*	*8*	*9*	*10*
FinalStateHeight	1	1	1.6	1.2	1.3	1.4	1	1.1	1	1.2
inner lu	0,1	1,1	0,5	0,8	0,8	0,7	0,9	0,8	0,8	0,8
Deviation	0,25	0,25	0,25	0,5	0,5	0,5	0,25	0,25	0,5	0,75
n-undulation	2	2	2	2	2	2	3	3	3	2
Mass	**7402**	**7421**	**7741**	**8056**	**8068**	**8126**	**8343**	**8350**	**8463**	**8643**

Table 4. The best results of the zipper bridge during motion states

self-weight [0.75]	ZIPPER BRIDGE									
	1	*2*	*3*	*4*	*5*	*6*	*7*	*8*	*9*	*10*
FinalStateHeight	1	1.,1	1,2	1	1,3	1,1	1	1,2	1	1
DriveThrough	5,0	5,0	5,0	4,9	5,0	4,9	5,1	4,9	4,3	5,2
Deviation	0,25	0,25	0,25	0,25	0,25	0,25	0,25	0,25	0,25	0,25
num undulation	2	2	2	2	2	2	2	2	2	2
Mass	**7505,31**	**7514,64**	**7526,52**	**7530,98**	**7537,18**	**7540,18**	**7551,05**	**7553,15**	**7554,67**	**7558,7**
self-weight [0.50]	ZIPPER BRIDGE									
	1	*2*	*3*	*4*	*5*	*6*	*7*	*8*	*9*	*10*
FinalStateHeight	1	1	1	1	1,1	1	1,1	1,1	1,1	1,2
DriveThrough	4,20	4,1	4	3,9	4,2	3,8	4,1	4	3,9	4,2
Deviation	0,25	0,25	0,25	0,25	0,25	0,25	0,25	0,25	0,25	0,25
num undulation	2	2	2	2	2	2	2	2	2	2
Mass	**7587,49**	**7590,78**	**7593,05**	**7597,15**	**7600,38**	**7601,9**	**7603,77**	**7606,17**	**7610,37**	**7614,06**
self-weight [0.25]	ZIPPER BRIDGE									
	1	*2*	*3*	*4*	*5*	*6*	*7*	*8*	*9*	*10*
FinalStateHeight	1,2	1,1	1	1,2	1,3	1,4	1	1.1	1,2	1
DriveThrough	2,70	4,5	4,5	4,5	4,5	4,5	4,5	4,5	4,5	4,3
Deviation	0,25	0,75	0,75	0,75	0,75	0,75	1,5	1,5	1,5	0,25
num undulation	2	2	2	2	2	2	2	2	2	3
Mass	**7773,32**	**7878,28**	**7889.58**	**7890,35**	**7906,21**	**7922,26**	**8007,02**	**8019,59**	**8030,62**	**8082,65**

3.2. Additional comparisons

If we compare the individual optimised solutions in all states, it turns out that we can differentiate between two sets of results: All variants optimised under self-weight have varying but comparable outcomes in all considered states (during folding under self-weight). When adding live loads to the structural models the optimized mass doubles or triples. Comparing solutions under live load to the states during unfolding, one sees, that the optimised mass is only in the fully folded, initial state higher.

Tables 5 and 6 show mass and displacement values calculated via Karamba3D before and after the cross-section optimisation.

Table 5. The best result of each state (red), investigated in all other states of the nested bridge

NESTED BRIDGE						
	Best Load	Best Eigen	Best 0,75	Best 0,5	Best 0,25	Best 0,00
FinalStateHeight	2,00	1	1	1	1	1,70
lu	0,25	0,08	0,25	0,08	0,08	0,83
a -Amplitude	0,25	0,25	0,25	0,25	0,25	0,75
n-undulation	4,00	2,00	2,00	2,00	2,00	2,00
Load [1]						
Mass	**10 462,95**	**19 728,45**	**18 898,83**	**19 728,45**	**19 728,45**	**16 348,59**
disp orig	5,58	9,53	9,31	9,53	9,53	7,74
disp	3,80	6,48	6,34	6,48	6,48	5,25
Self [1]						
Mass	**8 782,70**	**7 183,00**	**7 089,88**	**7 076,07**	**7 076,07**	**7 449,59**
disp orig	0,90	2,16	2,17	2,15	2,15	1,43
disp	0,66	1,60	1,61	1,59	1,59	1,06
Self [0.75]						
Mass	**9 155,70**	**7 437,20**	**7 325,49**	**7 437,20**	**7 437,20**	**7 726,34**
disp orig	0,40	0,66	0,68	0,66	0,66	1,20
disp	0,29	0,49	0,51	0,49	0,49	0,89
Self [0.5]						
Mass	**9 388,39**	**7 362,91**	**7 385,19**	**7 362,91**	**7 362,91**	**7 743,81**
disp orig	0,43	0,92	0,79	0,92	0,92	1,50
disp	0,32	0,68	0,58	0,68	0,68	1,11
Self [0.25]						
Mass	**9 238,39**	**7 385,82**	**7 382,45**	**7 385,82**	**7 385,82**	**8 453,49**
disp orig	1,83	1,28	1,25	1,28	**1,28**	4,93
disp	1,36	0,95	0,93	0,95	**0,95**	3,65

Table 6. The best result of each state (red), investigated in all other states of the zipper bridge

ZIPPER BRIDGE						
	Best Load	Best Eigen	Best 0,75	Best 0,5	Best 0,25	Best 0,00
FinalStateHeight	2,0	1,2	1	1	1	1
w - width	4,1	2	5	4,2	2,7	5,7
a - Amplitude	0,25	0,25	0,25	0,25	0,25	0,25
n-undulation	4	2	2	2	2	2
Load [1]						
Mass	**9 366,88**	**18 534,53**	**19 767,91**	**19 052,24**	**21 119,28**	**20 187,31**
disp orig	6,15	11,61	9,71	9,50	12,48	9,33
disp	4,14	7,88	6,41	6,46	8,49	6,36
Self [1]						
Mass	**6 843,16**	**5 805,52**	**6 016,25**	**6 026,54**	**5 881,13**	**6 091,97**
disp orig	0,74	5,43	2,45	2,36	4,34	2,55
disp	0,55	4,02	1,81	1,75	3,22	1,89
Self [0.75]						
Mass	**9 040,99**	**7 846,78**	**7 505,31**	**7 596,45**	**7 636,65**	**7 629,54**
disp orig	0,58	2,58	1,41	1,32	2,21	1,95
disp	0,43	1,91	1,04	0,98	1,64	1,45
Self [0.5]						
Mass	**9 031,67**	**7 619,46**	**7 632,51**	**7 587,49**	**7 682,78**	**7 659,92**
disp orig	0,56	6,00	0,98	1,00	3,00	1,11
disp	0,42	4,44	0,73	0,74	2,22	0,82
Self [0.25]						
Mass	**9 008,20**	**7 779,17**	**7 656,30**	**7 615,00**	**7 807,11**	**7 801,47**
disp orig	1,39	7,21	1,01	1,84	1,94	2,00
disp	1,03	5,34	0,75	1,36	1,43	1,48

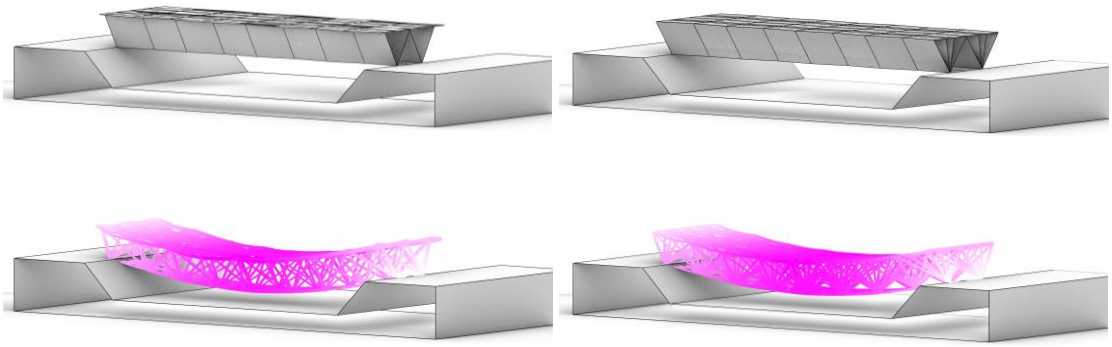


Figure 8. The zipper solution (left) and the nested solution (right) and their deformation under live load

4. Conclusion

The investigation shows that the zipper bridge option has advantages over the nested one in unfolded and final state. Although the zipper tubes are more rigid during the unfolding motion, the nested solution is in some states more efficient. The better performance seems to be linked to the fact that the zipper geometry allows for a slight cantilever of the bridge deck, that reduces the entire surface area and therefore the weight of the core structure.

The investigation shows that the bridge in its smallest possible package state behaves unstable. The reason for this behaviour requires additional investigations, to assess possible solutions to this problem. It can be assumed, that this small transportable package will require special treatment in the course of the erection process.

5. Outlook

This investigation constitutes a starting point for more detailed investigations on bridges based on T-hedral tubes. The presented results are promising and will be followed up by additional research.

In a further study the focus will be on the support conditions during unfolding. Using cantilevering instead of simply supported conditions, one has to control vertical deflections similarly to the analysis presented in [14]. This approach will require multi-objective optimisation to include additional objective functions as e.g. introduced by hinge design, support method, and positioning during unfolding. Another focus is the change from a repetitive pattern of the structural elements to a non-repetitive one that might be adapted for better motion and structural behaviour.

Obviously, future investigations should be refined by using shell elements instead of a simplified beam? model. The simulation problems encountered for the smallest foldable package state suggest a more detailed investigation in relation to the panel thickness, hinge solution, actuation and the temporary support during motion. If these problems can be solved, it is planned to build scaled demonstrators in a consecutive step.

Acknowledgements

The research is supported by grant F77 (SFB “Advanced Computational Design”) of the Austrian Science Fund FWF.

References

[1] D. Rutten, “Navigating Multi-Dimensional Landscapes in Foggy Weather as an Analogy for Generic Problem Solving,“ *Proceedings of the 16th International Conference on Geometry and Graphics*, pp. 826-839, 2014.

[2] C. Preisinger, "Linking Structure and Parametric Geometry," *Architectural Design*, vol. 83, pp. 110-113, 2013.

[3] K. Suto and K. Tanimichi, "Crane," Food4Rhino, 15 06 2022. [Online]. Available: https://www.food4rhino.com/en/app/crane. [Zugriff am 15 06 2022].

[4] R. Foschi, R. Kraft, R. Maleczek, K. Mundilova and T. Tachi, "Comparison of computational curved folding design methods," Proceedings of the IASS annual Conference 2020/21, Inspiring the next generation, pp. 2720-2730, 2021.

[5] R. Maleczek, G. Stern, A. Metzler and C. Preisinger, "Large Scale Curved Folding Mechanisms," *Impact: Design with all senses*, C. Gengnagel, O. Baverel, J. Burry, M. Ramsgaard Thomsen und S. Weinzier, Hrsg., Berlin, Springer, pp. 539-553, 2019.

[6] I. Ario, M. Nakazawa, Y. Tanaka, I. Tanikura and S. Ono, "Development of a prototype deployable bridge based on origami skill, " *Automation in Construction*, vol. 32, pp. 104-111, 2013.

[7] K. Sharifmoghaddam, R. Maleczek and G. Nawratil, "Generalizing rigid-foldable tubular structures of T-hedral type," arXiv:2301.09969, 2023.

[8] R. Sauer and H. Graf, "Über Flächenverbiegung in Analogie zur Verknickung offener Facetten-flache," *Mathematische Annalen*, vol. 105, pp. 499–535, 1931.

[9] E.T. Filipov, G.H. Paulino and T. Tachi, "Origami tubes with reconfigurable polygonal cross-sections," *Proceedings of the Royal Society A: Mathematical, Physical and Engineering Sciences*, vol. 472, Article ID. 20150607, 2016.

[10] M. Schenk and S.D. Guest, "Geometry of Miura-folded metamaterials," *Proceedings of the National Academy of Sciences of the United States of America*, vol. 110, pp. 3276–3281, 2013.

[11] E.T. Filipov, T. Tachi and G.H. Paulino, "Origami tubes assembled into stiff, yet reconfigurable structures and metamaterials," *Proceedings of the National Academy of Sciences of the United States of America*, vol. 112, pp. 12321–12326, 2015.

[12] Z. Wo, J.M. Raneses and E.T. Filipov, "Locking Zipper-Coupled Origami Tubes for Deployable Energy Absorption," *Journal of Mechanisms and Robotics*, vol. 14, Article ID. 041007, 2022.

[13] D.C. Webb, E. Reynolds, D.M. Halverson and L.L. Howell, "Asymmetric Zipper-Coupled Tubes and Smooth Sheet Attachments in the Design of Deployable Space-Filling Mechanisms," *Journal of mechanisms and Robotics*, vol. 16, Article ID. 011004, 2024.

[14] E.T. Filipov, T. Tachi and G.H. Paulino, "Coupled origami tubes for stiff deployable cantilevers," *Proceedings of the ASME 2019 International Design Engineering Technical Conferences and Computers and Information in Engineering Conference*, vol. 5B, Article ID. V05BT07A023, 2019.

IASS 2023
July 10–14 Melbourne
Integration of Design and Fabrication

Proceedings of the IASS Annual Symposium 2023
Integration of Design and Fabrication
10–14 July 2023, Melbourne, Australia
Y.M. Xie, J. Burry, T.U. Lee and J. Ma (eds.)

Design and evaluation of compliant hinges for deployable thick origami structures

Munkyun LEE[a], Tomohiro TACHI[*]

[*] Department of General System Studies, Graduate School of Arts and Sciences, The University of Tokyo
3-8-1 Komaba, Meguro-ku, Tokyo, 153-8902, Japan
tachi@idea.c.u-tokyo.ac.jp

[a] Department of Architecture, Graduate School of Engineering, The University of Tokyo

Abstract

Origami models are often idealized by discrete folding of zero-thickness sheets; however, the sheet thickness and the elastic limit of the material cannot be ignored in engineering practice. One solution for realizing thickness is the compliant hinge, which realizes the folding deformation in the elastic range of the material by replacing the crease line with a wide deformation zone where the compliant structure is installed. However, the compliant hinge has several limitations. First, it cannot maintain the center of rotation (CoR) between panels during the folding motion. This makes origami structures with interior vertices not transformable because the crease lines are no longer concurrent. Second, the play caused by the wide deformation zone increases the degree of freedom of the origami structure, leading to instability. To solve these problems, we propose three types of new compliant hinges. We provide two evaluation methods: the play is evaluated using eigenvalue analysis, and the change CoR under unideal load conditions is evaluated using FEM analysis.

Keywords: origami, thick origami, deployable structure, hinge, slit pattern, wood kerfing, compliant mechanism, eigenvalue analysis, structural morphology, hangai prize applicant

1. Introduction

1.1. Background

Origami, a technique of folding sheets that allows for the design of various shapes [1] and stiffnesses [2], can be used to create deployable structures at an architectural scale [1,3]. Origami structures have several advantages, such as the ability to transform from a flat state into a three-dimensional structure through folding, the capability for continuous shape transformation, and the ability to bear loading in the deployed state. These properties are designed based on the concept of rigid origami [1], which treats faces as rigid panels and creases as revolute hinges and allows for continuous transformation without panel deformation. During the design stage of rigid origami, panels are typically treated as ideal zero-thickness sheets. However, in engineering practice, the thickness of panels can cause self-intersection during folding and the elastic limit of panel materials must be considered.

The thickness problem has been typically solved by the geometric arrangement of the revolute hinge and thick panels [1]. However, these approaches require the use of mechanical parts and other materials for hinge structures, which can make fabrication and assembly difficult and potentially cause structural weaknesses such as breaks or delamination in connections between different materials. One solution to these fabrication problems is compliant hinges, i.e., setting the deformation zone and installing proper compliant structures [4,5]. This enables a folding motion within the elastic range of the material.

Copyright © 2023 by Munkyun LEE and Tomohiro TACHI. Published in the Proceedings of the IASS Annual Symposium 2023 with permission.

Compliant hinges can simplify the fabrication process when used in origami structures. However, the following challenges exist to realize a thick origami structure using compliant hinges.

1.2. Challenges

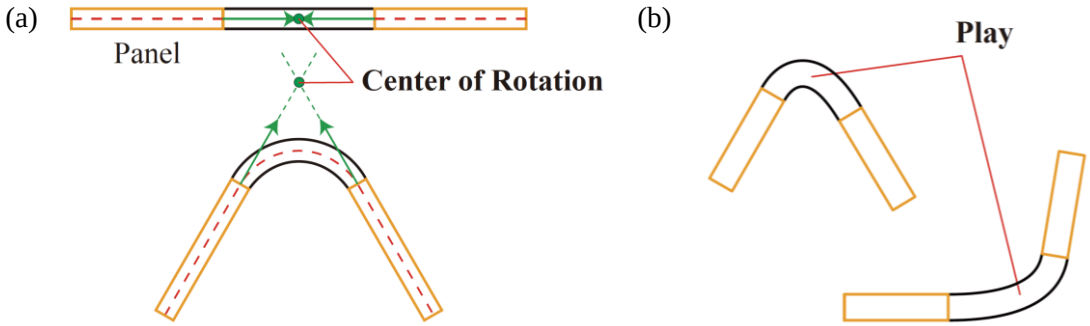


Fig.1 Challenges of compliant hinges. (a) The compliant hinges cannot maintain the center of rotation. (b) The wide hinge zone causes the play.

(a) Center of Rotation (CoR): The folding motion of the compliant hinge is not a perfect revolution about an axis, thus CoR is not maintained. This breaks the kinematics of rigid origami and blocks the deployment of origami structures with interior vertices where multiple crease lines meet.

(b) Play: Flexibility due to the wide deformation zone of the compliant hinge causes play or unwanted motion other than folding. This lowers the rigidity and stability of the origami structure and makes it difficult to control.

1.3. Purpose

In this paper, we aim to design compliant hinges that can maintain the kinematics of an ideal rigid origami. To compensate for both the CoR and play problems of compliant hinges, we propose three new types of compliant folding hinge structures by 1) combining existing compliant hinge designs [4,5], 2) aligning spherical compliant mechanisms, and 3) a hybrid of types 1 and 2. We propose two evaluation methods for compliant hinges from the perspectives of the center of rotation and play. We evaluate 1) the play through the eigenvalue bandgap of hinge structures in Section 5, and 2) the maintenance performance of the CoR under non-ideal loading conditions through finite element analyses in Section 6. The designed hinges are compared and evaluated with each other, and we select the best hinge structure that moves closest to the ideal with the least break to the kinematics of rigid origami.

2. Exiting joint design

2.1. LET hinge

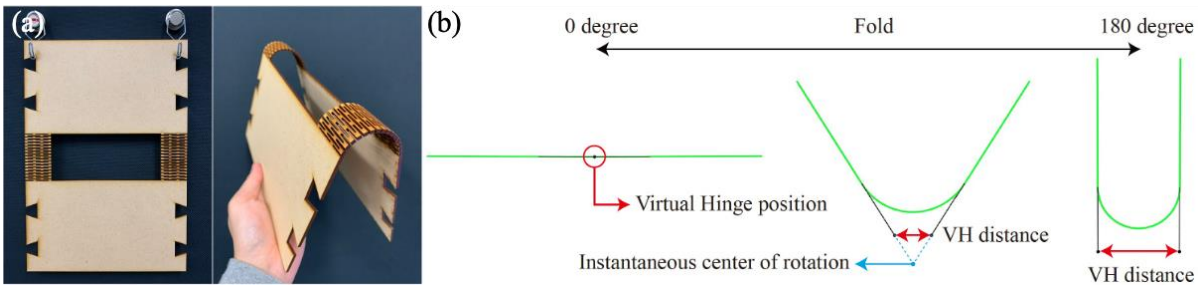


Fig.2 (a) Physical prototype of LET hinge, (b) Geometric model of LET hinge.

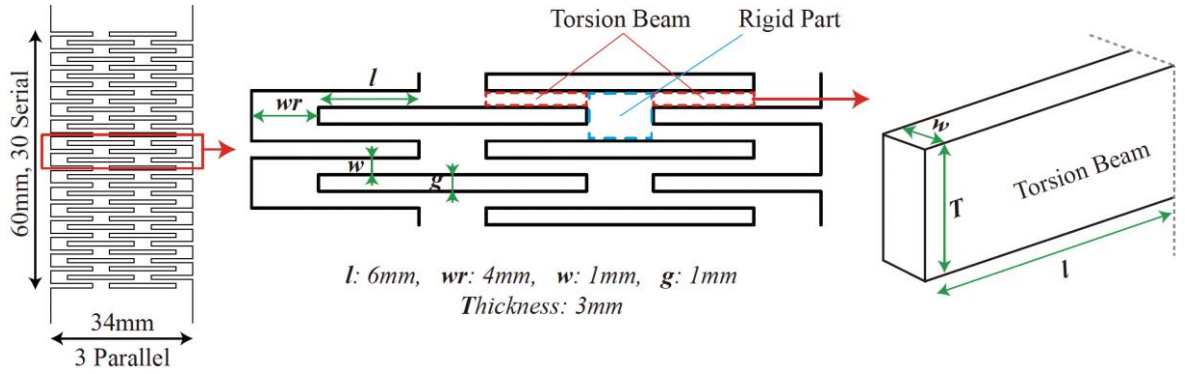


Fig.3 Common settings of LET pattern.

One of the most popular approaches for creating a hinge with patterns is the Laminar Emergent Torsion (LET) joint [4]. The LET joint (Fig.2 (a)) is a compliant hinge structure that allows for folding motion within the elastic range by lowering the stiffness of the corresponding part of the material. The LET pattern can be modeled as the composition of rigid bodies and torsion beams according to the model by Ohshima et al. [6] (Fig.3). With a proper proportion and repeating numbers, the flexible region only bends in parallel to the direction of torsion beams. This design method yields anisotropic stiffness property, making it flexible to folding deformation and rigid to other deformations, thereby partially solving the play problem.

The hinge motion under pure bending moment condition is represented by a circular arc as shown in Fig.2(b). This circular arc of finite curvature causes the loss of the CoR. The *Virtual Hinge (VH) position analysis* introduced by Lang et al. [5] is suitable to evaluate the geometrical maintenance performance of the CoR. The VH position for each panel is the position where the CoR should be for that panel. In the case of zero-thickness origami, the two VH positions coincide throughout the range of motion. However, in the case of the compliant hinge, the VH positions are separated during the folding motion (Fig.2(b)). We use the LET joint as the benchmark model to compare with our proposed joints. We models consist of two hinges that connect the panels. The height of the models is set to 300mm. The width is set to 209mm based on the Tomoe LET hinge, which has the largest horizontal width. All proposed models are made of a 3mm-thick MDF panel. The anisotropic layered composition of MDF is reported to be ideal for torsion beams [6]. The maximum torsion angle is set to 1 degree/mm to ensure that it twists within the elastic range. Under the pure bending condition of the LET hinge, the number of serial connections required for the LET pattern can be calculated as 30 when the folding angle is 180 degrees. The number of parallel connections of the LET pattern is set to 3. We call this LET pattern a "3P30S" LET array for short.

2.2. LEFF (Tomoe) hinge

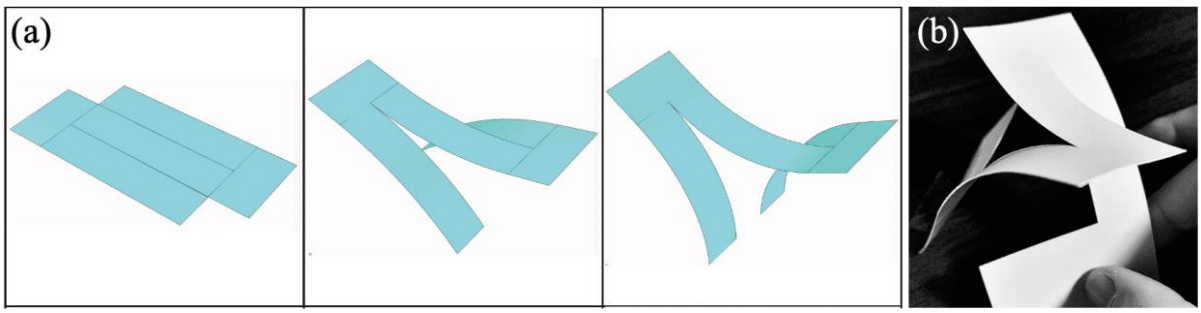


Fig.4 (a) Motion of LEFF joint. (b) example of the play of LEFF joint

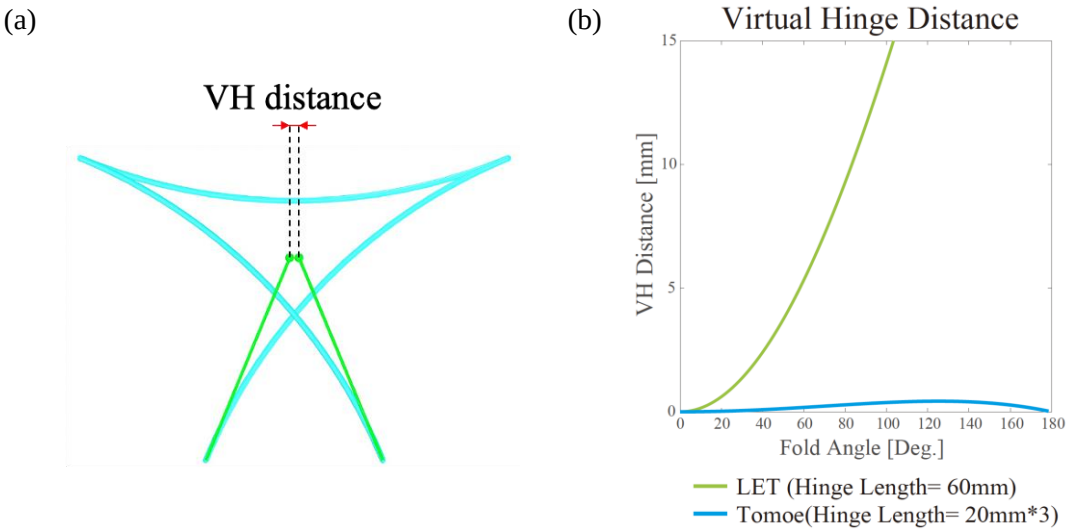


Fig. 5 (a) Geometric model of LEFF joint. (b) VH position analysis of LET and LEFF(Tomoe) joints.

The Laminar Emergent Flexural Fold (LEFF) joint, also known as the Tomoe-type Kirigami structure [5,7], exhibits excellent performance in maintaining the CoR under pure bending moment conditions (Fig.4(a)). Fig.5 (a) shows the geometric model of LEFF. Since the three beams of the LEFF hinge are designed with the same stiffness and length and connected in serial, the LEFF hinge shows symmetrical movements under the pure bending moment condition. The VH position analysis shown in Fig.5(b) compares the VH distances of LET and LEFF hinges, indicating that LEFF geometrically performs better at maintaining the CoR under a pure bending condition.

However, the flexibility of long narrow beams of LEFF slit causes play such as shear and twist, making it challenging to maintain the CoR under non-ideal loading conditions (Fig.4(b)). The reduction of the play is an important challenge for LEFF.

3. Proposed hinges

3.1. Approach 1: Tomoe LET hinge

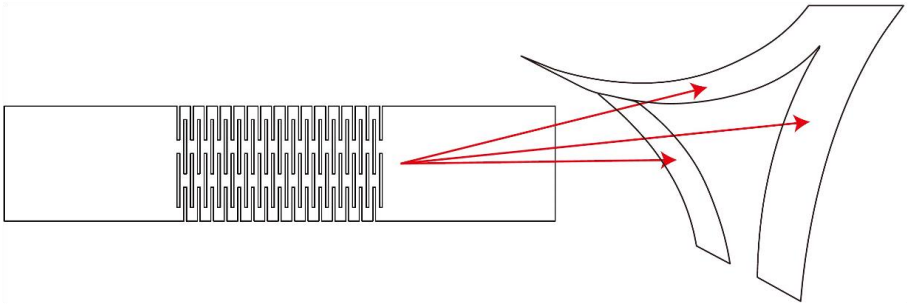


Fig.6 Concept of Tomoe LET Hinge combining LET and LEFF ideas.

The first approach for creating compliant hinges with CoR maintenance and reduced play we propose is the Tomoe LET hinge (Fig.6 (a)). Tomoe LET hinge is a combination of LET (Fig.2) and LEFF (Fig.4). By this combination, we expect that the advantages of LET to reduce the play and the advantages of LEFF of high CoR maintenance under the pure bending condition (Fig.5(a)). To further reduce the play, we join intermediate bodies of adjacent Tomoe LET hinges to unify the motion (Fig.7(b), Fig.8). We call this Joined-Tomoe LET Hinge. The joining technique was also used in the LEFF joint [5] and is expected to reduce the play. To make the folding stiffness similar to that of the LET hinge, we serially connect 3 times “3P10S” LET arrays (Fig.8).

(a) (b)

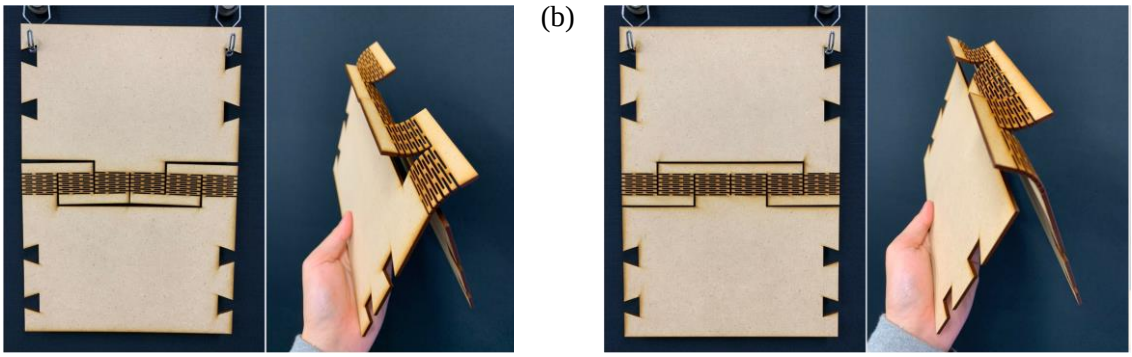


Fig.7 Physical prototypes of (a) Tomoe LET hinge and (b) Joined Tomoe LET hinge

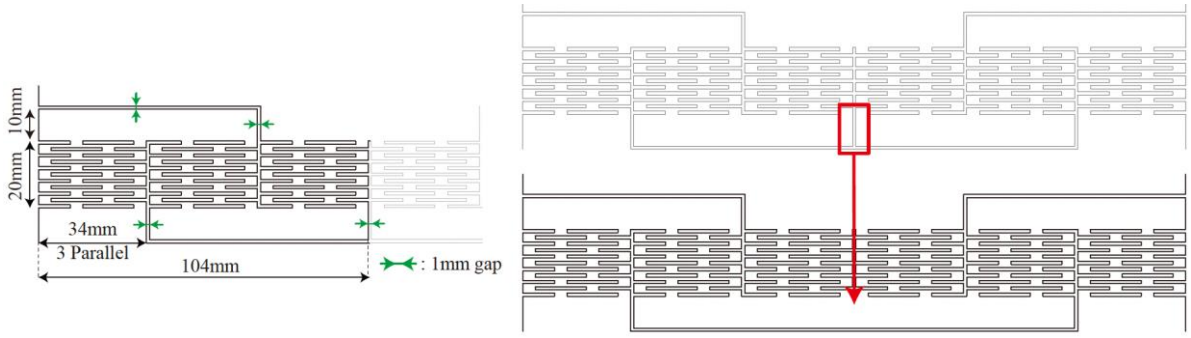


Fig.8 Experiment model settings of Tomoe LET and Joined Tomoe LET hinge (Right bottom).

3.2. Approach 2: Radial LET hinge

(a) (b)

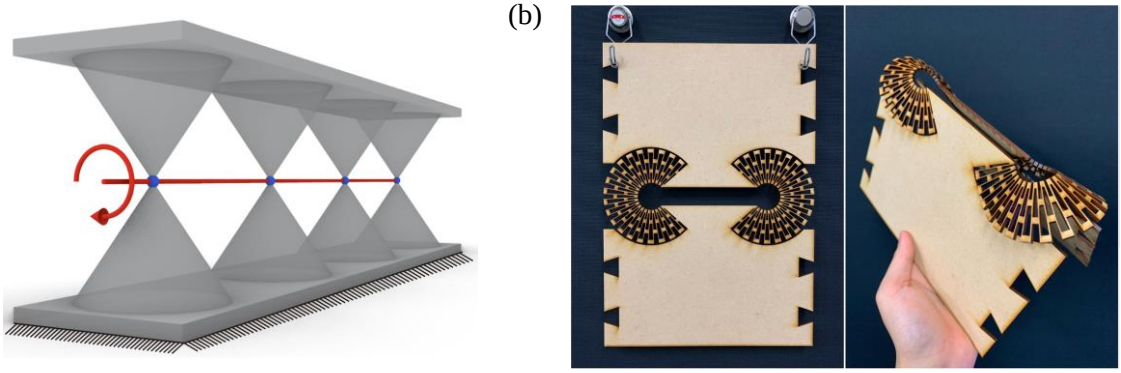


Fig.9 (a) The concept of the 1-DOF structure that consists of multiple spherical joints. (b) The physical prototype of the Radial LET hinge.

The second approach is to design the 1-DOF hinge structure using multiple spherical joints aligned on a straight line. The spherical joint can be designed by radially arranging the LET pattern so that the axis of all torsion beams passes through one point (Fig.9 (b)). Fig.9 (a) shows that placing the center points of spherical joints on a straight line and connected in parallel creates a hinge structure with 1-DOF. This straight line corresponds to the CoR. Using this method, we designed the Radial LET (RLET) hinge by connecting two Radial LETs in parallel.

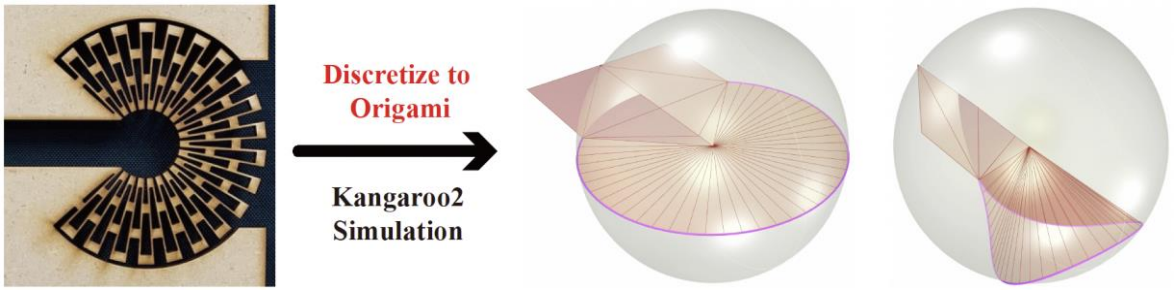


Fig.10 Single-vertex origami model of RLET hinge

Fig.9(b) shows that the curvature of the RLET hinge is not constant along the hinge surface. The curvature is negative (convex) and concentrated in the middle of the curved surface and has a positive value (concave) at its ends. The curvature distribution can be simulated by solving the equilibrium of the discrete shell model [8] as shown in Fig.10, where we consider beam axes as bending-resistant creases that are radially emanating from a single vertex.

For the evaluation model, we tune the number of serial connections of the LET pattern to have the same stiffness as the LET hinge. Based on the abovementioned discrete shell simulation, we chose "*3P40S*" radial (Fig.11(a)), so the average torsion angle of the torsion beams is as close as possible to 1 degree/mm. The average of the absolute values of torsion angles of RLET when folded by 180° was 1.02 degrees/mm. Having positive and negative curvature indicates that some torsion beams are not fully utilized to their capacity and are left unused. Here, we propose the third approach to fully utilize every torsion beam.

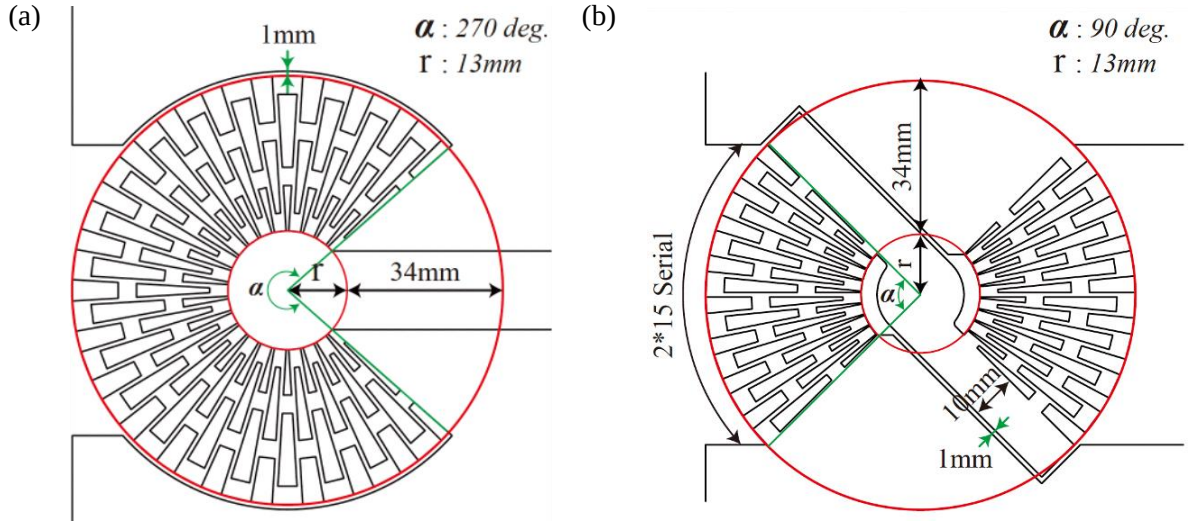


Fig.11 Settings of spherical joint hinge structures. (a) Settings of RLET and (b) S-shape hinge.

3.3. Approach 3: S-shape hinge

As the third approach, we combine the back-and-forth idea in Tomoe LET (Fig.7) with the idea of Radial LET (Fig.9) to propose the S-shape hinge (Fig.12(a)). Like the RLET hinge, the 1-DOF hinge structure is designed by connecting multiple spherical joints in a straight line in parallel (Fig.9(a)). Each spherical joint is composed of two symmetric Radial LETs connected with a rigid body. When we assume that each curved surface of the hinge has constant curvature, we obtain the geometric model in Fig.12(b) and Fig 13(a). From an analysis similar to the VH distance analysis on spherical geometry, we can measure the VH distance on the sphere (Fig. 13(b)).

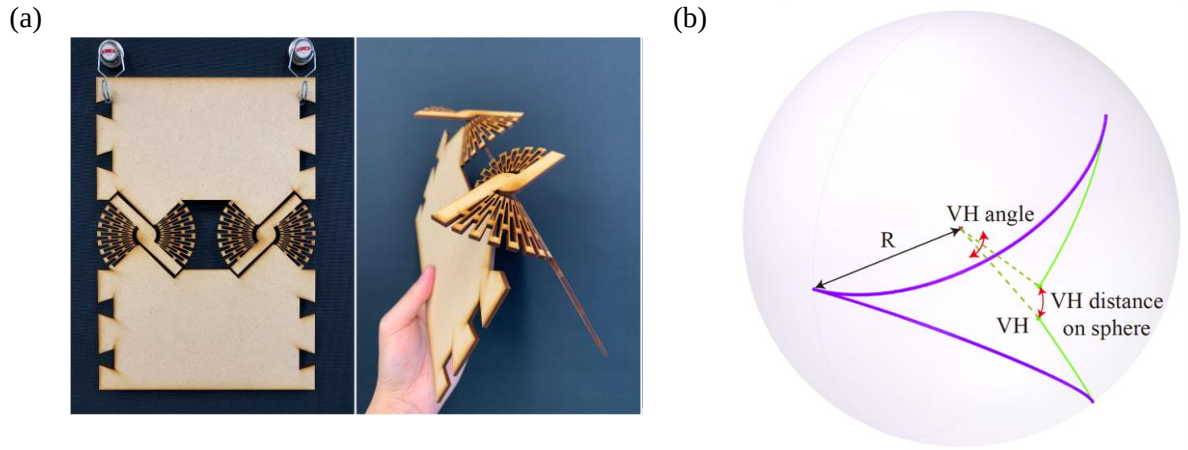


Fig.12 (a) The physical prototype and (b) the geometric model of the S-shape hinge.

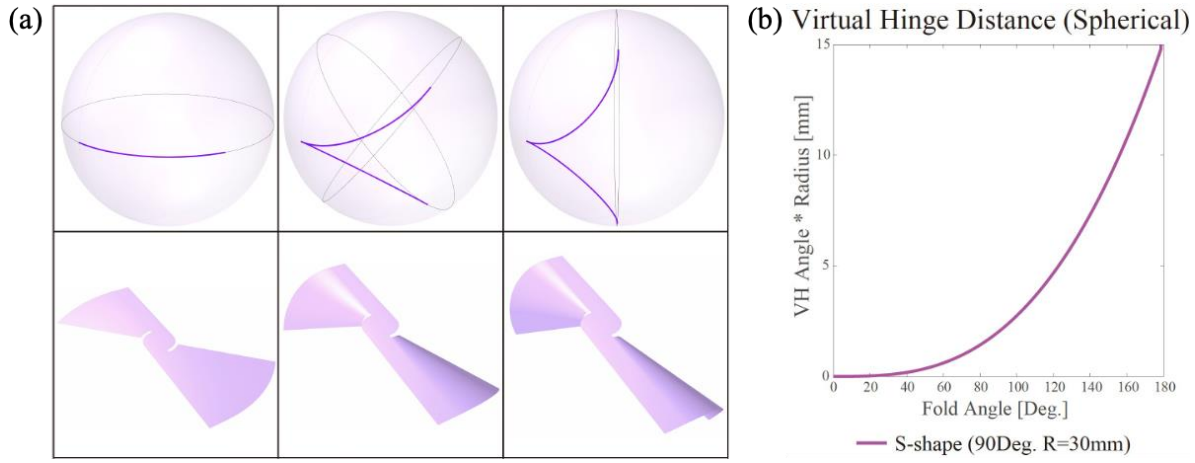


Fig.13 (a) Motion and Geometric model and (b) VH position analysis of S-shape hinge.

By parallel alignments of multiple spherical joints, the VH distance is supposed to disappear by modifying the curvature distribution of the surface. Fig 13(b) shows that the VH distance on a sphere is small ($< 3.86°$) for fold angle between 0° to 90°, indicating that when the joints are aligned in parallel, the curvature is still close to constant and that the curvature concentration problem of the RLET hinge is solved.

Assuming that the surface curvature is constant, the evaluation model is designed by coupling two "*3P15S*" Radial LETs as shown in Fig.11(b).

4. Play analysis

4.1. Eigenvalue bandgap analysis

In an ideal compliant hinge without play, the structure has low stiffness against the folding motion and high stiffness against any other motion. To identify the stiffnesses against different deformation modes, we perform an eigenvalue analysis to extract free vibration modes (eigenmode) and their corresponding frequency (eigenvalue). Each eigenvalue represents natural frequency corresponding to structural deformation modes (Fig.14). Structural deformation modes of compliant hinge structures consist of three out-of-plane modes (Bending Out-of-Plane (Fold), Twist, and Shear) and three in-plane modes

(Bending In-Plane (BIP), Stretch In-Plane (SIP), and Shear In-Plane (ShearIP)) (Fig.14). We evaluate the logarithmic difference between the eigenvalues, called the *eigenvalue bandgap*. Since the natural frequency is proportional to the square root of the stiffness of the structure, a large eigenvalue bandgap from the desired structural deformation mode (Fold-Mode) means that the hinge is stiffer in other modes; in other words, other modes are difficult to appear [9]. Therefore, eigenvalue analysis can evaluate the play of the compliant hinge in infinitesimal deformation.

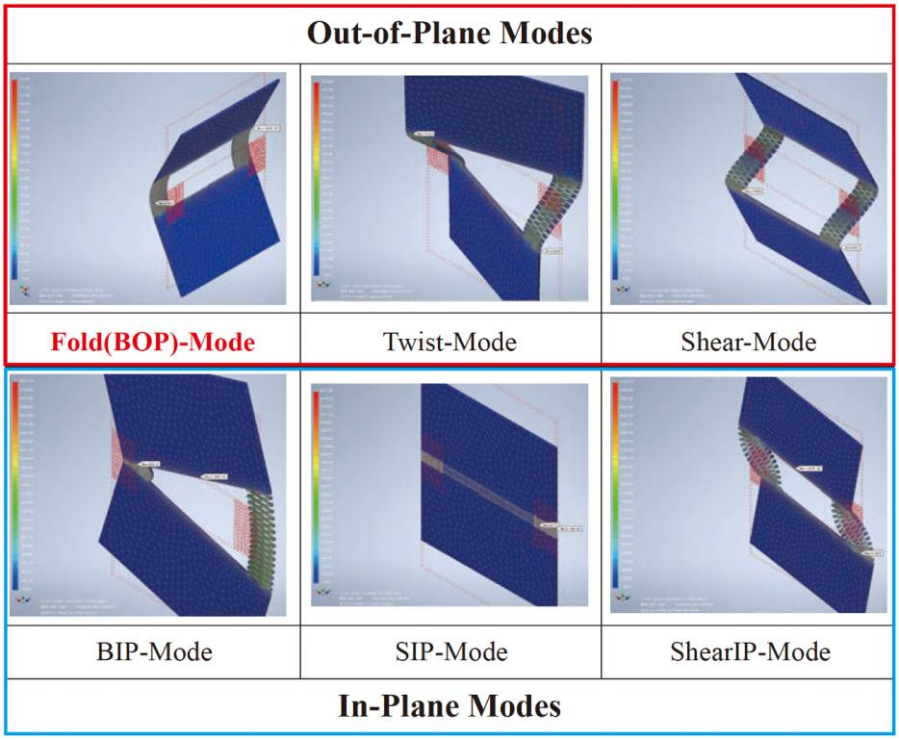


Fig.14 Structural deformation mode of hinge structure

The eigenvalue analysis is conducted without boundary conditions, and rigid body modes (1^{st}-6^{th} mode) are omitted from the analysis as they required zero energy. Table 1 shows the material setting for eigenvalue analysis. The 7^{th} mode and those following represent deformations requiring energy. We expect that the folding mode appear in the 7^{th} mode for the compliant hinge.

Table 1. The material setting for eigenvalue analysis and finite element analysis.

Plywood	Type	Young's Modulus	Poisson Ratio	Density
	Isotropic Material	7700 [N/mm^2]	0.25	5.52e-10 [t/mm^3]

4.2. Evaluation

Table 2 shows the ratio of the natural frequency of the 8^{th} mode and each deformation mode, relative to the 7^{th} mode. All proposed models represent folding mode at the 7^{th} mode. The Joined-TomoeLET hinge has the largest bandgap between the 7^{th} and 8^{th} modes, so it is expected that the play is difficult to occur. In addition, it has the highest stiffness for Twist and ShearIP modes, and the second highest stiffness for shear, SIP, and BIP modes. The S-shape hinge has high stiffness against shear mode but is flexible to in-plane modes, so play can occur easily.

Note that since the eigenvalue analysis is linear, it is limited to infinitesimal deformation. Also, we performed the analysis only at the flat state. Therefore, they may not correctly represent the play for large deformation.

Table 2. Natural frequency ratio from results of eigenvalue analysis

$f_{n(>7)}/f_7$	LET	TomoeLET	J-TomoeLET	RLET	S-shape
8thMode / 7thMode	3.91	3.94	**4.89**	2.94	3.9
Twist	3.91	4.87	**4.89**	2.94	4.57
Shear	5.74	10.11	11.44	7.55	**13.35**
SIP	**14.57**	4.93	8.58	4.95	4.49
BIP	**17.89**	3.94	5.8	4.78	3.9
Shear-IP	11.1	33.41	**33.82**	5.8	16

5. Compositive evaluation

5.1. Finite element analysis

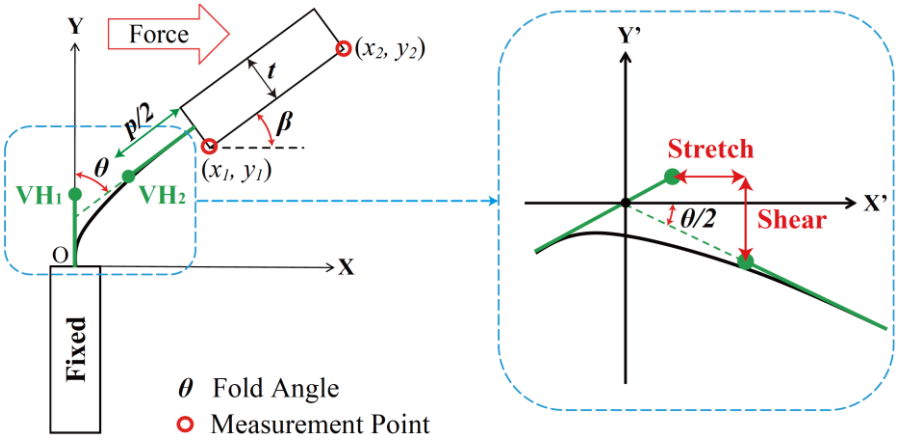


Fig.15 VH analysis under unideal load condition

To simultaneously assesses the CoR maintenance performance and play, finite element analysis is performed under an unideal load condition. The bottom panel is fixed as a boundary condition, and an incremental force of up to 5N is applied to the upper panel in a direction perpendicular to the panel surface as shown in Fig.15. Table 1 shows the material setting for analysis. Unlike the pure bending condition, this loading condition provides non-symmetric deformation due to the play of the mechanism. We decompose the stretch and shear effect by introducing the X'Y'-coordinate system that bisects the folding angle and measures the coordinates of the difference of VH positions, i.e., the VH vector. The X'-direction component of the VH vector represents the combination of the geometric separation of the hinge itself and the play in stretch direction, so we call it the VH-stretch. The Y'-direction component of the VH vector represents the play in the shear direction (Fig.15, right), so we call it the VH-shear.

5.2. Evaluation

Fig.16 (a), (b), and (c) show the plot of the VH-stretch, VH-shear, and VH distance. All proposed models have less play than the LET hinge. Especially, Joined Tomoe LET hinge has the least stretch and shear direction play during the folding motion, and it moved most similarly to rigid origami among the proposed models. The S-shape hinge shows equal to or better CoR maintenance and play performance than the Tomoe LET hinge. As expected through eigenvalue analysis, it showed good performance in the shear direction play.

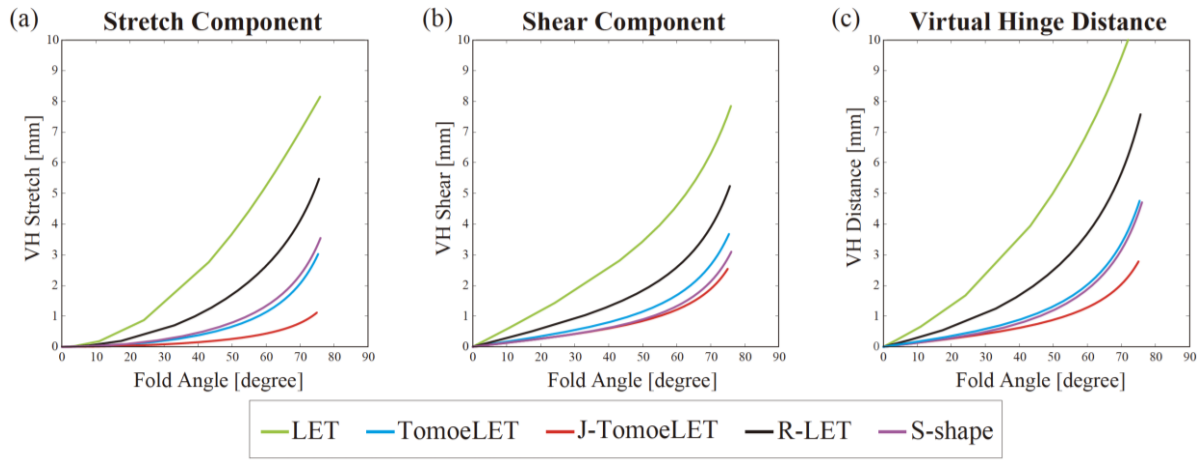


Fig.16 Results of Finite Element Analysis

6. Results

Based on the evaluation results, we conclude that the Joined Tomoe-LET hinge is the compliant hinge that best performs within our design. We consider that this excellence is due to the connection of the intermediate bodies of the two Tomoe LET hinges. This causes the motion of the hinges to be unified and makes it difficult to generate play. Therefore, the geometric maintenance performance of the Tomoe LET hinge is exhibited even under nonideal loading condition. It is expected that as the number of hinges increases, the performance of suppressing play due to unifying will increase. This hinge unifying technique cannot be used in the spherical joint hinge structure of Approaches 2 and 3. This is because points on the hinge move on a spherical surface and there is no motion for the intermediate bodies that are compatible with two neighboring spherical joints. Therefore, if the intermediate bodies are connected, the motion of the spherical joint cannot become realized.

Fig.17 shows the degree-4 vertex (top) and degree-6 vertex (bottom) pattern origami structures utilizing the Joined Tomoe LET hinge. Structures are fabricated by laser cutting machine and black connecting joints are fabricated by the 3D printer. The degree-4 vertex origami structure has one DOF, therefore it cannot deploy unless the CoR of the hinges intersects at the interior vertices. The motion appears to be well-interlocked, indicating that the CoR of the hinge is maintained to some extent. Similarly, the degree-6 vertex origami structure, which has three DOFs, moves well and spherical motion is also possible.

7. Conclusion

We designed four new types of compliant hinges that focus on CoR and Play using three different geometric approaches and evaluated their performance using methods proposed in this thesis. As a result, the Joined-Tomoe LET hinge was found to be the most effective at preserving the kinematics of rigid origami in our experimental condition. Using this compliant hinge, we were able to fabricate and actuate origami structures with internal vertices.

However, additional research is required under specific conditions (large deformation, load bearing, etc.) different from the conditions of this study. We need to evaluate play by performing eigenvalue analysis under large deformation conditions, and compositive evaluations under large deformation conditions of loads such as torsion, etc. that cause three-dimensional deformation are also required. Other hinges might perform better depending on the conditions. In addition, future works include optimizing the trade-off between hinge layout and stiffness to avoid interference with protruding hinge parts.

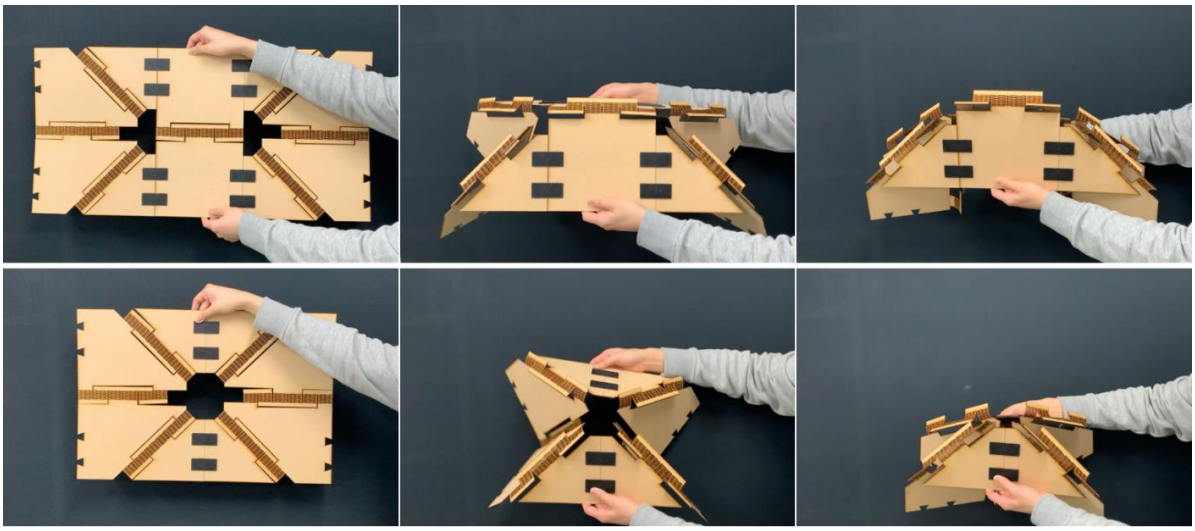


Fig.17 Origami structures with interior vertices. The structure of the top side is a degree-4 vertex pattern, and the bottom side is a degree-6 vertex pattern origami structure

Acknowledgments

This work is supported by JSPS KAKENHI 22H04954.

References

[1] Tomohiro Tachi. “Rigid-foldable thick origami”. In: AK Peters / CRC, 2011, pp. 253–264.

[2] Munkyun Lee, Yuki Miyajima, and Tomohiro Tachi. “Designing and Analyzing Multistable Mechanisms Using Quadrilateral Boundary Rigid Origami”. In: *Journal of Mechanisms and Robotics* 16.1 (Mar. 2023).

[3] David Melancon, Benjamin Gorissen, Carlos J García-Mora, Chuck Hoberman, and Katia Bertoldi. “Multistable inflatable origami structures at the metre scale”. In: *Nature* 592.7855 (2021), pp. 545–550.

[4] Joseph O Jacobsen, Guimin Chen, Larry L Howell, and Spencer P Magleby. “Lamina emergent torsional (LET) joint”. In: *Mechanism and Machine Theory* 44.11 (2009), pp. 2098–2109.

[5] Robert J Lang and Larry L Howell. “Laminar emergent flexural fold joints: Planar compliant mechanisms with large-angle near-revolute motion”. In: *Extreme Mechanics Letters* 52 (2022), p. 101657.

[6] Taisuke Ohshima, Tomohiro Tachi, Hiroya Tanaka, and Yasushi Yamaguchi. “Analysis and design of elastic materials formed using 2D repetitive slit pattern”. In: *Proceedings of IASS Annual Symposia*. Vol. 2015. 22. 2015, pp. 1–12.

[7] Dongchi Lee, Kazuya Saito, Takuya Umedachi, Tung D Ta, and Yoshihiro Kawahara. “Origami robots with flexible printed circuit sheets”. In: *Proceedings of the 2018 ACM International Joint Conference and 2018 International Symposium on Pervasive and Ubiquitous Computing and Wearable Computers*. 2018, pp. 392–395.

[8] Tomohiro Tachi. “Interactive form-finding of elastic origami”. In: *Proceedings of IASS Annual Symposia*. Vol. 2013. 12. 2013, pp. 1–4.

[9] Evgueni T Filipov, Tomohiro Tachi, and Glaucio H Paulino. “Origami tubes assembled into stiff, yet reconfigurable structures and metamaterials”. In: *Proceedings of the National Academy of Sciences* 112.40 (2015), pp. 12321–12326.

IASS 2023
July 10–14 Melbourne
Integration of Design and Fabrication

Proceedings of the IASS Annual Symposium 2023
Integration of Design and Fabrication
10–14 July 2023, Melbourne, Australia
Y.M. Xie, J. Burry, T.U. Lee and J. Ma (eds.)

Experimental study on a type of foldable structure with asymmetrical crease line pattern

Khai Seng CHEW*, Kok Keong CHOONG[a]

[a,*] School of Civil Engineering, Universiti Sains Malaysia
khaisengchew@student.usm.my

Abstract

This paper aims to highlight an experimental study of a light weight foldable structure that geometrically transforms from a flat planar state to a folded one with depth. The study was carried out to measure the folding behaviour of a foldable structure with a primary focus on an asymmetrical crease line pattern. The symmetry breaking pattern is key as it highlights the flexibility of origami pattern designs which can be adopted for foldable structures. The experimental model was made using light weight steel purlins that were boxed up using screws and assembled to form various panels. With a flat surface area footprint of 4m x 4m, the individual light weight panels are connected and arranged to form an asymmetrical pattern with hinges placed between these panels. Prior to the experimental study, a theoretical simulation of the folding process was carried out using Rhinoceros and Grasshopper to understand the transformation of the structure when it is being folded. The paper will also look into the various challenges faced during the fabrication and deployment of the actual model as well as lessons learnt throughout the process. The key points that will be discussed in this paper are the mechanisms of folding, hinges used to allow folding, method of data collection as well as an analysis of the data gathered comparing to the theoretical simulation. The paper will also discuss on the differences and impact of the folding of a physical model with finite thickness as a comparison to the simulation model which was made using surfaces with zero thickness.

Keywords: rigid origami, folded structure, asymmetrical crease line pattern

1. Introduction

Origami is the art of folding a thin sheet of material without cutting, stretching or shrinking the material. By folding a thin sheet of material, it transforms from a two dimensional surface to a three dimensional one with depth. In its folded state, the material would have a higher global stiffness than when it was flat. The additional stiffness and patterns formed from the folding are what draws engineers and architects to incorporate origami into the design of structures.

The folding process of a series of patterns can be simulated by following the mathematics of rigid origami as described by Belcastro and Hull (2002). Rigid origami describes a purely geometric mechanism in which the only flexure occurs along the crease lines. Through the simulation process, we have an understanding of the kinematic behaviour of a crease line pattern that is undergoing the folding process. This simulation provides a basis of comparison to the actual physical model that is being folded but it does not accurately exemplify the actual physical model especially after factoring the fabrication constraints, material thickness and the effect of self-weight.

Several studies have looked into the methods of incorporating thickness into the folding process. One of the studies were carried out by Tachi (2011) who demonstrated a method of hinge line arrangements and trimming by bisecting planes. Pehrson, Magleby, Lang and Howell (2016) also demonstrated the idea of a strained joint method which covers the trimming of the interior vertices. With regards to the

Copyright © 2023 by Khai Seng CHEW and Kok Keong CHOONG. Published in the Proceedings of the IASS Annual Symposium 2023 with permission.

effect of gravity on the simulation of folding, a more recent study by Zhang and Kawaguchi (2021) shows a method of incorporating the effect of gravity as a nodal force using the kinematic frame model.

This paper focuses on the experimental aspect of a foldable structure, with emphasis primarily on the fabrication processes and methods adopted to actuate the folding process. This study was carried out on a 4m x 4m foldable structure that is made using lightweight material. The findings of the experimental study from conception of the asymmetrical pattern, the fabrication of the physical model, the folding process and the interpretation of the data collected after folding are presented in the following sections.

2. Choosing the crease line pattern

The layout of the crease line pattern of an origami will determine the final shape of the material when folded. Figure 1 shows the chosen crease line pattern that was used for the development of the foldable structure in this experimental study along with the assignment of the Mountain and Valley folds. The considerations for the chosen asymmetrical pattern are highlighted in the subsections below.

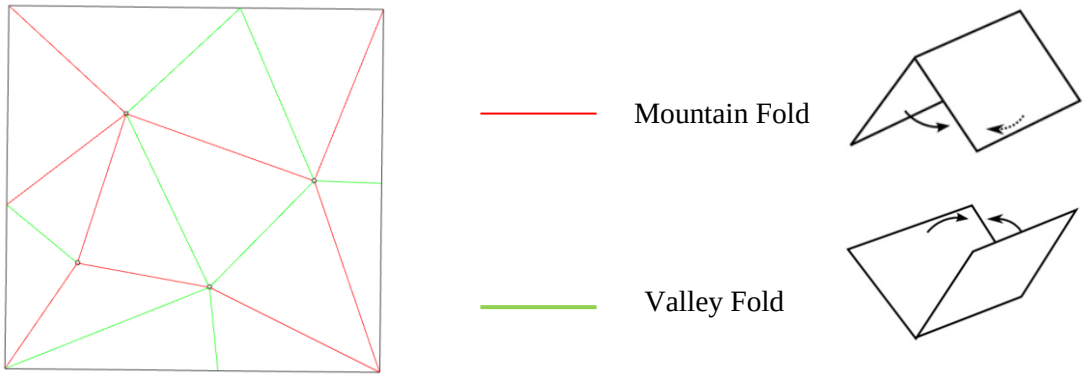


Figure 1. Crease line pattern that was used for the development of the foldable structure

2.1. Triangulation of individual faces

The crease line pattern assignment were intentional to create faces which were only triangular in shape to prevent in plane bending. A preliminary experiment was conducted using quadrilateral panel to test for in plane bending with pre-tension cross bracing and the result shows that the quadrilateral panel was not able to maintain planarity even with the addition of pretensioned bracing. Given the constraints of the folding simulation that follows rigid origami, the in-plane bending of a quadrilateral panel is undesirable and this is removed by triangulating every face forming the foldable structure.

2.2. Assembly and handling constraints

For ease of assembly, a continuous line of valley folds were introduced which effectively divides the model into two segments. The line of continuous valley hinges are necessary as they will be the final connection point between the two major segments as shown in Figure 2. Valley fold hinges can be installed from the top and the assignment of these continuous Valley fold hinges eliminates the need of flipping the fully connected 4m x 4m model around to install the Mountain fold hinges.

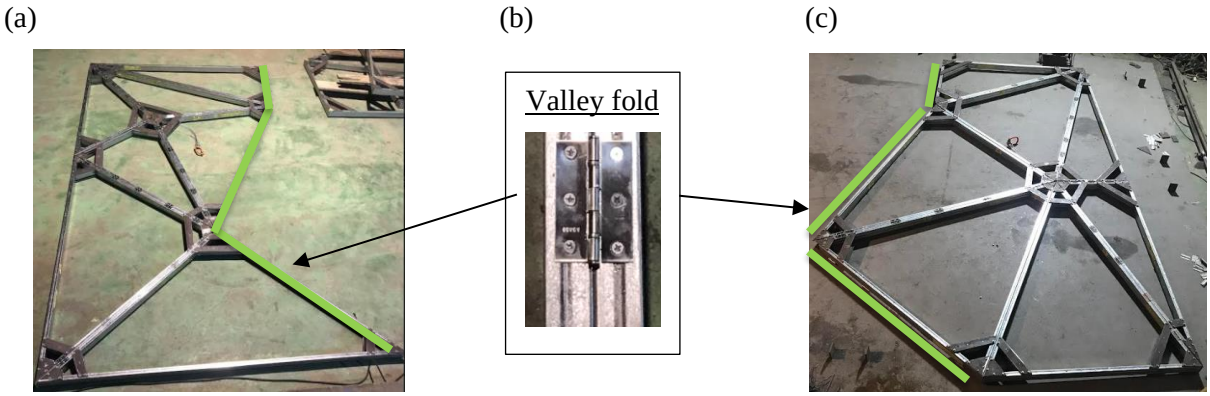


Figure 2. (a) First assembled segment of the foldable structure that comprise of continuous Valley folds (green) (b) Valley folds with hinges on the top side of the member (c) Second assembled segment of the foldable structure with continuous Valley folds (green) along the connecting edge to the first segment

3. Material used for foldable structure

The material that was chosen for this experimental study needed to be lightweight for ease of handling and to minimize the effect of self-weight. The material chosen for the panels were made from two 0.75mm thick steel C section that are combined and locked together using self-tapping screws. The self-tapping screws connect the top and bottom flanges of the C section and are spaced 100mm apart. Figure 3 shows the cross-sectional view of the cross section used.

Table 1. Mechanical properties of the C section used for the experimental study

Thickness of material, *t* (mm)	0.75
Cross-sectional Area, *A* (mm^2)	102.4
Weight, *W* (kg/m)	0.89
Major Second moment of inertia, *Ixx* (mm^4)	77760
Minor Second moment of inertia, I*yy* (mm^4)	10230

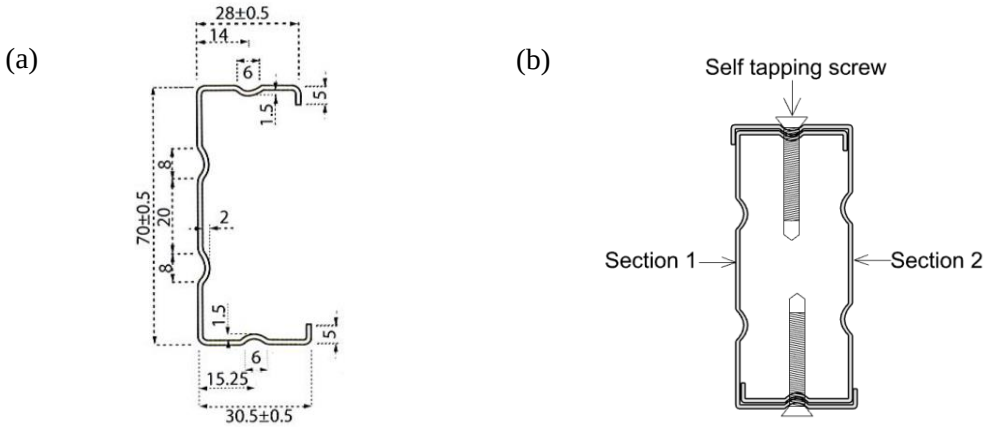


Figure 3. (a) Cross-section and dimensions of the 0.75mm thick steel section and (b) the connection between each member to form a closed box section

4. Fabrication of experimental model

The fabrication of the experimental model was carried out by connecting the combined steel C-section member to form individual triangular panels. These triangular panels were fabricated individually and assembled by connecting to the neighbouring panels along the designated Mountain or Valley fold hinges. The challenges faced during fabrication are highlighted in the subsections below.

4.1. Potential clash at vertices during folding

One of the considerations that needed to be made was on the potential clashing of the member during the folding process, specifically at the vertices. The members converging on the vertex needed to be trimmed back as shown in Figure 4 to allow for the rotation along the crease lines of the foldable structure.

4.2. Replicating a nodal support during the folding process

During the fabrication of the model, it was important to be able to create a node or a concentric point for the purpose of lifting. Additional 6mm triangular plates were connected above the trimmed members with holes drilled through for connection with the 6mm wire rope. These plates will be the points of attachment for the wire ropes that will be used to life the structure and commence the folding process. The setup and methodology of lifting and folding the experimental model is discussed in Section 6 of this paper.

(a) (b) (c)

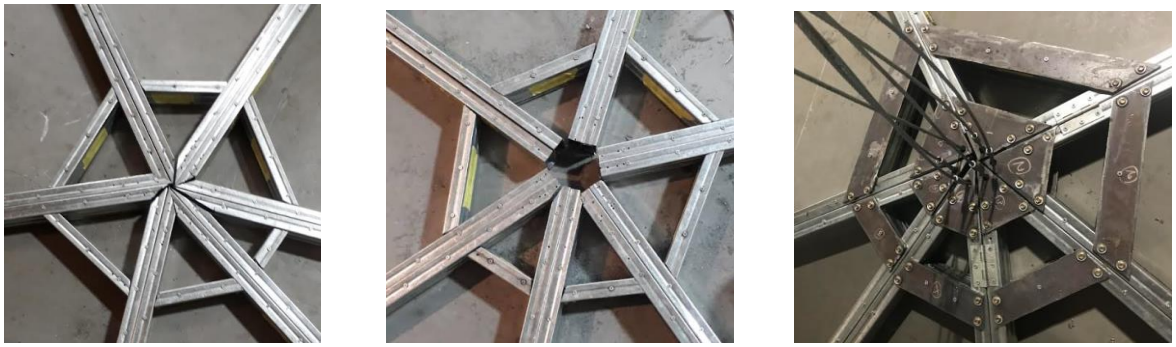


Figure 4. (a) Vertex of the experimental model with panels converging to a point (b) The vertex of the experimental model after trimming to prevent clashing during the folding process (c) The addition of triangular stiffener plates to replicate lifting or support at the nodal point of the vertex

5. Hinges

One of the most important decision that needed to be made was on the type of hinge to be used to enable the physical folding of the experimental model. A door hinge was chosen as the hinge mechanism as it is able to integrate into the fabricated experimental model and allows for the rotation along the crease lines. The hinges are spaced evenly along the length of the member as well as connect one triangular panel to another. The position of these hinges are dependant on whether the folds are designed to be a Valley fold or a Mountain fold. The hinges are located beneath the members for a Mountain folds and above the members for Valley folds. A pullout test was conducted on 4 types of hinges to understand the mechanical behaviour of these hinges when subjected to a lateral loading. Figure 5 shows the various door hinges tested as well as the set up to test the pullout capacity of the hinges.

(a) (b)

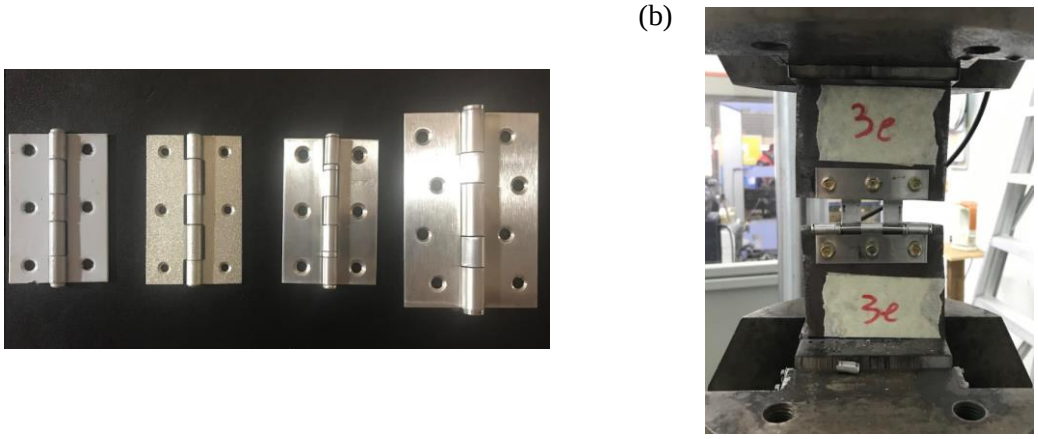


Figure 5. (a) Various door hinges were tested to understand the mechanical behaviour of the hinges under a pulling load. (b) The failure mechanism of the hinges are through the unrolling of the circular curved hook around the hinge bar

Figure 6 shows the comparison of the results from the pull out test on the hinges. The result of the tests shows that the hinges were able to support a horizontal loading perpendicular to the bar of about 7kN which is about 700kg. Although Hinge 2 showed a favourable pull out capacity, the variance in the pull out capacity was high after multiple testing which resulted in Hinge 3 being used in the experimental model.

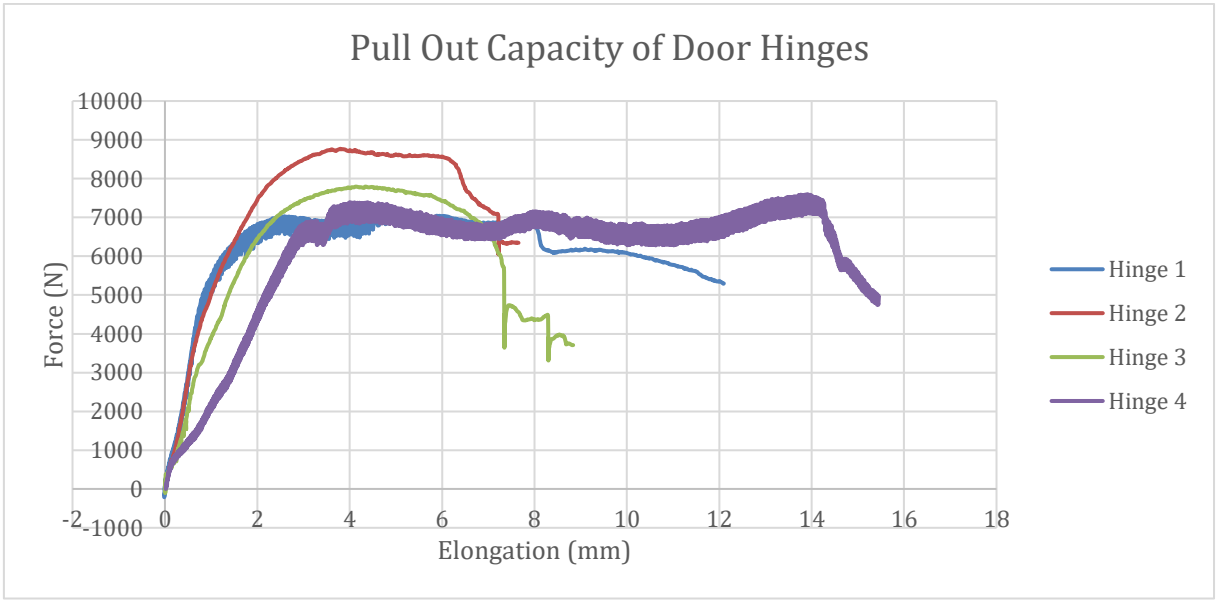


Figure 6. Result of the pull out test measuring the force exerted on the hinges against the elongation of the hinge

6. Folding the physical model

To physically fold the experimental model, an overhead framing system was built with four movable steel beams as shown in Figure 7. A chain block supported by rollers were placed on these steel beams to allow for movement. The moveable steel beams that were supporting the rollers allowed for the lifting points to cover almost all of the area within the steel frame which has a footprint of 5m x 6m, allowing for reusability in carrying out future works on foldable structure that has a different crease pattern.

(a) (b) (c)



Figure 7. (a) A 6m x 5m steel frame that supports the lifting mechanism used to fold the structure which comes with (b) moveable overhead steel beams supported by rollers and (c) moveable lifting hook which traverses along the length of the moveable steel beams

The folding was initiated by the vertical lifting of the experimental model at 3 vertices using chain blocks. These chain blocks were attached to movable beams which allowed for the horizontal movement of the lifting points in both East West and North South direction. The model will be lifted up in sequence to the desired height starting with the vertex that was estimated to be at the highest point in the simulations. The desired height for each of the lifted vertex was decided by the simulated shape and the relative height of these three points were set as the controlled points during the physical folding process. The folding of the physical model is stopped once these three points achieved their desired relative heights.

7. Measurement and gathering data

The important data to gather for the experimental study was the final shape of the folded structure after the folding process which can then be compared against the result of the simulation. Due to the suspended nature of the experimental foldable structure, any direct contact or an external force acting on the model could make the model sway.

To ensure accuracy of measurement and to minimize the impact of potential sway while collecting data on the final geometry of the model, a total station was used with a precision of up to 1mm. The folded nature of the model also made taking measurements tricky, especially due to there being no direct line of sight to the total station. A prism and ranging rods were used to mitigate the issue of direct line of sight to allow for adjustment in the height of the prism as shown in Figure 8.

(a) (b) (c)

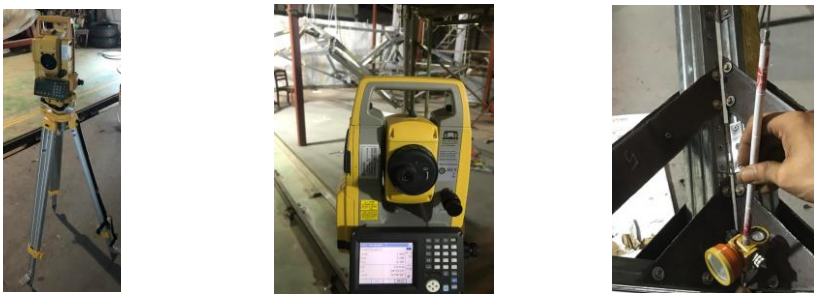


Figure 8. (a) A total station that was used to measure the geometry of the folded structure after folding by (b) establishing the coordinates of each point of interest with the aid of (c) a prism attached to a ranging rod.

8. Comparison of physical model and simulation

The result of the comparison shows that the physical experimental model has folded to a shape that is comparable to the simulation. Figure 9 shows a visualization of the data collected during survey which are represented by the annotated numbers as well as the coloured surfaces. The simulated folding of the experimental model is represented by the solid black lines and when this is put directly next to the collected survey data, the result shows there are difference between the data collected and the simulation, for the surfaces indicated in red to a maximum deviation of 500mm.

(a) (b) (c)



Figure 8. (a) The steel frame of the final folded shape of the experimental model with (b) lightweight surface covering made of foamboard to clearly define the folded surface of the experimental model. (c) The comparison of the simulated model with the actual physical model after folding.

The comparison of the model shows that higher degree of variations were shown in regions further away from the support which attributes the effect of self-weight as one of the factor that led to the variation to the simulated shape.

9. Conclusion

The folding behaviour of an experimental foldable structure with asymmetrical crease lines can be simulated with confidence to a comparable degree. However, the difference between folding a thin sheet of paper to folding a larger scale model brings about various challenges that can be overcome as shown in this paper to create a foldable structure. Through the vertical lifting of vertices which act as the control points, the desired shape of the model can be achieved. The outcome of the comparison between the shape of the simulation model and the folded structure shows a comparable result with higher degrees of variation shown in regions further away from the support which indicate the effect of self-weight on the final folded shape.

References

[1] S. Belcastro and T. Hull (2002). A mathematical model for non-flat origami. In Origami3: *Proceedings of the 3rd International Meeting of Origami Mathematics, Science, and Education, pp. 39-51*

[2] N.A. Pehrson,S.P. Magleby, R.J. Lang, L.L. Howell (2016). Introduction of monolithic origami with thick-sheet materials. *Proceedings of IASS Annual Symposia: International Association for Shell and Spatial Structure (IASS), pp. 1-10*

[3] T. Tachi, Rigid foldable thick origami, Origami 5 (2011) 253-264

[4] T. Zhang and K. Kawaguchi (2021). Folding analysis for thick origami with kinematic frame models concerning gravity. *In Automation in Construction, Vol. 127 (2021) 103691*

Proceedings of the IASS Annual Symposium 2023
Integration of Design and Fabrication
10–14 July 2023, Melbourne, Australia
Y.M. Xie, J. Burry, T.U. Lee and J. Ma (eds.)

Multi-layered curved folding

Marcus BERNHARD[a,*], Rupert MALECZEK[a,*]

[a,*] i.sd | Structure and Design | Department of Design, University of Innsbruck, Austria
Marcus.Bernhard@uibk.ac.at
Rupert.Maleczek@uibk.ac.at

Abstract

Curved folded shells made of thin materials find extensive application in architecture, design, and engineering due to their advantageous properties in design, fabrication, and structural performance. While folded shells typically consist of a single sheet of material, this may not always be sufficient to meet the required structural performance for certain applications. One solution is the use of structures composed of multiple layers, forming a hollow cross-section. In the field of technical folding or structural origami, these structures are commonly referred to as origami tubes [1] or multilayer tessellations [2]. This paper presents the authors' development of a (partially) multi-layered curved folding construction that generates one or more folded tubes during the folding process, thereby improving both the static properties and the folding mechanism. The tubes can be generated adjacent to two fold lines, resulting in a multi-layered structure that can have either a constant thickness throughout the folded configuration or explicit individual tubes attached to a specific folded configuration.

Keywords: curved folding, multi-layer folding, folded tubes; thin shells, structural origami

1. Introduction

Technical folding is an approach that enables the creation of three-dimensional spatial geometries using one or several flat sheets of material through folding and/or assembling. Typically, this method produces single-layer shells or tubes. In the construction industry, this approach offers advantages as building elements can be manufactured and assembled in a flat state under controlled conditions, reducing grey energy by minimizing transportation volume. These elements can then be folded on-site into their final form.

To enhance the strength of a shell, the material thickness becomes a crucial factor in addition to its overall geometry. Therefore, it is often beneficial to create shells with a certain thickness, providing them with increased stiffness. Depending on the geometry and fabrication method of the folded configuration, various types of structures can be distinguished, such as folded sandwich panels [3], thick folding [3] [4], and folded tubes [5] [1]. Klett [4] demonstrated that certain tessellations, featuring both straight and curved fold lines, allow for multilayering through coplanar joining, resulting in tube-like openings when in the folded state.

Copyright © 2023 by Marcus BERNHARD and Rupert MALECZEK. Published in the Proceedings of the IASS Annual Symposium 2023 with permission.

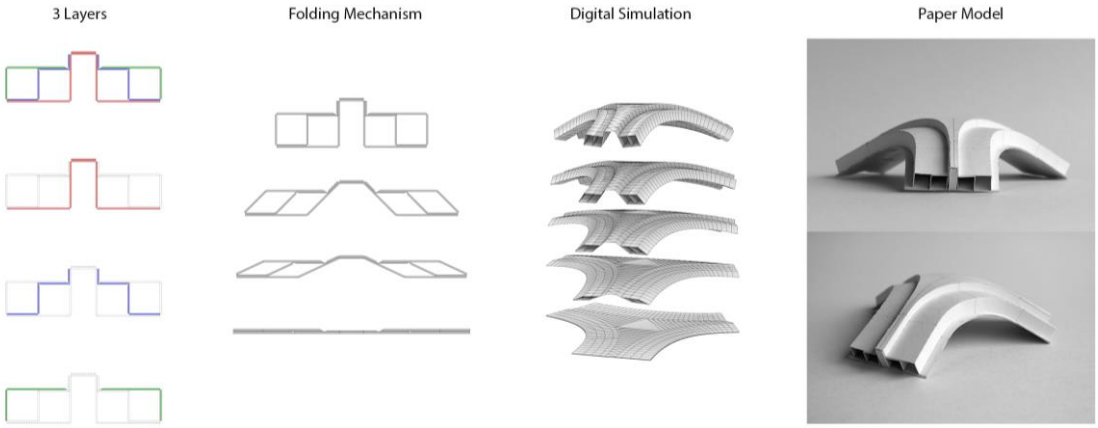


Figure 1. concept, digital and physical model of a multilayered foldable tripod

In this paper, multilayering refers to the incorporation of two or more layers of thin sheet material, where these layers have a coplanar contact area and one or more tubular spacers positioned between the top and bottom layers. Unlike classical sandwich structures where additional sheets are glued to the folded core, the top and bottom layers in this case are integral parts of the entire foldable geometry. The models presented in this study can be assembled in a flat state, making them fully developable. Furthermore, all models can be folded as a single entity in their multilayer configuration.

As depicted in Figure 2, the concept of multilayering can be viewed as a particular form of offset in the cross-section of a foldable component, where the spaced foldable patches remain parallel. Consequently, the multilayered curved folded configurations presented in this paper can also be regarded as foldable shells with an offset, enabling global developability.

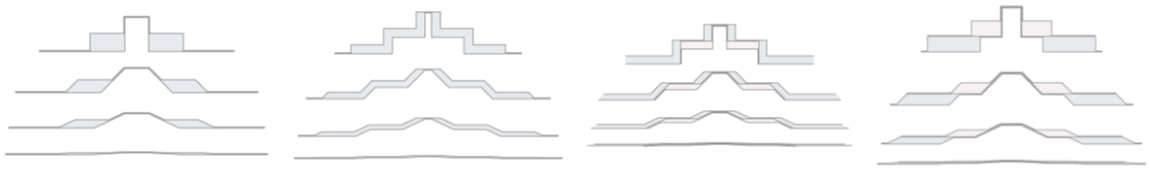


Figure 2. different types of the multilayer concept and its folding behaviour
with two layers (left) and three layers (right).

2. Geometric constraints

Offsetting a curved surface results in a surface with a different surface area compared to the original. However, in the case of multilayering, where globally developable surfaces with identical surface areas are required, additional constraints must be introduced into the process.

A straightforward way to illustrate this approach is through a multilayer shell composed of two identical folded configurations based on a cylindrical surface with parallel rulings, as depicted in Figure 3. By shifting one folded patch along the rulings, a tube emerges between the two patches. The surfaces of these tubes can be viewed as two interconnected offsets that share vertices at the rulings. When these components are joined together, the resulting configuration maintains its properties and can be both developed and rigidly folded.

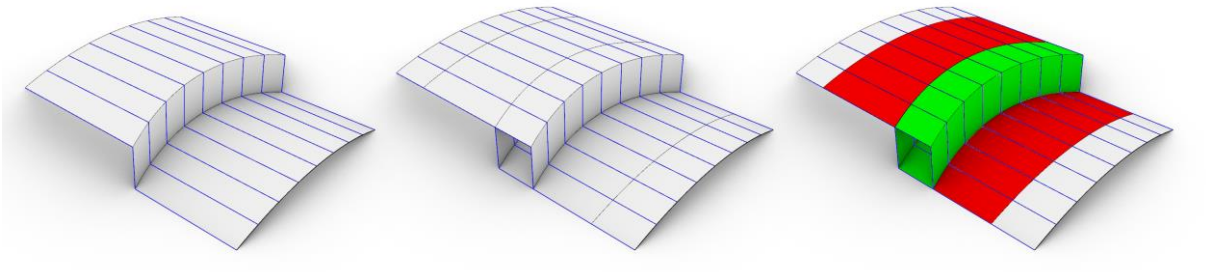


Figure 3. a simple example of a multilayer curved folded shell, with the tube in green and the glued connection surface patches in red

This process gives rise to a new type of curve on the surface, which serves as the fold line for the attached layer and marks the boundary of the surface patch that is glued to the other layer. When considering the entire geometry as a mesh, this curve is described as a manifold mesh edge with three adjacent faces. In the generation of the geometry, this curve becomes crucial as it needs to be defined in both meshes. Since it always represents a fold line but remains unfolded in one layer during motion, we refer to it as a "zero fold" (0-fold) or connection edge.

The distance between two zero folds on one side of the tube must be identical to the distance on the other side. This condition ensures the global developability of the interconnected multilayer structure.

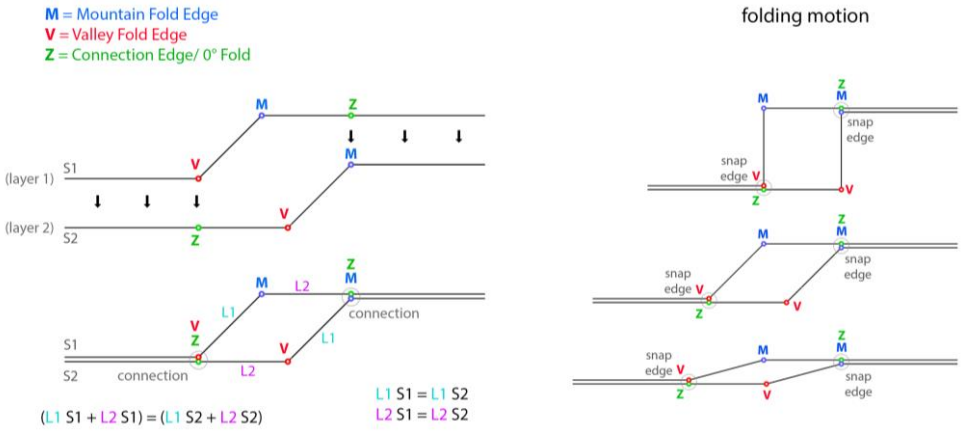


Figure 4. the concept in detail with the zero fold concept and the obligate lengths constrain

We can identify two approaches for generating multilayered shells with folded tubes along fold lines. The first approach involves starting from a folded configuration, as depicted in Figure 3. Alternatively, the tube can be initially generated along a fold line and then extended with surface patches. By combining both approaches, it becomes possible to create complex configurations that incorporate various types of developable surfaces, as well as planar and non-planar spatial curves.

2.1 Tubes in folded configurations

By utilizing a foldable tube as a starting point, there are multiple methods for generating multilayer surfaces. One approach involves extending the rulings of the foldable patches, which results in the creation of a 0-fold and a developable configuration. Two patches can then form different configurations, which can be illustrated as shown in Figure 5. When generated from two distinct sheets, the S- or Z-Types prove to be effective solutions as the tube features only one fold line between the 0-folds. Although other types are possible, they typically require additional fold lines and are not as straightforward to construct using two sheets of material. This paper primarily focuses on the investigation of S- or Z-Types.

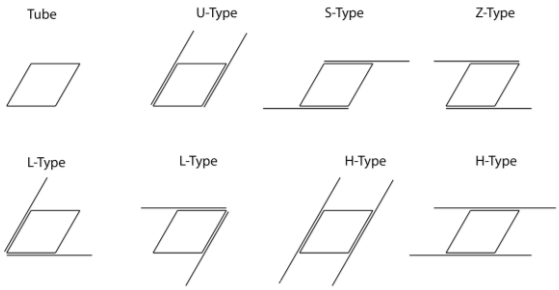


Figure 5. concept sketch of possible construction types, based on a single tube

As depicted in Figure 2, there are numerous possibilities for generating tubes and offsets along or connected to fold lines. Depending on the positioning and arrangement of the tubes, it becomes feasible to create partially or nearly constant offsets within a curved folded shell. When having one tube per fold line in a folded geometry, two layers are sufficient. However, for a constant offset consisting of a series of tubes, a minimum of three layers is required.

Model studies from the paper (Figure 6, left) demonstrate different configurations using various numbers of layers and fold lines between two 0-folds. The findings show that configurations with two layers and multiple fold lines are foldable, although controlling the folding angle precisely to achieve a constant distance between the layers can be challenging. Models from three or more layers allow for geometries whereas larger surface patches can be formed from a series of adjacent tubes that belong to the same fold line. These geometries seem to have 1 Degree of Freedom during folding. A notable example is the folded tripod (Figure 6, right), which serves as a proof of concept with three layers and two adjacent tubes forming the offsets along the fold lines.

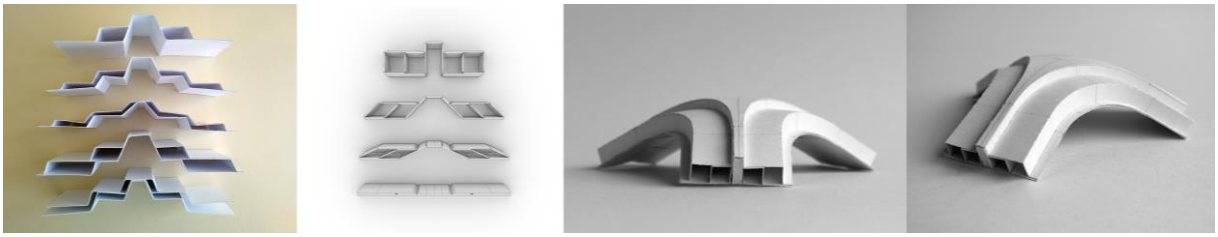


Figure 6. sandwich study (left) and a multilayered curved folded tripod (right)

2.2 Digital design constraints

To successfully achieve control over the numerous constraints involved in multi-layered shells with curved fold lines, it is necessary to adapt or develop new digital approaches and tools. As architects and designers often approximate design surfaces or low-poly meshes using various techniques, the authors of the paper propose a variation of an approach initially introduced by Bhooshan [7]. They combine this approach with the isometry enforcement technique described by Foschi et al. [8]. Starting from a given target geometry, two constrained guessed patches, a 2D development and a 3D guess, are adapted using Mesh relaxation with the help of Rhino3D [9] and Kangaroo [10] to become a foldable structure.

As mentioned earlier, each layer of the folded geometry can be viewed as an individual foldable shell created for the same target geometry but with variations in the positions of the curved fold lines. In order to generate a multilayer configuration, it is necessary to constrain the different layers into a single entity. This can be achieved by ensuring that the 0-folds align with their corresponding mountain or valley folds, and by enforcing the rulings of connected surface patches to be identical on both layers.

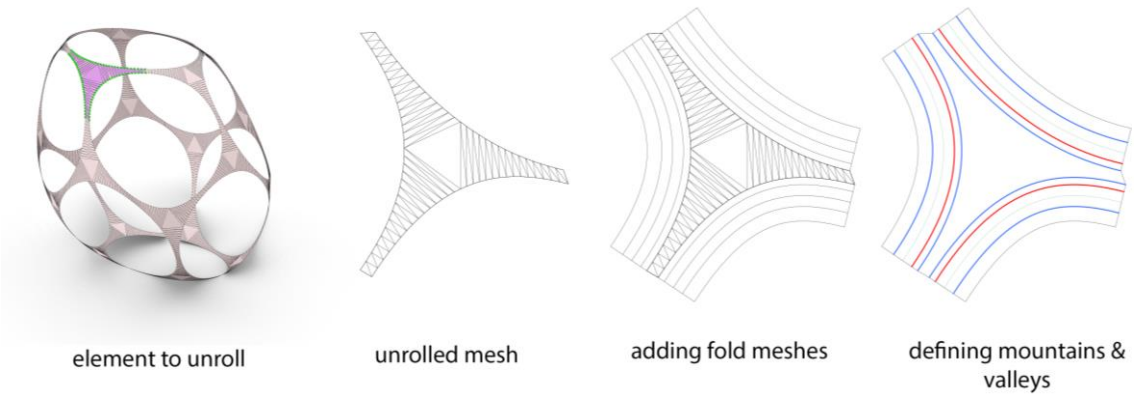


Figure 7. three-layer system applied on a planarized polyhedron

Similar to Bhooshan [7], we begin with a planarized chamfered polyhedron to create a collection of developable patches. These patches consist of planar polygons at the vertices connected by single curved patches. In this specific example, we divide the entire geometry into curved unfoldable meshes, which allow us to obtain 3-armed unfoldable modules in 2D. These are then used to construct the individual folded layers. Following the approach described by Foschi et al. [8], a good initial 2D geometry for the different layers is generated based on this patch. Initially, the outer edges are moved in parallel, and the mesh is extended with surfaces that can be folded in subsequent steps. To facilitate this process, the various fold lines (mountain, valley, and zero folds) must be assigned in 2D prior to guessing the rulings for the surfaces (refer to Figure 7).

The three-armed geometry, also referred to as a tripod [8], can be approximated as a foldable developable geometry through error distribution. At this stage of the process, it is crucial to define the rulings, as they will be enforced to be identical in the touching layers and allowed to change their positions during simulation. The rulings, along with the fold lines, contribute to the formation of a quad-mesh, where each face is required to be planar in both 2D and 3D configurations. Additionally, the surface area of each quad, as well as the entire surface patches, is maintained to be identical. To create tubes within the structure, each layer is assigned different positions for the mountain and valley folds. However, the zero folds are consistently constrained to their corresponding fold lines.

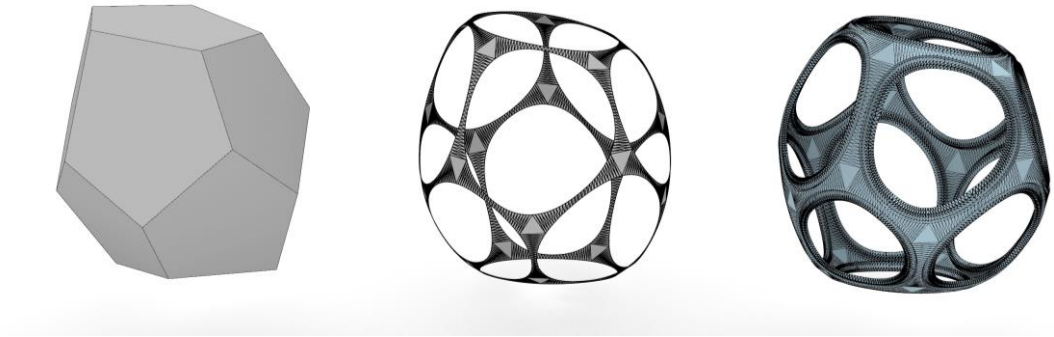


Figure 8. from polyhedron to curved folded multilyer structure with three layers

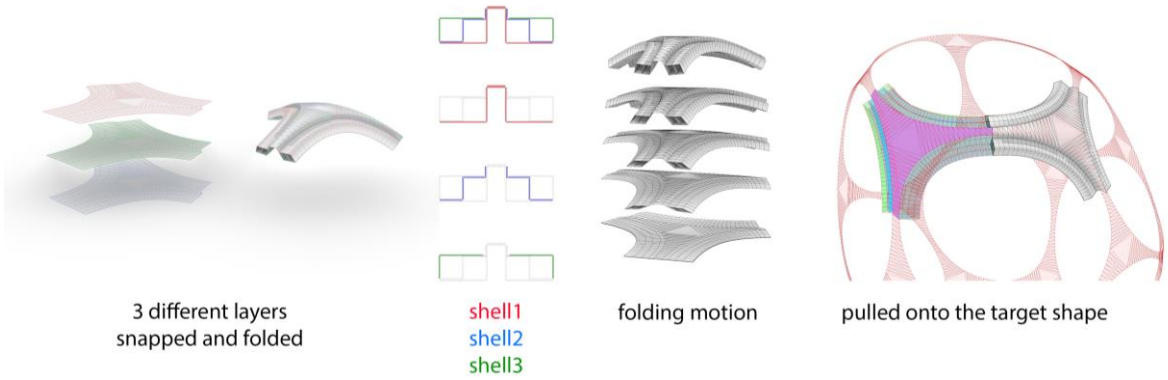


Figure 9. construction and application of the 3-shell construction in digital form

During the simulation, the lengths of corresponding edges and the areas of the planar quads are adjusted to be equalized in both the 3D and 2D states. The fold lines of each tube should be parallel offsets and superimposed in 2D as long as the 3D folding edges are planar curves. The outer boundaries of all layers within each tripod are identical, and the connections between the parts and neighboring tripods are constrained to ensure the formation of a seamless 3D folded geometry composed of multilayer tripods. The folded states of the individual layers can be observed in Figure 9, while the seamless structure and its cross-section are depicted in Figure 10.

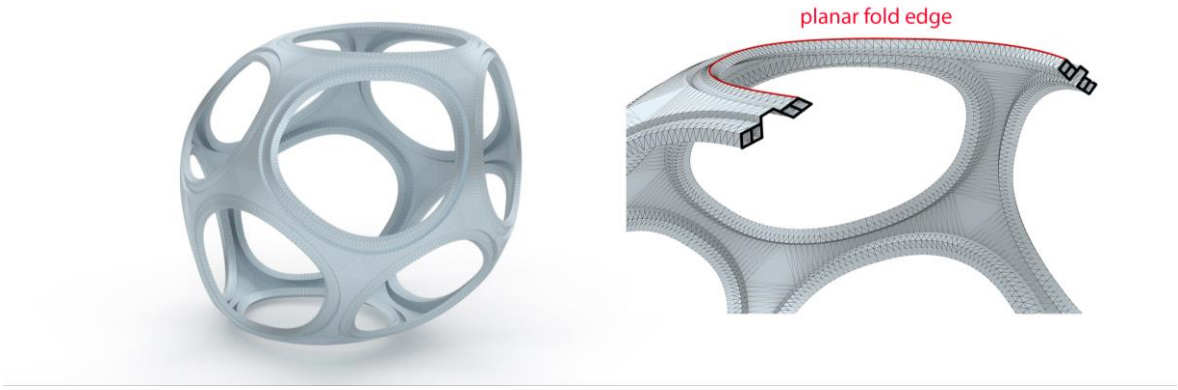


Figure 10. Digital Model of a multilayer curved fold with two adjacent tubes on a planarized polyhedron

2.3 Non-planar curved folds

The motivation for this investigation stemmed from the observation that certain artistic curved folded models utilize not only planar curves but also non-planar spatial curves as fold lines. It was inspired by Tachi's work [11], which demonstrated that such curves must be smooth and can be translated into a curved folding patch by generating consecutive rulings. However, the paper does not specifically address whether these surfaces correspond to cones, cylinders, or tangent developable surfaces, nor does it delve into an in-depth examination of the developed patches.

In this paper, our focus is on an approach that relies on isometry enforcement. By utilizing this technique, we can generate foldable surfaces consisting of planar quads without the need to predefine the surface patches or the parameters of the second patch, as required by the Lotus method [12].

If we apply the strategy described for planarized polyhedra and its resulting planar curves to a non-planar spatial curve, such as a helix curve, the physical models generated will still be foldable. However, the fold lines formed in these models will be planar instead of retaining the non-planar nature of the original curve. To address this, we propose adapting the approach presented by Tachi [11].

The first step involves generating a folded patch along the space curve, which is then unfolded to a 2D representation. In most cases, non-planar curved fold lines result in tangent developable surfaces that limit the extension along the rulings (as depicted in Figure 11, right) in terms of width. To create different 2D patches from the same space curve, the dihedral angle along the fold line can be varied (as shown in Figure 11, left).

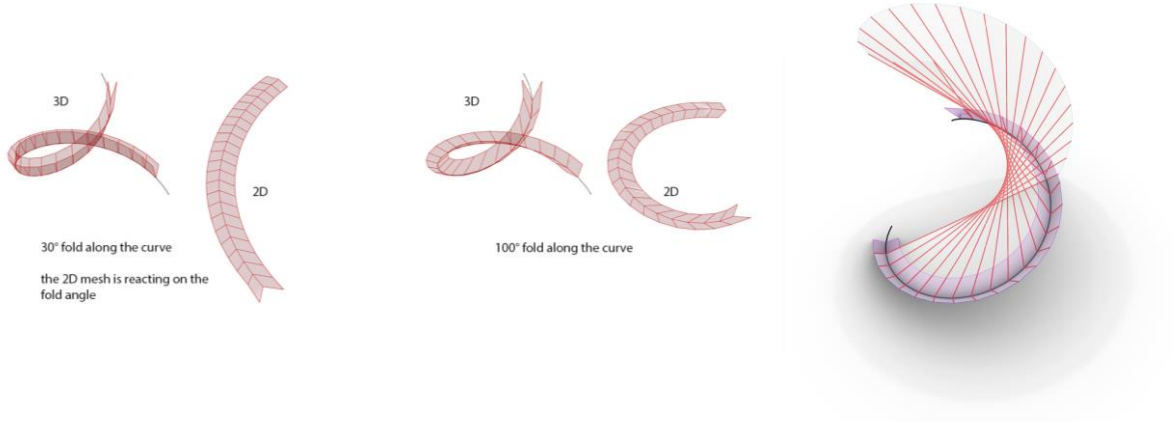


Figure 11. (left) strip out of planar quads folded on a helix curve; (right) extension of the rulings

As Tachi defines the entire tube-profile of the tube to generate it along the space curve, we propose a different approach that can be applied by isometry enforcement. In order to make a foldable tube from this first patch, two things need to be taken into account. The connection between the two strips and the rulings of the two strips.

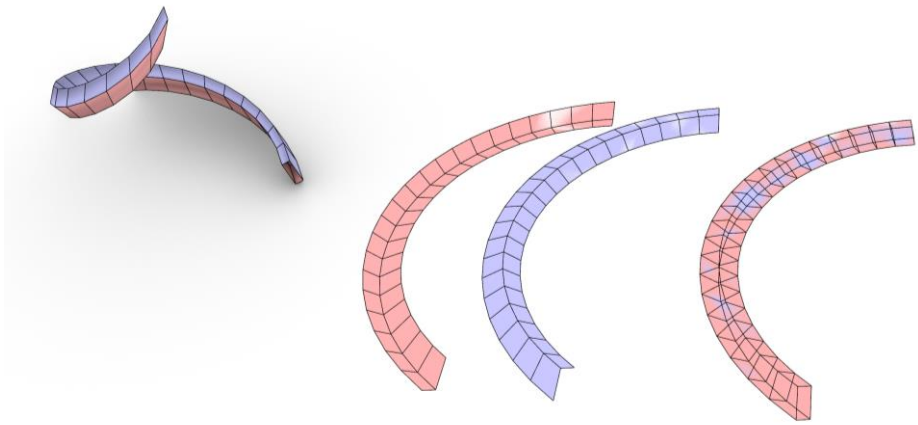


Figure 12. double shell tube along a helix curve in 3D (left) and its developed patches (right)

By considering the fold angle of the second patch as undetermined and utilizing the boundary edges of the first 2D patch as 0-folds to connect the two strips, we can generate a reasonable approximation by directly copying and defining the first patch as the second layer. This approach ensures the proper edge connection along the 0-fold and matching rulings of both patches there.

As the fold line and the rulings of two connected layers cannot be parallel for a non-planar fold line, the rulings and the fold line of the second layer will change position and length. These changes allow for the intersection of the two fold lines in the 2D patch while appearing 'parallel' in the 3D folded structure. As demonstrated by Tachi, the cross section of the resulting tube takes the form of parallelograms.

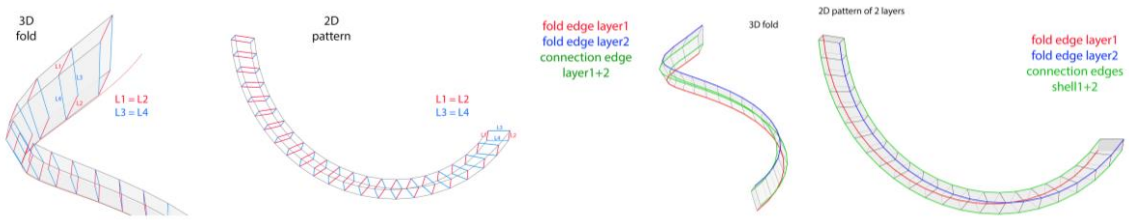


Figure 13. different section parallelograms

In the 2D pattern, the fold lines of a helix fold curve intersect once (Figure 13). In this particular case, the global dihedral angle was set to 120° and varied slightly along the fold line within the constraints of isometry enforcement. However, it has not been conclusively proven whether a consistent variation of the angle along the fold line is always possible. This remains an ongoing area of research.

When applied to other "nice" spatial curves, the authors were able to generate a wide range of foldable tubes. Various tests revealed that the fold lines of a helix intersect once in 2D, while other configurations may allow for multiple intersections in 2D. The authors hypothesize that this behavior is associated with the number of inflection points present in the non-planar space curve.

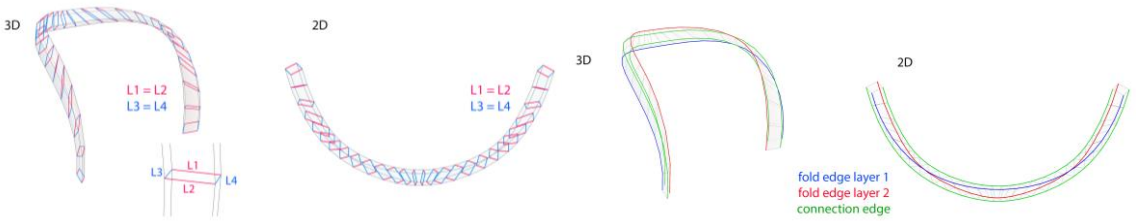


Figure 14. different section parallelograms and interscting foldlines in 2D

While the digital and physical models demonstrate the ability to create a wide range of tubes with varying folding angles, clear limitations have not yet been fully defined. It is evident that excessive changes in curvature along the space curve are not advantageous, as well as relatively wide tubes that may be constrained by resulting curves of regression. A comprehensive investigation into these limitations is currently a subject of ongoing research.

2.3 Tubes and shells from multiple fold lines.

If spatial curves serve as the foundation for a design process, it is essential to accommodate multiple spatial curves within that process. In contrast to Booshan's approach, which uses planar boundary curves of a developable patch as fold lines, the authors propose generating the developable patch between the curves. This patch, along with its rulings, is then utilized to create two connected tubes.

To illustrate this approach, two connected tripods can be employed as a design basis. By rotating one end of the tripod, one curve transitions from planar to non-planar. In Figure 15, a regular tripod with planar curves is discretized using planar quads. By rotating one end of the figure by 17°, the red curve transforms from planar to non-planar. The quads remain planar but undergo a change in the orientation of their rulings.

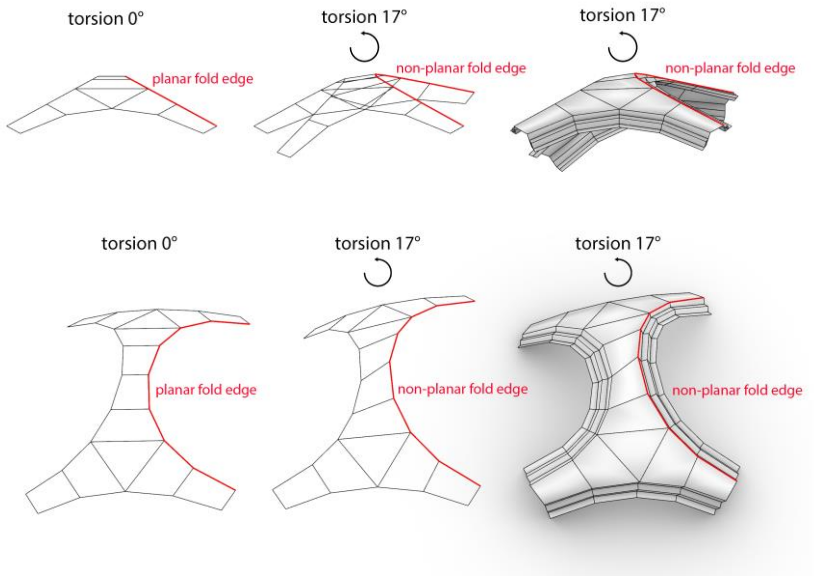


Figure 15. the tripod torsioned and materialized with a multilayer shell

By utilizing this base, a foldable shell with two layers can be generated, resulting in a structure with two tubes along each spatial curve. The original developable patch becomes in this configuration a connected one, that includes both layers with identical rulings and valley folds at the boundary (Figure 16).

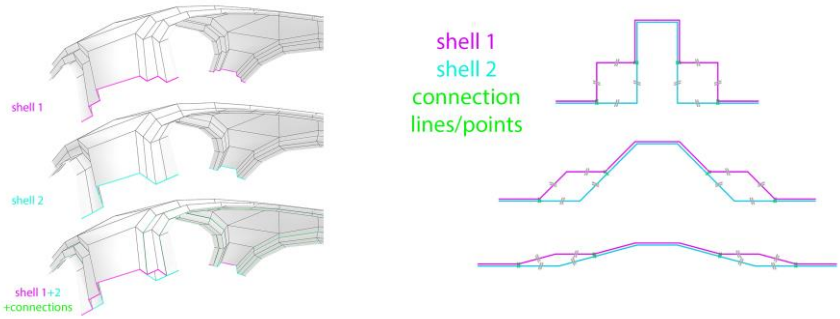


Figure 16. explanation of the layers

As described earlier, the cross-sections of the tubes exhibit unequal parallelograms in the simulation. This implies that the rulings and folded edges of both layers differ only at the tubes or the points where the tubes are formed. However, for the remaining patches, the layers are connected at all points and remain identical throughout and fulfill the multilayer condition.

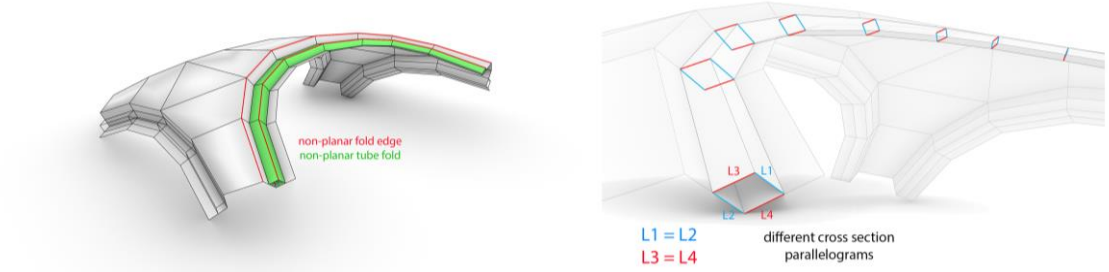


Figure 17. non planar fold edge and equalized tube ruling lengths

The non-planar curve also results in a transformation of the developable surface from a cylinder to a tangential developable one. In certain cases, the surface may exhibit characteristics of two conical surfaces with apexes located on opposite sides of the fold lines. However, defining the precise limits and underlying rules of this transformation is still a topic of ongoing research. By extending the rulings, the overall limits of the system can be readily identified without the need to generate the entire regression curve. The extension can be halted as soon as two non-neighboring faces intersect, allowing for a clear visualization of the limits (see Figure 18).

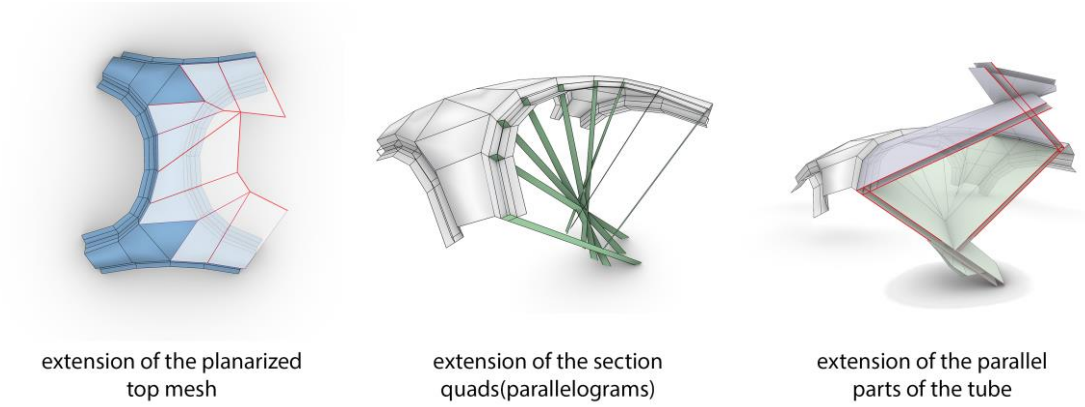


Figure 18. showing some extionsions of different parts of the folded object

2.4 Conclusion

The authors have provided an overview of their novel approach for generating multilayered foldable shells. They introduced the topic and presented two fundamental concepts for developing these new configurations. They discussed the constraints involved in connecting foldable tubes and constructing multilayer configurations. Additionally, they explained the application of isometry enforcement to both planar and non-planar curves, enabling the generation of intricate and complex configurations.

3. Outlook

The implementation of tubes through multilayering in curved folded shells holds great promise for various applications, ranging from architecture and design to fabrication and structural performance.

This paper serves as an initial starting point for a more comprehensive and detailed exploration of these shells. The design potential for spatial geometries is exemplified in Figure 19, showcasing a pavilion-like structure created by one of the authors using a set of spatial curves. Future research will delve further into not only geometric constraints but also manufacturing considerations and structural performance, aiming to advance the understanding and application of these innovative structures.



Figure 19. a pavilion proposition designed by a set of spatial curves

References

[1] F. Evguini T., T. Tomohiro und P. Glaucio H., „Origami tubes assembled into stiff, yet reconfigurable structures and metamaterials," *PNAS,* Bd. 112, Nr. 40, p. 12321–12326, 6 October 2015.

[2] Y. Klett und P. Middendorf, „Face to Face: Varieties and Properties of Coplanarly Joined Multilayer Tessellations," *IASS 2016 Annual International Symposium,* 09 2016.

[3] K. Sharifmoghaddam, R. Maleczek und G. Nawratil, „Generalizing rigid-foldable tubular structures of T-hedral type," *arXiv:2301.09969,* 2023.

[4] Y. Klett und D. K, „Designing Technical Tessellations," in *Origami 5,* London, CRC Press, 2011, pp. 305-322.

[5] T. Tachi, „Rigid-Foldable Thick Origami," in *Origsami 5,* Boca Raton, CRC Presse, 2011, pp. 253-264.

[6] J. S. Ku und E. Demaine, „Folding Flat Crease Patterns With Thick Materials," *Journal of Mechanisms and Robotics,* Bd. 8, Nr. 3, pp. 031003-1--6, 06 2016.

[7] S. Bhooshan, *Interactive Design of Curved-Crease_Folding,* Bath: University of Bath, 2015.

[8] R. Foschi, R. Kraft, R. Maleczek, K. Mundilova und T. Tachi, „Comparison of computational curved folding design methods," in *Inspiring the next generation,* Surrey, 2021.

[9] McNeel, „https://www.rhino3d.com/," McNeel. [Online].

[10] D. Piker, „https://www.food4rhino.com/app/kangaroo-physics," [Online].

[11] T. Tachi, „One-DOF Rigid Foldable Structures from Space Curves," in *Proceedings of the IABSE-IASS Symposium 2011,* London, 2011.

[12] K. Mundilova, E. Demaine, R. Foschi, R. Kraft, R. Maleczek und T. Tachi, „Lotus: A curved folded tool for Grasshopper," in *ACADIA 2021 Realignments: Toward Critical Computation: Proceedings of the 41st Annual Conference of the Association for Computer Aided Design in Architecture,* 2021.

Proceedings of the IASS Annual Symposium 2023
Integration of Design and Fabrication
10–14 July 2023, Melbourne, Australia
Y.M. Xie, J. Burry, T.U. Lee and J. Ma (eds.)

Multi-stability of hexagonal origami hypar structures based on group theory and symmetry breaking

Chenhao LU[a], Ruizhi XU[a], Yao CHEN[*], Ke LIU[a], Jian FENG[a], Pooya SAREH[b]

[*] Key Laboratory of Concrete and Prestressed Concrete Structures of Ministry of Education, and National Prestress Engineering Research Center.
Southeast University, Nanjing 211189, China
chenyao@seu.edu.cn

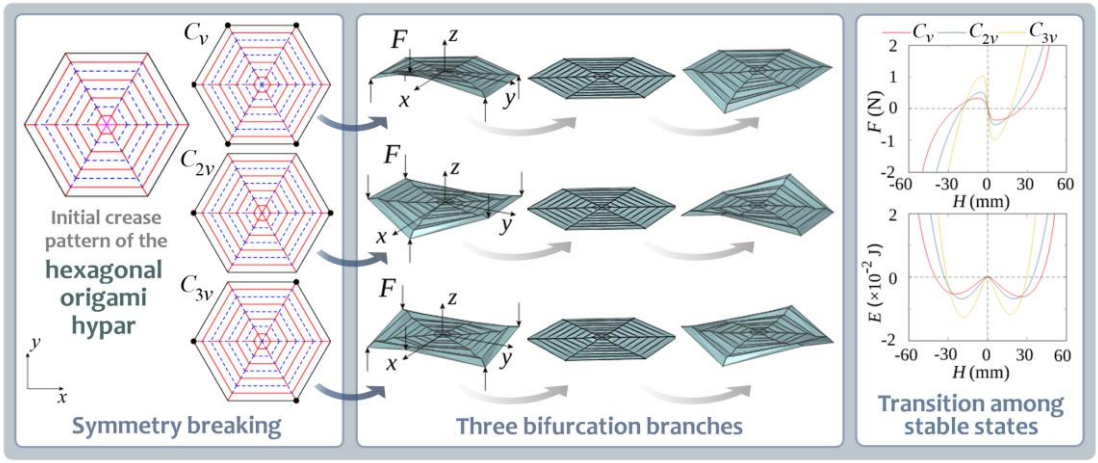
[a] Department of Advanced Manufacturing and Robotics, Peking University, Beijing 100871, China
[b] School of Engineering, University of Liverpool, Liverpool, L69 7ZX, UK

Abstract

Origami hyperbolic paraboloid (origami hypar) provides an avenue to be multi-stable via bifurcation branches of kinematic paths. However, some symmetry properties make origami hypar possess subtle multi-stability. The extensive application of symmetry properties will simplify the transition among various steady states in multi-stability study. Here, group theory and symmetry breaking are applied to the multi-stability analysis of hexagonal hypar to eliminate singularity in the stiffness matrix near the bifurcations. Results show a single hexagonal hypar has six steady states in total and the tessellation with three hexagonal hypar shows more stable states. Different bifurcation branches will convert to each other only if the structure is fully flattened. Notably, the energy barrier between the two stable states increases with the symmetry order of the branch. The ease of the transition among various steady states is determined by the difference between the potential energies of the initial steady state and the fully flatted state. This strategy will provide a basis for the multi-stability properties of origami hypar and promote the multi-stability study of origami structures with high order symmetry.

Keywords: origami hypar, multi-stability, group theory, bifurcation, symmetry breaking, tessellation, Hangai Prize applicant

Graphical abstract



Copyright © 2023 by Chenhao LU, Ruizhi XU, Yao CHEN, Ke LIU, Jian FENG and Pooya SAREH. Published in the Proceedings of the IASS Annual Symposium 2023 with permission.

1. Introduction

Non-trivial energy landscapes in multi-stable structures contribute to multiple stable equilibrium configurations. The transitions among stable states are often adopted to meet the geometric and functional requirements. Recently, multi-stable structures have received wide attention in bionics [1], metamaterials [2], robotics [3], engineering structures [4] and other fields. Typically, multi-stable structures originate from the combination of bistable units [5]. The overall properties of multi-stable structures depend on the local properties and composition of bistable units. For instance, a specific double-layer Kresling tube can transition between two different stable states without changing the total height [6]. Due to the abundant mechanics [7, 8], more origami structures have been utilized to develop bistable units and become an increasingly important approach to designing multi-stable structures.

Based on classic origami patterns, plenty of multi-stable origami structures have been derived (e.g., Miura-ori [9], Tachi-Miura polyhedron [10], and Kresling tubes [11, 12]). As representative multi-stable origami units, the square twist [13, 14], leaf-like origami [15], and origami hypar [16] are combined to acquire more numbers of stable states and richer programmability of origami structures. Notably, kinematics analysis of multi-stability origami is essential to ensure the folding process smoothly. The popular strategies for kinematic analysis of rigid and non-rigid origami include mechanism analysis and structural analysis. Compared with non-rigid folding, the conditions of rigid folding are much more severe. Consequently, rigid folding possesses a smooth kinematic analysis and can be handled with more computational models [17]. On the other hand, the non-rigid folding exists the deformation of the panel. However, mechanism analysis fails to deal with the deformation of the panel. Hence, analysis of non-rigid origami typically adopts the modified bar-and-hinge model [18], the membrane-and-hinge model [19], and the thin plate element [20].

In terms of the non-rigid and multi-stable origami units, origami hypar has attracted abundant attention, especially the square origami hypar and the circular origami hypar [21]. Two stable states of square origami hypar are macroscopically symmetric. Due to the competing folding, stretching, and bending energy [18], the square origami hypar first flat-unfold and then refold up during the transition between two stable states, going through a significant energy barrier. On the other hand, circular origami hypar possesses different stable states according to different approximate width conditions. For example, it will generate a saddle-like shape under the simplest condition. In addition to the two extreme cases, the multi-stability of polygonal origami hypar remains to be studied in-depth. Therefore, an investigation of the multi-stable properties of the hexagonal origami hypar will be performed.

An efficient and effective approach to identifying all stable states is essential to study multi-stability of the hexagonal origami hypar because experiments have proven it possesses at least two stable states. However, the approach to solving the bistability may be infeasible to handle with the global properties of the hexagonal origami hypar because the tangent stiffness matrix may become ill-conditioned. Kinematic bifurcation analysis of deployable structures can be adopted to simplify the simulation of the global process [22]. Singular value decomposition has been validated to be suitable for determining bifurcations [23]. Additionally, some studies [16, 24] have tackled the method of assuming the bifurcation parameters and the group theoretic approach to simplify multi-stability analysis by bifurcation branches. However, group theory and symmetry property are mostly applied in the design of novel crease patterns, whereas few attempts have been implemented in the field of stability studies.

Here, a new strategy will be proposed to study the multi-stability of hexagonal origami hypar by group theory and its representations. The whole folding process of origami structures will be simplified by the group-theoretic approach. In terms of origami structures with high-order symmetry as the hexagonal origami hypar, the bifurcation branches will be solved by symmetry breaking. Through kinematic analysis of different bifurcation branches, the corresponding stable states will be acquired. The multi-stability in the whole kinematic process is shown by the bifurcation branches and the corresponding stable states. In the following sections, we will study the multi-stability of the hexagonal origami hypar

in different bifurcation branches through the group-theoretic method. In addition, the potential stable states and the effect of geometric parameters will be discussed.

2. Methodology

It is assumed herein that the equivalent bar-and-hinge model will be leveraged to analyze the deformation of the hexagonal origami hypar. Based on group theory, the analysis process is simplified to bifurcation branches. The bifurcation branches can be obtained by symmetry breaking.

2.1. Principle of stationary potential energy

The establishment of the equivalent bar-and-hinge model is based on the potential energy approach. The total potential energy Π consists of strain energy U and external work W. In general, the strain energy U of non-rigid origami is decomposed into facet bending or twisting energy U_b, crease folding energy U_f and bar stretching energy U_s [25]. Thus, the total potential energy can be expressed as

$$\Pi = U - W = U_b + U_f + U_s - W \tag{1}$$

Based on the principle of stationary potential energy, the equilibrium condition can be derived as follows.

$$\mathbf{K}\boldsymbol{\Delta}_\mathbf{d} = \mathbf{F} \tag{2}$$

where $\mathbf{K}$, $\boldsymbol{\Delta}_\mathbf{d}$, and $\mathbf{F}$ denote the tangent stiffness matrix, the generalized displacement vector, and the force vector, respectively. The internal force vector and the tangent stiffness matrix consist of different components. It is essential to assemble them from equivalent nodal loads and elementary stiffness matrices.

The tangent stiffness matrix K includes the folding stiffness of the crease $\mathbf{K}_F$, in-plane stretching and shearing stiffness of the bar $\mathbf{K}_S$, and out-plane bending stiffness of the facet $\mathbf{K}_B$. In equivalent bar-and-hinge models, $\mathbf{K}_F$ is affected by the stiffness of rotational spring elements $\mathbf{K}_{spr}$ and the stiffness of bar elements $\mathbf{K}_{bar}$ is composed of $\mathbf{K}_S$ and $\mathbf{K}_B$. Namely, $\mathbf{K}_F = \mathbf{K}_{spr}$ and $\mathbf{K}_S + \mathbf{K}_B = \mathbf{K}_{bar}$. Hence, the stiffness components can be assembled as follows:

$$\mathbf{K} = = \ d\mathbf{f} \,/\, d\mathbf{u} = \mathbf{K}_F + \mathbf{K}_S + \mathbf{K}_B = \mathbf{K}_{spr} + \mathbf{K}_{bar} \tag{3}$$

To acquire the elementary stiffness matrices, we adopted the hyperplastic model to simulate the constitutive relationship of bar elements [26]. The elementary stiffness matrices have the following expression.

$$\begin{cases} \mathbf{K_F^e} = k_F^e \, d\theta/d\mathbf{u} \otimes d\theta/d\mathbf{u} + M_F \, d^2\theta/d\mathbf{u}^2 \\ \mathbf{K_B^e} = k_B^e \, d\theta/d\mathbf{u} \otimes d\theta/d\mathbf{u} + M_B \, d^2\theta/d\mathbf{u}^2 \\ \mathbf{K_S^e} = k_S^e \left(\mathbf{B}_1^T + \mathbf{B}_2\mathbf{u}\right)\left(\mathbf{B}_1^T + \mathbf{B}_2\mathbf{u}\right)^T + f_s\mathbf{B}_2 \end{cases} \tag{4}$$

2.2. A group-theoretic approach to the global bifurcation analysis

The tangent stiffness matrix near the bifurcations will become ill-conditioned when simulating the kinematic path. Group theory [27] is regarded as an effective method to avoid this problem. The essence of the global bifurcation analysis is to tackle the vector equilibrium equation.

$$\mathbf{f}\left(\mathbf{u}, m\right) = \mathbf{0} \tag{5}$$

where $\mathbf{u}$ belongs to an N-dimensional real vector space and m is a real number. Based on the symmetry-adapted coordinate system, the equation will be simplified by the successful implementation of Newton-Rapson procedure using block-diagonalization, as shown below.

$$\begin{bmatrix} \mathbf{K}_{v^{(1)}} & 0 & \cdots & 0 \\ 0 & \mathbf{K}_{v^{(2)}} & \cdots & 0 \\ \vdots & \vdots & \cdots & \vdots \\ 0 & 0 & \cdots & \mathbf{K}_{v^{(p)}} \end{bmatrix} \begin{bmatrix} \Delta\mathbf{u}_1 \\ \Delta\mathbf{u}_2 \\ \vdots \\ \Delta\mathbf{u}_n \end{bmatrix} = \begin{bmatrix} -\mathbf{f}_m \\ 0 \\ \vdots \\ 0 \end{bmatrix} \tag{6}$$

Thereafter, the vector equilibrium equation can be decomposed into independent problems associated with specific symmetry subspaces through the decomposition of matrices. Namely, Eq. (5) can be tackled by solving Eq. (7) involved with different subspaces.

$$\mathbf{K}_{v^{(1)}} \Delta\mathbf{u}_1 = -\mathbf{f}_m \tag{7}$$

In symmetric structures, symmetry subgroups are related to different symmetry subspaces. Hence, the bifurcation branches of the original structure will be composed of the bifurcation branches of the corresponding symmetry subgroups [28].

2.3. Symmetry breaking

Symmetry breaking behavior [7] exists in the transformation from the primary path to the bifurcation paths of deployable structures. That is, different bifurcation paths will be captured by reducing the symmetry order of structures.

The C_{nv} symmetry group contains a total of 2*n* independent symmetry operations [16].

$$C_{nv} = \left\{ C_n^j, \sigma_j \mid j = 1, 2, \cdots, n \right\} \tag{8}$$

where the rotation C_n^j represents that the original structure rotates an angle $2\pi j/n$ around the symmetry axis, $j \in [1, n]$, and σ_j donates the *j*th reflection along the vertical symmetry plane.

Without any constraints, the plane pattern of hexagonal origami hypar will be classified as C_{6v} symmetry group. The higher symmetry order of internal mechanism mode, compared with the self-stress state, will lead to kinematically indeterminate structures becoming mobile [29]. Hence, to ensure the foldability of origami hypar, the symmetry order of the self-stress state should be decreased less than that of the initial pattern [7]. The subgroups of C_{6v} group can be computed by

$$C_1, C_2, \ldots, C_6, C_v, C_{2v}, C_{3v} \subset C_{6v} \tag{9}$$

Based on theorems for mountain-valley assignments [30], the plane patterns possess a symmetric distribution of crease along the diagonals. That is, as a symmetry subgroup containing only cyclic rotations, C_6, C_3, C_2, and C_1 will be excluded. Hence, the subgroups with mirror symmetry, namely C_{3v}, C_{2v}, and C_v, will be studied.

When the symmetry order of the mechanism mode fails to meet the full symmetry, the origami structure will undergo a transition to a bifurcation branch with lower-order symmetry. Notably, the symmetry order of the related constraint modes matches the bifurcation branch. Namely, controlling the constraint mode is an effective method to programme the specific symmetry breaking of the structure.

By symmetry breaking, Figure 1A(b), (c), and (d) diagram C_{3v}, C_{2v}, and C_v symmetry origami configurations, respectively. In addition to constraint modes, the mountain-valley properties of the innermost creases are different among different bifurcation branches. The definitions of geometric and material properties are referred to the study of square origami hypar [18]. The geometric parameters include the fold spacing *d*= 8mm, the inner fold spacing *D*= 8mm, the number of the crease layers *n*= 8, and the thickness *t*= 127 μm. The material parameters consist of the elastic modulus *E*= 5GPa and the Poisson's ratio μ = 0.35.

2.4. Capture of stable 3D configurations

To track other stable states, it is urgent to capture a stable 3D configuration as the initial state 1. Because the tangent stiffness matrix near the bifurcations is often ill-conditioned. According to the folding of the square origami hypar [18], Figure 1B(a) shows the distribution of applied forces used to fold the initial pattern. Under this loading mode, the plane C_{3v} pattern will be transformed into an initial 3D configuration, see Figure 1B(b). Notably, this configuration is in a random state and remains existing the ill-conditioned possibility. Hence, the initial 3D configuration should be released from the loading and then transform into one of stable states, as shown in Figure 1B(c). Similarly, the capture of stable 3D configurations should be implemented to be used as an initial state 1 when we track the stable states of structures with different symmetry.

Thereafter, the structure will experience a complex transition from a stable state to a specific state with the imposition of displacement. The variations of configurations and equilibrium load versus displacement curves will be monitored during this process. On this basis, the number of stable states is judged according to the number of minimum in energy versus displacement curves and then validated by physical models. Figure 1C presents the flowchart of the multi-stabile investigation.

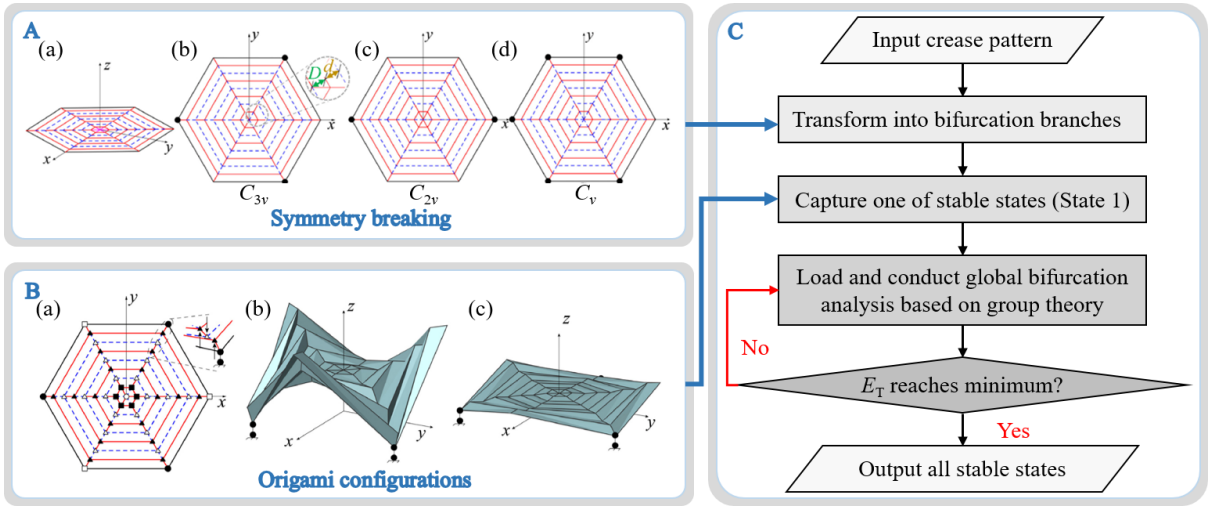


Figure 1 (**A**) Crease patterns of the hexagonal origami hypar: (a) Three-dimensional view of the crease pattern. (b) to (d) Different constraint modes and crease patterns corresponding to C_{3v}, C_{2v}, and C_v symmetry. (**B**) 3D origami configuration with C_{3v} symmetry. (a) Applied forces in the z-direction (the hollow circle ○ represents downward force F_0, the solid square ■ represents upward force $2.25F_0$, the hollow triangle △ represents downward force 4 F_0, the solid triangle ▲ represents upward force 4 F_0, the hollow square □ represents upward force 2 F_0, and the solid circle ● represents constraints in the z-direction) (b) Initial 3D configuration. (c) 3D configuration in a stable state. (**C**) Flowchart of the multi-stabile investigation.

3. Results

3.1. Multi-stability of hexagonal origami hypar

3.1.1. Hexagonal origami hypar with C_{3v} symmetry

According to Section 2.4, state 1 will be tackled as the initial state to find other stable states. In Figure 2(a), three lower vertices on the boundary are constrained, and downward displacements are imposed on the other vertices. In Figure 2(c), the equilibrium load will first increase from zero (state 1) to peak (state P1) and then decrease to zero (state 2) with the imposition of displacement. Subsequently, the equilibrium load experiences a roughly symmetric variation about state 2 as the center point. As for macroscopical configurations, the structure (state 1) will unfold to an approximately fully flat state (state

2). Subsequently, it continues to fold and achieves a new equilibrium (state 3). Notably, state 1 and state 3 are the null points of the equilibrium load-displacement curve as well as the minimum of the total potential energy. Based on the energy principle, it is considered that state 1 and 3 are two different stable states of the hexagonal origami hypar with C_{3v} symmetry.

The total potential energy E_T is composed of the folding energy E_F and the panel deformation energy $E_B + E_S$, which includes the tensile and shear energy E_s and the bending energy E_B. As shown in Figure 2(d), E_F is much larger than $E_B + E_S$. That is why the creases will be folded preferentially. However, $E_B + E_S$ accounts for a non-negligible proportion of E_T, especially when the configuration is close to state 1 and 3. Hence, the panel deformations remain to be taken into consideration during folding. In other words, the folding of hexagonal origami hypar is a non-rigid process.

During the folding process (i.e., the transition from state 1 to state 2), E_T and E_s increase with the folding angle, whereas E_B decreases with the flattening of the panels. On the contrary, the unfolding process (i.e., the transition from state 2 to state 3) undergoes an exactly opposite variation.

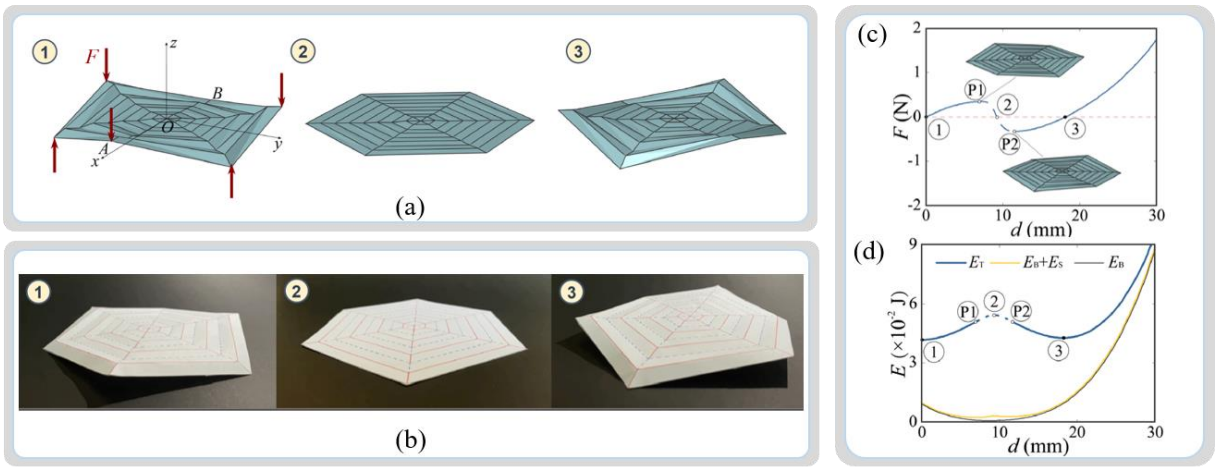


Figure 2 Multi-stability of hexagonal origami hypar with C_{3v} symmetry: (a) Key states. (b) Physical models. (c) Equilibrium load versus displacement curves of single load point. (d) Stored energy versus displacement curves.

3.1.2. Hexagonal origami hypar with C_{2v} symmetry

Notably, constraints and crease patterns in this case are distinguished from Section 3.1.1. Due to the variation of constraint conditions, the unconstrained outermost vertices are imposed downward loads. The loading mode of the remaining nodes is identical with Figure 1B(a).

With the increasement of displacements, the structure first unfolds to approximately fully flat State 2 and then folds to another stable State 3. As shown in Figure 3(d), the bending deformations $E_B + E_S$ dominate the deformations of facets during this transition. Hence, it can be demonstrated the non-rigid property of hexagonal origami hypar with C_{2v} symmetry. Similarly to hexagonal origami hypar with C_{3v} symmetry, the equilibrium load undergoes a symmetric variation about state 2 as center point. In addition, the total potential energy curves achieve two minimums, which indicates the bistability of hexagonal origami hypar with C_{2v} symmetry.

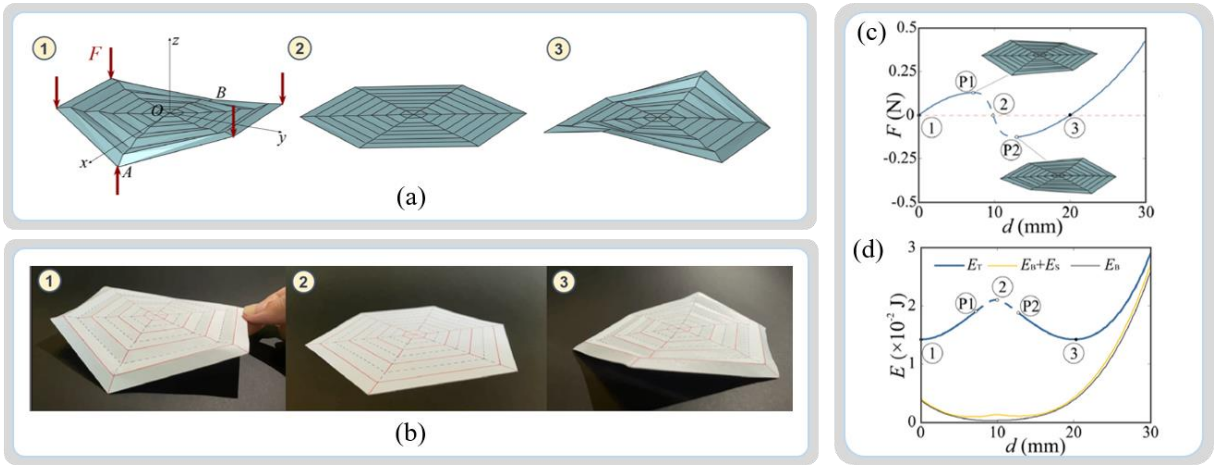


Figure 3 Multi-stability of hexagonal origami hypar with C_{2v} symmetry: (a) Key states. (b) Physical models. (c) Equilibrium load versus displacement curves of single load point. (d) Stored energy versus displacement curves.

3.1.3. Hexagonal origami hypar with C_v symmetry

With the further reduction of symmetry, the lowest symmetry mechanism mode is presented in Figure 1A(d). The stable state 1 is acquired according to the method explained in Section 2.4. Thereafter, the five outermost vertices are constrained and the remaining vertex is imposed a downward displacement, as shown in Figure 4(a).

Compared with Section 3.1.1 and 3.1.2, Figure 4 diagrams similar variations of macroscopical configurations, the equilibrium load, and the total potential energy. In other words, the properties of non-rigid and bistability are invariable regardless of any bifurcation paths.

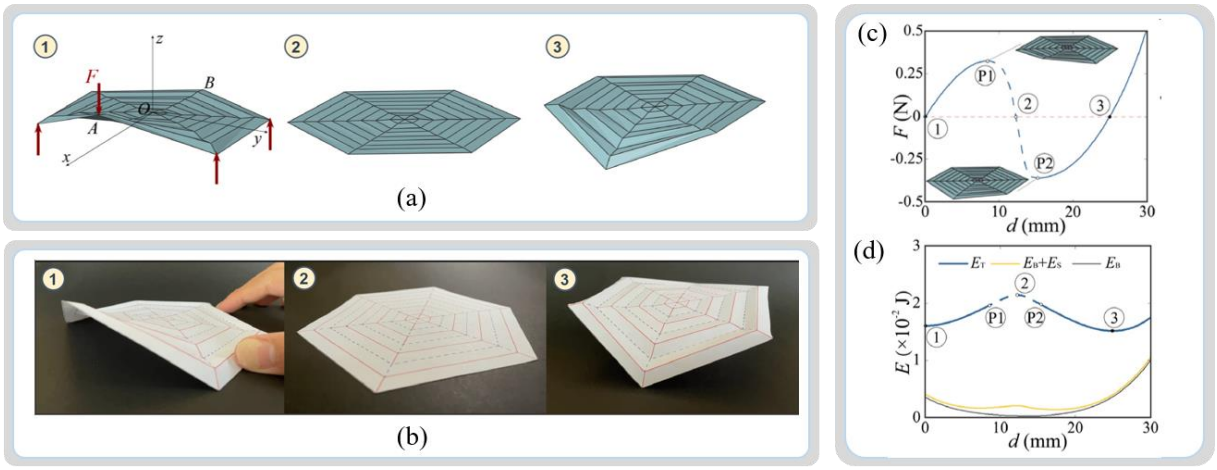


Figure 4 Multi-stability of hexagonal origami hypar with C_v symmetry: (a) Key states. (b) Physical models. (c) Equilibrium load versus displacement curves of single load point. (d) Stored energy versus displacement curves.

3.2. Comparisons of multi-stability among different bifurcation branches

To compare different bifurcation branches, a unified coordinate system is adopted in Figure 5. Points I_a, $P1_a$, $P2_a$, III_a, points I_b, $P1_b$, P2b, III_b, and points I_c, $P1_c$, $P2_c$, III_c correspond to the States 1, P1, P2, and 3 on the bifurcation branches with C_v, C_{2v} and C_{3v} symmetries, respectively. Considering the number of loading points is different among these bifurcation branches, the total equilibrium load is chosen to compare. Owing to the symmetry of loading conditions, the equilibrium loads are identical in terms of any loading points. Hence, the total equilibrium load will be equal to the equilibrium load of a single

loading point multiplied by the number of loading points. For example, the total equilibrium loads of the bifurcation branch with C_{3v} symmetry can be acquired by multiplying the equilibrium load of a single load point by three.

In Figure 5(a), the states of these bifurcation branches at the point X, Y, Z, X', Y', and Z' are different. As for Point II, it is the only intersection of these three bifurcation branches. On the other hand, it is observed in Figure 5(c) that there is no intersection except point II. In other words, point II is the only critical point of these three bifurcation branches. Therefore, the critical point II is considered as the zero potential energy state (i.e., fully flattened state).

The extreme values of the total energy curves reflect the differences of the energy barrier of conversion. Namely, the bigger extreme values are, the more difficult folding transformation will be. Figure 5(d) demonstrates the bifurcation branches with C_{3v} and C_v symmetry possess the biggest and slightest energy barrier against the transition to another stable state, respectively. The energy barrier of the bifurcation branch with C_{2v} symmetry falls in between.

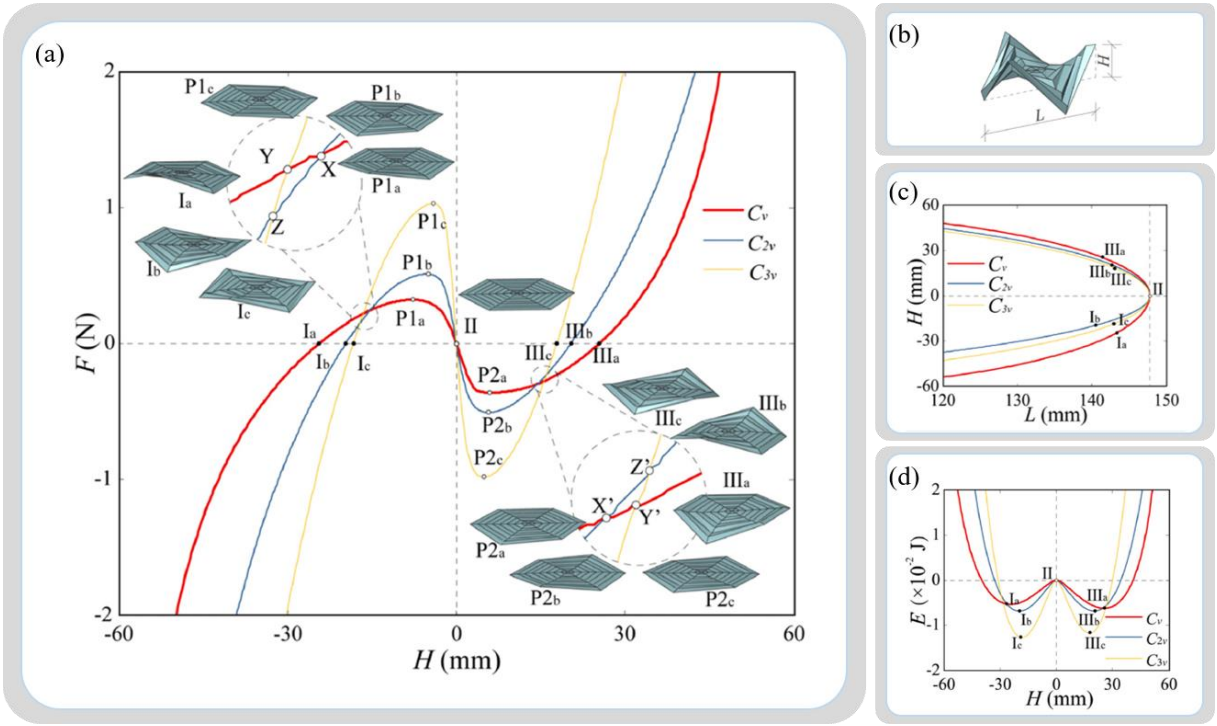


Figure 5 Comparison of various bifurcation branches. (a) Total equilibrium load-displacement curves. (b) Physical meaning of span (L) and height (H). (c) Span versus height curves. (d) Total energy versus height curves.

3.3. Influences of geometric parameters on multi-stability

3.3.1. Influence of material thickness t

The investigation of model T0 in Section 3.1 will be used as a reference to study the multi-stability of model T1 to T4 in Table 1. Figure 6(a), (c), and (e) depict the results of C_{3v}, C_{2v}, and C_v symmetries, respectively. Point $T0_I$, $T0_{II}$, $T0_{III}$ represents state 1, 2 and 3 in model T0, respectively. It is concluded that the bigger material thickness will lead to larger peak values of the equilibrium load during the transitions between two stable states. In Figure 6(b), (d), and (f), the curves of peak equilibrium load are centrosymmetric along the origin point. During the loading transition from state 1 to state 2, the peak equilibrium load is F_L. Similarly, F_R denotes the peak equilibrium load during the recovery transition from state 2 to state 3. The fitting operation demonstrates F_L and F_R are proportional to t^3.

Table 1 Parameters of numerical examples.

Model	T0	T1	T2	T3	T4	F1	F2	F3	F4	F5
L (mm)	64	64	64	64	64	60	60	60	60	60
D (mm)	8	8	8	8	8	12	12	12	12	12
d (mm)	8	8	8	8	8	4	6	8	12	16
t (μm)	127	40	76	200	240	127	127	127	127	127

The stable height H is defined by the height at which the structure reaches a stable state. Figure 6(a), (c), and (e) demonstrate H increases with t. H_I and H_{III} denote the stable height of stable State 1 and stable State 3, respectively. The absolute value of H indicates its structural height. If H increases along the positive z-axis, it is positive. Otherwise, H is negative. Hence, the farther the stable state from H=0 will contribute to the higher stable height. In summary, the bigger material thickness is, the larger peak equilibrium loads and the stable heights will be.

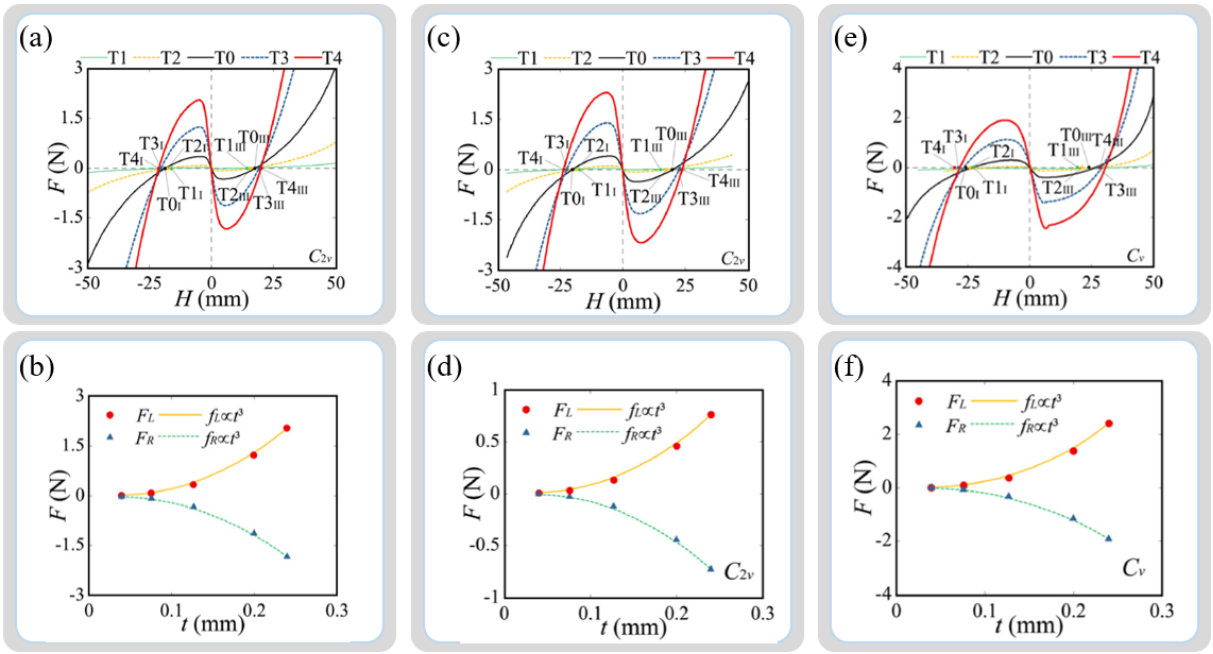


Figure 6 Effects of material thickness. (a), (c), and (e:) Equilibrium load versus height curves of a single load point. (b), (d), and (f): Relationship between the material thickness (t) and the peak equilibrium load (F).

3.3.2. Influence of crease length d

According to the variation of d, creases patterns of model F1 to F5 are presented in Figure 7. Figure 8(a) to (c) illustrate the equilibrium load versus height curves of C_{3v}, C_{2v}, and C_v symmetries, respectively. Point $F1_{P1}$ and $F1_{P2}$ represent State P1 and State P2 in model F1, respectively.

Figure 8 illustrates the peak equilibrium loads increase with d during the transition between stable states with the identical symmetry order. Since L remains constant, the variation of d will directly affect the change of n. Hence, the total length of all creases l is introduced to denote these two variables for simplicity. Figure 8(d) reflects the peak equilibrium loads in both the loading and recovery transitions increase with l. In other words, the longer crease length will lead to a more difficult folding process.

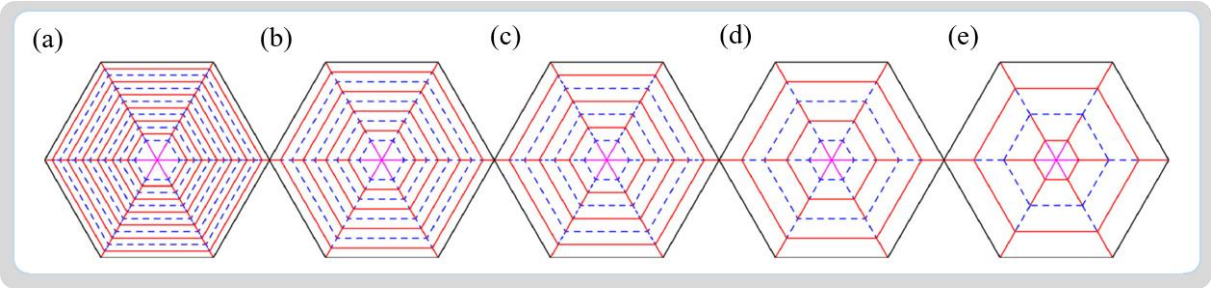


Figure 7 Crease patterns with different *d*.

In conclusion, the increasement of crease lengths will generate more significant energy barriers. The stable height is related to the *d*, *n* and *l* and remains to be further studied. In addition, it is essential for facilitating the design of novel programmable metamaterials to study the effects of different spans *L* and the number of initial polygon sides on the stable states.

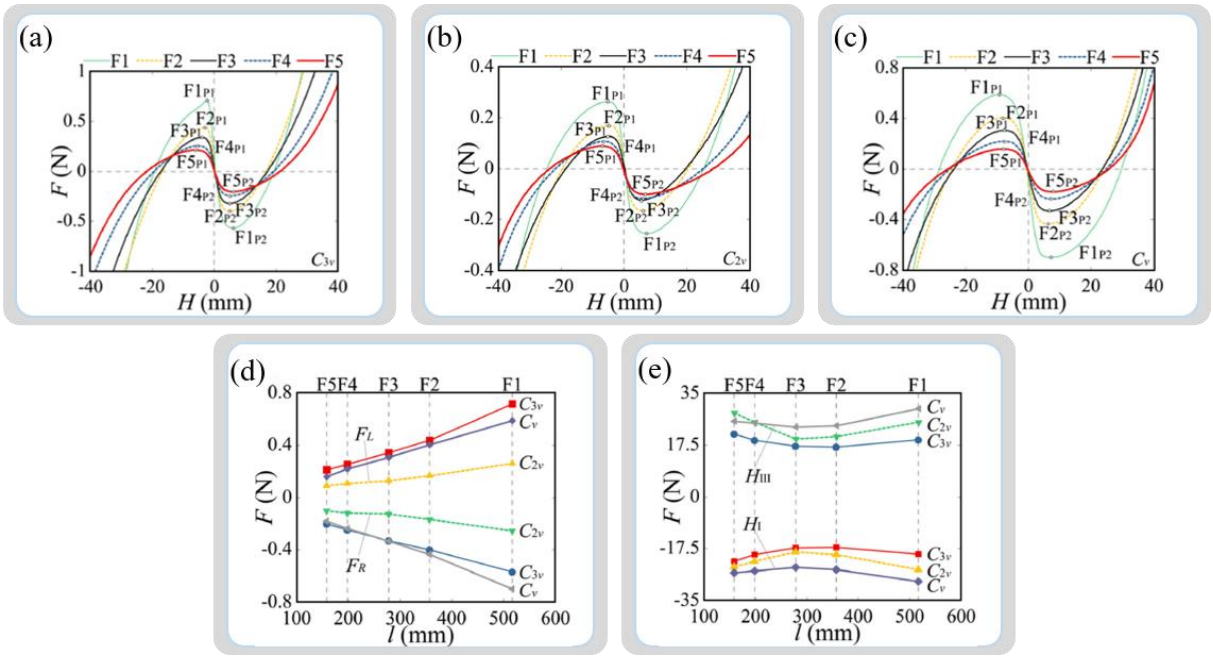


Figure 8 Effect of crease spacing. (a) to (c) Equilibrium load versus height curves of a single load point. (d) Relationship between the creases length *l* and the peak equilibrium loads F_L and F_R. (e) Relationship between the creases length *l* and the stable heights H_{I} and H_{III}.

4. Conclusion

In this work, we have adopted a group-theoretic approach and symmetry breaking for exploring the multi-stability of hexagonal origami hypar. The equivalent bar-and-hinge model was applied to simulate the whole folding and unfolding process. Concurrently, the group-theoretic approach was selected to avoid singularity in the stiffness matrix near the bifurcations. Based on symmetry breaking behaviour, the symmetry subgroups were obtained to trace bifurcation branches. The multi-stability of the structure can be obtained by analyzing the multi-stability of bifurcation branches.

Results illustrate the hexagonal hypar belongs to non-rigid origami due to the existence of non-rigid bending deformation. The bifurcation paths of the hexagonal origami hypar include C_{3v}, C_{2v}, and C_v symmetries. Every bifurcation branches exist bistability. Hence, the hexagonal origami hypar has six independent stable states. Notably, these stable states can be converted to each other only through the

fully flattened state. During the transition, the energy barrier of bifurcation branches with C_{3v}, C_{2v}, and C_v symmetries are in decreasing order. Meanwhile, the larger material thickness *t* or the crease length *l* will result in bigger energy barriers.

Note that the proposed method can convert the multi-stability of origami structures with high-order symmetry to multi-stability investigations in different bifurcation branches. By simplifying the complex folding analysis, this method has the potential to be extended for the multi-stability study of general origami structures.

Acknowledgements

This work has been supported by the National Natural Science Foundation of China (Grants No. 51978150 and 52050410334), Southeast University "Zhongying Young Scholars" Project, and the Fundamental Research Funds for the Central Universities. The corresponding author would like to acknowledge financial support from the Alexander von Humboldt-Foundation for his academic research at Max-Planck-Institut für Eisenforschung GmbH.

References

[1] K. Liu, T. Tachi and G. H. Paulino, "Bio-inspired origami metamaterials with metastable phases through mechanical phase transitions," *Journal of Applied Mechanics,* vol. 88, p. 091002, 2021.

[2] J. C. Ji, Q. Luo and K. Ye, "Vibration control based metamaterials and origami structures: A state-of-the-art review," *Mechanical Systems and Signal Processing,* vol. 161, p. 107945, 2021.

[3] X. Zhang, J. Ma, M. Li, Z. You, X. Wang, Y. Luo, K. Ma, and Y. Chen, "Kirigami-based metastructures with programmable multistability," *Proceedings of the National Academy of Sciences,* vol. 119, p. e2117649119, 2022.

[4] Y. Chen, C. Lu, W. Fan, J. Feng, and P. Sareh, "Data-driven design and morphological analysis of conical six-fold origami structures," *Thin-Walled Structures,* vol. 185, p. 110626, 2023.

[5] Y. Zhang, Q. Wang, M. Tichem, and F. van Keulen, "Design and characterization of multi-stable mechanical metastructures with level and tilted stable configurations," *Extreme Mechanics Letters,* vol. 34, p. 100593, 2020.

[6] H. Yasuda, T. Tachi, M. Lee, and J. Yang, "Origami-based tunable truss structures for non-volatile mechanical memory operation," *Nature Communications,* vol. 8, p. 962, 2017.

[7] Y. Chen, W. Ye, R. Xu, Y. Sun, J. Feng, and P. Sareh, "A programmable auxetic metamaterial with tunable crystal symmetry," *International Journal of Mechanical Sciences,* vol. 249, p. 108249, 2023.

[8] C. Lu, Y. Chen, J. Yan, J. Feng, and P. Sareh, "Algorithmic spatial form-finding of four-fold origami structures based on mountain-valley assignments," *Journal of Mechanisms and Robotics,* vol. 16, pp. 1-25, 2023.

[9] Y. Chen, J. Liang, P. Shi, J. Feng, P. Sareh, and J. Dai, "Inverse design of programmable Poisson's ratio and in-plane stiffness for generalized four-fold origami," *Composite Structures,* vol. 311, p. 116789, 2023.

[10] H. Yasuda and J. Yang, "Reentrant origami-based metamaterials with negative Poisson's ratio and bistability," *Physical Review Letters,* vol. 114, p. 185502, 2015.

[11] P. Bhovad, J. Kaufmann and S. Li, "Peristaltic locomotion without digital controllers: Exploiting multi-stability in origami to coordinate robotic motion," *Extreme Mechanics Letters,* vol. 32, p. 100552, 2019.

[12] L. Lu, X. Dang, F. Feng, P. Lv, and H. Duan, "Conical Kresling origami and its applications to curvature and energy programming," *Proceedings of the Royal Society A: Mathematical, Physical and Engineering Sciences,* vol. 478, p. 20210712, 2022.

[13] J. L. Silverberg, J. Na, A. A. Evans, B. Liu, T. C. Hull, C. D. Santangelo, R. J. Lang, R. C. Hayward, and I. Cohen, "Origami structures with a critical transition to bistability arising from hidden degrees of freedom," *Nature Materials,* vol. 14, pp. 389-393, 2015.

[14] J. Ma, S. Zang, H. Feng, Y. Chen, and Z. You, "Theoretical characterization of a non-rigid-foldable square-twist origami for property programmability," *International Journal of Mechanical Sciences,* vol. 189, p. 105981, 2021.

[15] H. Yasuda, K. Johnson, V. Arroyos, K. Yamaguchi, J. R. Raney, and J. Yang, "Leaf-like origami with bistability for self-adaptive grasping motions," *Soft Robotics,* vol. 9, pp. 938-947, 2022.

[16] Y. Chen, R. Xu, C. Lu, K. Liu, J. Feng, and P. Sareh, "Multi-stability of the hexagonal origami hypar based on group theory and symmetry breaking," *International Journal of Mechanical Sciences,* vol. 247, p. 108196, 2023.

[17] H. Feng, R. Peng, S. Zang, J. Ma, and Y. Chen, "Rigid foldability and mountain-valley crease assignments of square-twist origami pattern," *Mechanism and Machine Theory,* vol. 152, p. 103947, 2020.

[18] K. Liu, T. Tachi and G. H. Paulino, "Invariant and smooth limit of discrete geometry folded from bistable origami leading to multistable metasurfaces," *Nature Communications,* vol. 10, p. 4238, 2019.

[19] Y. C. Hu, Y. X. Zhou, K. W. Kwok, and K. Y. Sze, "Simulating flexible origami structures by finite element method," *International Journal of Mechanics and Materials in Design,* vol. 17, pp. 801-829, 2021.

[20] T. Yuan, L. Tang, Z. Liu, and J. Liu, "Nonlinear dynamic formulation for flexible origami-based deployable structures considering self-contact and friction," *Nonlinear Dynamics,* vol. 106, pp. 1789-1822, 2021.

[21] L. H. Dudte, L. Mahadevan, C. D. Santangelo, and M. A. Dias, "Geometric mechanics of curved crease origami," *Physical Review Letters,* vol. 109, p. 114301, 2012.

[22] P. Kumar and S. Pellegrino, "Computation of kinematic paths and bifurcation points," *International Journal of Solids and Structures,* vol. 37, pp. 7003-7027, 2000.

[23] Y. Chen and Z. You, "Two-fold symmetrical 6R foldable frame and its bifurcations," *International Journal of Solids and Structures,* vol. 46, pp. 4504-4514, 2009.

[24] Z. Lü, L. Chen and L. Duan, "Bifurcation analysis of mixed bursting in the pre-Bötzinger complex," *Applied Mathematical Modelling,* vol. 67, pp. 234-251, 2019.

[25] J. Tao and S. Li, "Asymmetric multi-stability from relaxing the rigid-folding conditions in a stacked Miura-ori cellular solid," *Thin-Walled Structures,* vol. 179, p. 109685, 2022.

[26] E. T. Filipov, K. Liu, T. Tachi, M. Schenk, and G. H. Paulino, "Bar and hinge models for scalable analysis of origami," *International Journal of Solids and Structures,* vol. 124, pp. 26-45, 2017.

[27] A. Zingoni, "On the best choice of symmetry group for group-theoretic computational schemes in solid and structural mechanics," *Computers & Structures,* vol. 223, p. 106101, 2019.

[28] K. Ikeda and K. Murota, "Bifurcation analysis of symmetric structures using block-diagonalization," *Computer Methods in Applied Mechanics and Engineering,* vol. 86, pp. 215-243, 1991.

[29] S. D. Guest and P. W. Fowler, "Symmetry Conditions and Finite Mechanisms," *Journal of Mechanics of Materials and Structures,* vol. 2, pp. 293-302, 2007.

[30] Y. Chen, C. Lu, J. Yan, J. Feng, and P. Sareh, "Intelligent computational design of scalene-faceted flat-foldable tessellations," *Journal of Computational Design and Engineering,* vol. 9, pp. 1765-1774, 2022.

IASS 2023
July 10–14 Melbourne
Integration of Design and Fabrication

Proceedings of the IASS Annual Symposium 2023
Integration of Design and Fabrication
10–14 July 2023, Melbourne, Australia
Y.M. Xie, J. Burry, T.U. Lee and J. Ma (eds.)

Panel-pin model for kinematic and equilibrium analysis of rigid origami

Kentaro HAYAKAWA[a,*], Makoto OHSAKI[a]

[a,*] Department of Architecture and Architectural Engineering, Kyoto University
Kyoto-Daigaku Katsura, Nishikyo, Kyoto 615-8540, Japan
se.hayakawa@archi.kyoto-u.ac.jp

Abstract

In this study, the mathematical model referred to as the panel-pin model is proposed for analyzing the infinitesimal-deformation mechanism and the large-deformation equilibrium path of a rigid origami composed of rigid faces (panels) and subjected to deformation only at its crease lines. The panel-pin model represents a rigid origami as a structure of rigid panels pin-connected at the vertices and has the following advantages: 1) consistent formulation of compatibility equations for any type of the rigid origami structure; 2) systematic computation of vertex displacements, folding angles, and their derivatives; and 3) ease of accounting for gravity acting on the panels. The infinitesimal mechanism of the panel-pin model is studied according to the standard procedure for mechanisms and linkages, and an equilibrium path is traced as the trajectory of equilibrium points obtained by minimizing the total potential energy of the model with a rotational spring along each crease line. The numerical examples with multiple degrees of freedom of the mechanism show that the multiple equilibrium paths can be obtained by assigning the initial imperfection, and this is also confirmed by the physical model.

Keywords: rigid origami, kinematics, equilibrium, energy minimization, geometrically nonlinear analysis

1. Introduction

Rigid origami is folded and unfolded within strict constraints, with its faces remaining undeformed during the folding process. It has wide range of potential engineering applications; e.g., solar panels on artificial satellites [1], robots [2], and transformable building envelopes [3]. Consequently, the analysis and simulation of folding properties are crucial to effectively exploit the deformation mechanisms of rigid origami, and numerous models and methods have been proposed in this respect [4].

The rotation hinge model [5, 6] in Fig. 1(b) and the truss model [7, 8] in Fig. 1(c) are commonly used for kinematic analysis of rigid origami. In the former model, folding angles are treated as independent variables, and a folding state can be expressed with fewer variables than other models. However, its complicated expression of vertex positions makes it difficult to incorporate displacement boundary conditions and external loads applied to vertices. In contrast, the latter model consists of rigid bars placed along the edges and treats the nodal translations as variables, making it easy to fix nodal displacements and to apply nodal loads. The disadvantage of this model is its complicated configuration for modelling a face with more than three edges; diagonal members must be arranged for the in-plane rigidity, and trigonometric geometric constraints [7] or the three-dimensional member assemblages [8] are necessary for the out-of-plane rigidity. The frame model in Fig. 1(d) has also been developed [9, 10], which consists of frame members hinge-connected at each crease line and rigidly connected at the node on each face. Although a folding path tracing method of this model has been proposed [10], this is not suitable for large models due to the high computational cost associated with a larger number of variables.

In this study, a *panel-pin model* is proposed for providing a simpler manner of ensuring the rigidity of faces compared to the truss model, while requiring fewer variables than the frame model. The

Copyright © 2023 by Kentaro HAYAKAWA and Makoto OHSAKI. Published in the Proceedings of the IASS Annual Symposium 2023 with permission.

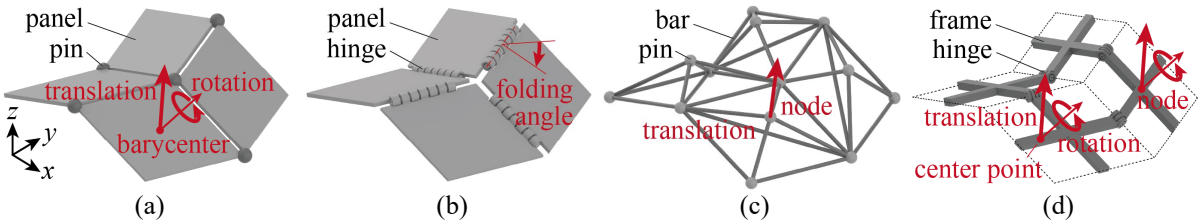


Figure 1. Models representing the deformation mechanism of rigid origami whose variables are indicated by red (a) Panel-pin model, (b) Rotation hinge model, (c) Truss model, (d) Frame model.

proposed model is highly versatile and can be applied to a wide range of analyses considering gravity, point loads, forced displacements and support conditions. This model offers following advantages;

1) consistent formulation of compatibility equations for describing the deformation mechanism of the model including holes or faces with more than three sides,
2) systematic computation of vertex displacements, folding angles, and their derivatives, and
3) ease of accounting for gravity acting on the panels.

The panel-pin model employs translation and rotation of the centers of gravity of rigid panels as independent variables, which are often used in the classical models of linkages. However, the formulation of the compatibility equations over these variables is different from that for linkages; the panels are pin-connected at the vertices instead of being joined by hinges. The vertex displacements and folding angles are treated as nonlinear functions of the panel displacements. The displacement boundary conditions on the vertices are incorporated as additional compatibility equations. The infinitesimal mechanism of the panel-pin model is determined from the derivatives of the compatibility equations. An equilibrium state under loads is determined by minimizing the total potential energy under the compatibility constraints after adding rotational springs along the crease lines. An equilibrium path is traced by sequentially updating the forced displacements, as proposed in Ref. [10].

2. Panel-pin model

2.1. Compatibility equations and folding angle at a single crease line

Suppose vertices 1 and 2 are the endpoints of the crease line, a unit vector directed from vertices 1 to 2 at the initial state is denoted by $\mathbf{e}^0 \in \mathbb{R}^3$. Note that the superscript 0 indicates the value at the initial state of the vector. In addition, let $\mathbf{n}_i^0$ and $\mathbf{d}_{i,j}^0 \in \mathbb{R}^3$ denote the unit normal vector of panel i and the vector from the barycenter of panel i to vertex j $(i,\ j=1,\ 2)$, respectively, at the initial state. The directions of the unit panel normal vectors are determined to the same side of the origami, and the local panel indices are determined so that panels 1 and 2 satisfies $\left\langle \mathbf{n}_1^0,\ \mathbf{d}_{1,1}^0 \times \mathbf{d}_{1,2}^0 \right\rangle > 0$ and $\left\langle \mathbf{n}_2^0,\ \mathbf{d}_{2,1}^0 \times \mathbf{d}_{2,2}^0 \right\rangle < 0$, respectively, where $\langle \bullet,\ \bullet \rangle$ stands for the inner product of two vectors. $\mathbf{b}_i^0 \in \mathbb{R}^3$ $(i=1,\ 2)$ is also defined such that $\mathbf{b}_i^0 = \mathbf{e}^0 \times \mathbf{n}_i^0$. Note that at the initial state, the crease lines may have non-zero folding angles.

Let $\mathbf{u}_i$ and $\boldsymbol{\theta}_i \in \mathbb{R}^3$ denote the translation and rotation vectors of panel i, respectively, in the global coordinate system $(x_1,\ x_2,\ x_3)$. As shown in Fig. 2(a), $\mathbf{n}_i$, $\mathbf{d}_{i,j}$, and $\mathbf{b}_i \in \mathbb{R}^3$ $(i,\ j=1,\ 2)$ are defined as

$$\mathbf{n}_i = \mathbf{R}(\boldsymbol{\theta}_i)\mathbf{n}_i^0, \quad \mathbf{d}_{i,j} = \mathbf{R}(\boldsymbol{\theta}_i)\mathbf{d}_{i,j}^0, \quad \mathbf{b}_i = \mathbf{R}(\boldsymbol{\theta}_i)\mathbf{b}_i^0 \tag{1}$$

where $\mathbf{R}(\boldsymbol{\theta}_i) \in \mathbb{R}^{3\times 3}$ is the Rodrigues' rotation matrix [11] with respect to $\boldsymbol{\theta}_i$. Using these vectors, the translation vector $\mathbf{v}_j^i \in \mathbb{R}^3$ $(i,\ j=1,\ 2)$ of vertex j can be written in two ways:

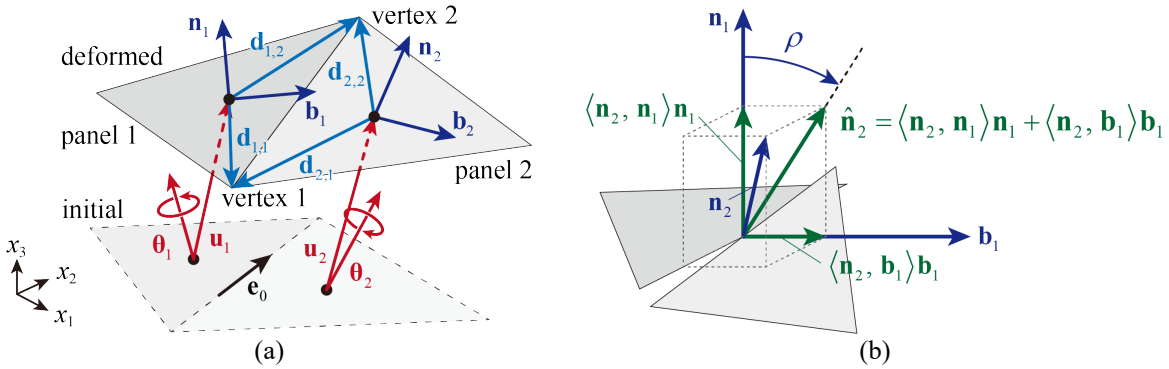


Figure 2. (a) Reference vectors of panels, (b) Reference vectors for calculating the folding angle

$$\mathbf{v}_j^i = \mathbf{u}_i + \mathbf{d}_{i,j} - \mathbf{d}_{i,j}^0 = \mathbf{u}_i + \left(\mathbf{R}(\boldsymbol{\theta}_i) - \mathbf{I}_3\right)\mathbf{d}_{i,j}^0 \quad (i = 1, 2) \tag{2}$$

where $\mathbf{I}_3 \in \mathbb{R}^{3\times 3}$ is the identity matrix. Since $\mathbf{v}_j^1 = \mathbf{v}_j^2$ should be satisfied, the compatibility equation for the displacements of panels 1 and 2 at vertex j $(=1, 2)$ is formulated as follows:

$$\Delta\mathbf{u}_j^{1,2} = \mathbf{u}_1 + \left(\mathbf{R}(\boldsymbol{\theta}_1) - \mathbf{I}_3\right)\mathbf{d}_{1,j}^0 - \mathbf{u}_2 - \left(\mathbf{R}(\boldsymbol{\theta}_2) - \mathbf{I}_3\right)\mathbf{d}_{2,j}^0 = \mathbf{0} \tag{3}$$

Furthermore, folding angle $\rho \in \mathbb{R}$ $(-\pi < \rho \le \pi)$ of the considering crease line is defined as

$$\rho = \operatorname{atan2}\left(\langle \mathbf{n}_2, \mathbf{b}_1 \rangle, \langle \mathbf{n}_2, \mathbf{n}_1 \rangle\right) \tag{4}$$

where $\operatorname{atan2}(y, x)$ is the 2-argument arctangent available in various programming languages. As shown in Fig. 2(b), ρ defined in Eq. (4) is the angle between $\mathbf{n}_1$ and $\hat{\mathbf{n}}_2 = \langle \mathbf{n}_2, \mathbf{n}_1 \rangle \mathbf{n}_1 + \langle \mathbf{n}_2, \mathbf{b}_1 \rangle \mathbf{b}_1$, which is a vector obtained by projecting $\mathbf{n}_2$ onto the plane spanned by $\mathbf{n}_1$ and $\mathbf{b}_1$. When $\Delta\mathbf{u}_1^{1,2} = \Delta\mathbf{u}_2^{1,2} = \mathbf{0}$, $\mathbf{n}_2 = \hat{\mathbf{n}}_2$, $\sin\rho = \langle \mathbf{n}_2, \mathbf{b}_1 \rangle$ and $\cos\rho = \langle \mathbf{n}_2, \mathbf{n}_1 \rangle$. According to Eq. (1), ρ is the function of only $\boldsymbol{\theta}_1$ and $\boldsymbol{\theta}_2$, and its derivatives can be systematically calculated using the derivatives of the rotation matrices.

Remark 1 By using $\operatorname{atan2}(y, x)$ function instead of arcsin or arccos function, ρ and its partial derivatives can be compatibly calculated even when $\Delta\mathbf{u}_1^{1,2} \neq \mathbf{0}$ or $\Delta\mathbf{u}_2^{1,2} \neq \mathbf{0}$.

2.2. Compatibility equations for entire rigid origami and displacements of vertices

Let N^{c}, N^{p}, and N^{v} denote the number of crease lines, panels (faces), and vertices of a rigid origami, respectively. The *generalized displacement vector* $\mathbf{X} \in \mathbb{R}^N$ is defined as the assemblage of the components of $\mathbf{u}_i$ and $\boldsymbol{\theta}_i$ for all $i = 1, \ldots, N^{\mathrm{p}}$ where $N = 6N^{\mathrm{p}}$. When adjacent panels i_1 and i_2 $(=1, \ldots, N^{\mathrm{p}})$ are connected at vertex j $(=1, \ldots, N^{\mathrm{v}})$ as shown in Fig. 3, the compatibility equation for the displacements of panels i_1 and i_2 at vertex j is formulated from Eq. (3) as

$$\Delta\mathbf{u}_j^{i_1,i_2}(\mathbf{X}) = \mathbf{u}_{i_1} + \left(\mathbf{R}(\boldsymbol{\theta}_{i_1}) - \mathbf{I}_3\right)\mathbf{d}_{i_1,j}^0 - \mathbf{u}_{i_2} - \left(\mathbf{R}(\boldsymbol{\theta}_{i_2}) - \mathbf{I}_3\right)\mathbf{d}_{i_2,j}^0 = \mathbf{0} \tag{5}$$

Its physical interpretation is indicated in Fig. 3. Since Eq. (5) is formulated at every endpoint of the crease line, there are in total $6N^{\mathrm{c}}$ compatibility conditions for the entire rigid origami. Here, all $\Delta\mathbf{u}_j^{i_1,i_2}(\mathbf{X})$ are assembled into a vector $\Delta\mathbf{U}(\mathbf{X}) \in \mathbb{R}^{6N^{\mathrm{c}}}$, and the compatibility equation for the entire rigid origami is formulated as $\Delta\mathbf{U}(\mathbf{X}) = \mathbf{0}$.

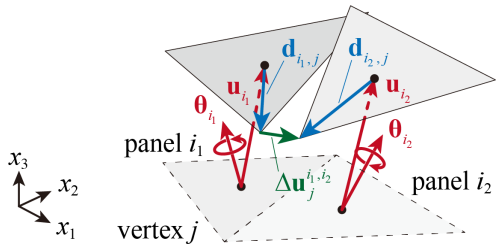


Figure 3. Incompatibility of the displacements of panels i_1 and i_2 at vertex j

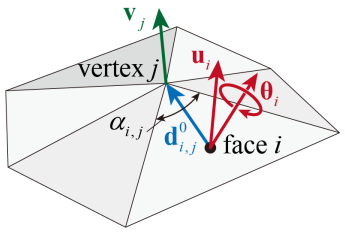


Figure 4. Translational displacement of vertex j

Next, we formulate the translation of a vertex. Although it can be written as in Eq. (2), the different formulation is used to include the case where $\Delta\mathbf{U}(\mathbf{X}) \neq \mathbf{0}$. Let $\mathcal{I}_j$ denote the set of indices of panels around vertex j $(=1,\ldots,N^{\mathrm{v}})$, and $\alpha_{i,j}$ $(i \in \mathcal{I}_j)$ denote the inner angle of panel i at vertex j as shown in Fig. 4. The translation vector $\mathbf{v}_j(\mathbf{X}) \in \mathbb{R}^3$ $(j=1,\ldots,N^{\mathrm{v}})$ of vertex j is calculated as follows:

$$\mathbf{v}_j(\mathbf{X}) = \frac{1}{A_j}\sum_{i\in\mathcal{I}_j}\alpha_{i,j}\left\{\mathbf{u}_i + \left(\mathbf{R}(\boldsymbol{\theta}_i) - \mathbf{I}_3\right)\mathbf{d}_{i,j}^0\right\}, \quad A_j = \sum_{i\in\mathcal{I}_j}\alpha_{i,j} \tag{6}$$

Remark 2 $\mathbf{v}_j(\mathbf{X})$ defined in Eq. (6) is the weighted average of the positions of panel vertices around vertex j, and reasonably estimates the position of vertex j when $\Delta\mathbf{U}(\mathbf{X}) \neq \mathbf{0}$. $\mathbf{v}_j$ and its partial derivatives with respect to the panel displacements can be compatibly calculated even when $\Delta\mathbf{U}(\mathbf{X}) \neq \mathbf{0}$.

Suppose the displacement of vertex j $(=1,\ldots,N^{\mathrm{v}})$ in the x_k-direction $(k=1, 2, 3)$ denoted by $v_j^{(k)}(\mathbf{X})$ is fixed, and let $\mathcal{J}^{\mathrm{f}}$ denote the set of index pairs of the vertices and the fixed directions. When the number of components of $\mathcal{J}^{\mathrm{f}}$ is N^{f}, $v_j^{(k)}(\mathbf{X})$ for all $\{j,k\} \in \mathcal{J}^{\mathrm{f}}$ are assembled into a vector $\Delta\mathbf{V}^{\mathrm{f}}(\mathbf{X}) \in \mathbb{R}^{N^{\mathrm{f}}}$. In addition, we also consider the forced vertex displacements, and let $\mathcal{J}^{\mathrm{d}}$ represent the set of index pairs of the vertices and the directions to which the forced displacements are applied. The non-zero target value of $v_j^{(k)}(\mathbf{X})$ $(\{j,k\} \in \mathcal{J}^{\mathrm{d}};\ j=1,\ldots,N^{\mathrm{v}};\ k=1, 2, 3)$ is denoted by $v_j^{\mathrm{d}(k)} \in \mathbb{R}$, and $v_j^{(k)}(\mathbf{X}) - v_j^{\mathrm{d}(k)}$ for all $\{j,k\} \in \mathcal{J}^{\mathrm{d}}$ are assembled into a vector $\Delta\mathbf{V}^{\mathrm{d}}(\mathbf{X}) \in \mathbb{R}^{N^{\mathrm{d}}}$ where N^{d} is the number of components of $\mathcal{J}^{\mathrm{d}}$. Here, $\Delta\mathbf{U}(\mathbf{X})$, $\Delta\mathbf{V}^{\mathrm{f}}(\mathbf{X})$, and $\Delta\mathbf{V}^{\mathrm{d}}(\mathbf{X})$ are combined into a column vector $\mathbf{C}(\mathbf{X}) = (\Delta\mathbf{U}(\mathbf{X})^{\mathrm{T}}, \Delta\mathbf{V}^{\mathrm{f}}(\mathbf{X})^{\mathrm{T}}, \Delta\mathbf{V}^{\mathrm{d}}(\mathbf{X})^{\mathrm{T}})^{\mathrm{T}} \in \mathbb{R}^M$ which is referred to as the *incompatiblity vector*. The number of components of $\mathbf{C}(\mathbf{X})$ is calculated as $M = 6N^{\mathrm{c}} + N^{\mathrm{f}} + N^{\mathrm{d}}$. Then, the compatibility equations representing the panel connectivity, fixed vertex displacements, and the forced vertex displacements are collectively written in a vector form as

$$\mathbf{C}(\mathbf{X}) = \mathbf{0} \tag{7}$$

3. Infinitesimal mechanism analysis

3.1. First-order infinitesimal mechanism

An infinitesimal mechanism of a panel-pin model is investigated to comprehend the degrees of freedom of the mechanism and the deformation modes in the range of infinitesimal deformation. It is evaluated in the same manner as the basic procedure for other models [2 – 5]. To compatibly incorporate the

degrees of freedom corresponding to the forced displacements, $\Delta\mathbf{V}^{\mathrm{d}}(\mathbf{X})=\mathbf{0}$ is replaced to constrain the relative displacements among the vertices where the forced displacements are assigned. When $N^{\mathrm{d}}=1$, the constraint for the forced displacement is not necessary. When $N^{\mathrm{d}}>1$, a single pair $\{\bar{j},\bar{k}\}$ is selected from $\mathcal{J}^{\mathrm{d}}$, and the constraint between $v_j^{(k)}(\mathbf{X})$ and $v_{\bar{j}}^{(\bar{k})}(\mathbf{X})$ is formulated as

$$\frac{1}{v_j^{\mathrm{d}(k)}}v_j^{(k)}(\mathbf{X})-\frac{1}{v_{\bar{j}}^{\mathrm{d}(\bar{k})}}v_{\bar{j}}^{(\bar{k})}(\mathbf{X})=0\quad(\{j,k\},\{\bar{j},\bar{k}\}\in\mathcal{J}^{\mathrm{d}};\{j,k\}\neq\{\bar{j},\bar{k}\}) \tag{8}$$

There are $N^{\mathrm{d}}-1$ constraints on the relative vertex displacements, and the left-hand sides of Eq (8) for all $\{j,k\}\in\mathcal{J}^{\mathrm{d}}\setminus\{\bar{j},\bar{k}\}$ are assembled into a vector $\Delta\bar{\mathbf{V}}^{\mathrm{d}}(\mathbf{X})\in\mathbb{R}^{N^{\mathrm{d}}-1}$. In the following, the argument $\mathbf{X}$ will be omitted for simple expression. Defining $\bar{\mathbf{C}}=\left(\Delta\mathbf{U}^{\mathrm{T}},\Delta\mathbf{V}^{\mathrm{fT}},\Delta\bar{\mathbf{V}}^{\mathrm{dT}}\right)^{\mathrm{T}}\in\mathbb{R}^{M-1}$, the *first-order infinitesimal mechanism* is represented by a vector $\mathbf{X}'\in\mathbb{R}^{N}$ satisfying

$$\frac{\mathrm{d}\bar{\mathbf{C}}}{\mathrm{d}\mathbf{X}}\mathbf{X}'=\mathbf{0} \tag{9}$$

$\mathrm{d}\bar{\mathbf{C}}/\mathrm{d}\mathbf{X}\in\mathbb{R}^{(M-1)\times N}$ is the *compatibility matrix* whose (i,j) component is $\partial\bar{C}_i/\partial X_j$ where the italic letter such as $\bar{C}_i$ and its subscript represent the component of a vector and its index, respectively. $\mathbf{X}'$ satisfying Eq. (9) is in the null-space of $\mathrm{d}\bar{\mathbf{C}}/\mathrm{d}\mathbf{X}$ whose dimension is $N-\mathrm{rank}(\mathrm{d}\bar{\mathbf{C}}/\mathrm{d}\mathbf{X})$, which is referred to as the number of kinematic indeterminacy, and its bases are referred to as the *infinitesimal mechanism modes*. Note that if the infinitesimal mechanism is investigated by using $\mathrm{d}\mathbf{C}/\mathrm{d}\mathbf{X}$ instead of $\mathrm{d}\bar{\mathbf{C}}/\mathrm{d}\mathbf{X}$, the forced displacements are regarded as the fixed displacements conditions. We can also define a *generalized self-equilibrium force* $\bar{\mathbf{F}}\in\mathbb{R}^{M-1}$ which satisfies

$$\bar{\mathbf{F}}^{\mathrm{T}}\frac{\mathrm{d}\bar{\mathbf{C}}}{\mathrm{d}\mathbf{X}}=\mathbf{0} \tag{10}$$

The self-equilibrium force $\bar{\mathbf{F}}$ satisfying Eq. (10) is in the left null-space of $\mathrm{d}\bar{\mathbf{C}}/\mathrm{d}\mathbf{X}$ whose dimension is $M-1-\mathrm{rank}(\mathrm{d}\bar{\mathbf{C}}/\mathrm{d}\mathbf{X})$, which is referred to as the number of statical indeterminacy.

3.2. Second-order infinitesimal mechanism

For a first-order infinitesimal mechanism $\mathbf{X}'$ satisfying Eq. (9), the *second-order infinitesimal mechanism* is represented by a pair of vectors $(\mathbf{X}',\mathbf{X}'')\in(\mathbb{R}^{N},\mathbb{R}^{N})$ satisfying

$$\frac{\mathrm{d}\bar{\mathbf{C}}}{\mathrm{d}\mathbf{X}}\mathbf{X}''+\left[\frac{\mathrm{d}^2\bar{\mathbf{C}}}{\mathrm{d}\mathbf{X}^2}\mathbf{X}'\right]\mathbf{X}'=\mathbf{0} \tag{11}$$

where $\mathrm{d}^2\bar{\mathbf{C}}/\mathrm{d}\mathbf{X}^2$ is the $(M-1)\times N\times N$ order-3 tensor whose (i,j,k) component is $\partial^2\bar{C}_i/\partial X_j\partial X_k$. The (i,j) component of $[(\mathrm{d}^2\bar{\mathbf{C}}/\mathrm{d}\mathbf{X}^2)\mathbf{X}']\in\mathbb{R}^{(M-1)\times N}$ is $\sum_{k=1}^{N}(\partial^2\bar{C}_i/\partial X_j\partial X_k)X_k'$. The second-order infinitesimal mechanism $(\mathbf{X}',\mathbf{X}'')$ exists if and only if $\mathbf{X}'$ satisfying Eq. (9) satisfies the following equation for any $\bar{\mathbf{F}}$ satisfying Eq. (10) [6]:

$$\bar{\mathbf{F}}^{\mathrm{T}}\left[\frac{\mathrm{d}^2\bar{\mathbf{C}}}{\mathrm{d}\mathbf{X}^2}\mathbf{X}'\right]\mathbf{X}'=\mathbf{X}'^{\mathrm{T}}\left[\bar{\mathbf{F}}^{\mathrm{T}}\frac{\mathrm{d}^2\bar{\mathbf{C}}}{\mathrm{d}\mathbf{X}^2}\right]\mathbf{X}'=0 \tag{12}$$

where the $(i,\ j)$ component of $[\overline{\mathbf{F}}^{\mathrm{T}}(\mathrm{d}^2\overline{\mathbf{C}}/\mathrm{d}\mathbf{X}^2)] \in \mathbb{R}^{N\times N}$ is calculated as $\sum_{k=1}^{M-1}\overline{F}_k(\partial^2\overline{C}_k/\partial X_i\partial X_j)$.

4. Equilibrium path analysis under gravity

4.1. Finding an equilibrium point

An equilibrium state of a panel-pin model is obtained by the energy minimization approach [10]. To stabilize and uniquely determine the equilibrium state, rotational stiffness is assigned to each crease line. The moment around crease line k $(=1,\ldots,N^{\mathrm{c}})$ is calculated as $K_k(\rho_k-\rho_k^0)$ for the constant $K_k\in\mathbb{R}$ where ρ_k^0 is the initial folding angle of crease line *k*. Let w_i and $u_i^{\mathrm{ref}(3)}\in\mathbb{R}$ denote the weight and the reference height of the barycenter of panel *i*, respectively, to determine the potential energy of the gravity in the x_3-direction. When the constant point load $\mathbf{p}_j\in\mathbb{R}^3$ $(j=1,\ldots,N^{\mathrm{v}})$ is applied to vertex j, the total potential energy of the panel-pin model is defined as the function of $\mathbf{X}$ as

$$\Pi(\mathbf{X})=\frac{1}{2}\sum_{k=1}^{N^{\mathrm{e}}}K_k\left(\rho_k(\mathbf{X})-\rho_k^0\right)^2+\sum_{i=1}^{N^{\mathrm{p}}}w_i\left(u_i^{(3)}(\mathbf{X})-u_i^{\mathrm{ref}(3)}\right)-\sum_{i=1}^{N^{\mathrm{v}}}\mathbf{p}_j^{\mathrm{T}}\mathbf{v}_j(\mathbf{X}) \tag{13}$$

where $u_i^{(3)}(\mathbf{X})$ is the component of $\mathbf{u}_i(\mathbf{X})$ corresponding to the x_3-direction.

In this study, the *path parameter* is introduced, and the magnitude of the forced displacements and/or the loads are assumed to be the function of the path parameter $\xi\in\mathbb{R}$ only. Then, an equilibrium state is obtained for a given ξ by solving the following energy minimization problem:

$$\begin{aligned}&\min_{\mathbf{X}}.\quad \Pi(\mathbf{X})\\ &\text{s.t.}\quad\ \mathbf{C}(\mathbf{X})=\mathbf{0}\end{aligned} \tag{14}$$

The pair of the path parameter ξ and the solution $\mathbf{X}$ to Problem (14) is referred to as the *equilibrium point*. Problem (14) is solved by the augmented Lagrangian method (ALM) [12]. The augmented Lagrangian $L(\mathbf{X})$ with the penalty parameter $\gamma\in\mathbb{R}$ and the Lagrange multipliers $\boldsymbol{\lambda}\in\mathbb{R}^M$ is defined as

$$L(\mathbf{X})=\Pi(\mathbf{X})+\mathbf{C}(\mathbf{X})^{\mathrm{T}}\left(\boldsymbol{\lambda}+\frac{\gamma}{2}\mathbf{C}(\mathbf{X})\right) \tag{15}$$

The solution to Problem (14) is obtained by repeatedly solving the following optimization problem:

$$\min_{\mathbf{X}}.\quad L(\mathbf{X}) \tag{16}$$

with constant $\boldsymbol{\lambda}$ while updating the multiplier as $\boldsymbol{\lambda}\leftarrow\boldsymbol{\lambda}+\gamma\mathbf{C}$ until the maximum absolute value among the components of $\mathbf{C}(\mathbf{X})$ becomes smaller than the user-specified tolerance C_{tol}. γ is automatically updated in the process of the ALM based on Ref. [12]. At an equilibrium point $(\mathbf{X},\xi)$, $\mathrm{d}L/\mathrm{d}X_j=0$ holds for all $j=1,\ldots,N$, and the convergence of Problem (16) is evaluated by comparing the maximum value among $\left|\mathrm{d}L/\mathrm{d}X_j\right|$ $(j=1,\ldots,N)$ to the user-specified tolerance E_{tol}.

4.3. Tracing an equilibrium path

An *equilibrium path* is the trajectory of the equilibrium point $(\mathbf{X},\xi)$ and traced by successively solving Problem (14) by the ALM while updating the path parameter as $\xi\leftarrow\xi+\mathrm{d}\xi$ where $\mathrm{d}\xi\in\mathbb{R}$ is the increment of ξ. In this study, the displacement control method is employed; i.e., each forced displacement $v_j^{\mathrm{d}(k)}$ $(\{j,k\}\in\mathcal{J}^{\mathrm{d}})$ is specified at each step of the equilibrium point search as

$$v_j^{\mathrm{d}(k)} = \xi \tilde{v}_j^{\mathrm{d}(k)} \tag{17}$$

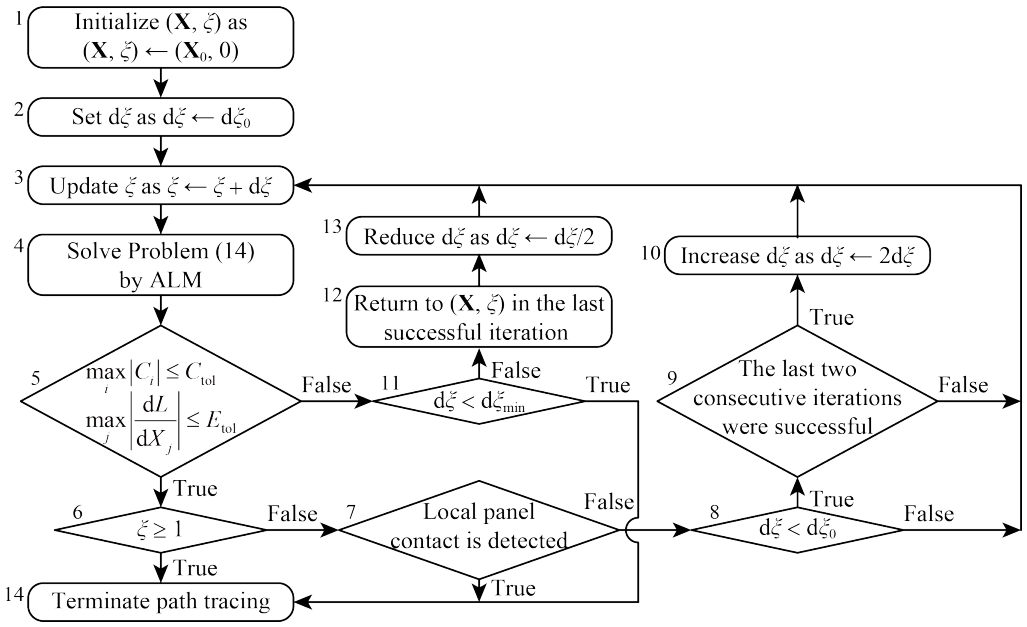


Figure 5. Flowchart of the equilibrium path tracing.

where ξ increases from 0 to 1 at the final step when $v_j^{\mathrm{d}(k)}$ reaches the target forced displacement $\tilde{v}_j^{\mathrm{d}(k)}$. The point loads $\mathbf{p}_j$ on vertices are assumed to be constant throughout the path tracing.

The procedure of the equilibrium path tracing is summarized in Fig. 5. At the initial step of the analysis (Step 1 in Fig. 5), $\mathbf{X}$ is initialized as $\mathbf{X} = \mathbf{X}_0$ where $\mathbf{X}_0$ represents the initial imperfection. Problem (14) is solved so that $\max_i |C_i| \le C_{\mathrm{tol}}$ and $\max_j |\mathrm{d}L/\mathrm{d}X_j| \le E_{\mathrm{tol}}$. However, if these conditions are not satisfied, the step size $\mathrm{d}\xi$ is reduced by half (Step 13). The reduced $\mathrm{d}\xi$ is restored to $2\mathrm{d}\xi$ if the equilibrium points are successfully found in the consecutive iterations (Step 10) to accelerate the analysis. The path tracing terminates when ξ reaches 1, $\mathrm{d}\xi$ decreases less than the specified lower bound $\mathrm{d}\xi_{\min} > 0$, or the local face contact between the panels adjacent to a crease line is detected.

5. Examples

5.1. Settings

The analysis is carried out by using a Python 3.9 program. Problem (16) in Section 4 is solved by using BFGS [13] available in scipy.optimize.minimize for the equilibrium path tracing. The units of length and force are omitted because they do not influence the analysis results.

Figure 6 shows the crease pattern to be analyzed. All the vertices are on the *xy*-plane in the initial shape. As indicated in green, the displacements of the vertices on the shorter boundaries are fixed, and the forced displacements are assigned along the *x*-axis as shown by the purple arrows. The orange arrows represent the loads in positive *y*-direction. The weight per unit area of each panel is 20, and the rotational stiffness per unit length of each crease line is 10. In the equilibrium path tracing, three types of initial imperfections based on sine functions are assigned to the panel translations in *z*-direction as shown in Fig. 7. The parameters are set as $C_{\mathrm{tol}} = E_{\mathrm{tol}} = 10^{-4}$ and $\mathrm{d}\xi_{\min} = 10^{-5}$ for all the following trials.

For an intuitive understanding of the path tracing results, a physical model has also been constructed as shown in Fig. 8. The model is hanged from the curtain rails at the hooks attached at the vertices, and the hooks in front are fixed to the rails. The curtain rail on the right side of the picture can move along

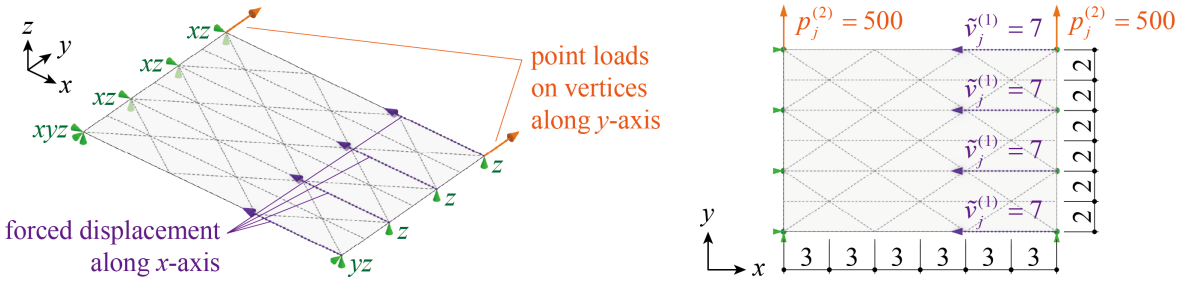


Figure 6. Initial flat shape, panel dimension, and boundary conditions.

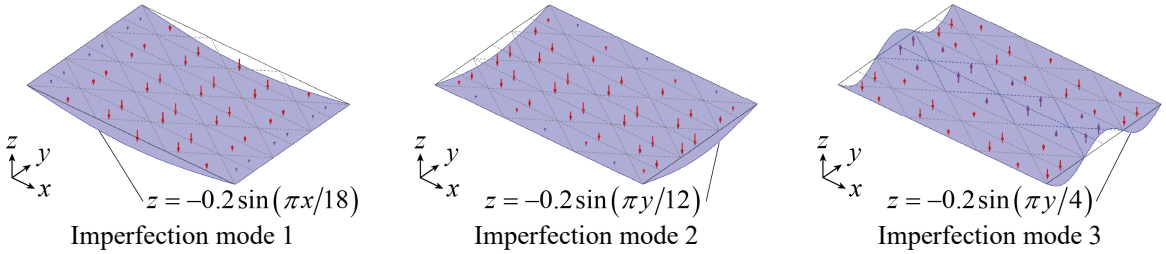


Figure 7. Initial imperfection of face displacements in z-direction based on a sine function.

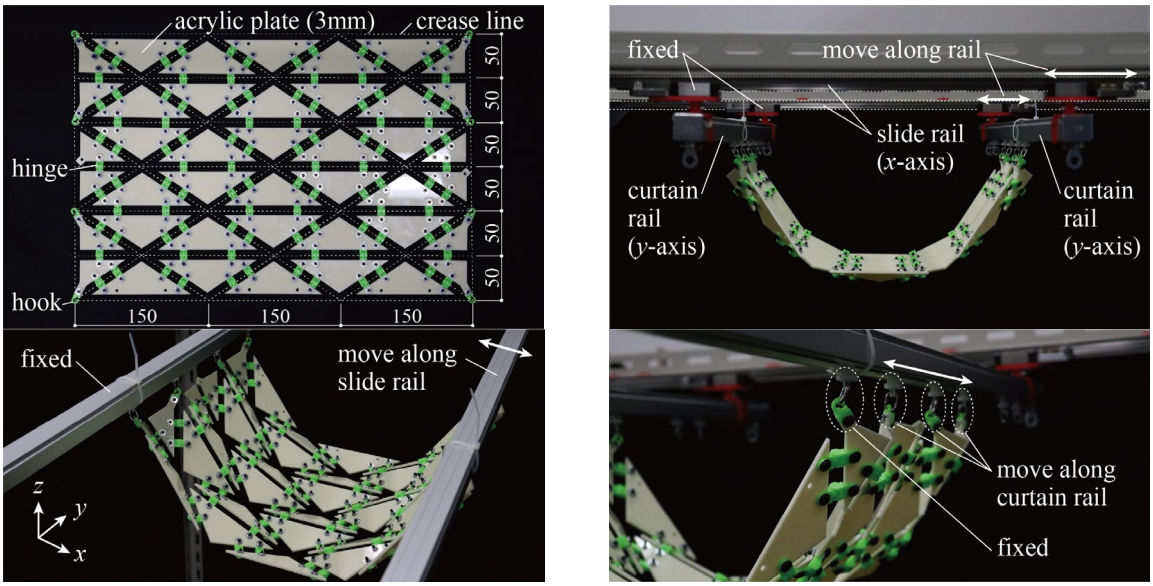


Figure 8. Experimental model.

the slide rails while remaining parallel to the left rail. As we focus on checking the deformation modes and the locking phenomenon of the crease lines, the vertex loads are not introduced in this model. However, friction provides resistance to the displacements in the direction along the curtain rails.

5.2. Infinitesimal mechanism analysis

The infinitesimal mechanism analysis introduced in Section 3 is carried out for the initial flat state. The size of compatibility matrix $\mathrm{d}\bar{\mathbf{C}}/\mathrm{d}\mathbf{X}$ is 341×252, and its rank is 229. Therefore, the number of kinematic and statical indeterminacies are 23 and 112, respectively. The orthonormal infinitesimal mechanism modes $\bar{\mathbf{X}}'_1,\ldots,\bar{\mathbf{X}}'_{23} \in \mathbb{R}^{252}$ cannot be uniquely determined only from Eq. (9), and we determine them as shown in Fig. 9 so that the following matrix is diagonalized and its diagonal elements are arranged in ascending order to reflect the bending stiffness of the model:

$$\begin{bmatrix} \bar{\mathbf{X}}'^{\mathrm{T}}_1 \\ \vdots \\ \bar{\mathbf{X}}'^{\mathrm{T}}_{23} \end{bmatrix} \begin{bmatrix} \partial\rho_1/\partial X_1 & \cdots & \partial\rho_{54}/\partial X_1 \\ \vdots & \ddots & \vdots \\ \partial\rho_1/\partial X_{252} & \cdots & \partial\rho_{54}/\partial X_{252} \end{bmatrix} \begin{bmatrix} K_1 & & 0 \\ & \ddots & \\ 0 & & K_{54} \end{bmatrix} \begin{bmatrix} \partial\rho_1/\partial X_1 & \cdots & \partial\rho_1/\partial X_{252} \\ \vdots & \ddots & \vdots \\ \partial\rho_{54}/\partial X_1 & \cdots & \partial\rho_{54}/\partial X_{252} \end{bmatrix} \begin{bmatrix} \bar{\mathbf{X}}'_1 & \cdots & \bar{\mathbf{X}}'_{23} \end{bmatrix}$$

Then, in the first-order infinitesimal mechanism, the stiffness of the crease pattern is lowest in the direction of $\bar{\mathbf{X}}'_1$. Any first-order infinitesimal mechanism $\mathbf{X}' \in \mathbb{R}^{252}$ can be represented by a linear combination of $\bar{\mathbf{X}}'_1,\ldots,\bar{\mathbf{X}}'_{23}$ with the arbitrary real coefficients $a_1,\ldots,a_{23} \in \mathbb{R}$ as

$$\mathbf{X}' = a_1\bar{\mathbf{X}}'_1 + \cdots + a_{23}\bar{\mathbf{X}}'_{23}$$

Note that the vertices move only along the *z*-axis in the first-order infinitesimal mechanism, and the displacements in the *x*- and *y*-directions are included in the higher-order infinitesimal mechanism. Eq (12) for the existence of the second-order infinitesimal mechanism turns into 19 independent quadratic equations for $a_1,\ldots,a_{23}$. Therefore, although it is difficult to analytically solve these equations, the degrees of freedom of the mechanism is expected to be 4 at a non-flat state as numerically confirmed in the following subsections. This significant reduction in the number of arbitrary coefficients leads to the bifurcation of the equilibrium path.

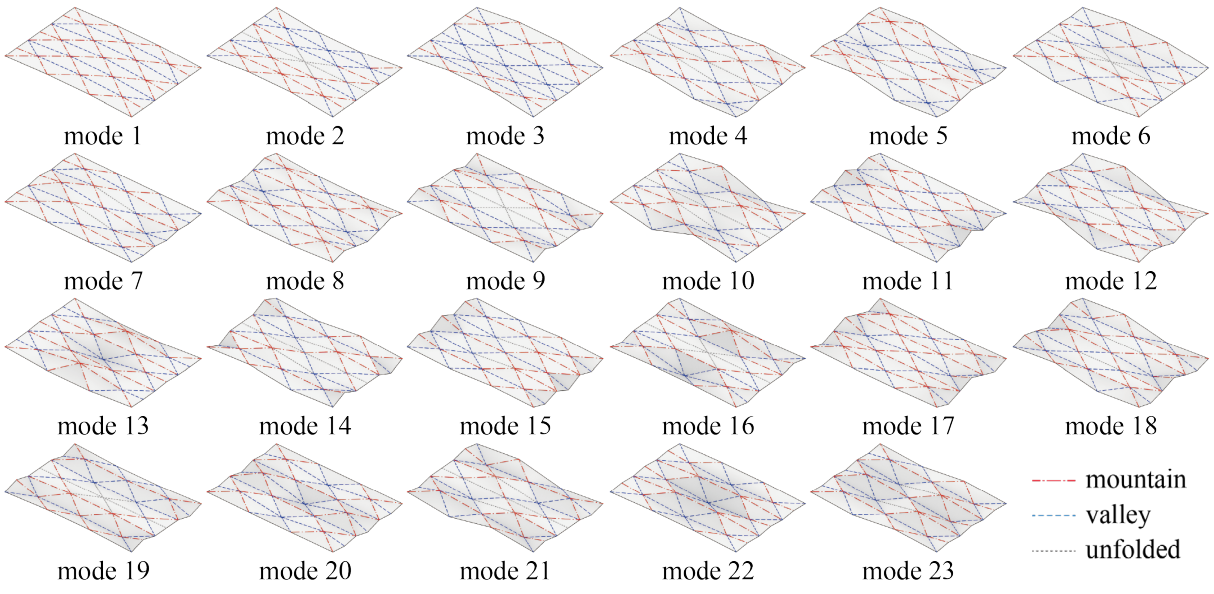
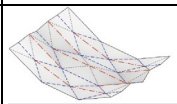
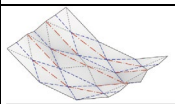
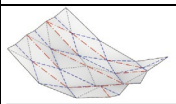
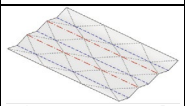
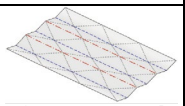
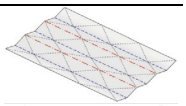
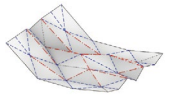
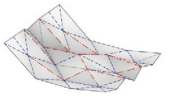
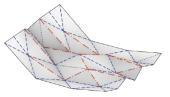
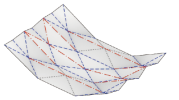
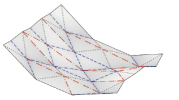
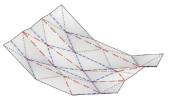
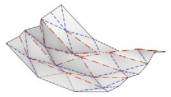
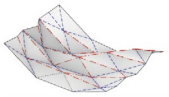
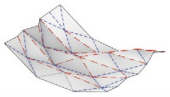
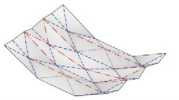
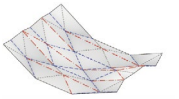
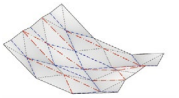
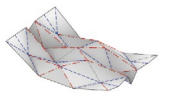
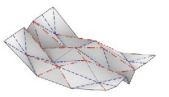
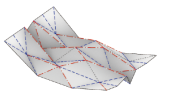
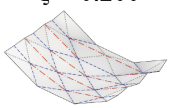
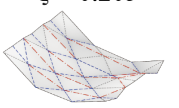
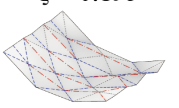


Figure 9. Orthonormal infinitesimal mechanism modes.

5.3. Instability and bifurcation at the flat state

This section demonstrates that the equilibrium path obtained by the method proposed in Section 4 is highly influenced by the size of the initial path parameter increment as well as the initial imperfection. As summarized in Table 1, we have carried out the path tracing without initial imperfection and with the imperfection mode 2 shown in Fig. 7 by changing the step size as $\mathrm{d}\xi_0 = 0.005, 0.010, 0.015$. To investigate the influence of the initial step size, the different step sizes $\mathrm{d}\xi_{\mathrm{ini}} = 0.005, 0.010, 0.015, 0.020$ are used to find the first equilibrium points. Since the deformation mode (assignment of the mountain and valley to the crease lines) hardly changes after $\xi = 0.2$, we show the deformed shape at the step around $\xi = 0.2$ or the final step if the analysis terminate before $\xi = 0.2$ in Table 1 to better illustrate the deformation. As shown in Table 1, different equilibrium paths are obtained by changing the initial step size $\mathrm{d}\xi_{\mathrm{ini}}$, while the regular step size $\mathrm{d}\xi_0$ does not significantly change the equilibrium paths.

Table 1. Deformed shapes around $\xi = 0.2$ or the final step of path tracing with different step sizes.

	Without initial imperfection			Imperfection mode 2		
	$\mathrm{d}\xi_0 = 0.005$	$\mathrm{d}\xi_0 = 0.010$	$\mathrm{d}\xi_0 = 0.015$	$\mathrm{d}\xi_0 = 0.005$	$\mathrm{d}\xi_0 = 0.010$	$\mathrm{d}\xi_0 = 0.015$
$\mathrm{d}\xi_{\mathrm{ini}} = 0.005$	 $\xi = 0.200$	 $\xi = 0.205$	 $\xi = 0.200$	 $\xi = 3.91\times10^{-5}$	 $\xi = 3.91\times10^{-5}$	 $\xi = 3.91\times10^{-5}$
$\mathrm{d}\xi_{\mathrm{ini}} = 0.010$	 $\xi = 0.200$	 $\xi = 0.200$	 $\xi = 0.205$	 $\xi = 0.200$	 $\xi = 0.200$	 $\xi = 0.205$
$\mathrm{d}\xi_{\mathrm{ini}} = 0.015$	 $\xi = 0.200$	 $\xi = 0.205$	 $\xi = 0.195$	 $\xi = 0.200$	 $\xi = 0.205$	 $\xi = 0.195$
$\mathrm{d}\xi_{\mathrm{ini}} = 0.020$	 $\xi = 0.200$	 $\xi = 0.200$	 $\xi = 0.200$	 $\xi = 0.200$	 $\xi = 0.200$	 $\xi = 0.200$

5.4. Path tracing with initial imperfection

In this section, we will show the result of the equilibrium path tracing from the perfectly flat state and the results with the initial imperfections shown in Fig. 7. The deformation modes and the locking phenomenon of the crease lines are also investigated by the physical experimental model.

Figure 10 shows the deformation path with $\mathrm{d}\xi_0 = 0.05$. The paths shown in Fig. 10(a) and (d) are approximately the same. By assigning the different initial imperfection, the different paths can be obtained. The deformed shape may contain the unfolded crease lines, and these crease lines may be locked; e.g., in the equilibrium path shown in Fig. 10(c) where the path tracing has been terminated with small ξ, the diagonal crease lines are locked under the forced displacements in the *x*-direction, and the forced displacements cannot increase due to the locked mechanism.

At every equilibrium point on the paths obtained without initial imperfection and with the imperfection modes 1 and 3, the rank of compatibility matrix is 248, and the number of kinematic indeterminacy is 4, while those are 247 and 5, respectively, at every equilibrium point on the path with imperfection mode 2. The values of coefficients of the first-order infinitesimal mechanism modes investigated in Section

5.2 at an equilibrium point $\mathbf{X}$ are computed by $a_i = \langle \mathbf{X}, \bar{\mathbf{X}}'_i \rangle$ $(i = 1, \ldots, 23)$, and the norm of the residual is computed as $\left\| \mathbf{X} - \sum_{i=1}^{23} a_i \bar{\mathbf{X}}'_i \right\|$. These values are plotted in Fig. 11. It can be seen that the coefficients of mode 1 is significantly larger than those of other modes in every path in Fig. 10, that is reasonable since the bending stiffness of the model is smallest in the direction of mode 1. In addition, since the infinitesimal mechanism modes do not include the vertex displacements in *x*- and *y*- directions, the norm of residual is quite large on every paths, which indicates the higher-order mechanisms. On the other hand, as shown in Fig. 11(c), modes 9, 18, 19, and 20 are not included in the path shown in Fig. 10(c).

The locking phenomenon of the crease lines is also confirmed by the physical experimental model shown in Fig. 12, which approximately reproduces each deformation mode in Fig. 10. In the experimental model, the curtain rail on the right side of the picture cannot move to the negative *x*-direction due to the locked hinges.

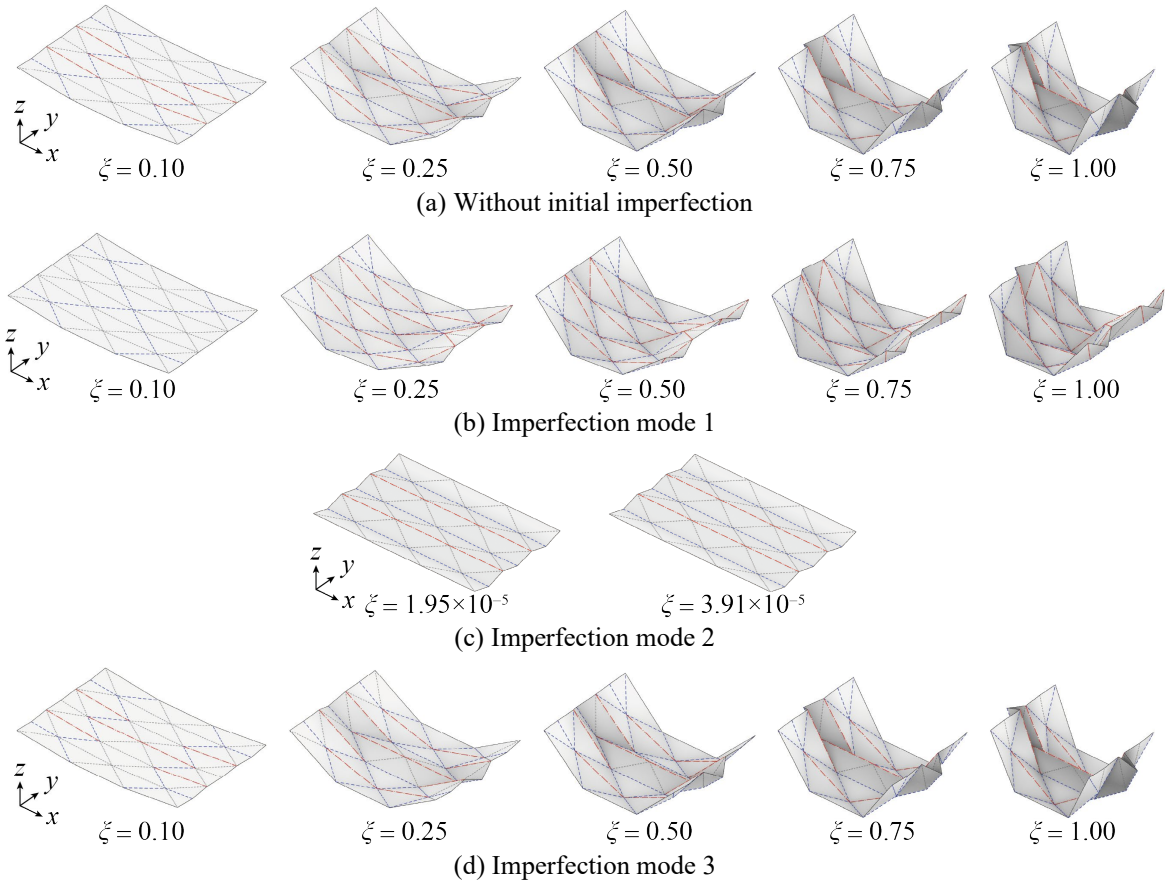
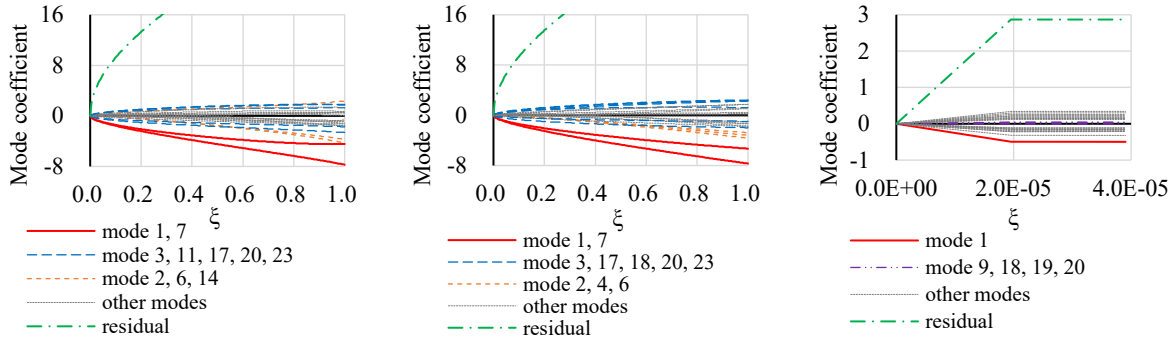
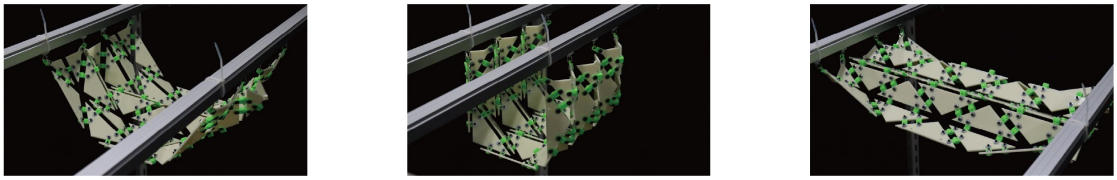


Figure 10. Deformation paths.



(a) Without imperfection / Mode 3 (b) Mode 1 (c) Mode 2

Figure 11. Value of coefficients of infinitesimal mechanism modes and the norm of residual vector.



(a) Without imperfection / Mode 3 (b) Mode 1 (c) Mode 2

Figure 12. Approximate reproduction of analysis results in Fig. 6 by experimental models.

6. Conclusions

This paper has presented the panel-pin model, which has been applied to the infinitesimal mechanism and the geometrically nonlinear equilibrium path analysis of the rigid origami with multiple degrees of freedom of mechanism. It has been shown that the multiple equilibrium paths can be obtained by assigning different initial imperfection in the investigated crease pattern.

Acknowledgements

This work is supported by JSPS KAKENHI Grant Numbers JP20J21650, JP19K04714 and JST CREST Grant Number JPMJCR1911.

References

[1] S. A. Zirbel, R. J. Lang, M. W. Thomson, D. A. Sigel, P. E, Walkemeyer, B. P. Trease, and S. P. Magleby, L. L. Howell, "Accommodating thickness in origami-based deployable arrays," *J. Mech. Design*, vol. 135, no. 11, paper no. 111005, Oct. 2013.

[2] C. H. Belke, and J. Paik, Mori: "A Modular Origami Robot," *IEEE/ASME Tran. Mechatron.*, vol. 22, no. 5, pp. 2153-2164, Oct. 2017.

[3] P. M. Reis, F. L. Jiménez, and J. Marthelot, "Transforming architectures inspired by origami," *Proc. Natl. Acad. Sci. U.S.A.*, vol. 112, no. 40, pp. 12234-12235, Oct. 2015.

[4] Y. Zhu, M. Schenk, and E. T. Filipov, "A review on origami simulations: from kinematics, to mechanics, toward multiphysics," *Appl. Mech. Rev.*, vol. 74, no. 3, paper no. 030801, Aug. 2022.

[5] T. Tachi, "Simulation of rigid origami," in *Proc. 4th international meeting of origami science, mathematics, and education (Origami4)*, R. J. Lang Ed., AK Peters, 2009, pp. 175-187.

[6] Z. He and S. D. Guest, "On rigid origami III: Local rigidity analysis," *Proc. Math. Phys. Eng. Sci.*, vol. 478, issue 2258, paper no. 20210589, Feb. 2022.

[7] M. Schenk and S. D. Guest, "Origami folding: A structural engineering approach," in *Proc. 5th international meeting of origami science, mathematics, and education (Origami5)*, P. Wang-Iverson, R. J. Lang, and M. Yim Eds., CRC Press, 2011, pp. 291-303.

[8] T. Zhang, K. Kawaguchi and M. Wu, "A folding analysis method for origami based on the frame with kinematic indeterminacy," *Int. J. Mech. Sci.*, vol. 146-147, pp. 234-248, Oct. 2018.

[9] K. Hayakawa and M. Ohsaki, "Form generation of rigid origami for approximation of a curved surface based on mechanical property of partially rigid frames," *Int. J. Solids Struct.*, vol. 216, pp. 182-199, May 2021.

[10] K. Hayakawa and M. Ohsaki, "Equilibrium path and stability analysis of rigid origami using energy minimization of frame model," *Front. Built Environ.*, vol. 8, Aug. 2022.

[11] M. Géradin and A. Cardona, *Flexible Multibody Dynamics: A Finite Element Approach*, London, Wiley, 2007

[12] E. G. Birgin and J. M. Martínez, "Augmented Lagrangian method with nonmonotone penalty parameters for constrained optimization," *Comput. Optim. Appl.*, vol. 51, pp. 941-965, Feb. 2012.

[13] J. Nocedal and S. J. Wright, *Numerical Optimization*, New York, Springer, 2006.

IASS 2023
July 10–14 Melbourne
Integration of Design and Fabrication

Proceedings of the IASS Annual Symposium 2023
Integration of Design and Fabrication
10–14 July 2023, Melbourne, Australia
Y.M. Xie, J. Burry, T.U. Lee and J. Ma (eds.)

Study on seismic behavior of origami-based buckling-controlled concentric braces with beam-column-brace connections

Yangqing LIU[a,*], Tian DENG[a], Dongping MEI[a], Qin YU[a]

[*] State Key Laboratory of Mountain Bridge and Tunnel Engineering, Chongqing Jiaotong University
No. 66, Xuefu Rd., Chongqing 400074, China
lyq19@cqjtu.edu.cn

[a] School of Civil Engineering, Chongqing Jiaotong University

Abstract

Compared with the conventional braces, origami-based buckling-controlled concentric braces (OBBCCBs) possess distinctive deformation capacity and load transmission path under axial load, like cross sectional twist at brace ends. Due to the specificity of OBBCCBs, the beam-column-brace connections should accommodate additional demands in load carrying capacity and deformation, which can hardly be met by the existing conventional connections. In this study, considering these features, based on the generalized uniform force method, a design method of the beam-column-brace connection is proposed to ensure the connection fails after the brace failure. Numerical study is conducted on the seismic behavior of the brace-connection subassembly under axial compression and reversed cyclic load. The effects of the connections on axial deformation capacity, lateral deformation, failure modes, and energy dissipation capacity of the OBBCCBs are investigated. The results show that the OBBCCBs with the connections can still prevent the global buckling and thus guarantee their energy dissipation capacity in the frame. The study results are expected to serve as a valuable reference for the design and application of the connections between OBBCCBs and frames.

Keywords: origami, concentric braces, connection design

1. Introduction

Conventional concentric braces in frame structures usually suffer from stability caused by globally flexural buckling during earthquake actions, which seriously deteriorates its energy dissipation capacity. To address the issue, origami-based buckling-controlled concentric braces (OBBCCBs) are proposed by Liu et al [1–3]. By applying the curved Miura origami, the OBBCCBs allows non-rigid deformation of the origami pattens to prevent the global buckling under axial compression and exhibit impressive energy dissipation capacity.

In braced frames, the connection plays a significant role in transferring axial force from the brace to the surrounding structure. However, undesirable failure of the connections may occur to the braced frame, limiting the brace to fully dissipate energy. Wu et al. [4] found that the potential out-of-plane rotation degraded the stability of the brace end near the gusset plate in cyclic and hybrid loading tests on the full-scale reinforced concrete (RC) frame with brace. Bai et al. [5] proposed and tested the perfobond strip and welded shear stub gusset connections to ensure the connection reliability by reducing frame action. Tan et al. [6] utilized the unconstrained gusset plates in the braced frame and found that the unconstrained gusset plates significantly reduced the damage to the RC members compared with the conventional gusset plates. Wang et al. [7] conducted subassemblage tests of buckling-restrained braced RC frames with various gusset connections. Results showed that the gusset plate connection type affected the rotation responses of the gusset plate and brace end zone. Thus, for the OBBCCBs, the

Copyright © 2023 by Yangqing LIU, Tian DENG, Dongping MEI and Qin YU. Published in the Proceedings of the IASS Annual Symposium 2023 with permission.

beam-column-brace connections must be properly designed so that they can sustain the maximum axial force capacities developed from the braces and exhibit good seismic performance.

In this paper, a design method for the connection of OBBCCB is developed by incorporating the generalized uniform force method [8] and the frame action forces computed from an equivalent strut model [9]. Finite element (FE) models are established by using software ANSYS to evaluate the seismic behavior of the brace-connection subassembly under axial compression and reversed cyclic load. The effects of the designed connections on axial deformation capacity, lateral deformation, failure modes, and energy dissipation capacity of the OBBCCB are investigated.

2. Connection Design

The connection design in this paper is based on a single-story single-bay monolithic precast concrete frame subassemblage with OBBCCB, as shown in Fig. 1. The upper gusset plate, noted as GP-A, is connected to the beam and column. The lower gusset plate, noted as GP-B, is connected to the column. The pinned connections are designed and checked for limit states based on the Chinese specification [10]. Considering the specificity of OBBCCBs, especially the twist of cross sectional at the brace ends, the clearance of the connection are deliberately designed.

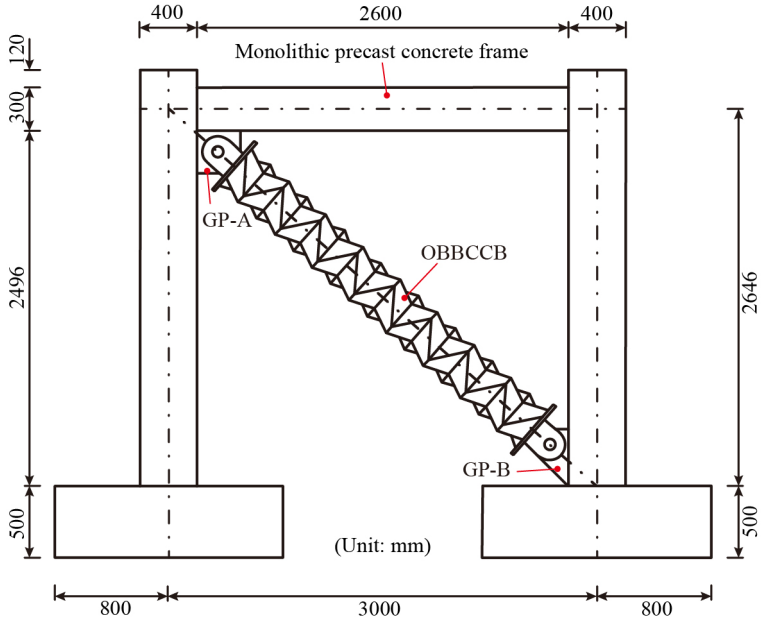


Figure 1. Monolithic precast concrete frame with OBBCCB.

2.1. Brace action

In this study, the generalized uniform force method [8] is adopted for considering the brace action of the gusset plate design. The horizontal and vertical force components at the gusset-to-beam (H_{ub} and V_{ub}) and gusset-to-column (H_{uc} and V_{uc}) interfaces that are caused by brace axial force are shown in Fig. 2 and the forces are calculated following Eq.s (1–4).

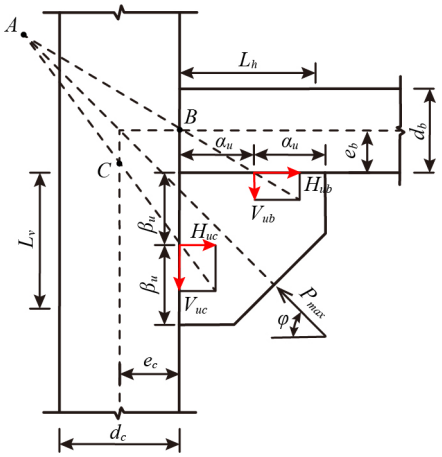


Figure 2. Generalized uniform force method.

$$H_{\mathrm{uc}}=P_{max}\,(e_c \sin\varphi)/(e_b+\beta_u) \tag{1}$$

$$V_{\mathrm{ub}}=P_{max}e_b\,[(e_b+\beta_u)\cos\varphi-e_c \sin\varphi]/[\alpha_u(e_b+\beta_u)] \tag{2}$$

$$H_{\mathrm{ub}}=P_{max}\cos\varphi-H_{\mathrm{uc}} \tag{3}$$

$$V_{\mathrm{uc}}=P_{max}\sin\varphi-V_{\mathrm{ub}} \tag{4}$$

Where α_u and β_u are half of the gusset length (L_h) and height (L_v), respectively; e_b and e_c are half of the beam and column depths, respectively; and φ is the incline angle of brace. The maximum brace axial force, P_{max}, can be obtained from the 1.2 times simulation results under axial load.

2.2. Framing action

To estimate the framing action force, the gusset plate is regarded as an equivalent strut [9] located at points of 0.6 times the gusset length and height from the column and beam flanges, respectively, as shown in Fig. 3. The relationship between the vertical component (V_{FA}) and horizontal component(H_{FA}) of the strut force is defined as follows in Eq.s (5–6):

$$H_{\mathrm{FA}}=\frac{d_bL_hV_{beam}(0.3L-0.18L_h)}{(4I_b/t_g)+d_bL_h(0.3d_b+0.18L_v)} \tag{5}$$

$$V_{\mathrm{FA}}=\frac{d_bL_vV_{beam}(0.3L-0.18L_h)}{(4I_b/t_g)+d_bL_h(0.3d_b+0.18L_v)} \tag{6}$$

Where t_g is the gusset plate thickness; I_b is the moment of inertia of the beam; L is the beam clear span, excluding the gusset region and column depth; V_{beam} is the beam shear when plastic hinge develops.

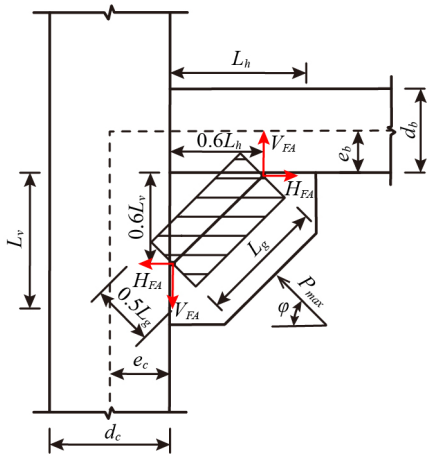


Figure 3. Equivalent strut model.

The combined action can be calculated to obtain the total gusset interface normal (σ) and shear (τ) stress distributions using the method proposed by Lin et al [11]. The maximum stresses on the gusset interfaces are used to calculate the demand-to-capacity ratios (DCRs), which must satisfy the design requirements. Table 1 lists the DCRs for gusset plates in compression (labelled as '-') and tension (labelled as '+') at three failure modes, namely von Mises yielding, tensile rupture, and shear rupture.

Table 1. Design demand-to-capacity ratio checks of design

DCRs	Location	Failure mode	GP-A		GP-B	
			-	+	-	+
$DCR_{m,b}$	Gusset-beam interface	Von Mises yielding	0.203	0.207		
$DCR_{t,b}$		Tensile rupture	0.106	0.101		
$DCR_{s,b}$		Shear rupture	0.290	0.297		
$DCR_{m,c}$	Gusset-column interface	Von Mises yielding	0.291	0.310	0.137	0.156
$DCR_{t,c}$		Tensile rupture	0.095	0.108	0.094	0.107
$DCR_{s,c}$		Shear rupture	0.431	0.457	0.186	0.211

2.3. Pinned design

According to specification [10], the pin connection can be made of the steel with the nominal yield strength of 335 MPa, and the geometric dimensions should meet the Eq.s (7–8). Where a is the minimum distance between the edge of the pin hole and the edge of the plate in the direction of force; b is the distance between the plate edge and the edge of the pin hole. The a, b and other parameters are depicted in Fig. 4.

$$a \geq \frac{4}{3} b_e \tag{7}$$

$$b_e = 2t_g + 16 \leq b \tag{8}$$

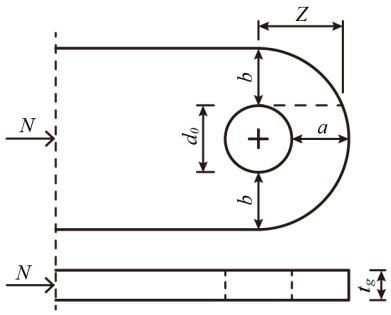


Figure 4. Design methodology of the pinned gusset plate.

Verification of the limit state of the pin connection is performed after determining the geometry. The tensile strength (σ_h) of the net section of the pinned gusset plate hole, the tensile strength (σ_e) of the section of pinned gusset plate end and the shear strength (τ) of the pinned gusset plate are checked by Eq.s (9–11):

$$\sigma_h = \frac{N}{2t_g b_1} \le f,\ b_1 = \min\left(2t_g + 16,\ b - \frac{d_0}{3}\right) \tag{9}$$

$$\sigma_e = \frac{N}{2t_g\left(a - \frac{2d_0}{3}\right)} \le f \tag{10}$$

$$\tau = \frac{N}{2t_g Z} \le f_v,\ Z = \sqrt{(a + d_0/2)^2 - (d_0/2)^2} \tag{11}$$

Where N is the design value of the axial force induced by the brace action, f and f_v are respectively the design value of the tensile strength and the shear strength of the gusset plate. The design values of tensile strength (f) and shear strength (f_v) of the 20 mm thick gusset plate steel are 295 N/mm^2 and 170 N/mm^2, respectively [10]. The dimensions of the pinned design in this study are illustrated in Fig. 5. The results all meet the design requirements mentioned above.

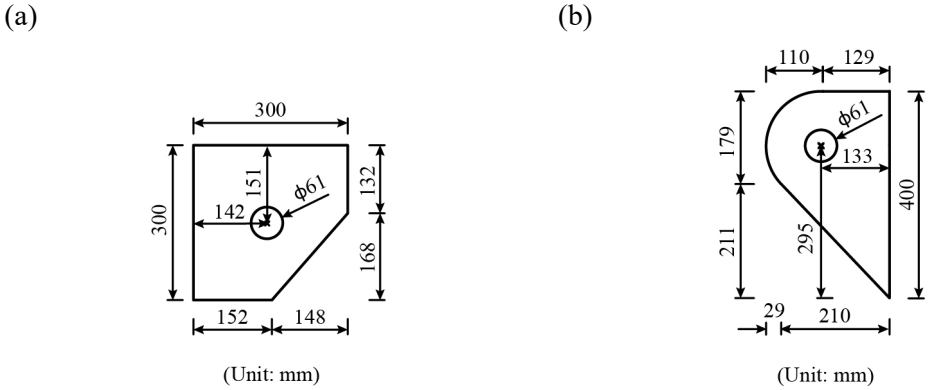


Figure 5. Dimensions of gusset plates: (a) GP-A, and (b) GP-B.

2.4. Clearance details

The OBBCCBs composed of multiple curved Miura origami tubular units longitudinally, possess distinctive deformation capacity and load transmission path under axial load, like cross sectional twist at brace ends. Due to the specificity of OBBCCBs, the beam-column-brace connections should accommodate additional demands in load carrying capacity and deformation. According to the preliminary simulation of the OBBCCB under axial load, the brace ends of OBBCCB may generate

rotational angles under axial force in the range of -3° to 3°. To accommodate the rotation, the clearance configuration is designed as shown in Fig. 6, where S_1 is the clearance between the gusset plate and the ring plate, S_2 is the clearance between the pin hole and the pin, and S_3 is the clearance between the ring plate and the pin cap.

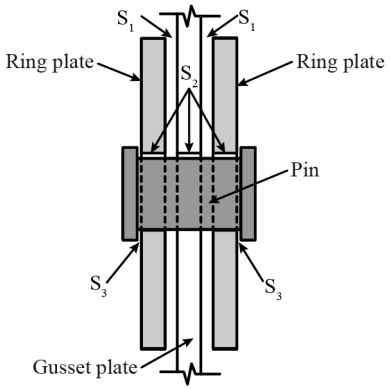


Figure 6. Clearance details.

The brace end rotation process consists of two stages: firstly, the ring plate is rotated by the brace until the ring plate hole is in contact with the pin surface, and then the ring plate is rotated together with the pin until the pin surface is in contact with the gusset plate hole wall. In consideration of the process, S_1, S_2 and S_3 are determined to be 8 mm, 1 mm, 1mm, respectively.

3. Numerical analysis

3.1. Finite element modelling

Nonlinear numerical simulations are conducted using general finite element (FE) package (ANSYS 19.2), aiming at investigating the seismic behavior of the OBBCCBs with designed connection. The finite element model of the brace-connection subassembly is shown in Fig. 7. Typical 4-node shell element SHELL181 is employed to simulate the 8 mm-thick panels of the origami pattern. The 8-node 3-D solid element SOLID45 is employed to simulate the end plates, ring plates, gusset plates and pins. In order to model the pin supports of the brace, MASS21 element is put at the supports, connecting the nodes of the ring plates, gusset plates and pins by constraint equations. The degree of freedom of rotation in the plane of connection is released. Firstly, the axial compression load is executed on the brace-connection subassembly to obtain mechanical properties such as yield displacement (Δ_y) and yield load (F_y); then the cyclic horizontal load is applied to simulate the earthquake action.

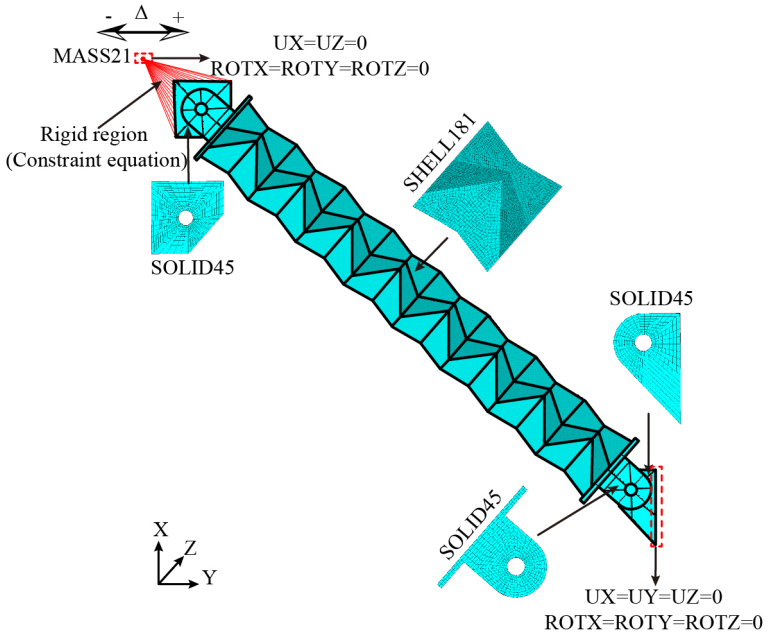


Figure 7. Finite element model.

The axial loading sequence recommended by ANSI/AISC 341-16[12] requires two quantities: D_{by} and D_{bm}. D_{by} is the axial displacement deformation at first yield of the specimen, which is the Δ_y obtained from the compression load simulation. D_{bm} refers to the axial deformation of the specimen at the design story drift (0.02 times the story height). In order to simulate the earthquake action, the horizontal loading protocol can be determined from the axial loading protocol based on the small deformation assumption, as listed in the Table 2.

Table 2. Loading protocol

Load level	Load magnitude	Cycle number
1	$\pm D_{by}$=±26.02	2
2	$\pm 0.5D_{bm}$=±26.67	2
3	$\pm 1.0D_{bm}$=±53.34	2
4	$\pm 1.5D_{bm}$=±80.01	2
5	$\pm 2.0D_{bm}$=±106.68	2

3.2. Results and observations

Fig. 8 shows the hysteretic and skeleton curves of the brace-connection subassembly. The main characteristic parameters (the effective stiffness K_{eff}, the yield load F_y, the yield displacement Δ_y, the ultimate load F_u and the ultimate displacement Δ_u) of the curves are quantified in Table 3 in accordance with FEMA P-795 [13]. The displacement ductility μ is obtained through Eq. (12). The parameters in the positive(labelled as '+') and negative(labelled as '-') directions are calculated respectively.

$$\mu = \frac{\Delta_u}{\Delta_y} \tag{12}$$

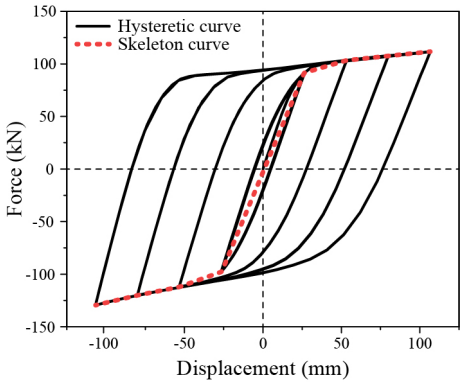


Figure 8. Hysteretic and skeleton curves.

Table 3. Characteristic parameters of skeleton curve

Direction	K_{eff}	F_y	Δ_y	F_u	Δ_u	μ
+	3.48	44.65	32.08	111.63	106.68	3.33
-	3.72	51.79	34.80	-129.47	-106.68	3.07

It can be seen from Fig. 8 that the brace behaves elastically at the early stage, for the curves perform almost linear in both directions. At this stage, the effective stiffness K_{eff} in the negative direction is marginally greater than that in the positive direction. No significant buckling occurrs on the brace-connection subassembly during the horizontal cyclic loading. Equivalent viscous damping ratio ζ_{eq} is obtained as defined in Eq. (13), where E_D is the hysteretic energy and E_{strain} is the equivalent strain energy [14]. The ratio reaches 39.13% at the final level, thus exhibiting stable, reliable and high-level energy dissipation capacity of the specimen.

$$\zeta_{eq} = \frac{E_D}{4\pi E_{strain}} \tag{13}$$

The von Mises stress distributions at the maximum load displacement is shown in Fig 9. It can be seem from the figure that no premature buckling of the gusset plates is found, satisfying the design principle of “strong connection and weak member”. Plasticity distribution is uniform, along the whole length of the OBBCCB. Within each unit, the deformation concentrates at the predetermined creases and plasticity develops there. Beyond a unit, each unit of the brace deforms simultaneously and uniformly and plasticity distributes along the full length of the brace, which prevents the global buckling of the brace.

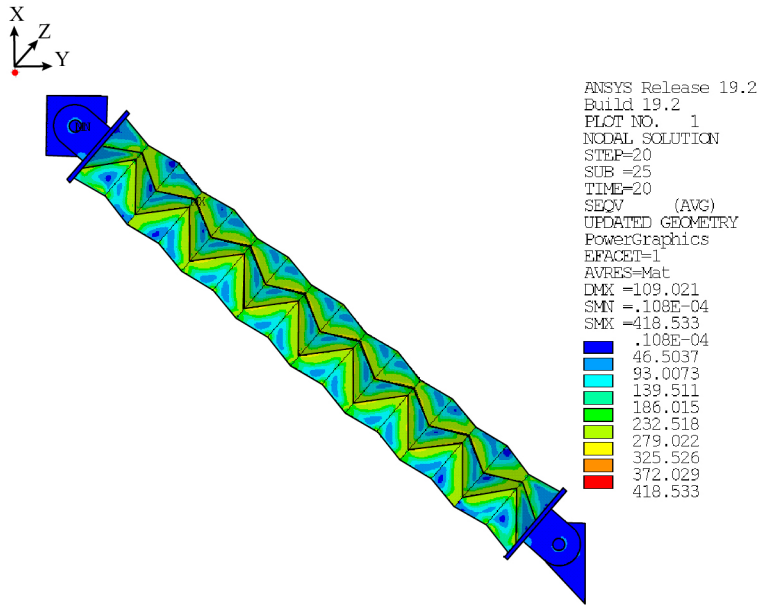


Figure 9. Stress distributions at maximum load displacement.

4. Conclusion

To guarantee that beam-column-brace-connections fail after energy dissipation braces, the connection design is a key issue for energy dissipation braces. The present work provides a design method of the beam-column-brace connection considering the specificity of OBBCCBs. According to the simulation results, the OBBCCB with designed connection exhibits satisfactory seismic performance. In follow-up study, the FE model will be further detailed to consider the actual actions of the concrete beam and column.

Acknowledgements

The authors gratefully acknowledge the financial support from the National Natural Science Foundation of China (Grant No. 52008064), and the Science and Technology Research Program of Chongqing Municipal Education Commission of China (Grant No. KJQN202000737).

References

[1] Y. Liu, X. Li, J. Cai and J. Feng, "Study on buckling resistance of Miura origami-based tube", *Journal of Southeast University (Natural Science Edition)*, vol. 51, no. 5, pp. 733-739, 2021. (in Chinese)

[2] Y. Liu, J. Cai and J. Feng, "Buckling suppression of a thin-walled Miura-origami patterned tube", *Plos One*, vol. 17, no. 7, pp. e0270228, 2022.

[3] Y. Liu, J. Cai and J. Feng, "A strategy to improve buckling resistance of a Miura origami-based tube," in *Form and Force: Proceedings of the IASS Annual Symposium 2019*, Barcelona, Spain, October 7–10, 2019, C. Lázaro, K. U. Bletzinger and E. Oñate, Eds.

[4] A. Wu, K. Tsai and H. Yang, "Hybrid experimental performance of a full-scale two-story buckling-restrained braced RC frame", *Earthquake Engineering & Structural Dynamics*, vol. 46, no.8, pp. 1223-1244, 2017.

[5] J. Bai H. Chen and J. Zhao, "Seismic design and subassemblage tests of buckling-restrained braced RC frames with shear connector gusset connections", *Engineering Structures*, vol. 234, pp. 112018, 2021.

[6] Q. Tan, B. Wu and P. Shi, "Experimental Performance of a Full-Scale Spatial RC Frame with Buckling-Restrained Braces Subjected to Bidirectional Loading", *Journal of Structural Engineering*, vol. 147, no. 3, pp. 04020352, 2021.

[7] J. Wang, F. Lu and B. Li "Subassemblage tests and analysis of buckling-restrained braced reinforced concrete frames with various gusset connections", *Structures*, vol.39, pp. 39-56, 2022.

[8] L. Muir, "Designing compact gussets with the uniform force method", *Engineering Journal*, vol.45, no.1, pp.13-19, 2008.

[9] C. Lee, "Seismic design of rib-reinforced steel moment connections based on equivalent strut model", *Journal of Structural Engineering*, vol.128, no.9, pp.1121-9, 2002.

[10] GB50017-2017, "Code for design of steel structures", Beijing: China Planning Press, 2017. (in Chinese).

[11] P. Lin, K. Tsai and A. Wu, "Seismic design and experiment of single and coupled corner gusset connections in a full-scale two-story buckling-restrained braced frame", *Earthquake Engineering & Structural Dynamics*, vol.44, no. 13, pp.2177-98, 2015.

[12] American Institute of Steel Construction (AISC), "Seismic provisions for structural steel buildings", Chicago, Illinois, U.S.A., 2016.

[13] Applied Technology Council (ATC), "Quantification of Building Seismic Performance Factors: Component Equivalency Methodology", Washington, D.C.: Federal Emergency Management 1 Agency (FEMA), 2011.

[14] A. Chopra, "Dynamics of structures, theory and applications to earthquake engineering", fifth ed., Pearson Education Inc, Upper Saddle River, 2017.

IASS 2023
July 10–14 Melbourne
Integration of Design and Fabrication

Proceedings of the IASS Annual Symposium 2023
Integration of Design and Fabrication
10–14 July 2023, Melbourne, Australia
Y.M. Xie, J. Burry, T.U. Lee and J. Ma (eds.)

Study on the performance of the space structure using CLT folded plate structure

Kaito IKAWA[a,*], Shinta YOSHITOMI[a]

[a,*] Ritsumeikan University
ru0085xk@ed.ritsumei.ac.jp

Abstract

In recent years, the wood materials are used widely in the building field, and various applications of CLT(Cross Laminated Timber) are being considered in Japan. This paper aims to be systematically clarified how each form design parameters of CLT folded parameters affects deformation, and unit stress. A analysis model of a 20m x 20m CLT folded plate catenary arch roof using three form design parameters: mountain height the folded plate, arch rise-span ratio, and the number of arch divisions is constructed. As for this model, the relationship between form design parameters and the maximum and average values of each of the fulcrum reaction forces, vertical displacements, and unit stress of the nodes due to their own weight will be investigated. Increasing the folded plate peak height suppresses thrust and reduces y-directional reaction forces, while the effect of different peak heights on the maximum vertical displacement is small. Because of increasing the rise, the maximum value of vertical displacement and unit stress will be smaller, preventing the concentration of deformation points. In addition, by increasing the number of arch divisions, shape of the model becomes closer to an arch and the joint springs increase, thus reducing the stress level of the CLT.

Keywords: CLT, folded plate roof, parametric design, LSB, FEM analysis

1. Introduction

Nowadays, the use of wood as a sustainable material has been actively promoted in the field of architecture, and among them, CLT (Cross Laminated Timber) has been attracting attention. In research on the structural performance of CLT, there has been much research on its use as a material to resist horizontal forces, such as in earthquake-resistant walls, and as a flooring material, taking advantage of its characteristics as a facing material, but there is relatively little research on its use in other ways. The previous studies that treated CLT as a space structural member of arches were small-scale, with spans as short as 6m [1], and there are not many examples of the application of CLT to roof members larger spans. The folded plate structure is an example of a structural form in which CLT is applied as a space structural member. Its folding frame structure increases rigidity and allows larger spans to fly.

This study analyzes the relationship between form design parameters and structural performance of a 20m span CLT folded plate arch structure and understands the mechanisms that cause this relationship. The goal is to understand the characteristics of CLT as a spatial structural member, thereby expanding the use of CLT and, ultimately, promoting the utilization of wood materials.

2. Study methods

2.1. Evaluation methods for structural performance

A model of a 20m x 20m CLT folded plate catenary arch roof is constructed using mountain height the folded plate, arch rise-span ratio, and the number of arch divisions as form design parameters as shown in Figure.1. The form design parameters are varied as shown in Table 1. For the design parameters of

Copyright © 2023 by Kaito IKAWA and Shinta YOSHITOMI. Published in the Proceedings of the IASS Annual Symposium 2023 with permission.

this model, the relationship between form design parameters and the maximum and average values of each of the fulcrum reaction forces, vertical displacements, and unit stress of the nodes due to their own weight will be investigated.

Structural performance is analyzed by static analysis of Midas iGen. The analysis method is finite element method (FEM), and nodes are generated at the point where the joint springs are inserted. Details of node generation points will be described later in *2.2.2.*

The long-term allowable stress of the CLT, the yield capacity of the joint springs, and the vertical displacement are used as constraints for the results of the analysis. The allowable stress and yield capacity are as shown in Tables 2 and 3, and the constraint of vertical displacement is assumed to be 80 mm (1/250 of the arch span). The fulcrums of the arch are a pin fulcrum, and they are restrained except for rotation around the y-axis.

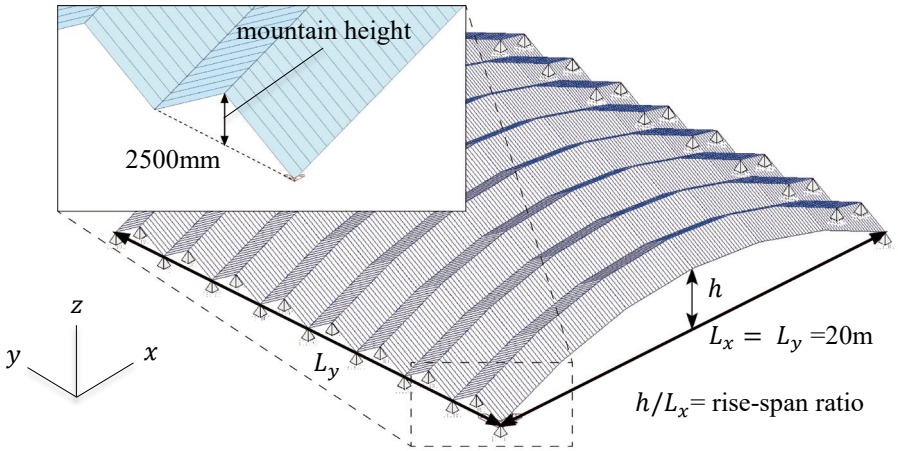


Figure 1. Model overview and form design parameters

Table 1. Changes of form design parameters

mountain height (mm)	500, 750, 1000
rise-span ratio	1/20, 1/12, 1/8, 1/6, 1/5
the number of arch divisions	3, 4, 5, 6, 7

Table 2. Long-term allowable stress of the CLT (N/mm^2)

direction	in-plane				out-of-plane	
	f_c	f_t	f_{bx}	f_{sx}	f_{by}	f_{sy}
strong-axis	4.55	3.38	4.55	1.32	4.88	0.44
weak-axis	3.04	2.26	3.04		1.28	

Table 3. Yield capacity of the joint springs

direction	P_x (kN)		P_y (kN)	P_z (kN)	M_r(kNm)
	compression	tension			
x	972	164	33	29.6	7.38
y	104.9	5.06	3.93	2.66	

2.2. Analysis model setup

2.2.1. CLT elements

The overall model shape is created by generating eight mountains of folded plate and extruding them to the division points of the arch. The width of mountains is 2500mm, the mountain height is determined by the form design parameter. The division points to be extruded are generated so that the length of the catenary arch is equally divided, and the folded plate is extruded in the form of fold lines connecting each the division points. The shape of the basic catenary arch is determined from the span between the two fulcrum points and the arch length.

The equation for determining the length of the catenary from the span to rise-span ratio is given below.

For the catenary as shown in the Figure 2, the span is L_x, the deflection is h, the total length of the curve is l, and the rise span ratio $h/L_x = \gamma$,

$$h = f\left(\frac{L_x}{2}\right) - a = \frac{{L_x}^2}{8a} \tag{1}$$

$$l = L_x + \frac{8h^2}{3L_x} \tag{2}$$

Since formula (1),

$$a = \frac{L_x}{8\gamma} \tag{3}$$

Substitute formulas (1) and (3) into formula (2),

$$l = \left(1 + \frac{8}{3}\gamma^2\right) L_x \tag{4}$$

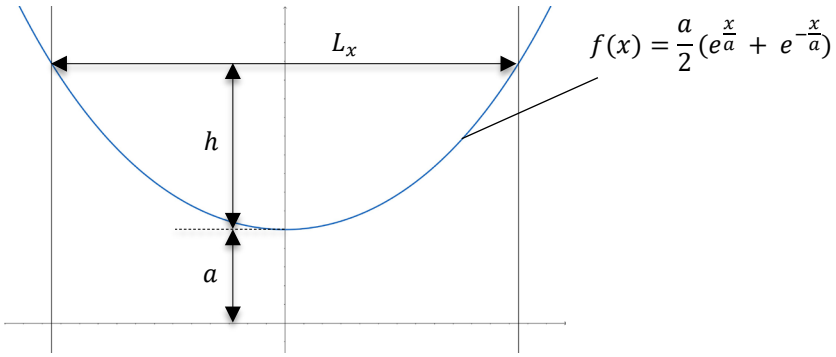


Figure 2. Catenary curve

The CLT in this study uses S90-5-5, 150mm thick, with weight of unit volume 5.0 kN/m^3. Table 4. shows the input material properties. In addition, a joint spring is inserted into the CLT and a 5mm gap is left between adjacent plates in the model so that stress is transmitted only by the spring.

Table 4. Properties of CLT (S90-5-5)

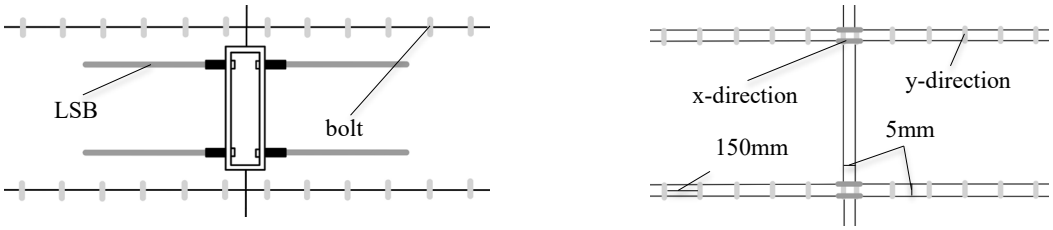
direction	E (N/mm^2)	G (N/mm^2)
strong-axis	5400	81.8
weak-axis	1872	40.9
thickness	6000	500

2.2.2. Joint spring elements

Joint springs are inserted in the strong-axis (x-direction) and weak-axis (y-direction). Three types of springs are inserted per joint: compression springs, tension springs, and general springs that include shear and bending stiffness.

The x-directional springs are joined so that the CLT plates are connected at the division points of the arch, and the type of joint is LSB joint. The four types of spring stiffnesses are axial spring D_x, in-plane shear spring D_y, out-of-plane shear spring D_z, and rotational spring R_y. For axial springs, compression is transmitted by the CLT bearing stiffness and tension by the LSB. The spring stiffnesses are determined by calculated values with reference to previous studies.

The y-directional springs are joined so that adjacent CLTs are connected at 150mm interval by bolted joints, using the existing building as a reference. There are three types of spring stiffnesses: axial spring D_x, in-plane shear spring D_y, out-of-plane shear spring D_z. The stiffnesses are the values obtained from experiments on the same building. The y-directional axial spring has the same transmission type as the x-directional spring, and at the same time, resistance to bending moment also is ensured. The schematic of the actual joints and the arrangement of the joint springs in the analysis model are shown in Figure 3, and the stiffness each joint springs in Tables 5.



(a) actual joints (b) analysis model

Figure 3. Schematic of the actual joints and the arrangement of the joint springs in the analysis model

Table 5. Stiffness of the joint springs

direction	Dx(kN/mm)		Dy(kN/mm)	Dz(kN/mm)	Ry(kNm/rad)
	Compression	tension			
x	901	105	7.30	14.8	352
y	63.6	4.74	1.73	1.07	-

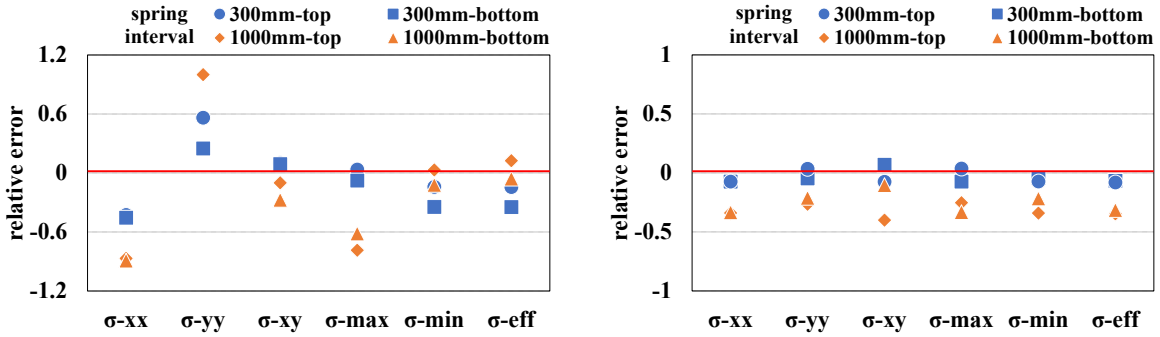
Since the joint springs in the model of this study are arranged at 150mm interval for a 20m roof, the number of elements and nodes is very large. Therefore, to reduce the number of them, it is considered that whether the analytical results are valid for the joint springs interval of 300mm and 1000mm. Only in this section, the length of L_y in the directional perpendicular to the arch is set to 10m. The design parameters are mountain height 750 mm, rise span ratio 1/6, and number of arch segments 6. The error is obtained by dividing the results of unit stress at 300mm and 1000mm interval at the nodes of the end of arch fulcrum and the center of arch top in the analysis model by the result at 150 mm.

3. Analysis results

3.1. Change of y-directional springs interval

Figure 4 shows the graph of unit stresses of CLT elements standardized by the 150mm result when the y-directional spring interval is varied from 150mm, 300mm, and 1000mm. Since the analytical model is a plate element, the results vary between the top and bottom of the plate at the same nodes.

In the end of arch fulcrum as there are no CLTs adjacent to each other and the error is relatively small. The error at the center of the top is the largest, with a maximum value of 3.125 and a minimum value of 0.110. In both cases, the error is larger for the 1000mm interval than for the 300mm interval. This is thought to be due to the fact that the size of each element changes as the y-directional spring interval changes, and the stresses are not equal inside the flat plate, but are biased.

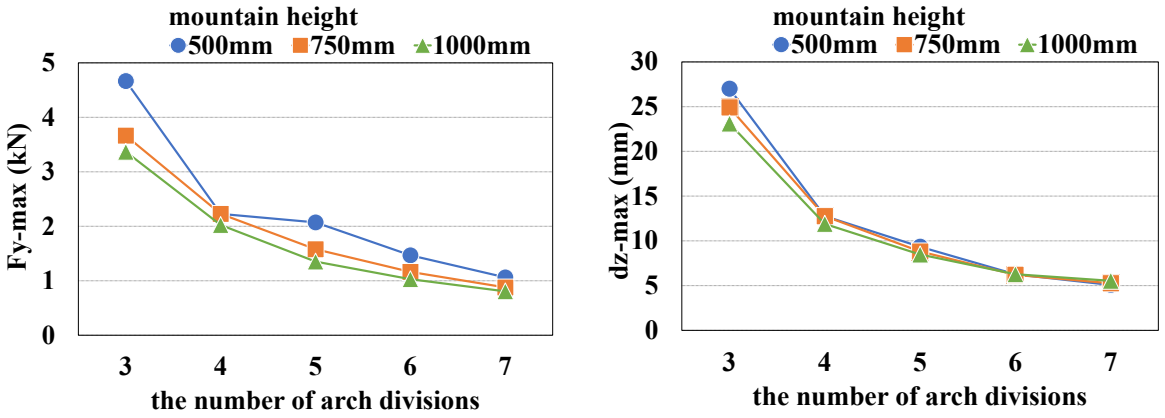


(a) end of arch fulcrum (b) center of top

Figure 4. Relative error of analysis results due to changes spring interval

3.2. Effect of mountain height of folded plate

Figure 5 shows the graph with rise-span ratio of 1/8 as a constant and the number of arch divisions as a variable. It shows how mountain height of folded plates affects from the sequence of lines in the graph. It can be seen from the sequence of lines in the graph that the y-directional reaction force is suppressed since the higher the mountain, the smaller the thrust. Since the sequence of lines of vertical displacement graph are generally same, it can be said that the effect of changing mountain height on vertical displacement is small.



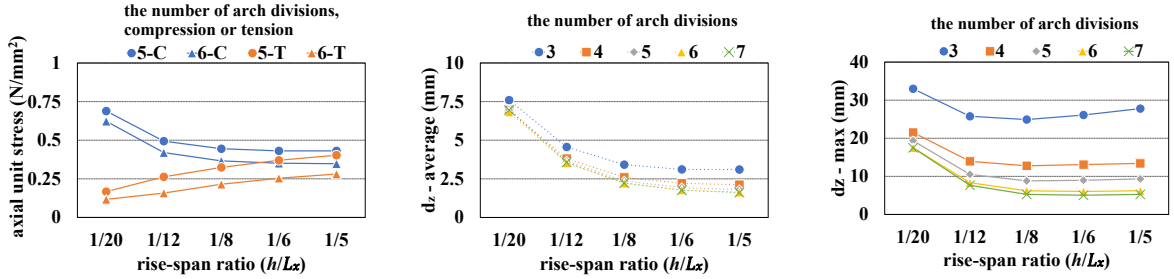
(a) y-directional reaction force (b) vertical displacement

Figure 5. Effect of mountain height

3.3. Effect of rise-span ratio of arch

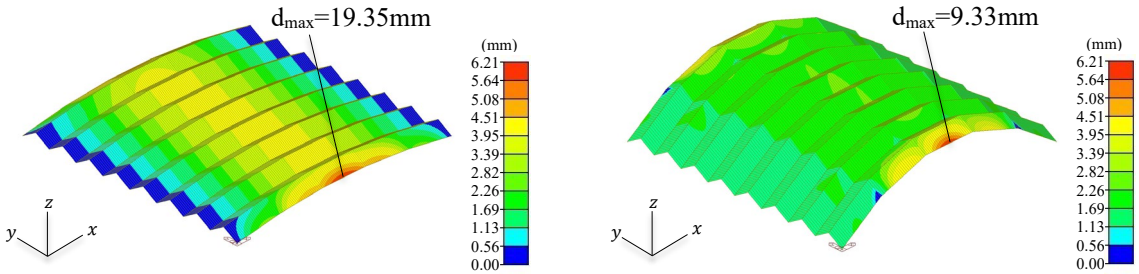
Figure 6 shows the effect of the rise-span ratio on each response when the mountain height is 750 mm. For the maximum value of the strong-axis unit stress, the higher the rise, the smaller the compression and the larger the tension. There is a trade-off between compression and tension, which can be controlled by the rise of the arch.

For vertical displacement, the higher the rise, the lower the average value. On the other hand, there is a rise-span ratio that is minimized the maximum value of vertical displacement along the way. The effect of the rise on the maximum vertical displacement becomes smaller when the rise span ratio exceeds 1/8, regardless of the number of arch divisions. Figure 7 shows contours of vertical displacement. Higher rise prevents deformation points from being concentrated in the center of the arch.



(a) strong-axis unit stress (b) d_z-average (c) d_z-maximum

Figure 6. Effect of rise-span ratio



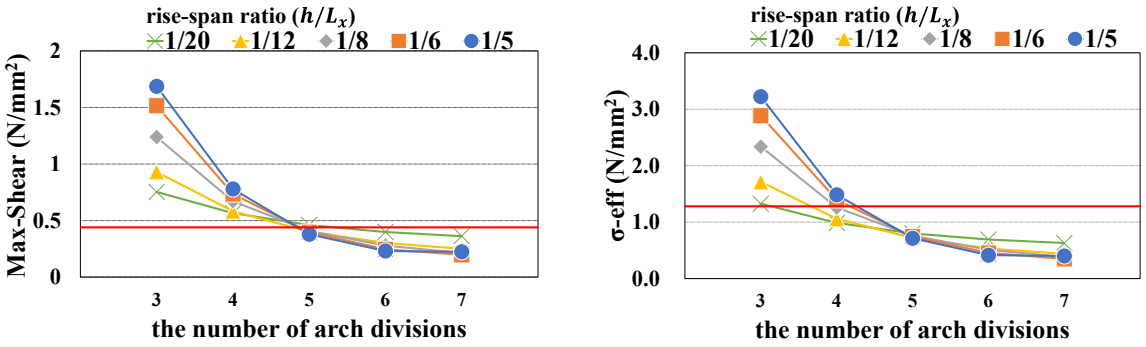
(a) h/L_x= 1/20 (b) h/L_x= 1/5

Figure 7. Contours of vertical displacement

3.4. Effect of the number of arch divisions

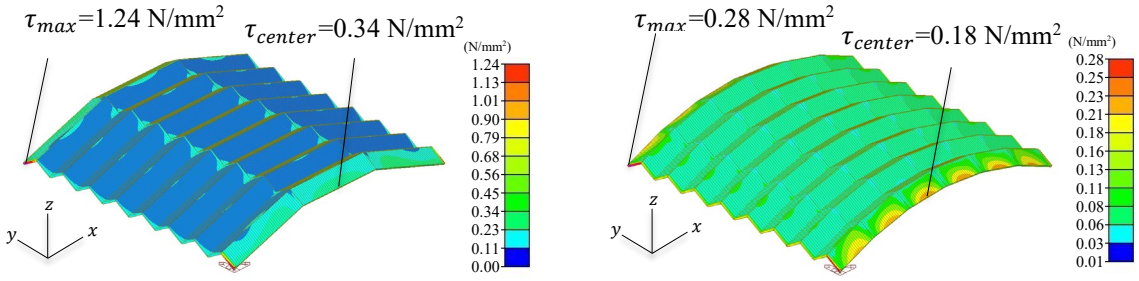
Figure 8 shows the effect of the number of arch divisions on the shear and bending unit stress when mountain height is 750mm. The maximum shear and bending unit stress values both decrease as the number of arch divisions increases. This is thought to be since the model shape approaches a catenary arch as the number of divisions increases and the number of x-directional springs are increase. The diminution of unit stresses increases as the rise increases and converges around 6 or 7 divisions for all rises.

Figure 9 shows contours of vertical displacement. Shear stress is concentrated at the four corners and is particularly pronounced in the case of the number of arch divisions: 3. In the case of the number of arch divisions: 6, the difference between the four corners and the rest of the image becomes smaller, as indicated by the contour tint.



(a) shear unit stress (b) bending unit stress

Figure 8. Effect of the number of arch divisions on unit stress

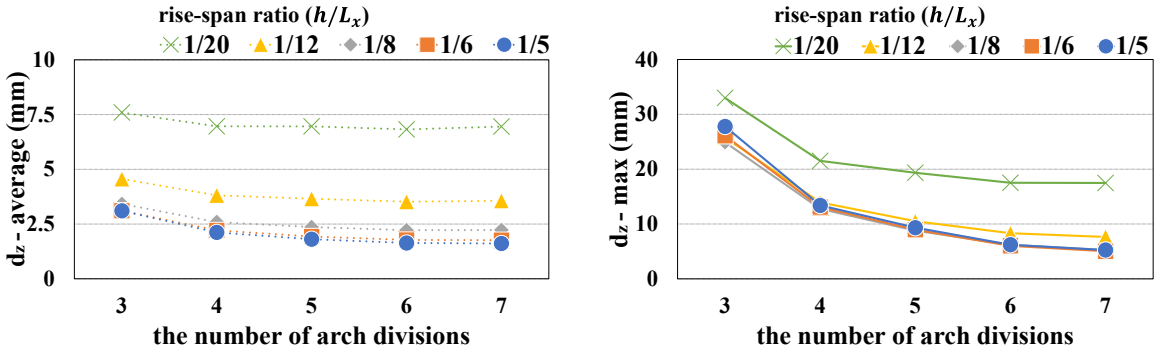


(a) the number of arch divisions : 3 (b) the number of arch divisions : 6

Figure 9. Contours of shear stress

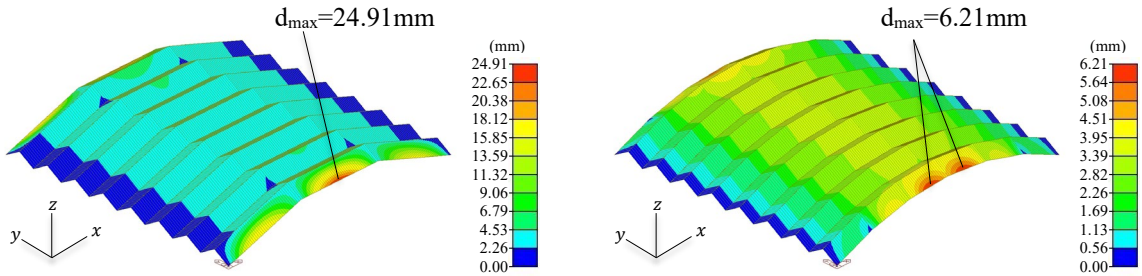
Figure 10 shows the effect of the number of arch divisions on vertical displacement when mountain height is 750mm. The maximum value of vertical displacement decreases as the number of divisions increase, and the amount of decrease also becomes smaller as the number of divisions increases. The average value shows a small change, indicating that the effect of the number of arch divisions is small.

Figure 11 shows contours of vertical displacement. The center of the long side of the CLT in the center of the arch will have the largest deformation, and if the number of divisions is even, two points of maximum vertical displacement will be represented.



(a) d_z-average (b) d_z-maximum

Figure 10. Effect of the number of arch divisions on vertical displacement



(a) the number of arch divisions : 3 (b) the number of arch divisions : 6

Figure 11. Contours of vertical displacement

4. Conclusion

The relationship between form design parameters and structural performance was analyzed for the CLT folded plate arch roof. Increasing the folded-plate peak height suppresses thrust and reduces y-directional reaction forces, while the effect of different peak heights on the maximum vertical displacement is small. By increasing the rise, the maximum value of vertical displacement and unit stress will be smaller, preventing the concentration of deformation points. In addition, by increasing the number of arch divisions, shape of the model becomes closer to an arch and the joint springs increase, thus reducing the stress level of the CLT. Future studies should consider the effects of horizontal forces, number of joints, and cost.

Acknowledgements

The materials necessary for spring modeling were provided by Mrs. Masuda of Tori-sha Co. The authors would like to express our gratitude to them.

References

[1] Ken NODA and Yoshiharu KANEBAKO, “Feasibility study on structural design for arched and interconnected CLT shells”, Architectural Institute of Japan, Journal of Structural Engineering, Vol67B, pp121-127, March 2021

IASS 2023
July 10–14 Melbourne
Integration of Design and Fabrication

Proceedings of the IASS Annual Symposium 2023
Integration of Design and Fabrication
10–14 July 2023, Melbourne, Australia
Y.M. Xie, J. Burry, T.U. Lee and J. Ma (eds.)

Tessellated origami surface and soft robotics

Youness YOUSEFI[a,*], Vera PARLAC[b]

[a,*] School of Architecture, Planning and Landscape, University of Calgary
Youness.yousefi@ucalgary.ca

[b] Hillier College of Architecture and Design, New Jersey Institute of Technology

Abstract

This project explores the kinetic capacity of a tessellated origami surface by incorporating pneumatic muscles into its structure. Folding surfaces such as origami are intrinsically dynamic and offer a promising approach to creating kinetic systems. They present an opportunity to design dynamic architectural spatial geometries capable of transforming in real-time through kinetic technologies. However, implementing this transformation requires meticulous experimentation and research on the origami system's materialization and actuation mechanism. This research project aims to activate a tessellated folding surface by proposing a novel approach to designing, fabricating, and integrating soft pneumatic actuators that enable complex multi-directional movements without complex mechanical systems. The research includes a computational investigation of the folding mechanism and physical experiments that integrate pneumatic silicone actuators into the origami structure. The focus of this research is to examine its foldability and structural stability. Strategic positioning of soft actuators produced distinct surface geometries by inflating and deflating different groups of actuators. The results reveal that the origami unit module scale and the actuator's position are two primary factors that impact the global deformation of the structure. The findings further highlight the potential of soft robotics to produce more intricate movements than their hard-bodied analogues.

Keywords: kinetic architecture, deployable origami structure, form finding, soft robotics

1. Introduction

The traditional approach to architecture has been to design and construct buildings that resist the influence of the changing environment, with a focus on stability and permanence. However, the current discourse in architecture is shifting towards a more sustainable and adaptable approach, which emphasizes the importance of establishing an active relationship between buildings, the environment, and building occupants. This approach recognizes that buildings should be designed to respond and adapt [1] to changing environmental conditions and the evolving needs of their occupants. One of the ways to make buildings adaptive is to include kinetic systems that can facilitate a dynamic relationship between the building and its environment/occupants. Integration of these systems can contribute significantly to the sustainability of the built environment by making it more adaptable and flexible, which can help reduce its energy consumption and minimize its environmental impact.

Dynamic systems require a level of movability of architectural elements and the actuation mechanism that would initiate and control the movement [2]. Most often, they are motor powered or hydraulic, which requires the inclusion of complex mechanical systems. This paper explores the kinetic capacity of origami tessellated surfaces actuated by integrated soft pneumatic muscles. One of the goals is to reduce the need for complex mechanical support.

Origami is a traditional Japanese art that involves folding uncut sheets of paper to produce a smooth

Copyright © 2023 by Youness YOUSEFI and Vera PARLAC. Published in the Proceedings of the IASS Annual Symposium 2023 with permission.

transformation between the flat and folded state by following specific predetermined folding pleats [3]. The folding surfaces of origami provide a kinetic mechanism that is a viable option for generating dynamic structures. Transformability and structural self-support make it a good choice for designing adaptable and deployable structures. The flat-foldability of origami makes it possible to achieve a compact folded state with parallel plate surfaces. This facilitates the deployment and transformation of structures, which is advantageous within an architectural context. Flat-foldable surfaces also retain impermeability during transformation, making them a potentially ideal component for building envelopes [4]. In certain origami patterns, panels are not subject to deformation and therefore qualify as rigid components. To implement kinetic surfaces in architectural applications, the three-dimensional transformation of the surface and its performance must be regulated to achieve the desired design configurations. This requires the application of actuators to provide physical force.

This research project focuses on origami tessellation surfaces with embedded actuating elements (force), that transform between several shapes through equilibrium configurations while preserving their geometric integrity. Producing controllable folding movement in an origami surface, such as the triangular tessellated pattern, can be exceedingly challenging due to the convergence of multiple folds at each vertex. Implementing automated folding motion at the scale of a building using conventional mechanical actuators would require a complex arrangement of sizable linear or rotary actuators. This would, in return, increase the weight of the structure, its energy consumption, and maintenance requirements [5]. This project uses soft pneumatic muscles (capable of movement in all three axes by inflation and deflation) [6] instead of mechanical actuators. A single pneumatic muscle (soft robotic) actuator can produce complex movements, contrary to its mechanical counterpart. In this way, complex movement trajectories of an origami surface can be supported by strategically positioned inflatable components. However, due to their nonlinear behaviour, these systems are challenging to design. The design and prototyping of the soft inflatable muscle have been explored in this research project.

1.1. Tessellated surfaces

The presented project employed a periodic triangular crease pattern, originally developed by Ronald Resch [7]. Resch defined tessellated structures as systems with two fundamental features: modularity and the ability to generate an infinite range of variable dispositions through the alteration of angles between faces [8]. Modularity can be particularly beneficial since it can reduce manufacturing complexity and cost and facilitate constructability [9].

However, Tachi emphasizes that although modular tessellations offer certain benefits, the act of folding periodic origami tessellations becomes increasingly inflexible and rigid as creases increase [10]. This phenomenon is due to the gathering of rigid panels (as they fold) that impede the seamless folding of the tessellations. Consequently, folding tessellations into intricate forms becomes more challenging. Accordingly, he characterized this origami design as periodic origami tessellations that have two degrees of freedom (DOF), namely the "folding-unfolding" motion and the "twisting" motion [10]. Contrary to this, the Resch tessellated structures comprise hinged panels that allow bending and twisting in multiple directions concurrently and can create Gaussian curvature in the form of the saddle or spherical shapes [11], shown in Figure 1, while presenting static equilibrium in both open and closed shapes [12]. Furthermore, the structural stability of folded triangular tessellations is attributed to their rigidity and inertia when erected, resulting in greater stiffness than non-triangular tessellations [13]. This means that it is possible to construct larger structures that sustain flexibility and mobility [14, 15].

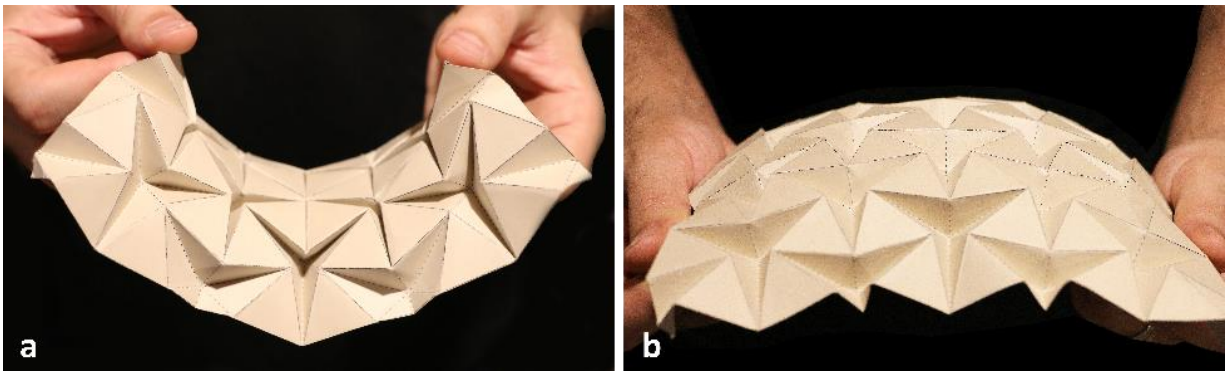


Figure 1. (a) Saddle and (b) spherical form the Gaussian curvature produced by warping tessellated triangular origami.

The foldability of paper origami is determined by the paper's thinness. Replacing paper with a thick, rigid material makes constructing a fully deployable tessellated structure challenging. In order to enhance the foldability of thick panels, Tachi proposed two approaches: relocating the rotational axis to the edges, Figure 2 (a), and trimming the solid of each facet by bisector planes of dihedral angles between adjacent pieces, Figure 2 (b), [16].

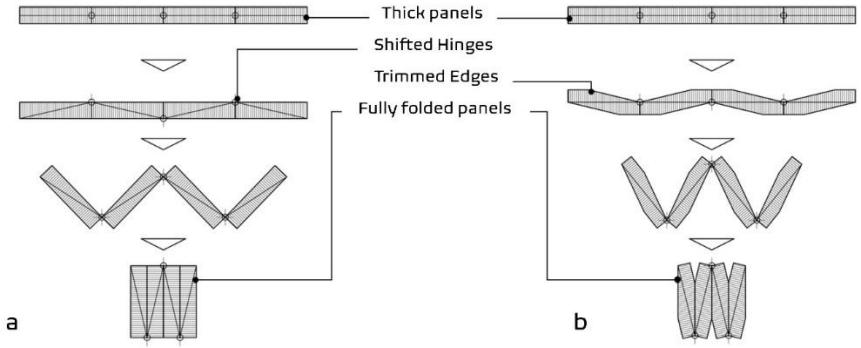


Figure 2. Optimizing foldability of thick panels in origami structures.

Thün et al. used Resch's triangular tessellation model [17] to create the "Resonant Chamber", an expressive acoustic envelope system. This folding structure prototype featured laminated membrane joints as hinges on the edges of the rigid panels [16]. Mechanical linear actuators between adjacent panels are used to animate the surface creating programmable spatial configurations based on sound analysis of the space. To explore the kinematics of a single unit module of the triangular tessellation pattern Mazzucchi developed a digital technique using a bespoke computer simulation [18]. He suggested two different kinds of hinges to make the rigid panels inside each unit cell more foldable. First, he used a system with hinges at the outer margins of the tapered panels, like Tachi [16] and Thün [17], that is similar to projection hinges. Second, he proposed a pin-joint-based hinge. By applying heat-sealing techniques to fabric sheets, Siéfert formed channel patterns that resulted in an anisotropic contraction in the plane and a potential alteration of Gaussian curvature [19]. This versatile single-step method for shaping stiff inflated structures can potentially be applied at a building scale, including deployable space structures and emergency shelters. Attempting to resolve the inflatability of origami structures Melancon et al. created a library of pneumatically actuated foldable origami shapes. The key here is inflatable cavities that, when inflated, preserve the shape of the structure [20].

1.2. Pneumatic actuation

Inspired by the inflatable structures in the early 1950s, the first generation of pneumatic artificial muscles was invented by J.L. McKibben in the late 1950s [21]. Since then, pneumatic muscles have been predominantly utilized in soft robotics to create flexible robots and soft actuators; their flexibility, inflatability, and high elasticity have added new performance capabilities for intricate movements. These inflatable muscles can be more fluidly integrated with moving components and can perform complex movements with a single action, outperforming multiple electromechanical actuators needed for a similar task. Their use simplifies the actuation mechanism, requires fewer mechanical components, and reduces manufacturing cost, assembly time, and operation energy consumption [6]. Due to their lifelike behaviour, soft muscles provide new functionality and improve the fluidity and safety of human and machine interaction [6, 22]. These qualities make them promising candidates for kinetic architecture applications as integrated actuators that generate movement of other elements [5, 23] or as sensor-embedded functional kinetic bodies that facilitate the interactivity of architectural systems [23-25].

The project presented in this paper explores the design, fabrication, and integration of soft inflatable muscles and their capacity to activate an origami-inspired structure. The project's initial phase involves examining the origami surface's folding mechanism, geometric morphology, and kinematic aspects. A computational design platform is utilized to model an origami-inspired folding structure. The spatial deformation of the folding triangular tessellated surface is simulated and systematically studied with the use of a physics engine. The later phase of the project centres on developing a soft pneumatic actuator that exhibits the capacity to generate multi-directional movement. The project also includes the development of a design prototype to test the folding and unfolding effectiveness of the actuator.

2. Methods

2.1. Simulation of surface kinematics

To better understand the geometry and kinematics of the origami tessellation, a surface is divided into unit modules. Simulating the movement of a single unit module enables a simulation of a much larger tessellated surface. The Rhinoceros 3D [26] modelling software was used to model the unit, while Grasshopper was utilized to determine the movement algorithm. Grasshopper's node-based visual programming and data management offer necessary mathematical and geometric functionalities for the development of algorithms.

The folding mechanism of a single unit module of Resch's triangular tessellation was simulated by the Kangaroo plugin – the particle physics engine that runs within the Grasshopper environment. The Kangaroo engine employs the dynamic relaxation method, which involves an iterative approach to compute the forces acting on nodes, followed by a pseudo-dynamic process over time to achieve a state of equilibrium. The nonlinearity of kangaroo simulations [27] renders them suitable for modelling origami structures that exhibit significant deformations. To imitate the folding mechanism, the model requires defining a mesh with its boundary that comprises all creases (valley and mountain), the rest angle of both valley and mountain folds, and the hinge strength.

The panels of the rigid origami surface were modelled as non-bendable mesh facets. Likewise, all the mesh edges, including the creases, were considered rigid beams to prevent elongation. Rigid beams were fabricated by utilizing the Length component. The strength parameter of this component determines the elasticity of the beam. A high numerical value indicates a beam that is rigid and exhibits minimal extension or compression, while a low numerical value indicates characteristics similar to those of a linear spring. All panels and their edges are subjected to compression and tension forces during the folding and unfolding simulation of the surface; therefore, rigid meshes and creases prevent the folding structure from collapsing. In order to simulate the hinges between folds, the rotational creases that link a pair of triangular facets were converted into spring elements using the Hinge component and assigned the strength parameter, which determines the hinges' stiffness. Tuning the strength parameter is crucial

for the simulation because it directly affects the quality of the origami's final deformation. The strength parameter in the Hinge component denotes the actuation force of the soft pneumatic actuators. In addition, a constraint is set using the NoFoldThrough component at all creases to prevent individual triangular faces from travelling through one another. Moreover, the Kangaroo plugin allows the application of virtual forces, such as gravity, translational, and rotational limitations, to the spring model, which helps control the folded pattern's global deformation.

We modelled the origami surface in a fully folded configuration, then started the actuation process by applying unbending forces on the creases locally in several patterns and globally on the entire folded surface. A digital workflow was developed to parametrically replicate inflation actuation through unfolding among the targeted units of the tessellation. The unfolding force is applied in a circular pattern, with the greatest force concentrated at the centre and diminishing outwards. The Kangaroo model simulates the surface deformation and results in a static equilibrium after a few iterations when applying the unfolding force and all predefined constraints. This simulation helps us to better understand the behaviour of the global surface geometry under various inflation-pattern scenarios. Triggered by various inflation rates, the unit module's different folding angles led to different origami surface deformations, as shown in Figure 3.

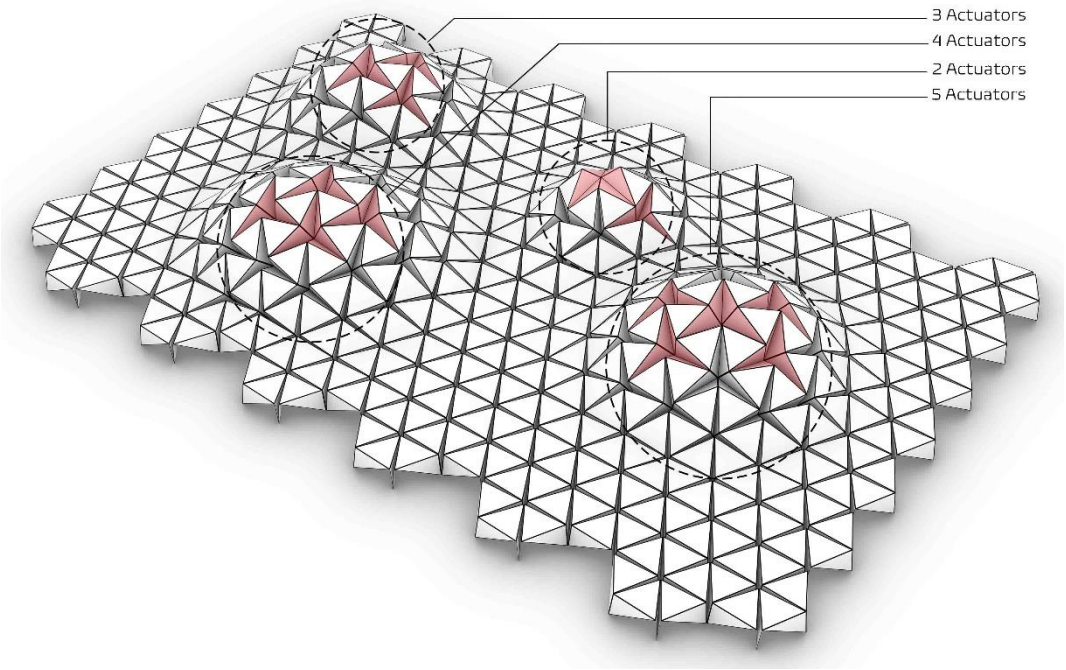


Figure 3. Origami surface deformation shows the surface behaviour caused by specific inflation patterns of actuators.

As mentioned earlier, the Resch origami tessellation is abstracted into an array of unit modules, Figure 4(a). The unit module exhibits a trifold symmetry, Figure 4(b), and includes two distinct vertices, A and B. Vertex A demonstrates a three-fold symmetry due to its six creases, Figure 4(c), while vertex B, also with six creases, displays plane symmetry, Figure 4(d) [13]. After primary analysis of the kinetic mechanism of the unit module of Resch origami, we divided its triangle panels into two kinds, namely, folding and non-folding, where the folding panels create the movement within the unit and the entire folding surface. Accordingly, two effective dihedral angles were recognized for the unit actuation. To move the unit facets from folded to a flat state, dihedral angles α and β, Figure 5(a), need to be increased from 0 to π and from $\pi/2$ to π, respectively. Consequently, if we were to use linear or rotary actuators to fold the unit module, up to nine actuators would be necessary to connect the panels on both sides of each hinge of the unit module, Figure 5(b).

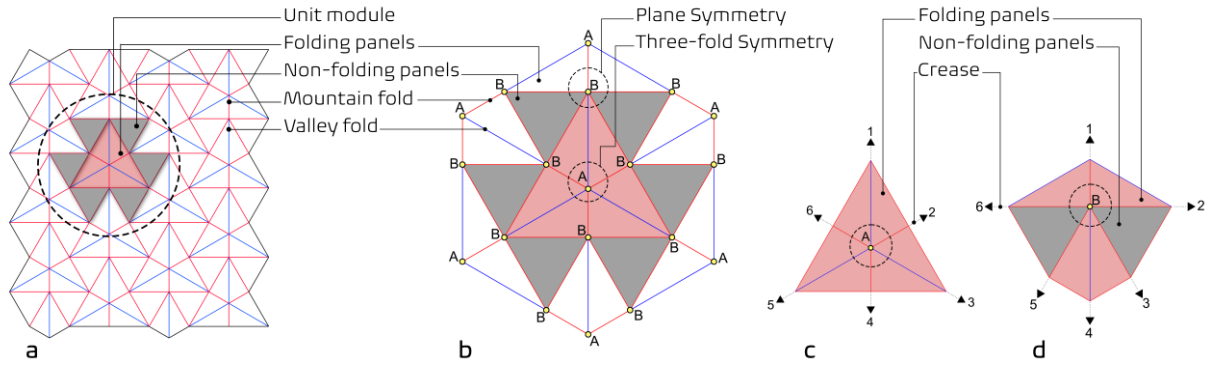


Figure 4. (a): The triangular tessellation of Resch with a single unit module. (b): a typical unit module of Resch tessellation. (c): Vertex A represents a three-fold symmetry. (d): Vertex B represents a plane symmetry.

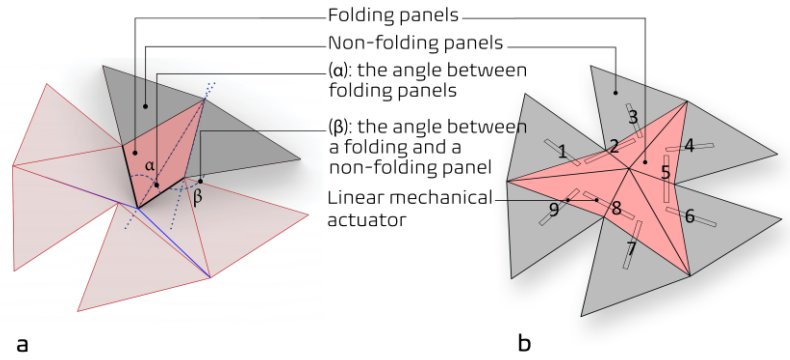


Figure 5. (a): diagram of the folding mechanism for a unit module. (b): Possible placements of linear actuators required for module movement.

2.2. Pneumatic muscle fabrication

The primary objective of this project is to replace linear actuators with a single soft robotic system integrated into a unit module capable of actuating its complex shape. Our proposed actuators are designed to prevent altering the origami pattern and interfering with the folding mechanism by taking into account the position of mountain and valley creases within the geometry of the folded module. Accordingly, two variations of a silicone actuator are created that function differently: (A) pushing and (B) pulling, Figure 6. Actuator A is installed within the foldable panels to push them to unfold when inflated. In contrast, actuator B is attached to the rear of the folding panels to pull them open when inflated.

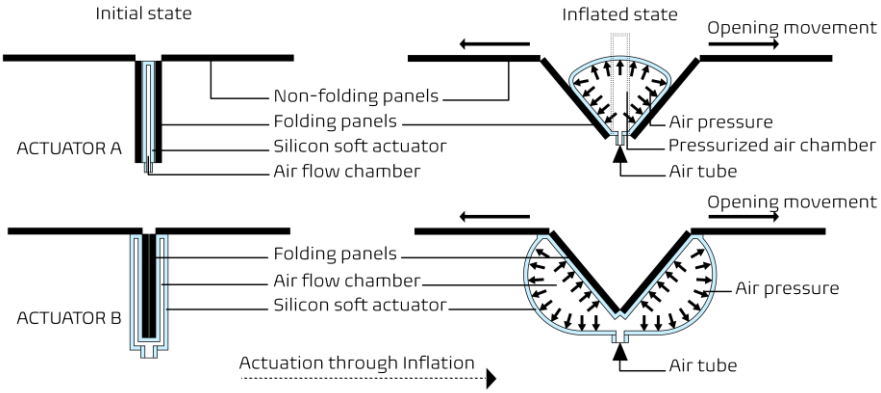


Figure 6. Two proposed actuators: type A functions as pushing, and type B functions as pulling.

Actuator A was designed to fit inside the tessellation folding pattern, Figure 7(A). It consists of three fins corresponding in size and shape to the unit module geometry. Three connected air chambers within the fins provide airflow for actuation. The casting procedure consisted of the main silicone body, made first and then cast with the cap to seal the air chambers. Accordingly, a ten mm wide gap was constructed between the folding panels to accommodate the three-fin silicone actuator with the unit module's folding pattern. Each fin of the soft actuator was attached to the fabric at the bottom of each crease, acting as a hinge between each pair of folding facets. Air was supplied for inflation through a polyurethane tube connected to the actuator from the rear of the unit module.

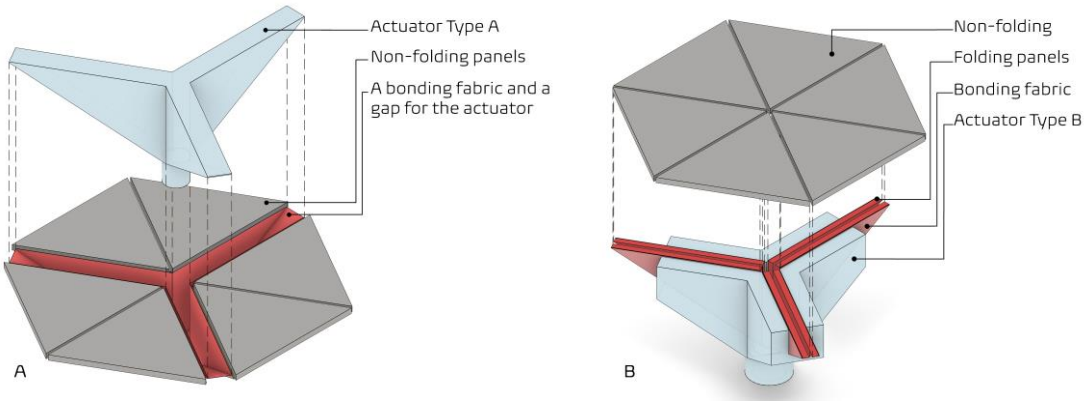


Figure 7. A and B actuators and their placement in a unit module of Resch's origami.

Actuator B was designed to hug the two folded faces of the module from the rare side of the surface., Figure 7(B). Similar to actuator A, its dimensions and shape are based on the origami unit module pattern and size. Unlike type A, however, each fin is divided into two sub-fins with distinct air chambers attached to both sides of the two folded panels. This structure provided larger bonding surfaces for the panels. In order to regulate inflation and attain the intended three-dimensional motion of the six chambers of actuator B, a constraining fabric layer was attached to the back side of the pneumatic actuator. This directed the force of movement toward the module's centre, which concentrated the force required to unfold the panel. The directed and constrained inflation force led to a notable reduction in air pressure requirements, Figure 8.

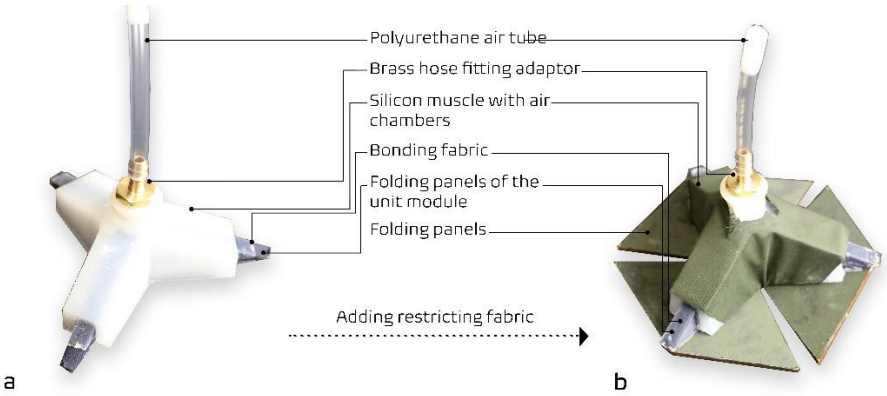


Figure 8. A restricting layer of fabric was attached over the pneumatic actuator.

2.3. Origami surface prototype

Soft actuators are cast using "Dragon SkinTM 10 Slow" silicone. Actuators are integrated into a wooden tessellation surface using the fabric matrix to create strong bonds between the surface and the silicone actuators. The gap layout between the triangular plywood elements is determined by considering the

plywood thickness and the edge hinge system [16, 17]. A prototype of 32 fully-folded unit modules is assembled in a four-by-eight grid, Figure 9(a). Twelve units are equipped with actuator B, Figure 9(b), and strategically grouped over the surface. This layout was used to explore the relationship between the folding mechanism and the local and global deformation of the origami surface. The non-actuated unit modules were kept in a folded position by embedded silicone clamps Figure 9(b). The entire tessellated structure was mounted on a 90 cm x 30 cm wood chassis, with two 30 cm and 60 cm–high walls on its two adjacent sides. The actuators were separated into six pairs, each connected to an independent air supply tube via pneumatic solenoid valves and an air compressor with an integrated air pressure sensor. They were commanded by an Arduino microcontroller with a MOSFET (metal-oxide-semiconductor field-effect transistor) driver module shield, Figure 9(c). Using pulse-width modulation, we programmed solenoid valves to perform six inflation patterns in a loop.

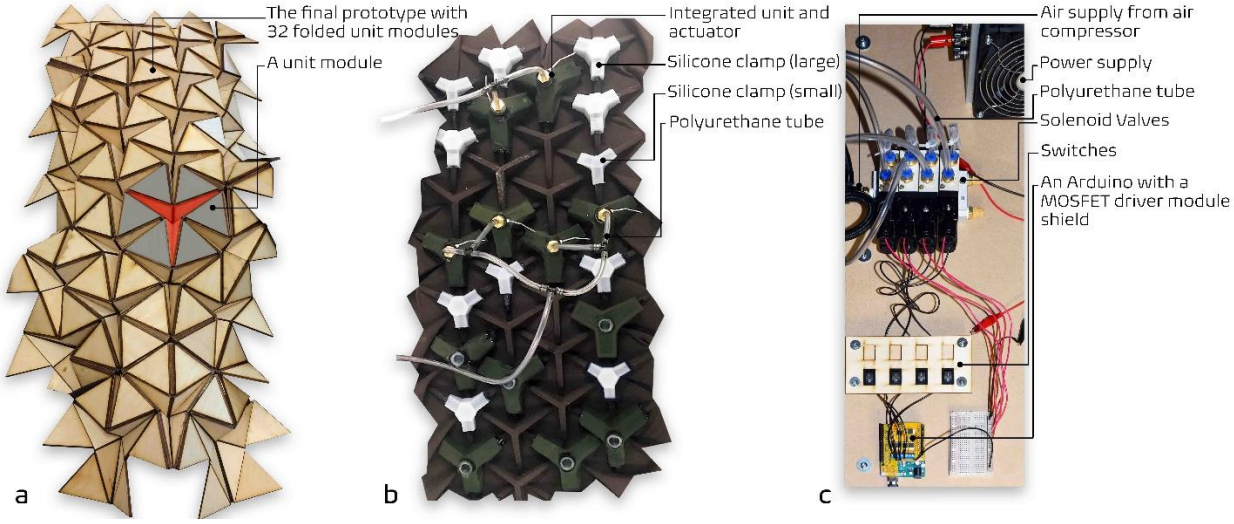


Figure 9. (a) The top surface of the final prototype of Resch's origami surface. (b) The reverse side of the completed prototype displays the locations of the actuators and clamps. (c): the control board containing Arduino and solenoid valves that regulate the air supply to the actuators.

3. Results and discussion

3.1. Simulation

The tessellated surface simulation assumes rigid and planar surface facets, as their bending is considered negligible. Despite the rigidity of the individual triangular facets, the mesh as a whole is regarded as a non-rigid and compliant body due to its ability to fold at the creases. The motion of the surface was generated within specific areas or across the entire model by modifying the angles of the folds, contingent on the distribution of the applied actuation. Regulating the magnitude of the angle constitutes a viable approach for managing the spatial changes of the creased surface. When no external forces or constraints were acting upon the surface, by increasing the angles α and β, the folding angles of both valley and mountain folds remained uniform due to the origami's inherent symmetry. Accordingly, the structure expanded only along X and Y axis at its equilibrium state without forming a spatial deformation. However, after local activation, as the angles of the fold increased, the α (angle between folding panels of each unit) decreased towards the edges of the deformation arch (Figure 10), indicating a greater compressive force at lower units due to their weight. Hence, the resting angle of α depends on the gravity stress on the folding panels, the stiffness of the hinge material, and the mechanical properties of the soft pneumatic actuator.

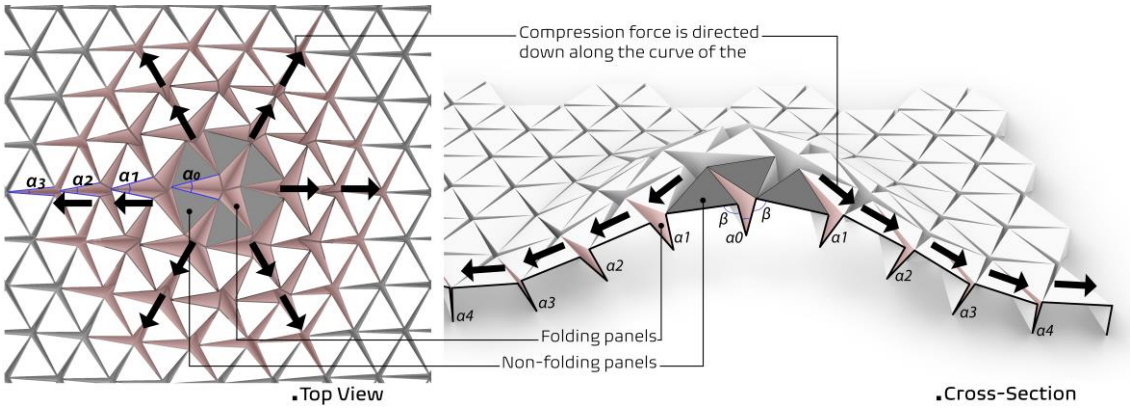


Figure 10. The angle between folding panels (α) was smaller towards the edges of the arch in each deformation.

The kinematics of the origami tessellation was simulated in vertical and horizontal positions using the particle engine of the Kangaroo plugin, Figure 11 and Figure 12. The simulation allowed for an easy change of the unit size within the surface. Scaling down the unit module increased the number of unit modules and, thus, the number of folds and actuators on the surface. More folds led to more varied deformation with more dramatic folding patterns of the origami surface that could be more easily calibrated. However, the increased number of unit modules compromised the structural stability of the surface. On the other hand, scaling up the unit module size reduced the number of unit modules on the surface and decreased the number of folds and actuators. This resulted in less varied deformation of the surface but more structural stability.

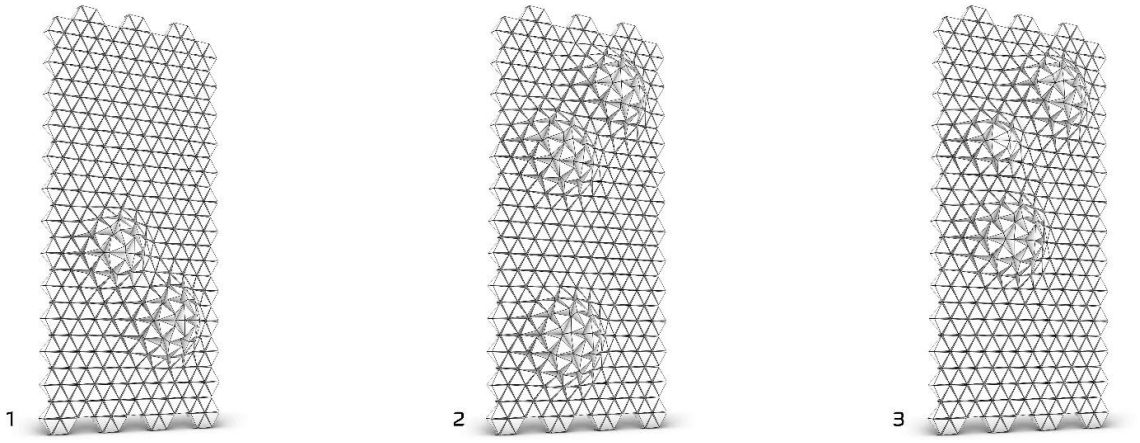


Figure 11. Simulation of various inflation patterns shows the surface's behaviour in the vertical position.

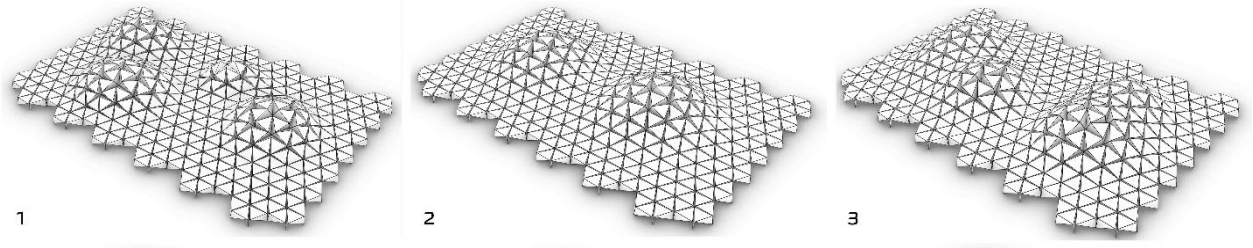


Figure 12. Simulation of various inflation patterns shows the surface's behaviour in the horizontal position.

3.1. Inflatable muscle performance

During the actuator inflation, several things were noted. Actuator A failed to fully open the unit module, as its inflation force was not fully utilized. Increasing the air pressure inflated the actuator in the opposite direction instead of increasing the pushing force. Because of its placement on the upper surface of the origami structure, this actuator would be exposed to possible damage, Figure 13(A). These observations obtained during the fabrication phase led to the design of the type B actuator.

Unlike actuator A, actuator B was fabricated as an integral part of the unit module's folding panels and placed under the surface. During the initial inflation test, the unit opened only partially, indicating that the actuator force must be more precisely directed. Applying a non-flexible fabric on the actuator enabled full inflation force towards the centre of the folding panels; thus, the amplified and directed force of the air unfolded the module, Figure 13(A).

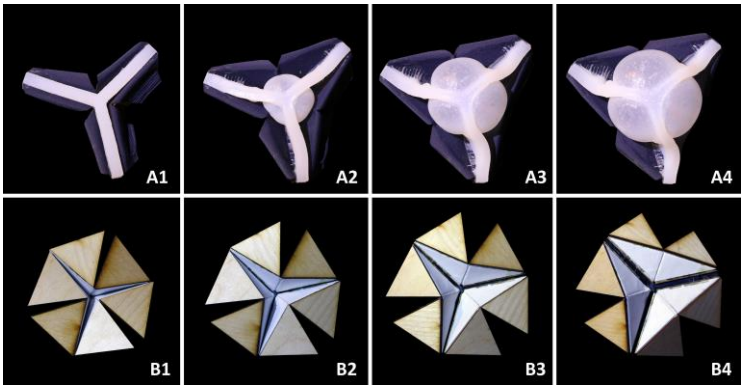


Figure 13. (A): Type A actuator opening sequence. (B): type B actuator opening sequence.

The final origami prototype consisted of 12 integrated actuators, while the rest of the unit modules remained closed with silicone clamps to provide the structural stability of the origami surface. Two sizes of silicone clamps were used on 11 non-actuated modules to help stabilize the origami surface in the folded state. The clamps allowed a minor folding/unfolding of each non-actuated module to enable a smooth global deformation of the entire origami surface. The size of the silicone clamps and their gripping force was critical in calibrating the surface deformation. If too large, clamps reduced the actuation force and caused a slight deformation, while small clamps resulted in structurally compromised and non-stable deformation.

The physical prototype inflation tests were carried out by orienting the prototype horizontally and vertically, Figure 14 and Figure 15. Various inflation patterns created different geometrical configurations, which helped examine the functionality of the actuators under the force of gravity. Although the actuators performed better in the vertical position, the folded units at the upper margin of the origami (where it was attached to the wood chassis) tended to unfold. In contrast, when in the horizontal position, the origami structure tended to remain folded due to the structure's weight. Therefore, actuating the units on the horizontal surface required higher air pressure. Furthermore, the analysis of the origami deformations in both positions determined that achieving a smoother global deformation would demand more actuators uniformly distributed through the surface.

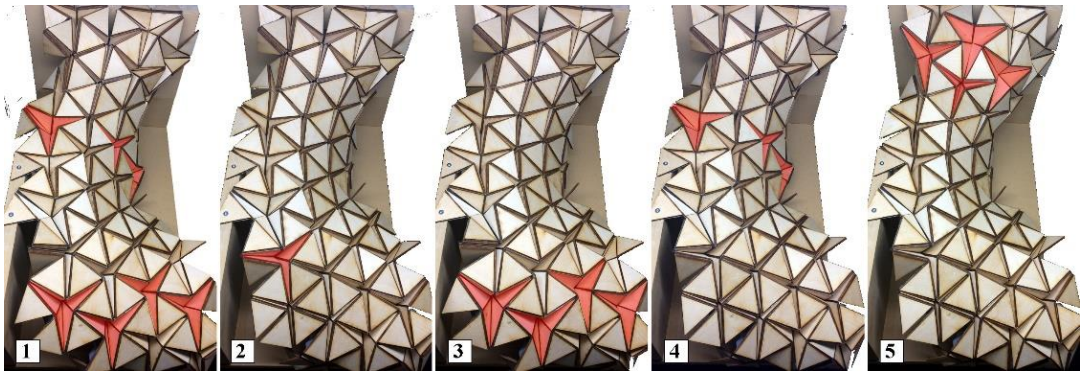


Figure 14. Prototype in a vertical position showing various inflation patterns.

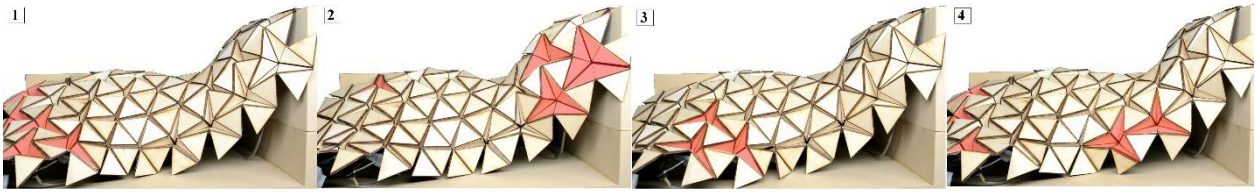


Figure 15. Prototype in horizontal position showing various inflation patterns.

4. Conclusion

This prototype-based study integrates soft robotics with Resch's triangular tessellation to exploit origami's kinetic properties. Compared to the linear actuation of the origami surface presented in the Resonant Chamber project [17], it was concluded that a single silicone actuator could replace up to six linear electromechanical actuators. Considering its folding kinematics, each unit module is divided into two parts: folding panels and non-folding panels. The final design embeds the folding panels in a soft actuator, enabling a one-step fabrication of the new module and actuator. Performing the inflation tests on the final prototype, equipped with 12 embedded actuators, underlined the significant influence of gravity on the surface deformation, its structural stability, and the unfolding function of the actuators. Designing an origami surface must account for its two intrinsic characteristics: flexibility and structural stability. The project strives to maintain both by integrating a soft actuator within a unit module of the origami pattern.

The outcome of this research highlights the possibility of making a tessellated origami structure kinetic by embedding soft robotics systems. Structures like these that include moving elements can be used in diverse architectural applications, such as adaptive facades or deployable shelters. For example, as a prefabricated deployable module, this design can aid in creating shelters for the survivors of natural disasters. The advantage of this folding system is that its prefabricated modules can be shipped to remote sites and assembled without any skilled labour. Once activated by specific air pressure, they would rapidly form a structurally stable shell.

This project is part of an ongoing study of actuating an origami surface. The authors believe further investigation is required to improve the efficiency of the soft pneumatic actuator and evaluate its nonlinear performance more precisely. In addition, given the compliant characteristics of Resch's origami, further structural analysis is necessary to evaluate its stability against different loads, including lateral loads.

Acknowledgements

The second phase of this project was a collaborative group effort for a course on responsive architecture offered at the School of Architecture, Planning, and Landscape at the University of Calgary. The authors

would like to thank Joseph Kaplan, Faraz Aghajafari, and Yanjinlkham Tumurbaatar for contributing to the fabrication of an early prototype.

References

[1] W. F. Preiser, A. E. Hardy, and J. J. Wilhelm, *Adaptive architecture: Changing parameters and practice*: Routledge, 2017.

[2] B. Kolarevic and V. Parlac, *Building dynamics: exploring architecture of change*. New York; London;: Routledge, 2015.

[3] G. L. Comstock, "Moisture diffusion coefficients in wood as calculated from adsorption, desorption and steady state data," *Forest Products Journal,* vol. 13, pp. 97-103, 1963.

[4] T. Tachi, "Freeform rigid-foldable structure using bidirectionally flat-foldable planar quadrilateral mesh," in *Advances in architectural geometry 2010*, ed: Springer, 2010, pp. 87-102.

[5] A. Körner, L. Born, A. Mader, R. Sachse, S. Saffarian, A. Westermeier, *et al.*, "Flectofold—a biomimetic compliant shading device for complex free form facades," *Smart Materials and Structures,* vol. 27, p. 017001, 2017.

[6] G. M. Whitesides, "Soft Robotics," *Angewandte Chemie International Edition,* vol. 57, pp. 4258-4273, 2018.

[7] R. Resch and H. N. Christiansen, "The design and analysis of kinematic folded plate systems," in *Proceedings of IASS Symposium on Folded Plates and Prismatic Structures, 1970*, 1970.

[8] R. D. Resch, "The topological design of sculptural and architectural systems," in *Proceedings of the June 4-8, 1973, national computer conference and exposition*, 1973, pp. 643-650.

[9] Mathieu Huard, Michael Eigensatz, and P. Bompas, "Planar Panelization with Extreme Repetition," in *In Book: Advances in Architectural Geometry 2014*, P. Block, J. Knippers, N. J. Mitra, L. e. M. Springer, and Statistics, Eds., 2015 ed Cham: Springer International Publishing, 2015, pp. 233-241.

[10] T. Tachi, "Rigid folding of periodic origami tessellations," *Origami*, vol. 6, pp. 97-108, 2015.

[11] M. Schenk and S. D. Guest, "Origami folding: A structural engineering approach," in *Origami 5: Fifth International Meeting of Origami Science, Mathematics, and Education*, 2011, pp. 291-304.

[12] L. Magliozzi, A. Micheletti, A. Pizzigoni, and G. Ruscica, "On the design of origami structures with a continuum of equilibrium shapes," *Composites Part B: Engineering,* vol. 115, pp. 144-150, 2017.

[13] F. Yang, M. Zhang, J. Ma, Z. You, Y. Yu, Y. Chen, *et al.*, "Design of Single Degree-of-Freedom Triangular Resch Patterns with Thick-panel Origami," *Mechanism and Machine Theory,* vol. 169, p. 104650, 2022/03/01/ 2022.

[14] D. Lee, "Self-Organizing Origami Structures (Research Poster)," in *ACADIA 13: Adaptive Architecture [Proceedings of the 33rd Annual Conference of the Association for Computer Aided Design in Architecture (ACADIA) ISBN 978-1-926724-22-5] Cambridge 24-26 October, 2013), pp. 421-422*, 2013.

[15] D. Baerlecken, R. Gentry, M. Swarts, and N. Wonoto, "Structural, Deployable Folds — Design and Simulation of Biological Inspired Folded Structures," *International Journal of Architectural Computing,* vol. 12, pp. 243-262, 2014.

[16] T. Tachi, "Rigid-Foldable Thick Origami," in *Origami 5: Fifth International Meeting of Origami Science, Mathematics, and Education*, 2011, p. 253.

[17] G. Thün, K. Velikov, C. Ripley, L. Sauvé, and W. McGee, "Soundspheres: Resonant Chamber," in *Leonardo*, 2012, pp. 348-357.

[18] A. Mazzucchi, "A Kinetic Module for Modular Structures Based on Rigid Origami," *Nexus Network Journal,* vol. 20, pp. 41-57, 2018.

[19] E. Siéfert, E. Reyssat, J. Bico, and B. Roman, "Programming stiff inflatable shells from planar patterned fabrics," *Soft Matter,* vol. 16, pp. 7898-7903, 2020.

[20] D. Melancon, B. Gorissen, C. J. García-Mora, C. Hoberman, and K. Bertoldi, "Multistable inflatable origami structures at the metre scale," *Nature*, vol. 592, pp. 545-550, 2021.
[21] J. McKibben, "Artificial muscle," *Life*, vol. 10, pp. 87-88, 1960.
[22] M. Decker, "Soft Robotics and Emergent Materials in Architecture," 2015.
[23] D. Fougere, R. Goold, K. Velikov, R. Goold, and K. Velikov, "Pneuma-Technics // Methods for Soft Adaptive Environments," in *ACADIA 2105: Computational Ecologies: Design in the Anthropocene [Proceedings of the 35th Annual Conference of the Association for Computer Aided Design in Architecture (ACADIA) ISBN 978-0-692-53726-8] Cincinnati 19-25 October, 2015), pp. 274-283*, 2015.
[24] D. Rossi, Z. Nagy, and A. Schlueter, "Soft Robotics for Architects: Integrating Soft Robotics Education in an Architectural Context," *Soft Robotics*, vol. 1, pp. 147-153, 2014.
[25] D. Park and M. Bechthold, "Designing Biologically-Inspired Smart Building Systems: Processes and Guidelines," *International Journal of Architectural Computing*, vol. 11, pp. 437-463, 2013.
[26] R. M. Associates. (2023). *Rhinoceros 3D*. Available: https://www.rhino3d.com
[27] D. Piker, "Kangaroo: form finding with computational physics," *Architectural Design*, vol. 83, pp. 136-137, 2013.

Other

Active bending
Additive manufacturing/ 3D printing
Architectural geometry
Bamboo for sustainable construction and quality of life improvement
Bio-inspired structures and architecture
Bridge structures
Computational form-finding
Conceptual design
Concrete structures
Construction techniques
Deployable and inflatable structures
Design competition (WG21)
Digital modelling and fabrication
Dynamic response of metal spatial structures
Dynamic response of other structures
Form-finding and structural optimisation of interlocking discrete assemblages
Graphical methods
Gridshell and lattice structures
Historical concrete shells
Historical structures
Lattice structures
Life-cycle design and assessment of structures
Metal gridshell structures, connections and stability
Methods and construction technologies for sustainable shell structures
Morphology and configuration processing
Next generation parametric design
Novel methods in modelling, optimisation and construction for reducing carbon footprint of continuous roof shells
Numerical methods for geometry, form-finding and optimisation of lightweight structures
Optimisation methods and applications
Origami
► **Other**
Teaching design uncertainty: working with unknown qualities/quantities of new and re-claimed materials
Teaching of shell and spatial structures
Tensegrity systems and cable structures
Tension and membrane structures
Tension structures in the Asia-Pacific
Timber and bio-based structures
Topology optimisation
Traditional masonry structures and innovation
Transformable structures

Proceedings of the IASS Annual Symposium 2023
Integration of Design and Fabrication
10–14 July 2023, Melbourne, Australia
Y.M. Xie, J. Burry, T.U. Lee and J. Ma (eds.)

A modified finite area element model for simulating the evolution of roof snow load

Huamei Mo[a,b,*], Zhiheng LUO[a,b], Ziwei TAI[c], Yuanyuan LI[c], Feng FAN[c]

[a,*] Key Lab of Structures Dynamic Behavior and Control of the Ministry of Education, Harbin Institute of Technology, Harbin 150090, China
[b,*] Key Lab of Smart Prevention and Mitigation of Civil Engineering Disasters of the Ministry of Industry and Information Technology, Harbin Institute of Technology, Harbin 150090, China
P.O. Box 2619, Harbin Inst. of Tech., No. 73 Huanghe Rd, Nangang District, Harbin, China
mohuamei@hit.edu.cn

[c] Gemdale Corporation, Shenzhen, 518026, China

Abstract

Long-span roofs are usually associated with a complex shape and are typically snow load-sensitive, but in most design codes, there is no specific guides for the design of roof snow load for these kinds of roofs. Therefore, it is of great significance to develop an algorithm or method to aid the design of roof snow load for long-span, complex roof structures. In this paper, the Finite Area Element (FAE) method proposed by Irwin and Gamble was modified to analytically simulate the evolution of roof snow load on a cylindrical roof. The modifications include three aspects: 1) the formula to estimate roof snow transport rate due to snow drifting; 2) the method of evaluating the wind field around the roof; and 3) the estimation of roof snow depletion. Using the modified model, the evolution of roof snow load on a cylindrical roof in Harbin China is simulated and analyzed for the period of 1971 – 2017. Results indicated that the modified model is easy to implement and could be a useful tool to aid the design of roof snow load for long-span, complex roofs.

Keywords: roof snow load, long-span complex roofs, finite area element, snow drifting

1. Introduction

The current load code for building structures in China specifies roof snow load factors for several conventional and simple roof types (shapes), so the roof snow load of these types of roofs could be designed by following the corresponding specifications. However, for roofs with complex shapes, such as that of many transportation hubs, stadiums, and exhibition centers that have been widely constructed in recent years in China, the roof snow load could hardly be designed by following the code since no specific guides are provided. The distribution of snow load on the roofs of such buildings are more complex than those on ordinary buildings. Therefore, it is of great significance to develop an algorithm or method to determine the design roof snow load for these long-span, complex roof structures.

At present, the research methods for studying roof snow load include field measurement [1-4], wind tunnel or water flume test [5-7], and numerical simulation [1,8,9]. In recent years, the Computational Fluid Dynamics (CFD)-based numerical simulation techniques have become a powerful tool in addressing the problem of snowdrift around/on buildings in snowy regions [10], and many applications of this technique could be found in the literature [11-13]. However, an overview of the current numerical models indicates that these models are mainly single event-based, i.e., the simulation result is associated with a single event of specific snowfall intensity, wind speed, and wind direction. Consequently, the simulation result cannot reflect the complex distribution of roof snow owing to the strong uncertainties

Copyright © 2023 by Huamei MO, Zhiheng LUO, Ziwei TAI, Yuanyuan LI and Feng FAN. Published in the Proceedings of the IASS Annual Symposium 2023 with permission.

in the combination of snowfall intensity, wind speed, and wind direction under natural conditions, so it could not be used directly to assist the design due to the lack of probabilistic implications.

Unlike the CFD-based simulation, analytical simulation such as Finite Area Element (FAE) method [14] incorporate historical meteorological variables in the simulation, so the result is a reflection of the time-history evolution of the roof snow load under actual climate condition and is associated with probabilistic implications, which is necessary for a structural design that is based on probability theory. Although the CFD-based simulation could also be extended to a time-history analysis, its high requirement in computational resources makes it not feasible under the current situation.

The FAE method was proposed by Irwin and Gamble [14] in their study of snow loading on the Toronto Skydome. The fundamental of this method is to carry out detailed computational simulations of snow deposition, erosion, and melting hour-by-hour, the absorption of rainwater and meltwater by snow is considered in the simulation. By carrying out the time-history analysis of roof snow load, the design value of roof snow load is determined through statistical analysis of the most unfavorable snow load in each winter.

In this paper, the FAE method is partially modified to simulate roof snow load on a cylindrical roof in Harbin China. In the modified model, the friction velocity on the roof surface, rather than the wind velocity at a height of 1 m above the roof surface suggested in the original model, is used to calculate the snow drifting rate at each node of the grid. Also, by considering the difficulties in measuring friction velocity in wind tunnel tests, numerical simulation is applied to determine the friction velocity on the roof surface. Additionally, since hourly records of meteorological variables are not available in China, daily records of snow and wind data were used in the simulations. Another major modification to the original FAE method is the method to estimate snow depletion due to melting and sublimation. The remaining part of the paper is organized as follows: details of the modifications to the model are presented in section 2, and the application of the model to simulate the roof snow load on a cylindrical roof is described in section 3. Finally, conclusions are drawn in section 4.

2. Modified FAE model

2.1. Summary of original FAE model

Assumptions and details of the FAE method could be found in Irwin and Gamble [14] and Irwin *et al*. [15], and a review of the steps of the method was given in Gamble *et al*. [16].Basically, to perform a FAE analysis, the roof is first divided into an orthogonal grid of elements, and a mass balance equation is performed on each area element of the grid to derive the snow load within the element. For an area element as shown in Figure 1, snow transport rate at each node of the element, $q_{i,j}$, is first calculated using an empirical equation between the wind speed and the snow transport rate. The two components of the snow transport rate are then estimated to be:

$$\begin{aligned} q_{xi,j} &= q_{i,j} \cdot \cos \alpha_{i,j} \\ q_{yi,j} &= q_{i,j} \cdot \sin \alpha_{i,j} \end{aligned} \tag{1}$$

where $\alpha_{i,j}$ is the angle of the local velocity vector to the grid at node (i, j). The snow transport rate normal to the four boundaries of the element is then calculated using:

$$\begin{aligned} q_1 &= 0.5 \times (q_{x(i,j)} + q_{x(i,j+1)}) \\ q_2 &= 0.5 \times (q_{y(i,j)} + q_{y(i+1,j)}) \\ q_3 &= 0.5 \times (q_{x(i+1,j)} + q_{x(i+1,j+1)}) \\ q_4 &= 0.5 \times (q_{y(i,j+1)} + q_{y(i+1,j+1)}) \end{aligned} \tag{2}$$

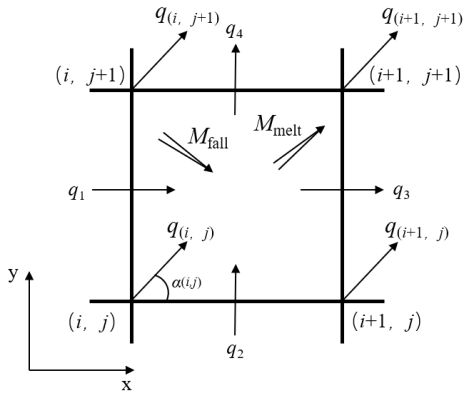


Figure 1. Schematic of snow mass balance for an area element

Finally, the change in snow mass, dm, in the element after a time interval, dt, is computed using:

$$\mathrm{d}\,m = \mathrm{d}\,t \cdot (q_1 l_1 + q_2 l_2 - q_3 l_3 - q_4 l_4) + M_{\text{fall}} - M_{\text{melt}} \tag{3}$$

where l_1 to l_4 are the lengths of the four sides of the element, M_{fall} and M_{melt} is snow mass caused by snowfall and snow melting during dt, respectively.

As a quick reference, the steps of the original FAE model are extracted from Gamble *et al*. [16]. The roof is divided into many area elements by a grid system.

a) The wind velocity distribution near the roof surface (1 m above the roof at full scale) is determined by wind tunnel tests on a model for a series of (typically16) wind directions, velocities are measured at each grid intersection point.

b) Snow drifting rates are then computed using empirical relationships for snow flux versus wind velocity. By computing the mass fluxes into and out of each element, the rate of build-up or depletion of snow mass in the element due to drifting is determined.

c) Time histories of meteorological data are used as input and the computations proceed in a time step manner in typically one hour time increments.

d) The mass balance computations at each time step include the additional mass from snowfall and the depletion due to melting. Hourly values of snowfall are produced from six-hour records of snowfall using a uniform rate of accumulation or weighted by qualitative snow flags if available. Melting calculations are performed by using hourly information on air temperature and cloud cover.

e) The result is a detailed time history of snow mass in each area element and the computed time histories extend over all the winters that are associated with sufficiently detailed meteorological data.

f) The snow mass time histories are analyzed statistically to determine various loading conditions of interest for design, 50-year return period value of the total imbalance in snow load between one half of the roof and the other for example.

2.2. Snow transport rate

In the original FAE method, the formula used to calculate the snow flux at a grid point is:

$$q = c \cdot U^2 \left(U - U_{\text{th}}\right) \tag{4}$$

where U is the wind speed at a height of 1 m above the roof; U_{th} is the threshold wind speed at a height of 1 m above the roof for the snow drift to occur, which is taken as 4 m/s, and c is a constant determined from field test results.

The formula was derived from field test [4], which were typically carried out on a flat, open ground. Since the actual roof geometry is much more complex than flat, open ground, the wind profile along the vertical direction on the roof should also differ a lot from those on the ground, this will result in different shear forces on the surface even when wind speed at 1m height is the same for the two cases. As a result, the snow transported by the wind will differ from each other. Consequently, it's considered in this study that the snow transport rate should be directly related to the shear force on the surface, and the equation given by Pomeroy and Gray [17] is used to obtain the snow flux at the grid nodes:

$$q = \frac{0.68\rho_a}{u_* g} u_{*t}(u_*^2 - u_{*t}^2) \tag{5}$$

$$u_* = \sqrt{\tau_0 / \rho_a} \tag{6}$$

where ρ_a is air density; u_{*t} is the threshold friction velocity which is taken as 0.2m/s in this study; u_* is the friction velocity that is calculated using Eq. (6), τ_0 is shear stress on the surface that could be derived from numerical simulations, and g is the acceleration of gravity that is taken as 9.8 m/s.

It should be noted that the relations given by Eq. (5) is also derived for flat, open ground, and it's assumed that the snow flux has reached a saturate or equilibrium state when developing the equation. Typically, a fetch length of about 200m to 350m [18] is required for the snow drift to reach a steady or saturated state, but for most buildings, the size of the roof is typically less than 200m. In addition, the development of the snow flux on the building roof is usually interrupted by obstacles on the roof such as roof steps. Consequently, a reduction factor, η, should be considered when applying Eq. (5) on building roofs, and the value of η should be case-dependent. The evaluation of η is out of the scope of this study and deserves further investigation. As a simplification, a value of 0.1 for η is considered for the roof considered in this study.

2.3. Utilization of daily wind speed

In the original FAE model, hourly records of meteorological data were required to run the simulation. However, historical meteorological data in China is daily at its highest temporal resolution. Consequently, an algorithm is required to estimate the daily snow transport using daily records of snow and wind data, such that the estimated snow transport should be as accurate as those estimated by hourly information. For this purpose, it's noted that the wind speed in the Chinese code is regarded as 10-min mean wind speed measured at 10-m height above the ground, U_{10}, and that the daily wind data provided by the China Meteorological Administration includes the daily average wind speed, U_{mean}, the daily maximum wind speed, U_{max}, and the daily maximum gust wind speed (3-s mean wind speed), U_{gust} [19-20]. Based on this situation, the 10-min mean wind speed U_{10} is regarded as a random variable in this study, and the two-parameter Weibull distribution was used to fit the probability distribution of U_{10}. According to the probability distribution model of U_{10}, the logarithmic law of wind speed profile that relates U_{10} and u_*, and the snow transport rate given by Eq. (5), the expected value of the daily snow transport, M_{exp}, can be obtained. Given this expected value of daily snow transport, an equivalent wind speed, U_{eqv}, is assumed and estimated, such that the snow transport caused by U_{eqv} for a period of 24 hours is equal to M_{exp}. In this way, the estimation of daily snow transport could be greatly simplified since only a single wind speed (U_{eqv}) is to be considered in the simulation for each day. Details of the probabilistic modeling of U_{10} and the estimation of U_{eqv} can be found in Li *et al.*[21].

2.4. Evaluation methods for snow depletion

In the original FAE model, the melting and sublimation of snow on the roof was estimated by considering an energy-balance-based snowmelt model, which works well but complicates the simulation. In the modified model, it is assumed that snow depletion on the roof is proportional to the reduction in snow depth on the ground:

$$\Delta M_{i,r} = M_{i-1,r} \cdot \left|\Delta h_{i,g}\right| / h_{i-1,g} \tag{7}$$

where $\Delta M_{i,r}$ is the reduction in snow amount on the roof for day i, $M_{i\text{-}1,r}$ is the snow mass on the roof on the previous day (day i-1), $\Delta h_{i,g}$ is the reduction in the ground snow depth on day i (compared to day i-1), and $h_{i\text{-}1,g}$ is the ground snow depth on the previous day.

Considering that the air temperature and solar radiation are the same for the roof snow and ground snow, and that air temperature and solar radiation are the main factors considered in the energy equation of the snowpack, the above-mentioned assumption is justified. Note that another important source of energy coming into the snowpack is the heating from the ground for ground snow and heating from the building for roof snow. Typically, the temperature inside the building is much higher than the temperature under the ground, consequently, the amount of snowmelt on building roofs is typically greater than those on the ground. The assumption adopted in this study would therefore underestimate the loss of roof snow, which is conservative to the structural safety.

2.5. Summary of the modified FAE method

Based on the considerations mentioned above, the steps of the modified FAE model are shown in Figure 4 and summarized as follows:

a) The roof is divided into many area elements by a grid system.

b) CFD simulations are run for a series of wind directions and wind speeds to establish a database for the friction velocity on the roof surface.

c) Starting from the first day of a snow season, snow drifting rates are computed using wind direction, equivalent wind speed, and Eq. (5). By computing the mass fluxes into and out of each element, the rate of build-up or depletion of snow mass in the element due to drifting is determined.

d) Snow depletion due to snow melting or snow sublimation is estimated using Eq. (7).

e) The result is a detailed time history of snow mass in each area element and the computed time histories extend over all the winters that are associated with sufficiently detailed meteorological data.

f) The snow mass time histories are analyzed statistically to determine various loading conditions of interest for design.

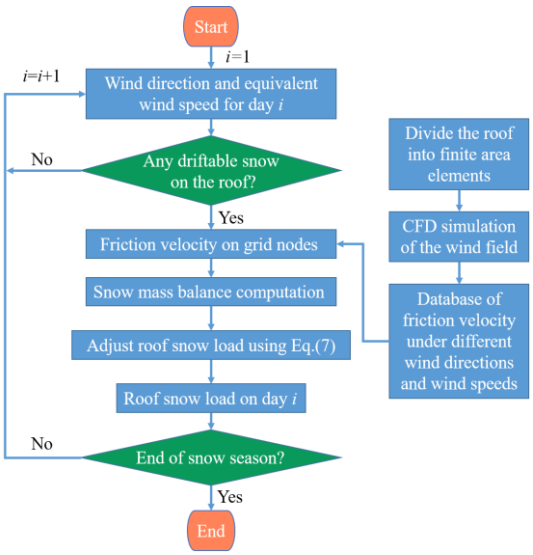


Figure 2. Flowchart of the modified FAE Method

3. FAE simulation of roof snow load for a cylindrical roof

3.1. Simulation of the wind field

As shown in Figure 3, the full-scale model of the cylindrical roof is 30 m in span, 50 m in length, 5 m in height at the eave, and associated with a rise-span ratio of 1/5. The computational domain is 400 m (length) × 300 m (width) × 60 m (height) in size, where the model is located 150 m downstream from the inlet section. The domain is divided by hexahedral mesh grids with a minimum size of 0.1m near the roof surface. An example of the mesh around the model is shown in Figure 4.

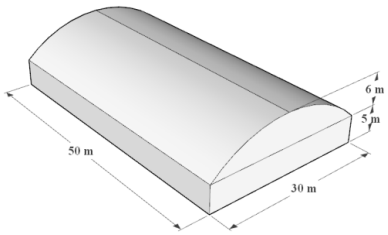


Figure 3. Size of the roof model

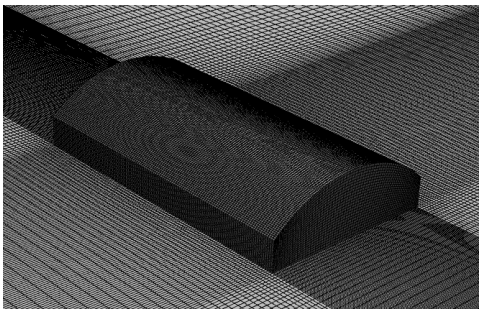


Figure 4. Mesh around the roof model

The boundary types used in the simulation are listed in Table 1, and the parameters of the inflow are given in Table 2. The Realizable *k-ε* model is selected for the turbulence model, and the solution is solved in the QUICK format. The iteration is treated as converged when the root means square residual reaches 1×10^{-5}.

In the simulation, 16 directions are considered as shown in Figure 5. Since the cylindrical roof is a biaxial-symmetric structure, wind fields for only five wind directions (0°, 22.5°, 45°, 67.5°, and 90°) are simulated in this study. The derived dimensionless friction velocity on the roof under different wind directions are presented in Figure 6, where the friction velocity on the roof is normalized using the corresponding friction velocity on the ground at the inlet. It can be seen from Figure 6 that, in general, the friction velocity is highest when the wind direction is taken as 0° and decreases gradually as the wind direction increase to 90°. This implies that more snow would be drifted when the wind is blowing from the radial direction (0°) than when the wind is blowing along the axial direction (90°).

Table 1: Boundary types of the computational domain

Boundary	Type
Inflow	velocity inlet
Outflow	pressure outlet
Lateral and top surfaces	symmetry boundary
Ground and building walls	non-slip wall boundary

Table 2: Formulas of the physical quantities

Parameter	Value
Inflow speed profile	$U(z)=U_0(z/z_0)^{\alpha}$ $z_0=10\text{m}$, $\alpha=0.16$ (B-type ground roughness) U_0 is the equivalent wind speed at the reference height
Turbulent kinetic energy	$k=1.5\left[\bar{U}(z)I(z)\right]^2$

Turbulent dissipation rate	$\varepsilon = C_\mu^{3/4} k(z)^{3/2} / l_u$
Turbulence intensity	$I(z) = \begin{cases} 0.1\left(\frac{z_b}{z_G}\right)^{-\alpha-0.05}, & z < z_b \\ 0.1\left(\frac{z}{z_G}\right)^{-\alpha-0.05}, & z_b < z < z_G \end{cases}$ $z_G = 350\text{m}$, $z_b = 5\text{m}$
Turbulence integral scale	$l_u(z) = \begin{cases} 100, & z < 30 \\ 100\left(\frac{z}{30}\right)^{0.5}, & 30 < z < z_G \end{cases}$ $z_G = 350\text{m}$

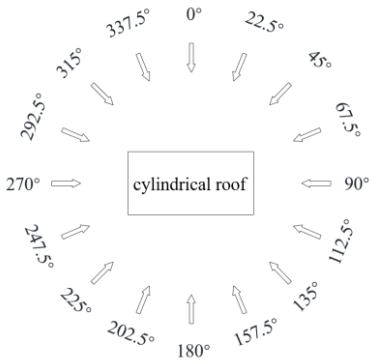
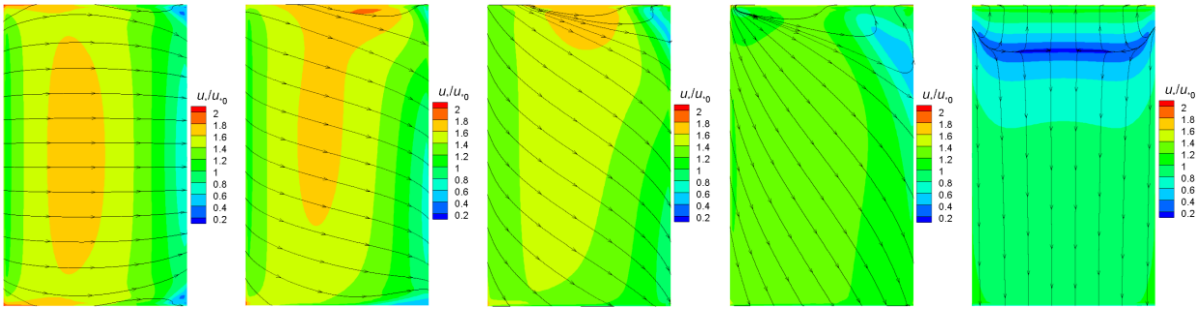


Figure 5. Schematic diagram of wind directions considered in the simulation

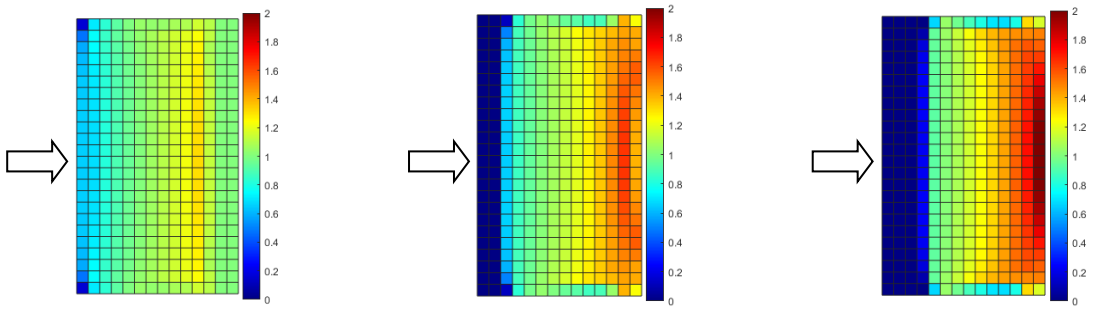


(a) 0° (b) 22.5° (c) 45° (d) 67.5° (e) 90°

Figure 6. Dimensionless friction velocity on the cylindrical roof under different wind directions

3.2. Patterns of roof snow load

Given the friction velocity on the roof and historical records of required meteorological data, daily roof snow load could be estimated by following the steps presented in section 2.5. As an example, Figure 7 presents the roof snow load factors (roof snow load normalized with ground snow load) on the roof when the wind direction is set at 0°, ground snow depth is taken as 6cm, and the threshold friction velocity u_{*t}=0.2 m/s. Figure 8 shows the snow load factors on the central horizontal cross-section. Note that snow sliding due to the angle of repose of snow particles near the eaves is not considered since the focus of this paper is the influence of wind speed and wind direction on the redistribution of roof snow.



(a) U_{10}= 4 m/s (b) U_{10}= 6 m/s (c) U_{10}= 8 m/s

Figure 7. Variation of roof snow load factors with wind speed when the wind direction is set at 0°, ground snow depth is taken as 6cm, and the threshold friction velocity u_{*t}=0.2 m/s

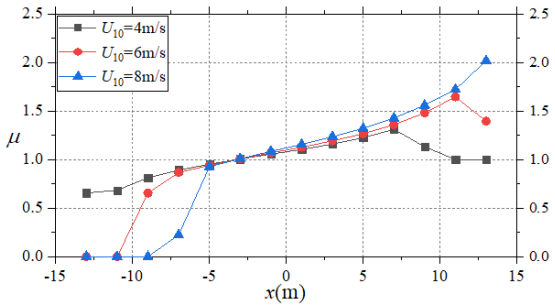
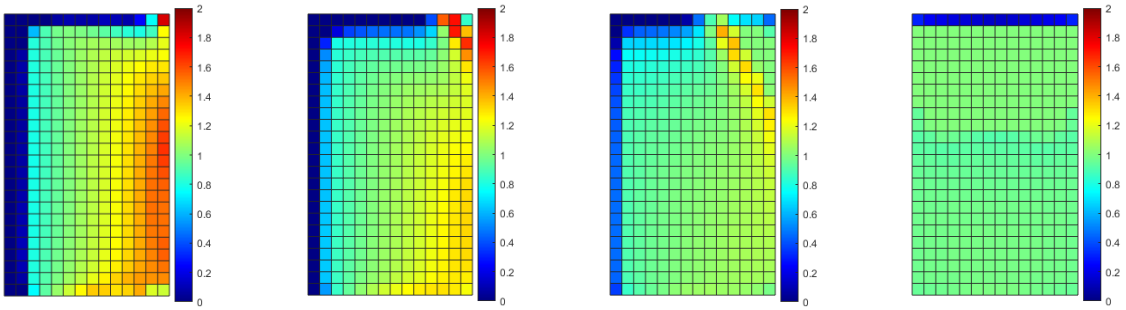


Figure 8. Comparison of roof snow load factors on the central horizontal cross-section for cases shown in Figure 7

It can be seen from Figure 7 and Figure 8 that the snow is tended to drift from the windward side of the roof to the leeward side, and more snow is drifted downstream when the wind speed increase. This is consistent with common sense in real life and can be explained by the distribution of friction velocity shown in Figure 6a. According to the basic assumption of FAE as presented in section 2.1, erosion or deposition of snow is related to the acceleration or deceleration of the wind, but not related to the absolute value of the wind speed. It's indicated by Figure 6a that the wind speeds up on the windward side, remains at a high level near the ridge, and decreases on the leeward side. Therefore, it's natural that erosion is observed on the windward side of the roof, and deposition is mainly observed on the leeward side. As the inlet wind speed increase, more area elements become erosive, and the peak of the deposition move downstream.

Figure 8 indicates that the roof snow load factor near the ridge is roughly 1.0, this implies that the snow is neither eroded nor deposited in this place. This phenomenon is not consistent with reality, where the snow near the ridge is typically eroded due to the relatively high wind speed. This is caused by the assumption in the FAE model that the snow transport rate is a constant for a given wind speed. In fact, the snow transport rate is an increasing function with the distance before the snow drift reaches its equilibrium state. Consequently, for an area element shown in Figure 1, the snow transport rate on the leeward edge should be greater than that on the windward edge even when the wind speed on the two edges is the same, such that the snow in this area element should be eroded but not keep unchanged as shown in Figure 8. This could be corrected by using a distance-dependent relation for the snow transport rate in the future.

Figure 9 and Figure 10 show the simulation results for different wind directions, where the initial snow depth h_0=6 cm, and the wind speed U_{10}=6 m/s. It can be seen from the figures that as the wind direction changes from 0° to 90°, the roof snow tends to become more evenly distributed. This indicates that the wind direction of 0° is the most unfavorable direction for snow drifting on cylindrical roofs.



(a) 22.5° (b) 45° (c) 67.5° (d) 90°

Figure 9. Variation of roof snow load factors with wind directions when the wind speed is taken as 6m/m, ground snow depth is taken as 6cm, and the threshold friction velocity u_{*t}=0.2 m/s

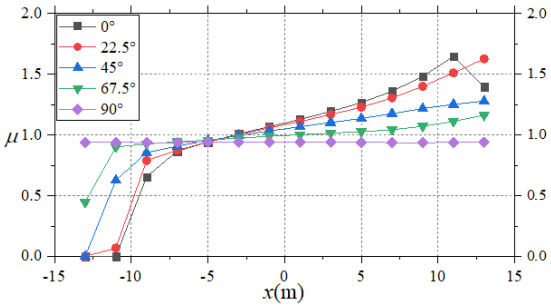


Figure 10. Comparison of roof snow load factors on the central horizontal cross-section for cases shown in Figure 9

3.3. Roof snow load considering historical meteorological data

To study the most unfavorable distribution of snow on the cylindrical roof under actual natural conditions, historical meteorological data of Harbin from 1971 to 2017 are considered to analyze the evolution of the snow on the cylindrical roof. Daily roof snow loads are estimated by following the steps presented in section 2.5 and a statistical analysis of the most unfavorable roof snow load is carried out to determine the representative value of the roof snow load. In the statistical analysis, the unbalanced roof snow load, S_u, defined in Figure 11 is considered, where $\bar{S}_A$ and $\bar{S}_B$ is respectively the average snow load on each half of the roof.

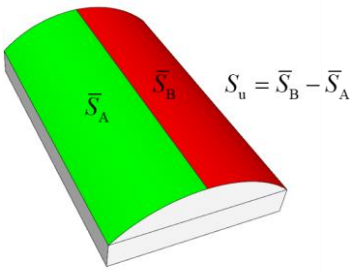


Figure 11. Definition of unbalanced roof snow load considered

Unbalanced roof snow load S_u is calculated for each day, and seasonal maximum value of S_u, $S_{u,max}$, is extracted for each snow season. The roof snow load on the date when $S_{u,max}$ is observed is then taken as the most unfavorable condition of the roof snow in the corresponding snow season. The roof snow load in each area element, $S_{r,ij}$, and the ground snow load, $S_{g,k}$, on that day is extracted and modeled as random

variables. A preliminary fitting exercise to the 43 samples of the variables indicates that both the $S_{r,ij}$ and $S_{g,k}$ could be modeled as a log-normally distributed variate. 50-year return period values of $S_{r,ij}$ and $S_{g,k}$, $S_{r,ij50}$ and $S_{g,k50}$, is then estimated from the fitted model and roof snow load factors for design are derived by normalizing $S_{r,ij50}$ with $S_{g,k50}$. As an example, Figure 12 shows the roof snow load factors for design when the roof is facing north-south and east-west. It can be seen from the figure that the roof snow load for cylindrical roofs in Harbin is more unfavorable when the roof is facing east-west.



(a) Roof facing north-south (b) Roof facing east-west

Figure 12. Roof snow load factors for design for a cylindrical roof in Harbin China: a) when the roof is facing north-south, and b) when the roof is facing east-west

Roof snow load factors for design on the central horizontal cross-section for different orientations of the roof are depicted and compared to the provisions specified in the Chinese load code in Figure 13. It can be seen from the figure that the distribution patterns of roof snow load for different roof orientations are quite similar, except that the magnitude of the roof snow load factors are slightly different. The estimated roof snow load factors are covered by the load provision in the middle of both halves of the roof but are greater than the code in the ridge. The reason for the overestimation of roof snow load near the ridge has been discussed in section 3.2 and is not repeated herein. Therefore, if the discrepancy near the ridge could be eliminated, the modified FAE could provide a reasonable estimation of roof snow load for design by considering the local climate condition.

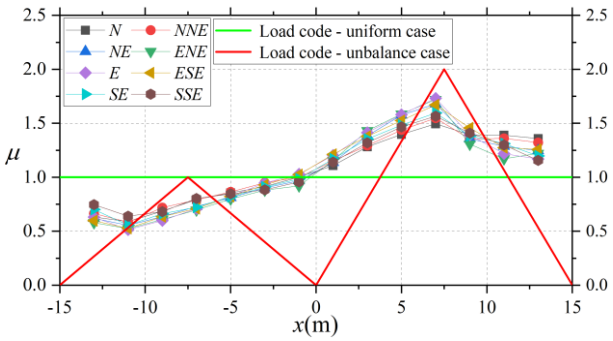


Figure 13. Roof snow load factors for design on the central horizontal cross-section for different orientations of the roof

4. Conclusions

A modified FAE model is proposed and used to simulate the evolution of roof snow load on a cylindrical roof in Harbin China for the period of 1971 – 2017. The modifications include the following aspects: 1) the friction velocity on the roof surface, rather than the wind velocity at a height of 1 m above the roof surface suggested in the original model, is used to calculate the snow drifting rate at each node of the grid; 2)by considering the difficulties in measuring friction velocity in wind tunnel tests, numerical simulation is applied to determine the friction velocity on the roof surface; 3) since hourly records of

meteorological variables are not available in China, daily records of snow and wind data were used in the simulations; and 4) the roof snow depletion due to melting and sublimation is estimated by assuming that the depletion is proportional to the decrease in ground snow depth. The application of the modified FAE model to a cylindrical roof in Harbin China indicates that the modified model is easy to implement and could be a useful tool to aid the design of roof snow load for long-span, complex roofs, except that the assumption that snow transport rate is solely related to the wind speed needs to be further improved by considering the fetch length of the snow drift development.

Acknowledgments

This study is funded by the National Natural Science Foundation of China (No. 51808169, No. 51921006, and No. 51927813) and Fundamental Research Funds for the Central Universities (Grant No. HIT. NSRIF. 2020083), which is gratefully acknowledged.

Reference

[1] H. Mo, *Numerical simulation and experimental study of snow distribution on typical roofs*: Harbin Institute of Technology, 2011.

[2] G. Zhang, *Research on snow load measurement and method of wind tunnel test*: Harbin Institute of Technology, 2015.

[3] M. Tsuchiya, T. Tomabechi, T. Hongo, and H. Ueda, "Wind effects on snowdrift on stepped flat roofs," *Journal of Wind Engineering and Industrial Aerodynamics*, vol. 90, pp. 1881-1892, 2002.

[4] D. Kobayashi, "Studies of snow transport in low-level drifting snow," *Contributions from the Institute of Low Temperature Science*, vol. 24, pp. 1-58, 1972.

[5] M. O Rourke, A. DeGaetano and J. D. Tokarczyk, "Snow drifting transport rates from water flume simulation," *Journal of Wind Engineering and Industrial Aerodynamics*, vol. 92, pp. 1245-1264, 2004.

[6] M. Liu, *Research on combined wind and snow test system and snow distribution on roofs*: Harbin Institute of Technology, 2020.

[7] R. J. Kind, "A critical examination of the requirements for model simulation of wind-induced erosion/deposition phenomena such as snow drifting," *Atmospheric Environment (1967)*, vol. 10, pp. 219-227, 1976.

[8] Y. Tominaga, T. Okaze and A. Mochida, "CFD modeling of snowdrift around a building: An overview of models and evaluation of a new approach," *Building and Environment*, vol. 46, pp. 899-910, 2011.

[9] G. Zhang, *Study on numerical simulation approach of snowdrifts and snow load characteristics on long-span roofs*: Harbin Institute of Technology, 2021.

[10] Y. Tominaga, "Computational fluid dynamics simulation of snowdrift around buildings: Past achievements and future perspectives," *Cold Regions Science and Technology*, vol. 150, pp. 2-14, 2018.

[11] Y. Tominaga, T. Okaze and A. Mochida, "CFD simulation of drift snow loads for an isolated gable-roof building," in *8th International Conference on Snow Engineering*, pp. 14-17, 2016.

[12] X. Zhou, L. Kang, M. Gu, L. Qiu, and J. Hu, "Numerical simulation and wind tunnel test for redistribution of snow on a flat roof," *Journal of Wind Engineering and Industrial Aerodynamics*, vol. 153, pp. 92-105, 2016.

[13] T. Thiis and A. D. Ferreira, "Sheltering effect and snow deposition in arrays of vertical pillars," *Environmental Fluid Mechanics*, vol. 15, pp. 27-39, 2015.

[14] P. A. Irwin and S. L. Gamble, "Prediction of Snow Loading on the Toronto Skydome," in *Proc. of the 1st International Conference on Snow Engineering, Santa Barbara*, pp. 118-141, 1988.

[15] P. A. Irwin, S. L. Gamble and D. A. Taylor, "Effects of roof size, heat transfer, and climate on snow loads: studies for the 1995 NBC," *Canadian Journal of Civil Engineering*, vol. 22, pp. 770-784, 1995.

[16] S. L. Gamble, W. W. Kochanski and P. A. Irwin, "Finite area element snow loading prediction - applications and advancements," *Journal of Wind Engineering and Industrial Aerodynamics*, vol. 42, pp. 1537-1548, 1992.

[17] J. W. Pomeroy and D. M. Gray, "Saltation of snow," *Water resources research*, vol. 26, pp. 1583-1594, 1990.

[18] M. Takeuchi, "Vertical profile and horizontal increase of drift-snow transport," *Journal of Glaciology*, vol. 26（94）, pp. 81-82, 1980.

[19] H. Mo, H. Hong and F. Fan, "Estimating the extreme wind speed for regions in China using surface wind observations and reanalysis data," *Journal of Wind Engineering and Industrial Aerodynamics*, vol. 143, pp. 19-33, 2015.

[20] H. Mo, H. Hong, S. Li, and F. Fan, "Impact of Annual Maximum Wind Speed in Mixed Wind Climates on Wind Hazard for Mainland China," *Natural Hazards Review*, vol. 23, p. 04021061, 2022.

[21] Y. Li, H. Mo, and F. Fan, "Probabilistic modeling of 10-min wind speed for the purpose of analytical simulation of snowdrift," in *Proceedings of the IASS Annual Symposium 2022 and APCS 2022*, Sep. 19-22, Beijing, China.

Proceedings of the IASS Annual Symposium 2023
Integration of Design and Fabrication
10–14 July 2023, Melbourne, Australia
Y.M. Xie, J. Burry, T.U. Lee and J. Ma (eds.)

Aeolus: a *Grasshopper* plugin for the interactive design and optimisation of acoustic shells

Gabriele MIRRA[a], Michael MACK[a,*], Alberto PUGNALE[a]

[a,*] Faculty of Architecture, Building and Planning, The University of Melbourne
Glyn Davis Building (133), The University of Melbourne, Masson Rd, Parkville VIC 3010, Australia
michael.mack@unimelb.edu.au

Abstract

The design of music venues, such as concert halls and open-air concert stages, requires an integrated approach in which the acoustic response of the space being created is evaluated at every stage of the process to inform its formal development and associated performance. Various software exists to assess acoustic performance: *Odeon* is considered by many as the industry standard standalone software for detailed and accurate acoustic analyses, whereas *Pachyderm* is a plugin for *Grasshopper* (*Rhinoceros 3D*), which provides architects and engineers with more rapid feedback on preliminary design ideas because of its integration with a parametric modelling environment. Although an experienced acoustic designer could rapidly learn to use any of these programs, their usefulness during conceptual design or teaching activities is limited by the computational power and time required to get acoustic performance results. In these instances, testing time is more valuable than accuracy. This paper introduces *Aeolus*, an acoustic modelling plugin for *Grasshopper*. Unlike other similar *Grasshopper* plugins, *Aeolus* allows users to control the simulation accuracy and can therefore be used to rapidly test the performance of design ideas. *Aeolus* can also easily be interfaced with various *Grasshopper* optimisation plugins. *Aeolus v0.1* was publicly released on 7 March 2023, and will be the focus of a Masterclass offered at the IASS Symposium 2023 in Melbourne, Australia.

Keywords: acoustic design, shell structures, computational morphogenesis, acoustic optimisation, conceptual design

1. Introduction

In architectural design, computational and performance-oriented approaches are no longer restricted to a niche number of large practices, engineering consultants and researchers: CAD software, particularly *Rhinoceros 3D* in recent years, has progressively facilitated the interface of architectural models with performance analysis software and optimisation algorithms. From Luigi Moretti's essays of the 40s and 50s about a future of parametric architecture and performance optimisation [1] to the Building Optimisation Procedure (BOP), developed by SOM Chicago in the 80s [2], software customisation and the integration of performance criteria in the design process have gone a long way [3-5].

For various reasons that are well beyond the scope of this paper, it can be said that *Rhinoceros 3D* has become a reference CAD environment over the past 20 years for many architects and engineers that make use of, or experiment with, computational design workflows. Whether the purpose concerned exploring and optimising complex geometries or automating design processes for fabrication, user-friendly scripting environments proved to be the answer to developing new tools and interfaces between design ideas and performance assessment. *Grasshopper* for *Rhinoceros 3D* is a visual scripting environment released between 2007 and 2008 [6]. Over the last decade, users have determined its success through numerous innovative performance-oriented design applications and by developing

Copyright © 2023 by Gabriele MIRRA, Michael MACK and Alberto PUGNALE. Published in the Proceedings of the IASS Annual Symposium 2023 with permission.

plugins to enhance its native features and functionalities. For example, thanks to *Karamba 3D*, architects and engineers can now perform finite element analyses and optimise structures directly within *Rhinoceros 3D*, without interrupting their creative design workflows because of annoying operations of exporting and reimporting geometric and performance data [7, 8]. With *Kangaroo*, a plugin focused on simulating physical phenomena, designers can perform structural form finding without using physical models [9]. Thanks to *LadyBug*, integrating environmental aspects during conceptual design has become easier than ever [10].

In this panorama, plugins that allow the optimisation of key building performance criteria, such as structural and environmental, or plugins that manage the flow of data between geometric models and fabrication machines, have been developed much faster than other tools to evaluate secondary – or even invisible – performance requirements. Acoustics falls into this category as it is rarely a performance aspect that informs the design of the built environment, with the only exception of music venues. Moreover, the computational power required to perform an accurate – and therefore useful – acoustic analysis is a major hurdle for developing simple plugins that can provide architects and engineers with real-time feedback within a parametric modelling environment.

Aeolus was conceived to address this problem precisely [11]. It was released as a *Grasshopper* plugin in March 2023 to allow designers, particularly architects and students, to rapidly explore and evaluate formal solutions for the design of acoustic shells [12]. According to acoustician experts, such as Beranek [13] and Long [14], an acoustic shell constitutes a temporary or permanent physical device, a surface as a minimum, either integrated into architectural systems or as a standalone object, designed to reflect sound both towards the audience and to the musicians themselves. The integration with industry-standard software and the extreme simplicity of *Aeolus*, which is based on the Image Source Method rather than FEM, are key features to bear in mind while comparing this product with other software to understand its value fully.

After a brief introduction to acoustic modelling strategies, and a description of commonly used current software and plugins in Section 2, the parametric design workflow with *Aeolus* is explained in detailed in Section 3. Given the applicability of *Aeolus* to the conceptual design of various building typologies, Section 4 focuses on potential uses of the tool inspired by real case studies to stimulate the reader's creativity. This paper should be considered a formal introduction and presentation of Aeolus, which will be complemented by a Masterclass at the IASS Symposium 2023 in Melbourne, Australia.

2. Acoustic modelling in parametric design environments

Acoustic modelling utilises the principles of geometric acoustics to simulate the propagation of soundwaves: at any given time *t*, a point on the wavefront is represented by a vector – an acoustic ray – with magnitude equal to the distance travelled by the sound. The interaction of an acoustic ray with architectural surfaces is modelled using the Snell Law, which states that the angle of reflection must be equal to the angle of incidence. A sound reflection path is computed using basic principles of descriptive geometry by recursively applying the Snell Law: each time the acoustic ray intersects a surface, the reflection angle is computed, and a new ray is cast. The ray casting process aims to either visualise the reflection paths or measure the sound pressure levels (SPLs) at a specific target location.

This process can be implemented through two different methods: "ray tracing" and "image source". The ray tracing method casts a pre-defined number of rays from the sound source in multiple directions [15]. After constructing a certain number of reflection paths, this method computes how many reflected rays intersect with a target surface representing the audience. The accuracy of this method heavily relies on the initial number of rays used, as the distance between two points on the wavefront increases with the square of the wavefront radius. In other words, the sample resolution decreases exponentially with the distance from the sound source. Conversely, the image-source method [16] constructs the reflection paths backwards from specific target points to the sound source. Having specified a reflection order *N*, i.e., how many times a ray bounces off surfaces before reaching the target, the method tests all possible

combinations of reflection paths, which will be equal to the number of surfaces composing the scene raised to *N*. Therefore, the image source method allows the computation of accurate SPLs at one or multiple target locations, which can be visualised as a 2D map. It is worth mentioning that both ray tracing and image source methods have pros and cons. Therefore, the acoustic analysis uses a combination of both methods to model early and late reflections, respectively.

These methods are currently integrated into plugins for *Grasshopper* to various extents. Excluding *Aeolus*, three other *Grasshopper* plugins are currently available: *Equissons*, *Snail*, and *Pachyderm*. *Equissons* focuses on auralisation, *Snail* on visualising ray tracing. However, they do not provide a quantitative analysis of acoustic measures. *Pachyderm* is the only plugin that allows users to visualise ray tracing but also implements the image source method to calculate early reflections. Standalone acoustic analysis software, such as *Odeon* and *Catt-Acoustic*, can simulate sound wave properties for calculating acoustic phenomena: for example, scattering and diffusion. Although the accuracy of these commercial standalone packages is higher than those of current *Grasshopper* plugins, they are primarily focused on detailed analysis: the learning curve is not necessarily practical in an architectural design setting, where simple computation and rapid feedback are required. Table 1 summarises the main features of all the plugins currently available for *Grasshopper*. *Odeon* and *CATT-Acoustic* are also included for comparison since they are commonly considered as the industry standards in acoustic engineering.

Table 1. Comparison of *Aeolus* against industry-standard acoustic analysis software and *Grasshopper* plugins.

	Odeon	**CATT-Acoustic**	**Equissions**	**Snail**	**Pachyderm**	**Aeolus**
Plugin for Grasshopper / Rhinoceros 3D			✓	✓	✓	✓
Native integration with parametric modelling			✓	✓	✓	✓
Quantitative analysis of acoustic data (e.g. SPL, RT)	✓	✓			✓	✓
Visualisation of acoustic analysis method	✓	✓	✓	✓	✓	✓
Auralisation	✓	✓	✓		✓	
Control of simulation method	✓	✓			✓	
Control over simulation accuracy	✓	✓				✓

Integrating acoustic modelling tools with parametric design software is essential to being able to design architectural spaces that are informed by acoustic performance. *Grasshopper* for *Rhinoceros 3D* allows the direct association between design parameters and acoustic outcome, letting designers receive acoustic feedback rapidly and interactively on preliminary formal ideas.

As mentioned above, *Pachyderm* is the only *Grasshopper* plugin that provides quantitative acoustic data, relatively accurate acoustic analysis, and visualisation and auralisation functionality. However, this plugin does not allow sufficient control over the acoustic simulation accuracy and speed, which makes it unsuitable for single and multi-objective optimisation algorithms.

Aeolus was developed in 2015 by Gabriele Mirra and Eduardo Pignatelli as part of the deliverables submitted with their master's thesis in Architecture (University of Naples Federico II) [11]. The purpose was to create an acoustic modelling plugin that could interface with multi-objective optimisation algorithms directly within the *Grasshopper* environment. At present, *Aeolus* only implements the image source method to accurately compute SPLs for early reflections. Even though the image source is a computationally expensive method, *Aeolus* allows users to select the level of the simulation accuracy to

produce a fast – but reliable – preliminary acoustic analysis. *Aeolus* can therefore be used in performance-oriented design workflows, where the resolution of the acoustic analysis can be reduced to prioritise the efficiency of optimisation algorithms.

It is worth underlining that *Aeolus* has been used in practice, research and teaching settings for the past eight years, even though it was only made publicly available as a free plugin for *Grasshopper* in March 2023. Regarding research, *Aeolus* was applied to the design and optimisation of a temporary acoustic shell in Acireale, Sicily. This acoustic shell, also known as "ReS", was first conceived in 2012 to be assembled and disassembled from wooden components and its design has then been improved and refined on a yearly basis [11], 17]. *Aeolus* was also used by Pugnale [18] in 2018 to study the acoustic performance of some of Frei Otto's most known tensile structures. In teaching and learning, *Aeolus* has been used for the past four years as the parametric acoustic analysis software in an architecture master's design studio at The University of Melbourne: the focus has been the acoustic design and optimisation of a music concert hall and school.

3. The design workflow with *Aeolus*

The section describes how *Aeolus* works and explains a typical acoustic analysis workflow with this plugin, from constructing the acoustic scene to visualising the simulation output as a 2D SPL map (Figure 1). The scene considered is simple to focus on the different stages of the workflow: it consists of a sound source, a curved surface acting as an acoustic reflector and an array of target/receiver locations evenly distributed over a hypothetical audience area (Figure 1, at the top).

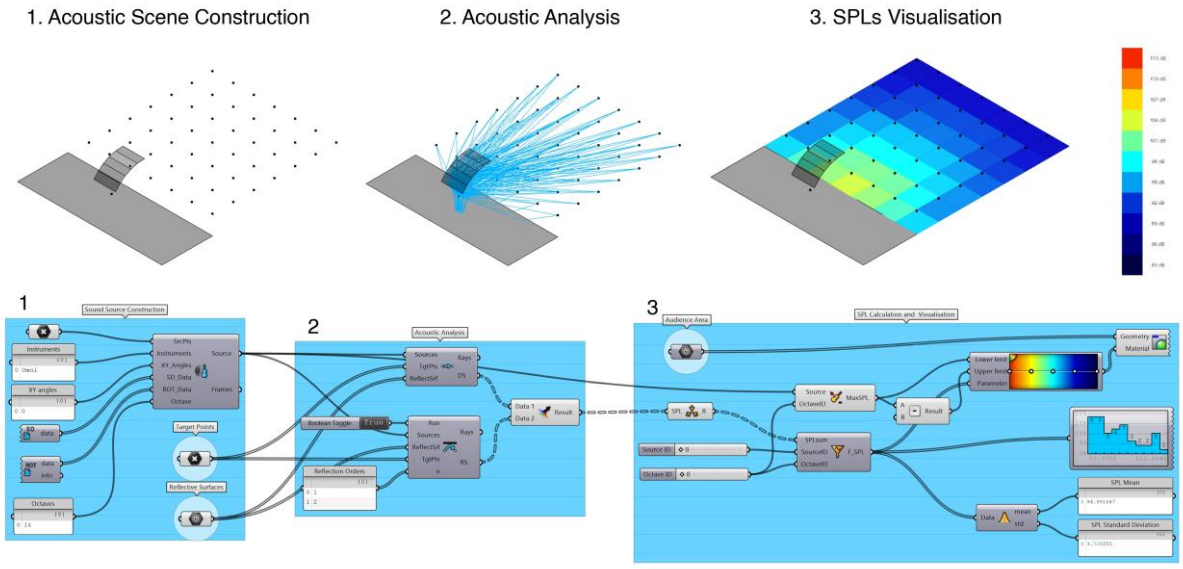


Figure 1. Overview of the design and analysis workflow with *Aeolus*, from constructing the acoustic scene to visualising the simulation output as an SPL map.

3.1. Constructing an acoustic scene

An acoustic scene configuration comprises, as a minimum, three geometric entities: a point, which represents the sound source location; a surface, which acts as an acoustic reflector; and a second point, which identifies the target or receiver location. Such a scene can be analysed with geometric acoustics to construct the sound reflection paths from a sound source to a target location. In acoustic modelling software, the three entities of a minimal acoustic scene can be assigned with physical properties to produce an accurate simulation. For instance, a sound source can be characterised by a sound directivity map, which assigns different SPLs to emission angles according to the instrument or loudspeaker

typology, whereas an acoustic reflector can have sound absorption coefficients which depend on the reflector material. *Aeolus* assumes that all surfaces are perfectly reflective, meaning they do not absorb sound. However, the plugin allows assigning a sound source with the directivity map of up to 15 instruments, which enables a more realistic analysis should the application require it. The following subsections describe how to construct the acoustic scene illustrated in Figure 1 using *Aeolus*: three steps are necessary, one for each of the entities listed above.

3.1.1. Defining the sound source

In *Aeolus*, a sound source object is constructed through a dedicated component by specifying: (1) a point location; (2) the instrument typology; (3) the sound source orientation in degrees; and (4) the octave band, which may include one or more of the seven reference values, i.e., 125, 250, 500, 1k, 4k, 8k, and 16k Hz. The sound directivity and orientation data of the supported instruments can be inputted through the components 'SD Database' and 'ROT Database', respectively. These two components import and perform the formatting of text files that are stored in the *Aeolus* installation folder. Such files reproduce information from the CATT-Acoustic sound directivity database and can be updated in future releases to include additional instruments.

Generally, a preliminary acoustic analysis would not require specifying instrument typology and the corresponding sound directivity values. An omnidirectional sound source can be used in *Aeolus* to perform an analysis that does not consider sound directivity. In this case, the specification of sound source orientation and octave band does not affect the simulation output.

3.1.2. Defining the acoustic reflectors

In *Aeolus*, acoustic reflectors are modelled as flat surfaces because the image source method requires a finite number of planes – one for each surface – to pre-compute all the possible reflection paths. Therefore, to analyse curved surfaces, these must be approximated by flat elements (Figure 1, stage 1).

Although there are no limitations to the number of surfaces that *Aeolus* can process, increasing this number can significantly affect the computational cost of the simulation. A trade-off between geometry approximation and simulation accuracy is required to keep the computational cost within manageable timeframes. It is worth mentioning that, as Section 3.4.1. will describe later, the approximation of a curved surface with flat elements does not overly affect the quality of the simulation. In some cases, a surface approximated by a few flat elements can perform better than a more refined one, thus suggesting alternative design solutions that might also be easier to build.

3.1.3. Defining the targets

In *Aeolus*, a target identifies the end point of sound reflection paths and can be considered as a listener's location in the audience area. The plugin accepts the specification of one or multiple targets to perform an acoustic simulation. If multiple targets are used, arranging them on an evenly spaced grid is preferable so that a map can be generated to visualise the distribution of SPLs.

3.2. Performing an acoustic analysis

Once the acoustic scene is defined, the three geometric entities – sound source, reflectors, and targets – are fed to the two *Aeolus* analysis components, 'Direct Sound' and 'Image Source', to construct the direct and reflected acoustic rays and calculate the SPLs.

The 'Direct Sound' component traces the direct sound paths, that is straight lines connecting the sound source with the target points. The paths that intersect any reflective surfaces in the scene are discarded. The component also computes the SPLs associated with the direct sound paths using the path length and the directivity values of the sound source object. The 'Image Source' component performs the main acoustic simulation. Given an acoustic scene and a reflection order *N*, this component tests all the reflected sound path combinations and keeps only those that connect the sound source with the targets

after *N* intersections with the acoustic reflectors. This component also computes the SPLs using the distance travelled by the reflected sound and the directivity values.

Upon completion of the analysis, these two components produce the direct and reflected sound paths, which can be visualised in the *Rhinoceros 3D* viewport as lines and polylines, respectively (Figure 1, stage 2). By visually inspecting the sound paths, the user can preliminarily assess the performance of the acoustic reflectors. Alternatively, the user can perform a more detailed analysis based on the SPLs computed from the direct and reflected sound paths. *Aeolus* allows users to combine and visualise the SPLs by following the procedure described below.

3.3. Visualising sound pressure levels

Aeolus provides a set of utility components to combine, filter and display the SPLs obtained through the direct and reflected sound analysis. The SPLs are combined using the 'SPL sum' component, which performs a logarithmic sum of the direct and reflected SPLs for every target. The output data structure has the following indices: frequency id, sound source id, and target id. These indices can be used to filter the SPLs by using either the standard data tree functionalities provided in *Grasshopper* or the *Aeolus* 'SPL filter' component.

An SPL map can be constructed from the filtered SPLs by applying a gradient of colours to the cells surrounding the targets (Figure 1, stage 3). *Aeolus* provides a utility component to extract the maximum SPL characterising a sound source object for a specific octave band, which can be used to set the upper bound of the gradient domain. Another component computes the standard deviation and the mean of the SPLs to capture their distribution over the audience area. These values can be used as objective functions for acoustic optimisation applications (see Section 3.5).

A typical use case of the visualisation workflow described above involves selecting a sound source id to extract the SPLs only for that specific sound source and comparing the results with the SPLs corresponding to the other sound sources used in the simulation. Figure 2 shows the SPL maps produced by switching the index of the sound source after completing the simulation of an acoustic scene that included two sound sources placed at the centre and one side of the acoustic reflector. The comparison reveals that the acoustic reflector evenly distributes sound only for the central sound source.

Alternatively, if the user has assigned the sound source object with an instrument and multiple octave bands at the beginning of the simulation, they can switch the frequency id to compare the SPLs for different octave bands. Figure 3 (at the bottom) illustrates the simulation outputs for an acoustic scene in which the sound source is assigned with the directivity values of a violin. The analysis focuses on the 1kHz-8kHz octave band range. By changing the frequency id, the user can visualise in real-time the SPL map associated with a specific sound directivity map (Figure 3 at the top).

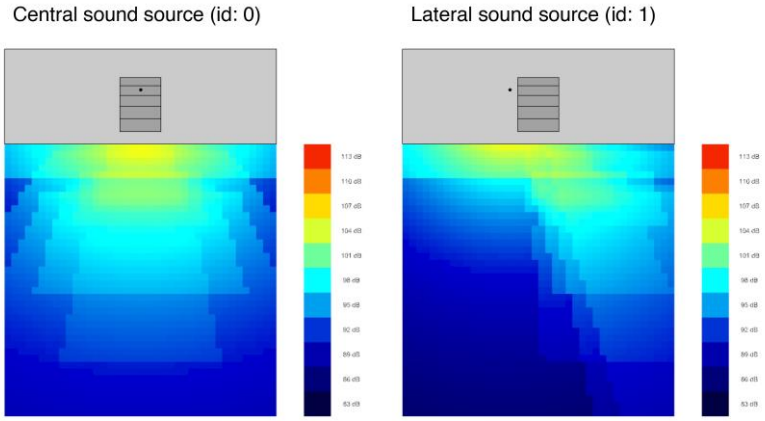


Figure 2. SPL maps produced by switching the sound source id after analysing an acoustic scene with two different sound source locations.

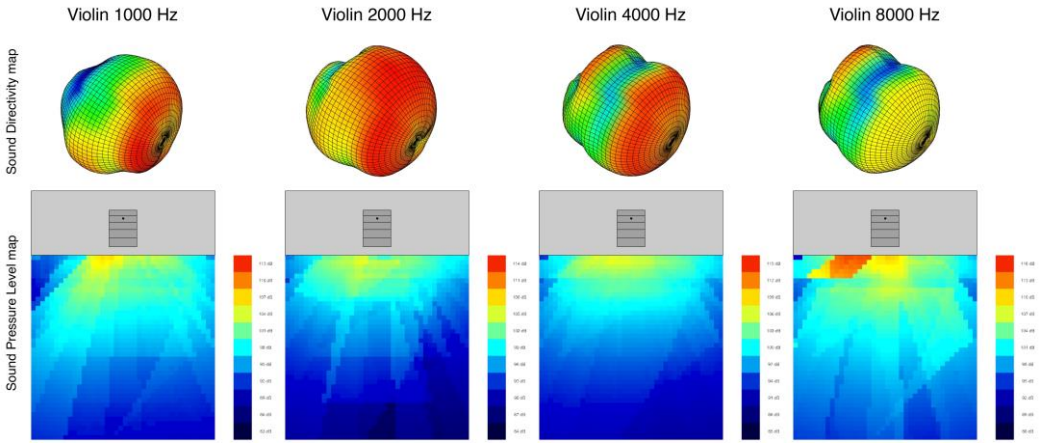


Figure 3. Simulation of an acoustic scene using sound source directivity. At the top: Sound directivity maps of a violin for four different octave bands; at the bottom: SPL maps produced by switching the frequency id after analysing an acoustic scene with a violin sound source for four different octave bands.

3.4. Adjusting the simulation settings

One of the main advantages of *Aeolus* is the possibility of fine-tuning the simulation settings to produce analyses with different degrees of accuracy. This is an essential feature of *Aeolus* because acoustic analyses are computationally expensive, limiting the interoperability of other plugins within parametric design software. This section describes the settings that reduce the computational cost of acoustic analysis in *Aeolus* and the effect these settings have on the simulation output. We do not provide a breakdown of the computational cost for each setting because this information depends on the computer hardware used. We instead compare the simulation outputs through the SPL maps.

3.4.1. Acoustic scene complexity

The complexity of the acoustic scene has a significant impact on the computational cost of the simulation. Increasing the number of acoustic reflectors, sound sources, and targets could provide very accurate information on the performance of a specific design but could also make exploring different formal configurations impractical.

Therefore, the number of acoustic reflectors is the first setting that can be adjusted to speed up the simulation. As mentioned at the beginning of this section, *Aeolus* require all geometries to be provided as flat elements. If the acoustic reflector/s are modelled as curved surfaces, these must be tessellated before running the simulation. The number of individual faces produced through the tessellation will be the actual number of acoustic reflectors used in the simulation. Figure 4 shows different subdivisions of the curved reflector considered in the previous analyses presented in the paper, and the effects these have on the SPL map. Since the reflector was described by a single-curvature surface, the tessellation only controlled the number of subdivisions along the surface V direction, which produced equally sized flat elements. The comparison of the SPL maps reveals that, for this particular geometry, a number of subdivisions of 25 is sufficient to simulate the performance of the original curved reflector accurately. In fact, a higher number of subdivisions did not considerably affect the SPL map, which is characterised by a trapezoidal area with a uniform sound distribution and almost no reflections at the final rows of the audience area. Conversely, tessellations produced from 5 and 10 subdivisions could spread sound to the entire audience area: though these do not capture the shadowing zone at the final rows that characterises the SPL maps obtained from a high number of subdivisions, and only approximate the trapezoidal shape of the strong reflections at the centre. It is worth mentioning that, although less accurate, the analysis suggests that a faceted reflector can be a better design choice since it can reflect sound more evenly.

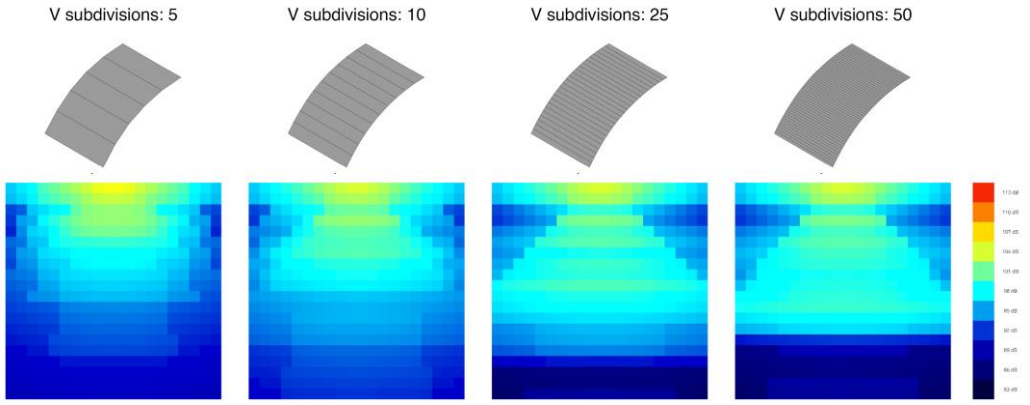


Figure 4. SPL maps for a single-curved reflector tessellated with an increasing number of flat elements.

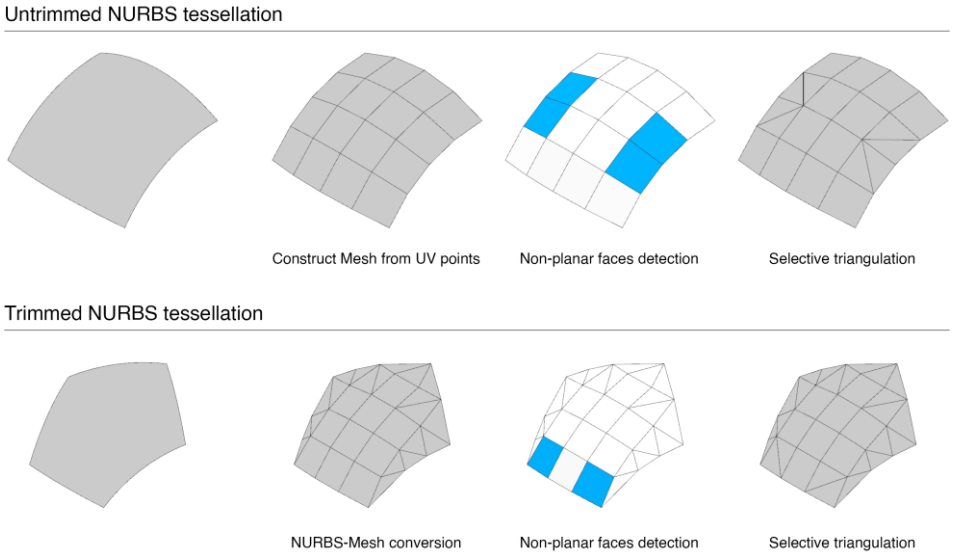


Figure 5. Stages for tessellating untrimmed and trimmed NURBS into a set of planar elements.

A tessellation based on UV subdivisions can also be applied for untrimmed doubly curved surfaces (Figure 5, at the top) by specifying the number of subdivisions for both U and V directions. However, if the surface is not ruled or extracted from a rotational surface, such as a sphere, the tessellation will not produce flat elements, and a planarity analysis is required to detect and triangulate non-planar faces.

Conversely, if the reflector is described by a trimmed surface, e.g., a NURBS with more than four edges, the tessellation cannot be performed through UV subdivisions. The user can convert the surface into a mesh object and control its resolution – i.e., the number of faces – by specifying the min and max length of the mesh edges. A planarity analysis and selective triangulation are also required to guarantee that all the faces are planar and suitable for the acoustic simulation (Figure 5, at the bottom).

Regardless of the input geometry and tessellation strategy, the selection of an appropriate number of faces should be guided by the purpose of the simulation. A low-resolution tessellation might be sufficient in the early exploratory stages of the design process, whereas a more detailed one can be useful to evaluate the performance of the final design accurately.

Another setting that affects the computational cost of the simulation is the number of targets. This parameter influences the resolution of the SPL map and can be controlled through the specification of the grid cell size. Figure 6 compares the SPL maps produced by analysing the same acoustic scene with a different number of targets. The maps are constructed with increasingly smaller grid cells, from 3 m to 0.5 m, in which each cell roughly corresponds to the footprint of a sitting area. The comparison shows

that as the map resolution increases, geometric patterns appear. These patterns are due to the reflections of the 5 panels composing the acoustic reflector and provide information about the contribution of each element to the SPL distribution.

In many cases, measuring the SPL for every point of the audience area might be unnecessary. If the objective of the simulation is assessing the overall distribution of SPLs, a low-resolution grid might be sufficient (see Section 3.5). Moreover, since a target identifies the listener position, the user may select only the actual seats as input for the simulation and discard irrelevant points from the audience area.

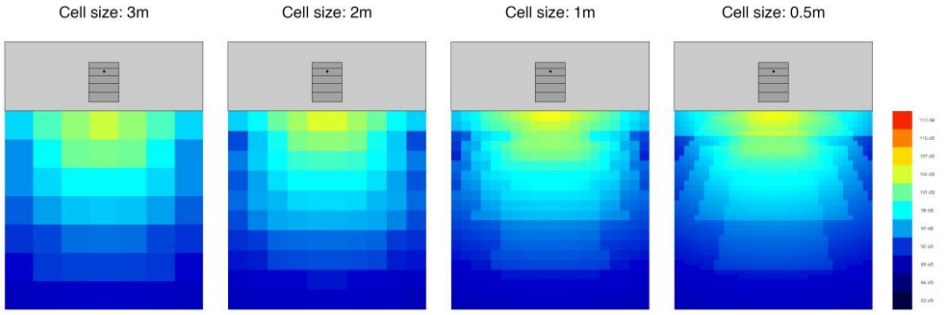


Figure 6. SPL maps at increasingly higher resolutions obtained by specifying a different cell size.

3.4.1. Acoustic analysis accuracy

In *Aeolus*, the accuracy of the simulation mainly depends on the reflection order, which affects the extension of the time domain in which sound waves propagate. A reflection order of 1 will only consider sound paths that arrive at the target location after one intersection with the acoustic reflectors. These paths are generally shorter than those reaching the target after multiple intersections with the reflective surfaces, and therefore do not provide much information about the SPLs associated with late reflections. Although a high reflection order *N* is required to produce a good estimate of the SPL in the time domain, and accurately compute important acoustic parameters such as sound clarity, definition and reverberation time (RT), the computational cost of the simulation grows exponentially with *N*. *Aeolus* can compute any number of reflection orders, but due to this limitation, a number higher than 4 is generally unmanageable even for simple acoustic scenes. Despite that, the information provided with an SPL map generated from up to 4 reflections can still be considered sufficient to evaluate a design option at the early design stages.

Figure 7 shows the effects of the reflection order *N* on the SPL map for two settings: a semi-reverberant field in which the acoustic scene comprises a curved reflector tessellated by 5 flat elements (Figure 7, at the top), and a reverberant field in which the acoustic reflector is surrounded by a rectangular box (Figure 7, at the bottom). Regarding SPL distribution, a reflection order of 2 returned a sufficiently detailed analysis for both settings. In the semi-reverberant field settings, *Aeolus* found no valid reflections for orders 3 and 4. Due to the absence of reflectors at the sides of the sound source, none of the acoustic rays could bounce more than twice before reaching the targets. Conversely, in the reverberant field settings, the reflectors constructed from the faces of the rectangular box always produced valid reflections. Nevertheless, the SPL distribution is almost identical for reflection orders 3 and 4, suggesting that, for this setting, a more appropriate analysis should have considered other acoustic parameters, such as RT, to determine the acoustic performance of the architectural volume. Although *Aeolus* does not currently support RT calculation, the analysis of the early reflections may still prove useful to determine the overall performance of an acoustic scene in a reverberant-field setting. In fact, strong early reflections correlate with good sound clarity and definition [11], and thus can effectively support a performance-oriented approach at the conceptual stages of the design process.

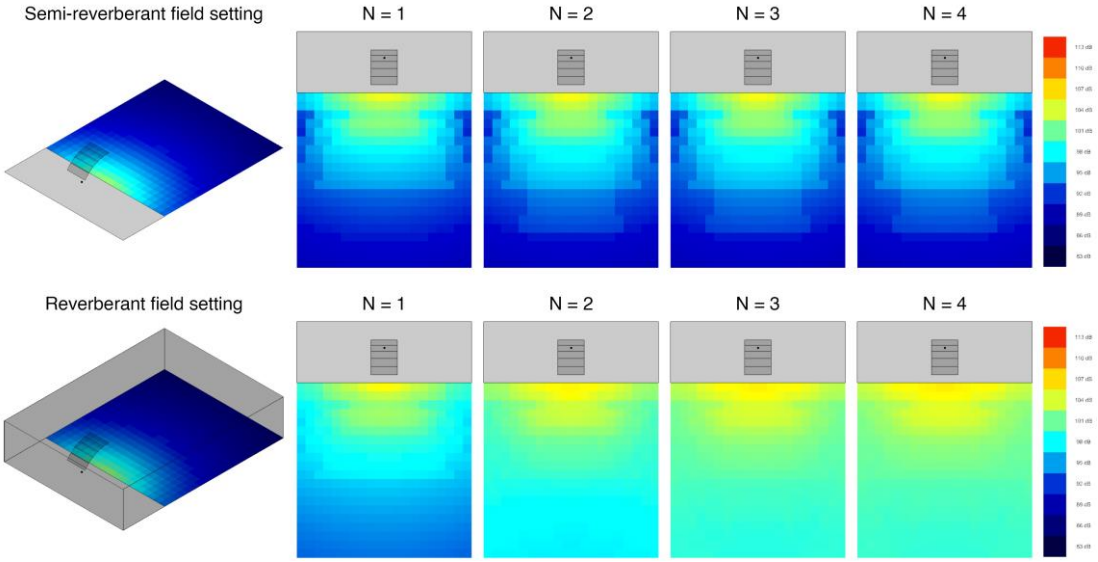


Figure 7. SPL maps for different reflection orders N. At the top, analysis of a single curved reflector (semi-reverberant field); at the bottom, analysis of a curved reflector inside a rectangular box (reverberant field).

3.5. Integration with optimisation plugins

As described in the previous sections, *Aeolus* allows performing more or less accurate analyses by fine-tuning the simulation settings, providing full control over the calculation time. With the appropriate settings, a user can rapidly test the acoustic performance of various design options within the *Grasshopper* environment. Alternatively, they can perform an optimisation process in *Grasshopper* using either the pre-built Genetic Algorithm (GA) component *Galapagos* or third-party plugins, such as *Octopus*.

Figure 8 illustrates a basic acoustic optimisation performed with *Galapagos*. The objective function was minimising the standard deviation of the SPLs distribution on the audience area. Three design variables were selected to control the z coordinate of the three control points defining the base profile of the curved reflector used for all the analyses described in this section (Figure 8, on the left). The acoustic reflector was tessellated with 5 flat elements, while a cell size of 2 m was used for the audience grid. The simulation considered reflections up to the second order. This setting kept the computational cost of each simulation below 100 ms.

The convergence graph in Figure 8 demonstrates that *Galapagos* could retrieve design options producing SPL maps with an increasingly lower standard deviation, which reduced from 3.67 (original design) to 2.36 (after 24 generations). The solution extracted from the 24th generation can be considered an improvement of the original design as the SPL is more uniform across the entire audience, meaning that the optimised design can reflect sound – for a specific sound source location – up to the last row of targets (Figure 8, at the bottom). Figure 8, at the right, compares the SPL maps of the original and optimal design obtained by increasing the resolution of surface tessellation and audience grid after the optimisation process. The optimal design still outperforms the original one in terms of SPL distribution, demonstrating that performing an analysis with *Aeolus* at a coarse resolution is a valid strategy for implementing an effective acoustic optimisation process.

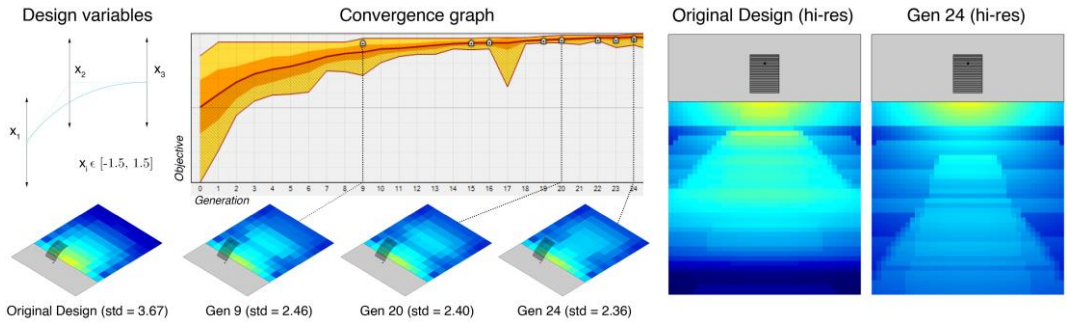


Figure 8. Example of an acoustic optimisation using *Aeolus* with the Genetic Algorithm *Galapagos* for *Grasshopper*; On the left, a representation of the design variables and convergence graph with selected design solutions; on the right, comparison between a high-resolution analysis of the original and optimised design.

4. Potential applications of *Aeolus*

The integration of *Aeolus* with architectural design and parametric modelling tools allows designers to use this plugin beyond applications that are specifically focused on acoustic performance. A brief survey of non-acoustic-oriented projects revealed that many architectural and structural forms could easily be recontextualised to perform as acoustic shells. We identified at least four different categories of architectural forms, which, even though unintendedly designed to be used as acoustic devices, impact the acoustic quality of the space they sit in. Figure 9 illustrates four example projects, and two abstracted variations of each are accompanied by an acoustic analysis to showcase the wider architectural applications of *Aeolus*. For the analyses, a single omnidirectional sound source was used at the centre of the design space, and the cell spacing for SPL analysis was set at 1m.

Facades [F] and openings in building envelopes are generally designed formally as invitational or gathering spaces providing opportunities for events. Naturally, this typology lends itself towards similarities with conventional acoustic performance shells encouraging mono-directional sound projection. In the examples, F1 mimics a canopy-like structure which can be adjusted to focus reflections intimately towards the opening or reflect sound away. [F2] proposes control over the lateral focusing of reflections, encouraging a linear approach towards the opening.

Gallery [G] spaces range from arcades to covered walkways, where sound is reflected from the ceiling treatment and perimeter walls and projected across the length of the primary circulation. The faceted example in [G1] gives a scattering-like effect at a larger scale resulting in an unfocused and lively environment. [G2] simulates a simple canopy or arched structure serving to reflect sound in the bi-lateral directions.

Canopies [C], promenades and marketplaces feature areas that are covered but open laterally for circulation. *Aeolus* can be used in these cases to understand the impact of the ceiling design and its performance in the multi-directional distribution or dispersion of sound in and away from the covered area. The example in [C1] produces similar scattering results to [G1] due to the asymmetrical ceiling treatment, and the density or regularity of the facets could be adjusted to control the level of scattering. The alternating wave canopy structure in [C2] creates clear horizontal banding of louder regions across the site. This analysis could serve to situate programs or functions across the site.

Pavilions [P] can be architecturally programmed for many purposes that vary in acoustic requirements. Using *Aeolus* to study the acoustic quality of pavilions may be useful to qualify the design for specific programs. While the faceted [P1] is larger by footprint, the active acoustic area is relatively smaller compared to the concave shell structure of [P2] which encourages a wider dispersion of acoustic reflections outside the footprint of the pavilion. Interestingly, both these examples also demonstrate a limitation of geometric acoustics, shown by the acoustic shadows generated by the pavilion elements that touch the ground.

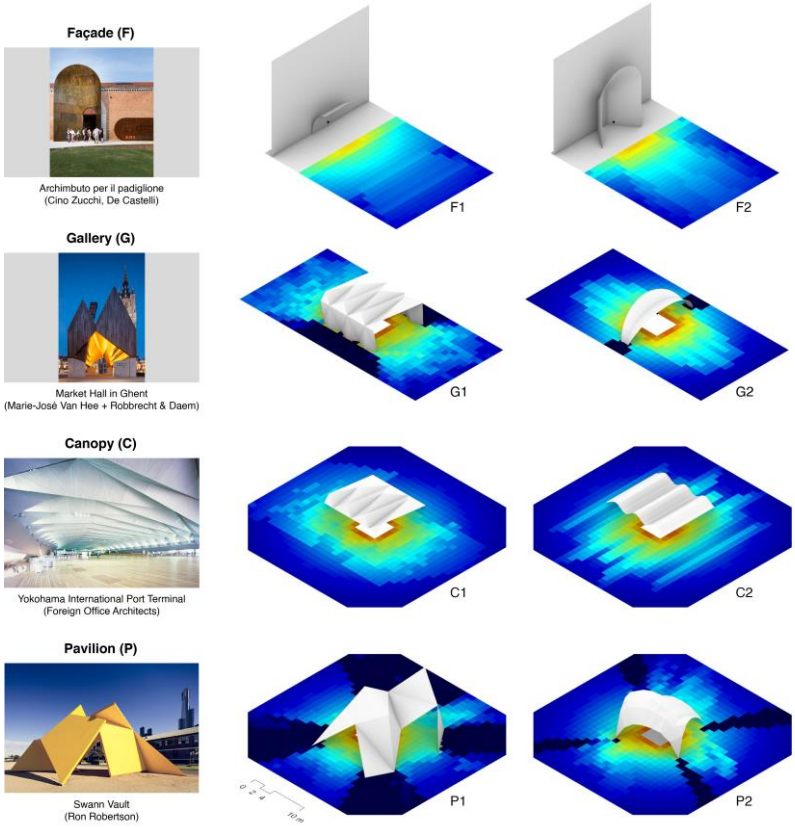


Figure 9. Example of potential applications of *Aeolus* with various architectural typologies. On the left, precedent projects illustrate each typology; on the right, comparison of SPL graphs of abstracted models.

5. Conclusions

This paper describes the development of *Aeolus* and its functionalities as an acoustic modelling software for the design, analysis and optimisation of acoustic shells. Its integration with *Grasshopper* for *Rhinoceros 3D*, i.e. an architectural parametric modelling software and associated optimisation plugins, makes it an effective tool for and performance-oriented design workflows, particularly at the conceptual design stages. Control over the degree of simulation accuracy, number of sound sources, and directivity allows the user to adapt the plugin precision level to different stages of the design process.

Like other available acoustic analysis tools, there are several shortcomings of *Aeolus*. The image source method requires surfaces to be modelled as flat, planar reflectors. This degree of approximation will always result in a trade-off between simulation accuracy, computational cost, and time. Particularly in a reverberant field setting, the reliance on the image source method also limits the accuracy of the SPL calculation and the lack of calculation for RT, though early reflections are suitable for measures of clarity and definition. Despite this, *Aeolus* can perform with a high enough accuracy and provide reliable analysis for preliminary stages in concept design, making it a suitable tool for architectural practice, research, and teaching. Future software development will incorporate additional algorithms to compute late reflections and construct a complete impulse-response graph.

Acknowledgements

We acknowledge Eduardo Pignatelli for contributing to the creation and development of the *Aeolus* plugin for *Grasshopper*. We also acknowledge Professor Sergio Pone, who supervised Gabriele Mirra's and Eduardo Pignatelli's master's thesis in 2015, through which *Aeolus* was developed. Professor Sergio Pone also financially supported the first practical application of *Aeolus*.

References

[1] L. Moretti, "Ricerca matematica in architettura e urbanistica", *Moebius*, no. 1, pp. 30-53, 1971. Also in: F. Bucci and M. Mulazzani, *Luigi Moretti: Opera e scritti*, Electa, 2000.

[2] N. Adams, *Skidmore, Owings & Merrill. SOM since 1936*, Electa, pp. 34-36, 2007. The use of computers within SOM has also been discussed at a conference entitled "Digital Design at SOM: The Past, the Present and the Future", accessible at the web address: vimeo.com/42786059 (accessed 13 April 2023).

[3] R. Aish and R. Woodbury, "Multi-level Interaction in Parametric Design", in: A. Butz, B. Fisher, A. Krüger, P. Olivier (eds.) *Smart Graphics. SG 2005. Lecture Notes in Computer Science*, vol. 3638, 2005.

[4] K. Besserud, N. Katz, A. Beghini, "Structural Emergence: Architectural and Structural Design Collaboration at SOM", *Architectural Design*, vol. 83:2, pp. 48-55, March/April 2013.

[5] G. Celani, C.E. Verzola Vaz, "CAD Scripting and Visual Programming Languages for Implementing Computational Design Concepts: A Comparison from a Pedagogical Point of View", *International Journal of Architectural Computing*, vol. 10:1, pp. 121-137, 2012.

[6] www.grasshopper3d.com/ (accessed 13 April 2023).

[7] C. Preisinger and M. Heimrath, "Karamba—A Toolkit for Parametric Structural Design", *Structural Engineering International*, vol. 24:2, pp. 217-221, 2014.

[8] C. Preisinger, "Linking Structure and Parametric Geometry", *Architectural Design*, vol. 83:2, pp. 110-113, March/April 2013.

[9] D. Piker, "Kangaroo: Form Finding with Computational Physics", *Architectural Design*, vol. 83:2, pp. 132-135, March/April 2013.

[10] M. Sadeghipour Roudsari, M. Pak, "Ladybug: A Parametric Environmental Plugin for Grasshopper to Help Designers Create an Environmentally-Conscious Design", in *Proceedings of the 13th International conference of Building Performance Simulation Association*, Chambery, France, 25-28 August, 2013.

[11] G. Mirra, E. Pignatelli and S. Pone, "Computational Morphogenesis and construction of an acoustic shell for outdoor chamber music", in *Proceedings of the IASS Annual Symposium 2016 "Spatial Structures in the 21st Century"*, Tokyo, Japan, 26-30 September, 2016.

[12] G. Mirra, *Aeolus*, www.food4rhino.com/en/app/aeolus (accessed 13 April 2023).

[13] L. L. Beranek, *Concert Halls and Opera Houses: Music, Acoustics, and Architecture (2nd Edition)*, Springer, 2003.

[14] M. Long, *Architectural Acoustics (2nd Edition)*, Elsevier Science & Technology, 2014.

[15] E. Haines, *Essential Ray Tracing Algorithms*, in A.S. Glassner (ed.), "An Introduction to Ray Tracing", Morgan Kaufmann Publishers, 1989.

[16] V. Martin and T. Guignard, Justification of the Image Sources in Ray-tracing Method, ICSV Congress 2005.

[17] G. Mirra, E. Pignatelli and S. Di Rosario. "An automated design methodology for acoustic shells in outdoor concerts", in *Proceedings of the Euronoise 2018 conference*, Hersonissos, Crete, 27-31 May, 2018.

[18] A. Pugnale, *Integrating Form, Structure and Acoustics: A Computational Reinterpretation of Frei Otto's Design Method and Vision*, "Journal of the International Association for Shell and Spatial Structures", vol. 59: 195, pp. 75- 86, 2018.

[19] A. van der Harten, "Pachyderm Acoustical Simulation: Towards Open-Source Sound Analysis" *Architectural Design*, vol. 83, pp. 138–139, 2013.

[20] A. van der Harten, Pachyderm Acoustic Simulation, www.food4rhino.com/en/app/pachyderm-acoustical-simulation (accessed 13 April 2023).

IASS 2023
July 10–14 Melbourne
Integration of Design and Fabrication

Proceedings of the IASS Annual Symposium 2023
Integration of Design and Fabrication
10–14 July 2023, Melbourne, Australia
Y.M. Xie, J. Burry, T.U. Lee and J. Ma (eds.)

Analytical simulation of roof snow load on flat roofs considering a probabilistic model of wind speed

Yuanyuan LI[a,b], Huamei Mo[a,b,*], Feng FAN[a,b]

[a,*] Key Lab of Structures Dynamic Behavior and Control of the Ministry of Education, Harbin Institute of Technology, Harbin 150090, China
[b,*] Key Lab of Smart Prevention and Mitigation of Civil Engineering Disasters of the Ministry of Industry and Information Technology, Harbin Institute of Technology, Harbin 150090, China
mohuamei@hit.edu.cn

Abstract

For analytical simulation of roof snow loads using historical meteorological data, meteorological data with high time resolution is required as input to obtain accurate results. Wind speed is the main factor in determining the distribution of roof snow load, and the simulated results are usually much more sensitive to the time resolution of the input wind speed. However, for the long-term historical meteorological dataset in China, only mean, and maximum values of 10-min average wind speed are available each day, which is hard to meet the simulation requirements. Therefore, a probability model of two-parameter Weibull distribution is proposed in this study to model the wind speed within each day finely. Then, based on the empirical relation between the transport rate of snowdrift and winds speed, the actual wind speed dataset from field measurement is used to validate the proposed model. Finally, based on the historical meteorological dataset of Harbin, an analytical simulation of snowdrift on a flat roof is carried out, and ground-to-roof conversion factors of snow load are derived.

Keywords: snow load, flat roof, analytical simulation, wind speed

1. Introduction

Snow load is one of the most critical loads that must be considered for structural design in cold and snowy regions, especially for long-span and lightweight structures. Failure of structures induced by snow overload frequently occurs for long-span and lightweight structures (Figure 1), severely threatening the structure's safety. To improve the snow load resistance of those structures, the proper design of roof snow load is of significant importance.



Figure 1. Some typical events of snow-induced structure collapse: (a) Marketplace in Russia, (b) Exhibition Hall in Poland, (c) Ice rink in Germany.

Plenty of research has been conducted to investigate snow distribution on roofs, and several approaches have been proposed and available till now. These methods include field measurements, wind tunnel/water flume tests, and numerical simulations (Figure 2). Field measurement is considered a

Copyright © 2023 by Yuanyuan LI, Huamei MO and Feng FAN. Published in the Proceedings of the IASS Annual Symposium 2023 with permission.

reliable approach to determining roof snow load, but it is time-consuming, and its results depend highly on the natural environment. Therefore, wind tunnel/water flume tests and numerical simulations, which are feasible to carry out and have more controllable working conditions, have become the mainstream research methods in the design of snow loads. These methods have also been applied to investigate the snow load around or above building for several structures, for example, the Concordia Scientific Research Station in Antarctica [1], Tongren Olympic Sports Center Stadium [2], and Beijing south station [3] et al. However, it is essential to note that these methods generally determine the roof snow load under the condition of a blizzard or storm, i.e., the design snow load is studied under the combination of heavy snowfall and strong wind as inflow condition, which failed to consider the evolution of roof snow load under the action of long-term natural climatic conditions. Thusly, the simulating result cannot provide a clear exceedance probability for roof snow load, and the result is hard to directly apply to structures' limit state design based on probability theory.



Figure 2. Methods for studying roof snow load: (a) field measurement, (b) wind tunnel test, (c) numerical simulation.

On the other hand, several researchers have studied the impact of actual meteorological conditions on roof snow loads and have proposed simulation methods based on historical meteorological data, such as the Finite Area Element Method (FAE) [4] and analytical simulation methods[5,6]. These methods simplify the process of roof snowdrift and make the simulation much more efficient. Thusly, this method can be combined with long-term meteorological data to analyze roof snow loads continuously over time. In contrast to the methods based on a single event, these methods consider the impact of actual meteorological conditions on roof snow loads and can provide a design roof snow load with a clear exceedance probability. Since these methods use meteorological data as inputs, the inputs significantly affect their results, especially wind speed. Hence, obtaining high-resolution meteorological data is necessary for more accurate simulation results. While for the historical meteorological dataset in China, daily wind speed data only include the maximum and mean value of 10-minute average wind speed and the maximum value of 3-second gust wind speed, which are coarse and cannot meet the requirements of simulation.

In this study, the analytical simulation method proposed by Qiang *et al*. [6] is used to study snow load on a flat roof. The historical meteorological data for Harbin, China, covering the time range of 1971 to 2018, are considered to study the evolution of roof snow load, and the two-parameter Weibull distribution is used to model the daily wind speed data. Finally, the time history of the snow load on the roof is derived, and the ground-to-roof conversion factors of the flat roof are also obtained.

2. Simulation setting and meteorological data

2.1. Simulation setting

The studied roof is shown in Figure 3. The snow transport model developed by Qiang *et al*. [6] is used to describe the snowdrift process on the studied roof. Considering the impact of threshold wind speed on snowdrift, this model classified snow transportation into snowdrift during snowfall and snowdrift without snowfall, and a sine function is used to describe the development of snowdrift on the roof. Following one of the cases studied by Qiang *et al*. [6], the studied roof is set as a two-dimensional

isolated flat roof without interference from nearby buildings, and the roof size is set as 50m in length and 10m in height and the inflow wind during the simulation is assumed to remain in a single direction.

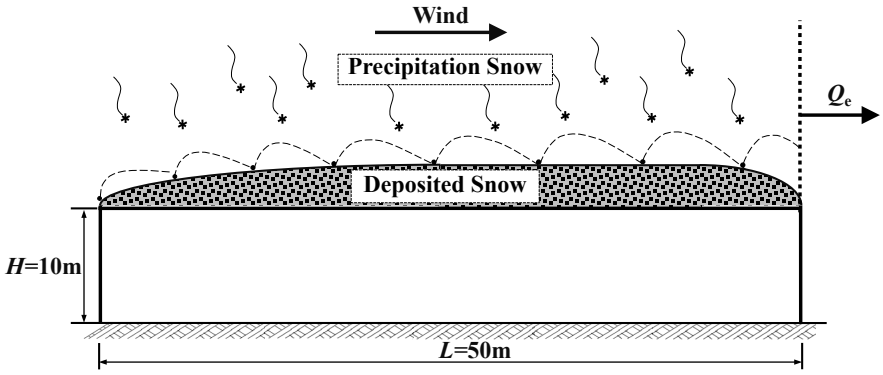


Figure 3. Schematic sketch of snow transport on flat roofs.

2.2. Meteorological data and data processing

2.2.1. Meteorological data

The historical meteorological data for Harbin, China, is used for snowdrift simulation. This dataset is collected from China Metrological Data Service Center (CMDSC) and contains daily records of wind speed, snow depth, air temperature, and precipitation lasting from 1971 to 2018.

The wind speed is measured at 10 m for open country exposure, corresponding to terrain categories B in the Chinese load standard. For roofs under different terrain categories, wind speed at roof height, V_H, can be calculated by:

$$V_H = G(\frac{H}{\delta})^{\alpha} \tag{1}$$

$$G = V_{600}(\frac{350}{10})^{0.15} \tag{2}$$

where V_{600} is the 10-min average wind speed at 10 m height from the meteorological dataset, H is the roof height, G is the geostrophic wind speed, δ is the thickness of the boundary layer, α is the power-law exponent. The value of δ and α for different terrain categories are shown in Table 1.

Table 1: Values of α and δ for the four terrain categories specified in the Chinese load code

Terrain category	Power-law exponent α	Boundary layer height δ (m)
Category A	0.12	300
Category B	0.15	350
Category C	0.22	450
Category D	0.30	550

Snow depth is measured for the days when more than half of the surrounding ground in vision is covered by snow, and the snow depth is converted to snow mass using a density of 150kg/m^3. Air temperature is observed at the height of 1.5m above the ground, and the data set for air temperature contains daily minimum, daily mean, and daily maximum air temperature. The precipitation data is recorded as the cumulative snow water equivalent (*SWE*, mm).

In Harbin, ground snow accumulation and subzero temperatures are rarely observed from May to September. Thusly, a winter season is defined as from October 1 to April 30 (of next year), and the meteorological data were partitioned into the winter season, resulting in a total of 47 complete seasons. The daily meteorological records for a typical winter season in Harbin are shown in Figure 4.

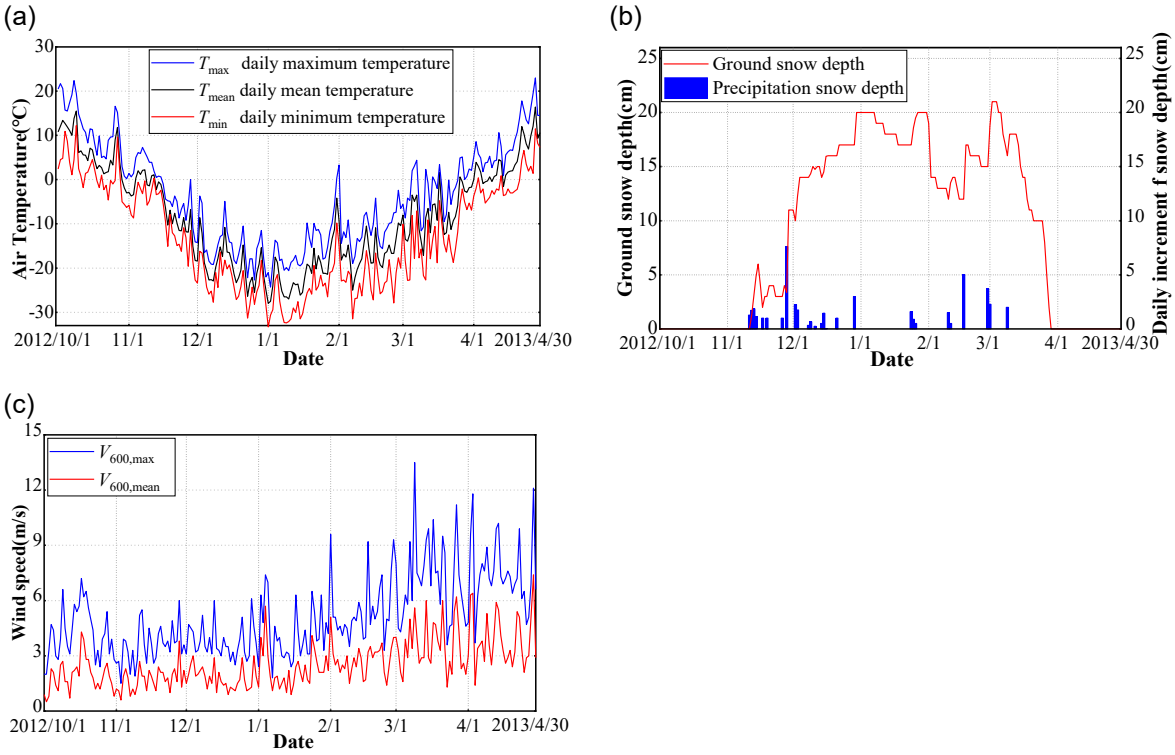


Figure 4. Daily meteorological records in Harbin for a typical winter season: (a) air temperature, (b) ground snow depth, (c) wind speed.

2.2.2. probabilistic modeling of wind speed

In this study, the two-parameter Weibull distribution (referred to as Wbl_2 hereafter) is used to model the frequency distribution of the daily wind speed, i.e., the frequency distribution of the 10-min average wind speed, V_{600}, within a whole day can be approximated by Wbl_2.

The probability density function (pdf), $f_w(x)$, and cumulative density function (CDF), $F_w(x)$, of Wbl_2 can be expressed by:

$$\begin{cases} f_W(x) = \dfrac{k}{\alpha}\left(\dfrac{x}{\alpha}\right)^{k-1}\exp\left[-\left(\dfrac{x}{\alpha}\right)^{k}\right] \\ F_W(x) = 1-\exp\left[-\left(\dfrac{x}{\alpha}\right)^{k}\right] \end{cases} \quad (x>0) \tag{3}$$

where x value of the random variable represents V_{600} in this study, α is the scale parameter; k is the shape parameter.

As mentioned above, the long-term historical wind speed dataset offers limited samples of $V_{600,}$ and only daily mean and maximum values of V_{600} are available daily. The commonly used parameter estimating methods, such as the method of moment (MOM), the method of maximum likelihood (MML), and the method of L-moments (MLM), cannot be applied. To fit Wbl_2 using $V_{600,max}$ and $V_{600,mean}$ offered in the daily wind speed dataset. We assume that: 1) the mean value of V_{600} represents the expectation of probability distribution of daily wind speed; 2) and the 144/145 percentile of the fitted distribution

equals $V_{600,\max}$. Based on those assumptions, a parameter estimation method, which combines the method of moment and method of cumulative probability, is proposed, and the parameters of Wbl_2 can be derived by:

$$\begin{cases} E(V_{600}) = k\Gamma[1+\dfrac{1}{\alpha}] = V_{600,\mathrm{mean}} \\ F_{\mathrm{W}}(V_{600,\max}) = 1-\exp[-(\dfrac{V_{600,\max}}{\alpha})^{k}] = \dfrac{144}{145} \end{cases} \tag{4}$$

where $\Gamma(\cdot)$ is the gamma function. An example of wind speed records during a whole day and its probabilistic modeling is shown in Figure 5.

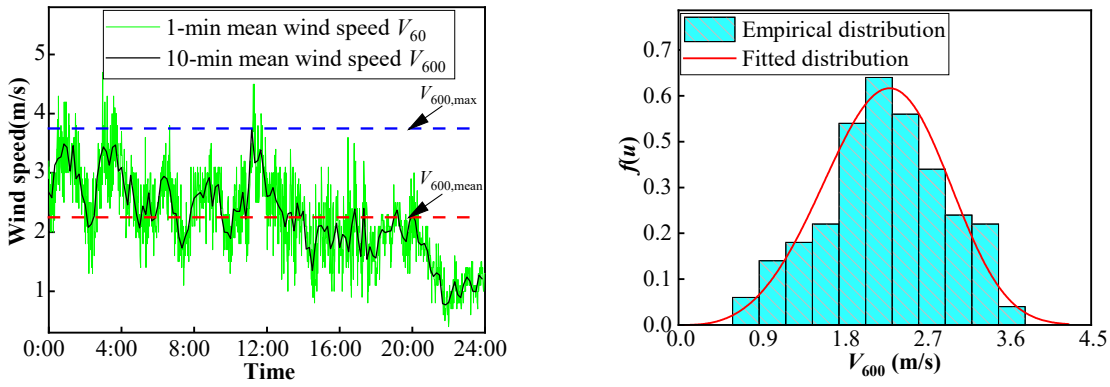


Figure 5. An example of wind speed records during a full day: (a) record and simple statistics of the wind speed, (b) frequency distribution of the wind speed and the fitted Wbl_2.

3. Results and discussion

3.1. Simulation results

Based on the long-term historical meteorological dataset and the proposed Wbl_2 of wind speed, the roof snow load for the studied case is simulated continuously. Figure 6 shows the time history of the roof and ground snow loads for typical winter seasons for category B. Due to the lower threshold friction velocity for snow particles during snowfall, snow particles are more likely to drift. Therefore, roof snow drift mainly occurs during snowfall, and the proportion of snow loads drifting off the roof after the snowfall is relatively small. Meanwhile, due to snow drift, precipitation snow cannot deposit on the roof, and the maximum ground snow load and the maximum roof snow load may appear on different dates.

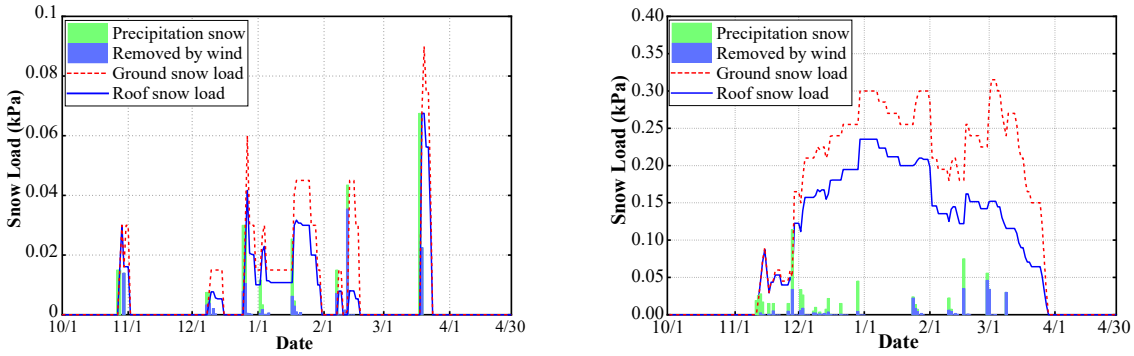


Figure 6. Ground and roof snow loads for typical winter seasons: (a) winter season of 1997-1998, (b) winter season of 2011-2012.

3.2. Ground-to-roof conversion factors

Simulations are also carried out considering other three terrain categories, i.e., categories A, C, and D. Based on the simulating result, the ground-to-roof conversion factors, C_s, defined as the ratio between the annual maximum roof snow load to the annual maximum ground snow load, are calculated for the studied roof, and the results are summarized in Table 2.

The result indicates that the conversion factor increases as the terrain category changes from A to D; since category A is typically associated with stronger winds, and category D usually leads to lower wind speeds. The opposite trend is observed for the deviation of the conversion factors, i.e., the deviation decreases with the terrain category changes from A to D. The different wind conditions in different terrain categories also cause this.

Table 2. Summary of ground-to-roof conversion factors C_s for the studied roof in Harbin, China

Terrain category	Mean	Standard deviation	COV
Category A	0.579	0.221	0.381
Category B	0.641	0.213	0.332
Category C	0.788	0.171	0.217
Category D	0.912	0.102	0.112
All Categories	0.730	0.223	0.306

We noted that some pioneering research had been conducted to investigate the conversion factors between the roof and ground snow load. For example, O'Rourke [7] analyzed the ground and roof snow load dataset across 199 United States buildings, suggesting conversion factors with a mean value of 0.67 and a standard deviation of 0.27. Furthermore, Thiis and O'Rourke [8] studied the snow load dataset measured in Norway and suggested a mean value of 0.73, with a standard deviation of 0.12, for the conversion factors.

The comparison of the conversion factors derived in the current study under all categories to that obtained by O'Rourke *et al*. [7] and Thiis and O'Rourke [8] is shown in Figure 7. The result indicates that the mean value of the conversion factors obtained in this study is close to those outlined in references[7,8], and the standard deviation is comparatively more significant. This standard deviation discrepancy is primarily attributable to the substantial differences in wind conditions across the four terrain categories.

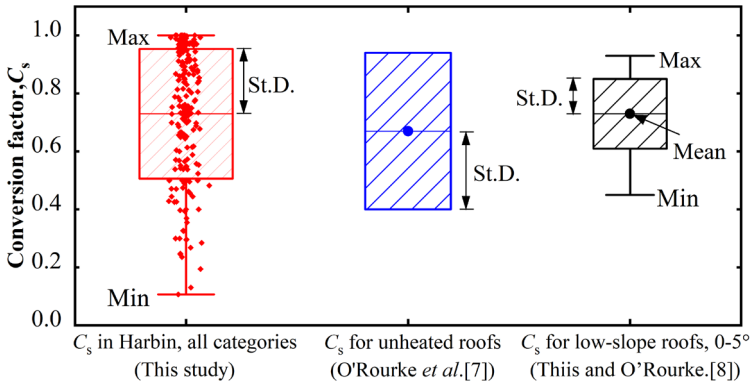


Figure 7. Comparison of C_s calculated in this study and some other studies.

4. Conclusion

In this study, an analytical simulation of snowdrift on a flat roof is carried out for a flat roof in Harbin, the long-term historical meteorological dataset for 47 winter seasons is used for the simulation, and daily wind speed records are modeled into higher time resolution by the proposed 2-parameter Weibull

distribution. Based on the simulation result, the ground-to-roof conversion factors, C_s, defined as the ratio between the annual maximum roof snow load to the annual maximum ground snow load, is calculated for the studied flat roof and the comparison of the conversion factors with that suggested by other studies illustrates the validation of the simulation.

Acknowledgments

Financial support received from National Natural Science Foundation of China (No. 51808169, No. 51921006, and No. 51927813) and Fundamental Research Funds for the Central Universities (Grant No. HIT. NSRIF. 2020083) is gratefully acknowledged.

References

[1] P. Delpech, P. Palier, and J. Gandemer, "Snowdrifting simulation around Antarctic buildings," *Journal of Wind Engineering and Industrial Aerodynamics,* vol. 74, pp. 567-576, 1998.

[2] G. Zhang, Q. Zhang, F. Fan, and S. Shen, "Research on Snow Load Characteristics on a Complex Long-Span Roof Based on Snow— Wind Tunnel Tests," *Applied Sciences,* vol. 9, p. 4369, 2019.

[3] X. Li, X. Zhou, M. Gu, "Study on snow loads on the roof of Beijing south station," *Building Structure,* vol. 38, pp. 109-112, 2008.

[4] S. L. Gamble, W. W. Kochanski, and P. A. Irwin, "Finite area element snow loading prediction-applications and advancements," *Journal of Wind Engineering and Industrial Aerodynamics*, vol. 42, pp. 1537-1548, 1992.

[5] M. O'rourke, A. Degaetano, and J. Tokarczyk, "Analytical Simulation of Snow Drift Loading," *Journal of Structural Engineering-ASCE*, vol. 131, pp. 660-667, 2005.

[6] S. Qiang, X. Zhou, M. Gu, and L. Kang, "A novel snow transport model for analytically investigating effects of wind exposure on flat roof snow load due to saltation," *Journal of Wind Engineering and Industrial Aerodynamics*, vol. 210, pp. 104505, 2021.

[7] M. O'rourke, "Snow Loads: Guide to the Snow Load Provisions of ASCE 7-16," 2017

[8] T. K. Thiis, M. O'Rourke, "Model for Snow Loading on Gable Roofs," *Journal of Structural Engineering (United States),* vol. 141, no. 12, 2015.

IASS 2023
July 10–14 Melbourne
Integration of Design and Fabrication

Proceedings of the IASS Annual Symposium 2023
Integration of Design and Fabrication
10–14 July 2023, Melbourne, Australia
Y.M. Xie, J. Burry, T.U. Lee and J. Ma (eds.)

Application of long span discontinuous curved lattice shell in Qingdao Airport design

Yuan FENG*, Xun XIA[a], Xiao-bing WU[a], Li-wei WANG[a], Zhi-qiang CHEN[a], Yan ZHANG[a]

[a,*]China Southwest Architectural Design and Research Institute CORP. LTD, Chengdu 610041, China
xnyfy@163.vip.com

Abstract

Qingdao International Airport is a regional airport hub and a portal to Japanese and Korean, with total area of 478,000 square meters. Its long span steel roof with side skylights brought challenges to structural engineers. We adopted the discontinuous curved lattice shell structure as the structure. By comparing multiple schemes, we found the discontinuous curved lattice shell ensured both structural stiffness and aesthetic effects by properly arranging V-shaped strut. This discontinuous curved lattice shell has now been used in many airports, including the brand new Chengdu Tianfu International Airport, the largest one in the 13th Five-Year Plan of China.

Keywords: discontinuous, lattice shell, skylight, Qingdao Airport, Chengdu Tianfu Airport

1. Introduction

The Qingdao Airport (Fig.1) is located 40 km northeast of Qingdao, on the west bank of the Da-gu River. This airport is positioned as a "regional airport hub and a portal to Japanese and Korean". The total architectural area of this airport is 478,000 square meters, and two runways have been constructed. Its annual passenger capacity is 35 million and cargo shipment capacity is 500,000 tons. Aircraft take-off and landing are 300,000 sorties. In the long run, its passenger capacity will reach 55 million.



Figure 1. Qingdao Airport

The plane size of the airport terminal is 948.3m×1090.2m. The terminal adopts a starfish layout and is divided into six independent structural units: the main hall (Zone F) and the five fingers (Zone A to E). The size of the main hall is 326m×388m (narrowest point) to 507m×415m (the widest point). Its steel

Copyright © 2023 by Yuan FENG, Xun XIA, Xiao-bing WU, Li-wei WANG, Zhi-qiang CHEN and Yan ZHANG. Published in the Proceedings of the IASS Annual Symposium 2023 with permission.

roof adopts an economically long span discontinuous curved lattice shell, with the lower part of the lattice shell supported on concrete filled tubular columns. The average column grid is 36m×62m in the main hall.

2. Architectural restrain

According to the requirements of natural lighting, ventilation, and architectural style, the architect required that a total of 9 skylight strips (Fig.2) should be placed on the long span steel roof. Due to aesthetic requirements, the skylight strip needed to be as transparent as possible and web members cannot be set (Fig.3). These skylight strips led to discontinuity of the roof shell and resulted significant reduction in strength and stiffness of the roof shell, which must be particularly strengthened.

3. Structural scheme

By comparing commonly used long span steel structures like unidirectional truss, bi-directional truss and spatial lattice shell, we selected spatial lattice shell as the roof structure. This structure has strong benefits in fitting complex curved surface, good structural integrity, high redundancy and ability to resist unexpected loads and to resist collapse. It is also with obvious advantages in fast construction and low cost.

However, where skylights strips are installed, the roof shell's continuity was broken. The discontinuity of the roof shell, as well as the removal of diagonal web members at skylight strips, has greatly weakened the performance of the roof lattice shell. So we had to adopt a new configuration for all skylight strips in order to strengthen the roof shell's load capacity. Further calculation and analysis indicated that it could meet the structural requirements. We call this lattice shell with new configuration at skylight strips the Discontinuous Curved Lattice Shell.

The key characteristic of this long span Discontinuous Curved Lattice Shell is the skylight strips of the shell are concise and transparent, and which can maximize the architectural effect. This configuration is to set a spatial truss at the skylight strip. The transverse section of the truss is a diamond shape and a steel connecting member is set on the diagonal of the diamond shape (Fig.4). The entire transverse section is a stable shape. The side surfaces of the skylight strip are covered by decorative planks, so diagonal rods can be arranged on two side surfaces to enhance the rigidity of the skylight strip. For the skylight strip's top and bottom surfaces, which directly facing passengers, diagonal web members must be removed, so the rigidity of the structure on the top and ground surfaces is greatly weakened. To ensure the rigidity of the top and bottom surfaces, we retain two diagonal web members at top and bottom surfaces on a certain spacing. These two retained web members form a V-shaped brace (Fig.5). When spacing of the V-shaped brace is proper, it can ensure the rigidity of the roof lattice shell, and hence achieves a transparent and concise architectural effect.

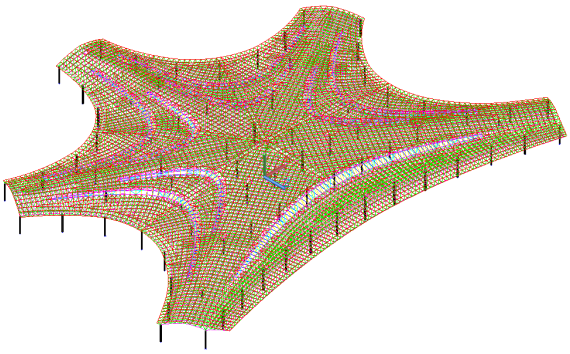


Figure 2. Analysis model

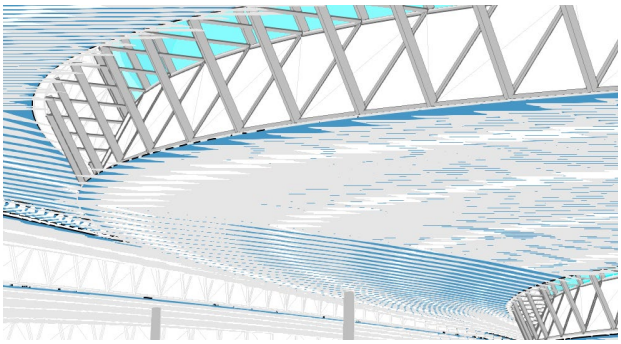


Figure 3. Skylight strip

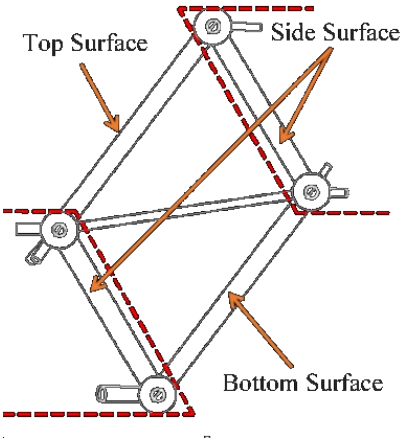


Figure 4. Section of skylight strip

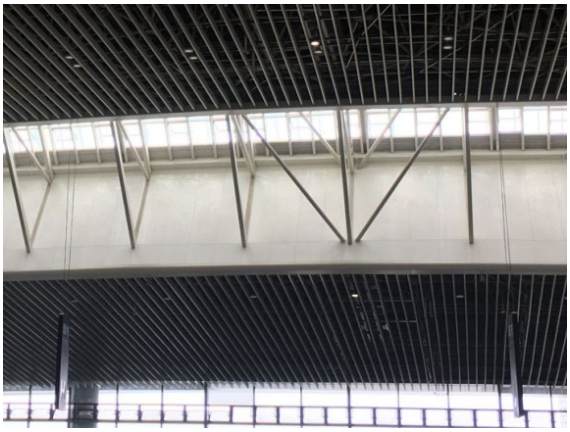
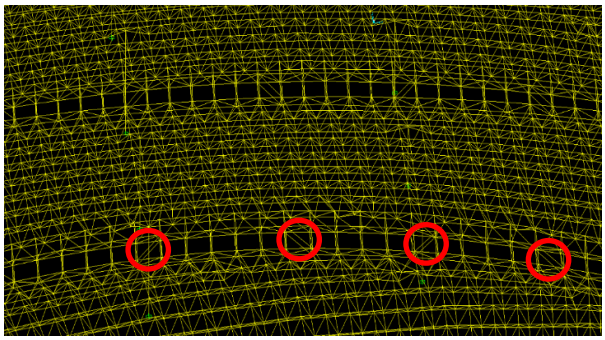


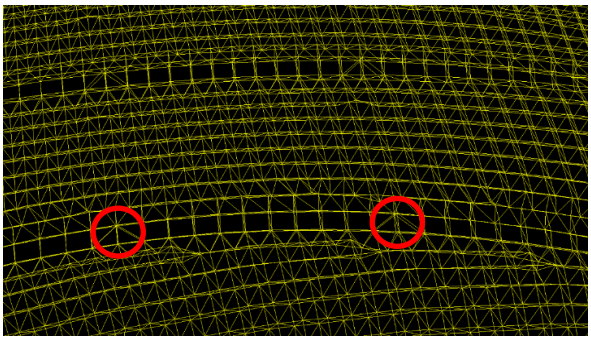
Figure 5. Skylight strip and V-shaped brace

The most important thing for this discontinuous curved lattice shell is to determine the spacing and position of V-shaped braces. In order to compare the mechanics differences between discontinuous curved lattice shells and ordinary curved lattice shells, designers have established several analytical models for ordinary curved lattice shells and discontinuous curved shells. Three respective schemes are considered for the discontinuous curved lattice shell. Scheme 1set one diagonal rod every 36m and Scheme 2 set two diagonal rods every 72m. Scheme 3 retain all diagonal rods. (Fig.6)

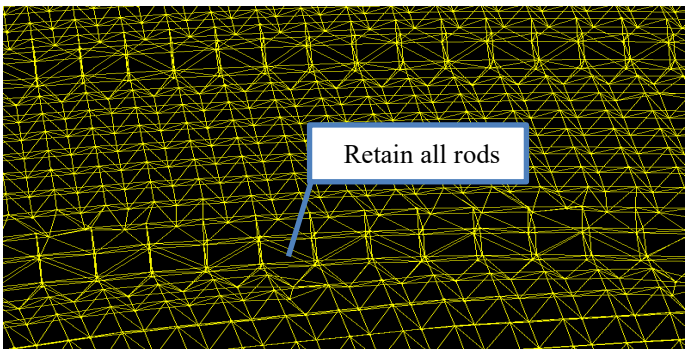
The analysis model includes the lattice shell and its supporting columns. The shell members employ truss elements, but the skylight strip and its adjacent members use beam elements to reflect their bending moments. The support columns use beam elements and are connected with the lattice shell by hinges. A supplementary model using beam elements for all grid shell members has also been established, and the results are consistent with the model with beam elements used only at the skylight strip and adjacent members.



(a). Scheme 1 - one rods every 36m



(b). Scheme 2 - two rods every 72m



(c). Scheme 3 – retain all diagonal rods

Figure 6. Three schemes for skylight strips

Calculation result shows that the natural vibration period of the discontinuous curved lattice shells are all slightly longer than that of the ordinary lattice shell, but the difference is not significant (only 8.3%). The first three order natural vibration periods of the three schemes are listed in the table below (Table 1). The natural vibration period of the scheme 1 and scheme 2 is almost the same. Comparing with these two schemes, scheme 3's natural vibration period slightly shorter, which means its stiffness is slightly higher. The stiffness of these three schemes is not significantly different from ordinary lattice shells.

Table 1. Natural period for discontinuous shell and ordinary shell

period（s）	Scheme1	Scheme2	Scheme3	Ordinary
Mode 1	2.690	2.690	2.673	2.467
Mode 2	2.462	2.458	2.435	2.453
Mode 3	2.107	2.095	2.088	2.345

Under 1.3D+1.5L load case, the stiffness of discontinuous curved lattice shell increases and the deflection decreases compared to ordinary grid structures in the skylight strip area. The reason is that the spatial truss is formed due to the height difference of the skylight strip, and hence increases thickness of the lattice shell at the skylight strip and improves the vertical stiffness of the shell here. In the skylight strip area, the deflection of discontinuous curved shell is 43.7% lower than the ordinary lattice shell. In the other area (no skylight strip area), the deflection of the discontinuous curved shell is the same as that of the ordinary shell. The deflection of scheme 1 is the same as that of scheme 2. And scheme 3's deflection is 10% lower than scheme 1 and scheme 2.

The comparison of the main mechanics and economic indicators between discontinuous curved lattice shells and ordinary lattice shells is listed in Table 2. The steel usage for a discontinuous curved lattice shell increases by 12% comparing to an ordinary lattice shell and its structural stiffness is equivalent to that of an ordinary lattice shell.

Table 2. Comparing for discontinuous shell and ordinary shell

index	Scheme1	Scheme2	Scheme3	Ordinary
Steel usage	6813	6827	6951	6001
Stress ratio	0.8	0.8	0.8	0.8
Period	2.690	2.690	2.673	2.467

From the above comparing, we see there is no significant difference for in-plane stiffness between discontinuous curved lattice shells and ordinary lattice shells (only 8.3%). Under vertical load, the discontinuous curved lattice shell's deflection in common areas (no skylight strip) is close to that of ordinary shell and deflection of the discontinuous curved lattice shell at skylight strip is smaller. The steel usage of the discontinuous curved lattice shell is about 12% higher than that of the ordinary lattice shell, but it can satisfy aesthetic requirement from architects. Three schemes of discontinuous curved lattice shells are compared, Scheme 3 shows the best mechanics performance. Scheme 1 and Scheme2 have almost the same mechanics performance and are slightly worse than the Scheme 3. For the Qingdao airport's long span steel roof, the discontinuous curved lattice shell is a reasonable structural solution. Through properly arranging V-shaped braces, we can ensure the mechanics capacity of a discontinuous curved lattice shell is similar to that of an ordinary lattice shell. And although its steel usage has slightly increased, a discontinuous curved lattice shell's overall architectural effect is better.



(a). Overall view (b). Inner view and skylight strip

Figure 7. Qingdao Airport after completion

Using discontinuous curved lattice shells have solved the key problem of the long span steel roof of Qingdao Airport and achieve good architectural effects on skylight strips. The airport was designed in 2017 and put in use in 2021. (Fig.7)

Discontinuous Curved Lattice Shell has a more transparent and aesthetically skylight strip than traditional grid shells. Compared with trusses, Discontinuous Curved Lattice Shell is more adaptable for complex curved surfaces. So it has better applicability and architectural performance when using for long-span buildings like airports, bus stations, exhibition hall and etc.

4. Other application

The discontinuous curved lattice shell provides a transparent and concise aesthetic effect at skylight strips by evacuating some diagonal rods, and meanwhile maintains the steel shell's in-plane and out-of-plane stiffness. It is particularly suitable for long span buildings like airports, railway stations and traffic hubs constructed in recent years. Therefore after being applied in Qingdao Airport, this structural form has been used in multiple projects as Chongqing Jiangbei International Airport and Chengdu Tianfu International Airport. All of these projects have achieved promising effects.



Figure 8. Chengdu Tianfu airport

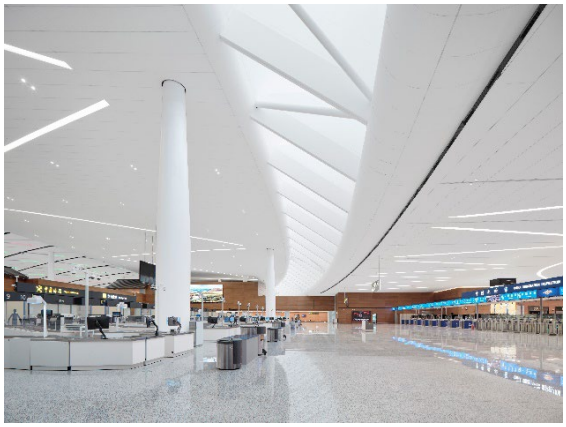


Figure 9. Skylight strip



Figure 10. Column free space and skylight strips

The newest Chengdu Tianfu International Airport (Fig.8~10) is located in city Chengdu of southwest China. It is the largest airport built during the 13th Five-Year Plan of China. Its terminal has a total area of 710,000 m^2 and opens up in April 2021. The biggest challenge for this airport is a 74 m×500m column-free space at the main hall and a large skylight strip with height difference of 7m is adopted there. The discontinuous curved lattice shell is used as the roof structure system and successfully forms the column-free space and also the skylight strip, which achieves decent architectural effects and aesthetic beauty.

IASS 2023
July 10–14 Melbourne
Integration of Design and Fabrication

Proceedings of the IASS Annual Symposium 2023
Integration of Design and Fabrication
10–14 July 2023, Melbourne, Australia
Y.M. Xie, J. Burry, T.U. Lee and J. Ma (eds.)

Bridging design and fabrication: BIM application in two prefabrication projects

Hing C. LAU*, Jingxiang ZHU[a]

[a,*] The Chinese University pf Hong Kong
Room 506, Lee Shau Kee Architecture Building,
The Chinese University of Hong Kong, Shatin, NT, Hong Kong
lauhingching@link.cuhk.edu.hk

Abstract

The paper introduces two prefabrication projects: New Lawuga School (2015) and Meili Transitional School (2018). These two projects have different scales and contexts: New Lawuga School is a charity school of 200 m^2 built in a plateau village; Meili Transitional School is a public transitional school of 5275 m^2 built in a high-density urban condition. The authors participated in the projects in person and applied Building Information Modelling (BIM) technology from design to construction. Details of BIM application in these two prefabrication projects, particularly those related to fabrication, are explained and reviewed to provide a springboard to explore the BIM potential in practice.

Keywords: building information modelling, prefabrication, modern construction, fabrication, case studies, architectural practice, supply chain

1. Introduction

Building Information Modelling (BIM) has been widely used in different regions of the world today. While the advantage of BIM adoption in promoting construction efficiency is widely recognised by the industry, there are also critiques of the approach. These criticisms are not only about the tool's functionality such as unintuitive user interfaces, but rather political in nature.

In the book "Atlas of Digital Architecture", the authors indicate an apparent condition that clients of big projects particularly like BIM as it "keep a handle on budgets, and nudges architects and engineers to work together towards optimising their use of materials [1]". This brings the BIM's strongest criticism of its "giving commercial interests, project management, and the bureaucracy of very large and therefore mighty clients the upper hand over architects as space creators [1]". Besides, BIM also entices "planners to use pre-defined construction elements [1]" and "liable to produce 'Lego architecture [1]'".

Yet, the authors rectify the criticisms by explaining that BIM is an approach with a mindset that changes the way of doing things, hence it is one of the cultural changes which tends to meet with resistance. They defend the technology by mentioning Zaha Hadid and AEC *Architectes* Rotzer & Kaempfer (from the French-speaking part of Switzerland) whose built creative and original projects with the help of the tool. They take the perspective that BIM after all is a technology in progress, and architects should determine the approach that takes to it.

This paper supplements the perspective by introducing two innovation projects: New Lawuga School, a charity school of 200 m^2 built in a plateau village in 2015, and Meili Transitional School, a transitional school of 5275 m^2 built in a high-density urban condition in 2018. Both schools are designed and built by a research team from the School of Architecture, The Chinese University of Hong Kong (CUHK) (Architecture Integrity and Innovation Association (AIIA) is the research team led by Prof Zhu Jingxiang in CUHK which has focused on lightweight prefabrication since 2008. UNITINNO is AIIA's

Copyright © 2023 by Hing C. LAU and Jingxiang ZHU. Published in the Proceedings of the IASS Annual Symposium 2023 with permission.

execution partner.) This paper's authors are the core architects who participated in both projects and applied BIM in the design and fabrication stages. This paper explains the details of BIM application in different stages to offer first-hand in-person experience illustrating how BIM technology could contribute to small-to-medium scaled innovative prefabrication projects.

2. New Lawuga school

2.1. Project introduction

In the 2010 earthquake in Yushu, Qinghai China, the one-storey brick-made buildings in the Lawuga School in a remote village in the Plateau area with an altitude of 3900m were damaged. Since then the school had used sandwich panel container houses as classrooms. In 2015, a philanthropist committed AIIA to design and build a charity schoolhouse to provide a better education environment for the local minority nomadic families.

The New Lawuga School is a 2-storey building with a floor area of 200 m2. It includes 4 classrooms, 1 stair hall and 1 storage, and serves around 160 students. It is constructed with a system of structural insulated panels (SIPs). The sectional profiles are I, C and Z. There are in total 81 panels in the main building structure system. These panels have widths of ~1.2m and lengths varied from 3m to 8m. Among the 81 panels, only two panels are identical. The differences among the other panels come from the geometry, opening, finish and connection detail. Besides the panels, the building includes other components such as lighting, windows and doors, and trombe wall units.

The New Lawuga School won the First Prize in the Local Academia Group of 3015 Construction Industry Council Innovation Award from Hong Kong, and the FuturArc Green Leadership Award (Institutional Group) in 2016.



Figure 1. New Lawuga School

2.2. BIM application in Lawuga

BIM was implemented in the New Lawuga School when the schematic design was finished. Because of the complicated geometries of the components, the project team recognised that BIM would be an appropriate tool to examine the components' detailed design. For example, the distribution of solid wood

trims in the SIPs should be guaranteed so that screws could be cut in; the finish materials of the SIPs should be designed to fit in other panels.

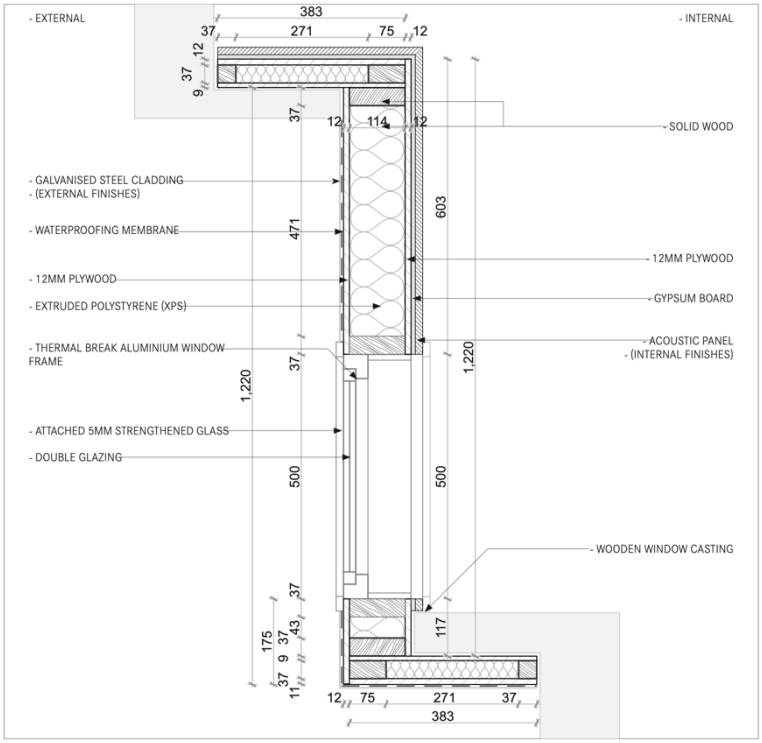


Figure 2. Details of SIPs

Then the BIM model was used to generate the two types of drawings. The first type was schematic drawings, which include plans, sections, and elevations. The second type was fabrication drawings, which were delivered to suppliers or manufacturers. In total there were around 260 drawings (regardless of revisions),which include:

- Composition drawings of SIPs for fabrication;
- Finishing drawings of SIPs for fabrication and installation;
- Geometrical drawings of steel cladding and steel connector for fabrication;
- Location drawings of metal claddings for installation;
- Schedules of windows and doors for purchasing metal frames;
- Composition drawings of wooden doors for fabrication;
- Composition drawings of wooden components (openings casting, staircase, etc) for fabrication;
- Geometrical drawings of PVC sheets (for trombe wall) for fabrication;
- Composition drawings of trombe wall units for fabrication;
- Schedules of solid wood trims for material cutting.

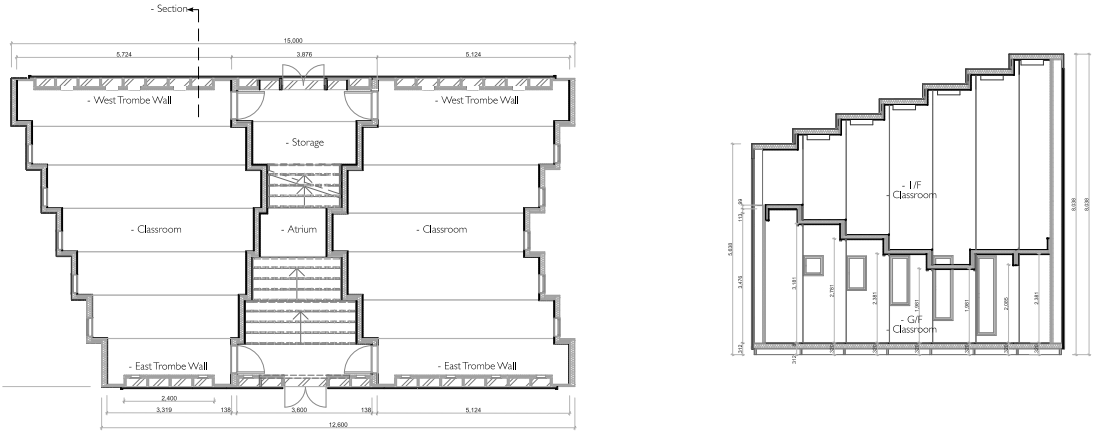


Figure 3. Schematic drawings: G/F plan & section

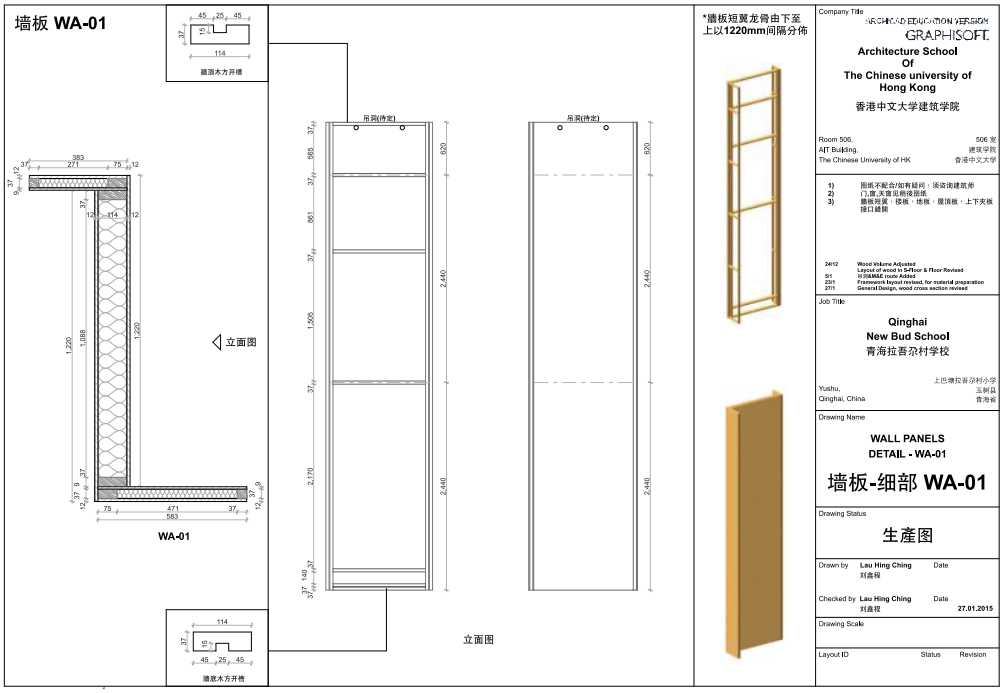


Figure 4. Fabrication drawings: Wall panel

The fabrication took place in Chengdu, a city 750km away from Yushu. There were two wood manufacturers involved: the big one with standard factories responsible for the SIPs production, and the small one which is a workshop responsible for the small wooden components (trombe wall units, staircase, doors, furniture). Another small manufacturer produced steel components and glass panels (for windows). The rest components such as window and door frames and electrical devices were purchased from the local building material market. Everything was delivered to Yushu by trunks, except the PVC Sheets which were sponsored by a Shanghai Company and delivered to the construction site from their warehouse.



Figure 5. Factory in Chengdu

3. Meili transitional school

3.1. Projects introduction

In 2018, the original Meili school located in Futian Shenzhen, China was planned to be deconstructed and rebuilt. The Planning Bureau invited the project team to design and build a transitional school on a nearby open space in an urban context to house the students during the construction period of the original school. The transitional school should be built fast, capable to be deconstructed and reassembled in other locations after use.

The Meili Transitional School commenced site work in mid of July 2018. The superstructure construction started on 29 July 2018. The school was ready to be used by 30 Nov 2018, but users only moved in on 25 Dec 2018. The two-storey school took 4.5 months to be built. It provides 32 standard classrooms (9.6m x 6.6m), and other supplementary facilities such as functional classrooms, offices and toilets, serving 1320 students.

The Meili Transitional School used a "Light Steel Post-and-Lintel System", which is a modular system characterised by the use of light steel members with small cross sections (80x80mm & 80x160mm) standardised bolt-and-nut joints. The system was later applied to build 4 more transitional schools in Shenzhen from 2019 to 2020, providing a total building floor area of 21610 $m^{2.}$

The Meili Transitional won the First Prize in the Science and Technology Award of the 2019 Guangdong Excellent Engineering Survey and Design Award, and the Highly-Commended Prize in Social Equality Award of the 2020 WA Awards for Chinese Architecture (WAACA). The other two transitional schools built in Longhua Shenzhen using the same system are shortlisted for the Technological Innovation Award and City Regeneration Award of 2020 WAACA.



Figure 6. Meili Transitional School

3.2. BIM application in Meili

BIM software had been applied in the project since the early design stage. It was used to build a "Scheme Model" which generated the overall basic drawings and 3D renderings for communication among different parties: bureaus, users and consultants. Schedules calculating the floor area and different materials were also produced from this model.

While the proposal was developing, another BIM model based on one standard classroom from the "Scheme Model" was built to study the detail of every component and the relationships between them. This "Unit Model" is composed of many independent "Component Models" which were used to generate the fabrication drawing. In the later stage, "Unit Models" of other facilities such as staircases, bridges, guard house, and water tower were also built.

In short, the "Scheme Model" was used for design and administration, while the "Unit Models" were used for fabrication. The two types of models were maintained by two different teams. Whenever there was a need for collaboration, the two teams abstracted the necessary parts of their models and exported them as "Intermediate Models" for the other team. Such practice could ensure efficient communication but not interfere with the working rhythm of two teams.

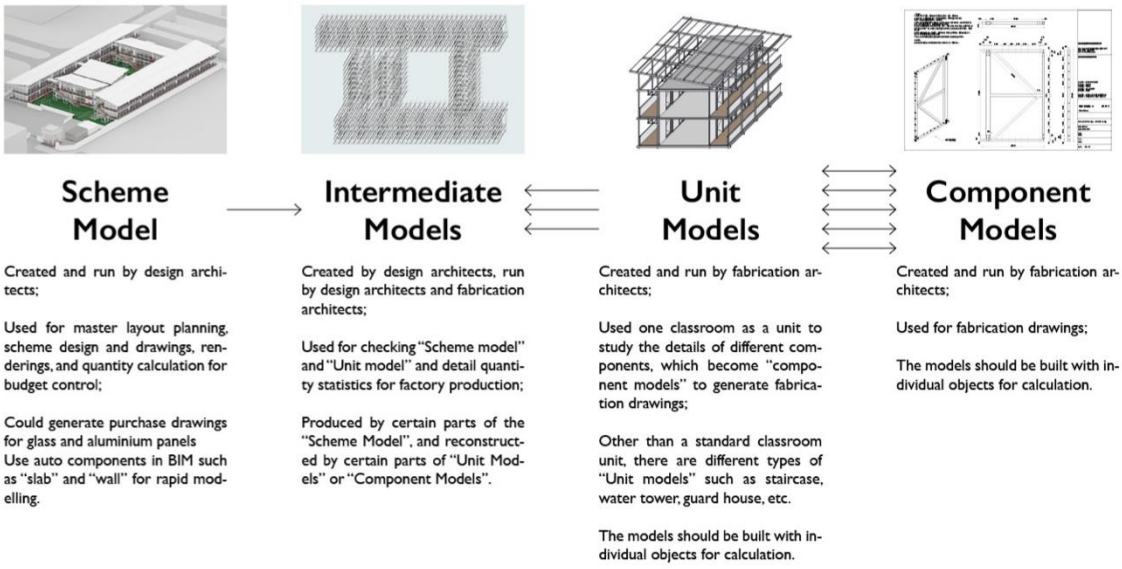


Figure 7. Bim models organisation

The main manufacturing factory was located in Henan Province, which could process both wood and steel components. It is worth mentioning that the factory used laser-cutting technology for machining the steel components. Even though direct output from BIM models to the laser cutting machines is theoretically practicable, the project team could not achieve this in this project, due to the incompatibility between the software formats.



Figure 8. Factory in Henan

4. Findings

These two projects, even though led by an academic team, are well grounded on local supply chains and embody generic value. Reviewing the projects could provide insights into academia and contribute to the practice industry.

Both schools use standardised industrialised products in the market and ordinary production technologies in common factories to develop innovative building systems fitting the specific project contexts. However, the SIPs in Lawuga School are differentiated panels with the same composition, while Meili Transitional School used a standard modular system for all the functions.

4.1. BIM merits

In the design stages, adopting BIM technology allowed the architects to generate comprehensive outputs under limited human resources and time. In the Meili Transitional School, the project schedule was very tight: it was established in February 2018 and the site work commenced in July 2018. Even though this project has a special nature that the project team was "invited" to solve a social problem and there was relatively less interference in the design compared to typical school projects, the comprehensive output still promoted effective communication among bureaus and users, which was critical to the project's success.

In the fabrication stages, there are several benefits of adopting the technology.

Firstly since 3D diagrams could be easily generated from the BIM model, they were used as a powerful communication tool to illustrate the design concepts with the local suppliers and factories during the quotation and fabrication stages. This was particularly critical as both the projects (Meil is a public project, Lawuga is a charity project) had strict budget control and could only involve ordinary suppliers, who basically manufactured according to the drawings.

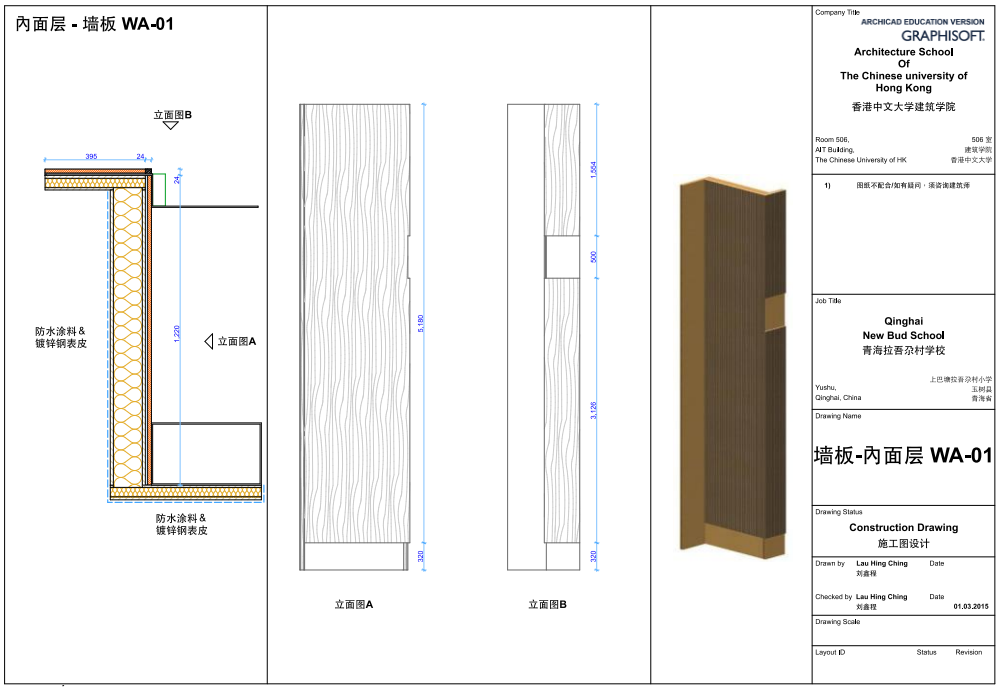
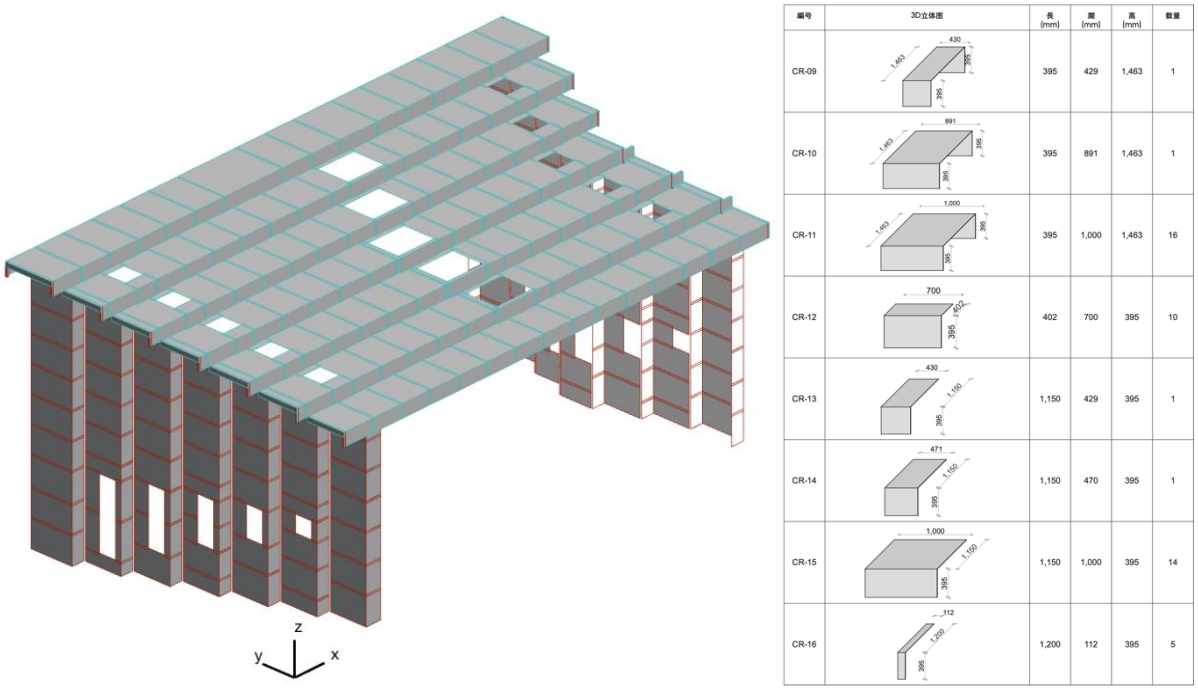


Figure 9. Wall panel finish drawing (Lawuga School)

Secondly, since the drawings were the direct output of the 3D model, the chance of errors in drawings was greatly reduced. For example, In Lawuga School, the most critical and complicated are the SIPs, which their composition and finishing drawings were found correct during the assembly stage.

Thirdly, the auto-generated schedules facilitated the fabrication process. In Lawuga School, schedules of solid wood trims inside the SIPs and metal claddings were generated from the BIM model, which listed out the requirements of form, dimension and quality. Workers could start preparing the materials once they received the schedules. These schedules also assisted the project team to calculate the budget cost and building weight.



編号	3D立体图	长 (mm)	闊 (mm)	高 (mm)	数量
CR-09		395	429	1,463	1
CR-10		395	891	1,463	1
CR-11		395	1,000	1,463	16
CR-12		402	700	395	10
CR-13		1,150	429	395	1
CR-14		1,150	470	395	1
CR-15		1,150	1,000	395	14
CR-16		1,200	112	395	5

Figure 10. Metal cladding model and auto-generated schedule (Lawuga School)

Fourthly, the BIM tool allowed all the fabrication drawings to be auto-updated when the model changed.

4.2. Discrepancies

Yet there are also lessons to learn. The followings are some observations about applying the BIM in the fabrication stage, specifically connecting to ordinary factories and workshops in the two mentioned projects, which may be regarded as reminds to improve the approach.

Although BIM software streamlines drawing production, it still requires tremendous effort to produce fabrication drawings, since each component is needed to be isolated and generated its own set of drawings. This process of isolation and drawing generation could be more intuitive. The best application of this aspect in the two cases is the steel cladding of the Lawuga School, in which the schedule generated from the BIM model was directly used for manufacture.

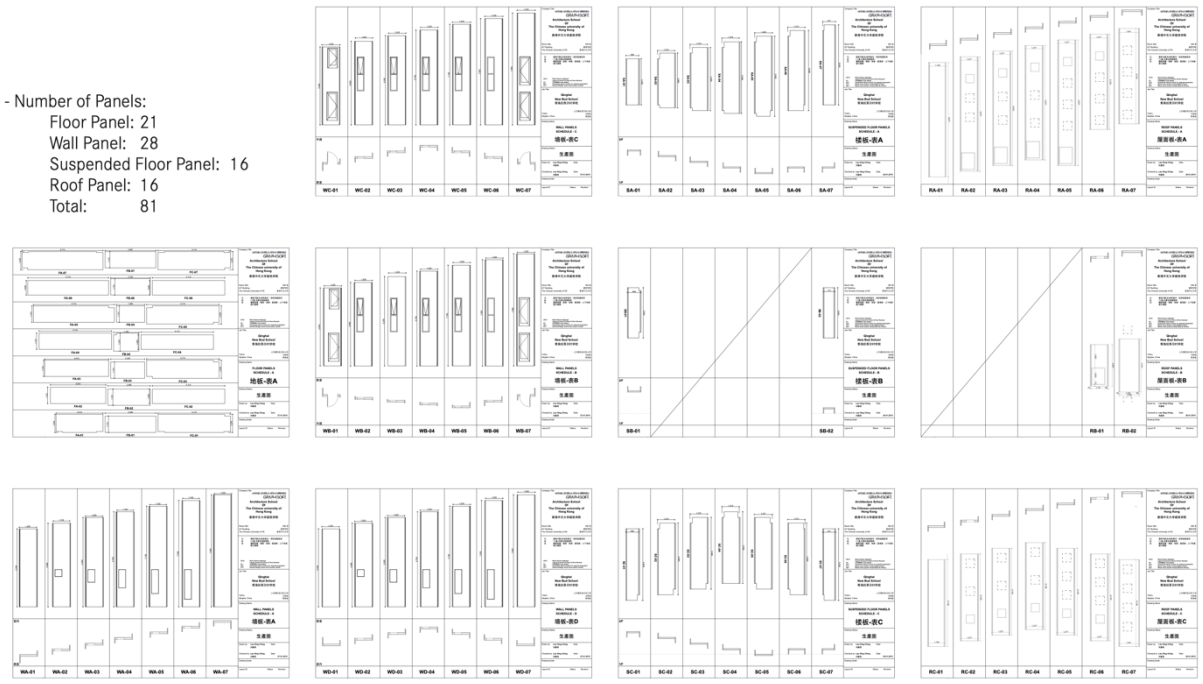


Figure 11. Lawuga School Schedule of all panels

The auto-generated schedule in the BIM calculates the components' quantity, which helps determine the material cost. However, the true materials used also include waste materials, which depend on the relationship between the raw materials and the designed components. Hence the project team should make studies of the raw materials and design accordingly to understand and control the discrepancy.

Another deviation comes from the tolerance and error from construction. The digital world is perfect and precise, but the real world is not. The fabrication drawings transfer the idealistic design into physical reality and hence should consider tolerance. For example in the New Lawuga School, 5mm space was reserved between the SIPs for error control (which was later proved insufficient). However, incorporating these imperfections in the BIM model makes it complicated. The Meili School had different models for design and fabrication. Measures against tolerance only appear in the fabrication model, hence keep the design model simple.

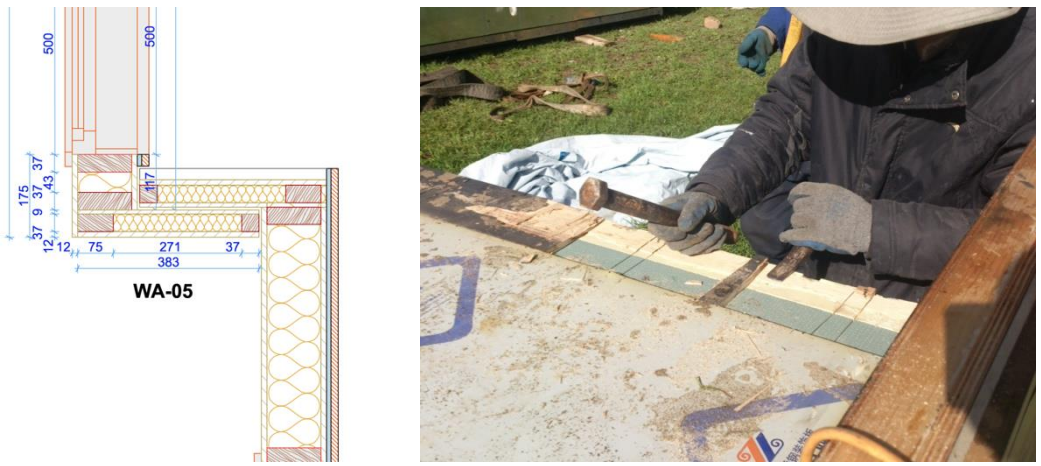


Figure 12. Tolerance in BIM model and reality

5. Conclusion

This paper explains the practices in two school projects to illustrate how BIM may contribute to small-to-medium scale innovative projects. They are first-hand experiences, as the authors participated actively in the projects throughout the design and build period.

The projects use standardised industrialised products in the market and ordinary production technologies in common factories to develop innovative building systems for specific project contexts. These design ideas persist as the BIM tool allows the project teams to control the fabrication effectively, thanks to its power to produce great visibility of design and consistent sets of information, and its streamlined outputting process.

This paper also discusses the demerits when applying BIM in the fabrication stage. These discrepancies between digital applications and reality provide an opportunity to improve the practice.

The emergence of BIM challenges the specialisation of the role of practitioners in the industry including the architects since the tool provides a platform to involve in different stages of the project. We have heard a metaphor from an architect that BIM is a “roadster” and practitioners need to be equipped to master the tool. This paper provides basics to extend the tools’ application in the connection with industrial supply chain and manufacturing technology, which is influential under the modernisation of the building industry in which integration of design, fabrication and assembly is taking place.

Acknowledgements

All of project drawings and images are from AIIA/ UNITINNO.

References

[1] O. Fritz, U. Hirschberg, L. Hovestadt, and G. De, Atlas of Digital Architecture : Terminology, Concepts, Methods, Tools, Examples, Phenomena. Basel: Birkhäuser (in English), pp.517-518, 523-525, 2020.

[2] Y. Zhai, J. Zhu, R. S. Diedering, and H. C. Lau, "Constructing form versus constructing architecture-A comparison of two modular buildings using irregular prefabricated panels," in Proceedings of IASS Annual Symposia, 2019, vol. 2019, no. 1: International Association for Shell and Spatial Structures (IASS), pp. 1-6.

IASS 2023
July 10–14 Melbourne
Integration of Design and Fabrication

Proceedings of the IASS Annual Symposium 2023
Integration of Design and Fabrication
10–14 July 2023, Melbourne, Australia
Y.M. Xie, J. Burry, T.U. Lee and J. Ma (eds.)

Built environment prototyping for design-value

Darcy ZELENKO[a,*], Duncan MAXWELL[a]

[a,*] Future Building Initiative, Monash University
darcy.zelenko@monash.edu

Abstract

The built environment is hindered by issues relating to laggard productivity, with practitioners looking to pursue sector-wide industrialisation and digitisation to improve this issue. Contrastingly, industries that have achieved widespread industrialisation and digitisation also possess developed prototyping cultures. Within these industries, prototyping approaches are tailored to suit the nature of the specific output product. Prototyping in the built environment acts as a tool for representation, testing, and communication. Prototyping approaches vary across the constituent disciplines with a lack of influential approaches or methods of the kind illustrated in other industries. This paper uses critical analysis to review prototyping literature from influential approaches found in engineering design, software development, and design management. These are compared to approaches used in the built environment disciples of architecture, engineering, and construction research. The findings confirm that prototyping is a value-adding activity, but suggest that prototyping cultures and outcomes in the built environment are inhibited by fragmentation that is inherent in the discipline. Future research could surround the development of prototyping approaches that enable practitioners to get the most out of the process. Such a protoyping approach would that also recognises that the creation of buildings requires both idea conceptualisation, and physical implementation to deliver quality outcomes.

Keywords: prototyping, design-value, built environment, architecture, engineering, construction

1. Introduction

The built environment is a production-based sector that creates high-cost goods that are produced in a one-off manner, at sites that change, and by teams that are temporary in nature [1]. The result is a fragmented project delivery process often leading to cost and time overruns that combine to negatively affect productivity in the sector [2]. There are efforts in the built environment to explore industrialisation and digitalisation to overcome these challenges. Within this context, prototyping is being specifically explored as a tool to mitigate these overruns, but is not commonly utilised in the built environment for purposes beyond representation, compared to other production-based sectors [3], [4].

Prototyping is defined broadly as "a first full-scale and usually functional form of a new type or design of a construction (such as an airplane)" [5]. The approach exists as a tool to explore product development and is used across a range of sectors with each developing specific definitions that are influenced by the needs of the field in which the approach is used. Sectors in which prototyping is common are: engineering design, software development, and design management, and some of these definitions will be explored by this paper as a means of developing a more critical and clear definition of prototyping for the varied requirements of the building industry [4], [6]. In their influential paper, 'What Do Prototypes Prototype?', Houde & Hill suggest that the main importance of prototypes lies in how the designer utilises them as part of an exploratory design process, or for demonstration purposes [7]. However, as noted, prototyping for the built environment (beyond representation) is a relatively uncommon endeavour, and a range of approaches and definitions exist that inhibit collaboration, knowledge sharing, and problem solving. This paper seeks to establish the value of prototyping in the

Copyright © 2023 by Darcy ZELENKO and Duncan MAXWELL. Published in the Proceedings of the IASS Annual Symposium 2023 with permission.

context of design for the built environment and by means of a critical review of literature to speculate on new prototyping definitions that will assist the building industry to build better buildings.

The critical review of this paper will develop an understanding of the variety of prototyping methods and terminology currently used by different practitioners in the built environment, and compare them to influential approaches developed in engineering design, software development, and design management. It is suggested that there is a link between the uncommon practice of prototyping in the built environment , and a lack of understanding about the benefits prototyping can provide. This is due to a lack of a built environment context-appropriate framework, to map prototyping purposes and classes, in ways similar to that found in disciplines where prototyping is a common practice. The critical review of literature undertaken from built environment disciplines helps to understand the different ways prototyping gets used. This is complimented by a review of prototyping literature from a three disciplines to understand more formalised approaches. This will be synthesised to propose a model for prototyping in the built environment that reflects the complex nature of building.

There are a number of unique factors that inhibit a greater uptake of prototyping in the built environment. The scale of construction often necessitates the production of large prototypes. Artefacts of such size require large amounts of materials, take time to produce, may require logistics to move, and storage space once completed. Built environment prototypes can be complex in nature, possessing a detailed scope, requiring input from multiple trades to complete, which can potentially be a costly endeavour. Even at a reduced scale, prototypes can also be costly to make[8]. Buildings are a high-cost product to create due to the sheer amount of materials and labour required. As construction tends to favour cost-minimisation over achieving best value, prototyping can be viewed as too costly [9]. Most conventional construction projects are one-off in nature which minimises the impact that prototyping can have, when compared to other industries that use mass production to create goods.
There is a sector-wide perception that the benefits to be gained from prototyping are low, especially on projects where perceived design complexity is low. When compared to the above-mentioned costs associated with built environment prototyping, the perceived cost-benefit ratio is skewed. As the built environment is fragmented in nature, the separation of the design and construction teams hampers the process of evaluation and subsequent learning associated with the prototyping. Prototyping in construction is observed to occur on projects possessing design complexity. It could be suggested that the construction sector doesn't consider prototyping on projects featuring conventional products and processes, as there is a view that there is nothing gleaned from the activity. The factors discussed above see prototyping carried-out in small amounts on construction projects. This hampers the development of prototyping cultures that would see built environment-specific methods could become more formalised.

2. Prototyping theory and uses outside built environment

While uncommon in the built environment, other fields such as engineering design, software development, and design management heavily rely on the use of prototypes as a part of their design process. Each discipline has developed frameworks and terminology that form a theoretical base to describe its use of prototyping. What has resulted is the the creation of varying definitions of the term prototyping that differ from the generalised definition stated above. This reflects in that they all highlight the act as a method employed as part of the design process.

2.1. Design engineering

An interpretation of prototyping from the perspective of technically-oriented industries like engineering or industrial design, is for it to be linked to predetermined design stages. This perspective sees prototyping defined as the process of creating a physical or digital embodiment of critical elements of an intended design, that is used as a tool to communicate and learn, and aid decision-making [10]. This approach recognises the ability of prototyping to act both as a learning tool, but also as a vessel through which to communicate a design to internal stakeholders. Prominent mechanical engineering academic

David G. Ullman describes four different classes of prototype being created that roughly correlate to different stages of the design process the field [11].

Table 1 - Ullman's classes of Prototyping

Prototype Function	Description
Proof-of-Concept	Undertaken in initial project stages to help direct design approach
Proof-of-Product	Used to refine components and subassemblies of a product
Proof-of-Process	Involves the production of samples that verifies both the geometry and manufacturing process
Proof-of-Production	Validates the entire production process where the prototype is the result of a pre-production run

The field of engineering design concerns the technical design of physical systems and machines, and heavily uses prototyping as part of the design process. The use of prototyping in mechanical engineering concentrates on the development of solutions to technical problems, as is reflected by the nature of the field itself, with less emphasis being placed on the overall use or form of the product.

Horton and Radcliffe detail the creation of a number of rapid proof-of-concept prototypes to create a pineapple de-topper that consisted of the designers experimenting with ways to remove the tops themselves [12]. Elverum et al. describe the use of rapid prototypes created with 3D printing that are created to assess size and appearance of parts early in the design process, that can be considered proof-of-product prototypes [13]. Liou describes the first complete Boeing 777 created that can be classified as a proof-of-production prototype as it required the entire manufacturing process to be defined to enable its creation [14]. These examples of prototyping are physical in nature, and possess varying levels of fiddelity, and workmanship.

2.2. Software development

Software development is a branch of computer science that concerns the design, programming, deployment, and maintenance of software. The nature of the products created in this industry differs from design engineering in that the scope of work leans more towards being more digital, so products tend to be virtual, with less of a physical presence. This has impacted the development of influential prototyping processes in the industry, in that they focus more around the development of the underlying concept that drives the product.

An evolutionary approach to software development is often employed, which sees a product built, then it is continually improved through feedback obtained from customers [15]. The need for such an approach reflects the fact that within software development, it is difficult to test a system that isn't fully complete, and that user needs change as projects evolve [16]. Within this context, prototyping is viewed as the production of early working versions of a future software application that are used for testing purposes [17]. Houde and Hill propose a model that helps designers ask what their prototypes 'prototype' and includes the classes; Role, Implementation, and Look and Feel [7]. They see their model helping to separate design problems into three classes of questions, that often require different kinds of prototypes to answer.

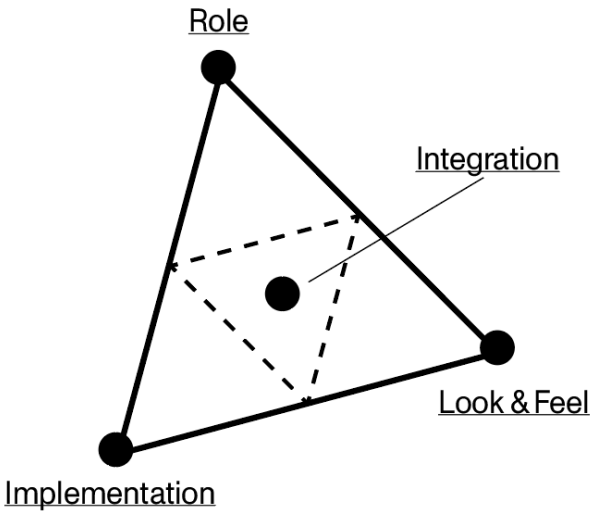


Figure 1. Houde and Hill's model of prototyping [7].

In this model, "Role" refers to questions surrounding what function a product (known as artefact) brings to the life of the user. "Look and feel" concerns questions about the physical sensory experience a user has when using a product. "Implementation" refers to the specific technology or programming that enables a product to perform its Role. "Integration" prototypes bring together the three classes to communicate an approxiamtion of the final product, and used to understand the design as a whole.

Bischofberger and Pomberger outline TOPOS, a software development environment that enables designers to prototype software in a controlled setting, separate from the real-life version [18]. Beaudouin-Lafon & Mackay define 'Paper and Pencil' prototypes as a way for developers to quickly answer questions relating to Look and Feel [19]. Camere et al. describe the prototype for an interactive mirror kit that was used to simulate the way a user interacted with the product, or "Role" according to Houde and Hill [20]. Their prototype consisted of a laptop and webcam that was used to run a specially-designed mirror software that tracked users facial expressions. These examples of prototypes from software development are a mix of physical and virtual, and tend to be low fidelity and possess low levels of workmanship. They also tend to be more nuanced and tailored to target specific aspects of the software design process, as defined by Houde and Hill.

2.3. Design management

Design Management is a broad field that concerns the organisational processes that are used to support the creation of new products and services [21]. Tom Kelley, a renowned design manager, defines prototyping broadly as a way to solve problems, further adding that anything can be prototyped [22]. Acklin describes the creation of a prototype model to guide and track the absorption of design knowledge in small and medium-sized enterprises [23]. This prototype is conceptual in nature, but was used to test and refine the underlying idea. Droz outlines the use of 'early-stage modeling' — a form of low fidelity and workmanship prototyping — by companies as a means of defining and strategising a new product [6]. He uses an example from Sony where small blocks of wood were used to envisage the design goals behind the creation of a Walkman; size and simplicity. The prototyping used by people working in design management is used to drive the conception of ideas, or ways of working in design, and does not necessarily have to be physical in nature. As these two examples are conceptual in nature, they can't be considered possess fidelity or workmanship.

2.4. Implications for built environment prototyping

The approaches to prototyping listed above can be thought of as defining a spectrum between idea conceptualisation, and physical implementation. As software development involves the creation of highly complex digital systems with limited physical engineering required, the approaches to prototyping have coalesced around the use of simple ways to tease-out ideas, and the creation of prototype virtual environments in which to test versions of software. Design engineering is a highly technical industry that concerns the creation of complex physical devices, and has seen its approaches to prototyping reflect this nature.

The above-mentioned spectrum illustrates that it is possible to prototype both conceptual and physical ideas. The creation of buildings requires both conceptual and physical embodiments of design. This suggests that a method of prototyping that utilises both ends of these poles is required to be able to adequately test all elements of a building. The development of such a method could be a useful tool to enable more comprehensive built environment prototyping.

3. Built environment prototyping

This section will now turn to analyse the use of prototyping in the built environment, through looking at the methods used by different professions that work in the discipline. The use of prototyping in the built environment is not as ubiquitous as in the above-mentioned fields, and more likely to be carried-out more extensively on projects possessing design complexity [24]. As a result, the literature concerning prototyping theory in the built environment is nascent. This has led to a lack of convergence in terms for prototyping in the same way Ullman's work has influenced mechanical engineering, or how the work by Houde & Hill has influenced software development. The design-focussed fields of architecture and engineering will be first analysed to understand how they approach and value prototyping, before turning to how these ideas are carried through into construction.

3.1. Architecture

Architectural design heavily relies on the creation of scale models as a tool in the design process [25]. Scale models explore form, spatial quality, and inform the design process of buildings [26], [27]. Scale models can be created to explore iterations of the actual built product, or can be made as a tool to explore concepts that inform the design process. They are created to varying levels of fidelity, but generally, scale models that are used in the design process tend to be created in haste, with low fidelity and varying degrees of workmanship. Scale models are also used to communicate the project to external stakeholders such as the client, local authorities or the wider community. This is most often for explanatory purposes at project presentations and are created with high levels of fidelity and workmanship [28]. However, there are instances where scale models can be used as a tool in a participatory design process, where models enable an exchange of ideas between laypeople, and designers. These are created with low-fidelity means and low levels of workmanship.

The term mock-up is also a term that is used commonly in the field to refer to a full-scale model, similar to a proof-of-process model. In their book on the topic, Burry and Burry acknowledge that in architecture, there is overlap in the use of the terms 'prototype' (in this case, a proof-of-process prototype) and 'mock-up', but add that level of fidelity can be used to further categorise mock-ups [29]. Naboni suggests that mock-ups enable a wide range of stakeholders to comprehend issues relating to building, in better ways than digital renderings, drawings, or 3D models are able to [30].

Özsel Akipek and Kozikoğlu offer a way to classify prototypes produced in a contemporary architectural education setting — in the digital era — as; Material, Conceptual, or Digital (Figure 2) [31]. They differentiate their model from Ullman's (Table 1), arguing that it concentrates mainly on process validation, and neglects the potential for the prototype to act as an ideator in a generative design process. Within their model, 'Material' prototypes are physical embodiments of a given complex system that is

being designed. The prototyping process serves to actualise the system, subject it to forces found in a materialised reality, and analyse the results. 'Conceptual' prototypes are seen to be diagrams of the input datasets, and their abstractions, that influence the design of a given complex system. The purpose of these prototypes is to act as a schematic for the entire system, such that it can be communicated and refined as a design tool. 'Digital' prototypes are vessels for design, where the tools of a chosen software are used by the designer to experiment and refine a given complex system. The nature of digital prototypes allows a range of design inputs, and serves to also introduce the student to computational design and programming concepts, through engaging with the interface. Özsel Akipek and Kozikoğlu's model offers a framework for designers to prototype an idea from concept, through to physical embodiement.

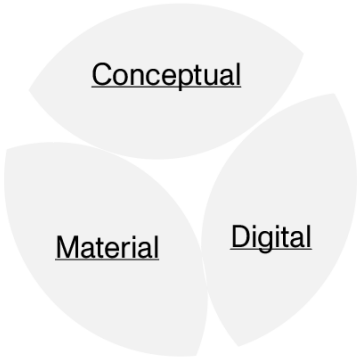


Figure 2. Özsel Akipek and Kozikoğlu's model of prototyping [31].

The advent of Building Information Modeling and computational design tools has enabled architects to undertake virtual prototyping more easily. A virtual prototype refers to a digital model that has been created using 3D modelling software, that is used for presentation, testing, or simulation purposes, and can be displayed in a variety of means [32], [33]. Tools like Ladybug for Grasshopper enable designers to simulate a number of environmental considerations relating to daylighting and climate [34]. When paired with powerful optimisation algorithms, many design iterations can be simulated and evaluated quickly, in ways physical models could never be used [35]. Virtual prototyping may be favoured over physical prototyping as they can be created with fewer resources, and in less time [36]. The underlying geometry used to virtual prototypes can be used across multiple testing environments in ways that physical prototypes cannot.

3.2. Engineering

Before the advent of computers, scale models were also used as important tools by engineers as part of the building design process, especially on projects possessing high design complexity. Addis defines four kinds of structural scale models that developed during the twentieth century by engineers;

- form-finding models that used by structural engineers as a method to arrive at a viable structural form and communicate its viability;
- small low fidelity elastic models made from homogenous materials for initial testing purposes;
- high fidelity strength models made at larger scale to yield more accurate test results; and,
- large low fidelity models for wind effects testing [37].

Azagra and Hay propose an alternative framework to categorise the use of scale models by engineers that concentrates mainly on the purpose of the model; conceptual models are created to explore design

ideas, form-finding models are used to determine a structure's shape according to predefined parameters, and experimental scale models are made to gather quantitative data about structural performance [38]. embodiement. This is similar to Ullman's prototyping model in that each component is linkeed to a stage of the design process

Virtual prototypes gained prominence as computers began to be utilised to perform structural analyses, and also began to be used in combination with experimental models [37]. As this endeavour became more expensive, virtual models superseded the use of the physical experimental model. The advent of software packages like Kangaroo and Karamba3D for the Rhino/Grasshopper environment provided designers with more instantaneous feedback than the real-word form-finding model [39], [40]. However, as these models can be time-consuming to create, conceptual scale models continue to be used in early project stages as a way to provide haptic feedback to the engineer [38]. While the use of virtual prototyping has become more prevalent in recent years, they cannot fully replicate their physical counterparts. For example, despite advances in computational fluid dynamics that has enabled the virtual simulation of the effect of wind on buildings and their surrounding context, physical prototypes are still used alongside them to counter a range of limitations [41].

3.3. Prototyping in construction research

There is a noticeable research gap in the prototyping cultures of those working in the construction trades. Gopinath & Messner suggest that the creation of prototypes can be used as a tool for; visualisation, identification of constructability issues, obtaining acceptance of design detail, and physical testing of specific products or systems [36]. Elvin notes the potential for onsite prototyping to act as an ideation tool, and to further foster direct communication and shared understanding across the wider project team [42].

The construction industry has been considered a low technology sector and has struggled to adopt digital technology [43]. This has hindered the amount of virtual prototyping occurring in construction. Sarshar and Christiansson also suggest that barriers to implementing virtual prototyping in construction relate to: culture and risk in information sharing, and a lack of pilot research projects [44]. Despite this lack of technology uptake, construction process (or 4D) planning has developed to enable practitioners to visualise drawings, and plan processes accordingly [45], [46].

Despite the research gaps that exist in academia concerning construction prototyping, there has been a recent increase in industry interest towards developing its culture of prototyping [47]. International engineering and construction company Laing O'Rourke have been utilising extensive prototyping to develop a system to 3D print complex concrete formwork at scale [48]. Vaz-Serra et al detailed a collaboration with an industry partner to produce a bathroom 'wet' wall for use in high rise construction, based on modular and design for manufacture and assembly (DfMA) principles and used prototyping as part of the development process [49].

4. Discussion

As shown in the literature and example cases above, prototyping is used as a tool in the design process by architectural designers and engineers to explore and refine conceptual ideas or aesthetic issues. It is also used to communicate these factors to internal and external stakeholders. This use of prototyping enables richer design outcomes to be realised that helps to increase the value of the built outcome. Prototyping can be used by project teams to test construction tectonics or building systems that serve to validate design decisions and resolve detail issues before construction commences. This minimises future time spent on site resolving issues at a time when many design decisions may already be locked-in. This enables buildings to be created more efficiently — in less time, or with fewer materials. The current purpose of prototyping in the built environment is aimed towards serving the needs of each specific field. While the fields mentioned above demonstrate that prototypes can add value to the built

outcome, the siloed nature of their prototyping prohibits knowledge from being shared with the wider team. Pietroforte et al. highlight that more integrated prototyping can play a social role in connecting projects teams; to help designers understand construction realities, and communicate design intent to tradespeople [50]. Integrated prototyping could be an enabler for DfMA in construction that shows promising benefits [51].

The goal of using prototyping in the built environment is to ultimately create better buildings that offer more output, from less input. However, design is the vessel through which data collected from the prototyping process flows. Each building created by a designer can be seen as a prototype to improve their design process, with the knowledge generated being utilised across future projects.

There are multiple terms for prototyping-like activities that are used within the built environment such as scale model, and mock-up. While there could be benefit gained from proposing a single system of definitions for all stakeholders to use, the chance of take-up is low because each term is ingrained into the profession that utilises them. What is of more use to built environment practitioners, is to communicate the range of benefits that possessing a strong prototyping culture affords — that this paper has done through using design value — and to propose techniques that enable stakeholders to get the most out of prototyping. The model of prototyping proposed by Houde and Hill (Figure 1) encourages users to formulate their design issues into questions that fall into three initial classes that culminate to a single Integration class. There is a slight similarity to the model proposed by Özsel Akipek and Kozikoğlu in that both models can be used to conceptualise the prototyping process. Both these models aren't directly applicable to the prototyping needs of built environment practitioners, however they would benefit from following a similar process. Practitioners should structure the issue to be prototyped as a question that needs to be answered, which will guide further decisions relating to the configuration of the prototype. Using such an approach helps to streamline prototyping endeavours to concentrate the scope to avoid unnecessary expenditures of time or money.

5. Conclusion



Figure 3. Potential conceptual approach to prototyping in the built environement.

This paper has reviewed literature in three industries about influential uses of prototyping. Future research work could expand on the number of industries analysed to develop a more comprehensive understanding about the use of prototyping. The findings of this paper has shown that prototyping is utilised in the built environment to varying amounts by different practitioners. The critical review of literature from other industries suggests the existence of research gaps concerning the comprehension of the use of prototyping in the sector as a whole. It is particularly pertinent to understand the use of prototyping activities by the construction trades. Future research activities could be used to quantify the use of prototyping by different practitioners in the built environment and understand their methods more deeply. The literature review also revealed two approaches to prototyping used by other industries as relating to; idea conceptualisation, and physical implementation, that are influenced by the main form of output of each respective field. As both approaches are required to create outcomes in the built environment (Figure 3), an approach to prototyping that accounts for this unique factor would be useful to encourage a more integrated approach. A quantitative study about built environment prototyping could also inform the development of an integrated model for prototyping that accounts for design conceptualisation, and implementation. Such a model could be tested on a subsequent pilot project to assess its validity.

References

[1] R. Vrijhoef and L. Koskela, "Revisiting the Three Peculiarities of Production in Construction," p. 10, 2005.

[2] A. H. Memon, I. A. Rahman, and A. A. A. Azis, "Preliminary Study on Causative Factors Leading to Construction Cost Overrun," *Int. J. Sustain. Constr. Eng. Technol.*, vol. 2, no. 1, Art. no. 1, Jul. 2011, Accessed: Apr. 05, 2023. [Online]. Available: https://publisher.uthm.edu.my/ojs/index.php/IJSCET/article/view/49

[3] R. Whitehead, *Model Behavior: The Evolving Use of Physical Prototypes in Structural Shell Design, 1959-1974*. 2016. Accessed: Apr. 06, 2023. [Online]. Available: https://www.acsa-arch.org/chapter/model-behavior-the-evolvinguse-of-physical-prototypes-instructural-shell-design-1959-1974/

[4] C. W. Elverum, T. Welo, and S. Tronvoll, "Prototyping in New Product Development: Strategy Considerations," *Procedia CIRP*, vol. 50, pp. 117–122, Jan. 2016, doi: 10.1016/j.procir.2016.05.010.

[5] "Definition of PROTOTYPE," Mar. 13, 2023. https://www.merriam-webster.com/dictionary/prototype (accessed Mar. 25, 2023).

[6] D. Droz, "Prototyping: A Key to Managing Product Development," *J. Bus. Strategy*, vol. 13, no. 3, pp. 34–38, Jan. 1992, doi: 10.1108/eb039491.

[7] S. Houde and C. Hill, "What do prototypes prototype?," in *Handbook of human-computer interaction*, Elsevier, 1997, pp. 367–381.

[8] S. Abdullah and R. Marasini, "An Analysis Of The Applications Of Rapid Prototyping In Architecture".

[9] R. Beach, M. Webster, and K. M. Campbell, "An evaluation of partnership development in the construction industry," *Int. J. Proj. Manag.*, vol. 23, no. 8, pp. 611–621, Nov. 2005, doi: 10.1016/j.ijproman.2005.04.001.

[10] C. Lauff, D. Kotys-Schwartz, and M. Rentschler, "What is a Prototype? What are the Roles of Prototypes in Companies?," *J. Mech. Des.*, vol. 140, Feb. 2018, doi: 10.1115/1.4039340.

[11] D. G. Ullman, *The mechanical design process: product discovery, project planning, product definition, conceptual design, product development, product support*, 4th Ed. Boston: McGraw-Hill, 2010.

[12] G. I. Horton and D. F. Radcliffe, "Nature of rapid proof-of-concept prototyping," *J. Engeering Des.*, vol. 6, no. 1, pp. 3–16, 1995.

[13] C. Elverum and T. Welo, "Leveraging prototypes to generate value in the concept-to-production process: a qualitative study of the automotive industry," *Int. J. Prod. Res.*, vol. 54, Feb. 2016, doi: 10.1080/00207543.2016.1152406.

[14] F. W. Liou, *Rapid Prototyping and Engineering Applications: A Toolbox for Prototype Development*. Boca Raton: CRC Press, 2007. doi: 10.1201/9781420014105.

[15] A. Pretschner, H. Lotzbeyer, and J. Philipps, "Model based testing in evolutionary software development," in *Proceedings 12th International Workshop on Rapid System Prototyping. RSP 2001*, Monterey, CA, USA, 2001, pp. 155–160. doi: 10.1109/IWRSP.2001.933854.

[16] C. Floyd, "A Systematic Look at Prototyping," in *Approaches to Prototyping*, Berlin, Heidelberg, 1984, pp. 1–18. doi: 10.1007/978-3-642-69796-8_1.

[17] R. Budde, K. Kautz, K. Kuhlenkamp, and H. Züllighoven, "What is prototyping?," *Inf. Technol. People*, vol. 6, no. 2/3, pp. 89–95, Jan. 1992, doi: 10.1108/EUM0000000003546.

[18] W. R. Bischofberger and G. Pomberger, *Prototyping-Oriented Software Development: Concepts and Tools*. Springer Science & Business Media, 2012.

[19] M. Beaudouin-Lafon and W. E. Mackay, "Prototyping tools and techniques," in *Human-Computer Interaction*, CRC Press, 2009, pp. 137–160.

[20] S. Camere, M. Bordegoni, and others, "A lens on future products: An expanded notion of prototyping practice," in *DS 84: Proceedings of the DESIGN 2016 14th international design conference*, 2016, pp. 155–164.

[21] K. Best, *Design Management: Managing Design Strategy, Process and Implementation*. AVA Publishing, 2006.

[22] T. Kelley, "Prototyping is the shorthand of innovation," *Des. Manag. J. Former Ser.*, vol. 12, no. 3, pp. 35–42, Jun. 2010, doi: 10.1111/j.1948-7169.2001.tb00551.x.

[23] C. Acklin, "Design Management Absorption Model: A Framework to Describe and Measure the Absorption Process of Design Knowledge by SMEs with Little or no Prior Design Experience: Design Management Absorption Model," *Creat. Innov. Manag.*, vol. 22, no. 2, pp. 147–160, Jun. 2013, doi: 10.1111/caim.12022.

[24] J.-H. Ock, "Testing as-built quality of free-form panels: Lessons learned from a case study and mock-up panel tests," *Appl. Sci.*, vol. 11, no. 4, p. 1439, 2021.

[25] N. Dunn, *Architectural Modelmaking Second Edition*. Hachette UK, 2014.

[26] M. E. Giacaglia, A. H. Lara, and N. C. da S. Moura, "Digital manufacturing terminology in the product and the construction industries," *Arquitetura Rev.*, vol. 7, no. 2, pp. 172–181, Dec. 2011, doi: 10.4013/arq.2011.72.07.

[27] A. Smith, *Architectural Model as Machine*. Routledge, 2007.

[28] I. Gibson, T. Kvan, and L. Wai Ming, "Rapid prototyping for architectural models," *Rapid Prototyp. J.*, vol. 8, no. 2, pp. 91–95, Jan. 2002, doi: 10.1108/13552540210420961.

[29] M. Burry, "Rapid prototyping, CAD/CAM and human factors," *Autom. Constr.*, vol. 11, no. 3, pp. 313–333, Apr. 2002, doi: 10.1016/S0926-5805(00)00107-2.

[30] E. Naboni, "The Use of Facade Mockups in LCA Based Architectural Design," *Procedia Eng.*, vol. 180, pp. 759–766, 2017, doi: 10.1016/j.proeng.2017.04.236.

[31] F. Özsel Akipek and N. Kozikoğlu, "Prototypes in Architectural Education: As Instruments of Integration in the Digital Era," *Mimarlık Eğitiminde Prototipler: Sayısal Çağ İle Bütünleşik Bir Yaklaşımın Temel Araçları*, Jun. 2007, Accessed: Mar. 17, 2023. [Online]. Available: https://open.metu.edu.tr/handle/11511/51042

[32] G. G. Wang, "Definition and Review of Virtual Prototyping," *J. Comput. Inf. Sci. Eng.*, vol. 2, no. 3, pp. 232–236, Sep. 2002, doi: 10.1115/1.1526508.

[33] S. Kalpakjian, *Manufacturing engineering and technology*, 2nd ed. Reading, Mass.: Addison-Wesley Pub. Co., 1992.

[34] M. Sadeghipour Roudsari, M. Pak, and A. Viola, "Ladybug: A Parametric Environmental Plugin For Grasshopper To Help Designers Create An Environmentally-conscious Design," presented at the 2017 Building Simulation Conference, Aug. 2013. doi: 10.26868/25222708.2013.2499.

[35] T. Wortmann, "Model-based Optimization for Architectural Design—Optimizing Daylight and Glare in Grasshopper," *Technol. Des.*, vol. 1, pp. 176–185, Nov. 2017, doi: 10.1080/24751448.2017.1354615.

[36] R. Gopinath and J. Messner, "Applying immersive virtual facility prototyping in the AEC industry," Jan. 2004.

[37] B. Addis, "'Toys that save millions' - A history of using physical models in structural design," *Struct. Eng.*, vol. 91, pp. 12–27, Apr. 2013.

[38] D. Azagra and T. Hay, "A case for physical models," *Struct. Eng. Lond. Engl. 1988*, vol. 90, no. 9, pp. 14–20, 2012.

[39] D. Piker, "Kangaroo: Form Finding with Computational Physics," *Archit. Des.*, vol. 83, no. 2, pp. 136–137, 2013, doi: 10.1002/ad.1569.

[40] C. Preisinger and M. Heimrath, "Karamba—A Toolkit for Parametric Structural Design," *Struct. Eng. Int.*, vol. 24, no. 2, pp. 217–221, May 2014, doi: 10.2749/101686614X13830790993483.

[41] D. A. Phillips and M. J. Soligo, "Will CFD ever Replace Wind Tunnels for Building Wind Simulations?," *Int. J. High-Rise Build.*, vol. 8, no. 2, pp. 107–116, Jun. 2019, doi: 10.21022/IJHRB.2019.8.2.107.

[42] G. Elvin, "Proven Practices in Design-Build and Fast-Track," pp. 1–8, May 2012, doi: 10.1061/40699(2003)33.

[43] T. Chowdhury, J. Adafin, and S. Wilkinson, "Review of digital technologies to improve productivity of New Zealand construction industry," *J. Inf. Technol. Constr.*, vol. 24, no. 2019VMAR, pp. 569–587, 2019, doi: 10.36680/j.itcon.2019.032.

[44] M. Sarshar and P. Christiansson, "TOWARDS VIRTUAL PROTOTYPING IN THE CONSTRUCTION INDUSTRY: THE CASE STUDY OF THE DIVERCITY PROJECT".

[45] T. Huang, C. W. Kong, H. L. Guo, A. Baldwin, and H. Li, "A virtual prototyping system for simulating construction processes," *Autom. Constr.*, vol. 16, no. 5, pp. 576–585, Aug. 2007, doi: 10.1016/j.autcon.2006.09.007.

[46] K. W. Chau, M. Anson, and J. P. Zhang, "4D dynamic construction management and visualization software: 1. Development," *Autom. Constr.*, vol. 14, no. 4, pp. 512–524, Aug. 2005, doi: 10.1016/j.autcon.2004.11.002.

[47] F. Barbosa, J. Woetzel, and J. Mischke, "Reinventing construction: A route of higher productivity," McKinsey Global Institute, 2017.

[48] J. B. Gardiner, S. Janssen, and N. Kirchner, "A Realisation of a Construction Scale Robotic System for 3D Printing of Complex Formwork," *Autom. Robot.*, 2016.

[49] P. Vaz-Serra, M. Wasim, and S. Egglestone, "Design for manufacture and assembly: A case study for a prefabricated bathroom wet wall panel," *J. Build. Eng.*, vol. 44, p. 102849, Dec. 2021, doi: 10.1016/j.jobe.2021.102849.

[50] R. Pietroforte, P. Tombesi, and D. D. Lebiedz, "Are Physical Mock-Ups Still Necessary to Complement Visual Models for the Realization of Design Intents?," *J. Archit. Eng.*, vol. 18, no. 1, pp. 34–41, Mar. 2012, doi: 10.1061/(ASCE)AE.1943-5568.0000060.

[51] S. Gao, R. Jin, and W. Lu, "Design for manufacture and assembly in construction: a review," *Build. Res. Inf.*, vol. 48, no. 5, pp. 538–550, Sep. 2019, doi: 10.1080/09613218.2019.1660608.

IASS 2023
July 10–14 Melbourne
Integration of Design and Fabrication

Proceedings of the IASS Annual Symposium 2023
Integration of Design and Fabrication
10–14 July 2023, Melbourne, Australia
Y.M. Xie, J. Burry, T.U. Lee and J. Ma (eds.)

CFD investigation of snow drifting on long-span dome roofs

Qingwen ZHANG[*,a,b], Guolong ZHANG[a,b], Feng FAN[a,b]

[*] School of Civil Engineering, Harbin Institute of Technology, Harbin, 150090, China
No.73 Huanghe Road, Harbin, China
zhangqw@hit.edu.cn

[a] Key Lab of Structures Dynamic Behavior and Control of the Ministry of Education, Harbin Institute of Technology, Harbin, 150090, China
[b] Key Lab of Smart Prevention and Mitigation of Civil Engineering Disasters of the Ministry of Industry and Information Technology, Harbin Institute of Technology, Harbin, 150090, China

Abstract

Under specific conditions of snowfall and wind, a large amount of snowdrift forms on buildings. At the worst, a significant amount of snowdrift will result in building collapse or cracking because of the unbalanced snow loads. This study aims to provide a new numerical approach, and apply it to the investigation of snowdrift development on a long-span dome roof. Firstly, the CFD prediction accuracy for snowdrifts was confirmed by comparing simulated results with field measurements. Then, the roof snow distribution characteristics on a long-span dome roof was predicted for different inflow wind velocities and roof spans. It is found that the uneven distribution of roof snow is weakened with the decreasing wind velocity and the increasing roof span.

Keywords: snowdrift, snow load, non-equilibrium, dome roof, inflow velocity, roof span

1. Introduction

Under specific conditions of snowfall and wind, a large amount of snowdrift forms on and around buildings. Snow blown by incoming flow on the windward side of an obstacle will accumulate in the regions around the obstacle, where the wind velocity is sufficiently low allowing snow to settle out and form a drift. Therefore, snowdrift is formed as the result of complicated interaction between snow particle motion and flow field affected by building geometry. At the worst, a significant amount of snowdrift will result in building collapse or cracking because of unbalanced snow loads and over-hanging snow on roofs [1]. Therefore, to develop suitable measures for handling difficulties and hazards due to snow in built-up environments, it is necessary to predict the spatial distribution of snowdrifts on and around buildings with high accuracy. Of all the methods, field measurements and experiments have been regarded as the most reliable approaches to deal with the complex interaction. However, their applicabilities are limited to specific weather conditions and similarity criterion, respectively. Fortunately, computational fluid dynamics (CFD) has been applied to simulate snowdrift around buildings recently, based on the dramatic increases in computational power together with advances in computer software [2].

The CFD method has been studied in the field of the applicability of turbulence models to a flow around a bluff body and in the field of the simulation of snowdrift process since 1990s. Much studies have focused on the aeolian sediment transport in a boundary layer flow developed on a flat terrain and snowdrifts around buildings. However, in the prediction of snow loads on building roofs, unbalanced snow accumulation due to wind flow is a difficult problem because it involves a complex interaction between snow particle motions and fluid flow affected by roof configurations [2]. So far, only a few

Copyright © 2022 by Qingwen ZHANG, Guolong ZHANG and Feng FAN. Published in the Proceedings of the IASS Annual Symposium 2023 with permission.

attempts have been made to apply CFD to roof snow issues. Thiis et al. [3,4] predicted the snow distribution on the curved roof of a sports hall located in Oslo and compared the results with field measurements. Generally, the simulated snow distribution pattern fit the measured shape well. Tominaga et al. [5] studied the CFD prediction of snowdrifts on a gable roofed building with different slopes. In the study, the predicted drift coefficients for different inflow velocities were compared against a series of observational results [6]. The simulation results generally corresponded well with the observational data for the exposed roof. Recently, Zhou et al. [7] proposed a quasi-steady method to simulate the redistribution of snow on a flat-roof building. In this method, the process of snow drifting was divided into several phases according to the characteristics of meteorological data. In each phase, the erosion or deposition of snow was regarded to occur in steady state. The snow redistributions obtained from the numerical simulation agreed well with those obtained in the wind tunnel tests.

It should be noted that the concepts and parameters used in the past snowdrift modeling have been mostly derived empirically from observations or experiments. Many of the observations and experiments were conducted based on a simple drifting boundary layer developed on a flat plane. For example, an estimation model for the transport rate of drifting snow attributable to saltation proposed by Pomeroy and Gray [8] has often been used in many previous CFD studies. The constant in the model was determined by the observation in a drifting boundary layer. Therefore, the proposed relation gives a saturated transport rate of drifting snow based on the assumption that drifting snow in the saltation layer has reached its equilibrium state, where neither wind velocity nor changes in the streamwise direction. However, Okaze et al. [9,10] investigated the change in the spatial distribution of for non-equilibrium flow in a developing saltation layer and its relationship with wind velocity by conducting a wind tunnel experiment using actual snow particles. Through comparison, the values obtained from Pomeroy's relation are greatly overestimated in almost the entire region. Thus, it is problematic to apply Pomeroy's relation (which is based on the equilibrium condition) to a flow around a building in which drifting snow is in non-equilibrium state because of acceleration and deceleration. It is necessary to further consider the applicability and validity of the modeling of the saltating process at the developing stage (non-equilibrium state). Tominaga et al. [11] lately proposed a new approach to account for the developing process of drifting snow with a one-way coupled drifting snow density transport equation, instead of the empirical saltation flux relationship. The new approach made some improvement, but some substantial deviations remained from experimental measurements. It was partly caused by the fact that the effect of snow particles on flow field and the increasing drifting snow density induced by building blocking were not fully considered, as the snow phase was simply treated as a scalar variable.

To fully account for the interaction between snow particle motion and fluid flow as well as the drifting snow density at a developing stage, a two-way coupled two-phase model was developed and adopted for the simulation of snowdrift development on a long-span roof. Besides properly accounting for two-way coupling of air and snow phases, this CFD model is free from all equilibrium assumptions used in the past approaches introduced above. In this study, the prediction accuracy of CFD on the snowdrift by comparing simulation results with field measurement results for a step roof was confirmed firstly. Next, the proposed snowdrift model was applied to predict snow distribution on the dome roofs. For this application, the snow load requirements of the ISO4355 ‘Basis for design of structures – Determination of snow loads on roofs’ [12] was compared with the simulated results. Finally, the snowdrift characteristics for different inflow velocities and roof spans were discussed.

2. CFD model for drifting snow

2.1. Governing equations

The air-snow flow is simulated by using the Mixture model in ANSYS FLUENT. The Mixture model equations consist of the continuity and momentum equations for the mixture phase, the continuity equation for the snow phase and the algebraic equation for the slip velocity between air and snow phases. Specifically, the transport equations for the air-snow mixture phase are given by.

$$\frac{\partial \rho_{\mathrm{m}}}{\partial t}+\nabla\cdot\left(\rho_{\mathrm{m}}\mathbf{u}_{\mathrm{m}}\right)=0 \tag{1}$$

$$\frac{\partial}{\partial t}\left(\rho_{\mathrm{m}}\mathbf{u}_{\mathrm{m}}\right)+\nabla\cdot\left(\rho_{\mathrm{m}}\mathbf{u}_{\mathrm{m}}\mathbf{u}_{\mathrm{m}}\right)=-\nabla p_{\mathrm{m}}+\nabla\cdot\left[\rho_{\mathrm{m}}c_{\mathrm{s}}\left(1-c_{\mathrm{s}}\right)\mathbf{u}_{\mathrm{as}}\mathbf{u}_{\mathrm{as}}\right]+\nabla\cdot\boldsymbol{\tau}_{\mathrm{Gm}}+\rho_{\mathrm{m}}\mathbf{g} \tag{2}$$

where, the subscripts "m", "a", "s" represent mixture, air and snow phases, respectively; $\boldsymbol{\tau}_{\mathrm{Gm}}$ is a generalized shear stress tensor, which is calculated according to Eq.(3); c_{s} is the mass fraction of snow phase; $\mathbf{u}_{\mathrm{as}}$ is the slip velocity vector between air and snow phases; ρ_{m} is the mixture density; $\mathbf{u}_{\mathrm{m}}$ is the mixture velocity vector; μ_{m} is the mixture viscosity.

$$\boldsymbol{\tau}_{\mathrm{Gm}}=\left(\mu_{\mathrm{m}}+\mu_{\mathrm{Tm}}\right)\left[\nabla\mathbf{u}_{\mathrm{m}}+\left(\nabla\mathbf{u}_{\mathrm{m}}\right)^{T}\right]-\frac{2}{3}\rho_{\mathrm{m}}k_{\mathrm{m}}\mathbf{I} \tag{3}$$

The snow volume fraction f_{s} is derived by solving the continuity equation for the snow phase, as shown in Eq.(4), where D_{Mp} is the diffusion constant. The third term on the left-hand side accounts for the slip between air and snow phases. Furthermore, based on the force balance and a local equilibrium assumption, the algebraic equation for the slip velocity $\mathbf{u}_{\mathrm{as}}$ is derived, as shown in Eq.(5).

$$\frac{\partial f_{\mathrm{s}}}{\partial t}+\nabla\cdot\left(f_{\mathrm{s}}\mathbf{u}_{\mathrm{m}}\right)+\nabla\cdot\left[f_{\mathrm{s}}\left(1-c_{\mathrm{s}}\right)\mathbf{u}_{\mathrm{as}}\right]=D_{\mathrm{Mp}}\cdot\nabla f_{\mathrm{s}} \tag{4}$$

$$\mathbf{u}_{\mathrm{as}}=\frac{t_{\mathrm{s}}}{f_{\mathrm{drag}}}\frac{\left(\rho_{\mathrm{s}}-\rho_{\mathrm{m}}\right)}{\rho_{\mathrm{s}}}\left[\mathbf{g}-\left(\mathbf{u}_{\mathrm{m}}\cdot\nabla\right)\mathbf{u}_{\mathrm{m}}-\frac{\partial\mathbf{u}_{\mathrm{m}}}{\partial t}\right] \tag{5}$$

In Eq.(5), t_{s} is the relaxation time of a particle; f_{drag} is the drag function, taken from Schiller and Naumann [13]; d_{s} is the diameter of snow particle; $\mathbf{g}$ is the gravitational acceleration. The k-ε turbulence model is applied to solve the flow turbulence quantities and turbulent viscosity for the mixture phase.

2.2. Treatment of deposition and erosion

The first grid adjacent to the snow surface is selected as a Control Volume (hereafter, CV) for evaluating the balance of snow concentration and calculating the total deposition. The total deposition flux q_{total} on the bottom surface of the CV is given by:

$$q_{\mathrm{total}}=q_{\mathrm{dep}}+q_{\mathrm{ero}} \tag{6}$$

Snow deposition per unit of time and unit of area q_{dep} is expressed as Eq.(7). Here, w_{f} is the snowfall velocity; Φ is the drifting snow density at the first grid adjacent to the snow surface, which is calculated as the product of the snow density ρ_{s} and snow volume fraction f_{s}.

$$q_{\mathrm{dep}}=-\Phi w_{\mathrm{f}}=-\rho_{\mathrm{s}}f_{\mathrm{s}}w_{\mathrm{f}} \tag{7}$$

Erosion flux q_{ero}, caused by the shear stress at the snow surface, is given by Eq.(8). This follows the expression, proposed by Anderson and Haff [14]. Here, c_{a} is a constant; u^{*} is the friction velocity; u^{*}_{t} is the threshold friction velocity.

$$q_{\mathrm{ero}}=\begin{cases}-c_{\mathrm{a}}\rho_{\mathrm{s}}u^{*}\left(1-\dfrac{u_{\mathrm{t}}^{*2}}{u^{*2}}\right) & for\ \ u^{*}>u_{\mathrm{t}}^{*}\\ 0 & for\ \ u^{*}\le u_{\mathrm{t}}^{*}\end{cases} \tag{8}$$

In this analysis, the total deposition mass q_{total} is incorporated into Eq.(4) as the source term to consider the snow concentration change within the saltation layer.

3. Validation of CFD model

3.1. Prototype

In order to validate the accuracy of the proposed snowdrift model, a field measurement of the snowdrift on a two-level step building model carried out by the authors was adopted as the analyzed flow field. The field measurements were carried out on an open flat base within the campus of Harbin Institute of Technology (HIT), Harbin, China. The prevailing wind experienced in this area was from south during winter, which was well suited for the measurements of snowdrifts. In previous researches of snowdrifts around buildings, the small precipitation condition was usually selected to only investigate the effects of wind flow on particle motion over the snow surface [15]. However, high precipitation condition shows a more complicated transport process in the case of the snowdrift formation on building roofs, as the source of snow on the roof is mainly limited to the precipitation and complex flow field around buildings seriously affects the transport of falling snow particles. Therefore, measurements were only carried out with high precipitation.

Before the snowstorm, a two-level step building model was placed on the measurement site with its lower edge facing against the prevailing wind, as shown in Figure 1. The dimension of the higher-level part was 1000 (x)×3000 (y)×1000 (z) mm, while the size of the lower-level part was 1500 (x)×3000 (y)×500 (z) mm. The wind profile was measured with three cup type anemometers, mounted on a 3 m mast and positioned 0.5, 1.0 and 3.0 m above the ground surface. The sampling interval was 10 minutes. Air temperature and humidity were measured by a PC-4 weather station, with an accuracy of 0.1 °C and 0.1 %. To measure the snow distribution on the building, a snow scale gauge was used to obtain the snow depth at each measuring point. Thereafter, the snow surface was generated using spatial interpolation. After each set of measurement, the remaining snow on the field was removed for the next set of measurement. Here, the snowfall event that occurred on 28th December 2018 was selected as the prototype to validate the snowdrift model. During the whole observational period, the mean wind velocity was approximately 1.1 m/s at 1.0 m height, and the snowfall volume fraction was 6×10^{-7}.

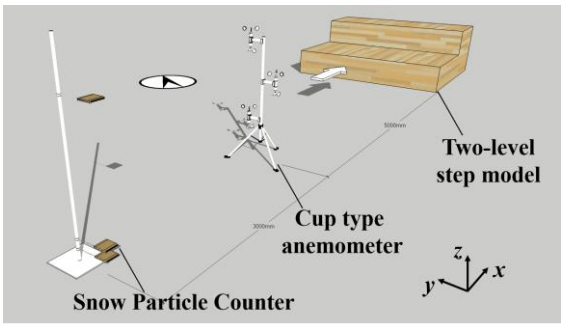


Figure 1: Schematic view of the field measurement site

3.2. Computational conditions

The computational domain and boundary conditions are summarized in Figure 2. The whole domain covers 14L (x-axis)×11B (y-axis)×6B (z-axis), where L represents the overall length of the two-level step model (2.5 m) and B represents the overall width of the two-level step model (3.0 m). Each side of the domain is assigned 201(x-axis), 172(y-axis) and 100(z-axis) grids, with the minimum size being 0.01H. The height of the first grid adjacent to the ground h_p is set to be 0.01H (0.01m). The computational conditions follow the guidelines provided by AIJ [16]. The Realizable k-ε model was employed as the base model to calculate the eddy viscosity. The semi-implicit method for the pressure-linked equation (SIMPLE) algorithm was used for the pressure-velocity coupling. The Green-Gauss cell based scheme was used for gradient discretization. The advection terms were discretized using a QUICK scheme.

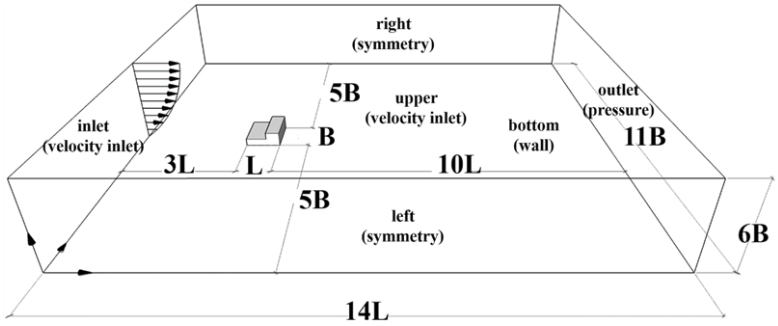
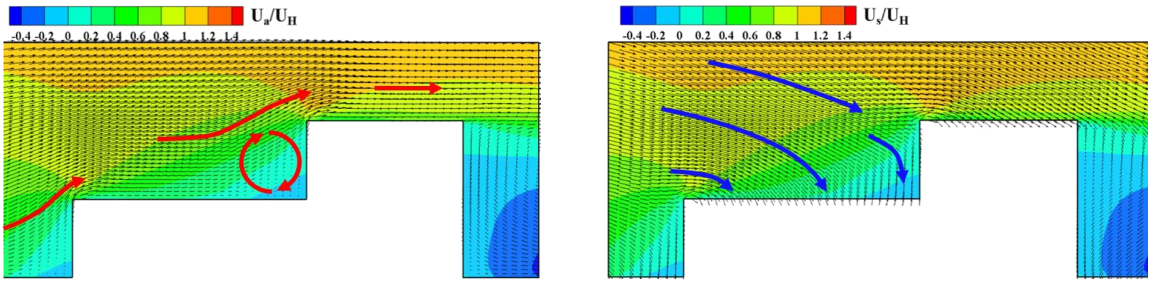


Figure 2: Computational domain and boundary conditions for the simulation of snowdrift on the two-level step building

3.3. Results and discussions

Figure 3 compares the vertical distributions of the streamwise velocities for air and snow phases, respectively. Obviously, the trajectory of air flow differs a lot from that for snow particles. The air flow moves upward and generates a strong separation flow from the end of the lower-level roof, forming an eddy current on the lower roof. Conversely, snow particles fall downward toward the building roof under the action of aerodynamic force and gravity. Figure 4 gives the spatial distribution of the drifting snow density Φ around the two-level step building. Due to the blocking of the high-level part, snow particles gather in large quantities at the windward edge of the high-level roof. High snow concentration leads to a peak value of snowdrifts formed right close to the foot of the high-level wall. Due the existence of upwind recirculation, a slight erosion is formed in front of the high-level wall. Generally, the snowdrift profiles obtained by the ratio of snow depths between the roof and open ground, shows good correspondence with the field measurements by comparison as shown in Figure 5.



(a) (b)

Figure 3: (a) Contours of dimensionless air streamwise velocity, (b) Contours of dimensionless snow streamwise velocity.

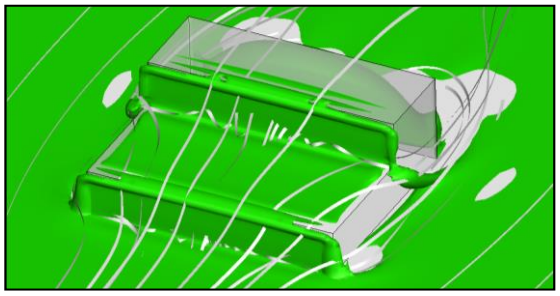


Figure 4: Iso-surface of drifting snow density Φ around the two-level step building

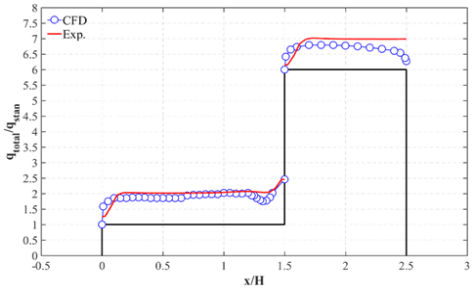


Figure 5: Comparison between normalized snow depths obtained from CFD results and field measurement along the streamwise direction (y/H=0)

4. Snowdrifts on dome roofs with various inflow velocities

4.1. Building configuration

Dome is a common roof shape for large-scale stadiums, exhibition halls, warehouses, etc. However, due to the light-weight roof structure, large roof area, complex building shape and other problems, it is extremely easy to cause snow-induced building collapse accidents. Therefore, It is very necessary to investigate the snow distribution characteristics on dome roofs in depth. Figure 6 provides a schematic view of the dome roofed building used in this study. An isolated dome roofed building, with an eave height (H_e) of 10 m and a span (L) of 50 m, was placed perpendicular to the approaching wind flow. The height of the dome roof (H_r) was 10 m with a rise-span ratio being 1:5.

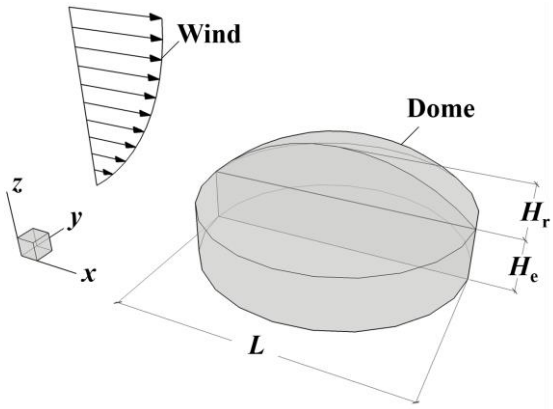


Figure 7: Schematic view of the dome roofed building

4.2. Computational conditions

The computational conditions used in this study were based on guidelines from the Architectural Institute of Japan (AIJ) [16]. The computational domain comprised a volume measuring 5L (x-axis)×5L (y-axis)×6(H_r+H_e) (z-axis). A power law profile with an index of 0.20 was assumed for inflow velocity; the profile for k was determined using a turbulent intensity equation proposed by the AIJ [18]. The ε values were determined from the local equilibrium assumption, P_k=ε. The mean wind velocity at the inflow boundary at the building height U_H was set to 2.0, 3.0, 4.0 and 5.0 m/s respectively to investigate the development of snowdrifts, referring to the requirements of snow distributions under various wind velocity conditions from AIJ guideline. The drifting snow density Φin at the inflow and top boundaries was given as a constant value by assuming that the standard snow depth, h^*, that resulted from snowfall

during the whole period of time. Here, the specific inflow snow volume fraction was set to 1.3×10^{-5}, referring to the snow disaster in Shenyang City, China in 2007. The parameters relating to the physical properties of snow were set as listed in Table 1.

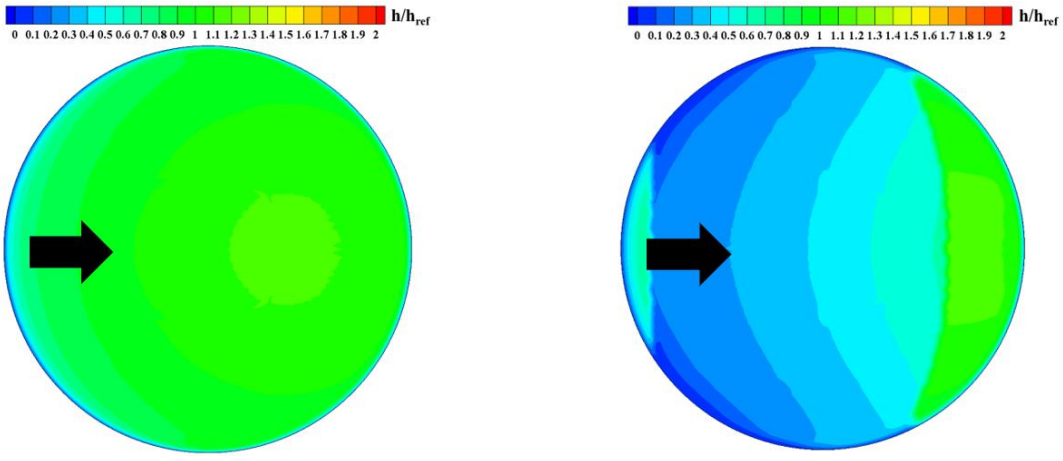
Table 1: Parameters relating to physical properties of snow

Threshold friction velocity u_t^*	0.2 m/s	Snowfall velocity w_f	-0.2 m/s
Snow paticle density ρ_s	250 kg/m^3	Diameter of snow particle d_s	5×10^{-4} m

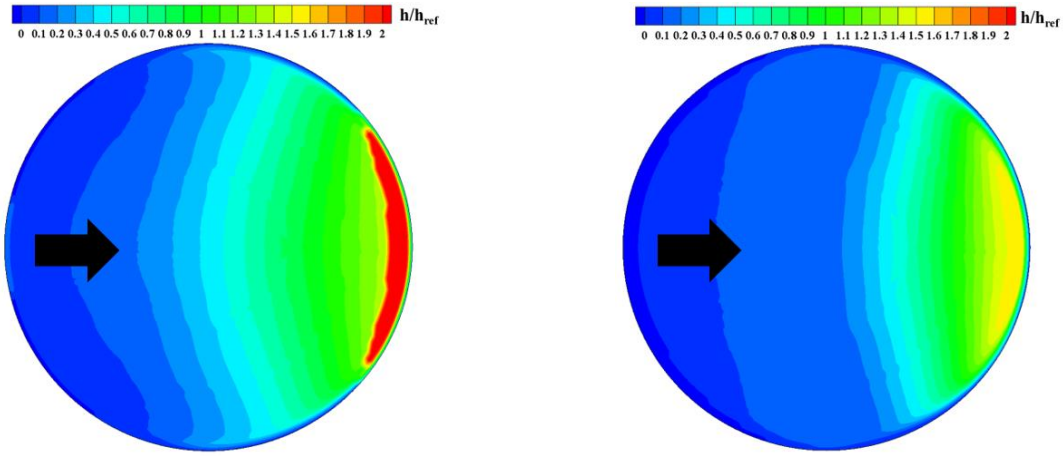
4.3. Results and discussions

Figure 8 indicates the contours of snow depth ratio q_{total}/q_{stan} on the dome roof for four different inflow velocities. The snow depth ratio was defined as the ratio between the total deposition flux q_{total} and the standard deposition flux q_{stan}. The standard deposition flux was calculated using the ground total deposition flux at a reference point, which was not affected by the building. For the case of lower inflow velocity (U_H=2 m/s), only very small undulations are observed due to the low friction velcotiy. No significant snow drifting occurs on the roof and the snow load on the dome is approximately evenly distributed. For U_H=3 m/s, erosion starts to occur in the windward area and extend in the lateal sides of the roof. However, a small accumulation of snow is formed on the windward eaves. For U_H=4 m/s, The windward erosion zone spreads further downstream and the deposition along the windward eave disappears. The uneven distribution of snow on the roof becomes more obvious, showing a half-span snow distribution pattern. For U_H>4 m/s, with more snow particles blown off the roof, the uneven distribution of snow on the roof begins to weaken, and the roof snow load turns to decrease.

In general, the snow load on the dome roof shows three kinds of distribution patterns, i.e., the full-span balanced distribution (U_H≤2 m/s), the half-span unbalanced distribution (U_H=4 m/s) and the transitional distribution between them (U_H=3 m/s). Snowdrift formed on the leeward side of the roof tends to increase with the increasing inflow velocity, when the inflow velocity is no more than 5m/s. Here, the inflow velocity (U_H=2 m/s) at which the snow distribution turns from uniform to non-uniform is defined as the lower critical inflow velocity, while the inflow velocity (U_H=5 m/s) at which the snow load turns from increasing to decreasing is defined as the upper critical inflow velocity. For this dome roofed building, the risking inflow velocity ranges from 2 m/s to 5 m/s, above which the snow load on the roof begins to decrease.



(a) (b)



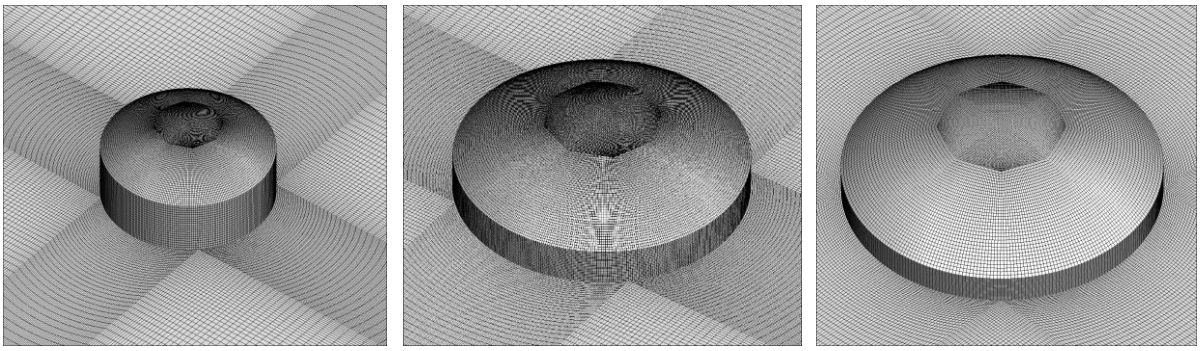
(c) (d)

Figure 8: Contours of normalized snow depth q_{total}/q_{stan} on the dome roof: (a) 2m/s; (b) 3m/s; (c) 4m/s; (d) 5m/s

5. Snowdrifts on dome roofs with various spans

5.1. Building configuration and computational conditions

In addition to the serious influence of inflow wind velocity on the snow distribution, O'Rourke and Auren [17] pointed out that the parameters of the roof shape, such as the roof slope, roof width, also have a significant impact on the drift size on roofs. Furthermore, the American Society of Civil Engineers (ASCE) [18] gave additional surcharges that extend downwind from the windward surface for some specified distance to account for the drifting snow load. Obviously, the roof snow load is not only related to the inflow conditions, but also related to the building dimensions. Considering that the dome roof is mostly applied to long-span structures, which are snow load sensitive, it is necessary to explore the size effect of the building roof on snowdrifts. Figure 9 provides a schematic view of the building model of different sizes used in this study. The same rise-span ratio of 1:5 and eave height (H_e) of 10 m were selected for all the buildings. The only difference is that the building model considers three different spans: 30 m, 70 m, and 110 m, respectively. Regarding computational conditions, The mean wind velocity at the inflow boundary at the building height U_H was set to 4.0 m/s, at which the snowdrift is obvious. Except for this, all the computational settings are the same as above.



(a) (b) (c)

Figure 9: Schematic view of building models with different spans: (a) 30m; (b) 70m; (c) 110m

5.2. Results and discussions

Fig. 10 indicates the contours of dimensionless snow depth ratio (q_{total}/q_{stan}) on the roof for different roof spans. Generally, erosion occurs in the windward area and extends along the lateal sides of the roof, while deposition is mainly formed in the leeward of the roof. However, with the increasing of roof span, too many snow particles accumulate on the roof to move downstream further under the same capacity of airflow to transport snow particles. Therefore, the uneven distribution of roof snow is weakened under the same inflow velocity condition. For example, the snow load on the dome roof shows a half-span unbalanced distribution when the span is 30 m, while it turns to become a full-span unbalanced snow load when the span expands to 110 m. As a result, for a long-span structure, a higher inflow wind velocity is required to achieve the same significantly uneven snow distribution pattern, that is, the upper critical inflow velocity at which the snow load turns from increasing to decreasing is higher, and the risking inflow velocity range will be wider. It should be noted at the structural design stage that the long-span roofs are more likely to experience the most adverse snow loads compared with the ordinary buildings.

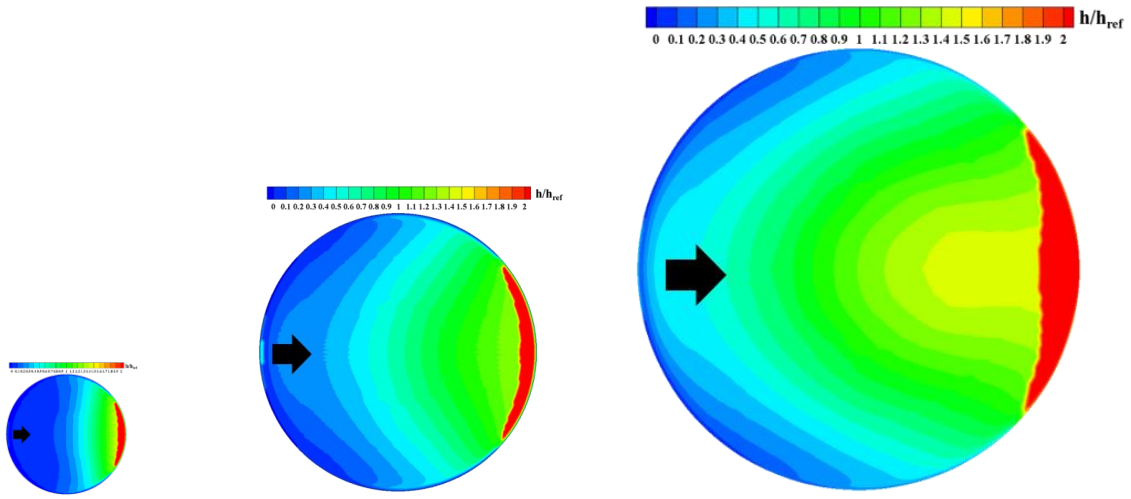


Figure 10: Contours of normalized snow depth q_{total}/q_{stan} on the dome roof: (a) 30m; (b) 70m; (c) 110m

6. Conclusion

This study proposed a new approach to account for the snowdrift in a non-equilibrium state. The simulated accuracy was examined by comparing results with the observational data. Based on this CFD model, the snowdrift development on an isolated dome roof with various inflow velocities and roof spans was explored. As a result of this work, the following conclusions can be drawn:

Through comparison, the proposed CFD simulation approach was generally able to reproduce the snowdrift on building roofs. Specifically, the snow accumulation on the windward side of the building due to building blocking and the trajectories of snow particles under the action of aerodynamic force and gravity are both well reproduced by adopting a two-way coupled multiphase flow model and considering the slip velocity between air and snow phases.

The snow load on the dome roof shows three kinds of distributions patterns, i.e., the full-span balanced distribution, half-span unbalanced distribution and transitional distribution between them. Snowdrift piled up on the leeward side of the roof tends to increase with the increasing inflow velocity. Here, the inflow velocity (2 m/s) at which the snow distribution changes from uniform to non-uniform is defined as the lower critical inflow velocity, while the inflow velocity (5 m/s) at which the non-uniform load changes from increasing to decreasing is defined as the upper critical inflow velocity. The risking inflow

velocity for this dome roof ranges from 2 m/s to 5 m/s, above which the snow load on the roof begins to decrease.

With the increasing roof span, the uneven distribution of roof snow is weakened under the same inflow velocity condition. Hence, for a longer roof span, the upper critical inflow velocity at which the non-uniform load changes from increasing to decreasing is higher. The risking inflow velocity range for a larger building will be wider, namely, the long-span roofs are more likely to experience the most adverse snow loads.

Acknowledgements

This study was funded by the Foundation for Chinese Creative Research Groups of National Natural Science Foundation (grant number: 51921006), National Natural Science Foundation of China (grant number 51978207, 51927813, 52208157), Postdoctoral Science Foundation of China (2022M710976), Heilongjiang Natural Science Foundation for Excellent Youth project (grant number YQ2021E030) and Heilongjiang Provincial Postdoctoral General Fund (grant number LBH-Z21161).

References

[1] M. O'Rourke, Lessons learned: structural collapse from snow loads, *Structure*, pp. 42-44, 2008.

[2] Y. Tominaga, Computational fluid dynamics simulation of snowdrift around buildings: Past achievements and future perspectives, *Cold Region Science and Technology*, vol. 150, pp. 2-14, 2018.

[3] T.K. Thiis, J.F. Ramberg, Measurements and numerical simulations of development of snow drifts of curved roofs, *Proceedings of the 6th International Conference on Snow Engineering, June 1-5, 2008*, Whistler, Canada, 2008.

[4] T.K. Thiis, J. Potac, J.F. Ramberg, 3D numerical simulations and full scale measurements of snow depositions on a curved roof, *Proceedings of the 5th European & African Conference on Wind engineering, July 19-23, 2009*, Florence, Italy, 2009.

[5] Y. Tominaga, T. Okaze, A. Mochida, CFD simulation of drift snow loads for an isolated gable-roof building, *Proceedings of the 8th International Conference on Snow Engineering, June 14-17, 2016*, Nantes, France, 2016. pp. 208-214.

[6] T.K. Thiis, M. O'Rourke, Model for snow loading on gable roofs, *Journal of Structural Engineering*, vol. 141 (12), pp. 04015051, 2015.

[7] X. Zhou, L. Kang, M. Gu et al., Numerical simulation and wind tunnel test for redistribution of snow on a flat roof, *Journal of Wind Engineering and Industrial Aerodynamics*, vol. 153, pp. 92-105, 2016.

[8] J.W. Pomeroy, D.M. Gray, Saltation of snow, *Water Resources Research*, vol. 26(7), pp. 1583-1594, 1990.

[9] T. Okaze, A. Mochida, Y. Tominaga et al., Modeling of drifting snow development in a boundary layer and its effects on wind field, *Proceedings of the 6th International Conference on Snow Engineering, June 1-5, 2008*, Whistler, Canada. 2008.

[10] T. Okaze, A. Mochida, Y. Tominaga et al., Wind tunnel investigation of drifting snow development in a boundary layer. *Journal of Wind Engineering and Industrial Aerodynamics*, vol. 104-106, pp. 532-539, 2012.

[11] Y. Tominaga, T. Okaze, A. Mochida, CFD modeling of snowdrift around a building: an overview of models and evaluation of a new approach, *Building Environment*, vol. 46 (4), pp. 899-910, 2011.

[12] ISO, *Bases for design of structures - Determination of snow loads on roofs*. Switzerland, 2013.

[13] R. Clift, J.R. Grace, M.E. Weber, *Bubbles, Drops, and Particles*. London, 1978.

[14] R.S. Anderson, P.K. Haff, Simulation of eolian saltation, *Science*, vol. 241, pp. 820-823, 1988.

[15] T.K. Thiis, Y. Gjessing, Large-scale measurements of snowdrifts around flat-roofed and single-pitch-roofed buildings, *Cold Regions Science and Technology*, vol. 30, pp. 175-181, 1999.

[16] Y. Tominaga, A. Mochida, R, Yoshie et al., AIJ guidelines for practical applications of CFD to pedestrian wind environment around buildings, *Journal of Wind Engineering and Industrial Aerodynamics*, vol. 96, pp. 1749-1761, 2008.

[17] M.J. O'Rourke, M. Auren, Unbalanced snow loads on gable roofs, *Snow Engineering: Recent Advances*, Izumi, Nakamura & Sack (Eds), 1997.

[18] ASCE, ASCE/SEI 7-05 Minimum Design Loads for Buildings and Other Structures. Reston, 2006.

IASS 2023
July 10–14 Melbourne
Integration of Design and Fabrication

Proceedings of the IASS Annual Symposium 2023
Integration of Design and Fabrication
10–14 July 2023, Melbourne, Australia
Y.M. Xie, J. Burry, T.U. Lee and J. Ma (eds.)

CLT requires a new approach to design: a case study in CLT folded-plate structure

Yoko MASUDA[a,*], Yuko MIYAMOTO[a]

[a,*] Tourisha Structural Design Office
4-4-12, Higashinoda, Miyakojima, Osaka, 534-0024, Japan
masuda@cd.wakwak.com

Abstract

The potential to produce CLT (Cross Laminated Timber) panels in sizes as large as 12m by 3m was key to all design and building processes for this project. By using such large panels, we could reduce the number of parts and joints, resulting in a shorter construction period. However, this large size panel is not robust enough for the anticipated bending forces. To overcome this issue, the first author developed a V-shaped beam composed of two 12m by 1.2m CLT panels bolted together at 90 degrees. When a flat CLT floor panel is fixed across the open arms of the V, the structure formed is robust enough to take the anticipated floor loads. To support the V-shaped beams, an open-grid diagonal lattice wall was developed. The V-shaped beams mate with the bottom corners of the diagonal grid modules to create a rational support structure. The roof is formed of 12m by 3m CLT panels fixed together in a V-shaped folded plate structure that is supported directly on the top ridges of the diagonal lattice walls. The whole architectural design process was governed by three specific solutions (V-shaped beam, V-shaped roof, and a diagonal lattice wall) to take full advantage of large-panel CLT construction. The other key element of the design process is the matrix chart, referred to as the INDEX. It was developed by the first author to help all parties involved come up with an optimal solution to the challenges of assembling these structural elements, and enables the implementation of a new design approach required by the use of CLT, where all disciplines work together in an integrated process.

Keywords: design and construction method, CLT, folded-plate structure

1. Introduction

The building presented in this paper is an office building with a floor area of 1000m^2 (Fig.1).

(a) (b)



Figure 1. Office building of MK: (a) Facade, (b) Building interior

Copyright © 2023 by Yoko MASUDA and Yuko MIYAMOTO. Published in the Proceedings of the IASS Annual Symposium 2023 with permission.

The owner of the office, MEIKEN LAMWOOD Corp. (hereafter MK), is a manufacturer of CLT and laminated timber, and also performs on-site assembly. The building is a showroom for CLT. The owner requested not only design quality but also a short construction period. The latter is one of the biggest advantages of CLT, and the authors tried to enhance construction speed further by using large panels in order to reduce the number of components. In addition, pre-build techniques were also used, in which insulation and moisture-proof sheets were pre-fitted to CLT panels at the factory.

2. Outline of structural system

The structural system is shown in Fig.2. Eight diagonal-lattice glulam walls are placed parallel to each other and a maximum of 10.5m apart. These walls act like bridge piers supporting V-shaped CLT beams and roof panels that span between them. The V-shaped beams and roof panels are connected to the diagonal-lattice walls using only dowels (Fig.2(c)), while CLT panels are fixed to each other with bolts and screws.

Earthquake-resistant elements are CLT walls and diagonal-lattice glulam walls. The former resists lateral forces in the X-direction and the latter in the Y-direction.

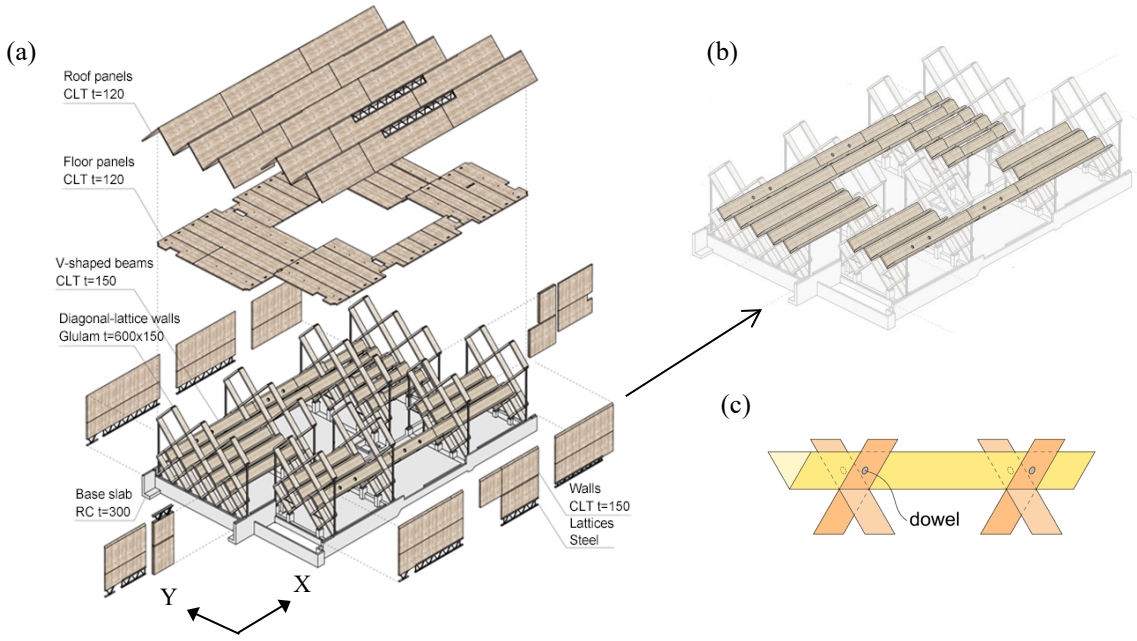


Figure 2. Structural system diagram:(a) whole, (b)arrangement of V-shaped beams, (c)concept of system

3. Design methods for each structural element

The key to structural design of wood construction is joints. The detail design of joints not only determines the performance of the structure, but also greatly affects workability on site. For large CLT panels in particular, the method of assembly determines the detail of the joints. Other factors that must be considered include ease of maintenance, aesthetics, coordination of structure and services, etc. The authors developed a new design approach to find the optimal solution for joint design that satisfied all conditions by bringing all parties together to discuss all issues (Fig.3). Section 4 briefly describes the main elements of the structure, with the joints which were determined by this new approach circled in red. The specific method is described in Section 5.

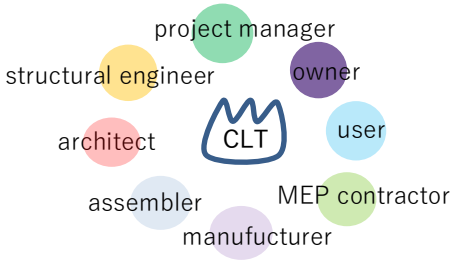


Figure 3. Participants in design discussions

4. Structural elements and the details

4.1. V-shaped beam

Details of V-shaped beams are shown in Fig.4. V-shaped beams are constructed of 150mm thick CLT panels a maximum size of 12 m long by 1.2 m wide. CLT floor panels run across the tops of the V-beams, with their long edge set at 90 degrees to the span direction of the beams (see Fig.2(a)andFig.4(a)). Steel dowels (diameter 90mm, length 120mm) connecting the V-beam to the diagonal-lattice walls are shown in Fig.4(b).

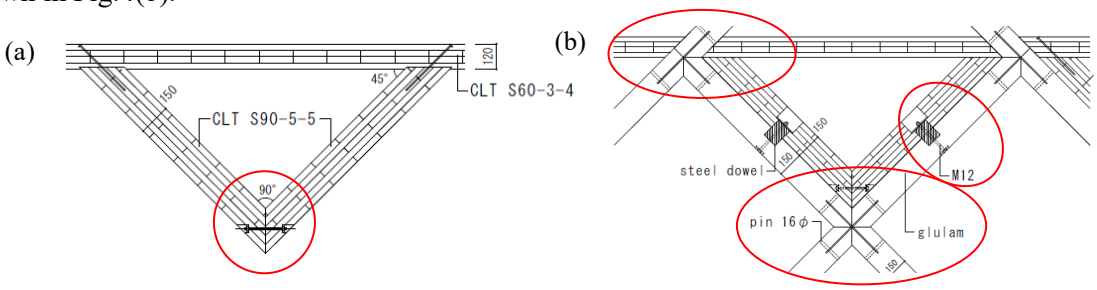


Figure 4. V-shaped beam: (a) detail, (b) V-shaped beam on diagonal-lattice glulam wall

4.2. Roof

The roof is a folded-plate structure made of CLT panels 120mm thick and 3m wide. Openings are formed in some roof panels for smoke exhaust and rooflights (Fig.2). These openings are reinforced with diagonal steel plates the same as those used at the lower part of CLT walls (Fig.7). Roof panels are connected to diagonal-lattice walls using the same dowels that connect V-beams to diagonal-lattice walls.

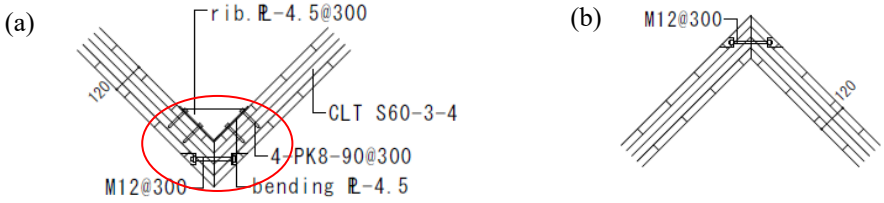


Figure 5. Detail of folded-plate roof panels: (a) valley junction (b) ridge junction

4.3. Diagonal-lattice glulam wall

To support the V-shaped beams and roof panels, the first author developed a diagonal-lattice glulam wall (Fig.6). The bottom corner of each grid can receive and support a V-shaped beam in a rational manner. Roof panels are supported directly on the top ridges of diagonal lattice walls. The lattice is composed of glulam members 150 mm thick by 600 mm wide. Four glulam members are connected at each node by inserted X-shaped steel flitch plates and drift pins (Fig.4(b)). The whole structure is supported by 75mm by 150mm solid steel columns at each end.

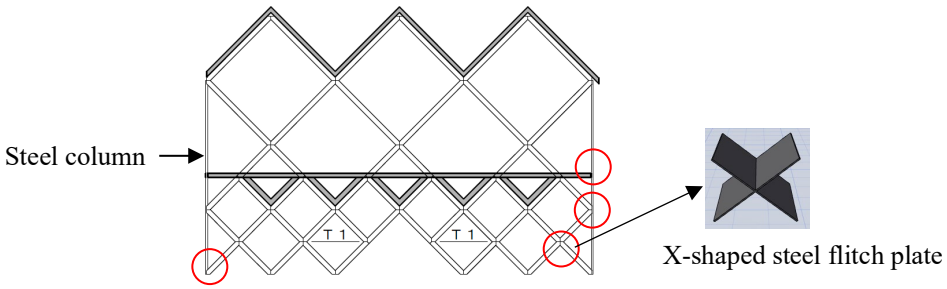


Figure 6. Diagonal-lattice glulam wall

4.4. CLT wall

CLT wall construction is shown in Fig.7. Axial forces resulting from the rocking of the walls during earthquakes are transmitted by bolts (indicated by the red circle). The walls are constructed of large horizontal panels with no openings. The steel lattice below the wall is a structural element that connects the wall to the foundation and also functions as a window.

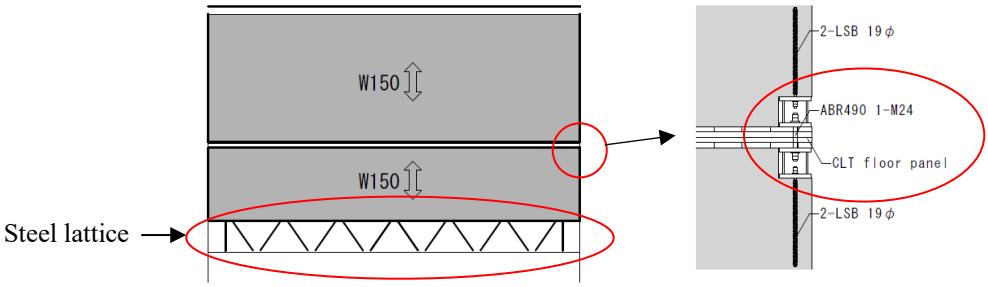


Figure 7. CLT wall construction

5. New approach to design

5.1. Controversy “Bolt or screw？”

Of all the joints, those forming the corner of the V-shaped beam had to be specified first (Fig.4(a)). This was crucial because no data existed for this type of construction and so full-scale testing was required for structural analysis. Therefore, details had to be determined during the schematic design phase in order to prepare the test specimens.

There were several possible methods of connecting panels, and the choice was not determined solely by mechanical rationality but through the integration of fabrication, assembly and design. The authors, along with the project manager, interviewed all project members, from the architect, builder, and manufacturer to users and the company president, focusing on the three joint possibilities shown in Fig.8.

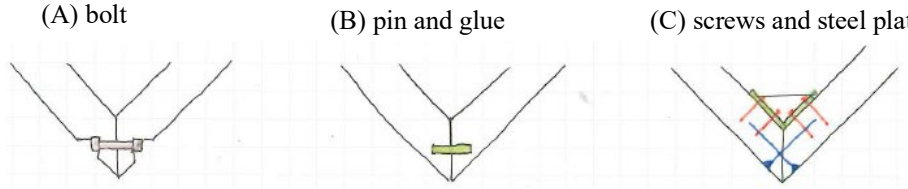


Figure 8. Detail of V-shaped beam

Advantages and disadvantages of each joint solution are shown in Table 1. The most advantageous is (A). However, the architect preferred (C) for its appearance, because in (C) only the heads of small

screws are visible. The authors argued that ease of construction and maintenance should be prioritized. Also, exposing bolts can express how the joint is made, and fits with the culture and character of the company.

To resolve the debate between the choice of bolts (A) or screws (C), respective full-scale mock-ups were made. It took two months to reach the conclusion that (A) should be chosen, based on the full-scale mock-ups. Following this decision, we decided to show, not hide, all jointing hardware.

Table1. Matrix for comparison of performance

	A	B	C
rationality of mechanics	simple	simple	complex
performance guarantee	very good	Dependent on construction	good
workability	very good	bad	midle
cost	low	high	midle
maintenance	easy	impossible	difficult
appearance	standing out	invisible	visible

5.2. INDEX MATRIX CHARTS and related meetings

Through the controversy over "Bolt or screw" during the schematic design phase, the authors realized that, in comparison to conventional materials, CLT challenges us to change our ways of thinking and working. Compared to conventional structures, CLT requires the design and assembly process, the details, and the overall structural system to be thought of holistically. The reason for this is the enormous size of the CLT panels. As most of the structural elements were designed to be visually exposed, these challenges needed to be considered carefully. (Fig.1(b))

To facilitate this, the first author developed a series of "INDEX MATRIX CHARTS" (hereinafter "the INDEX"), shown in Figure 9. This encouraged a new approach, and called for all the actors from design, fabrication, construction and maintenance phases to participate in regular joint discussions during the detailed design phase. [1]

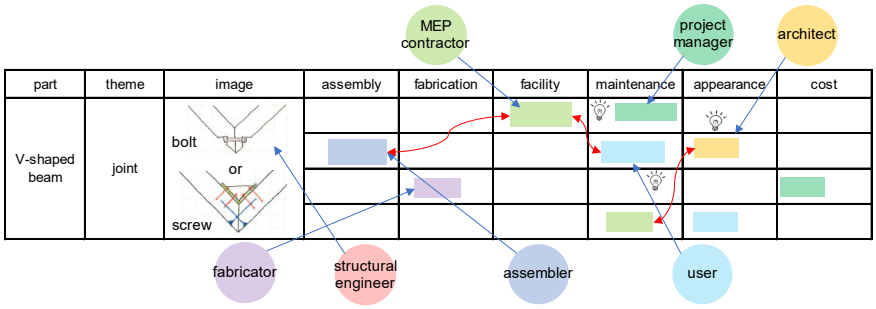
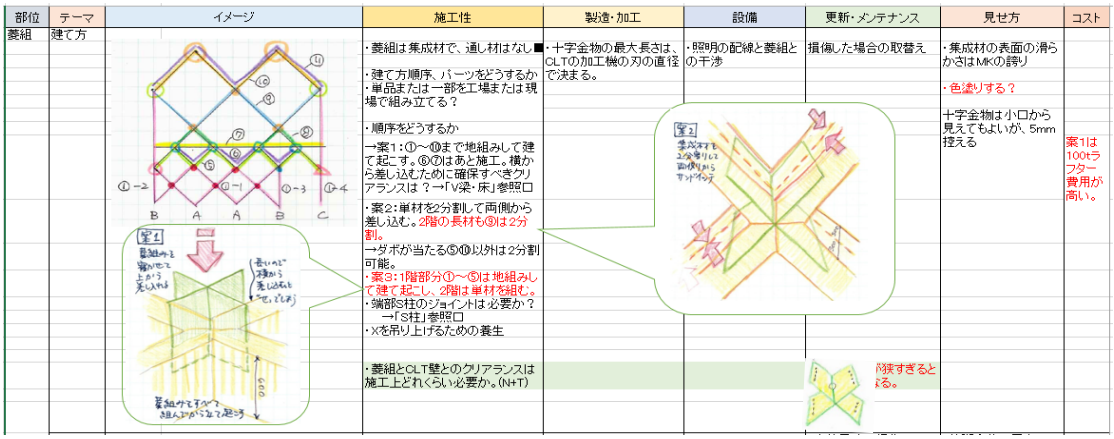


Figure 9. INDEX MATRIX CHARTS for the detail design of V-shaped beam

The authors produced separate INDEXES for respective structural themes, and the participants tried to reach the optimal solution for each theme. Themes were categorized by structural elements such as V-shaped beam or CLT slab, and participants discussed both design details and construction procedure in accordance with the factors listed in the INDEX. The importance of discussions for design integration with different parties has been addressed these days but it is not clarified who should chair and lead actual meetings. In this project, the first author chaired the meetings to ensure that design details were determined in the right order for structural analysis. The necessity for structural engineering resulted in design integration with fabrication and construction. The project manager drafted minutes to ensure the decisions and undecided issues at every meeting. An example from among many indexes is shown in Table.2. The assembly method of diagonal-lattice glulam walls was discussed using this INDEX. It was decided during this discussion that diagonal members should be split at the nodes. We noticed that some

members could not be inserted diagonally in the air due to geometry, so we decided to cut the width in half for these members and insert them from both sides of the X-shaped steel flitch plate. (See illustration on the right in Table.2.)

Table.2 Actual INDEX for erection of diagonal-lattice glulam wall



6. Analytical model

6.1. Specifications of CLT

The type and elastic modulus of CLT used in this design are shown below. The material of S90-5-5 is cypress, while the material of S60-3-4 and S60-5-5 are cedar. The elastic modulus (E) of cypress is 9000N/mm^2 and that of cedar is 7000N/mm^2. Table 3 shows that the elastic modulus decreases when made into CLT, and that the properties vary greatly depending on the direction.

Table 3. Elastic modulus of CLT

Used part	Thickness (mm)	Strength grade	Layer compositions	In-plane				Out-of-plane			
				E [N/mm^2]		G [N/mm^2]		E (N/mm^2)		G (N/mm^2)	
				Major axis	Minor axis	Major axis	Minor axis	Major axis	Minor axis	Major axis	Minor axis
V-shaped beams	150	S90-5-5	5-layer 5-ply	5400	3600	500	500	7128	1872	81.8	40.9
Floor panels	120	S60-3-4	3-layer 4-ply	3000	3000	500	500	5250	750	40.1	93.7
Roof panels	120	S60-3-4	3-layer 4-ply	3000	3000	500	500	5250	750	40.1	93.7
CLT walls	150	S60-5-5	5-layer 5-ply	3600	2400	500	500	4752	1248	54.5	27.2

*According to Building Standards Act of Japan

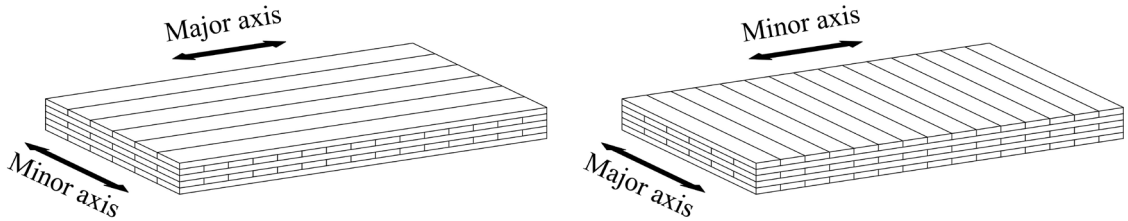


Figure 10. Axis orientation of CLT

6.2. Outline of analytical model

During structural analysis, the V-shaped beams with floor panels, roof panels, diagonal-lattice walls, and CLT walls were modelled separately. Finite element models were used for roof panels, V-shaped beams and floor panels shown in Fig.11 and Fig.12. The finite element mesh was approximately 150 mm. All fixings were treated as springs with appropriate stiffness.

The support points in Fig.11 and Fig.12 occur where roof panels or V-shaped beams and diagonal-lattice walls were connected with dowels, and at CLT walls at both ends. These supports were modelled as springs with appropriate stiffness. Long-term load and seismic load were applied to the roof in Fig.11, and floor in Fig.12. The reaction force occurring at the support points were applied as external forces on the diagonal-lattice walls and CLT walls. Diagonal-lattice walls and CLT walls are modelled by line component respectively.

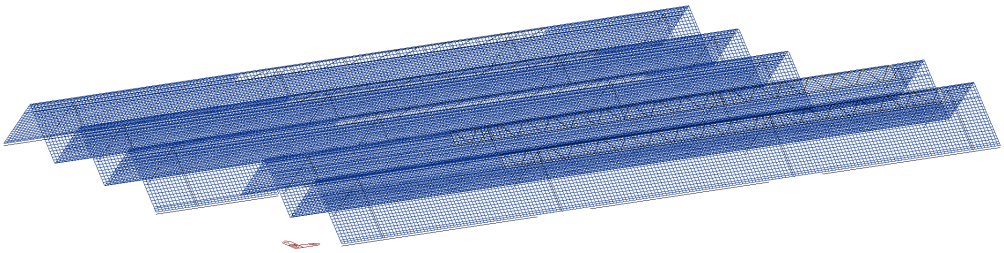


Figure 11. Finite element model of roof panels

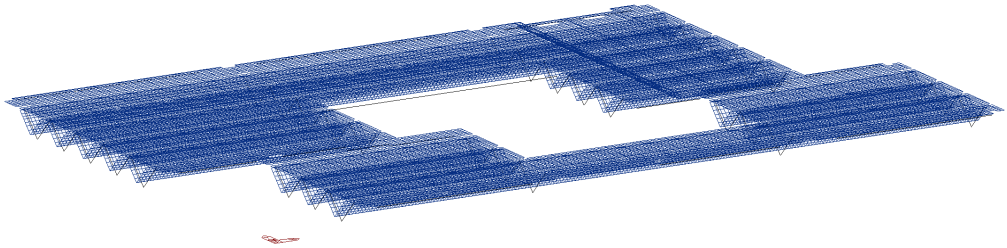


Figure 12. Finite element model of V-shaped beams and floor panels

6.3. Analytical model of joint

Joints in wood construction are less rigid than those in steel or reinforced concrete construction since stresses and deformations vary greatly depending on the stiffness of the joints. And so, joints were modelled as springs for the analysis. The detail of the roof joint is shown in Figure 13. The analytical model for Fig.13 is shown in Fig.14.

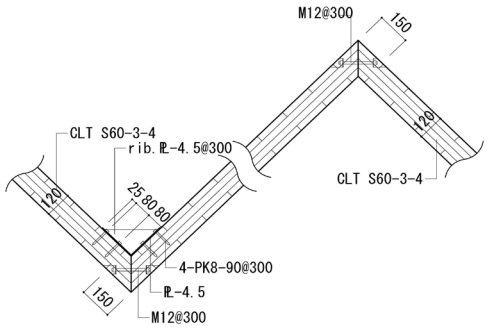


Figure 13. Cross-sectional view of roof panels

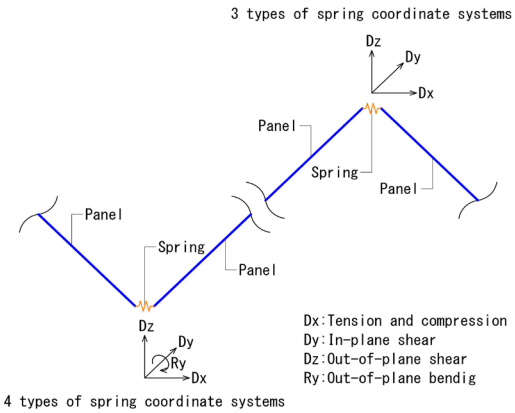


Figure 14. Analysis model diagram of roof panels

CLT has a short history in Japan and the CLT-related Building Standards Act was only enacted in 2016. Therefore, test data are usually used to design joints. As there are no test data for obliquely joined members like those in Fig.13., the authors conducted tests to obtain the yield strength and stiffness.

Tests were conducted with bolts, screws, and dowels. Using test data, the structural models for the roof were decided with spring stiffnesses for in-plane shear, out-of-plane shear, tension and compression, and out-of-plane bending.

6.4. Design load

Long-term load was assumed to be dead loads and live loads for the office floors. The specific gravity of CLT was assumed to be 4.9 kN/m^3. The construction site is in the inland area of Okayama Prefecture, and the snow load is assumed as the medium short-term load. A snow accumulation of 63 cm was assumed. Seismic load is assumed in accordance with the Building Standard Act. Wind load is not taken into account because it is smaller than seismic load.

7. Roof stress and deformation

The following figures show the stress contour map under snow load and the deformation contour map under long-term load. The deformation is after creep. Creep deformation is assumed to be twice the initial deflection.

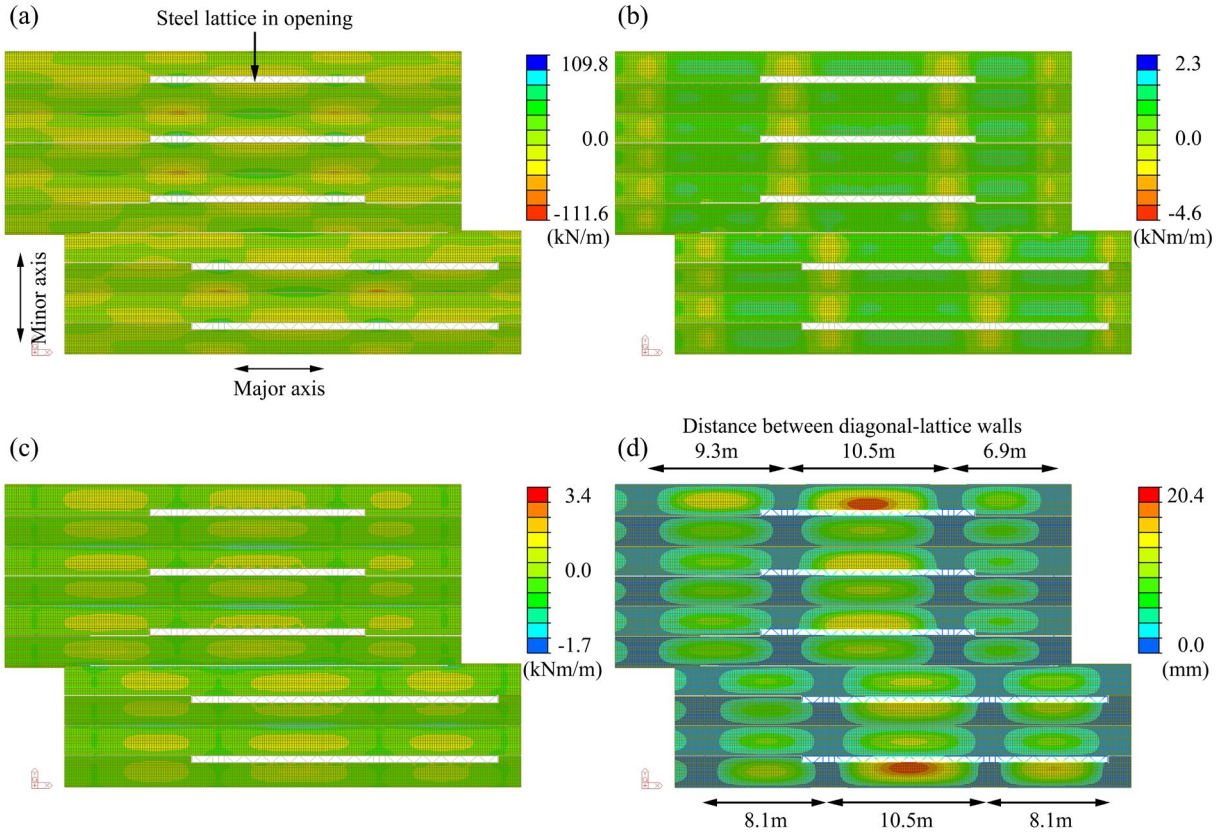


Figure 15. Stress contour map under snow load and Deformation contour map under long-term load: (a) axial stress in major axial direction, (b) out-of-plane bending stress in major axial direction, (c) out-of-plane bending stress in minor axial direction, (d) deformation after creep

Looking at the Axial stresses in major axial direction, it can be seen that tensile stresses of the upper panels are greater at the location supported by the diagonal-lattice walls, and the tensile stresses of the lower panels are greater in the center of the span. This is the stress state of a continuous beam. Out-of-plane bending stresses in major axial direction have similar trend. Out-of-plane bending stresses in minor axial direction are greater at the center of the panels and at valley junctions.

The deformation contour map shows that the maximum value is near the lattice in the center of the span, which is about 20 mm. The maximum deformation occurred at the outermost edge of the roof, the panel with the longest span. The reason is that the lower part of the panel is less restrained and the upper part is also less restrained due to the openings.

However, in the center of the roof for the same span, the panels are folded and continuous, so the deformation is about half. The fact that the deflection is about 1/1000 of the span with 120mm CLT panels spanning 10.5m shows the effect of the folded plate structure.

When CLT is used as flat panels, out-of-plane deformation increases due to the low modulus of elasticity of the out-of-plane minor axis. However, by folding it in the minor axial direction and making it continuous, as in this case, the weak point can be overcome.

8. Pre-build at the factory

Utilizing large-size CLT panels as a base, we tried several "pre-build" techniques in order to reduce the number of processes on site. V-shaped beams were made into a V shape at the factory and transported to the site. Ventilation ducts were installed inside the V-shaped beams at the factory (Fig.16). Insulation and waterproof sheets were attached to CLT panels for exterior walls at the factory (Fig.17). Pre-build not only shortened the construction period, but also improved quality because it was assembled in the factory with a good working environment.

Early involvement of an MEP contractor to the design discussion realized pre-installation of ventilation ducts. The location of ventilation duct joints on site, timing of onsite ducting works during erection, and air volume adjustment and maintenance method were reviewed using the INDEX.

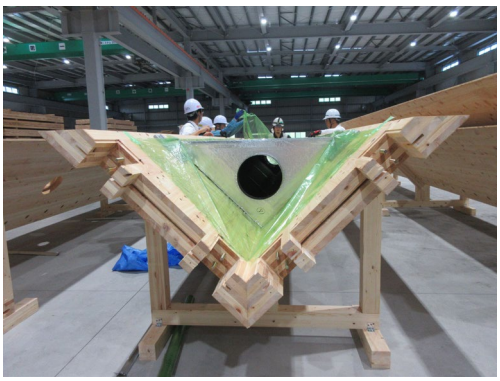


Figure 16. Duct installed in V-shaped beam



Figure 17. CLT wall covered with waterproof paper

9. Construction

A three-month preparation period was set aside prior to construction to ensure that there would be no rework. CLT construction is difficult to change or modify on site. Electrical wiring and piping for equipment were checked by the MEP contractor, the CLT fabricator and the architect using BIM.

Any issues expected during construction were reviewed by new INDEXES. Although a new general contractor joined at last, they smoothly communicated with the project members about the design intent of each detail through INDEX.

As constructability of timber joints were already studied in the design discussion using INDEX, structural timber erection works completed in 1 month as planned. In this way construction was completed in exactly 6 months. Fig.18. shows the construction site during the election.

(a) (b)



Figure 18. Construction:(a) Erection of diagonal-lattice glulam walls (b)Setting of V-shaped beams

10. Conclusion

Large size CLT panels are suitable for folded-plate construction and can lead to bold structural plans. When panels in the minor direction are made continuous by using a folded plate structure, the weak point of low bending stiffness can be overcome. Using larger size panels and reducing the number of pieces shortens the construction time of the building process. It is also possible to pre-build insulation and ductwork in a factory. Thus, CLT structural system can open up new construction process possibilities when off-site study is carefully done.

When encountering a new structural material such as CLT, it is important to think structurally in order to design a building that takes advantage of the material's specific features. CLT, due to its size, requires us to think carefully about how it is handled, assembled and joined. The authors invented a matrix chart (INDEX), which brought together not only the architect but also assembler, fabricator, and through discussion, they arrived at a method for finding the optimal solution that integrates design, assembly and fabrication.

Fig.19 shows that all jointing hardware is represented without being hidden. Joint is the key to wood construction. Only a structural engineer understands the mechanisms of joint. In this project, because the structural engineer, the first author, improved the quality of communication with the various parties involved, gathered their wisdom, and provided a platform, INDEX, for the optimal solution to the key issues, it was possible to create the building that was rationally constructed.

It was important for this project that the structural engineer had not only the capability of structural design and analysis but also the sensitivity to identify the critical issues in fabrication and construction phase through the communication with respective parties.

This report demonstrates how the structural engineer expanded her role beyond usual tasks, when CLT, the new structural material, was introduced. It implies a structural engineer’s potential key role when a new structural material is introduced in the future. By the efforts of structural engineer, never-before-seen of architecture may emerge which thoroughly represents the character of the new material.



Figure.19. Building interior

Acknowledgements

When the INDEX was born, it was project manager Ayako Omura (Naya Company) who quickly recognized its value. Because of her empathy and her efforts to manage this project, INDEX has evolved beyond my imagination.

Reference

[1] A. Omura and Y. Nakashima," Gradual changes on building production process in a CLT building project", *The 37th Building Production Symposium, organized by Architectural Institute of Japan, August 2022*

IASS 2023
July 10–14 Melbourne
Integration of Design and Fabrication

Proceedings of the IASS Annual Symposium 2023
Integration of Design and Fabrication
10–14 July 2023, Melbourne, Australia
Y.M. Xie, J. Burry, T.U. Lee and J. Ma (eds.)

Contribution of structural intuition at early conceptual stage in efficient workflow: A precedent study of Oscar Niemeyer

Irem SEREFOGLU[a,*], Luiza Souza WANDERLEY[b], Remo PEDRESCHI[c], Miguel Paredes MALDONADO[c]

[a,*] The University of Edinburgh
iserefog@ed.ac.uk

[b] Bouygues TP
[c] University of Edinburgh

Abstract

Complex forms necessitate a detailed understanding of form, structure, and architecture through a multi-disciplinary collaboration of the core players of the design team. The impact of design changes on the project's total cost becomes more detrimental as the project develops. The desired design efficiency is a result that is aesthetically pleasing, structurally efficient and easy to build for sustainable and innovative structures that comply with the budget [1]. Some scholars state that to optimise form, the designers need structural intuition, a skill that is explained as an innate understanding of the functional requirements of a structure [2]. This paper will explore how structural intuition affects design efficiency from an architectural point of view by looking at the work of the world-renown Brazilian architect Oscar Niemeyer. His work stands out with intrinsic detail to fine architecture, early-stage contribution of structural intuition and interdisciplinary design development. This paper identifies the critical elements of his design workflow which are exemplified through two case studies of his works: The University of Constantine (1972) and the National Congress (1960). Qualitative and quantitative analysis is conducted through a structured precedent analysis involving computational modelling, literature review and 3D printing to prove structurally intuitive design methods. The output of this evaluation demonstrates efficient workflow through learning from precedent studies and the application of parametric modelling.

Keywords: conceptual design, morphology, form finding, parametric design, digital fabrication, optimisation, concrete shells, precedent-based design, efficiency, workflow

1. Introduction

The disciplines of architecture and engineering have been inextricably linked throughout the history of the built environment. The evolution of new technologies, encompassing advanced tools, materials, and production techniques, has consistently spurred changes in these domains [3]. Moving away from the rectilinear paradigm, modern architectural trends push the limits of material and expression. The interaction between the two disciplines spans a broad range, from a cohesive vision of structure and architecture to a complete disregard for structural performance in favour of aesthetics [4]. This interplay is reflected in the collaborative relationship between architects and engineers during the design process.

The inseparable nature of the two disciplines merged within the work of master builders, single handedly designed, managed, and executed. In earlier times, architects or builders possessed only limited knowledge of construction but were ultimately responsible for all aspects of the building process. This required a multifaceted skill set, including artistic talent, materials expertise and an understanding of structural behaviour [5].

Copyright © 2023 by Irem SEREFOGLU, Luiza Souza WANDERLEY, Miguel Paredes MALDONADO and Remo PEDRESCHI. Published in the Proceedings of the IASS Annual Symposium 2023 with permission.

Despite the integration of complex forms and efficient design workflows, a prevailing trend exists where structural engineering considerations are seldom the primary focus at the beginning of an architectural design process, owing to the multitude of other concerns that need to be addressed. Conversely, architectural considerations are often not prioritized in structural engineering projects [6]. Key discussions within this interdisciplinary tension involve material selection, form and structure exploration, and proportion determination.

By incorporating complex forms and adopting efficient design workflows, architects and engineers can cultivate a stronger collaboration and develop more comprehensive solutions that effectively balance aesthetics, structural performance, and constructability [7]. This integrative approach has the potential to reshape the future of the built environment, as professionals from both disciplines work together to push the boundaries of design and engineering.

2. Workflow from the conceptual design phase

Modern construction projects often involve a linear design workflow where stakeholders possess separate goals and complications, leading to fragmented development of the project [8]. This fragmented process results in over-budget and inefficient buildings, particularly in large-scale complex projects where many stakeholders, materials, design challenges, and environmental impacts are involved [9].

Architects, structural engineers, civil engineers, and building services engineers have declared their commitment to addressing climate and biodiversity emergencies [10] [11]. However, achieving these common goals is challenging due to the fragmented nature of traditional linear workflow. Historically, architects and engineers have been associated with different parts of the building industry, leading to a lack of common design language [6] [12]. This fragmentation is reinforced by education and specialization of disciplines [13]. Despite advancements in modern digital tools and construction techniques, linear workflow fails to achieve a balance between aesthetic, structural, functional, and construction-related objectives. A more efficient and collaborative workflow model is required.

Modern architecture has introduced new dimensions to the traditional methods of construction, and it has had a tremendous effect on introducing new approaches to the aesthetic understanding of the built environment. Complex geometric forms in modern architecture can be designed more efficiently, cost-effective, and construction-friendly with minimal use of material when there is more structural intuition involved, and the project remains true to the early design decisions. Additionally, incorporating environmental considerations as early as the conceptual design phase can reduce the cost of later changes, as indicated by the MacLeamy Curve, shown in Figure 1.

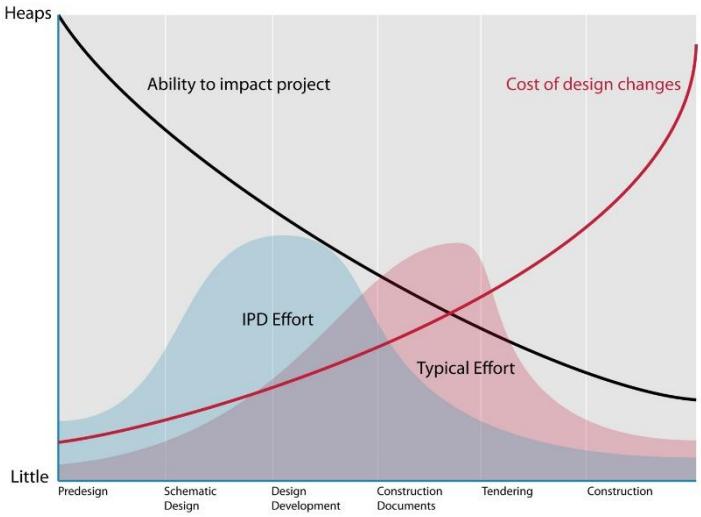


Figure 1. The MacLeamy Diagram [14]

The MacLeamy Design Effort/Effect Curve is a chart used to demonstrate the need to optimize the design process of complex design projects. According to the curve, the earlier in the design process that decisions are made, the more efficient the design process will be. This is because early decisions can be made that take account of structural intuition, which allows for a more accurate and efficient design process. The curve also suggests that the later in the design process that changes are made, the more costly and time-consuming they become.

Digital form-finding tools can facilitate efficient design of complex forms, but they require a change in workflow approach and seamless collaboration between architects and engineers. The Foundation Louis Vuitton by Frank Gehry, which exceeded its budget eight times, exemplifies the inefficiency that can result from post-rationalization of form despite using modern digital tools [15] [16].

3. Methodology and case study analysis

This paper focuses on Oscar Niemeyer and his works as contemporary examples of efficient design workflow that is demonstrated through a structured analysis of his distinguished projects. This study is a part of a broader research agenda that introduces a novel approach on how precedent and case studies can be used to address the issues that define efficient design, development, and production. The approach uses computational modelling and qualitative analysis of precedent case studies to determine the design workflow. A range of MEng Structural Engineering with Architecture (SEA) dissertation students was involved in understanding the possible impact of using digital tools and precedent studies and identifying the relationship between architecture, structure, and construction. This part of the research concentrates on the consistent collaboration between the architect Oscar Niemeyer and a small group of engineers throughout his career a conceptual design stage through exploring digital trends to extract information from case studies.

The two selected projects from Niemeyer demonstrate slightly different versions of Niemeyer's preferred workflow. The first one is the National Congress of Brasilia (1956) which relied on the expertise of the structural engineer Joaquim Cardozo [17]. The Congress was only one of the many buildings within the large-scale project that was the construction of the Brazilian capital, and due to its importance, it is also one of Niemeyer's most well-known projects. The second project is much less well known and it is the Auditorium of the University of Constantine 2 (1969) in Algeria. The university project is interesting as a whole because it is not one that immediately comes to mind when thinking of Niemeyer, but the story behind it contains valuable clues into Niemeyer's working dynamic with engineers.

4. Oscar Niemeyer

Oscar Niemeyer (1907-2012) is arguably Brazil's most renowned architect, with over 600 projects completed around the globe over the 78 years of his career [18]. He is widely considered one of the most significant names in modern architecture, with his use of concrete, glass, and curves as the main aspects of his signature style.

Niemeyer is often viewed through a primarily aesthetic lens. However, to fully understand his style and workflow, there are some important details in his early career that showcase a side to Niemeyer's works not often mentioned, a deep concern for both structure and construction.

4.1. Influences

4.1.1. Studies

Going as far back as his time in university the first detail is the courses he completed while studying at Escola Nacional de Belas Artes (ENBA), or National School of Fine Arts, 1930-34 [19] While there were curriculum changes during his time there, note that courses on construction, material sciences and

applied physics were always present while advanced mathematics was a later addition [20]. This alone shows that Niemeyer has some had been taught aspects structural behaviour. There are also interviews and letters from engineers that worked with Niemeyer where they mention having long discussions about the structural behaviour of Niemeyer's proposals from which the architect would learn from and then apply in subsequent projects [21]. This background of his studies provides an important clue as to his experience, as this background knowledge most likely played a part in his designs, meaning he knew when to push the materials and when to compromise for the sake of structural effectivness and practical construction.

4.1.2. Concrete revolution

The next major influence to be considered is the material Niemeyer used, which throughout his career was mostly reinforced concrete. The context required to understand the connection is both in the international and Brazilian scenarios of the time. The development of concrete began in the later years of the 18th Century in France but by mid-19th Century it had already become widespread with the evolution of reinforced concrete [18]. This new material could take advantage of the flexibility of concrete being moulded into varying shapes but also counted on the steel reinforcement taking the tensile stresses that concrete was weak against. Through this time several experiments and systems were developed finally in the 20th Century many key names in architecture and engineering were largely associated with the material, a few examples being Robert Maillart, Pier Luigi Nervi, Eugène Freyssinet amongst many others [22]. Meanwhile in Brazil, the document stating the standard for the calculation of reinforced concrete was first published in 1931, during Niemeyer's studies, therefore it would likely have been something discussed within his courses.

4.1.3. Le Corbusier

Finally, it is nearly impossible to talk of modern architecture without there being some reference to the Swiss-French architect, Le Corbusier (1887-1965) [18]. Niemeyer had the opportunity to work with Le Corbusier not long after graduating, and the influence on his style can be seen in the subsequent projects. Niemeyer, much like Le Corbusier gave importance to light, air, and space in his works, using the same five elements of Le Corbusier as the base of his early style. An example is the Obra do Berço (1938), where Niemeyer re-worked his preliminary study from 1935 after having worked on the building for Ministry of Health and Education in Rio de Janeiro with Le Corbusier [23]. However, it is also important to know that from those early works, Niemeyer developed his own language which he describes as being more suitable to Brazil, with curves and spaces to meld and reflect the curves of the country's rivers and mountains. In the documentary about his life and career titled "Life is a Breath", Niemeyer says: "Our architecture is very different from Le Corbusier's. We evolved to an architecture that has more to do with our weather: it's lighter, has more hollowed surfaces, more empty space." [24]

4.2. Style and workflow

This evolution from having Le Corbusier's five elements as a base to developing his own form of language in architecture can be seen through the different periods of Niemeyer's career. A study of thirty buildings from different periods of Niemeyer's career, ranging from 1943 to 2003, were analysed and one of the trends showed that through the years the control mechanisms he used became more sophisticated as he gained experience [25]. José Carlos Sussekind, a structural engineer that often worked with Niemeyer, says that despite not being an engineer, Niemeyer had an innate knowledge in addition to the many years of experience [26].

These events all explain how Niemeyer arrived at the aesthetic expression of his work, but these projects wouldn't be possible without the aid of structural engineers to fill in with their expertise on structural behaviour. Curiously, the architect himself recognised the importance of the engineers to the realisation of his projects and admitted in his own books that he would accept sacrifices to aesthetics for best result

[27]. Furthermore, he has repeatedly stated the sentiment that "once the structure is ready, the architecture is already there" [26]. Because of his long career it was inevitable that Niemeyer worked with many engineers on the hundreds of projects he completed, but there are also certain names that keep recurring in the list of collaborators. Early in his career it was Joaquim Cardozo, Bruno Contarini for his years in exile and return to Brazil and José Carlos Sussekind in the second half of his career [21] [26]. Niemeyer's long-standing connections to these engineers can be seen as an indication of cohesiveness of the unit of the design team and is often talked about by these people in their writings. Some examples are Contarini's biography, and the collection of letters exchanged between Sussekind and Niemeyer himself where they discuss Niemeyer's preferred workflow [21] [28].

5. Case studies

5.1 National Congress, Brasília, Brazil, 1960

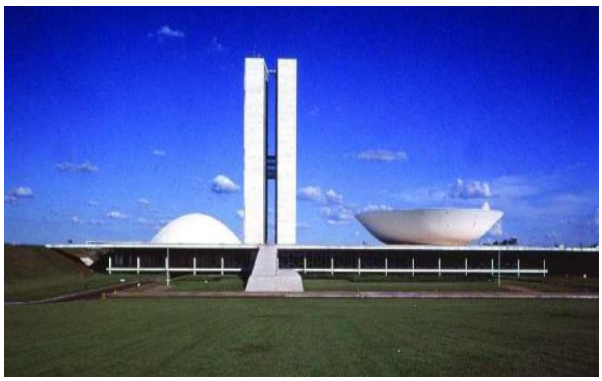


Figure 2. National Congress, Brasília, Brazil, 1960 [29]

The National Congress, shown in Figure 2, was one of the buildings commissioned in 1956 by President Juscelino Kubitschek within the larger scheme of what was to become the new capital of Brazil, Brasilia [30]. At the time, Niemeyer, with Lucio Costa (French-Brazilian architect and urban planner), prepared a plan that was eventually nicknamed the 'Monumental Axis' [31]. The congress is central to this plan, as the access ramp and the gap between the two towers align with the main axis of the city.

Niemeyer describes the design concept of the buildings in Brasilia as his search for structural purity, where structure and form are unified, a recurring theme in his work. The National Congress has in itself a few different parts to it: the two chambers (Federal Senate and Chamber of Deputies) shaped as a dome and a bowl sitting on a long horizontal building and the two office towers beside it.

Cardozo had already been working with Niemeyer for approximately a decade at this point and was considered an expert in the reinforced concrete within the country [17]. From Niemeyer's original sketches to the engineer's drawings some differences in shape can be noted, the main one being the inverted dome chamber, where the original intention was a paraboloid, but ultimately became an ellipsoid with a tangent of an inverted cone [32]. Precedent study did play a part here, as Cardozo introduced layers to the structure that resemble some of Robert Maillart's works [17].

Due to the magnitude of the project and the limited information released, there is no confirmed cost associated to the construction of Brasilia, although many scholars have made estimates, and this does therefore limit what can be said about the efficiency of the methods employed. However, there is some information on the workflow between Niemeyer and Cardozo related specifically to the congress, for example the story of Cardozo's morning call to Niemeyer to say he had found the ideal tangent to the inverted dome that would best suit Niemeyer's vision [21].

The congress building has been modelled in 3D multiple times and in multiple software, but going through the process based solely on the notes of the architect and engineer allow for a more practical insight into how the structure works. As mentioned before, the structure has several individual elements defined by Cardozo, these are shown in Table 1 and Figure 3:

Table 1. Structural Elements of the Chamber of Deputies as Defined by Joaquim Cardozo, see *[32]*

Number	Element
1	Lower Pillars
2	Concrete Curtains
3	Supporting Beams
4	Lower Compression Ring
5	First Shell
6	Intermediate Ring
7	Second Shell
8	Lining Slab
9	Ceiling Pillars
10	Third Shell
11	Upper Pillars
12	Upper Ring
13	Upper Slab

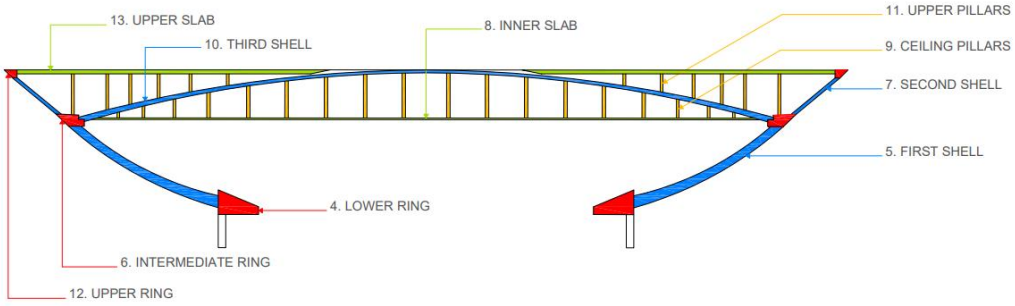


Figure 3. Section of the Chamber of Deputies with labelled elements corresponding to Table 1 [33]

Due to limitations in the modelling software (Rhino3D and Grasshopper) used certain aspects of the geometry had to be adapted and additional assumptions had to be made, and Figure *4* was the final result. For example, the software couldn't map the grid of pillars onto the surface of the third shell, and in their place imaginary support points were mapped onto the surfaces of the upper slab and third shell. Furthermore, the compression and intermediate rings also were divided into 1m segments and were called beams in the software. Lastly, the load cases were determined following the British Standard EN 1991-1-1 [33].



Figure 4. Rotated shape of the section of Figure 3 [33]

Elements 10 and 11 form a structure that resembles Maillart's Schwandbach Bridge (1933), with the thin bridge arch being equivalent to the inner shell and the stiff deck to be the upper slab. Therefore, when it came to analysing the structure, it was expected for these to act in a similar manner, where the

deck (or upper slab) would have a smaller deflection than the arch (or third shell). The results from the model confirm this, with the worst-case scenario having a deflection of 0.075cm in the upper slab and 0.567cm in the third shell [33].

From the results of the 3D model analysis, the other interesting occurrence was the behaviour of the intermediate ring. The deflection results of the third shell, show that the deflection was in the vertical direction, which is reasonable as the support conditions were set to be at the interface with the intermediate ring which restrained it from deflecting to the sides [33]. This resulted in the ring, defined as beams in the model, acted differently than it would have under pure gravity. Under normal conditions, the beams would sag, showing compression in the upper fibres and tension in the lower fibres. However due to the third shell pushing outwards, the opposite was observed, with upper fibres of the rings being under tension and the lower rings under compression.

5.2. University of Constantine, Constantine, Algeria, 1969

Commissioned by President Houari Boumediene, the Constantine University, now called Université Frères Mentouri de Constantine, is a large collection of educational and administrative buildings. Niemeyer was adamant to reduce the number of buildings from what was originally over twenty buildings to a simplified plan of only seven [24].



Figure 5. University of Constantine Auditorium, Constantine, Algeria, 1969 [34]

The auditorium, shown in Figure 5, is the most distinct looking of these buildings with the thin shell-like roofs, resembling a bird's wings or an open book, which meet in the middle with a single beam between them and contain no interior support. The 60 m long beam in the middle can be seen over the seam where the shells meet, while these span 30 m outwards. Niemeyer admits that he enjoyed pushing the limits of his preferred material of reinforced concrete.

One factor that seemed to be against Niemeyer's vision was the difference in technological advancements between Algeria and Brazil, which could have potentially set the construction back. However, the projects were designed in such a way that in addition with the cooperation between the Algerian and Brazilian workers it resulted in a smoother execution [35].

The information available on Niemeyer's process for the auditorium specifically is scarce as most of the literature available is surrounding the main classroom building. The story goes that when Niemeyer proposed the 50m span between columns the French engineers completing the calculations stated that a 1.5m thick wall would be required for structural stability. Niemeyer, unsatisfied with this, called in the Brazilian engineer Bruno Contarini who had worked with him in previous projects. Contarini then determined that only 0.3m thick walls were required and thus he was brought into the project [28].

The lack of information on this building meant that modelling it was a challenge and without anything to compare it to two versions were made, one following the tapering section as built in Constantine and a hypothetical version where the shell remains at a constant thickness. The tapering shell has a thickness

ranging from 3m where it meets the ground and 30cm at its highest point, while the uniform shell was chosen to be 30cm throughout [33].

The modelling software caused another limitation for this model where the program could not create the tapered shell as was designed, therefore the shell was broken up into strips with the average thickness of what it would have been. This seemed to have worked appropriately as the calculated mass of the adapted tapered shell was only 0.2% smaller than that of the hand calculated original tapered shell [33]. Once again, the load cases were determined following the British Standards EN 1991-1-1, and summarised in Table 2.

Table 2. Loading conditions for the tapered shell [33]

Load #	Name	Category	Eurocode	Value	Safety Factor
1, 2, 3	Self-Weight	Dead Load	-	Calculated from mass	1.35
2	Wind (x-dir)	Live Load	EN 1991-1-4	0.7 kN/m^2	1.5
3	Access	Live Load	Roof category H from EN 1991-1-4	0.4 kN/m^2	1.5



Figure 6. Complete model of the auditorium [33]

Since the two designs were so similar, the largest difference within the analysis was the self-weight of the tapered shell being larger than that of the shell with constant thickness. This proved to have a difference in deflection where the heavier, tapered shell had a deflection of 1 cm while the hypothetical shell only deflected 0.82 cm [33].

The more significant difference however is in the stress distribution across the shells. The wings become narrower on the side where it meets the ground, they go from 50 m wide in the middle where they meet the beam to 12m where it meets the ground [33]. This variation means that the stresses become more concentrated thus the expectation is that the model will show darker colours towards the foundations. This turns out to be true in the case of the shell with constant thickness, however the shell with tapered cross section, has a thicker section where it meets the ground which then counteracts the narrowing width [33].

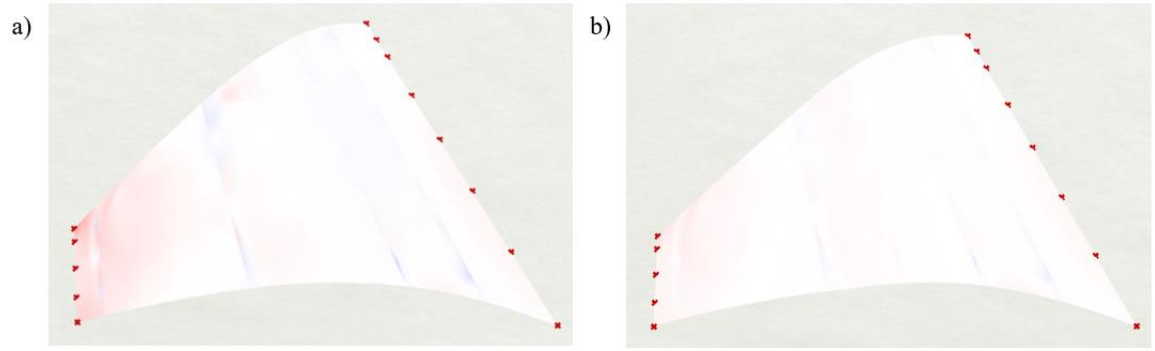


Figure 7 Principal stresses on the different shells a) constant 30cm thick shell b) variable thickness Shell [33]

Following this, the next point of concern would be the buckling of the constant thickness shell as the moments reach -81kNm/m, while the tapered section has a maximum bending moment of 27kNm/m at its thinnest point [33].

Unsurprisingly, the beams behave as would be expected, with displacement being at its highest in the middle of the beam, Figure 8.a , and compression on the top fibres and tension in the bottom fibres, Figure 8.b.

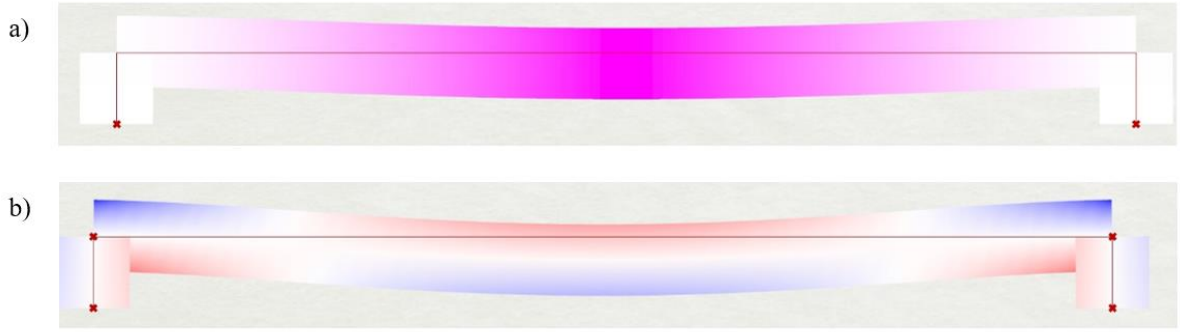


Figure 8. a) Displacement of beam b) Principal stresses on the beam. [33]

Recreating the 3D digital model of the case study and 3D printing of the structure provides great insights into design, behaviour and construction. In this case, individual shells and beam sections are printed separately giving clues in the complex nature of the tapered shells. The structure is designed for stability when the two shells work together. The beam stiffens as the tapered shells are attached to complete the two wings.

6. Discussion

"That in good architecture, when the structure is ready, architecture is already present." – Oscar Niemeyer [36]

This quote succinctly surmises Niemeyer's philosophy of design, where the structure and architecture are born together and coexist as a single entity. The engineers that worked with him, such as Contarini and Sussekind both repeatedly reaffirm this attitude in interviews and this is an example of Niemeyer's structural intuition at play [21] [28].

The structures observed in the case studies are visually different, however they do have similarities in terms of the rationalisation of their geometries. For the Congress, Niemeyer's design originally called for a parabola but he conceded to Cardozo's change to a revolved ellipsoid and tangential inverted cone, demonstrating Niemeyer's willingness to compromise his original idea for a more structurally intuitive option.

The way that Niemeyer designed these two buildings at the time used more conventional type of the design with hand calculations and drawings, while nowadays there are more advanced tools and softwares that allow for new ways of form-finding and faster iterative process. In this study the software used was Rhino3D, with the Grashopper, Karamba3D and other plugins to investigate how digital tools can be used to understand conventional structures with today's opportunities.

Despite the advancement in available tools there are still limitations to these that will affect the outcome and possibilities of the designs. In this particular set of case studies, the limitations with the software revolved around the geometric properties of the elements of the structure. For the National Congress the rings that had to be broken into 1m segments for the software to analyse them as beams, and for the auditorium, the tapered shell that had to be filleted into sections to show different thicknesses rather than a single continuous shell.

Whilst trying to understand the construction sequence and the rationalisation of form, the 3D model was useful to visualise and prove that the rationalised geometry was easy to build, thus fulfilling the ease of construction criteria of efficient design.

7. Conclusion

Ultimately, the examples of today's design explorations demonstrate that a more efficient and collaborative workflow is essential for modern construction projects. By addressing the fragmented nature of traditional linear workflow, stakeholders can work together to create buildings that simultaneously satisfy aesthetic, structural, functional, and construction-related objectives, while also contributing to climate change mitigation and sustainability.

Oscar Niemeyer, through his comprehensive education and the structural concern prioritised for his projects, carried a similar workflow throughout his career. He had a strong relationship and design collaboration with his engineers which allowed for cutting edge designs with the relatively new materials and techniques of the time. His innovation and precision to intrinsic detail rooted from the structurally intuitive nature of his design workflow.

There are many quotes from Niemeyer and his engineers on their collaboration process, perhaps one of the most insightful sources of these is the book with the collection of letters exchanged between Niemeyer and Sussekind [21]. In these Niemeyer writes: *"I attentively followed your explanations to the structural problems, not rarely caused by myself, certain that you always solve them in a masterful way."* and then continues *"I have felt how important you have been to me, in the development of my projects, a friendship that has seemed to do us both a lot of good."* [21]. The engineer also mentions a few projects where he and Niemeyer would discuss a design and come to a solution before submitting the final design to the client [21].

The structured analysis of two case studies have been demonstrated to provide an insight into a successful example of a collaborative workflow of aesthetically pleasing, structurally efficient and construction aware approach that results in Iconic architecture. Through physical modelling in this study, the fundamental principle behind the design and construction related challenges were identified. It was decided that 3D printing can serve as a valuable tool for feedback on the design at the early conceptual stages. Its implementation in the design workflow is recommended as it has been one of the earliest a tool for architectural design.

From the qualitative analysis in this study, it is seen that Niemeyer valued the engineers' point of view seeing them as a part of the initial design team to derive the concept. In the traditional design workflow where the architect receives the glory, often the engineer is responsible from facilitating the post-rationalisation of form to realisation where manufacturing becomes cumbersome and costly. Research into collaborative design strategies, learning from precedent and emphasis on practices with efficient design workflows becomes even more important when we consider the advantages of advanced digital opportunities in response to climate emergency.

References

[1] R. Prakesh, *Using digital form-finding methods to create innovative and sustainable structures,* 2020.

[2] A. MacDonald, Structure and Architecture, 3 ed., Routledge, 2019.

[3] N. Baldassini, "Architectural Structural Scheme," in *Structures and Architecture*, 2010.

[4] A. MacDonald, Structure and Architecture, 2 ed., Reed Elsevier, 2001.

[5] M. Taghavi, *The history of the relationship between architects and structural engineers,* 2010.

[6] M. Dunn, "Groundwork, Structure, Design: The Integrated Education of Architects and Engineers," in *Structures and Architecture*, 2010.

[7] I. Serefoglu, R. Pedreschi and M. Paredes Maldonado, "Consolidating Pedagogies In Between Architecture and Engineering," in *Structures and Architecture. A Viable Urban Perspective? (ICSA 2022)*, 2022.

[8] F. Bertagna, P. D'Acunto, P. Ohlbrock and V. Moosavi, "Holistic design explorations of building envelopes supported by machine learning," *Journal of Facade Design and Engineering,* vol. 9 (1), pp. 31-46, 2021.

[9] P. Jones, Ove Arup: masterbuilder of the twentieth century, London: Yale University Press, 2006.

[10] Architects Declare, "UK Architects Declare Climate and Biodiversity Emergency," 2019. [Online]. Available: https://www.architectsdeclare.com/. [Accessed 1 April 2023].

[11] Civil Engineers Declare, "UK Civil Engineers Declare Climate and Biodiversity Emergency," 2019. [Online]. Available: https://www.civilengineersdeclare.com/. [Accessed 01 April 2023].

[12] O. Arup, "Architects, Engineers and builders," *Journal of the Royal Society of Arts,* vol. 118, no. 5167, pp. 390-401, 1970a.

[13] C. Özmen and A. Ünay, "Architect – structural engineer collaboration in sustainable," *Gazi University Journal of Science,* vol. 24, no. 4, p. 919–925, 2011.

[14] E. Iacono, *Building Information Modelling for Construction Management,* 2018.

[15] O. Pritchard, "Gehry Monster: Foundation Louis Vuitton by Frank Gehry," *Architects' Journal.*

[16] R. Sacks, C. Eastman, G. Lee and P. Teich, "10.3 Foundation Louis Vuitton, Paris in BIM Case Studies," in *BIM Handbook,* Wiley, 2018, pp. 398-613.

[17] D. M. Macedo and E. G. Silva, "Contribuições De Joaquim Cardozo À Arquitetura De Oscar Niemeyer," in *11° SEMINÁRIO NACIONAL DO DOCOMOMO BRASIL*, Recife, 2016.

[18] J. Flemming, H. Honour and N. Pevsner, Dictionary of Architecture and Landscape Architecture, London: Penguin Books, 2007.

[19] M. Pawley and J. Glancey, "Oscar Niemeyer Obituary," *The Guardian,* 6 December 2012.

[20] M. Favero, "Dos Mestres Sem Escola a Escola Sem Mestre," Universidade Federal do Rio de Janeiro, 2009.

[21] O. Niemeyer and J. C. Sussekind, Conversas Entre Amigos, Revan, 2002.

[22] G. Tang, "An Overview of Historical and Contemporary Concrete Shells, Their Construction and Factors in Their Disappearance," *International Journal of Space Structures,* vol. 30, no. 1, 2015.

[23] Obra do Berço, "Obra do Berço: As Linhas do Jovem Niemeyer," [Online]. Available: https://aobradobercorj.org.br/niemeyer/. [Accessed 01 April 2023].

[24] F. Maciel, *A Vida é um Sopro,* 2007.

[25] R. Mayer, G. Edui Goncalez Martins and B. Turkienicz, "Niemeyer's Proportion Rules," Universidade Federal do Rio Grande do Sul, 2015.

[26] J. C. Sussekind, Interviewee, *@Divã Cultural (Archives Niemeyer) - Interview with the calculating engineer José Carlos Sussekind.* [Interview]. 15 August 2015.

[27] O. Niemeyer, "Forma e Função na Arquitetura," *Modulo,* vol. 18, 1960.

[28] N. C. Oliveira, O Mestre de Resolver Estruturas, São Paulo: Joseph Young Editorial, 2016.

[29] M. Moch, *National Congress Bras ́ılia..*

[30] S. Papadaki, Oscar Niemeyer, George Braziller, 1960.

[31] D. M. Macedo and E. G. Silva, "Congresso Nacional: Procedimentos Projectuais e Arquitura Brutalista," vol. 5, 2018.

[32] L. S. P. Inojosa, *O SISTEMA ESTRUTURAL NA OBRA DE OSCAR NIEMEYER,* Brasilia: Universidade de Brasilia, 2010.

[33] L. S. Wanderley, "The Influence of Structural Engineers in the Design Efficiency of Oscar Niemeyer's Works," 2022.

[34] *University of Constantine,* 2017.

[35] M. Bill, L. Cavalcanti, E. Kossel, C. Krohn, N. Maak, O. Niemeyer and J. C. Sussekind, Oscar Niemeyer, I. Flagge and P. Andreas, Eds., De Gruyter, 2013.

[36] J. Wolf, "Vôos e Vãos," *Revista AU,* pp. 15-23, 1987.

[37] X. Binjaku, "Joaquim Cardozo & Oscar Niemeyer," in *107th ACSA Annual Meeting Proceedings,* 2019.

[38] Structural Engineers Declare, "UK Structural Engineers Declare Climate and Biodiversity Emergency," 2022. [Online]. Available: https://www.structuralengineersdeclare.com/. [Accessed 01 April 2023].

[39] C. E. Porto, "Soluções Estruturais na Obra de Oscar Niemeyer," *paranoá,* vol. 15, pp. 22-51, 2015.

Proceedings of the IASS Annual Symposium 2023
Integration of Design and Fabrication
10–14 July 2023, Melbourne, Australia
Y.M. Xie, J. Burry, T.U. Lee and J. Ma (eds.)

Control objectives for adaptive slabs with integrated fluidic actuators, a comparison of effects

Markus NITZLADER*, Matthias J. BOSCH[b], Hansgeorg BINZ[b], Matthias KREIMEYER[b], Lucio BLANDINI[a]

* Institute for Lightweight Structures and Conceptual Design (ILEK) University of Stuttgart
Pfaffenwaldring 14, 70569 Stuttgart, Germany
markus.nitzlader@ilek.uni-stuttgart.de

[a] Institute for Lightweight Structures and Conceptual Design (ILEK) University of Stuttgart
Pfaffenwaldring 14, 70569 Stuttgart, Germany
[b] Institute for Engineering Design and Industrial Design (IKTD) University of Stuttgart

Abstract

The construction industry is responsible for much of the global resource depletion and greenhouse gas emissions. New methods are needed to significantly reduce resources and emissions associated with load-bearing structural elements. Conventional floor slabs embody up to 50% of the total structural mass in buildings to satisfy deflection limits and provide the required bending stiffness. Significant mass savings can be achieved by reducing actively the deflection response against loading using sensors and actuators. Fluidic actuators have been therefore developed to be embedded in the compression region of reinforced concrete slabs under bending action. Through the controlled expansion of such fluidic actuators, deflections and stresses caused by vertical loads are reduced within the required limits. This paper offers a benchmark study evaluating the effect of actuator placement and actuation forces for two different objectives: reduction of displacements and reduction of bending moments. A method to fulfil both objectives simultaneously has also been investigated. Depending on the direction of the actuation forces caused by pressurized regions within the cross-section of the slab, there are two main actuation modes: uniaxial and biaxial. Results show that the efficacy of uni- and biaxial actuation modes depend on the control objective. To compensate for displacements and moments simultaneously, biaxial actuation is most effective and requires the lowest actuation forces.

Keywords: adaptive floor slabs, adaptive structures, fluidic actuators, concrete slabs, multiaxial load-transfer

Copyright © 2023 by Markus NITZLADER, Matthias J. BOSCH, Hansgeorg BINZ, Matthias KREIMEYER and Lucio BLANDINI. Published in the Proceedings of the IASS Annual Symposium 2023 with permission.

1. Introduction

1.1 Motivation

The construction industry is responsible for much of the global resource depletion and greenhouse gas emissions [1, 2]. The construction industry is facing hard challenges to provide new living and working spaces required by population growth [3] and increasing urbanization [4] against resource scarcity of resources and the effect of climate change.

Structures are typically designed to take extreme loading events to satisfy safety and serviceability requirements [5]. Most structures, for example, flat roofs, car park slabs, stadiums, event halls, etc. are subject to variable loads. However, conventional methods such as prestressing and pre-cambering cannot respond to such variable loads, which, typically causes significant overdesign.

Conventional floor slabs embody up to 50% of the total structural mass in buildings [6, 7]. Floor slabs are typically built in reinforced concrete [6]. Large quantities of high-quality sand are required for the production of concrete. Such high-quality sand is already in short supply in some parts of the world [8]. In addition, CO_2 emissions from cement production account for 10% of the greenhouse gases of anthropic origin [9]. For this reason, one of the focuses of the research at ILEK is the development of lightweight and sustainable concrete structures. In concrete slabs, additional mass is typically required to provide sufficient bending stiffness to satisfy deflection limits under vertical loading [10]. Concerning structures subjected to bending stress, in general, the material near the neutral fibre is almost unused. To save mass, the load should be transferred using axial stiffness, as the bending stiffness is significantly lower. Material savings and thus weight reductions of reinforced concrete slabs can also help reduce the size of other components, such as columns and foundations.

Previous work has shown that the mitigation of the structural response through active control of stress and displacement (i.e., adaptation to loading), is an effective strategy to save the material mass required in load-bearing components [11–13]. Through the integration of sensors and actuators, structures can react against external loads to reduce deflections and stress peaks, which typically results in significant savings in mass and emissions [14, 15]. Adaptation offers great potential for material savings for stiffness-governed structures [16–18].

Previous design methodologies and experimental testing of adaptive structures have focused on truss and frame configurations including high-rise buildings and bridges [19–21]. Preceding work has also addressed the development of 2-dimensional thin-walled adaptive structures including shear walls, plates and shells [22–24]. The potential of adaptive concrete slab structures has received comparatively smaller attention.

1.2. Background, actuation through integrated fluidic actuators

New types of actuators for beam and slab components have been developed within the project "Integrated Fluid Actuators" [25–27] which is part of the Collaborative Research Centre (SFB) 1244 Adaptive Skins and Structures for the Built Environment of Tomorrow (University of Stuttgart).

Fluidic actuators have been strategically embedded in the cross-section of reinforced concrete components, within the compression zone, as shown in Figure 1. Referring to Figure 1 (a), the pressurization of the chambers and their consequent expansion causes a pair of opposite forces that, due to the eccentric position above the neutral fibre of the beam, results in a moment pair. This moment pair can counteract the bending moment caused by vertical loads. This way it is possible to artificially increase the bending stiffness which enables better use of the axial stiffness.

If the chambers are separated, several of them are needed to act over a certain distance. Due to dissipative effects, the force produced by a single actuator decreases gradually moving away from the chamber,

which has been modelled numerically in [25, 28]. Multiple actuators, in general, involve a more complex control system architecture, for example due to power distribution issues. As discussed for the uniaxial load transfer case (i.e., beam), to avoid increasing the number of chambers required to act over long distances, the distance between the application region of the actuation forces must be increased. This requires the development of new types of actuators that enable the generation of moment pairs acting over long distances without creating large cavities in the pressure chambers. Typically, large cavities affect negatively the load transfer in the passive state and, depending on the actuator shape (e.g., prismatic) could cause unwanted vertical actuator forces. A formulation to develop these new actuator types is given in [27]. However, if the distance between chambers is extended as shown in Figure 1 (b), the generated moment pair can act over a longer distance using only one actuator. To avoid the forces generated by the pressurization of the two ends of the chambers working against each other, one possible concept previously shown in [27] is to create a small gap filled with a low-stiffness material, which is indicated by empty regions in Figure 1 (b). This way, in principle, no force is applied onto the internal surfaces B and C when the chamber is pressurized resulting in the desired moment pair from the forces applied to the surface pair A-D. The actuation forces cause a compression zone on the outer sides of the surface-pair AD and a tension zone inside the region between B-C, as indicated in Figure 1 (b). For uniaxial load transfer, experimental verification of this actuation concept has been given in [26].

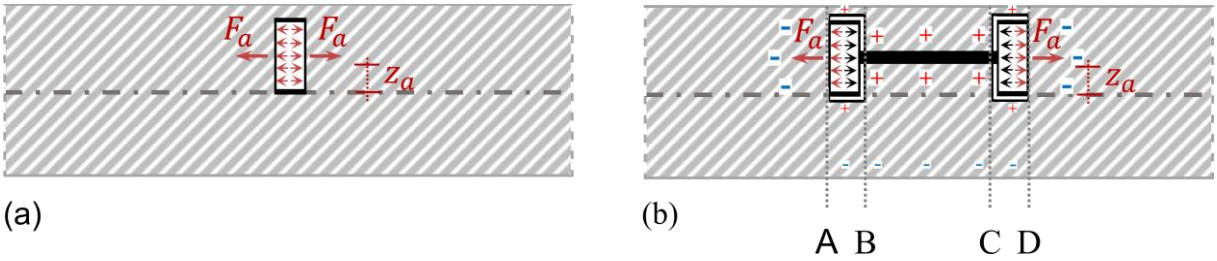


Figure 1: Actuation working principle in beam, a) single pressure chamber, b) extended pressure chamber.

An approach to developing such an actuation concept for slabs with multi-axial load transfer is given in [29]. Since this work focuses on numerical aspects, the actuator effect is simplified in the form of moment pairs (Figure 2).

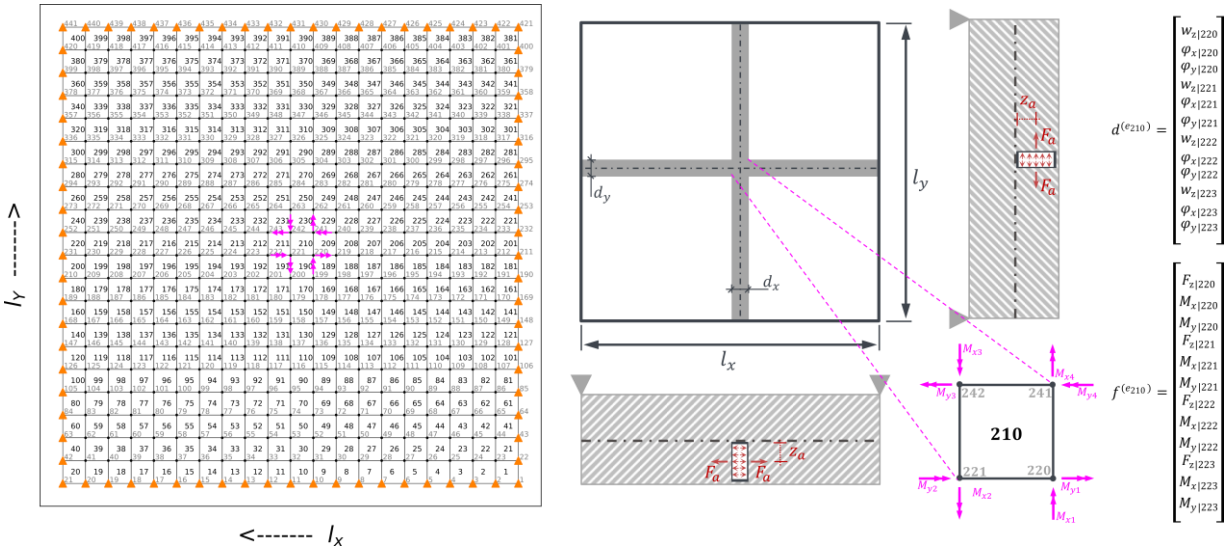


Figure 2 Actuation working principle in a plate. The actuator actions are illustrated as pairs of moments, Finite-Element-mesh, element labels are indicated in black and node labels in grey, deformation and force vector at element 210.

1.3. New contribution

This paper builds on the work presented in [29] which is summarized in section 2.1 to develop new actuation concepts for slabs. Actuation influence matrices [29, 30] are employed for deriving suitable placement, which includes the actuator form and topology as well as the control forces. The control objectives taken into consideration are displacement reduction and bending moment reduction. The effects of these two control objectives on actuator placement, actuation modes (i.e., the direction of applied actuation loads) and actuation loads are investigated. An approach to address both objectives simultaneously is also formulated. Simulations are carried out based on the dimensions of the floor slabs that will be installed in a prototype of an adaptive high-rise experimental building [21].

2. Analysis of a simply supported two-way slab

2.1. Summary of the general formulation of influence matrices

Assuming small strains and displacements, the adaptive state can be formulated as a superposition of a passive and an active state. The passive state is the structural response caused by conventional loads (e.g., self-weight and dead load) while the active state is the response caused by actuation forces. Influence matrices can be employed to analyse the effect of conventional and actuation loads on the different system states (active, passive, adaptive) [30]. For a chosen actuation mode (cf. section 2.3) the response caused by a unit actuation force can be quantified for each structural element. In other words, since the actuator layout is not known, each structural component is thought of as a candidate site to host an actuator. For the investigated slab, with *DOF* degrees of freedom and $i^{\#}$ active elements, equilibrium and compatibility conditions can be written as:

$$\boldsymbol{K}\boldsymbol{d} = \boldsymbol{f} = \boldsymbol{f}_{pas} + \boldsymbol{f}_{act} \tag{1}$$

Where $\boldsymbol{K} \in \mathbb{R}^{\mathrm{DOF\ x\ DOF}}$ is the stiffness matrix, $\boldsymbol{d} \in \mathbb{R}^{\mathrm{DOF}}$ is the deformation vector and $\boldsymbol{f} \in \mathbb{R}^{\mathrm{DOF}}$ is the force vector. The force vector can be separated into forces of the passive state $\boldsymbol{f}_{pas}$ and forces of the active state $\boldsymbol{f}_{act}$. In this work, the superscript # indicates the total number of the respective counting variable. An actuator allocation matrix $\boldsymbol{A} \in \mathbb{R}^{\mathrm{DOF\ x}\ i^{\#}}$ collates column-wise the forces produced by the unit actuation of each element in turn. The vector $\boldsymbol{u} \in \mathbb{R}^{\mathrm{DOF}}$is used as an actuation input:

$$\boldsymbol{f}_{act} = \boldsymbol{A}\boldsymbol{u} \tag{2}$$

If only the active system state is considered, for example, to generate influence matrices or influence surfaces, the actuation input vector $\boldsymbol{u}$ can be formulated as the identity matrix of dimensions $\mathbb{R}^{i^{\#}\mathrm{x}\ i^{\#}}$, which can therefore be omitted. Replacing Equation (2) in (1) yields the equation to compute the actuation influence matrix for displacements:

$$\boldsymbol{E}_d = \boldsymbol{K}^{-1}\boldsymbol{A} \tag{3}$$

By selecting every third global *DOF* of the influence matrix of displacements $\boldsymbol{E}_d \in \mathbb{R}^{\mathrm{DOF\ x}\ i^{\#}}$, the influence matrix for translational displacements, $\boldsymbol{E}_{d(w)} \in \mathbb{R}^{n^{\#}\mathrm{x}\ i^{\#}}$ is obtained (in the case of Finite-Element-mesh shown in Figure 3 $\boldsymbol{E}_{d(w)} \in \mathbb{R}^{2601\ \mathrm{x}\ 2500}$). $n^{\#}$ denotes the total number of element corner nodes. To compute actuation influence matrices for stress resultants, the element deformation vectors caused by unit actuation forces are multiplied with the strain-displacement as well as the stress–strain material matrices. A full description of the computation and use of the individual influence matrices is given in [29].

Influence matrices can be evaluated row or column-wise [31]. Each row indicates the influence of each element (considered active) on a component of the structural response, e.g., translational displacements or moments in the x-direction. Each column indicates the influence of the corresponding element on the structural response (i.e., on all DOFs).

As described in [30], influence matrices can also be used to calculate the actuation forces required to control the structure into a specific state $\boldsymbol{y}_{ada}$:

$$\boldsymbol{y}_{ada} = \boldsymbol{y}_{pas} + \boldsymbol{y}_{act} = \boldsymbol{K}^{-1}\boldsymbol{f}_{pas} + \boldsymbol{E}_d\boldsymbol{u} \tag{4}$$

Since influence matrices are typically not square, the Moore–Penrose pseudoinverse, denoted with $(\cdot)^+$, is employed to compute the actuation input $\boldsymbol{u}^*$:

$$\boldsymbol{u}^* = \left(\boldsymbol{E}_{d,comb}\right)^+ (\boldsymbol{y}_{ada} - \boldsymbol{y}_{pas}) \tag{5}$$

2.2. Adopted numerical model

The configuration considered in this work is a floor slab that is modelled as a quadratic plate with a span of 5 x 5 m, which is simply supported along all edges. The dimensions and material properties, indicated in Table 1, have been selected based on the floor slabs of the adaptive high-rise demonstrator D1244 [21]. The floor slab is discretized by subdividing each edge into 50 elements (2500 elements) as shown in Figure 3. All simulations have been performed using quadratic Elements with bilinear shape functions based on Reissner Mindlin Plate Theory, implemented in Python 3.7.8 [32].

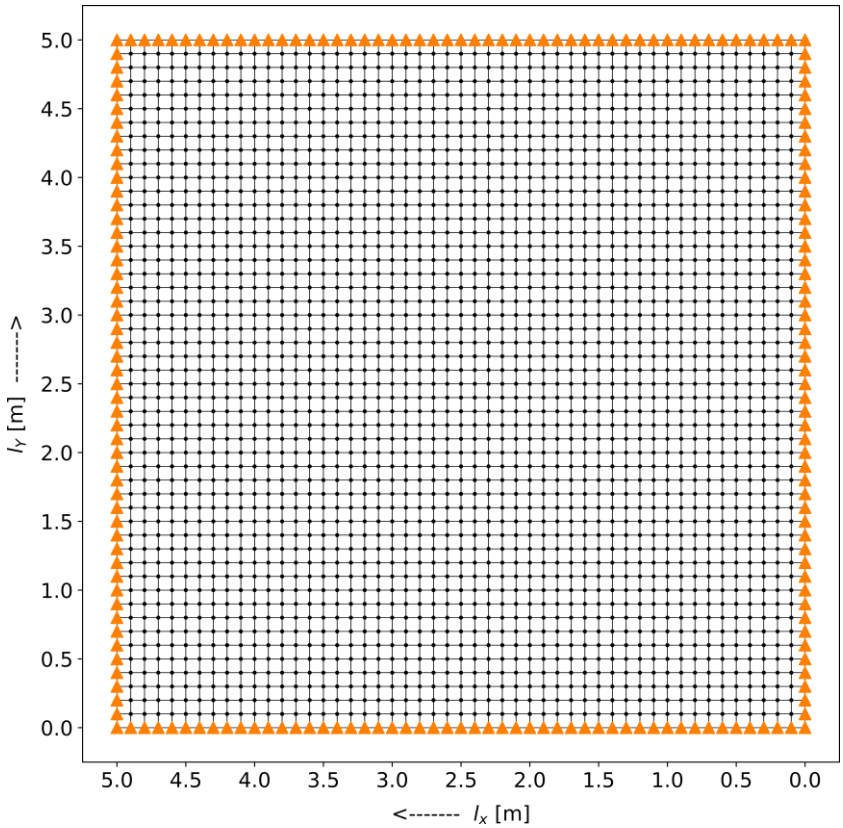


Figure 3: Finite-Element-mesh.

Table 1. Floor slab dimensions and material properties.

Properties	Value	Unit
Span $l_x = l_y$	5	m
Thickness	0.12	m
Element size $l_{a,x} = l_{a,y}$	0.1	m
E-modulus	37	GPa
Poisson's ratio	0.2	-

2.3. Actuation modes

Actuation modes are understood as the working direction of actuation forces caused by pressurized regions embedded within the cross-section of the slab. In this work, the effect of such pressurized regions is simplified with moments. Therefore, the actuation modes indicate the direction of the moments in the active state of an element. A general overview of possible actuation modes is given in [7]. Figure 4 gives an overview of the actuation modes considered in this work. The labels 45° and 135° refer to the axis of the resulting moments with reference to the coordinate system shown in Figure 4.

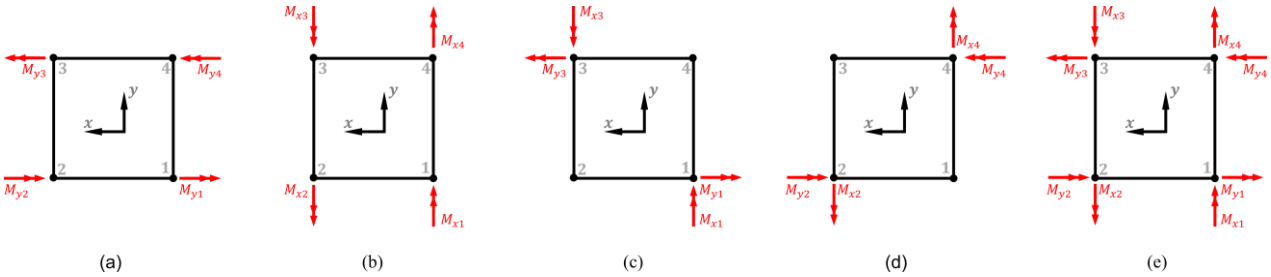


Figure 4: Considered actuation modes, (a) uniaxial actuation along Y-Axis, (b) uniaxial actuation along X-Axis, (c) uniaxial actuation 135°, (d) uniaxial actuation 45 °, (e) biaxial actuation.

The efficacy of the individual actuation modes depends on the control objective (cf. section 2.4). Summing the entries of a column yields a characteristic value of the influence of the corresponding element and actuation mode on the control objective which can be employed to evaluate the efficacy of a candidate site for actuation [29].

2.4 Control objectives

The choice of actuation mode depends on the control objective. First, each actuation mode presented in section 2.3 is evaluated by studying the efficacy of the actuation of each element on the reduction of deformations and bending moments. Figure 5 shows the plot of the summed influence on translational displacements *w* for all elements under (a) biaxial actuation, (b) uniaxial actuation 45° and (c) uniaxial actuation X-Axis. Due to symmetry, the plot for uniaxial actuation 135° and Y-Axis can be obtained by rotating that for 45° and X-Axis, respectively, by 90° degree. Figure 5 indicates that concerning displacement reduction, a biaxial actuation is effective in the centre of the slab and the uniaxial actuations 45° and 135° are effective on the diagonals. Uniaxial actuation X- and Y-Axis are comparatively ineffective to control displacements. Note that the actuation influence is independent of the effective of external loads. The summed influences indicate the effect of an actuation mode for each element of the slab (i.e., each element is assumed to be an actuator in turn) on the control objective.

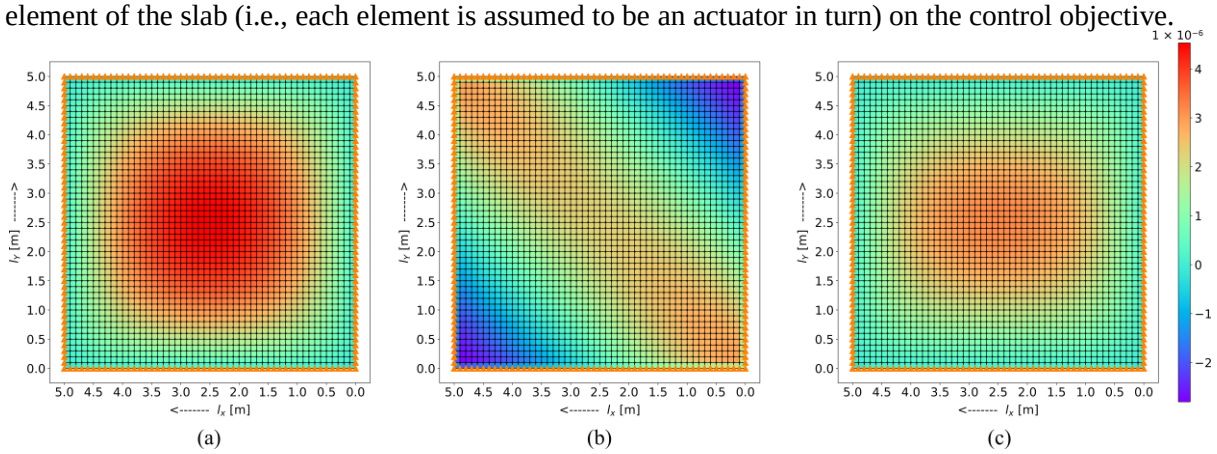


Figure 5: Summed influence on the displacements *w* for biaxial actuation (a), 45° (b) and X-Axis (c) uniaxial actuation.

For the analysis of the influence on the reduction of bending moments, the principal moments are considered. Figure 6 shows the summed influences on the principal moment m_1 for all elements of a biaxial actuation (a), uniaxial actuation 45° (b) and uniaxial actuation X-Axis (c). Due to symmetry, the plot for uniaxial actuation 135° and Y-Axis can be obtained by rotating that for 45° and X-Axis, respectively, by 90° degree. The same applies to the principal moment m_2. In this case, biaxial actuation is also effective along the diagonals. The uniaxial actuations 45° and 135° are only effective in the corners of the slab. In addition, the uniaxial actuations X- and Y-Axis are effective in the perimeter area along the respective main axes.

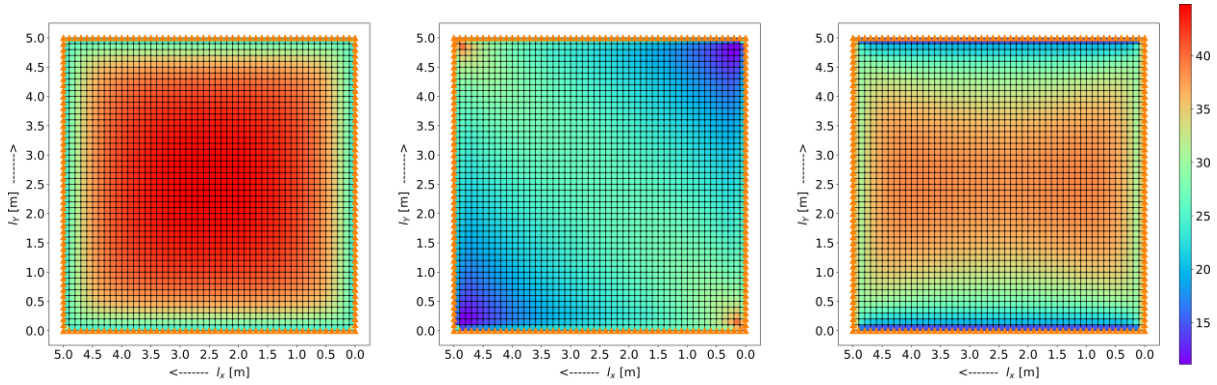


Figure 6: Summed influences on the principal moments m_1 of biaxial actuation (a), 45° (b) and X-Axis (c) uniaxial actuation.

A combination of the actuation modes with the highest influence for each control objective is shown in Figure 7. Actuation mode (a) combines elements with high actuation efficacy for the control of displacements and mode (b) for the control of principal moments m_1. Biaxial actuation is predominant for both control objectives, it avoids orientation issues of uniaxial actuation (cf. corner areas Figure 7 (a)) and the need for different actuator types is reduced. For these reasons, mode (c) which is a fully biaxial actuation mode is also considered in the following (Figure 7 (c)). Since no integrated fluidic actuators can be placed in the region of the supports (edges) and the influence is practically negligible regardless of the control objective, no active elements are placed along the edges (cf. Figure 7).

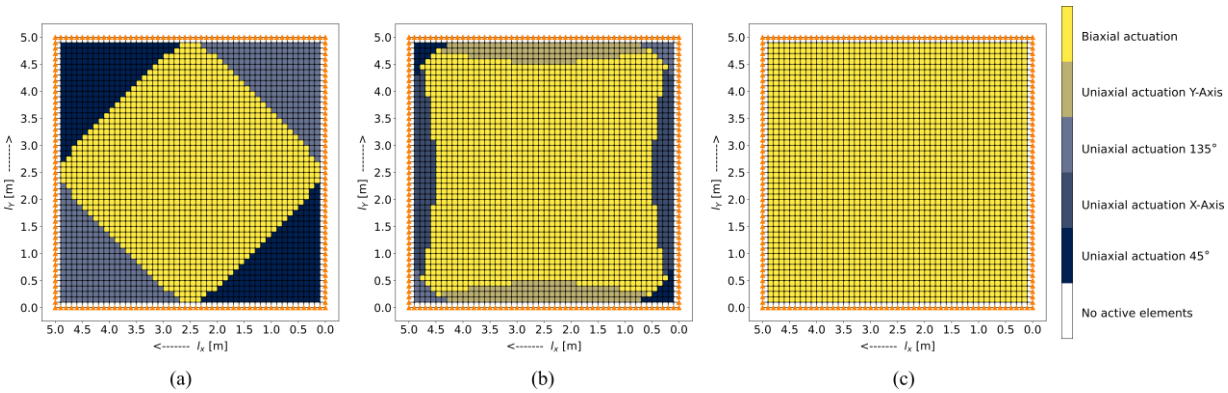


Figure 7: Actuation modes for reduction of deformations (a) reduction of bending moments (b) and complete biaxial distribution (c)

2.5 Adaptive system state

The efficacy of the combined actuation modes presented in section 2.4 is evaluated to reduce displacements and moments caused by vertical downward loading. A uniformly distributed load of 3 kN/m² and a quasi-point load of 3 kN applied on each element in turn are considered. To calculate the actuation input $\boldsymbol{u}^*$ (cf. equation (5)) the adaptive nominal state $\boldsymbol{y}_{ada}$ (control objective) is set to the negative passive state under the respective load case (i.e., complete reduction of translational and rotational deformations from the passive state). All three combined actuation modes (cf. section 2.4) are evaluated. Table 2 shows a summary of the results for the uniformly distributed load. The table indicates the maximum percentage reduction of translational displacements (column max. % red. *w*) in relation to the passive state, as well as an average value for all nodes to give an indicator of the global behaviour (columns avg. % red. *w* and avg. % red. m_1). A value of 100 % indicates complete compensation, and values below 100 % indicate that the target state is not fully achieved. Values above 100 % indicate a change of sign or deterioration from the passive state; for example, for the translational displacements, a value above 100 %, indicates an upward displacement or in the case of bending moments a change of sign or an increase of the respective bending moment. If only the node in the slab midspan, which shows the highest displacement and moment in the passive state is considered, all three approaches show very similar values near 100%. In some cases, the percentage change of principal moments m_1 is misleading. Large changes occur in areas where the bending moment is close to zero in the passive state. Therefore, the reduction of the maximum moment from the passive to the adaptive state is given (column homog. % red. m_1) as an indication of homogenization. To evaluate the effort required to achieve the adaptive state, table 2 also shows the required maximum actuation moments in the active system state. This value in column max. f_{act} indicates the maximum moment required for a single active element, which must be applied by an actuator. The average values refer to the average of the maximum moments of all active elements.

Table 2. Reduction of displacements and principal moment under a uniformly distributed load.

Control objective	**Uniformly distributed load 3 kN/m²**			
	max. % red. *w*	avg. % red. *w*	homog. % m_1	avg. % red. m_1
Displacements (mode a)	99.95	99.82	88.38	112.54
Principal moments (mode b)	103.09	99.68	69.54	124.59
Disp. + moment (mode c)	99.89	99.82	98.26	102.17

	max. f_{act} [Nm/m]	avg. f_{act} [Nm/m]
Displacements (mode a)	761.97	168.49
Principal moments (mode b)	1,363.98	285.89
Disp. + moment (mode c)	248.90	118.08

Table 3 shows a summary of the results under the quasi-point load and is structured analogously to table 2. As values close to the edges deviate strongly from the average, it is more informative to evaluate the maximum and the minimum reduction across all load cases instead of the average value. At the point of maximum displacement (slab midspan), all values are slightly above 100%, which indicates a marginal over-compensation.

Table 3. Reduction of displacements and principal moment under quasi-point load.

Control objective	**Point load 3 kN**			
	max. % red. w	min. % red. w	homog. % m_1	avg. % red. m_1
Displacements (mode a)	104.81	26.77	98.87	103.48
Principal moments (mode b)	„	„	98.88	„
Disp. + moment (mode c)	„	„	98,79	100.78

	max. f_{act} [Nm/m]	avg. f_{act} [Nm/m]
Displacements (mode a)	1.00	0.21
Principal moments (mode b)	4.00	0.88
Disp. + moment (mode c)	2.96	0.55

3. Result discussion

In most stiffness-dominated problems, compliance with deformation limits is the governing design criteria. However, if moments can be compensated at the same time, there is potential for reducing the required reinforcement. Compared to conventional slabs, the active load case plays a significant role in the design. The generation of the active moments through pressurization of the chambers can cause large in-plain stresses, (cf. Figure 1), making the actuation load dominant for the design. Concepts with low actuation loads are therefore advantageous.

As expected, the combined actuation mode based on the influence of displacement manipulation performs best in terms of displacement reduction. In comparison with the other actuation modes, the difference in displacement reduction is small while Larger differences can be observed in the moments and required actuation loads.

The summed influence plots provide information on how a single active element performs with regard to a control objective. However, no information can be gained about the interaction of several active elements with each other. Interaction means the superposition of the active moments as shown in Figure 8.

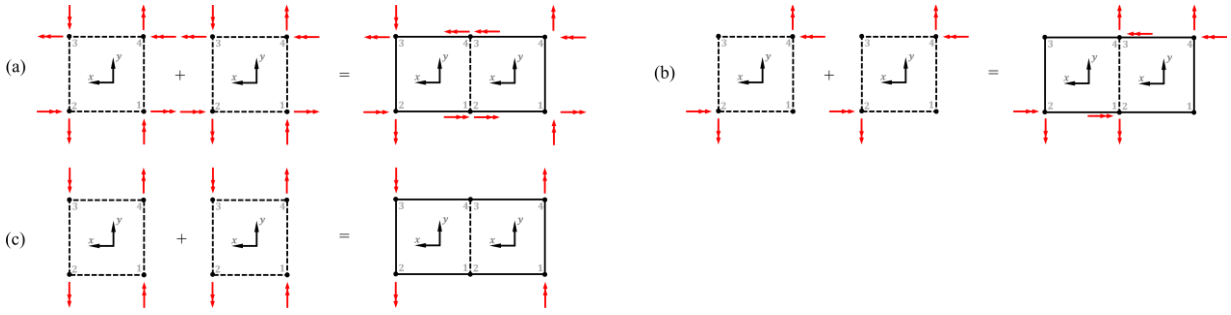


Figure 8: Superposition of actuation moments between adjacent elements using (a) biaxial actuation, (b) uniaxial actuation 45° and (c) uniaxial actuation along X-Axis.

This problem of superposition is also shown by the plots of the principal moment m_1 in the adaptive state (Figure 9). The least improvement in comparison to the passive state (Figure 9 (a)) is in the areas where different actuation modes interact.

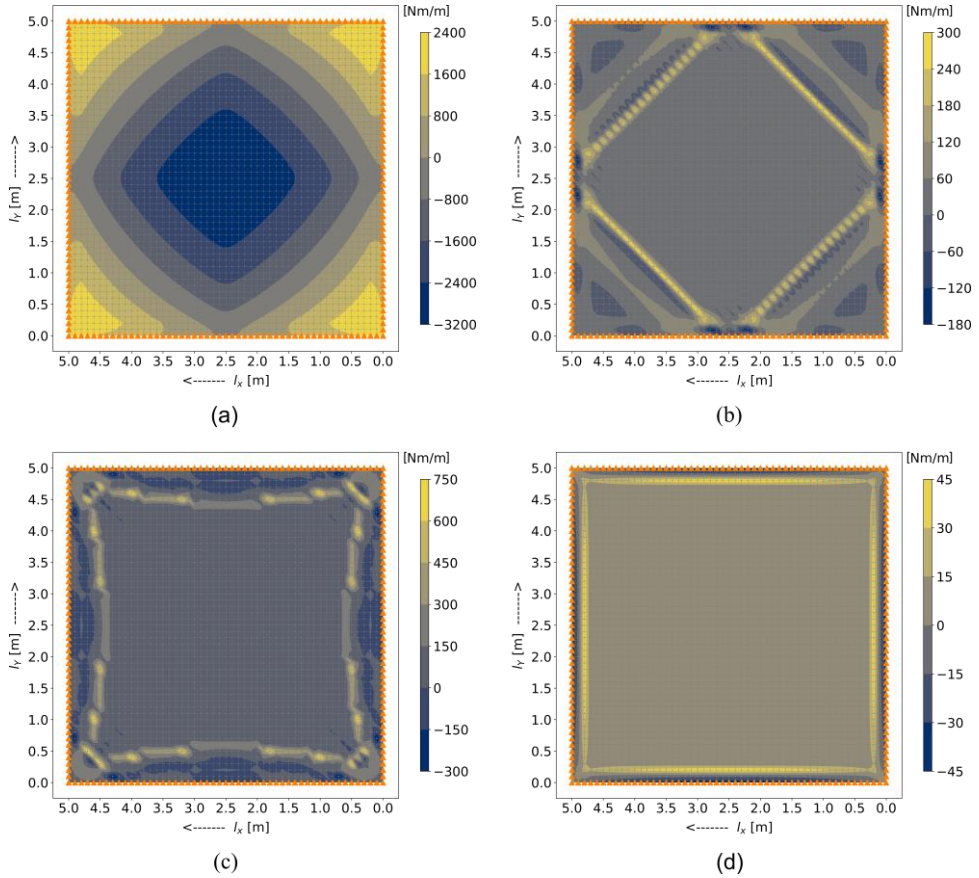


Figure 9: Plot of the principal moment m_1 under a uniformly distributed load of 3 kN/m² in the passive state (a) and in the adaptive state using the actuation mode for reduction of displacements (b) principal moment m_1 (c) and fully biaxial actuation (d)

A fully biaxial actuation has the greatest potential for an efficient superposition and therefore performs best. If biaxial actuation cannot be implemented for practical reasons (e.g., physical actuator limitations), uniaxial actuators can be placed according to their efficacy (i.e. influence) as shown in Figures 5 and 6.

4. Conclusion

This study shows that different combinations of actuation modes (directions of actuation) are advantageous depending on the choice of the control objective. Uniaxial actuation is more effective in certain regions of the slab when considering a single control objective.

To reduce simultaneously displacements and moments caused by external loads, biaxial actuation is the most effective strategy. In addition, the required actuation loads are lowest with pure biaxial actuation.

The theoretical investigations of this work can be used to specify requirements of the actuation concept on the actuator design.

Future work will evaluate the mass-savings potential for different actuation modes including simultaneous reduction of bending stresses and out-of-plane deflections. The actuation and actuator concept will also be investigated experimentally in future work.

Acknowledgements

This work is funded by the Deutsche Forschungsgemeinschaft (DFG, German Research Foundation) – Project-ID 279064222 – SFB 1244. The authors are grateful for the generous support.

References

[1] UNEP, *2020 Global status report for buildings and construction: towards a zero-emission, efficient and resilient buildings and construction sector*. Nairobi, 2020.
[2] W. Sobek, *Non nobis - über das Bauen in der Zukunft, Bd. 1: Ausgehen muss man von dem, was ist* (Bd. 1). Stuttgart: av edition, 2022.
[3] United Nations, Departments of Economic and Social Affairs, Population Division., *World Population Prospects 2019: Highlights*, 2019.
[4] United Nations, Departments of Economic and Social Affairs, Population Division., *World urbanization prospects: the 2018 revision*, 2019.
[5] F. Fingerloos, J. Hegger, and K. Zilch, Eds. *Eurocode 2 für Deutschland: DIN EN 1992-1-1 Bemessung und Konstruktion von Stahlbeton- und Spannbetontragwerken, Teil 1-1: Allgemeine Bemessungsregeln und Regeln für den Hochbau mit nationalem Anhang : kommentierte und konsolidierte Fassung*, 2nd ed. (Beuth Kommentar). Berlin, Wien, Zürich, Berlin: Beuth; Ernst & Sohn a Wiley brand, 2016.
[6] T. Berger, P. Prasser, and H. G. Reinke, "Einsparung von Grauer Energie bei Hochhäusern," *Beton- und Stahlbetonbau*, vol. 108, no. 6, pp. 395–403, 2013, doi: 10.1002/best.201300019.
[7] M. Nitzlader, M. Bosch, H. Binz, M. Kreimeyer, and L. Blandini, "Actuation of concrete slabs under bending with integrated fluidic actuators," in *15th World Congress on Computational Mechanics (WCCM-XV) and 8th Asian Pacific Congress on Computational Mechanics (APCOM-VIII)*, July 31 to Aug. 2022, doi: 10.23967/wccm-apcom.2022.014.
[8] P. Peduzzi, "Sand, rarer than one thinks," *UNEP Global Environmental Alert Service*, 2014.
[9] K. L. Scrivener, J. M. Vanderley, and E. M. Gartner, "Eco-efficent cements: Potential economically viable solutions for a low-CO2 cement-based materials industry," *Cement and Concrete Research*, 2018.
[10] L. Blandini, "Lightweight and Sustainable Concrete Structures: The ILEK Research Strategy," in *Proceedings of the fib International Congress 2022 in Oslo, Norway*, 2022.
[11] T. T. Soong and G. D. Manolis, "Active structures," *Journal of Structural Engineering*, vol. 113, no. 11, pp. 2290–2302, 1987, doi: 10.1061/(asce)0733-9445(1987)113:11(2290).
[12] G. Senatore, P. Duffour, S. Hanna, F. Labbe, and P. Winslow, "Adaptive structures for whole-life energy savings," in *International Association for Shell and Spatial Structures (IASS)*, 52nd ed., 2011, pp. 233–240.
[13] W. Sobek, "Ultra-lightweight construction," *International Journal of Space Structures*, vol. 31, no. 1, pp. 74–80, 2016, doi: 10.1177/0266351116643246.
[14] A. Ostertag, M. Dazer, B. Bertsche, F. Schlegl, and O. Sawodny, "Reliable Design of Adaptive Load-Bearing Structures with Focus on Sustainability," in *Proceedings of the 30th European Safety and Reliability Conference (ESREL)*, Venice, Italy, 2020, pp. 4703–4710, doi: 10.3850/978-981-14-8593-0_3806-cd.
[15] A. P. Reksowardojo, G. Senatore, A. Srivastava, C. Carroll, and I. F. C. Smith, "Design and testing of a low-energy and -carbon prototype structure that adapts to loading through shape morphing," *International Journal of Solids and Structures*, no. 252, 2022.
[16] F. Geiger, J. Gade, M. von Scheven, and M. Bischoff, "A case study on design and optimization of adaptive civil structures," *Frontiers in Built Environment*, vol. 6, p. 94, 2020, doi: 10.3389/fbuil.2020.00094.
[17] G. Senatore and A. P. Reksowardojo, "Force and shape control strategies for minimum energy adaptive structures," *Frontiers in Built Environment*, vol. 6, p. 105, 2020, doi: 10.3389/fbuil.2020.00105.
[18] S. Steffen, A. Zeller, M. Böhm, O. Sawodny, L. Blandini, and W. Sobek, "Actuation concepts for adaptive high-rise structures subjected to static wind loading," *Engineering Structures*, vol. 267, 2022, doi: 10.1016/j.engstruct.2022.114670.
[19] Y. Wang and G. Senatore, "Design of adaptive structures through energy minimization: extension to tensegrity," *Structural and multidisciplinary optimization : journal of the*

International Society for Structural and Multidisciplinary Optimization, early access. doi: 10.1007/s00158-021-02899-y.

[20] M. Schnellenbach-Held, A. Fakhouri, D. Steiner, and O. Kühn, *Adaptive Spannbetonstruktur mit lernfähigem Fuzzy-Regelungssystem: Bericht zum Forschungsprojekt 88.0107/2010* (Berichte der Bundesanstalt für Strassenwesen, Reihe B, Brücken- und Ingenieurbau 101). Bremen: Fachverlag NW, 2014.

[21] L. Blandini *et al.*, "D1244: Design and Construction of the First Adaptive High-Rise Experimental Building," *Frontiers in Built Environment*, vol. 8, 2022. doi: 10.3389/fbuil.2022.814911.

[22] S. Neuhäuser, M. Weickgenannt, C. Witte, W. Haase, O. Sawodny, and W. Sobek, "Stuttgart Smartshell - a full scale prototype of an adaptive shell structure," *Journal of the International Association for Shell and Spatial Structures*, vol. 54, no. 178, pp. 259–270, 2013.

[23] A. Weilandt, "Adaptivität bei Flächentragwerken," Dissertation, Universität Stuttgart, 2008.

[24] T. Kleine, J. L. Wagner, M. Böhm, and O. Sawodny, "Optimal actuator placement and static load compensation for a class of distributed parameter systems," *at - Automatisierungstechnik*, vol. 69, no. 9, pp. 739–749, 2021, doi: 10.1515/auto-2021-0027.

[25] C. Kelleter, T. Burghardt, H. Binz, L. Blandini, and W. Sobek, "Adaptive concrete beams equipped with integrated fluidic actuators," *Frontiers in Built Environment*, vol. 6, pp. 107–119, 2020, doi: 10.3389/fbuil.2020.00091.

[26] T. Burghardt *et al.*, "Investigations of a large-scale adaptive concrete beam with integrated fluidic actuators," *Civil Engineering Design*, vol. 4, 2022, doi: 10.1002/cend.202100037.

[27] M. Bosch *et al.*, "Design of integrated fluidic actuators for muti-axial loaded structural elements," in *8th European Congress on Computational Methods in Applied Sciences and Engineering*, 5th - 9th Jun. 2022, doi: 10.23967/eccomas.2022.081.

[28] M. Bosch *et al.*, "Effective range of integrated fluidic actuators in structural elements," in *15th World Congress on Computational Mechanics (WCCM-XV) and 8th Asian Pacific Congress on Computational Mechanics (APCOM-VIII)*, July 31 to Aug. 2022, doi: 10.23967/wccm-apcom.2022.046.

[29] M. Nitzlader, S. Steffen, M. J. Bosch, H. Binz, M. Kreimeyer, and L. Blandini, "Designing Actuation Concepts for Adaptive Slabs with Integrated Fluidic Actuators Using Influence Matrices," *CivilEng*, vol. 3, no. 3, pp. 809–830, 2022, doi: 10.3390/civileng3030047.

[30] S. Steffen, S. Weidner, L. Blandini, and W. Sobek, "Using influence matrices as a design and analysis tool for adaptive truss and beam structures," *Frontiers in Built Environment*, vol. 6, pp. 22–33, 2020, doi: 10.3389/fbuil.2020.00083.

[31] S. Steffen, L. Blandini, and W. Sobek, "Analysis of the inherent adaptivity of basic truss and beam modules by means of an extended method of influence matrices," *Engineering Structures*, vol. 266, 2022, doi: 10.1016/j.engstruct.2022.114588.

[32] A. Geiser, T. Oberbichler, and K. Sautter, *Theory of Plates - Version 1.0.1 Nov. 2017* (2017). TUM Statik.

Proceedings of the IASS Annual Symposium 2023
Integration of Design and Fabrication
10–14 July 2023, Melbourne, Australia
Y.M. Xie, J. Burry, T.U. Lee and J. Ma (eds.)

Effect of stochastic imperfections on the buckling of open-top storage tanks under wind loads

Liang LIU[a,*], Ying SUN[a], Ning SU[b], Zhenggang CAO[a]

[a,*] Key Lab of Structures Dynamic Behavior and Control of China Ministry of Education, Harbin institute of Technology
73 Huanghe Road, Nangang District, Harbin, Heilongjiang, China
liu_liang1112@163.com

[b] Key Laboratory of Environmental Protection Technology on Water Transport, Ministry of Transport, Tianjin Research Institute for Water Transport Engineering

Abstract

Open-top storage tanks are prone to buckling under wind loads due to the lack of top restraint. As a typical cylindrical shell, the buckling capacity is very sensitive to initial imperfections and the first buckling eigenmode is generally considered to be the most unfavorable imperfection shape, i.e., the consistent imperfection modal method (CIMM). However, this assumption has not been fully verified and the randomness of actual tank imperfections is not taken into account. In this study, a stochastic imperfection modal superposition method (SIMSM) is utilized to analyze the randomness of imperfections. The first ten buckling eigenmodes are superposed and corresponding participation coefficients are treated as random variables conform to normal distribution. Through Monte Carlo simulation, the stochastic structural buckling analyses are carried out on 1000 samples. The results show that the first buckling eigenmode is not always the most unfavorable initial imperfection shape, but the difference in buckling load factors between the two imperfect tanks can be minor. Besides, multi-parameter empirical formulas to accurately estimate the knock-down factor η of unstiffened and stiffened open-top tanks with different geometries are obtained through parameter fitting, which can provide safe guidance for structural design.

Keywords: open-top storage tanks, buckling of cylindrical shells, the most unfavorable imperfection, Monte Carlo simulation, knock-down factor

1. Introduction

Large petrochemical storage tanks mostly adopt the type of floating roof tank with open top, which are prone to buckling failure under empty conditions due to the combined effect of wind pressure on the outer and inner surfaces of tank walls and the lack of top restraint [1, 2]. It is difficult to repair the damaged storage tank, which will interrupt the production process, bring security risks, and may lead to serious economic losses and environmental pollution.

At present, many researchers have studied the wind-induced buckling characteristics of cylindrical tanks. For example, Flores and Godoy [3] analyzed the bifurcation buckling, nonlinear buckling and dynamic response of storage tanks damaged during hurricane Marilyn by numerical method. Portela and Godoy [4], Uematsu et. al [5] measured the wind pressure on grouped tanks in various arrangements through wind tunnel tests, and then the effects of arrangement pattern and gap spacing on the buckling of tanks were analyzed. The strengthening effects of the tank bottom were studied by Bu and Qian [6] and the optimal analysis to minimize the weight of wind girders for a given wind load was performed numerically. In addition, by conducting wind tunnel tests on elastic cylindrical shells, the relationship between the geometries and wind-induced buckling behavior has been studied in [7 - 9].

Copyright © 2023 by Liang LIU, Ying SUN, Ning SU and Zhenggang CAO. Published in the Proceedings of the IASS Annual Symposium 2023 with permission.

Since the diameter of a large storage tank can exceed 100 meters and the ratio of radius to thickness R/t is usually more than 2000, initial imperfections can greatly reduce the buckling capacity of this typical thin-walled structure. Godoy and Flores [10] studied the imperfection sensitivity of open-top storage tanks of four geometric sizes and compared the change of potential energy. Zhao and Lin [11] analyzed the wind-induced buckling of finite element tank models and found that short storage tanks are more sensitive to the first buckling eigenmode imperfection than the weld imperfection. In addition, in other studies covering initial imperfections of various shapes [10 - 13], it was also found that the first buckling eigenmode is more damaging. Regarding the first buckling eigenmode as the most unfavorable imperfection shape is called the consistent imperfection modal method (CIMM). The reduction of buckling capacity is usually represented by the knock-down factor η. In [11 - 15], the factor is between 0.5 and 0.9 for tanks with different geometries and imperfection amplitudes. In the American tank design standard API 650 [16], its value is fixed at 0.8, while Greiner and Derler [12] proposed that $\eta = 0.7$ under the effect of wind pressure, without considering changes in tank geometries and imperfection amplitudes. Chen and Rotter [17] discussed the influence of the first buckling eigenmode imperfections and obtained an empirical formula of buckling capacity for imperfect cylindrical shells, but only for the two cases of the aspect ratio $H/D = 1.5$ and 3.5. For large storage tanks with much smaller H/D, nonlinear buckling analysis based on the finite element method is usually required to predict the imperfection sensitivity.

However, the above studies only analyzed several imperfections of specific shapes and did not take into account the randomness of actual tank imperfections. For other structures such as spatial lattice shells, stochastic imperfection modal method considering the random imperfection of joints and members has been used in some studies [18, 19]. Although it has higher accuracy, the computing cost is usually large for complex structures. Liu et al. [20] proposed the stochastic imperfection modal superposition method (SIMSM) for a single-layer reticulated shell, which combines several modes to form the initial imperfection shape and takes the participation coefficients as random variables satisfying different probability distributions. The computing cost is lower than the traditional stochastic method.

Therefore, in order to reflect the randomness of tank imperfections and examine the reliability of CIMM and SIMSM, Monte Carlo simulations are firstly performed in this paper to sample the participation coefficients of buckling eigenmodes and determine the initial geometric imperfections. Then, an open-top cylindrical tank with $H/D = 0.2$ is selected as an example. The nonlinear buckling analysis is carried out to calculate the buckling capacity after applying the superposed initial imperfections. Based on the results of a large number of samples, the most unfavorable imperfection shape is determined and compared with the results of CIMM. Finally, considering the lack of quantitative method to evaluate the adverse effects of initial imperfections directly, the knock-down factor η of tanks with different geometric sizes and imperfection amplitudes are calculated through plenty of imperfection sensitivity analyses, and multi-parameter empirical prediction formulas are proposed to provide a reference for structural design.

2. Process of SIMSM

In the CIMM, only the first buckling eigenmode of the structure is applied with low computing cost, while the traditional stochastic imperfection modal method regards the imperfections of all nodes as random variables, which greatly increases the consumption of computing resources. The SIMSM combines these two thoughts, which uses the first m buckling eigenmodes of a tank, and coordinate deviations of all nodes are the stochastic superposition of the eigenmodes:

$$\{\Delta x\} = \sum_{i=1}^{m} c_i \{U\}_i \tag{1}$$

where $\{\Delta x\}$ is the node coordinate deviation caused by the imperfection, and c_i is the participation coefficient of the i-th eigenmode $\{U\}_i$, which is assumed to be a random variable conforming to normal

distribution. For each eigenmode, the modal displacement of all nodes should meet the following requirement:

$$\max\left(U_{1i},U_{2i},...,U_{ni}\right)=1 \tag{2}$$

where n is the total number of degrees of freedom of tank nodes. For the initial geometric imperfection with a given amplitude ξ, it is necessary to normalize the node coordinate deviation to obtain the imperfection $\{\Delta x\}'$:

$$\{\Delta x\}' = \xi * \Delta x / \max\left(\Delta x_1,\Delta x_2,...,\Delta x_n\right) \tag{3}$$

Then the node coordinates of the tank are:

$$\{x\} = \{x_0\} + \{\Delta x\}' \tag{4}$$

where $\{x_0\}$ is the initial node coordinate of the perfect tank, and $\{x\}$ is the modified coordinate with stochastic imperfection. Through Monte Carlo simulation, the geometric nonlinear finite element analysis is performed based on the j-th sampling result $\{c\}_j$, and then the critical buckling load factor λ_j is calculated. If the total number of samples is T, the load factor λ_{cr} corresponding to the most unfavorable imperfection shape obtained by the SIMSM is:

$$\lambda_{cr} = \min\left(\lambda_1,\lambda_2,...,\lambda_T\right) \tag{5}$$

3. Example analysis

3.1. Finite element model

The commercial software Abaqus is used for finite element analysis of the large open-top tank. The tank height H is 22.5m, diameter D is 112.5m, and the aspect ratio H/D = 0.2. The simplified uniform wall thickness is adopted as t = 15mm. The material is isotropic steel with elastic modulus E = 206Gpa, density ρ = 7850kg/m3, and Poisson's ratio v = 0.3. Since the buckling of the tank wall always occurs in the elastic range, the yield of material is not considered here [13].

The 4-node reduced integration element "S4R5" is used to avoid shear locking, and the thickness integration is calculated by the Simpson method with 5 integration points. Meshing the tank wall uniformly along the circumferential and axial direction. Through convergence analysis, the size of the quadrilateral element is about 0.5m × 0.5m, and the total number of elements is 28800. For the anchored tank with open top, the bottom of the finite element model is fixed and the top is free, as shown in Figure 1. The imperfection amplitude is set to $\xi = 1t$ and $\xi = 2t$.

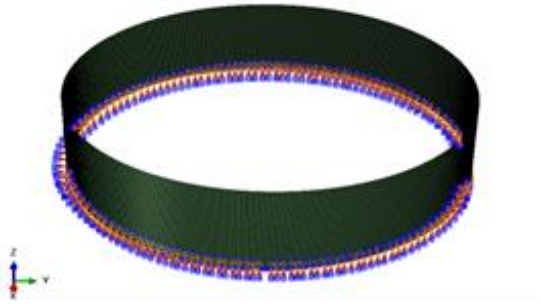


Figure 1. The finite element model of the open-top tank with H/D = 0.2.

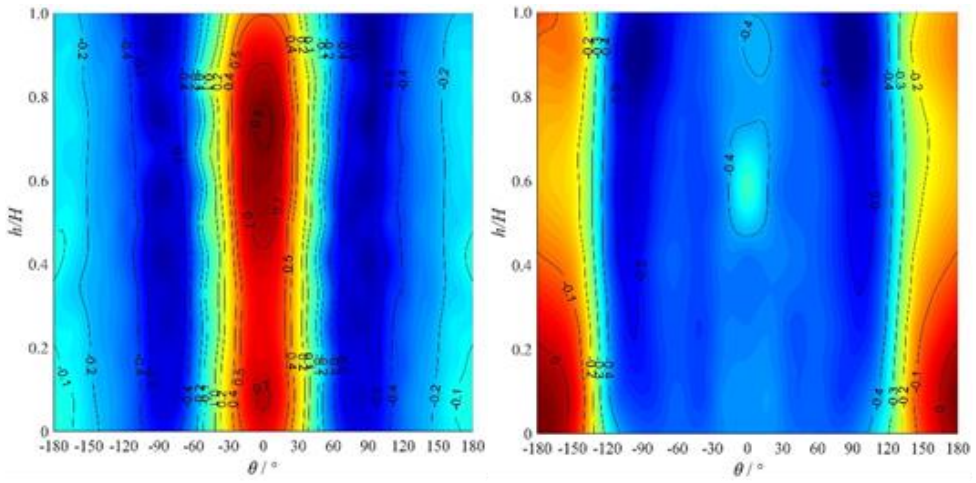
3.2. Wind load

The mean wind pressure on the outer and inner wall surfaces is obtained by wind tunnel tests on a rigid model with the same aspect ratio, as shown in Figure 2. Since the construction sites of large petrochemical storage tanks are mostly coastal ports, the boundary layer wind field of terrain type A (open country exposure) in Load Code [21] is selected. The scale ratio is 1:75, and the wind tunnel blocking rate is less than 5%. Pressure taps are arranged uniformly on the outer and inner surfaces to measure the wind pressure simultaneously. The effects of Reynolds number are not considered in the boundary layer flow field [22].



Figure 2. Wind tunnel test on the open-top tank model.

Taking the tank height H as the reference height, Figure 3 shows the mean wind pressure coefficient distribution on the outer and inner surfaces obtained from the test. It can be seen from the figure that the windward side of the outer surface is subject to large positive pressure, while the inner surface is subject to negative pressure. The superposition of the outer and inner wind pressure makes the thin-walled tank prone to buckling on the windward side.



(a) (b)

Figure 3. Mean wind pressure coefficient distributions on the tank surfaces: (a) outer surface, (b) inner surface.

3.3. Buckling analysis

Through eigenvalue buckling analysis, the first 10 eigenmodes of the tank are obtained and superposed stochastically. Change the initial coordinates of the finite element model nodes, and geometric nonlinear buckling analysis is carried out with the arc-length method. Figure 4 shows the buckling load factor for all samples when $\xi = 1t$ and $\xi = 2t$. The total number of samples is 1000 and the reference wind pressure is 100Pa.

It can be seen that when the imperfection amplitude $\xi = 1t$, the first eigenmode is the most unfavorable imperfection shape, indicating the reliability of CIMM. However, when $\xi = 2t$, the buckling load factor of samples moves down due to the increase of the imperfection amplitude, and even lower than the result

of CIMM, indicating that the first eigenmode is not always the most unfavorable imperfection shape. The lowest sample result of SIMSM is 1.756, and the result of CIMM is 1.772. The difference between the two is within 1%.

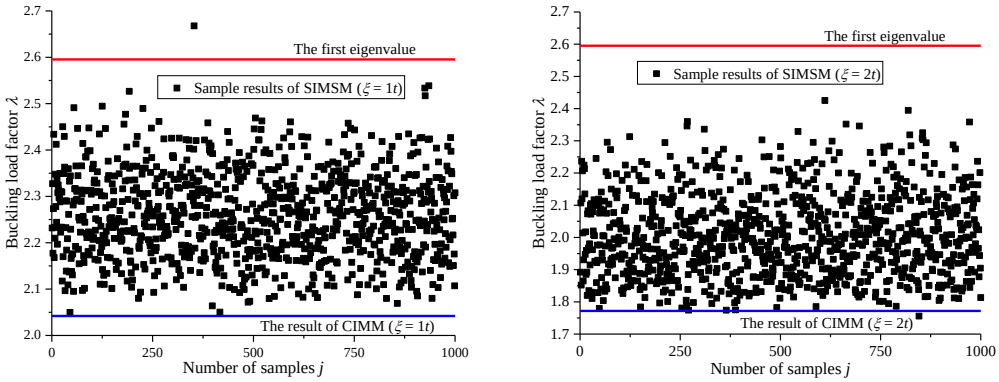
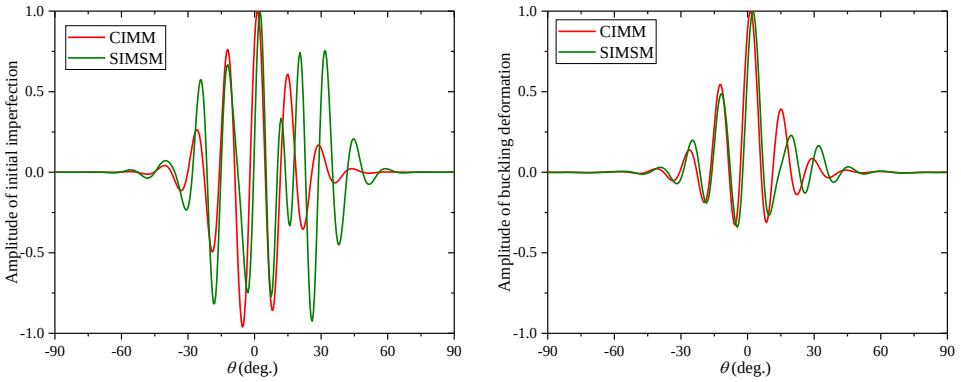


Figure 4. Comparisons of buckling load factors of the tank model.

Figure 5 shows the differences of the initial imperfection shape and the critical buckling deformation between the CIMM and the most unfavorable sample of SIMSM when $\xi = 2t$. The initial imperfection shape is obviously different, especially on the right side, and the deviation degree of the most unfavorable sample is higher than that of the first eigenmode. But from the perspective of critical buckling deformation, the difference between the two is relatively small. The buckling deformation is almost the same except for a slight difference on the right side. Therefore, the buckling capacity and deformation obtained from the two methods are very similar. It is reasonable to regard the first buckling eigenmode as the most unfavorable initial imperfection shape for convenience in practical engineering.

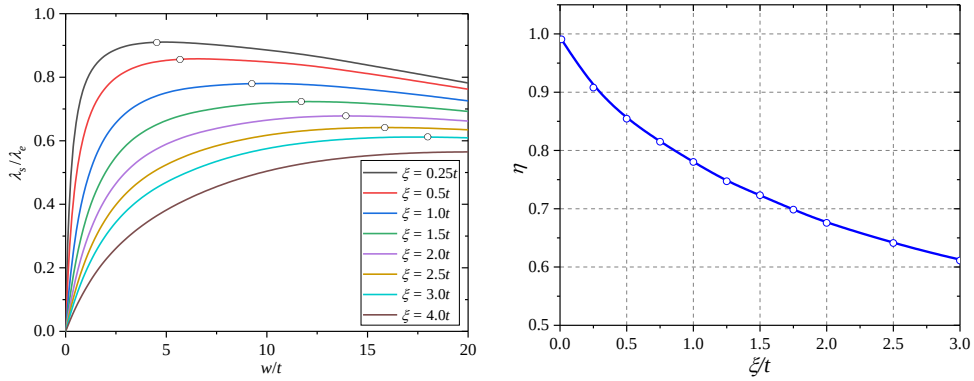


(a) (b)

Figure 5. Comparisons of the CIMM and the most unfavorable sample of SIMSM: (a) initial imperfection shape, (b) critical buckling deformation.

4. Quantitative analysis of imperfection sensitivity

Due to the lack of a direct evaluation method for the adverse effect of the initial imperfection, the change of wind-induced buckling capacity of storage tanks with different imperfection amplitudes ξ is studied by taking the first eigenmode as the initial imperfection shape. Figure 6(a) shows the load-displacement curves obtained by nonlinear analysis, where the vertical coordinate represents the ratio of the load factor λ_s to the first eigenvalue λ_e, and w represents the maximum radial displacement of the tank wall. The inflection point of the curve corresponds to the critical buckling state, where the knock-down factor η as shown in Figure 6(b) can be obtained.

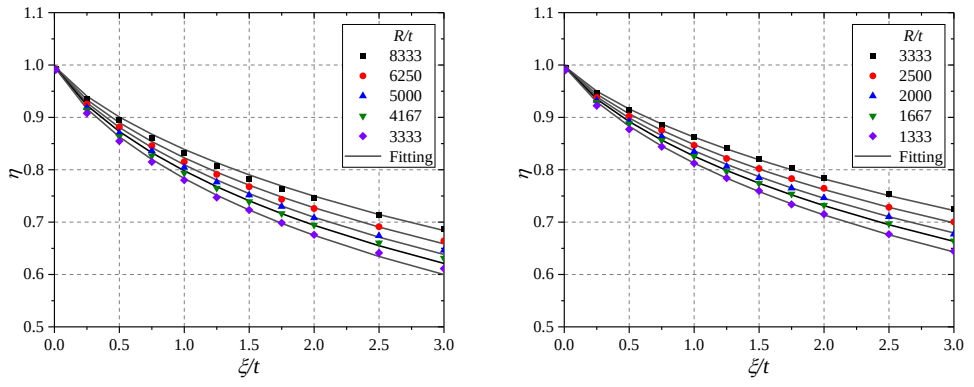


(a) (b)

Figure 6. Nonlinear analysis results of tanks with different imperfection amplitudes ξ: (a) load-displacement curves, (b) imperfection sensitivity curve.

As can be seen from Figure 6, the nonlinearity of load-displacement curves becomes more significant as ξ increases. The tank undergoes the limit-point buckling instead of bifurcation buckling, and the critical buckling load factor decreases gradually. When the imperfection amplitude $\xi = 0.25t$, the buckling capacity of the tank decreases by nearly 10%, and when $\xi = 2t$, the capacity decreases by about 32%, indicating that the tank is very sensitive to initial geometric imperfections. However, the decline of the knock-down factor η gradually slows down. With the further increase of ξ, no obvious downtrend of the load-displacement curve occurs, and the radial displacement of the inflection point is increasing. Taking $w/t = 20$ as a limit [23], if no inflection point appears before this value, it is considered to be a limit deformation problem rather than buckling, so only cases of $\xi/t \leq 3$ are discussed below.

In order to obtain empirical fitting results, a large number of parametric analyses are carried out. Considering the common size range, a variety of tanks with aspect ratios H/D = 0.2, 0.5, 1.0 and 1.5 and wall thicknesses t = 5, 6, 8, 10, 12, and 15mm are selected to analyze the influence of geometric parameters on imperfection sensitivity. The results of tanks with H/D = 0.2 and 0.5 are shown as the scatters in Figure 7. It can be seen that tanks with smaller R/t are more sensitive to initial imperfection. When R/t = 3333, η of the tank with H/D = 0.2 is lower than the result of H/D = 0.5 under the same imperfection amplitude, indicating that the initial geometric imperfection has a more significant adverse effect on the lower tank.



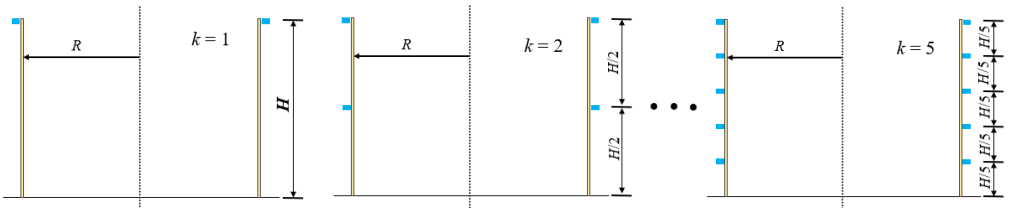
(a) (b)

Figure 7. Imperfection sensitivity and fitting results of tanks: (a) H/D = 0.2, (b) H/D = 0.5.

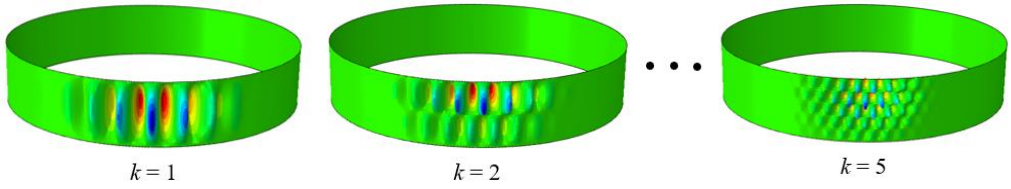
By fitting the geometric parameters of all analyzed cases, an empirical formula for the knock-down factor η is obtained as Equation (6). The fitting curves are shown in Figure 7, which are close to the scatters and have high accuracy.

$$\frac{1}{\eta}=1+4.2\left[\frac{\xi}{t}\left(\frac{H}{R}\right)^{-3/4}\left(\frac{R}{t}\right)^{-1/2}\right]^{4/5} \tag{6}$$

For actual tanks built according to the design standard [16], several wind girders (stiffener rings) are usually installed on the wall to strengthen the tank and improve its buckling capacity. The bending stiffness of wind girders are large, which can be regarded as rigid compared to the tank wall generally [24] and also change the imperfection sensitivity of the tank. Figure 8 shows the arrangement of wind girders and their different first buckling eigenmodes, where k represents the number of wind girders. k = 1 is to set the top wind girder, and other girders are arranged at equal intervals in the middle when k > 1.



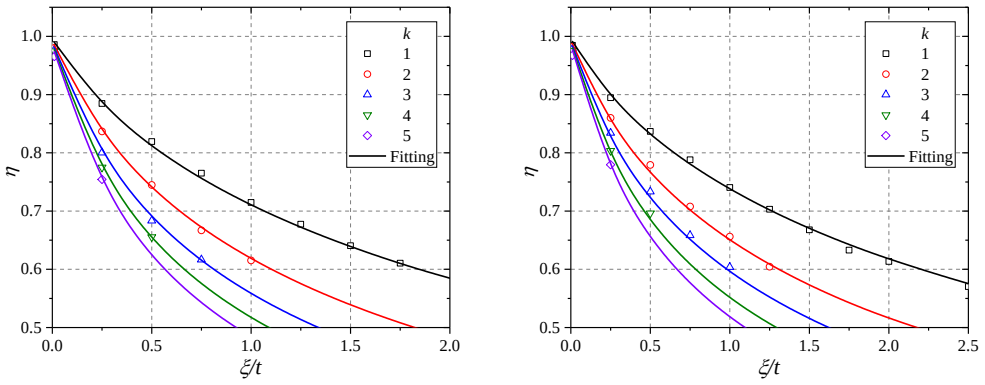
(a)



(b)

Figure 8. The arrangements of wind girders and their different first buckling eigenmodes: (a) arrangements with different k, (b) the first buckling eigenmodes.

The scatters in Figure 9 show the imperfection sensitivity of stiffened tanks with H/D = 0.5 and 1.0. Compared to the unstiffened tank in Figure 7, the stiffened tanks are significantly more sensitive to initial imperfections. For the case of the top stiffened tank with k = 1 in Figure 9(a), the knock-down factor η is about 0.71 when $\xi = 1t$, while the value for the unstiffened tank of the same size is about 0.86. It can be considered that wind girders can reduce the effective height of the tank, that is, a tank with smaller H/D and higher buckling capacity, which is more sensitive to initial imperfections with lower knock-down factors.



(a) (b)

Figure 9. Imperfection sensitivity and fitting results of stiffened tanks: (a) H/D = 0.5, R/t = 3333, (b) H/D = 1.0, R/t = 1667.

Through the parameter fitting of all cases, an empirical formula for the knock-down factor η of the stiffened tank with k wind girder(s) is obtained, as shown in Equation (7). The fitting curves in Figure 9 are in good agreement with the scatters, indicating that the formula has high prediction accuracy.

$$\frac{1}{\eta}=1+10.5\left[\frac{\xi}{t}\left(\frac{H}{kR}\right)^{-3/4}\left(\frac{R}{t}\right)^{-1/2}\right]^{4/5} \tag{7}$$

5. Conclusion

The SIMSM is utilized to analyze the effect of initial geometric imperfections on the buckling of open-top storage tanks, which can reflect the randomness of imperfections and save the computing cost. Nonlinear analysis results show that the first eigenmode is not always the most unfavorable imperfection shape, or even quite different from it, but the buckling capacity and critical deformation between the two imperfect tanks are relatively close. It is reasonable to apply the first eigenmode (the CIMM) for convenience in practical engineering.

Initial imperfections can result in a significant reduction in buckling capacity. For the unstiffened tank with H/D = 0.2, the knock-down factor η is about 10% when the imperfection amplitude $\xi = 0.25t$, and about 32% when $\xi = 2t$. In addition, tanks with smaller H/D and R/t, as well as stiffened tanks with wind girders are more sensitive to initial imperfections. Through plenty of case analysis and parameter fitting, empirical formulas to accurately estimate the knock-down factor of unstiffened and stiffened tanks with different geometries are obtained, which can provide safe guidance for structural design.

Acknowledgements

This study was financially supported by the National Natural Science Foundation of China (Grant Nos. 52202415, 52178132 and 52278167).

References

[1] L. A. Godoy, "Performance of storage tanks in oil facilities damaged by hurricanes Katrina and Rita," *Journal of Performance of Constructed Facilities*, vol. 21, no. 6, pp. 441–449, 2007.

[2] R. C. Jaca and L. A. Godoy, "Wind buckling of metal tanks during their construction," *Thin-Walled Structures*, vol. 48, pp. 453–459, 2010.

[3] F. G. Flores and L. A. Godoy, "Buckling of short tanks due to hurricanes," *Engineering Structures*, vol. 20, no. 8, pp. 752–760, 1998.

[4] G. Portela and L. A. Godoy, "Wind pressure and buckling of grouped steel tank," *Wind and Structures*, vol. 10, no. 1, pp. 23–44, 2007.

[5] Y. Uematsu, J. Yasunaga and C. Koo, "Design wind loads for open-topped storage tanks in various arrangements," *Journal of Wind Engineering and Industrial Aerodynamics*, vol. 138, pp. 77–86, 2015.

[6] F. Bu and C. F. Qian, "A rational design approach of intermediate wind girders on large storage tanks," *Thin-walled structures*, vol. 92, pp. 76–81, 2015.

[7] Y. Uematsu and K. Uchiyama, "Deflection and buckling behavior of thin, circular cylindrical shells under wind loads," *Journal of Wind Engineering and Industrial Aerodynamics*, vol. 18, pp. 245–261, 1985.

[8] K. Uchiyama, Y. Uematsu and T. Orimo, "Experiments on the deflection and Buckling behavior of ring-stiffened cylindrical shells under wind pressure," *Journal of Wind Engineering and Industrial Aerodynamics*, vol. 26, pp. 195–211, 1987.

[9] J. Yasunaga and Y. Uematsu, "Dynamic buckling of cylindrical storage tanks under fluctuating wind loading," *Thin-Walled Structures*, vol. 150, 106677, 2020.

[10] L. A. Godoy and F. G. Flores, "Imperfection sensitivity to elastic buckling of wind loaded open cylindrical tanks," *Structural Engineering and Mechanics*, vol. 13, no. 5, pp. 533–542, 2002.

[11] Y. Zhao and Y. Lin, "Buckling of cylindrical open-topped steel tanks under wind load," *Thin-Walled Structures*, vol. 79, pp. 83–94, 2014.

[12] R. Greiner and P. Derler, "Effect of imperfections on wind-loaded cylindrical shells," *Thin-Walled Structures*, vol. 23, pp. 271–281, 1995.

[13] Y. C. Chiang and Y. Guzey, "Influence of internal inward pressure on stability of open-top aboveground steel tanks subjected to wind loading," *Journal of Pressure Vessel Technology*, vol. 141, 031204, 2019.

[14] R. C. Jaca, L. A. Godoy and J. G. A Croll, "Reduced stiffness buckling analysis of aboveground storage tanks with thickness changes," *Advances in Structural Engineering*, vol. 14, no. 3, pp. 475–487, 2011.

[15] G. Portela and L. A. Godoy, "Wind pressures and buckling of cylindrical steel tanks with a conical roof," *Journal of Constructional Steel Research*, vol. 61, pp. 786–807, 2005.

[16] *Welded tanks for oil storage: API 650*. Washington, DC: API Publishing Services, 2016.

[17] L. Chen and J. M. Rotter, "Buckling of anchored cylindrical shells of uniform thickness under wind load," *Engineering Structures*, vol. 41, pp. 199–208, 2012.

[18] R. M. Tahamouli and G. Mehrdad, "Random imperfection effect on reliability of space structures with different supports," *Structural Engineering and Mechanics*, vol. 55, no. 3, pp. 461–472, 2015.

[19] G. B. Chen, H. Zhang, K. J. R. Rasmussen and F. Fan, "Modeling geometric imperfections for reticulated shell structures using random field theory," *Engineering Structures*, vol. 126, pp. 481–489, 2016.

[20] H. J. Liu, W. Zhang and H. Yuan, "Structural stability analysis of single-layer reticulated shells with stochastic imperfections," *Engineering Structures*, vol. 124, pp. 473–479, 2016.

[21] *Load code for the design of building structures: GB 50009-2012*. Beijing: China Architecture and Building Press, 2012 (in Chinese).

[22] L. Liu, Y. Shun, N. Su, Y. Wu and S. T. Peng, "Three-dimensional Reynolds number effects and wind load models for cylindrical storage tanks with low aspect ratios," *Journal of Wind Engineering and Industrial Aerodynamics*, vol. 227, 105080, 2022.

[23] *Eurocode 3: Design of Steel Structures-Part 4-1: Silos: EN 1993-4-1*. Brussels: European Committee for Standardization, 2007.

[24] Y. Uematsu, T. Yamaguchi and J. Yasunaga, "Effects of wind girders on the buckling of open-topped storage tanks under quasi-static wind loading," *Thin-Walled Structures*, vol. 124, pp. 1–12, 2018.

IASS 2023
July 10–14 Melbourne
Integration of Design and Fabrication

Proceedings of the IASS Annual Symposium 2023
Integration of Design and Fabrication
10–14 July 2023, Melbourne, Australia
Y.M. Xie, J. Burry, T.U. Lee and J. Ma (eds.)

Experimental study on estimation of water content and compaction of soil by SDS test

Tomoyuki SAKAMOTO*, Keisuke NOMURA[a]

* Architecture and Civil Engineering, Tokai University
2cckm008@mail.u-tokai.ac.jp

[a] Dept. of Architecture and Building Engineering, School of Architecture and Urban Planning

Abstract

Much of the land in Japan is mountainous, and embankments sites are often used.In new embankments, harmful settlement of buildings is often occurred.In Japan, when designing small buildings, the soil is often investigated by the screw weight sounding test (SWS test).This test is often used because it is quick and inexpensive.The purpose of the SWS test is to estimate the strength of the soil, and it cannot clearly estimate the soil type, water content ratio, and compaction degree, which greatly affect settlement.On the other hand, the screw driver sounding test (SDS test) is an improved version of the SWS test.The SDS test, the rotational resistance torque of the rod is measured. It provides more information about the soil than the SWS test.The authors considered that it is possible to estimate the water content ratio and the compaction degree of the soil from the measured torque. In order to verify the validity of this assumption, several simulated soils with different water content and compaction degree were created, and the correlation between the measured values of the SDS test, water content, and compaction degree was confirmed. The target soils were decomposed granite soil and Kanto loam, both of which have been frequently reported to cause settlement damage in Japan. The results showed that the ratio of vertical load energy to rotational resistance torque energy was correlated with the compaction degree, and that the amount of change in the ratio depended on the water content, and that the tendency of the correlation differed depending on the soil type.

1. Introduction

Japan has many mountainous areas. For this reason, buildings are often constructed on the ground with embankments. In this case, if the ground is not sufficiently compacted during construction, there is a possibility of harmful settlement occurring in the building. To verify this possibility, it is necessary to accurately understand the characteristics of the ground in question. To do this, it is necessary to perform indoor tests with samples collected, and to collect samples properly, extensive investigative equipment is required. For small-scale buildings where cost reduction is desired, a simple investigation method that can determine the presence or absence of subsidence on-site is required. On the other hand, there are construction standards for embankments[1], and the specified compaction degree varies depending on the purpose of the embankment. The specified value is determined based on past examples and numerous experiments to ensure that harmful subsidence does not occur for the weight of commonly-sized buildings according to their intended use. If this compaction degree can be estimated through a simple ground investigation, it would have significant social significance.

As a simple ground investigation method, there is the Screw Driver Sounding (SDS) test[2], which involves rotating a rod into the ground and measuring the resistance. The purpose of this paper is to estimate the compaction degree of the ground using the SDS test.The compaction degree of the ground is the ratio of the density of the ground to the density at which the ground is compacted to the limit. This

Copyright © 2023 by Tomoyuki SAKAMOTO and Keisuke NOMURA. Published in the Proceedings of the IASS Annual Symposium 2023 with permission.

limit state of compaction is reproduced by mechanically compacting the soil taken from the ground and reducing the internal air content as much as possible. At this time, the amount of air that can be reduced varies depending on the soil water content, so the density is determined by changing the water content. The water content at which the highest density is achieved is called the optimum water content. The dry density of the soil at the time when the highest density is achieved is called the maximum dry density. In this paper, a simulated ground was created using soil samples with varying compaction degrees and moisture contents. The SDS test was conducted on the simulated ground, and the relationship between the resistance energy obtained and the compaction degree and moisture content was investigated. In Japan, settlement damage often occurs when using either decomposed granite soil or Kanto loam as material for embankments. This paper focuses on these two types of soil samples. Decomposed granite soil is soil that is formed by the weathering of slowly cooled lava and has properties of sandy soil. Kanto loam is soil derived from deposited volcanic ash and has properties of clayey soil. The study investigates the effect of these differences on the SDS test and considers the possibility of soil classification based on these differences.

2. Strength measurement experiment by SDS test

2.1. Outline of experiment

We created model ground with varying water content and compaction degree, and conducted SDS tests. The properties of the test soils obtained from the soil test and the experimental conditions are shown in Table 1. The water content of the test samples was set to be higher or lower than the optimum water content. Hereafter, these conditions are referred to as high water content and low water content, respectively. The target values for the compaction degree of the test samples were set to 70%, 75%, 80%, 85%, and 90%. In the case of the decomposed granite soil, we were able to create test samples with a compaction degree of 90% with room to spare, so we also created test samples with a target compaction degree of 93%.

The preparation method of the test specimens is described. A steel mold (Figure 1, inner diameter 298.5 mm, height 985 mm, thickness 10 mm) was used as the soil tank. The sample soil was packed into the mold with a certain regularity, and the compaction degree of the sample soil was controlled by the density of the soil at that time. The mold was divided into 16 layers by height, and the weight of the sample soil to be packed in one layer was determined from the specified density. After placing the soil into a mold, a circular loading plate with a diameter of 280 mm was placed on top of it.The weight was repeatedly dropped onto the loading plate until the volume of the soil matched the volume of each layer. The volume of the soil was controlled by the distance from the top of the mold to the soil surface, and the distance was measured each time the weight was dropped. The weight of the compacted soil sample m_i was calculated using equation (1), where D_c is the degree of compaction, ρ_{dmax} is the maximum dry density, w is the water content, and V_i is the volume of each layer.

$$m_i = \frac{\rho_{dmax}\left(\frac{1+w}{100}\right)V_i D_c}{100} \tag{1}$$

Figure 1 shows photographs of the mold and test specimen used. The SDS test was performed using Geocarte III (manufactured by Nitto Seiko Co., Ltd.). An overview of the SDS test will be described in the next section. Three SDS tests were conducted on the same test specimen with the position changed. Figure 2 shows the appearance during the test.

Table 1. Experimental conditions

Soil name		Kanto loam	Decomposed granite soil
General	Density of soil particle ρ_s [g/cm^3]	2.680	2.702
	Natural water content ratio ω_n [%]	49.5	12.2
Particle size	Stone(over75mm) [%]	0	0
	Pellet(2~75mm) [%]	0.2	15.4
	Sand(0.075~2mm) [%]	17.1	62.1
	Silt(0.005~0.075mm) [%]	42.2	15.6
	Clay(under0.005mm) [%]	40.5	6.9
	Maximum grain size [mm]	4.75	19.00
Compaction	Maximum dry density $\rho_{d\max}$ [g/cm^3]	0.816	1.699
	Optimum water content ratio ω_O [%]	74.7	16.2
	Low water content ratio ω_L [%]	60.0	10.0
	High water content ratio ω_H [%]	85.0	20.0
	Target values for the compaction degree [%]	70,75,80,85,90	70,75,80,85, 90,93



Figure 1. Steel Mold (left) and test specimen (right)



Figure 2. During the test

2.2. Penetration energy by SDS test

Figure 1 shows the procedure of SDS test. The load is applied to the constantly rotating penetration rod, and the load is increased every rotation. The load increases in six steps from 0.25 kN to 1.00 kN until the penetration depth reaches 25 cm. After that, the load is kept constant at 1.00 kN while the penetration rod continues to rotate. When the penetration depth reaches 25 cm, the load is removed, and the reloading and rotation penetration begin. During this test, the load, rotation torque, and penetration depth are measured.

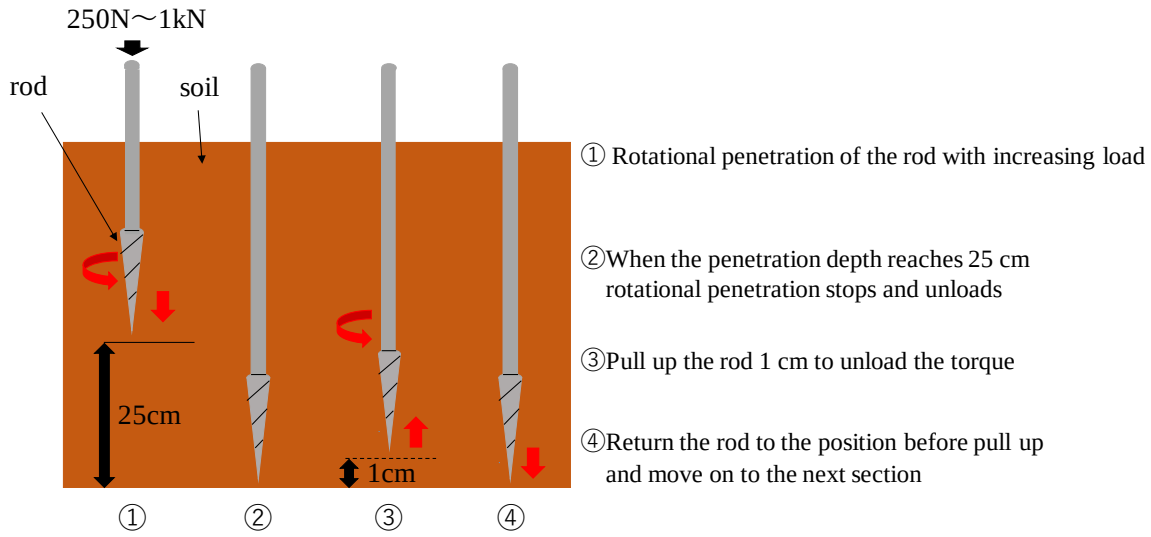


Figure 3. procedure of SDS test

In this paper, we focus on the energy *dE* required for penetration in each loading phase. *dE* is considered to be the sum of the energy weight *EW* obtained from the load *W* and the amount of penetration, and the energy torque *ET* obtained from the maximum torque *T* during one rotation. These values are defined as equations (2) through (4)[2].

$$ET = \pi T dn_{ht} \qquad T = T_a - T_f \tag{2}$$

$$EW = W ds_t \qquad W = W_a - W_f \tag{3}$$

$$dE = ET + EW \tag{4}$$

T is the corrected torque, T_a is the measured torque, T_f is the horizontal circumferential friction force and dn_{ht} is the number of half turns. W is the corrected load,W_a is the measured load, W_f is the vertical circumferential friction force and d_{st} is the 25 cm unit penetration.

2.3. Result of experiment

Figures 4 and 5 show examples of *ET* and *EW* obtained from SDS tests. Figure 4 is for a decomposed granite soil and Figure 5 is for a Kanto loam, both at 90% compaction degree. The vertical axis is the depth of penetration and the horizontal axis is *ET* or *EW*. Low water content is indicated by blue lines (legend GL, LL) and high water content by red lines (GH, LH). We focus on the range of 0.25 to 0.75 m because the penetration depths of 0.00 to 0.25 m and 0.75 to 1.00 m are immediately after penetration or close to the mold bottom plate, resulting in underestimation or overestimation of the values.

ET and *EW* increase as the load increases, and decrease when unloading occurs (when the penetration depth reaches 25cm). It can be seen that in the high water content sample, the penetration depth reached 25cm in the first or second load stage, whereas in the low water content sample, it reached the final load stage.

In *ET*, despite the same compaction degree, the values of low water content ratios are about 2-3 times higher than those of high water content ratios. In addition, it can be seen that *ET* shows a nonlinear relationship with penetration depth except for the Kanto loam, which has a small number of measurement points, indicating that decomposed granite soil has a larger variation in each 25cm interval.

In *EW*, both low and high water content ratios show a linear relationship with penetration depth. Since high water content ratios have a larger penetration depth even with a smaller load, *EW* is large from the initial load stage. Furthermore, there is no significant difference in the maximum values of *EW* based on water content ratios.

Indicating that the ratio of *ET* to *EW* varies with water content ratios. In particular, in the case of low water content ratios, there is a tendency for *ET* to increase significantly.

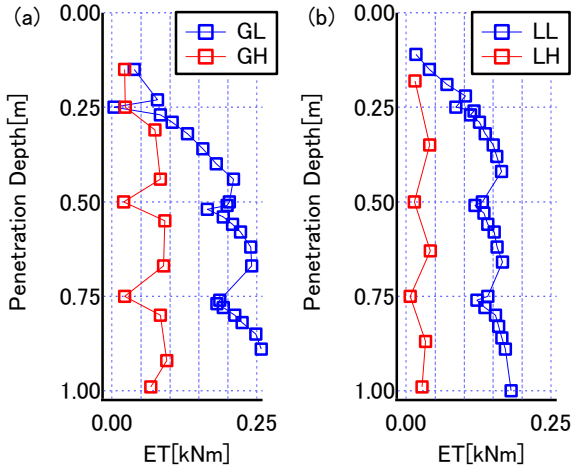


Figure 4. Variation of *ET* with depth of penetration
(a) decomposed granite soil, (b) Kanto loam

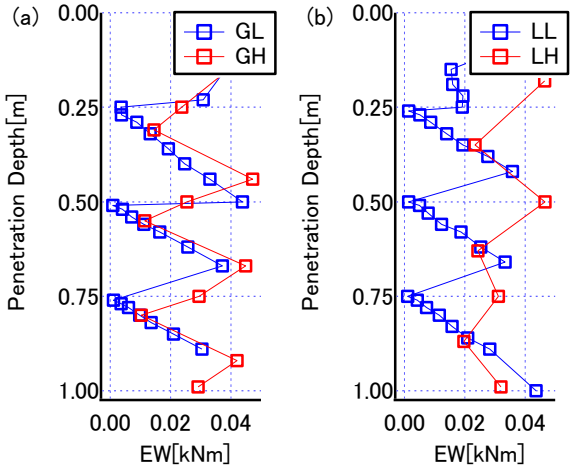


Figure 5. Variation of *EW* with depth of penetration
(a) decomposed granite soil, (b) Kanto loam

3. Determination of the compaction degree and soil texture by total penetration energy

3.1. Interpolation and evaluation methods for penetration energy

We investigate the relationship between energy (ET, EW) obtained from SDS testing and the degree of compaction or soil properties. In SDS testing, the load is gradually increased in stages, so in coarse soils, the penetration rod reaches 25cm in the initial load stages, while in dense soils, it may not reach 25cm even in the final load stage. Therefore, we considered that evaluating each energy at a specific load stage would not provide a consistent criterion. Instead, we decided to evaluate the total energy within each 25cm interval.

As mentioned above, the number of measurement points within each interval varies depending on the soil conditions. To evaluate the total energy under the same conditions, we normalized the area under the approximate curve for each measurement point by the length of the interval. The approximate curve was created using a power function for *ET* and a linear function for *EW* based on the distribution trend shown in Figure 3. When there were insufficient measurement points, interpolation points were added. Figure 4 shows a conceptual diagram of the process of creating an approximate curve. The vertical axis represents *ET* and the horizontal axis represents depth in 25cm increments. Figure 4(a) shows the case where there is only one measurement point, in which case the approximate curve is a linear function with a slope of 0. Figure 4(b) shows the case where there are two measurement points, with an interpolation point added at the midpoint of the two points. Figure 4(c) shows the case where there are three or more measurement points, and a power function was used to approximate all the measurement points. *EW* was also approximated using the same method with interpolation points added as necessary.

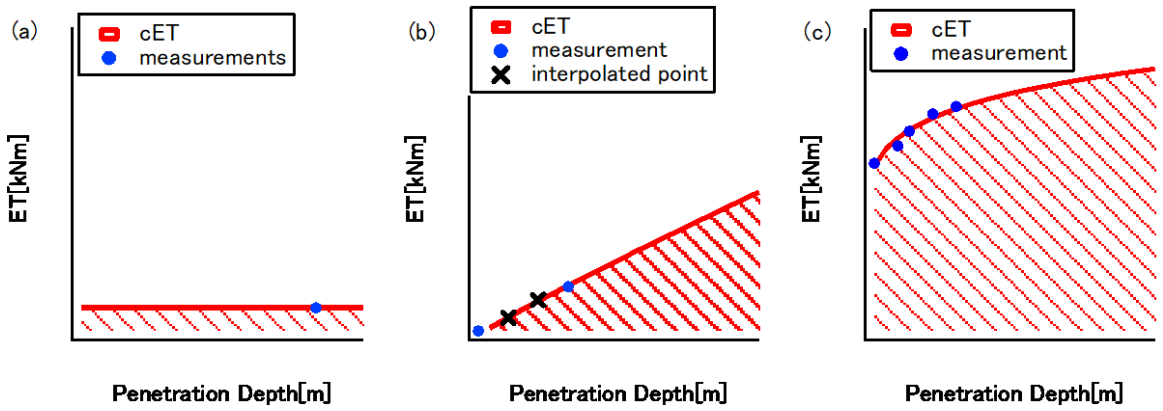


Figure 6. *ET* Approximate curves and interpolation points of *ET*:
(a) In the case of 1 point, (b) In the case of 2 points, (c) In case of 3 or more points

The total energy torque obtained from the *ET* through the above procedure is referred to as *cET*, and the total energy weight obtained from the *EW* is referred to as *cEW*. Furthermore, their sum is the total penetration energy, referred to as *cE*. *cET* and *cEW* are calculated using equations (5) and (6).

$$cET = \frac{\int_{0.25}^{0} az^b dz}{0.25} \tag{5}$$

$$cEW = \frac{\int_{0.25}^{0} (az + b) dz}{0.25} \tag{6}$$

The coefficients *a* and *b* in the equations are coefficients for creating approximate curves, and the values are obtained by the least-squares method using the measured *ET* and *EW* and the 25cm unit depth *z* at those measurement locations. The values of *a* and *b* are determined separately for each penetration point and each 25cm interval (depth range of 0.25 to 0.50 m and 0.50 to 0.75 m).

3.2. Relationship between compaction degree, water content ratio and total penetration energy

The relationship between total penetration energy *cE*, compaction degree *Dc*, and water content is shown in Figures 7 and 8. Figures 7 is for a decomposed granite soil and Figures 8 is for a Kanto loam. (a) is for the penetration depths of 0.25 m to 0.50 m and (b) is for the 0.50 m to 0.75 m. The vertical axis is *cE* and the horizontal axis is the compaction degree *Dc*. Although each specimen was prepared with the compaction degree in Table 1 as the target value, some specimens were over- or under-compacted because fine adjustment could not be made by dropping weights. In these cases, the density was recalculated using the amount of settlement caused by the falling of the weight, and the compaction degree was corrected. The red markers in the figures indicate specimens with high water content (legend names GH25, GH50, LH25, LH50), the blue markers are low water content (GL25, GL50, LL25, LL50) and the black markers are optimum water content (GO25, GO50, LO25, and LO50). The lines in each color in the figure are approximate curves obtained from those colored markers. The approximate curves were created using an exponential approximation for the decomposed granite soil and a linear approximation for the Kanto loam, based on the trend of their distributions.

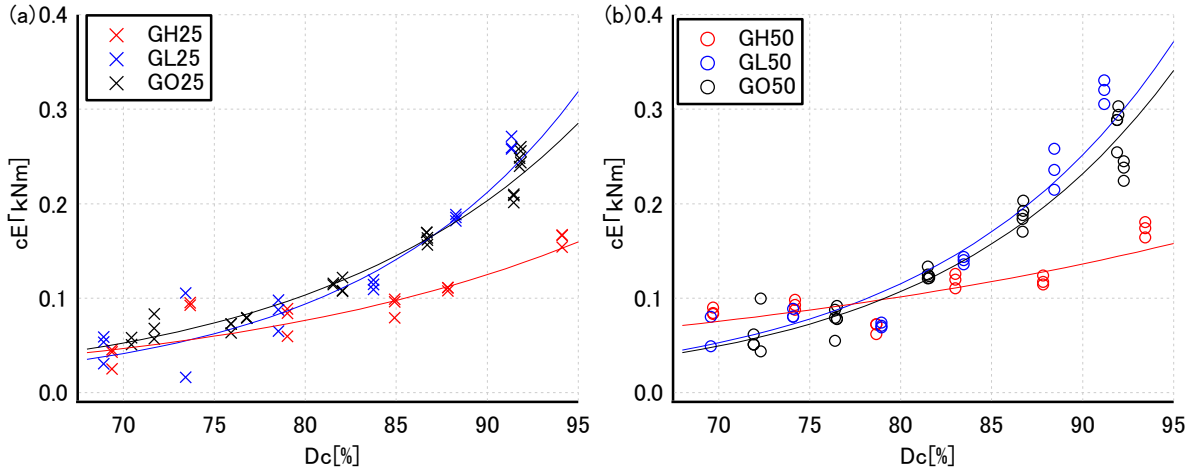


Figure 7. Relationship *cE* and compaction degree Dc of decomposed granite soil:
(a) 0.25～0.50m section, (b) 0.50～0.75m section

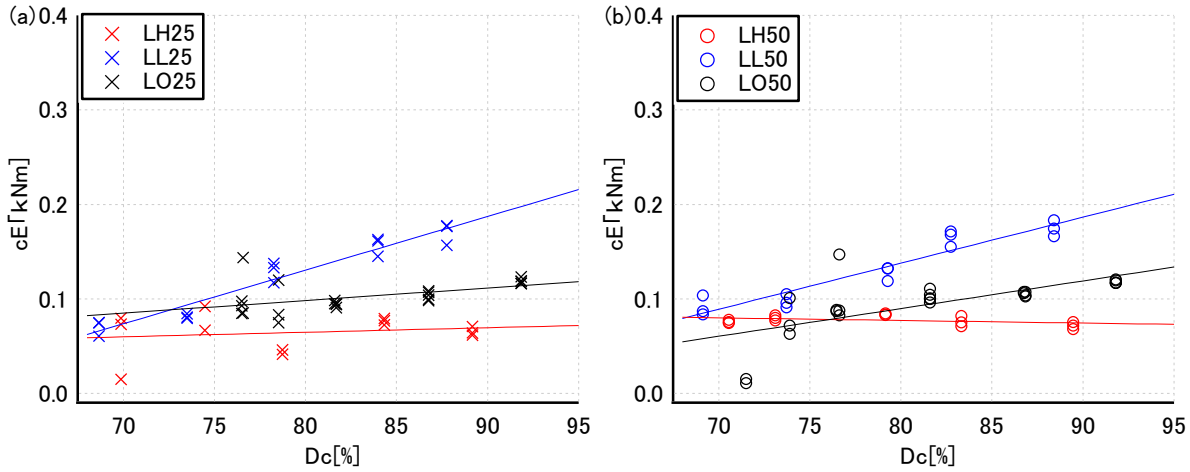


Figure 8. Relationship *cE* and compaction degree Dc of Kant loam:
(a) 0.25～0.50m section, (b) 0.50～0.75m section

In the case of decomposed granite soil, for all water contents, in specimens with a compaction degree of 70-80%, the penetrating rod reached 25cm at the first or the next stage of loading. As a result, the value of *cE* is very small and the change in *cE* with respect to the degree of compaction is minimal. When the compaction degree exceeded 80%, *cE* increased quadratically. *cE* values at low and optimum water contents were similar, while *cE* at high water contents was smaller than those at the other two levels. Therefore, it can be concluded that the strength does not decrease even if there is less water than the optimum water content, but it decreases with higher water content.

The *cE* for Kanto loam increased linearly. Differences due to the water content became apparent in *cE* from a compaction degree of 70%. In the case of high water content, the rod reached 25cm in the first or second load stage for all compaction degrees of the test specimens, resulting in a very small *cE* value. On the other hand, for low water content, the change in *cE* due to compaction degree was significant, and at a compaction degree of 90%, *cE* was about three times larger than that of the high water content case. This indicates that the strength decreases with higher water content than the optimum water content, and increases with lower water content.

Comparing the *cE* of the decomposed granite soil and the Kanto loam, the *cE* of the Kanto loam is larger at lower compaction degrees, and the *cE* of the sand becomes larger as the compaction degree increases. Furthermore, comparing (a) and (b), it can be seen that *cE* is larger at greater depths. This trend is particularly strong in the case of decomposed granite soil.

3.3. Soil identification by penetration energy

Next, we will discuss the possibility of soil identification. Figure 9 is a graph that summarizes the previous data with *cET*/*cEW* on the vertical axis and *Dc* on the horizontal axis. The circle markers represent the decomposed granite soil and the cross markers represent the Kanto loam. The dashed line is the approximate curve for decomposed granite soil, and the solid line is the approximate curve for Kanto loam.

For decomposed granite soil, *cET*/*cEW* increases rapidly from a compaction degree of around 80%, and changes exponentially. For Kanto loam, it changes linearly. In both cases, it can be seen that the slope changes depending on the water content. Therefore, it is possible to identify the soil type by using *cET*/*cEW* when the compaction degree is high and the water content is optimal or less. In cases where the compaction degree is low or the water content is high, it is difficult to identify the soil type because cET/cEW interferes with each other. In this paper, two type of soil was used, so the trend is limited. In the future, by increasing the number of soil samples, it is expected that more prominent trends can be confirmed.

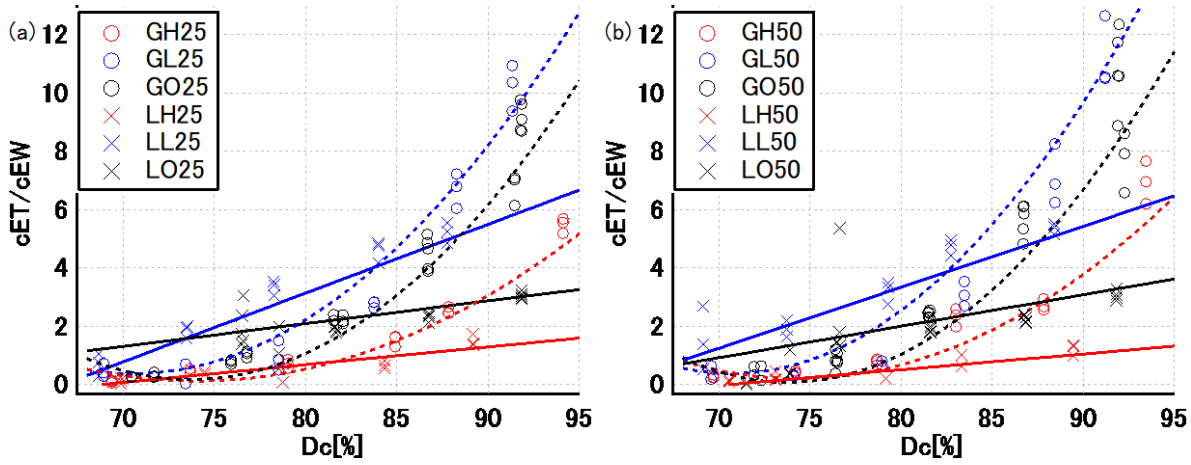


Figure 9. Relationship *cET*/*cEW* and *Dc*: (a) 0.25～0.5m section, (b) 0.50～0.75m section

4. Conclusion

The findings of this paper are as follows. When compaction is performed using the same type of soil, the lower the water content, the greater the strength, and differences in water content can result in a threefold or greater difference in penetration energy for the same compaction degree. In the case of decomposed granite soil, there is a difference in energy depending on the compaction depth of the soil, but there is not much difference in the case of Kanto loam soil.

When the vertical axis is *cET*/*cEW* and the horizontal axis is Dc, the energy increases quadratically for decomposed granite soil and linearly for Kanto loam, suggesting that *cET*/*cEW* may be able to discriminate between sandy soil and clayey soil. As a future prospect, we will conduct experiments at deeper depths to examine the correlation by depth method. We also plan to conduct experiments on soils other than decomposed granite soil and Kanto loam.

References

[1] Japan Riverfront Research Center, 2000., *Design and Construction Manual for High-Standard Levee Embankment*, Japan Riverfront Research Center

[2] T.Tanaka, N.Suemasa, T.Katada, S.Yamato and H.Tai, "Simple Estimation of Soil Liquefaction Using Screwdriver Sounding Test",*23nd ISOPE Conference*, pp. 567–571, 2013.

Proceedings of the IASS Annual Symposium 2023
Integration of Design and Fabrication
10–14 July 2023, Melbourne, Australia
Y.M. Xie, J. Burry, T.U. Lee and J. Ma (eds.)

Numerical simulations of snow loads on long-span curved roofs

Guolong ZHANG[a,b,*], Qingwen ZHANG[a,b], Feng FAN[a,b]

[*] School of Civil Engineering, Harbin Institute of Technology, Harbin, 150090, China
No.73 Huanghe Road, Harbin, China
zhanggl315@hit.edu.cn

[a] Key Lab of Structures Dynamic Behavior and Control of the Ministry of Education, Harbin Institute of Technology, Harbin, 150090, China
[b] Key Lab of Smart Prevention and Mitigation of Civil Engineering Disasters of the Ministry of Industry and Information Technology, Harbin Institute of Technology, Harbin, 150090, China

Abstract

Snow-induced building collapses are on the rise in long-span structures, as extreme weather events such as blizzards become more frequent. According to the accident investigation, the sudden increase in the snowfall and unbalanced snow distribution, which leads to an excessive snow load in a local area, are the main reasons for such collapses. However, due to the lack of related data, the rationality of Chinese load code for building structures need a further investigation. Therefore, based on a revised multiphase model, the numerical simulation of snowdrifts on a long-span curved roof was carried out with different inflow velocities and inflow directions. It is found that the unbalanced distribution of snow on the roof becomes more obvious with the increasing inflow velocity, showing a half-span snowdrift on the leeward side. Furthermore, for different inflow directions, the snow distribution pattern is mainly related to the building cross section parallel to the downstream direction. When the direction of the incoming flow is perpendicular to the eave, it is easier to form an uneven distribution.

Keywords: snow load, non-equilibrium, curved roof, inflow velocity, inflow direction

1. Introduction

Snow-induced building collapse often occurs in long-span structures, for example, the collapse of the Katowice Trade Hall (Poland, 2006), the collapse of the Minnesota Vikings membrane stadium (USA, 2010) and the collapse of an ice rink in Bad Reichenhall (Germany, 2006), etc. Generally, under specific conditions of snowfall and wind, a large amount of snowdrift will form on and around buildings, where the wind velocity is sufficiently low enough to allow snow particles to settle down. The uneven local snow load is believed as one of the main causes of building collapse or cracking (O'Rourke [1]). Therefore, it is very necessary to develop suitable methods to analyze and predict hazards due to snowdrift in built-up environments with high accuracy. Of all the methods, field measurements and experiments have been regarded as the most reliable approaches to deal with the snowdrift related problems. However, their applicabilities are limited to specific weather conditions and similarity criterion, respectively. Fortunately, computational fluid dynamics (CFD) has been applied to simulate snowdrift around buildings recently, based on the dramatic increases in computational power together with advances in computer software (Tominaga [2]).

Snowdrift on the ground is usually described as a solid particle transport process. Depending on whether the wind velocity reaches a threshold value, three different particle transport mechanisms are defined, namely, creep, saltation and suspension. Creep is a subprocess in which snow particles roll on the surface under a height below 0.01 m; saltation is a transport process at the height of around 0.01~0.1 m, in which

Copyright © 2023 by Guolong ZHANG, Qingwen ZHANG and Feng FAN. Published in the Proceedings of the IASS Annual Symposium 2023 with permission.

snow particles leap up and jump on the snow surface; suspension is a phenomenon in which particles are blown up into the air and transported far downwind. Among the subprocesses, saltation is the dominant particle transport process which causes approximately 67% of the overall drifted mass (Delpech et al. [3]). Therefore, many CFD studies have focused on the saltation transport process in a boundary layer flow developed on a flat terrain. However, snowdrift on a building roof is more complex because of the complicated interaction between snow particle motion and flow field affected by building geometry (Tominaga [2]). So far, only a few attempts have been made to apply CFD approach to roof snow issues. Thiis et al. [4] predicted the snow distribution on the curved roof of a sports hall under specific weather conditions and compared the results with field measurements. Generally, the simulated snow distribution pattern fit the measured shape well. Tominaga et al. [5] predicted the snowdrift on a gable roofed building with different roof slopes and wind velocities. In the study, additional snowdrifts formed on the leeward side under different inflow velocity conditions were compared against a series of field measurement results (Thiis et al. [6]). The simulation results generally corresponded well with the observational data for the exposed roof. Recently, Zhou et al. [7] proposed a quasi-steady method to simulate the redistribution of snow on a flat-roof building. The snow redistributions obtained from the numerical simulation agreed well with those obtained in the wind tunnel tests.

It should be noted that the relations and parameters used in the past snowdrift modeling have been mostly derived empirically from observations or experiments. Many of observations and experiments were conducted based on a simple drifting boundary layer developed on a flat plane. Among the empirical relations, an estimation model for the transport rate of drifting snow attributable to saltation Q_{sal} proposed by Pomeroy and Gray [8] has often been used to predict the snow concentration within the saltation layer. The proposed relation gives a saturated transport rate of drifting snow where the air-snow mixed flow has been fully developed. Okaze et al. [9] further investigated the prediction accuracy of the empirical relation for the non-equilibrium flow in a developing saltation layer by conducting a wind tunnel experiment. Through comparison, the values obtained from Pomeroy's relation were greatly overestimated in almost the entire region. Thus, it is problematic to apply Pomeroy's relation (which is based on the equilibrium condition) to a flow around a building in which drifting snow is in non-equilibrium state because of the complex flow field. It is necessary to further consider the applicability and validity of the modeling of the saltating process at the developing stage (non-equilibrium state). Tominaga et al. [10] lately proposed a new approach to account for the developing process of drifting snow with a one-way coupled snow concentration diffusion equation, instead of the empirical saltation flux relationship. The new approach made some improvement, but some substantial deviations remained from experimental measurements. It was partly caused by the fact that the effect of snow particles on flow field and the increasing drifting snow density induced by building blocking were not fully considered.

Besides the non-equilibrium developing process, the interaction between snow particle motion and fluid flow should also be accounted for. In this respect, Naaim et al. [11] introduced additional terms into the transport equations of k and ε to consider the turbulence damping by the presence of particles, based on a drifting snow density approach, which was firstly proposed by Uematsu et al [12]. Similarly, Okaze et al. [13] developed a new k-ε model to consider the aerodynamic effects of snow particles on the flow field, based on the canopy model concept for moving obstacles [14]. Three extra terms were added to the governing equations of air flow momentum, k and ε, respectively, to express the damping effect. Unfortunately, both approaches did not solve a snow phase momentum equation. Instead the snow velocity was set equal to a constant or a proportion value of wind velocity derived from empirical and experimental considerations [15]. This may be reasonable for a flow over a flat terrain but does not work appropriately for the flow around buildings. To fully account for the interaction between snow particle motion and fluid flow as well as the drifting snow density at a developing stage, a two-way coupled two-phase CFD model was developed and adopted for the simulation of snowdrift development on a long-span roof. Besides properly accounting for two-way coupling of air and snow phases, this CFD model is free from all equilibrium assumptions used in the past approaches introduced above.

In this study, Firstly, the CFD prediction accuracy for the snow distribution on a long-span curved roof was validated by comparing the simulated balanced and unbalanced results with the Chinese load code (MOHURD, [16]) and the design code developed by ISO4355 [1]. Thereafter, the snowdrift characteristics were investigated with different inflow velocities including 2 m/s, 3 m/s and 4 m/s, based on the validated CFD model. Finally, the effect of wind direction on snowdrifts was explored with three inflow directions including 0°, 45° and 90°.

2. CFD model for drifting snow

2.1. Governing equations

The air-snow flow is simulated by using the Mixture model in ANSYS FLUENT. The Mixture model equations consist of the continuity and momentum equations for the mixture phase, the continuity equation for the snow phase and the algebraic equation for the slip velocity between air and snow phases. Specifically, the transport equations for the air-snow mixture phase are given by.

$$\frac{\partial \rho_{\mathrm{m}}}{\partial t}+\nabla\cdot\left(\rho_{\mathrm{m}}\mathbf{u}_{\mathrm{m}}\right)=0 \tag{1}$$

$$\frac{\partial}{\partial t}\left(\rho_{\mathrm{m}}\mathbf{u}_{\mathrm{m}}\right)+\nabla\cdot\left(\rho_{\mathrm{m}}\mathbf{u}_{\mathrm{m}}\mathbf{u}_{\mathrm{m}}\right)=-\nabla p_{\mathrm{m}}+\nabla\cdot\left[\rho_{\mathrm{m}}c_{\mathrm{s}}\left(1-c_{\mathrm{s}}\right)\mathbf{u}_{\mathrm{as}}\mathbf{u}_{\mathrm{as}}\right]+\nabla\cdot\boldsymbol{\tau}_{\mathrm{Gm}}+\rho_{\mathrm{m}}\mathbf{g} \tag{2}$$

where, the subscripts "m", "a", "s" represent mixture, air and snow phases, respectively; $\boldsymbol{\tau}_{\mathrm{Gm}}$ is a generalized shear stress tensor, which is calculated according to Eq.(3); c_{s} is the mass fraction of snow phase; $\mathbf{u}_{\mathrm{as}}$ is the slip velocity vector between air and snow phases; ρ_{m} is the mixture density; $\mathbf{u}_{\mathrm{m}}$ is the mixture velocity vector; μ_{m} is the mixture viscosity.

$$\boldsymbol{\tau}_{\mathrm{Gm}}=\left(\mu_{\mathrm{m}}+\mu_{\mathrm{Tm}}\right)\left[\nabla\mathbf{u}_{\mathrm{m}}+\left(\nabla\mathbf{u}_{\mathrm{m}}\right)^{T}\right]-\frac{2}{3}\rho_{\mathrm{m}}k_{\mathrm{m}}\mathbf{I} \tag{3}$$

The snow volume fraction f_{s} is derived by solving the continuity equation for the snow phase, as shown in Eq.(4), where D_{Mp} is the diffusion constant. The third term on the left-hand side accounts for the slip between air and snow phases. Furthermore, based on the force balance and a local equilibrium assumption, the algebraic equation for the slip velocity $\mathbf{u}_{\mathrm{as}}$ is derived, as shown in Eq.(5).

$$\frac{\partial f_{\mathrm{s}}}{\partial t}+\nabla\cdot\left(f_{\mathrm{s}}\mathbf{u}_{\mathrm{m}}\right)+\nabla\cdot\left[f_{\mathrm{s}}\left(1-c_{\mathrm{s}}\right)\mathbf{u}_{\mathrm{as}}\right]=D_{\mathrm{Mp}}\cdot\nabla f_{\mathrm{s}} \tag{4}$$

$$\mathbf{u}_{\mathrm{as}}=\frac{t_{\mathrm{s}}}{f_{\mathrm{drag}}}\frac{\left(\rho_{\mathrm{s}}-\rho_{\mathrm{m}}\right)}{\rho_{\mathrm{s}}}\left[\mathbf{g}-\left(\mathbf{u}_{\mathrm{m}}\cdot\nabla\right)\mathbf{u}_{\mathrm{m}}-\frac{\partial\mathbf{u}_{\mathrm{m}}}{\partial t}\right] \tag{5}$$

In Eq.(5), t_{s} is the relaxation time of a particle; f_{drag} is the drag function, taken from Schiller and Naumann [17]; d_{s} is the diameter of snow particle; $\mathbf{g}$ is the gravitational acceleration. The k-ε turbulence model is applied to solve the flow turbulence quantities and turbulent viscosity for the mixture phase.

2.2. Treatment of deposition and erosion

The first grid adjacent to the snow surface is selected as a Control Volume (hereafter, CV) for evaluating the balance of snow concentration and calculating the total deposition. The total deposition flux q_{total} on the bottom surface of the CV is given by:

$$q_{\mathrm{total}}=q_{\mathrm{dep}}+q_{\mathrm{ero}} \tag{6}$$

Snow deposition per unit of time and unit of area q_{dep} is expressed as Eq.(7). Here, w_{f} is the snowfall velocity; Φ is the drifting snow density at the first grid adjacent to the snow surface, which is calculated as the product of the snow density ρ_{s} and snow volume fraction f_{s}.

$$q_{\mathrm{dep}} = -\Phi w_{\mathrm{f}} = -\rho_{\mathrm{s}} f_{\mathrm{s}} w_{\mathrm{f}} \tag{7}$$

Erosion flux q_{ero}, caused by the shear stress at the snow surface, is given by Eq.(8). This follows the expression, proposed by Anderson and Haff [18]. Here, c_{a} is a constant; u^* is the friction velocity; u^*_{t} is the threshold friction velocity.

$$q_{\mathrm{ero}} = \begin{cases} -c_{\mathrm{a}} \rho_{\mathrm{s}} u^* \left(1 - \dfrac{u_{\mathrm{t}}^{*2}}{u^{*2}}\right) & for \;\; u^* > u_{\mathrm{t}}^* \\ 0 & for \;\; u^* \le u_{\mathrm{t}}^* \end{cases} \tag{8}$$

In this analysis, the total deposition mass q_{total} is incorporated into Eq.(4) as the source term to consider the snow concentration change within the saltation layer.

3. Validation of CFD model

3.1. Computational conditions

As no measurement or experimental data of snow distribution on a curved roof was available, the balanced and unbalanced snow distributions in Chinese load code (MOHURD, [16]) and ISO load code (ISO, [19]) were selected for validation. For both distributions, the inflow velocities were determined by referring to the AIJ load code (AIJ, [20]), which elaborates the relationship between the velocity and the snow distribution.

Figure 1 a) provides a schematic view of the curved roof building used in this study, with an arc span of 50 m and a longitudinal span of 100 m. The height of the curved roof was 10 m with a rise-span ratio being 1/5. The eave was placed perpendicular to the approaching wind flow. The computational domain comprised a volume measuring 250 m (x-axis)×300 m (y-axis)×70 m (z-axis), as shown in Figure 1 b). In this study, special care was taken to allocate an adequate number of hexahedral cells along the curved roof. In order to simulate the saltating process, the height of the first grid adjacent to the roof surface was set to 0.01 m, approximately the height of the saltation layer.

a) b)

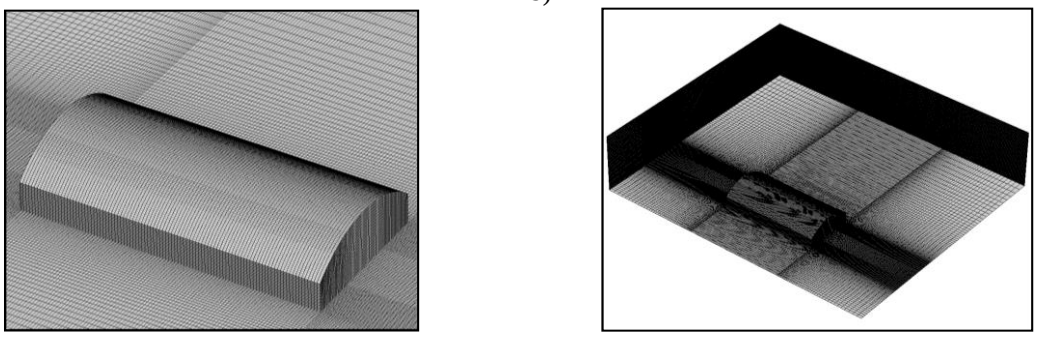


Figure 1. Grid overlay: a) schematic view of the curved roof building; b) schematic view of the domain

A power law profile with an index of 0.20 was assumed for inflow velocity; the profiles for k and ε were determined using the equations proposed by the AIJ [20]. The mean wind velocity at the inflow boundary at the building height U_{H} was set to 2.0 m/s, 3.0 m/s and 4.0 m/s, respectively to investigate the development of snowdrifts. The drifting snow density Φ_{in} at the inflow and top boundaries was given as a constant value by assuming that the standard snow depth, that resulted from snowfall during the whole period. Here, the specific inflow snow volume fraction was set to 1.3×10^{-5}, referring to the snow disaster in Shenyang City, China in 2007. The threshold friction velocity u^*_{t} was set to 0.2 m/s and snowfall velocity was set to 0.2 m/s. The snow particle density was selected as 250 kg/m^3.

3.2. Results and discussion

The distributions of friction velocity are shown in Figure 2. The friction velocity u^* was normalized by the threshold friction velocity u^*_t. For the case of 2 m/s, the friction velocity of the whole roof is lower than the threshold friction velocity; while for other cases, the friction velocity starts to exceed the threshold value from the windward area and increases with the increasing inflow velocity. Therefore, no snow drifting will occur on the roof with the 2 m/s inflow velocity. As for the distribution pattern, a high value of friction velocity is observed in the windward area for different inflow cases, and this area expands downstream with the increasing inflow velocity. However, a strip-shaped low friction velocity zone always exists along the leeward eave, where the wind velocity is low enough allowing snow to settle out and form a drift. Figure 3 illustrates the distribution of normalized drifting snow density Φ within the saltation layer. The drifting snow density shows small value along the windward eave. Much more snow particles are blown up and move further downstream under the action of strong shear stress in the windward area. Finally, the snow particles gather in the low velocity area along the leeward eave.

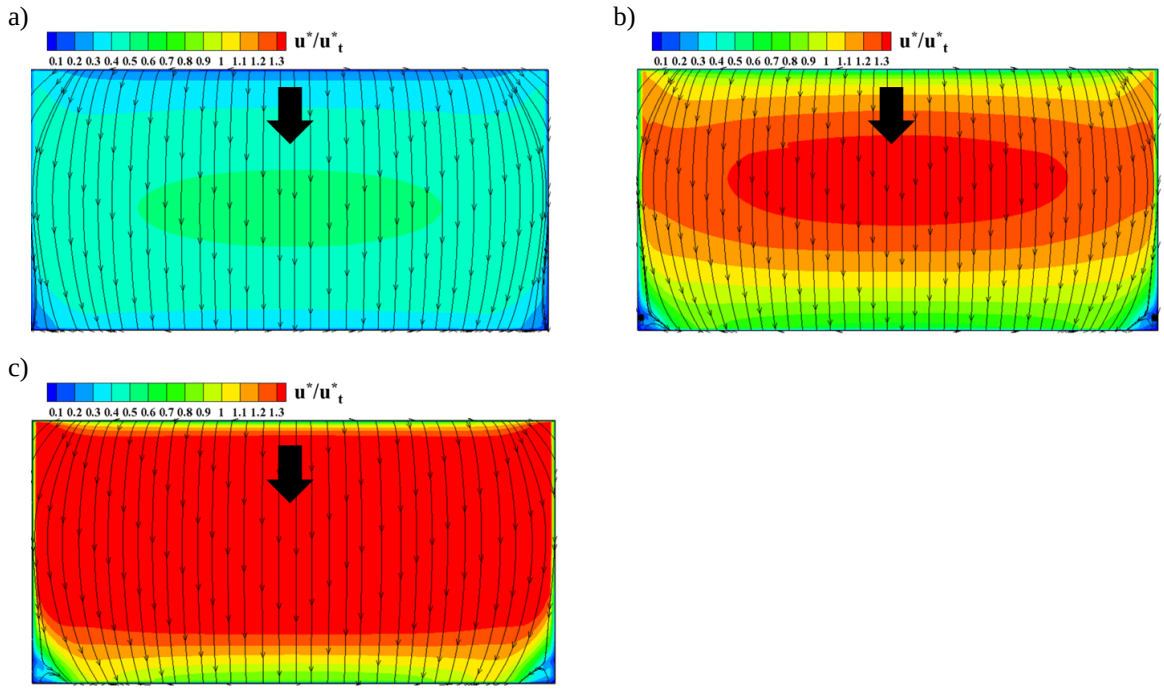


Figure 2. Contours of dimensionless friction velocity u^*/u^*_t: a) 2 m/s; b) 3 m/s; c) 4 m/s

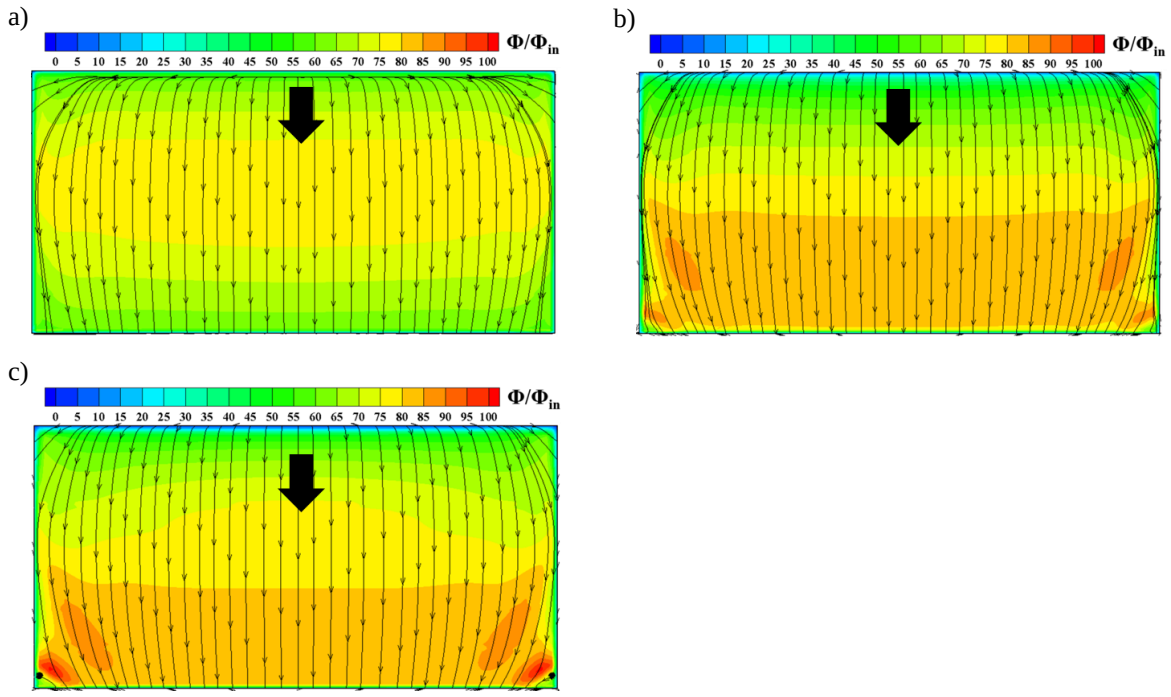


Figure 3. Contours of dimensionless snow concentration Φ/Φ_{in}: a) 2 m/s; b) 3 m/s; c) 4 m/s

Figure 4 indicates the contours of snow depth ratio h/h_{ref} on the curved roof. The snow depth ratio was defined as the ratio between the total deposition flux q_{total} and the total deposition flux q_{stan} at a reference point, which was not affected by the building. For U_H=2 m/s, only very small undulation is observed due to the low friction velocity. No significant snow drifting occurs on the roof and the snow load on the roof is approximately evenly distributed. For U_H=3 m/s, erosion starts to occur in the windward area. However, a small accumulation of snow is formed on the windward eaves. For U_H=4 m/s, the windward erosion zone spreads further downstream and the deposition along the windward eave disappears. The uneven distribution of snow on the roof becomes more obvious, showing a half-span snow distribution pattern. In general, the snow load on the curved roof shows three kinds of distribution patterns, i.e., the full-span balanced distribution (U_H=2 m/s), the half-span unbalanced distribution (U_H=4 m/s) and the transitional distribution between them (U_H=3 m/s).

Figure 5 shows the balanced and unbalanced snow distribution requirements for the curved roof provided in the Chinese load code (MOHURD, [16]) and the ISO 4355 load code (ISO, [19]). The balanced snow distributions in both codes correspond to the snowdrift with a lower inflow velocity (U_H=2.0 m/s). Consistent with ISO load code, the simulated snow depth continues to decrease gradually from the roof ridge to eaves. However, the snow depth remains the same in Chinese code as shown in Figure 5 a). The unbalanced snow distribution in ISO code is more likely the snowdrift formed at a higher wind velocity (U_H=4.0 m/s). The snow on the windward side is severely eroded, and a lot of snow accumulates on the leeward side. Different from the ISO code and CFD results, a large amount of snowdrift has formed in the high wind speed zone on the windward surface, which needs a further investigation.

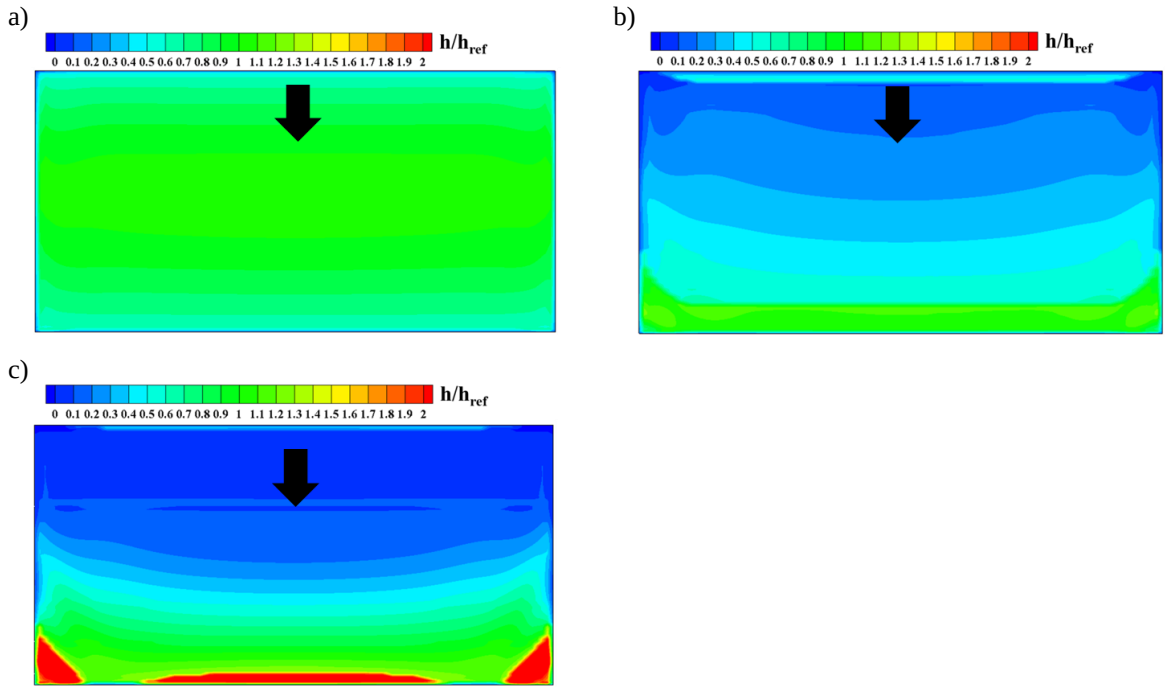


Figure 4. Contours of dimensionless snow depth h/h_{ref}: a) 2 m/s; b) 3 m/s; c) 4 m/s

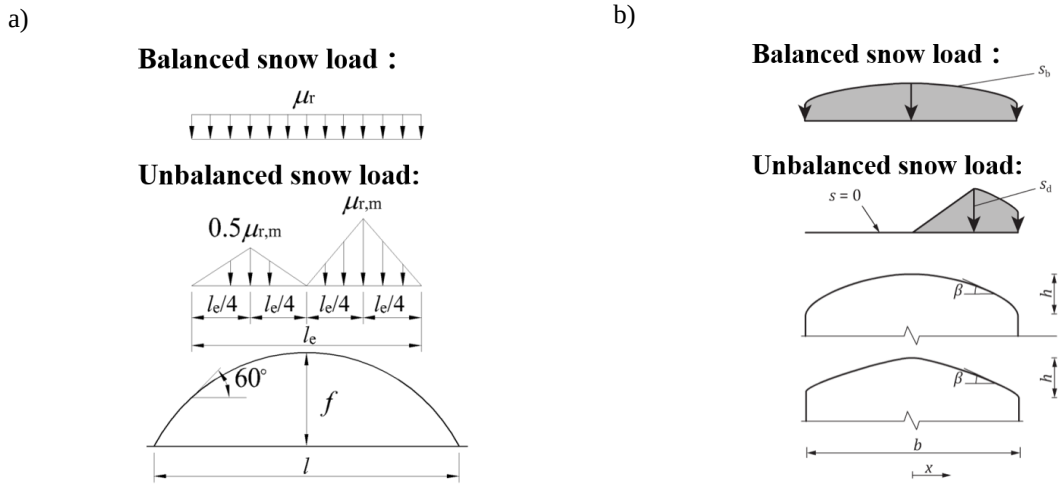


Figure 5. Snow load distribution in load codes: a) Chinese load code (GB 50009-2012); b) ISO 4355

4. Snowdrifts on curved roofs with various inflow directions

4.1. Computational conditions

In addition to the wind velocity, the wind direction also has a significant impact on the snow distribution parttern. In order to clarify the adverse wind direction, the snow distributions under three wind direction conditions were simulated, as shown in Figure 6. Regarding computational conditions, The mean wind velocity at the inflow boundary at the building height U_H was set to 4.0 m/s, at which the snowdrift was obvious. Except for this, all the computational settings were the same as above.

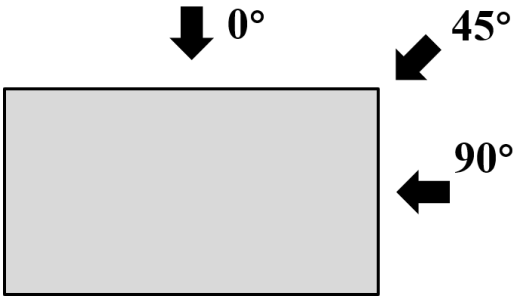


Figure 6. Computational cases for snowdrifts under different inflow direction conditions

4.2. Results and discussion

The distributions of friction velocity under different wind direction conditions are shown in Figure 7. The friction velocity u^* was normalized by the threshold friction velocity u^*_t. For the 0° inflow direction, the overall friction velocity exceeds the threshold friction velocity except for the low velocity zone along the leeward eave. The friction velocity is distributed in a strip shape parallel to the longitudinal eave. When the inflow direction turns to 45°, the strip-shaped friction velocity starts to tilt, and its value starts to decrease in the downstream region. For the 90° inflow direction condition, the overall friction velocity is below the threshold friction velocity, especially in the recirculation zone at the windward edge. Therefore, for the 0° inflow direction condition, the snow drifting phenomenon is more obvious; while for the 90° inflow direction condition, no snow drifting occurs on the roof. Figure 8 illustrates the distribution of normalized snow concentration within the saltation layer. A few snow particles gather in the windward region, while more particles are brought to the leeward area.

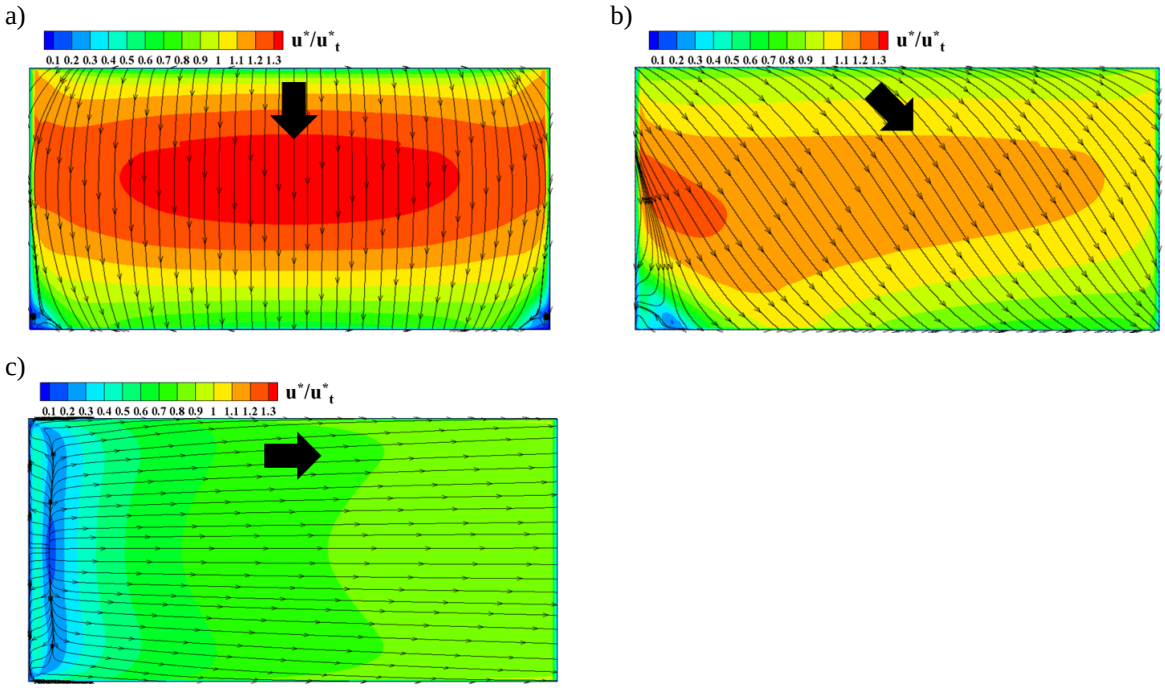


Figure 7. Contours of dimensionless friction velocity u^*/u^*_t: a) 0°; b) 45°; c) 90°

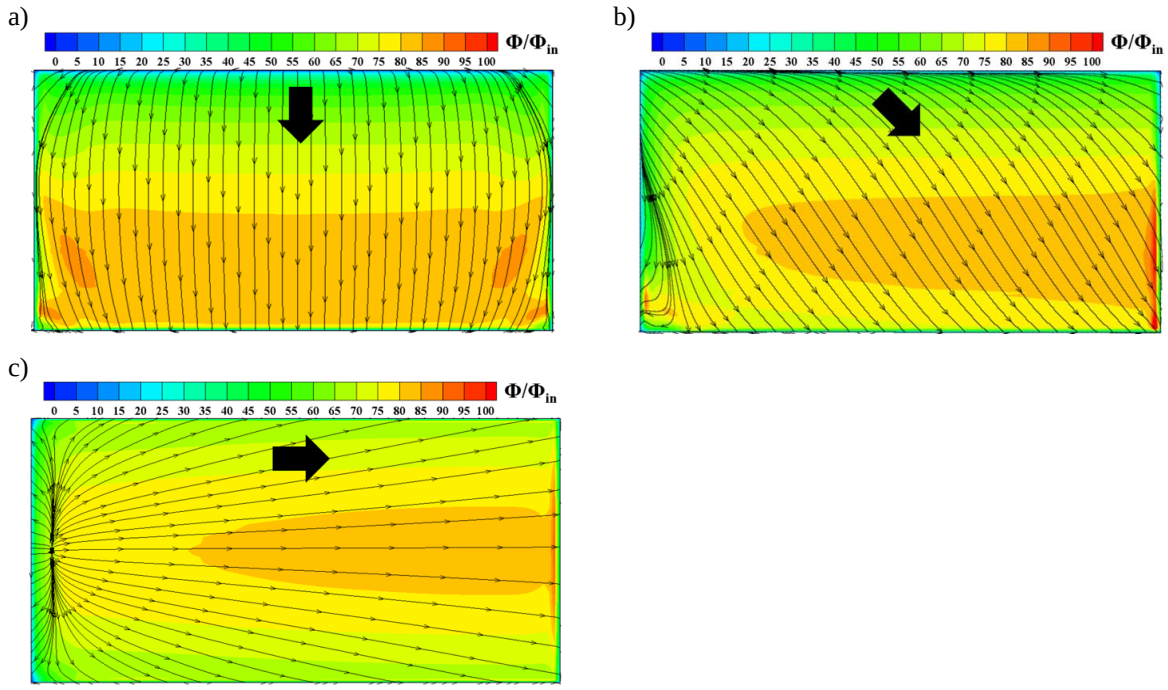
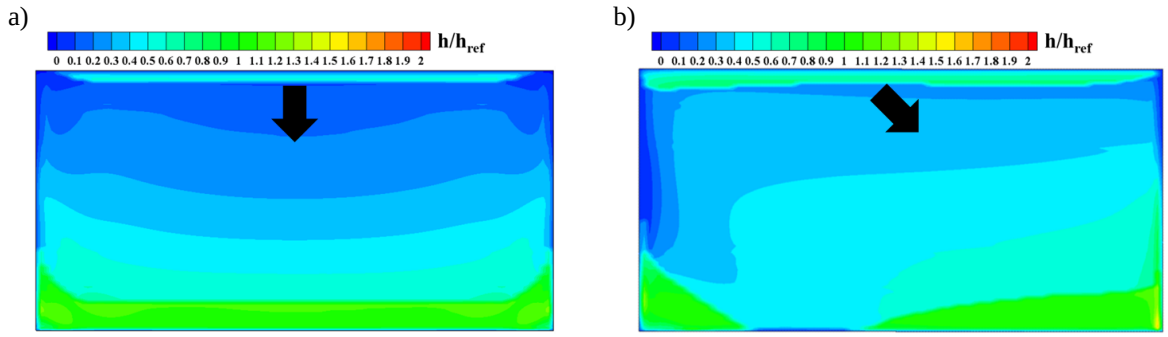


Figure 8. Contours of dimensionless snow concentration Φ/Φ_{in}: a) 0°; b) 45°; c) 90°

Figure 9 indicates the contours of snow depth ratio h/h_{ref} on the curved roof for different inflow directions. For the 0° inflow condition, since the friction velocity on the windward roof is much higher than the threshold friction velocity (as shown in Figure 7), many snow particles on the windward surface are carried to the leeward surface of the roof by the airflow (as shown in Figure 8). The snow distribution on the roof shows an obvious half-span distribution pattern. For the 45° inflow condition, due to the decrease in the value and area of the friction velocity on the windward surface, the uneven distribution of snow on the roof begins to weaken, and the overall pattern is triangular accumulations formed in the leeward corners. For the 90° inflow direction, as the friction velocity is lower than the threshold value, no snow drifting occurs on the roof. Only some falling snow particles from the sky are carried to the leeward side by the airflow. Therefore, the roof snow shows a uniform distribution, and only a small amount of snow accumulates around the leeward roof ridge. In general, for the curved roof, when the direction of the incoming flow is perpendicular to the eave, it is easier to form an uneven distribution.



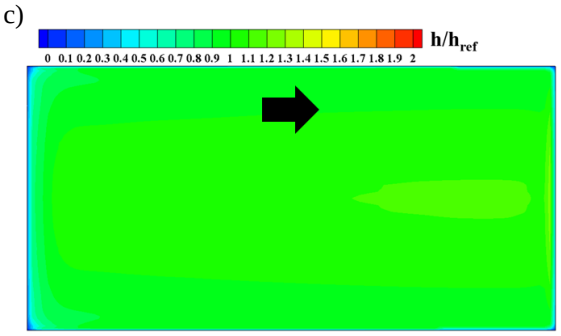


Figure 9. Contours of dimensionless snow depth h/h_{ref}: a) 0°; b) 45°; c) 90°

5. Conclusion

This study investigated the snowdrift development on an isolated curved roof with various inflow velocities and directions based on a revised multiphase model. As a result of this work, the following conclusions can be drawn:

1) By comparing with the Chinese load code and ISO load code, the revised CFD numerical model can accurately restore the balanced and unbalanced snow distribution pattern in the ISO code. Specifically, the movement of particles induced by airflow and the trajectorie of snow particle under the action of aerodynamic force and gravity are both well reproduced. However, some substantial deviations remain from the Chinese code, which needs a further investigation.

2) The snow load on the curved roof shows three kinds of distributions patterns, i.e., the full-span balanced distribution, half-span unbalanced distribution and transitional distribution between them. Snowdrift piled up on the leeward side of the roof tends to increase with the increasing inflow velocity.

3) With the change of wind direction from perpendicular to the eave to parallel to the eave, the uneven distribution of snow on the curved roof starts to weaken. In general, for the curved roof, when the direction of the incoming flow is perpendicular to the eave, it is easier to form an uneven distribution, which should be fully considered.

Acknowledgements

This study was funded by the Foundation for Chinese Creative Research Groups of National Natural Science Foundation (grant number: 51921006), National Natural Science Foundation of China (grant number 51978207, 51927813, 52208157), Postdoctoral Science Foundation of China (2022M710976), Heilongjiang Natural Science Foundation for Excellent Youth project (grant number YQ2021E030) and Heilongjiang Provincial Postdoctoral General Fund (grant number LBH-Z21161).

References

[1] M. O'Rourke, Lessons learned: structural collapse from snow loads, *Structure*, pp. 42-44, 2008.

[2] Y. Tominaga, Computational fluid dynamics simulation of snowdrift around buildings: Past achievements and future perspectives, *Cold Regions Science and Technology*, vol. 150, pp. 2-14, 2018.

[3] Ph. Delpech, P. Palier, J. Gandemer, Snowdrifting simulation around Antarctic buildings, *Journal of Wind Engineering and Industrial Aerodynamics*, vol. 74-76, pp. 567-576, 1998.

[4] T.K. Thiis, J.F. Ramberg, Measurements and numerical simulations of development of snow drifts of curved roofs, *Proceedings of the 6th International Conference on Snow Engineering*, Whistler, Canada, 2008.

[5] Y. Tominaga, T. Okaze, A. Mochida, CFD simulation of drift snow loads for an isolated gable-roof building, *Proceedings of the 8th International Conference on Snow Engineering*, Nantes, France, 2016. pp. 208-214.

[6] T.K. Thiis, M. O'Rourke, Model for snow loading on gable roofs, *Journal of Structural Engineering*, vol. 141(12), pp. 04015051, 2015.

[7] X. Zhou, L. Kang, M. Gu et al., Numerical simulation and wind tunnel test for redistribution of snow on a flat roof, *Journal of Wind Engineering and Industrial Aerodynamics*, vol. 153, pp. 92-105, 2016.

[8] J.W. Pomeroy, D.M. Gray, Saltation of snow, *Water Resources Research*, vol. 26(7), pp. 1583-1594, 1990.

[9] T. Okaze, A. Mochida, Y. Tominaga et al., Wind tunnel investigation of drifting snow development in a boundary layer, *Journal of Wind Engineering and Industrial Aerodynamics*, vol. 104-106, pp. 532-539, 2012.

[10] Y. Tominaga, T. Okaze, A. Mochida, CFD modeling of snowdrift around a building: an overview of models and evaluation of a new approach, *Building Environment*, vol. 46 (4), pp. 899-910, 2011.

[11] M. Naaim, F. Naaim-Bouvet, H. Martinez, Numerical simulation of drifting snow: erosion and deposition models, *Annals of Glaciology*, vol. 26, pp. 191-196, 1998.

[12] T. Uematsu, T. Nakata, K. Takeuchi et al., Three-dimensional numerical simulation of snowdrift, *Cold Regions Science and Technology*, vol. 20, pp. 65-73, 1991.

[13] T. Okaze, Y. Takano, A. Mochida et al., Development of a new k–ε model to reproduce the aerodynamic effects of snow particles on a flow field, *Journal of Wind Engineering and Industrial Aerodynamics*, vol. 144, pp. 118-124, 2015.

[14] A. Mochida, I.Y.F Lun, Prediction of wind environment and thermal comfort at pedestrian level in urban area, *Journal of Wind Engineering and Industrial Aerodynamics*, vol. 96, pp. 10-11, 2008.

[15] Y. Tominaga, T. Okaze, A. Mochida et al., PIV measurements of saltating snow particle velocity in a boundary layer developed in a wind tunnel, *Journal of Visualization*, vol. 16(2), pp. 95-98, 2013.

[16] Ministry of Construction of the People's Republic of China, *Load code for the design of building structures (GB50009-2012)*. Beijing, 2012.

[17] R. Clift, J.R. Grace, M.E. Weber, *Bubbles, Drops, and Particles*. London, 1978.

[18] R.S. Anderson, P.K. Haff, Simulation of eolian saltation, *Science*, vol. 241, pp. 820-823, 1988.

[19] ISO, *Bases for design of structures - Determination of snow loads on roofs*. Switzerland, 2013.

[20] AIJ, *AIJ Recommendations for Loads on Buildings*. Tokyo, 2004.

IASS 2023
July 10–14 Melbourne
Integration of Design and Fabrication

Proceedings of the IASS Annual Symposium 2023
Integration of Design and Fabrication
10–14 July 2023, Melbourne, Australia
Y.M. Xie, J. Burry, T.U. Lee and J. Ma (eds.)

Home reconstruction after the 2016 Kumamoto earthquake with a community focus

Yuuki KUROIWA[a,*]

[a,*] Kuroiwa Structural Engineers
6-3-5 Suizenji Chuo-ku, Kumamoto-shi, Kumamoto-ken, Japan
yuuki@kuroiwa-se.com

Abstract

In 2016, Kumamoto was struck by two earthquakes. The condominium I was living in was destroyed. We decided to search locally for a new section to build a home. The place we chose was a rich in groundwater so we thought to use it and so contributed to our hometown. The first floor would be an example of disaster relief architecture by using it as a public bath, and would provide water in times of disaster. The second floor would be our private home with no bath, we would use the public bath as ours. This report describes our construction process during which first floor ceiling, the latter using superimposed openwork beams of thinned wood. We designed the damaged structure to bear any subsequent earthquake. Since the remaining seismic capacity of a couple of nearby RC buildings dropped to about 60%, the analytical model for subsequent earthquakes assumed a reduced bearing capacity and an effective structural frame.The roof was designed using CLT arches. The joints have close fitting butterfly-shaped timber connectors without metal. Connector bending tests were performed. After the earthquake, construction costs skyrocketed. To reduce costs we took charge of site supervision, carpentry, and became the public bath operator. All this as a direct result of strong feelings for my Kumamoto hometown.

Keywords: timber fitting connector, CLT, superimposed openwork beam, thinned wood, high strength timber shear wall, timber frame structure, multiple earthquakes, disaster reconstruction, recovery utilizing a public bath, community preparedness

1. Introduction

In 2016, Kumamoto in South-Western Japan was severely damaged by a series of earthquakes (Figs.1).The condominium I was living in was destroyed and had to be rebuilt. However, the surrounding area was steadily becoming vacant and losing its liveliness. As the water supply was cut off for several months, I needed to regularly go to a public bath, However the washrooms were over-crowded and drains clogged with hair (Fig.2). My family searched locally for a new section on which to build our home. As there was an abundance of groundwater where we bought, we decided to use it and contribute` to our hometown. The first floor would involve relief architecture that could be used as a public bath and provide water in a disaster. The building would also serve as a small but useful example of community preparedness architecture.

2. Structural design

The building is a two-story, conventional post and beam timber structure. Since the use of the first floor is a public bath. It was constructed with the RC wall raised to a height to stop buckling. The first floor ceiling has superimposed openwork beams made of thinned wood to improve rigidity and strength. We designed the structure to bear any subsequent earthquake even if damaged. The roof is designed as an arch with CLT enabling a loft floor.

Copyright © 2023 by Yuuki KUROIWA. Published in the Proceedings of the IASS Annual Symposium 2023 with permission.



Figures 1. Consecutive Kumamoto earthquakes.



Figure 2. Public bath queue.

2.1. Timber frame with superimposed openwork beams

The area of the first floor public bath is small, so the ceiling height was set to 4.75m to allow for a more open bathing experience. Since the Kumamoto earthquake, the number of sub-contractors has increased, and construction costs have risen; so our policy was to consider low-cost construction. The unit price using small cedar square timber (ungraded, 4.0 m) is about 1/3 for that of engineered wood (E120-F330, 4.0 m). Thus 90 mm square cedar is widely used. Since bathers will look up at the ceiling for long periods of time, and also to make it interesting, the ceiling was made of superimposed openwork beams to improve rigidity and strength of the structure. Screw fastening was used for the small square and prop timbers, and the upper and lower flanges of the girders and the columns made of engineered wood (Fig.3,4). The girder was divided to increase bending strength.

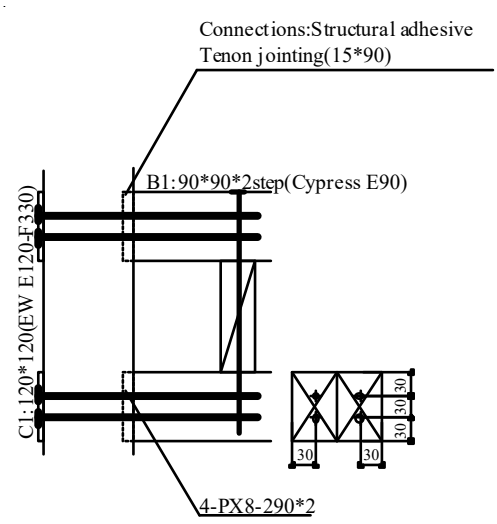


Figure 3. A column-girder joint

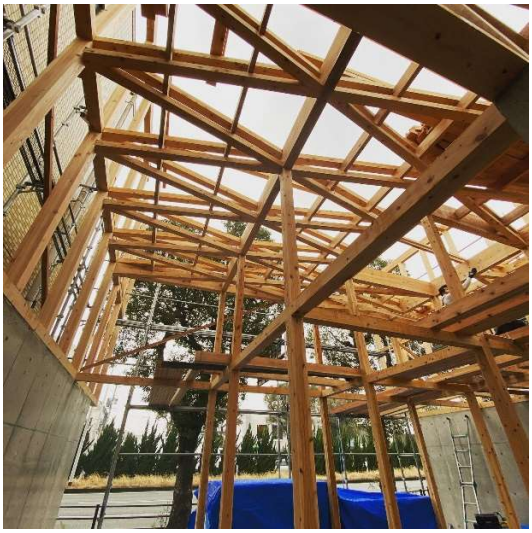


Figure 4. Superimposed openwork girders at the time of erection

Considering the possibility of subsequent earthquakes, high-strength bearing walls of structural plywood (Qa=19.6kN/m) that satisfy the Building Standard Law were used; any future earthquake impact would be borne by the timber frames with superimposed openwork beams. Since the remaining seismic capacity of a couple of nearby RC buildings dropped to about 60%, the analytical model for subsequent earthquakes assumed a reduced bearing capacity and an effective structural frame (Table 1). Framing was planned with the top of the RC wall as the rebound point, and the out-of-plane bearing strength of the RC wall at the bottom of the intermediate level was combined with the timber frame. RC wall tops, timber column legs, and intermediate beams were pinned together (Fig.6). The horizontal structure was borne solely by directly affixed structural plywood of t=24mm.

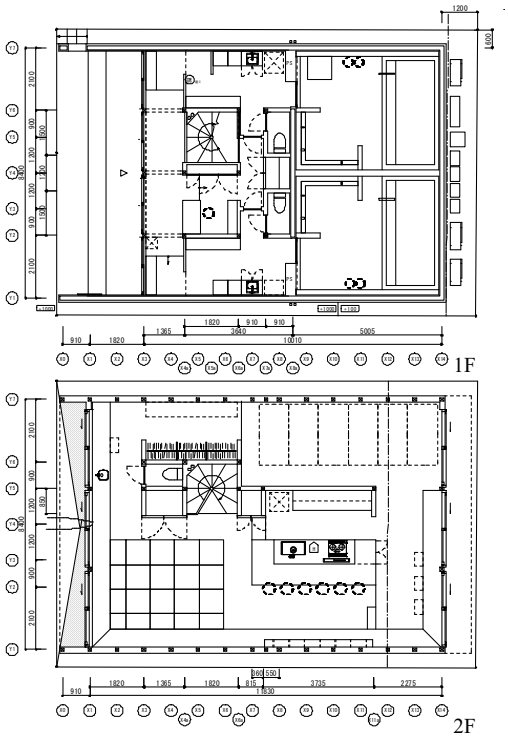


Figure 5. Floor plan

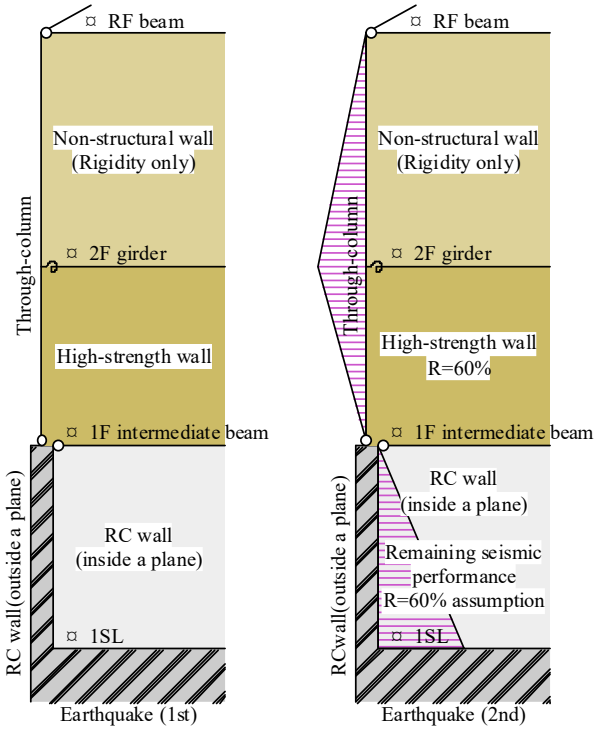
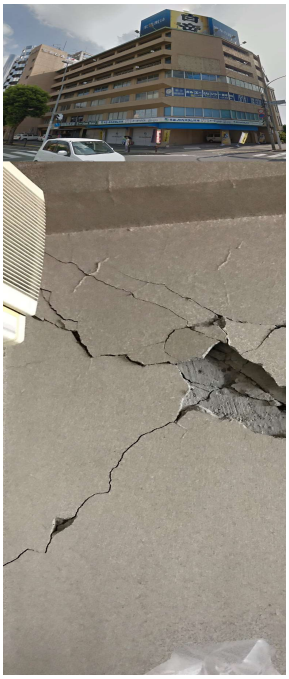


Figure 6. Second seismic analysis model

Table 1. Remaining seismic capacity after the disaster

	Y direction (+)													
Before disaster	Story	ΣWi	1/Ai	W/A	C	F	Collapse form	Eo	S_D	T	Is	C_{TU}・S_D	Judge
	PH2	213.3	0.333	10.16	5.71	1.00	WS	1.910 (2formula)	1.00	0.925	**1.767**		OK
	PH1	608.7	0.333	18.83	2.01	1.00	WS	0.669 (2formula)	1.00	0.925	**0.619**		OK
	7	4765.3	0.502	9.44	3.81	1.00	CB,WB,WS	1.914 (5formula)	1.00	0.925	**1.770**	**1.91**	OK
	6	9875.6	0.616	10.12	1.98	1.00	CB,WB,WS	1.222 (5formula)	0.85	0.925	**0.961**	**1.03**	OK
	5	14985.9	0.696	10.12	1.21	1.00	CB,WB,WS	0.848 (5formula)	0.75	0.925	**0.588**	**0.63**	OK
	4	19962.8	0.765	9.85	0.15 0.37	1.00 2.00	WB,WS CB	0.577 (4formula)	0.50	0.925	**0.266**	**0.14**	NG
	3	25252.8	0.834	10.41	0.68 0.19	1.00 2.60	WB,WS CB	0.715 (4formula)	0.96	0.925	**0.635**	**0.15**	NG
	2	30952.6	0.910	11.22	0.83	1.00	CB,WB,WS	0.754 (5formula)	1.00	0.925	**0.697**	**0.75**	OK
	1	37265.3	1.000	12.43	1.02	1.00	CB,CS,WB,WS,WCS	1.026 (5formula)	1.00	0.925	**0.949**	**1.02**	OK
After disaster	Story	ΣWi	1/Ai	W/A	C	F	Collapse form	Eo	DSD	T	DIs	DCTU・DSD	Judge (R%)
	PH2	213.3	0.333	10.16	5.71	1.00	WS	1.910 (2formula)	1.00	0.925	**1.767**		OK 100%
	PH1	608.7	0.333	18.83	2.01	1.00	WS	0.669 (2formula)	1.00	0.925	**0.619**		OK 100%
	7	4765.3	0.502	9.44	2.39	1.00	CB,WB,WS	1.203 (5formula)	1.00	0.925	**1.130**	**1.20**	OK 64%
	6	9875.6	0.616	10.12	1.11 0.20	1.00 3.00	WB,WS CB	0.778 (4formula)	0.82	0.925	**0.590**	**0.10**	NG 61%
	5	14985.9	0.696	10.12	0.52 0.12	1.00 2.60	CB,WB,WS CB	0.430 (4formula)	0.69	0.925	**0.274**	**0.06**	NG 47%
	4	19962.8	0.765	9.85	0.14 0.28	1.00 2.00	WB,WS CB	0.442 (4formula)	0.52	0.925	**0.212**	**0.11**	NG 80%
	3	25252.8	0.834	10.41	0.34 0.18	1.00 2.60	WB,WS CB	0.496 (4formula)	0.99	0.925	**0.454**	**0.15**	NG 71%
	2	30952.6	0.910	11.22	0.50	1.00	CB,WB,WS	0.462 (5formula)	0.85	0.925	**0.363**	**0.39**	NG 52%
	1	37265.3	1.000	12.43	0.63	1.00	CB,CS,WB,WS,WCS	0.631 (5formula)	1.00	0.925	**0.583**	**0.63**	OK 61%



2.2. CLT connecting arch with fitting

The roof has a loft floor with the CLT connected in an arched shape (Fig.7). Long engineered wood bore the long term thrust force. In the short term, tensile force would be generated between each CLT member, so the CLT were joined by butterfly-shaped close fitting timber connectors (Figs.8). To reduce costs, temporary girders were not used during erection; CLT sections were assembled in a curved shape at the factory and then installed by crane and human power. Joints were closely fitting timber connectors without any metal. Since the arches were cantilevered during erection, connector bending tests were performed (Figs.9,10). Interestingly, in 1968, the Japanese furniture designer George Nakashima made a desk using a butterfly-shaped timber fitting connector as a tensile member.

A total of 12 units were tested for the bending strength of the timber connectors, with and without structural adhesive (polyurethane resin adhesive); and with the strong and weak axial directions of shredding interchanged (Fig.11). To secure units, they were placed on top of the load bearing area and a pantograph was mounted at the center to prevent initial deflection. Force was applied using a

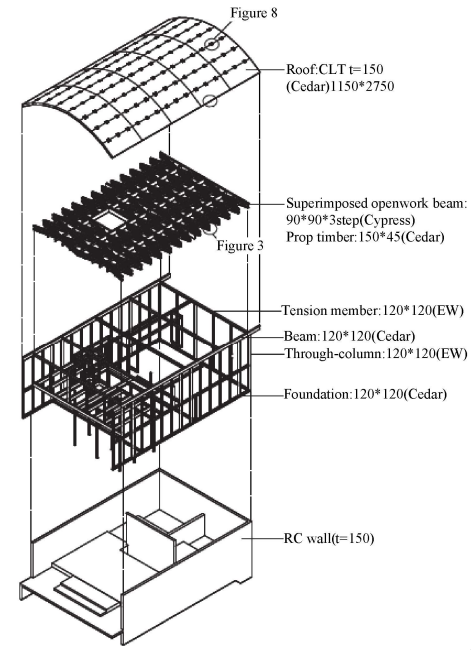
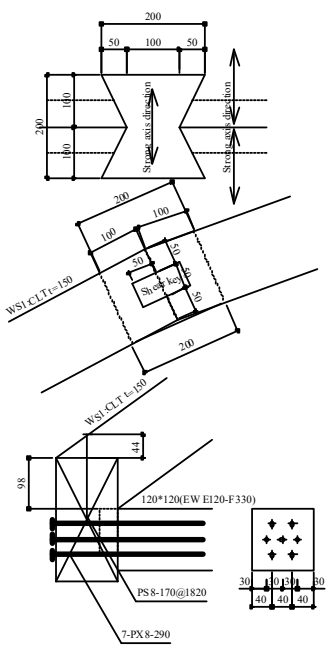
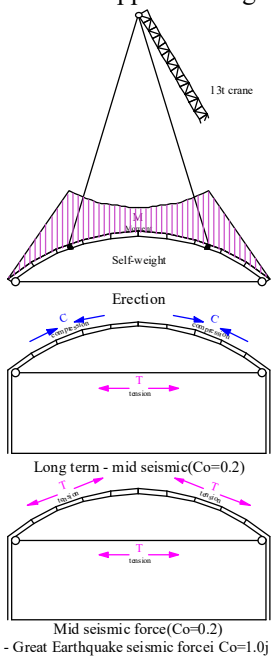


Figure 7. Axonometric drawing



Figures 8. Detail drawing of joint



Figures9. Changing Forces Flow



Cutting out CLT | Striking timber fitting connector | Unitized roof

Figures 10. Assembling CLT connecting arches

2000kN universal testing machine with four points with three equal loadings. The monotonic force rate was 5 mm/min until the max proof force was reached and the specimen displacement reached 50 mm. Displacement was measured using a strain gauge displacement transducer at the position shown in the figure. ["] indicates that the shreds are parallel to the CLT strong axis direction; without ["]. [Bond] indicates the application of structural adhesive. The test results confirm P max=12.0 kN (average value), and a long term allowable bending capacity Ma=1.54 kN· m (Fig.12, 13). Since the lamina widths were uncrimped, shear failure of the fitting connector snagging area occurred after rolling shear occurred. Resorcinol-phenol co-condensation resin was used as the structural adhesive joining the laminae. Although a structural adhesive was used, only stiffness increased without any increase in bending capacity. There was also a unit that suffered shear failure of the timber fitting connector after flexural failure of the shear key. The stiffness of the structural adhesive was higher than the stiffness of the timber fitting connector, so there no combined proof stress at the end of the test. Since cracking occurred only in the weak axial direction of the CLT layer, the bearing capacity would have increased if the fittings were in the strong axial direction (Fig.14).

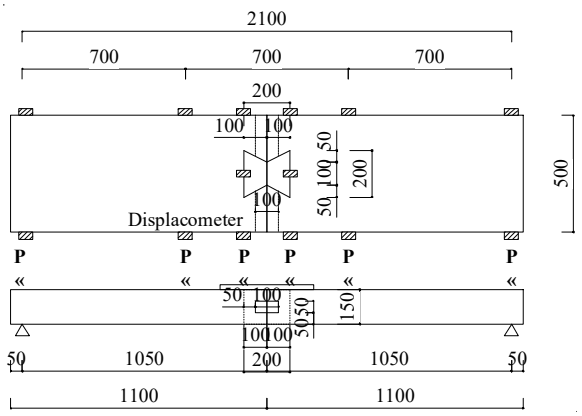
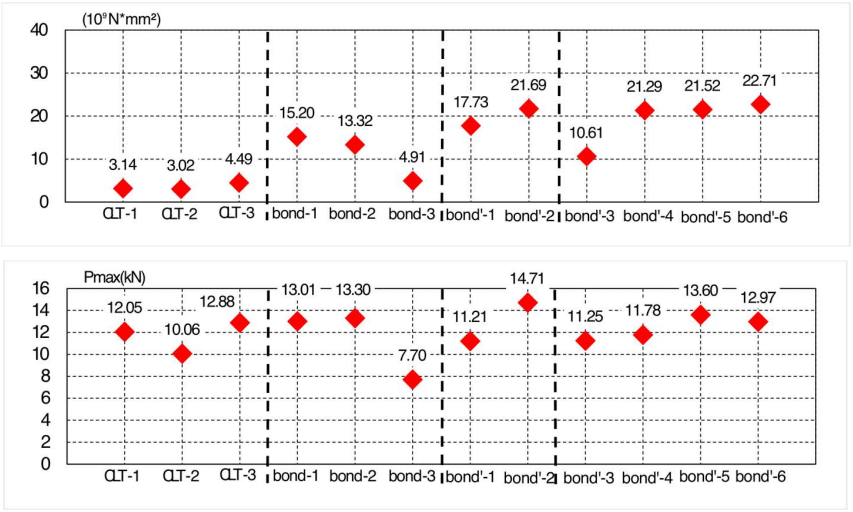


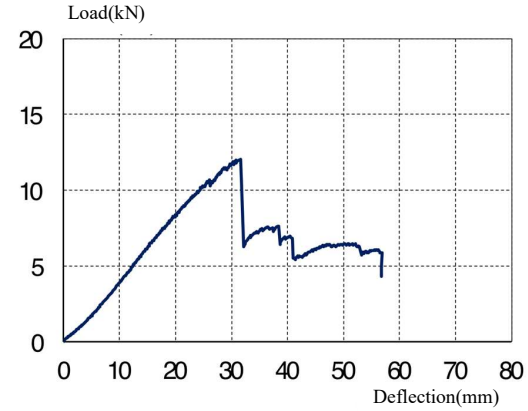
Figure 11. Bending test procedure

Table 2. Assessment Item Results

Specimen	Initial Deflection (mm)	Bending rigidity (10^9N*mm^2)	Maximum load Pmax(kN)
CLT-1	6	3.14	12.05
CLT-2	8	3.02	10.06
CLT-3	5	4.49	12.88
CLT-bond-1	2	15.20	13.01
CLT-bond-2	1	13.32	13.30
CLT-bond-3	3	4.91	7.70
CLT-bond'-1	0	17.73	11.21
CLT-bond'-2	0	21.69	14.71
CLT-bond'-3	0	10.61	11.25
CLT-bond'-4	0	21.29	11.78
CLT-bond'-5	0	21.52	13.60
CLT-bond'-6	0	22.71	12.97



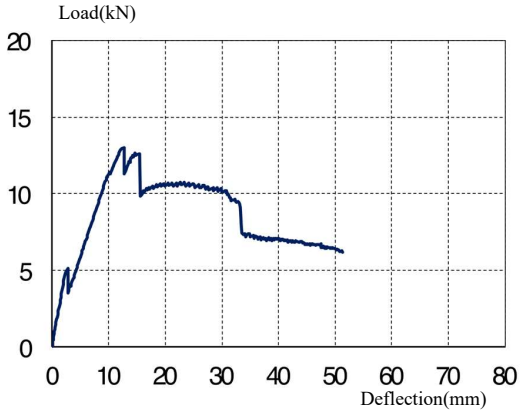
Figures 12. Bending rigidity and maximum load



CLT-1(Weak-axis direction, No adhesive)



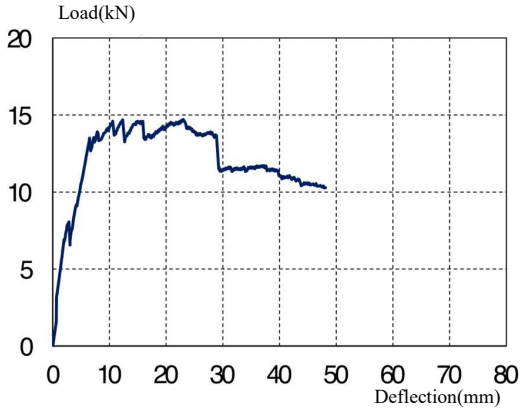
Crack fracture along fiber direction



CLT-bond-2(Weak-axis direction, with adhesive)



Shear failure for snagging



CLT-bond'-2(Strong-axis direction, with adhesive)



Weak axial crack with shear key

Figures 13. Load displacement curve

Figures 14. Specimen after completion of the test

The design equation (Architectural Institute of Japan) applies to the fitted timber connector for partial compressive stress perpendicular to the grain in the moment resisting joint equation. The existing

equation overestimates Ma=2.16 kN·m (long-term allowable bending capacity) as it has only three conditions [1] triangular compression to the grain displacement yielding strength, [2] equal compression to the grain displacement, yielding the strength of the wedge, and[3] wedge tensile yielding strength.

Since the type of failure was also different, [4] flexural shear strength at the snagging area and [5] shear strength at the snagging area were added. The design value Ma=1.36 kN·m was determined by the smallest value [5], which was close to the experimental value.

$$M_y=N_y \cdot j \tag{1}$$

$$N_y=\min(\Sigma N_y, N_{y1}, T_{y2})$$

$$\Sigma N_y=\frac{x_p y_p F_m}{2}\sqrt{\frac{C_x C_y}{C_{xm} C_{ym}}} \tag{1}$$

$$N_{y1}=x_0 y_0 F_m \sqrt{\frac{C_{y2}}{C_{yzm}}} \tag{2}$$

$$T_{y2}=A_e \cdot F_{ty} \tag{3}$$

$$Q_m=\frac{Z_c f_{bs}}{H} \cdot \sqrt{\frac{C_{y2}}{C_{y2m}}} \tag{4}$$

$$Q_s=A_s \cdot f_{ss} \tag{5}$$

2.3. Carpentry plan

To shorten the time for carpentry, the CLT connecting arches and the superimposed openwork beams were assembled in a factory and delivered to the site. Several mock-ups were made, and since it was necessary to account for swelling after application of the structural adhesive, the surface of the wood was pounded to temporarily compress wood cells (kigoroshi). The area compressed by kigoroshi swells back as a result of the wood's restorative force, thus increasing adhesion. The roof plate was divided into 5 units (1.5 t/unit) (Fig.17, 18). Manufacturing the CLT members (150 mm thick, S60 strength class, and ungraded cedar). And joint jigs, assembling the CLT connecting arches, and erecting the CLT connecting arches, each took one day. The construction was done by five carpenters.



Figures 15. Erection and horizontal sliding

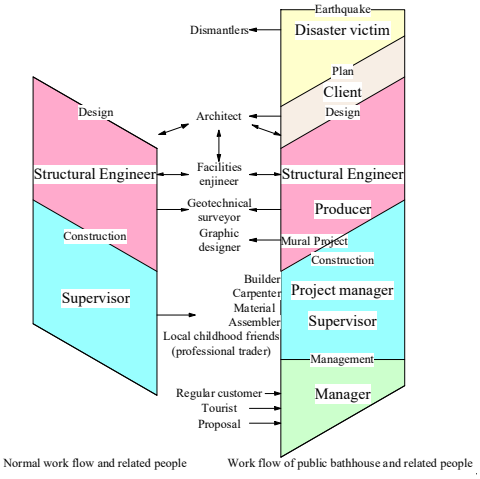


Figure 16. Author's Role

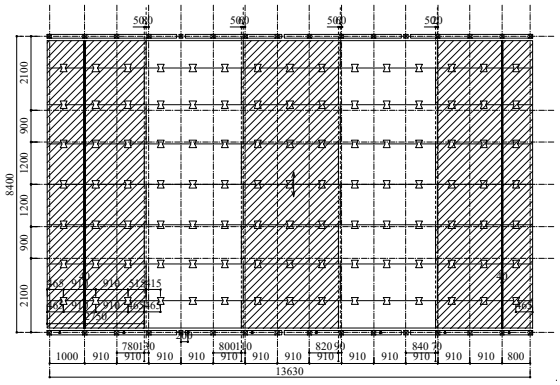


Figure 17. Unit layout

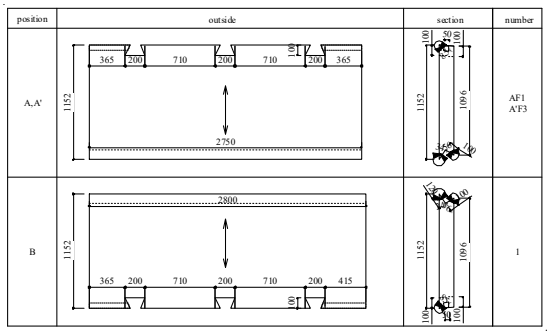


Figure 18. Single Item

The erection process was very difficult as the site was a narrow lot surrounded by power lines. Because CLT is light, the drop was completed by a single carpenter who manually manouvered the CLT connecting arch with a nylon sling (Fig.15). To reduce costs we took charge of site supervision, carpentry, and became the public bath operator. (Fig.16).



Figure 19. Interior and exterior views

3. Conclusion

In Japan CLT is still considered a new building material. Hence construction companies seek to avoid risk and involve a brokers. Thus, CLT construction costs approximate those of RC construction. This building reflected that double ordering. The CLT construction cost could be reduced to 1/3 (frame cost: 40,000 yen/m2) without the separate order. Although less strong, timber fittings are more reasonable than CLT-specific metal. Timber should also be considered as the fittings are easy to spread because they can be manufactured as long as there are trees. We successfully rebuilt our home. The public bath has been bustling with users, and we look forward to helping community preparedness in the future.

Acknowledgements

Six years have passed since the Kumamoto earthquake. It has not been a smooth road, and the support of my family and friends has been essential. I thank them.

References

[1] Japan Building Disaster Prevention Association, *Criteria for Determining the Degree of Damage to Earthquake-Damaged Buildings and Technical Guidelines for Restoration,* 2015.

[2] Architectural Institute of Japan., *Design Practice forEngineered Timber Joint*, 2012.

IASS 2023
July 10–14 Melbourne
Integration of Design and Fabrication

Proceedings of the IASS Annual Symposium 2023
Integration of Design and Fabrication
10–14 July 2023, Melbourne, Australia
Y.M. Xie, J. Burry, T.U. Lee and J. Ma (eds.)

Intelligent detection of ceiling damage in large public buildings based on semantic segmentation

Lichen WANG[a,*], Shihao YAN[a], Ken'ichi KAWAGUCHI[b]

[a,*] School of Civil Engineering, Tianjin University
No.135 Yaguan Road, Haihe Education Park, Jinnan District, 300350, Tianjin China
wanglc@tju.edu.cn

[b] Institute of Industrial Science, University of Tokyo

Abstract

Large public buildings are an essential part of the national earthquake emergency relief system, and detecting ceiling damage caused by earthquakes is a crucial part of evaluating the safety of large public buildings as emergency shelters. To overcome the limitations of human-based visual onsite inspections, a vision-based method using the semantic segmentation network Deeplabv3+ with transfer learning (TL) is proposed for the rapid detection of damaged ceilings in large public buildings after earthquakes. Damaged ceiling regions can be located and visualized accurately employing generating different pixel-level masks. A total of 1389 ceiling images of various scenes are used as the dataset after being manually labeled and categorized into four ceiling forms, including intact, fall-off, suspension, and crack. The final fine-tuned model achieved a pixel accuracy (PA) of 97.23% and a mean intersection over union (mIoU) of 84.18% in the test set, which shows that the proposed model has an excellent performance in terms of damage detection and location. The damaged regions of the ceiling can be localized accurately and visualized using generating different pixel-level masks. Some factors that have varying degrees of influence on the detection accuracy are explored. The results in this paper further promote rapid damage detection of post-earthquake ceilings in emergency relief work.

Keywords: ceiling damage detection, large public buildings, semantic segmentation, transfer learning, damage visualization

1. Introduction

Large public buildings, such as indoor stadiums, hospitals, and convention centers, are essential components of emergency shelters, which are transitional places for earthquake evacuees to live and rescue in a concentrated manner for some time after a disaster. Several investigations [1] demonstrated that the main structure of most buildings designated as a shelter can maintain normal service after an earthquake, but the damaged ceilings caused by earthquakes pose a substantial potential hazard to the safety of life and property during aftershocks [2]. Therefore, a rapid detection of the damaged ceiling is critical in evaluating the safety of a building used as a disaster shelter. Considering the limitations of transportation and communication in post-earthquake affected areas and the uncertainty of earthquake occurrence areas, implementing a rapid, reliable, and human-independent damage detection method for ceilings is of great practical significance for post-earthquake emergency relief work.

Nowadays, the visual detection method using convolutional neural networks (CNNs) is widely used [3] in structural damage detection, such as concrete cracks [4, 5], steel cracks [6, 7], masonry surface cracks [8], and road pavement cracks [9-12] due to their efficient and accurate feature extraction and representation of data. To detect ceilings damaged by earthquakes, Wang et al. [13] proposed a deep convolutional neural network (DCNN) method to detect whether the ceiling of a large-span structure is

Copyright © 2023 by Lichen WANG, Shihao YAN and Ken'ichi KAWAGUCHI. Published in the Proceedings of the IASS Annual Symposium 2023 with permission.

damaged or intact. A prediction accuracy of 86% is obtained, and the damaged ceiling regions can be visualized and localized using the Saliency-MAP method. In addition, Wang et al. [14] developed a YOLOX-based ceiling damage detection model which can detect different ceiling damage categories. Twelve detection models are established, trained, and compared by variable hyperparameter analysis. The model with the best performance reaches a mean average precision (mAP) of 75.28%, further promoting the automatic ceiling damage detection in large public buildings. The above two intelligent detection methods have gradually achieved rapid detection of whether post-earthquake damage occurred, damage categories, and damage locations of ceilings in large public buildings. However, existing detection methods are still incapable of achieving accurate detection of damage regions and quantitative measurement of the extent of damage.

Semantic segmentation [15] enables the accurate segmentation of pixel regions belonging to different categories in an image by assigning a category label to each pixel in the image. In tasks such as structural damage detection, segmentation results not only achieve classification and localization of targets but results such as the number of pixels in the target region can also be counted simultaneously. Pan et al. [16] developed a novel segmentation network for sewer defect detection based on an improved U-Net (i.e., PipeUNet). It detected the defect's type, location, shape, and boundary with high speed and accuracy and achieved the highest mean intersection over union (mIoU) of 76.37%. Yang et al. [17] established a soil diagnostic horizon identification method based on UNet++, with mIoU of 71.24% and pixel accuracy (PA) of 82.44% in the dataset of major soil types. Segmentation results accurately identified different soil types and delineated soil faults. Xu et al. [18] used SegNet to automatically segment retinal vessels and achieved 95.18%, 96.83%, and 96.53% accuracy on three public datasets, respectively. It effectively solved the problem of the need for more experienced ophthalmologists in remote areas and is important for clinical aid in diagnosing and treating ophthalmic diseases. Yangtao Li et al. [19] proposed a real-time pixel-level dam underwater crack automatic segmentation and quantification framework using the lightweight semantic segmentation network LinkNet and two-stage hybrid transfer learning (TL). The proposed method performed with 89.24% mIoU in the complex underwater scenario test set. Four advanced segmentation methods have been trained for sewer defect detection [20], including DeepLabv3+, FCN, U-Net, and SegNet. Compared to the three other methods, the DeepLabv3+ has the best performance with PA and mIoU of 0.90 and 0.53, respectively, for multiple types of defect detection results. In other studies, DeepLabv3+ has been successfully applied to solving challenges in several fields, including road cracks detection [21], biomedicine [22], automatic road-pothole extraction [23], and disaster prevention [24]. In summary, semantic segmentation methods, especially Deeplabv3+, perform satisfactorily in precise target localization, which can promote further development of damage detection work refinement and quantification.

Therefore, a damage detection method based on semantic segmentation for post-earthquake ceilings of large public buildings is proposed in this paper. It can achieve efficient and accurate damage detection by rapidly classifying and accurately locating the damage of ceilings in large public buildings. After the damage detection method is specifically described, the details of the dataset and the implementation details of the model in terms of training and validation are described. Based on the results of damage detection and visualized images, the effectiveness of damage detection and the influencing factors are analyzed. Finally, some concluding remarks are presented.

2. Methodology

2.1. Overview of detection method

The proposed detection method, as shown in Figure 1, is organized as follows: (1) Images are classified into different ceiling damage categories. (2) Images are preprocessed using damaged region marking and data augmentation. (3) The semantic segmentation model combined with transfer learning is trained using the preprocessed dataset. (4) A set of images that were not used in the training and validation are then applied to test the semantic segmentation model.

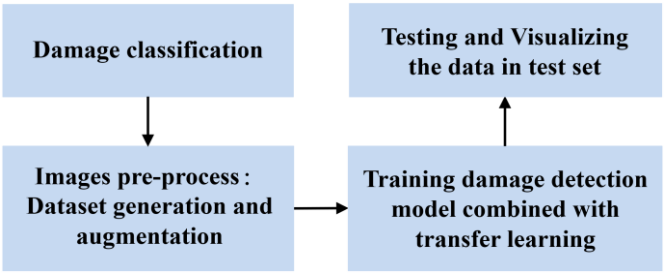


Figure 1. Overview of the proposed detection method.

2.2. Semantic segmentation algorithm

The DeepLabv3+ [25], as shown in Figure 2, is a current widely used semantic segmentation algorithm model that achieves target segmentation by assigning semantic labels to each pixel in an image. The model has an encoding-decoding structure. The rich context information can be captured by feature extraction with down-sampling at different resolutions, and then sharp object boundaries can be obtained by feature amplification with up-sampling.

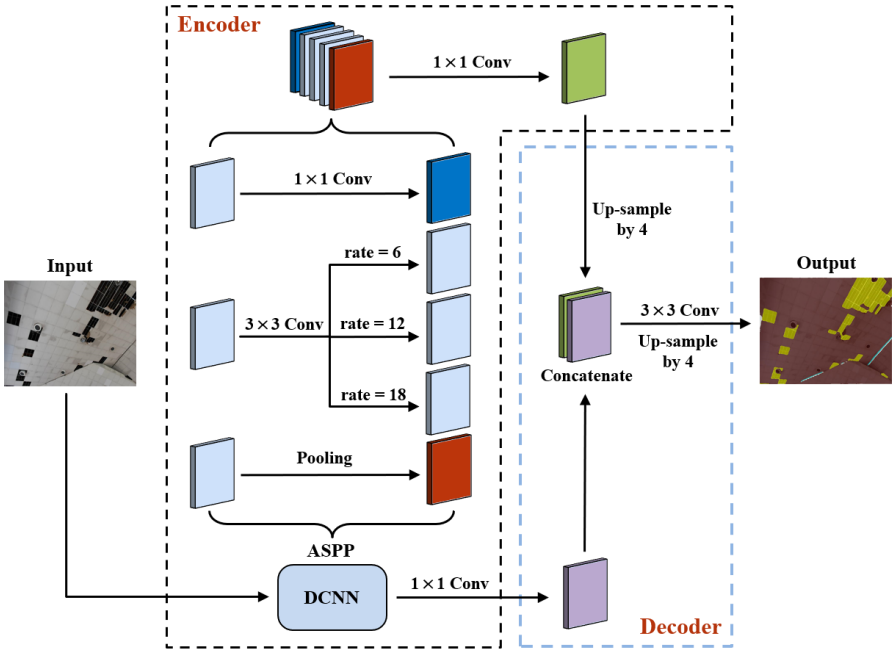


Figure 2. DeepLabv3+ architecture.

The encoder module mainly consists of an atrous space pyramidal pooling structure (ASPP). By combining several deep convolutional neural networks (DCNNs) which apply parallel atrous convolution with different rates, it can acquire multi-scale feature information of images. Compared with standard convolution, atrous convolution changes the size of the convolution kernel distribution by extracting feature points across pixels to increase the receptive field without decreasing the resolution. In the case of input image data, for each location i on the output feature map y and a convolution filter w, the atrous convolution is applied over the input feature map, x, as shown in Eq. (1):

$$y[i] = \sum_k x[i + r \cdot k] w[k] \tag{1}$$

Where the atrous rate r determines the sampling stride of the input signal. Figure 3 illustrates the difference between the atrous convolution with a dilation rate of 3 and the standard convolution. Standard convolution is a particular case in which rate r = 1. The filter's field-of-view is adaptively

modified by changing the rate value. More details are described in other articles. In this paper, the expansion rates are set to 6, 12, and 18 so that the receptive field is expanded to 13×13, 25×25, and 37×37 without changing the 3×3 convolution kernel with nine parameters to achieve the extraction of multi-scale information such as location and semantics. Five sets of features, including standard convolution and pooling layers, are concatenated to reduce the data dimensionality after obtaining multi-scale feature maps from ASPP.

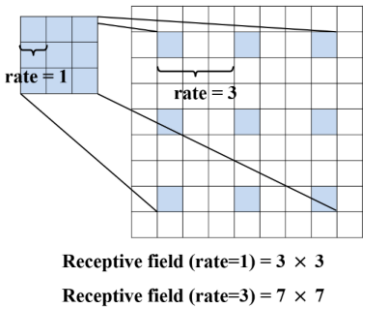


Figure 3. Example of the atrous convolution operation.

In the decoder module, the feature information from the ASPP input is up-sampled using bilinear interpolation to extend the dimensionality of the extracted features. The basic features extracted with the deep convolutional neural network are restored to the original spatial dimension after a series of cascading, convolution, and up-sampling processes to obtain semantically information-rich high-level feature information. Finally, in the output layer, the feature information is mapped to the corresponding pixel classes so that each pixel of the input image is labeled with the corresponding classification label to achieve semantic segmentation of the image.

2.3. Evaluation criterion for detection

This paper employs a group of mainstream evaluation indicators to evaluate the performances of semantic segmentation models in terms of rapid classification and accurate localization of damaged ceiling regions, including the (1) pixel accuracy (PA); (2) intersection over union (IoU); (3) mean intersection over union (mIoU); (4) precision (P); (5) recall (R). The detailed definition formulas for these indicators are defined in other articles [15].

In terms of the overall performance of the detection model, PA indicates the ratio of the number of all correctly detected pixels to the total number of pixels, which is used to evaluate classification correctness. The mIoU is the average value of IoU of each category, which indicates the degree of overlap between detection and true values and is used to evaluate the localization accuracy of the damaged ceiling region. For each different damage category, P and R denote the number of correctly detected true value pixels as a percentage of the total number of pixels in the recognition result and as a percentage of the total number of pixels in their category, respectively. As a result, P and R are used to evaluate the accuracy of the detection results and the completeness of the marked regions being successfully detected.

3. Data and implementation details

3.1. Dataset generation

A total of 1389 raw ceiling images with different pixel resolutions are used, including 760 damaged ceiling images caused by the earthquake. These images were taken from stadiums, indoor pools, transportation stations, lecture halls, industrial planets, and other structures with a large span, and have been collected by Kawaguchi Lab and Wang [13] since the Great Hanshin-Awaji Earthquakes in 1995. As shown in Figure 4, different types of ceiling regions in each image, namely intact, fall-off,

suspension, and crack, were marked as brownish-red, yellow, red, and cyan using the online annotation tool Labelme. Non-ceiling regions were automatically classified as background marking with no color.

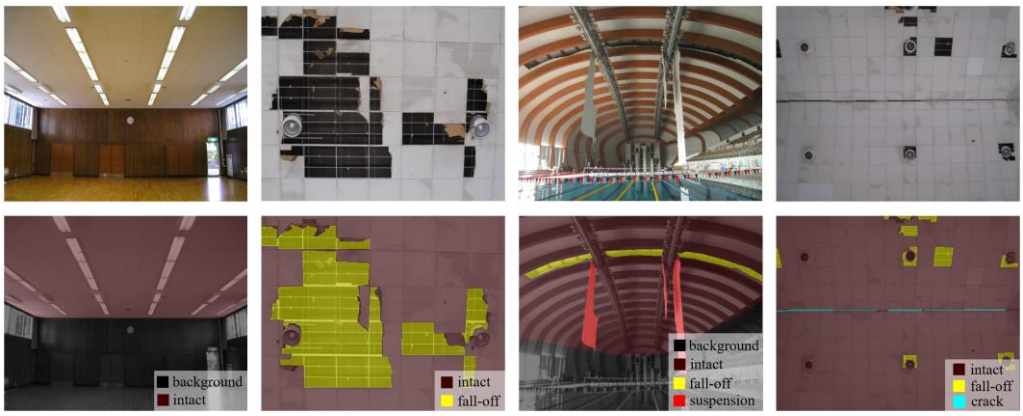


Figure 4. Example of original images and annotations of marked images.

To avoid overfitting, cross-validation was used in the training process. All images were randomly divided into a training dataset of 1111 images, a validation dataset of 139 images, and a test dataset of 139 images in a ratio of 8:1:1. The test dataset was not used in the training process except for the final test. Data augmentation (DA) can increase the number and diversity of samples and enhance the generalization of models [26]. Therefore, DA was used in the construction of datasets, including geometric transformations (e.g., rotation, flip, shift, scaling, etc.) with random combinations of color transformations (luminance, noise, contrast, etc.).

3.2. Implementation details

The code was programmed using Python 3.7 and Compute Unified Device Architecture (CUDA) v11.3. The virtual environment was established by Pytorch on the Pycharm IDE. All training and validation process was conducted on a computer with an Intel Core i9-10940X @3.30GHz CPU, and an NVIDIA Geforce RTX 2080Ti GPU.

The detection model contains several hyperparameters that have different effects on the performance. Batch size represents the number of samples involved in one forward propagation in training. By calculating the loss function in backpropagation, the model can continuously adjust the weights so that the output predictions keep approximating the true values. The optimizer can change how the loss function is calculated and the gradient drop in this process. In addition, the learning rate controls the convergence rate of the model.

More than 50 sets of hyperparameter combinations were trained and validated. Considering the time cost and features learning effect, the epoch of the training phase was set to 600. The details and validated results of four cases with excellent performance are shown in Table 1. All four cases achieved a PA of over 90% in the validation set, and the mIoU reached about 80%. Among them, Case 1 uses the original DCNN from the Deeplabv3+ model and randomizes the initial weights for training. Case 2 uses Mobilenetv2, a lightweight feature extraction network, to significantly reduces the number of training parameters while ensuring the detection effectiveness and improving operational efficiency. The maximum learning rate is set to 5e-4 during the training process while dynamically adjusting the decreasing rate of the learning rate in the form of a cosine function. Transfer learning (TL) can achieve the effect of improving [27] detection accuracy under the same conditions by using weights that have been successfully pre-trained in large-volume datasets (e.g., PASCAL VOC, ImageNet, and COCO, etc.). By comparing multiple sets of experiments, the model can achieve excellent results when the pre-training epoch exceeds 100. Compared with Case 2, the PA and mIoU of Case 3 are significantly improved by 2.42% and 7.06%, respectively, due to the optimization of each hyperparameter,

application of Focal_loss, Adam optimizer, and pre-training. When the pre-training epoch continued to increase to 200 in Case 4, the results of PA and mIoU have a slight decrease. As a result, the optimum value of the pre-training epoch is 100.

Table 1. Training details and validated results of four excellent cases.

	Backbone	Pretrained	Batch	Downsample	Focal_loss	Optimizer	Lr_decay	PA(%)	mIoU(%)
Case1	Xception	0	2	16	/	Sgd	Step	93.56	79.52
Case2	Mobilenetv2	0	2	16	/	Sgd	Step	94.81	80.19
Case3	Mobilenetv2	100	8	8	√	Adam	Cos	97.23	87.25
Case4	Mobilenetv2	200	8	8	√	Adam	Cos	97.11	86.68

Figure 5 shows the curves of the loss value and the mIoU of the validation set after each iteration for the four cases, which exhibit the learning process of the damage recognition model. In general, all cases have similar fitting trends and successfully achieve relatively stable convergence. Since Case 3 and Case 4 use TL, their loss curves do not show large oscillations, drop faster, and have significantly lower final fit loss values than Case 1 and Case 2. A rapid fit of the mIoU curve is also achieved at the early stage of training. The minimum validation set loss for the 562nd epoch in Case 3 is 0.118, and the maximum mIoU of the validation set is 87.25%, which is saved as the best weight.

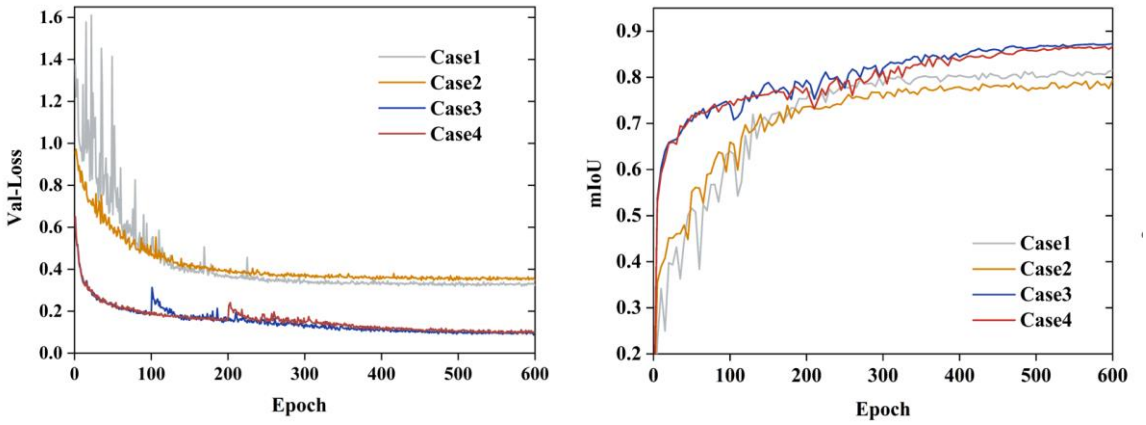


Figure 5. Validation loss and mIoU curve of four cases.

4. Results and discussion

4.1. Detection in the test set

Based on the optimal weights derived in the previous section, the ceiling damage detection model achieves 97.23% of the PA and 84.18% of the mIoU in the test set. The detection time of each image in the test set is about 0.02 s, which satisfies the need for emergency damage detection of ceilings after earthquakes. As shown in Figure 6, details of the detection results of each category can be known by the confusion matrix after normalizing. The main diagonal values of the matrices in Figure 6(a) and (b) represent the precision and recall of each category, respectively. It can be found that the precision and the recall of background, intact, and fall-off are above 95%. The precision and recall of suspension are 95.16% and 91.15%, respectively, and have a 4.17% and 3.70% probability of being incorrectly detected as intact or fall-off. The precision and recall of crack are 63.41% and 73.49%, respectively. The intact ceiling region has interfered with the detection performance of the ceiling crack to some extent. In summary, the testing results demonstrate that the model has excellent detection capabilities including classification and localization for the damaged ceiling region caused by the earthquake.

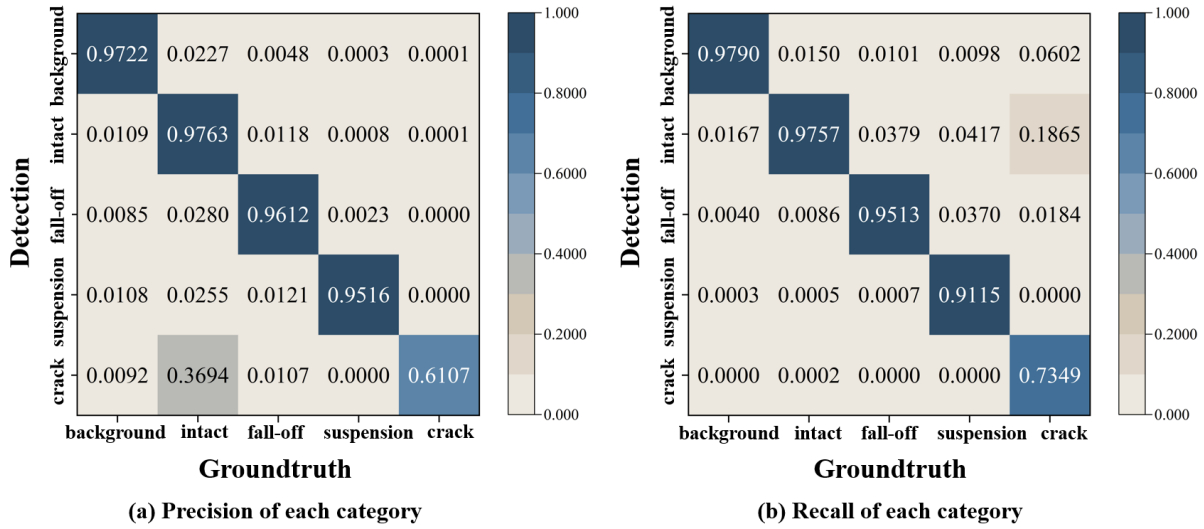


Figure 6. Normalization matrix of the test set.

4.2. Visualization of different categories

The classification correctness and localization accuracy in detection can be demonstrated intuitively using the visualization results. For the intact ceiling regions and backgrounds, 95.32% and 95.23% of the IoU are achieved, which means the detection results and marked region almost completely overlap, as shown in Figure 7(a) and (b). Even in the case of multi-target detection, the edges between the intact ceiling regions and other categories can be accurately identified and classified, as shown in Figure 7(c).

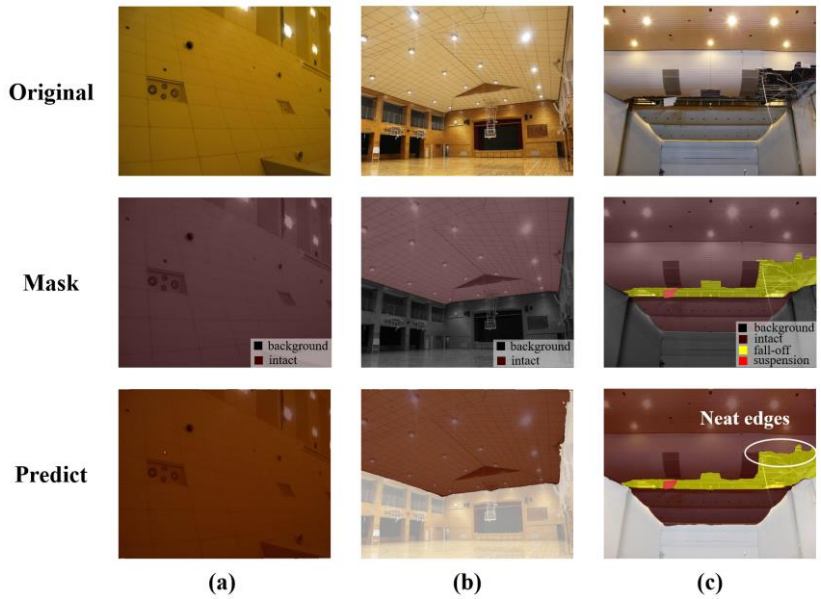


Figure 7. Examples of mask images and detection results of the ceiling intact region.

For the ceiling fall-off, the detection results and marked region overlap highly with the IoU of 91.61%. The fall-off regions have been detected accurately at different capture distances whether edge details and multiple targets, as shown in Figure 8(a)-(c). As shown in Figure 8(d), the model also performed outstandingly in the case of ceiling complete fall-off.

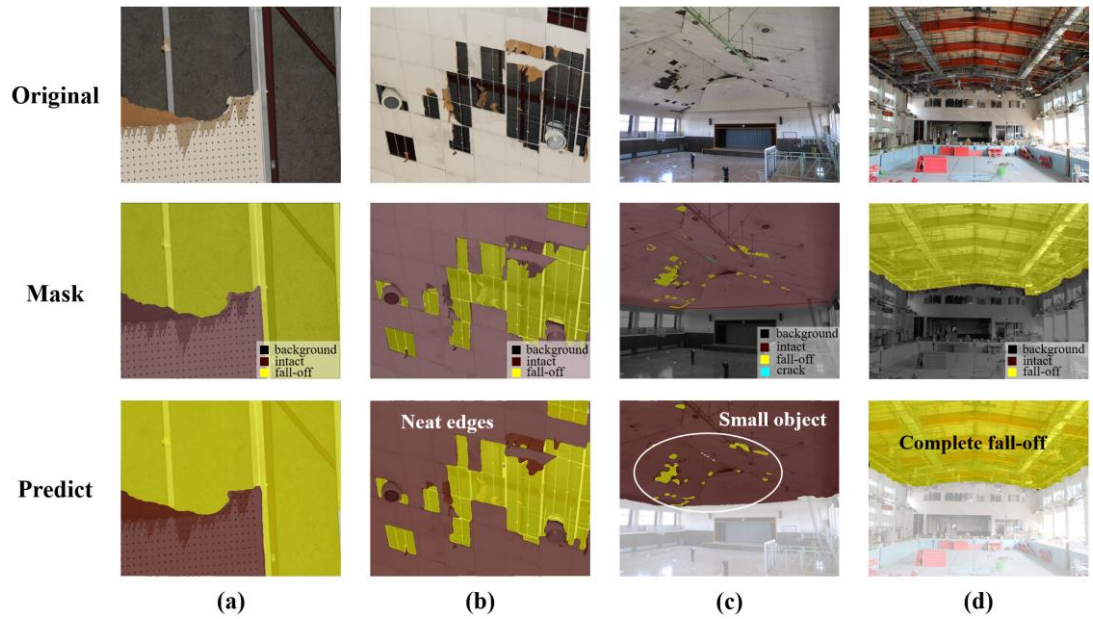


Figure 8. Examples of mask images and detection results of ceiling fall-off.

For the ceiling suspension, a similar high degree of overlap between the detection results and marked region compared with ceiling fall-off is achieved with the IoU of 87.11%. The suspension area can be detected well at different capture distances, as shown in Figure 9(a)-(c). When captured at a close distance, the edges of the suspension can be accurately detected, as shown in Figure 9(a) and (b). When the capturing distance is far, some factors can slightly affect the detection results. The colors of the two sides of the ceiling are sometimes different, as shown in Figure 9(c), and the model can well detect despite the darker color and smaller area of the suspension can visually confuse it with the fall-off region. In addition, since most of the suspensions are in the form of thin plates, their shapes are close to a thin line when captured at a specific angle, as shown in Figure 9(d), which may be missed detected and cause a certain degree of IoU reduction.

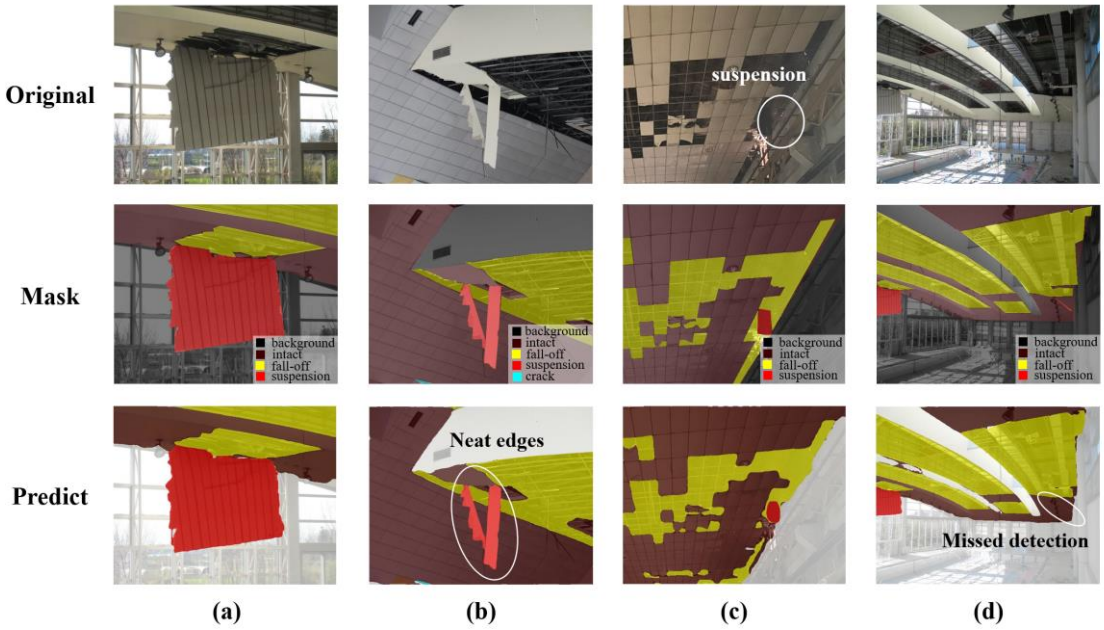


Figure 9. Examples of mask images and detection results of ceiling suspension.

For the detection of the crack, the IoU is 51.61%. Figure 10(a) and (b) reached an accurate detection, especially eight of the nine cracks labeled in Figure 10(b) are well detected although most of the cracks would be smaller targets in the long-distance capture. It indicates that the detection performance of the model is satisfactory at long distances and multiple targets. In addition, as the crack develops, it may cause part of the ceiling to fall off. At this time, the model is also able to achieve good detection for crack regions with adjacent locations and similar shapes to the fall-off, as shown in Figure 10(c). The relatively low IoU of crack compared to other categories are due to its shape which is mostly long or cracked. A significant increase in the area error could be caused by a small deviation in the direction of the short side in the case of a rectangle with a huge aspect ratio. In the example of the partially enlarged area of the crack in Figure 11, the green part represents the region where the detection result in overlaps with the cracked area, i.e., the correctly detected part. Due to the narrow geometry and small size of the crack, the increased area error reduces the IoU substantially when the detection results exhibit little deviation in the short side direction, i.e., the X direction in the figure. The detection areas in Figure 11(a) and (b) basically cover the damaged areas, with precision and recall achieving 90.72% and 83.02%, respectively. Nevertheless, their IoU is only 52.77% and 46.94%. The shape of the detected region in Figure 11(c) is very close to the damaged region, and the recall can reach 61.33% even if the IoU is lower than 50%. Therefore, this part of the error has little impact on the actual detection work. In addition, it can be observed from Figure 6 that the precision and the recall of crack are 63.41% and 73.49%, indicating that the detection has a great performance.

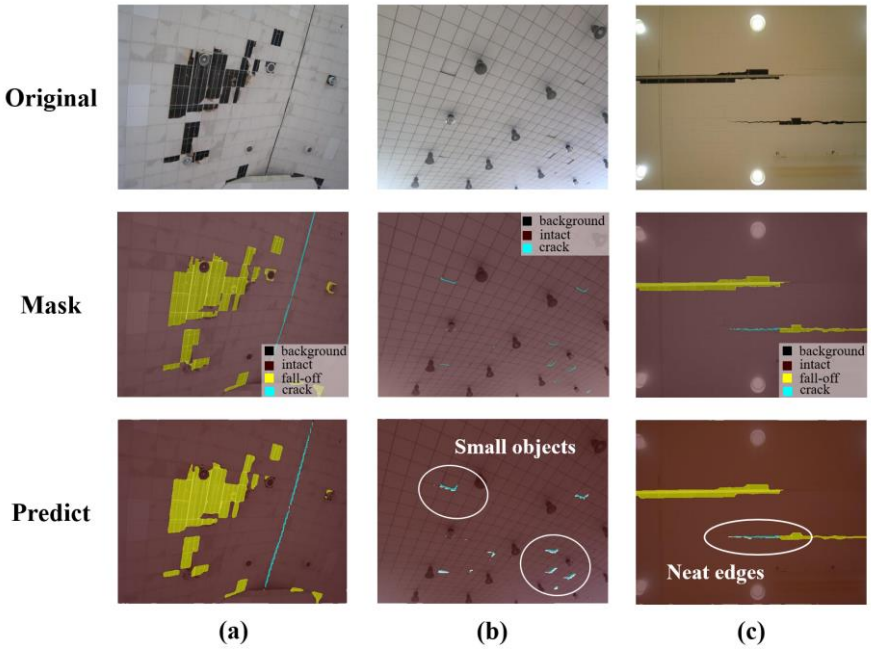


Figure 10. Examples of mask images and detection results of ceiling crack.

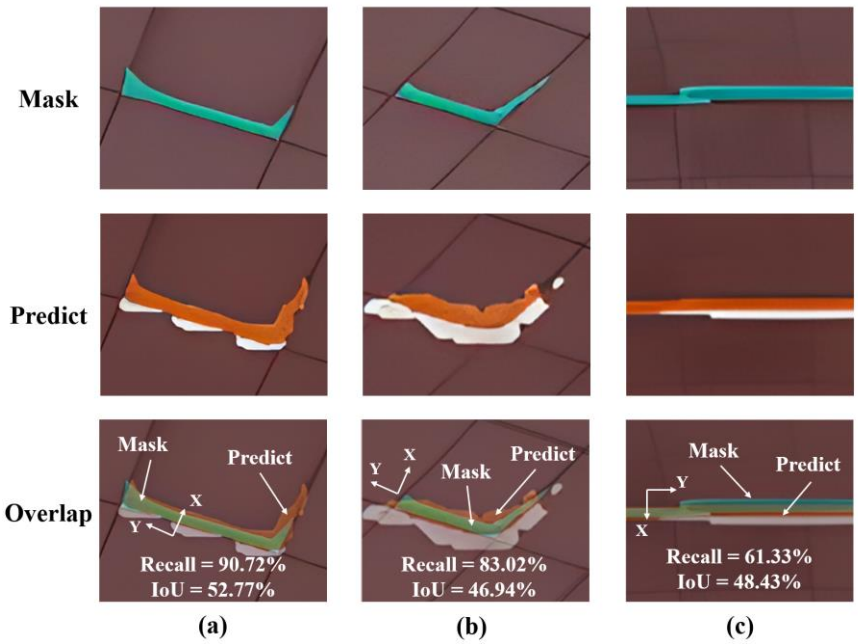


Figure 11. Examples of partially enlarged regions of the crack.

In most post-earthquake detection cases, as shown in Figure 12, several damages in multiple categories would appear in the image at the same time. Achieving accurate detection of small damage regions of different categories is challenging. A total of 36 damage regions with continuous boundaries were labeled in Figure 12(a), of which 31 were successfully detected with an accuracy of 86.11%. In Figure 12(b) and (c), with the shape and color of the suspensions similar to intact, the detection results achieved 70% and 88.89% accuracy despite some errors in some of the detected edges. In summary, the model can also achieve excellent detection results in challenging situations such as long-distance capture in the presence of multiple categories and several damages.

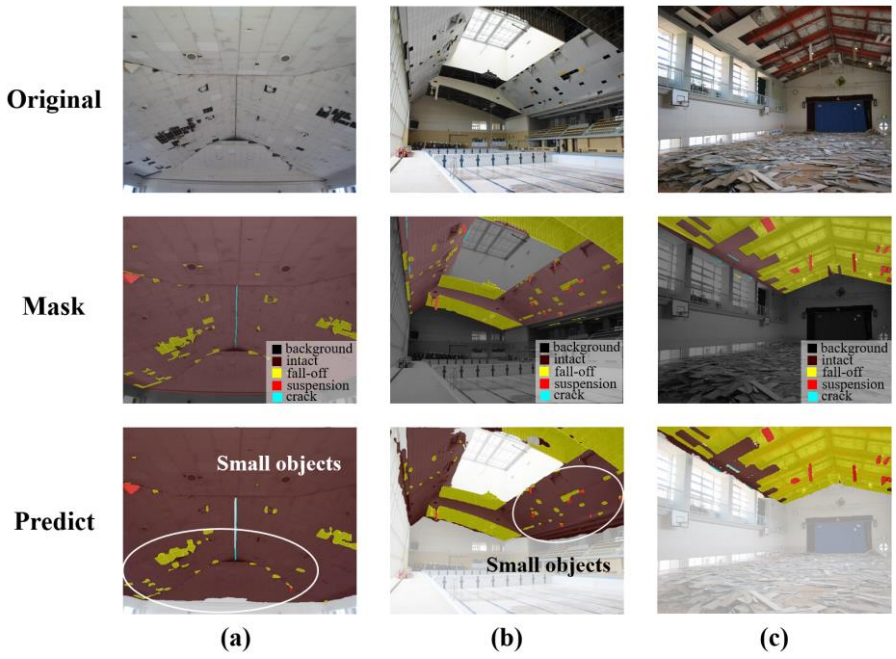


Figure 12. Examples of ceiling damage detection at long distances with multiple targets.

5. Conclusions

A damage detection method based on Deeplabv3+ is proposed for the rapid detection of damaged ceilings in large public buildings after earthquakes. A total of 1389 post-earthquake ceiling images were used to train, validate and test the model. Damage visualization was used to classify and localize the areas of different categories of damaged ceilings. The detection effects of different categories are analyzed based on the indicators of the test set and the results of damage visualization. The conclusions are summarized as follows:

(1) The damage detection model based on Deeplabv3+ obtained a PA of 97.23% and a mIoU of 84.18% in the test set. The proposed method has an excellent performance in correct classification and accurate localization in damage detection for the ceilings of large public buildings after an earthquake.

(2) The IoU of four ceiling categories and background achieved 95.32%, 91.61%, 87.11%, 51.61%, and 95.23%, respectively. The detection results in the test set were analyzed for a variety of situations, including capture distance, multiple categories, and small targets. Due to the narrow geometry and small size of the crack, the increased area error reduces the IoU substantially when the detection results exhibit little deviation in the short side direction. However, the results show that the detection regions for each category are almost identical to the marked real regions, achieving excellent detection performance. It shows that the method can accurately extract different categories of post-earthquake damage features of ceilings, display the contour shape of damaged regions.

References

[1] K. i. Kawaguchi, "Damage to Non-structural Components in Large Rooms by the Japan Earthquake," presented at the Structures Congress 2012, 2012.

[2] L. Xie and Z. Qu, "On the civil engineering disaster and its mitigation," *Journal of Earthquake Engineering and Engineering Vibration*, vol. 36, no. 1, pp. 1-10, 2016, Art no. 1000-1301(2016)36:1<1:Ltmgcz>2.0.Tx;2-z.

[3] T. D. Akinosho *et al.*, "Deep learning in the construction industry: A review of present status and future innovations," *Journal of Building Engineering*, vol. 32, 2020.

[4] Y.-J. Cha, W. Choi, and O. Büyüköztürk, "Deep Learning-Based Crack Damage Detection Using Convolutional Neural Networks," *Computer-Aided Civil and Infrastructure Engineering*, vol. 32, no. 5, pp. 361-378, 2017.

[5] Y.-J. Cha, W. Choi, G. Suh, S. Mahmoudkhani, and O. Büyüköztürk, "Autonomous Structural Visual Inspection Using Region-Based Deep Learning for Detecting Multiple Damage Types," *Computer-Aided Civil and Infrastructure Engineering*, vol. 33, no. 9, pp. 731-747, 2018.

[6] W. Hu *et al.*, "Machine vision-based surface crack analysis for transportation infrastructure," *Automation in Construction*, vol. 132, 2021.

[7] D. Soukup and R. Huber-Moerk, "Convolutional Neural Networks for Steel Surface Defect Detection from Photometric Stereo Images," in *10th International Symposium on Visual Computing (ISVC)*, Las Vegas, NV, 2014, vol. 8887, 2014, pp. 668-677.

[8] D. Dais, İ. E. Bal, E. Smyrou, and V. Sarhosis, "Automatic crack classification and segmentation on masonry surfaces using convolutional neural networks and transfer learning," *Automation in Construction*, vol. 125, 2021.

[9] L. Zhang, F. Yang, Y. D. Zhang, Y. J. Zhu, and Ieee, "ROAD CRACK DETECTION USING DEEP CONVOLUTIONAL NEURAL NETWORK," in *23rd IEEE International Conference on Image Processing (ICIP)*, Phoenix, AZ, 2016, 2016, pp. 3708-3712.

[10] H. Maeda, Y. Sekimoto, T. Seto, T. Kashiyama, and H. Omata, "Road Damage Detection and Classification Using Deep Neural Networks with Smartphone Images," *Computer-Aided Civil and Infrastructure Engineering*, vol. 33, no. 12, pp. 1127-1141, 2018.

[11] A. Zhang *et al.*, "Automated Pixel-Level Pavement Crack Detection on 3D Asphalt Surfaces Using a Deep-Learning Network," *Computer-Aided Civil and Infrastructure Engineering,* vol. 32, no. 10, pp. 805-819, 2017.

[12] Z. Tong, J. Gao, A. Sha, L. Hu, and S. Li, "Convolutional Neural Network for Asphalt Pavement Surface Texture Analysis," *Computer-Aided Civil and Infrastructure Engineering,* vol. 33, no. 12, pp. 1056-1072, 2018.

[13] L. Wang, K. i. Kawaguchi, and P. Wang, "Damaged ceiling detection and localization in large-span structures using convolutional neural networks," *Automation in Construction,* vol. 116, 2020.

[14] P. Wang, J. Xiao, K. i. Kawaguchi, and L. Wang, "Automatic Ceiling Damage Detection in Large-Span Structures Based on Computer Vision and Deep Learning," *Sustainability,* vol. 14, no. 6, 2022.

[15] S. O.-E. A. Garcia-Garcia, S.O. Oprea, V. Villena-Martinez, and J. Garcia-Rodriguez, "A Review on Deep Learning Techniques Applied to Semantic Segmentation," *arxiv,* 2017.

[16] G. Pan, Y. Zheng, S. Guo, and Y. Lv, "Automatic sewer pipe defect semantic segmentation based on improved U-Net," *Automation in Construction,* vol. 119, 2020.

[17] R. Yang, J. Chen, J. Wang, and S. Liu, "Toward Field Soil Surveys: Identifying and Delineating Soil Diagnostic Horizons Based on Deep Learning and RGB Image," *Agronomy,* vol. 12, no. 11, 2022.

[18] X. Xu *et al.*, "Retinal Vessel Automatic Segmentation Using SegNet," *Comput Math Methods Med,* vol. 2022, p. 3117455, 2022.

[19] Y. Li *et al.*, "Underwater crack pixel-wise identification and quantification for dams via lightweight semantic segmentation and transfer learning," *Automation in Construction,* vol. 144, 2022.

[20] Q. Zhou, Z. Situ, S. Teng, H. Liu, W. Chen, and G. Chen, "Automatic sewer defect detection and severity quantification based on pixel-level semantic segmentation," *Tunnelling and Underground Space Technology,* vol. 123, 2022.

[21] A. Ji, X. Xue, Y. Wang, X. Luo, and W. Xue, "An integrated approach to automatic pixel-level crack detection and quantification of asphalt pavement," *Automation in Construction,* vol. 114, 2020.

[22] M. Goyal, A. Oakley, P. Bansal, D. Dancey, and M. H. Yap, "Skin Lesion Segmentation in Dermoscopic Images With Ensemble Deep Learning Methods," *Ieee Access,* Article vol. 8, pp. 4171-4181, 2020 2020.

[23] H. Wu *et al.*, "Road pothole extraction and safety evaluation by integration of point cloud and images derived from mobile mapping sensors," *Advanced Engineering Informatics,* vol. 42, 2019.

[24] S. Cheng and J. Ma, "Smoke detection and trend prediction method based on Deeplabv3+ and generative adversarial network," *Journal of Electronic Imaging,* vol. 28, no. 03, 2019.

[25] L.-C. Chen, Y. Zhu, G. Papandreou, F. Schroff, and H. Adam, "Encoder-Decoder with Atrous Separable Convolution for Semantic Image Segmentation," in *15th European Conference on Computer Vision (ECCV)*, Munich, GERMANY, 2018, vol. 11211, 2018, pp. 833-851.

[26] Karen Simonyan and A. Zisserman, "VERY DEEP CONVOLUTIONAL NETWORKS FOR LARGE-SCALE IMAGE RECOGNITION," presented at the ICLR 2015, 2015.

[27] J. Yosinski, J. Clune, Y. Bengio, and H. Lipson, "How transferable are features in deep neural networks ?," in *28th Conference on Neural Information Processing Systems (NIPS)*, Montreal, CANADA, 2014, vol. 27, 2014.

Proceedings of the IASS Annual Symposium 2023
Integration of Design and Fabrication
10–14 July 2023, Melbourne, Australia
Y.M. Xie, J. Burry, T.U. Lee and J. Ma (eds.)

ReconWood Slab. Computational design and structural optimization of reconfigurable timber slabs

Anja KUNIC[a], Roberto NABONI[a,*]

[a,*] CREATE - University of Southern Denmark
Campusvej 55, 5230 Odense, DK
ron@iti.sdu.dk

Abstract

In timber buildings lately (re)gaining importance thanks to their environmental and structural performance, it is imperative to rethink material usage to reduce the pressure on the forests and optimize how the harvested material is used. Slab structures in buildings account for a significant amount of material employed due to their load-bearing requirements. To achieve environmental decarbonization and truly circular building construction, this work introduced a stress-driven computational workflow for the design and optimization of reconfigurable timber slabs which rely on automation-driven reversible joints and reusable building elements. The developed workflow was demonstrated on the *ReconWood Slab*, an experimental prototype featuring a stress-based multi-resolution timber frame of primary and secondary *ReconWood beams* stacked one upon the other. The developed research results and the constructed prototype showed the possibility of controlling and manipulating material organization and stress distribution in the structures, providing a virtually infinite automated re-configuration of varying slab structures in response to changing boundary conditions. The work findings show an enhancement of the reconfigurability of timber structures, which is discussed as a fundamental property to extend the life cycle of wood carbon sinks.

Keywords: reconfigurable wood slabs, carbon storage, stress-driven design, voxel-based design, robotic timber construction, circular wood architecture

1. Introduction

Human-induced climate change, exponential population growth, and the consequent increase in consumption and extraction of natural resources are challenging our living environment [1]. The construction industry alone is responsible for 40% of global CO2 emissions and large amounts of extracted non-renewable resources. For this reason, the significance of wood construction, due to its low embodied energy, carbon sequestration capabilities, and renewable nature, has returned to focus after a long history of industrialization. However, the forests are not an infinite resource either, and thus, design, architecture, and material practices are challenged to deal in new ways with complex interdependencies and trades between the forest to be preserved and the city to be built.

To achieve environmental decarbonization and truly circular building construction, it is fundamental to rethink material usage from the point of view of (1) *stress-driven* material allocation [2]; (2) *tectonic flexibility* that invokes disassembly, re-use, and reconfigurability [3]; and (3) *data-driven design workflows* that can accommodate specific features from variable timber sources and allow for material trackability [4]. Slab structures are of interest as they are responsible for the most significant amounts of material usage due to their load-bearing requirements.

Moreover, they are often produced in large sizes and combined with other material layers, making them less flexible for re-use and re-configuration.

Copyright © 2023 by Anja KUNIC and Roberto NABONI, University of Southern Denmark. Published in the Proceedings of the IASS Annual Symposium 2023 with permission.

In this work, we challenge the massive timber construction which relies on one-time-used and custom-tailored building elements by introducing the *ReconWood* system [5] made out of generic reconfigurable building blocks with reversible [6] and automation-driven [7] joinery (Fig. 1).

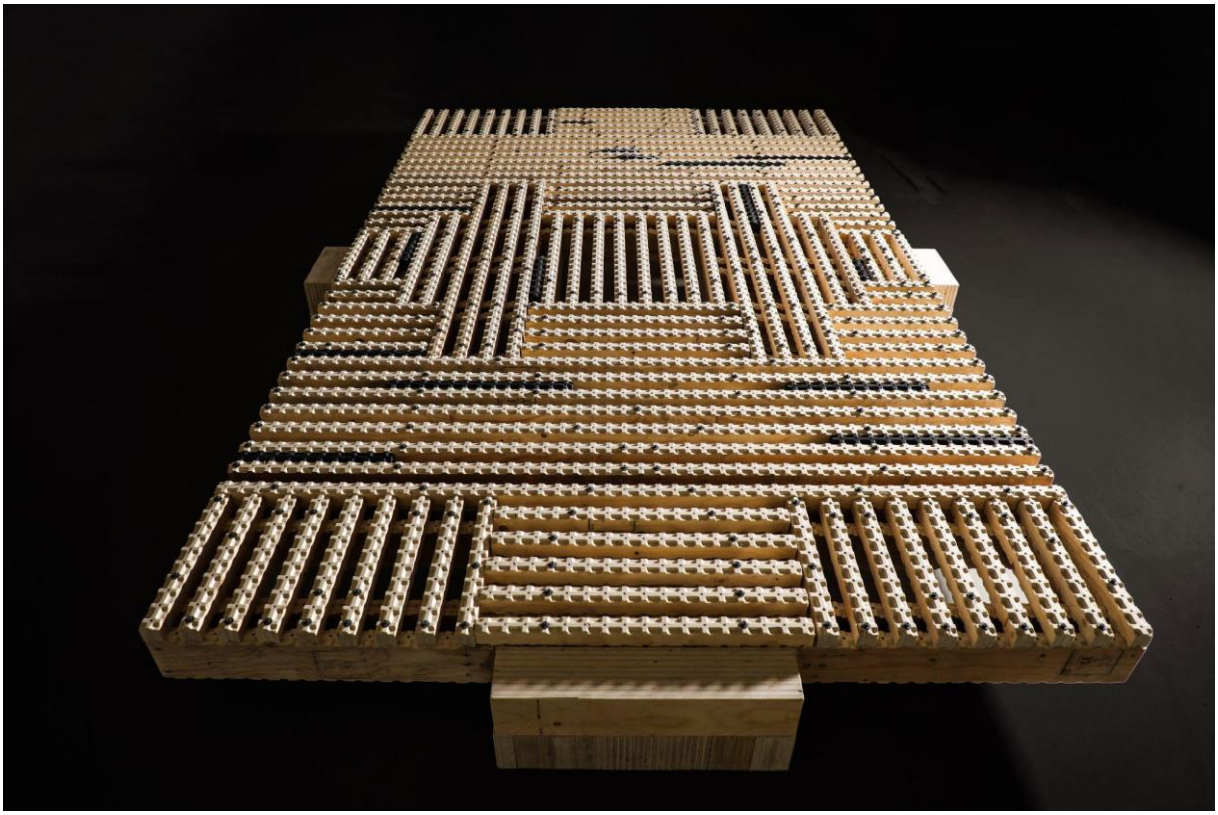


Figure 1. Picture of the ReconWood Slab prototype

2. Related work

Historically, due to the difficulty of finding, transporting, and handling long-span wood beams, the structural slabs were made of stacked and interlocked short beams, providing reciprocal supports [8]. Such systems offered an efficient method of covering large spans with short elements while assuring structurally efficient and durable floor structures.

Nowadays, eastern architecture such as the one of Kengo Kuma [9,10] still preserves the long-lasting tradition of stacking discrete timber girders into several layers to achieve the final load-bearing slab system. This layering of members avoids using massive beams while allowing light to pass through.

In academia, several contemporary research studies have been experimenting with stress-driven and robotically fabricated timber slabs to optimize material usage and structural efficiency. Here, the small-scale timber elements are positioned along principal stress flows in shape-and-span-adaptive stacked grids [11] or individual studs [12,13], reinforcing thin CLT plates and hollow slabs. However, reversibility and circularity properties are limited in these examples to facilitate the automation of the fabrication processes.

Our work is developed along the stress-driven approach, introducing a computational workflow for the design and structural optimization of novel automation and reconfigurability-driven timber slab structures, namely *ReconWood Slab(s)*. The ReconWood Slabs are based on layered stacking of discrete *ReconWood beams* with reversible joints that allow for a virtually infinite automated re-configuration of varying slab structures in response to changing boundary conditions.

3. Methodology

3.1. ReconWood Slab - system design and tectonics

The *ReconWood Slab* consisted of two stacked layers of laminated veneer lumber (LVL) beams, namely *primary* and *secondary ReconWood beams*, which formed a timber frame structure. Two lateral semi-threaded wood screws connected the primary beams at each intersection. On the other hand, the secondary beams were stacked on top of the primary ones by aligning three-dimensional male-female joints, facilitating automated assembly and disassembly while providing structural and positional stability during construction. 5 mm steel bolts fastened the joints with washers applied from the male side of the connection and steel insert nuts on the female side (Fig. 2). The cross-section height of the primary beams (117mm + 5mm joint height) was three times larger than the secondary ones (39mm + 5mm joint height), while the width of both was kept constant (39mm). The three-dimensional joints with holes in the middle were modularly repeated throughout the whole beam's length, with the distance between the holes equal to the width of the beams. This allows for many different connectivity patterns and high (re)configuration flexibility. The beams were discretized into a range of lengths divisible by the width value, ranging from 117 mm to 2028 mm, which allowed for variable structural resolution of the timber frame.

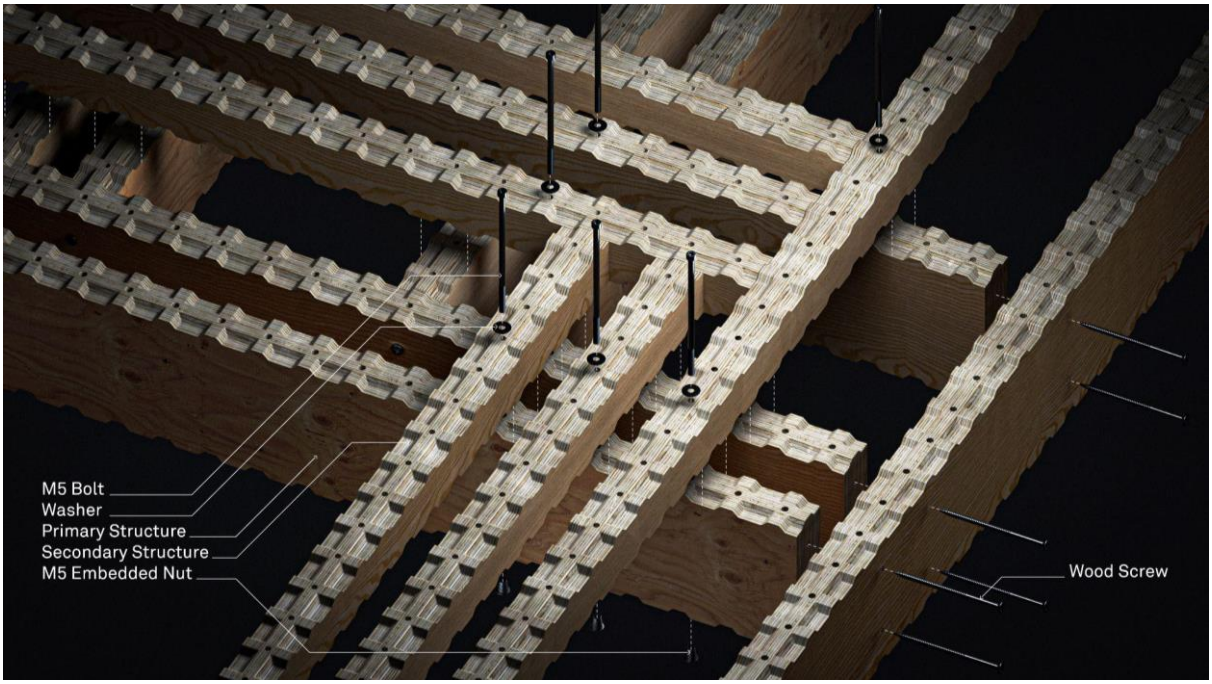


Figure 2. ReconWood construction system and joint types

3.2. Robotic fabrication of ReconWood beams

The ReconWood beams were robotically fabricated using a KUKA KR240 R3330 industrial robot arm that moves along a six-meter linear rail and is equipped with a 12 kW rotary spindle (Fig. 3). The building blocks of different lengths were nested into three-meter-long LVL beams which were clamped in front of the robot, parallel to the rail, and milled on the male side first, and female side afterwards.

Three milling tools were exchanged automatically during fabrication to produce the cross-shaped joints along the beam, and their respective Tool Centre Points (TCP) were defined in the toolpath programming algorithm. The 6 mm holes were drilled, providing additional space around the M5 bolts. This is desired both for facilitating the automated robotic assembly and disassembly [7] as well as for the mechanical performance of the joints [6]. Secondly, a V-shaped tool with a 45° inclined blade was

used to achieve oblique sides of the cross geometry in a single cut. Finally, a flat-end mill was employed to clear out the remaining material and even out all the horizontal sides of the joint.



Figure 3. (left) Robotic fabrication of a ReconWood beam; (right) Robotic milling toolpath of the male and female beam sides

3.3. Voxel-based computational design and structural optimization of ReconWood slabs

A computational workflow for the design and structural optimization of ReconWood slabs was developed through a voxel-based approach in Grasshopper for Rhino (Fig. 4). The voxelization method was used for computing the structural analysis, interpreting and discretizing its results and translating these into material layouts. The voxel size, and therefore the basic calculation unit, was based on the material unit itself, i.e., the length of the *ReconWood block*, significantly reducing computation time and allowing for a wide variety of design options. Implementing such an approach enables an easy and flexible iterative design process, where structurally optimized timber slabs are generated from simple user/designer inputs.

Karamba 3D [14] shell analysis was first performed to understand the slab deflection under given loading scenarios. The resulting data, such as the Principal shell forces and the Principal force directions, were discretized and used to determine the stress-driven material layout. The *Voxel* was a discretizing unit that stored self-pertaining structural data as design attributes. Thus the discretized Principal force direction was stored as a *direction* attribute and the Principal shell force as a *magnitude* attribute. A voxelized design space was generated from a given form or simply a set of inputs regarding structural boundary conditions. The corresponding materialized output was generated based on these, namely the *Maxel*.

Initially, a uniformly voxelized grid was computed, after which its *maxelized* counterpart was analyzed with Karamba3D beam analysis. If the beam displacement exceeded the targeted value (L/250), the voxels with larger *magnitude* attributes were subdivided. This procedure was repeated iteratively until

the maximum displacement conditions were met. Driven by the underlying voxel attributes, the optimized slab structure was characterized by a multi-resolution timber frame with a specific orientation of the primary beams and an optimized connectivity pattern between them.

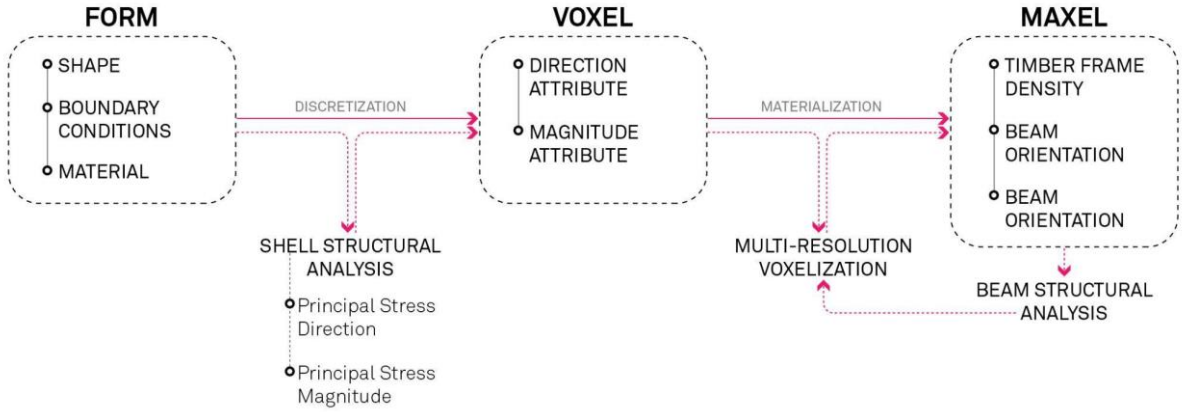


Figure 4. Computational workflow diagram for a stress-driven design and optimization of ReconWood slabs

3.4. Stress-based connectivity patterns

In the ReconWood slab, the reciprocal connectivity between the primary beams was crucial for the load transfer, while the secondary beams served as additional structural stiffeners. An algorithm that follows discretized Principal force directions and maximizes reciprocal connection points were implemented to optimize the force flow throughout the beams toward the supports.

In particular, a frame cell with a double beam was generated at each voxel's perimeter. The voxels with the same *direction* and *magnitude* attributes were joined into one frame cell. Considering the XY coordinate system to which the voxel grid was aligned, the beams of horizontal (along the X axis) and vertical (along the Y axis) were distinguished. Each beam was shortened or extended at both ends to meet its perpendicular neighbors most efficiently, allowing for a continuous and uninterrupted force flow. For each beam's endpoint, the algorithm first 1) checked the *direction* attribute of the voxel from which the specific beam is derived and 2) checked the *direction* attributes of the neighboring voxels. If the specific beam was oriented in the same direction as its correlated voxel and most neighboring voxels (e.g., vertical), it was extended until the first neighboring perpendicular beam. Else, if the beam was oriented in the opposite direction from its prevailing surroundings, it was shortened (Fig. 5). This control over the joinery layout was essential to ensure a stiff structure and maximize interconnectivity between the beams.

The secondary beams were consequently oriented perpendicular to their corresponding voxel's *directions.* Considering the span of the secondary beams and the number of primary beams upon which they lie, the number and positioning of the steel bolts were determined. The goal was to reduce the steel used while ensuring enough ties between the primary and secondary beams.

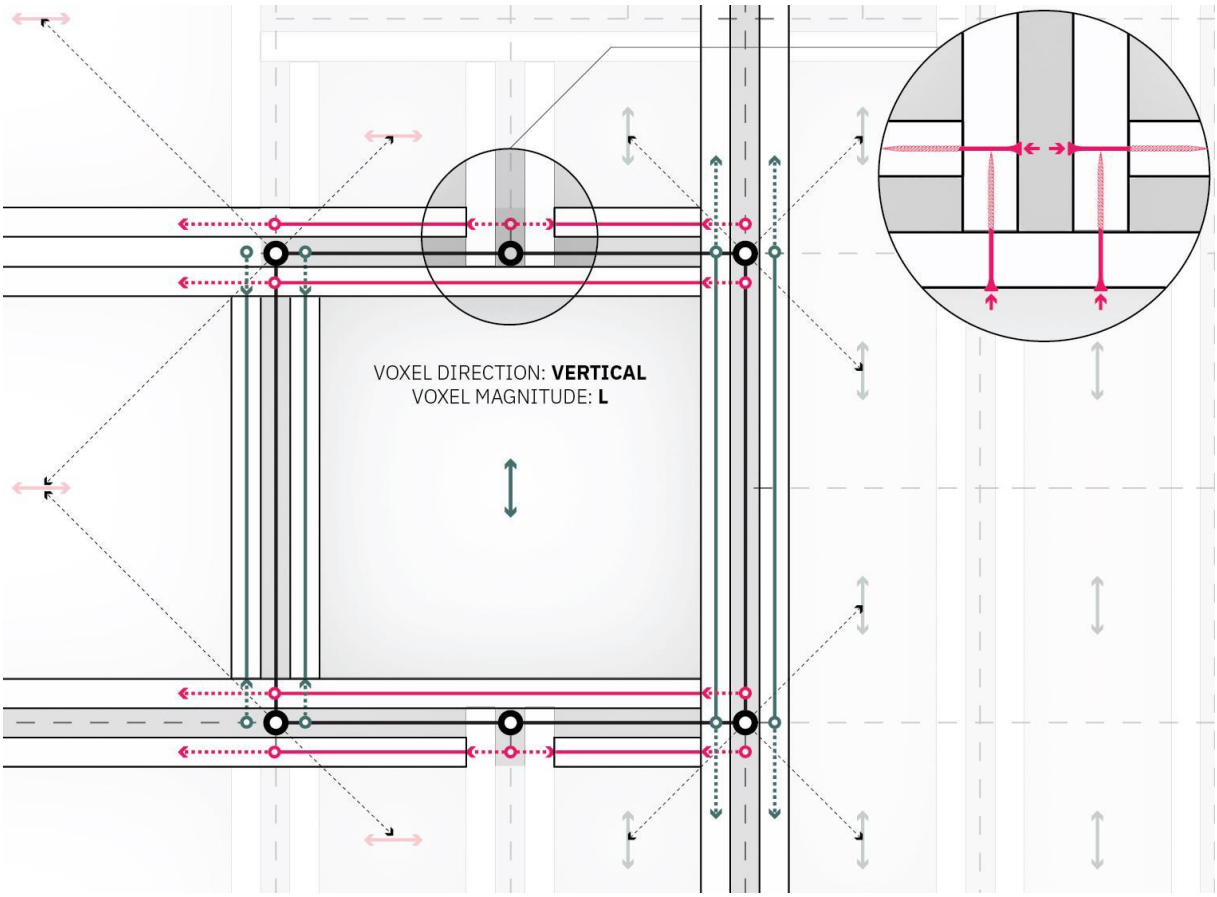


Figure 5. "Maxelization" process and connectivity optimization based on the stress-based Voxel attributes

4. Results

Design. Following the established workflow, a 3x2m ReconWood Slab was designed and structurally optimized. The slab was supported at four midpoints on each side, featuring cantilevering corners. The finite element model for the beam analysis (FEM) was developed, considering fixed supports and hinges at the connection points. To generate design iterations, a 200kg/m^2 distributed load and the self-weight of the structure were applied, and a maximum displacement limit was set. Considering the longest spanning beam of 1.5m starting from the support point on the longer side towards the cantilevered corner and following the Eurocode 5 [15] regulation for the instantaneous maximum deflection for cantilevering beams (W_{inst} = L/250), the value of 6mm was set as the optimization target. Different design options were generated and structurally simulated following a stress-driven multi-resolution voxelization, seeking an equilibrium between the material usage, maximum deflection, and stress distribution (Fig. 6).

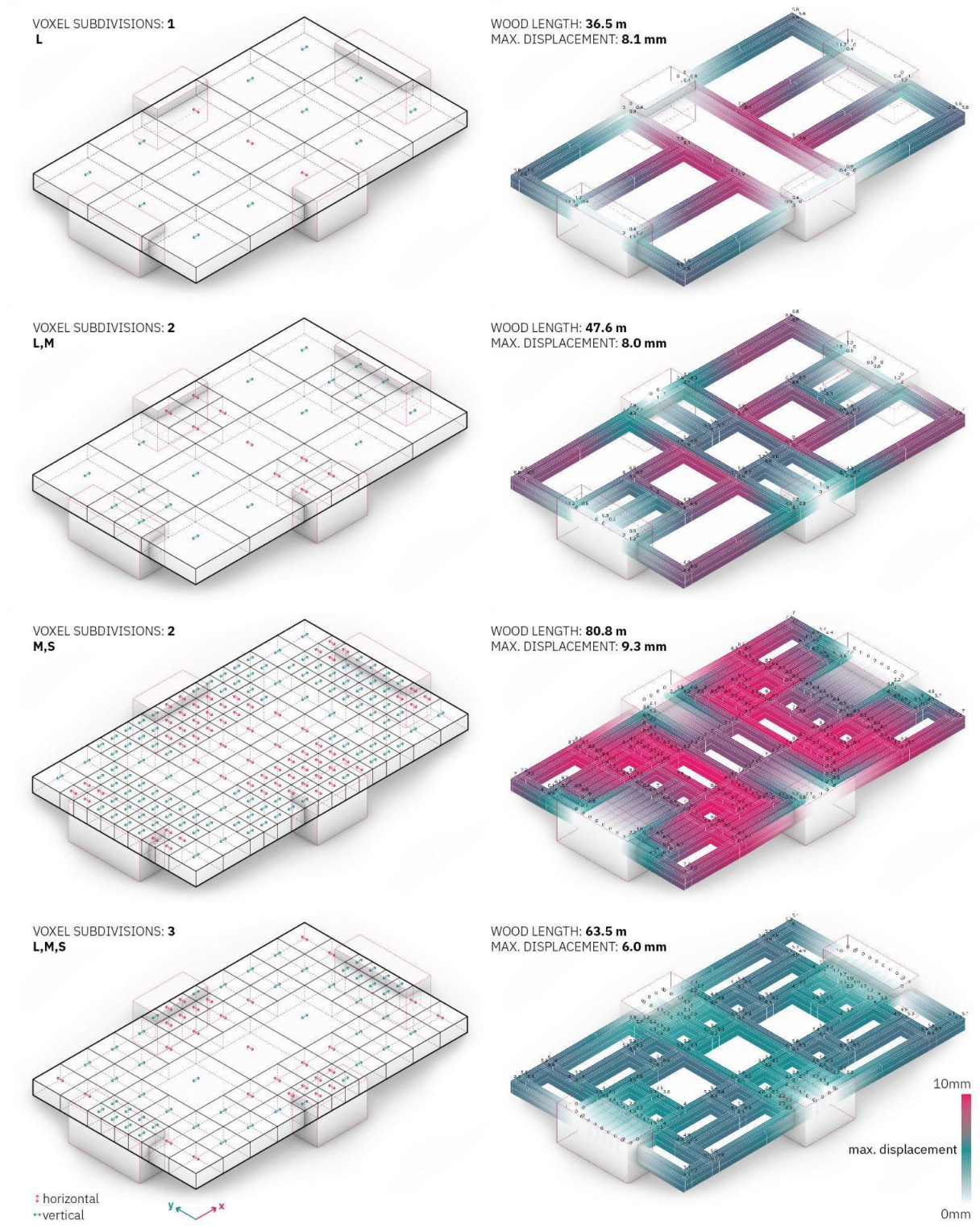


Figure 6. Iterative design and structural analysis of the ReconWood Slab prototype

The optimized slab resulted in 63.5 meters of wood for the primary beams and about 150 meters of wood for the secondary beams and a total weight of 210 kg. Since the goal of the ReconWood structures is reusability and reconfigurability, the structural layout with the most balanced stress distribution was selected, assuring that no joint or beam was overstressed and, therefore, unsuitable for use in further life cycles. Material redundancy and oversized safety factors are seen as an opportunity to provide long-lasting serviceability for each beam. Two semi-threaded structural wood screws were inserted at each connection between the primary and secondary beams. In contrast, the bolt-nut connections were minimized following the previously described principles (Fig. 7).

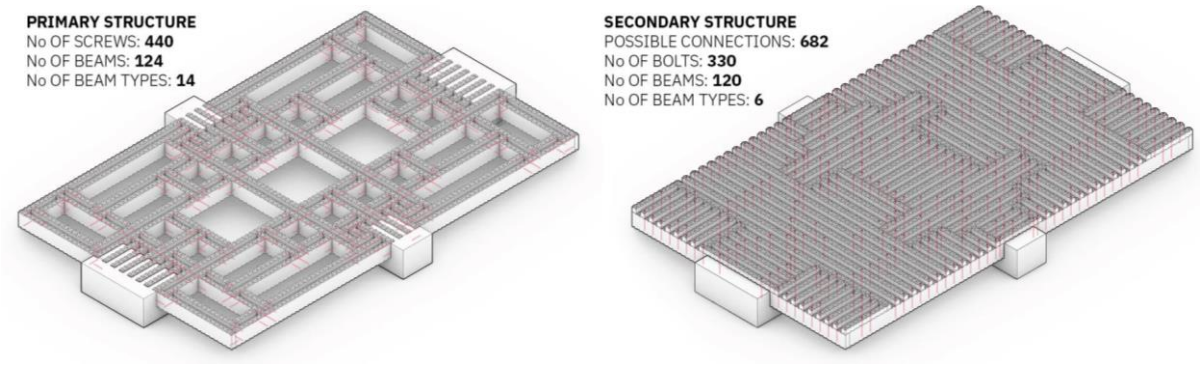


Figure 7. Final material configuration and optimized connections layout of the ReconWood Slab prototype

Workflow application. The flexibility of the established workflow was tested by applying the "calibrated" model for a specific loading condition to a wide range of design solutions that were generated to respond to different support layouts (Fig. 8A). For most of the generated slabs, the stress distribution and maximum deflection were already satisfying without the need for a further iterative optimization process (Fig. 8B). This means that the design optioneering and explorations can be done much faster. The iterative optimization can be done only at the beginning of the design process to calibrate the structural model and, in the end, refine the final design solution, thus saving much time.

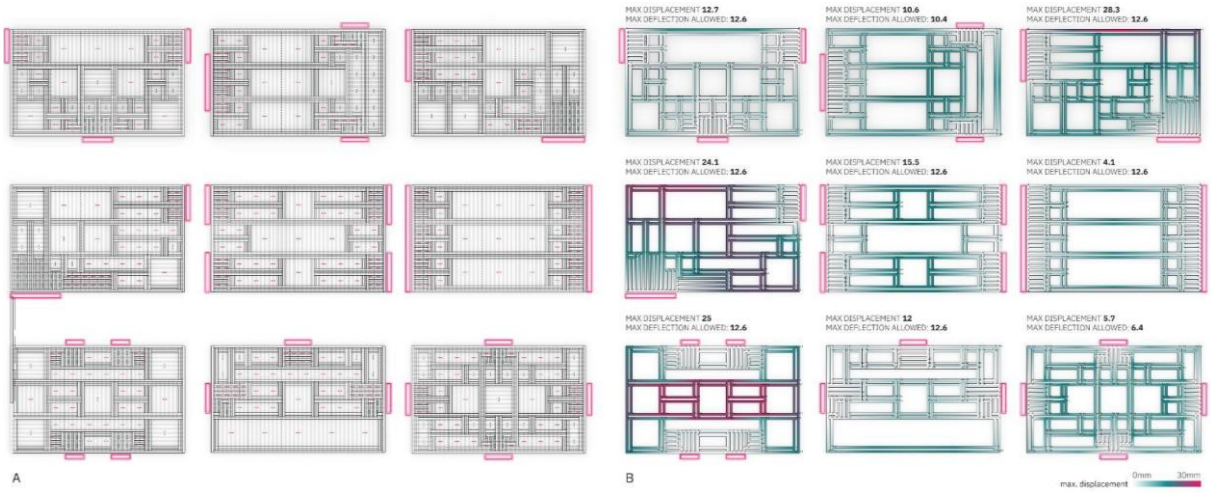


Figure 8. (left) Design optioneering of ReconWood slabs for a 200kg/m^2 + self-weight load and varying support locations; (right) Structural analysis outcomes based on a calibrated FE model

5. Conclusions and discussion

ReconWood is a system conceived for automated construction, de-construction, and re-construction of customized and data-informed prefabricated timber frame structures. This paper specifically described the computational design and structural optimization workflow for the generation of reconfigurable timber slabs using this system, following a stress-driven double-frame layout (Fig. 9). The process and constructed prototype results showed the possibility of obtaining structural layouts and controlling the stress distribution within the structure while ensuring the reusability of the building elements, thus extending the CO_2 capture within them. Disassembly and re-assembly of different configurations are made possible, enabled by closed data loops and a data-driven design approach. This construction system supports a more agile and transformable architecture without needing large and massive construction elements that limit spatial and operational flexibility and adaptation. Moving towards an application at a larger scale, the future work will further study and focus on mechanical characterization of the different joints, which will inform a new iteration of the FE modeling and simulation process. The ReconWood slab will be structurally benchmarked to CLT slabs to fully evaluate the potential of this construction concept. From an industrialization perspective, the fabrication process would require a redesign for parallel machining to reduce production time and costs.



Figure 9. ReconWood Slab prototype, seen below

Acknowledgements

The authors thank Davide Angeletti and Giuseppe Marrone for their active involvement in the project development, fabrication, and assembly. The work was supported by project partner Stora Enso (LVL Material).

References

[1] C. Ferrer, T. Hildebrand and C. Martinez-Cañavate, *Touch Wood: Material, Architecture, Future,* Lars Müller Publishers, 2023.

[2] P. L. Mayencourt, *Mass Reduction: Opportunities and Structural Optimization Methods to Reduce Material Use in Mass Timber Buildings*, Doctor of Philosophy in Architecture: Building Technology at the Massachusetts Institute of Technology, February 2020.

[3] K. G. Jensen and J. Sommer, *Building a Circular Future - 3rd Edition*, KLS PurePrint, 2018.

[4] A. Kunic, R. Naboni and R. Cognoli, "Re:Thinking Timber Architecture. Enhancing Design and Construction Circularity through Material Digital Twin", in *Proceedings of the UIA World Congress of Architects*, Copenhagen, Denmark, July 2-6, 2023, M. R. Thomsen and M. Tamke, Eds.

[5] A. Kunic and R. Naboni, "Reconfigurable Timber Construction in an Extended Reality Environment", in *Critical appropriations: Proceedings of the 25th SIGraDi Conference*, Lima, Perú, November 7-11, 2022, P. C. Herrera, et al. Eds.

[6] S. G. Hansen, A. Kunic and R. Naboni, "A reversible connection for robotic assembly of timber structures", *Engineering Structures*, vol. 245 (1-4): 112795.

[7] A. Kunic, A. Kramberger and R. Naboni, "Cyber-Physical Robotic Process for Re-Configurable Wood Architecture Closing the circular loop in wood architecture", in *Towards a new, configurable architecture: Proceedings of the 39th eCAADe Conference*, Novi Sad, Serbia, September 8-10, 2021, V. Stojakovic and B. Tepavcevic, Eds.

[8] F. Augelli, V. Nicola, F. Petracco and L. C. Ronchi, "The structural concept of the 16th century floors of the Ducal Palace in Sabbioneta (Mantua, Italy)", *Advanced Materials Research*, vol. 778, pp. 857–864, 2020.

[9] K. Kuma and Associates, *Rikuzentakata Amway House – Machi no Engawa*, Japan, 2020, Retrieved from https://kkaa.co.jp/project/rikuzentakata-amway-house-machi-no-engawa/

[10] K. Kuma and Associates, *Yusuhara Wooden Bridge Museum*, Japan, 2010, retrieved from https://kkaa.co.jp/project/yusuhara-wooden-bridge-museum/

[11] H. Chai, H. J. Wagner, Z. Guo, Y. Qi, A. Menges and P. F. Yuan, "Computational design and on-site mobile robotic construction of an adaptive reinforcement beam network for cross-laminated timber slab panels", *Automation in Construction*, vol. 142, August, 2022, 104536.

[12] O. Luis, A. Krtschil, H. J. Wagner, B. Simon, F. Amtsberg, L. Skoury, J. Knippers, and A. Menges, "Design Methods for Variable Density, Multi-Directional Composite Timber Slab Systems for Multi-Storey Construction" in *Towards a new, configurable architecture: Proceedings of the 39th eCAADe Conference*, Novi Sad, Serbia, September 8-10, 2021, V. Stojakovic and B. Tepavcevic, Eds.

[13] K. Schramm, C. Eppinger, A. Rossi, M. Braun, M. Brieden, W. Seim and P. Eversmann, "Redefining Material Efficiency Computational Design , Optimization and Robotic Fabrication Methods for Planar Timber Slabs", in *Towards Radical Regeneration: Proceedings of the Digital Modelling Symposium*, Berlin, Germany, September 26-28, 2022, C. Gengnagel et al., Eds.

[14] C. Preisinger, R. Vierlinger and M. Tam, *Karamba3D* (version 2.2.0), 2022, retrieved from https://www.karamba3d.com/

[15] The European Union, EN 1995-1-1 (2004) (English): Eurocode 5: Design of timber structures - Part 1-1: General - Common rules and rules for buildings

Proceedings of the IASS Annual Symposium 2023
Integration of Design and Fabrication
10–14 July 2023, Melbourne, Australia
Y.M. Xie, J. Burry, T.U. Lee and J. Ma (eds.)

Research of snow distribution on the long-span roof with local obstructions

Rui LI[a,b], Qingwen ZHANG[a,b,*], Yu ZHANG[a,b], Feng FAN[a,b]

[*] School of Civil Engineering, Harbin Institute of Technology, Harbin, 150090, China
No.73 Huanghe Road, Harbin, China
zhangqw@hit.edu.cn

[a] Key Lab of Structures Dynamic Behaviour and Control of the Ministry of Education, Harbin Institute of Technology, Harbin, 150090, China
[b] Key Lab of Smart Prevention and Mitigation of Civil Engineering Disasters of the Ministry of Industry and Information Technology, Harbin Institute of Technology, Harbin, 150090, China

Abstract

With the frequent occurrence of extreme ice and snow weather, engineering accidents such as the destruction and collapse of building structures have happened increasingly, resulting in huge economic losses and a large number of casualties. Due to functional requirements and building appearance, various forms of local obstructions are often arranged on long-span roofs. Such a structural form will exacerbate the uneven distribution of snow cover, which can more easily cause damage and destruction of the roof structures. Therefore, based on the wind-snow combined experiment facility and the similarity criteria based on snowfall, this paper systematically investigated the characteristics of snow distribution on long-span roofs with local obstructions under the effects of different inflow wind velocities, different lengths of the windward side of the obstructions, different heights of the obstructions, and different distances between obstruction center and long-span roof edge.

Keywords: long-span roofs, local obstructions, snow loads, wind-snow combined experiment

1. Introduction

In recent years, extreme ice and snow weather has occurred frequently worldwide, and the damage to building structures caused by snow disasters has become the focus of scholars [1]. With modern buildings in China becoming more and more diverse and complicated, long-span roofs are increasingly and widely used in civil, public, and industrial buildings. To satisfy the specific functional requirements and building appearance, it is often necessary to arrange various local obstructions on long-span roofs, such as daylighting and ventilation skylights, or air conditioning equipment. A long-span roof is a typical snow load sensitive structure due to the lightweight, complicated roof shape, huge roof area, and large proportion of snow load. Therefore, it is much more easily to form local snow accumulations on the roof, which is more likely to result in engineering accidents during snow disasters, causing more serious property losses and casualties. While the presence of local obstructions can exacerbate the uneven distribution of snow cover on the long-span roofs as shown in Figure 1, which will further increase the safety hazards of the structures and cause cracking and falling off of roof structural components, even resulting in severe engineering accidents such as structural overall collapse.

Currently, there is little research on snow distribution in long-span roofs with local obstructions, and the regulations on snow distribution coefficients for such roofs in the snow load codes lack sufficient data and empirical support. Therefore, based on wind-snow combined experiments, the important factors that affect the process of wind-induced snow drift on long-span roofs with local obstructions, such as the inflow wind velocity, the length of the windward side of the obstruction, the height of the obstruction,

Copyright © 2023 by Rui LI, Qingwen ZHANG, Yu ZHANG and Feng FAN. Published in the Proceedings of the IASS Annual Symposium 2023 with permission.

and the distance between obstruction center and long-span roof edge were systematically investigated in this paper, and the laws of snow distribution patterns and coefficients were summarized, which could provide for future building code revisions and practical engineering applications with a reference.



Figure 1. Uneven snow distribution on long-span roofs with local obstructions

2. Wind-snow combined experiment

2.1. Experiment facility

The experiments were carried out in an outdoor wind-snow combined experiment facility which was independently developed by the research team at the Harbin Institute of Technology [2], as shown in Figure 2. The experiment facility consists of a power system (fan matrix, guide tube, honeycomb, and damping net), a vibration-seeding snowfall simulator, an experimental platform, and a measurement system (thermal anemometer, PC-4 automatic weather station, box-type snow flux trapper). The experimental section is 4.5m×3.0m×10m and equipped with a laser positioning system, which can simulate any experiment cases under different wind directions. The power system consists of a 2×3 fan matrix, which can generate a stable and continuous wind field from 0.5m/s~11.5m/s. The snowfall simulator can seed snow particles into the experiment section through vibration, and different snowfall intensities can be simulated by adjusting the vibration frequency and the size of the sieve aperture.

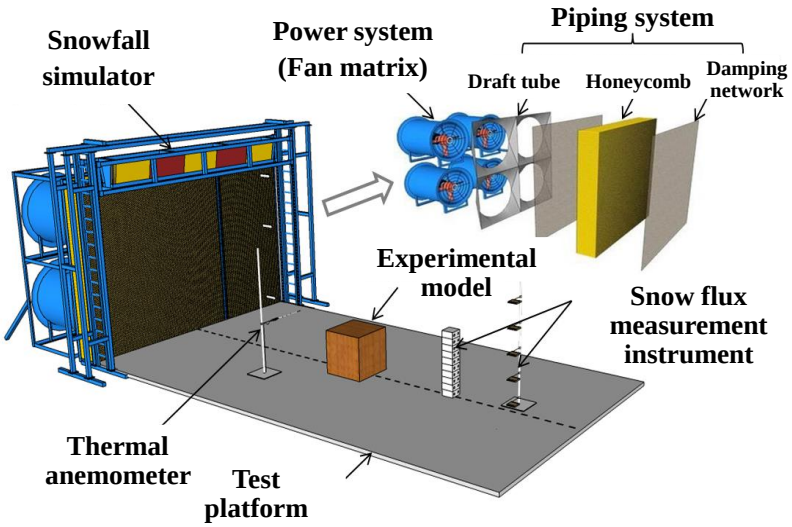


Figure 2. The design diagram of the wind-snow combined experiment facility

2.2. Validation of the experiment method

In order to validate the accuracy of the experiment method, the field observations of snow distribution around a standard cube model measured by Oikawa [3] (No. SN09) were selected as the prototype, and a comparative experiment was designed using the similarity criteria based on snowfall patterns [4]. The scale ratio of the experiment model was set as 1/5, the inflow wind velocity was set as 1.7m/s, the inflow

wind direction angle was set as 0 °, the snowfall rate was set as 25mm/h, and the experiment particles were artificial snow particles.

Figure 3 shows the comparison of SN09 measured results with those from different experimental results conducted by *Li et al*. Selecting the snow distribution in the standing vortex region at the front of the model of the windward direction as the focus to analyze, three essential characteristic points were divided: ① the peak value of snow deposition area on the windward side near the model; ② the minimum value of snow erosion area on the windward side of the model; ③ the peak value of snow deposition area on the windward side far away from the model. By comparing the snow distribution coefficients at three characteristic points obtained by different methods, the deviations among results of field observation and different experiments were shown in Table 1. It is obvious that the accuracy of snow distribution prediction using the wind-snow combined experiment method in this paper was higher than others, which validated the reliability of the experiment method.

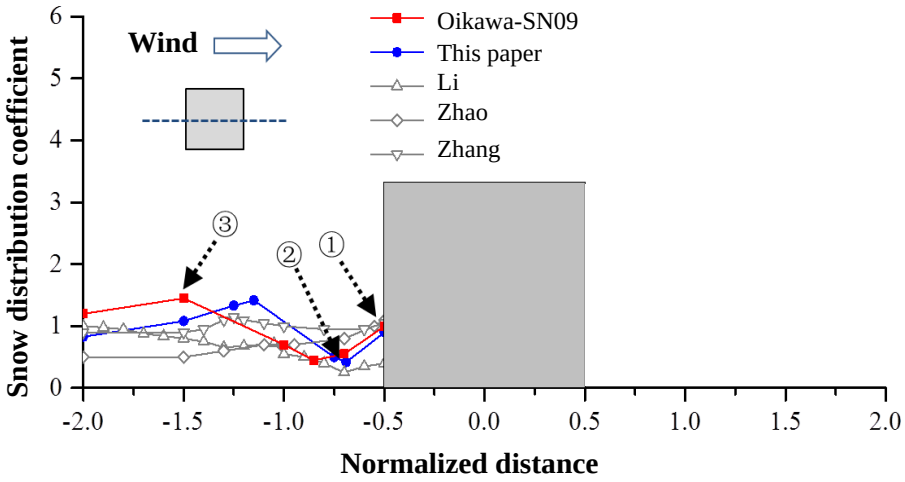


Figure 3. The comparison of snow distribution coefficients on the centreline obtained by different methods

Table 1 The deviations between the results of field observation and different experiments

	Coefficient at ①	Coefficient at ②	Coefficient at ③	Location of ②	Location of ③
This paper	17%	4.0%	24%	2.1%	34%
Li	60%	44%	24%	50%	41%
Zhao	20%	—	—	—	—
Zhang	18%	110%	65%	25%	32%

3. Wind-snow combined experiments of the long-span roof with local obstructions

3.1. Experiment settings

Since this paper aimed at investigating the influence of local obstructions on the snow distribution on the long-span roof, the same long-span roof was set for each experiment case, to eliminate the interference from different roof features on the snow distribution. The dimension of the long-span roof model was set as 2.0m×2.0m×0.5m with a scale ratio of 1/20. Considering the numerous factors that affect the snow distribution on the long-span roof with local obstructions, the inflow wind velocity, the length of the windward side of the obstruction, the height of the obstruction, and the distance between the obstruction center and long-span roof edge were selected as the investigated objects in this paper. Referring to the provisions in engineering applications, for the experiments, the width of the obstruction was set as 0.1m, the length of the windward side of the obstructions l_0 was set as 0.1m, 0.2m, 0.3m; the

height of the obstructions h was set as 0.1m, 0.125m, 0.15m; the distance between obstruction center and long-span roof edge l_u was set as 1.0m, 0.6m, 0.3m, as shown in Figure 4. The inflow wind simulated the environmental conditions of the Class B landforms. The wind velocities for the prototype building were set as 4.7m/s, and 6.6m/s, and the corresponding experiment wind velocities were 2m/s, and 2.5m/s calculated by the snowfall similarity criteria.

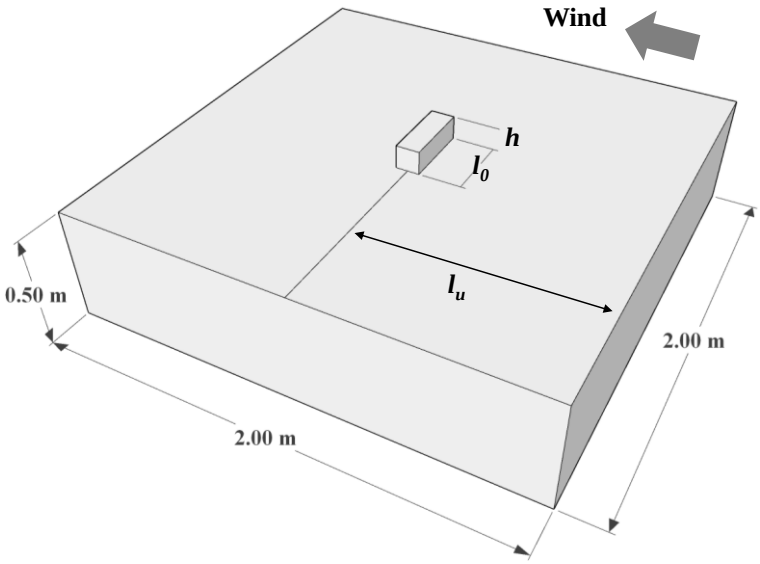


Figure 4. Experiment model

3.2. Experiment results

The experiment results were illustrated by the snow distribution coefficient, which was obtained by dividing the snow depth at any point by the mean snow depth on the ground without obstacles. Figure 5 shows the contours of the snow distribution coefficient under different wind velocities. It is illustrated that with the increase in wind velocity, the overall snow accumulation amount on the long-span roof decreases. However, an obvious snow deposition region appears on the windward side of the local obstruction, and the peak snow distribution coefficient increases, with a maximum of 3.8. In addition, there are two horseshoe-shaped snow erosion regions appearing on both sides of the local obstruction with wind velocity increasing, which exacerbates the uneven distribution of snow and causes a more adverse impact on the structure.

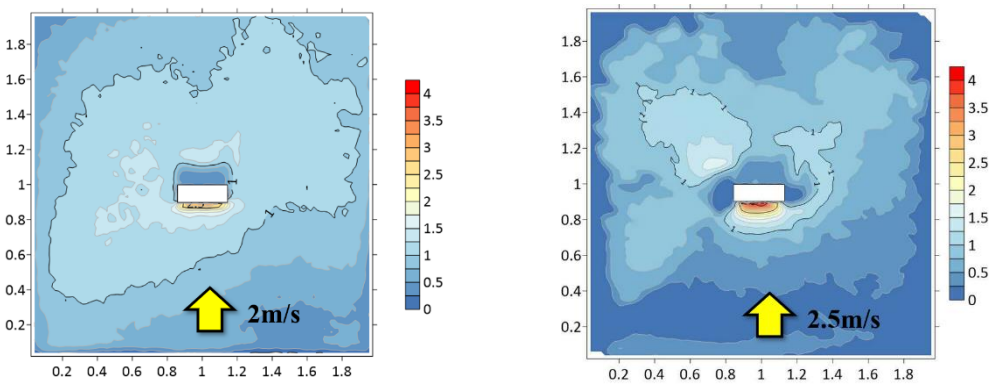
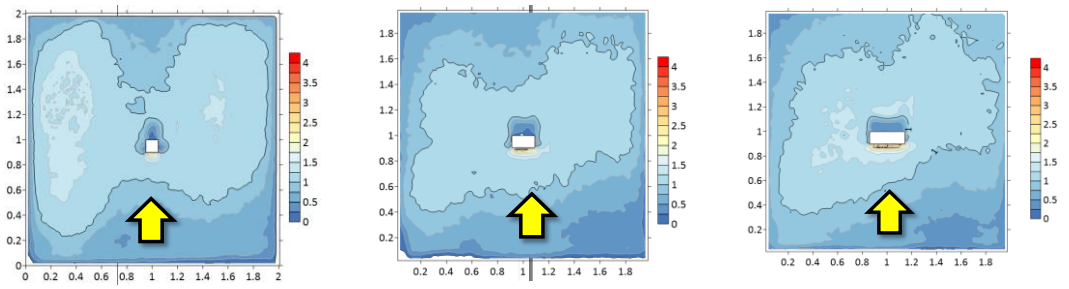


Figure 5. The contours of the snow distribution coefficient under different wind velocities

Figure 6 and Figure 7 show the contours and centerline values of the snow distribution coefficient under different lengths of the windward side of the obstructions. As the increase of the length of the local obstructions, the uneven snow distribution on the long-span roof on the windward side increases

gradually, and the maximum snow distribution coefficient could reach 3.3. Moreover, with the increase of the obstruction length, the obstructed cross-sectional area of inflow wind increases, which resulted in an increase of the overall snow accumulation amount in front of the obstruction at the windward side. Nevertheless, such influence on snow distribution only occurs within a certain range near the local obstruction, and there is nearly a change in the other area farther away from the local obstruction.



(a) l_0=0.1m (b) l_0=0.2m (c) l_0=0.3m

Figure 6. The contours of the snow distribution coefficient under different lengths at the windward side of the obstructions

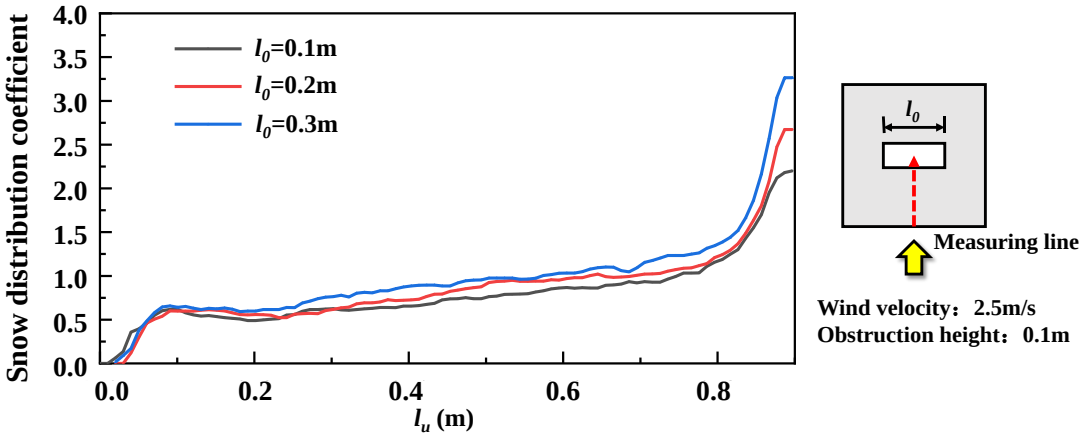
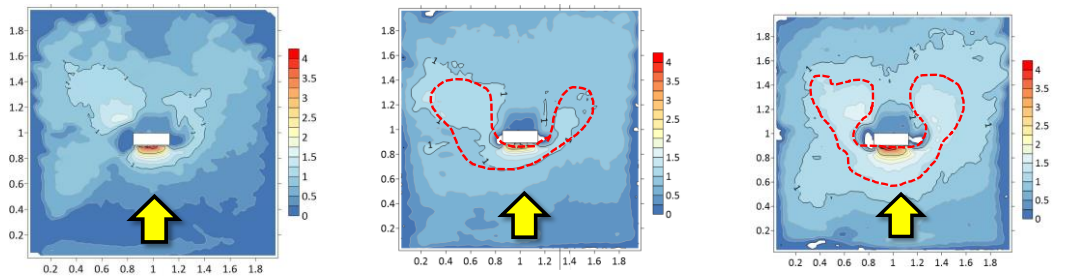


Figure 7. The centreline values of the snow distribution coefficient under different lengths at the windward side of the obstructions

Figure 8 and Figure 9 show the contours and centerline values of the snow distribution coefficient under different heights of the obstructions. It can be concluded that as the height increases, the area covered by snow particles increases, and two horseshoe-shaped erosion areas start to appear at both sides of the local obstruction, which are circled by red dotted lines in Figure 8. Besides, the range of uneven snow distribution grows with the increase of the obstruction height, and the peak snow distribution coefficient value could reach 4.2.



(a) h=0.1m (b) h=0.125m (c) h=0.15m

Figure 8. The contours of the snow distribution coefficient under different heights of the obstructions

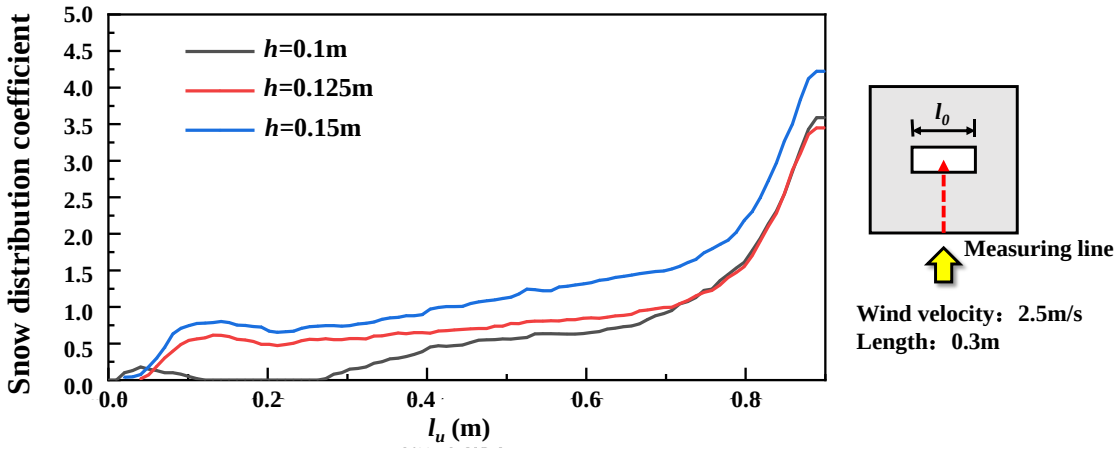


Figure 9. The centreline values of the snow distribution coefficient under different heights of the obstructions

Figure 10 shows the centerline values of the snow distribution coefficient under different distances between the obstruction center and long-span roof edge l_u. With the decrease of l_u, the amount of snow deposition in front of the local obstruction at the windward side also decreases. When l_u decreases to 0.6m, the peak value of the snow distribution coefficient decreases to 2.4; while when l_u decreases to 0.3m, there is a significant erosion region shown in front of the obstruction, with almost no accumulation of snow particles, and snow particles deposition occurs again at a distance from the obstruction. Through comparing different experiment cases, it can be found that when the l_u is $0.6l_u$~l_u (l_u=1.0m), with the increase of l_u, the area on the roof where snow particles can drift expands, and the peak value of snow distribution near the obstruction also increases; When l_u is within the range of 0.3 l_u to 0.6 l_u, due to the closer distance between the obstruction and the edge of the roof, the inflow wind field will generate vortices at the front of the obstruction at the windward, resulting in a significant erosion area at the windward side in front of the obstruction.

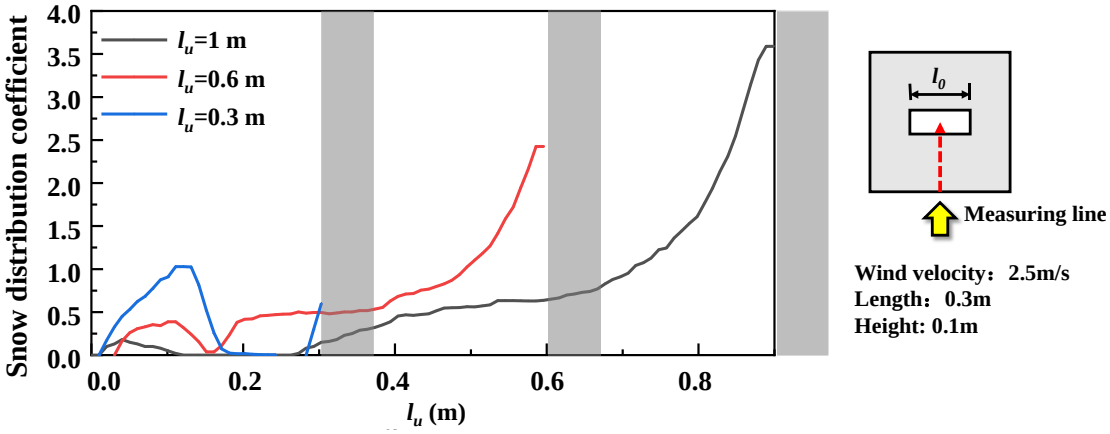


Figure 10. The centreline values of the snow distribution coefficient under different distances between the obstruction center and long-span roof edge

4. Conclusions

This paper systematically investigated the snow distribution characteristics on the long-span roof with local obstructions, the followings are the conclusions:

(1) The snow distribution on the long-span roof with local obstructions shows a typical pattern, with a horseshoe-shaped accumulation area around the center of the local obstruction. There is an obvious deposition area that appears on the windward side of the local obstruction, and erosion areas appear on

both sides of the obstruction. Such uneven snow distribution can result in adverse consequences for long-span roof structures.

(2) The snow distribution on the long-span roof with local obstructions is significantly affected by inflow wind velocity. Higher wind velocity can reduce the overall amount of snow particles on the roof, but it can exacerbate the uneven snow distribution on the long-span roof, with a maximum value of 3.8.

(3) For the long-span roof with local obstructions, the snow distribution coefficient on the roof is positively correlated with the height and length at the windward of the local obstruction. As the distance between the obstruction center and the long-span roof edge decreases, the snow distribution coefficient will also decrease, but there will be obvious erosion areas at the windward side of the local obstruction.

Acknowledgements

This study was funded by the Foundation for Chinese Creative Research Groups of National Natural Science Foundation (grant number: 51921006), National Natural Science Foundation of China (grant number 51978207, 51927813, 52208157), Postdoctoral Science Foundation of China (2022M710976), Heilongjiang Natural Science Foundation for Excellent Youth project (grant number YQ2021E030) and Heilongjiang Provincial Postdoctoral General Fund (grant number LBH-Z21161).

References

[1] W. X. Zhang, W.J. Yi, "Analysis of a one-story industrial factory building collapsed during snow disaster," *Journal of Natural Disasters*, vol.19(5), pp. 119-124, 2010.

[2] M. Liu, Q. Zhang, F. Fan, "Experiments on natural snow distribution around simplified building models based on open air snow-wind combined experimental facility," *Journal of Wind Engineering and Industrial Aerodynamics*, vol. 173, pp. 1-13, 2018.

[3] S. Oikawa, T. Tomabechi, "One-day Observations of Snowdrifts Around a Model Cube," *Journal of Snow Engineering of Japan*, vol.15(4), pp. 283-291, 1999.

[4] G. Zhang, Q. Zhang, H. Mo, R. Li, "Experimental Investigation of Snow Accumulations on Two-Span Single-Pitched Roofs Based on a New Similarity Criterion," *Frontiers in Earth Science*, vol.10, pp. 785010, 2022.

IASS 2023 July 10–14 Melbourne Integration of Design and Fabrication

Proceedings of the IASS Annual Symposium 2023
Integration of Design and Fabrication
10–14 July 2023, Melbourne, Australia
Y.M. Xie, J. Burry, T.U. Lee and J. Ma (eds.)

Rethink*Rotor, the reuse of rotor blades in the construction sector

Marcin ORAWIEC*, Thorsten HELBIG[a], Ina-Marie ORAWIEC[b]

* Department of Architecture at Darmstadt University of Applied Sciences
Schöfferstraße 1, 64295 Darmstadt, Germany
marcinorawiec@OX2.de, marcin.orawiec@h-da.de

[a] Department of Architecture at Darmstadt University of Applied Sciences, Germany
[b] OX2architekten GmbH, Aachen, Germany

Abstract

RETHINK ROTOR, the reuse of rotor blades in the construction sector promotes the circular economy that works across industries, which not only enables significant CO2 reductions by keeping the giant blades in the anthroposphere, but also shows a way out of the recycling dilemma. Thanks to the aesthetic potential and material properties such as durability, corrosion resistance, lightness and stability, added value is gained for the construction industry.

Keywords: fiber composites, shells, energy turnaround, architecture, climate turnaround, circular economy, wind energy, waste management, construction industry, urban mining

1. Introduction

The European Union's goal, as set out in the "European Green Deal", to reduce net emissions of greenhouse gases to zero by 2050, or to offset all unavoidable emissions with suitable processes and thus become the first continent to become climate-neutral, requires the transformation of the economy to circular systems (Circular Economy). The European fiber composite industry is facing major challenges in this context. On the one hand, the demand for lightweight materials in energy-intensive value chains such as the wind energy industry will increase; on the other hand, fiber composites have so far been difficult to reuse or recycle because the available technologies such as high-temperature pyrolysis or shredding (for use as a filler) are either not environmentally friendly or economically unattractive. In addition, it is forecast that from 2025 onwards, around 80,000 tons of material will be produced annually from end-of-life composite components - in Germany alone, around 7,500 discarded rotor blades are removed from wind turbines every year.But what happens to the discarded, in some cases over 80 m long, custom-made epoxy resin-bonded fiber-reinforced plastics (FRP) after their approx. 20 years of use in the wind farm?

REHINK*ROTOR supports the way out of the recycling dilemma: leaving the huge blades in the anthroposphere enables a significant CO2 reduction. The reuse of the complete rotor blades is many times more sustainable than their material recycling.

Upcycling: the aesthetic potential of the blades, their durability, corrosion resistance, lightness and stability are an added value for the construction industry.

New life cycle: the reuse of rotor blades reduces the consumption of raw materials and energy and the amount of waste generated.

The resource-conserving use of materials, building products and processes makes a significant contribution to climate justice and cannot be reduced to individual sectors. The cross-sectoral linking of

Copyright © 2023 by Marcin ORAWIEC and Ina-Marie ORAWIEC. Published in the Proceedings of the IASS Annual Symposium 2023 with permission.

circular value creation is a significant prerequisite for the success of the climate, construction, mobility and energy transformation. In this context, the socio-economic potential of the creative industries in particular can enrich and dynamize cross-innovative collaboration and the conviction that this will result in projects that solve man-made problems and do not create further ones. The RETHINK*ROTOR technical session will thus become a "best practice" example and an initial spark for comparable, transdisciplinary projects.

Promotion of acceptance: due to its sustainability, REHINK*ROTOR stands for a visibly comprehensible, social added value and has a positive influence on the public perception of wind energy.

2. Background information

2.1 Background information on the construction industry

approx. 90% of all mineral raw materials used in Germany are used for the production of building materials. The construction industry is a major contributor to waste generation (approx. 54%). Buildings account for 40% of the total energy demand, so that resource-saving construction is of particular importance.

2.2 Background information Wind energy

With approx. 22% of the gross electricity in Germany, wind energy is a fast growing market, but wind turbines have to be dismantled after 20 years. In Germany alone, 7,500 decommissioned rotor blades are produced annually. Their plastic matrix cannot be deformed. The material cocktail of the blades can only be partially recycled by means of costly, environmentally harmful processes. This is not done residue-free, neither CO_2-neutral, nor sustainable! Some are therefore shredded and metal residues contained therein are separated. The remaining waste is used as fuel or substitute in the cement industry or burned in small quantities in waste incineration plants.

2.3 Background information on political and social framework conditions

In December 2015, at the World Climate Conference in Paris, a climate agreement was reached in which 195 countries pledged to curb climate change and to transform the global economy in a climate-friendly way. Specifically, the agreement states that the global temperature increase should be limited to 1.5 degrees Celsius if possible, and in any case to well below two degrees Celsius compared to the pre-industrial era.

To achieve this goal, no more climate-damaging gases may be emitted in the second half of this century than are removed from the atmosphere by so-called carbon sinks, such as forests.

One of the most important principles for our handling of these findings is: the gray energy contained in every building but also in every manufactured part (e.g. rotor blade) is irretrievably lost if we do not reuse it. In order to reduce further exploitation of the earth's resources, the preservation or recycling of urban warehouses represents an important economic objective.

For this reason, a team of experts has been working for some time within the RETHINK*ROTOR project on the possibilities of finding a reuse for the discarded rotor blades in the construction industry - in the spirit of circularity.

2.4 Background information Processing

because of the high-performance but exclusively duromer-based material cocktail, the rotor blades are only partially recyclable through costly, environmentally harmful processes. Once cured, the epoxy resin-based plastic matrix of the huge blade surfaces can no longer be deformed. Some are therefore shredded after dismantling and metal residues contained therein are separated. The remaining waste is thermally recycled as fuel and sand substitute in the cement industry or incinerated in small quantities in conventional waste incineration plants. This form of thermal recycling is not residue-free, neither

CO_2-neutral, nor sustainable. The complex geometry of the rotor blades and their material properties, such as durability, combined with low weight and high rigidity, offer the way out of the recycling dilemma. The shapeliness of the components and the efficiency of the composite material can be "profitably" exploited in new applications. The construction industry, with its large material consumption, is therefore particularly predestined for the use of end-of-life (EoL) components.

Recycling is accompanied by a loss of quality of the non-degradable materials, which eventually end up in the waste. Common practice is therefore to store the rotor blades indefinitely. Due to their sheer size, this triggers a steadily increasing demand for space.

2.5 Background information on existing recycling processes

according to the evaluation of the recycling processes of the discarded rotor blades considered in various studies, it can be assumed that these processes will not achieve sufficient capacities in the foreseeable future to recycle the forecast GRP waste volumes. In addition, a large number of materials with insufficient data on toxicological effects are installed in rotor blades. A concrete example is the glass fibers, which may or may not be classified as carcinogenic depending on their type. Since critical fiber fragments with WHO geometry can be released during processing, the more dangerous case must always be assumed according to the precautionary principle.

3. Design principles

3.1 Initial situation design

RETHINK*ROTOR provides high-quality yet simple solutions for the complex task of giving disused rotor blades a second life in the construction sector and integrating them into the architecture of buildings.

The "second life applications" of the complex geometries of the rotor blades are supported by the beauty of the parts, but in order to guarantee their use in new applications, a whole series of creative and constructive ideas are required. Only then can the aesthetic potential of the repaired, used and reclaimed be fully realized.

The complex geometry of rotor blades and the fact that cutting them up is costly and sometimes harmful to health makes it necessary, when reusing the discarded custom-made products, to "profitably" transform the shape into a new form - a challenge for creatives that the team of the RETHINK*ROTOR project has taken on.

The challenge, which results from the complexity and a long-lasting use of the parts once produced, whether these are rotor blades or parts of a building, illustrates the urgency of solving the individual critical aspects. Without this, the vision of the building turnaround and the sustainable built world is only an illusion.

3.2 Static and design qualities

the wind turbine rotor blades, which are made of glass fiber-reinforced plastic, are subjected to static stresses - due to their own weight and wind - and, above all, dynamic stresses - in the form of vibrations - throughout their entire service life during initial use. Unlike most metals, fiber composites exhibit very good fatigue properties. Even under frequent load changes, the fatigue strength remains only slightly below the static strength.

No reduction in strength or other mechanical properties is to be expected after initial use. For the rotor blades intended for reuse, material properties can be assumed to be the same as for a newly manufactured GRP component. The rotor blade is designed as a hollow body, which is kept dimensionally stable by various stiffening ribs. Due to the variable oval shape over the length, there are clearly different geometric stiffnesses in the main directions (surface moments of inertia). The fiber scrims, which are

quite uniform over the surface, have local reinforcement areas and are reinforced with some compact chords. The bending, torsional and elongation stiffness has to be determined based on a specific analysis of the geometry and fabric formation, but can be well captured using simplified assumptions.

The rotor blades can be used as bending-stressed, torsion-stressed or normal-force-stressed components.

The necessary connection and joining points are advantageously realized by laminating stainless steel sheet segments. In this way, structural steel connections can be used for joining.

3.3 Scalability of possible uses

as already mentioned, about 7,500 of the rotor blades are currently disposed of as waste each year in Germany. In the near future, a much larger number can be expected.

For this reason, the focus of the Rethink*Rotor project is on a broad spectrum of possible new applications for rotor blades in the construction sector. Starting with 30 to 60 pieces for an industrial hall or 600 for a noise barrier up to 2000 or more for a pontoon construction as a floating support structure for a floating village. These are only three selected examples of many topics that the Rethink*Rotor project deals with. An important aspect is to find a secondary use near the original location of the wind turbine in order to minimize the transport distances. To this end, work is also being done on processing concepts that enable on-site feasibility. One of the prerequisites is that the joints for the components can be realized with low-tach methods.

Thanks to the prospects shown for subsequent use for the rotor blades, acceptance of the wind turbines in an urban context will also be increased.

3.4 General design starting point: the rotor blades of the wind turbines, which are made of glass fiber-reinforced plastic, are subjected to static stress - due to their own weight and wind - and, above all, dynamic stress - in the form of vibrations - throughout their entire service life during initial use. Unlike most metals, fiber composites exhibit very good fatigue properties. Even under frequent load changes, the fatigue strength remains only slightly below the static strength. No reduction in strength or other mechanical properties is to be expected after initial use. For the rotor blades intended for reuse, material properties can be assumed to be the same as for a newly manufactured GRP component. Of course, each component will have to be subjected to close inspection to determine that no mechanical damage such as localized fracture, delamination, etc. is present. The rotor blade is designed as a hollow body, which is held dimensionally stable by various stiffening ribs. Due to the variable oval shape over the length, there are clearly different geometric stiffnesses in the main directions (surface moments of inertia). The fiber scrims, which are quite uniform over the surface, have local reinforcement areas and are reinforced with some compact chords. The bending, torsional and elongation stiffness has to be determined based on a specific analysis of the geometry and fabric formation, but can be well captured using simplified assumptions. The rotor blades can be used as bending-stressed, torsion-stressed or normal-force-stressed components. The necessary connection and joining points are advantageously realized by laminating stainless steel sheet segments. In this way, structural steel connections can be used for joining.

4 Fields of application

An important aspect when deciding where to use the discarded rotor blades is the proximity to the site of the wind farm that is to be dismantled. This guarantees short transport distances.

For this reason, the applications are divided into onshore and offshore applications.

4.1 Onshore applications include:

4.1.1 Noise barriers

Similar to the initial application in the wind turbine, the rotor blades, which are set up in a row, are primarily loaded by wind transverse to the longitudinal axis. Therefore, no reinforcements to a significant extent should be necessary.



Figure 1. Noise barriers

4.1.2 Schuchow tower

The rotor blades are used as vertical members mainly transferring gravitational loads. The inner structural layer effectively stiffens the structure.

In this variant, the rotor blade segments are mainly subjected to normal force loads.

Depending on the specific design of the structure, longitudinally laminated GRP or CfK webbing supports the load transfer. Tie points to the inner cable structure can be designed as anchor points laminated to the inner belt layer.



Figure 2. Schuchow tower

4.1.3 Cantilever beams - Rotating roof support structure

The horizontal segments are mainly subjected to normal force (compression) and secondarily to bending due to the attached roof cladding. The chord reinforcement required for bending and normal force is combined in one element.

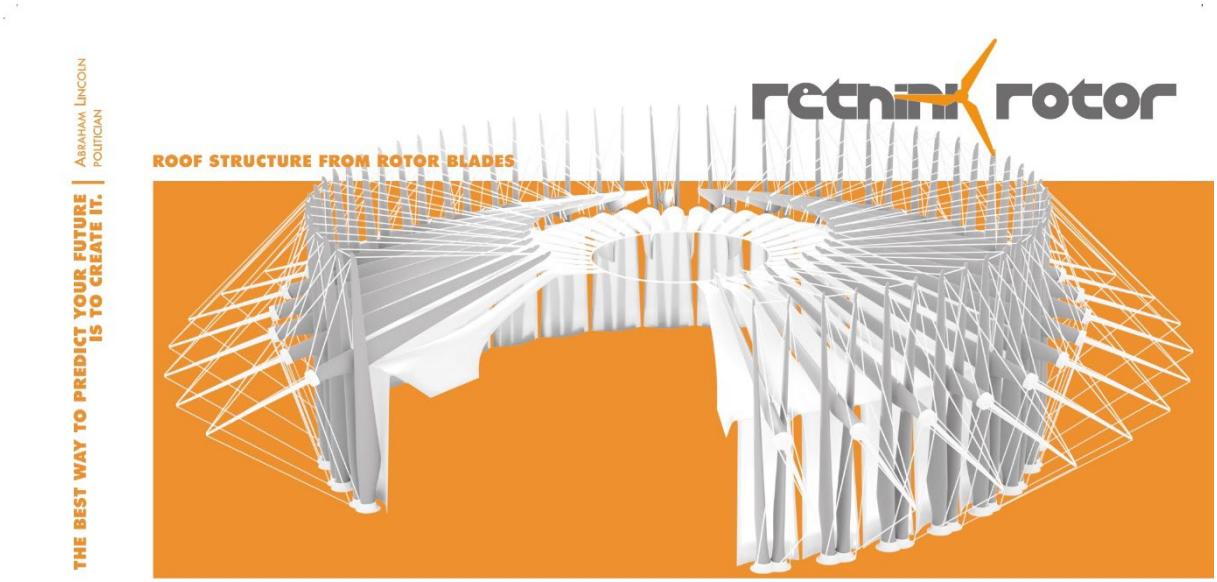


Figure 3. Cantilever beams - Rotating roof support structure

4.1.4 Saddle roof beam



Figure 4. Saddle roof beam

4.1.3 Cantilever beams - Parallel structure

The horizontal segments are mainly subjected to normal force (compression) and secondarily to bending due to the attached roof cladding. The chord reinforcement required for bending and normal force is combined in one element.

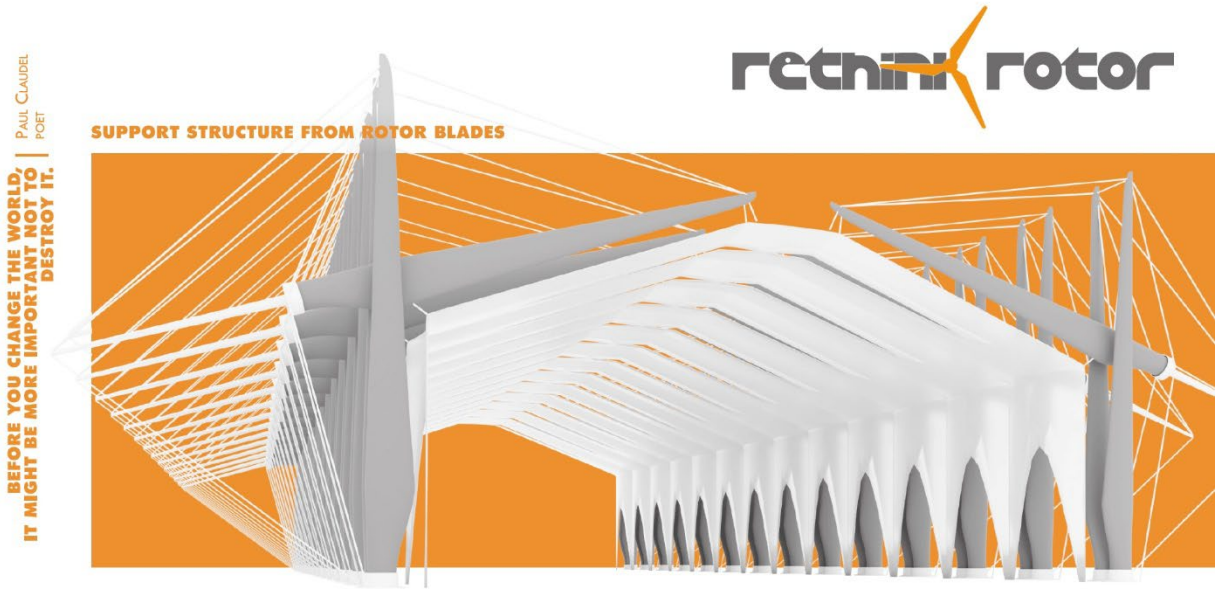


Figure 5. Cantilever beams - Parallel structure

4.1.5 Stadium roof

The cantilever beams are clamped at the base into the circumferential ring and carry only wind loads and the small dead loads. Reinforcement by laminated chord strips will only be necessary near the restraint in the bending compression and tension areas.

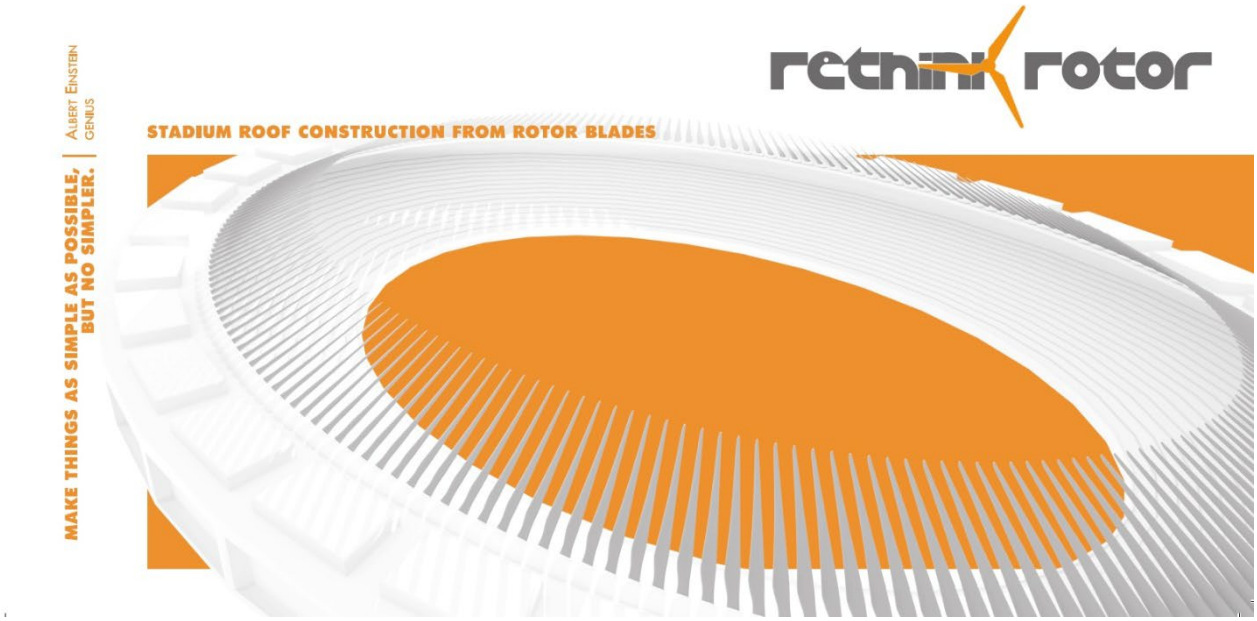


Figure 6. Stadium roof

4.2 Offshore applications include:

4.2.1 Coastal protection and retaining walls.

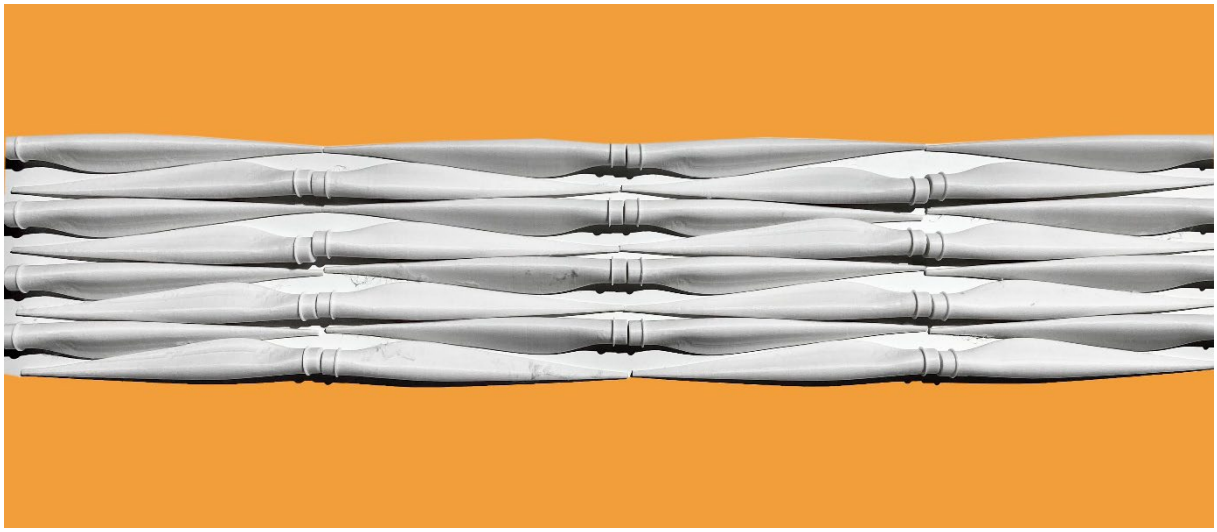


Figure 7. Coastal protection and retaining walls

4.2.2 Pontoons for floating islands

The calculation of the lift force is based on the rotor blade Enercon E66. The rotor blade type was installed in wind turbines between 1995 and 2005 and currently belongs to the type generation affected by decommissioning in Europe. The rotor blades are each 31m long. More recent models are sometimes 34m long. The 31 m long blade has a volume of 98.8 m3. The lift force, and thus the possible load capacity, is 94 tons after deducting the dead weight.

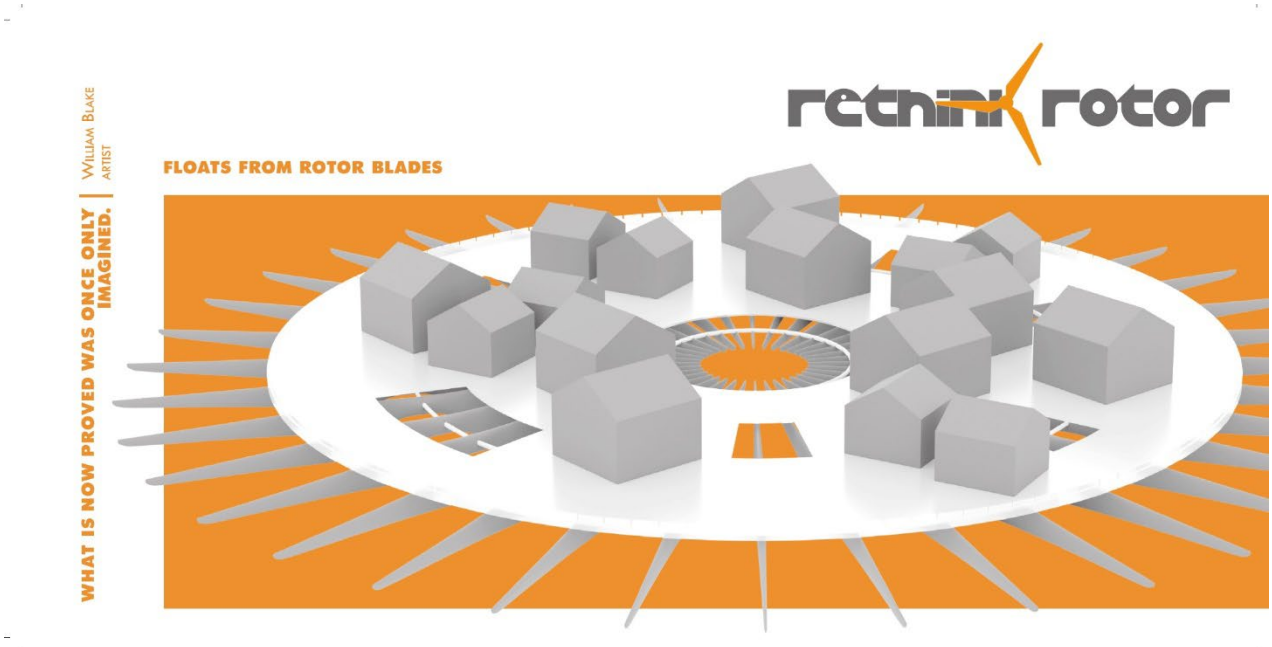


Figure 8. Pontoons for floating islands

Based on these fixed sizes, concepts for floating islands are being developed in the RETHINK*ROTOR project.

One of the possible uses is to provide a land substitute where natural islands are in danger of sinking due to rising sea levels. Tuvalu, for example, is affected. As early as 1989, the United Nations placed the country on a list of several island groups that are in danger of sinking into the sea in the 21st century due to global warming. Already today, two of Tuvalu's nine atolls are almost completely submerged. Because of its remote location in Oceania, the South Pacific island nation of Tuvalu is difficult to reach and massively threatened by rising sea levels. Only 11,500 people live on Tuvalu's nine islands - comparable to a small Central European town. On the densely populated atoll of Funafuti, which is one of the nine inhabited island groups of Tuvalu, live just over 6,000 inhabitants, about 60% of the total population. The atoll's 33 islands surround TeNamo Lagoon, which is also the largest lagoon in Tuvalu, covering 275 square kilometers.

The RETHINK*ROTOR project is now looking into the possibilities of creating a perspective for the future for the approximately 12 thousand inhabitants.

5. Conclusion

Using EoL wind power rotor blades as an example, RETHINK*ROTOR demonstrates that it is possible to create a closed loop of materials and further use EoL rotor blades in construction and give the process prominent visibility. The whole chain from the condition assessment of the EoL rotor blades: the logistics and the reprocessing, the planning of the recycling, the statics and implementation, must and will be profitably considered taking advantage of their aesthetic potentials. The knowledge and grey energy bound in each wind rotor blade will be definitively lost if it is not reused. With its project ideas, RETHINK*ROTOR aims to link a cross-sector repurpose of the blades, creative energy, new technologies and sustainability goals.

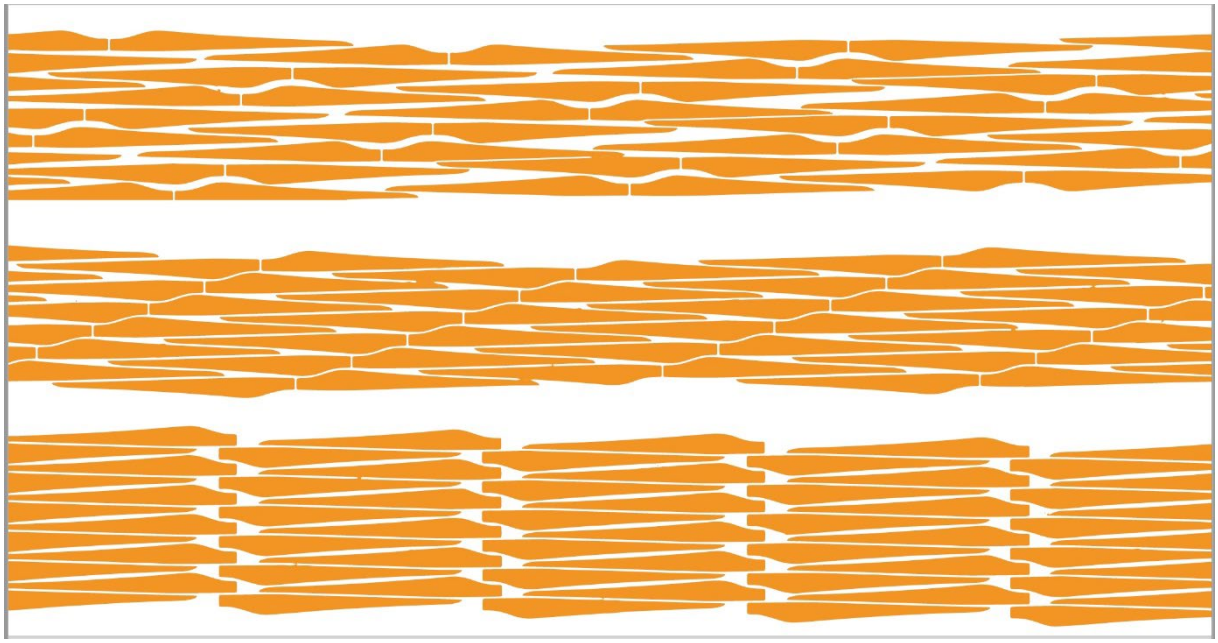


Figure 9. Coastal protection and retaining walls or noise barriers

References

[1] Final Report: Development of Deconstruction and Recycling Standards for Rotor Blades,Karlsruhe Institute of Technology (KIT), THINKTANK Industrial Resource Strategies, Institutfür Technische Chemie (ITC), Institut für Angewandte Geowissenschaften (AGW), Karlsruhe on behalf of the Federal Environment Agency, July 2022, ISSN 1862-4804 Dessau-Ro. lau, August 2022.

[2] Federal Ministry of Economics and Climate Protection, Germany.

[3] https://www.humanium.org/de/tuvalu/

[4] https://www.destatis.de/DE/Themen/Laender-Regionen/Internationales/Laenderprofile/tuvalu.pdf?__blob=publicationFile

[5] https://www.merkur.de/welt/tuvalu-geschichte-politik-bevoelkerung-und-geografie-92163215.html

[6] https://www.xflow.eu/de/2014/02/13/tuvalu-atoll-funafuti-pazifischer-ozean

Proceedings of the IASS Annual Symposium 2023
Integration of Design and Fabrication
10–14 July 2023, Melbourne, Australia
Y.M. Xie, J. Burry, T.U. Lee and J. Ma (eds.)

Structural design of a gymnasium with warren trusses in a grid arrangement supported by thin columns and damping braces

Eisuke MITSUDA[a,* (**)]

[a,*] Faculty of Design and Architecture, Kyoto Institute of Technology
[**] Former president, Mitsuda Structural Consultants Co., Ltd.
mitsuda@kit.ac.jp

Abstract

This paper describes the structural design of a gymnasium for a famous badminton team practice with a 36.36m x 36.36m sq. arena. The building is located in Kumamoto Prefecture, where a major earthquake occurred in 2016, and the structural design of the roof with long span as well as its seismic design was carefully considered. The ceiling height of this arena is 10.5 m to meet the standards for international badminton matches. A unique feature of this gymnasium project is that half of the arena's height is buried underground as a basement floor. On the ground floor, 5.5 m high steel columns are erected, on top of which the roof structure is placed. The roof structure consists of giridded warren trusses. The grid size is set at 6.06m, divided into six equal parts per side of the arena. All truss's sections were unified with H-beams of the 150-width series. φ165.2 steel pipes were used for the columns to match the H-beam trusses. In addition, buckling-restrained braces are used in order to grant a high energy absorption efficiency and toughness. The size of the brace core members was determined so that the stiffening tubes for buckling restraint were the same diameter as the columns, φ 165.2, and the total number of braces was determined backwards from the required bearing capacity of the building. In this gymnasium, all structural elements - trusses, columns and braces - are holistically designed.

Keywords: structural design, space structure, light construction, gridded warren trusses, seismic design, buckling-restrained brace



Figure 1. Interior view from the arena

Copyright © 2023 by Eisuke MITSUDA. Published in the Proceedings of the IASS Annual Symposium 2023 with permission.

1. Introduction

This building is a corporate's gymnasium in Kumamoto Prefecture, JAPAN. The company has a well-known women's badminton team with a World Championship winner, and this is their training base. The office and facotry of this company are located on a small hill near Kumamoto Airport. The company has spent a long time developing a beutiful green hill and the hill has become a favourite place for local people. This gymnasium was planned on the hillside.

The required effective ceiling height of 10.5 m was required for the arena. If a huge building were to be placed on top of the hill, it would destroy the beautiful site landscape that had been nurtured over the years, so the plan was to dig the ground to a certain depth and bury part of the building.

The basement floor of the building consists of a square arena measuring 36.36m x 36.36m, surrounded by changing rooms, lounges, equipment and machinery rooms in an L shape, which together form a rectangular shape measuring 48.48m x 42.42m. The ground floor consists of an atrium above the arena, as well as an entrance, a multi-purpose space, a gym and a viewing terrace. It is covered by a single large 54.54 m x 48.48 m truss roof that also serves as a cantilevered eave over the whole of the building.



Figure 2. Exterior view from down the hill



Figure 3. Bird's-eye view from the airplane

2. Architectural scheme

General information of this buiding

Name of buiding: SAISHUNKAN CIRCLARENA Architects: RYTHMDESIGN + KITOREPE

Location: Mashiki town, Kumamoto Prefecture Contractor: TAISEI CORPORATION

Building area: 2591.88m^2 Total floor area: 2766.86 m^2

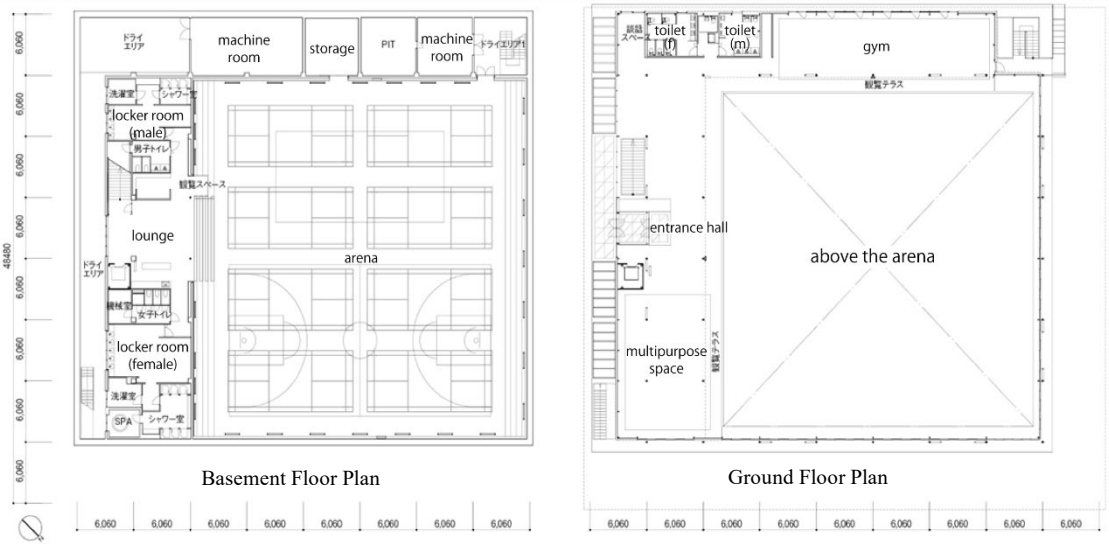


Figure 4. Plan of the gymnasium

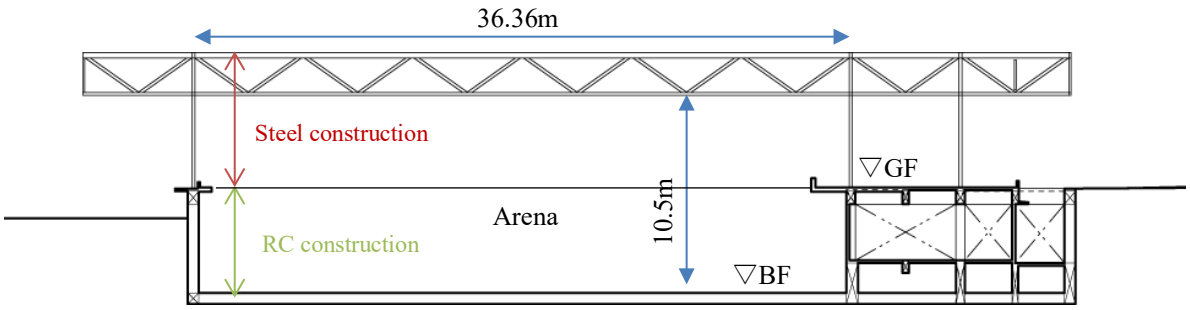


Figure 5. Cross sectional configuration

3. Structural scheme

General information about the structural planning

Structure of basement floor: Reinforced Concrete construction

Structure of ground floor: Steel frame construction with buckling-restrained braces

Foundation type: spread foundation (mat foundation)

Construction period: October 2016 to June 2017 (9 months)

3.1. Roof structure

To cover the 36.36m x 36.36m square arena, the roof has a grid of warren trusses in the form of lattice beams. The grid size is 6.06m x 6.06m to ensure that shuttles and balls do not hit the trusses as far as possible if they rise higher than the required ceiling height of 10.5m.

3.1.1. The configuration of the trusses

The truss cross-section was previously defined as 2.35 m externally, taking into account the transport unit from the factory to the site. The upper chords, which are subject to bending due to roof loads, are H-300x150x6.5x9, while the lower chords and diagonals, which are not subject to bending, are H-150x150x7x10. All H-beams in 150-width series are used.

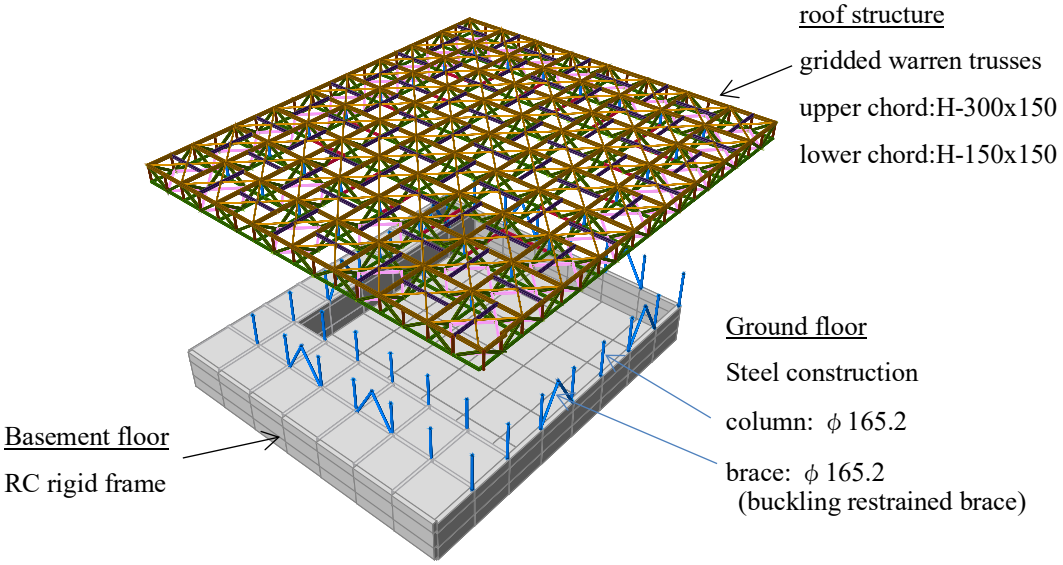


Figure 6. Building composition

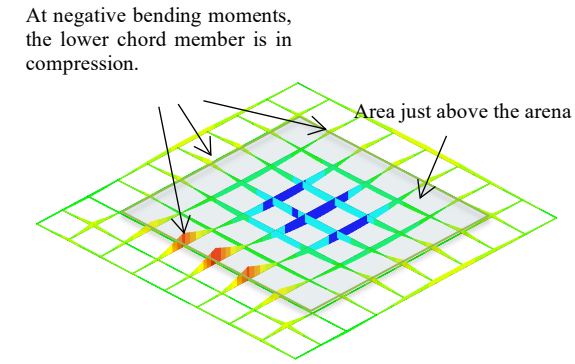


Figure 7. Moment diagram for grid beam model

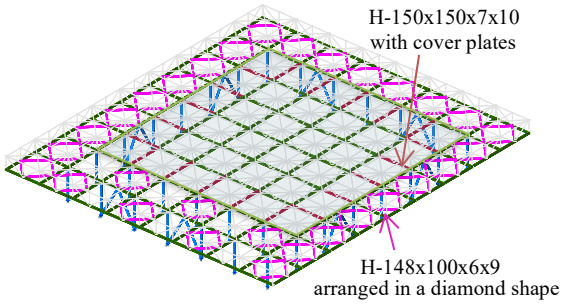


Figure 8. Buckling stiffening of truss lower chords



Figure 9. Specific examples of anti-buckling measures



Figure 10. Connect to the top of the seismic brace

3.1.2. Anti-buckling measures for truss members

The in-plane stiffness of the whole roof is ensured by in-plane bracing at the upper string level. Braces and beams reduce the buckling length of the upper chord by half to 3.03 m. During gravity action, compressive forces are also generated in the lower string members near the support point (Figure 7), which means that anti-buckling measures are also required for the lower string members. Outside the upper part of the arena, such as in gym and multipurpose spaces, the centres of the four sides of the grid are connected in a diamond shape with H-148x100x6x9 to reduce their buckling length by half (Figure 8,9). On the other hand, inside the arena, the arrangement of the diamond-shaped components is obstructed by the lighting, so the weak axis is supplemented by a cover plate (Figure 8,9). In addition, the diamond-shaped in-plane brace also serves to restrain the out-of-plane deformation of the head of the buckling-restrained braces, which are the elements that bear the seismic forces (Figure 10).

3.2. Supporting structure - column and brace

To give the impression of light, floating roof trusses, the columns and braces were designed to be moderately slender but with strong seismic performance.

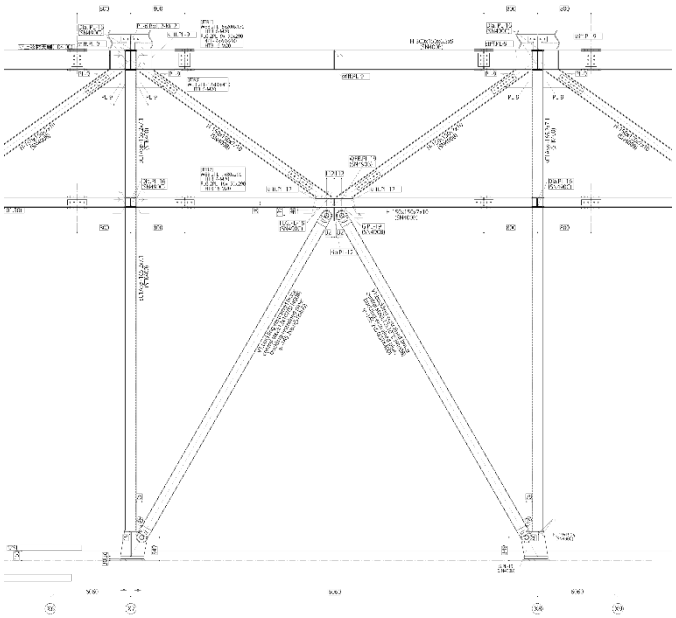


Figure 11. Detailed diagram of the steel frame structure

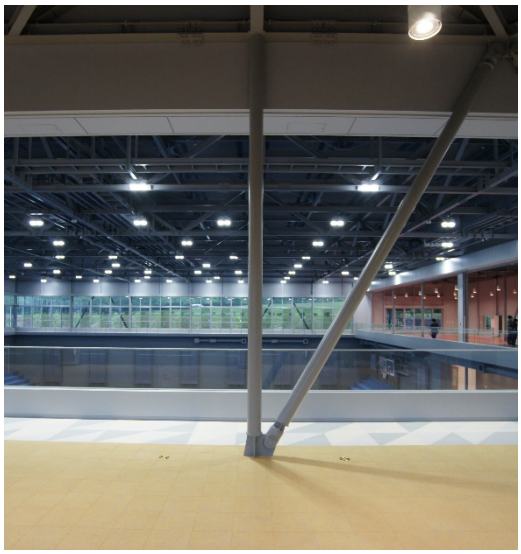


Figure 12. Column and buckling-restrained brace

3.2.1. Steel pipe columns with φ165.2 series

Where H-beam trusses with a unified 150 width join the columns, steel pipe columns of the φ 165.2 series are used to ensure that the diaphragm is of a suitable size to support the 150-width member (Figure 11). Steel pipe columns are erected at a pitch of 6.06m to support all the trusses covering the arena (Figure 13). Differences in the configuration of the outer side of the arena cause slight differences in axial forces in the columns. The thickness of some steel pipe columns is changed accordingly (standard thickness 7.1 mm, some 9.3 mm). The thickness of the steel pipes does not affect the truss-to-column joint details, so they all have a uniform detail.

3.2.2. Buckling-restrained bracing in a K-shaped arrangement

The seismic structure type of this building is braced, but with buckling-constrained bracing, which makes it a tough structure with high energy absorption efficiency. The buckling-restrained braces are selected in combination with a central steel member whose buckling-restrained pipe size is the same diameter as that of the columns, φ 165.2. The total number of braces is determined backwards from the required bearing capacity of the building (Figure 14). For design reasons, pin-type details are used at the ends of the braces instead of the high-strength bolt type (Figure 12).

The K-shaped arrangement of the braces allows horizontal forces during earthquakes to flow directly to the braces, resulting in almost no variable axial forces on the columns. Therefore, the φ165.2 columns, whose cross-sections are defined by long-term axial forces, are not affected. Furthermore, in the case of K-shaped arrangement bracing, the braces do not intersect at the truss-to-column joints, thus maintaining a uniform truss-to-column joint detailing.

An advantage of using buckling-restrained braces with K-shaped arrangement is that the pull-out and shear forces in the legs are determined by the brace yield axial force, thus reducing the need for complicated anchor bolts. Similarly, the design of the members in the brace frame is easier because the upper limit of the forces gathered at the connection between the brace and the truss is determined.

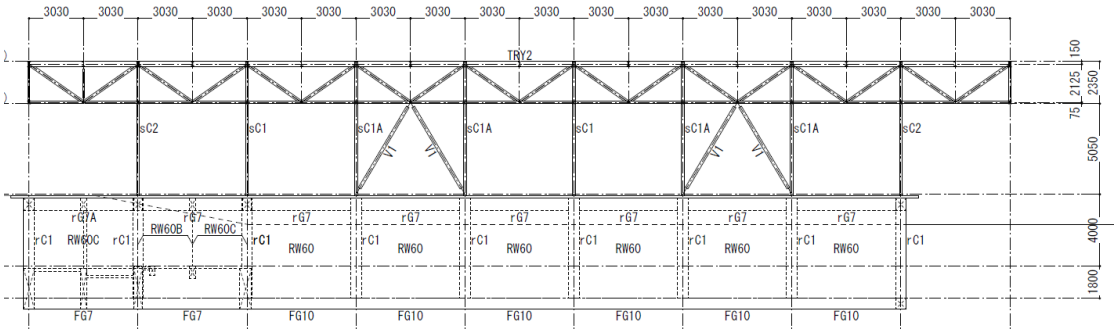


Figure 13. Framing elevation including K-shaped braces

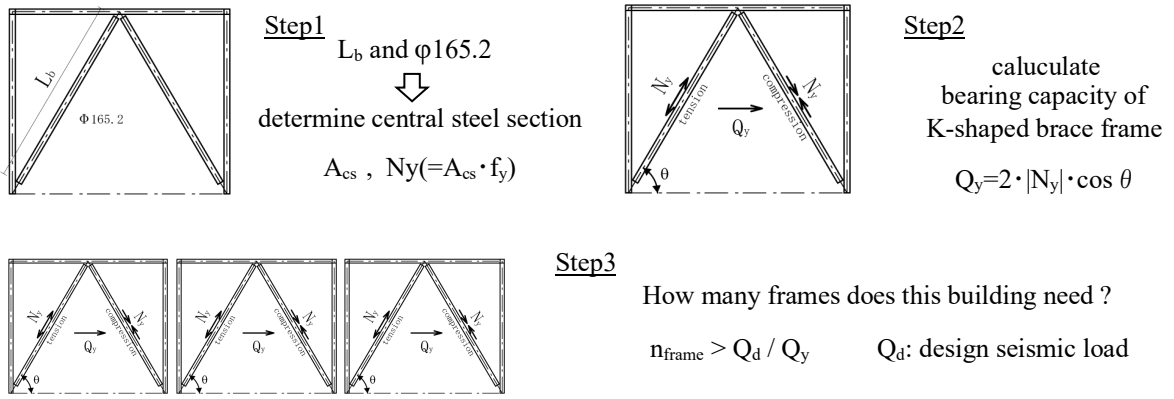


Figure 14. Design process of K-shaped buckling-restrained brace frame

3.3. Reinforcement concrete structure for basement floor

The basement floor is subject to soil pressure around the outside, and is therefore of RC construction. The 60 cm thick retaining wall circles the entire basement floor. The structure, including the retaining walls, is a rigid frame with columns and girders and earthquake-resistant walls (Figure 17), which is sufficiently rigid and strong. Two of the four sides surrounding the arena are directly in contact with the soil, and to prevent the retaining wall from being cantilevered, the top of the wall has a continuous strip of 2m to 2.5m wide slabs that also serve as a maintenance walkway.

3.4. Foundation structure

Although the site had soft ground, the weight of the soil removed by excavation was far heavier than the weight of the new building to be placed on it(Figure 18), so a direct foundation with mat slabs was applied. Due to the large size of the site, excavation was done by open cut and the surrounding area was backfilled after the retaining walls were constructed (Figure 15,16).



Figure 15. open cut excavation

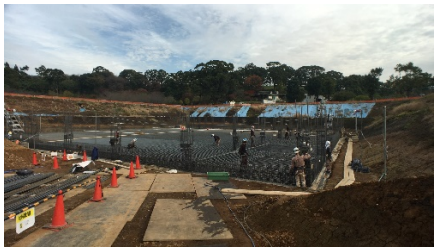


Figure 16. rebar construction of mat slab



Figure 17. RC skeleton in BF

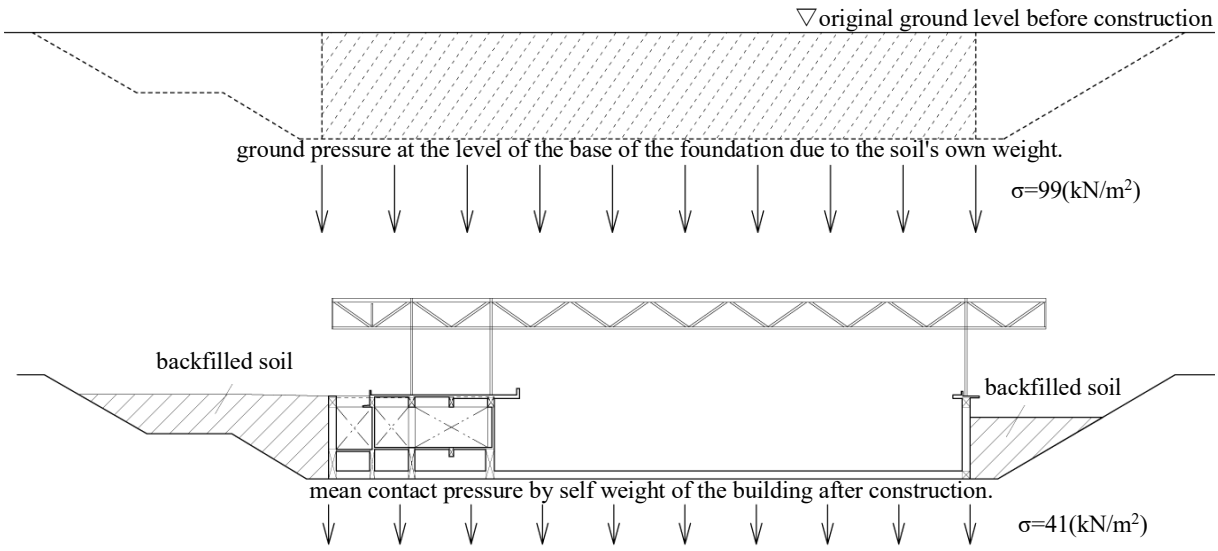


Figure 18. Comparison of contact pressure before and after construction

4. Construction plan of the roof structure

As noted in section 3.1.1, the external dimensions of the trusses were determined first so that a special permit under the Japanese Road Traffic Act would not be required. This allows the upper and lower string members to be transported as one unit, although they need to be divided in the longitudinal direction. The trusses were arranged in a grid pattern with the intention of distributing the stresses evenly.



Figure 19. Construction process of the warren truss. (a) transported by standard truck, (b) field assembling, (c) hanging the 36m long truss



Figure 20. Construction process with using four temporary support columns. (a) four temporary columns, (b) during the construction process, (c) after jacking-down

If longer trusses were installed first without support, they would become keel trusses and bear excessive stresses. Therefore, the use of four temporary columns was included in the design (Figure 20).

Two of the trusses delivered to the site were united in 36m lengths before being hoisted and hung in a position to be supported by temporary posts erected every 12m (Figure 19,20). The remaining trusses were installed in a sequential grid based on the two trusses supported by the temporary columns. After all trusses had been installed, the support columns were removed. Secondary components such as roof decking were installed after the removal of temporary columns.

5. Conclusion

This paper describes the structural design of a gymnasium with a 36mx36m square arena. It showed that the structural frame itself can make a high contribution to the design by making thorough and logical decisions.

・For roofs over square shapes, using grid trusses is effective in obtaining a homogeneous and smaller stress state.

・The overall size of the truss beams was determined in consideration of the transport size, and the components of the trusses were unified using H-beams of the 150-width series.

・In the compression zone of truss members, the buckling stiffening method can be switched according to the characteristics of the location, so that both design and structural performance can be achieved.

・Buckling-restrained braces were adopted so that the columns do not bear the seismic forces, and all the lattice trusses are supported by columns, so that a large roof can be supported by a thin column of Φ165, giving the design a light impression.

・A light and uniform design can be achieved by using column sizes according to the width of the truss members and sizing the buckling-restrained braces to match the column sizes.

・The design approach was to adjust the seismic performance by the number of braces by adopting braces that matched the column size, but this did not compromise the design quality compared to the conventional approach of determining the brace location first and then the performance required for the braces.

・By using excavation methods appropriate to the site's characteristics and efficient use of temporary columns, attractive internal spaces and an exterior appearance that is considerate of the surroundings were achieved without incurring extra costs.

It is important to develop the above logical thinking in a holistic way, which is also effective structural design as design.

References

[1] Eisuke MITSUDA, “Light spaces achieved by utilising the toughness of buckling-restrained braces,” *The Steel Structural Technology,* vol. 33, No.389, pp. 68–69, 2020.10

[2] Eisuke MITSUDA, Shingo YOSHIGI, “Simple and light structural design of the gymnasium - SAISHUNKAN CIRCLARENA-” *Proceedings of the JSCA Structural Design Presentations 2021*, pp.142-143, 2022.6

Proceedings of the IASS Annual Symposium 2023
Integration of Design and Fabrication
10–14 July 2023, Melbourne, Australia
Y.M. Xie, J. Burry, T.U. Lee and J. Ma (eds.)

Structural node of foundation for buildings located in seismic areas

Janusz RĘBIELAK[a,*]

[a,*] Chairman of the Committee for Architecture and Town Planning of Wroclaw Branch of the Polish Academy of Sciences, ul. Podwale 75, 50-449 Wroclaw, Poland

Email Address: j.rebielak@gmail.com

Abstract

The paper presents some proposals for the shaping of support nodes that can be an important part of the structural systems of foundations for buildings located in the seismically active areas. The proposed forms of such nodes are shown on examples of their use as not only the auxiliary but indeed the integral components of the system of composite foundation, however, they can also be applied in other commonly used types of the foundation structures. The structural system of the foundation of a building located in a seismically active area should ensure horizontal dilatation of this building from the ground and at the same time enable safe movement of the building in the horizontal and vertical directions, of course within an appropriate range of such displacements. The proposed forms of support nodes make possible to meet these requirements by using an appropriate arrangement of metal vertical ribs permanently connected to the metal main bodies of these nodes. These single ribs contain circular rollers with eccentrically placed holes where cylindrical pivots are located, due to which the load forces are transmitted to the adjacent body of the foundation node. Moreover suitable application of the proposed support nodes in the structures of floating platforms, where they can be appropriately connected with electricity generators, can contribute to obtaining the emission-free energy from the movement of sea waves.

Keywords: building, foundation structure, subsoil, load carrying capacity, seismic area, structural system, support node, structural node, floating platform, emission-free energy

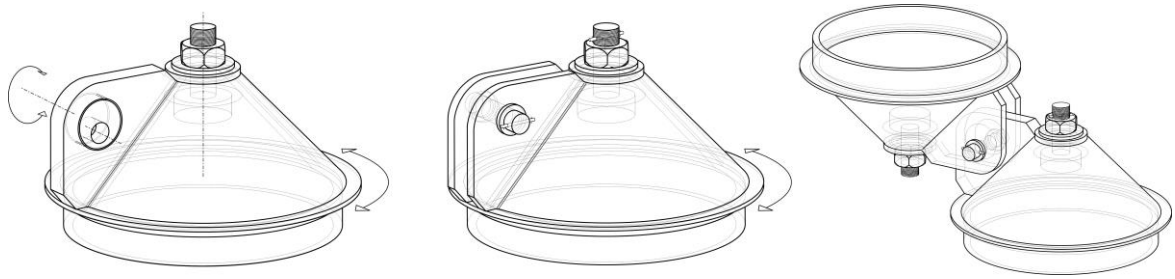


Figure 1. Views of exemplary shapes of conical bodies together with their mutual connection forming the basic type of the proposed structural node.

1. Introduction

There are numerous structural systems of foundation applied in the practice for a long time, which are permanently modified and gradually improved. They may be subdivided generally into two main groups of the shallow and the deep foundation systems. Systems of the shallow foundations are mostly applied when the passive earth pressure beneath the bottom surface of the foundation is also within the range of load carrying ability of the ground and usually these systems are not complex due to simplicity of their structural forms. Complexity of the deep foundations makes them often difficult to construct that is why

Copyright © 2023 by Janusz RĘBIELAK. Published in the Proceedings of the IASS Annual Symposium 2023 with permission.

they are the expensive technical solutions. In buildings erected in seismic areas, it is recommended to horizontally separate the load-bearing structures of the building from the ground, in order to enable appropriate horizontal displacements of the buildings [1 - 11]. The structural systems of support nodes presented in this paper are the results of the author's efforts to enlarge the range of possible applications of the system of composite foundation invented by him some time ago [12,13].

2. Structural concept of the system of composite foundation

The essential point of this system is to arrange the most important support nodes uniformly along the neutral axes of the main beams (1) placed on common base slab (BS), see Figure 2 and Figure 3. In a narrow space between two main beams, an intermediate system of straight structural members is arranged, while only its nodes situated along the neutral axis are connected to the main bodies of the horizontal beams. An outer concentrated force (F) is applied to an upper node (A) of a short vertical member put in vertical guides and having possibility to move only along the vertical direction. An intermediate system is built of two subsystems, the first one is called a cable system, see Figure 2(a) and Figure 1(d), while the second one is called an arch system, see Figure 2(b) and Figure 2(e). When these both subsystems are symmetrical arranged towards the neutral axes of the beams and they are combined together, see Figure 2(c) and Figure 2(f), then in the external central nodes act only vertical components of reactions, which in this case are directed down.

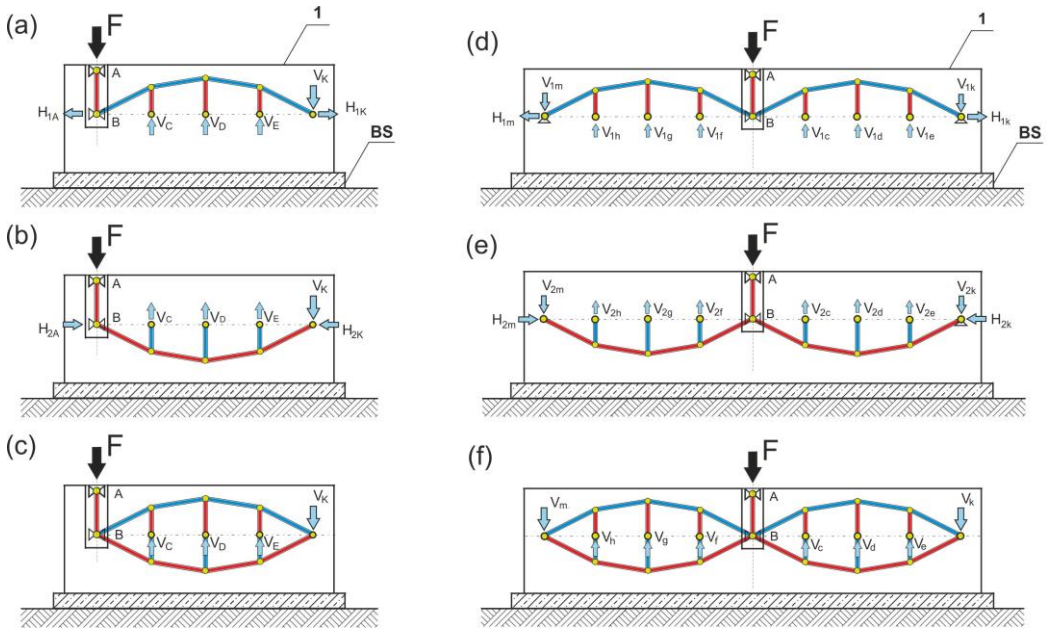


Figure 2. Structural analytic schemes of system of composite foundation

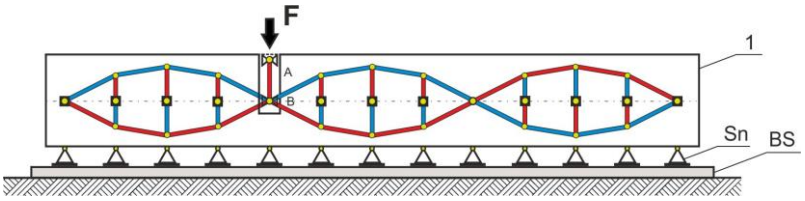


Figure 3. General scheme of an exemplary form of the more complex shape of system of the composite foundation with the way of arrangement of the proposed support nodes.

A lenticular set of two subtypes of the intermediate system, see Figure 2(c), is considered as a modular unit of this structural foundation system and it can be duplicated, see Figure 2(f). Number of its replications is optional, see Figure 3, what means that it can be replicated endlessly along the horizontal direction what further implies, that surface of this type of foundation structure can be theoretically unlimited. The application of the system of composite foundation makes possible to construct the very heavily loaded buildings, including the tall buildings, on the ground of very small load carrying ability on the main condition, that the available free terrain around the building is large enough. Due to the specific arrangement of components into the inner space the system of composite foundation is able to absorb a part of energy induced in the building structure by the earthquake. This ability can be enhanced e.g. by suitable application of computer controlled hydraulic actuators or for instance by application of system of appropriately designed support nodes.

3. Basic structural assumptions of the foundation supporting node

The structure of a building located in a seismically active area should be horizontally separated from the ground, and the foundation system under the influence of seismic loads should allow safe movement of the building structure in the horizontal and vertical directions, of course within the appropriate assumed ranges of such displacements. Currently, there are many types of construction solutions for foundations that make it possible to meet the above-mentioned requirements.

In all the presented proposals of shaping the new types of structures of such nodes, a structural configuration of a connector is used, which consists of a single vertical rib (R1), Figure 4(a), and a set of two vertical ribs (R2), Figure 4(b), which are connected together as it is shown in Figure 4(c). Inside the matter of a single rib, there is a relatively large cylindrical hole (2) inside which a circular roller (3) is placed in a tight manner and is freely rotatable around the horizontal axis X1. Moreover in the matter of this circular roller there is a much smaller cylindrical hole (4) intended for location a cylindrical pin (5), having the freedom of full rotation around the X2 axis parallel to the X1 axis, and applied to articulate connection of a single vertical rib with a set of two vertical ribs, also by help of similar holes (6), which are of the same diameter and present in each rib in the set of the two vertical ribs (R2) [14].

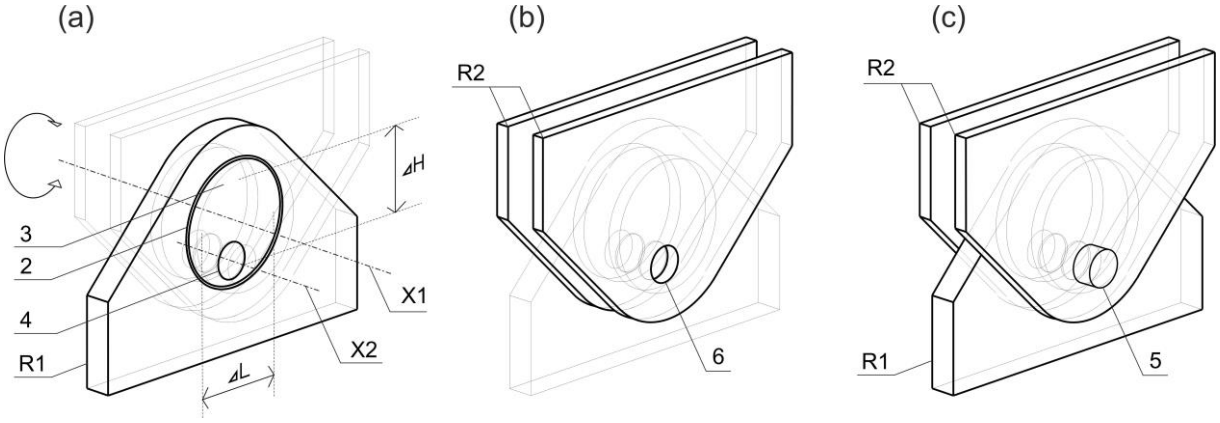


Figure 4. Structural configuration of basic component parts of a connector applied in all types of the proposed structures of the foundation support nodes.

All components of the basic structural set should be quite closely matched to each other, and their mutual contact surfaces should be covered with layers of e.g. Teflon or separated from each other with Kevlar spacers to facilitate their movements. The modular range of possible horizontal (ΔL) and vertical displacements (ΔH) is conditioned by the mutual relations of the geometric dimensions of the circular roller (3) and the distance between the axes X1 and Z2, however total range of the horizontal

displacement (ΔL) of the foundation can be enlarged by combining this basic structural configuration with suitably formed main bodies of the foundation node.

4. Support node with a conical form of the main body

From numerous observations of the effects of earthquakes follows that the greatest damages are usually caused by the action of horizontal seismic waves. Therefore, the structures of foundations called anti-seismic should enable the buildings to have the greatest value of safe displacements in the horizontal direction. The conical form and structure of the main body of the first of the proposed systems of support nodes, shown in Figure 5, enables such type of the displacements.

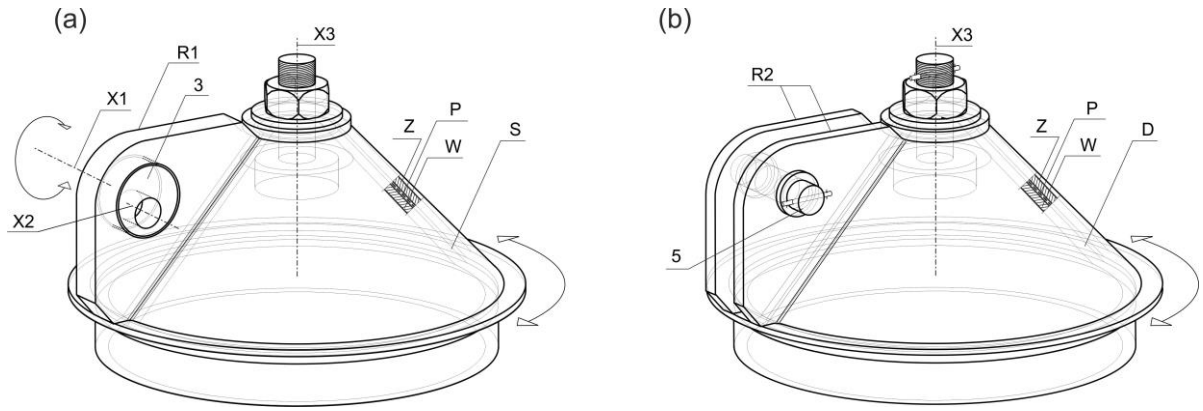


Figure 5. Conical form of main body of the support node with, (a) a single rib, (b) a set of two ribs.

In this case, an external conical structure (Z) is mounted on the internal conical structure (W), and between them there is, for example, a Teflon conical spacer (P) facilitating full rotation of the both main shells around the vertical axis X3. The outer conical structure (Z) is rigidly connected to a single rib (R1) or to a set of two ribs (R2). The main body with single rib (S) is connected to the main body with two rib set (D) by a cylindrical pin (5) as shown in Figure 6.

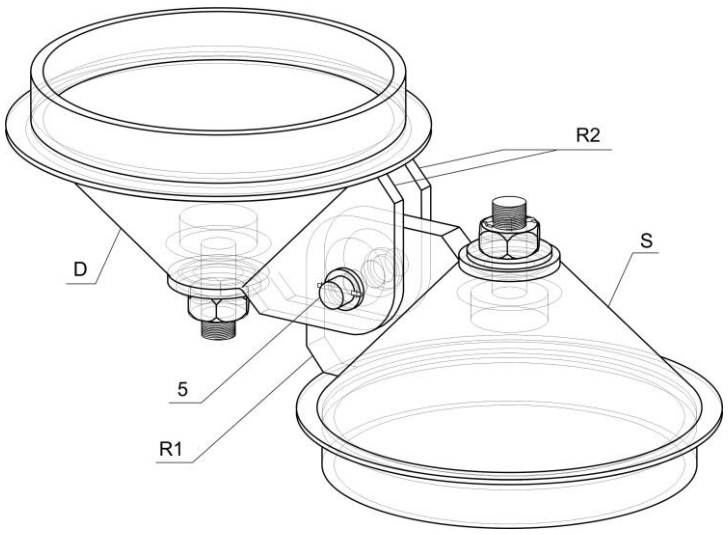


Figure 6. General view of the whole structure of the support node with conical forms of the main bodies.

In the configuration shown in Figure 6, Figure 7 and in Figure 8, the main body with a single rib (S) is fixed in the lower building structure (L) and the main body with a set of two ribs (D) is fixed in the upper building structure (U). The opposite configuration is equally valid, i.e. when the main body with a single rib (S) is fixed to the upper building structure (U) located above, and the main body with a set of two ribs (D) is fixed in the lower building structure (L) located below.

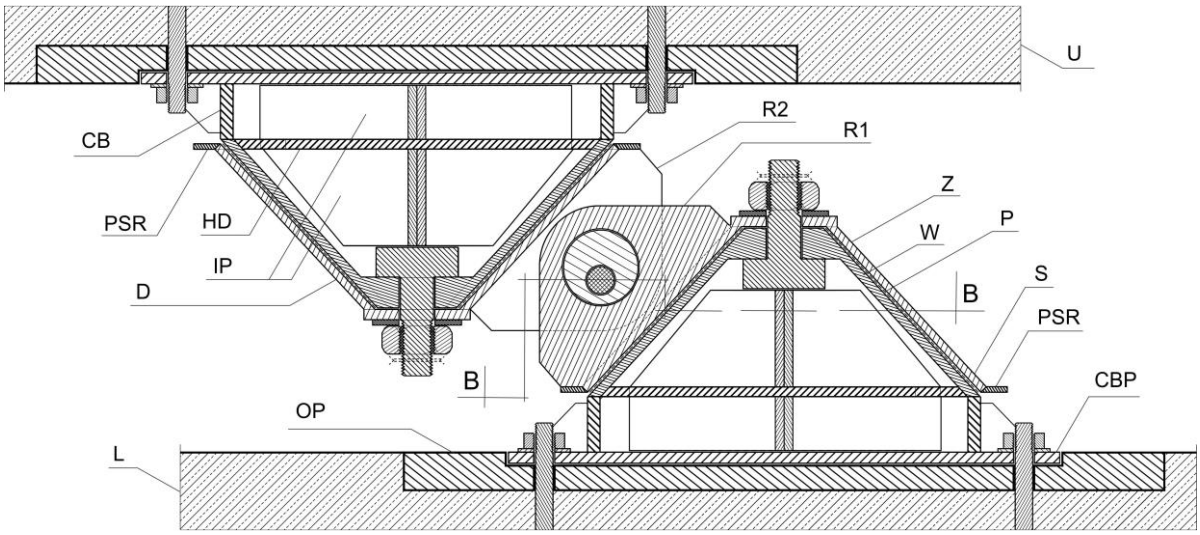


Figure 7. Vertical cross-section A-A of the whole support node with conical forms of the main bodies.

If the geometrical dimensions of the support node are significant, inside each body should be a horizontal disk (HD) and outside a peripheral stabilization ring (PSR), which is permanently connected to the lower edge of the external conical structure (Z). In the inner space there are located internal partitions (IP), see Figure 7, Figure 8, evenly spaced inside the conical structure, whose ends (IPE), see Figure 8(a), are permanently connected to the cylindrical base (CB), what base is also permanently connected to the metal, circular base plate (CBP), which is placed in a circular cavity of a metal outer plate (OP), while the last one can be of any shape. External plates (CBP) and (OP) are also permanently attached to the lower structure (L) or to the above-ground structure of the facility (U).

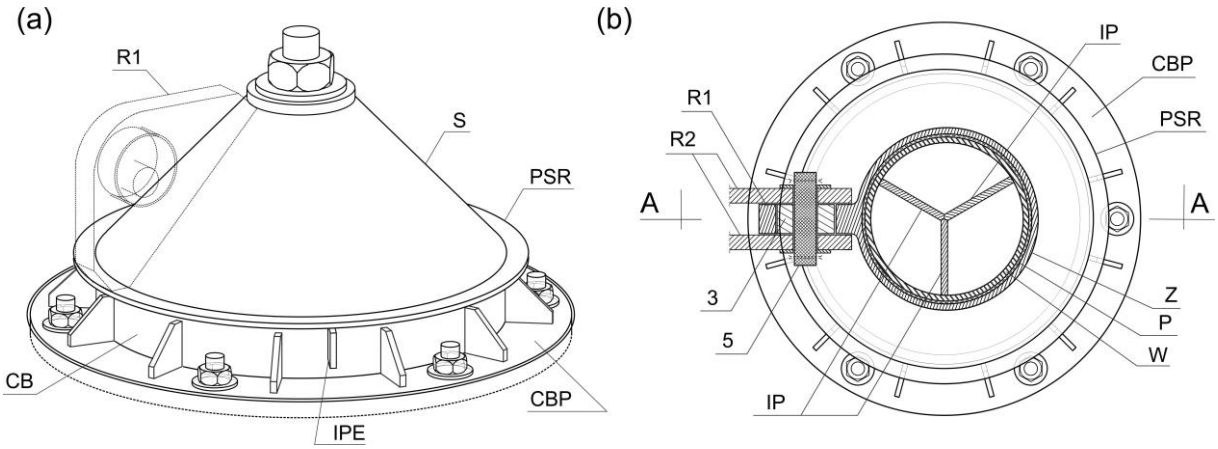


Figure 8. Support node with conical forms of the main bodies, (a) view of selected type the main body, (b) the horizontal offset cross-section B-B of the lower main body of the foundation support node structure.

One of the types of connectors joining these boards are fastening bolts located between circumferential ribs, and the fastening bolts are rigidly anchored in the structure of the lower object (L) or rigidly connected to the structure of the upper object (U). It is also possible to directly anchor cylindrical bases in the solid matters of the building structures located above or below the structure of the support node.

4.1. Example of possible applications

The main task of the structure of the support nodes made of conical bodies is to effectively suppress vibration energy caused by dynamic load applied from any direction through controlled movement of the lower and upper parts of the object connected with each other by a set of such nodes. If the values of dynamic loads are very large, then these displacements, mainly in the horizontal plane, consisting in the mutual rotation of conical solids relative to the vertical axes of the X3 type, see Figure 9, can sometimes be very fast.

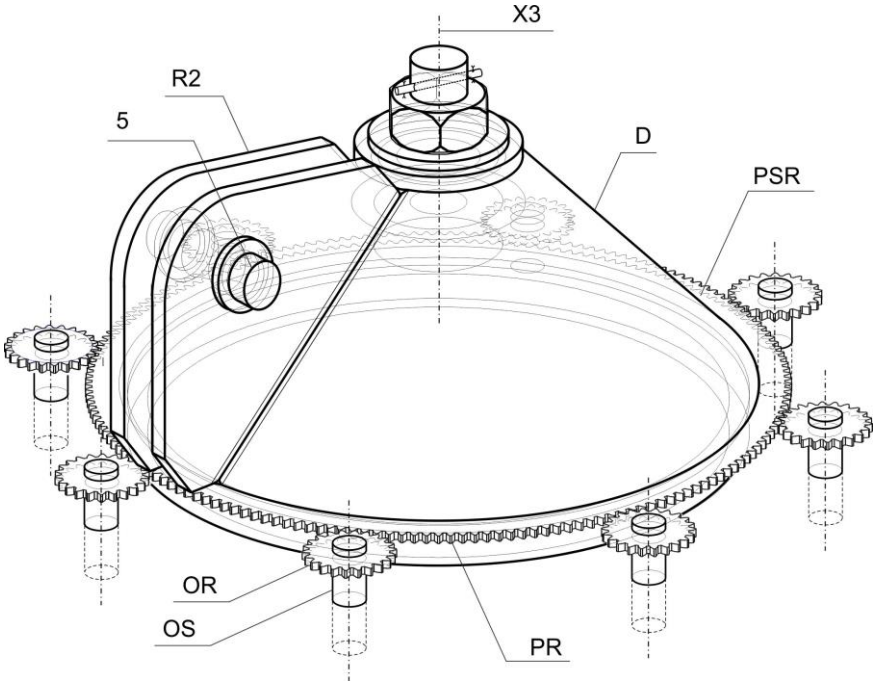


Figure 9. View of the conical body of the support node with a peripheral gear wheel and a set of external gears.

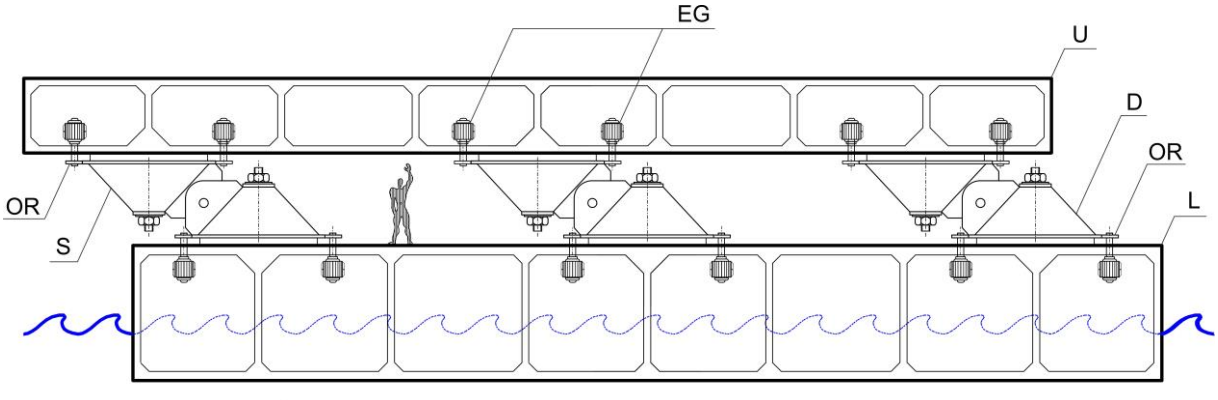


Figure 10. Scheme of a vertical cross-section of a dynamically loaded object built in the form of a floating platform consisting of the upper and lower parts of the object connected with each other by a system of the conical support nodes with the peripheral gears.

This may be hazardous, especially if the object has significant geometric dimensions. In this case, the geometrical dimensions of the support nodes and the conical solids constituting them can also be large. In order to make the vibration energy damping processes more effective, it will be beneficial to transfer the rotational energy of each of the conical bodies to the largest possible number of devices that can absorb this energy in a controlled and safely manner. This can be achieved, for example, by making a peripheral stabilization ring (PSR) in the form of a toothed wheel cooperating with external racks (OR) suitably located along the circumference of this wheel, see Figure 9. Each of these racks (OR) is mounted on an outer sleeve (OS), which in turn can be connected e.g. to friction discs, and these by controlled pressure force to similar discs mounted in the lower (L) and upper (U) structure of the object, what will enable more efficient dissipation of the vibration energy caused by the dynamic load [14].

A set of such support nodes can be a very efficient horizontal dilation of the upper part of the structure from its lower part. If the object constructed in this way is made as a floating horizontal platform, see Figure 10, then under the influence of the sea waves energy its lower (L) and upper (U) parts will move mutually. In this case, the receivers of the rotation energy of the conical bodies can be electric current generators (EG), then the electric energy generated in this way can be stored e.g. in battery packs located in the internal spaces of the lower (L) and upper (U) parts of the platform structure or this energy can be transmitted outside by special electric cables. This will enable emission-free production of ecologically clean electricity. The sizes of a single platform can vary and the number of platforms can be very large. The single platform itself can be anchored in the coastal zone or in the open sea, it can also be able to change its position on the surface of a lake, a sea or an ocean.

5. Support node with a cylindrical form of the main bodies

In the next presented type of the structural system of the support node the way of transmitting forces between the main bodies remains the same, it means they are transmitted from the single rib (R1) to the set of two ribs (R2) by means of horizontally located cylindrical pin (5), but now the upper part of the main body with a single rib is cylindrical (C1), Figure 11, likewise the upper part of the cylindrical main body with a set of two ribs (C2), and they are mounted on their lower parts in a way that allows the upper parts to rotate around the vertical axis X3, which is also the axis of the main vertical screw.

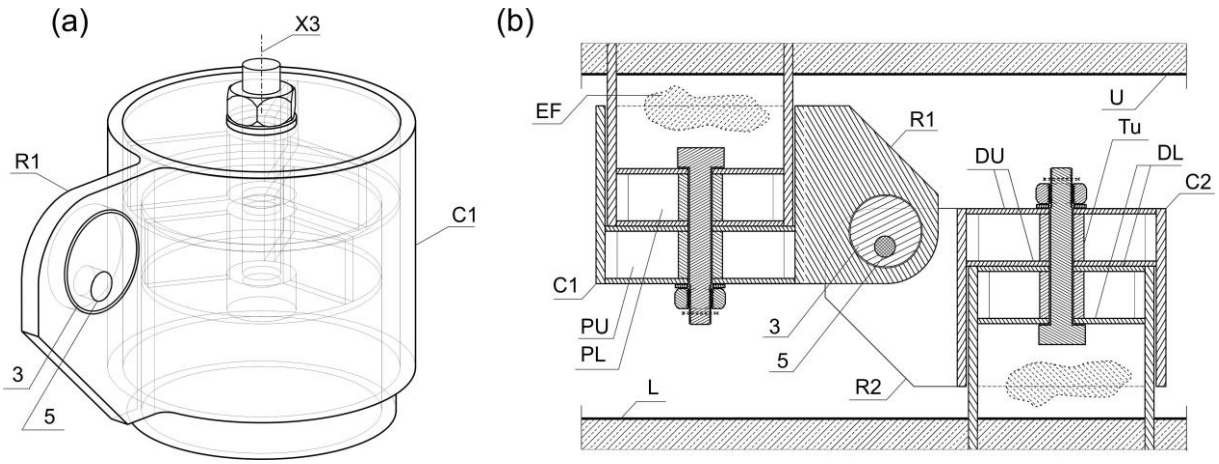


Figure 11. Support node with cylindrical forms of the main bodies, (a) general view of the main body with single rib, (b) vertical cross-section section of the support node with cylindrical forms of the main bodies.

Each of these main parts has its upper zone, and so the upper part of the cylindrical main body with a single rib (C1) has two circular horizontal discs (DU) vertically spaced apart by the value of the height of the stiffening ribs (PU), located between the vertical wall of the upper cylindrical component with

the single rib main body (C1), and the central sleeve (Tu). All these elements of the upper part are permanently connected to each other. The lower part of each main body is in this example rigidly fixed in the lower part of the object (L) or in the upper structure of the object (U). The upper zone of a single body is built in a similar way, i.e. it has two circular horizontal discs (DL) of a suitably smaller diameter than the horizontal discs (DU) and, as previously, are they are vertically spaced apart by the height of the stiffening ribs of the lower zone (PL) located between the vertical cylinder wall of the lower part of the cylindrical main body and the central sleeve (Tu). Empty spaces of lower parts of each main body of the foundation node can be also initially fulfilled e.g. by application of a cement mortar (EF).

6. Support node with a modular form of the main body

In the third proposed type of the structural system, the same form of a single vertical flat rib (R1) is used, see Figure 4(a), but now it is supplemented with two rectangular ribs (RR) located perpendicularly to its middle plane and permanently connected to it on both at its ends, Figure 12(a), the mirror image of which relative to its base and rotated by a right angle, then supplemented by a central horizontal plate

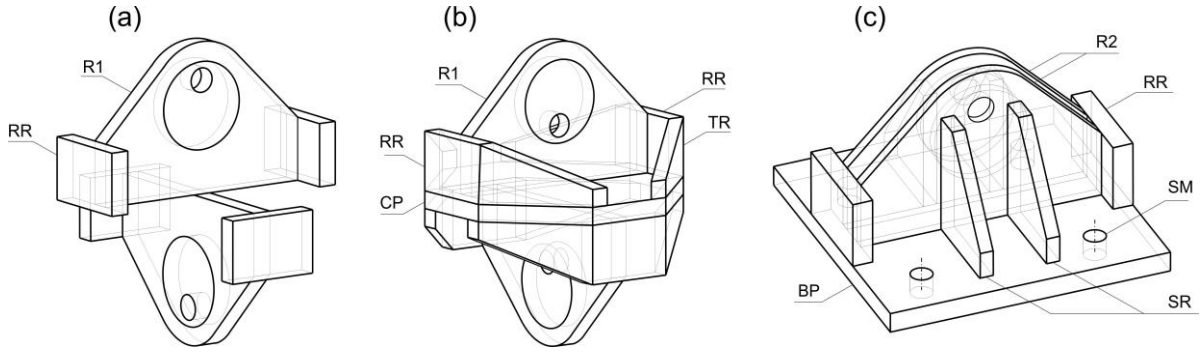


Figure 12. Component parts of third type of the support node, (a) basic modular configuration, (b) view of the central part, (c) shape of the border module of the support node.

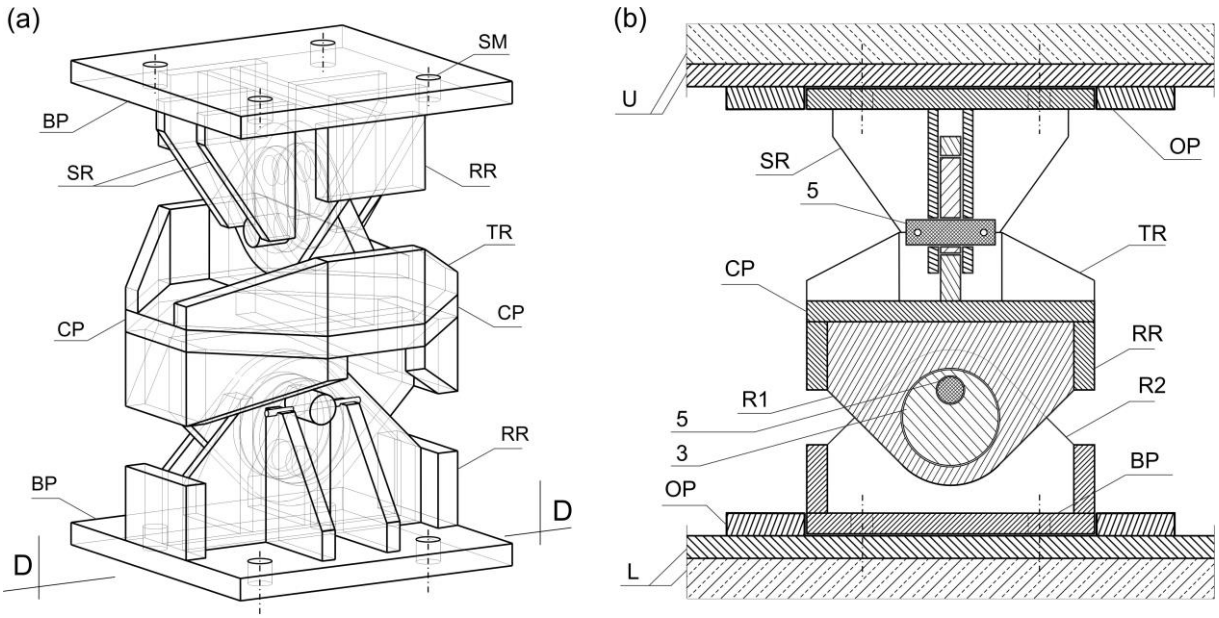


Figure 13. Modular support node, (a) general view, (b) vertical cross-section D-D.

(CP) and also suitably arranged trapezoidal ribs (TR), what together constitutes the structural module of the central part, see Figure 12(b), of this variant of the support node.

A set of two vertical ribs (R2) supplemented on each of its side sides with stabilizing ribs (SR) and front rectangular ribs (RR) located on a common base plate (BP) being with it and mutually between rigidly connected, form a border module, Figure 12(c), for the structure of such type of the support node, which is connected to the lower object structure (L) or to the upper structure of the object (U) by means of several anchor bolts placed in the screw holes (SM) with vertical axes, see Figure 13.

All the main components of this third and as well as the two previously presented types of the support node structure are made of metal, preferably of high-strength and corrosion-resistant steel. The range of vertical displacements possible to obtain with the use of the last presented form of the node is much larger than with the application of the two previously presented types of the support node structure, however range of horizontal displacements is relatively small. In addition, for the last described type of structural system, the mutual location of successive nodes need not be so precisely coordinated with each other, as it is required for nodes having structural systems presented in Chapter 4 and Chapter 5.

7. Conclusions

The presented structural systems of the support nodes are the results of the last stage of research undertaken in the past by the author through the development of system of the composite foundation. These types of nodes should be relatively close to each other and due to the recommended large number, they can be, e.g. horizontal dilatation of the building from the ground. Each of the developed variants of the structure of such the node has the ability to move within a certain range in the horizontal direction and at the same time in the vertical direction, which allows for the effective absorption of all or a significant part of the energy of vibrations, which in turn enables the safe operation of the building structure during an earthquake. The proposed forms of support nodes can be applied for almost all types of foundations for buildings located in seismically active areas. Initial studies of the forms of these nodes were carried out thanks to the analysis of their numerical models defined in the Formian programming language [15]. Important tasks in the next stages of research will include, among others: determining the optimal dimensions and geometric proportions of the movable components of the structural system of each of the proposed types of support nodes.

It seems that the support node with the conical form of the main bodies has the most advantageous structural, technological and utility features. The construction of the articulated joint placed along the inclined line, i.e. along the generatrix of the cone, makes the conical shape of the basic structure the most effective kind of this type of technical solution, since dynamic loads applied from each direction will cause rotation of the lower and upper part of the whole building structure about the vertical axes X3. The support node made of cylindrical bodies is similarly effective, the operational reliability of which is ensured mainly by the possibility of efficient rotation of the circular roller (3) relative to the horizontal axis X1. Conical or cylindrical joint bodies must be oriented in the same way between the lower part of the structure (L) and the upper part of the structure (U) in the entire area of the integral support field. On the other hand, the plate, metal bodies of the modular node can be freely oriented between the lower part of the structure (L) and the upper part of the object structure (U) in the area of the integral support field, but only in relation to the orthogonal axis system of such a support field.

The support nodes, especially those with a conical shape of the main bodies, can be applied in structures of floating platforms of various sizes designed as a kind of artificial islands, and in connections with appropriate power generators, the proposed support nodes should contribute to get of the emission-free electric energy. In addition, the upper surfaces of this type of platforms can be adapted to the cultivation of appropriate plant species. Moreover they can form the basis for photovoltaic panels or windmills, thus increasing the scope of the emission-free electricity production.

All the proposed types of foundation support nodes must be subjected to thorough and comprehensive static, dynamic and strength analyses, including tests of objects on a natural scale, in order to assess their practical suitability for the proposed purposes.

References

[1] A. Charleson, *Seismic Design for Architects. Outwitting the Quake*, Elsevier Ltd, 2008.

[2] A. S. Elnashai and L. Di Sarno, *Fundamentals of Earthquake Engineering*, John Wiley & Sons, Ltd, 2008.

[3] K. Biernatowski, *Foundation Engineering*, State Scientific Publishing House, 1984. (in Polish)

[4] D.P. Coduto, *Foundation Design. Principles and Practices*, Prentice Hall, 2001.

[5] M.J. Tomlinson and J. Woodward, *Pile Design and Construction Practice*, Taylor & Francis, 2008.

[6] R. Chudley and R. Greeno, *Building construction handbook*, Routledge, Taylor & Francis Group, 2014.

[7] R.O. Hamburger, "Earthquakes and Seismic Design," in *Facts for Steel Buildings*, 2009, American Institute of Steel Construction, USA.

[8] Z. Wiłun, *Outline of Geotechnology*, Publishers of Traffic and Communication, 1987. (in Polish)

[9] J.A. Ledwoń, *Construction in Mining Areas*, Arkady, 1983. (in Polish)

[10] K. Matso, "Lessons from Kobe," *Civil Engineering*, vol. 4, 42-47, 1995.

[11] R. Chudley and R. Greeno, *Building construction handbook*, 2014, Routledge, Taylor & Francis Group.

[12] J. Rębielak, *Systemowy fundament zespolony (Composite foundation system – in Polish)*, Patent No 221971, Patent Office of the Republic of Poland, 2016, Patent Application No P.394745, 2011.

[13] J. Rębielak, "System of combined foundation for tall buildings," *Journal of Civil Engineering and Architecture*, vol. 6, pp. 1627-1634, 2012.

[14] J. Rębielak, *Węzeł podporowy obiektu obciążonego dynamicznie (Support node of a dynamically loaded object – in Polish)*, Patent Office of the Republic of Poland, Patent application No P.444755, 2023.

[15] H. Nooshin and P. Disney, "Formex configuration processing," *International Journal of Space Structures*, vol. 17, 1-51, 2002.

Proceedings of the IASS Annual Symposium 2023
Integration of Design and Fabrication
10–14 July 2023, Melbourne, Australia
Y.M. Xie, J. Burry, T.U. Lee and J. Ma (eds.)

Sydney football stadium redevelopment – An efficient design, manufacturing and on-site assembly approach to a complex form-found roof shell structure

Michael CHERNYAVSKY*, Hudson KESTEL[a]

[a,*] Aurecon Australasia
michael.chernyavsky@aurecongroup.com

Abstract

The Sydney Football Stadium (SFS) is an $828m AUD state-of-the-art stadium near Sydney's CBD. This paper focuses on the collaborative approach to design, fabrication and erection that enabled the complex 2,000 tonne synclastic diagrid shell roof to be successfully brought to life in a fast-tracked design and construction programme whilst overcoming supply chain and lockdown challenges associated with COVID-19. The unique 25,000m^2 roof is constructed with inner arched trusses that span approximately 140m and 90m in length, a 680m long perimeter tension ring and a diagrid shell structure that includes arched sections spanning between the inner truss chord and tension ring. This structural behaviour and form-found geometry allow for an efficient and lightweight design for the roof. Prefabrication and modular construction techniques were adopted to limit working at heights and improve the erection efficiency on site, it enabled over 85% of steelwork installation to be undertaken at ground level. The roof consists of 5,000 individual pieces of steel, each with an associated pre-set length and geometry which required precise coordination, fabrication and planning through each stage of design and construction, a novel digital workflow was developed to enable the seamless translation of data between each sub-consultant. The connections of the roof are also some of the most intricate in Australia, the adoption of bi-directional digital workflows between structural engineers and steel detailers were essential to save time and improve quality assurance.

Keywords: case study, modular, preassembled, DfMA, sustainability, stadia, steel shells, steel diagrid, digital engineering, computational design

1. Project background and vision

Sydney Football Stadium (SFS), also known as Allianz Stadium is a state-of-the-art stadium, near Sydney's CBD. Designed to create a vibrant atmosphere with steep seating to bring 42,500 fans closer to the action, the world-class, multi-use rectangular stadium opened in August 2022 and has hosted football, rugby league, rugby union matches and concerts, as well as community and cultural events. The new stadium is a key component of the NSW Government's stadia strategy to promote a strong cultural and sporting sector by delivering a world-class venue within a parkland precinct for the state and Australia as a whole.

The previous Allianz Stadium on the same site was nearing the end of its economic and functional life and would not meet future safety and access requirements. Bringing the new $828 AUD million stadia to life were project partners Aurecon, as structural and civil engineers, John Holland Group, Cox Architecture and Schlaich Bergermann Partner (SBP), for the New South Wales (NSW) Government. The vision was to blend engineering and art through a 'sculpture', featuring a sweeping roof that covers 100 per cent of seats and a colosseum-like seating bowl that creates an electrifying atmosphere.
The stadium has been designed to achieve a US Green Building Council LEED gold rating. It features design for disassembly principles, a strong connection to the indigenous people of the land and involved

Copyright © 2023 by Michael CHERNYAVSKY and Hudson KESTEL. Published in the Proceedings of the IASS Annual Symposium 2023 with permission.

the recycling of over 85% of construction and demolition materials from the former Sydney Football Stadium to construct the new stadium.

The new stadium for Sydney allows Australia to continue offering fans some of the most memorable moments in Australian sports history. It is a stadium that strengthens Sydney as a destination for major sporting and entertainment events while enhancing the surrounding precinct with public places and spaces year-round. It has been delivered on time and on budget by the more than 7,000 personnel who contributed to the project despite disruptions to procurement and construction due to COVID-19, a proud achievement for the entire design and construction team.



Figure 1. Left: Aerial photo of SFS including Sydney context. Right: Photo from the North-Eastern corner.

2. Structural philosophy

Various stadia across Australia and the world have inspired the chosen design features in the redevelopment of SFS. The structural philosophy of this roof is based on the roof-ring principle. One of the first applications of this principle in large sporting arenas was in the redevelopment of the Stuttgart – Mercedes Benz Arena which paved the way for a new generation of stadia roof [2]. Relatedly, the roof of SFS utilises a tension ring and compression arch as an efficient global load path for the structure. The SFS roof is supported by four corner structures termed 'derricks' which are braced Circular Hollow Sections (CHS) that cantilever to support the arched trusses, this element was inspired from Suncorp Stadium in Brisbane [3]. The adoption of a diagrid shell structure contributes to the visual identify of the SFS roof, provides lateral stability and a secondary load path for the roof. Diagrid shell structures are prevalent in sports arenas globally and locally such as Adelaide Oval Western Grandstand redevelopment [4].

3. Adopted roof

The 25,000m^2 SFS roof transfers loads via axial forces with the use of arches and tensile mechanisms. The diagrid is supported on the inner chord via arched trusses that span 140m and 90m in length between the four corner 'derricks'. The trusses are arched in plan and elevation to efficiently transfer vertical and lateral loading. A 680m long perimeter tension ring is used to provide restraint to the diagrid, utilising the axial stiffness of the ring to prevent the diagrid from moving outwards. The diagrid shell adopts radial arched sections spanning between the inner compression arched truss and tension ring, with diagonal CHS members providing stability and support. The derrick's are braced CHS members which transfer approximately 50% of the roof vertical loads and 100% of the lateral loads to the superstructure.

Structural shells require stiff and, in this case, continuous edge elements in tension and compression. For SFS the outer boundary element is continuous and curved against the thrust forces from gravitational loads of the diagrid shell constituting a Tension Ring. The inner boundary element is curved in the same direction as the thrust constituting a Compression Arched Truss, see *Figure 2*. The primary structure of

the roof utilised mild steel CHS and Rectangular Hollow Sections (RHS). These hollow steel sections offer high strength-to-weight ratios and versatility, enabling Aurecon, SBP and Cox Architecture to devise an innovative and visually striking roof configuration that not only met the demands of a modern stadium design but also ensured long-lasting performance in an adverse coastal environment.

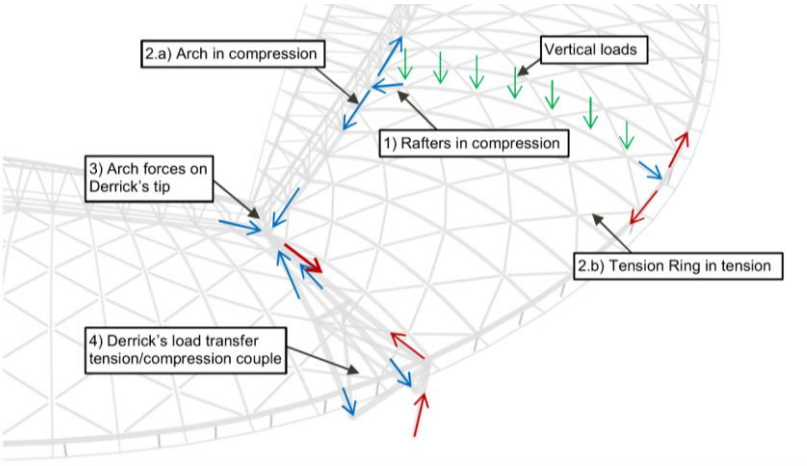


Figure 2. Structural load path of the Sydney Football Stadium Roof.

The extensive use of faceted steel sections for the 'arched' trusses and 'elliptical' tension ring created an efficient structural form compared to the traditional stadia roof philosophy such as deep flexural trusses. This structural behaviour allowed for an efficient and lightweight design for the adopted roof and the facetted geometry simplified fabrication without compromising the visual perception of curved elegant elements.

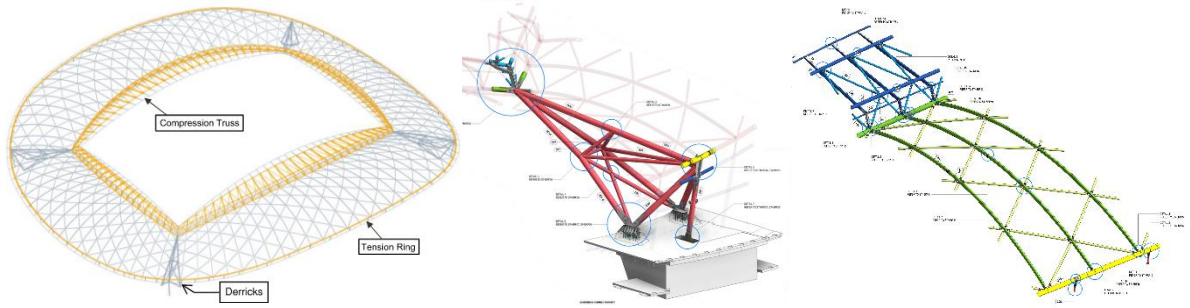


Figure 3. Roof Structure: (a) structure overview, (b) derricks, (c) typical diagrid segment.

4. Form finding

In the world of architecture and structural engineering, form-finding is an important methodology to improve efficiency, dematerialisation and unlock complex and organic shapes. Historical figures like Catalan architect Antoni Gaudí paved the way for modern form-finding. Gaudí's designs, which employ organic and biomimetic principles, demonstrate both visual appeal and structural efficiency. To study these forms, Gaudí often employed the use of hanging chain models, by suspending chains from points that represented the supports and applying weights to mimic loads, Gaudí could visualise the natural equilibrium shape for particular structures. He would then photograph the models, invert the images, and use them as a basis for his design [1]. Gaudi's form-finding techniques date back to the 1880s, but the principles he developed and demonstrated on projects such as Casa Vicens and Sagrada Familia form the basis of the form-finding implemented for the roof of Sydney Football Stadium.

The roof of Sydney Football Stadium adopted multiple methods of form-finding in the early geometry definition of elements and the overall structure. The *Stiffness Matrix form-finding* technique was one of the primary methods used and involved the following steps:

1. Define the initial geometry, including the position of nodes, the connectivity between nodes (any translational, rotation releases or offsets), and the structural elements such as beams or cables, for Sydney Football Stadium this was defined using Rhino and Grasshopper (a parametric modelling software) which enabled rapid geometry and design iterations.
2. Assign material properties, Elastic modulus and the cross-sectional areas of each element.
3. Define loads and boundary conditions which describe the constraints on the structure, for Sydney Football Stadium there was a maximum height limitation to respect the heritage Sydney Cricket Ground which is adjacent to the stadium as one example.
4. Develop the form-finding criteria, for Sydney Football Stadium, the six criteria were:
    I. Minimise bending actions to improve the efficiency of members
    II. Balance the forces of the trusses to align with the orientation of the derricks,
    III. Minimise the mass of the structure
    IV. Ensure the structure is stable and the global buckling behaviour is sufficient
    V. Create a structure with 2 axes of Symmetry
    VI. Minimise dead load displacements to span/500
5. Assemble the global stiffness matrix, in the case of Sydney Football Stadium this was undertaken using Strand7 Finite Element Analysis (Aurecon) and Oasys GSA (SBP).
6. Solve for nodal displacements, i.e. changes in the nodal coordinates after the loads are applied and the analysis is undertaken. This step results in the new positions of the nodes, which define the equilibrium shape of the structure.
7. Once the equilibrium shape was found, analyse the structural performance (stresses, deflections, and stability) and optimise the design, if necessary, by adjusting the geometry, member sizes, or material properties.
8. Iterate, if the optimised structure did not meet the desired objectives, then the initial geometry, or boundary conditions were adjusted, and steps 5 to 7 were repeated until the desired accuracy was achieved.

The form finding undertaken allowed for the efficient and accurate determination of equilibrium shapes under various load conditions, it resulted in a roof that is approximately 40% lighter than traditional long-span flexural systems, reducing cost and improving sustainability through dematerialisation.

5. Structural analysis and design

Due to the geometrical and loading complexity of the roof, the analysis and design required advanced engineering assessments and various sensitivity studies to ensure the roof was not only structural adequate but that sufficient fabrication and erection tolerances were allowed for. Due to the extensive number of load cases associated with wind tunnel testing and the fast-tracked procurement and erection program, a novel digital workflow was adopted. The analysis and design approach adopted for the design of the SFS roof is detailed below.

5.1 Global analysis

The structural analysis was partially completed in Strand 7 with a standalone roof model that had spring stiffness boundary constraints to represent the abutment cores and bored pile system supporting the roof. This more time-efficient model was used to inform the initial member selections and was validated with

a more detailed global analysis model in the detailed design which captured both the super and sub-structure behaviour of the stadium. Due to the 'arching' structural behaviour, the structure was sensitive to non-linear geometric analyses and softer boundary conditions which results in the compression arch flattening which induced higher axial loads. The design considered both upper-bound and lower-bound pile spring and concrete superstructure stiffnesses based on the available geological information. To optimise the applied loading, wind tunnel testing was conducted to provide more precise wind pressures and distributions. The wind tunnel test results were translated to the global and roof standalone models.

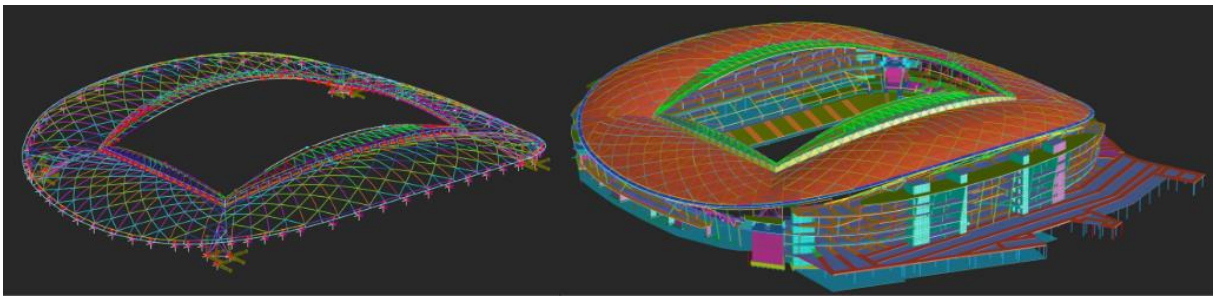


Figure 4. Analysis Models: (a) roof standalone model, (b) global model.

5.2 Digital workflow

The Stadium was designed and constructed within a two-and-a-half (2.5) year period. To meet this fast-tracked programme Aurecon developed a novel digital workflow that enabled exceptional collaboration, coordination and traceability on a level far beyond Federated Building Information Models. This digital workflow involved a 'single source of truth' database and computational design to produce models with 'smart' attributes and all relevant metadata in each of the preferred modelling software used by engineers, consultants, architects, builders, fabricators and shop detailers, this ensured rapid coordination and high quality assurance due to the common database, refer *Figure 5* below.

To ensure the full benefits of the workflow were realised, a unique, consistent and meaningful node and member numbering system was implemented for the traceability between all software (Rhino, Strand7, GSA, Revit, Tekla etc). Key building information attributes were also 'baked' into elements of every model ranging from the structural analysis, architectural and steel shop detailers model. Examples include the radii for the roof rafters or the translation from the fabrication geometry to the final installed geometry (which varied up to 300mm). This is estimated to have saved the project up to eight weeks as models could be updated and coordinated in a matter of hours, not days/weeks and helped automate the design, shop drawing review and verification process.

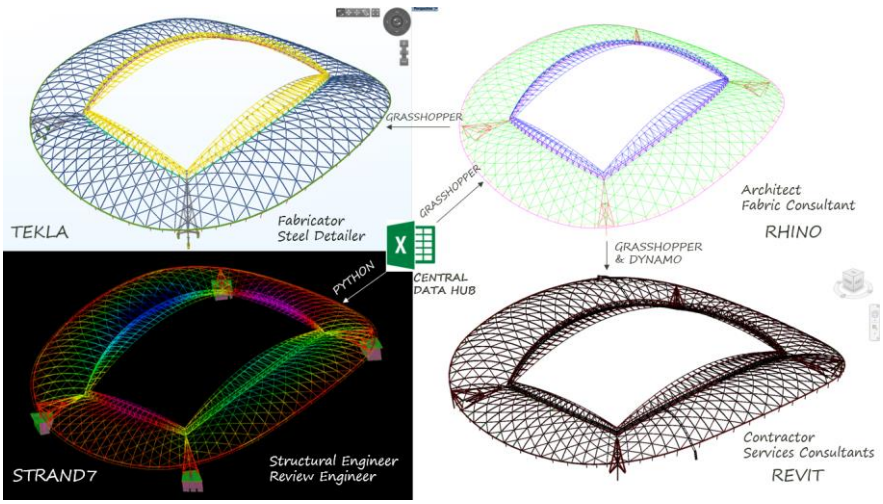


Figure 5. Digital workflow showing model interoperability.

5.3 Member design

The roof model consisted of approx. 5,000 beam elements and over 600 load cases. 10 data points per load case for each beam which were required to undertake the member design checks. Therefore approximately 30 million data points were required for each design iteration. In addition, the global analysis model required over 24 hours for analysis to be completed. The member design had two workflows adopted in the design process, the first of which was completed through excel via extracting the design actions and member properties from Strand 7. Data cleaning was conducted through queries in Excel to process the Strand 7 data into a suitable format for input into the VBA design scripts which were used to check each member for all load cases. The output summarised member utilisations, governing load case and output file which could be imported into Strand 7 to show design utilisations visually.

The second workflow used Python scripts, which were created with a variety of additional toolsets (pandas, jupyter, etc). The scripts were created to complete each task in the design process (data cleaning, member design, output files etc) independently during the debugging stage. This workflow had a significantly faster processing speed and was used in conjunction with the first workflow. Processing the two independent workflows allowed for internal validation of the design results.

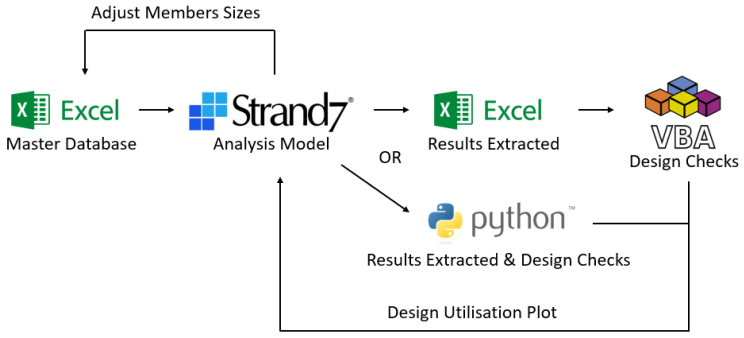


Figure 6. Member design workflow.

5.4 Connections

Due to the geometrical complexities of the roof, the steel connections are some of the most complex in Australian stadia. Large tubular, multi-noded connections exist throughout the roof package that required complex design and detailing. Aurecon and the DBM Vircon developed a bi-directional model workflow, enabling the design and shop detailing to work in parallel. The shop detailer worked with the structural engineers to help form connections suitable for the fabricator while incorporating the structural intent at an early stage. The shop detailer's model was then translated into analysis and design software to ensure design integrity.

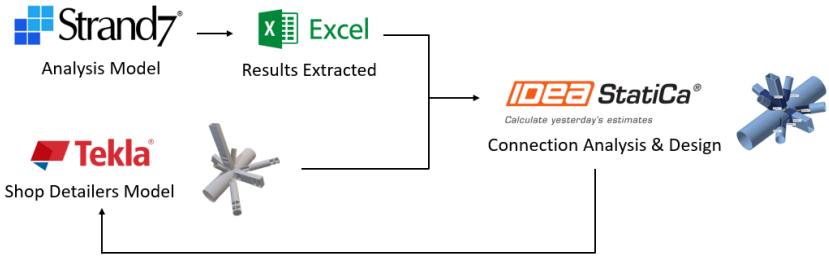


Figure 7. Typical connection design workflow.

The connections adopted were architecturally compact, avoiding bolts outside the cross-section of each member. This resulted in cruciform and bolted flange connections kept within the cross-section being

extensively used. Site welding was minimised as far as practically possible, for constructability and disassembly reasons, with 99% of all connections bolted. This enabled the erection of truss modules and diagrid segments to be installed with ease (refer to *Section 7. Erection and buildability* for more details on the erection staging of the roof).

Following the philosophy of the member design process, design actions and member properties were extracted from the global analysis and queried in Excel to have a suitable format for input into the connection analysis and design software. IDEA Statica was typically used for the majority of the roof connections, the associated design was accurate, and documentation was streamlined. The most critical and multi-elemental connections at the derricks were analysed through sub-modelling in Strand7 or local high-detail modelling within the global analysis model itself. Submodelling is a process which extracts a section of the global analysis model of interest to analyse in more detail. As global models typically make simplifications with the stiffness of connections, sub-modelling is an effective tool to validate the integrity of critical connections. Additionally, it removes any potential errors in translation between design software and provides greater confidence in the design. The design workflow for these connections is shown in the figure below.

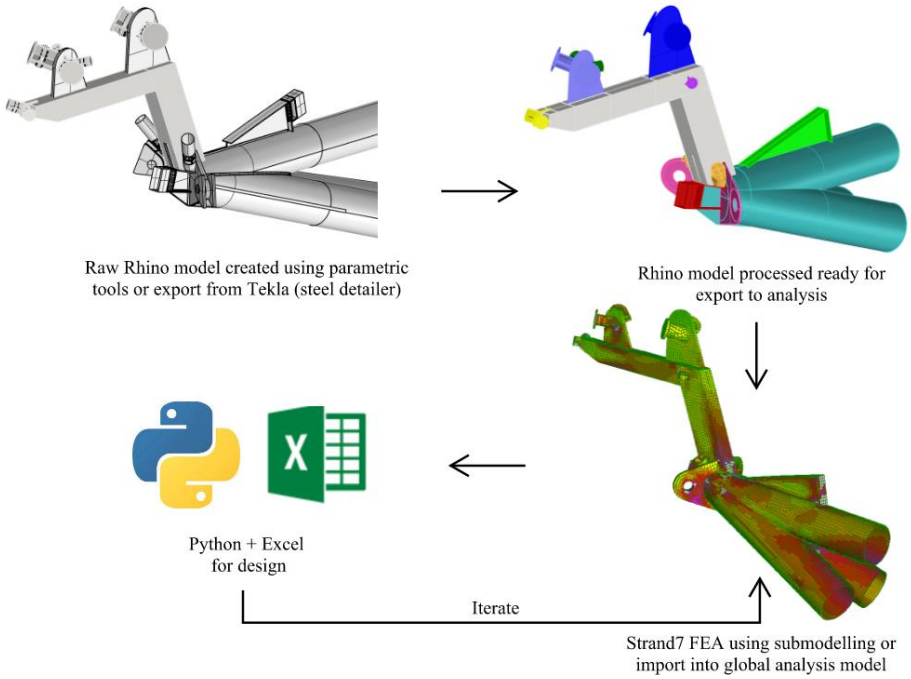


Figure 8. Connection design workflow for complex and stiffness sensitive connections.

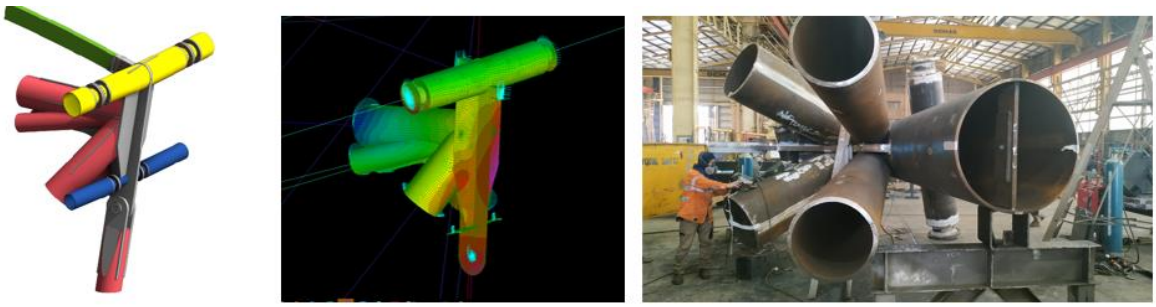


Figure 9. Derrick Rear Connections: (a) Tekla Model, (b) Finite Element Analysis Model, (c) Fabrication.

The digital workflow and bi-directional workflow between the structural engineer and the steel detailer (DBM Vircon) reduced iterations and ensured a very high standard of quality assurance, with over 95% of the shop drawings produced having no comments and proceeding straight to fabrication.

5.5 Buckling study

Long-span stadium roof structures can have trusses that exceed 100m in length, often fabricated in several segments which are erected and installed at elevated heights on site, creating a challenge for contractors to meet precise tolerances. The longest trusses in SFS span 140m and were erected in 3 segments with a nominated positional tolerance of 100mm. Typically when designing more standard structures, geometrical imperfections are captured in the design code buckling curves, (Some codes exclude the resistance, and are captured analytically through applied imperfections or notional loads). For key design elements, understanding sensitivity to tolerable geometrical imperfections may be necessary to provide confidence in the design for fabrication erection tolerances.
A study was undertaken at various design stages to assess the sensitivity of the SFS roof to geometrical imperfections. The workflow adopted is summarised below:

1. Using the base design geometry model, the Strand7 Application Programming Interface (API) was used to conduct a linear buckling analysis on all ULS load cases.
2. A Python script was run that extracted the buckling load factors for each load case.
3. The critical modes of interest were identified which related to the global buckling modes.
4. Geometrical imperfect models were created by adjusting the base design geometry to the shape of the global buckling modes. These models were created at 50mm, 100mm and 150mm imperfection magnitudes. Non-linear buckling analysis was run for each of these models.
5. A detailed assessment was undertaken to analyse the impact and sensitivity of geometric imperfections on the performance of the structure. This evaluation determined whether the roof was prone to buckling before yielding. This evaluation involved non-linear material and geometrical analyses to calculate the buckling load factors of the structure. Refer to *Figure 10*.

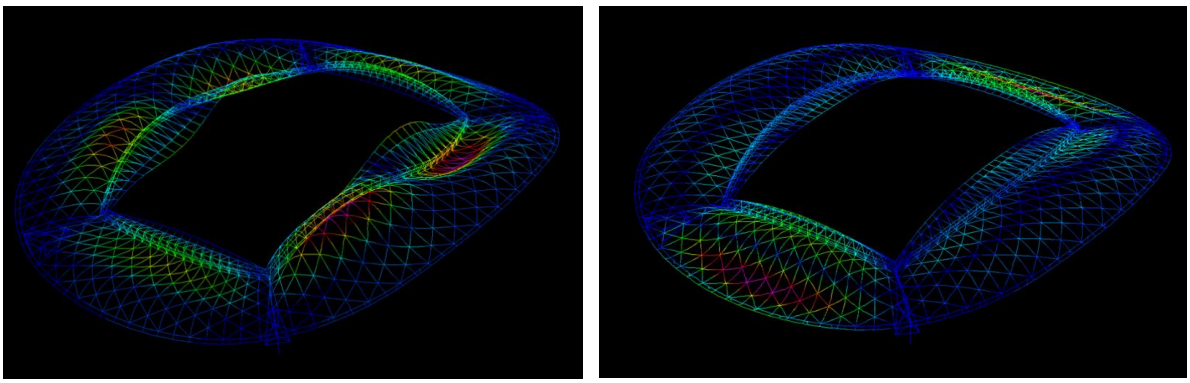


Figure 10. Roof buckling modes (a) Global buckling mode, (b) North-South diagrid buckling mode.

The buckling study indicated that the roof yielded before the first buckling mode occurred, exhibiting the desired structural behaviour, additionally the buckling load factors were within an acceptable range. The North-south bays, due to their pronounced curvature had a particular sensitivity to non-linear geometrical analysis and buckled via ‘snap-through buckling’. This form of buckling occurs when an arch is initially stable in compression, but as the vertical load progressively increases the arch flattens, which in turn increases the axial load in the arch due to the less optimal angle of the arch. The arch withstands the vertical load until buckling capacity is reached and ‘snaps-through’ as it reaches an inversed state that acts as a catenary.

6. Fabrication

The roof fabrication process for Sydney Football Stadium showcased cutting-edge techniques and exceptional collaboration among industry experts, resulting in a state-of-the-art stadium. A key focus during fabrication and procurement was to ensure precision and quality while adhering to the strict geometric tolerances of a form-found structural system. For the complex roof structure, steel fabricator S&L employed advanced processing methods for CHS members up to 762mm in diameter and the 400x200mm RHS members. Approximately 18 kilometres of steel members were sourced for the 2,000 tonne steel roof structure. The process of procurement took over 12 months and was staged to align with the lead times and critical path for erection, for example the structural design had to align with the procurement programme, particularly for the large diameter CHS members which were procured from South-East Asia, this fast-tracked programme enabled the first bulk order of steel to be made within three months of the commencement of design. The design and steel detailing of the members and connections aimed to standardise and simplify the complex geometry of the structure into an understandable and repeatable form, reducing material wastage while streamlining the shop detailing and fabrication process and improving the speed of erection within the confined site. The use of bolted connections allowed for simpler modifications or demountability in the future should the need arise, with over 99% of all steel site connections being bolted.

As with most form-found structures, the behaviour of the structure is sensitive to the geometry of the structure. The implementation of full-scale pre-assemblies of critical elements in the workshop validated the sensitive geometry and enabled any adjustments to be made before arriving on-site, improving the speed of assembly and installation on-site. This was critical to ensure all delivered steel was installed without the need for site modifications and enabled efficient use of the laydown and working areas on-site. The elements that were pre-assembled in the fabricator's workshop include; the Derricks, the Inner Arched Trusses, the Tension Ring and the Radial Arched Rafters.



Figure 11. Fabrication workshop (a) Roof truss pre-assembled, (b) Roof derrick pre-assembled.

Fabrication geometry requiring particularly high precision was the total length of each truss chord which was required to be within +/-10mm from derrick to derrick (up to 140m length), and similarly, the total length of the tension ring from derrick to derrick (up to 195m length) which was to be +/-10mm. This precision was defined based on sensitivity studies undertaken for the structure. This was a challenge to achieve as each element had multiple full strength butt welds with the potential for considerable weld contraction associated with heat and cooling cycles during the welding process. The cumulative effect of weld contraction could result in a significant change in the overall length or alignment. Therefore, multiple splice end plates were left unwelded until the final survey of the pre-assembled element was undertaken to enable adjustments in the root gaps of the welds, providing a method to compensate for any fabrication tolerances or weld contraction that may have occurred.

7. Erection and buildability

Prefabrication and modular construction techniques were adopted to limit the working at heights required and improve the erection efficiency on site, it also enabled multiple work fronts to progress on the pitch (working area) simultaneously without the use of a substantial tower or crawler cranes. The heaviest preassembled module was 130 tonnes which was assembled on the pitch and lifted onto temporary towers supporting the roof structure. The preassembled roof installation strategy enabled over 85 per cent of the roof steelwork installation to be undertaken at ground level, leading to substantial programme and safety benefits. The workshop modularisation or constructability extremities were governed by the overall transportation width and lengths. Each fabrication assembly was studied to ensure all structural members, assemblies and secondary items such as gutters, bull noses, gantries etc. could be installed in the fabricator's yard before transportation and to avoid overuse of the laydown areas on site.

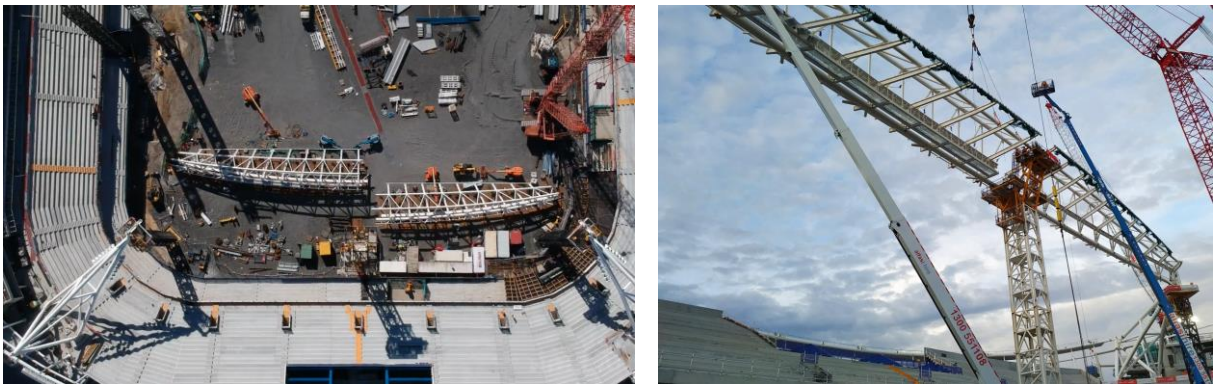


Figure 12. Roof truss erection (a) North truss preassembled on the pitch, (b) North truss installation of segment 2.

Early and collaborative involvement with the engineer, architect, contractor, fabricator and steel detailer was instrumental in achieving the tight design and construction timeframe of only two and a half years with the first steel ordered in less than three months from the commencement of the project. In contrast to many projects, direct relationships were formed through weekly design workshops with all stakeholders from the onset of the project. This is atypical as normally this type of feedback is only received once Issued Tender documentation is complete (i.e. 70% of the design). This early and crucial feedback ensured buildability and speed in fabrication and on-site assembly were at the centre of the design and modelling process.

7.1 Fabrication and design geometry

The design geometry is the agreed final architectural form. This geometry is achieved once all members are unpropped and all gravity loads from the permanent structure including superimposed loads from services, fabric and secondary steel are applied, this is the form-found structural geometry.

The fabrication geometry is the geometry for which the steel is fabricated and assembled in a stress-free state. It is established in such a manner, that the design geometry is achieved under permanent loads with as little deviation as possible.

To determine the fabrication geometry the following is undertaken for each element:

1. Lengthening of members to compensate for shortening through compression forces,
2. Shortening of members to compensate for lengthening through tension forces.

The force distribution in the roof structure follows this approach: The derricks, trusses and tension ring form the frame for the diagrid structure. The thrust from the curvature and intentional lengthening of the diagrid fabrication geometry ensures the tension ring and compression arched trusses are engaged and creates the desired load path. This pre-set geometry is not force-free contrary to an inversed gravity

approach that would be force free during installation but would not engage the derricks, trusses and tension ring as efficiently. The design geometry varies from the fabrication geometry by up to 300mm.

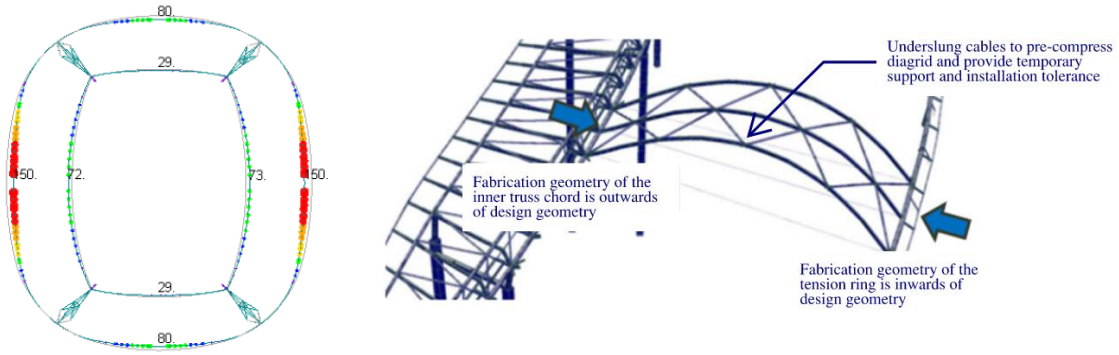


Figure 13. Design geometry and fabrication geometry for tension ring and inner truss chord.

7.2 Erection sequence

The main phases of roof construction were as follows:

1. Abutment cores and superstructure were constructed with associated cast-in anchors for the roof
2. The derrick structures were lifted into their pre-defined positions on the temporary tower at the tip and connected to the abutment cores at three points. The base points were grouted after a survey confirms the correct positions, refer to (a) of *Figure 14*.
3. Columns were installed and stabilised, the tension ring segments are installed and connected.
4. The Truss segments were lifted and connected to the derricks before being placed on temporary towers. As the lower truss chord is a highly compressed element (inner edge of the diagrid shell), the fabricated geometry is longer than the final geometry under force (refer to *Figure 13*). Therefore, to make the trusses fit and able to close the splice connections, vertical jacking operations were undertaken at the top of the towers to open and close the gaps of the end plates.
5. The diagrids were lifted into their positions in pre-assembled double bays. The curved radial arches were stabilised by temporary ties spanning between their ends. The lifted modules were connected by infill diagonals forming the shell structure.
6. Once the diagrid is completed, the radial cables were removed to activate the Tension Ring. Then the de-propping from the towers started by lowering the support to engage the Derricks and the trusses until the roof structure was self-standing and the towers could be dismantled.

The key erection stages are explained and illustrated below in *Figure 14*.

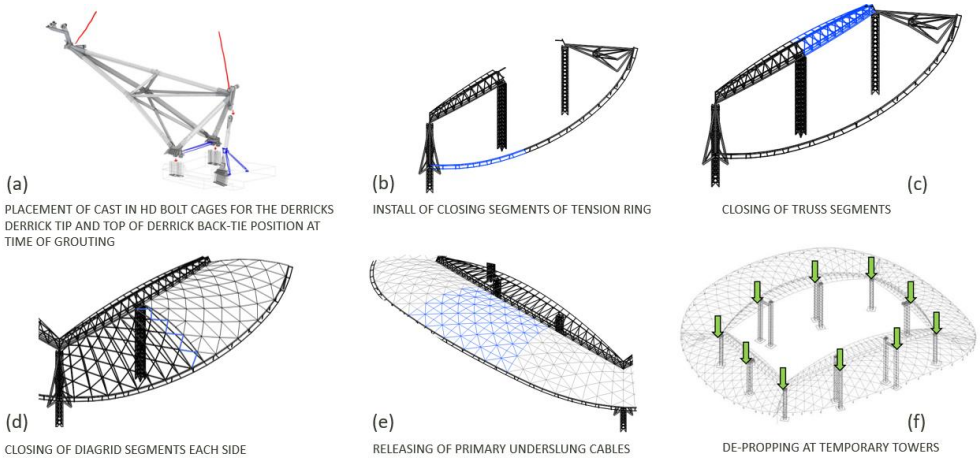


Figure 14. Key stages of erection.

Installing this complex roof with large spanning structures was a challenging task. Difficult access at height and a desire to preassemble as much as possible on the ground added a layer of complexity. Aurecon and Schlaich Bergermann Partner led the erection engineering, testing hundreds of possible deviations in sequence, temperature, geometry, jacking, de-jacking, site and fabrication tolerances, all of which were distilled into a series of simple 'rule books', which clearly outlined the procedures and bounds of what deviations are possible for each key erection stage. This provided substantial flexibility and ensured the roof was able to be fabricated and erected on programme. A key achievement, particularly considering the procurement and work constraints due to COVID-19.

8. Conclusion

Sydney Football Stadium stands as a testament to the power of collaboration, innovative design, and efficient construction techniques in the face of logistical and pandemic-related challenges. The state-of-the-art 2,000 tonne synclastic diagrid shell roof, with its unique geometry and intricate connections, was made possible through a combination of prefabrication, modular construction, and advanced erection engineering. The extensive use of bolted connections and ground-level assembly not only facilitated construction but also enabled future disassembly, adding to the structure's sustainability. The development of a novel digital workflow allowed seamless communication and coordination between various stakeholders, ensuring the successful integration of the roof's 5,000 individual steel pieces. The completion of the Sydney Football Stadium demonstrates the potential of modern engineering and construction techniques when they are employed within a cooperative and adaptive framework.

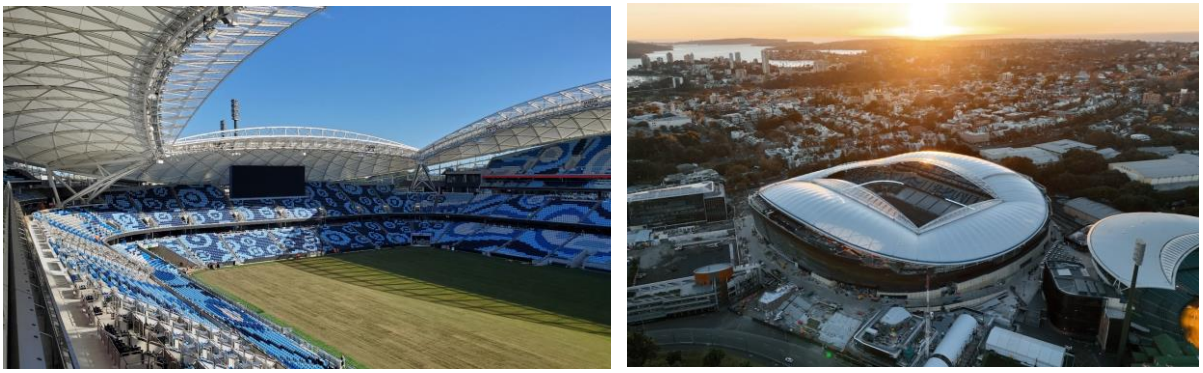


Figure 15. Photos of the completed Sydney Football Stadium.

Acknowledgements

The authors wish to make acknowledgement of the New South Wales (NSW) Government for commissioning this world class stadium. Together with principal contractor, John Holland Group, Aurecon delivered the structural and civil engineering design for the new stadium in collaboration with Schlaich Bergermann Partner and COX Architecture.

References

[1] M. S. a. R. S. Huerta, "Antoni Gaudí's Hanging Chain Models: A Case Study of the Church of Colònia Güell," Engineering Structures, vol. 194, no. 109766, pp. 1-16, 2021.

[2] K. Göppert, "Gottlieb-Daimler-Stadion, Stuttgart," Berlin Steel Construction Special, pp. 192-197, 2005.

[3] I. Ainsworth, "Suncorp Stadium Redevelopment," in Australian Structural Engineering Conference, Sydney, 2005.

[4] J. Bensen and G. Rowland, "Adelaide Oval - Western Grandstand Redevelopment," in Asian Region and Australasian Structural Engineering Conference, Sydney, 2010.

Teaching design uncertainty: working with unknown qualities/quantities of new and re-claimed materials

---

Active bending
Additive manufacturing/ 3D printing
Architectural geometry
Bamboo for sustainable construction and quality of life improvement
Bio-inspired structures and architecture
Bridge structures
Computational form-finding
Conceptual design
Concrete structures
Construction techniques
Deployable and inflatable structures
Design competition (WG21)
Digital modelling and fabrication
Dynamic response of metal spatial structures
Dynamic response of other structures
Form-finding and structural optimisation of interlocking discrete assemblages
Graphical methods
Gridshell and lattice structures
Historical concrete shells
Historical structures
Lattice structures
Life-cycle design and assessment of structures
Metal gridshell structures, connections and stability
Methods and construction technologies for sustainable shell structures
Morphology and configuration processing
Next generation parametric design
Novel methods in modelling, optimisation and construction for reducing carbon footprint of continuous roof shells
Numerical methods for geometry, form-finding and optimisation of lightweight structures
Optimisation methods and applications
Origami
Other
► Teaching design uncertainty: working with unknown qualities/quantities of new and re-claimed materials
Teaching of shell and spatial structures
Tensegrity systems and cable structures
Tension and membrane structures
Tension structures in the Asia-Pacific
Timber and bio-based structures
Topology optimisation
Traditional masonry structures and innovation
Transformable structures

IASS 2023
July 10–14 Melbourne
Integration of Design and Fabrication

Proceedings of the IASS Annual Symposium 2023
Integration of Design and Fabrication
10–14 July 2023, Melbourne, Australia
Y.M. Xie, J. Burry, T.U. Lee and J. Ma (eds.)

A modular approach to repurposing timber structural elements

Matthew TAM[*], Sascha BOHNENBERGER-FEHR[a,*], Chris FOX[b,c], Tommaso PAGANI[b]

[*] Bollinger+Grohmann
mtam@bollinger-grohmann.at

[a] Swinburne University of Technology
[b] Studio Chris Fox
[c] University of Sydney

Abstract

In the ever so prevalent drive to reduce the environmental impacts of the construction industry, the (re)emergence of opting for a circular economy through repurposing of structural elements is gaining traction [1]. Methodologies and tools are currently being established for more efficient inventory processing coupled with structural optimisation and cost evaluation to design structures entirely of reused components [2]. This paper builds off this past research and supplementarily explores an approach to develop modular systems that could be assembled and reassembled in a vast array of options thus further extending the lifespan of existing structural elements. The project consists of four individual modules (footing module, wall module, wall to roof module and a roof module) that were designed with a self-assembly process in mind that solely relies on the utilisation of bolted connections. This paper outlines the digital workflow working with inventories of reclaimed stock material to design the modules and methodologies to populate them in a three-dimensional framework. A live feedback loop was established to evaluate the structural integrity of the entire system in the various design iterations. The project demonstrates a viable solution for further investigation into the circular economy of our built environment.

1. Introduction

We no longer have the luxury to design and construct structures of the same calibre that we do today. The construction sector itself has the strongest impact on the environment, accounting for 40% of global carbon dioxide emissions alone [3]. According to the National Waste Report, Australia generated 29 million tonnes (Mt) of construction and demolition waste in the financial year of 2020-2021, 38% of total waste in the country [4]. A building's operation has a major influence on its total carbon emissions, but its materials and construction are expected to be responsible for up to 80% of its cumulative carbon emissions by 2050 [5]. In an effort the environmental impact, the (re)emergence of opting for a circular economy in the construction industry through repurposing of structural elements is gaining traction [6].

This paper explores a circular design methodology from concept through to the construction of a temporary pavilion for Summer Place, an annual event located in Albury, NSW Australia (Fig. 1). The "Re/place Pavilion" for the 2022-2023 edition was collaboratively designed by Studio Chris Fox (based in Sydney), Bollinger+Grohmann (based in Melbourne), the University of Sydney and Swinburne University of Technology, Melbourne, combining the expertise of architects, artists, students, engineers, and contractors. This paper outlines the design procedure from working with an existing material inventory through to developing discrete modular units to assemble as a global structure. The project demonstrates a viable solution for further investigation into the circular economy of our built environment.

Copyright © 2023 by Matthew TAM, Sascha BOHNENBERGER-FEHR, Chris FOX and Tommaso PAGANI. Published in the Proceedings of the IASS Annual Symposium 2023 with permission.



Figure 1. Re/place Pavilion constructed in 2022. © Jeremy Weihrauch.

2. Working with existing material stock

The main goal of a circular economy is to maximize the lifespan of existing products by ensuring they remain in use for as long as possible representing an alternate approach to recycling and simply using recycled materials. By repurposing building elements for new use, one can prolong the original intended lifespan of that element and significantly reduce waste and carbon emissions in the construction industry. Methodologies and tools have already been established for more efficient inventory processing coupled with structural optimisation and cost evaluation to design structures entirely of reused components [2]. With computational design, it is also possible to enhance the procedure to develop methods of optimising the reused stock for the design of frame structures subject to ultimate and serviceability limit states [7]. These new structures take on a totally new identity, building up upon the history of the repurposed elements which each of them has their own individual story to tell.

The re-use of building elements from an existing inventory is not a novel idea, being intensively implemented prior to the industrial revolution [8]. The Romans, for example, famously reused materials from conquered territories to construct their expansive empire [9]. The inherent material properties of the building elements play a significant role on its suitability for reuse. A common approach for concrete is to simply crush demolished concrete which, at best, can be recycled as an aggregate for new concrete. This process reduces construction waste but is itself very energy intensive [10]. Current trends focus on utilising entire elements such as reused precast concrete structures [11], salvaged timber beams as well as unconventional materials [12] or even parts of an element such as extracted concrete blocks from demolished concrete structures for a footbridge design [13].

In order to maintain a minimal carbon footprint, the entirety of the timber elements for the pavilion were sourced from existing and used materials. Salvaged timber (Fig. 2) from across multiple locations around Sydney and Melbourne as well as reclaimed elements from previous deconstructed pavilions of the Summer Place were collected, and their suitability for structural, footing and cladding capacity evaluated.

(a)  (b)  (c)  (d) 

Figure 2. Materials from various locations: (a) salvaged timber from a racecourse in Sydney, (b) structural timber from Timber Zoo, (c) timber beams from Albury City Council, (d) screw piles from previous pavilions.

3. Modular systems

Typically, the standard procedure when handling the reuse of building elements is often limited to its second life cycle. It was essential to extend the research to focus on how the elements could be reused in multiple lifecycles. In the process of DfDR (design for deconstruction and reuse) [14] a building is designed in a way that its parts can be easily dismantled and separated from each other for reuse or recycling. The research explored an approach to develop modular systems that could be assembled and reassembled in a vast array of options thus further extending the lifespan of existing elements.

With the city of Albury located at least three hours driving distance from Melbourne, and significantly longer from Sydney, it was essential to use prefabricated elements to minimize time on-site. The use of modular systems significantly reduces construction time on site, with most of the fabrication and assembly work largely completed off-site. They also offer increased flexibility in design: the components can be easily reconfigured or modified to accommodate changes in function or overall form.

Wasp is a plugin for Grasshopper that allows for "representing and designing with discrete elements" [15]. The toolkit allows for both the geometrical and topological description for each unit, as well as its inter-connectivity rules, to be defined. Researchers at the Frankfurt University of Applied Sciences used a similar approach to design a temporary pavilion with modular elements composed of discarded wire hangers, investigating the balance of achieving an "articulated morphological variation and a sufficient a level of design flexibility" [16]. Stochastic aggregation and field-driven aggregation methods in Wasp define instructions for the computational procedure to orient elements based on a set of connectivity rules [17] enabling the possibility to generate a vast array of design iterations in a short amount of time. Fig. 3 shows initial studies which looked at these aggregation methods based on the design of the individual discrete unit which themselves were designed based off stock material inventory.

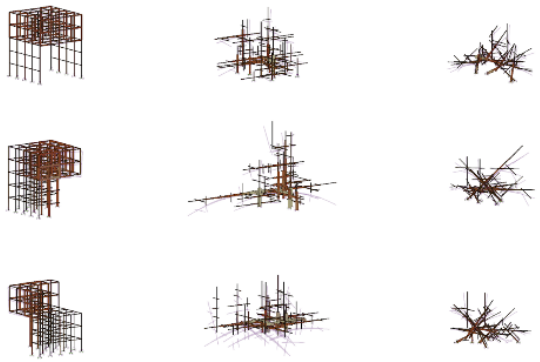


Figure 3. Design iterations using a discrete modular approach.

4. Identification of potential reusable elements

Bespoke computational workflows were developed in an initial case study that was presented at CAADRIA 2022. The workshop titled "Manipulating the VR space for the design of repurposed timber structures" set out to utilise the digital workflow working with inventories of reclaimed stock material to design the discrete units and methodologies to populate them in a three-dimensional framework. Techniques to 3d scan, archive, and document elements suitable for reuse were investigated during this workshop as depicted (Fig. 4). By studying several existing structures scheduled for demolition, it was possible to first identify and categorise specific elements to create a preliminary material database.



Figure 4. 3d scanning existing structure to create a digital archive and 3d model.

For the design of the new pavilion design, and its inherent structural properties and accessibility, timber was selected as the material of choice. There is an often-tedious process that involves analysing the salvaged timber elements for nails or foreign objects that need to be removed before processed with woodworking machinery. Initial prototyping, evaluation and processing of select timber beams that were over 100 years old were done at the University of Sydney. Due to time and resource limitations, an alternative approach was chosen were elements that were already dismantled and pre-processed were selected for the main structural elements, with those of less processing were used for non-structural elements such as the façade.

There was still a process to assess the acquired elements even if they are pre-processed beforehand. A surface assessment of the quality and defects of the timber helped to determine which elements could be used, which of them could be cut, where exactly it was appropriate to cut. This included a quite labour-intensive approach to manually evaluate whether there was warping, cracking, or bowing in the timber (Fig. 5). Any holes from nails and additional features were all entered in a Google Form which created an extensive Google Sheet of the sourced material (Fig. 6).



Figure 5. Identifying all the surface issues in the sourced timber.

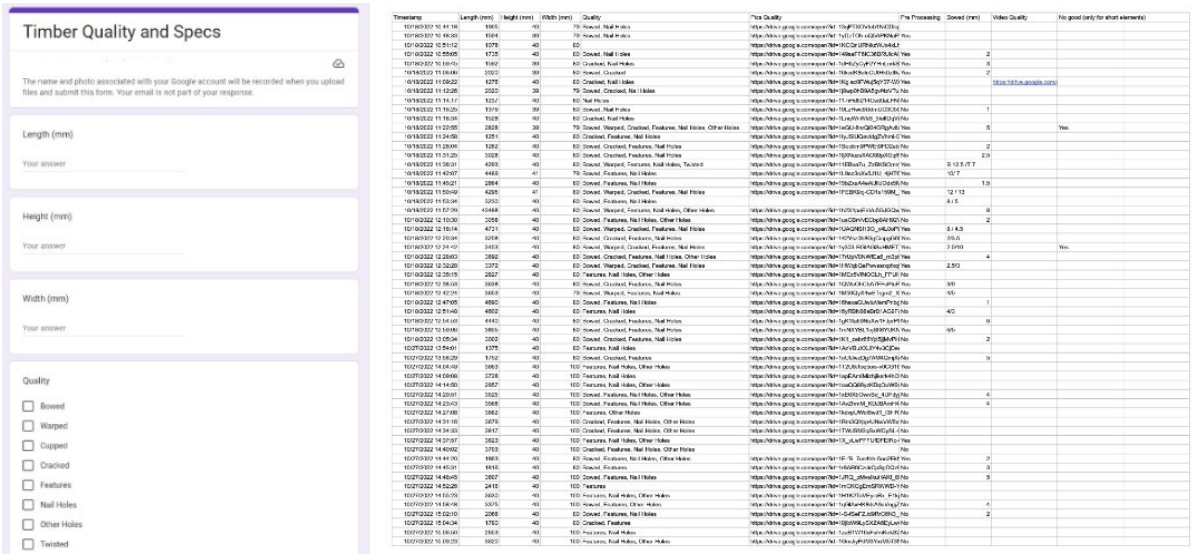


Figure 6. Google Form and Sheet to document the assessment of the timber quality.

5. Digital workflows

Setting up a computation workflow based on the findings from the CAADRIA workshop allow for quick sketches and 3d iterations based on the material database to be conceptualised. Simply adapting the starting input module and adjusting its connectivity rules, it was possible to generate many design iterations as depicted in Fig. 6. It was important to establish a dialogue with the new structure in its extended lifespan and its first intended function. Fig. 7 shows how elements from the digital model are able to be connected back its original position, allowing visitors to read the transition from old to new. The team of researchers led by Catherine De Wolf at the ETH Zurich explain that engraving QR codes on all repurposed elements "help people learn more about that building's history" [18].

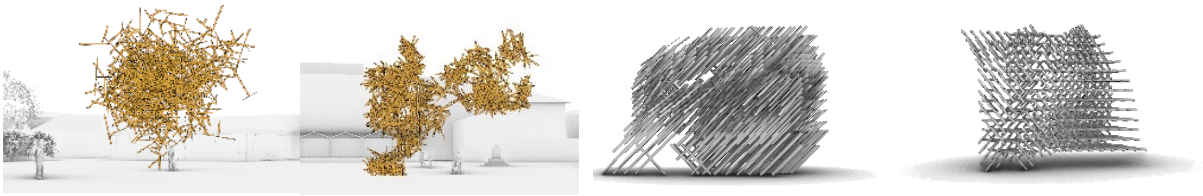


Figure 7. Early design iterations of the pavilions.

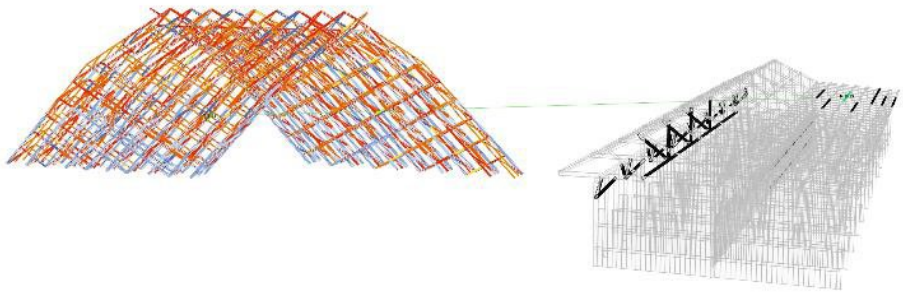


Figure 8. Design iteration relating to stock material.

5.1. Discrete modular elements

Several factors were at play in the design of the individual modules themselves (Fig. 8). They should be able to be lifted by hand by either one or two people without additional machinery, they needed to be transportable in the back of a small truck, the number of offcuts and material wastage should be minimized, and they needed to be self-supporting - able to carry its own weight and as well as other elements attached to it. With this design intent in mind, the team went through vigorous investigations of formal studies (Fig. 9) that coupled well with the modular design and to situate the pavilion within the context of the site of QE Square in the centre of Albury. Finally, a scheme depicting a deconstructed shed with a gable roof was chosen as point of inspiration.

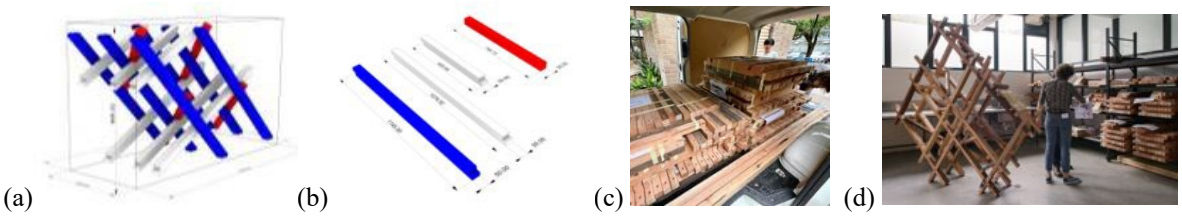


Figure 9. Module parameters: (a) Setting a module size, (b) Controlling the lengths and cuts, (c) Compact transportation of the elements, (d) Self-supporting modules lifted by hand.



Figure 10. Design iterations involving various predefined modular elements.

Enhancing the capabilities of a parametric design environment it was crucial to develop the geometry for the discrete units coupled with information about its structural axes that could be fed into a live analysis. Structural information in regard to cross sections and materials were also embedded to provide an accurate simulation of the structural integrity of the modules (Fig. 10). Any transformations to the starting module design would be immediately evaluated to provide quick live feedback.

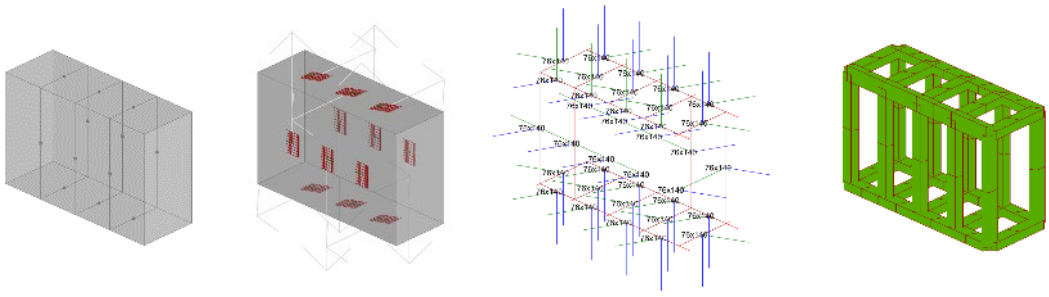


Figure 11. Modules embedded with geometry and structural information with live structural analysis.

Final design iterations resulted in individual modules for the pavilion design (footing module, wall module, wall to roof module and a roof module) that were designed with a self-assembly process in mind that solely relies on the utilisation of bolted connections. 20 wall modules, 12 roof modules, 10 footing modules, 6 wall to roof modules (Fig. 11). This would form the core structure of the pavilion, all elements self-supporting, and able to carry those adjacent to each other. Reclaimed timber strips from the previous pavilions were used as a final cladding element that helped to accentuate early key themes

of movement, dynamism, and texture, and also alleviate climbing potentials of the envisaged structure (Fig. 12).

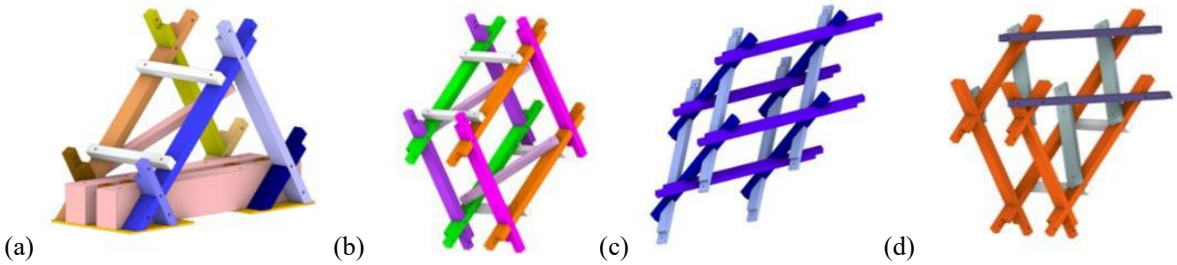


Figure 12. Final Modules (a) Footing, (b) Wall, (c) Roof, (d) Wall to Roof.

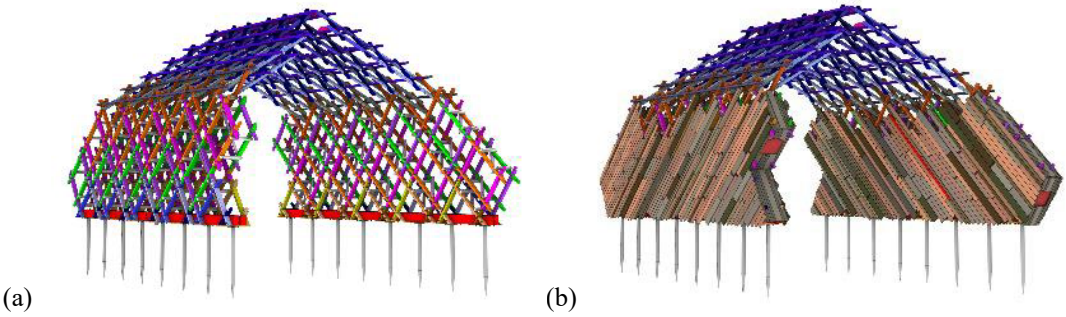


Figure 13. Final Pavilion (a) structural components, (b) with cladding.

5.2. Integrated structural analysis

The pavilion should provide some form of shelter, a portal where visitors could enter and experience the pavilion close up. With a clearly defined design concept, a grasshopper script was created to establish a live feedback loop to evaluate the structural integrity of the entire system in the various design iterations. The general form and silhouette of the project should remain consistent, but several parameters could be altered. The script allowed the size, angle, depth of the modules to be parametrically controlled (Fig. 13). Slight adjustments in the module design would have drastic effects on the global design as well as the overall structural capacity. It was crucial to be able to understand how the impact of the position and orientation of specific modules could affect the global structural behaviour (Fig. 14). During the structural design procedure, an optimisation was created to allow the algorithm to pick from the material database for a suitable cross section depending on its availability. The total amount of material could be easily extracted.

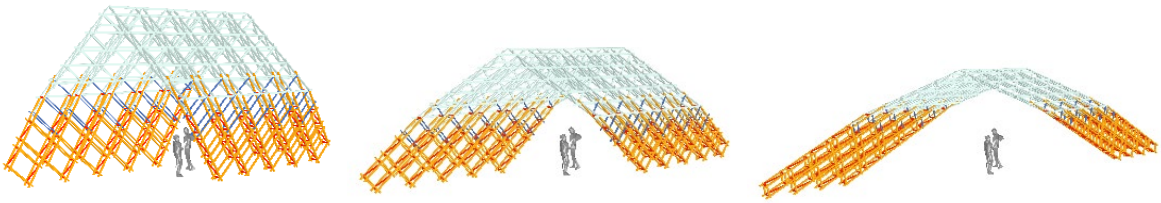


Figure 14. Parameters in the script-controlled size, angle of the module which affected the global shape.

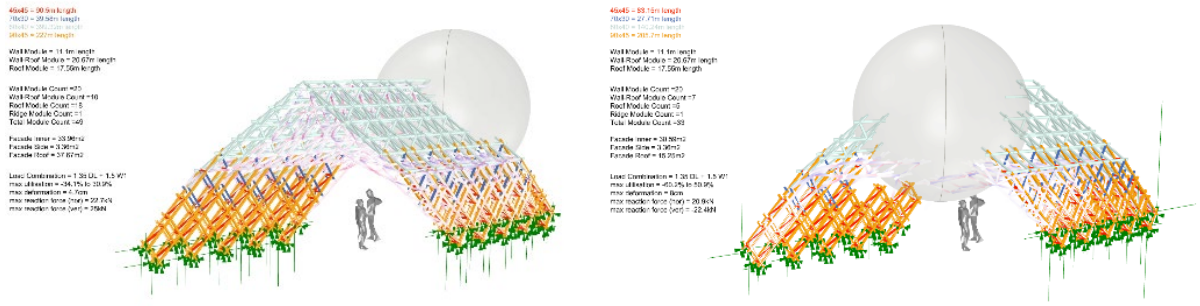


Figure 15. Design Iterations and their effect on the structural performance.

The pavilion measures 4.2m wide, 9.7m long and 4.2m high. Recycled screw piles were selected – 16 in total, 2 for each footing module. Calculations showed reaction forces of up to 4.65kN at the support positions meaning that the screw piles of 1.2m depth would be suitable. A timber base plate was attached onto the top of the screw piles where two recycled Kauri softwood beams (180x122mm) were fixed, onto which the footing modules would attach to. The roof and wall to roof modules are entirely constructed of 40x80mm hardwood members and the wall modules are composed of mainly 90x45mm softwood members with 45x45mm elements for bracing elements. Detailed structural calculations showed critical moments at the roof pitch junctions (Fig. 15).

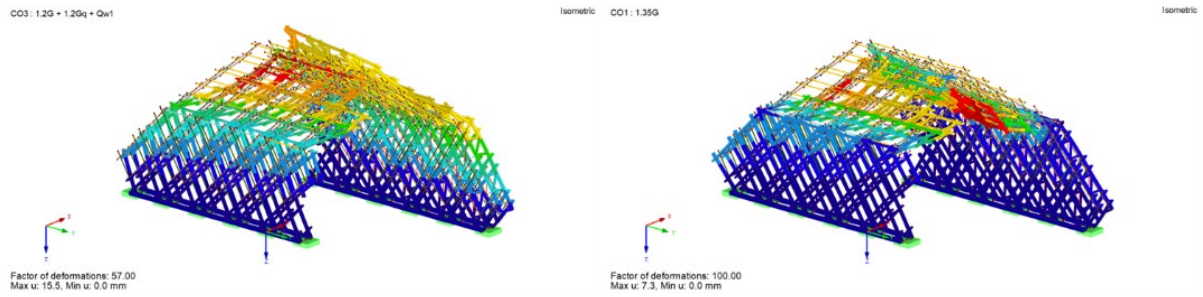


Figure 16. Structural analysis of the pavilion showing deformations under SLS loads.

6. Fabrication

The digital fabrication of the elements for the core structure was entirely done with a 3 axis CNC by the DMaF Lab in University of Sydney and Protolab in Swinburne University of Technology. For ease of assembly and fabrication, it was decided early on to use simple bolts and nuts to attach elements and modules to one another. Jigs were created to establish a seamless and efficient manufacturing line to cut, process and drill all the necessary components (Fig. 16). A distributed workflow allowed the separate universities to produce their subsequent modules, base and wall in Sydney and wall-roof and roof in Swinburne, and everything came together relatively easy on site even when they were fabricated in different locations.

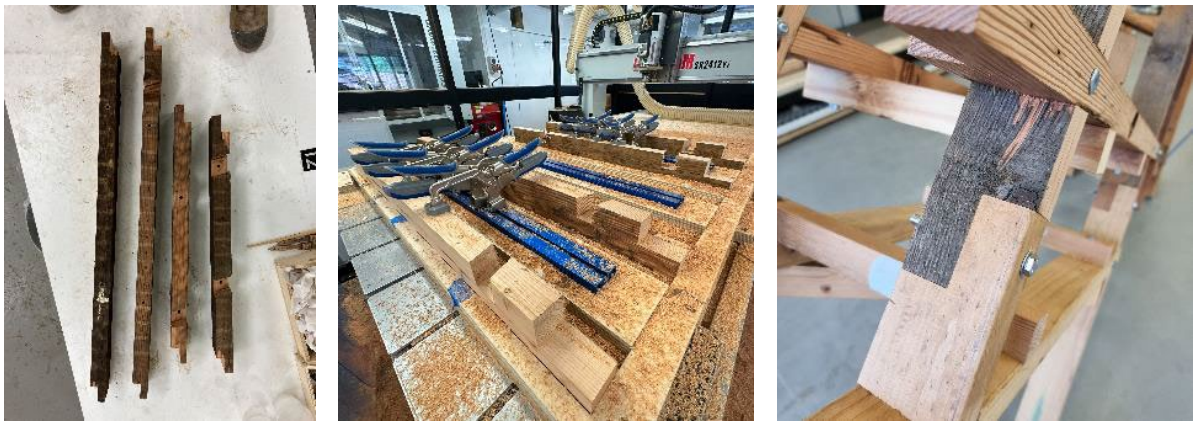


Figure 17. Fabrication of individual elements.

The individual elements were then transported in a small truck to Albury where all the modules were initially preassembled. A detailed assembly process was established in the planning process to allow the pavilion to be constructed from both walls simultaneously from the base. The wall-roof and roof modules would then be attached where the roof would eventually meet at its pitch. Individual elements were then used to join both sides of the pavilion together. This meant that no additional scaffolding was needed and only a mobile scissor lift was required to lift the uppermost modules into position. Fig. 18 shows the assembly process on site.



Figure 18. Assembly Process.

7. Sustainability aspects

The core structure of the pavilion has been built from entirely repurposed construction timber elements from various construction sites sourced by Among The Trees in Sydney and Timber Zoo in Melbourne. Oregon and Pine were used for the wall modules, originally sourced from USA, as was typical in the early 1900s. Messmate was used for the roof modules. The Oregon and Pine timber have been collected from different buildings built between 1920s and 1950s across the Sydney area. The Pavilion façade is composed of repurposed timber from Albury including reclaimed elements taken from the previous iteration of the Summer Place Pavilion. These timber boards were also originally salvaged from the Black Summer bushfires near Corryong in 2019-2020, blackened using an oxidizing process (Fig. 19).



Figure 19. "See the forest" by Akimbo Architecture, © Jeremy Weihrauch

With a life cycle analysis, it is possible to identify the environmental impact should have the structure been constructed of entirely new elements. Out of all the material used for the pavilion, the base plates, bolts and nuts were the only elements that were not sourced from an existing site, but rather purchased and are the only contributing value to the total embodied carbon of the structure. Table 1 outlines a comparison of all the materials and their embodied carbon or equivalent should they have had been newly sourced. All timber and screw piles were reclaimed from existing sites, and therefore do not contribute to the impact of this project. Only 14% of the total embodied carbon came from newly sourced materials (bolts, nuts, washers and base plates). Values are based on the ICE Database for Cradle to Gate Life cycle stages (A1-A3, C3+C4) [19].

Table 1. Values from Embodied Carbon - The ICE Database [19] and EPD-V/S/B [20]

Typology	New/Reclaimed	Material	Weight kg	CO_2 Emissions kg $C0_2e$/kg	Total CO_2 Emissions kg $C0_2e$
Timber Beams	Reclaimed	Softwood	220,5	0.263	57.99
Footing	Reclaimed	Softwood	126	0.263	33.14
Wall	Reclaimed	Softwood	328,5	0.263	86.40
Wall-Roof	Reclaimed	Hardwood	223,3	0.306	68.33
Roof	Reclaimed	Hardwood	408,1	0.306	124.88
Facade	Reclaimed	Softwood	454,5	0.263	119.53
Screw Piles	Reclaimed	Existing	62,8	3.75	235.50
				Subtotal	**725.77**
Base Plate	New	Steel	23,55	2.46	57,93
Bolts & Nuts	New	Steel	15,7	3.75	58.88
				Subtotal	**116.81**

Timber, when handled and treated properly, has great potential and durability, as seen in its ease when selecting it for repurposing. The dressing, cutting and drilling into the timber elements can affect its durability and continued processing can reduce its structural capacity. When addressing the idea of designing for a circular economy, it was therefore important to consider further potential for reuse where the pavilion could be disassembled into its separate modules and reassembled in different configurations (Fig. 20).

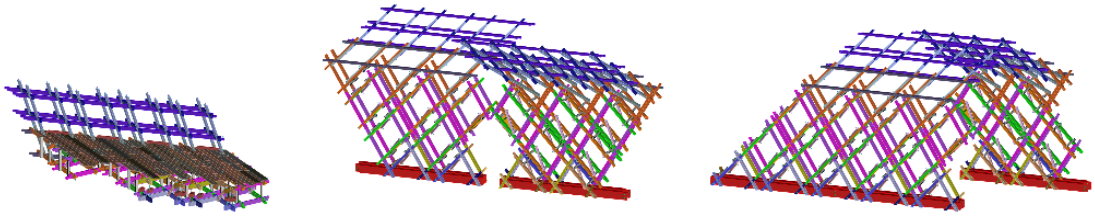


Fig. 20: Reconfigured elements.

8. Reflection & conclusion



Figure 21. Completed Structure © Jeremy Weihrauch.

The utilization of reclaimed timber for the construction industry is still challenging. Especially if it comes to liability clients and builders are concerned to use reclaimed timber since there are currently no standards or guidelines of how to proceed and design with this type of timber. Every source where the potential timber might come from has its own challenges whether it is accessibility, project management or lack of expertise. Most reclaimed timber elements are regarded not usable and classified as non-structural material and only fit for furniture making.

During the project development and the sourcing of the material, it became paramount to have one or in this case two reliable sources to purchase the material from. With a steady source of the material, a workflow was established that verified the quality of the timber delivered and its allocation in the design was assigned. This process is crucial and needs more research to improve on. For example, with vision control and AI technology smarter and faster ways of categorizing the material samples could be achieved in the future.

The design principles and the logic of reconfigurable modules will be further tested with the pavilion once it's reached its end of life at the current location. The idea is to relocate the pavilion and to give it a new life in a reconfigured way to extend the use of the pavilion and to showcase the next level of circular economy.

Acknowledgements

Studio Chris Fox: Chris Fox, Tommaso Pagani, Yuxiao Wang, Emma Hancock, Naomi Howell-Sivosh

Bollinger+Grohmann: Sascha Bohnenberger-Fehr, Matthew Tam, Ven Iyer

The University of Sydney Researchers: Chris Fox, Philip Gough, Elizabeth Duncan

Swinburne University of Technology Researchers: Sascha Bohnenberger-Fehr, Chen Canhui

Albury City Council: Megan Cullen, Yi Li

DMaF (The University of Sydney): Dylan Wozniak-O'Connor, Zoe Skinner, Paul Greedy, Majella Beck, Calvin Yeung, Prachi Patel, Julia Major,

Protolab (Swinburne University of Technlogy): Andrew Tarlinton, Ravi Bessabava, Nicole Farnell, Mark Whitehead, Elliot Henkel

Material Supply: Among the Trees, TimberZoo, *Summer Place 2021 See the Forest*

Installation: Marley Dawson, Max Volfneuk, Hugo Vos

Special thanks to: Murray Art Museum Albury (MAMA) Bernice Burke & Anthony Kilias (Urbis), Harriet Oswald (Grimshaw Architects), Imersian

References

[1] C. Fivet and J. Brütting, "Nothing is lost, nothing is created, everything is reused: structural design for a circular economy", *The Structural Engineer*, vol. 98, issue 1, pp. 74-81, 2020.

[2] Y. Huang, L. Alkhayat, C. De Wolf and C. Mueller, "Algorithmic circular design with reused structural elements: Method and Tool", *Proceedings of the International fib Symposium on the Conceptual Design of Structures*, vol. 66, pp. 457-468, 2021.

[3] ARUP & WBCSD, "Net-zero buildings: Where do we stand?", World Business Council for Sustainable Development, p. 5, July 8. 2021. [Online] https://www.wbcsd.org/Programs/Cities-and-Mobility/Sustainable-Cities/Transforming-the-Built-Environment/Decarbonization/Resources/Net-zero-buildings-Where-do-we-stand [Accessed February 22, 2023].

[4] National Waste Report 2022, Blue environment, Docklands, Australia, 2023 p.13.

[5] Kieran Timberlake, "Carbon Accounting", [Online] https://kierantimberlake.com/page/carbon-accounting [Accessed 22/3/2023].

[6] C. Fivet and J. Brütting, "Nothing is lost, nothing is created, everything is reused: structural design for a circular economy", *The Structural Engineer*, vol. 98, issue 1, pp. 74-81, 2020.

[7] J. Brütting, G. Senatore, M. Schevenels and C. Fivet, "Optimum design of frame structures from a stock of reclaimed elements", *Frontiers in Built Environment*, 2020-05-27, Vol. 6, num. 57, p. 1-18.

[8] B. Addis, *Building with Reclaimed Components and Materials: A Design Handbook for Reuse and Recycling,* Routledge, 2012.

[9] S. Barker, *Demolition, salvage and re-use in the city of Rome 100 BC-AD 315*, Ph.D. dissertation, University of Oxford, 2012.

[10] S. Marinković, V. Radonjanin, M. Malešev, and I. Ignjatović, "Comparative environmental assessment of natural and recycled aggregate concrete," *Waste Management*, vol. 30, no. 11, pp. 2255–2264, Nov. 2010.

[11] S. Huuhka, N. Naber, C. Asam, and C. Caldenby, "Architectural Potential of Deconstruction and Reuse in Declining Mass Housing Estates", *NJAR*, vol. 31, no. 1, 2019.

[12] S. Leblanc "From Humble Sources, Earthy Elegance Springs", *The New York Times*, April 18, 1996.

[13] C. Küpfer, M. Bastien-Masse, J. Devènes and C. Fivet, "Environmental and economic analysis of new construction techniques reusing existing concrete elements: two case studies," in *IOP Conference Series: Earth and Environmental Science,* 2022, vol. 1078.

[14] S. Moffatt, and P. Russell, "Assessing the Adaptability of Buildings," in *Annex 31, Energy-Related Environmental Impact of Buildings*, IEA Annex, 2001.

[15] A. Rossi and O. Tessmann, "Geometry as assembly-integrating design and fabrication with discrete modular units," in *ShoCK! - Sharing Computational Knowledge! Proceedings of the 35th eCAADe Conference, 2017*, Fioravanti, A., et al. Eds., vol. 2, pp. 201–210.

[16] T, Carl, T., S. Siefert, and A. Rossi, "Upcycling Shell: From Scrap to Structure," DMS 2022,

[17] A. Rossi, *Wasp v0.4.013 - Discrete Design for Grasshopper* (2021). [Online] https://github.com/ar0551/Wasp [Accessed February 15, 2023].

[18] R. Künzler, "A wooden dome made solely from waste", *ETH Zurich*, 26.04.2022 [Online] https://ethz.ch/en/news-and-events/eth-news/news/2022/04/globe-a-wooden-dome-made-solely-from-waste.html [Accessed March 2, 2023].

[19] Circular Ecology, *Embodied Carbon - The ICE Database*, 2019 [Online] https://circularecology.com/embodied-carbon-footprint-database.html [Accessed March 31, 2023]

[20] EPD, *V/S/B - Surface-treated steel screw for outdoor use*, January 4, 2023

IASS 2023
July 10–14 Melbourne
Integration of Design and Fabrication

Proceedings of the IASS Annual Symposium 2023
Integration of Design and Fabrication
10–14 July 2023, Melbourne, Australia
Y.M. Xie, J. Burry, T.U. Lee and J. Ma (eds.)

New master's education: innovative teaching of sustainable design approaches for handling uncertainty

Olga Popovic LARSEN*, Sander Løkkegaard BENNER*, Sebastian Bernhard SEIPELT*

* Royal Danish Academy: Architecture, Design, Conservation
olga.larsen@kglakademi.dk

Abstract

The climate emergency requires all sectors of Society to work together in seeking less polluting, better functioning, and more sustainable solutions. The building sector with a huge negative environmental impact currently is a segmented industry - with responsibilities, but also visions, values, and approaches that are fragmented. In the search for more holistic approaches/solutions that will reduce/revert the negative impacts of the building sector collaboration across disciplines is essential. This is both the vision, starting point and main aim of the new master's education at the Royal Danish Academy in Copenhagen - *Architectural Technology*. Designed as a two-year professional master's program for constructing architects, it started with new students in September 2021/22. Through the innovative teaching of sustainable design approaches, the graduates are better positioned to handling design uncertainty including scarcity of materials, structural robustness, adaptability, new design requirements etc. The paper presents the aims and vision for the program, the Nordic educational context, course structure and modules descriptions, project examples as well as a reflection for further developments.

Keywords: new education, teaching methods, sustainable approaches, holistic thinking, design uncertainty, materials reuse, structural robustness, adaptability

1. Introduction

Historic building design has created architectural masterpieces through a holistic approach. The glory of the Master builders and the embodiment of single leader- master in charge the project – dealing with aspects from technical to artistic, geometry, detailing, considerations about economy, planning and organising the construction process, as well as defining material choices, qualities and quantities manifests itself in the beautiful architectural examples. Whilst the huge development of technical knowledge and technology, made this was impossible to sustain, it is still the case that the collaboration in the design/construction team is what often "makes" or "breaks" a project. In more current projects facilitated by new collaborative tools and methods of working we can clearly follow the quality of outcome through the lenses of the quality and level of collaboration.

In the past collaboration was important for achieving good value building design and construction, which, to a large extent was relating to safety and durability. Today, building design and construction have additional requirements to fulfill. Yet, collaboration remains essential in seeking approaches that can address climate crisis we are facing [1]. The high level of uncertainty, lack of resources, complexity in design and huge environmental impacts of the building sector, are only some of the challenges we are encountering. On the one hand there is a need for a creative approach and thinking out of the box, on the another – high level of technical knowledge is required to fully foresee the consequences as well as opportunities. Perhaps the most important of all is to possess the ability for critical reflection and evaluation as well as holistic approach across all building design and construction phases. It is exactly out of these needs the idea for establishing the new master's education – Architectural Technology (AT) at the Royal Danish Academy was born.

Copyright © 2023 by Olga Popovic LARSEN, Sander Løkkegaard BENNER and Sebastian Bernhard SEIPELT. Published in the Proceedings of the IASS Annual Symposium 2023 with permission.

2. The vision for the new program – architectural technology (AT)

The following two statements encapsulate the AT's main aim:

from normative to critical

from convention to vision

Globally, the building sector is fully regulated to ensure quality and safety. As a result, most technical educations worldwide educate about how to work well within current regulations. AT as a master's program, is aimed for applicants who have already completed a 3.5 years' professional bachelor's degree with the title of "constructing architects". This education provides the graduates with a technical foundation and practical skills for working within the building sector. Constructing architects are a very respected profession in Denmark. They are highly employable and skilled in working with BIM, designing and drawing of technical details, supporting architectural design work in architectural practices, supporting engineering work in consultancies, also working as contractors and developers. They are highly skilled in many very relevant aspects needed in the building design and construction practice. Perhaps, one very important skill they come with is that they fully understand current and coming up building regulations and how to operate within them.

One of the main aims for the AT education is to work further with the normative aspects, to evaluate and challenge them. We would like the graduates, through the AT education to develop skills that enable them to move from the normative to the visionary. During the two years master's program we work with critical evaluation, analysis and critical thinking to develop the current conventions into new visions. The core of the AT aims is to develop critical and reflective practitioners who will be able in building design practice to support architectural quality and develop new ways of working that will address the climate crisis.

2.1. The Danish/Nordic educational context

It is evident that educational systems differ globally, yet these differences are greater within architectural education when compared to more technical educations within the building sector. That *"There are many ways of becoming an architect"* comes from the fact that an architectural education builds on design traditions, local building culture, context, by bridging artistic, practice-based and scientific knowledge creation methods.

The Danish/Nordic context typically builds upon the artistic tradition within architectural education. This has established Danish architecture globally with buildings that embrace building form, materiality and craftsmanship growing out of the context resulting in beautiful architectural masterpieces. Widely renown are buildings as the historic Kronborg Castle, Utzon's Sydney Opera House, Housing projects by BIG, Dorthe Mandrups's Wadden Sea Centre and many others.

Within the building sector globally, but also in Denmark/Nordic region we experience increasing need for documenting safety, performance, complying with new building regulation requirements, many of these challenging architectural quality. Many of the requirements are dealt with separately making it very difficult to retain the holistic approaches required for remaining true to the architect's design vision, but also, addressing the climate crisis. These aspects are exactly what AT graduates are educated to support: architectural quality and sustainable approaches within a circular context.

2.2. AT's programme structure, semester themes and module content

The education is organised in 4 semesters of 30 ECTS points each. Each semester is a mix of taught modules – so called "*shoulder modules*" that provide the knowledge basis for the project work. There is a clear progression with increased complexity from one semester to the next with each semester organised around a specific theme:

1. *Learning from history* – is the theme for the first semester. The taught modules offer lecture courses

that give insight into past examples of Danish and Nordic architecture and discuss the lessons to be learned. The 1st semester project is a study of a recognised historic building project where after learning about the history, period, context and architecture, the students take some aspects that are especially valuable and try to bring them into a current context. Some of these, due to current building regulations or because of current building practices would be impossible to build. Alternatives are investigated that achieve the same level of quality.

2. *Sustainable renovation* – is the theme of the second semester. Courses are offered to support the project that typically deals with a large renovation project. Strategies and approaches are investigated that challenge current practice, such as renovating with as much as possible reclaimed material harvested from the renovation project itself, or working with biodegradable materials, or seeking ways to have the lowest possible renovation footprint whilst supporting biodiversity. The specific projects that come as a result of these strategies, are then developed to detail level and represented through digital models and physical prototypes.

3. *From relative to absolute sustainability* – with this theme, the third semester is organised through seminars about how to design and stay within the planetary boundaries. The main design project and investigations are closely related to the themes that the faculty – teachers are working within their research, practice, or artistic development work, broadly addressing aspects of sustainability.

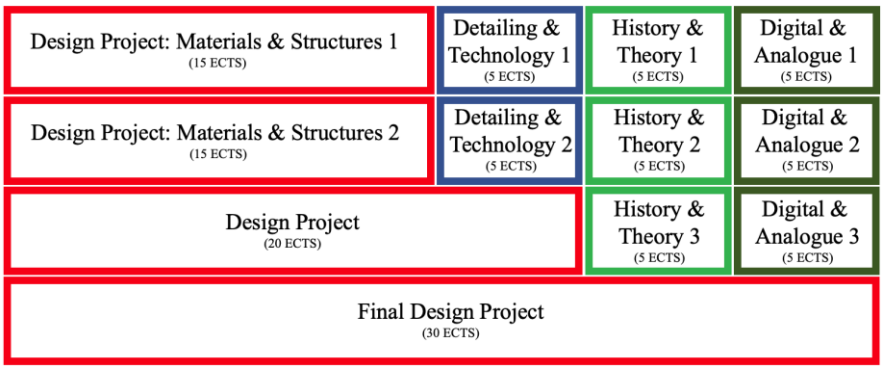
4. *Final project* – the final forth semester is used for a large independent project that will embrace all that has been learned in the previous three semesters. As a culmination the final project deals with a theme with substantial complexity and high level of development. Typically, the final project deals with a design or a research investigation that is relevant for current/future sustainable building practice where the student can show their critical thinking skills, investigation, and design skills. It is a crown - the finale of the two-year master's education.

In parallel with the taught modules and project work supervision, various workshops, including skill-building teaching is offered. These include:

- hands-on workshop skills building - working with wood, metal, concrete, glass, clay, etc.
- computation workshops: parametric tools, CFD modelling, acoustic and lighting modelling software, etc.
- hand sketching, artistic work, working with prints and paint, etc.

During the four semesters typically there are two trips, one in Denmark and one abroad as well as multiple visits to building projects under construction as well as completed ones, producers of materials, experimental practice offices etc.

Table 1. Architectural Technology – Course structure with modules overview



3. Project examples

First semester project, fall 2021: Islev church

At the very first semester, in the fall of 2021, students were divided into groups of four. Each group were assigned an existing building in the greater area of Copenhagen, where the main material consisted of either masonry, concrete, timber, or steel, which are frequently used materials for construction in Denmark. Typically, the buildings chosen were listed because of their recognised architectural qualities. The assignment was about analysing material use and construction, tendencies in contemporary architecture from when it was built, and then relate the acquired knowledge to today's construction methods, and technical requirements. It was about *learning from the past*.

One group was assigned Islev Church, a classic modern movement cubic church from 1970, with load-bearing masonry facades, and a long-span timber ceiling truss, spanning approx. eighteen meters (Figure 1). Compared to today's energy requirements in Denmark, the facades U-value (W/m^2K) would be inadequate, and even though the bonded ties with cavities require less bricks, compared to a massive masonry wall, a lot of bricks would still be needed. Therefore, theoretically, an alternative masonry wall was suggested: the diaphragm wall (Figure 2). Diaphragm wall, which means partition, separation, or division, is a form of traditionally known loadbearing masonry wall, where the inner- and outer walls are connected by bonded cross-ribs. The wall is a 2 – 2 ½ thick brick wall, between 466 – 570 mm. The cross-ribs, with a space distance between 800-1200 mm, give the wall an increased bending stiffness, dividing the wall into sections. The deeper the wall gets - the more load it can take, and more insulation can be added in the cavity. This makes it suitable for tall, single-storey buildings, such as Islev Church. Because of the length of the cross-ribs, the thermal loss through the ribs is limited and is generally assumed to have an 10% higher U-value than conventionally brick cavity walls [2], [3], which, theoretically, makes it possible to perform within the minimum U-value requirements in the Danish building regulations [4].

The roof loadbearing structure consists of four timber trusses in each direction. Because of the trusses being connected in both top and bottom in two directions, the calculated effective length of each member working in compression is halved [5]. This results in relatively slender timber members, forming a long span timber structure with relatively little material use.

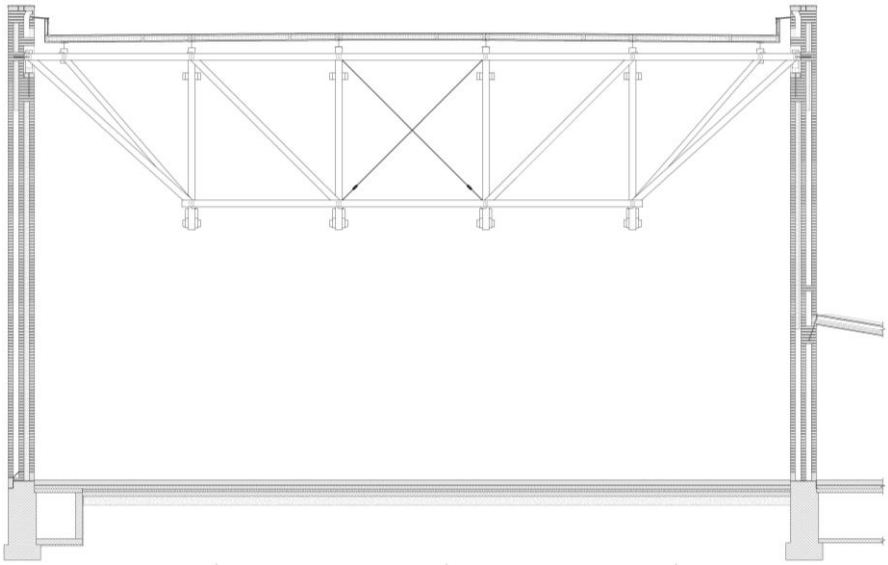


Figure 1. Cross section of Islev Church, with the original three-layer masonry walls. The masonry walls consist of three bonded layers of brick walls and two cavity spaces. The timber roof loadbearing structure, transferred the load onto the masonry walls, consists of four timber trusses in each direction that are connected. This increases the bending stiffness of the trusses.

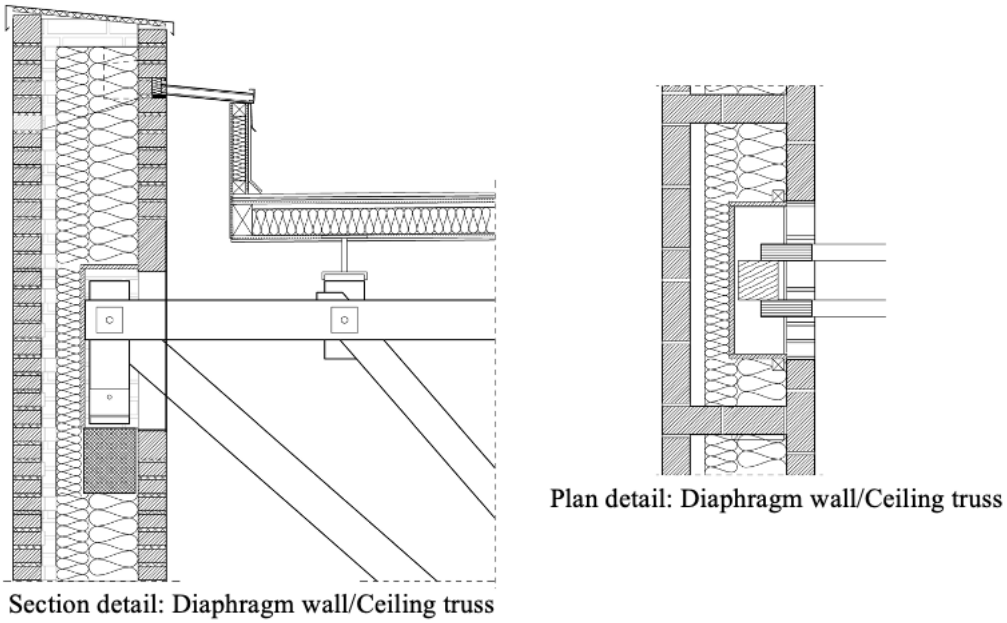


Figure 2. Connection and placement of a roof truss, with the diaphragm wall. Left: vertical detail section, showing the roof truss foot placed on a beam inside the diaphragm wall, supported by the cross ribs. Right: Horizontal detail view, showing the inner- and outer brick walls and the bonded cross ribs with insulation in the cavity.

Second semester project, spring 2022: The scarce & the reversible

In the second semester, the main theme was *sustainable renovation* and circular design approaches. The students were divided in groups, each group focusing on an existing building from between late 1940's and mid 1970's in, or near, Copenhagen, with different needs for renovation. The assignment was divided into two phases. The first was to investigate the needs for renovation, concerning poor insulation values, thermal bridges, and the general condition of the building; but also learning about architectural qualities and characteristics in the time when the buildings were constructed. The second phase was to make a renovation strategy, incorporating circular solutions. One group was assigned a two-story social housing area, build in 1948, called *Ved Kirken*.

After the second world war, in the second half of the 1940's and in the 1950's, there was a great need for social housing in Denmark. In this period a substantial number of apartment buildings were constructed, accounting for around 10% of all apartment buildings in Denmark in 2015. The 1940s and 1950s were a time with scarcity of energy and materials, which called for an optimization of traditional construction methods, where more could be obtained with less. The main characteristics for apartment buildings, from this period, are homogenic use of materials with masonry facades, and sloped roofs covered with tiles. Wall cavities were introduced in the masonry facades, reducing both material use, and construction time, as well as providing insulation properties to the wall, thus reducing the thermal loss. The façade now consisted of two brick walls connected with bonded bricks, making the wall 1 ½ brick thick, equivalent to 348 mm (Figure 3). Living rooms were often oriented towards south-west, often with a balcony, or there was a bay window, made from concrete. This period in Danish architecture, is known to have contributed with great architectural/aesthetic and cultural values, and therefore there is a wish for the architecture to be preserved. However, the buildings have issues with thermal bridges, also poor U-values (W/m^2K), mainly due to concrete in the walls crossing from the inside to the outside, also because of lack of insulation. This causes significant loss of energy, sometimes humidity with indoor mould growth, damaging the indoor climate. In many cases insulation has been added - blown into the cavity, but because of the relatively short length of the bonded ties, it is often an inadequate solution concerning thermal bridges and mould development [6], [7].

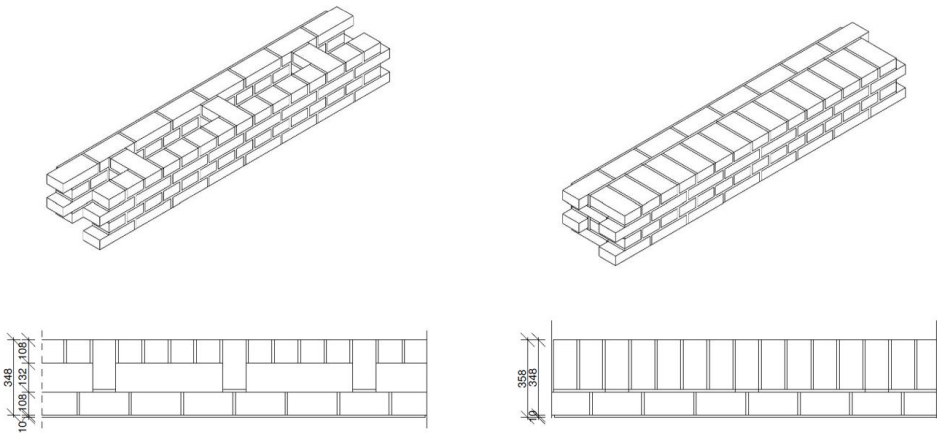


Figure 3. Left: The masonry wall, consisting of an inner- and outer brick wall, bonded together with brick ties, creating cavities inside the wall. Right: Where it was not possible to make the cavity due to structural reasons, a massive masonry wall was used instead, which is traditional in Denmark and a well-known solution

The group's main aim was to handle the poor insulation values, and cold bridges, while keeping the architectural characteristics and qualities, and to do so by adding as few new materials as possible. Danish studies have shown a short break-even time, for energy optimizing buildings from this Danish building period [8]. One aspect of the renovation strategy was to break down the outer brick layer, which, theoretically, would be possible due to the use of lime mortar used in this period [6], and "moving" the outer wall 30 mm out (because of the wish for using the existing foundation), cutting the bonded ties and eliminating the direct thermal bridges, and filling the cavity with insulation. The outer wall should then be built up again re-using the existing bricks, connected to the inner wall with mechanical mounted steel ties (Figure 4). A relevant discussion in terms of this solution was the long time -man hours needed for executing this approach. However, there is a successful precedent of a Danish demonstration project, using the same method of demolishing, insulating, and building up the wall again reusing the bricks, has been done. The results were positive both aesthetically, economically, and environmentally [9].

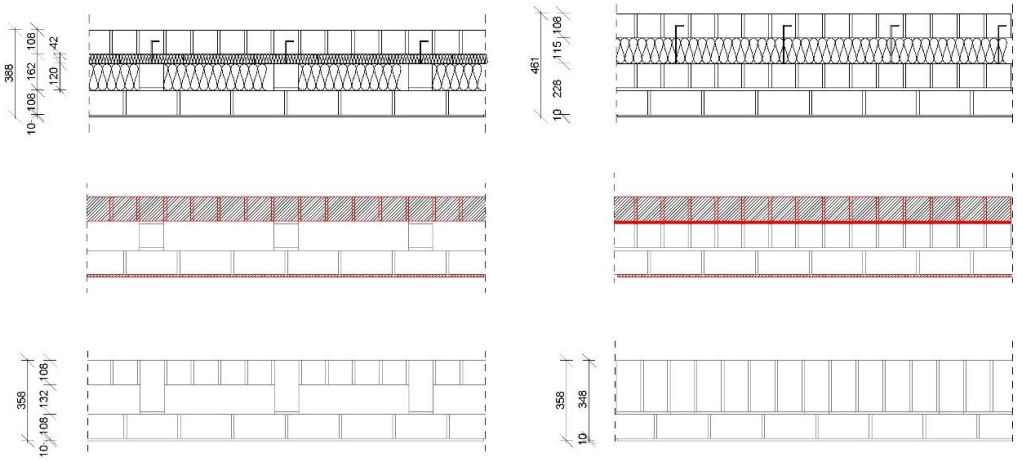


Figure 4. The process for demolishing the outer wall, insulating it, and building it up again connecting it with the inner wall using steel ties. Where there were no cavities, the students found the amount of insulation inadequate. They proposed the outer wall to be moved 30 mm. This however required further action and alterations to the foundation to be taken.

Third semester project, fall 2022: tectonics in industrialized timber structures

During the third semester, that addressed the theme *from relative to absolute sustainability*, the students were free to choose the topic of their project if it broadly related to sustainability in the building industry. One group focused on the opportunities and challenges of loadbearing timber structures between 5-8 storeys, for urban areas in Denmark. Their aim was to address local fire and acoustic regulations, deforestation tendencies globally, and carbon emissions from the building industry. In addition, the project investigated the potential for implementing re-used timber and enabling building transformations. The 5-8 storeys building height was chosen because of two main considerations:

(1) Based on studies investigating resource efficiency in different building typologies – including a 2-storey single-family house, 4 and 6-storey apartment buildings and 20 and 40-storey high-rise buildings - and various urban densities, it was identified as trend that there was higher resource efficiency in urban areas with higher density. The study identified the 4 and 6-storey apartment buildings with the lowest use of resources within the different building typologies that were studies. This was due to, among other things, a relatively low weight pr. m^2, and the greater number of people using common access ways [10].

(2) The second reason was relating to the Danish fire regulations. In Denmark, concerning fire, there are various prescriptive solutions for designing different building typologies. Here, there are two essential aspects: the calculated time for fire resistance, and the size of exposed area of wooden surfaces. Therefore, one aim for the project was to reduce the complexity of the building, by limiting the total area of exposed wooden surfaces to a maximum of 20 % of the indoor surface areas (excl. flooring). This, according to the prescriptive-accepted solutions, should not exceed 22 meters to the top floor which is the limit for the fire departments ladders in Denmark, and also, to limiting fire sections up to a maximum of 600 m^2 [11].The students choose to create an 8-storey case, consisting of a loadbearing glulam beam- and column structure considering the building's overall longevity [12]. The loadbearing parts in open plan structures, such as beam-column and beam-slab systems, don't partition the spaces, increasing the adaptability and building transformation potential.

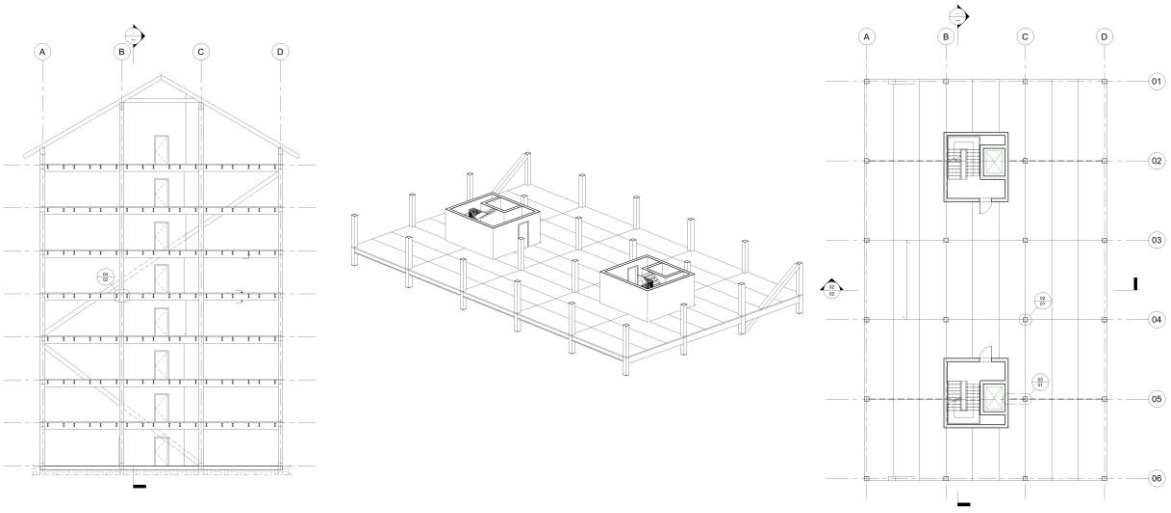


Figure 5. The students generated case. An 8-storey generic timber structure, consisting of glulam beams and columns with rib elements as slabs. The forces are transferred through the slab-elements and into loadbearing CLT-element cores. Bracing is achieved through diagonal members in the gables.

A proposal to substitute conventionally used CLT-slabs with glue less re-used timber components were introduced. For this there were several reasons. One was the environmental aspect where, regarding energy use from the production of timber products, the significantly higher consumption comes from the drying of green wood, and after that the adhesives used in e.g., glulam, plywood, and LVL [13]. Here, a large part of the total volume of materials used is related to the slabs, in the loadbearing structure. An overall wish for the case, was to articulate the loadbearing structure, keeping the beams and columns exposed, and with the assumption of difficulty in documenting re-used timber components properties concerning fire, the re-used timber could be protected by clay- or plasterboards. Here, it made sense to use re-used wood as slabs, because the ceilings would need to be covered anyway due to the 20% fire-related rule (Figure 4). The slabs used in this project case were inspired by already ongoing research projects with loadbearing, glue less, and waste wood components. The up-cycled floor-slabs consisted of structural waste wood beams, developed by PhD-student Xan Browne and the first author, which is inspired by a long-span beam system developed by Swedish Engineer Hilding Brosenius. Here, short members of reclaimed wood are put together in such a way that load is shared and transferred by each wood member. The beam members are screwed together without glue, making it suitable for disassembly and therefore each wooden peace reversable, thus reusable for further applications [14].The floor deck is a short-span re-used timber deck developed by the students themselves and inspired by a massive wood board element without glue, more suitable for longer spans, developed by Hüseyin Emre Ilgin and Markku Karjalainen [15].

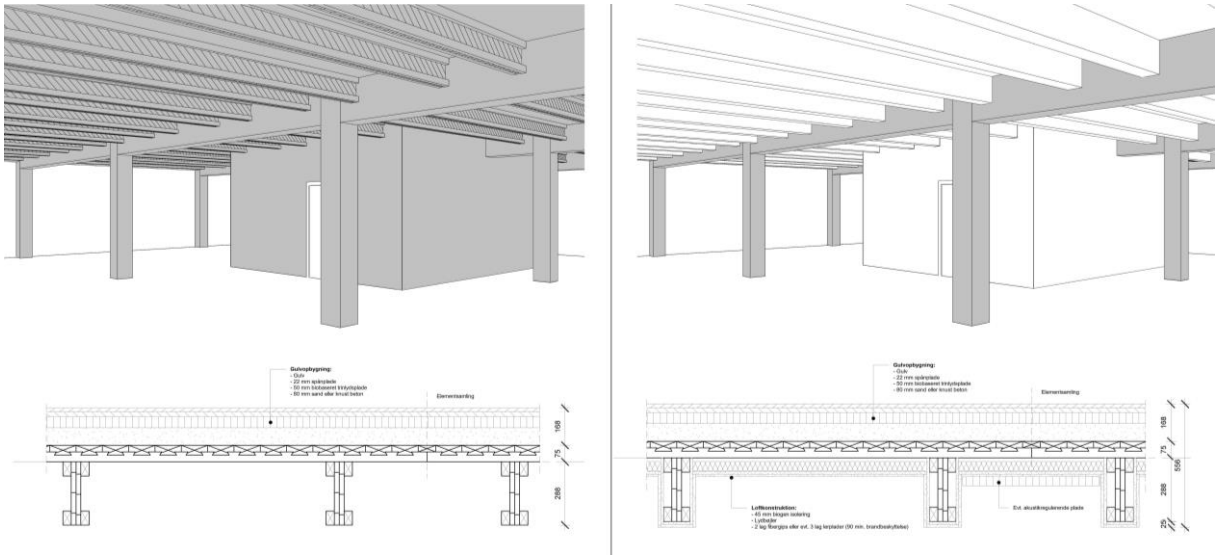


Figure 6. Top left: grey surfaces indicate exposed wooden surfaces in the case. Bottom left: section view of re-used slab-elements, with floor construction on top to reduce noise through different floor layers. A high-density aggregate was needed to reduce low transmission noise. Top right: a proposal that limiting the area of exposed wooden surfaces, by covering walls and ceilings with fire protecting clay- or plasterboards. This proposal left the glulam beams and columns exposed, articulating the loadbearing structure, while protecting the waste wood components from fire according to current Danish fire regulations.

4. AT within the Nordic, European and global educational environments

When one creates something new- it is never completely new as it has a context that it has grown out of. In creating AT it has always been a question of how this education compares with other educations within the Nordic, European and the global landscape. For us it is important what we can offer to other educational environments, but also, what can we learn from others. In that sense AT is fully new within

the Nordic context, that as described is very specific with the large knowledge/skills distance between the technical and artistic aspects within the building design professions. The evaluations of how we address the needs of the Nordic building design will show in time how we need to develop further and adjust the curriculum.

Within Europe and internationally the context is different. Even though this is true, we strongly believe that there are many good lessons to be learnt from other educations within Europe and more broadly. This is indeed our aim for the years to come to map the landscape of educations that we can compare with and offer and gain from each other's experiences that can inspire further developments for us and others, too.

5. Conclusion: submission of contributions

The paper presented the aims, vision, and program development of the new two- year master's education "Architectural Technology" at the Royal Danish Academy in Copenhagen. By outlining the module structure and module contents as well as describing some of the design projects, it is hoped that the reader will get a flavour of what the education offers. It is for the first time that we will have graduates finishing the program and graduating in the end of June 2023. It is a question time and following the graduates to see if they become the ones who integrate the building sector, support architectural quality and sustainable approaches. The fantastic project results we have seen so far give us faith that the coming up AT graduates are the ones who will challenge the normative and work further with the visionary, helping us build better and with more sustainable approaches in mind. We are looking forward to learning from other similar and different educations internationally.

Acknowledgements

Many have a great contribution in establishing and developing the Architectural Technology new education. The AT program would have not been possible without Natalie Mossin, architect and Institute leader at IBT, The Royal Danish Academy, Kirsten Nielsen chair and Jette Leth Djælund deputy chair of the Danish professional association of Architectural Technologists, Peter Hinsby – philosopher and PhD candidate at The Royal Danish Academy, Frans Drewniak, Architect and Associate Professor at The Royal Danish Academy, to name just a few. A huge thank you goes to the AT teaching team as well as the AT master's students for the great engagement, trust and input.

References

[1] O. P. Larsen, *Conceptual structural design: Bridging the gap between architects and Engineers*. London: ICE Publishing, 2023.

[2] W. G. Curtin, G. Shaw, J. Morton, W. A. Bray, and J. K. Beck, *Design of brick diaphragm walls*. Windsor, Berks.: Brick Development Association, 1990.

[3] M. J. Jensen, "Revitalisering af murværket," Ph.D. dissertation, Kunstakademiets Arkitektskole, Institut 1, Copenhagen, 2011.

[4] Bygningsreglementet, "Energiforbrug og klimapåvirkning (§ 250 - § 298)," *BR18*. [Online]. Available: https://bygningsreglementet.dk/Tekniske-bestemmelser/11/Krav/257#3e7c9938-9116-46a9-b468-2a571006ca9b. [Accessed: 21-Mar-2023].

[5] H. F. Mathiasen and E. Reitzel, *Grundtræk af Bærende Konstruktioner I Arkitekturen*. Kbh.: Kunstakademiets Arkitektskole, 1999.

[6] C. Bech-Danielsen, P. Heiselberg, and A. Høi, *Renoveringsguide: Kvaliteter, Udfordringer og Anbefalinger: 1940'erne og 1950'ernes murede boligbebyggelser*. Kbh.: Realdania, 2015.

[7] N. V. Riis, S. Petersen, J. D. Buhl, L. Ø. Pedersen, B. T. Eybye, H. E. Andersen, M. B. Lyhne, and M. A. Morgen, *Bygningskultur og Klima: Undersøgelse af Eksisterende Viden Om Livscyklusvurderinger og bevaringsværdier*. Realdania, Aarhus, 2021.

[8] K. Kanafani, A. M. Lund, A. S. Worm, J. D. Jensen, H. Birgisdottir, and J. Rose, *Klimaeffektiv renovering: Balancen mellem energibesparelse og materialepåvirkninger i bygningsrenovering*. København: Institut for Byggeri, By og Miljø (BUILD), Aalborg Universitet, 2021.

[9] Danakon, "Energirenovering af det murede boligbyggeri med genbrug af de oprindelige mursten," Industrial practice report, fsb, 2015.

[10] S. Weidner, R. Bechmann, and W. Sobek, "Why urban mining is inevitable: Analyzing the resource consumption of urban structures," 2022.

[11] Bygningsreglementet, "Brand (§ 82 - § 158)," *BR18*. [Online]. Available: https://bygningsreglementet.dk/Tekniske-bestemmelser/05/Vejledninger. [Accessed: 29-Oct-2021].

[12] A. Beim, Vibæk Kasper Sánchez, and T. R. Jørgensen, *Arkitektonisk Kvalitet & Industrielle byggesystemer*. Kbh.: Kunstakademiets Arkitektskole, CINARK, 2007.

[13] M. H. Ramage, H. Burridge, M. Busse-Wicher, G. Fereday, T. Reynolds, D. U. Shah, G. Wu, L. Yu, P. Fleming, D. Densley-Tingley, J. Allwood, P. Dupree, P. F. Linden and O. Scherman, "The wood from the trees: The use of timber in construction," ELSEVIER, Cambridge, 2017.

[14] H. Emre Ilgın and M. Karjalainen, "Massive wood construction in Finland: Past, present, and future," *Wood Industry - Past, Present and Future Outlook*, 2022.

[15] X. Browne, O. P. Larsen, N. C. Friis, and M. S. Kühn, "Material Value(s): Motivating the architectural application of Waste Wood," *Architecture, Structures and Construction*, vol. 2, no. 4, pp. 575–584, 2022.

Teaching of shell and spatial structures

Active bending
Additive manufacturing/ 3D printing
Architectural geometry
Bamboo for sustainable construction and quality of life improvement
Bio-inspired structures and architecture
Bridge structures
Computational form-finding
Conceptual design
Concrete structures
Construction techniques
Deployable and inflatable structures
Design competition (WG21)
Digital modelling and fabrication
Dynamic response of metal spatial structures
Dynamic response of other structures
Form-finding and structural optimisation of interlocking discrete assemblages
Graphical methods
Gridshell and lattice structures
Historical concrete shells
Historical structures
Lattice structures
Life-cycle design and assessment of structures
Metal gridshell structures, connections and stability
Methods and construction technologies for sustainable shell structures
Morphology and configuration processing
Next generation parametric design
Novel methods in modelling, optimisation and construction for reducing carbon footprint of continuous roof shells
Numerical methods for geometry, form-finding and optimisation of lightweight structures
Optimisation methods and applications
Origami
Other
Teaching design uncertainty: working with unknown qualities/quantities of new and re-claimed materials
► **Teaching of shell and spatial structures**
Tensegrity systems and cable structures
Tension and membrane structures
Tension structures in the Asia-Pacific
Timber and bio-based structures
Topology optimisation
Traditional masonry structures and innovation
Transformable structures

IASS 2023
July 10–14 Melbourne
Integration of Design and Fabrication

Proceedings of the IASS Annual Symposium 2023
Integration of Design and Fabrication
10–14 July 2023, Melbourne, Australia
Y.M. Xie, J. Burry, T.U. Lee and J. Ma (eds.)

Acoustic and structural design embedded in design studio pedagogy

Sofia COLABELLA*, Michael MACK[a]

* The University of Melbourne, Faculty of Architecture Building and Planning
s.colabella@unimelb.edu.au

[a] The University of Melbourne, Faculty of Architecture Building and Planning

Abstract

This paper presents a theoretical framework and pedagogical principles for performance-based design education focusing on acoustics and structural behaviour within the architectural context of the Melbourne School of Design of The University of Melbourne. Our architecture students have limited exposure to acoustics and structures, and both can be mistakenly perceived as engineering disciplines confined to specialists, taking place after a design idea is formalised. A design studio, *CDE Studio 45* [1], developed and taught by the authors for the past three years within the Master of Architecture Course of the Melbourne School of Design, is showcased in this paper to illustrate how structural behaviour, acoustics and music can drive design education and engage students intellectually and creatively, shifting between analytic, synthetic, and evaluative modes of design thinking (performance-based, model-making, computational design). Physical models of shell-like structures are developed and recursively tested through critical listening exercises and analogue acoustic simulations to visualise sound propagation (Figure 1). Proposals undergo acoustic analysis and optimisation via geometric acoustics methods and Multi-Objective Genetic Algorithms (MOGA) to evaluate and improve the final design's acoustic performance, allowing students to verify their design processes. Students' final designs demonstrate a capacity for critical design thinking driven by landscape, acoustics, structural and material systems, and detail considerations.

Keywords: Design studio pedagogy, shells, acoustics, structural behaviours, communication, design education, design research, research methods.

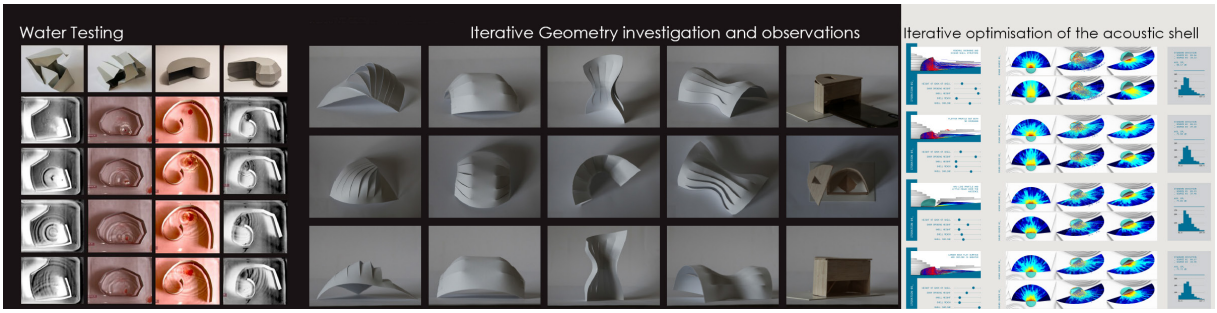


Figure 1. Amplify Your Phone exercise by Jeremy Bonwick. The physical models and listening tests informed the creation of digital models, run through a ray tracing simulation program to acoustically optimise the shells' final shape (reproduced by permission).

1. Context and background

The University of Melbourne adopted the *Melbourne Model* in 2008 to replace its 96 undergraduate courses; it involves seven undergraduate degrees supporting depth and breadth of knowledge. One of

Copyright © 2023 by Sofia COLABELLA and Michael MACK. Published in the Proceedings of the IASS Annual Symposium 2023 with permission.

the main aims is to develop a student's broad understanding across a range of disciplines. Introducing flexibility meant, specifically for a faculty of architecture, focusing on a wide range of disciplines instead of providing students with a strong technical background. On this aspect, teaching structures and acoustics within an architectural/design context poses a range of challenges in fine-tuning the way the technical content is conveyed in an appealing and meaningful manner. As Popovic described in 2015, "an engineer will spend a large proportion of their time studying how to minimise and optimise structural sections to achieve material economy through structural efficiency; these aspects of the structural concept design, for an architect, although relevant, may be secondary to other "more relevant" design aspects" [7].

This difference in values and approaches becomes even more delicate and complex when teaching acoustics, as vision dominates our relationship with architecture, both as users and designers. As prompted by Juhani Pallasmaa, in "Western culture, sight has historically been regarded as the noblest of the senses and thinking itself thought of in terms of seeing". According to the Finnish architect, that has long been entrenched in our culture as he quotes, "the eyes are more exact witnesses than the ears" [5]. The process of design and how we represent architecture through renders, diagrams, and drawings are all inherently visual exercises.

In response to this ocular-centric approach, we developed and taught a design studio (*CDE Studio 45*) within the *CDE Design Studios* coordinated by Professor Donald Bates in the Master of Architecture Course at the Melbourne School of Design for the past three years, based on the concept that structural behaviour and acoustics can drive design education and engage students intellectually from the early stages of design concepts. We aimed to expose our students to acoustics and structures not as engineering disciplines confined to specialists taking place after a design idea is formalised, but as creative tools to generate ideas at the inception of the design process. We purposely flipped the creative process to scaffold students' critical reflections and design thinking through tectonics, material, and performative investigations while enquiring "how to make the technical teaching content relevant, interesting and applicable" [10] [11].

Introducing students to acoustics seemed an obvious choice also because, despite the acoustic quality of buildings being vital to well-being, room acoustics are often the forgotten variable [5] of architectural design, resulting in an individualistic (and late) effort of acoustic engineers to correct or improve the acoustics of spaces. As recording and microphone technology, the arts of music, drama and public discourse have influenced and been influenced by the acoustics and architecture of their presentation environments [7] [1], we introduced basic concepts of music education to remove the instinctive relegation of acoustics to a pure engineering discipline.

2. Music and acoustics in architectural design education

CDE Studio 45 [1], is based on a recursive approach to design thinking through structural behaviour and acoustics as creative tools enabling design education and engaging students intellectually and shifting between analytic, synthetic, and evaluative modes of design thinking (performance-based, model-making, computational design). This design studio was conceived to expose students to a holistic understanding of architectural form, acoustics, and structural design, while considering the behaviour of materials to make informed design decisions that consider the technical and functional requirements of a building, along with its aesthetic qualities. Exposing students to engineering principles (both structures and acoustics) allows them to face opportunities, limitations, and implications of their design decisions; having this set of skills is meant to prepare them to collaborate with specialists and be more effective and well-rounded professionals in their field.

Despite the challenges of integrating technical aspects into the architectural design context, teaching structures in a design studio has long been trialled worldwide [10]. While we can learn from this integration, teaching architectural acoustics in a design studio has additional complications: (1) sound is invisible, and soundscape can change at any moment [12]; (2) how we experience and perceive sound

is a subjective process, and how, as architects, we design through it is still based on the intuitive approach and the trial-and-error experience on which knowledge about acoustic design is currently based [2]; (3) though computer simulations enabling the rapid testing of what-if scenarios alongside acoustic analysis and visualisation have been developed and made broadly available, there is a level of abstraction and understanding to overcome.

CDE Studio 45 is structured around these aspects, the outcomes of which are discussed and shown in section 4. A key element of the studio pedagogy is the intention to teach students to approach and understand sound and structural behaviour intuitively through the exercise *Amplify Your Phone* presented in section 3.

Introducing basic principles of music to design studio education acts to remove the distinction of acoustics as a purely engineering discipline. Alongside instruction in the physics of sound, acoustic, and lighting design, students receive a lecture on music performance and instrumentation, which ties acoustic principles and measures to aural effects. Some examples of this include acoustic measurements of reverberation time and initial time delay gap, which are chained to principles of clarity and articulation, and diffusion spacing in panels linked to harmonic and overtone frequencies.

Instruction on the relationship between music listening and acoustic outputs introduces students to the vocabulary needed to assess acoustic outcomes, providing them with the necessary skills to communicate with acoustic consultants and musicians. Through practical demonstration, key difficulties in designing performance venues can be more easily demonstrated. The level of subjectivity resulting from listening and observing music is also encouraged and discussed, softening the learning curve into approaching acoustics. This is a critical educative point, as students are demonstrated the importance of balancing visual intent with the acoustic outcome. Combined with prototyping and model-making, these initial observations become an essential method of design validation (Figure 1).

Prompted by David Byrne's exploration of the history of how context has led musical innovation [3], we have developed an all-rounded set of tools and workflow to allow students to shift between analytic, synthetic, and evaluative modes of design thinking through (1) model-making and grammar of sound; (2) digital models and performance-based design; (3) optimisation through MOGA and reflections on the final outcomes; (4) detailing of the main stage, both structurally and acoustically; final review of the festival program and design outcomes.

3. Theoretical framework and pedagogical principles

During the first three weeks of the semester, students investigate the basic concepts of acoustic and lighting design to explore the relationship between form and acoustic performance through physical models of acoustic shells. Students familiarise themselves with the reciprocal determinations between architectural forms and acoustic performance through the design group exercise, *Amplify Your Phone (AYP)*, to become aware of the geometric relationship between architectural form and acoustic performance. The AYP recursive exercise is based on a sequence of tasks: **listening** (A); **making physical models** (B); **evaluating acoustic qualities** (C); **making digital models through parametrisation** (D); **comparing the winning solutions and reflecting on the design thinking process** (E).

During this initial phase, each group of students is required to select three songs, varying in genre, instrumentation, and textures; students listening awareness is tested through their capacity to skilfully describe their listening experience using specialist terminology, the existence of which is unknown for the majority of them (A). Simultaneously, students are tasked with iteratively **making physical models** (B) to find a persuasive design and optimal acoustic shell geometry to amplify their phones. Listening to the chosen three songs with and without the acoustic shells allows them to test the amplification of their smartphones while refining their listening awareness. Figure 2 shows Alba's reflections on four iterative scale models based on the use of three different material systems and four shape variations.

Students usually focus on clarity and amount of amplification because detecting other parameters, such as reverberation, would be almost impossible at such a small scale. By using different materials, students learn to identify the unique qualities of each material and how they affect the overall performance of a given shape.

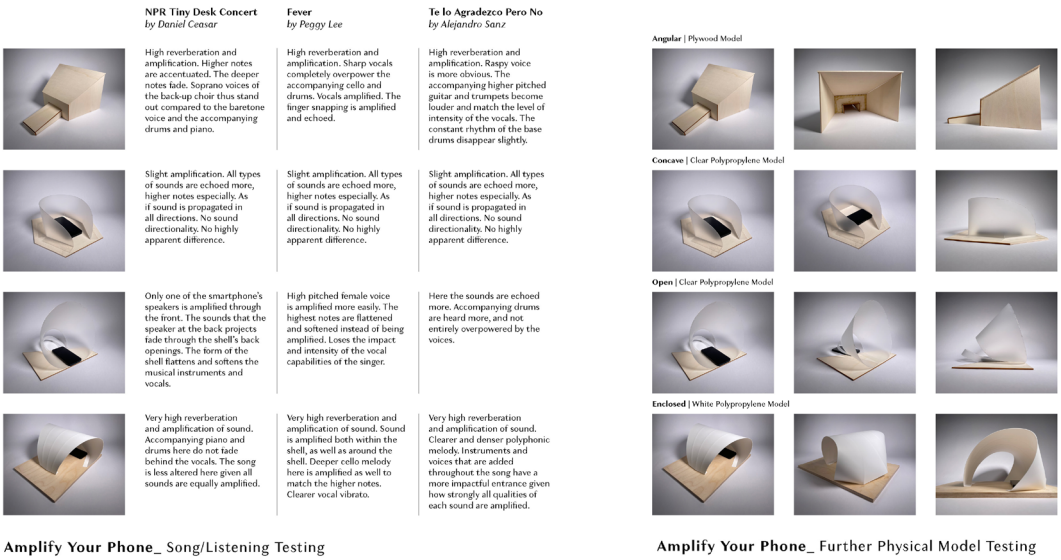


Figure 2. AYP, scale model studies and listening tests by Alba Moncau Munio and Michael Ming Park (reproduced by permission).

Alongside the listening exercises, students are introduced to **analogue evaluation techniques** (C) involving light and water, which simulate the ray and wave effects of sound. These tests consolidate students' understanding of sound interactions with geometry through visualisation. Students insert lights or a laser pointer into a reflective card or aluminium model for the lighting tests (based on those done by Alvar Aalto for the Municipal Library of Viipuri). To perform the water tests (based on the experiments by Jørn Utzon for the *Bagsværd Church*), students develop the shell profiles in sections out of aluminium or plexiglass and place them in a small pool of water. Coloured droplets generate waves, and a video is recorded in slow motion. Frames at consistent time periods can be extracted to compare the effects of different sections and annotate their observations. As shown in Figure 3, students fine-tune the shell profiles by adjusting them consistently as they repeat the tests.

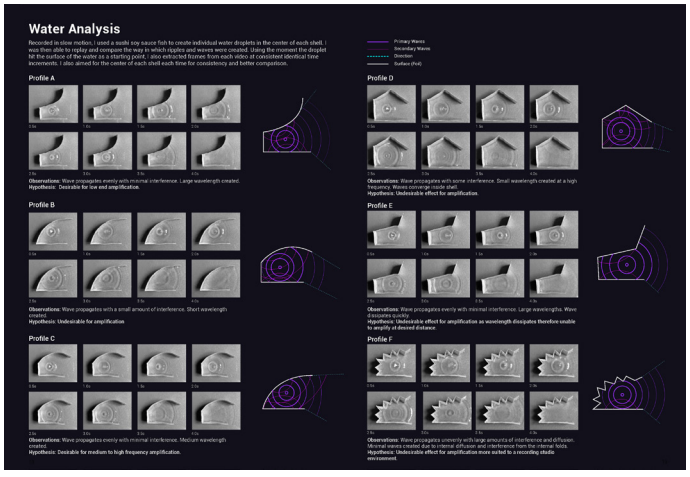


Figure 3. Observing sound through the water and light tests by Isabel Solin (reproduced by permission).

From these initial prototypes, students select and transform the best-performing shells, based on their observations, into a set of **digital models** by expressing their winning solutions as a function of specific quantities or parameters; they also select one or more invariances as the guiding principle of their design. Both invariances and parameters are essential to determine the next set of tests (D) through two acoustic simulators, *Pachyderm* 2020 and *Aeolus* 2021 and 2022, to compute the sound reflection paths and associated sound pressure levels (SPLs) at one or multiple target locations [8].

The final stage of this first assessment task is **comparing** the acoustic analyses and observations gathered from the physical models listening and testing phase for verification and validation (E). By comparing the two data sets, students can identify any discrepancies or inconsistencies between the objective and subjective observations. This analysis can also help students understand the relationship between the measurable qualities of acoustics and the subjective experiences of sound while developing a more nuanced understanding of the complexity of acoustics and how the human ear perceives it.

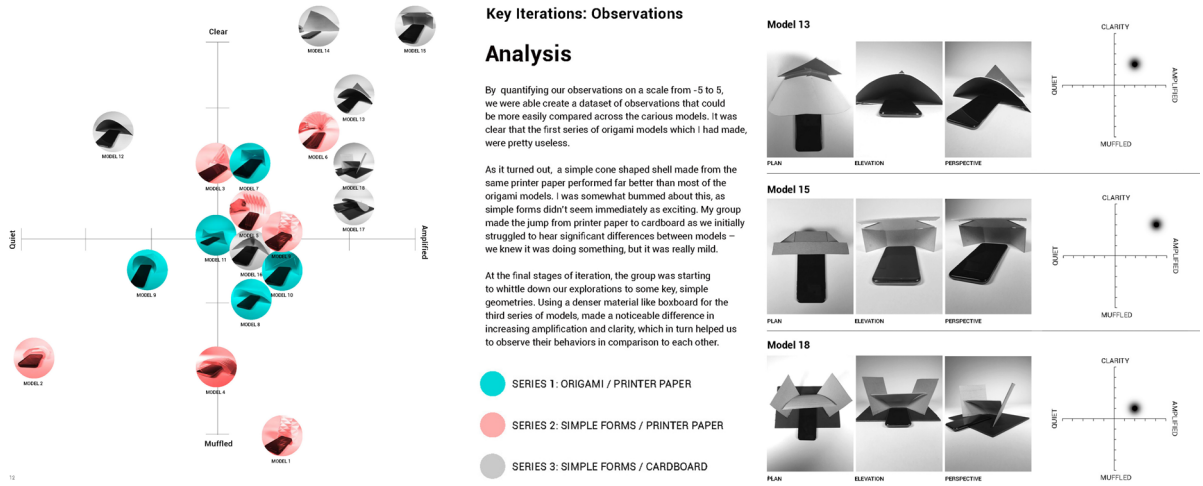


Figure 4. Dataset of listening observations by Isabel Solin, Michael Gentile, and Alessandro Antoci (reproduced by permission).

After the first three weeks, students apply their new knowledge to the given brief related to the requalification of an abandoned quarry in regional Victoria (AU) through the activation of a Music and Art Precinct comprising different programs. Performing Art Centres can contribute to community development in many ways, and students are also tasked with the redevelopment from a social and environmental standpoint. The design brief comprises 50% of the site to be revegetated for environmental sustainability and 50% for temporary activities for a range of community events linked with the Art Precinct and the Music Festival programs.

By the end of week 12, students will demonstrate to be able to: [1] develop the brief and the planning of a live art performance and events venue for a Music Festival; [2] simulate acoustic performance and lighting phenomena; [3] define and improve the acoustic and lighting qualities of their architectures; [4] communicate design ideas and propositions through a variety of media; [5] present their work verbally to an external panel of architects and engineers; [6] design a live-performing venue at different scales (1:1000 to 1:5). Overall, students will have learnt to use computational tools for acoustic analysis (the graphical algorithm editor *Grasshopper*® within *Rhinoceros*®) to evaluate and improve the acoustic performance of their design. The geometric acoustic analysis consolidates students' acquisition of how each variable impacts the shell performance, which in turn will generate a review and further refinement of their design, which includes all the BoH (Back-of-House) and FoH (Front-of-House) facilities of a performance venue (e.g. foyer, box office, food and toilet services, backstage facilities, car parking, etc.), and the ticket and audience area, which are discussed as a consequence of the effective audience

sight-lines to the stage and predicted acoustic qualities. The final challenge is balancing the architectural intent and aesthetics with the optimisation and performance of the acoustic shell. While the aesthetic aspects of a performance space are crucial for a visually appealing and immersive experience, its acoustic properties will massively impact its fruition and success. To strike this balance, students must consider the performance space's form and function, acknowledging that even if it is a common belief that acoustics can always be adjusted later, the best performance venues are the ones that prioritise acoustics at the early stages of the design process.

4. Acoustic design framework: in practice (CDE Studio 45)

The *CDE Studio 45* pedagogical framework is designed to encourage students to explore the multifaceted correlations between music, acoustics, structural design, and architectural design through 12-week activities. For the scope of this paper, we primarily focus on the outcomes of the first three-week exercise, *Amplify Your Phone*, based on the five tasks (A-E) explained in section 3 and how this exercise informed the translation into an architectural proposal. Over the last three iterations of this design studio activities, students have demonstrated and developed an affinity for specific aspects of the exercise, favouring parts of the acoustic testing methods over others, mostly based on their specific interests or passions and previous knowledge. Each student highlights different approaches to acoustic design thinking developed through the teaching framework.

Incorporating maker pedagogy into design studio education is a well-known tool to empower students to experiment, explore, and express themselves while developing critical thinking and problem-solving abilities [5]. In *CDE Studio 45*, the consequences of making and material choices are explored through the listening exercise in a recursive loop: students reproduce the same shell geometry with different materials to develop a more nuanced understanding of the properties (and possible uses) of acoustic materials. Given the small scale of the prototypes, echoes, reverberation, resonance, and reflection cannot be observed. Still, students generally get an initial understanding of the different capacities to absorb or reflect sound and noise due to the high and low density of materials. The exercise AYP doesn't provide a rigorous listening method for assessing acoustic performance, given the scale issues and external considerations such as surrounding objects and their materials. However, even with these constraints, prototypes still show noticeable differences. Repeating the listening exercise under the same conditions allows students to detect and identify the differences through aural observation.

The way students approach the given architectural design brief is illustrated below through a set of selected works produced by students within *CDE Studio 45.*

The first example (Figure 1) shows an initial workflow based on the rapid prototyping of structural forms. Hann Lynn Chan focused on broadly experimenting with a variety of structural configurations via a range of folded geometry. Qualitative analysis via listening and lighting tests was used to perform an initial survey to provide immediate feedback on the design iteration process. Trends between positive listening tests and lighting conditions were established through this prototyping process and used for further design iterations and narrowing of the design space. Eventually, a preliminary set of parameters for the shell's overall dimensions and form was developed.

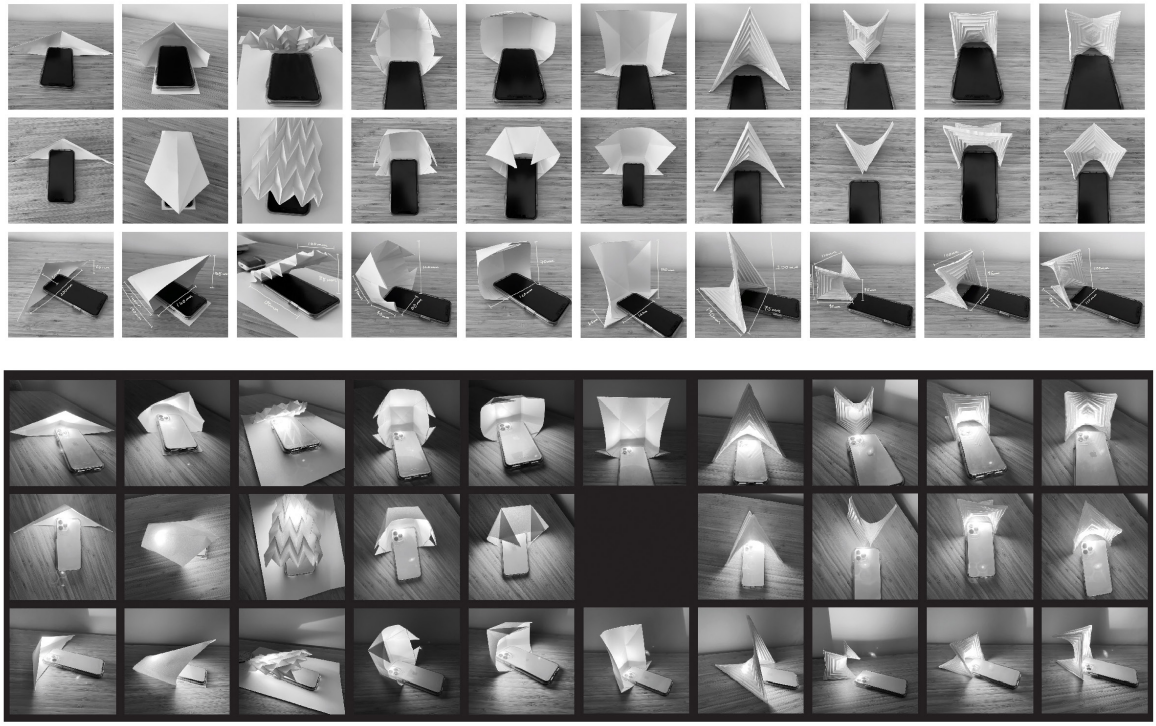


Figure 5. AYP, scale model prototyping and lighting testing by Hann Lynn Chan (reproduced by permission).

The best-performing examples based on Hann Lynn's qualitative evaluations are then converted to parametric models for acoustic analysis and optimisation, shown in Figure 6. This workflow proved useful for students less proficient with digital skills and parametric design tools: focusing on the model-making process provides them with a shortcut to iterate and optimise their designs through analogue methods before moving into the multi-objective optimisation process.

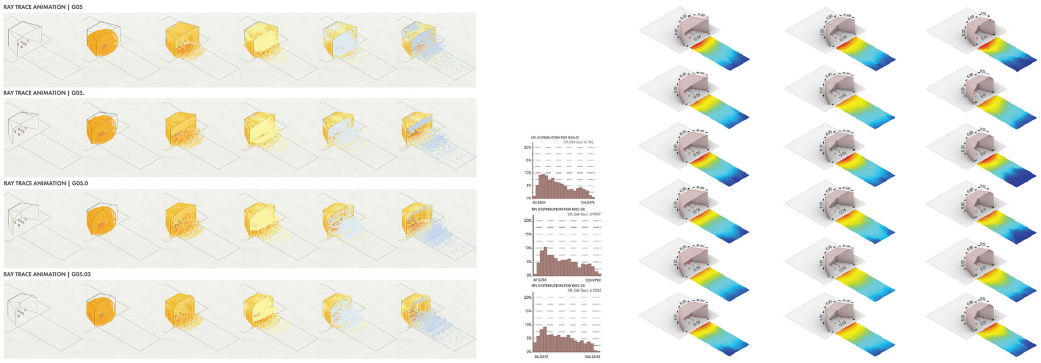


Figure 6. AYP, multi-objective optimisation of shortlisted designs by Hann Lynn Chan (reproduced by permission).

Figure 1 (page 1) shows Jeremy Bonwick's approach to the task, initially focused on the qualities of abstract architectural and sculptural forms: a wide variety of initial prototypes were tested and qualitatively ranked based on the initial impressions of their acoustic performance. Parallel to this, favourable samples were modelled in section using aluminium, placed in a shallow tub of water, and dropped with red food dye to visualise the wave propagation in each form (Figure 1, left). The flexibility of the aluminium models meant that several sections could be easily tested through adjustments in the model and repeating the test.

The outcomes of these analogue water tests from the AYP exercise informed Jeremy's approach to the architectural form in the following stage of the design process. He recognised that after scaling up the geometry to an architectural scale, the opening of the model's section where the projection of the waves occurred had to be developed geometrically and architecturally. By revolving the section around an axis, Jeremy could incorporate structural considerations into the shell-like structure. This process led to the development of the parametric model and optimisation process for the final acoustic shell structure shown in Figure 7.

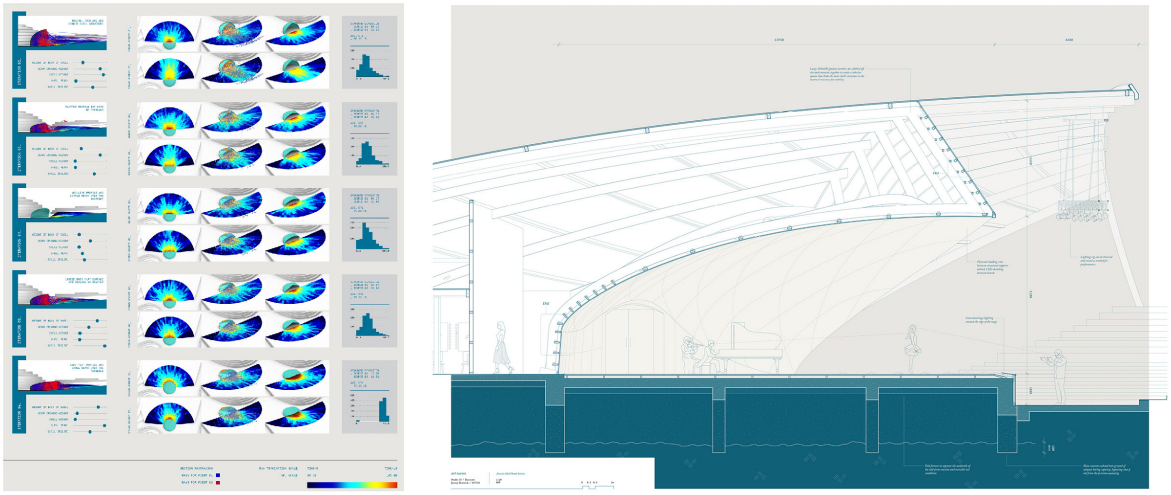


Figure 7. Translation of sectional model testing into an architectural proposal for an acoustic shell by Jeremy Bonwick (reproduced by permission).

Figure 8 shows a workflow largely based on material exploration: Alba and Michael's prototypes were constructed from cardboard, polypropylene, plywood, solid timber, and 3D-printed clay to explore the material impact on acoustic quality. Though the students acknowledged the materials were not necessarily translating full-scale acoustic properties, they observed a noticeable difference between the prototypes demonstrating their understanding of the relationship between material density and observed musical outcome.

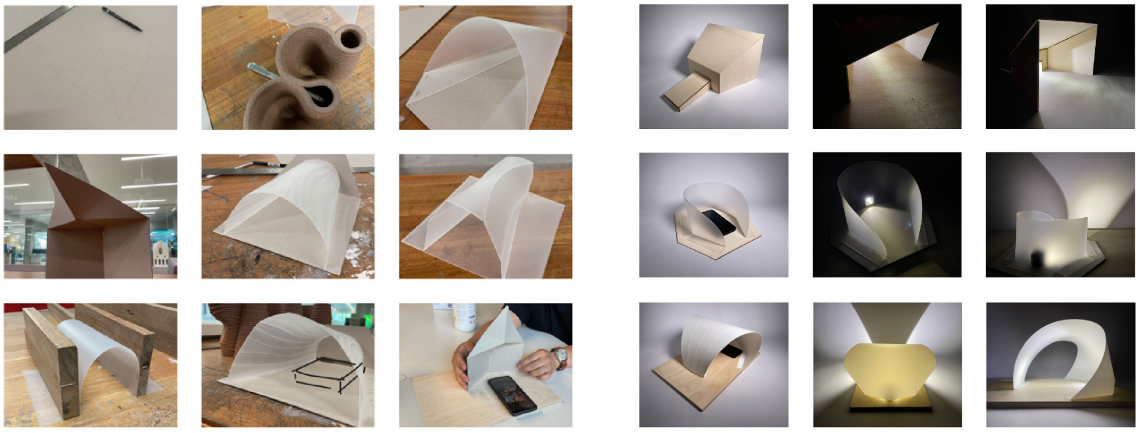


Figure 8. AYP material exploration and prototyping by Alba Moncau Munio and Michael Ming Park (reproduced by permission).

Michael and Alba selected the prototype to develop further based on the potentially novel architectural conditions of a laterally open audience area. The selected design shown in Figure 9 included strong rear reflections but necessitated an acoustic reflection strategy that improved the lateral distribution of sound.

The students recognised they could utilise the folding strategy developed in the AYP prototyping to accomplish and establish a discretisation approach that included both the acoustic and structural considerations for the ribs.

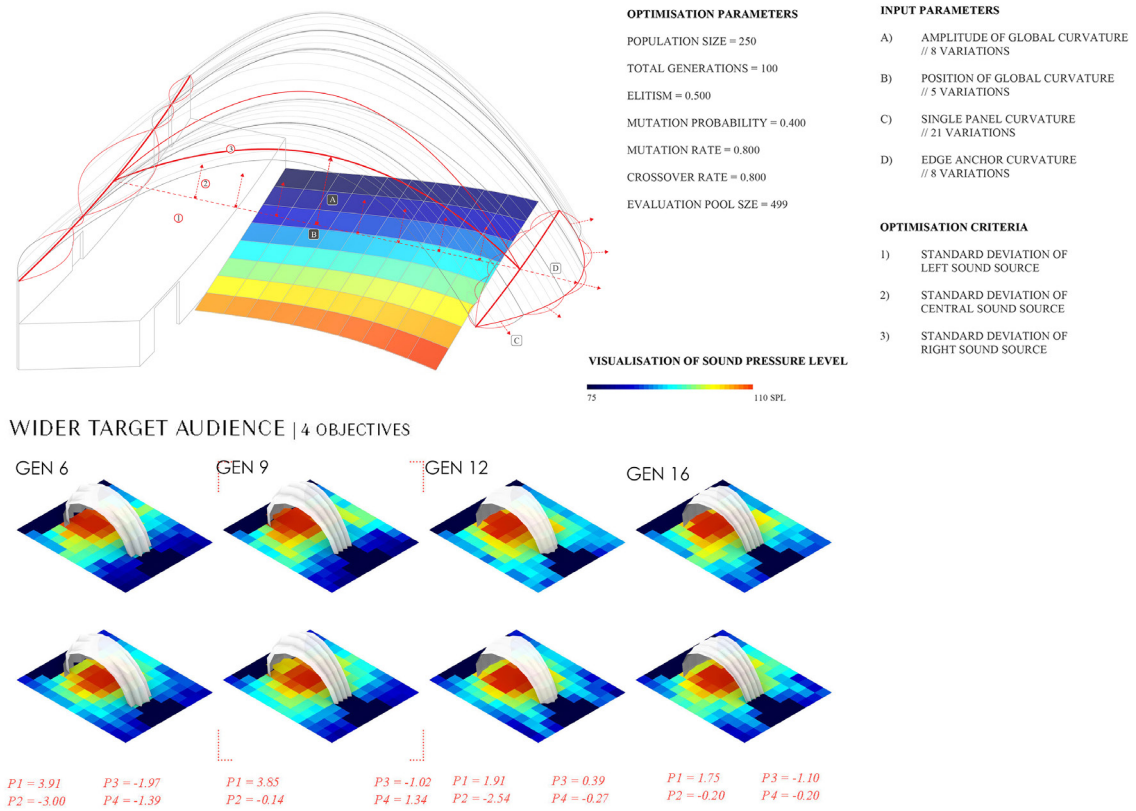


Figure 9. AYP material exploration and prototyping by Alba Moncau Munio and Michael Ming Park (reproduced by permission).

Unlike previous examples that developed the project formally or through the verification process, Vincent Heru's work (Figure 10) illustrates the development of an architectural proposal through an interest in acoustic principles. In his AYP exercise, Vincent prototyped a few panelised and folded geometries to attempt to observe the acoustic scattering effects. Unfortunately, this was largely unsuccessful as these effects could not be analysed at the scale at which the tests were being formed. Nonetheless, Vincent utilised learned principles of geometric acoustics to demonstrate a fundamental understanding of the acoustic ray tracing method through photos and sketches.

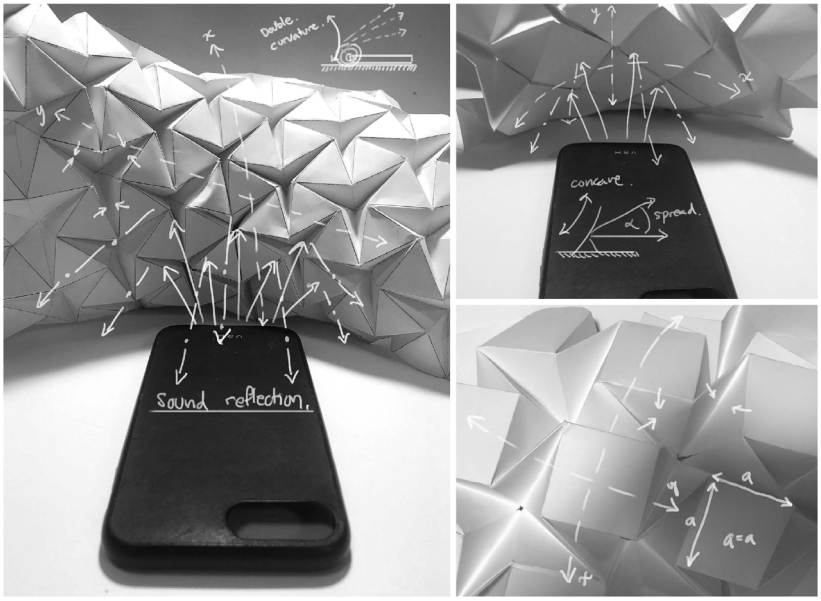


Figure 10. Preliminary sketches of ray tracing analysis of folded structures by Vincent Heru (reproduced by permission).

The models relied largely on three-dimensional representations and flexible materials for the scale of construction, making other analogue tests difficult to perform. However, an abstracted sectional model and water testing validated Vincent's understanding of the scattering effects (Figure 11). The analysis and diagramming of these tests further illustrate the development and consolidation of the relationship between acoustic principles and form.

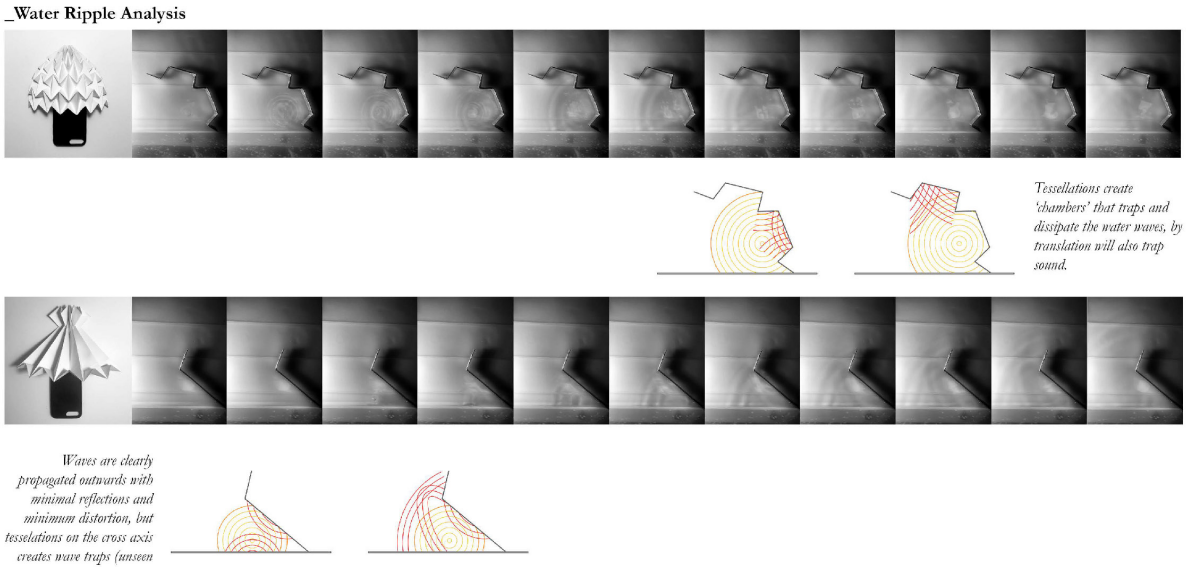


Figure 11. Water testing of diffusion and scattering-like effects by Vincent Heru (reproduced by permission).

For his architectural proposal, Vincent took the opportunity to explore scattering effects as a conceptual driver. Using a digital model for analysis and verification, Vincent developed a single reflector device suspended over the performance area, which distributed sound to the surrounding audience areas (Figure 12). Using precedents of vineyard-style concert halls, he recognised that acoustic performance could

also be compensated for by the lateral reflections of the side walls and back of the shells, resulting in the outdoor yet intimate performance setting.

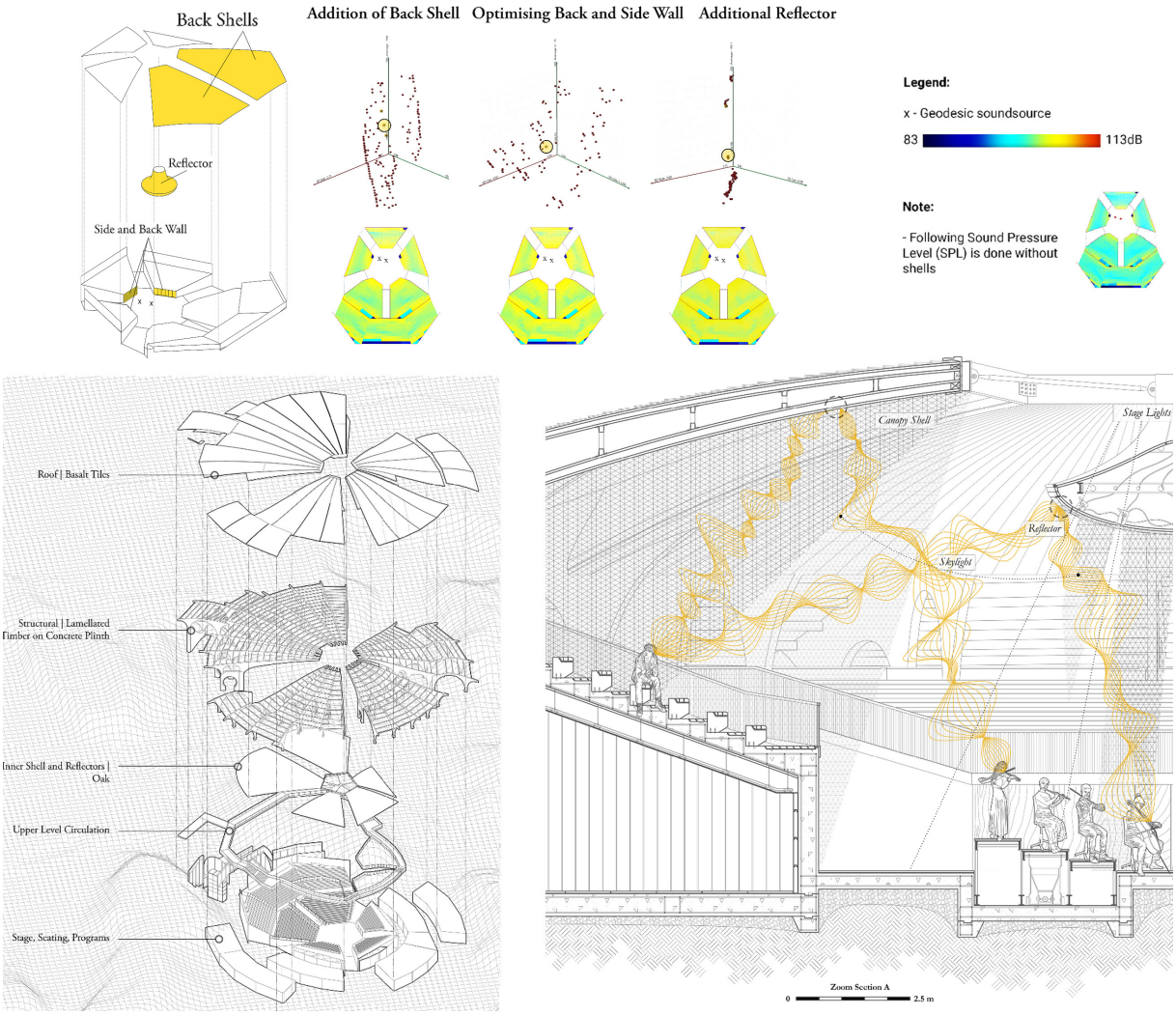


Figure 12. Architectural proposal of vineyard-style outdoor performance venue by Vincent Heru (reproduced by permission).

5. Conclusions

CDE Studio 45 presents a novel framework for teaching acoustic and structural design within Architectural discourse and embraces a radical removal of the boundaries between architecture and perforative, technical disciplines; it shows that a qualitative (and initially intuitive) approach to tectonics and acoustics can enable a creative approach to design and sustainable thinking. The examples in section 4 show how the pedagogical framework can successfully introduce students to acoustic design principles while remaining flexible enough to independently explore performance-based design solutions crafted around their individual interests and design propositions. As illustrated, students interested in structural techniques such as folding, or material exploration, can find accessible ways of developing acoustic design within their architectural education.

Though the early student explorations were largely within the scope of the AYP exercises, there is space for future research into how students utilise the ideas and develop them into the approach for their architectural proposals. Furthermore, the examples are taken from a Master of Architecture Course, with

students in their 4th and 5th year of architectural education. If applied earlier in the architectural curriculum, there may be an opportunity to understand how the framework may foster opportunities for acoustic design considerations and performance-oriented approaches, also at the undergraduate level.

Architectural education can easily provide opportunities for architecture students to learn about the relationship between performance-based design and aesthetics while providing a comprehensive education that includes both technical and creative aspects of building design, leading to a holistic understanding of the opportunities and limitations of their design decisions. Architecture students would then be able to graduate with the skills and knowledge needed to work collaboratively with engineers and develop more innovative and sustainable building designs.

Acknowledgements

We acknowledge the exceptional support of Professor Donald Bates, Chair in Architectural Design at the Faculty of Architecture, Building and Planning of The University of Melbourne, and master's studio coordinator at the same institution. We also acknowledge Peter Fearnside, former CEO and founder of Marshall Day Acoustics Australia, for the enthusiastic encouragement, patient guidance and useful critiques throughout the delivery of our teaching activities. His passion, knowledge and attention to detail inspired our students and us. We were lucky to have Gabriele Mirra as a technical tutor for our design studio because, on top of his technical knowledge, he allowed our students and us to use his work-in-progress version of *Aeolus*, a *Grasshopper* acoustic modelling plugin to analyse and optimise acoustic shells that was later made publicly available in March 2023.

References

[1] M. Asgaard Andersen, *Jørn Utzon Drawings and Buildings*, Princeton Architectural Press, 2013.

[2] L. Beranek, *Concert Halls and Opera Houses: Music, Acoustics, and Architecture*, Springer, 2004.

[3] D. Byrne, *How architecture helped music evolve*, TED Talk, 2010, https://www.ted.com/talks/david_byrne_how_architecture_helped_music_evolve/transcript?language=en.

[4] M. A. Crum, N. D. Matkin, "Room acoustics: The forgotten variable? Language, Speech, and Hearing Services in Schools", 7(2), pp. 106–110. https://doi.org/10.1044/0161-1461.0702.106.

[5] A. C. Gade, "Acoustics in halls for speech and music" in T. D. Rossing (ed.) *Handbook of acoustics*, Springer, 2007, p. 302.

[6] I. Harel, S. Papert, *Constructionism*, Praeger, 1991.

[7] M. Long, *Architectural Acoustics*, Elsevier Science & Technology, 2006.

[8] G. Mirra, https://www.food4rhino.com/en/app/aeolus and G. Mirra, E. Pignatelli, S. Di Rosario, "An automated design methodology for acoustic shells in outdoor concerts", Proceedings of the Euronoise 2018 conference, Hersonissos, Crete, 27-31 May 2018.

[9] J. Pallasmaa, *The Eyes of the Skin: Architecture and the Senses*, John Wiley & Sons, Incorporated, 2012, p. 18.

[10] O. Popovic, *Conceptual Structural Design: Bridging the gap between architects and engineers*, Thomas Telford Limited, 2003.

[11] O. Popovic, "Teaching spatial structures for complex requirements", in *Proceedings of the International Association for Shell and Spatial Structures (IASS) Symposium 2015*.

[12] M. Schafer, *The Soundscape, Our Sonic Environment and the Tuning of the World*, Simon & Schuster, 1977.

Proceedings of the IASS Annual Symposium 2023
Integration of Design and Fabrication
10–14 July 2023, Melbourne, Australia
Y.M. Xie, J. Burry, T.U. Lee and J. Ma (eds.)

Educational tools for arch and frame structures

Ayaka KONDO*, Shigehiro MOROOKA[a]

* Graduate Student, Graduate School of Engineering, Tokai University
2cckm006@mail.u-tokai.ac.jp

[a] School of Architecture and Urban Planning, Tokai University

Abstract

It is difficult for those new to structural mechanics to imagine a cross-sectional force diagram. For this reason, we have created structural educational tools aimed at deepening the understanding of structural mechanics for students studying structure. It is capable of vibrating a small model and visualizing the cross-sectional forces of the structure. To calculate the cross-sectional forces from the deformation of the structure, ArUco markers in OpenCV were pasted on the nodes to obtain the deformation. ArUco marker is a marker that can be detected and its coordinates obtained by taking a picture with a webcam. Calculate the cross-sectional force using the amount of rotation obtained from the coordinates of the four corners of the marker. The calculated cross-sectional forces can be viewed in real time by drawing them on the model in the shooting screen. The structures targeted in this study are arched and framed shapes.

Keywords: open CV, python, arch, ArUco marker, educational tools

1. Introduction

In understanding structure, it is very important to be able to visualize mechanical phenomena. Since forces are invisible, the only way is to imagine them. But it is difficult for beginners to imagine the cross-sectional forces that occur within the members when a structure is deformed. We believe that struggling with these basic areas and feel uncomfortable. For this reason, we have created a structural education tool that aims to deepen understanding of structural mechanics by enhancing the ability to visualize cross-sectional forces, and to stimulate their interest in structures. The system consists of two parts: a behavior display system created from Python and OpenCV that can display model behavior and cross-sectional forces in real time, and a model. We can observe changes in the sectional force of a model when it is vibrated. The model is captured by a webcam. And calculates cross-sectional force from the rotation angle of a node and draws a cross-sectional force diagram on the shooting screen. It is not important to see the exact cross-sectional force values, but to be able to see the distribution of cross-sectional forces and the relationship between ones. By using this educational tool to deform your own model and view cross-sectional force diagrams, you will acquire the ability to visualize cross-sectional forces, which we believe will help facilitate your subsequent study of structures. This part describes the creation of a behavior display system, a structural model, and a vibration table. The structures targeted in this study are arched and framed shapes.

2. Outline of behavior display system

2.1 Calculation of cross-sectional forces

Measuring deformations with strain gauges or displacement sensors can provide accurate values, but it is not practical to measure multiple points simultaneously. Therefore, in this study, we will capture deformations from a web cam. However, it is difficult to take a photograph and recognize the shape of

Copyright © 2023 by Ayaka KONDO and Shigehiro MOROOKA. Published in the Proceedings of the IASS Annual Symposium 2023 with permission.

the structure from the image data and draw a cross-sectional force diagram from the deformation of the structure, because depends largely on the accuracy of the webcam and takes a lot of time to recognize images of moving objects. It can also lead to misrecognition if the images are very confusing and difficult to judge. Since the deformation between nodes is small, it was decided to recognize the nodes of a structure with large deformations, and to calculate and visualize the sectional forces based on changes in node positions.

ArUco marker was used to recognize nodes (see in Figure 1). ArUco marker is an extension module of OpenCV. It can easily recognize a marker by simply capturing it with a webcam and the coordinate values of its four corners and the id number of the marker can be obtained. By attaching this to a node, it is possible to easily recognize the node and track its movement.

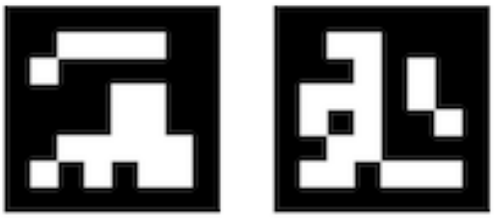


Figure 1. ArUco marker

First, I checked if it is possible to draw a sectional force diagram using Aruco markers. Two ArUco markers are recognized by taking a picture with a web cam.

Calculate the deformation v and the sectional force of a member based on the rotational angles θ_1 and θ_2 obtained from the coordinate values of the four corners of ArUco markers at both ends of the member (see in Figure 2).

$$M(x) = -EIv''(x) \tag{1}$$

$$v(x) = a_0 + a_1 x + a_2 x^2 + a_3 x^3 \tag{2}$$

$$a_0 = 0\ , a_1 = \theta_1 \tag{3}$$

$$a_2 = (-2\theta_1 - \theta_2)/L \tag{4}$$

$$a_3 = (\theta_1 + \theta_2)/L^2 \tag{5}$$

E is the Young's modulus, I is the moment of inertia, and L is the length of the member.

The bending moment M and the shear force Q can be calculated as follows by using the coefficients a_0, a_1, a_2, a_3 obtained from the above equations.

$$M = -(2a_2 + 6a_3 x) \times EI \tag{6}$$

$$Q = -6a_3 \times EI \tag{7}$$

In this case, the initial state is set as the shape recognized by the ArUco marker first, and the rotation amount from that state is used. By overlaying the calculated sectional forces onto the model in the captured image, a real-time sectional force diagram was displayed. (see in Figure 3)。 The performance of the webcam used in this study was 1920 x 1080p pixels at a frame rate of 30 fps.

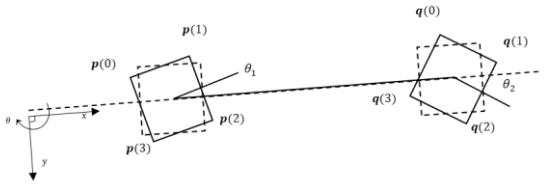


Figure 2. The rotation angle of the node

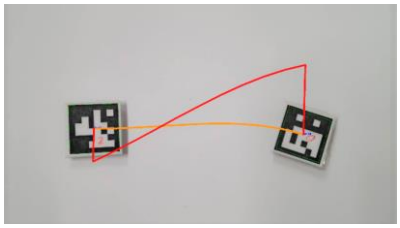


Figure 3. Bending moment calculated from the amount of rotation of the ArUco markers at both ends.

2.2 Arch shape

Create an arch model with ArUco markers and display a cross-sectional force diagram. The arch model was created using cardboard with a length of 450mm and a width of 20mm, a double clip with a width of 13mm, and magnets with a size of Φ5×3mm. A double clip was attached to a cardboard, and an ArUco marker was attached to the double clip with a magnet (see in Figure 4). An arch shape was created by bringing both ends of the cardboard close together and fixing them (see in Figure 5).

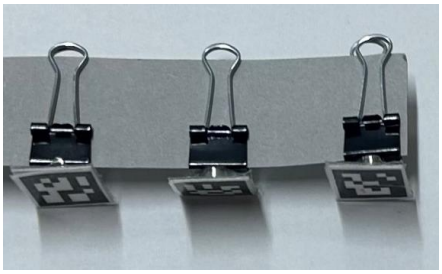


Figure 4. Details of combination

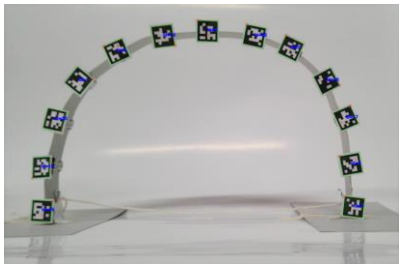


Figure 5. Overall view of arch model

The shape of the model before deformation is read and recognized as the initial state. By hanging a weight at the center of the model and deforming it, it is possible to see the bending moment diagram by calculating the sectional force from the change in the ArUco marker from the initial state.

Figure 6 displays a cross-sectional force diagram of a model divided into 12 parts using ArUco markers.

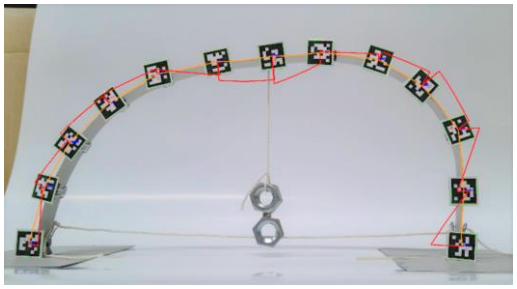


Figure 6. Bending moment of Arch model

2.3 Frame shape

To enable learners to create various shapes freely, model kits with frame shapes are constructed separately with nodes and members, rather than one frame model (see in Figure 7). Nodes require a 30mm square wooden material to attach ArUco markers and to provide enough mass for visible changes

in tremors to be observed by the eye. For members, we searched for materials that are easy to bend and decided to use PVC sheets. The widths of the members are changed so that the changes in the cross-sectional force diagram can be seen due to differences in stiffness. The difference in stiffness is distinguished in the program by changing the color of the member parts. This time, we prepared three types of members: green, blue, and red. The nodes and members were joined by inserting a 0.5mm-thick member into the nodes with a slit of 5mm depth and 0.5mm thickness on the fourth surface. However, problems occurred, such as members not being inserted completely or at an angle. Therefore, we changed the method of joining the nodes and members by partially shaving 0.2mm of a 0.7mm-thick PVC sheet with a CNC machine and inserting it from the side of the node part to avoid discrepancies caused by incomplete or angled insertion (see in Figure 8).

.



(a) Frame model (b) Parts of frame structure

Figure 7. Frame Model Structure

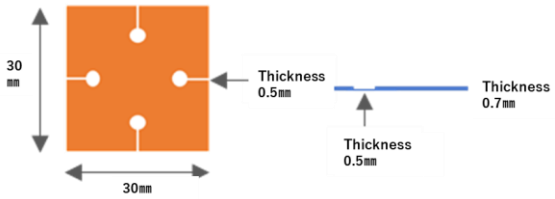
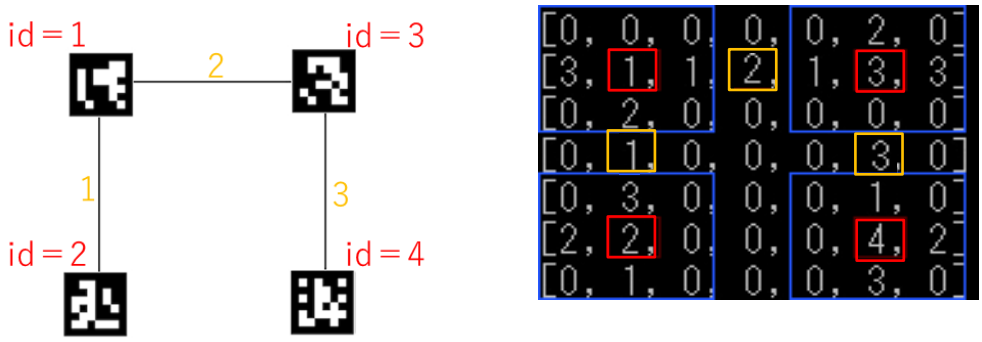


Figure 8. Details of node and member

The method of calculating cross-sectional forces for frame structures and arch models is the same, but it is designed to be able to handle various shapes of structures, so it is necessary to recognize the assembled shape by checking whether there are members between the recognized nodes with ArUco markers. To recognize the members, we searched for the specified color within the middle one-third range between the nodes to determine whether or not there were members. However, there were cases where parts could not be recognized well due to changes in color caused by the lighting conditions and the thinness of the parts.

Therefore, a new method for recognizing parts was considered. First, the model is vibrated. In this case, since the model is read from the state where it is being vibrated, the initial state of the structure is assumed to be one in which the columns and beams pass through the center. Using the image differencing, assuming that there are members in the moving parts in the image, we determine whether there are members between nodes. Then, if a member is recognized, the color of the member within the middle one-third range between the nodes is read, and a histogram is created. Then, we adopted the method of determining the color of the member as the one with the highest number of data in the histogram.

To facilitate data processing, the position relationship between the recognized nodes and members is stored on a table (see in Figure 9). The blue square area within the 3x3 table is where the node information is recorded. Put the id number of the ArUco marker in the red square, and the face number to know which side of the marker is connected to the member on the top, bottom, left and right of the id number. When a member is found between adjacent nodes, the member number is entered in the orange square in order of discovery, starting from 1. By following this procedure, the program is able to understand the shape of the structure.



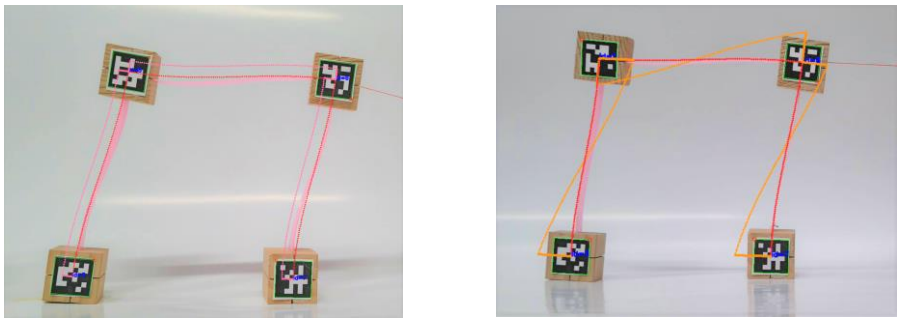
(a) Model to be read (b) location table of nodes and members

Figure 9. How to memorize structures on the program

After recognizing the shape, we calculated the sectional forces from the rotation angles of the nodes, and then plotted them on the captured image (see in Figure 10).

We also displayed the time history graph and the FFT results of the horizontal displacement of the specified nodes, and calculated the natural period (see in Figure 11).

By adopting a member recognition method using image differencing and identifying only the part of the member, we were able to recognize colors independently of the background of the model. On the other hand, while the column section can be recognized, there are times when the beam section cannot be recognized due to small differences in the differential. In addition, the nodes and members are created by hand, which slightly affects the cross-sectional forces depending on their accuracy. However, the distribution of the cross-sectional force diagram is displayed correctly, so there is no problem in terms of understanding the cross-sectional forces.



(a) shear force diagram (b) bending moment diagram

Figure 10. Cross-sectional force diagram of frame structure

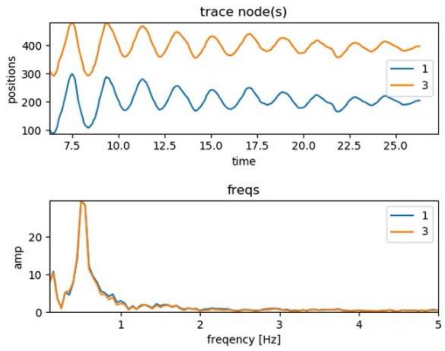


Figure 11. Time history change of nodal position (upper) and FFT (bottom)

2.4 Recognition of bracing material and calculation of axial force

To create a structural educational tool that allows for viewing of sectional force diagrams for various combinations of structural elements, we added bracing materials. We used rubber bands as bracing materials. Because the addition of brace materials required the ratio of stiffness between the brace and column-beam, experiments were conducted to determine the stiffness. We added brace members as shown in Figure 12. The recognition range is set slightly inside from the node. Search for the color specified as representing braces within the recognition range and determine the presence or absence of brace material. The axial force of braces cannot be calculated using the rotation angle of the nodes. Therefore, the axial force of the brace was calculated using the deformation amount of the brace length.

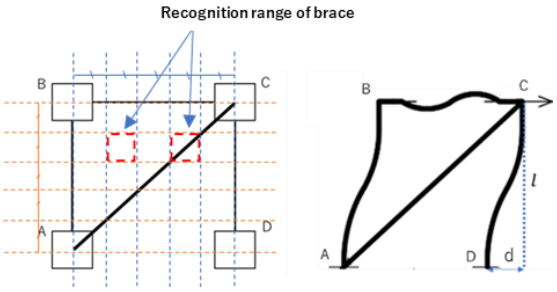


Figure 12. Deformation of structure with braces

Similarly, for the brace material, the braces are numbered from 1 in the order they are found in the positional relationship table and stored in the program. If there is a brace with a right diagonal line, put the number in the red square, and if it has a left diagonal line, put the number in the orange square (see in Figure 13).

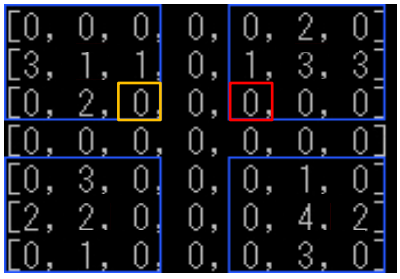


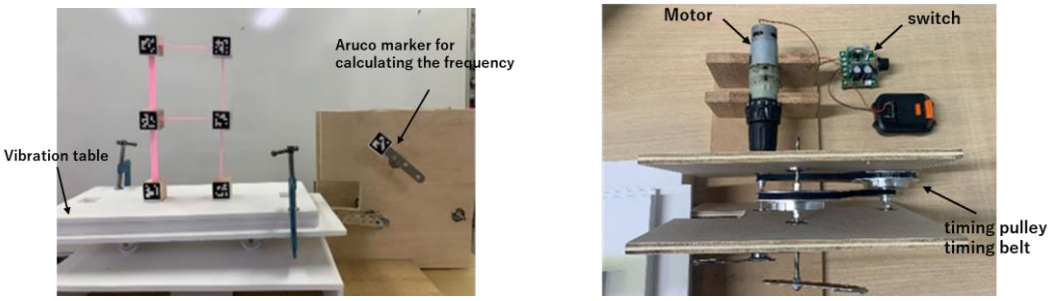
Figure 13. location table of brace

3. Vibrating table

A vibration table was created that can vibrate a model actually created (see in Figure 14). Styrofoam board is used for the foundation, and the power unit applies vibration using the motor of an electric drill.

To give a long-lasting vibration at a constant speed, the switch of the drill was replaced with a volume control type, allowing easy speed adjustment.

Furthermore, the vibration frequency of the vibration table was displayed on the shooting screen to match the behavior display system (see in Figure 15). Calculate the frequency from the coordinate values of an ArUco marker. However, it is difficult to obtain accurate values because the amplitude is small when tracking the behavior by attaching a marker to the vibration table. Therefore, we decided to install ArUco markers on the motor part to determine the vibration frequency. However, it is impossible to track the behavior of the ArUco marker because the rotation of the motor is too fast. By creating a mechanism to slow down the rotation using a timing pulley and timing belt, it became possible to track ArUco markers and determine the vibration frequency.



(a) Overall view of vibration table (b) Power unit and a mechanism

Figure 14. Vibrating table

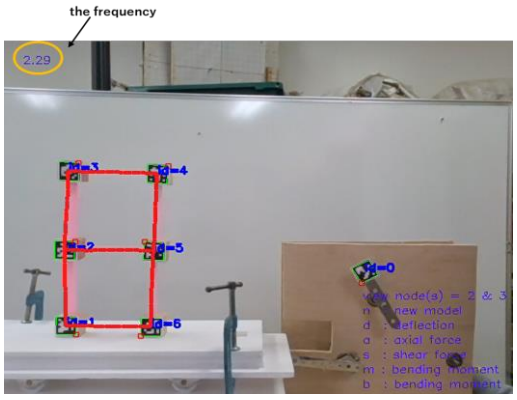


Figure 15. the frequency of the vibration table

4. Conclusion

As the model parts are made manually, there are variations in quality, which affect the cross-sectional force diagram. Furthermore, since the vibration table was made of styrofoam board to reduce weight, there is a possibility that there is a wobble due to the weight of the model. Therefore, it is necessary to improve the quality of the nodes and change the material of the vibration table. Another challenge for the future is to develop a method to easily recognize the model without using ArUco markers and to adapt to pin connections.

References

[1] OpenCV: Detection of ArUco Markers

IASS 2023
July 10–14 Melbourne
Integration of Design and Fabrication

Proceedings of the IASS Annual Symposium 2023
Integration of Design and Fabrication
10–14 July 2023, Melbourne, Australia
Y.M. Xie, J. Burry, T.U. Lee and J. Ma (eds.)

Mid-to-long term reflections on a project based learning initiative in civil engineering education

Ramsha SALEEM[a,*], S. Alireza BEHNEJAD[b], Anesa HOSEIN[c]

[a,*] Water, Energy, and Industry, WSP
Ramsha.Saleem@wsp.com

[b] Spatial Structures Research Centre, University of Surrey
[c] Surrey Institute of Education, University of Surrey

Abstract

This paper explores the state of flux within civil engineering education with universities facing demand from the ever-evolving industry to develop graduates with the desired skillsets and values. It discusses the transition in pedagogic approaches towards learner-centred models and evaluates the implementation of the Project-Based Learning (PBL) tool to shape the next generation of practicing civil engineers. A case study application of such a tool is explored in the form of the Design, Assemble and Dismantle (DAD) Project delivered during the first year of the civil engineering undergraduate programme at the University of Surrey. This Project is of an experiential nature where the student is placed at the centre of the pedagogic process. In order to fully understand the advantages of integrating this pedagogic tool in higher education in terms of enhancements it can make to the attributes developed and growth experienced by students, interviews with 20 participants of the DAD Project between 2015-2021 were conducted. The collated reflections depict the Project as an effective mechanism for developing an array of skills and values, including problem-solving, team working, leadership, communication, and cultivating a shift in mindset whereby students become more holistic, active, and conscious learners with a greater sense of accountability; all of which are paramount for the challenges of the 21st century.

Keywords: design, fabrication, spatial structures, civil engineering, tactile education, pedagogy, globalisation, collaboration

1. Introduction

'Tell me, and I will forget. Show me, and I may remember. Involve me, and I will understand.' The importance of a collaborative, interactive and engaging approach to pedagogy in which a hands-on student-centred model enhances the learning and retention process was recognised as early as 551 BCE by philosopher and politician Confucius.

There have been significant developments in civil engineering higher education over the last few decades with a shift in both the content delivered and pedagogic approaches adopted. The trend has transgressed from the traditional 'chalk-and-talk' format towards a more active learning, student-centered approach, focusing on the integration of engineering theory with hands-on practice in a multidisciplinary environment [1]. This transition is arguably steered by the increasing pressures placed on higher education institutions from of a multitude of external industrial, societal, and environmental challenges, to ensure that future generations of civil engineers are equipped with the skillsets required to overcome these. However, despite this increasing shift in teaching methods, civil engineering higher education is deemed to still consist predominantly of deductive one-way pedagogic frameworks [2].

Copyright © 2023 by Ramsha SALEEM, S. Alireza BEHNEJAD and Anesa HOSEIN. Published in the Proceedings of the IASS Annual Symposium 2023 with permission.

This paper discusses the main skillset domains that higher education institutions aim to develop within their students and the changing requirements within these relative to the wider changes in the civil engineering industry. It outlines the two main methods through which institutions can meet these changing demands; the content of their courses and the pedagogic methods through which they are delivered. The paper then explores the implementation of the PBL tool through a discussion and evaluation of the hands-on collaborative initiative, the DAD Project.

The DAD Project is a two-phase hands-on initiative which was developed at the University of Surrey in 2014 for civil engineering (and architecture) students, integrating both design and fabrication. The first phase of the Project involves groups of students designing a full-scale steel spatial structure and preparing all the required documents for assembly, including technical drawings, a list of requirements, method statements and risk assessments. During the second phase, a design exchange occurs in which each group is given the set of documents prepared by another group during phase one to assemble and dismantle the designed structure within a two-hour time limit. This example of PBL embodies all of the fundamental aspects of inductive pedagogy through its student-centred hands-on approach, developing team working and leadership skills, communication skills encompassing both verbal and written forms, interdisciplinary collaboration, problem solving skills and providing the freedom to cultivate creativity and independent thinking. The paper evaluates the benefits of the above initiative in terms of the skills and attributes it instills within its participants. In order to attain mid-to-long term reflections, the research conducted is in the form of a qualitative evaluative one-to-one interviews with selected participants who had participated the Project two or more years ago. Thematic content analysis is then undertaken to determine common patterns and trends, thus composing a holistic view on the value of PBL pedagogy.

2. Literature Review

Higher education is a pivotal stage in the development of civil engineers entering the industry. The abilities and attributes that higher education institutions aim to cultivate in their students can be categorised into two main domains: defining skills and enabling skills [3]. Unique to engineering students, the former encompasses technical skills consisting of sound disciplinary knowledge of fundamentals built on a strong mathematical foundation and the ability to apply that theory in practice in a creative and innovative manner [4]. The latter category consists of a set of abilities that are deemed to enable students to integrate and work capably within the industry through effective communication, problem solving, decision making, team working and leadership skills [5]. It is the combination of these two domains, as illustrated in Figure 1, that forms the 'core competencies' of a well-rounded engineering graduate and underpins their role in the industry today as a technical specialist who can work across boundaries in a complex environment, providing creativity, innovation, and effective leadership in the face of new challenges [4].

Of the aforementioned skills, those deemed most important for engineering graduates entering the industry are theoretical understanding, practical application, creativity, and innovation. However, one of the biggest current concerns is the lack of practical application within the theoretical framework delivered by civil engineering higher education institutions [3]. This integration of theory and practice within the learning experience is deemed critical in developing innovative graduates who can work through open-ended challenges [4]. While the primacy of the defining skills is clear, several studies also stress the equal importance of the enabling skills and deem those as the attributes that ultimately make a successful engineer in the long term [3]. Perhaps the criticality of the latter arises from their increasing importance within the wider evolving industry. The disciplinary fundamentals required of an engineer are of a more fixed nature, however the array and degree of enabling skills required continues to vary over time.

However, the critical aspect is not the shifting paradigm of what the challenge is for engineers but their ability to respond to it, which ultimately depends on the development of the relevant skillset and nurturing of the required mindset [3]. The Royal Academy of Engineering report [4] places the

responsibility of ensuring that graduates possess these skills upon entering the industry on higher education institutions. Thus, it is essential that these institutions constantly keep abreast with the evolving demands facing graduates in a wide range of professional contexts to ensure that future engineering graduates are able to tackle the challenges facing them [5].

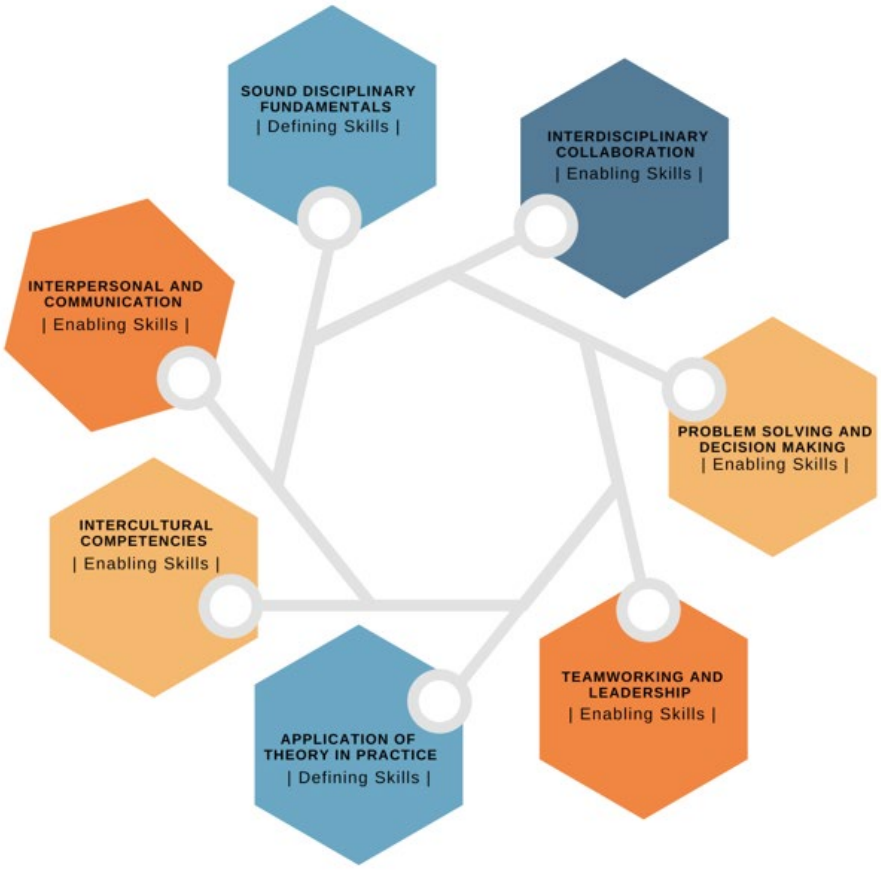


Figure 1. The Core Competencies of Engineers [4]

2.1. The Pedagogic Transition

In order to cultivate the desired skillset domains in future graduates, it is deemed that the pedagogic methods implemented by higher education institutions must be adapted. The pedagogic boundaries inherited from the 19th century have resulted in engineering courses being founded upon an instructor-centered model of teaching consisting of a deductive pedagogic manner, in which material is delivered through a highly structured framework. In this three-stage model, the lecturer would begin with an explanation of the general principles involved to a derive mathematical model. The next stage would be the application of the model to simple examples, reinforced by similar derivations and applications in tutorials. The third stage would then consist of more formal assessments. This model renders traditional pedagogic forms as predominantly auditory, deductive, passive, and sequential, promoting surface learning. However, engineering students are deemed to be visual, sensory, inductive, and active learners who reflect through action. These fundamental differences and imbalances are being recognised as preventing the full potential of effective pedagogy and as such, educational and cognitive research is increasingly encouraging the implementation of more inductive learning approaches [2].

Historic boundaries are now being transgressed with an increasing shift towards learner-centered models consisting of an inductive teaching manner based on the principle that knowledge can be developed and further enhanced through experience and interaction. This method of active and experiential teaching

consists of a fundamental shift in the pedagogical relationship between students and lecturers, to more symmetrical and interactive forms. It requires lecturers to assume the role of a facilitator encouraging students to navigate the 'indeterminate zones of practice', instinctively encouraging students to become active learners and impelling them to accept more responsibility for their own learning and development [6]. There is an array of inductive teaching methods that are gaining more recognition; inquiry learning, experiential learning, case-based teaching, discovery learning and PBL [2].

This paper will focus on the PBL approach which provides a framework of collaborative practical application to cultivate teamwork and leadership skills, independence, problem-solving skills, communication and interpersonal skills and creativity, within which the student is responsible for what needs to be learned and can influence the method by which it can be learned [3]. The model provides opportunities for deep learning and life-long learning [7]. It is argued that further benefits of this pedagogic approach are improved retention of knowledge, stronger reasoning and analytical skills, development of higher order skills, an enhanced ability to appreciate differing perspectives, greater motivation, and awareness of non-technical issues, all of which align to the demands of the evolving industry [2].

The following sections explore and evaluate the PBL approach through its application in the DAD Project, in order to ascertain the importance of integrating hands-on initiatives combining both design and fabrication in higher education to shape the future generations of civil engineers.

2.2 The Design, Assemble and Dismantle (DAD) Project

The DAD Project is fundamental in immersing first year students to the world of civil engineering and providing them with a unique experience of both the design and fabrication aspects of the industry across just one semester. The probability that knowledge and skills will effectively transfer to industrial settings has been argued to correlate to the similarity ratio of the two environments [2]. The DAD Project inherently mirrors the civil engineering industry, through the roles it assigns to students as consultants and contractors, as well as the project-long focus on health and safety, sustainability, and collaboration.

Over the course of its delivery, the DAD Project has undergone many developments in both its complexity and reach, in response to the evolving skillset demands from the civil engineering industry. The main developments are summarised in the timeline in Figure 2.

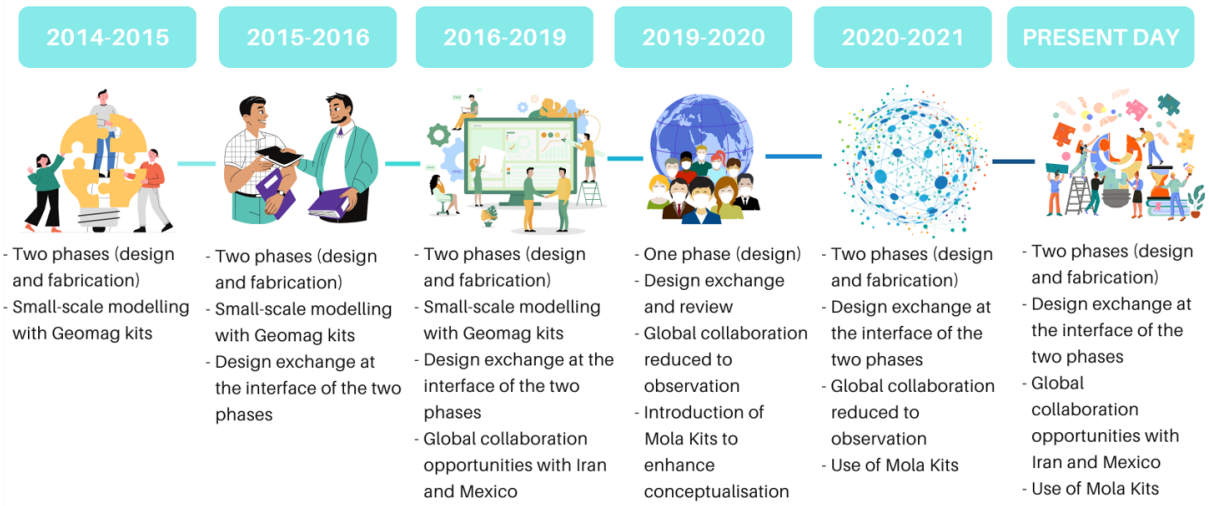


Figure 2. Development Timeline of the DAD Project

In the first year of its delivery each group of students designed a full-scale spatial structure, with the ability to develop a small-scale model, using Geomag kits and later Mola kits, as seen in Figure 3, and constructed the full-scale structure within a two-hour time limit, as can be seen in Figure 4. In its second

year across 2015-2016 a design exchange was introduced at the interface between phases one and two, whereby each group was given the set of documents prepared by another group in phase one to assemble and dismantle. This development aimed to increase the complexity of the Project and the communication and presentation skills required from the students through their design documents such that the required equipment, method of construction and relevant constraints and risks would be understood by another group.

In 2017 international collaborations were introduced into the design exchanges between students at the University of Surrey and civil engineering and architecture students in the 7th and 8th semester of their degrees at ITESO University in Mexico and with architecture students at the Ferdowsi University of Mashhad in Iran [8]. This development enabled students to cultivate a range of intercultural competencies, such as the ability to work across time, cultural and lingual differences, as well as an appreciation for different cultures, perspectives and of the wider globalising industry. As a result of the restrictions posed by the pandemic, in 2019-2020 and 2020-2021, no full-scale construction took place. However, the global design exchange and full-scale practice assembly were still achieved. To further facilitate conceptualisation of their designs in a virtual setting, students were provided with small-scale magnetic Mola kits. Furthermore, in 2020-2021, the design exchange was enhanced through competitive bidding whereby groups were able to choose which groups design they would construct, thereby reflecting some commercial elements of the industry. From 2021-2022, the DAD Project recommenced without the restrictions of the pandemic, with students being able to undertake the full-scale construction phase.

Since its conception, the DAD Project has extended even further throughout the world, through partnerships with the University of São Paulo in Brazil and Universiti Malaysia Pahang in Malaysia [8], offering even more opportunities for future global collaborations.

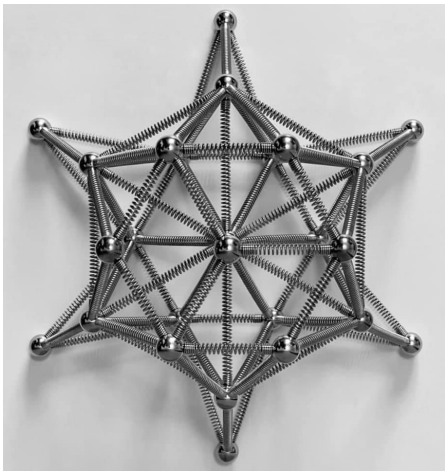


Figure 3. Small-Scale Model made with a Mola kit



Figure 4. Full-Scale Spatial Structure made with Steel Kit

3. Methodology

Module evaluation is an essential element of reflective practice models in higher education consisting of the collection of evidence which can be reflected upon to formulate actions for improvement in pedagogy [9]. Continuous evaluation of modules and academic programmes is deemed crucial for maintaining standards and promoting student engagement [7].

Student evaluations proving short-term reflections are integrated within the framework of the DAD Project through the videos they produce summarising their experience while undergoing the Project and through a short qualitative questionnaire that students are required to submit upon immediate completion of the Project. To assess the mid-to-long term reflections in this paper, the research conducted was in

the form of virtual one-to-one interviews with some participants who had undertaken the Project at least two or more years ago. The sample group consisted of participants from a range of cohorts in order to explore any patterns or correlations in the skills or values cultivated alongside the developments in the modules design since it was first introduced. The sample group aimed to have a balance between male and female participants to mitigate any bias. To explore the transferability of the skills acquired across other modules and industry, all selected participants had at least two months of industrial experience, whether through summer placements, yearlong placements, or graduate positions. A summary of the participants composing the sample group is presented in Table 1 below.

Table 1. Breakdown of Sample Group

Cohort	Sample Group							
2014-2015	Participant 1	F	Participant 2	F				
2016-2017	Participant 3	F	Participant 4	F				
2017-2018	Participant 5	M	Participant 6	M	Participant 7	F	Participant 8	M
2018-2019	Participant 9	F	Participant 10	M	Participant 11	F	Participant 12	F
2019-2020	Participant 13	M	Participant 14	F	Participant 15	M	Participant 16	F
2020-2021	Participant 17	F	Participant 18	M	Participant 19	M	Participant 20	F

The interview questions were designed to elicit qualitative data from participants, engaging responses that would go further than the surface approach of satisfaction-oriented surveys, and reveal the true perceptions, thoughts, and feelings of participants regarding the PBL approach [9]. A four-part series of questions were produced to determine the following:

- Prior exposure to civil engineering before participation in the DAD Project to ascertain the extent to which any skills developed were directly attributable to the Project
- Academic and professional journeys since the DAD Project, to explore any opportunities and applications that arose from their experience in the Project
- Personal or professional skills or values developed as a result of the DAD Project
- The transferability of those attributes to other modules or industrial experiences

While the above provided a framework for the interviews, it was an inherently open format with the potential for individual discussions to allow the emergence of questions not formerly contemplated, encouraging conversational flow attached to the emotions and experiences of each participant [6].

It is important to note that for the process of data collection, ethical considerations were adopted. Primarily, through fundamental communication ethics recognising all participants as voluntary interlocutors having understood the intentions and implications of the research being conducted. This was ensured through informed consents from all participants. Furthermore, confidentiality, anonymity, and data protection of all recordings and transcripts were guaranteed [6].

3.1 Data Processing

Upon completion of the data collection stage in which interviews were conducted, recorded and transcripted with all participants through Microsoft Teams, the data processing stage was commenced. Thematic content analysis was chosen as the method of data processing - in which the data set was analysed to identify common themes and patterns. Upon completion of the first interview, one initial scheme of variables was established, and after each subsequent interview this was redefined in terms of the categories and codes identified [6]. The final scheme consisted of 20 attributes and skills which had been commonly identified by at least two individual participants, which will be discussed in Section 4.

In order to efficiently manage, process and present all of the collected data, MAXQDA was adopted in the data processing stage in the following way:

1. All recordings and corresponding transcripts were imported into MAXQDA
2. Transcripts were reviewed to unify the written form through the removal of any non-verbal utterances, such as laughter, or nodding
3. Transcripts were corrected by making references to the recordings to fix grammatical mistakes and incomplete sentences to obtain a readable, concise, and clear transcript
4. A coding system was generated in which codes corresponding to the identified skills and attributes were created and assigned to the relevant segments of each transcript

Following this, the data was analysed to explore and visualise the progression of themes across the interviews both qualitatively and quantitatively.

4. Data Analysis and Discussion

Upon undertaking the thematic content analysis of all interviews conducted, there were several recurring skills and values that were attributed to the DAD Project. The most common themes and experiences across the entire dataset were extracted in MAXQDA and are presented in a word cloud as shown in Figure 5. The size of the attribute or reflection corresponds directly to its commonality across the interviews. As can be seen from the word cloud, most participants referred to the experiential nature of the DAD Project, which they deemed different to others in the course. The experience of partaking in the Project was described as immeasurable, insightful, and invaluable and one which '*helps shape the rest of your degree'* as stated by Participant 15.



Figure 5. Word Cloud of Recurrent Themes, Attributes, and Experiences

A broad array of common attributes was brought to the forefront including communication, leadership, team working, time management and organisation. Shifts in fundamental mindsets were also expressed in which there was an increased appreciation of industry relations and global collaboration, respect and appreciation of different perspectives, a more active and conscious learning approach, and a greater sense of accountability for work produced. The percentage of participants that mentioned each identified common attribute is shown in Figure 6. The following section will explore the reflections of the participants with regards to some of these attributes in more detail.

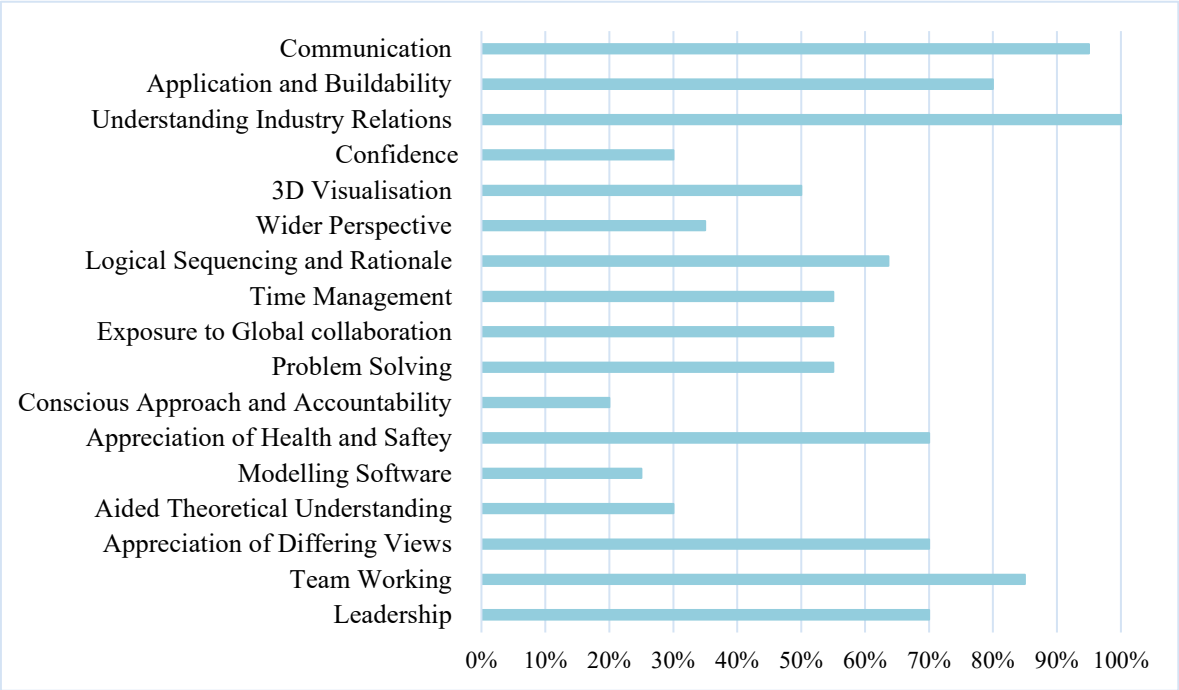


Figure 6. Percentage of Participants vs Attribute Developed

4.1 Industrial Awareness

The PBL tool allows students to understand the complex and multifactorial nature of professional practice, due to its inherent real life practical application [6]. This is in line with the findings in this study in which all participants agreed that they gained a deeper understanding of working in industry.

4.1.1 Consultant and Contractor Relations

Through the two phases of the DAD Project, in which students are able to first assume the role of a consultant and then of a contractor when working with the full-scale model, the interlinked and intricate relationship between the two are delineated and demonstrated to students. Participant 7 believed that *'the DAD Project mirrors what you get in the real world, because you have your consultant and contractor relationship, and I think it's really important to understand how that all works and how that will mesh together as early as possible'.* Being aware of the dynamic roles and relationships between the various stakeholders in the civil engineering industry is fundamental in providing wider context to the work undertaken and an insight into the systems of work in industry, which is reflected in Participant 13's view that the two phases enabled them *'to learn how projects are planned out and how they're efficiently done.'*

Furthermore, this arguably increases their insight into the considerations and challenges that each stakeholder faces, which they are then able to address more effectively through the design and construction processes. Participant 8 expressed that '*through the two phases, you got to see things from another perspective of not only designing something but being able to interpret someone else's designs and sketches'*, while Participant 5 believed that the Project '*definitely gave that awareness and thought process you need to have when designing something for construction'*. This implies a fundamental shift in the thought processes and approaches adopted by students from a purely theoretical mindset to one which can think ahead into the conceptualisation phases and the implications of decisions made. This was confirmed by Participant 11 who stated the following: '*I remember thinking to myself about whether the design would work in practice, which usually I wouldn't think about at all.'* The above reflections suggest that the Project was able to cultivate a development in mindset, whereby students were able to consider the challenge faced not only through one role, but through the multiple roles involved in the delivery of the solution, which according to Participant 3 was '*eye opening'*. Of the participants, 80%

expressed an increased awareness of buildability issues associated with the designs they produced or received. This was reflected in Participant 9's experience who stated that '*it made you realise the practicality of your designs; it's very easy to design things but not understand the implications of it'.* The 20% of participants who did not express a particular development in their awareness of buildability issues were those who were unable to participate in phase two of the Project due to the restrictions of the pandemic, highlighting the importance of the hands-on construction stage.

4.1.2 Globalisation

The era of globalisation in the civil engineering industry, which has gained significant momentum over the past couple of decades, has created demands and challenges for engineers to integrate efficiently into an increasingly complex and multicultural environment, with a particular focus on intercultural competencies consisting of the ability to collaborate in teams of individuals from various backgrounds, communicate effectively despite any lingual barriers and have cross-cultural knowledge. It is paramount for future generations of civil engineers to develop intercultural competencies across three tiers: a general understanding of cultural differences, awareness of cross-cultural differences within professional communication and the ability of effective cross-cultural communication in engineering practice [10].

Of the sample group, 100% of the participants involved in global design exchanges said that the DAD Project was fundamental in their exposure to global collaboration, the challenges it encompasses and the benefits it brings, predominantly through the international design exchanges. Participant 7 reflected that the Project '*really does mimic the industry, where we work with clients and colleagues abroad and that communication barrier can be quite a big challenge between different cultures, languages and regions.'* While global design exchanges were put on hold in 2019-2021, due to restrictions of the COVID-19 pandemic, participants were still able to experience some aspects of global collaboration as members of their teams were in other countries during lockdown. As such, they were still faced with some of the challenges associated with time differences and team working.

4.2 Practical Application

The unique hands-on approach adopted in the DAD Project through the use of both small-scale and full-scale models and the benefits that this brings was recognised by 80% of the participants. For most, this marked the first and only PBL project encountered in their higher education journeys and '*the first opportunity to put visions into realisation'* as noted by Participant 2. Prior to this, it was believed by Participant 6 that students '*don't think beyond the brief about how designs work and how it all comes together'*. This highlights how the interactive hands-on approach broadens the perspectives of students, enabling them to take on a more holistic view of the challenges posed and the steps needed to overcome them, ensuring that the work *'makes more sense and has more meaning'* as expressed by Participant 9, and reflected in Participant 8's views who stated that it gave them *'a better understanding of how a project works and how people work on a project'.*

Most students highlighted that there are few opportunities in higher education to address practical situations related to real-world practices, and that the realism reflected in the Project cultivated a more conscious approach. Participant 7 expressed that because of the Project, '*you're making more conscious decisions and having more conscious ideas and your perspective is slightly different throughout university,'* while Participant 14 stated that '*it was like the real world rather than coursework that you know is meaningless and you're just doing for a mark. It was nice to know that your design was going on to someone else and it made me want to perfect it, so they didn't come back with questions'.* It seemed the design exchange also instilled a sense of accountability for work produced as reflected by Participant 7's view: *'because the contracting team will come back to you with queries and clarifications, you have more accountability for your deliverables, they need to all join up to create the whole picture'*, while Participant 6 believed that '*being both consultant and contractor made me realise my design decisions really do matter'.*

In traditional pedagogy, the role of students is relegated to a receptive and passive one, where they encounter minimal challenges in which they can assume a pre-determined level autonomy to make decisions [6]. The student-centred approach places more responsibility on the student for their learning as they actively reconstruct their own reality, while the teacher merely acts as a facilitator [11]. This approach develops independent thinking, problem solving and logical reasoning, as confirmed by 64% of the participants. Participant 10 expressed that '*it gives you different skills that you need to be able to implement; the logistics of things and how you construct something in sequence'.* Furthermore, Participant 6 stated that the Project *'developed my logical reasoning skills and insight into systems of work, you see what needs to be done, you think about how to tackle the issue, then you move onto the next*.' It seems that it is in this process of PBL that real learning and problem solving resides [6].

It has been argued that PBL enables students to relate theory to practice and that the combination of the two produces enhanced results [9]. This is reflected in Participant 5's experience who noted that 'by *building the structure yourself you get an understanding of how the forces interact within the structure, you're not learning the calculations behind the structure, but in the long term when you're trying to learn the calculations you can apply it to a real life situation you've been in, it's easier to remember and understand it.'* Fundamental to the DAD Project is the use of physical models to understand structural behavior and construction requirements, which is first achieved through the use of the small-scale magnetic Geomag or Mola kits. For 50% of participants a key ability developed through the small-scale realisation of the designs was that of visualising a design in 3D space. Participant 6 mentioned that *'being able to visualise designs and see forms, doing it hands-on, really helps the initial understanding of scales; the tactile experience was invaluable.'* The above suggests that the assimilation of knowledge with application of theory in practice in different scales, during the formative undergraduate years of civil engineering offers greater benefits to overall educational development [11].

4.3 Communication

The DAD Project encourages effective communication not only verbally but through other means, such as written and visual forms, which is reflected in the experience of Participant 17 who mentioned: '*we had a few challenges trying to change the method statement and make it a bit easier to follow. Eventually, instead of just giving a written method statement, we had step-by-step photos and videos to explain how it works.'* Similarly Participant 4, who was involved in an international collaboration, stated the following: *'we had to ensure that the pictures and infographics made sense for them so that they could understand what we wanted them to do due to the language barrier'.* The ability to employ different means of communication has always been paramount for effective communication across a range of people, however even more so today due to the increasing virtual nature of collaboration in the industry which can limit some traditional forms of communication and understanding.

The design exchange shifts the focus of communication to whether the receiving group will be able to understand what is being expressed through the design documents. Participant 20 stated that this experience meant that when undertaking work, the predominant thought is '*if anyone ever looks at this from the outside, will they understand what I'm trying to say.'* The international collaboration aspect of the Project added a further level of communication required as Participant 15 believed that one of the most important takeaways was '*being able to communicate with different nationalities.'* Thus, interpersonal, and communicative skills constitute one of the main benefits of this form of pedagogy.

4.4 Collaboration

The DAD Project is based on a foundation of collaboration, whether that is within groups during phase one and two, across groups during the design exchange, or across the globe for those partnered with groups in Iran or Mexico. Collaboration is crucial within the civil engineering industry, and the DAD Project allows students to appreciate both the challenges and benefits it brings. Participant 8 expressed that '*the Project encouraged us to work with other people, which reflects the real-world experience really well – you don't work in silos, you have to work collaboratively to achieve the best results.'*

During the Project, students are required to collaborate effectively within their teams, managing group conflicts and varying levels of involvement from team members. Participant 14 stated that the experience '*gave me the idea that not everyone in your group is going to be as willing as you to play a part'.* This was embodied in the experience of Participant 17: '*it was easier to work with some people than others in the group. But then overtime you learn to put things in a way that everyone can understand.'* This confirms that the collaborative approach of PBL can cultivate the development of a range of managerial and team working skills, which is essential for engineers.

According to the perceptions of 85% of the participants, the teamworking aspect of the Project allowed them to consider points of view that, until then, had not been a part of their thinking schemes. This is reflected in the views of Participant 5: *'you develop new skills when trying to take into account new personalities and accommodate everyone's opinions.'* Participant 13 reflected that '*I learnt about becoming more open to listening to people's opinions',* and Participant 7 stated that *'it really opens up the spectrum to lots of different solutions and ideas.'* Thus, it seems that the PBL process is one of reconstructing participants knowledge schemes to integrate a more complex and polyhedral vision [6].

4.5 Health and Safety

This was the first encounter to health and safety within the civil engineering industry for most participants and learning about it in a practical framework through the full-scale construction meant that the responsibility to ensure it was on the students. Participant 19 expressed that '*coming to university, you don't care about health and safety, so being introduced to it at the start is really important',* thus indicating a fundamental shift in the attitudes and approaches of students which creates an important foundation for the rest of their careers. During the Project, every team assigns a health and safety manager responsible for ensuring that safety was inherent within the designs and method statements. Participant 6 confirmed that *'working on the design while being the health and safety officer allowed me to build safety into the design'.* Furthermore, the construction process requires students to think about how safety can be achieved on site, Participant 13 explained how '*because the structure designed was very tall, we had to figure out how to build it in a way which was within health and safety regulations.'*

4.6 Wider Benefits

The benefits for academic learning and professional development are tangible, with 100% and 75% of participants confirming that the skills developed through the DAD Project were transferrable to other modules and their industrial experiences respectively. Participant 3 stated the following: '*the Project gave us an appreciation for what needs to be done on both sides, which translates to the workplace because we always have to work with contractors, sub-contractors and clients'*. Many participants viewed the DAD Project as the sole experience in their higher education experience which allowed an insight into the world of contracting. Participant 7 believed that '*at university because we're not as practical, it's easy to fall into that design world rather than the contracting world'*, while Participant 18 stated that '*the Project helps you to decide which type of placements you want to do…and I think without it there is no way you could know'.* Participant 3 highlighted '*a lot of people are on the design side when leaving university, especially females, because contracting is more male dominated'.* As such it is believed that the Project gave a good insight into contracting even for whom it may seem less accessible in industry. Furthermore, several participants expressed that the Project sparked wider interests, as confirmed by Participant 14: '*without the DAD Project, I would not have gone to Mexico a few years later for a bamboo workshop and I wouldn't have been doing a dissertation on bamboo now'.*

Of the participants, 40% expressed that the Project enabled integration into their cohort at the start of their higher education journey, particularly crucial over the years affected by the pandemic. Another attribute highlighted by 30% of participants was that of confidence, predominantly in those who assumed the roles of project managers. Participant 17 reflected; *'I think that was probably the first group project that I was taking charge in, it gave me the confidence to do that more often'.* Furthermore, as

PBL reflects real world practice, students consider the work as relevant and thus are more motivated to [11]. This was a strong recurring theme in the data collected, with Participant 10 stating that *'it was amazing being able to see your design come to life and feeling that satisfaction',* highlighting a greater level of meaning and significance being associated to the work undertaken through the PBL approach.

5. Conclusion

The imbalance between theory and practical application is a systematic issue in civil engineering education; the challenge stands as the amalgamation of the two. However, the effectiveness of more hands-on approaches in engineering education is still open to question. This paper considers an application of such a method in the form of the DAD Project based on the PBL approach with small-scale and full-scale models. In order to fully understand its mid-to-long term implications and benefits, interviews with 20 participants of the Project are conducted and their reflections are subject to qualitative and quantitative analysis. Significant benefits are highlighted in the adoption of PBL as a pedagogical strategy, with improved attributes such as collaboration, communication, conceptualisation, and intercultural competencies. The observed benefits transgress beyond skills and attributes into shifted mindsets with greater appreciation of the wider context, health and safety considerations, different perspectives and students who assume the roles of active learners with an increased sense of accountability, motivation, and confidence.

References

[1] L. E. Carlson, J.F. Sullivan, "Hands-on Engineering: Learning by Doing in the Integrated Teaching and Learning Program", International *Journal of Engineering Education,* 20-31, 1999.

[2] T. A. Newson, N. J. Delatte, "Case methods in civil engineering teaching", *Canadian Journal of Civil Engineering,* 38(9): 1016-1030, 2011.

[3] N. Spinks, N. Silburn, D. Birchall "Educating Engineers for the 21st Century: The Industry View", 2006.

[4] The Royal Academy of Engineering, "Educating Engineers for the 21st Century", 2007.

[5] S. Mohammad, H. M. Nor, W. Omar and D. Mohamed. ″Enhancing teaching and learning through the incorporation of generic skills for civil engineering undergraduates.″, 2004.

[6] M. Marinda, A. Saiz-Linares, A. Costa, J. Castro, "Active, experiential and reflective training in civil engineering: evaluation of a project-based learning proposal." *European Journal of Engineering Education*, 45.6: 937-956, 2020.

[7] G. Kenneth, "Case study of a project-based learning course in civil engineering design.″ *European Journal of Engineering Education,* 36.6, pp. 547-558, 2011.

[8] S.A. Behnejad, "DAD Project: Leaning Experience for Students Around the World", *Spatial Structures Movers and Shakers,* 33–36, 2021.

[9] A. McNabola, C. O'Farrell, "Can teaching be evaluated through reflection on student performance in continuous assessment? A case study of practical engineering modules." *Innovations in Education and Teaching International,* 52.5:464-473, 2015.

[10] J. M. LaFave, H. Kang, and J. D. Kaiser, "Cultivating intercultural competencies for civil engineering students in the era of globalization: Case study." *Journal of Professional Issues in Engineering Education and Practice* 141.3, 05014008, 2015.

[11] T. McKenna, A. Gibney, M. G. Richardson. "Benefits and limitations of adopting project-based learning (PBL) in Civil Engineering education—A review." *Proceedings of the IV International Conference on Civil Engineering Education (EUCEET)*, 2018.

Proceedings of the IASS Annual Symposium 2023
Integration of Design and Fabrication
10–14 July 2023, Melbourne, Australia
Y.M. Xie, J. Burry, T.U. Lee and J. Ma (eds.)

Seismic retrofitting by double layer grids for HP suspension gymnasium

Kazuya MIYAGAWA[a,*], Yoshiya TANIGUCHI[a]

[a,*] Graduate School of Engineering, Osaka Metropolitan University
Sugimoto 3-3-138 Sumiyoshi, Osaka city, JAPAN
sk22075b@st.omu.ac.jp

Abstract

Many gymnasiums have been built with cable suspensions, and such buildings have roofs made of precast concrete and cables. As an example, this paper focuses on the gymnasium in the Kyushu region built with such the manner. The roof span of this building is 57 meters in the longitudinal direction, 51 meters in the short direction and 12 meters in ascending order. Since the main building will be used as a multipurpose hall from the gymnasium facility, we are considering the application of a double-layer lattice pattern that is resistant to additional loads for seismic reinforcement. If you are applying a double-layer lattice pattern, examine the square-on-square (SS), square-on-diagonal (SD), and diagonal-on-square (DS) meshes. In comparing these three types of lattice patterns, it is made clear that the SS type of mesh has the greatest material efficiency but is easily affected by boundary conditions. Although the material efficiency of the SD type is smaller than that of the SS type of mesh, it is revealed that the SD type of mesh is the shape that is least affected by boundary conditions.

Keywords: seismic retrofitting, hyperbolic paraboloid, cable suspension dome, double-layer grids

1. Introduction

The target is a suspension structure using cables with an HP curved roof structure as shown in Figure 1, which is composed of PC slabs and cables. As seismic retrofit, we are considering the application of double-layer lattice grids that could resist additional loads. In applying the double-layer lattice pattern, three types are investigated: Square-on-Square (SS), Square-on-Diagonal (SD), and Diagonal-on-Square (DS) meshes as shown in Figure 2.

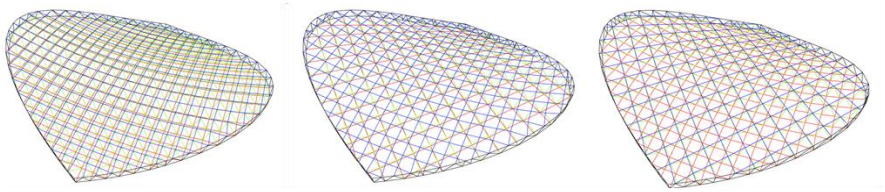
In previous studies, Yan [1] has clarified the influence of member placement on the elastic buckling behaviour of flat roofs, cylindrical roofs and domes, and Zhang [2] [3] has clarified the influence of member placement on the elastoplastic behaviour of flat roofs, cylindrical roofs, and domes.

To determine the extent to which the following lattice patterns can be applied to systems of suspended structures on HP curved surfaces, we specifically compare the load resistance system in the mesh and the flow of force to the boundary ring. Figure 2. (a), (b), and (c) show the mesh shape of the roof to be studied and they are composed of an upper chord member, a lower chord member, a web member, and an arch-shaped boundary ring beam.

Copyright © 2023 by Kazuya MIYAGAWA and Yoshiya TANIGUCHI. Published in the Proceedings of the IASS Annual Symposium 2023 with permission.



Figure 1. Exterior of the gymnasium



(a)SS (b)SD (c)DS

Figure 2. Lattice pattern

2. Roof shape

The arch-shaped boundary rings that make up the roof are provided for each upper and lower chord surface, which are composed of upper and lower chord members, respectively. The curve indicating the arch is expressed by the following Eq (1). The all nodes are yielded by the equation and the constituent members are straight and connecting two nodes.

$$y = \pm 18.0 \times \sqrt{\frac{28.5 - |x|}{14.25}} \tag{1}$$

The nodes of the upper chord of the roof are coordinated based on the following Eq (2) used in the design of the existing building.

$$z = 5.12 + \frac{5.0}{28.5^2} \cdot x^2 - \frac{4.0}{22.5^2} \cdot y^2 \tag{2}$$

The three plans of lattice patterns shown in Figure 2 are created: SS type, SD type, and DS type. The plan views of the upper and lower chord surfaces of the SS, SD, and DS types are shown in Figure 3.

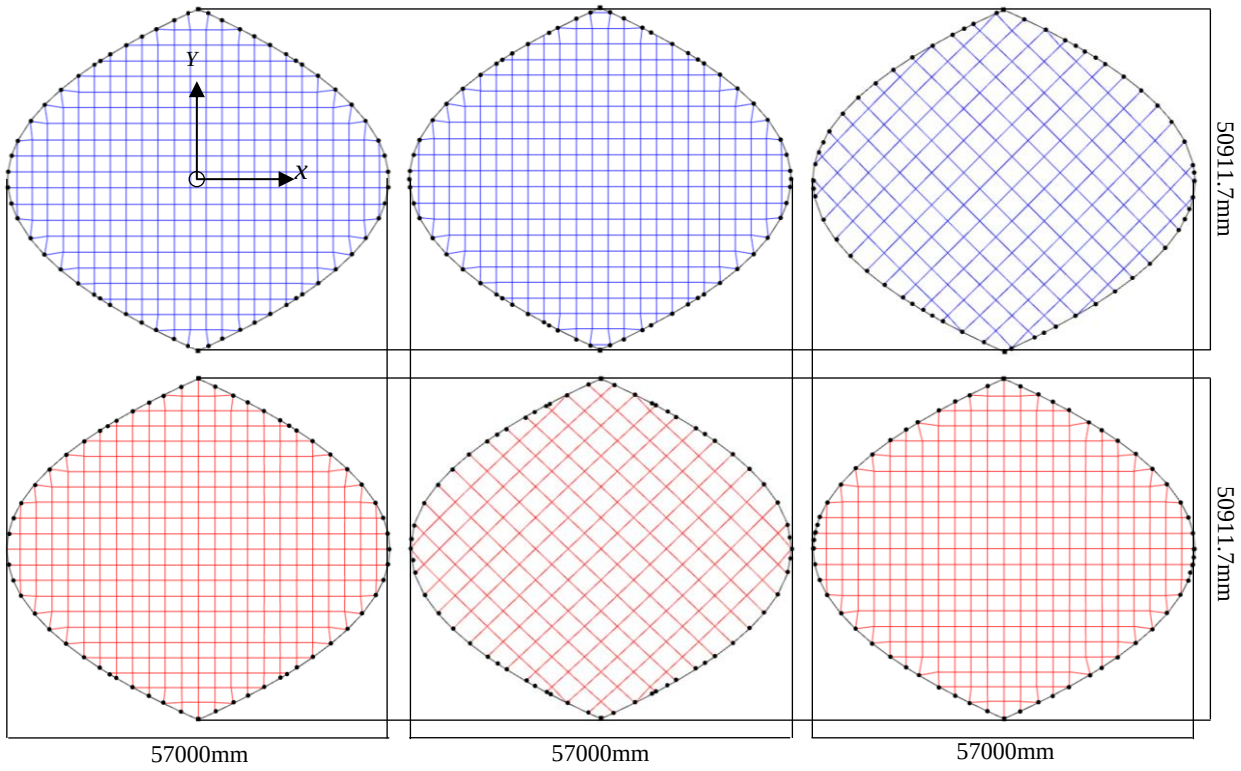


Figure 3. Plan

Table 1. Cross-sectional dimension

Member	Sectional Dimension (mm)	Cross Sectional Areas (cm^2)	Geometrical Moment of Inertia (cm^4)
Chord member	φ203.0×12.0	72.01	3300
Boundary ring member	φ298.5×16.0	142.0	14200
Young's Modulus	2.05×10^4kN/cm^2		

The cross-sectional dimensions of the HP shell roof are shown in Table 1. Except for the boundary ring, an upper chord node is provided so that the length of the SS type upper chord member is 240 cm. Starting at the intersection of the diagonals in the rhombic shape of the smallest unit composed of four upper chord nodes, the lower chord node is provided at a point 3394 mm (= 2400 mm $\times\sqrt{2}/2$: half the length of the diagonal) in the normal direction on the side toward the ground surface.

A square mesh is formed based on the upper and lower chord nodes for two layers of the SS type. Diagonal mesh is formed based on a above square mesh. To arrange web members, the tetrahedron consisting of four chord members and four web members is considered.

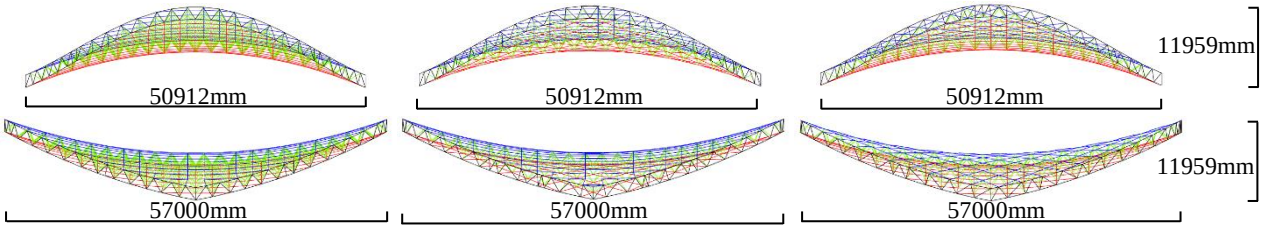


Figure 3. Elevation of upper and lower layers (a)SS type, (b)SD type and (c)DS type

It is necessary to design the tetrahedron to be formed so that the overall balance is not greatly disturbed even near the boundary ring. The boundary ring consists of two parallel chord members and web members. The constituent nodes are necessarily connected to chord members in each layer.

3. Loading and support conditions

There are two types of support conditions: pin support and roller support. The pin support is horizontal and vertical constraints at all the upper and lower nodes of the boundary ring beam. The roller support is only vertical constraints only except for the intersection of the two boundary ring beams. Therefore, the boundary ring intersection points are pin supported.

Table 2. Roof area and reference load

Roof area (m^2)	1935
Weight per area (kN/m^2)	2
Total reference load (kN)	3870

Table 3. Number of inside nodes on the top surface and load per node

Lattice Pattern	SS	DS	SD
Number of nodes	324	162	324
Load per node (kN)	12.0	23.9	12.0

In addition to the load due to the roof structure, it is assumed that the load of $2kN/m^2$ is applied to the roof area. As shown in Table 2, the total load on the roof is the reference load. In Table 3, it is assumed that the reference load is divided by the number of upper chord nodes and the divided load is applied on each node.

4. Analysis Results

Figure 4 is a diagram comparing vertical displacements in the pin support and roller support of the SS type, SD type, and DS type up to the reference load. The vertical displacements are values of the central nodes in the lower layers, and the vertical axis means the total loads on the upper layers. On the case of pin supports, SS type is the smallest and DS type is the largest. On the case of roller supports, SS type is smaller than the other types and the other two types are almost equal.

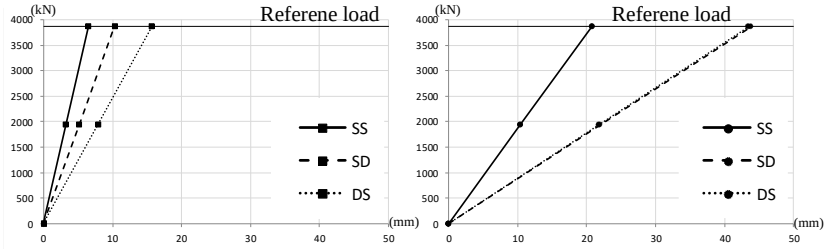
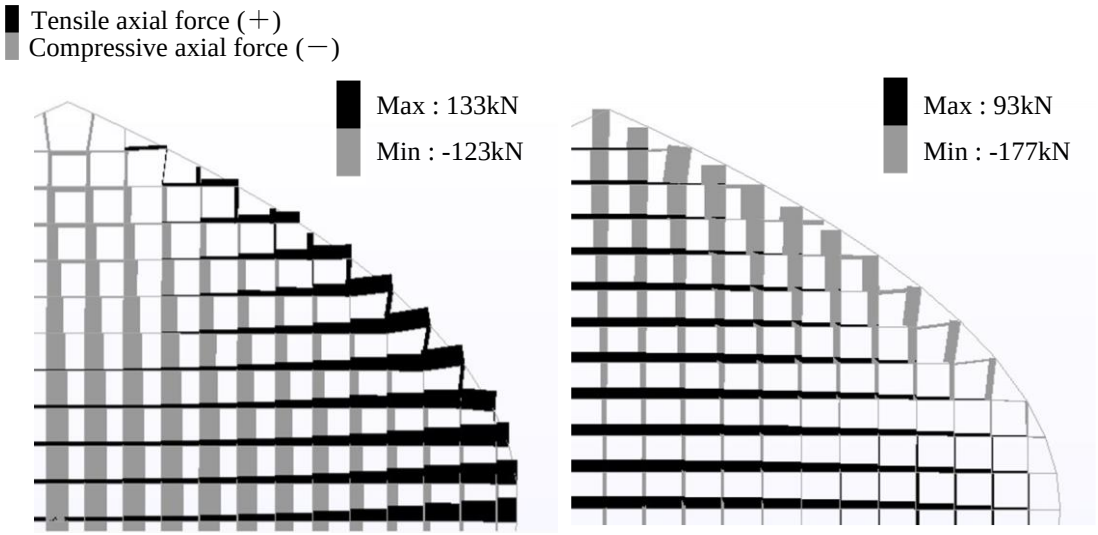
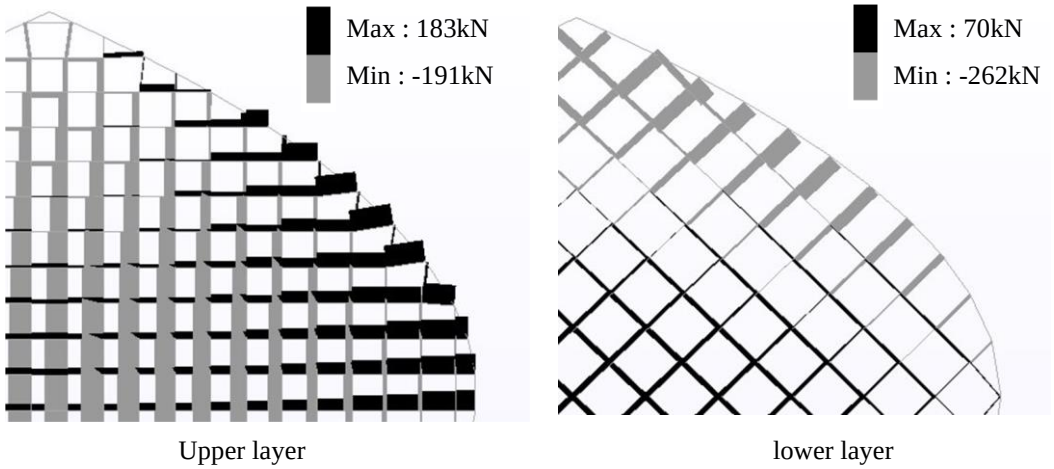


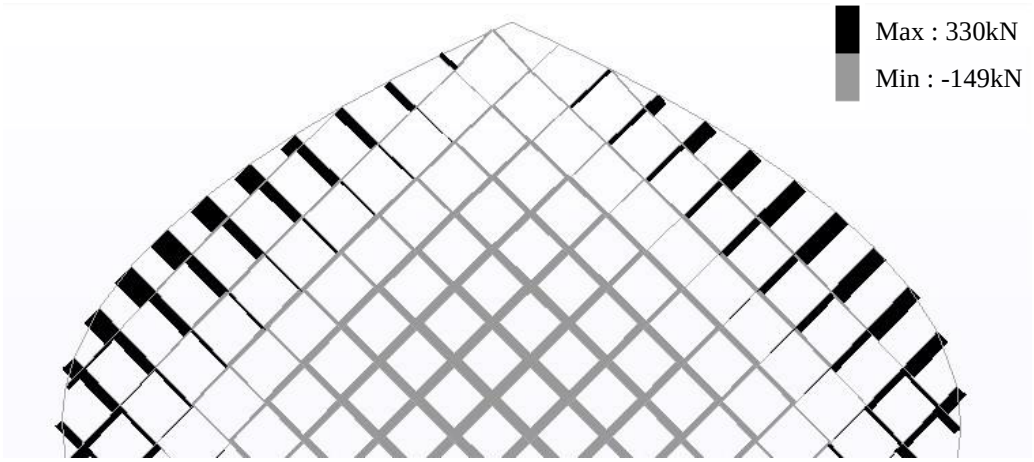
Figure 4. Vertical load displacement relationship



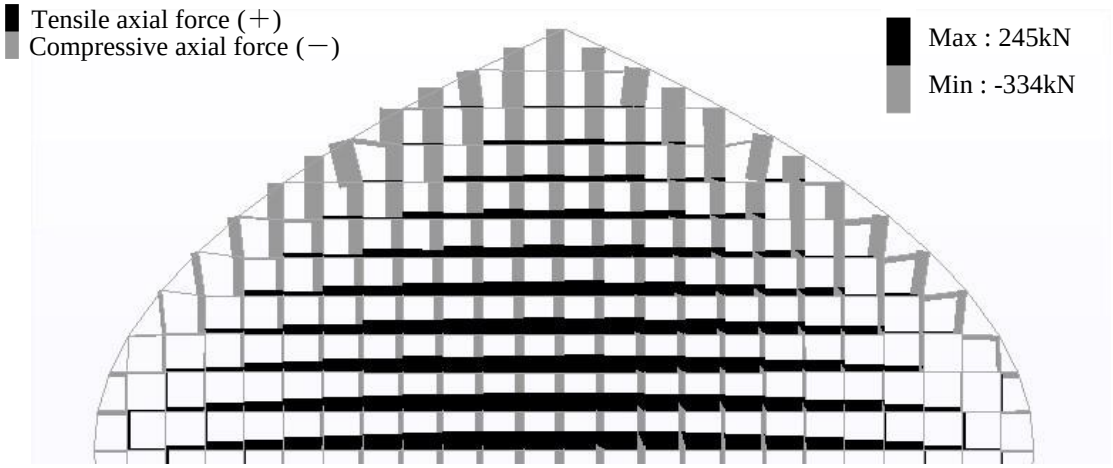
(a)Square-on-Square type



(b)Square-on-Diagonel type

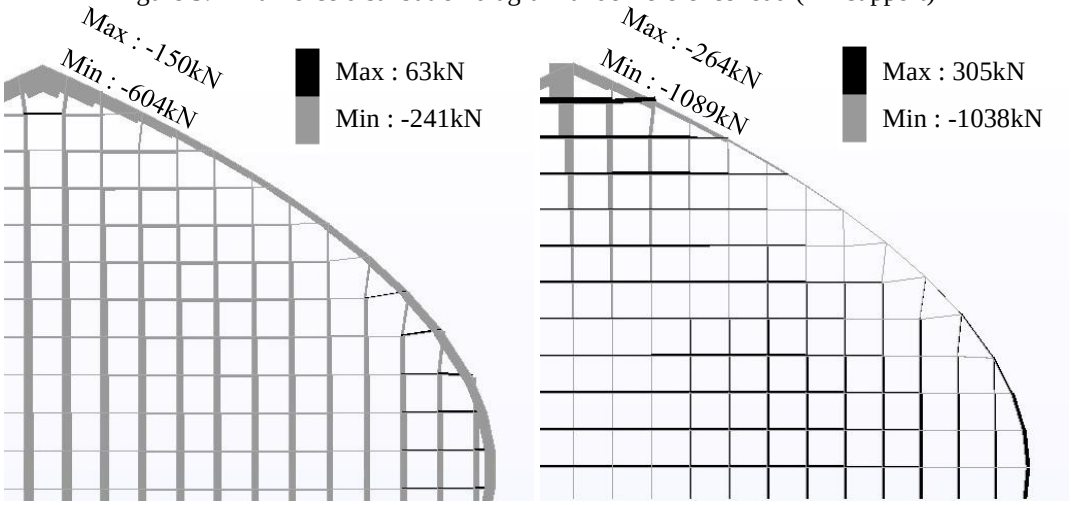


(c)Diagonal-on-Square type (upper layer)



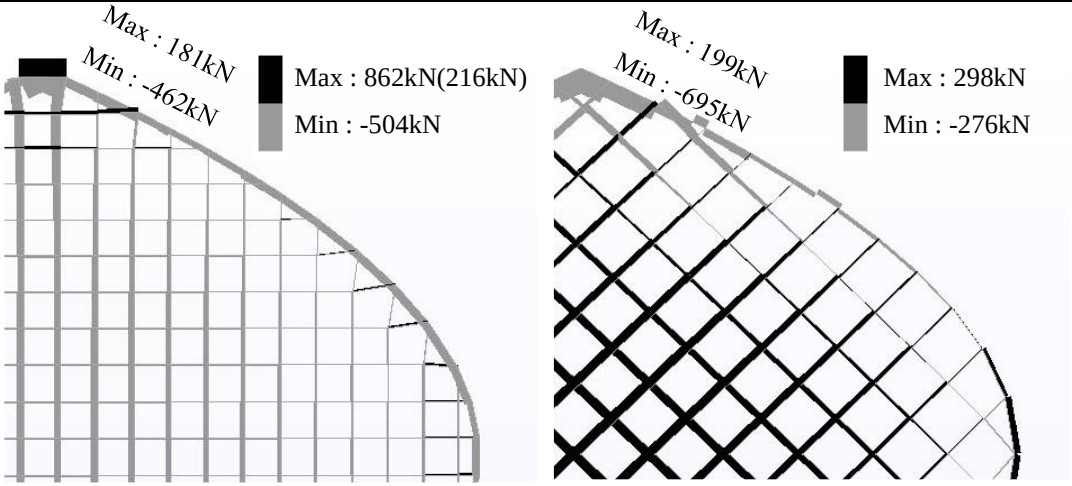
(d)Diagonal-on-Square type (lower layer)

Figure 5. Axial force distribution diagram under reference load (Pin support)



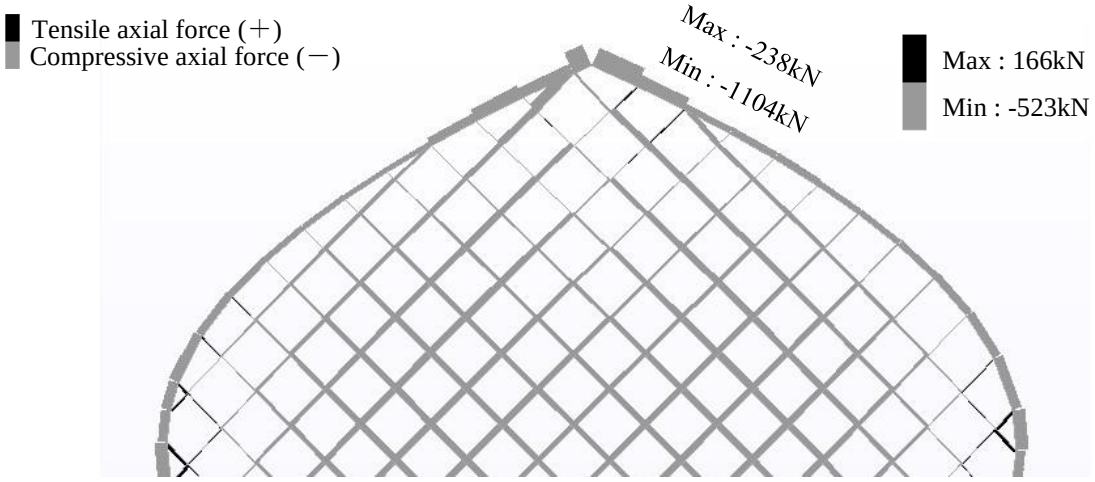
Upper layer lower layer

(a)Square-on-Square type

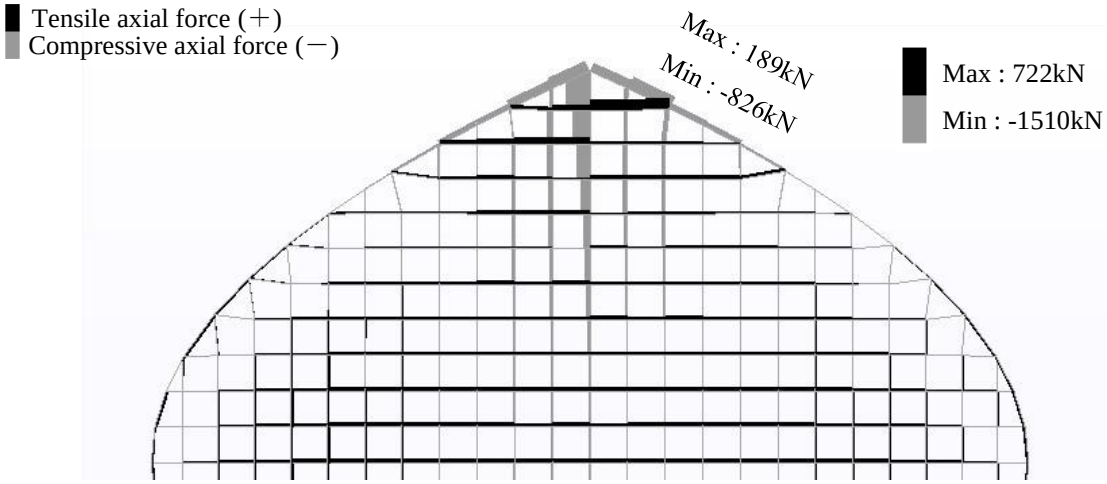


Upper layer lower layer

(b)Square-on-Diagonal type



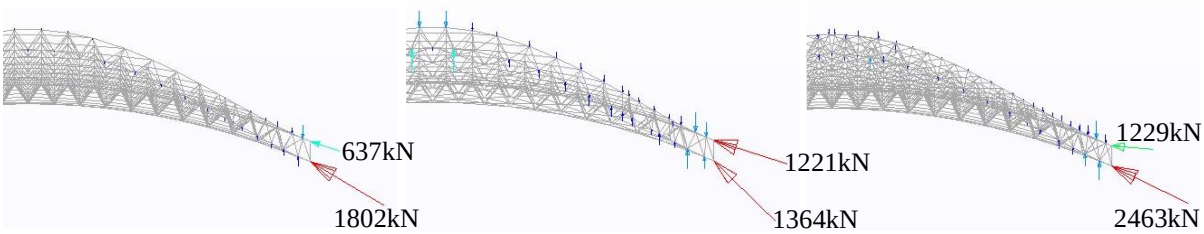
(c)Diagonal-on-Square type (upper layer)



(d)Diagonal-on-Square type (lower layer)

Figure 6. Axial force distribution diagram under reference load (Roller support)

Figures 5 and 6 show the axial force distribution under the reference load in which the tensile axial force is positive and compressive axial force is negative. In these figures, the maximum and minimum values shown in the chart are shown separately for the chord members and the ring beams, and the value of the chord member is shown in the upper right and the value of the boundary ring member is shown along the ring. The reaction forces of the buttress on the boundary ring intersection points are shown in Figure 7. In Figure 6(b), the value in parentheses expresses the maximum value except that of the neighbour member of the intersection (buttress) points. The member of 862kN is subjected to large tensile axial forces due to the roller support condition.



(a)Square-on-Square type (b)Square-on-Diagonal type (c)Diagonal-on-Square type

Figure 7. Reaction Forces (Roller support)

Figure 7 shows the magnitude of the reaction forces at the roller support. In any mesh model, the reaction forces at the boundary ring intersection (buttress) points are larger than the reaction forces at the other support points. The summation of the reaction forces in the upper and lower meshes in the DS type is about 1.5 times larger than the value of the other two meshes. The reaction force on the lower surface of DS type is greater than the reaction force on the upper surface of DS type. In comparing the reaction force in the two surfaces, the value of the lower surface is about 2.9 times of the upper surface for SS type (in Figure 7(a)), about 1.1 times for the SD type (in Figure 7(b)), and about 2.0 times that of the DS type (in Figure 7(c)).

5. Consideration

[Pin-support] At the case of pin support as shown in Figure 5, the x direction is tensile, and the y direction is compressive to resist the load for the SS type. For the SD type, the upper surface is similar as the SS type, but the lower surface is a diagonal mesh, and the axial force distribution is changed remarkably. The lower members near the boundary are in compression. The axial forces are smaller than the lower surface of SS type. For the DS type, the diagonal mesh of upper surface is tensile near the boundary ring and compressive in the central part, that is contrary to the SD type. The lower surface shows the tension in the central span of the x direction and the large compression near the ring beam of the y direction, such as SS type.

[Roller-support] At the case of roller support as shown in Figure 6, the upper surface of the SS type is compressive, and the lower surface is tensile, that is the resultant is a bending moment type. The upper chord members of the boundary ring are compressive, but a part of the lower chord members is tensile, except the members near the intersection (buttress) points. The same distribution is shown in the SD type, but most of the diagonal lower surface is tensile. For the DS type, most of the diagonal upper surface is compressive, and the lower surface is compressive near the intersection (buttress) points. The upper cord members of boundary rings are compressive for the 3 types, due to the horizontal freedom on the supports.

Tables 4 summarizes the maximum and minimum axial forces of Figures 5 and 6 under the reference load at both support conditions. The axial force of boundary ring at the pin support is omitted because it is approximately zero.

In comparing the axial forces of chord members at both support conditions, the ratios of Table 4 are shown in Table 5. The fluctuations of values are small in the SD type and large in the SS type. It can be said that SD type is relatively tough at the support conditions.

Table 4. Axial forces in Pin and Roller support (kN)

Lattice pattern	SS	DS	SD
Maximum value in chord member (Pin support)	133	330	183
Minimum value in chord member (Pin support)	-177	-334	-262
Maximum value in chord Member (Roller Support)	305	722	298
Minimum value in chord Member (Roller support)	-1038	-1510	-504
Maximum value in ring Member (Roller support)	181	189	199
Minimum value in ring Member (Roller support)	-604	-1104	-1089

Table 5. Axial force ratio of pin support and roller support

Lattice pattern	SS	DS	SD
Maximum value Roller/Pin	2.3	2.2	1.6
Minimum value Roller/Pin	5.9	4.5	4.2

6. Summary

The suspension system is replaced with double layer grid system for the purpose of seismic retrofit and multipurpose facility. Three typical lattice patterns, Square-on-Square (SS), Square-on-Diagonal (SD) and Diagonal-on-Square (DS) are compared from the viewpoint of the member axial force distributions.

At the same load level, Square-on-Square (SS) type shows the least deformation and high material efficiency at both the pin and roller support. However, it can be said that the Square-on-Diagonal (SD) type is stronger than the two others in the comparison with the axial force fluctuations by the differences of the two support conditions.

References

[1] C. Yan, Y. Taniguchi, and S. Yoshinaka, "Effect of Member Layout on Elastic Buckling Behavior for Square-and-Diagonal Double-Layer Lattice Domes," Proc. Of IASS Symposium 2009, Valencia, Spain Book of Abstracts, pp448~449, CD-ROM, pp.1941~1950, 2009.

[2] F.Zhang, Y.Taniguchi, T.Saka, and T.Ogawa, "Elastic Buckling and Elasto-Plastic Behavior of Double-Layer Latticed Structure with Various Forms and Mesh Patterns," IASS Symposium 2004, Monpellier, France, pp. 230~231, 2004.

[3] F.Zhang, Y.Taniguchi, and T.Saka, "Elastic Buckling Behavior of Double-Layer Latticed Structures Desingned by Allowable Stress Method," Smart Structures Technologies and Earth quake Engenerring 2004, Osaka Japan, pp 555~560, 2004.

Tensegrity systems and cable structures

Active bending
Additive manufacturing/ 3D printing
Architectural geometry
Bamboo for sustainable construction and quality of life improvement
Bio-inspired structures and architecture
Bridge structures
Computational form-finding
Conceptual design
Concrete structures
Construction techniques
Deployable and inflatable structures
Design competition (WG21)
Digital modelling and fabrication
Dynamic response of metal spatial structures
Dynamic response of other structures
Form-finding and structural optimisation of interlocking discrete assemblages
Graphical methods
Gridshell and lattice structures
Historical concrete shells
Historical structures
Lattice structures
Life-cycle design and assessment of structures
Metal gridshell structures, connections and stability
Methods and construction technologies for sustainable shell structures
Morphology and configuration processing
Next generation parametric design
Novel methods in modelling, optimisation and construction for reducing carbon footprint of continuous roof shells
Numerical methods for geometry, form-finding and optimisation of lightweight structures
Optimisation methods and applications
Origami
Other
Teaching design uncertainty: working with unknown qualities/quantities of new and re-claimed materials
Teaching of shell and spatial structures
► **Tensegrity systems and cable structures**
Tension and membrane structures
Tension structures in the Asia-Pacific
Timber and bio-based structures
Topology optimisation
Traditional masonry structures and innovation
Transformable structures

IASS 2023
July 10–14 Melbourne
Integration of Design and Fabrication

Proceedings of the IASS Annual Symposium 2023
Integration of Design and Fabrication
10–14 July 2023, Melbourne, Australia
Y.M. Xie, J. Burry, T.U. Lee and J. Ma (eds.)

Design and research on roof structure of the stadium of Sanya International Sports Industry Park

Chenyu LIANG[a,*], Zhongyi ZHU[a], Guangbo BAI[a], Yi CHEN[a], Xuyang DENG[a], Wei WANG[a], Xiaogang LIU[b]

[a,*] Beijing Institute of Architectural Design
62 South Lishi Road, Xicheng District, Beijing, China
liangchenyu@biad.com.cn

[b] University of Science and Technology Beijing

Abstract

The stadium is the main venue of the Asian Beach Games located in the tropical area where severe typhoon lands frequently. With a construction area of 86,000 m^2, the stadium can host up to 45,000 seats. The outline of stadium roof is 305m long and 270m wide. The long-span roof structure is composed of inner cable-membrane structure with a cantilever of 45m and outer steel structure. A spoke-type cable truss structure composed with Carbon Fiber Reinforced Polymer cables is designed. CFRP cable and high-strength cast steel G10MnMoV6-3 were used for the first time in large-scale spatial structures, realizing the lightweight of the structure and promoting the technological progress of the new material manufacturing industry. A horizontal truss structure supported by hinged columns is designed, and the section size of the ring beam is reduced by the overall action of the horizontal ring truss. Convex cable truss is used to deal with severe typhoon, which makes the structure safer, more comfortable and more economical. A kind of form analysis technology is used, which can significantly decrease the design duration of the entire project and increase the effectiveness of coordination between disciplines and avoid reworks. Connection detail of the arch supporting the PTFE membrane is designed, which has not only clear load path of transmitting vertical force and horizontal force, but also can provide out of plane support for the upper radial cable and improve the stability of the convex cable truss.

Keywords: spoke-type cable truss structure, CFRP cables, high-strength cast steel, convex cable truss, form analysis technology, connection detail design

1. Introduction

The stadium of Sanya International Sports Industry Park is the main venue of the Asian Beach Games located in the tropical area where severe typhoon lands frequently. With a construction area of 86,000 m^2, the stadium can host up to 45,000 seats. The outline of stadium roof is 305m long and 270m wide, shaped by an irregular pentagon with filleted corners. The shape of the inner oculus is composed of four arcs with different centers and radius, with a short axis of 134m, a long axis of 171.8m and a maximum elevation of about 46m.The long-span roof structure is composed of inner cable-membrane structure and outer steel structure. The inner cable-membrane structure has a cantilever of 45m, formed by spoke-type cable truss structure, which is consist of fully locked coil cable and CFRP cable; The outer steel structure is a ring-shaped plane truss structure composed of inner ring beam, outer ring beam and the cross-intersected beams between them, and sits on a supporting system formed by a series of hinged columns. The outer steel structure provides a reliable support for the inner structure. (Figure 1 to 3.)

Copyright © 2023 by Chenyu LIANG, Zhongyi ZHU, Guangbo BAI, Yi CHEN, Xuyang DENG, Wei WANG and Xiaogang LIU. Published in the Proceedings of the IASS Annual Symposium 2023 with permission.



Figure 1. Photo of the stadium after completion

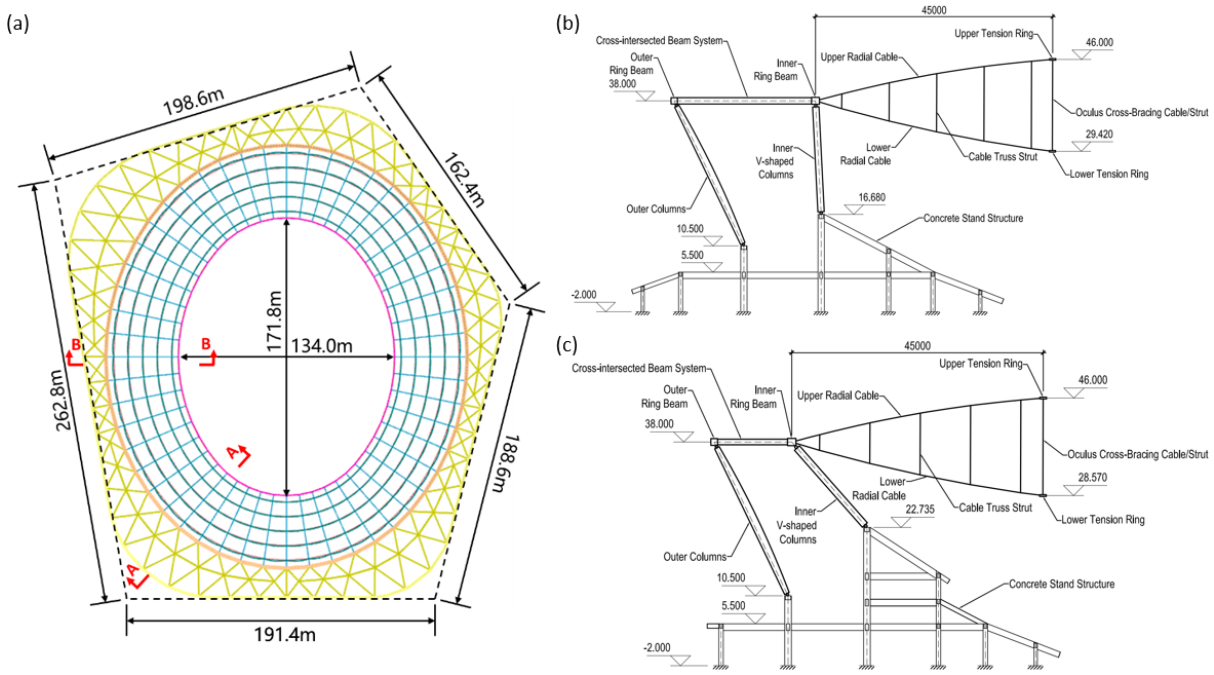
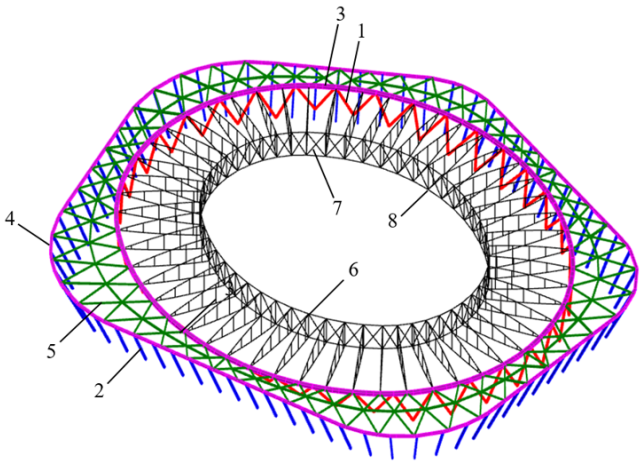


Figure 2. Layout of the roof structure of the stadium: (a) floor plan, (b) section A, (c) section B



1 – Inner hinged V-shape columns; 2 – Outer hinged columns; 3 – Inner ring beam; 4 – Outer ring beam;
5 – Cross-intersected beams; 6 – Cable truss; 7 – Cross-bracing cable (CFRP cable); 8 – Cable clamp (G10MnMoV6-3)

Figure 3. Compostion of the roof structure of the stadium

2. Key technologies in the design and research on this project

2.1. Application of CFRP cables

This project is located in the coastal area where severe typhoon lands frequently. According to the wind tunnel test, the wind load extreme values on this project are 3.8kN/m^2 and -3.7kN/m^2, and the Cp values are 2.2 and -2.3. The deformation caused by wind load is the governing factor of the lightweight roof structure design of the project. Setting cross-bracing cables between the upper and lower tension ring can significantly improve the stiffness of the roof structure and reduce the wind-induced deformation. (Figure 4.)

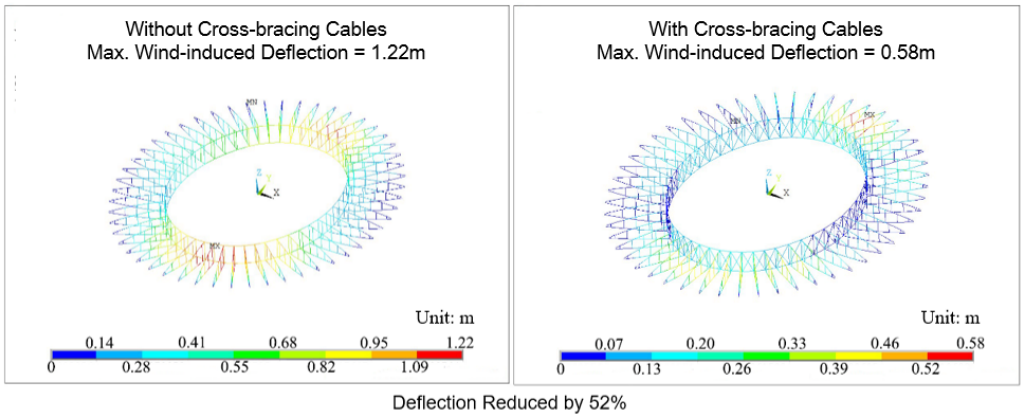


Figure 4. Benefit of setting cross-bracing cables between the upper and lower tension ring

The structural engineers noticed two important characteristics of the influence of cross-bracing cables on the structural performance (Figure 5):

a) a small axial stiffness (EA) of cross-bracing cables can significantly improve the structural stiffness, but further increasing of EA will have no obvious effect on further improving the structural stiffness.

b) The wind-induced unbalanced force at the cable clamp connection will increase along with the EA increases, which will consequently lead to increasing of the clamp size and weight on the roof.

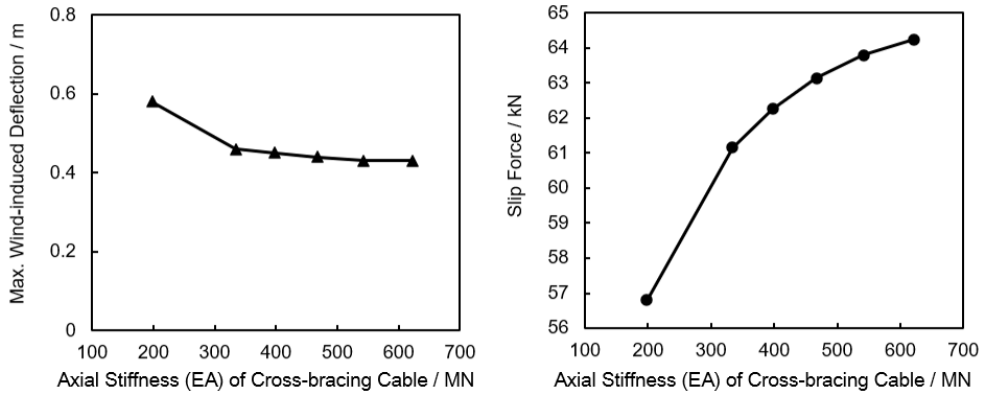


Figure 5. Influence of axial stiffness (EA) of cross-bracing cable

In this project, the designer selects CFRP cables as the cross-bracing cables. By making full use of its high strength and low elastic modulus characteristics [1], i.e., to keep smaller EA with small section area (A) and low elastic modulus (E), the contradiction between improving structural rigidity and reducing unbalanced force of cable clamp is creatively resolved. See the CFRP cable and its anchorage device of this project in figure 6.

This project is the first application of CFRP cable in large-scale spatial structure, which improves the

performance of the structure and is a beneficial attempt of new materials. After the completion of roof structural installation, the project team has invited 20 experts from universities, construction companies, steel and cable contractors to share all the acknowledge obtained from the project, including the design methods, technical standards, manufacture and installation specifications for CFRP cable in spatial structure. Together with a couple of patent and research papers which are all open to public, this project demonstrates and promotes the application of CFRP cable in the field of spatial structure. Yue Qingrui, academician of the Chinese Academy of Engineering, commented that "This project can be considered as an important milestone for a successful application of corrugated anchor CFRP parallel plate cable for the first time in the world, and is a breakthrough in the application of CFRP cable in long-span spatial structures."

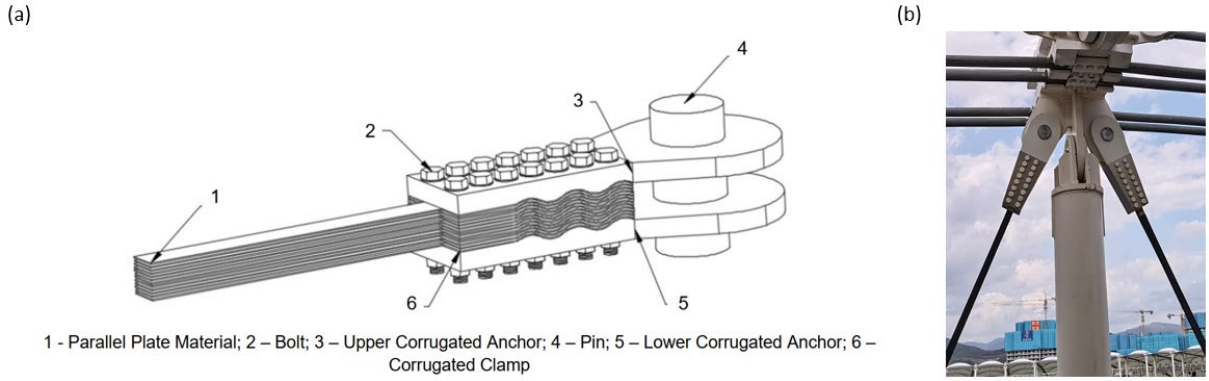


Figure 6. CFRP cable and its anchorage device: (a) schematic diagram, (b) live photo

2.2. Form selection of cable truss

The architect initially proposed to use concave cable truss as the roof structure. Although it has been successfully applied in many projects, the concave cable truss was proved having insufficient stiffness to deal with severe typhoons in this project. Therefore, the structural engineers suggested to change the form of cable truss from concave to convex, which has 33% higher stiffness. (Figure 7.) The advantage of the change includes: More economical - less material when achieving the same performance target; More safe – protect secondary structures from huge wind-induced deformation; More comfortable - the spectators will not suffer from insecure caused by large movement of the roof.

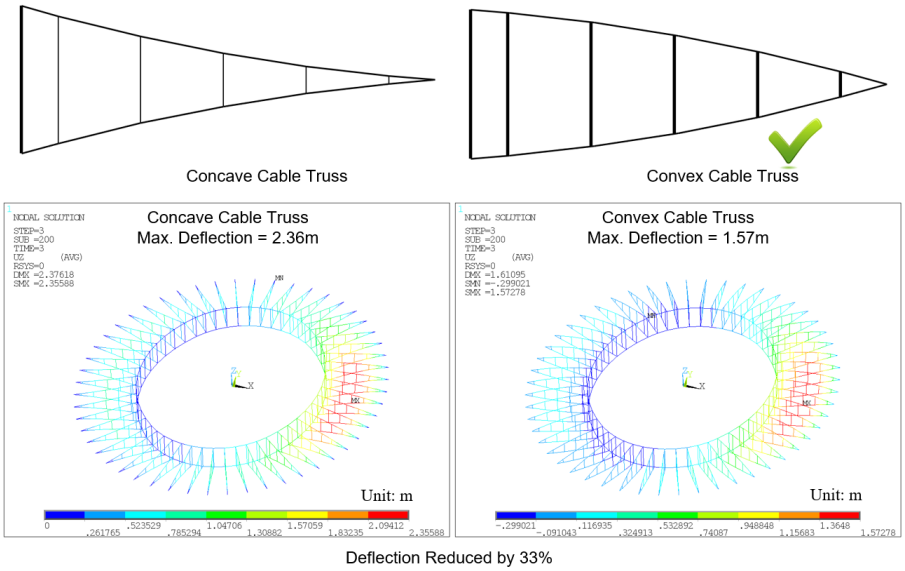
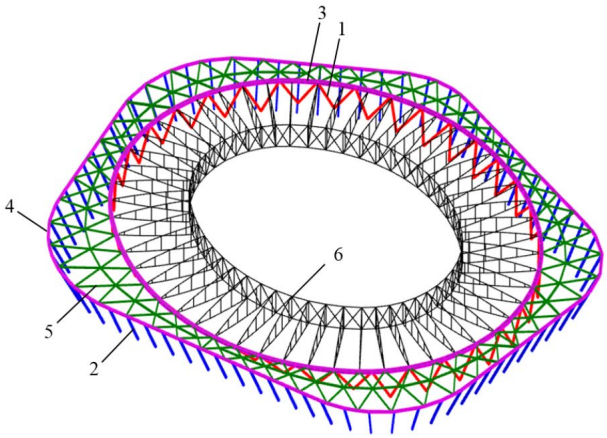


Figure 7. Comparison between concave and convex cable truss

2.3. Ring-shaped plane truss structure supported by hinged columns

The tension force of the cable truss of the inner roof is relatively large due to the location of the project which is coastal area with large wind load. According to the function of the building, the architect set up a ring of flat roof outside the inner ring roof. The structural engineer decided to use the bearing capacity of the entire outer roof to resist the horizontal force from the cables. As the support boundary of the cable truss, the ring-shaped plane truss structure was formed by arranging the inner and outer ring beams and the cross-intersected beams between them [2]. Meanwhile, all the supporting columns were designed as hinged at both ends, and the inner ring columns were arranged into continuous V-shape, which formed a reliable lateral force resistance system. (Figure 8 to 9.)



1- Inner hinged V-shape columns; 2 - Outer hinged columns; 3 - Inner ring beam; 4 - Outer ring beam; 5 – Cross-intersected beams; 6 - Cable truss

Figure 8. Layout of the ring-shaped plane truss structure supported by hinged columns



Figure 9. Live photo of the ring-shaped plane truss structure supported by hinged columns

By forming an integrated bearing system for the cable forces, the section size of the ring beam is reduced by 40%. By taking the axial force only and using the material strength in the most efficient way, the hinged steel columns reduce the amount of steel consumption and simplify the connection details between steel and concrete structure.

2.4. Advanced form analysis technology

In order to meet the requirements of architectural roof cladding geometry, the form of the cable structure roof in this project is determined by the balance between applied tension force and weight of the structure [3]. Once the weight of the roof structure is changed, the applied tension force should be adjusted to keep the position of the upper tiers consistent with their original position.

In the early stage of design, structural engineers can only make preliminary form finding based on an assumed weight of components on the roof. With the development of design and detailing, the weight value of each part of the roof become gradually determined. After all the weight of roof is finally determined, a final form finding is required to obtain the accurate theoretical shape of the roof after the construction. With advanced form analysis technology, when the weight of the roof changes, only the shape of the lower cable is required to be adjusted, while the position of the upper cable can maintain the shape and consistent with the form required by the architects. (Figure 10.) Therefore, the design of the roof cladding system, drainage and other related disciplines which depend on the cable position of the upper layer can be commenced from the early stage without being affected by the structural form found in the later stage. This technology can significantly decrease the design duration of the entire project and increase the effectiveness of coordination between disciplines and avoid reworks.

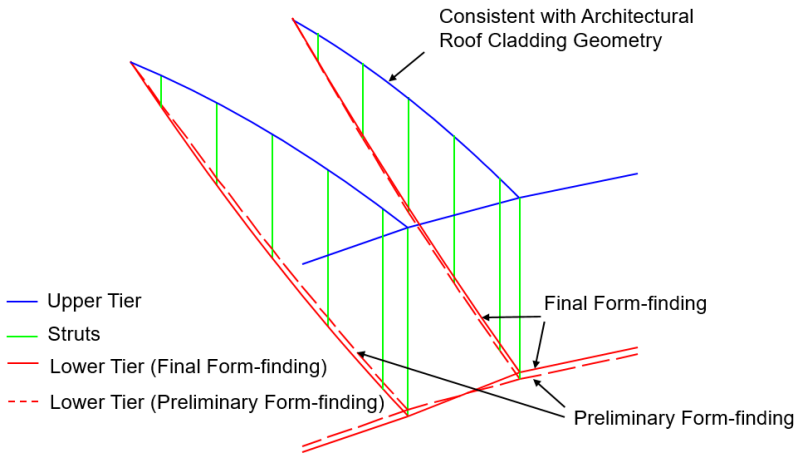


Figure 10. Schematic of the form analysis technology

2.5. Design of cable clamp with high-strength cast steel G10MnMoV6-3

The weight of cable clamp connection accounts for a large proportion of the self-weight of the whole cable-membrane structure, which has a great impact on the economic efficiency of the entire structure. The design needs high-strength cast steel to reduce the weight. The common structural cast steel materials G17Mn5 and G20Mn5 have a maximum yield strength of only 300MPa. Therefore, the structural engineers selected cast steel G10MnMoV6-3 with yield strength 33% higher than common material [4], which significantly reduced the weight of cable clamp by 30% while the same bearing capacity was maintained. By the use of G10MnMoV6-3, the weight of roof structure was reduced and the tension force of the cable truss was decreased. (Figure 11.)

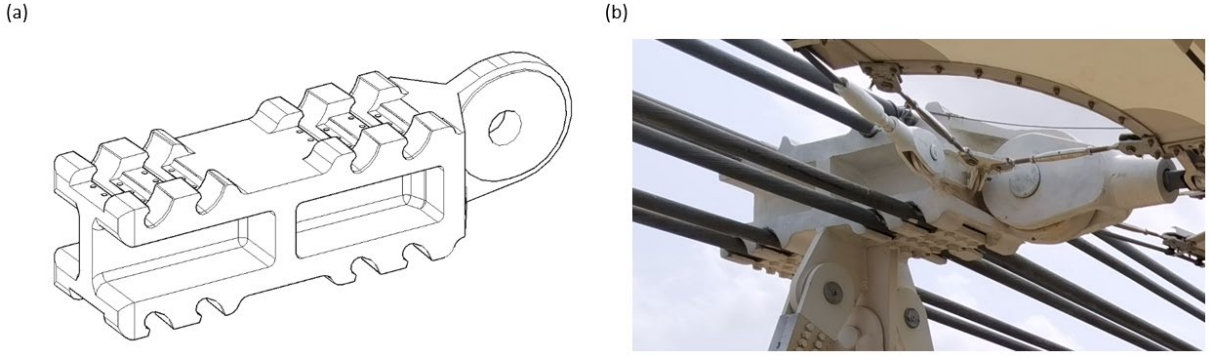


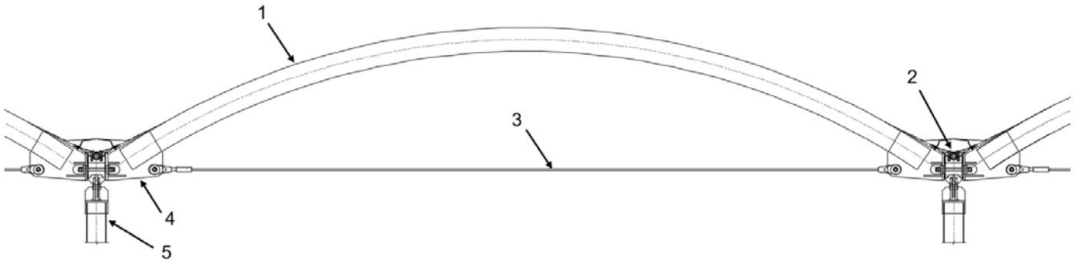
Figure 11. Cable clamp with G10MnMoV6-3: (a) schematic diagram, (b) live photo

G10MnMoV6-3 material is applied for the first time in China, which makes the casting connection to

be stronger and more lightweight. Driven by the design requirements of this project, Chinese cast steel foundries have conducted a lot of tests in the chemical constituent ratio and heat treatment process, formed a stable manufacturing process and met the performance requirements in European standard.

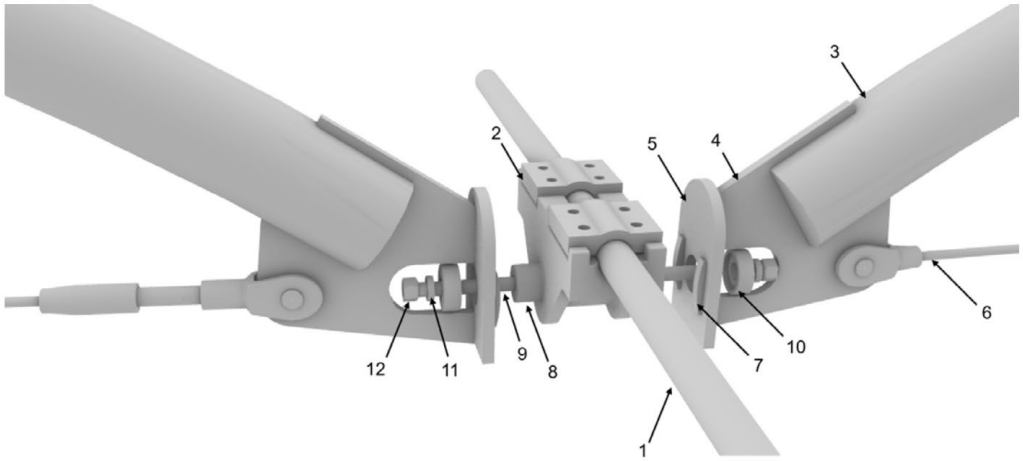
2.6. Creative type of connection detail at the support of the PTFE membrane

The PTFE membrane is supported by the arch with a balance cable set between the arch supports. (Figure 12.) In most of other projects with similar arch supporting membrane, the arch is designed to be relatively independent to the radial cable. However, for this project, a creative type of connection detail between the arch supports and radial cable clamps is designed in order to improve the stability of convex-shape cable truss. The radial cable clamp is designed to have a cylindrical cantilever bracket with bolt hole in the centre. The vertical reaction from the arch is transmitted to the bracket through the perforated end plate at arch support, where the cylindrical cantilever bracket can insert into. A high-strength bolt passes through the central hole of the bracket and is fixed through the convex nut and concave washer. By working together with a pair of chambered bosses designed on the end plate, both tension and compression can be transmitted reliably between the arch balance cable, arch and the upper radial cable while rotation ability between them is maintained to avoid the bending of the bolt due to structural deformation. (Figure 13 to 14.) This kind of connection detail has not only clear load path of transmitting vertical force and horizontal force, but also can provide out of plane support for the upper radial cable and improve the stability of the convex cable truss.



1 - Membrane shaping arch; 2 - Radial cable and clamp with cylindrical bracket; 3 - Arch balance cable; 4 - Arch support fin plate; 5 - Radial cable strut

Figure 12. Layout of arch and balance cable of the PTFE membrane



1 - Upper radial cable; 2 - Upper radial cable clamp cover plate; 3 – Membrane shaping arch; 4 - Arch support fin plate; 5 - Arch support end plate; 6 - Arch balance cable; 7 - Cambered boss on the end plate; 8 – Cylindrical bracket on radial cable clamp; 9 - High strength bolt; 10 - Perforated cover plate; 11 - Concave washer; 12 - Convex nut

Figure 13. Schematic of connection detail at the support of the PTFE membrane



Figure 14. Live photo of connection detail at the support of the PTFE membrane

3. Conclusion

a) The stadium of Sanya International Sports Industry Park is the main venue of the Asian Beach Games located in the tropical area where severe typhoon lands frequently.

b) A spoke-type cable truss structure composed with CFRP cables is designed. CFRP cable and high-strength cast steel G10MnMoV6-3 were used for the first time in large-scale spatial structures, realizing the lightweight of the structure and promoting the technological progress of the new material manufacturing industry.

c) A horizontal truss structure supported by hinged columns is designed, and the section size of the ring beam is reduced by the overall action of the horizontal ring truss. The use of hinged columns save the steel consumption and simplify the connection details between steel and concrete structure.

d) Convex cable truss is used to deal with severe typhoons, which makes the structure safer, more comfortable and more economical.

e) A kind of advanced form analysis technology is used, which can significantly decrease the design duration of the entire project and increase the effectiveness of coordination between disciplines and avoid reworks.

f) A creative type of connection detail of the arch supporting the PTFE membrane is designed, which has not only clear load path of transmitting vertical force and horizontal force, but also can provide out of plane support for the upper radial cable and improve the stability of the convex cable truss.

References

[1] L. H. Liu, Y. L. Zhu, J. W. Zhang and Z. B. Zhou, “Progress in the study on mechanical properties of anchorage system for cfrp cables,” *FRP/CM,* no. 2, pp. 81–86, 2015.

[2] C. Y. Liang, Z. Y. Zhu, G. B. Bai and et al, “Steel structure design on the stadium of Sanya International Sports Industry Park,” *Building Structure,* vol. 51, pp. 18–24, 2021.

[3] G. B. Bai, Z. Wang, B. L. Chen and et al, “Key issues in cable net form-finding of the national speed skating oval,” *Steel Construction (Chinese & English),* vol. 35, pp. 54–61, 2020.

[4] *Steel castings. Steel castings for general engineering uses (BS EN 10293: 2015),* British Standards Institution, 2015.

Proceedings of the IASS Annual Symposium 2023
Integration of Design and Fabrication
10–14 July 2023, Melbourne, Australia
Y.M. Xie, J. Burry, T.U. Lee and J. Ma (eds.)

Evaluation and improvement of bearing capacity of annular crossed cable net structure after local cable failure

Suduo XUE*, Xuanzhi LI[a], Xiongyan LI[a], Zaigen MU[b]

[a,*] The Key Laboratory of Urban Security and Disaster Engineering of Ministry of Education, Beijing University of Technology, 100 Pingleyuan, Beijing, China
xz.lee0713@foxmail.com

[b] University of Science and Technology Beijing 30 Xueyuan Road, Haidian District, Beijing, China, 100083

Abstract

The annular crossed cable net structure has strong collapse resistance and can continue to bear the load after local cable breaking. To quantitatively evaluate the bearing capacity of the structure after cable failure, a multiple-step loading and unloading method was proposed. The failure grades of cables were classified in the gradual cable breaking process. In addition, the bearing capacity reduction coefficient was put forward to quantitatively evaluate the reduction degree of bearing capacity. According to the curve of bearing capacity reduction coefficient, the residual ultimate load corresponding to different cable failure numbers can be quantitatively evaluated. The results show that delaying the failure of the grade I cables of the cable-net structure is the key to improving the ultimate bearing capacity. An effective way to change the bearing capacity of the structure is by adjusting the breaking order of the cables. Therefore, three effective design measures (using CFRP cables, increasing the cross-sectional area of load-bearing cables, and increasing the number and grade of cables) were put forward to improve the bearing capacity of the structure.

Keywords: annular crossed cable net structure, bearing capacity reduction coefficient, failure grades of cables, evaluate of bearing capacity, new design measures

1. Introduction

Cables, as members with stiffness and bearing capacity provided by pre-tension, have an important influence on the anti-collapse performance of these structural systems. Asghari R et al. [1] put forward a hybrid cable-strut system which is composed of tensegrity rings and a Levy cable dome and studied the initial collapse behavior of the structure by numerical simulation with ABAQUS software. Zheng J et al. [2] studied the failure mode of the cable dome structure and its mechanical performance after a cable rupture. Lu J et al. [3] investigated the failure effect of a planar truss string structure with a 6 m span through both experiments and numerical simulations. Zhou H et al. [4] analyzed the uncertainties of bearing capacity by combining the finite element method with the Monte Carlo simulation, proposed a simplified approach to establish a more realistic limit state equation of the beam string structure under both full-span load and half-span load, and carried out the bearing capacity reliability calibration considering the random properties of load ratio. However, little research has focused on the residual bearing capacity and anti-collapse mechanisms of the single-layer cable-net roof structure, such as cable force redistribution and configuration change after cable failure. Furthermore, the corresponding analysis methods and evaluation indexes for cable-net structures are rarely put forward.

The single-layer cable-net roof is a flexible full-tension structure system with all structural members consisting of prestressed cables. A the cable failure will lead to significant changes in cable force redistribution and configuration. Meanwhile, the cable force and configuration change characteristics,

Copyright © 2023 by Suduo XUE, Xuanzhi LI, Xiongyan LI and Zaigen MU. Published in the Proceedings of the IASS Annual Symposium 2023 with permission.

force transmission mechanism, and collapse resistance are quite different from those of other spatial structure systems. Therefore, this paper took the Annular Crossed Cable-net Structure (ACCN) as the research object and first puts forward the method of determining the load-bearing level of cable elements and the scheme of cable grade classification. To study the anti-collapse mechanism of the cable-net structure and to evaluate the bearing capacity of the structure after the cable failure, a collapse process analysis method of the cable-net structure is proposed. Finally, two effective design measures to improve the load-bearing capacity of the cable-net roof are presented.

2. Analysis model of ACCN

ACCN (Figure 1) [5] is a flexible full-tension saddle-shaped single-layer cable net system, in which both ends of the cables are directly connected to saddle-shaped outer ring beams. By arranging the cables in a circular cross, a large opening is formed in the center. This architectural shape is similar to a single-layer wheel-spoke cable-net, but there is no inner ring cable, so it is also called the single-layer cable-net structure without inner ring [6].

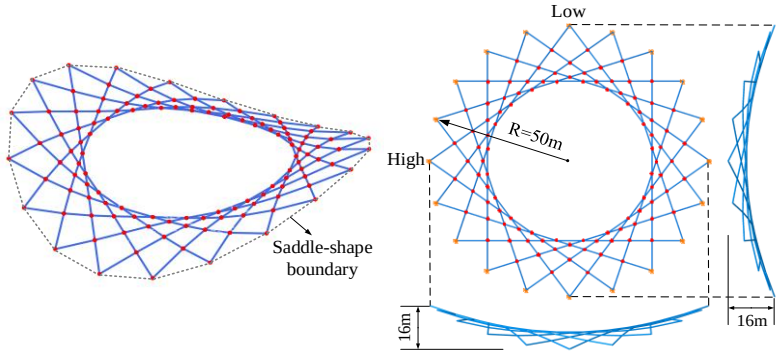


Figure 1 The model diagram of ACCN

The analysis model of ACCN was established with a structural span of 100m, the height difference of the hyperbolic outer ring boundary is 16m, and 20 cables are arranged in an annular direction. The structural layout is shown in Figure 1. The density, elastic modulus, and ultimate strength of the cable are 7850 kg/m^3, 160 GPa, and 1680 MPa, respectively. Considering the gravity of the membrane roof and equipment, the dead load is 0.15kN/m^2 and is equivalent to node concentrated load. The density of the cable is enlarged 1.2 time considering the gravity of the cable clamps at the node. The live load is considered to be 0.3 kN/m^2. The diameter of the cables that meet the structural design requirements [7,8] is 64mm, and all of the cables share the same size. Only the cable net is analyzed, and the boundary constraints are hinge constraints. The load combination (1.2 dead loads + 0.5 live loads) is used according to the code [9]. The cable element between nodes was divided, so that each cable has 11 elements, thus the total element number of 20 cables is 220.

3. Classification of load-bearing grades of cables

The strain energy is selected as the parameter by considering the cable force and deformation from the energy point of view. The greater the proportion of the strain energy increment of a cable element in the cable net to the total strain energy increment when the load is increased under normal conditions, indicating that the bearing grade of this cable element is higher. The corresponding Eq. (1) is as follows:

$$\gamma_i = \frac{U_{1i} - U_{0i}}{\sum_{i=1}^{n}(U_{1i} - U_{0i})} \tag{1}$$

where, γ_i is load-bearing coefficient of cable element i, U_{0i} is the strain energy of the cable element i at the normal state, U_{1i} is the strain energy of the cable element i after increasing the load ΔF. The cable element is in an elastic state and only bears the axial tension, and the strain energy can be expressed as follows:

$$U_i = \frac{0.5{F_i}^2 L_i}{E_i A_i} = \frac{0.5{\sigma_i}^2 V_i}{E_i} \tag{2}$$

where, F_i is the cable force of the element i, L_i is the cable length of the element i at the zero-stress state, σ_i is the stress of the element i, V_i is the volume of the element i at the zero-stress state, and E_i and A_i are the elastic modulus and cross-sectional area of the element i, respectively. Substituting Eq. (2) into Eq. (1), the load-bearing coefficient γ_i can be obtained as follows:

$$\gamma_i = \frac{({\sigma_{1i}}^2 - {\sigma_{0i}}^2)V_i}{\sum_{i=1}^{n}({\sigma_{1i}}^2 - {\sigma_{0i}}^2)V_i} \tag{3}$$

Eq. (3) indicates that the change degree of stress square difference of the cable element before and after increasing the load ΔF. The larger γ_i is, the higher of load-bearing the corresponding cable element is. According to the model shown in Figure 1, the load increment is 1 time of the live load. The load-bearing coefficients of the cable elements are calculated according to Eq.(3) by the incremental load method.

It is illustrated in Figure 2 that the load-bearing coefficients are obviously divided into two parts. The ones greater than 0 are the load-bearing cable elements, and the other ones less than 0 are the stable cable elements. The maximum load-bearing coefficient of all elements in each cable is selected and ranked for all cables in descending order, as shown in Figure 3. The maximum load-bearing coefficient of the elements in each grade of cables is listed in Table 1. The load-bearing value of cables from grade I to grade VI decreases step by step. Grade I to grade III are load-bearing cables and grade IV to grade VI are stable cables. The elements (122, 132, 166, 167) with the greatest load-bearing coefficient appear at the two ends of the grade I cable (C12, C16) (Figure 3). They are the most load-bearing elements of the whole cable-net structure.

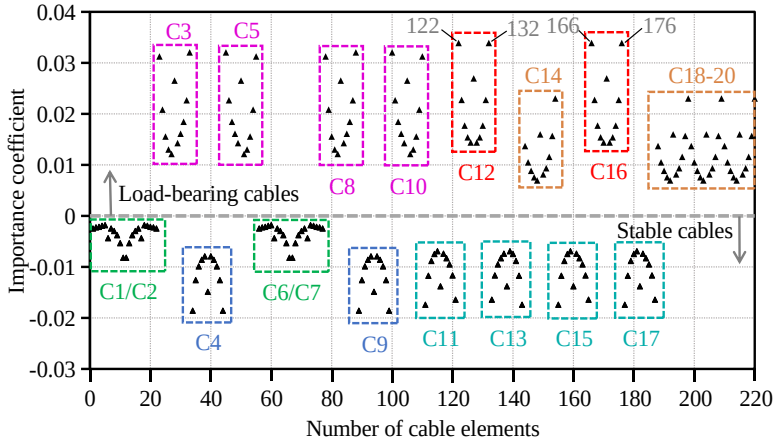


Figure 2 The load-bearing coefficients of cable elements

Table 1 Maximum load-bearing coefficient of each grade for cables

Grade	I	II	III	VI	V	VI
Max importance coefficient	0.034	0.032	0.023	-0.0018	-0.0070	-0.0079

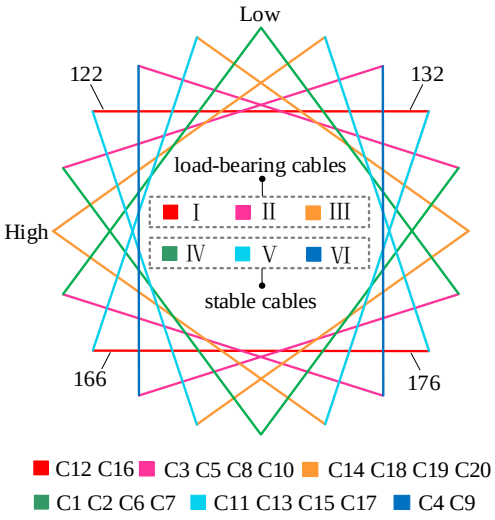


Figure 3 Load-bearing grades for cables

4. Evaluation of load-bearing capacity for ACCN

4.1. Multi-Step loading-unloading method

The key to the load-bearing capacity analysis is to determine the ultimate load and residual ultimate load of the structure, which can effectively analyze the structural performance in each stage of cable failure. Due to the changing trend of F_n (n = 0,1,2,···), a multi-step loading-unloading method is proposed to calculate the residual ultimate load at each stage of cable failure. The algorithm steps are as follows:

1) The dead and weight load of the cable-net structure in the normal state are included, and the incremental load is equivalent to the node concentrated load according to the full live load. The incremental load is calculated by the Bisection method. First, the cable force is calculated by taking a larger load F_p which ensures that F_0 is between 0 and F_p. The load range is reduced so that F_0 is between $F_p/2$ and F_p, and then this range is continuously reduced until F_0 is obtained.

2) The first group of failed elements reaching their ultimate strength (1680MPa) is deleted. The residual structure is loaded step by step from 0 to F_0 in small increments, i.e., the increment force $\Delta F = F_0/m$ (m=1000). When certain elements reach their ultimate strength in step n, these elements are the second group of failed elements, and the load at this step is calibrated as F_1, i.e., $F_1 = n_1 \Delta F = \beta_1 F_0$,

   where n_1 is the step number of the load increment, β_1 is the reduction coefficient of bearing capacity at the failure of the first group of cables.

3) The second group of failed elements is deleted. According to the same method used in step 2, the load F_2 and the corresponding failed elements are obtained. This process is repeated, until the structure loses bearing capacity and collapses. The corresponding loads $F_0[1, \beta_1, \beta_2, \cdots, \beta_n]$ and failed elements at each stage are obtained.

The failure mechanism of the cable-net structure is analyzed according to the cable force redistribution and configuration changes in each stage of the cable failure. Two indexes both average and maximum displacement are used to reveal the changing trend of configuration of the structure. The curve of the reduction coefficient of bearing capacity is used to evaluate the anti-collapse performance of the cable-net structure.

4.2. Collapse process analysis for ACCN

The ultimate load F_0 obtained by the above method is 6.3 kN/m^2. The curves of displacement change, and the reduction coefficient for bearing capacity are shown in Figure 4, and Figure 5, respectively.

It can be seen from Figure 4 that the order of cable failure follows the grade standard defined by the load-bearing coefficient in Figure 3. Grade I cables, as the most important load-bearing cables, fail first, and then it is grade II to grade V in turn. After the fifth group of cables fails, the cable net deformation increased sharply (from 5.3m to 9.5m in Figure 4), and only two cables (grade VI) were left to connect, and the structure lost bearing capacity. The trend of average displacement (Figure 5) shows a parabolic decline. With the increase in failure times, the displacement increment gradually increases. The maximum displacement (3.3m) before the cable failure is smaller than that (2.5m) when Grade I cables fail. This is mainly because F_1 is less than F_0, which makes the middle area of grade VI cables suffer from large node forces.

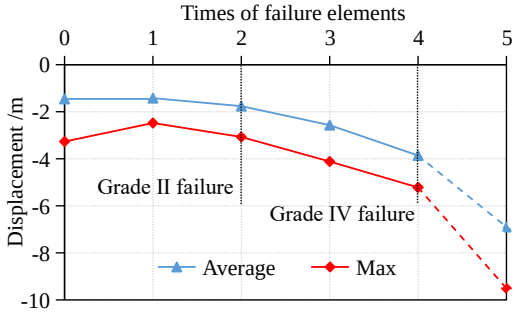


Figure 4 Curve of displacement change.

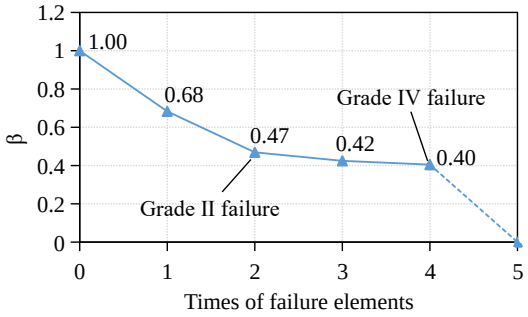


Figure 5 Curve of the reduction coefficient of load-bearing capacity.

It is possible to evaluate the structural bearing capacity in any cable failure through the curve of reduction coefficient for bearing capacity (Figure 5). Table 2 shows the residual ultimate loads corresponding to the number of failed cables.

Table 2 Residual ultimate loads corresponding to numbers of failed cables

Number of failed cables	0~2	3~6	7~10	11~14	15~18
Residual ultimate loads /F_0	1~0.68	0.68~0.47	0.47~0.42	0.42~0.40	0.40~0

5. Load-bearing performance improvement

It can be found from the above analysis that delaying the failure of the grade I cables of the cable-net structure is the key to improving the ultimate bearing capacity. An effective way to change the collapse failure mode of the cable-net structure is by adjusting the breaking order of the cables. Therefore, three effective ways to improve load-bearing performance are presented.

5.1. Improve the strength of cables and use CFRP cables with high tensile strength

The density, elastic modulus, and ultimate strength of CFRP cables are 1500kg/m^3, 160GPa and 2.4GPa, respectively. The density of CFRP cables is 0.19 times that of steel cables, and their ultimate strength is 1.43 times that of steel cables. Under the same conditions except for the replacement of cable materials, the importance grade of cables is not changed. The failure sequence of the cables is the same as that in Figure 3. Thus, only the ultimate bearing capacity is analyzed here.

The ultimate load F_0 calculated by the steel cable structure is taken as the unit comparative value. The curve of reduction coefficient of bearing capacity for the structure with CFRP cables is shown in Figure 6. The ultimate load of the CFRP cable structure is about 1.74 times higher than that of the steel cable structure. After the first group of cables fail, the residual ultimate load F_1 of the CFRP cable structure is still greater than the ultimate load F_0 of the steel cable structure. The changing trend of both curves is similar. The residual ultimate load of the CFRP cable structure in each stage is obviously improved. This indicates that replacing steel cables with CFRP cables can effectively improve the bearing capacity and collapse resistance of the structure.

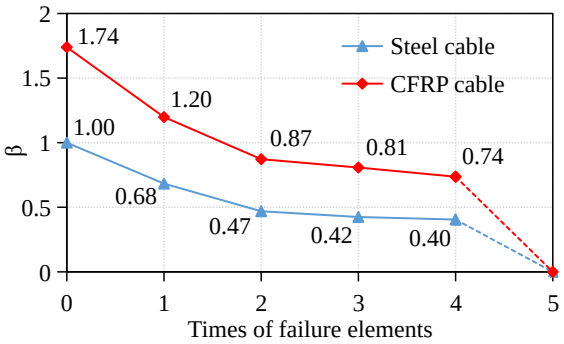


Figure 6 Comparison of bearing capacity curves between CFRP cables and steel cables

5.2. Increase the cross-sectional area of the load-bearing cable

Based on the model in Figure 2, the cross-sectional area A of the cable is doubled according to the three situations of the grade I cables (A1), the grade I cables to grade II cables (A12), and the grade I to grade III cables (A123) in Figure 3. It can be seen from Eq. (3) that the importance grade of the cable is unchanged. The ultimate cable forces of some cables are doubled, however, which will change the order of cable failure. At the same time, the ultimate load and the residual ultimate load in each stage also change accordingly, as seen in Figure 7. The reduction coefficient of bearing capacity and failure order of the cables have been listed in Table 3.

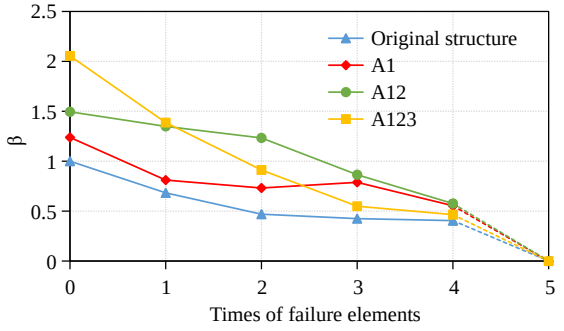


Figure 7 Influence of increasing cross-sectional area of load-bearing cables on bearing capacity

It can be seen from Figure 7 and Table 3 that the ultimate load F_0 gradually increases with the increase of the cross-sectional area from the grade I cables to the grade III cables. Meanwhile, the residual

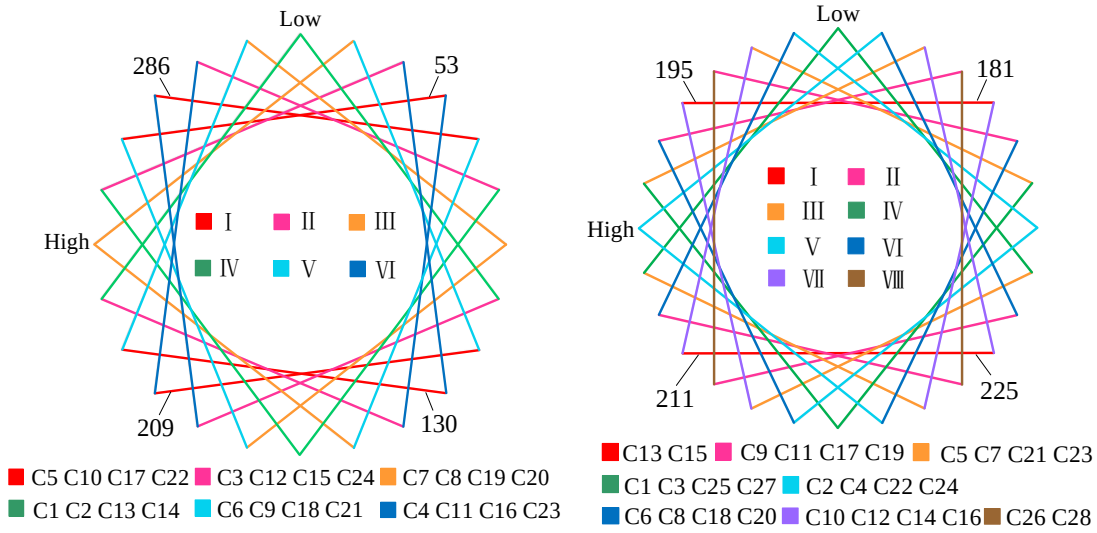
ultimate loads of each stage in the three schemes are higher than the corresponding value of the original structure. This indicates that increasing the cross-sectional area of the load-bearing cable according to the rank order can effectively improve the collapse resistance of the structure. For scheme A1, the residual ultimate loads from the first failure to the third failure are all close (0.81,0.73,0.79). The residual ultimate load for A1 decreased significantly after the fourth failure, i.e., after the grade I cable was broken. This illustrates that the increase of the ultimate cable force of the grade I cable can improve the residual bearing capacity of the structure. For scheme A123, the ultimate load has increased to twice that of the original structure and the failure sequence of the cables is the same as that of the original structure. When the second group of cables fail, the residual ultimate load for A123 is already smaller than that of the corresponding A12. The residual ultimate load for A123 is close to that of the original structure when the third cable fails.

Table 3 Changes of bearing capacity of the structure by increasing the cross-sectional area of the load-bearing cable

Failure times		0	1	2	3	4	5
Reduction coefficient of bearing capacity	Original structure	1.00	0.68	0.47	0.42	0.40	0.00
	A1	1.24	0.81	0.73	0.79	0.55	0.00
	A12	1.50	1.35	1.23	0.86	0.58	0.00
	A123	2.06	1.39	0.91	0.55	0.46	0.00
Failure cable	Original structure	None	grade I	grade II	grade III	grade IV	grade V
	A1	None	grade II	grade III	grade IV	grade I	grade V
	A12	None	grade III	grade IV	grade II	grade I	grade V
	A123	None	grade I	grade II	grade III	grade IV	grade V
Number of failed elements	Original structure	0	4	4	4	16	32
	A1	0	4	4	16	4	32
	A12	0	4	16	4	4	32
	A123	0	4	4	4	16	32

5.3. Increase the number and grade of cables

The number of cables in the original structure (Figure 1) is 20. Two new models were designed, named M1 and M2 respectively. The number of cables in M1 is 24. Each cable is divided into 13 elements (Figure 8a). The number of cables in M2 is 28. Each cable is divided into 15 elements (Figure 8b). The rest of the conditions are the same as the original structure. For the two new schemes, the cable grades obtained by the importance coefficient of the cable elements according to Eq. (3) are shown in Figure 8. Their maximum importance coefficients are 0.028 and 0.023 respectively, and the corresponding cable elements are also shown in Fig. 8. Compared with the original structure, the maximum importance coefficient decreases with the increase of the number of cables, which shows that the influence of a single cable failure on the structure is gradually decreasing.



(a) (b)

Figure 8 Schematic diagram of cable importance grade for two new schemes:(a) M1 (24 cables), (b) M2 (28 cables).

For scheme M1 (24 cables), the cable importance grade is divided into 6 levels, which are the same as the original structure, but the quantities of grade I and grade VI cables have increased from two to four. For scheme M2 (28 cables), the cable importance grade is divided into 8 levels. The number of grade I and grade VIII cables is two, which is the same as the number of grade I and grade VI cables in the original structure. Due to the increase in the number of cables and nodes, the cable net becomes denser, the load shared by each cable decreases, and the bearing capacity will be improved, as shown in Figure 9.

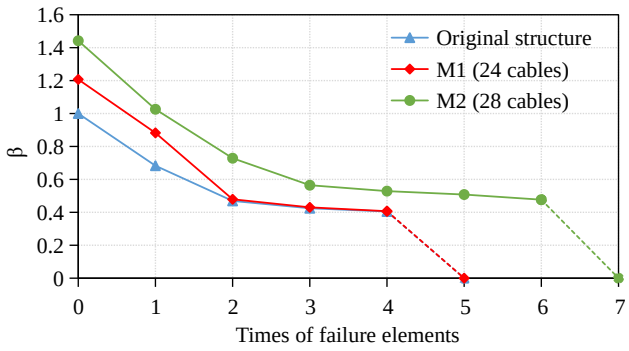


Figure 9 Influence of increasing number of cables on bearing capacity of structures

The failure sequence of the cables of the two new structures also follows the ranking of cables. The grade I cables are the first to break, their failure positions are the same as those of the original structure, and they all appear at the ends of the cables (Figure 3). With the increase in the number of cables (20,24,28), the ultimate load increases proportionally (1:1.21:1.44), as seen in Table 4. The residual ultimate load for M1 after the failure of the grade II cables is close to that for the original structure. Adding grade VI cables has no effect on the bearing capacity of the structure, and structural collapse still occurs after the failure of the grade V cables. For M2, as the cable grade increased by two levels, the structure collapsed only after the failure of the grade VII cables. The whole collapse stage of M2 is prolonged with the increase of cable grades, and the residual ultimate load of each stage is higher than that of the original structure.

Table 4 Comparison of reduction coefficients of bearing capacity for different cable numbers

Cable failure grade	None	I	II	III	VI	V	VI	VII
Original structure	1.00	0.68	0.47	0.42	0.40	0.00	—	—
M1 (24 cables)	1.21	0.88	0.48	0.43	0.41	0.00	—	—
M2 (28 cables)	1.44	1.03	0.73	0.56	0.53	0.51	0.48	0.00

6. Conclusion

This paper took the annular crossed cable-net roof structure (ACCN) as the research object and put forward the load-bearing grading method of cables and the evaluation of load-bearing capacity according to the characteristics of the cable-net structure. The bearing capacity and failure mode of ACCN were detailed. Three effective measures to improve the load-bearing performance of the structure were put forward. Some important conclusions are as follows:

(1) The load increment method is used to calculate the strain energy increment of the cables for the cable-net structure. This method can effectively judge the load-bearing level of the cable elements, divide the load-bearing cables and stabilizing cables, and determine the load-bearing grade of the cables. The load-bearing grade of the cables for ACCN is mainly related to the number of cables and the saddle-shaped boundary conditions.

(2) The ultimate load and the residual ultimate load in the collapse process analysis of the cable-net structure can be calculated by using the multi-step loading-unloading method. Through drawing the curve of reduction coefficient of bearing capacity, the failure sequence of the cables can be sorted out and the bearing capacity of each stage can be evaluated. The load-bearing grade of the cables is the key index to determine the failure sequence of the cables.

(3) Using CFRP cables, increasing the cross-sectional area of the load-bearing cables and increasing the number and grade of cables can effectively improve the load-bearing capacity of the cable-net structure. For ACCN, increasing the section area of all load-bearing cables is the most effective way to improve the ultimate load, followed by using CFRP cables; increasing the number of important grades of cables is the most effective way to increase the residual ultimate load and delay the collapse of structures, followed by using CFRP cables.

References

[1] R. Asghari, M. R. Chenaghlou, B. Shekastehband, “Investigation into Collapse Behavior of Cable Dome with Hybrid Form and Improvement of behavior with Force Limiting Devices,” *Journal of Civil and Environmental Engineering*, 2022.

[2] J. H. Zheng, X. F. Yuan, S. L. Dong, “Failure modes and mechanical properties of two types of cable domes,” *Engineering Mechanics*, 2007(01):44-50.

[3] J. Y. Lu, H. Y. Zhang, X. L. Wu, “Experimental study on collapse behaviour of truss string structures under cable rupture,” *Journal of Constructional Steel Research*, 185 (2021): 106864.

[4] H. Zhou, Y. Jiang, S. Adhikari, et al, “Comparisons of design methods for beam string structure based on reliability and progressive collapse analysis,” *Structures*, 33 (2021):2166-2176.

[5] S. D. Xue, X. S. Tian, Y. Liu, X. Y. Li, R. J. Liu, “Mechanical behavior of single-layer saddle-shaped crossed cable net without inner ring,” *Journal of Building Structure*, 2021,42(01):30-38. (in Chinese)

[6] S. D. Xue, X. Z. Li, Y. Liu. “Advanced form finding of cable roof structures integral with supporting frames: Numerical methods and case studies.” *Journal of Building Engineering* 60 (2022): 105204.

[7] Load code for the design of building structures: GB50009-2012. Beijing: China Architecture & Building Press, 2012. (in Chinese)

[8] Technical specification for cable structures: JGJ257-2012. Beijing: China Architecture & Building Press, 2012. (in Chinese)

[9] Department of Defense, Design of buildings to resist progressive collapse UFC 4-023-03[S]. Washington DC : Department of Defense,2013.

IASS 2023
July 10–14 Melbourne
Integration of Design and Fabrication

Proceedings of the IASS Annual Symposium 2023
Integration of Design and Fabrication
10–14 July 2023, Melbourne, Australia
Y.M. Xie, J. Burry, T.U. Lee and J. Ma (eds.)

Exploration on the shape and force of large-span steel structure of Chengdu open-air music park

Yuan FENG, Lian LIAO[a,*], Guangpo ZHAO[a], Xinyu CHE[a], Xiaolong DENG[a], Kaiguo DENG[a]

[a,*] China Southwest Architecture Design & Research Institute Co., LTD
499322641@qq.com

Abstract

The main stage of Chengdu Open-Air Music Park is one of the iconic projects in Chengdu's effort to build a music city. It is the world's largest semi-open-air and semi-indoor double-sided theater with panoramic sound and will also serve as the main venue for the closing ceremony of the 31st World University Games. The main stage roof is composed of two parts: an independent canopy and a grandstand canopy. This article focuses on the independent canopy. The independent canopy adopts a system of inclined plane arches, single-layer cable nets, and double-sided covering membranes. The arch span is 180 meters, and a pentagon-shaped solid rib arch with a jewel cross-section was used through boundary stiffness calculation and morphological comparison analysis. Hyperbolic paraboloid cable nets were used between the inclined arches, with a load-bearing span of 90 meters and a stable span of 136 meters. By optimizing the parameters of the cable net, such as sag, arch height, initial tension ratio between the load-bearing cable and the stable cable, and cable net spacing, the structural force, material consumption, and construction difficulty were all optimized to achieve the best comprehensive state. A reinforcing ring was installed between the arches at a height of 15 meters above the ground, which effectively reduced the outward bending moment of the arch surface by 50%. This not only saved materials and reduced the weight but also enriched the building facade effect. The cable net is covered with an inner and outer double-layer membrane, with an inner membrane of about 5,000 square meters of smooth surface, forming a projection canopy for music performances. The outer membrane, combined with the parameterized simulation of drainage, uses a bamboo-shaped arch membrane. The roof form of cable and membrane significantly reduces the weight of the structure and is advantageous to the foundation design. The support adopts a gravity-type anti-push foundation scheme, embedded in medium-weathered sandy mudstone.

Keywords: large-span spatial structure, polygonal solid-rib steel arch, hyperbolic paraboloid cable net, membrane structure, arch and cable net combination structure, gravity-type anti-push foundation

1. Introduction

Chengdu Open-Air Music Park is located in the northern third ring road of Chengdu City, Sichuan Province, and is one of China's top cultural and artistic theme park. The main stage has a projected area of approximately 14,400 square meters, making it the world's largest semi-open-air and semi-indoor double-sided theater with panoramic sound. The roof is mainly composed of two independent structural units: a grandstand canopy supported on the concrete grandstand and an independent canopy, as shown in Figure 1. The following highlights the independent canopy.

Copyright © 2023 by Yuan FENG, Lian LIAO, Guangpo ZHAO, Xinyu CHE, Xiaolong DENG and Kaiguo DENG. Published in the Proceedings of the IASS Annual Symposium 2023 with permission.

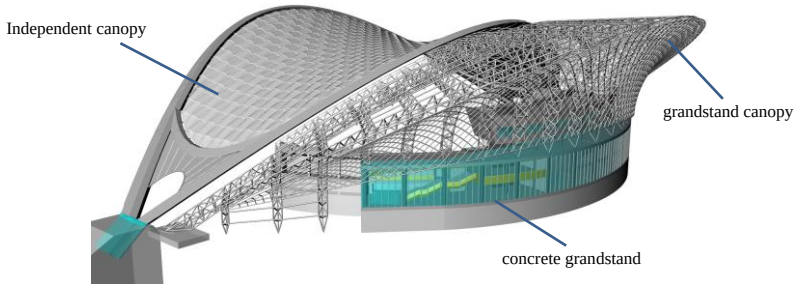


Figure 1: Schematic Diagram of Main Stage Composition

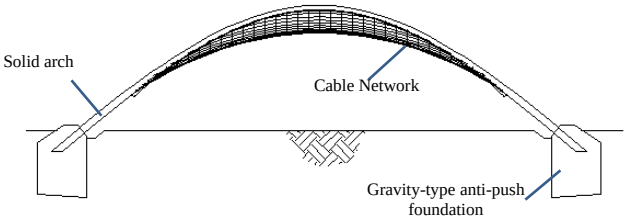
2. Structural system

The stage design for outdoor performances with varying formats has no precedent to draw on. The strategy for architectural design is to provide a sufficiently large space and well-reserved conditions to meet the demands of different forms of performances. The coverage area of the main stage canopy is over 10,000 square meters, which can be used for semi-outdoor performances of up to tens of thousands of people in the space under the roof, or outdoor performances using the terrain. The stage position can be adjusted according to different performance needs, creating the concept of a double-sided viewing experience.

The design philosophy of the building requires a large, transparent roof that can provide shade and shelter. The weight of the roof and the components that transmit wind and seismic forces to the foundation should be as small as possible, to achieve an outdoor-like viewing experience under the roof.

To realize the above design philosophy of the architect, the independent canopy adopts a large-span space structure with only two ground supports and a span of 180 meters between supports. This structure is composed of multi-sided steel arches with full-section support, intersecting at two oblique planes, and supporting a single-layer hyperbolic paraboloid cable net. The two main arches on the left and right are oblique arches, and their axes are obtained by the intersection of oblique planes and hyperbolic paraboloids. The angle between the oblique plane and the horizontal plane is 46.548°. The two oblique arches are connected by two strengthening rings to enhance the overall performance of the structure. The longitudinal span of the main arch is 180 meters, the horizontal distance between the top axes of the two main arches is 90 meters, and the height of the arch is 47.5 meters (±0.000, above 44.5 meters). The overall structural diagram is shown in Figure 2.

The hyperbolic paraboloid cable net is supported on the oblique arches and strengthening rings, with 33 horizontal load-bearing cables and 21 vertical stabilizing cables. The maximum span of the central load-bearing cable is 90 meters, the sag is 9 meters, and the sag-to-span ratio is 1/10. The maximum span of the central stabilizing cable is 136 meters, the arch degree is 22 meters, and the arch span ratio is 1/6.2. The horizontal projection distance between the load-bearing cable and the stabilizing cable is 4 meters, and both use Φ48 high-vanadium cables.



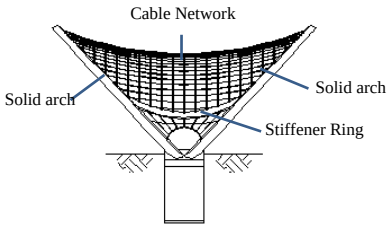


Figure 2: Schematic diagram of double oblique arches supporting a single-layer hyperbolic paraboloid cable net structure

The arch is located in the inclined plane, and the gravity points away from the arch plane. In addition to the force component within the arch plane, gravity also has a component pointing outside the arch plane, causing bending stress on the arch. For a sloping arch with a top height of about 45 meters and a vector height of about 65 meters within the arch plane, this bending moment is significant. The tensile force of the cable located on the other side of the arch plane is such that its external force component largely cancels out the gravity's external component. As shown in Figure 2, by adding a stiffening ring to the appropriate position of the arch, the calculation span of the bending moment outside the arch can be significantly reduced. At the same time, the maximum bending moment inside the arch and the maximum bending moment outside the arch occur at different positions, greatly reducing the demand for the arch section and making the material more effectively utilized. Adding stiffening rings also enriches the building's elevation.

The single-layer cable net provides balance for the gravity load's external component for the sloping arch, and the solid steel arch of the sloping plane, with a large external stiffness, in turn serves as the rigid boundary of the single-layer cable net. The single-layer cable net and the solid steel arch of the sloping plane work together to form a stable spatial structural system.

The upper and lower surfaces of the canopy's single-layer cable net are covered with a PVDF film. The outer film uses a bamboo joint-type arch film combined with drainage in a parametric simulation, serving as a sunshade and rain shelter. The inner film forms a smooth inner surface of about 5,000 square meters, which, when used for performances, projects changing and stunning light and shadow effects in conjunction with the sound effects.



Figure 3: Actual performance scene

3. Analysis and design

The project is located in an area prone to earthquakes, and the effects of seismic motion on the structure cannot be ignored. The project is adjacent to the city viaduct and hills, with a complex wind environment, and the response of the structure under wind loads needs to be carefully studied. The exposed polygonal solid ribbed steel arch is subjected to significant temperature differences between the sunny and shady sides due to solar radiation, which may significantly affect the structure. Individual cables should not break and cause continuous collapse of the structure due to accidental factors. The effect of construction procedures on the distribution of internal forces in the structure needs to be understood clearly before determining the final construction method. The structural engineer needs to have a precise and clear understanding of the mechanical behavior of the structure under all possible loads and actions during

construction and use throughout the entire life cycle before adopting targeted design strategies and using them to guide structure construction.

The designer conducted various static analysis or quasi-static analysis, dynamic analysis, stability analysis, and other calculation analyses for the structure under various working conditions. The following mainly introduces the calculation and analysis of the static and seismic performance of the structure and the analysis and design of the steel arch.

3.1 Static analysis

Static analysis or quasi-static analysis is the basis for other analyses. The analysis considers dead, live, and wind loads, and unfavorable situations such as non-uniformly distributed live loads.

Under typical working conditions of the double inclined arch carrying a hyperbolic paraboloid cable net structure, the maximum stress ratio of the main arch is 0.753, the maximum stress ratio of the stiffening ring is 0.668, the bearing cable is 0.289 times the breaking force, and the stability cable is 0.498 times the breaking force. Under each typical working condition, the maximum deflection in the arch plane is 123mm, and the deflection-to-span ratio is 1/1453; the maximum deflection outside the arch plane is 356mm, and the deflection-to-span ratio is 1/505; the maximum vertical displacement of the cable net is 576, and the deflection-to-span ratio is 1/236. The stress ratio of each component (breaking force of the cable) and the vertical displacement of the structure are all smaller than the limit values in the Chinese specifications.

Supplementary analysis was performed using plate shell elements for the solid ribbed steel arch. Near the nodes of the solid arch and the stiffening ring, and near the nodes of the arch feet, the stress level of the plate shell element model is significantly smaller than that of the beam element model. The reason is that when modeling with plate shell elements, the size effect of the nodes can be reflected, and the solid arch and the stiffening ring near the nodes have been merged into a common cross-section under the same force, which cannot be reflected by the beam calculation.

3.2 Seismic performance

The project is located in an area prone to earthquakes, and to ensure the safety of the project under seismic action, the structure was analyzed under earthquake action.

The first 300 modes of vibration of the structure were calculated. The first 6 modes of vibration are mainly in-plane or out-of-plane vibration of the arch. The first mode has a period of 2.40s and is an out-of-plane vibration of the two arches in phase. The second mode has a period of 1.54s and is an in-plane anti-phase vibration of the two arches. The third mode has a period of 1.51s and is an in-plane in-phase vibration of the two arches.

The combination of the effects of three-directional seismic actions, with horizontal earthquakes as the main component, and the combination of effects of three-directional seismic actions, with vertical earthquakes as the main component, were considered separately and analyzed using the response spectrum method. Under rare earthquake actions, all components remained elastic, and the maximum stress ratio of the arch foot was approximately 0.727.

Two sets of ground motion records and one set of artificial waves were selected for rare earthquake time history analysis. Under rare earthquake actions, the stress ratios of all critical components were within 0.66, meeting the performance objectives of elastic behavior during large earthquakes.

3.3 Analysis and design of boundary arches

The hyperbolic paraboloid cable net has no stability issues. The stability of the boundary arches of the cable net and stiffening rings in the structural system should be investigated.

Taking into account the buckling characteristics of the arch and applying initial defects, when applying "half-span longitudinal (along the direction of the arch span)" live loads, the first-order eigenvalue

buckling mode (internal buckling of the arch surface) is used as the initial defect for calculation. When applying "half-span transverse" live loads, the third-order eigenvalue buckling mode (external buckling of the arch surface) is used as the initial defect for calculation.

Considering the arch as nonlinear and applying half-span live loads along the arch span, the minimum safety factor obtained through elastic-plastic full process analysis using the first-order eigenvalue buckling mode as the initial defect was 4.24.

The 180m-span steel arch requires a large section to bear the load. After visual analysis, both the main arch and stiffening rings use diamond-shaped pentagonal cross-sections, with the acute angles of the pentagonal cross-sections pointing towards the audience's line of sight, making the structure visible but not bulky. The cross-section gradually decreases from the arch foot to the arch top according to the internal force of the arch. The maximum contour size of the arch foot section is approximately 5m, and the contour size is reduced to approximately 3.2m at the arch top. The entire structure appears lightweight and dynamic.

The rigid-jointed hingeless arch scheme with arch feet connected was adopted. After the two arch feet were combined into one, they were directly inserted into the slot of the gravity anti-sliding foundation cast in place. The anti-sliding foundation was embedded in the rock to reliably transmit the vertical force, thrust, bending moment, and shear force from the arch to the foundation.

4. Conclusion

Through analyzing the structural system, force characteristics, static and dynamic properties, and seismic performance of the independent canopy of Chengdu Open-Air Music Park, the following main conclusions can be drawn:

(1) The addition of stiffening rings between the two arches can significantly reduce the out-of-plane bending moment of the arch, and the maximum bending moment inside the arch and the maximum bending moment outside the arch occur at different locations. As a result, the stress on the arch section is greatly reduced, balancing architectural aesthetics and structural economy.

(2) The structure has good seismic performance. Even under rare earthquake conditions, the arch remains elastic.

(3) Although the arch and cable network structure have only two ground supports, they still have high safety.

The main stage of Chengdu Open-Air Music Park was put into use in May 2019 and has successfully held many performances and public welfare activities. The canopy has become a place for daily family activities, rest, and entertainment for many people. The closing ceremony of the 31st World University Summer Games will also be held on the main stage, and it is believed that this uniquely designed building will leave a deep impression on young athletes and audiences from all over the world.



Figure 4: Photos of Main Stage Completed in Chengdu Open-Air Music Park



Figure 5: Photos during the construction of the main stage of Chengdu Open-Air Music Park

IASS 2023
July 10–14 Melbourne
Integration of Design and Fabrication

Proceedings of the IASS Annual Symposium 2023
Integration of Design and Fabrication
10–14 July 2023, Melbourne, Australia
Y.M. Xie, J. Burry, T.U. Lee and J. Ma (eds.)

Kinematic performance of a vibration-driven six-bar tensegrity structure

Ruhe MEI [a,b], Xian XU[*], Ruizhi LIU[a,b]

[a,b,*] College of Civil Engineering and Architecture, Zhejiang University, Hangzhou 310058, China
Space structures key laboratory of Zhejiang Province, Hangzhou 310058, China
xianxu@zju.edu.cn

Abstract

Vibration excitation can take full advantage of the characteristics of high strength-to-weight ratio, low modal frequency and natural impact resistance of tensegrity structure. Resonance-based amplification of dynamic response of structure is a simple and low-cost method to achieve efficient structure driving. This paper proposes a six-bar tensegrity structure based on vibration driving and applies it to the rescue and search scene after a disaster. Through high-altitude delivery, the vibration-driven tensegrity structure can be dropped on the ruins on a large scale and explore the unknown environment. Using numerical simulation method to explore the parameters that affect the kinematic performance of this tensegrity structure, it is found that the low-order vibration modes of the structure exhibit significant vertical and horizontal motion, which can excite the potential jumping, creeping and rotating gaits of the structure by vibration. Besides, it can be observed that the location of motors at the lower edge of the lower group of struts is the best initial position to promote structural locomotion. In addition, directional movement can be achieved by controlling the switching state of motors at different positions. A small low-cost prototype of wireless vibration-driven tensegrity structure is established, which can move freely in the designed two-dimensional and three-dimensional spatial paths to find an exit. It is verified that the success rate for finding the exit is increased by changing the vibration strategy.

Keywords: six-bar tensegrity structure, vibration-driven, finite element numerical simulation, kinematic performance, prototype, multiple gaits

1. Introduction

Tensegrities are pre-stress stable structures, consisting of a set of discrete struts suspended in a network of continuous cables, which fits the natural law of continuous tensioning and intermittent compression [1]. This high-efficiency principle can be found at all scales of nature organisms from cellular cytoskeleton, the structure of proteins up to the tendinous network of the human hand [2], [3]. Because of tensegrity system's inherent ability to distribute external forces through a synergistic interplay of inner axial force, it possesses many appealing traits, which are impressive strength-to-wight ratio, high redundancy, natural resistance to impact and controllable morphology. Meanwhile, multiple degrees of freedom means that the structure is dynamic and displays a diversity of locomotive gaits. Thus, there are promising applications for tensegrities in the emerging fields of robotics engineering [4] for aerospace exploration technology [5], [6] and disaster rescue scenes [7]. Since 2011, UC Berkeley and the NASA Ames Research Center had been conducting research on next-generation space exploration robots — the tensegrity-based "SuperBall", which can fulfill folding, buffering and scrolling functions [8]. In 2019, a tensegrity robot prototype from Agogino's research team performed a disaster rescue test where it was dropped from a height of 180m into a rock pile by a drone and then searched the site and sent feedback immediately from the rugged terrain.

Copyright © 2023 by Ruhe MEI, Xian XU and Ruizhi LIU. Published in the Proceedings of the IASS Annual Symposium 2023 with permission.

Due to the flexible characteristics of tensegrities, small changes in shape or internal forces can cause complex nonlinear dynamic responses in structures, such as vibration resonances and tight dynamic coupling between components. In conventional research, tensegrity-based structures or robots are considered quasi-static, implying high precision requirements of structural morphology controlling. Therefore, traditional engineering approaches take initiative control measures to avoid or suppress vibration to stabilize the structures in their equilibrium states and reduce harmful large deformations caused by resonance [9]. However, tensegrities with low and dense model frequencies are, by their very nature, highly sensitive to kinetic effect, which easily leads to high levels of vibration inspired by disturbance of external excitation [10]. Subsequently, a novel concept was proposed that exploiting complex dynamics of tensegrities as an advantage to facilitate their locomotion, rather than suppressing them at abundant cost [11].

Khazanov *et al*. [12], [13] designed a small (with 9.4cm struts) physical robot based upon a canonical six-bar tensegrity shape with open-loop actuation using three low-voltage vibration motors. The maximum linear locomotion speed of the robot was 4cm/s, and diverse gait behaviors were uncovered by changing the frequencies of motors. Liang from Zhejiang University revealed that the locomotive capabilities of vibration-driven tensegrity structure which include mode, linear speed and angular velocity have a discrete mapping relationship with the frequency parameters of vibration. Research at Union College lead by Professor John Rieffel [14] firstly fabricated a low-cost (approximately $100 for each strut with length of 15.5cm) wireless modular tensegrity robot with every self-contained module consisting of a vibration motor, a microprocessor capable of wireless communication, a three-axis motion sensor and two batteries. John Rieffel's research team [15] employed a Quality Diversity Algorithm to autonomously generate a behavioral repertoire of this robot, displaying110 distinct gaits, which is useful for adapting to changeable and complex conditions.

In addition to physical model tests, numerical simulation methods are also used for the study of the vibration characteristics of tensegrity structure. The results of research show that self-vibration properties of a tensegrity including natural frequency and its corresponding vibration modes depend on the equilibrium configuration of structure, the modulus of elasticity of material, and the magnitude of initial stress [16]. Besides, the parameters of excitation, including amplitude and frequency of vibration and the arrangement of actuators (position and number) will significantly affect vibration-driven dynamic response of structure, such as the direction and regularity of motion [17], [18].

Because of the complex dynamics of the tensegrity, vibration-driven motion exhibits a certain randomness, which is suitable for scenarios with low requirement for motion control accuracy, such as disaster rescue search. In the earthquake rescue, in order to prevent unknown danger, the tensegrity structures carrying infrared sensors, wireless communications and other devices can be dropped from high altitude into the large area of ruins and be used as the advance force performing a search mission to improve the efficiency and safety of the rescue. Besides, the scale of tensegrity structure can be miniaturized to enable them to enter inaccessible small space to humans, expanding the scope of rescue in depth and breadth. Benefitting by high impact-resistance of tensegrity, the structure and the devices carried can be well protected for repeated uses. Vibration driving is a simple method and only needs low-cost actuators, greatly reducing the expenses of rescue. Thus, research on kinematic performance of a vibration-driven tensegrity structure is promising both in its social and economic value.

Current studies on vibration-driven tensegrity are limited to a known and barrier-free level plane without considering the interaction between unknown and rugged terrain and the structure, which may influence the dynamic response of the structure. Furthermore, the control strategy of the tensegrity structure to explore within complex environments has not been systematically studied.

In this paper, in order to optimize the design of the physically vibration-driven tensegrity structure prototype and provide guidance for its motion control, we first investigate the effects of self-vibration characteristics, excitation parameters and the arrangement of motors on dynamic responses of a canonical six-bar tensegrity structure by using finite element numerical simulation methods. Next, we

develop a small low-cost and fully untethered tensegrity structure prototype excited by vibration, of which the total price will not exceed $20. Then, we construct two-dimensional and three-dimensional spatial paths with horizontal and vertical channels to simulate the complex terrain of disaster rescue search and conduct kinematic performance tests on prototype in the above environment. Finally, we summarize the control strategy for the vibration-driven tensegrity structure through experimental results to further promote the search capabilities of it in disaster rescue scenario.

2. Numerical simulation and analysis of vibration-driven tensegrity structure

A key point of using vibration excitation to drive the tensegrity structure and to fully exploit potential and beneficial dynamic response is to produce a resonance phenomenon. The tensegrity structure is a structural system with multi degrees of freedom, which has multiple inherent frequencies corresponding to multiple vibration modes. Some vibration patterns can help the structure jump higher and some can control the movement direction. Only if the pre-stress modal analysis of the tensegrity structure is carried out can we determine the appropriate vibration frequency range to accurately and safely guide the tensegrity structure to realize various functions. Through transient dynamic analysis, the effect of vibration frequency and vibration amplitude on the dynamic response of the tensegrity structure should be further investigated after considering the influence of the collision between the structure and the ground. Moreover, the location and quantity of motors have profound effect on efficiency and directionality of structural motion, so it is necessary to determine the optimal initial arrangement of motors and guide the motor switching strategies for changing the structural moving behaviors by numerical simulation.

A canonical six-bar tensegrity structure we based upon consists of six 10cm length carbon-fibre material struts that is connected to 24 identical springs and each strut end emanates four springs. Struts have tubular cross-sectional size of 6mm*8mm. Carbon-fibre material used for struts has awesome property with modulus of elasticity of 230GPa density of 1.67g/cm^3, significantly reducing the weight of structure. The spring selected with elasticity factor of 1.05N/cm will provide 3.28N pre-tension to the tensegrity structure.

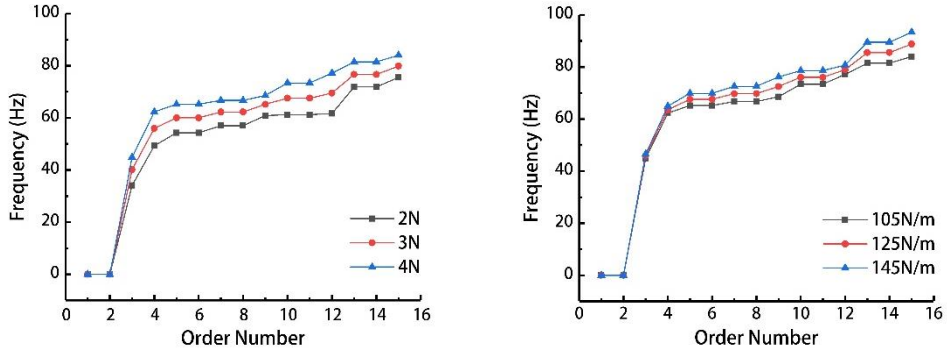
2.1. Modal analysis based on Ansys Workbench

Modal analysis of above tensegrity structure is performed using the Pre-Stress Modal procedures in ANSYS Workbench. The plane where a closed triangle on the surface of the structure is located is positioned as the X-Y plane of local coordinate system. The mesh of each strut is divided into individual beam elements and springs connect strut ends according to the topology of structure. Subsequently, gravity fields are applied and the freedom of touchdown nodes at the vertical direction are constrained. Static solution is performed first, and then modal analysis is carried out considering the effect of structural deformation and its pre-stress stiffness on the natural frequency and vibration modes.

The results of the static analysis show that the ratio of tension to pressure accords with the theoretical value of 0.4082 and the inner forces are redistributed under gravity, which proves the validity of the numerical simulation model. Then, from the outcomes of structural pre-stress modal analysis, it can be concluded as follow:

(1) The first two orders of vibration modes are rigid body displacement, and the third shows bouncing up and down, the resonance of which may improve the jump height of structure;
(2) In the fourth to sixteenth vibration modes, the stretch and swing in X and Y directions appear in pairs corresponding to the same vibration frequency, which may explain the linear creeping gait, and the torsional pattern will appear randomly between above vibration patterns, which may be the essential reason for rotating gaits;
(3) The frequencies for different vibration modes have obvious gaps, which is conducive to controlling the structural locomotion characteristics by distinct frequency sets and carrying out regular motion of tensegrity structure;

(4) Starting from the sixteenth order, a completely new vibration mode that rigid struts swing in place appears, leading to an abrupt enlargement in the frequency values.



(a) different pre-stress under 105N/m (b) different spring elasticity factor under 4N

Figure 1. Comparison of natural frequencies of the first fifteen orders of tensegrity structures

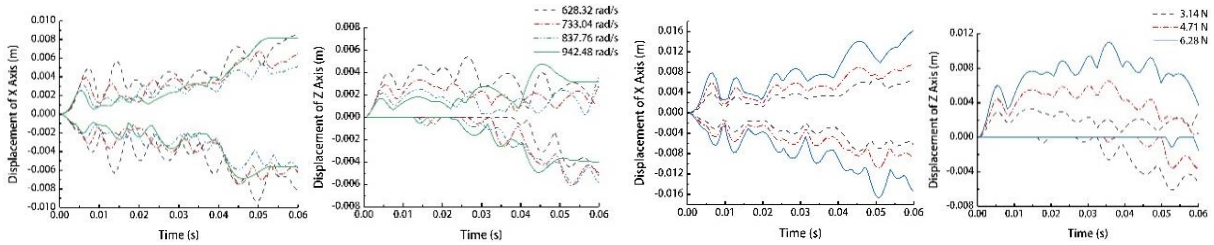
The overall stiffness of the tensegrity structure is composed of the initial stress stiffness and the elastic stiffness. Through further investigation, we find that in the first fifteen orders of vibration modes, increasing the pre-stress can significantly enhance the low-order natural frequency, which suggests that the initial stress stiffness contributes drastically to the overall stiffness of the lower-order vibration modes. Besides, improving the spring elasticity factor causes growth in the natural frequency with the increase of the order by raising the elastic stiffness of the structure. Above the sixteenth order, the overall stiffness of structure is controlled by elastic stiffness of strut which is much larger than pre-stress stiffness and spring elasticity stiffness. The conclusions indicate that the spring modulus and pre-stress of the tensegrity structure should be selected properly so that the natural frequency range of the low-order useful vibration modes falls within the vibration frequency range of motors.

2.2. Transient dynamic analysis based on Ansys Workbench

In this model, a rectangular rigid body with fixed bottom surface is used to simulate the ground and the struts with hemispherical ends are created as solid elements. Then, the contact with frictional factor of 0.02 is set between the touchdown faces of structure and the ground. In a local coordinate system with the ground as the X-Y plane, a gravity load and cyclic vibration loads perpendicular to the axis of struts are applied to the structural model. The cyclic vibration load is decomposed by the inertial force of an eccentric mass block performing circular motion, which can be express as $F_I = m_1 e\omega^2$ from D'Alembert's principle (the mass of the block is m_1, the eccentric distance is e, and the angular velocity is ω). Its components in the X-axis and Y-axis can be represented by $F_{Ix} = F_I\cos(\omega t)$, $F_{Iy} = F_I\sin(\omega t)$ respectively. Since the tensegrity structure will emerge large nonlinear deformation when simple harmonic loads are applied at struts, the direct-integration method (Newmark method) is chosen to calculate. The total analysis time is set to 0.06s with automatic time step activated.

2.2.1. Analysis of the effect of vibration frequency and vibration amplitude on structural dynamic response

For physically wireless vibration-driven tensegrity structure, the vibration frequency selection is limited by the mechanical properties of the vibration motors, and the vibration amplitude is also influenced by vibrator mass and eccentric distance. The rotating speed of the vibration motor is between 6000RMP and 9000RMP after measured, so we take the circular frequencies ω of simple harmonic loads as 628.32rad/s, 733.04rad/s, 837.76rad/s, 942.48rad/s. The vibration amplitude is taken as 3.14 N for m_1=2g, e=1.768mm, ω=942.48rad/s, and at the same frequency, the amplitude of the vibration will vary in multiples to carry out the research.



(a) different vibration frequency (b) different vibration amplitude

Figure 2. Displacement-Time diagram in the X-axis and Z-axis for models

Figure 2(a) shows displacement-time diagrams in the X-axis and Z-axis for models with different vibration frequency applied under the same amplitude. The lower the vibration frequency, the larger the displacement of the structure, the reason of which maybe that the lower vibration frequency is closer to the low-order natural frequency of the structure. The spatial symmetry of the structural geometric configuration and applied loads leads to roughly symmetrical displacement in the x-direction. The reason for the negative value of the minimum displacement on the Z-axis is that part of the structure continues to move downward after collision of the structure with the ground, the figure also shows that the larger the vibration frequency, the earlier the structure falls and collides with the ground.

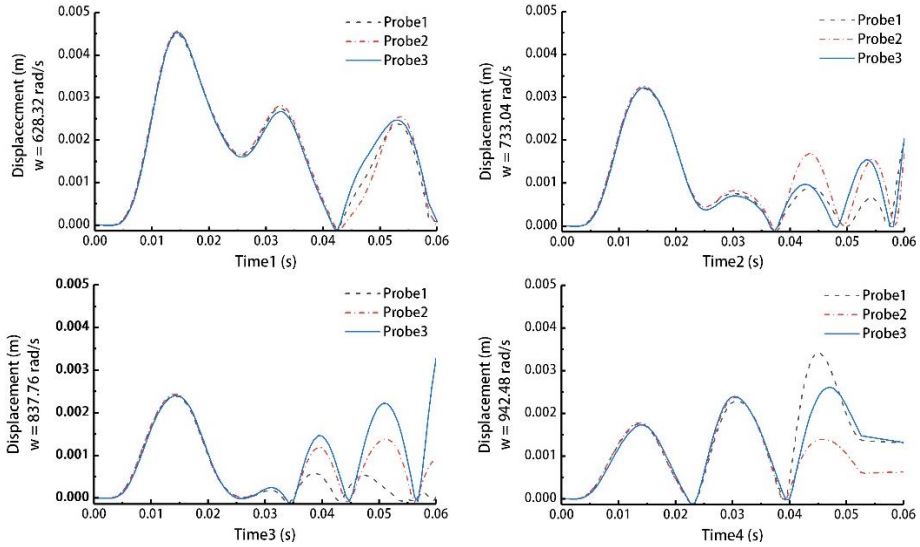


Figure 3. Displacement-Time diagram of the touchdown nodes in the Z-axis under different vibration frequency

According to displacement-time diagram of the touchdown nodes in the Z-axis, we can find that the displacements of different touchdown nodes deviate after the initial collision with the ground, and the difference gradually grows with the increase of vibration frequency. It indicates that the structure tends to be unstable and asymmetric under the excitation of high vibration frequency. Under different vibration frequency, the peak displacement of different touchdown nodes is ordered randomly. The displacement of the structure with high frequency vibration becomes larger after the collision with the ground. It implies that the reaction force of the ground can further promote the movement of the structure.

Figure 2(b) shows that the displacement of the structure multiples according to the variation of vibration amplitude. The smaller the vibration amplitude, the sooner the structure falls and collides with the ground.

2.2.2. Analysis of the effect of the location and quantity of motors on structural dynamic response

When a closed triangle surface of the structure contacts with the ground, the six struts can be divided into upper and lower groups. The loads are set at the middle (Site 1,2) and the lower edge (Site 3,4) of these two groups of struts respectively. When the research object is the quantity of motors, "one motor" load is applied at the middle of the upper strut connected to the node where Probe 3 is located, "two motors" loads are applied at the middle of the upper struts connected to the Probe 3 and Probe 2 respectively, and "three vibrations" all act in Site 1.

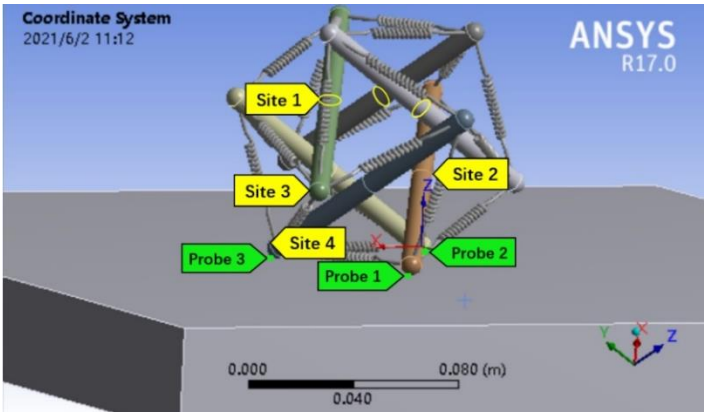


Figure 4. Vibration load position diagram

It can be concluded from the simulation results that the motor loads act at the lower edge of the struts cause much larger displacements than that acting in the middle, and its growth rate is significantly higher. The displacements also increase when loads act in lower group of struts. Minimum displacements on Z-axis caused by loads acting in Site 3 and Site 4 fluctuate immediately, the reason is that the vibration at the lower edge of the struts incurs rotation on the upper edge in the opposite direction. This leads to the lateral expansion and contraction of the structure. Therefore, it can be inferred that the location of motors at the lower edge of the lower group of struts is the best initial position to promote the dynamic response of structure. Meanwhile, the research presents that the larger the quantity of motors, the larger the displacement of the structure.

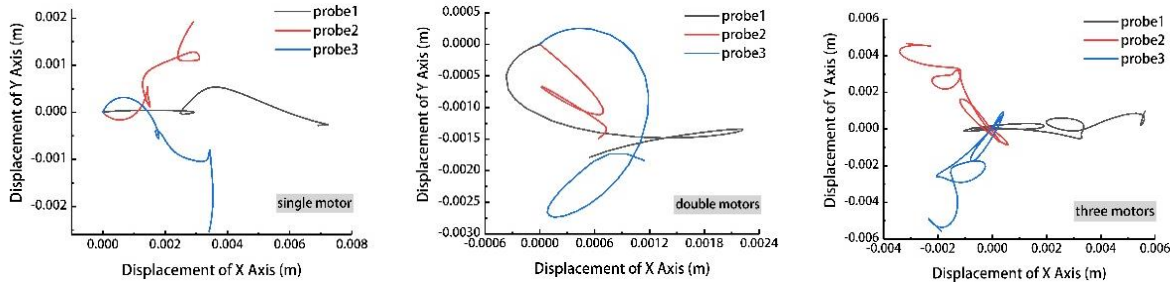


Figure 5. Trajectories of three touchdown nodes in the X-Y plane

Figure 5 shows that when exciting a single motor or double motors, the locomotion of three touchdown nodes is clearly directional while the trajectory under three vibration motors exhibits spatial symmetry. The results indicate that structural locomotion can be controlled by the switching state of the vibration motors.

3. The design of physically wireless vibration-driven tensegrity structure prototype

Our design criteria for this wireless vibration-driven tensegrity structure are as follows:

• **High Strength-Weight Ratio** - According to theoretical calculations, load provided by the vibration motor does not exceed 5N, so the lighter the weight of the structure, the smaller the energy loss of the

vibration drive. Considering that the tensegrity structure is used in disaster rescue scenarios where there exists a lot of hard debris which will cause severe wear on material, a tubular carbon-fibre strut with a cross-sectional size of 5mm*7mm is chosen.

• **Appropriate Natural Frequency -** In order to realize resonance-based motion control, a spring with an elasticity factor of 97 N/m and original length of 30 mm is selected as the tensile element of the structure, combining the experience of numerical simulation and the actual model parameters.

• **Modular –** The tensegrity structure possesses simple and equal-length elements, the assembly process can be expedited through modular joint design. The integrated joints are produced by 3D printing using nylon material. They are convenient for positioning, installing, and disassembling the components, increase the stability of the structure touching the ground and significantly reduce the mass of the joints. The prototype is built in the order from line to surface then from surface to body, which only takes 10 minutes for a single person.

• **Wireless-Driven –** It is important for the tensegrity structure to explore untethered in unknown and complex environments. So, a distributed self-powered vibration motor is used for wireless driving. The vibration motor is circuit welded to the button battery box with switch, and they are fixed to the strut with epoxy ab glue, so that the force of the vibration motor is steadily transferred to the structure.

• **Small Scale -** the length of each strut is 10cm, which allows this tensegrity structure to enter the narrow passages inside the ruins of the building.

• **Low Cost –** the actuate method of vibration-driven tensegrity structure is simple and the price of dynamical system is extraordinarily cheap compared to conventional actuator. The overall prototype only cost about $20, which is affordable for disaster rescue scenarios.

4. Kinematic performance tests against the tensegrity structure

The main purpose of the model tests is to verify the multi-directional motion performance, multi-gait kinematic performance and impact resistance of the vibration-driven tensegrity structure. After ensuring that the prototype is in normal working condition, the vibration motor is positioned at the lower edge of the lower group of struts as the optimal initial position, the motors are switched on and the prototype is placed at the beginning of the spatial path. The locomotion of the prototype is observed and intactly recorded by a stable fixed camera device. Each test will be stopped if the prototype stays at a position for more than one minute. It is seen that whether the tensegrity structure could change locomotion direction when encountering obstacles, whether it could find the exit smoothly, and what the influence is on structural dynamic response after the tensegrity structure falls and collisions with rigid slab.

4.1. Two-dimensional spatial path test

The wireless vibration system can control the switching state of vibration motors at different positions to achieve changes in vibration strategies of the tensegrity structure. We use the initial number of vibration motors as a variable in the two-dimensional spatial path test, and add a “combination” working conditions, that is, if the structure is trapped in the process of movement for more than 30s, the switching state of the motors are changed randomly to alter the dynamic behavior of the structure.

The two-dimensional spatial path test device is built with large particle blocks which can be freely assembled and a transparent acrylic panel encapsulating one side of the device which makes it easy to observe the locomotion of the prototype. The device possesses two horizontal motive directions and vertical falling spaces with maximum height difference of 25.6cm. The detailed dimensions are shown in Figure 6.

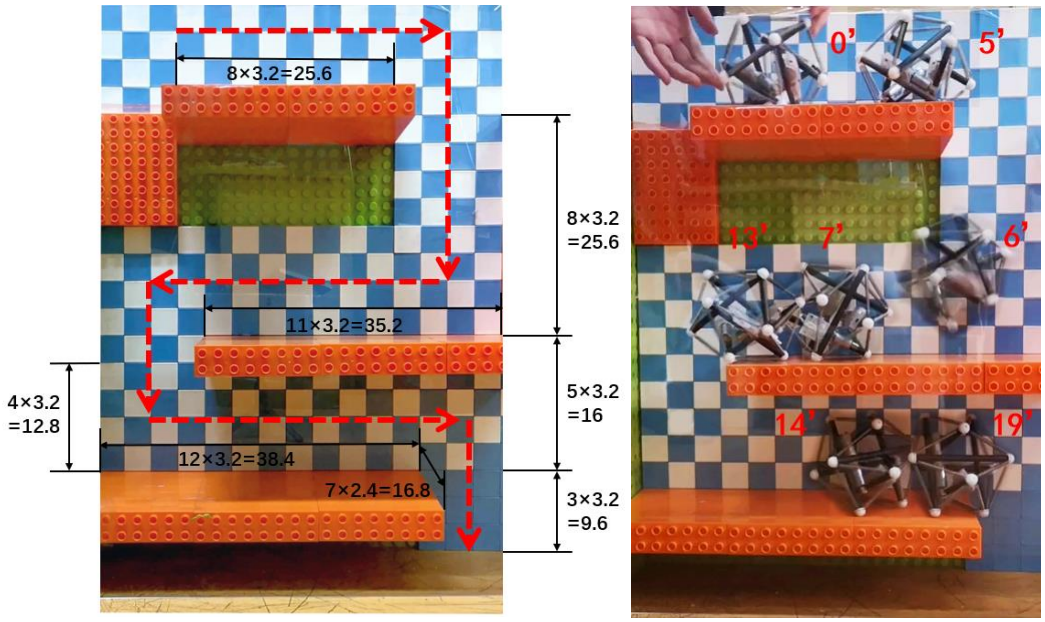


Figure 6. Dimensional diagram of the two-dimensional test device (left) and the record of the locomotion of the vibration-driven tensegrity structure (right)

We can conclude the kinematic performance of the vibration-driven tensegrity structure moving in the two-dimensional spatial path by repetitive experiments as follow:

(1) The speed test results shows that $V_{\text{triple-motor}} > V_{\text{dual-motor}} > V_{\text{single-motor}}$, the fastest unidirectional motion driven by three motors can reach 12.55 cm/s.
(2) The tensegrity structure will rotate anticlockwise or clockwise. The initial rotation direction is influenced by the vibration strategy. Then the structure will adjust the moving direction on its own based on the surrounding obstruction, moving forward or backward along the wall panel.
(3) The tensegrity structure performs stable vibration creeping gait before drops. Bouncing gait occurs after structure falls and collides with the rigid slab, and position of each strut changes correspondingly. When the structure continues moving and collides with the surrounding wall panels, the counterforce and gravity cause a rolling gait of the structure to adjust its gestures. Although there is no advanced control system, the vibration-driven tensegrity structure is sensitive to the surrounding environment and can find the exit successfully for its multiple degrees of freedom, multi-gait nature and easy perturbation of structural characteristics.
(4) The deformation of the tensegrity structure can buffer the collision impact, which ensures that it can move normally after falling. This exhibits high impact resistance of the tensegrity structure.
(5) If no manual control is applied to the vibration of the prototype during its locomotion, the success rate of the vibration-driven tensegrity structure in finding the exit is 65%. In the "combination" working condition, the prototype can stop ineffective movement in a dilemma and excite the complex dynamic response by changing the vibration strategy, after which it will alter the kinematic performance and find a way to move on. In this way, the success rate increases to 100 %.

4.2. Three-dimensional spatial path test

The three-dimensional spatial path test device is built by three uncovered boxes with a square bottom and a notch in one corner as the falling position. Different numbers of clapboards are arranged in the box under the principle of maximizing the travel routes of the prototype from the starting point to the notch, forming planar motion paths of different complexity. By adjusting the stacking order of the three boxes and changing the relative positions of the notches by rotation, we can achieve three-dimensional spatial paths of different complexity. The falling heights of this device are both 20cm and other detailed

dimensions are shown in Figure 7. The material used in this device is transparent acrylic for the convenience of observation.

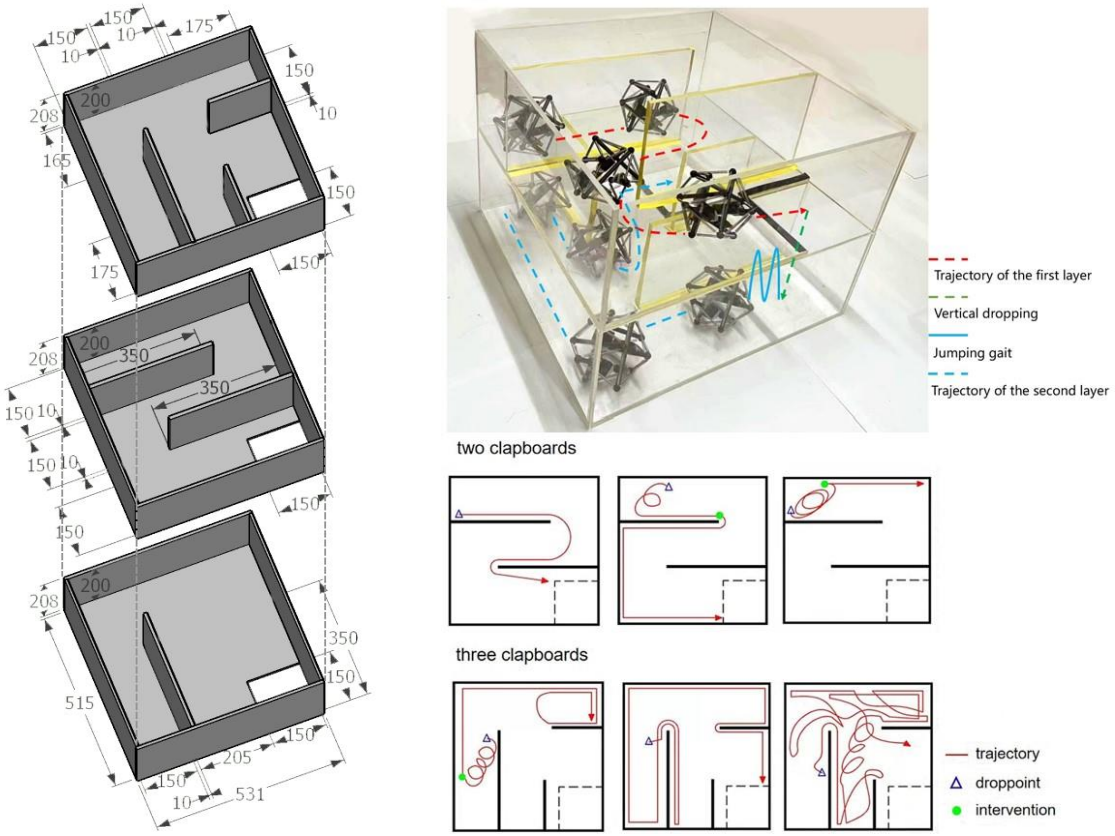


Figure 7. Dimensional diagram of the three-dimensional test device (left) and the record of the trajectory of the vibration-driven tensegrity structure (right)

We first place the prototype in single-layer box with different complexity for plane motion tests with obstacles. Based on the test results, we can conclude that the complex dynamic response of the tensegrity structure allows it to spontaneously adjust its motion angle by rotating gait to explore the passable path under the action of vibration motors and the interaction with the surrounding obstacles. At the same time, this dynamic complexity also adds randomness to the structural locomotion. After repetitive tests are carried out in the same environment, large discreteness of the time it takes to find the exit is observed for each experiment. Overlapping trajectories for each experiment can basically cover the whole plane space, which means full coverage of the exploration environment can be achieved by launching this tensegrity structure on a large scale. As the complexity of the planer paths increases, there is no significant difference in the success rate of the prototype in finding the exit, indicating that the vibration-driven tensegrity structure is highly adaptable to complex environments.

Three boxes are stacked together for three-dimensional spatial path tests, we are currently focusing on a fixed three-dimensional complex environment to discuss the strategy for controlling the vibration-driven tensegrity structure. The intervention scheme is used to adjust the switching state of the motors at different positions when the structure enters a dead end for a long period of time and cannot get out of the trap. Since the driving force of a single motor is too small, it is necessary to ensure that at least two motors are in working condition when adjusting. The results show that the success rate of the vibration-driven tensegrity structure in finding an exit in a 3D complex space without active intervention is only 30%; however, the success rate increases to 60% after intervention, indicating the necessity of

adding a controlled intervention module to the prototype. We also explore a more appropriate adjustment time, and finally decide to take 10s as the time criterion for performing active intervention.

5. Conclusion and future work

In this paper, the vibration modes obtained from numerical simulation reasonably explain the locomotion gaits exhibited by the vibration-driven tensegrity structure in the tests. Moreover, the transient analysis also verifies the complex dynamic responses of structure after collision, indicating the randomness of the structural motion. Further, the optimal initial arrangement of the vibration motor is determined, which can promote steady and efficient structural locomotion. Finally, the vibration-driven tensegrity structure shows awesome adaptation to complex environments, and its success rate in finding exits is significantly improved by the active intervention scheme.

We look forward to applying a closed-loop control strategy to the vibration-driven tensegrity structure, which can give feedback from on-board sensors such as accelerometers and carry out active intervention without manual operation. In addition, we are interested in using machine learning to further explore better control strategy and improve the ability of the structure to explore complex environments. It is also one of our ambitions to further enhance functions of the structure in real disaster rescue scenarios.

Acknowledgement

This work was supported by the National Natural Science Foundation of China (Grant No. 52178175) and the National Natural Science Foundation of Zhejiang Province (Grant No. LZ23E080003).

References

[1] R. B. Fuller, "Tensile integrity structures," *U.S. Patent* 3 063 521, Nov. 13, 1962.
[2] N. Wang, K. Naruse, D. Stamenović, et al, "Mechanical behavior in living cells consistent with the tensegrity model," *Proceedings of the National Academy of Sciences*, vol. 98, pp. 7765–7770, 2001.
[3] F. J. Valero-Cuevas, J. -W. Yi, D. Brown, R. V. McNamara, C. Paul and H. Lipson, "The Tendon Network of the Fingers Performs Anatomical Computation at a Macroscopic Scale," *IEEE Transactions on Biomedical Engineering*, vol. 54, pp. 1161-1166, June 2007.
[4] Y. Koizumi, M. Shibata and S. Hirai, "Rolling tensegrity driven by pneumatic soft actuators," *2012 IEEE International Conference on Robotics and Automation*, Saint Paul, MN, USA, May 14-18, 2012. pp. 1988-1993.
[5] G. Tibert, "Deployable Tensegrity Structures for Space Applications," Ph.D. thesis, Dept. Mech., KTH, Stockholm, 2002.
[6] L. -H. Chen *et al*., "Inclined surface locomotion strategies for spherical tensegrity robots," *2017 IEEE/RSJ International Conference on Intelligent Robots and Systems*, Vancouver, BC, Canada, Sept. 24-28, 2017. pp. 4976-4981.
[7] D. Lu, J. Liu, H. Gao, "Integrated exploration robots for planetary surface landing and patrolling: A review," *Acta Aeronautica et Astronautica Sinica*, vol. 42, pp. 523742- 523742, 2021.
[8] A. Agogino, V. SunSpiral, and D. Atkinson, "Super ball bot-structures for planetary landing and exploration," NASA Innovative Advanced Concepts (NIAC) Program, Final Report, 2013.
[9] X. Feng, G. Jiang, S. Du, "Seismic response and vibration control of a planar tensegrity beam," *Proceedings of the 26th national conference on structural engineering*, Changsha, Hunan, China, Oct. 20, 2017. pp. 44-50.
[10] J. Jiang, T. Li, "Optimal configuration of actuators for optimal control of vibration of tensegrity structures," *Journal of Xidian University*, vol. 41, pp. 170-175, 2014.
[11] V. Bohm and K. Zicermann, "Vibration-driven mobile robots based on single actuated tensegrity structures," in Robotics and Automation (ICRA), 2013 IEEE International Conference on. IEEE, 2013, pp. 5475–5480.
[12] M. Khazanov, B. Humphreys, W. Keat et al., "Exploiting Dynamical Complexity in a Physical

Tensegrity Robot to Achieve Locomotion," *ECAL 2013: The Twelfth European Conference on Artificial Life*, Sicily, Italy. Sept. 2-6, 2013. pp. 965-972.
[13] M. Khazanov, J. Jocque, and J. Rieffel, "Evolution of locomotion on a physical tensegrity robot," in *ALIFE 14: The Fourteenth Conference on the Synthesis and Simulation of Living Systems*, 2014, pp. 232–238.
[14] J. Kimber, Z. Ji, A. Petridou, T. Sipple, K. Barhydt, J. Boggs, L. Dosiek, and J. Rieffel, "Low-cost wireless modular soft tensegrity robots," in *2019 2nd IEEE International Conference on Soft Robotics (RoboSoft)*. IEEE, 2019, pp. 88–93.
[15] K. Doney, A. Petridou, J. Karaul et al., "Behavioral Repertoires for Soft Tensegrity Robots," *2020 IEEE Symposium Series on Computational Intelligence (SSCI)*. IEEE, 2020, pp. 2265-2271.
[16] L. Jia, Z. Chen, H. Liu et al., "Analysis of structural dynamic characteristics and seismic response of a tensegrity tower," *Building Structure*, vol. 47, pp. 16-20, 2017.
[17] P. Schorr, V. Böhm, L. Zentner et al., "Motion characteristics of a vibration driven mobile tensegrity structure with multiple stable equilibrium states," *Journal of Sound and Vibration*, vol. 437, pp. 198- 208, 2018.
[18] D. He, Q. Gao, W. Zhong, "An accurate method for the dynamic behavior of tensegrity structures," *Engineering Computations*, vol. 35, pp. 1250-1278, 2018.

Proceedings of the IASS Annual Symposium 2023
Integration of Design and Fabrication
10–14 July 2023, Melbourne, Australia
Y.M. Xie, J. Burry, T.U. Lee and J. Ma (eds.)

Locomotive performance evaluation of the spherical tensegrity robots

Meijia WANG[a,*], Xian XU[a], Yaozhi LUO[a]

[a,*] Key Laboratory of Space Structures of Zhejiang Province, Zhejiang University
Anzhong Building, 886 Yuhangtang Road, Hangzhou, Zhejiang, China
229150@zju.edu.cn

Abstract

A tensegrity robot is a type of locomotive robot that is based on the principle of tensegrity, which can change their shape by adjusting their internal tension. Tensegrity robots can be classified into different categories according to their shape, such as spherical, quadruped, or spine-like, of which the spherical tensegrity robot has received the most attention. However, current designs tend to be relatively simple and lack standardized criteria for evaluating their locomotion capabilities. To address this issue, we propose an optimization approach using the force density method to generate new spherical regular tensegrity configurations. This is achieved by parameterizing the topology and configuration of the structure, while taking into account structural symmetry and evenness of internal forces. Our proposed approach not only generates classical tensegrities but also novel configurations suitable for locomotive robots. To evaluate the locomotion adaptability of these tensegrity configurations, we propose an evaluation method based on several geometric indicators such as inner space, foldability, prestress evenness, path rectilinearity, and geometrical instability. These indicators reflect the ability of tensegrity robots to move efficiently in different environments as well as manufacturing difficulty, storage ratio, and other characteristics, of different tensegrity configuration as potential robot candidates. A comparison study between existing tensegrity configurations and those obtained from optimization design is conducted.

Keywords: optimization design, spherical tensegrity, form finding, locomotive evaluation, geometric indicators

1. Introduction

The tensegrity is a kind of self-stressed pin-jointed system consisting of compression struts and tensile cables [1]. “Self-stress” means pre-stress equilibrated by itself. A distinguishing feature is that they change shape by adjusting their prestress, and they have advantages such as high resilience, adaptability, and energy efficiency, which makes it have potential applications as shape controllable and motion systems, such as smart structures, deployable structures, and locomotive robots.

Tensegrity robots can be divided into different categories such as spherical, prismatic, or spine-like according to their shapes. There have been many studies on these different types of tensegrity in recent years, among which the study on motion control of spherical tensegrity robots has received the most attention. This is due to the fact that spherical structures have a smoother outer shape, which makes it easier to rolling by changing their rest length. Shibata et al. experimentally validated the rolling behaviors of six-strut spherical tensegrity robots [2]. Wang et al. proposed a light-powered six-strut spherical tensegrity robot using liquid crystal elastomer-carbon nanotube composites as the light-powered actuator [3]. A novel spherical tensegrity robot based on a rhombicuboctahedron-like 12-strut tensegrity, i.e., T12-R, was able to move in a straight line and prevent the loss of momentum associated with the zig-zag path [4]. Baines et al. discussed the effect of the outer shape of different spherical tensegrity robots on motion ability [5].

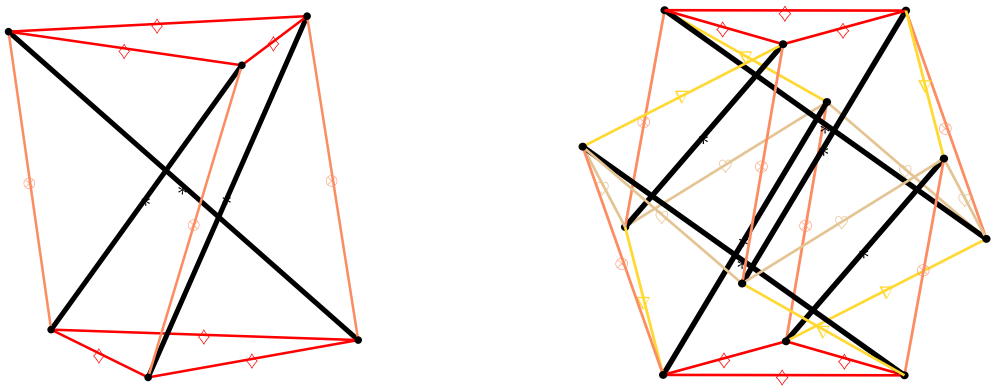
Copyright © 2023 by Meijia WANG, Xian XU and Yaozhi LUO. Published in the Proceedings of the IASS Annual Symposium 2023 with permission.

Tensegrity robots are often limited to 6-strut and 12-strut structures due to control difficulties caused by increasing strut numbers and limitations of spherical tensegrity types, as the common spherical structures are generally derived from Archimedean polyhedra and Platonic polyhedra. In fact, there are many methods to find new tensegrities. Wang et al. proposes a method for determining the optimal topology and positions of struts and cables in a tensegrity structure [6]. Liu et al. proposes a method that seeks a topology of the tensegrity that is within a given geometry [7]. The design of tensegrities with better motion performance and the evaluation of different tensegrity configurations as spherical possible tensegrity robot candidates are likely to further extend the application prospects of such structures. In this paper, the optimization design problem is simplified as a form-finding problem with given member topology using the force density method. An evaluation method based on several geometric indicators, i.e., foldability, inner space, prestress evenness, path rectilinearity, and geometrical instability that reflect the locomotive ability and other characteristics is put forward to evaluate not only the existing tensegrities but also the designed tensegrities as locomotive robots.

2. Topology and configuration design of a new spherical tensegrity

2.1. Topology of a new spherical tensegrity

Snelson's patent "Continuous Tension, Discontinuous Compression Structures" describes the construction of highly complex tensegrities from simple modules, a typical example of which is a two-layer, 6-strut tensegrity (Figure 1(b)). These two unit tensegrities can be deemed as a combination of two reciprocal counterpart single 3-strut prismatic tensegrity, i.e., a right-handed prismatic tensegrity (Figure 1(a)) and a left-handed prismatic tensegrity, with the combined overlap replacing the triangular cables with saddle-like cables, and the addition of diagonal cables. All nodes of the structure are constrained on a sphere.



(a) (b)

Figure 1. (a) 3-strut prismatic tensegrity, and (b) 2 3-strut prismatic tensegrities combine a modular 6-strut tensegrity. The nodes, cables and struts are represented by black dots, thin colored lines, and thick black lines respectively.

This approach can be extended to the topology of any higher dimensional tensegrity. For a combined tensegrity with m unit tensegrities of which each has n struts, there are $2mn$ nodes, arranged on $2m$ layers. Each basic unit tensegrity with $2n$ nodes in upper and lower bottom surfaces, respectively, is constrained to the interior of a sphere (Figure 1(a)). All struts in the same unit tensegrity have equal deflection angles. The unit is a prismatic tensegrity if the radii of the node distribution circles on the upper and lower surfaces are equal, and a conical tensegrity if they are different. A new modular tensegrity can be obtained by sequentially combining the right-handed and left-handed prismatic/ conical tensegrity units. The concept of this design is as follows (Figure 2): all the horizontal cables in the middle layer are replaced with saddle cables in wavy arrangement, and diagonal cables connecting two adjacent units are added to ensure the stability of the structure; in addition, the vertical cables on the initial units are arranged accordingly. The nomenclature of the nodes as well as the relationship in which nodes are

subordinate to layers is shown in the Figure 2, and finally a *n*-stage *m*-torus modular tensegrity containing 4*mn* cables, *mn* struts, and 2*mn* nodes can be obtained. Each node connects to 1 strut and 4 cables.

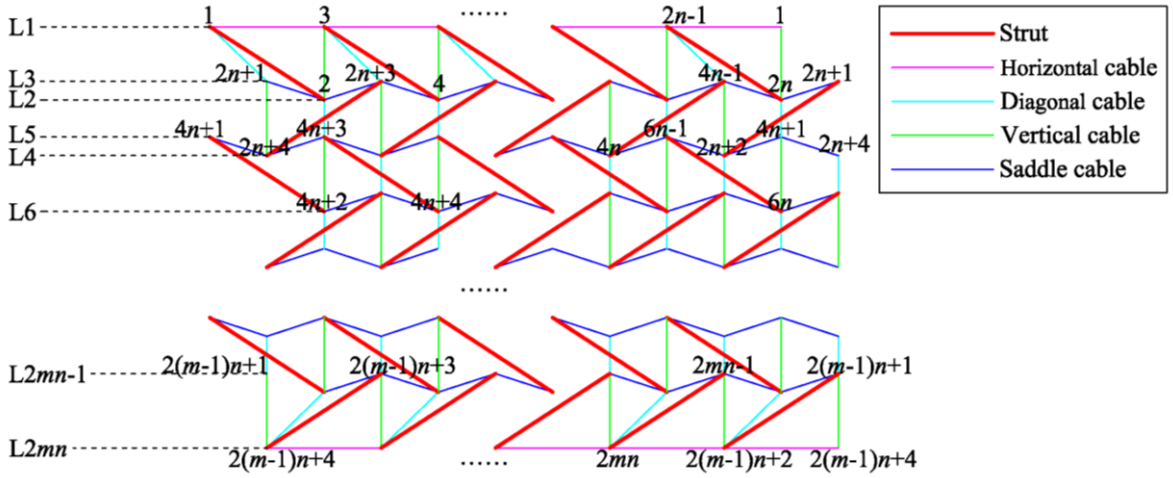


Figure 2. Topological connection of spherical tensegrity

2.2. Node coordinates

In this paper, the node coordinates are first represented by a spherical coordinate. The parameters required to determine the node coordinates of the spherical tensegrity are as follows: the number of modules *m*, the number of compression struts per module *n*, the nodal radial distance ***r***, and the polar angle $2m\times1$ matrix $\boldsymbol{\theta}$ and azimuthal angle $2m\times1$ matrix $\boldsymbol{\varphi}$ of the first nodes of each layer in the spherical coordinate system, which together determine the torsional angle of each unit and the offset angle between adjacent layers. The node numbering and coordinate definition of a 6-strut tensegrity is shown as an example in Figure 3. As for the remaining nodes in each layer, their polar angle remains the same as the first node, while azimuthal angle is added $2\pi/n$ by in clockwise order according to the azimuthal angle of the first node

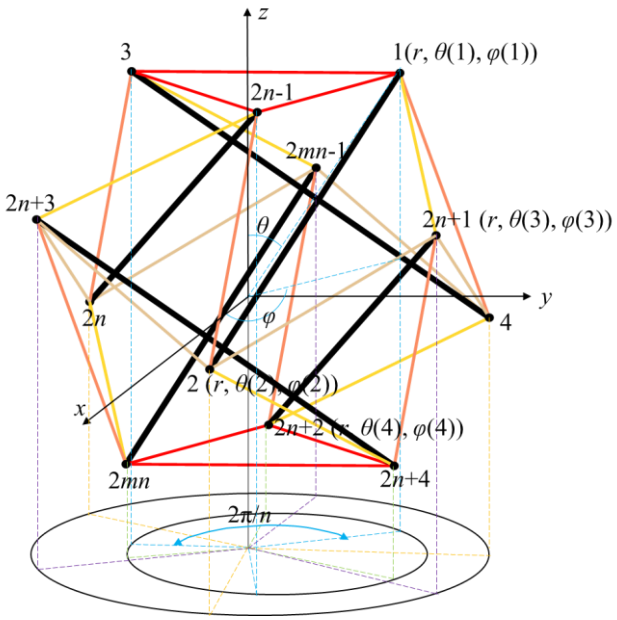


Figure 3. Coordinate representation of a 2-layer 6-strut spherical tensegrity

To ensure the symmetry of the tensegrity, constraints are also placed on the two units that are symmetric to each other in the upper and lower. For example, the first unit of the top layer is symmetric with the *m*th unit of the bottom layer. Therefore, the polar angles of the first and last layers should correspond to each other, i.e., $\theta(1)+\theta(2mn)=\pi$; similarly, $\theta(2)+\theta(2mn-1)=\pi$, etc. In addition, the strut torsional angles of the two corresponding units should also remain equal, and when *m* is an even, $\varphi(1)-\varphi(2)=\varphi(2mn)-\varphi(2mn-1)$, or $\varphi(1)-\varphi(2)=\varphi(2mn-1)-\varphi(2mn)$ when *m* is odd. The relationship between intermediate units are also in the same rule. And all the nodes are also constrained on a sphere. These constraints guarantee in advance that the tensegrity obtained to be spherical, regular and symmetric as well as have more uniform internal force.

2.3. Constraints and objective function

In this paper, the following properties are assumed for the tensegrity structures: (a) Members are in elastic range, and buckling or yielding is not considered; (b) No external load is applied and the self-weight is neglected; and (c) Members are connected by pin joints. In addition to the constraint on node coordinates as well as topology, the following conditions are also constrained.

2.3.1. Equilibrium constraint

For a 3-dimensional structure with n_e members, n_c nodes, its member connectivities can be expressed by a connectivity matrix $\mathbf{C}\in\mathbb{R}^{m\times n}$ defined in the field of graph theory [9]. By converting the spherical coordinates $\boldsymbol{r}$, θ , and $\boldsymbol{\varphi}$ to Cartesian coordinates, **X**, **Y**, and **Z** which represent the coordinate components in *X*-, *Y*-, and *Z*- directions respectively. And $\mathbf{Q}(\in\mathbb{R}^{m\times m})$ is a diagonal square matrix which is given by $\mathbf{Q}=diag(\mathbf{q})$, where $\mathbf{q}=(q_1,q_2,\cdots,\ q_m)\in\mathbb{R}^m$ is the force density vector determined as internal force per unit length. For simplicity, matrix **D** is defined $\mathbf{D}=\mathbf{C}^{\mathrm{T}}\mathbf{Q}\mathbf{C}$. Without external load, the equilibrium equation can be written as

$$\begin{aligned}\mathbf{D}\mathbf{X}&=0\\ \mathbf{D}\mathbf{Y}&=0\\ \mathbf{D}\mathbf{Z}&=0\end{aligned}\tag{1}$$

2.3.2. Member length evenness constraints

To control the evenness of member lengths, a set of constraints as follows are appointed

$$\begin{aligned}&l^s s_i+\varepsilon_l(1-s_i)\le l_k^2\le(l^s+e_l^s)s_i,\forall k\in E\\ &\underline{l}_s^2\le l^s\le\bar{l}_s^2,\underline{l}_s^2\le l^s+e_l^s\le\bar{l}_s^2,\\ &e_l^s\ge 0\\ &l^c c_i+\varepsilon_l(1-c_i)\le l_k^2\le(l^s+e_l^c)c_i,\forall k\in E\\ &\underline{l}_c^2\le l^c\le\bar{l}_c^2,\underline{l}_c^2\le l^c+e_l^c\le\bar{l}_c^2,\\ &e_l^c\ge 0\end{aligned}\tag{2}$$

where $\underline{l}_s$ and $\bar{l}_s$ are the lower bound and upper bound of strut lengths respectively; $\underline{l}_c$ and $\bar{l}_c$ are the lower bound and upper bound of cable lengths respectively. e_l^s and e_l^c are auxiliary continuous variables. In this way, smaller e_l^s or e_l^c means more even strut lengths or cable lengths respectively.

2.3.3. Force density evenness constraints

To control the evenness of force densities of struts or cables, a set of constraints is defined as

$$\begin{aligned}
&(q^s - e_q^s)s_k + \underline{q}_c c_k \le q_k \le q^s s_k + \bar{q}_c c_k, \forall k \in E \\
&\underline{q}_s \le q^s \le \bar{q}_s, \underline{q}_s \le q^s + e_q^s \le \bar{q}_s, \\
&e_q^s \ge 0 \\
&\underline{q}_s s_k + q^c c_k \le q_k \le \bar{q}_s s_k + (q^c + e_q^c)c_k, \forall k \in E \\
&\underline{q}_c \le q^c \le \bar{q}_c, \underline{q}_c \le q^c + e_q^c \le \bar{q}_c, \\
&e_q^c \ge 0
\end{aligned} \tag{3}$$

where $(s_k, c_k) = (1,0)$ indicates that member *k* is a strut, while $(s_k, c_k) = (0,1)$ indicates that member *k* is a cable. $\underline{q}_s$, $\underline{q}_c$ are lower bounds of force densities of struts and cables respectively, while $\bar{q}_s$ and $\bar{q}_c$ are upper bounds of force densities of struts and cables respectively. e_q^s and e_q^c are auxiliary continuous variables. In this way, smaller e_q^s or e_q^c means more even strut force densities or cable force densities.

2.3.4. Objective function

In order to minimize the number of cables and get more even member lengths and force densities, the objective function can be written as

$$f = \alpha_1 e_l^s + \alpha_2 e_l^c + \alpha_3 e_q^s + \alpha_4 e_q^c \tag{4}$$

Member topology (s, c), nodal positions (**X**, **Y**, and **Z**), and force density (**q**) are given as conditions for optimization in this model, which makes it effective for optimization of tensegrity structures. In addition, the stability of the tensegrity structures will be checked after they are identified by the optimization process. A flowchart for the proposed approach is shown in Figure 4.

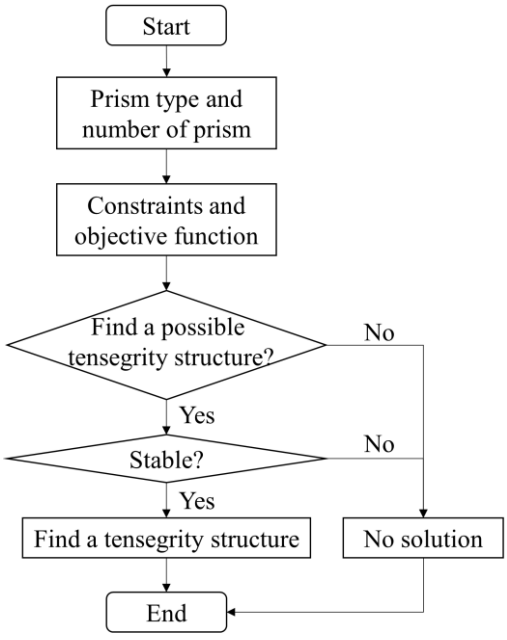
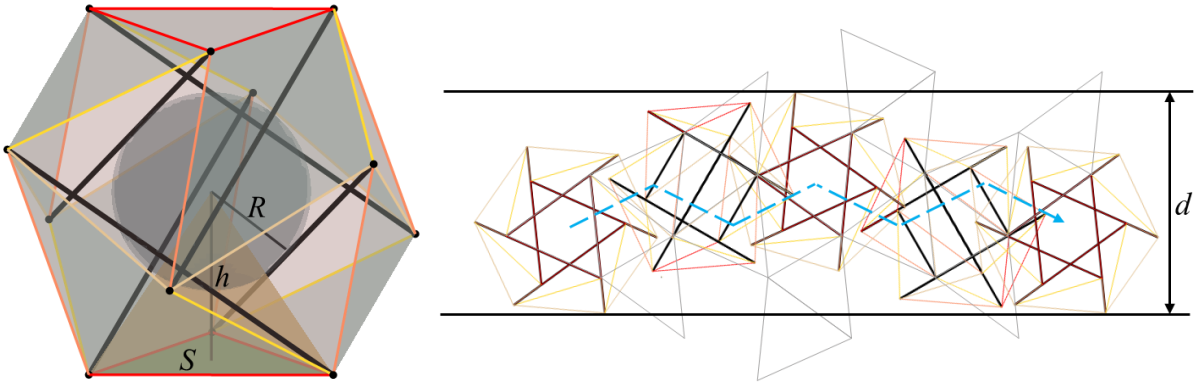


Figure 4. Flowchart of optimization process

3. Design of geometric evaluation indicators

This paper aims to generate more tensegrity configurations suitable for locomotive robots and provide a practical way to evaluate them. To be exact, the design a locomotive robot candidate that can not only meet the basic locomotive needs, but also conform to the current trend of robot development, with advantages such as lightweight, efficient, highly redundant, motion controllable, and so on, is our concern. In such needs, we propose several evaluation indicators that combines both theoretical locomotive capabilities and other geometric indicators that reflect the structural characteristics.



(a) (b)

Figure 5. (a) Inner space of 6-strut tensegrity, and (b) the 6-strut tensegrity traveling along the theoretical zigzag path generated by the surface expansion from a top view.

3.1. Inner space

The inner space is quantified as the ratio of the volume of the free inner ball with radius R that does not come into contact and collision with any component to the volume of the robot in its initial state. This can be useful for tensegrity robots or protectors design in which a central space may need to contain some functional devices. The geometry of the inner space of 6-strut tensegrity is illustrated in Figure 5.

3.2. Foldability

The foldability assesses the ability of the robot to survive in extreme terrain such as narrow spaces and is defined as the ratio of the volume of the robot when all struts are reduced to the minimum driven lengths to the volume of the robot in its initial state.

3.3. Prestress evenness

This prestress evenness is defined as the variance of the absolute value of the normalized prestress forces of all components. It measures the degree of uniformity of internal forces in each member and reflects the symmetry and regularity of the structure. In addition, more uniform internal prestress in the robot indicates it's easier to manufacture, and more controllable.

3.4. Path rectilinearity

The path rectilinearity embodies the degree of straightness of the theoretical motion path obtained from the surface expansion, which is defined as the ratio of the width d in the X-Y plane along the theoretical path to the length of the robot.

3.5. Geometrical instability

The geometric meaning of instability is the ratio of the height h of the robot's mass center to the area of touching-ground surface S [8]. It can assess the stability of the structure under a certain touching-ground state and the degree of susceptibility to rolling.

These five evaluation indexes identified above are all related to the geometric shape and the initial prestress state of the tensegrity only.

4. Evaluation of different tensegrity configurations as robot candidates

In Chapter 2, a method to develop modular spherical tensegrity configurations as optional locomotive robots is presented, which can be obtained for any tensegrity with *m* unit prismatic tensegrities of which each has *n* struts. However, as the unit number *m* or the number of compression struts per unit *n* increases, the difficulty of fabrication increases as well. According to the previous research, the control as well as construction difficulty of tensegrities with the number of compression struts more than 15 will be greatly increased. Therefore, we carried out the optimization design mainly for the cases of two and three units, i.e. *m*=2 or 3. In this paper, the 2-layer 8-strut tensegrity (Figure 6(b)), 3-layer 12-strut tensegrity (Figure 6(c)), and 3-layer 15-strut tensegrity (Figure 6(e)) are chosen as the robot candidates.

On the other hand, the 6-strut tensegrity is often studied because it is simple to construct and its external appearance resembles the Icosahedron, which is a classic polyhedron. Other tensegrity configurations based on the known Platonic and Archimedean polyhedron have been developed as well, such as the 12-strut tensegrity based on the Rhombicuboctahedron (Figure 6(d)), and the 30-strut tensegrity based on Snub Dodecohedron (Figure 6(f)), both of which have been discussed for their locomotion capacity. In fact, the aforementioned 3-layer 12-strut tensegrity (Figure 6(c)) can also be obtained based on the Snub Cube through form-finding.

Based on this, the above 6 tensegrity configurations are taken as the evaluation objects. The evaluation is carried out for the indicators in Chapter 3, and the characteristics of the different configurations are compared as shown in Figure 6. It can be seen that the characteristics of different configurations are also various. If the indicator of path rectilinearity is considered as the priority indicator, the motion paths of configurations (c), (d), (e), (f) both conform to a better straightness. Both configurations (a) and (b) do appear to have a less smooth motion path due to the small number of components. However, these two configurations are more controllable, and the foldability is also one of their advantages. In addition, the 30-strut tensegrity has a more balanced and outstanding performance, but too many actuating members can complicate the actuation and limit its development. Although the motion path of configuration (d) as a robot candidate could be a normal straight line, the inner space is small and the folding ability is not that good, and the existence of contact and collision between the struts is also a problem that needs to be solved. Among the several configurations put forward, it is considered that the 3-layer structures (e.g., (c) and (e)) have potential as robot candidate, since they can basically travel along a straight line, and all indicators are relatively balanced. The number and distribution of actuating members are reasonable, so that their motion capability can be further analysed and discussed.

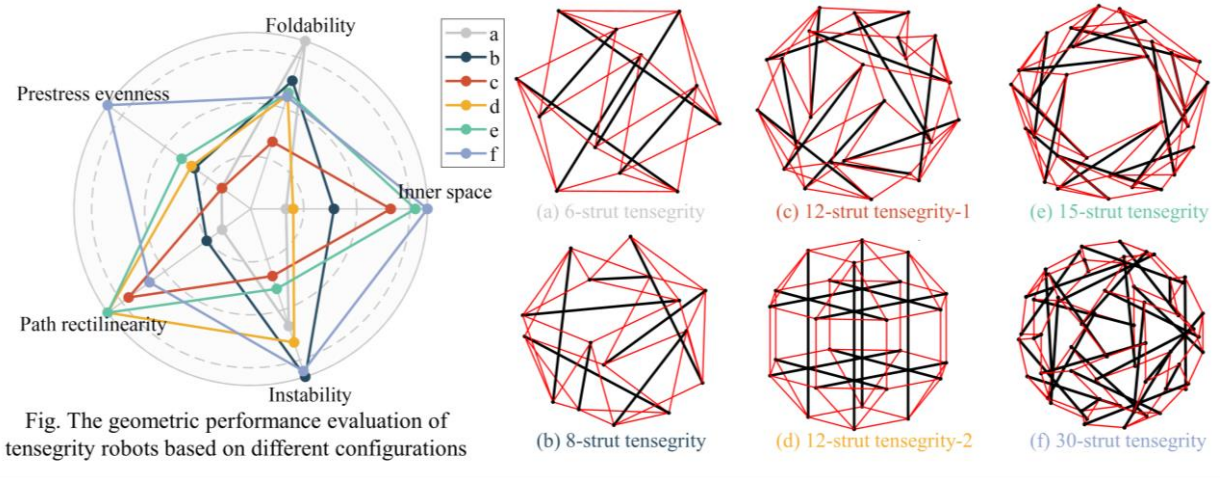


Fig. The geometric performance evaluation of tensegrity robots based on different configurations

Figure 6. The geometric performance evaluation of tensegrity robots based on different configurations

5. Conclusion

In this paper, an optimization approach aimed to generate spherical regular tensegrity structures is proposed. It provides a practical way to design the initial configuration of a regular spherical tensegrity that not only classical tensegrities but also novel spherical regular tensegrities are obtained by the proposed method. In order to generate more tensegrity configurations suitable for locomotive robots and evaluate the adaptability of different tensegrity configurations as robot candidates, an evaluation method based on several geometric indicators, i.e., foldability, inner space, prestress evenness, surface smoothness and geometrical instability is put forward. It assesses not only the locomotive capacity but also manufacturing difficulty, storage ratio, and so on, of different tensegrity configuration. Based on this evaluation, the 12-strut tensegrity and 15-strut tensegrity are identified as the most promising designs for future study.

Acknowledgements

This work was supported by the National Natural Science Foundation of China (Grant Nos. 52178175 and 51908492) and Center for Balance Architecture, Zhejiang University.

References

[1] R. E. Skelton and M. C. de Oliveira, “Tensegrity systems,” Springer, 2009.

[2] O. Omer, S. Offer, A. Amir, and B. Uri, "A model of caterpillar locomotion based on assur tensegrity structures," Proceedings of ASME International Design Engineering Technical Conferences and Computers and Information in Engineering Conference 2011, vol 6, pts A and B, p. 739-745.

[3] Z. Wang, K. Li, Q. He, and S. Cai, "A light-powered ultralight tensegrity robot with high deformability and load capacity," Advanced Materials, vol. 31, p. 1806849, 2019.

[4] K. Kim, D. Moon, J. Y. Bin, and A. M. Agogino, "Design of a spherical tensegrity robot for dynamic locomotion," in *2017 IEEE/RSJ International Conference on Intelligent Robots and Systems (IROS)*, 2017, pp. 450-455.

[5] R. L. Baines, J. W. Booth and R. Kramer-Bottiglio, "Rolling soft membrane-driven tensegrity robots," IEEE Robotics and Automation Letters, vol. 5, pp. 6567-6574, 2020.

[6] X. Xu, Y. Wang and Y. Luo, "Finding member connectivities and nodal positions of tensegrity structures based on force density method and mixed integer nonlinear programming," *Engineering Structures*, vol. 166, pp. 240-250, 2018.

[7] K. Liu and G. H. Paulino, "Tensegrity topology optimization by force maximization on arbitrary ground structures," *Structural and Multidisciplinary Optimization*, vol. 59, pp. 2041-2062, 2019.

[8] W. Du, S. Ma, B. Li, M. Wang, and S. Hirai, "Force Analytic Method for Rolling Gaits of Tensegrity Robots," *IEEE/ASME Transactions on Mechatronics*, vol. 21, pp. 2249-2259, 2016.

[9] Kaveh A. Structural mechanics: graph and matrix methods (No. 1). *Research Studies Press Ltd*; 2004.

IASS 2023
July 10–14 Melbourne
Integration of Design and Fabrication

Proceedings of the IASS Annual Symposium 2023
Integration of Design and Fabrication
10–14 July 2023, Melbourne, Australia
Y.M. Xie, J. Burry, T.U. Lee and J. Ma (eds.)

Static performance of an open Levy cable dome with partial CFRP cables

Weijing ZHANG[a,*], Yizhou HU[a]

[a,*] Beijing University of Technology, Beijing 100124, China
zhangweijing@bjut.edu.cn

Abstract

Carbon fiber reinforced polymer (CFRP) has the advantages of high tensile strength, low weight, corrosion resistance and fatigue resistance, which is suitable for cable domes. In order to study the static performance of the cable dome after the application of CFRP cables, part of the steel cables in a Levy type open cable dome with span of 120m was replaced with CFRP cables. The cables in the cable dome can be divided into three kinds of ridge cables, diagonal cables and ring cables according to their functions, and ten groups of cables according to their positions, such as outer ridge cables, middle ridge cables, inner ridge cables, outer ring cables, middle ring cables, etc. The simulation results show that: In all cases, the static performance of Levy open cable dome with part CFRP cables is little different from that of steel cable dome structure. The stress of each group of cables decreases within 8%, and the maximum vertical displacement of nodes changes within 10%. The replacement of ridge cables and upper inner ring cable with CFRP cables can increase the structure stiffness and reduce the vertical displacement of Levy type open cable dome. The research in this paper can provide reference for the application of CFRP cables in cable domes.

Keywords: cable dome, CFRP cables, static performance

1. Introduction

As a kind of long-span spacial structure, cable dome structure is widely used in exhibition facilities, transportation hubs, sports venues and other important projects because of its light weight, large span, beautiful structure and other advantages [1]. At present, most types of cable dome structures are full coverage systems without openings, which are rarely used in long-span stadiums requiring openings. Chengdu Fenghuangshan Stadium is the first football stadium building in China to adopt a large opening Levy type cable dome structure [2]. Combining the opening demand of the stadium roof with the cable dome structure is an innovation in the form of cable dome structure.

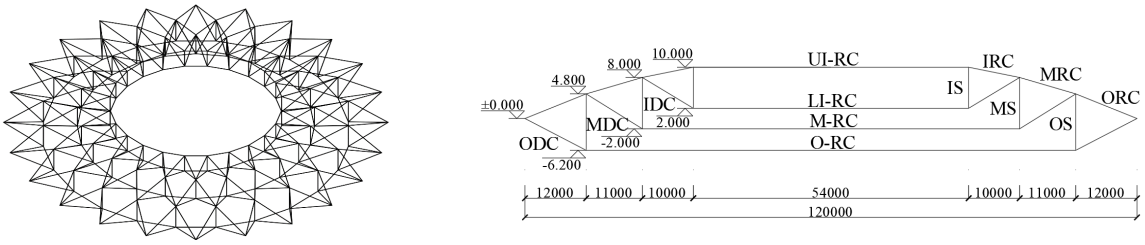
The materials of cable in cable dome structure have also been studied extensively.Compared with steel, CFRP has advantages such as light weight, high strength and good corrosion resistance, and is an ideal material for constructing long-span structures. At present, the application and research of CFRP in long-span structures are mainly focused on bridges [3]. The research of CFRP in spatial structure has just started [4], and there are few studies on CFRP cable dome structure. Due to the great difference between CFRP and steel in material properties, it is necessary to study the static performance of CFRP cable dome structure. Considering the current application degree of CFRP cable, it is difficult to realize the cable dome structure with all CFRP cables. A Levy open cable dome with 120m span is taken as the object, the mechanical properties of the cable dome structure with part of CFRP cables are studied and compared with steel cable dome.

Copyright © 2023 by Weijing ZHANG and Yizhou HU. Published in the Proceedings of the IASS Annual Symposium 2023 with permission.

2. Finite element analytical model of open Levy cable dome

2.1. Introduction of structural model

As shown in Figure 1, the open Levy cable dome structure [5] has a span of 120m, a rise height of 10m, a rise-span ratio of 1/12, and an opening diameter of 54m. The cable dome is composed of 10 groups of cable members and 3 groups of strut members. There are inner ridge cable (IRC), middle ridge cable (MRC) and outer ridge cable (ORC). Diagonal cable has inner diagonal cable (IDC), middle diagonal cable (MDC) and outer diagonal cable (ODC). The ring cable includes upper inner ring cable (UI-RC), lower inner ring cable (LI-RC), middle ring cable (M-RC) and outer ring cable (O-RC).The strut has inner strut (IS), middle strut (MS) and outer strut (OS). The cables are made of 1670 grade 7mm steel wire bundle, and the steel pipes are made of Q345 grade steel.The bar CFRP cable of equal diameter was obtained. The carbon fiber prefilament was made of standard high-performance carbon fiber, and the ultimate tensile strength was 2500MPa and the elastic modulus was 172GPa. The specific specifications and parameters of the component are shown in Table 1.The material parameters of components are shown in Table 2.



(a) (b)

Figure 1. Structural diagram of cable dome: (a) axonometric drawing, (b) sectional drawing.

Table 1. Member specifications and initial prestress of Levy type open cable dome structure

Member Type	Group Number	Materials Specification	Area/mm^2	Initial Prestress/kN
UI-RC	1	Φ7×139	5349	2696.70
LI-RC	2	Φ7×55	2117	963.50
M-RC	3	Φ7×151	5811	1979.50
O-RC	4	Φ7×439	16895	5295.70
IRC	5	Φ7×19	731	400.00
IDC	6	Φ7×13	500	160.69
MRC	7	Φ7×31	1193	606.01
MDC	8	Φ7×31	1193	343.01
ORC	9	Φ7×55	2117	1044.20
ODC	10	Φ7×61	2348	916.02
IS	11	Φ285×10	8639	-151.57
MS	12	Φ360×10	10996	-322.01
OS	13	Φ450×12	16512	-720.19

Table 2. Material properties used for structural analysis

Member Type	Materials	Density (kg/m^3)	Modulus of Elasticity (MPa)	Ultimate Tensile Strength(MPa)
cables	CFRP	1600	1.72×10^5	2500
	Steel	7850	1.95×10^5	1670
struts	Steel	7850	2.06×10^5	345

According to the relevant specifications, considering the design requirements of rigid roof, the dead load is 0.6kN/m^2, live load is 0.5kN/m^2, the roof load is equivalent to the concentrated load on the strut node.

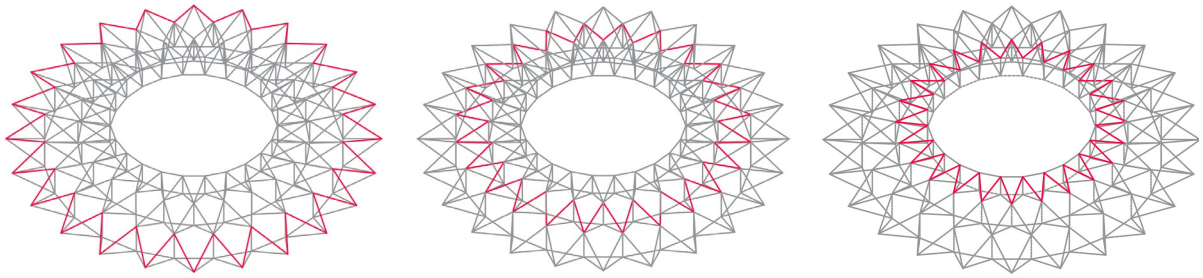
The static analysis of the Levy type cable dome structure with large opening was carried out by ANSYS. The cables were simulated by LINK10 element, and the struts were simulated by LINK8 element. The support was simplified to be fixed hinged support, and the initial prestress was applied by adding initial strain. Geometric nonlinearity of the system was considered in the analysis process.

3. The static behaviour of structure before and after the replacement

CFRP has the advantages of light weight, high strength and good corrosion resistance, but its elastic modulus is smaller than that of steel cables. When applied to structures, it may lead to structural stiffness reduction and displacement increase. In order to study the static properties of the structure after the application of CFRP cables, cable replacement was carried out for the Levy open cable dome structure, and the influence of cable replacement at different positions on the static properties of the structure was studied.

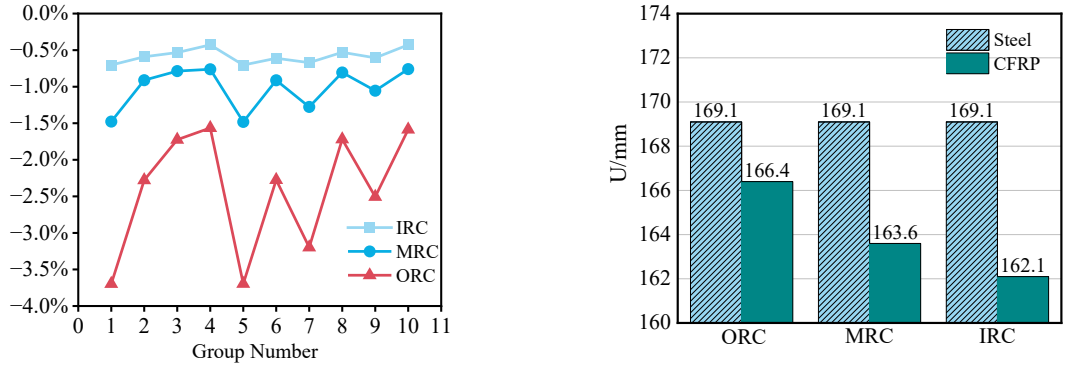
3.1. Replacement of ridge cables

According to different positions of ridge cables, three replacement cases were considered: 1) replacement of ORC 2) replacement of MRC 3). replacement of IRC, as shown in Fig.2. The cable stress changes of each group in the open Levy cable dome structure (group number is shown in Table 1) and the maximum vertical displacement of the inner ring nodes is shown in Fig.3.



(a) ORC (b) MRC (c) IRC

Figure 2. Replace the ridge cables in different positions: (a) outer ridge cables, (b) middle ridge cables, (c) inner ridge cables.



(a)The percentage change in cables stress (b)The change in nodes displacement(in mm)

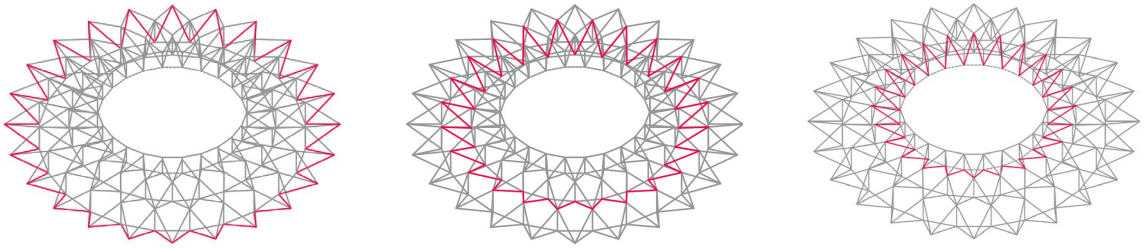
Figure 3. Member stresses and displacements before and after the replacement of ridge cables

As can be seen from Fig. 3 (a), when the ridge cables at different positions were replaced, the cable stress in each group decreased somewhat, and the range of stress reduction gradually increased from inside to outside with the replacement of ridge cables. The variation of cable stress in each group was roughly the same:(1) The stress reduction reached the maximum at the upper inner ring cable (Group number 1) and the inner ridge cable (Group number 5), which was 3.7% when the outer ridge cable was replaced, and 1.5% when the middle ridge cable (Group number 7) was replaced. (2) On the whole, the stress reduction rate of ring cable was upper inner ring cable (Group number 1) > lower inner ring cable (Group number 2) > middle ring cable (Group number 3) > outer ring cable (Group number 4), and the stress reduction trend of diagonal cables and ridge cables was similar to that of ring cable. (3) Except for the upper inner ring cable, the stress reduction of ridge cables is greater than the other two kinds of cables.

Vertical displacement of nodes on the innermost ring of cable dome structure was selected for comparison, and its changes before and after replacement were shown in Fig.3 (b).As can be seen from the figure, when the ridge cables at different positions are replaced, the node displacement of the cable dome with part of CFRP cables is smaller than that of the original cable dome structure. In conclusion, although the elastic modulus of CFRP cable is lower than that of steel cable, the structural stiffness increases and the displacement of the node decreases when the ridge cables at different positions are replaced with CFRP cables.

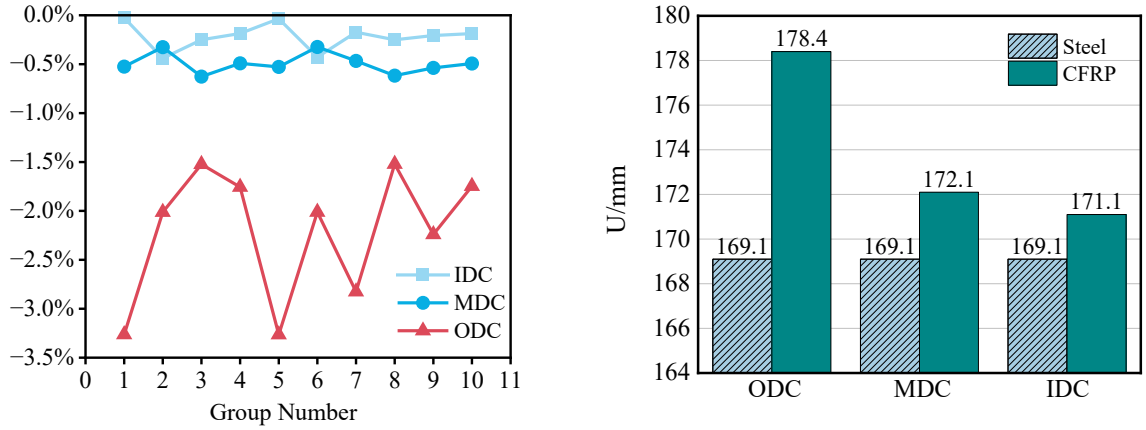
3.2. Replacement of diagonal cables

When replacing steel diagonal cable with CFRP cable, three cases are considered: 1) Replace the outer diagonal cables 2).Replace the middle diagonal cables 3). Replace the inner diagonal cables, as shown in Fig. 4. Fig. 5 shows the cable stress changes of each group (group numbers are shown in Table 1) and the maximum vertical displacement of inner ring nodes.



(a)ODC (b)MDC (c)IDC

Figure 4. Replace the diagonal cables in different positions: (a) outer diagonal cables, (b) middle diagonal cables, (c) inner diagonal cables.



(a)The percentage change in cables stress (b)The change in nodes displacement (in mm)

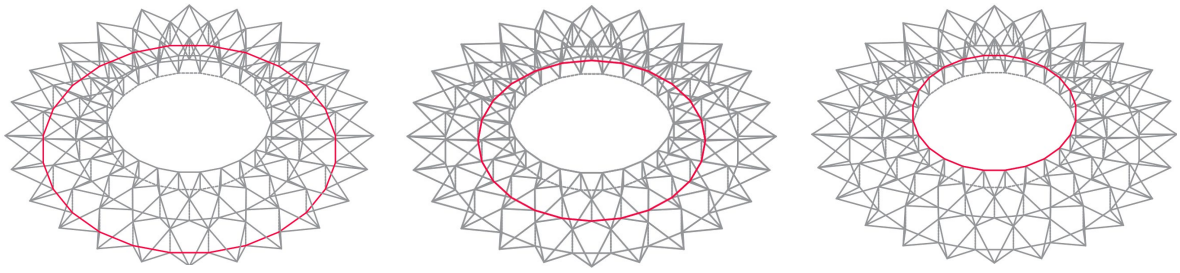
Figure 5. Member stresses and displacements for open Levy cable dome before and after the replacement of diagonal cables with CFRP cables

As can be seen from Fig.5 (a), the cable stress of each group in the structure decreases after the diagonal cables are replaced by CFRP cables. When the outer diagonal cables are replaced, the cable stress drop in the cable dome structure is significantly greater than that when the other two kinds of diagonal cables are replaced. When the CFRP cable replaces the outer diagonal cable, the maximum cable force reduction of the cable dome structure appears in the upper inner ring cable (Group number 1) and the inner ridge cable (Group number 5), reaching 3.3%. When middle diagonal cables or inner diagonal cables are replaced by the CFRP cables, the overall cable force of cable dome structure does not decrease by more than 1%.

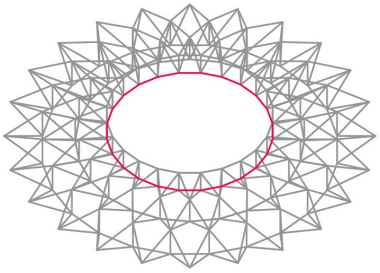
Before and after replacing the CFRP cable, the vertical displacement changes of the nodes on the innermost ring of the cable dome structure are shown in Fig.5(b).As can be seen from the figure, when different diagonal cables are replaced by CFRP cables, the node displacements are all larger than those of the original structure, and the joint displacements increase by 9.3mm when the outer diagonal cables are replaced by the CFRP cables, showing the largest increase. Contrary to the stress variation trend, the node displacement increases from inner to outer with the replacement cable position.When CFRP cablea are used to replace steel diagonal cables, the structural stiffness decreases and the joint displacement increases.

3.3. Replacement of ring cables

When replacing ring cable with CFRP cable, four conditions are considered: 1). Replace outer ring cable 2).Replace central ring cable 3). Replace upper inner ring cable 4). Replace lower inner ring cable, as shown in Fig6. Fig. 7 shows the cable stress change diagram of each group of Levy cable dome structure with opening (group number is shown in Table 1) and the maximum vertical displacement diagram of the inner ring node when the four types of ring cables are replaced.



(a)O-RC (b)M-RC (c)UI-RC



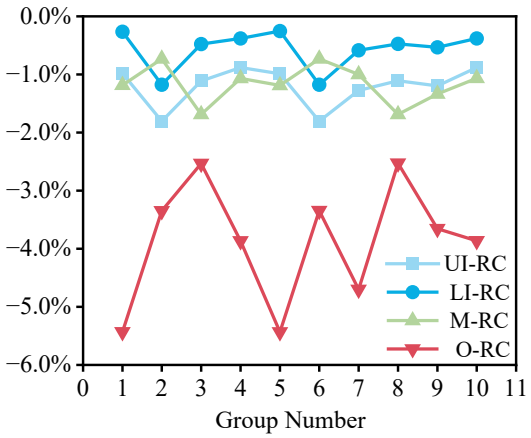
(d)LI-RC

Figure 6. Replace the ring cables in different positions: (a) outer ring cables, (b) middle ring cables, (c) upper inner ring cables, (d) lower inner ring cables.

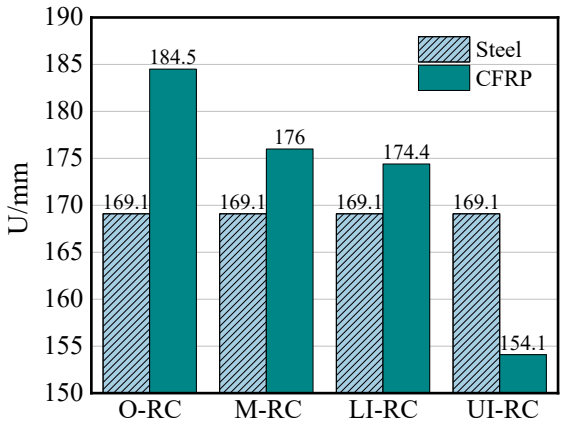
As can be seen from Fig.7 (a), the cable stress in the cable dome structure decreases after the replacement of the ring cable with CFRP cable. When the outer ring cable is replaced, the cable stress drop in the cable dome structure is significantly greater than that in the replacement of the other three kinds of ring cable. The cable force drop is close to that in the replacement of the middle ring cable and the upper inner ring cable, and the cable stress drop is the lowest when the lower inner ring cable is replaced.

When CFRP cable is used to replace the outer ring cable, the maximum stress drop occurs at the upper inner ring cable and the inner ridge cable, reaching 5.4%, which is the maximum stress drop when single group of cable is replaced. When the ring cable is replaced, the outer ring cable has a great influence on the internal force distribution of each group cables, while the other ring cables have little change on the stress of each group cables.

The vertical displacement of nodes on the innermost ring of cable dome structure was selected as the research object, and its changes before and after replacement were shown in Fig.7 (b). As can be seen from the figure, when the upper inner ring cables are replaced by CFRP cables, the vertical displacement of nodes decreases by 15mm compared with the vertical displacement of the original structure, and when other ring cables are replaced, the vertical displacement of nodes increases. When the outer ring cable is replaced, the node displacement increases 15.4mm, with the largest increase of 9.1%.When the ring cable is replaced, the displacement increase of the structure vertical decreases from inner to outer.The effect of upper inner ring cable on the vertical displacement of structure is different from that of lower inner ring cable.



(a)The percentage change in cables stress

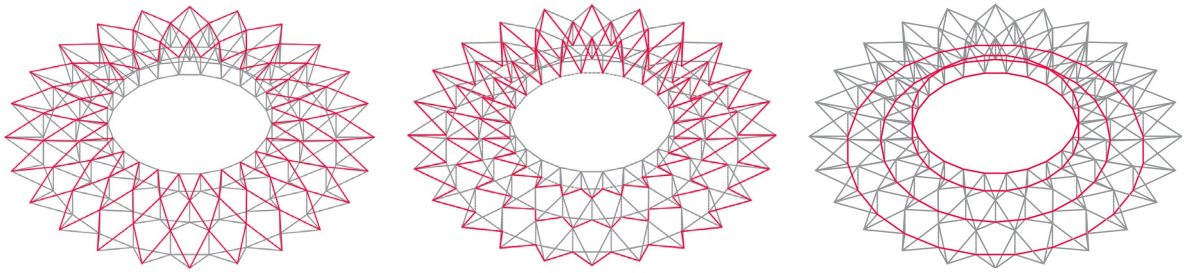


(b)The change in nodes displacement (in mm)

Figure 7. Member stresses and displacements for open Levy cable dome before and after the replacement of ring cables with CFRP cables

3.4. Replacement of different types of cable

Three cases were considered when all the same type cables were replaced with CFRP cables: 1).Replace the ridge cables 2).Replace the diagonal cables 3). Replace the ring cables, as shown in Fig. 8. Fig. 9 shows the maximum vertical displacement of the open Levy cable dome structure and the change of cable stress in each group when three kinds of cables are replaced.

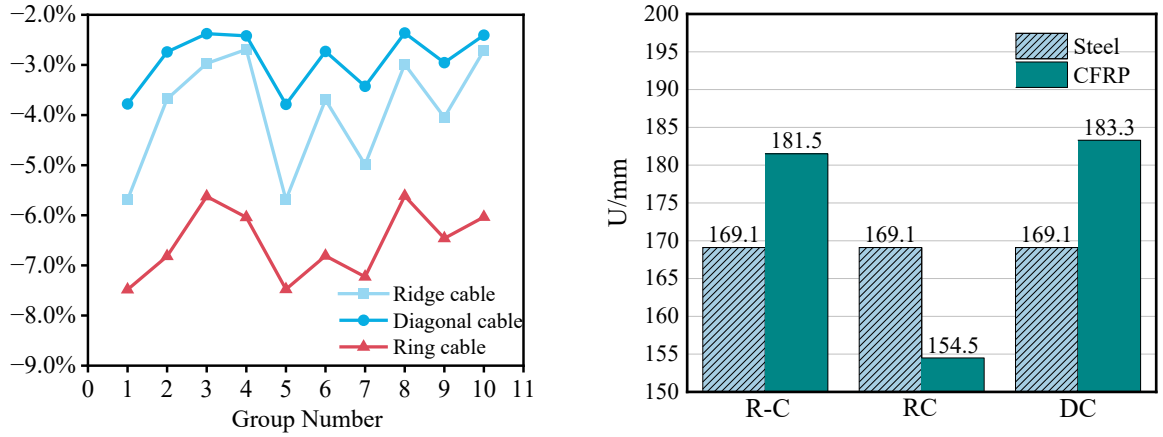


(a)RC (b)DC (c)R-C

Figure 8. Replace different types of cables: (a) ridge cables, (b) diagonal cables, (c) ring cables

It can be seen from Fig. 9 (a) that when single type of cables are replaced, the stress of each group decreases, and the change trend is roughly the same. The change range of the stress of each group is the largest when the ring cable is replaced, while the change range is the smallest when the diagonal cable is replaced. When the three kinds of cables were replaced, the maximum amplitude of stress change appeared in the upper inner ring cable (Group number 1) and the inner ridge cable(Group number 5), which decreased by 7.5%.

The vertical displacement changes of nodes on the innermost ring before and after replacement are shown in Fig.9 (b).As can be seen from the figure, when all ring cables and diagonal cables are replaced, the node displacement increases by 12.5mm and 14.2mm respectively.When the ridge cables are replaced, the structural stiffness increases and the maximum displacement of the node decreases by 14.5mm.



(a)The percentage change in cables stress (b)The change in nodes displacement (in mm)

Figure 9. Member stresses and displacements for open Levy cable dome before and after the replacement of different types of cables with CFRP cables

4. Conclusion

(1) Compared with the steel cable dome, the stress level of the cable dome structure with partial CFRP cables is reduced, but the reduction range of the cable stress is less than 8% for each group cables.

(2) The maximum vertical displacement of nodes changes within 10%. The replacement of ridge cables and upper inner ring cable with CFRP cables can increase the structure stiffness and reduce the vertical displacement of Levy type open cable dome

(3) The open Levy cable dome structure with partal CFRP cables has little difference in static performance with the traditional steel cable dome structure. Meanwhile, CFRP has the advantages of corrosion resistance and fatigue resistance, so CFRP cable has a promising application prospect in cable dome structure.

Acknowledgements

The authors would like to thank the National Natural Science Foundation of China for financial support (Grant No 51178009).

References

[1] S. L. Dong, D. Xing and Y. Zhao, "Application and development of modern long-span space structures in China," *Spatial Structures,* vol. 18, pp. 3-16, 2012. (in Chinese)

[2] Y. Feng, L. W. Wang, Y. Zhang, T, Qiu, W. Yang, X. A. Xiang, X. Liu and S. Y. Liao, "Structural design of Chengdu Fenghuangshan professional football field," Building Structure, vol. 50, pp. 15-21+14, 2020. (in Chinese)

[3] X. Wen, C. S. Cai, Y. Zhang, and R. C. Xiao, "Study of super long span cable-stayed bridge with CFRP components," *Engineering Structures,* vol. 33, pp. 330-343, 2011.

[4] I. O. Olofin and R. G. Liu, "Research on the Static Behaviour of a Suspen Dome with Carbon Fiber Reinforced Polymer (CFRP) Tensegrity System," Iranian Journal of Science and Technology, Transactions of Civil Engineering, vol, 45, pp. 795-813, 2021.

[5] W. J. Zhang and P. W. Li, "Progressive collapse analysis of Levy type open cable domes," in *Proceedings of the IASS 2022 Symposium affiliated with APCS 2022 conference*, BeiJing, China, September 19-22, 2022, Su-duo Xue, Jin-zhi Wu and Guo-jun Sun(eds.)

Proceedings of the IASS Annual Symposium 2023
Integration of Design and Fabrication
10–14 July 2023, Melbourne, Australia
Y.M. Xie, J. Burry, T.U. Lee and J. Ma (eds.)

Structural behaviours of arch SCS with “pin-pin” support

Akira TANAKA*

* Department of Industrial Information Tsukuba University of Technology, Japan
Amakubo 4-3-15, Tsukuba City, Ibaraki, 305-8520 Japan
akira@a.tsukuba-tech.ac.jp

Abstract

String Crescent Structure (abbreviated as SCS) is the unique masonry structure with consisting of the blocks, lower strings, and connecting members or Cables, and this was proposed by the presenter. In previous studies, the experiments and analysis had shown that SCS with pin-roller support is stable structures. Build upon these results, in the paper, the arch shape with pin-pin support was adopted to ensure higher stability of SCS. Experimental and analytical results for this structure showed that no tension is generated in the lower strings under all load, but this tension is generated near the load point under partial distributed load. Although unstable deformation was expected to occur in SCS under partial distributed load, this did not happen. This stable state is due to the tension of the lower strings preventing the progression of slipping between the blocks. Next, the prestress effect of SCS with pin-pin support was studied. The prestressing members are made of strand rope, and the prestressing introduction component are the eyebolts that are set near the support points. The prestress effect of SCS with pin-pin support has never been studied before. Detailed experiments and analyses were done to confirm these.

Keywords: string crescent structure, reuse, kinetic system, unique masonry structure, arch with “pin-pin” support, all load, half load, prestress, analysis, load experiment

1. Introduction

1.1. Lightweight structure derived from traditional masonry arch

Elements of structural safety are strength, stiffness, and stability [1]. The structure must be strong enough to resist the loads and must not cause excessive deflection or unstable displacement. If these three elements can be full, the structure can be used as a building structure. However, in the design of masonry arches in the Middle Ages, only stability was considered among these elements. Before to the publication of "Dialogues Concerning Two New Sciences" by Galileo, the existence of stresses was not recognized [2]. Specifically, the stresses generated in the stone blocks of the masonry arches are small, and buckling measures are not considered. On the other hand, destruction due to slipping between blocks and unbalance forces is easy to occur, and it was necessary to ensure "stability" against this risk.

One of the most important factor for structural design in the 20th century was the balance between safety and economy. As a result, lightweight structures such as shell structures flourished, but masonry arches did not. This reason for this is that traditional masonry arches were not only vulnerable to earthquakes, and it was also difficult to manage a balance between economy and safety.

The structure that solve this weakness and improved the economics of the masonry arch exists [3]. This is the vault roof with hollow cells and extant on Djerba island, Tunisia (Figure 1). The basic shape of this hollow cell is a trapezoidal tube and its material is clay. After these blocks are assembled into the vaulted roof, the top of this roof is coated with mortar. This vault has many advantages such as light

Copyright © 2023 by Akira TANAKA. Published in the Proceedings of the IASS Annual Symposium 2023 with permission.

weight, economy, and heat insulation. Blocks such as Tube type need to be checked for strength and stiffness, and application to vast roofs is difficult.

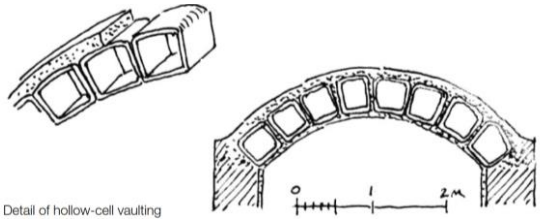


Figure 1. The vault roof with hollow cells

1.2. Development from the traditional masonry arch to the unique masonry arch

In the 21st century, the issue of the global environment has come under close scrutiny. The requirements for a technology to address this issue include not only stability and economy, but also environment-conscious performance (Figure 2). Environment-conscious performance is an important keyword for a sustainable society. CO2 emissions from large-lot production and consumption lead to climate variation, threaten global biodiversity, deplete natural resources, and cause environmental pollution. To prevent this, environment-conscious technologies and product approaches are needed. One of these environment-conscious features is 3R such as recycle, reuse, and reduce. Do these increasingly complex conditions make the design of masonry arches difficult?

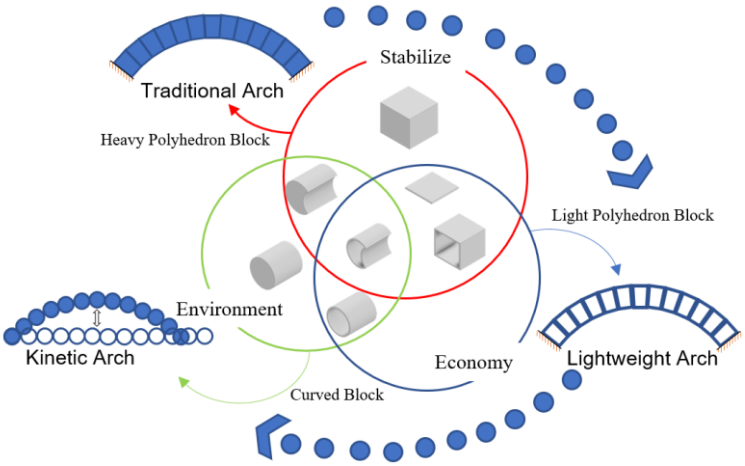


Figure 2. Development of block and masonry arches

Architectural shapes and scales are extremely diverse. In order to easy block diversion between different shape structures, the remanufacturing process such as combination process or a cutting process is need. The combination process is a remanufacturing process that combines parts of different geometries. However, this leads to an increase in the number of different types of parts, make complex joints and unnecessary materials. The cutting process is a remanufacturing process in which the blocks are cut after disassembly. However, the large volume of a single block increases the amount of waste during the cutting process and fuel for transportation. The requirement for environment-conscious blocks is that they can be reused into different shape structures while reducing the aforementioned processes (Figure3). To achieve this object, it is advisable to introduce blocks with curved surfaces such as bone joints, and to construct a kinetic system that allows rotational sliding between blocks. An example of a block with a curved surface is a cylindrical block. The structure with this block is free to move structural shape. An example of this is the arch proposed by Hiroishi et al [3]. The disadvantage of this structure is that the contact area between the blocks is very small, which tends to occur stress concentration.

To ensure both environmentally friendly performance and stability, the block must have contact curved surface and a sufficient contact area. The block shape that can satisfy this condition is the crescent column shape. In order to achieve both lightness and rigidity of this block, it was further developed into

a wheel-shaped block. The structure with crescent block becomes unstable structure. To stabilize this, the lower strings and PS Cables are needed. The name of this unique masonry structure with the crescent block and tension members is SCS.

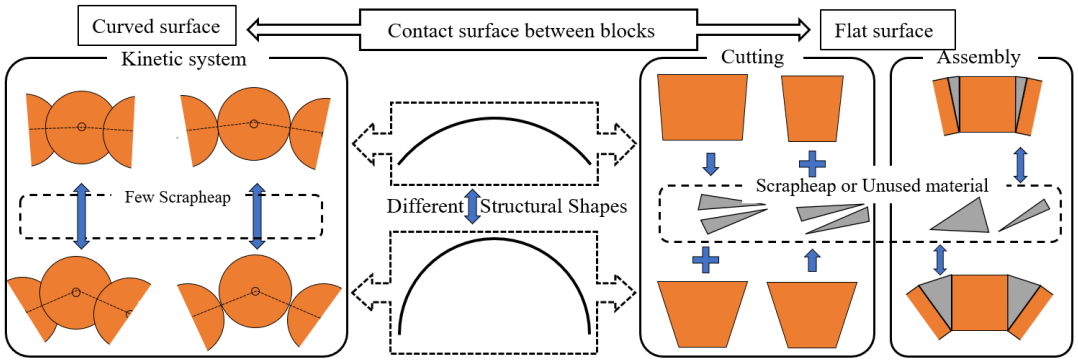


Figure 3. Block remanufacturing process

1.3. Assumptions of SCS structural properties and research objectives

Before a description of the structural characteristics of SCS, the block contact problem is considered. Regardless of the shape of the block, the supporting pressure of the block during compression may easily maintain the stability of the arch during All loading. However, the joints between the blocks under moment or shear may be unstable.

First, the contact states between the blocks under the moment are described. In trapezoidal blocks, bearing pressure occurs on the compression side and separation occurs on the tension side, and in crescent-shaped blocks, rotational slipping occurs between the blocks (Figure 4a). The case of shear forces is described next. Shear slip occurs when trapezoidal blocks are subjected to shear, while bearing pressure and separation occur for crescent-shaped blocks. Different shapes of blocks may lead to different destruction mechanism of the structure.

These contact state between crescent block become the unstable structure. To solve this problems, tension member is needed. The role of this member is to prevent separation for trapezoidal blocks and prevent rotational slipping for crescent-shaped blocks.

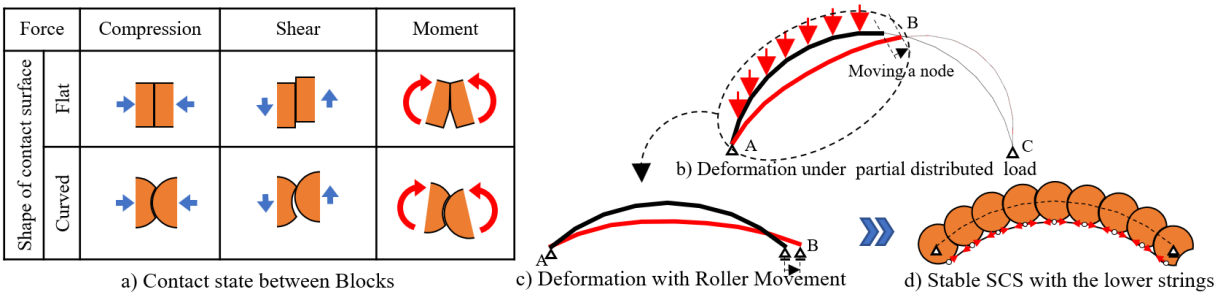


Figure 4. Stabilization of SCS considering contact condition between blocks

Figure 4b shows the deformation of ArchABC with pin-pin support under partial distributed load. Arch AB in the area of load application is detached from this arch, and this is replaced by the arch with pin-roller support (Figure4b-c). Then the deformation of arch AB is caused by the thrust of B (Figure4c). If Arch AB were replaced by a masonry arch with crescent-shaped blocks, this arch become an unstable structure with rotational slipping between blocks. To stabilize this structure, the lower chords are required. The effectiveness of Addition of the low string has already been demonstrated by load experiments of SCS with pin-roller support[5]. The description returns to the deformation of the entire arch (Figure4b). Upward deformation occurs at the area of non-load B-C. Will this deformation adversely affect the stability of the entire arch? Based on this assumption, the stability of SCS with pin-pin support under partial distributed load must be tested. This is one of the study objectives.

The results of studies already showed that the structural behavior of SCS with pin-pin support is more stable under cyclic load than that of SCS with pin-roller support [7]. But that of SCS with pin-pin support has not yet been studied.

The subject of this study is SCS with pin-pin support, and the objective of the study is to verify the differences in structural behavior and PS effects that occur between all and partial distributed loads. For this purpose, the load experiments and structural analysis were done.

2. Experimental and analytical models

2.1. Experimental models

The components of the experimental model are (1) Blocks and (5) Lower Strings, (3) PS Cables, and (6) Lower Joint (Figure5). The rise-span ratio of the arch based on the shape of "(3)PS Cable" is 0.2. "(3)PS Cable" passes directly through the eye bolt placed in the center of "(1)Block" and is fixed by "(4)PS Eye Bolt" provided at both ends of SCS. To reduce friction between "(1)Block" and "(7)Support Plate", the rolling bearings are installed between the through-bolt of the block and the bolt hole.

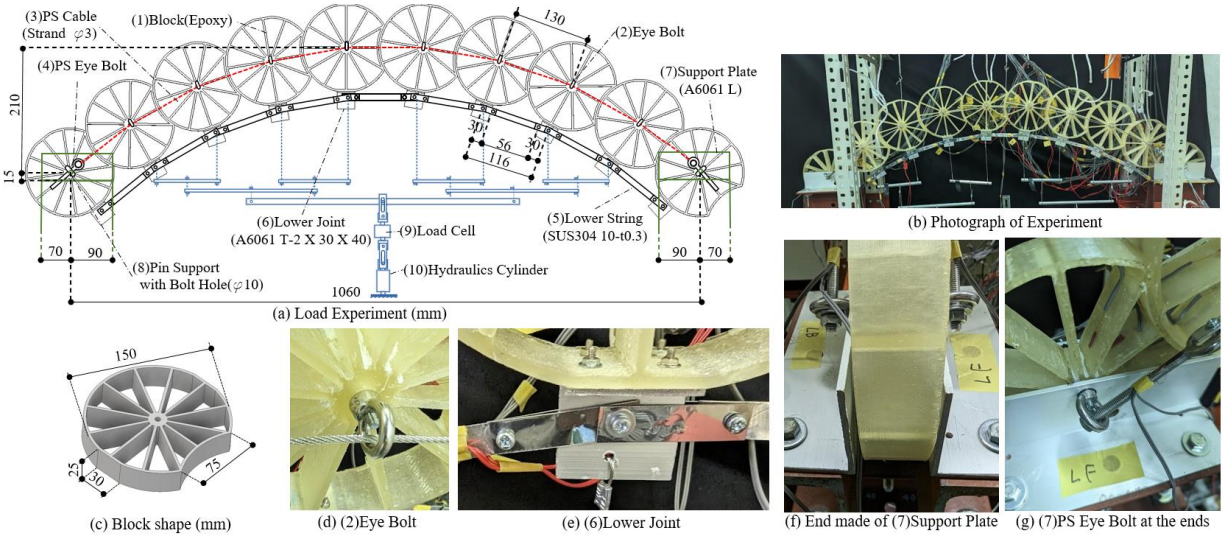


Figure 5. Experimental model

2.2. Analytical models

The geometry of the analytical model are determined based on the experimental model, and the structural specifications are given in Table 1. The block material is epoxy resin and was fabricated by the presenter. The difference in environmental conditions during this manual work affects Young's modulus. For this reason, the following work was performed to determine the Young's modulus of the epoxy resin. First, poor quality blocks are selected from among many "(1) Blocks". The indication of poor quality is the presence of cracks or large bubbles inside the block. A reinforcing member is cut from the selected block and used as a beam specimen (span: 50 mm, thickness: 3.0 mm, width: 21 mm). Twelve experiments were conducted in which the beams under concentrated loads. Based on this results, Young's modulus was calculated. Based on these results, the average value of Young's modulus was decided 1500 N/mm2, and this value was entered into the analysis software. However, this material property does not take into account the plastic range. Truss elements such as "(5) Lower Strings" and "(3) PS Cables" resist only tension. "(11) rods" is introduced in the center of "(1) Block" and "(12) Contact Element" are installed between "(3) PSCable" and "(11) rods" (Figure6). The pin joint between "(3) PS Cable" and "(12) Contact Element". The sliding joint was installed between "(11) rods" and "(12) Contact Element". Based on the results of the IASS 2021 friction tests, the friction coefficient of the sliding joint was set to 0.2 [6] and the stiffness factor was set to 1. This stiffness factor is not a

contact stiffness but a parameter for convergence of the analysis with Inventor Nastran [8]. This analytical model was made and used for nonlinear analysis including contact analysis with NASTRAN.

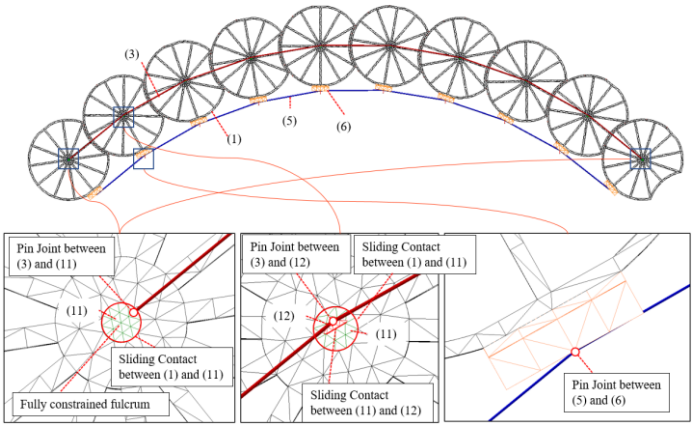


Figure. 6 Analytical model

Table.1

Name	Colour	Material	E (N/mm^2)	Shape, Cross-sectional Area
(1)Block		Epoxy	1500	
(3)PS Cable		Strand Cable	$6.7X10^4$	$4.8mm^2$
(5)Lower String		Stainless	$2.0X10^5$	$3.0mm^2$
(6)Lower Joint		AL6061	$6.9X10^4$	T-2X30X9
(11)Rod		Steel	$2.1X10^5$	φ6.0mm
(12)Contact Element			$1.0X10^6$	

2.3. Load Condition

A.L., H.L.L., or H.R.L. is selected as the load condition, and P.S. is used in addition (Figure7). These applies to experiments and analysis. The load method is pressurization by "(10) Hydraulics Cylinder", and "(9) Load Cell" and a tournament are set between the SSS and the "(10) Hydraulics Cylinder". Two partial distributed load conditions are prepared. This reason is that the choice of H.L.L. and H.R.L. may make different structural behavior of SSS. The reason for this assumption is that the shape of the SSS with asymmetric blocks is asymmetric.

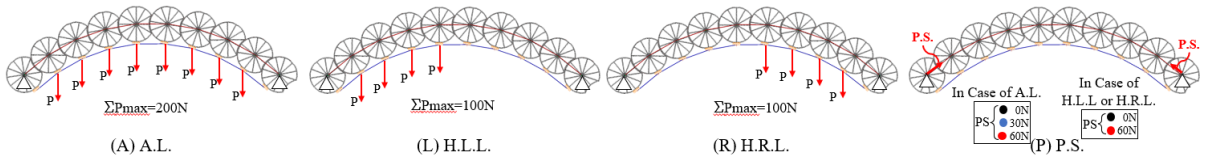


Figure. 7 Load Contidion

3. Result

3.1. Tension in the lower strings

Regarding the generation of tension in the lower strings under A.L.. It is already understood that these tension are generated when the boundary condition is pin-roller [6]. On the other hand, in this experiment, no tension was generated regardless of the presence or absence of P.S. because the support condition was pin-pin (Figure 7A). This result was consistent with the analysis and the experiment, showing that the lower string under A.L. had no mechanical role. Regardless of H.L.L. or H.R.L., the tension in the lower string occurred in the area load application, whereas that did not occur in the area of non-load (Figure. 7LR). This result tended to be consistent with the analysis and the experiment.

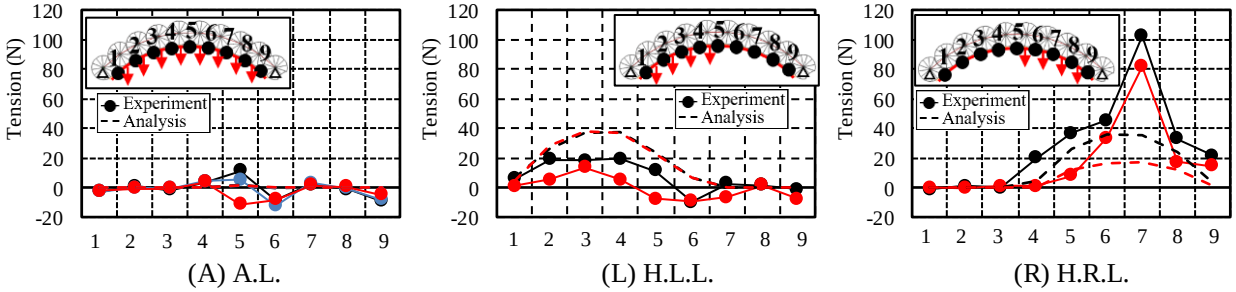


Figure. 7 Tension distribution of the lower strings

Experimental results show that P.S. reduce the generated tension. This cause was that P.S. leads to a state of close contact between the blocks, reducing slipping.

3.2. Tension in PSCable

The shape of PS Cable overlaps the axis of the entire arch. As a result, the tension of PS Cable under A.L. did not increase. An increasing P.S. led to the increasing load level that the slackness in PS Cable occurs. This result was consistent with the analysis and the experiment (Figure. 8A).

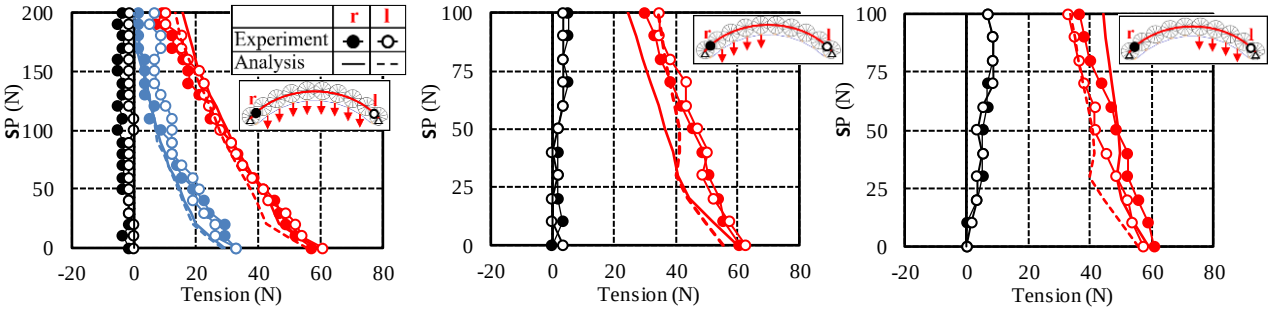


Figure. 8 Tension in PS Cable

Regardless of H.L.L. and H.R.L., P.S. led to a loosening of PS Cable tension under load. In contrast, no-P.S. led to the generation of this tension (Figure 8LR). This cause can be explained as follows: this generation is caused by the reduction of both the progressive separation between the blocks (Figure 10) and the upward deformation in the area of non-loaded (Figure 9).

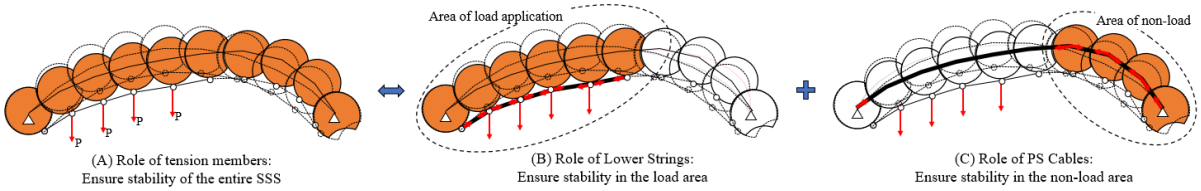


Figure. 9 Mechanical role of tension members in SCS

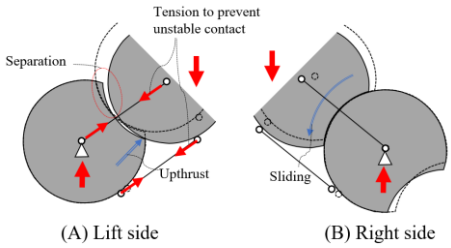


Figure. 10 Detail view of contact state between blocks

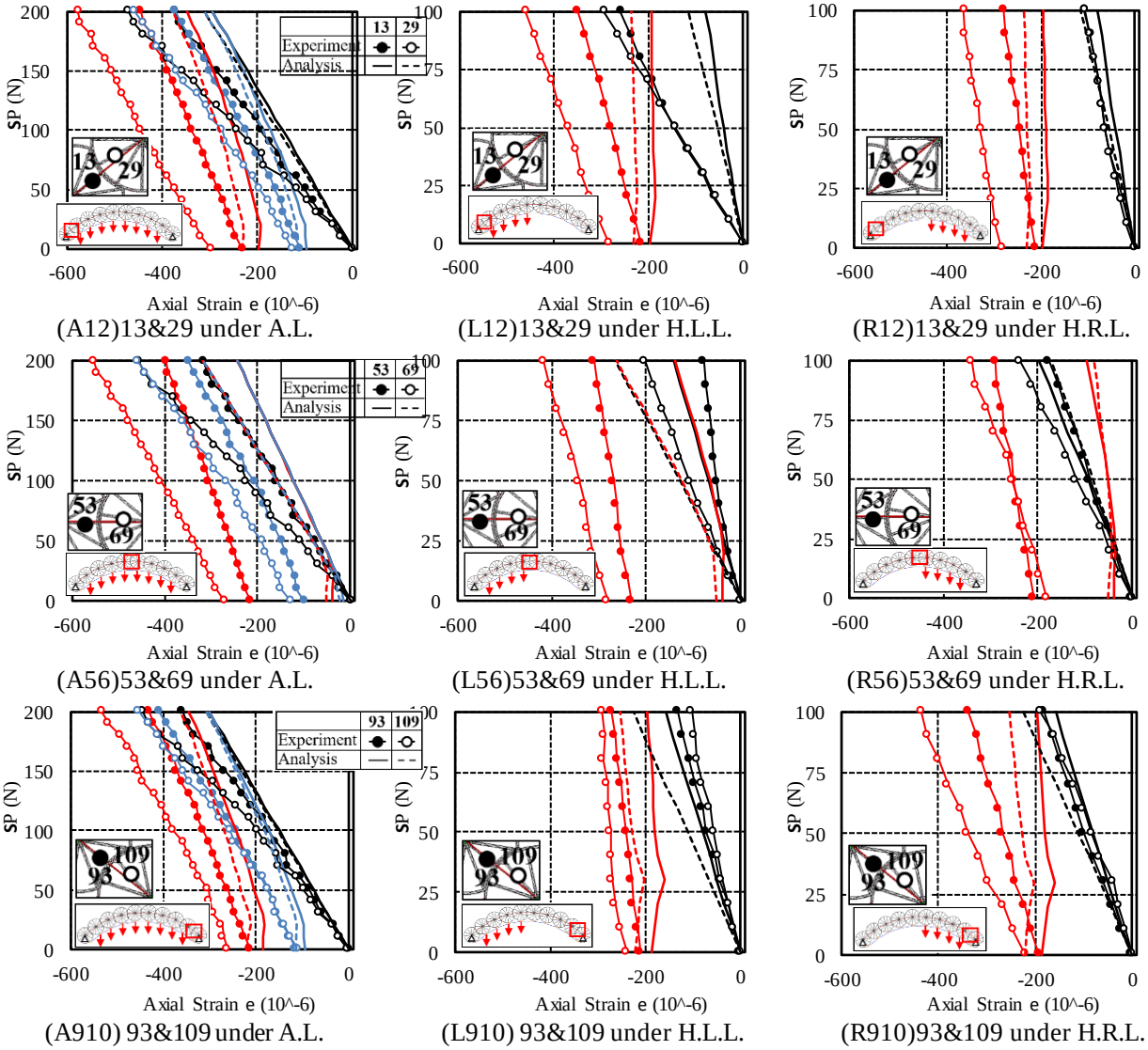
However, the analytical model without P.S. did not generate tension unlike the experimental model. The cause of this difference can be attributed to the incompleteness of the analytical model.

3.3. Axial strain of the block near axis of the entire arch

In both the experimental and analytical results, compressive strains occurred at all measured points regardless of the load conditions, and P.S. led to increasing compressive strain before load (Figure 11). This result indicates that the blocks must be designed under conditions that reducing stress due to P.S. is not expected.

The total amount of load ΣP as load condition is narrowed down to 100N, and the strain between each load is compared. There was no significant difference between the strains on the area subjected to loading under H.L.L or H.R.L. and strains under A.L.. In contrast, the strain at the non-load-bearing area under H.L.L or H.R.L. tended to be slightly smaller than the strains under A.L..

In the case of models without P.S., the results of the analysis and the experiments were in close agreement, but in the case of models with P.S., this tended to be not the case. The cause of this may be the initial imperfection of the experimental model and the incomplete analytical model pointed out in Section 3.2.



(A12)13&29 under A.L. (L12)13&29 under H.L.L. (R12)13&29 under H.R.L.

(A56)53&69 under A.L. (L56)53&69 under H.L.L. (R56)53&69 under H.R.L.

(A910) 93&109 under A.L. (L910) 93&109 under H.L.L. (R910)93&109 under H.R.L.

Figure. 11 Axial Strain in Block

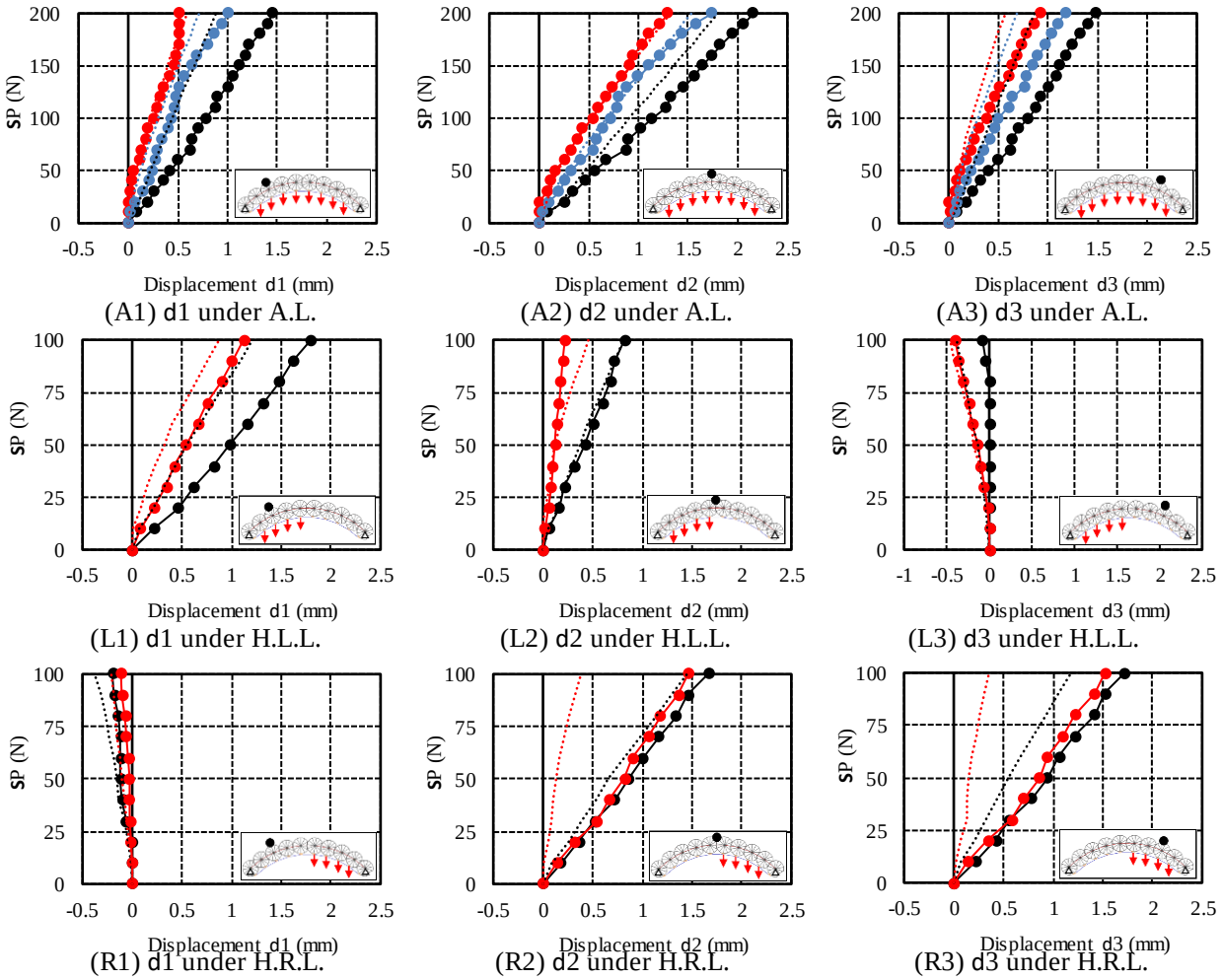
3.4. Displacement

P.S. led to the reducing displacement of SSS under A.L. (Fig. 12A1A2A3). However, the model without P.S. showed symmetrical deformation, while increasing P.S. leds to asymmetrical deformation, such that the displacements on the left side are reduced more than those on the right side. This cause is the different contact conditions between the blocks, shown in Figure 10. For example, the convexity of the block at left end pushes up the neighboring block on the right. In contrast, the non-convexity in the block at the right end does not pushing up the neighboring block on the left. The increasing P.S. makes these differences in contact conditions clear.

In the case of H.L.L., P.S. reduced the maximum displacement (Figure 12L1L2), but not in the case of H.R.L. (Figure 12R1R2). In addition, a comparison between H.L.L. and H.R.L. showed a difference in

the state of upward deformation in the area of non-load. For example, P.S. reduced the upward displacement under H.L.L. (Figure 12L3), but not so under H.R.L. (Figure 12R3).

The cause of the different H.L.L. and H.R.L. displacements is the contact state in Figure 10, which were discussed in detail in the discussion of displacement under ALL.



(A1) d1 under A.L. (A2) d2 under A.L. (A3) d3 under A.L.

(L1) d1 under H.L.L. (L2) d2 under H.L.L. (L3) d3 under H.L.L.

(R1) d1 under H.R.L. (R2) d2 under H.R.L. (R3) d3 under H.R.L.

Figure. 12 Displacement

5. Conclusion

The structural behavior of SCS with pin-pin support is different from that of SCS with pin-rollers. These are explained as follows based on analytical and experimental results.

*Since SSS under A.L. is the axial resisting system, the lower string has no mechanical role. However, the lower string under half load has the role of stabilizing the contact state between the blocks.

* The role of PS Cable is to reduce the separation between the blocks and the upward deformation of the entire SCS and to stabilize SSS under partial distributed load.

* The PS effects such as increasing stiffness of SCS can be expected in the case of A.L.L., but this may not be expected in the case of H.R.L.

* The PS effects under partial distributed load is to reduce the tension of the lower string under load.

* The introducing PS leads to an increasing compressive strain of the block. This shows that the adequate PS must be need so that the amount of PS is not excessive.

Future tasks are as follows: experimentally verify the fracture of the SSS and design the geometry of the block based on these results. Specifically, the thickness of each part and the arrangement of each parts in the block must be considered. Differences between experimental and analytical values are observed in the case of partial distributed loads, and a complete analytical model must be developed.

References

[1] Jacques Heyman, *The Stone Skeleton: Structural Engineering of Masonry Architecture*, Cambridge University Press, 1997.

[2] Stephen P. Timoshenko, *History of Strength of Materials*, Dover Publications,1983

[3] Friedrich Ragette, *Traditional Domestic Architecture of the Arab Region*, Axel Menges, 2003.

[4] N. TSUTSUMI, A. OKADA, N. MIYASATO and S. HIROISHI, "*Study on basic structural characteristics of prestressed beads-on-string structure",* Architectural Institute of Japan, Journal of Structural Engineering, Vol. 62B, March 2016, pp01-06.

[5] A. Tanaka, "Load and Constructional Experiments on Beam-shape String Crescent Structure with Pretension Cables fitted to the neutral surface", *IASS Annual Symposium 2019*, Barcelona, Spain, October 7-10, 2019, pp1741-1748.

[6] A. Tanaka, "The effect of friction coefficient of the structural behavior of String Crescent Structure", *IASS Annual Symposium 2021*, Guilford, UK, August 23-27, 2021, pp2941-2952

[7] A. Tanaka, "The effect of changing boundary conditions at the arch End on the structural behavior of String Crescent Structure", *IASS/APCS Annual Symposium 2022*, Beijing, China, August 19-22, 2022.

[8] "Autodesk Inventor Nastran 2023 help , Surace contacts" ,https://help.autodesk.com/view/NINCAD/2023/ENU/?guid=GUID-797778BD-E6EC-49BC-B8A4-2D9F6E1DC1BA/,20 Jan 2023

IASS 2023
July 10–14 Melbourne
Integration of Design and Fabrication

Proceedings of the IASS Annual Symposium 2023
Integration of Design and Fabrication
10–14 July 2023, Melbourne, Australia
Y.M. Xie, J. Burry, T.U. Lee and J. Ma (eds.)

Suspended tensegrity: the anthropomorphic machine

Paul LOH[*], David. LEGGETT[a], Sascha BOHNENBERGER[b], Matthew TAM[c]

[*] Bond University
Abedian School of Architecture, Gold Coast, Queensland, 4229, Australia
ploh@bond.edu.au

[a] LLDS Architects | Architectural Research Laboratory
[b] Swinburne University of Technology
[c] Bollinger+Grohmann

Abstract

The paper presents a suspended tensegrity "cloud" structure as an interactive art installation with computer vision. Actuated by 12 pneumatic rubber muscles, the research discusses the design, engineering and fabrication challenges of a dynamic tensegrity "cloud". Through material testing and physical prototyping processes, the design workflow enables a cross-disciplinary approach to the problems with feedback and an iterative static analysis approach. The project demonstrates a cross-disciplinary design collaboration between artists, architects, engineers, and the fabricator towards refinement in the engineering of dynamic structures. Using a pneumatic actuation system combined with tensegrity structures, the project demonstrated a method to develop active, controlled, deployable and form-changing envelopes and structures on a larger scale.

Keywords: tensegrity, fabrication, prototyping, automation, dynamic structure, interactive structure

1. Introduction

A tensegrity structure is typically used for large, spanning self-equilibrium systems composed of continuous prestressed tension cables and individual compression struts, such as the Georgia Dome by Levy [1]. Its use as a dynamic structure to shape space is rare. While there is much speculation about its interactive potential in architecture, typically through a single cell or a spine-like array, to explore transformational (as movements) or collapsible structures as soft robotics [2]. They are usually built as small-scale prototypes as proof of concept [3]. Actuations generally are limited to replacing the tension members to produce movement and are constrained by strut congestion, poor load response, and fabrication complexity.

This paper presents a suspended tensegrity structure actuated by a set of pneumatic muscles driven by a computer vision feedback system. The paper examined the engineering and fabrication of the design with a focus on the tensegrity "cloud". The project, titled the Anthropomorphic Machine, is an interactive art installation, in collaboration with the artist STELARC, that responds to the crowd's behaviour in a gallery setting, see figure 1. The paper outlines the design process balancing structural stability, integrity, and dynamic performance through prototyping. The physical prototyping process incorporates feedback from the system's virtual stress analysis and reaction forces, as well as tensile stress testing of the typical connection joints. The paper concludes with the assembly procedure of the tensegrity structure. It points towards the new potential of using tensegrity structure to modulate spatial experience through automation and machine visions. The project's significance is in demonstrating how to achieve a large-scale dynamic tensegrity structure that is atypical of its use in architecture and engineering.

Copyright © 2023 by Paul LOH, David. LEGGETT, Sascha BOHNENBERGER and Matthew TAM. Published in the Proceedings of the IASS Annual Symposium 2023 with permission.

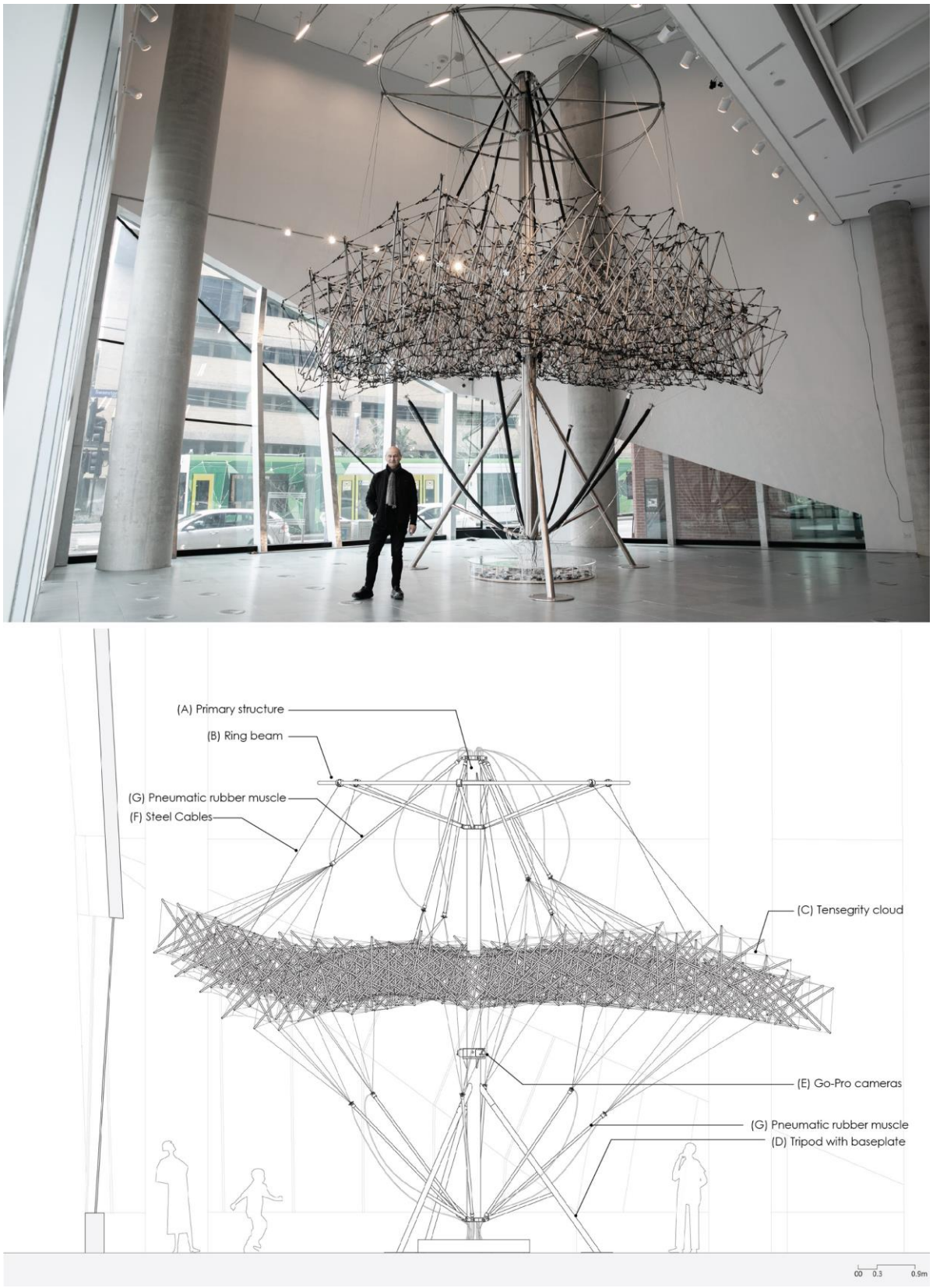


Figure 1. The 8-meter tall Anthropomorphic Machine installation in an art gallery with an actuated suspended tensegrity "cloud".

2. Background

The Anthropomorphic Machine is an interactive art installation presented as part of the Swarm exhibition at the Science Gallery Melbourne. The research was a two-year collaborative project with multiple contributors, as acknowledged at the end of the paper. Led by LLDS architects in collaboration with the artist STELARC, the structure analysis was performed by Bollinger+Grohmann engineers with the cooperation of the fabricator, Pelican Studio. The fabrication team was given a 5-month period to fabricate the structure. The installation needed to be operational 24 hours, seven days a week, as the installation was also linked to a proposed web interface that allows remote interaction. The project was intended to be in the Gallery for three months, and this was extended to 12 months post-installation.

2.1. Design of the anthropomorphic machine

The project consists of an 8-meter-tall stainless-steel primary structure with a circular ring boom and supporting struts at the top from which the tensegrity "cloud" is suspended, figure 1A, B and C. The structure sits on the raised floor of the Gallery on a tripod support structure with baseplates, figure 1D. The tensegrity "cloud" is 8 meters in diameter and consists of 204 tensegrity cells. It is suspended 4 meters off the ground using 5mm diameter stainless-steel cables, see figure 1F. Twelve pneumatic rubber muscles actuate the "cloud", each 2.5m long, that take advantage of the dynamic quality of the tensegrity to create a set of choreographed movements, see figure 1G.

2.2. Problems with tensegrity structures

A tensegrity system consists of a set of discontinuous compression components (struts) interacting with continuous tensile members (cable or cords) to define a stable 3-dimensional form. Buckminster Fuller first used the term in his 1959 patent on "Tensile-Integrity Structures" [4]. Its geometries (in various configurations) and mathematics have since been widely studied. However, the design and fabrication of tensegrity structure remain challenging. Burkhardt [5] highlighted the four obstacles in the design and fabrication of a tensegrity structure, namely: (1) strut congestion, (2) poor load response (with high deflection), (3) fabrication complexity and (4) inadequate design tools. This research utilised the high deflection of the system to produce an interactive artwork. The strut congestion becomes part of the design intent – designing opportunities for the stainless-steel struts to generate sound as they strike each other when actuated. The later section will discuss the fabrication complexity, primarily around the dynamic behaviour and connection details. As the system are difficult to predict [1], the research team develops prototypes throughout the build process to test and counteract issues around fabrication, assembly, and installation. Typically, tensegrity is designed as either a single cell (with unique arrangement) or part of dome geometry (either as a higher frequency sphere or double-layer system); a planar array is limited in its configuration [5].

3. Suspending tensegrity for interaction

The early concept of the Anthropomorphic Machine took inspiration from Loren Carpenter's Audience Participation project based on his Cinematrix Interactive Entertainment System presented at the 18th Annual Conference on Computer Graphics and Interactive Techniques [6]. Carpenter pioneered the deployment of computer vision, moving from bi-directional one-on-one interaction between a human and a computer towards multiple audience participation using images captured with a conventional camera and a computer to process the image as data [7]. In SIGGRAPH 1991, the system was tested on an audience of participants, each provided with a green and red paddle to collectively play the classic computer game, Pong [8].

3.1. Computer vision for interaction

In this project, we used an open-source software called OpenPose connected to three go-pro cameras to provide a 360 degrees vision of the Gallery, see figure 1E. OpenPose is a real-time multi-person human pose detection library [9]. The interactivity in the Gallery was based on the overall dynamic of the

human crowd movement; their speed and density (number of people) were mapped to four pre-defined sets of choreographed performances. Each set of performances creates a seamless behaviour that changes the cloud shapes and form, with a typical play length varying from 10s to 15s. The performance was caused by actuating the pneumatic rubber muscles at different speeds and frequencies. Six pneumatic muscles hung from the top to actuate the top surface of the cloud, and a further six pneumatic muscles were located below the "cloud". Aside from its self-weight, the tensegrity "cloud" must withstand the dynamic forces resulting from the performances. The design of the performance and actuation sequences are outside the scope of this paper.

3.2. Actuation system

Early experiments with students at the Melbourne School of Design explored using OpenPose to trigger a pneumatic rubber muscle - a single-action actuator which contracts up to 25% of its nominal length, actuated using compressed air (typically at 6 bar pressure) regulated by valves with no mechanical system. Figure 2 illustrates early prototypes that explored the actuation of a one-cell and 12-cell tensegrity prototype. The positioning of the pneumatic muscles is critical in maximising the dynamic effect of the cloud. When the actuator replaces one of the tension cords, the movement is precise, but its impact is minimal as a network. When the pneumatic muscle is located outside the system, its action is amplified across the network. The latter is used in the gallery installation; each muscle has a set of 2mm diameter steel cables (called tendons with 6 to 12 arrays) that connect the "cloud" as a network. The initial test also identified that all the tension members should be elastic as this help to amplify the movement; we used an industrial multi-strands shock (or bungee) cord for the installation.



Figure 2. Left, pneumatic muscle interaction with OpenPose. Right, the 12-cell tensegrity prototype actuated through OpenPose.

The final installation used twelve 2.5 meters long, 40mm diameter pneumatic muscles, with a 250 kg freely suspended additional load capacity. Each weighs 2kg with wrought aluminium alloy press-fitted connections.

3.3. Detailing of the T-prism cell

As discussed in 2.2, the tensegrity structure has several fabrication limitations and constraints. With five months to engineer and fabricate the steel structure and the 204 tensegrity cells, the design and detailing of the cell were critical to the success of the project. The design team developed a system where the individual cell was prefabricated and joined together to form a planar assembly on site.

The design team proposed using a tensegrity prism (also known as the T-Prism) as the primary cell for the planar assembly. The planar arrangement repeats rows of T-Prism with a half-cell offset; see figure 3-left. Each cell comprises of three 22.2mm diameter stainless-steel tubes acting as the compression struts (figure 3A). Two end connectors are fitted to both ends of the struts (figure 3B). The tension cables are 8mm diameter multi-strand industrial shock cords (figure 3C) with hooked connector fixtures to both ends (figure 3D). The hook is connected to the end connectors enabling the fabricator to pre-assemble the unit. A triangular arrangement of cords is on the top and bottom planes of the cell (figure 3E). These triangular cords are connected with temporary connectors (figure 3F), allowing neighbouring cells to attach and expand as an array. Once the neighbouring cells are added, the triangular cord forms part of the tensegrity network. Figure 3-right illustrates the prefabrication of a three cells cluster. With dynamic forces acting on the connectors and the cords (figure 3B, C and D), these components were tested to satisfy the dynamic load of the system, see 4.2.

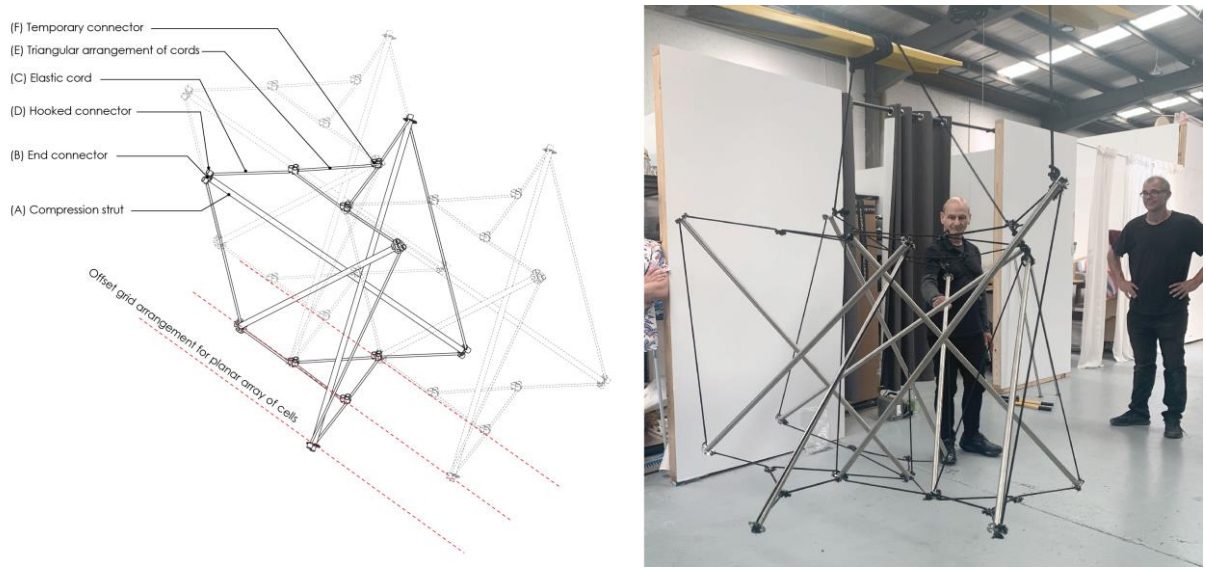


Figure 3. Left, Single T-Prism and planar arrangement of the "cloud". Right, the 3-cell cluster prototype at Pelican Studio.

4. Engineering dynamic system

This section focuses on designing and engineering the tensegrity "cloud". It comprised 204 prefabricated T-Prism cells with 612 struts, each 1340mm long. There were 1400 meters of 8mm diameter multi-stands industrial elastic (shock) cord cables that acted as tension members. In addition, 50 meters of 5mm diameter stainless-steel wire cables supported the "cloud" structure. A further 50 meters of 2mm diameter steel (tendon) wires spread the linear actuation force from the pneumatic muscle to the tensegrity network. The tensegrity "cloud" weighs 780kg. The dynamic performance of the tensegrity "cloud" posed challenges in structural evaluation. Critically, much of the materials used to fabricate the T-Prism were non-standard or unknown, particularly the elastic cord and connectors.

4.1. Testing material and connection details

The first author conducted three sets of tensile strength tests at the mechanical lab at the University of Melbourne using an Instron 5569A electromechanical Universal Testing Machine – (1) industrial elastic cord, see figure 4A, (2) strut's end connectors, see figure 4B, and (3) hooked connector fixtures to the elastic cord, see figure 4C & 4D. The data collected in the tests inform the design of the connection details and engineering analysis.



Figure 4. Ultimate Tensile Strength testing of connectors and elastic cords.

4.1.1 Tensile tests of elastic cord

The shock cord manufacturer cannot provide the material's tensile strength. The research team conducted two-sample tests; both samples were 8mm diameter industrial elastic cords with a rest length of 95mm. Sample 1 yields an Ultimate Tensile Strength (UTS) of 3.6MPA and elongation of 200.5%.

Sample 2 produces a UTS of 3.3MPA, and elongation of 183%, see figure 4A. Both samples have similar break patterns—for example, in Sample 1, the outer shell fabric tears at 190.46mm displacement at the clamps. Between 350-375mm, the individual strain of rubber breaks one at a time. In the final displacement calculation of the structure, a typical elongation of 140% was permitted, with the maximum permissible elongation of 200%.

4.1.2 Tensile tests of connecting fixtures.

The initial design for both ends of the compression struts consisted of a bespoke end connector using a 3mm laser-cut steel profile, see figure 4B. The open hook end was to connect the tensile cords. The steel distorted at 0.65kN and released the elastic cord at 0.89kN when displacement reached 455mm.

The weakness came when we tested the fixture to the tensile cord's ends. Figure 4C illustrates the initial design with a 6mm diameter stainless steel tube and a crimp joint to the end of the cord. It yielded a UTS of 1.7MPA and elongation of 152%. The worst-case scenario illustrated that the crimp connection is half as effective as the elastic cord itself. The fabricator and the architects need to reconsider the detail.

The fabricator required a quick-to-assemble solution and proposed a proprietary PET plastic hooded fixture with a compression-fit as a solution, see figure 4D. It yielded a UTS of 6.1MPA and elongation of 280%. In Sample 1, we observed the outer fabric of the elastic cord failed at the claws of the clamp. In Sample 4, the fabric failed at the compression-fit joint; we suspect this explains the higher UTS and elongation.

4.2. Structure evaluation

Typically tensegrity structures are categorised as non-linear structures. For a large arrangement of cables and struts, it is computationally complex to find its equilibrium state, especially if it is a kinematic-driven and controlled shape in continuous flux. Therefore we decided to apply a static analysis approach at various critical positions of the different shapes. The evaluation was concerned with finding the maximum internal stresses of the tension cables, compression forces in the struts to its dimension and suitable material thickness for the cables.

The overall behaviour of the different states also governed the dimensions and design of the supporting stainless steel column with its tripod legs and circular boom structure for the suspended cables. The five different states were as follows:

- Static (figure 5A). None of the muscles is activated. All the tendons (cables) are loose and should not receive any force. The main structural cables (figure 1F) support the tensegrity structure.
- Dynamic All (figure 5B): all the muscles are activated, and the tendons receive various forces.
- Dynamic V1 (figure 5C): some muscles are activated, and some tendons receive various forces.
- Dynamic V2 (figure 5D): some muscles are activated, and some tendons receive various forces.
- Dynamic V3 (figure 5E): some muscles are activated, and some tendons receive various forces.

The simulation considered a maximum of 200% elongation for the multi-strand elastic cord. The results showed the highest reaction forces nearest the "cloud" centre at 9kN. The highest displacement of the structure came from the splicing of the support legs, resulting in a maximum deformation of 40mm. The stainless steel support structure reached a maximum of 60% utilisation, and the support cables had a maximum normal force of 1.6 kN. The analysis showed that some suspension cables would fail under tension forces during dynamic behaviour. However, due to the redundancy in the system, the structure was always predicted to be stable.

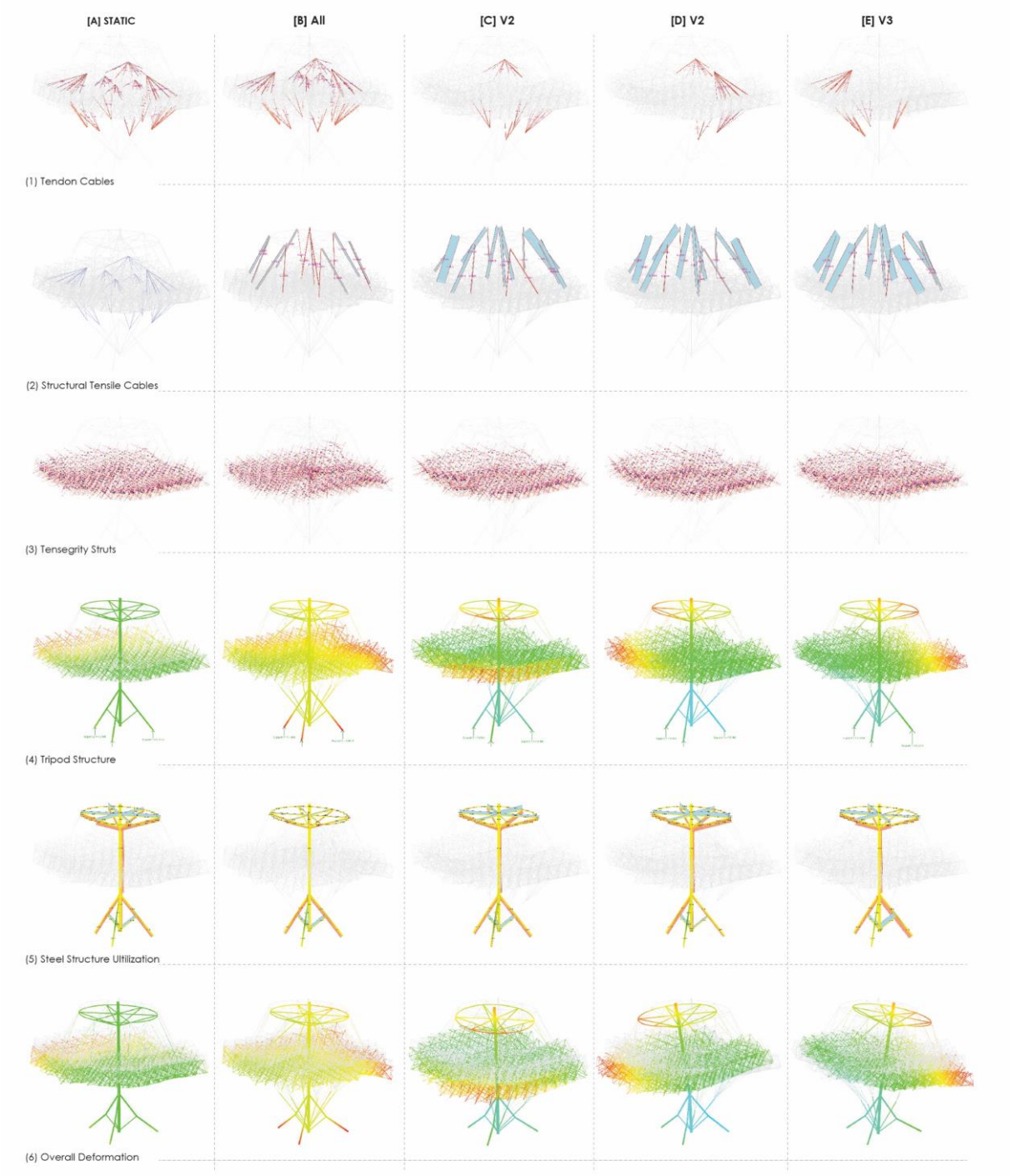


Figure 5. Matrix of static analysis across the five different states. (1) Forces on tendon cables caused by pneumatic muscle actuation. (2) Maximum internal stresses of the tension cables at the various states. (3) Compression forces in the tensegrity struts. (4) Forces on the tripod support structure and its impact on the raised gallery floor. (5) Steel utilisation of the primary structure. (6) Overall deformation at the various states.

5. Assembly of the tensegrity cloud

The primary frame was erected in the Gallery in two parts. Figure 6 illustrates the assembly of the tensegrity "cloud". The design of an individual cell allowed all the parts to be prefabricated off-site and assembled in the Gallery. As the cells were assembled, parallel lines denoting the row alignments were set out on site. Rows of tensegrity were built and then connected together. Once the cloud was completed on the ground, it was lifted 300mm higher than its final position and suspended with 12 steel cables connected to the circular ring boom. This allowed the installer to slowly adjust the "cloud" into position after installing the pneumatic muscles. The pneumatic muscles must remain in a "relaxed" position and not take the tensegrity load until it is inflated with air. The bunching of the tensegrity cell was challenging for the installation when it was suspended. The configuration is unpredictable, despite the best effect to simulate it in Grasshopper 3D. It resulted in an uneven load distribution across the 12 supporting steel cables, causing them to twist and tangle. The suspension cables and the positioning of the wires were manually adjusted; this amplified the human error affecting the "relaxed" state of the "cloud". These effects are hard to predict and simulate, and as Knippers stated, physical prototypes are necessary when engaging with new materials and material systems [10]. Therefore, during the installation phase, the engineer checked and worked with the installer to adjust the cable positions to ensure an evenly distributed load. The installation took over five days, followed by one week of testing with the dynamic performance.

During the testing phase, three shock cords broke, resulting from the actuated movement. The congested struts, predominantly around the central column of the primary structure, caused some of the elastic cords to rub against the steel connectors and tear its outer fabric. Additional stay cables were introduced to pull the tensegrity away from the column. Three inner cells were also removed during the testing process.

5.1. Discussions

When actuated, the Anthropomorphic Machine produces a variety of dynamic performances. The most compelling is the slow inhalation and exhaustion of air mimicking 'breathing'. This results in the 'cloud' animating slowly above the visitors, changing the experience of the space. Since installation, prominent Australian dancers, artists and musicians have created performances interacting with the structure.

There are several key lessons learnt in this project. First, the project could only be possible through interdisciplinary knowledge and collaboration. The architects have also taken on a significant role in prototyping the design and developing the actuation system – this interdisciplinary bridge is critical. Second, the project results from design and engineering research through testing and prototyping. The knowledge gained through the fabrication process informed the final design. Last, the project demonstrates a refinement in engineering towards dynamic structural design. The use of pneumatic elements in combination with tensegrity structures illustrates a method to develop active, controlled, deployable and form-changing envelopes and structures on a larger scale. However, the system still requires a level of maintenance (visual inspection and replacing shock cords). The shock cords seem to rapture in an irregular pattern while the Machine is operational. The team believes this might be because the dynamic load on the cord and the increased state of change in elongation (cycling through the different performance modes) are causing the cords to break faster than expected. Further on-site testing and investigation, especially into the shock cord layout and material composition, should be conducted to identify the issues and to be able to suggest improvements to extend the life expectations of the structure.

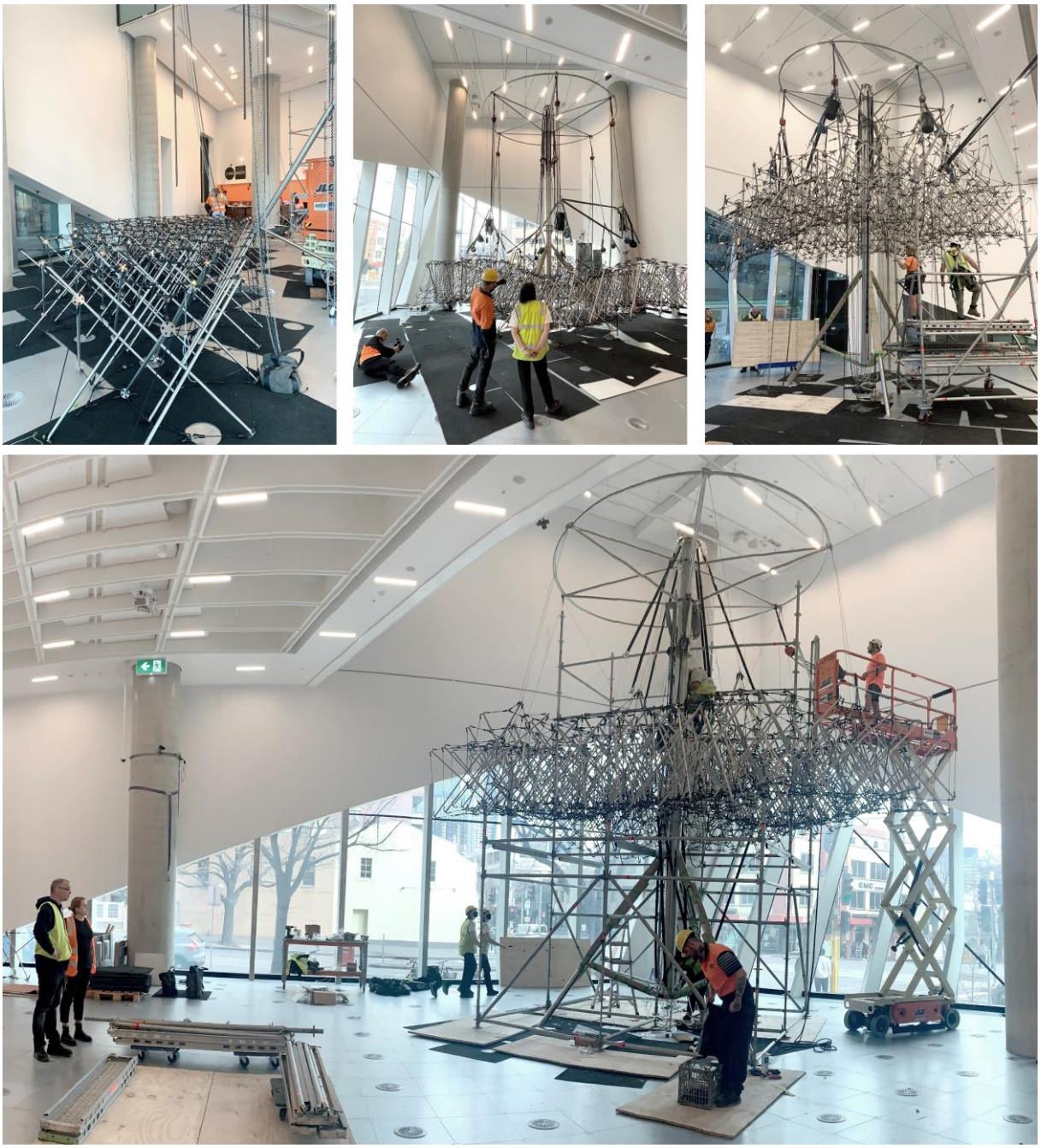


Figure 6. Top left, setting up of T-Prism planar array for the tensegrity cloud. Top centre, Suspension of tensegrity cloud. Top right, lifting of tensegrity cloud into position. Bottom, adjustment to tension cable to distribute the load evenly. Pneumatic muscles are in relaxed mode without air inflation.

6. Conclusion

The paper presents an unconventional use of tensegrity structure as a suspended and dynamic interactive installation. The high deflection of the tensegrity is maximised as part of the performance design, which creates challenges in the system's design, prototyping, fabrication and installation. The design and fabrication of the tensegrity were refined through material testing, and data was used to evaluate its dynamic behaviour through an iterative static analysis approach. The project illustrated a method of assembling T-Prism tensegrity cells into a planar arrangement and discussed the challenges of the

assembly process. It demonstrates a successful cross-disciplinary design collaboration between artists, architects, engineers, installers and fabricators.

Acknowledgements

The project acknowledges the generous commission of Science Gallery Melbourne with support from Festo, Melbourne School of Design and School of Computing and Information Systems, the University of Melbourne. Special thanks to Dr Jeffrey Ryan, Elise Brokensha and Philippa Brumby for coordinating and making the project possible. Design and Pneumatic system: Paul Loh, David Leggett, Psyche Hou. Model Making: Haoyu Chen. Electrical and Electronic Engineering: Dr Eric Schoof. Computing and Information Systems: Dr Eduardo Velloso, Qiushi Zhou and Gabriele Marini. The Architectural Association Visiting School Melbourne 2021, led by Paul Loh, David Leggett and Psyche Hou with students Mason Mo, Ying Lee, Lu Bai, Mingjia Shi and Yichen Sheng.

References

[1] F. Fu, *Design and Analysis of Tall and Complex Structures*. Saint Louis, UK: Elsevier Science & Technology, 2018. [Online]. Available: http://ebookcentral.proquest.com/lib/bond/detail.action?docID=5257306

[2] A. Musaffar and A. Agogino, "Scalability and Design of Six Rod Tensegrity Soft Robotic Structure," 2021. [Online]. Available: https://ntrs.nasa.gov/api/citations/20210014844/downloads/AgoginoTensScale.pdf

[3] J. Won, M. Silverio, J. Llubia, A. Markopoulou, A. Chronis, and A. Dubor, "Remembrane: A Shape Changing Adaptive Structure," 2017.

[4] R. B. Fuller, "Tensile-integrity structures," 3,063,521, 1962 [Online]. Available: https://patentimages.storage.googleapis.com/ab/cb/74/362b8cd8c7b88b/US3063521.pdf

[5] Robert William Burkhardt, *A Practical Guide to Tensegrity Design*, 2nd ed. Cambridge, Massachusetts, 2008. [Online]. Available: https://www.angelfire.com/ma4/bob_wb/tenseg.pdf

[6] SIGGRAPH, "'Audience Participation' by Carpenter," *ACM SIGGRAPH Infomration and Artifacts History*, 1991. https://history.siggraph.org/animation-video-pod/audience-participation-by-carpenter/ (accessed Mar. 25, 2023).

[7] L. Carpenter, "Cinematrix, Video Imaging Method and Apparatus for Audience Participation," US Patents #5210604, 1994

[8] D. Maynes-Aminzade, R. Pausch, and S. Seitz, "Techniques for interactive audience participation," in *ACM SIGGRAPH 2002 conference abstracts and applications*, Jul. 2002, pp. 257–257. doi: 10.1145/1242073.1242270.

[9] B. Gaudenz, "The Complete Guide to OpenPose in 2023 Read more at: https://viso.ai/deep-learning/openpose/," *viso.ai*, 2023. https://viso.ai/deep-learning/openpose/ (accessed Mar. 24, 2023).

[10] J. Knippers, "The Limits of Simulation: Towards a New Culture of Architectural Engineering," *Technol. + Des.*, vol. 1, no. 2, pp. 155–162, Nov. 2017, doi: 10.1080/24751448.2017.1354610.

Tension and membrane structures

Active bending
Additive manufacturing/ 3D printing
Architectural geometry
Bamboo for sustainable construction and quality of life improvement
Bio-inspired structures and architecture
Bridge structures
Computational form-finding
Conceptual design
Concrete structures
Construction techniques
Deployable and inflatable structures
Design competition (WG21)
Digital modelling and fabrication
Dynamic response of metal spatial structures
Dynamic response of other structures
Form-finding and structural optimisation of interlocking discrete assemblages
Graphical methods
Gridshell and lattice structures
Historical concrete shells
Historical structures
Lattice structures
Life-cycle design and assessment of structures
Metal gridshell structures, connections and stability
Methods and construction technologies for sustainable shell structures
Morphology and configuration processing
Next generation parametric design
Novel methods in modelling, optimisation and construction for reducing carbon footprint of continuous roof shells
Numerical methods for geometry, form-finding and optimisation of lightweight structures
Optimisation methods and applications
Origami
Other
Teaching design uncertainty: working with unknown qualities/quantities of new and re-claimed materials
Teaching of shell and spatial structures
Tensegrity systems and cable structures
► **Tension and membrane structures**
Tension structures in the Asia-Pacific
Timber and bio-based structures
Topology optimisation
Traditional masonry structures and innovation
Transformable structures

IASS 2023
July 10–14 Melbourne
Integration of Design and Fabrication

Proceedings of the IASS Annual Symposium 2023
Integration of Design and Fabrication
10–14 July 2023, Melbourne, Australia
Y.M. Xie, J. Burry, T.U. Lee and J. Ma (eds.)

Active control of hybrid string structure

Wucheng XU[a,b,c], Xuanhe ZHANG[a,b,c], Yanbin SHEN[a,b,c,*], Xian XU[a,b,c], Yaozhi LUO[a,b,c]

[*] College of Civil Engineering and Architecture, Zhejiang University
Zijingang Campus, Zhejiang University, Hangzhou 310058, China
ybshen@zju.edu.cn

[a] College of Civil Engineering and Architecture, Zhejiang University, Hangzhou 310058, China
[b] Innovation Center of Yangtze River Delta, Zhejiang University, Jiashan 314102, China
[c] Key Laboratory of Space Structures of Zhejiang Province, Hangzhou 310058, China

Abstract
Active control has been increasingly used in civil engineering to improve the performance of structures in service and to avoid serious damage to structures. Hybrid string structure is an efficient hybrid system composed of upper chord rigid components, lower chord flexible components, and struts. Based on an optimization-based model, this paper proposes a set of active control approach for hybrid string structures including the beam string structure (BBS) and suspen-dome structure (SDS) by applying the genetic gradient algorithm (GGA) and multi-population genetic algorithm (MPGA). To verify the validity of GGA and MPGA in terms of search control strategies, an experimental case and two numerical cases are investigated. The test and simulation results show that the active control based on the GGA and MPGA can effectively optimize the mechanical properties of BBS and SDS (e.g., the stress, displacement, and strain energy), which validates the validity of GGA and MPGA. The research methods and conclusions of this paper can provide valuable references for the active control of hybrid string structures or similar structures.

Keywords: active control, hybrid string structure, member stress, nodal displacement, strain energy, genetic gradient algorithm, multi-population genetic algorithm

1. Introduction

According to the tension elements, the tension structures is divided into two types: (1) membrane structures and (2) string structures [1]. Tension members such as cables, rods, and chains belong to strings. The string structures includes pure tension structures and hybrid tension structures, where pure tension structures are those made up of strings only, and hybrid tension structures is the structures created by mixing tension and rigid members (e.g., arches, beams, and struts), which mainly includes the beam string structures (BBS) and suspen-dome structures (SDS). Because of good mechanical properties and high utilization rate of material strength, the BBS and SDS have been extensively applied in various civil infrastructures and large construction structures [2,3], for example, the Shanghai Pudong International Airport Terminal, National Indoor Stadium, Tianjin Sports Center Bicycle Gymnasium, and Xuancheng Stadium, as shown in Fig.1.



(a) Shanghai Pudong International Airport Terminal (BBS)

(b) National Indoor Stadium (BBS)

(c) Tianjin Sports Center Bicycle Gymnasium (SDS)

(d) Xuancheng Stadium (SDS)

Fig. 1. Representative engineering of BBS and SDS

Copyright © 2023 by Wucheng XU, Xuanhe ZHANG, Yanbin SHEN, Xian XU and Yaozhi LUO. Published in the Proceedings of the IASS Annual Symposium 2023 with permission.

The civil structures are traditionally designed to remain static and passively endure external loading, resulting in heavy structures, high material consumption, and significant CO2 emissions. The statistical research indicates that this sector is responsible for a significant amount of global non-renewable material consumption and energy-related CO2 emissions [4]. However, incorporating active adaptation to civil structures could lead to lightweight structures that autonomously adjust to changing environmental conditions. While this poses challenges, it also presents an opportunity to address industry issues [5]. Active structures have sensors and actuators that detect and respond to external loading, improving the structure's performance [6]. Yao originally introduced active control to civil engineering [7], and Soong and Manolis put forward a modern concept of active civil structures for the first time [8]. Through decades of sustained development, a large number of active control devices and technologies (e.g., the hybrid active mass damper, shape memory alloy actuator, and magnetorheological damper) have been developed for vibration control [9-12]. Furthermore, active control has also been applied to various applications such as retractable roofs [13], antenna structures [14], and daylight regulation in buildings [15].

Previous researches have focused on active spatial structures. Senatore et al. proposed a set of design and control methods for active truss structures based on whole-life energy minimization systematically, and tests of two active trusses and various numerical cases provided strong evidence of the validity of the method [16-19]. Wang et al. presented an integrated formulation for achieving the total energy optimization of active tensegrity structures [20]. Besides, a general approach for designing the active tensegrity structure with minimal mass is also provided by Wang et al., and active designs can reduce material usage compared to passive designs, resulting in lighter tensegrity structures [21]. Korkmaz extended the study on active control of tensegrity structures to self-repair of structural damage, utilizing active components to implement an intelligent control method based on the stochastic search, the repair function meets the requirements for safety and availability in the event of cable damage [22,23]. Fest et al. created an active structure consisted of five tensegrity units, in which some compression bars were constructed as linear actuators and proactive modifications based on preset procedures well fulfill the structure's usage needs in various operating modes [24]. Lu et al. developed an internal force control method using ant colony algorithm for cable dome structures and discussed the effect of optimizing the internal force under different actuator arrangement strategies [25]. With sensors for force detection and active components for modifying the stiffness configuration and stress properties of the structure, Kmet et al. applied a Levy cable dome to investigate how sensing and actuation systems can adapt a structure to changes in external loads [26]. As far as BBS and SDS are concerned, a great deal of researches has been carried out for their static and dynamic analysis, thermal analysis, wind effects, seismic behavior and parameter optimization [27-32], but little research has been done for their active control.

In this paper, a set of active control approach for hybrid string structures including the BBS and SDS by using the genetic gradient algorithm (GGA) and multi-population genetic algorithm (MPGA) based on an optimization-based model. To verify the validity of GGA and MPGA for searching control strategies, an experimental case and two numerical cases are investigated, and the validity of GGA and MPGA are validated through analysis of numerical and experimental results.

2. Active control model

The BBS and SDS are both made up of upper chord rigid components (i.e., the beams of BBS and latticed shell of SDS), lower chord flexible components (i.e., the cables), and struts connecting the upper and lower chords. The rigid components withstand external loading directly, and the prestressing is introduced into the cables to improve the mechanical properties of upper chords. Struts play an important role in the structural systems of BBS and SDS, and changes in their length can lead to the significant redistribution of internal forces. Therefore, the active control of BBS and SDS is able to be achieved through the length changes of struts. In this paper, the struts are embedded in the actuators so that they can change lengths linearly.

The equilibrium of BSS and SDS under external loading is expressed as

$$KU = P \tag{1}$$

Where K is the stiffness matrix, U is the nodal displacement matrix, and P is the external loading matrix.
The active control process of BBS and SDS is limited by the material characteristics of components, specification of actuators, and overall synergy of the structure, and the following constraints should be satisfied:

$$d^l \le d \le d^u \tag{2}$$
$$\sigma_u^c \le \sigma_u \le \sigma_u^t \tag{3}$$
$$\sigma_s^c \le \sigma_s \le \sigma_s^t \tag{4}$$
$$\sigma_l^m \le \sigma_l \le \sigma_l^t \tag{5}$$
$$-F_s^b \le F_s \tag{6}$$
$$\Delta L^l \le \Delta L \le \Delta L^u \tag{7}$$

Where d is the nodal displacement, σ_u, σ_l, and σ_s are the stresses of rigid components, cables, and struts, d^u and d^l are the upper and lower limits of allowable node displacement, σ_u^c and σ_u^t are the allowable compressive and tensile stresses of the rigid component, σ_s^c and σ_s^t are the allowable compressive and tensile stresses of the strut, σ_l^m is the minimal stress at which the cable do not quit working, σ_l^t is the allowable tensile stress of the cable, F_s is the internal force of strut, F_s^b is the buckling load of strut, ΔL is the linear change of the strut, and ΔL^u and ΔL^l are the upper and lower limits of the actuator.
Without loss of generality, the active control objective of BSS and SDS is defined as $f(x)$, which can be the stress, displacement, or strain energy, etc. The active control model for BBS and SDS with the objective minimized is shown below:

$$\min f(x) \qquad \text{s.t. Eqs. } (1)\sim(7) \tag{8}$$

3. Search algorithm

3.1. Standard genetic algorithm

Standard genetic algorithm (SGA) originates from the computer simulation of biological system and is a random global search approach that simulates the selection, crossover, and mutation in natural selection and genetic evolution. Starting from any initial population, the population evolves to an increasingly better region of the search space through random selection, crossover and mutation operations to produce a group of individuals that are better suited to the environment, so that the population continues to reproduce and evolve from generation to generation, eventually converging on a group of individuals that are best suited to the environment and thus finding a quality solution to the problem. The main features of SGA are as follows:
(1) SGA is able to operate directly on the structure objects without derivation and function continuity restrictions;
(2) SGA has intrinsic implicit parallelism and good global search capability;
(3) In the absence of definite rules, SGAs use probabilistic optimization methods to automatically acquire and guide an optimized search space and adaptively adjust the search method.
The flow chart of SGA is shown in Fig. 2.

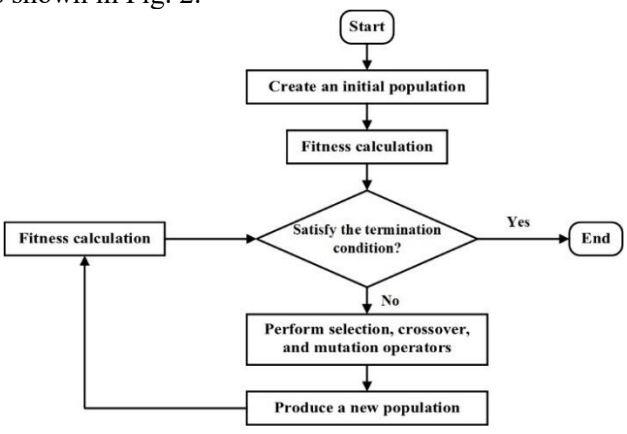


Fig. 2. Flow chart of SGA

3.2. Genetic gradient algorithm

Gradient descent (GD) is a type of iterative method that can be used to solve least squares problems. It iteratively searches for the minimum value along the gradient descent direction and can converge quickly to the optimal result. The general steps of GD are as follows:

Step 1: Specify the initial point $x^0 \in R^n$, set the termination error ε and maximum iterations N;

Step 2: For x^k, solve the gradient of the objective function $\nabla f(x^k)$, calculate the step size λ^k and move in the direction of the negative gradient for $\lambda^k \nabla f(x^k)$, thus $x^{k+1} = x^k - \lambda^k \nabla f(x^k)$.

Step 3: Cycle Step 2 until $f\left(x^{k+1}\right) - f(x^k) \leq \varepsilon$;

Step 4: Output x^k and x^{k+1}.

GD is shown schematically in Fig. 3. GD is fast and can easily obtain local optimal solutions near the iteration point, but for optimization problems with multiple local optimal solutions, this method is difficult to find other local optimal solutions far away from the current location point, making it difficult to search for the global optimal solution. It is noteworthy that SGA is good at global search, but have limited local convergence. Genetic-gradient algorithm (GGA) is a global search algorithm established by combining SGA and GD, and it has good local convergence as well as ensuring global search capability. The flow chart of GGA is shown in Fig. 4.

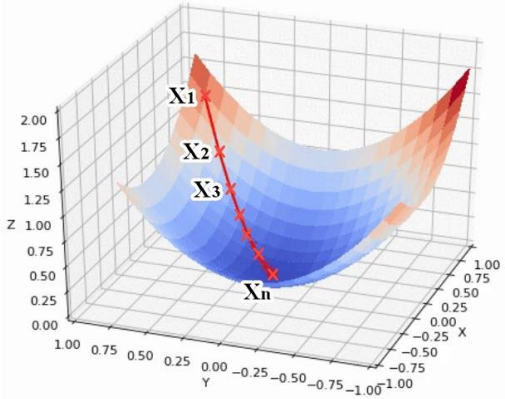


Fig. 3. Schematic diagram of GD

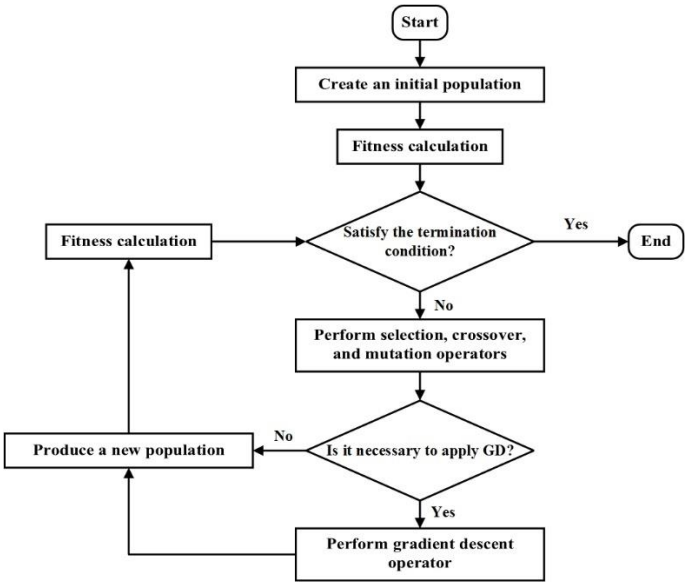


Fig. 4. Flow chart of GGA

3.3. Multi-population genetic algorithm

Multi-population genetic algorithm (MPGA) is based on SGA and introduces the concept of multi-population, which can solve the premature convergence problem of SGA. The main improvements of MPGA are as follows:

(1) MPGA breaks away from the framework of SGA, which only relies on a single population for the genetic evolution, and introduces multiple populations for the simultaneous optimization search, and different populations are assigned different control parameters to achieve different search purposes;

(2) The populations are connected by the transport operator, enabling the co-evolution of multiple populations, and the optimal solution is obtained as a combined result of co-evolution;

(3) The optimal individuals in each evolutionary generation of the various populations are preserved by the artificial selection operator and are used as a basis for judging the convergence of the algorithm.

Fig. 5 presents the flow chart of MPGA. In MPGA, the populations are relatively independent and are linked to each other by the transport operator, and the transport operator regularly introduces the best individuals from each population into other populations during the evolutionary process, enabling the exchange of information between populations; the elite population are not like other populations, and at each generation of evolution the best individuals from other populations are selected by the artificial selection operators and placed in the elite population for conservation; and the elite population is also the basis for judging the termination of the algorithm.

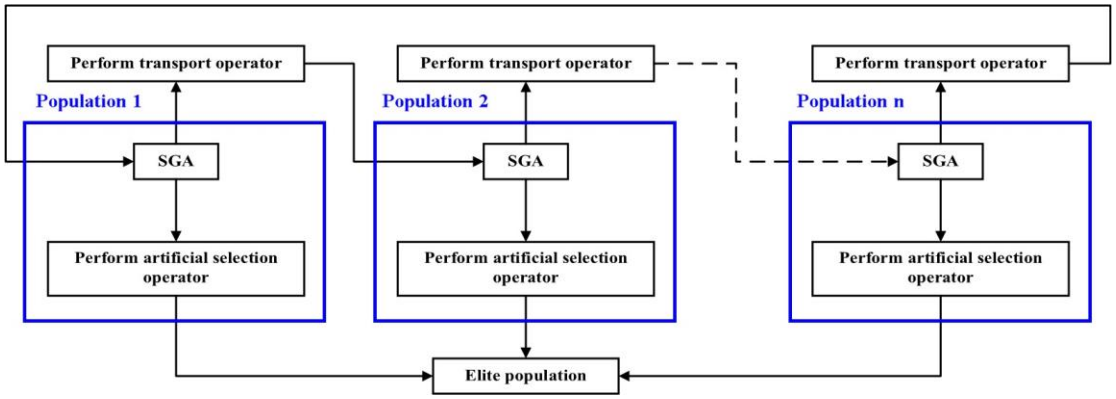


Fig. 5. Flow chart of MPGA

In this paper, GGA and MPGA are used to search for active control strategies of BBS and SDS, respectively.

4. Experimental case: single-span BBS model

A single-span BBS model with a span and sag of 4 m and 0.68m is developed for active control research. The model consists of a beam made of aluminum alloy, a cable made of carbon steel, and three struts made of cast iron. To measure the stresses and vertical displacements of the rigid beam directly subjected to load, four strain gauges are installed on the upper surfaces of spans 1/8, 3/8, 5/8, and 7/8 of the beam, while other four strain gauges are installed on the lower surfaces in the same position; and three displacement gauges are installed uniformly on the lower surfaces of the beam. As active elements, the three struts with the incipient lengths of 0.54 m, 0.68 m, and 0.54 m are specially customized, their total strokes are 100 mm, 150 mm, and 100 mm separately, and the extension and contraction strokes are the same for each strut. The installed BBS model is displayed in Fig. 6, and the layout of measurement points are shown in Fig. 7, where Si and Di denote the i^{th} stress measurement point and i^{th} displacement measurement point.

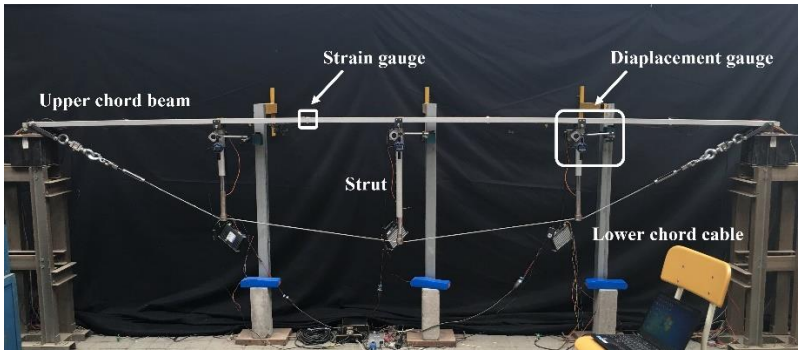


Fig. 6. Single-span BBS model at the experimental site

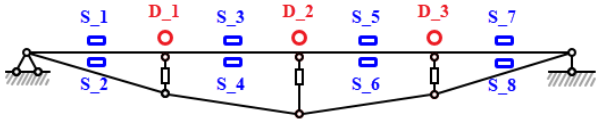


Fig. 7. Layout of measurement points

In this case, GGA is adopted for searching control strategy, and the active control objective is set to minimize the vertical displacement of the beam, which is expressed as

$$f(x) = \max d_i^v \tag{9}$$

Where d_i^v is the vertical displacement of the i^{th} observation point.

To simulate the external load acting on the test model, two loading scenarios are defined, as shown in Fig. 8. The tests are carried out using a nodal load loading method with the loading points evenly spaced on the beam, and nodal loads are simulated by means of weight blocks. Fig. 9 shows the loading schematics of two loads.

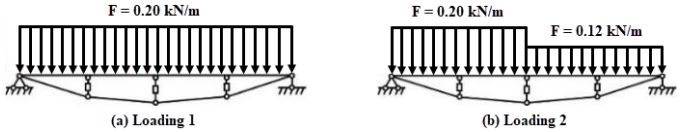


Fig. 8. Definition of loading scenarios



Fig. 9. Loading schematics of two loads

Fig. 10 illustrates the change in vertical displacement of the measurement points before and after the control, where the upward and downward vertical displacements are positive and negative, respectively. From the figure, for loading 1, the vertical displacements of the measurement points before control are -4.2 mm, -6.0 mm and -4.2 mm, which change to -0.2 mm, 0.5 mm and -0.1 mm after control; and for loading 2, the vertical displacements of the measurement points before control are -6.3 mm, -4.3 mm, and -0.2 mm, which change to 0.7 mm, 0.7 mm, and -0.1 mm after control. The average reduction in vertical displacement of the measurement points is 84.5%, with a maximum reduction of 97.6%. It shows that the implementation of active control strategy can significantly reduce the vertical displacement of the beam. Fig. 11 shows the variation in stress of the measurement points before and after the control, where the tensile and compressive stresses are positive and negative, respectively. From the figure, for loading 1, the maximum and mean stress of the measurement points are up to 5.8 MPa and 4.5 MPa, and they fall to 4.9 MPa and 2.9 MPa; and for loading 2, the maximum and mean stress of the measurement points are up to 9.2 MPa and 5.2 MPa, and they fall to 4.9 MPa and 2.6 MPa. The

results indicate that the process of controlling the vertical displacement also optimizes the stresses in the beam to some extent.

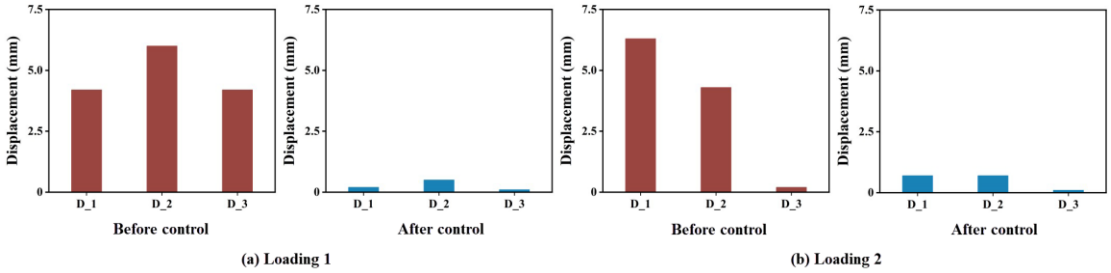


Fig. 10. Vertical displacements of measurement points before and after control

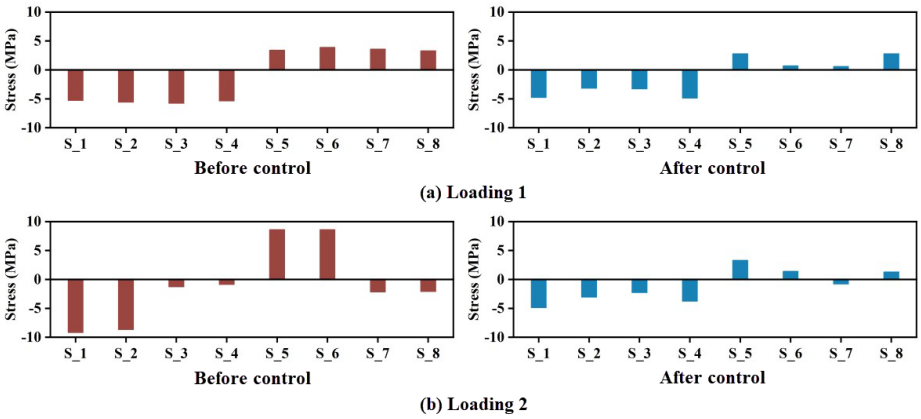


Fig. 11. Stresses of measurement points before and after control

5. Numerical case 1: Bi-directional BSS

In the structural analysis module of the software ANSYS, a 3D dimensional parametric finite element model of a bi-directional BBS is established. The bi-directional BBS has the size of 24 m×24 m×2.4 m. The simulation of the beams adopts the 3D linear finite strain beam element Beam188, the linear actuator element Link11 is applied to model the struts, and the 3D finite strain bar element Link180 is used for simulating the cables. The supports on each side of each span of the BBS are set as fixed and sliding supports separately. Fig. 12 presents the schematic diagram of bi-directional BBS. To simulate the external load acting on the bi-directional BBS, two loading scenarios are defined, as shown in Fig. 13.

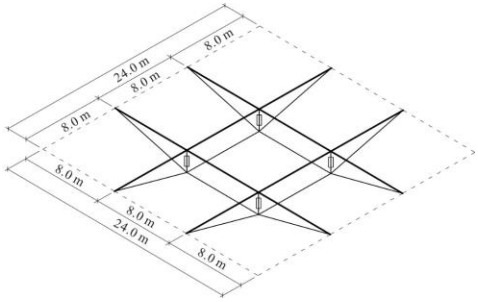


Fig. 12. Schematic diagram of bi-directional BBS

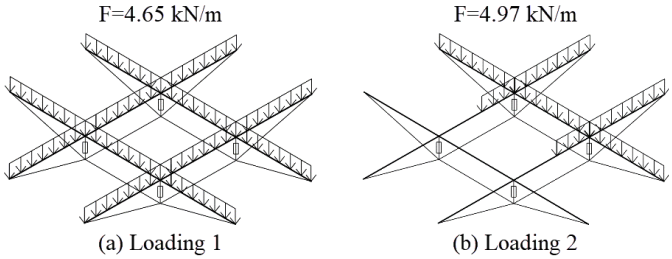


Fig. 13. Definition of loading scenarios

In this case, GGA is adopted for searching control strategy, and the active control objective is set to minimize the vertical displacement of the beam, which is expressed as

$$f(x) = \max \sigma_i \tag{10}$$

Where σ_i is the stress of the i^{th} observation point.

Table 1 lists the change in the maximum stress and displacement of the beams before and after the control. From the table, for loading 1, the maximum stress and displacement of the beams are 89.4 MPa and 95.9 mm, with the implementation of active control strategies they are decreased by 21.0% and 82.6% to 70.6 MPa and 16.7 mm; for loading 2, the maximum stress and displacement of the beams are 113.8 MPa and 76.4 mm, with the implementation of active control strategies they are decreased by 15.7% and 73.4% to 95.9 MPa and 20.3 mm. In general, after active control, the peak internal forces of the beams are effectively controlled and the beam deformation is also substantially improved.

Table 1. Simulation results before and after control

	Loading 1		Loading 2	
	Before control	After control	Before control	After control
Maximum stress (MPa)	89.4	95.9	113.8	76.4
Maximum displacement (mm)	70.6	16.7	95.9	20.3

6. Numerical case 2: Kiewitt SDS

In the structural analysis module of the software ANSYS, a 3D dimensional parametric finite element model of a Kiewitt SDS. The Kiewitt SDS has the size of 12 m×12 m×1.2 m. The latticed shell is simulated through the Beam188 elements, the cables are modelled by the Link180 elements, and the struts are simulated though the Link11 elements. The supports at the bottom of the structure are set as fixed supports. The schematic diagram of Kiewitt SDS is shown in Fig. 14, where the blue, red, and green elements denote the latticed shell, cables, and struts separately. To simulate the external load acting on the Kiewitt SDS, one loading scenario is defined, as shown in Fig. 15.

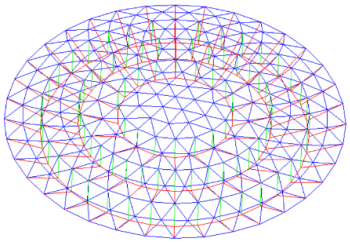


Fig. 14. Schematic diagram of Kiewitt SDS

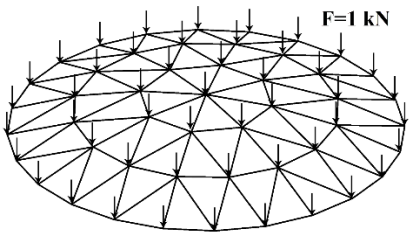


Fig. 15. Definition of loading scenario

In this case, MPGA is adopted for searching control strategy, and the active control objective is set to minimize the strain energy of the beam, which is expressed as

$$f(x) = \text{sum}\, U_i \tag{11}$$

Where U_i is the strain energy of the i^{th} element.

Based on the virtual work principle, the strain energy of SDS is equal to the work of the external forces. The density ratio of strain energy and strain energy of volume can be expressed by Eqs. (12) and (13) separately.

$$A = \frac{1}{2}\left(\sigma_x\varepsilon_x + \sigma_y\varepsilon_y + \sigma_z\varepsilon_z + \tau_{xy}\gamma_{xy} + \tau_{xz}\gamma_{xz} + \tau_{yz}\gamma_{yz}\right) \tag{12}$$

$$U = \iiint_V A\mathrm{d}V = \frac{1}{2}\iiint_V \left(\sigma_x\varepsilon_x + \sigma_y\varepsilon_y + \sigma_z\varepsilon_z + \tau_{xy}\gamma_{xy} + \tau_{xz}\gamma_{xz} + \tau_{yz}\gamma_{yz}\right)\mathrm{d}x\mathrm{d}y\mathrm{d}x \tag{13}$$

In term of the beam elements, strains and displacements can be expressed by the shape function and nodal displacement, as given in Eqs. (14) ~ (16).

$$\{f\} = [N]\{\delta\}^e \tag{14}$$

$$\{\varepsilon\}=\begin{Bmatrix}\varepsilon_x\\ \varepsilon_y\\ \varepsilon_z\\ \gamma_{xy}\\ \gamma_{xz}\\ \gamma_{yz}\end{Bmatrix}=\begin{Bmatrix}\frac{\partial u}{\partial x}\\ \frac{\partial v}{\partial y}\\ \frac{\partial w}{\partial z}\\ \frac{\partial x}{\partial y}+\frac{\partial y}{\partial x}\\ \frac{\partial z}{\partial y}+\frac{\partial y}{\partial z}\\ \frac{\partial z}{\partial x}+\frac{\partial x}{\partial z}\end{Bmatrix}=\begin{bmatrix}\frac{\partial}{\partial x} & 0 & 0\\ 0 & \frac{\partial}{\partial y} & 0\\ 0 & 0 & \frac{\partial}{\partial z}\\ \frac{\partial}{\partial y} & \frac{\partial}{\partial x} & 0\\ 0 & \frac{\partial}{\partial z} & \frac{\partial}{\partial y}\\ \frac{\partial}{\partial x} & 0 & \frac{\partial}{\partial z}\end{bmatrix}\begin{Bmatrix}u\\ v\\ w\end{Bmatrix}=\begin{bmatrix}\frac{\partial}{\partial x} & 0 & 0\\ 0 & \frac{\partial}{\partial y} & 0\\ 0 & 0 & \frac{\partial}{\partial z}\\ \frac{\partial}{\partial y} & \frac{\partial}{\partial x} & 0\\ 0 & \frac{\partial}{\partial z} & \frac{\partial}{\partial y}\\ \frac{\partial}{\partial x} & 0 & \frac{\partial}{\partial z}\end{bmatrix}[N]\{\delta\}^e \tag{15}$$

$$[B]=\begin{bmatrix}\frac{\partial}{\partial x} & 0 & 0\\ 0 & \frac{\partial}{\partial y} & 0\\ 0 & 0 & \frac{\partial}{\partial z}\\ \frac{\partial}{\partial y} & \frac{\partial}{\partial x} & 0\\ 0 & \frac{\partial}{\partial z} & \frac{\partial}{\partial y}\\ \frac{\partial}{\partial x} & 0 & \frac{\partial}{\partial z}\end{bmatrix}[N] \tag{16}$$

Where $[N]$ is the shape function, and $\{\delta\}^e$ is the nodal displacement vector.
Therefore, the strain energy is described by

$$\begin{aligned}U^e &= \iiint_V \{\varepsilon\}^T\{\sigma\}\mathrm{d}V = \iiint_V (\{\delta\}^e)^T[B]^T[D][B]\{\delta\}^e\mathrm{d}V\\ &= (\{\delta\}^e)^T\iiint_V [B]^T[D][B]\mathrm{d}V\{\delta\}^e\end{aligned} \tag{17}$$

$$U=\sum_{i=1}^{n}U_i^e \tag{18}$$

Where n is the element number.
As the strain energy contains both stress and displacement, it is reasonable to set the strain energy as an objective function. Table 2 lists the change in the maximum strain energy of SDS before and after the control. From the Table, the strain energies of SDS are 481.7 J and 289.7 J before and after executing the active control strategies, and a significant reduction of 39.9% in strain energy is achieved. The good control efficiency shows that the active control optimizes the structural strain energy, which also demonstrates that both member stresses and nodal displacements are improved.

Table 2. Simulation results before and after control

	Before control	After control
Stain energy of SDS (J)	481.7	289.7

7. Conclusions

In this paper, an active control method for hybrid string structures including the beam string structure (BBS) and suspen-dome structure (SDS) is proposed based on the genetic gradient algorithm (GGA) and multi-population genetic algorithm (MPGA), and the validity of the method is verified by tests and simulations. Some conclusions and salient observations are as follows:
(1) The concept of active control of hybrid string structures is presented by introducing active struts that can change length linearly. An optimization-based control model is established to minimize the active

control objective (e.g., the stress, displacement, and strain energy) to improve the mechanical properties of BBS and SDS.
(2) Standard genetic algorithm (SGA), genetic gradient algorithm (GGA), and multi-population (MPGA) are introduced, and their advantages and disadvantages are also analyzed. Among them, the GGA and MPGA are applied to search the active control strategies of BBS and SDS under loading.
(3) A single-span BBS model with a span and sag of 4 m and 0.68m is developed and constructed for active control research. With the minimization of vertical displacement as the control objective, the active control of the test model is achieved through the use of GGA. Test results indicate that the implementation of active control strategy can significantly reduce the vertical displacement of the beam, and the control process also optimizes the stresses in the beam to some extent.
(4) A bi-directional BBS with the size of 24 m×24 m×2.4 m is used for numerical analysis. With the minimization of stress as the control objective, the active control of the bi-directional BBS is achieved by applying the GGA. Simulation results show that after active control the peak internal forces of the beams are effectively controlled and the beam deformation is also substantially improved.
(5) A Kiewitt SDS with the size of 12 m×12 m×1.2 m is used for numerical analysis. With the minimization of strain energy as the control objective, the active control of the Kiewitt SDS is achieved by applying the MPGA. Simulation results show that the active control optimizes the structural strain energy, which also demonstrates that both member stresses and nodal displacements are improved.

Acknowledgments
The authors gratefully acknowledge the support from the National Natural Science Foundation of China (Grant No. 51578491 and 52238001), and the Funding of Center for Balance Architecture, Zhejiang University.

References
[1] Saitoh, M., and Okada, A. 1999. “The role of string in hybrid string structure.” Eng. Struct. 21 (8): 756-769.
[2] Shen, Y.B., Zheng, J.H., and Luo, Y.Z. 2010. “Experimental study on truss string structure of Beijing North Station.” J. Build. Struct. 31 (11): 51-57.
[3] Chen, Z. H. 2012. “Cable-supported structure system.” Beijing: Science Press.
[4] Organization for Economic Co-operation and Development. 2019. “Global material resources outlook to 2060: Economic drivers and environmental consequences.” France: OECD Publishing.
[5] Korkmaz, S. 2011. “A review of active structural control: Challenges for engineering informatics.” Comput. Struct. 89 (23-24): 2113-2132.
[6] Senatore, G., Duffour, P., and Winslow, P. 2018a. “Exploring the application domain of adaptive structures.” Eng. Struct. 167: 608-628.
[7] Yao, J.T.P. 1972. “Concept of structural control.” J. Struct. Div. 98 (7): 1567-1574.
[8] Soong, T.T., and Manolis, G.D. 1987. “Active structures.” J. Struct. Eng. 113 (11): 2290-2302.
[9] Xu, Z.D., Shen, Y.P., and Guo, Y.Q. 2003. “Semi-active control of structures incorporated with magnetorheological dampers using neural networks.” Smart Mater. Struct. 12 (1): 80-87.
[10] Li, G., and Fahnestock, L.A. 2013. “Seismic response of single-degree-of-freedom systems representing low-ductility steel concentrically braced frames with reserve capacity.” J. Struct. Eng. 139 (2): 199-211.
[11] Cao, L.Y., and Li, C.X. 2018. “Enhanced hybrid active tuned mass dampers for structures.” Struct. Control. Health Monit. 25 (2): e2067.
[12] Zhang, D.H., Zhao, X.J., Han, J.D., Li, X.G., Zhang, B. 2019. “Active modeling and control for shape memory alloy actuators.” IEEE Access. 7: 162549-162558.
[13] Pellegrino. S. 2001. “Deployable structures.” New York: Springer Wien.
[14] Jenkins. C.H.M. 2005. “Compliant structures in nature and engineering”. Boston: WIT Press.
[15] Lienhard, J., Schleicher, S., Poppinga, S., Masselter, T., Milwich, M., Speck, T., and Knippers, J. 2012. “Flectofin: a hingeless flapping mechanism inspired by nature.” Bioinspir. Biomim. 6 (4):

045001.
[16] Senatore, G., Duffour, P., and Winslow, P. 2019. "Synthesis of minimum energy adaptive structures." Struct. Multidiscip. Optim. 60 (3): 849-877.
[17] Senatore, G., Duffour, P., and Winslow, P. 2018. "Exploring the application domain of adaptive structures." Eng. Struct. 167: 608-628.
[18] Reksowardojo, A.P., Senatore, G., and Smith, I.F.C. 2020. "Design of structures that adapt to loads through large shape changes." J. Struct. Eng. 146 (5): 04020068.
[19] Reksowardojo, A.P., Senatore, G., Srivastava, A., Carroll, C., and Smith, I.F.C. 2022. "Design and testing of a low-energy and -carbon prototype structure that adapts to loading through shape morphing." Int. J. Solids. Struct. 252: 111629.
[20] Wang, Y.F., and Senatore, G. 2020. "Minimum energy adaptive structures - All-In-One problem formulation." 236: 106266.
[21] Wang, Y.F., Xu, X., and Luo, Y.Z. 2021. "Minimal mass design of active tensegrity structures." Eng. Struct. 234: 111965.
[22] Korkmaz, S.; Ali, N.B.H.; and Smith, I.F.C. 2011. "Determining control strategies for damage tolerance of an active tensegrity structure." Eng. Struct. 33 (6): 1930-1939.
[23] Korkmaz, S.; Ali, N.B.H.; and Smith, I.F.C. 2012. "Configuration of control system for damage tolerance of a tensegrity bridge." Adv. Eng. Inform. 26 (1): 145-155.
[24] Fest, E., Shea, K., Domer, D., and Smith, I.F.C. 2003. "Adjustable tensegrity structures." J. Struct. Eng. 129 (4): 515-526.
[25] Lu, J.Y., and Lu, M. 2017. "Application of ant colony algorithm in internal force control of adaptive cable dome." J. Southeast Univ. (Nat Sci Ed). 47 (6): 1161-1166.
[26] Kmet, S., and Mojdis, M. 2015. "Adaptive cable dome". J. Struct. Eng. 141 (9): 04014225.
[27] Wu, M.E. 2008. "Analytical method for the lateral buckling of the struts in beam string structures." Eng. Struct. 30(9): 2301-2310.
[28] Chen, D.S., Xu, W.C., Qian, H.L., and Wang, H.J. 2021. "Thermal behavior of beam string structure: Experimental study and numerical analysis." J. Build. Eng. 40: 102724.
[29] Chen, F., Li, Q.S., Wu, J.R., and Fu, J.Y. 2011. "Wind effects on a long-span beam string roof structure: Wind tunnel test, field measurement and numerical analysis." J Constr. Steel Res. 67(10):1591-1604.
[30] Xue, W.C., and Liu, S. 2009. "Design optimization and experimental study on beam string structures." J. Constr. Steel. Res. 65(1): 70-80.
[31] Cai, J.G., Feng, J., and Jiang, C. 2014. "Development and analysis of a long-span retractable roof structure." J. Constr. Steel. Res. 92: 175-182.
[32] Lee, S., Seo, M., Baek, K.Y., Jeong, J., Kim, S.M., and Lee, J. 2019. "Experimental study of two-way beam string structures." Eng. Struct. 191: 563-574.

IASS 2023
July 10–14 Melbourne
Integration of Design and Fabrication

Proceedings of the IASS Annual Symposium 2023
Integration of Design and Fabrication
10–14 July 2023, Melbourne, Australia
Y.M. Xie, J. Burry, T.U. Lee and J. Ma (eds.)

Application of partial factors to actions in case of membrane structures

Wolfram JÄGER[a,*], Tammam BAKEER[a], Andreas NIEMEIER[b]

[a,*] Planungs- und Ingenieurbüro für Bauwesen Radebeul
Wichernstr. 12, D-01445 Radebeul, Germany
w.jaeger@jaeger-ingenieure.de

[b] Dlubal Software GmbH
Am Zellweg 2, D-93464 Tiefenbach, Germany
support@dlubal.com

Abstract

The use of partial safety factor method has become a prevalent practice in designing membrane structures. However, the application of standard partial safety factors for actions presents a challenge as membrane structure calculations are inherently nonlinear. If the relative increase in the effect of action exceeds the relative increase in the action itself, the solution is straightforward: apply the partial safety factors to the actions before calculating their effects. However, membrane and cable structures often include elements or areas where the relative increase in effect is less than the relative increase in action, raising concerns about safety deficits. In 1960, Basler's conclusion [2] was somewhat empirical, as the highly nonlinear nature of the problem made it impossible to simply calculate the safety index for the ultimate limit state function. The presumed safety deficit was incorporated into the Basis of Structural Design according to EN 1990:2012 [1], with further explanation provided by *Calgaro, Gulvanessian, and Holický* in the background document [3]. This standard suggests that, when relative increase in the effect is less than the relative increase in action, effect should be calculated first and then multiplied by their corresponding partial safety factor before conducting the verification. During the recent revision and expansion of EN 1990, some engineers working on membrane structure design raised objections [4]. The authors were able to resolve this issue prior to the introduction of prEN 1990:2022 [5] in practice, thus simplifying the process and promoting practical acceptance.

Keywords: architectural membranes, verification, partial safety factors, hybrid structures, non-linear behaviour, semi-probabilistic approach, reliability, Eurocodes, basis of design.

1. Introduction

EN 1990:2012 [1] provides guidelines, under provision 6.3.2.(4), on how to handle partial factors when dealing with non-linear problems and in special cases such as cable and membrane structures:

> (4) For non-linear analysis (i.e. when the relationship between actions and their effects is not linear), the following simplified rules may be considered in the case of a single predominant action:
>
> a) when the action effect increases more than the action, the partial factor g_F should be applied to the representative value of the action. (over-linear behaviour)
>
> b) When the action effect increases less than the action, the partial factor g_F should be applied to the action effect of the representative value of the action. (under-linear behaviour)

Copyright © 2023 by Wolfram JÄGER, Tammam BAKEER and Andreas NIEMEIER. Published in the Proceedings of the IASS Annual Symposium 2023 with permission.

NOTE Except for rope, cable and membrane structures, most structures or structural elements are in category a).

Figure 1 illustrates how to interpret these provisions. According to the Note, cable and membrane structures are generally classified as exhibiting under-linear behavior, and most other structures or structural elements are classified as exhibiting over-linear behavior. However, this categorization may not always be applicable, particularly in the case of membrane structures, where both under-linear and over-linear behaviors may be observed depending on the specific design conditions. Additionally, non-linear structures may exhibit both under-linear and over-linear behavior at different design points, making it difficult to classify them under a single unique category.

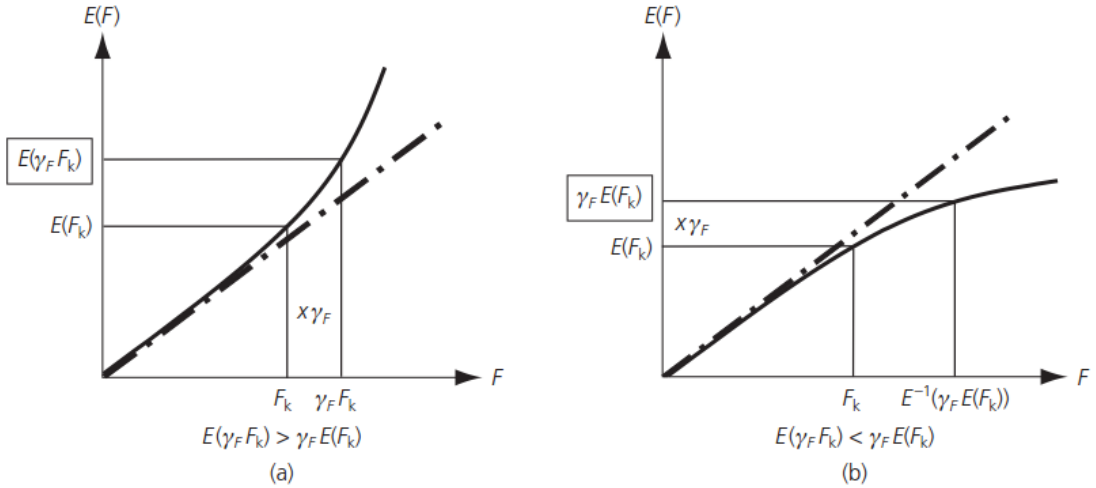


Figure 1. Application of the partial factor γ_F in the case of non-linear analysis (single action). (a) The non-linear action effect $E(\gamma_F F_k)$ increases more than the linear action effect $\gamma F_E(F_k)$ proportional to the action. (b) The non-linear action effect $E(\gamma_F F_k)$ increases less than the linear action effect $\gamma F_E(F_k)$ proportional to the action [3].

During the revision and extension of the standard, the corresponding passages in EN 1990 were subjected to a more detailed examination by the authors [6–8]. They started from the following hypothesis:

Hypothesis:

The safety is influenced by both:
1) The nonlinearity which is a characteristic of the system at the design point and it is preserved with the system;
2) The statistical properties of the basic parameters (normally characterized by the coefficient of variation and the distribution).

2. Nonlinearity and safety

The initial question to be addressed how the level of non-linearity in a structural system influences its reliability index. To address this, we employed the Monte Carlo method to ascertain the reliability index for varying degrees of non-linearity *n*

$$n = \frac{E(\gamma_F \cdot F_k)}{\gamma_F \cdot F_k} \quad (1)$$

taking into account the effect of different materials and actions (Figure 2).

The partial safety factors of actions γ_F were applied on the action side, regardless of the system's over-linear or under-linear behavior. The blue lines or points represent the Monte Carlo simulation (MCS) results for each combination of material and action. The red lines correspond to the maximum and minimum possible values of the reliability index β. The vertical dashed line separates the under-linear behavior from the over-linear behavior. The horizontal dashed black line corresponds to the value $\beta = 3.8$, which is the target reliability index.

The range between the two vertical lines, from $n = 0.8$ to 1.5, represents the safe range as it results in $\beta > 3.8$ for all possible combinations of materials and actions. For non-linear problems with $n < 0.8$, applying the partial safety factors on the action side results in unsafe outcomes. The behavior over the dashed red line on the right side is asymptotic, which means it tends not to deviate far from $\beta = 3.8$. This confirms the correctness of applying on the action side, without incurring any safety risk as previously assumed in [2].

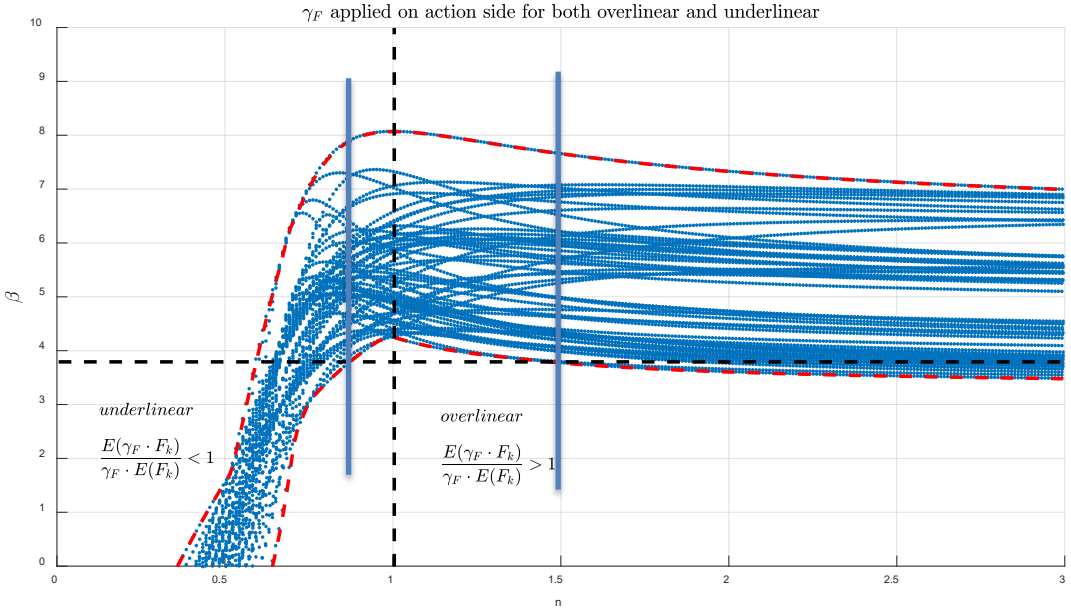


Figure 2. The variation of the reliability index ß with respect to the degree of nonlinearity n for different material-action combinations.

The subsequent phase involved identifying the areas in construction practice where non-linearities may emerge, particularly in cable and membrane structures. To accomplish this, we employed a simple cable system, as illustrated in Figure 3, to conduct our investigation.

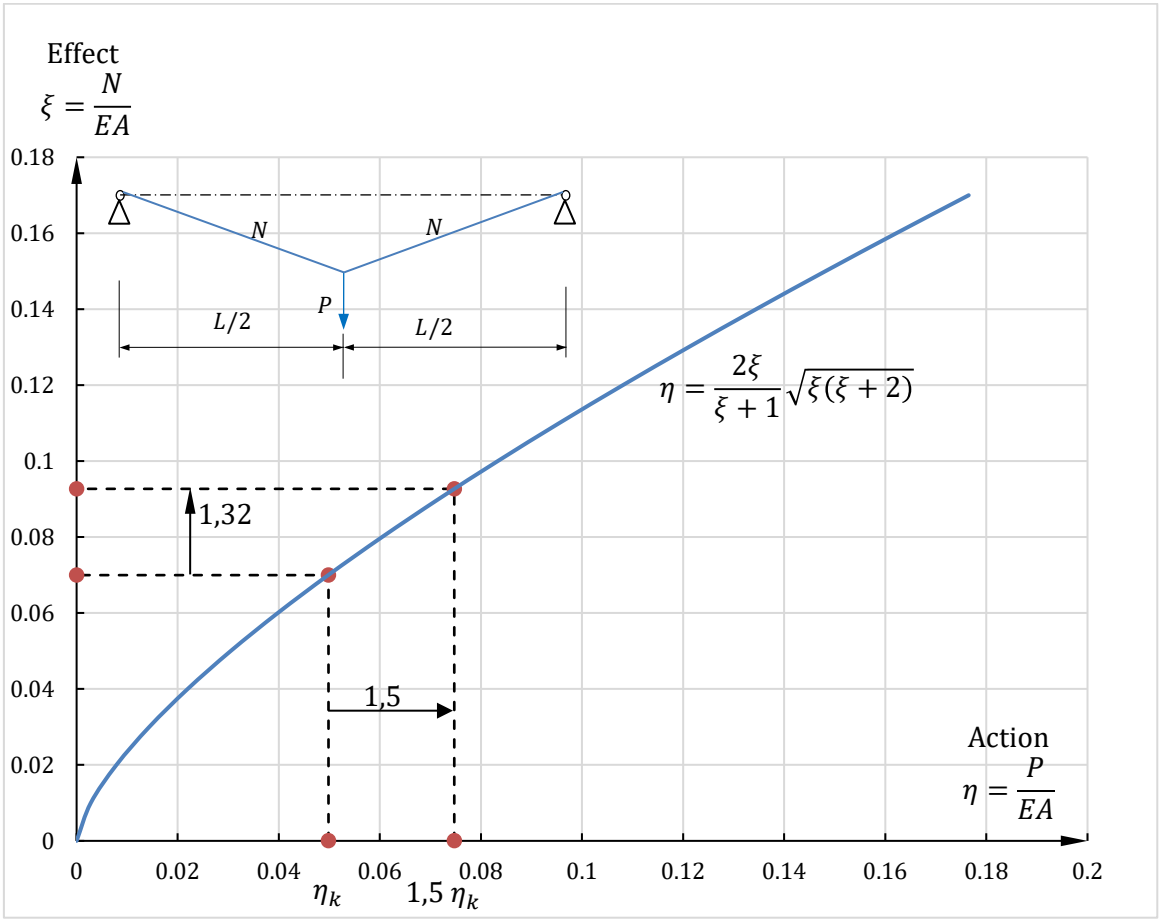


Figure 3. Horizontal cable with one vertical force. Representation of the effect and action relationship.

The system is deemed under-linear at every possible action point, as per the definition provided in 6.3.2 (4) of EN 1990:2012 [1]. This characteristic is evident in Figure 4, where the degree of nonlinearity is plotted against several characteristic actions.

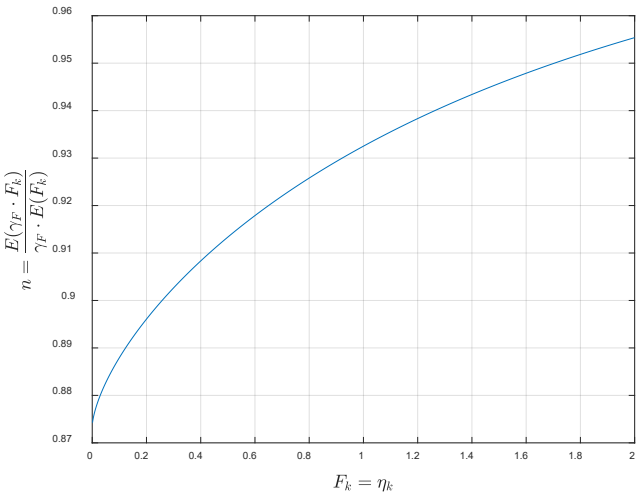


Figure 4. Calculation of degree of nonlinearity *n* at several characteristic loads.

The information conveyed by Figure 4 is crucial for interpreting the results of the reliability analysis presented in Figure 2 for cable and membrane structures in general. Specifically, Figure 4 shows that the degree of nonlinearity (n) for the cable system does not fall below 0.87.

Figure 5 illustrates another example of a simple double cable system created by simplifying a hyperbolic membrane, which has been previously discussed in the literature [6].

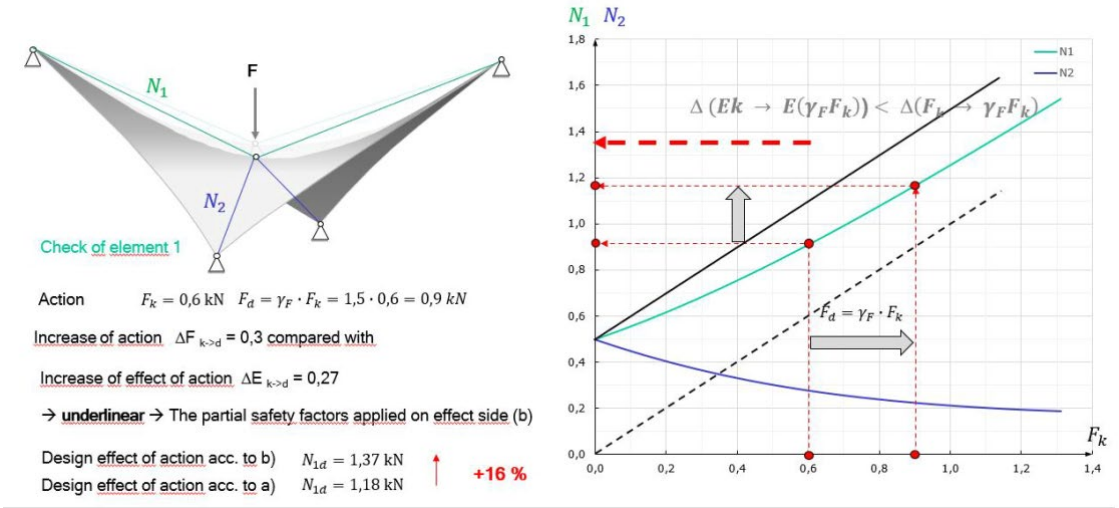


Figure 5. Simplified membrane structure and check of element 1 with concrete figures.

In case of element 1 the provisions of EN 1990:2010, 6.3.2 (4) lead to an over-design, which cannot be justified by the point of view of safety (see Figure 5; red dashed line).

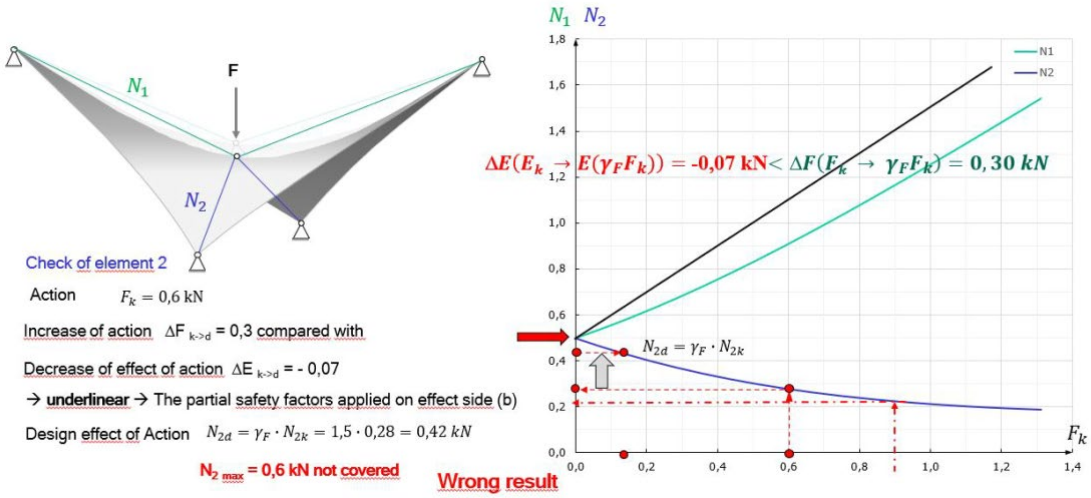


Figure 6. Simplified membrane structure and check of element 2 with concrete figures.

Conversely, applying the same provisions to Element 2 misleads the applicant (see Figure 6).

A closer examination of the non-linear effect course of Element 2 in Figure 5 suggests the need to determine whether the decisive design point is still being met or if another load combination should be

verified instead. The example of pre-tensioning in membrane structures serves as a relevant illustration. While Element 2 must be verified in the ultimate limit-state for the highest internal force that arises, it is essential to ensure that the structure does not experience folds or withdraw from the force distribution during relaxation. This state is more likely to be associated with the verification of serviceability.

Bakeer in his general theory [7–8] provides a compelling mathematical and theoretical proof that validates the hypothesis advanced by the authors. This important result serves to further confirm the accuracy of the hypothesis and solidifies its significance in the field of cable and membrane structures.

3. Example

A simple hyperbolic paraboloid example demonstrates that the regulations regarding the factoring of effects instead of actions, which were previously included in EN 1990:2010, are impractical and cannot be executed strictly. Instead, it is correct to always allocate partial safety factors to actions before calculating their effects. This necessitates the distinction between favorable and unfavorable actions, including those related to prestressing.

3.1. Input data

3.1.1. Geometry and Materials

Figure 7 presents an example of a membrane structure, where the membrane is stretched between boundary cables running between the top and bottom points. The top points are supported by steel columns, which are in turn stabilized by three cables each.

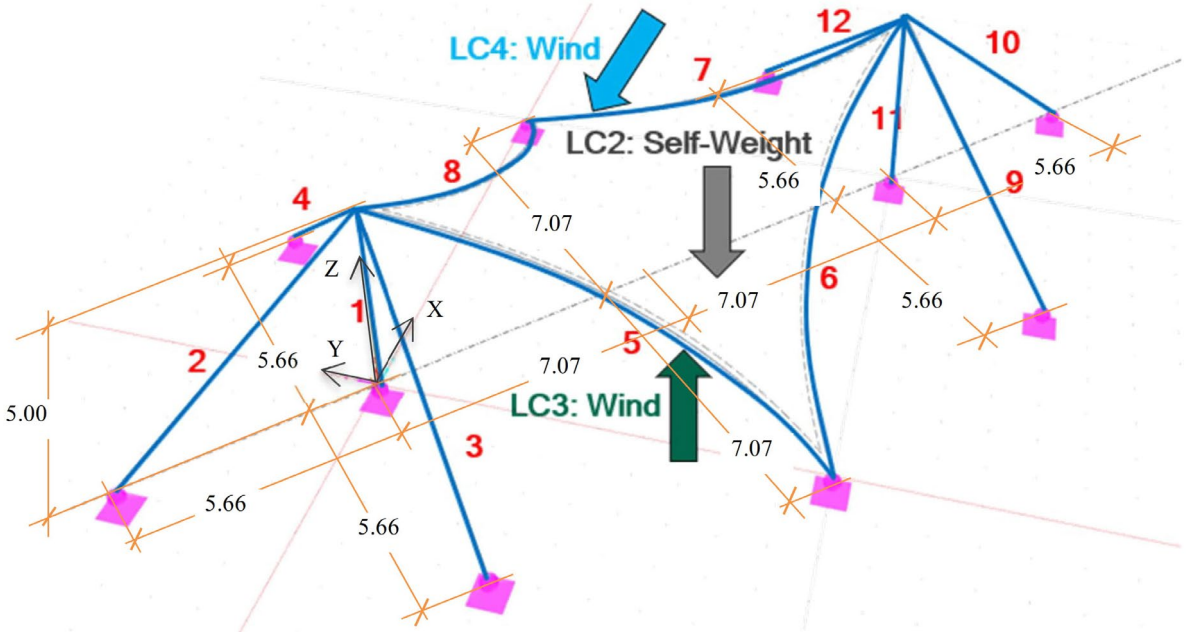


Figure 7. Geometry and load cases used as input for the Dlubal RFEM 6.0.

The material data are given in Table 1.

Table 1. Material data.

No.	Structural member		Type	Dimension / Area / Inertia	E-Mod	G-Mod.	ν	Specific weight
					[N/mm²]	[N/mm²]	[--]	[kN/m³]
1	column	1, 11	A36 (AISC 360-16) CHS 250/4.8/H	It=5544.90 cm² Iy=Iz=2783.88 cm² A=36,98 cm²	199948	77221	0,295	78,49
2	cable	2, 3, 4, 5, 6, 7, 8, 9, 10, 12	Cable PE Pfeiffer	A=1,54 cm² It=0,38 cm4 Iy=Iz=0,19 cm4	130000	50000	0,3	80,00
3	membrane	membrane between 6, 7, 8, 9	PES-PVC (theoretical assumed, orthotropic)	d= 2 mm	448	153	0,464	10,70

3.1.2. Load cases & load combinations

The principal load cases considered, namely LC1: pre-stressing, LC2: self-weight, LC3: suction wind, and LC4: side wind, are depicted in Figure 7 and given in Table 2.

Favorable and unfavorable values are presented for both LC1 and LC2. However, only unfavorable values are provided for the actions in LC3 and LC4. Although the wind load case's actions were manually introduced for this example, there are more efficient ways to determine them, such as utilizing specialized software like the "wind tunnel" software [9].

Table 2. Magnitudes of actions considered.

Actions	Direction (local, global)	Magnitude
LC 1: Prestressing	local	$L_{c,rel}$=102% (6, 7) $L_{c,rel}$=102,65% (4, 5, 10, 11, 12, 13), membrane 1,0 kN/m
LC 2: Self weight	Z global	automatically considered
LC 3: Wind	Z global	0,2 kN/m²
LC 4: Wind	X global	-0,2 kN/m²

3.2. Results

In accordance with the provisions of EN 1990:2010, 6.3.2 (4), the analysis was conducted in two ways:

- Determining the effects of unfactored actions and then factoring those determined effects.
- Factoring the actions and then determining the effects of the factored actions.

An overview of some of the results obtained from these two methods is shown in Figure 8.

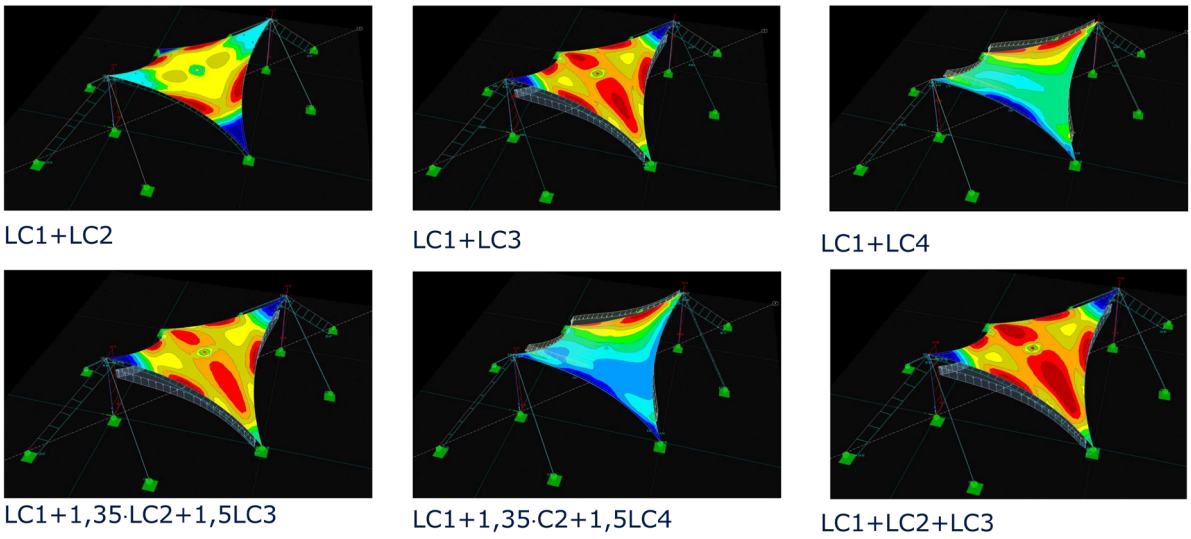


Figure 8. Results of the load combinations in Dlubal RFEM 6.0 [10]:
The top row shows the effects without factoring in the actions, whereas the bottom row presents the effects with the action factors accounted for.

It's crucial to note that load case 1 and load case 2 cannot be regarded as separate load cases due to stability considerations. Instead, they are jointly computed as part of the form-finding process when designing membrane structures. Without prestressing, it's impossible to independently analyze LC2, LC3, and LC4 load cases as the structure's stability relies on the prestressing load.

Table 3 and Table 4 demonstrate that LC 1 + LC 2 indicate that prestressing is taken into account as the initial form. Conducting separate calculations of load cases without prestressing is unfeasible due to the structure's instability.

Table 3. Results of the effects without factoring of the actions.

Effect	N1	N2	N3	N4	N5	N6	N7	N8	N9	N10	N11	N12
LC1	27.77	26.57	0.04	0.04	11.09	11.09	11.09	11.09	0.04	26.57	27.77	0.04
LC2	x	x	x	x	x	x	x	x	x	x	x	x
LC3	x	x	x	x	x	x	x	x	x	x	x	x
LC4	x	x	x	x	x	x	x	x	x	x	x	x
LC1+LC2	28.05	27.31	0.03	0.03	17.61	17.61	17.61	17.61	0.03	27.31	28.05	0.03
LC1+LC3	21.65	17.62	4.46	0.03	3.02	12.22	22.25	12.99	5.12	39.26	43.78	0.03
LC1+LC4	33.01	29.39	1.54	1.54	12.34	12.34	12.34	12.34	1.54	29.39	34.45	1.54

Due to instability, it is impossible to determine the effect

Table 4. Results of the effects with factoring of the actions.

Effect	N1	N2	N3	N4	N5	N6	N7	N8	N9	N10	N11	N12
LC1	27.77	26.57	0.04	0.04	11.09	11.09	11.09	11.09	0.04	26.57	27.77	0.04
LC2	x	x	x	x	x	x	x	x	x	x	x	x
LC3	x	x	x	x	x	x	x	x	x	x	x	x
LC4	x	x	x	x	x	x	x	x	x	x	x	x
LC1+1.35LC2+1.5LC3	30.69	25.47	1.84	1.84	18.79	18.79	18.79	18.79	1.84	25.47	30.69	1.84
LC1+1.35LC2+1.5LC4	25.56	17.29	6.16	1.03	1.67	11.74	29.83	13.8	8.68	48.72	58.45	0.86

Due to instability, it is impossible to determine the effect

In order to be able to apply the specifications of EN 1990:2010 6.3.2 (4), we assume that the initial state is defined with the form finding and that the individual loads are then applied separately to this (see Table 3). The results – the effects - are then multiplied by the partial load factors and combined into the respective load combination. These numbers are now compared with the result of the calculation of the membrane with factored and combined actions (see Table 4).

In case of member 1 and the combination of the effects of prestressing, self-weight and horizontal wind leads to the following effects:

Application of the combination on the effect

28.05	*1,35+	33,01	*1,5 =	87,38	≫	25,56

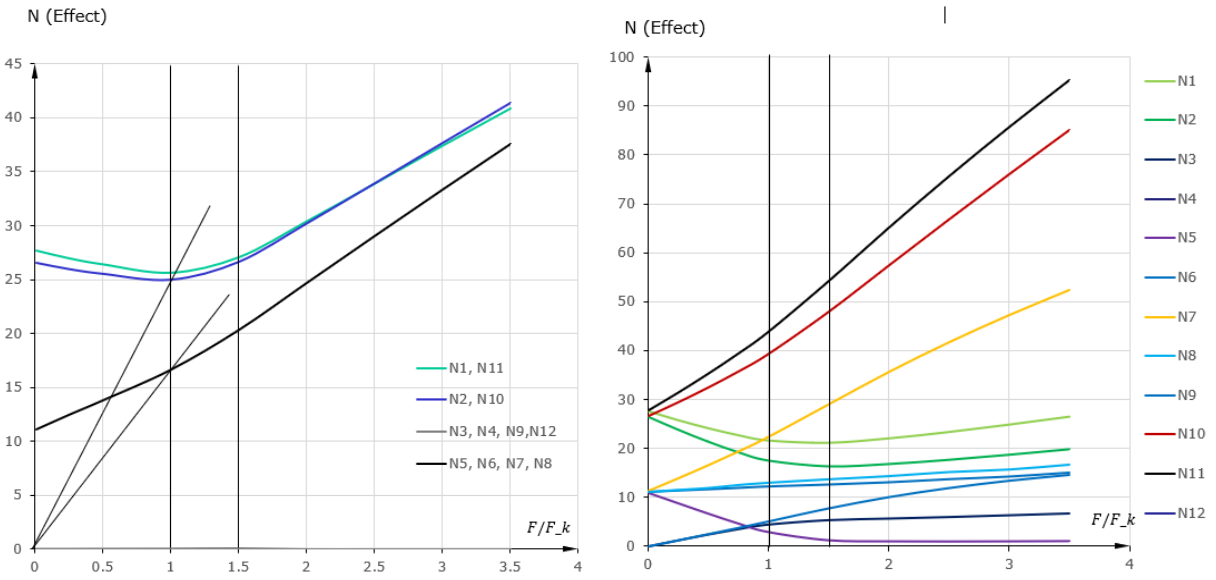
The combination of the effects for member 1 therefore results in significantly larger values than the combination of the factored actions. In case of member 9 this leads to inverse effects:

Application of the combination on the effect

0.03	*1,35+	1.54	*1,5 =	2,35	<	8,68

The combination of effects for member 9 results in significantly lower values than the combination of factored actions.

The recommended way of applying the partial factors of EN 1990:2010 can be misleading as shown by the fact that if one factors the initial state of self-weight with prestressing by 1.35, it leads to a simultaneous increase in the prestressing and does not account for any loss or uncertainty of the prestress. Moreover, the ratio of prestress to dead weight is not proportional.



(a) (b)

Figure 9. Effect-Action curves as the action increases (a) increasing the wind action LC3, (b) increasing the wind action LC4.

Figure 9 presents the effect-action curves for all the key elements in the considered membrane structure. The following observations can be made:

1- The safety contribution of the action is dependent on the design point. For instance, in Figure 9 (a) under LC3, the effect in element 1 and 11 initially decreases as the wind load LC3 increases, then it increases. This indicates that the LC3 increase was favorable in the initial loading stage and later became unfavorable. This reaffirms that the safety assessment should be based on the system's non-linearity and design points.
2- The behavior of the membrane structure cannot be classified as under-linear. Many of the plotted effect-action curves in Figure 9 (a) and (b) indicate that both behaviors are possible, and this must be verified at the design point.
3- Over-linearity and under-linearity are typically used to describe the impact of unfavorable loads. However, the behavior under favorable loads can also exhibit both over- and under-linearity.

4. Conclusions

The paper highlights a misleading provision in the EN 1990:2010 guidelines regarding the application of partial safety factors to membrane structures. The definitions provided for over-linearity and under-linearity are based solely on the comparison of the increase of the effect with the increase of action, which differs from the mathematical definition in the background document [3].

Typically, membrane structures involve multiple actions with different partial safety factors. If the system is found to be underlinear according to EN 1990:2010, and the partial safety factor should be applied to the effect side, determining the appropriate partial safety factor becomes challenging. Even if the partial safety factor of the leading action is applied to the effect side, it could produce unsafe results, especially if the actions involved in the system have different statuses (favorable and unfavorable), which is quite common in membrane structures.

Furthermore, the over-linearity and under-linearity alone do not sufficiently characterize a nonlinear system without considering the design point. However, under the practically existing range of nonlinearity, applying partial safety factors on the action side is sufficient to achieve the target reliability index. This applies to both over-linear and under-linear cases.

Moreover, the study suggests that the exception for membrane and cable structures in clause 8.3.2.4(a) of FprEN 1990 is unnecessary, and the provisions for these structures in EN 1990:2010 are outdated and not expedient. The recommended approach of applying partial factors can be misleading as it fails to account for the loss or uncertainty of the prestress, leading to a disproportionate increase in the prestressing compared with the dead load. The aim of the contribution was to confirm the validity of the first part of the starting hypothesis.

These findings emphasize the importance of revising current guidelines to ensure accurate and reliable design values for membrane structures. Therefore, it is recommended that future research addresses the issues highlighted in this study to improve the safety and reliability of structural designs.

Acknowledgements

The study's findings were the result of a combination of our own research at the office and investigations conducted by Tammam Bakeer, utilizing Dlubal RFEM 6.0 [10] software to analyze the membrane example. We express our sincere appreciation to Dlubal Software GmbH Tiefenbach for their valuable support and collaboration throughout this work.

References

[1] EN 1990: 2012: Eurocode: *Basis of structural design*. CEN, Brussels 2010.

[2] E. Basler, *Untersuchungen über den Sicherheitsbegriff von Bauwerken*. Diss. ETH Zürich. Solothurn: Vogt-Schild AG, 1960.

[3] H. Gulvanessian, J.-A. Calgaro and M. Holický, *Designers' Guide to Eurocode: Basis of Structural Design EN 1990*. Second edition. London: Thomas Telford Limited; 2012.

[4] N. Stranghöner, J. Uhlemann et al., *Scientific and Policy Report „Background Documentation for a European Structural Design of Tensile Membrane Structures Made from Fabrics and Foils".* CEN/TC 250/WG 5 Membrane Structures. 10th Draft, 13th of February 2015, JRC 2015.

[5] FprEN 1990:2021: *Eurocode - Basis of structural and geotechnical design*; CEN / TC 250 / SC 10, Brussels 2022.

[6] T. Bakeer and W. Jäger, *The underlinear problem of systems with cable elements.* Unpublished working document, Ad-hoc-group "Reliability background of prEN 1990:2021" of CEN/TC 250/ SC10, 10.09.2021.

[7] T. Bakeer, General partial safety factor theory for the assessment of the reliability of nonlinear structural systems. *Reliability Engineering & System Safety* 2023:109150. https://doi.org/10.1016/j.ress.2023.109150

[8] T. Bakeer, *The theory of homogeneity of nonlinear structural systems - A general basis for structural safety*. https://arxiv.org/abs/2212.01423. 31.12.2022

[9] *Program RWIND2* - PC-Progress s.r.o., Dlubal Software GmbH und CFD Support s.r.o. - https://www.dlubal.com/de/produkte/eigenstaendige-statiksoftware/rwind

[10] *Program RFEM 6* - Dlubal Software GmbH - https://www.dlubal.com/de/produkte/fem-statik-software-rfem/was-ist-rfem

IASS 2023
July 10–14 Melbourne
Integration of Design and Fabrication

Proceedings of the IASS Annual Symposium 2023
Integration of Design and Fabrication
10–14 July 2023, Melbourne, Australia
Y.M. Xie, J. Burry, T.U. Lee and J. Ma (eds.)

Construction of developable freeform membrane tensegrity structures

Yuta SHIMODA[a,*], Sei HAYASHI[b], Hiroki AWAJI[c], Taichi NAKAMURA[b], Haruto KAMIJO[b], Tomoyuki GONDO[b], Tomohiro TACHI[b], Jun SATO [a,*]

[a,*] Jun Sato Structural Engineers Co. Ltd.
simo4mo314@gmail.com

[b] The University of Tokyo
[c] Asahi Building-Wall Co., Ltd.

Abstract

The construction of complex buildings, such as tensegrity structures and freeform shapes, can be costly, labor-intensive, and time-consuming due to the challenge of reproducing the geometry of the shape and assembling the structure. This paper proposes an automation method for designing arbitrary freeform tensegrity structures by solving the inverse problem using freeform origami tessellations. This approach allows for easy construction of freeform tensegrity structures by even unskilled workers, using a single planar membrane as a guide. Developable membrane tensegrity structures are structures formed from single planar membranes used as tensile and struts used as compression members. They have advantages in manufacturing in that freeform surfaces can be erected by simply attaching struts to a single planar membrane while applying initial tension. We propose a design method of membrane tensegrity structures by solving the inverse problem using freeform origami tessellations by generalizing Resch's patterns proposed by Tachi [1]. In this paper, we demonstrate the feasibility of our method by constructing a full-scale mock-up. Specifically, we place the mountain creases of the tessellation with struts and the other parts with a membrane under initial tension, and show the tessellation can be formed as a tensegrity structure. In constructing the structure, we sewed pockets, shorter in length than compression members, into the mountain creases and applied tensile force across the membrane by inserting carbon fiber reinforced plastic (CFRP) rods as the compression members while pulling the membrane material. Since the joints between the CFRP rods and the basement are at an arbitrary angle, we created rotatable joints by three-dimensional (3D) printing. After inserting the CFRP rods, we clamped them to create a single, freely rotatable joint. Finally, we measured the coordinates of each joint of the structure with a three-dimensional laser distance meter. We compared them with the design model to assess the reproducibility of its geometry.

Keywords: membrane structure, freeform shape, origami tessellation, Resch's pattern, structural optimization

1. Introduction

Developable membrane tensegrity structures are tensegrity structures formed from single planar membranes used as the tensile member and struts used as the compression members. They have advantages in the manufacturing process as they can be constructed in planar states by laying out struts on a single pre-tensioned membrane and erected by releasing the pretensions. Several methods for "forward problems" to find the output, i.e., the three-dimensional resulting shape from the input, i.e., a two-dimensional layout pattern have been proposed.

Copyright © 2023 by Yuta SHIMODA, Sei HAYASHI, Hiroki AWAJI, Taichi NAKAMURA, Haruto KAMIJO, Tomoyuki GONDO, Tomohiro TACHI and Jun SATO. Published in the Proceedings of the IASS Annual Symposium 2023 with permission.

However, the inverse problem, i.e., designing the planar pattern when the target shape is given, has not been solved. In this paper, we propose a design method of membrane tensegrity structures by solving the inverse problem using freeform origami tessellations by generalizing Resch's patterns proposed by Tachi (2013).

2. Related works

Several methods for “forward problems” to find the three-dimensional resulting shape from a two-dimensional layout pattern have been proposed.

One example is the MOOM Pavilion [2], created by students of the Tokyo University of Science under the supervision of Kazuhiro Kojima and Jun Sato(Ratschke et al. [3]). They developed a staggered arrangement of parallel struts and a tunnel-like structure with arches in the direction parallel to the struts and cables pulling in the transverse direction. The pavilion consists of 131 aluminum tubes and an elastic polyester mesh, and was successfully constructed as an 8 x 26 m.

Shigematsu et al. [4] presented the the basic configurations of Diamond and Zigzag models and confirmed that this structure could be established by static non-linear finite element analysis.Gupta et al. [5] extended the designable structure by placing compression struts in a reciprocal pattern on the membrane. They also demonstrated a workflow for accurately producing knits using CNC-produced knittings as the main tensile element. The process of creating these structures is form-finding through mechanical simulation and model making, solving forward problems to determine what 3D shape can be obtained from a given 2D strut pattern.

However, the inverse problem, i.e., designing the planar pattern when the target shape is given, has not been solved. In this paper, we propose a design method of membrane tensegrity structures by solving the inverse problem using freeform origami tessellations by generalizing Resch's patterns proposed by Tachi [1].

3. Geometry

In this study, we aim to make use of the universality of computational origami design, i.e., origami-based patterns can be computed for given polyhedral meshes for the design of membrane tensegrity structures that can be deployed from flat states. Specifically, we show that if we generate an origami tessellation by generalizing Resch's patterns proposed by Tachi, and replace the mountain crease of the tessellation with struts and the other parts with a membrane under initial tension, the tessellation can be formed as a tensegrity structure (Figure1).

The flow of membrane tensegrity structure generation is as follows,

1. Provide a target shape as a polyhedral mesh.
2. Origamise, i.e., apply the algorithm of Tachi [1]to create a generalized Ron-Resch pattern. We choose star-shaped wrinkle patterns inserted on the edges of the given mesh and let the corrugated surface be developable using an optimization scheme. Here, either Freeform Origami (Tach[1]) or Crane (Suto et al.[6])can be used for optimization calculations.
3. Replace the mountain crease lines of the obtained mesh with compression members and the other creases with tension members under initial tension by setting the target length to its scaled version by some scale factor $s<1$ (empirically chosen $s \fallingdotseq 0.90$). Support points are provided around the boundary of the mesh. To obtain the equilibrium position, we use dynamic relaxation. Kangaroo2 (Piker[7]) was used in our analysis.

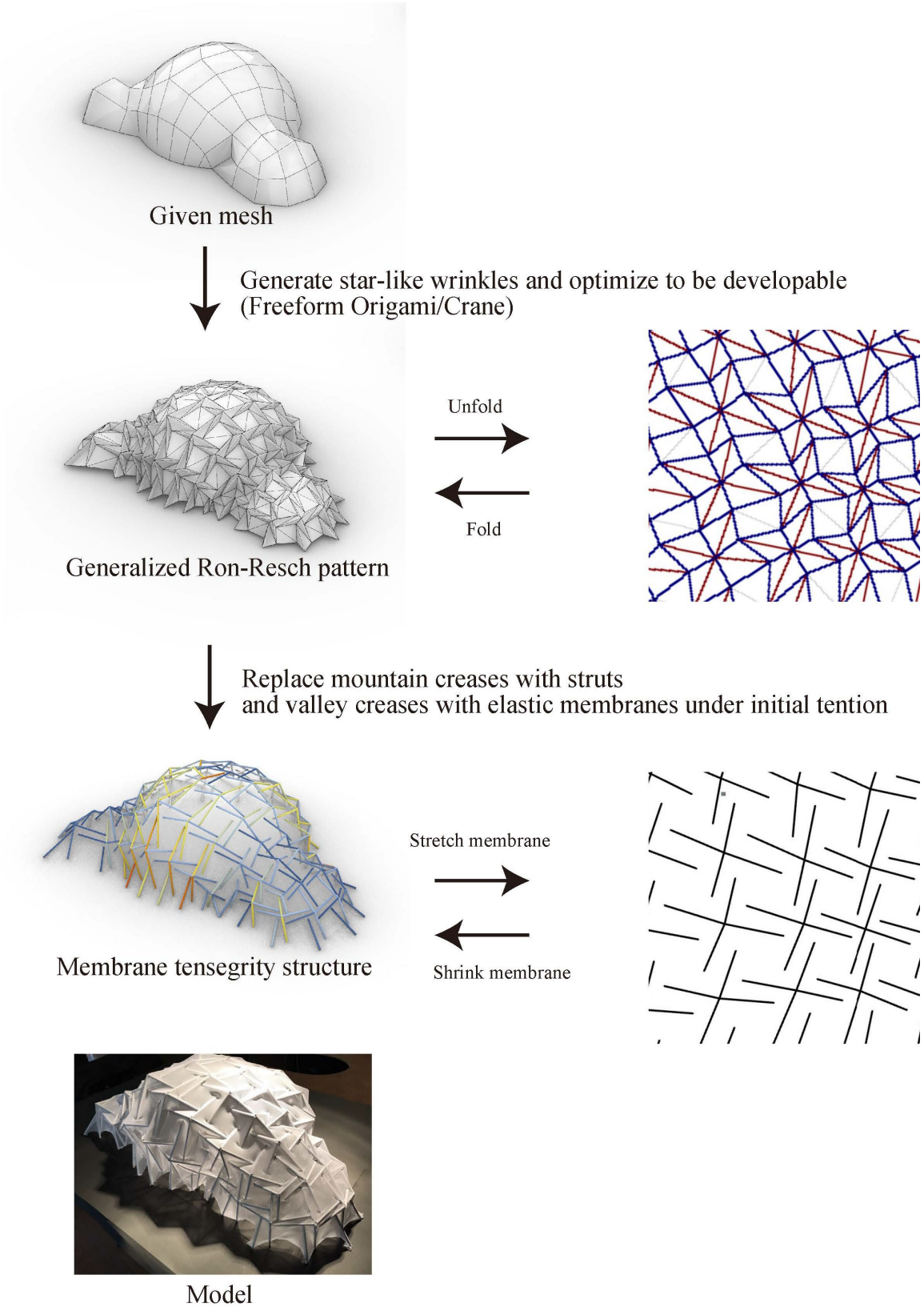


Figure 1. The process of solving inverse program of a membrane tensegrity structure.

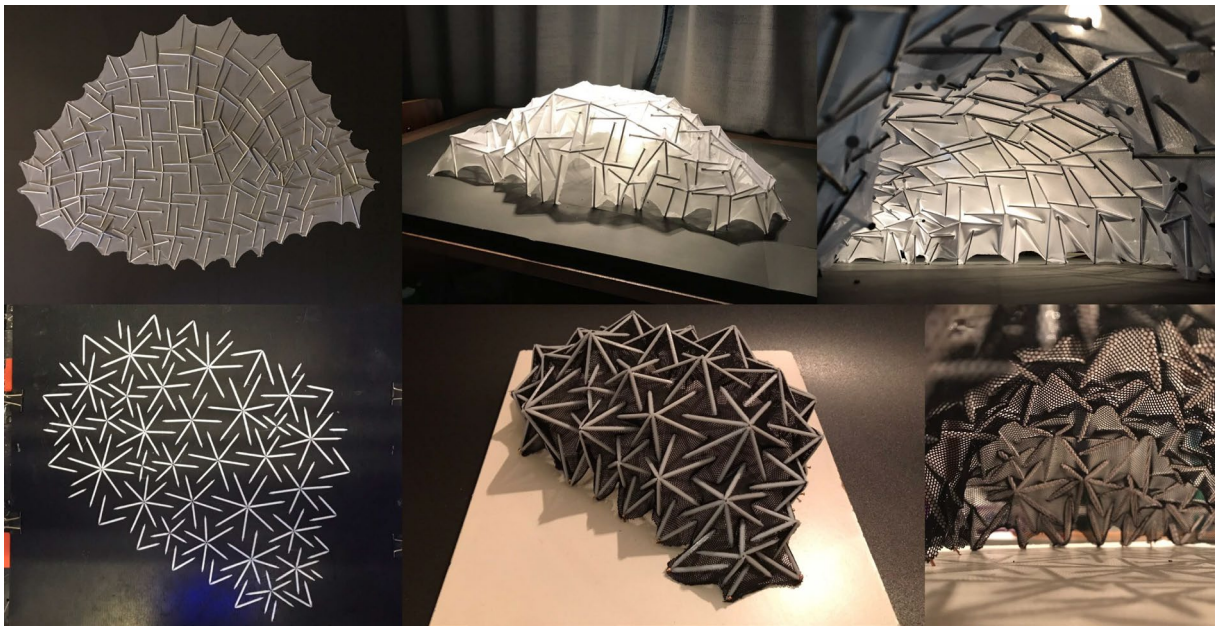


Figure 2. Process of model making. (Top left) Fixing aluminum pipes to stretched stretchable nylon cloth. (Top right) When the boundary is cut out and the foot is fixed, the structure stands up in the same shape as the given curved surface. (Bottom left) 3D printing PLA directly onto stretched stretchable nylon fabric.(Bottom right) When the boundary is cut out and the foot is fixed, a structure with the same shape as the given curved surface rises up.

After verifying the form under equilibrium, we stretch the membrane in a planar state by some scale factor 1/s and attach rigid material along the mountain creases of the crease pattern. Here, for a small-scale model, the attachment of rigid bars can be replaced by 3D printing directly to the membrane as in Tibbits [8]; Jourdan et al. [9](Figure2). We release the prestress by cutting out the boundary of the crease pattern; then the membrane's tension produces the curvature and after a small adjustment and the pinning at the support point. We obtain the desired membrane tensegrity structure.

A feature of this structure is that the star shaped “spikes” can snap-through. It is important to avoid snap-through because it can lead to the collapse of the entire structure. One parameter that affects the ease of snap-through is the number of rods that gather around a single spike.

Considering the increase or decrease in energy in snap-through in a simplified model, the energy is proportional to $n*\sin(\pi/n)$, which increases as the number of struts increases. For example, a quad mesh consists of degree-4 vertices and thus gathers 4 struts, while a triangle mesh consists of degree-6 vertices and thus gathers 6 struts. Considering the ease of snap-through, we will proceed with the design based on a triangular mesh (Figure 3).

4. Verification of construction methods and details

4.1. Selection of membrane material

Considering its future deployment in outdoor structures, the need for durability to withstand localized forces at the ends of the compression members, and to allow tensile forces to be preloaded by human-powered pulling on site, “Shade Azul” manufactured by Taiyo Kogyo Corporation, an material with high elasticity can be used outdoor, was selected for the membrane material. Shade Azul is strong enough not to tear even when the fabric is pulled strongly in both the longitudinal and transverse directions, with a longitudinal tensile strength of 791 N/cm and a transverse tensile strength of 604 N/cm.

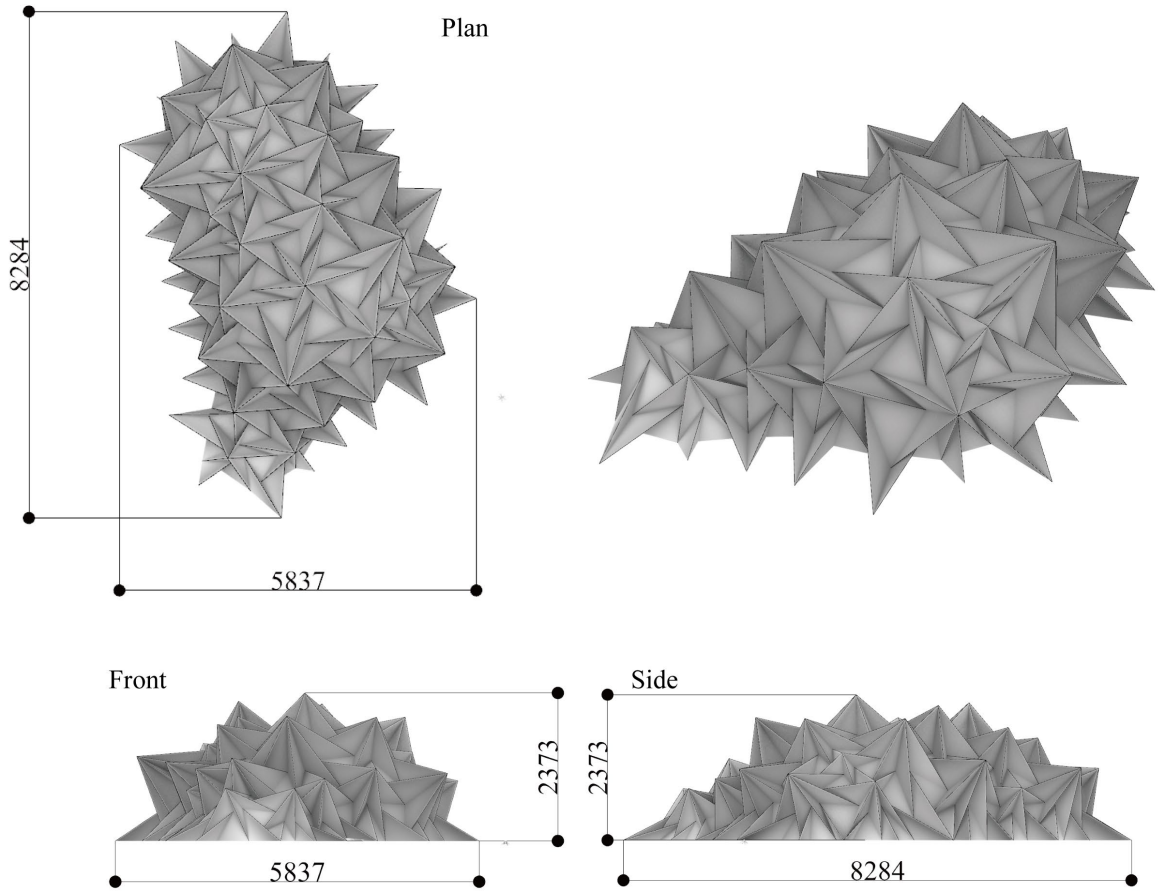
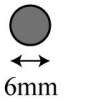


Figure 3. Dimensions of the pavilion designed and constructed for this project.

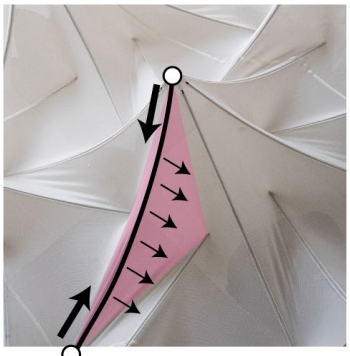
The longitudinal tensile stiffness is 62 kN/m and Poisson's ratio is 0.675. The performance of elongation against tension is homogeneous in both directions.

4.2. Selection of material for compressed members

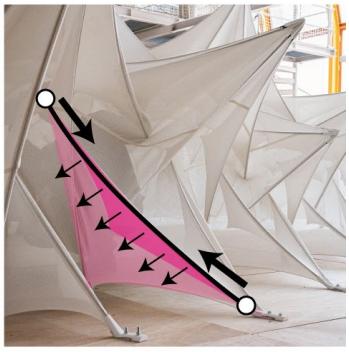
Carbon fiber reinforced plastic(CFRP) rods was used as the compression member because it is lightweight and a hard material with a high Young's modulus. 218 rods ranging from 581mm to 1627mm was used. The geometry around the rods is the same in the floating part and the ground part of the structure, and the stresses do not change significantly, so the same cross section is used for all of them (Figure 4).



Length	Young' s modulus	Moment of inertia
L mm	E kN/mm²	I mm⁴
581~1627	390.4	63.6



Geometry and stresses of floating rod



Geometry and stresses of ground rod

Figure 4. Material and section of compressed members

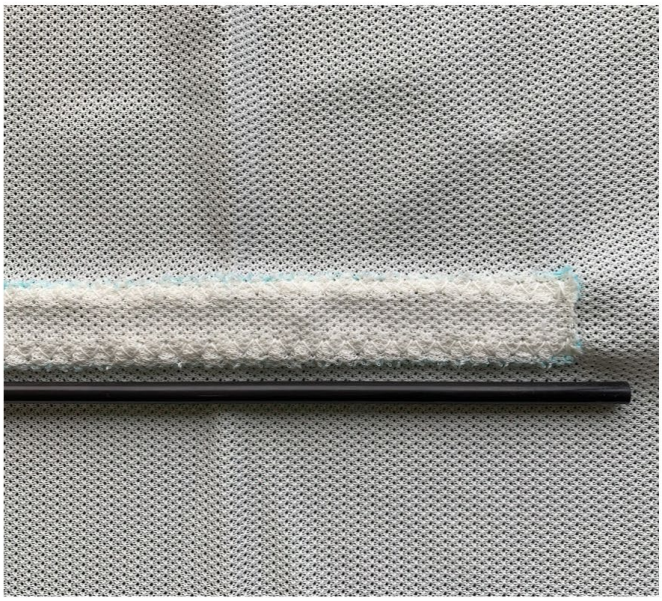




Figure 5. (Left) CFRP rod and pocket for rod attachment. (Right) Mock-up for rod attachment verification

4.3. Fixing method of compression members

In order to apply tension evenly to the membrane between the compressions and to prevent them from coming off, long pockets of the same material as the membrane is sewn in and the CFRP rods are inserted into the pocket, thereby securing the compressions to the membrane (Figure 5). A fold is provided at the edge of the pocket, and the inserted CFRP rod is hooked and attached to the pocket. The pocket is 19% shorter than the membrane when no load is applied, and the tension is applied into the membrane by inserting and securing the CFRP rods while pulling on this textile. For this method, we refer to a previous case study, the MOOM project's method[2] of fastening aluminum compression material.

4.4. Design and verification of compression member joints

Although the vertices where the compression members meet were structurally pin-jointed, there was concern that the contact points at the ends of the CFRP rods would shift due to expansion and contraction of the membrane when the it is attached to the compression members. In this experiment, the ends of the compression members were joined to each other with a Thermoplastic polyurethane (TPU) joint produced by 3D printing, and the joint was bolted to the membrane material to fix this contact point so that it would not shift from the membrane. TPU was used because it is a flexible material and shows flexible behavior in response to the movement and load of the membrane. If a load is applied to the apex in the out-of-plane direction of the membrane, snap deformation may happen. Therefore, we took one sample of the vertex, produced it, and applied a load to the vertex from above to see how much load the deformation could be caused by. When the elongation of the membrane was 19%, the load in the out-of-plane direction that could cause snap deformation was 4kgW, confirming that the membrane was sufficiently resistant to deformation even in full-scale tests (Figure 5).

4.5. Design and verification of 3D printed legs

The legs, which are the joints of the ground, were also made of TPU material by 3D printing. They were fixed to the floor surface with bolts in two places so that they would not rotate on the plane. Membrane material was wrapped around the inner bolt, and the bolt was hooked to the pigeonholes on the membrane, so that the leg could be held under tension.

5. Construction

5.1. Preparation for construction

In preparation for installation, the joints and legs were 3D printed with generic small size 3D print machine. Two joints were printed in pairs, and 24 hours were required for each pair. The legs took 6 hours. The joint number and branch number were engraved on the 3D printed outputs to prevent misplacement and misorientation during construction. A development drawing of the membrane was made, was sewn, the pockets were attached, and the pigeonholes were attached in the cooperative factory of Taiyo Kogyo Corporation (Figure.6).

5.2. Installation of floor panels and marking of leg bolts

The construction experiment was conducted indoors on March 25, 2023. The construction work was done by 15 people over a period of nine hours. First, a floating floor was created by lining the floor with a square timber and then lining it with 910 x 1820, 12 mm plywood. The coordinates of where the legs were to be fixed were marked, holes were drilled at the bolt locations on the plywood, and the bolts were temporarily placed from the downside.

5.3. Load of tensile force to the membrane material

In this experiment, the compression member was simultaneously fixed and tension was load by inserting the compression members into pockets pre-sewn on the membrane and hooking the end of the rods while stretching the pocket. The installation procedure was as follows.

(1) Bolt the 3D printed joint at the apex where the CFRP rod gathers on the membrane material.

(2) The CFRP rods are threaded through a pocket sewn on the membrane and then the tip is inserted into the hole in the joint.

(3) Pull the membrane material along the CFRP rods and hook the folded end of the pocket onto the opposite end of the CFRP rod, securing the membrane material with tensile force applied to it.

(4) (1) to (3) were performed sequentially from the centre of the membrane to the periphery (Figure.7).



Figure 6. (Left) 3D printed joints and legs. (Right) One flat membrane with pockets attached



Figure 7. (Top left) Bolt the 3D printed joint (Top right) insert CFRP rod to pocket on the membrane (Bottom left) Assembled joint by joint and stand vertices. (Bottom right) 3D printed joints and legs on membrane.

5.4. Fixing membrane to floor

After all joints and CFRP rods were installed, the membrane was inserted between the legs and the floor panel and bolted in the same manner as the joints, securing the membrane material to the floor panel. As with the joints, CFRP rods were inserted through the pockets and into the holes in the legs, and tensile forces were loaded by pulling the membrane and hooking the opposite end onto the fold of the membrane (Figure 8).



Figure 8. Self-supporting membrane tensegrity structure



Figure 9. (Left) Large deflected rod members (Right)Twisted and broken joint with rod protruding

6. Analysis of shape accuracy

6.1. Visual observation

Visual observation showed that the center of the rod deflected significantly and appeared to be more deformed than expected. In addition, some of the joints were found to be twisted and greatly deformed. Some of the joints were damaged and the rods were exposed through the joints, so the rods were reinforced to prevent further damage (Figure 9).

6.2. Measured by 3D laser distance-measuring machine

The 3D coordinates of the apex using a 3D laser distance-measuring machine. We used a fixed-type surveying instrument that can calculate the 3D coordinates and angles of any point on the measurement object's surface through laser irradiation. The distance error between each point on the specimen and the 3D model's apexes were then measured, and the accuracy of the sample's shape was analyzed . Figure 10 shows the amount and direction of deformation at each of the 27 vertices for the actual design model. The outward deformation is shown in red and the inward deformation in blue for the freeform dome shape. Of the 27 vertices, the vertex in the center of the span was highly deformed downward, dropping a maximum of 469 mm. On the other hand, the vertex in the second row from the perimeter had relatively small displacement from the design model and moved in the outward opening direction. In this range, the apexes were settled with a displacement of about 60-100 mm (maximum 161mm).

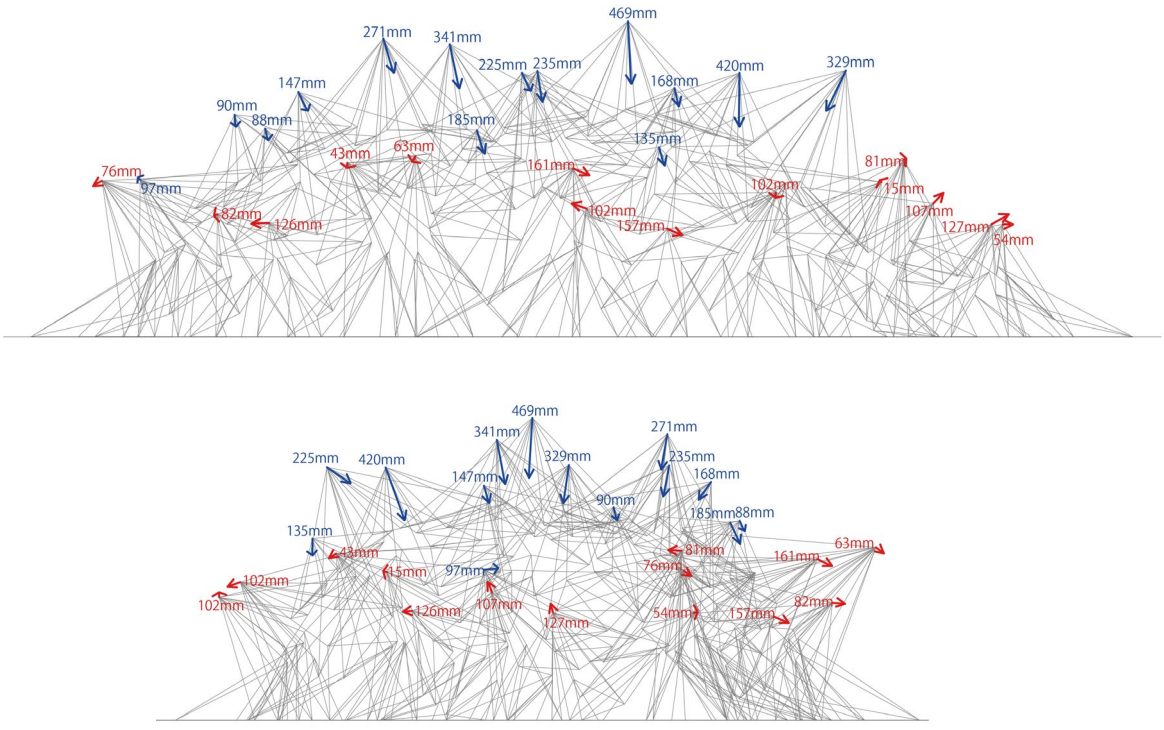


Figure 10. Error of each vertex in the design model and mock-up

7. Discussion and conclusion

This paper proposes a design method for membrane tensegrity structures by solving the inverse problem using freeform origami tessellations by generalizing Resch's patterns. Moreover, we demonstrated the feasibility of our method by constructing a full-scale mock-up. In constructing the structure, we sewed pockets, shorter in length than compression members, into the mountain fold lines and applied tensile force across the membrane by inserting CFRP rods as the compression members while pulling the membrane material. Furthermore, we measured the coordinates of each joint of the structure with a three-dimensional laser distance meter. Finally, we compared them with the design model to assess the reproducibility of its geometry. A comparison of the shape of the constructed mock-up and the model shows that the apex in the center of the span is much lower than in the model. In addition, observation of the test specimen showed that the compression material deflected significantly. Issues to be addressed include building a design model that considers the bending of the compression material and the stable sculpting of the 3D-printed joints.

Acknowledgements

This research is funded by Nohmura Foundation for Membrane Structure's Technology.

References

[1] T. Tachi, “Designing freeform origami tessellations by generalizing Resch’s patterns,” *Journal of mechanical design*, vol. 135, 2013.

[2] Coelacanth and Associates(n.d.), Moom, https://c-and-a.co.jp/en/projects/moom/, accessed 2023/3/11

[3] N. Ratschke, A. Bögle, and J. Lindenberg, "Parametric analysis of tensegrity-membrane-structures." *Proceedings of IASS Annual Symposum 2017,* Hamburg, Germany, September 25 - 28, 2017.

[4] M. Shigematsu, M. Tanaka, and H. Noguchi. "Form finding analysis of tensegrity membrane structures based on variational method." *Proceeding of 6th International Conference on Computation of Shell & Spatial Structures 2008* , New York, USA, May 28-31, 2020.

[5] S. S. Gupta, Y.Y. Tan, P. Z. Chia, C. P. Pambudi, Y. H. Quek, C. Yogiaman, and K. J. Tracy, "Prototyping knit tensegrity shells: a design-to-fabrication workflow." *SN Applied Sciences 2*, pp.1-13, 2020.

[6] K. Suto , Y. Noma , K. Tanimichi , K. Narumi , and T. Tachi, "Crane: An Integrated Computational Design Platformfor Functional, Foldable, and Fabricable Origami Products." *ACM Transactions on Computer-Human Interaction*, 2022, https://doi.org/10.1145/3576856.

[7] D. Piker, "Kangaroo: form finding with computational physics." *Architectural Design.* Vol.83, Issue 2, pp. 136-137, 2013.

[8] S. Tibbits, *Self-assembly lab: experiments in programming matter*, Taylor & Francis, 2016.

[9] D. Jourdan, M. Skouras, E. Vouga, and A. Bousseau, "Printing-on-fabric meta-material for self-shaping architectural models", *Proceeding of Advances in Architectural Geometry 2020* , Paris, France, August 30 – Sptember , 2020.

IASS 2023
July 10–14 Melbourne
Integration of Design and Fabrication

Proceedings of the IASS Annual Symposium 2023
Integration of Design and Fabrication
10–14 July 2023, Melbourne, Australia
Y.M. Xie, J. Burry, T.U. Lee and J. Ma (eds.)

Defining design limits for ETFE foils determined in bubble inflation tests

Felix SURHOLT[*], Jörg UHLEMANN[a], Natalie STRANGHÖNER[a]

[a,*] University of Duisburg-Essen, Institute for Metal and Lightweight Structures
Universitätsstr. 15, 45141 Essen, Germany
felix.surholt@uni-due.de

Abstract

With the understanding of the mechanical behaviour of membrane materials, the popularity steadily increases. Membrane materials can be distinguished between technical (coated) textiles and technical foils, oftentimes ETFE foils. Recently, the final draft of the technical specification (TS) prCEN/TS 19102 has been submitted to CEN, which focuses on the design of tensioned membrane structures. Herein, rules for the design of textiles and foils are given, distinguishing between the Ultimate Limit State (ULS) and the Serviceability Limit State (SLS). For ETFE foils, the ULS and SLS design are based on uniaxially determined material properties. However, the majority of membrane structures exhibit biaxial stresses. Therefore, the material behaviour under biaxial tension is crucial. To evaluate the biaxial mechanical behaviour of membrane materials, generally biaxial tension tests on cruciform specimen are conducted. Yet, due to the cruciform geometry, a biaxial yield stress f_y cannot be determined. Bubble inflation tests can be performed to determine the biaxial stress-strain behaviour of ETFE foils especially after yielding. To determine the biaxial material behaviour of ETFE foils, bubble inflation tests are performed on materials from three different producers and one foil thickness. The evaluated data are presented and used to formulate design limits considering the material behaviour under biaxial tension up to the plastic deformation stage.

Keywords: ETFE foils, uniaxial, biaxial, bubble inflation test, mechanical behaviour, design, design limits

1. Introduction

With its first use of Ethylene/Tetrafluoroethylene (ETFE) foils as façade and cladding materials in the 1980ies, their convention in membrane structures steadily increased. Today, the building material ETFE is applied in cladding systems of prestigious buildings, such as stadiums, atriums or market halls. They are characterised by their low dead weight and transparency. All these membrane structures – technical textiles, technical foils – have in common, that they are usually built in synclastic or anticlastic shapes to activate their membrane stiffness. Generally, membranes are multiaxially prestressed and are exposed to multiaxial stresses due to external loads. Herein, the prestress can be applied either mechanically or pneumatically to form the anticlastic and synclastic shapes. Mechanical prestress is used to form anticlastic, single-layer shapes. To obtain synclastic shapes, oftentimes foil envelopes are produced and prestressed with an internal pressure, so that cushions are formed. Figure 1 illustrates two exemplary foil structures, which are mechanically (left) and pneumatically (right) prestressed. Comparing these two prestress application types, pneumatically prestressed multi-layer structures excel due to their capacity to compensate occurring plastic deformations by adjusting the internal air volume while keeping the pressure constant. Plastic deformation occurring in mechanically prestressed, single-layer structures leads to a loss in pretension and therefore to a loss of structural integrity.

Copyright © 2023 by Felix SURHOLT, Jörg UHLEMANN and Natalie STRANGHÖNER. Published in the Proceedings of the IASS Annual Symposium 2023 with permission.



Figure 1. Mechanically and pneumatically prestressed ETFE foil structures (left: Ruhr Park Bochum, Bochum, Germany, © Taiyo Europe GmbH; right: Nuova Sede Regione Puglia, Bari, Italy, © Taiyo Europe GmbH)

Regardless of the prestress application, all membrane structures must be designed in the Ultimate Limit State (ULS) and Serviceability Limit State (SLS) with external loads in mind. The newly developed final draft of the technical specification prCEN/TS 19102 [1] includes the design, execution and testing of membranes using the k-factor concept. With the use of the k-factor concept, which bases on the A-factor concept, see e. g. Minte [2], the strength characteristics of the used materials are divided by corresponding k-factors, which are chosen depending on the design condition, e. g. a slowly accumulating long-term load at T = 0 °C is taken into account for the load case "snow". For ETFE foil structures, decisive characteristics are the Young's Modulus E, the elastic limit f_{el}, which is defined by the first inflexion point f_{ip} in the stress-strain diagram, the yield point f_y, and the ultimate tensile strength f_u, which are highly dependent on the strain rate and temperature due to ETFE being a thermoplastic. To derive these material characteristics, typically uniaxial tensile tests or more rarely biaxial tensile tests are performed, simplifying the multiaxial stress states occurring in membrane structures into two principle stresses. Uniaxial tensile tests are carried out due to the ease of processing and the comparatively low costs. However, knowledge about material properties and characteristic values under multiaxial – or simplified biaxial – loading conditions are crucial. Under multiaxial tension, ETFE foils show a stiffer and at the same time stronger material behaviour compared to the material response under uniaxial tension. If the strains in the material directions are compared in uniaxial and biaxial/multiaxial stress conditions, higher forces and thus higher stresses result in equivalent material strains in the biaxial stress state.

In the ULS design of ETFE foils, according to the submitted final draft of prCEN/TS 19102 [1], no difference is made between the ultimate tensile strength of ETFE foils in uni- and biaxial stress states resulting in a k-factor of $k_{biax} = 1.0$. However, previous studies on the biaxial mechanical behaviour of ETFE foils in bubble inflation tests showed, that under biaxial tension, ETFE foils exhibit a stiffer material behaviour. Schiemann [3] performed bubble inflation tests on 200 µm ETFE foils revealing that the ultimate tensile strength of a ETFE foil in a bubble inflation test occurs at approx. 10 % to 12 % strain with a mean tensile strength of 29 MPa and a characteristic tensile strength of 26.6 MPa. Thus, according to Schiemann the k_{biax}-factor for the ULS as a quotient between the characteristic tensile strength of welded ETFE foils ($f_{uw,k,uni} = 30$ MPa) and the characteristic tensile strength in his welded bubble inflation tests ($f_{uw,k,bubble} = 26.6$ MPa) equals $k_{biax} = 30/26.6 \cong 1.15$. In SLS-design, Schiemann refers to the yield strength of ETFE foils, thus determining a factor of $k_{biax} = 1.0$. Moritz [4] suggested a factor to consider the biaxial tensile strength of ETFE foils of 1.2 for ULS-design and 1.4 for SLS-design. In uniaxial tensile tests on ETFE foils, the yield point occurs at approximately 18 % strain.

2. The tensile behaviour of ETFE foils

2.1. General

In the framework of the German DFG research project "Characterisation of the nonlinear viscoelastic material behaviour of ETFE- and ECTFE-foils for the use in building membrane structures" (STR482/6-

1), the mechanical behaviour of ETFE foils was analysed in short-term tensile tests as well as in long-term creep and relaxation tests, both in uniaxial and biaxial stress states. To evaluate the influence of the material thickness, two commonly used foil thicknesses were examined: 100 µm and 250 µm ETFE foils. Herein, 100 µm foils are usually applied as the middle layers of multi-chamber cushion systems. 250 µm foils typically form the envelope of those structures. Additionally, to investigate the producer's influence on the material behaviour, materials from three different producers were included in the project: Fluon ETFE Film 250NJ-1550NT and 100NJ-1550NT, Nowoflon ET 6235 Z in 250 µm and 100 µm, ETFE AG 250 µm and ETFE AG 100 µm. This order does not reflect the allocation of producers I, II, and III in the following, respectively. In this paper, the results achieved for the 250 µm foils are presented and discussed.

2.2. Uniaxial tensile behaviour

To derive the uniaxial mechanical behaviour of ETFE foils, uniaxial tensile tests were performed according to EN ISO 527-1 [5] and -3 [6]. Special provisions are mentioned in prCEN/TS 19102 [1] regarding the specimen's geometry, prestress application and the strain rate. According to prCEN/TS 19102, uniaxial tensile tests should be performed on strip specimens with an initial measuring length of 50 mm and a width to length ration of 1:5 with linear fixation at the top and bottom. The tensile test results include the recorded force F and elongation $\Delta L = L\text{-}L_0$ obtaining an engineering stress-engineering strain diagram (σ_{eng}-ε_{eng}-diagram), relating to the initial cross-section area A_0 and initial measuring length L_0 with $\sigma_{eng} = F/A_0$ [MPa] and $\varepsilon_{eng} = \Delta L/L_0$ [%].

Figure 2 represents a typical σ_{eng}-ε_{eng} diagram of 250 µm ETFE foils at room temperature and at $d\varepsilon/dt$ = 200 %/min from three different material producers I, II and III, featuring the material characterising parameters. In the left diagram, the overall uniaxial tensile behaviour up to the break is shown. For ETFE foils, the ultimate tensile strength f_u occurs at the rupture of the specimen. At the inflexion point f_{ip} as well as the yield point f_y, the material stiffness significantly decreases. These two points are commonly called first and second yield point, $f_{y,1}$ and $f_{y,2}$ respectively. However, EN ISO 527-1 defines the yield point as the σ_{eng}-ε_{eng} point, where the strain increases without any further increase in stress, so that the first inflexion point is called f_{ip} here. Simultaneously, f_{ip} and f_y divide the material behaviour of the thermoplastic ETFE into three different stages. The first stage represents the viscoelastic stage ranging up to the stress f_{ip} including elastic and viscoelastic deformations. After the stress f_y, ETFE foil is viscoplastic. The foil material yields and mainly plastic, viscous deformations are present. Between f_{ip} and f_y, the material is viscoelastic-plastic with significant viscoelastic and viscoplastic deformation.

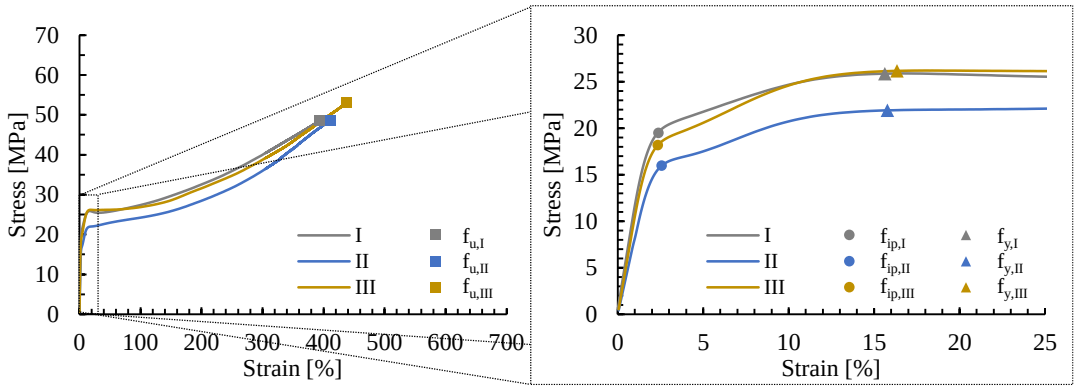


Figure 2. Engineering stress-engineering strain diagram of ETFE foil in ED under uniaxial tension for three different producers I, II and III (250 µm, 23 °C, 100 mm/min ≙ 200 %/min).

Additionally, Figure 2 shows the material producer dependency on the foil product. Material from producer II shows significantly lower strength values, even at the elastic and viscoelastic limit, which is

decisive for the design of ETFE foil structures. prCEN/TS 19102 defines the characteristic tensile strength of ETFE foil base material to $f_{u,k}$ = 40 MPa (T = 23 °C) for ULS design, and the elastic limit to f_{el23} = 15 MPa for SLS design. Figure 3 shows the temperature and strain-rate dependent material behaviour of ETFE foils. With an increase in the test temperature, the material shows a considerably weaker and slightly softer tensile behaviour. An equivalent response can be observed with a decrease in the strain-rate. For a detailed discussion on the temperature- and strain-rate dependent uniaxial material behaviour see Surholt et al. [7]. In the past several investigations into the strain rate and temperature dependent material behaviour of ETFE foils were conducted, e.g. by Moritz [4], Galliot and Luchsinger [8], Hu et al. [9], [10], Zhao and Chen [11], [12], Saxe [13], Sun et al. [14], and Lippke [15].

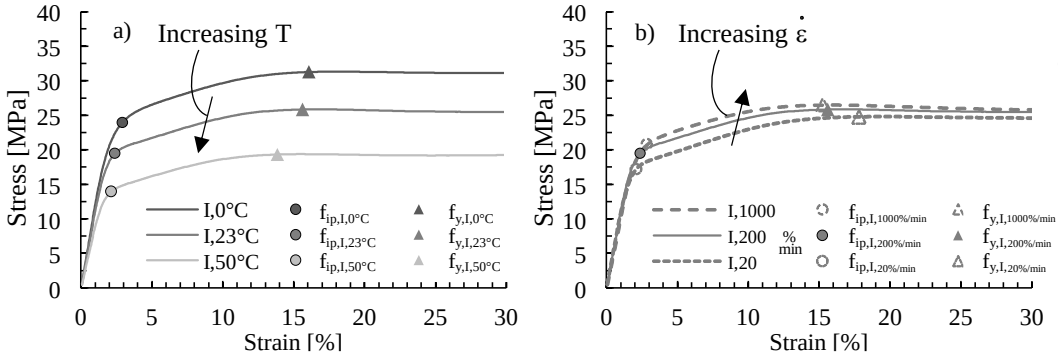


Figure 3. Section of an engineering stress-engineering strain diagram of ETFE foil in ED under uniaxial tension for producer I up to 30 % strain; a) 0 °C, 23 °C and 50 °C (250 µm, 100 mm/min ≙ 200 %/min); b) 10 mm/min ≙ 20 %/min, 100 mm/min ≙ 200 %/min and 500 mm/min ≙ 1000 %/min (250 µm, 23 °C).

To consider environmental effects on site, the previously mentioned design concept in prCEN/TS 19102 introduces additional k-factors to modify the material behaviour at T = 23 °C to the material behaviour under the considered design condition, e. g. $k_{temp,50\,°C}$ to consider the strength reducing effect of an environmental temperature of 50 °C on site on the foil surface or the surface of adjacent components like clamping profiles.

2.2. Biaxial tensile behaviour using cruciform specimens

Uniaxial stress states rarely occur in built membrane structures. The necessary prestress as well as the stresses due to external loads are multiaxially and transferred to the primary steel-, aluminium- or timber-structure. These multiaxial stresses can be simplified to biaxial stress states considering the principle stresses σ_1 and σ_2. Therefore, to design membrane structures overall and ETFE foil structures in particular, the load bearing behaviour in multiaxial stress states is crucial. To evaluate this material behaviour, biaxial tensile tests and bubble inflation tests were performed. Using plane cruciform specimens, defined loads can be applied via arms, which transfer the uniaxial stresses to a measuring field, which is thus biaxially loaded. Figure 4 illustrates such a plane cruciform specimen.

Figure 5 presents the response of biaxial tensile tests in stress ratio 1:1 (extrusion direction:transverse direction, short ED:TD) of ETFE foil material of the three different producers at room temperature. The tests were performed with a constant stress rate of 1.5 MPa/min, which equals an average strain rate of approximately 0.33 %/min. The stress rates refer to the first principal direction of stress (ED). The σ_{eng}-ε_{eng} diagram shows the stress-state dependent material behaviour of the ETFE foils investigated. It illustrates that for all three ETFE foil materials under biaxial tension, a stiffer mechanical response can be observed compared to uniaxial stress, cf. Figure 2. A distinct yield point f_y cannot be identified due to early specimen rupture. The specimen arms are loaded uniaxially as mentioned above. When they begin to yield, the biaxially loaded measuring field cannot be loaded further by the test machine and the test is terminated. All investigated ETFE foils show an isotropic material behaviour in a 1:1 stress ratio, and – compared to uniaxial behaviour – the three analysed materials stiffen, referring to the Young's modulus E and the hardening modulus E_{ve}. Moreover, they harden, referring to f_{ip} and f_y. Here, the

engineering stresses σ_{eng} are determined as a quotient of the measured forces F and the initial specimen area A_0: $\sigma_{eng} = F/A_0$ [MPa].

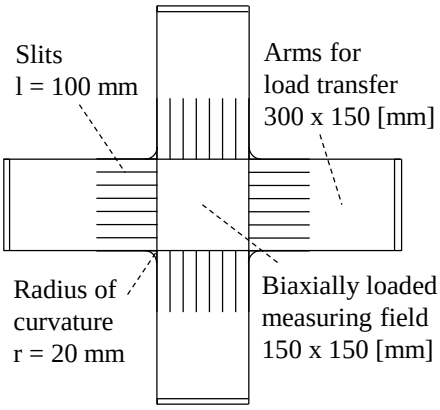


Figure 4. Used cruciform specimen geometry.

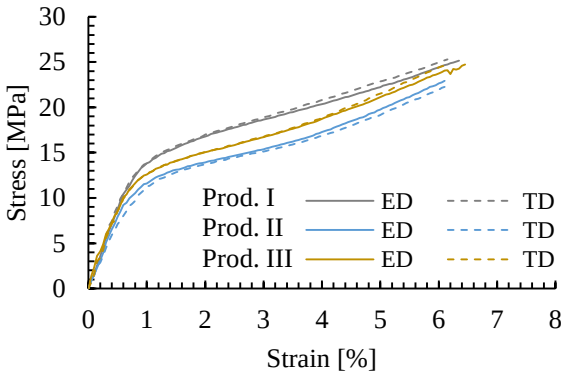


Figure 5. Biaxial mechanical behaviour of ETFE foils of three different producers under stress ratio 1:1 (mean value curves; 250 µm; $d\sigma/dt$ = 1.5 MPa/min ~ $d\varepsilon/dt \cong 0.33$ %/min).

2.3. Multiaxial tensile behaviour using bubble inflation specimens

To characterise ETFE foils in the viscoelastic-plastic as well as the viscoplastic material stages, bubble inflation tests are required. For this purpose, circular test specimens with a clear diameter of 500 mm were used. In bubble inflation tests, the forces F cannot be measured directly. In these tests, the specimens are loaded pneumatically, so only the internal pressure is known. In the performed tests, the inner pressure was constantly raised with a rate of dp_i/dt = 16.67 Pa/min to achieve a strain rate of approximately $d\varepsilon/dt \cong 0.33$ %/min. The strains were determined using a photogrammetric 3D deformation measurement system. To derive the stresses at the bubble peak in stress ratio 1:1 induced by the internal pressure, the Barlow's formula can be used. In the bubble inflation test, a rotationally symmetric shape is assumed. This leads to an identical stress in both material directions ED and TD:

$$\sigma_{eng,bubble,ED} = \sigma_{eng,bubble,TD} = \frac{p_i r_i}{2t_0} \tag{1}$$

with p_i being the internal pressure [MPa = N/mm^2], r_i the radius of curvature at the peak [mm], and t_0 the initial foil thickness [mm]. Schiemann [3] used Eq. 1 to derive the foil stresses in his bubble inflation tests. However, in bubble inflation tests, ETFE foils show an inhomogeneous material behaviour in its deformation after reaching the yield point. The specimen's peak elongates at first up to the point, when its mechanical capabilities are exhausted. To compensate the still increasing air volume in the pressure chamber and to allow for further elongation, material from further down the line is pulled in reducing the material's thickness at the locations from where it is drawn. Murphy [16] (cited in [17]) as well as Javořik and Dvořàk [18] performed bubble inflation tests on elastomers and calculated the stresses at the peak considering the occurring "stretch ratio" λ ($\lambda = \varepsilon+1 = L/L_0$ [-]). Under the assumption that ETFE foils are incompressible, the engineering stresses at the peak can be determined under the consideration of the stretches in ED (λ_{ED}) and TD (λ_{TD}):

$$\sigma_{eng,bubble,ED} = \frac{p_i r_i}{2t_0}\lambda_{ED} \tag{2}$$

$$\sigma_{eng,bubble,TD} = \frac{p_i r_i}{2t_0}\lambda_{TD} \tag{3}$$

In both cases, the radius at the pole r_i is determined evaluating the deformation in ED and TD axis using a polynomial fit of 6th degree ($f(x) = ax^6+bx^5+cx^4+dx^3+gx^2+hx+j$). As an example, Figure 6 illustrates

the deformation and strain along ED and TD of test no. BIT-II250-23_16,67-II (Bubble Inflation Test, producer II, t_0 = 250 µm, T = 23 °C, dp_i/dt = 16.67 Pa/min, test number II) at recording step 1 000 with an internal pressure of p_{1000} = 32 812 Pa, at the recording step 1 290 with the maximum internal pressure of $p_{i.max}$ = 42 150 Pa, and at the last recording step (1 305) with an internal pressure of p_{1305} = 33 620 Pa close before fracture. The tests were recorded with 0.5 Hz. Figure 6 illustrates the general good fit of the polynomial fit for the material from Producer II, 250 µm.

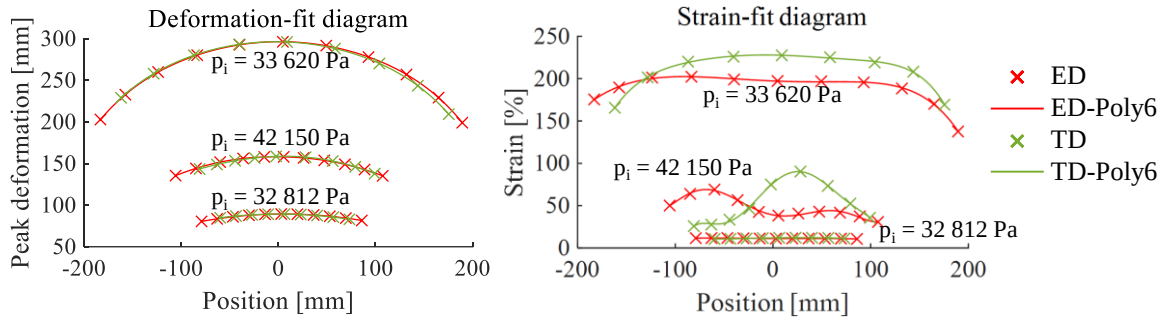


Figure 6. Comparison of the polynomial fit to the measured deformation stages (left) and strains (right) for the bubble inflation test BIT-II250-23_16,67-II at specific points X in both material directions at p_{1000} = 32 812 Pa, and at p_{1305} = 33 620 Pa.

Figure 7 illustrates the load-deformation curves of the performed bubble inflation tests for all three producers. In all tests, the internal pressure was constantly rising until the maximum internal pressure was reached. Reaching their individual maximum internal pressure, the specimen's volume increased drastically, so that the pressure system could not maintain the programmed pressure rate. This way, the internal pressure decreased until specimen fracture occurred.

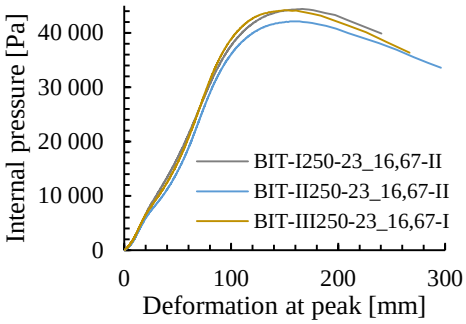


Figure 7. Load-deformation diagram of the performed bubble inflation tests.

Using the fitted curves (Poly6), the radius of curvature in each recording step, each point, in each direction and for each test can be calculated. Here, the radius of curvature was calculated at the peak deformation of the test specimen for ED and TD separately to derive the stresses of the ETFE foil in the two material directions using the following formula:

$$r = \frac{1}{\kappa} = \frac{\left(1+\left(\frac{df}{dx}\right)^2\right)^{\frac{3}{2}}}{\frac{d^2 f}{dx^2}} \tag{4}$$

In addition to the calculation of the radius, the strains in ED and TD were calculated at the peak. This does not mean that the highest strains must occur at the peak deformation, see Figure 6 (right). The occurring strains in ED and TD of the illustrated bubble inflation test demonstrate the anisotropic behaviour in the last recording stage close before rupture. Over a wide span of the test specimen, the

strains equalize, so that a strain "plateau" is observed. The specimen gathers material from the region closer to the clamps. During bubble inflation tests, the centre region around the peak exhibits the highest strains in both material directions. Approaching the maximum bearable inner pressure, the strain at the pole does not increase drastically anymore; the strains further away from the centre region raise while the strains in the centre region stay stable. In the present paper, the strains were calculated using the polynomial fit at the location with the highest peak deformation. As an example, for test BIT-II250-23_16,67-II, the strains were calculated at the centre of the peak which lays at position approximately 5 mm, see Figure 6.

To obtain the strains in both material directions, the specimens have to be prepared for the photogrammetric measurement system. The photogrammetric measurement system generates facets on the specimen surface based on a black and white stochastic pattern. Therefore, the transparent ETFE foils to be tested were primed white and then dabbed with black paint, cf. Figure 10. The photogrammetric measurement system then tracks the generated facets during the inflation test and calculates the distances of their centres from which the strains are obtained.

With the calculated parameters, which are mentioned above, a σ_{eng}-ε_{eng} diagram can be generated for the peak location on the bubble using Equations (2), (3) and (4). For the tests performed on the 250 µm ETFE foils of three different producers at room temperature, Figure 8 illustrates the determined σ_{eng}-ε_{eng} curves up to 200 % strain and in a cut-out up to 25 % strain.

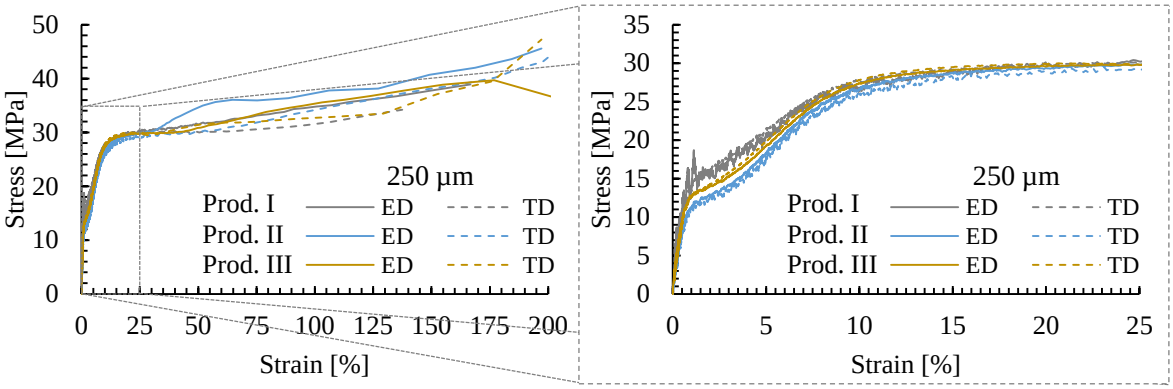


Figure 8. Calculated σ_{eng}-ε_{eng} curves of the bubble inflation tests performed on 250 µm ETFE foils from three different producers (T = 23 °C).

The results show the different material behaviour of the three foils already observed in the uniaxial and biaxial test results. Material from producer I exhibits the strongest characteristic first inflexion point f_{ip}, and material from producer II the weakest. Table 1 lists the measured breaking strains ε_u and calculated ultimate tensile stresses f_u as well as the material characterising strength points f_{ip} and f_y in addition to their strain values ε_{ip} and ε_y. The first inflexion point was determined by calculating the point where the slope of the σ_{eng}-ε_{eng} curves reaches 80 % of its initial slope calculated in the elastic material region, and f_y where the slope reaches less than 1.5 % of its initial slope, respectively. Reaching the second material characteristic f_y between 10 % to 15 % strain, depending on the material producer, the material shows a similar yielding stage as known from uniaxial tensile tests but with less pronounced hardening after yielding, cf. Figure 2. After reaching f_y, the strain rate drastically increases while the pressure regulator tries to maintain the programmed pressure rate. This effect was so strong that the pressure system could not reach the desired pressure rate in this stage. In the yielding process, an extremely high strain rate occurs, which leads to the recording of only a few measuring steps due to the fixed measuring rate of 0.5 Hz. After reaching the yield point f_y, hardening effects can be observed in the σ_{eng}-ε_{eng} curves. Finally, the ultimate tensile strength is reached at several hundred percent strain with stresses higher than the yield point, which again resembles the σ_{eng}-ε_{eng} curve of uniaxial tensile tests. After rupture, the nominal specimen thicknesses of 250 µm decreased to 40 µm, 39 µm, and 35 µm for producers I, II,

and III, at the pole, respectively. Ruptures occurred diagonally between ED and TD as well as in TD, with crack sizes between approximately 230 mm, 320 mm, and 285 mm for producers I, II, and III, respectively.

Table 1. Measured strains [%] and calculated tensile stresses [MPa] of the performed bubble inflation tests on 250 µm ETFE foil.

Test	BIT-I250-23_16,67_II		BIT-II250-23_16,67_II		BIT-III250-23_16,67_I	
Producer	I		II		III	
Direction	ED	TD	ED	TD	ED	TD
f_{ip} [MPa]	14.4	14.4	11.3	11.0	12.3	12.5
ε_{ip} [%]	0.8	1.1	1.0	1.1	0.9	1.0
f_y [MPa]	27.7	28.6	28.6	28.1	28.6	29.1
ε_y [%]	11.7	12.3	15.0	15.2	12.7	13.1
f_u [MPa]	43.4	39.7	45.6	49.4	50.5	47.2
ε_u [%]	205	182	197	228	255	197

It should be noted that not every bubble inflation test specimen reached its theoretical maximum load bearing capacity due to the occurrence of early "small cracks" which appeared approximately in the middle between the pole and clamping region, see Figure 10. It is assumed that a small defect in the foil can lead to this type of crack/leakage in the specimen when the defected area is strongly strained and the thickness reduced. These small cracks, however, do not propagate further. As soon as there was such a crack/leakage in the specimen, the internal pressure dropped, so that the specimen could not be loaded further. In 1/3 of the tests, the full capability of the foils was not achieved because of such small cracks. In these tests, the crack occurred shortly after yielding at the pole region. It can be concluded for practical construction applications, that yielding of foils used in cushion structures under internal pressure should be strictly avoided. Figure 9 shows the derived σ_{eng}-ε_{eng} curve of a bubble inflation test (test BIT-I250-23_16,67-I), where a small crack occurred after reaching f_y. Figure 10 shows the plastic deformed specimen and the crack detail.

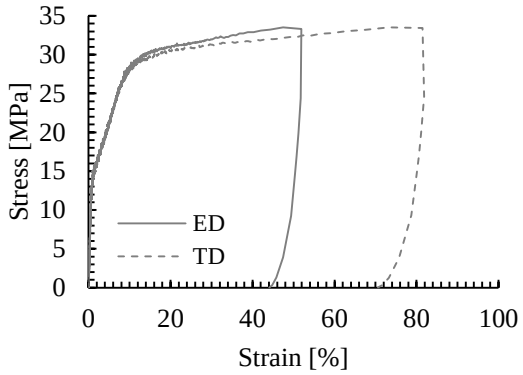


Figure 9. Calculated σ_{eng}-ε_{eng} curves of BIT-I250-23_16,67-I terminated early due to a small crack.

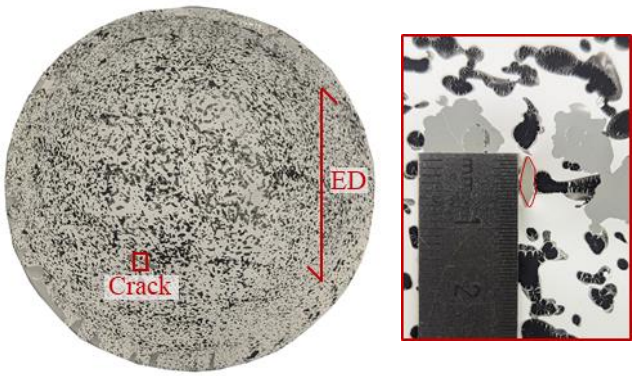


Figure 10. Small crack in the deformed test specimen BIT-I250-23_16,67-I leading to the termination of the test.

3. Comparison of the uniaxial and multiaxial/biaxial mechanical behaviour using strip, cruciform and bubble inflation specimens

Figure 11 shows the mechanical behaviour of ETFE foils in a uniaxial and two biaxial stress states using strip, cruciform and bubble inflation specimens, respectively. Additional information is presented in Table 2 regarding the derived material characteristics. Comparing the biaxial mechanical behaviour of the foils investigated using cruciform and bubble inflation specimens, the stress-strain diagrams show qualitatively equal stress-strain curves of ETFE foils independent of the stress state. In the stress range up to f_{ip} also quantities are comparable. Moreover, cruciform and bubble inflation specimens behave

similar up to the point where records for the cruciform specimens end. This verifies the applicability of bubble inflation tests for the determination of biaxial mechanical properties. Cruciform specimens exhibit slightly less strains at equal stress levels greater than f_{ip}. A biaxial yield stress f_y cannot be measured using these specimens. Even though a yield strength cannot be measured in this way, these specimens find application for the determination of the biaxial material behaviour for building purposes. According to prCEN/TS 19102 [1], single layer foil structures should not exhibit plastic deformation which can lead to a loss of prestress and thus to a loss of its load bearing capabilities. Thus, the elastic limit should be used for the SLS verification of single layer structures. Special provisions are mentioned for the SLS design of foil cushion structures. If no limitation is defined by contractual agreement, the plastic strain may be limited to 1.0 %, which opens the applicable stress to stresses higher than the elastic limit. Therefore, cruciform specimen can be used to determine the biaxial material behaviour with measurable strains of approximately 6 % to 7 %, cf. Figure 5.

Figure 11 and Table 2 show that under multiaxial tension, ETFE foils show a less ductile material behaviour than under uniaxial tension. Regarding strength characteristics, the different materials behave different, at least with regard to f_{ip}. It can be stated that at f_{ip} the material of producer I exhibits increased stresses while materials of producers II and III exhibit slight decreases in stresses in bubble inflation tests compared to uniaxial tests. The amount of differences are $((f_{ip,bubble}-f_{ip,uni})/f_{ip,uni} =)$ 5.9 %, -1.7 %, and -1.6 % in ED for producers I, II, and III, respectively. At f_y, these differences are $((f_{y,bubble}-f_{y,uni})/f_{y,uni} =)$ 14.0 %, 26.5 %, and 17.7 % also in ED for producers I, II, and III, respectively. In TD the differences in stresses equal 8.3 %, 0 %, and 5.0 % at f_{ip}, and 15.8 %, 28.3 %, and 22.8 % at f_y for producers I, II, and III, respectively. This shows that in the preliminary bubble inflation tests, small differences in the range between 8 % and -2 % are recorded for f_{ip}, while an increase of at least 10 % is observed for f_y. Regarding the ultimate tensile strength of the investigated materials, percentile deviations at f_u equal $((f_{u,bubble}-f_{u,uni})/f_{u,uni} =)$ 0.2 %, -4.2 %, and 12.2 % in ED and -13.1 %, 5.8 %, and -8.3 % in TD for producers I, II, and III, respectively. However, with only one bubble inflation test made per producer, statements about an increasing or a decreasing ultimate tensile strength due to multiaxial loading cannot be made keeping in mind that at f_u relatively high coefficients of variation (COV) are observed in the uniaxial tensile tests with 6.2 %, 8.0 %, and 17.5 % in ED and 3.9 %, 2.8 % and 3.5 % in TD for producers I, II, and III, respectively. While the breaking stresses roughly maintain their level, the breaking strains are approximately halved.

The findings in these preliminary experiments that f_u does not change noticeably in a uniform biaxial stress state indicates that the current modification factor $k_{biax} = 1.0$ considering biaxial/multiaxial stresses is justified in the ULS design. For SLS design, the current modification factor $k_{biax} = 1.0$ is applicable for $f_{ip,uni}$. For safety reasons, $f_{y,bubble}$ should not be used in SLS design, due to the possibility of occurring small cracks in the specimens at stresses slightly higher than $f_{y,bubble}$ and at strains of approximately three times $\varepsilon_{y,bubble}$. With other words, when the yield point $f_{y,uni}$, is used for the stress verification of cushion structures, the current modification factor $k_{biax} = 1.0$ should still be used and not reduced to reflect $f_{y,bubble}$. By this way, a safety margin towards the chance of occurring small cracks after yielding of at least 10 % remains, when using $f_{y,uni}$ in combination with $k_{biax} = 1.0$. Additionally, the usage of $f_{y,uni}$ in SLS design leads to huge strains in cushion structures, which are generally not desired. In the performed bubble inflation tests, strains of approximately 7 % are measured at stresses equal to the uniaxially determined yield strengths $f_{y,uni}$ for all the analysed materials from producers I, II, and III. These values align with the maximum strains measured in the biaxial tensile tests using cruciform specimens.

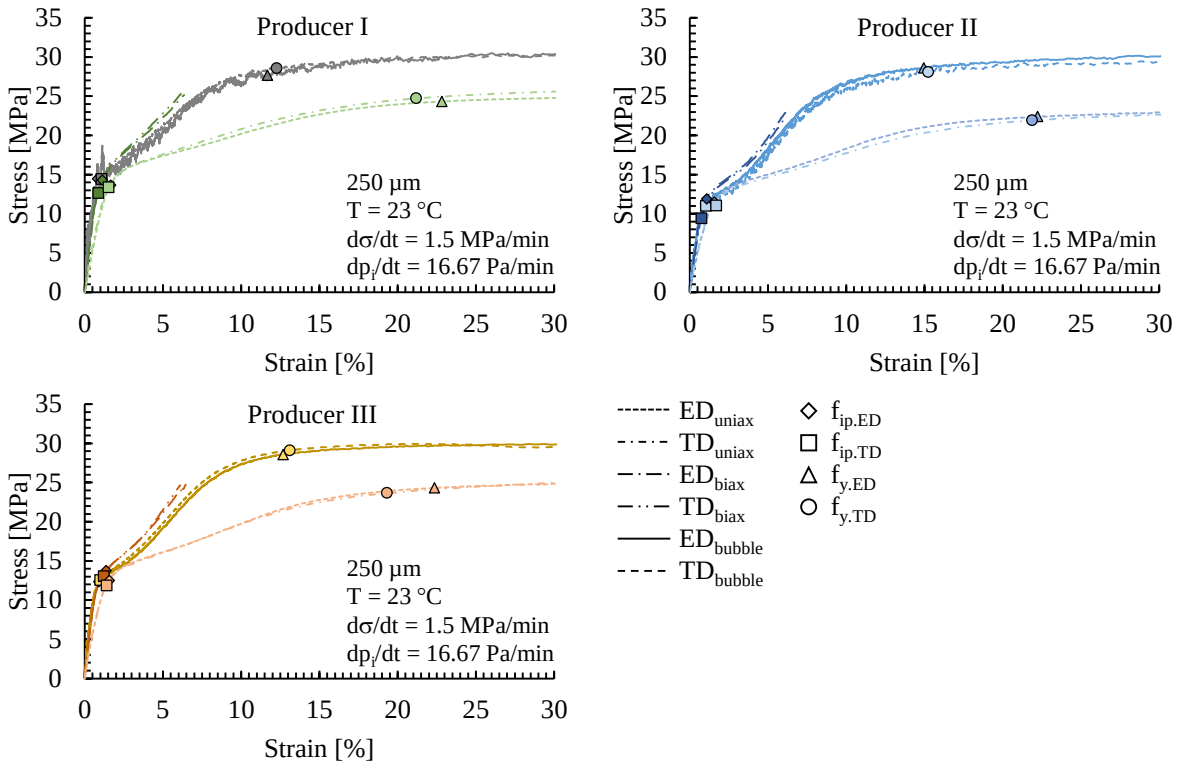


Figure 11. Comparison of the mechanical behaviour of ETFE foils derived in uniaxial, biaxial and multiaxial tensile tests using strip, cruciform and bubble inflation specimens of producers I, II, and III.

Table 2. Comparison of ETFE foils' tensile behaviour using different types of specimens in a uniaxial (1.5 MPa/min), biaxial (1.5 MPa/min) and multiaxial (16.67 Pa/min) stress state (250 µm, T = 23 °C).

Producer		I			II			III		
Test type		Uniaxial[1)]	Biaxial[2)]	Bubble inflation[3)]	Uniaxial[1)]	Biaxial[2)]	Bubble inflation[3)]	Uniaxial[1)]	Biaxial[2)]	Bubble inflation[3)]
f_{ip}	ED	13.6	14.3	14.4	11.5	11.9	11.3	12.5	13.7	12.3
[MPa]	TD	13.3	12.6	14.4	11.0	9.4	11.0	11.9	13.0	12.5
ε_{ip}	ED	1.7	1.1	0.8	1.6	1.1	1.0	1.6	1.4	0.9
[%]	TD	1.5	0.9	1.1	1.7	0.8	1.1	1.4	1.2	1.0
f_y	ED	24.3	-	27.7	22.6	-	28.6	24.3	-	28.6
[MPa]	TD	24.7	-	28.6	21.9	-	28.1	23.7	-	29.1
ε_y	ED	22.8	-	11.7	22.2	-	15.0	22.4	-	12.7
[%]	TD	21.2	-	12.3	21.9	-	15.2	19.3	-	13.1
f_u	ED	43.3	-	43.4	47.6	-	45.6	45.0	-	50.5
[MPa]	TD	45.7	-	39.7	46.7	-	49.4	51.5	-	47.2
ε_u	ED	405	-	205	424	-	197	430	-	255
[%]	TD	373	-	182	416	-	228	466	-	197

[1)] Mean values; n = 5; Determination of ε_{ip} and ε_y using optical measurement and ε_u by traverse travel
[2)] Mean values; n = 3; stress ratio ED:TD 1:1; optical strain measurement
[3)] n = 1; circular base; optical strain measurement

Extensive research is demanded, characterising the strength effects caused by multiaxial loading to formulate more accurate k-factors for the ULS and SLS design. Herein, additional parameters influencing the mechanical behaviour such as the strain rate and test temperature have to be analysed simultaneously. A design method should be developed that allows the use of increasing strengths and

load bearing capabilities of ETFE foils due to multiaxial loading derived in bubble inflation tests, while maintaining safety against small cracks.

4. Conclusions

In the draft technical specification prCEN/TS 19102 [1] just recently submitted to the standardisation body, ETFE foil structures have to be designed in the ultimate limit state (ULS) and the serviceability limit state (SLS). In these design situations, different mechanical properties are required, which are typically determined in uniaxial tensile tests. To consider various effects such as multiaxial stresses occurring in ETFE foil structures, the k-factor concept is introduced, which is based on the A-factor concept, see e. g. Minte [2]. In prCEN/TS 19102, the modification factor considering biaxial/multiaxial stresses k_{biax} is set to 1.0 for ULS and SLS. In the frame of this contribution, a comparison is conducted between the mechanical behaviour of ETFE foils under uniaxial and biaxial/multiaxial tension using strip, cruciform and bubble inflation specimens. The tests performed reveal that the derived stress-strain diagrams show qualitatively equal stress-strain curves of ETFE foils independent of the stress state with three decisive strength characteristics, f_{ip}, f_y, and f_u.

ETFE foils exhibit a higher strength and stiffness under biaxial/multiaxial tension in comparison to the behaviour under uniaxial tension regarding the first and second inflexion point, f_{ip} and f_y. In the bubble inflation tests performed, specimen rupture occurred at several hundred percent strain with an average of 219 % strain in ED and 202 % strain in TD at stresses higher than f_y with average ultimate tensile stresses f_u of 47 MPa in ED and 45 MPa in TD. As the numbers of f_u are similar to those measured in uniaxial tensile tests, these preliminary tests confirm the current assumption of a k-factor considering biaxial/multiaxial stresses of $k_{biax} = 1.0$ for ULS design. In SLS design, the modification factor of $k_{biax} = 1.0$ is applicable for the first strength characteristic f_{ip}. The test series revealed that small damages/cracks can lead to leakages in the specimen. This occurred in 1/3 of the tests, each time shortly after reaching the yield point ε_y/f_y. With the occurrence of a leakage, the pressure system could not maintain the internal pressure, so that the internal pressure decreased to 0 Pa leading to a loss of prestress and thus to a loss of the load bearing capabilities of the specimen. It was concluded for practical structural applications that the yield stress should not be exceeded to avoid this type of failure. To ensure stresses not reaching the yield strength determined in bubble inflation tests, the modification factor for the uniaxially determined yield strength $f_{y,uni}$ is also proposed as $k_{biax} = 1.0$. By this way, the strength increase of at least 10 % at the yield strength under multiaxial loading compared to uniaxial is used as a safety margin to avoid the risk of appearance of small cracks.

To specify the modification factor k_{biax} more reliably, more bubble inflation tests are required. Simultaneously, influencing parameters such as the temperature and strain rate as well as different stress ratios should be investigated leading into a design method considering the strength increasing effects due to multiaxial loading.

Acknowledgements

The authors wish to express thanks for the funding of this research by the Deutsche Forschungsgemeinschaft (DFG – German Research Foundation) in the framework of the research project “Characterisation of the nonlinear viscoelastic material behaviour of ETFE and ECTFE foils for the use in membrane structures in the building industry” (project STR 482/6-1).

AGC Chemicals Europe Ltd., Amsterdam, Netherlands (Fluon ETFE Film 250NJ-1550NT, Fluon ETFE Film 100NJ-1550NT), Nowofol GmbH & Co. KG, Siegsdorf, Germany (Nowoflon ET 6235 Z in 250 µm and 100 µm) and Textiles Coated Europe GmbH (TCI), Kaarst, Germany (ETFE AG 250 µm, ETFE AG 100 µm), provided the investigated 100 µm and 250 µm ETFE foil materials. The materials provided by AGC were shipped from Japan, the materials from Nowofol came from Germany, and the materials from TCI were shipped from USA.

The provision of test material by AGC Chemicals Europe Ltd., Amsterdam, Netherlands, NOWOFOL® Kunststoffprodukte GmbH & Co. KG, Siegsdorf, Germany, and Textiles Coated Europe GmbH (TCI), Kaarst, Germany is gratefully acknowledged.

References

[1] prCEN/TS 19102:2022, "Design of tensioned membrane structures", Final draft submitted to NEN (unpublished).

[2] J. Minte, „Das mechanische Verhalten von Verbindungen beschichteter Chemiefasergewebe", Dissertation, RWTH Aachen, Aachen, Germany, 1981.

[3] L. Schiemann, "Tragverhalten von ETFE Folien unter biaxialer Belastung", Dissertation, TU Munich, Munich, Germany, 2009.

[4] K. Moritz, „ETFE Folie als Tragelement", Dissertation, TU Munich, Munich, Germany, 2007.

[5] EN ISO 527-1:2019-12, Plastics – Determination of tensile properties – Part 1: General principles (ISO 527-1:2019); German version EN ISO 527-1:2019.

[6] EN ISO 527-3:2019-12, Plastics – Determination of tensile properties – Part 3: Test conditions for films and sheets (ISO 527-3:2018); German version EN ISO 527-3:2018.

[7] F. Surholt, J. Uhlemann and N. Stranghöner, "Temperature and strain rate effects on the uniaxial tensile behaviour of ETFE foils", in *Polymers*, vol. 14, pp. 3156, 2022.

[8] C. Galliot, L. Luchsinger, "Uniaxial and biaxial mechanical properties of ETFE foils", in *Polymer Testing*, vol. 30, pp. 356-365, 2011.

[9] J. Hu, W. Chen, B. Zhao, K. Wang, „Uniaxial tensile mechanical properties and model parameters determination of eth-ylene tetrafluoroethylene (ETFE) foils", in *Construction and Building Materials*, vol. 75, pp. 200-207, 2015.

[10] J. Hu, W. Chen, B. Zhao, D. Yang, „Buildings with ETFE foils: A review on material properties, architectural performance and structural behaviour", in *Construction and Building Materials*, vol. 131, pp. 411-422, 2017.

[11] B. Zhao, W. Chen, „Experimental study and constitutive modeling on viscoelastic-plastic mechanical properties of ETFE foils subjected to uniaxial monotonic tension at various strain rates", in *Construction and Building Materials*, vol. 263, pp. 120060, 2020.

[12] B. Zhao, W. Chen, "Rate-dependent mechanical properties and elastic modulus of ETFE foils used in inflated forming of transparency air-inflated cushion membrane structures", in *Engineering Structures*, vol. 227, pp. 111404, 2021.

[13] K. Saxe, "Zur Berechnung und Bemessung von ETFE-Folientragwerken", in: *Proceedings of the Essener Membranbau Symposium*, Essen, Germany, 28. September 2012, Shaker Verlag, Aachen, Germany, 2012.

[14] G. Sun, M. Wu, X. Qu, S. Xue, "Experimental investigation of the uniaxial tensile properties and thermal deformation of the ETFE membrane at different temperatures", in *Construction and Building Materials*, vol. 327, pp. 126944, 2022.

[15] R. Lippke, „Folien als transparente Elemente in der Fassade: Mechanische und bauphysikalische Eigenschaften", Dissertation, Technische Universität Berlin, Berlin, Germany, 2009.

[16] N. Murphy, "Providing Stress Controlled Equi-biaxial Fatigue Test Data for Elastomers Using the Bubble Inflation Method", PhD Dissertation, Dublin Institute of Technology, Ireland, 2009.

[17] M. Johnson, N. Murphy and R. Ekins, "Equi-biaxial fatigue testing of EPM utilising bubble inflation", in *Polymer Testing*, vol. 53, pp. 122–131, 2016.

[18] J. Javořik and Z.Dvořàk, "Equibiaxial Test of Elastomers", in *KGK*, November 2007.

IASS 2023
July 10–14 Melbourne
Integration of Design and Fabrication

Proceedings of the IASS Annual Symposium 2023
Integration of Design and Fabrication
10–14 July 2023, Melbourne, Australia
Y.M. Xie, J. Burry, T.U. Lee and J. Ma (eds.)

Effect of temperature on strength of PVC coated fabrics

Chengjun GAO[b], Zilong ZHOU[b], Sen WANG[b], Wujun CHEN[a,*], Bing ZHAO[b], Jianhui HU[b]

[a,*] Space Structures Research Center, Shanghai Jiao Tong University
No. 800 Dongchuan Road, Minhang district, Shanghai 200030, China
cwj@sjtu.edu.cn

[b] School of Aeronautics and Astronautics, Shanghai Jiao Tong University, Shanghai 200030, China

Abstract

PVC coated polyester fibre membrane is one of the most widely used materials since its good mechanical properties and durability. In this paper, the strength of PVC coated polyester fibre membrane under different temperature were studied. The results showed the strength and stiffness decreased significantly with the increasement of test temperatures, which may be the cause of stress relaxation and wrinkles of the membrane structure. This study can provide reference for fire safety design, as well as for product design of material manufacturers.

Keywords: fabric membrane, temperature, strength, stiffness

1. Introduction

The architectural membrane structure has flourished, not only widely used in stadiums, transportation hubs, commercial exhibitions, but also in special application such as shelter hospitals, stockyards, logistics centres, and so on. However, with the expansion of application scenarios and the increase of fire risk factors faced during the service life of architectural membrane structures, fire prevention of architectural membrane structures becomes more and more important.

The key to fire protection in architectural membrane structures is the mechanical properties of the fabric membrane under high temperature, especially the strength and stiffness have an important impact on structural safety. Inevitably, the strength of the membrane material decreases under fire, and this drastic decrease in strength can lead to structural damage as it is difficult to maintain the original load-bearing capacity in a fire environment. The high temperature of fire also causes softening of the fabric membrane, making it difficult to maintain the original structural shape due to the loss of membrane surface pretension.

Ambroziak et al. [1] conducted uniaxial tensile tests at different temperatures and determined the variation of nonlinear elastic parameters with temperature in the range of -30°C to +70°C, which is far from the fire temperature. Ma [2] studied the tensile strength and elongation at break of PVC and PTFE coated fabrics by uniaxial tensile tests at different temperatures; PVC coated fabrics showed a 44% ~ 52.5% reduction in strength at 170°C and an increase in elongation at break of more than 20%; PTFE coated fabrics showed a 17.5% to 19.1% reduction in strength at 220°C and an increase in elongation at break of 6% to 11%. Sun et al. [3] conducted an experimental study of four kinds of PVC coated fabrics with uniaxial loading from 23°C to 250°C. The results showed that the elastic modulus at 230°C was only 1/10 of that at room temperature, and the ultimate tensile strength (UTS) at 200°C was about 1/2 of that at room temperature. Thus, both PVC and PTFE coated fabrics shown significant elastic modulus and strength reduction problems at high temperatures.

In this paper, the mechanical properties of PVC coated fabrics and weld seam at high temperature was tested in uniaxial tensile test method, and the test temperature was gradually increased from room

Copyright © 2023 by Chengjun GAO, Wujun CHEN, Sen WANG, Zilong ZHOU and Bing ZHAO. Published in the Proceedings of the IASS Annual Symposium 2023 with permission.

temperature (20℃). The mechanical properties of coated fabrics and weld seam at high temperature were obtained in this study. The weld was more prone to damage in fire damage since the strength of the weld at high temperatures is lower than the strength of coated fabrics.

2. Specimen

In this case, rectangular specimens with twisted clamp were used to avoid breakings at the gripped ends [28]. The rectangular specimen with a length of 1 m and width of 50 mm, and the lap length was 50 mm in weld specimen. The longer specimen was for an extra loop at the twisted clamping to prevent slippage caused by melting coating. The detailed dimensions of the two specimens were illustrated in Fig. 1. The material in this study was two kinds of PVC coated fabrics, JD5500 from Zhejiang Jinda New Material Co., Ltd and the basic parameters of materials was shown in Table 1.

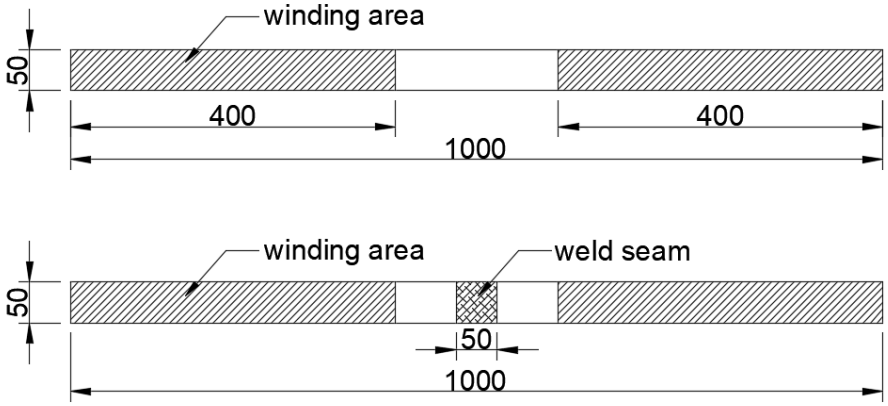


Figure 1. Dimensions of rectangular specimen

Table 1. Basic parameters of materials

Material	JD5500
Total thickness	0.84 mm
Total mass	1055 g/m^2
Tensile strength (warp/filling)	110/105 N/mm
Tear strength (warp/filling)	780/770 N

3. Test method

Mechanical tests were carried out on a single axis servo-hydraulic test machine UTM 400 with computer control and acquisition. Specimens were twisted at the twisted clamps and were preloaded with 1.0 N in order to ensure the removal of slack just prior to the tests. The displacements were measured between two ends of the rectangular specimens and load was measured by a standard force transducer. After mounting the retangular specimen, the target temperature was reached in 15 minutes and maintained for 15 minutes. Then apply tensile force to the specimen until failure, and record the tensile force and fixture displacement

The temperature chamber used for the test was shown in Fig. 2. Four electric heating tubes were placed inside the environmental chamber to directly heat the specimen, and the maximum temperature can reach 300°C. The temperature was controlled by PID control strategy with a control accuracy of ±2°C. The clamp was located outside the temperature chamber, and the hole of temperature chamber was sealed with asbestos to prevent heat escape. The thermocouple was lightly attached to the specimen to collecte the temperature, and the value of temperature was sent to temperature control system.

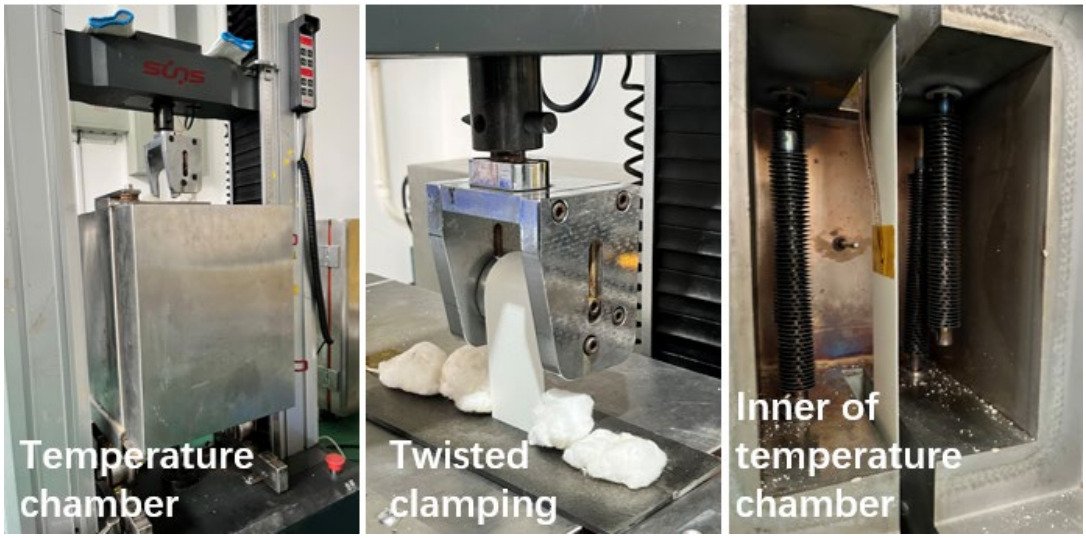


Figure 2. Temperature chamber and specimen installation method

4. Test result

4.1 Failure form

All of the specimens were broken in the middle of the test piece, except that no valid data was obtained at 80 °C since the coating of PVC partially softened and on the twisted clamping. The fracture pattern of the warp specimen at different temperatures were shown in Fig. 3. The fracture was relatively smooth at 20 °C, while the port flatness decreased with the increase in temperature and the yarn peeling phenomenon became more serious. When the temperature was between 20 °C and 60 °C, the apparent quality of the specimen did not change significantly. Further increasing the temperature, the surface color of the specimen to deepen, which was accompanied by the emission of white smoke and a pungent odor. The specimen became charred black and exhibited complete loss of strength at 250 °C.

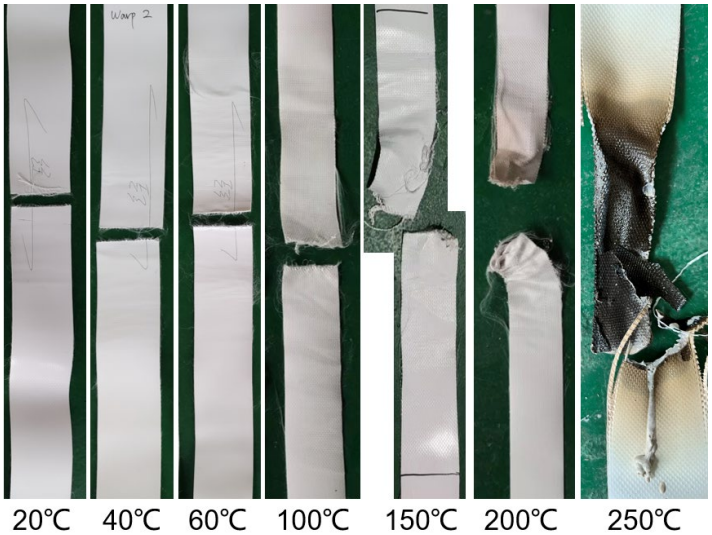


Figure 3. Fracture pattern of warp specimens at each temperature

The fracture pattern of the welded specimens was shown in Fig. 4. The fractures were flush and occurred in the same direction as the weld. At 20℃ and 40℃, the fracture were located at the intersection of the

weld and the membrane and the weld joint remaining intact. The strength at edge of the weld was reduced due to the high temperature of the welding knife. The weld specimens were damaged in the form of joint separation from 60℃, and the weld strength was gradually reduced. Weld joint were separated and the surface of the specimens were blackened at 200℃。

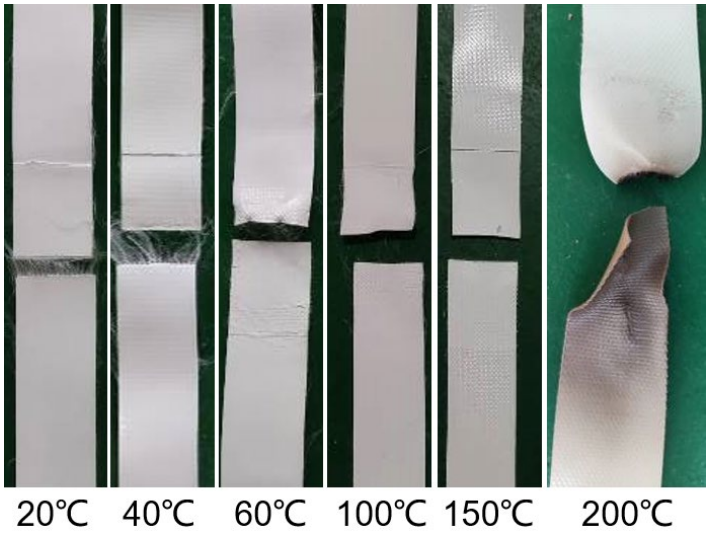
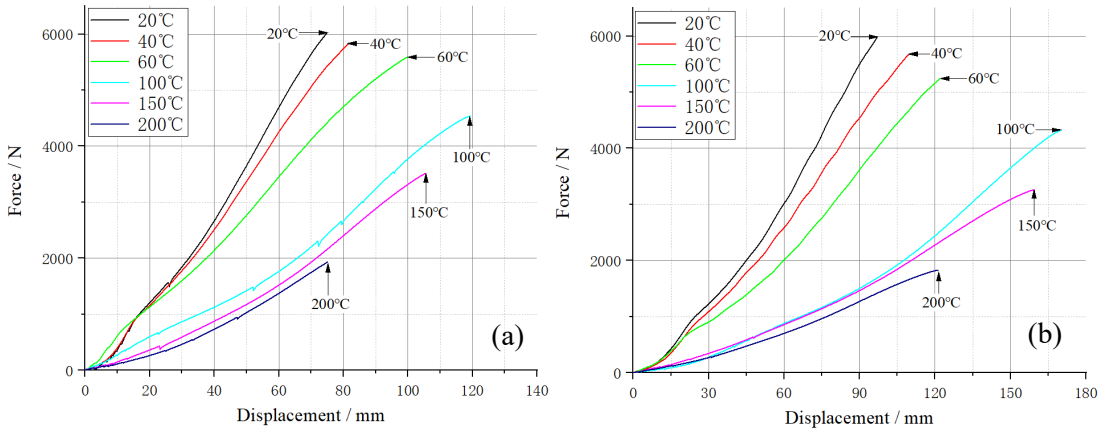


Figure 4. Fracture pattern of weld specmens at each temperature

4.2 Force-displacement curves

The weld joint failed at 200℃, while the fabric underwent charring at 250℃. Tensile tests were performed on the specimens in both the warp and weft directions, ranging from 20 ℃ to 200℃, as well as on the weld joint specimens, ranging from 20 ℃ to 150℃.

The curves in Fig. 5 exhibited non-linear behaviour, with stiffness gradually decreasing. Chen et al. [4] described non-linear concave-convex changes in the tensile behaviour of the yarns in the membrane material, which were also observed below 60℃. However, at temperatures exceeding 100℃, the initial portion of the curve exhibited concave behaviour, with a subsequent trend towards convex behaviour, without the concave-convex behaviour observed at temperatures below 60℃.



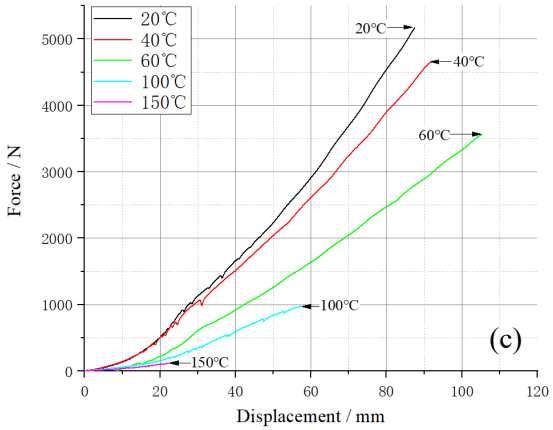


Figure 5. Force-displacement curves: (a) warp, (b) weft, (c) weld.

4.3 Uniaxial tensile strength

The tensile force at the time of fracture was recorded, and the uniaxial tensile strength of specimens at each temperatures were listed in Table 2 and Fig. 6. The strength of both the fabric and the weld was significantly reduced.

Table 2. The uniaxial tensile strength of specimens at each temperatures

Temperature (°C)	Warp		Weft		Weld joint	
	Strength (N/mm)	Percentage of 20 °C strength	Strength (N/mm)	Percentage of 20 °C strength	Strength (N/mm)	Percentage of 20 °C strength
20	118.11	100%	117.20	100%	101.26	100%
40	114.06	97%	111.35	95%	90.94	90%
60	109.63	93%	102.74	88%	70.46	70%
100	88.90	75%	84.70	72%	18.77	19%
150	68.93	58%	66.02	56%	2.28	2%
200	37.87	32%	35.84	31%	Separated	-
250	Burned	-	Burned	-		

Temperature has a significant effect on the strength of the membrane. When the temperature was below 60°C, the specimen was able to maintain 90% of its initial strength, but only about 30% of strength remaining at 200°C. When higher than 250 °C, the specimens were burned out. Ma [2] studied that the tensile strength of PVC coated fabircs in the warp and weft directions decreased 44% and 52.5% of its initial strength at 170°C respectively, which was similar to the results of this test.

The strength of the weld joint was found to be more sensitive to temperature, with a 30% reduction in strength observed when the temperature increased from 20°C to 60°C. At a temperature of 150°C, the strength decreased to only 2%, rendering it unable to withstand the pre-tension of the membrane structure. The weld joint failed completely at 200°C.

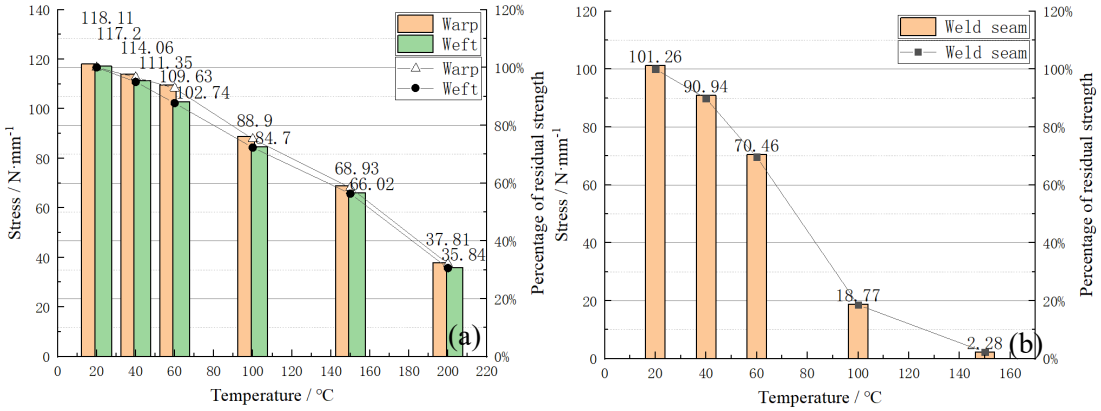


Figure 6. Uniaxial tensile strength and the percentage of residual strength: (a) warp and weft, (b) weld.

5. Conclusions

Temperature plays a crucial role in the strength of the specimen. This study provides important insights into the thermal behaviour of PVC coated fabrics and has potential applications in the field of fire performance analysis of membrane structures. PVC coating exhibited a softening phenomenon at a temperature of 80℃, resulting in slippage of the membrane material during the tensile testing process. The strength reduction of the weld was significantly greater than that of fabric membrane, so more attention needs to be paid to weld damage during fires

Acknowledgements

The authors acknowledge the financial support from the National Natural Science Foundation of China (Nos. 52278193, 52278191). The fabrics and specimens used in the tests were supplied and fabricated by Zhejiang Jinda New Material Co., Ltd.

References

[1] A. Ambroziak, P. Kłosowski, "Influence of thermal effects on mechanical properties of PVDF-coated fabric," *Journal of Reinforced Plastics and Composites,* vol. 33(7), pp. 663-673, 2013.

[2] J. Ma, "Experimental study on high temperature mechanical properties of building membranes," Master Degree in Engineering, Harbin Institute of Technology, Harbin, 2018.

[3] G. Sun, L. Li, S. Xue and Y. Yang, "Mechanical properties of polyester-coated fabric membrane material subjected to uniaxial loading at elevated temperatures," *Journal of Materials in Civil Engineering,* vol. 33(7), pp. 4021169, 2021.

[4] J. Chen, W. Chen and D. Zhang, "Experimental study on uniaxial and biaxial tensile properties of coated fabric for airship envelopes" *Journal of Reinforced Plastics and Composites,* vol. 33(7), pp. 630-647, 2013.

IASS 2023
July 10–14 Melbourne
Integration of Design and Fabrication

Proceedings of the IASS Annual Symposium 2023
Integration of Design and Fabrication
10–14 July 2023, Melbourne, Australia
Y.M. Xie, J. Burry, T.U. Lee and J. Ma (eds.)

Experimental methods and performance of membrane structures: A systematic literature review

Haonan HUANG[a], Yaozhi LUO[a,*]

[a,*] College of Civil Engineering and Architecture, Zhejiang University
866 Yuhangtang Rd, Hangzhou 310058, P.R. China
luoyz@zju.edu.cn

Abstract

Membrane structures have become popular in public, civil, and industrial buildings due to their diverse appearance, adaptability, low cost, and durability. However, the application of membrane structures and the precise assessment of their structural qualities are constrained by the fact that only a small number of studies have been conducted on them using experimentally obtained response data and environmental factors of models or actual structures. An effective method for analyzing the properties of membrane structures involves directly obtaining response data or environmental characteristics from a model or building. This method can also aid in the advancement of theoretical studies and simulation techniques, as well as the implementation of specifications. This paper provides a thorough discussion of the mechanical, thermal, and energy performance of membrane structures, as well as the deployment and deflation of inflatable varieties. The composition of the structure is the most essential component influencing its performance, and appropriate design can lead to improvements in mechanical characteristics, thermal environment, and energy consumption. The advantages and challenges of the current literature are also discussed.

Keywords: membrane, performance, thermal environment, energy, deployment, deflation

1. Introduction

Membrane structures have gained significant attention in recent decades due to their versatility in appearance and their ability to be constructed quickly as permanent or semi-permanent buildings [1]. They are also highly portable and adaptable for use in temporary construction projects [2]. In recent years, there has been a significant increase in the use of membrane structures, which can be attributed to the advancements in architectural membrane materials and improvements in construction technology.

The significant deformation of the membrane under external loads is a distinctive feature. Consequently, the mechanical performance of the membrane structure has become a major concern. The building sector is responsible for 40% of primary energy consumption, highlighting the importance of energy efficiency in construction [3]. As green concepts become increasingly prevalent, achieving a balance between energy consumption and maintaining a comfortable internal temperature environment is a key focus in the advancement of membrane buildings. Additionally, the deployment efficiency and safe deflation of inflatable membrane structures have been analyzed in recent studies [4, 5].

Membrane structures possess unique properties that distinguish them from traditional building materials, resulting in challenges when determining their architectural performance through conventional research methods [5]. Due to the significant geometric nonlinearity caused by the lightweight and flexible nature of membrane structures [6], precise structural analysis is vital for the formulation of design principles and the successful implementation of these structures [7]. Theoretical studies and numerical simulations

Copyright © 2023 by Haonan HUANG and Yaozhi LUO. Published in the Proceedings of the IASS Annual Symposium 2023 with permission.

have shed some light on the structural properties of membrane structures. However, the reliability of the results may be impacted by the simplification of structural aspects or the application of models during the analysis process, raising concerns about the accuracy of the findings [8]. Understanding the structural performance of membrane structures can be improved by examining data gathered from models or real structures. This procedure also contributes in the improvement of finite element models and the verification of theoretical equations.

In this paper, a systematic review of the performance of membrane structures is conducted from five perspectives: mechanics, thermotics, energy, deployment, and deflation. A comprehensive understanding of these topics is crucial for the development of membrane structure specifications and for promoting their application in a wide range of fields.

2. Application of membrane structure

Polyvinylchloride (PVC), polyvinylidene fluoride (PVDF), ethylene tetrafluoroethylene (ETFE), and polytetrafluoroethylene (PTFE) are among the commonly used membrane materials in construction [9, 10]. Different combinations of materials result in various membrane types with distinct characteristics. Although there is a broad selection of membrane materials to choose from, a few dominant production types have dominated the market, accounting for 90% of membrane structures used in building construction [11]. As illustrated in Figure 1, the purpose of a building plays a significant role in determining the choice of membrane material. Membranes are more commonly utilized in enclosed permanent buildings than in other structures.

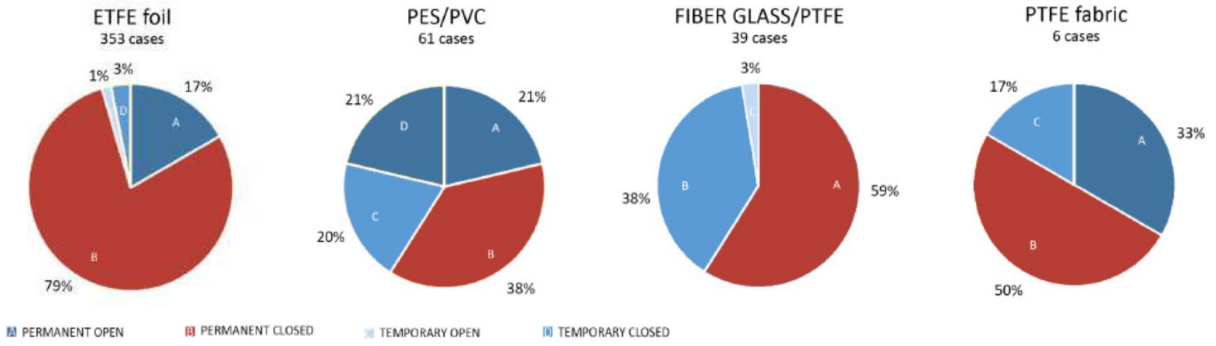


Figure 1. The utilization of membrane materials [11].

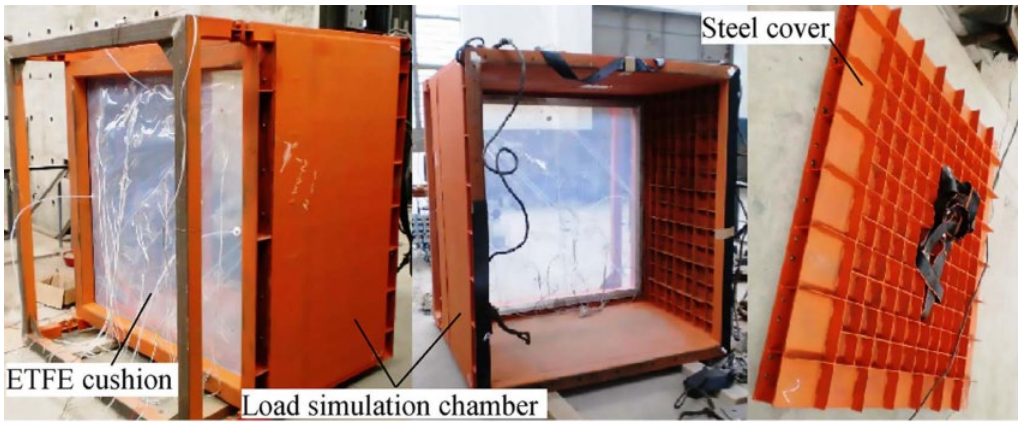
Depending on the building shape and supporting conditions, membrane structures are classified into tensioned, skeleton, cable membrane, and inflatable structures in the engineering field [12]. Engineers have also developed various derivative structures to cater to specific service requirements [13, 14].

3. Mechanical performance

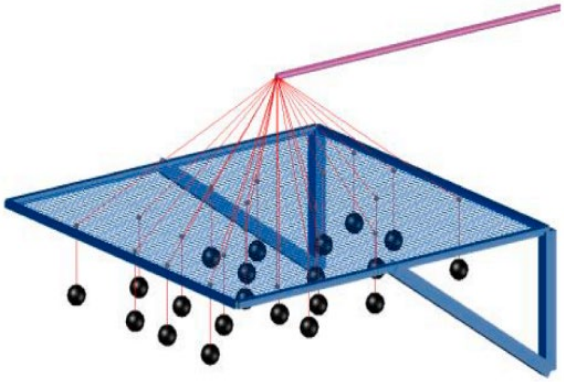
The mechanical behavior of membrane structures can be primarily determined by analyzing their response to external loads. Membrane structures are subjected to external loads, which can be caused by natural phenomena (for actual buildings) or induced by human activities (for test models). The progress in technology has made it achievable to mimic the external loads that membrane structures might confront in actual environments under controlled laboratory conditions. Several load simulation devices are depicted in Figure 2, which are utilized for replicating external loads on membrane structures.

The unique properties of membrane materials necessitate consideration of load distribution across the structural elements, as variations in loads can greatly affect the load-carrying capacity of the structure [15]. One method to address this is by adding an auxiliary structure to the exterior of the membrane, which can improve load-bearing performance while also retaining the flexibility and other desirable characteristics of the membrane structure [16]. The stiffness of a membrane structure is closely linked

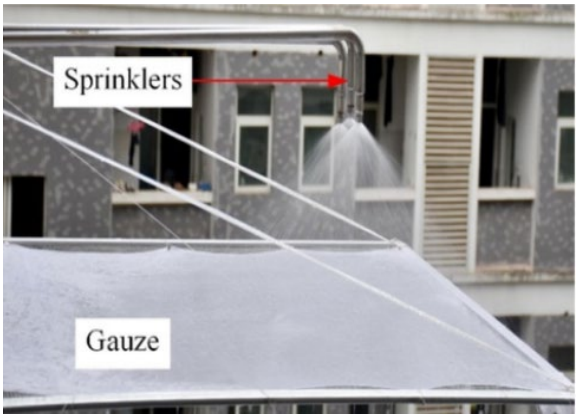
to the magnitude of prestress or internal pressure. However, the relationship between these factors is non-linear, and as the prestress or internal pressure increases, the corresponding increase in stiffness gradually decreases [17]. The long-term stress on membrane structures during regular use can result in a creeping phenomenon, which causes the material to experience increased deformation and reduced maximum structural stress over time [18, 19]. The welds that connect the membranes function as local reinforcement for the structure, but the distribution of stresses is not significantly affected by them [20]. Due to the significant impact of shear stress, the deformation of an air beam under external load is best calculated using the Timoshenko beam theory rather than the Bernoulli beam theory [21].



(a) Load simulation device.



(b) Hail simulation device.



(c) Rainfall simulation device.

Figure 2. Experimental devices [22-24].

The oscillation of the structure during wind-induced vibration is affected by the alteration of the surrounding airflow pattern, resulting in a lower frequency of oscillation than in a vacuum, referred to as added mass [25, 26]. As the wind speed increases, the added mass also increases, significantly influencing the structure's displacement [27]. Wind-induced vibration can excite multiple vibration modes, and the amplitude and damping ratio are positively correlated with wind speed [28]. In the case of aeroelastic instability in tension membranes due to vortex-induced resonance, only one vibration mode is excited and leads to periodic destabilization [29]. Flutter occurs when the membrane deflects in a divergent direction and takes on the shape of standing waves [30]. The deformation of the structure was more prominent in the lateral and vertical directions along the airflow than in the longitudinal direction [8]. The membrane structure has different failure modes when subject to wind pressure and suction. Edge tearing is the primary cause of failure under wind pressure, while holes in the weld are the main cause of failure under excessive wind suction [31]. Wind tunnel is one of the most common experimental devices used for wind response of membrane structures. The deformation behavior of the

membrane structure under external loads makes it inappropriate to use a rigid model with an undeformed construction shape, as this may result in considerable discrepancies between the measured data and the actual state of the structure.

The properties of impact loads on the structure in nature are unknown, resulting in stochastic vibration and deformation [32]. Large deformations may cause the structural pretension to decrease, making the structure unserviceable when exposed to wind loads below the design value [23]. Moreover, structures with a low tear strength in the membrane are susceptible to scratches and punctures from impact objects [33]. The interaction of incident and reflected waves from the boundary triggered high-frequency vibrations during the early stages of vibration caused by an impact.

Wrinkling is a common issue that arises when compressive or shear stresses are applied to membranes, and it occurs locally when the maximum stress exceeds a critical threshold [34]. This phenomenon, which is a form of localized buckling, can significantly compromise the structural stability and performance. The prediction of the buckling behavior through theoretical and numerical methods is complicated by the complex wrinkling effect. Therefore, it is crucial to consider the wrinkling effect in the design and analysis of membrane structures. The creation of new wrinkles is driven by the local buckling of pre-existing wrinkles, in addition to changes in local modes [35]. The distribution of wrinkles is greatly influenced by the initial imperfections in membrane thickness, and the shapes of wrinkles cannot be uniquely determined when the membrane undergoes repeated deformations under identical conditions [36]. Wrinkles in the membrane affect its vibration modes and create areas of high stress at the wave peaks. The critical wrinkle strain can be calculated using the membrane's out-of-plane displacement and in-plane stress, with the mean principal stress increasing as shear displacement increases [37, 38].

4. Thermal environment

The thinness and high transparency of membrane structures make them less thermally insulated than traditional structures, with limited temperature inertia. Consequently, membrane structures rely heavily on temperature influences and usually have poor thermal comfort [39, 40]. Onsite measurements are the most appropriate method for acquiring building performance due to the solid space- and time-dependent characteristics of the structural temperature environment [41].

The temperature distribution in non-enclosed areas is affected by wind speed and direction, solar radiation, and the convective heat transfer coefficient on the membrane surface. As a result, the temperature inside the building is primarily dependent on the outdoor temperature and indoor heat sources. For enclosed spaces, the temperature is positively correlated with height and varies depending on the horizontal position, while the peak temperature occurs later as height decreases [42, 43]. Under natural ventilation conditions, the temperature distribution in a room is more influenced by solar irradiation than by airflow, given that the latter remains mostly stationary. Temperature fluctuations within membrane structures are significantly impacted by periodic changes in outdoor temperatures, with indoor air temperatures exhibiting a delay of less than 60 minutes compared to outdoor air temperatures [44, 45]. The correlation between the indoor and outdoor temperatures of an industrial membrane warehouse over time is visualized in Figure 3. Changes in outside temperature can cause more dramatic temperature fluctuations inside the building.

The temperature inside and outside of membrane structures plays a crucial role in their functionality and serviceability. In multilayer structures, the temperature on the side facing hot or cold air undergoes drastic variations, while the other side experiences minor differences due to the low thermal conductivity of the material and air between the membranes [4, 46]. A decrease in temperature reduces the degree of deformation in a structure under external loads, but the load-carrying capacity does not vary significantly [4]. The temperature difference has a significant impact on the internal pressure. Furthermore, a drop-in temperature leads to a decrease in the natural frequency of the structure and the internal force of the cable, affecting their performance and stability [47, 48]. Attaching elements comprised of insulating

materials to the structure is one way to lessen the effect of temperature on membrane systems. Despite the poor heat resistance of membrane materials, the use of retractable membrane structures can be a viable solution for improving the temperature conditions within pre-existing buildings.

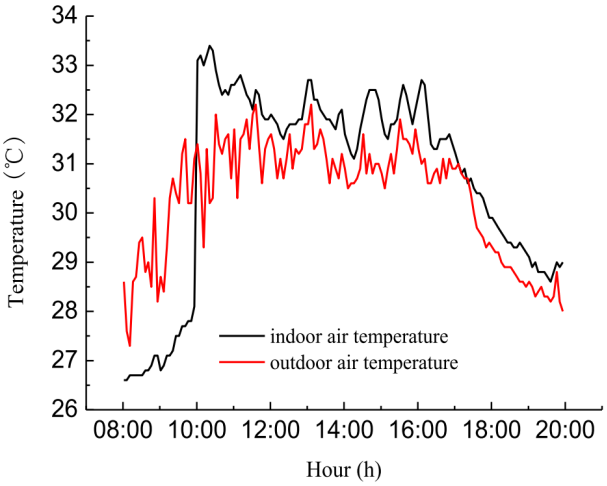


Figure 3. Indoor and outdoor temperature variation time course [45].

5. Energy performance

The numbers reveal that the building industry uses up almost a third of the world's energy resources [49]. With the increasing focus on energy conservation, it is becoming increasingly popular to enhance the energy efficiency of buildings. Energy performance in buildings is largely determined by the building's design. Natural lighting through the light transmission of membrane material can help lower the energy needed for artificial lighting, which is a key factor in improving energy efficiency in buildings. Additionally, the use of energy-efficient heating, ventilation and air conditioning (HVAC) systems, such as geothermal or solar-powered systems, can also significantly reduce energy consumption. A comparison of three membrane structure designs - single-layer, double-layer with cushions, and double-layer with a continuous air gap - showed differences in energy consumption. The energy savings achieved by the second and third designs were 11% and 18% respectively, in comparison to the single-layer design. Nonetheless, the same results as the single-layer design can be achieved by reducing infiltration losses or adding a low-emissivity coating [40]. The addition of photovoltaic (PV) panels to membrane structures allows for the conversion of solar energy to electrical energy, which can be harnessed to power the membrane, reduce the reliance on external energy sources, and promote sustainability.

6. Deployment and deflation

Inflatable structures, such as arches and tubes, have the potential to be rapidly deployed and provide temporary shelter in emergency situations, such as natural disasters or refugee camps [15]. The quick setup time is crucial in these scenarios, as it allows for immediate relief efforts to take place. Geometric configuration and ground placement prior to inflation are crucial for the successful deployment of inflatable arches. A larger diameter and lower height of the arch can facilitate easier deployment and lower peak pressures during inflation. In-plane deployment is more challenging than out-of-plane, and self-erection without external support can be problematic [4]. The location of wrinkles during inflation is variable and can differ between subsequent inflations. Assistance during the deployment phase, such as the use of elevation or other methods, can be beneficial in enhancing the efficiency of structural deployment.

Unlike traditional buildings that rely on rigid components for stability, inflatable membrane structures depend on internal pressure to provide adequate stiffness. Consequently, deflation-induced loss of load-

bearing capacity can lead to the complete collapse of the entire structure. Thus, the evacuation of occupants must be considered during the assessment of the dynamic deflation of the structure. The internal pressure of inflatable arches and tubes during deflation is typically lower than during deployment, due to a hysteresis effect that occurs when they reach a similar deformation state [50]. The internal pressure of the inflatable membrane structure undergoes a nonlinear shift, initially exhibiting a sharp decrease and then stabilizing as the deflation time increases. This leads to the structural displacement exhibiting a nonlinear increase followed by stabilization into a linear trend. Although the internal pressure of the structure drops rapidly during the early stages of deflation, the change in volume of the structure is negligible, as depicted in Figure 4. If a certain level of positive pressure is maintained within the structure, its shape can be largely retained, providing enough time for personnel to evacuate during an emergency. Wrinkling of the membrane usually initiates at the corners of the structure and subsequently propagates across the surface. n the case of sudden deflation, the membrane deformation around the entrance/exit area occurs faster, which may decrease the visibility of emergency access [51]. The appearance of wrinkles in the inflatable structure is directly influenced by the distribution of the load, which is an important factor in determining the residual pressure needed for the structure to maintain its deflated form [52].

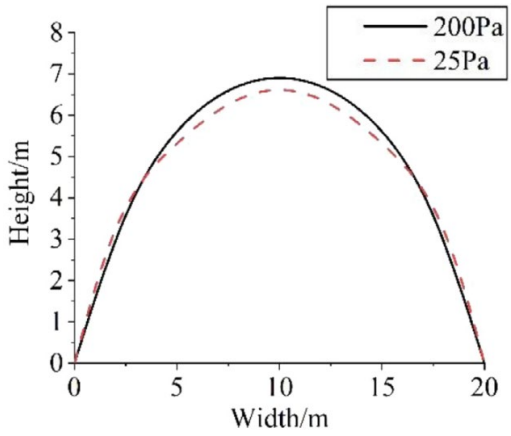


Figure 4. The structural profile at the beginning of deflation [51].

7. Measurement devices

Traditional contact measuring methods are no longer appropriate for measuring membrane structures, given their thinness and lightness, which may be influenced by the weight of the instrument. Instead, non-contact measuring instruments, such as lasers, cameras, and 3D scanners, have clear advantages when it comes to measuring membrane structures. Laser sensors can provide data on the stress and pre-stress of the membrane structure, among other factors relevant to the structure's performance by measuring the deformation of the membrane surface at a specific point. The structural pretension level can be estimated accurately using a laser sensor, which measures the maximum response amplitude of the membrane under impact load excitation. The accuracy of the estimation is directly proportional to the actual pretension magnitude. The excitation process using steel pellets results in higher accuracy than using glass and plastic pellets [53]. Devices such as 3D scanners, laser scanners, and cameras are capable of measuring multiple points at the same time, enabling the determination of the displacement field for the entire structure. This feature proves advantageous for accurately assessing the response of structures with considerable deformation and flexibility. Measuring the dynamic shape of small buildings can be achieved using 3D scanners. Laser scanning is capable of providing highly precise static profiles of structures regardless of their size. By adjusting the number of cameras, different structural data can be obtained. A static shape of the structure is obtained with a one-camera system, whereas a dynamic shape is obtained with a multi-camera system. The system's accuracy is constrained by systematic and statistical errors, although calibration algorithms based on MATLAB or OpenCV can

be utilized to reduce system errors. To reduce potential inaccuracies in data acquisition and fault detection, increasing the number of cameras and applying the least-squares method are recommended [54, 55].

The advancement of sensing technology, computing, and structural control methods has enabled the more extensive adoption of structural health monitoring (SHM) in recent years [56], but there is still a shortage of SHM applications in membrane structures, particularly in large-span ones. The monitoring system comprised of a sensor system, data acquisition and transmission system, data management system, and early warning system. The selection of measurement points is dependent on the economic and practical constraints, as well as the influence of each building component on structural safety. The key to realizing early warning of structural anomalies in the monitoring system is to achieve simultaneous processing of multiple signals from various sensors. Two approaches are used to identify anomalies in the structure: comparing the monitored data magnitude with prescribed upper limits and analyzing the structural modalities and correlation between variables [57]. The structural health monitoring system framework for a large-span membrane structure is depicted in Figure 5.

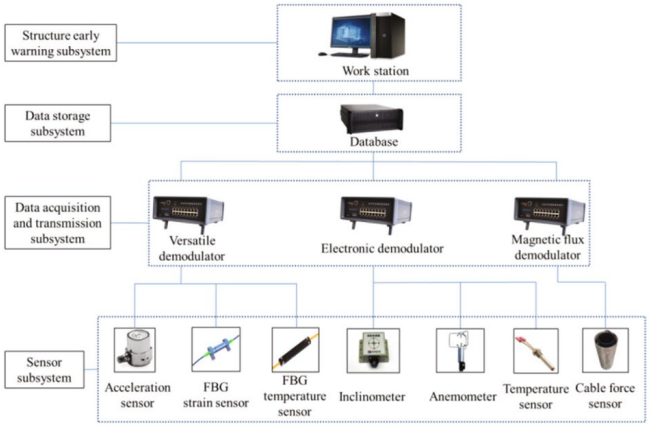


Figure 5. The framework of the SHM system for a membrane structure [57].

8. Conclusions

This paper provided an overview of the performance of membrane structures and measuring tools, which can be summed up as follows:

1) The mechanical behavior of membrane structures is closely related to their specific structural forms. Failure of membrane structures under external loads is mainly caused by damage to the joints between the membrane and the rigid boundary, as well as the seams between the membranes. The most effective approach to improving the mechanical performance of the structure is through proper design of the building configuration.

2) Optimal placement of uninflated inflatable membrane structures and assisted lifting during inflation can greatly enhance the efficiency of deployment.

3) Structural design and natural light utilization are passive methods that effectively alter the thermal environment within the building and decrease energy consumption, while ventilation systems and retractable devices are active methods that achieve similar results.

4) Contactless sensors that do not interfere with the membrane are more appropriate, and utilizing tools like cameras permit low-cost multi-point measurements.

References

[1] B. Forster and M. Mollaert, *European Design Guide for Tensile Surface Structures*, TensiNet, 2004.

[2] X. Guo, Q. Li, D. Zhang and J. Gong, Structural behavior of an air-inflated fabric arch frame." *Journal of Structural Engineering*, vol. 142, 04015108, 2016.

[3] R. Chenni, M. Makhlouf, T. Kerbache, and A. Bouzid, "A detailed modeling method for photovoltaic cells." *Energy*, vol. 32, pp. 1724–1730, 2007.

[4] Q. Li, X. Guo, J. Gong, Q. Qing, and Z. Li, "Experimental deployment behavior of air-inflated fabric arches and a full-scale fabric arch frame." *Thin-Walled Structure*, vol. 103, pp. 90–104, 2016.

[5] Q. Qing, S. Shen and J. Gong, "Deflation behavior and related safety assessment of an air-supported membrane structure." *Thin-Walled Structure*, vol. 129, pp. 225–236, 2018.

[6] X. Zhou, Z. Han, M. Gu, A.A. Zhang, W. Zhang and W. Fang, "Research on wind-induced responses of a large-scale membrane structure." *Earthquake Engineering and Engineering Vibration*, vol. 12, pp. 297–305, 2013.

[7] A. Kandel, X. Sun and Y. Wu, "Wind-induced responses and equivalent static design method of oval-shaped arch-supported membrane structure." *Journal of Wind Engineering and Industrial Aerodynamics*, vol. 213, 104620, 2021.

[8] Y. Yin, W. Chen, J. Hu, B. Zhao and Q. Wang, "In-situ measurement of structural performance of large-span air-supported dome under wind loads." *Thin-Walled Structure*, vol. 169, 108476, 2021.

[9] J. Llorens, *Fabric Structures in Architecture*, Elsevier, 2015.

[10] T. Tanigami, K. Yamaura, S. Matsuzawa, M. Ishikawa, K. Mizoguchi and K. Miyasaka, "Structural studies on eth-ylene-tetrafluoroethylene copolymer: 2. Transition from crystal phase to mesophase." *Polymer,* vol. 27, pp. 1521–1528. 1986.

[11] C. Monticelli and A. Zanelli, "Life Cycle Design and Efficiency Principles for Membrane Architecture: Towards a New Set of Eco-design Strategies." *Procedia Engineering*, vol. 155, pp. 416–425. 2016.

[12] CECS. *Technical Specification for Membrane Structures*, China Planning Press, 2015.

[13] J. Estephan, C. Feng, A.G. Chowdhury, M. A. Chavez, Baskaran and M. Moravej, "Characterization of wind-induced pressure on membrane roofs based on full-scale wind tunnel testing." *Engineering Structures*, vol. 235, 112101. 2021.

[14] J. Roekens, L.D. Laet, M. Mollaert and R. Luchsinger, "Experimental and numerical investigation of a tensairity arch." *Thin-Walled Structure*, vol. 105, pp. 112–120. 2016.

[15] K.E. Brayley, W.G. Davids and J.D. Clapp, "Bending response of externally reinforced, inflated, braided fabric arches and beams." *Construction and Building Materials*, vol. 30, pp. 50–58, 2012.

[16] C.G. Malm, W.G. Davids, M.L. Peterson and A.W. Turner, "Experimental characterization and finite element analysis of inflated fabric beams." *Construction and Building Materials*, vol. 23, pp. 2027–2034, 2009.

[17] T.S. Plagianakos, U. Teutsch, R. Crettol and R.H. Luchsinger, "Static response of a spindle-shaped tensairity column to axial compression." *Engineering Structures*, vol. 31, pp. 1822–1831, 2009.

[18] B. Zhao, J. Hu, W. Chen, J. Chen and Z. Jing, "Dynamic geometrical shape measurement and structural analysis of inflatable membrane structures using a low-cost three-camera system." *Automation in Construction*, vol. 96, pp. 442–456, 2018.

[19] B. Zhao, J. Hu, W. Chen, J. Chen, Z. Qiu and Z. Jing, "Computational method for in-situ finite element modeling of inflatable membrane structures based on geometrical shape measurement using photogrammetry." *Computers and Structures*, vol. 224, 106105, 2019.

[20] L. Gu, P. Wang, S. Chen and H. Wang, "Experimental study and FEA of ETFE cushion." *Journal of Building Engineering*, vol. 33, pp. 46–52, 2012.

[21] J. C. Thomas and C. Wielgosz, "Deflections of highly inflated fabric tubes." *Thin-Walled Structure*. vol. 42, pp. 1049–1066, 2004.

[22] B. Zhao, J. Hu, W. Chen, J. Chen, Z. Qiu, J. Zhou and C. Gao, "An automatic system for pressure control and load simulation of inflatable membrane structure." *Automation in Construction*, vol. 90, pp. 58–66, 2018.

[23] C. Liu, X. Deng, J. Liu, T. Peng, S. Yang and Z. Zheng, "Dynamic response of saddle membrane structure under hail impact." *Engineering Structures*, vol. 214, 110597, 2020.

[24] C. Liu, F. Wang, L. He, X. Deng, J. Liu and Y. Wu, "Experimental and numerical investigation on dynamic responses of the umbrella membrane structure excited by heavy rainfall." *Journal of Vibration and Control*, vol. 0, pp. 1-10. 2020.

[25] Q. Yang, Y. Wu and W. Zhu, "Experimental study on interaction between membrane structures and wind environment." *Earthquake Engineering and Engineering Vibration*, vol. 9, pp. 523–532, 2010.

[26] Z. Han, M. Gu and X. Zhou, "Aerodynamic parameters of tensioned membrane structure based on aeroelastic wind tunnel test." *Journal of Tongji University*, vol. 43, pp. 830–837, 2015.

[27] Y. Zhou, Y. Li and A. Yoshida, "Effect of Added Mass on Wind-Induced Vibration of a Circular Flat Membrane by Wind Tunnel Tests." *International Journal of Structural Stability and Dynamics*, vol. 12, 1850156, 2018.

[28] Y. Wu, Z. Che and X. Sun, "Research on the wind-induced aero-elastic response of closed-type saddle-shaped tensioned membrane models." *Journal of Zhejiang University-SCIENCE A*, vol. 16, pp. 656–668. 2015.

[29] X. Sun, Z. Chen and Y. Wu, "Aeroelastic experiment of one-way tensioned membrane structure." *Journal of Building Engineering*, vol. 34, pp. 63–69, 2013.

[30] R. Sygulski, "Stability of membrane in low subsonic flow." *International Journal of Non-Linear Mechanics*, vol. 42, pp. 196–202, 2007.

[31] B. Zhao, W. Chen, J. Chen and Z. Jing, "Experimental Evaluation on Structural Behaviors of ETFE Cushion Structures Subjected to Progressive Loading." *Journal of Structural Engineering*, vol. 147, 04021205, 2021

[32] J. Guo, J. Cai and W. Chen, "Inertial effect on RC beam subjected to impact load." *International Journal of Structural Stability and Dynamics*, vol. 17, 1750053, 2017.

[33] Y. Zhang, J. Xu, Y. Zhou, Q. Zhang and F. Wu, "Central tearing behaviors of PVC coated fabrics with initial notch." *Composite Structures*, vol. 208, pp. 618–633, 2019.

[34] Y. Liu, C. Wang, H. Tan and M.K. Wadee, "The interactive bending wrinkling behaviour of inflated beams." *Proceedings of the Royal Society A*, vol. 472, 20160504, 2016.

[35] Y. Lecieux and R. Bouzidi, "Experimental analysis on membrane wrinkling under biaxial load–Comparison with bifurcation analysis." *International Journal of Solids and Structures*, vol. 47, pp. 2459–2475, 2010.

[36] Y. Luo, J. Xing, Z. Kang, J. Zhan and M. Li, "Uncertainty of membrane wrinkling behaviors considering initial thickness imperfections." *International Journal of Solids and Structures*, pp. 191–192, 264–277, 2020.

[37] Y. Li, M. Lu, H. Tan and Y. Tan, "A study on wrinkling characteristics and dynamic mechanical behavior of membrane." *Acta Mechanica Sinica*, vol. 28, pp. 201–210, 2012.

[38] X. Dai, T. Yuan, Z. Zu, X. Shao, L. Li, X. Cheng, J. Zhou, F. Yang, X. He, "Experimental study of wrinkling behavior of membrane structures via visual method." *Thin-Walled Structure*, vol. 149, 106537, 2020.

[39] J. He and A. Hoyano, "Measurement and simulation of the thermal environment in the built space under a membrane structure." *Building and Environment*, vol. 44, pp. 1119–1127, 2009.

[40] H. Suo, A. Angelotti and A. Zanelli, "Thermal-physical behavior and energy performance of air-supported membranes for sports halls: A comparison among traditional and advanced building envelopes." *Energy Buildings*, vol. 109, pp. 35–46, 2015.

[41] J. Hu, W. Chen, S. Zhang, Y. Yin, Y. Li and D. Yang, "Thermal characteristics and comfort assessment of enclosed large-span membrane stadiums." *Applied Energy*, vol. 229, pp. 728–735, 2018.

[42] Y. Yin, J. Hu, W. Chen, Y. Li, "Indoor Thermal Environment Measurement of Enclosed Gymnasium with Membrane Structure in Winter." *Journal of Shanghai Jiaotong University*, vol. 52, pp. 1452–1458, 2018.

[43] Y. Yin, Y. Song, W. Chen, Y. Yan, X. Wang, J. Hu, B. Zhao and S. Ren, "Thermal environment analysis of enclosed dome with double-layered PTFE fabric roof integrated with aerogel-glass wool insulation mats: On-site test and numerical simulation." *Energy Buildings*, vol.254, 111621, 2022.

[44] Y. Bai, L. Zhao, R. Tang and X. Kang, "Study on winter thermal comfort of membrane structure gymnasium in severe cold region of China." *Science and Technology for the Built Environment*, vol. 28, pp. 1–14, 2020.

[45] G. Tian, Y. Fan, H. Wang, K. Peng, X. Zhang and H. Zheng, "Studies on the thermal environment and natural ventilation in the industrial building spaces enclosed by fabric membranes: A case study." *Journal of Building Engineering*, vol. 32, 101651, 2020.

[46] R. Bouzidi, S. Buytet and A. le Van, "A numerical and experimental study of the quasi-static deployment of membrane tubes." *International Journal of Solids and Structures*, vol. 50, pp. 651–661, 2013.

[47] J.Y. Kim, E. Yu, D.Y. Kim and Y. Tamura, "Long-term monitoring of wind-induced responses of a large-span roof structure." *Journal of Wind Engineering and Industrial Aerodynamics*, vol. 99, pp. 955–963, 2011.

[48] P. Fajman, M. Polák, J. Máca and T. Plachý, "The Experimental Observation of the Prestress Forces in the Structural Elements of a Tension Fabric Structure." *Applied Mathematics and Mechanics*, vol. 486, pp. 189–194, 2014.

[49] E. Beusker, C. Stoy and S.N. Pollalis, "Estimation model and benchmarks for heating energy consumption of schools and sport facilities in Germany." *Building and Environment*, vol. 49, pp. 324–335, 2012.

[50] J. Hu, K. Kawaguchi and J. Ma, "Long-term building thermal performance of enclosed large-span swimming stadiums with retractable membrane ceilings." *Energy Buildings*, vol. 207, 109363. 2020.

[51] S. Xue, F. Yan and G. Sun, "Deflation and collapse of air-supported membrane structures." *Thin-Walled Structure*. vol. 169, 108338, 2021.

[52] Q. Qing, X. Guo, J. Gong and Z. Li, "Structural behavior of joined hemispherical-cylindrical air-supported membrane structure under vertical loading deflation." *Advances in Structural Engineering*, vol. 23, pp. 549–564, 2020

[53] C. J. Liu, M.D. Todd, Z. L. Zheng and Y. Y. Wu, "A nondestructive method for the pretension detection in membrane structures based on nonlinear vibration response to impact." *Structural health monitoring*, vol. 17, pp. 67–79, 2018.

[54] T. Sibert, T. Becker, K. Spiltthof, I. Neumann, R. Krupka, "High-speed digital image correlation: Error estimations and applications." *Proceedings – SPIE*, vol. 46, 051004, 2007.

[55] E. Zappa, A. Matinmanesh and P. Mazzoleni, "Evaluation and improvement of digital image correlation uncertainty in dynamic conditions." *Optics and Lasers in Engineering*, vol. 59, pp. 82–92, 2014.

[56] B. Basu, O.S. Bursi, F. Casciati, S. Casciati, A.E. del Grosso, M. Domaneschi, L. Faravelli, J. Holnicki-Szulc, H. Irschik and M. Krommer, et al. "A European association for the control of structures joint perspective. Recent studies in civil structural control across Europe." *Structural Control and Health Monitoring*, vol. 21, pp. 1414–1436, 2014.

[57] T. Tang, D. H. Yang, L. Wang, J. R. Zhang and T. H. Yi, "Design and application of structural health monitoring system in long-span cable-membrane structure." *Earthquake Engineering and Engineering Vibration*, vol. 18, pp. 461–474, 2019.

IASS 2023
July 10–14 Melbourne
Integration of Design and Fabrication

Proceedings of the IASS Annual Symposium 2023
Integration of Design and Fabrication
10–14 July 2023, Melbourne, Australia
Y.M. Xie, J. Burry, T.U. Lee and J. Ma (eds.)

FDMremote: Interactive inverse design of tensile structures with differentiable FDM

Adam BURKE*, Keith LEE[a], Janet ECHELMAN[b], David FELDMAN[b], Caitlin MUELLER[a]

[a,*] Building Technology Program, Massachusetts Institute of Technology
77 Massachusetts Avenue, Room 5-418, Cambridge, MA, USA
Aburke3@mit.edu

[b] Studio Echelman

Abstract

We present FDMremote [1], an interactive inverse form-finding tool based on the force density method for the design of tensile networks by non-specialist users in the fields of art and architecture. We use gradient-based optimization to find force density distributions that best satisfy given objectives and automatic differentiation (AD) tools are deployed to provide exact gradients with respect to objective functions. This functionality is wrapped with a graphical interface built as a plugin for Grasshopper for real-time design and optimization of tensile structures. We review the functionality of our tool, demonstrate our workflow for optimization of a single objective and the composition of multiple design optimization objectives. We conclude with a case study demonstrating the use of FDMremote to develop a structure from design to fabrication during a short workshop.

Keywords: form-finding, force density method, inverse design, optimization, tensile structures, cable nets, interactive design tools

1. Introduction

Cable and rope net structures are lightweight structures that are designed to carry loads with only tensile forces and cannot resist compression or bending. This means that the entire cross section of the material is used efficiently, resulting in materially efficient structures that can be constructed from a variety of modern materials (wire rope, steel cables, UHMWPE rope, composites, etc.) which have high tensile strength-to-weight ratios. They have found applications in both art and architecture due to their visual lightness and they offer opportunities for transparency when combined with membranes or other cladding systems. Additionally, they can span large distances without intermediate supports which is often desirable in architecture and infrastructure. Key examples of note include the work of architect Frei Otto (e.g. the Munich Olympic Stadium)[2] and contemporary artist Janet Echelman (e.g. As If It Were Already Here, Boston, MA)[3].

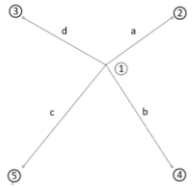
Despite their advantages, tensile structures are difficult to model and manipulate in design. Their form cannot be directly imposed since an arbitrary geometry is not necessarily guaranteed to be in tensile equilibrium. Instead, a process of *form-finding* must be used to discover an appropriate shape that can work structurally in pure tension.

Prior to the 1970s, physical models were the primary tool for form-finding explorations. However, these models were difficult to adjust and not accurate enough for the engineering of large scale structures[2]. To address these issues, computational methods for form-finding were developed. The applicable methods can be grouped into three major categories: stiffness matrix methods, geometric stiffness methods, and dynamic equilibrium methods[4]. Within the category of geometric stiffness methods is an approach called the Force Density Method (FDM) which is well suited for the form-finding of tensile

Copyright © 2023 by Adam BURKE, Keith LEE, Janet ECHELMAN, David FELDMAN and Caitlin MUELLER. Published in the Proceedings of the IASS Annual Symposium 2023 with permission.

structures [5]. Unlike other methods, it does not require iteration to find an equilibrium configuration of a tensile network, instead using a single linear solve, which makes it very computationally efficient.

This paper works with the original force density method proposed by Linkwitz and Schek (1971)[6]. The formulation is as follows: To solve for an equilibrium configuration of nodes using the force density method, it is required to build a branch-node connectivity matrix of the network [C] where each edge start is indicated with -1 and edge end is 1. Once assembled, each bar can be assigned a force density value, *q*, which is defined as the bar's force divided by length in the final equilibrium configuration. Various designs in tensile equilibrium can be found by varying the distributions of *q* values throughout the network (or by changing boundary conditions, which is not considered in this paper but could be included in future work). The branch-node matrix for a simple network is shown here:



$$C = \begin{bmatrix} -1 & 1 & 0 & 0 & 0 \\ -1 & 0 & 0 & 0 & 1 \\ -1 & 0 & 0 & 1 & 0 \\ -1 & 0 & 1 & 0 & 0 \end{bmatrix} \begin{matrix} a \\ b \\ c \\ d \end{matrix} \quad (1)$$

Then it is possible to solve:

$$\boldsymbol{XYZ_{free}} = \left(\boldsymbol{C_{free}^T\, Q\, C_{free}}\right)^{-1}\left(\boldsymbol{p_{free}} - \boldsymbol{C_{free}^T\, Q\, C_{fixed}\, XYZ_{fixed}}\right) \quad (2)$$

Where:

$\mathbf{C} = [\boldsymbol{C_{free}}\ \boldsymbol{C_{fixed}}]$
$\boldsymbol{XYZ_{free}}$ is a matrix of free node coordinates to be found
$\boldsymbol{XYZ_{fixed}}$ is a matrix of fixed node coordinates
$\boldsymbol{C_{free}}$ is a matrix with only the free nodes in C
$\boldsymbol{C_{fixed}}$ is a matrix with only the fixed nodes in C
$\boldsymbol{Q}$ is a diagonal matrix of force densities (*q*) with one value for each edge in the network
$\boldsymbol{p_{free}}$ is a matrix of force vectors acting on the free nodes in the network

Once the $\boldsymbol{XYZ_{free}}$ positions have been found, the network can be redrawn using the same connectivity. Additionally, since *q* = force/length, the force in each edge can be found by $q *$ length = force.

Although FDM provides a direct method for finding a single equilibrium solution, it does not provide a means for adjusting the structure after the initial form-finding. Due to the nonlinear relationships of the force density values *q*, it is not clear how one should redistribute them to achieve a modified network structure in a directed manner towards a particular desired outcome, such as the best fit of a target surface or force and length constraints based on fabrication requirements. This describes an inverse problem where the approximate goal outcome is known and can be defined as some objective to minimize, but the exact parameters to achieve this are unknown. Optimization techniques can be used to find a suitable set of force densities which do move an entire network towards some directed objective or compound objective [7]; however in practice, these techniques are largely inaccessible to designers who wish to work with form-found structures. A key to working with such techniques in an interactive manner is the ability to use gradient-based optimization techniques with accurate, fast evaluations of the gradient of the goal objective (i.e. matching a target shape) with respect to the design variables (i.e. the force densities).

To increase the accessibility the inverse design of tensile structures, we propose FDMremote, which abstracts away the technical implementation of the optimization of form-found networks, integrates fast and accurate gradients, and provides a user interface using Rhino/Grasshopper that allows for intuitive

network topology specification, node-based objective assignment and composition, and visualization of form-found networks for interactive iteration and fabrication.

2. Prior work

There are a variety of existing tools and approaches that can be used to approach the inverse form-finding problem for tensile structures. Notable non-FDM approaches include the use of the commercial Kangaroo2 tool for Grasshopper, which adapts techniques from the ShapeOp physics solver and constrained-optimization tool to provide a fast and robust design tool for a variety of physical simulation scenarios [8]. It implements its physics solver within the visual programming environment, Grasshopper and allows assignment of geometric and force goals in an intuitive manner. Although it can be used for form-finding, it does not ensure that the solutions reached are funicular, which can lead to physically impossible results. Additionally, finding a best fit funicular shape to an approximate target shape is not feasible since static equilibrium cannot be established as a hard constraint in the problem construction. Another technique, Thrust Network Analysis [9], was developed primarily for the design of compression-only structures, but can also be applied to the inverse form-finding of tensile structures [10]. This approach works by projecting the form network onto a horizontal plane and then modifying the reciprocal force diagram with an optimization loop to adjust the 3D form network. Authors of this work note several key restrictions: loads may only be applied vertically, and nodes are only allowed to move vertically during the form-finding process.

In contrast to these techniques, inverse form-finding with FDM is especially attractive because of the convenient parameterization via the force density q values, which indeed was originally noted by Schek in his 1974 overview of FDM (he called inverse form-finding via nested loops "a nonlinear [method]") [5]. However, it has only recently been demonstrated how to implement this approach with fast gradient evaluations. Cuvilliers et al. apply inverse design with FDM for the form-finding of compression structures that match target shapes using gradient-based optimization [11]. In this work, the authors derive the gradient and Hessian analytically for a single objective, but in doing this also demonstrate the complexity and challenges of including additional objectives.

The inclusion of additional objectives is necessary to enable more sophisticated design explorations and to deal with fabrication constraints. Fortunately, due to the rise of machine learning and the requirement of computing gradients of complex computational graphs, there are several software libraries that enable the easy implementation of automatic differentiation (AD), which allows for the computation of exact derivatives of arbitrary functions by breaking them down into elementary mathematical operations and composing them using the chain rule.

There are two primary modes that AD can operate in: *forward* and *reverse*. In forward mode, as a program is evaluated its directional partial derivatives with respect to a single input is also computed simultaneously. The decomposition of a function into its basic constituent parts can be represented as a directed acyclic graph also called the trace. If there are multiple inputs, then a forward evaluation pass is required for each input variable. For some function $f : \mathrm{R}^n \rightarrow \mathrm{R}^m$ where $n \leq m$, forward-mode will be the most efficient method. Reverse-mode, also referred to as adjoint mode, requires an initial forward evaluation pass. Then the gradient (if the output of the function is a scalar) can be computed in a single traversal of the graph in the opposite direction of forward mode. In general, if $m >> n$ then reverse-mode will be more efficient. For the optimization of a large vector of force densities with a scalar loss function output, reverse-mode is the most appropriate method to use [12].

In more recent work from 2020, Cuvilliers utilized the AD library *autograd* [13] written for the python programming language to extend the set of objective functions for use in conjunction with FDM as a core form-finding method[7]. He demonstrated a number of examples where multiple objectives, expressed only in code, were composed and returned a single scalar objective score that could be efficiently minimized using a general-purpose gradient-based optimization algorithm since the gradients of the functions were automatically computed by the *autograd* library. Most recently, an open-source

implementation called JAX FDM [14] takes a similar approach using the JAX [15] library for automatic differentiation and provides an API for inverse form-finding using gradient-based optimization written in python.

While an API approach to tool development does enable exploration and experimentation by advanced users, its reach to a more general user base is limited. A programming-based approach to geometric modelling also can hinder rapid user iteration in an uninterrupted flow state or creative expression of design intent. In contrast, this paper proposes a tool and design workflow that are integrated into a GUI-based 3D modelling environment, allowing the inverse form-finding process to respond to designer input in a rapid and natural manner.

3. Interactive Inverse Design

FDMremote is algorithmically structured as a triple nested loop. It integrates the intuitive problem setup style of Kangaroo2 with the fast form-finding and efficient optimization of multiple objectives possible with FDM and automatic differentiation.

The outer loop is where the user interacts with FDMremote and specifies their network topology, anchor locations, applied loading, and any objectives they wish to incorporate into their form-finding process. Then, a middle loop automatically sets up the optimization problem and iteratively and efficiently searches for the combination of design variables (force density q values for each bar) that minimize the defined objective. At each iteration of the middle loop, an inner loop is executed where updated force densities are used to form find a network and a new objective value is computed with respect to the updated network configuration.

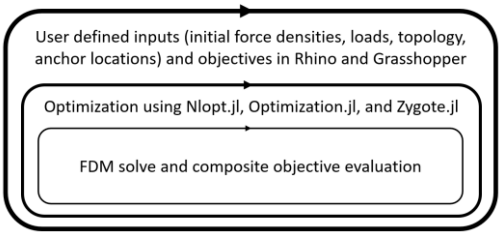


Figure 1. Triple nested loop program structure.

FDMremote implements a client-server model where the client (Rhino/Grasshopper) provides the graphical user interface (GUI) for the definition of objective, constraints, and network topology. This information is formatted into a single JSON message which can be passed via WebSocket messaging protocol to a server running the optimization loop and FDM form-finding. This separation is implemented out of necessity since Rhino 7 and Grasshopper do not have native support for high-performance linear algebra and automatic differentiation, which are essential features to provide a near-real-time workflow.



Figure 2: Client-Server program model

We chose to develop the server side of FDMremote using Julia [16]. Julia is an open-source, high-performance general purpose programming language with libraries that support automatic differentiation of sparse matrix operations. This allows for more efficient execution of the inner FDM solve, which is typically a very sparse problem. The library Nlopt.jl [17] is utilized for its L-BFGS optimization algorithm implementation, Optimization.jl [18] for optimization problem setup, and

Zygote.jl [19] for automatic differentiation. We used HTTP.jl to set up the WebSocket protocol for efficient inter-program communication. Since FDMremote utilizes a standard network protocol, the more computationally intensive part of the program can be run on a remote machine with more computational power if required.

3.1 User defined topology, anchor locations, and initial force densities

The first step in using the tool is the definition of a connected bar network on the client side in Rhino 7 and Grasshopper. A network in this context is a set of nodes which can either be fixed or free and a set of edges (lines) which connect pairs of nodes (points). Note that the topology (or connectivity) of the network remains constant in this paper's approach.

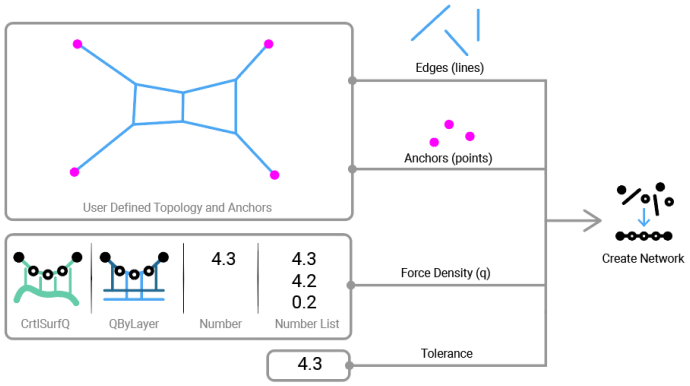


Figure 3. Creating a network

A network is defined using the inputs outlined in Figure 3. A user draws a set of lines which may share some end points. These lines may be drawn in the 3D modeling environment of Rhino or generated programmatically within Grasshopper. Once these lines are input to the *Create* component, endpoints closer than a specified tolerance will be fused together and become a node. Lines that connect nodes become edges.

The boundary conditions for the problem are points that will remain fixed during the form-finding process. A set of points to be used as anchors are input into the *Create* component. The closest points in the set of nodes generated from the lines input to *Create* will be flagged as fixed points. A minimum of two anchors are required to prevent the FDM problem from collapsing all points to a single location, however a minimum of three anchor points is recommended. A network with no anchor points is not well defined and is not permitted by FDMremote.

The initial force densities can be specified in multiple ways. If no objectives are provided, these assigned force densities will be used directly for FDM form finding. If objectives are provided, then these will be the initial variable values for the optimization. *CtrlSurfQ* is a component which allows the use of a control surface to spatially vary the initial force densities. *QByLayer* is another component that allows assignment of force densities to lines which are grouped by drawing them on separate layers in Rhino. If a single value is provided, the force densities for all edges will be set to the same value. If a list of values (matching the number of edges in the network) is provided, each edge will have a unique force density value.

The *Create* component will convert the lines, anchors, and force densities (q) into a description in suitable for the form-finding process.

3.2 User defined objectives and optimizer settings

To specify objectives and settings for the optimization algorithm there are a set of components. These are broken down into a set of 8 objective components and one *Params* component.

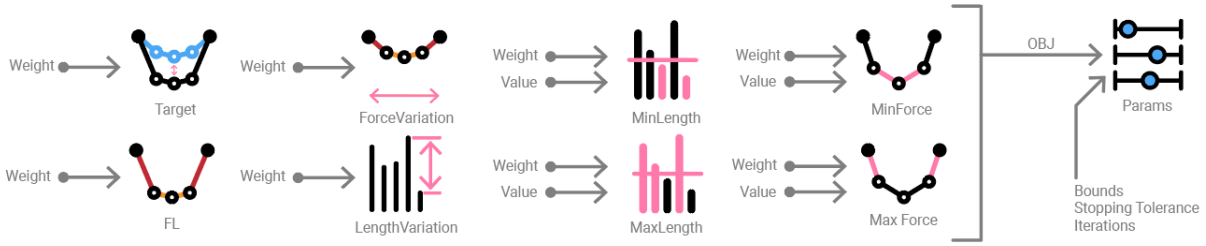


Figure 4: Optimizer settings and objective assignment

For each objective function available in FDMremote there is a corresponding objective function component. Each objective component has a *weight* input that can be used to scale the relative importance of an objective in the optimization process. The min/max force and length components have an additional *value* input used to specify a cutoff threshold above or below which the objective will be penalized. To compose multiple objective functions the output of each objective component is simply added to the *OBJ* input of the *Params* component. Because the objective values are not normalized, the weighting may require some experimentation to find a range where the influence of different objectives are relatively balanced. The current objectives include the following functions to minimize:

Table 1. Objectives for minimization in FDMremote.

Force Variation	$OBJ = \max(\boldsymbol{F}) - \min(\boldsymbol{F})$
Length Variation	$OBJ = \max(\boldsymbol{L}) - \min(\boldsymbol{L})$
Maximum Force	$\boldsymbol{t} = [F_i - v]\ \forall\ i\ ,\ OBJ = \sum(t_i + \lvert t_i \rvert)$
Minimum Force	$\boldsymbol{t} = [v - F_i]\ \forall\ i\ ,\ OBJ = \sum t_i + \lvert t_i \rvert$
Maximum Length	$\boldsymbol{t} = [L_i - v]\ \forall\ i\ ,\ OBJ = \sum t_i + \lvert t_i \rvert$
Minimum Length	$\boldsymbol{t} = [v - L_i]\ \forall\ i\ ,\ OBJ = \sum t_i + \lvert t_i \rvert$
Structural Performance	$OBJ = \sum_{i=1}^{N_e} (\lvert F_i \rvert L_i)$
Target	$OBJ = \lVert \boldsymbol{XYZ_0} - \boldsymbol{XYZ_f} \rVert$

Where:

$\boldsymbol{F}$ is a vector of edge forces for all edges in the network
$\boldsymbol{L}$ is a vector of lengths for all edges in the network
v is a thresholding value for min/max force or length objectives
N_e is the number of edges in the network
$\boldsymbol{XYZ_0}$ is a matrix of initial nodal coordinates from the user specified topology drawing (target shape)
$\boldsymbol{XYZ_f}$ is a matrix of nodal coordinates after an FDM solve

Additional settings for the optimization algorithm can also be specified in the *Params* component. These include upper and lower bounds for allowable force densities, stopping tolerance for the optimizer, and number of iterations before the optimization halts. In general, it is best to rely on relative improvement of the loss function between optimization steps falling below a threshold and not on the objective value falling below an absolute threshold since many of the objectives will not be able to reach zero and will instead simply cease to improve.

3.3 Full problem assembly for sending to the server for form-finding and optimization\

Once network creation and parameter specification have been completed, these components, along with any loads to be applied to the free nodes can be assembled with the *FDMsend* component in Figure 5. The loads can be applied in multiple ways, similarly to the force densities. The *CtrlSurfP* component can be used to assign varying loads controlled by a parameterized surface. Additionally, a single force vector or list of force vectors matching the number of free nodes can be applied to the network. The *FDMsend* component handles compiling all the inputs into a single JSON message to send via WebSocket protocol to the server in Julia.

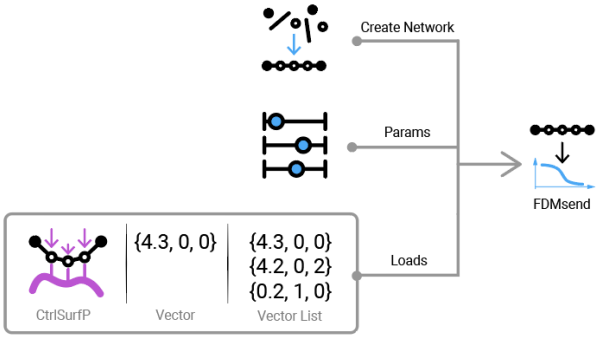


Figure 5. Assembly of inputs to send to be form-found using FDMremote

3.4 Optimization in Julia

In Julia once a new message is received the form-finding and optimization is performed. If no objectives are provided then a single FDM solve using user provided force density values is performed using equation (2) and the form found nodal positions are returned to grasshopper.

If objectives are provided, then a minimization problem is set up in the form:

$$\min_{\boldsymbol{x}} f(\boldsymbol{x}) \tag{3}$$

$$s.t.\ \boldsymbol{lb} \leq \boldsymbol{x} \leq \boldsymbol{ub}$$

Where:

$\boldsymbol{x}$ is a vector of force densities (q) which are the variables in the optimization
$f(\boldsymbol{x})$ is a composite objective function $\sum_{i=1}^{N_{OBJ}} w_i\ OBJ_i(\boldsymbol{x})$
OBJ is the set of user defined objectives to minimize
w are the corresponding user defined weights for each objective
lb is a vector of lower bounds for the force densities (always at least 0)
ub is a vector of upper bounds for the force densities

When the stopping criteria specified in the *Params* component are met the optimization will halt and the final nodal coordinates, final $\boldsymbol{x}$ force density values, final objective value, and the history of the objective values during the optimization are sent back to Grasshopper.

3.5 Visualization and fabrication of a form-found network

Once a form-found network is returned to Grasshopper, a user has a few options for proceeding. There are a set of utility functions outlined in Figure 5 to assist with iteration, documentation, and fabrication.



Figure 6. Utility Functions for Extracting Additional Information, Saving Networks, and Fabrication

To view the form-found network, the *Visualize* component can be used and different display modes are available to investigate force and force density distributions visually. *Info* will provide additional information about the form-found network.

If further design iteration is desired, the *Update* component can be used to match lines drawn in Rhino with their new form-found position. This is a very rapid way to iteratively form-find and then make incremental adjustments to a target shape. The *Freeze* and *Load* components are used to save a form-found network for later use or to save an option during a design session. *Tagger* and *Make* provide different ways of viewing additional information about a form-found network such as element forces (these are relative values dependent on the units of the rhino model), element lengths (accounting for expected elongation during installation), node names, and edge names required to fabricate a form-found network.

4. Results

The simplest form-finding possible with FDMremote is to directly use FDM to find an equilibrium configuration. In this situation, no optimization is required. The force densities for each edge are set manually and a network form-found using those values is returned.

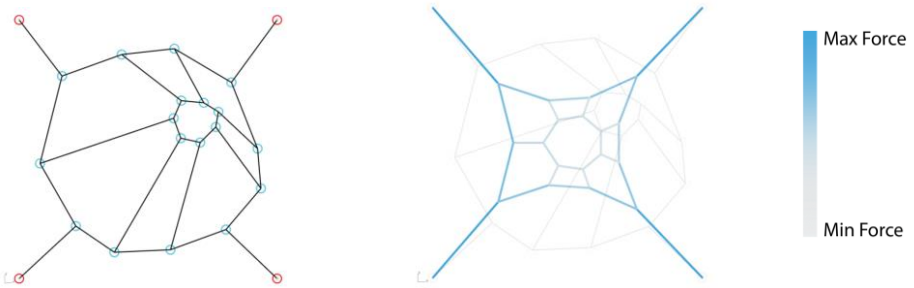


Figure 7. A simple network topology (left) with fixed (red) and free (cyan) nodes highlighted, and a form-found solution using equal force density values for all edges (right).

In the initial network specification in Figure 7, all the anchor points and free nodes lie on the XY plane. The initial locations of free nodes in the network topology diagram have no impact on the form-found solution on the right. Also note that even though the force densities prescribed for each edge are all equal, in the form-found solution the forces vary throughout the network.

4.1 Single-objective optimization

In Figure 8, a minimum length objective has been introduced. Now the optimization loop is required. In this case there is a feasible minimum solution where all edge lengths are longer than the prescribed

minimum length. After five steps the objective value reached zero and the network (right) was returned for visualization in Rhino/Grasshopper.

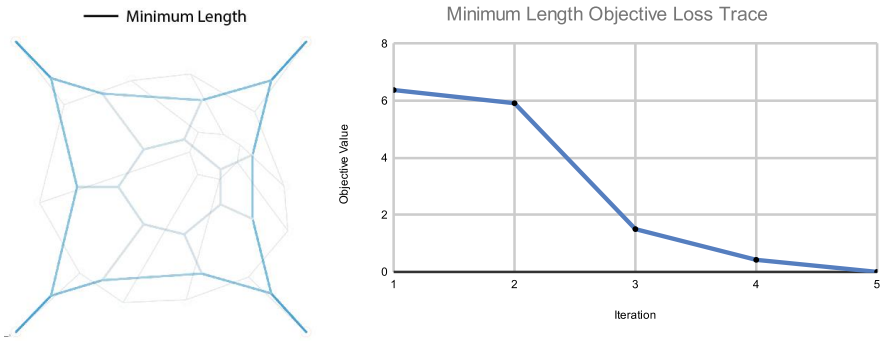


Figure 8. Use of a minimum length objective.

In Figure 9, a target objective has been used. In this example the optimized form-found network is trying to match nodal locations of the topological diagram while also ensuring that all the edges are in tension. Some of the node locations are impossible to reach if the edges are only in tension, which results in a slow convergence at the end of the optimization process.

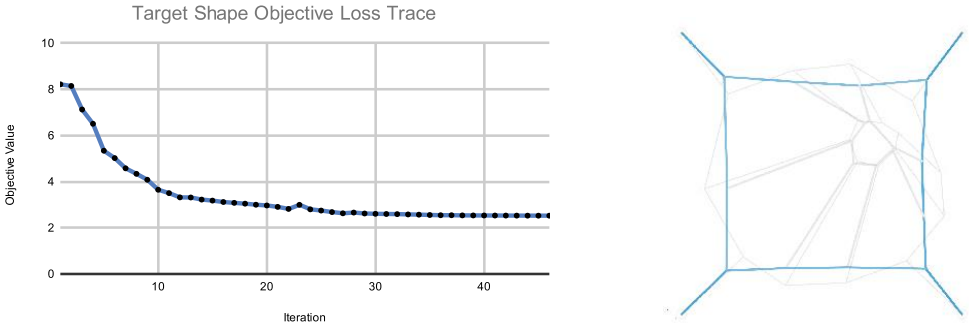


Figure 9. Use of a target shape objective.

4.2 Composite objective optimization

It is also possible to combine multiple objectives and to interpolate between them, using the objective weights to influence the relative importance of each objective. This provides a unique way to explore a large spectrum of design options. The form-found solutions are guaranteed to be in tensile equilibrium since the force densities have been restricted to be strictly positive; however, the visual outcome and force density distributions can vary across an infinite spectrum. In Figure 10 a more complex initial network has been defined and a tensile equilibrium solution using uniform force densities is shown.



Figure 10. An initial network constructed from the outline of the letter A (left) and its form-found shape with uniform force densities (right). This network has 588 edges, 8 fixed nodes, and 410 free nodes.

This generates an interesting form, however if a form-found shape which is shares more visual similarity to the initial input network is desired, additional objectives can be added to drive the form towards a different shape.

In Figure 11 multiple objectives are introduced to adjust the form-found network shape. In 11(a) two objectives (minimum length and maximum length) have been added to limit the extension or collapse of edges. In 11(e) only a structural performance objective is used. Alone, this objective results in form visually similar to the FDM only solution with uniform force densities. In 11(b-d) all three objectives are used, however in 11(b) the structural performance component has a weight of 1 while the min and max length components have weights of 16 and 8, respectively. In 11(c) the weight of the structural performance objective has been raised to 5 while the other weights remain constant. In 11(d) it is raised again to 10 at which point it dominates the optimization. In this example all optimization loops are initialized with uniform force densities and after a change is made by a user in Grasshopper the initial force densities are re-initialized as a uniform set.

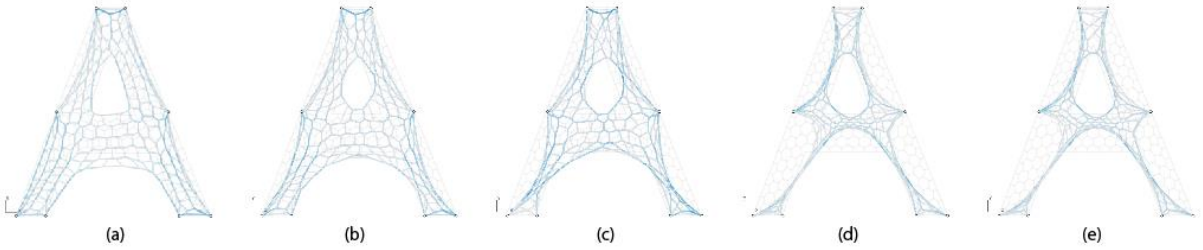


Figure 11. A range of alternative form found shapes can be explored using multiple objectives and their relative weights to interpolate between objective importance

4.3 Complex 3D Tensile Forms

Previous examples have explored tensile form-finding in 2D, however FDMremote can also be used for the exploration of 3D tensile forms. In Figure 12 a structural performance objective and target shape objective were used to drive the shape generation. The shown form is the result of performing multiple iterations, updating the target geometry using the *Update* component to set a new target geometry and making incremental adjustments to anchor locations and topology (deleting or adding edges before performing another form-finding and optimization pass). In Figure 13 a minimum edge length and target shape objective were used. The target geometry (left) was generated in a hybrid fashion between Rhino (black lines) and Grasshopper (red lines) to allow for direct control over some aspects of the structure, but also allowing for parametric control over others (such as number of subdivisions from end to end) all integrated into a single workflow.

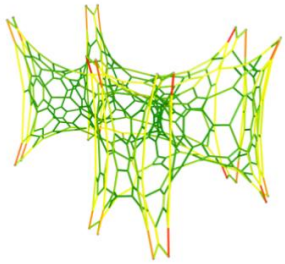


Figure 12. Structure with 814 edges

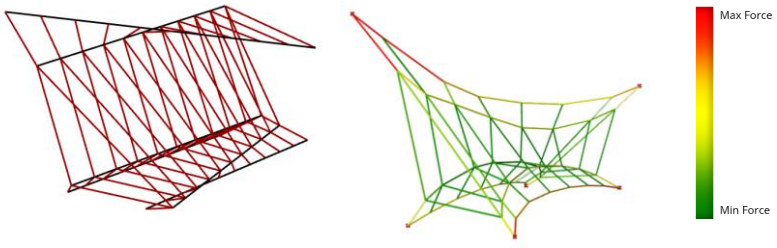


Figure 13. Structure with 90 edges - Target (left) and form-found (right)

4.4 Workshop participant designs and tensile network fabrication

In January 2023, we conducted an academic workshop, called *In Tension*, to introduce new users to FDMremote and to explore its use for the development of tensile sculptural works. The workshop took place over four half-day sessions. Participants first explored form-finding using physical models, and then worked with FDMremote to develop digitally form-found tensile structures.

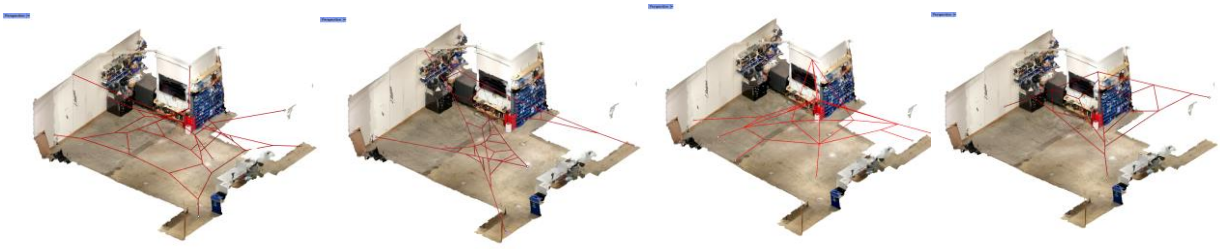


Figure 14. A selection of digital designs from the workshop.



Figure 15. Design selected for fabrication (left), students splicing (center), and installation of the structure (right)

The final design charette was to develop a site-specific tensile network structure. The participants were limited to eight anchor points and asked to consider the range of forces, number of nodes, and total length of rope when developing their designs (Figure 14). One design was selected by the group for fabrication (Figure 15, left) and installation in a teaching space on the MIT campus. Student participants were able to use the tool to design and construct a large-scale tensile sculpture in 24 hours, and worked collaboratively as a group to build the final piece. Students worked with traditional hand-splicing techniques (Figure 15, center) to translate the design from the computational environment to built reality (Figure 15, right), with minimal errors. The results showed that the FDMremote tool can be used by designers (including novices) to interactively explore buildable, lightweight structures in tensile equilibrium with a high diversity of possible outcomes.

5. Conclusion: Summary of contributions

In this paper, we reviewed the computational methods that enabled the development of FDMremote, an interactive tool for the inverse form-finding of cable structures. We showed the optimization of a simple network with a single objective. We then showed the composition of multiple objective functions on a more complex network and form-found solutions that interpolate between them through user adjustment of weighting parameters. Finally, we showed designs by non-specialist workshop participants and the physicalized outcome of one form-found design. Future work will focus on the assignment of objectives to subsets of the network, optimization of the boundary conditions, and the development of additional objective functions. We believe that this physically informed inverse design process can be a powerful tool for non-specialists to explore the design of form-found funicular structures.

Acknowledgements

We would like to thank the workshop participants Adam Snowdon, Albertine Van Marcke, Bernardo Gonzalez, Bill McKenna, Doris Duanmu, Gabrielle Moore, Harris Chowdhary, Jenny Zhang,

Jeonghyun Yoon, Karl-Johan Soerensen, Leon Kamp, Lingyi Qiu, Manavi Dixit, Morgan Johnson Quamina, Susan Williams, Tananya Prankprakma, and Thomas King for testing our tool and collaborating with us to design and fabricate a tensile structure. Additionally, we would like to thank Alessandro Beghini and Nicole Wang from SOM for their feedback on the development of our form-finding tool and contribution of time to the *In Tension* workshop, and MIT CAST staff, including Katherine Higgins and Leila Kinney, for their support of the workshop.

References

[1] "FDMremote," *Food4Rhino*, Jan. 09, 2023. https://www.food4rhino.com/en/app/fdmremote?lang=en (accessed Mar. 28, 2023).
[2] J. Tomlow, "Designing and constructing the Olympic roof (Munich 1972)," *Int. J. Space Struct.*, vol. 31, no. 1, pp. 62–73, Mar. 2016, doi: 10.1177/0266351116642078.
[3] "Janet Echelman," *Janet Echelman*. https://www.echelman.com (accessed Mar. 30, 2023).
[4] D. Veenendaal and P. Block, "An overview and comparison of structural form finding methods for general networks," *Int. J. Solids Struct.*, vol. 49, no. 26, pp. 3741–3753, Dec. 2012, doi: 10.1016/j.ijsolstr.2012.08.008.
[5] H.-J. Schek, "The force density method for form finding and computation of general networks," *Comput. Methods Appl. Mech. Eng.*, vol. 3, no. 1, pp. 115–134, 1974, doi: https://doi.org/10.1016/0045-7825(74)90045-0.
[6] K. Linkwitz and H.-J. Schek, "Einige Bemerkungen zur Berechnung von vorgespannten Seilnetzkonstruktionen," *Ing.-Arch.*, vol. 40, no. 3, pp. 145–158, May 1971, doi: 10.1007/BF00532146.
[7] P. E. Cuvilliers, "The constrained geometry of structures : optimization methods for inverse form-finding design," Thesis, Massachusetts Institute of Technology, 2020. Accessed: Oct. 17, 2022. [Online]. Available: https://dspace.mit.edu/handle/1721.1/127853
[8] M. Deuss, A. H. Deleuran, S. Bouaziz, B. Deng, D. Piker, and M. Pauly, "ShapeOp—A Robust and Extensible Geometric Modelling Paradigm," in *Modelling Behaviour: Design Modelling Symposium 2015*, M. R. Thomsen, M. Tamke, C. Gengnagel, B. Faircloth, and F. Scheurer, Eds., Cham: Springer International Publishing, 2015, pp. 505–515. doi: 10.1007/978-3-319-24208-8_42.
[9] P. Block and J. Ochsendorf, "Thrust Network Analysis: A New Methodology for Three-Dimensional Equilibrium," *J. Int. Assoc. Shell Spat. Struct.*, vol. 48, no. 3, pp. 167–173, Dec. 2007.
[10] T. Van Mele and P. Block, "A Novel Form Finding Method for Fabric Formwork For Concrete Shells," *J. Int. Assoc. Shell Spat. Struct.*, vol. 52, no. 4, pp. 217–224, Dec. 2011.
[11] P. Cuvilliers, R. Danhaive, and C. Mueller, "Gradient-based optimization of closest-fit funicular structures," *Proc. IASS Annu. Symp.*, vol. 2016, no. 8, pp. 1–10, Sep. 2016.
[12] C. Margossian, "A review of automatic differentiation and its efficient implementation," *Wiley Interdiscip. Rev. Data Min. Knowl. Discov.*, vol. 9, Jul. 2019, doi: 10.1002/widm.1305.
[13] "Autograd." Formerly: Harvard Intelligent Probabilistic Systems Group -- Now at Princeton, Mar. 28, 2023. Accessed: Mar. 28, 2023. [Online]. Available: https://github.com/HIPS/autograd
[14] R. Pastrana, "JAX FDM." Nov. 06, 2022. Accessed: Dec. 14, 2022. [Online]. Available: https://github.com/arpastrana/jax_fdm
[15] J. Bradbury *et al.*, "JAX: composable transformations of Python+NumPy programs." 2018. [Online]. Available: http://github.com/google/jax
[16] "The Julia Programming Language." https://julialang.org/ (accessed Dec. 19, 2022).
[17] "The NLopt module for Julia." JuliaOpt, Dec. 15, 2022. Accessed: Dec. 19, 2022. [Online]. Available: https://github.com/JuliaOpt/NLopt.jl
[18] "Optimization.jl." SciML Open Source Scientific Machine Learning, Dec. 19, 2022. Accessed: Dec. 19, 2022. [Online]. Available: https://github.com/SciML/Optimization.jl
[19] "FluxML/Zygote.jl." FluxML, Dec. 15, 2022. Accessed: Dec. 19, 2022. [Online]. Available: https://github.com/FluxML/Zygote.jl

IASS 2023
July 10–14 Melbourne
Integration of Design and Fabrication

Proceedings of the IASS Annual Symposium 2023
Integration of Design and Fabrication
10–14 July 2023, Melbourne, Australia
Y.M. Xie, J. Burry, T.U. Lee and J. Ma (eds.)

Fundamental study on form-finding of tensegrity-membrane structures using a dynamic relaxation method

Yohei NAGANO*, Takuo NAGAI[a]

* Graduate School of Environmental Science, The University of Shiga Prefecture
2500, Hassakacho, Hikone-city, Shiga, Japan
oe13ynagano@ec.usp.ac.jp

[a] Department of Architecture and Design, The University of Shiga Prefecture

Abstract

In this study, we explore a method for form-finding in tensegrity-membrane structures by substituting membrane materials with truss elements, and we propose a technique for estimating the structure's behavior under external forces in a simple and accurate manner. We employ the dynamic relaxation method, a numerical analysis technique commonly utilized in form-finding for tensegrity structures. The analysis model is generated by replacing the membrane material with truss elements, referred to as equivalent membrane elements, based on the physical model. However, determining the properties and cross-sectional dimensions of the equivalent membrane elements solely from the physical model observation proves to be challenging. Consequently, we perform form-finding using the load-strain relationship obtained from tension tests on the membrane material. By comparing the experimental measurements from the physical model with the form-finding outcomes, we evaluate the efficacy of the analysis method presented in this study.

Keywords: tensegrity, membrane structures, form-finding, dynamic relaxation method, Hangai Prize applicant

1. Introduction

A tensegrity structure comprises continuous tension forces and discontinuous compressive forces. This structure can be composed solely of small members without using large members like conventional building materials. As a result, tensegrity structures offer the benefits of lightweight construction and efficient material utilization. Furthermore, their discontinuous compressive materials create a unique and captivating spatial experience. Nevertheless, achieving equilibrium states and predicting behavior under external forces can be challenging. A recent study introduced a method for obtaining equilibrium states through the dynamic relaxation method [1]. Additionally, tensegrity structures are difficult to use in structures like walls or roofs due to their low rigidity and large displacement.

To address this issue, several projects have explored tensegrity-membrane structures, where multiple tension elements are replaced with a single membrane material. A notable example is the "MOOM Pavilion" designed by C+A [2]. This design demonstrates advantages such as lightweight construction, straightforward assembly, and compact storage for transport. However, assessing tension stress and stiffness quantitatively is difficult because the membrane members do not form minimal surfaces, and there is significant variation in tension stress on the membrane. Consequently, tensegrity-membrane structures inherently present challenges in analyzing their equilibrium states and accurately evaluating their behavior under external forces. While numerous studies have investigated the form-finding and stability of membrane tensegrity structures [2]-[4], few have quantitatively assessed their behavior against external forces. To actualize tensegrity-membrane structures, it is essential to develop an analysis method that accurately evaluates their stiffness. As such, we conducted research aimed at

Copyright © 2023 by Yohei NAGANO and Takuo NAGAI. Published in the Proceedings of the IASS Annual Symposium 2023 with permission.

establishing a simple and precise analysis method for assessing the stiffness of tensegrity-membrane structures by substituting membrane materials with truss elements. In this study, we created a physical model of a tensegrity-membrane structure to examine its mechanical properties. Form-finding was executed using the dynamic relaxation method, and the results were compared with actual phenomena. We also discussed the evaluation method for the stiffness of tensegrity-membrane structures.

2. Physical model creating method

Fig. 1 illustrates the physical model created for this study. To investigate the fundamentals of tensegrity-membrane structures, we conducted experiments and analyses using a simplified model with as few members as possible. The model depicted in the figure is referred to as a "planar arch model." The compression materials employed were 3 mm diameter aluminium rods, and the membrane material consisted of highly elastic fabric.



Figure 1. Photos of the physical model (planar arch model).

Fig. 2 presents the process of creating the physical model. To produce a natural condition view of the membrane material, a 3D model (initial form) was generated based on geometric rules, as demonstrated in Fig. 2(a). The position of the compression members was determined by the sides of the regular polygon, and their lengths were calculated by extending each side of the regular polygon based on the angle θ at the center. The initial form was then flattened to create a rectangular development view, as displayed in Fig. 2(b), and a natural condition view was generated by scaling down the development view using a similarity factor of 0.65. The X direction of the natural condition view corresponded to the warp direction of the membrane material, the Y direction to the weft direction, and the compression members were parallel to the X direction. The compression members were fabricated to the same length as the initial form, and the membrane material was made according to the natural condition view. Finally, the compression members were inserted into the cut membrane, and tension was applied to the membrane by pulling both ends until the span of the column base in the initial form was reached, as illustrated in Fig. 2(c).

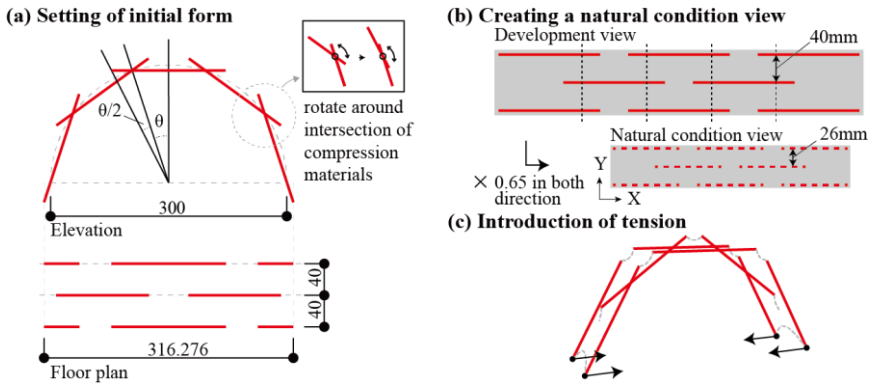


Figure 2. Creating method of physical model.

3. Modeling and analysis method

3.1. Modeling of tensegrity-membrane structures

Typically, in the analysis of tensegrity-membrane structures, the modeling of membrane materials is conducted by dividing the membrane surfaces into triangular meshes [5]. However, estimating the stiffness of the replaced membrane elements is difficult due to the anisotropic nature of the membrane materials and the complex stress distribution in the tensegrity-membrane structure. In tensegrity-membrane structures with scattered discontinuous compression members, dividing the membrane material into meshes necessitates a considerable amount of computational time due to the large number of elements, rendering it impractical for use in actual architectural design. Consequently, we focused on simplifying the modeling of membrane materials by referring to the physical model. The membrane materials are replaced with truss elements placed on parts of the membrane material where tension is particularly strong with straight lines, as illustrated in Fig. 3. The blue lines in the figure represent the equivalent membrane elements (EME).

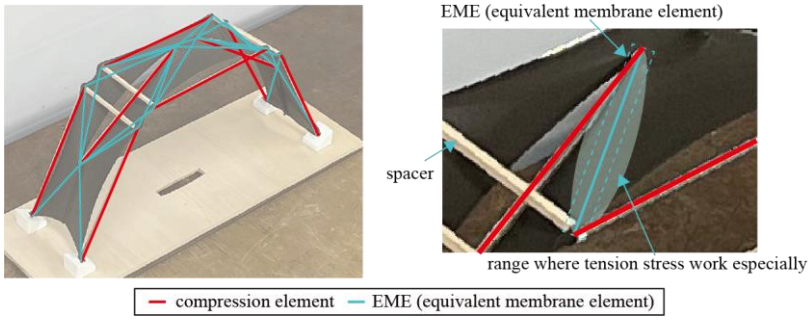


Figure 3. Method of replacing the tensioned membrane with EMEs (equivalent truss elements).

Fig. 4 displays a plan view of the analysis model used for form-finding, illustrating the element numbers and boundary conditions. Elements 1 to 3 in the figure represent compression elements (red lines), while the others are EMEs (blue lines). In accordance with the physical model, the compression elements are assumed to be 3 mm diameter aluminum rods with a Young's modulus set to 70,000 N/mm². Conversely, since the EMEs' properties cannot be determined solely based on the physical model's appearance, they were examined through tension tests. The boundary conditions include pin-supports at four points of the column bases, and to maintain the model's width of 80 mm, the Y-axis movement is constrained at eight points, as shown in the figure.

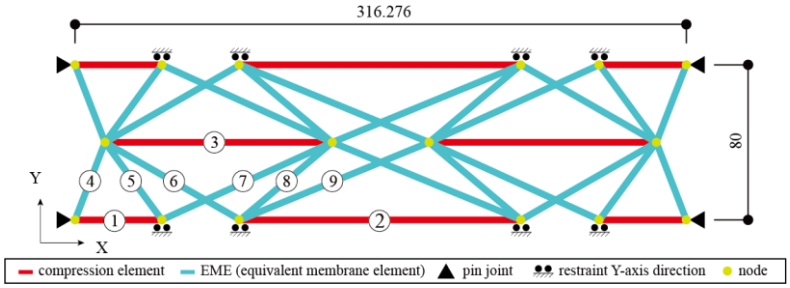


Figure 4. Plan view of numerical model: index of elements and boundary conditions.

3.2. Dynamic relaxation method (DRM)

In this study, form-finding using the dynamic relaxation method (DRM) was performed. DRM transforms a static equilibrium problem into a pseudo-dynamic problem and solves the original static problem by artificially damping the dynamic system to achieve a steady state [1]. Numerous studies have been conducted on form-finding and stress analysis using DRM [1], [6]-[8].

The following outlines the detailed calculation process for form-finding of tensegrity-membrane structures using DRM in this study. First, Eq. (1) is formulated based on Newton's second law of motion and is transformed into Eq. (2). Then, the accelerations $\boldsymbol{a}(\mathrm{t}+\Delta\mathrm{t})$ at time $\mathrm{t}+\Delta\mathrm{t}$ are obtained from the velocities $\boldsymbol{v}(\mathrm{t})$ and the out-of-balance forces $\boldsymbol{f}(\mathrm{t})$ at time t.

$$-\boldsymbol{D}\boldsymbol{v}-\boldsymbol{f}=\boldsymbol{M}\boldsymbol{a} \tag{1}$$

$$\boldsymbol{a}(\mathrm{t}+\Delta\mathrm{t})=-\boldsymbol{M}^{-1}\left(\boldsymbol{D}\boldsymbol{v}(\mathrm{t})+\boldsymbol{f}(\mathrm{t})\right) \tag{2}$$

Here, $\boldsymbol{D}$ represents the viscous damping matrix, $\boldsymbol{M}$ denotes the mass matrix, and $\Delta\mathrm{t}$ signifies the analysis time interval. Although these values have little connection with the analysis result, they are closely related to the calculation's convergence rate. Thus, we search for values that increase the convergence speed and utilize them. The out-of-balance forces $\boldsymbol{f}(\mathrm{t})$ at time t are obtained from the axial force $s(\mathrm{t})$ acting on each element. The axial force s acting on each element can be determined from the change in length of the elements. The axial force $s_{\mathrm{c}}(\mathrm{t})$ acting on the compression elements at time t can be expressed as Eq. (3). However, the membrane materials used in this study exhibit strongly nonlinear characteristics, necessitating their consideration when determining the axial force of the EMEs. Consequently, the axial force of the EMEs was calculated using the load-strain relationship expressions shown in Eq. (8)-(11), which are obtained in the following chapter, and the analysis was conducted using the EMEs as nonlinear springs.

$$s_{\mathrm{c}}(\mathrm{t})=\mathrm{EA}\varepsilon_{\mathrm{c}}(\mathrm{t}) \tag{3}$$

$$\varepsilon_{\mathrm{c}}(\mathrm{t})=\frac{\mathrm{L_c}(\mathrm{t})-\mathrm{L_{N,c}}}{\mathrm{L_{N,c}}} \tag{4}$$

Here, E represents Young's modulus, A denotes the cross-sectional area, and $\mathrm{L_c}(\mathrm{t})$ is the length of the compression elements at the t step, and $\mathrm{L_{N,c}}$ is the natural length of the compression elements. Fig. 5 illustrates the definition of the length of elements. $\mathrm{L_E}(0)$ is the initial length of the EMEs, $\mathrm{L_{N,E}}$ is the natural length of the EMEs, $\mathrm{L_c}(0)$ is the initial length of the compression elements. The natural condition view is obtained, similar to the creation method of the physical model. The length of the compression elements, $\mathrm{L_c}(0)$, are set to equal $\mathrm{L_{N,c}}$ in the initial form.

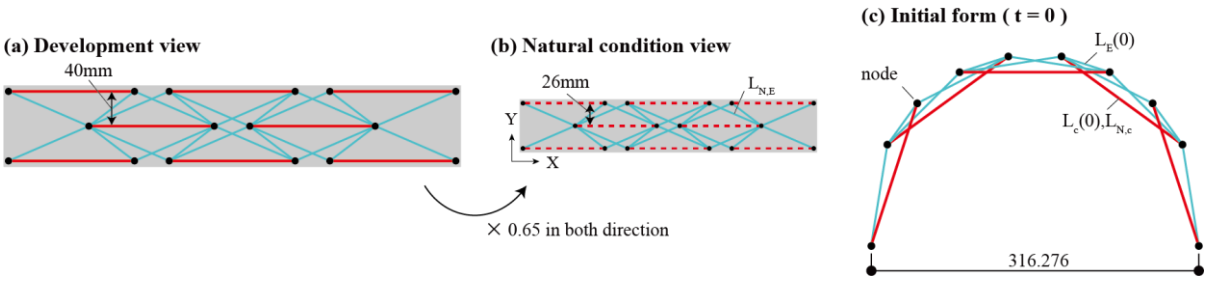


Figure 5. Definition of the length of elements and initial condition for form-finding analysis.

Utilizing the obtained acceleration $\boldsymbol{a}(\mathrm{t}+\Delta\mathrm{t})$ we can calculate the velocity $\boldsymbol{v}(\mathrm{t}+\Delta\mathrm{t})$ and displacement $\boldsymbol{\delta}(\mathrm{t}+\Delta\mathrm{t})$ simultaneously from Eq. (5) and (6). These calculations are repeated until the out-of-balance forces approach zero. The convergence condition for this iterative calculation is set as shown in Eq. (7). Here, R represents the convergence value, and n refers to the number of nodal degrees of freedom.

$$\boldsymbol{v}(\mathrm{t}+\Delta\mathrm{t})=\boldsymbol{v}(\mathrm{t})+\boldsymbol{a}(\mathrm{t}+\Delta\mathrm{t})\Delta\mathrm{t} \tag{5}$$

$$\boldsymbol{\delta}(\mathrm{t}+\Delta\mathrm{t})=\boldsymbol{\delta}(\mathrm{t})+\boldsymbol{v}(\mathrm{t}+\Delta\mathrm{t})\Delta t \tag{6}$$

$$\mathrm{R}\leq\sqrt{\boldsymbol{f}^{\mathrm{T}}\boldsymbol{f}/\mathrm{n}} \tag{7}$$

In addition, kinetic damping is employed alongside viscous damping. When the kinetic energy reaches a maximum value at a certain step, the calculation continues with the value of velocity at all nodes set to zero at the next time step.

3.3. Parameter setting of DRM analysis

The values employed in the numerical analysis were based on a mass matrix $\boldsymbol{M}$ that was 0.2 times the identity matrix, meaning that the mass of each point was taken to be 0.2 kg. The viscous damping matrix $\boldsymbol{D}$ was 1.0×10^{-5} times the identity matrix, and since the period was 1.2×10^{4} seconds, this value corresponds to a damping constant of 4.8% when interpreted as mass-proportional damping. The time interval for the analysis, Δt, was set to 2.0×10^{-4} seconds, and the convergence criterion was set to $R = 1.0 \times 10^{-3}$.

4. Tension test of membrane materials

4.1. Uniaxial tension test

In the modeling of the EMEs, there is an issue that it is difficult to estimate the properties and cross-section by only observing the physical model. Therefore, we conducted tests by pulling both ends of the membrane material under the same conditions as the EMEs in the structure. Fig. 6(a) shows the specific method for preparing the test pieces. The test pieces were cut in the directions of angles θ_A and θ_B, with the test pieces in the direction of angle θ_A denoted as test piece A1 and the test pieces in the direction of angle θ_B denoted as test piece B1 (θ_A is 23.3 degrees relative to the X-axis and θ_B is 37.2 degrees). The length of each test piece was set to 50 mm. The adhesive area between the membrane material and the compression members in the physical model was circular with a 5 mm diameter, as shown in Fig. 6(b). To create the same boundary conditions as the physical model, jigs with a 5 mm diameter were attached to each test piece. Additionally, since it was expected that the stiffness would differ depending on the width of the test pieces, even with the same boundary conditions, three types of test pieces were created with widths of 5, 10, and 15 mm. Test pieces were also prepared in the X-Y direction under the same conditions and were denoted as test piece X and test piece Y, respectively.

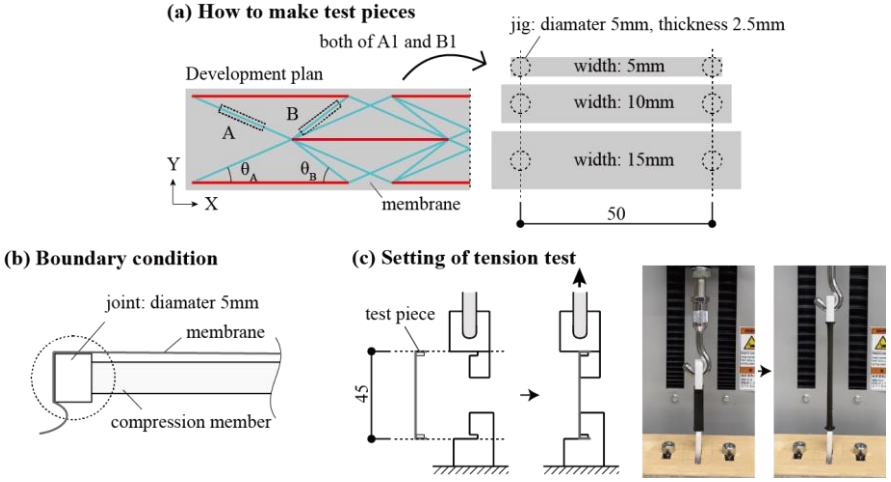


Figure 6. Uniaxial tension test of membrane materials used in the physical model.

Fig. 7 shows the results of the tension tests. The points represent the measured data, and the solid lines represent the curve obtained by the least squares method using the measured data. Here, the strain is calculated as linear strain that is obtained by dividing the displacement by 45 mm. From the graphs (a) and (b), it can be seen that the membrane material used in this study has a large difference in stiffness

between the X and Y directions. In addition, from the graphs (c) and (d), both test pieces A1 and B1 tended to be similar to the results of test piece X.

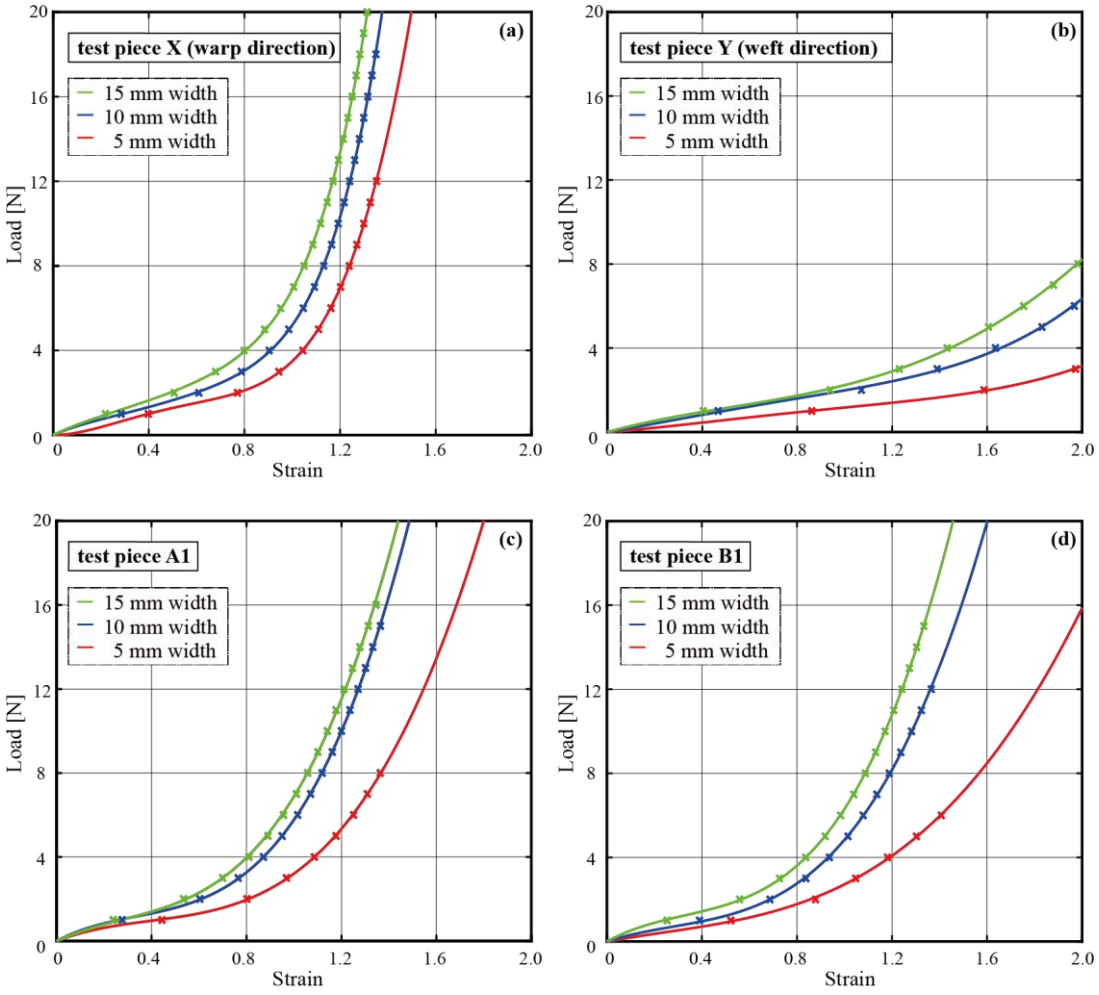


Figure 7. Results of uniaxial tension test.

As a general trend, the greater the width of test pieces, the greater the stiffness, and the differences in stiffness due to differences in width can be seen to be smaller for 10 mm and 15 mm compared to 5 mm and 10 mm. From these observations, it can be anticipated that even if the width of the test pieces exceeds 15 mm, load-strain relationships are unlikely to change significantly. Therefore, it is considered that the test results of the test pieces with a width of 15 mm best represent the properties of the EMEs. Eq. (8) is the load-strain relationship expression of test piece A1 (EME-A) obtained from the measurement data by the least squares method, and Eq. (9) is that of test piece B1 (EME-B).

$$s_{\mathrm{A1}}(\varepsilon) = 9.9\varepsilon^3 - 8.2\varepsilon^2 + 5.2\varepsilon \quad [\mathrm{N}] \tag{8}$$

$$s_{\mathrm{B1}}(\varepsilon) = 11.0\varepsilon^3 - 10.9\varepsilon^2 + 6.2\varepsilon \quad [\mathrm{N}] \tag{9}$$

4.2. Repeated uniaxial tension test

Since there is a possibility that the stiffness may change due to residual deformation occurring when the membrane material used in this study undergoes a large strain, we conducted the repeated loading-unloading test for the test pieces A1 and B1 within a range of strain up to 1.0 using the same testing

method as in the previous section. Fig. 8 shows the results of the tests. It is difficult to accurately grasp how much the stiffness changes because it is not possible to quantitatively grasp the range of strain for the EMEs in the structure, but it can be seen that the stiffness of both test pieces decreases from the graphs (a) and (b).

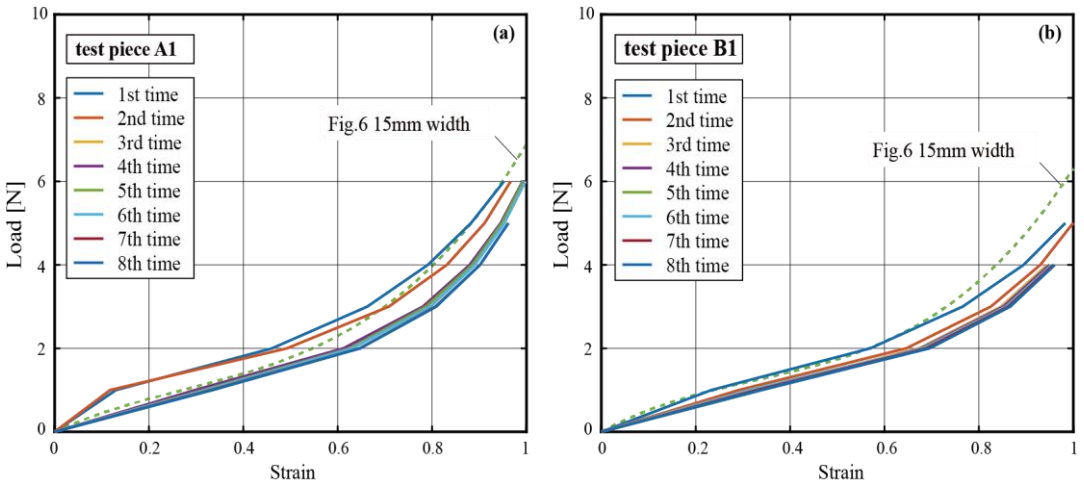


Figure 8. Result of repeated uniaxial tension test.

4.3. Biaxial tension test

In the equilibrium state of tensegrity-membrane structures, the membrane material is subjected to tension forces in various directions, not just in a single direction. As a result, it is uncertain whether the stiffness of the EME can be accurately estimated using only the load-strain relationship expressions derived from the uniaxial test in the previous section. To address this issue, a biaxial tension test was conducted, which involved applying tension forces in orthogonal directions to the EME-A and B. The change in stiffness was then compared to the results from the previous section. Test pieces were prepared by cutting the membrane material as shown in Fig. 6(a) and inserting a compression rod vertically into the test pieces, as illustrated in Fig. 9(a). It can be predicted that the stiffness of membrane will change depending on the length of the rod, but it is difficult to predict how much tension will act in the orthogonal direction of the EME in the actual model. Therefore, the length of the rod was set according to the same method of making the physical model as shown in the figure. By doing that, a test piece was thoght to be created in which the orthogonal tension force of roughly the same as the physical model. The test piece cut to match the EME-A is referred to as test piece A2, while the test piece cut to match the EME-B is referred to as test piece B2.

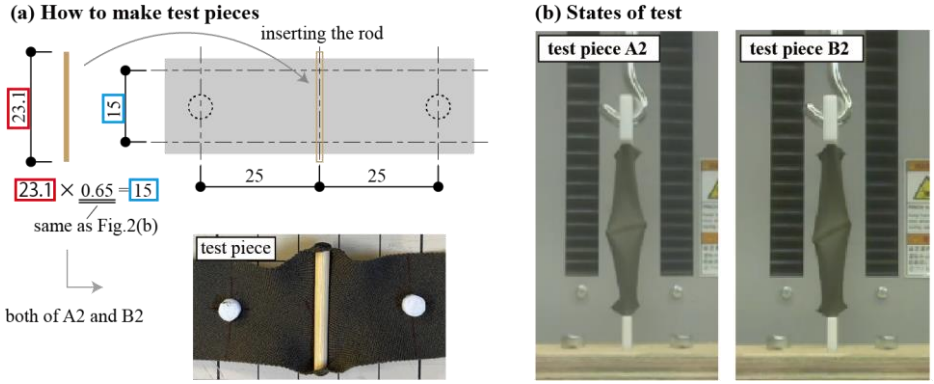


Figure 9. Biaxial tension test of membrane.

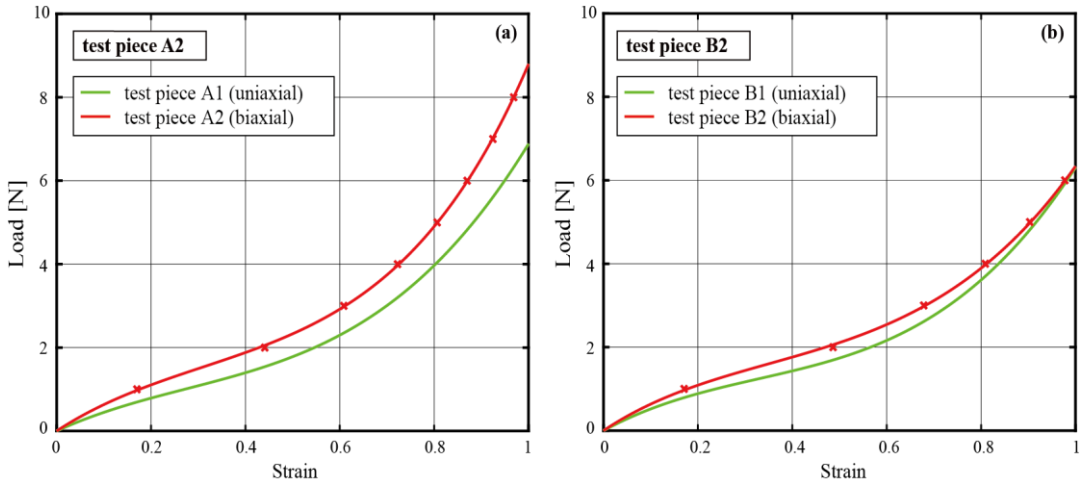


Figure 10. Results of biaxial tension test.

The graph comparing the results of the test and the Eq. (8) and (9) obtained in the previous section is shown in Fig. 10. Eq. (10) represents the load-strain relationship expression for test piece A2 (EME-A), obtained from the measured data using the least squares method, while Eq. (11) represents the load-strain relationship expression for test piece B2 (EME-B). From graphs (a) and (b), it can be observed that both test pieces exhibit higher stiffness than the results obtained in the previous section. This finding suggests that to accurately estimate the stiffness of the EME, it is crucial to consider the tension forces acting in directions other than the member axis and to understand the load-strain relationship accordingly.

$$s_{A2}(\varepsilon) = 5.4\varepsilon^5 - 8.6\varepsilon^4 + 17.3\varepsilon^3 - 12.7\varepsilon^2 + 7.4\varepsilon \quad [\mathrm{N}] \tag{10}$$

$$s_{B2}(\varepsilon) = 3.4\varepsilon^5 - 8.4\varepsilon^4 + 17.6\varepsilon^3 - 13.8\varepsilon^2 + 7.6\varepsilon \quad [\mathrm{N}] \tag{11}$$

5. Form-finding and structural analysis against external forces

5.1. Comparison of equilibrium states

Fig. 11 presents a comparison of the equilibrium state obtained from the form-finding using DRM and the physical model. Model-1 employs Eq. (8) and (9) as the load-strain relationship for the EME-A and B, while Model-2 utilizes Eq. (10) and (11). Both results are in good agreement with the physical model; however, it was found that the maximum height value of Model-2 is slightly closer to the value of the physical model form.

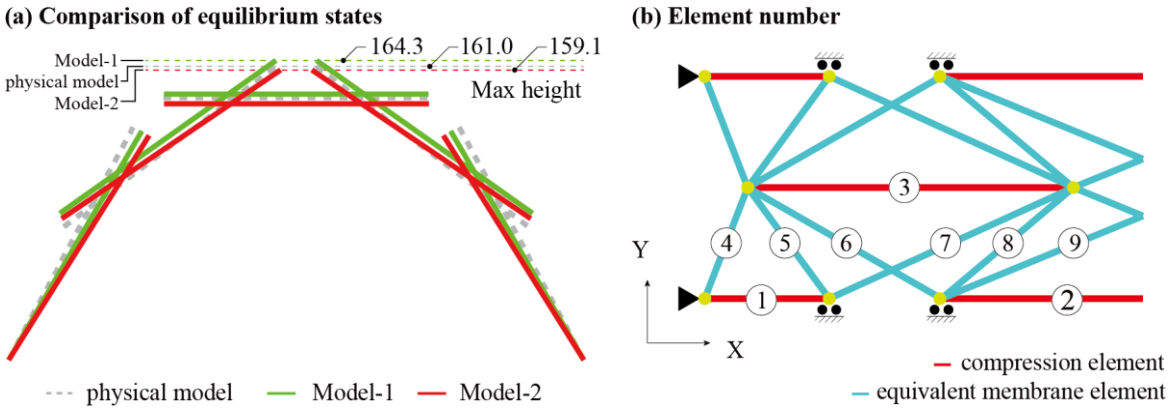


Figure 11. Comparison of equilibrium states and axial forces in the members.

Table 1 displays the axial force and strain acting on each element in the equilibrium state of Model-1 and Model-2. It is observed that the tension forces acting on the EMEs in the equilibrium state are greater in Model-2 than in Model-1.

Table 1. The axial force and strain in each element.

	Model-1		Model-2	
Element number	axial force[N]	strain	axial force[N]	strain
1 (compression element)	-1.50	0	-1.88	0
2 (compression element)	-3.05	0	-3.77	0
3 (compression element)	-5.86	0	-7.28	0
4 (EME-A)	1.52	0.43	1.89	0.40
5 (EME-B)	3.16	0.75	3.90	0.80
6 (EME-A)	1.60	0.46	1.98	0.42
7 (EME-A)	1.42	0.41	1.77	0.37
8 (EME-B)	3.24	0.76	3.98	0.81
9 (EME-A)	1.55	0.44	1.92	0.41

5.2. Comparison of behaviour against external force

The behavior of Model-2 under applied external forces is investigated using DRM, and the results are compared with the physical model experiment. Fig. 12(a) presents the comparison of the deformed forms between the physical experiment and the numerical result when an external force was applied in the vertically downward direction, as shown in the figure. The photos demonstrate that both forms during deformation match well.

Fig. 12(b) displays the relationship between the load and vertical downward displacement at the loading point. In the physical experiment, the first test was conducted approximately 5 months after the physical model was completed, followed by the second test about 15 months later. Both tests used the average of multiple trial results. It can be observed that the stiffness of the second result has decreased compared to the first result. This is considered to be due to the loss of tension in the membrane material from maintaining it under tension for an extended period, resulting in a decrease in stiffness. Therefore, it is highly likely that the stiffness of the first test result has decreased compared to just after the completion of the physical model. In fact, when comparing the analysis results of Model-2, assuming it was just after the physical model's completion, and the physical model experiment results, the analysis results exhibit a higher stiffness than the experimental results.

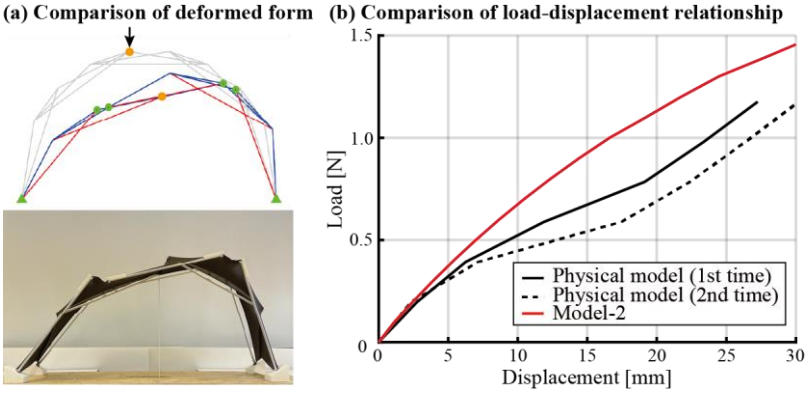


Figure 12. Results of experiment and numerical analysis applying external force

6. Conclusion

In this paper, we investigated the modeling and form-finding method for simple tensegrity-membrane structures. It was determined that the equilibrium state of the planar arch model could be accurately identified by performing form-finding using DRM through the replacement of equivalent membrane elements (EMEs) and tension testing of membrane materials.

On the other hand, due to the overall stiffness of the tensegrity-membrane structure decreasing over time, it was found that the behavior against external forces could not be accurately predicted using the analysis method that assumes the condition just after the completion of the physical model. As discussed above, it was discovered that the stiffness of the EME increases or decreases due to various factors. Therefore, it is essential to investigate the mechanism of stiffness change in membrane materials to determine the load-strain relationship for the EMEs.

Acknowledgements

A portion of this research was conducted with the support of a research grant from the Nohmura Foundation for Membrane Structure's Technology. We also received valuable advice and collaboration from Dr. Masaaki MIKI (The University of Tokyo), Kenji OHYA and Tatsushi HEGURI (Taiyo Kogyo). We would like to express our sincere gratitude here to all those involved.

References

[1] J. Zhang and M. Ohsaki, "Form-finding of complex tensegrity structures by dynamic relaxation method," *Journal of Structural and Construction Engineering, Architectural Institute of Japan*, Vol. 81, No. 719, pp. 71-77, 2016. (in Japanese)

[2] Y. Yu and C. Lin, "Tensegric membrane structure with radiated struts," *in Proceedings of IASS Annual Symposia, IASS 2016 Tokyo Symposium: Spatial Structures in the 21st Century – Tension & Membrane Structures*, pp.1-10, 2016.

[3] S. S. Gupta, Y. Y. Tan, P. Z. Chia, C. P. Pambudi, Y. H. Quek, C. Yogiaman and K. J. Tracy, "Prototyping knit tensegrity shells: a design-to-fabrication workflow," *SN Applied Sciences 2,* No. 1062, 2020.

[4] K. Tracy, S. S. Gupta, L. Y. N. Stella, S. J. Wen, A. Pal, T. Wortmann, R. Bamford, "Tensile configurations: exploring spatial membrane tensegrity shell structures," *in Proceedings of ACADIA 2019*, Austin, USA, 2019.

[5] E. Henrysson, J. Olsson, A. Fisher and M. Ander, "CONCEPTUAL DESIGN AND ANALYSIS OF MEMBRANE STRUCTURES," *29th Nordic Seminar on Computational Mechanics*, Issue S8:2:c, 2016.

[6] L. Rhode-Barbarigos and S. Adriaenssens, "Investigating the influence of bending in the structural behavior of tensegrity modules using dynamic relaxation," *Proceedings of the International Conference on Computational Methods, Fitzwilliam College Cambridge, England*, Vol. 1, 2014.

[7] N. B. H. Ali, L. Rhode-Barbarigos, I. F. C. Smith, "Analysis of clustered tensegrity structure using a modified dynamic relaxation algorism," *International Journal of Solids and Structures*, Vol. 48, Issue. 5, p.637‑647, 2011.

[8] M. R. Pajand and M. T. Hakkak, "Nonlinear Analysis of Truss Structures Using Dynamic Relaxation," *International Journal of Engineering*, Vol. 19, Issue. 1, p.11‑22, 2006.

IASS 2023
July 10–14 Melbourne
Integration of Design and Fabrication

Proceedings of the IASS Annual Symposium 2023
Integration of Design and Fabrication
10–14 July 2023, Melbourne, Australia
Y.M. Xie, J. Burry, T.U. Lee and J. Ma (eds.)

Large span membrane architecture: how to accomplish carbon neutral with innovative photovoltaic and adaptive control strategy

Yongsheng YAN[a], Wujun CHEN[a,*], Jianhui HU[a,*]

[a,*] Space Structure Research Center, Shanghai Jiao Tong University
No.800 DongChuan Road, Shanghai 200240, China
cwj@sjtu.edu.cn

Abstract

Membrane structure has encountered some problems in the development of photovoltaic integration, and its engineering practicability has not been well verified, such as low energy conversion efficiency, and the integration of photovoltaic modules and structural system. A membrane structure system integrated photovoltaic is designed and manufactured to verify the practical engineering applicability of these new green building technologies. The system consists of roof, facade, insulation, semiconductor air conditioner and monitoring cabinet. The photovoltaic membrane structures made of three kinds of building membrane materials (PTFE\ETFE\PVC) are used as the roof. The south facade is a photovoltaic glass curtain wall made of CdTe cells. The indoor wall is equipped with PCM materials to achieve heat storage and insulation. The indoor temperature is controlled through the air conditioning made of semiconductor chips. The monitoring cabinet is used to monitor the structural performance, photovoltaic temperature, membrane film temperature, indoor air temperature and humidity, solar energy generation and other indicators all day for a long period continuously. Through the testing system, the engineering feasibility and economy of a variety of new photovoltaic integrated building technologies can be verified, providing a basis for the promotion of new technologies and the development of new membrane buildings integrated photovoltaic.

Keywords: new PV integrated building technologies, photovoltaic glass, photovoltaic membrane structures, PCM materials, semiconductor refrigeration, Hangai Prize applicant

1. Introduction

Membrane structures have become increasingly popular for large-span public buildings due to their lightweight, high efficiency, and aesthetically pleasing architectural shapes.[1] With global energy scarcity and climate change, green buildings have gained significant attention. large-span public buildings with membrane structures[2] typically consume a substantial amount of energy in human activities, such as lighting and regulating the thermal environment of the building due to their size, facing significant energy pressure and having great potential for low-carbon optimization.

Moreover, the large roof area of membrane buildings presents a significant potential for laying photovoltaic (PV) modules, although the curved shape of membrane structures creates significant resistance to the installation of PV modules.[3] In addition to photovoltaic energy storage measures, low-carbon solutions can also be sought in building energy consumption, such as building thermal insulation and regulating the thermal environment within the building. Currently, new low carbon technologies for membrane building are emerging, but their engineering feasibility has not yet been fully verified.

Many studies have researched the new technologies that porperbily can be used in large span membrane structures, such as flexible thin-film solar cells composites with different substrates. Weerasinghe *et al.*[4] studied the fabrication process and electrical properties of flexible thin-film solar cells with plastic

Copyright © 2023 by Yongsheng YAN, Wujun CHEN and Jianhui HU. Published in the Proceedings of the IASS Annual Symposium 2023 with permission.

substrates. Chenni *et al*.[5] studied the photoelectric performance of photovoltaic cells. Armstrong *et al*.[6] analyzed the photothermal performance of photovoltaic cells under different conditions, which proves that flexible photovoltaic cells can be used in high temperature condition and can be integrated into building surfaces. Fukushige[7] analyzed the change law of temperature of OPV cells. Asano *et al*.[8] studied the electrochemical properties of flexible thin-film solar cells with PSE films as substrates. Zhao *et al*.[9] Concern the field experiments and numerical modeling on the temperature characteristics and temperature value of the a-Si PV integrated in a double-layer ETFE cushion structure. Zhou *et al*.[10] gained the force-electrical properties of flexible thin-film solar cells during uniaxial stretching. Hu[11] developed the heat transfer model and carried out experimental verification. Xu *et al*.[12] measured the force-electrical properties of flexible thin-film solar cells laminated with polyvinylidene fluoride film materials. Yin *et al*.[13] conducted an experimental study on the electro-thermal-mechanical properties of the composition of flexible organic thin-film solar cells with ETFE foils. Geng *et al*.[14] studied the heat transfer performance of photovoltaic cells under different environments through modeling and simulation. M. Gloeckler et al.[15] showed that laboratory conversion efficiencies up to 22.1% have been achieved for CdTe solar cells, and large-area module efficiencies of 19% have been achieved. Corina Stetiu et al.[16] conducted a study on the energy-saving effect of phase change materials through numerical simulations and experiments, showing that the use of a cooling system with phase change materials can achieve an average energy saving of about 30%, regardless of the location or climate in the U.S. A.K. Athienitis[17] also conducted a study on phase change gypsum board and found through experiments that it can reduce energy consumption by storing solar energy during the heating period. Similarly, Dariusz Heim et al.[18] conducted research on phase change gypsum board and confirmed its energy-saving capabilities.

This study aims to design and fabricate a PV-integrated membrane structure system that validates the practical engineering utility of new PV building technologies, including various PV membrane structures, CdTe PV glass, phase change materials (PCM), and semiconductor air conditioner, in line with the trend of the development of the current low-carbon membrane structure concept. The system comprises a roof cover, facade, insulation, interior regulation, and monitoring cabinet, with the latter offering long-term, all-weather monitoring of structural response, temperature of membrane surface and PV modules, indoor temperature and humidity, PV power generation, and other critical parameters to evaluate the engineering practicality and economy of each new green building technology.

2. Membrane structure integrated innovation PV

Membrane structures are a popular choice for the roofs of large-span public buildings [19] as they offer ample space for PV utilization, with PV modules mainly installed on the roof and façade, while the curved shape of these structures presents challenges for PV module arrangement.

In recent years, glass curtain wall designs have become commonplace, and membrane curtain walls are gaining traction among architects. Fabric curtain walls and ETFE tensioned grids offer several advantages, including lightweight, transparency, and aesthetic appeal, making them a potential replacement for glass of the architectural curtain wall.

2.1. New flexible PV membrane structure

Membrane roofs are typically curved, making it challenging to lay rigid supports for PV modules. As a result, coordinating the flexible PV modules with the membrane structure's geometric shape is crucial. However, the low photoelectric conversion efficiency of the current flexible OPV modules is a major obstacle that hinders the development and promotion of the integration of PV module and membrane structure.

Unlike the approach of attaching PV modules to the structure after the membrane structure construction is completed, material integration design is considered more reasonable. Using crystalline silicon solar cells made via an ultra-thin cutting process, the PV modules are flexible due to their ultra-thin thickness

while maintaining high photovoltaic conversion rates. Before the structure is formed, the PV modules are integrated into the membrane structure materials, such as ETFE, PVC, and PTFE, which are commonly used for membrane architecture, creating a flexible surface that ensures the mechanical reliability of membrane structures while allowing the solar energy to be converted into electricity through the composite PV modules.

The composite material is consisting of a laminated structure comprising three layers, from top to bottom: encapsulation film, cell layer, and base film. The encapsulation film is 25μm thick ETFE film with excellent light transmission, while the base film is made of ETFE, PVC, and PTFE, which are common building film materials. The cell layer is 140μm thick monocrystalline silicon cell.

Table 1. Properties of each layer of PV membrane materials

	Material	Thickness(μm)	Features
cover	ETFE	25	
PV	a-Si	140	0.4V×2.5A，conversion efficiency 21%
substrate	PVC	780	Fabric film 120kN/m
	PTFE	800	Fabric film 140kN/m
	ETFE	250	Polymer film 12kN/m

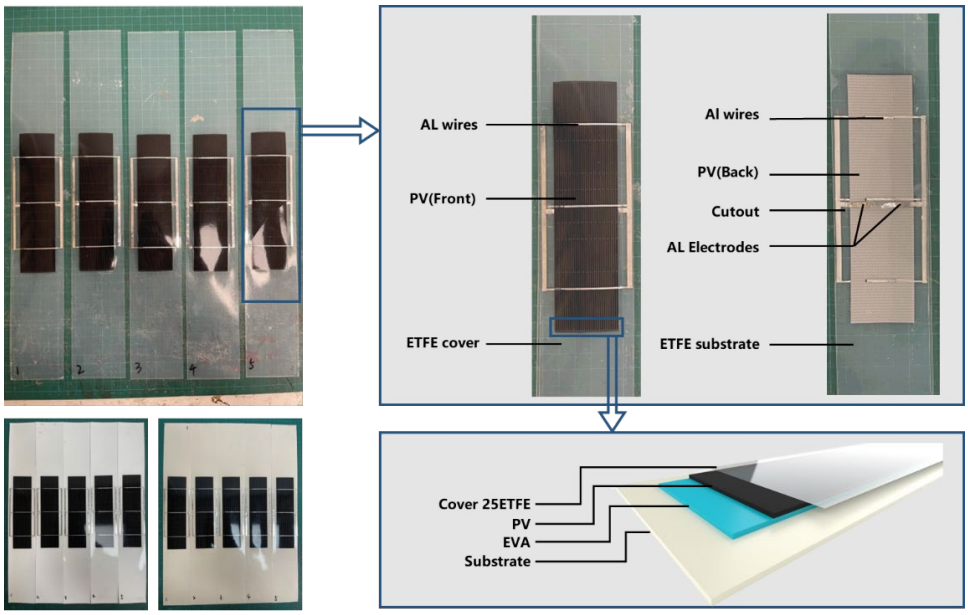


Figure 1. PV-membrane strip specimen

Membrane materials are flexible and sensitive to temperature, and their mechanical properties and structural performance are closely related to the geometry. PV-integrated membrane structure buildings unify structural force and photovoltaic function, but the temperature increase of PV modules under sunlight radiation can impact power generation efficiency, mechanical properties of the materials, and overall force of the structure. When laminated with crystalline silicon solar cells, the close fit between the PV module and membrane structure materials can further affect the material properties and geometry of the membrane structure due to temperature changes brought about by solar radiation. To address this issue, this study designed a test system to evaluate the temperature distribution and changes, as well as stress relaxation of this new PV-integrated membrane structure under solar radiation.

The test system uses three common membrane materials, namely PVC, ETFE, and PTFE, to create composite membrane materials, which are tensioned and formed into a single-layer plane with a negative

Gaussian curvature surface. The PV modules occupy 20.4% of the membrane structure area and consist of 30 monolithic packages measuring 160mm × 40mm. Under standard laboratory test conditions (AM1.5, 25°C), the module has an open-circuit voltage of 19.5V, a short-circuit current of 2.54A, an operating voltage of 16.5V and operating current of 2.4A, meaning 40W output power.

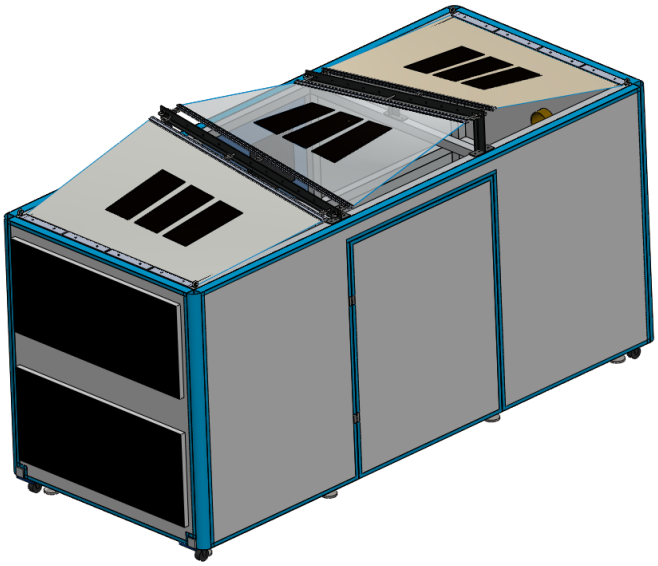


Figure 2. PV membrane testing mock-up

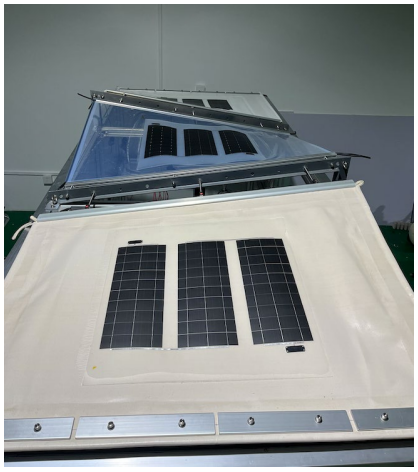


Figure 3. PV-PTFE/PV-ETFE/PV-PVC membrane roofs



Figure 4. Facade of mock-up

In the case of Shanghai 2022, the average daily solar radiation energy reaching the ground in August is 5.77kWh/m^2, which can be converted into approximately 791Wh of electricity through PV membrane structures. In January, the average daily solar radiation energy reaching the ground is 2.58kWh/m^2 due to heavy clouds and rainy weather, which can be converted into approximately 354Wh of electricity through PV membrane structures.

Since the membrane material has been compounded with the PV module before installation, this test system employs a planar tensioning process for the installation construction of the PV membrane structure. This process verifies the applicability of the planar forming process and ensures that the PV membrane structure is well tensioned after installation, with a smooth surface, uniform stress, and no damage to the PV modules. The results demonstrate the feasibility of planar tensioning and forming of PV integrated membrane structures and provide a reference for the application of planar tensioned membrane structures to building facades.

The test system can also evaluate the performance of the three membranes laminating the new flexible crystalline silicon photovoltaic modules. The photovoltaic power generation performance and the impact of temperature change on the membrane structure performance can be simultaneously examined, thereby verifying the structural suitability and energy efficiency of this flexible crystalline silicon photovoltaic integrated membrane structure for building roof and facade applications.

2.2. CdTe PV Glass

Tensioned membrane structures are typically used for roofing in membrane buildings, but building facades are also exposed to solar radiation and offer significant potential for the use of photovoltaic modules. While membrane facades are gaining attention from architects, glass remains the most used facade material. The primary method of integrating PV modules into glass facades involves using the glass as the base plate and panel, with the PV modules placed in the middle layer. However, the use of crystalline silicon solar cell arrays in these modules can negatively affect the transparency and aesthetics of the glass due to their thickness, as well as create challenges in waterproofing.

To address these issues, this test system employs chromium telluride (CdTe) material photovoltaic glass, which offers a solution to these problems. The sprayable nature of the chromium telluride photovoltaic material allows for customization of the transparency of the photovoltaic glass based on the spraying concentration. The resulting teal glass achieves both photovoltaic power generation and transparency, while also avoiding direct glare and other potential issues. The thickness of the chromium telluride photovoltaic modules is thin, and their coatings can be customized with patterns and colours to enhance the aesthetic appeal of the building. The temperature coefficient of CdTe cells is 0.20%/°C, which is lower than that of crystalline silicon (0.45%/°C), so that the output power of CdTe cells is not easily affected by temperature as Si cells.[20]

Table 2. Properties of CdTe PV modules

ASP-S1		
	P_m	105W
	V_{oc}	124V
	I_{sc}	1.28A
	V_m	92.9V
	I_m	1.13A
	Size	1200*600*6.8mm
	Weight	12kg

The test model presented in this paper features two chromium telluride photovoltaic glass modules installed on the south elevation. For instance, based on statistical data from the national meteorological station in Shanghai, the highest and lowest average daily solar radiation values are recorded in August and January, respectively, at 5.77kWh/m^2/day and 2.58kWh/m^2/day. Based on these values, the average daily power generation of the two PV modules in August and January can be calculated to be 1557Wh and 696Wh, respectively. The energy utilization rate of the PV modules is estimated to be around 18.7%.

The combination of chromium telluride photovoltaic modules and glass aligns with the current trend in the building market, which favours glass curtain walls that maximize the use of building facades for photovoltaic power generation, while also considering aspects such as light transmittance and aesthetics.

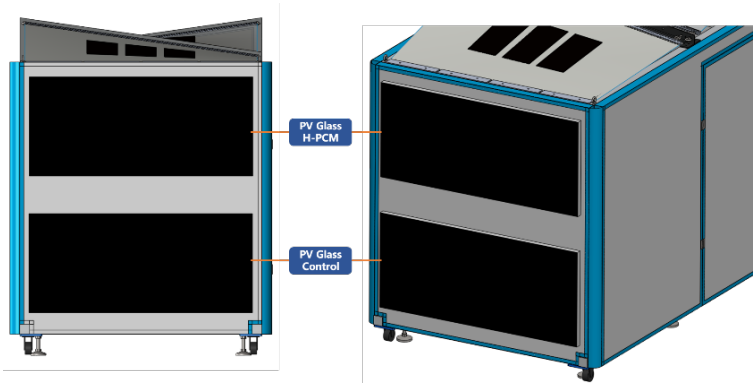


Figure 5. PV Glass module design



Figure 6. PV Glass Modules

3. Thermal regulation in membrane buildings

The indoor temperature is a crucial factor affecting human comfort. Traditionally, air conditioning and heating systems are used to regulate indoor temperature, which often results in significant energy consumption and reliance on fossil fuels. However, by incorporating solar power and heat storage systems, a significant portion of energy consumption can be reduced, resulting in a more sustainable and eco-friendly approach to regulating indoor temperature.

3.1. Semiconductor air conditioning

Summer presents a great opportunity to utilize solar air conditioners due to the high radiant sunlight energy during this period. The compressor, which uses Freon as its refrigerant, is the main component of conventional air conditioners. The release of Freon into the atmosphere contributes to ozone layer destruction. However, recent advancements in semiconductor materials have made it possible to develop eco-friendly air conditioners. Semiconductor cooling sheets create a significant temperature difference between the two sides when activated, which can be utilized to regulate room temperature. Although the effectiveness and energy efficiency ratio of semiconductor air conditioning in larger building spaces are yet to be proven, a small refrigerator has already been designed and produced using the idea of using semiconductors.



Figure 7. Semiconductor air conditioner

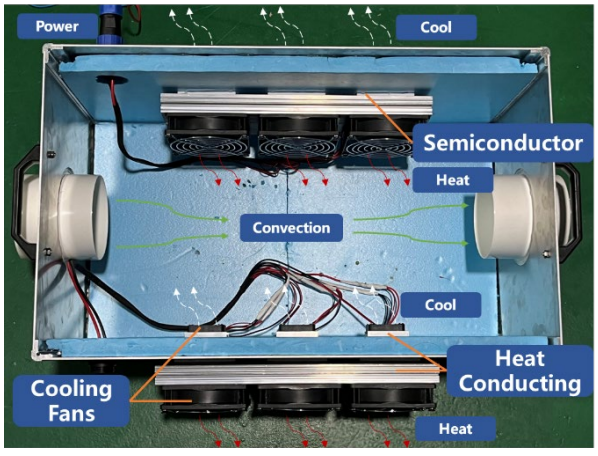


Figure 8. Configration of semiconductor air conditioner

This paper presents the design and construction of a semiconductor air conditioner that considers both cooling and heating. The semiconductor air conditioner consists of a semiconductor chip, a heat transfer chip, a cooling fan, a cabinet, and an extractor fan. Six semiconductor chips are used in this study, with

three forming a cooling group and another three forming a heating group. A single group has a power of 150W.

The semiconductor air conditioner has been tested and shown to meet the cooling and heating needs within 3.6m^2. Its advantage is that it consumes only electrical energy, produces no exhaust gas or pollution, and provides equal cooling and heating power. However, the inflow measures are not yet optimized, and temperature control is less efficient.

3.2. Phase change materials (PCM)

Besides air conditioning, thermal insulation is also crucial for maintaining a stable environment inside membrane buildings. While PV modules on the market have an efficiency of around 20%, which means only a fraction of the solar energy can be utilized for PV power generation, a significant portion of the radiant energy is converted into thermal energy, leading to a rise in the temperature of the PV modules. High temperatures can compromise both the lifetime of the PV modules and the comfort of the building's occupants in PV-integrated buildings.

To address this issue, phase change materials (PCM) with excellent thermal storage capacity, thanks to their special thermodynamic properties, can be added to the backside of PV modules. This addition not only reduces the peak temperature of the modules but also stores the thermal energy generated by the sunlight radiation for later use. Additionally, the adjustable phase change temperature of the PCM material allows for building insulation, providing a new way of thinking about building insulation and heating in the winter. During the day, solar energy is absorbed by the photovoltaic modules and stored in the phase change material. At night, when the temperature drops, the phase change material releases the stored heat to maintain a comfortable indoor temperature.

Table 3. Properties of PCM

Material	Temperature	Enthalpy	Heat conductivity	Density
PCM	Variable	220J/g	0.21W/(m K)	0.86g/cm3

As an example, a 10mm thick phase change material (PCM) weighs 8.6kg/m^2 and has a thermal storage capacity of 525Wh/m^2. PV glass modules can reach a maximum surface temperature of 80°C under solar radiation. Therefore, PCM materials with a higher phase change temperature can be used to reduce the high temperature zone and peak of PV modules. In contrast, the building facade can be made of PCM materials with a lower phase change temperature to achieve the building insulation effect of storing energy during the day and releasing it at night.

If a 10mm thick solid-solid PCM with a phase change temperature of 18°C is used as insulation for the building facade during winter, the energy utilization rate can reach 20.3% based on the enthalpy of the PCM material for heat storage.

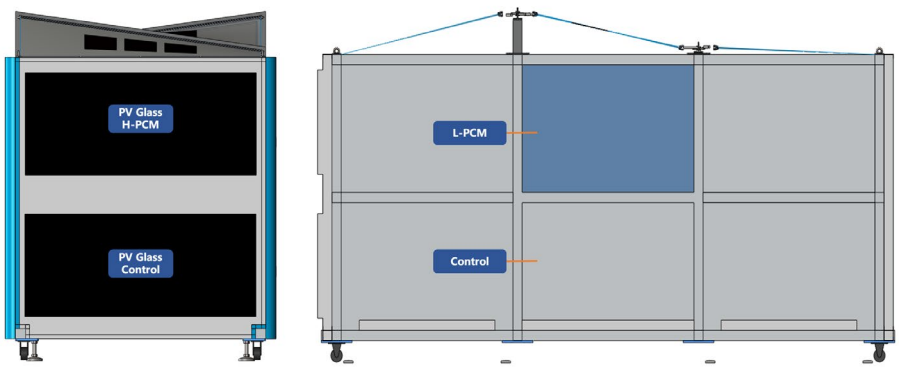


Figure 9. PCM in the mock-up design

Therefore, utilizing the remarkable energy storage capacity of phase change materials, incorporating PCM materials as insulation in buildings can provide numerous benefits. Firstly, using high-temperature PCM on the backside of PV modules can decrease the temperature peak of the modules, which protects them and prolongs their lifetime. Secondly, using low-temperature PCM on the building façade can help regulate the thermal environment inside the building and serve as a buffer when the temperature fluctuates, thereby decreasing the need for air conditioning or heating and saving energy.

4. Monitoring and control system for membrane buildings integrated PV

To achieve intelligent health testing of buildings and to verify the reliability and applicability of the low carbon technologies mentioned in long-term operations of large-span membrane structures, an integrated test system has been developed. This system addresses membrane structure safety, building energy efficiency, comfort, and intelligence. Equipped with a design control cabinet, the system enables health monitoring and control of the building structure, energy storage, and cloud data transmission. This integrated approach ensures a comprehensive and effective means of testing the performance of the low carbon technologies used in large-span membrane structures.

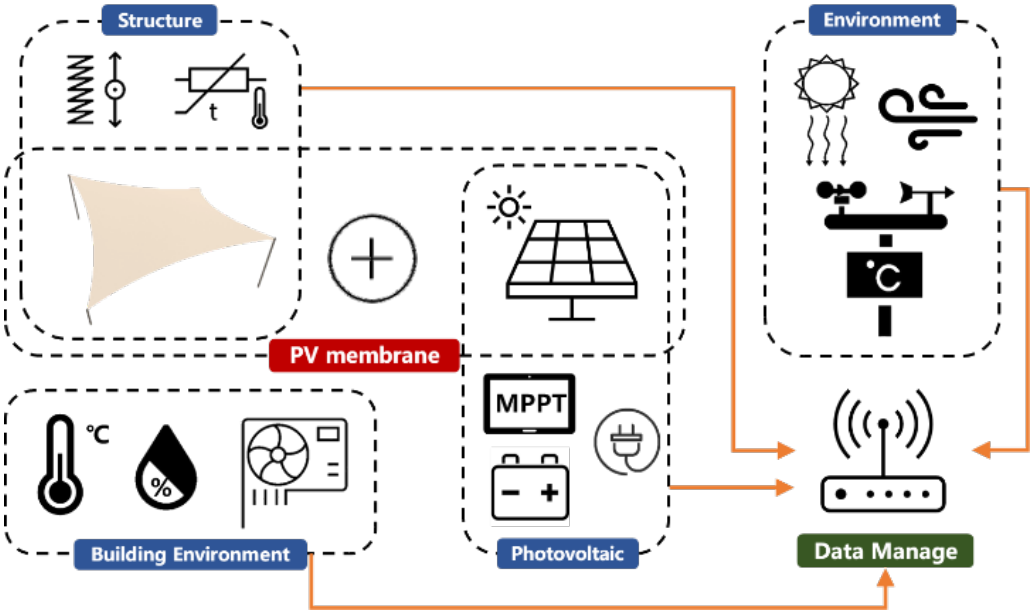


Figure 10. Data acquisition and management system

The structural monitoring system outlined above enables the monitoring of key indicators of photovoltaic membrane buildings over long periods of operation in natural environments. By assessing the economic efficiency of photovoltaic power generation, membrane structure relaxation, and thermal environment of the building, the feasibility and cost-effectiveness of various low-carbon technologies in membrane buildings can be evaluated. The monitoring system comprises five main components:

(1) Photovoltaic system, which includes monitoring of power generation from photovoltaic modules, battery storage, and load energy consumption.

(2) Membrane system, which includes monitoring of tension in the PV membrane structure and temperature of the membrane surface.

(3) Building environment, which includes monitoring of temperature and humidity, as well as air conditioning control.

(4) External environment, which includes measurement of sunlight radiation intensity, wind speed, wind direction, ambient temperature, humidity, and other meteorological data.

(5) Data acquisition and transmission, which includes data acquisition and internet transmission modules.

To realize the above ideas, a monitoring cabinet for the test system is designed and built. The structural monitoring system is capable of monitoring the main indicators of photovoltaic membrane buildings for a prolonged period of time.

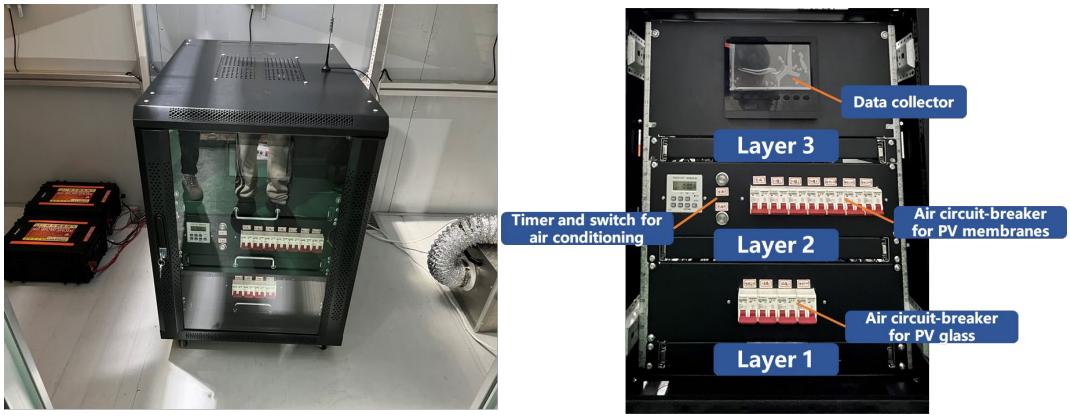
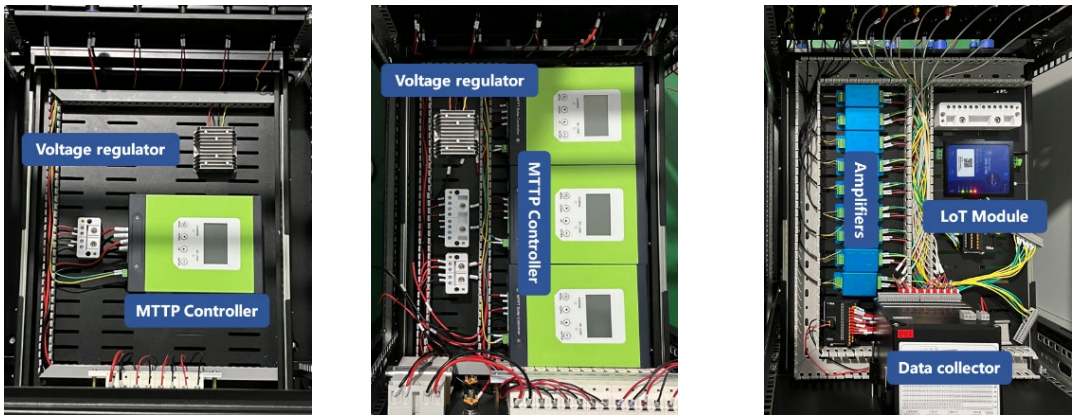


Figure 11. Monitoring and Control Cabinet



(a) Layer 1 Control of PV glass modules

(b) Layer 2 Control of PV membrane modules

(c) Layer 3 Data Collector and Internet modules

Figure 12. Layout of the control cabinet

The monitoring cabinet is equipped with data acquisition and internet cloud transmission capabilities, enabling the acquisition of various data types, including temperature, tension, current, voltage, and meteorological data such as solar radiation intensity and wind speed. By monitoring various aspects of the photovoltaic membrane building, including building safety, energy economy, and comfort, the applicability of a broad range of low-carbon membrane technologies can be verified.

Concerning building structural safety and reliability, the system collects data on membrane surface temperature, tension relaxation, and ambient wind speed to monitor the membrane's structural safety and to analyse the effect of temperature changes, wind pressure, and other factors on membrane tensioning.

For building energy and economy, the system monitors the generation, storage, and energy consumption of photovoltaic modules to achieve a balance between energy acquisition and consumption for the test installation's long-term operation and to reach carbon neutrality in the membrane structure.

Regarding building comfort, the system monitors ambient temperature and humidity and controls the switching time of air conditioning using energy from solar power storage to adjust the indoor environment.

In order to ensure the safety and stability of the test system while working outdoors for extended periods and to avoid any interference with the sensors, all devices within the monitoring cabinet, including sensors, data acquisition components, IoT modules, time control switches, and building loads, are powered by DC. Power is generated by the photovoltaic membrane structure and photovoltaic glass modules through solar energy and is stored in batteries. The batteries then power the test system and loads such as the air conditioning, enabling the test system to operate off-grid for long periods of time.

Table 4. Energy consumption of testing system

	Power/W	Amount	Energy consumption/(Wh/Day)
Data collector	8	1	192
Tensile sensor	0.3	9	2.7
Temperature sensor	0.1	3	0.3
MTTP	2	4	192
LoT Module	0.86	1	21
Time-controlled switch	1	1	1
SUM			409

According to the statistical monitoring of the test system's power consumption, the system requires a continuous energy supply that is obtained through the PV glass modules absorbing solar energy and converting it into electrical energy. The PV glass can supply a minimum of 696Wh per day, which is sufficient for the system's continuous operation, and any excess energy is stored in the battery. The air conditioner operates at a power of 150W, which is powered by the solar energy absorbed by the PV membrane structure. Throughout the year, the PV membrane structure generates a maximum of 791Wh per day and a minimum of 354Wh per day. This provides approximately 5 hours and 2.5 hours of power respectively for the air conditioner. A time-controlled switch can be used to turn the air conditioner on and off depending on the amount of solar radiation and the indoor temperature during different seasons.

In summary, this monitoring cabinet combines data monitoring, control, and transmission into a single unit, capable of collecting data and transmitting it to the cloud for the low-carbon membrane structure testing system. The monitoring system operates with long-term autonomous energy supply, effectively monitoring membrane structures' safety, economy, comfort, and energy efficiency, and assessing the applicability of low-carbon technologies across a broad range of membrane structures.

5. Conclusion

This paper presents four low-carbon building technologies that can be applied to large-span membrane structures and explains their characteristics.

Membrane structure integrated photovoltaic, which achieves an integrated structure of membrane and photovoltaic module, can convert solar energy into electricity through the photovoltaic module on the composite while ensuring the mechanical properties of the membrane material itself. The ultra-thin crystalline silicon flexible photovoltaic module used in the testing mock-up can reach a photoelectric conversion efficiency of 21%, with a measured 23.8%.

CdTe photovoltaic glass provides a new option for membrane structure building facades. Cadmium telluride photovoltaic material is sprayed onto the glass, forming photovoltaic modules. The spraying concentration can customize the transparency and pattern of photovoltaic glass, ensuring the

transparency of the glass while absorbing solar energy into electricity. Its photoelectric conversion efficiency is 19%, measured at 18.7%.

With the advance of semiconductor material, semiconductor air conditioning system is designed for membrane building. When a semiconductor cooling material is energized, a temperature difference is generated on both sides of the material. Using this temperature difference, equipped with a thermal conductor, cooling fan, and ventilation fan, it can play a simple air conditioning effect of cooling and heating. The process consumes only electrical energy and does not rely on refrigerants such as Freon, thus avoiding damage to the atmosphere.

Phase change material (PCM) has a good thermal storage effect due to the presence of a plateau section in the phase change process, whose phase change temperature can be adjusted according to demand. It can act as a buffer during temperature changes, and it can be used for high-temperature protection of photovoltaic modules and as an insulation material for building facades.

To test and verify these low-carbon technologies, a carbon neutral test system for long period off-grid operation has been designed and fabricated, which includes an integrated control cabinet that allows for long-term and all-weather monitoring of structural response, PV temperature, membrane surface temperature, indoor temperature and humidity, PV power generation, and other indicators. This testing system will provide a basis for the application and development of new low-carbon building technologies in large-span membrane structures.

Acknowledgement

The authors acknowledge the financial support from the National Natural Science Foundation of China (Nos. 52278193, 52278191). The PV membrane materials and PV glass used in the tests were fabricated by Hunan Pro space Power Technology Co., Ltd and Advanced Solar Power (Hangzhou) Inc.

References

[1] W. J. Chen, J. H. Hu, and H. Song, “Novel BIPV/T ETFE cushion,” presented at the Textiles composites and inflatable structures VI : proceedings of the VI International Conference on Textile Composites and Inflatable Structures, Barcelona, Spain. 9-11 October, 2013, CIMNE, 2013, pp. 363–374. Accessed: Jun. 16, 2022.

[2] V. Milošević and J. Marchwiński, “Photovoltaic Technology Integration with Tensile Membrane Structures - a Critical Review,” *Tehnički vjesnik*, vol. 29, no. 2, pp. 702–713, Apr. 2022.

[3] J. Hu *et al.*, “Structural behavior of the PV–ETFE cushion roof,” *Thin-Walled Structures*, vol. 101, pp. 169–180, Apr. 2016.

[4] H. C. Weerasinghe, F. Huang, and Y.-B. Cheng, “Fabrication of flexible dye sensitized solar cells on plastic substrates,” *Nano Energy*, vol. 2, no. 2, pp. 174–189, Mar. 2013.

[5] R. Chenni, M. Makhlouf, T. Kerbache, and A. Bouzid, “A detailed modeling method for photovoltaic cells,” *Energy*, vol. 32, no. 9, pp. 1724–1730, Sep. 2007.

[6] S. Armstrong and W. G. Hurley, “A thermal model for photovoltaic panels under varying atmospheric conditions,” *Applied Thermal Engineering*, vol. 30, no. 11, pp. 1488–1495, Aug. 2010.

[7] S. Fukushige, K. Ichida, T. Minemoto, and H. Takakura, “Analysis of the temperature history of amorphous silicon photovoltaic module outdoors,” *Solar Energy Materials and Solar Cells*, vol. 93, no. 6, pp. 926–931, Jun. 2009.

[8] T. Asano, T. Kubo, and Y. Nishikitani, “Electrochemical properties of dye-sensitized solar cells fabricated with PVDF-type polymeric solid electrolytes,” *Journal of Photochemistry and Photobiology A: Chemistry*, vol. 164, no. 1, pp. 111–115, Jun. 2004.

[9] B. Zhao *et al.*, “Photothermal performance of an amorphous silicon photovoltaic panel integrated in a membrane structure,” *Journal of Physics D: Applied Physics*, vol. 49, no. 39, p. 395601, 2016.

[10] N. Zhou and Y. Luo, "Force electrical parameter testing of flexible thin film solar cells," Experimental mechanics, vol. 25, no. 06, pp. 717–722, 2010.
[11] J. Hu *et al.*, "Electrical-thermal-mechanical properties of multifunctional OPV-ETFE foils for large-span transparent membrane buildings," *Polymer Testing*, vol. 66, pp. 394–402, Apr. 2018.
[12] X. Xu, N. Zhou and Y. Luo, "Experimental study of the force-electric properties of flexible thin film solar cells laminated with polyvinylidene fluoride membranes," Journal of Building Structures, vol. 32, no. 08, pp. 127–132, 2011.
[13] Y. Yin, J. Hu, W. Chen, and Y. Li, "Experimental study of the electrical-thermal-force performance of flexible thin-film solar cells with ethylene-tetrafluoroethylene thin-film composites," Manned Spaceflight, vol. 24, no. 01, pp. 73–78, 2018.
[14] S. Geng, S. Su, Y. Zou, and X. Mu, "Heat transfer characteristics of stratospheric blimp photovoltaic cells," Science, Technology and Engineering, vol. 20, no. 14, pp. 5849–5855, 2020.
[15] M. Gloeckler, I. Sankin, and Z. Zhao, "CdTe Solar Cells at the Threshold to 20% Efficiency," *IEEE Journal of Photovoltaics*, vol. 3, no. 4, pp. 1389–1393, Oct. 2013.
[16] C. Stetiu, "Energy and peak power savings potential of radiant cooling systems in US commercial buildings," *Energy and Buildings*, vol. 30, no. 2, pp. 127–138, Jun. 1999.
[17] A. K. Athienitis, C. Liu, D. Hawes, D. Banu, and D. Feldman, "Investigation of the thermal performance of a passive solar test-room with wall latent heat storage," *Building and Environment*, vol. 32, no. 5, pp. 405–410, Sep. 1997.
[18] D. Heim and J. A. Clarke, "Numerical modelling and thermal simulation of PCM–gypsum composites with ESP-r," *Energy and Buildings*, vol. 36, no. 8, pp. 795–805, Aug. 2004.
[19] Q. Li and A. Zanelli, "A review on fabrication and applications of textile envelope integrated flexible photovoltaic systems," *Renewable and Sustainable Energy Reviews*, vol. 139, p. 110678, Apr. 2021.
[20] L. Ma *et al.*, "Progress in research and industrialization of CdTe thin film solar cells," Journal of Silicates, vol. 50, no. 8, pp. 2305–2312, 2022.

IASS 2023
July 10–14 Melbourne
Integration of Design and Fabrication

Proceedings of the IASS Annual Symposium 2023
Integration of Design and Fabrication
10–14 July 2023, Melbourne, Australia
Y.M. Xie, J. Burry, T.U. Lee and J. Ma (eds.)

Numerical and experimental modelling of pneumatic structures

Ruy Marcelo O. PAULETTI[a,*], Karina B. ROCHA[b]

[a,*] Department of Structural & Geotechnical Engineering, Polytechnic School, University of São Paulo, Brazil
pauletti@usp.br

[b] Department of Mathematics, Mauá Institute of Technology, São Paulo, Brazil

Abstract

As other types of tensile structures, pneumatics rely on geometric stiffness for stability. However, pneumatic structures are also endowed with a 'pneumatic stiffness', which corresponds to a reluctance of the pressure envelope to change its volume. The higher the inside pressure, the more relevant this component can be. Most civil and architectural applications of pneumatic structures are low to moderate-energy systems, for which simplified material models may suffice, if a sound model to cope with membrane wrinkling is also considered. This paper presents a simple yet effective model to cope with the nonlinear analysis of pneumatic membranes under wind loads, incorporating an effective wrinkling criterion into a simple membrane element, and deriving new expressions for its pneumatic stiffness. The model was tested through an inexpensive experiment, comprising the compression of an exercise ball, which corroborated the importance of considering variable inside pressures for moderate-energy systems. The relevance reduces, however, as the dimensions of the structures increase, especially in the case of large, insufflate domes, which are also discussed in the paper.

Keywords: pneumatic structures, membranes, finite elements, nonlinear analysis, pneumatic stiffness, membrane wrinkling

1. Introduction

Pneumatic structures are paradigms of tension structures, since only in them it is possible to have all structural elements working exclusively in tension. Practical applications of pneumatic structures started at the beginnings of the 20th century, to become rather customary nowadays, in many distinct areas, as large stadia roofs, building façades, or everyday furniture, like sofas, boats and toys. Although the use of large, insufflated pneumatics for permanent applications has been superseded by other light structural systems in the last decades, the use of smaller inflated or insufflated domes, as well as inflated beams and cushions, combined with gridshells and other rigid systems, is becoming increasingly popular worldwide [1].

In this paper we present a simple model, of easy implementation and yet able to cope with a broad range of civil and architectural applications, which usually employ (almost) impermeable fabrics or films, whose material behaviors might be quite complex. Typical materials present nonlinear, anisotropic and hysteretic behaviors, very much dependent on the fabric internal structure and load history. The orientation of orthotropy directions in double curvatures surfaces is not a trivial matter, not least because fabric patterning usually aims to minimizing waste, a conflicting objective with optimizing the yarns lay-out. Consequently, industry strives to provide the market with fabrics the more isotropic and linear elastic as possible, and so follows design and analysis software. Furthermore, wind loads might induce

Copyright © 2023 by Ruy M.O. PAULETTI and Karina B. ROCHA. Published in the Proceedings of the IASS Annual Symposium 2023 with permission.

wrinkling on the pneumatic envelope, and practical strategies to cope with wrinkling supersede concerns about other types of nonlinear material behavior [2].

2. Nonlinear equilibrium

Upon discretization, the problem of *equilibrium of a membrane structure* can be expressed as finding *a displacement vector* $\boldsymbol{u}^*$ such that $\boldsymbol{g}(\boldsymbol{u}^*) = \boldsymbol{p}(\boldsymbol{u}^*) - \boldsymbol{f}(\boldsymbol{u}^*) = \boldsymbol{0}$, where $\boldsymbol{u} = \boldsymbol{x} - \boldsymbol{x}_r$ is the *global displacement vector* with respect to an initial configuration $\boldsymbol{x}_0$, $\boldsymbol{g}(\boldsymbol{u})$ is *a residual force vector*, $\boldsymbol{p}(\boldsymbol{u})$ is the *internal load vector* and $\boldsymbol{f}(\boldsymbol{u})$ is the *external load vector*, all of order n_{dof}, the number of degrees of freedom of the system. The equilibrium problem can be solved –within a vicinity of a solution $\boldsymbol{u}^*$– iterating Newton-Raphson's recurrence formula, $\boldsymbol{u}_{k+1} = \boldsymbol{u}_k - \left(\frac{\partial \boldsymbol{g}}{\partial \boldsymbol{u}}\Big|_{\boldsymbol{u}_k}\right)^{-1} \boldsymbol{g}(\boldsymbol{u}_k)$, where the *tangent stiffness matrix* is defined as $\boldsymbol{K} = \frac{\partial \boldsymbol{g}}{\partial \boldsymbol{u}}$. It is usual to assemble the global quantities from their elements' counterparts, with the element tangent stiffness given by $\boldsymbol{k}^e = \frac{\partial \boldsymbol{g}^e}{\partial \boldsymbol{u}^e}$, where $\boldsymbol{u}^e$ is the element displacement vector and $\boldsymbol{g}^e$ is the element residual vector.

Whenever analytical expressions for the tangent stiffness matrices are not at hand, a convenient option is given by *finite-difference approximations,* which achieve the same convergence rate and precision as the consistent tangent stiffness matrices, with acceptable extra computational cost, provided calculations are performed at the element level. Using a *central-difference* scheme, each column of the tangent stiffness matrix can be evaluated according to $\breve{\boldsymbol{k}}_j^e = \frac{1}{2h}\left[\boldsymbol{g}^e\left(\boldsymbol{u}^e + h\delta_j^e\right) - \boldsymbol{g}\left(\boldsymbol{u}^e - h\delta_j^e\right)\right]$, where $\pm h\delta_j^e$ are backward and forward perturbations of the j^{th} degree of freedom, which can be taken as small as allowed by the machine precision [3].

The *Newton-Raphson Method* (NRM) usually yields the best algorithm for the solution of non-linear static equilibrium of cable and membrane structures, since it then presents quadratic convergence rate, in a sufficiently narrow vicinity of the solution. However, cables and membranes have no bending stiffness and in the absence of a proper tension field, the structure's tangent stiffness matrix may become non-positive definite, leading to divergence of the method. In many cases, the *Dynamic Relaxation Method* (DRM) offers a convenient alternative, replacing the equilibrium problem by a pseudo-dynamic analysis, where fictitious mass and damping matrices are arbitrarily chosen to control the stability of the time integration process. The definition of an arbitrary damping matrix may be circumvented by the process of *kinetic damping*, whereby the undamped movement of the system, governed by $\boldsymbol{M}\ddot{\boldsymbol{u}} + \mathbf{g}(\boldsymbol{u}) = \boldsymbol{0}$, is followed until a maximum of the total kinetic energy is reached, whence all the velocity components are cancelled, and the analysis is restarted, until new kinetic energy maxima (usually smaller than the precedent ones) are found, and all velocities are zeroed again. Although DRM shows no advantage for small to medium sized problems, whenever NRM shows good convergence, there might be economy for large problems. Both methods have been implemented into a coherent computational framework named SATS – A System for the Analysis of Taut Structures, which has been applied to several problems involving the shape finding and analysis of cable and membrane structure. Details can be found in [4].

2.1. Argyris' membrane element

Figure 1(a) shows the Argyris' natural triangular membrane finite element defined in an initial configuration Ω_0, in which it is already under an initial stress field. A *reference configuration* Ω_r usually considers stress-free conditions but, for small strains, we assume $\Omega_r \equiv \Omega_0$. The element's *current configuration* is denoted by Ω. Element nodes and edges are numbered anticlockwise, with edges facing nodes of same number.

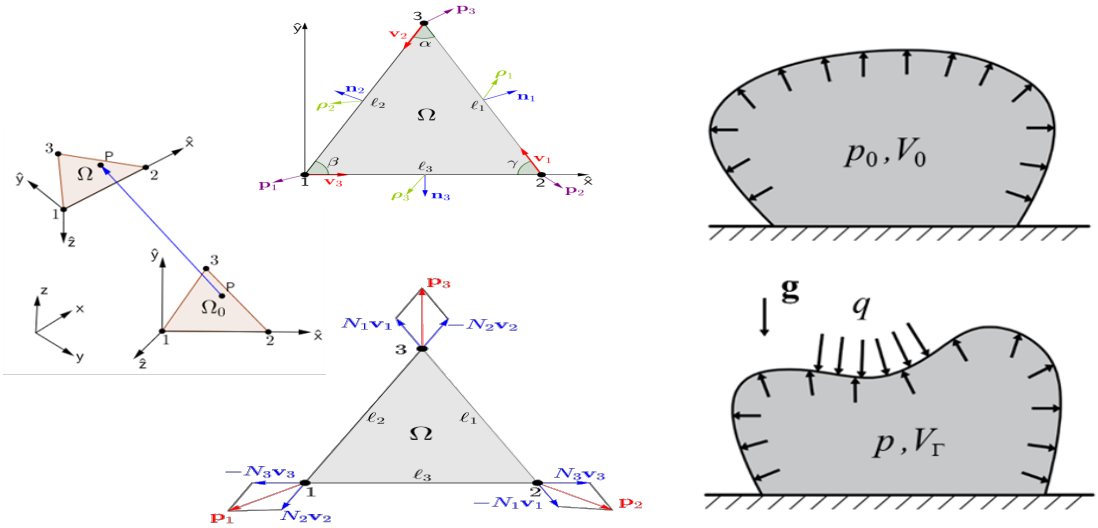


Figure 1. (a) definitions of Argyris membrane element quantities: An element is defined at a configuration Ω_0, which may also be used as reference configuration, i.e. $\Omega_r \equiv \Omega_0$; (b) initial and current configuration of a pneumatic envelope.

Nodal coordinates are referred to a global Cartesian system and at the current configuration are given by $\boldsymbol{x}_i = \boldsymbol{x}_i^0 + \boldsymbol{u}_i$ where $\boldsymbol{u}_i$ are the element's nodal displacements. The lengths of element edges are given by $\ell_i = \|\boldsymbol{\ell}_i\| = \|\boldsymbol{x}_k - \boldsymbol{x}_j\|$, with indexes $i,j,k = 1,2,3$ in cyclic permutation. Unit vectors parallel to the element edges are denoted by $\boldsymbol{v}_i = \boldsymbol{\ell}_i/\|\boldsymbol{\ell}_i\|$. At the current configuration Ω , side length ℓ_i and the unit vector $\boldsymbol{v}_i$, parallel to the nodes are shown in Figure 1, as well as the unit vector normal to the sides $\boldsymbol{n}_i$, and the resultant of the stress acting on each element side, $\boldsymbol{\rho}_i$. These results are added up to the nodal loads $\mathbf{p}_i$, which may be decomposed into natural load, i.e., components of loads parallel to the element sides see [2] and [4] for further details).

With these definitions, the *vector of internal nodal forces* can be decomposed into forces parallel to the element edges, according to

$$\boldsymbol{p}^e = \begin{bmatrix}\boldsymbol{p}_1\\ \boldsymbol{p}_2\\ \boldsymbol{p}_3\end{bmatrix} = \begin{bmatrix}N_2\boldsymbol{v}_2 - N_3\boldsymbol{v}_3\\ N_3\boldsymbol{v}_3 - N_1\boldsymbol{v}_1\\ N_1\boldsymbol{v}_1 - N_2\boldsymbol{v}_2\end{bmatrix} = \begin{bmatrix}\mathbf{0} & \boldsymbol{v}_2 & -\boldsymbol{v}_3\\ -\boldsymbol{v}_1 & \mathbf{0} & \boldsymbol{v}_3\\ \boldsymbol{v}_1 & -\boldsymbol{v}_2 & \mathbf{0}\end{bmatrix}\begin{bmatrix}N_1\\ N_2\\ N_3\end{bmatrix} = \boldsymbol{C}\boldsymbol{N}, \qquad (1)$$

where $\boldsymbol{C}$ is a *geometric operator*, which collects the unit vectors parallel to the element edges and $\boldsymbol{N} = [N_1 \quad N_2 \quad N_3]^T$ is the *vector of natural forces*.

We assume that the behavior of the element in taut conditions is linear elastic, thus a relationship exists, such that $\boldsymbol{N} = \boldsymbol{k}_n^0\boldsymbol{a} + \boldsymbol{N}_0$, where $\boldsymbol{a} = [\Delta\ell_1 \quad \Delta\ell_2 \quad \Delta\ell_3]^T$ is the *vector of natural displacements* (with $\Delta\ell_i = \ell_i - \ell_i^0$ and the *element natural stiffness* is a constant matrix given by

$$\boldsymbol{k}_n^0 = t_0 A_0 \boldsymbol{L}_0^{-1}\boldsymbol{T}_0^{-T}\widehat{\boldsymbol{D}}\boldsymbol{T}_0^{-1}\boldsymbol{L}_0^{-1}, \qquad (2)$$

where t_0A_0 is the element volume, $\boldsymbol{L}_0 = \mathrm{diag}\{\ell_i^0\}$, $\widehat{\boldsymbol{D}}$ collects the coefficients of Hooke's law for plane stresses, such that $\widehat{\boldsymbol{\sigma}} = \widehat{\boldsymbol{D}}\widehat{\boldsymbol{\varepsilon}}$, and $\widehat{\boldsymbol{T}}_0$ is a classical transformation matrix, relating the linear Green strains $\widehat{\boldsymbol{\varepsilon}}$ to the *natural strains , i.e.*, $\boldsymbol{\varepsilon}_n = \widehat{\boldsymbol{T}}_0\widehat{\boldsymbol{\varepsilon}}$, highlighting the fact that Argyris' natural membrane element is akin to a *strain gauge rosette*.

Since $\boldsymbol{k}_n^0$ has only six independent components, its storage is economic, reducing the number of operations required to calculate the internal loads and tangent stiffness, and thus the overall computing time. The vector of internal forces at each configuration is given by

$$\boldsymbol{p}^e = \boldsymbol{C}(\boldsymbol{k}_n^0 \boldsymbol{a} + \boldsymbol{N}_0). \qquad (3)$$

Assembling these loads into the global residual vector is all it takes to pose the equilibrium equation of a taut membrane structure via DRM or NRM, using finite differences. It is also a matter of simple derivation to obtain the *internal stiffness matrix of the taut membrane element*, given by:

$$\boldsymbol{k}_{int} = \boldsymbol{C}\boldsymbol{k}_n^0\boldsymbol{C}^T + \begin{bmatrix} \left(\frac{N_2}{\ell_2}\boldsymbol{M}_2 + \frac{N_3}{\ell_3}\boldsymbol{M}_3\right) & -\frac{N_3}{\ell_3}\boldsymbol{M}_3 & -\frac{N_2}{\ell_2}\boldsymbol{M}_2 \\ -\frac{N_3}{\ell_3}\boldsymbol{M}_3 & \left(\frac{N_1}{\ell 1}\boldsymbol{M}_1 + \frac{N_3}{\ell_3}\boldsymbol{M}_3\right) & -\frac{N_1}{\ell 1}\boldsymbol{M}_1 \\ -\frac{N_2}{\ell_2}\boldsymbol{M}_2 & -\frac{N_1}{\ell 1}\boldsymbol{M}_1 & \left(\frac{N_1}{\ell 1}\boldsymbol{M}_1 + \frac{N_2}{\ell_2}\boldsymbol{M}_2\right) \end{bmatrix}, \quad (4)$$

where, for brevity, we have defined some *projection matrices*, $\boldsymbol{M}_i = \boldsymbol{I}_3 - \boldsymbol{v}_i\boldsymbol{v}_i^T$. See details of the above formulation in [2] and [4].

2.2. External nodal loads and stiffness for pneumatic envelopes

We consider that the pressure envelope displayed in Figure 1(b) is under pressure on both sides. We denote the total *outside pressure* as q, and we strongly simplify the problem by assuming that its magnitude is not dependent on displacements. For the *inside* pressure p, we assume Boyle-Mariotte's law, for an ideal gas under adiabatic conditions, such that $p = p_0 V_0 / V_\Gamma$, where p_0 and p are the absolute values of the pressure acting inside the pneumatic envelope, at the initial and current configurations, of total volumes V_0 and V_Γ, respectively.

The total volume of the pneumatic envelope at some current configuration Γ can be calculated as $V_\Gamma = \frac{1}{3}\int_\Gamma (\boldsymbol{x}\cdot\boldsymbol{n})dA \simeq \frac{1}{3}\sum_{k=1}^{n_{el}} \boldsymbol{x}_1^k \cdot A_k \boldsymbol{n}_k$, where n_{el} is the number of elements of the mesh, A_k is the k^{th} element area, $\boldsymbol{n}_k$ its unit normal vector, and where we arbitrary picked $\boldsymbol{x}_1^k$ (the coordinates of node 1 of the element), but could have chosen $\boldsymbol{x}_2^k$ or $\boldsymbol{x}_3^k$ as well. If positive p acts parallel to $\boldsymbol{n}$, outwards the envelope, and outside pressure q is positive inwards, the external load vector acting on the element is given by

$$\boldsymbol{f} = \boldsymbol{f}_g + \boldsymbol{f}_p = \frac{\boldsymbol{m}}{3}\left[\boldsymbol{g}^T \,|\, \boldsymbol{g}^T \,|\, \boldsymbol{g}^T\right]^T + \frac{(p-q)A}{3}\left[\boldsymbol{n}^T \,|\, \boldsymbol{n}^T \,|\, \boldsymbol{n}^T\right]^T, \quad (5)$$

where $\boldsymbol{f}_g$ are forces due to self-weight, $\boldsymbol{f}_p$ are forces due to the transversal inside and pressures, $\boldsymbol{m}$ is the mass of the membrane element, $\boldsymbol{g}$ is the gravity acceleration vector. The awkward double transpositions were used to allow a single line notation.

Eq. (5) assembled for each element is all what is needed to include the external pressure loads on the equilibrium problem, solved through DRM or NRM, with finite-difference approximations $\widetilde{\boldsymbol{k}}_{ext}$. A somewhat lengthy derivation is required to arrive at the analytical expression for the external tangent stiffness under wind and pneumatic loads, given by:

$$\boldsymbol{k}_{ext} = \frac{q-p}{6}\begin{bmatrix} \boldsymbol{\Lambda}_1 & \boldsymbol{\Lambda}_2 & \boldsymbol{\Lambda}_3 \\ \boldsymbol{\Lambda}_1 & \boldsymbol{\Lambda}_2 & \boldsymbol{\Lambda}_3 \\ \boldsymbol{\Lambda}_1 & \boldsymbol{\Lambda}_2 & \boldsymbol{\Lambda}_3 \end{bmatrix} + \frac{pA}{18V_\Gamma}\begin{bmatrix} \boldsymbol{\Phi}_1 & \boldsymbol{\Phi}_2 & \boldsymbol{\Phi}_3 \\ \boldsymbol{\Phi}_1 & \boldsymbol{\Phi}_2 & \boldsymbol{\Phi}_3 \\ \boldsymbol{\Phi}_1 & \boldsymbol{\Phi}_2 & \boldsymbol{\Phi}_3 \end{bmatrix} = \boldsymbol{k}_\Lambda + \boldsymbol{k}_\Phi\,, \quad (6)$$

where $\boldsymbol{\Lambda}_i = skew(\boldsymbol{\ell}_i)$ are skew-symmetric matrices, whose axial vectors are given by $\boldsymbol{\ell}_i = \ell_i \boldsymbol{v}_i$ and where $\boldsymbol{\Phi}_i = \boldsymbol{n}\left(\boldsymbol{x}_j \times \boldsymbol{x}_k\right)^T$, with indices $i, j, k = 1,2,3$ in cyclic permutation. The Appendix provided in [2] presents the deduction of Eq. (6).

Several authors present alternative ways to handle pneumatic loads and stiffness [2], but there is limited exploration on the relative importance of the resulting terms. Especially in the case of insufflated structures, due to the envelope permeability and the limited power of the mechanical blowers, a constant inside pressure might be a more realistic assumption, in which case $\boldsymbol{k}_{ext} = \boldsymbol{k}_\Lambda$. Moreover, the examples explored in Section 3 suggest that the external stiffness can be approximated by $\widetilde{\boldsymbol{k}}_{ext} \cong \boldsymbol{k}_\Lambda$, alleviating computations without degrading convergence. We also remark that although $\boldsymbol{k}_{ext}$ is an asymmetric

matrix at the element level, if the boundary nodes are constrained, all the non-symmetric stiffness terms cancel out on the global external stiffness $\boldsymbol{K}_{\text{ext}}$, therefore the system is conservative. If, however, free borders exist, or pressure varies along the surface in a generic way, there is no guaranty on the symmetry of $\boldsymbol{K}_{ext}$.

2.3. A simple wrinkling model

Matrix $\boldsymbol{k}_n^0$ defined in (2) provides an efficient scheme to compute the internal loads and stiffness of a taut membrane, avoiding explicit calculation of strains or stresses, which may be evaluated at the postprocessing stage. However, before undergoing compressive stresses, a membrane becomes wrinkled or slack. When wrinkles ought to be accurately represented, a shell-like formulation is required, demanding relatively heavy computation. Nonetheless, in most civil and architectural applications, there is no exacting requirement for tautness, nor it is required the knowledge of the precise wrinkle patterns. What does is required is the knowledge of the basic load transfer mechanisms, which may be incorrectly assessed, if spurious compression is not averted. Moreover, if wrinkling or slackening are allowed, for some operational conditions, the resulting anchorage loads might be reduced, because smaller initial stresses are then required, and because larger displacements of the membrane usually contribute to a more favorable load distribution. Criteria for identification of the *status* of a membrane element (*taut*, *wrinkled,* or *slack*) require consideration of either stresses or strains, or both. When wrinkling or slackening are likely, equations (3) and (4) ought to be replaced for lengthier calculations. For isotropic materials, principal stress and strain directions are parallel, and stress, strain or mixed wrinkling criteria are equivalent. Herein, we choose a *pure stress criterion* and calculate the element stresses directly from the natural displacements.

In order to speed up calculations, we first decompose the element natural stiffness according to $\boldsymbol{k}_n^0 = \left(t_0 A_0 \boldsymbol{L}_0^{-1} \widehat{\boldsymbol{T}}_0^{-T}\right)\left(\widehat{\boldsymbol{D}}\widehat{\boldsymbol{T}}_0^{-1}\boldsymbol{L}_0^{-1}\right) = \boldsymbol{k}_\sigma^0 \boldsymbol{k}_a^0$, where we observe that $\boldsymbol{k}_\sigma^0$ and $\boldsymbol{k}_a^0$ are two constant matrices that can be conveniently stored during the pre-processing phase. Then stresses at any configuration can be evaluated according to $\widehat{\boldsymbol{\sigma}} = \boldsymbol{k}_a^0 \boldsymbol{a} + \boldsymbol{\sigma}_0$ and, after calculating the principal stresses (σ_1, σ_2) and the "principal angle" θ_1 (between the element local axis $\hat{x}$ and the σ_1 direction), we determine the element status, and whether it is necessary to modify stresses, according to the following *wrinkling criterion*:

$$\begin{cases} \sigma_2 > 0 & \Rightarrow \text{TAUT} & \Rightarrow & \tilde{\boldsymbol{\sigma}} = \widehat{\boldsymbol{\sigma}} \\ \sigma_1 > 0 \ \wedge \ \sigma_2 \leq 0 & \Rightarrow \text{WRINKLED} & \Rightarrow & \tilde{\boldsymbol{\sigma}} = \frac{\sigma_1}{2}[(1+\cos\theta_1) \quad (1-\cos\theta_1) \quad \sin(2\theta_1)]^T \\ \sigma_1 \leq 0 & \Rightarrow \text{SLACK} & \Rightarrow & \tilde{\boldsymbol{\sigma}} = \boldsymbol{0} \end{cases} \tag{7}$$

Thereafter, we consider a *modified element internal force vector* $\tilde{\boldsymbol{p}}^e = \boldsymbol{C}\boldsymbol{k}_\sigma^0 \tilde{\boldsymbol{\sigma}}$. A mixed stress-strain criterion could avoid the intermediate calculation of negative stresses, which have no physical meaning for membranes, but in our framework, we determine stresses and internal loads without the explicit calculation of strains. Once again, assembling the element internal load vectors into the global residual vector is all it takes to pose the equilibrium of a wrinkled membrane structure via DRM or NRM using finite differences. An analytical expression for the internal stiffness, according to the above criterion is still possible, as given in [5], but it is not as immediate as for the taut element, so we avoid bringing forth its consideration. Reference [6] details the above formulation.

3. Applications

We present in this section some selected problems to assess the performance of our simplified kinematic assumptions and the relevance of the pneumatic stiffness for modelling low to moderate-pressure systems. Initially experimental and numerical results of two small-scale pneumatics are compared, to assess the performance of the proposed membrane element, and the Boyle-Mariotte's Law. Then two pneumatic domes under inside and outside pressures are numerically modeled, one of moderate and another of large dimensions, under different hypothesis for the inside pressure. Results allow relevant conclusions about the importance of modeling the variation of inside pressure and considering the pneumatic stiffness term.

3.1. Henky's problem

We first consider Hencky's problem (1915), on the deformation of an initially flat, circular membrane fixed at the border and pressurized at one side. Bouzidi *et al*. [7] compared analytical solutions given by different authors with a numerical solution using an axisymmetric membrane element and considering large deformations and hyperelastic material. Figure 2(a) depicts the profiles assumed by a flat membrane with radius $R = 0.1425$ m, a product $Et = 311488\ Nm$, Poison ratio $\nu = 0$, under inflation pressures $100\ kPa$, $250\ kPa$ and $400\ kPa$. Up to moderate deformations, isotropic strains are approximately $\varepsilon \cong 2(\delta/r)^{2/3}$, thus, strains are about 3.5%, 7% and 10%, for these three pressures intensities. We modeled the same problem in SATS, considering the mesh shown in Figure 2(b). For each pressure intensity, our model took five NRM iteration to achieve equilibrium, for $\max(\|\boldsymbol{g}_i\|)/\max(\|\boldsymbol{g}_i^0\|) \leq 10^{-3}$, starting from a flat disc configuration. Our results, superimpose well with those provided in [7], with increasing, but small differences up to the maximum tested load, showing that our model is applicable to problems up to moderate deformations, which comprises a broad range of structural applications ((Figure 2(c)).

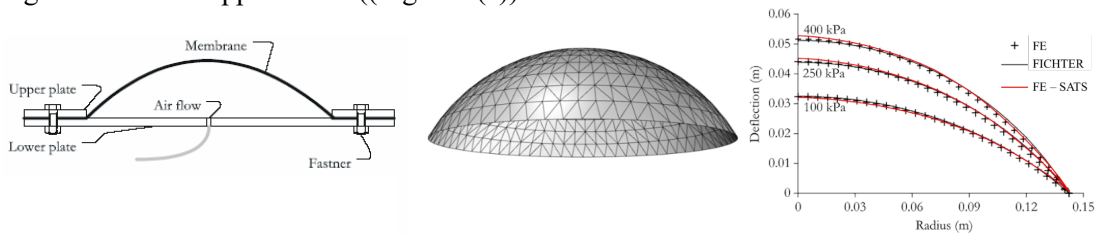


Figure 2. (a) experimental set up of an axisymmetric pressurized membrane; (b) SATS finite element model (flat initial configuration); (c) comparison between FE and theoretical results.

3.2. A Swiss ball experiment

The problem of the equilibrium of a spherical balloon under axisymmetric loads has become a benchmark for theoretical and numerical methods on the modelling of pneumatic membranes, and Swiss balls provide for ready and inexpensive experimental setups. In this section we compare the numerical modelling of a typical Swiss ball compressed between two parallel planes with experimental results. The test was freely inspired by Liu *et al.* [8], where a semi-analytical formulation was solved numerically, for different contact conditions, comparing numerical results with experimental ones.

We experimentally obtained an average elasticity modulus $E = 7.23$ MPa and a density $\rho = 0.88\ \mathrm{g/mm^3}$ for the ball's material, as well as an average membrane thickness $t = 1.3$mm. The tests were made according to ASTM D638-14. We started the experiment inflating the ball with an initial inside pressure $p_0 = 2.413$ kPa (0.35 psi). The precision of this measurement was limited by the low resolution of the available pressure gauge ($\Delta p = 0.01$psi). The initial inflated geometry was then measured with a digital ruler. Due to slight orthotropy of the material and the presence of some reinforcement rings, the inflated shape was a slightly prolate spheroid, of equatorial radius $R_{E,0} = 0.2775$ m and polar radius $R_{P,0} = 0.2800$ m, with an initial volume $V_0 = \pi R_E^2 R_P/3 = 9.0318 \times 10^{-2}$ m^3. The reinforcement rings were located at symmetrical distances, parallel to the equator and the air inlet was located at the lower pole. To connect the pressure gauge, the original PVC inlet was replaced by a metal valve stem.

We tested the ball for a vertical compression load, preserving the rotational symmetry of the problem. A gap was provided below a stiff base plate, to accommodate the pressure gauge, and the ball was pushed downward by the top plate. An ink layer was sprayed over the ball's top hemisphere, and a sheet of paper was glued to the lower face of the top plate, to obtain an imprint of the contact area. An initial vertical load of 50 N was required to stabilize the set, before a final vertical load $F = 535$ N could be applied, (encompassing both the applied external load and the weight of the top plate). The final pressure

measured by the pressure gauge was $p = 4.481$ kPa (0.65 psi). Thus, considering the BML, a final volume $V_{BM} = 4.8633 \times 10^{-2}$ m^3 was estimated.

Using a digital ruler, we measured the ball's final equatorial radius $R_{E,f} = 0.313$ m, equivalent to a radial displacement $\Delta R_E = 0.0355$ m. It was then possible to estimate the meridional stress $\sigma_\theta = \left(p\pi R_{E,f}^2 - F\right)/\left(2\pi R_{E,f} t\right) \cong 0.32$ MPa. The downward displacement of the top plate was $\Delta_{Z,NP} = 0.189$m. The vertical coordinate of the circular contact disc, with respect to ball equator, was $z_{DISC} = \left(R_{P,0} - \Delta_{Z,NP}\right)/2 = 0.1855$ m. The diameter of the imprint of the contact disc was also measured with a digital rule, resulting $D_{disc} = 0.39350$ m. Disregarding any bending stiffness of the ball, the coherence between these measurements can be verified by considering that the ratio of the measured vertical force by the measured inside pressure should equate the area of the contact imprint. That yields and estimated diameter $D'_{disc} = 0.38987\ m$, with a 0.92% error compared to the measured imprint diameter.

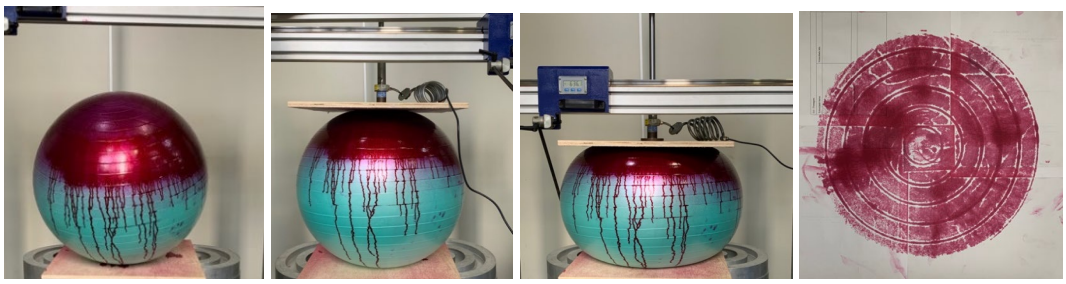


Figure 3. Several stages of the testing of the Swiss ball before, at the onset and at the end of the compression test and imprint of the contact área.

Figure 4(a) displays our numerical model, which considered the symmetry with respect to the equatorial plane. Boundary conditions avoided any rigid body movements and preserved the rotational symmetry. The volume of faceted approximation was $\tilde{V}_0 = 9.03690 \times 10^{-2}$ m^3, with an error of 0.39%, compared to the analytical volume of the spheroid. We assumed a membrane material with $E = 7.23$ MPa and a zero Poison ration, as well as a membrane thickness $t = 1.3$ mm.

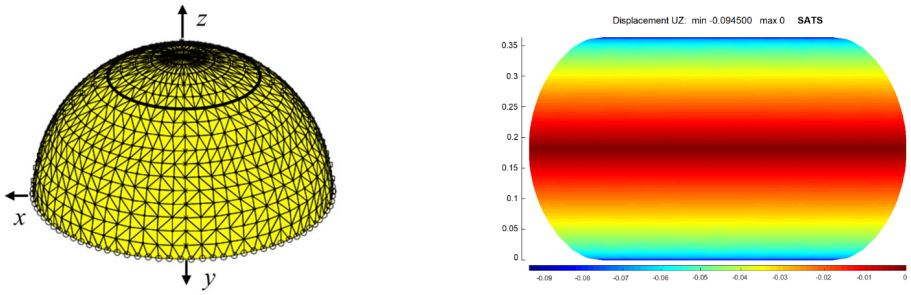


Figure 4. Numerical model: (a) discretization of the ball's top hemisphere; (b) Lateral view of the deformed numerical, reflect with respect to the equatorial plane.

We opted for controlling the vertical displacements of the nodes belonging to the spheroidal cap, which would become in contact with the top plate. To estimate the size of this cap, we assumed that both the sag of the cap and the material deformation were small, thus the cap perimeter could be approximated by the intersection of the spheroid with the plane $z = z_{cap} = R_{P,0} \times \cos\left(R_{disc}/R_{P,0}\right) = 0.2137$m. We enforced a set of nodes of our finite element mesh to conform to this perimeter, highlighted with a thicker parallel shown in Figure 4(a) . We then deformed the top cap into a flat disco, imposing vertical displacements such that the final vertical coordinates of the cap's nodes were all equal to $z_{disc} = 0.1855m$, as experimentally measured. Thus, the node located at the upper pole was displaced of $u_{z,P} =$

$z_{disc} - R_{P,0} = -0.0945m$, whilst the nodes at cap's perimeter were displaced of $u_z^{\partial cap} = z_{disc} - z_{cap} = -0.02817m$, with intermediate u_z values for the intermediate nodes. We remark that this procedure implies frictionless contact between the membrane and the compression plates. We considered that the reference experiment reported in [8] actually indicated that the effect should be relatively small, moreover because in our case the membrane was partially lubricated by the ink layer and because the contact occurred gradually, so that the contact disc would become stretched even for high friction conditions. Anyway, the validity of the frictionless assumption could be verified afterward, by inspecting the results of our model.

Figure 4(b) displays the resulting equilibrium shape. Although only the top hemisphere was modelled. For easier interpretation, the deformed geometry mirrored with respect to the equatorial plane. Colors indicate the magnitude of the vertical displacement. Only minor differences were observed using ether NRM and DRM. Moreover, equal values were obtained, through NRM, either with the analytical tangent stiffness or its finite-difference counterpart, requiring the same number of 6 iterations, with $\epsilon_{\boldsymbol{g}} \leq 10^{-3}$. The third column of Table 1 compares the NRM solution with respect to the experimental values. A discrepant error on maximum $\sigma_1$compared to the meridional stress estimated from the experimental results, may be associated to the coarseness of the mesh. Nonetheless, a maximum deformation $\varepsilon_{max} \approx max(\sigma_1)/E = 4.7\%$ is still within the applicable range of our simplified kinematic model.

Table 1. Results for the Swiss ball, $\boldsymbol{V_0 = 9.0318 \times 10^{-2}\, m^3}$, $\boldsymbol{p_0 = 2.4132\ kPa}$

Hypothesis on inside pressure:	BML: $p = p_0 V_0 / V_\Gamma$			$p = p_0$
Solution method:	NRM	Error NRM vs. expr.	DRM	NRM & FDM
$p\ [kPa]$:	4.4870	0.1%	4.4913	2.4132
$V_\Gamma\ [\times 10^{-2}\ m^3]$:	9.6980	0.3%	9.7494	13.1740
Equator displacement ΔR_E [cm]:	3.532	0.5%	3.553	5.5259
Total vertical reaction $\sum F_z$ [kN]:	0.5368	0.3%	0.5359	0.5364
max (σ_1) [MPa]:	0.3392	5.1%	0.3457	0.4748
min (σ_1) [MPa]:	1.9393	--	2.027	0.2644
max (σ_2) [MPa]:	2.4504	--	2.5739	3.2119
min (σ_2) [MPa]:	1.5894	--	1.8917	0.2143

To highlight the importance of considering the BML for this system, we repeated the analyses assuming a constant inside pressure $p_0 = 2.413$kPa. Results for this case are summarized at the fourth column of Table 1. Both NRM and DRM provides the same numerical results, requiring 4 iterations to achieve converge, for the same criterion as before. However, large errors are observed with respect to the experimental values, of about 32% for the final volume, 46% for the final pressure, 56% for the equator's displacements and 33% for the final maximum stress. The comparison between the numerical and experimental results indicates that the assumption of frictionless contact was acceptable, and that at the scale of a Swiss ball, compliance to BML is required to provide satisfactory results.

3.2. A hemispherical pneumatic dome under wind loads

As a further example, Figure **5**(a) shows a model of hemispherical pneumatic dome with radius $R = 10.0$ m, All the nodes at the base of model are constrained, and we assumed an elastic modulus $E = 0.5$ GPa, zero Poisson ratio, and membrane thickness $t = 0.5$ mm. An initial isotropic stress field $\sigma_0 = 0.2$ MPa was imposed, coherent to an initial inside pressure $p_0 = 0.2$ kPa. We considered two load cases, superimposed with the inside pressure: *(a)* a *low wind velocity* $v_a = 47$km/h , equivalent to a *low dynamic wind pressure* $q_a = 0.1$ kPa $< p_0$ and *(b)* a *high wind velocity* $v_b = 147$ km/h, equivalent to a *high dynamic wind pressure* $q_b = 1.0$ kPa $> p_0$, Figure **5**(b) shows the wind pressure

coefficients, determined using Ansys/Fluent software, considering a uniform inlet velocity profile. Positive pressures coefficients were obtained at both the weather and leeward sides, which is somewhat against common knowledge, but coherent with recent research [9]-[11], which indicate that for Reynold's numbers $Re > 10^6$ a separation region appears, where the flow detaches from the surface of the dome, leading to a recirculation area at leeward. Thus, for the current geometry and wind velocities, with $Re \approx 10^7$, compression at this region can indeed appear. The precise location of flow detachment depends not only on Re, but also on the turbulence intensity at boundary layer and the surface roughness.

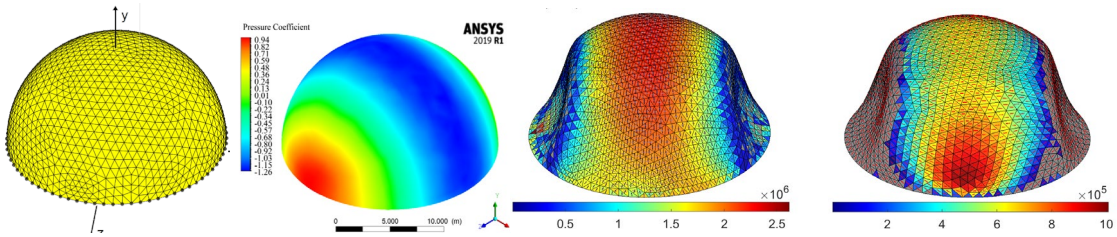


Figure 5. (a) FE model; (b) pressure coefficients determined using Ansys/fluent; (c/d) field of principal stresses $\boldsymbol{\sigma_1}$ and $\boldsymbol{\sigma_2}$, plotted over the deformed shape. Maximum values are given in Table 2.

Table 2 - Selected results for a hemispherical dome, $\boldsymbol{V_0 = 2.0892 \times 10^3\ m^3}$, $\boldsymbol{p_0 = 0.2\ kPa}$

Basic wind pressure	Hypothesis on inside pressure	BML: $p = p_0 V_0 / V_\Gamma$	Constant: $p = p_0$
$v_a = 47\ k$m/h $q_a = 0.1$ kPa	p (kPa):	0.1994	0.2000
	V_Γ ($\times 10^3$ m^3):	2.0898	2.0898
	$max\ (\sigma_1)$ (MPa):	0.4174	0.4175
	$min(\sigma_1)$ (MPa):	1.6841	1.6847
	$max\ (\sigma_2)$ (MPa):	0.2886	2.8887
	$min(\sigma_2)$ (MPa):	0.0262	0.0262
	$max\ (\|\boldsymbol{u}\|)\ (m)$:	0.0048	0.0048
$v_b = 147$ km/h $q_b = 1.0$ kPa	p (kPa):	0.2161	0.2000
	V_Γ ($\times 10^3$ m^3):	1.7987	1.9336
	$max\ (\sigma_1)$ (MPa):	2.6224	2.6846
	$min(\sigma_1)$ (MPa):	0	0
	$max\ (\sigma_2)$ (MPa):	1.0073	1.0115
	$min(\sigma_2)$ (MPa):	0	0
	$max\ (\|\boldsymbol{u}\|)\ (m)$:	2.2094	2.2660

For the low wind velocity case, the analysis converged in only 3 NRM iterations, with $\epsilon_u \leq 10^{-3}$. Very small displacements were observed, $\|\boldsymbol{u}\| < 5$ mm , with all elements in taut or marginally taut conditions. For the high wind velocity case, however, convergence by NRM becomes problematic, since large wrinkling areas developed over the membrane, with a ring of elements effectively becoming slack, at the transitions between the convex and concave regions of the membrane at the deformed configuration, as can be seen on the plotting of the σ_1 field (Figure **5**(c)). The onset of slackness renders the system's tangent stiffness $\boldsymbol{K}$ non-positive definite. To circumvent this nuisance using NRM, we have implemented a naïve, yet enough penalty method, simply adding artificial nodal stiffnesses $\bar{k}$ for every degree of freedom and gradually reducing it until artificial reactions becomes either null or small, if compared with the external forces $\boldsymbol{f}$ .Assuming as correct the results obtained using BML, shown at the 2nd column of Table 2 , we compare them with the results obtaining with constant inside pressure, shown at the 3rd column of Table 2. We find an error about 7.5% for the inside pressure and the final volume. The maximum displacement becomes 6 cm smaller, with an error about 2.6%. Maximum σ_1 and σ_2 principal stresses present errors of 2.32% e 0.41%. It is seen that in comparison to the Swiss ball experiment, the consideration of BML in this example is not as relevant, although not insignificant.

3.3. A large, insufflated dome reinforced by meridian cables

As a final example, we will consider the '*Megadome*', a large, inflated dome built for the 2022 Christmas and New Year's celebrations in the city of *Canela*, in the South of Brazil. Figure 6(a/b) depict the installed structure. Only the main dome, with a diameter of $D = 60\text{m}$ and a height $H = 30\text{m}$, was modeled. The pneumatic envelope is constituted by single layer of PVC-polyester fabric, reinforced with 40 meridian steel cables anchored to a perimeter concrete ring. The inside pressure was guaranteed by a set of fans with enough redundancy and capacity to vary the internal pressure for different operational scenarios.



Figure 6. The Canela's *Megadome*, Brazil (2022).

The meridian cables converge to a parallel upper cable ring, with a diameter of 5m. The spacing between the cables varies from 4.7m at the base of the dome to 0.40m at the top. Although a larger number of smaller diameter cables might be desirable to increase the rigidity of the dome and minimize the wrinkles of the membrane, they would also significantly increase the practical difficulties of detailing and assembling the structure. The internal surface of the Megadome was designed for cinematographic projections, and to avoid significant creases in the pneumatic envelope under normal operational conditions, the reinforcing cables should be installed with small initial loads, which should however suffice to prevent cable slippage, under normal operating conditions. Morover, the inside pressure under normal operational conditions should not be as high as to excessive, to avoid an excessiveley scaloped surface.

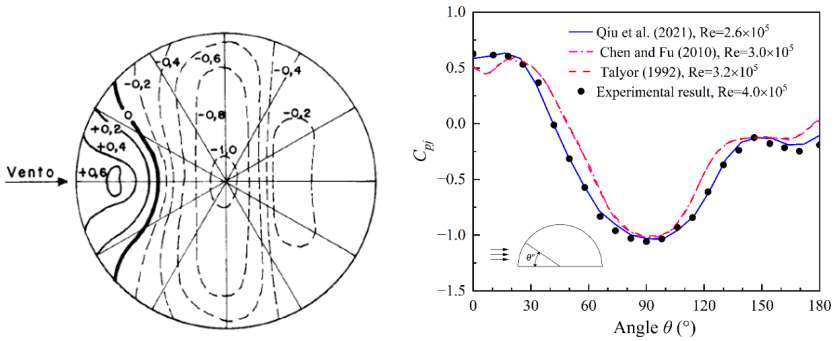


Figure 7. Wind pressure coefficients for a semispherical dome; (a) NBR-6123 standard; (b) reference [12].

Reference [12] lists some of the most notable spherical domes in the world. The dimensions of the Megadome place it among the largest pneumatic domes in the world, and while there are domes with larger diameters, those that reach its height and aspect ratio are rare. It is common for large spherical domes to be reinforced by cables, with the most frequent option being a meridian arrangement, although in some cases, cross-cable arrangements are also used. The option of pneumatic envelopes without reinforcement cables is less frequent, usually limited to domes with smaller diameters. Although the response of pneumatic domes to wind actions is a dynamic phenomenon, the consideration of equivalent

static analyses is reasonable for typical dimensions [12]. Moreover, in this case we considered constant inside pressure, since in [2] we concluded that this hypothesis suffices for large, insufflated domes.

Wind loads were defined considering Brazilian NBR6123 Standard. A characteristic wind speed $v_k = 37\text{m/s}$ = 133km/h was defined. The dome was classified as a temporary building, since public access is restricted for operational wind speeds $v_{op} > 30\text{m/s}$. A dynamic wind pressure $q = 0.613 v_k^2 = 0.85\text{kPa}$ was defined. The external pressure coefficients were assumed by considering an envelope of the coefficients provided by the NBR-6123 and [12], see Figure 7.

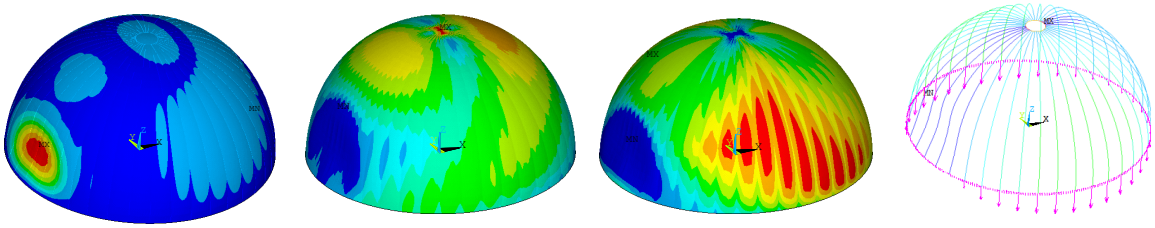


Figure 8. field distributions for Concern conditions: (a) norm of the displacements; (b/c) principal σ_1 and σ_2 stress fields; (d) normal loads on cables and achorages. Maximum values are given in Table 3 for different operational conditions.

Table 3. Some selected maximum results for different operational conditions (without partial safety factors)

Conditions	Beauford wind Scale	v_{op} $[km/h]$	p_0 [mmH2O]	Max. Membrane Displacements [m]	Max. Membrane stress [kN/m]	Max cable loads N_{max} [kN]	
				$\|\|\boldsymbol{u}\|\|_{max}$	$S_1 = \sigma_1 \times t$	Meridian	Ring
Assembling	--	0	30	0,03	4,7	0	0
Attention	Fresh Gales	70	30	0,36	11,4	23,4	37,6
Concern	Storms	100	30	2,02	18,0	47,4	87,9
Preservation	Violent Storms	134	40	2,70	25,0	87,8	196,6

The operational conditions of the Magadome are associated to daily wind forecasts. Several conditions have been considered, including Testing, Instalation, Maintenance, Normal Operation, Attention, Concern and Preservation. The *Concern* condition corresponds to 'Storms' on the Beaufort Scale and, in antecipation of that forescat, the structure must be closed to the public, with access allowed only to the maintenance team. In the *Preservation* conditions, corresponding to 'Violent Storms', the inside pressure must be increased to p_0=0.4kPa, the structure must be sealed, and access allowed only to tackle the envelope's jeopardy. We remark that even moderate winds can generate projectiles such as fallen tree branches [13], which might puncture the pnaumetic envelope, but with low probability of tearing the membrane, under normal operational conditions. At Conservation conditions, the membrane will be under high stresses, and tear progagation cannot be precluded.

Figure 8 shows the overal spatial distribution of main quantities for Concern condition. Maximum values, relevant to the design, are given in Table 3 for differet operational conditions. Since the direction of the wind can be any, all the cables and anchorages must be designed to withstand maximum loads.

4. Conclusions

We have presented a simple yet effective model to cope with the nonlinear static analysis of pneumatic membranes under wind loads, incorporating an effective wrinkling criterion into Argyris' triangular membrane element and deriving a new expression for its pneumatic stiffness, $\boldsymbol{k}_{ext} = \boldsymbol{k}_{\Lambda} + \boldsymbol{k}_{\Phi}$. The model was tested through an inexpensive experiment, comprising the compression of a typical exercise

ball, which corroborated the relevance of the variation of the inside pressure, for moderate-energy systems. However, further numerical explorations, on domes of realistic dimensions and pressure intensities, indicated that this relevance decreases, as the dimensions of the pressure envelopes increase. In the case of a large, insufflated dome, have found that although $\boldsymbol{k}_{\Phi}$ did complete $\boldsymbol{k}_{ext}$, its contribution did not improve convergence of NRM. On the other hand, when wrinkling occurs, $\boldsymbol{k}_{\Lambda}$ was required to guaranty converge, but it was not necessary while the pressure envelope was fully taut. The relative influence of these stiffness terms is an open subject, but our results indicate that, at least for low to moderate-energy pneumatic systems, the external stiffness is fairly approximated by $\widetilde{\boldsymbol{k}}_{ext} \cong \boldsymbol{k}_{\Lambda}$, without degrading convergence, while alleviating computations.

References

[1] Pauletti RMO. "Some issues on the design and analysis of pneumatic structures". *Int J Struct Eng* 2010; 1(3/4): 217-240.

[2] R.M.O. Pauletti, K.B. Rocha, "A simple finite element framework for modelling pneumatic structures". *Engineering Structures* vol. 235 (2021) 111812 https://doi.org/10.1016/j.engstruct.2020.111812

[3] Pauletti RMO, Almeida Neto ES. "A finite-difference approximation to Newton's Method Jacobian Matrices". *IABSE-IASS Symposium, London, 2011*.

[4] Pauletti, RMO. "Static Analysis of Taut Structures. in *Comput Meth Appl Sci 2008; 8: p.117-139. Textile Composites and Inflatable Struct II*, E. Oñate, B. Kröplin (eds). Springer, Dordrecht.

[5] Akita , Nakashino K, Natori MC, Park KC. "A simple computer implementation of membrane wrinkle behaviour via a projection technique". *Int J Numer Meth Eng 2007; 71(10): 1231–1259*.

[6] Pauletti RMO, Guirardi DM. "Implementation of a simple wrinkling model into Argyris' membrane finite element". *VI International Conference on Textile Composites and Inflatable Structures 2013*; Munich.

[7] Bouzidi R, Ravaut Y, Wielgosz C. "Finite elements for 2D problems of pressurized membrane". *Comput Struct 2003*; 81(26–27): 2479–2490.

[8] Liu MX, Wang CG, Li XD. "Rigid-flexible contact analysis of an inflated membrane balloon with various contact conditions". *Comput Meth Appl Mech Eng 2018*; 144–145: 218-229. Elsevier BV.

[9] Sun Y, Su N, Wu Y, Jin Q. "Experimental Investigation of the Aerodynamic Forces and Pressures on Dome Roofs: Reynolds Number Effects". *World Congress on Advances in Civil, Environmental and Materials Research (ACEM16). Jeju Island, Korea; 2016.*

[10] Wood JN, De Nayer G, Schmidt S, Breuer M. "Experimental Investigation and Large-Eddy Simulation of the Turbulent Flow past a Smooth and Rigid Hemisphere". *Flow, Turbulence and Combustion 2016*; 97(1): 79–119.

[11] Wood JN, Breuer M, De Nayer G. "Experimental studies on the instantaneous fluid–structure interaction of an air-inflated flexible membrane in turbulent flow". J of Fluids Struct 2018; 80: 405–440. Elsevier BV.

[12] Chen, Z.; Wei, C.; Li, Z.; Zeng, C.; Zhao, J.; Hong, N.; Su, N., Wind-Induced Response Characteristics and Equivalent Static Wind-Resistant Design Method of Spherical Inflatable Membrane Structures. Buildings 2022, 12, 1611.

[13] J. D. Holmes, Wind Loading of Structures, Taylor & Francis, London, 2001.

Proceedings of the IASS Annual Symposium 2023
Integration of Design and Fabrication
10–14 July 2023, Melbourne, Australia
Y.M. Xie, J. Burry, T.U. Lee and J. Ma (eds.)

Numerical simulation of snowdrift on a membrane structure

Jialin ZOU[*], Xiaoying SUN[a], Yue WU[a]

[a,*] Harbin Institute of technology
Key Lab of Structure Dynamic Behaviour and Control of the Ministry of Education, 150090 Harbin, China
zerogress195217@163.com

Abstract

In snowy and windy regions, snowdrift may lead to uneven snow distribution on the roofs. Uneven snow distribution cause snow sliding from the edge of roofs and frequent collapsing, which threatens people's lives and properties. With the rapid development of membrane structures, an increasing number of these structures have been built in cold regions at high latitudes and altitudes. In recent years, climate-related disasters including heavy snow on membrane structures for roofing have increased globally. Therefore, the snowdrift on membrane structures has received increasing attention. In this paper, based on the Euler-Euler method in multi-phase flow theory, the Mixture model using the secondary development method for commercial CFD software Fluent is adopted. Based on this simulation approach, the snowdrift on a long-span membrane structure is simulated under different wind velocities and wind directions.

Keywords: snowdrift, membrane structure, numerical simulation, mixture model

1. Introduction

With the rapid development of construction technology, an increasing number of membrane structures have been built in cold regions at high latitudes and altitudes. Considering the wind action, snowdrift may result in uneven snow distribution on the roofs which ultimately leads to structural collapse. Although the membrane structures have great advantages in unique shape and rapid construction, it has deficiencies in bearing the unbalanced snow loads. Thus, accurate prediction of snow distribution on the membrane roof is indispensable to membrane structure design.

In the investigation process of the snowdrift, there are three methods to estimate snowdrift namely field measurement, wind tunnel test, and numerical simulation. Based on the restrictions of uncontrollability of field measurements and similarity requirements of wind tunnel tests, Computational Fluid Dynamics (CFD) takes more attention from researchers. Uematsu[1] conducted a pioneering study suggesting a three-dimensional. numerical simulation for snowdrift and took saltation as well as suspension into consideration. Sundsbø[2] proposed a two-dimensional numerical model for the transient simulation of snow drift where snow transport by saltation and suspension is considered. Okaze[3] develop a new k–ε model that incorporates the effects of snow particles on a flow field. The spatial distributions of the mass flux of drifting snow, wind velocity, and turbulence were simultaneously measured under several different wind-speed conditions. Zhou[4] proposed a quasi-steady method to simulate the redistribution of snow on roofs, which is considered the calculated results of the change rate of snow depth in the previous phase.

On the account of the treatment of the snow phase, the numerical simulation method of CFD can be classified into two methods i.e. the Eulerian-Lagrangian method and the Eulerian-Eulerian method. The Eulerian-Lagrangian method is used to track each trace of snow particles while the snow is regarded as the continuous phase of the air phase in the Eulerian-Eulerian method. It makes the Eulerian-Eulerian method has high computational efficiency.

Copyright © 2023 by Jialin ZOU, Xiaoying SUN and Yue WU. Published in the Proceedings of the IASS Annual Symposium 2023 with permission.

In recent years, with the rapid development of construction technology of membrane structures, the annual construction quantity of the membrane structure increases year by year. And there are few studies and relevant codes on snow distribution of membrane structures. In this paper, to investigate the snow distribution on membrane structure, a series of numerical simulations are conducted. Based on the Euler-Euler method in multi-phase flow theory, the Mixture model in FLUENT is adopted. Firstly, the governing equation, deposition and erosion, and turbulence model are briefly introduced. Then, the geometrical modelling and computational settings, which are used in the numerical simulation, are recommended. In the final section, the impacts of wind direction and velocity on snow distribution on the air-supported membrane structure are discussed.

2. Numerical modelling

2.1. Governing equations

Simulation methods for snow drifting progress on the roof include the Euler-Euler method and the Euler-Lagrangian method. In this simulation, the snow is taken as a continuous phase in the flow field with multiphase flow theory using the Euler-Euler method. On account of the Euler-Euler method, there are three typical models named the VOF model, the Mixture model and the Eulerian model, respectively. The Mixture model could take the speed difference between the snow and air phase into account, which has higher computational stability[7]. The governing equations consist of the mass continuity equation and momentum conservation equation as Eq.(1) and Eq.(2). The Mixture model is equivalent to one-way coupling, in which the snow phase has no impact on the mass continuity equation and momentum conservation equation of the air phase. The snowdrift simulation is done with the Computational Fluid Dynamics (CFD) software —— FLUENT.

$$\frac{\partial \rho_m}{\partial t} + \nabla\cdot\left(\rho_m u_m\right) = 0 \tag{1}$$

$$\frac{\partial\left(\rho_m \overrightarrow{v_m}\right)}{\partial t} + \nabla\cdot\left(\rho_m v_m \overrightarrow{v_m}\right) = -\nabla p + \nabla\cdot\left[\mu_m\left(\nabla\overrightarrow{v_m} + \nabla\overrightarrow{v_m}^T\right)\right] + \rho_m \vec{g} + \vec{F} \tag{2}$$

where ρ_{m} is the density of the mixture phase, v_{m} is the velocity of the mixture phase of air and snow, and μ_{m} is the mixture dynamic viscosity.

2.2. Deposition and erosion model

The wall shear stress is a significant parameter which can determine whether erosion and deposition occur. When the wall shear stress is more than the gravity and internal force of snow particles, deposition takes place. However, it is difficult to obtain the wall shear stress during snowdrift. In most of the previous studies on snow drifting, the wall shear stress is generally calculated from the friction velocity through logarithmic law. Hence the discriminant method of erosion and deposition is transformed to whether the friction velocity is larger than the threshold friction velocity or not.

The relationship between friction velocity and snow mass flux has been investigated. Beyers[8] indicated that snow erosion would occur on the occasion that the friction velocity exceeds the threshold friction velocity, as shown in Eq.(3).

$$q_s \begin{cases} q_{ero} = A_{ero}\left(u_*^2 - u_{*t}^2\right) & u_* > u_{*t} \\ q_{dep} = \rho_s f w_f \dfrac{u_{*t}^2 - u_*^2}{u_{*t}^2} & u_* \le u_{*t} \end{cases} \tag{3}$$

where f is the snow concentration, A_{ero} is the empirical constant which is set as 7.0×10^{-4}, and w_f is snowfall velocity.

2.3. Turbulence model

The turbulence model has been widely explored to predict complex turbulent flow fields around a bluff body and the validity of turbulence models has been verified. The turbulence model used for snow drifting includes the RSM model, SST *k-ε* model, *k-ε* model[8] and *k-kl-ω* mode[7]. And the results of the turbulence model mentioned above are in good agreement with filed observation data or test data. The model can effectively describe the transition from laminar to turbulent flow in the boundary layer, and the transition from saltation to suspension motion during snowdrift is similar to the transition from laminar to turbulent. Hence the model is suitable for simulating snowdrift on roofs. To better reproduce the movement of snow particles on the roof, an approach based on the Realizable *k-kl-ω* model is adopted in this study. Specifically, the turbulence equations are as follows.

$$\frac{Dk_T}{Dt} = P_{k_T} + R + R_{NAT} - wk_T - D_T + \frac{\partial}{\partial x_j}\left[\left(v + \frac{\alpha_T}{\alpha k}\right)\frac{\partial k_T}{\partial x_j}\right] \tag{4}$$

$$\frac{Dk_L}{Dt} = P_{k_L} - R - R_{NAT} - D_L + \frac{\partial}{\partial x_j}\left[v\frac{\partial k_L}{\partial x_j}\right] \tag{5}$$

$$\frac{D\omega}{Dt} = C_{\omega 1}\frac{\omega}{k_T}P_{k_T} + \left(\frac{C_\omega R}{f_\omega} - 1\right)(R + R_{NAT})\frac{\omega}{k_T} - C_{\omega 2}\omega^2 + C_{\omega 3} f_\omega \alpha_T f_\omega^2 \frac{\sqrt{k_T}}{d^3} + \frac{\partial}{\partial x_j}\left[\left(v + \frac{\alpha_T}{\alpha_k}\right)\frac{\partial k_T}{\partial x_j}\right] \tag{6}$$

where k_T is the turbulent kinetic energy, k_L is the laminar kinetic energy, ω is the inverse turbulent time scale, P_{kT} and P_{kL} are the production term of turbulence and laminar kinetic energy respectively. D_T and D_L are diffusion terms. $C_{\omega 1}$, $C_{\omega 2}$ and $C_{\omega 3}$ are constant terms.

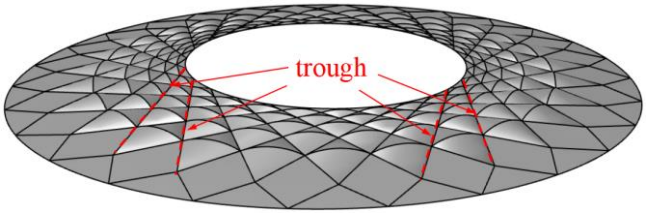
3. Numerical simulation of snowdrift

3.1. Geometrical modelling

The membrane structure is located in Dalian, northeast China, a representative cold region with heavy snowfall. This cold region has a medium-latitude monsoon climate. Referring to meteorological history data, Dalian has an extremely high temperature of 35.3 °C extremely low temperature of -20.1 °C, and a maximum snow depth of 136 mm. This membrane structure adopts an oblique double-cable system, and the roof material is PVC-coated fabric, as shown in Figure1 (a). The span of the membrane structure is about 253 m with a covered area of 42994 m^2, and the highest point of the membrane part is about 54.25 m. Because the curvature of the membrane structure is small and it has fan-shaped bulges locally, snow stacks in the trough between the bulges (Figure1(b)). For safety, it was necessary to simulate the snow distribution on this membrane structure.



(a) photo of the long-span membrane structure



(b) Lateral view of membrane structure

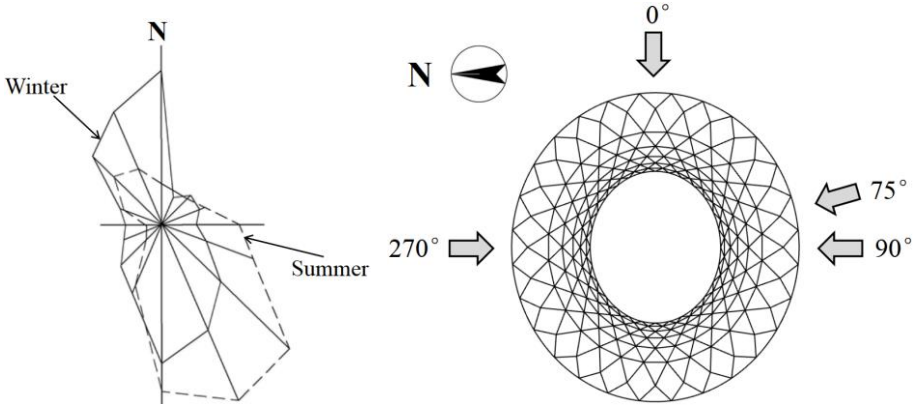
Figure 1. Membrane structure.

3.2. Computational settings

Figure 2 shows the wind rose map of Dalian and the orientation of the membrane structure. Because the dominant wind direction of Dalian in winter is north to south, we selected wind directions of 90 ° and 270 ° to simulate the snowdrift. Considering the symmetry of the structure, 0 ° is also a significant wind direction that affects snow distribution. This membrane structure was built on the seaside, and wind often blows from land to the ocean during the winter. Hence, a wind direction of 75 ° is the prevailing wind direction in the winter. Considering the asymmetry of the structure and the prevailing wind direction of Dalian in the winter, snowdrift under four wind directions was simulated. The wind directions were 0 ° , 75 ° , 90 ° , and 270 ° , as shown in Figure 2.

A full-scale model is established for the membrane structure in Figure 3. To ignore the impact of the boundary of the computational region, the size of the computational region of the numerical simulation is 10L(x)×21B(y)×7H(z). L, B, and H represent the length and width and height of the membrane structure, respectively. Considering the efficiently developed flow field, the model is placed at 7B from the entrance of the computational region. The computational domain and boundary conditions are summarized in figure 3. The total number of the unstructured mesh employed in this study is around 4.8 million cells and the growth factor of the grid is 1.2.

The SIMPLE algorithm is used to simulate the transportation of snow particles. Convergence is assumed to be obtained when all scaled residuals level off and reach a minimum of 10^{-7} for continuity, 10^{-7} for x velocity, y velocity, and z velocity. The height of the saltation layer is 0.05 m. The snow particle density is 150 kg/m^3, the snow particle diameter is 0.0005 m, and the threshold friction velocity is 0.2 m/s.



(a) Dalian wind rose map (b) Wind direction

Figure 2. The schematic diagram of the wind rose map and wind direction.

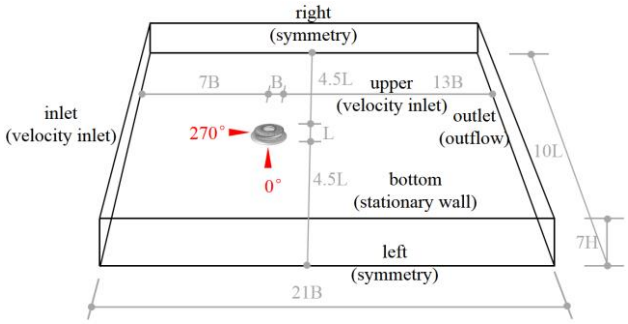
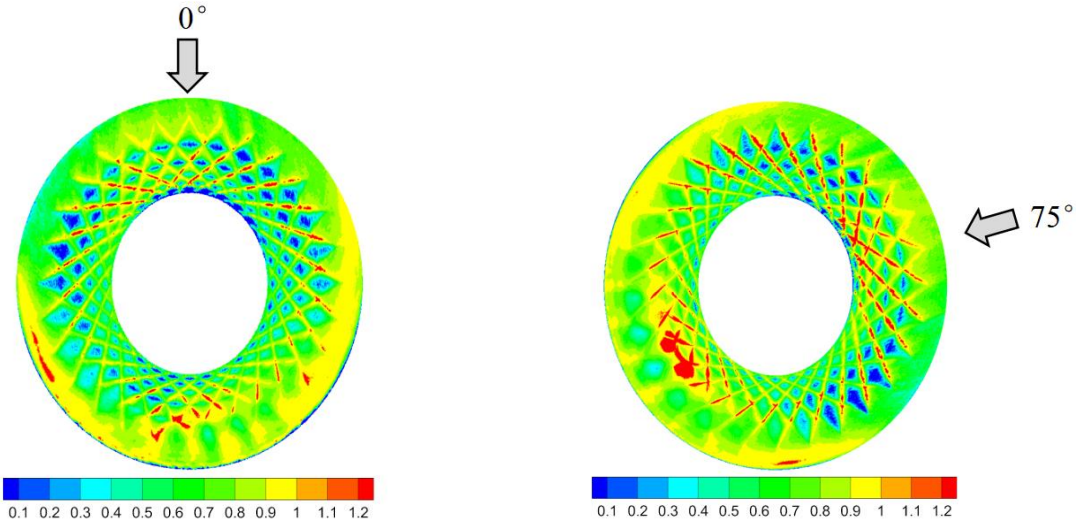


Figure 3. Computational domain and boundary conditions.

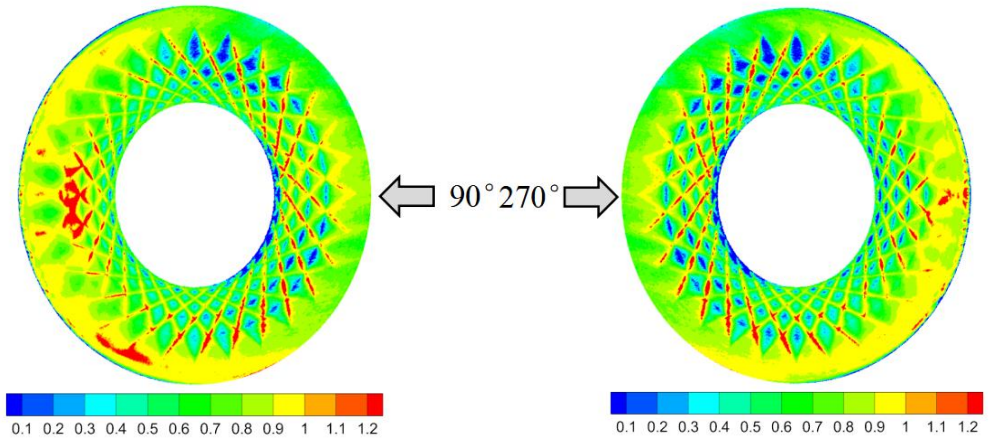
3.2. Results and discussion

3.2.1. Impact of wind direction

Wind direction is a dispensable parameter which influences the snow distribution on the air-supported membrane structure. That is attributed that wind direction has an impact on the flow field around the roof. Figure 7 shows the snow distribution on the air-supported membrane structure under the wind direction of 0, 75, 90, and 270° with the wind velocity of 10m/s, respectively. Under all wind directions, the windward section of the roof presents to be erosion. The value of the snow distribution trend is 0.4. The deposition occurs throughout the entire region of the leeward side. The maximum normalized dimensionless snow depth occurs in the trough between the bulges which reaches 1.2. In the leeward area, considering the flow separation, the snow particles blown away from the windward area reattach to the surface of the structure in the leeward area which leads to snow deposition in the leeward area and snow erosion in the windward area.



(a) 0° (b) 75°

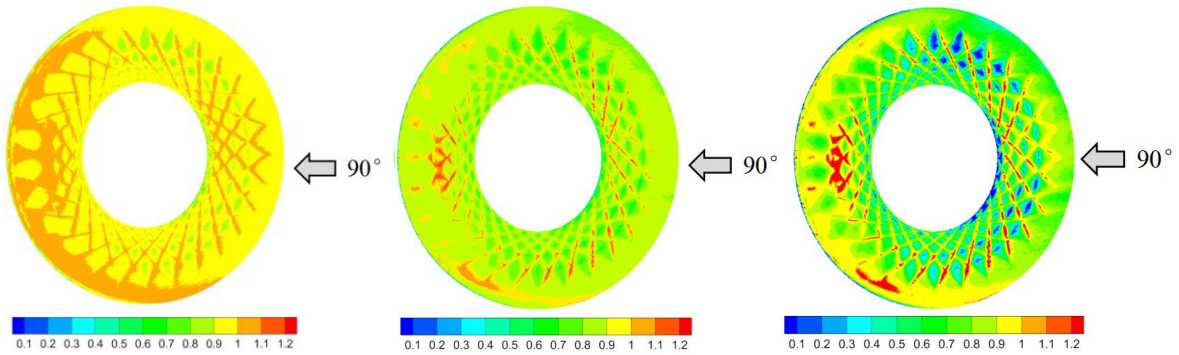


(c) 90° (d) 270°

Figure 4. Snow distribution under different wind directions.

3.2.2. Impact of wind velocity

Wind velocity is the significant influential factor determining snow distribution. Figure 8 shows the snow distribution under wind velocity of 6, 8, and 10m/s with the wind direction of 90 ° . When the wind velocity is 6m/s, nearly no erosion and deposition occurs on the structure and the normalized dimensionless snow depth is around 1 in most areas of the air-supported membrane structure. A significant increase in snow deposition and erosion with the increase in wind velocity can be concluded from figure 5. Meanwhile, the difference in the region of the erosion area between different wind velocities may not be obvious. This is because the wind velocity does not affect the position of separation of the flow which influences whether snow particles are blown away or not. For the wind velocity of 6m/s, the normalized dimensionless snow depth in the snow erosion area reaches 0.83. Additionally, the minimum normalized dimensionless snow depth with the wind velocity of 8m/s and 10m/s is 0.41 and 0.19.



(a) 6m/s (b) 8m/s (c) 10m/s

Figure 5. Snow distribution under different wind velocities.

4. Conclusion: submission of contributions

The numerical simulation based on the Mixture multiphase model was conducted to analyse the relationship between the wind direction, wind velocity and normalized dimensionless snow depth. The snowpack is mainly eroded on the windward side and deposited on the leeward of the structure under

wind action. Meanwhile, it is noticed that the maximum and minimum normalized dimensionless snow depth has a positive correlation with wind velocity and the difference in the region of the erosion area between different wind velocities may not be obvious. The reason could be wind velocity does not affect the position of flow separation.

Acknowledgements

The authors would like to acknowledge the National Natural Science Foundation of China (Grant No.52178134) for the financial support of the research.

References

[1] SATO T., UEMATSU T. & NAKATA T. et al., "Three dimensional numerical simulation of snowdrift," Journal of Wind Engineering and Industrial Aerodynamics, No.46(1993), pp.741-746.

[2] Sundsbo P., "Numerical simulations of wind deflection fins to control snow accumulation in building steps," Journal of wind engineering and industrial aerodynamics, Vol.74(1998), pp.543-552.

[3] Okaze T , Takano Y , Mochida A , et al. Development of a new k–ε model to reproduce the aerodynamic effects of snow particles on a flow field[J]. Journal of Wind Engineering and Industrial Aerodynamics, 2015, 144:118-124.

[4] Gu, Ming, Qiu, et al. Numerical simulation and wind tunnel test for redistribution of snow on a flat roof[J]. Journal of Wind Engineering & Industrial Aerodynamics the Journal of the International Association for Wind Engineering, 2016.

[5] T. U. Lee and Y. M. Xie, “From ruled surfaces to elastica-ruled surfaces: New possibilities for creating architectural forms,” *Journal of the International Association for Shell and Spatial Structures*, vol. 62, pp. 271–281, 2021.

[6] J. Burry and M. Burry, *The New Mathematics of Architecture*, Thames & Hudson, 2010.

[7] Sun X., He R. & Wu Y., "Numerical simulation of snowdrift on a membrane roof and the mechanical performance under snow loads," Cold Regions Science and Technology, Vol.150(2018), pp.15-24.

[8] Beyers J. H. M., Sundsbø P. A. & Harms T. M., "Numerical simulation of three-dimensional, transient snow drifting around a cube," Journal of Wind Engineering and Industrial Aerodynamics, Vol.92, No.9(2004), pp.725-747.

[9] Tominaga Y., Okaze T. & Mochida A., "CFD modelling of snowdrift around a building: An overview of models and evaluation of a new approach," Building and Environment, Vol.46, No.4(2011), pp.899-910.

Proceedings of the IASS Annual Symposium 2023
Integration of Design and Fabrication
10–14 July 2023, Melbourne, Australia
Y.M. Xie, J. Burry, T.U. Lee and J. Ma (eds.)

PTFE membrane privacy screen structure for National Palace Malaysia

Migico SING[a], Kok Keong CHOONG[*], Azri Hariz CHE MALID[a], Chong Kiat NG[a]

[*] School of Civil Engineering, Universiti Sains Malaysia
14300 Nibong Tebal, Penang, Malaysia
cekkc@usm.my

[a] Tensioned Fabric Structure Sdn Bhd, Kuala Lumpur, Malaysia

Abstract

This paper presents a unique application of tensile membrane as a shield for privacy protection purpose. The privacy protection membrane structure is located within the compound of National Palace in Kuala Lumpur Malaysia. The necessity for the privacy screen arises from the fact there are highrise condominium buildings surrounding the compound of National Palace and privacy protection of an outdoor private area within the palace is needed. The project was managed by Public Work Department of Malaysia. The final design of the privacy screen is a frame supported PTFE membrane structure. The height of the membrane screen structure is 11.36 m with cantilever parts of 8.53 m(front) and 3 m(back). The total length of the screen is about 25 m in plan. Several challenges were faced during the construction. First and foremost was the lack of information on the supporting RC structure. Rebound hammer, determination of reinforcement using ferroscan equipment and concrete coring were carried out. Other challenge was site accessibility for logistic and installation purpose which called for solution of using high capacity crane (120T) and smaller individual segments for the ease of steel frame structure erection. These challenges together with strict rules regarding working time and entry check for security reason into compound of National Palace are described in the paper.

Keywords: PTFE membrane, privacy screen structure

1. Introduction

Due to its lightweight and flexible characteristic, tensile membrane is suitable to be formed into surface with large area. Such large-surface-area membrane can be used in application such as outdoor screen, all-weather purpose cover over construction site, sunlight shields over surface of building etc. With proper form-finding and design, the membrane surface can be formed into anti-clastic surface which adds element of aesthetic apart from serving its intended function.

Figure 1 shows the National Place of Malaysia which is located in the city of Kuala Lumpur. The location of the National Palace is surrounded by highrise buildings as shown in Figure 2. Due to the necessity of privacy protection of an outdoor area within the compound of the palace, Public Works Department of Malaysia as project management consultant was tasked to design a privacy protection structure. The design called for a structure in the form of a privacy screen. Figure 3 shows the conceptual idea of the privacy screen.

This paper describes the planning work and construction of this unique application of tensioned fabric structure as a privacy screen. Challenges faced and solutions adopted are presented.

Copyright © 2023 by Migico SING, Kok Keong CHOONG, Azri Hariz Che MALID and Chong Kiat NG.
Published in the Proceedings of the IASS Annual Symposium 2023 with permission.

2. Structural system of the privacy screen

The final design of the privacy screen is a frame supported PTFE membrane structure. The height of the membrane screen structure is 11.36 m with cantilever parts of 8.53 m(front) and 3 m(back). The total length of the screen is about 25 m in plan. Figure 4 shows the overall structural system.



Figure 1. National Palace of Malaysia.



Figure 2. Highrise buildings surrounding National Palace Malaysia.

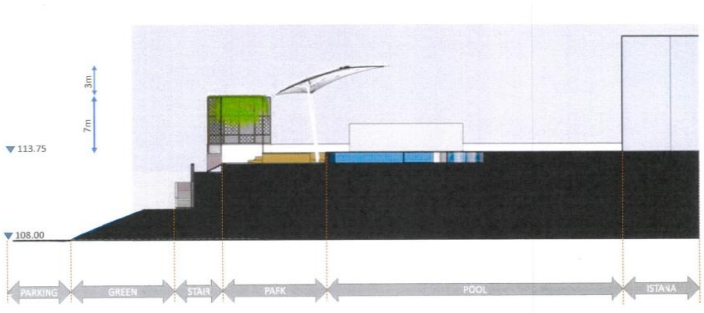


Figure 3. Conceptual idea of a privacy protection structure for a private area within National Palace Malaysia.

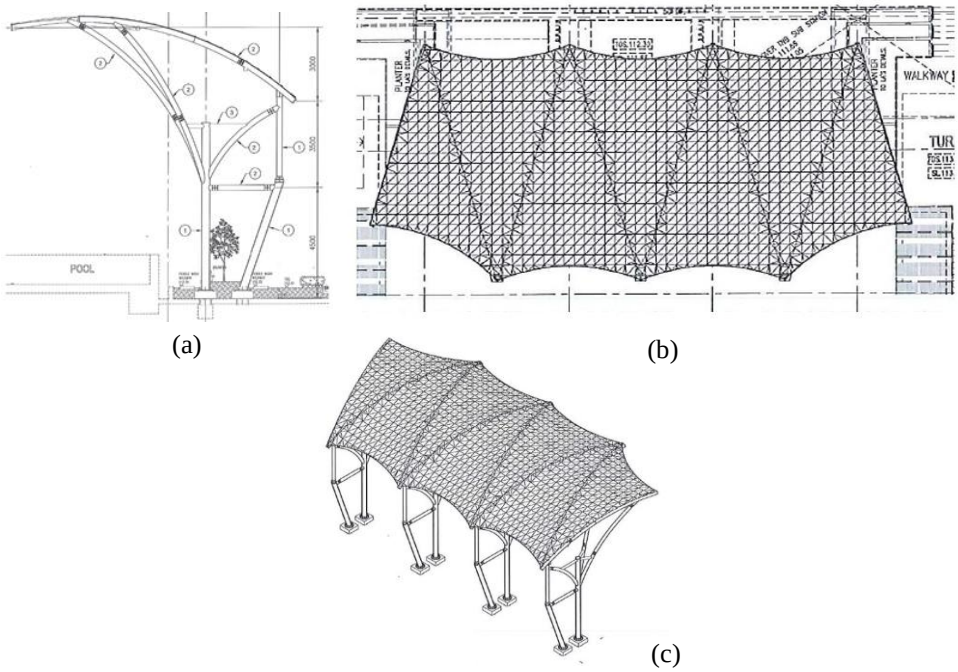


Figure 4. PTFE membrane privacy screen structure of National Palace Malaysia: (a) plan view, (b) site view and (c) 3D view.

The whole project took six month to complete. Several challenges were faced during the planning of the structure. First of foremost was the lack of information regarding the structural conditions of existing RC beams to be used as supporting or anchoring points of the tensioned fabric structure(see Figure 4a). Figure 5 shows another view of the RC beams where the frame of the privacy screen structure was to be supported. The support details is also shown.

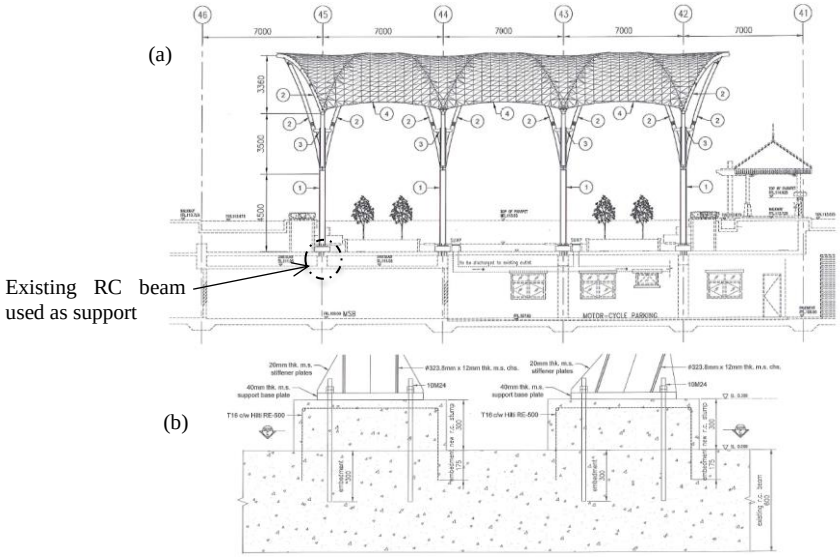


Figure 5. (a) Existing RC structure supporting the frame of privacy screen structure; (b) Details of the support.

Non-destructive tests such as rebound hammer test and ferroscan were carried out on existing structure to ascertain the strength and to obtain more information about the structures – e.g. location of reinforcement bars. Concrete coring was also carried out in order to further confirm the compressive capacity of concrete of the existing structure. Site accessibility and logistic were other problems faced. In order to overcome this problem, crane with capacity of 120 T was used for better reach purpose. At the same time, steel members were split into smaller individual components for ease of lifting during installation. Figure 6 shows the information about size of members used for the frame of the privacy screen structure. Details of fabric to frame connections are also shown.

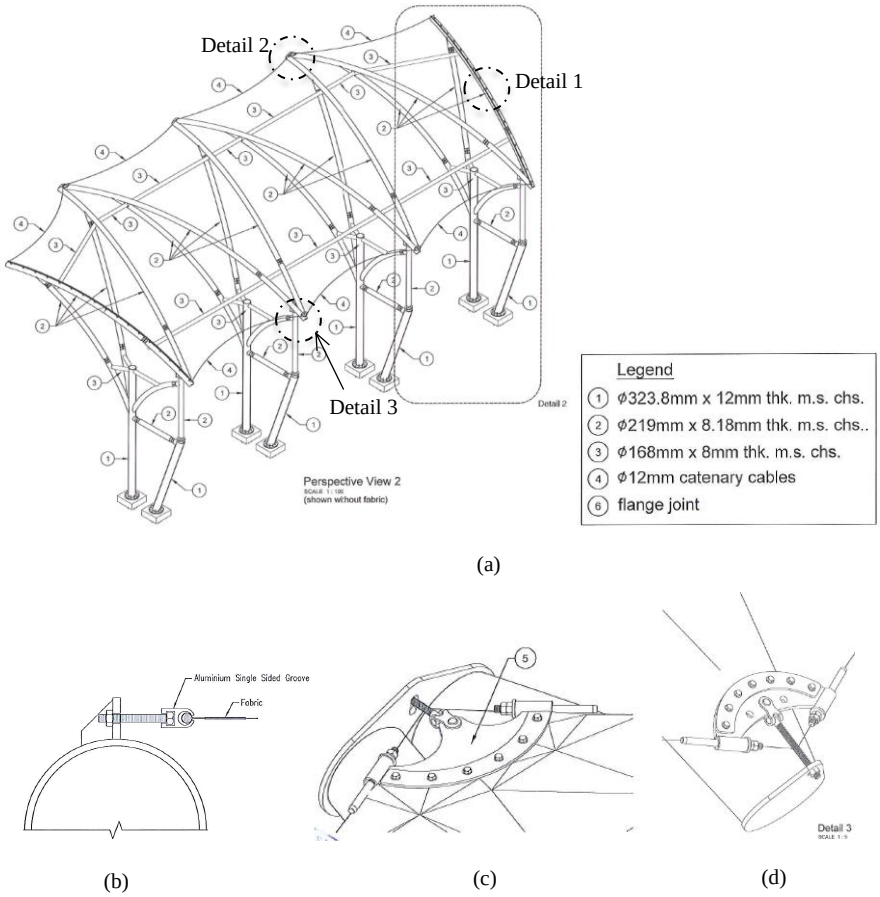


Figure 6. (a) Member sizes used for the different parts of the frame of the privacy screen structure; (b) Detail 1; (c) Detail 2; (d) Detail 3.

Apart from technical issues mentioned above, there was also problem due to strict working time according to requirements of National Palace which has resulted in longer project duration. Strict workers' background check prior to entering work site was another rule that has to be adhered to for security of National Palace.

4. Construction process

All components of the steel frames and fabrics were first fabricated in the factory and later transported to site (Figure 7). With the use of 120 T crane, the frame was first erected(Figure 8). After the completion of the frame, tensioned fabric was then installed on the frame structure(Figure 9). The final completed PTFE privacy screen tensioned fabric structure is shown in Figure 10.



Figure 7. Fabrication of components of steel frame.



Figure 8. Erection of steel frame at site.



Figure 9. Installation of tensioned fabric on the steel frame.



Figure 10. Completed PTFE privacy screen tensioned fabric structure.

5. Conclusion

The planning and construction of PTFE privacy screen tensioned fabric structure within the compound of National Palace Malaysia has been described. It can be considered as a unique application of tensioned fabric structure for privacy protection. It also showcases the diverse application of tensioned fabric structure – from large span roof structure to small scale flexible screen structure.

Proceedings of the IASS Annual Symposium 2023
Integration of Design and Fabrication
10–14 July 2023, Melbourne, Australia
Y.M. Xie, J. Burry, T.U. Lee and J. Ma (eds.)

Study on the wind response properties of roof structures composed of radially arranged cables considering roof deformation

Akira OSHIUMI [a,*], Naoya MIYASATO[a], Akira OKADA[a], Shuzo HIROISHI[a], Daisuke SHINOHARA[a]

[a,*] Nihon University
3-11-2 Kanda Surugadai, Chiyoda-ku, Tokyo, 101-8308, Japan
oshiumi.akira@nihon-u.ac.jp

Abstract

Roofs of stadium buildings generally require a large opening in the center of the roof, and many examples of roof structures composed of radially arranged cables have been constructed in recent years in stadium buildings outside of Japan. This structure is a lightweight structure in which cables are radially arranged between the inner tension ring and the outer compression ring. In a previous report [1] considering this structure for Japan, the authors reported on wind tunnel tests and numerical analyses of a model with one tension ring and two compression rings. However, the wind tunnel tests in the previous papers used rigid models of the initial geometry, so the deformation of the roof surface was not taken into consideration in the wind load evaluation. In addition, with recent improvements in computer processing power, the use of computational fluid dynamics (CFD) analysis is expected to be utilized in the wind-resistant design of buildings. Therefore, in this paper, the authors proposed a convergence calculation to obtain the response after deformation of the roof based on CFD analysis and static analysis iterations to understand the effects of roof deformation on the wind pressure characteristics and structural behavior of this structure.

Keywords: lightweight structure, stadium, tension structure, cable, CFD analysis

1. Introduction

Roofs of stadium buildings generally require a large opening in the center of the roof, and many examples of roof structures composed of radially arranged cables have been constructed in recent years in stadium buildings outside of Japan. This structure is a lightweight structure in which cables are radially arranged between the inner tension ring and the outer compression ring. In previous papers [1, 2], the authors have investigated the structural behavior using wind tunnel tests and numerical analysis with a view to adopt this structure in Japan. In those previous papers, it was reported that the deformation of this structure under wind load is more than 1/100 of the cantilever length, which is large deformation. There are also some cases outside Japan where deformation of more than 1/20 of the cantilever length is allowed [3, 4]. On the other hand, the wind tunnel test in the previous paper [1] was conducted on a rigid model with initial geometry, so the deformation of the roof surface was not considered in the wind load evaluation.

Therefore, in this paper, the authors consider roof deformation from convergence calculations based on computational fluid dynamics (CFD) analysis and static analysis iterations to understand the effect of roof deformation on the wind pressure characteristics and structural behavior of this structure.

Copyright © 2023 by Akira OSHIUMI, Naoya MIYASATO, Akira OKADA, Shuzo HIROISHI and Daisuke SHINOHARA. Published in the Proceedings of the IASS Annual Symposium 2023 with permission.

2. Study methodology and model overview

The study flow is shown in Figure 1. First, a CFD analysis (CFD-1; hereinafter, called CFD-*n*) is performed on the initial shaped roof model to determine the mean wind force coefficient C_f. The *n* in CFD-*n* indicates the number of iterations of the calculation. Next, a static numerical analysis (FEM-1; hereinafter, called FEM-*n*) is performed using the obtained C_f to determine the structural behavior. Then, CFD analysis (CFD-2) and static numerical analysis (FEM-2) are performed again using the deformed roof shape from FEM-1 as the model. This iteration was performed five times (*n*=1-5). Roof deformation is evaluated as a time-averaged value during the analysis time (equivalent to 10 minutes on a real scale). In this paper, the convergence calculation was judged to have converged when the displacement difference (δ_n-δ_{n-1}) between the displacements δ_n and δ_{n-1} obtained from the n^{th} and $(n\text{-}1)^{th}$ FEMs were less than 1/300 of the cantilever length 50 m.

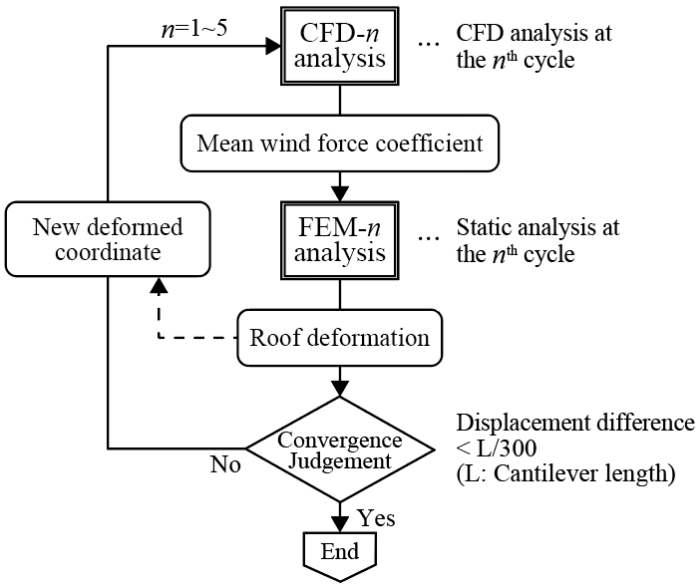


Figure 1. Consideration flowchart

The study model is shown in Figure 2. In this paper, only the roof structure is considered, and it is circular. Two roof configurations were used: Model A has one tension ring and two compression rings, and model B has two tension rings and one compression ring. The roof membrane material was attached to the lower radial cable in model A and to the upper radial cable in model B. The height of the roof surface was 24 m at the eaves.

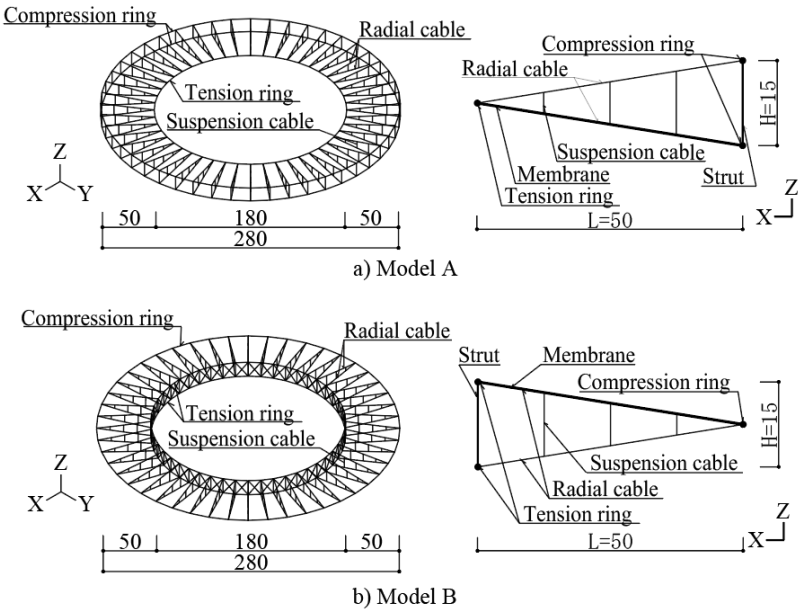
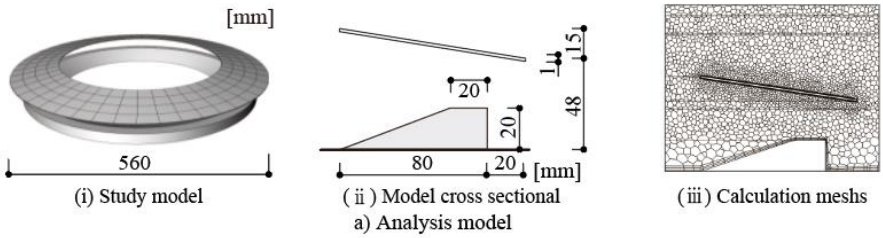


Figure 2. Outline of model (unit: m)

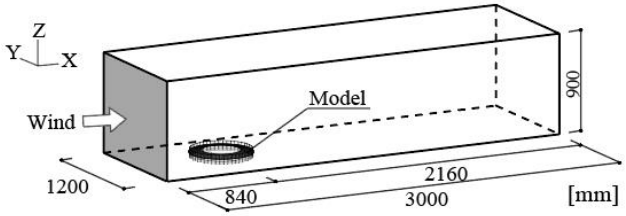
3. Numerical analysis overview

3.1. CFD analysis overview

An overview of the CFD analysis is shown in Figure 3. The model for the CFD analysis is assumed to be 1/500 of the actual size, with a total length of 560 mm and a cantilever length of 100 mm. This scale was adjusted to the model of the wind tunnel test conducted separately. In addition, only the roof and stand were used to reduce the analysis load. The CFD analysis was performed using scFlow (ver. v2020) and the turbulence model is the Smagorinsky model of LES. The governing equations were the incompressible Navier-Stokes equations and the continuity equation. The lattice system is an unstructured lattice with polyhedral. The discretization method was the finite volume method, with a gamma scheme for the discretization of the spatial term and a second-order precision implicit method for the discretization of the time term. The inflow condition is a uniform flow simulating only the vertical profile of wind velocity in surface roughness category III in Japan. The outflow condition was static pressure = 0. The evaluation time was set to be equivalent to approximately 10 minutes on the real scale, and the time increments for the calculations were 1.3×10^{-3} seconds. The analysis area was 1.2 m x 0.9 m and 3 m in length. The boundary conditions were set as no-slip boundaries on the ground surface and model surface, and free-slip boundaries on the sky and sides. The number of elements is approximately 4 million.



a) Analysis model



b) Analysis area

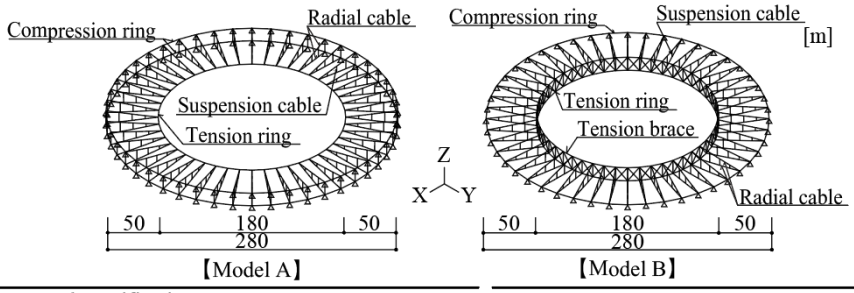
c) Analysis conditions

Turbulence model	LES [Smagorinsky model(Cs=0.15)]	
Air flow	Uniform flow(α=0.2)	
Boundary condition	Ground・Model surface	no - slip
	Upper・Side surface	free - slip
Time step	1.3×10^{-3}sec	

Figure 3. CFD analysis overview

3.2. Static numerical analysis overview

A static numerical analysis (FEM) overview is shown in Figure 4. The radial cable was modeled as an incompressible material and divided into eight sections. The suspension cables connecting the upper and lower radial cables were placed at equal intervals and were made of incompressible material. The boundary condition was pin support at the joints of the compression rings and radial cables. The wind load was calculated from a reference wind speed of 41 m/s at the roof eave height to a design velocity pressure of 1,000 N/m². In addition, considering the mean wind force coefficient and burden area, loads were placed as concentrated loads at eight nodes of the radial cable. The self-weight and the membrane weight of 20 N/m^2 are considered as the fixed load (long-term load). The self-weight is divided by 1.2 times the cable self-weight of the tension ring to account for the weight of the cable joint. The initial tension force was set at 2,000 kN and 4,000 kN, the sum of the upper and lower cable axial forces of the radial cable under long-term loading.



■Structural specifications

		model A	model B
Compression ring	STKN400	φ850.0×36.0	φ850.0×36.0
Bundle of steel	STKN400	φ406.4×12.7	φ318.5×10.3
Initial tensile force	2,000 , 4,000kN (total of radial cable tensile force)		

■Loading conditions

・Weight of membrane: 20 [N/m²]
・Wind load
Reference velocity pressure q: 1,000 [N/m²]
・Wind coefficient
Mean wind force coefficient C_f

■Structural specifications of the cable

		Model A	Model B
Tension ring	Structural locked coil rope	10-φ100	5-φ100
Radial cable	Structural locked coil rope	φ94	φ94
Suspension cable	Structural spiral rope	φ22.4 (1×19)	φ22.4 (1×19)
Tension brace	Structural spiral rope		φ33.5 (1×37)

Figure 4. Static numerical analysis overview

4. Numerical analysis results

4.1. CFD analysis results

The mean wind force coefficient C_f obtained from the CFD analysis at an initial tension of 2,000 kN is shown in Figure 5. Focusing on model A, CFD-1 through CFD-2 showed properties with larger positive C_f on the windward side. This is thought to be due to deformation from the initial shape in FEM-1, creating areas where wind tends to stagnate on the roof surface. After CFD-2, C_f tended to increase at the points where there were no suspension cables (even points in Fig. 5). On the other hand, no significant changes were observed from CFD-1 on the leeward side. Focusing on model B, the positive C_f was larger in the center of the roof on the windward side. This is thought to be due to the loss of tension force in the suspension cables due to the windward blowdown load. On the other hand, on the leeward side, no significant changes were observed from CFD-1 as in model A. This suggests that the upward convex deformation shape has a small effect on the wind pressure characteristics.

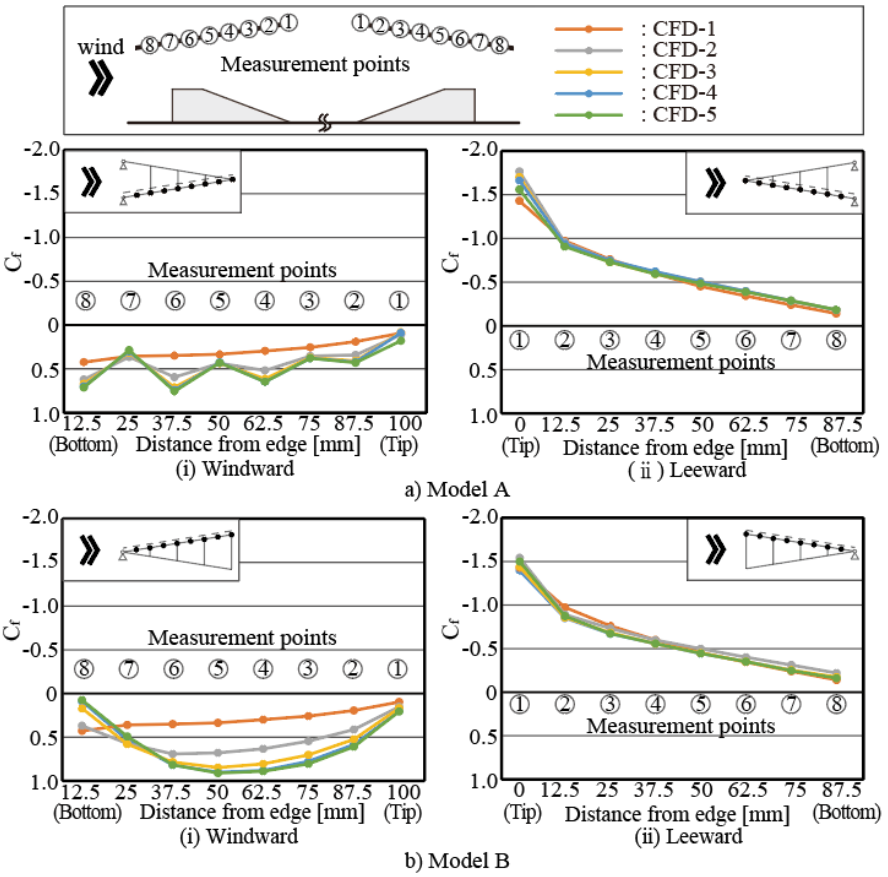


Figure 5. Mean wind force coefficient (Initial tension force 2,000 kN)

The convergence conditions of the displacements with the number of iterations are shown in Figure 6. For both models, the number of convergence calculations decreased as the initial tension increased. The displacement tended to decrease rapidly from FEM-1 to FEM-2.

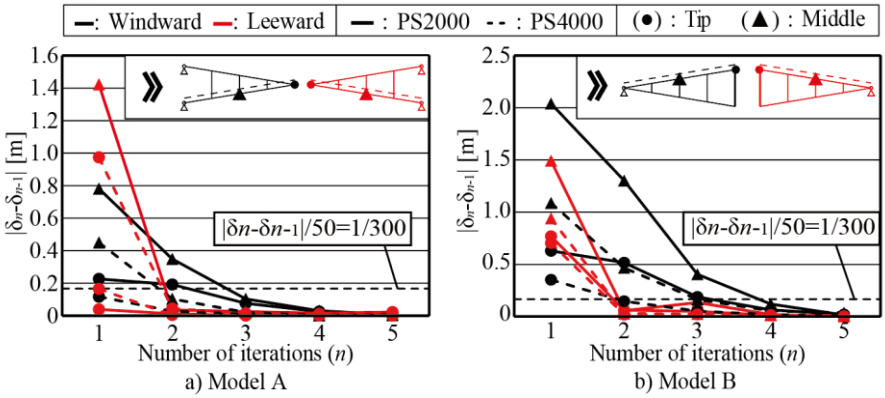


Figure 6. Convergence conditions of the displacements

Figures 7, 8 and Table 1 show that the roof deformation and the radial cable axial force after convergence increased from orthogonal to windward direction for both models A and B. No significant deformation changes were observed on the leeward side. The radial cable axial force showed an overall increasing trend with deformation.

Focusing on model A, the vertical displacement was 1.78 times the value at convergence compared with FEM-1 for an initial tension force of 2,000 kN at the windward tip. For the initial tension force of 4,000 kN, the windward tip was 1.12 times the initial tension force of 2,000 kN, and the rate of increase was smaller than for the initial tension force of 2,000 kN. For these roof deformations, the radial cable axial force increases by about 1.10 times the upper radial cable axial force for both windward and leeward sides at an initial tension force of 2,000 kN. On the other hand, at an initial tension force of 4,000 kN, the increase in axial force of the upper radial cable was less than 1.02 times.

Focusing on model B, the vertical displacement was 1.77 times the deformation at the windward tip at convergence compared with FEM-1 for an initial tension force of 2,000 kN, whereas for an initial tension force of 4,000 kN, the windward tip was 1.30 times the deformation. The radial cable axial force increases more than 1.12 times for the upper and 1.21 times and lower radial cable axial forces in all regions at an initial tension force of 2,000 kN. On the other hand, the increase in axial force at an initial tension force of 4,000 kN was less than 1.04 times for both the upper and lower radial cables.

The above results suggest the need for a wind load evaluation that takes deformation into account, since models with small initial tension force and initial deformation (FEM-1) of more than about 1/40 of the cantilever length for model A and more than about 1/20 of the cantilever length for model B may experience increased deformation and axial force due to repeated calculations. On the other hand, when the initial deformation (FEM-1) is less than about 1/60 of the cantilever length for model A and 1/40 of the cantilever length for model B, the wind load evaluation considering the deformation suggests that the deformation only affects the deformation.

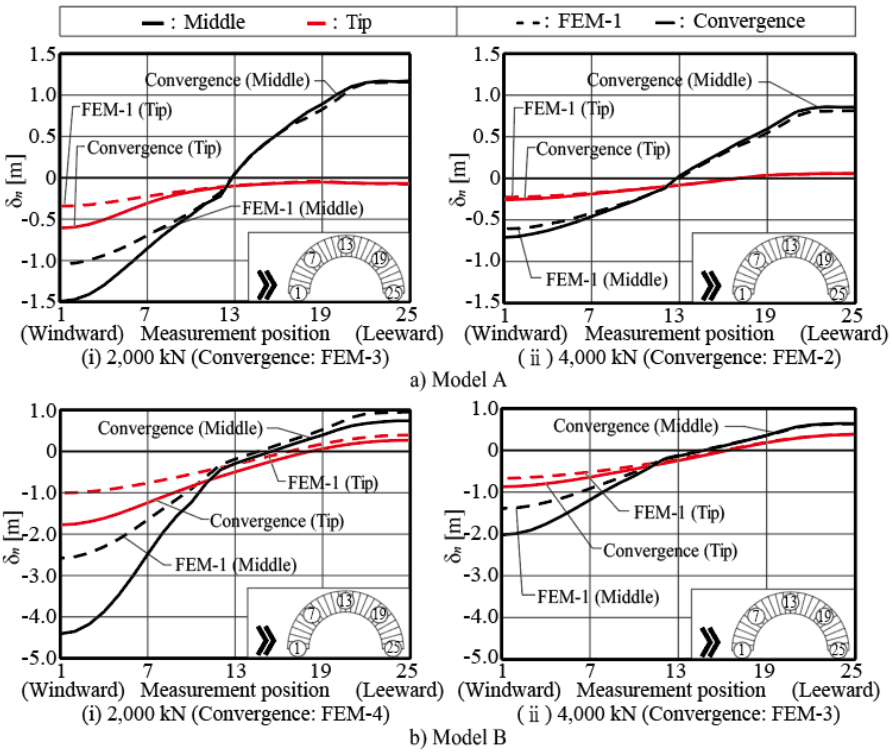


Figure 7. Vertical displacement at each location

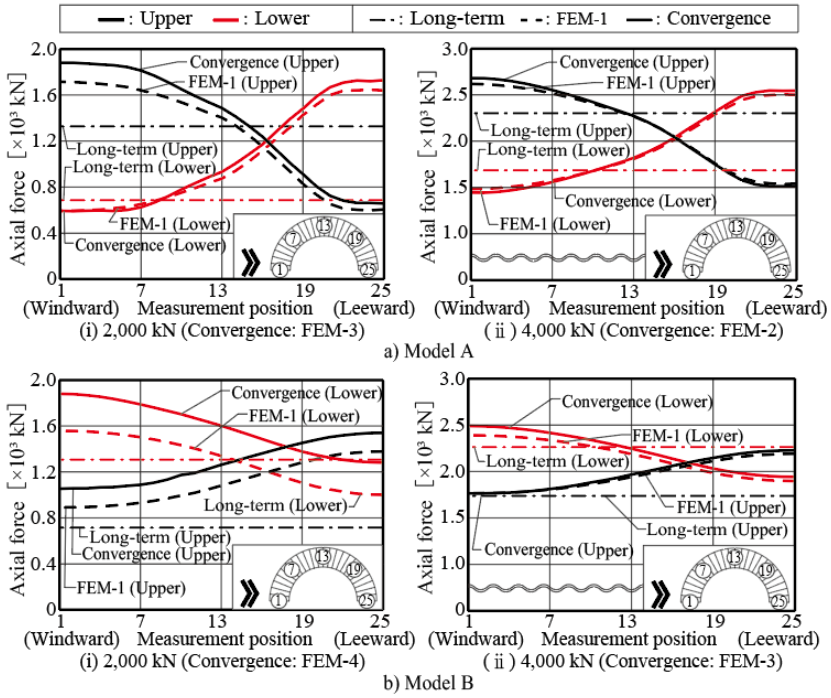


Figure 8. Radial cable axial force at each location

Table 1. Vertical displacement and radial cable axial force

			Vertical displacement [m (FEM-*n*/FEM-1)]				Radial Cable [kN (FEM-*n*/FEM-1)]			
			Windward		Leeward		Windward		Leeward	
			Tip	Middle	Tip	Middle	Upper	Lower	Upper	Lower
Model A	PS2,000	Long-term load	-0.116	-0.262	-0.116	-0.262	1,328	687	1,328	687
		FEM-1	-0.342	-1.042	-0.078	1.161	1,715	593	605	1,640
		FEM-3	-0.608 (1.78)	-1.494 (1.43)	-0.068 (0.87)	1.172 (1.01)	1,879 (1.10)	593 (1.00)	658 (1.09)	1,729 (1.05)
	PS4,000	Long-term load	-0.110	-0.158	-0.110	-0.158	2,302	1,686	2,302	1,686
		FEM-1	-0.227	-0.609	0.055	0.815	2,620	1,483	1,542	2,502
		FEM-2	-0.255 (1.12)	-0.712 (1.17)	0.058 (1.07)	0.858 (1.05)	2,681 (1.02)	1,445 (0.97)	1,512 (0.98)	2,547 (1.02)
Model B	PS2,000	Long-term load	-0.375	-0.541	-0.375	-0.541	716	1,308	716	1,308
		FEM-1	-1.004	-2.581	0.395	0.952	893	1,560	1,380	1,001
		FEM-4	-1.774 (1.77)	-4.410 (1.71)	0.270 (0.68)	0.739 (0.78)	1,055 (1.18)	1,881 (1.21)	1,541 (1.12)	1,283 (1.28)
	PS4,000	Long-term load	-0.317	-0.304	-0.317	-0.304	1,737	2,263	1,737	2,263
		FEM-1	-0.671	-1.392	0.387	0.636	1,765	2,391	2,192	1,898
		FEM-3	-0.872 (1.30)	-2.023 (1.45)	0.383 (0.99)	0.640 (1.01)	1,764 (1.00)	2,491 (1.04)	2,229 (1.02)	1,942 (1.02)

4. Conclusion

In this paper, the effects of the roof deformation of this structure and wind response characteristics were investigated. The results suggest the need for wind load evaluation that takes deformation into account, since models with low initial tension force and large initial deformation may experience increased deformation and axial force due to repeated calculations. On the other hand, when the initial deformation (FEM-1) is less than about 1/60 of the cantilever length for model A and 1/40 of the cantilever length for model B, the wind load evaluation considering the deformation suggests that the deformation only affects the deformation.

Acknowledgements

The authors would also like to express their gratitude to Jonathan Harrison and Kota Ayusawa for assistance in the editing of this paper.

References

[1] A. Oshiumi, T. Yagasaki, A. Okada, N. Miyasato and S. Hiroishi, "Study on structural behavior of roof structures consisting of radially arranged cables under strong winds and evaluation method of wind load for structural design, *Journal of Structural and Construction Engineering (Transactions of AIJ)*, Vol. 87, No. 795, pp. 454-463, 2022 (In Japanese).

[2] K. Kiuchi, N. Miyasato, A. Okada, S. Hiroishi and A. Oshiumi, "Basic study on wind response properties of roof structures consisting of radially arranged cables," *Summaries of Technical Papers of Annual Meeting, Architectural Institute of Japan, Structures-I*, pp. 923-928, 2022 (In Japanese).

[3] J. Bong-Soo and L. Jae-Hynk, "Cable membrane roof structure with oval opening of stadium for 2002 FIFA World Cup in Busan," in APCS2000.

[4] Z. Shi-chang, X. Xiao-ming, G. Feng, H. Peng, L. Bin, S. Wei-zhon and F. Qing, "Analysis and design of the accessory structure under the large deformation of a flexible roof," in IASS2022, Beijing, China, pp.190-201, 2022.

IASS 2023
July 10–14 Melbourne
Integration of Design and Fabrication

Proceedings of the IASS Annual Symposium 2023
Integration of Design and Fabrication
10–14 July 2023, Melbourne, Australia
Y.M. Xie, J. Burry, T.U. Lee and J. Ma (eds.)

Temperature field analysis of air-supported membrane structure for coal storage sheds

Xiuliang Lu[a], Cong Zhang[a], Xiongyan Li[a,b,*], Fei Yan[a], Suduo Xue[a,b]

[a,*] Faculty of Urban Construction, Beijing University of Technology, Beijing 100124, P.R. China.
Email: xiongy2006@126.com

[b] The Key Laboratory of Urban Security and Disaster Engineering, Ministry of Education, Beijing University of Technology, Beijing 10012, P.R. China.

Abstract

This study focuses on the temperature field analysis of air-supported membrane structures. A numerical model under various fire conditions of rectangular air-supported membrane structures for coal storage sheds was established using the Pyrosim field simulation software. An empirical formula for the relationship between the maximum temperature and the spatial position was proposed. This paper analysed flue gas emissions and construction. The influence of building height and the power of the fire source on the maximum temperature was also investigated.

This study shows that the R-squared for the maximum temperature curve obtained by the numerical simulation and the established mathematical model falls within 0.92-0.94, indicating that the proposed empirical formula correlates well with the simulation. The paper also discusses the relationship between the maximum temperature and the spatial position of the fire source in the combustion process. The power of the fire source is found to be the main factor affecting the maximum temperature. Under the same conditions, the maximum temperature is found to be inversely proportional to the building height. Results also indicated that the mechanical smoke extraction system has a specific cooling effect, but this effect is limited for the air-supported membrane structure coal storage shed with large space.

Keywords: space structure, air supported membrane structures, mathematical model, temperature field

1. Introduction

Over the past few years, the importance of environmental protection has significantly increased in China, leading to the closure of many coal yards in power plants. During this time, the use of air-supported membrane structures has become increasingly popular due to their flexible space, simple construction, and economic benefits. As these structures rely on inflation to provide a stable closed structure, understanding the temperature field during a fire is crucial. Domestic and foreign scholars have used relevant software to simulate fires in small and large-scale structures and analyze temperature field characteristics. For example, Li Guoqiang [1-2] et al. used a two-region model and temperature unsteady model to analyze the fire numerical analysis of large-span spatial structures and fitted an empirical temperature rise model for specific structures. However, this model is not universal and needs to be re-fitted for different projects. Other researchers [3] have used computational fluid dynamics software to simulate different fire scenarios in large space buildings, considering factors such as smoke exhaust systems. Xue Suduo[4-5] simulated fire scenes using the FDS program and established a mathematical model of the temperature field related to time, taking into account the influence of smoke emission on air temperature rise in large space building fires. Finally, other scholars [6-7] have studied the temperature distribution and smoke diffusion law of cylindrical inflatable membrane structures under fire using CFD numerical models, obtaining temperature distribution and smoke diffusion laws for membrane structures with different ignition points and smoke exhaust measures.

Copyright © 2023 by Xiuliang LU, Cong ZHANG, Xiongyan LI, Fei YAN and Suduo XUE. Published in the Proceedings of the IASS Annual Symposium 2023 with permission.

2. Fire model

2.1. Fire simulation parameters

In the context of closed renovation projects of coal yards in power plants, gas film structures are commonly used, particularly rectangular gas-supported membrane structures. Gas film coal storage sheds require fire-fighting equipment and a certain spray area. Experience has shown that the actual combustion area during a warehouse fire is generally between 10m2-20m2. Therefore, assuming a stable fire source, a cube of 4m × 4m × 1m with a combustion area of 16m2 is used to simulate a fire. Previous research on combustion tests and simulations have shown that adverse fire conditions mostly occur during the beginning and full combustion stages. However, the ignition and recession stages of fire are not typically considered. The heat release rate of a fire is proportional to the square of time, which is known as 't square fire'. The coal stored in these sheds tends to burn at a medium speed, and the simulation uses the fast fire coefficient with a growth coefficient α of 0.044kw/s2 to ensure the structure's safety. According to the technical standard of building smoke prevention and exhaust system [8] GB51251-2017, the heat release rate of the fire is determined to be 4MW and 20MW.

The coal shed is equipped with 6 evacuation doors, 16 air supply outlets, and 10 exhaust outlets. The door opening size is 1.5m × 2m, while the air inlet and outlet sizes are 1m × 1m and 0.85m × 0.85m, respectively. The setting of the supplementary air volume and exhaust air volume is based on the condition that the structure does not collapse due to air leakage without burning through. The pressure difference between the interior and exterior of the structure remains constant, and the parameters are established such that the intake air volume is equivalent to the total air leakage.

The mechanical smoke exhaust volume of the smoke outlet is determined using the calculation method provided in the American standard NFPA 92B [9]. It is important to note that the parameters for the intake air and exhaust air are determined with the safety of the structure in mind, such that it can withstand the air leakage without collapsing.

$$m_p = 0.071 Q_c^{1/3} Z^{5/3} + 0.0018 Q_c \tag{1}$$

$$V = m_p / \rho_0 + Q_c / \rho_0 T_0 C_p \tag{2}$$

In the formula: the mass flow rate of the plume, kg / s ; convective heat release rate (about 0.7 Q), KW ; is the height above the burning surface, m ; the volume flow rate of plume, smoke exhaust volume, m3 / s ;

ambient air density, kg / m3; for the ambient temperature (take 293K), K; is the specific heat capacity of air, 1.02KJ / (kg °C). The air leakage at the door opening is calculated according to the formula in the ' Air Membrane Structure Design and Construction Guide '[8] :

$$P = 1/2 \times \rho \times v^2 \tag{3}$$

In the formula: for the pressure difference between the inside and outside of the inflatable membrane, Pa ; for air velocity ; m / s ; the air density is 1.205kg / m3 at 20 °C.

The position of the air supply outlet is shown in Figure1. When the top surface exhausts, the fan is evenly arranged on the top surface of the membrane, and the size and number of the exhaust outlets are the same as the side wall exhaust. The setting of the air intake and exhaust volume of the fan is shown in table 1.

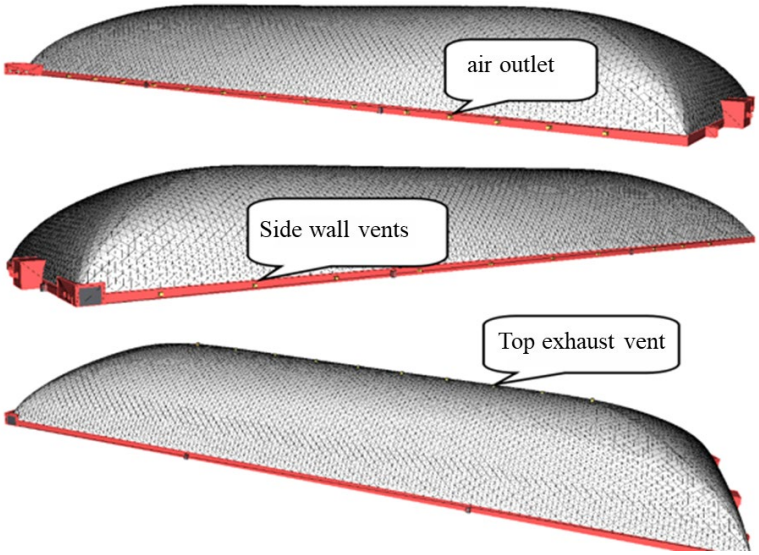


Figure1. Location of fan

Table 1. Fan inlet air volume and exhaust air volume setting

smoke exhaust mode	Leakage velocity of door opening(m^3/s)	inlet air velocity /(m^3/s)	Exhaust rate / (m^3/s)
Evacuation door smoke	251	15.68/each	
Side wall mechanical smoke exhaust	251	21/ each	8.5/ each
Top mechanical smoke exhaust	251	21/ each	8.5/ each

The model takes the grid as the minimum calculation unit. The finer the grid division, the more accurate the calculation results. Practice has proved that the influence of the grid on the calculation results will increase with the shortening of the distance from the fire source. Considering the running time and calculation accuracy of the computer, the model mesh is divided into four regions in the numerical simulation. The mesh size of the region with fire source is 1m × 1m × 1m, and the mesh size of other regions is 2m × 2m × 1m. The actual fire will burn completely within 15 minutes (experience). Considering the calculation running time, the combustion time is 2000 s.

2.2. Fire source location

The coal storage shed of the power plant divides the coal storage area into four areas], and a 10 m wide fire isolation belt is set between the coal piles. The partition is shown in Figure 2. Han Hongbin [10] studied the spontaneous combustion phenomenon of coal yard in thermal power plant. The results show that the flammable area of coal pile is the surrounding of the bottom layer of coal pile and the intersection of coal pile. Lyu Mu [11] and Gu Haijun [12] found that coal pile is easy to spontaneous combustion in the internal oxide layer of coal pile. Tang Zhong and Du Yunfeng [13] optimized the determination process of coal calorific value in the process of long-term coal storage on the basis of the study of the law of coal oxidation temperature rise in the field, and concluded that the flammable oxide layer of coal pile is located 1-3 meters below the coal surface. It is stipulated in the safety regulations of coal preparation plant [14] that the stacking height of coal pile should not exceed 6 meters. Based on the study of the stacking height of the coal pile in the ' Coal Preparation Plant Safety Regulations ' and the

flammable position of the oxide layer by Tang Zhong and Du Yunfeng, the ignition height of the oxide layer of the coal pile is roughly within 3-5 meters from the ground. After calculation and discrimination, the 10 m wide fire isolation belt can meet the safety needs. A pile of coal is on fire, and theoretically it will not ignite adjacent coal piles. This situation is not considered in the study. In summary, take two fire source points of fire source one and fire source two, and the plane position is shown in Figure2.

Based on the numerical simulation results of the previous foundation, the hot smoke in the center of the fire source rises vertically after the fire, and the top surface of the film directly above the fire source is directly impacted by the hot smoke airflow and is in a relatively unfavorable position. After the hot smoke flow rises to the top surface of the film, it gradually diffuses around the film and then decreases layer by layer. There are workers in the coal shed, and the limit temperature that the human body can tolerate is 60 °C. Inhalation of superheated smoke by the human body will cause heat stroke, skin burning or other injuries. The temperature of the smoke layer in the area affected by the evacuation of the researchers is particularly important for the safety of evacuation. NFPA 92B stipulates that the 2m high plane is a clear height plane, and the temperature of the smoke layer on this plane is studied to provide suggestions for the safe evacuation of personnel.

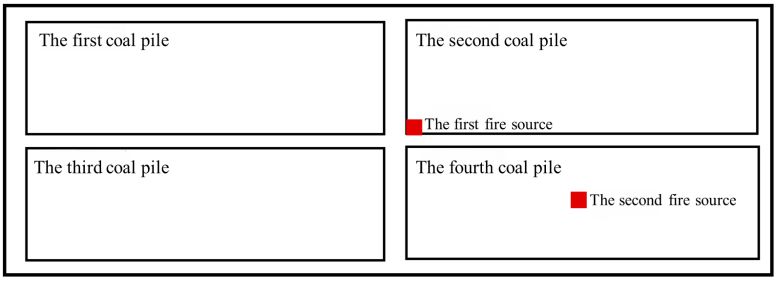


Figure2. Coal heap zoning and fire source location map

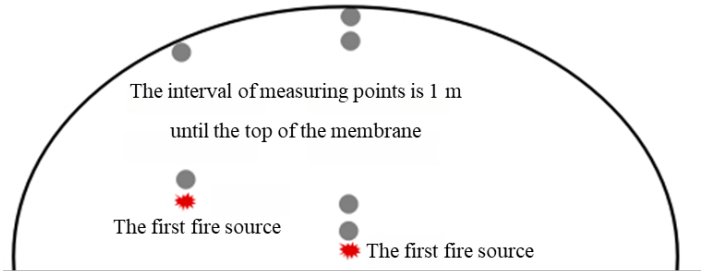


Figure3. Layout of longitudinal measuring points

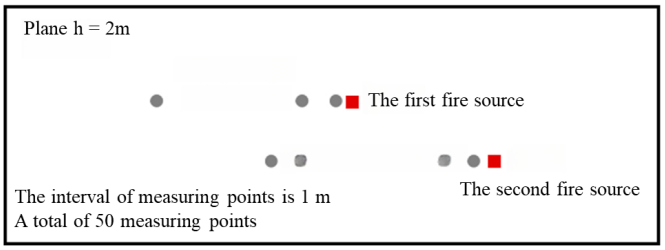


Figure4. Layout of horizontal measuring points on clear height plane

Table 2. Fire area and space longitudinal position of different fire sources

combustion source	fire area /m	Longitudinal position of fire source /m
First Fire source	4×4	0-1
Second Fire source	4×4	4-5

2.3. Fire conditions

The building area and building height of the gas film structure coal storage shed in the existing power plant coal yard closed renovation project are summarized. The building area of the gas film structure coal storage shed of most power plants is 30000m2-40000m2, and the building height is 30m-40m. The building area is 30000m2,35000m2,40000m2, the building height is 30m, 35m, 40m, the fire power is 4MW, 20MW, the smoke exhaust methods are evacuation door smoke exhaust, side mechanical smoke exhaust and top mechanical smoke exhaust. The above different factors are arranged and combined to obtain 54 different fire conditions, see table 3. The following fire conditions were simulated for fire source one and fire source two.

Table.3 Fire condition

building area /m^2	building height /m	fire power /(MW)	smoke exhaust mode	working condition
30000	30	4	Evacuation door smoke	1
			Side wall mechanical smoke exhaust	2
			Top exhaust mechanical smoke	3
		20	Evacuation door smoke	4
40000	40	20	Top mechanical smoke exhaust	54

3. The relationship between maximum temperature and spatial location

3.1. The relationship between the highest position above the fire source center and the longitudinal height

The numerical simulation of the combined fire conditions was carried out. Through the collation and analysis of the data, the relationship curve between the maximum temperature and the longitudinal height above the fire source is shown in Fig.6. During the combustion process, the trend of the highest temperature at different heights is as follows : between 2m and 8m, the highest temperature at each position decreases very rapidly ; as the height increases, the temperature gradient at each position gradually decreases ; between 10 m and 14 m, the maximum temperature at each position is not much different, and the curve shows a smooth downward trend ; when the height is 16 m and above, the maximum temperature at each position basically shows a horizontal linear trend. When the ignition point is the second fire source, the characteristic trend of the relationship curve between the maximum temperature above the fire source and the longitudinal height is the same as above. The characteristic curve is shown in figure5: 6m to 20m, and the maximum temperature gradient at each position is large ; as the height increases, the maximum temperature gradient decreases and the curve tends to be gentle.

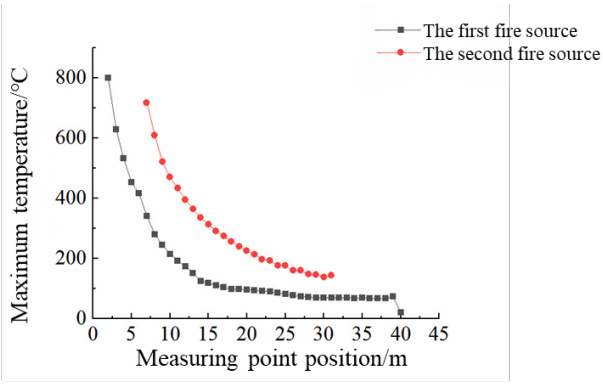


Figure5. Relationship between maximum temperature and vertical height

Figure 6 show the temperature cloud diagram on the center plane of the fire source under one of the fire conditions. It can be seen from the figure that the temperature of the flue gas layer above the fire source center has obvious stratification in the height range near the fire source point, and the temperature gradient is large. As the height increases, the temperature gradient difference decreases, and the stratification law is consistent with the previous curve characteristics.

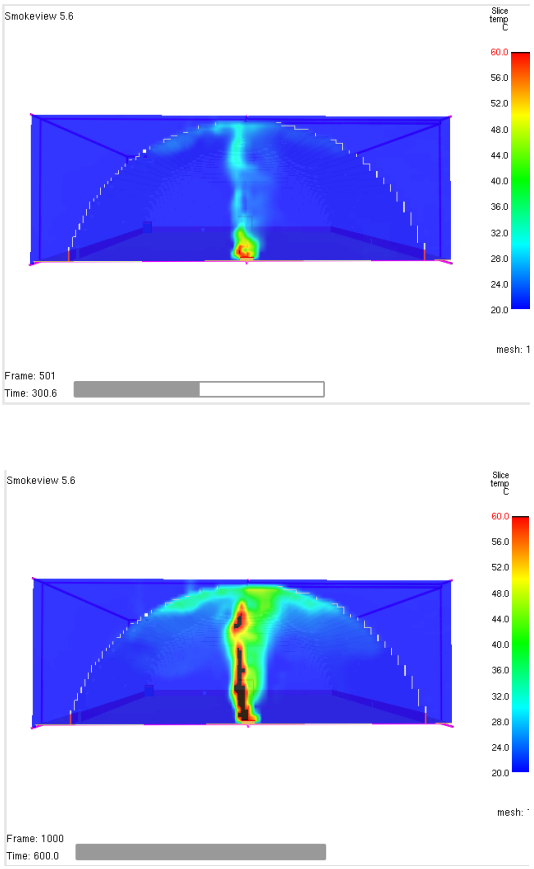


Figure6. Temperature nephogram of longitudinal section in the center of fire source (fire source 1)

The empirical formula of the relationship between the maximum temperature above the fire source and the longitudinal height is obtained by fitting the maximum temperature characteristic curve of each working condition, as shown in Equation 4 :

$$T_{\max} = \theta_1 \ln(h - z) + \theta_2 + T_0 \tag{4}$$

where : : the maximum temperature at the height of the fire source center ; °C Height of measuring point directly above the fire source ; m : the highest surface height of the fire source ; m The initial ambient temperature inside the structure ; 20 °C The height of the fire source surface of fire source 1 and fire source 2 is different. The parameters in the empirical formula are explained : see table 4.

Table.4 Fire condition

	z	h	$h-z$
First Fire source	1m	≤ height of film surface above fire source	≥1m
Second Fire source	5m	≤ height of film surface above fire source	≥1m

3.2. The relationship between the maximum temperature on the clear height plane and the transverse position

The fire numerical simulation of the combined fire conditions is carried out. Through the collation and analysis of the data, it is concluded that the relationship between the maximum temperature and the transverse position on the clear height plane of fire source one and fire source two is different. The characteristic curves are shown in Figure7 and Figure 8 respectively.

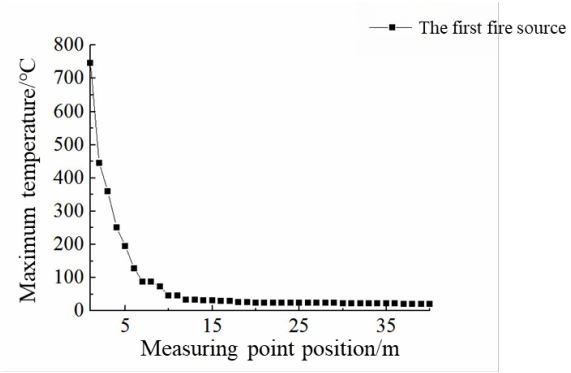


Figure7. Relationship between maximum temperature and transverse direction

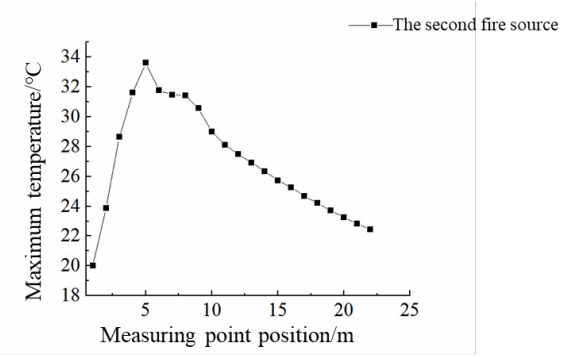


Figure8. Relationship between maximum temperature and transverse direction

When the ignition point is a fire source, the relationship between the maximum temperature on the clear height plane and the lateral position is roughly the following characteristics : in the range of 0-4m from the center of the fire source, the maximum temperature decreases rapidly with the increase of distance, and the curve almost shows a 90 ° downward trend ; in the range of 4m-10 m, the change of maximum temperature with distance is no longer obvious, especially after 12 m, the curve tends to be almost horizontal. When the ignition point is fire source two, the relationship between the maximum temperature and the lateral position on the clear height plane is roughly the following characteristics :

between 1m and 6m from the center of the fire source, the maximum temperature increases with the increase of distance ; the maximum temperature decreases with the increase of distance when the distance from the fire source center is greater than 6m. Basically at about 6m from the fire source, the temperature reached during the combustion process is the highest, roughly at 35 °C.

The study of the highest temperature on the clear height plane mainly considers the safety of personnel evacuation. When the ignition point is the second fire source, the highest temperature within the measuring point range under each working condition does not reach the human tolerance limit temperature of 60 °C, and its highest temperature will not affect the evacuation of personnel. The relationship between the maximum temperature and the transverse position when the ignition point is the fire source is studied in detail. The empirical formula of the relationship between the maximum temperature and the lateral position on the clear height plane is obtained by fitting the characteristic curves of each working condition, as shown in Formula 5.

$$T_{\max} = \theta_1 \times r^{\theta_2} + \mathrm{T}_0 \tag{5}$$

Where : Maximum temperature, °C Room temperature, 20 °C : Distance from the fire center ($1 \leq \leq 50$), m

It is determined according to different fire conditions, which is related to building area, building height, fire power and smoke exhaust mode. The practical verification of the formula and the determination of the parameters are shown in Chapter 4.

4. Effects of different factors on the maximum temperature above the fire center

The effects of building height, smoke exhaust mode and fire source power on the maximum temperature above the fire source center of rectangular air-supported membrane structure coal shed in super large space were studied. Due to too many working conditions, the paper is limited in space. Only some of the working conditions are listed for analysis and explanation, and the remaining results are essentially the same as the listed results.

4.1. Effect of building height

Figure 9 is the comparison of the highest temperature data when the fire source power is 20MW, the building area is 30,000m2, the smoke exhaust mode is evacuation door smoke exhaust, and the building height is 30m, 35m and 40m respectively. It can be seen from Fig.11 that within the height range of 0m-8m, the maximum temperature does not show a clear characteristic relationship with the height due to the instability of the fire source power near the fire source. When the height of the position rises, roughly from 8m, the relationship between the maximum temperature and the height shows regularity, that is, under the same other conditions, the higher the building height, the lower the maximum temperature at each height of the fire source center.

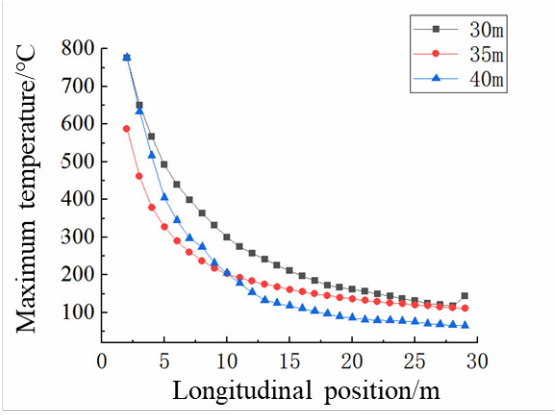


Figure9. Comparison of building height impact

4.2. Impact of smoke exhaust methods

Table 5 is the comparison of data results when the fire source power is 20MW, the building height is 40m, the building area is 40,000m2, and the smoke exhaust methods are evacuation door smoke exhaust, side wall mechanical smoke exhaust, and top surface mechanical smoke exhaust (working condition 1). Table 6 is the comparison of the data results of the fire source power of 20 MW, the building height of 30 m, and the building area of 40,000 m2. The smoke exhaust methods are evacuation door smoke exhaust, side wall mechanical smoke exhaust, and top surface mechanical smoke exhaust (working condition 2). From Table 5 and Table 6, it can be seen that the highest temperature obtained by different smoke exhaust methods is slightly different under the same building area, the same building height and the same fire source power. Compared with the evacuation door exhaust method, the mechanical exhaust method has a slight cooling effect, and the cooling effect of the top mechanical exhaust method is slightly better than that of the side mechanical exhaust method. However, the actual cooling of the two smoke exhaust methods is not much. At the same position, the side wall mechanical smoke exhaust is about 5 ° C lower than the evacuation door smoke exhaust, and the top surface smoke exhaust is about 10 ° C lower than the evacuation door smoke exhaust. In practical engineering, the smoke exhaust method is not an efficient cooling solution.

Table.5 Situation (1)

	8m	16m	24m
Evacuation door smoke	369.90℃	235.46℃	173.79℃
Side wall mechanical smoke exhaust	357.92℃	228.40℃	169.93℃
Top mechanical smoke exhaust	354.19℃	215.84℃	154.01℃

Table.6 Situation (2)

	8m	16m	24m
Evacuation door smoke	355.80℃	232.52℃	171.77℃
Side wall mechanical smoke exhaust	358.17℃	226.20℃	166.57℃
Top mechanical smoke exhaust	355.79℃	221.25℃	160.20℃

4.3. Effect of fire power

Figure 10 shows the data comparison diagram when the building area is 30000m2, the building height is 30m, the smoke exhaust mode is evacuation door, and the fire source power is 4MW and 20MW respectively. It can be seen from Fig.12 that the fire source power has a great influence on the maximum temperature compared with the influence of the smoke exhaust mode on the temperature. The maximum temperature difference under different fire power at the same position reaches about 400 °C. The closer to the fire source point, the greater the temperature difference. As the position increases, the difference becomes smaller, but even close to the height of the top surface of the film, the temperature difference reaches about 50 °C. The fire power is the main factor affecting the maximum temperature at different heights of the fire center.

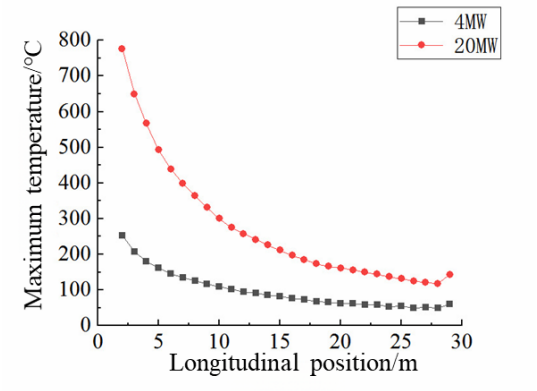


Figure10. Comparison chart of fire source power influence

5. Practical verification of empirical formula

Chapter 3 analyzes the influence of different factors on the maximum temperature. From chapter 3, it can be seen that the higher the building height, the greater the fire source power, the smoke exhaust mode is the evacuation door smoke exhaust, that is, the fire condition is the building height of 30 m, the fire source power is 20 MW, and the smoke exhaust mode is the evacuation door smoke exhaust. The coefficients of each working condition are summarized, and the coefficients of the highest temperature empirical formula of the following three most unfavorable working conditions are described in detail. The highest temperature calculated by the empirical formula is compared with the highest temperature obtained by numerical simulation to verify the practicability of the empirical formula.

5.1. Practicability verification of empirical formula for the relationship between maximum temperature and longitudinal height

The empirical formula coefficients, evaluation function R2 and corresponding empirical formulas of the relationship between the maximum temperature and the longitudinal height of the three working conditions are summarized in Tables 7 and 8.

Table 7 Working conditions

Condition	building area /m^2	building height /m	smoke exhaust mode	fire power /KW
The first condition	30000	30	Evacuation door smoke	20
The Second condition	35000	30		20
The Third condition	40000	30		20

Table 8. Fire source

		θ_1	θ_2	R^2
First Fire source	The first condition	-203.90	747.12	0.98
	The Second condition	-190.70	653.54	0.97
	The Third condition	-174.5	692.08	0.99
Second Fire source	The first condition	-160.80	527.56	0.94
	The Second condition	-211.90	788.68	0.99
	The Third condition	-208.70	746.18	0.99

The maximum temperature results obtained by numerical simulation are compared with the maximum temperature results calculated by empirical formula to verify the reliability of empirical formula, see table 9.

Table 9. Results comparison table

		Loaction/m	Numerical simulation of the highest temperature /℃	Empirical formula to calculate the highest temperature /℃
First Fire source	The first condition	8	364.16	370.35
		16	197.22	214.95
		24	137.20	127.79
	The Second condition	8	293.78	302.46
		16	159.10	157.12
		24	114.68	77.00
	The Third condition	8	355.80	372.52
		16	232.52	239.53
		24	171.77	164.94
Second Fire source	The first condition	8	369.36	370.94
		16	137.53	161.96
		24	80.93	74.16
	The Second condition	8	576.42	576.01
		16	284.61	300.54
		24	180.18	184.85
	The Third condition	8	550.90	537.03
		16	263.48	201.02
		24	181.34	151.76

6. Conclusion

According to the numerical simulation results and analysis results, the conclusions are as follows:

(1) The characteristic curve of the relationship between the maximum temperature and the spatial position was obtained, and the empirical formula was fitted. The evaluation function R2 was above 0.92, which indicated that the formula was simple and practical.

(2) When other conditions are the same, the higher the building height, the lower the maximum temperature above the fire center.

(3) For the large space rectangular air-supported membrane structure coal storage shed, the cooling effect of mechanical smoke exhaust is not obvious. In practical engineering, smoke exhaust is not an efficient cooling method.

(4) The fire power is the main factor affecting the maximum temperature. The higher the fire power, the higher the maximum temperature.

References

[1] C. Zhang, G. Q. Li. Simple formula for building large space fire simulation and temperature rise calculation [J]. Fire Science, 2012,21 (02) : 84-91.

[2] Y. Bai, Y. Shi, Y. Q. Wang. Numerical simulation analysis of temperature field of large space structure under fire [J]. Chinese Journal of Safety Science, 2006, (01) : 34-38 + 0 + 2.

[3] S. D. Xue, J. Liang, X. Y. Li. Influence of smoke exhaust mode on air temperature rise in large space building fire. Journal of disaster prevention and Mitigation Engineering,2010,30(5).

[4] S. D. Xue, J. Liang, X. Y. Li. Empirical formula of air temperature rise in large space building fire. Journal of Beijing University of Technology,2013,39(2).

[5] Y. K. Shen, Z. P. Wang, C. B. Peng.Temperature field distribution characteristics of semi cylindrical gas film under different fire scenarios. Structural engineer,2014,30(5).

[6] Y. K Shen, Z. P. Wang, C. B. Peng.Fire temperature field and smoke distribution of rectangular inflatable membrane structure[J]. Industrial Building,2014,44(9):78-82.

[7] S. L. Yi, Zeng B. Study on temperature field characteristics of inflatable membrane structure in fire[J]. Fire science and technology,2016,35(11):1507-1510.

[8] NFPA 92B.Guide for smoke management system in malls, atria and large area. Quincy,Mass National Fire Protection Associatioon,1995.

[9] H. B. Han. Formation characteristics and prevention and control methods of spontaneous combustion in coal yard of thermal power plant[J]. China Electric Power，2013，46(04)：98-103.

[10] M. Lv. Cause and prevention of spontaneous combustion of coal pile in coal storage yard of thermal power plant[J]. Science and technology information,2013,(12):135.

[11] H. J. Gu. Discussion on the cause, prevention and treatment of coal spontaneous combustion in thermal power plant[J]. enterprise's technology development,2012,31(32):170-172.

[12] Z. Tang, Y. F. Du, G. Liu, et al. Study on Optimization of long period calorific value determination process of coal[J]. Coal science and technology,2016,(S2):226-228.

[13] S. D. Xue. Technical Guide for Design and Construction of Inflatable Membrane Structures [M]. Beijing : China Construction Industry Press, 2019.

[14] GB 50229 - 2019. Fire protection standard for thermal power plant and substation design [S]. Beijing, China Plan Press, 2019.

Proceedings of the IASS Annual Symposium 2023
Integration of Design and Fabrication
10–14 July 2023, Melbourne, Australia
Y.M. Xie, J. Burry, T.U. Lee and J. Ma (eds.)

The constitutive model of STFE membrane material

Ye YUAN[a], Qilin ZHANG[a,*], Xiaoqun LUO[a], Ruijie GU[a]

[a,*] Dept. of Structural Engineering, College of Civil Engineering, Tongji University
No. 1239, Si Ping Rd. Shanghai 200092 P. R. China
zhangqilin@tongji.edu.cn

Abstract

STFE membrane material is a new kind of building material developed these years, it combines the high transparency of fluoropolymer film as ETFE, and the high strength of coated fabric membrane materials as PVC and PTFE, which makes it a high-strength transparent roof material for membrane structures. However, the constitutive model of STFE material has not been studied yet. In this paper, uniaxial tensile test and biaxial tensile test in different load scales between warp and weft directions (with 1:1,1:2,2:1,1:0,0:1) were carried out, gaining the stress-strain relationship curve of warp and weft directions. Resulting from the structure of the fabrics, the stress-strain curve in weft direction are approximately linear, while the curve in warp direction are non-linear. An in-plane orthotropic anisotropy linear constitutive model is established, calibrating the elastic modulus and Poisson's ratio for two directions, furthermore, a non-linear biaxial constitutive model is proposed, which has a higher accuracy for the description of stress-strain relationship.

Keywords: tensioned membrane structures, STFE membrane materials, uniaxial tensile test, biaxial tensile test, constitutive model

1. Introduction

Membrane structure is an important type of spatial tensile flexible structure, which is lightweight in appearance and easy to construct. They have been widely used in various types of architectures such as public buildings and transportation facilities [1]. The emergence of structural systems is closely related to the invention of building materials. The promotion and application of membrane structures are developed from the invention of architecture membrane materials. After decades of development, two different types of membrane structures have gradually emerged based on different membrane materials: coated fabric membrane structures and polymer membrane structures, which correspond to coated fabric membrane materials and polymer membrane materials, respectively.

Coated fabric membrane materials are made of high-strength fibers woven into a base cloth, covered and protected by a polymer coating. According to the type of the fibers that bear the tension, they are generally divided into polyester fiber fabric and glass fiber fabric, corresponding to P-type membrane materials and G-type membrane materials, respectively. Depending on the type that polymer coating used, they can be classified as PVC membrane materials, PVDF membrane materials, PTFE membrane materials, etc. The thickness of coated fabric membrane materials are generally in the range of 0.3mm-1.5mm, and are characterized by high strength, easy welding, and resistance to high tensile and tear forces, making them suitable for use in large-span tensile membrane structures, such as the Shanghai Hongkou Stadium and other buildings (Figure 1).

Copyright © 2023 by Ye YUAN, Qilin ZHANG, Xiaoqun LUO and Ruijie GU. Published in the Proceedings of the IASS Annual Symposium 2023 with permission.



Figure 1. The coated fabric membrane structure: Hongkou Stadium

The most commonly used polymer membrane material in membrane structures is ETFE membrane material, which has strong light transmission and is suitable for use in various types of buildings that require transparency, particularly the famous National Aquatics Center "Water Cube" in Beijing (Figure 2). The thickness of ETFE membrane material is generally between 0.05mm and 0.3mm, much thinner than coated fabric membrane materials, and its strength is far lower than that of coated fabric membrane materials. For ETFE membrane materials, tearing strength is generally not considered, making it difficult to use for large-span tensile membrane structures. Generally, it is attached to the rigid or other tensile building facade in the form of air cushions.



Figure 2. The polymer membrane structure: National Aquatics Center "Water Cube"

In order to meet the demands of large-span tension and transparency in membrane structures, Serge Ferrari Company has developed a new type of transparent tensile membrane material called STFE, which stands for Structural, Transparent, Fluorinated, Envelope. The material composition of this membrane is polyarylate structural mesh with high tenacity yarn and Transparent hybrid fluoropolymer film. Due to the high strength of the fibers, which is higher than that of general polyester fibers and glass fibers, sparse fiber arrangement can be adopted on the membrane surface, leaving a large area of transparent film uncovered, thus keep a certain degree of translucency of the membrane material (see Figure 3). It has been measured that the light transmittance of STFE membrane material can reach more than 50%, which is less than the high light transmittance of ETFE membrane material (usually above

90%). Since the fibers are relatively thick (about 1mm in diameter), the fibers on the membrane surface can be clearly seen from close distance. However, at a distance of more than 5m from the membrane surface, the fibers are basically invisible and difficult to see clearly, and the effect of viewing the membrane surface from a distance is very similar to that of transparent membrane materials(as Figure 4 shows).

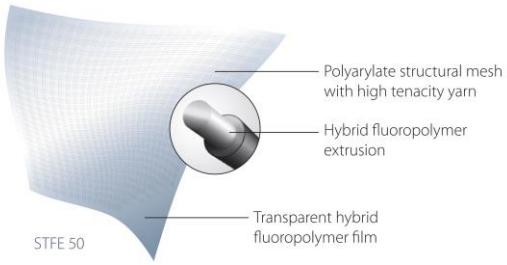


Figure 3. The composition of STFE



Figure 4. Transparent view effect from different distance

2. The constitutive model of traditional membrane

In the design and calculation of membrane structures, the stress-strain relationship of materials is the most important mechanical model, which forms the basis for calculating the displacement of membrane structures under various loads. For traditional coated fabric membrane materials and polymer membrane materials, there are already many mechanical models that describe their stress-strain relationships.

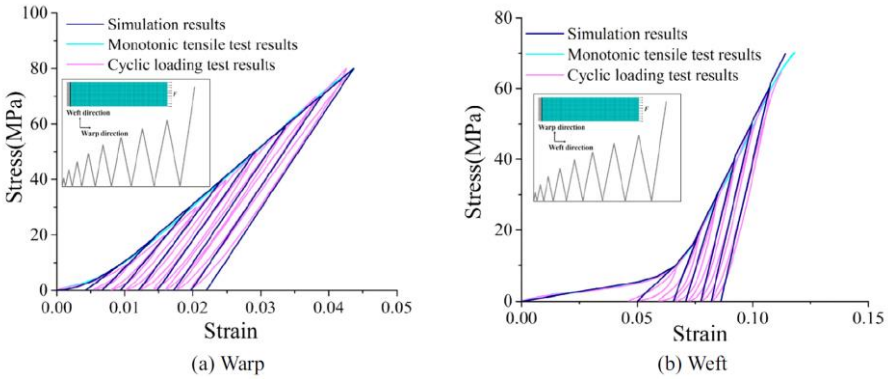


Figure 5. Comparison between the stress-strain curve of warp and weft directions [3]

The stress-strain relationship of coated fabric membrane materials is influenced by their material composition. The base fabric of this type of membrane is woven from high-strength fibers that intersect in two perpendicular directions, the warp and weft directions, resulting in two material principal axes that correspond to the mechanical properties in the warp and weft directions. In various codes/standards, the orthogonal anisotropic model of linear elasticity is commonly used to describe the mechanical properties of coated fabric membrane materials, but this model cannot reflect the nonlinear stress-strain relationship of the membrane material. As a result, other nonlinear models have been developed, such as nonlinear orthotropic material model [2], segmented model [3], hyperelastic model [4], and models

that consider the crimp interchange of the warp and weft directions [5]. These models to some extent reflect the differences in stress-strain relationships between the warp and weft directions and the nonlinearity of the two direction curves (as shown in Figure 5). To determine the stress-strain curves in the warp and weft directions, biaxial tests are usually performed by applying different proportions of loads in the warp and weft directions to obtain the curves of the membrane material under different stress states [6].

The stress-strain relationship of ETFE membrane material is generally considered to be isotropic, although it is greatly influenced by temperature. Under certain temperatures, the membrane material can be approximately regarded as a homogeneous material in-plane, and described using a fixed constitutive model [7]. At room temperature, a three-segment model shown in Figure 6 is commonly used to describe the stress-strain relationship of ETFE membrane material, which has two characteristic points on the curve representing the first and second yield strengths of the material. It is generally believed that ETFE material is elastic only on the curve before the first yield strength.

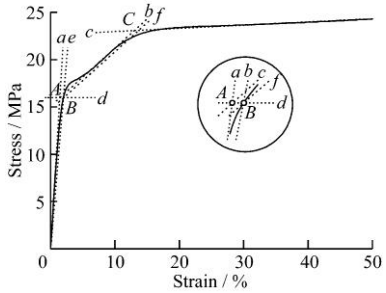


Figure 6. The stress-strain curve of ETFE [7]

3. The uniaxial tensile test and biaxial tensile test

To obtain the stress-strain relationship of STFE membrane material, uniaxial and biaxial tests of the membrane material must be performed. Since the main tension component of STFE membrane material is its fibers, similar to coated fabric membrane materials, the test specimen processing method of coated fabric membrane materials is used when testing STFE membrane materials.

The uniaxial test of STFE membrane material use the clamping test method, and the specimen uses a rectangular strip specimen with a length of 300mm and a width of 50mm, cut from warp and weft directions. The clamping area at both ends is 50mm long, and the strain elongation area in the middle is 200mm long, as shown in Figure 7. The uniaxial test is carried out on an electronic universal testing machine, and the clamping end of the specimen is clamped with a clamping fixture at a loading speed of 10mm/min, as shown in Figure 8.

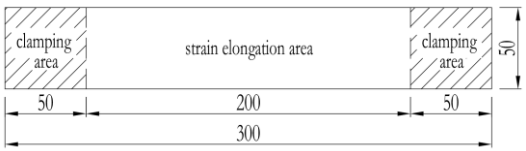


Figure 7. The size of uniaxial specimen

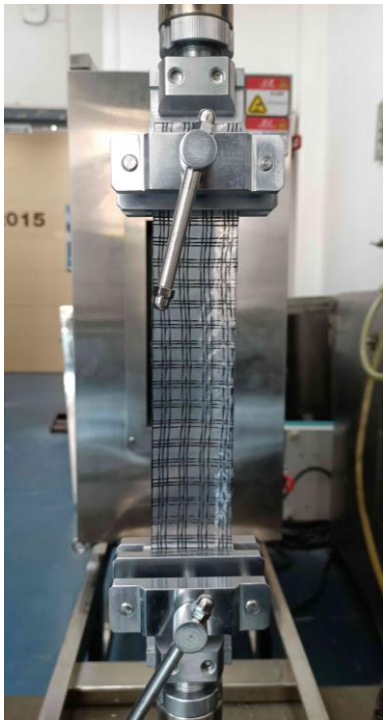


Figure 8. Uniaxial test

The biaxial test of STFE membrane uses a cross-shaped biaxial specimen with a core area of 160mm×160mm. The strain in the core area is measured by digital image correlation (DIC), and the tensile force of the warp and weft arms is measured in the clamping area to obtain the biaxial stress-strain curve. The biaxial test adopts a reciprocating loading system and performs five different ratios of longitudinal to transverse loading in turn: 1:1, 2:1, 1:2, 1:0, and 0:1. Before each loading, three 1:1 reciprocating loading cycle are conducted to eliminate strain. The stress and core area displacement field are measured and recorded in each formal loading. The loading speed of the high-stress side in the test is 10mm/min.

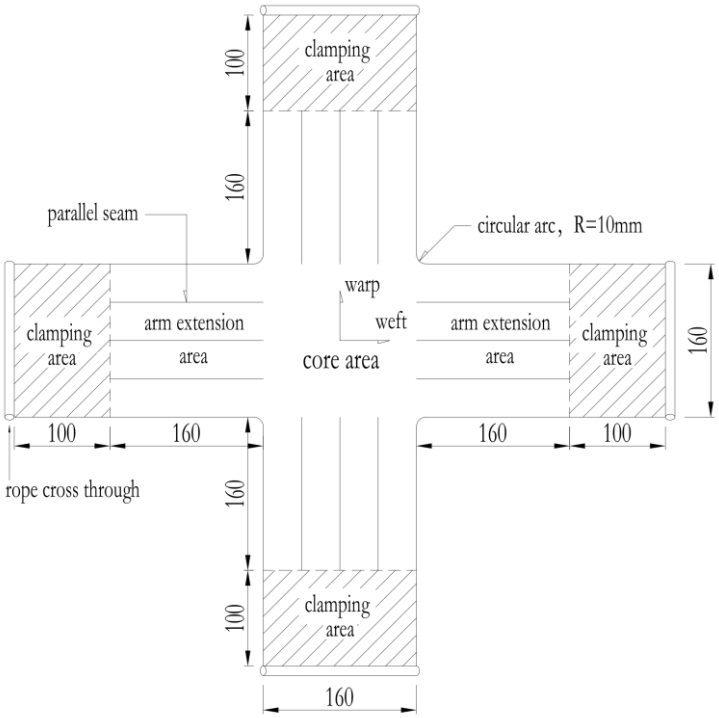


Figure 9. The size of biaxial specimen

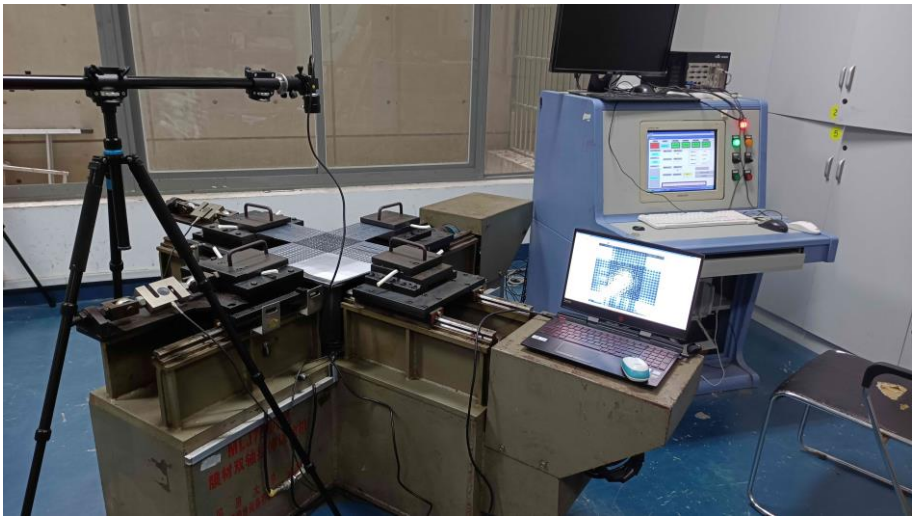


Figure 10. Biaxial test

4. The constitutive model of STFE

4.1 The uniaxial stress-strain model

From the uniaxial test, the uniaxial stress-strain curves of STFE membrane in the warp and weft directions can be obtained, as shown in Figure 11. The stress-strain curve in the warp direction is nonlinear, while that in the weft direction is linear. They are fitted with a quadratic polynomial and a linear function, respectively, as shown in equation (1), in the equation, σ_X is the stress in warp direction, σ_Y is the stress in weft direction, ε_X is the strain in warp direction, ε_Y is the strain in weft direction. In the stress-strain relationship in the warp direction, there are two material parameters a_1, a_2, while in the stress-strain relationship in the weft direction, there is only one linear material parameter b_1, These material parameters can be calibrated according to the test data, the fitting parameters are shown in table 1, and the fitted curves are also shown in Figure 11. It can be seen that the constitutive models of the quadratic function in the warp direction and the linear function in the weft direction have high fitting accuracy to the test results.

$$\begin{aligned} \sigma_X &= a_1 \cdot \varepsilon_X + a_2 \cdot \varepsilon_X^2 \\ \sigma_Y &= b_1 \cdot \varepsilon_Y \end{aligned} \tag{1}$$

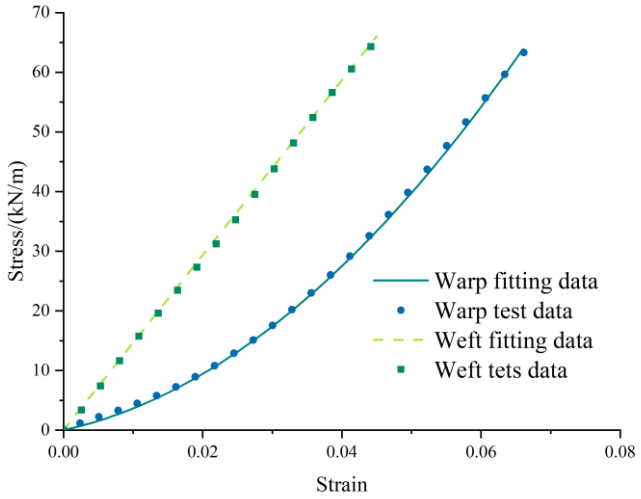


Figure 11. Uniaxial stress-strain curve

Table 1. The material parameters of uniaxial constitutive model

Direction	Linear parameter (a_1, b_1) (kN/m)	Non-linear parameter (a_1, b_1)(kN/m)
Warp	256	10780
Weft	1467	——

4.2 The linear biaxial stress-strain model

According to the current membrane structural design standards/specifications of most countries, the most commonly used mechanical model for coated fabric membrane materials is the in-plane orthotropic linear constitutive model. This mechanical model describes the biaxial stress-strain relationship in the warp and weft directions through the elastic modulus and Poisson's ratio in the warp and weft directions,

as well as their mutual influence under different stress ratios. The general formula for this type of mechanical model is shown in equation (2), where E_X denotes the warp elastic modulus, E_Y denotes the weft elastic modulus, v_X denotes the warp Poisson's ratio, v_Y denotes the weft Poisson's ratio, and the Poisson's ratio in the warp and weft directions satisfies the relationship in equation (3). By calculating the sum of squared strain residuals for the five curves, the biaxial mechanical model parameters (elastic moduli and Poisson's ratio) of the membrane material can be determined using the least squares method. The calibrated parameters are shown in table 2. The biaxial stress-strain test data in the warp and weft directions at various stress ratios are plotted on the same graph with the fitted curves, as shown in Figure 12 and 13. It can be seen that the weft test data is approximately linear and fits the mechanical model well, while the warp test data is nonlinear and has some deviation from the mechanical model.

$$\varepsilon_X = \frac{\sigma_X}{E_X} - \frac{\sigma_Y}{E_Y} v_Y \qquad (2)$$

$$\varepsilon_Y = \frac{\sigma_Y}{E_Y} - \frac{\sigma_X}{E_X} v_X$$

$$\frac{v_X}{E_X} = \frac{v_Y}{E_Y} \qquad (3)$$

Table 2. The material parameters of biaxial linear model

Direction	Elastic modulus (E_X, E_Y) (kN/m)	Poisson's ratio (v_X, v_Y)
Warp	1510	0.13
Weft	2350	0.20

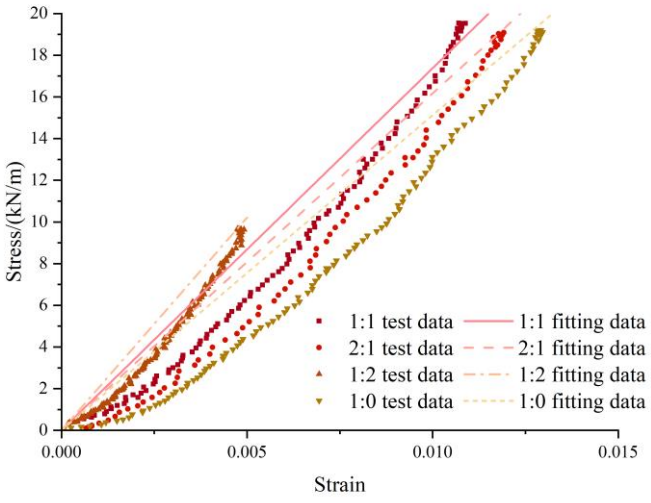


Figure 12. Biaxial stress-strain curve in warp direction with linear model

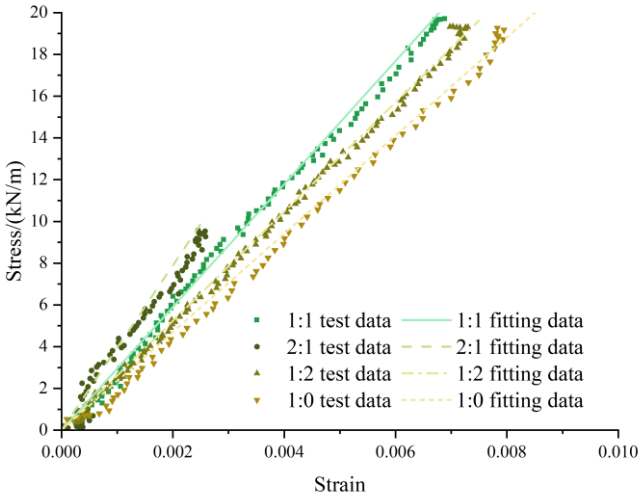


Figure 13. Biaxial stress-strain curve in weft direction with linear model

4.3 The non-linear biaxial stress-strain model

As mentioned in the previous section, the axial stress-strain curve of STFE membrane material is nonlinear at various loading ratios. In order to improve the model accuracy, a second-order term is introduced based on the linear orthogonal anisotropic constitutive model to describe the nonlinearity of the warp axial curve, as shown in equation (4). This mechanical model expresses stress as a function of strain, with material parameters (C values with subscripts) having the same unit as elastic modulus. The warp direction includes three material parameters: linear parameters C_{11}, C_{12} and nonlinear parameter C_{111}, while the weft direction includes two material parameters: C_{22} and C_{21}. By calculating the sum of the squared stress residuals for each curve and using the least squares method to calibrate the material parameters in the formula, the resulting data is recorded in Table 3. When the experimental data is plotted against the fitted curves in Figures 14 and 15, it can be seen that the nonlinear model fits the axial curve much more accurately than the linear model.

$$\begin{aligned} \sigma_X &= C_{11}\varepsilon_X + C_{12}\varepsilon_Y + C_{111}\varepsilon_X^2 \\ \sigma_Y &= C_{22}\varepsilon_Y + C_{21}\varepsilon_X \end{aligned} \tag{2}$$

Table 3. The material parameters of biaxial non-linear model

Direction	Parameter this side (C_{11}, C_{22}) (kN/m)	Parameter opposite side (C_{12}, C_{21}) (kN/m)	Second order Parameter (C_{111}) (kN/m)
Warp	693	572	65670
Weft	2352	251	——

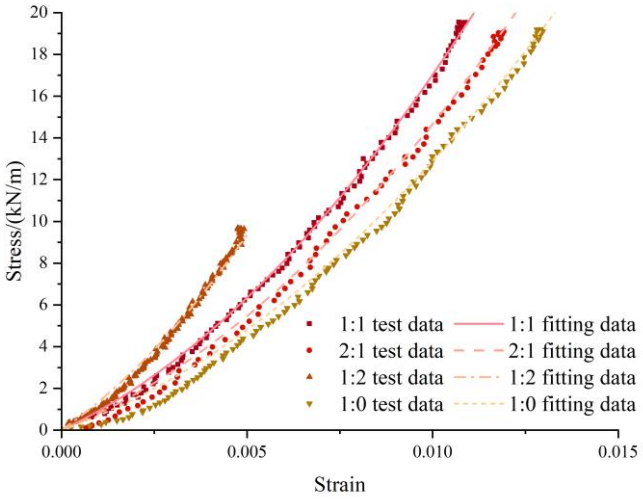


Figure 14. Biaxial stress-strain curve in warp direction with non-linear model

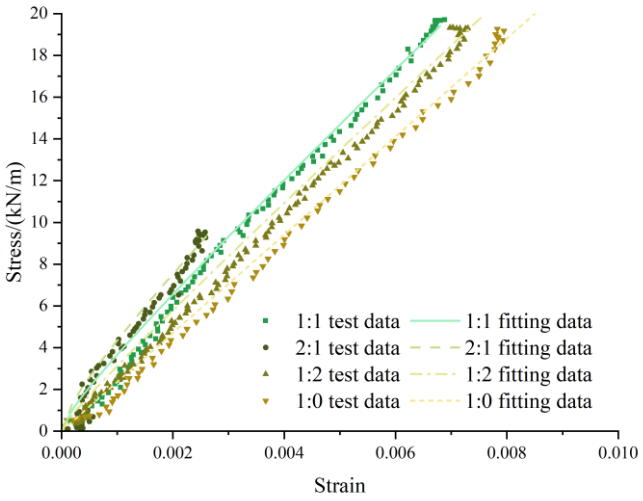


Figure 15. Biaxial stress-strain curve in weft direction with non-linear model

5. Comparison of elastic modulus between STFE and traditional membrane materials

As the most important parameter of the linear orthogonal anisotropic model, the elastic modulus approximately represents the ability of the membrane material to resist deformation in the warp and weft directions. A comparison of the elastic moduli of STFE membrane material with traditional membrane materials, including PVC, PTFE, ETFE, etc., is shown in Table 4. It can be seen that the elastic modulus of polyester fiber fabric membrane material is relatively low, while that of glass fiber fabric membrane material is relatively high. The elastic modulus of STFE membrane material is higher than these two, and the data for ETFE membrane material is taken as its tangent modulus. Compared with other materials, its elastic modulus is the lowest, less than 15% of that of STFE.

Table 4. The elastic modulus of different membrane materials

Direction	PVC membrane [2] (kN/m)	PTFE membrane [8] (kN/m)	STFE membrane (kN/m)	ETFE membrane [7] (kN/m)
Warp	730-917	1270	1510	223
Weft	565-714	866	2350	223

Compared with traditional building membrane materials, STFE membrane material has a higher elastic modulus, stronger in-plane resistance to deformation, a simpler form of stress-strain curve, and is more convenient to calculate in design, which is determined by the sparse arrangement and high strength characteristics of its fibers.

6. Conclusion:

This article conducted uniaxial and biaxial tensile tests on STFE membrane material, measuring the stress-strain curves in the warp and weft directions under uniaxial loading, and the stress-strain curves at different loading ratios under biaxial loading. Based on the test data, the uniaxial and biaxial constitutive mechanical models of STFE membrane material were established, and the parameters in the models were calibrated.

The test results showed that the stress-strain relationship in the warp direction of the STFE membrane material was nonlinear, while that in the weft direction was linear. The material had a high elastic modulus and good resistance to in-plane deformation, making it suitable for use in large-span tension membrane structures.

References

[1] Q. L. Zhang. Application review and future development of membrane structures in China[J]. Building Structure, 2019,49(19):55-64.

[2] B. Yang, Z. L. Yu, Q. L. Zhang, et al. The nonlinear orthotropic material model describing biaxial tensile behavior of PVC coated fabrics[J]. Composite Structures, 2020, 236: 111850.

[3] J. H. Xu,Y. Y. Zhang, M. Wu, et al. A phenomenological material model for PTFE coated fabrics[J]. Construction and Building Materials, 2020, 237: 117667.

[4] X. Peng, Z. Guo, T. Du, et al. A simple anisotropic hyperelastic constitutive model for textile fabrics with application to forming simulation[J]. Composites Part B: Engineering, 2013, 52: 275-281.

[5] Y. Yuan, Q. L. Zhang, R. J. Gu. A non-linear constitutive model describing uniaxial andbiaxial performance of PVC coated fabrics[C]. *Proceedings of IASS Annual Symposium 2022*, Beijing, China, September 19-22,2022.

[6] Standard for inspection of membrane structures: DG/TJ08-2019-2019 [S]. Shanghai: Tongji University Press,2020.

[7] M. E. WU, J. M. LIU, T. MU et al. Uniaxial tensile properties of ETFE foils[J]. Journal of Building Materials, 2008, 48(02):241-247.

[8] H. WANG. Study on Evaluation Methods for Fiberglass Fabric Architectural Membranes [J]. Fiber Glass, 2010, 235(06):18-25.

Proceedings of the IASS Annual Symposium 2023
Integration of Design and Fabrication
10–14 July 2023, Melbourne, Australia
Y.M. Xie, J. Burry, T.U. Lee and J. Ma (eds.)

The mechanical properties of membrane material STFE

Ruijie GU[a], Qilin ZHANG[a,*], Xiaoqun LUO[a], Ye YUAN[a]

[a,*] Dept. of Structural Engineering, College of Civil Engineering, Tongji University
No. 1239, Si Ping Rd. Shanghai 200092 P. R. China
zhangqilin@tongji.edu.cn

Abstract

STFE studied in this paper is a new kind of building membrane material, which is composed of polyarylate structural mesh with high tenacity yarn and transparent hybrid fluoropolymer film. Compared with fabric membrane materials, its non-tightly woven mesh makes STFE have better light transmission performance (53%); Compared with ETFE, the high tenacity polyester yarn grid provides a higher structural strength for STFE, making it suitable for tensile membrane structure. At present, there is no systematic experimental study on the mechanical properties of STFE membrane. In this paper, four mechanical properties of STFE are studied: The tensile strength of STFE membrane was measured by uniaxial tensile test based on winding method; The tearing strength of STFE membrane was measured by trapezoidal tearing method; The connection strength of STFE was measured by uniaxial tensile test; The creep of STFE within 24h was measured by uniaxial tensile test. On the basis of the above test data, STFE membrane materials are compared with traditional membrane materials, and the following conclusions are obtained: The tensile strength of STFE membrane is between that of traditional fabric material and ETFE material, while the tearing strength is higher than that of the above two types of materials; The butt joint of STFE is covered by black film. The connection strength is higher than the strength of base material. Therefore, the connection reliability is better than traditional membrane materials; The creep of STFE membrane is lower than that of the traditional membrane materials. This study shows that STFE membrane material has superior mechanical properties and can be an alternative material for membrane structure. Meanwhile, Material parameters given in this paper can provide reference for the design and application of membrane structure made of STFE.

Keywords: STFE, uniaxial tensile test, mechanical properties

1. Introduction

As a kind of spatial structure, membrane structure is favored by many architects and structural engineers due to its graceful architectural appearance and reliable structural system. Nowadays membrane structure is frequently used in large-scale public building such as stadiums, museums, airport terminals and railroad stations as shown in the Figure 1. Meanwhile, the development of membrane structure is inseparable from the innovation of membrane materials. There are two main categories of common membrane materials: one is coated fabric materials (e.g. PVC, PTFE, PVDF materials), which consist of bi-woven fibre substrate and self-cleaning coating; the other is polymeric membrane materials (e.g. ETFE materials). In terms of architectural performance, because of the poor light transmission performance of coated fabric materials, they do not meet the requirements of some building facades. In contrast, the light transmission rate of ETFE material is greater than 90%, which can meet the architects' requirements for light and landscape. However, ETFE is a single-layer polymer film, and its in-surface strength is much lower than that of coated fabric materials, so it is only applicable to inflatable membrane structures.

Copyright © 2023 by Ruijie GU, Qilin ZHANG, Xiaoqun LUO and Ye YUAN. Published in the Proceedings of the IASS Annual Symposium 2023 with permission.



(a) Shanghai Stadium (PTFE) (b) National Aquatics Center (ETFE)

Figure 1. Famous membrane structures

As shown in Figure 2. STFE membrane material (Structural Transparent Fluorinated Envelope) is a new type of architectural membrane material produced by Serge Ferrari, which is composed of polyarylate structural mesh with high tenacity yarn and transparent hybrid fluoropolymer film. Specifically, the structural mesh of STFE is made in groups of three fibres, with each group of fibres staggered along both warp and weft directions. The fibres are arranged symmetrically along the warp direction and anti-symmetrically along the weft direction which is shown in Figure 3. The center distance between two adjacent fibre groups is about 12.5mm, and the fibre spacing within the group is about 2mm.

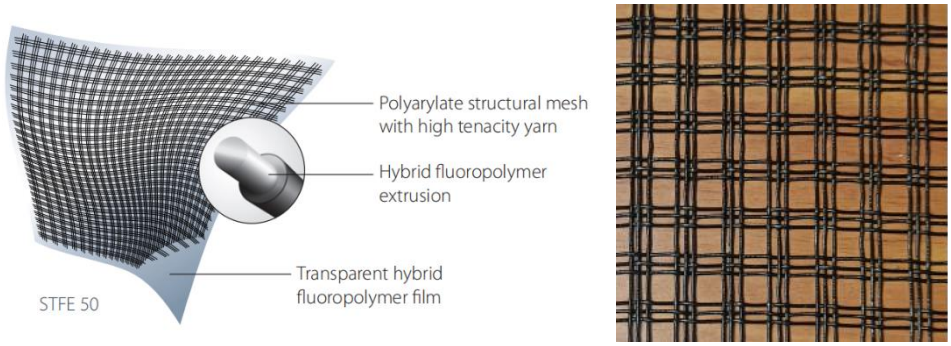


Figure 2. STFE membrane material

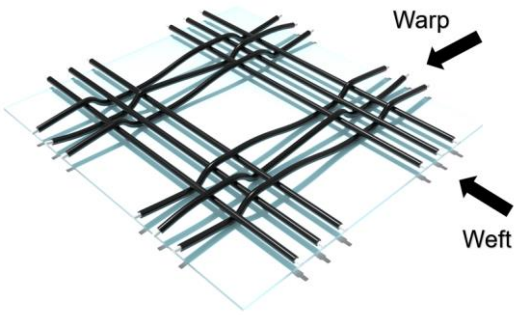


Figure 3. Microstructure diagram of STFE

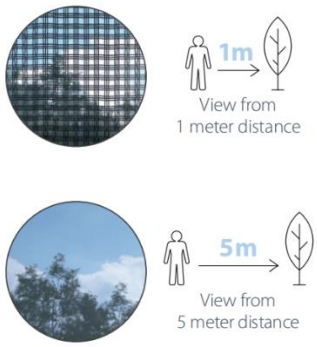


Figure 4. Visual performance of STFE

STFE uses non-tightly woven mesh instead of the dense weave of traditional coated fabric material. However, the strength of its single fibre is high enough, the global in-plane strength is sufficient to

ensure its application in tensioned membrane structures. In the light transmission performance test, the light transmission rate of STFE membrane is greater than 53%, which is a significant improvement compared to traditional coated fabric membrane materials. At the same time, though the black fiber groups on the surface of the STFE can be seen from a distance of 1m, this blocking field of view no longer occurs when the distance is extended to 5m and above as shown in Figure 4. In terms of structural and architectural performance, STFE is a new type of membrane material with superior performance. At present, STFE has been applied in some projects. As shown in Figure 5, the outer courtyard of the Royal Orthopaedic Hospital and the crosswalks of Istanbul Airport both use STFE as the membrane structure material.



(a) Royal Orthopaedic Hospital (b) The crosswalks of Istanbul Airport

Figure 5. Application projects of STFE

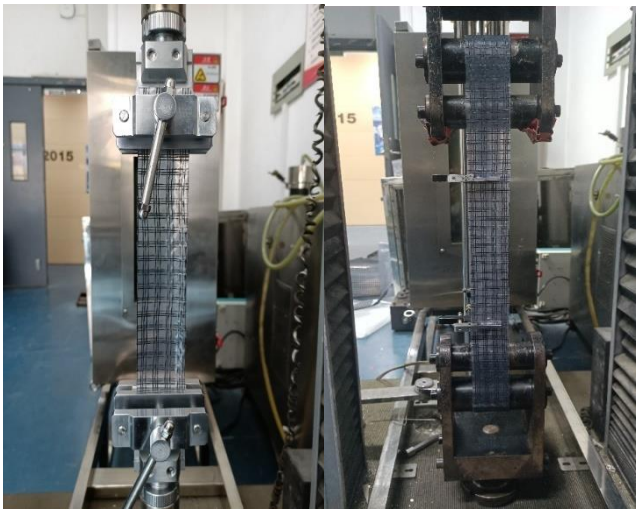
Nowadays, numerous test methods have been proposed for fabric and polymeric membrane materials. However, the mechanical properties of STFE membranes have not yet been systematically studied by scholars in the field of membrane structures. It is essential to provide standard test methods and material mechanical parameters for projects designed with STFE. Therefore, in this paper, four mechanical properties of STFE and the parameters are investigated: 1) tensile strength of STFE 2) tearing strength of STFE 3) connection strength of STFE 4) creep properties of STFE. The test method in this paper is based on the traditional test method for coated fabric membrane materials in Standard for inspection of membrane structures (DG/TJ08-2019), with some improvements to the sampling and test method based on the unique characteristics of STFE material. The test data are obtained under the adjusted test methods, different test methods may lead to some deviations from the test results.

2. Tensile strength

Tensile strength is an important parameter of the in-plane strength of membrane materials. Uniaxial tensile tests are commonly used to determine the tensile strength of traditional fabric and ETFE membrane materials [1–3]. Some scholars also proposed the use of biaxial tensile test to determine the tensile strength of membrane materials. Even though the biaxial tensile test reflects the actual force conditions of membrane materials in engineering better, the failure usually occurs at the edge of the cross specimens, so the accuracy of biaxial test is lower [4].

In this paper, the uniaxial tensile test method is used to determine the tensile strength of STFE. As shown in Figure 6, there are two different test method according to the types of holders: winding method and clamping method. The winding method fixes the specimen on the uniaxial tensile apparatus by the friction between the specimen and the holders, while the clamping method fixes the specimen by the gripping force of the holders. The advantages of the clamping method are easy operation and low material consumption. However, due to the stress concentration effect, specimen fracture often occurs at the edge of holders, so that the tensile strength of the material is underestimated. On the contrary, the stress of specimen fixed by winding holders is more uniform, which leads to more accurate tensile strength of the material. The disadvantage of winding method is the high material consumption and is

more complicated to operate. On balance, the winding method was chosen for the study to guarantee the accuracy of test results.



(a) clamping method (b) winding method

Figure 6. Uniaxial tensile strength test

For traditional coated fabric membrane materials, the tensile strength is mostly tested on long specimens of 50±0.5mm width and 300±1mm length (50mm on both sides of the gripper zone + 200mm in the core measurement zone), while for ETFE membrane materials, in consideration of the effect of stress concentration in the gripper, dumbbell-shaped specimens are often used. The strength of STFE membranes is mainly provided by the structural mesh with high tenacity yarn, from which the fibre groups should not be cut through during sampling to compromise the membrane strength. Therefore, it is necessary to ensure that the specimen has enough intact fibre groups during the sampling process. In the actual sampling, 4 groups of fibres are taken in the width direction and the width of the specimen is 50±0.5mm. Due to the selection of winding method, enough length need to be left at both sides to ensure that the size of the friction surface is sufficient to fix the specimen in the test, and the actual length was taken as 1200±5mm (500mm on both sides + 200mm in the core measurement zone). The specimen of tensile strength test is shown in Figure 7.

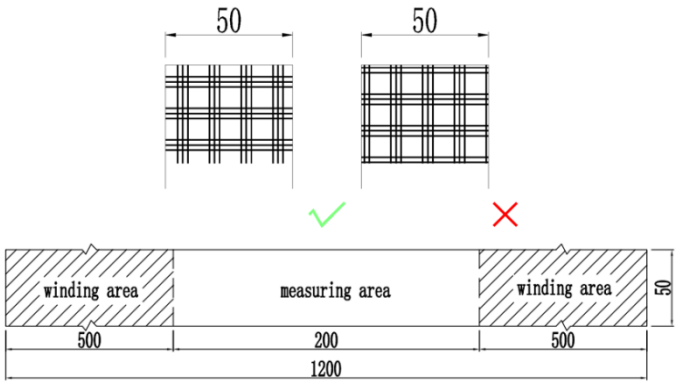


Figure 7. Specimen of tensile strength test

The experiments were carried out at a temperature of (20±2) ℃ and a relative humidity of (65±4) %. A uniaxial tensile test machine and an extensometer was used for recording the load and displacement

of the specimen. At the beginning of the experiment, the specimen was first tensioned to a pre-tension of 10N, and then stretched at a constant rate of 100mm/min until the specimen fractured. When the specimen fractures, if the fracture position is in the middle of the specimen, it is regarded as a valid result. If the specimen slips or the fracture does not occur in the core measurement area during the loading process, it is regarded as an invalid result and the test value of the specimen is discarded. In this test, five valid values were obtained in the warp and weft directions for the calculation of tensile strength. The elongation after fracture was determined based on the deformation of the core area measured by the extensometer.

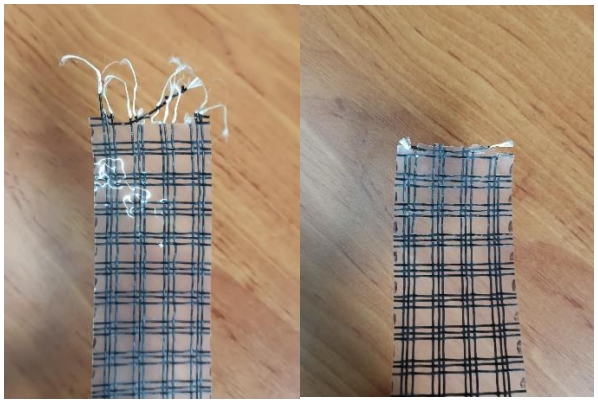


Figure 8. Two damage modes of STFE tensile test

According to the Figure 8, two damage modes were shown in the test of STFE: one is the longitudinal fibre fracture with a relatively straight fracture surface, which occurs relatively quickly and belongs to the brittle damage; under the other condition, firstly the longitudinal fluoropolymer coating yarn is pulled out from the black fibre shell, then the fracture of yarn leads to the damage of material, in which damage process is relatively slow. The main reason for the occurrence of the two damage modes may depend on whether the internal yarn is reliably connected with the fibre shell.

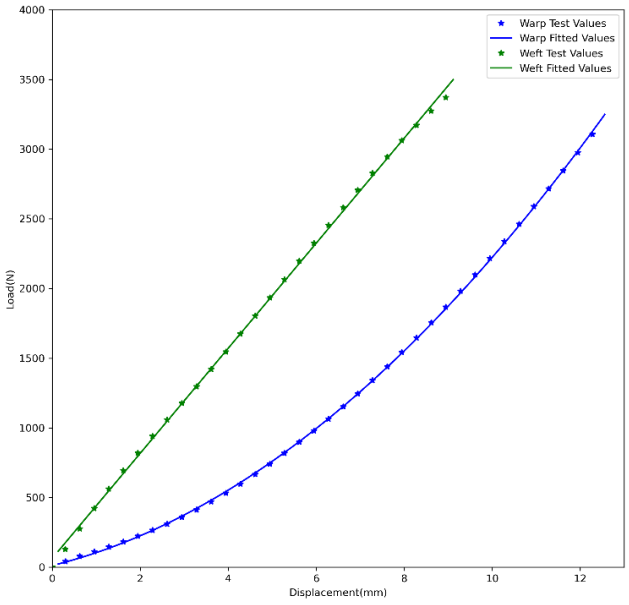


Figure 9. Uniaxial load-displacement curves of STFE

The uniaxial load-displacement curves of STFE in both warp and weft directions were obtained in this test. As shown in the Figure 9, STFE material is anisotropic. Nonlinear performance is obvious in the

warp direction under lower loads. With the loading process, the stiffness gradually increases and nonlinearity gradually decreases; while the material shows linear performance in the weft direction.

After calculation, the tensile strength of STFE is about 3136.42N/5cm in the warp direction and 4243.31N/5cm in the weft direction. The elongation rate after fracture is about 3.5%-4% in the warp direction and 3.0%-3.5% in the weft direction. The tensile strength of STFE in the weft direction is significantly higher than that of the warp direction, while the elongation rate after fracture in the weft direction is lower than that of the warp direction.

Compared with traditional materials, the tensile strength of STFE is slightly lower than that of coated fabric membrane materials such as PVC, PTFE, while higher than that of ETFE materials. The elongation rate after fracture is much lower than that of traditional coated fabric and ETFE materials. The data is shown in the Table 2, PVC material of Ferrari 1202T2, Ferrari 1002T are tested by Yang Li [5], PTFE material is tested by Tengfei Wang [6], and the data of ETFE is provided by Minger Wu [7].

Table 1. Results of STFE tensile strength test

Tensile strength (warp) N/5cm	3318.07	3159.35	3242.43	2868.33	3093.91
Tensile strength (weft) N/5cm	4207.69	4584.62	3579.10	4337.75	4507.37
Elongation rate (warp)	4.01%	3.46%	3.81%	3.75%	3.46%
Elongation rate (weft)	3.17%	3.34%	3.19%	3.32%	3.28%

Table 2. Comparison of tensile strength among different membrane materials

Material	STFE	PVC (1202T2)	PVC (1002T)	PTFE	ETFE
Tensile strength (warp) N/5cm	3136.42	5269	4125	5231.50	600-900
Tensile strength (weft) N/5cm	4243.31	5174	4485	4127.50	600-900
Elongation rate (warp)	3.70	22.41	20.91	5.86	400
Elongation rate (weft)	3.26	23.06	20.59	7.92	400

3. Tearing strength

Tearing failure is a common damage mode of membrane structure. At present, there are several test methods for tearing performance of membrane material based on previous research: single tongue tearing method, double tongue tearing method, trapezoidal tearing method, center tearing method. The tearing strength obtained by the trapezoidal tear method are more stable, so the trapezoidal tear method was used in this study to determine the tearing strength of STFE membrane materials.

As shown in Figure 10, the size of the specimens and the crack are based on the Standard for inspection of membrane structures (DG/TJ08-2019). The specimens are in the form of long strips, and the length direction of the cut specimens should be parallel to the warp or weft direction of the membrane. The width of each specimen is (50±0.5) mm and the length is (180±1) mm, in which the middle tearing area is isosceles trapezoid, the upper bottom is 50 mm wide, the two waists are clamping lines, and the angle between the clamping lines and the length direction is 75°. The incision starts from the center of the upper bottom and the length of the incision is (25 ± 0.5) mm. In order to ensure the stable of the tearing experiment, the end of the incision should be required in the position of the film instead of the middle of a group of fibres, Also, the lower part of the incision should be left with two groups of parallel fibres.

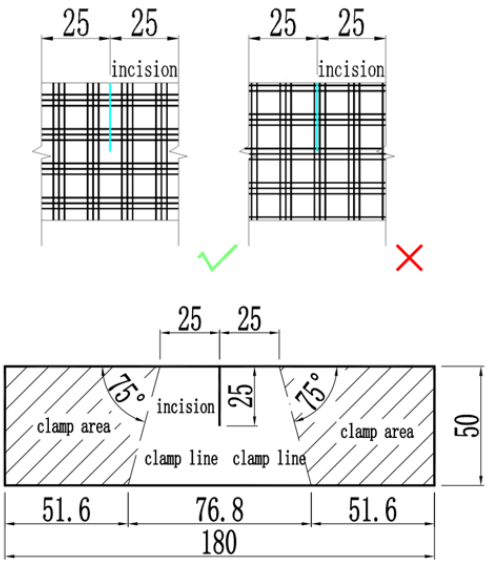


Figure 10. Specimen of tearing strength test

The experiment was carried out at the temperature of (20±2) ℃ and the relative humidity of (65±4) %. Before the test begins, keeping the short side of the trapezoid tensioned and the long side in a creased state, as shown in Figure 11. After the test begins, the specimen is stretched at a constant rate of 100 mm/min. If the specimen is torn along the middle incision direction, it is regarded as a valid result, while the specimen is not torn along the middle incision direction or slipped out of the jaws, it is regarded as an invalid result and the test value of the specimen is discarded. The processing of the test is shown in Figure 11.



(a) Before the test begins (b) After the test begins

Figure 11. The processing of tearing strength test

The processing of tearing failure starts with the film tearing along the incision line, then the crack quickly spreads to the fibre nearest to the incision. With the fibre gradually stressed, it slowly fractures

or its yarn is extracted. The tearing of film continues and spreads to the next fibres until all fibres are destroyed. Below the incision line, there are two intact fibre groups, each containing three fibres. Therefore, during the tearing process, six fibres are damaged in sequence. As shown in Figure 12, the tearing load-displacement curve shows a six-wave peak pattern in two regions.

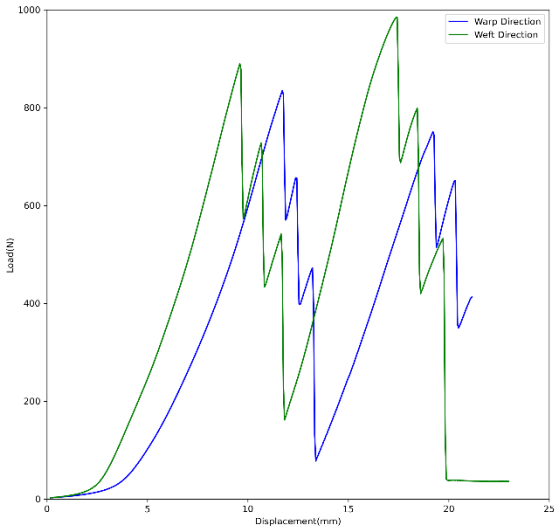


Figure 12. Tearing load-displacement curves of STFE

Based on the load-displacement curves of STFE specimens, this paper suggests using the mean value of six peaks to characterize the tearing strength of STFE. Seven groups in the warp direction and six groups in the weft direction are obtained. The tearing strength is 645.68 N in the warp direction and 754.96 N in the weft direction. The tearing strength in the warp direction was slightly lower than that in the weft direction, which is consistent with the conclusion of tensile strength.

Table 3. Results of STFE tearing strength test

Tearing strength (warp) N/5cm	629.64	623.78	695.42	616.13	640.70
	637.58	676.50			
Tearing strength (weft) N/5cm	714.73	760.25	745.69	772.12	707.28
	829.71				

Table 4. Comparison of tearing strength among different membrane materials

Material	STFE	PVC	PTFE (FGT-800)
Tearing strength (warp) N/5cm	645.68	552	418
Tearing strength (weft) N/5cm	754.96	540	407

From the Table 4, it can be seen that the tearing strength of STFE is higher than that of traditional coated fabric material. This result is reasonable since the tearing strength depends mainly on the local strength of individual fibres rather than the global strength of the material. The high tenacity polyarylate yarn used in STFE is stronger than glass fibre or polyester fibre used in traditional coated fabric material.

Compared to ETFE, the local tearing strength of its single-layer polymer structure is much lower than that of STFE. The data of PVC is provided by Han Bao [8] and PTFE is provided by Yaqin Wang [9].

4. Connection strength

Due to the limitation of material processing size, multiple pieces of STFE should be spliced together for membrane structures. A reliable connection strength is necessary for the construction of membrane structures. In this study, the connection strength of butt-joint of STFE is investigated experimentally. The STFE butt-joint are constructed by welding the fibre at both ends with a black covering film added, as shown in Figure 13, which can effectively protect the connection nodes, enhance the durability and make the appearance more attractive.

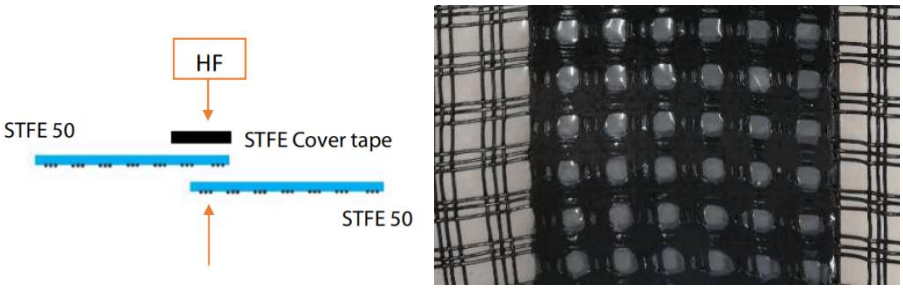


Figure 13. Butt-joint of STFE

The experiment was carried out at the temperature of (20±2)℃ and the relative humidity of (65±4)%. Samples are taken in long strips as shown in Fig. 14. Each specimen consists of two short samples. The width of short samples is (50 ± 0.5) mm and the length is (175 ± 1.0) mm. The length of connection area is (50 ± 0.5) mm and the total length of the specimen is (300 ± 1.0) mm. The samples should be cut parallel to the warp direction and through the center of the two adjacent groups of fibres.

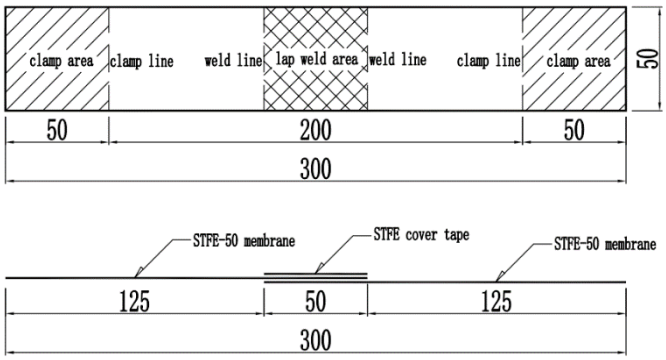


Figure 14. Specimen of connection strength test

After the test begins, the specimen is stretched at a constant rate of 100 mm/min. As a matter of fact, the failure of the specimen takes place in the junction of welding and non-welding area shown in Figure 15, which means the connection strength of STFE is higher than tensile strength. The conclusion is also confirmed by the test data which is shown in Table 5. The calculation check is unnecessary for the design of membrane structures made of STFE.

Table 5. Results of STFE connection strength test

Connection strength (warp) N/5cm	3744.67	3680.38	3288.26	3155.44	3423.01
	3423.01	3129.42	3414.35	2932.75	2688.90

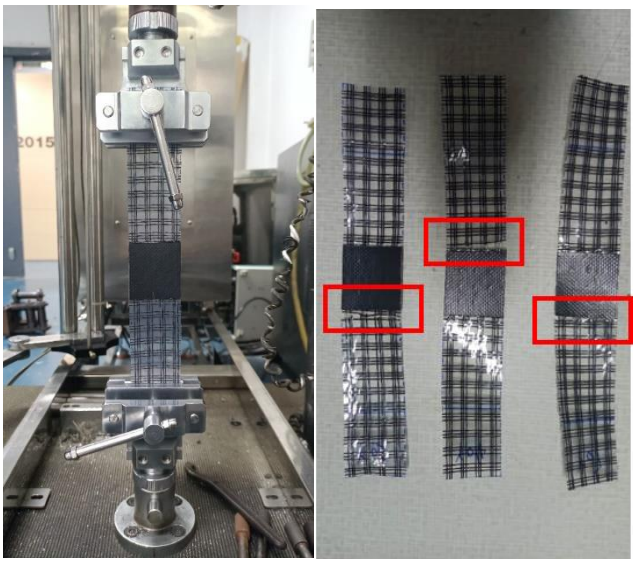


Figure 15. The connection strength test

5. Creep performance

The creep of membrane materials refers that the deformation of membrane materials gradually increases while the holding force remains constant over a long period of time. In project applications, the creep of membrane materials may lead to slackening or deformation of the membrane surface, so it is necessary to determine the creep elongation of membrane materials. Both traditional coated fabric materials and ETFE have the effect of creep. In general, the creep elongation of ETFE membranes is greater than that of coated fabric materials. The main influencing factors of creep include the type of material, temperature, holding force, etc. In this paper, based on the Standard for inspection of membrane structures (DG/TJ08-2019), the creep performance of STFE material at room temperature for 24h at 1/4 tensile strength is tested.

The size of specimen is exactly the same as the specimen for tearing strength test without incision. The experiments were conducted under the conditions of temperature (20±2) ℃ and relative humidity (65 ±4) %. After the experiment started, the specimen was stretched to 1/4 tensile strength at a stretching rate of 100 mm/min, after which the constant tension was maintained for 24 h. The distance between the two clamps at the beginning of the application of constant tension and at the end of the application is recorded. The creep elongation is calculated following the formula shown below:

$$\varepsilon_{cf} = \frac{L_2 - L_1}{L_0} \tag{1.}$$

L_2: Distance between two clamps at the end of constant tension application (mm).

L_1: Distance between two clamps at the beginning of constant tension application (mm).

L_0: Length of spacing, $L_0 = 200mm$.

ε_{cf}: Creep elongation.

As shown in Fig. 16, the creep time-strain curve indicates that the warp creep elongation is slightly higher than the weft creep elongation, which is consistent with the results of the fracture elongation rate. The test data is shown in Table 6, the absolute creep elongation in the warp direction is 0.85%, and the creep in the weft direction is 0.73%.

Compared to traditional coated fabric materials, the creep elongation of STFE is close to that of PVC in the warp direction (the higher creep elongation of STFE in the Table 7 is due to the higher stress), while

lower than PVC in the weft direction. Compared to ETFE, STFE has a much lower creep elongation in both directions than ETFE. In conclusion, STFE has better creep performance than traditional membrane materials. The data of PVC is provided by Yucong Yin [10] and the data of ETFE is provided by Minger Wu [11].

Table 6. Results of STFE creep test

Creep elongation (warp)	L_1 (mm)	4.72	4.51	4.56	4.78	5.30
	L_2 (mm)	6.47	6.07	6.30	6.37	7.14
	ε_{cf}	0.88%	0.78%	0.87%	0.80%	0.92%
Creep elongation (weft)	L_1 (mm)	3.52	3.87	3.49	3.68	3.81
	L_2 (mm)	5.00	5.29	5.10	5.17	5.14
	ε_{cf}	0.74%	0.71%	0.80%	0.75%	0.67%

Table 7. Comparison of creep elongation among different membrane materials

Material	STFE (20kN/m)	PVC (12kN/m)	ETFE (2.7kN/m)
Creep elongation (warp)	0.85%	0.38%	2.24%
Creep elongation (weft)	0.73%	1.30%	2.24%

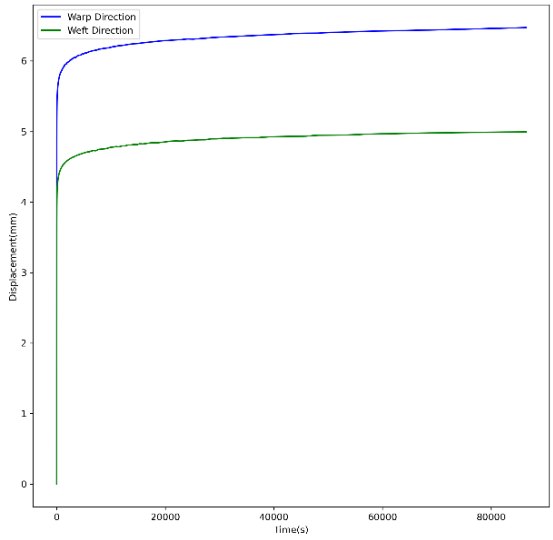


Fig. 16. Creep time-displacement curves of STFE

6. Conclusion

1) The tensile strength of STFE membrane is between that of traditional coated fabric material and ETFE material, while the tearing strength is higher than that of the above two types of materials.

2) The butt-joint connection strength of STFE is higher than the strength of base material. Therefore, the connection reliability is better than traditional membrane materials.

3) STFE has better creep performance than traditional membrane materials.

Acknowledgements

The author is grateful to Serge Ferrari who gave material STFE for the above tests.

References

[1] Mollaert M, Forster B. European design guide for tensile surface structures[M]. TensiNet, 2004.

[2] MSAJ (Membrane Structures Association of Japan). Testing method for elastic constants of membrane materials[J]. 1995.

[3] DG/TJ 08-2019-2019, Membrane Structure Testing Technical Regulations, Tongji University, Shanghai, 2020.

[4] T.B. Shi, W.J. Chen, C.J. Gao, J.H. Hu, B. Zhao, P.A. Wang, M. Wang, Biaxial constitutive relationship and strength criterion of composite fabric for airship structures, Compos. Struct. 214 (2019) 379–389, http://dx.doi.org/10.1016/j.compstruct.2019.02.028.

[5] Y. Li, Study and applications on mechanical properties of membrane materials and structures[D]. Tongji University, 2007.

[6] T. F. Wang, Research on the tensile and tearing properties of architectural coated fabric[D]. Harbin Institute of Technology, 2018.

[7] M. E. Wu. ETFE foil for architecture [J]. World Architecture, 2009(10):104-105.

[8] H. Bao, X. B. Zhang, M. E. Wu. Experimental study on tearing behavior of PVC coated polyester fibre membrane[J]. Journal of Building Materials, 2020,23(03):631-641.

[9] Y. Q. Wang, Experimental study on mechanical properties of PTFE membrane[D]. Tongji University, 2009.

[10] Y. C. Yin. PVC creep properties of PVC coated fabric [D]. Ludong University, 2022.

[11] M. E. Wu, T. Mu, J. M. Liu. Cycle loading and creep tests of ETFE foil[J]. Journal of Building Materials, 2008,11(06):690-694.

Proceedings of the IASS Annual Symposium 2023
Integration of Design and Fabrication
10–14 July 2023, Melbourne, Australia
Y.M. Xie, J. Burry, T.U. Lee and J. Ma (eds.)

The roof structure design of the professional football stadium of Chengdu phoenix mountain sports center

Yuan FENG[a,*], Tian QIU[a], Liwei WANG[a], Yan ZHANG[a], Xin An XIANG[a]

[a,*] China Southwest Architectural Design and Research Institute Corp., LTD
866 Tianfu Avenue North Section, Chengdu, China
xnyfy@vip.163.com

Abstract

The professional football stadium of Chengdu Phoenix Mountain Sports Center will host the 31st World University Games in 2023. The number of seats designed for professional football stadiums has reached 60000. The stadium roof is about 279 meters long in the north-south direction and 234 meters long in the east-west direction. The maximum overhanging length of the roof is 64 meters. The roof covering material is ETFE membrane material in the inner circle area and metal material in the outer circle area. An attempt was made to use a cable dome structure in a non enclosed roof in a football stadium. By using an inner ring steel truss at the edge of the central large opening, the weakening of the stiffness and integrity of the cable dome structure due to the large opening is compensated, ensuring the effective transmission of the force system of the tension structure. The practice of this project has expanded the application scope of cable dome structures to achieve lightweight and unique architectural effects. This article introduces the selection of the roof structure in detail, explains how the structure can be efficiently, economically, and aesthetically implemented, and ultimately completes the structural expression of the architectural form.

Keywords: large opening, rigid inner ring, cable dome, parametric analysis, anti-continuous collapse

1. Project overview

The Chengdu Phoenix Mountain Sports Center project was designed in 2019 and completed in February 2021. The project includes a 60000 seat football stadium and a 18000 seat comprehensive stadium. The project is located in the northern new city of Jinniu District, Chengdu, China, about 12 kilometers from the center of Chengdu.

The professional football stadium is located on the south side of the base, with a two-storey grandstand and a one-storey box, which can host large-scale football matches and large-scale performance activities. The total aboveground construction area of football stadium is 123500 square meters, and the total height of the building is 64.000 meters; The comprehensive stadium is located on the north side of the base, with a two-storey grandstand and a two-storey box. It can host different types of competitions such as basketball, ice hockey, badminton, gymnastics, and meet functional requirements such as performing arts, conferences, and exhibitions. The total aboveground building area of the building is 83200 square meters, and the total building height is 51.4m.

Copyright © 2023 by Yuan FENG, Tian QIU, Liwei WANG, Yan ZHANG and Xin An XIANG. Published in the Proceedings of the IASS Annual Symposium 2023 with permission.

(a) (b)

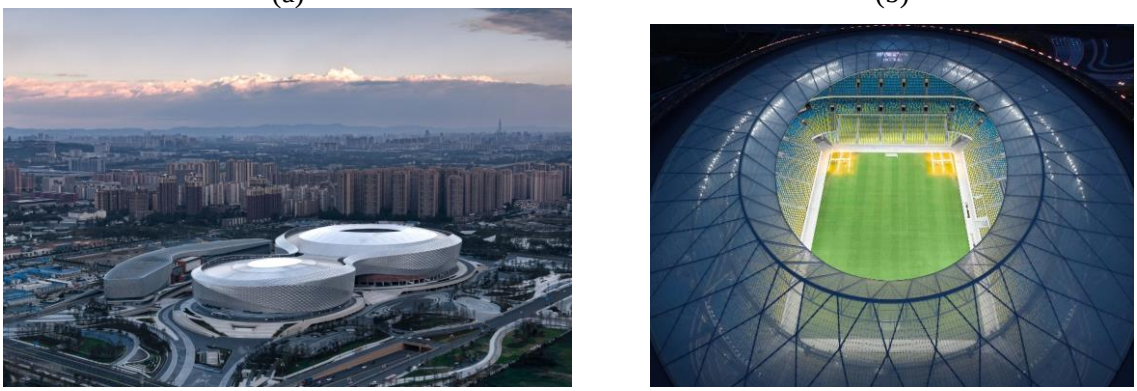


Figure 1. Chengdu Phoenix Mountain Sports Center: (a) aerial view of completed project, (b) night view of football stadium

Through two structural seams, the professional football stadium, the comprehensive stadium, and the Tianfu Club, which connects the football field and the stadium, are divided into three independent structural seismic units above the ground, ensuring that each part of the structure has reasonable dynamic characteristics and seismic capacity, while reducing the impact of temperature on the structure. After dividing the structural units, the structural units of the professional football stadium have a total length of 202m in the east-west direction and a total width of 242m in the north-south direction above the 7m platform. A typical structural layout plan is shown in Figure 2(a); The overall length of the comprehensive stadium structural unit above the 7m platform from east to west is 142m, and the total width in the north-south direction is 167m. The typical structural layout plan is shown in Figure 2(b).

(a) (b)

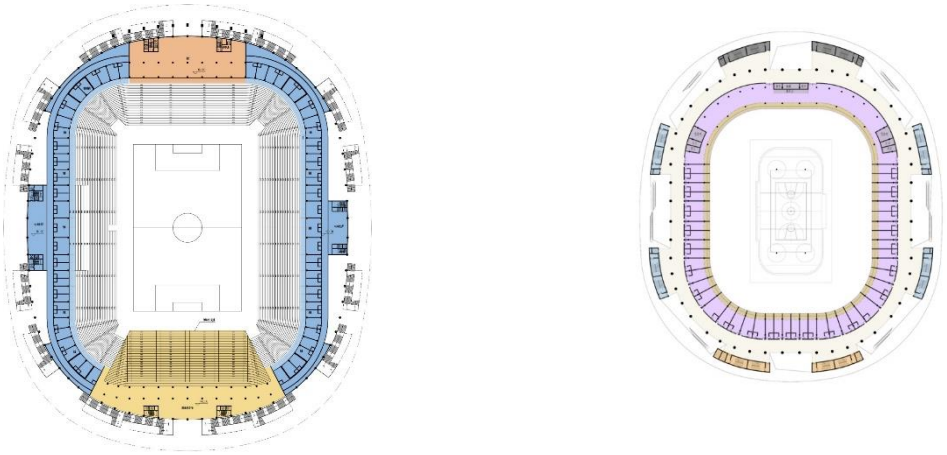


Figure 2. layout plan of Chengdu Phoenix Mountain Sports Center structure: (a) typical layout plan of football stadium, (b) typical layout plan of stadium

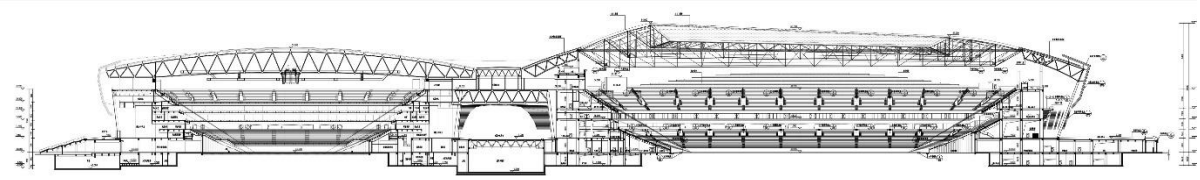


Figure 3. Overall profile of Chengdu Phoenix Mountain Sports Center

2. Architectural characteristics

2.1. Irregular shape of the roof

For structural design, concise and symmetrical shapes tend to be more uniformly stressed, and have better static and dynamic performance. Especially for large span spatial structures, the symmetrical shape allows the structure to adopt a symmetrical layout, simplifying the design difficulty of the main structure. The architectural design scheme of this project is novel. The overall shape of the roof is inclined, with a north-south inclination and an angle of about 2.5 ° with the horizontal plane. The projection of the roof shape is oval like, symmetrical from east to west, but asymmetric from north to south. The overall shape is high in the north and low in the south, with a gradient shape. The irregular shape has brought certain difficulties to the structural design of the project.

(a) (b)

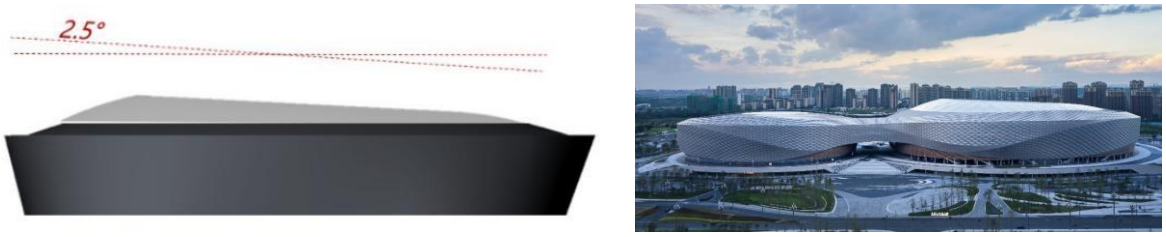


Figure 4. roof form: (a) schematic diagram of the north-south inclination of the football field roof, (b) elevation drawing of building project

2.2. Various roof covering materials

When designing the covering material for the roof, the architect chose two materials, one is traditional metal covering material, and the other is membrane material with high permeability. Choosing a transparent and lightweight membrane material as the covering material not only reduces the load and reduces the impact on the main structure, but also facilitates the maintenance and maintenance of high-quality lawns with a transparent and lightweight roof. Combined with the metal roof on the periphery, it can completely illuminate the lawn surface while avoiding the main stand from being exposed to sunlight, ensuring the audience's watching experience. Due to the different characteristics of the covering materials, it will have an impact on the selection of the main structure. Metal roof construction is convenient, with strong modeling ability and rich colors, but the overall load is large and cannot adapt to the large deformation of the main structure. Therefore, the main structure often adopts rigid systems, such as rigid trusses. The construction of membrane roofing is relatively difficult and its modeling ability is not strong, but the overall load is small and can adapt to large deformation of the main structure. Therefore, flexible systems such as cable trusses or rigid systems such as trusses can be selected for the main structure. The construction of this project adopts metal roofing and membrane roofing, which puts forward higher requirements for structural selection. Whether to adopt a simple rigid system, a flexible structural system, or a hybrid system of rigidity and flexibility is a question that needs to be considered in the design phase of the structure.

(a) (b)



Figure 5. Roof covering membrane material: (a) sunlight transmission film material, (b) interior drawing of construction project

2.3. Non enclosed roof

Unlike buildings such as stadiums and natatoriums, football stadiums often have large openings in the middle of the roof due to their architectural functions and audience line of sight. The size of the openings is close to or even exceeds half the length or width of the structure. How to give full play to the spatial performance of the structure with large openings is also a problem that structural engineers need to consider at the beginning of the scheme. At the same time, the project has designed 60000 audience seats. In order to meet the seating requirements, the overhang length of the roof has finally reached 64m. How to achieve the overhang economically and efficiently poses a challenge for structural engineers.

(a) (b)



Figure 6. Non enclosed roof: (a) top view of building project, (b) roof opening size

2.4. The position of the column grid does not correspond to the shape of the roof

The grandstand design of this project not only meets the requirements of FIFA, but also combines with China's security operation strategy, and tries to shorten the distance between the grandstand and the stadium to improve the proportion of high-quality grandstands. The grandstand design of the project is in a square and rounded shape, so the column network of the structure is closely related to the circumferential shape of the grandstand, and has an equidistant offset relationship with the edge line of the grandstand. However, the projection of the project roof shape is similar to an oval shape (red line in Figure 7), resulting in a problem of inconsistency between the structure column grid connection line (blue line in Figure 7) and the roof structure shape.

(a) (b)

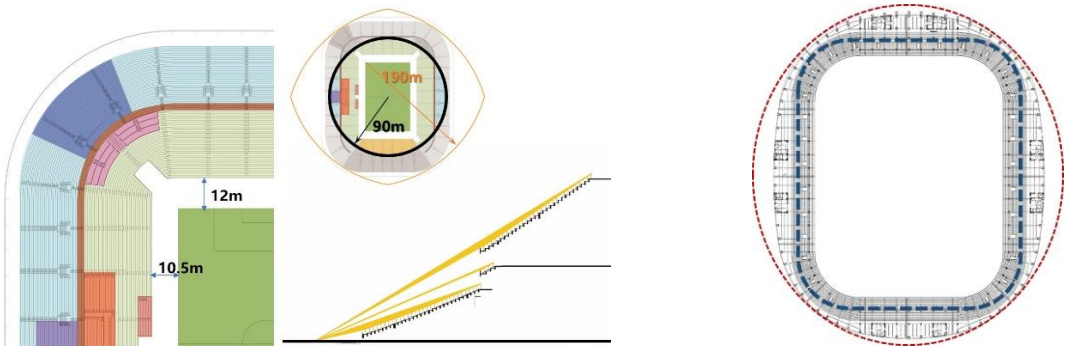


Figure 7. Stand column network relationship: (a) stand form, (b) column grid and roof form

3. Roof structure selection

Based on the architectural characteristics of the project, the roof structure system of the project should meet the requirements of safety, rationality, aesthetics, applicability, and economy. When seeing that

the roof covering material of the building roof is membrane material, the first thought of structural engineers is to use a flexible cable structure system. The most classic of cable structure system is the large opening spoke cable truss structure system[1]. The upper and lower inner ring steel cables of this structural system connect the radially arranged open web cable trusses together (as shown in Figure 8). The structural system has the following characteristics: 1) The planar cable truss is connected as a whole through inner ring cables to form a spatial stable system; 2) There are few structural members and a large number of members are tension cables, while a small number of members are compression members; 3) Structural stiffness is provided by prestress[2]; 4) The structure has a mechanical displacement mode, but can become a geometrically stable system under the action of prestress. However, with the increase of the cantilever length, in order to ensure the structural stress efficiency, the distance between the upper and lower chords at the cantilever end of the cable truss increases, and the height of the compression brace is high, causing certain design difficulties and easily affecting the audience's visual field. Especially in this project, as the structural overhang reaches 64m, if a cable truss structure is adopted, it will affect the audience's view of the game (as shown in Figure 8(b)).

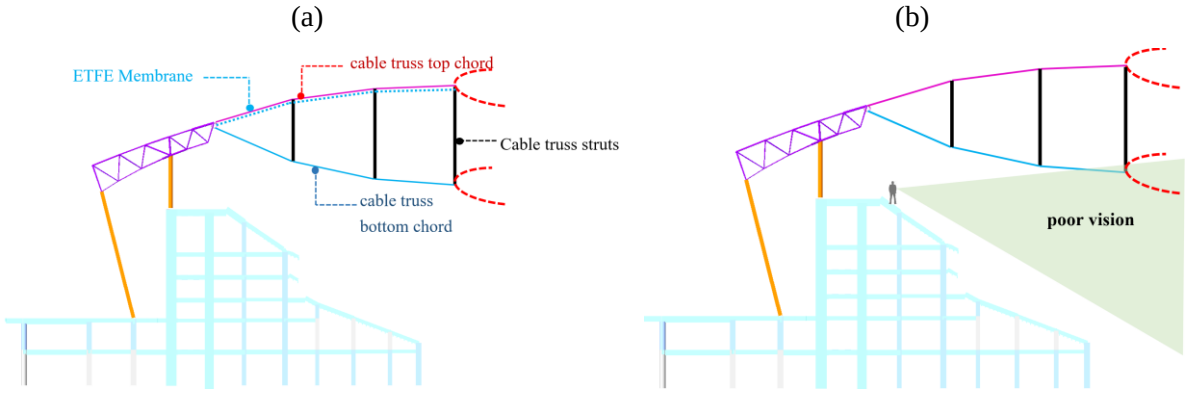


Figure 8. Cable truss structure: (a) cable truss structure composition, (b) audience ;ine of sight analysis

At this time, it is considered to lift the lower stay cable up while reducing the height of the strut. In order to ensure the transmission of force flow, the stay cable is arranged circumferentially at the end of the lower stay cable. At this time, the structural force is transmitted step by step from the inside to the outside. The height of the strut at each level of the structure is limited, and combined with a flexible lightweight membrane roof, not only the structural force is efficient and reasonable, especially suitable for large span spaces, but also can solve many adverse effects caused by the high height of the innermost ring strut, Improve the visual effect within the audience. This structural system is a cable dome structure[3] (see Figure 9).

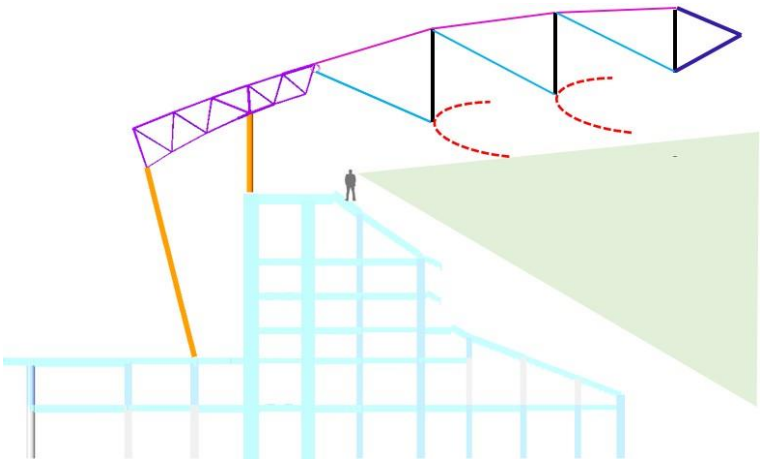
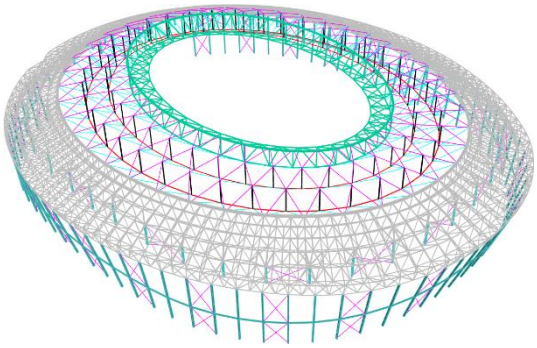


Figure 9. Cable dome structure

A rigid pull ring is arranging in the center of the closed tension cable dome structure, but the size of the pull ring opening is relatively small compared to the overall size of the structure. Generally, it is designed according to ordinary components, which can ensure the effective transmission of tension in the structural system; However, compared to the overall size of the structure, the size of the inner pull ring opening in the central large opening non closed tension cable dome structure cannot be ignored. The large opening significantly weakens the overall stiffness of the structure, and the inner pull ring needs to have sufficient stiffness to ensure effective transmission of tensile force. Therefore, an inner ring steel truss with good stiffness is provided at the edge of the large opening to solve the problem of weakening the overall structure and transmission of tensile force by the large opening.

The plane of the roof of the Chengdu Phoenix Mountain Sports Center is elliptical, with a length of about 279 meters in the north-south direction (long axis) and 234 meters in the east-west direction (short axis). The highest point of the roof is about 64 meters high. The maximum overhang length of the roof roof is 64m, and the minimum overhang length is 55m. In the outer metal material area, a double layer grid structure is adopted, which simultaneously serves as the edge member of the cable dome. The average width of the grid is 27m, and the width of the cable dome is 46m. The cable dome structure in the inner membrane area is provided with two loops of cables, each loop being provided with 40 support rods, with a maximum height of about 14m. The outer ring of the cable dome structure is connected to a steel grid as a compression ring, and the inner ring is provided with a triangular three-dimensional pull ring truss. The lower end of the steel column supporting the roof is hinged to the concrete grandstand structure. The lower end of the outer ring facade steel column is hinged on a 7m elevation concrete structure. The composition of the roof structural system is shown below.

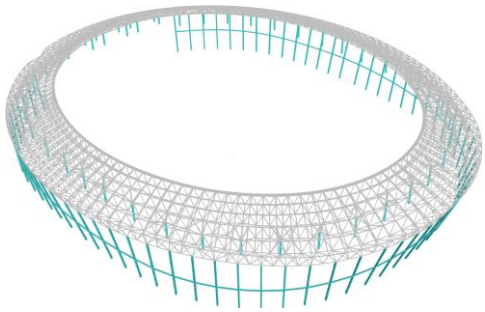
(a)



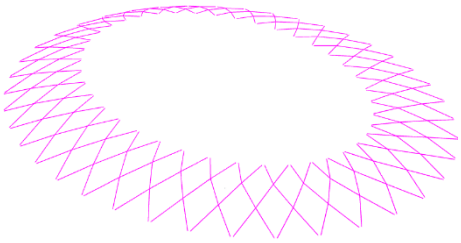
(b)



(c)



(d)



(e)

(f)

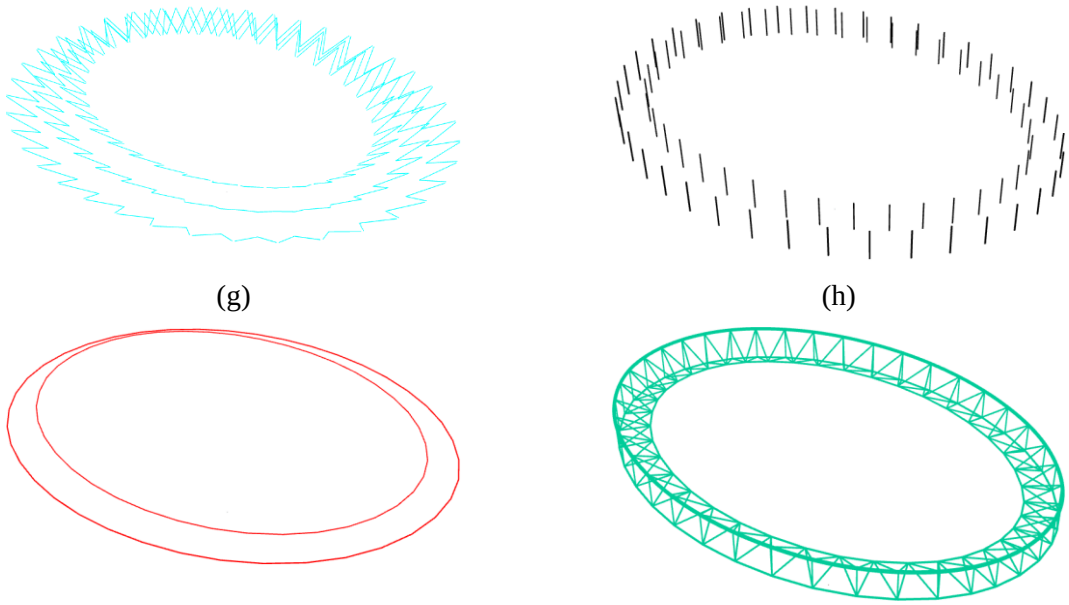


Figure 10. The structure composition of the football stadium roof: (a) the overall structure of the roof, (b) the roof structure during construction, (c) the peripheral grid structure, (d) the upper spine cable of the cable dome, (e) the lower diagonal cable of the cable dome, (f) the cable dome support rod, (g) the cable dome ring cable, (h) the inner rigid pull ring of the cable dome

4. Calculation and analysis of roof structure

4.1. Static analysis

Establish a finite element analysis model in Midas Gen analysis software and conduct static analysis considering geometric nonlinearity. The analysis results show that gravity load and temperature play a major control role. The maximum vertical displacement of the large opening inner ring truss cable dome structure under 1.0 times the dead load and 1.0 times the live load is -388mm, and the maximum vertical displacement under 1.0 times the dead load and 1.0 times the wind load is 323mm. The calculation results show that the structure has good stiffness. The maximum stress of the cable in the roof structure is less than 0.5 times the breaking force, and the stress ratio of the main steel members is less than 0.75. The roof cable dome structure has sufficient safety.

The cross-sectional dimensions of the main steel structure components are: the maximum radial cable is a sealing cable with a diameter of 92 mm, and the maximum circumferential cable is a sealing cable with a diameter of 4 pieces of 125 mm; The maximum cross section of the support rod is a circular tube with a diameter of 426mm.

4.2. Stability analysis

Stability performance is the focus of attention for large span spatial structures. The stability performance of the structure under various operating conditions such as 1.0 dead load+1.0 live load, 1.0 dead load+1.0 half span live load was calculated and analyzed in Ansys finite element software through a full process analysis considering both geometric and material nonlinearities of the structure. The analysis shows that due to the use of a sunflower shaped cable dome structure, the structure has a high stiffness out of plane and is insensitive to defects. The ultimate bearing capacity state is controlled by strength. The most unfavorable working condition for stability analysis is 1.0 dead load+1.0 live load, and the safety factor for ultimate bearing capacity is 2.6.

(a) (b)

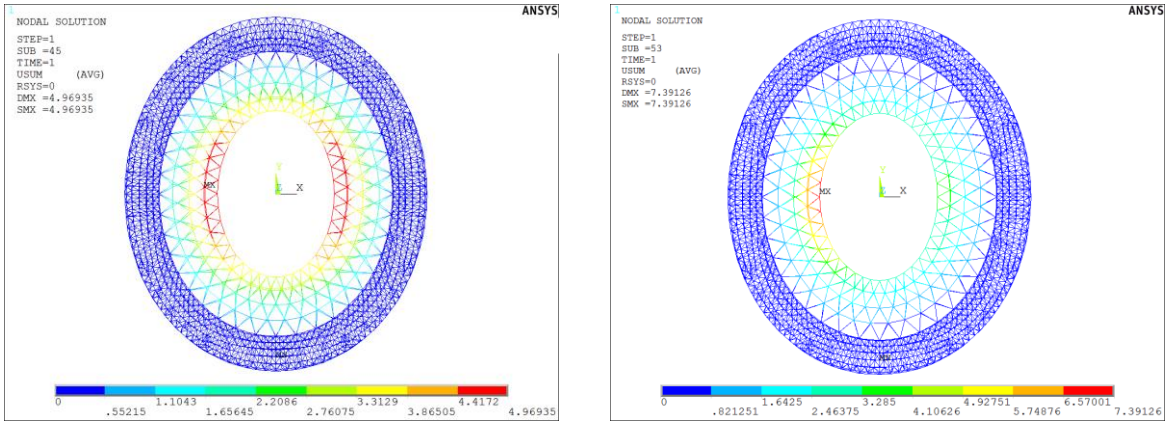


Figure 11. Structural stability analysis: (a) Instability mode under 1.0 dead load+1.0 live load condition, (b) Instability mode under 1.0 dead load+1.0 half span live load condition

4.3. Node analysis

This project has carried out detailed analysis and design on various types of key nodes to ensure reliable force transmission of the nodes. Due to limitations, only the connection nodes between the upper end of the strut and the notochord are listed.

The calculation results are shown in Figure 14. From Figure 13, it can be seen that the ultimate bearing capacity of this node is approximately 2.6 times the control case load, indicating that this node has sufficient safety reserves. As can be seen from Figure 14, under the control working condition, the node is in an elastic state, with the stress in most areas below 200Mpa, and the maximum stress value of 296Mpa appears at the side wall of the pin hole.



Figure 12. Node Realistic View

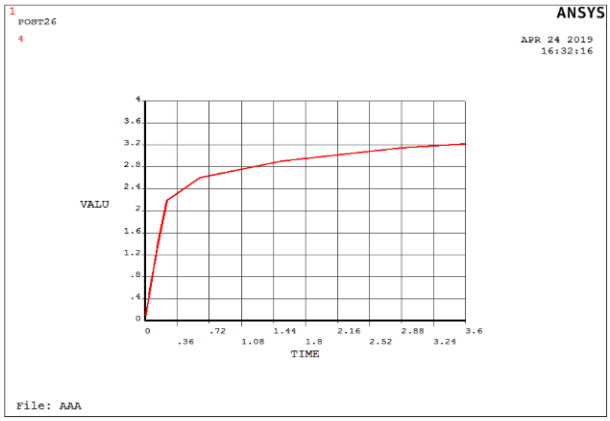


Figure 13. Node load displacement curve

(a) (b)

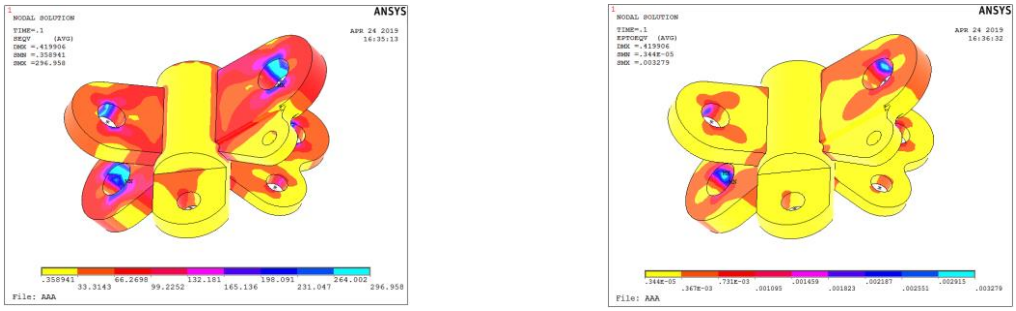


Figure 14. Node analysis results: (a) node stress diagram under 1 time control condition, and (b) node strain diagram under 1 time control condition

4.4. Analysis of resistance to continuous collapse

The cables of the football stadium roof structure play an important role in the entire structural system. If any one of the cables fails and causes the structure to collapse, it will bring serious consequences. Therefore, ANSYS finite element software is used to analyse the collapse resistance of the structure under the condition of broken cables using the transient analysis method of removed components. The location of structural cable breaks is shown in Figure 15.

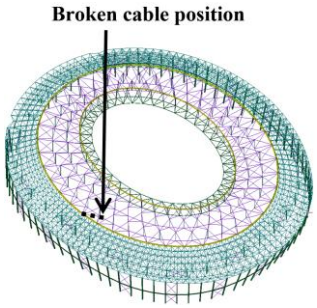


Figure 15. Broken cable position

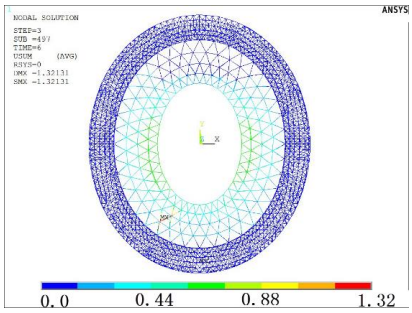


Figure 16. Cloud map of the maximum deformation of the notochord structure on the southwestern side of the fault /m

The fracture of the upper spinal cord on the southwest side was calculated and analysed. As can be seen from Figure 17, after one upper spine cable was broken in the southwest, a large horizontal deformation occurred in the local cable dome in the horizontal direction. After the vibration stopped, the maximum horizontal deformation of the structure was 1.5m, and the maximum stress during the radial cable breaking process of the adjacent upper spine cable was 463MPa, which was less than the cable breaking stress of 1670MPa. During the process of cable breakage, the internal force of the brace decreases and the internal force of the loop cable remains basically unchanged.

(a) (b)

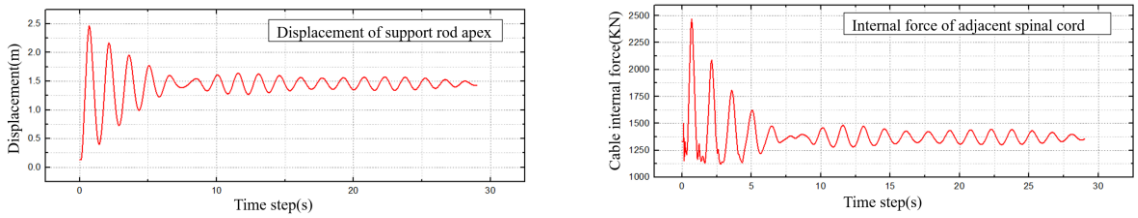


Figure 17. Analysis results of broken cable: (a) displacement of strut vertex/m, (b) axial force time history of adjacent spinal cables on the southwest side of the broken cable/KN

5. Conclusion

The professional football stadium of Chengdu Phoenix Mountain Sports Center will host the 31st World University Games in 2023. In the structural design of football stadiums, cable dome structures are used in non enclosed roof, and a large opening inner ring steel truss cable dome structure is proposed, expanding the application range of cable dome structures. The project compensates for the weakening of the stiffness and integrity of the cable dome structure due to the large opening by arraging an inner ring steel truss at the edge of the middle large opening; By adopting a sunflower shaped cable dome structure and conducting force finding analysis and applying reasonable prestress, the problem of uneven structural stress caused by structural asymmetry, oblique placement of the overall structure, and complex boundaries has been solved. At the same time, according to the building covering materials, the grid structure system was adopted, solving the contradiction between the boundary requirements of the column grid and the tensioning structure, achieving the architect's plan efficiently, economically, and aesthetically, and ultimately completing the structural expression of the architectural form.

References

[1] Y. L. Guo, “Research and design of spoke tension structure”, Journal of Building Structures, vol. 34, pp. 1-10, 2013. (in Chinese)

[2] R. J. Shang, “The form-finding method based on the form of composition of forces for spoke structure”, Engineering Mechanics, vol. 1, pp. 145-152, 2011. (in Chinese)

[3] M. P. Levy, “Georgia dome and beyond achieving lightweight-long span structures”, Proceedings of the IASS-ASCE International Symposium. International Association for Shell and Spatial Structures, Atlanta, USA, 1994.

Tension structures in the Asia-Pacific

Active bending
Additive manufacturing/ 3D printing
Architectural geometry
Bamboo for sustainable construction and quality of life improvement
Bio-inspired structures and architecture
Bridge structures
Computational form-finding
Conceptual design
Concrete structures
Construction techniques
Deployable and inflatable structures
Design competition (WG21)
Digital modelling and fabrication
Dynamic response of metal spatial structures
Dynamic response of other structures
Form-finding and structural optimisation of interlocking discrete assemblages
Graphical methods
Gridshell and lattice structures
Historical concrete shells
Historical structures
Lattice structures
Life-cycle design and assessment of structures
Metal gridshell structures, connections and stability
Methods and construction technologies for sustainable shell structures
Morphology and configuration processing
Next generation parametric design
Novel methods in modelling, optimisation and construction for reducing carbon footprint of continuous roof shells
Numerical methods for geometry, form-finding and optimisation of lightweight structures
Optimisation methods and applications
Origami
Other
Teaching design uncertainty: working with unknown qualities/quantities of new and re-claimed materials
Teaching of shell and spatial structures
Tensegrity systems and cable structures
Tension and membrane structures
► **Tension structures in the Asia-Pacific**
Timber and bio-based structures
Topology optimisation
Traditional masonry structures and innovation
Transformable structures

IASS 2023
July 10–14 Melbourne
Integration of Design and Fabrication

Proceedings of the IASS Annual Symposium 2023
Integration of Design and Fabrication
10–14 July 2023, Melbourne, Australia
Y.M. Xie, J. Burry, T.U. Lee and J. Ma (eds.)

Structural analysis of steel structure of a 60,000-seats stadium

Yuan FENG[a], Yan ZHANG[a,*], Liwei WANG[a], Xinan XIANG[a], Tian QIU[a]

[a,*] China Southwest Architectural Design and Research Institute Corp. Ltd
No. 9 Shuxiu West Road, Wuhou District, Chengdu City, Sichuan Province, China
12489411@qq.com

Abstract

The Zhengzhou Olympic Center Sports Stadium has 60000 seats. The steel structure of the Stadium roof is 291.5m in the north-south direction, 311.6m in the east-west direction and the maximum length of cantilever is 54.1m. The steel structure of roof is composed of four components: the canopy of large-opening spoke-wheel-type cable-supported grid structure with the largest cantilever length in the world, the double-layer grid roof, plane truss and the spatial corridor of triangular mega truss with largest span in China. In order to optimize the large opening spoke-wheel-type cable supported grid structure, 8 main influencing factors on static performance are studied by parametric analysis. The rigid inner ring members is identified as the stable sensitive area of the structure by elastoplastic nonlinear whole process analysis. The load case of snow under extreme climate is considered to ensure the safety of the structure. The ability of the structure to resist progressive collapse is studied by alternative path analysis. Based on the time-varying of construction process and BIM technology, the integrated technology of design and construction is achieved. The seismic performance of the Stadium steel structure is investigated by using the assembly model, and the results show that the steel structure can keep elasticity under the action of frequently occurred earthquakes or precautionary earthquakes, and can achieve the objective of performance about non-yielding under the action of rarely occurred earthquakes.

Keywords: spoke-wheel-type cable-supported grid structure, static performance, influencing factor, nonlinear analysis, progressive collapse, integration, seismic design

1. Introduction

The project of Zhengzhou Olympic Sports Center, which includes Stadium, Gymnasium, Natatorium, and Commercial Facilities, is located in the core region of Zhengxi New District, Zhengzhou City, Henan Province, China (Figure 1). The Stadium has 50000 fixed seats and 10000 movable seats. It is a large-scale Grade A Stadium with a total construction area of 138,500 square meters. The plane size of the concrete structure is about 330m×362m and the roof is about 292m×311m. There are 11 floors above the ground, and the total building height is 54.390m. The standard track and field are located in the middle of the Stadium, which can host football matches and track and field competitions. There are badminton and table tennis courts on the west side of the west stand. The badminton and basketball training courts are located in the northern underground of the north stand. There is an hotel with eight-storey on the east side of the east stand, which is a complex and comprehensive multi-functional Stadium.

Copyright © 2023 by Yuan FENG. Published in the Proceedings of the IASS Annual Symposium 2023 with permission.



Figure 1. Aerial view of Zhengzhou Olympic Sports Center.

The steel structure of the Stadium roof is about 291.5m long in the north-south direction and 311.6m in the east-west direction, and the plane shape is approximately circular. The cantilever length of the stand canopy is 54.1m in the east-west direction and 30.8m in the north-south direction. The plane shape is approximately elliptical (Figure 2).

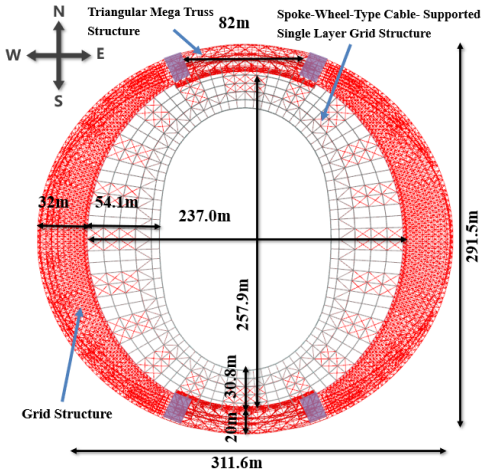


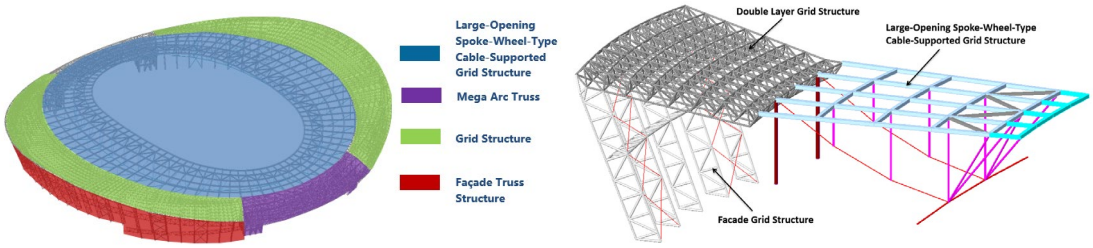
Figure 2. Plan of the Stadium roof.

2. Analysis and research of design

2.1. Structural system and layout

The roof steel structure consists of 4 components (Figure 3a). 1) The stand canopy of Stadium adopts the large opening spoke-wheel-type cable-supported grid structure. 2) The outer roof of Stadium adopts the square pyramid double layer grid structure, which is placed on the outer edge of the roof in the ring shape, and the width is 20m-32m. 3) The spatial corridors adopt the triangular mega truss structure at the north and south ends of the Stadium. 4) The façade adopts the plane truss structure. As shown in Figure 3b, the stand canopy is supported by the steel columns around the stands and the triangular mega truss at the north and south ends. One end of the grid structure is supported on the steel column, and the other end is supported on the facade truss. the lower end of the facade truss is hinged and placed on the

concrete structure with the elevations of 7m and 43.9m. The large opening spoke-wheel-type cable-supported grid structure is adopted for canopy, which is the self-balancing tension structural system [1]. The high-strength material characteristics of the cables are fully utilized, and the impacts on the main structure is also greatly reduced. It can economically and effectively realize the application of large spans, and at the same time obtain the simple design of architecture. The grid structure, as the outer roof of Stadium, also acts as the ring of external compression for cable-supported grid structure. The functional requirements of the building are satisfied by the layout of the facade truss structure and triangular mega truss structure, making the structural selection and architectural requirements harmonious and unified.



(a) (b)

Figure 3. Composition diagram of Stadium steel structure.

The main loads acting on the structure: 1) Self-weight, which should be considered according to the actual weight; 2) The additional dead load of the metal roof is 0.8kN/m^2, sunlight roofing sheets is 0.5kN/m^2， façade system is 1.5kN/m^2; 3) The reference wind pressure is 0.5kN/m^2 (100-year return period). The terrain roughness is Class B. The factor of height is determined according to the code for design. The shape factor and wind vibration factor are determined according to the results of wind tunnel test; 4) The reference snow pressure is 0.45kN/m^2 (100-year return period); 5) The temperatures are considered to be ±35; 6) The live load shall be selected according to the load code based on the building function of the specific location; 7) The seismic precautionary intensity is 7 degrees. The design basic acceleration of ground motion is 0.15g. The group of seismic design is the second group. And the category of seismic precaution is the key precautionary category. The load combination considers the combination of the normal service limit state and the combination of bearing capacity limit state.

According to the importance and distribution of members， the steel structural members of the Stadium are divided into key members (Table 1) and general members, and the indicators of stress control are developed respectively as shown in Table 2 and 3. The control criterions of displacement are simultaneously developed.

Table 1. Key members of Stadium steel structure.

Steel Structure of Stadium	Key Members
Spoke-Wheel-Type Cable-Supported Grid Structure（Canopy）	Ring Cable、Radial Cable、Inner ring truss strut、Upper Ring Beam of Inner Ring Truss、Outer Ring Beam、Stand Column
Double Layer Grid Structure（Roof）	Members Around the Support
Façade and Plane truss	Floor-Standing Column and Chords Connected with Grid Structure
Triangular Mega Truss（Spatial Corridor）	Upper Chord、Lower Chord、Web Members Connected to Steel Frame、Steel Frame Column

Table 2. Stress ratio criterion of steel members.

Type of Function	Stress Ratio	
	Key Members	General Members
Static Force	0.75	0.90
Frequently Occurred Earthquake	0.75	0.90
Precautionary Earthquake	0.90（Elasticity）	1.00（Elasticity）
Rarely Occurred Earthquake	1.00（Elasticity）	1.00（Bending Yield Only）
Extremely Accidental Load	1.00	1.00

Table 3. Stress ratio criterion of cables.

Type of Function	Stress Ratio	
	Hoop Cable	Radial Cabel
Static Force	0.40	0.40
Frequently Occurred Earthquake	0.40	0.40
Precautionary Earthquake	0.50	0.50
Rarely Occurred Earthquake	0.50	0.50
Extremely Accidental Load	0.50	0.50

Table 4. Displacement criterion.

Steel Structure of Stadium	Deflection-Span Ratio
Spoke-Wheel-Type Cable-Supported Grid Structure（Canopy）	1/125
Triangular Mega Truss（Spatial Corridor）	1/400

2.2. Canopy design of large opening spoke-wheel-type cable-supported grid Structure

2.2.1. Structural system

The shape of the canopy in the Stadium stand area is saddle-shaped, high in the east-west direction and low in the north-south direction. It adopts the large opening spoke-wheel-type cable-supported grid structure with internal ring trusses. The large opening spoke-wheel-type cable-supported grid structure reference to the mechanical characteristics of spoke-wheel-type tensioned cable truss structure [3] and beam-string structure [4-6], which is the new type of self-balancing and rigid-flexible composite structure. As shown in Figure 4, the upper chord of the structural system is the rigid single-layer grid, and the lower chord is the tensioned cable-strut system in the spoke-wheel-type layout; Diagonal web members connecting the ring cable and the upper chord single-layer grid are arranged along the ring cable to form the stereoscopic inner ring truss; Based on the combination of the requirement by architectural daylighting, the innermost ring is set with the cantilevered grid; The entire structural system is supported on the stand columns and the north-south triangular mega truss. The upper chord rigid grid of this project is arranged in the ribbed ring type, with 6 ring beams and 84 radial beams in total. Diagonal web members are set between the two ring beams corresponding to the inner truss. 1 ring cable and 42 radial cables are set in the lower chord cable-strut system, and 3 vertical struts on the upper side of each radial cable.

The mechanism of the structural system: By tensioning the lower chord cable, the upward support force is generated in the strut and elastic support for the upper single layer grid; The wide compressed ring is formed by the upper chord single layer grid, and the external compressed ring is formed by the

grid outside the stand and the north-south triangular mega truss, which further increases the horizontal stiffness and effectively resists the horizontal force caused by radial cables. This is the self-balancing structural system.

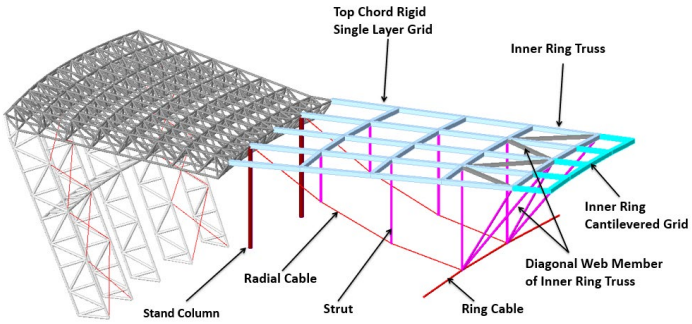


Figure 4. Composition diagram of large opening spoke-wheel-type cable-supported grid structure.

2.2.2. Statics analysis

Through a series of analysis and research on the static force influencing factors of the large opening spoke-wheel-type cable-supported grid structure, the mechanical characteristics under the static force are grasped. According to the basic principle of structural mechanism, there are two aspects by analysis about the influencing factors of structural static performance:

1) For the cable-strut system (Figure 5): Pretension is the necessary element in cable-strut system. Therefore, the magnitude of pretension was set as the analysis parameter; The support of the cable-strut to the rigid grid is mainly provided by the radial cables, and the stiffness of the radial cables is related to the inclination angle of the cables. Therefore, the height of the struts that characterizes the inclination angle of the radial cables was set as the analysis parameter; The function of the ring cable is balancing the horizontal force of the radial cable in the inner ring, and adjustment of the internal force distribution of the cable-strut system. Therefore, the shape of the inner ring cable was set as the analysis parameter; The form-finding of the cable system depends on the layout of the boundary. Therefore, the height difference of the outer ring beam at the boundary of the rigid grid was set as the analysis parameter.

2) For rigid grid: As the upper chord rigid member of the structural system and the “compressed ring” of the lower chord cable system, the rigid grid provides the certain stiffness and bearing capacity. Therefore, the height of the rigid grid surface and the rigid grid form were set as the main analysis parameters (Figure 6). At the same time, the influence of the height difference which about the inner ring of the rigid grid and the curvature of the ribbed beam on the structural performance were analysed.

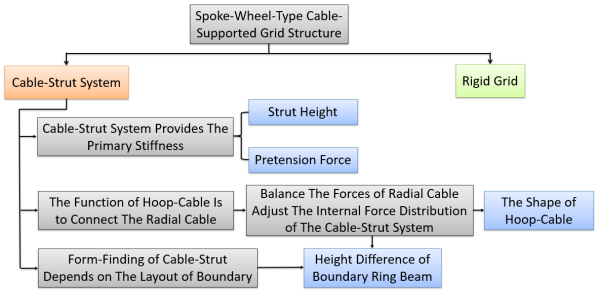


Figure 5. Parameter setting according to cable-strut system.

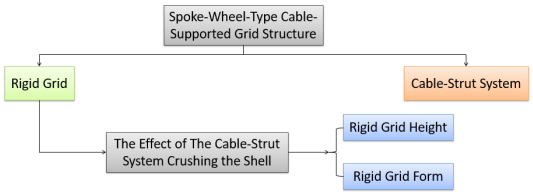


Figure 6. Parameter setting according to rigid grid.

Through the study of the factors which affecting the static performance, the principle of structural optimum design was obtained [2]. Therefore, based on the satisfaction of architectural requirements, the optimized parameters could be used to design and analyse the large opening spoke-wheel-type cable-supported grid structure roof of Zhengzhou Olympic Sports Center Stadium.

Through the modelling of the finite element analysis in Midas Gen analysis software, considered the influence of geometric nonlinearity, and analysed the static performance of the structure. The gravity load and temperature are the major controlling as shown in analysis results. The maximum vertical deformation of the cable-supported grid structure under displacement control conditions (1.0 dead love+ 1.0 live load+ 0.6 temperature reduction) is -427.4mm. The deflection-span ratio is 1/126 less than the limitation of 1/125 in design code. The maximum vertical deformation is occurred at the edge of the east-west inner ring of the cable-supported grid (Figure 7). The stress ratios of all members meet the requirements of Table 2 and Table 3.

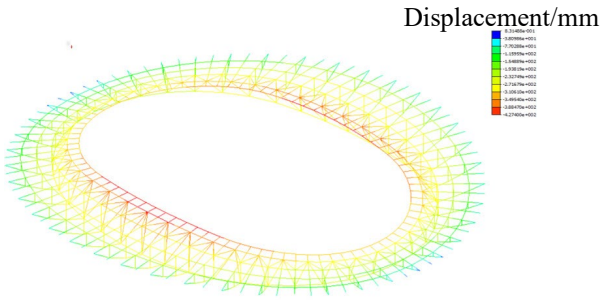


Figure 7. Displacement distribution of large opening spoke-wheel-type cable supported grid structure.

The cross-sectional dimensions of the main steel structural members are shown in Table 5. The maximum radial cable is 2×Φ119 of vanadium cable，and the ring cable is 8×Φ130 full locked coil rope; The maximum cross-section of the radial member is □750×500×20×20 and the ring member is □750×700×30×30 in upper chord grid; The maximum cross-section of the strut is Φ500×25.

Table 5. Sectional dimension of main steel members.

Function		Section Type	Section specification
Cable-Supported Grid Roof	Radial Cable	Round	Φ116、Φ140、2×Φ119
	Radial Cable	Round	8×Φ130
	Rigid Grid Radial Member	Rectangular Tube	□750×400×16×16、□750×500×20×20 etc.
	Rigid Grid Radial Member	Rectangular Tube	□750×450×20×20、□750×700×30×30 etc.
	Strut	Circular Tube	Φ315×16、Φ426×16、Φ500×16、Φ500×25
Roof Support Column		Circular Tube	Φ800×35

2.2.3. Stability analysis

Stability is the focus of the large-span space structure. In the Ansys software, the stability of the structure was studied by analysing the whole process of geometry and double-nonlinear analysis of material, and examined the load-displacement curve of the whole process. The stability of the structure was considered under various working conditions, such as 1.0 dead load + 1.0 live load, 1.0 dead load + 1.0 half-span live load, 1.0 dead load + 1.0 wind load, 1.0 dead load + 1.0 temperature rise and 1.0 dead load + 1.0 temperature reduction performance. Analysis shows that the stability of the structure is better, insensitive to defects, and control by strength. Due to the large axial pressure and weak out-of-plane stiffness of the inner ring beam, it is the sensitive area for stability and loses stability first (Figure 8). The most unfavourable working condition for stability analysis is 1.0 dead load + 1.0 live load, and the safety factor of ultimate bearing capacity is 2.6.

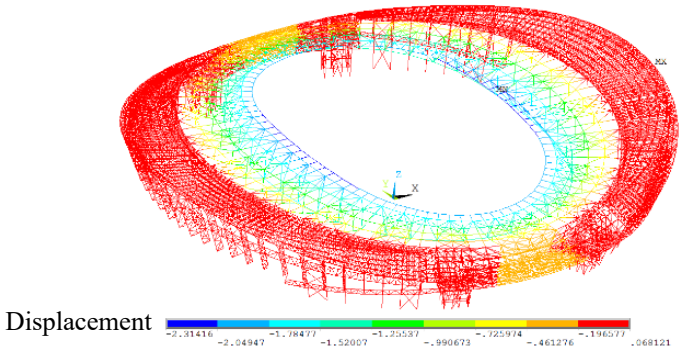
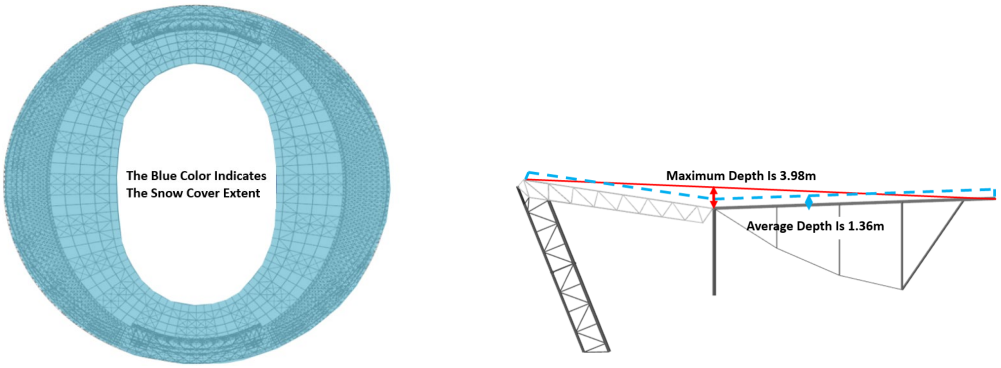


Figure 8. Buckling mode based on the load case of 1.0 dead load+1.0 live load.

2.2.4. Analysis of snow load in extreme climate

The elevation of the outer ring beam of the spoke-wheel-type cable-supported grid roof is lower than the outer edge of the grid and the inner edge of the cable-supported roof. Therefore, it is easy to cause the snow accumulation near the position. Based on the importance of the Stadium, the unfavourable condition of snow accumulation was considered in the extreme climate. In Midas Gen, the nonlinear finite element method was used to conduct static analysis on the structure. The snow accumulation range during the calculation is shown in Figure 9. According to the maximum snow accumulation, the average depth of snow accumulation is about 1.36m after calculation, and the snow load is 3.4kN/m^2.



（a）Plane　　（b）Section

Figure 9. Snow Distribution Range

The accidental combinations were considered of dead load, snow accumulation and temperature reduction conditions. The maximum stress of the ring cable is 575MPa and the radial cable is 675MPa. And the maximum stress ratio is 0.48, which is less than the limit value of 0.5 in Table 3. The stress ratios of the upper chord rigid grid also meet the requirements of Table 2. It can be seen from the analysis results that the structure can still guarantee the safety under the consideration of snow load in extreme climate.

2.2.5. Progressive collapse resistance analysis

The Stadium is the Densely populated place, and reliable measures should be taken in the design to avoid the progressive collapse of the structure due to the failure of local members. The spoke-wheel-type cable-supported grid structure resists external loads by applying of prestress to the cables. Therefore, the cables play a vital role in the entire structural system, and it is necessary to avoid the progressive collapse of the structure caused by the failure of the cables. The method of removing members (alternate load path method) can analyse the response of the structure after partial members

failure, to ensure that after partial members failure, the remaining members can redistribute internal forces and resist external loads without progressive collapse. Therefore, the member removal method was adopted, and the dynamic elastoplastic time-history analysis was used in Ansys software to study the progressive collapse resistance of the structure under the condition of broken cables [7-9].

The ring cable is the most important load bearing cable. This project guarantees the safety by controlling the stress ratio to be less than 0.4, and 8 parallel sub-cables are adopted to form the ring cable in structure. Assuming that the sub-cables of the 5 ring cables are damaged, the remaining 3 sub-cables bear the total force of the original 8 sub-cables. The stress ratio is 0.4/（3/8）=1.06, which just exceeds the breaking force. Therefore, when less than 5 sub-cables are broken, the ring cable will not be damaged as a whole, and the safety of margin is high.

Radial cables consist of single or double cables and are relatively easier to be damaged. Therefore, one and two radial cables are broken respectively at the maximum cantilever and tension to examine the progressive collapse resistance of the structure. The case where the cable breaks at the maximum cantilever as an example in Table 6. The stability value in the Table is after the dynamic impact effect of the broken cable disappears and the structure is stable; The peak value is the maximum value during the dynamic process of breaking the cable; The amplification factor is the ratio of the stable value, the peak value and the value before the broken cable. It can be seen that after the radial cable is broken, the displacement of the broken cable and the internal force of the adjacent radial cable will increase significantly, and the increased rate of breaking two radial cables is greater than one radial cable. Due to the dynamic effect, the maximum increasing of the adjacent cable force is 2.82 times when two radial cables are broken, and 2.23 times after stabilization. The maximum increasing in displacement is 7.7 times, and 5.0 times after stabilization. However, the internal force of the cable is still smaller than the breaking force, and the structure will not be progressive collapse.

Table 6. Results of alternative path analysis.

Condition	One Cable Broken				Two Cable Broken			
	Vertical Displacement		Stress of Radial Cable		Vertical Displacement		Stress of Radial Cable	
	Value/ m	Amplification Coefficient	Value/ MPa	Amplification Coefficient	Value/ m	Amplification Coefficient	Value/ MPa	Amplification Coefficient
Before Breaking the Cable	0.170	-	221	-	0.170	-	221	-
After Breaking the Cable (Stable Value)	0.250	1.47	327	1.47	0.857	5.0	501	2.23
After Breaking the Cable (Stable Value)	0.320	1.89	449	2.03	1.310	7.7	623	2.82

2.3. Integration technology of design and construction

The engineering project has two main stages from start to finish, design and construction. The construction stage includes the processing state, construction and installation state and forming state; The design stage includes the forming state and the working state; The forming state, as the junction between the design and construction stages, is the end of the construction stage and the start of the design stage (Figure 10).

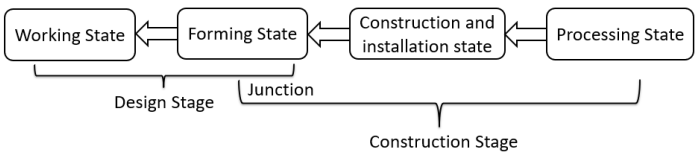


Figure 10. Design and Construction Stage.

In the process of manufacturing for complex steel structures, if the connection details are not fully considered in the design stage, it may cause processing difficulties, or even impracticability. At the same time, during the construction and installation process, the structure is the time-varying structure [10-11]. The composition, boundary conditions, internal force and deformation of the members are all changing, which affecting the structural forming. If the construction forming deviates too much from the original design, it will lead to problems, such as large geometric deviations, reduced mechanical properties, and even modification and adjustment of the structural plan. So, the design stage and the construction stage should be considered in the integrated manner.

In the steel structural design of Zhengzhou Olympic Sports Center Stadium, the design and construction were considered comprehensively. And the integrated technology of design and construction was formed, mainly including the following two points: 1) Tension numerical analysis based on time-varying structure; 2) Steel structure design based on BIM technology.

2.3.1. Tension numerical analysis based on time-varying structure

The large opening spoke-wheel-type cable-supported grid structure is set with inner ring truss. Due to the diagonal braces of inner ring, the tensioned cable-strut system is the statically indeterminate structure. And the time-varying installation will significantly affect the forming state of the structure. Analysis, calculation and consideration about the generation path of the members. The cumulative effect of stress and deformation. Tracking and analysis the whole process of tensioning and forming. And understanding the internal forces and displacement changes of the structure. With the objective of minimizing the difference between the forming state and the design target, the feasibility of the structure and the appropriate tensioning and forming method were evaluated during the design stage. The following 5 tensioning and forming methods were considered (Figure 11).

1) Tensioning of the complete structure with diagonal braces of inner ring; After diagonal braces of inner ring are installed, the radial cables are directly tensioned for forming.
2) Tensioning + in-situ installation of diagonal braces: Tension the radial cables, and then install the diagonal braces in-situ.
3) Tensioning + installation of the front-end diagonal bracing section: Tension the radial cables, and then install the diagonal braces of inner ring and the corresponding upper rigid grid.
4) Tensioning + installation of diagonal braces + jacking up of diagonal braces: Tension the radial cables, install the diagonal braces, and then install the jacks on the diagonal braces and push the diagonal braces in place.
5) Tensioning + end jacking + installation of diagonal braces: Tension the radial cables. After the tensioning is completed, jacking the cantilever section of the front-end of the roof by jacks, and then install the diagonal braces after the jacking is in place.

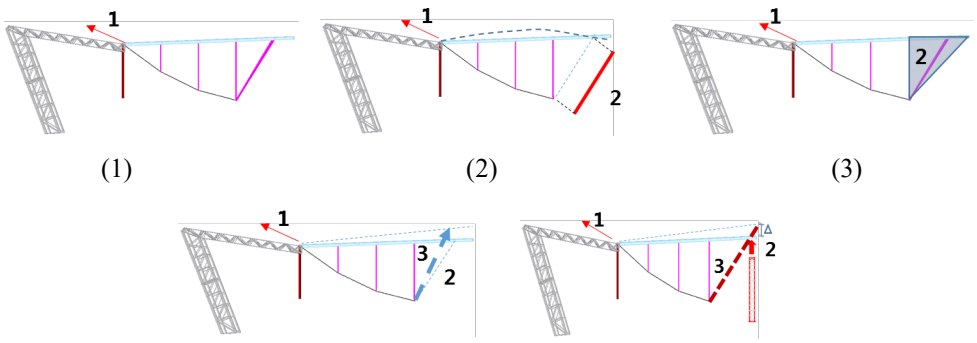


Figure 11. Five Tensioning Methods.

Table 7 is the comparison of each tensioning method. Method 1 has the largest deviation of cable force, and the maximum deviation of ring cable force is 11.5%; Method 3 has the largest displacement deviation which is 872mm; In method 2, the deviation of cable force is small, but the displacement and stress deviation of steel members are large; In method 4 and 5, the displacement, cable force and stress deviation of steel members are all very small, which meet the actual engineering requirements and can be used as the better implementation method. Method 5 was finally adopted for the construction.

Table 7. Comparison of Tensioning Methods.

Tensioning and forming method	Displacement Deviation/mm	Ring Cable		Radial Cable		Stress Difference of Rigid Member Value/MPa
		Cable Force Deviation/KN	Percentage of Cable Force Deviation/%	Cable Force Deviation/KN	Percentage of Cable Force Deviation /%	
Method 1	-270~86	-1924~-1241	-11.5~-7.5	-37~41	-1.36~1.4	-150~73
Method 2	-341~153	-1036~-856	-6.3~-5.1	-48~147	-1.5~6.3	-165~88
Method 3	-872~265	-1254~726	-7.5~-4.4	-202~-48	-6.3~-4.2	-104~96
Method 4	-2~16	176~226	1.1~1.4	-34~17	-2.6~0.6	-10~35
Method 5	-47~49	-65~-6	-0.4~-0.04	-51~70	-1.6~2.9	-33~36

2.3.2. Steel structure design based on BIM technology

Based on BIM technology, the digital 3D of structural model was built in the design stage (Figure 12). The BIM model can solve the problems, such as dimension matching and collision of members, and obtain joints that satisfy the calculation assumptions, are easy to process and beautiful. For the joints obtained by BIM technology, elastoplastic finite element analysis was carried out with application of Ansys software to ensured that the design of the joints met the force requirements (the ring cable clamp as an example, as shown in Figures 13 and 14). Through the application of BIM technology, the detailed design in the processing and production is advanced, which promotes the integration of design and construction, reduces the repeated work of adjustment, and greatly improves the quality of design.

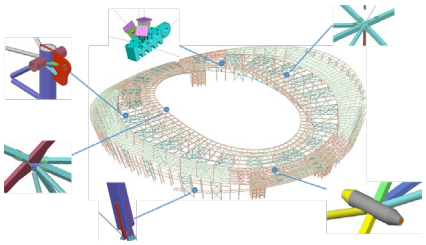


Figure 12. Application of BIM technology.

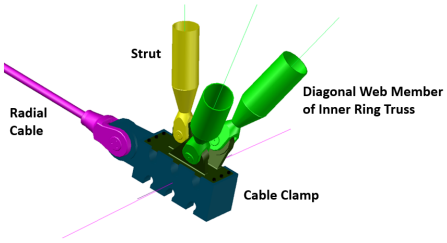
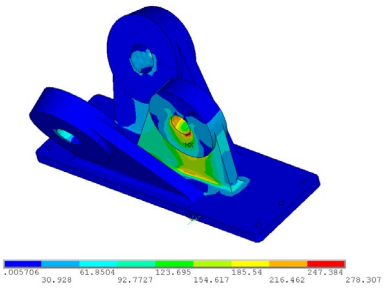
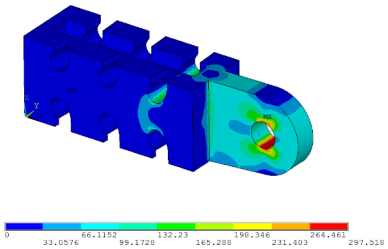


Figure 13. BIM Model of ring cable clamp joint.



Stress/Mp

（a）Analysis result on upper section



Stress/Mp

（b）Analysis result on lower section

Figure 14. Analysis result of ring cable clamp joint

2.4. Steel structure analysis of seismic performance

In order to accurately reflected the impact of the concrete structure on the upper steel structure under the seismic action, the concrete structure and upper steel structure were combined to the integration which was the collaborative finite element model in Midas Gen (Figure 15). The model considered the seismic action of three-dimensional dominated by horizontal and vertical earthquakes. And the seismic performance was analysed by elastic response spectrum method and time-history analysis method.

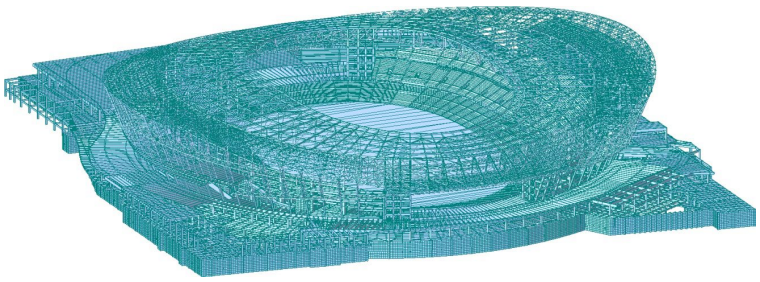


Figure 15. Collaborative analysis model of the Stadium.

The analysis results of elastic response spectrum are shown that: Under frequently occurred earthquake, the maximum stress ratio of the key members occurs at the struts of the cable-supported grid structure, which is 0.568 and less than the limit value of 0.75 (elasticity) in Table 2; The stress ratio of general members is less than the limit value of 0.9 (elasticity) in Table 2; The maximum stress ratio of the cable is 0.26, which is less than the limit value of 0.4 in Table 3. Under the precautionary earthquake, the maximum stress ratio of the key members occurs at the struts of the cable-supported grid structure, which is 0.854 and less than the limit value of 0.9 (elasticity) in Table 2; The stress ratio of general members is less than the limit value 1.0 (elasticity) in Table 2; The maximum stress ratio of the cable is 0.28, which is less than the limit value of 0.5 in Table 3. Under rarely occurred earthquake, the maximum stress ratio of the key members occurs at the struts of the cable-supported grid structure, which is 0.989 and less than the limit value of 1.0 (elasticity) in Table 2; The stress ratio of general members is less than the limit value 1.0 (non-yielding) in Table 2; The maximum stress ratio of the cable is 0.26, which is less than the limit value of 0.5 in Table 3. All kinds of members meet the objectives of performance under different seismic levels.

The results of time-history analysis method are shown that: Under rarely occurred earthquake, the maximum stress ratio of a small number of key members is 1.04, which is slightly greater the 1.0, but within 5%. The occurrence location is the web member connecting the grid and the façade truss. The stress ratios of the cables are all lest than the limit value of 0.5 in Table 3. And the members basically meet the objectives of performance. In general, the results of time-history analysis method are close to the elastic response spectrum.

The analysis shows that the roof structure can maintain the elasticity under frequently occurred earthquake or precautionary earthquake. Under the action of rarely occurred earthquake, roof structure can achieve the objective of performance about non-yielding, and has the good seismic performance.

3. Conclusion

1) The inner ring beam of the large opening spoke-wheel-type cable-supported grid has the large axial compression and weak out-of-plane stiffness, which is the sensitive area for stability and will lose the stability first. In general, the stability is good and controlled by strength.

2) Unfavourable snow accumulation condition in extreme climate should be considered in combination with the shape of roof. The safety can still be guaranteed of the structure by considering the snow accumulation at the depth of 1.36m in this project.

3) The large opening spoke-wheel-type cable-supported grid has the better performance against progressive collapse. The progressive collapse of the structure will not be occurred when two radial cables are broken.

4) For the complex steel structure, the design and construction stages should be considered in the integrated manner. Otherwise, the problems will be easily occurred, such as processing difficulties, large geometric deviations and reduced mechanical properties, and even modification and adjustment of the structural plan. The steel structure of Zhengzhou Olympic Sports Center Stadium takes into account the influence of time-varying during construction process, and combines BIM technology to achieve the integrated technology of design and construction.

5) The roof structure can maintain the elasticity under frequently occurred earthquake or precautionary earthquake. Under the action of rarely occurred earthquake, roof structure can achieve the objective of performance about non-yielding, and has the good seismic performance.

References

[1] Y. Feng, X. Xiang, H. Wang and W. Chen, "Mechanical behaviour and form-finding research on large opening spoke-wheel-type cable supported grid structure," *Journal of Building Structures,* 2019, 40(3): 69-80. (In Chinese).

[2] Y. Feng, X. Xiang and H. Wang, "Static performance parameter analysis of large opening spoke-wheel-type cable supported grid structure," *Journal of Building Structures*, 2019, 40(3): 81-91. (In Chinese).

[3] Y. Guo, K. Wang, G. Tian and et al, "Research and design of structural form of spoke structure[J]," *Journal of Building Structures*, 2013,34(5):1-10. (In Chinese).

[4] Z. Zhang, M. Zhang and S. Dong, "Discussion on some problems of beam-string structures[J]," *Engineering Mechanics*, 2004, 21(6):26-30. (In Chinese).

[5] W. Xue, S. Liu, X. Su and et al, "Design optimization and experimental study on prestressed beam string of Shanghai Yuanshen Arena[J]," *Journal of Building Structures,* 2008, 29(1):16-23. (In Chinese).

[6] Z. Zhang, S. Dong and H. Deng, "Computational analysis and shape determination problem of Beam-String Structures[J]," *Spatial Structures*, 2011, 17(1): 8-14. (In Chinese).

[7] B. Tu and D. Zhao, "Research review of basic problems of progressive collapse[J]," *Spatial Structures*, 2013, 19(3): 20-26. (In Chinese)

[8] Q. Han, C. Wang and J. Xu, "Progressive collapse mechanism analysis of large-span double-layer latticed domes[J]," *Spatial Structures*, 2014,20(2):29-36. (In Chinese)

[9] Y. Ding, J. Ge and Z. Li, "Instantaneous Component-Removing Method for Analysis of Progressive Collapse of Space Grid Structure[J]," *Journal of Tianjin University*, 2011,44(6):471-476. (In Chinese)

[10] G. Wang, "On mechanics of time-varying structures[J]," *China Civil Engineering Journal*, 2000, 33(6): 105-108. (In Chinese)

[11] Z. Cao, "Construction mechanics and time-varying mechanics in civil engineering [J]," *China Civil Engineering Journal*, 2001(03): 41-46. (In Chinese)

Timber and bio-based structures

Active bending
Additive manufacturing/ 3D printing
Architectural geometry
Bamboo for sustainable construction and quality of life improvement
Bio-inspired structures and architecture
Bridge structures
Computational form-finding
Conceptual design
Concrete structures
Construction techniques
Deployable and inflatable structures
Design competition (WG21)
Digital modelling and fabrication
Dynamic response of metal spatial structures
Dynamic response of other structures
Form-finding and structural optimisation of interlocking discrete assemblages
Graphical methods
Gridshell and lattice structures
Historical concrete shells
Historical structures
Lattice structures
Life-cycle design and assessment of structures
Metal gridshell structures, connections and stability
Methods and construction technologies for sustainable shell structures
Morphology and configuration processing
Next generation parametric design
Novel methods in modelling, optimisation and construction for reducing carbon footprint of continuous roof shells
Numerical methods for geometry, form-finding and optimisation of lightweight structures
Optimisation methods and applications
Origami
Other
Teaching design uncertainty: working with unknown qualities/quantities of new and re-claimed materials
Teaching of shell and spatial structures
Tensegrity systems and cable structures
Tension and membrane structures
Tension structures in the Asia-Pacific
► **Timber and bio-based structures**
Topology optimisation
Traditional masonry structures and innovation
Transformable structures

IASS 2023
July 10–14 Melbourne
Integration of Design and Fabrication

Proceedings of the IASS Annual Symposium 2023
Integration of Design and Fabrication
10–14 July 2023, Melbourne, Australia
Y.M. Xie, J. Burry, T.U. Lee and J. Ma (eds.)

Compression resistance of digitally fabricated hollow timber columns

Stephan RAPLEY[a], Dan V. BOMPA[a,*], Suryakanta BISWAL[a]

[a,*] School of Sustainability, Civil and Environmental Engineering,
University of Surrey, Guildford, GU2 7XH, UK
d.bompa@surrey.ac.uk

Abstract

This paper investigates the experimental response of digitally manufactured hollow timber columns incorporating dry mechanical connections (DMC). Timber plates were cut to complementary geometries and mechanically attached to interlock and form an integral joint. For this research, from existing DMC, rectangular tab and slot geometries were considered. Four sets of columns with different aspect ratios, were tested to assess the influence of member slenderness on the structural response, which has not been yet investigated. Complementary compression and tension samples, as well as single tab and slot joint shear and pull-out samples were also tested. After describing the design rationale and manufacturing methodology, the test results from more than forty material and structural tests are given. A full account of the deformational response, stiffness, strength and post-peak characteristics of each configuration is given. The material tests indicate both the compression and tension strengths of the plywood sheet are of similar magnitude in the range of 25 MPa. As expected, the tension failure was relatively brittle whilst crushing in compression was rather gradual due to the inherent properties of the engineered timber. The tab and slot joint shear strength was consistently above 6 MPa, whilst the friction strength around 0.5 MPa. Brittle failure was observed in all the column tests. The predominant failure modes were crushing close to the top or bottom of the columns, buckling of the tab-panels or slot-panels around mid-height, and separation of plies in the failed region. The load-shortening response indicated that the stiffness and strength of the DMC hollow timber columns reduces gradually with increasing slenderness. Relatively slender columns with an aspect ratio of 5.0, had about 22% less strength than stub columns with an aspect ratio of 1.0. These results provide a detailed insight into the structural performance of digitally manufactured hollow timber columns which can be employed in temporary lightweight structures that can be disassembled and reused.

Keywords: digital manufacturing, timber joints, dry mechanical connections, disassembly, compression members

1. Introduction

Engineered wood materials like glulam, laminated veneer lumber (LVL) or plywood (PW) overcome issues such as strength, durability, natural defects, and scalability occurring in sawn timber [1]. These were applied in a number of digital fabrication projects such as, The Vida Theatre in Switzerland, which adopts integral mechanical attachments or dry mechanical connections (DMC) inspired by traditional cabinetmaking, showcasing the potential of combining digital and timber technologies. Another example, the ICD/ITKE Research Pavilion (Figure 1a), was designed with birch PW strips utilising the elastic bending behaviour of the material. The strips were robotically manufactured as planar elements, and subsequently connected so that elastically bent and tensioned regions alternate along their length [2]. WikiHouse shown in Figure 1b is one of many prototypes designed worldwide using a unique digitally fabricated open-source building system that started development in 2014 and demonstrates the capabilities of typical off the shelf PW and OSB sheets in building compliant, affordable houses with minimal erection time and labour required. The concept of building blocks exploits the benefits of CAD

Copyright © 2023 by Stephan RAPLEY, Dan V. BOMPA and Suryakanta BISWAL. Published in the Proceedings of the IASS Annual Symposium 2023 with permission.

and CNC (3-axis) technologies to produce accurate and jigsaw-like components, to enable people with no foreknowledge of the construction industry to construct a WikiHouse [3]. The Hexbox shelter in Sydney depicted in Figure 1c, adopted tusk mortise and tenon/tab joints to construct a curved shell PW canopy with an assembly of 201 unique hexagon box-like segments with PW wedge connectors [4].

The DMC method is a conventional technique of joining timber without using additional connectors such as screws or bolts, as commonly used in building structures [5]. With time it became unfeasible due to high labour costs and the need for specialized workmanship. But with modern digital fabrication, this technique has been resurrected. It is also known as 'dry wood joints' or 'wood-wood connections,' and include different types of joints such as mortise and tenon/tab, notched, lap, and scarf joints [6] (Figure 2). DMC was used in computer-controlled fabricated folded CLT plate structures made to create a bidirectionally folded surface construction, joined using a customised single-degree-of-freedom (1DOF), multi tab and slot joint (MTSJ) DMC similar to those used in this paper and shown in Figure 3 [7]. Compared to the configuration in Figure 3, the geometry of the tabs and slots was trapezoidal [8].

On the fixity provided by DMCs, Ref. [9] explored the MTSJs with dovetail joints (DJ) for the joinery of LVL panel hollow beams. It was shown that DJ provide a highly feasible alternative to the traditional screwed connection, obtaining 96% of the rigidity comparing it to reasonable screw spacing, with a much shorter assembly time. Experiments comprised ten series of hollow beams, produced from 21mm thick LVL panels with spruce ply, and incorporating different connection types. Sensitivity analyses were conducted with respect to varying the tab length (41mm to 221mm) and the tab face angle (0, 15, and 25 degrees). The slot lengths were equal to the tab lengths for each configuration. It was concluded that increasing the tab face angle to 15 or 25 degrees increases rigidity by 26% and 38%, respectively. Larger angles, such as 25 degrees, increase transverse stresses and loads perpendicular to the panel grain.


(a)

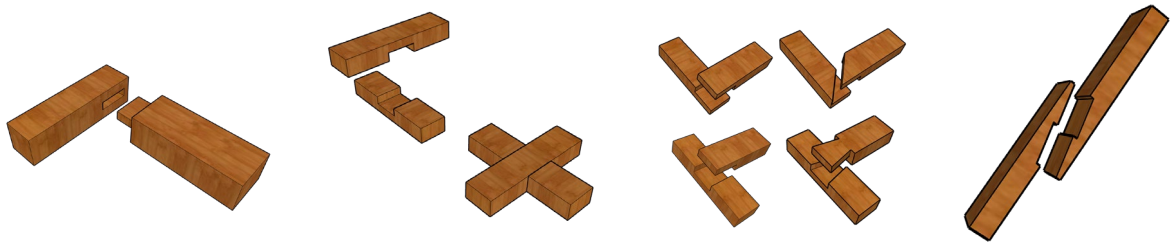
(b)

(c)

Figure 1. Structures incorporating DMC, a) ICD/ITKE Research Pavilion 2010 [2]; b) Example of Wiki House construction [3]; c) Hexbox Shelter [4].

Two types of MTSJs were investigated, showing that the closed slot MTSJ was more efficient and structurally robust compared to the open slot MTSJ [10,11]. Closed slot (CS) MTSJ are like those from Figure 3, whilst open slots are joined at the edge of the two plates; i.e. the tabs and slots are in contact at three interfaces. The load-carrying capacity of the CS joint was studied in an experiment using five types of wood products, including OSB and LVL, and varying tab lengths [12]. Robeller et al. [10] tested the assembly of a folded timber plate structure with oversized DMCs of 0.05- 0.25mm.

They discovered that the force required for inserting tabs significantly increased for oversizing above 0.15mm. They also found that tilting the joint faces at a 1° angle across the edge greatly reduced the wedging effect. An investigation into the CS connection explored three different tab insertion angles (45, 60 and 90 degrees) with specimens loaded in the parallel and perpendicular fibre orientations, and the use of two LVL types. The in-plane strength was highest in specimens with a 60-degree tab insertion angle, as it activated both tension and shear capacities perpendicular to the grains in the tabs. The study also found that the tab insertion angle strongly influenced joint stiffness, while the fibre orientation had a significant impact on joint strength [6].



(a) (b) (c) (d)

Figure 2. Joint types a) mortise and tenon/tab; b) notch; c) lap; d) scarf.

Elsewhere, the structural response of an OSB roof (slab) components composed of large top and bottom panels (1.25 × 2.5m) separated and joined by web elements, and employing DMC CS joints. A fully robot-automated process was used for manufacturing and assembly. Shear tests showed that the CS joint behaviour is elastic and brittle, the panel thickness does not significantly influence the resistance and stiffness, but the machining of the panel does, and the joint spacing affects the shear stiffness up until an effective number of joints is reached [13].

DMCs called elastic interlocks or snap-fit joints were also developed [7]. These were used to join 21 mm thick Spruce Kerto-Q panels with a box beam that was CNC manufactured. The snap-fits only carried tensile forces, while prismatic tab-and-slot joints provided the share resistance, making the connection behave like a screwed joint. The snap-fit joints were only necessary during construction to keep the panels together, so they were not designed for high traction forces. Changing the hook geometry and the number of hooks could improve the shear capacity of the joint. Although DMCs have been studied in various applications, limited research has been conducted on its use for structural applications in typical framed buildings such as beams and columns. This study aims to investigate the structural performance of digitally manufactured hollow timber columns incorporating DMC, which has not been explored before. Such systems can be employed in temporary lightweight structures that can be disassembled and reused.

2. Methods and materials

To analyse the behaviour of DMC timber hollow columns in compression, four sets of columns were designed with different aspect ratios, to capture the effects of slenderness. Three specimens for each configuration were built. In addition to the column tests, material (tension and compression) and DMC (shear and pull-out) tests were also conducted to obtain the mechanical properties of the 18 mm hardwood plywood (PW) poplar core. These tests assess the compressive and tensile strengths of the material, and the shear strength of and adhesion (friction) of each tab and slot joint in the columns. A minimum of three material tests per configuration were carried out, in accordance with current procedures. The moisture content of the PW was obtained using the existing guidance [14]. This was 5.76 %. All samples were taken from PW sheets of 1220 × 2440 × 18 mm sheets. The methodology comprised the following stages: design, cutting of the material, preparation for testing, and testing, and post-processing. These are explained in more detail below.

2.1. Design and fabrication

Three-dimensional representations were developed using SketchUp, and AutoCAD 2022 was employed to produce the exploded columns in 2D drawings form, for CNC machining [15, 16, 17]. The specimen designs were constrained by the 3 axes of the CNC machine. Thus, the tab and slot DMC was chosen for these experiments. Column designs were also constrained by the CNC machine bed dimensions (600 mm × 900 mm), and a further reduction due to the spindle not reaching the full length of the bed. A schematic column design configuration (AR4), along with the other test specimens, are shown in Figure 3. Material/connection sample ID adopts the format xxx-y, in which xxx=Ten, Com, Shr, Pul for tension, compression, shear or pull-out, respectively, whilst y is for the sample repeat. Columns specimen ID

includes the definition Col-ARx-y, in which Col stands for columns, ARx is for aspect ratio with x=1,2,3,4,5, and y is for the specimen repeat. For example, Col-AR1-2, is the second column with aspect ratio of 1 (i.e. height to width ratio of 1).

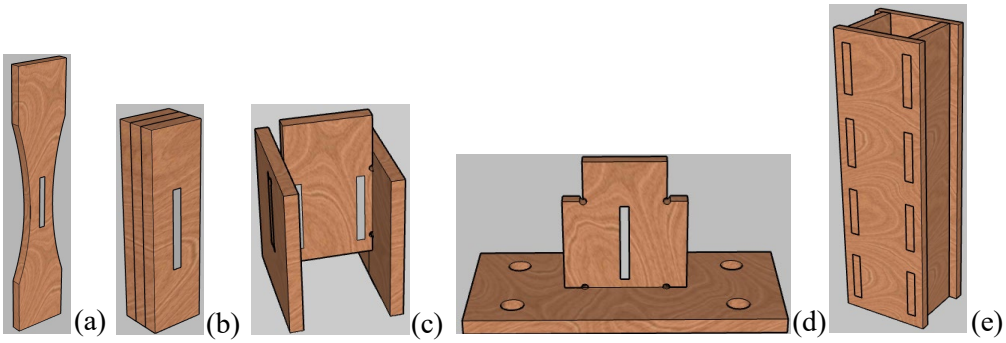


Figure 3. Material and column test specimens with location of transducers shown by grey shaded areas for: a) tension, b) compression, c) shear, d) pull-out, e) hollow column (AR4) (note: not to scale)

After the schedules were ready, they were opened on the CNC's VCarve Pro software ~~and~~ where the cut runs were configured [18]. Between 2 and 6 tabs of length 10 mm and thickness 4 mm were added to each element, to keep them secure while being cut. The router was configured to 7 passes at 3 mm depth for each element, corresponding to half the diameter of the router cutter. The first pass, however, was set to 0.5mm depth, to provide a clean finish. The entire cutting depth was set to 18.5 mm, 0.5 mm larger than the thickness to allow for cutter penetration. A sacrificial MDF board was used below the plywood boards to protect the CNC bed (Figure 4). A Spartan 6090, 3-axis CNC router, equipped with a straight, 2-flute cutter with a radius of 6mm, operated at a feed rate of around 3800 millimetres per minute (mm/min), corresponding to a chip load of 0.38mm, and a spindle speed of 10,000 revolutions per minute (RPM). The plunge rate was set to 254 mm/min. The cutting time for the scheduled board was around 35 to 50 mins, depending on the quantity and complexity of components per board. After each cut job was complete, the elements were marked with their identification code.

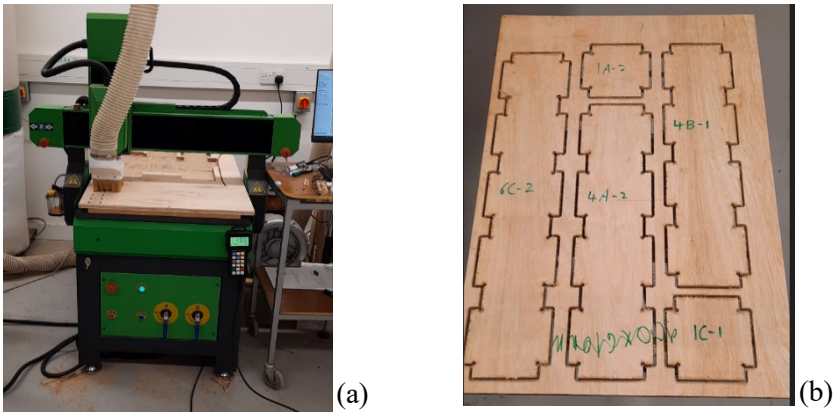


Figure 4. Digital fabrication of the specimens: a) CNC cutter operating on a cutting schedule; b) plywood board with column tab-panels post-cutting.

Once the schedules were finished on the CNC, the tabs were severed using a chisel and mallet, placing the plywood panels on a flat surface, and striking the chisel once for a clean cut. Sandpaper was used to lightly smooth down the rough surfaces where needed, particularly around tabs and slots. The perimeter of the components was also sanded to remove any sharp edges. A block plane was used to create a small (1 to 2 mm) taper on the edges of all the tabs on every panel to allow for easy assembly of the tab and slot joints. Specimens were prepared for digital image correlation (DIC) capture.

To assemble the hollow columns, the individual panels were grouped together according to their ID markings. A panel with the slots (slot-panel) was placed on a clean, flat surface, then one of the corresponding tab-panels was placed on top of the slot panel with the tabs and slots aligned. A rubber mallet was used to hit the tabs into the slots, beginning at one end of the panel, and incrementally hitting each tab downwards so that the panels join evenly, firmly applying pressure to the tab panel to limit any see-saw action. An inspection of all the joints was carried out, to ensure all the joints were fully connected. A block plane was used to smooth the top and bottom surfaces, where the column bases were slightly uneven. The same assembly process was undertaken for the shear and pull-out tests.

2.2. Testing arrangements and procedures

An Instron 600 kN testing machine was used for all the tests. The machine was fixed to the ground and applied load to/from the top of the specimens (Figure 5). For the compression-loaded specimens (compression shear, and columns tests), a base plate was mounted to the bottom jaw, with a round spring head attachment with a steel plate to distribute the load over the top. These enabled the uniform, concentric loading of the specimens with minimal eccentricities. For the tensile tests, the specimens were first mounted in the bottom grip at 50 mm from the bottom of the cavity, prior to the grips being closed. Once the top grips were lowered into position, they too were closed onto the top part of the dog-bones. The pull-out tests required the base (slot-panel) component to be attached to the base of the testing machine with four bolts; four holes were drilled to facilitate this. The upper machine grips were fixed onto the tab-component of the pull-out tests over round 25 mm depth. For the columns, a loading rate of 1 mm/min was used. For the material and DMC tests, a loading rate of 0.5 mm/min was used. These displacement rates are typical for monotonic testing of construction materials [19, 20].

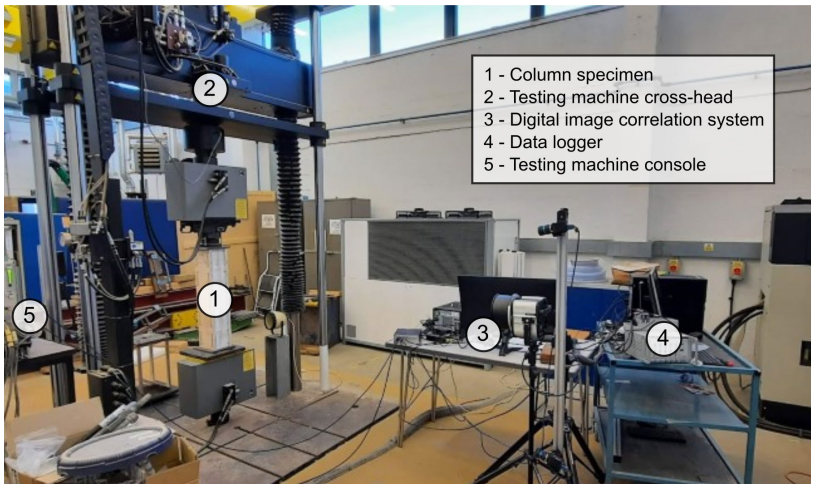


Figure 5. Test set-up for the columns.

3. Results and discussion

3.1. Material tests

Figure 6 shows the tensile stress-strain curves and typical representations of the dog-bone specimens after testing. The stress was evaluated by dividing the machine recorded force by the smallest cross-section of the sample, whilst the strain was evaluated from transducer data using a gauge length of 80 mm. From Figure 6, there appears to be a kink at a stress of 3.0-5.0 MPa in all the tension curves, exhibiting a bilinear response of the plywood. Subsequently, the stiffnesses of the lower and upper parts of the curves are calculated separately. Respectively, these are taken as E_1 (0 to 5 MPa), and E_2 (5.0 to 10.0 MPa). The average modulus of elasticity, E was 3.5 GPa. The average tensile strength exhibited by the plywood specimens was 22.4 MPa. The highest stress reached at 25.0 MPa at a strain of 0.0013, for Ten-1. The lowest stress was 19.9 MPa at a strain of 0.0096, for Ten-3.

The average tensile strength also agrees with the range of typical values for plywood, with variations due to differing plywood timber and moisture content [20]. Ten-2 shows a fracture line close to the centre of the specimen, which is expected (Figure 6b,c). From the second photo for Ten-2, the last few plies of the back face have separated from the specimen, with the crack propagating through a ply just above the transducer bracket. The fracture in Ten-3 was slightly lower than that of Ten-2, but a more visible fracture can be seen through the plies, with some separation between them. The failure of Ten-4 was similar to Ten-2, with the fracture occurring at 20-30 degrees at the centre.

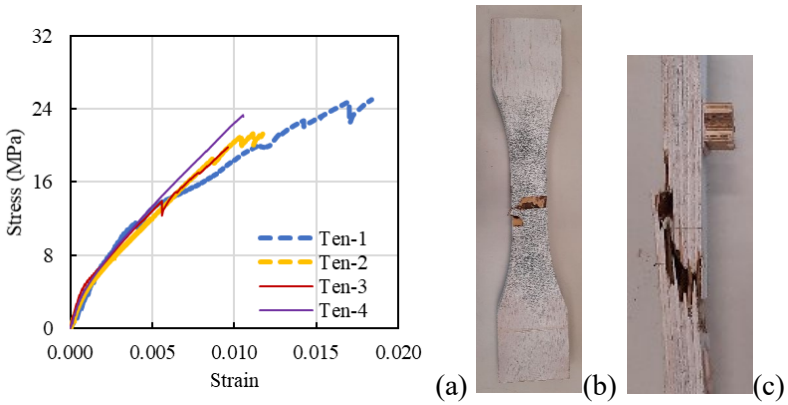


Figure 6. Tension tests: a) stress-strain curves; tension specimen Ten-4: b) after testing; c) side face fracture.

The results from the four compression tests showed the plywood to have an average compressive strength of 24.2 MPa. The compressive strength was evaluated by dividing the machine load by the cross-section of the sample, whist the strains were evaluated using the same approach as for the tension coupons. As a comparison, this value is close to the characteristic compression strength of other plywood materials [5, 20]. As shown in Figure 7, Com-2 achieved the highest peak stress at 25.7 MPa, with a strain of 0.0082. A shear failure occurred at the top of the specimen with an approximate angle of 45-degrees. Com-3 exhibited the lowest peak stress, 21.7 MPa at a strain of 0.0072. A modest crushing at the bottom of the specimen and some separations of the plies were observed.

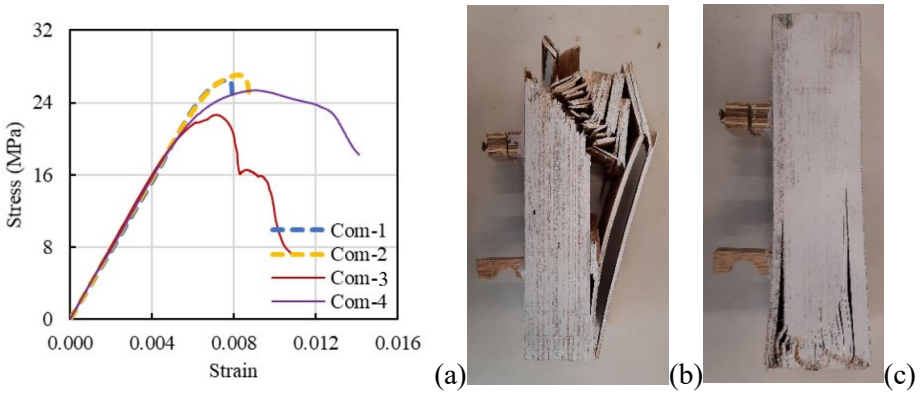


Figure 7. Compression tests: a) stress-strain curves, b) Com-1 after testing; c) Com-2 after testing.

Com-2 experienced severe separation of the plies during loading, which contributed to the inverted V-shaped crushing at the bottom of the specimen. Com-4 experienced a shear failure at the top of the specimen, along with partial separation of the plies at the back face of the specimen. This shear failure was similar to that of Com-1, but the shear angle propagated in the opposite direction. A large linear region is observed in the compression stress-strain curve, from 0 to 20 MPa. The average modulus of elasticity was 4.1 GPa, with a maximum of 4.7 GPa and a minimum of 3.9 GPa. These correspond to Com-3 and Com-2, respectively. The low standard deviation of 0.39 in the linear elastic range agrees with the stress-strain plot in Figure 7 as the curves of each specimen follow a similar path.

3.2. DMC tests

The results from the shear tests are shown in Figure 8. The highest peak load was 26.9 kN, corresponding to a shear stress of 3.8 MPa, and a displacement of 25.1 mm. This was exhibited by Shr-3, which also absorbed the most energy. The shear stress was evaluated based on the section of the tabs, and the energy refers to the area under the stress-displacement curve. The average peak load was 23.0 kN, but a standard deviation of 3.6 was calculated, reflecting some variance of these values. In terms of specimen kinematics, Shr-1 showed crushing and shearing of the right joint, but the left joint only showed crushing of the tab at the base of the slot. The same failure mode was demonstrated for Shr-2. Similarly, Shr-3 showed crushing of the tab on both the right and left side joints, but a more defined crack at the right joint propagated from the bottom right notch to the base of the panel, at a steep angle between 75 and 85 degrees. However, by observation of the curve in Figure 8, the linear region of the curve only reached 1 kN, although with a small displacement of less than 1 mm. This curve is somewhat different compared to curves from literature for LVL DMCs [6], which had a longer initial linear section beyond 5.0 MPa.

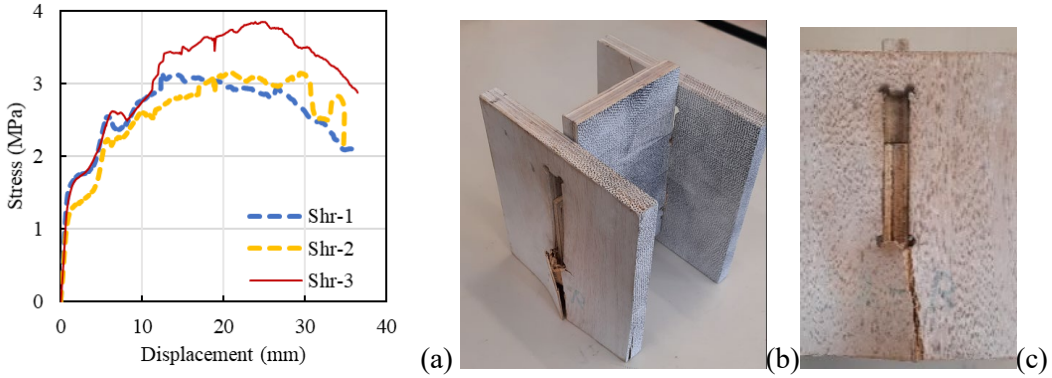


Figure 8. DMC shear tests: a) stress-displacement curves; Shr-3 specimen: b) after testing, c) left side fracture.

As shown in Figure 9, the maximum stress from pull-out tests was around 0.73 MPa, corresponding to 2.2 kN and a displacement of 2.04 mm, for Pul-2. The pull-out stress is the force divided by the contact area between the tab and the slot. On the other hand, Pul-1 sustained the smallest pull-out load, 0.27 kN. Although the displacement is only 0.43 mm, the capacity of the joint is significantly less than that exhibited by Pul-2. Despite the low magnitude, the tab does not have to sustain a large friction resistance, because its primary function is to secure the column panels together. Moreover, a very large friction resistance will induce difficulties in dismantling the columns.

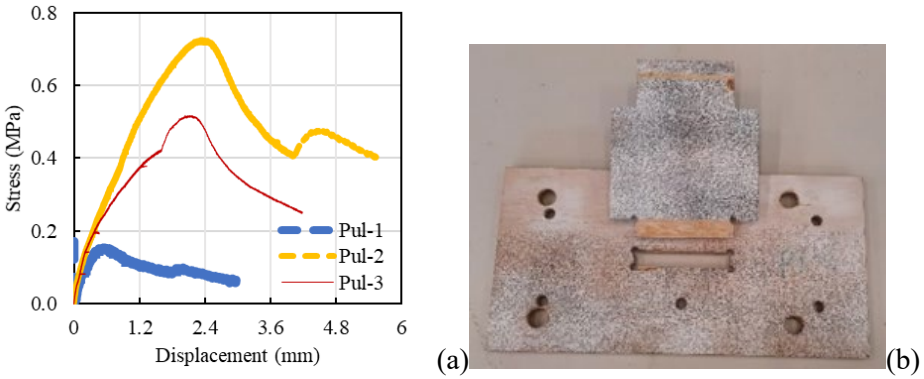


Figure 9. DMC pull-out tests: a) stress-displacement curves, b) specimen Pul-2 after testing.

The high standard deviation is likely to be due to the manual process of preparing and assembling the specimens. The total energy absorbed by each specimen varied substantially, with the lowest value, for Pul-1, and the highest value, for Pul-3. This is reflected in the curves; Pul-1 experienced a very short

curve which reached its maximum load very early compared to Pul-3, which gave a longer, but shallower curve, with a well-defined curved section at its peak. Overall, the results from the pull-out tests demonstrate that DMC tab and slot joints can vary substantially in load capacity by a factor of 5.1 and in displacement at the peak load of 4.1.

3.3. Column tests

Figure 10 shows the load-shortening curves and selected column specimens after failure. Table 1 depicts the main results as the average of the three tested specimens per configuration, as well as the standard deviation. Specimens Col-AR1 tests achieved a peak load between 195.9 kN and 216.4 kN, with an average capacity of 208.3 kN, equating to a stress of 19.3 MPa. The peak load, achieved by Col-AR1-2, was reached at a displacement of 2.3 mm. The failure mode had local crushing at the top of the specimen. Both findings could be expected, due to the stocky nature of the column, which, internally, has the form of a cube. The results from the Col-AR2 tests showed a decrease in the average peak load by 13.0%, compared with Col-AR1. Furthermore, a slightly larger displacement was observed in all the specimens, around 2.3 mm. The highest peak load, 185.5 kN, (17.2 MPa in stress), was achieved by Col-AR2-3; this is 10.4 kN less than the lowest capacity of the AR1 columns. Col-AR2-3 also experienced local crushing at the top of the specimen on one side.

Table 1. Main results for the column tests

Specimen ID	Length (mm)	Width (mm)	Height (mm)	Tabs/ slots (-)	Peak load P_{max} (kN)	Peak stress (MPa)	Displacement at P_{max} (mm)
Col-AR1	186	150	150	4	208.3±10.9	19.3±1.0	2.2±0.1
Col-AR2	186	150	300	8	181.3±3.7	16.8±0.4	2.3±0.2
Col-AR4	186	150	600	16	180.7±22.5	16.7±2.1	3.6±0.5
Col-AR5	186	150	750	20	166.4±13.9	15.4±1.3	3.9±0.6

From the Col-AR4 tests, a higher overall peak load was observed, in comparison to Col-AR2 tests, with the force reaching 201.5 kN, with a stress of 18.7 MPa, for Col-AR4-1. The deflection, 4.00 mm, was nearly double that of the Col-AR2 tests. A well-defined buckling on one of the panels was observed just above mid-height. The lowest peak load for Col-AR4, however, only reached 156.8 kN (14.5 MPa), by Col-AR4-3; a 12% reduction in capacity compared to the Col-AR2-2, which achieved the smallest peak load from the AR2 tests. This observation is reflected in the higher standard deviation of 22.50, compared to 3.73 for Col-AR2. Overall, a reduction of 13.3% in the average capacity, compared to ColAR1, was observed.

In parallel with the decreasing capacity trend from the previous column results, the results for the three AR5 columns showed a 7.9% reduction in the average capacity between Col-AR4 and Col-AR5, and an overall reduction of 20% between Col-AR1 and Col-AR5. The highest capacity, 176.5 kN (16.4 MPa) was achieved by Col-AR5-3, and the lowest, 150.6 kN (13.9 MPa), by Col-AR5-2. This was also the overall lowest peak load. Similar failure modes in plate buckling were observed in all three AR5 specimens; buckling occurred at the midpoint of Col-AR5-3.In relation to the material compression test, the strongest hollow column (Col-AR1-2, with a capacity of 20.0 MPa), is 17.0% lower than the average stress, 24.2 MPa. All other hollow columns achieved a lower compression capacity, particularly as the slenderness increases. This indicates a loss of capacity in the hollow columns, which would be increased through design changes, such as the addition of stiffeners or end plates.

With regard to the failure modes and specimen kinematics, Col-AR1-1 showed outward buckling of slot-panel at mid-height with some crushing near the bottom edges of tab-panel and slot-panel, Col-AR1-2 showed crushing at top of tab-panels and severe separation of slot-panel plies, whilst Col-AR1-

3 crushing at top of tab-panel and slot-panel, and fracture at top of slot-panel propagating from the notch. Specimens with an aspect ratio of 2 showed crushing at top of the tab-panel and slot-panel and some separation of plies in the failed region (Col-AR2-1), or buckling of tab-panel and vertical cracks at the mid-point of the slot-panel (Col-AR2-2), or 30° shear failure at the top edge of slot panel; some buckling at mid-height of tab panel (Col-AR2-3). All Col-AR2 specimens showed some separation of the plies.

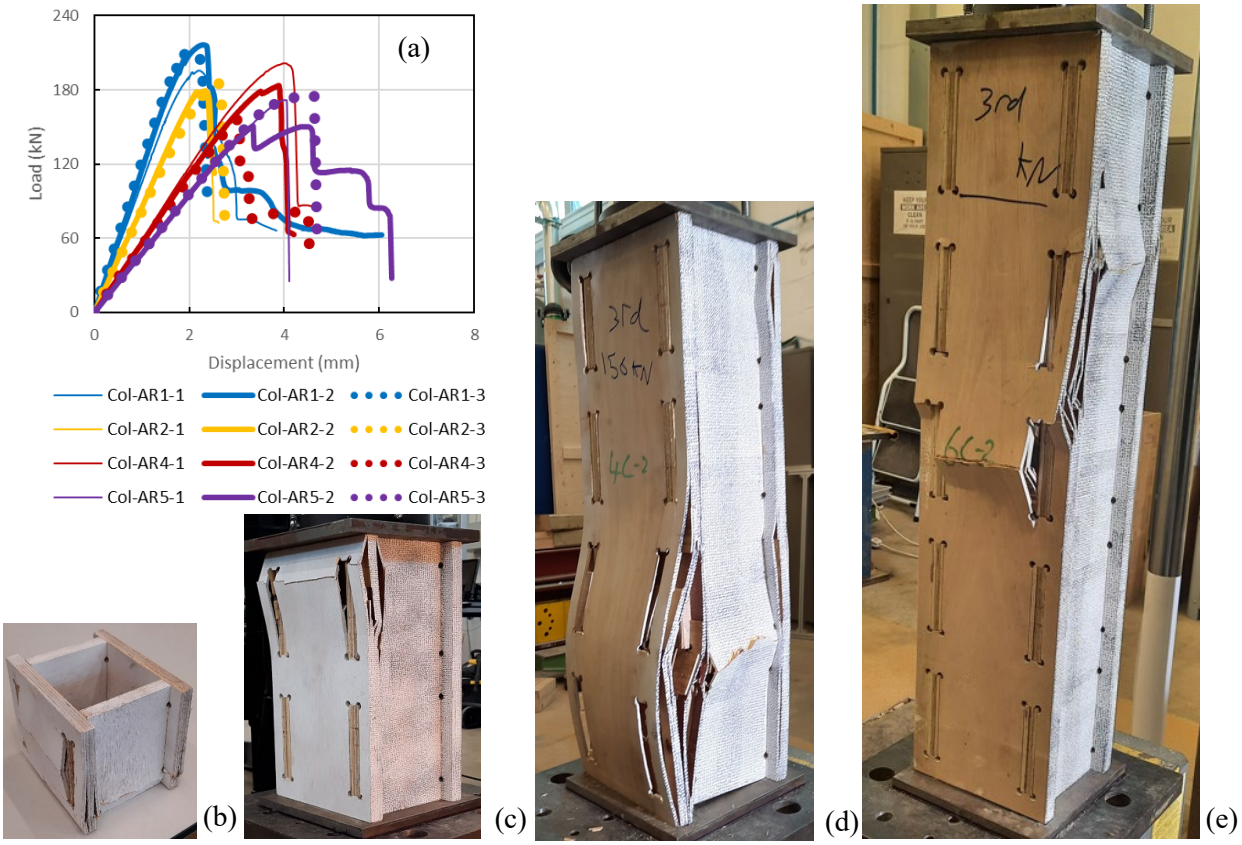


Figure 10. Results from column tests: a) Graph showing load-displacement curves for all the column tests; DMCges of failed specimens, b) Col-AR1-1; c) Col-AR2-1; d) Col-AR4-3; e) Col-AR5-3.

With an increase in height, a well-defined plate buckling just above mid-height of slot-panel or tab-panel with a fracture at the edge of slot-panel was observed (Col-AR4-1, Col-AR4-2). Col-AR4-3 failed with substantial separation of slot-panel plies, buckling of tab-panel at mid-height, and global flexural buckling of the column. Finally, the tallest columns (Col-AR5) had well-defined buckling modes at the tab-panel and slot-panel, with various levels of ply separation or splitting. Overall, the DMC hollow columns tend to experience brittle failure, with either crushing close to the top or bottom of the columns, buckling of the tab-panels or slot-panels close to mid-height, and separation of plies in the failed region.

4. Concluding remarks

This paper investigated the experimental response of digitally manufactured hollow timber columns incorporating dry mechanical connections (DMC). Timber plates were cut to complementary geometries and mechanically attached to interlock and form an integral joint. For this research, from existing DMC, rectangular tab and slot geometries were considered. Four sets of columns with different aspect ratios, were tested to assess the influence of member slenderness on the structural response, which has not been yet investigated. Complementary compression and tension samples, as well as single tab and slot DMC shear and pull-out samples were also tested. The main concluding remarks are below.

The material tests indicate both the compression and tension strengths of the plywood sheet are of similar magnitude in the range of 20-25 MPa. The tab and slot joint shear strength was consistently above 6 MPa, whilst the friction strength was around 0.5 MPa. Brittle failure was observed in all the column tests. As expected, the tension failure was relatively brittle whilst crushing in compression was rather gradual due to the inherent properties of the engineered timber.

The load-shortening response indicated that the stiffness and strength of the DMC hollow timber columns reduces gradually with increasing slenderness. Relatively slender columns with an aspect ratio of 5.0, had about 22% less strength than stub columns with an aspect ratio of 1.0. This corresponds to an axial peak stress at crushing of 63% and 80% of the compression strength of the material, respectively. The predominant failure modes were crushing close to the top or bottom of the columns, buckling of the tab-panels or slot-panels around mid-height, and separation of plies in the failed region.

These results provide a detailed insight into the structural performance of digitally manufactured hollow timber columns which can be employed in temporary lightweight structures that can be disassembled and reused. Additional benefits come from geometry optimisation and material minimisation for efficient transportation.

Acknowledgements

This research has been supported by internal funding provided by the School of Sustainability, Civil and Environmental Engineering at the University of Surrey. The support is gratefully acknowledged.

References

[1] Lendlease, "Timber Pavilion at IQL has 'outstanding' sustainability credentials," *www.lendlease.com,* 2021. https://www.lendlease.com/better-places/timber-pavilion-at-iql-has-outstanding-sustainability-credentials/ (accessed Aug. 15, 2022).

[2] J. Knippers and A. Menges, "ICD/ITKE Research Pavilion 2010," *www.icd.uni-stuttgart.de*, 2010. https://www.icd.uni-stuttgart.de/projects/icditke-research-pavilion-2010/ (accessed Aug. 22, 2022).

[3] WikiHouse, "WikiHouse," 2022. *https://www.wikihouse.cc* (accessed Aug. 22, 2022).

[4] P. Pintos, Hexbox. 2019. Accessed: Aug. 22, 2022. [Online image]. Available: https://www.archdaily.com/942876/hexbox-canopy-dtc-plus-codetoproduction

[5] D. V. Bompa, G. Dance, A. Chira, M.G. Walker. 2023. Structural response of hybrid timber - cold formed steel floors. *In Proceedings of Eurosteel 2023.*

[6] A. Rezaei Rad, Y. Weinand, H. Burton, Experimental push-out investigation on the in-plane force-deformation behavior of integrally-attached timber Through-Tenon joints. *Construction and Building Materials,* vol. 215, pp.925–940. 2019

[7] C. W. M. Robeller, "Integral Mechanical Attachment for Timber Folded Plate Structures," *École Polytechnique Fédérale de Lausanne (EPFL*), Switzerland, 2015.

[8] S. Roche, J. Gamerro, and Y. Weinand, "Multiple Tab-and-Slot Joint : Improvement of the Rotational Stiffness for the Connection of Thin Structural Wood Panels," in *World Conference on Timber Engineering*, Vienna, Austria, August 22-25, 2016, pp. 1–9.

[9] S. Roche, C. Robeller, L. Humbert, and Y. Weinand, "On the semi-rigidity of dovetail joint for the joinery of LVL panels," *European Journal of Wood and Wood Products*, vol. 73, no. 5, pp. 667–675, Jun. 2015, doi: https://doi.org/10.1007/s00107-015-0932-y.

[10] C. Robeller, V. Helm, A. Thoma, F. Gramazio, M. Kohler, and T. Weinand, Y. (2017). Robotic Integral Attachment. In: *Fabricate 2017*. UCL Press, pp.92–7.

[11] A. Stitic, C. Robeller, and Y. Weinand, 2018. "Experimental investigation of the influence of integral mechanical attachments on structural behaviour of timber folded surface structures," *Thin-Walled Structures*, vol. 122, pp. 314–328, doi: https://doi.org/10.1016/j.tws.2017.10.001.

[12] J. Gamerro, J. F. Bocquet, and Y. Weinand, 2020. "Experimental investigations on the load-carrying capacity of digitally produced wood-wood connections," *Engineering Structures*, vol. 213, p. 110576, doi: 10.1016/j.engstruct.2020.110576.

[13] J. Gamerro, I. Lemaıtre, and Y. Weinand, "Mechanical Characterization of Timber Structural Elements Using Integral Mechanical Attachments integral mechanical attachments," in *World Conference on Timber Engineering 2018*, Soeul, Republic of Korea, Jun. 2018.

[14] CEN (European Committee for Standardisation). 2022. EN 13183-1:2002. Moisture content of a piece of sawn timber - determination by oven dry method. 2022.

[15] Trimble. 2022. SketchUp (2022). [Software]. [Accessed 20 June 2022].

[16] Autodesk. 2022. AutoCAD (2022). [Software]. [Accessed 20 June 2022].

[17] Ventric. 2022. VCarve Pro V10.5 (2022). [Software]. [Accessed 20 June 2022].

[18] D.V. Bompa, B. Xu, O. Corbu, 2022. "Evaluation of One-Part Slag–Fly-Ash Alkali-Activated Mortars Incorporating Waste Glass Powder". *Journal of Materials in Civil Engineering*, 34(12), p.05022001. doi:10.1061/(ASCE)MT.1943-5533.0004532

[19] D.V. Bompa, B. Xu, A.Y. Elghazouli, 2021. "Constitutive modelling and mechanical properties of cementitious composites incorporating recycled vinyl banner plastics". *Construction and Building Materials*, 275, p.122159. doi: 10.1016/j.conbuildmat.2020.122159

[20] F. Latvijas. 2020. *Plywood Handbook.* 3rd ed. [online] pp.59–64. Available at: https://www.finieris.lv/docs/Produkti/Bukleti/Handbook_2017.pdf [Accessed 20 Aug.2022].

Proceedings of the IASS Annual Symposium 2023
Integration of Design and Fabrication
10–14 July 2023, Melbourne, Australia
Y.M. Xie, J. Burry, T.U. Lee and J. Ma (eds.)

Cross laminated plywood construction of a free-form roof

Paul LOH*, David. LEGGETT[a]

* Bond University
Abedian School of Architecture, Gold Coast, Queensland, 4229, Australia
ploh@bond.edu.au

[a] LLDS Architects | Power to Make

Abstract

The paper discusses the design, fabrication and assembly of a free-form roof structure constructed using a hybrid method of cross-laminating structural plywood. The research outlined the roof's design, fabrication and engineering workflow within an integrated fabrication environment led by the architect in collaboration with the engineer. Such workflow constructed resilience in the design and manufacturing process. The digital fabrication of the structure was developed in a single parametric model informed through 3 sets of physical prototypes. By incorporating as-built site information through digital scans, the assembly process was enhanced with feedback to ensure precision in manufacturing, thereby demonstrating care in construction through digital technology.

Keywords: timber structure, integrated design and fabrication, cross-laminated, designing for assembly, plywood, digital fabrication, prototyping

1. Introduction

Structural plywood and Laminated Veneer Lumber (LVL) are common building materials in construction, typically used as bracing and beam, respectively [1]. In recent years, Cross Laminated Timber (CLT) as a structural wood panel has increased usage globally and in Australia [2]. This paper expands on the research on timber laminated panel systems using digital fabrication and robotics [3] to explore a hybrid fabrication method called Cross Laminated Plywood (CLP). The CLP forms a structural wood panel and is an alternative to CLT.

The paper outlined CLP's integrated design, fabrication, and assembly workflow for a house project with a free-form roof structure, see figure 1. The roof design had multiple performative requirements. It provided a flat roof deck as a private open space, addressed overlooking issues from neighbours and diffused sunlight to the interior, see figure 2. Structurally, the roof was designed to support a biodiverse brown roof. It consisted of a set of CLP rafter beams and bracing plates as the primary structure, sheathed with plywood, insulated, and topped with a brown roof build-up. Through prototyping and structural testing, design information and construction parameters were integrated into the computation model to manage the complex geometry and the fabrication workflow. The paper concludes with the assembly methods, including in-situ templating and digital scans to accurately position each roof beam within a +/-2mm tolerance on site.

The research's significance lies in manufacturing the CLP within a small-to-medium enterprise (SME) context to reduce the design-to-production supply chain. The fabrication methods are relevant during and after the COVID-19 pandemic, where construction is often delayed due to an extended production chain and lack of human resources in Australia. CLP fabrication and construction methods provide an

Copyright © 2023 by Paul LOH and David. LEGGETT. Published in the Proceedings of the IASS Annual Symposium 2023 with permission.

alternative to CLT's large-scale production. The research highlights the need to integrate design, engineering and fabrication within a continuous construction ecology tested through a built project.

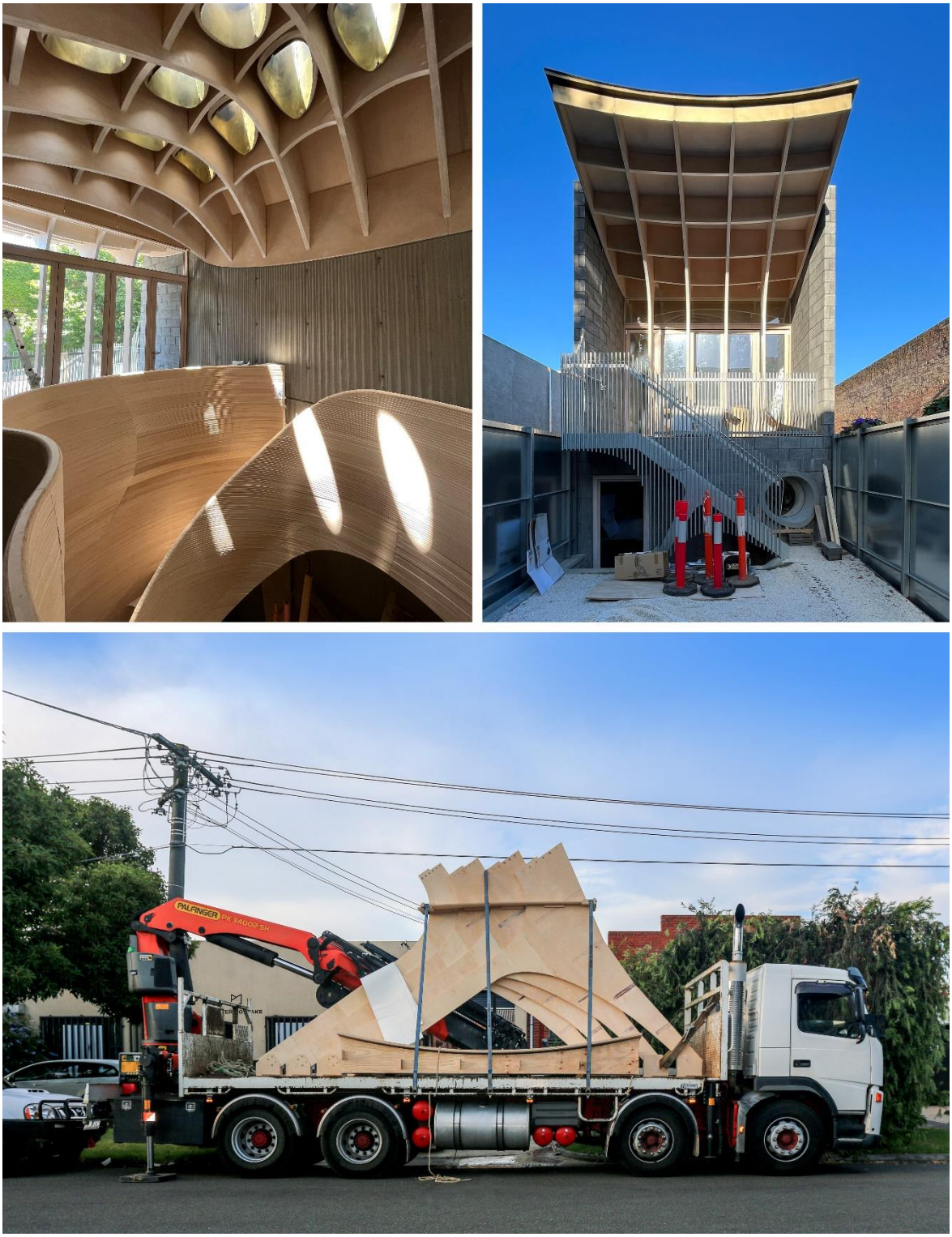


Figure 1. Top Left, the roof's soffit with skylights supported by the concrete boundary wall. Top Right, front elevation of the house with a cantilevered roof. Bottom, urban manufacturing facility of Power to Make. Image showing the loading of CLP roof rafters ready for site delivery.

2. Background

LVL is similar to plywood except that there is no cross-banding in LVL. CLT is fundamentally a large format plywood with individual layers between 12-45mm thick in three, five or seven layers [4]. The larger dimension of CLT over a standardise structural plywood sheet (typically of 2.4 x 1.2m) allows for its application as full-size wall, floor and linear components with the ability to bear load in and out of plane. Both CLT and plywood have high dimensional plane stability due to cross-layering. In CLT, a single layer is typically finger-jointed. The cross layering of lumber is quasi-rigidly connected using annular ringed shank nails or hardwood dowels [5].

Since its development in the 1990s, CLT has shaped building design. It challenges structure and superstructure design replacing concrete as the primary material. While solid timber construction has significantly accelerated in the past two decades, the first CLT building was not completed in Australia till 2012 [6]. In 2015, Australia produced its first CLT panel, and manufacturing plants were established in 2017 [7], [8]. Before this, most CLT panels are imported from New Zealand or Europe (using Spruce and Pine species).

2.1. Project background and fabrication context

The Northcote House by LLDS architects was designed in 2015-18, with construction commencing on site in 2019-2023. The roof design and fabrication result from an integrated collaboration between LLDS architects and TGA engineers, a specialist timber engineering practice based in Melbourne. While it is common for engineers to develop design and fabrication within the same environment (such as specialist fabricators in steel and timber), architecture practices are often removed from the fabrication environment. While significant efforts to bridge the gap exist through direct file-to-manufacturing in the past two decades, the integration is often only through data management and rarely through physical manufacturing [9], [10].

The significant difference in this project is the fabrication context. The architect operates a 500-square-meter fabrication workshop located within 7km of Melbourne CBD called Power to Make, specialising in timber joinery and architectural components, see figure 1. The practice operates its own CNC machinery, including a large format Computer Numeric Controlled (CNC) router (suitable for standard 1.2 x 2.4m plywood panel), a Kuka KR120 robotic arm, traditional woodwork and metalwork machinery.

2.2. Roof design

Two 150mm thick concrete walls on the site's boundary support the timber roof. At its thickest point, the roof is 3 meters deep and tapered to the cantilever edge of 205mm. The roof was designed as a trafficable landscape (live load of 3kPa). It functioned as a brown roof that contributes to the site's biodiversity (500kg/m2), shedding water to the edge gutters, and the symmetrical apex is used to block views from the neighbouring buildings. Figure 2 illustrates the geometric parameters used to set up the roof design. The underside of the roof is an exposed waffled (or coffered) structure that gives the main living area of the house its dramatic volumetric form. It is defined by a centrally located parabolic curve which blends into the two (short) parameter straight edges, see figure 2A. The two straight edges interface with the opening of the façade identified as Beam 1 and 15; Beam 1 is conditioned by the concrete beam that ties the two concrete walls together; Beam 15 is required to interface with the entrance door.

The roof consisted of 19 rafter beams and 76 bracing plates. It was designed to be assembled in two phases. The first phase is from Beam 1 to Beam 15; see figure 2. The second phase forms the cantilever roof from Beam 16 to Beam 19; see Figure 2. Two waling plates designed with mortises were anchor-bolted to the concrete walls to receive the primary beams. The area covered by Beam 1 to 15 forms the main roof over the interior. Beam 15 marks the transition between inside and outside. After Beam 15, the primary beams changed orientation from north-south to east-west and cantilevered out to form the overhanging roof. These east-west beams rested on the first-floor slab for two reasons. First, it ties the

uplift forces of the cantilever roof to the first-floor slab. Second, the depth of these beams acts as vertical brise soleil and privacy screening from the street.

Thirteen cone-shaped roof lights in the coffered roof structure draw daylight to the interior, see figure 2b. The depth of the coffered soffit is driven by the need to (1) diffuse daylight during winter and (2) block direct sunlight during summer. The roof light's fabrication detail is outside the scope of this paper.

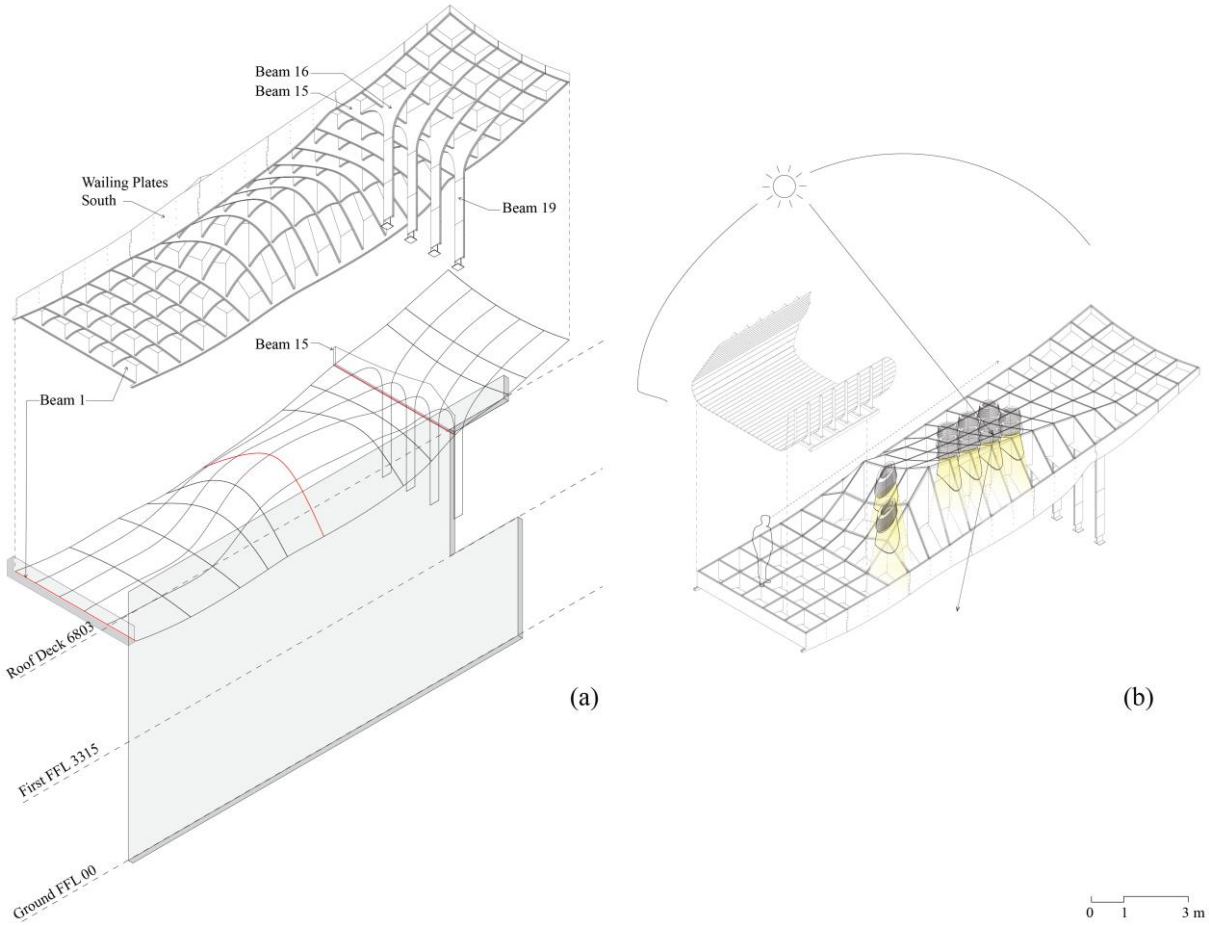


Figure 2. Left, (a) worm-eye isometric view of roof indicating the interior geometry parameters. Right, (b) isometric view of the roof illustrating the exterior requirements that shaped the roof design, including the 13 roof lights that bring diffuse lighting to the interior.

2.3. Motivations to reduce supply chain

During the schematic design phase in 2015, the nearest CLT supplier was based in New Zealand. The design team consciously shifted away from CLT, motivated by the need to reduce the roof's supply chain and the transportation cost (and carbon footprint). Two other design alternatives were considered, including (1) using LVL as a beam and rafter to construct a portal frame structure with plywood gussets or (2) constructing the roof using plywood-stressed skin panels [1]. The design team rejected these options as the width of the rafter will increase significantly from 54mm to 150mm. Further motivation to reduce the supply chain comes from the design team to integrate the design and fabrication of the roof structure within the manufacturing facilities of Power to Make. The workshop setup allows the design team to develop three sets of prototypes with the engineers. The testing and prototypes subsequently led to Power to Make fabricating and assembling the CLP onsite with the assistance of a licensed builder.

Reducing the supply chain has other implications. For example, the design team can monitor and control the cost of the CLP through its design. In-house production also allows the team to manage the quality of the finish, especially when the entire interior surfaces are visual. Structural plywood comes in five veneer grades (A, S, B, C and D), and the appearance can be further specified with ten different combinations of grading to the facing and back veneer (AA, AB, AC, AD, BB, BC, BD, CC, CD and DD). The structural plywood used in the project was specially pressed with the grain running along the panel's length and a BB/BB-facing veneer. The COVID-19 pandemic hit in January 2020 in Australia, halting all global supply chains. The roof was manufactured at Power to Make between March – August 2020, and installation on site commenced later that year.

3. Cross laminated plywood (CLP)

Standard plywood sheets come in 2400 x 1200mm. Each roof beam and bracing plate are glue laminated like a CLT - comprised of three layers of 18mm birch plywood laminated using structural polyurethane adhesive at 4MPA or a minimum of 500 PSI. Each layer was designed to be staggered vertically and horizontally, so there was no continuous joint line across the entire panel. Similar to CLT fabrication, each layer was edge-jointed with finger joint, $L \geq 45$mm, to reduce resistances and bend out of plane. The finger joints were CNC milled with 0.1mm tolerance.

The architects decided to use European Birch plywood as it was the most economical and dimensionally stable (compared to Hooped pine) in Australia. TGA engineers converted data for structural plywood performance certified to AS/NZS 2269.0:2012, in an equivalent of F17 grade timber to satisfy the Building Code Australia (Class 1) and simulated plate displacement and stress calculation analysis, see figure 3.

The main advantage of CLP is (1) it can be locally manufactured using a standard CNC router and (2) a single person can manually handle the standard-size plywood sheet. In this project, the authors fabricated the CLP under the guidance of TGA engineers. The largest panel fabricated was nominally 3.63m x 3m. In practice, the panel size is only limited by the constraints of the lifting equipment in the manufacturing facilities.

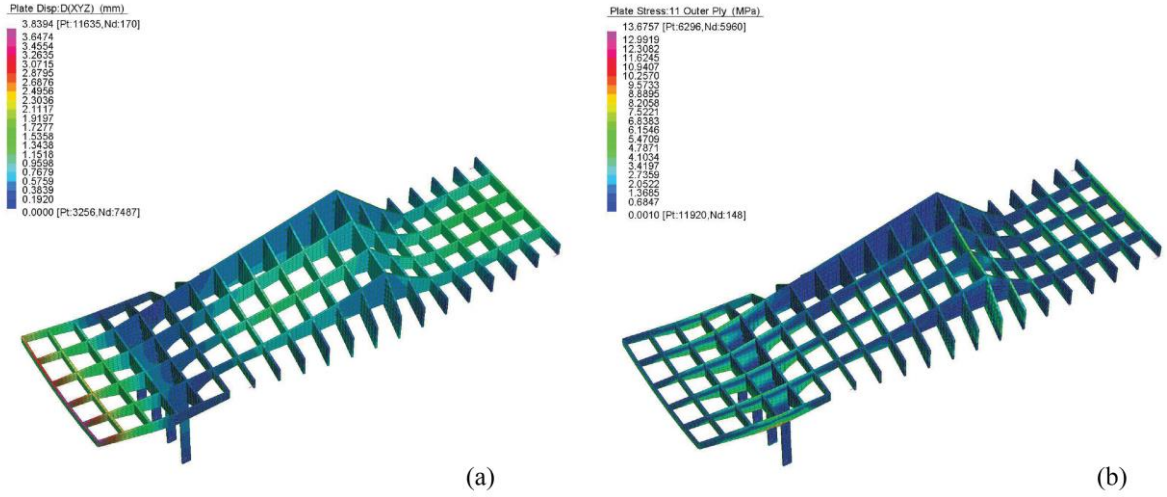


Figure 3. (a) Plate displacement analysis of 3-layer CLP. (b) Stress displacement analysis of 3-layer CLP. Image by TGA engineers.

3.1. Engineering and design feedback

The roof design evolved over two years, from initial sketch design to fabrication. To be resilient to the data updates and design changes, LLDS developed a single parametric model that processes the design constraints, detailing, engineering inputs, fabrication and assembly information into a continuous

workflow using Grasshopper 3D, see figure 4. The roof design was denoted by a set of base parameters, including a base grid, a collection of input curves and a surface (figure 4a). The input curves and surface respond to the criteria outlined in section 2.2. The model was evaluated through two sets of analysis: the minimal structural depth provided by the engineer (figure 4b) and the planarisation of the sheathing panels, refer to section 4.2. Rooflight detailing and its distributions were separately developed and integrated into the model (figure 4c). The structural members were separated into their assembly sequenced, and construction detail (figure 4c:11, 12 and 13) was added to the modelling, further expanded in section 4.1. The data was then checked against the as-build information (figure 4d:15); refer to section 5.1. The splitting of the CLP into its layers and joints was automated for CNC fabrication (figure 4d). The model enables LLDS to incrementally build design knowledge as the research team understands the roof's limitations and opportunities. In this instance, care in construction was created through the feedback system embedded in the parametric model, designed as an open system.

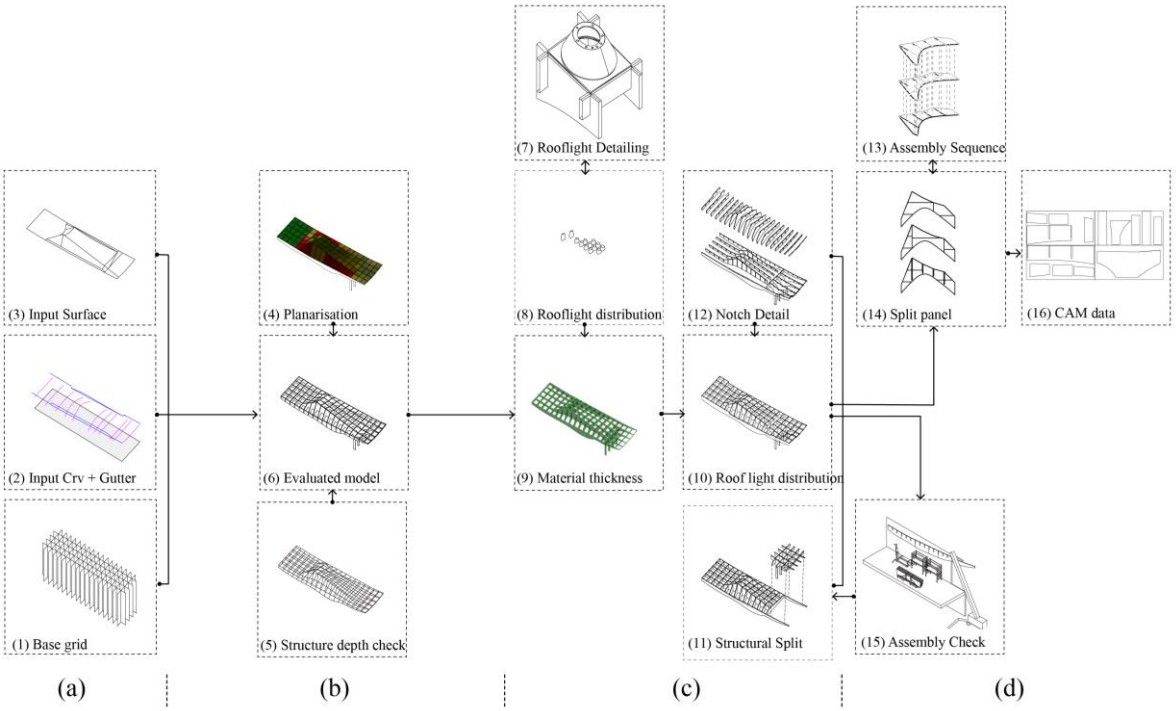


Figure 4. Integrated parametric design workflow. (a) Design input and criteria used to shape the roof geometry. (b) Evaluation of material and engineering requirements. (c) Inclusion of details developed through prototyping and construction sequencing. (d) Automation of fabrication information.

4. Learning from prototyping

Three prototypes are developed: (1) a 1m long junction with the 3-layer CLP composition, (2) a 1:1 prototype of a typical cell with a roof light and (3) a full-scale CLP Beam 1 for point load testing by TGA engineers. The purpose of these prototypes was to understand the fabrication sequence and technique of the CLP. Critically, the development led to Power to Make fabricating all the beams and plates in-house.

4.1. Prototype 1: fixing and lamination

Prototype 1 allowed LLDS to test the finger joints' tolerance, lamination techniques, and the junction between the beam and the bracing plate, see figure 5. The engineer specified 120mm long annular ringed shank nail to be screwed into the junction at a 45-degree angle, leaving little room for errors. Any deviation by +/- 3 degrees will cause the screws to penetrate the plywood on the other side. A jig was

designed to hold the screw at the correct angle. The screw hole positions were CNC piloted with an asymmetrical ellipse, used as a guide to orientate the screw fixing. It was pocketed so the fixing can be concealed with a plug. All the above are visual considerations.

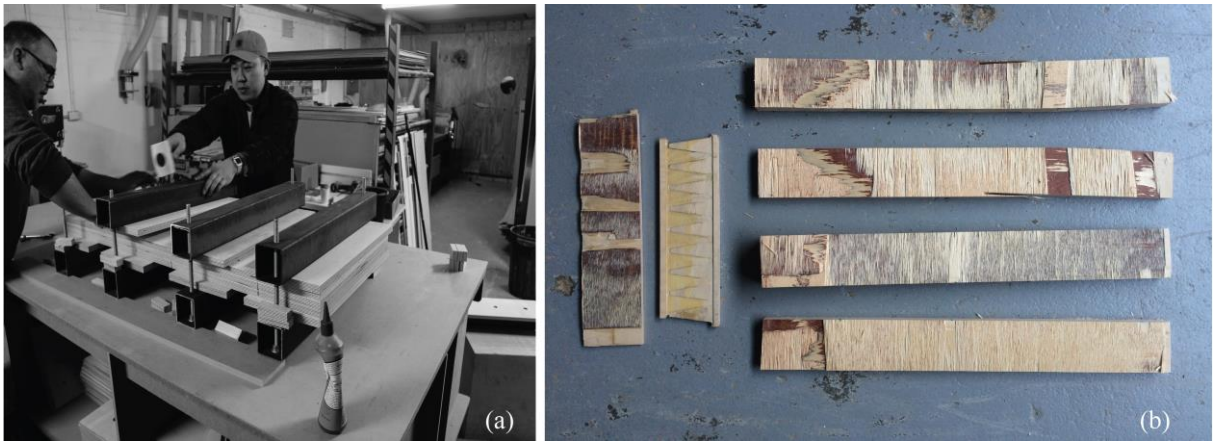


Figure 5. Left, lamination of prototype 1 illustrating the clamping device. Right, a splitted CLP demonstrates the glue bond quality between plywood layers.

A key aspect of CLP is the lamination techniques, particularly the consistent pressure required during the pressing process, as this needs to be proportional to the timber properties [11]. The engineer split the prototype with a chisel as a visual check. The glue is stronger than the timber, so the split did not yield a clean surface. Instead, it revealed the ply of each layer. Figure 5 illustrates the outcome, which indicates the lamination process was adequate.

4.2. Prototype 2: active bending

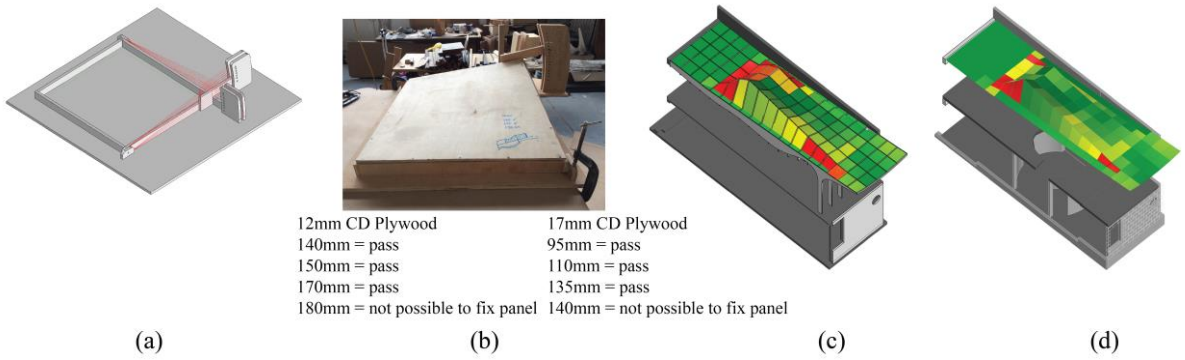


Figure 6. (a) Device used for testing the warp property of plywood. (b) Physical testing of plywood. (c) Roof model correlating sheathing geometry to plywood warp property. Red indicates the surface warp is out of range, and the dark green panel is flat. (d) The roof model was optimised to reduce the number of extremely warp panels to 8.

The second prototype is an entire roof cell with a roof light detail. This prototype illustrates the complexity of the sheathing to the roof. As the roof was subdivided into square cells (730 x 730mm), 75% of the 95 sheathing panels were doubly curved hyperbolic surfaces. Triangulating the sheathing panel into a planar surface was not an option without introducing another complicated structure to the cell and impacting the interior's visual quality.

LLDS developed a simple device to test the bending capacity of 12mm and 17mm plywood, see figure 6a & b. The physical tests provided data as input to the parametric model of the roof, see figure 6c. After several modifications to the surface geometry, the number of panels outside the active bending capacity of the plywood was reduced from 18 to 8 panels with the most extreme curvature, see figure 6d. These

panels are kerf and laminated separately. This results in all the sheathing panels being CNC milled and brought to the site, which speeds up the installation process.

4.3. Prototype 3: point load and deflection

The third prototype is a full-length beam, laminated with all the details captured in Prototype 1. LLDS designed a bespoke, flexible table clamp system to provide even compression pressure across the beam surface, see figure 8. The 3.63m long beam was point-load tested at the TGA workshop. It was designed to take up to 30kN. The result indicates the beam deflected by 21mm at 65.7kN (6.7 tonnes) with visible tear to the plywood core, see figure 7. The beam outperforms the design by over 200%.

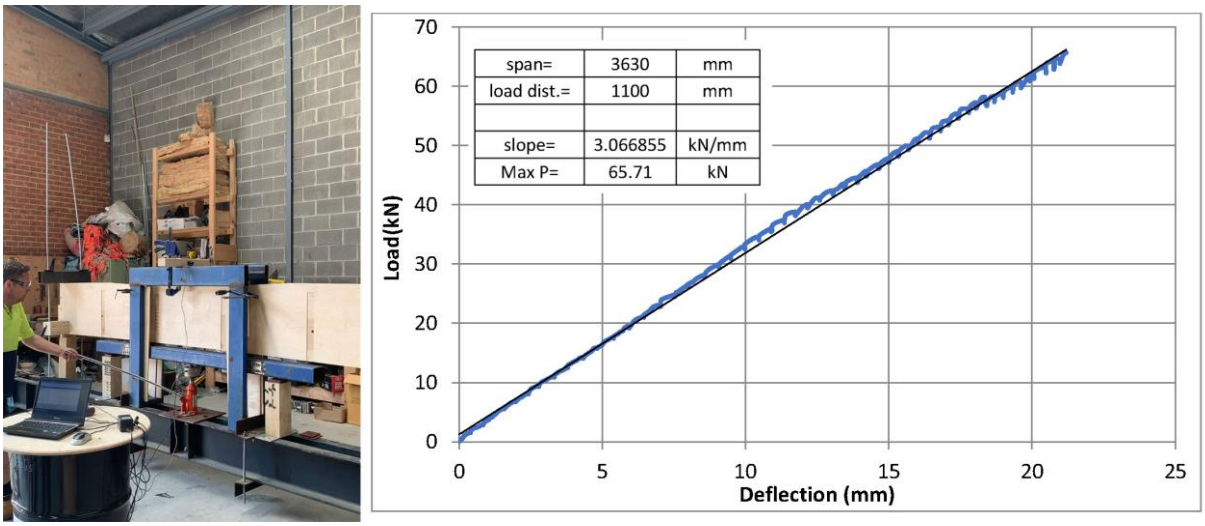


Figure 7. Left, point load deflection testing at TGA workshop. Right, load–deflection curve indicates the beam outperforms the design deflection by over 200%.

5. Assembly of the CLP roof

The authors installed the CLP roof structure with assistance from a registered builder. Before the final wailing plates were delivered to the site, LLDS architects produced a full-scale template of the waling plate in MDF. The templating process was critical as it allowed a final check on the wailing plates' alignment using laser levels and for the anchor bolt holes to be pre-drilled. Each wailing plate comprises five segments with a notch joint between each panel. Four segments were fully anchored to the concrete wall to receive Beam 1 to 15. The last segment was supported with 1/3 of its length fixed to the concrete wall (supported by a concealed steel bracket) and the rest cantilevering.

5.1. Site feedback

Once the final wailing plates were installed, the site was digitally scanned with a Z+F IMAGER 5016 terrestrial laser scanner with a maximum of 160m reach and a resolution of 0.8mm. A series of sections were extracted from the point clouds to check the as-built against the digital model, see figure 8. The scan data were used to (1) adjust the CNC fabrication information of the beams and (2) allowed Power to Make to trim the tenon ends of the beams to ensure the entire structure would fit before delivery to the site. With the scanning technique, LLDS comfortably work to a tolerance of +/- 2mm, just enough for the beam to wiggle into the mortise with a snug fit. The authors used this incremental construction technique in the concrete package previously published in another article [12].

Once all Beam 1 to 15 were installed, the bracing plates followed. The beam and bracing plates were mechanically screw-fixed at a diagonal per the prototype. The jig for the screw fixing and the pocketing to orientate the screw become useful onsite. The same operation applies to the second installation phase for the cantilever roof.



Figure 8. Top Left, clamping device developed by Power to Make. Top Center, Installation of the roof beam on site. Top Right, Installation of sheathing panels, showing both the pre-curved panels and active bending of the sheathing onsite. Bottom, point cloud of as-built concrete walls checked against the digital model of the roof.

6. Conclusion

The paper outlined the design and fabrication of a free-form roof using an integrated design and fabrication workflow, embedding architectural practice within a fabrication environment in collaboration with engineering. The research used CLT fabrication techniques to explore an alternative method using structural plywood as lumber layers, called CLP. CLP is designed to be manufactured within an SME context and to reduce the supply chain. Through 3 sets of prototypes, the design and engineering information was integrated within a single parametric model, allowing resilience in the design and manufacturing process. As-built site information was looped back into the fabrication data to ensure precision in site assembly, demonstrating care in construction.

Acknowledgements

The research acknowledged the contribution of the dedicated staff at LLDS: Ryan Huang, Psyche Hou, Darren Ng and Kyle Kwon. Special thanks to Rob Nestic and TGA Engineers for their engineering vision and faith in the project.

References

[1] EWPAA, "Design Guide Structural Plywood and LVL," Australia, 2018.

[2] IndurtryEdge, "Australia's growing CLT market," *Indurtry Edge*, 2020. https://industryedge.com.au/new-cross-laminated-timber-facility-in-australia/ (accessed Dec. 22, 2022).

[3] A. Menges, T. Schwinn, and O. D. Krieg, *Advancing Wood Architecture*. New York : Routledge, 2016.: Routledge, 2016. doi: 10.4324/9781315678825.

[4] XLam, "Australian Cross Laminated Timber Panel Structural Guide," Australia, 2017.

[5] R. Brandner, G. Flatscher, A. Ringhofer, G. Schickhofer, and A. Thiel, "Cross laminated timber (CLT): overview and development," *Eur. J. Wood Wood Prod.*, vol. 74, no. 3, pp. 331–351, May 2016, doi: 10.1007/s00107-015-0999-5.

[6] N. Johnson, "The time is now for CLT in Australia: developments, barriers and our first CLT house explored," *Architecture & Design*, 2016. https://www.architectureanddesign.com.au/features/product-in-focus/cross-laminated-timber-construction-in-australia-d (accessed Mar. 15, 2023).

[7] P. Kemp, "About CrossLam Australia," 2023. http://www.crosslamaustralia.com.au/about/#:~:text=CLT (Cross Laminated Timber) is,Panels in Australia in 2013.

[8] Editorial, "Australia to get its first CLT & GLT plant," *Architecture & Design*, Jan. 2021. https://www.architectureanddesign.com.au/news/timberlink-to-build-first-aussie-clt-and-glt-plant#:~:text=The new state-of-the,sawmill in Tarpeena%2C South Australia. (accessed Mar. 15, 2023).

[9] F. Scheurer, “Materialising Complexity,” pp. 86–91, 2010.

[10] J. Burry *et al.*, "Modelling Hyperboloid Sound Scattering The Challenge of Simulating, Fabricating and Measuring," in *Computational Design Modelling*, 2012, pp. 89–96.

[11] H. Behm, "The effect of clamping pressure and orthotropic wood structure on strength of glued bonds," *Wood Fiber Sci.*, vol. 24, no. 3, pp. 260–273, 1992.

[12] P. Loh and D. Leggett, "HOUSE #05 Incremental Construction in Digital Practice," in *Fabricate 2020 Making Resilient Architecture*, J. Burry, J. Sabin, B. Sheil, and M. Skavara, Eds. London, England: UCL Press, 2020, pp. 280–285.

IASS 2023
July 10–14 Melbourne
Integration of Design and Fabrication

Proceedings of the IASS Annual Symposium 2023
Integration of Design and Fabrication
10–14 July 2023, Melbourne, Australia
Y.M. Xie, J. Burry, T.U. Lee and J. Ma (eds.)

Derivation of wind loads for shell structures using CFD analyses

Christian HEIDENREICH[*], André KILIAN[a], Josephin BÜTTNER[b], Sophie SCHERER[a]

[a,*] HTW Dresden, Statics and Structural Analysis
Friedrich-List-Platz 1, 01069 Dresden, Germany
christian.heidenreich@htw-dresden.de

[b] HTW Dresden, Research Project TimberPlan+

Abstract

The construction and operation of buildings consumes a large proportion of the energy and raw materials available worldwide. In order to increase sustainability in construction, high-performance structural systems are required. Especially load-flow-adapted and form-optimized shell structures can bridge large spans with low material consumption. The asymmetric snow and wind loads are to be regarded as relevant for the design. Based on a comparison of international standards, it is shown that the lateral wind flow on shell structures is represented very differently or not at all. This leads to uncertainties among planners with regard to the loads to be applied. On the safe side, values are then set too high and the structure is overdimensioned. However, an individual and specific handling of the wind loads is essential against the background of ensuring structural safety, serviceability and sustainability. In this study, an approach to determine the wind load pressure coefficients for a timber shell support structure using computational fluid dynamics (CFD) is presented. Using a parametrically generated structure, different geometries can be generated and analyzed for wind load coefficients. Depending on the characteristic values, an algorithm is developed to derive a zoning coefficient according to wind load standards. In this way, an application without further CFD analysis is possible. Due to the variable approach, the developed algorithm can also be applied to free-form shell structures.

Keywords: Zollinger, wood construction, shell structure, lightweight construction, structural design, resource efficiency, arch roof, board-rip-construction, optimization, wind load analysis, computer fluid dynamics

1. Introduction

1.1. Determination of wind loads for sharpe-edged buildings

The wind loads to be considered are essential input parameters for the dimensioning of the structure within the framework of a static as well as a dynamic analysis. Due to the wide range of influencing factors, such as wind speed, wind direction, turbulence intensities and roughness, these parameters must be determined individually for each structure to be investigated. Against the background of engineering practice, national and international wind load standards specify wind load parameters in the form of tables and diagrams for typical applications. These include, above all, geometric shapes of classical building components such as walls and common roof shapes (flat roof, gable roof, ...). The characteristic values given here are based on wind tunnel tests. The size of the investigated building and the wind tunnels makes it necessary to scale the model. For this reason, in addition to the geometric scaling, the other boundary conditions of turbulence, roughness and force ratios must also be considered.

$$Re = \frac{\rho v d}{\eta} \tag{1}$$

Where ρ = density, υ = flow velocity, d = characteristic length, η = dynamic viscosity.

Copyright © 2023 by C. HEIDENREICH, A. KILIAN, J. BÜTTNER and S. SCHERER. Published in the Proceedings of the IASS Annual Symposium 2023 with permission.

In particular, the consideration of a correct mapping of the Reynolds number is essential for realistic and meaningful results. The Reynolds number describes as a dimensionless quantity whether a flow is laminar or turbulent, see eq. 1.

According to [1], the wind loads on sharp-edged profiles are usually independent of the flow-physical parameters, so that the wind loads can be determined on geometrically similar models in the wind tunnel. The preparation and execution of physical wind tunnel tests is time-consuming and costly, especially for complex geometries. This fact is of particular importance when several tests are carried out as part of parameter studies and thus wind tunnel series investigations. In [2], a comparative study of physical and numerical wind analyses is presented.

1.2. Determination of wind loads for curved buildings

In contrast to the previously described standard-based wind load characteristics for sharp-edged structural components, curved roof shapes, such as shell structures, are only represented in a few standards. Barrel-shaped roof structures, for example, are described in the Eurocode with respect to a lateral wind inflow, see fig. 1 (left), but not under longitudinal inflow. In contrast, this wind loading direction is considered in selected standards [AS/NZS: 1170.2: 2022 (2005), NBC: 1995 (2002), ASCE/SEI 7-05 (2006), IS: 875 (part 3): 1987 (1989)], see fig. 1 (right).

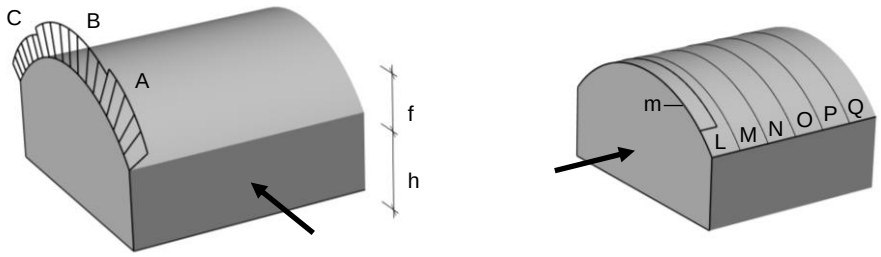


Figure 1. shell with lateral inflow (left) [DIN EN 1991-1-4]; longitudinal inflow (right) [NBC 1995 (2002)].

The wind load parameters can be determined on the basis of numerical flow simulations (CFD analyses). The modelling can follow all geometrically complex shapes. In [3] and [4], a procedure for curved roof structures is discussed. With regard to the calculation results, suitable turbulence models must be selected. In contrast to physical wind tunnel tests, no scaling problems are encountered. Special attention has to be paid to the detachment behaviour of the flow of curved surfaces [1, 5]. The resulting vortices or turbulences cause non-uniform pressure distributions.

In this study, the wind load characteristics of a shell structure, based on the Zollinger-System, are determined, see fig. 2. The basis for this study is laid in a master's thesis [6]. On these structures, previous investigations [7-10] have determined the basic properties and structural improvements. In this context, the relevance of half-sided loads, such as wind loads, for shell structures could be worked out. The workflow described in detail focuses on the underlying parametric modeling, the necessary input and calculation parameters as well as the derived conclusions. Thus, this study contributes to the further establishment of digitalization in the construction industry and the increase of sustainability capacities in timber construction.

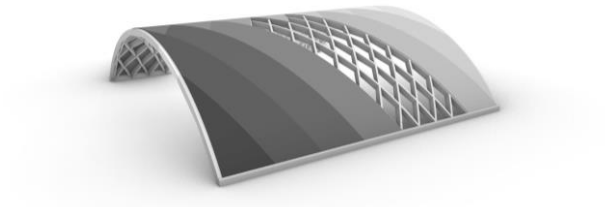


Figure 2. Timber grid shell structure, Project TimberPlan+.

2. Hypothesis and method

2.1. Hypothesis

The further development and resource-saving dimensioning of the Zollinger system and other curved shell structures is only possible on the basis of specific and exact wind load parameters. The relevant wind load standards do not fully describe these geometric shapes. If the user does not want to resort to the blanket use of "similar" classical geometry shapes, which are chosen on the safe side - and thus accompanied by higher material expenses - the application of wind tunnel tests or numerical computer fluid dynamic calculations becomes necessary.

Based on the research of standard-based wind load characteristics for curved shell structures and the computational preliminary investigations, the main hypothesis can be formulated as follows: The determination and definition of wind load characteristics for shell structures should be favoured using a CFD analysis in view of practical engineering use. In this way, load values can be generated that are more realistic and depend on the individual shape.

2.2. Method

The main hypothesis is investigated and evaluated on the basis of a specific timber grid construction, see Figure 3 (left). The methodological procedure described below is explained in detail and is suitable for transfer to other fields of application.

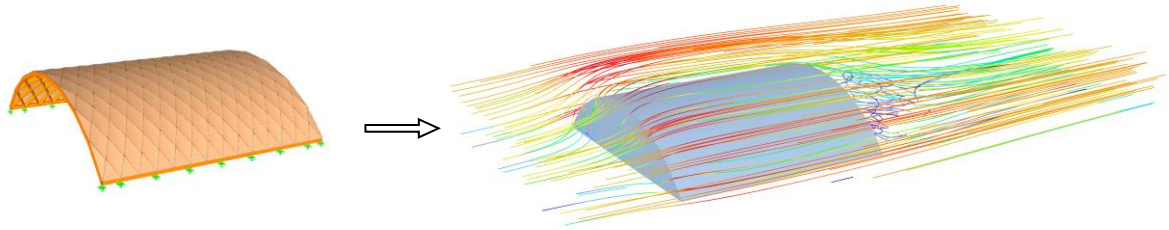


Figure 3. Parametric Finite Element Model (left) with lateral wind load (right), Project TimberPlan+.

The timber shell structure to be investigated is described with a parametric overall model, see fig. 4, with respect to the architectural dimensions (length, width, arch height and shape) and the statically relevant parameters (material grades, cross section dimensions, stiffnesses in the component connections, permanent loads and snow loads, etc.). For this purpose, the parametric programming platform Grasshopper3D is used. The further determination of the wind loads is carried out using the computer fluid dynamic calculation tool RWIND, which is based on OpenFOAM®. For this purpose, the developed parametric model can be directly transferred and analysed. The determined wind load parameters can be added to the overall model. Subsequently, the static finite element model can be merged for further analyses and transferred to the finite element calculation program RFEM, see fig. 3 (right). The parameter-based approach is highly flexible with regard to possible parameter variations due to architectural-planning and structural-constructional modifications. The automatic model data adjustment carried out in this context also enables variant investigations and parameter studies.

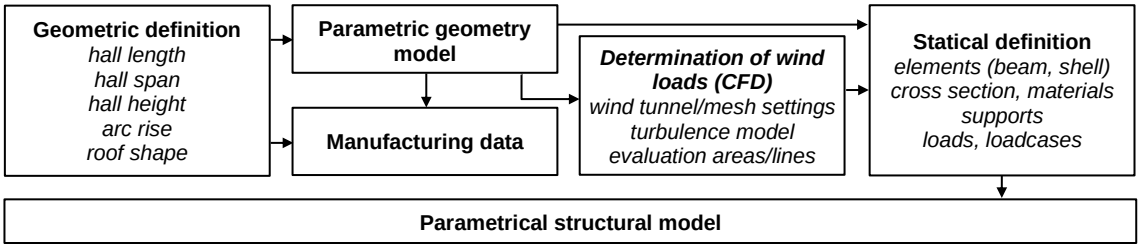


Figure 4. Basic structure of the holistic parametric model considering a CFD wind analysis.

3. Concept of investigation

The aim of the investigation is to determine wind load characteristics for shell surface structures with longitudinal inflow. On the basis of the parametric overall model, see section 2, the object of study can be developed considering parameters to be adjusted. In this way, the influence of the different component dimensions can be determined in relation to the generated wind load characteristics.

Against the background of non-uniform wind load characteristics distributed over the shell surface, suitable evaluation methods and ranges have to be analysed. Furthermore, the occurring turbulences have to be discussed.

3.1. Definition of the object of investigation

Different calculation models are generated for the wind load analysis. Here, a variation of span, length and height is applied, see Figure 5 and Table 1. The shell structure is modelled as supported on the floor, closed on the face side and without openings in the roof area. Dormers or discontinuities in the roof area are also excluded. The aim of the investigation is to determine the specific wind loads and, if necessary, to show conclusions about possible wind load characteristics to be standardized.

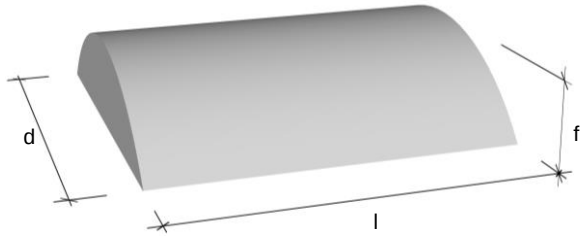


Figure 5. Visualization of the objects of study in principle.

According to Table 1, it can be noted that five different spans are investigated. In addition, a variation of the length to span ratio as well as the rise to span ratio is investigated. Due to the large number of models to be investigated, it is possible to identify the same or similar effects. Furthermore, the reproducibility and transferability of the approach chosen here can be investigated.

Table 1. Dimensions of the investigated structures.

Span d [m]	Length-span ration l/d [-]	Rise-span ration f/d [-]
5.0 / 10.0 / 15.0 / 20.0 / 30.0	1.0 / 2.0 / 3.0 / 4.0 / 5.0	0.125 / 0.25 / 0.375 / 0.5

3.2. Parameters of the CFD-analysis

For the computational fluid dynamics analysis, the generated models are supplemented by information on the wind tunnel dimensions and roughness parameters. Furthermore, the site parameters are defined, whereby the wind load zones and wind load profiles defined according to the standard are taken into account.

Since the accuracy of the results of a CFD analysis is very strongly dependent on the simulation accuracy in the area of detachment effects, see also section 1.2, a suitable turbulence model must be applied. The most widely used method for this purpose represents the application of the "Reynolds-averaged Navier-Stokes equations" (RANS) [11]. In contrast to direct numerical simulation (DNS), which place high demands on computational resources, turbulent flow is modelled here by averaged values and variance of velocity and pressure [12, 13]. Due to these generated equations, the computational time decreases. Here, the k-ε turbulence model is used in RWIND [14].

The size of the wind tunnel is determined depending on the object size to be investigated, always balancing between short calculation times and well-mapped flow conditions. In general, the distance on

the inlet side is shorter than on the back side, see Figure 6. Furthermore, the surface roughness can be defined for the floor surface, which also influences the flow properties around the object under investigation.

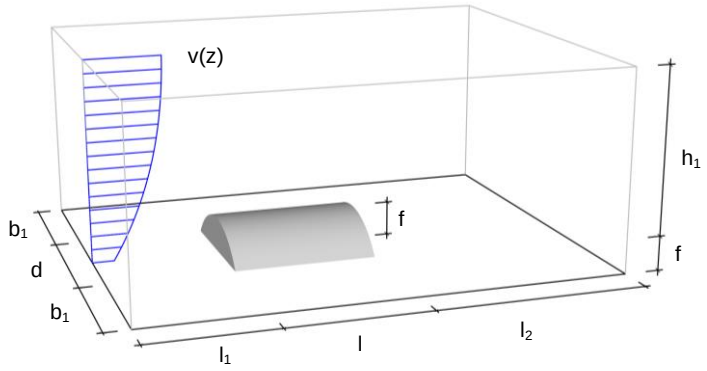


Figure 6. Wind tunnel dimensions and wind profile.

The wind profile to be used, taking into account the wind load velocity distribution over the height, corresponds to the specifications of the wind load standard applied. This is applied to the inlet zone of the wind tunnel within the framework of the computational fluid dynamics calculation, see Figure 6.

3.3. Determination for result evaluation

On the basis of the numerical wind load characteristic value determination, the evaluation and determination of the wind pressure coefficients (c_{pe}) on the shell structure can be carried out. Due to the symmetrical design of the structure and the longitudinal inflow, an evaluation can be carried out along defined lines, see Figure 7. For this purpose, the shell structure is divided into uniform sections along the arc. The number of these lines is freely definable. Against the background of a practical engineering application, a subdivision into two sections is sufficient. This takes into account the observation in the ridge and eave curvature areas. A further reduction in the scope of the evaluation can be achieved by considering only the left-hand and right-hand evaluation lines. On the basis of these lines, the pressure coefficients (c_{pe}) are displayed as a curve, which can be converted into c_{pe} zones by regions.

The c_{pe} curves and the evaluation of the flow lines illustrate any turbulence that may occur on the structure under investigation. In this case, adjustments with respect to the meshing or the specifications of the calculation parameters must be checked, if necessary.

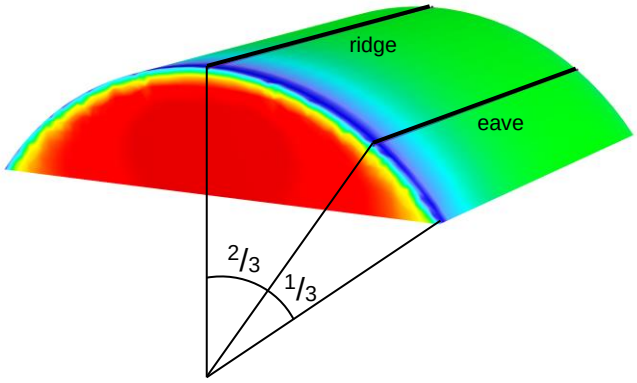


Figure 7. Shell structure with evaluation lines.

4. Results

The determination of wind loads of a shell structure considering different dimensions is performed on the basis of computer fluid dynamic calculation and evaluated in the form of diagrams.

4.1. Determination of the relevant evaluation line

Section 3.3 describes the defined evaluation lines. The possibility of half-sided observation (evaluation lines *ridge* and *eave*) is pointed out. In the following, the course of the c_{pe} characteristic values along the evaluation lines is examined for all variants according to Table 1. Figure 8 shows an example of the results for the variant d = 20 m, f/d = 0.5.

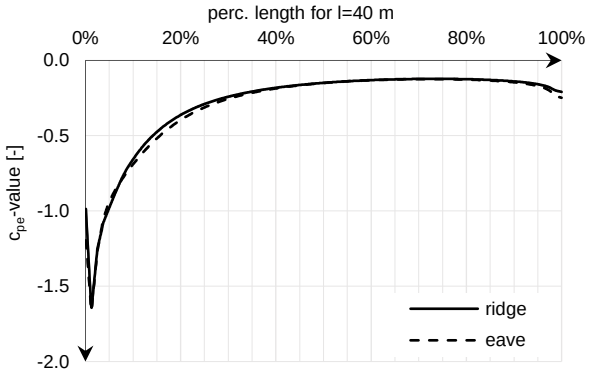


Figure 8. Course of the pressure coefficients (c_{pe}) of evaluation lines (*ridge* and *eave*).

It can be seen that both evaluation lines have similar courses. From this it can be concluded that the wind conditions are uniform in large areas and that the dimension of the selected wind tunnel is of sufficient size for the present investigation. The further investigation can be carried out only on the decisive evaluation line *ridge*.

4.2. Investigation of the pressure coefficients (c_{pe}) for variable length to span ratios

In the following, the further influence of different shell heights is considered. Figure 9 compares the c_{pe} characteristics for the 20 m span shell for a span-to-height ratio of 0.5 (left) and 0.125 (right). The following effects can be described: The shell with greater height has greater pressure coefficients (c_{pe}) (Fig. 9, left), with the maximum values occurring at the same distance from the side exposed to the wind. The greatest turbulence occurs in this region. Subsequently, the c_{pe} courses converge to a minimum value, with convergence occurring earlier at smaller f/d ratios (Fig. 9, right). The shell is affected in larger areas by the minimum wind loads. Increasing pressure coefficients (c_{pe}) are determined at the end of the shell. This is due to turbulence and detachment behaviour.

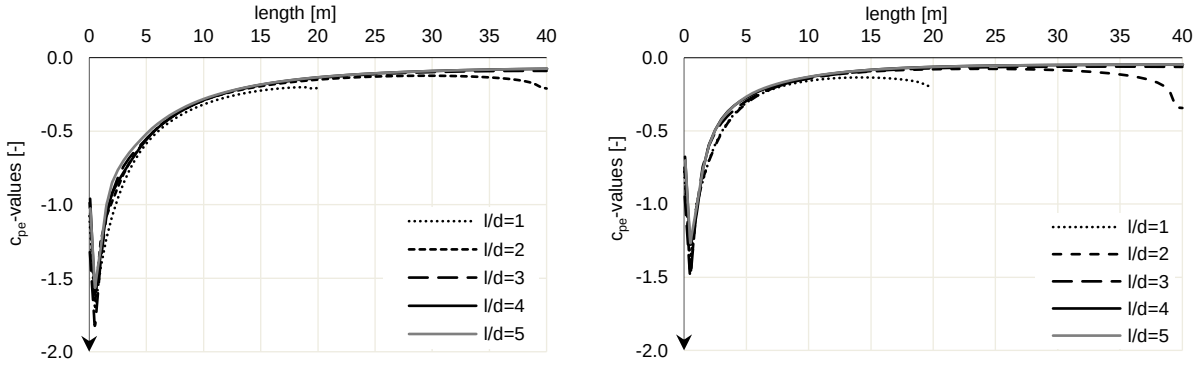


Figure 9. pres. coefficients (c_{pe}) for different l/d-ratios, fixed span (d=20 m); f/d=0.5 (left) and f/d=0.125 (right).

For further verification of the investigation approach, especially of the turbulence model and detachment behaviour, a comparative observation with a sharp-edged structure (cuboid) is conducted, see Fig. 10. The result curves show similar tendencies, which underline the possible applications of the chosen approach.

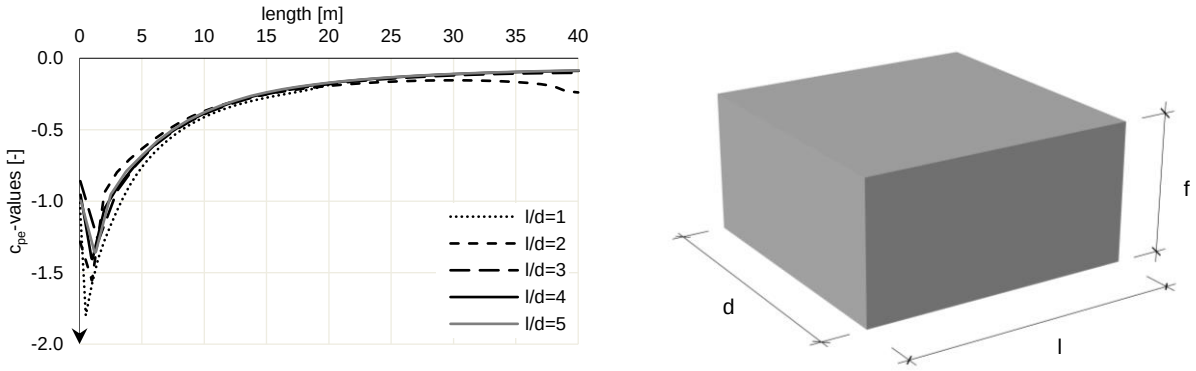


Figure 10. pressure coefficients (c_{pe}) for cuboid (d = 20.0 m and f = 10.0 m).

The c_{pe} characteristic values plotted in diagrams 9 and 10 can be used for a static analysis. Nevertheless, special attention must be paid to the turbulence and detachment behaviour at the beginning and end of the shell. The pressure coefficients (c_{pe}) given here represent absolute maximum values. The analysis of the turbulence behaviour in these areas can be performed with specially meshed numerical models.

With respect to a safe, engineering approach, further investigation is performed for the global regions of the shell structure. For this purpose, in the following considerations, the graphs are presented in the main continuity region, without considering the input region (5% of the total length) and the final region (10% of the total length).

4.3. Investigation of the pressure coefficients (c_{pe}) for variable height to span ratios

The further investigation of the c_{pe} characteristic values is carried out in dependence of the rise to span ratio exemplarily for the spans 20.0 m and 30.0 m considering geometric similarity on the basis of the length-span ratio l/d = 2.0, see Fig. 11 (left and right). The determined pressure coefficients (c_{pe}) are identical for the investigated variants. It becomes clear that the largest pressure coefficients occur at f/d=0.5. Thus, these characteristic values can also be assumed to be on the safe side for designs with f/d < 0.5.

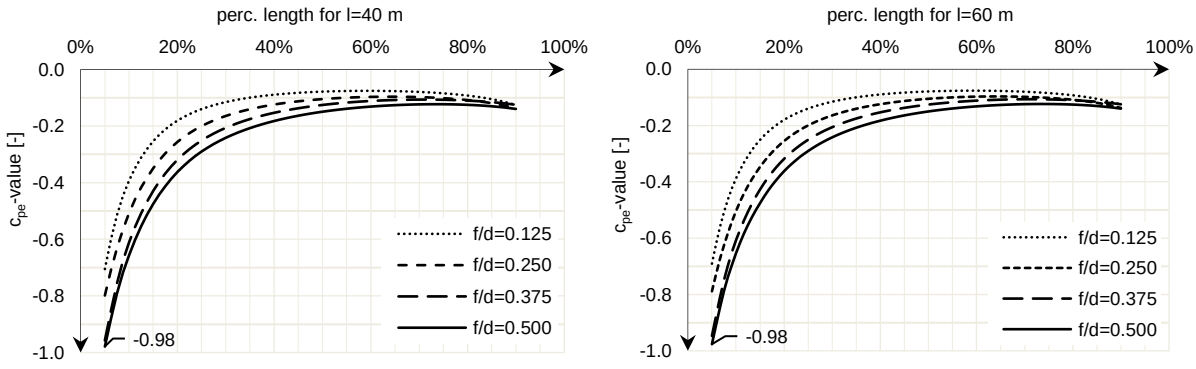


Figure 11. pressure coefficients (c_{pe}) for different f/d-ratios, fixed span; d=20.0 m (left) and d= 30.0 m (right).

4.4. Investigation of the pressure coefficients (c_{pe}) for different spans

The analysis of the wind pressure coefficients (c_{pe}) due to different span lengths is shown in the following Fig. 12 (left and right). Fig. 12 (left) shows a percentage length representation and Fig. 12 (right) a representation of the specific shell lengths in meters. For identical geometry ratios, a qualitatively and quantitatively uniform progression of the pressure coefficients (c_{pe}) over the longitudinal direction of the shell can be observed, irrespective of the span length, see Fig. 12 (left). The maximum wind load values due to initial turbulence decrease continuously with the shell length. For longer shell structures, this "harmonically" loaded region is more pronounced. Nevertheless, it can be seen that a convergence to the load minimum is reached for all shells considered.

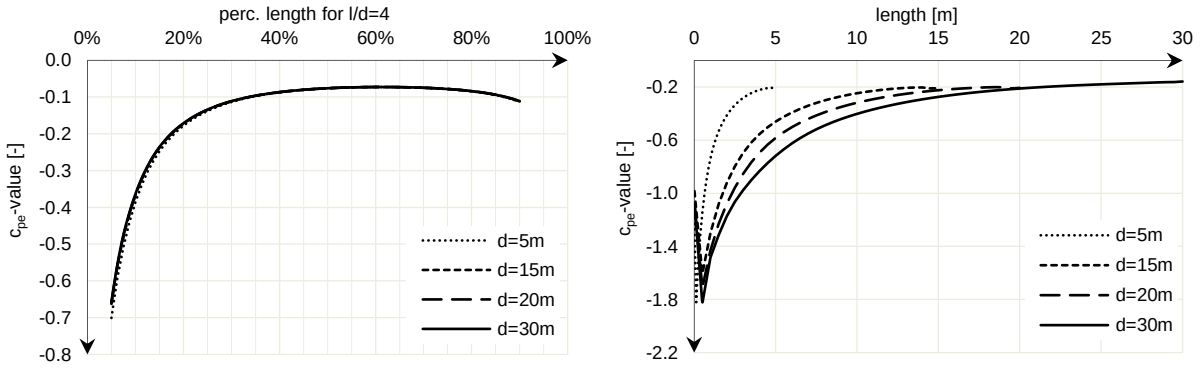


Figure 12. pressure coefficients (c_{pe}) for different spans, l/d=4 and f/d=0.5 (left) and l/d=1.0 and f/d=0.5 (right).

4.5. Derivation of applicable pressure coefficients (c_{pe}) and normative classification

From the previous analyses, the determined c_{pe} characteristics for the shell structure studied here can be classified and summarized.

Figure 9 clearly shows that an increase in the height-span ratio leads to an increase in the pressure coefficients (c_{pe}). In this study, this ratio was limited to f/d = 0.5. Figure 13 (left) illustrates an exemplary spatial representation of the wind load distribution on the shell structure. This wind load envelope is transformed into averaged zone areas in Fig. 13.

The pressure coefficients (c_{pe}) determined here are assumed to be on the safe side and are subsequently compared with the normative approaches according to DIN EN 1991-1-4. For this purpose, the characteristic values for flat roofs, see Fig. 14 (left), and gable roofs, see Fig. 14 (right), are used. The pressure coefficients (c_{pe}) specified in the standard are compared with the pressure coefficients determined in this study, see Table 2.

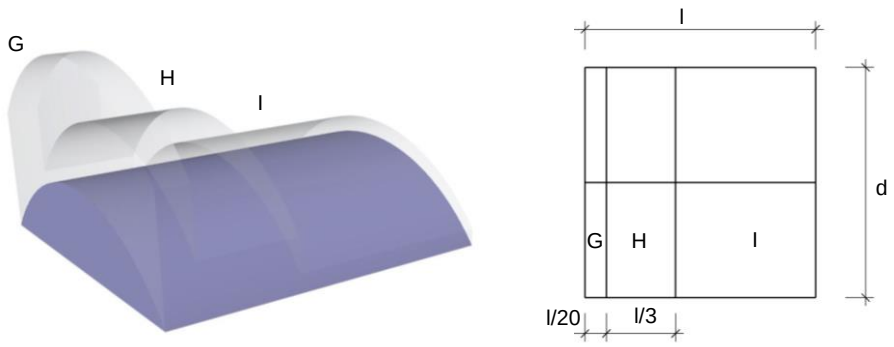


Figure 13. Exemplary wind load distribution on shell structure, determined values (left), averaged zones (right).

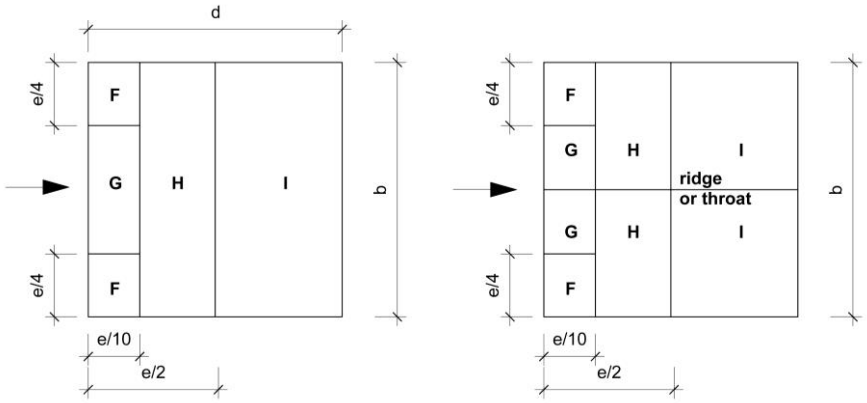


Figure 14. Division of the roof areas for flat roofs (left) and gable roofs (right) according to [EC1].

Table 2. Compilation of the pressure coefficients (c_{pe}).

Geometry or roof shape	Area			
	F ($c_{pe,10}$) [-]	G ($c_{pe,10}$) [-]	H ($c_{pe,10}$) [-]	I ($c_{pe,10}$) [-]
Shell		-1.8	-0.7	-0.2
Flat roof	-1.8	-1.2 ($c_{pe,10}$) -2.0 ($c_{pe,1}$)	-0.7	-0.2
Gable roof (inflow 90°, roof pitch 5°)	-1.8	-1.2	-0.7	-0.6

According to Table 2, it can be shown that the determined pressure coefficients (c_{pe}) correspond in the range of the normative characteristic values for flat and gable roofs.

On the basis of the previous investigations, see section 3, it should be noted that lower values can be determined in some cases if the exact geometric conditions are taken into account. Based on the geometry-dependent wind load values, a more sustainable design of shell structures can be carried out.

5. Summary and outlook

In this article, a contribution is made to the wind load determination of longitudinal shell roof structures. Based on extensive research, the current status of wind load standardization at European and international level is elaborated. It can be shown that the standardization approaches for these structural forms are very different. Furthermore, methods and fundamentals for individual wind load determination based on physical wind tunnel tests and numerical computer fluid dynamic analyses are researched.

Shell structures can cover large spans with low material expenses. On the other hand, these structures are highly sensitive to asymmetric loads. For this reason, exact, real expected wind loads are essential in the course of the design. The procedure for determining wind loads is presented using a Zollinger roof structure based on a computational fluid dynamics calculation. With the aid of a parameter study, the calculation accuracy, result reproducibility and transferability can be clarified. By considering specific evaluation lines and areas, a direct comparison to standard approaches can be drawn. The determined wind load coefficients of shell structures are compared with those of available roof shapes. Here, a reference is drawn to flat roofs or gable roofs. It can be shown that the results determined here follow the courses of the standards, but that lower wind load values can be achieved.

The results obtained are to be verified in further investigations. In addition to physical wind tunnel tests, comparative calculations with other CFD systems can also be carried out. Especially the consideration of the further influence of the CFD wind tunnel dimension, discretization of the finite volume mesh and the detachment and turbulence properties especially at the curved roof edges are to be focused. In

conclusion, specific wind load assumptions are essential with regard to material-saving and resource-efficient roof structures. For this purpose, approaches of further topology optimization and sustainability investigation of supporting structures should be mentioned, for example.

Acknowledgements

The German Federal Ministry of Food and Agriculture (Agency for sustainable raw materials) funded the project (funding code: 2220HV003B). The authors are responsible for the content of this publication.

The authors would like to thank the project partners FLEX-Research-Team at HTWK Leipzig (Prof. Dr.-Ing. Alexander Stahr, Marius Zwigart, M.A. and Hannes Löschke, M.A.) and Institute of Building Construction and Timber Structures at Technical University Braunschweig (Prof. Dr.-Ing. Mike Sieder and Katrin Vögele, M.Eng.).

References

[1] G. Rosemeier, "Windbelastung von Bauwerken. Hoch- und Brückenbauten, Schalen, leichte Flächentragwerke, neue Windlastnorm DIN 1055-4, Baudynamik, Aerodynamik, Luftturbulenzen," Bauwerk-Verlag, Berlin, 2008.

[2] M. Werth, "Vergleichende Studie zu Windlastmodellen im Hochbau: Numerische Strömungsberechnung vs. Druckmessungen im Windkanal", Master Thesis, TU Graz, 2019.

[3] A. Abraham et. al., "Wind loads on curved roofs: Effect of side walls", in *Proceedings of the Eighth Asia-Pacific Conference on Wind Engineering*, 2013, Chennai, India, 2013.

[4] P. A. Blackmore, E. Tsokri, "Wind loads on curved roofs", *Jorunal of Wind Engineering and Aerodynamics*, vol. 94, pp. 833-844, 2006.

[5] C. Katz, "Analysis of the wind load with CFD for an assembly of high rise buildings in Moscow", SOFISTIK-Seminar, 2007

[6] S. Scherer, "Beitrag zu Windlastannahmen von längsangeströmten Tonnendächern mittels computerfluiddynamischer Untersuchungen", Master Thesis, HTW Dresden, 2022.

[7] C. Heidenreich, A. Hollberg and J. Ruth, "Big Shells | Small Footprint – Evolutionary Optimized Concrete Shell Structures", in *Proceedings of the IASS Symposium* 2014, Brasilia, 2014.

[8] L. Franke, A. Stahr, C. Dijoux and C. Heidenreich, "How Does the Zollinger Node Really Work?", in *Proceedings of the IASS Symposium* 2017, Hamburg, 2017.

[9] C. Dijoux, A. Stahr, L. Franke and C. Heidenreich, "Parametric Engineering of a Historic Timber-Gridshell-System", in *Proceedings of the IASS Symposium* 2017, Hamburg, 2017.

[10] A. Stahr, C. Heidenreich, A. Kilian, C. Dijoux, L. Franke and R. Hallahan, "Load test on ribbed timber shells for medium span roofs", in *Proceedings of the IASS Symposium* 2020/21, Guilford, 2021.

[11] C. R. Maliska, "Fundamentals of Computational Fluid Dynamics", Springer 2023.

[12] F. Moukalled, L. Mangani, M. Darwish, "The Finite Volume Method in Computational Fluid Dynamics – An Advanced Introduction with OpenFOAM® and Matlab®, Springer International Publishing AG, 2016.

[13] P. Panneer Selvam, "Computational Fluid Dynamics for Wind Engineering", Wiley Blackwell, 2022.

[14] Dlubal, "RWIND Generation of Wind-Induced Loads on General Models", User Manual, 2021

Proceedings of the IASS Annual Symposium 2023
Integration of Design and Fabrication
10–14 July 2023, Melbourne, Australia
Y.M. Xie, J. Burry, T.U. Lee and J. Ma (eds.)

Digital twins of wooden shingle envelopes

Farzaneh ESKANDARI[*], Yves WEINAND[a]

[a,*] École Polytechnique Fédérale de Lausanne
GC H2 711, Station 18, 1015, Lausanne, Switzerland
Farzaneh.eskandari@epfl.ch

Abstract

Wooden shingles have long been used as a vernacular roofing technique in many well-wooded areas. Despite the fact that shingles, as local raw materials, are low in embodied energy, nowadays they are not much used in construction, as the specific craft knowledge for building shingle roofs and facades has not been well-documented. Consequently, it is now becoming more difficult to find a new generation of skilled workers who can perform this task. As a result, this type of architecture is gradually disappearing. This research aims to provide a technical approach for digitization and generation of an as-built three-dimensional (3D) reconstruction of wooden shingle envelopes. Towards this aim, digital twins of wooden shingle envelopes are generated based on step-by-step real-time 3D scanning of shingles and point-cloud processing of the obtained scans, while they are placed by craftspeople. Two experiments on two different types of wooden shingles are conducted to validate the proposed method, and a precise digital model of this valuable type of vernacular architecture is produced. Furthermore, the exact geometrical configuration, assembly rules, installation patterns, and technical details of the construction process are documented and explained in detail. This work concludes with potential future research directions including design automation and optimization of wooden shingle envelopes which could help the industry re-introduce the use of local raw wood in contemporary architectural constructions, and revive this cultural and artisanal heritage.

Keywords: wooden shingles, bio-based local raw material, digital twins, point-cloud processing, vernacular architecture, sustainable architecture

1. Introduction

Emissions of carbon dioxide and other greenhouse gases continue to rise rapidly [1], with a considerable amount coming primarily from the building and construction sector due to the manufacture of building materials and products such as steel, cement, and glass [2]. Additionally, the dramatic growth of the world population will require significant construction efforts which compel the building industry to implement more sustainable materials. Among all construction materials, wood as a natural material for construction purposes is in a highly advantageous position and has recently been promoted to the center of interest [3]. However, engineering wood for the production of timber panels and beams consumes a large amount of energy and requires unsustainable processing and modification techniques. Additionally, if treated with chemical substances, it will eventually increase the carbon footprint, and consequently, reduce the inherent sustainability of raw wood [4]. Indeed, raw wood as a local material is low in embodied energy and has been widely used in traditional and vernacular constructions, and has become part of the cultural heritage of many well-wooded areas. Vernacular architecture with local raw wood has always relied on the technique [5], and expertise of craftspeople. Regrettably, this knowledge of craftspeople for these kinds of vernacular constructions has been passed down from generation to generation only practically, yet has not been well-documented and archived scientifically in terms of technical details, geometrical configurations, and construction rules. As a result, many of these

Copyright © 2023 by Farzaneh ESKANDARI and Yves WEINAND. Published in the Proceedings of the IASS Annual Symposium 2023 with permission.

worthwhile traditional building systems are disappearing, and industries mainly tend not to use local raw wood due to labour shortages and construction difficulties with such irregular unprocessed material. Even in rare cases where these traditional building systems are implemented in contemporary constructions, they are of lower caliber with a lack of attention to the culture, context, and building performances in response to the environment.

Wooden shingles are one of these sustainable vernacular building materials and were widely used by expert craftspeople to cover building roofs and facades. This roofing technique greatly depends on craft knowledge and nowadays only a limited number of artisans know this technique. Subsequently, wooden shingle envelopes have remained unknown to many contemporary architects and have been being replaced with unsustainable materials such as metal or cement, even in areas where local wood resources are abundant (Figure1). This is mainly due to a lack of proper documentation and reliable 2D and 3D drawings to guide non-specialized builders to use this type of material.

The emergence of the "digital twin" concept in the fields of manufacturing, and production [6], along with advances in the field of computational design and computer vision has assisted the progress of digitization of local building systems and cultural heritages [7] to make thorough documentation of them. Digital twins are defined as three-dimensional virtual models of a system [8], which indicate the physical characteristics and functional attributes of that system. This type of information from the buildings can be obtained by real-time monitoring of the construction process using advanced sensing technologies such as laser scanning (LIDAR) and photogrammetry [9], which can provide useful data for architects, engineers, and builders. The obtained data from the sensors are processed using computer vision algorithms and libraries such as PCL [10], Open3D [11], CGAL [12], and Cilantro [13], as cutting-edge libraries that provide comprehensive functions to post-process the aforementioned data for digitization of the systems. Digital twins for construction are highly beneficial not only for the automated data acquisition from construction sites and supply chains, but also for surveying and virtual reconstruction of archaeological sites [14, 15], and acquisition of as-built geometry and documentation of traditional building systems [7]. However, the current state of the art in digital surveying of traditional buildings mostly centers on the protection, maintenance, and preservation of cultural heritages, without providing much information on technical details of the step-by-step construction procedure, assembly sequences, and material properties, with no guiding principles or plans.

In this paper, we present an approach for the digitization of traditional wooden shingle envelopes for two types of shingles, known as Bardeaux and Tavillons, which are used as roof and facade tiles in well-wooded areas. Our methodology contains a step-by-step as-built three-dimensional reconstruction of shingles, based on obtained point clouds from a 3D scanner. One scan is taken for each element during the assembly process, following that, the point cloud is post-processed by our algorithm, and the three-dimensional model of the element is retrieved. Two prototypes are built by expert craftspeople to validate the proposed methodology. Subsequently, the proposed approach enables us to make the digital twin of shingle envelopes, document and archive all the details for the assembly sequence, installation patterns, material properties, horizontal and vertical overlaps, size of elements for each row of shingles, and the quantity and position of nails for fastening the shingles. The outcomes could guide builders to use this type of natural raw material in contemporary architectural constructions, respecting traditional rules.

To the best of our knowledge, this is the first time a digital twin of wooden shingle envelopes has been developed in accordance with craft knowledge and traditional standards.

2. Related works

In the past few years, a number of projects in the field of architecture and engineering have attempted to make digital twins of various historical buildings such as bridges, churches, theaters, etc., with the help of 3D scanning and photogrammetry techniques. Projects and research of this type have assisted the progress of prediction of damages, preservation, and restoration of monuments and archaeological

sites. Bilis et al. [16] made thorough documentation and conducted a graphic restoration study of the ancient theatre of Nikopolis, with the aid of 3D scanning and image-based 3D reconstruction. The study on the object dimensional imprinting of the Byzantine church of the holy apostles in Thessaloniki by Katsoulis et al. [17] provides the data collection of the geometric information, such as the shape, the size and the location of the monument. "Cyclopean Cannibalism", a traditional masonry technique, was translated into a contemporary digital procedure by Clifford et al. [18], through scanning and virtual algorithms. Betrocci et al. [15] also presented a digital survey for the archaeological analysis and enhancement of Gropina site, by integrating data from laser scanning and photogrammetric instruments. In addition to the aforementioned projects for the digitization of cultural properties, the digital twin technique has also gained increased popularity in the domain of on-site construction, for automating building processes [19], autonomous navigation, object detection, real-time robotic assembly [20, 21, 22], and also the autonomous robotic fabrication of raw wood [23]. However, there is no proof of concept on the digitization of traditional wooden shingles, and this type of architecture is investigated in this article.

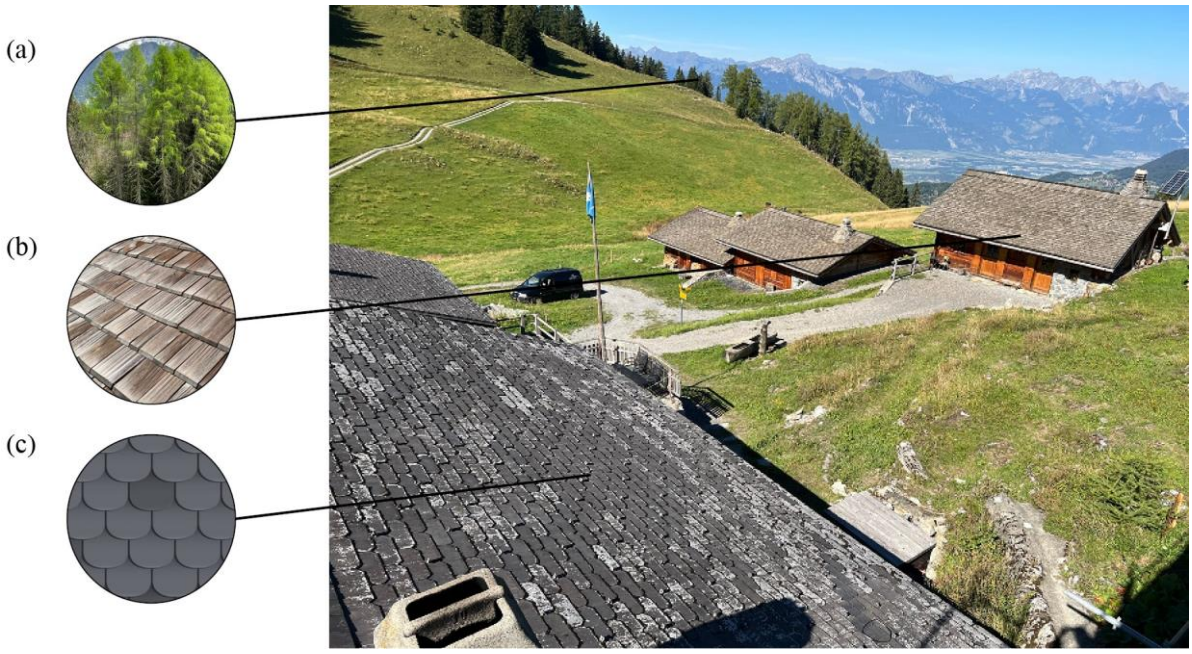


Figure 1. Implementation of unsustainable materials such as metal shingles in the construction of contemporary buildings, in areas where there are abundant wood resources that were traditionally used by local people in the past to construct age-old wooden shingle roofs: (a) Available material resources, such as larch trees, for wooden shingles, (b) Age-old wooden shingle roofs from 25 years ago constructed by local craftspeople and (c) a contemporary metal shingle roof built by present-day industries [Gryon, Switzerland].

3. Age-old wooden shingle envelopes

In this section, some general information is provided on the material characteristics and assembly rules of the historical wooden shingle envelopes according to some ancient references.

Shingles have long been used as a vernacular roofing technique in well-wooded areas. Attentively and dexterously done, shingles are superior to many other roofing methods in terms of durability, sustainability, exquisiteness, and monumentality [24]. The specific fabrication process of the material, makes the roofs and facades watertight and highly resistant against weather-induced decay, without using any chemical coatings [25]. Historically, shingled roofs were of immensely high caliber and were built by eminently expert craftspeople. There are two types of wooden shingles, known as tavillons and

bardeaux in French. The key differences that distinguish these two types of wood are mainly the overlapping method and material resources, which will be explained in the following.

The thin nature of the shingle, its fabrication process, and its exposure to rain, snow, and sun necessitate high-quality wood. An ideal tree for this application should be straight, and must not be twisted. Additionally, it has to be mature and fine textured, without too many knots, and free from rot and blue stain fungi, with a large proportion of heartwood in relation to sapwood. Trees for this application should not be cut during spring or summer but in winter as it ensures high-quality wood. Tree felling is also bound to the phase of the moon. Thus, felling has to occur when there is a new moon, as it would make the timber more resistant to rot and to the depredations of insects. Trees should be barked immediately after felling, and definitely before spring to avoid the risk of rot and damage by insects. After bark removal, the trunks are sawn into log sections with the desired length, known as bolts [24, 26]. Afterward, each bolt is split in quarters from which sapwood is removed, all of which then is chamfered at one corner to avoid over-thickness during installation [24]. Following that, they would be split into rough shingles with a wedge and mallet [24, 27]. Tavillons are left submerged in the water to make them flexible for assembly, as they are naturally quite brittle when dried. Shingles are quite thin (0.7-1.9 cm), relatively narrow (7.6-20 cm), and with varying lengths (35-90 cm). The final products are always irregular with disparate geometry and size, and bumpy surfaces. The laying process is conducted by a series of rules conveyed by oral transmission and collaborative practice, without any execution drawings or technical documentation. A specific frame has to be built as the structure underneath, on which shingles are laid and nailed. The main constraint for the sub-structure is the slope which should not be less than 27◦, due to water tightness issues. What should be taken into consideration, first and foremost, is the consistency of the rows of shingles. Tavillons are placed over the previous one laterally with a side overlap corresponding to 1/3 of their width, this leads to three thicknesses per row. Each row vertically overlaps the previous one so that only 1/4 of the tavillon length would remain exposed, this ensures 12 thicknesses of the shingles. Mechanical fasteners are used for connecting tavillons, at least one nail is used per two tavillons. Some craftspeople use a different method, in such a way that instead of placing tavillons one by one, they place the tavillons in pairs and fasten them with one nail. On the other hand, bardeaux are placed beside each other with no horizontal overlapping. However, it is important to stagger each bardeaux by a minimum of 30 mm to avoid a seam alignment and a direct path for water leakage and thus ensure water tightness. Additionally, leaving a small space (3-12 mm) between two neighboring bardeaux is necessary for free swelling, due to the extreme variations of temperature and humidity they undergo. The same vertical overlapping as explained for tavillons is considered for bardeaux as well [26].

4. Digitization of wooden shingle envelopes

4.1 Methodology

In this section, a technical approach is presented for automating the as-built three-dimensional (3D) reconstruction of the wooden shingle envelopes in real-time based on point cloud processing. In this work, the already developed functions for point cloud processing from three main libraries including Open3D [11], CGAL [12], and Cilantro [13] were used to develop the digital twin. Furthermore, other functions were also developed by the authors. The main objective of the proposed approach is to achieve a reliable CAD model of the vernacular shingle envelopes by which we can detail all the specifications of shingled roofs and facades. As mentioned in the previous section, the shingle's geometry is uncertain, and each of them is of a different size and curvature, so the generation of CAD models cannot be carried out manually in CAD software such as Rhinoceros, or AutoCAD. Moreover, as shingles are laid over each other with horizontal and vertical overlaps and cover one another, it is not feasible to obtain an accurate 3D model of the roofs by 3D scanning of existing buildings with the conventional digital twin generation methods (see Section 2). Figure 2 shows a 3D model of an existing shingled roof covered with tavillons, generated by 3D scanning of the building using a Faro Focus 3D scanner, which was

conducted as the first step for this research [28]. This 3D model could only provide some general information about the roof such as the size, the minimum required slope for the roof, and also a general

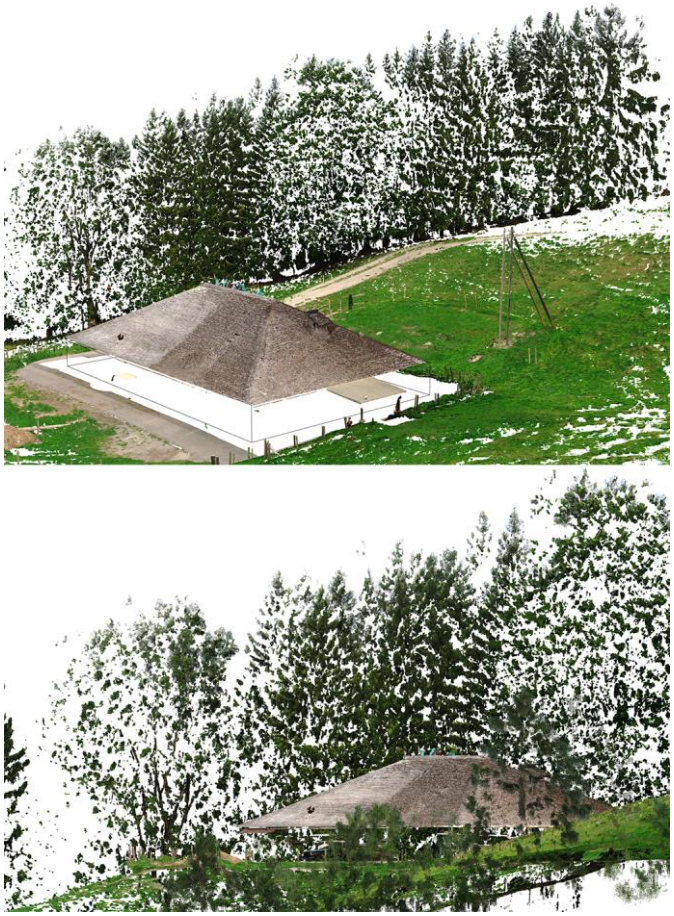


Figure 2. Three-dimensional model of an existing age-old wooden shingle roof in Rossiniére, Switzerland, 2022.

overview of shingles, without any specific details on the laying sequence and installation patterns. Therefore, in order to generate an accurate and complete 3D reconstruction of these envelopes, an approach is presented to scan and digitize the shingles during the assembly one by one in order to extract the individual 3D models of each of them. Subsequently, an experiment is set up as shown in Figure 3-a. To detect the in-progress shingles and the sub-structure, a Faro Focus 3D scanner is mounted statically on top of the workspace to provide the 3D scans. The scanner is connected online via computer, in order to transfer the captured point clouds in real-time [29]. A sub-structure, composed of rafters (known as contre-lattage in French) with an 800*600 mm section and battens (known as Lattage in French) with a 27*100 mm section (the first row of battens has to be of a 27*160 mm section) and 100 mm spacing, which are installed on rafters, is fixed on the worktable with four targets at the corners. One scan is taken per shingle right after it is positioned by a craftsperson (Figure 3-b), and then it is imported into our C++ project to be post-processed in order to extract only the detached 3d point cloud of the last assembled shingle (Figure 4). The surrounding environment is filtered out (Figure 4-a) and the points belonging to the last assembled shingle are clustered (Figure 4-b). This process is repeated for all the shingles until the full 3D model of the prototype is obtained. The result could elucidate all assembly techniques which are performed by craftspeople.

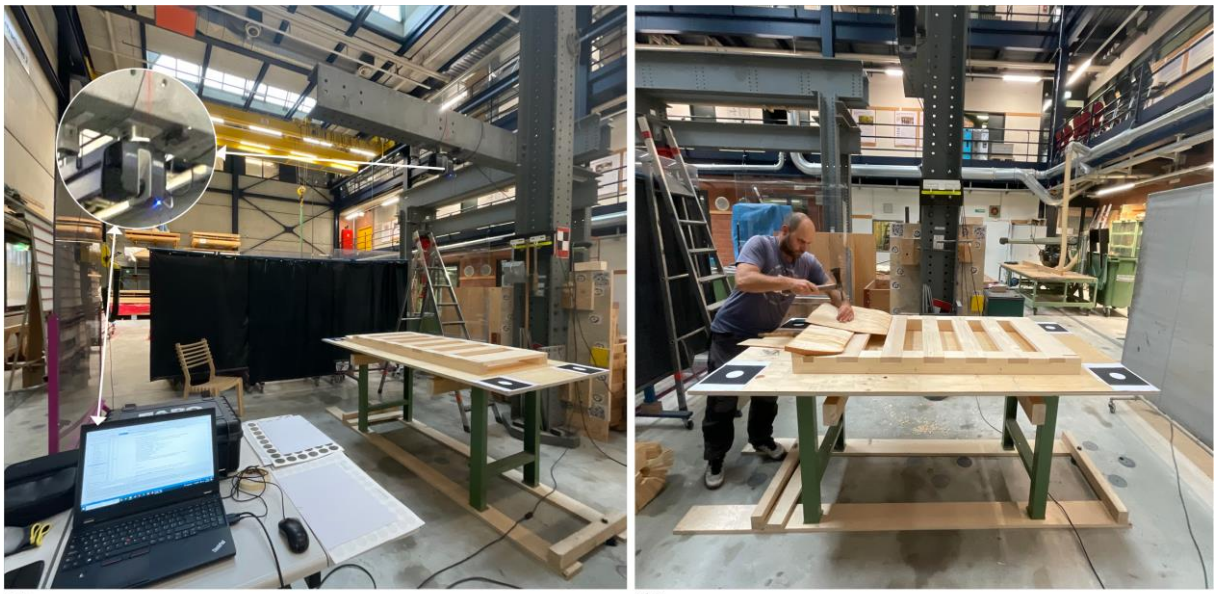


Figure 3. Experiment set-up for the real-time 3D scanning of shingles assembly: (a) A 3D scanner that is connected online via a computer and mounted statically on top of the workspace to provide the 3D scans and transfer the captured point clouds in real-time, (b) A craftsperson assembles the shingles one by one as the process is recorded.

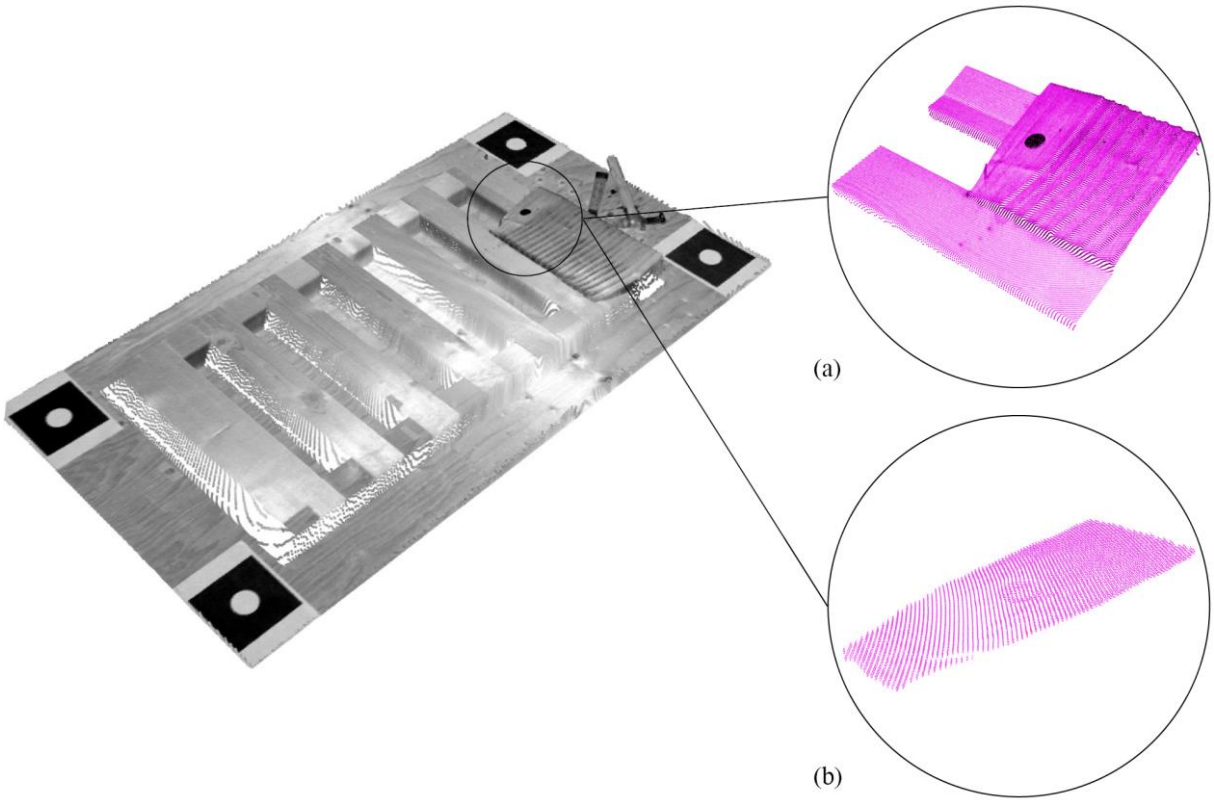


Figure 4. Scanning each shingle after it is placed by the craftsperson: (a) Filtering out the surrounding environment, (b) Clustering the last assembled shingle.

4.2 Experiments and results

Two prototypes are designed and built with two skilled craftspeople, on two types of wooden shingles including tavillons and bardeaux, in order to both validate the proposed methodology and document the details of the two types of shingles. Both prototypes are of a width of 80 cm and a length of 140 cm. A craftsperson builds the prototype in accordance with traditional techniques, and the shingles are scanned one by one. The obtained scans are then post-processed with the above-mentioned methodology, the accurate digital twins of two prototypes were made [30] and the details of the prototypes are documented and will be explained below.

4.2.1 Tavillon

For the first experiment, a prototype was built with tavillons and the following assembly rules were extracted. The first row of tavillons is laid at the lowest point of the substructure, and elements are placed one by one from left to right. The first batten has an inclined surface with a gentle slope, which provides the proper inclination angle for the envelope, thus ensuring the rain drips off the roof. The first row of tavillons consists of elements with a length of 25cm and a width of 10 cm. Each tavillons is placed over the previous one laterally with a side overlap corresponding to 1/5 of their width, such that only 2cm of the tavillon width is exposed. Each tavillon always covers 3/5 of the second last one. The second layer is made up of longer tavillons with a length of 45 cm, and a width of 12cm. The horizontal offset is 2.5-3.0 cm (1/4 of the tavillons width). Additionally, the second row should begin 2.5 cm further back from the first row. From the third row on, each layer is composed of tavillons of the same size as the second row. However, the horizontal overlaps correspond to 1/3 of the tavillons width, meaning that only 4cm of each tavillon is exposed and each tavillon covers 1/3 of the second last one. Furthermore, each row is placed over the previous one, with a vertical overlap corresponding to 1/4 of the tavillon length.

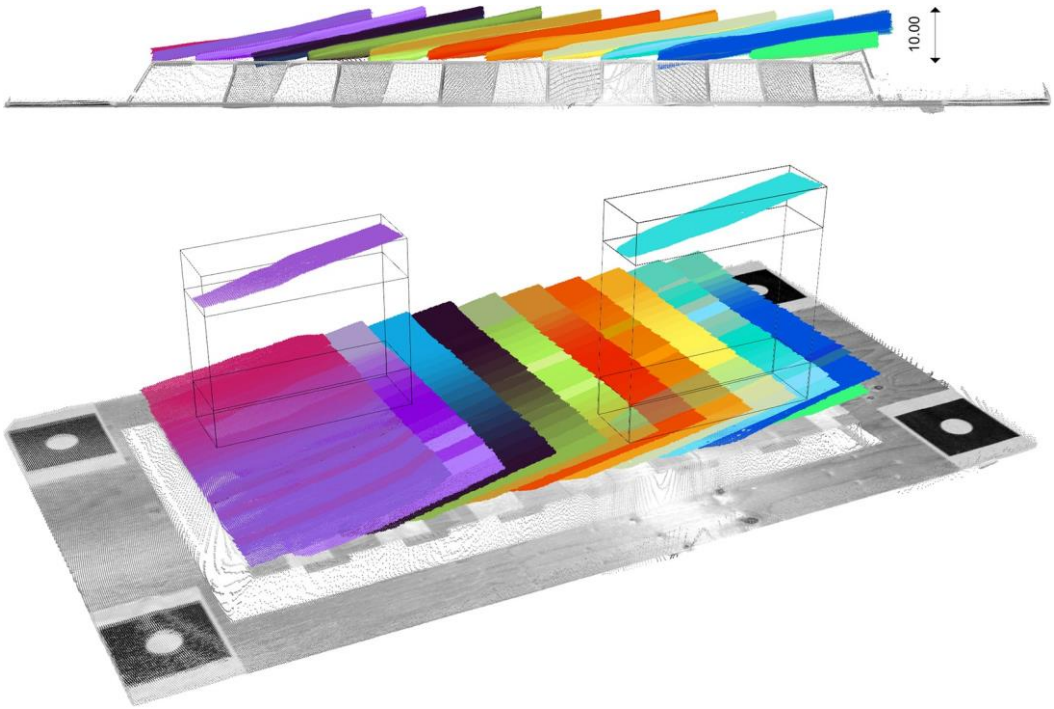


Figure 5. Digital twin of tavillons envelopes

Finally, for the last row, tavillons are placed with the same horizontal and vertical overlaps, but in the opposite direction, such that the thicker side of the material would be placed at the end. In the end, we

always have 12 layers of wood (10 cm thickness) at each point of the prototype, which is essential to ensure the water-tightness of the envelopes (Figure 5). Each tavillon is fastened to the substructure with galvanized nails with a minimum length of 5 cm. the nails must be intersected with battens underneath in order to fix the tavillons properly. Additionally, nails can only be applied in the regions that are covered with the next layer, which indicates that we cannot have any nails in the first quarter of the tavillons length (below the exposure line), otherwise, the nails are exposed to rain and would rot, which results in wood decay. Moreover, the position of nails is different for each layer, as the position of the tavillons changes in each layer in relation to the position of the battens underneath.

4.2.2 Bardeaux

For the second experiment, a same-size prototype was built with Bordeaux. Each bardeau was scanned and post-processed using the same methodology as the one used for tavillons. However, the assembly rules are quite different. Just like tavillons, the first row of Bardeaux is built with shorter elements, with a length of 25cm. The elements are placed next to each other with a minimum spacing of 3mm, but unlike tavillons, with no horizontal overlapping (Figure 6). The second row consists of elements with a length of 35cm which are aligned with the bottom of the first row. The elements are selected based on their width, such that they stagger by a minimum of 30 mm, so no seam alignment occurs. The third and fourth rows begin 2.5 cm further back from the two previous rows, with a length of 45cm, and the same staggered pattern. From the fifth row to the third last row, the elements with the same length as the previous row, with a 12cm vertical offset and with the same staggered order are used. For the two last rows, elements with a length of 30-35 cm are used and are placed over each other with no vertical offset, and with a 12cm vertical offset in relation to the previous row. In the end, we have 8-10 cm thickness at each point of the envelope, which is necessary for water tightness concerns. Nails are also positioned with the same rules as for the tavillons.

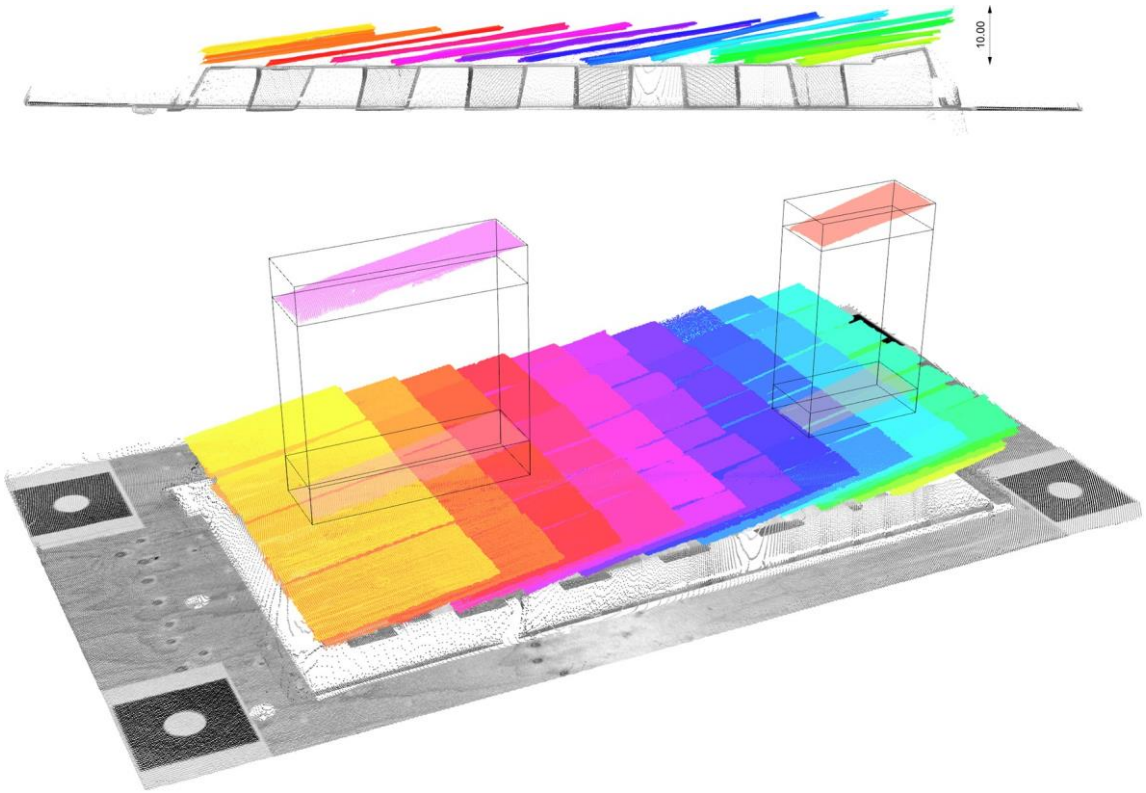


Figure 6. Digital twin of bardeaux envelopes

5. Conclusion

This research demonstrates the first digital three-dimensional reconstruction of vernacular wooden shingle envelopes, along with the details of installation patterns, assembly sequences, and material properties for two types of wooden shingles, known as tavillons and bardeaux, in conformity with craft knowledge. We present a real-time mapping algorithm combined with a vision system that enables the detection of in-progress shingles while a craftsperson assembles them, based on point cloud processing techniques. Unlike most common digital twins of historical buildings, which only provide the exterior surface of the existing buildings' envelopes, in this research, the step-by-step approach for the 3D scanning of the assembly process of shingles produces a fully 3D model of all individual objects, even the elements in the lower layers of the envelope which are covered with topmost layers. The described mapping tools and algorithms could be used for the design automation of wooden shingle envelopes by present-day industries to re-introduce this local raw material in contemporary constructions, which not only would help revive this traditional building system and cultural properties but would also help achieve more sustainable buildings and reduce the carbon footprint of the building and construction sector.

Acknowledgements

This study was supported by the Swiss National Science Foundation (SNSF) through the National Centre of Competence in Research Digital Fabrication (NCCR DFAB).

References

[1] IEA. Global co2 emissions rebounded to their highest level in history in 2021. [Online]. Available: https://www.iea.org/news/ global-co2-emissions-rebounded-to-their-highest-level-in-history-in-2021

[2] UNEP. 2021 global status report for buildings and construction. [Online]. Available: https: //globalabc.org/resources/publications/2021-global-status-report-buildings-and-construction

[3] Y. Weinand, Design of integrally-attached timber plate structures. Routledge, 2021.

[4] C. Goldhahn, E. Cabane, and M. Chanana, "Sustainability in wood materials science: an opinion about current material development techniques and the end of lifetime perspectives," Philosophical Transactions of the Royal Society A, vol. 379, no. 2206, p. 20200339, 2021.

[5] D. Pye, The nature and art of workmanship. Herbert Press, 1968.

[6] F. Tao, F. Sui, A. Liu, Q. Qi, M. Zhang, B. Song, Z. Guo, S. C.-Y. Lu, and A. Y. Nee, "Digital twin-driven product design framework," International Journal of Production Research, vol. 57, no. 12, pp. 3935–3953, 2019.

[7] Z. Manžuch, "Ethical issues in digitization of cultural heritage," Journal of Contemporary Archival Studies, vol. 4, no. 2, p. 4, 2017.

[8] R. Sacks, I. Brilakis, E. Pikas, H. S. Xie, and M. Girolami, "Construction with digital twin information systems," Data-Centric Engineering, vol. 1, p. e14, 2020.

[9] I. Brilakis, M. Lourakis, R. Sacks, S. Savarese, S. Christodoulou, J. Teizer, and A. Makhmalbaf "Toward automated generation of parametric bims based on hybrid video and laser scanning data," Advanced Engineering Informatics, vol. 24, no. 4, pp. 456–465, 2010.

[10] R. B. Rusu and S. Cousins, "3d is here: Point cloud library (pcl)," in 2011 IEEE international conference on robotics and automation. IEEE, 2011, pp. 1–4.

[11] Q.-Y. Zhou, J. Park, and V. Koltun, "Open3d: A modern library for 3d data processing," arXiv preprint arXiv:1801.09847, 2018.

[12] CGAL. Computational geometry algorithms library. [Online]. Available: https://www.cgal.org/

[13] K. Zampogiannis, C. Fermuller, and Y. Aloimonos, "Cilantro: A lean, versatile, and efficient library for point cloud data processing," in Proceedings of the 26th ACM international conference on Multimedia, 2018, pp. 1364–1367.

[14] G. Guidi, M. Russo, and D. Angheleddu, "3d survey and virtual reconstruction of archeological sites," Digital Applications in Archaeology and Cultural Heritage, vol. 1, no. 2, pp. 55–69, 2014.

[15] S. Bertocci and S. Parrinello, "Digital survey and documentation of the archaeological and architectural sities," Firenze, Italy: Edifir, 2015.

[16] T. Bilis, T. Kouimtzoglou, M. Magnisali, and P. Tokmakidis, "The use of 3d scanning and photogrammetry techniques in the case study of the roman theatre of nikopolis. surveying, virtual reconstruction and restoration study," The International Archives of the Photogrammetry, Remote Sensing and Spatial Information Sciences, vol. 42, pp. 97–103, 2017.

[17] G. Katsoulis, P. Tokmakidis, and K. Tokmakidis, "Object – dimensional nument imprinting with laser scanner. the case study of the byzantine church of the holy apostles in thessaloniki," in Pan-Hellenic Conference on Digital Cultural Heritage, 2015.

[18] B. Clifford, W. McGee, and M. Muhonen, "Recovering cannibalism in architecture with a return to cyclopean masonry," Nexus Network Journal, vol. 20, no. 3, pp. 583–604, 2018.

[19] K. S. D. Ravi, J. M. Ib´an˜ez, D. M. Hall et al., "Real-time digital twin of on-site robotic construction processes in mixed reality," in ISARC. Proceedings of the International Symposium on Automation and Robotics in Construction, vol. 38. IAARC Publications, 2021, pp. 451–458.

[20] R. Mascaro, M. Wermelinger, M. Hutter, and M. Chli, "Towards automating construction tasks: Large-scale object mapping, segmentation, and manipulation," Journal of Field Robotics, vol. 38, no. 5, pp. 684–699, 2021.

[21] R. L. Johns, M. Wermelinger, R. Mascaro, D. Jud, F. Gramazio, M. Kohler, M. Chli, and M. Hutter, "Autonomous dry stone: On-site planning and assembly of stone walls with a robotic excavator," Construction Robotics, vol. 4, 12 2020.

[22] M. Wermelinger, R. Johns, F. Gramazio, M. Kohler, and M. Hutter, "Grasping and object reorientation for autonomous construction of stone structures," IEEE Robotics and Automation Letters, vol. 6, no. 3, pp. 5105–5112, 2021.

[23] P. Vestartas and Y. Weinand, "Laser scanning with industrial robot arm for raw-wood fabrication," in ISARC. Proceedings of the International Symposium on Automation and Robotics in Construction, vol. 37. IAARC Publications, 2020, pp. 773–780.

[24] K. Tollestén, "Shingles and shingled roofs," in Nessun futuro senza passato. 6th ICOMOS General Assembly and International Symposium. Atti. Roma: ICOMOS, 1981, pp. 347–363.

[25] S. S. Niemiec, T. D. Brown et al. Care and maintenance of wood shingle and shake roofs. [Online]. Available: https://ir.library.oregonstate.edu/concern/administrative_report_or_publications/k930bx234

[26] S. C. Park. The repair and replacement of historic wooden shingle roofs. [Online]. Available: https://www.nps.gov/tps/how-to-preserve/briefs/19-wooden-shingle-roofs.htm

[27] V. Olivier and G. Piere, Tavillons et Bardeaux. Editions Favre SA, 2010.

[28] F. Eskandari and Y. Weinand, "Three dimensional reconstruction of an existing age-old wooden shingle roof," Mar. 2023. [Online]. Available: https://doi.org/10.5281/zenodo.7752044

[29] P. Vestartas. Farofocussdk. [Online]. Available: https://github.com/ibois-epfl/FaroFocusSDK1

[30] F. Eskandari and Y. Weinand, "Digital twin of wooden shingle envelopes," Mar. 2023. [Online]. Available: https://doi.org/10.5281/zenodo.7748986

IASS 2023
July 10–14 Melbourne
Integration of Design and Fabrication

Proceedings of the IASS Annual Symposium 2023
Integration of Design and Fabrication
10–14 July 2023, Melbourne, Australia
Y.M. Xie, J. Burry, T.U. Lee and J. Ma (eds.)

Experimental investigation on the bending response of reuse-ready timber slabs – The Pixel Slab System

Xavier ESTRELLA[a,*], Johnny SYRIANI[a], Corentin FIVET[a]

[a,*] École Polytechnique Fédérale de Lausanne (EPFL), Structural Xploration Lab (SXL)
Passage du Cardinal 13b, 1700 Fribourg, Switzerland
edisson.estrellaarcos@epfl.ch

Abstract

Current construction practices follow linear economic models of "take-make-dispose" that result in substantial material landfilling after the end-of-life of buildings. This issue takes relevance given the construction industry's significant stake in the high levels of resource depletion and waste production observed today. As an attempt to address the problem, this paper presents an experimental investigation on the bending behavior of glue-laminated timber (GLT) slabs -Pixel Slab System- designed for open-ended reuse following Circular Economy principles. The system employs an arrangement of orthogonally intersecting GLT beams to form a reuse-ready grid slab, relying on adjustable static heights, reversible connections, and modular elements to guarantee easy disassembly and reassembly in unknown configurations. To evaluate the system performance, twelve full-scale GLT beams were tested under bending load, employing different spans, depths, and connection placements. Results showed that the system has adequate performance under 3- and 4-point loads; however, the use of notches at the intersections reduced its stiffness and moment capacity by 23% and 29%, respectively. Using reversible steel connections to join consecutive slab modules proved to deliver a proper mechanism to transfer axial, shear, and bending loads, while not affecting the elastic response or failure mode of the beams. Finally, a constructability analysis showed that the concept poses no constraints to on-site construction/deconstruction, since low-tech procedures are used for assembly/disassembly.

Keywords: component reuse, design for deconstruction, circular economy, sustainable buildings, wooden beams

1. Introduction

The Pixel Slab is a new slab-column system designed for deconstruction and open-ended reuse over several lifespans. By employing modular elements and reversible connections, the proposed concept allows effortless assembly/disassembly procedures and subsequent reuse in diverse architectural layouts, including ones requiring greater static height [1]. As Figure 1 shows, the system is comprised of modular timber slab elements (2.4×2.4 m) made up of orthogonally intersecting beams that transfer loads to adjacent slabs or columns. Slabs are arranged horizontally by means of in-plane “IP” connections to create a lateral surface. If required by design, the slab’s thickness can be increased by vertically attaching additional slab elements with out-of-plane “OoP” connections to reach longer spans or greater loads. Columns can be placed at any position within the slabs to allow flexible layouts, and their length can vary to satisfy different story heights. This way, the structural elements pose no restrains to flexible architectural requirements, making room for future open-ended reuse. Finally, non-structural elements, such as tiles or insulation, can be assembled on top of the slab elements to provide a flat surface and disassembled for replacement or reuse.

Slab elements are manufactured using glue-laminated timber (GLT) beams with half-lap joints (beam-to-beam "B2B" connectors) at the orthogonal beam intersections, forming a uniform grid across the slab. This allows standardizing the manufacturing by using a single beam geometry for all elements in the modules while being compatible with the current GLT manufacturing process.

Copyright © 2023 by Xavier ESTRELLA, Johnny SYRIANI and Corentin FIVET. Published in the Proceedings of the IASS Annual Symposium 2023 with permission.

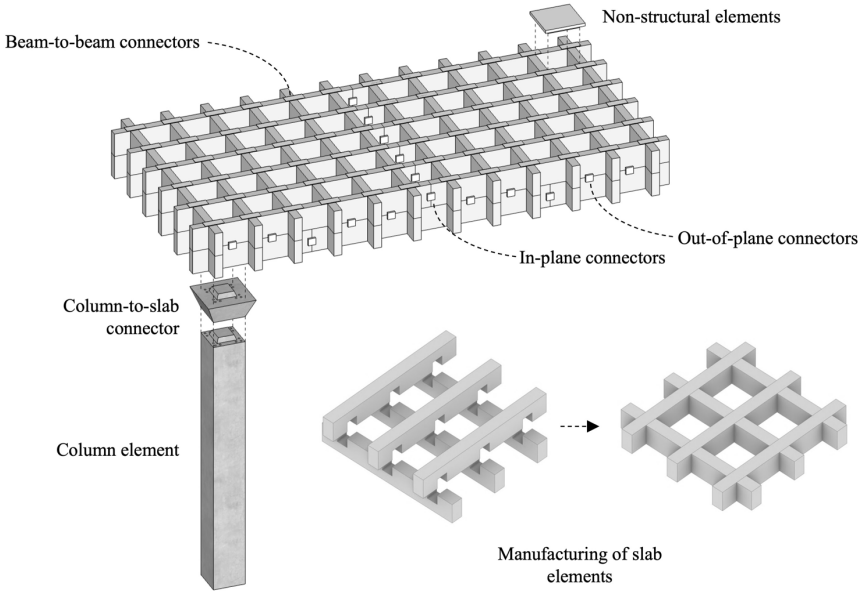


Figure 1. Elements of the Pixel Slab system and manufacturing of slabs.

To better understand the structural performance of the Pixel Slab under vertical loads, this paper presents an experimental investigation on the bending behavior of two main system components: (1) superimposed GLT beams with OoP connectors, and (2) GLT beams with notched B2B connectors. Test results provided insightful information on the load-carrying capacity of the system, geometry/capacity connections compatibility, and suitable design strategies for component design. A full understanding of these phenomena is key for proper implementation of the Pixel Slab, since the slab's behavior, strength, stiffness, and deflection are governed by the mechanical properties of the beams and their connections.

2. Connection design

2.1. Out-of-plane OoP connections

The Knapp MEGANT connector [2] is proposed for the OoP connection. To achieve the composite action between two beams, the connectors need to be placed horizontally at the interface between the top and bottom beams as Figure 2(a) shows. To minimize the impact on the B2B connections, only the smaller Knapp connector length of 310 mm was selected. Three width variants exist for this length, with capacities ranging from 97 to 156 kN and slip modules from 40 to 88 kN/mm. To determine the connection capacities, the MEGANT connector variant was maximized for each cross-section width.

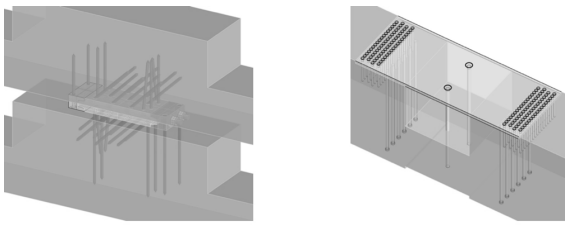


Figure 2. (a) Out-of-plane OoP connection, and (b) beam-to-beam B2B connection.

One drawback of this connection as it is available, is that while it is reversible, it does require to be oriented in the right direction to achieve its highest capacity and slip modulus as provided by the manufacturer. Indeed, in order to benefit from the 45° screws working in withdrawal (tension), they need to be oriented in the direction of the shear force. Alternatively, the screws would work mainly in shear and compression, which are significantly weaker. The load-carrying capacity in this "weak"

orientation is 30-40% that obtained in the "strong" orientation [3]. The slip modulus for the connection in the "weak" orientation is not given in the manufacturer specifications.

To calculate the composite action between elements the gamma-method was used as presented in EN1995.1.1 - Annex B [4]. This method requires the definition of the connection's slip modulus, spacing and element length. For serviceability limit state calculation, the above slip modulus K_{ser} can be used, while for ultimate limit state calculations, a reduced slip modulus $K_u = 0.66\ K_{ser}$ needs to be used as per EN1995.1.1 – 2.2.2 (2) [4]. These are then used to determine gamma coefficients relating to the degree of shear transfer at the interface between two elements. Using these coefficients, the effective bending stiffness $(EI)_{eff}$ can be obtained for direct use in standard calculations. Besides, since all elements have the same rectangular cross-section and modulus of elasticity, the effective height can be calculated as:

$$(EI)_{eff} = E\frac{bh_{eff}^3}{12} \Longrightarrow h_{eff} = \left(\frac{12\cdot(EI)_{eff}}{Eb}\right)^{(1/3)} \quad (1)$$

The results for the obtained effective bending stiffnesses and heights for the considered cross-sections and MEGANT connectors are summarized in Figure 3. Figure 3(a) shows that for two-layer elements, i.e., when two slabs are superimposed, the effective bending stiffness obtained from the gamma-method for the 800 mm connector spacing was 33% of the maximum theoretical stiffness compared to 17% for three-layer elements. This corresponded to effective heights of two-layer elements being on average 69% of the maximum theoretical value compared to 55% for the three-layer elements.

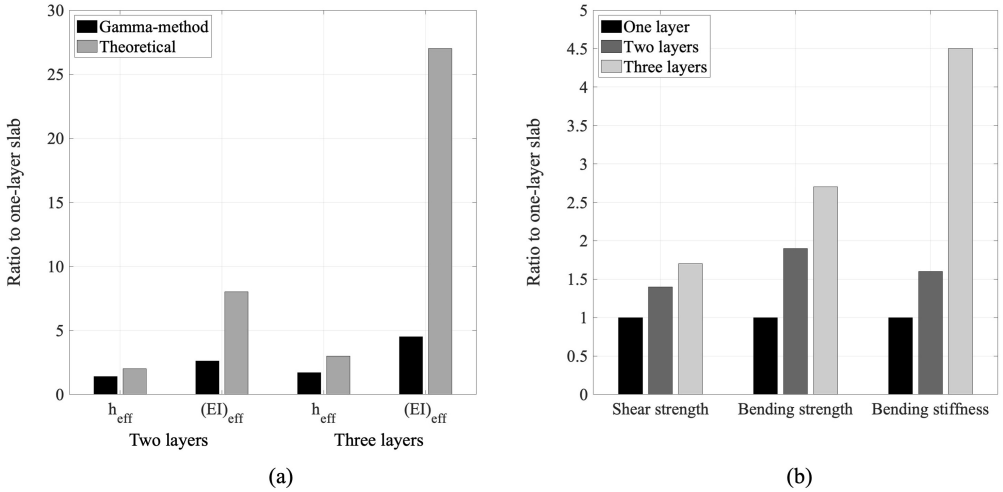


Figure 3. (a) Comparison between theoretical and calculated values for a MEGANT connector spacing of 800 mm, and (b) comparison between strength and stiffness for different element layers.

Compared to single layer elements in Figure 3(b), these gains represent a 38% increase in height for two-layer elements and 65% for three-layer elements. In terms of strength, this would translate to a 38% increase in shear strength and 91% increase in bending strength for two-layer elements. For three-layer elements, those gains would equate to a 65% increase in shear strength and 173% increase in moment resistance. These gains are much lower than the maximum theoretical 2 and 4 times increase in shear and bending strength respectively for the two-layer elements, and 3 to 9 times increase in shear and bending strength respectively for the three layers. In terms of stiffness, the OoP connection results in a 160% and 350% improvement for two- and three-layer elements over the single element layer.

2.2. Beam-to-beam B2B intersection connections

The proposed solution consists in using 90º nails working in shear through a steel plate to transfer the normal forces from the bending moments across the discontinuity. This connection benefits from nails having a smaller diameter and minimum spacings requirements to obtain a significantly higher the

number of fasteners within the limited space available. Here for both tensile and compressive forces, the nails work in shear between the timber beam and the steel plate. The latter then transfers these normal forces across the beam intersection. The steel plate's capacity in tension is defined by the net area, or block shear capacity while its compressive capacity is controlled by the flexural buckling capacity. To this end, fully threaded countersunk head "stability" screws are positioned at the plate centerline to halve the effective length and keep the steel plate as thin as possible. These "stability" screws also serve a fabrication purpose in tying the intersection beam together. Here, again, the connection configuration has the normal force transmitted at the top fiber of the cross-section resulting in an equivalent moment resistance of $M_{Rd} = 5Nh / 6$.

Regarding the shear strength, it is defined by the minimum of the shear capacity of half of the beam cross-section, or the augmented capacity obtained using the reinforcement screws on both sides of the joint. The B2B connection is illustrated in Figure 2(b).

3. Experimental testing

3.1. Out-of-Plane OoP connections

Three-point bending tests were carried out to investigate the capacity of the double beams assembled using the OoP connectors. In total, five tests were conducted: for the first three tests (OoP1, OoP2 and OoP3) the double beams were linked using two MEGANT connectors spaced at 2300 mm, while for the last two tests (OoP4 and OoP5) the beams used six MEGANT connectors spaced at 767 mm along the beams. The specimens were two 4800 mm long GLT elements with a cross-section of 180×280 mm and a GL24h strength class. For the connections, two or six Knapp MEGANT 310×100×40 mm were used. Each connection consists of two connector plates, two clamping jaws, 4–8×240 mm fully threaded screws, 26–8×160 mm fully threaded screws and 2–16×340 mm threaded rods with washers and nuts.

The testing setup is shown in Figure 4. To prevent crushing perpendicular to the grain at the supports, 180×300×5 mm steel plates were screwed on the underside of the bottom GLT beam. At the load application point, located at midspan, the jack head area of 180×300 mm was sufficiently large to avoid crushing perpendicular to grain for the given load and no bearing plate was added. Deformations were recorded at several locations in the beams employing linear variable differential transformers LVDTs.

The testing procedure was divided in two parts. The first part consisted of three loading cycles up to 10 kN and down to 1 kN with a two-minute interval between each cycle. The results from the last two loading cycles were used to determine the effective elastic bending stiffness $(EI)_{eff}$ of the specimens. The obtained elastic bending stiffness can then be used to calculate the effective height of the composite cross-section, as shown previously. The second part consisted in loading the specimen until failure. The loading rate was set to 0.02 mm/s (1.2 mm/min) for both parts of the test.



Figure 4. Three-point testing setup for OoP specimens and failure modes.

The elastic bending stiffness was computed for all specimens from the results of the first part of the test. For the specimens OoP1-2-3, the average effective bending stiffness was of $(EI)_{eff,avg}$ = 6.93e12 N/mm^2 with a coefficient of variation (CoV) of 19.1%. This high CoV value is explained by the higher performance observed for specimen OoP3. The obtained effective bending stiffness translates an average effective height of $h_{eff,avg}$ = 432 mm, assuming the mean elastic modulus E = 11 500 N/mm^2. This is below the theoretical values obtained using the gamma-method, for both serviceability and ultimate limit states. In addition, this average effective height is lower than the theoretical value for two vertically stacked beams having no shear transfer between them. Superimposing two beams would result in doubling the stiffness which result in an effective height equal to $h_{2,eff} = 2^{1/3} \cdot h$ = 353 mm Therefore, the large 2300 mm connector spacing shows an effective reduction in overall bending stiffness of the system. This could, however, not entirely be caused by the presence of the connectors and may be also explained by the elastic modulus of specimens OoP1 and OoP2 being lower than the mean value due to the high natural variability of timber elements. Another possible explanation for such observation could relate to the fact that the ends of the top beam, past the connection point, do not contribute to the overall stiffness of the system. Indeed, since all the internal forces are transferred at the connector point, only the central half of the top beam is being solicited.

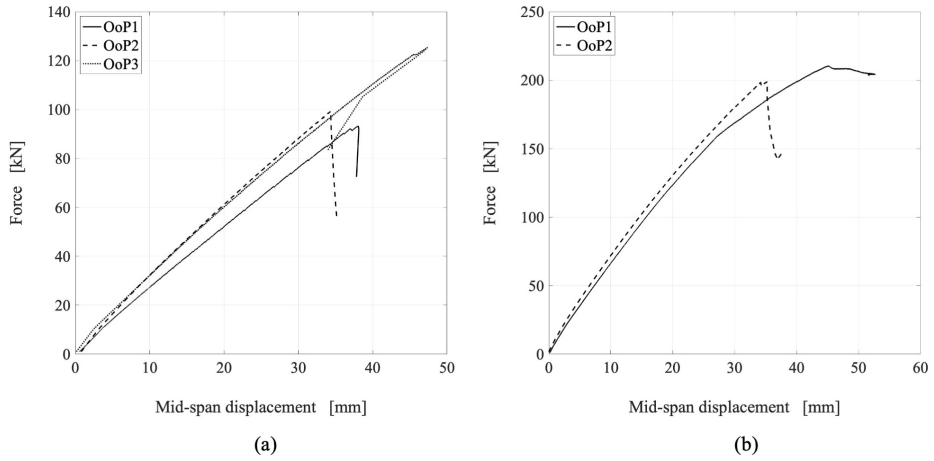


Figure 5. Force-displacement results for OoP specimens.

For the second part of the test, the specimens were loaded up to failure. From the force-displacement results in Figure 5, it can be observed that for specimens OoP1-2-3 there was a higher initial stiffness which reduced slightly around a midpoint deflection of 4-5 mm and remained constant throughout the test. All three specimen exhibited a linear elastic behaviour up to failure. Specimen OoP1 showed the lowest stiffness and ultimate load of 93.3 kN. Specimens OoP2 and OoP3 showed a very similar stiffness throughout the test, however the specimen OoP2 failed at a load of 99.3 kN compared to 125.3 kN for specimen OoP3. The failure mechanism was the same for the three specimens with the bottom beam failing on the underside due to tension from the bending stresses (Figure 4). In all three cases the tension crack originated at a knot on the bottom lamella which then propagated across the cross-section. This failure mode was extremely brittle as can be observed in the graphs by the instantaneous drop in force following the ultimate load.

For specimens OoP4 and OoP5, the latter can be seen to have a higher stiffness overall. For both specimens however, the force-displacement relationship is not as linear as for the specimens OoP1-2-3. After reaching 165 kN, a decrease in stiffness can be observed, which is more apparent in OoP4. This can be due to cracks forming in the beams as the loading increases. However, the post-peak behaviour of specimen OoP4 was not representative since towards the end of the test, the steel bearing plates at the supports yielded, resulting in crushing of the bottom beam at the supports. This therefore limited the beam develop additional bending stress and the specimen simply exhibited larger support settlement before the test was stopped. Nonetheless, both specimens reached a peak load around 200 kN which is

roughly twice that of specimens OoP1-2-3, while exhibiting similar midpoint deflections. For both specimens OoP4 and OoP5, the failure mechanism was the same with the bottom beam reaching its tension capacity on the bottom lamella due to bending.

A similar strength performance was observed for specimens OoP1 and OoP2 with peak bending moments around 110 kN-m. Specimen OoP3 on the other hand, again exhibited a higher performance reaching a maximum bending moment of 144.1 kN-m. This leads to an average bending resistance of 121.9 kN-m and translates to a CoV of 16.1% for these three specimens. With regards to mid-span deflection, the average for specimens OoP1-2-3 was 39.9 mm, with a CoV of 16.8%. The high CoV values here are due to the relatively high performance of specimen OoP3. In the second series of tests, specimens OoP4 and OoP5 performed very similarly with an average ultimate bending moment of 235.1 kN-m and a CoV of 4.0%. With regards to maximum mid-span deflection, the resulting average deflection was found to be 40.2 mm for a CoV of 17.5%. This high CoV value can be attributed to the bearing plate failure for specimen OoP4, as discussed previously.

3.2. Beam-to-beam B2B intersection connections

Four-point bending tests were carried out to investigate the capacity of the B2B connection. In total, seven tests were conducted: the first test was done on a reference beam with no notches or connection (Ref), then three tests had the connection on the tension side of the beams (T1, T2, T3) while the last three tests had the connection on the compression side of the beams (C1, C2, C3). The specimens were made using 2400 mm long GLT elements of cross-section 180×280 mm and strength class GL24h. The specimens T1-2-3 and C1-2-3 had two notches of dimension 180×180×140 mm located at 300 mm on each side of the beam centerline. Those notches were filled using GLT blocks of the same dimension as the notches and were oriented with the grain perpendicular to the beam direction to replicate the intersecting beam. The connections consisted of 180×480×6 mm steel plates of grade S355, fastened using 66–6 mm diameter × 100 mm long LBA nails, and 2–9 mm diameter – 260 mm long fully threaded countersunk-head VGS screws. The shear reinforcement screws used 6–7 mm diameter – 260 mm long fully threaded cylindrical head screws per side of the notches, for a total of 24 screws per specimen.

Figures 6 and 7 show the testing setups for specimens C and T, respectively. As for OoP specimens, steel plates were installed at the edges to prevent crushing of the wood. Similarly, the testing procedure was divided in two parts. The first part consisted of three loading cycles up to 10 kN and down to 1 kN at each jack. A two-minute pause was made between each cycle. The results from the last two loading cycles were used to determine the effective elastic ending stiffness. The second part consisted of loading the specimen until failure. The loading rate was set to 0.02 mm/s (1.2 mm/min) for both parts of the test.



Figure 6. Three-point testing setup for C specimens and failure modes.

The elastic bending stiffness was computed for all B2B specimens. For the reference specimen this value is a characteristic property since the geometric properties of the element are uniform over its length. On the other hand, for the specimens with the half-lap notches, these obtained values represent effective properties. The effective nature of the obtained bending stiffness can be attributed to the elastic modulus E_{eef} or to the moment of inertia I_{eff}. Therefore, two alternatives were evaluated.

First, the effective elastic modulus E_{eef} was determined considering the full height of the beam h = 280 mm in the calculation of the moment of inertia $I = b \cdot h^3/12$. It was found that for the specimens with the B2B connection in tension and in compression, the obtained values are between 33% and 45% the theoretical mean value of $E_{0,mean}$ = 11 500 N/mm^2 from the GL24h material properties. Comparatively, the reference beam had a 44% higher stiffness compared to the expected mean value. However, it is important to note that since only one reference beam was used in the testing, no statistical relevance can be derived from the obtained results. Alternatively, for the notched specimens, the effective height h_{eff} can be calculated from the effective moment of inertia assuming the theoretical mean modulus of elasticity. These results show, the effective height was lower than the actual beam height by 23% to 31%. Therefore, the notches in the beams have a negative impact the bending stiffness.

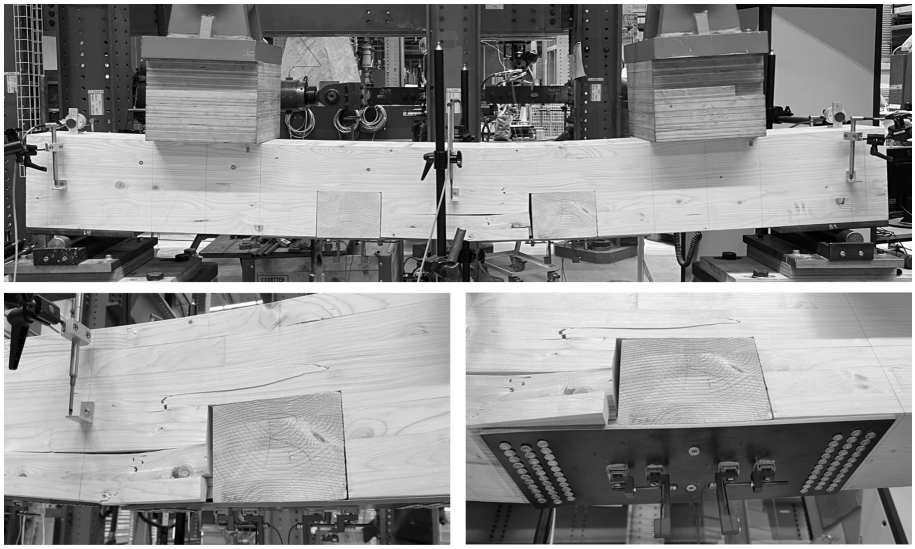


Figure 7. Three-point testing setup for T specimens and failure modes.

As Figure 8(a) shows, the three specimens C1, C2 and C3 exhibited different force-displacement relationships. First, the ultimate load for the specimens C2 and C3 was just above 80 kN while specimen C1 reached 50% higher load at 126.6 kN. This can be attributed to the fact that the failure occurred in the tension fibers between the lines of reinforcement screws in specimen C1. Comparatively, the failure line in specimens C2 and C3 occurred at the shear reinforcement screw location (Figure 6). This discontinuity in the bottom fibers due to the presence of the screws could have resulted in the creation of weaker lines across the width of the beam having a reduced net section to resist the tension force. Therefore, the different failure line could be partly responsible for the observed difference in strength between the specimens. Furthermore, the failure mode of specimens C1 and C3 can be observed to be more ductile.

These specimens show a marked stiffness reduction after reaching around a load 90 kN and 70 kN respectively. From the force-displacement graph, it can be observed that these specimens exhibited sudden strength drops due to crack formation inside the cross-section as the loading increased which reduced the element stiffness. On the other hand, specimen C2 failed in a more brittle manner immediately after reaching its ultimate load. Nonetheless, all three specimens showed a very similar stiffness throughout the testing up to failure and a linear elastic behaviour until cracking occurred.

For specimens T1-2-3, as shown in Figure 8(b), it can be observed that there was a relatively large difference in stiffness between the three specimens up to the onset of the first crack. Following cracking of the beams, failure did not occur immediately. Rather, the specimens exhibited relatively high levels of ductility, especially compared to specimens C1-2-3 as can be observed in Figure 8. The specimens were able to maintain some load-carrying capacity, albeit a very low, or null stiffness, by continuing to deform under constant or slightly increasing load by up to 47 mm for specimen T1 before reaching ruin. This ductility can be attributed to the B2B connections which, due to the shearing of nails-timber interface, resulted in an initial local splitting without the fibers reaching their capacity (Figure 7).

The nailed connection still had load carrying capacity due to the high number of nails in the connection, providing a high degree of redundancy thus translating to the observed ductility. Then, once the deformation reaches a critical point the ruin occurs by the crack propagating perpendicular to the grain. Furthermore, the ultimate load reached by the three specimens was between 70 kN and 80 kN, showing less variability compared to the specimens C1-2-3.

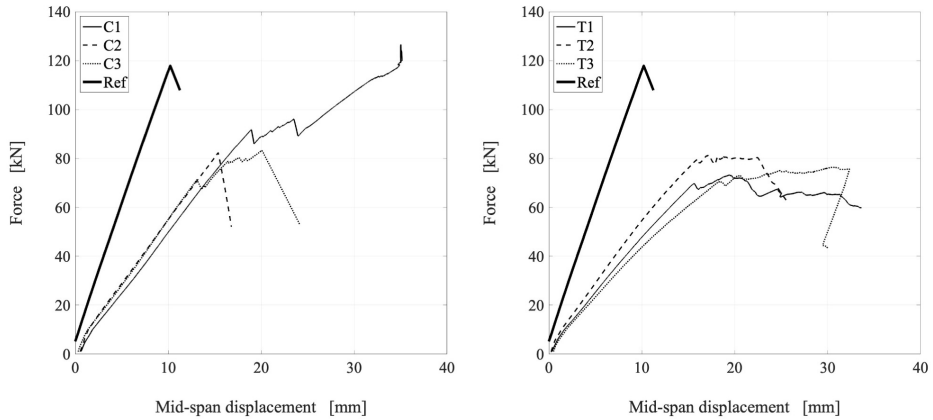


Figure 8. Force-displacement results for B2B specimens.

The reference beam exhibited a linear elastic behaviour throughout the test. The higher stiffness of the beam is apparent in the steeper slope of the force-displacement relationship presented in Figure 8. The failure occurred at the bottom fiber due to the tension stress from the bending moment. While the specimen reached a high ultimate of load, at 117.9 kN, its displacement capacity was limited by the brittle nature of the failure mechanism.

The results for the maximum bending moment and associated jack load and mid-span deflection were computed for all beams from the test data. With regards to the maximum bending moment, all the specimens fitted with the B2B connection reached a similar value around 30 kN-m with the exception of specimen C1 which exhibited a significantly higher performance attaining a bending moment of 50.6 kN-m. This discrepancy leads to a high CoV of 26.0% for the maximum bending moment for specimens C1-2-3. In comparison, specimens T1-2-3 all performed similarly in this regard and displayed a CoV of 5.3%. The reference specimen reached a peak bending moment of 47.2 k-Nm.

For the peak mid-span deflection, the average for specimens C1-2-3 was of 25.4 mm while for T1-2-3 was 33.2 mm, which represents a 31.0% increase compared to specimens C1-2-3. Both series of tests exhibited high variability and dispersion around the mean with a CoV of 36.4% and 24.3% for specimens C1-2-3 and T1-2-3, respectively. For the former, this value can be explained in part by the high performance of specimen C1. For the latter, since in all three tests the maximum bending moment was reached during the plateau region of the force-displacement, the corresponding mid-span deflection values varied according to the propagation of cracks cause by the nail-timber shear failure. This ductile behaviour also explains the higher average for those specimens, which deformed more significantly before reaching their peak capacity.

4. Performance review and design implications

4.1. Out-of-Plane OoP connections

The initial stiffness results show that the gamma-method can be suitable to estimate the effective composite cross-section properties but only at smaller spacings. Indeed, in the first tested configuration with two connectors spaced at 2300 mm, the internal force transfer between the two beams relies solely on those two discrete points. This, in turn, limits the contribution of the top beam since only the central portion of the beam between the two connectors is utilized. In comparison, the second configuration has six connectors evenly distributed along the lengths at one third the spacing of the first configuration. This allows the two beams to be utilized over a longer length and benefits from three times the number of points of force transfer thus distributing the internal forces more gradually along the element length.

Overall, these tests demonstrate that for the OoP connection system to work well for a connector spacing equal to the beam grid spacing, 800 mm or less, corresponding to the second tested configuration. Comparatively, the first configuration with the connector spacing of 2300 mm, would be equivalent to having one connector per beam grid module. This would therefore not be sufficient as the resulting stiffness gains are insufficient to justify the addition of an out-of-plane module.

Therefore, while not achieving a completely rigid connection between the elements, the system can be calculated and analysed easily using the gamma-method. Combined with the reversible nature of the connection, this improved performance compared to the current design of this connection, as presented in Section 2.1, and validated by the testing, and easily implementable calculation methodology makes the Knapp MEGANT connector a viable option for the OoP connection.

4.2. Beam-to-beam B2B intersection connections

A comparison can be made to the expected theoretical failure mechanisms and maximum loads. The unfactored bending capacity of a full 180×280 mm GLT beam is $M_{y,Rd}$ = 60.9 kN-m, which under a 4-point bending setup, should have been reached for a jack load of P = 152.2 kN. For specimens C1, C2 and C3, the expected failure mechanism was the plate buckling under the compression due to bending. The calculated buckling capacity of the 6 mm steel plate was $N_{b,Rd}$ = 120,1 kN, which would have been reached for a bending moment equal to $M_{y,C,Ed}$ = 28.0 kN-m corresponding to a jack load of PC = 70.0 kN. However, those specimens all failed in tension on the underside due to the bending moment (Figure 6). A few reasons can explain this discrepancy.

The first being the potential weakening of the cross-section on the bottom fiber due to the reinforcement screws as discussed previously. The second reason could be the reduced bending stiffness (or corresponding effective cross-section height), which reduced the bending strength of the beams. Indeed, the unfactored bending capacity of a beam of dimensions 180×206 mm – corresponding to the average of the effective heights from specimens C-1-2-3 – can be calculated to be $M_{y,Rd,C,eff}$ = 33.6 kN-m, corresponding to a jack load of $P_{C,eff}$ = 84.0 kN. This effective capacity is, however, still higher than the expected failure load for buckling of the steel plate. Therefore, in addition to the B2B connection, another compression force transfer mechanism must be involved around the notch, since the B2B connection did not reach its expected buckling capacity.

Indeed, upon reaching higher curvature and slip in the connection due to the increased beam deformation and bending force respectively, the notch and transverse beam "block" were seen to be in contact. The compressive stresses could therefore be transferred by compression perpendicular to grain between those elements. This would explain the observed failure mechanism in bending and the ultimate loads around 80 kN for specimens C2 and C3 corresponding to the effective strength of the element. For specimen C1, the failure load corresponds to that of the reference beam which failed at about 80% of the expected jack load. This could be explained by variability in the timber beams with the presence of knots on the bottom fiber where the failure occurred in specimen C1, or by the high stiffness of the tested reference beam.

For specimens T1, T2 and T3, the failure mechanism was expected to be the shear failure of the nail-timber connection, with a capacity of V_{Rd} = 174.2 kN, which would be reached for a bending moment equal to $M_{y,T,Ed}$ = 40.7 kN-m at a jack load of P_T = 101.7 kN. This failure mode corresponds to the observations from the testing as Figure 7 shows. In all three cases, the failure initiated from a lengthwise splitting of the cross-section at the edge nail locations closest to the notch, which then propagated across the cross-section. This can be due to the shear capacity of the beam being reached at this point. However, the failure load only reached 70 to 80% of the expected value. This could again be due to the reduced stiffness of the beams, as discussed above. Using the average h_{eff} = 203 mm for the three specimens, the equivalent bending moment required to develop the connection's shear capacity V_{Rd} = 174.2 kN can be calculated as $M_{y,Rd,T,eff}$ = 29.5 kN-m. This bending moment is reached at a jack load $P_{T,eff}$ = 73.8 kN. For these specimens, calculating the unfactored effective bending capacity using the average h_{eff} results in $M_{y,Rd,eff}$ = 32.6 kN-m. Thus, the beam's effective moment capacity is higher than the equivalent effective connector's moment resistance and relates to the observed failure mode of the nail-timber connection.

4. Conclusions

This paper presents the results of an experimental investigation on the bending behavior of reusable timber slabs – The Pixel Slab System. Twelve beam specimens with different spans, depths, and connections were tested with 3- and 4-point bending setups. Two connection methods were studied: (1) superimposed GLT beams with OoP connectors, and (2) GLT beams with notched B2B connectors.

The proposed OoP connection employed a Knapp MEGANT connector at the interface between the vertically arranged beams. Test results of this connection show that the wider connector spacing did not successfully achieve full composite action between two beams. The smaller spacing however, exceeded the theoretical expectations with regard to the effective heights obtained with the gamma-method. While not achieving full shear transfer between two beams due to the connection slippage, the performance still was found suitable for the application thanks to the reversibility potential of the Knapp MEGANT connector. Yet, the connector's directionality and constructability constraints could be further refined.

The proposed B2B connection uses half-lap geometry to join the intersecting beams together. To achieve the element continuity, a nailed plate is installed on one side of the beams to tie the discontinuous beam ends around the half-lap notch. The results from the experimental testing for this connection shows a significant reduction in stiffness up to 66% of the expected mean value, due to the half-lap notches and the connection slip. In tension, the B2B connection performed as expected. However, in compression, the connection slip induced bearing perpendicular to the grain between the notched ends and the perpendicular block. Hence, care should be taken to dimension the notch to account for this issue.

Acknowledgements

This research was partially funded by the EPFL - ENAC Innovation Seed Grants 2022 program. The steel connectors employed in this research for the OoP tests were facilitated by KNAPP GmbH.

References

[1] A. Muresan, J. Brütting, J. Cañada, D. Redaelli, and C. Fivet, "Design Space of Modular Slab Systems with Discrete Stiffness Distribution and Irregular Column Layout," in *Proceedings of the IASS Symposium 2018*, Boston, USA, 2018.

[2] Knapp-Verbinder, "MEGANT (R) - heavy duty system | Knapp Connectors," *[Online]. https://www.knapp-verbinder.com/en/produkt/megant-heavy-duty-system/?v=11486*, 2021.

[3] Austrian Institute of Construction Engineering, "European Technical Assessment ETA-15/0667 of 22.07.2019," Austrian Institute of Construction Engineering, 2019.

[4] European Committee for Standardization, "Eurocode 5: Design of timber structures - Part 1-1: Common rules and rules for buildings," European Committee for Standardization, 2004.

IASS 2023
July 10–14 Melbourne
Integration of Design and Fabrication

Proceedings of the IASS Annual Symposium 2023
Integration of Design and Fabrication
10–14 July 2023, Melbourne, Australia
Y.M. Xie, J. Burry, T.U. Lee and J. Ma (eds.)

Integrative approach to a timber gridshell formed on-site

Evy Laura SLABBINCK[*], Hermann BLUMER[a], Stefan RICK[c], David RIGGENBACH[b], Martin ANTEMANN[d], Fabian SCHEURER [d]

[*] Design-to-Production, Seestrasse 78, 8703 Erlenbach, Switzerland
slabbinck@designtoproduction.com

[a] Création Holz, Tobelackerstrasse 6, 9100 Herisau, Switzerland
[b] Blumer-Lehmann AG, Erlenhof, 9200 Gossau, Switzerland
[c] SJB Kempter Fitze, Zürcherstrasse 239, 8500 Frauenfeld, Switzerland
[d] Design-to-Production, Seestrasse 78, 8703 Erlenbach, Switzerland

Abstract

This paper describes the integrative approach of timber experts to achieve an innovative bent on-site timber gridshell in a combined effort and focusses on the different challenges and how each discipline responded to them, including workflow, exchange, and an interdisciplinary digital master model. The timber gridshell 'Wisdome Stockholm' is an extension of the Tekniska Museet in Stockholm, Sweden. The gridshell is constructed out of five crossing layers supported by pre-tensioned timber columns. The lower layer acts as falsework and is assembled from pre-curved, CNC-machined beams, while the upper four beam layers are bent on-site from laminated-veneer-lumber (LVL), a planar sheet material, held in place by wooden dowels and screws enabling loads to be transferred via contact. This innovative construction method was developed due to a central prerequisite: the mandatory usage of LVL as main material due to sponsorship. Finding this solution could only be achieved by early on integration of knowledge along the whole process chain. The collaborative team consisted of timber experts in digital planning and timber construction, engineering, and fabrication and assembly.

Keywords: integrative approach, timber gridshell, collaboration, interdisciplinary solutions, wood-only constructions, free-form structures, timber construction, digital fabrication

1. Introduction

The 'Wisdome Stockholm' is an extension of the National Museum of Science and Technology (Tekniska Museet) in Sweden, designed by the local architects Elding Oscarson. The building consists of an interior wooden dome, housing a 3D-cinema, covered by a conditioned free-form timber roof. This innovative gridshell covers 1,128 m^2 and is constructed out of five crossing layers with a maximum span in the longitudinal direction of 47 metres, supported by pre-tensioned timber columns (see figure 1).



Figure 1. Wisdome Stockholm project, bent on-site timber gridshell currently under construction

Copyright © 2023 by Evy Laura SLABBINCK, Hermann BLUMER, Stefan RICK, David RIGGENBACH, Martin ANTEMANN and Fabian SCHEURER. Published in the Proceedings of the IASS Annual Symposium 2023 with permission.

The five crossing layers (layers ‘A’ to ‘E’, see figure 2) span alternating along the short and long section of the building, which leaves three layers along the short distance of the building and two layers along the long distance. In contrast to other timber gridshells, like the Centre Pompidou-Metz or the recent Swatch Headquarters in Biel [1], only the lowest layer (layer ‘A’) is assembled from pre-curved, CNC-fabricated beams, and works as falsework. The upper four beam layers (layer ‘B’ to ‘E’) are bent on-site from five LVL sheets (sublayer ‘a’ to ‘e’) each, with bending and torsion held in place by 3,500 wooden dowels and screws enabling loads to be transferred via contact. Stora Enso sponsored the project and mandated the use of LVL, which was also the key to enable this innovative construction method.

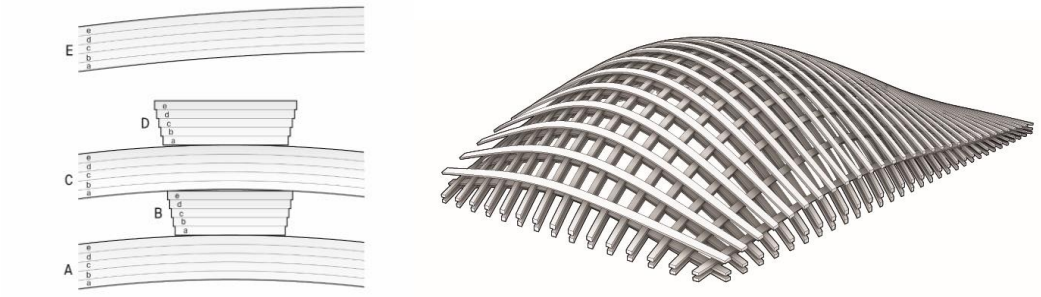


Figure 2. Gridshell layer and sublayer overview

1.1. Background and context

Gridshell structures have the advantage of covering large spans without intermediate supports, enabled by their geometry. In the past decade, there has been an increased development in the design and construction of innovative and advanced timber gridshells [1][2]. Timber is the ideal material for shell structures and has several advantages over other materials: excellent strength to weight ratio; machinability; elasticity; environmentally friendly and sustainable; structural flexibility by customisation possibilities of the material; adaptability to geometric demands; and it is a light and dry construction material making it ideal for prefabrication. Timber gridshells, and in particular timber elastic gridshells, e.g. Mannheim Multihalle, Weald and Downland Museum and PEMADE gridshell [3], use thin, slender members and by doing so, the geometrical torsion in the members is reduced [4]. To be able to control the horizontal thrust of bending the members, these gridshells are often continuous facades of a building starting at ground level and covering wall and roof geometry. Apart from the following examples, Savill Garden Gridshell and Flimwell Woodland Enterprise Centre are solely a roof on columns with either a ring beam transferring the forces to the ground via inclined columns, or by having columns tangentially oriented to the roof surface [1].

In ‘Construction 4.0’, the use of advanced building materials and prefabrication is key, by combining digital planning and fabrication, time and resources can be managed more efficiently [5][6]. Due to the advances in digital fabrication, timber gridshell design has shifted away from bending elements on-site to prefabricating glued laminated (glulam) beams. This is largely due to new CAD, CAE, CAM and CNC technologies. Furthermore, these technologies enable curved glulam beams to expand the design space, and avoid difficulties encountered during the design and construction of elastic gridshell structures [7]. A range of alternative timber gridshell types and connection systems were developed using glulam beams, among others: Zollinger system (Toskana Thermal Springs), use of lap joints (Swatch Headquarters), hierarchical beam directions (the French Pavilion Expo 2015) and the use of timber dowels (Centre Pompidou Metz) [1].
In order to overcome the limited design freedom, construction constraints and complexity of the design, research evolved by bending continuous elements in timber gridshells in an innovative way. Bend-plate gridshells, such as the 2010 ICD/ITKE research pavilion, enabled the use of single curvature locally [8]. Ribbed and cross-ribbed shells are constructed by means of falsework and the members are doweled or nailed together [9]. Alternatively, wood's hygroscopic properties can be used to form surface-active plates [10].

The use of a single material that speaks the same language for connection and structural member is crucial in timber construction. In recent decades, extensive research has been conducted on the use of dowels to mechanically laminate timber. As early as the 18th century Hans Ulrich Grubenmann built bridge arches with dowelled solid beams. Later in the 19th century Amand-Rose Emy illustrated mechanical lamination of timber by bending timber elements in a jig and fixing them with bolts and clamps [11][12]. Research conducted more recently has shown how dowel laminated timber (DLT), ribbed shells with doweled planks, and shear keyed beams, improve the overall stiffness and efficiency of beams [13][9][14][15].

Wisdome Stockholm is part of Construction 4.0 and extends the state-of-the-art structural design method of elastically curved, bent-on-site gridshells and addresses the design freedom and construction constraints.

1.2. Challenges requiring cross-disciplinary collaboration

The winning design of the Wisdome Stockholm competition was a rectangular floor plan housing a dome-shaped, wooden lattice structure as roof. Due to the free-form geometry of the roof outlining the interior dome, the loadbearing behaviour deviates from an ideal dome where the structural components are mainly subjected to pressure. The shape of the roof is very flat on one side and very steep in the other direction. This has the consequence that on-site assembly is more complex in the steep areas, and that the complexity of components is increased due to the requirement of more flexibility in the connection details in order to ensure engagement of all elements. The Wisdome roof is elevated from the ground by vertically oriented timber columns, which can only take limited horizontal thrusts from the roof. This results in a gridshell structure that is mainly subject to bending stress in the flatter area. In gridshell design, this is mostly managed with glulam elements with a large cross-section height. Due to the material supply of Stora Enso, a solution based on planar LVL panels of limited thickness needed to be found. The challenges and facilitations that this new prerequisite entails had to be balanced to ensure time, cost, risk, and quality.

This project pushed boundaries. The 5 layers of the gridshell in LVL in itself was an experiment, this was exacerbated by the grid organisation to be able to transfer the loads to the columns, such that they were rigid in the key areas and the pre-tensioning of the columns themselves. The experiment was embedded in the framework of an executed, real large-scale project. The entrepreneurial aspects of the client and the executing companies limited the scope and brought the constructive pressure for healthy pragmatism for the development, planning and implementation of the project.

The first challenge in the development of complex experimental projects was the alignment of the team of specialists. The goal was to get a holistic view of the project and the process behind it. The project should be a success for both client and users. In addition to the architectural and constructive ideas, the time and financial framework in which the project must be implemented are fundamental to the success of the project. Topics such as local value chains and the cross-generational reuse of components are increasingly used by decision-makers and are more and more influencing the solution space.

1.3. Cross-disciplinary collaboration

The success and completion of this challenging experimental project could only be achieved through early integration of knowledge throughout the whole process chain and required a close-knit cross-disciplinary team.

The collaborative team consisted of timber experts in digital planning, timber construction, engineering, fabrication, and assembly. Timber contractor Blumer-Lehmann AG, responsible for planning and execution of the timber construction, contracted long-term partners Création Holz, SJB Kempter Fitze

and Design-to-Production early on in the project. Création Holz and SJB Kempter Fitze are the timber construction engineers, involved in structural concept design and development. Design-to-Production delivered timber consulting, project management support and digital planning. The team has extensive experience with collaborating on free-form projects, for example Swatch Headquarters in Biel in 2019, Cambridge Mosque in Cambridge in 2017, and Nine Bridges Golf Club in Yeoju in 2008.

Requirements for cross-disciplinary collaboration are understanding the needs and interests of all parties and incorporating them into solutions and suggestion, a high degree of openness and transparentness in discussions, trust between all parties, knowing what the others are capable of, and taking responsibility. As the solution space is unclear and undefined in the concept phase of a project, all ideas and solution approaches from different specialist shall be considered and analysed to create an in-depth synergistic and iterative solution process. In addition to improving quality and achieving project completion on time, cross-disciplinary collaborations encourage teamwork, stimulate information sharing, and enhance communication among project members [16].

2. Integrative design concept

A design concept always starts from the architectural intent. The whole team was focused on the vision of the architect to realise a prefabricated supporting and enveloping structure made of wood. The development and documentation process lasted one and a half years and involved a series of physical mock-ups at a 1:1 scale alongside a thorough analytical approach to validate progress.

2.1. Trade-offs

Processing in the constructional development started with solution approaches in assembly and worked its way "backward" via transport and logistics, pre-assembly, CNC production, material procurement, execution planning, digital planning, structural engineering all the ways to architecture. For the sake of the story of this paper, the approach is reversed.

2.1.1. Structural concept

Modern timber constructors have the opportunity to be inspired by engineers of the last centuries. Hans Ulrich Grubenmann and Amand-Rose Emy created arches by doweling beam elements [11][12], while Arthur Vierendeel designed and implemented bridges without diagonals according the well-known Vierendeel girders [17]. These two solutions were the initial step to the concept of the Wisdome.

On the one hand the first mock-up (see chapter 2.2) has shown that is not useful to dowel the lamellae into ready-made structural elements. This is due to a large recoil after release from the fabrication jig and the effort that goes into the assembly for the subsequent lack of accuracy. Ensuring that the five-by-five (in total 25) lamella layers all meet exact points in space for idealised load transfer is an unwieldy challenge. On the other hand, production of the LVL lamellae according to the glulam technology, does not bring the required accuracy we expect from the elements. All-round milling, like with glulam blanks, would be very costly and not an efficient option. With their various advantages and disadvantages, both approaches have found their way into the project. The glued LVL beams for the bottom layer (layer A), as part of the falsework and, so to speak, the template for all subsequent layers (layers B to E). With the four additional beam layers, the advantages of the individual lamellae bending on-site outweighed the disadvantages, even though the bending on-site of individual lamellae into the required shape quintuples the number of components and is a new construction method in type and size. This means that two different construction principles had to be implemented in this roof construction. In this scope of the project, this affects the processing intensity for development and production, from assembly to planning. The width of the lamellae is stepped to visually circumvent any visual tolerances during bending of the elements. The minimum width of 380 millimetres, and the maximum width of 500 millimetres, with a step of 7.5 millimetres on each side were defined by the architectural intent. To be able to bend the

lamellae, the LVL thickness of 31 millimetres was chosen. The large width of the lamellae allowed for enough structural cross-section to be left after cut-outs were made for the dowels.

Besides the beams, the structural concept consists of five different elements. Firstly, for the dowels there are two main types in the roof, namely the cross-dowel and the shear-dowel. The cross-dowels ensure that the different layers of beams are held in position, are connected, and transfer loads at the crossing points, while every other layer is connected with a shear-dowel to transfer shear loads between the layers to achieve the same principle as shear keyed beam [13]. The tenons of the shear-dowels are tapered to make the assembly easier and to ensure a tolerance-free connection and therefore transfer loads at the contact face between dowel and lamella. The fibre direction of these dowels is in the longitudinal direction (see figure 3). The cross-dowels are cone shaped to simplify the assembly and create a tolerance-free connection. No fibre direction was specified as forces were coming from two different directions, and calculations were performed with cross-grain values.

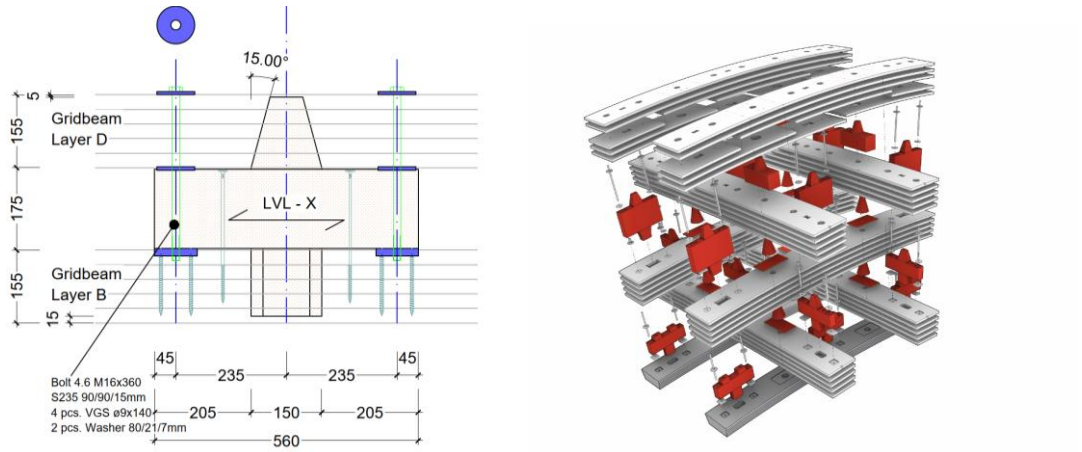


Figure 3. Overview shear-dowel and detailed roof build-up

Secondly, along the edge of the building, three-metre-high up to seven-metre-high hybrid timber columns are supporting the roof. Due to the asymmetrical arch-shape of the roof, the horizontal thrusts deform the columns individually (see figure 4). By pre-tensioning the timber columns the horizontal deformation is absorbed. As a fixed connection at the column foot was not sufficient, the vertical deflection of the roof is reduced and custom pretension of the columns allowed for a uniform deflection along the whole facade. Pre-tensioning of the columns is done by embedding steel rods without bond and connecting them to the concrete at the bottom of the base plate. Non-linear behaviour is introduced by the individual behaviour of each column, either the steel rod absorbs the forces for the deformation, or the E-modulus of the wood does.

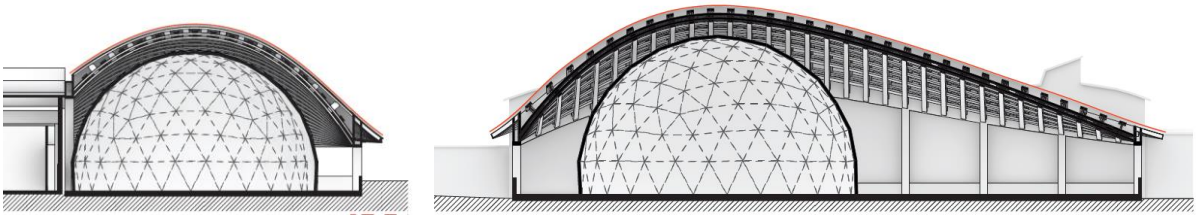


Figure 4. Cross-section through the roof in the short and longitudinal direction

Thirdly, running along the edge, the edge beam and edge panels transfer the vertical and horizontal forces from the received roof layers to the columns. A shear panel is located between the grid beams that directly arrive at the column. These panels, connecting layer C and E, create a frame connection with the column to further stiffen the elements for the roof structure and building. Lastly, to the edge beam and edge panels, rafters are connected to build a cantilevering canopy for the roof.

2.1.2. Engineering

In the early design phase, the balance between simplified calculation models and adequate detail needed to be balanced. One wants to draw quick decisions but still have all elements in the model that impact the structural behaviour. Possible solutions to the different challenges for early structural design decisions were strengthened by the experience of the different parties.

The engineering of the gridshell was done in a two-step calculation process. First, internal stresses, due to bending and torsioning of the beams from layer B to E needed to be calculated. Because each member of the roof has a slightly differing geometry, the internal stresses differentiate along the whole roof. The internal stresses were taken into account by applying (in a parametric matter) a torsional and bending force on the lamellae to approximate the final geometry. These loads were transferred to the second step in the calculation process, namely, the final geometry of the lamellae, to simulate the recoil. It is important to consider these recoil forces for the connections that keep the lamellae in the desired shape. Relaxation of the lamellae is advantageous for the structure as internal stresses will be reduced over time; no relaxation reduction was taken into consideration. While creeping effects of the structure were considered within the analysis.

Due to the structural concept of individual lamellae, lots of single individual members had to be modelled, which increased the importance of tolerances. Even though larger tolerances were helpful for assembly, in the case of structural design it complicated the process due to different connection properties between each connecting element. This emphasized the collaboration between engineer and manufacturer to define a manageable tolerance for both fields.

The shear- and cross-dowels are main connection details within the roof. Depending on their location, a different size of forces is received by the dowels. To maximise standardisation, but avoid waste of material, a certain number of dowel types are defined. This involves an iterative process, as choosing a dowel type in a certain location, influences the stiffness and the size of the forces attracting the dowel compared to the rest of the roof. Even though layers B to D are offsets from layer A, the dowel height needed to be adaptable to accommodate a small height difference at each dowel due to local curvature and torsion. Each dowel type uses the smallest required height in the roof, and the variable height is achieved by steel washers partially sunken into the lamella. Slack and slip between the different elements and connections were applied in the structural model through member hinges.

The most complex connection in the building was the connection from the roof to the column (see figure 5). This connection was structurally used to get more stiffness into the roof structure by creating a frame through transferring bending moments from the roof to the column. Layers A, C and E are connected to the column head, while layer A would mainly deliver a compression force, layer E delivers a tension force. Due to the fact that each column received a different size of forces, and a different geometry arrived at each column, and these are not aligned thus there is no worst case to calculate. This resulted in a calculation of every individual column, which was made possible by using a parametric process. The compilation of all connections of the roof beams, edge beams, edge plates and shear panel, made the overview of the stresses within the column head complicated and obscure. On top of that, all these connections needed to be designed in a way that assembly on-site can happen in the most efficient way possible, see chapter 2.1.6.

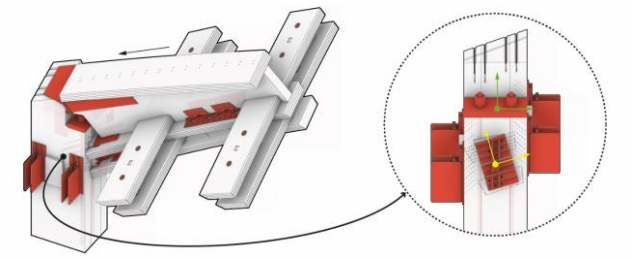


Figure 5. Column head and all its connections to take the forces from the roof

2.1.3. Constructional development

Wisdom is an extension of the museum and is to be built alongside an existing building (Wallenberghallen). This had to be taken into the consideration for the construction process and limits the accessibility to the components and connections. Another restriction is the 3D-cinema dome. With a diameter of approximately 20 metres, the dome extends up to 1 metre below the roof structure and therefore had to be integrated into the falsework construction.

The interface between the foundation and the timber column is a concrete support base where the pre-tensioned rods of the columns are connected to. A zero tolerance between concrete and wood is required to avoid slack, and for architectural aesthetic reasons.

2.1.4. Digital planning

Geometric description of a free-form gridshell requires advanced geometry and modelling knowledge. It was clear from the start that pre-fabricating all parts of such a complex structure could only be achieved by means of digital CNC-production. Thus, the objective for digital planning always was to eventually create production-ready data. Based on the multi-scalar modelling-process developed by Design-to-Production [18], not just one but a stack of four digital 3D-models was developed over the different stages of the project (see figure 6):

1. A **context-model**, defining the relevant surroundings (outside the project scope) and the building-grid-and-levels defined by the architects. This served as a common reference for all subsequent digital modelling within the project.
2. A **reference-model**, defining the geometry of the roof surface and its different layers (as precise NURBS-surfaces), the beam axis grid, and placeholders for all connection nodes. This was used to identify geometrical worst cases and provide initial input for other digital modelling efforts (e.g. by the engineering team).
3. A **coordination-model**, fixing all component dimensions and breaking the continuous beams of the reference-model down into segments and lamellae, so that the necessary raw-material for all components could be evaluated and ordered. Also, collision testing for the numerous connection details was done at this level, to find collisions between neighbouring joints and to ensure that assembly was possible despite the complex geometry.

All but the first of these models were parametrically generated from their respective predecessor (after this was carefully checked and approved) with only very little manual modelling involved. Thus, very low error rates could be achieved in the overall process. Likewise, changes (e.g. in the detailing) could easily be accommodated by altering parameters and re-executing the respective step of the parametric modelling process – based on the stable model of the previous detailing level.

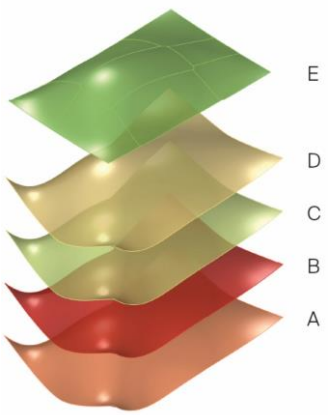
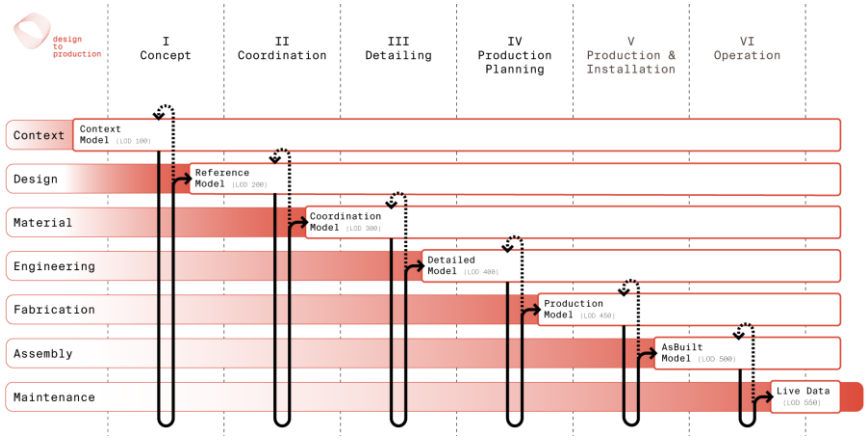


Figure 6. Left: Agile Design-to-Production process. Right: Reference-surfaces of all 5 beam layers

From the last model, production data in various formats could then be extracted and delivered to various fabricators. A special challenge in this final step was the two-fold unrolling of the curved LVL-lamellae: first from the undetailed coordination model, in order to nest the lamellae on flat LVL-panels and order raw-material, which had a lead-time of several weeks. During this time, detailing was finalised, and the lamellae were subsequently unrolled a second time, now including all their complex detailing, production-ready for 5-axis CNC-fabrication.

2.1.5. Machining and fabrication

The decision to only glue beam-layer A, led to a significant streamlining of the production process for layers B to E. The fabrication process of all layers started the same with the 3-axis contour milling of the lamellae out of standard flat LVL panels. The aim of layer A was to avoid contour 5-axis machining along the longitudinal edges, like with glulam blanks, which made precise positioning of the CNC milling a challenge. An individual gluing formwork for each beam segment was created. As there were only end cuts and machining where connection points need to be created, the positioning and gluing of the lamellae needed to be accurate. As a last step, 5-axis milling of the beam segment was performed: the end sections, connections to the edge beams, longitudinal joints, screw holes and spacers for plates and washers were milled. Positioning of the beam to the CNC system was done by re-using the gluing formwork which were placed in a rigid frame and thus the exact planned geometry could be imposed on the bendable beams on the machine table. For layer B to E an additional 5-axis CNC milling was added to mill the connections to the edge beam, cut-outs for dowels, drills for screws and pocket milling for spacer plates and washers. A challenge here was how the visible lamella (sublayer a) was processed from the bottom, while other lamellae were processed from the top. To help sorting the five lamellae that belong together in the correct order, orientation and correct displacement in relation to the longitudinal direction (overlapping longitudinal joint), a milling mark was introduced in the process.



2.1.6 Assembly

It was already clear in the early phases of the project that the assembly of the entire wooden structure would take place in a closed tent. This tent covered about one and a half times the floorplan of the building and included a powerful gantry crane which operates the entire tent area. This was taken into account from the beginning when developing the production and assembly concept. Usually, the quickest possible assembly of the supporting structure is encouraged so the building envelope can be closed within a short amount of time, and side-to-side (e.g. left to right) assembly process is recommended. The tent ensures a weather-independent installation, even during winter, so that the gridshell beams could be installed layer by layer, namely bottom to top.

Important for a smooth assembly of the gridshell was a very precise assembly of the columns and edge beams, which had to be held in position by temporary struts to prevent displacement during the assembly of the roof structure. Also important was a temporary substructure (precise, 5-axis milled templates

placed on surface scaffolding) which enabled precise positioning of the layer A beams. The timber columns were placed over the rebars of the concrete base, formwork was built, and concrete was poured. With the assembly of the layer A, in which all connection dowels were pre-assembled as an interface to layer B and C, a perfect template was created for the other layers of the gridshell. All beams of layers B to E were delivered as flat lamella packs in the correct order, and automatically found their final position when attached through the conical plug-in connections, namely cross dowel. In case of more curved areas in the roof, the segment length was limited by the entry vectors of the dowels. In flatter areas, a maximum segment length of 13.30 metres was chosen. On the one hand, this enables standard transport (including the raw panels) with closed trailers, but on the other hand, the handling of 31-millimetre-thick panel strips with greater lengths is very difficult. The load required to force the plate packs into the desired curvature could be applied using screw clamps (see figure 7). Once in the final position, the parts were screwed together to secure the position.

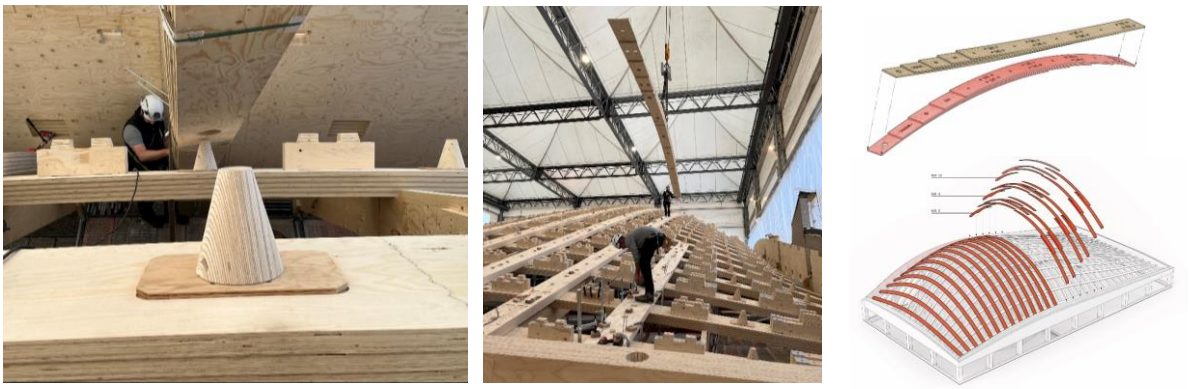


Figure 7. Assembly of the roof structure

2.1.7. Logistics and transport

The goal of every timber project is to reduce transport to a minimum, and optimise truckloads to the fullest, and make logistics as straight forward as possible.

Similar to transporting curved glulam beams, the 93 beam segments of layer A could not be stacked due to their double curvature. The formwork was reused from previous projects for transportation in a bespoke designed frame, but even then, the loading capacity of the truck was still limited in size. The load sequence of the truck was coordinated with the assembly process to guarantee an efficient assembly on site. In contrast, the lamellae for layer B to E could be stacked in a flat packed configuration, transporting significantly more material per truckload (see figure 8). In total 22 closed truck trailers were loaded for transportation to the building site, including columns, dowels, edge beams and panels, and rafters. In order to keep track of the 2,186 lamellae and the resulting 444 beam segments, a numbering system was developed already in the concept phase, which allowed a logical assignment of each individual component without having to consult a list or plan. Each of the individual lamellae were labelled accordingly.

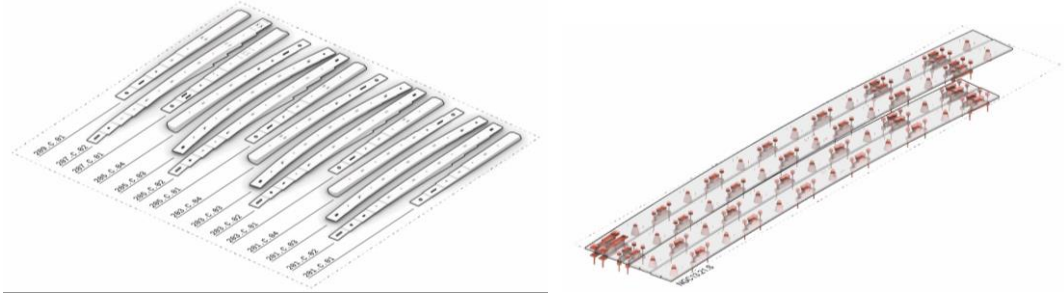


Figure 8. Flat packed beam segments and production export per sheet

2.2. Process and methodology

In the early stages of the project a feasibility study was conducted by the whole team as the project reached beyond the experience of the experts. This included a digital 3D model of the shell structure, analyses of the 3D model, and structural concepts which were tested and quantified by three 1:1 mock-ups, all within a period of 4 months. First, the *design mock-up* is a cut-out of the roof and was made out of eight beams which consist of four crossed layers of two beams each (see figure 9). With this mock-up, the client and architects were able to validate the aesthetic, as well as the connection between the different beam layers. Second, two *technical mock-ups* of each one beam segment were fabricated. These two beams had respectively the highest amount of torsion (8,4 degrees per meter) and bending (radius of 10 metres) in the entire roof. With these mock-ups, the recoil of the elements, the fabrication and assembly process of the beams, drilling holes in the high-tension zone of the beam, dowel connection holding the shape, and feasibility of the input force to bend and twist the beam were tested.



Figure 9. (From left to right) Technical mock-up, design mock-up and constructional mock-up

A fourth mock-up was made 10 months after the start of the project to test the construction development. The mock-up was a cut-out of the roof in an area where the torsion value was high. A variation of tolerances of all dowels, connection and tolerance of the shear panel, fabrication of all dowels, digital planning process, resolving all details and collision detection was tested and quantified. This mock-up served as a dry-run for the final construction and involved the whole team including the subcontractors. The mock-up was a success and allowed for further optimisation of the constructional development and collaborative teamwork.

3. Collaboration between disciplines according to an integrative approach

Success of the concept and the feasibility to complete this experimental project with a high quality and within budget and short time frame was only possible with the close collaboration and commitment of the cross-disciplinary team of experts [16].

During the development process of the project, questions, objectives, and basic rules of the individual project stages resulted in concepts and possible solution spaces in which the different experts contributed with arguments, and these arguments are the basis for the realisation of the project. These were evaluated qualitatively and quantitatively and compared with the objectives and basic rules of every discipline. To verify the solution approaches, built mock-ups were verified. In addition to the physical result of the mock-up, feedback was received from the whole team and an overall assessment could be made to achieve a compromise. With the help of this evaluation, decisions could be made on a broad basis, or the solution approach could be corrected at an early stage. From the start, everyone understood that the level of uncertainty would remain high throughout a large part of the process. However, despite the lack of total confirmation, everyone continued to work on the project. Otherwise, the specified tight timeline would not have been feasible.

When the solution area became narrow enough, all project participants had the basis for their technical elaboration, the project framework conditions (e.g.: budget, deadlines, and local use of resources) were aligned, the project guidelines were formulated and set. During the further planning of the project, it

was necessary to coordinate the ensuing questions and adjust proposals based on in-depth knowledge with the project guidelines and thus to ensure the quality assurance of the timber construction planning and execution.

To be able to speed up the overall workflow, the process was divided into multiple branches during the coordination stage to allow parallel coordination, detailing, and production of component types defined by the order of production and assembly (pull planning) [19].

The narrow collaboration, the iterative process and the back and forward exchange was made possible by balancing business, technology and people, where trust and engagement played a crucial role [20]. Communication was mainly done digitally by means of email, project management software and video calls. On a few occasions, the different parties had in-person discussions during visits to the production facilities. The form of information exchange between the parties were set at the beginning of the collaboration, and included excel sheets, 3D models, 2D drawings, and a component and detail catalogue.

4. Conclusion and discussion

The complexity of the experimental Wisdome Stockholm project is evident. Thanks to the excellence (both professionally and personally) of everyone involved in the project, from the carpenter on the construction site to the architect, the project was successfully completed. Its success can be seen from different perspectives. Firstly, the structure is built, and learning is done successfully. Secondly, the network was strengthened by the great performance and collaboration. Thirdly, the project was completed within time and with high quality. And finally, the vision of the client and architect was realised.

The project requested a higher investment of working hours compared to traditional glulam gridshells, mainly due to the many challenges and unknowns, discussed throughout this paper. The challenges and facilitations that this new approach of bending LVL on-site entails had to be balanced to ensure time, cost, and quality. Logistics, structural concept, engineering calculations and details, digital planning, and assembly were found to be more difficult, while transport, machining, and material efficiency proved to be advantageous. In addition, the standard challenges such as geometric boundary conditions, architectural intent, extremely tight timeline, etc. were contemplated.

Acknowledgements

The Wisdome Stockholm, designed by Elding Oscarson and commissioned by Tekniska Museet, is a collaboration between different companies: Florian Kosche, Stora Enso, SJB Kempter Fitze, Création Holz, Design-to-Production, Blumer-Lehmann, Roth, Balteschwiler, Mueller, Olijbe and Oberholzer.

Special thanks to the core team of the Wisdome Stockholm: *Stora Enso* (Carl Humble and Jessika Szyber) for the material sponsorship; *Elding Oscarson* (Johan Oscarson and Arin Alia) for believing in the timber team, always being enthusiastic and being the initiative of this building; *Tekniska Museet* (Astrid Stenberg and Frederik Eriksson as representative of the client) for aiming high and investing in innovation and the future, *Blumer-Lehmann AG* (David Riggenbach, Valentin Künzle, Martin Looser-Frey, and Kai Strehlke) for all the valuable input, for coordinating and trusting the team and execution of the project; *Création Holz* (Hermann Blumer) for the great initial concept development of the building, as always, and thinking about timber construction in a novel way; *SJB Kempter Fitze* (Christoph Meier, Stefan Rick and Dominik Fischinger) for being able to analyse and calculate this complex building, for realising Hermann's ideas and being open to innovation and pushing the boundaries; *Design-to-Production* (Fabian Scheurer, Martin Antemann, Sylvain Usai, Moritz Niebler, Matthias Hornung, Valeriia Vlasenko and Evy Slabbinck) for timber consulting, parametric and digital planning and supporting the project management.

We would also like to thank Claes Nyberg of Olijbe, Herbert Schmid and Sven Bill of Balteschwiler, Thomas Brühlmann of Gebhard Müller for collaborating on the project. And Valentin Kubatta and Daniel Christev for their contribution to this paper.

References

[1] J. Chilton and G. Tang, Ed. *Timber Gridshells: Architecture, Stucture and Craft*, New York: Routledge, 2017.

[2] J. Lara-Bocanegra, A. Roig, A. Majano-Majano and M. Guaita, "Innovative developments in the design and construction of a permanent elastic timber gridshell," *Word Conference of Timber Engineering*, 2018.

[3] V. Tomei, E. Grande and M. Imbimbo, "Design optimization of gridshells equipped with pre-tensioned rods," *Journal of Building Engineering*, vol. 52, 2022.

[4] E. Slabbinck, A. Koerner and J. Knippers, "Torsion as a design driver in plate-bending-active tensile structures," *Proceedings of the IASS Annual Symposium 2017*, Hamburg, Germany, September 25-28, 2017, A. Bögle and M. Grohmann, Eds.

[5] P. Krupik, "Advanced building materials – prefabricated and modular designs as part of Construction 4.0 with a focus on transport constructions," *IOP conference series: Material Schience and Engineering*, 2021.

[6] H.J. Wagner, M. Alvarez, A. Groenewolt and A. Menges, "Towards digital automation flexibility in large-scale timber construction: integrative robotic prefabrication and co-design of the BUGA Wood Pavilion," *Construction Robotics*, vol. 4, 2020 pp. 187-204.

[7] A. J. Lara-Bocanegra, "Elastic timber gridshells, from material to construction," Doctoral thesis, Polytechnic University of Madrid, 2022.

[8] G. Quinn, "Pneumatic erection of elastic gridshells, design, simulation and realisation," Doctoral thesis, Berlin University of the Arts, 2018.

[9] K. Gliniorz, K.M. Mosalam and J. Natterer, "Modeling of layered timber beams and ribbed shell frameworks," *Composites part B: engineering*, vol. 33, 2022, pp. 367-381.

[10] S. Bechert, L. Aldinger, D. Wood, J. Knippers and A. Menges, "Urbach Tower: Integrative structural design of a lightweight structure made of self-shaped curved cross-laminated timber," *Structures*, vol. 33, pp. 3667-3681.

[11] A. Emy, *Traité de l´art de la charpenterie*. Paris: Carilian-Goeury (etc.), 1837

[12] R. Widmann and A. Mueller, "History and development stages in timber bridge construction in Switzerland," *Conference Proceedings 4th International conference of timber bridges 2022*, Biel, Switzerland, May 9-12, 2022.

[13] J. F. Miller and W. M. Bulleit, "Analysis of Mechanically Laminated Timber Beams Using Shear Keys," *Journal of Structural Engineering (ASCE)*, vol. 137, 2011, pp. 124-132.

[14] A. Sotayo, et al., "Review of state of the art of dowel laminated timber members and densified wood materials as sustainable engineered wood products for construction and building applications," *Developments in the Built Environment*, vol. 1, 2020.

[15] C. O'Ceallaigh, A. M. Harte and P. J. McGetrick, "Dowel Laminated Timber Elements Manufactured using Compressed Wood Dowels," *Civil Engineering Research in Ireland*, 2022, pp. 222-227.

[16] S.H.A. Rahman, I.R. Endut, N. Faisol and S. Paydar, "The importance of collaboration in construction industry from contractor's perspectives, *Procedia – Social and Behavioral Sciences*, vol. 129, 2017, pp. 4114-421.

[17] J.M. Pons-Poblet, "The Vierendeel truss: past and present of an innovative technology," *Arquitetura Revista*, vol. 15, no. 1, 2019.

[18] F. Scheurer, H. Stehling, F. Tschümperlin and M. Antemann, "Design for Assembly –Digital Prefabrication of Complex Timber Structures," *Proceedings of the IASS Annual Symposium 2013,* Wroclaw, Poland, September 23-27, 2013, J.B. Obrebski and R. Tarczewski, Eds..

[19] S. Ghosh, M. Reyes, A. Perrenoud and M. Coetzee, "Increasing the productivity of a construction project using collaborative pull planning," *Proceedings of the Architectural Engineering Conference,* Oklahoma City, USA, April 11-13, 2017, J.S Volz, Eds.

[20] M. A. Shelbourn, et al. "Planning and implementation of effective collaboration in construction projects." *Construction Innovation: Information, Process, Management*, vol. 7, 2007, pp. 357-377.

Proceedings of the IASS Annual Symposium 2023
Integration of Design and Fabrication
10–14 July 2023, Melbourne, Australia
Y.M. Xie, J. Burry, T.U. Lee and J. Ma (eds.)

Inventory-constrained design of a variable small diameter round timber structure

Kim R. BABER[a,*], Aaron BARTON[a,*], Jane R. BURRY[b], Canhui CHEN[b] , Joseph M GATTAS[c], Christoph KOCH[a,*], Hengyi REN[a,*]

[a,*] School of Architecture, University of Queensland
St Lucia, QLD 4067, Australia
k.baber@uq.edu.au

[b] School of Design, Swinburne University of Technology
Hawthorne, VIC 3122, Australia
[c] School of Civil Engineering, University of Queensland
St Lucia, QLD 4067, Australia

Abstract

To improve the overall supply of renewable building materials, forestry industries around the world are seeking better ways to yield structural timber products from low diameter logs. Such logs are produced in large volumes, from both plantation thinnings and as the crowns of harvested saw log. However, they are marginally valued for use in conventional structures due to their small diameter, high dimensional tapering, and relatively low recovery volume and structural capacity when milled into sawn boards. This paper investigates the design of an optimised branched timber structure that utilises minimally processed round logs in their near-to natural dimensions, using a digital form-finding tool that combines the dual processes of *Inventory-Constrained Design* and *Combinatorial Equilibrium modelling (CEM)*. A material inventory was generated directly from small diameter logs harvested from a plantation, giving a unique series of member lengths with associated diminishing diameters. The CEM model was used to optimise the geometric assignment of the inventory in a branched column structure, that also inherently benefits from members with diminishing diameter. This geometry was then developed into a proposition for a full scale branched column structure, with proof-of-concept design and prototyping of the intersecting geometry at the connection nodes undertaken. The development of this optimisation tool and the prototyping of the nodes, demonstrates feasibility for a novel application of this marginally valued forest resource that reduces material waste within the forestry and wood product value chains.

Keywords: inventory-constrained design, form-finding, round timber structures, combinatorial equilibrium modelling, timber connection design

1. Introduction

Structural form finding models such as Combinatorial Equilibrium Modelling (CEM) are designed to reduce material in structures through the optimisation of force path geometry. CEM is a sophisticated and powerful design tool for form finding of reticulated structures such as branched tree and truss structures [1]. It allows the designer to iterate through alternative equilibrated options for structural geometry based on input and constraint criteria such as member length, node position, force quantum and direction. Adjustments of one or more of the inputs will trigger a responsive and precise adjustment of the overall geometry and force paths to approach or reach equilibrium.

Inventory Constrained Design is a process whereby a given inventory of available material is consumed in an optimised configuration, based on a set of prescribed selection criteria, or heuristics, typically targeting minimisation of material waste [2]. With the global urgency to reduce carbon emissions,

Copyright © 2023 by Kim R. BABER, Aaron BARTON, Jane R. BURRY, Canhui CHEN, Joseph M GATTAS, Christoph KOCH and Hengyi REN. Published in the Proceedings of the IASS Annual Symposium 2023 with permission.

building designers also have the opportunity to directly influence the carbon footprint of a given structure. Being involved in the early stages of the design process, they are in a decisive position to measure and control the embodied carbon, and to design structures that maximise the quantity of carbon that can be locked-up in a structure, instead of releasing it back into the atmosphere. Toward this goal, recent studies have suggested the use of *inventory constrained* or *stock constrained* [1] design processes to enable the use of timber and forestry by-products as value-added structural components. This optimisation process customises the geometry of the structure through assignment of unique member lengths as in [3], or adaptations of unique connection intersection angles as in [4] in order to utilise the maximum amount of available resource, and minimise waste through the manufacturing process.

The research therefore develops a tool that employs three parallel material optimisation processes. It optimises the structural distribution of material, minimises waste from the material source, and maximises the carbon locked up in a structure for its given structural capacity. The first part of this paper discusses the design of the digital form finding tool and the second demonstrates the feasibility of the construction of a novel connection node.

2. Small diameter round timber members as an inventory

In any natural forest ecosystem, variation of tree size and form occurs between individual specimens. The degree of variation is reduced in plantation forests grown for timber harvesting, through close and regular planting of controlled genetic tube stock. There is however, a percentage of dimensional variation between specimens due to variable tree health, local soil and water availability, location within the stand, and damage due to animals or adverse weather conditions [5]. As such, even within regularly planted stands of trees of the same age, substantial variation occurs in the length and tapering diameters of harvested logs.

The forest selected for this project is a plantation of native Australian hardwoods in Queensland, Australia. The plantation is young, ranging 12 to 15 years old, and as a result, logs are relatively small in diameter (90-150mm) as shown in Figure 1. This is due to initial planting at high densities forcing trees to grow straight and thin as they compete for available light. When the stand reaches the age of 12 to 15 years, a percentage of trees (40-60%) are removed or ‘thinned out’ in order to allow the remaining straight trees to slow their growth in height, and increase their girth [5]. As a output of this thinning process, a significant volume of timber is harvested, however due to the relatively small diameter of the logs, there is only marginal market value realised by current processing practises. Given the abundance of small diameter logs within the plantation industry, increasing their utilisation is a particularly relevant opportunity for designers of timber structures [6].



(a) (b)

Figure 1. Juvenile hardwood trees prior to thinning (a) Typical stand (b) individual specimen.

Current timber processing practises are largely driven by market demand for sawn timber sections. When logs are sawn into dimensional rectangular sections, the process is a calculated compromise between the maximum structural timber yielded from the log and the economies of dimensional standardisation of cross sections profiles. When round (or near round) logs are sawn into rectangular or square sawn profiles, there is resultant waste in the outer flitches or 'cheeks' of the logs, and in the accounting for the natural taper of the log along its sawn length (the smallest end diameter will determine the maximum resultant cross-section) [7]. Modern harvesting and transportation logistics also mean that trees are cut into logs of regular length (typically six or eight metres) and the remaining top of the stem, along with the branches, are typically left on the ground in the forest to return to the ecosystem as mulch, or otherwise chipped to be used as fibre for chipboard or pulp. Whilst this paper does not deny the practice of mulching after harvest is valuable in terms of ecology and biodiversity [8], the process does release carbon into the atmosphere. Many fibre-based products also have short carbon lifecycles. By utilising as much of the usable timber from the tree in permanent timber structures, carbon can be stored for a longer period of time.

This paper investigates the opportunities for maximising the utilisation of a plantation's available timber in building structures, by addressing this material compromise in two ways. Firstly, the structures investigated are proposed to utilise logs in their near to natural round geometry, where only minimal processing is employed to turn the 'natural round' log into a 'true round' cross section, principally for reasons of manufacturing standardisation, but also for reasons of aesthetic preference[1]. Secondly, the structures will be parametrically optimised to utilise the complete length of each harvested log. In this way, the resultant waste from the processed stand of trees is minimised, whilst the quantity of CO2 locked up in the structure is maximised.

3. Tree geometry and part assignment

A generic branched tree structure was investigated as the test case for combining an Inventory Constrained design process with CEM form finding. The goal for this structure was to utilise the entirety of a given log in the inventory and apply CEM to maintain structural equilibrium. The initial base geometry of the tree structure was explicitly modelled with 3 levels of branches. Part lengths per level were arrayed at the ratio of 2:2:1, with bifurcation angles of 90 and 60 degrees between levels 1 and 2, and levels 2 and 3, respectively.

Provisional tension members were applied horizontally between the nodes at the intersection of level 2 and level 3 branches and between the tops of branches in level 3. As described later, these represent a transverse load carrying capacity, which was later replaced by a semi-rigid flexural capacity designed into the physical node prototype as part of this test case.

The part assignment heuristic based on this ratio could be applied to any of the unique logs in the inventory and the resultant tree's branch length (and associated large and small end diameters), assigned accordingly. When tested on the range of logs in the inventory, the overall tree structure's aggregate part length established a range of potential heights from 3.6m to 4.5m. Applying a constraint to the

[1] Logs could be used in their natural, unprocessed form. Whilst this paper does not evaluate the economic value of a 'natural round' timber member with natural features (such as branch stumps and remnants of bark, along with natural geometrical variations) compared with a 'true round' (that has been peeled to remove bark and some sapwood to create a true cylindrical member) it does take the position that the 'true round', in addition to being more readily deployable in structures with array of joined members, is likely more aesthetically desirable and result in a higher uptake in industry.

overall tree structure height (in this case 4.0m was chosen as a median height) resulted in a relative increase or decrease to the bifurcation angles when longer or shorter logs from the inventory were used.

When applying the part assignment heuristic to a unique log in the inventory, each part within the tree was assigned a unique section from the log, with a unique large and small end diameter and a corresponding unique mass, even when lengths with each level remained identical. Thus, when distributed throughout the tree structure symmetrically, the imbalance of masses between the elements would result in disequilibrium.

CEM was then applied to the part assigned geometry to re-equilibrate the overall tree structure, whilst maintaining the original total aggregate log length. As can be seen in Figure 2, this was achieved by allowing the branch in level 1 and its node between levels 1 and 2 to move location in the x, y plane. The lengths of all members in level 3 were constrained to their original length, but the nodes between levels 2 and 3, and the location of the top node of level 3, were allowed freedom in the x, y plane only. This allowed adjustment of the individual branch lengths in levels 1 and 2, whilst maintaining the original aggregate length of members in levels 1 and 2, and arriving at a state of equilibrium. With re-assigned inventory lengths for branch level 2 (and corresponding masses) applied, the CEM model was then run again for a final re-calibration of the geometry.

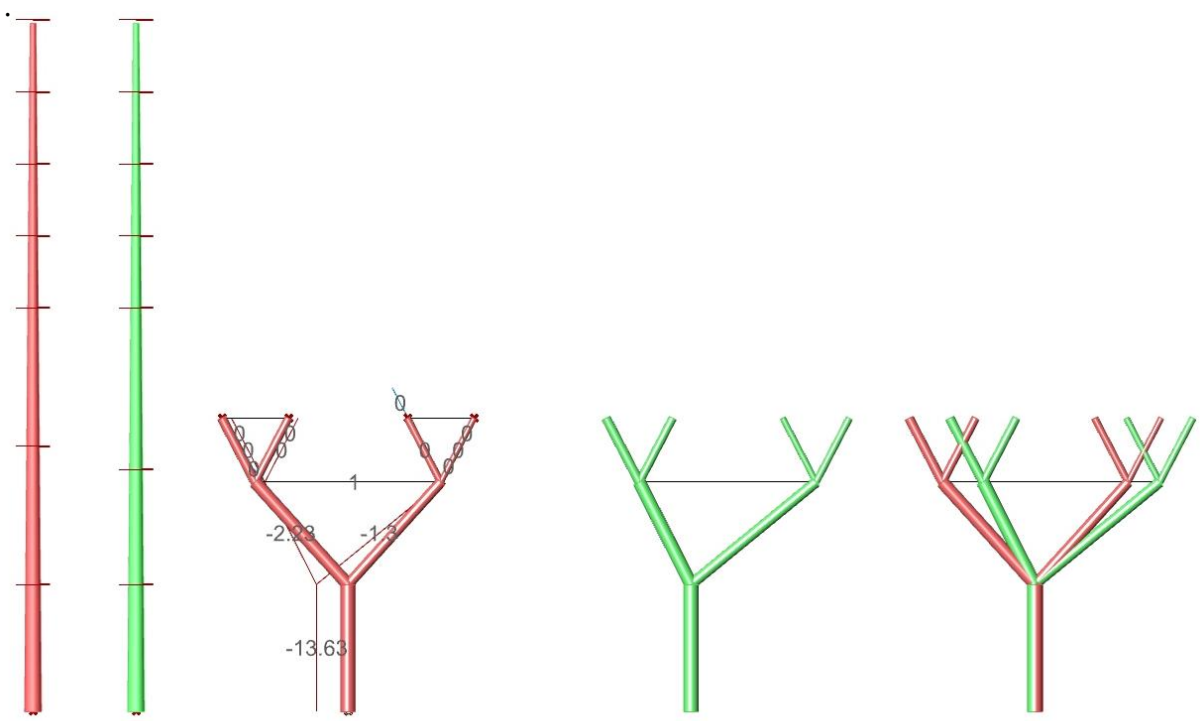
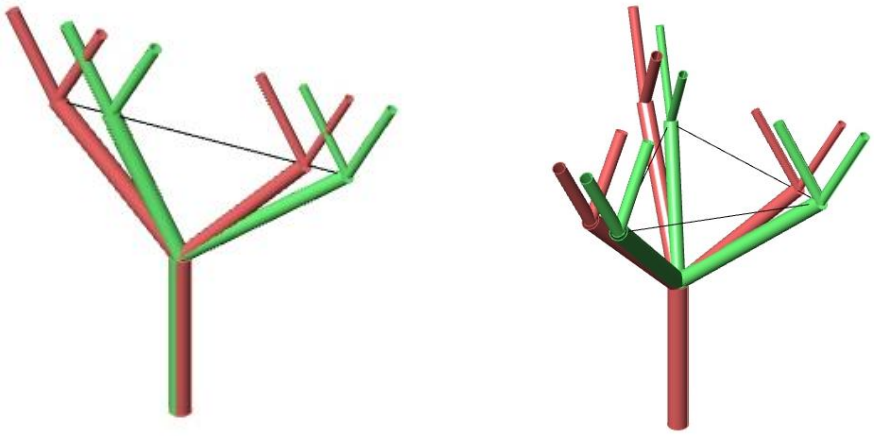


Figure 2. (a) and (c): Log inventory part assignment and correlating tree structure based on initial explicit definition of geometry, (b) and (d): log inventory part assignment and correlating tree structure after CEM adjustment to reach equilibrium (e): superimposition of (c) and (d).

After testing this form finding model in a co-planar branched tree structure with 2-way branches, a second structure was modelled using a non co-planar branch connection using 3-way branches between levels 1 and 2, utilising 3 more branch lengths on the overall structure. In this case, when the same part assignment heuristic was applied, iterations resulted in either: *i.* when applying the same initial log from

the inventory, the overall tree structure was shorter; or *ii.* an alternate, taller log was selected from the inventory for the assignment, such that the overall tree structure could reach an equivalent height.



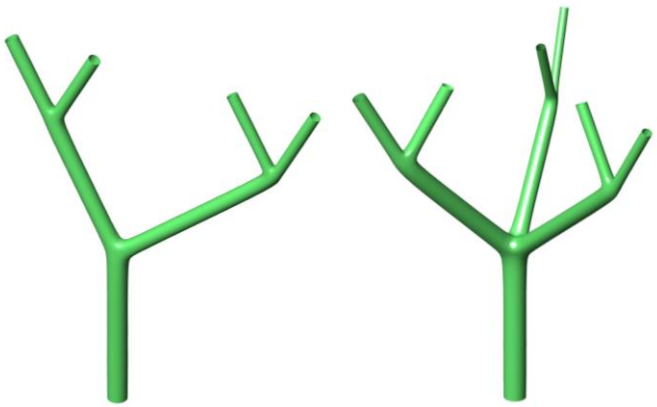
(a) (b)

Figure 3. (a) co-planar tree structure with three levels of 2-way co-planar branches, (b) non co-planar tree structure with 3-way non co-planar branch between levels 1 and 2, and 2-way co-planar branches between levels 2 and 3

4. Node design and prototyping

4.1 Node modelling

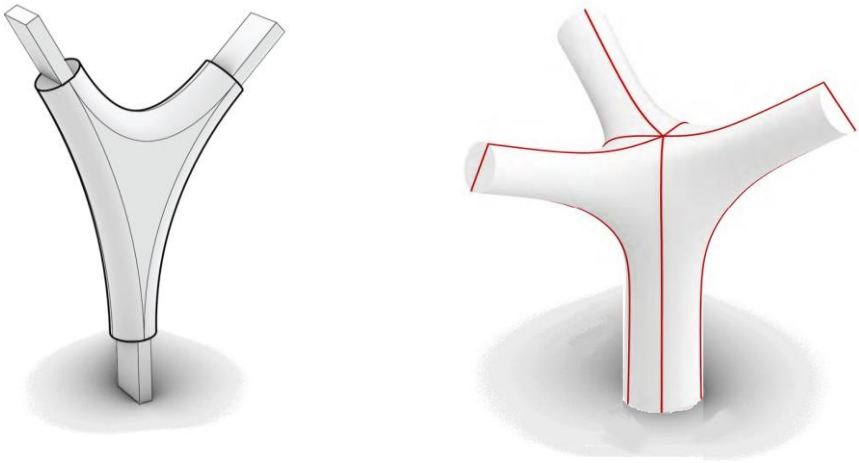
Once the tree structure geometry had been optimised through part assignment and CEM, the intersecting geometry of the co-planar and non-coplanar node types was resolved through the design of node that performs as a semi-rigid connection, alleviating the need for a tension member at the intersection of level 2 and level 3 branches and between the tops of branches in level 3. A custom laminated timber node utilising short length timber offcuts with a similar design approach as used in [9] was developed to create a smoothly blended node form that could parametrically resolve the intersecting branch geometries.



(a) (b)

Figure 4. (a) co-planar tree structure with 2-way co-planar branch nodes modelled, (b) non co-planar tree structure with 3-way non co-planar branch nodes modelled

In this demonstration, both 2-way co-planar and 3-way non co-planar nodes were designed using the process of mediating convergent centreline vectors. Geometries of both co-planar and non co-planar nodes were designed through parametric NURBS modelling within Rhino and Grasshopper. In both strategies, a solid geometry was generated to correspond to resolve the varying cross section diameters of the part-assigned branches. Planes perpendicular to the centreline geometries then bisected the branched node arms with defined length offsets, allowing enough material for future connection featuring, as shown in Figure 5.

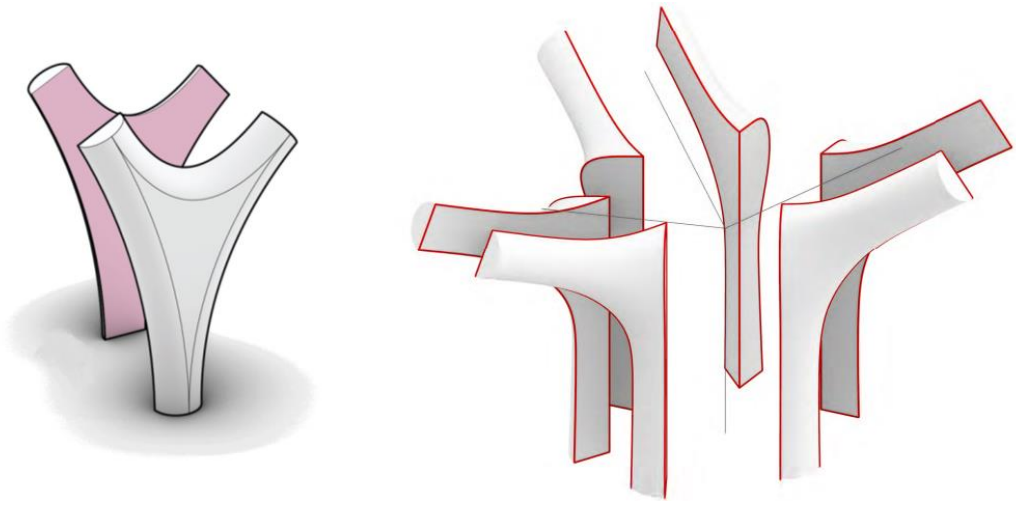


(a) (b)

Figure 5. NURB modelling based on mediating convergent centreline vectors in (a) co-planar node and (b) non co-planar node

4.2 Rationalisation for fabrication

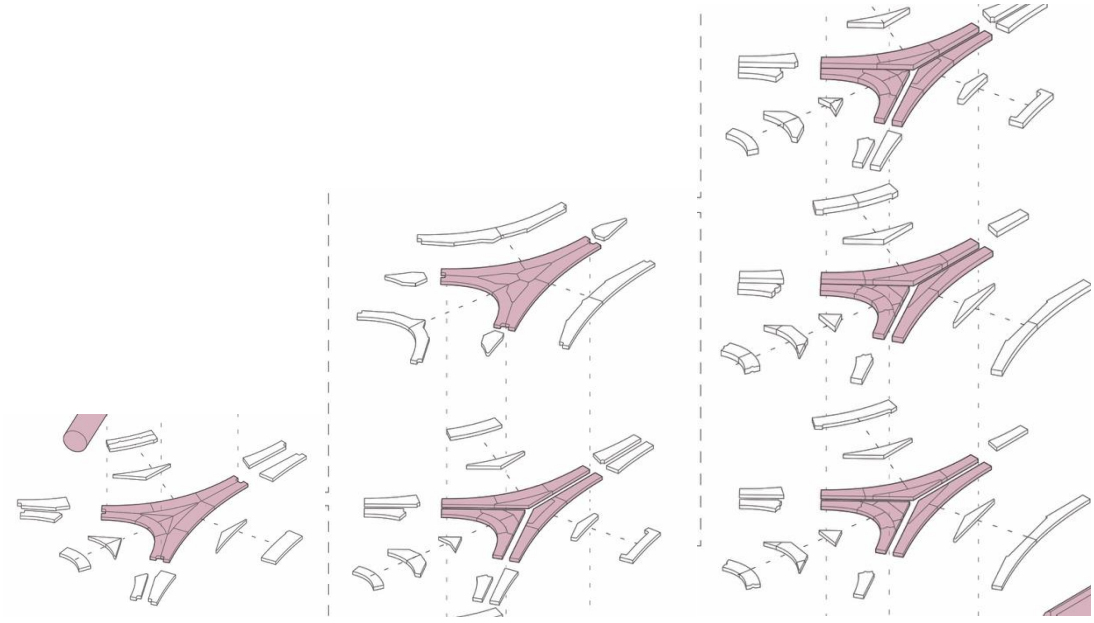
For the purposes of custom lamination and machining, nodes were bisected about identified common planes. This enabled the timber parts to be laminated with grain running parallel to the force direction, and also for the parts to be simply machined on a 3-axis router, with the bisected plane laid on the flatbed of the router. The co-planar node was bisected into two mirrored parts about the plane formed by the 3 centrelines of the co-planar branches, whilst the non co-planar node was bisected into six parts based on the 3 planes formed between the common centreline axis of the lower level branch, and each of the 3 intersecting branches respectively, as shown in Figure 6.



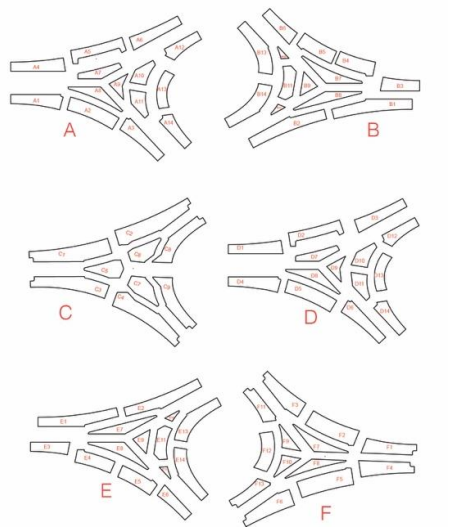
(a) (b)

Figure 6. Bisecting the nodes about common symmetrical planes (a) co-planar node, (b) non co-planar node.

From here, the process for fabricating both the co-planar and non co-planar node parts was similar, the flat face of each part corresponding to the plane of bisection, is rotated in 3D to orient to the x, y plane corresponding to the machine bed of CNC router. Each part was then further subdivided through contouring parallel to x, y axis (laying flat) to generate a series of laminations, or lamellas, to be constructed from edge glued timber members. The lamellas were in-turn further subdivided for edge gluing through the introduction of custom alternating layups of short-length dressed timber boards. These were arranged to ensure sufficient overlap of individual boards between the lamellas, ensuring grain direction is aligned to the compressive load path through each part as shown in Figures 7 and 8. Where timber boards changed direction to follow the geometry of the overall part, an internal lapped dovetail connection was pre-featured, primarily to aid in accurate assembly of the lamellas, but also to contribute some stiffening to the overall assembly. Locating holes for dowels were also machined to aid in positioning assembly in the following stages. Boards were then pre-glued into lamellas and then laminated and press glued to complete the rough billet for CNC machining.

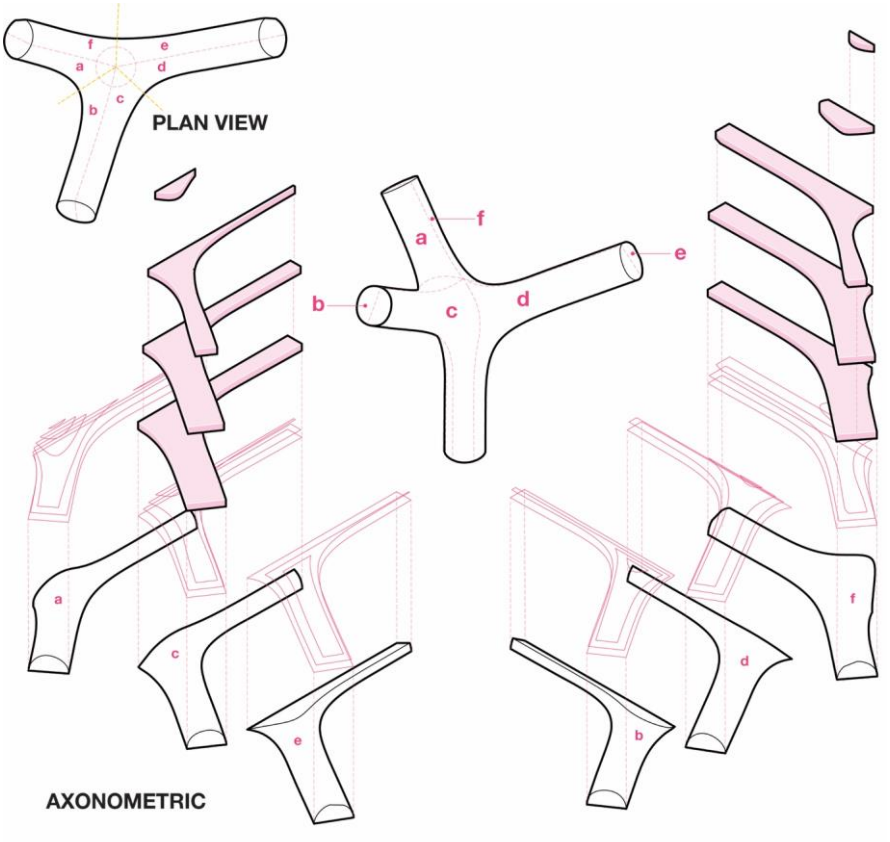


(a)

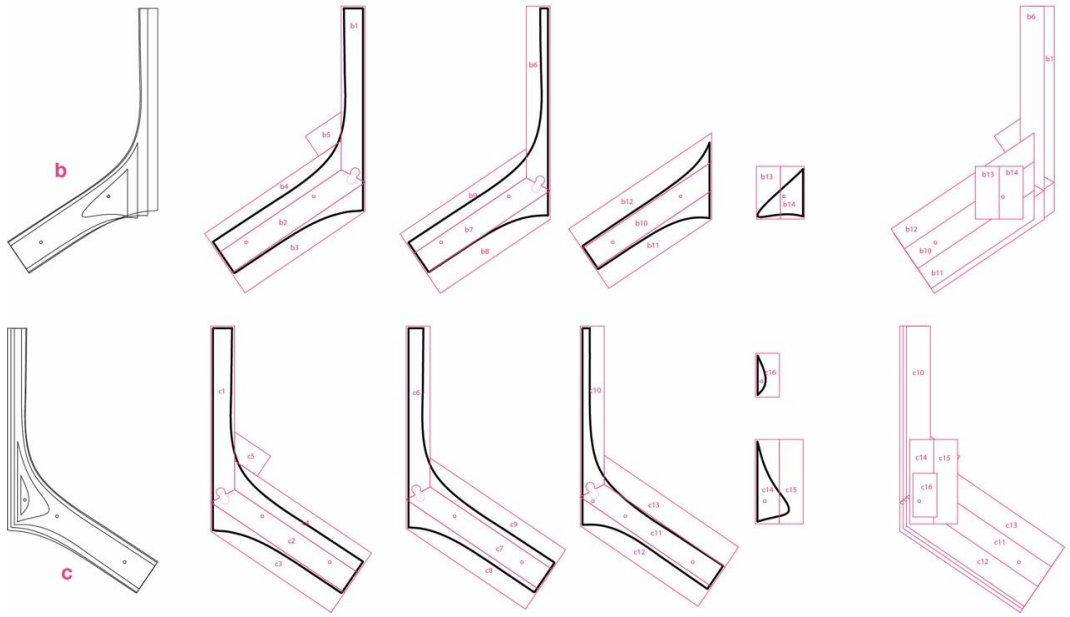


(b)

Figure 7. Contouring and subdivision of the co-planar node into lamellas of custom arranged short length timber boards for fabrication. Diagram shown in (a) axonometric view and (b) plan view.



(a)



(b)

Figure 8. (a) Contouring of the non co-planar node into lamellas, shown in axonometric and plan views. (b) Custom arrangement of short length timber boards for fabrication.

4.2 Machining sequence and assembly

Machining of the parts from the laminated billet was tool pathed through RhinoCAM, which directly integrated into the Rhino interface for a continuous workflow. The previously machined pockets for locating dowels in the billet were then matched to their corresponding positions cut into a sacrificial sheet on the CNC bed for coordination. The machine sequence was then executed in two processes, first a rough-mill was programmed to remove excess stock, followed by a final contoured parallel finishing pass with a ball nose to complete the process to higher level of finish. Utilising the locating dowels, the completed segments were then assembled, with hand finishing on a linisher where required. Finally, all parts were glued together at their bisecting planes. Prototypes of both co-planar and non co-planar nodes are shown in Figures 9-11.



(a) (b) (c)

Figure 9. Prototyping of a Co-planar node at 1:1 scale showing (a) gluing of the lamellas, (b) an assembled node test fit prior to contour machining, and (c) a final assembled node showing connections to branches, with a tenon (top left) and mortised branches connected (top right and bottom)



(a) (b) (c)

Figure 10. Prototyping of a non co-planar node at 1:5 scale, showing (a) the 6 individual node elements machined prior to assembly, (b) assembly of the 3 upper branches about their individual common planes, and (c) assembly of the complete node with the all branches assembled about the single common axis of the primary lower branch

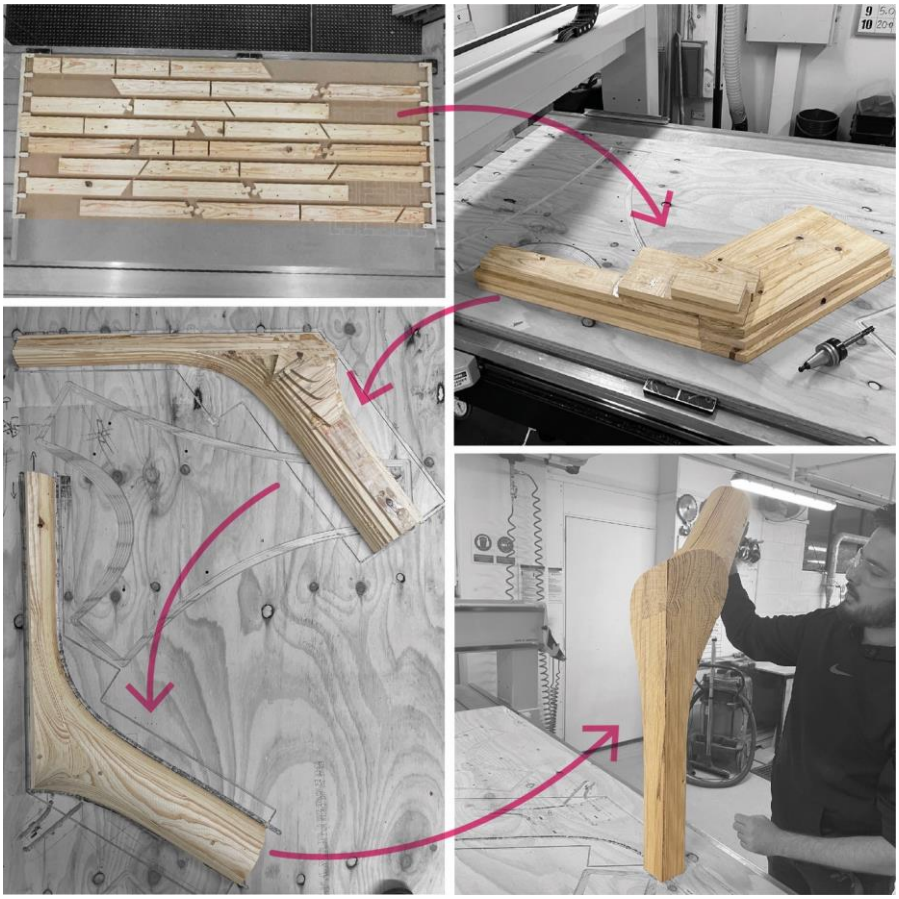


Figure 11. Prototyping of an individual non co-planar node element at 1:1. Sequence showing individual lamella boards machined, laminated into the billet, first pass and second pass CNC machining, and completion of one of the 6 node elements.

5. Discussion

The CEM modelling developed was shown to be an effective and agile tool for ensuring an equilibrated solution is reached for a range of tree structures, based on variable log length with corresponding variable branch diameters and masses. The applied part assignment heuristic was able to ensure the structures could utilise the entirety of the material in the log inventory. The effective combination of both of these tools, however, is of most significance, as it demonstrates the capability to simultaneously optimise for material usage based on structural efficiency, waste minimisation due to an inventory constraint, and minimisation of the structure's carbon emissions. Finally, the modelling and prototyping of the semi-rigid nodes demonstrates feasibility for complex three dimensional intersections to be resolved in timber, providing an elegant connection solution for round timber members of variable diameters.

References

[1] J. Brütting, P. O. Ohlbrock, J. Hofer, and P. D'Acunto, "Stock-constrained truss design exploration through combinatorial equilibrium modeling," *International Journal of Space Structures*, vol. 36, no. 4, pp. 253-269, 2021.

[2] A. Bukauskas, "Inventory-constrained structural design," University of Bath, 2020.

[3] K. R. Baber, J. R. Burry, C. Chen, J. M. Gattas, and A. Bukauskas, "Inventory constrained design of a timber funicular structure," *SN Applied Sciences*, vol. 2, pp. 1-19, 2020.

[4] I. Desai, "Designing structures with tree forks: mechanical characterization and generalized computational design approach," Massachusetts Institute of Technology, 2020.

[5] T. Lewis *et al.*, "Tree growth relationships and silvicultural tools to assist stand management in private native spotted gum dominant forests in Queensland and northern New South Wales," 2010.

[6] R. Burton, M. Dickson, and R. Harris, "The use of roundwood thinnings in buildings–a case study," *Building Research & Information*, vol. 26, no. 2, pp. 76-93, 1998.

[7] A. Bukauskas *et al.*, "Whole timber construction: A state of the art review," *Construction and Building Materials*, vol. 213, pp. 748-769, 2019.

[8] S. Seibold *et al.*, "The contribution of insects to global forest deadwood decomposition," *Nature*, vol. 597, no. 7874, pp. 77-81, 2021.

[9] K. R. Baber, J. R. Burry, C. Chen, J. M. Gattas, and A. Bukauskas, "Inventory constrained funicular modelling," in *Proceedings of IASS Annual Symposia*, 2019, vol. 2019, no. 5: International Association for Shell and Spatial Structures (IASS), pp. 1-10.

IASS 2023
July 10–14 Melbourne
Integration of Design and Fabrication

Proceedings of the IASS Annual Symposium 2023
Integration of Design and Fabrication
10–14 July 2023, Melbourne, Australia
Y.M. Xie, J. Burry, T.U. Lee and J. Ma (eds.)

Material efficiency in local timber construction: unlocking the potential of English timber

Dario MARINO[a], Harry F. MILLS [a,*], Antiopi KORONAKI[a], Darshil U. SHAH[a], Michael H. RAMAGE[a]

[a,*] Centre for Natural Material Innovation, Department of Architecture, University of Cambridge, 1-5 Scroope Terrace, Cambridge CB2 1PX, UK
hfm35@cam.ac.uk

Abstract

The rising demand for low-embodied carbon materials and supply chain disruptions, such as climate change impacts and global crises, necessitate a sustainable wood supply for building products. Supporting local capacity to grow, manufacture, and supply timber-building products can surmount international trade barriers. In the UK, the market is import-oriented, with forests in England primarily utilised for short-term purposes. This study explores material-efficient, optimisation-driven structural timber systems using local underutilised English timber for low to mid-rise buildings and retrofitting. Adding value to this timber offers long-term carbon sequestration, addresses the demand for low-embodied carbon materials, and provides socio-economic benefits through local education and employment. We present designs and simulations of structural prototypes using underutilised English timber and analyse timber-based truss system performance. Preliminary results show effective and scalable approaches for optimised truss, beam, and joist systems relevant to those interested in material-efficient timber structures with underutilised timber resources.

Keywords: nature-based solutions; harvested wood products; wood utilisation; topology-optimised structures; material-efficiency; underutilised timber; timber design; robotic construction

1. Introduction

The global built environment is projected to expand by 230 billion square meters by 2060, approximately double its current size [1]. By 2030, this increase is expected to reach 20%, with the majority of growth occurring in emerging and developing regions [2]. The materials used for constructing these buildings will profoundly impact the environment and how we live. Raw material consumption nearly doubled by 2016, and based on current trends, the global demand for natural, replenishable materials is anticipated to more than double to 190 billion tons [1], [3].

Traditional construction practices often rely on carbon-intensive resources such as steel and concrete. Nature-based solutions (NBS) offer alternatives such as timber, bamboo, hemp, or earth, which are both renewable and carbon-sequestering. By adopting NBS in construction and substituting high embodied carbon materials like steel and concrete with natural alternatives like wood, it is possible to reduce carbon emissions by 0.9 kilograms for each kilogram of carbon sequestered in the wood [4]. Thus, due to the urgent need to reduce greenhouse gas emissions and promote carbon sequestration strategies, there is a need for a rapid shift in practices across the construction industry.

Timber, the most advanced natural material in use, is processed for various purposes, from packaging and building products to fuel, food, and textiles. The demand for structural timber is significant, and the desire for an increase in engineered wood construction, such as mass timber, is substantial. The United Kingdom (UK), is the second-largest net importer of timber globally, with 82% of its timber imported [5]. However, the timber global trade is vulnerable to supply chain disruptions resulting from climate

Copyright © 2023 by Dario MARINO, Harry F. MILLS, Antiopi KORONAKI, Darshil U. SHAH and Michael H. RAMAGE. Published in the Proceedings of the IASS Annual Symposium 2023 with permission.

events, forest disease and impacts, pandemics, invasions, and wars; therefore, ensuring the continuous and affordable supply of sustainably harvested wood for building products is a pressing issue. One way to meet demand and overcome international trade barriers is to support local and sovereign capacity to grow, manufacture, and supply timber-building products.

The UK, comprising roughly 3.24 million hectares of woodland, representing 13% of its total land area, boasts a vast array of forest types and management practices [6], [7]. These span from small private landowners and extensive monoculture plantations to progressively mixed, biodiversity conservation-focused forests. Conifer plantations, primarily situated in the North and West of England, Scotland, and Wales, supply the majority of domestically-produced structural softwood sawn boards utilised in building and construction.

In England specifically, forests account for 10% of land cover and exhibit a diverse assortment of species. Conifer plantations typically include Scots or Corsican Pine, Sitka or Norway Spruce, Larch, and Douglas Fir. Conversely, broadleaf stands may encompass Oak, Elm, Sycamore, Chestnut, Beech, and Ash species, which are particularly favoured by private small-lot landowners in the South. Conifer resources, particularly pines, are predominantly used for bio-energy, pallet and packaging production, and agricultural fencing [8]. Broadleaf species are preferred for specialised construction, boat building, and furniture markets; however, their value can be challenging to optimise for larger sawmills due to factors such as location, proximity, volume, and species diversity within each forest stand. Characteristics like log size, quality variance, and the extended processing time required for drying broadleaf species contribute to the limited adoption of structural broadleaf-sawn boards in building products. As a result, the majority of structural sawn board supplies for building products are imported, whilst locally-grown English timber remains underutilised and reserved for short-term applications.

In addition to supply chain challenges and lack of sovereign capacity to produce timber building products, like many regions worldwide, England and the UK are facing an increasing population, rising inflation and expenses, infrastructure and a building crisis, characterised by outdated and energy-intensive building stock, poor-performing public infrastructure, and an under-supply of housing [9]–[15]. There is an urgent need for new construction, retrofitting and renovation of existing buildings that incorporate NBS that are structurally capable and carbon-sequestering. Although the substitution of timber in structural building design is increasing and is heralded as the material of the future [16], [17], an increased demand requires greater material efficiency and lower-consuming timber products [18]. Focusing on residential buildings, material efficiency strategies can reduce emissions in the material cycle by over 80% by 2050 [4], [19].

This research adopts a material-efficient approach to investigate optimisation-driven structural systems using local underutilised English timber for low to mid-rise buildings to meet housing supply and retrofit existing poor-performing buildings. Adding value to local underutilised English timber through building products offers long-term carbon sequestration, supports the growing demand for low-embodied carbon construction material and brings a raft of socio-economic benefits to communities through local and regionalised education and employment. In the following sections, we present the structural performance of a timber-based truss system, looking at member utilisation, material volume and embodied carbon. The paper contains preliminary findings that inform a larger project looking to add value to English underutilised timber for use in construction.

2. Methods

This study aims to promote more efficient uses of homegrown local underutilised English timber, to provide opportunities to generate the local supply chains and industry and thus enable low-embodied carbon options for locally manufactured construction products through efficient structural design. The study was based on the properties of available materials, which are discussed in the following sections.

2.1 Material-efficient design development

A computational workflow has been developed using a parametric 3D modelling environment to design and analyse truss-like structures. Timber trusses are considered efficient structural typologies because they are primarily subject to axial stresses (tension and compression) rather than bending moments. The optimisation of these structural typologies to improve material efficiency has been extensively investigated, originating in the studies of A. G. M. Michell (1904) [20]. Recently, thanks to advances in computational power and software development that allow faster calculations [21], its potential is being explored further. For instance, Fairclough, Gilbert and Thirion [22] have demonstrated through a case study of a large transfer truss, industry-ready design solutions that enable reducing embodied carbon (EC) by customising the truss layout based on project-specific variables

Ching and Carstensen recently explored the optimisation of member layout in truss systems to reduce EC using the Ground Structure (GS) approach [21]. This approach consists of a dense structure populated with multiple potential elements, undergoing a sizing optimisation that allows the minimum bar area to approach zero. The GS method's first step is to define the design domain, load application, and boundary conditions. The domain is then populated with a grid of points, all connected to form potential truss elements. The optimisation criteria focus on minimising the weight and, in mono-material trusses, the volume of the employed resource. A material-agnostic method has recently been developed and made accessible to designers and engineers through a user-intuitive interactive design tool [23].

Using parametric modelling platforms, such as the Peregrine plugin [24] in the Rhino-Grasshopper environment, users can run a structural simulation that indicates the best truss layout given design boundary conditions and load cases. The contribution of a layout optimisation method in trusses for weight and volume savings can vary based on several variables, such as domain configuration, buckling of compressed members, load cases, allowed deflections, and manufacturing constraints. In some practical cases, this optimisation method can achieve up to a 40% volume reduction compared to a traditional Warren-truss layout with optimised cross-sections [22]. The primary trade-off for volume reduction lies in the layout complexity and related manufacturing constraints. The employed plugin (Peregrine in Rhino-Grasshopper) allows for post-processing rationalisation to simplify the design by reducing the number of joints and members.



Figure 1. Typical floor joists with open steel webs. The top and bottom chords are made of softwood-graded TR26.

This study leverages the Peregrine plugin in the Rhino-Grasshopper environment to design and analyse truss-based floor joists suitable for low- to mid-rise applications in multistorey residential, office, or school buildings, addressing the high demand for such structures in England and the UK [23]. Secondary structural elements, such as floor joists, are the primary focus and explore the potential of implementing English timber by replacing steel web joists with wooden alternatives. The industry benchmark for comparison is the conventional steel web joist with wooden top and bottom chords, a design widely employed in the UK construction market for timber-framed buildings (Fig. 1).

The workflow, developed within the Rhino-Grasshopper environment, integrates layout optimisation with Peregrine and structural analysis in Karamba 3D[25]. The process can be summarised in four main steps: i) defining the domain and boundary conditions (joist dimensions, material properties, load cases) and performing layout optimisation using Peregrine; ii) selecting the minimum cross-section according to maximum utilisation values for members and manufacturing constraints (e.g., joint typology); iii) optimising the cross-section and conducting structural analysis with Karamba 3D; and iv) comparing the results with the industry benchmark in terms of embodied carbon and timber volume through an A1-A4 life-cycle assessment.

2.2.1 Material properties

The primary factor influencing the design of structural timber is the grading system. The top and bottom chords in steel web joists typically comprise TR26-graded softwood, often imported from Scandinavia. Compared to the C-grading system, TR26 characteristic values closely resemble C27[26]. Utilising high-grade timber versus low-grade timber can significantly impact structural performance.

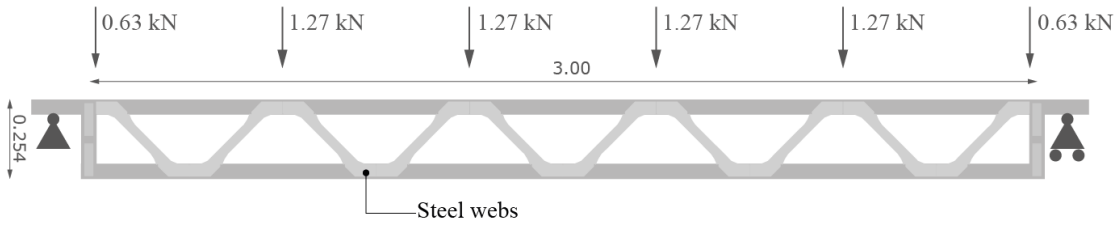


Figure 2. Typical floor joists are used as an industry benchmark for prototype design analysis. Chords cross-section 47x72mm softwood graded TR26, with open steel webs.

Earlier research on English timber has found potential for structural yield of strength classes around C16 [27], [28]. Thus, the study constrains availability to C16-graded softwood timber as the primary resource and considers underutilised and out-of-grade softwood sawn boards [29], [30], looking to existing agriculture and pallet and packaging markets to evaluate their potential structural performance. In England, more than 70% of sawn softwood processed goes to pallets, packaging, and fencing [7]. Additionally, broadleaf stands account for approximately 70% of English woodland, and therein lies potential for how more significant volumes can be value-added to long-lasting timber-building products.

By examining alternative timber sources and grading systems, this research aims to promote sustainable and locally sourced materials in the construction industry, fostering a more material-efficient approach to designing timber building products.

2.2.2 Prototype design

The prototypes are 3-metre-long joists with 20 cm supports at both ends of the top chord and a 25 cm distance between the chord axes. These dimensions were established based on examples of timber-framed three and four-bedroom houses featuring open-web floor joists, where 3 metres is a typical small span, while also considering the ease of manufacturing and manoeuvrability within a testing laboratory. The design optimisation objective is to reduce volume, with the minimum cross-sections of each member determined primarily by two parameters: a numerical factor, the utilisation of members in tension and compression (capped at 85%), and an empirical factor, manufacturing constraints such as joints.

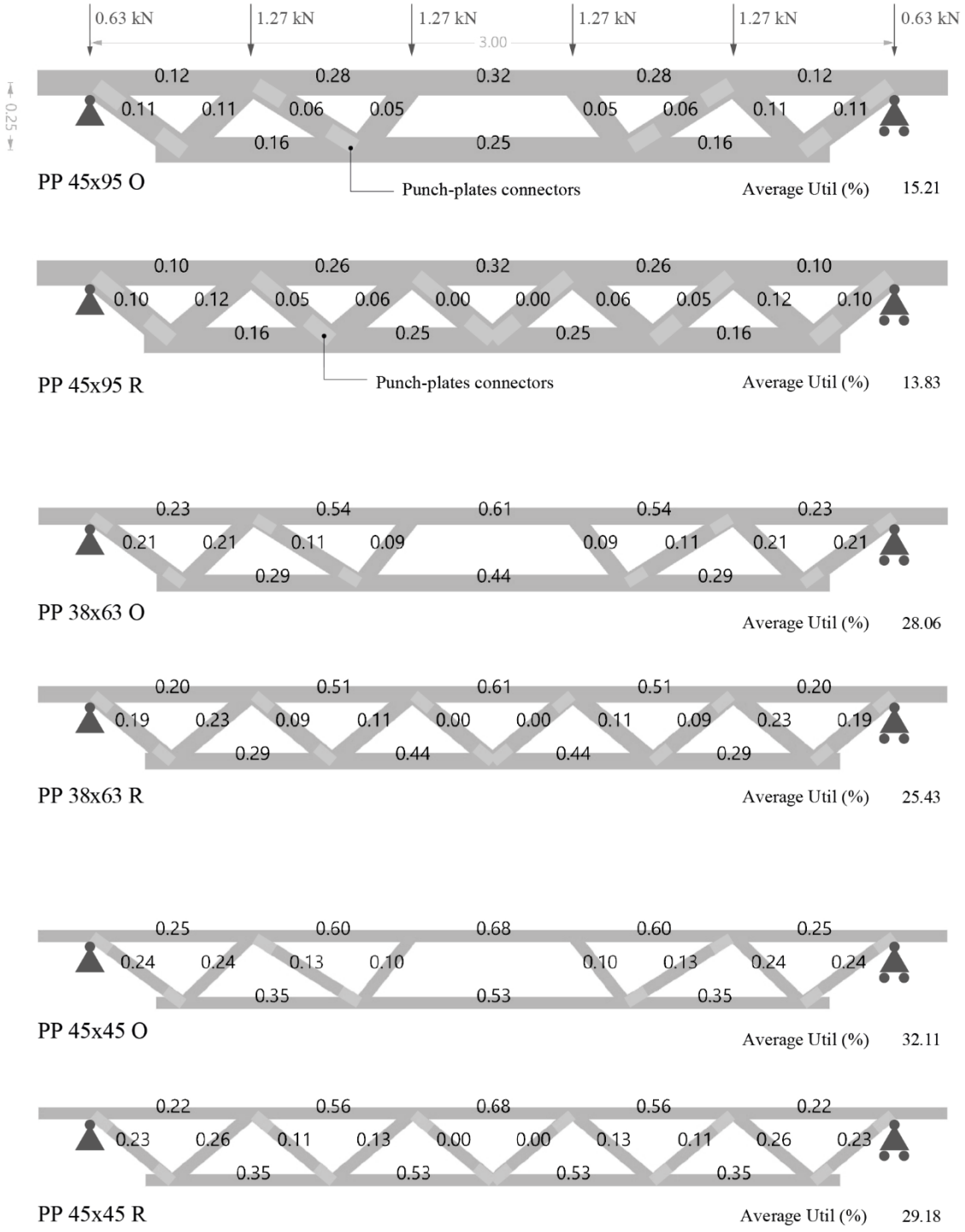


Figure 3. Prototype design proposals joined with steel punch-plates to assess the effects of cross-section variations according to commercially available industry standards (45x95mm treated wood, 38x63mm untreated wood).

Due to the limited truss domain height (25 cm), the grid division for layout optimisation has points only at the top and bottom chords to prevent the generation of complex nodes in between. The applied loads include 1.5 kN/m2 for live loads, 0.6 kN/m2 for top chord dead loads (timber floor and framed walls),

and 0.25 kN/m2 for bottom chord dead loads (ceiling), each multiplied by a safety factor of 1.5. A single 3-metre joist with 60 cm centre spacing is designed to support 6.34 kN or 3.52 kN/m^2. The loads are applied at nodes of the top chord spaced every 60 cm along the chord for consistency with the industry benchmark (steel web joist) and to maintain the same setup for mechanical testing to be conducted in subsequent research phases.

Regarding potential applications in the construction industry, the cross-section specification for C16 carcassing timber is typical for industrial softwood producers in the UK. A series of design tests have been developed for both currently available commercial cross-section sizes and speculative future sizes, which could be more diverse and vary in scale. For the 3-metre prototype, the minimum cross-sections tested in the simulation are 45x95 mm and 38x63 mm for the graded ones and 45x45 mm for the ungraded ones. In the examples presented in Figure 3, the chords and webs are designed with the same width for each case (45 or 38 mm). The connections of tension webs to the chords are intended as steel punch plates. This impacts the EC calculation, with 63x152 mm plates for the 45x95 mm case and 38x76 mm plates for the other two cases (38x63 and 45x45 mm). Connection details can significantly influence structural performance, embodied carbon, or volume data, leading to the proposal and implementation of two alternative joining systems in distinct prototypes.

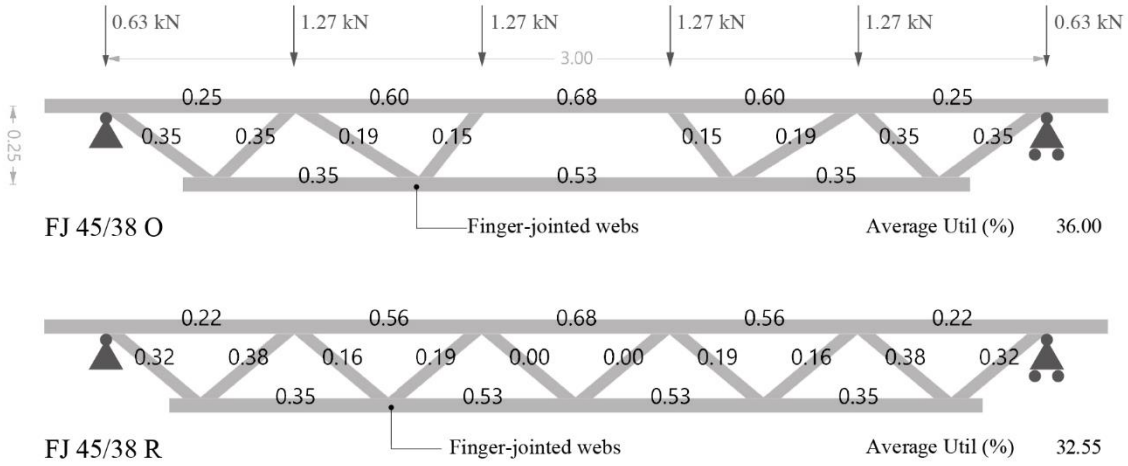


Figure 4. Prototype design proposal for finger-joint floor joist to assess steel-free connections' contribution to embodied carbon. In this case, an adaptation of the commercially available cross-sections is considered for the webs (38x38mm).

Prototype 1 – Steel punch-plates

The first prototype, depicted in Figure 3, features chords and webs connected through steel punch plates, a method currently prevalent in the construction industry. To minimise EC, the punch plates are strategically employed only for joining the tension chords. This selective application of punch plates serves to contain both the EC and volume when compared to industry benchmarks, showcasing an innovative approach to balance material use and environmental impact in the construction process. By refining traditional methods in this manner, the first prototype demonstrates the potential for improving the efficiency of widely used construction techniques.

Prototype 2 – Finger-joint

The second prototype features a truss system with finger-jointed webs and chords, a method commonly employed in the North American construction industry [31]. This design permits using more minor webs

than chords, potentially leading to additional material savings. Although the absence of steel connectors significantly reduces EC values (as shown in Table 1), industry-based examples often utilise resorcinol resin containing formaldehyde for gluing, raising health concerns. As an alternative, polyurethane-based glue will be used for assembling this prototype in future investigations.

For both prototypes, two alternative member layouts have been considered: an optimised layout, in which member distribution is derived from the Peregrine method and each diagonal has a different angle, and a regular layout, in which all diagonal webs maintain the same angle, similar to a Warren truss.

Since the prototypes are relatively small and subject to minor loads as secondary structural elements, the primary distinction between the two layouts is the absence of two central tension webs in the optimised version, which are omitted due to their near 0% utilisation factor. However, for ease of manufacturing and considering the potential improvement in overall stability during truss handling, the initial prototypes to be tested will be based on a regular layout.

Table 1. Overview of the design proposals compared with the industry benchmark. PP stands for Punch-plates connected, FJ stands for Finger-joint, R is the Regular layout of webs, and O is the Optimised layout of webs.

	Standard joist	PP 45x95 O	PP 45x95 R	PP 38x63 O	PP 38x63 R	PP 45x45 O	PP 45x45 R	FJ 45/38 O	FJ 45/38 R
Volume Δ (%)	-	65.70	77.05	-2.58	5.02	-15.30	-8.32	-18.59	-12.39
EC Δ (%)	-	-35.74	-17.73	-67.99	-60.11	-73.76	-67.63	-74.57	-72.80
EC + Seq Δ (%)	-	270.26	252.83	135.84	137.32	110.03	114.87	101.65	117.57
Volume (m3)	0.0203	0.0336	0.0359	0.0198	0.0213	0.0172	0.0186	0.0165	0.0178
EC ($kgCO_2eq$)	11.21	7.21	9.23	3.59	4.47	2.94	3.63	2.85	3.05
EC+Seq ($kgCO_2eq$)	-3.56	-13.21	-12.58	-8.41	-8.46	-7.49	-7.66	-7.18	-7.75
Average Util. (%)	-	15.21	13.83	28.06	25.43	32.11	29.18	36.00	32.55
Ratio (V/Av Util.)	-	2.21	2.60	0.70	0.84	0.54	0.64	0.46	0.55

2.2.3 Life-cycle assessment

To evaluate the carbon impact of the design, a Life-Cycle Assessment (LCA) calculation has been performed considering the stages A1-A4, which are from cradle (A1: raw material supply) to gate (A3), and then adding the transportation to the construction site (A4). In this context, there is no information on the emissions during the construction phase (A5). The comparison between a typical floor joist with metal webs and the proposed prototypes would not affect the comparison since the installation procedure should be the same.

For timber, the LCA is performed using the Inventory of Carbon & Energy (ICE) database [32]. The calculations are based on the weight of the timber, and the EC values refer to "Timber, Softwood, No Carbon Storage", where the EC for the modules A1-A3 is 0.263 (kgCO2e/kg); this value has been used for both the prototype and the industry benchmark. The A4 module is calculated using the table of transport emission factors for the UK [33], which identifies "European manufactured" 1500km by road, 0.160 (kgCO2e/kg), and "nationally manufactured" 300km by road, 0.032 (kgCO2e/kg). The biogenic carbon as the contribution of timber to sequester atmospheric carbon is -1.64 (kgCO2e/kg). Two EC values are analysed, with and without biogenic carbon, EC+Seq (kgCO2eq) and EC (kgCO2eq).

A ratio (V/Av Util.) was developed, as shown in Table 1, normalising the volume against material utilisation, showing the importance of considering both aspects of biogenic carbon and material utilisation to maximise material efficiency.

For the steel components, the webs and punch plates, the EPD data are derived from one of the available manufacturers on the market. For the selected manufacturer, the embodied carbon (A1-A4) for both is 2.297 (kgCO2e/kg). The carbon impact of the polyurethane glue for the considered LCA modules is 0.876 (kgCO2e/kg), and the average amount considered is 0.3 kg of glue per finger-jointed joist. To give a reference value, the glue accounts for an increase of about 2% in the EC calculation.

3. Results

This research adopts a material-efficient approach to investigate optimisation-driven structural systems using local underutilised English timber for low to mid-rise buildings, to address housing supply challenges and retrofit existing poor-performing buildings. The study focuses on the structural performance of optimised truss systems, analysing various parameters for comparison, including member utilisation, timber volume, and embodied carbon, both with and without sequestration. All data are expressed as increased or decreased percentages relative to an industry benchmark for the same span load case (Table 1). The developed algorithm will serve as a fundamental basis for studying and designing larger building products, such as truss beams employed as primary structural elements. The simulation results show promising outcomes, with expected structural performance according to initial inputs such as geometry, loads, and material properties.

For the design of floor joists, the research analyses several combinations of member cross-sections and joining techniques. All proposed solutions demonstrate a lower EC compared to standard systems. The reductions in EC range from approximately -17% to -74% without accounting for carbon sequestration. This reduction can be attributed to substituting steel webs with timber and the lower impact of the LCA A4 module for local timber transportation. Concurrently, the use of steel in the designed prototypes is minimised and restricted to tension webs.

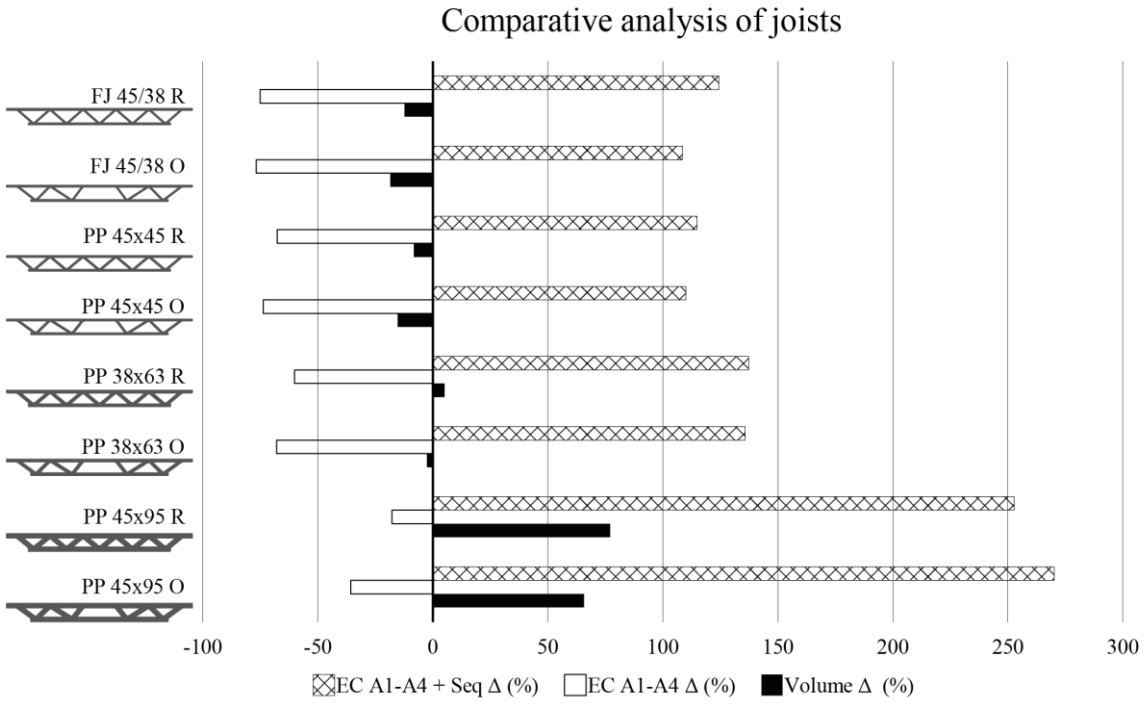


Figure 4. Overview of the design proposals compared with the industry benchmark. PP stands for Punch-plates connected, FJ stands for Finger-joint, R is the Regular layout of webs, and O is the Optimised layout of webs.

In contrast, the volume of timber employed in the prototypes varies between approximately +77%, with an average member utilisation of 14% and a maximum of 32%, to -18.5%, with an average member utilisation of 36% and a maximum of 68%.

In the comparative analysis of joists (Figure 4), the EC+Seq (kgCO2eq) reveals a significant rise in the sequestered carbon within each joist. Compared to the industry benchmark joist (-3.56 kgCO2eq), PP 45x95 O showed the highest level of carbon sequestration (-13.21 kgCO2eq) due to larger dimensions in the chords, and the use of timber rather than steel in the webbing.

4. Discussion and conclusion

This study employed an optimisation-driven approach to develop material-efficient structural systems that utilise locally underutilised English timber for low to mid-rise buildings. The aim was to address housing supply issues and retrofit existing poorly-performing structures employing local resources. The research analysed optimised truss systems, considering parameters such as member utilisation, timber volume, and embodied carbon. The developed workflow can potentially design more significant building components, such as truss beams used as primary structural elements.

The findings revealed that the proposed solutions exhibited lower embodied carbon than standard systems, which can be attributed to substituting steel webs with timber and reducing the impact of local timber transportation. However, timber volume and member utilisation demonstrated broader values among the prototypes. The prototypes represent viable alternatives to current practices. Future structural testing is required to evaluate their potential for application in real-life scenarios. As the larger project, which this study is a part of, evolves, these promising alternatives will be assessed through manufacturing and structural testing, examining real-world applicability. Following the testing results, subsequent phases of the research will focus on larger primary structural elements such as beams, walls, and columns, as well as the supply of local resources.

In summary, this study establishes the foundation for the development of material-efficient timber structural systems for low to mid-rise buildings, employing locally grown and manufactured English timber. These systems have the potential to contribute to addressing housing demand and the retrofit of poorly performing and outdated existing buildings. The material-efficient design workflow is transferable and relevant to audiences interested in material-efficient topology-optimised timber structures, which can apply the insights to regions where stocks of underutilised timber resources exist. The research findings present a promising avenue for promoting sustainable and regionally-sourced solutions within the construction industry.

Acknowledgments

This research forms work from the Timber in Construction (TIC) project funded by the Forestry Commission, and the Growing the Future Project funded by the Laudes Foundation. The authors would also like to thank and acknowledge TIC partners Timber Frame Management, Smith and Wallwork Engineers, Rothoblaas, and Ecosystems Technologies for their insights and constructive feedback on this work.

References

[1] Global Alliance for Buildings and Construction, International Energy Agency, and United Nations Environment Programme, 'Global Status Report 2017', *World Green Building Council*, 2017. https://worldgbc.org/article/global-status-report-2017/
[2] IEA, 'Buildings', *IEA*, 2022. https://www.iea.org/reports/buildings
[3] *The State of the World's Forests 2022*. FAO, 2022. doi: 10.4060/cb9360en.

[4] U. N. Environment, ‘2022 Global Status Report for Buildings and Construction', *UNEP - UN Environment Programme*, Sep. 11, 2022. http://www.unep.org/resources/publication/2022-global-status-report-buildings-and-construction
[5] Forest Research, 'Forestry Facts and Figures 2022', *Forest Research*. https://www.forestresearch.gov.uk/publications/forestry-facts-and-figures-2022/ (accessed Sep. 29, 2022).
[6] 'Forest Management Plans', *Forestry England*. https://www.forestryengland.uk/forest-planning (accessed Apr. 27, 2022).
[7] Forest Research, 'Forestry Statistics 2022', *Forest Research*. https://www.forestresearch.gov.uk/tools-and-resources/statistics/forestry-statistics/forestry-statistics-2022/ (accessed Apr. 13, 2023).
[8] Forest Research, 'Woodland Statistics', *Forest Research*. https://www.forestresearch.gov.uk/tools-and-resources/statistics/statistics-by-topic/woodland-statistics/ (accessed Sep. 06, 2022).
[9] C. Barton, L. Booth, and W. Wilson, 'Tackling the under-supply of housing in England', 2022, Accessed: Jul. 14, 2022. [Online]. Available: https://commonslibrary.parliament.uk/research-briefings/cbp-7671/
[10] S. O. S. E. zu Ermgassen *et al.*, 'A home for all within planetary boundaries: Pathways for meeting England's housing needs without transgressing national climate and biodiversity goals', *Ecological Economics*, vol. 201, p. 107562, Nov. 2022, doi: 10.1016/j.ecolecon.2022.107562.
[11] Office for National Statistics, 'Overview of the UK population: 2020', 2022. https://www.ons.gov.uk/peoplepopulationandcommunity/populationandmigration/populationestimates/articles/overviewoftheukpopulation/2020 (accessed Aug. 14, 2022).
[12] Office for National Statistics, 'Household projections for England: 2018-based', 2020. https://www.ons.gov.uk/peoplepopulationandcommunity/populationandmigration/populationprojections/bulletins/householdprojectionsforengland/2018based (accessed Apr. 14, 2023).
[13] The Independent, 'Cost of fixing "crumbling" NHS hospitals soars to record £10bn', *The Independent*, Oct. 13, 2022. https://www.independent.co.uk/news/health/cost-nhs-hospital-buildings-b2202118.html (accessed Apr. 14, 2023).
[14] T. Helm, 'England's crumbling schools are a "risk to life", officials warn No 10', *The Guardian*, May 14, 2022. Accessed: Apr. 14, 2023. [Online]. Available: https://www.theguardian.com/education/2022/may/14/england-crumbling-schools-risk-warn-no-10-education-department-treasury
[15] United Nations, 'Population', *United Nations*, n.d. https://www.un.org/en/global-issues/population (accessed Apr. 14, 2023).
[16] TOG and Financial Times, 'How timber buildings can save the world'. http://www.ft.com/partnercontent/tog/how-timber-buildings-can-save-the-world.html (accessed Jan. 27, 2023).
[17] A. Neslen, 'Timber cities "could cut 100bn tons of CO2 emissions by 2100"', *The Guardian*, Aug. 30, 2022. Accessed: Jan. 27, 2023. [Online]. Available: https://www.theguardian.com/environment/2022/aug/30/timber-cities-could-cut-100bn-tons-of-co2-emissions-by-2100
[18] M. Pramreiter, T. Nenning, L. Malzl, and J. Konnerth, 'A plea for the efficient use of wood in construction', *Nat Rev Mater*, pp. 1–2, Jan. 2023, doi: 10.1038/s41578-023-00534-4.
[19] E. Hertwich, R. Lifset, S. Pauliuk, and N. Heeren, 'Resource Efficiency and Climate Change: Material Efficiency Strategies for a Low-Carbon Future', International Resource Panel, Nov. 2020. Accessed: Apr. 14, 2023. [Online]. Available: https://www.resourcepanel.org/reports/resource-efficiency-and-climate-change
[20] A. G. M. Michell, ‘LVIII. The limits of economy of material in frame-structures', *The London, Edinburgh, and Dublin Philosophical Magazine and Journal of Science*, vol. 8, no. 47, pp. 589–597, Nov. 1904, doi: 10.1080/14786440409463229.

[21] E. Ching and J. V. Carstensen, 'Truss topology optimisation of timber–steel structures for reduced embodied carbon design', *Prof. Carstensen*, 2022, Accessed: Apr. 15, 2023. [Online]. Available: https://dspace.mit.edu/handle/1721.1/150023
[22] H. Fairclough, M. Gilbert, C. Thirion, A. Tyas, and P. Winslow, 'Optimisation-driven conceptual design : case study of a large transfer truss', p. 17, 2019.
[23] H. Lu and Y. M. Xie, 'Reducing the number of different members in truss layout optimisation', *Struct Multidisc Optim*, vol. 66, no. 3, p. 52, Feb. 2023, doi: 10.1007/s00158-023-03514-y.
[24] 'Peregrine', *LimitState*. https://www.limitstate.com/peregrine (accessed Apr. 15, 2023).
[25] 'Karamba3D', *Karamba3D*. https://karamba3d.com/ (accessed Jan. 14, 2022).
[26] TRA Trussed Rafter Association, Ed., 'Characteristic Properties of TR26'. 2017. [Online]. Available: http://www.crtc.ie/wp-content/uploads/2018/03/strength-classes-for-softwood-based-on-edgewise-bending-tests.pdf
[27] J. French *et al.*, 'Low carbon supply chains for forest products in the East of England', 2010.
[28] D. Ridley-Ellis, D. Gil-Moreno, and A. M. Harte, 'Strength grading of timber in the UK and Ireland in 2021', *International Wood Products Journal*, 2022, doi: 10.1080/20426445.2022.2050549.
[29] R. Cherry, A. Manalo, W. Karunasena, and G. Stringer, 'Out-of-grade sawn pine: A state-of-the-art review on challenges and new opportunities in cross laminated timber (CLT)', *Construction and Building Materials*, vol. 211, pp. 858–868, Jun. 2019, doi: 10.1016/j.conbuildmat.2019.03.293.
[30] H. F. Mills, 'Underutilised Timber (UUT) Acceptance Through North America & Europe', *Gottstein Trust*, 2020, [Online]. Available: https://gottsteintrust.org/projects-reports/report/1-underutilised-timber-uut-acceptance-through-north-america-europe
[31] 'TRIFORCE® Open Joist: Peace of Mind Underfoot', *TRIFORCE® Open Joist*. https://www.openjoisttriforce.com/ (accessed Apr. 14, 2023).
[32] C. Jones, 'Embodied Carbon Footprint Database', *Circular Ecology*. https://circularecology.com/embodied-carbon-footprint-database.html (accessed Feb. 15, 2021).
[33] J. Orr and O. Gibbons, 'How to calculate Embodied Carbon'. The Institution of Structural Engineers, 2020.

IASS 2023
July 10–14 Melbourne
Integration of Design and Fabrication

Proceedings of the IASS Annual Symposium 2023
Integration of Design and Fabrication
10–14 July 2023, Melbourne, Australia
Y.M. Xie, J. Burry, T.U. Lee and J. Ma (eds.)

Multi-material components for a sustainable built environment: integration of design by topology optimisation and fabrication by 3D printing

Hèrm HOFMEYER[a,*], Motahareh YOUSHI[a], Arjen H. DEETMAN[a]

[a,*] Eindhoven University of Technology
Groene Loper 3, 5612 AE, Eindhoven, The Netherlands
h.hofmeyer@tue.nl

Abstract

For a sustainable built environment, there is an increasing need for optimised (new or renovated) designs, including the customisable fabrication of their components. This paper (i) presents a general approach to translate design problems into a Topology Optimisation (TO) strategy; (ii) shows multi-disciplinary TO for multi-material components, including concrete, which behaves differently for compression or tension; and (iii) addresses issues in the process from design to fabrication. Applying the general approach and TO, two cases are studied: a part of a façade panel and a sandwich panel. A TO design for the sandwich panel was tested for fabrication by black-and-white printing and functional grading. These tests revealed that design by TO requires specific print path plans and tweaking of system dynamics for the fabrication by 3D printing. Vice versa, fabrication requires modifications to the design by TO, e.g., geometrical adjustments. In the future, TO density filtering using a print path shaped inclusion zone can be studied, and mass minimisation with a stiffness constraint.

Keywords: topology optimisation, 3D printing, multi-material components, multi-disciplinary optimisation, sustainability, built environment

1. Introduction

For the built environment, quite some challenges are ahead. With a world population growing fast, many new buildings should be constructed for living, work, and care. At the same time, energy resources are getting depleted, and for sustainability reasons, existing buildings should be renovated. Consequently, the built environment should be optimized, either by design if new, or by (design of) renovation of the existing building stock.

Within the above framework, this paper presents an approach to design and fabricate multi-material components, specifically for renovation. The approach ensures that structural and thermal performances are optimised. The multi-material setup delivers an optimal amount of each material to be used. Also, the approach is flexible and adaptable, since for each specific building, dedicated components can be designed, fabricated, dismounted, and reused. This all contributes to a sustainable built environment. The research presented is part of the Dutch governmental RVO financed MMIP program, with seeks to enable the energy transition of the existing residential building stock in The Netherlands.

In section 2, the translation will be discussed of a design problem into a so-called Topology Optimisation (TO) strategy, which finds designs for (conflicting) objectives and boundary conditions. TO implementation and multi-material aspects will be covered in section 3. Section 4 presents two cases studies: The first study shows the functionality of the TO developed, whereas the second tackles a realistic sandwich panel. Finally, Section 5 and Section 6 discuss fabrication and conclusions and future work respectively.

Copyright © 2023 by Hèrm HOFMEYER, Motahareh YOUSHI and Arjen H. DEETMAN. Published in the Proceedings of the IASS Annual Symposium 2023 with permission.

2. The translation of a design problem into a TO strategy

A design problem for a building component can often be regarded as finding a geometry with a material distribution. This fits TO well, as it basically generates the optimal (given objectives and boundary conditions) distribution of a certain amount of material within a spatial domain. For structural applications, in civil engineering, the method was pioneered by Bendsøe and Kikuchi [1], and several approaches can be used, as reviewed by Sigmund and Maute [2]. In the beginning, often a maximum structural stiffness, i.e. a minimum compliance, was used as the objective, together with a certain amount of material as the constraint. Later, also constraints related to allowable stresses were studied, in combination with the objective to minimise the amount of material, the practical implication being a design in which all material is fully utilised. In this latter case, as long as e.g. Von Mises stress constraints were used, it showed to be relatively easy to steer solutions into the right direction. However, for concrete, which has quite different strengths for compression or tension, for which e.g. the Drucker-Prager yield criterion can be used, solutions need further attention: Van de Werfhorst-Bouw *et al.* [3] demonstrated that for volume minimisation, some TO approaches result in designs with most parts in tension, whereas better minimisation would be achieved with so-called Traditional TO (TTO), yielding a design with most parts under compression, More recently, TO has been studied and applied in several other domains like heat transfer (Cho and Choi [4]), fluid flow, and acoustics, and increasingly for multi-material design variables, multi-physics objectives, and complex constraints. Examples are the work by Das and Sutradhar [5], which involved TO for optimally designing structurally stiff and heat-dissipating (porous) structures, and research by Tavakoli and Mohseni [6] that involved multi-material problems in the structural and thermal domains. Even more close to this paper, Bruggi and Taliercio [7] studied the optimisation of the insulation performance of masonry blocks, at the same time maximizing their structural rigidity, resulting in a new internal block layout.

In this section, first a case representing a design problem will be introduced (discussed in detail in Section 4.2), whereafter it will be translated into a TO strategy. The design problem involves a sandwich panel, meant for the renovation of terraced houses, planned to be 3D printed with two materials: concrete and insulation. Except for architectural voids, e.g. a window opening, the panel is solid, which means in TO terms that the sum of the relative densities of concrete and insulation always equals 1.0. The involved structural engineering firm defines the requirements: (a) a stiffness requirement, the maximum panel's horizontal deflection being smaller than 1/150 of the height; (b) a strength requirement, the concrete maximum stress being 3 MPa in tension and 30 MPa in compression; and (c) a minimal thermal resistance of 4.7 m^2K/W. No explicit objectives are given, however, TO needs at least one objective. So, to translate the design problem into a TO strategy, first combinations of TO objectives and constraints are studied, as shown in Table 1.

Table 1. Combinations of TO objectives and constraints [8].

Objectives → / Constraints ↓	Minimal strain energy	Maximal thermal compliance	Minimal volume
Volume equality	A1	n.a.	n.a.
Volume inequality	A2		n.a.
Maximum stress	n.a.		A4
Maximum stress + volume inequality	A3		n.a.

Combination A1 and A4 represent strategies found in literature, as mentioned above. For the case studied here, only requirements, no objectives, are formulated, and so there is complete freedom in

selecting the objectives. However, minimal volume cannot be used, as two materials are involved, together always occupying the complete TO design space, and the volume of one of the materials is used to control the ratio between the materials. Thus, a weighted sum of the minimal strain energy and maximal thermal compliance is selected, so the trade-off between structural and thermal objectives can be studied. With respect to the constraints, it should be noted that the stiffness requirement and minimal thermal resistance cannot be cast into TO constraints, as their nature is equal to the selected objectives. However, the strength requirement can be represented by constraints, to be presented later. Looking at Table 1, a volume inequality can be used, which defines a minimal or maximal ratio between concrete and insulation, making possible a systematic study of the influence of this ratio. The resulting strategy, here defined as A2, is simple to implement and computationally cheap. As a more advanced alternative strategy, also the stress at each location can be constrained to the maximum allowable stress, strategy A3. This is computationally expensive, however, it relieves postprocessing from checking the strength requirement later. Namely, for both strategies, inevitably results should be checked against the requirements (except for the strength requirement for A3), and adjustments should be made for a following TO attempt. These adjustments may concern: (a) a different geometrical design space, e.g. a thicker panel; (b) a different weighting of the objectives: or (c) a different volume inequality (i.e. more concrete or insulation on average). As a generalization of the above considerations, design problems always have requirements, which can possibly be reformulated as TO objectives and constraints. If no objectives can be found, TO should be driven in an artificial fashion, e.g. by requirement related objectives as used in literature, and preferably in weighted form, so the requirements to be tested afterwards can possibly be met by investigating trade-off solutions. Then, further TO constraints can be formulated to control and study variables that have a strong influence on the requirements: In the above case, the ratio between concrete and insulation was used, via a volume inequality constraint [8].

3. Multi-disciplinary TO for multi-material components

This section presents relevant details of TO strategies A2 and A3. Both strategies use two materials, instead of a more commonly used single material. For a single material, TO defines the so-called relative density x_e, which by a value between 0.0 and 1.0 indicates how much material is thought to be present in each finite element *e* (finite elements explained later). As mentioned before, here the summed relative densities of the two materials always equal 1.0, which allows for the following relation between the ratio of two materials, and the structural and thermal properties of the material mix:

$$E\left(x_e\right) = x_e^p E_{mat1} + (1 - x_e)^p E_{mat2} \tag{1}$$

$$k_{th}\left(x_e\right) = x_e^p k_{mat1} + (1 - x_e)^p k_{mat2} \tag{2}$$

In these equations, x_e is the relative density of material 1 within element *e*; *p* is the so-called penalization factor, an integer to be determined; *E* is the structural Young's modulus [N/mm^2] and *k* is the thermal conductivity [W/(mK)], both for the material mix (no subscript or *th*) or of one of the materials (subscript *mat1* or *mat2*).

The 3D spatial domain, in which TO distributes the ratio between material 1 and 2, is discretised in 3D eight-node orthogonal finite elements, according to the finite element method. Mechanically, each element node has three displacement Degrees Of Freedom (DOF); each finite element is represented by an element stiffness matrix that relates the nodal forces and displacements; and the element matrices are assembled into the structural stiffness matrix, which is part of a linear set of equilibrium equations as follows:

$$\mathbf{K_s u = f} \tag{3}$$

where $\mathbf{K_s}$ is the structural stiffness matrix, **u** the vector of global nodal displacements and **f** the vector of the sum of all nodal forces (from the surrounding elements + external). Thermally, each node has a single DOF, the temperature, and similar reasoning as for the mechanical part results in a linear set of thermal equilibrium equations:

$$\mathbf{K_{th}}\boldsymbol{\varphi} = \mathbf{q} \tag{4}$$

In Equation (4), $\mathbf{K_{th}}$ is the global conductivity matrix, $\boldsymbol{\varphi}$ the vector of nodal temperatures, and **q** a vector in which each term represents the sum of all thermal fluxes (from the surrounding elements + external) at a node. Details on how the mechanical and thermal element stiffness matrices are derived and assembled are given in a report by Youshi [8].

A design can be defined as the discretised spatial domain with for each element a value x_e (implying a certain mix of materials 1 and 2), these values grouped in a vector **x**. With this vector and appropriate loads and boundary conditions, Equations (3) and (4) can be solved, predicting the structural and thermal behaviour of the design. Strain energy c_s, related to the first objective (see Section 2) is then found by:

$$c_s(\mathbf{x}) = \mathbf{f}^{\mathbf{T}}\mathbf{u} = \mathbf{u}^{\mathbf{T}}\mathbf{K_s}(\mathbf{x})\mathbf{u} \tag{5}$$

And thermal compliance c_{th}, related to the second objective (see Section 2) by:

$$c_{th}(\mathbf{x}) = \mathbf{q}^{\mathbf{T}}\boldsymbol{\varphi} = \boldsymbol{\varphi}^{\mathbf{T}}\mathbf{K_{th}}(\mathbf{x})\boldsymbol{\varphi} \tag{6}$$

Finally, a weighted sum of (normalised) objectives is defined; maximal (instead of minimal) thermal compliance is required; and the total amount of material 1 (and so material 2) is controlled via a volume inequality constraint, which together leads to TO strategy A2:

$$\begin{cases} \min f = w_s \dfrac{c_s(\mathbf{x})}{c_{s,max}} - (1-w_s)\dfrac{c_{th}(\mathbf{x})}{c_{th,max}} \\ \text{subject to} \begin{cases} \dfrac{\sum_{e=1}^{n} x_e v_e}{V_f} \le 1 \\ 0 < x_{min} \le x_e \le 1 \end{cases} \end{cases} \tag{7}$$

In this equation (7), f is the function to be minimised, w_s is the weight factor, to be set, $c_{s,max}$ and $c_{th,max}$ the maximal occurring values for the objectives (taken from test runs using w_s = 0.01 and 0.99), n the number of elements, v_e the volume of element e, V_f the required total volume for material 1, to be set, and x_{min} a minimum value to avoid numerical singularities (as the stiffness of material 2, insulation, is very low).

For strategy A3, additionally the stress in each finite element is constrained. As in this paper concrete is used as the structural material, for the constraints the well-known Drucker-Prager yield criterion is used. This leads to a constraint for the stress state in the middle (found via the solution of Equation (3) and precursors of the element stiffness matrix) of each finite element e:

$$\sqrt{\frac{(\sigma_{xx}-\sigma_{yy})^2 + (\sigma_{yy}-\sigma_{zz})^2 + (\sigma_{zz}-\sigma_{xx})^2 + 6\sigma_{xy}^2 + 6\sigma_{yz}^2 + 6\sigma_{zx}^2}{6}} + \alpha(\sigma_{xx}+\sigma_{yy}+\sigma_{zz}) - \beta \le 0 \tag{8}$$

In which σ is the stress, with conventional subscripts for its type and direction, and constants α and β are functions of the concrete's compression and tension strengths. Two issues should be addressed. Firstly, the Drucker-Prager yield criterion is applicable to a finite element fully consisting of concrete (i.e. x_e = 1.0), however, if the relative density is lower, the element can be regarded as porous concrete, for which local stresses will be higher than the average stresses as predicted as explained above. This

can be solved by interpolation, see Duysinx and Bendsøe [9]. Secondly, it can be demonstrated that if the finite element's density becomes very low, local stresses keep a certain value, however, for an element with hardly any material, the stress constraints should not apply, and so stresses are set to zero. This discontinuity (finite vs. zero stress) may lead to solution problems, which can be avoided by the use of so-called relaxation, see Duysinx and Bendsøe [9].

For both strategies A2 and A3, multiple load cases see the objectives being formulated as the sum of the objective values for each load case, and the constraints require that stresses are below the required value for all individual cases. Also, relative densities are filtered, i.e. smoothened across the domain, to reduce the sensitivity of the outcomes for the finite element mesh, and to avoid checkerboard patterns.

The solutions of the linear systems of equations as given by Equations (3) and (4) are found by the proprietary MATLAB functions "mldivide, \", which may use different type of solvers (e.g. QR, LU, Cholesky), depending on the problem. For the optimisation itself, the Method of Moving Asymptotes (MMA) by Svanberg [10] is applied. MMA needs the derivatives of the two objective functions, the total volume, and all stress constraints (one for each finite element) with respect to the element relative densities. Details on the formulation and implementation of interpolation, relaxation, multiple load cases, density filtering, and derivatives can be found in Youshi's report [8], which also includes the complete MATLAB (version 2021b) script used.

4. Case studies

Two case studies are presented, related to the renovation of terraced houses. If these houses have load-bearing party walls, and non-load-bearing façades, they can be renovated by new 3D printed façade panels, either with complete freedom of the concrete/insulation mix across the spatial domain, a case in Section 4.1, or as a sandwich panel with predefined concrete faces, Section 4.2. In the future, it may be possible to completely print houses on site, and a related third case study on a continuous wall-floor system is presented in Youshi's report [8].

4.1. Façade panel

The method presented in Section 3 is used to find an optimal design for a (small part of a) façade panel, for which the design domain, boundary conditions, and loads are shown in Figure 1 on the left. This case is a first academic exploration, and unit loads (1N per node) are taken, which is fine as objectives are normalised, see Equation (7). With respect to the volume inequality, on average max. 50% of concrete can be used for the panel. The Young's modulus of concrete equals 30,000 N/mm^2, and for the insulation it is 19 N/mm^2. Poisson's ratio equals 0.2 for both materials. Equally important, the thermal conductivity of concrete equals 1 W/(mK), and for the insulation 0.06 W/(mK) is taken. Using strategy A2, figure 1 on the right shows the suggested design for w_s = 0.75. Note that elements have an x_e anywhere between 0.0 and 1.0, but for clarity, the visualisation is black-white (in fact: grey-yellow). The exterior surface (shown top right) is almost purely concrete, to distribute the load to the constrained sides in the stiffest way. However, also space is reserved for insulation material, mostly located near the influx of heat, to maximise the thermal compliance. Not shown, but for w_s = 0.99, much more concrete is suggested, e.g. using a thicker exterior face and more concrete along the sides, whereas for w_s = 0.01, a solid piece of insulation is proposed. Figure 2 on the left shows the objectives' values versus the sequence of iterations for w_s = 0.5 and w_s = 0.75. Cleary a trade-off can be seen between the two objectives: If w_s goes from 0.5 to 0.75, the structural compliance decreases (so better performance), whereas the thermal compliance (multiplied by -1) increases from about -1.8 to -1.3, which resembles worse performance. The same case study is also carried out using approach A3, so including stress constraints, with for the concrete's compression and tension strength values of 30 and 3 N/mm^2 respectively. Outcomes are similar, with respect to the TO suggested designs (qualitatively) and convergence behaviour (like in Figure 2 on the left). For a typical example, w_s = 0.75, Figure 2 on the right shows the number of finite elements (on the vertical axis) against the stress constraint function on

the horizontal axis. The stress constraint function's range equals -1 to 0, with "-1" representing zero stress, and "0" indicating that the maximum allowable stress state has been reached.

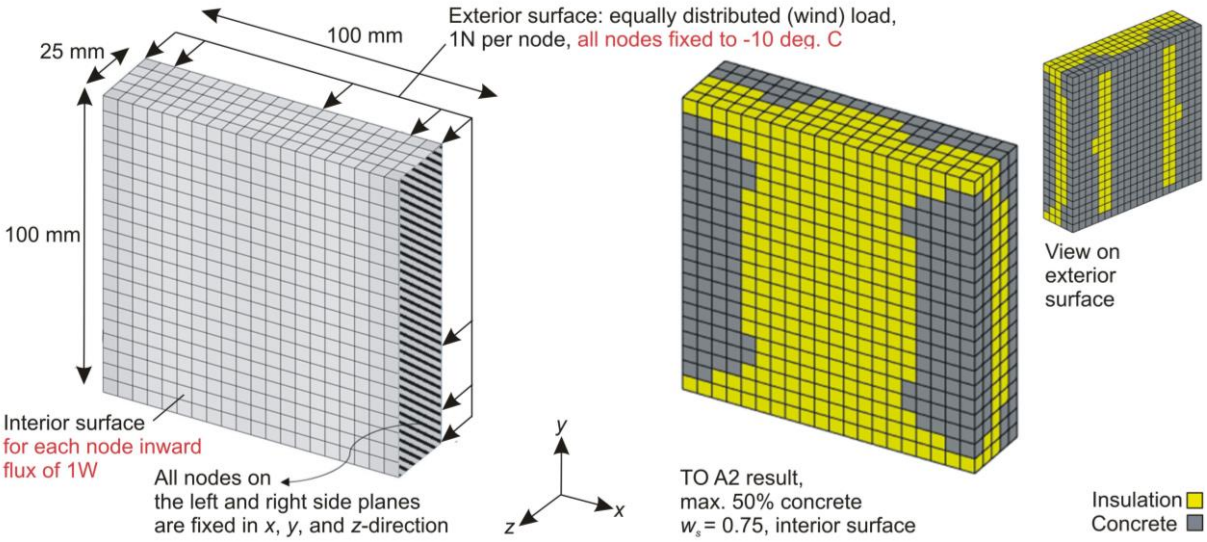


Figure 1. Façade panel case study. Left: finite element model. Right: TO A2 result visualised as a black-white solution (grey "Concrete" if $x_e \geq 0.5$, yellow "Insulation" if $x_e < 0.5$).

As figure 2 shows, all stresses are on the very safe side, and this is also the case for the other A3 simulations (w_s = 0.01, 0.5, and 0.99). This indicates that the maximal allowable average amount of concrete (now 50%) may be reduced in favour of higher insulation performance, or the panel may be designed thinner, all to be presented in the next section.

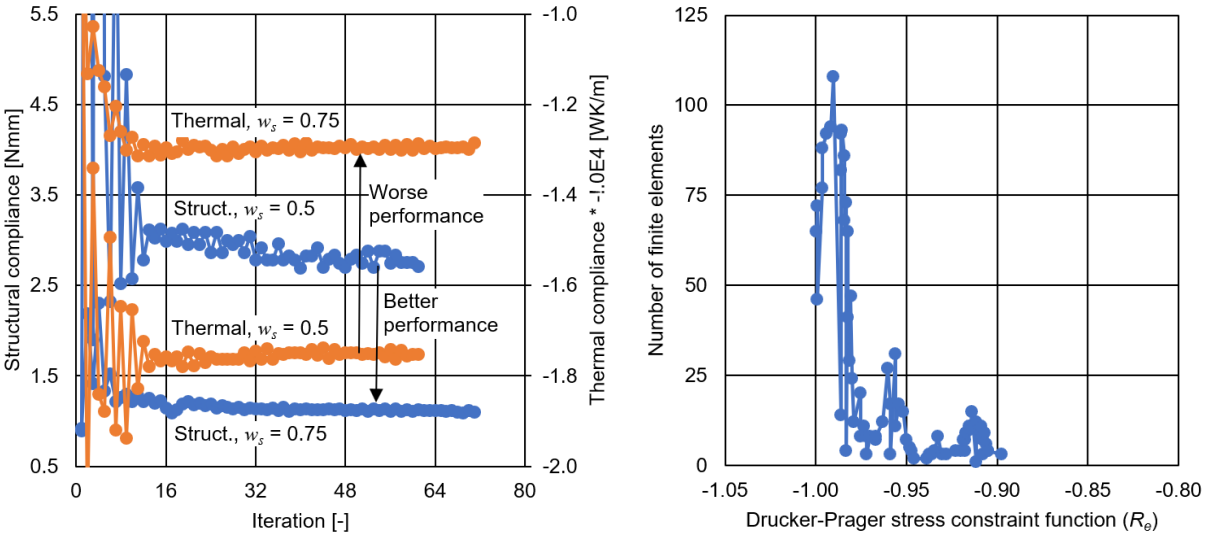


Figure 2. Left: Strategy A2 convergence of structural compliance (blue, left ver. axis) and thermal compliance (orange, right ver. axis) for different weight factors. Right: Strategy A3, w_s = 0.75, number of finite elements vs. the stress constraint function (R_e = -1.0 implies no stress, R_e = 0.0 indicates fully stressed).

As a conclusion, the "multi-disciplinary TO for multi-material components" functions, for it: (i) suggests the multi-material layout of a design; (ii) shows trade-offs between objectives; (iii) accounts for volume and stress constraints.

4.2. Sandwich panel

In Section 3, a design problem was introduced for a sandwich panel, requiring (a) its horizontal deflection being smaller than 1/150 of the height; (b) all concrete stresses being within the limits of 3 MPa in tension and 30 MPa in compression; and (c) a minimal thermal resistance of 4.7 m^2K/W should be achieved. For this problem, the TO (finite element) model is shown in Figure 3 on the left. Pure concrete faces are default for the interior and exterior surfaces, whereas the interior core is subject to TO. The panel is 3 meters wide and 2.5 meters high, including a 1×1 meter window opening, exactly in the middle. The core is modelled by 100×100×100 mm finite elements, and each concrete face by two layers of 100×100×25 mm elements, respecting a 1:4 element aspect ratio. Structurally, on the exterior surface, an equally distributed wind load is put, equal to 2 kN/m^2, together with a line load of 12.5 kN/m^2 on the top side, with an offset of minus 20 mm in *z*-direction following common design standards, representing the load of a floor on top of the panel. The bottom sides of the concrete faces are completely fixed, whereas all nodes along the interior top edge of the concrete face are fixed in *x* and *z*-direction. Thermally, all nodes on the exterior surface are temperature set at minus 10 deg. C., and each node at the interior surface has imposed on it an inward flux of 1W. No further conditions are prescribed for the sides, so fluxes are zero all around there.

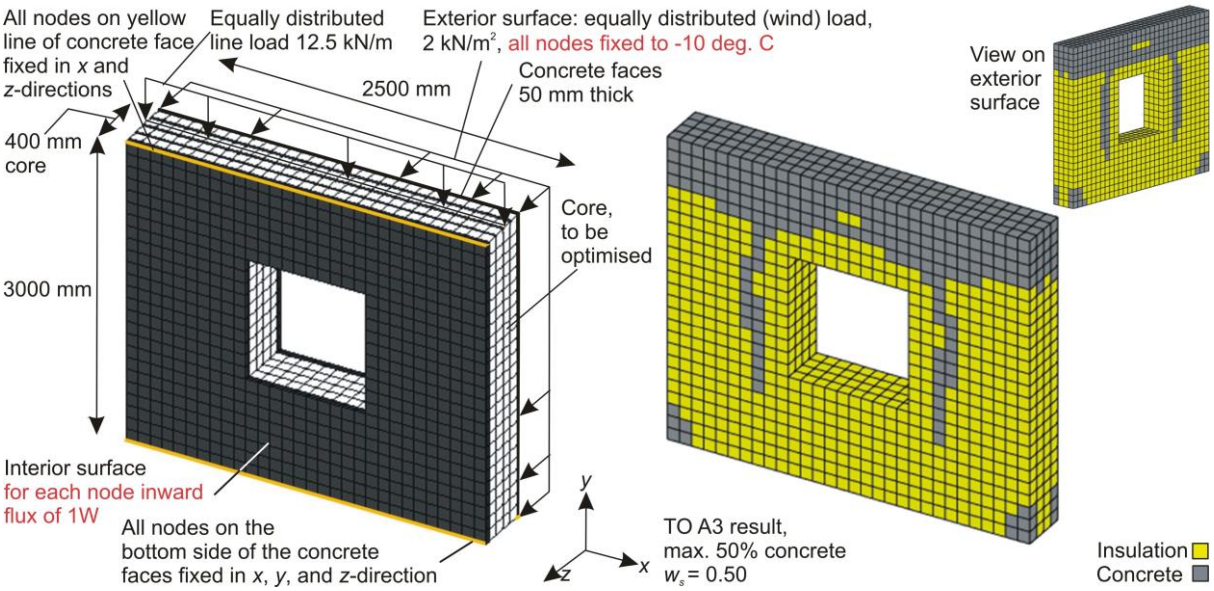


Figure 3. Sandwich panel case study. Left: finite element model. Right: TO A3 result visualised as a black-white solution (grey "Concrete" if $x_e \geq 0.3$, yellow "Insulation" if $x_e < 0.3$).

The initial thickness of the panel (later this thickness will be varied) is determined by simple engineering equations: The sandwich panel is regarded as a linear elastic beam, spanning from top to bottom, with core and faces fully connected. Given the wind and floor loads, the structural requirements (a) and (b) can be plotted as a function of the face thickness versus the core thickness. This shows that the face thickness is (i) dictated by the strength requirement (b); and (ii) a function of the core thickness. Therefore, the core thickness is predicted by the thermal requirement (c), which leads to a thickness of 400 mm. In turn, this leads with requirements (a) and (b) to a face thickness of only 0.5 mm, which is complicating the finite element model setup, impossible to print, and vulnerable in practice, and so for the faces a thickness equal to 50 mm is used.

Similar to the previous case study, strategies A2 and A3 are used, both for the weight factors $w_s = 0.01$, 0.50, 0.75, and 0.99. A typical outcome is shown in figure 3 on the right, for A3 and $w_s = 0.50$. Note that for clarity the solid concrete faces are not visualised, and interior parts of the core, e.g. the second and third layers of elements, are hidden and may have a different layout than as shown for the outer layers.

Not all outcomes can be presented visually here, but strategy A2 shows window opening interior edges of concrete (resulting in stress concentrations). This is avoided by strategy A3, which also results in smoother geometries at other locations. Nevertheless, in general strategy A3 leads to less stiff designs, but for similar insulation performance, see Table 2. Furthermore, this table shows quantitatively the same conclusions as for the first case study: TO is successful in handling the weight factor for a multi-material mix, and results show consistently a clear trade-off between structural and thermal objectives. For the face and core thicknesses initially selected, the stiffness requirement is easily met for all cases, however, the requirement for thermal resistance is only satisfied for a high weight on thermal performance (equals a low weight on structural performance: $w_s = 0.01$). Results in the table are based on successfully finished TO runs, and so for strategy A3 stress constraints are met in all cases.

Table 2. Overview of all TO generated designs for the sandwich panel case [8].

Strategy → / Constraints ↓	A2	A3	A2	A3	A2	A3	A2	A3
Weight factor w_s	0.99		0.75		0.5		0.01	
Maximum deflection [mm] (<16.6)	0.0079	0.0138	0.0409	0.0542	0.1126	0.1238	0.1619	0.1653
Structural compliance [Nmm]	161.6	179.8	465.8	569.4	1010.7	1022.1	1635.1	1918.9
Thermal resistance [m^2K/W] (>4.7)	0.92	0.92	3.47	3.42	4.69	4.67	5.18	5.26

4.2.1. Sandwich panel thickness variations

As Table 2 indicates all requirements can be met (in the last two columns), it can be tried to search for even more efficient designs, by lowering the core thickness (face thickness is fixed, as explained earlier). To investigate this, the previous simulations (total panel thickness 500 mm) are repeated for two other panel thicknesses, 300 and 400 mm, effectively changing the core thickness to 200 and 300 mm respectively. Using strategy A2 and a larger number of weight factors w_s, Figure 4 shows the three resulting Pareto fronts, and for illustrative purposes, three TO suggested designs for thickness = 500 mm. To obtain a classic orientation of the Pareto front, the reciprocal value of the thermal resistance is taken. Again, a too high deflection is not an issue, but the required thermal performance can only be achieved by (a) a sufficiently high weight on its objective in combination with (b) a sufficient thickness, and not by further optimisations, since the solution is optimised already.

Although strategy A2 is used, so stresses are not checked during TO, results still allow for the calculation of the average equivalent Drucker-Prager stress afterwards. As such, it can be shown that for the simulations in Figure 4: (i) the average stress decreases for higher w_s, i.e. structural stiffness is deemed to be more important and more concrete material is used; (ii) average stress increases for thinner panels, for deflections are larger as less material is available; (iii) for all cases the average stress is much lower than the maximal allowable stress, due to the limited load and its distributed character.

5. Fabrication by 3D Printing

Related to the fabrication of multi-material building components by 3D printing, research has been carried out by Herrmann and Sobek [11] on so-called shotcrete printing (for which concrete is sprayed rather than extruded [12]). They used two different concrete mixtures, one with a normal density, and the other one being an ultra-lightweight mixture for insulation purposes. One of their approaches was to blend the two mixtures (allowing variable ratios during printing) before the spray nozzle. Another approach was to apply for each type of mixture a separate spray nozzle. Small concrete prisms were fabricated with controlled densities (and so properties) across their volume. Similar research was carried out by Craveiro *et al*. [13], who followed an approach using extrusion, in which before the single nozzle normal concrete and concrete with cork instead of sand (for insulation purposes) was mixed. Finally,

Ahmed *et al*. [14] experimented with a system to add dry fibres or light-weight granular materials to the wet concrete in the extrusion nozzle, part of several large-scale research projects [15]. Different from the experimental work in academia, in the built environment printing technology is still limited to fabricate components using a single material. Therefore, here two strategies are explored to fabricate multi-material components by 3D printing: (i) functional grading and (ii) printing black-and-white solutions.

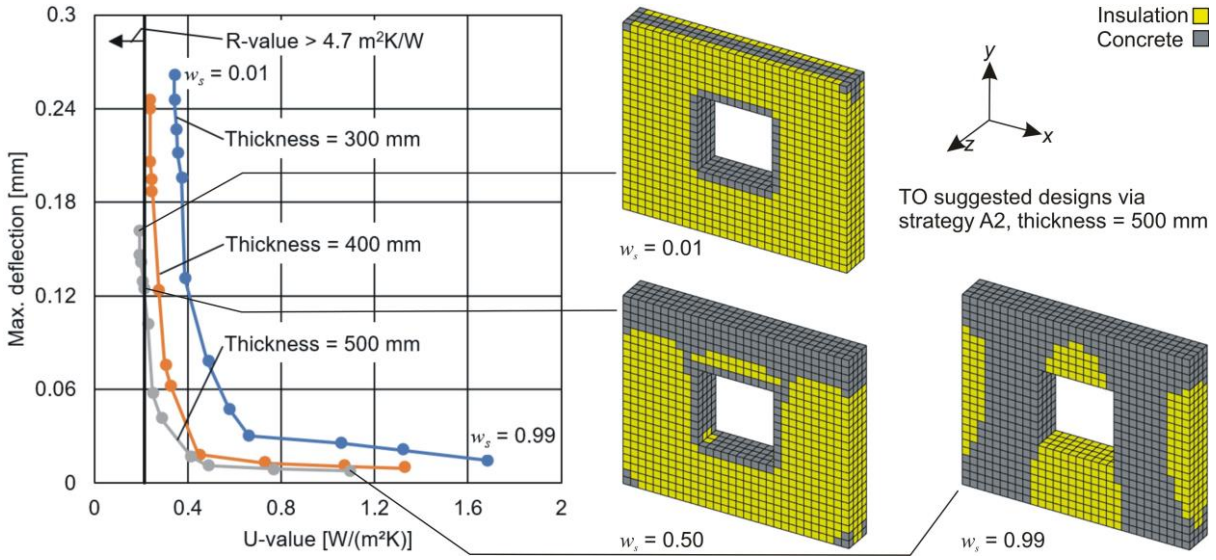


Figure 4. Pareto fronts for different sandwich panel thicknesses, using strategy A2. For all three Pareto fronts, end points refer to w_s = 0.01 and 0.99 respectively (only indicated for the blue curve).

5.1. Functional grading

Relative densities of designs can be shown to all vary continuously between 0.0 (full insulation) and 1.0 (full concrete). Functional grading allows for the printing of all these different densities, by varying the mix of insulation and concrete materials real time during printing. For further study, a TO suggested design is taken based on the problem definition in Figure 3 on the left. Strategy A2 is used, with w_s = 0.75, however, the window opening width is increased to 1.4 m to allow for a circular print path, avoiding 180 degree turns. The resulting finite element mesh is illustrated in Figure 5 on the left for layer 1, with for each element a relative density between 0.0 (full white) and 1.0 (full red).

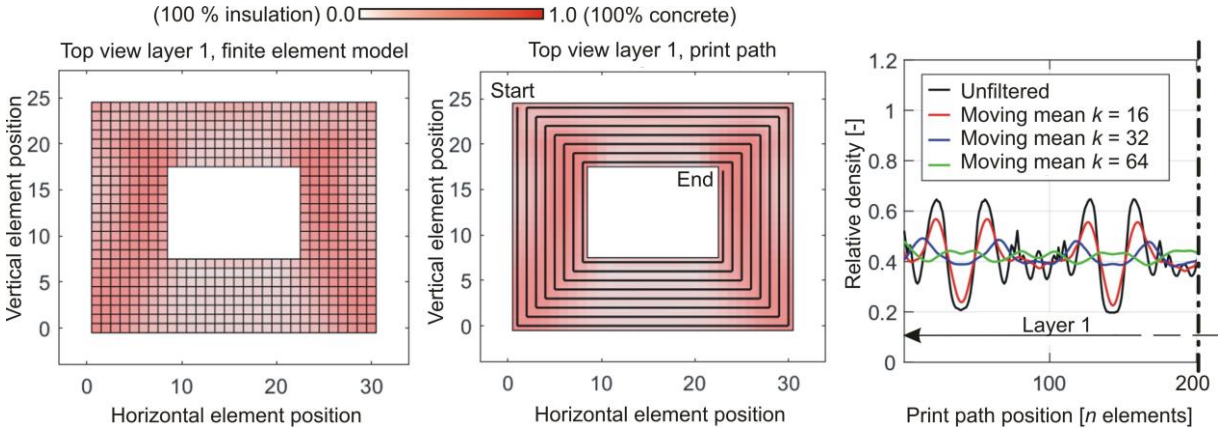


Figure 5. Left: finite element model with continuous relative densities between 0.0 and 1.0. Middle: print path for first layer. Right: required relative densities along the print path (shown for first 200 elements only).

Assuming that the panel is printed in its horizontal (flat) position, a (spiral-like) print path is planned through the entire infill of the panel, see Figure 5 in the middle. Subsequently, the finite elements are sorted along the print path and a graph can made of the relative density vs. the location at the print path, see the black line ("Unfiltered") in Figure 5 on the right. Rapid changes along the print path (and so in time) exist for the relative density, which cannot always be realised due to system dynamics (damping due to mixing, acceleration of the dosing system, etc.). The effects of system dynamics are simulated in Figure 5 on the right by moving mean filters. Practically, the filtered outcomes show that the concrete-insulation mix as fabricated (e.g. green line) is different from the design by TO (i.e. black line), as such compromising the structural and thermal performance. At least, the fabricated distribution should be checked against the design requirements, but better, density filtering, as discussed near the end of Section 3, could be modified to work with a print path shaped inclusion zone, instead of the common spherical inclusion zone [16].

5.2. Printing black-and-white solutions

Similar to the visualisation of densities in Figure 1,3, and 4, for the strategy that prints black-and-white solutions a threshold is used, here 0.50. This practically means that all relative densities equal or above 0.5 are regarded as solid concrete; and everything below 0.5 is solid insulation. There are several strategies to fabricate this type of designs. First, two printing systems, e.g. a gantry printer and a robotic arm, can be used simultaneously or sequentially. However, interference of movements needs to be controlled. Second, like functional grading in the previous section, a print path can be planned (the same as in Figure 5 in the middle) and relative densities can be set along the print path as shown in Figure 6 on the left. Figure 6 uses the same TO suggested design as Section 5.1.

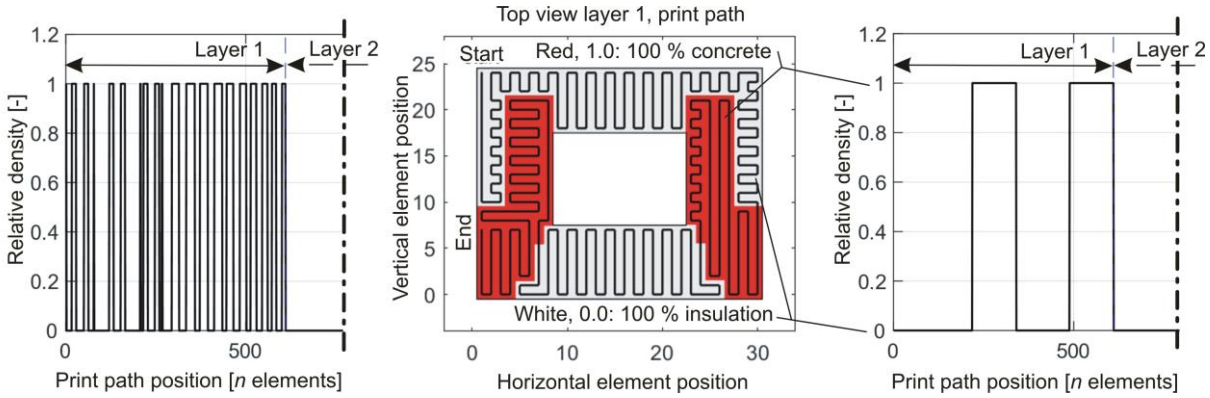


Figure 6. Left: Relative densities on the print path of Figure 5. Middle: optimised print path for black-and-white densities (threshold = 0.50). Right: Required relative densities using the print path of this Figure 6 in the middle.

Even if a printing system is available that can extrude real time the selected materials following the graph (in Figure 6 on the left), the rapid changes in material selection imply issues with system dynamics and fabrication quality. As a possible solution, each layer is divided into different zones based on the element relative densities, and the print path is planned accordingly, as shown in Figure 6 in the middle. The resulting relative densities along the print path clearly show fewer changes, Figure 6 on the right.

5.3. Experiments

Related to the above presented strategies, in 2022 several experiments have been carried out in the Structures Laboratory Eindhoven. First of all, for printing black-and-white solutions, the concrete part was printed of the first layer of the design from Figure 3, with strategy A2 and $w_s = 0.75$, on top of the solid concrete face. This with the assumption that two printing systems are used, and that the concrete system is tested. The result is shown in Figure 7 on the left, where the inset shows irregular printing, caused by the low stiffness of the gantry robot. For functional grading, first the print path was optimised (e.g. avoiding 180 degree turns and reduced flow in 90 degree turns) for the specific gantry robot, by

printing a solid version of the first layer shown in Figure 5. Then calibration prints were carried out, using mortar and a colour dye, instead of insulation material, to tune the flow rate of the dye dosing pump with respect to the print path. Finally, the full interior of four layers of the TO suggested design presented in Sections 5.1 and 5.2 was printed (using a black-white design). A spiral print path similar to Figure 5 was used, since it was more fitting to the used equipment. For practical reasons some scaling was used, projecting each finite element surface to 70×70 mm^2 in practice, and the thickness of each layer of finite elements seen as the printer filament thickness of 10 mm. Results are shown in Figure 7 on the right. Despite a black-white design, gradual transitions occur, and the TO strategy could be advanced by e.g. density filtering using a print path shaped inclusion zone [16].

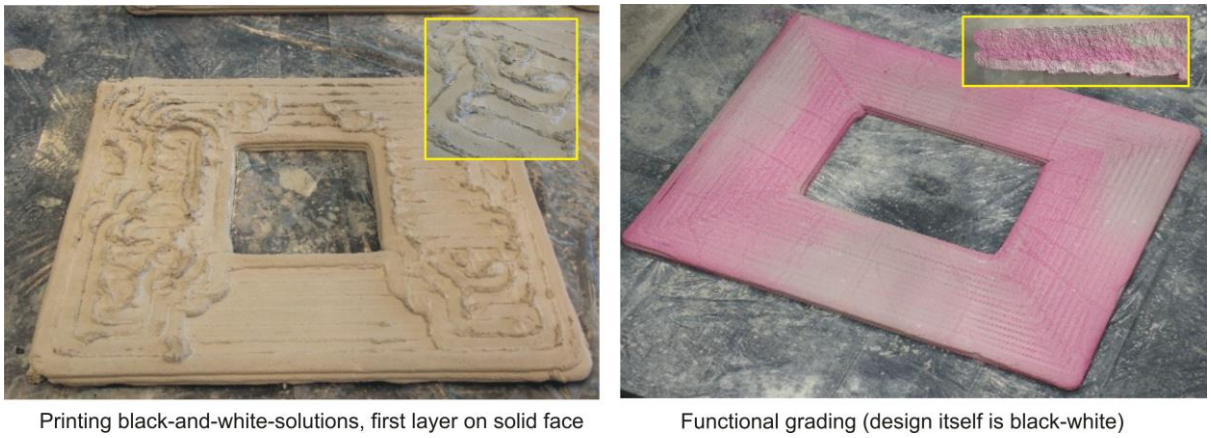


Figure 7. Left: Black-white printing only the first layer's concrete on a solid face. Right: functional grading able printing of a black-white design, full sandwich panel interior.

6. Conclusions and future research

Engineering design problems can be formulated in terms of objectives and constraints. However, if TO is used to create solutions, often the practical objectives and constraints cannot be applied directly. One or preferably more practical constraints should be reformulated as TO objectives, so trade-off solutions can be explored.

Using existing TO strategies with a redefined relative density, multi-disciplinary TO for multi-material components is able to suggest the multi-material layout of a design, to show trade-offs between the objectives, and to account for volume and stress constraints. Mass minimisation with a stiffness constraint [17] can be investigated in the future.

Experiments have revealed that design by TO requires specific print path plans and tweaking of system dynamics for the fabrication by 3D printing. Vice versa, this fabrication requires modifications in the design by TO, e.g by geometrical adjustments (here another window size) or by future density filtering using a print path shaped inclusion zone, both for functional grading and black-white printing [16]. As such, interaction is shown between design by TO and fabrication by 3D printing.

Acknowledgements

This research was financed by the Dutch "RVO" under "Meerjarige Missiegedreven Innovatie Programma's" (MMIP). Jan Blaakmeer (Saint-Gobain Weber Beamix), Marijn Bruurs and Maartje Hoogeveen (Witteveen+Bos), and Sandra Lucas, Theo Salet, and Payam Poorsolhjouy (Eindhoven University of Technology) are acknowledged for their valuable contributions to this project. The authors also thank the staff of the Structures Laboratory Eindhoven for their assistance in setting up the printing system, and Derk Bos and Lauri Hass for their support during printing.

References

[1] M. P. Bendsøe and N. Kikuchi, "Generating optimal topologies in structural design using a homogenization method," *Comput. Methods Appl. Mech. Eng.*, vol. 71, pp. 197–224, 1988.

[2] O. Sigmund and K. Maute, "Topology optimization approaches," *Struct. Multidiscipl. Optim.*, vol. 48, pp. 1031–1055, 2013.

[3] I. van de Werfhorst-Bouw, H. Hofmeyer, S. Boonstra, and R. J. M. Wolfs, "Stress-Constrained Topology Optimization of Concrete Structures: preliminary study for combining topology optimization and 3D concrete printing," *Heron*, vol. 66, pp. 199–237, 2021.

[4] S. Cho and J. Y. Choi, "Efficient topology optimization of thermo-elasticity problems using coupled field adjoint sensitivity analysis method," *Finite Elem. Anal. Des.*, vol. 41, pp. 1481–1495, 2005.

[5] S. Das and A. Sutradhar, "Multi-physics topology optimization of functionally graded controllable porous structures: Application to heat dissipating problems," *Mater. Des.*, vol. 193, 2020, Art. no. 108775.

[6] R. Tavakoli and S. M. Mohseni, "Alternating active-phase algorithm for multimaterial topology optimization problems: a 115-line MATLAB implementation," *Struct. Multidiscipl. Optim.*, vol. 49, pp. 621–642, 2014.

[7] M. Bruggi and A. Taliercio, "Design of masonry blocks with enhanced thermomechanical performances by topology optimization," *Constr. Build. Mater.*, vol. 48, pp. 424–433, 2013.

[8] M. Youshi, "Topology Optimization for Multiple Materials with Structural and Thermal Objectives to Design 3D Printed Building Elements," Eng.D. thesis, Department of the Built Environment, Unit SED, Eindhoven University of Technology, The Netherlands, 2022. [Online]. Available: https://research.tue.nl/files/210386279/20220713_SBC_Youshi_M.pdf

[9] P. Duysinx and M. P. Bendsøe, "Topology optimization of continuum structures with local stress constraints," *Int. J. Numer. Methods. Eng.*, vol. 43, pp. 1453–1478, 1998.

[10] K. Svanberg, "The method of moving asymptotes—a new method for structural optimization," *Int. J. Numer. Methods. Eng.*, vol. 24, pp. 359–373, 1987.

[11] M. Herrmann and W. Sobek, "Functionally graded concrete: Numerical design methods and experimental tests of mass-optimized structural components," *Struct. Concr.*, vol. 18, pp. 54–66, 2017.

[12] F. Heidarnezhad and Q. Zhang, "Shotcrete based 3D concrete printing: State of art, challenges, and opportunities," *Constr. Build. Mater.*, vol. 323, 2022, Art. no. 126545.

[13] F. Craveiro, S. Nazarian, H. Bartolo, P. J. Bartolo, and J. Pinto Duarte, "An automated system for 3D printing functionally graded concrete-based materials," *Addit. Manuf.*, vol. 33, 2020, Art. no. 101146.

[14] Z. Y. Ahmed, F. P. Bos, M. C. A. J. van Brunschot, and T. A. M. Salet, "On-demand additive manufacturing of functionally graded concrete," *Virtual Phys. Prototyp.*, vol. 15, pp. 194–210, 2020.

[15] F. Bos, R. J. M. Wolfs, Z. Ahmed, and T. A. M. Salet, "Additive manufacturing of concrete in construction: potentials and challenges of 3D concrete printing," *Virtual Phys. Prototyp.*, vol. 11, pp. 209–225, 2016.

[16] A. H. Deetman, "3D Printing Technology for Multiple Materials with Structural and Thermal Objectives for Building Elements," MMIP/IEBB/WP4.3-report (confidential), Department of the Built Environment, Unit SED, Eindhoven University of Technology, The Netherlands, 2022.

[17] D. Li and I. Y. Kim, "Multi-material topology optimization for practical lightweight design," *Struct. Multidisc. Optim.*, vol. 58, pp. 1081–1094, 2018.

Proceedings of the IASS Annual Symposium 2023
Integration of Design and Fabrication
10–14 July 2023, Melbourne, Australia
Y.M. Xie, J. Burry, T.U. Lee and J. Ma (eds.)

Post-tensioned strapping connections for rapid assembly of low-cost timber structures

Joseph M. GATTAS*, Shaobo XU[a], Zhengtao LU[a], Zhuo-Yang XIN[b]

* School of Civil Engineering, University of Queensland, Brisbane, Australia
j.gattas@uq.edu.au

[a] School of Civil Engineering, University of Queensland, Brisbane, Australia
[b] School of Architecture, University of Queensland, Brisbane, Australia

Abstract

This paper explores the development of novel post-tensioned strapping connections for low-cost and high-speed timber framed construction. The strapping is made from a cheap and widely-available polyester packaging material, which can be tensioned and sealed using inexpensive hand tools. The connections are designed conceptually as adaptions of semi-rigid post-tensioned or mortise-and-tenon connections used for permanent timber constructions. Two types of semi-rigid joints were developed which achieve a rotational stiffness via different mechanical behaviours. The first joint uses a force couple between offset straps, developed for a truss frame structure built using utility-grade timber as the component material. The second joint induces a mechanical clamping between adjacent timber elements, developed for a sway frame structure built using engineered timber I-joists as the component material. For both designs, connection rotational stiffness and strength capacity is established with experimental testing. Full-scale prototypes are also built to establish connection suitability for the rapid structural assembly of lightweight timber elements and prefabricated panels.

Keywords: timber framing; timber connections, rapidly-assembled structures, emergency and temporary housing, lightweight structures

a) b)



Figure 1: Timber-framed structures built using post-tensioned strapping connections. (a) Truss frame structure with force couple developed between offset strap connection. (b) Sway frame structure with mechanical clamping induced by strap connections between adjacent elements.

Copyright © 2023 by J.M. GATTAS, S. XU, Z. LU and Z.Y. XIN. Published in the Proceedings of the IASS Annual Symposium 2023 with permission.

1. Introduction

1.1. Timber-Framed Construction and Out-of-Grade Timber

Timber is a popular construction material for residential housing as it is renewable, low-cost, and highly workable. In Australia, lightweight timber framing is used for 76% of detached dwelling construction [1]; this building typology comprises sawn timber and engineered wood product structural members, specified to a particular material grade. Grading is intended to classify a timber product into a defined grouping with similar visual and mechanical material characteristics. Grading methods vary by country and resource type; taking Australian sawn pine board as an example, a machine-stress grading process will assign an 'MGP' stress grade, based on allowable thresholds for minimum stiffness and maximum size and frequency of observable defects [2].

The residential timber construction supply chain is highly industrialised; for sawn framing boards, it is also highly optimised to deliver typical rectangular framing sizes in the best attainable structural grade. However, due to the high variability in utilised Australian softwood species, a large volume of sawn softwood fails to attain a structural grade, estimated at 1.2 million m^3 in 2015/16 [3, 4]. These 'out-of-grade' boards have no existing market use and are consequently sold at a loss by millers.

Out-of-grade timber may be classified as such due to low stiffness or due to the large size or higher prevalence of natural defects. These defects could include sloping grain, wane, knots, shakes, splits, checks, or resin. Defects will locally reduce certain structural capacities of a timber member, for example reduced tensile or shear capacity, but the member may otherwise still have excellent performance. More critically though, localised defects prevent the practical connection of out-of-grade timber members. In typical residential housing, timber elements are connected by steel mechanical fixings, such as nails, nail plates, and strapping, which interlock with timber fibres for load transfer. As fibres are more likely to be disrupted or even removed by defects in out-of-grade timber, they are unsuited to assembly using conventional connector types.

1.2. Timber-framed emergency and temporary housing

In a post-disaster context, emergency and temporary housing is used to provide short-term shelter for displaced populations. The frequent and increasing occurrence of worldwide disasters in recent years, including recent bushfire and flood disasters in Australia, has highlighted the need to develop more scalable delivery models for post-disaster housing responses. Scalability of existing systems is limited by their need to access to conventional supply chains for sourcing new construction materials and skilled construction labour, which may be highly limited, and thus expensive, in regional disaster areas. Such systems also have limited ability to integrate or adapt to local material and labour, and thus limited scope for building cost reduction and a high dependence on external support.

Timber framing is beneficial in being lightweight, workable, demountable, and versatile with regards to the structural form and finishing level. These properties make timber stick-framed construction suitable for emergency and temporary housing in tropical and sub-tropical locations with appropriate material availability and climate suitability[5]. Successful recent examples of timber-framed housing systems for low-cost modular construction have also allowed for very rapid assembly, with a single house built in one weekend by a small team of people[6].

The economic viability, transportability, and construction speed of timber housing is strongly dependent on local availability and understanding of connector components. As such, novel connection approaches are frequently proposed to enable a greater flexibility in emergency housing design and delivery, and to make better use of local materials and supply chains. Recent examples have proposed the utilisation of post-tensioned strap joints for high-speed, low-cost, and reversible timber constructions, where reversible refers to a de- and re-constructable structural system [7]. The Liina Transitional Shelter [8] connects individual wooden frames with a nylon hoop strapping, to create an $18m^2$ structure that can be assembled in just 6 hours. A semi-rigid frame structure [9] was proposed by the authors to connect

engineered timber I-joists with polyester (PET) packaging straps, with a 1.5m^2 housing segment assembled in 30 minutes. The connection rotational stiffness in this case was insufficient to meet serviceability requirements for a permanent housing use case.

1.3 Aim

This paper aims to explore two novel connection systems that allow for: i) rapid construction with out-of-grade structural timber; and ii) improved rotational stiffness as compared to existing systems. The new connection methods will also aim to retain the capacity of existing systems in being low-cost, rapidly constructable and de-constructable. The design rationale for the two new 'Strap Truss' and 'Strap Clamp' connection systems are presented in Sections 2 and 3, respectively. For each system, a structural performance assessment is conducted from experimental connection testing, and a constructability performance assessment is conducted from fabrication and assembly of a full-scale building prototype.

2. Strap truss connection system

2.1 Connection design

2.1.1. Out-of-grade timber truss connections

To facilitate a structural assembly of out-of-grade timber, a novel pair of strap-based connection methods was developed as shown in Fig. 2. The first method is based on traditional 'birdsmouth' roof truss connections, which transfer compressive bearing and shear action via a notched recess [10]. These can be additionally reinforced by a metallic binding strip or through-bolt to resist tensile action [4].

The present study introduces a modified form of the strap-reinforced birdsmouth joint, which uses post-tensioned PET packaging strap to connect truss chord and vertical web members as shown in Fig. 2a-b. Inclined truss web members were slightly over-sized, such that they were pre-compressed by the strap tensioning action to remain stable in-plane. Inclined web members also used small double-ended nails at the mitred surfaces for transverse stability.

This connection method is well-suited to assembly of utility-grade timber members, as it relies on pre-compressed bearing action, rather than fibre interlock, for load transfer. For fibre orientation defects such as knot, shake, or resin, the strapping pre-compresses truss chords in the cross-grain direction, reducing the potential for transverse splitting when the member is loaded in axial tension or compression. For geometrical defects such as bowing or twisting, the progressive assembly of strapped locations pulls connected members into structural alignment.

2.1.2. Semi-rigid truss frame connections

A second strapping connection is also introduced to facilitate the semi-rigid connection of adjacent trusses into truss frame structures. With reference to Fig. 2b-c, continuous tensile straps are looped around an entire truss module to anchor to a rigid ground support. When loaded in flexure, semi-rigid load transfer occurs from the force couple between top and bottom anchor locations; due to the applied pre-compression, this will initiate as compressive bearing in both interfaces, and progress to compressive bearing in one interface and tensile strap loading at the other interface. This load transfer mechanism is similar to post-tension timber connection systems for engineered wood products, such as the QuickConnect system [11].

Shear transfer can occur via shear keys located proximate to interface, in the case of connection to a rigid ground support. In the case of connection to an adjacent truss assembly, these shear keys can be introduced as integral notched recesses, similar to that used within the truss for chord and web attachment. These options will be discussed further in below sections.

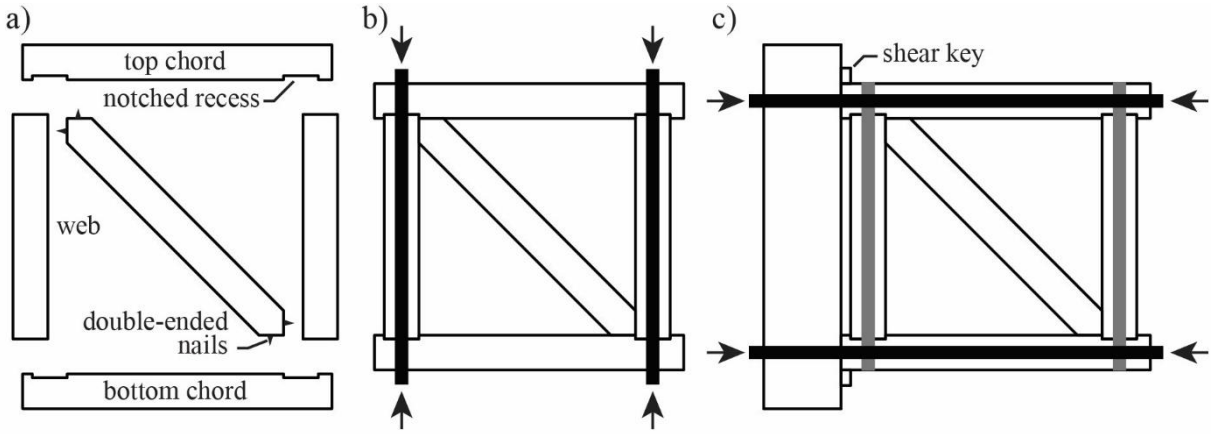


Figure 2: Strap Truss connection system. a) Truss parts. b) Tensioned strap connection of chord and web members. c) Tensioned strap connection to rigid ground support.

2.2 Structural performance assessment

2.2.1 Specimen fabrication and testing

An experimental testing methodology was adopted to evaluate the structural performance capacity of the strap truss connection system. Experimental tests were designed to establish the semi-rigid rotational capacity of truss frame connection straps, which were judged to be the most likely to influence global structure behaviour. With reference to Fig. 3a, specimen geometry was designed to utilise 1.5 full-length (2400mm long) out-of-grade timber boards. Boards was cut into two 795 mm top chords, two 562mm vertical web member, and one 792mm include web member. Parts were assembled into truss modules with two vertical straps, tensioned to 2.7kN and welded with a FROMM P329 strapping tool. Truss modules were then fixed to a pseudo-rigid glue-laminated timber base part, using horizontal straps fixed in the same way. Plywood shear keys were added to the base part at location shown using brad nails.

Three specimen groups were tested, using out-of-grade timber with different Young's Moduli. Specimen Groups A, B, and C utilised boards with average Young's Modulus of 5600 MPa, 7850 MPa, and 11900 MPa, respectively. 90x35 boards were provided by Hyne Timber with average board stiffness values provided based on continuous flatwise bending stiffness measurement. Three samples were fabricated and tested for each specimen group.

Specimens were tested using the apparatus shown in Fig. 3b. The base part was fixed to a rigid steel column and a vertical load was applied at the module end by hydraulic actuator. Side plates were used to prevent lateral instability and force, displacement, and rotation data was recorded by the actuator, a string potentiometer, and an inclinometer, respectively. Load was applied based on European standard EN26891 for timber joints [12], with an initial loading to 40% of predicted peak force (obtained from an initial sample test), an unloading, and a final loading until failure. Force data was multiplied by a 540mm lever arm to convert to a moment about the base support.

2.2.2 Results

Moment-rotation curves for the three tested groups are plotted in Fig. 4a-c. A mean group response curve is obtained as the average of all specimen responses and plotted in Fig. 4d. It can be seen that all specimens exhibit a similar response profile, with an initial pseudo-elastic region with approximately linear stiffness, followed by a non-linear softening behaviour and large rotation. Response values are summarised in Table 1a, with initial stiffness obtained from linear trendlines in pseudo-elastic regions.

The initial region was observed to correspond to the release of the compressive bearing stress on the bottom surface. The only observable material damage in the initial stage is the perpendicular-to-grain crushing where the strap anchors onto the base part during initial pre-tensioning, Fig. 3a. This is consistent with the response shape described in [9] for an I-joist strap joint, which also found that joint

initial stiffness is sensitive to timber flatwise MOE. In the softening region, the truss module underwent a large rotation, with additional progressive material failures. Some samples with material defects at the notched recess in the top chord member showed a shear fracture at the notch location. This caused a sharp force reduction but, in most cases, the vertical web member was caught by the rigid base part to give a force restoration. Ultimate failure then occurred from tensile strap fracture. There was little difference between specimen groups, indicating that out-of-grade timber member stiffness had little impact on connection performance.

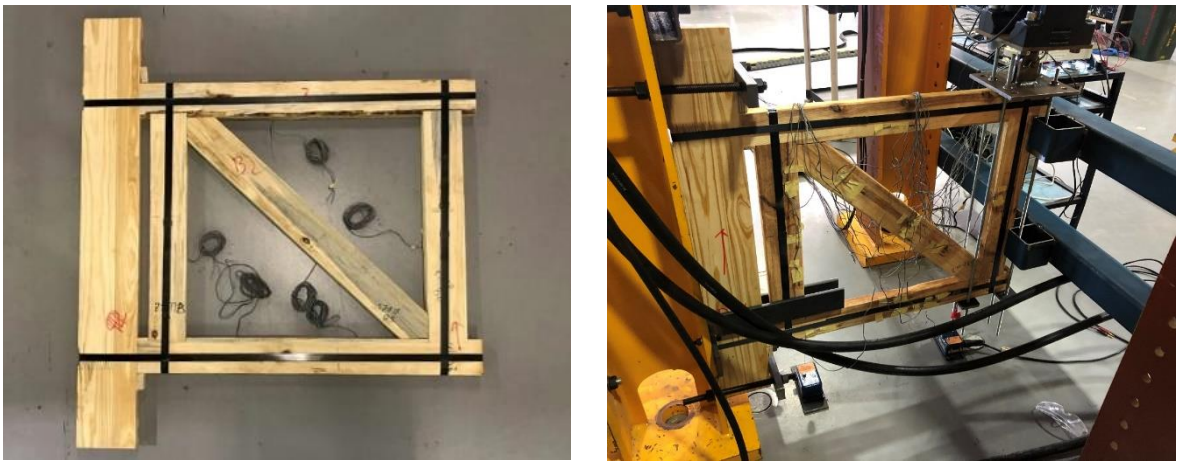


Figure 3: Strap Truss Connection testing. a) Fabricated specimen and b) testing apparatus.

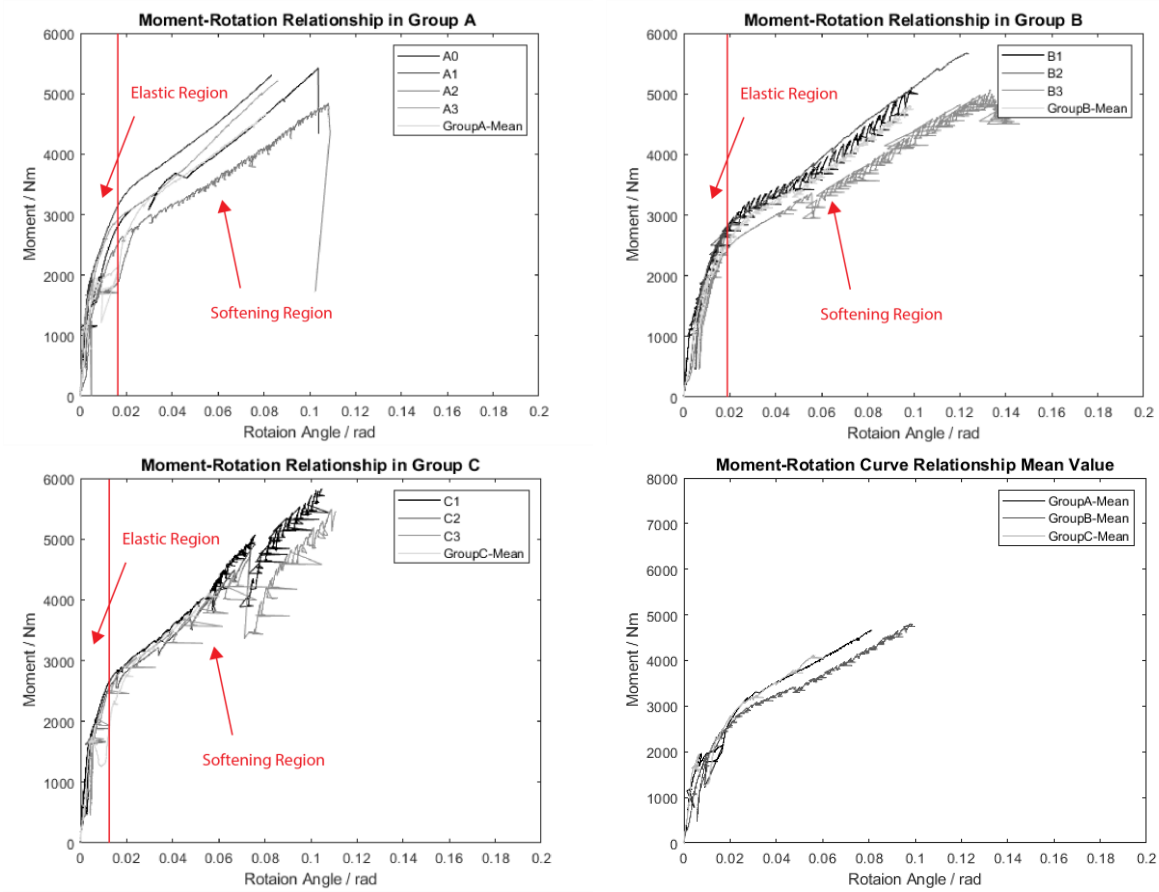


Figure 4: Moment–rotation curves of strap truss connections. From left-to-right, top-to-bottom: Group A, B, and C specimens; and Group mean values.

Table 1. Summary of key experimental testing values. a) Truss Frame connections and b) Clamp connections.

a) Truss Frame Connections

Specimen	Max Rotation (rad)	Max Moment (Nm)	Initial Stiffness (kNm/rad)
A1	0.0833	5302	215
A2	0.1087	4834	142
A3	0.0859	5493	170
B1	0.1018	5097	130
B2	0.1234	5668	159
B3	0.1524	5653	114
C1	0.1077	5837	219
C2	0.0757	5039	195
C3	0.1107	5493	179
A(avg)	0.0926	5210	176
B(avg)	0.1258	5473	135
C(avg)	0.0980	5456	198

b) Clamp Connections

Specimen	Max Rotation (rad)	Max Moment (Nm)	Initial Stiffness (kNm/rad)
A1	0.0024	2923	62
A2	0.0021	2952	55
A3	0.0021	2928	52
B1	0.0024	3030	56
B2	0.0028	3293	53
B3	0.0023	2859	67
B0a	0.0024	3030	56
B0b	0.0019	2343	49
B0c	0.0026	4443	121
A(avg)	0.0022	2934	56
B(avg)	0.0025	3061	59

2.3. Constructability performance assessment

A full-scale temporary structure was built using the truss strap connection system, to investigate the fabrication effort, assembly effort, and system cost. The structure was designed to use a single repeated truss module, Fig. 5a, comprising four repeating parts: top/bottom chord and vertical/inclined web members. Assembled modules were connected at 600mm spacings with timber battens to create prefabricated wall and roof cassettes. Battens used a small notch to locate frames at the correct transverse spacing and were connected with batten screws.

Prefabricated cassettes were connected side-on in the truss frame strap arrangement shown in Fig. 5b, with semi-rigid connections between roof, wall, and base surfaces. Roof sheeting was screwed onto the outer batten layer and the frame was then tilted up for transport. Upright frames were self-stable and could be transported by using a pallet truck or forklift, lifting from under the floor cassette. A complete structure, Fig. 5c, used two mirrored frames to create a pentagonal envelope, connected by plywood gussets at the apex.

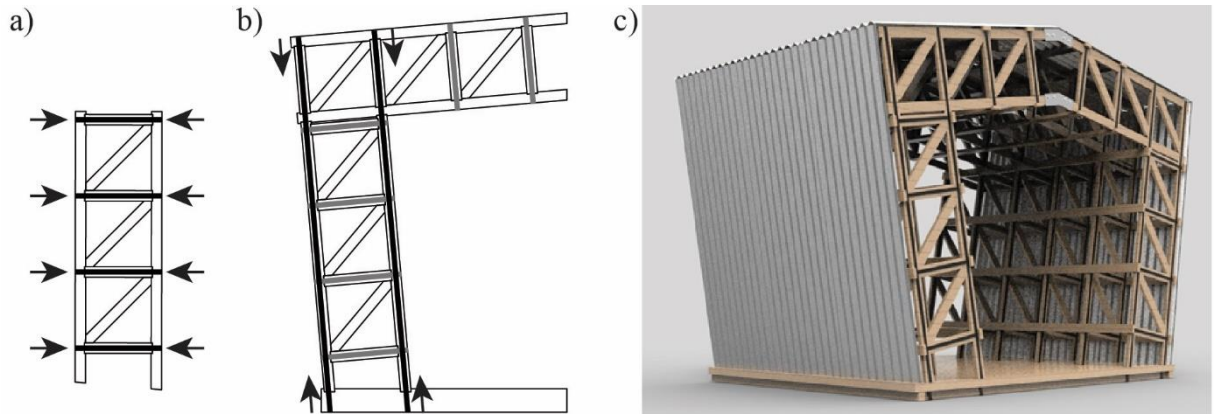


Figure 5: Truss frame temporary structure prototype. a) Repeated truss module (arrows indicate tension strap locations). b) Roof, wall, and floor cassette assembly. c) Complete structure.

The final structure had an internal width and height of 2.66m and 2.46m, respectively, and maximum external width and height of 4.72m and 3.21m, respectively. A single truss module used four 90mm x 35mm x 2400mm out-of-grade timber boards and 6m of strap. A paired frame, Fig. 1a, was 1.2m deep and used 12 truss modules and 36m of strap. Parts were fabricated in approximately 1 day by two people, using typical timber power tools (mitre saw, router). Truss modules were assembled in approximately

ten minutes each by two people; prefabricated cassettes were assembled in approximately four hours by three people; and the full structure took approximately two hours to assemble by four people. The fabrication and assembly effort relative to other systems will be discussed further in Section 4.

3. Strap clamp connection system

3.1 Connection design

In prior strap-based connection designs, both for the truss frame connection above and the system in [9], stiffness is limited by perpendicular-to-grain bearing stiffness and ultimate strength is limited by tensile strap capacity. A new connection system was thus developed to avoid primary load transfer through these components, instead using the strapping elements to facilitate connection assembly.

With reference to Fig. 6, the 'Strap Clamp' connection is an adapted form of a mortise-and-tenon joint, modified to allow low-effort fabrication from engineered timber member. The system considers an entire timber member as the 'tenon'; plywood plates are nailed onto adjected members to build up a 'mortise' to receive the tenon. When subject to flexure, load transfer occurs as shear load into nails and plywood plates, and then compressive bearing between plywood plates and tenon members.

For symmetric load distribution, the connection requires a double-member arrangement in one of the connecting members. Two options for this are shown in Fig. 6. In Fig. 6a, the mortise is split between outer and inner surfaces of a single vertical member, to receive two horizontal tenon members. In Fig. 6b, the mortise is contained within two vertical members, to receive a single horizontal tenon member. Assuming the same plywood width for both cases, the connection bearing area is the same and so joints are expected to have a similar capacity.

The split member arrangement helps to simplify the practical construction of the joint; members can be attached separately in the transverse direction, rather than having to align and insert the full-length member as a pseudo-tenon. Assembly effort and structural performance are also strongly influenced by joint tolerance, controlled here by spacing of the plywood plates. A tighter fit will create a stiffer connection [13, 14], make manual assembly more difficult. Thus, the straps are used to apply a clamping stress that forces parts into a correct and snug-fit alignment, while being removable for disassembly.

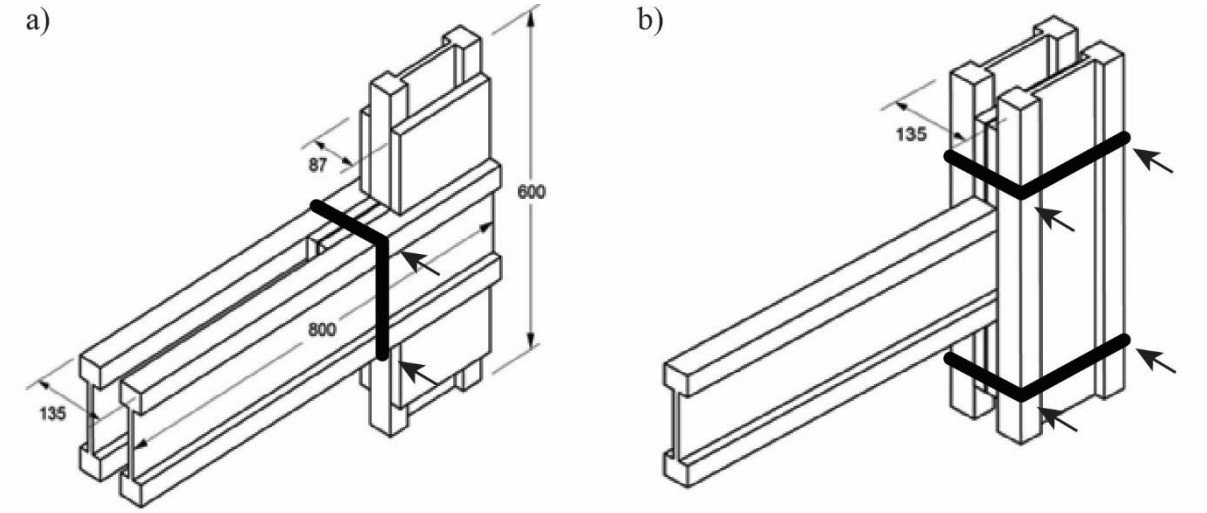


Figure 6: Strap Clamp connection system, with a) double-tenon or b) double-mortise split member arrangement. Strap clamp and assembly direction indicated by arrows.

3.2 Structural performance assessment

3.2.1 Specimen Fabrication and Testing

Strap clamp joints were tested using a similar methodology to that described above for strap truss connections. Three samples each of two specimen groups, A and B, were fabricated to correspond to connection arrangements in Fig. 6a and b, respectively. Connections utilise 'ej20045' timber I-joists, provided by Wesbeam and with flange width w_f = 43 mm, flange height h_f = 38.5 mm, web width w_b = 10 mm and total height h = 200 mm. Plywood plates are 200mm x 150mm x 22.5mm and fixed with six 50mm x 2.87mm D-head strip nails (three nails per I-joist flange). Specimens were hypothesised to be sensitive to this nail arrangement. Three additional specimens were fabricated to conduct a preliminary investigation of this: B0a, B0b, and B0c types with six, four, and ten nails, respectively. Due to time restrictions, only a single specimen for each type was fabricated, noting however that B0a is equivalent to Group B specimens.

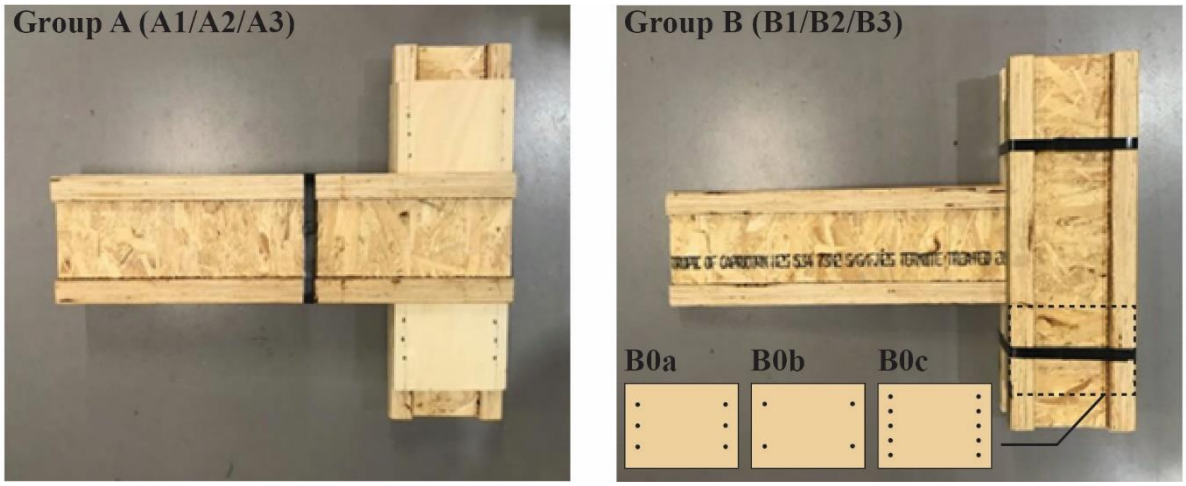


Figure 7: Figure 3: Strap Clamp connection test specimens.

3.2.2 Results

Moment-rotation curves for Strap Clamp connection Groups A and B are plotted in Fig. 8a-b. Curves for nail-varied specimens B0a-c are plotted in Fig. 8c, and alongside all specimens in Fig. 8d. Response values are summarised in Table 1b.

Group A and B responses are very similar, confirming that the distribution of the bearing area, via internal or external attachment, does not strongly influence connection behaviour. Overall, the strap clamps are less stiff than strap truss and prior strap connections; the stiffness range of 62-121kNm/rad for Strap Clamp connections is also smaller than values reported for traditional mortise and tenon connections with similar dimensions[15]. For most specimens, failure occurred as ductile shear failure and rotation of the plywood plates, with local crushing of the timber and some nail withdrawal. In a single specimen, B0c with ten nails, some perpendicular-to-grain crushing was also observed in the flange of the tenon member. The observed response shape is consistent with similar ductile failure modes in direct shear loading of dowel-type timber fasteners [16], with an initial elastic region and subsequent softening. Structural capacity can be seen to be strongly influenced by the nailed plate, with the lowest and highest strength and stiffness recorded for 4-nail B0b and 10-nail B0c specimens, respectively. The performance of the joint could likely be further improved with closer design consideration of these connection components.

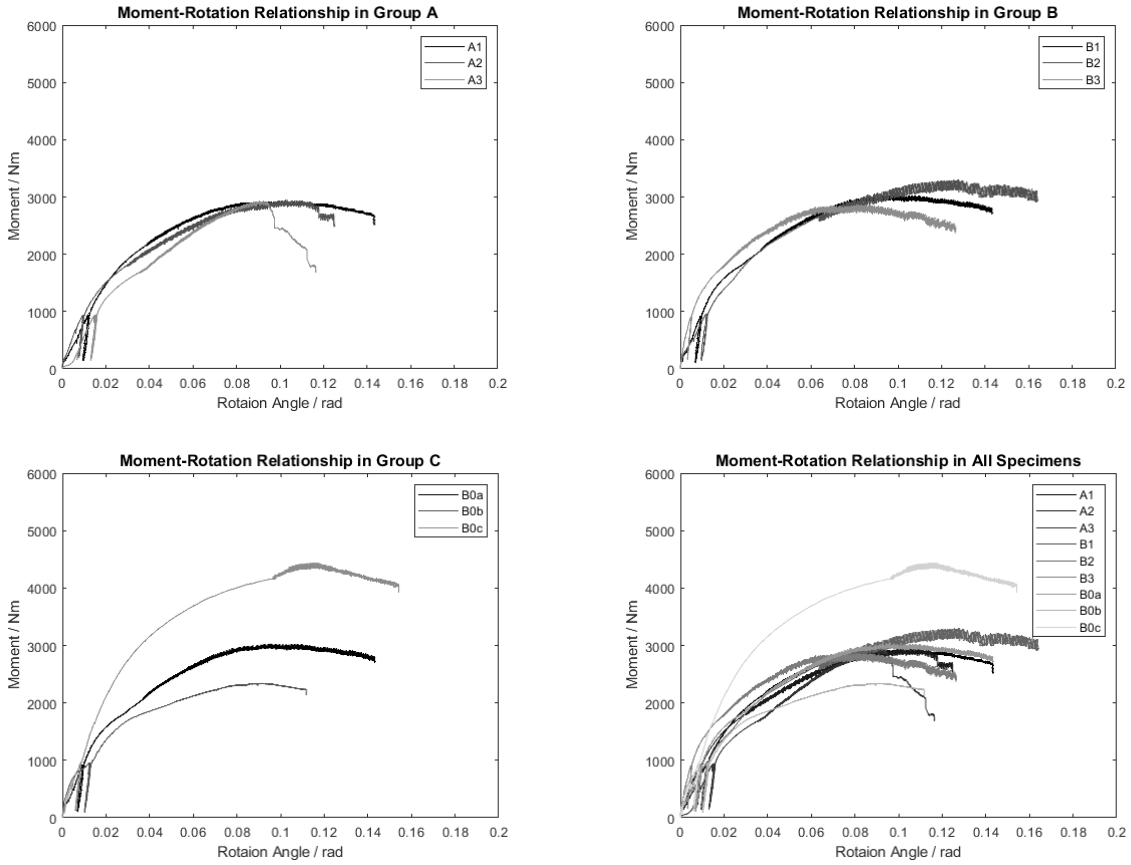


Figure 8: Moment–rotation curves of strap clamp connections. From left-to-right, top-to-bottom: Group A, B, and B0a-c specimens; all specimens.

3.3. Constructability performance assessment

A full-scale temporary structure was built using the strap clamp connection system, termed the 'Bush Hut' and pictured in Fig. 1b. The structure used a sway frame construction, with floor joists connected to wall elements using the double-mortise split member arrangement; and wall elements connected to roof beams using the double-tenon split member arrangement. With reference to the construction sequence shown in Fig. 9, ground anchors and bearers were first installed on a 2400mm x 2400 mm grid. Sway frame parts were fabricated offset, assembled on-site, and lifted onto floor bearers at 1200mm centres. Additional floor joists were placed at 600mm spacing to support floor sheeting and battens were installed at approximately 600mm centres to support wall and roof sheeting. To avoid having to work at height; roof sheeting was pre-fixed to battens while on-ground; a lifting mechanism was then used to lift up the ceiling to slide onto the primary structure. The ceiling was then fixed from underneath using tension straps wrapped around battens and roof beams.

The final structure had an internal width and height of 2.4m and maximum external width and height of 2.9m and 3.1m, respectively. A single sway frame used three 6m long timber I-joists (2.8m + 3.0m floor and wall part; 3.2m + 2.7m roof and wall part; 3.0m + 2.7m wall parts), eight plywood plates as sized for connection tests, and approximately 8m of strap. Frame parts were fabricated in approximately 1 day by 2 people, using typical timber power tools (mitre saw, nail gun). The entire structure was assembled in approximately 1 day by 6 people, including foundations but excluding wall sheeting. Wall sheeting was installed later in 4 hours by 3 people. Frame parts were assembled in 10 minutes each, on the uneven site ground and without issue, as the clamp joint was able to correct for small misalignments.



Figure 9: Construction sequence of 'Bush Hut' temporary housing sway frame structure built with strap clamp connections. From left-to-tight, top-to-bottom: footings and bearers; first strap clamp frame; all strap clamp frames; battens; floor sheeting; roof lifting mechanism; prefabricated roof cassette; lifted roof; installed roof.

4. Discussion

The relative performance of the Strap Truss (ST), Bush Hut (BH) and Strap House (SH) housing prototype previously reported in [9] is summarised in Table 2. Relative material cost, Table 2a, is evaluated using 2023 retail prices of constituent materials. The out-of-grade timber materials used for the ST prototype ($217/m^2) significantly reduce the housing cost as compared to BH ($587/m^2) and SH ($713/m^2) systems. The BH system is also cheaper than the SH system by requiring fewer I-joist components per square meter of building.

Relative labour effort, Table 2b, is evaluated as build time multiplied by the number of required people, and of 1 day being equal to 8 hours. It can see that the lower material cost of out-of-grade stud comes at the expense of a much higher labour effort for the ST (22.6 person-hours/m^2) as compared to the BH (13.2p.h./m^2) and SH (6.3p.h./m^2) systems. The SH system is relatively slower that the BH system as cladding layers could be partially pre-assembled to include structural frame elements. Finally, relative structural performance is summarised in Table 1c from connection experimental test results.

Table 2. Comparison of Strap House (SH) [9], Strap Truss (ST) and Bush Hut (BH) temporary housing prototypes: a) material cost, b) labour effort, and c) structural performance. Note: SH price updated to 2023 material cost.

a)

Element	Material	Cost		
		SH	ST	BH
Structure	I-beam	$ 793	$ -	$ 2,331
	90 x 35 Stud (out-of-grade)	$ -	$ 343	
	21mm Plywood	$ -	$ -	$ 58
Cladding & Flooring	PET Strap	$ 4	$ 8	$ 2
	90 x 35 Stud (out-of-grade)	$ 19	$ 51	$ 95
	Corrugated roof sheet	$ 179	$ 220	$ 769
	19mm Particleboard Flooring	$ 32	$ 71	$ 128
	Total	*$ 1,026*	*$ 693*	*$ 3,384*
	Total per sqm	*$ 713*	*$ 217*	*$ 587*

b)

Stage	Person-Hours		
	SH	ST	BH
Fabrication	8	16	16
Pre-Assembly (Offsite)		48	-
Final Assembly (Onsite)	1	8	60
Total	*9*	*72*	*76*
Total per sqm	*6.3*	*22.6*	*13.2*

c)

Structural Performance	Connection test		
	SH	ST	BH
Initial Stiffness (kNm/rad)	111-141	114-219	49-121
Ult. Moment (kNm)	1.3-1.4	4.8-5.8	2.9-4.4

5. Conclusion

This study has proposed two new connection systems for low-cost and rapid assembly of temporary timber structures. A Strap Truss connection system enabled connection between out-of-grade timber materials and thus achieved a very low cost overall cost for final building assembly. A Strap Clamp connection system used a strap-fixed, pseudo mortise-and-tenon joint to create a fast, deconstructable, and low-effort assembly system using engineered wood products.

Acknowledgements

The authors gratefully acknowledge Wesbeam, Hyne Timber, and Queensland Sheet Metal for donation of material used in testing and prototyping.

References

[1] Australian Construction Insights, "Framing Material Use in Residential Construction". Project Report, Forest and Wood Products Australia, 2018.

[2] *AS/NZS 1748.1:2011 Timber-Solid_stress-graded for structural purposes*, 2011.

[3] R. Cherry, A. Manalo, W. Karunasena, and G. Stringer, "Out-of-grade sawn pine: A state-of-the-art review on challenges and new opportunities in cross laminated timber (CLT)," *Construction and Building Materials*, vol. 211, pp. 858-868, 2019.

[4] H. Bailleres, D. J. Lee, C. Kumar, S. Psaltis, G. Hopewell, and L. Brancheriau, "Improving returns from southern pine plantations through innovative resource characterisation,". Project Report, Forest and Wood Products Australia, 2019.

[5] J. Ashmore, C. Treherne, J. da Silva, E. Parker, E. Roberts, and I. B. Hill, "Transitional shelters: Eight designs," International Federation of Red Cross and Red Crescent Societies, 2011. [Online]. Available: https://www.humanitarianlibrary.org/sites/default/files/2014/02/900300-transitional_shelters-eight_designs-en-lr.pdf

[6] M. Cecila. "Techo's Modular Shelter Works for Guatemalans Made Homeless After Fuego's Eruption." [Online]. Available: https://www.engineeringforchange.org/news/techos-modular-shelter-works-guatemalans-made-homeless-fuegos-eruption/.

[7] Z. Yan, L.-M. Ottenhaus, P. Leardini, and R. Jockwer, "Performance of reversible timber connections in Australian light timber framed panelised construction," *Journal of Building Engineering*, vol. 61, p. 105244, 2022.

[8] Aalto University Wood Program. "Liina Transitional Shelter." [Online] https://www.archdaily.com/174909/liina-transitional-shelter-aalto-university-wood-program.

[9] Z.-Y. Xin, K. Baber, and J. M. Gattas, "A novel tension strap connection for rapid assembly of temporary timber structures," *Engineering Structures*, vol. 262, p. 114320, 2022.

[10] P. Palma, H. Garcia, J. Ferreira, J. Appleton, and H. Cruz, "Behaviour and repair of carpentry connections–Rotational behaviour of the rafter and tie beam connection in timber roof structures," *Journal of Cultural Heritage*, vol. 13, no. 3, pp. S64-S73, 2012.

[11] F. Scheibmair and P. Quenneville, "The quick connect moment connection for portal frame buildings–an introduction and case study," in *World Conference on Timber Engineering, WCTE*, 2012.

[12] *BS EN 26891:1991 Timber structures -Joints made with mechanical fasteners-General principles for the determination of strength and deformation characteristics*, E. C. f. Standardization, 1991.

[13] Y. Alqaryouti, D. Fernando, and J. Gattas, "Structural behavior of digitally fabricated thin-walled timber columns," *International Journal of Structural Stability and Dynamics*, vol. 19, no. 10, p. 1950126, 2019.

[14] N. Quinn, D. D'Ayala, and T. Descamps, "Structural characterization and numerical modeling of historic Quincha walls," *International Journal of Architectural Heritage*, vol. 10, no. 2-3, pp. 300-331, 2016.

[15] Y. P. Prihatmaji, A. Kitamori, and K. Komatsu, "Rotation performance of Javanese traditional timber joint," *Procedia Environmental Sciences*, vol. 20, pp. 154-161, 2014.

[16] M. Yurrita and J. M. Cabrero, "On the need of distinguishing ductile and brittle failure modes in timber connections with dowel-type fasteners," *Engineering structures*, vol. 242, p. 112496, 2021.

Proceedings of the IASS Annual Symposium 2023
Integration of Design and Fabrication
10–14 July 2023, Melbourne, Australia
Y.M. Xie, J. Burry, T.U. Lee and J. Ma(eds.)

Research on clay mixtures for sustainable building materials

Andreea-Terezia MIRCEA*, Gabriela CĂLĂTAN[a]

* Department of Civil Engineering and Management, Technical University of Cluj-Napoca, Romania
andreea.mircea@ccm.utcluj.ro

[a] INCD URBAN-INCERC Bucharest (Cluj-Napoca Branch), Romania

Abstract

Developing new solutions from the historical and traditional experience, in order to provide superior performance, is currently become a priority in civil engineering research. The most important features of sustainable building are represented by materials derived directly from surroundings, obtained from local, often family-run businesses, supporting the local development and cultural independence of the region. The objectives are to build with simple techniques that do not further pollute the environment, do not consume more fossil fuel, and do not extract unnecessarily resources. Earthen architecture can be linked to a technological continuity common all over the world, dating back to ancient periods. In this aim, clay mixtures are able to be successfully used to build masonry bricks, mortars, plasters and finishes. The paper presents experimental studies and results made in the field of eco-friendly building materials, emphasizing significant contributions for revaluation of traditional and local construction materials, along with conservation of natural resources, protection of landscape and bionetwork.

Keywords: sustainability, natural resources, eco-friendly building materials, recycling, environmental compatible structures, structural materials

1. Introduction

The present global economic and social context has a high impact on the built environment. The full life-cycle of a building has to be considered from early design phase [1], with reference to: integration in the urban environment, planning with regard to economical land use and inclusion of green spaces, placing and shaping the building in relation to natural light, wind effects and passive solar heating, using local, traditional building materials, preservation of the site and vegetation integrity during all construction activities, along with the selection of native plants in landscape design. This approach involves and sustains protection of natural resources, minimizes emission levels and waste production, by achieving energy efficiency, and allowing materials and equipment to be reused.

An ever-increasing turn towards tradition arises from the need of society to have its own identity, to keep in touch with the identity of the nation it originates from, and not to lose the traditions that define it [2]. Constructions made of earthen materials can be found all over the world, mainly in rural areas, both in less developed countries as well as in economically developed ones [3], therefore, many countries have proposed and implemented standards and regulations for earth housing construction.

The recent trend of green-building construction concept underlines the importance of an environment-friendly management of materials throughout their entire life-cycle [4], from resource extraction, during the fabrication phase, on-site installation, use, maintenance and post- utilization. By supporting the local development and cultural independence of the region, the use of these materials meet the objectives to build with simple techniques that don't further pollute the environment, don’t consume more fossil fuel, or unnecessarily extract resources. For the ease of recycling, as well, the natural materials are preferred.

Copyright © 2023 by Andreea-Terezia MIRCEA and Gabriela CĂLĂTAN. Published in the Proceedings of the IASS Annual Symposium 2023 with permission.

2. Materials and methods

The terms related to natural building refers to any sort of construction that is accomplished with the use of materials, and techniques with reduced environmental impact, as well as building measures that minimize the use of products that require considerable embodied energy for their manufacture or transportation.

Earthen architecture can be linked to a technological continuity common all over the word, dating back to ancient periods. Incorporating ancient and traditional construction techniques into contemporary sustainable building practices offers several opportunities to address modern challenges in the construction industry, the reason why many countries have proposed and implemented standards and regulations for earth housing construction [5], [6], [7]. By understanding the advantages of these time-tested methods, architects, engineers, and other professionals can develop innovative, environmentally friendly, and culturally sensitive building solutions:

- Climate-responsive design: Ancient construction techniques have evolved to suit specific local climates and environmental conditions. By studying these techniques, designers can develop climate-responsive buildings that efficiently regulate indoor temperatures, reducing the reliance on mechanical heating and cooling systems and minimizing energy consumption.

- Local material sourcing: Traditional construction methods often employ locally sourced materials, reducing the need for transportation and associated carbon emissions. Embracing these practices can support local economies, minimize environmental impacts, and promote the use of sustainable, low-impact building materials.

- Bioclimatic architecture: By analyzing ancient building methods, designers can learn how to create structures that harmonize with their natural surroundings. Bioclimatic architecture integrates passive design strategies, such as natural ventilation, day lighting, and solar gain, reducing energy consumption and enhancing occupant comfort.

- Community engagement and empowerment: Ancient construction techniques often involve community participation, fostering social cohesion and empowering communities in the building process. Integrating these practices into modern construction projects can promote affordable, inclusive, and culturally sensitive housing solutions.

- Preservation and adaptation of traditional skills: Integrating ancient techniques into contemporary building practices helps preserve traditional knowledge and craftsmanship. By adapting these techniques to modern requirements and materials, designers can develop innovative solutions that merge the best of both worlds, creating durable, sustainable, and culturally relevant structures.

- Circular economy in construction: Ancient techniques often employ biodegradable and recyclable materials, minimizing waste and promoting resource efficiency. Incorporating these practices into modern construction projects can support the transition towards a circular economy in the industry [8], where materials are reused, repurposed, or recycled at the end of their life cycle.

- Resilience and durability: Traditional building techniques have proven their durability and resilience over time [9]. By integrating these methods and principles into modern sustainable construction, designers can create structures that withstand the test of time and adapt to changing environmental conditions.

Advantages of clay based compositions are mentioned in literature [10], [11], [12], as being environmentally friendly, easy obtained with little financial and energy effort, adaptable to users' needs, helping to regulate indoor air relative humidity, with no toxic emissions, being fire resistant, as well as resistant to insects, rodents and mold attack. Clay mixtures can be successfully used to build masonry bricks, mortars, plasters and finishes. There are various benefits and advantages of traditional clay-based construction techniques in the context of sustainability and environmental concerns:

- Local and natural material sourcing: Traditional clay-based construction techniques often utilize locally sourced materials, reducing the need for transportation and their associated carbon emissions. This approach supports local economies and minimizes the environmental impact of material extraction and production.

- Low-cost and community-driven construction methods: Traditional clay-based construction techniques are often cost-effective and rely on community participation, making them accessible to a wide range of people. This promotes social cohesion and empowers communities to be involved in building their own homes and public spaces.

- Adaptation to local climate and environmental conditions: Traditional clay-based construction techniques have evolved over time to suit specific local climates and environmental conditions. This adaptation ensures that buildings are resilient and well-suited to their surroundings, minimizing the need for additional energy inputs and reducing the overall environmental impact of the building.

- Energy efficiency and thermal properties: Clay-based materials have good thermal properties, providing natural insulation and temperature regulation. This helps to maintain comfortable indoor environments with minimal reliance on mechanical heating and cooling systems, reducing energy consumption and greenhouse gas emissions.

- Biodegradable and recyclable materials: Clay-based construction materials are often biodegradable and recyclable, making them an environmentally friendly choice. They can be easily reused or repurposed at the end of their life cycle, reducing waste and promoting the circular economy in the construction industry.

Despite of many advantages, some shortcomings and limitations are indicated by the literature [13], [14], [15], including the reduced resistance to water and moisture, being susceptible to erosion and damage, requiring proper site selection, drainage, and maintenance to ensure durability, the reduced resistance to seismic actions, being not suitable for regions with high seismic activity, as they can be prone to structural damage during earthquakes, the necessity of more frequent maintenance and repairs than in case of industrial construction materials, as well as the effort to establish the optimal composition of clay-sand-additions, which are varying from one extraction site to another [16], [17].

The research was performed in order to improve the mechanical performance of adobe bricks and the workability of local fresh clay mixtures. In this intend, a wide span of natural additives was studied, and different samples of clay mixtures material have been used in adobe bricks, mortar, and plaster for eco-friendly construction elements, made with products and resources from the nearby geographic area [18]. The clay material extracted from a natural deposit, usually referred to as loam, is a product of erosion of feldspar and other minerals, and as expected, does not represent a standardized composition. In order to determine the suitability of loam for a specific application, it is necessary to know its composition.

Depending on the site of extraction it contains varying amounts of clay, silt, sand, aggregate and water, resulting in specific properties. According to their ratio there are defined several types of clay based compositions and consequently, different samples of clay mixtures material have been used in adobe bricks, mortar, and plaster for eco-friendly construction elements.

The clay mixtures were made with products and resources from the nearby geographic area. The experimental mixes were made with soil extracted from a Transylvanian site. The granulometric analysis was determined according to prescriptions [19], by sieving method.

The granulation characteristics in correlation with data from the literature indicate that this soil is in accordance with the chosen purpose, having a sandy loam-type composition [20], as pointed out in Figure 1.

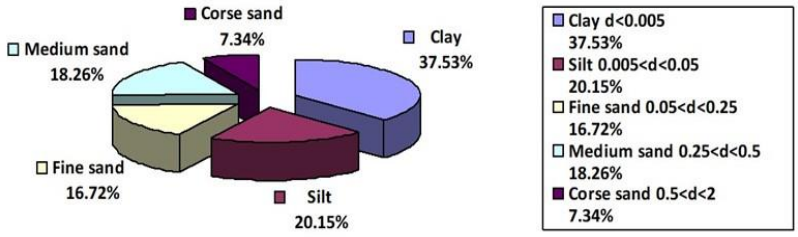


Figure 1. Characteristic texture and size distribution of the clay composition, see Călătan et al. [20]

The sand has a bulk density of 1500 kg/m3 and a size distribution presented in Table 1:

Table 1. Sand size distribution, determined by sieving method

Sieve size [mm]	0.063	0.125	0.25	0.5	1	2	4	8
Past [%]	0.5	1.6	8.8	28.5	59.6	82.4	98	100

A wide range of additions were studied, both theoretically and experimentally, throughout more than 50 mix recipes, and the use of following was highlighted: paste lime, bone glue, sodium hydroxide (NaOH), and salt (NaCl). In this regard, paste lime was analyzed according to SR EN 4592 [21], bone glue was purchased in granular form and dissolved in water, while sodium hydroxide (NaOH) and salt (NaCl) were procured as maximum purity substances, which are routinely used in the laboratory.

Experimental studies regarding the effectiveness of natural fiber disperse reinforcement in adobe bricks were conducted previously [2], [18], [20], [22]. The primary clay mixture was modified by introducing the vegetal fibers (hemp fibers and wheat straw, Figure 2).

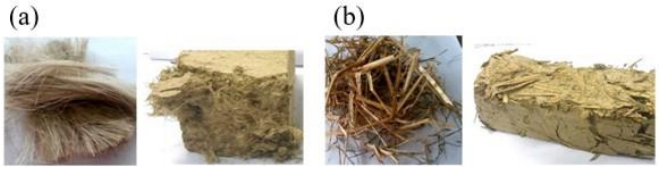


Figure 2. Fibers used in the preparation of clay mixtures: a) Hemp fibers; b) Wheat straw fibers, see Călătan [18]

Hemp (industrial hemp) is a species of plant that is grown specifically for the industrial uses of its derived products. It can be refined into a variety of commercial items including paper, textiles, clothing, biodegradable materials, paint, insulation, bio-fuel, food, and animal feed. The fibers are extracted from the hemp stem which is straight and has branches at the bottom. The stem's length varies between 1 and 3 m, and the thickness ranges from 4 to 8 mm. Hardness, durability and resistance to decay are included among the many characteristics of the hemp fibers.

Wheat straw is a harvesting agricultural by-product, rich in cellulosic fibers, available from the annually renewable crops, produced in large quantities, in numerous regions all over the world. Used as addition to building materials' composition, neither their production nor their use, even at the end of their life service, does harm the environment or health. Having high water absorption capacity, straw fibers have to be immersed in water in advance to avoid the phenomenon of water absorption from the clay matrix.

In order to determine the physical - mechanical parameters, samples have been made by casting in molds. Prismatic specimens of 40x40x160 mm were used to determine the bulk density of the material reached to equilibrium moister, the axial contractions, the flexural tensile strength and the compressive strength. Also prismatic specimens of 300x300x40 mm were used to determine the thermal conductivity based on the heat transfer property of the samples, through the thermofluxmetric method, for an average temperature between plates, of 10ºC, as shown in Figure 3.

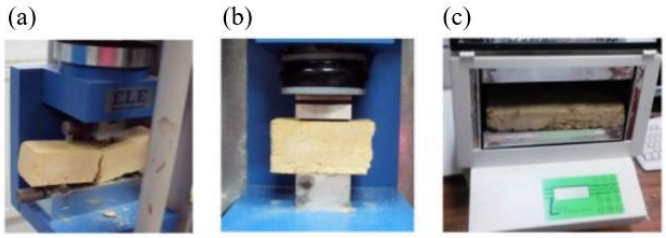


Figure 3. Specimens in test devices: a) Testing of the flexural tensile strength (Rf); b) Testing of the compressive strength (Rc); c) Determination of the thermal conductivity, see Călătan [18]

The witness specimen was conceived from the established composition, as the optimal one from the experimental research. The mix included sandy loam, sand, bone glue and paste lime, in proportions of 35% sand and 65% binder (composed of 79% sandy loam, 1% bone glue and 2% paste lime). The required water was established as 33% reported to the dry material mass. There were made three sets of witness specimens: optimal mixture, optimal mixture with straw addition and optimal mixture with hemp fiber addition. The proportion of vegetal fibers was determined as well, during experimental research [18], [22]. The composition was prepared by hand mixing of raw materials. After preparation the mix was placed in molds, in form of successive layers, each layer was then rammed until its thickness was reduced to half. After unmolding, the specimens were stored under laboratory conditions, at +23 ^{o}C, until reaching the equilibrium moister.

The specimens tested for mechanical strength were evaluated in following combinations: mixture of recycled clay material without vegetal fibers, mixture of recycled clay material with straw addition and mixture of recycled clay material with hemp fiber addition. The flexural tensile strength (Rf), was determined by applying a concentrated load at half of the distance between the supports, and the compressive strength (Rc), on the two resulted halves of the specimen.

The research aims to determine furthermore the optimal addition of vegetal materials, hemp fibers or straw, taking into account the main factors that must be observed in the production of sandy clay bricks: axial contractions, eventuality of appearance and evolution of cracks, bulk density, mechanical strength and thermal performance. For this purpose, vegetal materials were introduced into the clay matrix in various amounts, expressed as percentage by volume of the clay mixture. Thus, 3%, 8%, 9%, 10%, 12% or 15% volume of hemp fiber, respectively 10%, 20%, 30%, 40%, 50% or 60% volume of straw. Hemp fibers were used as such. Straws, having a high water absorption capacity, were used after being immersed in water for an hour, in order to avoid the water absorption phenomenon from the clay matrix.

From each mixture, a set of three prismatic specimens of 40x40x160 mm was made, to determine the bulk density, axial contractions and mechanical resistances. Another set of prismatic specimens, of 300x300x40 mm was dried in an oven until to a constant mass, and then placed in the apparatus to determine and to record the thermal conductivity. All specimens were kept under laboratory conditions until equilibrium humidity was reached. The workability of the mixture was tracked during the preparation of the mixtures and during the manufacture of the specimens. The appearance and evolution of the cracks was visually tracked as well.

3. Experimental data and results

By comparing the experimental results obtained for clay mixtures with paste lime, with the admissible limit values indicated in the literature [23], [24], it has been found that an addition of up to 3% paste lime in the mixture keeps the compressive strength within limits that meet the required conditions. The addition of paste lime has positive influences by reducing the axial contractions and thus, the risk of cracks, as the amount of paste lime used in the mixture increases. All these achieved mixes had axial contractions falling within the range of values recommended in the literature.

Gathering the obtained experimental results, it can be remarked that in the case of the using paste lime as a single additive material, the results are not satisfactory for more than 2% of paste lime because it induces significant reduction of the mechanical resistances. Bulk density is negatively influenced in this case; none of the tested mixtures reached the minimum density limit indicated in the literature.

From the view of mechanical strengths recorded in case of replacement of the mixing water with solutions of NaOH and/ or bone glue, it can be said that an improvement was generally found, with peak values for the mixtures made with 0.7% to 1.25% bone glue, as well as for the mixture made with 1.5% bone glue and 2% sodium hydroxide (NaOH) solution. Comparing the obtained experimental results with the admissible limit values indicated in the literature, it has been found that all mixing variants analyzed are in this case higher in value than the minimal compression resistance specified in the literature, which indicates that they are suitable for the intended purpose.

Following the analysis of the obtained results, it may be appreciated that in the case of sandy clay materials, for the identification of an optimal composition meant for building masonry elements of vernacular structures, it is advisable to consider the use of additions of sand and paste lime, along with the possibility of substituting the mixture water with a solution of bone glue and NaOH. This combination of several additive materials creates the possibility of identifying the mix to meet at best the criteria of thermal resistance by a satisfactory bulk density, and the criteria for the strength and durability (mechanical strength, axial shrinkage and water resistance), along with the need of minimum effort (in terms of energy consumption and resource efficiency) required in production and utilization.

The research emphasizes that the most beneficial additives were the bone glue and sodium hydroxide (NaOH). The optimal concentration of bone glue is 1.25% to achieve compressive strengths of about 4.1 MPa at 40 days (higher concentrations leads to mold grow). Bone glue was purchased in granular form and dissolved in water. An addition of 2% sodium hydroxide (NaOH) provides a better workability of the mixture and helps dissolve the bone glue faster. Also, the research revealed that the variation of the observed physical-mechanical parameters is influenced by the type of the organic material, hemp fiber or straw, and of the amount entered in the mixture. In conformity with literature [2], [3], [20], [22] an amount of minimum 5% but no more than 50% clay in the loam extracted from the natural deposit is optimal for obtain proper adobe bricks. By analyzing simultaneously all watched physical-mechanical parameters, for the used clay mixture, it was set an optimum addition of hemp fibers, of 9-10% by volume, respectively an optimal straw addition, of 30-40% by volume. Thus, it contributes to the completion of the information reported up to date in literature, and indicates the possibility of diminishing the dimensions of earthen walls, as well as maintaining the safety operation characteristics along with the thermal efficiency. The variation of compressive strength, flexural tensile strength, and thermal conductivity, depending on the amount of vegetal fibers included in the clay mixture is presented in Figure 4.

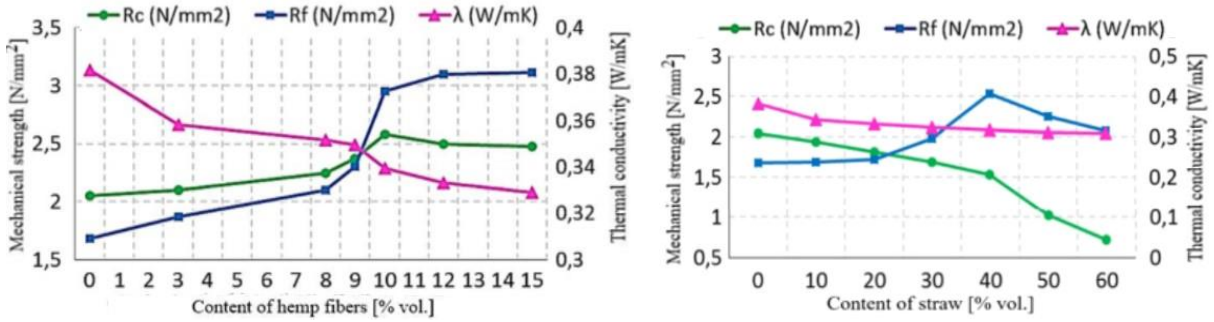


Figure 4. Variation of compressive strength, flexural tensile strength, and thermal conductivity (depending on the content of hemp fibers and straw), see Călătan et al. [22]

4. Conclusion:

In recent years, the circular economy has been endorsed as a policy to minimize burdens to the environment and stimulate the economy, and especially to reduce the redundant resource exploitation. There are promoted innovative business models that go beyond product preservation, along with strategies for multifunctionality [25], or use intensification of products, in order to prevent the unreasonably consumption of new products and consequently to prevent the unnecessarily exploitation of resources and generation of waste. Life Cycle Assessment should be used as a technique for determining the potential environmental aspects associated with products, processes and activities, through production, usage, and disposal, by identifying and quantifying energy and materials used, and wastes released to the environment [1], [26], [27].

Constructions made of earthen materials can be found all over the world, mainly in rural areas, and an ever-increasing turn towards tradition arises from the need of society to have its own identity, and not to lose the origins that define it. In this reason, the use of organic waste in building materials' production takes part directly in the field of sustainable construction. Adobe bricks composition for masonry contains different proportions of clay (as main row material, extracted from natural deposit), sand and various organic matter additive of animal or vegetal provenience, being dispersed reinforced with animal or vegetal fibers.

Using low cost materials and vegetal by-products, which are as well located close to the production centres, along with the possibility of recycling and introducing them again into the manufacturing processes (through the use of waste), could become an opportunity for improvement and sustainable development. The research contributes to the completion of the information reported up to date in literature, and indicates the monitoring possibility of earthen walls dimensions, along with the maintaining of safety operation characteristics, and their thermal efficiency. Integrating ancient construction techniques into contemporary sustainable building practices offers a wealth of opportunities for addressing modern challenges. By embracing the wisdom and expertise of the past, professionals can develop innovative, environmentally friendly, and culturally sensitive solutions that promote a more sustainable future for the construction industry.

References

[1] A.T. Mircea, "Environmental and Economic Benefits from Construction and Demolition Waste", in *From Spatial Structures to Space Structures: Proceedings of the IASS 2012*, Seoul, Korea.

[2] C. Mircea, G. Călătan, A.T. Mircea, "Research on adobe bricks for sustainable/ traditional building", in *Form and Force: Proceedings of the IASS 2019*, Barcelona, Spain.

[3] G. Minke, *Building with earth. Design and technology of a sustainable architecture*, Birkhäuser, Publishers for Architecture Basel Berlin Boston, 2006.

[4] J.A. Lozano-Miralles, M.J. Hermoso-Orzáez, C. Martínez-García, J.I. Rojas-Sola, "Comparative Study on the Environmental Impact of Traditional Clay Bricks Mixed with Organic Waste Using Life Cycle Analysis". *Sustainability* 2018, 10, 2917.

[5] Waitakere City Council, Sustainable home guidelines: Earth building, Oakland, 2008.

[6] Standards New Zeeland, NZS 2497, Engineering Design of Earth Buildings, Wellington, 1996.

[7] Standards New Zeeland, NZS 2498, Materials and Workmanship for Earth Buildings, Wellington, 1996.

[8] A.T. Mircea, "Selecting Environmentally Compatible Materials for Priority Integration into the Design Process", in *SGEM 2017 Conference Proceedings, Vol. 17-62, Section Green Buildings, Technologies and Materials*, Albena, Bulgaria 2017.

[9] D. Sucala, S.A. Ciplea, I.N. Sucala, "Management of historical building rehabilitation", in *Proceedings of the 6th RMEE International Management Conference: Performance management or Management Performance*, Abrudan I. (Ed.), pp. 51-62, Cluj-Napoca, 2018.

[10] F. Pacheo-Torgal, S. Jalili, "Earth construction: Lesson from the past for future eco-efficient construction", *Construction and Building Materials*, 29, 2012, pp. 512-519.

[11] M.R. Parra-Saldivar, W. Betty, "Thermal behaviour of adobe construction", *Building and Environment*, 41, 2006, pp. 1892-1904.

[12] J. Revuelta-Acosta, A. Garcia-Diaz, G.M. Soto-Zarazua, E. Rico-Garcia, "Adobe as a sustainable material: A thermal performance", *Journal of Applied Sciences*, 10 (19), 2010, pp. 2211-2216.

[13] M. Blondet, G.G. Villa, S. Brzev, "Earthqake-resistant construction of adobe buildings: A Tutorial", *EERI/ IAE, World Housing Encyclopedia*, Oakland, California, 2011.

[14] A.S. Elnashai, B. Gencturk, O.S. Kwon, Y. Hashash, et al., "The Maule (Chile) Earthquake of February 27, 2010. Consequence assessments and case studies", *Urbana (IL), Mid-America Earthquake Center*, 2010.

[15] M.L. Germana, "Early modern adobe period in Sicily: Recent finds, Earthen Architecture: Past, Present and Future", Mileto, Vegas, Garcia Soriano & Cristini (Eds), *Taylor & Francis Group London*, 2015, pp. 163-168.

[16] D. Silveira, H. Varum, A. Costa, "Influence of the testing procedures in the mechanical characterization of adobe bricks", *Construction and Building Materials*, 40, 2013, pp. 719-728.

[17] D. Silveira, H. Varum, A. Costa, T. Martins, H. Pereira, J. Almeida, "Mechanical properties of adobe bricks in ancient constructions", *Construction and Building Materials* 28, 2012, pp. 36-44.

[18] G. Călătan, "Contributions on implementation of local and traditional solutions in sustainable housing", PhD Thesis, *Technical University of Cluj-Napoca*, Romania, 2018.

[19] SR EN ISO 14688:1-2018, Geotechnical investigations and tests.

[20] G. Călătan, A. Hegyi, C. Dico, C. Mircea, "Experimental research on the recyclability of the clay material used in the fabrication of adobe bricks type masonry units", *Procedia Technology*, 181, 2017, pp. 363-369.

[21] SR EN 4592 Lime for constructions; Part 2; Testing Methods.

[22] G. Călătan, A. Heghyi, C. Dico, C. Mircea, "Determining the optimum addition of vegetable materials in adobe bricks", *Procedia Technology*, 22, 2016, pp. 259-265.

[23] BS 3921:1985, Specifications for clay bricks, 1998.

[24] ASTM E2392/ E2392 M-10e1, Standard guide for design of earthen wall building system, 2010.

[25] G. Moraga, S. Huysveld, F.M. Gian, A. Blengini, L. Alaerts, K.V. Acker, S. Meester, J. Dewulf, "Circular economy indicators: What do they measure?", *Resources, Conservation and Recycling*, Vol. 146, 2019, pp. 452-461.

[26] A.T. Mircea, S.A. Ciplea, "Identifying opportunities to sustain environmental compatibility for construction projects", in *Proceedings of the 34th IBIMA Conference: Vision 2025: Education excellence and management of innovations through sustainable economic competitive advantage*, Madrid, Spain, 2019.

[27] P. Vegh, "Designing Environmentally Compatible Structures", in *Proceedings of the 11th International Seminar on Environmentally Compatible Structures and Structural Materials 2014*, A.T. Mircea (Ed.), IASS WG 18 on ECS, pp. 13-22, Cluj-Napoca, Romania, 2014.

Proceedings of the IASS Annual Symposium 2023
Integration of Design and Fabrication
10–14 July 2023, Melbourne, Australia
Y.M. Xie, J. Burry, T.U. Lee and J. Ma (eds.)

Reversible timber only connections – an investigation into the potential of threaded dowels and swelling for reconfigurable truss components

Xan BROWNE*, Olga Popovic LARSEN[a]

[a,*] Royal Danish Academy- Architecture, Design, Conservation
Philip de langes alle 10, 1435, Copenhagen, Denmark
xbro@kglakademi.dk

Abstract

Current design for disassembly strategies largely rely on geometry relations between parts, with little thought given to the potential of inherent material properties to foster reversibility. This study investigates low-tech and low-energy methods for the assembly and disassembly of timber only structures, utilising reclaimed timber and wood's swelling and shrinkage to create reversible connections. The paper contributes with experimental data to demonstrate ideal assembly, in-use, and disassembly conditions, with significant changes in joint tightness between conditions. This practical approach is then applied in a truss structure, a component-based typology that is reconfigurable to different spans, geometries and scales. This specific design is evaluated using diagrammatic Statistical Entropy as well as reflections/considerations of the approach's opportunities and challenges. Finally, the paper offers insights into how the project can contribute to a more sustainable building practice, in balance with the resources it depends on.

Keywords: timber only structures, reclaimed wood, timber trusses, design for disassembly , timber connections

1. Introduction

Current pressures on the building sector to reduce its impact have provoked a necessity for materials to last longer than building lifetimes, requiring effective design for disassembly strategies [1]. This is important for materials like wood, that require relatively long regeneration periods compared to faster growing bio-based materials, such as hemp and straw. Therefore, design strategies that work towards material lifetimes in harmony with forest renewal is essential for creating regenerative building practices.

Structural parts of buildings are considered the most culturally and technically long lasting, as highlighted by Stewart Brand's Layers of Change principle [2]. This durability makes structural functions an ideal application for materials such as timber that require long service lives. The demolition and disassembly of long-lasting components invokes the dilemma of predicting future technologies, priorities, and scarcities. Therefore, design strategies that recognise this, and enable the greatest variety of future scenarios through either the direct reuse of entire components, their elemental parts, or through cascading are optimal for enabling extended material lifetimes.

Effective examples of biomass cascading succeed in keeping material in its solid form for as long as possible [3]. The cascading of timber in practice is currently limited, with the associated challenges of fixings, fasteners, adhesives, and contaminants contributing to low material yields in investigations applying salvaged material to structural applications [4] [5]. Furthermore, these aspects have contributed to low motivation from current industry to introduce reclaimed material to their existing timber product production [6].

Copyright © 2023 by Xan BROWNE and Olga Popovic LARSEN. Published in the Proceedings of the IASS Annual Symposium 2023 with permission.

Today's popular environmental impact assessments, such as LCA (Life Cycle Assessment) prioritise material volumes as a metric to evaluate impact, offering little indication of how effectively materials can be reused or repurposed. The types of interfaces and fixings between materials are more important parameters than volumetric quantities when assessing disassembly potential of building parts [7]. An alternative approach, Statistical Entropy, is a method that models how intertwined materials are, and subsequently a quantifiable indication of their separability [8]. The method models how material is distributed within a component or structure, therefore enabling recyclability to be assessed. This promotes mono-material design solutions and mechanical connections as an alternative to the predominant irreversible complications of multi-layered, multi-material, and adhesive oriented construction.

Today, the predominant focus in research into design for disassembly has revolved around geometric relations between parts. This is exemplified in the *design for dissassemly alphabet*, that outlines a series of interfacing strategies for enabling components to be separated from one another [9]. More radical architectural investigations include the complex spatial assemblies of discrete parts by Retsin et, al. and Kunic et, al. [10], [11]. Whilst these offer rich tectonic taxonomies and morphological potentials, they regard components as neutral, neglecting the capacity for materials to morph over time in response to their environment.

The investigative foundation of this study is two-fold. Firstly, to investigate the potential role of timber's inherent properties in design for disassembly strategies. Secondly, to investigate the potential of timber only connections for enabling the reconfigurability and reversibility of components, providing a greater material availability in future scenarios. The study is centred around trusses and multi-shear connections, both existing typologies that already demonstrate potential for utilising reclaimed timber in its solid form [12].

2. Swelling and shrinking in timber design

Swelling and shrinking occurs in timber during changes to relative humidity (RH) due to its hydroscopic properties, finding moisture content (MC) equilibrium with its environment. This phenomenon is well studied from science to craft and is included as a consideration in many applications for wood. In typical buildings, the most significant changes to RH are seasonal, however, there are also daily fluctuations. Wood is well known for its anisotropic structure, significantly impacting its mechanical properties. Anisotropy also causes non-uniform swelling and shrinkage during changes in MC, as a consequence of fluctuating RH. This trait is typically regarded as a deficiency in the design of timber structures and components. The Engineered Wood Product (EWP) Cross Laminated Timber (CLT) is an example where anisotropic movement is mitigated through the perpendicular laminating of lamellae. This works against rather than with a fundamental material characteristic, arguably leading to inefficient allocation of timber in building design.

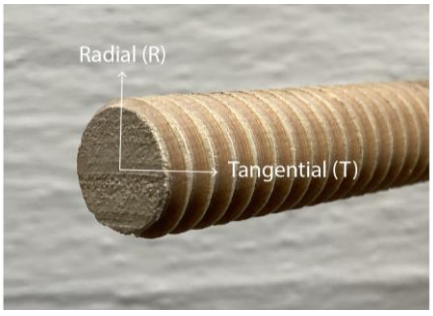


Figure 1. The radial and tangential axes of a threaded wood dowel, each with their own expansion coefficients.

3. Threaded timber dowel connections

Threaded timber dowels are less commonplace in building design than regular timber dowels and threaded steel dowels. They have however been applied to many technologies, such as early forms of fruit press, and remain in some examples of adjustable height timber stools today. In buildings, the *Nur Holz* product is an example of a deck type EWP utilising threaded dowels as an alternative to adhesives [13]. Whilst this succeeds in delivering a single material component, it is unclear as to whether this system is designed to be reversible, enabling dowels and boards of two different wood species to return to their component parts.

Steel bolts are well established as an optimal solution for reversible connections, as well as offering high strength to weight ratio and ductile structural behaviour. However, design contexts featuring large quantities of connections are disadvantaged by steel's high environmental impact.

This study aims to combine the reversibility made possible by threads with the renewability and low embodied energy of wood. Today, threaded timber dowels are available commercially, often intended for machines where metals must be avoided. Alternatively, they can be produced using simple, inexpensive tap and die hand tools in a variety of diameters (Figure 2). Earlier explorations have demonstrated the variety of possible threaded dowels, as well as their application in connecting irregular timber feedstock [12].



Figure 2. The tap and die set for wood used in this study.

4. Design Context

This study investigates the potential of threaded timber dowels for connections in structural members from reclaimed timber. Multi-shear truss connections are the specific focus, motivated by a need to develop alternatives to the adhesive dependent EWPs common today, and the steel connections typical in traditional trusses. Furthermore, the paper expands on the potential of reversible threaded dowel connections in full scale component design. This demonstrates how reclaimed timber can be efficiently allocated to timber trusses, and later reconfigured for second and third building applications.

Previous studies investigating the potential of reclaimed timber for structural applications have demonstrated the potential of threaded dowels to connect elements with irregular surface geometries. Many of today's EWPs are dependent on reliable material feedstock, toxic adhesives, and centralised fabrication; each of which have an impact on environmental performance. The proposed multi-shear truss layup (Figure 3) aims to challenge these three aspects by featuring irregular timber feedstock, mechanical timber fastenings, and low-tech fabrication techniques.

Geometric irregularities, physical contaminants, and short lengths often determine timber's rejection from EWP production, leading to significant quantities meeting premature energy recovery. Strategies for utilising this material for EWPs with minimum processing have shown potential at a prototype level [12]. This demonstrates that the accurate interfaces required for adhesive connections can be alternatively achieved with threaded dowel fastenings, that lock elements along the fastener, as well as in shear. A system can be designed to work with a domain of element cross section dimensions. This domain can be calibrated with a constrained stock, especially as reclaimed material typically falls into dimension categories informed by sawing standards, as opposed to being completely randomised [14].

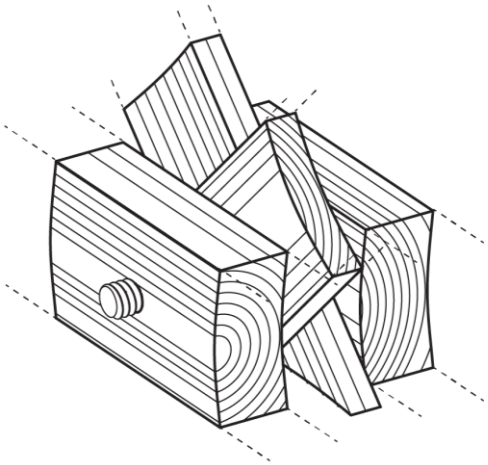


Figure 3: Truss elements with irregular timber stock featuring *cupping*, preventing proper interfacing.

At the component scale, maintaining the inherited properties and qualities of salvaged timber has two aims. Firstly, processing of imperfect geometry is minimised, meaning the volume of material yielded from the waste stream is as high as possible. This provides optimum carbon storage, reduced energy usage, minimal processing infrastructure, as well as maximising the volume of material available for future uses. Secondly, the spectrum of tones and textures inherent to timber and developed over time is retained. This presents the opportunity for components to express the diversity of material origins, offering a visual representation of salvaged timber's provenance- a notion that contrasts to the relative aesthetic homogeneity of single specie EWPs.

Furthermore, short lengths are a common attribute of undervalued reclaimed timber, aligning well with truss typologies. This further enables salvaged timber to be utilised in its inherited from, without the need for processing and finger jointing to elongate elements.

Despite the general functioning of threaded dowels in previous studies, inserting dowels demanded inconsistent torque and in some cases resulted in spiral fractures of dowels, causing them to be immobile and presenting a production problem for the remainder of the component. These challenges, and unpredictable behaviours motivate a need to develop a more calculated production approach to utilising threaded dowels, with calibrated relations between the parts and the varying stages of a components' lifetime: assembly, in-use, and disassembly.

Lastly, the development of structural components that are optimised based on a constrained stock is gaining momentum. Bruttning et, al have developed numerous studies on structurally optimal morphologies from a constrained stock of steel elements [15], [16].

5. Materials and testing method

A method was devised to measure the torque of threaded dowels in multi-shear connections after exposure to contrasting environmental conditions. Through testing, the study intends to determine ideal conditions for the assembly, in-use, and disassembly of connections. With the in-use condition resembling the domain of typical indoor RH, where tight connections are considered optimal.

Capitalising on the dimensional change occurring when exposed to varying RH and temperature environments, threaded dowels can be assembled with a designed level of torque. To reduce variables in the study, virgin single species timber for the truss elements combined with single species and dimension dowels was selected.

Grade C14 spruce samples and 19mm birch dowels were conditioned at (20 ± 2) °C and (65 ± 5) % relative humidity until they reached constant mass. This conditioning space is hereafter referred to as *ambient* for the duration of the study. The spruce was planed and cut into pieces to resemble single multi-shear connections (Figure 4), followed by a 16mm hole drilled into the centre. The birch dowels settled at an average of 12.3% MC during conditioning. These dowels were cut into 200mm lengths, before having threads cut with the die. The die is adjustable and was calibrated after initial assembly tests. It is important to note the limited accuracy of the tool's adjustability, making precise thread sizes challenging to define. Lastly, threads were cut into the spruce connection samples with two passes of a tap.

Torque was measured using a customised attachment between the birch dowels and a torque wrench with a measurement range of 1.6-14 newton meters (Nm). Ca. 2Nm is considered hand tight, and therefore an optimal target for assembly and disassembly readings. During assembly, an oven at 60c was used to induce shrinkage. This temperature reduced RH to ca. 10%, and ensured dowels were cool enough to handle. Measurements were taken every 15 minutes, recording maximum torque and distance from complete assembly if torque exceeded 6Nm prior to full assembly. This maximum is introduced due to drier, more brittle dowels splitting under torque higher than 6Nm during pre-experiments.

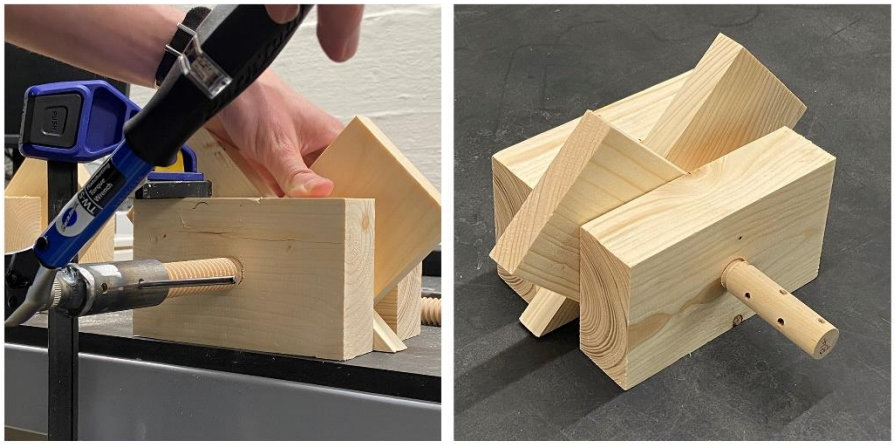


Figure 4. Torque measuring setup (left) and assembled sample (right).

During in-use, the assembled samples are returned to ambient condition. Timing is less critical in this stage, as the conditions are less extreme, and a production scenario needn't require an instantaneous tight joint during equilibrating with ambient conditions.

For disassembly, the oven's temperature was reduced to 45c, as the dowels are insulated by the spruce and are expected to require a more extended and slower drying period prior to dowel removal.

6. Results

6.1 Initial experiments (Figure 5)

After determining the average MC of a batch of uniform dimension birch dowels, an assessment was made of how quickly the MC would decrease. Initial tests, recording moisture content changes, by weighing samples at 15-minute intervals when exposed to 60c, demonstrated that significant moisture losses occur in the first 30-45 minutes. It is also shown that this is where the most significant dimensional change takes place, although reductions in the transverse direction are minimal, and undetectable in the radial direction.

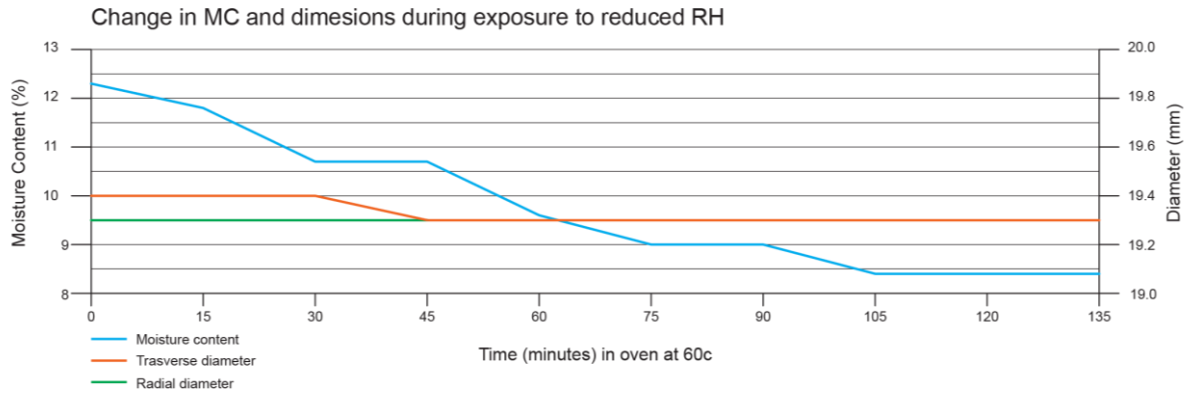


Figure 5: Change in MC and dowel diameter dimensions during exposure to reduced RH.

6.2 Assembly results (Figure 6)

The 5 sets of spruce samples with corresponding dowels each show the same trend despite noticeable torque variation between sets. Some samples required longer drying times to reach the target torque of 2Nm, such as B2. Earlier tests demonstrated slowed reduction in MC after 90 minutes, this corresponds with the torque reduction shown in the assembly tests, exemplified by B2 and B4.

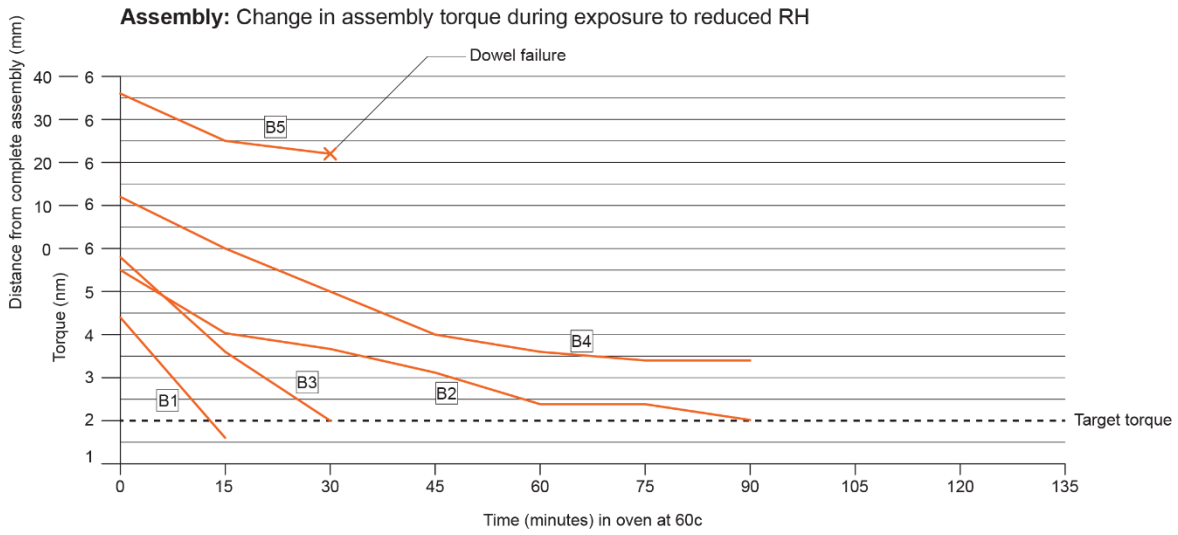


Figure 6. Change in dowel assembly torque during shrinkage due to exposure to reduced RH. Dowel B5 failed in torsion at the third measurement. The y axis shows two scales as some samples could not be fully assembled with 6Nm of torque.

6.3 In-use results (Figure 7)

Upon returning the samples to the ambient environment previously used for conditioning, the threaded dowels swelled, returning the torque readings to a similar value shown in beginning of assembly. A single dowel sample that had followed the environments of B1-B4 returned to its original MC after 1 day. The four assembled samples follow a similar trend, though the highest recorded torque is inconsistent, and almost all samples showed a reduction in tightness towards the end of the measurement period.

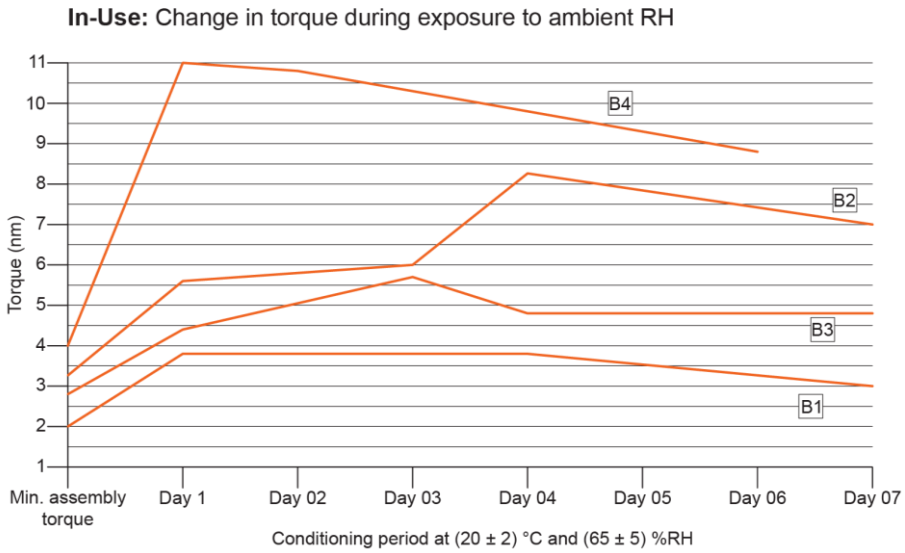


Figure 7. Change in dowel torque during swelling due to ambient exposure to RH. The first values correspond to the last values in figure 6.

6.4 Disassembly results (Figure 8)

The disassembly results show that all samples reached the target torque of less than 2Nm after 3 days.

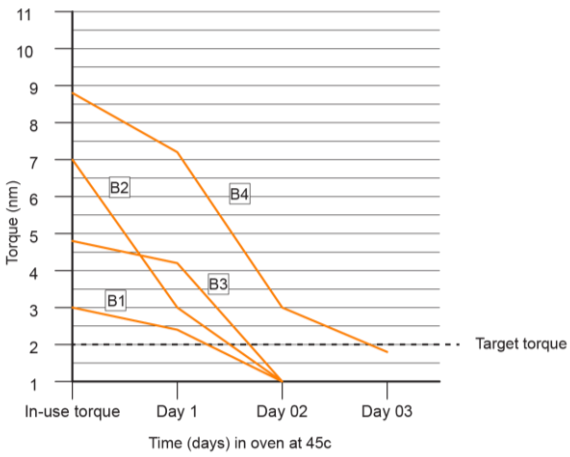


Figure 8. Change in dowel torque during shrinking in oven at 45c. The first values correspond to the last values in figure 7.

7. Applying the connection to a component

The reversible connection is contextualised in multi-layer truss type structures, Figure 9 shows a truss concept that applies the multi-shear threaded dowel connection. Truss component typologies can be applied to a spectrum of scales and building types, subsequently making them appropriate for applying a variety of reclaimed wood dimensions.



Figure 9. Truss concept with threaded dowel connections, featuring a variety of timber tones and geometries, assimilated into a rectilinear component. - Rendered elevation

MC is a crucial parameter to the success of the approach and can be challenging to accurately record and monitor in an industrial context as devices depending on probes and surface readings are not always reliable.

To overcome this, a *tracer* element with a known weight and MC can be continuously weighed to monitor fluctuations in MC of the dowels, providing that the tracer is always exposed to the same conditions as the dowel group. This would enable fabrication staff to know when MC is optimum for cutting dowel threads, and for how long they should be dried prior to assembly. The reliability of this approach would require a further study, as well as an investigation of its suitability in production environments.

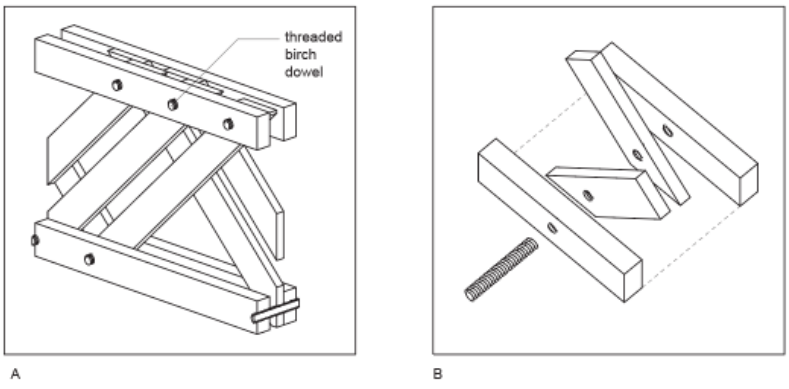


Figure 10. A: Multi-layered truss – isometric. B: Truss connection, using threaded wood dowels – exploded isometric.

The truss concept utilises semi-standard web elements, each of which are cut to the same length with 45° end angles. This intends to negotiate a balance between the irregular characteristics of timber waste streams and the standardisation preference of current production practices. Furthermore, as the assembly system is forgiving of variability, it can be applied to a variety of production methods, from low-tech crafting to full automation. This responds to the introductory problematic of predicting the future

technologies, priorities, and scarcities that ultimately determine how components are assembled, used, and disassembled.

7.1 Evaluating reversibility- Statistical entropy

A study by Roithner et, al., presents methods for making a recyclability assessment of two case study buildings [8]. This introduces methods for quantifying how materials are spatially distributed, how they are connected, and ultimately how easily they can be recovered for future applications. They apply Statistical Entropy (SE) as a means to measure how *mixed* materials are, and therefore their recoverability potential. A lower SE corresponds to fewer parts or materials, and a higher SE the opposite, the former being considered more ideal for recyclability.

SE is applied in this study in diagrammatic form (Figure 11) to make a comparison between the truss concept and a conventional glulam element from three perspectives: Complexity, Disassembly, and Material Concentration. From a complexity perspective, the truss is shown to have higher SE, due to its larger number of parts. From a disassembly perspective, glulam is shown to have higher SE due to the parts being inseparable. Finally, from the perspective of material concentration, the glulam is shown to have higher SE due to the two different materials, wood and glue, being intertwined, whereas the truss is a mono-material component. These three perspectives provide an alternative method to conventional LCA for approaching the reversibility of building elements, as well as what might be prioritised. For example, the truss's complexity may require significant steps to take a part, but it is made possible due to the type of fastening.

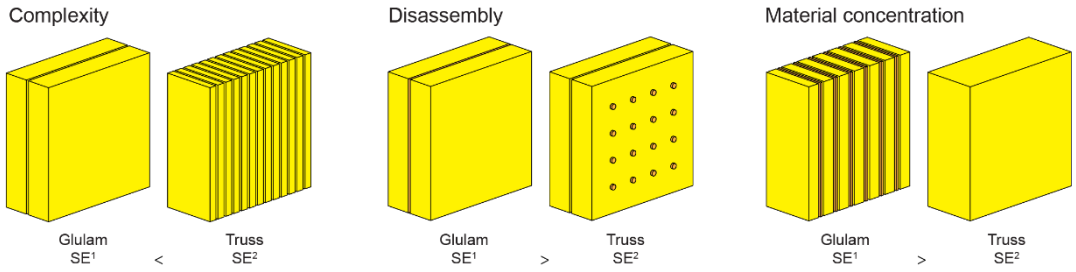


Figure 11. Statistical entropy diagrams of the truss concept compared to a glulam, from the perspective of Complexity, Disassembly, and Material Concentration.

8. Reconfigurability in context

To further the contextualisation of the reversible joints, the study continues to demonstrate how reconfigured elements might work in practice. The same stock of component parts can be applied to a range of structural requirements, with each truss retaining the same exterior component geometry. This contrasts to conventional glulam practises, that although graded, generally require geometric changes to match design loads. Here, web elements can be allocated to create distributions of material and quality to meet specific functional demands. This approach can be applied to a series of components, each with the same geometry, that have varying load cases within a single building. Alternatively, as a series of load cases across a series of buildings over time.

Reconfigurability can take place during changing requirements to a building's programme, or after disassembly, to reallocate material for a future structural function. This approach enables the same

material to cater to multiple building applications over time, each with their own specific performance demands, and with little or no loss of material between applications. Below, two examples are given showing the same component type with unique load cases. These load cases define how a varied stock of material is allocated, and due to the flexibility of the truss concept, each web member can be of a different dimension. The two examples could represent individual components within the same building, or two components produced from the same elements, a building lifetime apart.

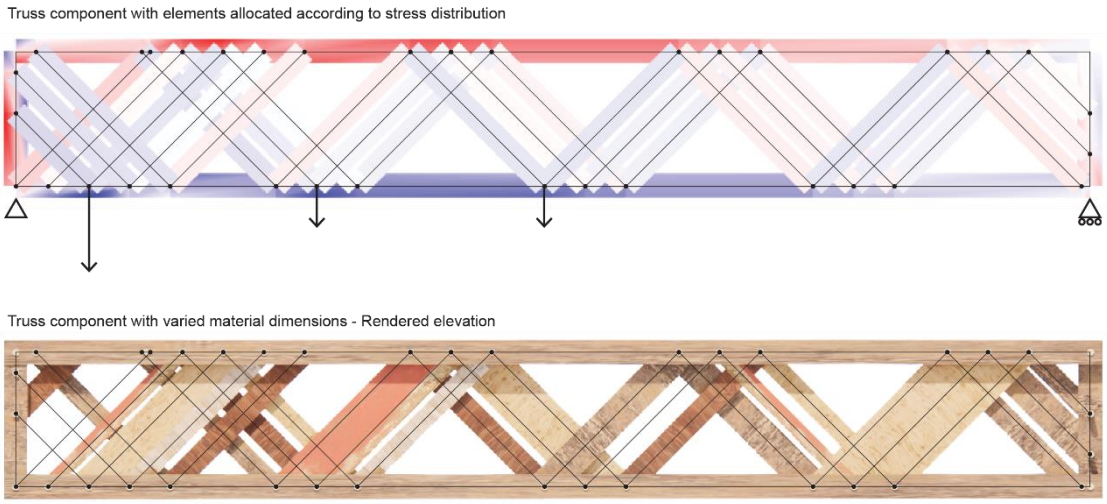


Figure 12. Building application 01- optimum material distribution for a specific load case

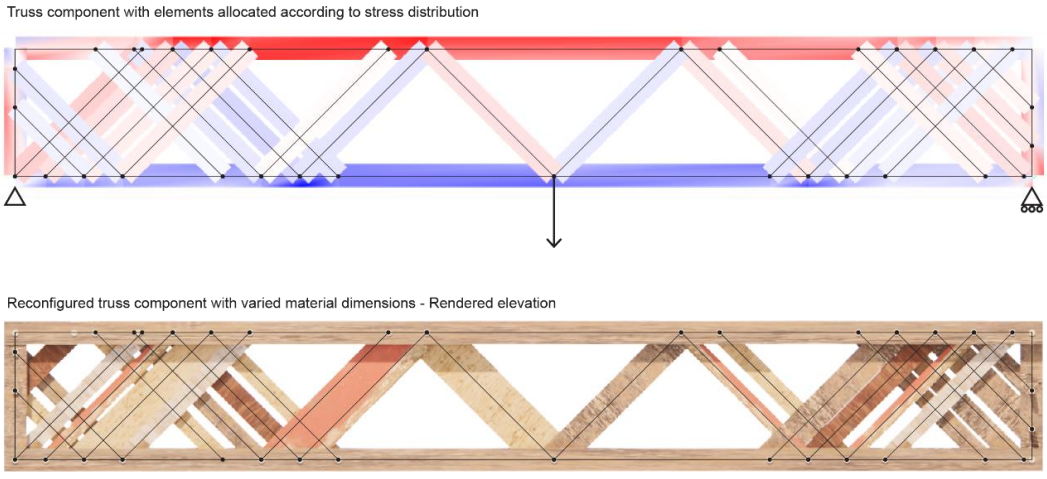


Figure 13. Building application 02- optimum material distribution for a second specific load case

9. Discussion

The study offers an initial investigation into a method for applying reclaimed timber to structural applications. This combines the opportunities of integrating timber's movement in joints with a reconfigurable component design. Together, these intend to enable components to meet the specificity of their function, in close dialogue with the inherited forms of secondary materials.

Within the presented project, the principle aim of harnessing timber's geometry fluctuations to create reversible connections has been demonstrated. The investigation achieved an increased understanding of optimum drying times, swelling 'tightness', and the reversibility of threaded dowel joints. It is important to state that the time periods required to create effective geometry changes are within practical domains. For example, a drying period of less than 2 hours is required prior to assembly, and joints become tight after only one day. Furthermore, disassembly is achievable within a short period, increasing the feasibility of such an approach to be adopted at a larger scale.

Working with fundamental material properties, that have been known and utilised for centuries, leads to the conclusion that the relevant knowledge to reverse these connections will be available in the future. This challenges design for disassembly solutions that require new technologies or highly specific knowledge, often becoming obsolete after a time period relatively short compared to a potential building's lifetime.

Further work would benefit the reliability of the approach, that showed surprising variability considering the consistency of materials and method. This may include other impacting parameters not found or considered in this investigation. Reliability is likely to be more challenging when applying the approach to reclaimed material, where material heterogeneity is more acute. The range of properties occurring in waste materials is likely to present varying performances. A future study with increased scope would benefit from longer term monitoring of dowel joints, with comparisons between controlled conditioning environments and the real-life RH fluctuations of a building's interior- ideally tested over the course of 1 year, to include the full spectrum of RH conditions.

This investigation proposes an alternative to the recent traditional paradigms of efficiency, that tend to prioritise a reduction of material volumes, an increase in material strength, and focus on a single application. In contrast, the approach investigated and presented in this paper demonstrates a strategy to effectively apply materials for current and future applications by considering the required material footprint, how they are combined (SE), and how they can be adapted for future uses. Whilst this may lead to components that are over dimensioned, it intends to offer effective utilisation of available reclaimed material, as well as maximise the material availability for future scenarios.

Furthermore, aspects other than structural performance are important considerations for material allocation in structures. Aesthetics, partitioning, light, acoustics, servicing, and fire are equally involved parameters in the design of components and their arrangement in buildings. Future investigations of the approach would benefit from diversifying optimisation parameters to include aspects other than structural performance and material utilisation, leading to more holistically considered applications for waste timber materials.

10. Conclusion

This research demonstrates that rethinking the scope of design for disassembly, structural components from reclaimed timber can be designed with timber only reversible joints. This enables discarded material to be utilised in high value building parts, with a situated relationship between discarded materials and a building's needs.

The results show that the principle of defining assembly, in-use, and disassembly conditions for timber only joints is practical and feasible. This integration of principles from wood science can be further enhanced to achieve more reliable production. For the purpose of this study, these joints have been applied to a hypothetical building application in the form of a truss, a component-based structural system.

Lastly, the study contributes with a general approach to sustainability, where undervalued materials are utilised, allocated as they are needed, and designed to achieve service lives that extend beyond the regeneration periods of the ecosystems they depend upon.

References

[1] A. Beim, 'Tectonic thinking in contemporary industrialized architecture', *Journal of Facade Design and Engineering*, vol. 1, no. 1–2, pp. 85–95, 2013, doi: 10.3233/fde-130003.

[2] S. Brand, *How buildings learn: what happens after they're built*. New York, NY: Viking, 1994.

[3] M. Hughes, Y. Niu, K. Rasi, M. Hughes, M. Halme, and G. Fink, 'Prolonging life cycles of construction materials and combating climate change by cascading : The case of reusing timber in Finland Resources , Conservation & Recycling Prolonging life cycles of construction materials and combating climate change by cascad', no. July, 2021, doi: 10.1016/j.resconrec.2021.105555.

[4] M. Risse, G. Weber-Blaschke, and K. Richter, 'Eco-efficiency analysis of recycling recovered solid wood from construction into laminated timber products', *Science of the Total Environment*, vol. 661, pp. 107–119, 2019, doi: 10.1016/j.scitotenv.2019.01.117.

[5] C. M. Rose, D. Bergsagel, T. Dufresne, E. Unubreme, and T. Lyu, 'Cross-Laminated Secondary Timber : Experimental Testing and Modelling the Effect of Defects and Reduced Feedstock Properties sustainability Cross-Laminated Secondary Timber : Experimental Testing and Modelling the Effect of Defects and Reduced Feedstock P', no. November, 2018, doi: 10.3390/su10114118.

[6] R. Husgafvel, L. Linkosalmi, M. Hughes, J. Kanerva, and O. Dahl, 'Forest sector circular economy development in Finland: A regional study on sustainability driven competitive advantage and an assessment of the potential for cascading recovered solid wood', *Journal of Cleaner Production*, vol. 181, pp. 483–497, 2018, doi: 10.1016/j.jclepro.2017.12.176.

[7] A. M. Manelius, S. Nielsen, and J. Schipull Kauschen, 'Rebeauty - Artistic Strategies for Repurposing Material Components', *IOP Conference Series: Earth and Environmental Science*, vol. 225, no. 1, 2019, doi: 10.1088/1755-1315/225/1/012023.

[8] C. Roithner, O. Cencic, M. Honic, and H. Rechberger, 'Recyclability assessment at the building design stage based on statistical entropy: A case study on timber and concrete building', *Resources, Conservation and Recycling*, vol. 184, p. 106407, Sep. 2022, doi: 10.1016/j.resconrec.2022.106407.

[9] Pelle Munch Pederson, 'Circular Facade Design - THE TECTONICS OF CIRCULAR ECONOMY', 2020.

[10] G. Retsin, M. Jimenez, M. Claypool, and V. Soler, *Robotic Building: Architecture in the Age of Automation*. Detail, 2019.

[11] A. Kunic, R. Naboni, A. Kramberger, and C. Schlette, 'Design and assembly automation of the Robotic Reversible Timber Beam', *Automation in Construction*, vol. 123, no. April 2020, p. 103531, 2021, doi: 10.1016/j.autcon.2020.103531.

[12] X. Browne, O. P. Larsen, N. C. Friis, and M. S. Kühn, 'Material Value(s): Motivating the architectural application of waste wood', *Archit. Struct. Constr.*, vol. 2, no. 4, pp. 575–584, Dec. 2022, doi: 10.1007/s44150-022-00065-6.

[13] M. Wójcik and J. Strumiłło, 'Behaviour-based Wood Connection as a Base for New Tectonics Behaviour-based Wood Connection as a Base for New Tectonics BEHAVIOUR-BASED WOOD CONNECTION AS A BASE FOR NEW TECTONICS'.

[14] G. Ruan, 'An integrated architectural and structural design concept by using local , salvaged timber An integrated architectural and structural design concept by using local , salvaged timber', no. October, 2021.

[15] J. Brütting, G. Senatore, and C. Fivet, 'Form Follows Availability – Designing Structures Through Reuse', *Journal of the International Association for Shell and Spatial Structures*, vol. 60, no. 4, pp. 257–265, Dec. 2019, doi: 10.20898/j.iass.2019.202.033.

[16] W. Nadir, I. Y. Kim, D. Hauser, and O. de Weck, 'Multidisciplinary Structural Truss Topology Optimization for Reconfigurability', in *10th AIAA/ISSMO Multidisciplinary Analysis and Optimization Conference*, Albany, New York: American Institute of Aeronautics and Astronautics, Aug. 2004. doi: 10.2514/6.2004-4337.

Proceedings of the IASS Annual Symposium 2023
Integration of Design and Fabrication
10–14 July 2023, Melbourne, Australia
Y.M. Xie, J. Burry, T.U. Lee and J. Ma (eds.)

Structural design of Mukogawa women's university canoe club house

Naoyuki TAKAYAMA*

* Takenaka Corporation, 4-1-13, Honmachi, Chuo-ku, Osaka-Shi, Osaka 541-0053, Japan
takayama.naoyuki@takenaka.co.jp

Abstract

Normally, timber is used for compression or bending members, where the allowable stress can be evaluated to be high. However, for a structural frame in which the axial forces are dominant, this material can also be fully utilized as tensile members because the entire sections of the members can be effectively used. This paper presents the structural design of a club house with a catenary-shaped wooden roof. Use of a catenary shape for the roof has created a column-free space for the training room by making use of the small section of wood and ensuring that the main stresses in the members are axial forces. The author has determined the roof shape by considering the creep deformation properties of wood, and parametrically verifying the shape with a computer, to meet various constraints such as the required roof drainage slope and smoke exhaust area, building height restrictions, and effective ceiling height requirements. Furthermore, the application of a system that combines tensile bolts and timber to the member joints that tend to be complicated minimizes the partial losses of the member areas at the joints to improve the architectural design, productivity, and structural performance of the building.

Keywords: catenary-shaped wooden roof, triangular grid, computational design, geometric nonlinear analysis, computer numerical control (CNC) machining

1. Introduction

In this project, we relocated the boathouse of the Mukogawa Women's University's canoe club known for its strong canoe racing team and built a new building ("Building"). The project site is located in the residential area where the canoe club has been active for years, and very close to the old boathouse used by the club. The Building was required not only to provide an easy-to-use club room and boathouse, but also to create a memorable space that brings the club members back the memories of their club activities. To meet the requirements, we took a structural approach using generally available lumber.



Figure 1. Bird's-eye view of Building



Figure 2. Building's interior view (2nd-floor training room)

Copyright © 2023 by Naoyuki TAKAYAMA. Published in the Proceedings of the IASS Annual Symposium 2023 with permission.

2. Building overview and structural planning

2.1. Architectural planning and design

The Building is two-storied with a plane shape of 17.34 meters by 13.65 meters. It has a boathouse at the first-floor level and a training room at the second-floor level. The Building can accommodate up to 20 club members for training and store up to 77 canoes (2.95 to 11 meters long each).

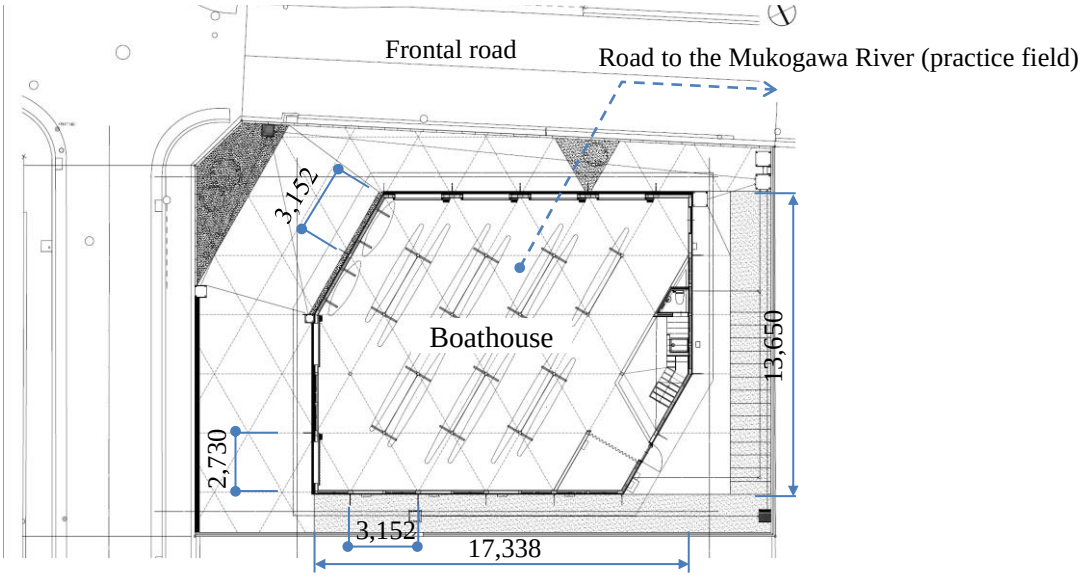


Figure 3. Site plan / first floor plan

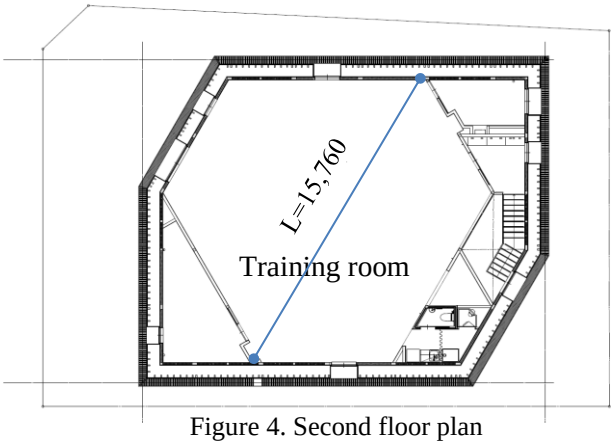


Figure 4. Second floor plan



Figure 5. Exterior view of Building (north side)

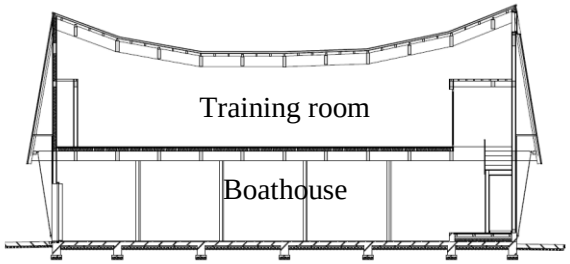


Figure 6. Section

2.2. Structural planning

In planning the Building, we used three distinctive planning elements: "timber," "triangular grid," and "catenary-shaped roof" to solve the issues faced in the planning. The details of the elements are as follows.

2.2.1. Timber

In recent years, the promotion of using timber has attracted attention because it requires less energy for processing than other materials and is an environmentally friendly material. There was another reason for choosing timber. The club house is not only a place for training but also a place for the girls to relax after practicing on the river. Therefore, we designed a wooden structure with small section members as used in ordinary houses so as to make them feel at home on a human scale, aiming to create a space with a friendly ambience rather than a place for strict training.

2.2.2. Triangular grid

The first-floor boathouse was required to be easy to maintain because canoes are frequently taken out of and into it. Therefore, we adopted a triangular grid (Figure 7), instead of the conventional orthogonal grid, in consideration of the narrow road in front of the boathouse. The triangular grid, inclined at 30 degrees to the frontal road, has made it possible to move them from the boatyard to the Mukogawa River, then to the canoe maintenance area, and back to the boatyard in a single uninterrupted movement. The triangular grid also enhances the rigidity of the wooden floor.

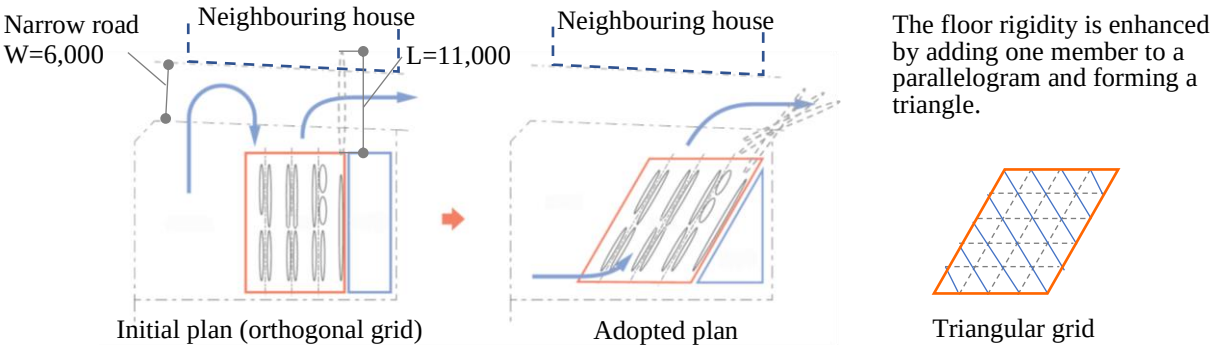


Figure 7. Planning of grid

2.2.3. Catenary-shaped roof

The training room required a large column-free, partition-free space to accommodate various types of training activities. It was also necessary to minimize the pocket created by the structural framework in order to secure the required training room space while meeting the building height limitations in the residential area although truss beams and string beams are often used when planning a long-span wooden structure. Accordingly, we considered the use of a wooden catenary structure to meet the required spatial shape while reducing the member heights as much as possible to meet the building height limitations.



Figure 8. Selection of roof structure type

Thus, we planned to place a wooden catenary structure, derived from the "timber," "triangular grid," and "catenary-shaped roof," over a structure with wooden seismic walls all around the building. Figure 9 shows a diagram of the structural frame.

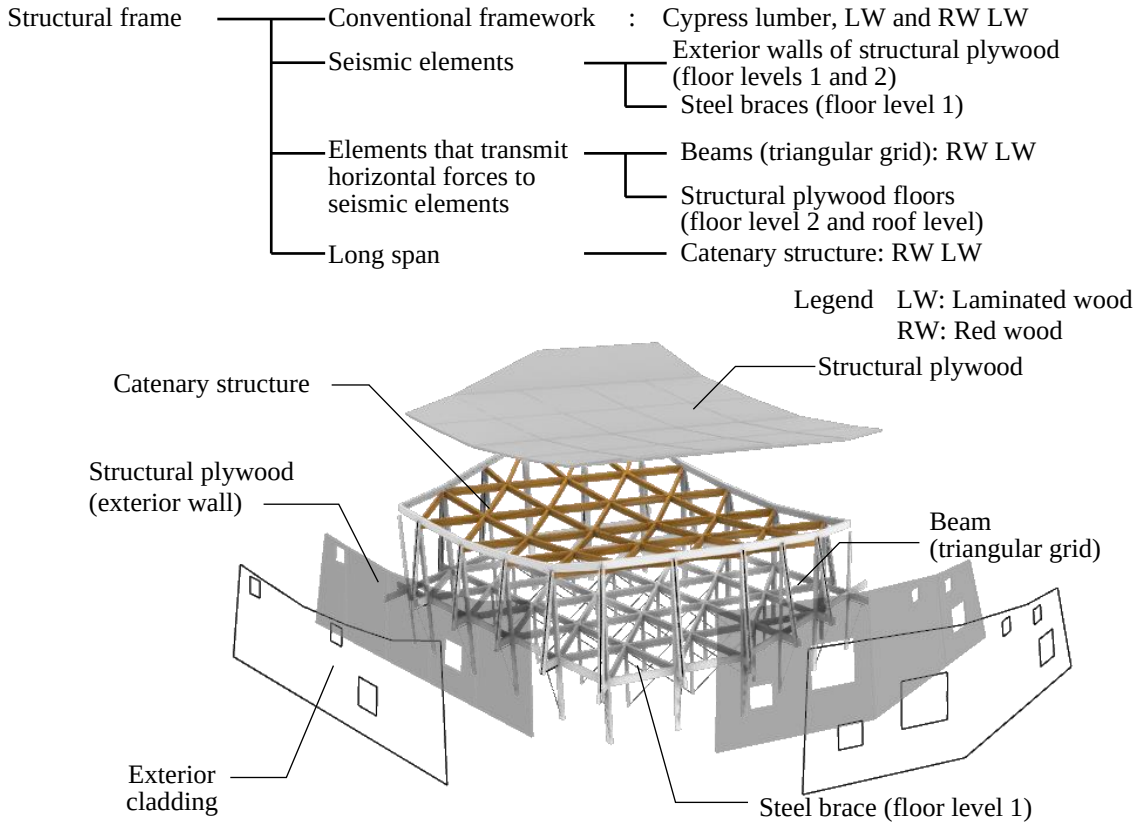


Figure 9. Diagram of structural frame

3. Catenary-shaped wooden roof

3.1. Determination of roof shape by simulation

A catenary-shaped wooden roof needed to be established under the constraints including the building height restrictions on the site, required ceiling height for the training room, opening dimensions and location required for smoke extraction, and required roof drainage slope. The computational design method using "grasshopper" was helpful in the situation where many conditions had to be validated concurrently. We used the following structural validation flow to determine the roof shape.

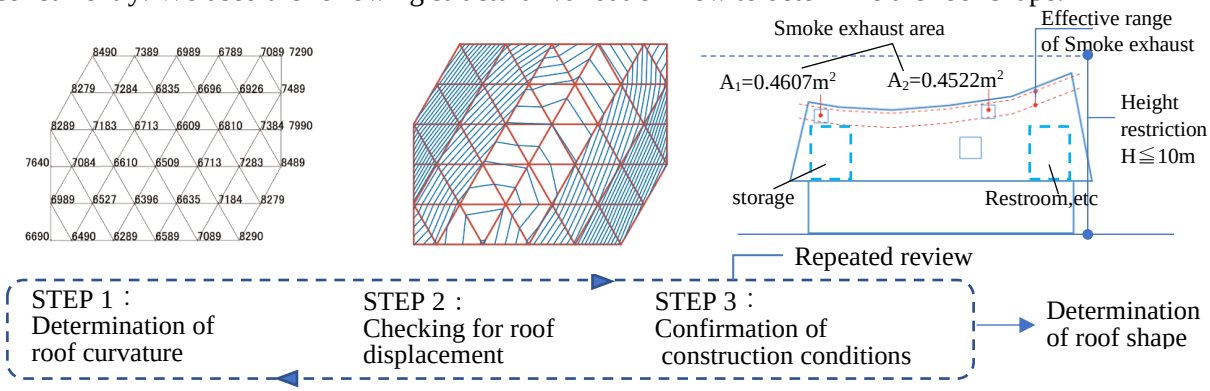


Figure 10. Structural validation flow

3.2. Study on application of wooden catenary beam structure consisting of wooden members and tensile bolts

The sizes of locally sourceable lumber ranged from [120 mm by 120 mm] to [120 mm by 390 mm]. In the architectural planning, the roof span was as long as 15.7 meters when the beams were planned in a grid pattern. Therefore, there was an issue that if the beams were planned in a usual way, the roof beams would have been large to the extent that the beam height would be about 140 cm.

First, we explored possibilities of using a suspended wooden roof with small timber beams for the Building.

Then we considered the use of a catenary-shaped wooden frame with a combination of tensile bolts and a wooden member for each grid of no more than 4,000 mm in order to use local timber with a maximum length of 4,000 mm.

3.3. Invention and design of wooden catenary beam structure consisting of wooden members and tensile bolts

Normally, the allowable stress of wood is lower in the tensile direction than in the bending direction. Therefore, it is generally considered inefficient to apply members against tensile forces. In this project, however, the stresses of the roof structure are designed to be axial, which makes it possible to use the entire sections of the members, bringing a larger effect. Moreover, the pin-joined structure using tensile bolts at the joints between wooden members has created a wooden frame conforming to the roof curvature, suspended from the two ends of the roof like a string of beads.

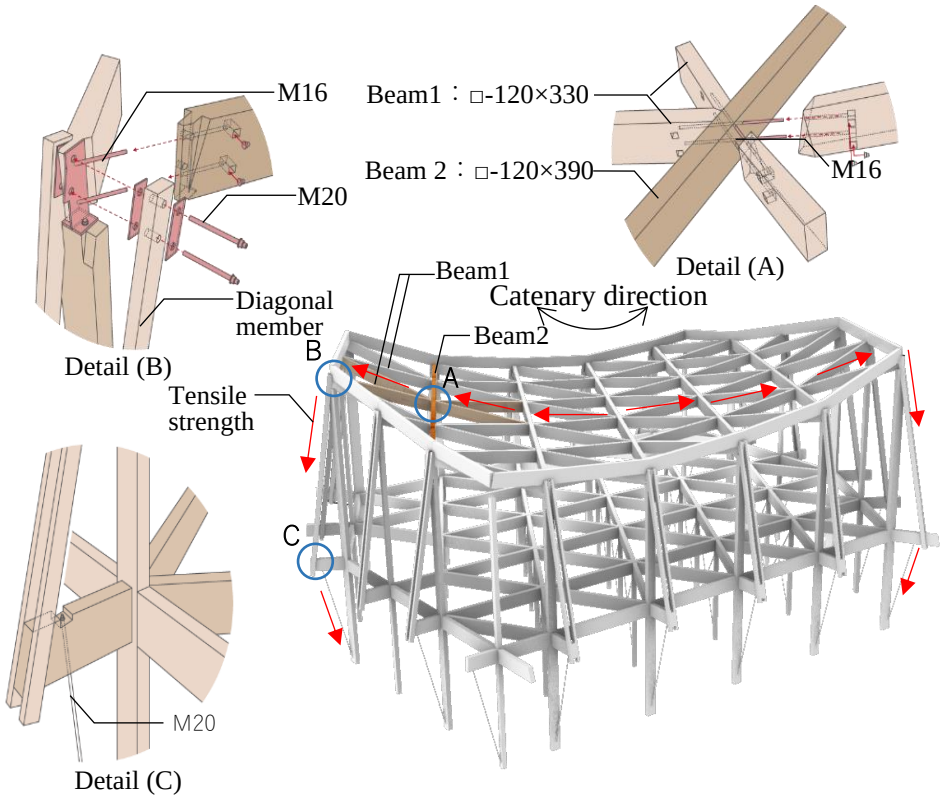


Figure 11. Structural frame

3.4. Analytical results of catenary-shaped wood frame

The author performed a static geometric nonlinear incremental analysis of the catenary-shaped wood frame and obtained the data concerning the deformation and stresses of the members, considering the geometric nonlinearity caused by the roof deformation. The results of the analysis have revealed that approximately 70% of the loads were transferred by axial forces in a suspended roof structure (Beam 1 in Figure 11), and the remaining loads were transferred in an orthogonal beam framing structure (Beam 2 in Figure 11).

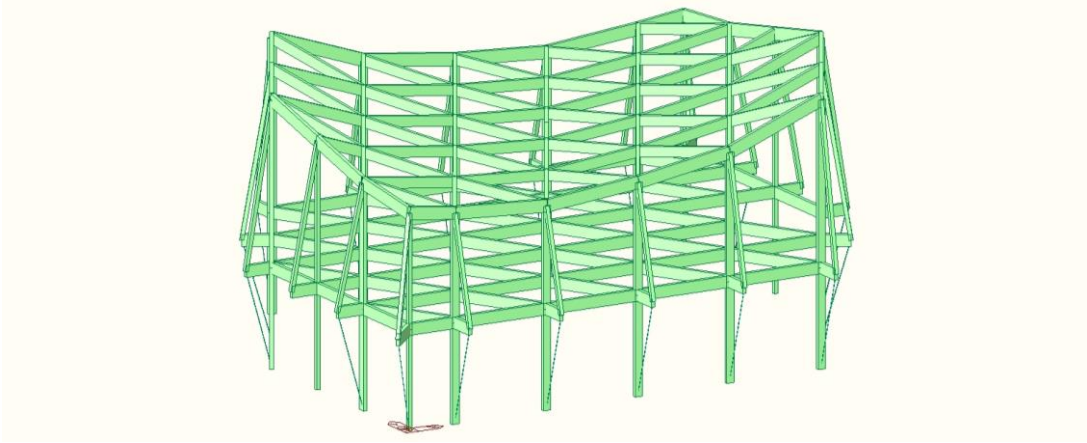


Figure 12. Analysis model

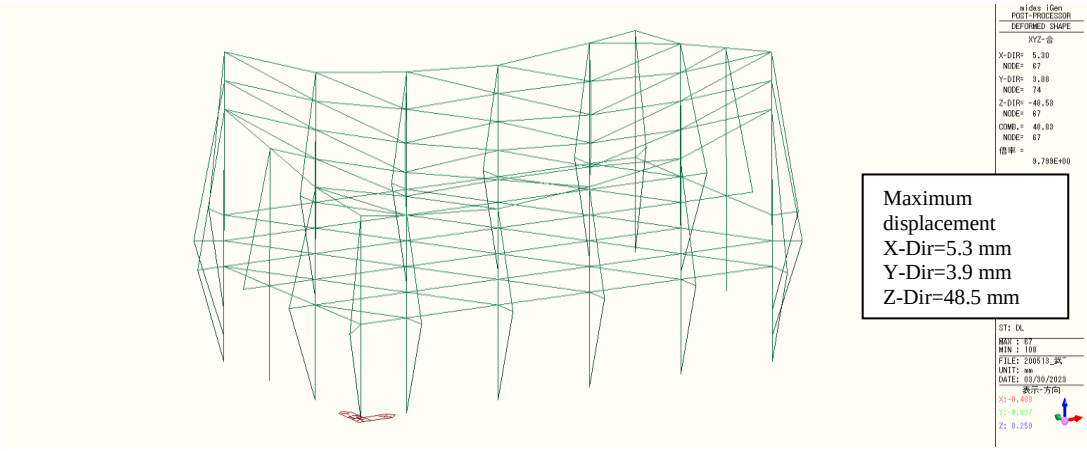


Figure 13. Deformations under dead load

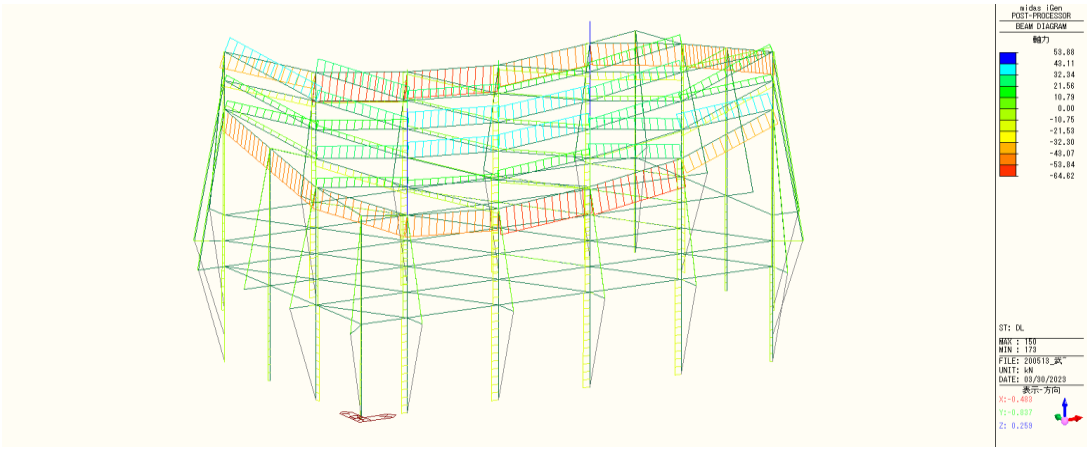


Figure 14. Axial forces under dead load

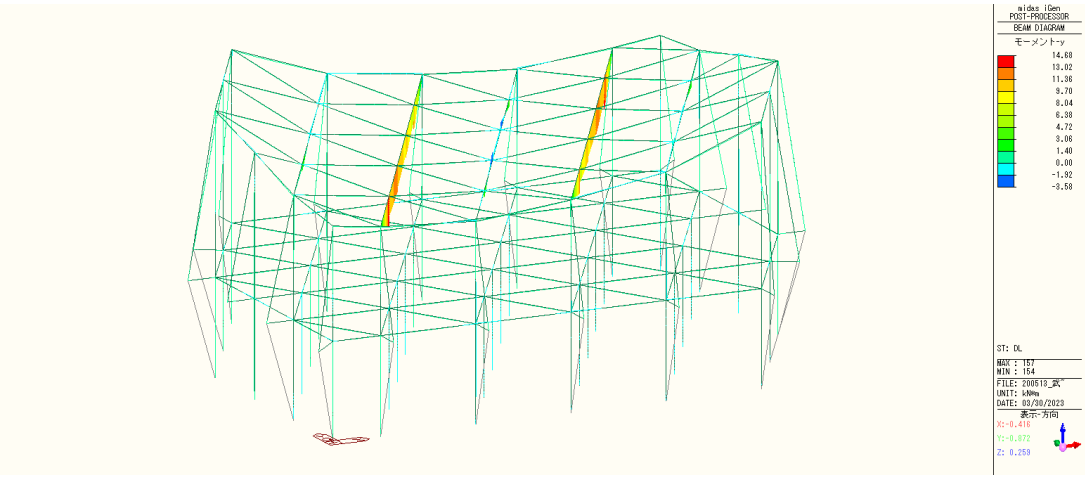


Figure 15. Bending moments (My) under dead load

4. Computational design and handwork

4.1. Digital fabrication and handwork

In the catenary structure used in this project, the shapes of intersecting members vary from joint to joint. Since the main force to be transmitted is a tensile force in this structure, the author has invented a simple rule for the joints that the sectional area of a member should be secured up to a position of 190 mm from a tensile bolt fixing point. The parts exceeding 190 mm are treated as a finishing material. We have developed an interior elevation of every member joint as shown in Figure 17. Although CNC machines were used for processing the members as much as possible, the parts that could not be shaped by machining were processed by hand.

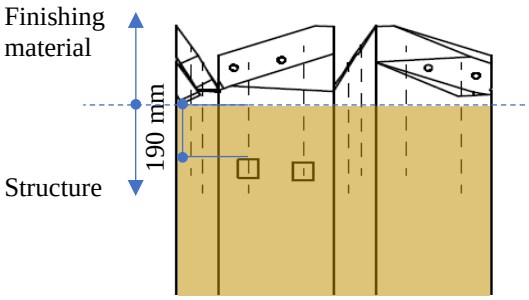


Figure 16. Joint rule

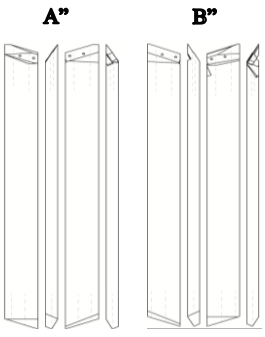


Figure 17. Interior elevation of processed shapes

Since the continuous beam (Beam 2 in Figure 11) material passing through joints was as long as 15.7 meters, it was necessary to join two timbers after transportation. The Japanese traditional joint system called *Okkake Daisen* (Figure 17), which can transmit bending stress, was used for the joints. We upgraded the traditional system by inserting an oblique plug in the centre of each joint as the measure against the axial shrinkage over time and filling the gaps which may be generated between the members.



Figure 18. Processed shapes

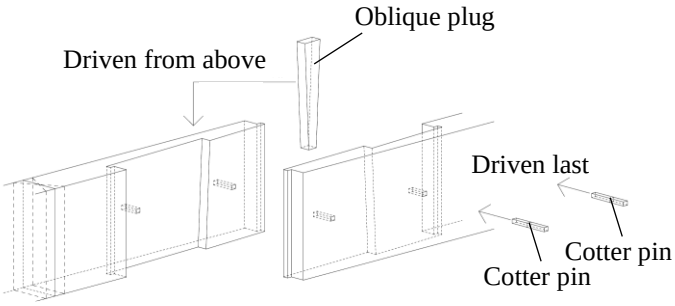


Figure 19. *Okkake Daisen* joint detail

4.2. Erection

Prior to erection, we assembled members temporarily at the fabricator's factory to check the processing accuracy of the members (Figure 20). We erected members on scaffolding, assembling the roof structural frame members and then purlins (Figures 21-23).



Figure 20. Verification of assembled members



Figure 21. Bird's-eye view of erection



Figure 22. Erection: Timber joints ((A) in Figure 11)



Figure 23. Erection: Timber joints (triangular grid)

5. Conclusion

We have developed a catenary-curved roof with a triangular grid of wood for roof structures. Generally available lumber will do to achieve this special system. In addition, a hybrid combination with tensile bolts allows forces to be transmitted only in the direction of the wood fibres, which is helpful against future creep deformation specific to wood and enables simple member joining. Our analysis and measurements verified that the developed beams have sufficient strength and stiffness to meet the requirements.



Figure 24. Training in training room (second floor)



Figure 25. Canoes maintenance (first floor)

Acknowledgments

The author would like to express his gratitude to all the people related to the Mukogawa Women's University Canoe Club for their cooperation from planning to construction. The author would also like to thank the people at Nagase Construction Co. and Tanigaki Co. who involved in the construction of the Building.

References

[1] S. Furuichi and J. Sato, “Design of timber suspension roof pretensioned to reduce deformation under snow load,” in *Proceedings of IASS Annual Symposia, IASS 2016 Tokyo Symposium: Timber Structures & Environmental Compatibility*, 2016, pp. 1-9 (9).

Proceedings of the IASS Annual Symposium 2023
Integration of Design and Fabrication
10–14 July 2023, Melbourne, Australia
Y.M. Xie, J. Burry, T.U. Lee and J. Ma (eds.)

Systematically ranking of mycelium composites used for facade construction via a fuzzy comprehensive evaluation

Yaning WEI*, Seyed Ali HADIGHEH[a], Zicheng HUANG[b], Anastasia GLOBA[c], Phillip GOUGH[c], Anusha WITHANA[d]

* School of Civil Engineering, Faculty of Engineering, The University of Sydney
The University of Sydney, NSW 2006, Australia
yaning.wei@sydney.edu.au

[a] School of Civil Engineering, Faculty of Engineering, The University of Sydney
[b] School of Built Environment, Faculty of Arts, Design & Architecture, UNSW Sydney
[c] School of Architecture, Design and Planning, Faculty of Engineering, The University of Sydney
[d] School of Computer Science, Faculty of Engineering, The University of Sydney

Abstract

There has been a growing interest in advancing the use of mycelium composite in recent years, due to their eco-friendliness, affordable cost, low density, and excellent acoustic and thermal insulation properties. This study compares various mycelium composites manufactured using different fungal species and provides a decision-making guide for selecting the most suitable material of secondary structure member for built environment applications. To determine the most important variables in the selection process, the analytic hierarchy process (AHP) was employed, revealing that tensile strength is the most critical factor (52%), followed by flexural strength (19%), manufacturing period (17%), density (9%), and water absorption (3%). It shows that both the mechanical properties and manufacturing duration significantly affect project delivery, emphasizing the need to consider these factors in the selection process. This study also used the Fuzzy Comprehensive Evaluation (FCE) approach to establish a rational rating system for making the decision of material selection. The FCE results indicate that Ganoderma lucidum is the most promising material, as it has an optimal balance of material performance and material manufacturing time. The combination of AHP and FCE methods is shown to be an effective tool for establishing a comprehensive evaluation for selecting mycelium composites for specific purposes in construction.

Keywords: circular economy, sustainability, living materials, analytic hierarchy process, fuzzy comprehensive evaluation

1. Introduction

In recent decades, there has been a growing focus within the international community on reducing energy usage and achieving universal sustainable development [1]. According to recent studies, approximately one-third of all global carbon emissions can be attributed to the built environment, with fossil fuel combustion accounting for 71% of these emissions [2, 3]. In Australia, the construction sector alone accounts for 36% of the country's carbon balance [4]. As a result, decarbonization of the built environment has become a crucial undertaking in achieving sustainable urbanization and climate neutrality [5]. Traditional building materials, such as concrete and steel, are not conducive to environmental conservation, since their production increases energy consumption and contributes around 10 percent of the world's carbon dioxide emissions [6, 7]. Therefore, it is crucial to encourage the adoption of “green engineering materials” that can minimise non-renewable energy consumption, greenhouse gas emissions, and land and water contamination during the fabrication, transportation, and

Copyright © 2023 by Yaning WEI, Seyed Ali HADIGHEH, Zicheng HUANG, Anastasia GLOBA, Phillip GOUGH, and Anusha WITHANA. Published in the Proceedings of the IASS Annual Symposium 2023 with permission.

deconstruction process [8]. Mycelium-based composites (MBC), a type of renewable and biodegradable engineering material, have attracted considerable interest as a sustainable alternative to conventional synthetic materials in the field of civil engineering (Figure 1) [9]. It is a biomaterial formed from the development of fungi on diverse substrates, such as agricultural waste, forestry leftovers, and cellulosic materials at the end of their useful life [10, 11]. In the sector of construction, MBCs provide various benefits over conventional materials. For example, it has a reduced carbon footprint, which presents an opportunity to improve the sustainability of built environments while also ensuring aesthetic appeal [12]. In addition, their low density, excellent acoustic and thermal insulation, reasonable cost, and minimal environmental effect make them highly competitive in the material market for non-primary structural members [13].

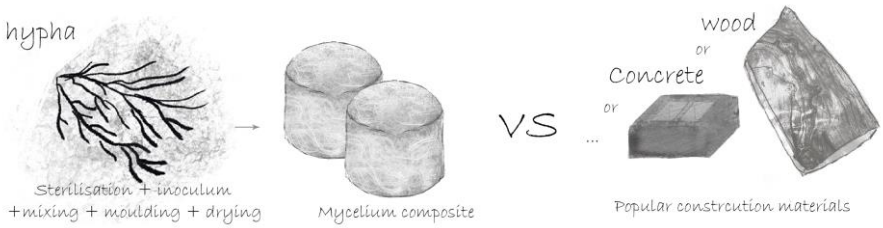


Figure 1. Different construction materials.

Mycelium-based composites are gaining prominence in facade construction owing to their exceptional material properties. For example, the production of the exterior facade panel of the Growing Pavilion by Pascal Leboucq and Erik Klarenbeek involved the use of MBCs [14]. However, despite the increasing popularity of mycelium-based composites in the construction industry, there remains a dearth of comprehensive evaluation guides that thoroughly assess the properties of different types of MBCs manufactured with various fungal species. This poses significant challenges for architects in selecting appropriate materials, as they may lack sufficient foresight regarding the balance of product satisfaction and construction period. To address this gap, this study aims to compare and contrast the key characteristics of different mycelium composites produced from a range of fungal species, while also offering a decision-making guide for the selection of materials used as the secondary structural members in the construction of facades. In this paper, fuzzy comprehensive evaluation (FCE) technique will be employed to provide a systematic ranking of different MBCs. Throughout this process, the study will consider and assess the key properties of MBCs, including density, water absorption, tensile strength, and flexural strength, as well as manufacturing periods. Also, the weight proportions of these evaluation factors in the context of facade applications will be evaluated using the analytic hierarchy process (AHP).

2. Research methodology

2.1. Analytic hierarchy process

The AHP decision-making approach [15] can facilitate an accurate and straightforward determination of the weight vector for multivariable systems, particularly those with more than three variables. Instead of performing a laborious and ill-defined process of cross-comparison, this technique enables the creation of a pairwise comparison matrix, which can then be used to evaluate the relevance of each aspect that was taken into consideration [16]. Discovering the primary key factors for assessment, building the pairwise comparison matrix using the Saaty scale (Table 1), calculating the eigenvector and major eigenvalue and transferring the result to the weight vector are the five procedures that are necessary to generate the weight fraction. Following the calculation of the weight fraction, the

consistency of the created matrix must be evaluated by determining its value using the consistency ratio (CR). The calculation for CR can be found in Equation 1, as indicated. If the value of CR is more than the restriction of 0.1, it is possible that a mistake caused by poor human judgement occurred during the building of the matrix. In every other case, the outcome is considered rational [17].

$$\mathrm{CR} = \frac{CI}{RI} = \frac{\sum_{i=1}^{n} \frac{(A\vec{\omega})_i}{n\omega_i} - n}{RI\ (n-1)} \leq 0.1 \tag{1}$$

where A is the formed pairwise matrix, ω_i is the weight vector, n is the number of variables, RI is an average random index and CI is the consistency index.

Table 1. Saaty scale used to form comparison matrix.

The number for A/B	Definition
1	Factor A has the SAME importance as B in the assessment.
2	Factor A is SLIGHTLY more important than B in the assessment.
3	Factor A is MODERATELY more important than B in the assessment.
4	Factor A is MODERATELY PLUS more important than B in the assessment.
5	Factor A is STRONGLY more important than B in the assessment.
6	Factor A is VERY STRONGLY more important than B in the assessment.
7	Factor A is DEMONSTRATED more important than B in the assessment.
8	Factor A is VERY VERY STRONGLY more important than B in the assessment.
9	Factor A is EXTREMELY more important than B in the assessment.

2.2. Fuzzy comprehensive evaluation

Fuzzy comprehensive evaluation was created based on Zadeh's fuzzy mathematics theory [18, 19]. The benefit of this technique is delivering the quantified full evaluation for each choice without needing exact numerical criteria and resources. The complete technique might be separated into three steps: (i) establishing the variable set and scale set, (ii) building the fuzzy evaluation matrix, and (iii) determining the rank by applying the weight vector obtained in the AHP. The evaluation level with the greatest likelihood of the outcome reflects the final projected grade of assessment [16]. The detailed process is summarised in Figure 2.

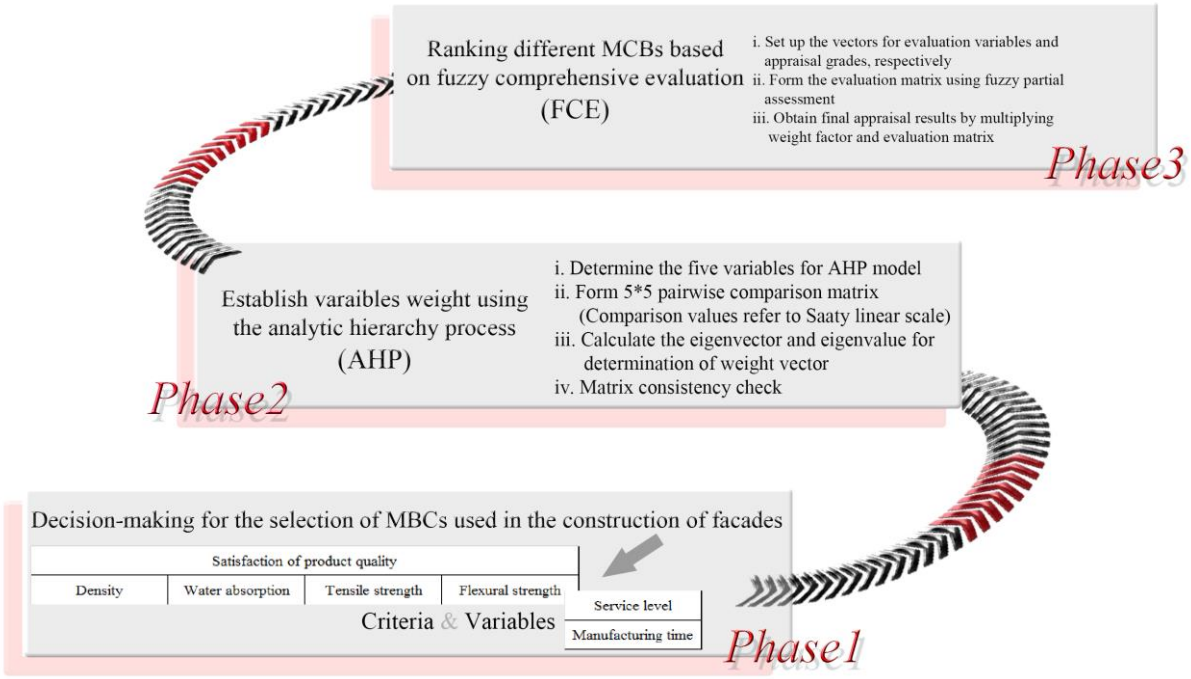


Figure 2. Systematical scoring process for different MBCs.

3. Result and discussion

3.1. Weight vector determination for multi-variables

The Analytic Hierarchy Process (AHP) allows to divide complex cross-comparisons into a series of pairwise evaluations. By adopting a numerical scale for pairwise comparison, it is feasible to establish the degree of significance of each variable through an easy, methodical, and accurate technique. The steps required to acquire the weight vector that will be used to evaluate the various realignment methods are outlined below.

At the variable determination phase, which is the initial stage, all five variables needed for decision-making - density, water absorption, tensile strength, flexural strength, and manufacturing period - are acquired from existing research to evaluate and compare properties of different MBCs. The second phase focuses on the development of matrices for pairwise comparisons. This study focus to evaluate the overall performance of mycelium composites as a material for secondary structural members in both outer-frame and inter-frame configurations, whose findings provide significant insight into the possibilities of each mycelium composite as the material for facade construction

The AHP approach provides the option to break down complicated cross-comparisons into a series of pairwise assessments. It would be possible to determine the degree of significance of each variable using a procedure that was straightforward, methodical and exact if one used a numbering scale for pairwise comparison. The following process is used to obtain the weight vector that will be used for rating the different realignment methods. The pairwise relationship between every two variables for both conditions is defined based on the studies conducted by Chen [20], Patnaik et.al. [21] and Lee et al.[22]. The matrix is created following the procedure outlined in Table 2. To assess the relative relevance of each variable, it is compared with its counterpart. Using the Saaty linear scale, this relative relevance is then mapped onto numerical data, as illustrated in Table 3 [17].

Table 2. Pairwise comparison matrix.

Matrix Framework		Satisfaction with product quality				Service level
		Density (D)	Water absorption(WA)	Tensile strength (TS)	Flexural strength (FS)	Manufacturing period (MP)
Satisfaction with product quality	Density (D)	1	D/WA	D/TS	D/FS	D/MP
	Water absorption (WA)	WA/D	1	WA/TS	WA/FS	WA/MP
	Tensile strength (TS)	TS/D	TS/WA	1	TS/FS	TS/MP
	Flexural strength (FS)	FS/D	FS/WA	FS/TS	1	FS/MP
Service level	Manufacturing period (MP)	MP/D	MP/WA	MP/TS	MP/FS	1

Table 3. Pairwise comparison matrix with data input.

Matrix Framework		Satisfaction with product quality				Service level
		Density (D)	Water absorption(WA)	Tensile strength (TS)	Flexural strength (FS)	Manufacturing period (MP)
Satisfaction with product quality	Density (D)	1	5	1/7	2	1
	Water absorption (WA)	1/5	1	1/9	1/9	1/9
	Tensile strength (TS)	7	9	1	4	4
	Flexural strength (FS)	3	9	1/4	1	1
Service level	Manufacturing period (MP)	2	9	1/4	1	1

The third phase involves calculating the eigen system and weight vector for each variable. The eigenvector (ν) and principal eigenvalue (λ_{max}) are determined to be (0.436, 0.143, 2.599, 0.949, 0.873) and 5.276, respectively. Additional transformations can be performed to determine the weight proportion of each consideration factor: 8.772% for density, 2.857% for water absorption, 51.978% for tensile strength, 18.979% for flexural strength, and 17.464% for manufacturing period. The result shows the selection of suitable materials for secondary structure members in facade construction is a crucial aspect of engineering design. Among the various factors considered in this process, mechanical properties hold a key significance due to their impact on the structural integrity and safety of the built environment. In addition to mechanical properties, AHP results highlight the manufacturing period of a material also plays a significant role in project delivery. The duration of the manufacturing process can have considerable impacts on the timeline of a project. Hence, it is essential to consider the manufacturing period of a material during the material selection process, to ensure that the selected material can be manufactured and delivered within the project's timeframe, while also meeting the required performance specifications during its expected lifetime.

The fourth stage of matrix consistency inspection entails calculating the CR (*CR = CI/RI*) to validate the precision of the comparison matrix. The consistency index, also known as CI, can be calculated using Equation 2. The RI, or average random index, is 1.12, as shown in Table 4 [23]. The calculated CR is 0.062, which is below the threshold of 0.1. Therefore, it is possible to conclude that the matrix's consistency level is sufficient.

$$\mathrm{CI} = \frac{\lambda_{max} - n}{n - 1} = 0.069 \tag{2}$$

where *n* is the size of the matrix.

3.2. Fuzzy comprehensive evaluation model

The FCE approach offers a comprehensive analysis of the fuzzy evaluation of each criterion, making it a valuable tool for cross-comparisons across various methodologies. In this study, the FCE approach was employed to establish a logical ranking system for suitable mycelium composites used as material of secondary structural members in facade construction. The factors/variables set (U) in this study comprised density, water absorption, tensile strength, flexural strength, and manufacturing periods. The assessment levels (V) were categorized as excellent, very good, good, fair, or poor according to the established scale. The specific ranking criteria are presented in Table 4 along with the corresponding assessment levels. By considering both mechanical properties and the manufacturing period during the material selection process, architects can make informed decisions that ensure the optimal balance between performance and time for their projects.

Table 4. Evaluation scale used in FCE.

Level	Excellent	Very Good	Good	Fair	Poor
Density, D (kg/m3)	D<100	100 ≤D<200	200≤D<300	300≤D<500	D≥500
Water absorption, WA (%）	WA<100	100 ≤WA<150	150≤WA<200	200≤WA<300	WA≥300
Tensile strength, TS (MPa)	TS>1	0.5<TS≤1	0.1 <TS≤0.5	0.05 <TS≤0.1	TS≤0.05
Flexural strength, FS (MPa)	FS>1	0.5<FS≤1	0.1 <FS≤0.5	0.05 <FS≤0.1	FS≤0.05
Manufacturing period, MP (days)	MT<15	15 ≤MT<20	20≤MT<25	25≤MT<30	MT≥30

This study aimed to evaluate seven different types of mycelium composites for their suitability as facade construction materials. These tested composites were composed of *trametes multicolor*, *pleurotus ostreatus*, *ganoderma fornicatum*, *ganoderma williamsianum*, *lentinus sajor-caju*, *schizophyllum commune*, and *ganoderma lucidum*, respectively. Physical and mechanical properties of these composites as well as their production time were collected from relevant literature sources, which are summarized in Figure 3 [24-34]. The results indicate that there is a high degree of uncertainty regarding all five properties of mycelium composite with *pleurotus ostreatus*, while the behaviour of *ganoderma williamsianum* is relatively stable. Additionally, the difference in physical properties between the seven different types of mycelium composites is less significant compared to the difference in mechanical properties.

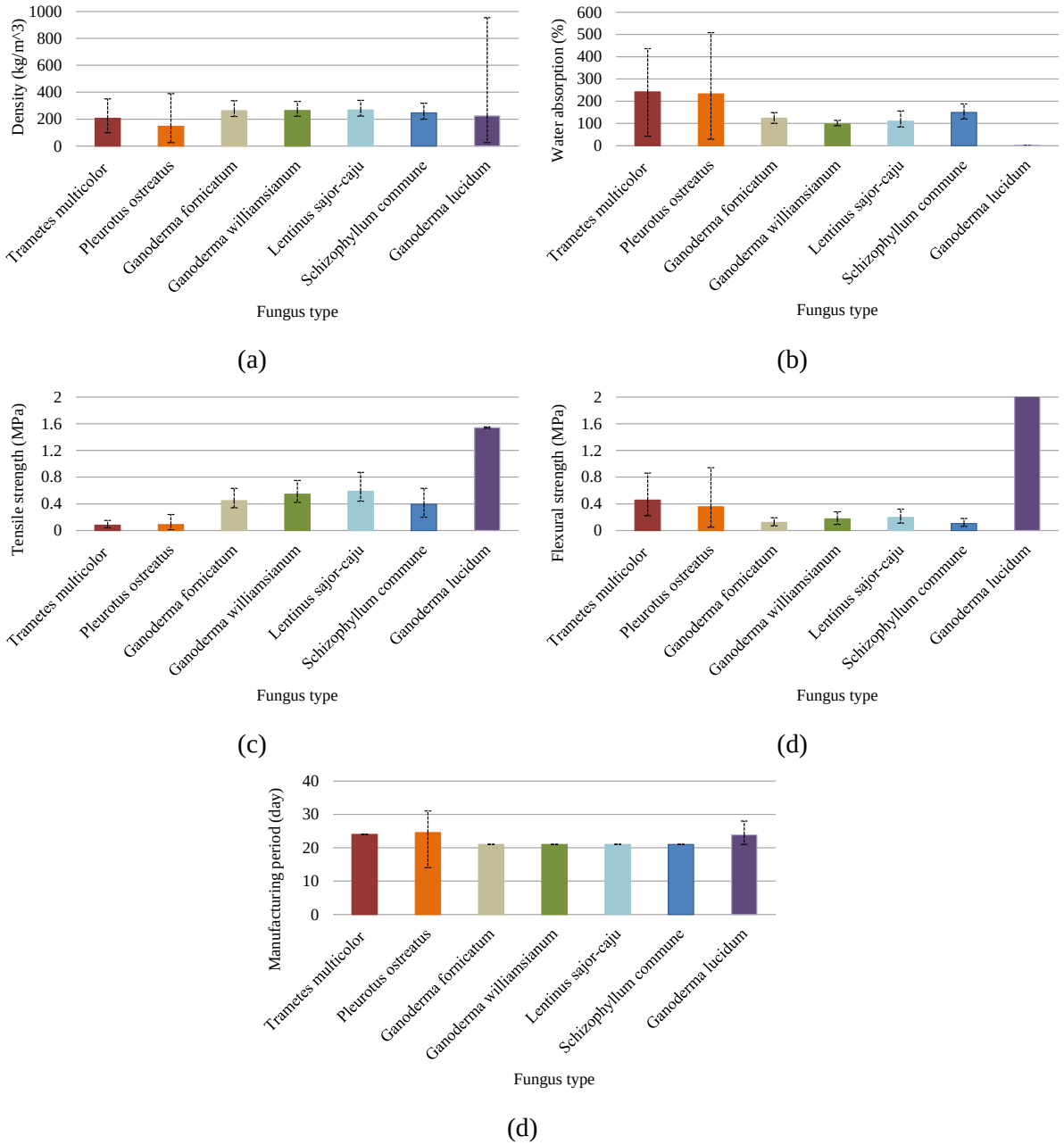


Figure 3. Five characteristics of mycelium composites manufactured with different fungi: (a) Density, (b)Water absorption, (c) Tensile strength, (d) Flexural strength and (e) Manunfacturing period.

The fuzzy matrix R, which includes entries $u_i v_i$, was constructed using the findings from existing literature. The dot product of the weight vector and the fuzzy matrix presented in Figure 4 was used to create the complete assessment set. According to the results, *ganoderma lucidum* appears to be the most promising fungus for the manufacture of mycelium composites used in facades. This type of MBC boasts outstanding water resistance and tensile strength, relative light density but longer production period. However, given the limited data available in the literature, this study acknowledges the

uncertainty of the range for each variable. Future studies can improve upon these findings by expanding the database.

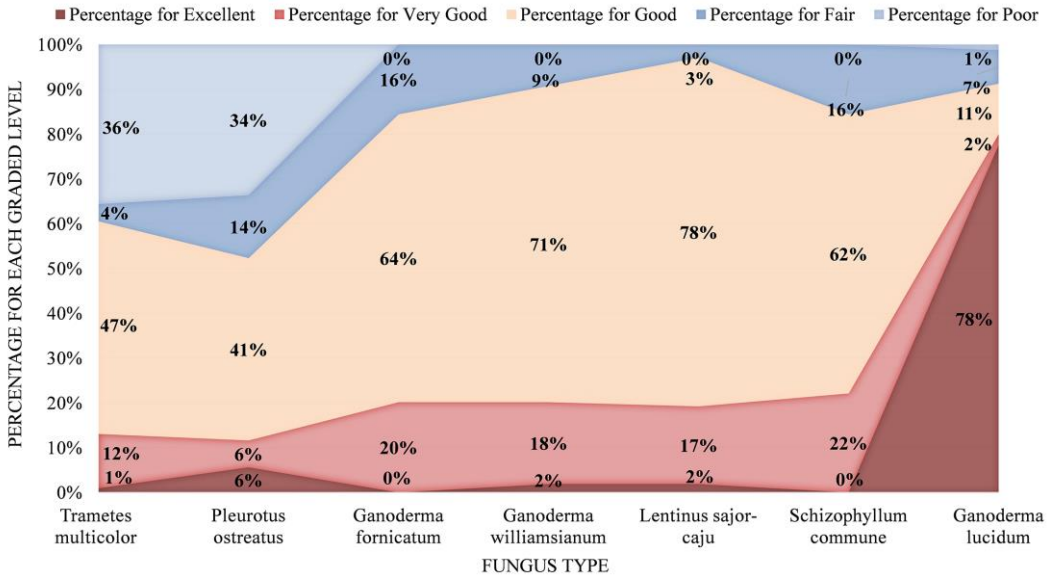


Figure 4. Evaluation results for mycelium composites manufactured with a different fungus.

4. Conclusions

This research employs the Analytic Hierarchy Process and Fuzzy Comprehensive Evaluation methods to identify the most suitable mycelium composites for use in facade construction. The research presents a comprehensive evaluation to assess the suitability of each typed mycelium composites and their potential to enhance practical application in civil engineering. The AHP results reveal the weight proportion of each variable considered in the study, with density accounting for 8.8%, water absorption for 2.9%, tensile strength for 52.0%, flexural strength for 19.0%, and manufacturing period for 17.5%. The study underscores the significance of mechanical properties in the selection of materials for secondary structure members, as these properties have a crucial impact on the structural integrity and safety of the built environment. Moreover, the analysis emphasizes that material manufacturing duration and mechanical properties are two significant factors that affect project delivery.

The FCE approach has been utilised to establish a rational rating system for mycelium composites used in facade construction. This study examines five key factors that influence the suitability of mycelium composites. Architects and engineers can use the FCE results to make informed decisions that balance performance and time while ensuring optimal material selection. Based on the FCE findings, Ganoderma lucidum appears to be the most promising fungus for mycelium composites for built environment applications, for both external and internal spaces. This typed MBC has excellent water resistance and tensile strength, a relatively light density, but takes longer to produce. Nevertheless, this analysis acknowledges the range uncertainty for each variable due to the limited literature available. Therefore, future studies can improve upon these findings by expanding the database. However, it is clear to show that the FCE approach can provide a reasonable rational ranking system for the selection of mycelium composites used for the specific purpose of construction. This study improves the architect's predictive abilities in material selection, resulting in better control over both structural and aesthetic features during the early stages of design. In addition, the proposed methodology is adaptable, allowing for a variety of material selection purposes by modification of factors and alternative material assessments.

Acknowledgements

We would like to acknowledge the support and encouragement that our team has received from the Sydney Nano Institute through their Kickstarter program.

References

[1] W. Feng, Q. Zhang, H. Ji, R. Wang, N. Zhou, Q. Ye, B. Hao, Y. Li, D. Luo, and S. S. Y. Lau, "A review of net zero energy buildings in hot and humid climates: Experience learned from 34 case study buildings," *Renewable and Sustainable Energy Reviews*, vol. 114, p. 109303, 2019.
[2] IEA, *Transition to Sustainable Buildings*, International energy agent, 2013.
[3] C. Rosenzweig, W. Solecki, S. A. Hammer, and S. Mehrotra, "Cities lead the way in climate–change action," *Nature*, vol. 467, pp. 909-911, 2010.
[4] B. Huang, K. Xing and S. Pullen, "Carbon assessment for urban precincts: Integrated model and case studies," *Energy and Buildings*, vol. 153, pp. 111-125, 2017.
[5] B. Huang, K. Xing, D. Ness, L. Liao, K. Huang, P. Xie, and J. Huang, "Rethinking carbon–neutral built environment: Urban dynamics and scenario analysis," *Energy and Buildings*, vol. 255, p. 111672, 2022.
[6] M. V. Madurwar, R. V. Ralegaonkar and S. A. Mandavgane, "Application of agro-waste for sustainable construction materials: A review," *Construction and Building Materials*, vol. 38, pp. 872-878, 2013.
[7] H. Italia, I. Patel and J. Shah, "Experimental study of bacterial self-healing effect on concrete: a review," *Journal of Civil Engineering and Environmental Technology*, vol. 3, pp. 78-81, 2016.
[8] D. Alemu, M. Tafesse, A. K. Mondal, and A. Seifalian, "Mycelium-Based Composite: The Future Sustainable Biomaterial," *International Journal of Biomaterials*, vol. 2022, p. 8401528, 2022.
[9] M. Fairus, E. Bahrin, E. Natasha, E. Arbaain, and N. Ramli, "Mycelium-based composite: A way forward for renewable material," *Journal of Sustainability Science and Management*, vol. 17, pp. 271-280, 2022.
[10] C. Girometta, A. M. Picco, R. M. Baiguera, D. Dondi, S. Babbini, M. Cartabia, M. Pellegrini, and E. Savino, "Physico-Mechanical and Thermodynamic Properties of Mycelium-Based Biocomposites: A Review," *Sustainability*. vol. 11, 2019.
[11] M. Sydor, G. Cofta, B. Doczekalska, and A. Bonenberg, "Fungi in Mycelium-Based Composites: Usage and Recommendations," *Materials*. vol. 15, 2022.
[12] M. Jones, T. Huynh, C. Dekiwadia, F. Daver, and S. John, "Mycelium Composites: A Review of Engineering Characteristics and Growth Kinetics," *Journal of Bionanoscience*. vol. 11, 2017, pp. 241-257.
[13] L. Yang, D. Park and Z. Qin, "Material Function of Mycelium-Based Bio-Composite: A Review," *Frontiers in Materials*, vol. 8, 2021.
[14] A. Ghazvinian, *A Sustainable Alternative to Architectural Materials: Mycelium-based Bio-composites*, Georgia Institute of Technology, 2021.
[15] R. W. Saaty, "The analytic hierarchy process—what it is and how it is used," *Mathematical Modelling*, vol. 9, pp. 161-176, 1987.
[16] R. Zhou and A. H. S. Chan, "Using a fuzzy comprehensive evaluation method to determine product usability: A proposed theoretical framework," *Work*, vol. 56, pp. 9-19, 2017.
[17] T. Saaty, "Decision making with the Analytic Hierarchy Process," *International Journal of Services Sciences*, vol. 1, pp. 83-98, 2008.
[18] J. A. Goguen, "Similarity relation and fuzzy orderings," *Journal of Symbolic Logic*, vol. 38, pp. 656-657, 1973.
[19] L. A. Zadeh, "Fuzzy sets," *Information and Control*, vol. 8, pp. 338-353, 1965-01-01 1965.
[20] C. Chen, "A Novel Multi-Criteria Decision-Making Model for Building Material Supplier Selection Based on Entropy-AHP Weighted TOPSIS," *Entropy*. vol. 22, 2020.
[21] P. K. Patnaik, P. T. R. Swain, S. K. Mishra, A. Purohit, and S. Biswas, "Composite material

selection for structural applications based on AHP-MOORA approach," *Materials Today: Proceedings,* vol. 33, pp. 5659-5663, 2020.
[22] D. Lee, D. Lee, M. Lee, M. Kim, and T. Kim, "Analytic Hierarchy Process-Based Construction Material Selection for Performance Improvement of Building Construction: The Case of a Concrete System Form," *Materials(Basel),* vol. 7, p. 1738, 2020.
[23] T. Saaty, *The analytic hierarchy process*, McGraw Hill, 1980.
[24] F. V. W. Appels, S. Camere, M. Montalti, E. Karana, K. M. B. Jansen, J. Dijksterhuis, P. Krijgsheld, and H. A. B. Wösten, "Fabrication factors influencing mechanical, moisture- and water-related properties of mycelium-based composites," *Materials & Design,* vol. 161, pp. 64-71, 2019.
[25] L. Gou, S. Li, J. Yin, T. Li, and X. Liu, "Morphological and physico-mechanical properties of mycelium biocomposites with natural reinforcement particles," *Construction and Building Materials,* vol. 304, p. 124656, 2021.
[26] A. Ghazvinian, P. Farrokhsiar, F. Rocha Vieira, J. Pecchia, and B. Gursoy, "Mycelium-Based Bio-Composites For Architecture: Assessing the Effects of Cultivation Factors on Compressive Strength," *in Form and Force: Proceedings of Event37th Conference on Education and Research in Computer Aided Architectural Design in Europe and 23rd Conference of the Iberoamerican Society Digital Graphics*, Porto, Portugal, September 11–13, 2019, J. P. Sousa, G. C. Henriques and J. P. Xavier, Eds.
[27] T. Kuribayashi, P. Lankinen, S. Hietala, and K. S. Mikkonen, "Dense and continuous networks of aerial hyphae improve flexibility and shape retention of mycelium composite in the wet state," *Composites Part A: Applied Science and Manufacturing,* vol. 152, p. 106688, 2022.
[28] H. Vašatko, L. Gosch, J. Jauk, and M. Stavric, "Basic Research of Material Properties of Mycelium-Based Composites," *Biomimetics*. vol. 7, 2022.
[29] L. Peng, J. Yi, X. Yang, J. Xie, and C. Chen, "Development and characterization of mycelium bio-composites by utilization of different agricultural residual byproducts," *Journal of Bioresources and Bioproducts,* vol. 8, pp. 78-89, 2023.
[30] N. Thatchanamoorthy, V. Rukumani Devi, S. Chandramathi, and S. T. Tay, "Candida auris: A Mini Review on Epidemiology in Healthcare Facilities in Asia," *Journal of Fungi*. vol. 8, 2022.
[31] Z. Tacer-Caba, J. J. Varis, P. Lankinen, and K. S. Mikkonen, "Comparison of novel fungal mycelia strains and sustainable growth substrates to produce humidity-resistant biocomposites," *Materials & Design,* vol. 192, p. 108728, 2020.
[32] X. Y. Chan, N. Saeidi, A. Javadian, D. E. Hebel, and M. Gupta, "Mechanical properties of dense mycelium-bound composites under accelerated tropical weathering conditions," *Scientific Reports,* vol. 11, p. 22112, 2021.
[33] H. Vašatko, L. Gosch, J. Jauk, and M. Stavric, "Basic Research of Material Properties of Mycelium-Based Composites," *Biomimetics*. vol. 7, 2022.
[34] H. Schritt, S. Vidi and D. Pleissner, "Spent mushroom substrate and sawdust to produce mycelium-based thermal insulation composites," *Journal of Cleaner Production,* vol. 313, p. 127910, 2021.

Proceedings of the IASS Annual Symposium 2023
Integration of Design and Fabrication
10–14 July 2023, Melbourne, Australia
Y.M. Xie, J. Burry, T.U. Lee and J. Ma (eds.)

Testing on the shear performance of embedded steel tube glulam joints in arched timber structures

Chengyang HE[a], Minjuan HE[*], Zheng LI[a], Yongliang SUN[a]

[*] Department of Structural Engineering, Tongji University
1239 Siping Road, Yangpu District, Shanghai, 200092, China
Hemj@tongji.edu.cn

[a] Tongji Architectural Design(Group) Co., Ltd., Shanghai, 200092, China

Abstract

Glulam arches have promising in-plane stability due to the high compression efficiency of wood. As the span becomes large currently, well attention should be paid to the out-of-plane mechanical property of the structure. In some cases, several arches are connected with each other with members, where the connections between web members and arches come into place. This paper studies the mechanical properties of a type of embedded steel-tube glulam joint applied in a real arched glulam structure. Experimental tests were conducted on three full-scale joint specimens with two dimensions of steel tubes. Two loading protocols were considered, i.e. the monotonic and cycling loading. Tshe failure mode, force-displacement responses, shearing capacities, shearing stiffnesses, and ductility factors of the specimens were compared. The test results proved the shearing capacity to be reliable compared to the design forces. The enhancing screws effectively restricted the crack propagation which enabled the specimens to fail in a ductile manner. Finally, standard codes were utilized to calculate the theoretical capacities of the specimens. The theoretical results prove to be too conservative mainly because such large steel tubes in glulam joints were seldom considered.

Keywords: arched glulam structures, steel-tube glulam joints, mechanical performance, experimental tests, analytical models

1. Introduction

Arched glulam structures are widely used for the construction of gymnasiums, industrial and agricultural buildings, etc. Such structural systems possess superiorities in aesthetical attractions and structural efficiency, which is associated with the unique arch-type configuration that reduces the bending moment demand on structural members. Recently, glulam arched structures are gaining increased popularity owing to the positive environmental impact of wood, and the high strength-to-weight ratio of glulam. The exposure of wood members can further improve the aesthetic appearance of the structure. As the span of glulam arches becomes large, the length challenge of glulam members associated with the manufacturing and transportation limits needs to be well addressed. For example, for the Tianfu Botanical Garden project, which includes five large-span glulam arches ranging from 11 m to 50 m in height and 88 m to 128 m in diameter (one of them shown in Figure 1(a)), it is quite challenging for a single arch to resist various loads. For this reason, several arches are connected to each other with steel triangles to become an arch truss. This has raised concerns regarding the mechanical performance of the connection properties between the steel members and the glulam arch since they may greatly influence the response of the entire structure, especially in shearing force.

Various connection techniques have been developed to connect timber elements or sometimes even steel members. These techniques involve the use of slotted-in steel plates and dowels [1, 2], glued-in steel

Copyright © 2023 by Chengyang HE, Minjuan HE, Zheng LI and Yongliang SUN. Published in the Proceedings of the IASS Annual Symposium 2023 with permission.

rods or plates [3, 4], direct adhesive bonding [5, 6], self-tapping screws (STSs) [7, 8], lagscrewbolts [9], long threaded rods (LTRs) [10, 11], etc. Each splice connection technique has pros and cons, as discussed in [12]. From the perspectives of aesthetic appearance and on-site assembly efficiency, using a steel tube to embed into the glulam arch from one side is preferred in the project. In such a joint, the embedment performance of the glulam material is challenged. The embedment performance of dowel-type connections have been investigated sufficiently [13–17] for small diameter fasteners. Previous work elaborately considered the influence of diameter of fasteners, wood density, loading degree, moisture etc. to the embedment strength. Many equations have been refined from tests and theoretical studies and been proved to be feasible within common range in practice.

However, previous work mainly focused on dowel-type fasteners whose diameters are mostly within a limited range where the diameter of fasteners is commonly small. There is not enough research as to large-sized fasteners or even large steel-tubes as mentioned in this paper. Therefore, this paper carried out a series of steel-tube embedded glulam joint with three replicates taken from a real large-span arched glulam project to investigate the shear performance of this kind of joint.

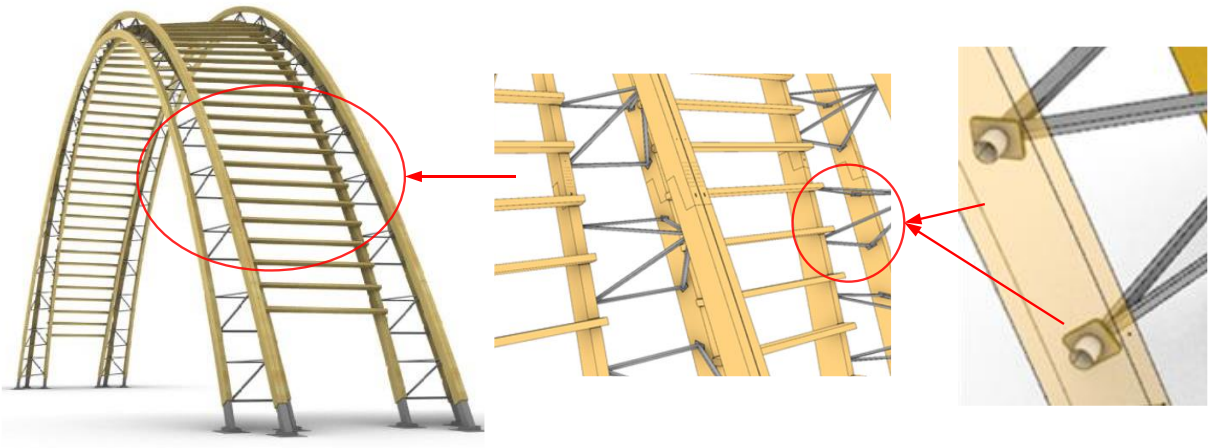


Figure 1. The joint sketch in real structure

2. Test program

2.1. Specimen design

In order to investigate the shear performance of the steel-tube glulam joint, three specimens were tested under quasi-static load. The specimens were full-scale replicates extracted from a real long-span arched glulam structure - Tianfu Agricultural Expo. project. The three specimens were labelled as AM, BM and BC. The first letter in the label represents the cross section and the second letter refers to the loading type. Thus, there were two types of cross-sections and two types of loading modes in the testing program. All the wood in three specimens were glulam in grade GL-24h, with an average density and moisture contents in 460 kg/m3 and 12.6%. The steel tubes were manufactured with Q235B low-carbon steel. Furthermore, self-tapping screws (STS) were set in the direction perpendicular to grain near the joint area to restrict the crack propagation. The product in the type of VGS from a famous company Rothoblaas [18] was adopted. Specimens are designed as shown in Figure 2.

Specimen AM has a glulam cross section in 660mm x 200mm. A prefabricated hole was cut in the middle of the specimen by 135mm in diameter. The steel tube was 133mm in diameter, slightly smaller than the hole for installation convenience. The specimen was 2.5m in length. The specimen design of AM is shown in Figure 3(a), along with the STS configuration. Specimen AM was loaded with a monotonic mode.

Group B contains two specimens, both of which were made of glulam in cross-section of 920mm x 200mm, with a prefabricated hole in the middle of the specimen by 275mm in diameter. The steel tubes were 273mm in diameter. The specimens were 2.5m in length and the design was shown in Figure 3(b), (c), along with the detailed STS configuration. Similar to AM, specimen BM was loaded monotonically, while BC was loaded with a cyclic mode.

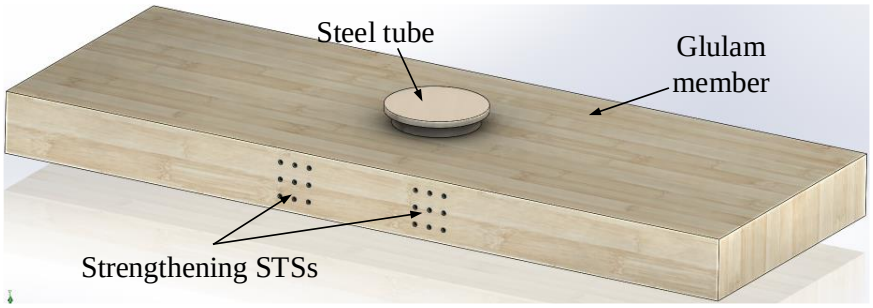


Figure 2. Joint appearance

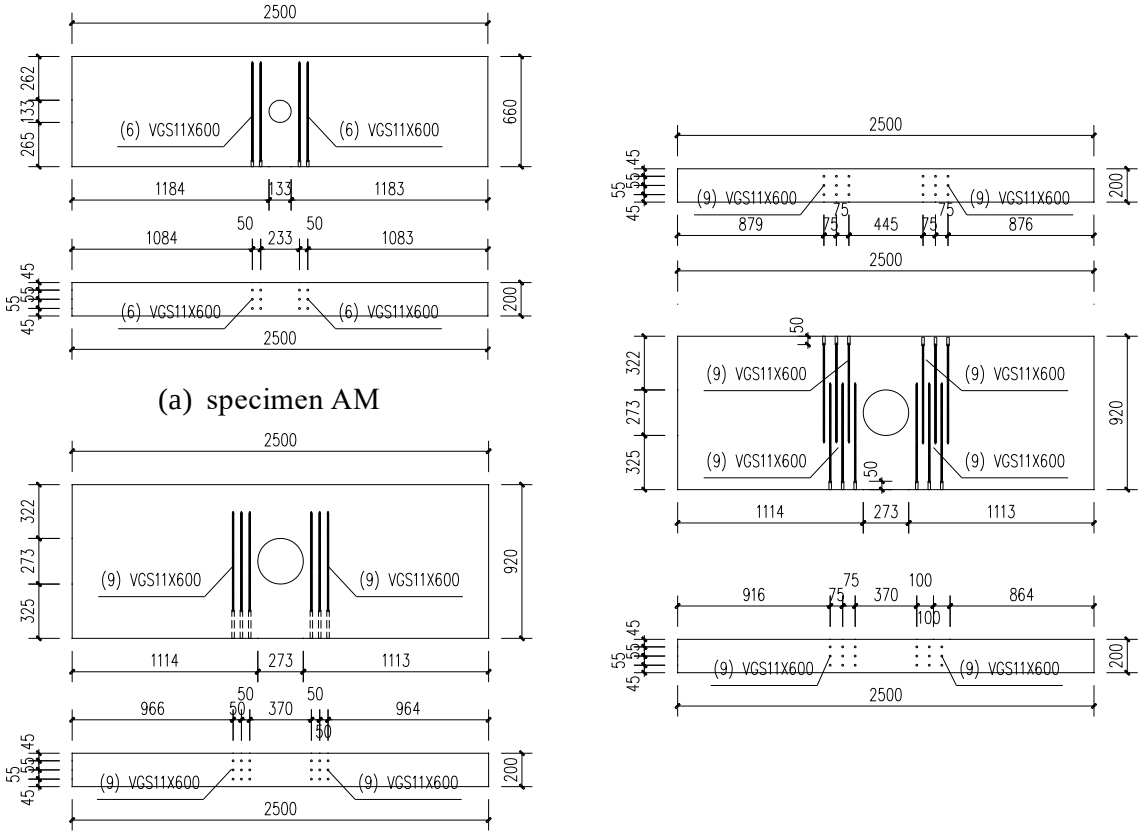
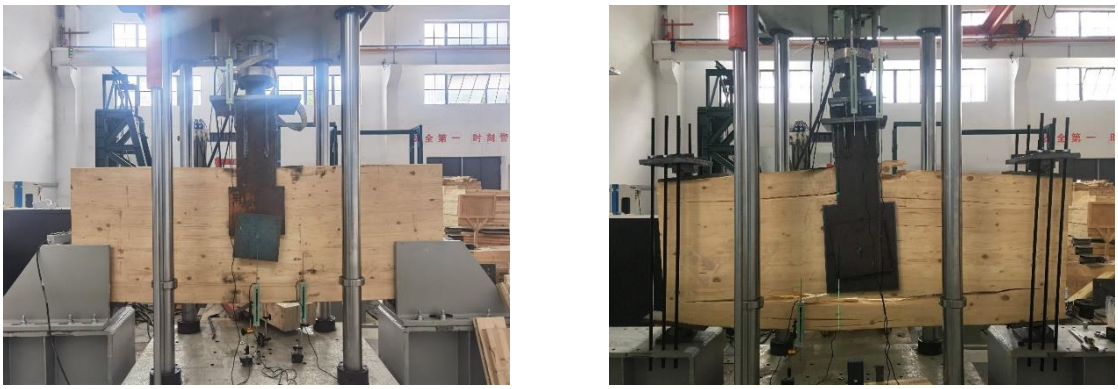


Figure 3. Specimen sketches

2.2. Test setup

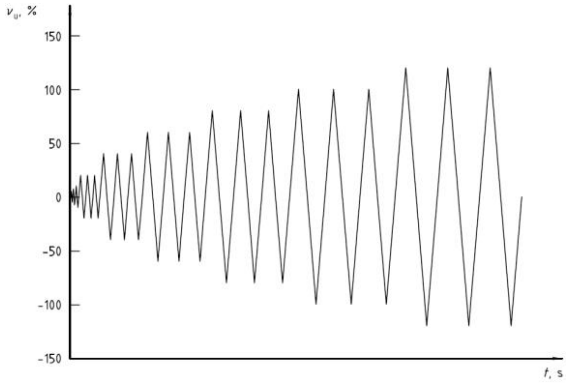
Generally speaking, the mechanical properties for wood in the direction perpendicular to grain was often challenged. Therefore, the loading direction follows this way perpendicular to grain, namely vertical according to the set of the actuator. Figure 4 shows the test installation. There was a difference between the specimens BM and BC, as to the loading device between the steel tube and the actuator. The difference simply came from the loading mode between the two specimens, namely monotonic or cyclic loading.

In the monotonic loading mode, the loading speed was set to be 3mm/min. If the force drops suddenly or it decreases to 80% of the peak load. In the cyclic loading mode, the quasi-static reversed-cyclic test method was adopted which follows the standard ISO-16670-2003, as shown in Figure 5 and Table 1.



(a) Group A (b) Group B

Figure 4. Test installation



Step	No. of cycles	Amplitude
1	1	1,25 % of v_u
2	1	2,5 % of v_u
3	1	5 % of v_u
4	1	7,5 % of v_u
5	1	10 % of v_u
6	3	20 % of v_u
7	3	40 % of v_u
8	3	60 % of v_u
9	3	80 % of v_u
10	3	100 % of v_u
11	3	increments of 20 % of v_u
NOTE Some of the initial steps (1,25 % to 10 % v_u) may be omitted or repeated (or new steps may be added) depending on the stiffness of the joint or accuracy of the measurement system, as long as the principles given in 6.2 are satisfied. Clause A.2 identifies cases where modification of the standard cyclic displacement schedule may be warranted.		

(a) Displacement-time curve (b) Amplitude of each loop

Figure 5. ISO cyclic loading program

Since the specimen BM and BC are same replicates as to dimensions and material. Therefore, BM can be the monotonic reference specimen for BC. The predicated ultimate displacement $v_u = 148mm$ as obtained by the curve of BM. In this way, the loading protocol of BC can be determined as Table 1.

The arrangement of the Linear Voltage Displacement Transducers (LVDTs) were displayed in Figure 6 L1 and L2, L3 and L4. L2, L3 detect the moment of the steel-tube, and the displacement can be the average of the results of L2 and L3. L1 and L2 separately record the displacement of the wood, within which L1 on the top and L2 the bottom.

Table 1. Detailed loading protocol

Step	Amplitude(%)	displacement(mm)	No. of cycles	Speed(mm/min)
1	1.25	1.85	1	5
2	2.50	3.7	1	5
3	5	7.4	1	10
4	7.50	11.1	1	20
5	10	14.8	1	20
6	20	29.6	3	40
7	40	59.2	3	60
8	60	88.8	3	60
9	80	118.4	3	60
10	100	148	3	60
11	120	177.6	3	60

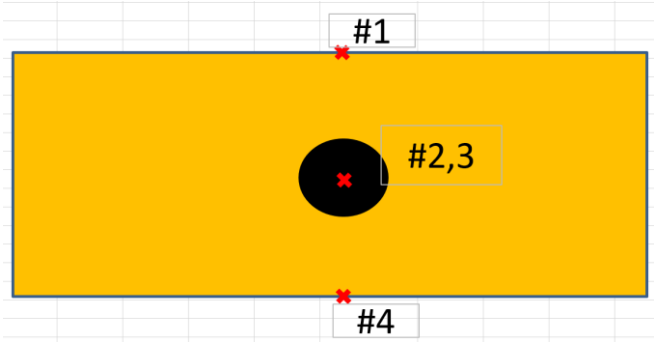


Figure 6. LVDT arrangement

3. Test results

3.1 Experimental observations

The photos of the specimens AM and BM which were both loaded monotonically are shown in Figure 7, respectively. It was observed that for specimen AM, a longitudinal crack initiated in the middle of the hole, when the load reached about 300kN and the displacement of the steel tube was about 40mm. As the load increased, the crack propagated along the longitudinal grain, which inevitably met with the strengthening screws perpendicular to the grain, as shown in Figure 7(a),(b). At the meantime, with the continuing vertical movement of the tube, the squeezing deformation at the embedded area was simultaneously observed. When the load approached the peak load (around 340kN), an obvious longitudinal crack was formed throughout the whole specimen to the end of one side, leading to a significant damage in the specimen as shown in Figure 7(b).

As for specimen BM, similar pattern at the early stage of the loading was observed, where some cracks caused from the squeezing of the steel tube initiated at the hole. With the increasing of the load, similar squeezing area as that of specimen AM was noticed at the embedded region. However, when the load continued to increase, no obvious brittle failure was observed except that the embedded region continued to be squeezed. Figure 7(c),(d) indicated that the cracks around the hole were restricted by the strengthening screws perpendicular to the grain.

The pictures exhibiting the failure mode of specimen BC were listed in Figure 7(e). At a low magnitude of loading when the force was around 50% of the peak load, the steel tube kept squeezing the embedded region of the hole, causing small cracks to propagate. When the peak load was reached (about 450kN),

a longitudinal crack below the hole was observed, as shown in Figure 7(e). The crack continued to open as the actuator continued to move down at the seventh cycle level (i.e. 59.2mm). When the actuator moved in the reverse way, namely upward, another crack symmetrically occurred at the upper region of the wood member above the hole, as shown in the photo. Since the wood member has some initial defect near the upper crack, the crack was observed to propagate to the uppermost layer of the member. With the loading continued to progress, the upper and lower cracks alternatingly propagated until the capacity decreased to 80% of the peak load, which was popularly viewed as the failure point of wood joints.

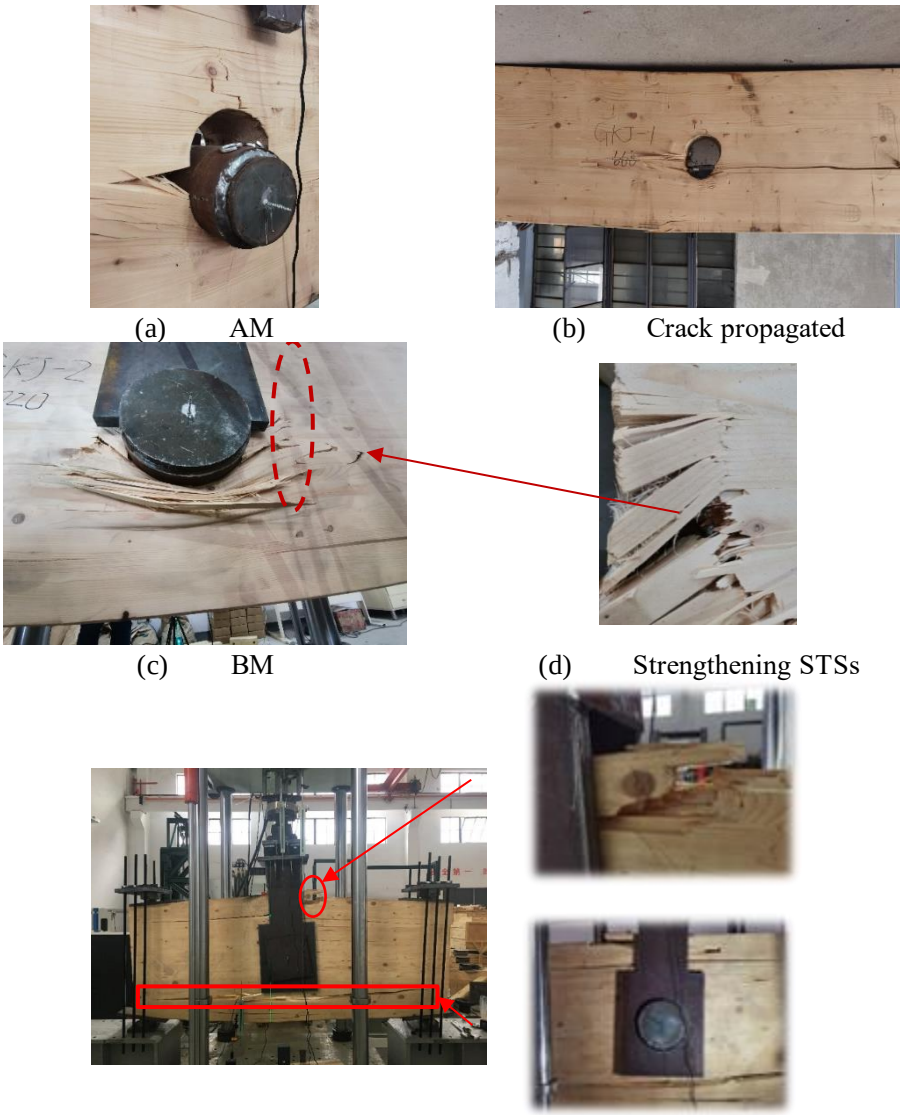


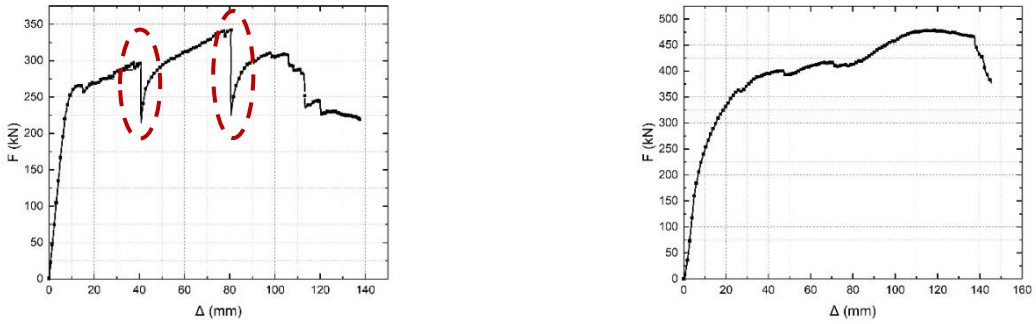
Figure 7. Test observations

3.2 Load-displacement curves

The load-displacement curves for the specimens under monotonic loading were plotted in Figure 8,. Figure 8(a) represents the curve of specimen AM, which is consistent with the experimental observation. At the early stage of loading, the curve progressed linearly when the joint deformed in an elastic way. Then the curve experienced two sudden declines in sequence. The first decline happened at the point where the displacement of the steel tube was 40mm and the shear force reached about 300kN, which corresponds to the first crack initiated at the hole. The capacity continued to increase until the displacement reached 80mm when the peak load of 342.6kN was reached. The second decline

corresponds to the perfoliate crack as stated in section 3.1. After the summit point, the curve increased to a certain rate lower than the summit and then decreased gradually.

As is shown in Figure 8(b), the curve of specimen BM showed a different characteristic than specimen AM. No obvious decrease was observed in the curve. At the early stage of the loading, the force increased linearly along with the displacement of the steel tube before the yield point (about 20mm, 350kN). Then the stiffness decreased significantly after the yield point. The force increased slowly along with the displacement. After the joint reached the peak load (478.2kN), the curve began to decline gradually until 80% of the peak load.



(a) GKJ-1 (b) GKJ-2

Figure 8. Monotonically loaded specimens (i.e. AM, BM)

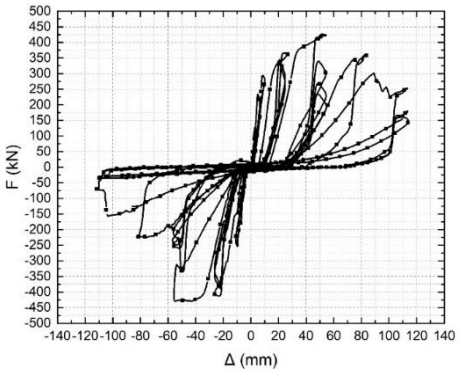


Figure 9. Cyclically loaded specimen BC

Table 2. Connection properties matrix

Specimen No.	Stiffness kN/mm	Yield point		Peak point	
		displacement(mm)	shear(kN)	displacement(mm)	force(kN)
AM	33.0	5.2	171.4	77.7	342.6
BM	27.9	7.9	220.2	118.4	478.2
BC	28.3	7.5	212.6	90.4	428.9

Figure 9 shows the force-displacement hysteretic curve of specimen BC, which was loaded cyclically. The early hysteretic loops showed relatively high and stable stiffness. The later loops were relatively full, which indicates that the energy dissipation ability was good for specimen BC. During the declining

stage of the loading, the curve decreases gradually after the peak load of the certain loop and decreases to zero when the loading direction reverses. The specimen failed at the nineth hysteretic loop, where the capacity of the joint decreased to 80% of the peak load.

All of the connection properties are listed in Table 2.

3.3 Capacity calculation method

Many countries have already put design codes into practice that provide the specific equations to calculate the embedment capacity of wood in various cases. This section arranges these calculating approaches together and compare them with each other, in order to investigate the feasibility of the calculating methods in current codes.

Chinese standard GB50005-2017 provides the calculation for the embedment strength in the direction perpendicular to grain as Eq. (1)

$$f_{e,90} = \frac{212G^{1.45}}{\sqrt{d}} \tag{1}$$

Where G represents the total dry relative density of the wood (10^3kg/m^3), d represents the diameter of the fastener (mm). The equation provided here is similar to that in American code [19].

In European standard EN1995-1-1:2004 [20], embedment strength at an angle α to grain is obtained according to Eqs. (2)~(3):

$$f_{e,\alpha} = \frac{f_{e,0}}{K_{90}\sin^2\alpha + \cos^2\alpha} \tag{2}$$

$$K_{90} = \begin{cases} 1.35 + 0.015d\,(soft\ wood) \\ 1.30 + 0.015d\,(LVL) \\ 0.90 + 0.015d\,(hard\ wood) \end{cases} \tag{3}$$

Furthermore, Canadian standard [21] CSA(O86-09-2009) provides the embedment strength relative to the density as well as the diameter of fasteners as follows:

$$f_{e,90} = 22G(1 - 0.01d) \tag{4}$$

As is easily noticed that, for European and Canadian standards, the embedment strength of wood is directly or indirectly relative to the diameter of the fastener And it can be inferred that no embedment strength can be calculated using current equations with diameter over 100mm since the part (1-0.01d) can't be negative obviously. Therefore, only Chinese or American standards can currently calculate the embedment strength for such large steel-tube joints discussed in this paper. Calculation results are listed below in Table 3 and the comparison with test results are also obtained.

Table 3. Calculation and test results

d(mm)	Test results(kN)	GB50005-2017/NDS-2005(kN)	Error(%)
133(for group A)	342.6	158.6	53.7
273(for group B)	478.2	227.2	52.5

According to Table 3, even if some certain standards can calculate the shear performance for large steel-tube connections, the accuracy is doubted with an error up to 50%. This error means that the test results can be almost two times over calculation results, which indicates that for large steel-tube joints, the capacities are over underestimated.

4. Conclusion

A series of three embedded steel-tube glulam joint have been tested and the results have been compared to the current standards. The conclusions are listed as follows:

(1) The embedded steel-tube glulam joints applied in arched timber structures can achieve high shear capacity and stiffness, which can be a good method of connecting arches together in the out-of-plane direction;

(2) It can be a valuable approach to apply self-tapping screws (STSs) near the joint area perpendicular to the wood grain to help the joint to perform in a more ductile way;

(3) The current standards cannot exactly predict the capacity of large embedded steel-tube glulam joint since the embedment strength cannot be applied to fasteners larger than 100mm in diameter.

References

[1] D. Lathuillière, L. Bléron, T. Descamps, J.-F. Bocquet, Reinforcement of dowel type connections, Constr. Build. Mater. 97 (2015) 48–54. https://doi.org/10.1016/j.conbuildmat.2015.05.088.

[2] Z. Shu, Z. Li, X. Yu, J. Zhang, M. He, Rotational performance of glulam bolted joints: experimental investigation and analytical approach, Constr. Build. Mater. 213 (2019) 675–695. https://doi.org/10.1016/j.conbuildmat.2019.03.002.

[3] J. Thamboo, S. Navaratnam, T. Ponnampalam, Pull-out resistance of glued in rod connection in timber: Reliability analyses using an experimental database, Constr. Build. Mater. 344 (2022) 128291. https://doi.org/10.1016/j.conbuildmat.2022.128291.

[4] Z. Li, F. Chen, M. He, W. Long, J. Ou, M. Li, Experimental investigation on self-centering steel-timber hybrid beam-column connections, J. Struct. Eng. 149 (2023) 04022256. https://doi.org/10.1061/JSENDH.STENG-11570.

[5] P. Rapp, Computational model of adhesive scarf joints in timber beams, Drewno. 57 (2014) 5–35. https://doi.org/10.12841/wood.1644-3985.070.01.

[6] A. Morin-Bernard, P. Blanchet, C. Dagenais, A. Achim, Glued-laminated timber from northern hardwoods: Effect of finger-joint profile on lamellae tensile strength, Constr. Build. Mater. 271 (2021) 121591. https://doi.org/10.1016/j.conbuildmat.2020.121591.

[7] U.A. Girhammar, N. Jacquier, B. Källsner, Stiffness model for inclined screws in shear-tension mode in timber-to-timber joints, Eng. Struct. 136 (2017) 580–595. https://doi.org/10.1016/j.engstruct.2017.01.022.

[8] Y. Liu, Z. Yao, F. Wang, H. Huang, Z. Que, Effect of arrangement distances on stiffness of shear-tension mode in timber-to-timber connections with inclined screws, Constr. Build. Mater. 314 (2022) 125592. https://doi.org/10.1016/j.conbuildmat.2021.125592.

[9] T. Mori, M. Nakatani, S. Tesfamariam, Performance of semirigid timber frame with Lagscrewbolt connections: Experimental, analytical, and numerical model results, Int. J. Adv. Struct. Eng. 7 (2015) 387–403. https://doi.org/10.1007/s40091-015-0107-4.

[10] Z. Shu, B. Ning, J. Chen, Z. Li, M. He, J. Luo, H. Dong, Reinforced moment‐resisting glulam bolted connection with coupled long steel rod with screwheads for modern timber frame structures, Earthquake Engng. Struct. Dyn. (2022) eqe.3789. https://doi.org/10.1002/eqe.3789.

[11] M. Cepelka, K.A. Malo, Moment resisting splice of timber beams using long threaded rods and grout-filled couplers – Experimental results and predictive models, Constr. Build. Mater. 155 (2017) 560–570. https://doi.org/10.1016/j.conbuildmat.2017.08.089.

[12] M. Cepelka, K.A. Malo, Review on on-site splice joints in timber engineering, in: Proceedings of COST Timber Bridge Confetence - CTBC 2014, Biel, Switzerland, 2014.

[13] Uibel T, Blaß H J. Load carrying capacity of joints with dowel type fasteners in solid wood panels. Proceedings. CIB-W18 Meeting. 2006.

[14] Uibel T, Blaß H J. Edge joints with dowel type fasteners in cross laminated timber. Proceedings. CIB-W18 Meeting. 2007.

[15] Kennedy S, Salenikovich A, Munoz W, et al. Design equations for dowel embedment strength and withdrawal resistance for threaded fasteners in CLT. Proceedings of the world conference on timber engineering, Quebec. 2014.

[16] Dong W, Li Q, Zhang H, et al. Embedment Strength of Cross-Laminated Timber for Smooth Dowel-type Fasteners. MATEC Web of Conferences. EDP Sciences, 2019, 275: 01020.

[17] Dong W, Wang Z, Zhou J, et al. Embedment strength of smooth dowel-type fasteners in cross-laminated timber. Construction and Building Materials, 2020, 233: 117243.

[18] Rothoblaas, VGS - Fully threaded screw with countersunk or hexagonal head, Cortaccia, Italy: Rothoblaas design manual, 2022.

[19] ANSI, American Forest, Paper Association. ANSI/AF&PA NDS-2005. National design specification for wood construction. U.S: American Forest & Paper Association,2005.

[20] British Standards Institution. EN1995-1-1. Eurocode 5-Design of Timber Structures-Part 1-1: General-Common Rules and Rules for Buildings. London, UK: British Standards Institution, 2004.

[21] Canadian Standards Association. CSA O86-09. Engineering design in wood. Mississauga, Canada: Canadian Standards Association,2009.

Topology optimisation

Active bending
Additive manufacturing/ 3D printing
Architectural geometry
Bamboo for sustainable construction and quality of life improvement
Bio-inspired structures and architecture
Bridge structures
Computational form-finding
Conceptual design
Concrete structures
Construction techniques
Deployable and inflatable structures
Design competition (WG21)
Digital modelling and fabrication
Dynamic response of metal spatial structures
Dynamic response of other structures
Form-finding and structural optimisation of interlocking discrete assemblages
Graphical methods
Gridshell and lattice structures
Historical concrete shells
Historical structures
Lattice structures
Life-cycle design and assessment of structures
Metal gridshell structures, connections and stability
Methods and construction technologies for sustainable shell structures
Morphology and configuration processing
Next generation parametric design
Novel methods in modelling, optimisation and construction for reducing carbon footprint of continuous roof shells
Numerical methods for geometry, form-finding and optimisation of lightweight structures
Optimisation methods and applications
Origami
Other
Teaching design uncertainty: working with unknown qualities/quantities of new and re-claimed materials
Teaching of shell and spatial structures
Tensegrity systems and cable structures
Tension and membrane structures
Tension structures in the Asia-Pacific
Timber and bio-based structures
► **Topology optimisation**
Traditional masonry structures and innovation
Transformable structures

IASS 2023
July 10–14 Melbourne
Integration of Design and Fabrication

Proceedings of the IASS Annual Symposium 2023
Integration of Design and Fabrication
10–14 July 2023, Melbourne, Australia
Y.M. Xie, J. Burry, T.U. Lee and J. Ma (eds.)

A boundary-finite element coupling framework for topology optimisation in unbounded media

Aldemar SIQUEIRA[*], Pérsio L.A. BARROS[a], Renato PICELLI[b], Josué LABAKI[a]

[a,*] School of Mechanical Engineering, University of Campinas,
200 Mendeleyev St, 13083-860, Campinas SP, Brazil
a235583@dac.unicamp.br

[b] Department of Mining and Petroleum Engineering, University of São Paulo, Narciso de Andrade Sq, Mathias Vlg, 11013-560, Santos SP, Brazil

Abstract

This article presents a framework for topology optimisation in unbounded media. The air in electromagnetic and acoustic problems and the soil in soil-structure interaction problems are examples of unbounded media. Unbounded media have characteristics that require special methods to describe them properly. Domain discretization methods such as the classical Finite Element Method (FEM) resort to truncation of the unbounded domain, which not only results in computational cost issues, but also violates radiation conditions for the unbounded domain. In this paper, we focus on the case of a soil-structure interaction problem and present a strategy to design via topology optimisation. The unbounded region surrounding this domain is modelled via Boundary Element Method (BEM). Coupling between the two methods is obtained by imposing continuity and equilibrium conditions at their interface. We also present a strategy to describe this coupling in the case in which the finite and boundary element meshes have different orders. The paper discusses the derivation of sensitivity and filtering schemes based on the coupled FEM-BEM equilibrium equation. As an illustrative example, this framework is used in this paper to compute optimised designs for buried foundations. In order to show the flexibility of the framework, we have used both the Solid Isotropic Microstructure with Penalization (SIMP) and the Bi-Directional Evolutionary Structural Optimisation (BESO) methods to solve this foundation optimisation problem. The results show that the present framework is computationally efficient and yields physically consistent results.

Keywords: soil-structure interaction, topology optimisation, coupled methods, foundations

1. Introduction

Topology optimisation (TO) algorithms have become widely used in recent years. The popularisation of these powerful design tools has occurred in conjunction with intense research in different methods [1,2] and applications [3,4], culminating in the possibility of applying topology optimisation to a wide range of engineering problems. However, problems involving unbounded domains, such as soil-structure interaction, have not been studied as extensively as those with finite domains.

Most works involving the structural optimisation of structure-soil systems focus on the problem of a completely buried structure, specifically, deep buried tunnels and excavations [5,6]. More recently, the work of [7] expanded the set of applications of TO in soil-structure interaction by investigating the structural optimisation of buried foundations. All these works have in common that the soil is represented through a large finite element mesh that needs to be truncated at a significant distance from the design domain.

Copyright © 2023 by Aldemar SIQUEIRA, Pérsio L.A. BARROS, Renato PICELLI and Josué LABAKI. Published in the Proceedings of the IASS Annual Symposium 2023 with permission.

The recent works of [8] and [9] have utilised boundary-element formulations to accurately model the soil and avoid the use of huge meshes in problems of soil-structure interaction. By coupling a finite-element-modelled design domain with the unbounded soil response, they were able to demonstrate that the presence of the soil strongly affects the optimisation of structures on the soil surface. Although these results are encouraging, there is still room for further investigation and improvements in the current approaches.

The present work aims to expand the use of coupled formulations in topology optimisation of soil-structure systems by investigating the optimisation of half-buried structures. Classical four-noded isoparametric finite elements are used to model the optimisation design domain, which is defined at a specific portion of the soil that surrounds the buried part of the structure. The soil is modelled as a semi-infinite elastic medium using an Indirect Boundary Element formulation based on the superposition of influence functions. The two formulations are coupled through the imposition of continuity and equilibrium conditions at the interface. The optimisation is carried out using the BESO and SIMP algorithms. The present results illustrate the effect of applied load position, available material and the coupling scheme on the optimisation final solution.

2. Numerical model

2.1. Problem statement

Consider a linear-elastic, two-dimensional structure of Young's modulus E_c and Poisson ratio ν_c, which has an arbitrary shape and is partially buried in a linear-elastic layer of Young's modulus E_s and Poisson ratio ν_s. The layer extends horizontally without bounds, has a depth of H, and is placed on a rigid bedrock. The optimisation problem can be stated as: given a static load applied over the structure, determine the optimal topology for the buried section of the structure that maximises the stiffness of the soil-structure system, while keeping the volume of material fixed.

2.2. Soil-structure interaction model

The methodology employed in this study involves utilising a boundary-finite element coupling scheme to model the interaction between the soil and the structure. The proposed method employs classical four-noded finite elements to model a rectangular-shaped domain denoted by Ω, which encompasses the embedded portion of the structure (Fig. 1b). This allows each finite element within Ω to be assigned material properties of either the structure (denoted by the sub-index *c*), the surrounding soil (denoted by the sub-index *s*), or to represent voids in the structure. The remaining portion of the semi-infinite soil layer is modelled using an Indirect Boundary Element Method formulation, in which the interface $\Gamma=\Gamma_1+\Gamma_2+\Gamma_3$ (Fig. 1c) is discretized with piecewise constant boundary elements representing a superposition of non-singular influence functions.

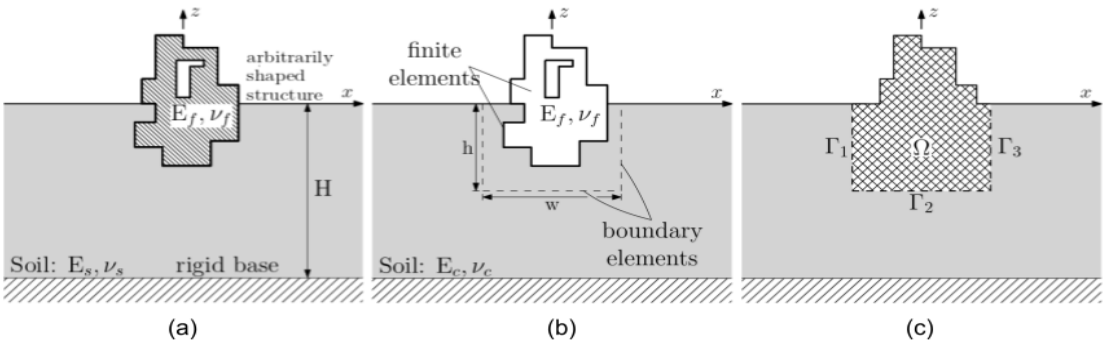


Figure 1. Problem statement: (a) arbitrarily shape half-buried in the soil, (b) subdomains used in the finite- and boundary-element models and (c) subdomain notation.

2.3. Model of the structure

The optimizable domain Ω is modelled with linear-elastic, isoparametric quadrilateral finite elements (FE), with four nodes and two degrees of freedom per node. A plane-strain condition is assumed. The elemental stiffness matrix is given by $\mathbf{k}_c = \int_{-1}^{+1} \int_{-1}^{+1} \mathbf{B}\mathbf{C}^T\mathbf{B} \det[\mathbf{J}] d\xi d\eta$, where **B** is the strain–displacement transformation matrix, **C** is the constitutive matrix for the plane-strain case and **J** is the Jacobian operator of the transformation between natural $(x - z)$ and parametric $(\xi - \eta)$ domains. The global stiffness matrix $\mathbf{K}_c$ of Ω is assembled from $\mathbf{k}_c$ according to the classical assembly algorithm [10]. The equilibrium equation for Ω is given by:

$$\mathbf{K}_c \mathbf{u}_c = \mathbf{f}_c, \tag{1}$$

in which $\mathbf{u}_c$ and $\mathbf{f}_c$ are the vector of nodal displacements and forces, respectively.

2.4. Model of the soil layer

To model the unbounded soil layer, the IBEM formulation involves the discretization of the interface Γ by piecewise constant boundary elements (BE). These elements have a single node located at their center, and the displacements and tractions measured at these nodes are connected via a series of fictitious loads. In the present model, Γ is discretized by $N_s = N_h + 2N_w$ elements, in which N_w is the number of vertical elements at Γ_1 and Γ_3, and N_h is the number of horizontal elements at Γ_2. The displacements and tractions for each element can be written as

$$\mathbf{u}_b = \mathbf{U}\mathbf{q}, \tag{2}$$

$$\mathbf{t}_b = \mathbf{T}\mathbf{q}, \tag{3}$$

in which $\mathbf{u}_b = \{u_x^1\ u_z^1\ u_x^2\ u_z^2 \ldots u_x^{Ns}\ u_z^{Ns}\}^T$ is the vector of nodal displacements, $\mathbf{t}_b = \{t_x^1\ t_z^1\ t_x^2\ t_z^2 \ldots t_x^{Ns}\ t_z^{Ns}\}^T$ is the vector of nodal tractions, $\mathbf{q} = \{q_x^1\ q_z^1\ q_x^2\ q_z^2 \ldots q_x^{Ns}\ q_z^{Ns}\}^T$ is the vector of fictitious loads, and **U** and **T** are displacement and traction influence matrices that incorporate the response of the soil layer. A general term $u_{r,s}^{i,j}$ of matrix **U** represent the displacement of an element *i* of the BE mesh in the *r*-direction due to a unit load uniformly distributed over an element *j* in the *s*-direction $(i, j = 1, \ldots, N_s; r, s = x, z)$. The same convention holds for a general term $t_{r,s}^{i,j}$ of matrix **T**. The solution for the unknown contact loads **q** is obtained by imposing prescribed continuity and equilibrium conditions throughout the element nodes at the Γ interface.

2.4.1. Influence functions

General solutions for stress and displacements in the semi-infinite soil are expressed in terms of non-singular Green's functions, which are commonly referred to as influence functions. The solutions proposed by [9], which take into account loads applied within the soil, are employed in this study. The displacement and stress inside the soil layer are written in terms of improper integrals in the Fourier transformed space:

$$u_i(x, z) = \int_{-\infty}^{\infty} \bar{u}_i\ e^{i\zeta x} d\zeta \tag{4}$$

$$\sigma_{ij}(x, z) = \int_{-\infty}^{\infty} \bar{\sigma}_{ij}\ e^{i\zeta x} d\zeta, \quad i, j = x, z, \tag{5}$$

where $\underline{u_i}$ and $\underline{\sigma_{ij}}$ are functions of the constitutive properties of the soil and load depth. These solutions are computed numerically, as they do not have an explicit solution, demanding a high computational cost. This is due to the integrands containing regions with singularities, and an oscillatory-decaying tail which necessitate the use of specific integration techniques. Details of the numerical evaluation of these functions are presented in [9].

To account for the geometric orientation of the boundary in the problem, the stress terms calculated in Eq. (5) need to be converted into traction terms. This can be achieved with the Cauchy's formula $t_{rt}^{i,j} = \sigma_{rst}^{i,j} n_r^i$, $(r,s,t = x,z;\ i,j = 1,\ldots,N_s)$, in which $\mathbf{n}^i = \{\boldsymbol{n_x^i}\ \boldsymbol{n_z^i}\}^T$ is the unit normal vector at the BE where the traction is being determined, and pointing outward from the soil domain. At Γ_1, Γ_2 and Γ_3, $\mathbf{n}^i = \{1\ 0\}^T$, $\mathbf{n}^i = \{0\ 1\}^T$, $\mathbf{n}^i = \{-1\ 0\}^T$, respectively. Influence functions for loads that are uniformly distributed in the vertical direction are computed for elements located at $\Gamma_{1,3}$, while influence functions for loads that are uniformly distributed in the horizontal direction are computed for elements located at Γ_2.

2.5. Coupling scheme

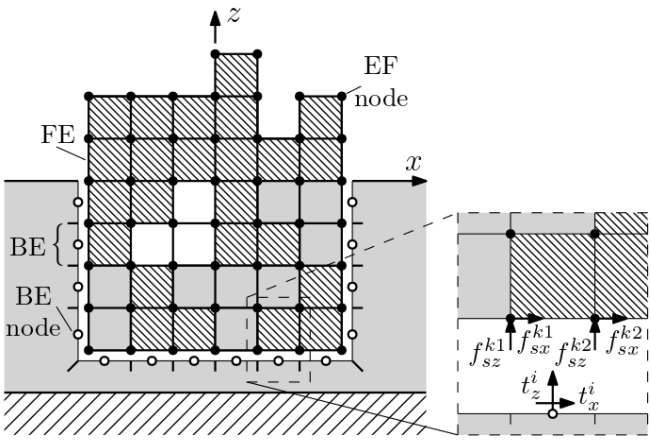


Figure 2. Coupling.

To incorporate the soil response on the design domain, one can implement a finite-boundary coupling scheme. The unbounded soil response over Ω can be expressed in terms of a set of equivalent nodal contact forces $\mathbf{f}_s$ (Fig. 2), acting on the finite element nodes at the Γ interface. Thus, the equilibrium equation of Ω can be written as:

$$\mathbf{K}_c\mathbf{u}_c = \mathbf{f}_c - \mathbf{f}_s. \tag{6}$$

The coupling of Ω and the surrounding soil is achieved by imposing continuity and equilibrium conditions at the interface Γ. The equilibrium condition represents that the equivalent nodal contact force over a finite element can be expressed in terms of the fictitious loads applied over the corresponding boundary element. As the elements used have different orders of approximation, a nodal equivalence transformation given by $\mathbf{f}_s$=**ATq**, is used to represent equilibrium. In this equation, $\mathbf{f}_s = \{f_{sx}^1\ f_{sz}^1\ f_{sx}^2\ f_{sz}^1 \ldots f_{sx}^{n\prime}\ f_{sz}^{n\prime}\}$, **A** is a transformation matrix and *n'* is the number of nodes at the interface Γ. Considering this nodal equivalence transformation, Eq. (6) can be rewritten as

$$\mathbf{K}_c\mathbf{u}_c + \mathbf{ATq} = \mathbf{f}_c. \tag{7}$$

The continuity condition ensures kinematic compatibility of the correspondent FE-BE. This can also be achieved by a linear transformation such as:

$$\mathbf{u}_b = \mathbf{D}\mathbf{u}_c, \tag{8}$$

where **D** is a transformation matrix. In view of Eq. (2), the continuity condition yields

$$\mathbf{D}\mathbf{u}_c - \mathbf{U}\mathbf{q} = \mathbf{0}. \tag{9}$$

Rewriting Eq. (7) and Eq. (8) into a single matrix equation gives

$$\begin{bmatrix} \mathbf{K} & \mathbf{AT} \\ \mathbf{D} & -\mathbf{U} \end{bmatrix} \begin{Bmatrix} \mathbf{u}_c \\ \mathbf{q} \end{Bmatrix} = \begin{Bmatrix} \mathbf{f} \\ \mathbf{0} \end{Bmatrix}, \tag{10}$$

which represents the equilibrium for nodes at the interface Γ. Extending to the entire domain Ω, yields

$$\begin{bmatrix} \mathbf{K} & \begin{Bmatrix} \mathbf{AT} \\ \mathbf{0} \end{Bmatrix} \\ \{\mathbf{D} \quad \mathbf{0}\} & -\mathbf{U} \end{bmatrix} \begin{Bmatrix} \begin{Bmatrix} \mathbf{u}_c \\ \mathbf{0} \end{Bmatrix} \\ \mathbf{q} \end{Bmatrix} = \begin{Bmatrix} \begin{Bmatrix} \mathbf{f} \\ \mathbf{0} \end{Bmatrix} \\ \mathbf{0} \end{Bmatrix}, \tag{11}$$

in which **0** are matrices of zeros of compatible dimensions. Equation (11) represents the present coupled IBEM-FEM formulation, and its solution for a set of applied forces **f** yields the nodal displacements $\mathbf{u}_c$ of Ω, as well as the set of fictitious loads **q**.

3. Topology optimisation

In this work, the focus is on optimising the topology of the buried part of the structure in order to obtain the structure-soil system with the maximum possible stiffness, thus resulting in an optimal foundation design. This is addressed by considering the optimisation problem as one of compliance minimization with a prescribed volume constraint. In the sense of the present IBEM-FEM implementation, this problem can be formulated as

$$\begin{aligned} &\text{Minimise } C(\boldsymbol{x}) = \mathbf{f}^T\mathbf{u}_c, \\ &\text{Subject to } V^* - \textstyle\sum_{i=1}^{Nd} \quad V_i x_i = 0, \\ &\qquad x_i \in \{1,0\}, \\ &\qquad \begin{bmatrix} \mathbf{K} & \mathbf{AT} \\ \mathbf{D} & -\mathbf{U} \end{bmatrix} \begin{Bmatrix} \mathbf{u}_c \\ \mathbf{q} \end{Bmatrix} = \begin{Bmatrix} \mathbf{f} \\ \mathbf{0} \end{Bmatrix}, \end{aligned} \tag{12}$$

in which x_i is the vector of design variables, V^* is the specified maximum of the structure material, N_d is the number of elements in the design domain, and $C(x)$ is the structural compliance, which is the objective function. A value of x_i = 1 corresponds to a structure element and x_i = 0 corresponds to a soil element. In this article, the BESO algorithm [11] is mainly used for the optimisation process.

Considering the problem's two-phase nature, the material interpolation scheme applied is defined by the following power law [12]:

$$E(x_i) = E_s + x_i^p (E_s + E_c), \tag{13}$$

where $p = 3$ is a penalty coefficient.

3.1. Sensitivity numbers

Sensitivity numbers represent the gradient of the objective function with respect to the design variables. The influence matrices **U** and **T**, as well as the transformation matrices **A** and **D**, are not dependent on the elastic properties of the optimizable domain Ω. This implies that the sensitivity analysis is solely dependent on the coupled structural stiffness. For a two-phase material problem, the elemental sensitivities can be written as [11]

$$\alpha_i = \begin{cases} \left[1 - \dfrac{E_s}{E_c}\right] \mathbf{u}_i{}^T \mathbf{k}_i \mathbf{u}_i, & \text{for structure element} \\ 0, & \text{for soil element,} \end{cases}, \tag{14}$$

where $\mathbf{k}_i$ and $\mathbf{u}_i$ are the elemental stiffness matrix and the vector of nodal displacements of element *i*, respectively. These numbers are derived considering the hard-kill BESO algorithm, in which the penalty factor *p* in Eq. (13) approaches infinity.

3.2. BESO algorithm

The Bi-directional Evolutionary Structural Optimisation method (BESO) [11] is a well-established optimisation algorithm [3] that consists of an iterative material removal scheme based on the ranked elemental sensitivity numbers (Eq. (14)). The method applies a binary approach, in which, starting from a given initial design, elements with the lowest sensitivities are iteratively removed (switching x_i from 1 to 0). Elements that have been removed from the design domain can also be reintroduced (switching x_i from 0 to 1) to prevent local minimum solutions. The net amount of material removed at each iteration is controlled by an evolutionary ratio (*ER*), given as a percentage of the design domain volume. The maximum of added material is also controlled by a maximum admission ratio (AR_{max}) parameter.

Traditional structural optimisation problems like checkerboard patterns and mesh-dependent solutions are avoided by applying a smoothing filter to the elemental sensitivities. In this work, the filtered sensitivity number of element *i* is given by:

$$\hat{\alpha}_i = \frac{\sum_{j=1}^{N_d} \alpha_i H_{ij}}{\sum_{j=1}^{N_d} H_{ij}}, \tag{15}$$

Where $H_{ij} = \max\{0, r_f - r_{ij}\}$, r_f is the filter radius and r_{ij} is the distance between the centers of the *i*-th and *j*-th elements.

A historic stabilisation scheme is also employed in order to enhance optimisation convergence properties [11]. This is obtained by taking the average sensitivity number of two consecutive iterations:

$$\hat{\alpha}_i^k = \frac{\hat{\alpha}_i^k + \hat{\alpha}_i^{k-1}}{2}, \tag{16}$$

in which *k* denotes the current iteration. It is assumed that optimisation reaches convergence when the value of the objective function remains stable for at least 10 consecutive iterations. This is formulated by the following equation

$$\text{error} = \frac{\left|\sum_{i=1}^{N}(C_{k-i+1} - C_{k-N-i+1})\right|}{\sum_{i=1}^{N} C_{k-i+1}} \leq \tau, \tag{17}$$

where the relative convergence error must be less than a small value $\tau = 10^{-4}$, and $N = 5$.

4. Numerical results

This section presents some numerical examples of the present implementation. The problem considered is that of the foundation of a rigid strip footing resting on the soil surface. The footing has a width of *a* and is subjected to vertical symmetric and eccentric static loads (Fig. 3). The optimizable domain Ω was defined as a square with $w = h = 4a$. The plate and the design domain are discretized with a homogeneous mesh of quadrilateral finite elements with size of $0.04a$ (total of 10^{-4} elements). All results consider a rigid base with depth of $H = 40$, a foundation 100 times stiffer than the soil, $E_c = 100E_s$, and with the same Poisson ratio of $\nu_c = \nu_s = 0.25$. The BESO parameters used were $ER = 0.02$ % and $AR_{max} = 0.05$ %, with a filter radius of 2.5 times the size of the element. The SIMP algorithm was applied with a continuation method following the approach proposed by [7]. Results illustrate the effect of the foundation volume, applied load position and coupling scheme on the optimisation results.

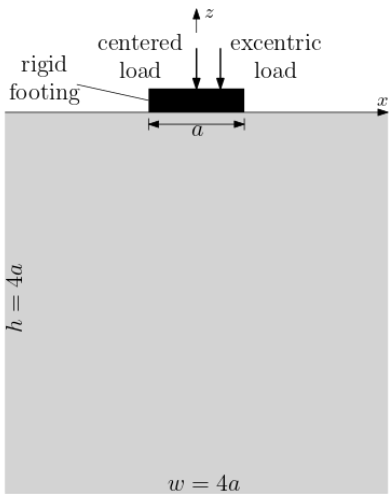


Figure 3. Design domain.

4.1. Effect of the applied load position

Figure 4 shows the final optimisation solution for a foundation under the effect of a symmetric and an eccentric applied load. The target volume for the foundation is 4.5 % of the design domain volume for both scenarios. In the symmetrical load case, the foundation material is concentrated symmetrically at both footing edges, which is physically consistent, as at these points the stress reaches its maximum value over the entire domain. The final topology of the foundation resembles the shape of a traditional piled-foundation, but with a slight inclination from the vertical. In the eccentric load case, the pile-like structures are not symmetrical, and it is observed that there is a noticeable greater concentration of material at the most demanded end of the footing.

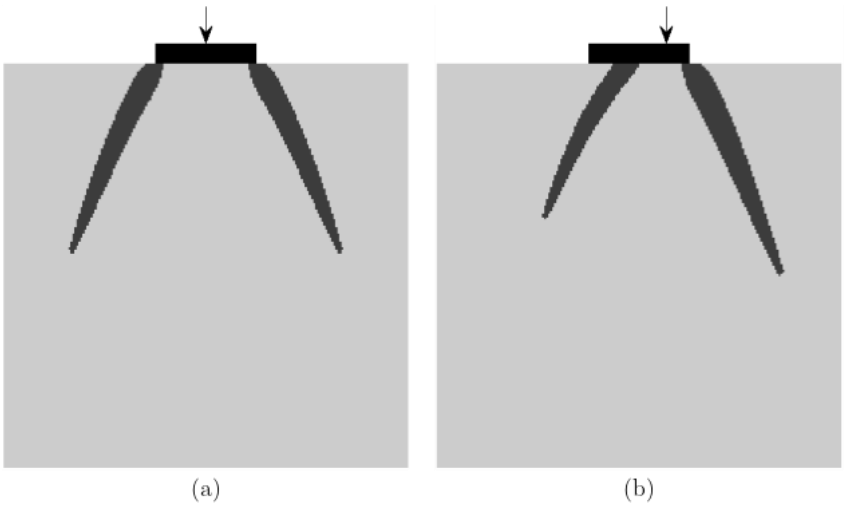


Figure 4. Effect of the applied load position on the optimisation solution: (a) symmetrical load and (b) eccentric load.

The evolution of the objective function for both load cases is presented in Fig. 5. Note that the structural compliance value is significantly increased throughout the iterations as the foundation material is replaced by soil. The objective function value for the centered load case is C = 0.1905 and for the eccentric load case is C = 0.2111, which indicates that the asymmetrical foundation configuration is more flexible than the symmetric configuration.

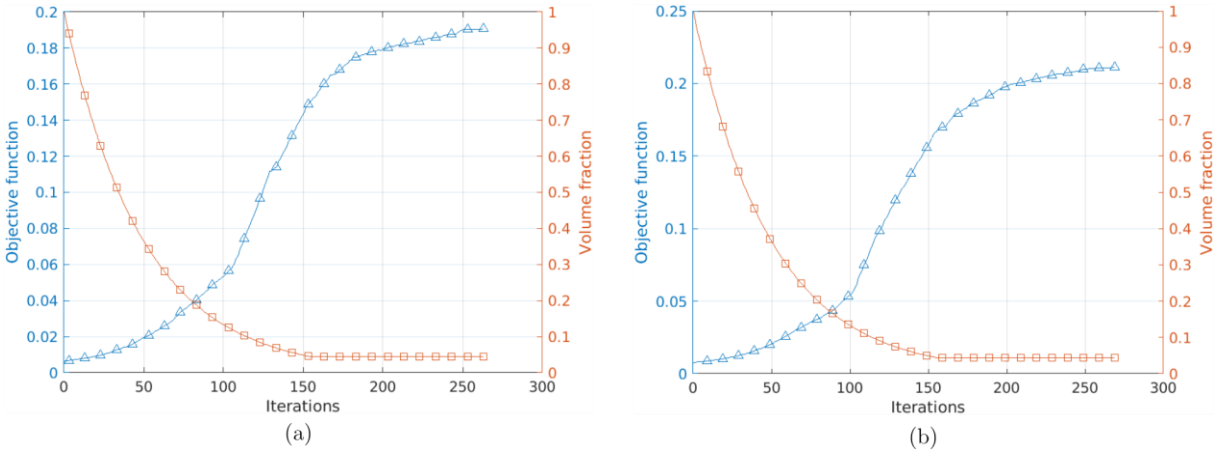


Figure 5. Objective function evolution: (a) symmetrical load and (b) eccentric load.

Figure 6 illustrates the final solution obtained for both load cases using the SIMP method. These results are mostly similar to the results obtained with the BESO method, but with the difference of the formation of thin horizontal bars at the soil surface around the footing, which are absent in the BESO solution. Also, the pile-like structures obtained with the SIMP method are a little more deeper and straighter than those obtained with BESO. The final solutions obtained with the SIMP method present a stiffer configuration than those obtained with BESO method, as the objective function value for the centered load case is C = 0.1590 and for the eccentric load case is C = 0.1824. This is directly related to the fact that the solutions obtained by the SIMP are deeper.

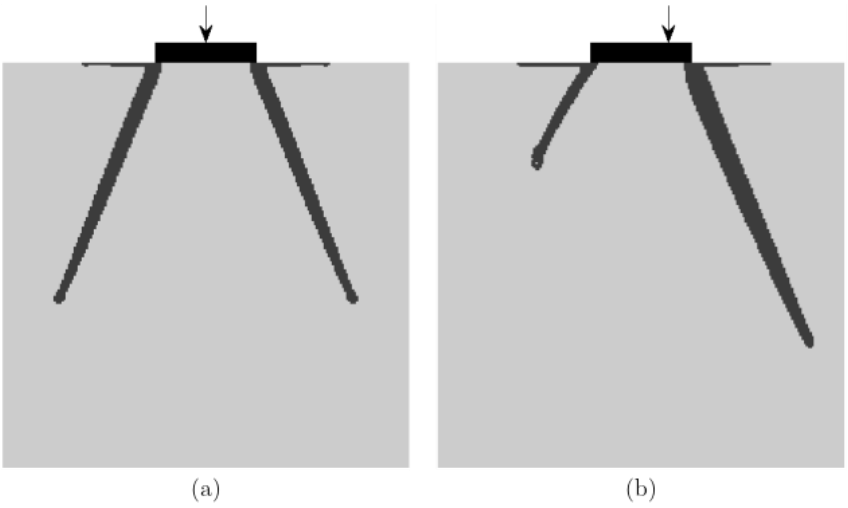


Figure 6. Final solutions obtained with the SIMP method: (a) symmetrical load and (b) eccentric load.

4.2. Effect of foundation volume

Figure 7 shows the influence of the foundation prescribed volume. The results consider a footing under centered load and two prescribed foundation volumes of 4.5% and 10% of the design domain, respectively. It is observed that the more material available, the deeper the optimised foundation is. This is physically consistent with the engineering practice, as deeper foundations present more contact area with the soil which increases the capacity of load transfer from the structure to the soil.

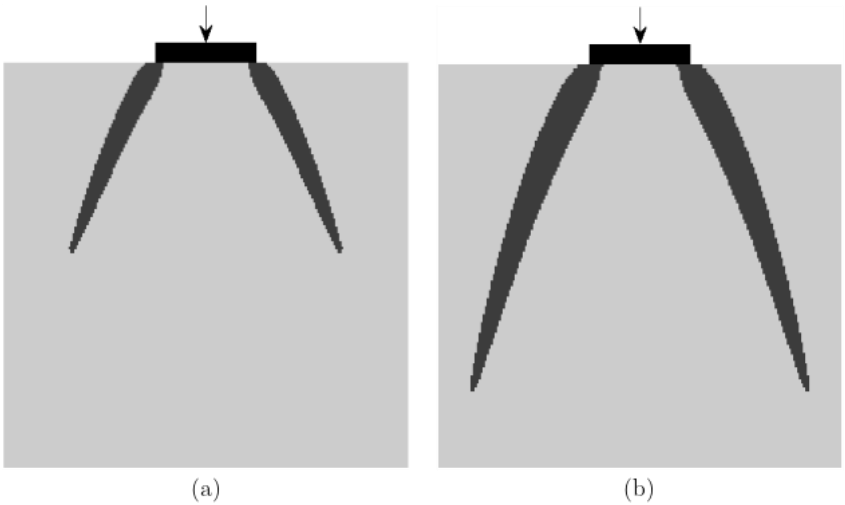


Figure 7. Effect of prescribed foundation volume on the optimisation solution: (a) foundation with a volume of 4.5% of design domain and (b) foundation with a volume of 10% of design domain.

4.2. Effect of coupling

In general, coupling a single finite element to a single neighbour boundary element provides the accurate solution to Eq. (11), but one can use different orders of mesh correspondence to reduce the computational cost at the expense of some accuracy. Figure 8 presents the difference between the final optimised solution for the foundation of a rigid footing subject to a centered vertical load using a 1-1 FE-BE and a 2-1 FE-BE correspondence. The foundation prescribed volume is 4.5% of the design domain volume. Note that both solutions are nearly identical, but the solution obtained with the 2-1 correspondence is on average five times faster, demonstrating the advantage of this approach for computational efficiency.

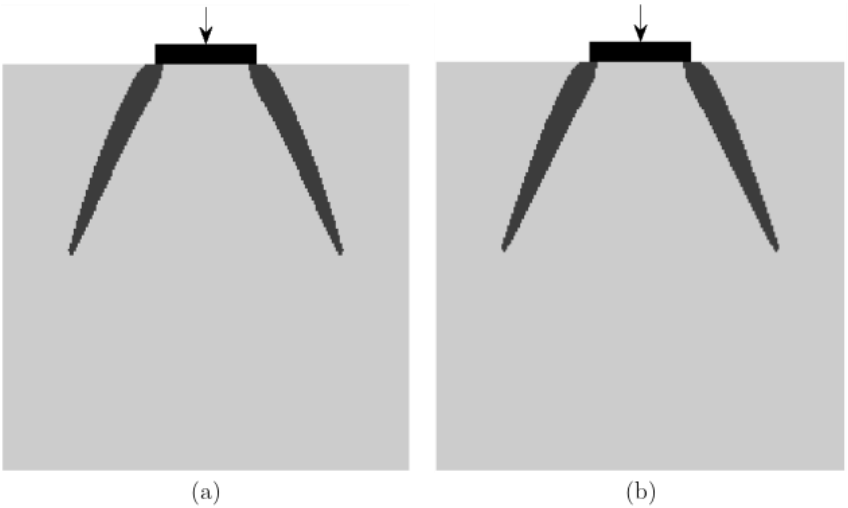


Figure 8. Effect of different orders of coupling correspondence on the optimisation solution: (a) one finite element coupled with one boundary element and (b) two finite elements coupled with one boundary element.

5. Final remarks

This work investigated the topology optimisation of buried foundations. The soil-structure system was modelled via an IBEM-FEM formulation which was used in conjunction with BESO and SIMP algorithms to optimise the material distribution of the buried structure. The soil was modelled through

an Indirect-BEM formulation and was considered a homogeneous semi infinite linear-elastic layer resting over a rigid bedrock. The optimisation domain was defined as a square region in the soil, modelled via classical quadrilateral finite elements. The representative case of the foundation of a rigid strip footing under vertical static loads is investigated. The optimised structure topology resembles that of a piled-foundation, indicating consistency with the engineering practice. It was observed that the position of the applied load significantly affects the optimisation solution. Additionally, increasing the available material resulted in a deeper optimised foundation. Lastly, results have shown that one can choose different coupling configurations to improve the algorithm efficiency without compromising the optimisation results.

5. Acknowledgements

The research leading to this article has been funded in part by the São Paulo Research Foundation (Fapesp) through grant 2022/02753-5.

References

[1] X. Huang, "Smooth topological design of structures using the floating projection," *Engineering Structures,* vol. 208, pp. 110330, 2020.

[2] R. Sivapuram and R. Picelli, "Topology optimization of binary structures using Integer Linear Programming," *Finite Elements in Analysis and Design,* vol. 139, pp. 49-61, 2018.

[3] L. Xia, Q. Xia, X. Huang, and Y. M. Xie, "Bi-directional evolutionary structural optimisation on advanced structures and materials: A comprehensive review," *Archives of Computational Methods in Engineering,* vol. 25, no. 2, pp. 437–478, 2016.

[4] B. C. Souza, P.V.M. Yamabe, L.F.N. Sá, S. Ranjbarzadeh and E.C.N. Silva, "Topology optimization of fluid flow by using Integer Linear Programming,", *Structural and Multidisciplinary Optimization,* vol. 64, pp. 1221-1240, 2021.

[5] K. Ghabraie, Y. M. Xie and G. Ren, "Shape and reinforcement optimization of underground tunnels," *Journal of Computational Science and Technology,* vol. 4, pp. 51-63, 2010.

[6] T. Nguyen, K. Ghabraie and T. Tran-Cong, "Applying bi-directional evolutionary structural optimisation method for tunnel reinforcement design considering nonlinear material behaviour," *Computers and Geotechnics,* vol. 55, pp. 57-66. 2014.

[7] K. F. Seitz and J. Grabe, "Structural optimization in geotechnical engineering: basis and application," *Computers and Geotechnics,* vol. 80, pp. 41-48, 2016.

[8] I. Cavalcante, E. Tavares, R. Picelli and J. Labaki, "Influence of foundation flexibility on the topology optimization of piled structures," *International Journal for Numerical and Analytical Methods in Geomechanics,* vol. 46, pp. 659-673, 2021.

[9] R. Cortez, R. Sivapuram, P. L. A. Barros, R. Picelli and J. Labaki, "On the influence of soil flexibility in structural topology," *Computer Methods in Applied Mechanics and Engineering,* under review.

[10] K. J. Bathe, *Finite element procedures,* 2006.

[11] X. Huang and Y. M. Xie, "Convergent and mesh-independent solutions for the bi-directional evolutionary structural optimization method," *Finite elements in analysis and design,* vol. 43, pp. 1039-1049, 2007.

[12] M. P. Bendsøe and O. Sigmund, "Material interpolation schemes in topology optimization," Archive of applied mechanics, vol. 69, pp. 635-654, 1999.

IASS 2023
July 10–14 Melbourne
Integration of Design and Fabrication

Proceedings of the IASS Annual Symposium 2023
Integration of Design and Fabrication
10–14 July 2023, Melbourne, Australia
Y.M. Xie, J. Burry, T.U. Lee and J. Ma (eds.)

A reaction diffusion-based B-spline level set method using body-fitted mesh for structural topology optimisation

Cong WANG[a], Zicheng ZHUANG[b], Xuyu ZHANG[a], Yi Min XIE[a], Shiwei ZHOU[a,*]

[a,*]Centre for Innovative Structures and Materials, School of Engineering, RMIT University, Melbourne 3000, Australia
shiwei.zhou@rmit.edu.au

[b] Department of Building and Real Estate, The Hong Kong Polytechnic University, Hong Kong, China

Abstract

The level set-based optimisation method generally uses the rectangular/hexahedral mesh in finite element analysis despite its zero-level contour crossing these elements. The work uses adaptive triangular mesh to improve the similarity of the finite element model with the smooth structure presented by the level set method. Also, the level set function is a linear combination of cubic B-spline basis functions to increase optimisation flexibility and structural smoothness. The edges of the triangular mesh are equivalent to a balanced truss network, with its adaptivity adjusted by the distance between the nodes to the boundaries. The sensitivity of design variables, the coefficients of the B-spline basis functions, is analysed using the adjoint variable method. Their values should be interpolated from the nodes of the body-fitted mesh to the nodes of rectangular elements. A reaction-diffusion method and void elements-excluding scheme are used to update and reduce the design variables. Numerical examples illustrate that elegant structures with ultra-smooth boundaries can be generated with high efficiency.

Keywords: topology optimisation, adaptive triangular/tetrahedral mesh, B-spline functions, level set method, reaction-diffusion method, Hangai Prize applicant

1. Introduction

Structural topology optimisation involves the computational layout of material within a design domain based on minimising a costing function and fulfilling various constraints. The approach to structural representation is a critical factor in optimisation as it greatly impacts the final results. The homogenisation method [1] controls material occupancy in an element by using the size of a rectangular void. The solid isotropic material with the penalisation (SIMP) method [2, 3], and bi-directional evolutionary optimisation method (BESO) [4–7] all use the volume ratio of solid material in a local element to represent the structure. The SIMP method imposes a penalty factor greater than or equal to 3 to allow for either complete material occupancy or void in an element, while the grey element with a volume ratio between 0 and 1 is sometimes necessary. In contrast, the level set method [8–10] assumes the structural profile as the zero-level contour of a higher-dimensional level set function. Although this guarantees continuous boundaries, the application of rectangular/tetrahedral elements in finite element analysis makes it meaningless. Therefore, automatic adaptive mesh generation is essential for topology optimisation, as a high-quality body-fitted mesh can accurately describe and discretise the design domain geometry. In the past, various techniques have been proposed for adaptive mesh generation, including polygonal mesh [11], fluid relaxation analogy [12], and feature-aware smoothed particle hydrodynamics [13]. More recently, level-set-based mesh adaptation methods [14, 15] have been proposed and applied in topology optimisation. Closed-source re-meshing tools like MMG, Rhino, and ZBrush have been used to generate body-fitted meshes.

Copyright © 2023 by Cong WANG, Zicheng ZHUANG, Xuyu ZHANG, Yi Min XIE, Shiwei ZHOU.
Published in the Proceedings of the IASS Annual Symposium 2023 with permission.

In addition to body-fitted mesh, a proper structural representation method can also be considered to provide smooth boundaries. For example, B-spline and non-uniform rational basis spline (NURBS) are widely used methods for expressing geometry in computer-aided design/manufacturing (CAD/CAM). They offer global control over the design domain while allowing for local adjustments. In the pursuit of bridging structural topology optimisation with CAD/CAM, researchers have explored using spline functions in structural topology optimisation. One such attempt involved Wall et al. [16], who combined isogeometric analysis (IGA) with shape optimisation, using NURBS to create an exact geometry model. However, the quality of the mesh deteriorated as optimisation progressed due to the high reliance on control points. To address this issue, researchers have turned to parametric representation on the level set function, rather than on the structure directly, to achieve clear and smooth boundaries.

Therefore, the B-spline level set representation method and body-fitted mesh are combined in this article. We propose a reaction diffusion-based B-spline level set method that uses a body-fitted mesh and nonlinear diffusion regularisation. The algorithm updates the positions of vertices iteratively by finding a solution to force equilibrium in the bars, generating a high-quality triangular mesh that captures the boundaries. Delaunay triangulation is used to connect the nodes, forming the body-fitted mesh. The sensitivities generated by adaptive mesh are interpolated to produce B-spline coefficients of sensitivities. Simultaneously, the B-spline coefficients of the level set function is regarded as the designed variables, updated by the reaction-diffusion method. Numerical examples illustrate that elegant structures with ultra-smooth boundaries can be generated with high efficiency.

2. Problem statement

2.1. Optimization problem

The objective of this study is to minimise the mean compliance in order to showcase the advantages of using a B-spline-based level set function using adaptive mesh for structural topology optimisation. The mathematical representation of this optimisation problem, illustrated in Figure 1, can be expressed as:

$$\begin{cases} -\mathrm{div}(\boldsymbol{\sigma}(\mathbf{u})) = f_a(\mathbf{x},\mathbf{u}) & \text{in } D \\ \mathbf{u} = 0 & \text{on } \Gamma_D \\ \boldsymbol{\sigma}(\mathbf{u})\cdot\mathbf{n} = f_b(\mathbf{x},\mathbf{u}) & \text{on } \Gamma_N \\ \boldsymbol{\sigma}(\mathbf{u})\cdot\mathbf{n} = 0 & \text{on } \Gamma_H \end{cases} \tag{1}$$

where $\mathbf{x}$ represents a point situated in the design domain D, $\mathbf{n}$ is the outward normal to the boundary, $\mathbf{u}$ is the displacement field, Γ_D is the Dirichlet boundary that indicates the fixed displacement, Γ_N is the non-homogeneous Neumann boundary that implies the imposed surface traction load with Γ_H being the homogeneous Neumann boundary.

Hooke's law allows us to calculate the stress tensor $\boldsymbol{\sigma}(\mathbf{u})$ and is expressed as:

$$\boldsymbol{\sigma}(\mathbf{u}) = \mathbf{C} : \boldsymbol{\varepsilon}(\mathbf{u}) = 2\mu_1\boldsymbol{\varepsilon}(\mathbf{u}) + \mu_2\mathrm{tr}(\boldsymbol{\varepsilon}(\mathbf{u}))\mathbf{I} \tag{2}$$

where the strain tensor $\boldsymbol{\varepsilon}(\mathbf{u})$ is calculated as 0.5 times the sum of the gradient of displacement $\mathbf{u}$ and its transpose, which is represented as $\boldsymbol{\varepsilon}(\mathbf{u})=0.5(\nabla\mathbf{u}+(\nabla\mathbf{u})^T)$. The fourth-order elasticity tensor $\mathbf{C}$ is used in Hooke's law to calculate the stress tensor $\boldsymbol{\sigma}(\mathbf{u})$. The Lamé coefficients μ_1 and μ_2 are related to Young's modulus E and Poisson's ratio v. The term $\mathrm{tr}(\boldsymbol{\varepsilon}(\mathbf{u}))$ represents the trace of the strain tensor $\boldsymbol{\varepsilon}(\mathbf{u})$.

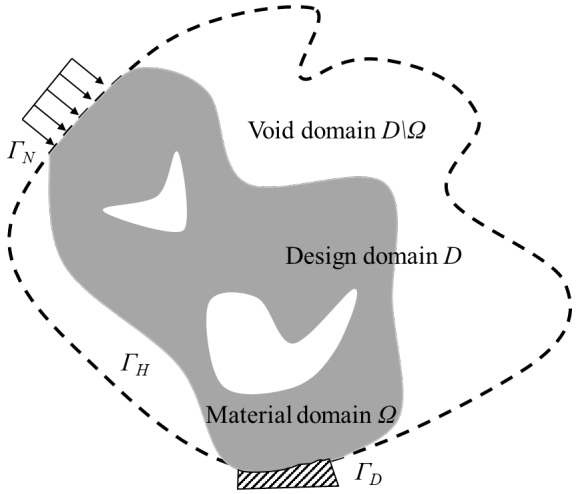


Figure 1. Schematic of the optimisation problem.

An optimisation problem with an objective functional F subject to a volume constraint functional G can be generally represented as:

$$\begin{aligned} &\inf_{\chi_\Omega} F(\chi_\Omega(\mathbf{x})) = \int_D f_a(\mathbf{x},\mathbf{u})\chi_\Omega(\mathbf{x})d\Omega + \int_{\Gamma_N} f_b(\mathbf{x},\mathbf{u})\chi_\Omega(\mathbf{x})d\Gamma_N \\ &\text{subject to } G(\chi_\Omega(\mathbf{x})) = \int_D \chi_\Omega(\mathbf{x})d\Omega - V_{\max} \le 0 \end{aligned} \tag{3}$$

The material distribution problem can be transformed using a characteristic function $\chi_\Omega \in L^2$, which is defined as follows:

$$\begin{cases} \chi_\Omega(\mathbf{x}) = 1 & \text{if } \mathbf{x} \in \Omega \\ \chi_\Omega(\mathbf{x}) = 0 & \text{if } \mathbf{x} \in D \setminus \Omega \end{cases} \tag{4}$$

Then, the analysis in Section 2.1 shows that the characteristic function $\chi_\varphi(\varphi)$ is generated by a level set function expressed by B-splines.

The Lagrange function for the classical level set-based topology optimisation method can be constructed as follows:

$$\inf_{\varphi} L(\chi_\varphi(\varphi),\varphi) = F_d(\chi_\varphi(\varphi),\varphi) + \lambda\left(\int_D \chi_\varphi(\varphi)d\Omega - V_{\max}\right) \tag{5}$$

where L represents the Lagrangian, λ is the Lagrange multiplier of the volume constraint, and F_d is the objective function with a fictitious interface energy term:

$$F_d(\chi_\varphi(\varphi),\varphi) = \int_D f_a(\mathbf{x},\mathbf{u},\chi_\varphi(\varphi))d\Omega + \int_{\Gamma_N} f_b(\mathbf{x},\mathbf{u},\chi_\varphi(\varphi))d\Gamma_N + \int_D \frac{1}{2}\tau\left|\nabla\varphi\right|^2 d\Omega \tag{6}$$

2.2. Structures representation

The conventional level set method utilises a level set function to represent a structure in higher dimensions. Figure 2 illustrates how the zero-level contour $\partial\Omega$ of the level set function φ ($\mathbf{x}$, t) divides the design domain D into regions Ω and $D\backslash\Omega$ based on its sign. This can be expressed mathematically as:

$$\begin{cases} \varphi(\mathbf{x},t) = 0 & \forall \mathbf{x} \in \partial\Omega \\ \varphi(\mathbf{x},t) < 0 & \forall \mathbf{x} \in D \setminus \Omega \\ \varphi(\mathbf{x},t) > 0 & \forall \mathbf{x} \in \Omega \end{cases} \tag{7}$$

where $\mathbf{x}=(u, v)\in R^2$ denotes the global coordinates of a point in Ω and t represents the pseudo-time for the evolution of the level set function.

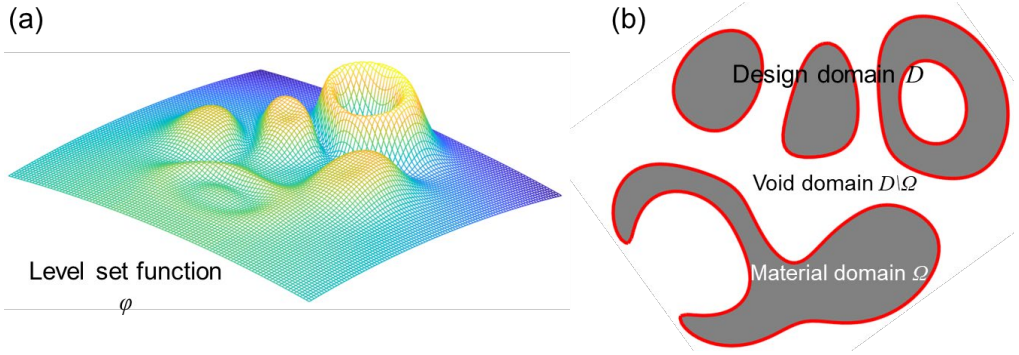


Figure 2. (a) The level set function and (b) its zero-level contour.

The characteristic function χ can be used to represent material presented at a local point and is defined as:

$$\begin{cases} \chi_\varphi\left(\varphi(\mathbf{x},t)\right) = 1 & \text{if } \varphi(\mathbf{x},t) \geq 0 \\ \chi_\varphi\left(\varphi(\mathbf{x},t)\right) = 0 & \text{if } \varphi(\mathbf{x},t) < 0 \end{cases} \tag{8}$$

According to the tensor product of B-spline functions, the level set function is implicitly expressed as the linear combination of cubic B-spline basis functions in our work as:

$$\varphi(\mathbf{x},t) = \sum_{i=1}^{m}\sum_{j=1}^{n} c_{ij}(t)\cdot N_{ij}(\mathbf{x}) = \sum_{i=1}^{m}\sum_{j=1}^{n} c_{ij}(t)\cdot B_i(u)B_j(v) \tag{9}$$

Where the bivariate B-spline function N_{ij} can be expressed as $B_i(u)\ B_j(v)$, where $B_i(u)$ and $B_j(v)$ are the B-spline basis functions defined on the knot vectors in the x and y directions. The coefficient c_{ij} parameterises the level set function.

The standard B-spline shape function in an element can be generated by the Cox-de-Boor formula, the corresponding curves are shown in Figure 3. The detailed generation process can be referred to [17].

$$\begin{aligned} B_1(\xi) &= \frac{1}{6}\left(1-\frac{\xi}{a}\right)^3 \\ B_2(\xi) &= \frac{1}{6}\left[3\left(\frac{\xi}{a}\right)^3 - 6\left(\frac{\xi}{a}\right)^2 + 4\right] \\ B_3(\xi) &= \frac{1}{6}\left[-3\left(\frac{\xi}{a}\right)^3 + 3\left(\frac{\xi}{a}\right)^2 + 3\left(\frac{\xi}{a}\right) + 1\right] \\ B_4(\xi) &= \frac{1}{6}\left(\frac{\xi}{a}\right)^3 \end{aligned} \tag{10}$$

The $B_j(\eta)$ has similar formulae to $B_i(\xi)$, so they are not presented herein.

With 4×4 B-spline shape functions of x and y directions, Eq. (9) in each element becomes:

$$\varphi^e(\xi,\eta,t) = \sum_{i=1}^{4}\sum_{j=1}^{4} c_{ij}(t)\cdot N_{ij}(\xi,\eta) = \sum_{i=1}^{4}\sum_{j=1}^{4} c_{ij}(t)\cdot B_i(\xi)B_j(\eta) = \mathbf{N}(\xi,\eta)\cdot\mathbf{C}_\varphi(t) \tag{11}$$

where $\underbrace{\mathbf{N}(\xi,\eta)}_{1\times16}$ is the row vector form of $\underbrace{\mathbf{N}_0(\xi,\eta)}_{4\times4}$ and $\underbrace{\mathbf{C}_\varphi(t)}_{16\times1}$ is the column vector of $\underbrace{\mathbf{C}_{0\varphi}(t)}_{4\times4}$. Thus, the design variables become the coefficients c_{ij}.

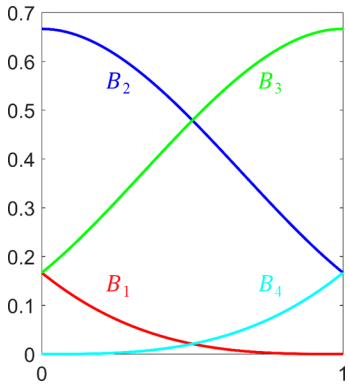


Figure 3. Standard B-spline shape function in an element of x direction.

3. Numerical implement

3.1 Body-fitted mesh generator

In this paper, the adaptive triangular mesh generation method proposed by Persson and Strang [18] is utilised to improve the quality of the boundaries. The node sensitivity field obtained from the bi-sectioning method is not only utilised for redistributing the solid and void domain but also for determining the material boundaries based on its zero-level isosurface. A 2D Gaussian filter is applied to further refine the material boundaries within the design domain. To generate a point set on the boundary, the MATLAB function "contour" is used, and the spacing between these nodes is adjusted before being fixed as the element vertices. Points with narrow spacing are merged to avoid singularity, and additional points are inserted between points with ample spacing to capture the smooth interface accurately.

An initial pattern is generated using Delaunay triangulation with uniformly distributed nodes located on the boundaries. To satisfy user-defined mesh density, the positions of nodes are iteratively changed by solving the force-displacement function for the edges. Hooke's law is used to calculate the repulsive force in bars F_e, based on the current length l and the expected unextended length l_0 of each bar, as follows:

$$F_e(l,l_0) = k_0(l_0 - l) \tag{12}$$

where k_0 is the modulus of elasticity. The expected bar length l_0 specified by the user is used to control the mesh density. The resultant force $\boldsymbol{F}_p$ for each node is the sum of force vectors from the connected bars, except for the fixed nodes where the force is zero to prevent movement. With the node coordinate matrix $\boldsymbol{p}$, the ODE system can be expressed as follows:

$$\frac{d\boldsymbol{p}}{dt} = \boldsymbol{F}_p(\boldsymbol{p}) \tag{13}$$

The approximate solution can be updated iteratively using the forward Euler method starting from the regularly distributed nodes as:

$$\boldsymbol{p}_{n+1} = \boldsymbol{p}_n + \Delta t \boldsymbol{F}_p(\boldsymbol{p}_n) \tag{14}$$

where Δt is the artificial time, set to 0.2 in the MATLAB code. After a prescribed maximum number of iterations, an elegant triangular mesh with the desired density is generated by the unstructured mesh generator, as shown in Figure 4. The red curve represents the smooth interface between the solid

(yellow) and void (grey) domains, with each triangular element being either fully solid or fully void to avoid intermediate densities in the design domain. For a detailed description of the mesh generation process, please refer to [19, 20].

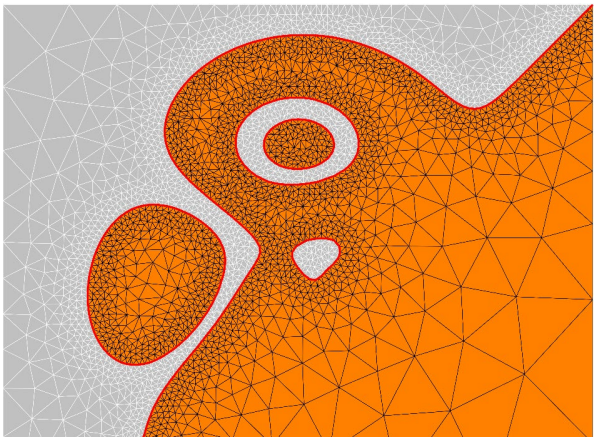


Figure 4. The adaptive triangular elements produced by the unstructured mesh generator.

Then, finite element analysis and sensitivity analysis are both launched based on the generated adaptive triangular mesh. To integrate with the B-spline level set method, the shape sensitivities must be interpolated to generate the corresponding B-spline coefficients.

3.2 Update scheme

In order to minimise the number of iterations and manage the geometrical complexity of the optimised structure, the reaction-diffusion equation is applied to modify the design variables, specifically the B-spline coefficients. This methodology is detailed below.

It is assumed that the variation of the level set function is proportional to the derivative of Lagrangian L' with a coefficient of K=1, resulting in the following equation.

$$\frac{\partial \varphi}{\partial t} = -K \cdot L' = -L' \tag{15}$$

Substituting Eqs. (5) & (6) into Eq. (15) yields:

$$\frac{\partial \varphi}{\partial t} = -(\bar{F}' + \tau \cdot \nabla^2 \varphi) \tag{16}$$

The finite difference approach can be employed to discretise Eq. (16) in the time direction as follows:

$$\frac{\partial \varphi}{\partial t} = \frac{\varphi(t+\Delta t) - \varphi(t)}{\Delta t} = -(\bar{F}' + \tau \cdot \nabla^2 \varphi) \tag{17}$$

where Δt is the step for fictitious time t. Then, substitute Eq. (11) into the reorganised Eq. (17) in weak form, the B-spline based reaction-diffusion equation is generated as:

$$\mathbf{T} \cdot \mathbf{C}_{\varphi}(t+\Delta t) = \mathbf{Y} \tag{18}$$

where $\mathbf{T}$ and $\mathbf{Y}$ are:

$$\mathbf{T} = \frac{1}{\Delta t} \underbrace{\int_V \mathbf{N}^T \mathbf{N}_g dV}_{\mathbf{NN}} + \tau \underbrace{\int_V \nabla^T \mathbf{N} \nabla \mathbf{N}_g dV}_{\mathbf{dNdN}} \tag{19}$$

$$\mathbf{Y} = \underbrace{\int_V \mathbf{N}^T \mathbf{N}_g dV}_{\mathbf{NN}} \cdot \underbrace{\left(-\mathbf{C}_{\bar{F}'}(t) + \frac{\mathbf{C}_\varphi(t)}{\Delta t} \right)}_{\mathbf{C_Y}} \tag{20}$$

NN and **dNdN** can be pre-calculated when parameters Δt and τ are decided, thus resulting in saving time when updating B-spline coefficients iteratively. Detailed updating process can be referred to [17].

4. Numerical examples

In both cases, the time step size for fictitious time t is set to 2, and all initial B-spline coefficients are initialised to 1. The initial body-fitted mesh is created using a uniform-distributed pore pattern. The convergence check is performed after reaching the minimum number of iterations, and the optimisation stops if the previous five iterations of the objective function differ by less than 1%. The precision of l_1 and l_2 in the bi-section method is set to 10^{-6}.

The first example involves a Messerschmitt-Bölkow-Blohm (MBB) beam with 240×80 B-spline elements, and symmetric boundary conditions are applied. The optimisation result for the MBB beam is presented in Figure 5. A regularisation parameter τ of 0.6 is used for the diffusion term, and a volume fraction upper limit of 0.5 is applied. The mean compliance problem converges within 20 iterations and takes 707.4 seconds to complete.

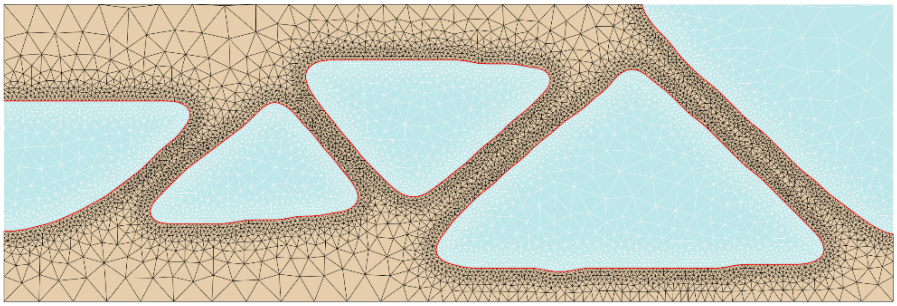


Figure 5. The optimised MBB beam.

The second example deals with a cantilever beam consisting of 200×100 B-spline elements. The optimisation result for the cantilever beam is shown in Figure 6, with a volume fraction upper limit of 0.3. The regularisation parameter τ for the diffusion term is set to 0.1, and the program converges within 20 iterations, taking 1026.0 seconds to complete.

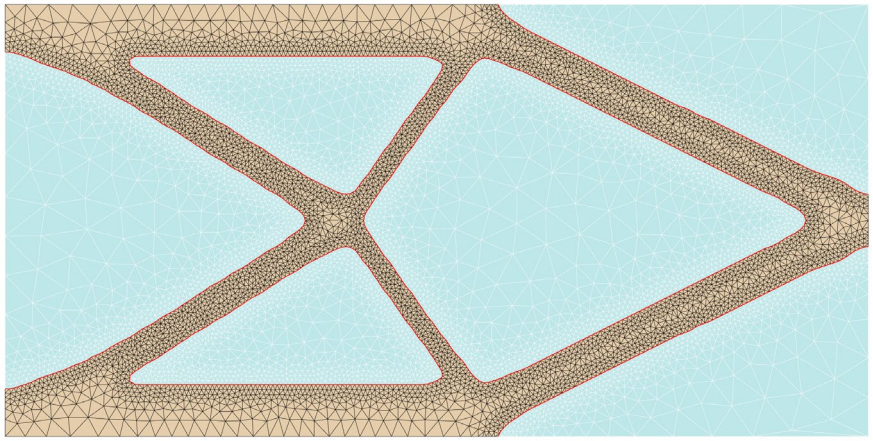


Figure 6. The optimised Cantilever beam.

5. Conclusions

In conclusion, the combination of RDBLS and body-fitted mesh is a promising approach for topology optimisation problems. RDBLS provides a powerful parametric representation method that allows for precise control of the level set function through B-spline coefficients, while the body-fitted mesh with an adaptive mesh generator can efficiently increase the flexibility of topology optimisation with a denser mesh around boundaries and a coarser mesh away from them. The synergy of these two methods has demonstrated significant improvements in the accuracy and efficiency of topology optimisation and it has the potential to be applied to fluid and optic problems, which require smooth boundaries for accurate physical performance calculations. Therefore, we believe that this combined approach will have a significant impact on the field of topology optimisation and will be beneficial for future research and practical applications.

Acknowledgements

This project was supported by the Australian Research Council (DP200102190, FL190100014).

References

[1] M. P. Bendsoe and N. Kikuchi, "Generating optimal topologies in structural design using a homogenisation method," *Computer Methods in Applied Mechanics and Engineering,* vol. 71, pp. 197–224, 1988.

[2] M. P. Bendsøe, "Optimal shape design as a material distribution problem," *Structural optimization,* vol. 1, pp. 193–202, 1989.

[3] G. I. N. Rozvany, M. Zhou and T. Birker, "Generalized shape optimization without homogenization," *Structural optimization,* vol. 4, pp. 250–252, 1992.

[4] M. Querin, G. P. Steven and Y. M. Xie, "Evolutionary structural optimisation (ESO) using a bidirectional algorithm," *Engineering Computations,* vol. 15, pp. 1031–1048, 1998.

[5] X. Y. Yang, Y. M. Xie, G. P. Steven and O. M. Querin, "Bidirectional evolutionary method for stiffness optimization," *AIAA Journal,* vol. 37, pp. 1483–1488, 1999.

[6] X. Huang and Y. M. Xie, "Convergent and mesh-independent solutions for the bi-directional evolutionary structural optimization method," *Finite Elements in Analysis and Design,* vol. 43, pp. 1039–1049, 2007.

[7] X. Huang and Y. M. Xie, *Evolutionary Topology Optimization of Continuum Structures: Methods and Applications*, Chichester: John Wiley & Sons, 2010.

[8] J. A. Sethian and A. Wiegmann, "Structural boundary design via level set and immersed interface methods," *Journal of Computational Physics,* vol. 163, pp. 489–528, 2000.

[9] M. Y. Wang, X. Wang and D. Guo, "A level set method for structural topology optimization," *Computer Methods in Applied Mechanics and Engineering,* vol. 192, pp. 227–246, 2003.

[10] G. Allaire, F. Jouve and A. M. Toader, "Structural optimization using sensitivity analysis and a level-set method," *Journal of Computational Physics,* vol. 194, pp. 363–393, 2004.

[11] C. Talischi, G. H. Paulino, A. Pereira and I. F. M. Menezes, "PolyMesher: a general-purpose mesh generator for polygonal elements written in Matlab," *Structural and Multidisciplinary Optimization,* vol. 45, pp. 309–328, 2012.

[12] L. Fu, L. Han, X. Y. Hu and N. A. Adams, "An isotropic unstructured mesh generation method based on a fluid relaxation analogy," *Computer Methods in Applied Mechanics and Engineering*, vol. 350, pp. 396–431, 2019.

[13] Z. Ji, L. Fu, X. Hu and N. Adams, "A feature-aware SPH for isotropic unstructured mesh generation," *Computer Methods in Applied Mechanics and Engineering,* vol. 375, pp. 1–26, 2021.

[14] G. Allaire, C. Dapogny and P. Frey, "A mesh evolution algorithm based on the level set method for geometry and topology optimization," *Structural and Multidisciplinary Optimization,* vol. 48, pp. 711–715, 2013.

[15] G. Allaire, C. Dapogny and P. Frey, "Shape optimization with a level set based mesh evolution method," *Computer Methods in Applied Mechanics and Engineering,* vol. 282, pp. 22–53, 2014.

[16] W. A. Wall, M. A. Frenzel and C. Cyron, "Isogeometric structural shape optimization," *Computer Methods in Applied Mechanics and Engineering,* vol. 197, pp. 2976–2988, 2008.

[17] C. Wang, Y. M. Xie, X. Lin and S. Zhou, "A reaction diffusion-based B-spline level set (RDBLS) method for structural topology optimization," *Computer Methods in Applied Mechanics and Engineering,* vol. 398, pp. 1–36, 2022.

[18] P.-O. Persson and G. Strang, "A simple mesh generator in MATLAB," *SIAM Review,* vol. 46, pp. 329–345, 2004.

[19] Z. Zhuang, Y. M. Xie and S. Zhou, "A reaction diffusion-based level set method using body-fitted mesh for structural topology optimization," *Computer Methods in Applied Mechanics and Engineering,* vol. 381, pp. 1–37, 2021.

[20] Z. Zhuang, Y. M. Xie, Q. Li and S. Zhou, "Body-fitted bi-directional evolutionary structural optimization using nonlinear diffusion regularization," *Computer Methods in Applied Mechanics and Engineering,* vol. 396, pp. 1–27, 2022.

Proceedings of the IASS Annual Symposium 2023
Integration of Design and Fabrication
10–14 July 2023, Melbourne, Australia
Y.M. Xie, J. Burry, T.U. Lee and J. Ma (eds.)

Efficient steel-concrete slab designed using multi-material topology optimisation

Yu LI[a,b], Hao WU[a], Xingjie XIE[a], Philip F. YUAN[a,*], Yi Min XIE[b,*]

[a,*] College of Architecture and Urban Planning, Tongji University, Shanghai, 200092, China

philipyuan007@tongji.edu.cn; mike.xie@rmit.edu.au

[b,*] Centre for Innovative Structures and Materials, School of Engineering, RMIT University, Melbourne, 3001, Australia

Abstract

Recent years have seen rapid developments in advanced concrete construction techniques, such as 3D-printed moulds and 3D concrete printing, enabling the construction of free-form concrete structures. However, due to the poor tensile capacity of concrete, it has been a great challenge to design structurally efficient concrete structures that are applicable to automated construction. To address this challenge, the multi-material bi-directional evolutionary structural optimisation (MBESO) method, which arranges two different materials suitable for tension and compression in the respective tensile and compressive regions of the structure, can be used to design efficient composite structures. In this study, an 800 mm × 800 mm × 120 mm steel cable-supported concrete slab is designed using the MBESO method. Furthermore, the structural analysis confirms the efficiency of the composite slab, demonstrating its potential for use in future practical engineering. The proposed steel-concrete composite model in this paper maximises concrete's compressive properties and circumvent its poor tensile ability, offering an innovative and efficient structural design strategy for concrete structures and potentially other materials such as clay and gypsum.

Keywords: topology optimisation, concrete slab, multi-material topology optimisation, composite structure, form finding

1. Introduction

Structural optimisation is crucial for architectural structural design, particularly for the design of concrete structures [1]. Reasonable design and optimisation of concrete structures can effectively reduce the amount of concrete used, lower the structural self-weight, save material usage, and reduce carbon emissions [2]. Since the application of concrete materials in architecture, designing efficient concrete structures has been an important research topic [3, 4]. The ancient Roman Pantheon, constructed in 120 AD, is an excellent example of a large-span dome built using concrete materials, fully utilizing the compressive performance of concrete [5].

Since the 19th century, with the continuous improvement of concrete technology, it has been widely used in construction. Thin slab structures are a common type of architectural structure that differs from other structures, such as arches and shells. They can achieve large-span coverage within a limited height range. The design of efficient concrete slabs has different methods and solutions in different eras, and it remains an important area of research in the field of structural engineering.

In the Gatti Wool Factory, Nervi and Arcangeli [6, 11] collaborated to design a rib-reinforced concrete floor system based on the curved isostatic pattern of the factory floors (Figure 1a). This method has similarities with some of the modern construction practices. Based on stress trajectories, Yuan's team

Copyright © 2023 by Yu LI, Hao WU, Xingjie XIE, Philip F. YUAN and Yi Min XIE. Published in the Proceedings of the IASS Annual Symposium 2023 with permission.

at Tongji University designed ribs on the opposite side of the floor prototype and used a 3D concrete printing method assisted by a robotic arm for construction (Figure 1b). Similarly, Dillenburger's research group [8] at ETH Zurich designed and constructed "Smart Slabs" using 3D-printed sand casts, laser-cut timber formwork, and concrete spraying (Figure 1c). In addition to stress trajectory-based optimisation, topology optimisation technology is also a very effective tool for concrete slab optimisation design. For example, Dillenburger's research group [12] used the Solid Isotropic Material Penalization (SIMP method [13, 14], a type of topology optimisation method) to obtain an optimized design for a 1.8 m × 1 m × 0.15 m slab and used a template for concrete casting (Figure 1d). Combining the modified BESO method, Xie's group from RMIT University developed a digital design and construction process for large-scale ribbed floor systems [10].

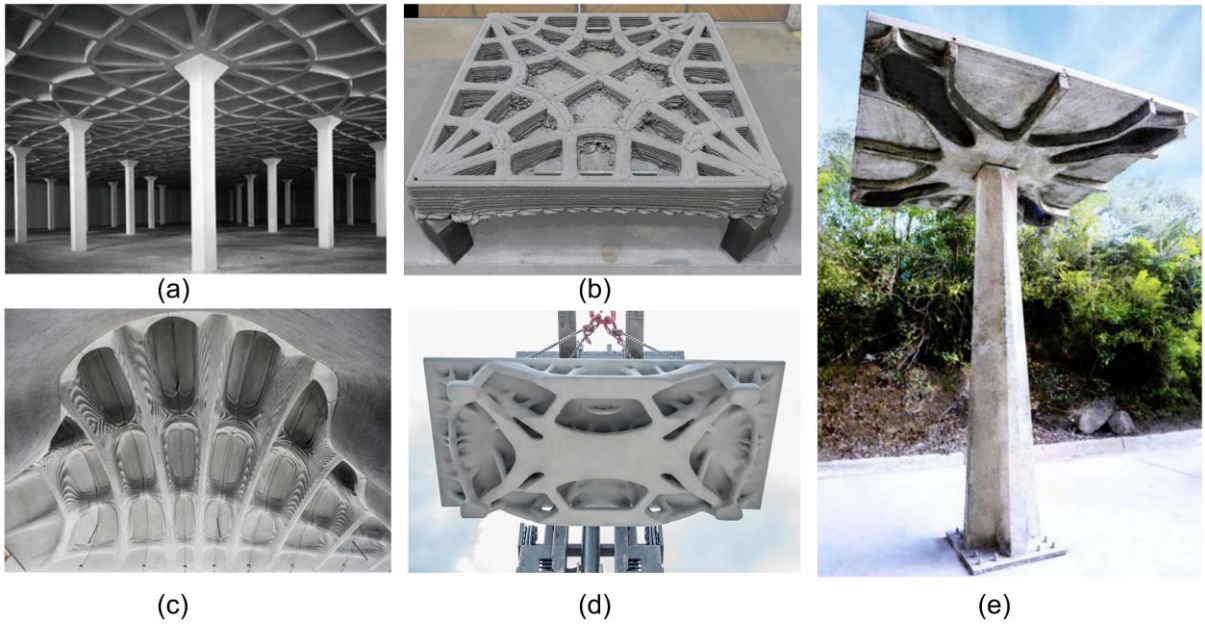


Figure 1. Concrete slabs designed based on structural performance: (a) The Gatti Wool Factory designed by Nervi [6]; (b) a 3D-printed high-performance concrete slab designed and constructed by Yuan's team at Tongji University [7]; (c) "Smart Slabs" designed by Dillenburger's research group at ETH Zurich [8]; (d) concrete slab designed based on topology optimisation, also by Dillenburger's research group at ETH [9]; (e) ribbed floor system designed and constructed by Xie's team at RMIT University using topology optimisation [10].

It is evident that both methods are effective in achieving lightweight design for slab structures, ensuring structural strength while maximizing material efficiency. Among these methods, topology optimisation based on continuum models can present more intricate 3D structural details while optimizing the structure, making it more suitable for intelligent construction methods such as 3D concrete printing or concrete casting with 3D-printed moulds.

Most studies on topology optimisation have been developed for single-material structures, which are effective for materials like metals that exhibit similar mechanical properties in both tension and compression. However, for concrete, which has significantly better compressive performance compared to its tensile performance, single-material topology optimisation algorithms that do not consider the performance differences between the two stress states are not applicable.

Recently, developed from the single-material BESO method based on stress, Li and Xie [15, 16] proposed the MBESO method. By considering the performance differences of materials in tension and compression, this technique has shown great potential in improving the structural efficiency of multi-material structures, such as steel-concrete structures. This method is very simple but effective for the

form-finding of composite structures, providing a new approach to concrete structure design [17]. In this paper, this method is used for the topology optimisation design of a thin steel-concrete slab prototype, which is then constructed using digital fabrication methods.

2. Design of the steel-concrete slab based on multi-material topology optimisation

2.1 Multi-material topology optimisation

In this research, we adopt the relative stress level of a structure as the standard for evaluating the importance of each element to the entirety of the structure. To this end, we use the utilization of material as an indicator. For the *i*-th element in the design domain, its utilization η_i can be determined as follows:

$$\eta_i = \begin{cases} \sigma_{i,Mises}/[\sigma_s^t] & \text{(for steel)} \\ \sigma_{i,Mises}/[\sigma_c^c] & \text{(for concrete)} \end{cases}, i = 1, 2, \dots, N \tag{1}$$

where $[\sigma_s^t]$ and $[\sigma_c^c]$ indicate the allowable tensile stress for steel and the allowable compressive stress for concrete, respectively. The von Mises stress of the *i*-th element is denoted by $\sigma_{i,Mises}$, and *N* represents the total number of elements in the design domain.

Regarding how to determine the tensile or compressive stress state of the elements in the structure, this study utilizes a complex stress indicator: the first invariant of the stress tensor. In terms of physic meaning [18, 19], the first invariant I_1 of the stress tensor represents the change in volume of the element. $I_1 \geqslant 0$ indicates that the volume of the element has increased, which can be considered as a tensile stress. Conversely, $I_1 < 0$ signifies that the volume has decreased, indicating a compressive stress state. In composite structures with intricate stress states, this approach facilitates the classification of each element as a tensile or compressed element based on whether the sum of the principal stresses exceeds 0. To represent the variable, I_1 is calculated as:

$$I_1 = \sigma_{11} + \sigma_{22} + \sigma_{33} \tag{2}$$

where σ_{11}, σ_{22} and σ_{33} denote the maximum principal stress, the second principal stress, and the minimum stress, respectively.

This method allows for the easy classification of elements in composite structures into two distinct types that match two different materials, such as steel and concrete. Although this approach is heuristic, it has been demonstrated to be effective in identifying a more suitable material for each element between two distinct materials.

To describe the solid-void design and the material properties of each element in our study, we define two variables x_i and m_i as follows:

$$x_i = \begin{cases} 1 & \text{(solid)} \\ x_{min} & \text{(void)} \end{cases}, i = 1, 2, \dots, N \tag{3}$$

$$m_i = \begin{cases} 1 & \text{(steel)} \\ 2 & \text{(concrete)} \\ 0 & \text{(void)} \end{cases}, i = 1, 2, \dots, N \tag{4}$$

where $x_i = 1$ or x_{min} (0.001 is used in this study) means that the *i*-th element is solid (including steel and concrete) or void, and $m_i = 1$, 2 or 3 indicates the type of the material. For void elements, material 3 with a small Young's modulus is introduced, and its Young's modulus is calculated as

$$E_{min} = x_i^p E_2 \tag{5}$$

where *p* is the penalty coefficient set as 3 in our study. Huang and Xie [20] have shown that the contribution of a material like material 3 in solid-void design can be ignored when $p \geqslant 3$.

To address the mesh-dependency problem and checkerboard patterns [21, 22], filter techniques can be employed for raw utilization. Besides, to enhance the convergence of the process, it is possible to incorporate historical data into the topology optimisation, similar to some previous work [23, 24]. One approach is to calculate the average utilization value by combining the current utilization with the historical data obtained in the previous step. The details of the filter and stabilisation processes can be found in [16, 17].

To begin the optimisation process, the volume of the solid elements in the *k*-th iteration, denoted as $v^{(k)}$, can be calculated using Equation (6).

$$v^{(k)} = v^{(k-1)} \times (1 - er) \ \ (v^{(0)} = 1, k = 1, 2, \dots) \tag{6}$$

Here, $v^{(k)}$ represents the volume of solid elements in the (*k*-1)-th iteration, and *er* is the evolutionary ratio, which is set to 0.001 in this study. Initially, the volume of solid elements is set to 1 in the first iteration, i.e., $v^{(k)} = 1$, and for all subsequent iterations, the volume is updated using Equation (6).

Once the volume of solid elements is determined, all the elements are ranked based on their utilizations, from maximum to minimum. The top $v^{(k)}$ elements are designated as solid elements, represented by $x_i = 1$, while the elements ranked after top $v^{(k)}$ are set as void, represented by $x_i = x_{min}$. This step-wise reduction in the volume of solid elements gradually decreases the volume of solid material from 1 to the preset volume fraction v_f.

After the updating of inefficient solid elements and efficient void elements in each iteration, the material type of each solid element can be determined as follows:

$$m_i = \begin{cases} 1 & (\sigma_e > 0, \ x_i = 1) \\ 2 & (\sigma_e \leq 0, \ x_i = 1) \\ 0 & (\ x_i = x_{min}) \end{cases}, i = 1, 2, \dots, N \tag{7}$$

where only the solid elements with $x_i = 1$ need to be classified. This process results in a new multi-material design for the structure.

The optimisation calculation stops when the volume of the optimized structure is reduced to the volume fraction v_f, and the compliance satisfies the following condition:

$$\frac{|C^{(k)} - C^{(k-1)}|}{C^{(k)}} \leq \tau \tag{8}$$

Where $C^{(k)}$ and $C^{(k\text{-}1)}$ are the compliance of the optimized structure calculated in the *k*-th and the (*k* -1)-th iterations, respectively, and τ is a small preset value set to 10^{-4} in this study.

2.2 Topology optimisation and post-design process of the steel-concrete slab.

2.2.1 Material properties

The mechanical properties of the two materials, steel and concrete, used to construct the composite concrete slab in this study are shown in Table 1. Based on the MBESO algorithm, the steel material only exists in the tensile region of the structure, while the concrete is only subjected to compression. Therefore, only the mechanical properties of the steel in the tensile state and the concrete in the compression state are included as the actual properties of the two materials in Table 1. For the void element (Material 3), there are two allowable stress values because, similar to the solid element, the void elements are also divided into tensile and compressed elements in the multi-material topology optimisation calculation, respectively serving as candidate elements for steel and concrete elements. Therefore, the material utilization calculation standards and the threshold for becoming a solid element differ between these two types of elements [25].

Table 1: Material properties of the structures (material 3 is introduced to represent void elements).

Material	Young's modulus E (GPa)	Poisson's ratio μ	Allowable stress $[\sigma]$ (MPa)
Steel	E_1 = 200	μ = 0.3	$[\sigma_s^t]$ = 250 (in tension)
Concrete	E_2 = 20	μ = 0.3	$[\sigma_c^c]$ = 50 (in compression)
Material 3	$E_3 = E_{min}$	μ = 0.3	$[\sigma_{m3}] = [\sigma_s^t]$ = 250 (in tension)
(void elements)			or $[\sigma_{m3}] = [\sigma_c^c]$ = 50 (in compression)

2.2.2 Topology optimisation process and results

As shown in Figure 2(a), the experimental prototype in this study is a rectangular slab with four corners simply supported, where only one corner is fixed as a hinge support, and the other corners are only fixed in the vertical direction. The size of the slab design domain is 800 mm × 800 mm ×120 mm, where the upper surface with a thickness of 20 mm is set as a non-design domain. The elements in this area will always be reserved during the topology optimisation process to ensure the effective transmission of the uniform load above.

Due to the symmetry in both the structural model and load conditions, 4 symmetric planes are set in the design domain to accelerate calculations. With the presence of symmetry boundaries, only a minimum of 1/8 of the structure needs to be computed to achieve the topology optimisation of the rectangular concrete slab. In this study, 1/4 of the structure is actually used for calculation and subsequently reassembled into a complete slab.

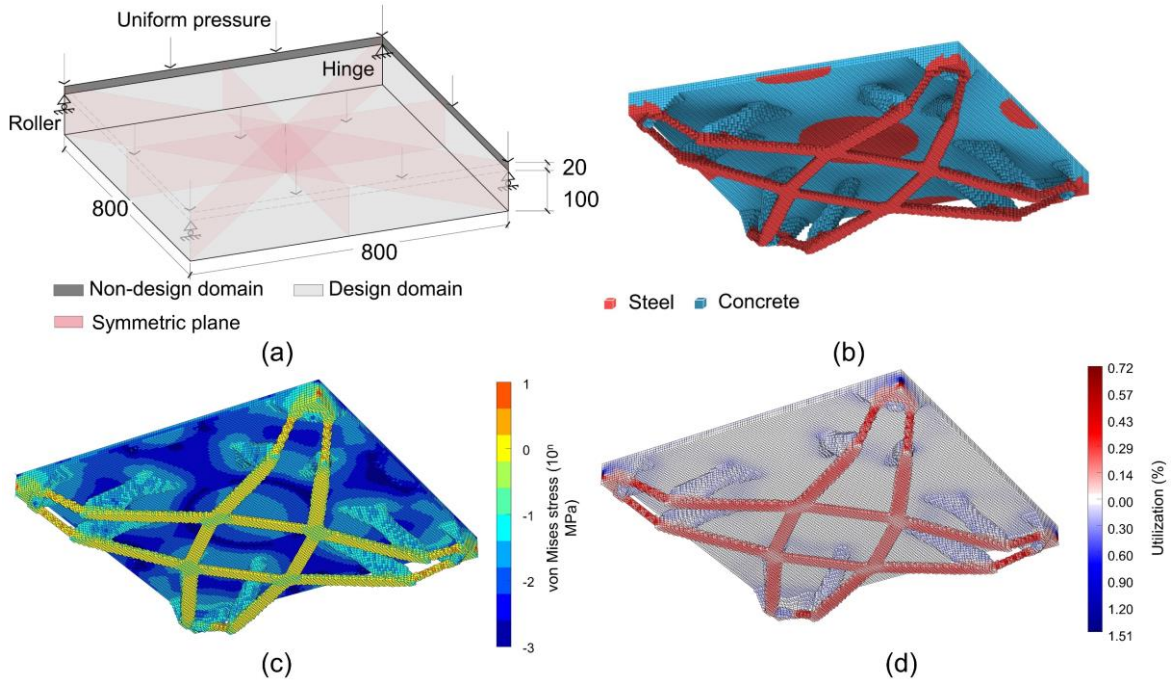


Figure 2. Topology optimisation settings and corresponding results of the multi-material concrete slab: (a) design domain, loads, and support conditions; (b) optimized material layout of the multi-material slab; (c) von Mises stress distribution; (d) material utilization distribution.

For the design domain shown in Figure 2(a), one quarter of it is discretised using 66 × 66 × 20 eight-node hexahedral elements. A total of 348,480 finite elements are used to represent the whole structure. The target volume fraction for the final structure is set at 0.2, meaning that the solid material in the final structure occupies 20% of the initial design domain. Other topology optimisation parameters are set as follows: uniform load q = 1 kN/m^2, evolution rate er = 0.01, and filter radius $r_1 = r_2$ = 45 mm.

The topologically optimized slab obtained based on the above settings is shown in Figure 2(b). In this structure, the concrete material is mainly distributed in the upper part, and 8 inclined short columns are supporting the red steel components beneath the concrete part. The steel material mainly forms 4 intersecting cable-like components below the superstructure, with each cable end connected to one support point. The cable turns at the lower end of each inclined short column. In addition to the steel material in the lower part of the structure, there is also a small amount of steel material below the mid-span area, indicating tension in this area. During the topology optimisation of the concrete slab, the stress distribution (Figure 2c) and material utilization distribution (Figure 2d) in the structure can be calculated simultaneously. From these two figures, it can be seen that, except for the stress concentration at the 4 support points, the stress in the bottom cable is much higher than that in the upper concrete slab. However, from the distribution of material utilization, the maximum material utilisation of the steel and concrete parts is similar, indicating both materials are well utilised.

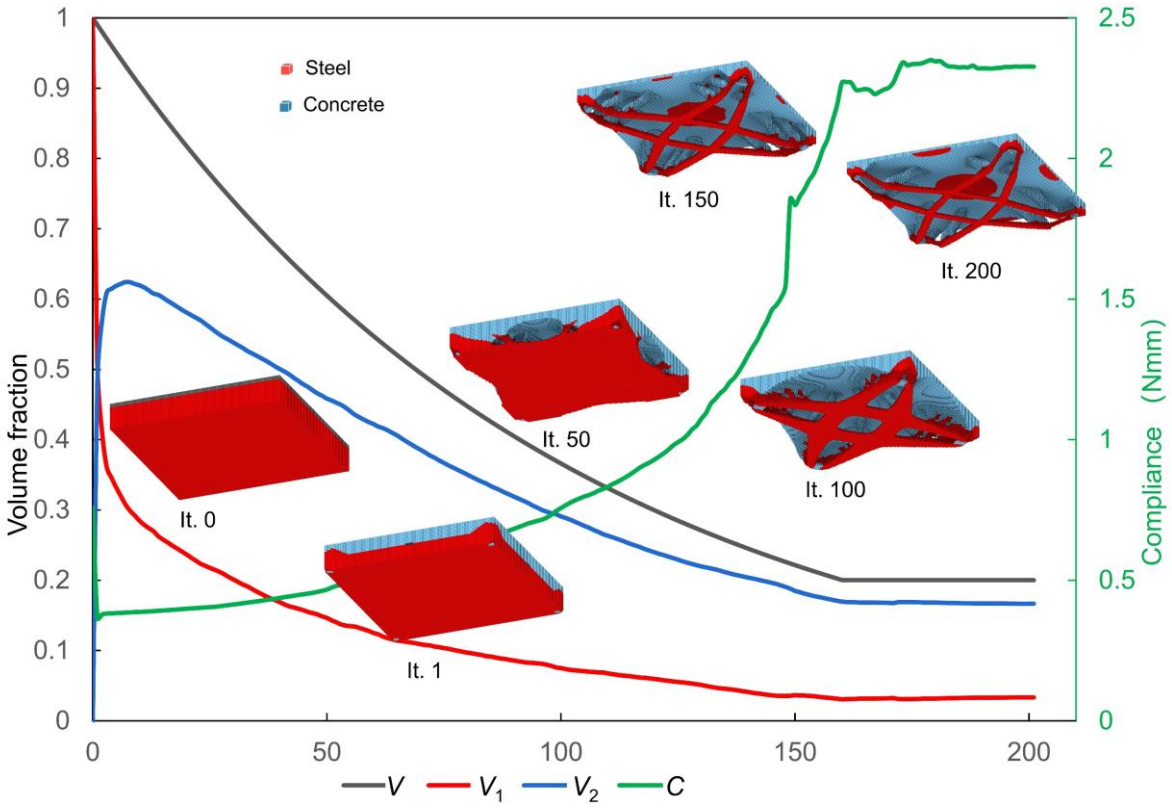


Figure 3. Evolution history of the relevant parameters during the topology optimisation of the composite slab (where V represents the total volume of the material, v_1 represents the volume of steel, v_2 represents the volume of concrete, and C represents the compliance of the structure).

The evolution history of the relevant parameters during the topology optimisation of this composite slab is shown in Figure 3. The entire design domain consists solely of steel in the initial stage of topology optimisation (Iteration 0). In the first iteration, steel or concrete materials are assigned based on the tension or compression state of each element, and 2% of solid materials are removed simultaneously.

The iteration continues until the material volume reaches the target volume fraction and the structural compliance converges. It can be observed that the volume fraction of steel gradually decreases from 1 and finally stabilizes at around 0.033, while the volume fraction of concrete rapidly increases from 0 to a peak of about 0.624, and then gradually decreases to 0.167. The total material volume fraction gradually decreases from 1 to the target volume fraction of 0.2 and remains stable. In this process, the compliance of the structure first decreases rapidly (the all-steel structure becomes a dual-material structure in the first iteration), then gradually increases, and finally reaches a relatively stable state.

2.2.3 Comparison of slabs with different thicknesses

Topology optimization outcomes for composite slabs exhibit considerable variation across varying thicknesses. In this regard, exploring slabs with distinct thicknesses can aid in identifying the suitable thickness for topology optimization results in post-design procedures. Figure 4 showcases the topology optimization outcomes for four different thicknesses of steel-concrete composite slabs: 80, 120, 160, and 200 mm.

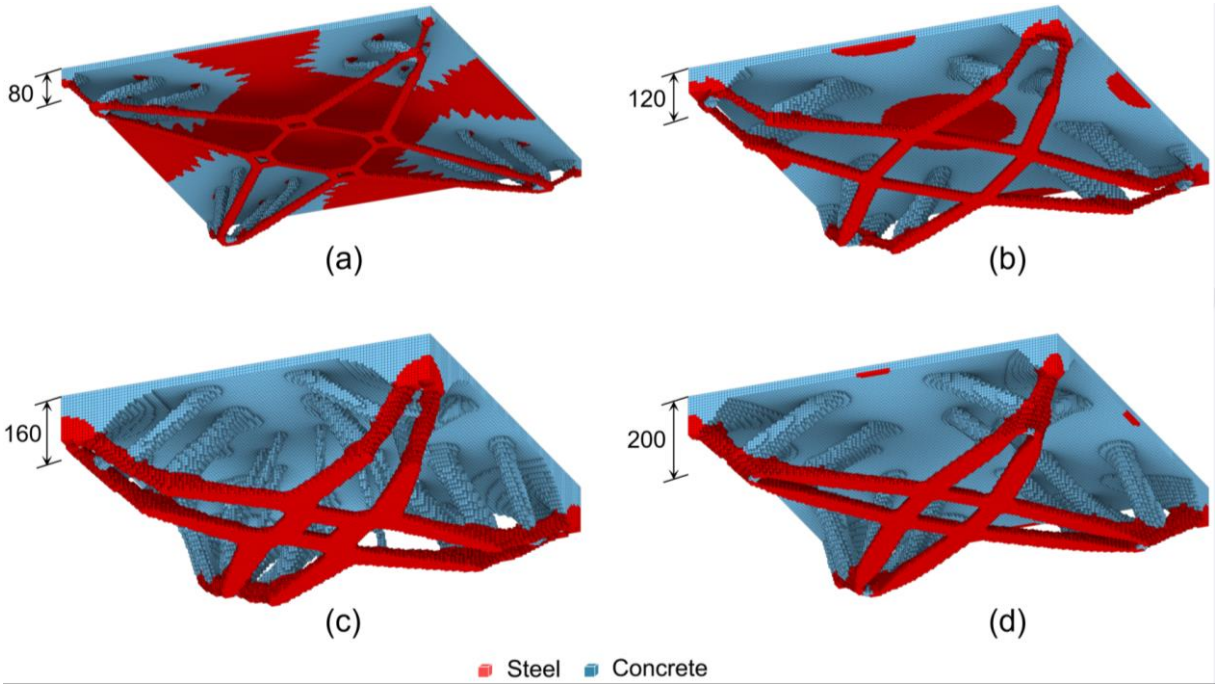


Figure 4. Topology optimization results for steel-concrete composite slabs with different thicknesses: (a) h = 80 mm; (b) h = 120 mm; (c) h = 160 mm; (d) h = 200 mm.

The results reveal both commonalities and differences among them. For instance, in the composite slab with an 80 mm thickness (Figure 4a), the steel parts and inclined columns used to reinforce the slab are inadequate to provide sufficient support for the thin slab. As a consequence, there are significant proportions of tensile regions (in red) and compression regions (in blue) in the upper structure of the slab. Given this situation, relying solely on concrete for the construction of the upper slab is inappropriate.

On the other hand, by increasing the thickness to 120 mm (Figure 4b), the proportion of tensile regions in the upper slab decreases, and a large surface area of the upper structure comes under compression. Consequently, in such a scenario, it is possible to employ concrete reinforcement measures to construct the upper slab. As the thickness increases further to 160 mm (Figure 4c) and 200 mm (Figure 4d), the tensile regions in the upper structure fade away, and the superstructure transforms into a pure

compressed component. Thus, in these models, the upper slab is suitable for construction using unreinforced concrete.

Following a comprehensive comparison and analysis of these outcomes, the topology optimization result with a thickness of 120 mm (Figure 4b) was selected as the prototype for further design and analysis. This prototype meets the fundamental requirement of ensuring that the upper plate is mostly under compression while maintaining a relatively thin thickness.

2.2.4 Post-design process

As shown in Figure 5(a), although the upper structure is not purely under compression, it mainly consists of compressed concrete. If the upper concrete components are constructed as a whole, they can, to some extent, satisfy the local bending conditions. Therefore, in this paper, the upper structure is simplified as a complete concrete slab (Figure 5b), and the eight inclined short columns are also made of concrete. The lower tensioned steel structure is simplified as four intersecting steel cables, each of which is connected to the two diagonal support bases.

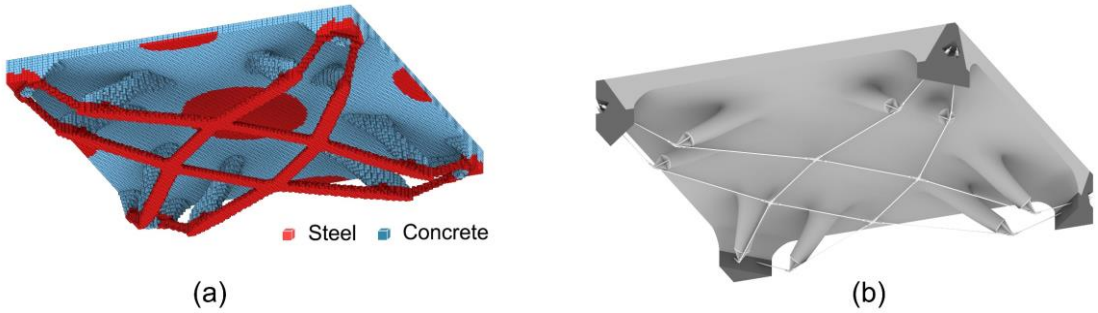


Figure 5. Post-design process based on the multi-material topology optimisation result: (a) dual-material topology optimisation result; (b) constructible model after the post-design process.

4 Structural analysis

In this structural model, the cable-support system formed by intersecting steel cables and inclined columns is the key component that reduces the deformation of the concrete slab. To validate the strengthening effect of this system, the stress and strain distributions of two concrete slabs, one with cable support and one without, are compared in Figure 6.

Figures 6(a) and (b) show the von Mises stress distribution of the two slabs without and with cable support, respectively, with the same legend values in both figures. While little difference is observed in the stress distribution of the upper concrete portion, in the slab with cable support (Figure 6b), the stress in the tension cable at the bottom of the slab is very high but still within the safety range of the steel material. Figures 6(c) and (d) present the vertical deformation distribution of the two slabs, also with the same legend values in both figures. In Figure 6(c), due to the lack of reinforcement components, the deformation of the concrete slab mainly depends on itself, and there is a significant deformation in the mid-span area of the slab. On the contrary, in Figure 6(d), due to the support of steel cables and inclined columns, the deformation of the central part of the concrete slab is relatively reduced, with the maximum deformation being 36% lower than that in Figure 6(c).

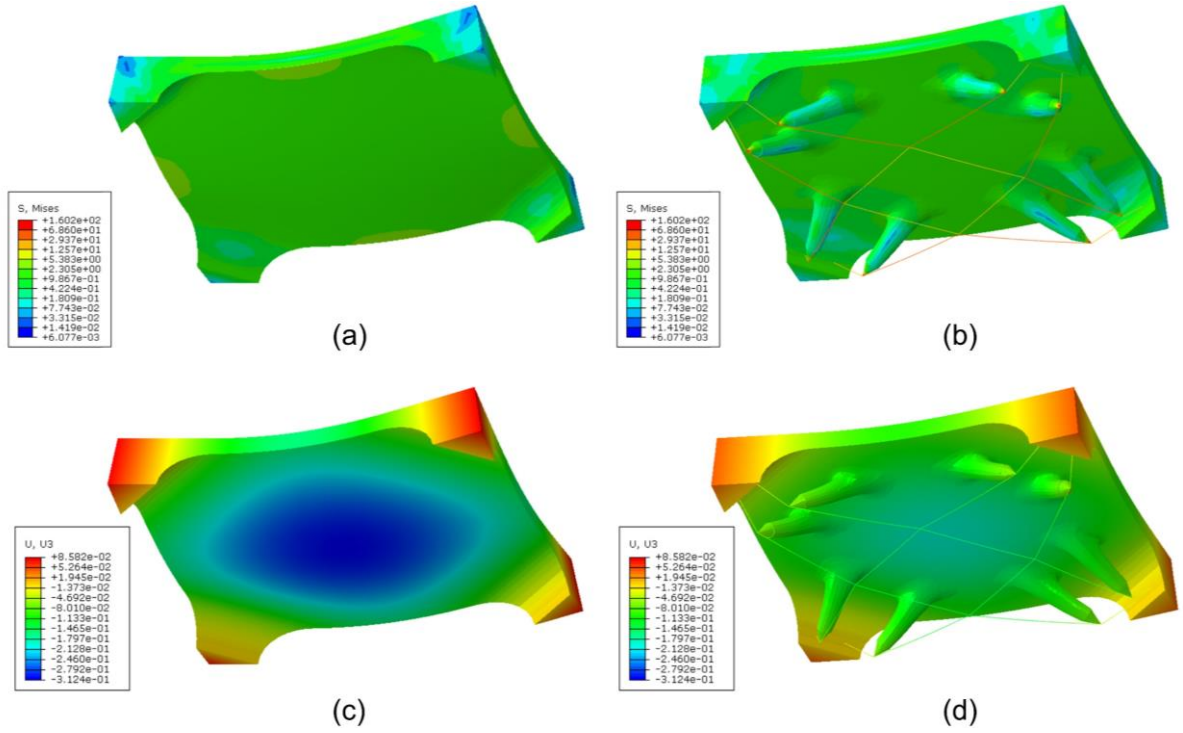


Figure 6. Comparison of stress and strain analysis results of two concrete slabs with and without cable-support systems (units: mm, MPa): (a) von Mises stress distribution of the concrete slab without cable-support system; (b) von Mises stress distribution of the concrete slab with the cable-support system. (c) deformation distribution of the concrete slab without a cable-support system; (d) deformation distribution of the concrete slab with a cable-support system.

5 Conclusions

In this study, the multi-material bi-directional evolutionary structural optimisation (MBESO) method was applied to design an efficient steel-concrete slab, resulting in a composite structural system that effectively utilises steel for tension and concrete for compression. During the post-design process based on the multi-material topology optimisation result, the tensile portion of the structure was simplified into crossed steel cables that connected diagonal support bases, and the compressed upper portion was streamlined into freeform concrete casting components. The connection between the steel cables and the concrete was reinforced by metal nodes to accommodate the transmission of significant forces. Furthermore, the numerical analysis comparing the stress and strain of slabs with and without cable-support systems showed that cable reinforcement reduced the maximum deformation of the concrete slab by about 36%, effectively enhancing its structural rigidity. This innovative approach simplifies the design process, and provides valuable guidance for digital design and intelligent construction of complex-shaped concrete structures in the future. The development of the steel-concrete composite slab model highlights the immense potential and significance of utilising multi-material topology optimisation methods for efficient structural design of similar materials such as gypsum, clay, or concrete. The process demonstrated how these techniques can assist in streamlining the construction of complex-shaped structures while optimising their performance.

Acknowledgements

This project is supported by the Shanghai Municipal Science and Technology Major Project (2021SHZDZX0100), the National Key Research and Development Program “Inter-governmental

Cooperation in International Science and Technology Innovation" (2022YFE0141400) and the National Natural Science Foundation of China (U1913603).

References

[1] N. Stoiber and B. Kromoser, "Topology optimization in concrete construction: a systematic review on numerical and experimental investigations," *Structural and Multidisciplinary Optimization*, vol. 64, pp. 1725–1749, 2021.

[2] D. Yeo and R. D. Gabbai, "Sustainable design of reinforced concrete structures through embodied energy optimization," *Energy and Buildings*, vol. 43, pp. 2028–2033, 2011.

[3] T. Wangler, N. Roussel, F. P. Bos, T. A. M. Salet and R. J. Flatt, "Digital concrete: a review," *Cement and Concrete Research*, vol. 123, 105780, 2019.

[4] F. Bester, M. van den Heever, J. Kruger and G. van Zijl, "Reinforcing digitally fabricated concrete: A systems approach review," *Additive Manufacturing*, vol. 37, 101737, 2021.

[5] G. R. H. Wright, *Ancient building technology, volume 3: construction*, Brill. 2009.

[6] Architectural Research Centers Consortium, *Considering Research: Reflecting upon current themes in Architecture Research*, Lawrence Technological University, 2011.

[7] H. Wu, S. Gu, X. Gao and P. F. Yuan, "Extrusion-to-Masoning: Robotic 3D concrete printing of concrete shells as building floor system," in *28th International Conference of the Association for Computer-Aided Architectural Design Research in Asia 2023*, Ahmedabad, India, Mar 18–24, 2023.

[8] M. Marani, "This experimental concrete roof is half the weight of its peers." The Architect's Newspaper. https://www.archpaper.com/2018/08/eth-zurich-concrete-roof/ (accessed Mar. 23, 2023).

[9] A. Jipa, H. Kwon, M. Bernhard and P. Steiner, "Topology optimization for a concrete slab." dbt.arch.ethz.ch. https://dbt.arch.ethz.ch/project/topology-optimisation-concrete-slab/ (accessed Mar. 23, 2023).

[10] J. Ma, M. Gomaa, D. W. Bao, A. Rezaee Javan and Y. M. Xie, "PrintNervi – Design and construction of a ribbed floor system in the digital era," *Journal of the International Association for Shell and Spatial Structures*, vol. 63, pp. 241–251, 2022.

[11] A. B. Halpern, D. P. Billington and S. Adriaenssens, "The ribbed floor slab systems of Pier Luigi Nervi," *Journal of the International Association for Shell and Spatial Structures*, vol. 54, pp. 176–177, 2013.

[12] M. A. Meibodi, M. Bernhard, A. Jipa and B. Dillenburger, "The Smart Takes from the Strong," *Fabricate Rethinking Design and Construction*, vol. 3, pp. 210–217, 2017.

[13] M. P. Bendsøe and O. Sigmund, "Material interpolation schemes in topology optimization," *Archive of Applied Mechanics*, vol. 69, pp. 635–654, 1999.

[14] A. Rietz, "Sufficiency of a finite exponent in SIMP (power law) methods," *Structural and Multidisciplinary Optimization*, vol. 21, pp. 159–163, 2001.

[15] Y. Li and Y. M. Xie, "Evolutionary topology optimization for structures made of multiple materials with different properties in tension and compression," *Composite Structure*, vol. 259, 113497, 2021.

[16] Y. Li and Y. M. Xie, "Evolutionary topology optimization of spatial steel-concrete structures," *Journal of the International Association for Shell and Spatial Structures*, vol. 62, pp. 102–112, 2021.

[17] Y. Li, Y. Lai, G. Lu, F. Yan, P. Wei, and Y. M. Xie, "Innovative design of long-span steel – concrete composite bridge using multi-material topology optimization," *Engineering Structures*, vol. 269, 114838, 2022.

[18] B. McGinty, "Principal Strains & Invariants." Continuum Mechanics. https://www.continuummechanics.org/principalstrain.html (accessed Mar. 23, 2023).

[19] T. H. G. Megson, "Structural and Stress Analysis, Second Edition," *Academic Commons*, Butterworth-Heinemann, 2011.

[20] X. Huang and Y. M. Xie, *Evolutionary Topology Optimization of Continuum Structures: Methods and Applications*, Wiley, 2010.

[21] Q. Li, G. P. Steven and Y. M. Xie, "A simple checkerboard suppression algorithm for evolutionary structural optimization," *Structural and Multidisciplinary Optimization*, vol. 22, pp. 230–239, 2001.

[22] O. Sigmund and J. Petersson, "Numerical instabilities in topology optimization: A survey on procedures dealing with checkerboards, mesh-dependencies and local minima," *Structural Optimization*, vol. 16, pp. 68–75, 1998.

[23] Y. M. Xie and G. P. Steven, "A simple evolutionary procedure for structural optimization," *Computers and Structures*, vol. 49, pp. 885–896, 1993.

[24] S. Liu and H. Qiao, "Topology optimization of continuum structures with different tensile and compressive properties in bridge layout design," *Structural and Multidisciplinary Optimization*, vol. 43, pp. 369–380, 2011.

[25] Y. Li, P. F. Yuan and Y. M. Xie, "A strategy for improving the safety and strength of topologically optimized multi-material structures," *Acta Mechanica Sinica*, vol. 39, 422134, 2023.

IASS 2023
July 10–14 Melbourne
Integration of Design and Fabrication

Proceedings of the IASS Annual Symposium 2023
Integration of Design and Fabrication
10–14 July 2023, Melbourne, Australia
Y.M. Xie, J. Burry, T.U. Lee and J. Ma (eds.)

Non-penalization topology optimization for maximizing natural frequency using SEMDOT

Yun-Fei FU[a], Bernard ROLFE[b,*]

[a] Institute for Frontier Materials, Deakin University, Geelong, VIC 3216, Australia.
[b,*] School of Engineering, Deakin University, Geelong, VIC 3216, Australia.
Email Address: bernard.rolfe@deakin.edu.au

Abstract

This work aims to conduct the topological design for the natural frequency maximization problems using non-penalization Smooth-Edged Material Distribution for Optimizing Topology (SEMDOT) algorithm. Pin-pin, fix-pin, and clamped beams are used to demonstrate the effectiveness of the proposed non-penalization SEMDOT algorithm in solving natural frequency maximization problems. Comparisons with Evolutionary Topology Optimization (ETO) and Floating Projection Topology Optimization (FPTO) algorithms, which are capable of generating smooth boundaries, are conducted, showing that non-penalized SEMDOT can obtain comparable results.

Keywords: natural frequency maximization, non-penalization, smooth boundary, topology optimization

1. Introduction

Topology optimization is a powerful virtual tool that can find the optimal material distribution and geometry within a predefined design domain [1]. Topology optimization, an important branch of the light-weight design, has been extensively used in mechanical design, weight reduction in industry and multiple other physics fields [2-4]. Element-based topology optimization algorithms are the most widely used methods because of their easy implementation and ability to remove materials freely across the design domain. There are some representative element-based topology optimization algorithms, including Solid Isotropic Material with Penalization (SIMP) [5], Evolutionary Structural Optimization (ESO) [6], Bi-directional Evolutionary Structural Optimization (BESO) [7], and Floating Projection Topology Optimization (FPTO) [8-11].

Traditional element-based methods such as SIMP and BESO will generate zigzag or blurry boundaries, which will require the post-processing method such as shape optimization to obtain smooth boundaries before fabrication. To avoid extra efforts, Da et al. [12] proposed an elemental volume fraction-based approach named Evolutionary Topology Optimization (ETO) algorithm in which the smooth topological boundaries can be formed during optimization. Since ETO is developed based on the BESO framework, only the Optimality Criteria (OC) method can be used as the optimizer. However, the Method of Moving Asymptote (MMA) proposed by Svanberg [13] performs better than OC in solving some complicated optimization problems [14]. Therefore, Fu et al. [15,16] proposed a new elemental volume fraction-based method named Smooth-Edged Material Distribution for Optimizing Topology (SEMDOT) based on the SIMP framework, and hence the MMA optimizer can be used in SEMDOT. Since the use of the material penalization scheme will artificially change the relationship between material properties and elemental values, the authors developed a non-penalization SEMDOT algorithm using discrete variable sensitivities [17]. Compared to penalized SEMDOT, non-penalized SEMDOT can generally lead to better performance and stronger convergence [17]. Another advantage of non-penalized SEMDOT is that the complexity of the algorithm is reduced. Therefore, non-penalization SEMDOT will be used as the optimization platform in this work.

Copyright © 2023 by Yun-Fei FU and Bernard ROLFE. Published in the Proceedings of the IASS Annual Symposium 2023 with permission.

Natural frequency is an important performance index for numerous engineering structures. Compared with stiffness optimization, topology optimization for natural frequency is more challenging due to the possible localized modes [18], and hence the natural frequency maximization case is a representative problem used to validate the effectiveness of a topology optimization algorithm [18-20]. To date, non-penalized SEMDOT is not yet used for maximizing natural frequency.

This work aims to conduct the topological design for the natural frequency maximization problems using the non-penalization SEMDOT algorithm. In addition, comparisons with existing element-based algorithms (i.e., ETO and FPTO) will be presented.

2. Topology optimization for maximizing natural frequency

The smooth boundary strategy of SEMDOT is schematically illustrated in Figure 1 where X_e is the elemental volume fraction (design variable), $\rho_{e,g}$ is the density (value) of the grid points, and $\rho_{\min}$ is a small value, for example, 0.001. SEMDOT pursues the solid and void design of grid points, and then the obtained solid and grid points will be used to assemble the elements. As the number of grid points is higher than that of elements, the smooth topological boundary can be formed. As shown in Figure 1, the solid element ($X_e = 1$) is full of solid grid points ($\rho_{e,g} = 1$); the void element ($X_e = \rho_{\min}$) is full of void grid points ($\rho_{e,g} = \rho_{\min}$); and the boundary element ($\rho_{\min} < X_e < 1$) is a mixture of solid and void grid points.

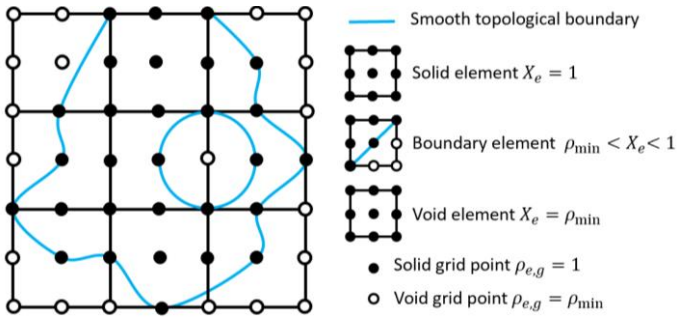


Figure 1. Smooth boundary representation in SEMDOT.

The relationship between X_e and $\rho_{e,g}$ is

$$X_e = \frac{1}{N}\sum_{g=1}^{N} \rho_{e,g} \tag{1}$$

where e is the number of the element, g is the number of the grid point in the eth element, and N is the total number of grid points in each element.

This work focuses on maximizing the first natural frequency of the structure. The optimization problem is therefore mathematically stated as:

$$\begin{aligned} &\min: C = -\varphi_1 = -\omega_1^2 \\ &\text{s.t.}: \begin{cases} (\mathbf{K} - \varphi_1 \mathbf{M})\mathbf{u}_1 = 0 \\ \dfrac{\sum_{e=1}^{n} X_e V_e}{\sum_{e=1}^{n} V_e} - V^* \le 0 \\ 0 < \rho_{\min} \le X_e \le 1; \quad e = 1,2,\cdots,n \end{cases} \end{aligned} \tag{2}$$

where C is the objective function, φ_1 and ω_1 are the first eigenvalue and natural frequency, respectively; $\mathbf{u}_1$ is the eigenvector related to φ_1; $\mathbf{K}$ is the global stiffness matrix; $\mathbf{M}$ is the global mass matrix; V_e is the volume of the eth element; V^* is the target volume; and n is the total number of elements.

According to the Rayleigh quotient, the first eigenvalue can be calculated by

$$\varphi_1 = \frac{\mathbf{u_1^T K u_1}}{\mathbf{u_1^T M u_1}} \tag{3}$$

The linear interpolation in non-penalization SEMDOT is used to calculate the global stiffness matrix $\mathbf{K}$ such that

$$\mathbf{K} = (1 - X_e)\rho_{\min}\mathbf{K}^1 + X_e\mathbf{K}^1 \tag{4}$$

where $\mathbf{K}^1$ is the stiffness matrix of solid elements.

Using the same form, the global mass matrix $\mathbf{M}$ is given by

$$\mathbf{M} = (1 - X_e)\rho_{\min}\mathbf{M}^1 + X_e\mathbf{M}^1 \tag{5}$$

where $\mathbf{M}^1$ is the mass matrix of solid elements.

The sensitivity analysis is then calculated by

$$\frac{\partial \varphi_1}{\partial X_e} = \mathbf{u_1^T}\left(\frac{\partial \mathbf{K}}{\partial X_e} - \varphi_1 \frac{\partial \mathbf{M}}{\partial X_e}\right)\mathbf{u_1} \tag{6}$$

where

$$\frac{\partial \mathbf{K}}{\partial X_e} \approx (1 - X_e)\frac{\partial \mathbf{K}}{\partial X_e}\Big|_{X_e=\rho_{\min}} + X_e \frac{\partial \mathbf{K}}{\partial X_e}\Big|_{X_e=1} \tag{7}$$

$$\frac{\partial \mathbf{M}}{\partial X_e} \approx (1 - X_e)\frac{\partial \mathbf{M}}{\partial X_e}\Big|_{X_e=\rho_{\min}} + X_e \frac{\partial \mathbf{M}}{\partial X_e}\Big|_{X_e=1} \tag{8}$$

It should be noted that the sensitivity analysis in SEMDOT is very different with traditional methods such as SIMP and BESO. In SEMDOT, the sensitivity is approximated using the linear combination of solid and void phases. More details can be found in [17].

3. Numerical examples

This section will use pin-pin, fix-pin, and clamped beams to demonstrate the effectiveness of non-penalization SEMDOT in solving natural frequency maximization problems. Unless otherwise stated, the parameters of SEMDOT in [15] and default MMA parameters are adopted. It is noted that the default move limit in MMA is 1. Different versions of the MMA optimizer will result in different results. For all numerical cases, the Young's modulus is set to 1, and the Poisson's ratio is set to 0.3.

The first optimization case is the pin-pin beam whose design domain and boundary conditions are shown in Figure 2. In Figure 2, M represents the concentrated mass, and L and W represent the length and width of the design domain, respectively. Here, M is set to 1×10^{-4}; the mass density ρ_M is set to 1×10^{-9}; L is set to 240; and W is set to 60. The filter radius $r_{\min}$ is set to 2, and the final volume V^* is restricted to be 30% of the design domain.

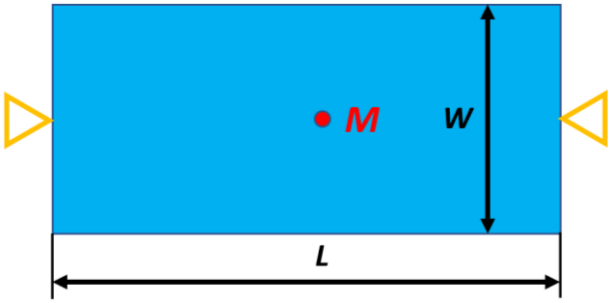
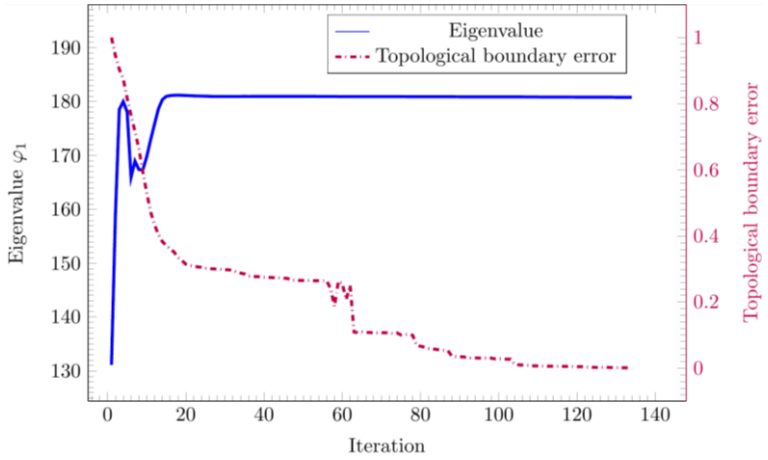


Figure 2. Design domain of a pin-pin beam.

Figure 3a shows that the optimization process converges at the first eigenvalue of 180.7897 after 134 iterations, and the topological boundary error value reaches zero. Figure 3b,c shows the element and smooth designs of the optimized topology, respectively.



(a) Convergence process



(b) Element design



(c) Smooth design

Figure 3. Convergence process and element and smooth designs of a pin-pin beam.

The second optimization case is the fix-pin beam whose design domain and boundary conditions are shown in Figure 4. It is noted that the fix-pin beam case uses the same parameter setting as the pin-pin beam case.

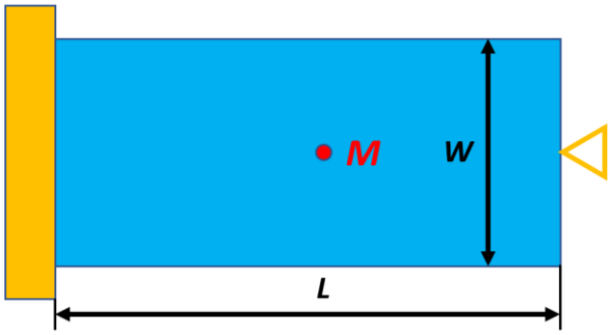
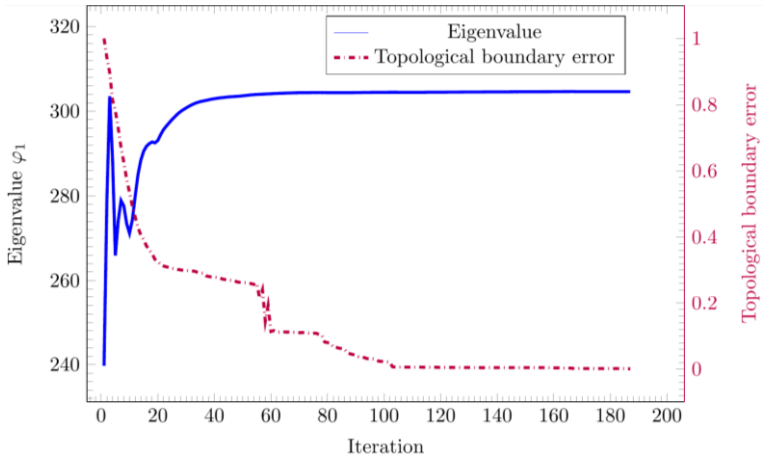


Figure 4. Design domain of a fix-pin beam.

Figure 5a shows that the optimization process converges at the first eigenvalue of 304.6251 after 187 iterations, and the topological boundary error value reaches zero. Figure 5b,c shows the element and smooth designs of the optimized topology, respectively.



(a) Convergence process



(b) Element design



(c) Smooth design

Figure 5. Convergence process and element and smooth designs of a fix-pin beam.

The third optimization case is the clamped beam whose design domain and boundary conditions are shown in Figure 6. The clamped beam case is used to compare SEMDOT with two representative smooth topological design algorithms (ETO and FPTO) with the purpose of further showing the capability of non-penalization SEMDOT. It is noted that FPTO is also a non-penalization topology optimization algorithm.

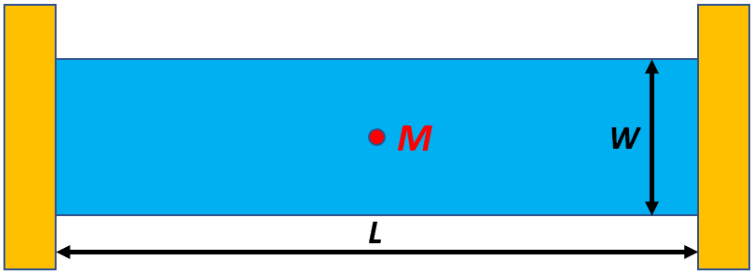
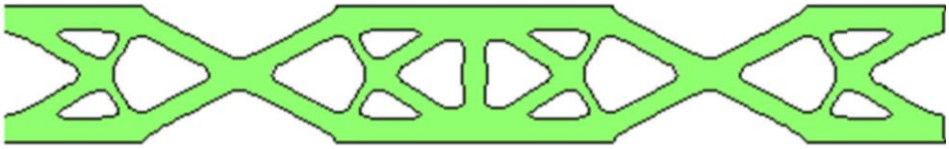


Figure 6. Design domain of a clamped beam.

To make a fair comparison with ETO, the same parameters are used, namely, $L = 140$, $W = 20$, $M = 1 \times 10^{-3}$, $\rho_M = 1 \times 10^{-9}$, $r_{\min} = 2$, and $V^* = 0.5$. The optimization process of SEMDOT converges at the first eigenvalue of 21.7045 after 235 iterations, and the optimization process of ETO converges at the first eigenvalue of 21.75 after 61 iterations [12]. Although ETO performs better than SEMDOT in both performance and convergence, the topology obtained by SEMDOT (Figure 7a) is smoother than that obtained by ETO (Figure 7b). Similar topologies can be observed in Figure 7.



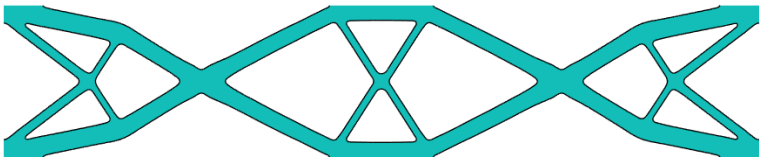
(a) SEMDOT with $\varphi_1 = 21.7045$



(b) ETO with $\varphi_1 = 21.75$ [12]

Figure 7. Comparison between SEMDOT and ETO [12] for a clamped beam.

To ensure the fairness of the comparison with FPTO, the parameters are set to $L = 500$, $W = 100$, $M = 0.1$, $\rho_M = 1 \times 10^{-6}$, $r_{\min} = 3$, and $V^* = 0.3$. The optimization process of SEMDOT converges at the first eigenvalue of 0.2340 after 149 iterations, and the optimization process of FPTO converges at the first eigenvalue of 0.23289 after 186 iterations [11]. The SEMDOT performs better than FPTO in both performance and convergence. The topology obtained by SEMDOT (Figure 8a) is almost the same with that obtained by FPTO (Figure 8b).



(a) SEMDOT with $\varphi_1 = 0.2340$



(b) FPTO with $\varphi_1 = 0.23289$ [11]

Figure 8. Comparison between SEMDOT and FPTO [11] for a clamped beam.

Based on the above discussion, it can be concluded that non-penalization SEMDOT can obtain comparable results and similar topological layouts compared to ETO and FPTO. However, it is hard to determine which algorithm is better as a systematic comparison is required.

4. Concluding remarks

This work used the newly developed non-penalization SEMDOT algorithm to solve the natural frequency maximization problems. Maximizing the first natural frequency of the structure is the focus of this study. Pin-pin, fix-pin, and clamped beams are used to demonstrate the effectiveness of non-penalization SEMDOT. Comparisons with ETO and FPTO show that non-penalized SEMDOT can obtain comparable results and similar topologies. Future work will consider the 3D cases.

Acknowledgements

The authors would like to thank Prof. Krister Svanberg for providing the MMA optimizer code. Dr. Yun-Fei Fu would like to thank Prof. Xiaodong Huang from Swinburne University of Technology (Australia) for the discussion on non-penalization topology optimization.

References

[1] O. Sigmund, "On benchmarking and good scientific practise in topology optimization," *Structural and Multidisciplinary Optimization*, vol. 65, no. 11, p. 315, 2022.

[2] L. Xia, Q. Xia, X. Huang and Y. M. Xie, "Bi-directional evolutionary structural optimization on advanced structures and materials: A comprehensive review," *Archives of Computational Methods in Engineering*, vol. 25, pp. 437-478, 2018.

[3] J. Alexandersen and C. S. Andreasen, "A review of topology optimisation for fluid-based problems," *Fluids*, vol. 5, no. 1, p. 29, 2020.

[4] J. Zhu, H. Zhou, C. Wang, L. Zhou, S. Yuan and W. Zhang, "A review of topology optimization for additive manufacturing: Status and challenges," *Chinese Journal of Aeronautics*, vol. 34, no. 1, pp. 91-110, 2021.

[5] O. Sigmund and J. Petersson, "Numerical instabilities in topology optimization: A survey on procedures dealing with checkerboards, mesh dependencies and local minima," *Structural and Multidisciplinary Optimization*, vol. 16, no. 1, pp. 68-75, 1998.

[6] Y. M. Xie and G. P. Steven, "A simple evolutionary procedure for structural optimization," *Computers and Structures*, vol. 49, no. 5, pp. 885-896, 1993.

[7] X. Huang and Y. M. Xie, "Convergent and mesh-independent solutions for the bi-directional evolutionary structural optimization method," *Finite Element in Analysis and Design*, vol. 43, no. 14, pp. 1039-1049, 2007.

[8] X. Huang, "Smooth topological design of structures using the floating projection," *Engineering Structures*, vol. 208, p. 110330, 2020.

[9] X. Huang, "On smooth or 0/1 designs of the fixed-mesh element-based topology optimization," *Advances in Engineering Software*, vol. 151, p. 102942, 2021.

[10] X. Huang and W. Li, "Three-field floating projection topology optimization of continuum structures," *Computer Methods in Applied Mechanics and Engineering*, vol. 399, p. 115444, 2022.

[11] X. Huang, "A Matlab code of topology optimization by imposing the implicit floating projection constraint," DOI: 10.21203/rs.3.rs-2219853/v1, 2022.

[12] D. Da, L. Xia, G. Li and X. Huang, "Evolutionary topology optimization of continuum structures with smooth boundary representation," *Structural and Multidisciplinary Optimization*, vol. 57, pp. 2143-2159, 2018.

[13] K. Svanberg, "The method of moving asymptotes: A new method for structural optimization," *International Journal of Numerical Methods in Engineering*, vol. 24, no. 2, pp. 359-373, 1987.

[14] M. Langelaar, "An additive manufacturing filter for topology optimization of print-ready designs," *Structural and Multidisciplinary Optimization*, vol. 55, no. 3, pp. 871-883, 2017.

[15] Y. F. Fu, B. Rolfe, L. N. Chiu, Y. Wang, X. Huang and K. Ghabraie, "SEMDOT: Smooth-edged material distribution for optimizing topology algorithm," *Advances in Engineering Software*, vol. 150, p. 102921, 2020.

[16] Y. F. Fu, B. Rolfe, L. N. Chiu, Y. Wang, X. Huang and K. Ghabraie, "Smooth topological design of 3D continuum structures using elemental volume fractions," *Computers and Structures*, vol. 231, p. 106213, 2020.

[17] Y. F. Fu, K. Long and B. Rolfe, "On non-penalization SEMDOT using discrete variable sensitivities," *Journal of Optimization Theory and Applications*, pp. 1-34, 2023.

[18] X. Huang, Z. H. Zuo and Y. M. Xie, "Evolutionary topological optimization of vibrating continuum structures for natural frequencies," *Computers and Structures*, vol. 88, no. 5-6, pp. 357-364, 2010.

[19] B. Xu, Y. S. Han, L. Zhao and Y. M. Xie, "Topology optimization of continuum structures for natural frequencies considering casting constraints," *Engineering Optimization*, vol. 51, no. 6, pp. 941-960, 2019.

[20] Y. Zhang, L. Gao and M. Xiao, "Maximizing natural frequencies of inhomogeneous cellular structures by Kriging-assisted multiscale topology optimization," *Computers and Structures*, vol. 230, p. 106197, 2020.

IASS 2023
July 10–14 Melbourne
Integration of Design and Fabrication

Proceedings of the IASS Annual Symposium 2023
Integration of Design and Fabrication
10–14 July 2023, Melbourne, Australia
Y.M. Xie, J. Burry, T.U. Lee and J. Ma (eds.)

Optimisation of a satellite antenna bracket using the BESO method

Joshua RODRIGUES[a,*], Simon BARTER[a], Raj DAS[a]

[a,*] Space Industry Hub, RMIT University, Melbourne, VIC 3000, Australia
joshua.rodrigues@student.rmit.edu.au

Abstract

Structural optimisation plays a significant role in the development of innovative structures for the aerospace and space sectors. The advancement of technology and research in the space domain has sparked interest towards increasing the efficiency and duration of satellite operations for Earth-orbit missions. The ability to reduce the weight of structures by removing inefficient material whilst maintaining essential strength and stiffness qualities is highly advantageous in such weight-conscious applications. Structural optimisation combined with the deployment of additive manufacturing technology further enables the production of these highly optimised and complex structures. This paper presents a case study for the optimisation of a non-tertiary, satellite antenna bracket structure using the bi-directional evolutionary structural optimisation (BESO) method. It is observed that the BESO method can reduce the weight of a structure through inefficient material removal whilst maintaining critical strength and stiffness qualities. The findings of this study inform the ability of the BESO method as a functional tool for the future design optimisation of spacecraft structures.

Keywords: satellite antenna bracket, topology optimisation, BESO, finite element method, additive manufacturing

1. Introduction

Satellite bracket structures are essential to the design and functionality of satellite systems. Various types of brackets are used to support satellite components including electronics, batteries, cameras and antennae [1]. The primary function of these structures is to support the load and ensure the stability of these systems during various operational phases including launch, deployment and service. Antennas are fundamental to satellites for communication and navigation purposes through sending and receiving signals. The size and mass of the antenna significantly influences the supporting bracket structure required. Whilst the bracket must have the required strength and stiffness to bear the mass of the antenna, conventional supporting brackets are often simplistic and utilise unnecessary and excessive material in their design. With mission costs known to exceed €10,000 (approximately AUD $15,000) per kilogram, minimising the use of non-essential material can enable more efficient structures and hence overall mission profiles [2].

Additive manufacturing (AM) is a fabrication method that creates structures through a sequential layering process. A variety of AM processes exist that can be understood as consisting of two main actions; the first being material deposition followed by material solidification [3]. Various types of metal AM processes are used in the aerospace field including powder bed fusion and directed energy deposition. The generative nature of AM enables significant design freedom to be achieved by removing constraints often imposed by traditional, subtractive manufacturing methods [4]. This further extends to providing fine control over the shape, composition and functionality of structures that is unparalleled by other methods [5].

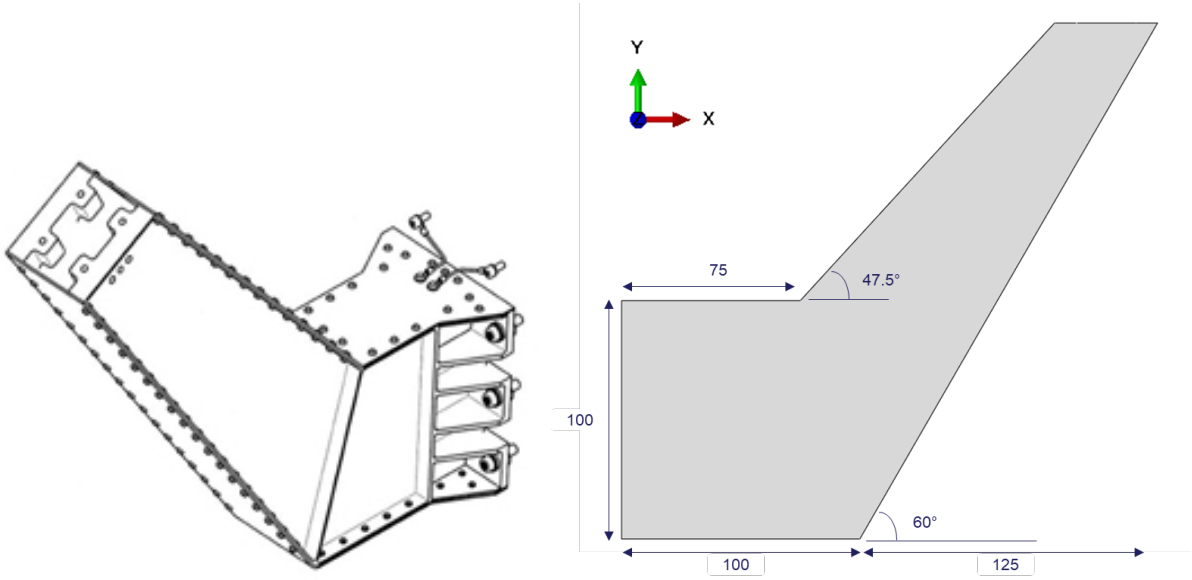
Copyright © 2023 by Joshua RODRIGUES, Simon BARTER and Raj DAS. Published in the Proceedings of the IASS Annual Symposium 2023 with permission.

The realisation and potential of AM technology have led to significant research in methods and application of structural optimisation techniques. As structures with complex, porous and internal features can now be manufactured with relative ease, methods of structural optimisation have become widely utilised across various industries including the automotive, civil and aerospace sectors. Structural optimisation refers to a technique where the material distribution of a structure is spatially changed (such as the elimination of excess material or the addition of new material) to increase structural efficiency for a given application. This is quite appealing to the space sector where weight-conscious designs are paramount. Common methods of optimisation include size, shape and topology changes, with associated levels of complexity [6]. Topology optimisation focuses on determining the optimal layout of material within a structure whilst considering a set design objective(s) and constraint(s) [7]. The bi-directional evolutionary structural optimisation (BESO) method is a finite element-based topology optimisation technique that is an extension of the evolutionary structural optimisation (ESO) method [8, 9]. Compared to ESO which is limited in its approach to material removal, the BESO method not only removes inefficient material from a structure but can simultaneously add efficient material to regions that require strengthening, making it much more material efficient [10].

In this paper, we apply the BESO algorithm to optimise a realistic satellite antenna bracket through finite element modelling using Abaqus software (ver. 2020). The original design of the satellite antenna bracket will be presented and used as inspiration for the design domain. Relevant loading and boundary conditions will then be applied to the structure, where it will be meshed and the BESO method will be performed, specifically using the compact 100-line Python code as presented in [8] due to its simplicity and use for educational purposes. The outcome of this study will be used to assess the applicability of such a method for the design optimisation of satellite components, in this case, an antenna bracket structure.

2. Satellite antenna bracket design

Here the applicability of the BESO algorithm is demonstrated to obtain an improved material layout for a satellite antenna bracket. This optimisation aims to produce a lighter bracket structure whilst still adhering to the geometric and strength requirements. The structure of choice is based on the antenna bracket used in the RUAG Sentinel 1 radar satellite as per Fig. 1a. The structure is simplified to a 3D plate model in which complicated features, such as the rivets and fasteners, were neglected as their effects on the main analysis results of interest were negligible. It is also noted that the exact parameters of the RUAG bracket are not publically available, hence representative dimensions are used, as per Fig. 1b. The thickness of the structure is assumed to be 1 mm.



(a) (b)

Figure 1. (a) RUAG Sentinel 1 satellite antenna bracket and (b) representative structure with dimensions in millimetres (mm) [11].

A lightweight AM aluminium alloy (AlSi10Mg) is used as the material for this analysis as it is common in AM processes. The Poisson's ratio (v) was taken as 0.33. Prior tensile testing of AM coupons has been completed on this alloy, giving a Young's modulus (E) of 58.571 GPa, assuming a vertical build direction. The density of this material is 2.597 g/cm^3. Typically aluminium alloys such as 6061-T6 and 6063-T6 extrusions are used for this application, which have comparable density and mechanical properties. A linear-elastic finite element analysis was performed throughout.

3. Finite element modelling

The bracket structure was created in finite element software Abaqus as a solid, 3D model using the graphical user interface (Abaqus CAE). The aluminium alloy AlSi10Mg material was created and the properties were assigned as a homogeneous, solid section. A static general step was applied to the structure with an increment size between 0.01 and 1. Optimisation problems require a fine mesh to achieve accurate results. In this analysis, the solid model was meshed with a seed size of 2.0 mm which resulted in 100,138 elements and 201,730 nodes. Type C3D8 elements were used, which are 8-node linear brick elements. This is due to the BESO code requiring hexahedral elements to perform the optimisation process. The meshed part is displayed in Fig. 2.

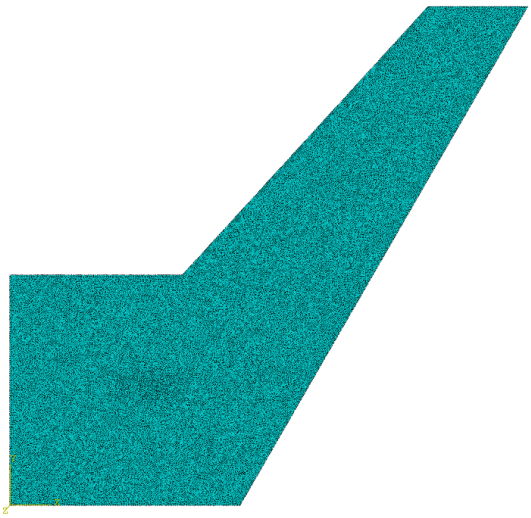
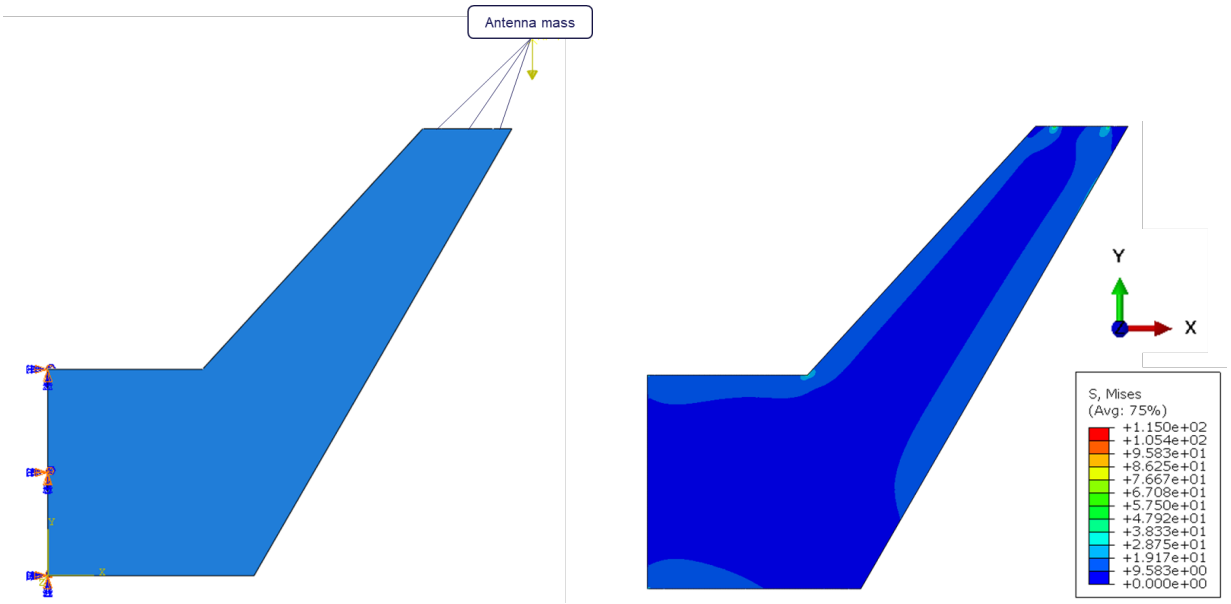


Figure 2. Meshed antenna bracket structure.

The purpose of this bracket structure is to support the load of an antenna system. To enhance the simplicity of the computational model, the antenna is considered as a singular point mass of 1.00 kg at the location of its centre of gravity. A simple static case is considered for this analysis where the weight of the antenna is considered to be under the force of gravity (10g). Therefore, a singular point load of 100 N is applied vertically downwards (the negative y-direction). As seen in Fig. 1a, the antenna is mounted to the original bracket using fasteners. In this analysis, it is assumed that the loading of the antenna is applied evenly across the middle area of this section. A 25 mm partition along the top surface of the model is applied to represent potential fasteners at this location. A multi-point constraint (MPC) of type beam is used to constrain the mass load evenly across this partitioned region of the structure.

The original structure is also fixed to the main satellite body using fasteners at the base of the bracket. The precise locations of these mounting points, however, are not fundamental to the design and optimisation process. Therefore, this entire edge of the bracket is considered fully fixed (encastre) to the satellite in all six degrees of freedom but is still part of the overall design domain. The results from this optimisation can then inform the potential location of these fastener interfaces, rather than excluding unnecessary regions from the optimisation. The von Mises stress is chosen as the criterion for this optimisation and will hence be used throughout. Fig. 3a exhibits the loading and boundary conditions applied to the structure and Fig. 3b displays the initial von Mises stress analysis of the applied load.



(a) (b)

Figure 3. (a) loading and boundary conditions applied to the finite element model and (b) the von Mises stress distribution of static analysis.

The von Mises stress distribution of the structure under a static analysis is depicted in Fig. 3b, where a maximum stress of 100.970 MPa is observed occurring at the corner of the edge where the antenna load is applied. It is observed that the fixed edge of the structure has elevated stress at the top and bottom locations along the edge. An elevated stress region is also seen at the oblique corner angle in the bracket. The majority of the structure has minimal stress of approximately 5 MPa throughout, represented by the deep blue region. This suggests that there is a large portion of inefficient material used to transfer the load in the part, indicating that a more optimum layout of the material will be beneficial to saving weight.

4. Optimisation using BESO

Once the model was developed, the BESO method was performed by running the Python code in Abaqus. Abaqus CAE was used to monitor the progress of the iterative jobs. This study considers a compliance minimisation objective (stiffness maximisation) with respect to a volume constraint. The BESO method used in this analysis is based on the 'soft-kill' approach. This treats elements as relative densities as either being 1.0, which indicates the presence of a solid element, or a small prescribed value of 0.001, to indicate void elements. In contrast to a 'hard-kill' approach that completely removes the elements from the model, the soft-kill can filter between each material type instead of entire element deletion. The void material can then be excluded when viewing the results whilst remaining in the part, which is the case for the results presented in this paper. The von Mises stress field was used to modify the topology of the structure. At each iteration, the von Mises stress was calculated, whereby elements were deemed void if they were lower than a reference stress value. A target volume fraction was set to 0.3, with a minimum filter radius of 3 mm and an evolutionary ratio of 2%. The gradual evolution of the optimisation process is presented in Fig. 4 by a few intermediate topologies. A volume fraction (W/W_0) is also denoted, representing the current iteration volume (W) to the initial volume of the structure (W_0).

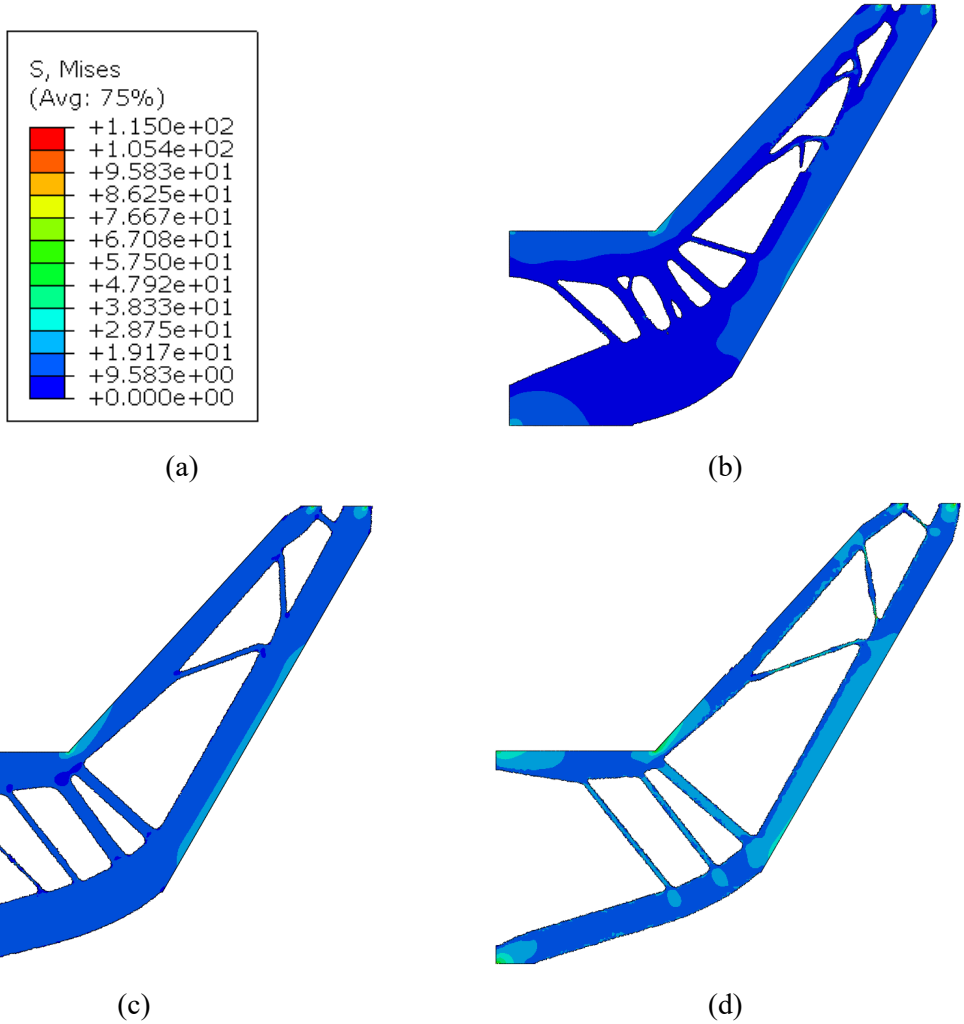


Figure 4. Intermediate results of the satellite antenna bracket optimisation process using the BESO method including (a) von Mises stress legend, (b) iteration 17: $W/W_0 = 70.93\%$, (c) iteration 34: $W/W_0 = 50.32\%$ and (d) iteration 53: $W/W_0 = 34.28\%$.

The 'optimum' solution was determined based on the maximum stress of the structure and the weight savings achievable within a prescribed domain. As described in [7], a maximum design allowable stress (σ_a) was selected that is usually based on failure criteria, material properties and operating conditions. In this analysis, the maximum allowable stress was set to 110 MPa, which is approximately 10% greater than the maximum initial von Mises stress. The iteration with the greatest weight savings whilst remaining under σ_a is considered to be the optimum solution for this analysis. Fig. 5a and Fig. 5b show the variation of the maximum von Mises stress and volume fraction, respectively, of the satellite antenna bracket with a change in topology layout (iteration number). A dashed horizontal line is drawn to represent the prescribed maximum allowable stress of 110 MPa. The topology layout of the structure that immediately precedes the point of intersection between this line and the stress history curve represents the most optimum solution. This was determined to be the 43rd iteration, represented by the red dot denoted as the 'design point'.

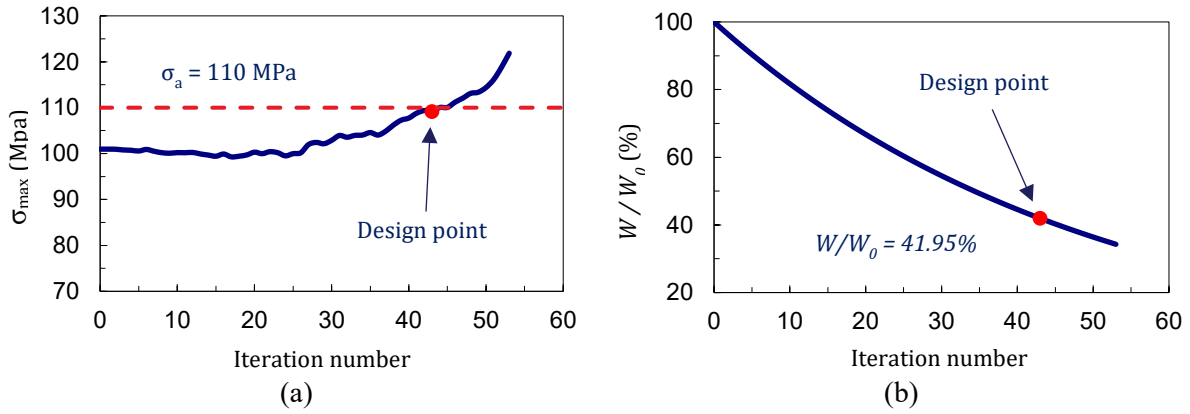


Figure 5. (a) Variation of the maximum von Mises stress in the antenna bracket with change in topology layout, and (b) change in volume fraction of the bracket with change in topology layout.

Under the prescribed loading and boundary conditions, the topology layout at this iteration resulted in a maximum von Mises stress of 109.142 MPa. The next iteration had a maximum von Mises stress of 110.036 MPa, which exceeds the allowable limit of 110 MPa. This design point also yielded a weight fraction of 41.95% compared to the weight of the original structure. This implies that the optimum design yielded a weight reduction of around 58%, whilst only increasing the maximum von Mises stress by approximately only 8 MPa. This weight saving could have a significant impact on the efficiency and performance of, not only this sub-component but the holistic satellite structure, signifying the importance that design optimisation can have for spacecraft structures.

The resultant optimal topology is exhibited in Fig. 6, where several layout and stress changes can be observed compared to the initial design in Fig. 3b. The key features of the optimal topology are listed below:

- The bulk of the lowly stressed material that was present in the middle of the initial structure has been removed and replaced with strut-like connections between the upper and lower edges of the bracket.
- The top and bottom sides of the fixed edge remain whilst the middle section has been removed. This indicates that potential fasteners should be applied at the top and bottom corners of the fixed edge and that no fasteners are required in the middle.
- The highest stress occurs at the location where the antenna mass is constrained to the partitioned edge at the top of the antenna bracket. The material on either side of this partition was inefficient as it did not support much load and was hence removed.
- The average lowly stressed regions have increased from 5 MPa in the initial structure to approximately 15 MPa in the optimum design.
- The inclined portion of the bracket where the antenna is mounted appears to represent a truss section with diagonal struts present between the upper and lower edges.
- In the original design, an oblique 60° angle was present at the lower edge of the bracket. Whilst this incline remains, the bottom edge of the structure appears to have a more filleted section with a more gradual transition radius that reduces the stress concentrations in this corner. This further reduces the potential for crack initiation at this location due to launch vibrations.

It is noted that the derived optimal design using BESO is a conceptual design and requires significant post-processing to effectively implement this design. This can be in the form of local modifications to the geometry, shape optimisation of features and more accurate geometries for fastener interfaces.

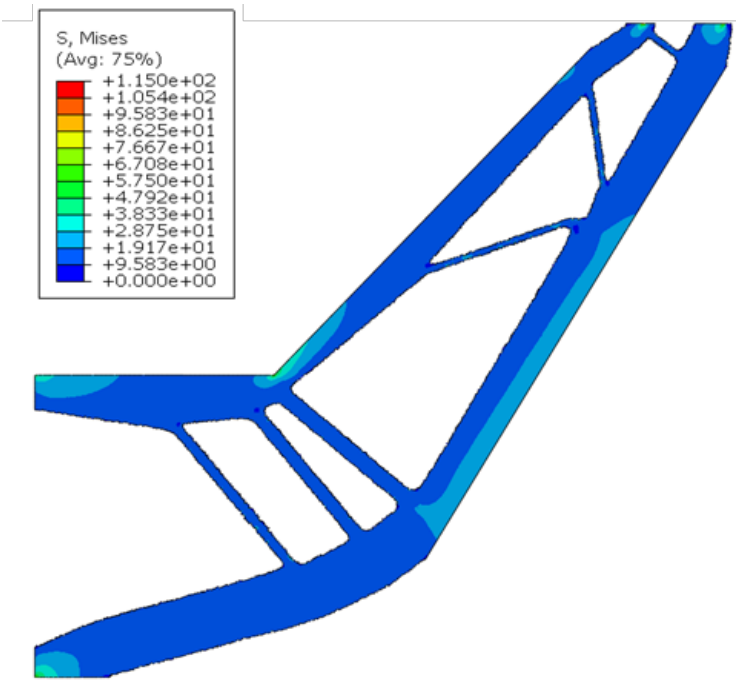


Figure 6. Optimal topology layout of the satellite antenna bracket with von Mises stress distribution.

6. Conclusions

This paper investigated the use of the BESO method for the topology optimisation of a spacecraft structure. The capabilities of the BESO algorithm were demonstrated by considering the design optimisation of a satellite antenna bracket structure. The BESO algorithm was applied to the initial design of the structure to generate an improved topological layout by the gradual removal and addition of material using the soft-kill approach. An approximate 58% decrease in the weight of the structure was achieved whilst having a maximum stress below the allowable design stress limit of 110 MPa that was set for this optimisation. The BESO algorithm was found to be an efficient and practical tool for the optimisation of realistic spacecraft structures. This technique can serve as a valuable starting point for further design considerations and other optimisation techniques that are not easily realised using conventional methods. The BESO method can be applied to various spacecraft applications to reduce the weight of structures without compromising their critical strength and stiffness characteristics. Variations in stress levels can also be reduced and lead to a more uniformly stressed structure with more optimum material usage.

References

[1] Samal, S.K., Vishwanatha, H.M., Saxena, K.K., Behera, A., Nguyen, T.A., Behera, A., Prakash, C., Dixit, S., and Mohammed, K.A., 2022, 3D-Printed Satellite Brackets: Materials, Manufacturing and Applications, *Crystals,* vol. 12 (8).

[2] Mitchell, A., Lafont, U., Hołyńska, M., and Semprimoschnig, C., 2018, Additive manufacturing — A review of 4D printing and future applications, *Additive Manufacturing,* vol. 24, pp. 606-626.

[3] D'Angelo, O., Kuthe, F., Liu, S.-J., Wiedey, R., Bennett, J.M., Meisnar, M., Barnes, A., Kranz, W.T., Voigtmann, T., and Meyer, A., 2021, A gravity-independent powder-based additive manufacturing process tailored for space applications, *Additive Manufacturing,* vol. 47, pp. 102349.

[4] Dordlofva, C., and Törlind, P., 2017, Qualification challenges with additive manufacturing in space applications, In *2017 International Solid Freeform Fabrication Symposium,* pp. 2699-2712. University of Texas at Austin.

[5] Huang, Y., Leu, M.C., Mazumder, J., and Donmez, A., 2015, Additive Manufacturing: Current State, Future Potential, Gaps and Needs, and Recommendations, *Journal of Manufacturing Science and Engineering,* vol. 137 (1).

[6] Tejani, G.G., Savsani, V.J., Patel, V.K., and Savsani, P.V., 2018, Size, shape, and topology optimization of planar and space trusses using mutation-based improved metaheuristics, *Journal of Computational Design and Engineering,* vol. 5 (2), pp. 198-214.

[7] Das, R., and Jones, R., 2011, Topology optimisation of a bulkhead component used in aircrafts using an evolutionary algorithm, *Procedia Engineering,* vol. 10, pp. 2867-2872.

[8] Zuo, Z.H., and Xie, Y.M., 2015, A simple and compact Python code for complex 3D topology optimization, *Advances in Engineering Software,* vol. 85, pp. 1-11.

[9] Xie, Y.M., and Steven, G.P., 1993, A simple evolutionary procedure for structural optimization, *Computers & Structures,* vol. 49 (5), pp. 885-896.

[10] Tang, Y., Kurtz, A., and Zhao, Y.F., 2015, Bidirectional Evolutionary Structural Optimization (BESO) based design method for lattice structure to be fabricated by additive manufacturing, *Computer-Aided Design,* vol. 69, pp. 91-101.

[11] RUAG, Additive Manufacturing for Space Application. 2015.

IASS 2023
July 10–14 Melbourne
Integration of Design and Fabrication

Proceedings of the IASS Annual Symposium 2023
Integration of Design and Fabrication
10–14 July 2023, Melbourne, Australia
Y.M. Xie, J. Burry, T.U. Lee and J. Ma (eds.)

Topology optimisation considering buckling in architectural design

Tao XU[a], Xiaoshan LIN[a], Yi Min XIE[a,*]

[a,*] Centre for Innovative Structures and Materials, School of Engineering
RMIT University, Melbourne 3001, Australia
mike.xie@rmit.edu.au

Abstract

Topology optimisation techniques have been increasingly employed in architectural designs to achieve efficient and elegant structures with minimal material. Current architectural applications of topology optimisation typically consider structural stiffness as the main design objective. However, buckling is a critical phenomenon that should not be ignored in structural designs, as it could lead to catastrophic failure of a structure. In this study, a buckling-constrained bi-directional evolutionary optimisation (BC-BESO) algorithm is presented for designing buckling-resistant structures. The proposed algorithm aims to minimise the compliance of a structure under predefined buckling constraints, thus ensuring both stiffness and stability of the structure. To validate the proposed algorithm, a benchmark example is presented to compare the numerical result with the analytical solution. The application of the proposed method in the structural design of high-rise buildings demonstrates that the algorithm can significantly enhance buckling resistance with a slight sacrifice of stiffness.

Keywords: topology optimisation, bi-directional evolutionary structural optimisation, architectural design, buckling, structural stability

1. Introduction

Topology optimisation has emerged as a powerful tool in the architecture community over the past few decades, enabling the design of high-performance structures with minimal material [1]. Among various topology optimisation techniques, the bi-directional evolutionary structural optimisation (BESO) method is one of the most commonly used methods, which removes inefficient material from a structure and adds material to the most-needed locations [2, 3]. The BESO method has been employed to design buildings and bridges that are optimised for efficiency, environmental sustainability, and aesthetical appeal [4–10].

Notwithstanding the growing interest of architects in topology optimisation, practical applications of this technique in large-scale projects remain limited [1]. One of the main reasons is the fact that the current BESO algorithm for architectural design primarily focuses on maximising structural stiffness, generating forms that may be susceptible to buckling issues. The lack of consideration for the buckling effect in topology optimisation can lead to poor stability and unexpected structural failures [11]. To address this issue, this paper introduces a buckling-constrained BESO (BC-BESO) algorithm for architectural design, allowing architects to obtain more practical solutions with improved stability and buckling-resistant performance.

The BESO algorithm benefits from having only two discrete states (solid and void) for the design variables, which helps alleviate the issues related to so-called pseudo-buckling modes that often occur in other density-based topology optimisation algorithms [12, 13]. In this study, the proposed BC-BESO algorithm is validated through a benchmark example, where the numerical result obtained by the algorithm is compared to the analytical solution presented by Haftka and Gürdal [14]. Besides, this

Copyright © 2023 by Tao XU, Xiaoshan LIN and Yi Min XIE. Published in the Proceedings of the IASS Annual Symposium 2023 with permission.

paper presents an example of topology optimisation considering buckling effect in the design of a high-rise building, highlighting the importance of this consideration for achieving practical and buckling-resistant solutions.

The rest of the paper is organised as follows. In Section 2, the formulas and the procedure of the BC-BESO algorithm are given. Section 3 studies a benchmark example that demonstrates the effectiveness of the BC-BESO algorithm. In Section 4, the application of the algorithm in the design of a high-rise building is presented, and a comparison is made between the results obtained from the BC-BESO and the conventional BESO methods. Lastly, concluding remarks are given in Section 5.

2. Buckling-constrained BESO method

In this section, the BC-BESO method for architectural optimisation is presented. By considering buckling constraints in topology optimisation, the proposed method enables architects to achieve more efficient and buckling-resistant structures for their designs.

2.1. Problem statement

The topology optimisation for minimising compliance subject to buckling constraints can be stated as follows:

$$\begin{aligned} &\text{min: } C = \boldsymbol{F}^T \boldsymbol{u} \\ &\text{s.t.: } \begin{cases} \boldsymbol{K}\boldsymbol{u} = \boldsymbol{F} \\ V(x) = \sum x_i v_i - V^* = 0 \\ x_i = x_{min} \text{ or } 1,\ i = 1,\ 2,\ ...,\ N. \\ \lambda_1 \geq \underline{\lambda} \end{cases} \end{aligned} \tag{1}$$

where C is the mean compliance, $\boldsymbol{K}$ and $\boldsymbol{u}$ are the global stiffness matrix and the displacement vector, respectively. $\boldsymbol{F}$ is the load applied to the structure. v_i is the volume of the corresponding element and V^* is the predefined volume fraction. λ_1 is the lowest buckling load factor (BLF) and $\underline{\lambda}$ is the prescribed buckling constraint. x_i is the binary design variable of an individual element, which equals to either x_{min} (void) or 1 (solid).

2.2. Optimisation procedure

Linear buckling analysis is used to conduct sensitivity analysis to save computational cost. Linear buckling analysis is defined as

$$\mu_j = -\frac{\boldsymbol{\varphi}_j^T \boldsymbol{G} \boldsymbol{\varphi}_j}{\boldsymbol{\varphi}_j^T \boldsymbol{K} \boldsymbol{\varphi}_j} \tag{2}$$

where $\boldsymbol{G}$ is the stress stiffness matrix. μ_j and $\boldsymbol{\varphi}_j$ are the inverse value of the j-th BLF λ_j and its corresponding buckling mode vector, respectively. Two different material interpolation schemes are used for stiffness and the stress stiffness matrix to restrain pseudo-buckling modes [15], which are given as follows.

$$\begin{cases} E_K(x_i) = \left[\dfrac{x_{min} - x_{min}^p}{1 - x_{min}^p} (1 - x_i^p) + x_i^p \right] E \\ E_G(x_i) = x_i^p E \end{cases} \tag{3}$$

The sensitivity of BLF is calculated as

$$\frac{\partial \mu_j}{\partial x_i} = -\left[\boldsymbol{\varphi}_j^T \left(\frac{\partial \boldsymbol{G}}{\partial x_i} + \mu_j \frac{\partial \boldsymbol{K}}{\partial x_i} \right) \boldsymbol{\varphi}_j - \boldsymbol{v}_j^T \frac{\partial \boldsymbol{K}}{\partial x_i} \boldsymbol{u} \right] \tag{4}$$

The second term on the right side is the adjoint term, which can be solved by

$$\boldsymbol{K}\boldsymbol{v}_j = \boldsymbol{\varphi}_j^T \frac{\partial \boldsymbol{G}}{\partial \boldsymbol{u}} \boldsymbol{\varphi}_j \tag{5}$$

Multiple buckling constraints are aggregated into a single one by the KS function. The KS-aggregated buckling sensitivity is written as [16]

$$\frac{\partial \mu^{KS}}{\partial x_i} = \frac{\sum_{i=1}^{q} e^{\rho(\mu_j - \mu_1)} \frac{\partial \mu_j}{\partial x_i}}{\sum_{i=1}^{q} e^{\rho(\mu_j - \mu_1)}} \tag{6}$$

The above sensitivity of buckling constraints is added to compliance sensitivity via an augmented Lagrangian multiplier Λ reported in the literature [11]. The overall sensitivity can be found as

$$\frac{\partial f}{\partial x_i} = \frac{\partial C}{\partial x_i} + \Lambda \frac{\partial \mu^{KS}}{\partial x_i} = -\frac{1}{2}\boldsymbol{u}^T \frac{\partial \boldsymbol{K}}{\partial x_i}\boldsymbol{u} - \Lambda \frac{\sum_{i=1}^{q} e^{\rho(\mu_j - \mu_1)} \left[\boldsymbol{\varphi}_j^T \left(\frac{\partial \boldsymbol{G}}{\partial x_i} + \mu_j \frac{\partial \boldsymbol{K}}{\partial x_i} \right) \boldsymbol{\varphi}_j - \boldsymbol{v}_j^T \frac{\partial \boldsymbol{K}}{\partial x_i} \boldsymbol{u} \right]}{\sum_{i=1}^{q} e^{\rho(\mu_j - \mu_1)}} \tag{7}$$

Therefore, the sensitivity of element *i* in the BESO method is calculated as

$$\alpha_i = -\frac{\partial f}{\partial x_i} = \frac{1}{2}\boldsymbol{u}^T \frac{\partial \boldsymbol{K}}{\partial x_i}\boldsymbol{u} + \Lambda \frac{\sum_{i=1}^{q} e^{\rho(\mu_j - \mu_1)} \left[\boldsymbol{\varphi}_j^T \left(\frac{\partial \boldsymbol{G}}{\partial x_i} + \mu_j \frac{\partial \boldsymbol{K}}{\partial x_i} \right) \boldsymbol{\varphi}_j - \boldsymbol{v}_j^T \frac{\partial \boldsymbol{K}}{\partial x_i} \boldsymbol{u} \right]}{\sum_{i=1}^{q} e^{\rho(\mu_j - \mu_1)}} \tag{8}$$

To avoid a mesh-dependent solution, the sensitivity values are averaged by a filtering scheme, which is determined as [17]

$$\tilde{\alpha}_j = \frac{\sum_{i=1}^{N} \omega_{ij} \alpha_i}{\sum_{i=1}^{N} \omega_{ij}} \tag{9}$$

where $\tilde{\alpha}_j$ is the averaged sensitivity value of the *j*-th element. *N* denotes the number of neighbouring elements. ω_{ij} is the linear weight factor related to r_{ij}, which is the distance between the centroids of the centred element *j* and its neighbouring elements *i*

$$\omega_{ij} = r_{min} - r_{ij} \left(j = 1, 2, ..., \mathrm{N} \right) \tag{10}$$

where r_{min} is the filter radius. To enhance the optimisation stability and convergence, the sensitivity value is averaged by the previous three historical information as

$$\tilde{\alpha}_j^k = \frac{\tilde{\alpha}_j^k + \tilde{\alpha}_j^{k-1} + \tilde{\alpha}_j^{k-2}}{3} \tag{11}$$

where *k* is the current iteration number, and afterwards, the design variables are updated according to the scheme described in [11].

The optimisation process is conducted until buckling constraints, the volume constraint and the convergence criterion are all met. The convergence criterion is defined as the change in the objective function over the last ten iterations being sufficiently small, e.g., 10^{-3} to 10^{-5}. The overall procedure of the proposed BC-BESO method is illustrated in Figure 1.

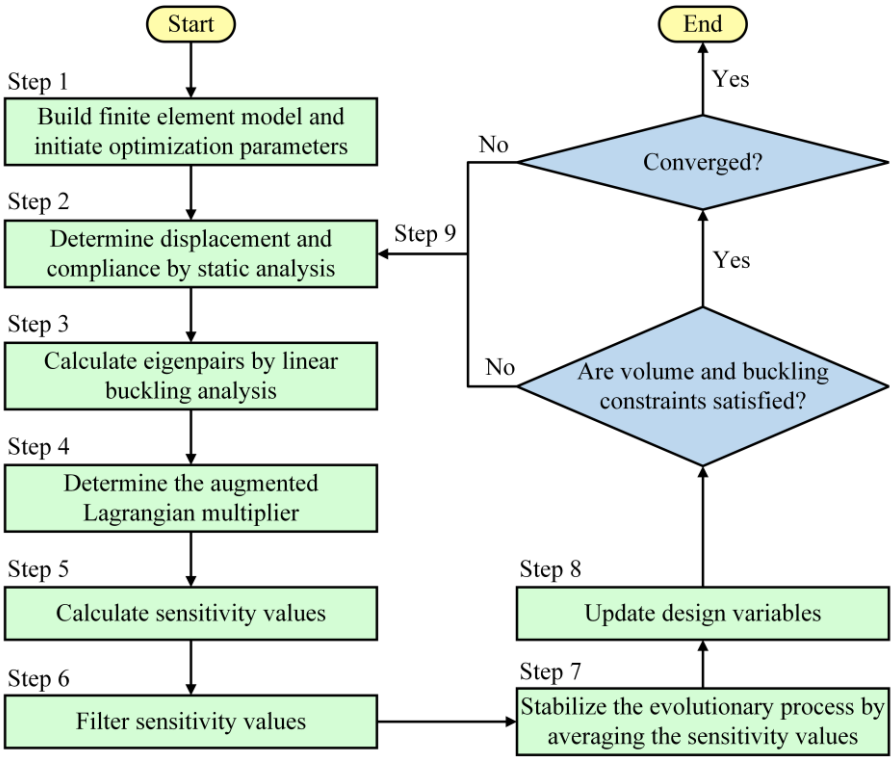


Figure 1. Flowchart of the BC-BESO method.

3. Benchmark example

To validate the BC-BESO algorithm, a benchmark example reported by [14] is studied in this section. The objective of this example is to maximise the lowest BLF λ_1 of a simply supported column with a length of L subjected to the constant volume constraint (Figure 2a). The optimum analytical column from the literature has zero cross-sectional areas at both ends, and the cross-sectional area gradually increases towards the middle section. The analytical solution of the lowest BLF of the optimised column is given as follows [14].

$$\lambda_1^{opt} = \frac{125}{9}\frac{EI_0}{L^2} = 1.407\frac{\pi^2 EI_0}{L^2} = 1.407\lambda_1^0 \tag{12}$$

where I_0 and λ_1^0 are the moment of inertia and the lowest BLF of the initial constant area column, respectively.

In this study, a continuum model is employed, which has a discretised rectangular design domain with a high aspect ratio. Shape optimisation is performed with a constant volume. The parameters are set as $E = 1$, $\nu = 0$, $p = 3$, $x_{min} = 10^{-6}$, and $r_{min} = 2 \times$ the element side length. The ideal slender column has an approximately infinite aspect ratio, whereas different aspect ratios (L_x/L_y) are adopted for the rectangular design domain, i.e., 20, 30, 50 and 80. Besides, it was reported by [18] that the discretisation could influence the accuracy of λ_1 approximations. Thus, different discretisation levels are used in this study. The numerical results obtained from the proposed buckling-constrained BESO method are compared with the analytical solution [14] in Table 1.

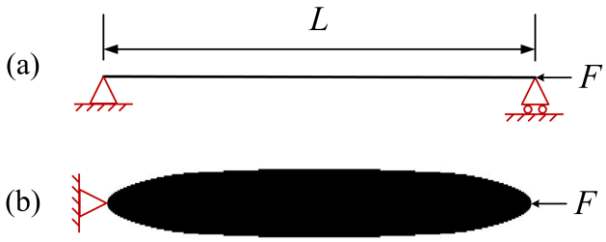


Figure 2. Benchmark example: (a) boundary conditions of the simply supported column, and (b) optimum design obtained from the continuum model. Note that the length of the optimum design is scaled for easy viewing.

Table 1. λ_1 obtained based on different discretisation levels and aspect ratios of the design domain. (Both λ_1 and $\lambda_1^{uniform}$ are the numerical results obtained with the discretisation shown in the same row.)

Aspect ratio L_x/L_y	Discretisation	$\lambda_1/\lambda_1^{uniform}$	Error (%)
20	200×10	1.339	-4.9
	400×20	1.368	-2.8
	600×30	1.370	-2.6
	800×40	1.376	-2.2
30	600×20	1.372	-2.5
	900×30	1.380	-1.9
	1200×40	1.381	-1.9
50	1500×30	1.390	-1.2
	2000×40	1.392	-1.1
80	4800×60	1.396	-0.8

The shape of the optimum column (Figure 2b) exhibits consistent characteristics with the analytical solution, i.e., infinitesimal widths at the ends and wider dimensions in the middle. Such a width-tapered column leads to a higher moment of inertia and stronger resistance to buckling. Nevertheless, as shown in Table 1, the accuracy of the numerical results is dependent on the discretisation level and the aspect ratio of the design domain.

The error decreases when a finer discretisation level is applied. For instance, when the aspect ratio is 20, the error reduces from -4.9% for 200 × 10 elements to -2.2% for 800 × 40 elements; when the aspect ratio is 30, the error reduces from -2.5% for 600 × 20 elements to -1.9% for 1200 × 40 elements.

The aspect ratio of the design domain also affects the accuracy of the optimisation results. With a discretisation of 30 × the aspect ratio $=$ 30, the errors are -2.6%, -1.9% and -1.2% when the aspect ratios are 20, 30 and 50, respectively. With a large aspect ratio of 80 and an extremely fine mesh of 4800 × 60, an error of only -0.8% can be achieved. Besides, it is worth mentioning that the same numerical results are obtained with $\nu = 0.3$.

The comparison between the analytical solution and the numerical results indicates that satisfactory results can be obtained with a small error margin. The proposed algorithm has been demonstrated to be valid and accurate.

4. Numerical examples

A high-rise building with a width of 20 m and a height of 100 m is considered, as illustrated in Figure 3a. It is assumed that the building is subjected to lateral wind loads at five different heights, where the wind load *P* at the height of 20 m is 1000 kN and increases linearly with height. Two wind load cases

are considered. In the first case, the building is subjected to the wind load from the left, while in the second case, it experiences the wind load from the right. The design domain is discretised into 80 × 400 elements.

The stiffness optimisation is firstly conducted with $V^* = 50\%$, $ER = 1\%$, and $r_{min} = 1$ m. The corresponding stiffness design is presented in Figure 3b. The design exhibits a concentration of material in the lower part of the structure, while the upper part features thinner structural members. Upon applying the wind load on both sides, the first buckling modes are observed in Figure 3c and 3d, where a localised buckling is clearly evident at the top of the structure (indicated by the red circle). Additionally, a high level of strain energy density is observed in the upper part of the structure, while the lower part possesses relatively low strain energy density. The lowest BLF λ_1^C of the stiffness design is only 0.127, corresponding to a critical load $P_{cr} = \lambda_1^C \times P = 127$ kN. Therefore, the obtained stiffness design cannot be used in practical architectural applications, as it may be susceptible to severe buckling issues.

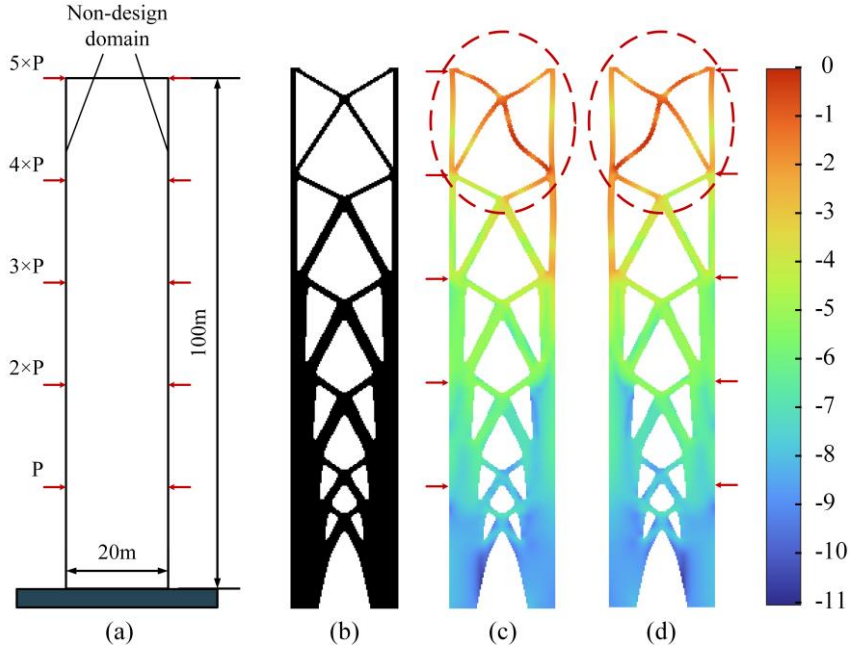


Figure 3. High-rise building: (a) boundary conditions; (b) stiffness design; (c) first buckling mode under left wind load; and (d) first buckling mode under right wind load. Buckling modes are coloured from blue to red, corresponding to the logarithm of normalised strain energy density from low to high.

To achieve a structure resistant to buckling, the buckling-constrained optimisation is then conducted based on the stiffness design with $ER = 0.1\%$, $r_{min} = 0.75$ m, and $\underline{\lambda} = 10 \times \lambda_1^C = 1.27$. The resulted buckling-reinforced structure is shown in Figure 4a, where the material is relocated from the lower part of the structure to the upper part. Thin members in the upper part are separated, and additional members are generated to resist buckling (as indicated by the red circle). The first buckling modes, illustrated in Figure 4b and 4c, show that the buckling-reinforce structure exhibits a more global buckling mode, and the strain energy density distributes more evenly compared to that of the stiffness design (Figure 3c and 3d). The lowest BLF λ_1^B of the buckling-reinforced design is increased to 1.27, corresponding to a much higher critical load $P_{cr} = \lambda_1^B \times P = 1{,}270$ kN. Moreover, the stiffness of the buckling-reinforced structure is decreased by only 1.0% compared to that of the stiffness design.

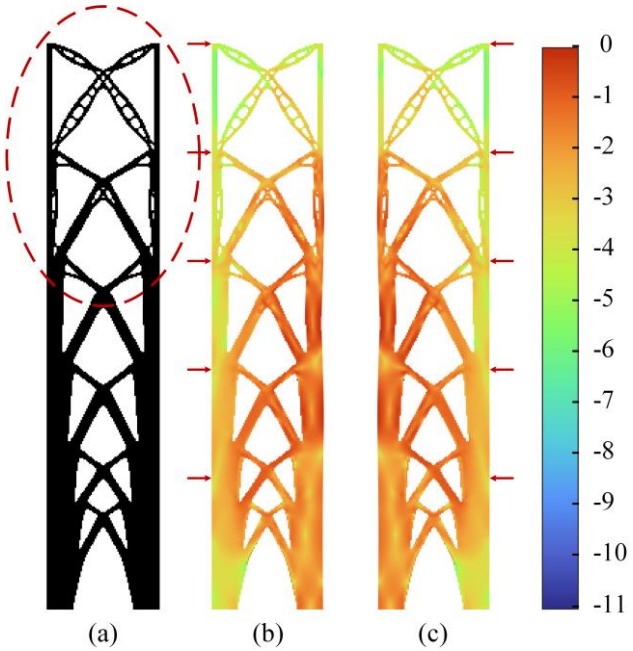


Figure 4. Buckling-constrained optimisation: (a) optimisation result and (b) first buckling mode under left wind load; and (c) first buckling mode under right wind load. Buckling modes are coloured from blue to red, corresponding to the logarithm of normalised strain energy density from low to high.

This example highlights the importance of considering the buckling effect in architectural design, as the stiffness design generated by conventional BESO can face severe buckling issues. The proposed BC-BESO algorithm offers a promising solution to achieve more efficient and stable architectural designs by incorporating buckling constraints in the optimisation process.

5. Conclusion

In this study, a buckling-constrained bi-directional evolutionary structural optimisation (BC-BESO) algorithm is presented for architectural design to enhance structural stability. The algorithm is validated through a benchmark example, demonstrating its effectiveness in generating efficient and buckling-resistant structures. The application of the algorithm to the design of a high-rise building demonstrates its ability to significantly improve buckling resistance with minimal stiffness reduction. Furthermore, the research contributes to the body of knowledge on topology optimisation with buckling constraints in architectural design. In future research, it is worthwhile to investigate the inclusion of additional constraints, such as vibration or thermal performance, and to apply the algorithm to optimise different types of structures, such as bridges and large-scale infrastructure.

Acknowledgements

The authors gratefully acknowledge the financial support from the Australian Research Council (FL190100014, DP200102190).

References

[1] Y. M. Xie, “Generalized topology optimization for architectural design,” *Architectural Intelligence*, vol. 1, no. 1, 2, 2022.

[2] Y. M. Xie, K. Yang, Y. He, Z. L. Zhao and K. Cai, “How to obtain diverse and efficient structural designs through topology optimization,” in *Form and Force: Proceedings of the IASS Annual Symposium 2019*, Barcelona, Spain, October 7–10, 2019, C. Lázaro, K. U. Bletzinger and E. Oñate, Eds.

[3] X. Huang and Y. M. Xie, "Bi-directional evolutionary topology optimization of continuum structures with one or multiple materials," *Computational Mechanics*, vol. 43, no. 3, pp. 393–401, 2008.

[4] X. Huang and Y. M. Xie, *Evolutionary Topology Optimization of Continuum Structures: Methods and Applications*, John Wiley & Sons, 2010.

[5] Y. He, Z. L. Zhao, K. Cai, J. Kirby, Y. Xiong and Y. M. Xie, "A thinning algorithm based approach to controlling structural complexity in topology optimization," *Finite Elements in Analysis and Design*, vol. 207, 103779, 2022.

[6] J. D. Deaton and R. V. Grandhi, "A survey of structural and multidisciplinary continuum topology optimization: post 2000," *Structural and Multidisciplinary Optimization*, vol. 49, no. 1, pp. 1–38, 2014.

[7] L. Xia, Q. Xia, X. Huang and Y. M. Xie, "Bi-directional Evolutionary Structural Optimization on Advanced Structures and Materials: A Comprehensive Review," *Archives of Computational Methods in Engineering*, vol. 25, no. 2, pp. 437–478, 2018.

[8] Y. Li, P. Yuan and Y. M. Xie, "Topology optimization of structures composed of more than two materials with different tensile and compressive properties," *Composite Structures*, vol. 306, 116609, 2022.

[9] Y. Li and Y. M. Xie, "Evolutionary topology optimization for structures made of multiple materials with different properties in tension and compression," *Composite Structures*, vol. 259, 113497, 2021.

[10] T. Xu, W. Shen, X. Lin and Y. M. Xie, "Additively manufactured thermoplastic polyurethane (TPU) mold for concrete casting of complex structure," *Rapid Prototyping Journal*, vol. 28, no. 9, pp. 1717–1730, 2022.

[11] T. Xu, X. Lin and Y. M. Xie, "Bi-directional evolutionary structural optimization with buckling constraints," *Structural and Multidisciplinary Optimization*, vol. 66, no. 4, 67, 2023.

[12] X. Gao and H. Ma, "Topology optimization of continuum structures under buckling constraints," *Computers & Structures*, vol. 157, pp. 142–152, 2015.

[13] A. Dalklint, M. Wallin and D. A. Tortorelli, "Structural stability and artificial buckling modes in topology optimization," *Structural and Multidisciplinary Optimization*, vol. 64, no. 4, pp. 1751–1763, 2021.

[14] R. T. Haftka and Z. Gürdal, *Elements of Structural Optimization*, Springer Dordrecht, 1992.

[15] X. Huang, Z. H. Zuo and Y. M. Xie, "Evolutionary topological optimization of vibrating continuum structures for natural frequencies," *Computers & Structures*, vol. 88, no. 5–6, pp. 357–364, 2010.

[16] C. G. Raspanti, J. A. Bandoni and L. T. Biegler, "New strategies for flexibility analysis and design under uncertainty," *Computers & Chemical Engineering*, vol. 24, no. 9–10, pp. 2193–2209, 2000.

[17] X. Huang and Y. M. Xie, "Convergent and mesh-independent solutions for the bi-directional evolutionary structural optimization method," *Finite Elements in Analysis and Design*, vol. 43, no. 14, pp. 1039–1049, 2007.

[18] F. Ferrari and O. Sigmund, "Revisiting topology optimization with buckling constraints," *Structural and Multidisciplinary Optimization*, vol. 59, no. 5, pp. 1401–1415, 2019.

IASS 2023
July 10–14 Melbourne
Integration of Design and Fabrication

Proceedings of the IASS Annual Symposium 2023
Integration of Design and Fabrication
10–14 July 2023, Melbourne, Australia
Y.M. Xie, J. Burry, T.U. Lee and J. Ma (eds.)

Topology optimisation considering subjective preferences: current progress and challenges

Zhi LI [a], Ting-Uei LEE[a], Yi Min XIE[a,*]

[a,*] Centre for Innovative Structures and Materials, School of Engineering,
RMIT University, Melbourne, 3001, Australia
mike.xie@rmit.edu.au

Abstract

Topology optimisation techniques can redistribute given materials to their most-needed locations to generate efficient and innovative structural designs. However, these techniques are typically performed based purely on structural performance. Hence, the solutions could be of low value in specific practical applications, as they may not always satisfy all design requirements, including factors like aesthetic quality. Recently, a few studies have reported that introducing subjective preferences into topology optimisation techniques can result in more satisfying structural designs so that users do not need to passively accept the conventional optimisation results. This paper provides a brief overview of the state-of-the-art in topology optimisation techniques that consider subjective preferences. The techniques are classified into three groups based on when subjective interventions are introduced: pre-processing, post-processing and interactive processing strategies. The advantages and limitations of each group are discussed, as are the technical challenges involved in extending these new techniques. Overall, this paper aims to serve as a helpful guide for future developments of topology optimisation techniques that consider subjective preferences, hoping to create more practical and customised structural designs that better meet the needs of users.

Keywords: topology optimisation, subjective preferences, structural design, interactive design

1. Introduction

Topology optimisation is an effective strategy to generate lightweight, efficient and innovative structural designs by redistributing underutilised materials to their most-needed locations in continuous design domains [1]. Conventional topology optimisation techniques are typically performed based on finite element analysis (FEA) with the elements used to represent the given materials. A widely used topology optimisation technique is the bi-directional evolutionary structural optimisation (BESO) method; it allows inefficient and efficient elements to be simultaneously removed and added, generating clear 0/1 designs to represent material density distributions [2]. As shown in Figures 1(a)–(e), the BESO method has been employed in numerous novel practical applications, including bridges [3], furniture [4] and architectural designs [5,6].

According to [7], topology optimisation that focuses only on improving structural performance may not achieve solutions that meet all design requirements, such as aesthetics. Therefore, recent studies have extended the BESO method (i.e., multi-solution strategies) to produce diverse and competitive solutions, offering users a variety of design choices [7]. Specifically, such strategies trade off a minor decrease in the structural performance (e.g., 3% stiffness) of the 'best design' in exchange for multiple topologically different and structurally efficient solutions. Multi-solution strategies include parameter-based [8,9], sub-domain-based [5,10,11], constraint-based [12,13] and weight-based strategies [10,11,14].

It should be noted that design options generated from multi-solution strategies may include many undesired candidates due to differences in personal preferences [15]. Hence, designers must spend

Copyright © 2023 by Zhi LI, Ting-Uei LEE and Yi Min XIE. Published in the Proceedings of the IASS Annual Symposium 2023 with permission.

significant time and effort to evaluate each option to select a satisfactory one, leading to a costly design exploration process [15]. As reported in [16], a piece of design work can reflect the designer's personality, taste and thoughts, emphasising the need to introduce subjective preferences into the design process rather than selecting from multiple options. To this end, recent studies have developed various computational design methods incorporating subjective preferences [16–19]. However, only a few studies have implemented the concept of 'subjective preferences' into topology optimisation [5,14,16]. In this context, a comprehensive review of the current topology optimisation methods considering subjective preferences is necessary to better understand the progress, potential and challenges.

The objective of this paper is to offer a clear understanding of topology optimisation methods that incorporate subjective preferences. To achieve this goal, we conduct a critical review of state-of-the-art research in this field. By examining the progress made so far, the potential and challenges of these methods can be better understood. This will help to improve the development of future topology optimisation techniques that can produce structural designs that better reflect subjective preferences and ultimately lead to more efficient and effective design processes. Section 2 provides a detailed review of these methods, while Section 3 discusses the existing challenges and future possibilities. Finally, Section 4 presents a conclusion.

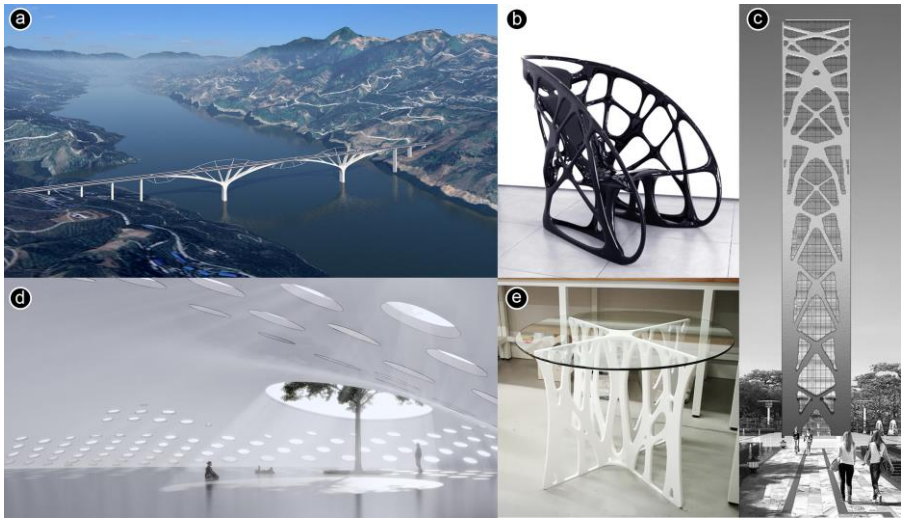


Figure 1. Applications of the BESO method in structural design: (a) bridge [3]; (b) chair [4]; (c) high-rise building [5]; (d) roof [6]; (e) table [4].

2. Topology optimisation techniques considering subjective preferences

2.1. Selection criteria

Shortlisted research papers discussed in this paper are selected based on the following criteria:

- The underlying computational design method must be topology optimisation, such as the BESO, SIMP and level-set methods.
- The topology optimisation method must allow users to input their subjective preferences, such as aesthetics, design concepts and artificial intervention, among others.
- The incorporation of subjective preferences must have an impact on the generation of optimal structural topologies.

Note that the term 'subjective preferences' may be expressed in different ways in different studies. A few phrases were useful in finding the shortlisted research papers: 'topology optimisation based on artificial intervention', 'preference-based topology optimisation' and 'topology optimisation considering aesthetics'.

Based on the above criteria, we have found three most-related research papers about 'topology optimisation considering subjective preferences', including [5], [14] and [16]. The three interrelated studies put forward a total of five topology optimisation methods that incorporate subjective preferences. These methods can be classified into three groups based on the conditions of subjective interventions in topology optimisation, as shown in Figure 2. They include 'pre-processing', 'post-processing' and 'interactive processing' strategies, corresponding to subjective interventions 'before', 'after' and 'during' topology optimisation, respectively. Details of each group are summarised in Sections 2.2–2.4.

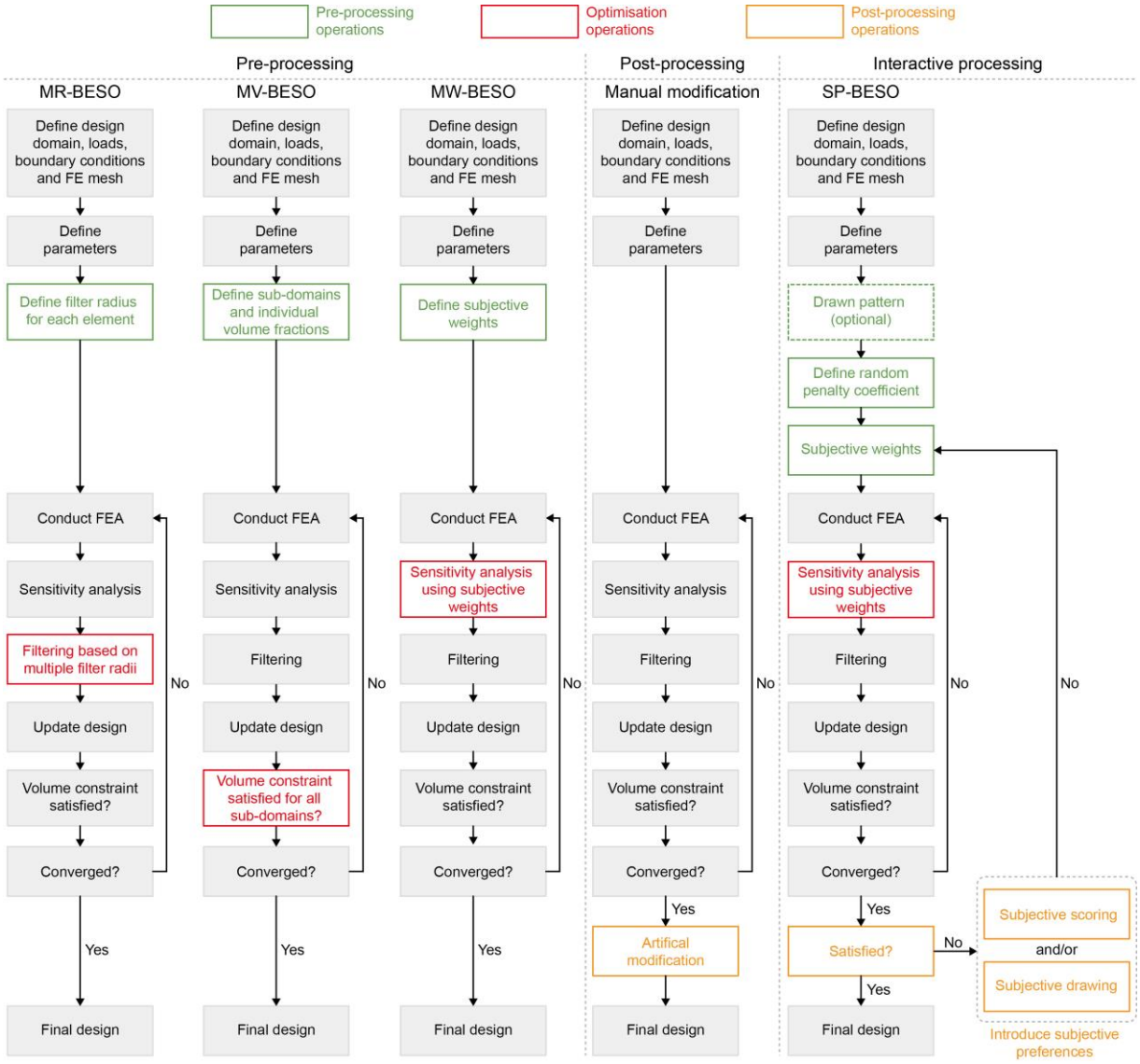


Figure 2. Computational workflow of topology optimisation methods considering subjective preferences. These five methods can be categorised into three groups: pre-processing, post-processing and interactive processing strategies.

2.2. Pre-processing strategy

In the pre-processing strategy, users are required to subjectively define local settings, such as weights of elements and optimisation parameters, before carrying out topology optimisation. Yan et al. [5] proposed three extensions of the BESO method based on the pre-processing strategy to consider subjective preferences, including multi-radius BESO (MR-BESO), multi-volume BESO (MV-BESO) and multi-weight BESO (MW-BESO). Figure 3 provides a clear graphical comparison of these three

methods with the original BESO method. Note that in the original BESO method (see Figure 3(a)), there is only a uniform filter radius, a global volume constraint and equal weights for all elements (i.e., one weight). However, in [5], the number of these optimisation parameters is increased to expand design freedom to include subjective preferences.

- MR-BESO (see Figure 3(b)) empowers designers to specify multiple filters of different sizes in different areas of the design domain. This feature enables designers to regulate the minimum sizes of structural members based on their subjective preferences and ensure that the design requirements of member sizes at specific regions are met.
- MV-BESO (see Figure 3(c)) first divides the design domain into multiple sub-domains, where the elements in each sub-domain are independently added or removed during topology optimisation in the same evolutionary iteration [10]. Using MV-BESO, designers can pre-define different local volume fractions for each sub-domain based on their subjective preferences or design requirements, resulting in customised structural designs.
- MW-BESO (see Figure 3(d)) allows designers to adjust the importance of elements by introducing elemental weights based on subjective preferences. By assigning higher weights to specific elements, users can influence the outcome of the optimisation process and potentially achieve a design that better meets their needs. These weighted elements are given a higher rank during sensitivity analysis, which increases their likelihood of being retained in the final topology. Notably, the importance level of subjective preferences in MW-BESO is controlled by two weighting coefficients, enabling the final structural topology to be subjective- or performance-driven, depending on the design requirements.

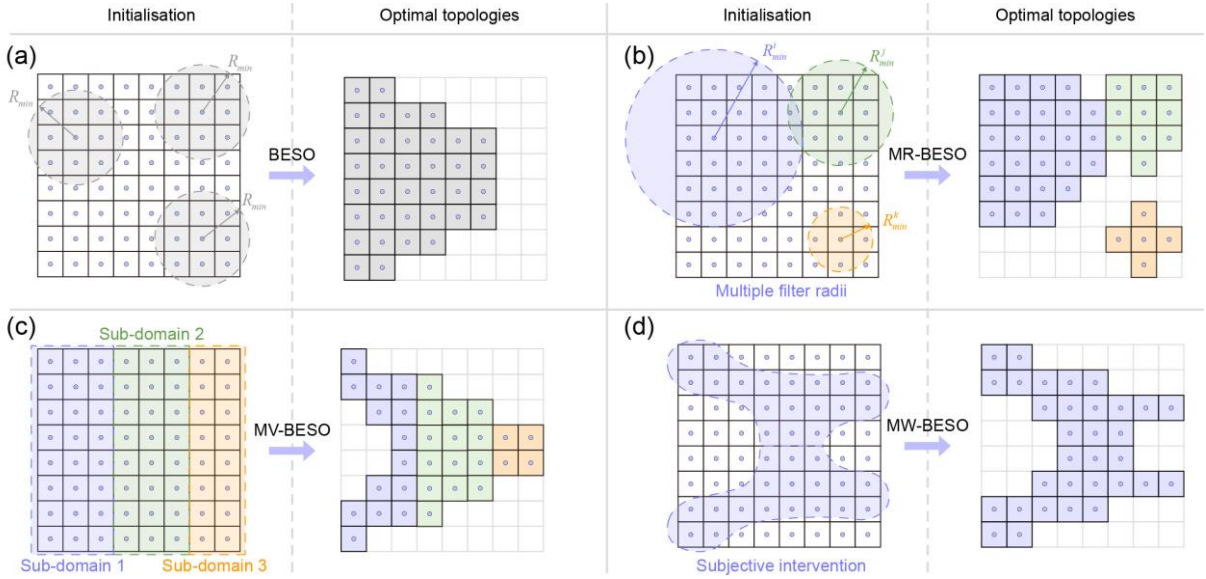


Figure 3. Comparison of the BESO method with its extensions developed based on pre-processing strategies to include subjective preferences: (a) original BESO; (b) MR-BESO; (c) MV-BESO; (d) MW-BESO [5].

The pre-processing strategies can produce efficient structural designs while including subjective preferences, as the final structural topologies are ultimately determined by the optimisation algorithm. However, there are a few limitations to this strategy. For example, as discussed in [5], MR-BESO cannot control the locations of high-stressed areas in a specific topology because the filter radius can only control the minimum sizes of structural members. As for MV-BESO and MW-BESO, although they can directly manipulate locations of high-stressed regions by altering the topologies, the use of subjective preferences may result in significant performance losses because the preferred topologies may deviate from the global optimum. Moreover, the pre-processing strategies are all performed only once, hoping to produce satisfactory designs. However, designers may wish to further refine their subjective

preferences to find a better design option. Therefore, modification based on existing designs is considered a necessary process in design exploration, which is beyond the capability of the pre-processing strategies.

2.3. Post-processing strategy

The post-processing strategy involves manual processing of the optimal topologies to align with the Unity-in-Variety design principle [16]. Specifically, subjective preferences are introduced after topology optimisation is performed. Unity refers to the level of coherence that can be perceived in a design, while variety serves as a source of inspiration for designers by arousing their interest [20]. Striking a balance between unity and variety in a design can enhance the aesthetic quality and meet the design requirements of subjective preferences [21].

The manual modification involves extracting the optimised structures' contours and editing the control points to adjust the design based on subjective Gestalt principles, such as similarity, closure and continuity [16,22]. This process allows for the incorporation of subjective preferences into the optimal topology, resulting in designs that align with the desired aesthetic qualities.

In Figure 4, two pairs of optimal topologies (i.e., chairs) and their modified counterparts are reproduced from [16]. The highlighted areas demonstrate that the modified designs are edited by designers according to the continuity and similarity principles. As reported in [16], their survey claim that artificial modification can significantly improve the unity of the designs. Specifically, a majority of participants perceived the modified designs as visually more appealing. This instance exemplifies how the integration of optimal topologies with subjective preferences can further enhance structural forms to meet design requirements.

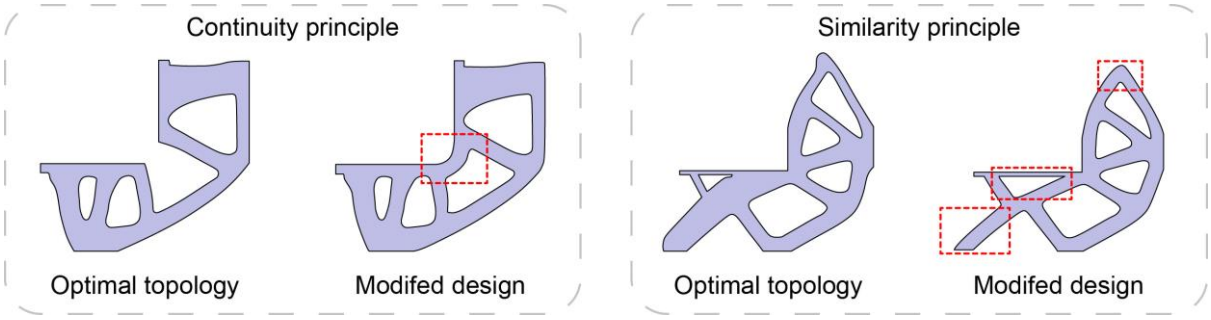


Figure 4. Two 2D chairs designed using the post-processing strategy. The highlighted areas are artificially modified based on the continuity and similarity principles. The figures are modified versions of [16].

It is worth noting that applying overly subjective intervention may be contrary to the original goal of topology optimisation, as the manual post-processing method is purely based on designers' preferences, which ignores the volume constraint and compromises structural performance. Therefore, the obtained designs may fail to fulfil objective design requirements, such as structural efficiency.

2.4. Interactive processing strategy

The two strategies above (pre-processing and post-processing) create structural designs through 'single-execution topology optimisation'. However, these strategies still face challenges in exploring satisfactory designs. In detail, while the pre-processing strategies can generate efficient structural topologies considering subjective preferences, they do not support designers in further explorations based on these results. On the other hand, the post-processing strategy requires strong artificial intervention, which ignores the volume constraint and structural performance. To address these issues, Li et al. [14] proposed an interactive topology optimisation method, SP-BESO, which considers subjective preferences (SP). This strategy introduces scoring and drawing systems that allow users to iteratively explore desired designs by alternately inputting quantified subjective preferences and

performing topology optimisation. The interactive approach enables designers to balance their subjective preferences and structural performance by refining the design through an iterative process.

The SP-BESO method employs three weight-based approaches to generate preference-driven designs by affecting the ranking of elemental sensitivity numbers in BESO:

- SP-BESO uses a random perturbation technique to generate unexpected initial structural topologies (i.e., before introducing subjective preferences), enhancing the design diversity [9].
- Subjective evaluation of an existing design can be converted into weights by integrating design variables and artificial scores; these scoring weights can be used to alter the subsequent topology optimisation outcomes.
- Drawing weights are introduced that translate hand-drawn sketches into weights, guiding the next topology optimisation process to produce efficient designs similar to the inputted pattern.

It should be noted that the scoring and drawing systems can be independently executed during optimisation. Adjusting parameters, λ_e, λ_s and λ_d, can control the importance level of *structural performance*, *subjective scoring* and *drawing*, respectively. Repeatedly running the SP-BESO method allows designers to dynamically adjust subjective preferences and create improved solutions based on existing designs. However, designers may need to make refinements more than once, so the entire interactive design exploration process can be time-consuming.

Figure 5 shows a 2D chair example designed by the authors using SP-BESO. The optimisation problem is shown in Figure 5(a), with details described in [14]. For comparison purposes, the reference design (see Figure 5(b)) is obtained from the standard BESO method without considering subjective preferences. Each optimisation produces four child designs as potential design options. After optimisation, zig-zag boundaries of the child designs are smoothed to improve visual quality, assisting subjective evaluation of design options [23]. The iterative design exploration process is detailed as follows.

A preferred pattern is first drawn to connect the two supports and the backrest as the initial subjective preferences to generate the first set of solutions, as shown in Figure 5(c), where the optimisation parameters are $\lambda_e = 1$, $\lambda_s = 0$ and $\lambda_d = 0.3$. Among the four solutions shown in Figure 5(c), solutions C and D are subjectively selected as preferred designs, so they are imparted with higher scores (2 and 4); undesired solutions have lower scores (-5 and -2). From here, the optimisation parameters are updated to $\lambda_e = \lambda_s = 1$ and $\lambda_d = 0.3$ to generate a new set of designs, as shown in Figure 5(d). If one wishes to further modify the preferred design in Figure 5(d) (i.e., solution A), the drawn pattern can be modified to include the key geometrical features of solution A, with optimisation parameters adjusted to $\lambda_e = 0.8$, $\lambda_s = 0$ and $\lambda_d = 1$. Among the four solutions shown in Figure 5(d), Solution D may be selected as the final solution due to the best structural performance with the highest stiffness (i.e., the lowest C); the final 3D simulation is shown in Figure 5(f). Compared with the original BESO result (see Figure 5(b)), the final design has a 42% of performance loss (see Figure 5(e)). Nevertheless, it is still structurally efficient due to the use of topology optimisation, and the shape can fulfil subjective design requirements based on an iterative design exploration process.

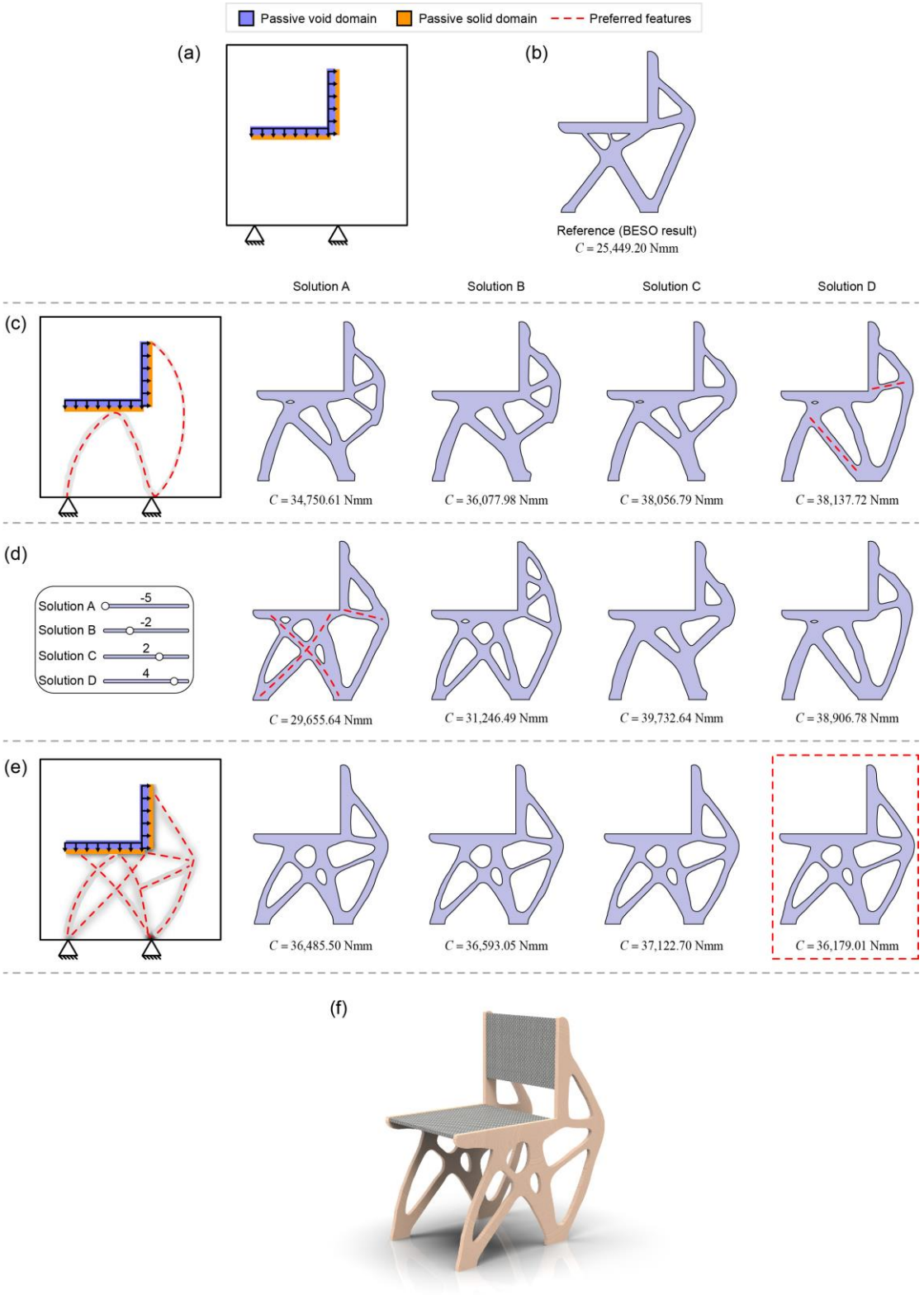


Figure 5. 2D chairs designed using the SP-BESO method: (a) loading and boundary conditions; (b) the standard BESO result; (c) child designs obtained using the drawing system ($\lambda_e = 1, \lambda_s = 0, \lambda_d = 0.3$); (d) updated designs obtained by scoring the previous child designs ($\lambda_e = \lambda_s = 1, \lambda_d = 0.3$); (e) final generation of designs ($\lambda_e = 0.8, \lambda_s = 0, \lambda_d = 1$); (f) 3D simulation of the desired design.

3. Discussion

3.1. Other topology optimisation methods

The abovementioned pre-processing and interactive processing strategies are based on the BESO method, whereas the post-processing strategy is independent of the method of topology optimisation. It is worth noting that the key advantage of using the BESO method is its simplicity in employing discrete design variables. However, the use of discrete design variables may not be sufficient to address some mathematically more complex structural design problems, such as multi-objective optimisation problems.

The pre-processing and interactive processing strategies are straightforward. They can be easily integrated into other element-based topology optimisation methods that use continuous design variables. For example, multiple filters (MR-BESO) and multiple local volume constraints (MV-BESO) can be combined with other topology optimisation methods, such as SIMP and level-set methods, to produce solutions considering subjective preferences. The same concept can be applied to MW-BESO and SP-BESO, where the weights of elements are a scalar field to penalise the sensitivity numbers independent of the underlying element-based topology optimisation method. Together, it can be understood that these potential extensions sacrifice the simplicity of the BESO method in exchange for the capability of solving complex structural design problems; future studies are needed to develop such possible extensions.

3.2. Objective functions

For certain practical applications, the overall stiffness of the structure may be less important, as the designers could be more concerned about the local performance, such as local displacement, stress and buckling. Existing topology optimisation methods that consider subjective preferences only focus on compliance minimisation (i.e., stiffness maximisation) problems. There is potential to extend these methods for optimisation of local performance while ensuring subjective preferences. The key challenge is to formulate the objective function of local performance, but mathematically possible. Furthermore, some structural designs are sensitive to minor local changes, making it crucial to carefully apply subjective interventions. Therefore, future research is needed to investigate the influence of subjective interventions in sensitive areas. Overall, there is a need for future research to consider different design objectives than just compliance minimisation to develop topology optimisation techniques that can be applied to diverse real-world scenarios while ensuring subjective preferences.

3.3. Structural complexity control

To enhance the effectiveness of pre-processing and interactive processing strategies, quantified subjective preferences can be supplemented with additional geometric constraints, similar to the structural complexity control technique [12]. For instance, the number and location of holes can be explicitly pre-defined before carrying out topology optimisation, which enables users to manage manufacturing difficulty and costs according to fabrication limitations. However, too many holes can pose significant challenges in fabrication [13]. Besides, some designers consider the number of holes a valuable aesthetic contribution as they can modify how light interacts with the structure, creating unique lighting and shadow effects that enhance the design's visual appeal.

It is worth pointing out that existing topology optimisation techniques that consider subjective preferences do not yet use geometric constraints to impact the complexity of final outcomes based on fabrication limitations or functional aesthetic requirements. Therefore, future research could explore ways to utilise geometric constraints to address diverse demands in practical applications while ensuring other subjective preferences are met.

3.4. 3D applications

Designing a structure in 3D space provides more flexibility and richer geometric details, resulting in more accurate real-world representations [24]. It should be noted that the three strategies outlined in this paper have not yet been extended to 3D cases. Addressing this goal requires overcoming three technical challenges.

The first challenge is visualisation. Specifically, accurately observing and evaluating a given 3D structure can be difficult for inexperienced designers, as it requires strong spatial awareness skills to look at many 3D geometric details. Therefore, precisely determining subjective preferences based on these observations becomes a demanding task.

The second challenge is interaction. Some manual-based interactive operations, such as drawing, struggle to work in 3D. That is because 3D structures often include numerous internal elements that cannot be directly visualised and edited from the outside. That is to say, concisely and accurately interacting with 3D structures to include specific subjective preferences can be a complex task.

The third challenge is structural performance. Subjective intervention in 3D topology optimisation may result in more significant performance losses than in 2D cases. The increased design degrees of freedom provide greater opportunities for subjective intervention to deviate from the globally optimal solution, meaning that even minor modifications may severely compromise the structural performance.

These three technical challenges require further exploration in future research, aiming to develop a practically useful 3D topology optimisation tool that can create appealing, efficient and reliable structures based on subjective preferences.

4. Conclusion

This paper presents a review of the latest topology optimisation methods considering subjective preferences. Existing methods are classified into three groups, pre-processing, post-processing and interactive processing strategies, depending on the conditions of subjective interventions in topology optimisation. The pre-processing strategies can generate diverse and competitive structural designs, but they may not be able to obtain a satisfactory solution. This is because the optimisation is performed only once, with subjective preferences specified beforehand without allowing any further refinement, leading to the hope of achieving satisfactory designs in a single attempt. The post-processing strategy involves manual modifications to the optimal structural topologies based on subjective design principles, resulting in highly preferred customised designs. However, this approach may overlook objective design requirements such as volume constraints and structural performance, potentially compromising the overall effectiveness of the optimisation. The interactive processing strategy enables designers to iteratively explore desired designs by inputting quantified subjective preferences and performing topology optimisation in alternation. This approach forms an iterative design exploration process that strikes a balance between structural performance and subjective preferences. However, refinements of subjective preferences may be made more than once, so the entire process can be time-consuming.

This paper also proposes four potential extensions of the strategies discussed above. Firstly, all existing strategies have the potential to be extended to other topology optimisation methods, expanding their applicability to other structural design problems. Secondly, extending the existing strategies to consider design objectives other than compliance minimisation may be useful for specific applications; the overall stiffness may be less important, as the designers could be more concerned about the local performance. Thirdly, incorporating geometric constraints into the existing strategies may lead to more useful solutions that can simultaneously satisfy diverse design requirements, such as fabrication limitations and aesthetic requirements. Lastly, it is highly desirable to extend existing strategies to 3D structural design problems for more realistic applications. However, the 3D extension faces challenges related to visualisation, interaction and structural performance loss, highlighting the need for further research. Undoubtedly, there is significant potential for further development of topology optimisation

techniques considering subjective preferences that can be applied in real-world scenarios to create innovative, efficient and satisfactory structural designs.

Acknowledgements

This project was supported by the Australian Research Council (grant number FL190100014). The authors would like to thank Dr Xin Yan and Dr Xianchuan Meng for their helpful advice on various technical issues examined in this paper.

References

[1] M. P. Bendsøe and O. Sigmund, *Topology Optimization: Theory, Methods, and Applications*, Springer, 2004.

[2] X. Huang and Y. M. Xie, *Evolutionary Topology Optimization of Continuum Structures: Methods and Applications*, John Wiley & Sons, 2010.

[3] Y. Li, Y. Lai, G. Lu, F. Yan, P. Wei and Y. M. Xie, "Innovative design of long-span steel–concrete composite bridge using multi-material topology optimization," *Engineering Structures*, vol. 269, 114838, 2022.

[4] J. Ma, Z. Li, Z. L. Zhao and Y. M. Xie, "Creating novel furniture through topology optimization and advanced manufacturing," *Rapid Prototyping Journal*, vol. 27, pp. 1749–1758, 2021.

[5] X. Yan, D. Bao, Y. Zhou, Y. M. Xie and T. Cui, "Detail control strategies for topology optimization in architectural design and development," *Frontiers of Architectural Research*, vol. 11, pp. 340–356, 2021.

[6] X. Meng, L. Y. Zhang, Z. L. Zhao and Y. M. Xie, "A direct approach to achieving efficient free-form shells with embedded geometrical patterns," *Thin-Walled Structures*, vol. 185, 110559, 2023.

[7] Y. M. Xie, "Generalized topology optimization for architectural design," *Architectural Intelligence*, vol. 1, pp. 1–11, 2022.

[8] X. Huang and Y. M. Xie, "Convergent and mesh-independent solutions for the bi-directional evolutionary structural optimization method," *Finite Elements in Analysis and Design*, vol. 43, pp. 1039–1049, 2007.

[9] Y. He, K. Cai, Z. L. Zhao and Y. M. Xie, "Stochastic approaches to generating diverse and competitive structural designs in topology optimization," *Finite Elements in Analysis and Design*, vol. 173, 103399, 2020.

[10] X. Yan, Y. Xiong, D. Bao, Y. M. Xie and X. Peng, "A Multi-volume constraint approach to diverse form designs from topology optimization," *Engineering Structures*, vol. 279, 115525, 2023.

[11] K. Yang, Z. L. Zhao, Y. He, S. Zhou, Q. Zhou, W. Huang and Y. M. Xie, "Simple and effective strategies for achieving diverse and competitive structural designs," *Extreme Mechanics Letters*, vol. 30, 100481, 2019.

[12] Y. He, Z. L. Zhao, K. Cai, J. Kirby, Y. Xiong and Y. M. Xie, "A thinning algorithm based approach to controlling structural complexity in topology optimization," *Finite Elements in Analysis and Design*, vol. 207, 103779, 2022.

[13] Z. L. Zhao, S. Zhou, K. Cai and Y. M. Xie, "A direct approach to controlling the topology in structural optimization", *Computers & Structures*, vol. 227, 106141, 2020.

[14] Z. Li, T. U. Lee and Y. M. Xie, "Interactive structural topology optimization with subjective scoring and drawing systems," *Computer-Aided Design*, vol. 160, 103532, 2023.

[15] D. Davis, "Generative design is doomed to fail," www.danieldavis.com. https://www.danieldavis.com/generative-design-doomed-to-fail/ [Accessed Mar. 23, 2023].

[16] S. Loos, S. v. d. Wolk, N. d. Graaf, P. Hekkert and J. Wu, "Towards intentional aesthetics within topology optimization by applying the principle of unity-in-variety," *Structural and Multidisciplinary Optimization*, vol. 65, 185, 2022.

[17] J. Qi, J. Hu and Y. Peng, "Modified rough VIKOR based design concept evaluation method compatible with objective design and subjective preference factors", *Applied Soft Computing*, vol. 107, 107414, 2021.

[18] C. T. Mueller and J. A. Ochsendorf, "Combining structural performance and designer preferences in evolutionary design space exploration," *Automation in Construction*, vol. 52, pp. 70–82, 2015.

[19] J. Michalek and P. Papalambros, "Interactive design optimization of architectural layouts," *Engineering Optimization*, vol. 34, pp. 485–501, 2002.

[20] P. Hekkert, "Design aesthetics: principles of pleasure in design," *Psychology Science*, vol. 48, 157–172, 2006.

[21] P. A. G. Post, J. Blijlevens and P. Hekkert, "'To preserve unity while almost allowing for chaos': Testing the aesthetic principle of unity-in-variety in product design," *Acta Psychologica*, vol. 163, pp. 142–152, 2016.

[22] J. Wagemans, J. Feldman, S. Gepshtein, R. Kimchi, J. R. Pomerantz, P. A. Van der Helm and C. Van Leeuwen, "A century of Gestalt psychology in visual perception: II. Conceptual and theoretical foundations," *Psychological Bulletin*, vol. 138, 1218–1252, 2012.

[23] Z. Li, T. U. Lee, Y. Yao and Y. M. Xie, "Smoothing topology optimization results using pre-built lookup tables," *Advances in Engineering Software*, vol. 173, 103204, 2022.

[24] O. Sigmund, "On benchmarking and good scientific practise in topology optimization," *Structural and Multidisciplinary Optimization*, vol. 65, 315, 2022.

IASS 2023
July 10–14 Melbourne
Integration of Design and Fabrication

Proceedings of the IASS Annual Symposium 2023
Integration of Design and Fabrication
10–14 July 2023, Melbourne, Australia
Y.M. Xie, J. Burry, T.U. Lee and J. Ma (eds.)

Topology optimisation of support-free structures for multi-axis additive manufacture

Qichen GUO[a], Hongjia LU[b], Jun YE[a,*]

[*] College of Civil Engineering and Architecture, Zhejiang University, Hangzhou, 310058, China
B303, Anzhong Building, Zhejiang University, No. 866 Yuhangtang Road, West Lake District, Hangzhou, Zhejiang Province, China
jun_ye@zju.edu.cn

[a] Centre for Balance Architecture, Zhejiang University, Hangzhou, 310014, China
[b] Centre for Innovative Structures and Materials, School of Engineering, RMIT University, Melbourne, 3001, Australia

Abstract

The overhang problem remains a critical issue that prevents components with complex geometry from being fabricated by additive manufacture (AM) without support structures. To address this problem, previous studies have extensively investigated the design of support-free structures by including overhang constraints in topology optimisation approaches. However, the previous research mainly focused on AM machines with 3-axis (i.e., movable printing nozzle in x, y, and z directions), and the recently developed multi-axis machines (i.e., with rotatable base platform) were not considered. In addition, it was reported that the performance sacrifice brought by the overhang constraints for 3-axis AM could be high in structures with low volume fractions (i.e., the ratio between structure and domain volume). Therefore, to reduce the performance sacrifice, this paper proposes an optimisation approach that considers the overhang constraints for multi-axis AM. This approach starts with an optimised structure obtained by using the free-form topology optimisation approach. Firstly, the design domain is divided into several zones. Then a novel linear optimisation problem is solved to determine the local build directions for each zone, aiming to maximise the optimised structure's printable proportion. Several examples are presented to demonstrate the effectiveness of the proposed approach. It is found that the previous significant performance sacrifice brought by the 3-axis approach can be reduced to a negligible level with the novel approach based on multi-axis AM.

Keywords: topology optimisation, multi-axis additive manufacture, overhang constraint, Hangai Prize applicant

1. Introduction

Topology optimisation aims to identify structures with optimised performance while satisfying specified conditions and constraints [1-3], and it has been applied to many different fields [4-5]. However, although topology optimisation can be used to create ultra-high-performance structures, the optimised free-form shapes are often difficult to fabricate with traditional manufacturing technique. To address the problem, additive manufacture (AM) have been frequently employed [6].

Although AM can be used to print complex geometries, current technologies do not guarantee that structures with arbitrary geometries are printable. One foremost reason is the overhang effect [7-9]. As illustrated in Figure 1, if the overhang angle ϕ_{ov} of the component exceeds the maximum threshold angle ϕ_{max}, the deposited part cannot consolidate due to gravity [10]. To address this problem, temporary support structures can be used [11]. However, support structures consume additional materials and are difficult to remove in certain cases (e.g., metal AM).

Copyright © 2023 by Qichen GUO, Hongjia LU and Jun YE. Published in the Proceedings of the IASS Annual Symposium 2023 with permission.



Figure 1. The overhang effect: (a) structure failing to consolidate when the overhang angle ϕ_{ov} is larger than the threshold ϕ_{max}; (b) structure successfully consolidating when the overhang angle ϕ_{ov} is smaller than ϕ_{max}.

In order to avoid the overhang effect while not using support structures, some studies have modified the geometrical shape of the components to be printable. In this thread, Leary et al. and Li et al. used a post-processing approach to design efficient support-free structures for optimised solutions [12-13]. However, since the resulting structures required additional materials, the volume fraction constraint of the optimisation formulation was violated. Therefore, other studies added the overhang constraints into the topology optimisation formulation. This concept has been extensively studied via filtering out the elements violating overhang constraints or adding explicit overhang constraints to the optimisation formulation. For example, Gaynor et al. considered overhang constraints through projection methods [14]. Zhang et al. applied the overhang constraints by restricting the orientation of elemental density gradients [15]. Garaigordobil et al. used a SUSAN algorithm to extract the structural boundaries and then controlled the structural boundary to avoid the overhang effect [16]. Although these studies can eliminate the overhang parts, the overhang constraints considered are all based on 3-axis AM. Consequently, the performance sacrifice caused by overhang constraints was usually high, especially in problems with low volume-fraction values.

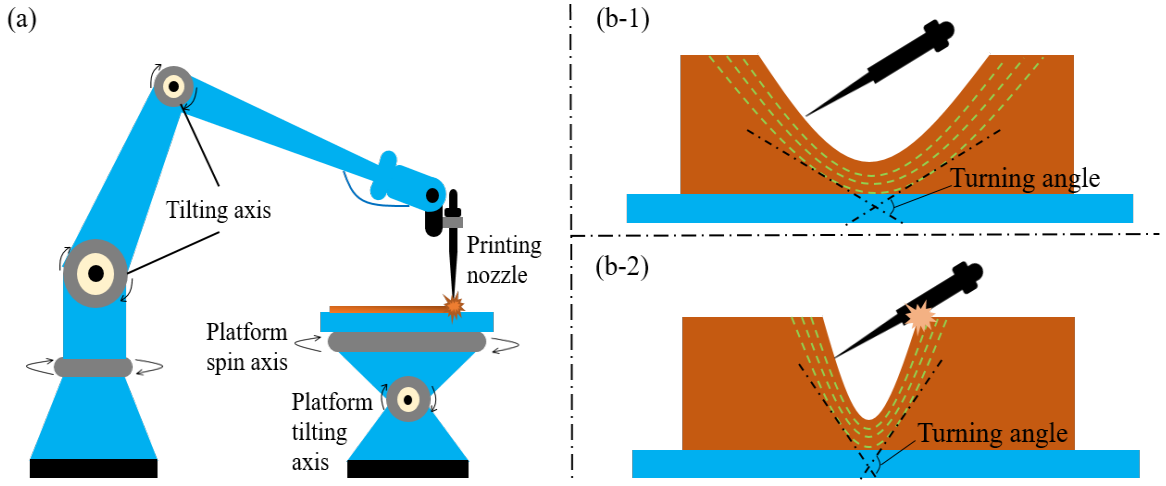


Figure 2. Multi-axis AM: (a) Multi-axis AM machine; (b) potential collision problem of concave printing surfaces: (1) less likely with small turning angle; (2) more likely with increased turning angle.

Besides the aforementioned optimisation-related studies, other research focused on addressing the overhang problem by improving the machine flexibility; hence AM machines with multi-axis configuration were developed in recent years [17-18]. Multi-axis machines differ from 3-axis machines by having rotatable platforms that allow for continuous build direction adjustments, thus enabling the printing of curved surfaces [19]. Compared with 3-axis printing, multi-axis printing can reduce the component's overhang angle and improve the quality of fabrication [10]. Therefore, some studies have focused on reducing the overhang effect by decomposing the structure into several parts and applying different build directions for each part [20-22]. Further studies customised the curved printing surfaces

to reduce the overhang effect [23]. However, in multi-axis AM, concave printing surfaces can lead to potential collisions between the printing nozzle and the printed component when the turning angle of the printing surface is large (Figure 2 (b-2)). These studies related to multi-axis AM can significantly reduce the support materials.

Whilst multi-axis AM can effectively reduce the overhang effect, most studies in the topology optimisation area considered the overhang constraints for 3-axis AM. Therefore, to achieve support-free designs that have higher performance, this study proposes an optimisation approach that considers the overhang constraints for multi-axis AM. This approach starts with an optimised design obtained through the traditional topology optimisation, then a novel approach is developed to identify the curved printing surfaces that can make the optimised structure printable as much as possible. With the proposed workflow, the optimised structures and their associated curved printing surfaces can both be identified.

The following parts of the paper are organised as follows: in Section 2, the previous topology optimisation approach is reviewed; in Section 3, the new approach for multi-axis AM is introduced; two examples are given to demonstrate the effectiveness of the proposed approach in Section 4 and conclusions are drawn in Section 5.

2. Review of topology optimisation and 3-axis overhang constraints

2.1. Review of free-form topology optimisation

The approach proposed in this paper is based on SIMP (Solid Isotropic Material with Penalty), which is briefly reviewed in this section. SIMP uses the finite element discretisation approach to divide the domain into many elements, with the existence of each element is determined by its density ρ_i, which is 0 for void and 1 for solid. The traditional topology optimisation formulation is:

$$\text{find: } \boldsymbol{\rho} = (\rho_1, \rho_2, ..., \rho_{n_{ele}}) \tag{1.a}$$

$$\text{min: } C = \boldsymbol{F}^T \boldsymbol{U} \tag{1.b}$$

$$\text{s.t.: } \boldsymbol{K}(\rho)\boldsymbol{U} = \boldsymbol{F} \tag{1.c}$$

$$\frac{\sum_{i=1}^{n_{\text{ele}}} \rho_i v_i}{\sum_{i=1}^{n_{\text{ele}}} v_i} \le f \tag{1.d}$$

$$0 \le \rho_i \le 1,\ i=1,2,\ldots,n_{\text{ele}} \tag{1.e}$$

where n_{ele} is the number of elements, v_i is each element's volume; f is the allowable volume fraction; $\boldsymbol{K}(\rho)$, $\boldsymbol{U}$ and $\boldsymbol{F}$ are the structural stiffness matrix, displacement and load vector, respectively.

Young's modulus E_i of element i can be obtained by Eqn. (2) [24]:

$$E_i = E_{\min} + \rho_i^p (E_0 - E_{\min}) \tag{2}$$

where p is the penalisation factor (typically p=3); E_0 is the material's Young's modulus; $E_{\min}$ is a near 0 parameter used to avoid numerical singularity problems.

In addition, element filters are frequently employed to overcome the check-board problem, and Heaviside projection can be used to guarantee a black-and-white solution. More details of these approaches can be found in [25] and [26].

2.2. Review of 3-axis overhang constraint

For the concerned element i, with its neighbour element densities equal to ρ_1^i to ρ_9^i as shown in Figure 3, its density gradient direction $\nabla\rho_i = (a_i, b_i)$ is:

$$a_i = -\frac{1}{6}\rho_1^i + \frac{1}{6}\rho_3^i - \frac{1}{6}\rho_4^i + \frac{1}{6}\rho_6^i - \frac{1}{6}\rho_7^i + \frac{1}{6}\rho_9^i \tag{3.a}$$

$$b_i = \frac{1}{6}\rho_1^i + \frac{1}{6}\rho_2^i + \frac{1}{6}\rho_3^i - \frac{1}{6}\rho_7^i - \frac{1}{6}\rho_8^i - \frac{1}{6}\rho_9^i \tag{3.b}$$

With the density gradient obtained, a boundary element is self-supportable when its boundary orientation λ_i (i.e., perpendicular to the density gradient direction) lies within the allowable range associated with the build direction (Figure 3), that is [15]:

$$\tau_i = \nabla\rho_i \cdot \gamma - \sin(\phi_{\max}) < r_{i1} \tag{4}$$

where τ_i is the overhang value, γ is the build direction and r_{i1} is a near 0 parameter used to avoid numerical problems.

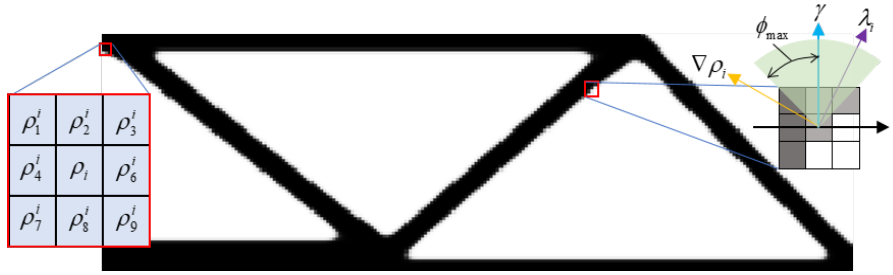


Figure 3. A boundary element *i* considered as self-supported since its boundary orientation λ_i lies within the allowable overhang range (i.e. green region).

3. Printing plan optimisation for multi-axis AM

3.1. Domain subdivision

To reach a favourable zone arrangement, we first identify structural corner positions (Figure 4 (a)). Subsequently, the structure is subdivided at the structural corner position; with this approach, members with different orientations are separated into different zones. Nevertheless, it is found that the zone arrangement that can lead to a (near) 100% printable proportion is not unique, and the effect of different zone arrangements is discussed in detail later in Section 4.2.

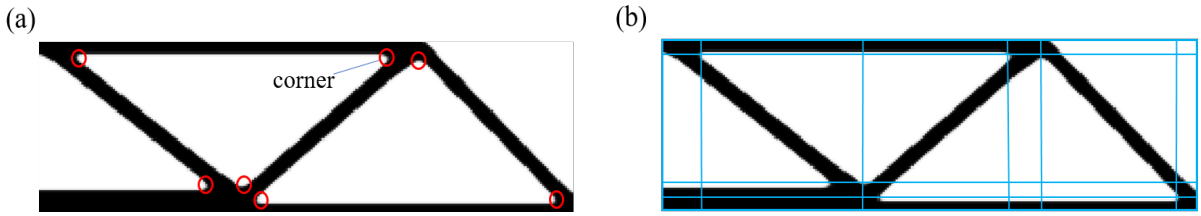


Figure 4. Construct zones based on structural corner locations; (a) structural corners; (b) zone boundaries on the structural corner positions.

3.2. Determination of build direction in each zone

Similar to the approach in the 3-axis AM, we consider the structure fully printable when all the boundary elements are support-free. If a boundary element *i* whose incline angle is $\phi_{i,g}$ in zone *j* whose build direction is ϕ_j satisfy:

$$\left|\phi_j - \phi_{i,g} - \phi_{\max}\right| + \left|\phi_j - \phi_{i,g} + \phi_{\max}\right| = 2\phi_{\max} \tag{5}$$

element i is determined to be support-free. Note that if a boundary element is not support-free, the left side of Eqn. (5) becomes greater than $2\phi_{\max}$, causing an overhang violation. Therefore, to maximise the printable proportion of the structure, the following optimisation problem can be formulated:

$$\text{find: } \boldsymbol{\phi} = (\phi_1, \phi_2, ..., \phi_{n_z})^T \tag{6.a}$$

$$\min: \boldsymbol{\eta} \cdot \tilde{\boldsymbol{\rho}} \tag{6.b}$$

$$\text{s.t.: } \boldsymbol{\eta} \geq \left| \boldsymbol{M}\boldsymbol{\phi} - \boldsymbol{\phi}_g - \phi_{\max} \right| + \left| \boldsymbol{M}\boldsymbol{\phi} - \boldsymbol{\phi}_g + \phi_{\max} \right| \tag{6.c}$$

where $\boldsymbol{\phi} = (\phi_1, \phi_2, ..., \phi_{n_z})^T$ is the local build direction vector with n_z denotes the number of zones; $\boldsymbol{\eta} = (\eta_1, \eta_2, ..., \eta_{n_{ele}})^T$ is the vector of elements' overhang violation; $\tilde{\boldsymbol{\rho}} = (\tilde{\rho}_1, \tilde{\rho}_2, ..., \tilde{\rho}_{n_{ele}})^T$ with $\tilde{\rho}_i \in \{0,1\}$ and $\tilde{\rho}_i = 1$ for boundary elements and $\tilde{\rho}_i = 0$ for others; $\boldsymbol{M}$ is a 0-1 mapping matrix used to link the corresponding zone to each element; $\boldsymbol{\phi}_g = (\phi_{1,g}, \phi_{2,g}, ..., \phi_{n_{ele},g})$ is the elemental incline angle vector. If the proportion of unprintable elements r_{un} is less than a threshold r_s, the structure can be considered as fully printable.

3.3. Collision between the printing nozzle and the structure

In multi-axis AM, the printing nozzle and the already printed component may collide if the printing surfaces are concave and have a large turning angle, as shown in Figure 2 (b-2). To avoid this problem, the turning angle of the printing surfaces are required to be restricted:

$$\phi_{\text{next}} - \phi_{\text{first}} < \phi_{\text{t,max}} \tag{7}$$

where ϕ_{next} and ϕ_{first} is defined as the build direction of two adjacent zones (see Figure 5), $\phi_{\text{t,max}}$ is the allowable turning angle.

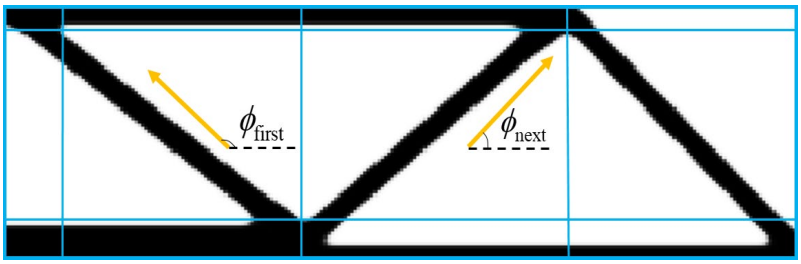


Figure 5. The local build direction ϕ_{first} and ϕ_{next} of two adjacent zones.

3.4. Consideration of always printable elements

If Problem (6) is directly solved to determine the local build directions, two types of "always-printable" elements will affect the quality of the optimised result, leading to solutions with lower printable proportions. The first type of the "always-printable" elements is illustrated in Figure 6. The highlighted elements are always printable by using a vertical build direction since they are directly attached to the base platform. To identify this type of element, a scanning process is conducted, as illustrated in Figure 6, where a vertical build direction $\boldsymbol{\gamma}_v$ is used to evaluate the printability of each element using Eqn. (4).

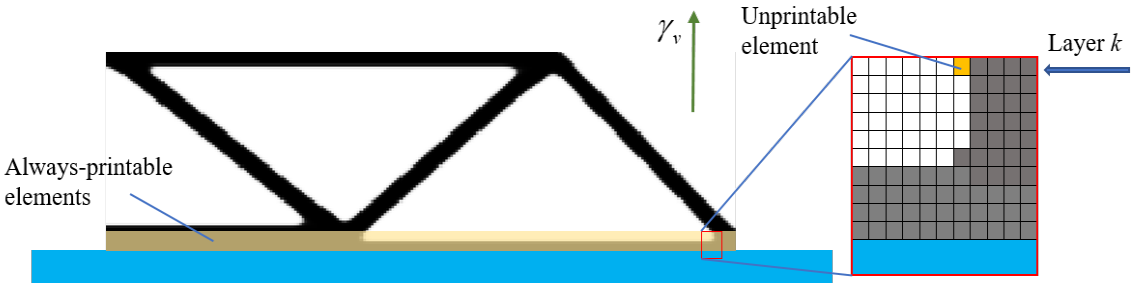


Figure 6. Elements attached to the base platform considered as "always-printable" elements.

The scan process starts from the elements on the first layer that are directly attached to the base platform and ends when an unprintable element appears in the kth layer. Then all the elements under the kth layer are considered "always-printable" elements and excluded from Problem (6).

The second type of "always-printable" elements are illustrated in Figure 7, whose density gradient are always within the printable range if the platform's allowable rotatable angle is ϕ_{allow}.

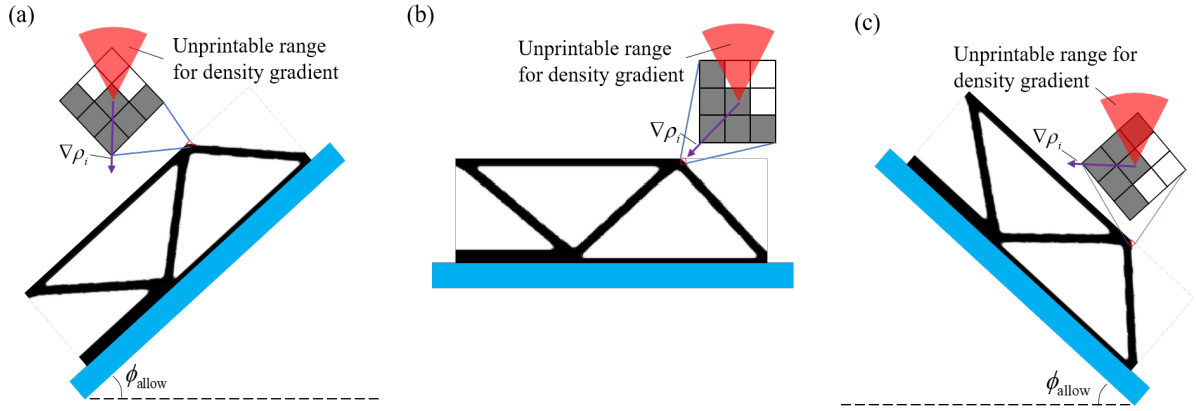


Figure 7. "Always-printable" elements for all base platform orientations within [- ϕ_{allow} , ϕ_{allow}].

3.5. Optimization of local printing directions

By combing (6) and (7), the following optimisation problem can be used to obtain the build directions of all the printing zones:

$$\text{find: } \boldsymbol{\phi} = (\phi_1, \phi_2, ..., \phi_{n_z})^T \tag{8.a}$$

$$\text{min: } \boldsymbol{\eta} \cdot \tilde{\boldsymbol{\rho}} \tag{8.b}$$

$$\text{s.t.: } \boldsymbol{\eta} \geq \left| \boldsymbol{M}\boldsymbol{\phi} - \boldsymbol{\phi}_g - \phi_{\max} \right| + \left| \boldsymbol{M}\boldsymbol{\phi} - \boldsymbol{\phi}_g + \phi_{\max} \right| \tag{8.c}$$

$$\boldsymbol{\phi}_{\text{next}} - \boldsymbol{\phi}_{\text{first}} < \phi_{\text{t,max}} \tag{8.d}$$

where $\tilde{\boldsymbol{\rho}} = (\tilde{\rho}_1, \tilde{\rho}_2, ..., \tilde{\rho}_{n_{\text{ele}}})^T$ with $\tilde{\rho}_i \in \{0,1\}$ and $\tilde{\rho}_i = 1$ for non-always-printable boundary elements and $\tilde{\rho}_i = 0$ for others. Since Problem (8) is a linear programming problem. Modern interior point solvers such as *MOSEK* can be used to solve this problem efficiently. In addition, the optimized solutions are guaranteed to be the global optimum.

4. Numerical examples

In this section, two numerical examples are presented to demonstrate the effectiveness of the proposed approach. Young's modulus E_0 and the Poisson's radio v are assumed to be 1.0 and 0.3, respectively; the minimum Young's modulus $E_{\min}$ is 1×10^{-9}; the parameter p is 3. All design domains are meshed by quadrilateral elements. The allowable rotatable angle for the platform ϕ_{allow} is taken as 90°. The maximum turning angle $\phi_{\text{t,max}}$ is 90° and the unprintable threshold r_s is taken as 1.5% by default.

4.1. Influence of the maximum overhang angle

To investigate the influence of $\phi_{\max}$ on results, the half MBB (Messerschmitt-Bölkow-Blohm) beam is studied. The case description is shown in Figure 8 (a). The size of the design domain are 180×60, the maximum volume fraction is 0.2, and the magnitude of F is taken as 1. In the printing plan optimisation, the zone arrangement is shown in Figure 8 (b), and $\phi_{\max}$ = 60°,45° and 30° are considered.

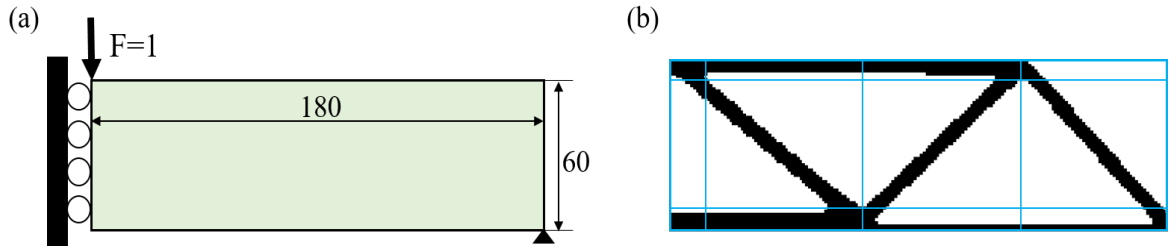


Figure 8. MBB beam example: (a) design domain, load and boundary conditions; (b) solution of traditional topology optimisation (Compliance C=86.18) and the zone arrangements in multi-axis AM optimisation.

The optimised results are shown in Figure 9 (a-c), and the corresponding r_{un} are 0.55%, 0.74%, 0.92%. r_{un} increases as $\phi_{\max}$ decreases, which suggests that the structures are more challenging to be printed in situations with low $\phi_{\max}$. In addition, the optimisation difficulty brought by low $\phi_{\max}$ is also reflected in the reduction of always-printable elements, as shown in Figure 9 (a). It is worth noting that the unprintable elements are mainly distributed near the corners of the structure. As expected, by excluding the second type of always-printable elements, the proportion of the unprintable elements at these corner positions is reduced to a negligible level.

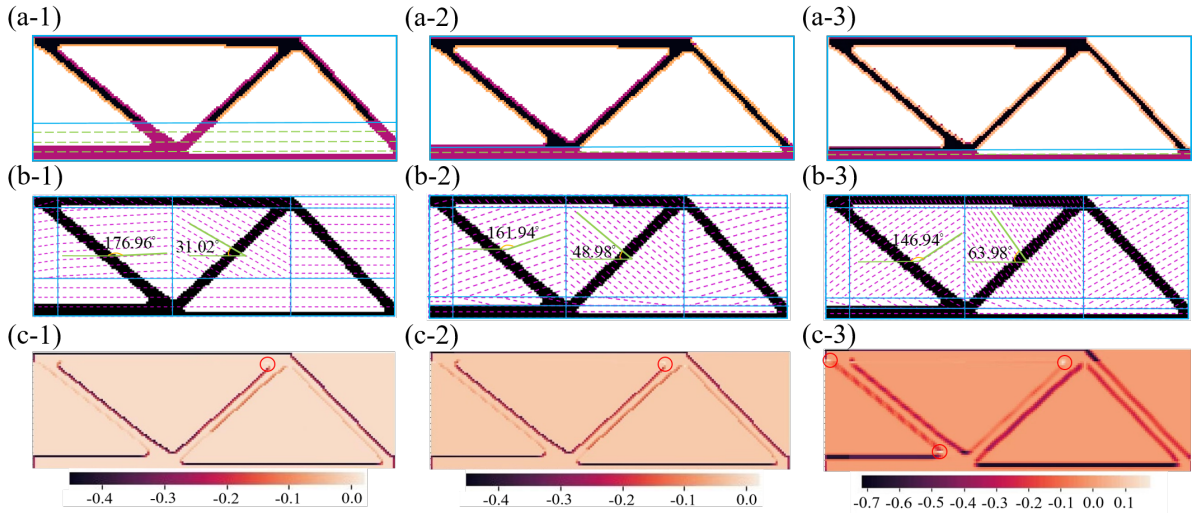


Figure 9. Optimised results of the MBB example: (a) The always-printable elements (i.e., coloured in purple) and non-always-printable boundary elements (i.e., coloured in orange); (b) optimised solutions for multi-axis

printing; (c) value τ_i for the structure, where few unprintable elements are marked within the red circles, when the maximum overhang angle ϕ_{max} is (1) 60°; (2) 45°; (3) 30°; purple lines represent printing surfaces.

A similar MBB example with $\phi_{max} = 45^{\circ}$ has been investigated by Gaynor using the approach for 3-axis in [14]. The sacrifices of structural performance are 10.43% and 20.64% when volume fraction is 0.4 and 0.25, respectively, which is far greater than the sacrifices using the approach proposed in this paper.

4.2. Influence of different zone arrangements

Since it is mentioned in Section 3.1 that different zone arrangements may be used on the same structure, their influences are investigated in this section with the cantilever example. The case description is shown in Figure 10 (a). The length L=160 and the height H=80, the load F=1.0, and the allowable volume fraction f is 0.2. The optimised solution from the traditional SIMP method is shown in Figure 10 (b).

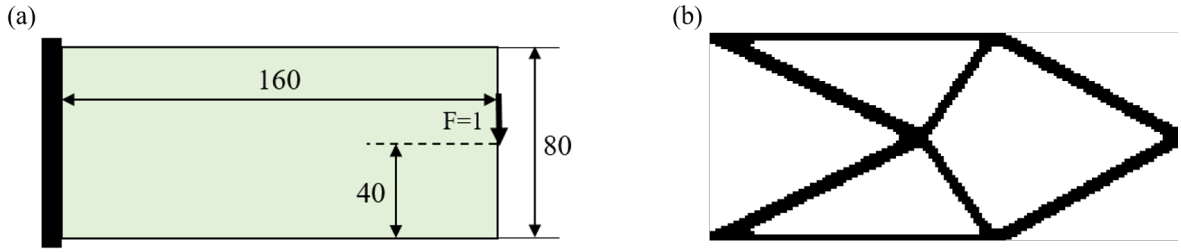


Figure 10. Cantilever example: (a) design domain, load and boundary conditions; (b) solution obtained with the traditional topology optimisation (structural compliance C=145.25).

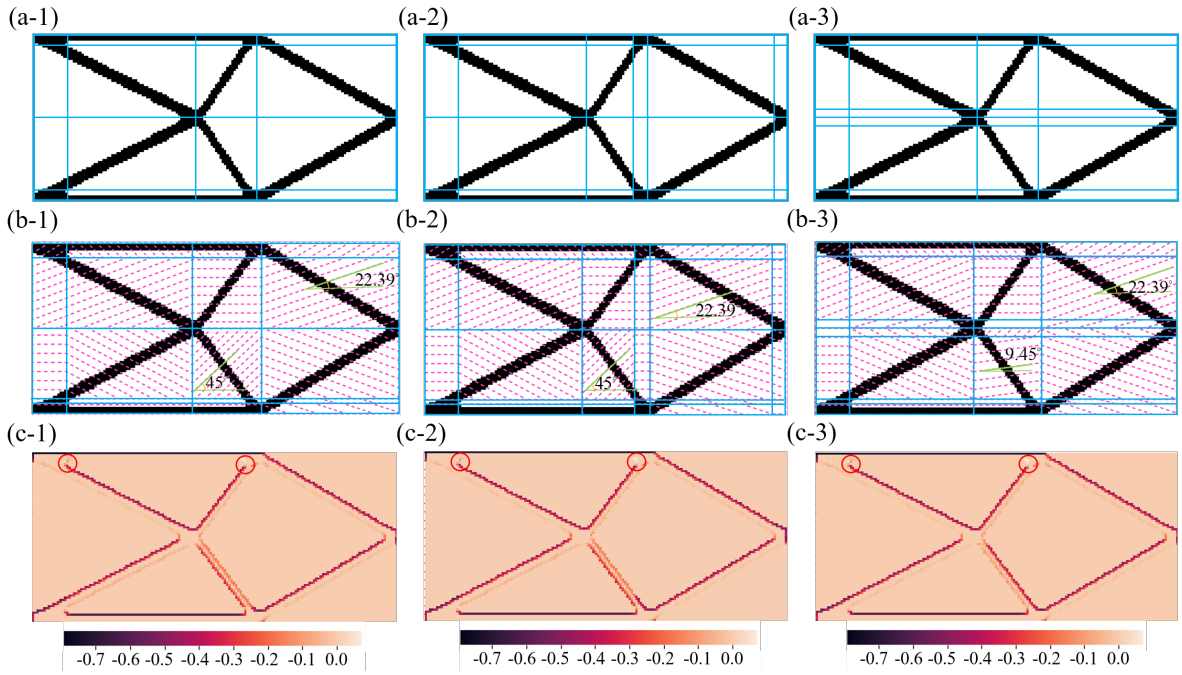


Figure 11. Optimised results of the cantilever example: (a) three different zone arrangements; (b) optimised printing surfaces with different zone arrangements; (c) value τ_i for the structure, where few unprintable elements are marked within the red circles.

In the printing plan optimisation step, ϕ_{max} = 45° is considered, and we study three different zone arrangements, as shown in Figure 11 (a). The associated unprintable ratios r_{un} are 0.69%, 0.69% and 0.49%, which are all far less than the threshold 1.5%. The achieved r_{un} values for Figure 11 are

remarkably close, which is as expected since members with different orientations are all arranged into different zones in the three zone arrangements.

5. Conclusion

This paper proposes a novel optimisation approach to consider the overhang constraints for multi-axis AM (i.e., machines with rotatable base platforms). Different from the previous studies for 3-axis printing, the design domain is subdivided into a number of zones and each zone is assumed to correspond to one build direction. Two numerical examples have been presented to demonstrate the effectiveness of the proposed approach, and the following conclusions can be drawn:

1) Compared to the 3-axis-based approaches, the proposed multi-axis-based approach can significantly reduce the structural compliance increase caused by overhang constraints.
2) Since each zone corresponds to one build direction, the proportion of printable elements will be low if two structural members with vastly different orientations are allocated in the same zone. Therefore, we propose to subdivide the domain at the structural corner positions. The results show by following the proposed corner subdivision approach, the zone arrangement that can lead to a satisfactory proportion of printable elements is not unique.
3) Unlike the 3-axis AM, collisions can happen in multi-axis AM when a concave printing surface is used. To reduce the possibility of potential collisions, an angle constraint is used to restrict the maximum turning angle $\phi_{\mathrm{t,max}}$ of the optimised printing surface.

The approach proposed in this paper has the potential to be extended to three-dimension cases and can be applied to the design of complex metal structures (e.g. steel nodes, aeronautical structures and medical titanium alloy bones) and their multi-axis printing plans. With this design approach, structural performance and fabrication quality can both be effectively improved, and it can promote the application of 3D printing in the fabrication of structures with high performance.

However, due to the possible impact of potential collisions, it is hard to ensure that the structure is support-free in certain cases. A possible solution to overcome the collision problem is to suppress the unprintable elements based on the identified optimal printing plan, that is, the local build directions obtained from solving Eq. (8) are used, and the structure is adjusted accordingly to avoid the overhang effect. Further research is required in the future.

Acknowledgements

The authors would like to acknowledge the financial support from the Excellent Young Talent Fellowship Program of the National Natural Science Foundation of China (NSFC), the National Natural Science Foundation of China (Grant Number: 52208215), the Natural Science Foundation of Zhejiang Province (Grant Number: LQ22E080008), the Centre for Balance Architecture of Zhejiang University and the Australian Research Council (Grant Number: FL190100014).

References

[1] E. Andreassen, A. Clausen, M. Schevenels, B.S. Lazarov, O. Sigmund, “Efficient topology optimization in MATLAB using 88 lines of code,” *Structural and Multidisciplinary Optimization,* vol. 43, pp. 1-16, 2011.

[2] M. Bendsøe, N. Kikuchi, “Generating optimal topologies in structural design using a homogenization method,” *Computer Methods in Applied Mechanics and Engineering,* vol. 71, pp. 197-224, 1988.

[3] M.P. Bendsøe, O. Sigmund, *Topology Optimization: "Theory, Methods, And Applications"*, Springer Berlin, 2011.

[4] Y. Zhang, Y. Shan, X. Liu, T. He, "An integrated multi-objective topology optimization method for automobile wheels made of lightweight materials," *Structural and Multidisciplinary Optimization,* vol. 64, pp.1585-1605, 2021.

[5] J.-H. Zhu, W.-H. Zhang, L. Xia, "Topology optimization in aircraft and aerospace structures design," *Archives of Computational Methods in Engineering,* vol. 23, pp. 595-622, 2016.

[6] A. Delissen, E. Boots, D. Laro, H. Kleijnen, F. van Keulen, M. Langelaar, "Realization and assessment of metal additive manufacturing and topology optimization for high-precision motion systems," *Additive Manufacturing,* vol. 58, pp. 103012, 2022.

[7] M. Bi, P. Tran, L. Xia, G. Ma, Y.M. Xie, "Topology optimization for 3D concrete printing with various manufacturing constraints," *Additive Manufacturing,* vol. 57, pp. 102982, 2022.

[8] W. Gao, Y. Zhang, D. Ramanujan, K. Ramani, Y. Chen, C.B. Williams, C.C.L. Wang, Y.C. Shin, S. Zhang, P.D. Zavattieri, "The status, challenges, and future of additive manufacturing in engineering," *Computer Aided Design,* vol. 69, pp. 65-89, 2015.

[9] Z. Mu, Y. Yang, A.T. Gaynor, J.K. Guest, "Considering constructability in structural topology optimization," in *Proceedings of the Structures Congress 2014*, Boston, Massachusetts, United States, April 3-5, 2014, S. Gumpertz and Heger, Eds.

[10] D. Wang, Y. Yang, Z. Yi, X. Su, "Research on the fabricating quality optimization of the overhanging surface in SLM process," *The International Journal of Advanced Manufacturing Technology,* vol. 65, pp. 1471-1484, 2013.

[11] G. Strano, L. Hao, R.M. Everson, K.E. Evans, "A new approach to the design and optimisation of support structures in additive manufacturing," *The International Journal of Advanced Manufacturing Technology,* vol.66, pp. 1247-1254, 2013.

[12] M. Leary, L. Merli, F. Torti, M. Mazur, M. Brandt, "Optimal topology for additive manufacture: A method for enabling additive manufacture of support-free optimal structures," *Materials and Design,* vol. 63, pp. 678-690, 2014.

[13] Z. Li, D.Z. Zhang, P. Dong, I. Kucukkoc, "A lightweight and support-free design method for selective laser melting," *The International Journal of Advanced Manufacturing Technology,* vol.90, pp. 2943-2953, 2017.

[14] A.T. Gaynor, J.K. Guest, "Topology optimization considering overhang constraints: Eliminating sacrificial support material in additive manufacturing through design," *Structural and Multidisciplinary Optimization,* vol. 54, pp. 1157-1172, 2016.

[15] K. Zhang, G. Cheng, L. Xu, "Topology optimization considering overhang constraint in additive manufacturing," *Computers and Structures,* vol. 212, pp. 86-100, 2019.

[16] A. Garaigordobil, R. Ansola, J. Santamaría, I. Fernández de Bustos, "A new overhang constraint for topology optimization of self-supporting structures in additive manufacturing," *Structural and Multidisciplinary Optimization,* vol. 58, pp. 2003-2017, 2018.

[17] B.T. Gibson, P. Mhatre, M.C. Borish, C.E. Atkins, J.T. Potter, J.E. Vaughan, L.J. Love, "Controls and process planning strategies for 5-axis laser directed energy deposition of Ti-6Al-4V using an 8-axis industrial robot and rotary motion," *Additive Manufacturing,* vol. 58, pp. 103048, 2022.

[18] F. Wulle, O. Gorke, S. Schmidt, M. Nistler, G.E.M. Tovar, O. Riedel, A. Verl, A. Weber, A. Southan, "Multi-axis 3D printing of gelatin methacryloyl hydrogels on a non-planar surface obtained from magnetic resonance imaging," *Additive Manufacturing,* vol. 50, pp. 102566, 2022.

[19] K. Xu, Y. Li, L. Chen, K. Tang, "Curved layer based process planning for multi-axis volume printing of freeform parts," *Computer Aided Design,* vol. 114, pp. 51-63, 2019.

[20] Y. Gao, L. Wu, D.M. Yan, L. Nan, "Near support-free multi-directional 3D printing via global-optimal decomposition," *Graphical Models,* vol. 104, pp. 101034, 2019.

[21] E. Karasik, R. Fattal, M. Werman, "Object partitioning for suppor‐free 3D‐printing," *Computer Graphics Forum,* vol. 38, pp. 306-316, 2019.

[22] C. Wu, C. Dai, G. Fang, Y.J. Liu, C.C.L. Wang, "General support-effective decomposition for multi-directional 3-D Printing," *IEEE Transactions on Automation Science and Engineering,* vol. 17, pp. 599-610, 2020.

[23] F. Xie, X. Jing, C. Zhang, S. Chen, D. Bi, Z. Li, D. He, K. Tang, "Volume decomposition for multi-axis support-free and gouging-free printing based on ellipsoidal slicing," *Computer Aided Design,* vol. 143, pp. 103135, 2022.

[24] M.P. Bendsøe, O. Sigmund, "Material interpolation schemes in topology optimization," *Archive of Applied Mechanics,* vol. 69, pp. 635-654, 1999.

[25] O. Sigmund, J. Petersson, "Numerical instabilities in topology optimization: A survey on procedures dealing with checkerboards, mesh-dependencies and local minima," *Structural and Multidisciplinary Optimization,* vol. 16, pp. 68-75, 1998.

[26] S. Xu, Y. Cai, G. Cheng, "Volume preserving nonlinear density filter based on heaviside functions," *Structural and Multidisciplinary Optimization,* vol. 41, pp. 495-505, 2010.

IASS 2023
July 10–14 Melbourne
Integration of Design and Fabrication

Proceedings of the IASS Annual Symposium 2023
Integration of Design and Fabrication
10–14 July 2023, Melbourne, Australia
Y.M. Xie, J. Burry, T.U. Lee and J. Ma (eds.)

Topology optimization of dynamic stiffness response of constrained damping laminate structures

Teng Xiao YAN*, Chen Xiang YANG[a], Jiang Xu DONG[b]

* Laboratory 2035, Building 61, Harbin Engineering University, Heilongjiang Province, China
tengxiaoyan@hrbeu.edu.cn

[a] Laboratory 2035, Building 61, Harbin Engineering University, Heilongjiang Province, China
[b] Harbin University of Science and Technology, Heilongjiang Province, China

Abstract

The constrained damping laminate structure is used as an optimization object in this paper, the optimization of the optimal layout of the constrained damping in the substrate is taken as the research problem, a finite element model of a 7-degree of freedom constrained damping laminate structure is established, on this basis, the dynamic load acting on the structure is transformed into a static load in multiple analysis steps by using the basic principle of equivalent static load, so this dynamical problem is transformed into a static problem. The BESO optimization method is combined with the finite element analysis model to analyse the optimal topological configuration of the constrained damping on the substrate structure with the optimization objective of maximizing the dynamic stiffness, and a MATLAB program is written for the topological optimization algorithm of the dynamic stiffness response based on the equivalent static load method. The optimal layout of the restrained damping on the substrate under different iterative processes is obtained.

Keywords: topology optimization, BESO, multi-objective, power flow, stiffeners, constraint damping

1. Introduction

The constrained damping structure is formed by laying a viscoelastic layer on top of the plate and shell structure and then laying a constrained layer on top of the viscoelastic layer. The structure corresponding to the constrained damping plate is the free damping structure, and Kerwin [1] verified the difference in action between the free damping structure and the constrained damping structure by means of an experiment. DiTaranto [2] established a multi-order partial differential equation for the mathematical modeling of constrained damped beams as the object of study. On the basis of DiTaranto's study Mead [3] et al. further derived the sixth-order partial differential equations and derived the corresponding transverse displacements at different boundaries. Rao [4] derived the dynamic equations and boundary condition equations for constrained damped structures and proposed design algorithms with practical implications through the process of solving them by numerical methods. Zhang and Sainsbury [5] et al. analytically studied the vibration characteristics of sandwich plates when subjected to loads by combining the traditional finite element model and the basic principle of Gerlerkin's orthogonal function. The reinforced laminate shell structure can improve the overall stiffness and other mechanical properties of the structure, while the constrained damped laminate shell structure can suppress the overall vibration response amplitude of the structure [6]. In this paper, a finite element model of a 7-degree-of-freedom constrained damped laminate structure is established to optimize the optimal layout of the substrate for the constrained damped laminate structure [7]. The BESO optimization method is combined with the finite element analysis model to analyze the optimal topological configuration of the constrained damping on the substrate structure with the optimization objective of maximizing the dynamic stiffness.

Copyright © 2023 by Teng Xiao YAN, Chen Xiang YANG and Jiang Xu DONG. Published in the Proceedings of the IASS Annual Symposium 2023 with permission.

2. Finite element modeling and verification of constrained damped laminate

In the process of structural topology optimization, it is necessary to establish the overall stiffness matrix and mass matrix of the constrained damped structure, which are the basis for solving the structural dynamics and static response. Finally, a finite element model with 7 degrees of freedom of constrained damped finite units is developed.

2.1. Structural description and assumptions of the constrained damped laminate

The overall schematic diagram of the constrained damped composite structure is shown in Figure 1 below, which consists of three superimposed layers, namely the substrate structure layer, the intermediate damping layer, and the constrained layer structure. The subscript c represents the constraint layer, the subscript v represents the damping layer, and the subscript p represents the substrate layer. As shown in the figure below h indicates the thickness of each layer and the other dimensions are shown in the figure.

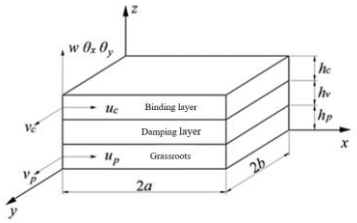


Figure 1. Schematic diagram of the structural model of the constrained damped laminate

In order to establish the finite element model of the constrained damped laminate simply and easily and to facilitate the calculation, the following assumptions are made in this paper.

(1) It is assumed that the overall restrained damping plate in this study is a thin plate structure, and the deformation is small after the force is applied.

(2) It is assumed that the base and restrained plates conform to the Kichhoff assumption and the damping layer conforms to the Mindlin assumption.

(3) Neglecting the relative movement between the layers of the restrained damping plate structure;

(4) Assume equal lateral displacements of the layers at the same location;

(5) It is assumed that the rotational inertia of each layer of material is neglected.

In order to facilitate the study of the geometric displacement relationships within the constrained damping plate structure, Figure 2 is used as an example to illustrate the geometric displacement relationships between the different material layers during deformation. Where u_c, u_v, and u_p represent the displacement in the x-direction of the neutral plane of each layer respectively, and similarly represents the displacement in the y-direction of each layer.

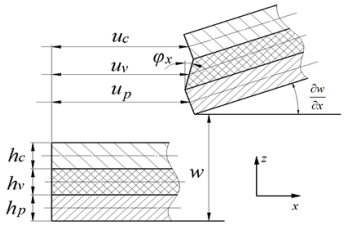


Figure 2. Geometric deformation relationship of the constrained damping plate model

The in-plane displacement of the constrained damped laminate in the direction of x can be obtained from the first-order shear deformation theory u as

$$u = u_0 + s\frac{\partial w}{\partial x}(-\frac{h}{2} \le s \le \frac{h}{2}) \tag{1}$$

In the above equation u is the displacement of the restrained damping laminate in an arbitrary plane and s is the distance between that arbitrary plane and the neutral plane.

The in-plane displacements u_1, u_2 of the upper and lower ends of the intermediate damping layer in the direction of x can be obtained from equation (1) as

$$u_1 = u_c - \frac{h_c}{2}\frac{\partial w}{\partial x} \tag{2}$$

$$u_2 = u_p - \frac{h_p}{2}\frac{\partial w}{\partial x} \tag{3}$$

From the deformation relationship, it is obtained that the rotation angle of the intermediate damping layer around the y-axis direction φ_x is

$$\varphi_x = \frac{u_1 - u_2}{h_v} \tag{4}$$

The angle of shear deformation generated by the intermediate damping layer around the y-axis can be expressed as in equation (5):

$$\beta_x = \frac{\partial w}{\partial x} + \varphi_x \tag{5}$$

Bringing (1), (2), (3), and (4) into (5) yields the following transformation equation:

$$\beta_x = \frac{u_c - u_p}{h_v} + (\frac{h_c + h_p}{2h_v} + 1)\frac{\partial w}{\partial x} \tag{6}$$

From the geometric relationship in Figure 2, the plane displacement in the direction of the damping layer a x xis can be obtained u_v and by bringing equation (2) into (5) we can obtain equation (7):

$$u_v = \frac{1}{2}\left[(u_c + u_p) + \frac{h_c - h_p}{2}\frac{\partial w}{\partial x}\right] \tag{7}$$

β_y The shear deformation of the middle damping layer of the constrained damping laminate around the x axis can be obtained from the above reasoning process in the same way as equation (8):

$$\beta_y = \frac{u_c - u_p}{h_v} + (\frac{h_c + h_p}{2h_v} + 1)\frac{\partial w}{\partial y} \tag{8}$$

Similarly the plane displacement in the direction of the intermediate damping layer y is

$$-\frac{d}{dx}\frac{\partial F}{\partial y'} + \frac{d^2}{dx^2}\frac{\partial F}{\partial y''} = 0 \tag{9}$$

2.2. Displacement patterns and their shape functions

In the process of finite element analysis of the constrained damping laminate structure, the unit division is consistent with the conventional unit division, and the division rule in this paper adopts the general principle of plate unit division, each unit includes four physical nodes, and each node includes seven degrees of freedom, including the displacement of the base plate and the constrained plate in the neutral

plane in the direction of x axis and y axis, which can be expressed as u_p, v_p, u_c, v_c; the transverse displacement of the overall unit of the constrained damping laminate w; and The angle of rotation of the constrained damped laminate unit around the x, y axis θ_x, θ_y, the above seven degrees of freedom are used as all the degrees of freedom in the finite element analysis to describe the displacements of each unit, and their displacement interpolation functions are Eqs. (10):

$$\begin{aligned}
u_c &= a_1 + a_2 x + a_3 y + a_4 xy \\
v_c &= a_5 + a_6 x + a_7 y + a_8 xy \\
u_p &= a_9 + a_{10} x + a_{11} y + a_{12} xy \\
v_p &= a_{13} + a_{14} x + a_{15} y + a_{16} xy \\
w &= a_{17} + a_{18} x + a_{19} y + a_{20}\,\mathrm{x}^2 + a_{21} xy + \\
&\quad a_{22} y^2 + a_{23} x^3 + a_{24} x^2 y + a_{25} xy^2 + \\
&\quad a_{26}\,\mathrm{y}^3 + a_{27}\,\mathrm{x}^3\,\mathrm{y} + a_{28}\,\mathrm{xy}^3 \\
\theta_x &= \frac{\partial w}{\partial \mathrm{y}} \qquad \theta_y = \frac{\partial w}{\partial \mathrm{x}}
\end{aligned} \tag{20}$$

where the displacement vector of each cell can be approximated by the four nodal displacements in the following equation (11):

$$u = \left[\mathrm{u}_1 \;\; \mathrm{u}_2 \;\; \mathrm{u}_3 \;\; \mathrm{u}_4\right]^{\mathrm{T}} \tag{31}$$

In the above equation u_i represents the displacement vector of each cell node, where $i = 1,2,3,4$ is the sequential number of the node.

$$u_{\mathrm{i}} = \left[\mathrm{u}_{\mathrm{ci}}\ \mathrm{v}_{\mathrm{ci}}\ \mathrm{u}_{\mathrm{pi}}\ \mathrm{v}_{\mathrm{pi}}\ \mathrm{w}_{\mathrm{i}}\ \theta_{\mathrm{xi}}\ \theta_{\mathrm{yi}}\right] \tag{42}$$

Therefore, in order to obtain all the displacements within a cell can be achieved by interpolating the displacements of the four nodes to satisfy the displacement solution at any position within the cell with the interpolation function shown in (10) below, which can be obtained by the association of (10), (11) (12):

$$\left[\mathrm{u}_{\mathrm{c}}\ \mathrm{v}_{\mathrm{c}}\ \mathrm{u}_{\mathrm{p}}\ \mathrm{v}_{\mathrm{p}}\ \mathrm{w}_{\mathrm{i}}\ \theta_{\mathrm{xi}}\ \theta_{\mathrm{yi}}\right]^{\mathrm{T}} = Nu \tag{53}$$

In the above equation (4-13) N is the matrix of form functions, where the form function N contains seven column vectors from N_1 to N_7.

The above displacement expressions and the corresponding components of the form functions are brought into Eqs. (7) and (9) to obtain the form functions N_8 and N_9 for the two directions of displacement on the neutral surface of the middle damping layer . x, y

$$N_8 = \frac{1}{2}\left[\left(N_1 + N_3\right) - \left(\frac{\mathrm{h}_c - \mathrm{h}_p}{2}\right)N_7\right] \tag{64}$$

$$N_9 = \frac{1}{2}\left[\left(N_2 + N_4\right) - \left(\frac{\mathrm{h}_c - \mathrm{h}_p}{2}\right)N_6\right] \tag{75}$$

Similarly, the shape functions of the intermediate damping layer around the x axis and the shear strain β_x, β_y around the y axis can be obtained at N_{10}, N_{11}.

$$N_{10} = \frac{1}{\mathrm{h_v}}\left[\left(N_1 - N_3 \right) - \left(\frac{\mathrm{h}_c - \mathrm{h}_p}{2} + \mathrm{h_v} \right) N_7 \right] \tag{86}$$

$$N_{11} = \frac{1}{\mathrm{h_v}}\left[\left(N_2 - N_4 \right) - \left(\frac{\mathrm{h}_c - \mathrm{h}_p}{2} + \mathrm{h_v} \right) N_6 \right] \tag{97}$$

Use right tabs at the right margin to justify equation numbers to that edge, and the equation numbers shall be sequential and in parentheses. Simple equations and assignments, like $v = 0$, may appear within the text. The equation editor shall be used to produce equations.

2.3. Structural principal structure relationship

From equation (1), the positive strain in the direction of x, y for each ply in the constrained damped laminate can be obtained by taking the partial derivative of x, y for that ply respectively, so the positive strain in the direction of x and y at any point in the base ply can be expressed by the following equations (18) and (19): The

$$\varepsilon_{px} = \frac{\partial u}{\partial x} = \frac{\partial u_p}{\partial x} + s\frac{\partial^2 w}{\partial x^2} \tag{108}$$

$$\varepsilon_{py} = \frac{\partial u}{\partial y} = \frac{\partial u_p}{\partial y} + s\frac{\partial^2 w}{\partial y^2} \tag{119}$$

The shear strain is expressed as equation (20):

$$\gamma_{pxy} = \frac{\partial u}{\partial y} + \frac{\partial v}{\partial x} = \frac{\partial u_p}{\partial y} + \frac{\partial v_p}{\partial x} + 2s\frac{\partial^2 w}{\partial x \partial y} \tag{20}$$

Relying on the basic assumptions, Hooke's law is used to express the stress-strain relationship at any point within the base plate in the constrained damping plate, so the positive stress at any point within the base plate is

$$\sigma_{px} = \frac{E_p}{1-\nu_p^2}\left(\varepsilon_{px} + \nu_p \varepsilon_{py}\right) \tag{212}$$

$$\sigma_{py} = \frac{E_p}{1-\upsilon_p^2}\left(\varepsilon_{py} + \upsilon_p \varepsilon_{px}\right) \tag{22}$$

The shear stress can be expressed as follows: equation (23)

$$\tau_{pxy} = G_p \gamma_{pxy} = \frac{E_p}{\left(1-\upsilon_p\right)}\gamma_{pxy} \tag{23}$$

As above, the positive and shear strains at any point within the constraint level can be obtained as in Eqs. (24), (25):

$$\varepsilon_{cx} = \frac{\partial u}{\partial x} = \frac{\partial u_c}{\partial x} + z\frac{\partial^2 w}{\partial x^2} \tag{24}$$

$$\varepsilon_{cy} = \frac{\partial u}{\partial y} = \frac{\partial v_c}{\partial y} + z\frac{\partial^2 w}{\partial y^2} \tag{25}$$

$$\gamma_{cxy}=\frac{\partial u}{\partial y}+\frac{\partial u}{\partial x}=\frac{\partial u_c}{\partial y}+\frac{\partial v_c}{\partial x}+2z\frac{\partial^2 w}{\partial x\partial y} \tag{26}$$

The positive stress-strain relationship in the direction of the confining layer x, y can be found by Hooke's law as follows:

$$\sigma_{cx}=\frac{E_c}{1-\upsilon_c^2}\left(\varepsilon_{cx}+\upsilon_c\varepsilon_{cy}\right) \tag{27}$$

$$\sigma_{cy}=\frac{E_p}{1-\upsilon_c^2}\left(\varepsilon_{cy}+\upsilon_c\varepsilon_{cx}\right) \tag{28}$$

$$\tau_{cxy}=G_c\gamma_{cxy}=\frac{E_c}{\left(1-\upsilon_c\right)}\gamma_{cxy} \tag{29}$$

Similarly the positive and shear strains at any point within the intermediate damping level can be expressed as Eqs. (30), (31), (32):

$$\varepsilon_{vx}=\frac{\partial u}{\partial x}=\frac{\partial u_v}{\partial x}+z\frac{\partial^2 w}{\partial x^2} \tag{30}$$

$$\varepsilon_{vy}=\frac{\partial u}{\partial y}=\frac{\partial v_v}{\partial y}+z\frac{\partial^2 w}{\partial y^2} \tag{313}$$

$$\gamma_{vxy}=\frac{\partial u}{\partial y}+\frac{\partial u}{\partial x}=\frac{\partial u_v}{\partial y}+\frac{\partial v_v}{\partial x}+2z\frac{\partial^2 w}{\partial x\partial y} \tag{32}$$

From the two-bit Hooke's law, the positive stress in the intermediate damping layer in the direction of x, y and the shear stress are obtained as shown in the following equations (33), (34), and (35):

$$\sigma_{vx}=\frac{E_v}{1-\upsilon_v^2}\left(\varepsilon_{vx}+\upsilon_v\varepsilon_{vy}\right) \tag{33}$$

$$\sigma_{vy}=\frac{E_v}{1-\upsilon_v^2}\left(\varepsilon_{vy}+\upsilon_v\varepsilon_{vx}\right) \tag{34}$$

$$\tau_{vxy}=G_v\gamma_{vxy}=\frac{E_v}{\left(1-\upsilon_v\right)}\gamma_{vxy} \tag{35}$$

The symbol E represents the modulus of elasticity of each layer and G represents the shear modulus of each material.

2.4. Kinetic equations

Based on the theoretical knowledge of elastic mechanics, the kinetic and potential energy of the bound damping plate unit in each layer of the laminate is solved using the principle of energy method, and the kinetic and potential energy principles are used to represent the dynamic equations of the bound damping plate structure. The expressions for the kinetic and potential energy of each laminate unit are derived specifically below, where the kinetic energy of the substrate layer unit is:

$$\mathrm{T}_{\mathrm{p}}^{\mathrm{e}}=\frac{1}{2}\rho_{\mathrm{p}}\iiint_{\mathrm{V}}\left[\left(\frac{\partial u_{\mathrm{p}}}{\partial \mathrm{t}}\right)^2+\left(\frac{\partial v_{\mathrm{p}}}{\partial \mathrm{t}}\right)^2+\left(\frac{\partial w}{\partial \mathrm{t}}\right)^2\right]\mathrm{d}\,\mathrm{V} \tag{36}$$

In the grassroots level, u_p , v_p , w are used to represent the internal displacement of the cell, and the shape functions corresponding to the above three displacement components are substituted into the above equation (36) to obtain the following expression (37).

$$\begin{aligned} \mathrm{T}_{\mathrm{p}}^{\mathrm{e}} &= \frac{1}{2}\left\{\dot{u}^{\mathrm{e}}\right\}^{\mathrm{T}} \rho_p \, \mathrm{h}_{\mathrm{p}} \int_{-\mathrm{a}}^{\mathrm{a}} \int_{-\mathrm{b}}^{\mathrm{b}} \left(N_3^{\mathrm{T}} N_3 + N_4^{\mathrm{T}} N_4 + N_5^{\mathrm{T}} N_5\right) \mathrm{d}\,\mathrm{x}\,\mathrm{d}\,\mathrm{y} \left\{\dot{u}^{\mathrm{e}}\right\} \\ &= \frac{1}{2}\left\{\dot{u}^{\mathrm{e}}\right\}^{\mathrm{T}} m_{\mathrm{p}} \left\{\dot{u}^{\mathrm{e}}\right\} \end{aligned} \tag{37}$$

The mass matrix of the substrate layer cell in the above equation is $\boldsymbol{m}_{\boldsymbol{p}}$, and

$$m_{\mathrm{p}} = \rho_{\mathrm{p}} \, \mathrm{h}_{\mathrm{p}} \int_{-\mathrm{a}}^{\mathrm{a}} \int_{-\mathrm{b}}^{\mathrm{b}} \left(N_3^{\mathrm{T}} N_3 + N_4^{\mathrm{T}} N_4 + N_5^{\mathrm{T}} N_5\right) \mathrm{d}\,\mathrm{x}\,\mathrm{d}\,\mathrm{y} \tag{38}$$

From the theory of elasticity, the strain potential energy of the base plate is given by equation (39)

$$\begin{aligned} \mathrm{E}_{\mathrm{p}}^{\mathrm{e}} &= \frac{1}{2} \iiint_V \varepsilon_{\mathrm{p}} \sigma_{\mathrm{p}} \mathrm{d}\,\mathrm{V} \\ &= \frac{1}{2} \iiint_V \left(\varepsilon_{\mathrm{px}} \sigma_{\mathrm{px}} + \varepsilon_{\mathrm{py}} \sigma_{\mathrm{py}} + \tau_{\mathrm{pxy}} \gamma_{\mathrm{pxy}}\right) \mathrm{d}\,\mathrm{V} \left\{\dot{u}^{e}\right\}^{\mathrm{T}} k_p \left\{\dot{u}^{e}\right\} \end{aligned} \tag{39}$$

Bringing the equations (18)-(20) into the above equation (39) and bringing the shape functions corresponding to the three displacement components of the base plate into the above equation yields

$$\begin{aligned} \mathrm{E}_{\mathrm{p}}^{\mathrm{e}} &= \frac{1}{2}\left\{\dot{u}^{e}\right\}^{\mathrm{T}} \left(\mathrm{h}_p \int_{-a}^{a} \int_{-b}^{b} B_{\mathrm{p}}^{\mathrm{T}} D_{\mathrm{p}} B_{\mathrm{p}} \mathrm{d}\,\mathrm{x}\,\mathrm{d}\,\mathrm{y} + \frac{\mathrm{h}_{\mathrm{p}}^3}{12} \int_{-a}^{a} \int_{-b}^{b} B^{\mathrm{T}} D_{\mathrm{p}} B \mathrm{d}\,\mathrm{x}\,\mathrm{d}\,\mathrm{y} \right) \left\{\dot{u}^{e}\right\} \\ &= \frac{1}{2}\left\{\dot{u}^{e}\right\}^{\mathrm{T}} k_p \left\{\dot{u}^{e}\right\} \end{aligned} \tag{40}$$

Therefore, the stiffness matrix of the base plate is

$$k_{\mathrm{p}} = h_{\mathrm{p}} \int_{-\mathrm{a}}^{\mathrm{a}} \int_{-\mathrm{b}}^{\mathrm{b}} B_{\mathrm{p}}^{\mathrm{T}} D_{\mathrm{p}} B_{\mathrm{p}} \mathbf{d}\,\mathrm{y}\,\mathbf{d}\,\mathrm{x} + \frac{h_{\mathrm{p}}^3}{12} \int_{-\mathrm{a}}^{\mathrm{a}} \int_{-\mathrm{b}}^{\mathrm{b}} B^{\mathrm{T}} D_{\mathrm{p}} B \mathbf{d}\,\mathrm{y}\,\mathbf{d}\,\mathrm{x} \tag{41}$$

According to the above reasoning process of mass matrix and stiffness matrix, the damping layer mass matrix and stiffness matrix can be obtained.

$$m_{\mathrm{v}} = \rho_{\mathrm{v}} \, \mathrm{h}_{\mathrm{v}} \int_{-\mathrm{a}}^{\mathrm{a}} \int_{-\mathrm{b}}^{\mathrm{b}} \left(N_8^{\mathrm{T}} N_8 + N_9^{\mathrm{T}} N_9 + N_5^{\mathrm{T}} N_5\right) \mathrm{d}\,\mathrm{x}\,\mathrm{d}\,\mathrm{y} \tag{42}$$

$$k_{\mathrm{v}} = h_{\mathrm{v}} \int_{-\mathrm{a}}^{\mathrm{a}} \int_{-\mathrm{b}}^{\mathrm{b}} B_{\mathrm{v}}^{\mathrm{T}} D_{\mathrm{v}} B_{\mathrm{v}} \mathbf{d}\,\mathrm{y}\,\mathbf{d}\,\mathrm{x} + \frac{h_{\mathrm{v}}^3}{12} \int_{-\mathrm{a}}^{\mathrm{a}} \int_{-\mathrm{b}}^{\mathrm{b}} B^{\mathrm{T}} D_{\mathrm{v}} B \mathbf{d}\,\mathrm{y}\,\mathbf{d}\,\mathrm{x} \tag{43}$$

Similarly, the stiffness matrix and mass matrix of the constrained layer cells are shown below

$$m_{\mathrm{c}} = \rho_{\mathrm{c}} \, \mathrm{h}_{\mathrm{c}} \int_{-\mathrm{a}}^{\mathrm{a}} \int_{-\mathrm{b}}^{\mathrm{b}} \left(N_1^{\mathrm{T}} N_1 + N_2^{\mathrm{T}} N_2 + N_5^{\mathrm{T}} N_5\right) \mathrm{d}\,\mathrm{x}\,\mathrm{d}\,\mathrm{y} \tag{44}$$

$$k_{\mathrm{c}} = h_{\mathrm{c}} \int_{-\mathrm{a}}^{\mathrm{a}} \int_{-\mathrm{b}}^{\mathrm{b}} B_{\mathrm{c}}^{\mathrm{T}} D_{\mathrm{c}} B_{\mathrm{c}} \mathbf{d}\,\mathrm{y}\,\mathbf{d}\,\mathrm{x} + \frac{h_{\mathrm{c}}^3}{12} \int_{-\mathrm{a}}^{\mathrm{a}} \int_{-\mathrm{b}}^{\mathrm{b}} B^{\mathrm{T}} D_{\mathrm{c}} B \mathbf{d}\,\mathrm{y}\,\mathbf{d}\,\mathrm{x} \tag{45}$$

where the elasticity matrix of the constrained damping plate structure can be expressed as equation (46)

$$D = \frac{\mathrm{E}}{1-\mu^2}\begin{bmatrix} 1 & \mu & 0 \\ \mu & 1 & 0 \\ 0 & 0 & \dfrac{1-\mu}{2} \end{bmatrix} \tag{46}$$

The strain conversion matrix for each layer of the constrained damped laminate is

$$B_{\mathrm{p}} = \begin{bmatrix} \dfrac{\mathrm{d}\,\mathrm{N}_3}{\mathrm{d}\,\mathrm{x}} & \dfrac{\mathrm{d}\,\mathrm{N}_4}{\mathrm{d}\,\mathrm{y}} & \dfrac{\mathbf{d}\,\mathrm{N}_3}{\mathbf{d}\,\mathrm{y}} + \dfrac{\mathbf{d}\,\mathrm{N}_4}{\mathbf{d}\,\mathrm{x}} \end{bmatrix}^{\mathrm{T}} \tag{47}$$

$$B_{\mathrm{c}} = \begin{bmatrix} \dfrac{\mathrm{d}\,\mathrm{N}_1}{\mathrm{d}\,\mathrm{x}} & \dfrac{\mathrm{d}\,\mathrm{N}_2}{\mathrm{d}\,\mathrm{y}} & \dfrac{\mathbf{d}\,\mathrm{N}_1}{\mathbf{d}\,\mathrm{y}} + \dfrac{\mathbf{d}\,\mathrm{N}_2}{\mathbf{d}\,\mathrm{x}} \end{bmatrix}^{\mathrm{T}} \tag{48}$$

$$B_{\mathrm{v}} = \begin{bmatrix} \dfrac{\mathrm{d}\,\mathrm{N}_8}{\mathrm{d}\,\mathrm{x}} & \dfrac{\mathrm{d}\,\mathrm{N}_9}{\mathrm{d}\,\mathrm{y}} & \dfrac{\mathbf{d}\,\mathrm{N}_8}{\mathbf{d}\,\mathrm{y}} + \dfrac{\mathbf{d}\,\mathrm{N}_9}{\mathbf{d}\,\mathrm{x}} \end{bmatrix}^{\mathrm{T}} \tag{49}$$

$$B = \begin{bmatrix} \dfrac{\mathrm{d}^2\,\mathrm{N}_5}{\mathrm{d}\,\mathrm{x}^2} & \dfrac{\mathrm{d}^2\,\mathrm{N}_5}{\mathrm{d}\,\mathrm{y}^2} & \dfrac{2\mathbf{d}^2\,\mathrm{N}_5}{\mathbf{d}\,\mathrm{y}^2} \end{bmatrix}^{\mathrm{T}} \tag{50}$$

Since the middle damping plate of the constrained damping laminate structure will not only generate positive strain, but also shear deformation will occur in the transverse direction while deforming, the potential energy of shear deformation can be determined according to the assumptions started in the text as

$$\mathrm{E}_{\mathrm{p}}^{\mathrm{e}} = \frac{1}{2}\iiint_{V}\left(\mathrm{G}_{v}\,\beta_{v}^{2} + \mathrm{G}_{v}\,\beta_{y}^{2}\right)\mathrm{d}\,\mathrm{V} \tag{51}$$

Bringing the form function corresponding to β_v, β_y in the above equation yields the following relation:

$$\mathrm{E}_{\beta}^{\mathrm{e}} = \frac{1}{2}\left\{\dot{u}^{e}\right\}^{\mathrm{T}}\left(\mathrm{G}_{\mathrm{v}}\mathrm{h}_{\mathrm{v}}\int_{-a}^{a}\int_{-b}^{b} N_{10}^{\mathrm{T}}N_{10} + N_{11}^{\mathrm{T}}N_{11}\,\mathrm{d}\,\mathrm{x}\,\mathrm{d}\,\mathrm{y}\right)\left\{\dot{u}^{e}\right\} = \frac{1}{2}\left\{\dot{u}^{e}\right\}^{\mathrm{T}} k_{\mathrm{v}\beta}\left\{\dot{u}^{e}\right\} \tag{52}$$

The shear stiffness of the constrained damping plate structure can be obtained from the above equation as

$$k_{\mathrm{v}\beta} = \frac{1}{2}\mathrm{G}_{\mathrm{v}}\mathrm{h}_{\mathrm{v}}\int_{-a}^{a}\int_{-b}^{b}\left(N_{10}^{\mathrm{T}}N_{10} + N_{11}^{\mathrm{T}}N_{11}\right)\mathrm{d}\,\mathrm{x}\,\mathrm{d}\,\mathrm{y} \tag{53}$$

The kinetic energy, potential energy and shear energy of the three-layer laminate structure of the constrained damped laminate structure are brought in according to the variational equation of Hamilton's principle, and the kinetic equation of the laminate unit can be obtained;

$$m\left\{\ddot{u}^{\mathrm{e}}\right\} + k\left\{u^{\mathrm{e}}\right\} = \left\{F\right\} \tag{54}$$

In the above equation, $\boldsymbol{m}$ is the mass matrix, $\boldsymbol{k}$ is the stiffness matrix, and F is the external excitation force. Where the stiffness matrix and mass matrix of each cell are integrated in the form of a total assembly into the overall mass matrix and stiffness matrix.

$$M = \sum_{\mathrm{i}=1}^{\mathrm{N}}\left(m_{\mathrm{p}}^{\mathrm{i}} + m_{\mathrm{c}}^{\mathrm{i}} + m_{\mathrm{v}}^{\mathrm{i}}\right) \tag{55}$$

$$K=\sum_{\mathrm{i}=1}^{\mathrm{N}}\left(k_{\mathrm{p}}^{\mathrm{i}}+k_{\mathrm{c}}^{\mathrm{i}}+k_{\mathrm{v}}^{\mathrm{i}}+k_{\mathrm{vb}}^{\mathrm{i}}\right) \tag{56}$$

From the above series of equations the kinetic equations of the bound damping plate as a whole can be determined:

$$M\{\ddot{u}\}+K\{u\}=\{F\} \tag{57}$$

3.Equivalent static load fundamentals

Equivalent static load is a method of solving the dynamic response of a structure under dynamic load, which works by converting the dynamic problem into a static problem through multiple analysis steps, so that the displacement response generated in the same time and the displacement generated by the dynamic load is the same, so that the dynamic response problem is converted into a multi-case static problem by multiple analysis steps to solve [11]. The specific equivalent process can be represented by Figure 3, and the equivalent process of vibration control equation 58 is shown below:

$$\mathbf{M}\ddot{\mathbf{d}}+\mathbf{K}\mathbf{d}=\mathbf{f}=\{0 \quad \ldots \quad f_i \ldots f_{i+l-1} 0 \ldots 0\} \tag{58}$$

In the above equation, M represents the overall mass matrix of the structure, K represents the overall stiffness matrix of the structure, d is the displacement response under load, $\ddot{d}$ is the corresponding acceleration response, f is the applied load on the structure, where l is the number of equivalent static loads.

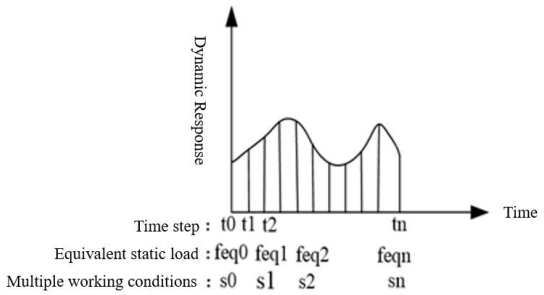


Figure 3. Schematic diagram of the equivalent process

4. Optimization Example and Analysis

4.1 Mathematical modeling of the optimization problem

In this section, with maximization of stiffness as the optimization objective, dynamic loads are applied to the structure with volume as the constraint objective, and the equivalent static load method approach is used to solve for the structural dynamic response, with the following mathematical model:

$$\begin{cases} \text{Minimize} & C=\sum_{u=1}^{l} w_u\left(\frac{1}{2} f_{tu}^{T} z_{\mathrm{ou}}\right); & u=1,\ldots,l \\ \text{Subject to} & V^{*}-\sum_{i=1}^{N} V_i x_i=0 & \\ & \mathbf{K}(\mathbf{x})\mathbf{z}(s)-\mathbf{f}_{eq}(s)=0; \quad s=1,\ldots,l & \\ & x_i \in \{x_{\min},1\} & \end{cases} \tag{59}$$

In the above equation, l is the total time step, w_u is the time step weight factor, which is 1 if the time analysis steps have the same time. $1/2*(f^T z_{tu})$ is the stiffness value of the structure during the time step, V^* is the volume constraint, x_i is the relative cell density, z_{tu} is the displacement at the u time step, and f_{tu} is the dynamic load.

4.2 Unit sensitivity and optimization process analysis

4.2.1. Unit sensitivity calculation

The sensitivity of the cell under equivalent static load is calculated by the following equation:

$$\begin{cases} dc_{ij} = \dfrac{1}{2} p x_{ij}^{p-1} \mathbf{u}_{ij}^T \mathbf{K}_i \mathbf{u}_{ij} \\ dc_i = \dfrac{1}{2} \displaystyle\sum_{j=1}^{l} p x_{ij}^{p-1} \mathbf{u}_{ij}^T \mathbf{K}_i \mathbf{u}_{ij} \end{cases} \tag{60}$$

In the above equation, dc_{ij} is the sensitivity of the i cell at the j step, dc_i indicates the cell sensitivity, p is the total time step of the penalty factor expressed by l , and x_{ij} indicates the relative density of the i cell at the j time step.

4.2.2 Optimization process analysis

a) first need to assign values to the initial variables of the structure as well as to the initial optimization parameters;

b) Calculation of the dynamic response at each analysis step time under dynamic load using the Newmark method of analysis;

c) Solving the load values for each analysis step time using the equivalent static load method;

d) Establish the mathematical model of the objective function in the optimization model:

$$\begin{cases} \text{Minimize} & C = \displaystyle\sum_{u=1}^{l} w_u \left(\frac{1}{2} f_{tu}^T z_{tu} \right); \quad u = 1, \ldots, l \\ \text{Subject to} & V^* - \displaystyle\sum_{i=1}^{N} V_i x_i = 0 \\ & \mathbf{K}(\mathbf{x})\mathbf{z}(s) - f_{eq}(s) = 0; \quad s = 1, \ldots, l \\ & x_i \in \{x_{\min}, 1\} \end{cases} \tag{61}$$

e) Combined with the BESO method to add and delete structural units, the cycle ends when the convergence conditions are met; the criteria for determining convergence are as follows:

$$\left(\left| x_i^{k+1} - x_i^k \right| \geq \varepsilon_1 \right) \leq n \times \varepsilon_2; \quad i = 1, \ldots, n \tag{62}$$

In the above equation ε_1 , the ε_2 is the defined minimal value.

4.3 Analysis of dynamic stiffness optimization algorithm based on equivalent static load method

In this section, the dynamic response of the structure under dynamic load is solved by using the equivalent static load method to construct the optimal topology of constrained damping with dynamic stiffness as the optimization objective. $f(t)$ Based on the theory of equivalent static load and the theoretical knowledge of the finite element model of the restrained damped laminate, Matlab is used to

write the above analysis and calculation process. The specific parameters are as follows: plate length is 0.3480m, plate width is 0.3048m, volume constraint is 0.3, cell division is 40×40 , three-layer material parameters are shown in Table 2.1, set the total time step is 20, material penalty factor is 3, in order to avoid the singular matrix to take the virtual cell $x_{\min}$ value is 0.0001

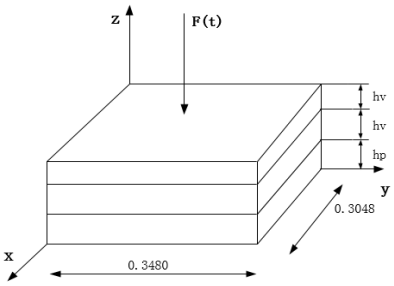


Figure 4. Laminate under equivalent static load

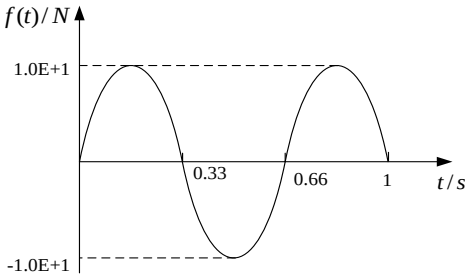
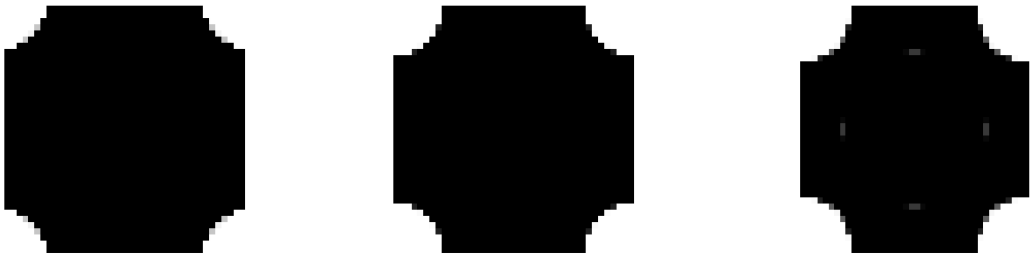


Figure 5. Simple harmonic excitation load diagram

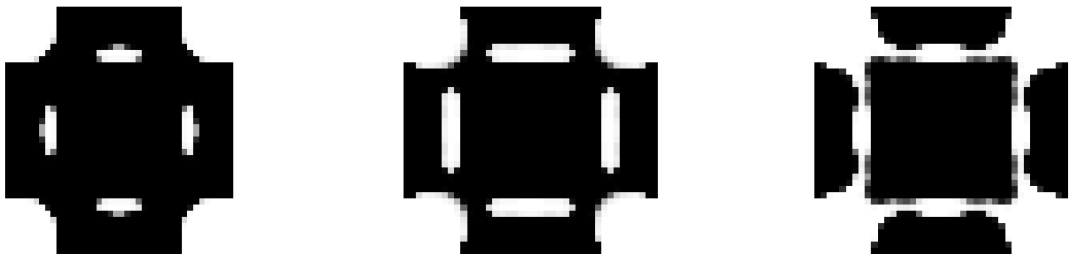
By writing the BESO optimization algorithm program, a topology optimization program with the minimum flexibility as the optimization objective is established, and the constrained damping volume ratio is used as the constraint, and the topology diagram of each stage iteration and the final constrained damping optimal topology configuration are obtained through multiple iterations, and the topology diagram of the whole iteration process is shown in Figure 6 below.



(a) Iterative optimization of the 10th constrained damping layout configuration

(b) Iterative optimization of the 15th constrained damping layout configuration

(c) Iterative optimization of the 20th constrained damping layout configuration



(d) Iterative optimization of the 30th constrained damping layout configuration

(e) Iterative optimization of the 50th constrained damping layout configuration

(f) Final constrained damping layout configuration

Figure 6. Topology optimization process of four-sided solid support constrained damped laminate layout

In the above figures 6 represent the constrained damping topology after optimization of the four-sided fixed-supported constrained damping laminate, where the dynamic load is loaded in the middle of the

constrained damping laminate, and the dynamic stiffness is maximized under the action of the dynamic load as the optimization objective. The restrained damping material is uniformly distributed in the four sides and the middle of the plate. The above distribution of the restrained damping reflects the transmission path of the center load plate under the restrained condition of four-sided solid support.

5. Conclusion

In this paper, the topological optimization method of BESO optimization is used to optimize the constrained damping laminate structure, and the dynamic stiffness is used as the optimal design objective to distribute the constrained damping material in the best position. In order to obtain the stiffness matrix and mass matrix of the restrained damping structure as a whole, a finite element analysis model of the restrained damping laminate is developed and verified. In order to convert the problem of dynamics analysis into a static problem for calculation, the equivalent static load method combined with BESO topology optimization is applied to solve this problem. In order to obtain the final topological distribution of the constrained damping during the optimization iterations, a MATLAB program based on the topological optimization algorithm of the dynamic stiffness response of the equivalent static load method is written, and finally the optimal layout of the constrained damping on the substrate under different iterations is obtained.

Acknowledgements

This research is supported by the National Natural Science Foundation, of China (Grant No.51505096), and National Natural Science Foundation of Heilongjiang Province of China (Grant No.LH2020E064). This paper is funded by the International Exchange Program of Harbin Engineering University for Innovation-oriented Talents Cultivation.

References

[1] M. Edward and Kerwin, “Damping of Flexural Waves by a Constrained Viscoelastic Layer,” *The Journal of the Acoustical Society of America*, vol. 31, 952–962, 1959.

[2] R. A. Ditaranto, “Theory of Vibratory Bending for Elastic and Viscoelastic Layered Finite-Length Beams,” *Journal of Applied Mechanics*, vol. 32, 881-886, 1965.

[3] D. J. Mead and S. Markus, “The forced vibration of a three-layer, damped sandwich beam with arbitrary boundary conditions,” *Journal of Sound and Vibration*, vol. 10, 163-175, 1969.

[4] M. D. Rao, “Recent applications of viscoelastic damping for noise control in automobiles and commercial airplanes,” *Journal of sound and vibration*, vol. 262, 457-474, 2003.

[5] Q. J. Zhang and M. G. Sainsbury, “The Galerkin element method applied to the vibration of rectangular damped sandwich plates,” *Computers & Structures*, vol. 74, 717-730, 2000.

[6] W. Hare, N. Julie, S. Tesfamariam, “A survey of non-gradient optimization methods in structural engineering,” *Advances in Engineering Software*, vol. 59, 19-28, 2013

[7] D. E. Grierson and W. H. Pak, “Optimal sizing, geometrical and topological design using a genetic algorithm,” *Structural optimization*, vol. 6, 151-159, 1993.

Proceedings of the IASS Annual Symposium 2023
Integration of Design and Fabrication
10–14 July 2023, Melbourne, Australia
Y.M. Xie, J. Burry, T.U. Lee and J. Ma (eds.)

Topology optimization of spatial grid structures considering member stability based on linear allowable stress iteration

Ruoqiang FENG*, Hui WANG[a], Qi CAI[a]

[a,*] Key Laboratory of Concrete and Prestressed Concrete Structures of Ministry of Education, Southeast University, Nanjing, Jiangsu Province 211189, China
hitfeng@163.com

Abstract

In order to solve the problems of low efficiency and inaccurate identification of member stability in structural topology optimization model with section area as design variable considering member stability, a linear allowable stress iteration method considering member stability limit is proposed. In this paper, the nonlinear structural optimization problem considering member buckling is transformed into a linear optimization problem, and an optimization model and program for spatial grid structures are established. Finally, the effectiveness of the algorithm in spatial grid structures is explored through numerical examples. The results show that topology of the structure can be changed by using the iterative allowable stress method to meet the requirements of the stable buckling of members. In addition, the linear allowable stress iteration method considering the stability limit of members not only can optimize the topology of spatial grid structures based on Euler buckling, but also through the buckling of Chinese codes, making the practical engineering application of topology optimization of spatial grid structures possible.

Keywords: spatial grid structure, topology optimization, member stability, linear allowable stress iteration

1. Introduction

Topology optimization is one of the most important and challenging areas in structural optimization, as it allows for the optimization of both the topology structure and geometric shape of trusses, providing an effective method for generating optimized truss designs. The ground structure method is a commonly used method in topology optimization. Based on the ground structure method, many truss optimization methods are achieved by reducing or increasing the number of truss members while keeping the node positions unchanged.

However, in topology optimization using the ground structure method, two existing challenges are the low computational efficiency and inaccurate stability criteria for the design variable of cross-sectional area of the bar and the consideration of bar stability constraints [1,2]. Firstly, due to the nonlinear function of bar stability constraints as optimization variables, the optimal solution may be located in the degenerate domain of the feasible domain, making the solution efficiency of optimization problems considering bar stability very low [3,4]. Secondly, because the Euler buckling criterion is relatively simple compared to the more complex requirements of structural design standards, previous studies mainly relied on the Euler buckling criterion rather than actual structural design standards to determine whether bars buckle.

However, many studies have shown that the critical buckling force of bars calculated using the Euler buckling criterion algorithm may be overestimated, which could lead to unsafe optimized structures [5]. Most national and regional structural design standards not only consider the length and cross-sectional shape of bars, but also initial defects when determining whether bars buckle. For example, the British

Copyright © 2023 by Ruiqiang FENG, Hui WANG and Qi CAI. Published in the Proceedings of the IASS Annual Symposium 2023 with permission.

steel design standard BS5950 [6] and the European steel design standard Eurocode 3 [7] require consideration of the influence of the slenderness ratio when determining bar stability.

Due to the high number of bars in spatial grid structures, optimization algorithms are required to have high computational efficiency. A feasible approach is to set the allowable compressive stress of the material to a relatively small value, which transforms the nonlinear optimization problem of considering bar stability into a linear optimization problem that only considers stress constraints [8]. However, determining the appropriate value for the allowable compressive stress remains a challenge [9]. If the allowable compressive stress is set too high, it may result in instability of the optimized structure, while setting it too low may cause material waste and affect optimization performance [10, 11].

Building upon the aforementioned modifications to the allowable stress method, this study proposes a linear iterative method for allowable stress. This method iteratively modifies the material allowable stress for each rod, transforming the non-linear rod stability constraints into linear constraints, thereby improving computational efficiency. Additionally, this method can use either the Euler buckling criterion or the "Code for Design of Steel Structures" (GB 50017) as the criterion for rod buckling.

2. Theoretical methods

2.1. Structural optimization formula considering the stability of members

Although the Euler buckling criterion and the "Code for Design of Steel Structures" (GB 50017) have different formulas for calculating the critical buckling force of a member, both require the axial force of the member to be greater than the negative value of its corresponding critical buckling force in the structural optimization model, i.e., satisfying Equation (1). We define the cross-sectional area of the member in the buckling state as the critical buckling cross-sectional area. Therefore, the critical buckling cross-sectional areas calculated by the Euler buckling criterion and the "Code for Design of Steel Structures" (GB 50017) are:

$$a_i^{Euler} = 2l_i\sqrt{\frac{S_i^{Euler}}{\pi E}} \tag{1}$$

$$a_i^{code} = \frac{S_i^{code}}{\varphi\sigma_f} \tag{2}$$

In the above equations, a_i^{Euler} and a_i^{code} represent the Euler critical section area and the specification critical section area, respectively. Therefore, during the optimization process, as long as the cross-sectional area of the member is not less than the critical section area, it can be considered that the member satisfies the local buckling constraint, that is: $a_i \geq a_i^{cr}$.

Based on the above discussions, the optimization formula for three-dimensional space grid structures, with the minimum structural weight as the optimization objective and stress, static equilibrium, and member stability as the constraint conditions, can be expressed as:

Objective function: $\min\limits_{\mathbf{A,q}} M = \rho \mathbf{A}^{\mathrm{T}}\mathbf{L}$

constraint condition: $\mathbf{BS}^k = \mathbf{f}^k$

$$-\sigma^{-}\mathbf{A} \leq \mathbf{S}^{\alpha} \leq \sigma^{+}\mathbf{A} \qquad \alpha = 1, 2, \ldots, k+6$$

$$\mathbf{BS}^{k+1}=\mathbf{f}_x \qquad \mathbf{BS}^{k+2}=-\mathbf{f}_x \qquad \mathbf{BS}^{k+3}=\mathbf{f}_y$$

$$\mathbf{BS}^{k+4}=-\mathbf{f}_y \qquad \mathbf{BS}^{k+5}=\mathbf{f}_z \qquad \mathbf{BS}^{k+6}=-\mathbf{f}_z$$

$$\mathbf{f}_x \geq \frac{1}{2} r \mathbf{T}_x \mathbf{S}^k \qquad \mathbf{f}_y \geq \frac{1}{2} r \mathbf{T}_y \mathbf{S}^k \qquad \mathbf{f}_z \geq \frac{1}{2} r \mathbf{T}_z \mathbf{S}^k$$

$$a_i \geq a_i^{cr} \qquad \mathbf{A} \geq 0$$

In the formula, ρ represents material density, **A**, **L**, and **S** represent the cross-section, length, and axial force vector of the member, respectively. **B** is the static moment matrix of the structure, $\mathbf{f}^k$ is the external load matrix, and k represents the number of external load cases. $\mathbf{S}^{\alpha}$ represents the member axial force under k external load cases and 6 nominal disturbance force cases. $\mathbf{f}_x$, $\mathbf{f}_y$, and $\mathbf{f}_z$ represent the nominal disturbance force vectors along the positive x, y, and z directions, respectively, while $-\mathbf{f}_x$, $-\mathbf{f}_y$, and $-\mathbf{f}_z$ represent the nominal disturbance force vectors along the negative x, y, and z directions, respectively. Here, "$\geq$" indicates that the nominal disturbance force should satisfy k external load cases. $\mathbf{T}_x$, $\mathbf{T}_y$, and $\mathbf{T}_z$ represent the conversion matrices that convert the member axial force to the x, y, and z directions, respectively. r is the disturbance force coefficient, and in this study, r is set to 0.02. $\mathbf{M}_{com}$ represents the set of compression members.

2.2. Linear allowable stress iteration method

In this section, we propose a linear permissible stress iteration method for linearizing the stability constraints of beam elements in structural optimization problems. The feasible domain of such problems is nonlinear and difficult to solve. The proposed method is illustrated in Figure 1.

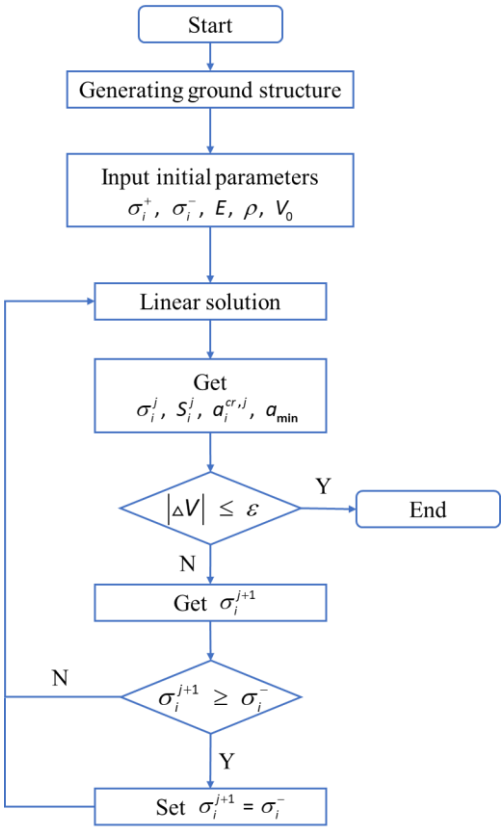


Figure 1. Linear Allowable Stress Iteration Process.

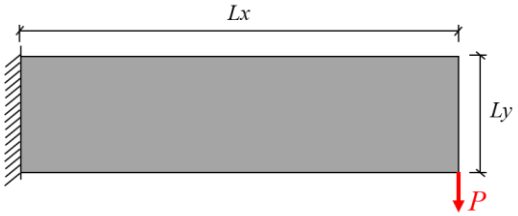
3. Numerical examples

In this section, numerical examples are presented to demonstrate the effectiveness of the linear allowable stress iteration method proposed in this study. The material used in the numerical examples is Q 345 steel with allowable compressive and tensile stress values of $\sigma^+ = \sigma^- = 305$ MPa, yield strength $\sigma_y = 345$ MPa, density $\rho = 7.85$ g/cm3, and elastic modulus E = 206 GPa. As short bars are commonly encountered in practical engineering, a first-order connectivity is adopted in the construction of the base structure, where only adjacent nodes are connected to form bar elements. Consequently, overlapping bar elements do not exist in the base structure. Unless specified otherwise, the solid circular bar section is selected. The minimum section is chosen to be 10% of the average effective section in the previous iteration. Moreover, to address the issue of unstable nodes, the nominal perturbation method proposed in Chapter 5 of this study is employed, with a perturbation force coefficient of r = 0.02. In the optimized structure, the blue, red, and green bars represent bars subjected to compression, tension, and support, respectively. A support bar is a bar with zero axial force under the main external loading condition, which serves to maintain node stability.

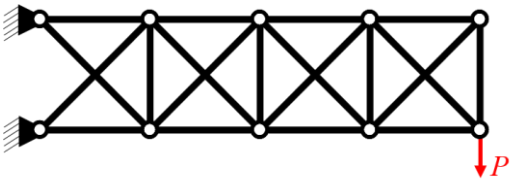
3.1. Two-dimensional cantilever beam

As shown in Figure 2 (a), this study optimizes the design domain of a classical cantilever beam subjected to concentrated loads at its ends. The size of the cantilever beam design domain is $L_x \times L_y$ = 2000 mm × 500 mm。 The left end of the design domain is hinged to limit the horizontal and vertical movement of the structure, and the lower part of the right end bears a vertical concentrated load P = 8 kN. Uniformly arrange node elements within the design domain, with a distance of 500 mm between any two adjacent node elements. Connecting two adjacent node elements to form a member element, together forming a base structure containing 10 node elements and 20 member elements, as shown in Figure 2 (b). In order to better reflect the difference between the optimization results obtained based on the Euler buckling algorithm and the algorithm based on the Design Standard for Steel Structures (GB 50017) (hereinafter referred to as the code), the minimum section and minimum allowable stress are not set in this calculation example.

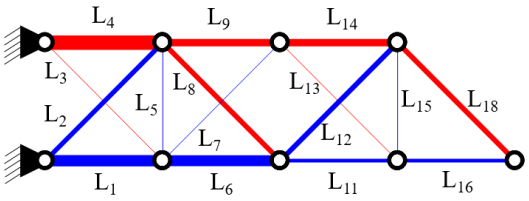
The optimization result without considering the stability of the member is shown in Figure 2 (c), with a structural mass of 2.491 kg and a calculation time of 2.1 *s*. The optimized structure considering the stability of the member according to the Euler buckling criterion is shown in Figure 2 (d). The structural mass is 5.356 kg, with a total of 23 iterations and a calculation time of 10.5 seconds. Finally, the optimized structural mass obtained by the algorithm for judging the buckling of the rod according to the regulations is 5.898 kg, the program has been iterated 12 times, and the running time is 6.8 seconds. In the three cases, the axial force, cross-sectional area, and buckling critical force of the effective member of the optimized structure are shown in Table 1.



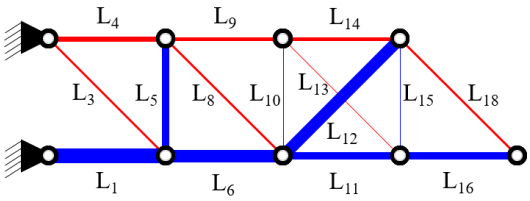
(a) Design area



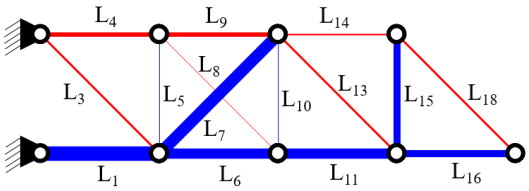
(b) Ground Structure



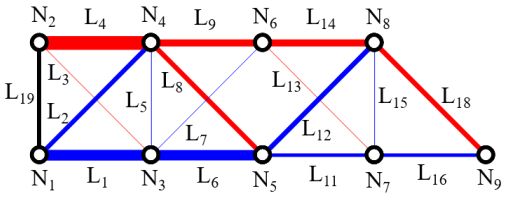
(c) Optimal structure without stability of members



(d) Optimal Structure considering euler buckling



(e) Optimal structures considering code buckling



(f) Optimized structure after simplification

Figure 2. Optimization model of cantilever beam

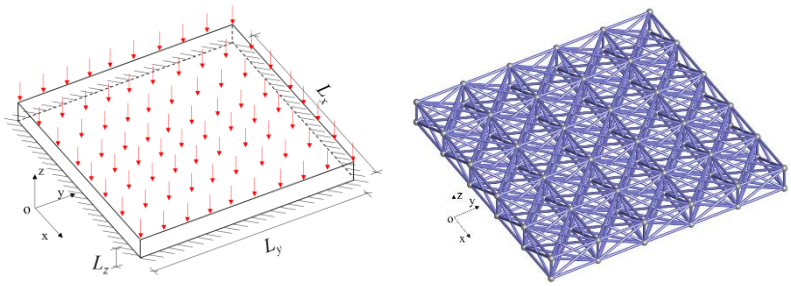
Table 1. Optimization results of cantilever beam

		Without local buckling			With Euler local buckling				With code local buckling		
No.	*l*/mm	*a*/mm²	*S*/ kN	S^{Code} / kN	*a*/mm²	*S*/ kN	S^{Euler} / kN	S^{Code} / kN	*a*/mm²	*S*/ kN	S^{Code} / kN
L_1	500	79.7	-24.322	3.413	222.4	-32	32	24.702	255.5	-32	32
L_2	707	35.6	-10.858	0.353	0	—	—	—	—	—	—
L_3	707	1.5	0.456	—	37.1	11.314	—	—	37.1	11.314	—
L_4	500	103.9	31.678	—	78.7	24	—	—	78.7	24	—
L_5	500	0.8	-0.242	0	111.2	-8	8	6.534	1.0	-0.001	0.001
L_6	500	78.4	-23.919	3.303	192.6	-24	24	18.826	176.8	-16.001	16.001
L_7	707	0.4	-0.114	0	0	—	—	—	206.5	-11.312	11.313
L_8	707	36.7	11.199	—	37.1	11.314	—	—	1.5	0.002	—
L_9	500	52.7	16.081	—	52.5	16	—	—	78.7	24	—
L_{10}	500	—	—	—	0.5	—	—	—	1.0	-0.001	0.001
L_{11}	500	26.5	-8.08	0.388	111.2	-8	8	6.534	176.8	-16	16
L_{12}	707	36.7	-11.2	0.375	187.0	-11.314	11.313	9.320	—	—	—
L_{13}	707	0.4	0.114	—	0.7	—	—	—	37.1	11.314	—
L_{14}	500	52.2	15.92	—	52.5	16	—	—	26.2	8	—
L_{15}	500	0.3	-0.08	0	0.5	—	—	—	123.4	-8	8
L_{16}	500	26.2	-8	0.380	111.2	-8	8	6.534	123.4	-8	8
L_{17}	707	—	—	—	0	—	—	—	—	—	—
L_{18}	707	37.1	11.314	—	37.1	11.314	—	—	37.1	11.314	—
L_{19}	500	—	—	—	0	—	—	—	—	—	—
L_{20}	500	—	—	—	0	—	—	—	—	—	—

Note: The calculation accuracy is 0.1%.

3.2. Grid structure

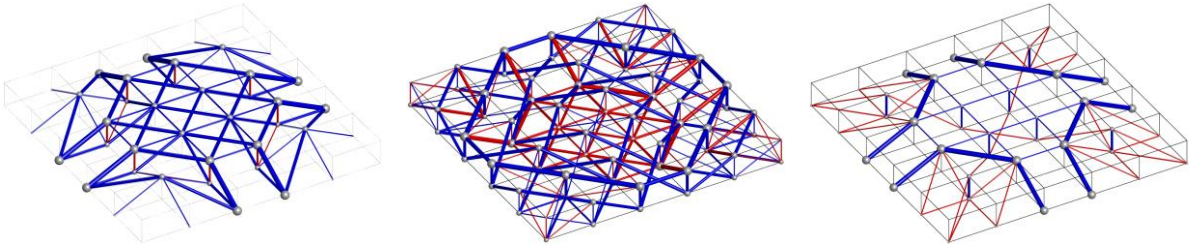
This study optimizes the design domain of the bottom chord supported grid structure shown in Figure 3 (a). The design domain size is $L_x \times L_y \times L_z = 10\ m \times 10\ m \times 1\ m$, the upper surface bears a vertically downward uniform surface load of 1.5 kN/m^2. Uniformly arrange nodes within the design area, with a horizontal spacing of 2 m and a vertical spacing of 1 m. In the study, the uniformly distributed surface load was converted into a concentrated load acting on the upper surface node, with a load value of 6 kN. Due to the fact that node loads around the upper surface can be directly transferred to the support through the maintenance structure, which has a small impact on the overall topology of the structure, in order to simplify the calculation, no concentrated loads are applied to the surrounding nodes. Set the member connection level to Lvl=1, that is, connect only adjacent nodes in the base grid, and the resulting base structure is shown in Figure 3(b). The base structure contains 476 rod elements and 72 node elements. The nominal perturbation method is used to consider the impact of node stability, and the nominal perturbation coefficient is set to r=0.02.



(a) Design area (b) Ground Structure

Figure 3. Design area of bottom chord braced grid structure

Without considering the stability of the rod, the optimized structure is shown in Figure 4(a), with a structural mass of 33.59 kg. At this point, most of the members in the structure are under pressure. Figure 5 shows the comparison of the actual axial force value, Euler buckling critical force, and gauge buckling critical force of the compression rod in Figure 4 (a). As can be seen from Figure 5, none of these compression rods can meet the requirements for rod buckling. Therefore, it is necessary to consider member buckling in structural topology optimization.



(a) Structure before iteration (b) Structure after iteration 1 (c) Structure after iteration 36

Figure 4 Optimization results of grid structures based on Euler buckling

When using the Euler buckling criterion to assess the local buckling of the truss members, the resulting topology of the optimized structure at different iterations is shown in Figure 4, while the corresponding structural quality changes after each iteration are demonstrated by the black line in Figure 6. Figure 4 indicates that the topology of the structure changes significantly in the early stages of the iterations. As the number of iterations increases, the topology of the structure tends to be stable, which explains the significant changes in the structural quality in the early iterations. The optimized structure with a mass of Me = 374.502 kg is obtained as shown in Figure 4 (c) at the end of the process. In addition, there are relatively few truss members (shown by green lines) used solely for supporting unstable nodes in the

final optimized structure, indicating that the structure gradually converges towards a topology with high material efficiency.

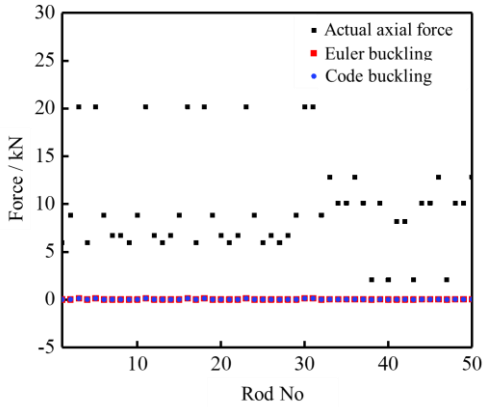


Figure 5. members without rod buckling

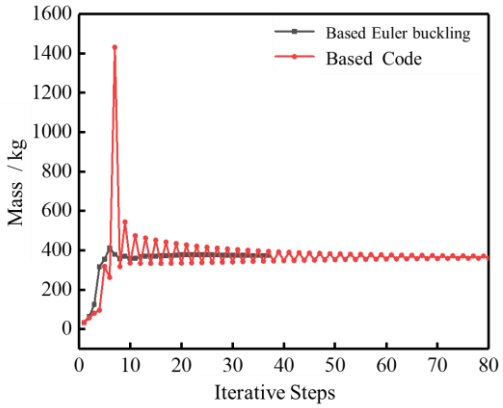
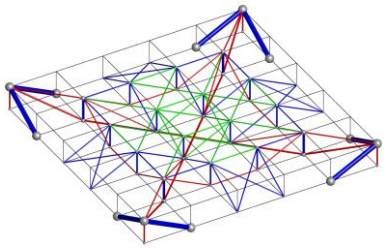


Figure 6. Structural mass of each iteration step

When using the code buckling method to determine the local buckling of a member, the structural topology corresponding to different iteration steps is shown in Figure 7, it is similar to the optimization process considering the Euler buckling criterion, the topology of the structure changes greatly in the early stages of the iteration process. With the increase of the number of iterations, the topology of the structure tends to stabilize, and the optimized structure mass is Mc=360.447 kg. In addition, the optimized structure obtained using the gauge buckling method is lighter than the structure obtained using the Euler criterion method.



(a) Structure after iteration 79

Figure 7. Optimization results of grid structures based on code buckling

The compression bar in the topological optimization structure obtained by using the Euler buckling method cannot meet the requirements of structural specifications for the buckling of the bar. However, the compression bar in the topology optimized structure obtained by using the standard buckling method can not only meet the structural code requirements for member buckling, but also meet the requirements of the Euler buckling criterion. Comparing the optimized structures generated by the two optimization types, it can be seen that the topological forms of the optimized structures obtained by the two methods considering the buckling of the members differ greatly. This indicates that using the iterative allowable stress method can meet the buckling requirements of members by changing the topology of the structure. This also shows that the iterative allowable stress method has the ability to globally search for the optimal solution.

5. Conclusion

This paper proposes a linear permissible stress iterative method for considering the stability constraints of truss members in spatial grid structure optimization, and establishes a structural optimization model. The linear permissible stress iterative method uses an iterative approach to convert the nonlinear stability

constraints of truss members into linear constraints, making it possible to solve topology optimization problems of spatial grid structures containing a large number of members. The main conclusions are as follows:

(1) Compared to the traditional structural optimization models that rely solely on the Euler buckling criterion to assess the stability of members, the linear permissible stress iteration method proposed in this study can evaluate the stability of members based on both the Euler buckling criterion and the design code. This versatility makes the proposed method applicable to practical engineering design.

(2) Through the comparison of optimization results, it can be seen that the optimized topology of the structure based on the Euler buckling criterion and the one based on actual design standards may differ in the optimization model. Additionally, the optimized structure obtained through the Euler buckling-based optimization algorithm may not meet the requirements of the actual structural design standards for rod stability. Therefore, it is recommended to directly use a rod stability judgment algorithm based on structural design standards in structural optimization calculations.

(3) The quality of the optimized structure using the actual design specifications may be lower compared to the one optimized using the Euler buckling-based method. This indicates that the linear iterative allowable stress method proposed in this study has the ability to perform global optimization search.

Acknowledgements

This research was financially supported by the National Natural Science Foundation of China (Grant numbers: 51978151).

References

[1] L. W. He, M, Gilbert, X. Y. Song, "A Python script for adaptive layout optimization of trusses," *Structural and Multidisciplinary Optimization*, vol. 60, pp. 835-847, 2019.

[2] H. Wang, W. Du, Y. Zhao, Y. Wang, M. Yang, "Optimization and experimental research on treelike joints based on generative design and powder bed fusion," *Engineering Structures*, vol. 278, pp. 115564, 2023.

[3] X. Guo, G. Cheng, K. Yamazaki, "A new approach for the solution of singular optima in truss topology optimization with stress and local buckling constraints," *Structural and Multidisciplinary Optimization*, vol. 22, pp. 364-372, 2021.

[4] G. D. Cheng,Guo X, "A note on a jellyfish-like feasible domain in structural topology optimization," *Engineering Optimization*, vol. 31, pp. 1-24, 1998.

[5] Q. Cai, R. Feng, Z. Zhang, "Topology optimization of trusses incorporating practical local buckling stability considerations," *Structures*, vol. 41, pp. 1710-1718, 2022.

[6] British Standards Institution. BS 5950-1 Structural use of steelwork in building. Milton Keynes: British Library, 2000.

[7] British Standards Institution. Eurocode 3: Part 1. Design of steel structures, general rules and rules for buildings. Milton Keynes: British Library, 1992.

[8] National Standard of the People's Republic of China, GB/T 50017-2017, Standard for Design of Steel Structures, China Standard Press, Beijing, 2017.

[9] K. Mela, "Resolving issues with member buckling in truss topology optimization using a mixed variable approach," *Structural and Multidisciplinary Optimization*, vol. 50, pp. 1037-1049, 2014.

[10] Q. Cai, L. W. He, Y. M. Xie, "Simple and effective strategies to generate diverse designs for truss structures," *Structures*, vol. 32, pp. 268-278, 2021.

[11] L. He, M. Gilbert, "Rationalization of trusses generated via layout optimization," *Structural and Multidisciplinary Optimization*, vol. 52, pp. 677-694, 2015.

IASS 2023
July 10–14 Melbourne
Integration of Design and Fabrication

Proceedings of the IASS Annual Symposium 2023
Integration of Design and Fabrication
10–14 July 2023, Melbourne, Australia
Y.M. Xie, J. Burry, T.U. Lee and J. Ma (eds.)

Topology optimization of truss structure with nodal stability and local buckling of member constraints

Qi CAI[a,*], Yiyi ZHOU[a]

[a,*] The College of Mechanics and Materials, Ho Hai University
Nanjing, Jiangsu Province 211189
caiqi302@126.com

Abstract

In this study, the nominal perturbing force (NPF) method and the allowable stress iteration (ASI) method are proposed to address nodal instability and local buckling instability problems in truss topology optimization, respectively. In the NPF approach, an infinite number of disturbing forces that a node may suffer are considered by a finite number of nominal perturbation force conditions whose magnitude and direction are analyzed to capture the worst-case perturbation. In the ASI method, the allowable compressive stresses in the members are recalculated according to Euler buckling criterion in each iteration to make the buckling constraint active. Finally, a truss topology optimization formulation incorporating the NPF and ASI methods is proposed and demonstrated through two numerical examples.

Keywords: conceptual design, topology optimization, truss, local buckling, nodal stability

1. Introduction

A typical truss topology optimization problem might comprise a design domain containing an array of fixed nodal points connected by potential members, called the ground structure. Typically, the truss topology optimization based on the ground structure method is mainly divided into four steps. Firstly, as shown in Figure 1a, the design domain with appropriate supports and loads is determined. Secondly, as shown in Figure 1b, the nodes are arranged, usually evenly, to discrete the design domain. Thirdly, as shown in Figure 1c, these nodes are connected with potential members to generate the ground structure. Finally, as shown in Figure 1d, some optimization algorithms are used to remove the redundant members to generate the optimal structure. However, the optimized structure obtained by using the ground structure method always contains unstable nodes within successive parallel compression members, such as node N_5 in Figure 1d, which may lead to structural instability.

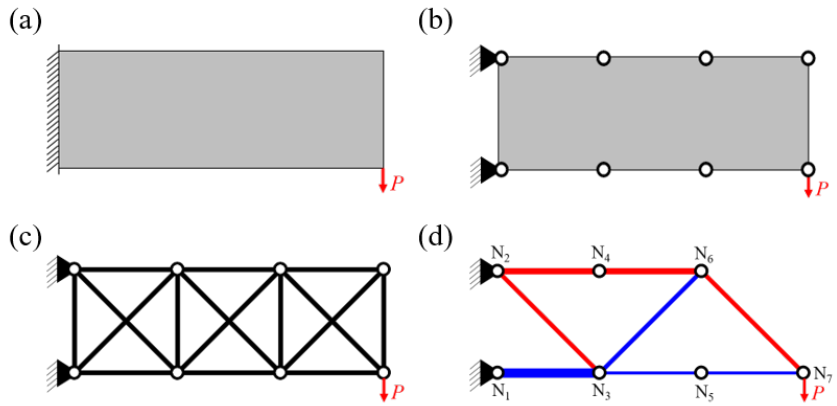


Figure 1. Optimization of truss structure based on ground structure method. (a) Design domain, (b) Node arrangement, (c) Ground structure, (d) Optimal structure.

Copyright © 2023 by Qi CAI and Yiyi ZHOU. Published in the Proceedings of the IASS Annual Symposium 2023 with permission.

In previous studies, lots of attempts had been made to solve the nodal instability problem. An intuitive approach is to eliminate unstable nodes and merge these consecutive members into a single long member. However, the inclusion of local buckling in an optimization formulation means that any method which involves this approach is highly unlikely to obtain an optimal design. Another approach is to add constraints on the minimum number of active members connected to the active nodes in the truss topology optimization problem. The original intention of this approach is to add enough bracings to the unstable nodes to limit the node motion. However, in this approach, it may be neither guaranteed that all directions of freedom of the nodes are constrained nor that the bracings can provide sufficient support forces. The inclusion of a global elastic stability criterion in the optimization algorithm can also, to some extent, solve the nodal stability problem in truss topology optimization, since the global stability of the structure requires nodal stability by default. However, due to the low computational efficiency of solving the semidefinite programming, only ground structures containing a relatively small number of members can be solved in this way. Therefore, the nodal stability problem in truss optimization still needs to be addressed.

In addition to nodal stability, local buckling of members should be considered in the optimization of truss structures. The first observation on Euler buckling constraints is that they exhibit similar behavior as stress constraints that are known for making the feasible set non-convex and for inducing degenerated regions, where the optimal point may lie. These regions can be treated in the solution process by the so-called ε-relaxed approach [1], a technique adapted from a similar idea for stress constraints. However, even though the disjointness and degeneracy of the feasible set can be solved, one still has to face the numerical difficulties related to non-convexity and choosing the parameter ε. Furthermore, it has been shown that this method may not yield reasonable optimization results for pressure constraints. Therefore, in many studies of truss structure optimization, the local buckling problem of the members is neglected. In order to use the optimized structure in the practical structural design, an intuitive approach is to increase the cross-sectional area of the buckling member after optimization. However, since this approach cannot take the local buckling stability into account in the optimization process, it does not lead to better optimization results. A rudimentary approach for taking member local buckling stability into account is to set the allowable stress in compression to be some specified constant fraction of the tensile stress. This reduces the problem to one with unequal permissible stresses in tension and in compression, and no further modifications are needed for member local stability. However, in general, it is very difficult to choose a correct constant lower stress constraint for members with different lengths or axial forces. Therefore, this method does not provide a practical means for taking member local buckling stability into account in truss optimization. In summary, the local buckling of members still needs to be addressed in the optimization of truss structures.

This study mainly addresses the nodal instability and the local buckling of member problems in topology optimization of truss structures, which is organized as follows. In section 2, the framework for truss topology optimization with constraints on member stress is present. Then, in section 3, the nominal perturbing force method and the allowable stress iteration method are introduced, respectively. In Section 4, the effectiveness of the proposed methods is demonstrated on numerical examples. Finally, the paper is summarized in Section 5.

2. Truss topology optimization

For convenience, the structures studied in this section are plane trusses defined by N_n nodal points and N_b members. For spatial trusses, there is a similar derivation. The number of supports is denoted N_s and the number of degrees of freedom of the nodes is $N_{dof} = d \times N_n - N_s$, where $d = 2$ for plane truss. The sectional area of the member i is given as a_i collected in $\mathbf{a} \in \mathrm{R}^{N_b \times 1}$. Similarly, the lengths of members are collected in $\mathbf{l} \in \mathbf{R}^{N_b \times 1}$. The plastic formulation for the minimized truss volume with member stress constraint subjected to M external load conditions can be formulated as,

$$\begin{aligned} &\min_{\mathbf{a},\mathbf{q}} \; V = \mathbf{a}^{\mathrm{T}}\mathbf{l} && \\ \text{s.t.} \quad &\mathbf{B}\mathbf{q}^{t} = \mathbf{f}^{t} && t = 1, 2, ..., M \\ &-\sigma^{-} a_i \le q_i^{t} \le \sigma^{+} a_i && \\ &a_i \ge 0 && i = 1, 2, ..., N_b \end{aligned} \tag{1}$$

where $\mathbf{B} \in \mathrm{R}^{N_{dof} \times N_b}$ is the equilibrium matrix, built from the directional cosines of the members, $\mathbf{q}^{t} \in \mathrm{R}^{N_b \times M}$ is a matrix containing the axial force for all members under M external load conditions, and $\mathbf{f}^{\mathbf{t}} \in \mathrm{R}^{N_{dof} \times M}$ is a matrix containing the external loads, $\sigma^{+} > 0$ and $\sigma^{-} > 0$ are limiting tensile and compressive yield stresses respectively, q_i^{t} is the axial force of the member i under loading case f^{t}. The optimization variables are the cross-sectional areas in **a** and the internal force in **q**. It can be observed that the element in matrix **B** is determined by the positions and connectivity of the nodes in the ground structure. Therefore, the optimization formulation is a linear programming problem, which can be solved very efficiently by a state-of-the-art solver.

2.2 Nominal perturbing force method

In order to address the nodal instability problem in the optimized structure, the Nominal perturbing force (NPF) approach is proposed in this study. In the NPF approach, an infinite number of disturbing forces at nodes in the ground structure are incorporated into the truss topology optimization problem in the form of nominal perturbing force conditions, whose magnitude and direction will be determined in the following section.

2.2.1 Magnitude of the nominal perturbing force

Considering a single primary external load case, each of these axes is considered in turn with the sum of all the components of axil forces pushing onto the node normal to this axis being determined, and a nominal force taken as some specified proportion of this sum.

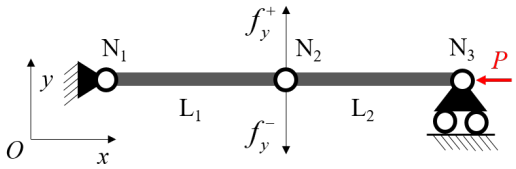


Figure 2. Two-member structure parallel to the coordinate axis

Using the two-member structure shown in Figure 2 as an example, the nominal perturbing forces can be calculated from the following equation,

$$f_y^{+} = f_y^{-} = \frac{1}{2} r \sum_{i=1}^{m_j} q_i d_i^{x} \tag{2}$$

where f_y^{+} and f_y^{-} are two nominal perturbing force conditions at node N_2 in the same and opposite directions to the y-axis, respectively, m_j is the number of members connected to node j, d_i^{x} is the direction cosine of the member i relative to the x-axis, r is the nominal perturbing force coefficient, which reflects the ratio of the magnitude of the bracing force to the axial force of the braced members. In this paper, the nominal perturbing force calculated by using formula (2) is called calculated nominal force. The magnitude of the perturbing force required to stabilize the internal nodes within compressive members can be reflected in the requirements of the practical design code that stipulates the strength

standards of bracings. For example, both BS5950[2] and EC3 code[3] require that, the bracing force should be not less than 1% of the compression force that is being resisted. Therefore, the magnitude of the nominal perturbing force perpendicular to the braced members is taken as 1% of the magnitude of the compression force of the braced members.

2.2.2 Direction of the nominal perturbing force

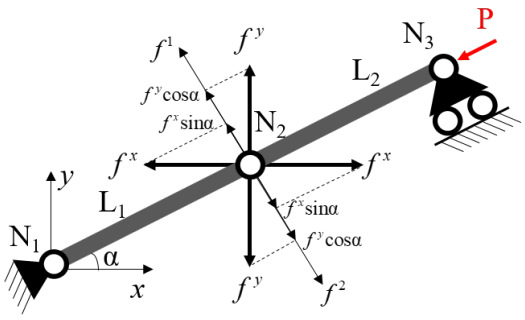


Figure 3. Two-member structure not parallel to the coordinate axis [4]

When the orientation of the members does not necessarily coincide with the Cartesian axis, one of the main concerns is how to evaluate the direction and magnitude of the nominal perturbing forces. In the following, we discuss this issue using the two-member structure shown in Figure 3. Four perturbing force conditions are applied to node N_2, which are load conditions f^x and $-f^x$ along with the positive and negative directions of the *x*-axis, and f^y and $-f^y$ along with the positive and negative directions of the *y*-axis, respectively. According to formula (2), the perturbing forces can be stated as,

$$f^x = rP\sin\alpha \qquad \alpha \in [0,\ \pi/2] \tag{3}$$

$$f^y = rP\cos\alpha \qquad \alpha \in [0,\ \pi/2] \tag{4}$$

where P is the axial force of the compression member, α is the angle between the member and the *x*-axis. Then, the maximum component forces of the nominal perturbing force perpendicular to the members L_1 and L_2 can be given as

$$f^1 = f^2 = \max\left\{rf^x\sin\alpha, rf^y\cos\alpha\right\} \qquad \alpha \in [0,\ \pi/2] \tag{5}$$

Adding equations (3) and (4) to equation (5), the nominal perturbing force perpendicular to the braced members can be stated as

$$f^1 = f^2 = \max\left\{rP\sin^2\alpha, rP\cos^2\alpha\right\} \qquad \alpha \in [0,\ \pi/2] \tag{6}$$

Therefore, as the angle between the member and the Cartesian coordinate axis varies from 0 to $\pi/2$, the perturbing force perpendicular to the braced members can be stated as

$$\frac{1}{2}rP \le f^1 = f^2 \le rP \tag{7}$$

This shows that when the member dose not coincide with any Cartesian coordinate axis, the effective component of nominal force in the direction perpendicular to the member axis is 0.5 to 1 time the calculated nominal force. According to equation (6), when the angle α is $\pi/4$, the nominal force perpendicular to the direction of the member obtains the minimum value, which is 0.5 times the calculated nominal force.

In this study, as an approximation, four nominal perturbing forces cases projected in either direction to the two Cartesian axes in plane truss are adopted. To ensure the axial force that can be provided by the bracing is at least 0.01 times the axial force of the braced member, the nominal perturbing force coefficient r is taken as 0.02.

2.3 Local buckling of member constraint

By introducing the critical Euler buckling load for a simply supported member, the local buckling constraint for the member i can be given as

$$-q_i \le P_i^{cr} = \frac{\pi^2 E I_i}{l_i^2} \tag{8}$$

where P_i^{cr} and I_i are the critical buckling load and the second moment of the sectional area of the member i, respectively, E is Young's modulus. For the tension member, formulation (8) is automatically satisfied since the axial force $q_i \ge 0$. Therefore, inequality (8) is only active for the compression members. For a member with a solid circular section, the second moment of sectional area can be expressed as,

$$I_i = \frac{a_i^2}{4\pi} \tag{9}$$

Adding the second moment of sectional area (9) into the local buckling constraint, the critical buckling area can be expressed as,

$$a_i^{cr} = \sqrt{\frac{4P_i^{cr} l_i^2}{\pi E}} \tag{10}$$

Obviously, the critical buckling load is a concave function on the cross-sectional area, which is difficult to obtain the optimal solution. Therefore, in this study, a novel iteration approach is used to make the local buckling problem into a linear expression on the cross-sectional area, as shown in Figure 3.

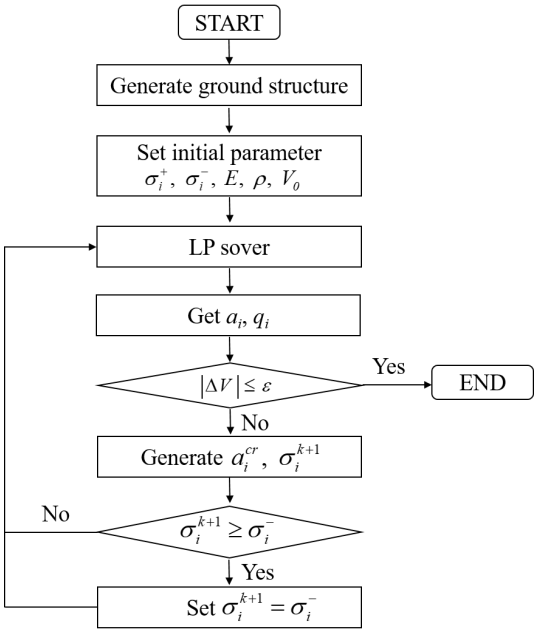


Figure 4. Flowchart of ASI method

where $|\Delta V|$ is the change in structural volume between four consecutive iteration steps, which can be expressed as

$$\left|\Delta V\right| = \left|\left(V^k + V^{k-1}\right) - \left(V^{k-2} + V^{k-3}\right)\right| \tag{11}$$

where V^k , V^{k-1} , V^{k-2} , V^{k-3} ($k \geq 4$) are the volume of structure at iteration *k, k*-1*, k*-2 and *k*-3, respectively. In addition, ε is taken as 0.001 in this study. If the convergence criteria are not met, for each member that is active in the solution, the limiting compressive yield stress for the next iteration *k* + 1 can be obtained by

$$\sigma_i^{k+1} = \sigma_i^k \frac{a_i}{a_i^{cr}} \tag{12}$$

where σ_i^k is the compressive stress in the member *i* at iteration *k*, a_i^{cr} is the critical buckling area of the member *i*, which can be stated as

$$a_i^{cr} = \sqrt{\frac{4\left|q_i^k\right| l_i^2}{\pi E}} \tag{13}$$

where q_i^k is the axial force of the member *i* at iteration *k*, $\left|\ \right|$ indicates the absolute value. However, direct use of σ_i^{k+1} obtained by (12) in the iterations is likely to cause cycling to occur. Therefore, a relaxation term η, the value of which is to be taken within zero to one, is introduced in the calculation, then the limiting compressive stress can be expressed as

$$\sigma_i^{k+1} = \eta\sigma_i^k \frac{a_i}{a_i^{cr}} + \left(1-\eta\right)\sigma_i^k \tag{14}$$

For members with other sectional areas, it is sufficient to modify the second moment formula (9).

It should be noted that the cross-sectional area of the bracing is generally small, and the minimum cross-sectional area of the member is limited in the structure design according to practical codes. Therefore, in this study, the local buckling of the bracing member is not considered.

3. Numerical applications

3.1 2D column

In this section, a two-dimensional column subjected to a vertical concentrated load are studied in order to verify the validity of the nominal perturbing force method. The bottom boundary of the design domain is hingedly constrained, where the horizontal and vertical displacements of the nodes are constrained. The middle of the top boundary of the column design domain is subjected to a vertical downward load $P = 1$. The design domain, boundary conditions and load are shown in Figure 5(a), where $H = 5$, $W = 1.6$. In addition, the height of the mesh grid is 1 and the width is 0.4. As shown in Figure 5(b), the ground structure contains 89 bars and 30 nodes.

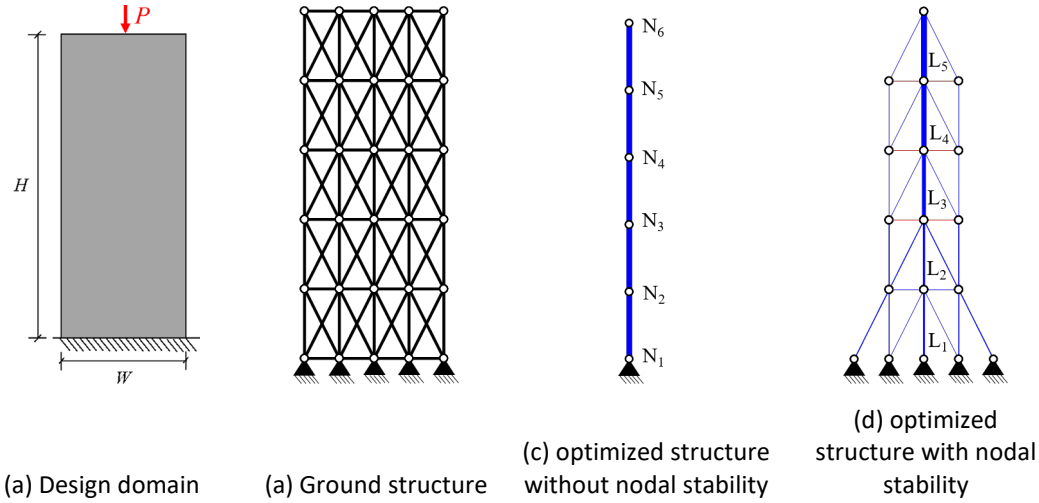


Figure 5. Topology optimization of 2D column design domain

Without considering the node stability, the optimized structure is shown in Figure 5(c), and the volume of the structure is $V_0 = 4$. Obviously, nodes $N_2 \sim N_5$ are all unstable nodes due to lake of lateral supports. When the nominal perturbing forces are applied to the ground structure, the optimized structure is obtained as shown in Figure 5(d). The volume of the structure is $V_1 = 4.286$, which is only $(V_1 - V_0)/V_0 = 7.15\%$ more than the volume of the structure shown in Figure 5(c).

As can be seen in Figure 5 (d), the cross-sectional area of the vertical bars of the structure gradually increases from bar L_1 to the upper L_5. This is because the lateral support bars provide not only lateral support but also vertical support for the unstable nodes. Obviously, the topology of the optimal structure considering node stability is completely different from that of the optimal structure without considering node stability. This shows that the use of the nominal perturbing forces method can ensure node stability by adjusting the topological form of the structure during the optimization process. It also shows that the optimization algorithm has the ability to globally search for optimal solutions.

3.2 Crane domain

As shown in Figure 4a, a crane design domain example is studied in this section, where L is 0.2 m. As shown in Figure 4 a, in the design domain, pinned supports are present on the bottom face and four-point loads P = 20 kN is applied downwards at the tip of the upper beam. Limiting tensile and compressive stresses are taken as 355 MPa. The design domain is discretized using 38 neighboring nodes (Figure 4b) connected by 173 potential members to generate an adjacent connectivity ground structure (Figure 4c).

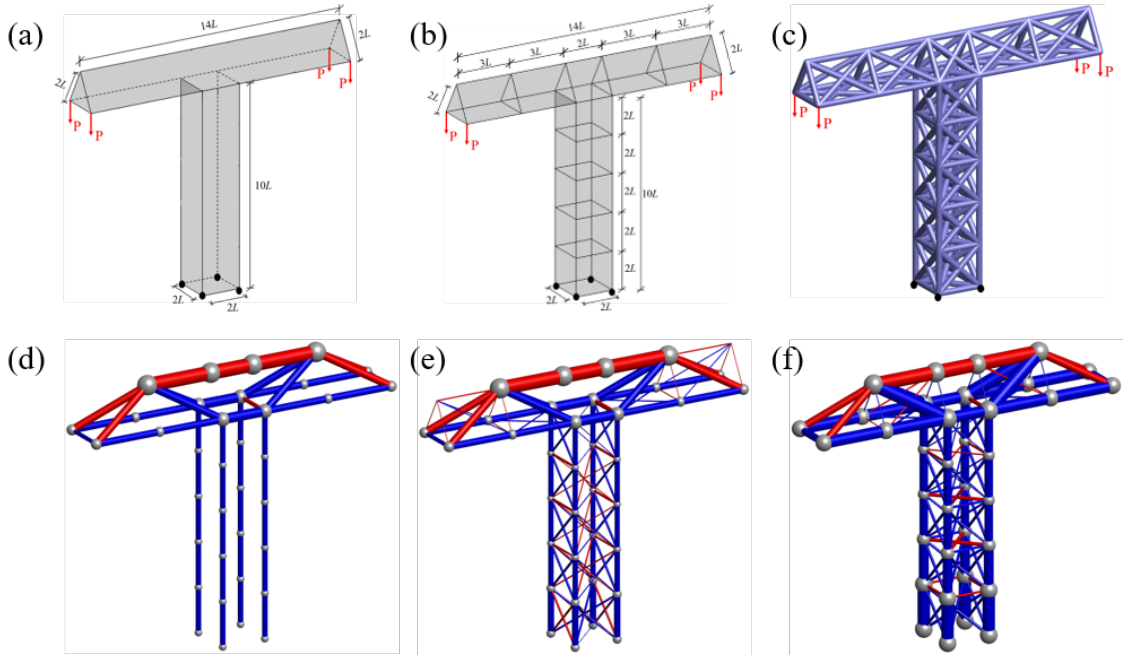


Figure 6. Optimization of crane [5]. (a) Design domain, (b) Mesh grid, (c) Ground structure, (d) optimized structure without stability, (e) optimized structure with nodal stability, (f) optimized structure with nodal stability and local buckling stability

The optimized structure with a volume of $V_{OSW} = 2.428 \times 10^6$ mm^3 is shown in Figure 4d when neither the nodal stability nor local buckling stability is considered in the optimization. However, almost all the nodes within compressive members are unstable, which cannot be used in practical applications, obviously. As shown in Figure 4e, when only the nodal local buckling stability is considered in the optimization, an optimized structure with a volume of $V_{OSN} = 2.635 \times 10^6$ mm^3 is obtained, where $\left(V_{OSN} - V_{OSW}\right)/V_{OSW} \times 100\% = 8.526\%$ more material is used to make the nodes stable. As shown in Figure 4f, an optimized structure with volume $V_{OSNL} = 5.607 \times 10^6$ mm^3 is obtained with both nodal and local buckling stability, where $\left(V_{OSNB} - V_{OSW}\right)/V_{OSW} \times 100\% = 130.931\%$ more material is used to make the nodes and local buckling stable.

Figure 6 shows two comparisons of the axial and critical buckling forces of the optimized structures. As shown in Figure 6a, when local buckling stability is not considered, the magnitudes of the axial forces of many members in the optimized structure exceed their critical buckling forces. When local buckling is considered in the optimization using the ASI method, the axial force and critical local buckling force of all compression members in the optimized structure are shown in Figure 6b. It can be seen from Figure 6b that the magnitudes of the axial forces of all the compression members do not exceed their critical buckling forces, which demonstrates the effectiveness of the ASI method proposed in this study.

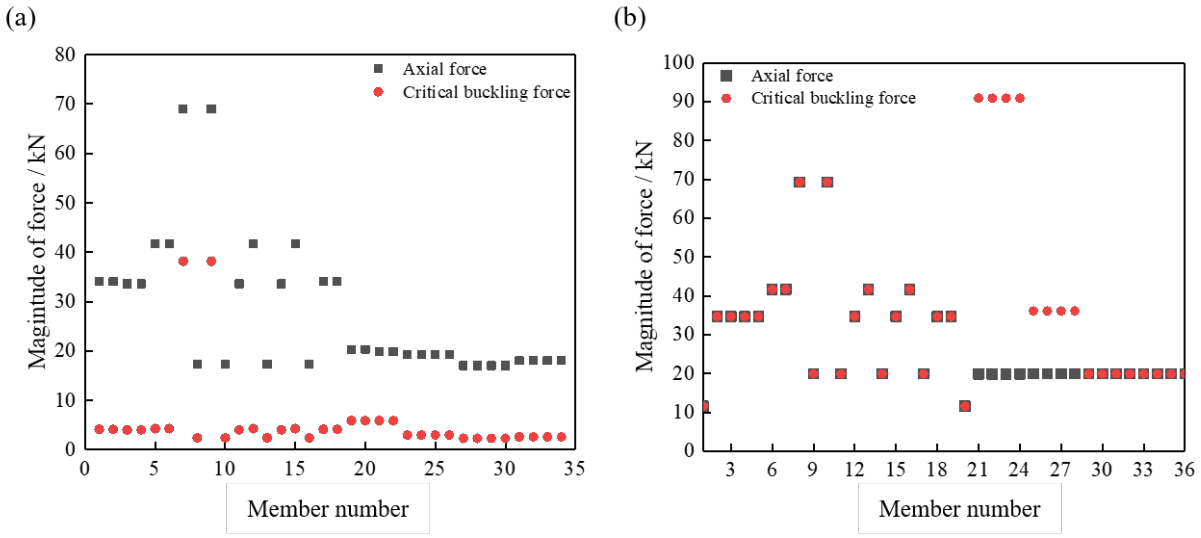


Figure 7. Comparison of axial force and critical buckling force of the crane. (a) optimized structure with nodal stability, (b) optimized structure with nodal stability and local buckling of members.

4. Conclusions

The nominal perturbing force (NPF) approach has been proposed to address the nodal instability in the truss topology optimization problem. In the NPF approach, nominal perturbing forces consistent with the directions of the Cartesian axes are used to model the possible perturbations of the unstable nodes. Compared with the conventional nominal lateral force (NLF) approach, (a) the NPF approach has higher computational efficiency because it contains fewer optimization variables; (b) the effect of tension members connected to the nodes is considered in determining the unstable nodes, which can lead to a better optimization result. In addition, the nominal allowable stress iteration (ASI) approach is proposed to address the local buckling instability in the truss topology optimization problem. In this way, the concave local buckling instability problem is linearized in each iteration and can be solved efficiently by a linear programming solver. Numerical examples have shown the practical applicability of the proposed method for the preliminary design of truss structures.

References

[1] X Guo, G. D. Cheng and K. Yamazaki, "A new approach for the solution of singular optima in truss topology optimization with stress and local buckling constraints," *Structural and Multidisciplinary Optimization*, vol. 22, pp. 364-372, 2001.

[2] BS 5950: Part 1. Structural use of steelwork in building. Code of practice for design.

[3] Eurocode 3: Part 1. Design of steel structures, general rules and rules for buildings.

[4] Q Cai, R. Q. Feng and Z.J. Zhang, "Topology optimization of truss structure considering nodal stability and local buckling stability," *Structures*, vol. 40, pp. 64-73, 2022.

[5] Q Cai, R. Q. Feng and Z.J. Zhang, "Topology optimization of trusses incorporating practical local buckling stability considerations," *Structures*, vol. 41, pp. 1710-1718, 2022.

IASS 2023
July 10–14 Melbourne
Integration of Design and Fabrication

Proceedings of the IASS Annual Symposium 2023
Integration of Design and Fabrication
10–14 July 2023, Melbourne, Australia
Y.M. Xie, J. Burry, T.U. Lee and J. Ma (eds.)

Truss topology optimisation considering constructability constraints

Ajmal Babu MAHASRANKINTAKAM*, Allan L. MARBANIANG[a], Sounak KABASI[a], Siddhartha GHOSH[b], Subhrajit DUTTA[c]

[a,*] Department of Civil Engineering, Indian Institute of Technology Bombay, Mumbai 400076, India
ajmalbabums@gmail.com

[b] Structural Safety, Risk & Reliability (SSRR) Lab, Department of Civil Engineering, Indian Institute of Technology Bombay, Mumbai 400076, India
[c]Department of Civil Engineering, National Institute of Technology Silchar, Silchar 788010, India

Abstract

Trusses are efficient structures that have been widely employed for stadiums, large-span bridges, and roofs among other numerous structural applications. In addition to being reasonably simple to build and maintain, trusses can also be aesthetically beautiful. Discrete topology optimisation focuses on finding the optimal truss configuration and cross-sectional dimension for the truss members within a particular domain, for given boundary and loading conditions. In most cases, the optimal structures (e.g. Michell trusses) may not be easily constructible or conceptually feasible. In actual practice, other design constraints and restrictions that are specified by regulatory (structural design and construction) standards also come into play. In this study, the discrete topology optimization is applied on different types of truss structures using a heuristic optimiser. Structural and architectural constraints are formulated based on structural design codes and constructability considerations for each structure type. A parametric study is then conducted to understand and compare the effects and importance of different constraints on the final optimal solutions, with respect to their feasibility and constructability.

Keywords: discrete topology optimisation, ground structure, buildability, design standards, optimization for design and fabrication, layout optimization

1. Introduction

The known history of structural optimization can be traced back to Galileo, who in 1638 determined the optimal parabolic shape of a cantilever beam with a point load at its free end [1]. Structural optimization of truss like structures began with the pioneering work by Michell [2]. Different structural optimisation problems have been solved including both continuous and discrete approaches. Discrete topology optimization problems are mostly used for topology optimization of frame like structures such as trusses. Frame like structures (including trusses) achieve the most optimal or economic design when every member in the structure is completely utilised with respect to its available strength. Truss optimisation methods can be categorised into size, shape and topology methods. The most common approach for topology optimization is to use a domain discretization such as the ground structure method which employs removal of elements from the ground structure [3]. Alternatives approaches include adaptive member adding methods [4] and growth methods [5].

The topology optimization problems are generally non-convex where gradient evaluations are impractical to solve by traditional optimization methods. In the last few decades many non-gradient optimization methods have been developed. Heuristic optimization methods are class of non-gradient

Copyright © 2023 by Ajmal Babu MAHASRANKINTAKAM, Allan L. MARBANIANG, Sounak KABASI, Siddhartha GHOSH and Subhrajit DUTTA. Published in the Proceedings of the IASS Annual Symposium 2023 with permission.

methods in which only function evaluations are employed. They are often inspired from natural phenomenon or behaviour of animals, birds or insects. Some of the popular heuristic methods are particle swarm optimization (PSO), genetic algorithm (GA), simulated annealing (SA), differential evolution (DE). The grey wolf optimiser (GWO) has been shown to be relatively performant and more robust with respect to the other heuristics [6]. The advantage of these methods is that the gradient of the objective function and constraints need not be found, while also ensuring a global solution. More insight about the heuristic methods can be found from the review article [7].

Most of the topology optimisation methods, however, focus heavily on minimising the total weight or the compliance of the system. Displacement, stress and buckling constraints are usually included as constraints [7], but the constraint limits are usually constant and simplified. However, most code limits are highly nonlinear. Structural design standard checks also include other factors such as member imperfection, slenderness, etc. Directly minimising the weight or maximising the stiffness may also lead to optimal solutions that are impractical or difficult to construct. There can be interest regions which are may be taken as infeasible or regions of interest. There are a few limited studies focusing on the constructability aspect of a topology optimisation process [8].

In this study, the ground-structure optimisation process is used for the discrete topology optimisation problem. The study also includes more realistic constraints based on the Indian standard on structural steel buildings (IS 800:2007) [9] for steel structures. The Grey Wolf (GWO) optimiser is employed to solve the minimal weight problem with the nonlinear code constraints and discrete cross-section variables. GWO has been shown to be relatively performant with respect to other common heuristic solvers [6]. A new constraint is proposed to include the regions of interest where structural members are required to present. This allows for the inclusion of constructability constraints that may be an important criterion by the designer. An optimisation formulation for topology optimisation is developed based on the proposed constraints.

The paper is organised as follows. Sec. 2 gives the formulation of the topology optimisation used in this study. The Grey Wolf optimiser is detailed in Sec. 3. This is followed by a numerical case study in Sec. 4. In Sec. 5, the final and concluding remarks are presented.

2. Topology optimisation

2.1. Standard constrained formulation

The most common objective function in truss optimization is the total cost of the structure. This may be expressed as the total weight or volume of members as scaling of the objective does not affect the optimizer. The standard constrained formulation can be formulated as [7]

$$\begin{aligned} &\text{Minimise: } W(\mathbf{A}) = \sum_{i=1}^{m} \rho A_i l_i \\ &\text{subject to: } -\min(\sigma_i^{cr}, \sigma_y) \le \sigma_i \le \sigma_y \\ &\qquad\qquad d_{\max} \le d_{\text{limit}} \end{aligned} \tag{1}$$

where the member cross-sectional areas comprises the design variable $\mathbf{A}=[A_1, A_2, \ldots, A_m]$ and bounded as $\epsilon \le A_i \le A_{\max}$, ρ is the density of steel, σ_i is the member stress for the i^{th} element, $d_{\max}$ is the maximum absolute nodal displacement due to the external loading, the strength in compression is the minimum of the Euler buckling stress (σ_i^{cr}) and yield strength (σ_y). The buckling stress for the i^{th} element is found using the known equation $\sigma_i^{cr} = \frac{\pi^e E I_i}{A_i l_i^2}$. Furthermore, the tensile strenght is taken as the yield strength σ_y with the displacement limit denoted by d_{limit}. The value of ϵ is taken to be a very small number so as to ensure the stiffness matrix is non-singular.

2.2. Implemented constraints

In this study, the optimization problem aims to minimize the total weight by selecting optimal discrete design variables from a database subset of cross-sections provided in IS 1161:1998 [10]. Apart from the constraints corresponds to strength and serviceability limit states of IS 800:2007, constraints based on regions of interest are also defined.

2.2.1 Design standard constraints

The IS 800:2007 is used to derive the design strengths used for the strength limits. The design tensile strength is similar to the constraint given in Equation (1) with the only difference being a reduction in the yield strength due to a partial safety factor. The tensile strength σ_t of a member is given as

$$\sigma_t = \frac{\sigma_y}{\gamma_{m0}} \tag{2}$$

where γ_{m0} is the material partial factor and is given as 1.1.

In the calculation of the compressive strength, the design strength formulation is more complex with the inclusion of the geometric imperfection parameter and the yield strength in the slenderness parameter. The design compressive strength σ^i_c of an i^{th} member is given as

$$\sigma_c = \min\left(\frac{\sigma_y / \gamma_{m0}}{\phi + [\phi^2 - \lambda^2]^{0.5}}, \sigma_y / \gamma_{m0} \right) \tag{3}$$

$$\phi = 0.5[1 + \alpha(\lambda - 0.2) + \lambda^2]; \qquad \lambda = \sqrt{\sigma_y / \sigma_i^{cr}} \tag{4}$$

where α is the imperfection factor dependent on the cross-sectional type and manufacturing process.

The displacement constraint is taken as the serviceability constraint given as

$$d_s = \frac{L}{100} \tag{5}$$

where L is the total span.

2.2.1 Interest regions

In most ground structure implementations, cross section area of all the members in the ground structure are taken as design variables for minimising the objective function. However, there can be constructability considerations such as infeasible regions where structural members are refrained to be present or regions of interest where non-loading building components such as service ducts in roof trusses may require members for connection or support. A simplified region can be defined by a rectangular region given as $I = [x_1, x_2] \times [y_1, y_2]$, where certain members in the ground-structure pass through. In the case the region represents an infeasible region, the ground structure can be generated so that no structural members are present within I [4].

This study introduces a new concept of including a region of interest in the domain. This constraint penalises the solution when there are no or very few members that cross a region of interest. This can ensure that the optimal solution may come out to a local solution, which may be of interest to the designer. The steps for enforcing the interest region are

Step 1. Find ground structure members within the region I denoted as $\mathbf{A}_I$

Step 2. Find number of members (c) in $\mathbf{A}_I$ with the tolerance minimal area given as

$$c = |\{A \in \mathbf{A}_I : A \leq \upsilon\}| \tag{6}$$

where $|\ .\ |$ denotes the number of elements or cardinality of the set and υ is the minimal tolerance cross-section value.

Step 3. The constraint is given such that

$$c < c_N \tag{7}$$

where c_N is a parametric value that limits the number of elements that should not have an area less than the tolerance area υ within the region of interest I. c_N can be regarded as the number of elements that can vanish from the ground structure in the region I.

2.3. Proposed optimisation formulation

The formulated topology optimisation formulation in this study is therefore given as

$$\begin{aligned} &\text{Minimise: } W(\mathbf{A}) = \sum_{i=1}^{m} \rho A_i l_i \\ &\text{subject to: } -\sigma^i{}_c \leq \sigma_i \leq \sigma^i{}_t \\ &d_{\max} \leq d_s \\ &c < c_N \end{aligned} \tag{8}$$

where $\mathbf{A}$ is the set of available cross sections that can be used in the truss structure.

3. The Grey Wolf Optimiser (GWO)

The Grey Wolf Optimiser (GWO) is a type of swarm-based optimisation algorithm inspired by the hunting behaviour of grey wolves [6]. The algorithm consists of a population or pack of grey wolves, where each grey wolf represents a candidate solution. The heuristic models the social behaviour and leadership hierarchy of the pack where an alpha wolf leads the pack. The update process of the

population is dependent on a searching step, circling prey step, attacking prey step and updating the alpha wolf position step. The population of the optimisation algorithm is given as

$$\mathbf{P} = [\mathbf{X}_1, \mathbf{X}_2, \ldots, \mathbf{X}_n] \tag{9}$$

where $\mathbf{P}$ is the population is categorised into α, β, δ and ω individuals, $\mathbf{X}_i$ is the i^{th} wolf candidate solution with fitness W_i. The individual positions of these enlist wolfs is given as $\mathbf{X}_\alpha^t$, $\mathbf{X}_\beta^t$ and $\mathbf{X}_\delta^t$ respectively. The α wolf is having the best fitness, followed by β and δ wolfs. The rest of wolfs are identified as ω which follows their superior wolfs while hunting. The pseudo-code for GWO is shown in Algorithm 1 with the detailed implementation given in [6]. An objective function $W(\mathbf{X})$ with a constraint $g_i \leq 0$ is formulated using a penalty approach where any violation in the constraint leads to the objective function being penalised as

$$W(\mathbf{X}) + W_{penalty} \tag{10}$$

$$W_{penalty} = W \sum k \max(g_i, 0)$$

where k is a constant.

Algorithm 1. GWO pseudo-code [6]

Initialize *Grey wolf population* $\mathbf{X}_i$ *(i = 1, 2, ..., n)*
Initialize t =1, a, A, and C
Calculate the fitness of each search agent $\mathbf{X}_i$
$\mathbf{X}_\alpha^t$ *= best search agent*
$\mathbf{X}_\beta^t$ *= second best search agent*
$\mathbf{X}_\delta^t$ *= third best search agent*
while *(t < Max number of iterations)*
for *each search agent*
Update the position of the current search agent
end
Update a, A, and C
Calculate the fitness of all search agents $\mathbf{X}_i$
Update $\mathbf{X}_\alpha^t$, $\mathbf{X}_\beta^t$, *and* $\mathbf{X}_\delta^t$
t=t+1
end
return $\mathbf{X}_\alpha^t$

4. Numerical study

In this section, the topology optimisation problem defined in Equation (8) is demonstrated using two truss problems. The initial ground structure considered and final optimal solutions is shown. In all the case studies, the values of $\sigma_y = 250\,\text{MPa}$, $E = 200000\,\text{MPa}$ and $\rho = 7750\,\text{kg/m}^3$ corresponds to E250 grade steel. GWO (Sec. 3) is used to minimise the penalized weight of the ground structure. The

constraints are added to the total weight using a penalty approach as shown in Equation (10). The number of search agents is taken as 30 and 6000 iterations have carried out for each run. A series of 20 runs is preformed, with the best solution from the above runs shown in the results. The problems are implemented in *MATLAB* in a Linux system having 8GB RAM. The set for available cross sections, $\mathbf{A}$ is taken from a subset of discrete tubular sections listed in IS 1161:1998.

4.1. Example 1

The first truss problem consists of a 5486.4 mm wide domain having a height of 2743.2 mm. Two loads of 445 kN are applied at the two points as shown in Figure (1a). The used ground structure is shown in Figure (1a). The diagonal members in the ground structure cross each other without a node, where physically the members may cross besides each other but not connected at that point. The optimal solution by solving the standard problem in Equation (1) is shown in Figure (1b). The formulated optimisation problem in Equation (8) results in the optimal solution shown in Figure (1c). In this problem, the region of interest constraint is not considered. The total weight for the two structures is 555.11 kg and 614.50 kg for the first and second case respectively. It can be seen that the weight of the standard solution is lesser than the constructable solution using the IS code constraint. The solution in Figure (1c) has thicker section, specifically along the diagonal as the constraint due to the design compressive strength is more conservative. The more conservative and lesser design strength with respect to global buckling causes the section to be thicker than the simplified Euler bucking constraint. Using the formulation based on a constant constraint limit can be therefore problematic especially in the case of structures that are optimally designed.

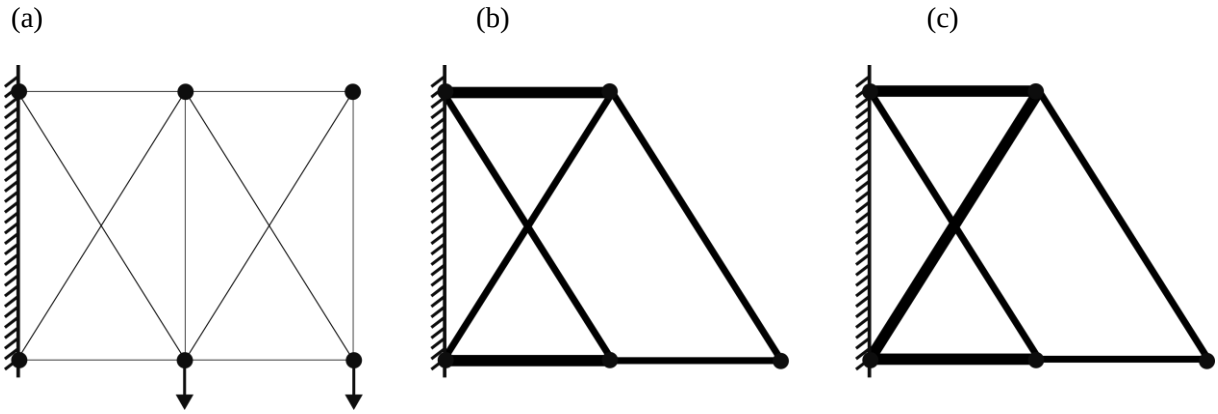


Figure 1. (a) Initial ground-structure with loading; (b) Optimal solution with standard constraints; (c) Optimal solution with codal constraints

4.2. Example 2

The second case study consists of 18.288 m $\times$ 18.288 m. A ground structure with a higher connectivity topology is taken as shown in Figure (2b). A single load of 445 kN is applied at the mid-point of right edge of the domain. The region of interest I is shown in Figure (2b) by the shaded region. The region of interest is constructed on the basis that some service lines pass through that region which needs to be supported by the members. The minimal area is taken as υ. Therefore, the constraint imposes that there should be at-least $c_N = 4$ members in the region I. The optimal solution while solving Equation (1) without the interest region constraint is shown in Figure (2c). The optimal solution for the constrained solution ($c \leq c_N$) is shown in Figure (2d). It should be noted that both cases consider the code design constraints. The total weight in the first case is 1855.7 kg and in the second case is 2051.3 kg. It is

observed that the truss in the second case has members present in the grey interest region. The weight of the structure is also not significantly different from the unconstrained case. Therefore, the proposed approach can help in finding local solutions that satisfy the defined constructability constraints.

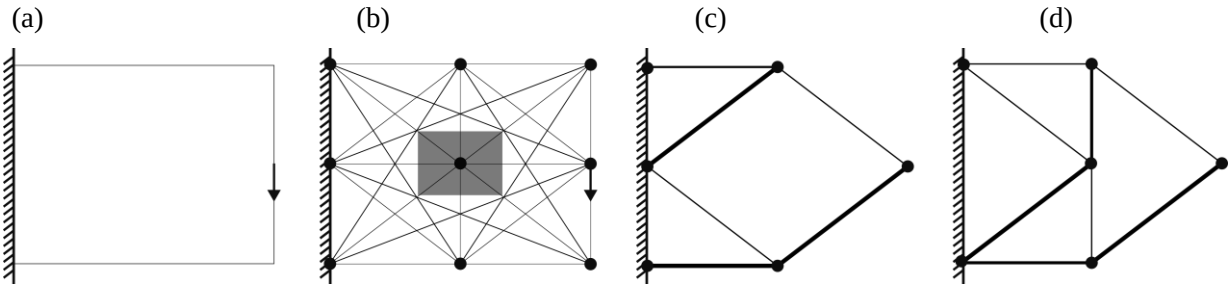


Figure 2. (a) Initial domain; (b) Ground-structure with region of interest I (shaded area); (c) Optimal solution without interest region constraint; (d) Optimal solution with interest region constraint

5. Conclusion

Topology optimization can be an elegant tool in finding the most optimal form of structures particularly for discrete truss systems. This study introduces a topology optimisation formulation based on Indian standard design limits and additional constructability constraints. The concept of interest regions is introduced to shift the optimal solution to slightly local solutions having members located at the specified regions of interest. This is advantageous as different local solutions can be attained by the designer on the basis of construction and service requirements. The optimal solution is found using a GWO heuristic solver which is overall found to be relatively robust. Overall, the proposed study is shown to highlight the importance of using actual design constraints. The use of the interest regions is also shown to be helpful in providing an alternative constraint defined by the designer in the topology solution.

References

[1] J. Heyman, *Structural Analysis: A Historical Approach*. Cambridge, United Kingdom: Cambridge University Press, 1998.

[2] A. Michell, "LVIII. The limits of economy of material in frame-structures", *The London, Edinburgh, and Dublin Philosophical Magazine and Journal of Science*, vol. 8(47), pp. 589–597, 1904.

[3] W. S. Dorn, R. E. Gomory and H. J. Greenberg, "Automatic design of optimal structures", *Journal de M´ecanique*, vol. 3(1), pp. 25–52, 1964.

[4] L. He, M. Gilbert, and X. Song, "A Python script for adaptive layout optimization of trusses," *Structural and Multidisciplinary Optimization*, vol. 60, pp. 835–847, 2019.

[5] P. Martínez, P. Martí, and O. M. Querin, "Growth method for size, topology, and geometry optimization of truss structures," *Structural and Multidisciplinary Optimization*, vol. 33, no. 1, pp. 13-26, 2006.

[6] S. Mirjalili, S. M. Mirjalili, and A. Lewis, "Grey Wolf Optimizer," *Advances in Engineering Software*, vol. 69, pp. 46-61, 2014.

[7] Stolpe, M. Truss optimization with discrete design variables: a critical review. Struct Multidisc Optim 53, 349–374 (2016). https://doi.org/10.1007/s00158-015-1333-x

[8] M. Zhu, Y. Yang, A. T. Gaynor, and J. K. Guest, "Considering Constructability in Structural Topology Optimization," in *Structures Congress 2014 - Proceedings of the 2014 Structures Congress*, pp. 2754-2764, 2014.

[9] Bureau of Indian Standards, *IS 800:2007 General construction in steel -- Code of practice*. New Delhi, India: Bureau of Indian Standards, 2007.

[10] Bureau of Indian Standards, *IS 1161:1998 Steel tubes for structural purposes*. New Delhi, India: Bureau of Indian Standards, 1998.

Traditional masonry structures and innovation

Active bending
Additive manufacturing/ 3D printing
Architectural geometry
Bamboo for sustainable construction and quality of life improvement
Bio-inspired structures and architecture
Bridge structures
Computational form-finding
Conceptual design
Concrete structures
Construction techniques
Deployable and inflatable structures
Design competition (WG21)
Digital modelling and fabrication
Dynamic response of metal spatial structures
Dynamic response of other structures
Form-finding and structural optimisation of interlocking discrete assemblages
Graphical methods
Gridshell and lattice structures
Historical concrete shells
Historical structures
Lattice structures
Life-cycle design and assessment of structures
Metal gridshell structures, connections and stability
Methods and construction technologies for sustainable shell structures
Morphology and configuration processing
Next generation parametric design
Novel methods in modelling, optimisation and construction for reducing carbon footprint of continuous roof shells
Numerical methods for geometry, form-finding and optimisation of lightweight structures
Optimisation methods and applications
Origami
Other
Teaching design uncertainty: working with unknown qualities/quantities of new and re-claimed materials
Teaching of shell and spatial structures
Tensegrity systems and cable structures
Tension and membrane structures
Tension structures in the Asia-Pacific
Timber and bio-based structures
Topology optimisation
► **Traditional masonry structures and innovation**
Transformable structures

IASS 2023
July 10–14 Melbourne
Integration of Design and Fabrication

Proceedings of the IASS Annual Symposium 2023
Integration of Design and Fabrication
10–14 July 2023, Melbourne, Australia
Y.M. Xie, J. Burry, T.U. Lee and J. Ma (eds.)

Tile patterning on free-form surfaces that reduces tile cutting

Chaoyu DU[a,*], Tom VAN MELE[a], Philippe BLOCK[a]

[a,*] Block Research Group, ETH Zurich
Stefano-Franscini-Platz 1, 8093 Zurich, Switzerland
chaoyu.du@arch.ethz.ch

Abstract

We propose a new strategy for generating staggered patterns for standard, rectangular tiles on free-form surface. The given input surface is firstly tessellated into near-square quadrilateral faces using a re-meshing algorithm. Afterwards, we run a matching algorithm that assigns each tile to two adjacent faces. We use binary integer programming to find a tessellation on the surface that minimises the number of unique tiles and tiles that are not staggered. Lastly, we generate the tiles and post-process the tessellation result.

Keywords: tile vaulting, tile pattern, free-form surface, quadrangulation, binary integer programming

1. Introduction

Shells and vaults are efficient structures whose form follows the flow of forces. They emerge again in contemporary architecture because of the emergence of computational form-finding techniques to design them as well as for their sustainability. Specifically, for longer spans, shell structures require less material quantities and for funicular vaults lower-strength materials, which typically have reduced embodied carbon coefficients [1–3].

Among the methods of constructing shells and vaults, thin-tile vaulting is a 600-year-old Mediterranean technique that requires minimum formwork during its construction and relies on traditional manufacturing of the tiles. The flexibility offered by non-uniformly spacing of the tiles, by using small offset deviations in the mortar joints, a wide range of shell geometries can be achieved with standard tile shapes. However, tile vaulting dropped in popularity due to (among many factors) the high cost of skilled labour, emerging competitive materials, namely steel and concrete, modern building codes and the onset of modernism that favoured straight lines [4–6] . The construction of tile vaults involves skilled masons adjusting the direction of the tile, handling the mortar thickness, and cutting the tiles on site dextrously to follow the curvature and gradually fill the surface. This process can become especially challenging when the surface is geometrically intricate [7], [8].

Recent research suggests that this complexity can be partially overcome with the help of robotic fabrication and augmented reality, as the tiles can be precisely registered in 3D. The craft-specific tasks can be executed in a fully automated manner or by collaboration between humans and machines [9–11]. However, the main challenge remains in the generation of tiling patterns, i.e., where, and how to place the single-sized tiles on a free-form surface.

This paper focuses on how to compute a tiling pattern on a free-form surface and tries to find a global solution to the tiling pattern that can achieve both aesthetic requirements and reduce fabrication complexity, which means a minimal amount of customised cutting on-site. Specifically, this paper focuses on the shells and vaults with small to medium span and surface curvature large compared with the tile size.

Copyright © 2023 by Chaoyu DU, Tom VAN MELE and Philippe BLOCK. Published in the Proceedings of the IASS Annual Symposium 2023 with permission.

2. Related work

2.1. Surface geometry and tile pattern

The process of traditional tile laying involves a series of technical decisions that impact various aspects of a structure, such as its strength, stability, aesthetics, constructability, and cost-effectiveness [1], [6], [8]. This section will discuss two examples of tile-laying patterns, examining the challenges and opportunities they present in terms of research and construction.

Guastavino vaulting is not only structural but also decorative [6]. The sophisticated decorative tile patterns exposed in their buildings (Figure 1. left) are accomplished by highly skilled masons by applying a final decorative layer from below. This step allowed the creation of more complex tile patterns without consideration of the construction sequence. However, in some cases, it's simply impossible to use a single pattern to fill a surface, for example, using a herringbone pattern to construct a dome without compensating for the smoothness and customised cutting (Figure 1. middle). In such situations, Guastavino uses multiple pattern patches instead of using a single pattern, which not only makes the vault decorative but also resolves the tiling problem for the three-dimensional forms.

The method of separating the shell in a full or partial manner also exists in other designs, to accommodate the surface aesthetics and tessellation pattern. For example, the glass vault is a doubly-curved barrel vault built by two robotic arms without a centring [10]. It adopts a herringbone pattern to interlock the bricks and defines a clear construction sequence for the robots to build alongside the first arch, and from bottom to top. To accommodate the amplified gap sizes due to curvature changes at the scale of the final structure, the tessellation pattern is shifted by half a brick along the reset lines (Figure 1. right), along which the herringbone pattern stops. Moreover, the vault uses irregular tiles at the boundary to ensure compete pattern on the shell surface.



Figure 1. left: some examples of Guastavino tiling patterns[6]; middle: the dome at the Chapel of Our Lady (photo credits: Michael Freeman); right: tiling pattern and reset lines of the glass vault [10].

2.2. Computational tile and brick laying

A few researchers have tackled the problem of tile laying to find a suitable mediation between aesthetics and structural behaviour. Shaghayegh [12] developed a design tool that can semi-automatically tessellate bricks on a curved surface by sequentially projecting the tiles. The workflow requires the designer to first choose a pattern in 2D and the start point of the first tile. Afterwards, the algorithm can compute the location of the adjacent tile by referring to the previous ones. However, the transformation and projection of the next tile is based on the local positions of the previous tiles, and thus globally, cutting the tiles is inevitable.

Adiels et al. [13] compute the geodesic distance on the curved surface to guide their tessellation process. This approach yields several benefits, such as effectively aligning patterns with boundaries and enabling the creation of running bond designs. However, this method faces challenges to accommodate other tiling patterns and singularities, where tiles need to be arranged circularly.

Unlike these methods based on geometry, Panozzo et al. [14] formulate the patterning as a 2-colouring graph problem on a quad mesh, i.e. the staggered pattern is created by removing every second edge of a regular grid. Although this research does not focus on tessellation with rectangular tiles, the approach of combining geometric and topological methods serves as an inspiration for our research.

2.3. Surface paneling and rationalisation

Surface panelling, a related topic to tile laying, involves filling a curved surface with geometric or manufacturing constraints. The problem is typically tackled through a two-step process: first, segmenting the shape into smaller pieces, and then, approximating each segment with a panel within a given tolerance [15], [16].

According to Pottmann et al. [17], good segmentation is crucial to achieving an accurate approximation. This can be accomplished through techniques such as polygonal mesh layout, re-meshing, and patch decomposition. Though segmentation is usually a decision driven by the designers, a good segmentation can lead to a good approximation.

One typical approximation task is driven by the need to fabricate the panels with a limited number of moulds to reduce the overall cost. Eigensatz et al. [16] assign the panel type, such as planar, cylindrical or custom, to each segment and interleave discrete and continuous optimisation steps to improve the quality of the panelling and to reduce the number of moulds while still keeping the kink angles and gaps within tolerance.

Approximation can also be driven by a desired panel shape. Shape-up [18] is an optimisation framework for geometry processing that enforces shape constraints in a local-global iterative algorithm. In the local step, the distance between each vertex in the mesh and its projections under multiple constraints is encoded. The global step then minimally relocates the vertices on the mesh to match the projected fragments and solves a single energy function to minimise deviation from the local shape approximation, input surface, and surface smoothness.

3. Proposed approach

In this paper, we propose a three-step method to generate tile-laying patterns on a free-form surface, as shown in Figure 2. This method finds a global solution to tessellate the surface and while keeping the need for unique cutting small.

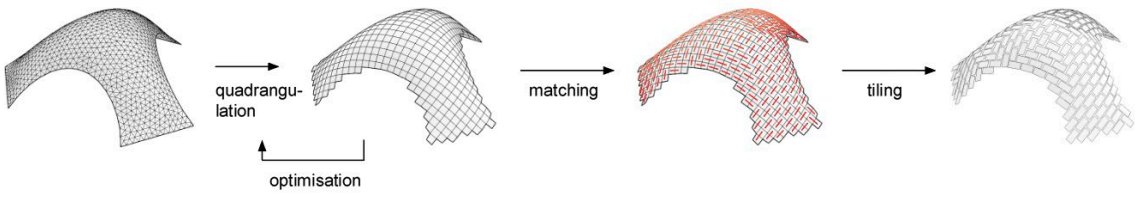


Figure 2. The proposed three-step tile patterning workflow.

The three steps are:

1. quadrangulation: generating a global quad mesh from the input surface;
2. matching: finding a (mostly) surface-covering combination of pairs of two neighbouring quadrilateral faces; and,

3. tiling: generating tile geometries.

3.1. Quadrangulation

We first convert the input surface into a quad mesh. Quadrangulation is an important topic in computer graphics and architectural geometry [19]. Similar to the panelling task described in Section 2.3, a good initial quadrangulation can reduce the efforts of post-processing and further optimising the mesh surfaces. We aim to partition our reference surface into a semi-regular quad mesh, whose quadrilateral faces are close to squares of equal size and where the number of singularities remains small.

We have considered two approaches. The first one is based on parametrisation, which means mapping the surface embedded in 3D to a domain in 2D and tessellating the 2D domain by regular grids. However, to reduce distortion, we need to find a correct set of seams either to cut the geometry and restitch it or the correct placement of singularities, which is challenging to compute and easily leads to areas with locally high distortion. These situations are not ideal for our tile arrangement in the next steps.

Thus, we instead adopt a field-guided approach, which uses an orientation field and prioritises higher distortion reduction. This approach is typically composed of three steps:

1. Generate an orientation field. This orientation field is driven by principal curvature and defined continuously over the surface. If the field is locally not smoothly aligned in a region, a singularity can occur, resulting in an irregular vertex in the quad mesh, which in our case, means an irregular tile.
2. Compute a position field, determining where the vertices are placed. Since square faces are preferred, the sizing function should be isotropic.
3. Synthesise the quad mesh.

We use the QuadriFlow algorithm without boundary constraints for this re-meshing step [20]. It allows for the efficient production of scalable quad meshes with minimal distortion while maintaining a low number of singularities. We use the tile dimension to estimate the target mesh edge length. In general, the algorithm provides a reasonable approximation of the half-tile locations; however, some level of distortion is inevitable. Here we present two quadrangulation outcomes for a surface (as illustrated in Figure 3, left and middle), and evaluate their area and angle distortion with respect to the squares. For this surface, the presence of the singularity can cause the faces near it to become smaller and more distorted, resulting in overlapping tiles. If the singularity is removed, bigger gaps will appear in the middle of the shell. If neither of the two solutions is satisfactory, we can further enhance the mesh quality by imposing square shape constraints. For the latter, we use the shapeup optimisation solver implemented in libigl [21], and the outcome is displayed in Figure 3, right. It is important to note though that due to the shapeup optimisation the shape of the mesh deviates from the original input shape.

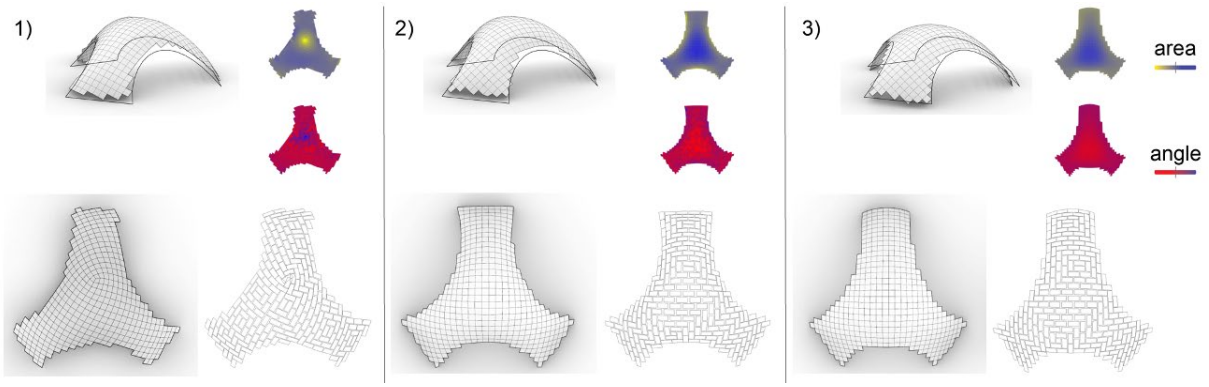


Figure 3. Left and middle: quadrangulation result with singularities without singularities; right: quadrangulation result after shapeup optimisation.

3.2. Maximal matching

Section 3.1 has discussed how to generate a high-quality quadrilateral mesh with faces close to squares of equal size. Based on this mesh, an arrangement of rectangles can be generated by connecting pairs of adjacent faces. One face can only be connected either 1 time or 0 times. If it is not connected, the face represents a half-tile, which needs additional cutting. Thus, maximising the pair of adjacent faces to generate as many tiles as possible can be formulated as a graph-matching problem.

Given the set of faces F and the possible edges E that connect adjacent faces, the goal is to find the maximal number of matched edges E', where E' is a subset of E, such that no two edges in E' share an adjacent face.

This problem can be formulated as a binary integer program:

Let edge connectivity $\mathrm{x_e} \in \{0,1\}$, $x_e = 1$ if $e \in E'$, else $x_e = 0$. For one face, let $E(f)$ denote all edges that connect a face f. Taking Figure 4. left as an example. For face f_4, the edges that connect to it are listed in $E(f_4) = \{e_{14}, e_{34}, e_{45}, e_{47}\}$. One face can be at most connected to one adjacent face. If f_4 and f_7 are connected, for example, $x_{47} = 1$ and $\mathrm{x_{14}} = \mathrm{x_{34}} = \mathrm{x_{45}} = 0$.

Our problem can be written as follows:

$$\begin{aligned} &\max \sum_{e \in \mathrm{E}} x_e \\ &s.t. \sum_{e \in \mathrm{E(f)}} x_e \leq 1, \forall f \in \mathrm{F} \end{aligned} \tag{1}$$

We use the Gurobi Optimizer [17] to solve the binary integer program (1). Figures. 3-2, middle and right, show the matching result for a 10x10 grid and an 11x11 grid. The total number of faces for an 11x11 grid is odd, resulting in one unmatched face. Note that many edges are parallel, which can cause continuous mortar joints in real tile-laying. We address this problem in the next section.

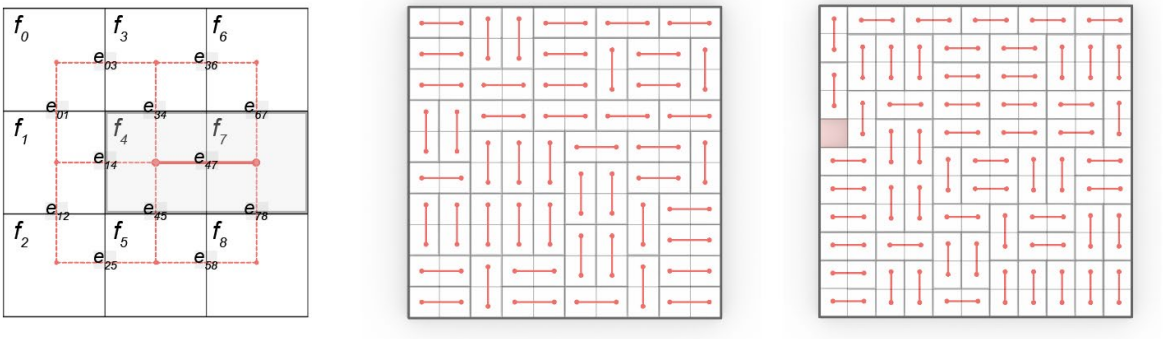


Figure 4. left: A mesh composed of nine faces and the connectivity between them. f_4 and f_7 are a connected face pair; middle and right: the matching result for a 10x10 grid and an 11x11 grid using binary integer program (1).

3.3. Staggered pattern

In tile vaulting, the tiles are often staggered to avoid continuous mortar. To avoid parallel edges, as is the case in Section 3.2, we can formulate them as penalties in the objective function.

We introduce a new set of variables $\mathrm{y_{e1,e2}}$ to describe neighbouring parallel edges. Let $\mathrm{y_{e1,e2}} \in \{0,1\}$, $\mathrm{y_{e1,e2}} = 1$ if and only if both $e_1, e_2 \in E'$, else $\mathrm{y_{e1,e2}} = 0$. Taking the example in Figure 4. left, edge e_{47} has only two neighbouring parallel edges e_{36}, and e_{58}. We know that f_4 and f_7 are connected, so

$x_{47} = 1$. Assume f_3 and f_6 are connected, $x_{36} = 1$. Now, we have a pair of parallel neighbouring edges, so $y_{e47,e36} = 1$. In our objective, we can penalise this situation.

The optimisation problem with penalties can be written as follows:

$$\begin{aligned} &\max \sum_{e\in E} x_e - w * \sum y_{e1,e2} \\ &s.t. \sum_{e\in E(f)} x_e \leq 1, \forall f \in F, \\ &x_{e1} + x_{e2} - y_{e1,e2} \leq 1, \forall y_{e1,e2} \end{aligned} \tag{2}$$

The weight w for the penalty term can be chosen to tell the optimiser how it should balance between avoiding unmatched faces and parallel edges if no solution is possible that avoids both.

The solutions found by Gurobi for the 10x10 and 11x11 grids are shown in Figure 5. The results show high similarities to state-of-the-art patterns observed in tile vaults built by expert masons. Our algorithm can also generate a staggered pattern for mesh with singularities (Figure.5 right).

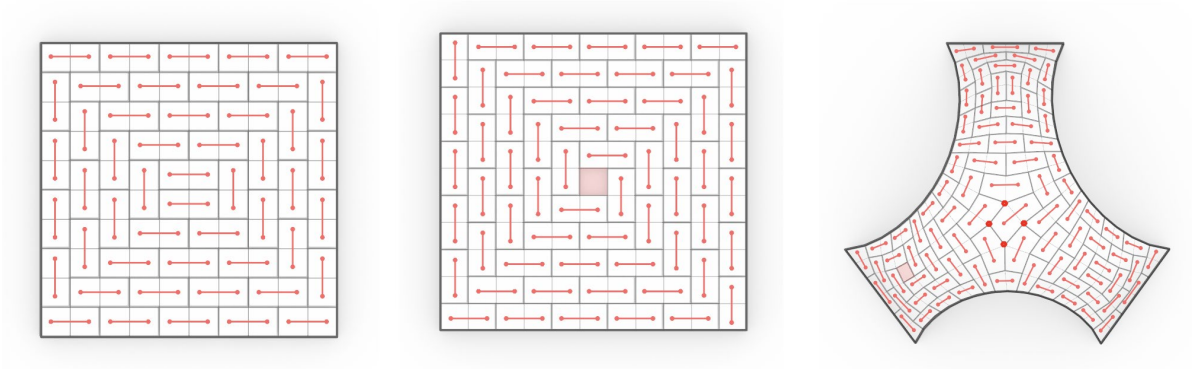


Figure 5. left and middle: staggered pattern for a 10x10 grid and an 11x11 grid, respectively; and right: staggered pattern for mesh with singularities, which are shown as red dots.

3.4. Other patterns

Other tile patterns, e.g., a running-bond or herringbone pattern, can be targeted by replacing the penalty term for parallel edges described in Section 3.3 with a different term that penalises or rewards certain combinations of edges.

For example, we can optimise for a running-bond pattern by using a term that rewards pairs of parallelly shifted edges, as shown in Figure 6. left (i.e. the edges are in neighbouring columns or rows of the grid but "shifted" by one row/column). This can be done by introducing a new set of binary variables $z_{e1,e2} \in \{0, 1\}$, which exists for every neighbouring shifted pair $e_1, e_2 \in E$. Again, as in Section 3.3, we add a set of constraints that enforces $z_{e1,e2} = 1$ if and only if both $e_1, e_2 \in E'$. These constraints look different because the $z_{e1,e2}$ contributes positively to the objective function while the $y_{e1,e2}$ in Section 3.2 contribute negatively. Our problem is written as follows:

$$\begin{aligned} &\max \sum_{e\in E} x_e + w_R * \sum z_{e1,e2} \\ &s.t. \sum_{e\in E(f)} x_e \leq 1, \forall f \in F, \\ &z_{e1,e2} \leq x_{e1}, z_{e1,e2} \leq x_{e2}, \forall z_{e1,e2} \end{aligned} \tag{3}$$

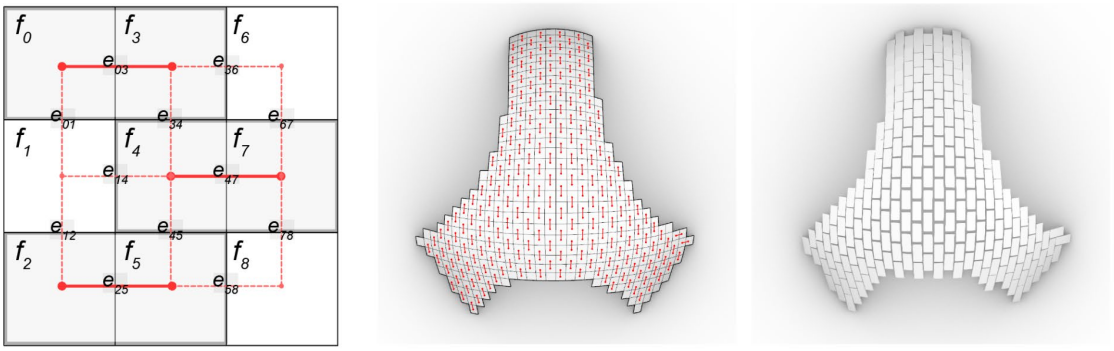


Figure 6. Running bond pattern and the connected face pairs; middle and right: running bond pattern outcome using quad mesh from Figure 3. right.

3.5. Generate tiles

After the matching process, the tile geometries can be generated using the facial information of the matched faces. We establish the origin of the tile by determining the midpoint of the line that connects the two centroid points of the face, and consider the direction of the line as the tile's length direction. Next, we compute the best-fit plane of all the vertices on the two faces, with the plane's normal being used as the thickness direction of the tile. By calculating the cross product of these two directions, we obtain the height direction, allowing us to construct the tile using these three directions. We implemented this step in Rhino 7 using the COMPAS framework [22]. The results are displayed in Figure 3. and Figure 6., right.

4. Results and discussion

4.1. Results

We apply the tile laying method explained in section 3 to the doubly curved free-form shells shown below. Our method produces satisfactory results for the shallow shell with small curvature (as depicted in Figure 7.), accurately computing the quadrilateral mesh and staggered pattern without any noticeable gaps or overlaps. However, for the shell shown in Figure 8., taking the geometry of [8], we observe larger gaps in regions with higher curvature, as explained in Section 3.1.

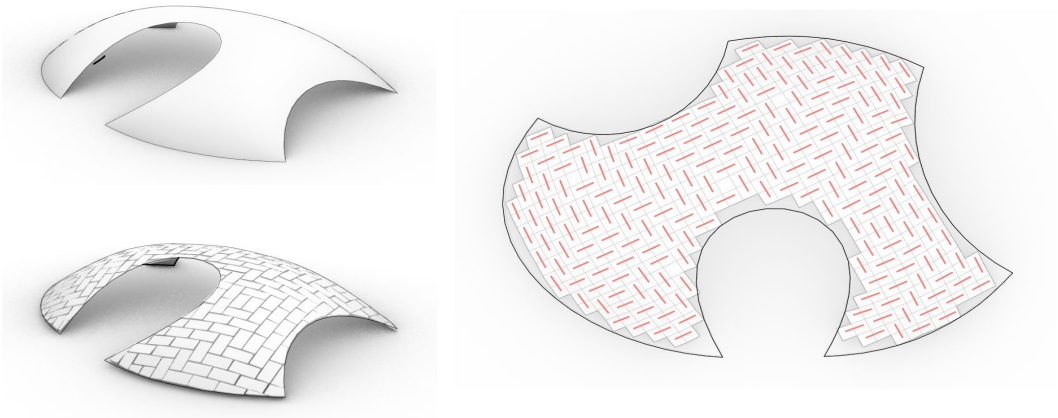


Figure 7. input mesh, tiled surface with irregular tiles at the boundary, and quadrangulation and matching outcome of a shallow shell.

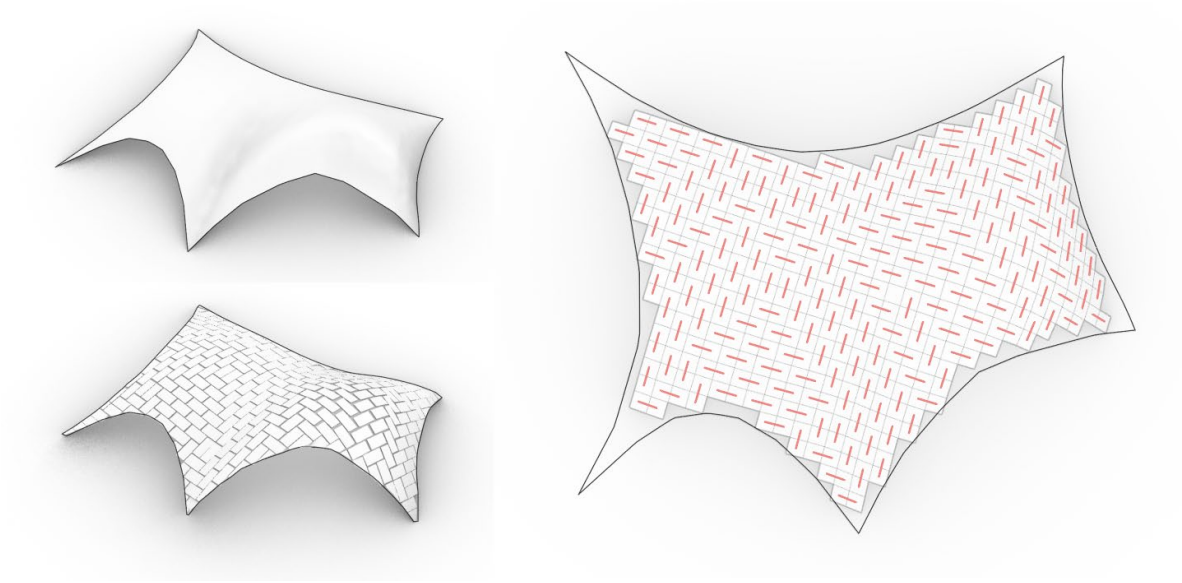
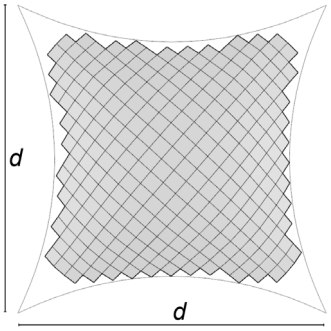


Figure 8. input mesh, tiled surface with irregular tiles at the boundary, and quadrangulation and matching outcome of a shell with higher curvature.

4.2. Performance

To evaluate the performance of our method in section 3, we conduct tile patterning on a shell with dimensions (d) as shown in Figure 9. left. The shell is supported at its four corners and tessellated with tiles measuring 280 × 140 × 15 mm. We ensure that all the quadrilateral faces have edge lengths greater than 140 mm. The dimension of the shell and the number of the faces are shown in Figure 9. right. The experiments are performed on a MacBook Pro (2020) with macOS 13.2.1, Apple M1 CPU and 8 physical cores. The computing time for section 3.1 is less than 1 second, and the computing time for section 3.2 using Gurobi Optimiser v10.0.0rc2 is listed in Figure 9. right. The time is the total (real) time reported by the time command. Our results indicate that the computing time grows exponentially with the input size. For a shell covering an area of approximately 50 m^2, the computing time is about 3 minutes.



Shell dimension	Number of faces	Time (section 3.2)
1.5 m	89	0.01 sec
2.5 m	185	0.20 sec
3.0 m	270	1.29 sec
4.5 m	531	8.85 sec
5.8 m	1192	30.58 sec
7.2 m	1679	183.19 sec

Figure 9. left: The input shell geometry; right: comparison of different shell dimensions, number of faces derived from section 3.1, and the corresponding computing time for section 3.2.

4.3. Contribution

Our approach tackles tile laying as a three-step global problem instead of a sequence of local problems. The presented approach allows us to adapt to different laying patterns by modifying the objective function in the matching step (as described in Section 3.4). Compared to other state-of-the-art methods, our approach can significantly reduce the need for customised cutting in the tiling pattern, particularly for smaller shell surfaces where the curvature is high in comparison to the tile dimension. For nearly developable surfaces, our approach can almost automate the tile-laying process, with little decision-making from the designers. For other free-form surfaces, our approach requires the designer to run an optimisation step after the variable quadrangulation to find a tileable mesh or separate the input surface into more developable patches.

4.4. Discussion

Our method relies purely on geometry and topology. We can compute different design solutions by changing the direction of the orientation field, such as changing it by 45 degrees or modifying the objective function in our matching step. However, our method cannot avoid distortion at the singularities, and in most cases, the resulting quadrangulation cannot align with the input surface boundary. The responsibility of balancing constructability and aesthetics still lies with the designer.

Additionally, solving the matching problem using a binary integer program solver can be prohibitively expensive for larger inputs (as discussed in Section 4.2). To deal with larger input sizes, one can split the input into smaller parts and solve the problem one part at a time.

Finally, our method does not consider structural behaviour. If we extend this method for tessellation patterns in masonry structures, there is potential for improvements by aligning the orientation field with the direction of force flow within the structure.

Acknowledgement

This research is supported by the A/T doctoral fellowship at ITA, ETH Zurich. Thanks to Ziqi Wang for the discussions and the suggestion for using Shape-Up for the shape optimisation step. Thanks to Stephan A. Kollmann for the discussion about the binary integer program, and correcting the notations in Section 3.

Code

Source code for reproducing the case studies is available from the corresponding author upon request.

Reference

[1] D. López, T. Mele, and P. Block, “Tile vaulting in the 21st century.,” *Inf. Constr.*, vol. 68, p. 162, Dec. 2016, doi: 10.3989/ic.15.169.m15.

[2] C. De Wolf, M. Ramage, and J. Ochsendorf, “Low Carbon Vaulted Masonry Structures,” *J. Int. Assoc. Shell Spat. Struct.*, vol. 57, no. 4, pp. 275–284, Dec. 2016, doi: 10.20898/j.iass.2016.190.854.

[3] D. López López, T. Van Mele, and P. Block, “The combination of tile vaults with reinforcement and concrete,” *Int. J. Archit. Herit.*, vol. 13, no. 6, pp. 782–798, Aug. 2019, doi: 10.1080/15583058.2018.1476606.

[4] M. W. A. Asali, “Craft-inclusive Construction,” p. 248.

[5] M. Ramage, “Guastavino’s Vault Construction Revisited,” *Constr. Hist.*, vol. 22, pp. 47–60, 2007.

[6] J. Ochsendorf and M. Freeman, “Guastavino Vaulting: The Art of Structural Tile,” Feb. 2010. Accessed: Mar. 31, 2023. [Online]. Available:

https://www.semanticscholar.org/paper/Guastavino-Vaulting%3A-The-Art-of-Structural-Tile-Ochsendorf-Freeman./8c3f0fa2a96ab059a0441190450dc45c74a54850

[7] S. Rajabzadeh, "On the Computational Design of Free-form Masonry Vault," 2015, doi: 10.6092/POLITO/PORTO/2616850.

[8] L. Davis, M. Rippmann, and T. Pawlofsky, "Innovative funicular tile vaulting: A prototype vault in Switzerland," 2012.

[9] T. Bonwetsch and F. Gramazio, "Digitally Fabricating Non-Standardised Brick Walls," 2007. Accessed: Mar. 31, 2023. [Online]. Available: https://www.semanticscholar.org/paper/Digitally-Fabricating-Non-Standardised-Brick-Walls-Bonwetsch-Gramazio/9e38ea121835b2eb5f8464cddf6f06bf215d4fd3#citing-papers

[10] S. Parascho, I. X. Han, S. Walker, A. Beghini, E. P. G. Bruun, and S. Adriaenssens, "Robotic vault: a cooperative robotic assembly method for brick vault construction," *Constr. Robot.*, vol. 4, no. 3–4, pp. 117–126, Dec. 2020, doi: 10.1007/s41693-020-00041-w.

[11] D. Mitterberger *et al.*, "Augmented bricklaying: Human–machine interaction for in situ assembly of complex brickwork using object-aware augmented reality," *Constr. Robot.*, vol. 4, no. 3–4, pp. 151–161, Dec. 2020, doi: 10.1007/s41693-020-00035-8.

[12] S. Rajabzadeh and M. Sassone, "Brick Patterning on Free-Form Surfaces," *Nexus Netw. J.*, vol. 19, no. 1, pp. 5–25, Apr. 2017, doi: 10.1007/s00004-016-0305-9.

[13] E. Adiels, M. Ander, and C. Williams, "Brick patterns on shells using geodesic coordinates," 2017.

[14] D. Panozzo, P. Block, and O. Sorkine-Hornung, "Designing unreinforced masonry models," *ACM Trans. Graph.*, vol. 32, no. 4, pp. 1–12, Jul. 2013, doi: 10.1145/2461912.2461958.

[15] M. Eigensatz *et al.*, "Case Studies in Cost-Optimized Paneling of Architectural Freeform Surfaces," in *Advances in Architectural Geometry 2010*, Vienna, 2010, pp. 49–72. doi: 10.1007/978-3-7091-0309-8_4.

[16] M. Eigensatz, M. Kilian, A. Schiftner, N. J. Mitra, H. Pottmann, and M. Pauly, "Paneling architectural freeform surfaces," *ACM Trans. Graph.*, vol. 29, no. 4, p. 45:1-45:10, 2010, doi: 10.1145/1778765.1778782.

[17] H. Pottmann, M. Eigensatz, A. Vaxman, and J. Wallner, "Architectural geometry," *Comput. Graph.*, vol. 47, pp. 145–164, Apr. 2015, doi: 10.1016/j.cag.2014.11.002.

[18] S. Bouaziz, M. Deuss, Y. Schwartzburg, T. Weise, and M. Pauly, "Shape-Up: Shaping Discrete Geometry with Projections," *Comput. Graph. Forum*, vol. 31, no. 5, pp. 1657–1667, Aug. 2012, doi: 10.1111/j.1467-8659.2012.03171.x.

[19] D. Bommes *et al.*, "Quad-Mesh Generation and Processing: A Survey," *Comput. Graph. Forum*, vol. 32, no. 6, pp. 51–76, 2013, doi: 10.1111/cgf.12014.

[20] J. Huang, Y. Zhou, M. Niessner, J. R. Shewchuk, and L. J. Guibas, "QuadriFlow: A Scalable and Robust Method for Quadrangulation," *Comput. Graph. Forum*, vol. 37, no. 5, pp. 147–160, Aug. 2018, doi: 10.1111/cgf.13498.

[21] A. Jacobson *et al.*, "libigl: A simple C++ geometry processing library," 2013, Accessed: Mar. 31, 2023. [Online]. Available: https://opus.lib.uts.edu.au/handle/10453/167463

[22] "COMPAS." https://compas.dev/index.html (accessed Nov. 30, 2022).

Transformable structures

Active bending
Additive manufacturing/ 3D printing
Architectural geometry
Bamboo for sustainable construction and quality of life improvement
Bio-inspired structures and architecture
Bridge structures
Computational form-finding
Conceptual design
Concrete structures
Construction techniques
Deployable and inflatable structures
Design competition (WG21)
Digital modelling and fabrication
Dynamic response of metal spatial structures
Dynamic response of other structures
Form-finding and structural optimisation of interlocking discrete assemblages
Graphical methods
Gridshell and lattice structures
Historical concrete shells
Historical structures
Lattice structures
Life-cycle design and assessment of structures
Metal gridshell structures, connections and stability
Methods and construction technologies for sustainable shell structures
Morphology and configuration processing
Next generation parametric design
Novel methods in modelling, optimisation and construction for reducing carbon footprint of continuous roof shells
Numerical methods for geometry, form-finding and optimisation of lightweight structures
Optimisation methods and applications
Origami
Other
Teaching design uncertainty: working with unknown qualities/quantities of new and re-claimed materials
Teaching of shell and spatial structures
Tensegrity systems and cable structures
Tension and membrane structures
Tension structures in the Asia-Pacific
Timber and bio-based structures
Topology optimisation
Traditional masonry structures and innovation
► **Transformable structures**

IASS 2023
July 10–14 Melbourne
Integration of Design and Fabrication

Proceedings of the IASS Annual Symposium 2023
Integration of Design and Fabrication
10–14 July 2023, Melbourne, Australia
Y.M. Xie, J. Burry, T.U. Lee and J. Ma (eds.)

Design and development of a hybrid deployable spherical shield based on foldable plate structures and scissor systems

Kevin MORENO GATA[a,*], Alex SEITER[a], Juan MUSTO[a], Martin TRAUTZ[a]

[a,*] Chair of Structures and Structural Design – RWTH Aachen University
Schinkelstr. 1, 52062 Aachen
morenogata@trako.arch.rwth-aachen.de

Abstract

The manufacturing industry is undergoing rapid changes, requiring flexible and adaptable production environments. Mobile transformable structures, based on rigid folding origami, offer a solution for creating self-supporting rigid enclosures that can be easily transported and opened. Longitudinal folding systems allow for compactness by reducing the thickness of the axes, and origami-based patterns can be modified to adapt enclosures made of lightweight composite materials. Spherical scissor systems offer constant trajectories for actuating the transformable system. This study presents the design and implementation of a hybrid folding and scissors system enclosure for manufacturing tasks. The enclosure can be manually opened and closed and compacts to less than one-third of its original size. The lightweight and rigid folding shield is composed of composite panels with elastic hinges. A scaled prototype was developed and tested, demonstrating the potential of the system for use in manufacturing tasks. This study highlights the potential of the system for providing protection in manufacturing environments and suggests that it could be further optimized for a range of applications.

Keywords: deployable structures, folded plate structures, origami, scissor systems

1. Introduction

Mobile transformable structures can adapt to different environments, allowing easy transport or opening. With rigid folding origami, these structures generate self-supporting rigid enclosures [1] suitable for dividing spaces or as movable walls or roofs. Longitudinal folding systems tolerate great compactness due to the ability to slide hinges and reduce the thickness of the axes [2]. These origami-based patterns are modified to adapt enclosures that may be composed of lightweight composite materials [3]. A study of the movement of its deployment allows us to design specific trajectories for actuating the transformable system. Spherical scissor systems can adapt to constant trajectories with spherical mechanisms [4]. Implementing several transformable hybrid systems enables its deployment and limits the number of degrees of freedom.

1.1. Protection enclosures

Integrating digital manufacturing techniques in construction has revolutionized the creation of personalized designs that cater to specific procedures, such as cutting, milling, assembling, and welding. These procedures are often carried out by industrial robots, which exhibit exceptional scalability and versatility but require specific installation specifications. However, the current approach to creating manufacturing spaces typically involves static elements like sturdy walls or enclosures that are challenging to modify to meet new requirements, especially when frequent assembly and disassembly are necessary. With the rapid development of the manufacturing industry, there is a growing demand for flexible production environments.

Copyright © 2023 by Kevin MORENO GATA, Alex SEITER, Juan MUSTO and Martin TRAUTZ. Published in the Proceedings of the IASS Annual Symposium 2023 with permission.

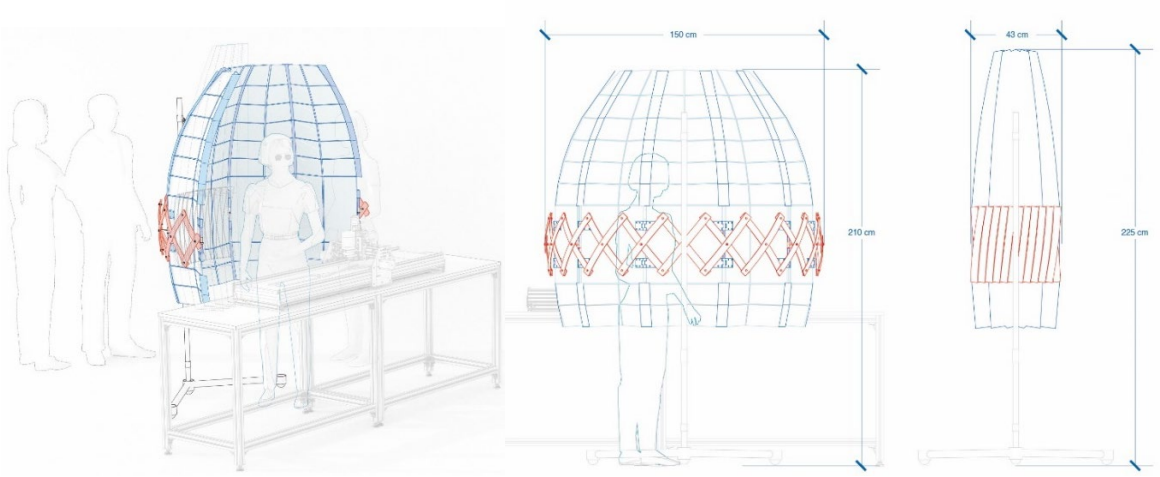


Figure 1. Concept of a foldable spherical shield for manufacturing.

To meet the demands of the industry, protection elements such as transportable shields are necessary to provide a safe working environment, either for machines or workers during manual labour. The shields aim to contribute for a safe environment protecting from hazards that may arise during manufacturing: flying sawdust chips, grinding sparks, intense welding lights or others.

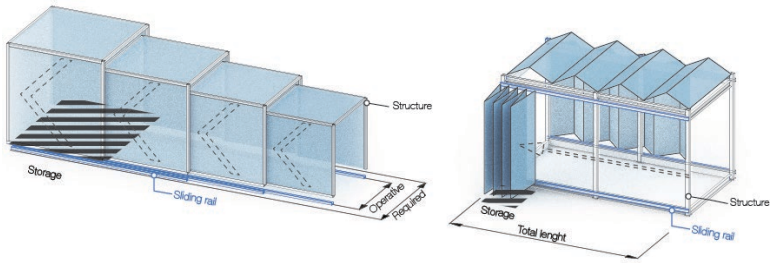


Figure 2. Standard sliding and folding transformable enclosures in manufacturing and industrial production cells.

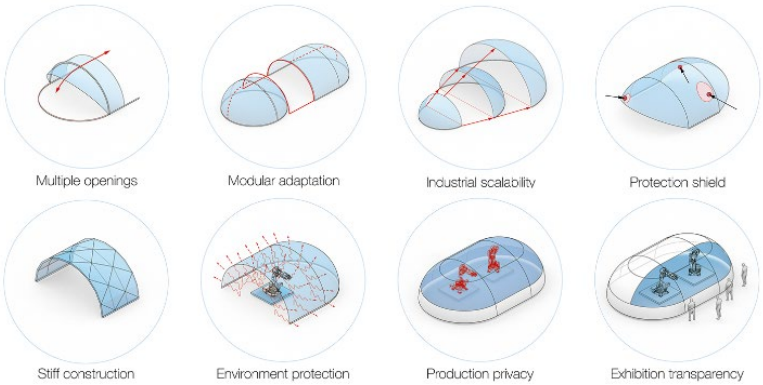


Figure 3. Characteristics of deployable enclosures and protective shields for manufacturing environments

To keep pace with the evolving manufacturing industry, the design of mobile enclosures and protection shields has become increasingly critical (Figure 2). The flexibility of production processes requires the use of highly adaptable and transportable elements. These enclosures allow manufacturing processes to be carried out in different locations, reducing the need for extensive capital investments in permanent

facilities. Mobile and deployable enclosures and shields can be easily reconfigured to suit different production needs and are ideal for responding quickly to changing market demands.

1.2. Technical origami and folded plate structures

The combination of origami patterns and quasi-rigid plates with finite thickness can be called technical origami or technical folding [5]. The efficient load transfer of such structures is known to this effect. If a locking of defined states is ensured for convertible folding structures, the load-bearing behavior is identical to rigid folding structures. For locking, frames and/or guides are necessary which also have to fulfill complex movement tasks due to the connection with the folding surfaces. In the case of non-parallel folding lines, the folding mechanisms for finite-thickness panels must be assigned to spherical or even spatial gears.

The folding mechanisms can be designed in such a way that they can be easily assembled and disassembled. Due to these properties, there is a high potential for their use in the manufacturing industry.

Example [6], [7] shows how the presented process can be applied in production environments. By incorporating a spherical geometry, a folding pattern can be brought closer to the workspace in question (Figure 2). Folding units with convertible frames offer advantages over conventional motion devices with rigid frames. However, the complex kinematic and dynamic dependencies involved complicate the design and planning process. Motion task-oriented design processes [8] incorporate the kinematic and kinetostatic metrics. The integration of a folding mechanism toolbox for multibody simulations ensures that the folding mechanism is designed to effectively perform the necessary motion tasks.

2. Deployable foldable design

In the following, the design and its geometrical optimization of a spherical folding unit including the frame for a protective shield that can be used flexibly in production is explained.

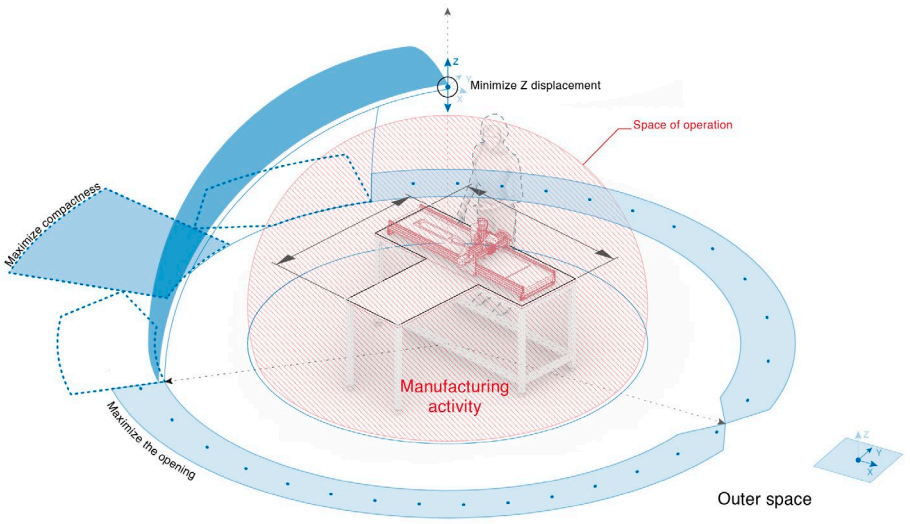


Figure 4. Design constraints: definition of the space for manufacturing tasks (red), the definition of the opening ways on the floor (blue), the definition of the storage area to maximize the compactness (left).

2.1. Geometry definition

The geometry design starts by defining design constraints (see Figure 4). In this phase, we define which zones must be protected in order to design the shield. The spherical shield is the closest to all trajectories of harmful substances, such as flying chips or sparks, emitted from one or more specific zones.

The folding is defined through the given surface. This surface is discretized, and different origami patterns were applied (see Figure 5). The procedure is as follows.

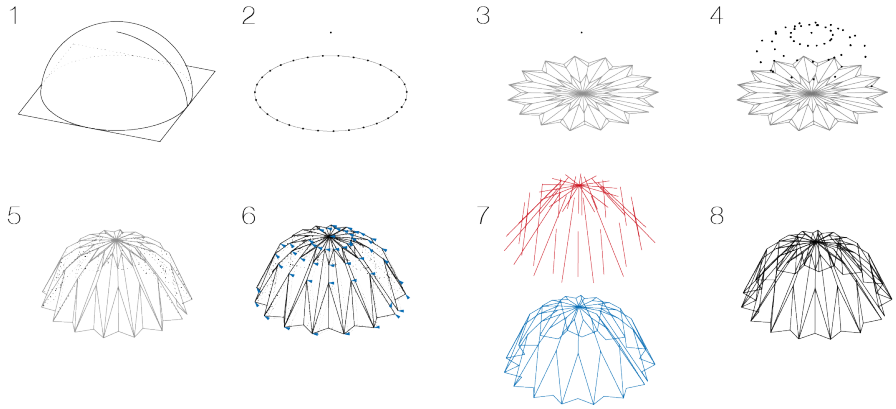


Figure 5. Folding pattern definition for a given surface.

First, the spherical base surface (1) is generated, then the folding path is subdivided in the XY plane (2), pattern definition (3), projection on the base surface (4), folding definition (5), geometry relaxation (6), the definition of the folding lines (7) and simulation of the folding (8). The development of the design was carried out using Rhinoceros ® [9], with the support of relaxation and planarization optimizations with Kangaroo [10] and constraints and rigidity definitions using Crane [11]. FE Analysis was carried out with Ansys [12]. After the automation and generation of the final model, a kinematic check using the MATLAB suite [13] was performed to validate the motion of the model.

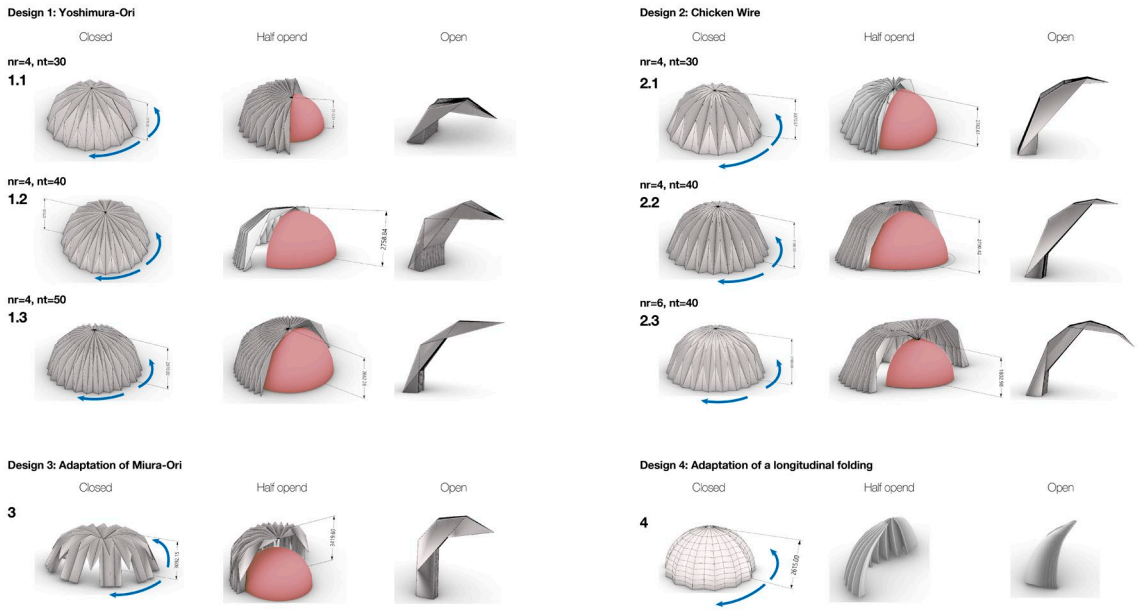


Figure 6. Geometry generation: 3 iterations of Design 1 and 2, and 1 iteration of Design 3 and 4 were generated.

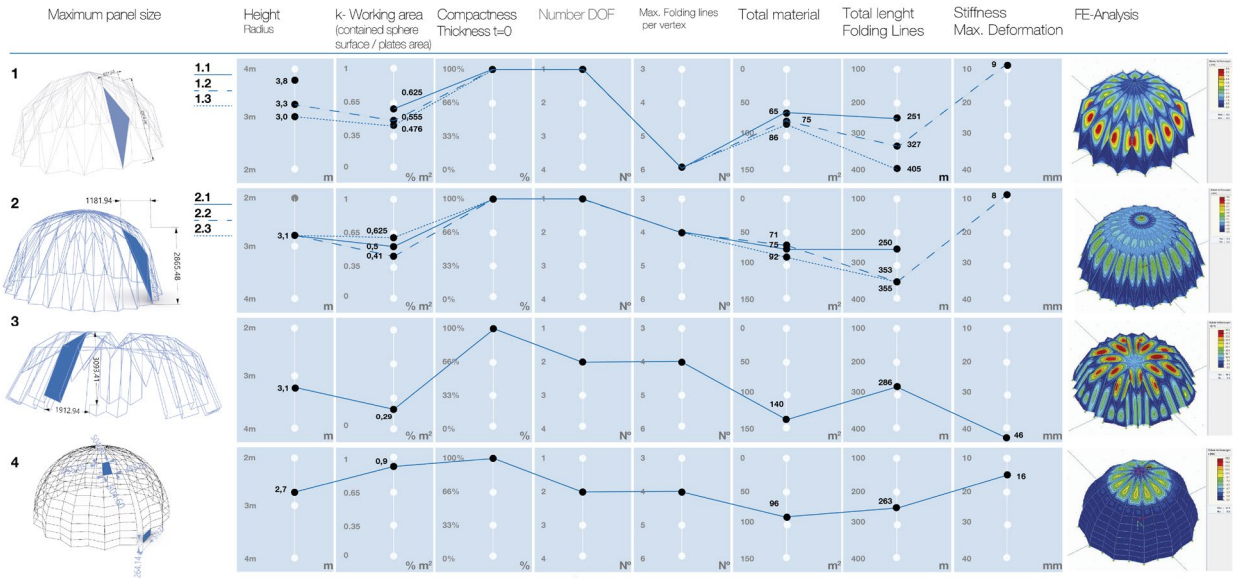
In this project, four types of origami patterns that can be adapted into a spherical geometry were studied: Yoshimura-Ori (Design 1), Chicken Wire (Design 2), and two from the literature: an adaptation of Miura-Ori [14] (Design 3), and an adaptation of a longitudinal folding [3] (Design 4). Here we study different factors that may lead to selecting one pattern or another, such as the displacement of the apex or center point, which is influenced by the subdivision of panels (see Figure 6, Design 1 and 2). Design

4, however, does not interrupt or collide with the workspace since that pattern only moves its center point upwards. In contrast to the previous ones, Design 3 does not move its center point.

2.2. Pattern design analysis

Table 1 shows the manly geometrical characteristics that were investigated: the dimensions of the largest panels, the maximum height of the structure, the working-area coefficient (obtained by dividing the surface of the contained sphere and the area of the total panels), the compactness (for a panel thickness of 0), the degrees of freedom, the maximum number of folding lines per vertex, the total area of the panels, and the length of all folding lines. Finally, the maximum deformation and support forces (self-weight and impact) were determined by FE analysis.

Table 1. Comparison of folding patterns.



It can be observed that designs 1, 2, and 3 are the ones that require larger panels. In contrast, Design 4 has smaller panels and, therefore with, a higher k- coefficient since it is closer to the working space. Further on, it can be seen how design 3 is the one that requires the most material, needing up to 140 m^2, the other designs remaining in a range from 65 to 96m^2. It can be seen that Design 1 and 2 are the stiffest, followed by Design 4, and Design 3 is the one with the most significant deformation, due to the geometric configuration, largest panels and cantilever.

In addition, other issues based on Figure 6 were observed: In Design 1 and 2, the central point moves downward when opening; circular trajectory only with mountain or valley folds possible circular trajectory approximately maintained; low degree of difficulty. In Design 3 it is observed that the circular trajectory not possible with rigid surfaces, the lower end open and therefore special solution for open areas in the base is necessary; construction is only stable to semi-open; and medium degree of difficulty.

Finally, it is observed that Design 4, the pattern does not correspond to the principles of folding (mountain-valley ratio is not equal to 3 to 1). It is a necessarily well-faceted geometry not to be full longitudinal folding. It is only possible with very flexible material. The circular trajectory is maintained and has a high degree of difficulty due to the number of joints.

For these reasons, it was concluded that the most suitable designs for a realization would be 1 and 2. Later it was supposed that the Chicken-Wire pattern would be the most suitable because it has less folding lines in the same vertex (4 in contrast to 6 of the Yoshimura-Ori). The realization and development of this design is described in [7].

On the other hand, in this project we wanted to explore design 4, since it does not comply with the folding conditions. Therefore, a construction concept was developed with flexible hinges and a semi-opening of the panels to allow folding. This would allow us to explore a more spherical design, with a more optimal k- ratio (see Table 1), and a smaller overall panel size.

3. Hybrid concept integrating scissor systems

In order to design actuation and supports of deployable structures, the motion trajectories of individual surfaces and points must be determined on a coordinate basis. This can be done e.g. with the Folding Mechanisms Library for Simulink [15]. Scissor systems with telescopic motors as in [16] can reduce the degrees of freedom of entire structures and simplify actuation. In contrast to the trivial geometry of the scissor system for parallel folding lines, the design of actuation systems for spherical or spatial gears is much more complex.

3.1. Movement trajectory analysis

The examples analyzed (see part 2), which were optimized with the [9] [10] tools, differ from the initial circular trajectory required. We can visualize the trajectory in the image, where we can see how the trajectory of the pattern lower points (on the floor) tends to be linear until we exceed 30º of folding. This non-linear area is then not considered, since the thickness of the panels would not allow that folded position.

This trajectory, with rigid panels, varies in the radius of the circle at 2.8 cm at its outer points and 12.9 cm at its inner points, with a z-displacement of 7.5 cm of the outer points. According to this analysis, it is observed that, by placing actuation at the outer points, the deviation of 2.8 cm can be absorbed with the flexibility of the panels (see construction in part 4). The inner points are suitable for support in z-direction. This consideration can be applied to the different patterns analyzed in Table 1.

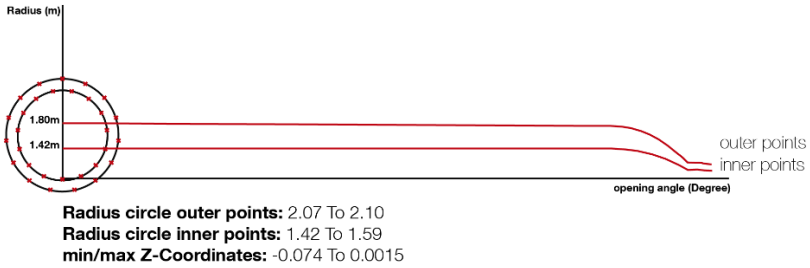


Figure 7. Trajectory analysis of the lower points.

3.1.1. Flat scissors

Simple symmetrical flat scissors, consisting of only two elements, can be inscribed in circles, which, however, vary in radius during their deployment. For this reason, a simple circular motion cannot be executed with this mechanism. Alternatively, independent scissors can be generated which, when actuated simultaneously with a linear actuator, can accomplish this operation. Design 2 (Figure 5) is executed with this consideration in the project [6].

3.1.2. Spherical scissors development

Scissors based on spherical geometries [4] are a variation of the geometry of a flat scissors. These scissors are projected onto the target sphere with a result of curved elements [17].

The center of the spherical scissors is identical to the center of the same sphere that generates the folding, with a larger radius, accommodating the external anchor points (see Figure 8). The connection of the scissor construction to the folding construction must allow rotations in all three directions.

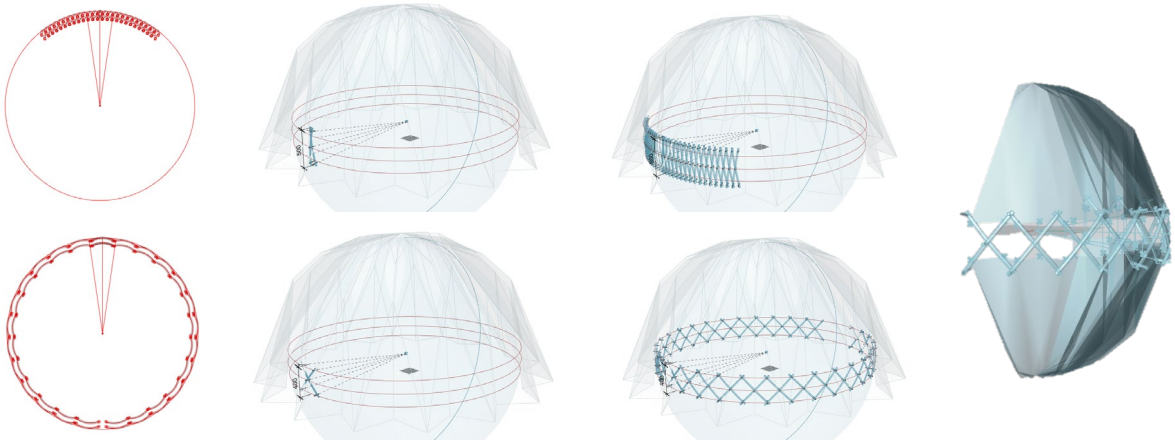


Figure 8. Development of spherical scissors. (Left to right): Top view of the scissor folded and unfolded. View of the scissor in combination with the folding. Positioning of the scissor according the outer points.

4. Construction development

The construction concept is divided into two main elements: folding and scissors. For the folding, following the methodology in [6], the material used was the composite material "Thermhex-Organosandwich" (6THPP120-CP820) (3-), composed of two 0.5 mm fiberglass face sheets and a honeycomb polypropylene core, was used for the 6mm thick rigid panels. Its stiffness satisfies static and dynamic calculations without compromising the overall structure's compatibility, and its low weight of 2.4 kg/m² limits stress on joints, frames, and drives. To avoid compatibility restrictions, low thickness continuous joints were developed using "Hylite" (4- and 5-), a 2 mm thick material with 0.2 mm aluminum cover layers and a 1.6 mm polypropylene core. A two-sided milling process with a width of 5 mm and a depth of 0.6 mm was used to give the material its joint properties, with an additional engraving milling of 0.6 mm and 0.2 mm widths on all valley folds for improved joint activation. CNC-drilled screw and rivet connections were used for surface connection to ensure spatial precision. The detachable connections of surfaces and joints allow for easy replacement of individual elements and material separation for complete disassembly e.g. for transportation or reusability of single parts or elements. Discontinuous 5- hinges were included to facilitate the deployment of this particular geometry.

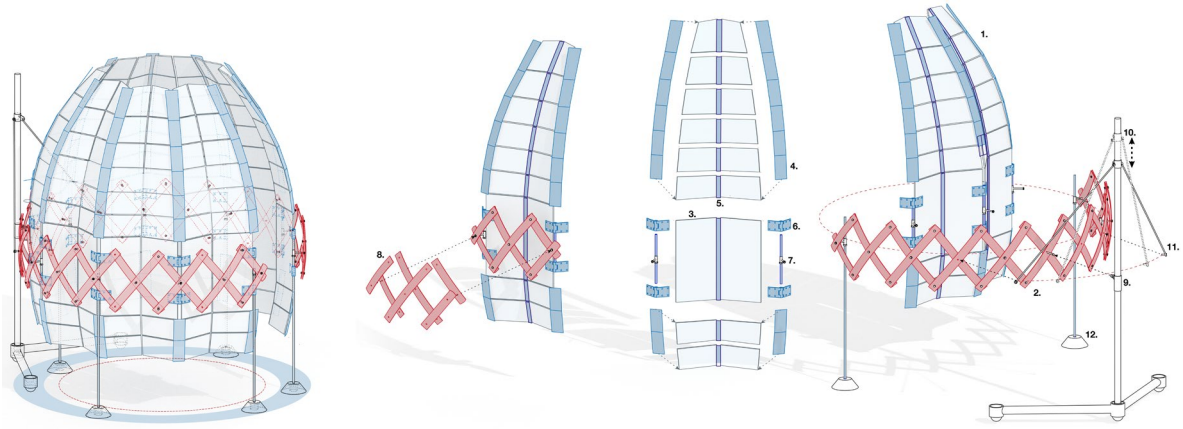


Figure 9. Construction concept and assembly: 1- Folding elements, 2- Spherical scissor, 3- Composite panels, 4- Continuous composite hinges, 5- Discontinuous composite hinges, 6. Aluminium hinge, 7-Vertical rod and scissor connector, 8-Scissors elements (internal and external). 9- Horizontal connector, 10- Vertical connector, 11- Diagonal rods and spherical joint connector, 12-Additional supports with spherical wheels.

The scissor system (8-) is composed of 4mm "Alucobond" (ALUCOBOND® PLUS) aluminum composite elements, which were precisely bent using a metal bending machine. The assembly is done with bearings and screws. Its assembly with the folding is carried out with through rods that are anchored to integrated vertical rods (7-).

The tripod that supports the structure integrates a horizontal connector (9-), which is anchored to the scissors, as well as a vertical connector (10-) which is mobile. The vertical connector (10-), by means of a vertical slide, activates the opening and closing movement of the scissors.

4.1. Construction demonstration and set-up

The construction of the prototype was carried out on a 1:1 scale (Figure 9), and was tested as a shield for grinding operations (Figure 10).

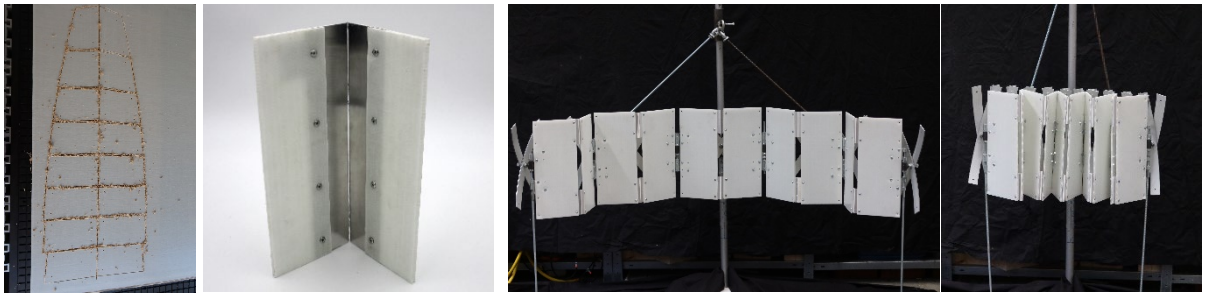


Figure 10. (left to right) Fabrication of the panels, photo of the connection, assembly of the folding and scissor.

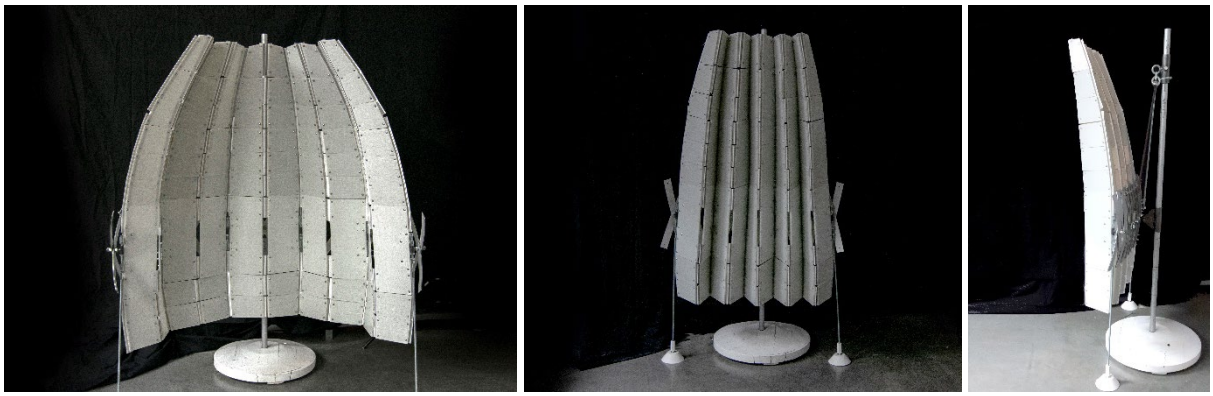


Figure 11. Proof of concept (left to right): Deployed shield, folded shield, lateral view of the folded shield.

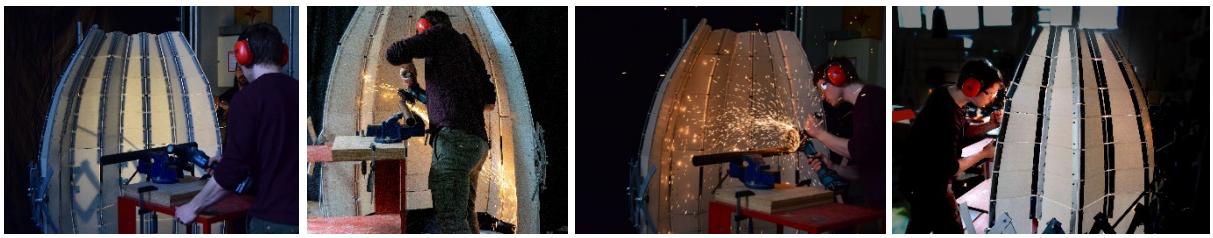


Figure 12. Proof of concept (left to right): grinding preparation, protection from downward sparks protection, upward sparks protection, rear view of the action.

5. Conclusions

This paper shows the design and implementation of a novel enclosure as a protective shield for manufacturing tasks, where a working environment in a workshop must be protected. The structure comprises a hybrid folding and scissors system, which opens and closes manually and compacts itself

in less than one-third of the surface. The lightweight and rigid folding shield consist of composite panels with elastic hinges. The spherical scissor system follows a pattern of parallel axis bent in aluminium on a specific radius to deploy the circular trajectory. The two systems demonstrate the ability to collaborate to generate a self-supporting system with one degree of freedom, which simplifies the use of multiple motors to drive the mechanism. The project presented here has been executed with a scaled prototype that can be integrated into workshops environments.

Acknowledgements

This project was carried out complementary to the E^2F project, which was funded by the Deutsche Forschungsgemeinschaft (DFG) Project: 289387994, aimed at designing and developing transformable folding structures, conducted during the period of 2020-2021[6]. This project realization also involved the collaboration of student research assistants Sheldon Stephens, Clemens Braumann, Viktor Wages and Tobias Grüters, as well as students who contributed to its assembly during the elective course Transformable Structures held in the summer semester 2022 at the Faculty of Architecture of the RWTH-Aachen University.

References

[1] A. Künstler and M. Trautz, 'Wandelbare Faltungen aus biegesteifen Faltelementen', *Bautechnik*, vol. 88, no. 2, pp. 86–93, 2011, doi: 10.1002/bate.201110008.

[2] M. Trautz and A. Künstler, 'Deployable folded plate structures - folding patterns based on 4-fold-mechanism using stiff plates', presented at the IASS Symposium 2009, Ed. UPV, Oct. 2009. Accessed: Mar. 31, 2022. [Online]. Available: https://publications.rwth-aachen.de/record/99886

[3] K. Ando, B. Izumi, M. Shigematsu, H. Tamai, J. Matsuo, Y. Mizuta, T. Miyata, J. Sadanobu, K. Suto, and T. Tachi, 'Lightweight rigidly foldable canopy using composite materials', *SN Appl. Sci.*, vol. 2, no. 12, p. 1994, Nov. 2020, doi: 10.1007/s42452-020-03846-0.

[4] C. H. Chiang, *Kinematics of Spherical Mechanisms*, 2nd Ed. 2nd Ed.Cambidge, UK: Cambridge UniversityPress, 1988.

[5] T. Tachi, 'Rigid-Foldable Thick Origami', vol. 5, Jun. 2011, doi: 10.1201/b10971-24.

[6] K. Moreno Gata, 'Deployable folding enclosures for robotic manufacturing processes', *Chair of Structures and Structural Design - RWTH-Aachen*, 2023. https://trako.arch.rwth-aachen.de/cms/TRAKO/Forschung/Tragsysteme-Strukturformprinzipien/~bazscm/Copy-of-E-F-Entwurf-und-Entwicklung-vo/?lidx=1 (accessed Apr. 14, 2023).

[7] K. Moreno Gata, A. Seiter, J. Musto, F. Wieja, J. U. Merz, B. Corves, G. Jacobs, and M. Trautz, 'A design concept for deployable folding enclosures for robotic manufacturing processes (Submitted paper)', *CDRF*, no. The 5th International Conference on Computational Design and Robotic Fabrication, Jun. 2023.

[8] J. Paris, J. U. Merz, H. Buffart, S. Hoffman, J. Siebrecht, C. Weigel, M. Hsing, M. Trautz, and B. Corves, 'Kinematic and kinetostatic classification for motion-task-oriented synthesis of folding mechanisms', in *The International Meeting on Origami Science, Mathematics, and Education, Oxford*, 2018.

[9] R. McNeel and others, 'Rhinoceros 3D, Version 6.0', *Robert McNeel & Associates, Seattle, WA*, 2010.

[10] D. Piker, 'Kangaroo: Form Finding with Computational Physics', *Architectural Design*, vol. 83, Mar. 2013, doi: 10.1002/ad.1569.

[11] K. Suto, Y. Noma, K. Tanimichi, K. Narumi, and T. Tachi, 'Crane: An Integrated Computational Design Platformfor Functional, Foldable, and Fabricable Origami Products', *ACM Trans. Comput.-Hum. Interact.*, Dec. 2022, doi: 10.1145/3576856.

[12] 'Ansys® Ansys Mechanical, Release 18.1'. https://www.ansys.com/products/structures/ansys-mechanical (accessed Mar. 30, 2023).

[13] *MATLAB version 9.10.0.1613233 (R2021a)*. Natick, Massachusetts: The Mathworks, Inc., 2021.

[14] M. Barej, S. Hoffmann, C. Knief, M. Trautz, and B. Corves, 'Design and Application Studies for a Cupola Forming Orbital Arrangment of Miura-Ori Basic Units'.
[15] J. Paris, J. Merz, H. Buffart, S. Hoffmann, C. Weigel, M. Husing, M. Trautz, and B. Corves, 'Classification, Collection, and Simulation of Folding Mechanisms', in *2018 International Conference on Reconfigurable Mechanisms and Robots (ReMAR)*, 2018, pp. 1–8. doi: 10.1109/REMAR.2018.8449857.
[16] 'Convertible Folding Structures, (Faltbare Bühnenüberdachung Kennedypark Aachen - RWTH AACHEN UNIVERSITY Chair of Structures and Structural Design - English'. https://trako.arch.rwth-aachen.de/cms/TRAKO/Forschung/Tragsysteme-Strukturformprinzipien/~isbh/Wandelbare-Faltwerke/lidx/1/ (accessed Mar. 31, 2023).
[17] USPTO.report, 'Compact Spherical 3-dof Mechanism Constructed With Scissor Linkages Patent Application', PA 2017 70789, Apr. 16, 2020 Accessed: Mar. 31, 2022. [Online]. Available: https://uspto.report/patent/app/20200238542

IASS 2023
July 10–14 Melbourne
Integration of Design and Fabrication

Proceedings of the IASS Annual Symposium 2023
Integration of Design and Fabrication
10–14 July 2023, Melbourne, Australia
Y.M. Xie, J. Burry, T.U. Lee and J. Ma (eds.)

Snap-through buckling detection and analysis method for multi-stable structures

Ruta STANKEVICIUTE[a,*], Jun SATO[a]

[a,*] Graduate School of Frontier Sciences, The University of Tokyo
Chiba, Kashiwa, Kashiwanoha, 5-1-5
ruta@g.ecc.o-tokyo.ac.jp

Abstract

Buckling is usually observed in structural engineering as a failure of the structure. However, using snap-through buckling, a multi-stability can be achieved in animated structures. While there is numerous research on analysing structural behaviour when snapping-through occurs, there is little study on detecting snap-through buckling occurrence, which is essential to multi-stable structures. In this paper, we propose a computational method for detecting snap-through buckling events, which analyses the critical load estimated through eigenvalue buckling analysis. The workflow was developed by first simulating the multi-stable structure using the dynamic relaxation method and capturing the structure's behaviour while transforming from one state to another by recording iterations of the animation. Since simulation produced a high number of geometric models, we used a linear buckling analysis, which proved to be faster than a non-linear analysis. By observing results throughout the animation, we detected a drastic fluctuation in eigenvalue, which correlated with geometry changes from the simulation and physical experiment. A sudden drop in eigenvalue corresponded with large deformation of the structure, indicating snap-through occurrence. The results suggest that our proposed analysis method can be a fast way to detect the occurrence of snap-through buckling in multi-stable structures.

Keywords: snap-through buckling, buckling analysis, eigenvalue, multi-stability

1. Introduction

Thin structures tend to bend rather than stretch; therefore, this tendency often results in elastic instability. Designing thin and lightweight structures using high-strength materials is inherently prone to instability due to this behaviour [1]. Once an unwanted phenomenon in structural engineering, elastic instability is now employed in making structures multi-stable. With the need for deployable compact, lightweight structures growing, architects and engineers draw inspiration from nature, designing structures ranging from metamaterials [2] and micro-robotics [3] to meter-scale structures like emergency shelters [4]. The field of multi-stable structures has never been as influential and growing as now.

Although there has been extensive research on employing snap-through buckling to create multi-stable structures, a limited amount of study focuses on detecting such a phenomenon. There are ways to detect snap-through occurrence physically, by measuring the strain distribution along the structure with a fibreglass sensor [5] or by measuring the voltage of the energy produced during the snap-through event [6]. In addition, the snap-through signature can be observed digitally by measuring the change in the tilting angles of the members in buckled regions [7].

However, the research on the effect of snap-through buckling and post-event focuses on one stage of the structure, usually the final deployed shape, rather than analysis throughout the deployment. It is possible to acquire pre-snap-through and post-snap-through states, as well as the iterations in between, by using the incremental displacement numerical method [8]. Even so, there are no tools for detecting

Copyright © 2023 by Ruta STANKEVICIUTE and Jun SATO. Published in the Proceedings of the IASS Annual Symposium 2023 with permission.

snap-through occurrences during deployment animation, which is essential to multi-stable structures since snap-through can occur anytime throughout the deployments and change the structural integrity and behaviour of the structure.

Although structural analysis tools can animate incremental displacement or even visualise snap-through phenomena, they cannot simulate deployment animation. The most common approach towards analysing animated structures is developing a simulation and analysis using two different software, which often results in the incompatibility of models and interruption of the workflow [9]. While geometry animation and buckling analysis have been seen as separate methods, we bridge the gap by proposing a computational method for multi-stable structures, which simulates the deployment and analyses the structure in parallel. Using linear eigenvalue buckling analysis, we enable quick computation and unburdened workflow to detect snap-through buckling occurrence throughout the animation process.

2. Method basis

The fundamental mathematical difference between a bifurcation and a snap-through phenomenon lies in how the structure responds to instability: bifurcation entails a shift to a new equilibrium path, while snap-through involves a sudden jump to a new point on the same equilibrium path [1]. Bifurcation is characterized as a gradual deformation, while snap-through buckling results in a rapid, discontinuous deformation that involves an instability phase [6]. Additionally, the critical load threshold for bifurcation refers to the point where the structural stability transitions from its current stable state to a new equilibrium, which could be either stable or unstable, emanating from the original equilibrium state [10] [11]. Concurrently, the critical points for snap-through buckling signify the instance when the structure transitions abruptly to a new point of stability whilst maintaining stable equilibrium. [12]. This transition drastically changes the structure's integrity, resulting in collapse or, in the case of multi-stable structures, a new stable state. Therefore, observations of any sudden change in the stability of the structure during deployment could identify a snap-through event.

Multi-stable structures require a critical load to snap through between deployed states [13]. In the case of snap-through buckling, structural stability changes drastically, sometimes leading to significant stress reversals [14] [15]. Therefore, the critical load changes significantly at the snap-through buckling occurrence, which would reflect in the eigenvalue that identifies the stability of the structure through buckling analysis [16] [17] [18]. Based on our study, the rapid, significant displacement and drastic change in stability reflected in eigenvalue are proposed to be used as a signature for detecting snap-through events.

Since snap-through buckling is a complex non-linear problem, it is commonly solved using non-linear analysis methods, such as the arc-length method [7] or the Newton-Raphson method [19]. However, fundamental linearised buckling analysis is sufficient for predicting the collapse load. Specifically, the linear eigenvalue approximation is just as precise as both the analytical and rigorous non-linear pre-buckling analysis [20]. Moreover, even though eigenvalue buckling analysis may over-predict the critical buckling strength, it needs less computational effort compared with a non-linear buckling analysis [21]. Therefore, our hypothesis is focused on using linear eigenvalue analysis for quick detection of possible snap-through occurrence by reading eigenvalue fluctuations throughout the deployment of a multi-stable structure.

3. Deployment simulation

Our study uses an inflatable origami structure as a deployable multi-stable structure. The origami geometry is composed of sharp and soft folds. Sharp folds are curve-creased folds, which are folded

along a curve instead of a straight line and can store elastic strain energy [22]. Using curved-creased folds enables us to control snapping [23] by increasing the crease curvature raising the critical force needed for snap-through instability [24]. Soft folds are folded along an edge using a radius. Thus, their behaviour is more similar to the surface than the crease.

3.1 Physical set-up

A physical experiment was conducted to validate the proposed computational method for simulating and detecting snap-through sequences. The origami structure is built using a 0.3mm aluminium sheet. Inflated, it spans 2m in length and 1m in width and rises to 0.5m (see Figure 1(a)). The freestanding structure was inflated via a tube attached at the top of the model. The primary folds, sharp edges of the geometry, are created by cutting the sheets of aluminium and joining the creases using hinges, which gives the fold almost no resistance when folding. Secondary folds, soft edge folds, are created by bending the sheet without making a cut or joining with hinges. Therefore, they have bending stiffness inherited from the material. The behaviour of the structure observed during the deployment of the physical experiment was used to tune up the deployment simulation.

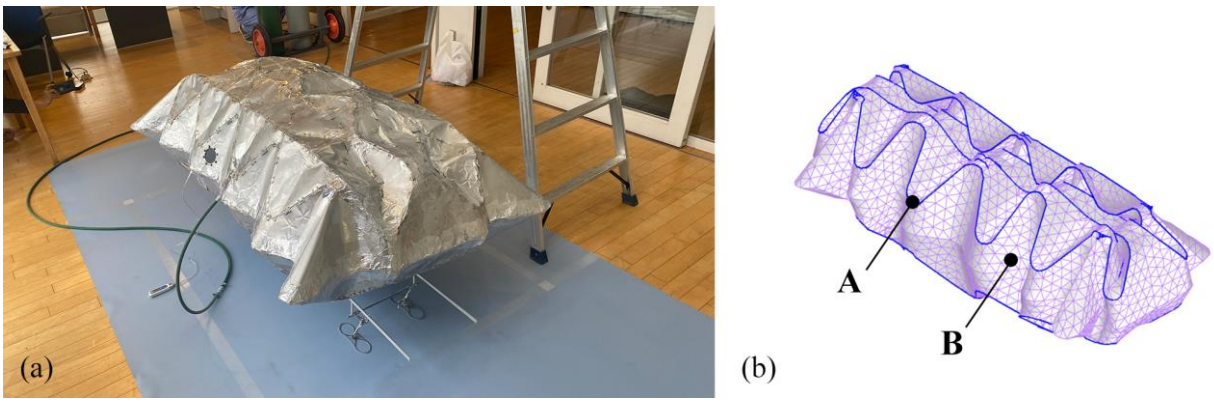


Figure 1. Inflatable multi-stable origami structure: (a) physical set-up, (b) simulation set-up, indicating: A – primary, sharp folds, B – secondary, soft folds.

3.2 Simulation set-up

It is essential to analyse the structure throughout the deployment process. Therefore, a simulation was used to produce the geometry at multiple stages of the animation. The method was built using Rhinoceros software, commonly used by architects and engineers. It houses various plug-ins that can be used together within one environment called Grasshopper. This makes workflow between different software uninterrupted.

Deployment of the origami structure was simulated using Kangaroo physics plug-in – an interactive physics engine that reaches set goals using a form of dynamic relaxation. A technique that, through an iterative solving process, combines all the acting forces and transforms geometry accordingly until the equilibrium of forces can be reached [25]. The Kangaroo physics components are used to set up goals for the simulation while Kangaroo solvers run the simulation and provide the result.

A ‘Plastic Hinge’ component was used for sharp folds, which acts as an angular spring [26] and allows deformation of the crease once the plastic angle is exceeded. However, for the soft folds, – the ‘Hinge’ component was more suitable because, although similar to Plastic Hinge, it has no deformation angle constraint, allowing the fold to recover to its original state. The length component is used to transform

the origami structure into a network of springs, representing rigid beams. The 'NoFoldThrough' component ensures that no faces can pass through each other during animation.

All goal components used in setting up the geometry of the origami structure can be assigned a strength parameter corresponding to axial stiffness. Value can be calculated based on the structure's material using the formula: EA/L, where E is the elastic modulus, A is the cross-sectional area, and L is the length of the element [24].

In the simulation set-up, the strength parameter of the Hinge and Plastic Hinge components was tuned to match the behaviour observed during the physical experiment.

The origami structure is deployed by inflation. For that purpose, air pressure was represented using a Pressure component. However, the pressure is assumed to be constant throughout the simulation, and animation using a Kangaroo solver component or step solver component only represents the iteration solutions or deformation until a final solution is achieved. Thus, it is impossible to know how pressure changes throughout the deployment.

Seeing that it is essential to the study to know the exact pressure at a given point throughout the deployment of the structure, it was crucial to set up a recursive flow that allows an incremental increase in pressure during simulation. Therefore, a loop was created using an Anemone plug-in, which enabled the incrementation of the pressure. Each loop runs one simulation using the Zombie solver at a given pressure, which is increased in each loop until recursion is broken once the model is fully deployed.

4. Buckling analysis

The key point of the multi-stable structure is the ability to lock in place after deployment; thus, it is essential to transition from one stable state to another using snap-through buckling and not folding. It is hard to detect which buckling mode the crease underwent simply by observing the deformation scale; therefore, it is necessary to conduct a buckling analysis.

4.1 Analysis set-up

For buckling analysis, an in-house software Hogan was chosen. Hogan solves the generalised eigenvalue problem using the bisection method. It is a fast linear buckling analysis solver capable of detecting the smallest eigenvalue and corresponding mode.

Hogan can be linked directly within the Grasshopper environment via a plug-in called GHogan. Therefore, buckling analysis can be set up inside the Anemone loop and run simultaneously with the Kangaroo simulation. First, GHogan components are used to construct a file Hogan uses for buckling analysis. Afterwards, an output file can be read in the Grasshopper environment to observe the eigenvalue result.

Assuming that the model is symmetrical on the x and y-axis, only one-quarter of the geometry was used for structural analysis to make the calculations faster (see Figure 2(a)). As a result, points on the xz plane were locked on the y-axis, while points on the yz plane were locked on the x-axis, respectively (see Figure 2(b)).

Inner pressure applied during inflations is used as a load for the buckling analysis. First, it is calculated using plankton mesh, which uses a half-edge data structure to create polygon mesh. Afterwards, vertices and vortex normal are used to define the vector for the nodal load (see Figure 2(c)).

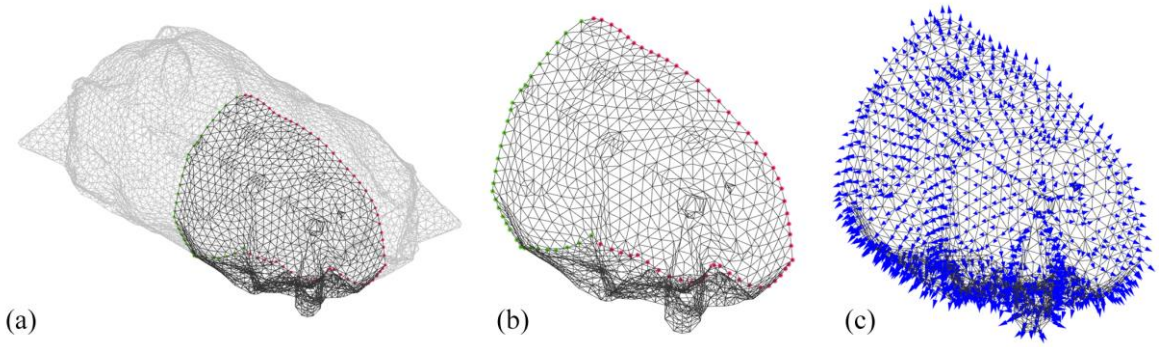


Figure 2. Buckling analysis set-up: (a) quarter model, (b) red - points fixed on the xz plane, green – points fixed on the yz plane, (c) blue – nodal load vectors representing internal pressure.

5. Results

5.1 Snap-through detection and sequence observing deformation throughout the physical experiment

During the physical deployment test, Snap-through occurrence was confirmed. 12 snaps were detected (see Figure 3), and three different snap-through sequences were recorded (see Figure 4(a)). Due to imperfections of the prototype model, deployment was asymmetrical. Therefore, it is hard to determine the correct sequence.

Furthermore, air leakage occurred during inflation, which might have affected the deployment and the sequence of snapping. After pressure was removed, some snaped areas reversed to the original state, indicating that snap-through might not have occurred or the critical load for deformation was too low to sustain the shape. However, most of the model stayed deployed, validating the multi-stability of the structure.

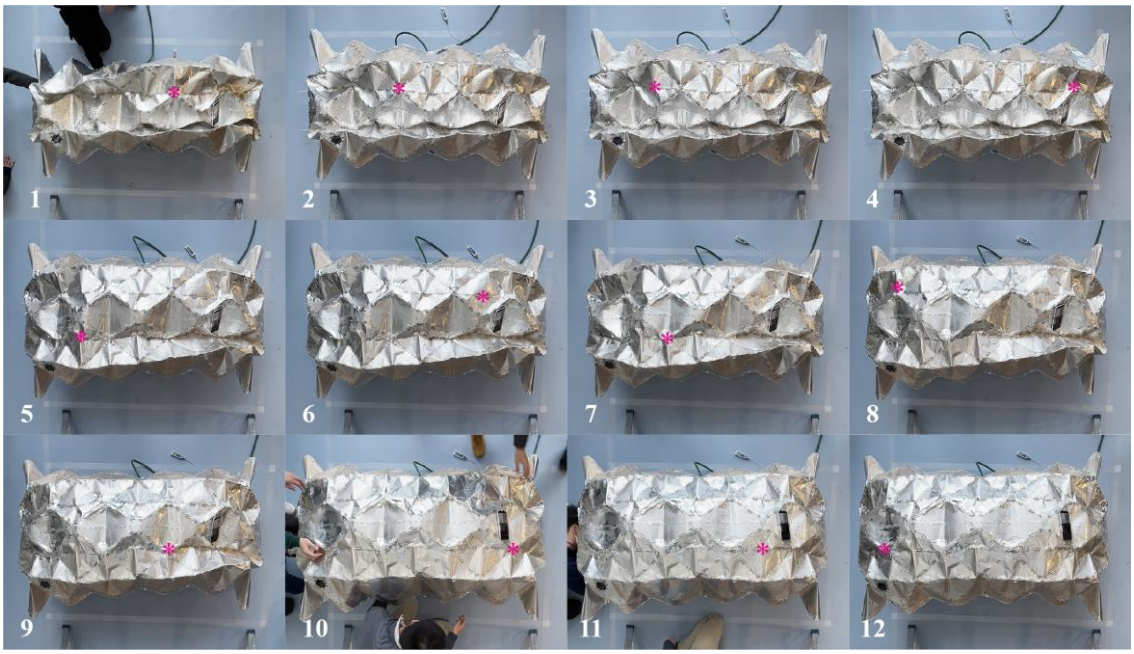


Figure 3. Physical experiment result: 12 snap-through events recorded in sequence.

5.2 Snap-through detection and sequence observing large deformation throughout the simulation

The snap-through-like motion could be detected by measuring the deformation vector between iterations. Tracking how points moved after pressure was increased indicated possible snap-through occurrence. Since vector length changed drastically between iterations, it is more likely reflected as a snap-through deformation rather than folding. However, after decreasing pressure incrementation to make the deployment simulation more accurate, detecting snap-through-like events became harder because deformation became more subtle. Compared to the physical experiment, the geometry could be deployed symmetrically. Only one snap-through sequence was recorded, which correlated to one of the sequences observed during the physical experiment (see Figure 4(b)).

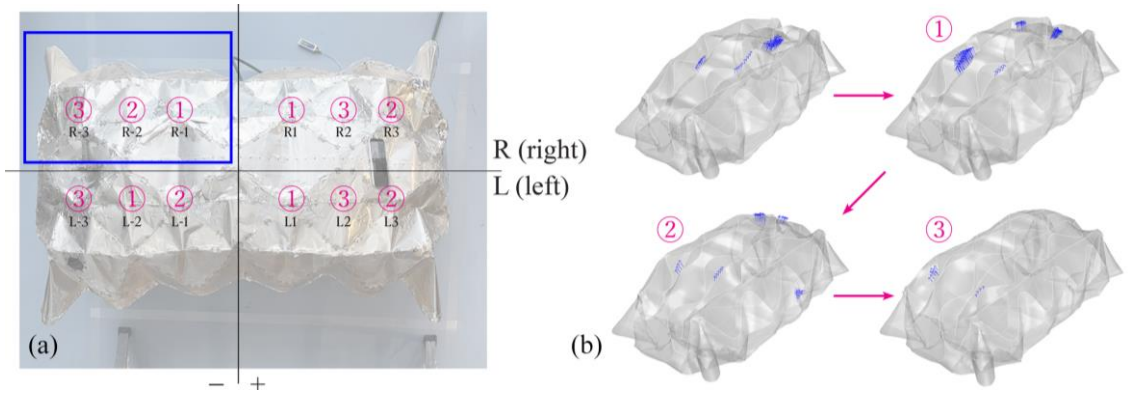


Figure 4. Comparison between physical experiment result and simulation result: (a) 3 different snap-through sequences occurred during physical model deployment, (b) only one snap-through sequence was recorded during the deployment simulation.

5.3 Snap-through detection using eigenvalue buckling analysis

The first simulation and analysis were conducted in 0.1atm (10.1325kPa) pressure increments. A drastic fluctuation in eigenvalue was detected by observing buckling analysis results throughout the animation (see Figure 5(a)), which correlated with geometry changes from the simulation. A sudden drop in eigenvalue corresponded with large deformation of the structure, previously indicated as a snap-through event.

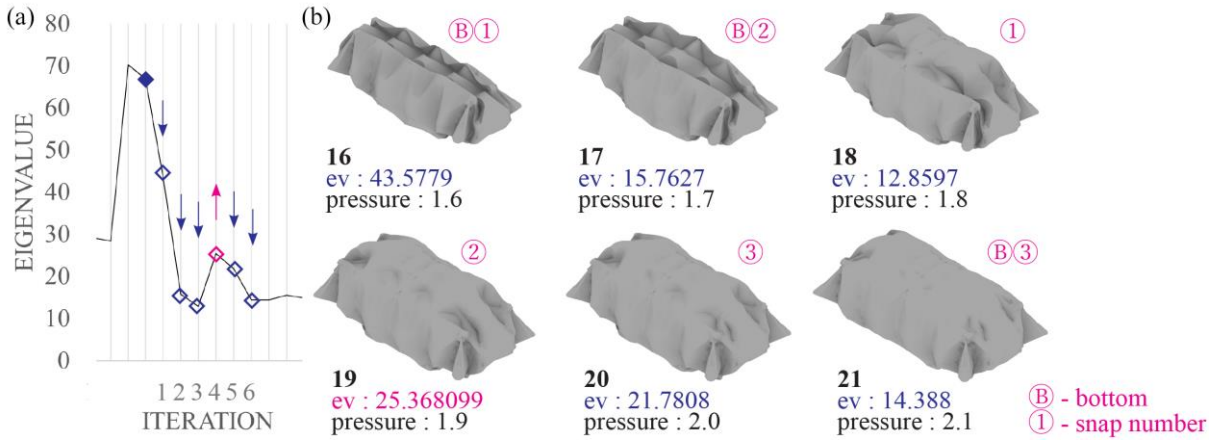


Figure 5. 0.1 incremental pressure simulation eigenvalue buckling analysis result: (a) eigenvalue fluctuation indicating 6 snap-through events, (b) snap-through sequence.

A sequence of 6 snaps was recorded (see Figure 5(b)). The first two snaps indicated rapid deployment and snap-through-like behaviour at the bottom of the shape. Afterwards, 3 snaps occurred on the top of the structure. The final snap appeared on the bottom. Each snap was followed by a drastic change in eigenvalue.

While 5 out of 6 snaps were indicated by the drop in eigenvalue, an increase was detected around the 4th snap occurrence, which did not follow the proposed hypothesis. For in-depth research, a more precise analysis was conducted.

The second simulation and analysis were conducted in more precise 0.02 atm (2.0265kPa) pressure increments. Compared with the first simulation and analysis, more fluctuations in eigenvalue could be recorded, providing more data regarding the deployment sequence (see Figure 6(a)). Eight eigenvalue spikes were recorded. Six spikes indicated a rise of eigenvalue and then afterwards a sudden drop, which suggests snap-through-like behaviour. After observing the 3D model, we could confirm that the eigenvalue spikes matched the snaping seen during the deployment animation.

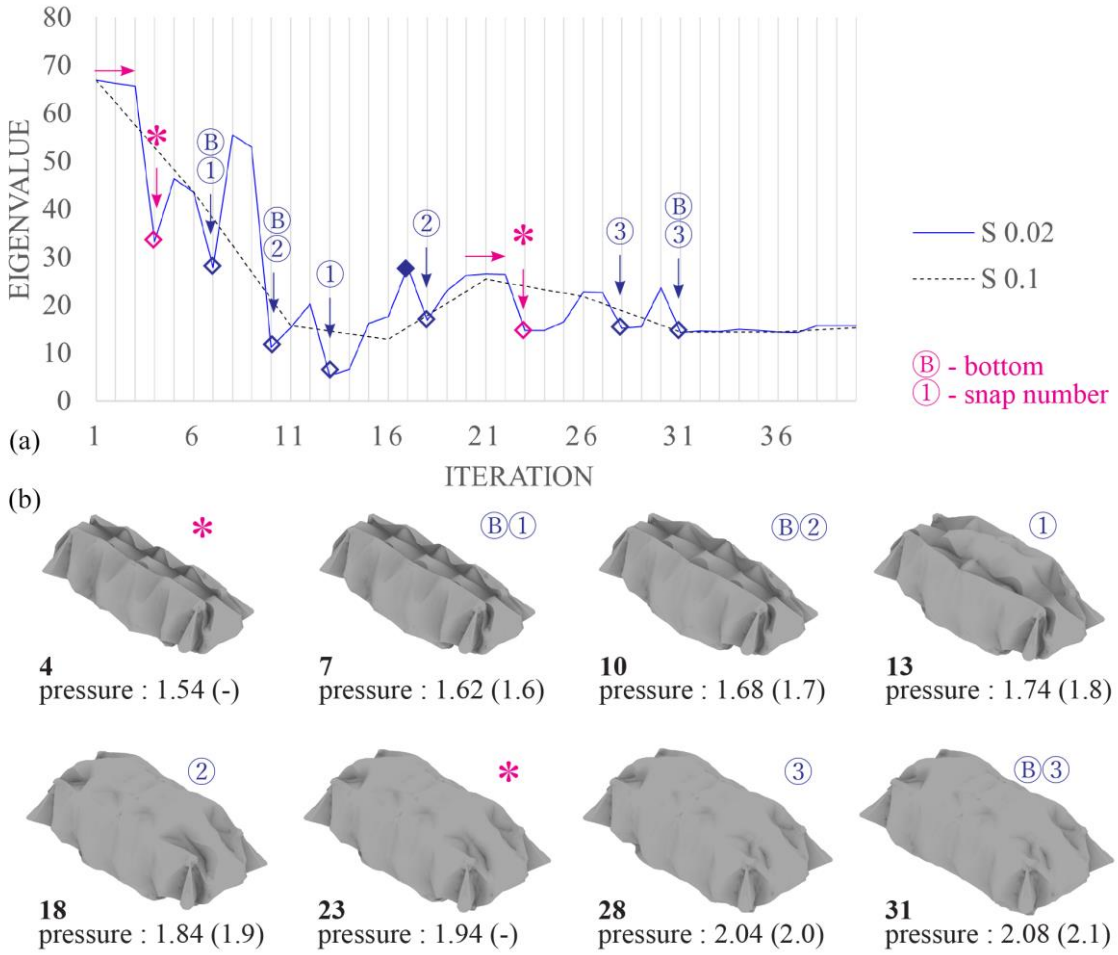


Figure 6. 0.02 incremental pressure simulation eigenvalue buckling analysis result: (a) eigenvalue fluctuation indicating 6 snap-through events and 2 unidentified events, (b) snap-through sequence.

However, around iterations no. 4 and no. 23, no snap-through could be identified from simulation images, while the eigenvalue from buckling analysis spiked (see Figure 6(b)). The rise of eigenvalue was smoother than the spikes associated with snap-through events. However, the value dropped just as rapidly. By observing the eigenvalue analysis result, a large deformation was visible at the front of the model (see Figure 7). Two more snaps happened afterwards in the area indicated by the analysis, which suggests that folding motion or a different type of buckling might have occurred during the unidentified eigenvalue spike.

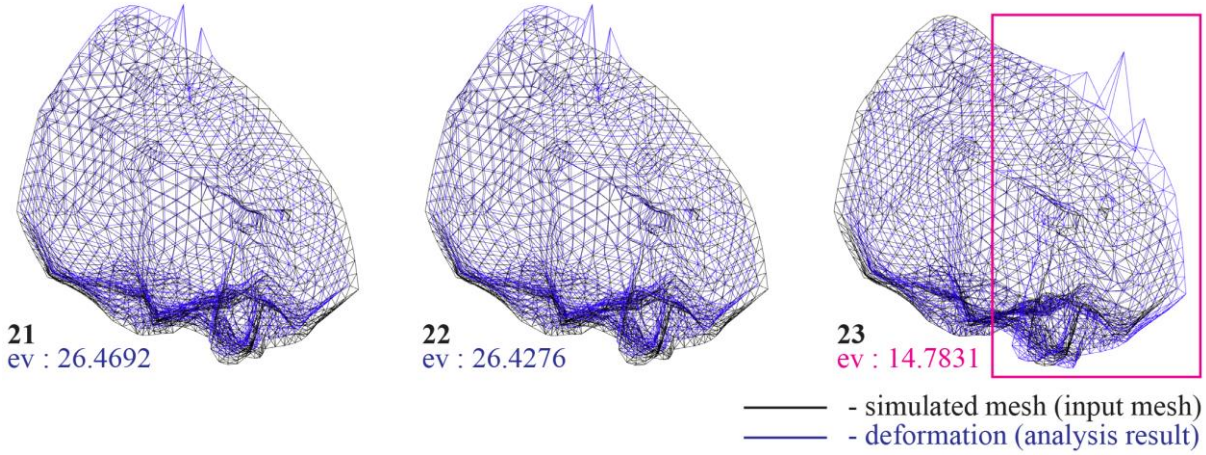


Figure 7. Iteration no. 23 eigenvalue buckling analysis result indicating large deformation.

Using smaller increments, more precise snap-through detection could be achieved using our developed method. Furthermore, the pressure required for each snap-through to occur could be specified. Finally, the results showed that rapid, significant displacement and change in eigenvalue are strong indicators of snap-through buckling occurrence.

6. Conclusion

This paper presents a computational method for simulating and analysing the deployable structure using linear eigenvalue buckling analysis for snap-through buckling detection. It is based on the fact that eigenvalue drastically increases just before the snap-through buckling occurs; therefore, it can be used as a signature detecting snap-through phenomenon. We achieved a realistic simulation correlating with the behaviour of the structure observed during the physical experiment. Furthermore, this study is the first to demonstrate an animated linear eigenvalue buckling analysis for deployable multi-stable structures with snap-through detection. However, there is much scope for improvement of our proposed method. While we could identify most of the eigenvalue spikes as snap-through buckling by observing the physical experiment as well as data from the simulation, there were unknown fluctuations that need more thorough study in the future. Additionally, the deformation result from the analysis could be used to identify the location of the snap-through occurrence.

Being able to work with geometry and quickly detect snap-through sequences in parallel allows us to use the method with geometry optimisation, presenting an opportunity for innovative ways to work with multi-stable structures.

References

[1] D. P. Holmes, "Elasticity and stability of shape-shifting structures," *Current Opinion in Colloid & Interface Science*, vol. 40, pp. 118–137, Apr. 2019.

[2] K. Liu, T. Tachi, and G. H. Paulino, "Bio-Inspired Origami Metamaterials With Metastable Phases Through Mechanical Phase Transitions," *Journal of Applied Mechanics*, vol. 88, no. 9, p. 091002, Sep. 2021.

[3] X. Zhang *et al.*, "A bioinspired snap-through metastructure for manipulating micro-objects," *Science Advances*, vol. 8, no. 46, p. eadd4768, Nov. 2022.

[4] D. Melancon, B. Gorissen, C. J. García-Mora, C. Hoberman, and K. Bertoldi, "Multistable inflatable origami structures at the metre scale," *Nature*, vol. 592, no. 7855, pp. 545–550, Apr. 2021.

[5] X. Tan, P. Guo, X. Zou, and Y. Bao, "Buckling detection and shape reconstruction using strain distributions measured from a distributed fiber optic sensor," *Measurement*, vol. 200, p. 111625, Aug. 2022.

[6] Y. Kessler, B. R. Ilic, S. Krylov, and A. Liberzon, "Flow Sensor Based on the Snap-Through Detection of a Curved Micromechanical Beam," *Journal of Microelectromechanical Systems*, vol. 27, no. 6, pp. 945–947, Dec. 2018.

[7] G. Yan, Q. Duan, and X. Hua, "Instability signature for detecting snap-through buckling of dome structures," in *Sensors and Smart Structures Technologies for Civil, Mechanical, and Aerospace Systems 2016*, SPIE, Apr. 2016, pp. 1100–1106, Apr. 2016.

[8] J. Zhao, J. Jia, X. He, and H. Wang, "Post-buckling and Snap-Through Behavior of Inclined Slender Beams," *Journal of Applied Mechanics*, vol. 75, no. 4, p. 041020, Jul. 2008.

[9] D. Baerlecken, R. Gentry, M. Swarts, and N. Wonoto, "Structural, Deployable Folds — Design and Simulation of Biological Inspired Folded Structures," *International Journal of Architectural Computing*, vol. 12, no. 3, pp. 243–262, Sep. 2014.

[10] Y. Grabovsky and D. Harutyunyan, "Rigorous asymptotic analysis of buckling of thin-walled cylinders under axial compression." arXiv, Jan. 25, 2013.

[11] N. Olhoff and A. P. Seyranian, "Bifurcation and post-buckling analysis of bimodal optimum columns," *International Journal of Solids and Structures*, vol. 45, no. 14, pp. 3967–3995, Jul. 2008.

[12] M. Gomez, D. E. Moulton, and D. Vella, "Critical slowing down in purely elastic 'snap-through' instabilities," *Nature Phys*, vol. 13, no. 2, pp. 142–145, Feb. 2017.

[13] B. S. Yeow *et al.*, "Origami-Inspired Snap-through Bistability in Parallel and Curved Mechanisms Through the Inflection of Degree Four Vertexes," in *2021 IEEE International Conference on Robotics and Automation (ICRA)*, May 2021, pp. 10863–10869, Oct. 2021.

[14] Y. D. Sha, Z. J. Gao, and F. Xu, "Influences of Thermal Loads on Nonlinear Response of Thin-Walled Structures in Thermo-Acoustic Environment," *Applied Mechanics and Materials*, vol. 105–107, pp. 220–226, 2012.

[15] A. Przekop, S. A. Rizzi, and K. A. Sweitzer, "An investigation of high-cycle fatigue models for metallic structures exhibiting snap-through response," *International Journal of Fatigue*, vol. 30, no. 9, pp. 1579–1598, Sep. 2008.

[16] M. A. Crisfield, "A fast incremental/iterative solution procedure that handles 'snap-through,'" *Computers & Structures*, vol. 13, no. 1, pp. 55–62, Jun. 1981.

[17] J. Mäkinen, R. Kouhia, A. Fedoroff, and H. Marjamäki, "Direct computation of critical equilibrium states for spatial beams and frames," *International journal for numerical methods in engineering*, vol. x, pp. 1–21, Jan. 2012.

[18] A. Steinboeck, X. Jia, G. Hoefinger, H. Rubin, and H. A. Mang, "Remarkable Postbuckling Paths Analyzed by Means of the Consistently Linearized Eigenproblem," *International Journal for Numerical Methods in Engineering*, vol. 76, no. 2, pp. 156–182, 2008.

[19] Y. Zhang, Y. Liu, P. Chen, and K. D. Murphy, "Buckling loads and eigenfrequencies of a braced beam resting on an elastic foundation," *Acta Mechanica Solida Sinica*, vol. 24, no. 6, pp. 510–518, Dec. 2011.

[20] S. Malek, "The effect of geometry and topology on the mechanics of grid shells," PhD diss., Massachusetts Institute of Technology, Oct. 2012.

[21] G. Yan, T. Li, R. Feng, G. Chen, X. Hua, and Q. Duan, "Detection of Nodal Snap-through Instability in Reticulated Shell Structures Using Tilt Sensing of Members," *Journal of Applied Nonlinear Dynamics*, vol. 7, pp. 25–44, Mar. 2018.

[22] K. Rzeszut, "Post-Buckling Behaviour of Steel Structures with Different Types of Imperfections," *Applied Sciences*, vol. 12, p. 9018, Sep. 2022.

[23] R. Swaminathan, C. J. Cai, S. Yuan, and H. Ren, "Multiphysics Simulation of Magnetically Actuated Robotic Origami Worms," *IEEE Robot. Autom. Lett.*, vol. 6, no. 3, pp. 4923–4930, Jul. 2021.

[24] J. Flores, L. Stein-Montalvo, and S. Adriaenssens, "Effect of crease curvature on the bistability of the origami waterbomb base," *Extreme Mechanics Letters*, vol. 57, p. 101909, Oct. 2022.

[25] D. Piker, *Lecture about architecture, based on physical laws*, Sep. 17, 2011.

[26] D. Piker, "How does Kangaroo solver work?," *McNeel Forum*, Nov. 14, 2019.

Acknowledgements

Diamond Sponsor

LANDREAM

Platinum Sponsors

一造科技 FAB-UNION

MOR Melbourne Australia

Silver Sponsors

EUREKA TECHNOLOGY Innovation & Investment

THE UNIVERSITY OF QUEENSLAND AUSTRALIA

TTW

Bronze Sponsor

EZSTEEL

Gala Dinner Sponsor

THE UNIVERSITY OF MELBOURNE

Supporters

VICTORIA State Government

MELBOURNE Convention Bureau

Nohmura Foundation for Membrane Structure's Technology

RMIT UNIVERSITY

SWINBURNE UNIVERSITY OF TECHNOLOGY

LSAA Lightweight Structures Association Australasia Inc.

Technical Supporters

eolus

ameba

BOLLINGER+GROHMANN

Fologram

KARAMBA3D

PolyFrame

TENSYS Engineering • Analysis



IASS 2023

July 10–14 Melbourne

Integration of Design and Fabrication

ISBN 978-0-646-87830-0